ICTAM 2016
MONTRÉAL

24th International Congress of Theoretical and Applied Mechanics

Palais des congrès, Montréal, Canada

August 21 – 26, 2016

Book of Papers



IUTAM International Union of Theoretical and Applied Mechanics

Official IUTAM Congress

Photos © NASA and Tourisme Montréal

www.ictam2016.org

Preface

This volume contains all ICTAM 2016 Papers presented as:
- Plenary Lectures,
- Prize Lectures - Batchelor and Hill
- Sectional Lectures
- Mini-symposia presentations
- Thematic Session presentations, and
- Short Talk with Poster presentations.

The content of this book is available electronically only and will be archived on the IUTAM permanent site as follows:

ISBN: NR16-127/2016E-EPUB
Catalogue Number: 978-0-660-05459-9

Foreword

The organizers are proud to present the ICTAM2016 papers.

The electronic collection contains all submissions accepted for either oral or poster presentation as of July 8, 2016.

Papers received after this date, as well as those included here, can be accessed using the m*yICTAM2016* congress mobile app.

After the Congress itself all papers will be archived on the permanent IUTAM website.

We would like to thank all the members of the International Program Committee, for generating the content for such an inspiring scientific program. We would also like to acknowledge the tremendous work performed by the National Research Council of Canada and Legend Conference Planning for converting all our ideas into an actual Congress program.

Papers are presented as they were submitted. The organisers take no responsibility for the content language and errors in the texts.

The International Program Committee
ICTAM 2016
Montreal, Canada

GOLD

Virginia Tech
Invent the Future®

Department of Biomedical Engineering and Mechanics

SILVER

UNIVERSITY OF TORONTO
FACULTY OF APPLIED SCIENCE & ENGINEERING

BRONZE

McMaster University
ENGINEERING

SPECIAL

WATERLOO | ENGINEERING

UNIVERSITÉ Concordia UNIVERSITY

2016 BATCHELOR PRIZE Journal of Fluid Mechanics

ELSEVIER

Pacific Institute for the Mathematical Sciences

CANADIAN CONGRESS FOR APPLIED MECHANICS CANCAM CONGRÈS CANADIEN DE MÉCANIQUE APPLIQUÉE

uOttawa Faculté de génie Faculty of Engineering

McGill

Western Engineering

FACETS

Canada NRC·CNRC

Index Codes

Opening Lecture:

OL

Closing Lectures:

CL

Batchelor Prize Lecture

BP

Hill Prize Lecture

HP

Sectional Lectures

SLnn-x

nn= Topic

-x= order of the lecture within topic

Thematic Sessions (Orals)

TS.FMxx-x.mm

TS = Presentation Type

MSxx/FMxx/SMxx/FSxx = Thematic Session and topic

-x = block order within session

.**mm** = speaking order within block

Short Talks with Poster

PO.MSxx-x.mm.xxx

PO = Presentation Type

MSxx/FMxx/SMxx/FSxx = Thematic Session and topic

-x = block order within session

.**mm** = speaking order within block

xxx = Board #

Table of Contents

Opening Lecture
Paper 01

Closing Lecture
Paper 03

Hill Prize Lecture
Paper 05

Batchelor Prize Lecture
Paper 07

Sectional Lectures
Papers 08
Fluids Papers 09
Solids Papers 21
Fluids/Solids Papers 35

Thematic Sessions and Short Talks with Poster
Papers 41

MS01 - Bypass Transition 41
MS02 - Fluid Active Matter 71
MS03 - Multiphase Flow in the Processing Industry 88
MS04 - Nonlinear Dynamics of Engineering Systems 99
MS05 - Soft Solid Active Matter 242
MS06 - Topology Optimization 334
FM01 - Biological Fluid Mechanics 406
FM02 - Boundary Layers 478
FM03 - Combustion and Flames 583

FM04 - Compressible Flow 645
FM05 - Convection 707
FM06 - Drops, Bubbles and Multiphase Flows 771
FM07 - Flow Instability and Transition 908
FM08 - Flow in Thin Films 1027
FM09 - Geophysical and Environmental Fluid Dynamics 1086
FM10 - Low Reynolds Number Flow 1139
FM11 - Micro- and Nano-fluidics 1190
FM12 - Non-Newtonian and Complex Fluids 1250
FM13 - Computational Fluid Dynamics 1328
FM14 - Turbulence 1390
FM15 - Vortex Dynamics 1502
FM16 - Waves in Fluids 1580
FM17 - Other Topics in Fluid Mechanics 1644
SM01 - Biomechanics and Biomaterials 1655
SM02 - Contact and Friction 1753
SM03 - Damage Mechanics 1804
SM04 - Elasticity 1885
SM05 - Fracture Mechanics 2004
SM06 - Geophysics and Geomechanics 2143
SM07 - Impact Mechanics and Wave Propagation 2188
SM08 - Multi-component Materials and Composites 2285
SM09 - Phase and Chemical Transformations and Thermomechanical Phenomena 2388
SM10 - Sizescale Effects in Materials 2458
SM11 - Multibody and Vehicle Dynamics 2558
SM12 - Nanostructures and MEMS 2603
SM13 - Plasticity, Viscoplasticity and Creep 2676
SM14 - Stability of Structures 2764
SM15 - Computational Solid Mechanics 2850
SM16 - Vibrations and Control of Structures 2961
FS01 - Acoustics 3035
FS02 - Exascale Computing 3093
FS03 - Experimental Methods in Mechanics 3125
FS04 - Chaos and Pattern Formation 3166
FS05 - Porous Media 3175
FS06 - Fluid Structure Interactions 3224
FS07 - Actuating and Smart Materials 3285
FS08 - Granular Materials and Flows 3339
FS09 - Foams and Cellular Materials 3417
FS10 - Education in Mechanics 3466

OCEAN TURBULENCE AND CLIMATE HISTORY

W. Richard Peltier
Department of Physics, University of Toronto, Toronto, Ontario, Canada

Summary The global oceans play a critical role in the climate system, not only in the transport of heat from the equator towards the poles but also in the global carbon cycle. Although the wind driven component of this circulation continues to be of interest, the thermohaline or Meridional Overturning Circulation (MOC) component is of particular importance and interest from a fundamental fluid mechanical perspective. This is because its existence depends upon the continuous generation of small scale turbulence engendered primarily by the breaking of hydrodynamic waves. A primary source of excitation of these waves is the flow of the lunar barotropic tide over ocean bottom topography. The turbulence produced by wave breaking effects a vertical flux of mass that may be characterized by an effective turbulent diffusivity and it is this vertical flux of mass that enables the high density deep water that forms at the poles to return to the surface. Following a review of recent advances in the characterization of this diffusivity, it will be demonstrated that a previously unexplained phenomenon in climate system history, the so-called Dansgaard-Oeschger oscillation (see Figure 1), can be understood in terms of a global-scale relaxation oscillation of the Atlantic MOC. It is furthermore shown that this nonlinear oscillation is highly sensitive to the representation of stratified turbulence. This is an extreme example of a multi-scale dynamical phenomenon in which small scale turbulence controls not only the existence but also the millennium timescale of a truly global scale climate related oscillatory phenomenon.

BREAKING WAVE INDUCED MIXING: MODEL PROBLEMS

Our interest is in the high Reynolds number regime that is appropriate for environmentally relevant circumstances, specifically but not exclusively for the oceans. Since we are interested in phenomenology in which the turbulence of interest develops in a background that is stably stratified in density, appropriate model problems will consist of "parallel" flows in which the background is destabilized by shear, in which case the primary instability leading to transition will be governed by the Miles-Howard Theorem which asserts that a necessary condition for instability is that the gradient Richardson number be less than 0.25 somewhere in the vertical. Although there are several distinct types of instability that may occur in such circumstances, the primary types are those first identified by Kelvin and Helmholtz (hereafter KHI) and by Holmboe (hereafter HI) which differ from one another by the ratio of the depth of the shear zone to that of the coincident density inversion. Both mechanisms generate waves which inevitably break at sufficiently high Re and the turbulence thereby produced may be analysed through DNS analyses to infer the diapycnal diffusivity that is characteristic of the typical life-cycle of such an event [we employ the spectral element software of Fischer et al., 1, to obtain the DNS results to be described]. This requires careful distinction between the irreversible "mixing" associated with the event and the entirely reversible "stirring" that can contribute nothing to diapycal turbulent diffusion. This requires explicit use of the concept of Available Potential Energy (APE) that was originally introduced by Lorenz in the context of his analysis of the atmospheric general circulation [eg. 2]. We employ the results from these model problems to compare the turbulent diffusivities inferred on the basis of analyses of the associated stratified turbulence to reveal explicitly the nature of the errors incurred when these diffusivities are determined on the basis of several commonly employed models including the simplest model based upon the Prandtl mixing length idea as well as more sophisticated but nevertheless inaccurate models such as that due to Osborn [3] which continues to be widely employed in the area of physical oceanography [4].

A critical issue that cannot be avoided in the inference of irreversible mixing is that of mixing "efficiency", an estimate of which Osborn believed to be provided by the "flux" Richardson number and which he imagined could be assumed to be fixed to a constant value of 0.2 for practical oceanographic applications. It is now widely understood, however, that mixing efficiency is a strong function of at least two characteristics of the turbulence, respectively a measure of turbulence intensity as provided by the buoyancy Reynolds number and a parameter dependent upon the shear that is perhaps best represented by "bulk" Richardson number. In the oceans, where density may be strongly controlled by salinity due to the highly nonlinear nature of the equation of state, especially under cold temperature conditions, the Prandtl number may also exert a further impact upon mixing efficiency [5]. Its inference on the basis of the DNS data requires a complete sorting of the individual density elements of which the flow is comprised at each time step in its evolution so as to determine the evolution of the minimum potential energy state that could be reached by adiabatic rearrangement and thereby the extent to which irreversible processes associated with the destruction of small scale density variance have occurred.

DIAPYCNAL TURBULENT DIFFUSIVITY AND MOC TIME DEPENDENCE

Although it is well understood that the existence of the MOC depends entirely upon the action of small scale diapycnal turbulent diffusivity, it is an interesting issue as to what role this physical process might play, if any, in the time dependence of this global scale component of the ocean general circulation and thereby climate. Although such time dependence has often been invoked in the understanding of isolated events in the Climate System, it has only recently proven possible to

[a] Corresponding author. Email: peltier@atmosp.physics.utoronto.ca

make a connection between observations of climate variability and MOC time dependence. This has been possible by providing a detailed fluid mechanical understanding of the so-called Dansgaard-Oeschger oscillation phenomenon, an oscillation with a timescale of approximately a millennium in the temperature of the North Atlantic sector of the climate system which has been inferred to have occurred under cold glacial climate conditions. The data, shown on Figure 1, in terms of which the existence of the phenomenon has been inferred, consist of measurements of oxygen isotopes in ice cores extracted by drilling into the Greenland ice sheet, the modern data shown on this figure being derived from holes drilled at the Summit location. Inspection of the figure will show that the individually numbered D-O cycles appear to be triggered by events labelled “H” in the individual time series. These so-called “Heinrich” events correspond to intense inputs of floating ice from the eastern flank of the ice sheet that covered all of Canada at the last maximum of glaciation approximately 21,000 years ago. When measured in an ice-core, the oxygen isotopic signal is a proxy for the temperature of the air from which the precipitation over Greenland derived. It is therefore a climate related signal that requires explanation.

The hydrodynamic explanation of this phenomenon, one that connects it unambiguously to the time dependence of the MOC, proves to be quite sensitive to the representation of turbulent diapycnal diffusivity employed in a global ocean model. In order to establish this fact, a modern coupled climate model that includes a detailed representation of ocean hydrodynamics, the CESM1 model of the US National Center for Atmospheric Research, has been integrated at high spatial resolution over a period of multiple millennia with the surface boundary conditions of ice cover and land-sea distribution appropriate to cold glacial maximum conditions. The results of this analysis have demonstrated that, when the surface ocean under these conditions is struck by a Heinrich event related transient forcing that causes intense cooling of the northern hemisphere, a fibrillation in the strength of the MOC on the observed millennium timescale occurs. The model also explains the temperature signal inferred on the basis of Greenland oxygen isotopic data as well as the related signal derived from ice cores drilled from the Antarctic ice sheet in the opposite hemisphere. I have referred to the D-O phenomenology as involving the action of a “kicked” salt oscillator in the Atlantic [6], the details of which I will explain in the presentation

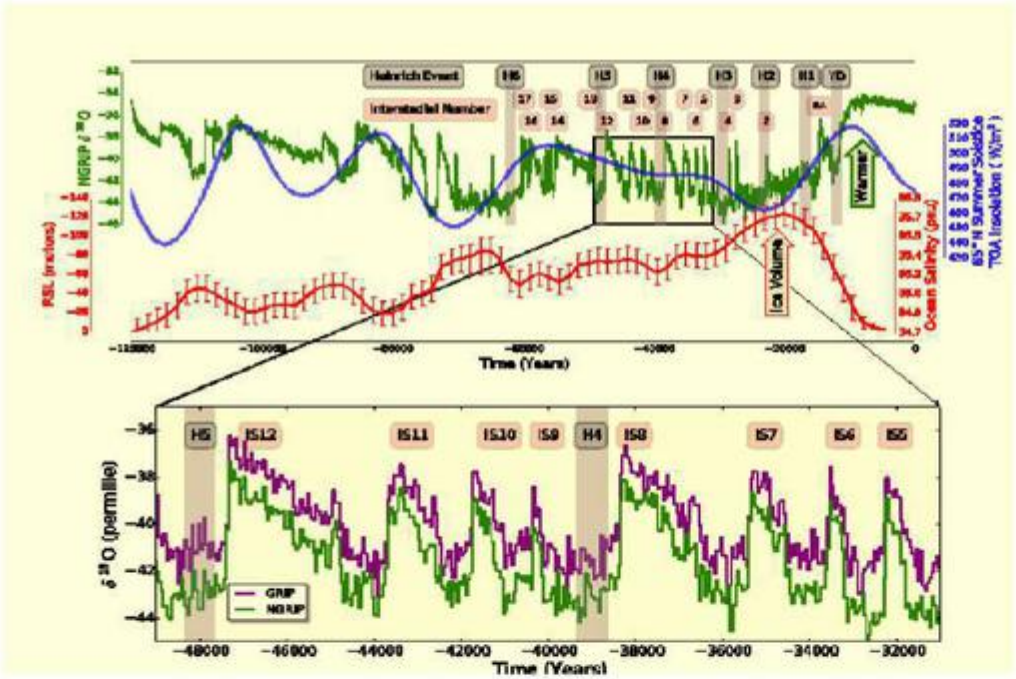

Figure 1. The upper frame illustrates the evolution of a number of climate related variables over the most recent 100,000 years of Earth history including northern hemisphere summer solar insolation at 65 degrees north latitude (in blue), continental ice volume (in red) and the oxygen isotopipc signal from the NGRIP ice core from summit Greenland (in green). The lower frame shows a blow-up of the oxgen isotopic signal from NGRIP compared to that from the GRIP hole which was drilled some km distant, a comparison that demonstrates that the signals are very highly correlated. The numbered shaded regions correspond to Heinrich events while those number IS (for InterStadial) correspond to individual D-O cycles.

References

[1] Fischer, P.F. et al. J. Sci. Comput. 17, (1-4), 2002.

[2] Peltier, W.R. and Caulfield, C.P. Ann. Rev. Fluid Mech.. 35, 135-167, 2003.

[3] Osborn, P.F. J. Phys. Oceanogr. 10, 83-89, 1980.

[4] Salehipour, H. and Peltier, W.R. J. Fluid Mech. 775, 464-500, 2015.

[5] Salehipour, H., Peltier, W.R. and Mashayek, A. J. Fluid mech. 773, 178-223, 2015.

[6] Peltier, W.R. and Vettoretti, G. Geophys. Res. Lett. 41, 7306-7313, 2014.

MICROARCHITECTURED MATERIALS: ARE THEY EFFECTIVE?

Norman Fleck[1a],
[1]*Cambridge University Engineering Dept., Trumpington St., Cambridge, CB2 1PZ, UK*

Summary An overview is presented of the role of microarchitecture in dictating the properties of engineering materials, ranging from the bulk to coatings and adhesive joints. Some properties (modulus, strength) are remarkably insensitive to imperfections, whilst others (toughness and ductility) can be severely degraded by imperfections. There is scope to reinforce by the addition of a second phase, and indeed to prestress, akin pre-stressed concrete. The presentation considers 3 inter-related topics: the effective properties of bulk lattices, microacrhitectured adhesive joints and the significance of boundary layers in composite coatings.

FROM BRITTLE FOAMS TO TOUGH AND DUCTILE LATTICES

Lattice materials are emerging with a broad range of properties due to their combination of microarchitecture, length scale and composition. They have impressive properties: as bulk materials, as the cores of sandwich panels and as engineered surfaces. Toughness knows no bounds, and high toughness can be achieved by the successive renucleation of fracture in the lattice ahead of a macroscopic crack tip. Likewise, there are no theoretical bounds for tensile ductility. There is a recent emergence of multi-phase lattice materials due to a combination of two or more constituent lattices. Extreme properties, such as high strength are evident with a diminishing length scale, but new challenges (such as adhesion of neighbouring cell walls and low toughness) also appear.

The sensitivity of toughness and ductility to microstructure of elasto-plastic lattices are assessed. A range of imperfections are considered in order to attempt to explain the remarkably low tensile ductility of metallic and polymeric foams; these include randomly displaced joints, missing cell walls and Plateau borders for the case of foams. The formation of densification bands in compression is explored, and it is shown that buckling and volumetric lock-up can protect a lattice from failure of the struts.

Reinforcement (and pre-stressing) of foams (and lattices) is possible by the addition of a second phase as an inter-penetrating lattice. This is explored for the case of a foam-cored sandwich beam with pre-stressed faces.

MICROARCHITECTURED ADHISIVE JOINTS

Adhesive joints are used increasingly structural engineering components. There is a challenge to control the strength and toughness of the joint (under remote tension and under remote shear), by suitable design of the microarchitecture of the joint. A joint of 'square-wave' topology is manufactured using aluminium substrates and a silicone-based elastomeric adhesive layer. Under remote tensile loading of the joint, the top and bottom faces of the square-wave behave as butt joints, while the side faces behave as lap joints. The overall tensile strength and work of fracture of the 'square-wave' joint can thereby be predicted, see Fig. 1. Maps are constructed to show the sensitivity of joint strength, toughness and transition flaw size to joint architecture (amplitude/wavelength of square wave). Additionally, the crack resistance of the square-wave joint is measured by testing a double cantilever beam specimen. Accurate macroscopic crack growth predictions are made by taking the tensile response of the square-wave joint to define a cohesive zone law between elastic substrates.

EFFECTIVE PROPERTIES OF COMPOSITE LAYERS – FROM COATINSG TO ADHESIVE LAYERS

Surface coatings and embedded layers are ubiquitous in engineering components, and serve a wide range of functions from environmental protection to low friction and wear resistance. A related geometry to the surface coating is the embedded layer sandwiched between two substrates. This geometry is also ubiquitous and is representative of adhesive joints, the mortar between the bricks of a building, and interphases at grain boundaries *inter alia*.

Frequently, a coating comprises a multi-phase composite with, for example, particulate reinforcement in order to increase its stiffness and strength. *The question arises: what are the effective properties of a composite coating?* A common assumption is to use the effective properties of the *bulk* composite for that of the *coating*. Whilst this assumption is accurate when the correlation length of each phase is much less than the coating thickness, it is less accurate when the two length scales are of comparable magnitude. The presence of the substrate or a free surface perturbs the stress field within the composite coating. This can be re-phrased in a more mathematical manner, as follows. The usual Hashin-Shtrikman variational approach for the bulk properties of a composite makes use of the infinite-body Greens function in order to determine the ensemble-averaged strain field in terms of a polarization in stress from one phase to the next. For the embedded layer, the

[a)] Corresponding author. Email: naf1@eng.cam.ac.uk

infinite-body Greens function is employed, whereas for a surface coating the half-space Greens function is exploited. The presence of the substrate or free surface perturbs the 'interaction stresses' from phase to phase, and consequently the effective properties of the coating differ from those predicted for the bulk composite of equal thickness. Boundary layers emerge within the coating, adjacent to the substrate and free surface.

The purpose of this study is to make accurate predictions for the effective properties of a *surface composite coating* or an *embedded composite* layer, taking into account the presence of the substrate of differing properties, whether *linear* or *non-linear*. Effective properties and associated bounds are generated for composite coatings and for composite sandwich layers of finite thickness, based on the Hashin-Shtrikman approach, but suitably modified to account for the presence of a free surface in the case of a coating and of substrates in the case of a sandwich layer. First, the linear properties are generated and then the method is modified to generate bounds and estimates for a non-linear composite coating. We limit our scoping study to two-dimensional problems by considering anti-plane shear of an isotropic 2-phase composite on a single-phase substrate, with microstructure prismatic along the direction of anti-plane shear.

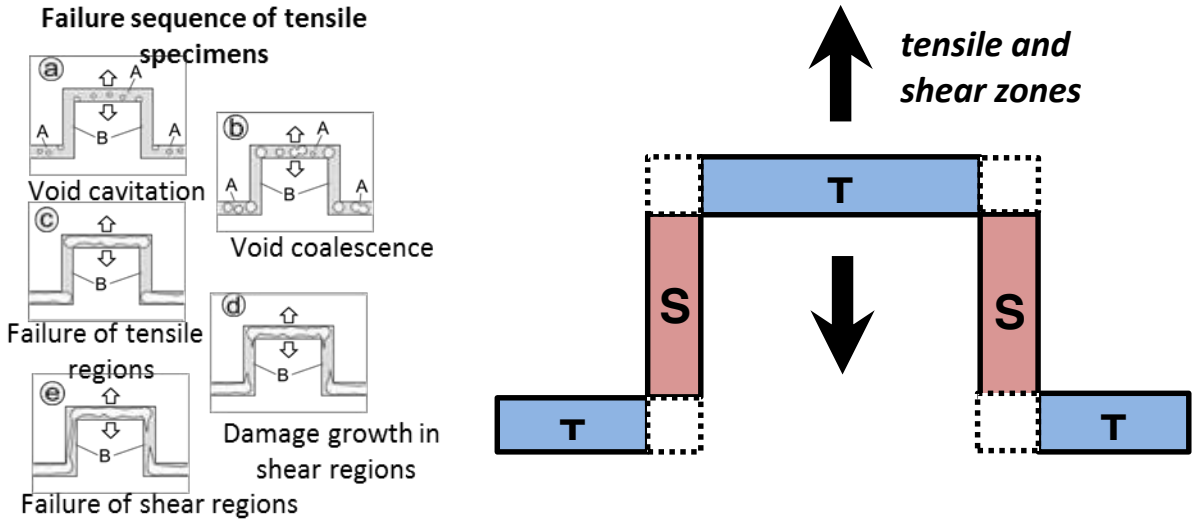

Fig. 1 A microarchitectured adhesive joint

CONCLUSIONS

There is scope to develop microarchitecture lattice materials with a wide range of topologies, and engineering properties. Recent advances in additive manufacture and in nanoscale manufacture have stimulated this activity, due to the ability to co-deposit two or more lattices. The effective properties for a wide range of topologies have been determined, and defect sensitivity assessed. Reinforcement and pre-stressing by a second phase can be used to increase strength and toughness. Finally, the effective properties of composite coatings is explored, and the role of boundary layers emphasised.

APPLICATION OF NONLINEAR ELASTICITY TO SOFT TISSUE BIOMECHANICS

Ray W. Ogden [1] and Gerhard A. Holzapfel[2]

[1]School of Mathematics and Statistics, University of Glasgow, Glasgow, UK
[2]Institute of Biomechanics, Graz University of Technology, Graz, Austria

Summary After a short background discussion, this lecture will focus on the application of anisotropic nonlinear elasticity theory to the modelling of the mechanical properties of soft biological tissues, with particular attention paid to the properties of artery walls and their layered fibrous structure. We shall describe how our models have developed in sophistication as more and more experimental data have become available to inform the modelling process, with particular reference to the details of collagen fibre dispersion and the most recent model involving non-symmetric fibre dispersion. We shall also touch on recent work that shows how omitting the contribution of fibres within a dispersion that are compressed during deformation makes a significant difference to the stress response of the material.

BACKGROUND

The theory of nonlinear elasticity was developed largely by Rivlin in the 1940s and 1950s because of the need to describe the properties of rubberlike materials and to predict the behaviour of these materials for different geometries and under various loading regimes. Rivlin's substantial works are contained in the two-volume collection of papers edited by Barenblatt and Joseph [1] and are a continuing source of reference for researchers in the area. In more recent years, while significant interest in the application of the theory of elasticity, and also inelasticity, remains, much attention has turned towards applications in the field of biomechanics, in particular for applications to the mechanics of soft biological tissues such as artery walls and heart tissue, as exemplified in Humphrey's book [2]. Further stimulus for the theory has been found relatively recently in the need to analyze the properties of so-called 'smart materials', which include electro-sensitive and magneto-sensitive elastomers capable oflarge elastic deformation induced by applied electric or magnetic fields. Such materials have been developed for applications to sensors, actuators and artificial muscles, for example, and to fully understand their behaviour the theories of nonlinear electro-elasticity and magneto-elasticity are required, as summarized in the recent volume [3]. This presentation, however, focuses entirely on the biomechanics applications.

Soft biological tissues have a very complicated structure, only some of which can be seen depicted in this widely used schematic figure from [4]. Within the structure the collagen fibres have a very important role since they are considerably stiffer than the surrounding material in which they are embedded and they endow the material with anisotropic properties. To describe the elastic properties of soft materials with a fibrous structure the theory of nonlinear elasticity that incorporates preferred directions, the local fibre directions, is required. The two main solid mechanically relevant layers of a healthy artery wall, the media and adventitia, typically contain families of collagen fibres that are arranged symmetrically in two helical structures, and this (idealized) structure was the basis for our first contribution to the elasticity of arteries described in [4]. Subsequently it became apparent that a slightly more sophisticated model that accounted for the dispersion in the fibre orientations about the mean helical structure was required, and to accommodate this we introduced the notion of a generalized structure tensor that incorporated a measure of the dispersion, and this was published in [5].

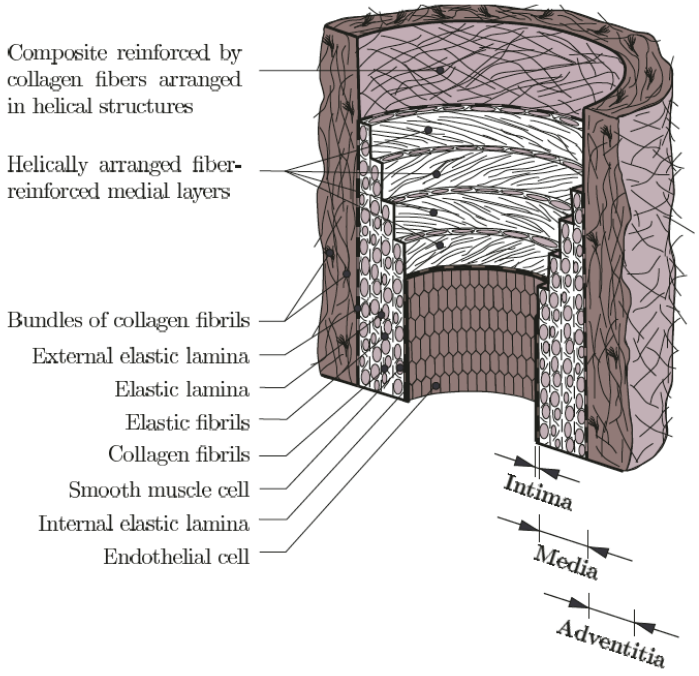

Both papers have been very successful and the models they contain have been applied to a wide range of soft biological tissues. However, recent very detailed and extensive experimental work [6, 7] highlighting the collagen fibre dispersion in a range of different arteries has shown that a more general model is needed to account for the three-dimensional dispersion. In particular, the rotationally symmetric dispersion model in [5] cannot account for these data. This prompted us to develop a non-symmetric fibre dispersion model to accommodate the new findings, and this was published recently in [8].

Corresponding author. Email: raymond.ogden@glasgow.ac.uk

CONTENT OF THE LECTURE

In this lecture we shall describe the development of our constitutive models of arterial elasticity starting from the model with two helically arranged families of fibres in [4] and then going on to the models of fibre dispersion in [5, 8]. The non-symmetric fibre dispersion model in [8] is based on a bi-variate von Mises distribution of fibres and introduces new structure tensors, one for each fibre family, which are incorporated into the constitutive law to model the fibre dispersion. Necessarily we shall cover some background material on nonlinear anisotropic elasticity and constitutive laws that govern the nonlinear elastic response of fibrous solids. Then, with reference to experimental data, models that have a specific structure but are special cases within the general constitutive framework will be described, and their predictions will be examined for particular simple deformations. The non-symmetric fibre dispersion model, in particular, will be described in detail. We shall also make reference to the important effect that residual stresses in unloaded arteries have on their response when loaded.

In the literature it is often considered that collagen fibres do not support significant stress when under compression and so should be excluded from constitutive models when the material is subject to deformations for which they are compressed. It is debatable to what extent this notion should be applied since multiple fibres in the matrix within which they are embedded may well support at least some compressive stress. Nevertheless, in recent (as yet unpublished) work we have explored the effect of omitting compressed fibres within a dispersion from the analysis and we have found that this makes a considerable difference to the stress response of the material when there is significant dispersion. This will be discussed briefly during the lecture.

References

[1] Barenblatt G.I., Joseph D.D.: Collected Papers of R.S. Rivlin. Springer, New York 1997.

[2] Humphrey J.D.: Cardiovascular Solid Mechanics. Springer, New York 2002.

[3] Dorfmann L., Ogden R.W.: Nonlinear Theory of Electroelastic and Magnetoelastic Interactions. Springer, New York 2014.

[4] Holzapfel G.A, Gasser T.C., Ogden R.W.: A new constitutive framework for arterial wall mechanics and a comparative study of material models. J. Elasticity 61:1-48, 2000.

[5] Gasser T.C., Ogden R.W., Holzapfel G.A.: Hyperelastic modelling of arterial layers with distributed collagen fibre orientations. J. R. Soc. Interface 3:15-35, 2006.

[6] Schriefl A.J., Zeindlinger G., Pierce D.M., Regitnig P., Holzapfel G.A.: Determination of the layer-specific distributed collagen fiber orientations in human thoracic and abdominal aortas and common iliac arteries. J. R. Soc. Interface 9:1275-1286.

[7] Schriefl A.J., Reinisch A.J., Sankaran S., Pierce D.M., Holzapfel G.A.: Quantitative assessment of collagen fiber orientations from two-dimensional images of soft biological tissues. J. R. Soc. Interface 9:3081-3093, 2012.

[8] Holzapfel G.A., Niestrawska J., Ogden R.W., Reinisch A.J., Schriefl A.J.: Modelling non-symmetric collagen fibre dispersion in arterial walls. J. R. Soc. Interface 12: 2015.0188, 2015.

FLUID DYNAMICS AT THE SCALE OF THE CELL

Raymond E. Goldstein*
Department of Applied Mathematics and Theoretical Physics, University of Cambridge, United Kingdom

Summary The world of cellular biology provides us with many fascinating fluid dynamical phenomena that lie at the heart of important aspects of physiology, development, and ecology. Advances in imaging, micromanipulation, and microfluidics over the past decade have allowed for high-precision measurements of such flows, providing tests of fundamental theories about microhydrodynamics and also revealing a wealth of new phenomena which call out for explanation. In this lecture I summarize this progress in the context of four issues: cytoplasmic streaming in plant and animal cells, synchronization of eukaryotic flagella, collective behaviour in dense suspensions of microswimmers, and the interaction between swimming cells and surfaces. Throughout, I emphasize the role of fluid dynamics in an interdisciplinary approach to the mysteries of biology.

*Email: R.E.Goldstein@damtp.cam.ac.uk

Sectional Lecture in Fluids

SL.FM-1	Colonius, Tim - Models of coherent structures in turbulent jets and their radiated sound	9
SL.FM-2	Smits, Alexander - Turbulent drag reduction using liquid-infused surfaces	11
SL.FM-3	Jimenez, Javier - Coherent structures in wall-bounded turbulence	13
SL.FM-4	Hosoi, Anette - Hydrodynamics and Hairy Surfaces	15
SL.FM-5	Bodenschatz, Eberhard - The Transition to the Ultimate State in Turbulent Thermal Convection	17
SL.FM-6	Bush, John - Hydrodynamic quantum analogs	19

Sectional Lecture in Solids

SL.SM-1	Audoly, Basile - The non-linear mechanics of slender deformable bodies	21
SL.SM-2	Hunter, Peter - Biomechanics and the physiome project	23
SL.SM-3	Fang, Daining - Deformation and Fracture of Electromagnetic Thin Films and Laminates under Multi-field Loading	25
SL.SM-4	Rogers, John - Concepts in mechanics for 3D, bio-integrated electronics	27
SL.SM-5	Suo, Zhigang - Soft Machines	29
SL.SM-6	Forest, Samuel - The micromorphic approach to gradient crystal plasticity and damage	31
SL.SM-7	Onck, Patrick - Protein mechanics: from amino acid to swimming cells	33

Sectional Lecture in Fluids-Solids

SL.FS-1	Hu, Haiyan - Soft machines: challenges to computational dynamics	35
SL.FS-2	Farhat, Charbel - Computational framework for multi-material FSI, shocks, turbulence and fracture	37
SL.FS-3	Haller, George - Can solid mechanics help in understanding fluid vortices?	39

MODELS OF COHERENT STRUCTURES IN TURBULENT JETS AND THEIR RADIATED SOUND

Tim Colonius*[1], Aaron Towne[1], and Oliver Schmidt[1]
[1]*Department of Mechanical and Civil Engineering, California Institute of Technology, Pasadena, CA USA*

Summary This paper provides an overview of recent research aimed at modeling the coherent structures that comprise the dominant source of mixing noise in high-speed, turbulent jets. A trove of new data from numerical simulations and state-of-the-art measurement techniques are being fruitfully combined with computationally-enabled access to the eigenspace of large, non-normal, linear systems, in order to provide tools whereby turbulent structure and mechanism can be reliably educed, and through which quantitatively accurate models are now emerging. Beyond jet noise, these models have a role to play in controlling turbulence in a variety of free and wall-bounded shear flows.

Background

Enormous progress has been made towards the accurate prediction, via large-eddy simulation (LES), of jet turbulence and its associated radiated sound, a problem of profound and sustained interest in commercial and military aviation. While LES is computationally expensive, motivating the continued pursuit of theory and reduced-order models, the realism of the predictions makes its data a key resource for understanding the physics and modeling the relevant phenomena.

In high Reynolds number turbulent jets, coherent large-scale structures in the form of wavepackets (reminiscent of linear instability waves in transitional flow) have long been observed (see the extensive review in [1]). Their length and time-scales far exceed the integral scale of turbulence, and they propagate with a coherent wavelength and phase speed that is slowly varying with downstream position along the jet potential core and beyond. Their spatiotemporal coherence renders them more acoustically efficient than smaller-scale, more random turbulent fluctuations, especially in high subsonic and supersonic jets. The signatures of these structures can be most clearly identified from modern multi-point measurements such as near-field microphone arrays [2, 3] and time-resolved particle image velocimetry [3]. Within the turbulent jet itself, the envelope, wavelength, and phase speed of these wavepackets have been accurately modeled, compared with these experiments, using a variant of weakly nonparallel spatial linear stability analysis, namely parabolized stability equations (PSE) [2]. A key aspect of the work has been using techniques such as proper orthogonal decomposition, which involve averaging, to extract the coherent wavepacket from more random fluctuations present in the measurements in order to compare to the analytical models; models should therefore be regarded as predicting the *average* wavepackets.

Unfortunately, particularly in subsonic jets, these linear models fail to accurately predict a consistent acoustic signature of wavepackets in the far-field. Random variations in the wavepacket characteristics in different short-duration realizations of the flow lead to preferential amplification to the acoustic field. Simply put, the average wavepacket does not necessarily make the average sound. Thus to predict the acoustic field, it becomes necessary to model the "jitter" [4] of the wavepackets through their stochastic forcing, either at the nozzle exit or in a distributed way throughout the jet.

Input/output models

In our recent work, we consider a more general modeling framework that is based on the full equations of continuity, momentum, and energy, and the Reynolds decomposition separating the flow into mean and fluctuating components. Once spatially discretized and specialized to the case of statistically stationary flow, these equations take the form of a set of large, linear systems (one for each frequency and azimuthal wavenumber) driven by the (generalized) Reynolds stresses representing triadic interactions coupling the frequency/wavenumber components.

In the absence of right-hand-side forcing, the linear system is then identical to that which would be used in modal or transient stability analysis, but linearized about the turbulent mean rather than an equilibrium (laminar) solution. This provides a commonality with previous models built around the weakly parallel flow theory, but allows for the full spectrum of modes associated with the non-parallel flow to also be considered. Further, with nonzero forcing, the input/output (resolvent) behavior of the system can be studied, similar to that being developed for wall-bounded flows [5]. The SVD can be used to extract the highest-gain modes of the multiple-input, multiple-output system, forming a reduced-order (low rank) basis that can be expected to span the energetic, large-scale coherent structures [6].

This approach, while computationally intensive in non-parallel flow, provides new insights into the wavepackets and their associated noise radiation [7]. We note without elaboration that we have recently proposed more computationally efficient solutions to these systems based on the notion of parabolization, or streamwise marching, of the equations [8]. Such methods are in fact necessary if we are to develop "reduced-order" models of turbulence, since the SVD associated with the full complement of frequencies and wavenumbers has a cost approaching LES.

*Corresponding author. Email: colonius@caltech.edu

Ramifications for wavepackets and their radiated noise

The present analysis is fueled by an extensive LES database and companion experiment created by our collaborators for a canonical Mach 0.9 jet [9] with Reynolds number 10^6 issuing from a round, converging nozzle. The LES model was carefully developed to replicate, as closely as possible, the turbulent boundary layers emanating from the nozzle exit in the experiment. Within the nozzle, synthetic turbulence injection and wall modeling were found to be of prime importance in accurately predicting the overall jet turbulence and especially the spectrum of radiated sound [9]. Another critical aspect of the LES was to assemble very long-duration records of the entire flow field to allow for adequate convergence of the low-frequency statistics associated with the largest flow structures.

Based on the LES mean flow field, we have computed global and resolvent modes associated with the linear operator, restricting our attention to the jet region downstream of the nozzle exit. Both analyses produce dominant modes in the form of wavepackets over a wide range of frequencies. An interesting twist, however, is that over a range of frequencies, these modes are coupled to what can be understood as trapped acoustic waves within the potential core. These modes appear as discrete lightly damped modes in the global spectra, and their frequencies have also been observed as tones in the near nozzle acoustic field of recent experiments, as will be reported in forthcoming publications.

The extensive LES data allows us to assess the impact of the nonlinear forcing term on wavepacket evolution by directly tabulating, over a range of frequencies, both sides of the forced input/output system described in the previous section. In order to focus the analysis on the dominant coherent structures, we have developed a data decomposition technique that we call *empirical resolvent-mode decomposition* [10]. Given an ensemble of realizations for both the forcing and response, two sets of linked, mutually orthogonal modes can be formed–one for the forcing (inputs) and one for the response (outputs)–that maximize the respective gain between them. For a full-rank dataset these would naturally reproduce the standard resolvent modes associated with the input/output transfer function. For data constrained to lie in the space visited by the LES simulations, the empirical modes are biased towards high-gain "events" that actually occurred, thereby serving as a diagnostic to determine which kind of nonlinear interactions led to the observed coherent structures.

The results of this analysis were striking, in that the forcing modes that produced the highly coherent large-scale wavepackets lacked a coherent wave structure, instead appearing more random and smaller-scale in nature, and particularly concentrated in the near-nozzle thin shear layer region. Whereas a relatively small subset of the response modes were responsible for a large fraction of the flow fluctuations, the forcing modes were essentially no more efficient than white noise in reconstructing their total forcing. These observations support the view that the dominant large-scale structures arise stochastically from uncorrelated forcing from other scales, the structure being associated with the high-gain linear operator itself rather through coherent nonlinear interactions amongst the dominant modes at other frequencies. This provides justifications for the earlier PSE models, which are based on the premise that the waves are initiated stochastically in the near-nozzle region.

By restricting the output of the linear system to be the far-field pressure, acoustically dominant structures and their related forcings can also be characterized. Again it is found that the wavepackets associated with the dominant (low-rank) far-field structures are produced by incoherent, small scale fluctuations, dominant near the nozzle exit but also through the jet shear layers, particularly near the region that would be marked as the critical layer (for a given frequency) in a weakly non-parallel framework. To state the result in cartoon form, both the near-field-dominant wavepackets and far-field-dominant wavepackets are the result of incoherent fluctuations amplified through the low-rank, non-normal operator associated with the mean of the turbulent flow field. This suggests the potential for linear models that capture both the coherent flow and acoustic fields. One approach would be to use RANS to predict the turbulent mean flow field, resolvent analysis (made computationally efficient via the aforementioned spatial marching method), together with parameterizations of the stochastic forcing terms.

Acknowledgements: This research is the result of a collaboration spanning multiple institutions. The Caltech portion of this work has been supported by NAVAIR, the Office of Naval Research. The authors acknowledge the key contributions made by Dr. Peter Jordan and his students and associates at Institut Pprime, University of Poitiers, Dr. André Cavalieri and students at ITA Brazil, Dr. Guillaume Brès of CASCADE Technologies, Inc, and Dr. Aniruddha Sinha of IIT Bombay. Our views have also been deeply influenced by Drs. Kristján Guðmundsson, Takao Suzuki, and Arnab Samanta, and Prof. Sanjiva Lele.

References

[1] Jordan P., Colonius T.: Wave packets and turbulent jet noise. Annu. Rev. Fluid Mech. 45:173-195, 2013.
[2] Guðmundsson K., Colonius T.: Instability wave models for the near-field fluctuations of turbulent jets. J. Fluid Mech.
[3] Cavalieri A. V. G. *et al.*: Wavepackets in the Velocity Field of Turbulent Jets. J. Fluid Mech. 730:559-592, 2013
[4] Cavalieri A. V. G., Jordan P., Agarwal A., Gervais Y.: Jittering wave-packet models for subsonic jet noise. J. Sound Vib. 330(18):4474-4492.
[5] McKeon B. J., Sharma A.S.: A critical-layer framework for turbulent pipe flow. J. Fluid Mech. 658:336-382, 2010. 689:97-128, 2011.
[6] Bagheri S: Computational Hydrodynamic Stability... Arch. of Comput. Meth. Engrg. 19(3):341-379, 2012.
[7] Nichols J., Jovanović M.: Input-output analysis of high speed jet noise, Proceedings of the Center for Turbulence Research summer program, 2014.
[8] Towne A., Colonius T: One-way spatial integration of hyperbolic equations. J. Comput. Phys. 300:844-861, 2015.
[9] Brès G. *et al.*.: LES for jet noise: the importance of getting the boundary layer right. AIAA 2015-2535, 2015.
[10] Towne A.: Ph.D. Thesis, California Institute of Technology, 2016.

TURBULENT DRAG REDUCTION USING LIQUID-INFUSED SURFACES

Alexander J. Smits*[1,2] and Tyler Van Buren[1]

[1]*Princeton University, Princeton, NJ 08544, U.S.A. and* [2]*Monash University, Melbourne, Australia*

Summary Liquid-infused surfaces are textured surfaces that have a lubricating liquid impregnated in the surface features. When these surfaces are exposed to the flow of an immiscible liquid, it is possible to achieve substantial drag reduction in fully turbulent flow. Liquid-infused surfaces may overcome some of the shortcomings associated with conventional superhydrophobic surfaces, namely failure under turbulent flow fluctuations and conditions of high hydrodynamic pressure. Results are presented for turbulent Taylor-Couette flow with longitudinal grooves. A number of different lubricating liquids are tested, and we find a strong dependence on the ratio between the viscosity of water and that of the lubricating liquid. The drag reduction, remains fairly constant over the Reynolds number range tested ($100 \leq Re_\tau \leq 140$) with a maximum of about 14%, as reported by [6]. The current study extends this previous work to examine the effects of changing the characteristics of the surface features.

INTRODUCTION

It has variously been shown that modifications of the surface can lead to drag reduction for turbulent wall-bounded flows. For example, [1] showed that for V-shaped grooves (riblets) drag was reduced when $h^+ < 25$ and $b^+ < 30$, with the maximum drag reduction of 8% occurring for $h^+ = 10$ and $b^+ = 15$. Here, $h^+ = \rho h u_\tau/\mu$, $b^+ = \rho b u_\tau/\mu$, where h is the riblet height, b is the riblet pitch, $u_\tau = \sqrt{\tau_w/rho}$ is the friction velocity, τ_w is the surface shear stress, and ρ and μ are the fluid density and viscosity, respectively. Shark-skin surfaces, which are broadly similar to riblet surfaces, have been reported to reduce drag by up to 10% [2]. Superhydrophobic surfaces, where water flows over a grooved surface with air infused in the grooves, has shown particular promise for drag reduction, with some researchers reporting up to 75% drag reduction in turbulent flows [3]. However, the air pockets may fail when they are under high pressure and under high shear, and turbulent pressure fluctuations can also cause failure at high Reynolds numbers [4].

Recently, a new technology that uses liquid-infused surfaces has been developed that exhibits negligible contact angle hysteresis when in contact with various polar and non-polar fluids, low sliding angles for drops on the surface, rapid and repeatable self-healing, and extreme pressure stability (at least 675 atm) [5]. These liquid/liquid systems are stable as long as the two liquids are immiscible, the impregnating liquid preferentially wets the substrate compared to the working liquid, and interfacial tension is stronger than destabilizing body and surface forces. Here, we report how this new surface treatment responds to flow, and demonstrate that such liquid-infused surfaces can lead to sustainable drag reduction in turbulent flows. The current study extends the recent work by [6] to examine the effects of changing the characteristics of the surface features on the level of drag reduction that can be achieved. In addition, we discuss related analytical and numerical model development, and preliminary results obtained in large-scale tests.

EXPERIMENTS

A Taylor-Couette flow was used to study the drag reducing characteristics of liquid-infused surfaces. The Taylor-Couette flow was generated using a commercial rheometer (Brabender Rheotron). The inner cylinder was stationary, while the outer cylinder was rotated over a range of angular frequencies ω (rad/s). The radial gap between the outer and inner cylinders, d was $1.982 \pm 0.013\ mm$ and the height of the inner cylinder H was $80.0 \pm 0.1\ mm$. The working fluid, deionized water, was maintained at constant temperature to within $\pm 0.1^\circ$C for each experiment using a cooling jacket.

In the original experiments reported by [6], the surface of the aluminum inner cylinder was engraved with grooves aligned in the flow direction that had a pitch $b \approx 106\ \mu m$. A confocal microscope (Olympus LEXT OLS4000) was used to measure the surface topography (see figure 1a), and the features had an average height of $h = 75 \pm 3\ \mu m$.

Three configurations of the $h = 75\ \mu m$ surface were tested, as illustrated in figure 1b. These preparations were called "hydrophilic," "superhydrophobic," and "oil-filled," respectively. For the hydrophilic or "control" case, the surface was made wettable so that the water completely filled the texture. For the superhydrophobic case the same cylinder was then placed in an ethanol-based solution containing Masurf FS100 (Mason Chemical Co.), resulting in a strong repellency to water and the entrapment of air in the grooves. For the liquid-infused cases using perfluorinated oils, the oils have a high chemical affinity for the fluorinated aluminum. For the cases using alkanes such as heptane, the surface was made wetting with respect to alkanes by removing the fluorination treatment in the plasma cleaner and then functionalizing the surface with n-Octadecyltrichlorosilane (OTS). The physical and chemical properties of all test surfaces are summarized in table 1.

Figure 1c show the torque measured on the inner cylinder as a function of Reynolds number Re based on the gap size and the outer cylinder speed ($Re = \rho_w d\omega R_o/\mu_w$). The Reynolds number range corresponds to turbulent flow with $100 \leq$

*Corresponding author. Email: asmits@princeton.edu

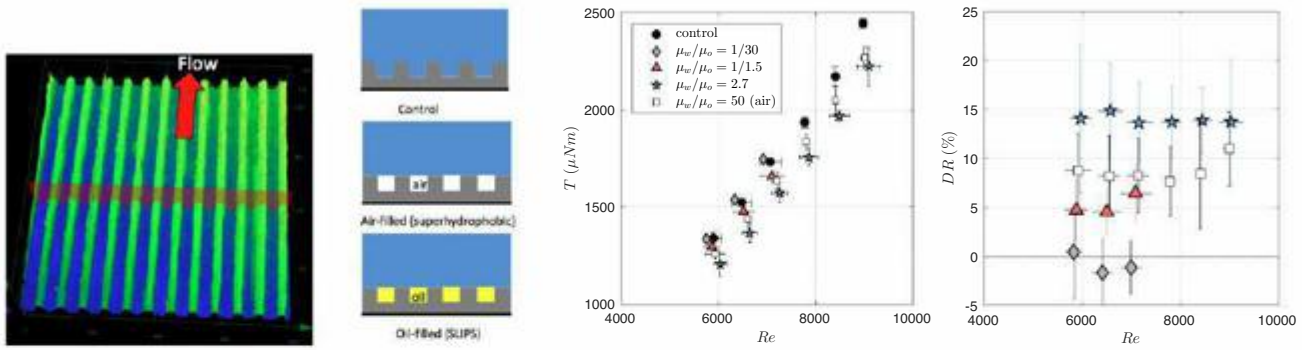

Figure 1: (a) Confocal microscope images of streamwise ridges fabricated by finely threading an aluminum cylinder; (b) Control, superhydrophobic (air-filled), and liquid-infused configurations; (c) Measured torque data for each test surface; (d) Drag reduction over the superhydrophobic and three liquid-infused surfaces. Figures (c) and (d) from [6].

Impregnating fluid	Surface functionalization	μ_w/μ_o	$\rho_o\ (kg/m^3)$	$\gamma_{ow}\ (mN/m)$
Dupont Krytox GPL-101	fluorinated	1/30	1850	$55-56$
3M Fluorinert FC-3283	fluorinated	$1/1.5$	1830	$55-56$
Heptane	OTS	2.7 or 1/0.37	684	$51-52$
Air	fluorinated	50	1.2	72.8

Table 1: Physical and chemical properties of each air- or liquid-infused surface at $20^\circ\ C$. Data from [6].

$Re_\tau \leq 140$, where $Re_\tau = \rho_w d u_\tau / \mu_w$. In figure 1d, we show the percentage drag reduction achieved, where the torque measurements have been corrected for the extraneous drag exerted by the water on the base of the cylinder. Both sets of data indicate that substantial drag reduction is achieved, with the level of drag reduction increasing with decreasing μ_w/μ_o, that is, for less viscous oils. The best performance achieved in these tests were given by the liquid-infused surface using heptane.

In previous work exploring riblet surfaces, the dimensions of the riblets were found to be critical in determining the level of drag reduction, with some surfaces exhibiting drag increases (recall that the maximum drag reduction of 8% occurred for $h^+ = 10$ and $b^+ = 15$) [1]. Similarly, the model developed by [7] for the drag reduction obtained using liquid-infused surfaces indicates that, in addition to the viscosity ratio, the characteristic value of b^+ is a governing parameter. Our current experiments are directed to verifying this model, and are focused on the role of b^+. These results will be reported in the presentation.

The support of ONR-MURI Grants N00014-12-1-0875, N00014-12-1-0962, and ONR Grant N00014-13-1-0458, Progam Manager Ki-Han Kim, is gratefully acknowledged.

References

[1] WALSH, MICHAEL J 1983 Riblets as a viscous drag reduction technique. *AIAA Journal* **21** (4), 485–486.

[2] DEAN, BRIAN & BHUSHAN, BHARAT 2010 Shark-skin surfaces for fluid-drag reduction in turbulent flow: a review. *Philosophical Transactions of the Royal Society of London A: Mathematical, Physical and Engineering Sciences* **368** (1929), 4775–4806.

[3] PARK, HYUNGMIN, SUN, GUANGYI & KIM, CHANG-JIN 2014 Superhydrophobic turbulent drag reduction as a function of surface grating parameters. *Journal of Fluid Mechanics* **747**, 722–734.

[4] ALJALLIS, ELIAS, SARSHAR, MOHAMMAD AMIN, DATLA, RAJU, SIKKA, VINOD, JONES, ANDREW & CHOI, CHANG-HWAN 2013 Experimental study of skin friction drag reduction on superhydrophobic flat plates in high reynolds number boundary layer flow. *Physics of Fluids* **25** (2), 025103.

[5] WONG, TAK-SING, KANG, SUNG HOON, TANG, SINDY K. Y., SMYTHE, ELIZABETH J., HATTON, BENJAMIN D., GRINTHAL, ALISON & AIZENBERG, JOANNA 2011 Bioinspired self-repairing slippery surfaces with pressure-stable omniphobicity. *Nature* **477** (7365), 443–447.

[6] ROSENBERG, B. J., VAN BUREN, T., FU, M. K. & SMITS, A. J. 2016 Turbulent drag reduction over air- and liquid-impregnated surfaces. *Physics of Fluids* in print.

[7] FU, M. K., SAMAHA, M. A., ROSENBERGB. J., HULTMARK, M. 2016 A model for turbulent drag reduction over fluid infused surfaces. Under review.

COHERENT STRUCTURES IN WALL-BOUNDED TURBULENCE

Javier Jiménez*

School of Aeronautics, Universidad Politécnica Madrid, 28040 Madrid, Spain

Summary As a consequence of the recent explosion in the amount and quality of data on turbulent flows, due in large part to direct numerical simulations, the emphasis has moved from what information is available to the choice of how to analyse it. In particular, the deterministic description of turbulence, although still a distant goal, does not appear any longer to be unreachable. We review recent advances in the description of wall-bounded turbulence in terms of identifiable structures that remain coherent for substantial times. We outline their properties and temporal evolution, and trace their connections with other descriptions of turbulence. We enumerate successes and failures, and speculate on the future development of the field.

INTRODUCTION

As far as we know, the flow of Newtonian fluids is well described by the deterministic Navier–Stokes equations. This includes turbulence, and its usual stochastic description can be seen as an admission of our inability to handle complex solutions rather than as an intrinsic property of the flow. Even the usual argument that engineering is primarily interested on mean quantities is disingenuous. While the point-to-point instantaneous description of an industrial flow may never be required, a robust deterministic description would open the door to better prediction and even to control. To give an example, full-scale weather control may always be impractical, but the prevention of individual tornadoes is a simpler proposition that would still be very useful.

Coherent structures have always been part of these descriptive attempts. Ideally, they would be local flow configurations that can be easily recognised and that stay recognisable for a while in a way that can be predicted from the equations. Unfortunately, this is unlikely to be true in general, because pressure in incompressible flows satisfies an elliptic equation that spreads globally the effect of local initial conditions, but it may work locally for strong events. This hope probably stems from the observation of free-shear flows [3] or of eddies in rivers and in the atmosphere, although we now understand that coherence in these systems is linked to fast inviscid instabilities that locally overwhelm the nonlinearity and chaos of the equations.

WALL-BOUNDED FLOWS

Most wall-bounded turbulent flows lack inviscid instabilities in the sense just mentioned, but they don't lack structures that can be 'visually' identified as coherent. That identification can be automated, and most of the results below have good statistical support. Popular examples are streaks [11], hairpins[1], sweeps and ejections [14] and vortex clusters [5]. They differ from the free-shear structures in that we lack a clear theory for their origin, although we believe that we know why they survive once they have been created. For the same reason that there are no strong instabilities to create them, they are only weakly damped once they form.

These structures have often been used as descriptive devices in wall turbulence, and each of them has fierce defenders and, in some cases, detractors. The absence of a fast generation mechanism probably means that no single structure is likely to dominate the flow everywhere. Most reasonable definitions imply a low-dimensional manifold in phase space towards which the flow tends, and in whose neighbourhood it stays for some time, but the intrinsic dimensionality of even very-low-Reynolds number turbulence is high [10]. Moreover, recent results suggest that the inertial range of turbulence is essentially attractorless, and temporal tracking of the growth and decay of individual structures is more consistent with a memoryless process than with an organised evolution. On the other hand, the visually identified structures are far from being negligible. Streaks carry a large fraction of the fluctuating kinetic energy, and the same is true of the momentum transfer (i.e. drag) by sweeps and ejections.

A wealth of data, and a paucity of models

Some of the ambiguities plaguing coherent structures can be traced to the incomplete information that experiments provide about extended objects. Until the recent appearance of time-resolved PIV, experiments were mostly restricted to time traces at a few points. Even today, experiments rarely extend beyond two-dimensional sections. This left a lot of scope for interpretation and hypothesising, and has been largely superseded by direct simulations that routinely provide three-dimensional time-resolved fields of all flow variables. Numerical Reynolds numbers are also now comparable to experiments, although it is striking that efforts to relate experimental with numerical structural data remain relative rare.

A case that has been studied in some detail are the carriers of intense 'bursts' of momentum transfer, originally defined from point velocity data in terms 'quadrants' in a u–v diagram [14]. They were later generalised to a self-similar hierarchy

*Corresponding author. Email: jimenez@torroja.dmt.upm.es

of irregular three-dimensional objects [12], each of which contains, on average, a short streamwise roller and a side-by-side pair of a sweep and an ejection. They have lifetimes of the order of the local eddy turnover, and owe much of their growth and decay to a series of mergers and splits between objects of comparable size [13]. A sub-family of 'wall-attached' eddies spanning the whole boundary layer carry 60% of the total momentum flux, even if they fill less than 8% of the total volume.

Unfortunately, while data are very useful to determine which hypotheses are untenable, they do not amount to a theory of turbulence. Models incorporating structures are also being developed. For example, we have reasons to believe that the origin of the observed bursts is the quasi-linear transient growth of perturbations to the mean profile [4, 6], and we know that these transient structures exist in all the linearly stable turbulent shear flows in which they have been sought [7]. Linear processes are thus excellent candidates for the driving engine of wall-bounded flows, and they can be easily analysed and predicted. They are also fast and inviscid in the sense of free-shear flows, even if transient. However, it is unclear whether our enthusiasm for these desirable properties simply reflects our inability to deal with fully nonlinear behaviour. A recent analysis in our group reveals that only 10% of the volume and 40% of the drag are represented by 'linear' bursts.

Nonlinear exact solutions of the Navier–Stokes equations, such as permanent waves, cycles [9], and homoclinic and heteroclinic connections [2, 15], are also tantalisingly similar to some of the visual features of low-Reynolds number turbulence, but they are hard to observe at higher Reynolds numbers, and it is even unclear how they could be recognised in a fully chaotic flow if they were present. As long as this continues to be the case, we do not know how significant they are.

A worrying possibility is that we may be looking at the wrong objects. Structures are presently defined in terms of variables, such as the Reynolds stresses, whose main justification is that they can be measured experimentally. But only their divergence enters the equations, and the stresses themselves can be modified by an arbitrary divergence-less 'gauge' [8]. Most present analyses use a particular 'experimental' gauge, but this needs not be the case with numerical data. It is intriguing whether other gauges, or even gauge-invariant quantities, may give results that are easier to interpret.

CONCLUSIONS

The flood of data provided by numerical simulations, and up to a point by experiments, is shifting the focus of turbulence research away from observation and back to theoretical modelling. In particular, coherent structures offer a promising path to the deterministic description of at least the most energetic parts of the flow. This in turn may lead to practical applications in control and modelling. There is by now a virtually unlimited supply of relevant data, including at Reynolds numbers comparable to most experiments in which detailed measurements are possible. On the other hand, theoretical understanding is still limited. In particular, we do not know how to restrict our analysis to a local region. We have argued that part of the problem may be that our methods have inherited the limitations of experiments, and that adapting them to the new numerical capabilities could be a first step in resolving the theoretical impasse.

This preparation of this paper was partially supported by the Multiflow and Coturb advanced grants of the European Research Council. I am grateful to S. Dong, M.P. Encinar, C. Huertas–Cerdeira, A. Lozano–Durán and A. Vela–Martín for much of the research cited here.

References

[1] R. J. Adrian: Hairpin vortex organization in wall turbulence. Phys. Fluids, 19:041301, 2007.

[2] N. Aubry, P. Holmes, J. L. Lumley, E. Stone: The dynamics of coherent structures in the wall region of a turbulent boundary layer. J. Fluid Mech., 192:115–173, 1988.

[3] G. L. Brown, A. Roshko: On the density effects and large structure in turbulent mixing layers. J. Fluid Mech., 64:775–816, 1974.

[4] K. M. Butler, B. F. Farrell: Optimal perturbations and streak spacing in wall-bounded shear flow. Phys. Fluids A, 5:774–777, 1993.

[5] J. C. del Álamo, J. Jiménez, P. Zandonade, R. D. Moser: Self-similar vortex clusters in the logarithmic region. J. Fluid Mech., 561:329–358, 2006.

[6] J. Jiménez: How linear is wall-bounded turbulence? Phys. Fluids, 25:110814, 2013.

[7] J. Jiménez: Direct detection of linearized bursts in turbulence. Phys. Fluids, 27:065102, 2015.

[8] J. Jiménez: Optimal fluxes and Reynolds stresses. J. Fluid Mech., submitted.

[9] G. Kawahara, M. Uhlmann, L. van Veen: The significance of simple invariant solutions in turbulent flows. Ann. Rev. Fluid Mech., 44:203–225, 2012.

[10] L. Keefe, P. Moin, J. Kim: The dimension of attractors underlying periodic turbulent Poiseuille flow. J. Fluid Mech., 242:1–29, 1992.

[11] S. J. Kline, W. C. Reynolds, F. A. Schraub, P. W. Runstadler: Structure of turbulent boundary layers. J. Fluid Mech., 30:741–773, 1967.

[12] A. Lozano–Durán, O. Flores, J. Jiménez: The three-dimensional structure of momentum transfer in turbulent channels. J. Fluid Mech., 694:100–130, 2012.

[13] A. Lozano–Durán, J. Jiménez: Time-resolved evolution of coherent structures in turbulent channels: characterization of eddies and cascades. J. Fluid Mech., 759:432–471, 2014.

[14] S. S. Lu, W. W. Willmarth: Measurements of the structure of the Reynolds stress in a turbulent boundary layer. J Fluid Mech, 60:481–511, 1973.

[15] L. Van Veen, G. Kawahara: Homoclinic tangle on the edge of shear turbulence. Phys. Rev. Lett., 107:114501, 2011.

HYDRODYNAMICS AND HAIRY SURFACES

A. E. Hosoi*[1]
[1]*Department of Mechanical Engineering, Massachusetts Institute of Technology, Cambridge, MA*

Summary Flexible slender structures in flow are everywhere. While a great deal is known about individual flexible fibers interacting with fluids, considerably less work has been done on fiber ensembles, such as fur or hair, in flow. These hairy surfaces are abundant in nature and perform multiple functions from thermal regulation to water harvesting to sensing. Motivated by these biological systems, we consider two examples of hairy surfaces interacting with flow: (1) air entrainment in the fur of diving mammals and (2) symmetry breaking in hairy microchannels.

THERMAL REGULATION VIA AIR ENTRAINMENT IN SEMI-AQUATIC MARINE MAMMALS

Arctic mammals are faced with the challenge of maintaining body temperature in extremely cold environments. The task is further complicated by the fact that many of these animals must find solutions that are effective both on land and under water. Unlike fully aquatic mammals which rely on blubber for insulation, semi-aquatic mammals (such as fur seals, otters, and beavers) have specially adapted fur that serves as an effective insulator both above and below water. Many of these animals have evolved pelts that naturally entrap air when they dive. This air: (1) provides additional insulation under water, (2) provides added buoyancy, and (3) facilitates water shedding when the animals resurface. In this study we investigate diving conditions and fur properties which amplify air entrainment in fur.

Our toy model of a furry animal diving into water consists of a textured surface plunged into fluid [1]. Studies of both withdrawal and submersion of rigid surfaces into fluids have a rich history beginning with the pioneering work of Landau-Levich-Derjaguin (LLD) [2]. Here we extend LLD to surfaces with mesoscale textures which are relevant to diving mammals. Hairy surfaces are fabricated using laser cut molds and casting samples with PDMS (Figure 1, Middle). The sample is lowered into a bath of silicone oil at a constant speed, simulating a dive. A representative snapshot of the dive is shown in Figure 1 (Right) in which the dark region indicates a wedge of air entrained by the hairs. The shape of the wedge is set by a dynamic balance between fluid entering from the left between the hairs and air escaping out at the top of the wedge.

To estimate conditions under which we expect air entrainment, we construct a model in which hairs of length L are plunged into liquid at a speed V. The x-direction is defined parallel to the hairs. As the hairs are plunged into the bath, liquid penetrates between the hairs, forming a wetting front. This flow between hairs is analogous to flow in a capillary tube and the balance of pressure at the liquid/air interface is given by

$$\rho g y + \frac{1}{2}\rho \dot{x}^2 = \gamma\kappa + \frac{\mu}{k}\frac{xx}{r^2}$$

where γ represents surface tension, κ is the meniscus curvature, μ is the dynamic viscosity, k the effective permeability, r the spacing of the hairs, and ρ is the density of the fluid. In our experiments, bending of the hairs, capillary forces, and inertial

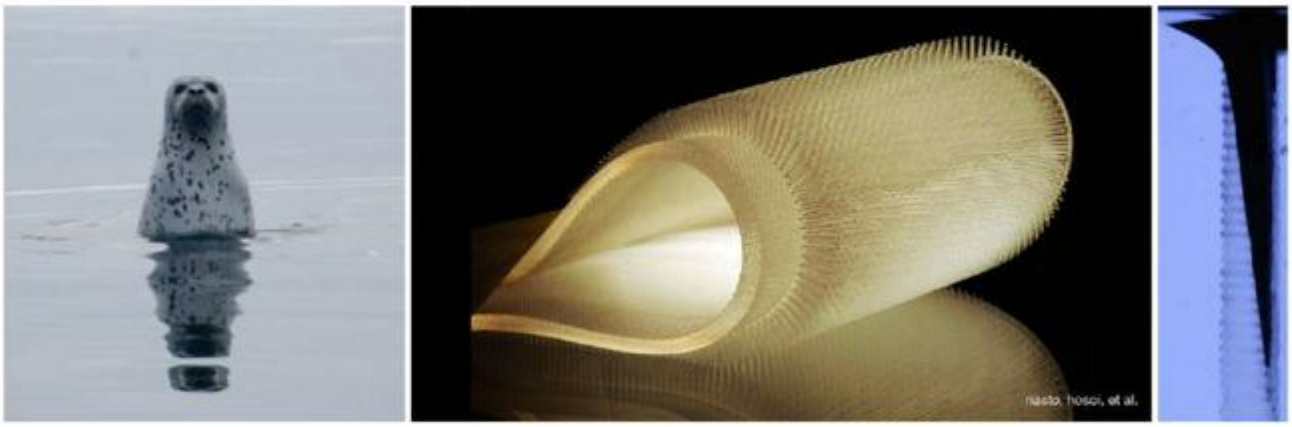

Figure 1: (Left) Spotted seal. Photo credit M. Cameron [3]. (Middle) Fabricated PDMS hair surface. Photo credit Felice Frankel. (Right) PDMS hair surface plunging into a silicon bath. Dark wedge shows a region of entrained air.

*Corresponding author. Email: peko@mit.edu

effects are all negligible. Balancing hydrostatic pressure and viscous resistance we solve for the speed of the advancing front. By comparing this speed with the diving speed, we find a maximum diving depth that can be achieved while maintaining an insulating layer of air given by:

$$\frac{h_{max}}{L} = \left(\frac{V\mu}{k\rho g r^2}\right)^{1/2}.$$

The model is compared with experimental data from our toy system as well as with typical biological data from seals and otters.

LOW REYNOLDS NUMBER SOLID STATE FLOW RECTIFIERS

A fundamental component in hydraulic systems is the flow rectifier in which resistance varies with the direction of the flow. One of the simplest ways to generate such an asymmetry is with a ball valve in which flow is completely obstructed in one direction and free to flow in the other. In this work we seek a variation that: (1) allows the designer to modulate the relative resistances in the rectifier and (2) can be achieved with solid state state components (i.e. no moving parts). Such a device was first proposed by Nikola Tesla who patented the "valvular conduit" in 1920 [4]. Tesla's device relied on fluid inertia to break symmetry in the rectifier. Later Groisman and Quake [5] demonstrated a microfluidic rectifier for viscoelastic fluids in which the non-Newtonian properties of the working fluid break symmetry in the flow via nonlinear effects.

In this project, we design a fluid rectifier for low Reynolds number Newtonian flows [6]. In order to circumvent the time-reversal symmetry inherent in Stokes flow, we again turn to mesoscale elastic hairs that are affixed to the channel walls. Hairs are angled such that flow aligned with the hairs bends them towards the channel walls increasing the effective height of the channel; flow in the other direction bends hairs away from the walls decreasing the effective height.

Consider a channel coated with a bed of elastic fibers, each of radius a and length $L \gg a$. The fibers are anchored to a rigid substrate wall, and tilted at an angle θ_0 to the z-axis. Flow is driven through the channel by an externally imposed pressure differential. The channel, of height $2R$, can be modeled using two zones. The interior zone corresponds to the space in the center of the channel which is free of hairs, hence the flow corresponds to Poiseuille flow. The second zone is comprised of flow through the fiber bed near the wall and is modeled as a porous medium using Darcy flow with a permeability that is dependent on the local orientation of the fibers [7]. Coupling the two zones, we assume that the shear stress is supported by the elastic fibers and that the flow velocity is continuous at the fiber tip. Finally, to close the system we require a model for the deformation of the fibers. We consider two alternate models for fibers: (1) a linear elastic beam and (2) a rigid fiber attached to the substrate via a torsional spring. This system can now be solved to find the equilibrium shape of the fibers which can then be used to find flow rates and resistances.

For the torsional spring model, fiber orientation θ is given by the transcendental equation

$$\cos\theta\left(1 - \frac{\alpha}{2}\cos\theta\right) = \mathrm{Te}(\theta - \theta_0).$$

Hence the system response is characterized by three dimensionless groups: $\mathrm{Te} = (K_s\phi_s)/(\pi a^2 L\mu v)$ which represents the ratio of elastic to viscous stresses, $\alpha = L/R$ the ratio of fiber length to channel height, and θ_0 the undeformed angle of the fiber. Here K_s represents the torsional spring stiffness, ϕ_s is the density of fibers, and v is the average fluid velocity. This equation can be solved numerically to map and optimize impedance asymmetry. Note that in the limit of large Te the fibers are nearly rigid and, owing to the time-reversal symmetry in Stokes flow, there is no impedance asymmetry. At the other extreme, $\mathrm{Te} \to 0$, the fibers are extremely flexible and fold down to the walls regardless of the flow direction, again resulting in no asymmetry. However, there is a region of parameter space in which elastic and viscous forces on the fibers are comparable, maximizing the anisotropic resistive properties of the channel. These predictions are tested by constructing a fiber bed using the fabrication techniques described above and directly measuring resistance asymmetries.

References

[1] Nasto, Regli, Brun, Alvarado, Clanet, Hosoi. PREPRINT, 2015.

[2] Landau, Levich.:Entrainment of fluid by the driven plate, *Acta Phys.-Chim. USSR* **17**: 42, 1942.

[3] Wikimedia Commons, source http://www.ecofoci.noaa.gov/cruiseWeb/ice08/Ice2008_seals.html.

[4] Tesla.: Valvular Conduit, Patent # US 1,329,559 A, 1920.

[5] Groisman, Quake.: A Microfluidic Rectifier: Anisotropic Flow Resistance at Low Reynolds Numbers, *PRL* **92**:094501, 2004.

[6] Alvarado, Comtet, Hosoi. PREPRINT, 2015.

[7] Gopinath, Mahadevan.: Elastohyrodynamics of wet bristles, carpets and brushes, *Proc. Roy. Soc. A* **467**: 1665-1685, 2011.

THE TRANSITION TO THE ULTIMATE STATE IN TURBULEN THERMAL CONVECTION

E. Bodenschatz *, G. Ahlers, D. Funfschilling, D. van Gills, X. He, H. Nobach, and S. Weiss
Max Planck Institut für Dynamik und Selbstorganisation, Göttingen, Deutschland

Summary We report measurements on turbulent Rayleigh-Bénard convection using three cylindrical samples with aspect ratios (diameter/height) $\Gamma = 1.00, 0.50$ and 0.33. All samples had the same diameter $D = 1.12$ m, but different heights L. Compressed sulfur hexafluoride gas (SF_6) at pressures up to 19 bar was used as the fluid at the Göttingen Turbulence Facility (see www.EuHIT.org). The measurements were conducted over the Rayleigh-number range $10^{12} \lesssim Ra \lesssim 4 \times 10^{15}$ and for Prandtl numbers Pr near 0.8. In three independent measurements, namely global heat transport, local turbulent Reynolds numbers, and large-scale-circulation dynamics, we observed a transition over a range of Ra from the classical regime to a new regime which has been referred to as "ultimate". We discuss the properties of the classical and the ultimate state, as well as the influence of rotation on this system.

INTRODUCTION

Rayleigh-Bénard convection (RBC), where fluid mass and heat are convected due to a vertical temperature difference ΔT in the presence of gravity, has long been a model system for the study of thermal convection [1]. The fluid is contained between two parallel horizontal plates and heated from below. The dynamics of the system depends on the Rayleigh number $\mathrm{Ra} \equiv \alpha g \Delta T L^3/(\kappa\nu)$ and the Prandtl number $\mathrm{Pr} \equiv \nu/\kappa$. Here g is the gravitational acceleration, L is the sample height, and α, ν and κ are the thermal expansion coefficient, the kinematic viscosity and the thermal diffusivity respectively. When Ra is moderate, there are two thin laminar boundary layers (BLs), one adjacent to each of the plates. This system is referred to as the "classical state". Each BL emits plumes that rise or fall towards the opposite plate under the influence of buoyancy. The plumes drive, and in turn are carried by, a large-scale circulation (LSC). When L and the diameter D of the sample are not too different, then the LSC consists of a single convection roll occupying the bulk region between the BLs. As Ra increases and exceeds a critical value Ra^*, the LSC mean flow, as well as fluctuations on somewhat smaller scales, will apply shear to the BLs and, at sufficiently large $\mathrm{Ra} > \mathrm{Ra}^*$, will cause the BLs to become turbulent as well. Since no further structural changes are anticipated as Ra increases beyond Ra^*, the system above Ra^* is referred to as the "ultimate state". The value of Ra^* was predicted to be of the order of 10^{14} for $\mathrm{Pr} \simeq 1$ [2], and to increase as Pr increases.

Various properties, such as the Nusselt number Nu (a dimensionless form of the heat transport), the Reynolds numbers Re, and aspects of the the LSC dynamics are expected to have different Ra dependences in the classical and ultimate states. In agreement with the model of Grossmann and Lohse (GL) [2], measurements at the Göttingen Turbulence Facility gave $\mathrm{Nu} \propto \mathrm{Ra}^{0.32}$ and $\mathrm{Re} \propto \mathrm{Ra}^{0.43}$ for the classical state. For the ultimate state they yielded $\mathrm{Nu} \propto \mathrm{Ra}^{0.38}$ and $\mathrm{Re} \propto \mathrm{Ra}^{0.50}$, as predicted also by GL [3]. Recent measurements of the Reynolds number Re_{θ_m} (which describes the LSC azimuthal diffusivity) revealed a transition from $\mathrm{Re}_{\theta_m} \propto \mathrm{Ra}^{0.28}$ for the classical state to $\mathrm{Re}_{\theta_m} \propto \mathrm{Ra}^{0.40}$ for the ultimate state [4].

EXPERIMENTAL FACILITIES AND MEASUREMENTS

The experiments were conducted with three large RBC samples known as the High-Pressure Convection Facilities (HPCFs) which were located in an even larger pressure vessel known as the Uboot of Göttingen at the Göttingen Turbulence Facility. The samples were cylindrical with diameter $D = 1.12$ m and heights $L = 1.12$, 2.24, and 3.40 m, corresponding to aspect ratios $\Gamma \equiv D/L = 1.00$, 0.50, and 0.33. The fluid was gaseous pressurized sulfur hexafluoride (SF_6) at ambient temperatures. For a perfect gas $\mathrm{Ra} \propto P^2$ (P is the pressure). Thus, increasing P up to the maximum Uboot design pressure of 19 bar yielded the highest possible Ra values. For $L = 3.40$ m $\mathrm{Ra} = 4 \times 10^{15}$ was reached. The value of Pr was close to 0.8. Details about the facilities and experimental procedures were reported elsewhere [5].

EXPERIMENTAL RESULTS

Figure 1(a) shows Nu measurements for the $\Gamma = 1.00$ sample (known as "HPCF-IVb") which cover the range $10^{12} \lesssim \mathrm{Ra} \lesssim 1.5 \times 10^{14}$. For $\mathrm{Ra} < \mathrm{Ra}_1^* \simeq 2 \times 10^{13}$ one sees that $\mathrm{Nu} \propto \mathrm{Ra}^{0.321}$, consistent with the classical-state prediction [2] and previous measurements. For $\mathrm{Ra} > \mathrm{Ra}_2^* \simeq 8 \times 10^{13}$ we find $\mathrm{Nu} \propto \mathrm{Ra}^{0.37}$, consistent with the prediction for the ultimate state [3]. In the range $\mathrm{Ra}_1^* < \mathrm{Ra} < \mathrm{Ra}_2^*$ Nu gently increases from values corresponding to one state to those of the other, indicating the existence of a transition range between the classical and the ultimate state.

Figure 1(b) shows the reduced Reynolds number $\mathrm{Re}_V/\mathrm{Ra}^{0.5}$ from a different $\Gamma = 1.00$ sample (known as "HPCF-IV") [5]. Here $\mathrm{Re}_V \equiv VL/\nu$ where V is the rms velocity fluctuation in the vertical direction. While the data do not give an obvious indication of Ra_1^* (except for a slight increase of the scatter), they clearly show a discontinuity and a change of the Ra

*Email: Eberhard.Bodenschatz@ds.mpg.de

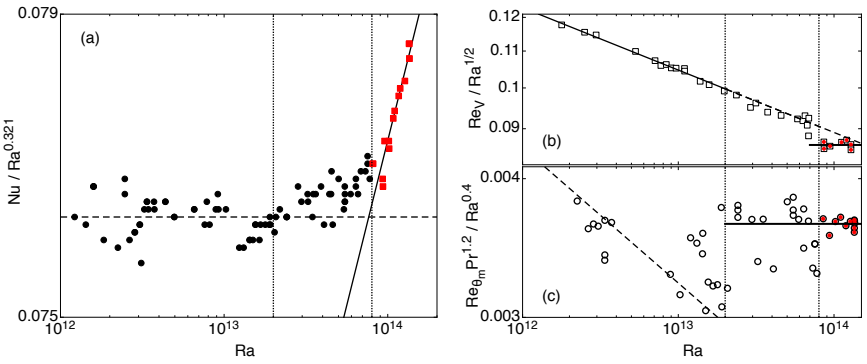

Figure 1: (a) The reduced Nusselt number $\mathrm{Nu}/\mathrm{Ra}^{0.321}$ as a function of Ra on logarithmic scales. The solid line is the power-law fit $\mathrm{Nu} = 0.0159 Ra^{0.37}$ to the red squares, and the horizontal dashed line is at $\mathrm{Nu}/\mathrm{Ra}^{0.321} = 0.0763$. (b) The reduced velocity-fluctuation Reynolds number $\mathrm{Re}_V/\mathrm{Ra}^{0.5}$ as a function of Ra [5]. The solid line is the power-law fit to the data with $\mathrm{Ra} \leq \mathrm{Ra}_1^* = 2 \times 10^{13}$, which gave an exponent of 0.43. The dashed line is the extrapolation of that fit beyond Ra_1^*. The horizontal solid bar corresponds to 0.0863. (c) The reduced Reynolds number $\mathrm{Re}_{\theta_m}\mathrm{Pr}^{1.2}/\mathrm{Ra}^{0.4}$ as a function of Ra. Dashed line: $\mathrm{Re}_{\theta_m}\mathrm{Pr}^{1.2} = 0.124\mathrm{Ra}^{0.278}$ as determined using the data from Ref. [6] for $\mathrm{Pr} = 4.38$. The horizontal solid bar corresponds to $\mathrm{Re}_{\theta_m}\mathrm{Pr}^{1.2} = 0.00364\mathrm{Ra}^{0.40}$. In all panels the data are for $\Gamma = 1.00$ and vertical dotted lines represent $\mathrm{Ra}_1^* \simeq 2 \times 10^{13}$ and $\mathrm{Ra}_2^* \simeq 8 \times 10^{13}$.

dependence at Ra_2^*. Above Ra_2^* the data give $\mathrm{Re}_V \propto \mathrm{Ra}^{0.50\pm0.02}$, in excellent agreement with the prediction for the mean-flow Reynolds number Re_U in the ultimate state [3] (to our knowledge there is no prediction for Re_V).

The orientation θ_m (measured at the height $z = L/2$) of the LSC plane diffuses in the azimuthal direction because of the stochastic action of the small-scale fluctuations. From the LSC azimuthal diffusivity D_{θ_m} one can construct a Reynolds number $\mathrm{Re}_{\theta_m} \equiv L\sqrt{D_{\theta_m}/\nu}$ as a quantitative measure of the stochastic azimuthal dynamics of the LSC. In figure 1(c) we show $\mathrm{Re}_{\theta_m}\mathrm{Pr}^{1.2}/\mathrm{Ra}^{0.4}$ measured with HPCF-IVb. In the classical regime the Ra dependence agrees well with the extrapolation of the result $\mathrm{Re}_{\theta_m} \propto \mathrm{Ra}^{0.28}$ obtained from a physically smaller $\Gamma = 1.00$ sample for $\mathrm{Ra} \lesssim 10^{11}$ and $\mathrm{Pr} = 4.38$ [6]. In the ultimate state the data scatter much less than in the transition range, and yield $\mathrm{Re}_{\theta_m}\mathrm{Pr}^{1.2} = 0.0036\mathrm{Ra}^{0.40\pm0.03}$. While a theoretical explanation of the scaling of $\mathrm{Re}_{\theta_m}(\mathrm{Ra}, \mathrm{Pr})$ remains a challenge for both the classical and the ultimate state, our measurements of Nu, Re_V and Re_{θ_m} for $\Gamma = 1.00$ clearly reveal the ultimate-state transition and yield consistent values of Ra_1^* and Ra_2^*.

Measurements of Nu and Re for $\Gamma = 0.50$ [7] and $\Gamma = 0.33$ also showed the same ultimate-state transition. As Γ increased, the onset of the transition at $\mathrm{Ra}_1^* \simeq 2 \times 10^{13}$ remained almost unchanged, while Ra_2^* decreased. This leads to a shorter transition range at larger Γ. The data suggest that $\mathrm{Ra}_1^* = \mathrm{Ra}_2^*$ for $\Gamma \gtrsim 1.5$, implying a sharp transition at a unique value Ra^* of Ra.

ACKNOWLEDGEMENTS

We are grateful to the Max Planck Society and the Volkswagen Stiftung, whose support made the establishment of the Uboot facility and the experiments possible. We thank the Deutsche Forschungsgemeinschaft (DFG) for financial support through SFB963: “Astrophysical Flow Instabilities and Turbulence”.

References

[1] Ahlers G., Grossmann S., Lohse D.: Heat transfer and large scale dynamics in turbulent Rayleigh-Bénard convection. Rev. Mod. Phys. **81**, 503 (2009).

[2] Stevens J.A.M., van der Poel E.P., Grossmann S. and Lohse D.: The unifying theory of scaling in thermal convection: The updated prefactors. J. Fluid Mech. **730**, 295 (2013); and references therein.

[3] Grossmann S. and Lohse D.: Multiple scaling in the ultimate regime of thermal convection. Phys. Fluids **23**, 045108 (2011).

[4] He X., Bodenschatz E., Ahlers G.: Azimuthal diffusion of the large-scale-circulation plane, and absence of significant non-Boussinesq effects, in turbulent convection near the ultimate-state transition. J. Fluid Mech. **791**, R3 (2016).

[5] He X., van Gils D.P.M., Bodenschatz E., Ahlers G.: Reynolds numbers and the elliptic approximation near the ultimate state of turbulent RayleighBénard convection. New J. Phys. **17**, 063028 (2015).

[6] Brown E., Ahlers G.: Rotations and cessations of the large-scale circulation in turbulent Rayleigh-Bénard convection. J. Fluid Mech. **568**, 351 (2006).

[7] He X., Funfschilling D., Nobach H., Bodenschatz E., Ahlers G.: Transition to the Ultimate State of Turbulent Rayleigh-Bénard Convection. Phys. Rev. Lett. **108**, 024502 (2012).

HYDRODYNAMIC QUANTUM ANALOGS

John W. M. Bush *[1]
[1]*Department of Mathematics, MIT, Cambridge MA, USA*

Summary A decade ago, Yves Couder and Emmanuel Fort discovered that a millimetric droplet may self-propel on the surface of a vibrating bath by virtue of a resonant interaction with its own wave field. This hydrodynamic system is unique in that it exhibits several features, both dynamical and statistical, previously thought to be exclusive to the microscopic, quantum realm. Moreover, its dynamics are reminiscent of an early realist model of quantum dynamics, Louis de Broglie's pilot-wave theory. In my Sectional Lecture, I shall discuss prior and ongoing work in the experimental and theoretical modeling of this rich hydrodynamic pilot-wave system, and its relation to the modern extensions of de Broglie's mechanics.

When a fluid layer is subjected to vertical vibration, its surface goes unstable to a field of Faraday waves when a critical forcing acceleration is exceeded (Figure 1A-B). Below this Faraday threshold, millimetric drops can bounce indefinitely on the surface (Figure 1C). Ten years ago, Yves Couder and Emmanuel Fort discovered that a droplet bouncing in this fashion may destabilize into a dynamic state, interacting with its own wave field in such a way as to walk steadily across the surface [4] (Figure 1D). These walking droplets, or 'walkers', are composed of both the droplet and an extended wave field. The propulsive wave force imparted to the walker during impact is proportional to the local slope of the interface. Since the wave field depends on both the walker's history and environment, the walker dynamics are implicitly non-local in both space and time, said to depend on the system's 'path-memory' [9]. By virtue of this dynamical non-locality, as is most pronounced in the high-memory limit when the waves are most persistent, the walkers exhibit several features previously thought to be peculiar to the microscopic, quantum realm.

The walkers exhibit single-particle diffraction when they pass through a slit, on the basis of which one can infer an uncertainty principle in position and momentum [5]. Single-particle interference has also been reported in the double-slit geometry [5], although these results have recently been contested [1]. The walkers can tunnel across barriers consisting of submerged obstacles, with the tunneling probability decreasing exponentially with barrier width [8]. Walkers in confined geometries follow complex chaotic trajectories, but exhibit coherent statistics reminiscent of electrons in a quantum corral [13]. When the droplets walk in a rotating frame, quantized inertial orbits analogous to Landau levels may emerge owing to the droplet interacting with its own wake [11, 14]. Hydrodynamic spin states and analog Zeeman splitting have also been explored [18]. Walkers in a harmonic potential execute orbits that are quantized in both energy and angular momentum, analogous to the quantum simple harmonic oscillator [20].

When several bouncing or walking droplets interact, they couple through their wave fields to form a variety of static or dynamic bound states. Pairs of identical walkers may either scatter, lock into circular orbits [4, 21] (Figure 1E), walk together with one trailing the other, or walk side by side in the so-called promenade mode [2] (Figure 1F). Atom-like structures can form from small drops near larger ones, with walkers orbiting static bouncers (Figure 1G). Multiple bouncers or walkers may also lock into a stable lattice[7] (Figure 1H). All such multiple droplet arrangements, or 'bound states', are stable below a critical forcing acceleration, beyond which wobbling instabilities set in, followed by the collapse of the compound structure.

Recent experimental studies have been directed towards an improved understanding of walker-boundary interactions. When walkers interact with a planar boundaries, enigmatic reflection laws emerge. Specifically, the reflection angle depends only weakly on the system memory and angle of incidence: for a broad range of incident angles, the angle of reflection is nearly 70°. When a walker scatters off a submerged pillar, it may lock onto a logarithmic spiral. The effective force required to generate such a spiral is found to be proportional to the Coriolis force that would act on the walker if it were in a frame rotating with its instantaneous angular velocity. The equivalent form of the Lorentz force acting on a charge in a uniform magnetic field and the Coriolis force acting on a mass in a rotating frame suggests that the walker is behaving as would a moving charge responding to the magnetic field generated by the current associated with its own motion. These scattering experiments have thus revealed a surprising new behavior analogous to mechanical self-induction.

A hierarchy of theoretical models of increasing sophistication have been developed to describe the walkers [11, 16, 17, 15] Theoretical models now allow for a quantitative description of the walker dynamics, and reveal a strong dependence of the bouncing behavior on drop size and driving acceleration [16]. These models allow for a robust assessment of the stability of a number of dynamical states, including straight line walking and circular orbital motion [17, 18]. The studies of orbital dynamics have provided insight into the origins of quantization and quantum-like statistics in this hydrodynamic pilot-wave system. Quantization arises by virtue of the dynamic constraint imposed on the walker by its monochromatic wave field. When the orbital states destabilize, the chaotic walker drifts between unstable orbital states, the result being multimodal, quantum-like statistics. A similar physical picture provides rationale for the statistical behavior reported for walkers in a circular corral [13], wherein concentric circles may be considered as the quantized orbital states [12]. Current theoretical models are being extended in order to consider walker-boundary interactions and the stability of multiple-walker states.

*Corresponding author. Email: bush@math.mit.edu

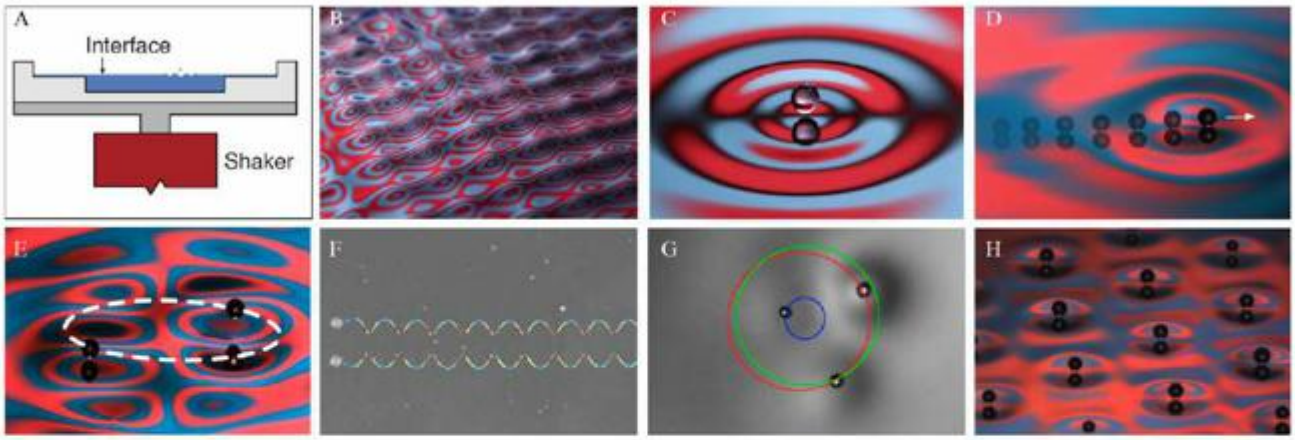

Figure 1: (A) Schematic illustration of the experiment: a drop walks on the surface of a vibrating fluid bath. (B) Faraday waves emerge on the bath when the Faraday threshold is exceeded. (C) A millimetric oil droplet bounces in place on a vertically vibrating fluid bath just below the Faraday threshold. (D) An oil droplet walks due to a resonant interaction with its own wavefield. E) A pair of identical walkers locked in orbit. (F) A pair of identical droplets walk from right to left in the 'promenade mode', their trajectories color coded according to speed. (G) Three drops form a bound state marked by nearly circular orbits for each. (H) A stable lattice of identical bouncing droplets.

In an attempt to reconcile quantum mechanics and relativity, Louis De Broglie proposed that quantum objects such as electrons consist of a localized vibrating particle moving in sync with a spatially extended particle-centered wave field [6]. The particle vibration is characterized by an exchange between rest mass energy and wave energy at the Compton frequency. He proposed that the guiding or 'pilot' wave field consists of a monochromatic wave field with the de Broglie wavelength, and asserted that the resulting pilot-wave dynamics could give rise to a statistical behavior consistent with the predictions of standard quantum theory. While de Broglie did not specify the physical origins of his pilot-wave field, others have sought it in the electromagnetic vacuum field [19]. The walking-droplet system, when considered in light of these modern, vacuum-based pilot-wave theories, would seem to suggest the possibility of an unresolved quantum dynamics on the Compton scale, that a successful non-local hidden-variable theory might be based on the physical picture of particles interacting with the vacuum, and propagating in an equilibrium state of energy exchange within it [3].

References

[1] Andersen A, Madsen J, Reichelt C, Ahl S, Lautrup B, Ellegaard C, Levinsen M, and Bohr T: Double-slit experiment with single wave-driven particles and its relation to quantum mechanics, *Phys. Rev. E* 92, 013006, 2015.

[2] Borghesi C, Moukhtar J, Labousse M, Eddi A, Fort E and Couder Y: Interaction of two walkers: Wave-mediated energy and force. Phys. Rev. E, 90:063017, 2014.

[3] Bush, JWM: Pilot-wave hydrodynamics, *Ann. Rev. Fluid Mech.* 47: 269–292-996, 2015.

[4] Couder Y, Protière S, Fort E, Boudaoud A.: Walking and orbiting droplets. *Nature* 437: 208, 2005.

[5] Couder Y, Fort E.: Single particle diffraction and interference at a macroscopic scale. *Phys. Rev. Lett.* 97: 154101, 2006.

[6] de Broglie L: Interpretation of quantum mechanics by the double solution theory. *Annales de la Fondation Louis de Broglie* 12: 1-23, 1987.

[7] Eddi A, Decelle A. Fort E and Couder Y: Archimedean lattices in the bound states of wave interacting particles, *Europhys. Lett.*, 87: 56002, 2009.

[8] Eddi A, Fort E, Moisy F. Couder Y.: Unpredictable tunneling of a classical wave-particle association. *Phys. Rev. Lett.* 102: 240401, 2009.

[9] Eddi A, Sultan E, Moukhtar J, Fort E, Rossi, M, Couder Y.: Information stored in Faraday waves: the origin of path memory. *J. Fluid Mech.* 674: 433-463., 2011

[10] Eddi A, Moukhtar J, Perrard J, Fort E, Couder Y.: Level splitting at a macroscopic scale. *Phys. Rev. Lett.* 108:264503, 2012.

[11] Fort E, Eddi A, Boudaoud A, Moukhtar J, Couder Y.: Path-memory induced quantization of classical orbits. *PNAS* 107:41: 17515–17520, 2010.

[12] Gilet, T. Dynamics and statistics of wave-particle interactions in a confined geometry. *Phys. Rev. E.* 90: 052917, 2014.

[13] Harris DM, Moukhtar J, Fort E, Couder Y, Bush JWM: Wavelike statistics from pilot-wave dynamics in a circular corral. *Phys. Rev. E* 88, 011001, 2013.

[14] Harris DM, Bush JWM: Droplets walking in a rotating frame: from quantized orbits to multimodal statistics. *J. Fluid Mech.* 739: 444-464, 2014.

[15] Milewski P, Galeano-Rios C, Nachbin A, Bush JWM: Pilot-wave hydrodynamics: modeling and computation. *J. Fluid Mech.*, 778: 361–388, 2015.

[16] Mol´cek J, Bush JWM: Droplets walking on a vibrating fluid bath: towards a hydrodynamic pilot-wave theory. *J. Fluid Mech.* 727: 612-647, 2013.

[17] Oza A, Rosales RR, Bush JWM. A trajectory equation for walking droplets: hydrodynamic pilot-wave theory. *J. Fluid Mech.* 737: 552-570, 2013.

[18] Oza A, Harris DM, Rosales RR, Bush JWM: Pilot-wave dynamics in a rotating frame: on the emergence of orbital quantization. *J. Fluid Mech.* 744: 404–429, 2014.

[19] de la Pena L, Cetto AM, Valdes Hernandez A: The emerging quantum: The physics behind quantum mechanics, Springer, 2015.

[20] Perrard S, Labousse M, Fort E, Couder Y.: Chaos driven by interfering memory, *Phys. Rev. Lett.* 113:104101, 2014.

[21] Protière S, Bohn S and Couder Y: Exotic orbits of two interacting wave sources. *Phys. Rev. E*, 78:036204, 2008.

THE NON-LINEAR MECHANICS OF SLENDER DEFORMABLE BODIES

Basile Audoly[1]

[1]*Laboratoire de mécanique des solides, Ecole polytechnique and CNRS, Palaiseau, France*

Summary We discuss some challenges arising in the mechanics of slender (quasi-1D) deformable bodies, such as a thin thread of polymer, curly hair, or a carpenter's tape for example. Slender bodies can exhibit a number complex and intriguing behaviors that are accessible through simple experiments. The analysis of slender bodies exposes one to many of the fundamental concepts of 3D non-linear mechanics, albeit in a simpler setting where explicit analytical solutions and fast numerical methods can be proposed. Based on examples, we review some problems arising in the analysis of deformable bodies, including the derivation of accurate 1D mechanical models by dimensional reduction, the solution of non-linear 1D models by analytical or numerical methods, and the analysis of material or geometrical instabilities.

There are many examples of slender (quasi-one dimensional) bodies around us, including computer cables, human hair, sailing and climbing ropes. Being flexible, slender bodies commonly undergo large rotations. As a result, they are prone to instabilities and can display complex behaviors, some of which are illustrated in the figure. In this talk, we will discuss the specific challenges arising in the mechanics of slender deformable bodies. They include the derivation of dimensionally reduced models and their analytical or numerical solution, especially in the non-linear range.

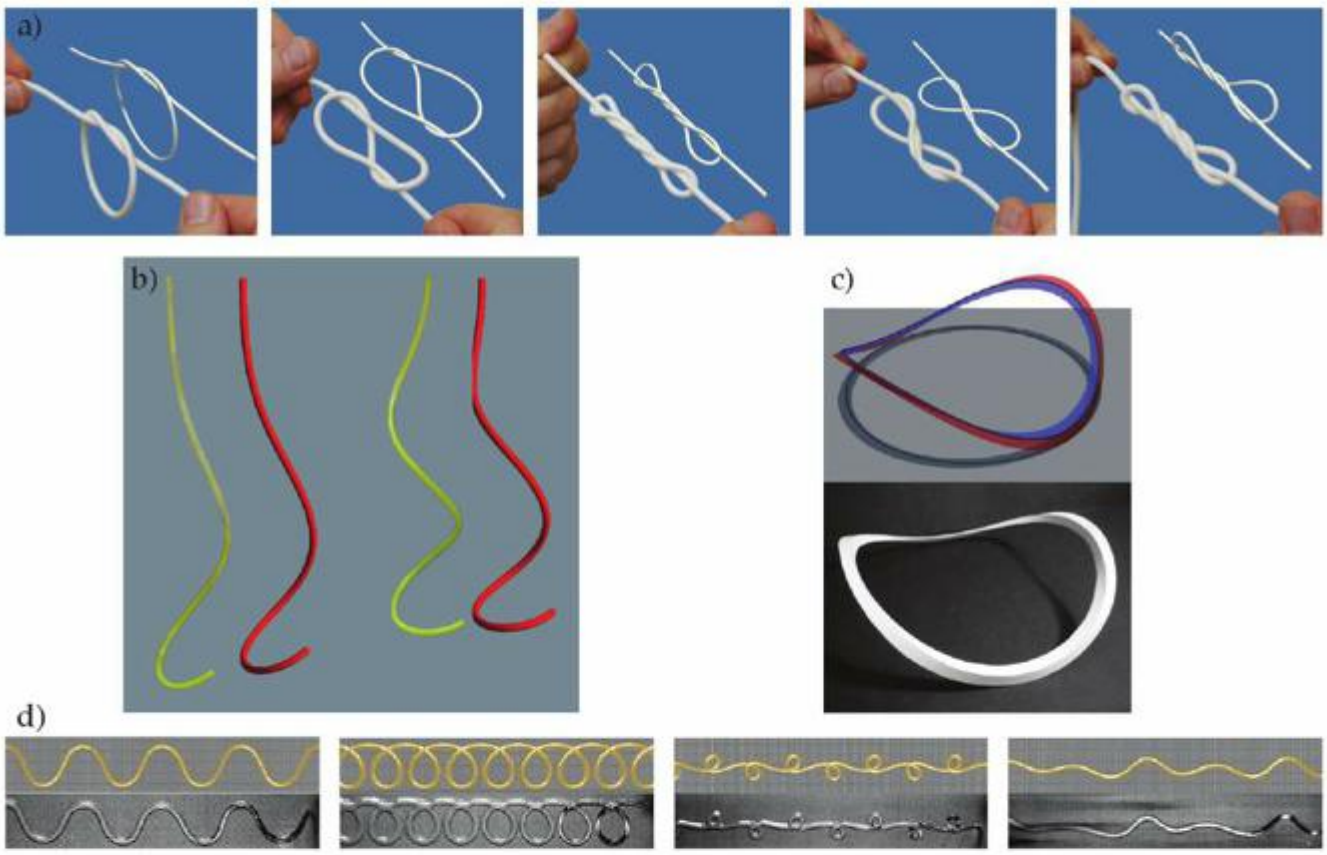

Figure 1: (a) Shapes obtained by twisting a simple knot in both directions: comparison of experiments using a silicone filament and numerical simulations using the Discrete Elastic Rods method [3]. (b) Curly hair: equilibria of a naturally curved rod under its own weight, experiments (green) versus simulation (red) for different values of the natural curvature [8]. (c) 3D origami obtained by pleating a flat annular piece of paper along a central ridge [7, 6]. (d) Patterns produced by a thin jet of viscous fluid stretched by its own weight and impinging on a moving substrate, for different fall heights and substrate velocities: comparison of dynamic simulations based on the theory of viscous rods (yellow) and experiments (black and white) [2, 5, 1, 4].

Even though many aspects of the beam and rod theories are classical and well understood, fundamental (and often simple) problems have been solved recently only, or have remained unsolved to date. This includes for instance the derivation of accurate 1D models for curved strips (*i.e.* narrow shells) such as a carpenter's tape, and for filaments made of non-purely

elastic materials (such as elasto-plastic or visco-plastic materials), the design of robust and efficient simulation methods, and the derivation of explicit solutions to non-linear self-contact problems.

Being effectively one-dimensional, slender bodies are governed by equations that are simpler to write down, more likely to have analytical solutions, and easier to solve numerically than the corresponding equations of 3D continuum mechanics. This allows one to address problems that would be impossible to tackle otherwise. In this talk, we will illustrate the derivation of solutions of this kind.

References

[1] B. Audoly, N. Clauvelin, P.-T. Brun, M. Bergou, E. Grinspun, and M. Wardetzky. A discrete geometric approach for simulating the dynamics of thin viscous threads. *Journal of Computational Physics*, 253:18–49, 2013.

[2] C. Batty, B. Audoly, and E. Grinspun. Discrete viscous sheets. *Transactions on Graphics*, 31(4):113:1–7, 2012.

[3] M. Bergou, M. Wardetzky, S. Robinson, B. Audoly, and E. Grinspun. Discrete elastic rods. *ACM Transactions on Graphics*, 27(3):63:1–63:12, 2008.

[4] P.-T. Brun, B. Audoly, N. Ribe, T. S. Eaves, and J. R. Lister. Liquid ropes: a geometrical model for thin viscous jet instabilities. *Physical Review Letters*, 114(17):174501, 2015.

[5] P.-T. Brun, N. M. Ribe, and B. Audoly. A numerical investigation of the fluid mechanical sewing machine. *Physics of fluids*, 24(4):043102, 2012.

[6] M. A. Dias and B. Audoly. A non-linear rod model for folded elastic strips. *Journal of the Mechanics and Physics of Solids*, 62:57—80, 2014.

[7] M. A. Dias, L. H. Dudte, L. Mahadevan, and C. D. Santangelo. Geometric mechanics of curved crease origami. *Physical Review Letters*, 109(11):114301, 2012.

[8] J. T. Miller, A. Lazarus, B. Audoly, and P. M. Reis. Shapes of a suspended curly hair. *Physical Review Letters*, 112:068103, 2014.

BIOMECHANICS AND THE PHYSIOME PROJECT

Peter Hunter[1]
[1]*Auckland Bioengineering Institute, University of Auckland, New Zealand*

ABSTRACT

Biomechanics underpins many areas of physiology. Anatomically based continuum models of the heart, lungs, skin and musculo-skeletal system have been developed and are essential for a quantitative understanding of the physiological function of these organs and organ systems. Solving the equations of large deformation continuum mechanics and three dimensional viscous fluid mechanics via finite element methods is now a relatively mature discipline. The challenge at the continuum level is to capture the nonlinear, anisotropic and inhomogeneous nature of the biological tissues and to link their constitutive properties to microstructural models. The bigger challenge is to understand the molecular processes that regulate tissue function and the processes of adaptation and growth that characterise all biological tissues. This talk will present work being done for the Physiome Project on these challenges at both the tissue scale and the molecular scale.

THE PHYSIOME PROJECT

The Physiome project was initiated by the International Union of Physiological Sciences (IUPS) in 1997 in order to bring multiscale engineering modelling approaches to the physiological interpretation of the wealth of molecular data becoming available at that time [1]. The interaction between gene expression and the physical environment into which the genes are expressed is key to understanding physiological function. While diseases and drugs operate at the molecular level, the regulation of genetic transcription and hence the assembly of proteins (the building blocks of life) are both highly dependent on environmental factors governed by the physical world in which molecular biology operates. Engineering, and in particular the rapidly growing field of bioengineering, is the discipline that has the integrative skills and tools to put the molecular pieces back together again.

In 2003, six years after the establishment of the Physiome Project by IUPS in 1997, the US 'Interagency Modeling and Analysis Group' (IMAG) began funding physiome project grants. Four years later, in 2007, a consortium of European scientists and engineers published a roadmap 'Seeding the EuroPhysiome: A Roadmap to the Virtual Physiological Human' (VPH) that persuaded the European Commission to call for research proposals under Framework 7 on healthcare related modelling. A VPH Institute (VPH-I) was subsequently established to provide continued global leadership for the VPH/Physiome Project with the goal of '*using computational modelling of biological processes to integrate quantitative biological knowledge from molecular to cell, tissue, organ and whole body scales in order to understand physiological systems in terms of both their molecular components and their interaction with the environment and translate this understanding into clinical practice*' [2].

Mathematics is the language of quantitative science and every scientific discipline should analyse its experimental data in the light of physical laws encapsulated in mathematical equations. The challenge facing the Physiome Project is the enormous complexity, including spatial and temporal scales, of molecular and physiological systems. Mathematical models of these processes quickly become difficult for anyone other than the author of a model to reproduce let alone understand. The engineering solution to this problem is to build models based on 'standards' and 'modularity'. Data and modelling standards, with tools and model repositories based on these standards, ensure reproducibility and testability. And models must be built from modules that define the functional components of a system. To link models of proteins to physiological scale models (i.e. cells, tissues, organs and organ systems) also requires a hierarchy of models that are semantically rich so that an imported component module can be assembled automatically into the right place in the parent model.

A typical multiscale model is shown in Figure 1 [3]. Four spatial scales are shown: the cell (cardiac myocyte), tissue (myocardium), organ (heart) and whole body (torso). The cell model shown here is in fact made up of many individual protein models. Heart disease and heart drugs operate at the protein level, but the diagnosis of disease usually made at the level of the intact organ (e.g., the EKG for electrical function or ultrasound images for mechanical function). The challenge is to link models across these scales.

The talk will describe multiscale modelling work on the heart, lungs and musculo-skeletal system. It will also describe the framework being developed to ensure reproducible modelling using standards and standards-based tools developed for the Physiome Project.

[a)] Corresponding author. Email: **p.hunter@auckland.ac.nz**

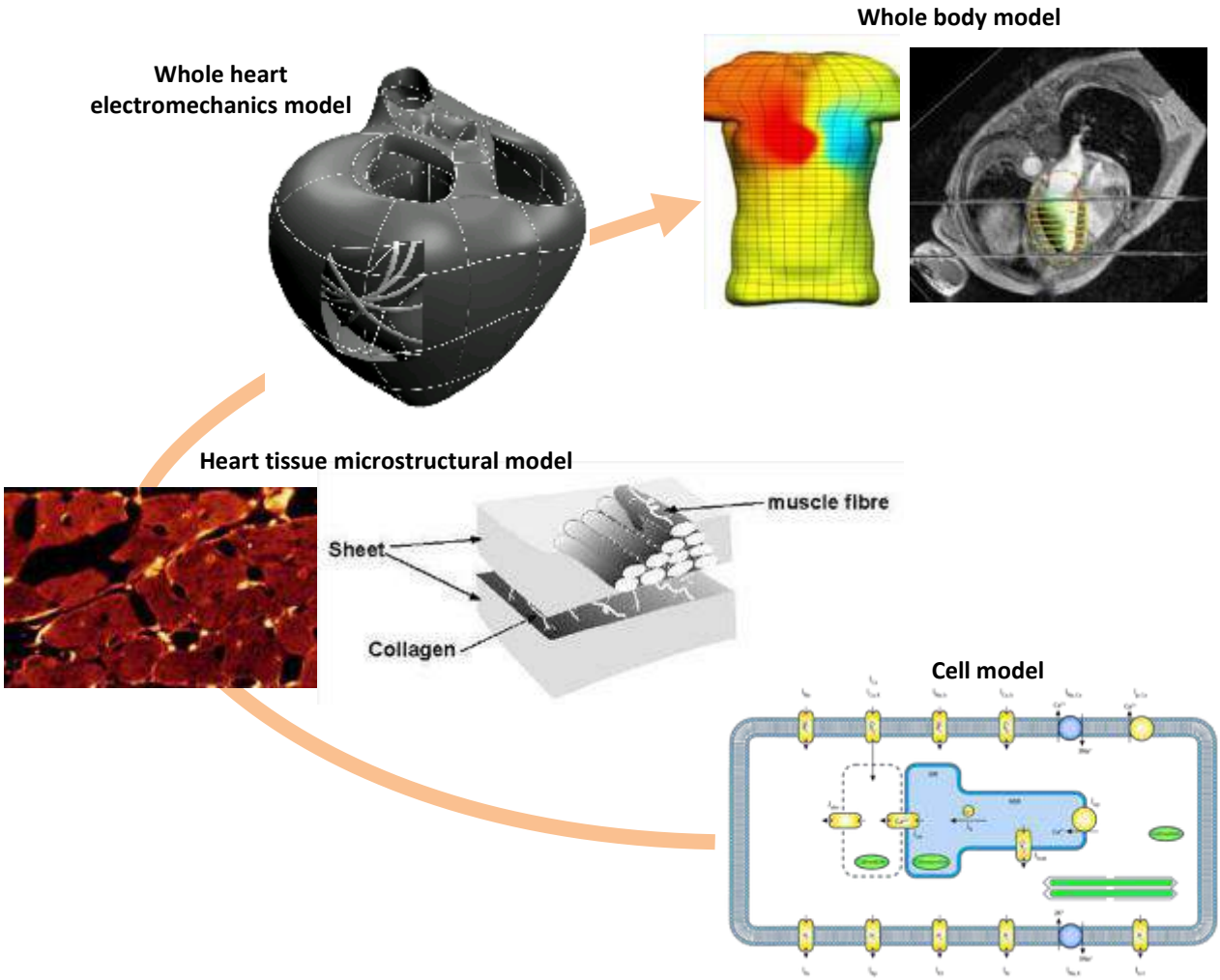

FIGURE 1 A multiscale model for electromechanics in the heart. The cell, tissue, organ and torso scales are shown here. The cell model is made up of many imported modules – corresponding, for example, to the individual membrane protein ion channels, pumps and exchangers, and to signalling pathways that control gene expression and growth processes. A microstructural model at the tissue level is used to derive constitutive laws that are used with the field equations of physics at the organ and whole body levels.

The initial focus for the Physiome Project has been on the establishment of standards, based on modular components, that help ensure reproducibility of models [4]. The syntax for the model equations is MathML, the w3c standard for both content and presentation of mathematics. The need for semantically rich metadata is addressed through RDF (Resource Description Framework), another w3c standard, using ontologies such as ChEBI for chemical identifiers, GO for cell components, the CellType ontology, the Foundation Model of Anatomy (FMA), and OPB for biophysical annotation. Based on these, two XML standards have been developed: one called CellML for lumped parameter (not spatially varying) algebraic and ODE models (e.g. the cell model shown in Fig.1) and another called FieldML for spatially varying (typically finite element) models (e.g. the tissue, organ and torso models shown in Figure 1).

References

[1] Hunter P.J., Borg T.K. Integration from proteins to organs: The Physiome Project. *Nature Reviews Molecular and Cell Biology*, 4(3):237-243, 2003.

[2] Hunter P., Chapman T., Coveney P.V., de Bono B., Diaz V., et al. A vision and strategy for the virtual physiological human: 2012 update. *Interface Focus* 3:20130004, 2013.

[3] Hunter P.J., Pullan A.J., Smaill B.H. Modeling total heart function. *Annual Review of Biomedical Engineering*, 5:147-177, 2003.

[4] Cuellar, A.A., Lloyd, C.M., Nielsen, P.F., Halstead, M.D.B., Bullivant, D.P., Nickerson, D.P., Hunter, P.J. An overview of CellML 1.1, a biological model description language. *SIMULATION: Transactions of The Society for Modeling and Simulation Internationa*l, 79(12):740-747, 2003.

DEFORMATION AND FRACTURE OF ELECTROMAGNETIC THIN FILMS AND LAMINATES UNDER MULTI-FIELD LOADING

Daining Fang[1a)], Yongmao Pei[2] , Faxin Li[2] & Haosen Chen[1]
[1] *Institutes of Advanced Technology, Beijing Institute of Technology, Beijing, China*
[2]*State Key Laboratory for Turbulence and Complex Systems, College of Engineering, Peking University, Beijing, China*

Abstract

Electromagnetic functional materials, such as ferroelectrics, ferromagnetics and magnetoelectric thin films and laminates, have been widely used in modern industries. Their deformation and fracture behaviors under mechanical loading are affected considerably by an external electric or magnetic field. To provide a deep understanding of the intrinsic coupling properties, a novel electro-magneto-mechanical multi-field nanoindentation apparatus and a novel multi-field bulge-test instrument were designed and constructed. The corresponding characterization method for the thin-film electromagnetic materials was also established. The experimental results reveal the size-dependency of various mechanical properties, ranging from the Young's modulus, to the hardness as well as fracture toughness. Notably, these properties can be well controlled by applying external electric/magnetic fields. Furthermore, a new size-dependent nonlinear constitutive model is developed for the magnetoelectric laminates to account for the coupling mechanisms under multi-field loading. This model is managed to study the dynamic harmonic magnetoelectric response and the microwave magnetoelectric effect.

Main text

With the rapid advances in the materials science and technologies, the characteristic dimensions of electromagnetic functional materials have been pushed down to micro or even nanoscale, creating great challenges in the characterization of their multi-field coupling properties [1,2]. In this work, a novel electro-magneto-mechanical multi-field nanoindenter with powerful functions [Fig. 1(a)] was designed and constructed to study the local mechanical properties of electromagnetic materials [3]. The dependence of Young's modulus and hardness of ferroelectric/ferromagnetic materials on applied electric/magnetic fields were systematically investigated [4]. The field tunable fracture behavior of thin-film structures was studied as well [Fig. 1(b)], which is found to be size-dependent. A new method is proposed to characterize the electro-magneto-mechanical coupled performances resulted from the nanoindentation experiment, based on the field tunable scaling laws. This method can avoid the testing errors encountered in the Oliver-Pharr method for the estimation of contact area [5]. Moreover, a multi-field bulge-test instrument [Fig. 1(c)] was designed and constructed to explore the electro-magneto-mechanical coupling properties of the electromagnetic thin films [6]. The corresponding characterization method for the elastic property and fracture toughness of thin films was also established. A few interesting phenomena were found, including the evident effect of mechanical deformation on the electric/magnetic behaviors (e.g., the ferroelectric hysteresis loops, butterfly curves, magnetization loops and magnetostrictive curves), as well as the underlying dependences of the fracture toughness of the magnetic thin films on both the thickness and the external magnetic field [Fig. 1(d)].

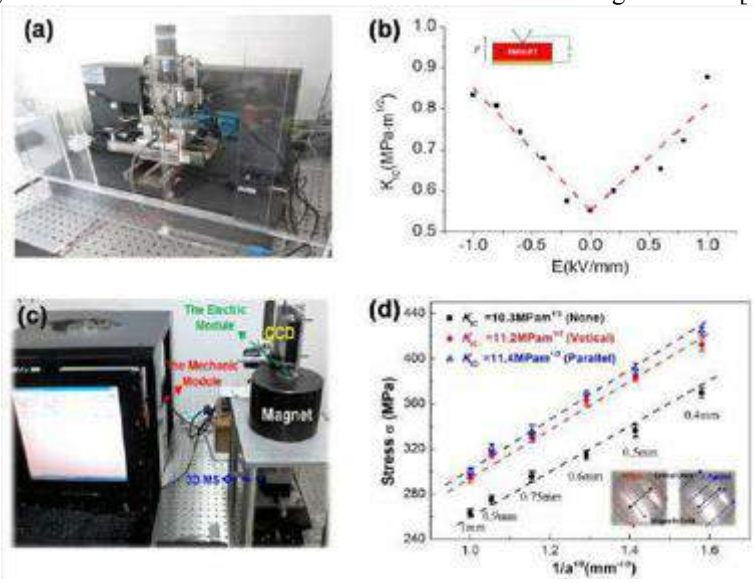

[a)] Corresponding author. Email: fangdn@pku.edu.cn.

Fig. 1. (a) Photo of the multi-field nanoindenter. (b) Electric-filed dependency of fracture toughness of relaxor ferroelectric Pb(Mn1/3Nb2/3)O3-PbTiO3 crystals measured by nanoindentation. (c) Multi-field bulge-test instrument setup. (d) Fracture toughness of Ni thin films under different magnetic fields.

In order to describe the multi-field coupling deformation behavior of magnetoelectric composites laminates, we develop a nonlinear constitutive model, which can reveal size dependency of coupling behaviors, by use of a probabilistic criterion of domain switching [7]. The various responses (e.g., the polarization, magnetization as well as strain) under combined electro-magneto-mechanical loading were investigated. The results demonstrate quantitatively the electric-field control of magnetization and magnetic-field tuning of polarization, as shown in Fig. 2, which can serve as a guideline for practical device applications. The size effect of the magnetoelectric coupling was also explored, which demonstrates the competition of the strain-mediated and charge-driven effects. Finally, the model is successfully extended to study dynamic harmonic magnetoelectric response and nonlinear microwave magnetoelectric effect.

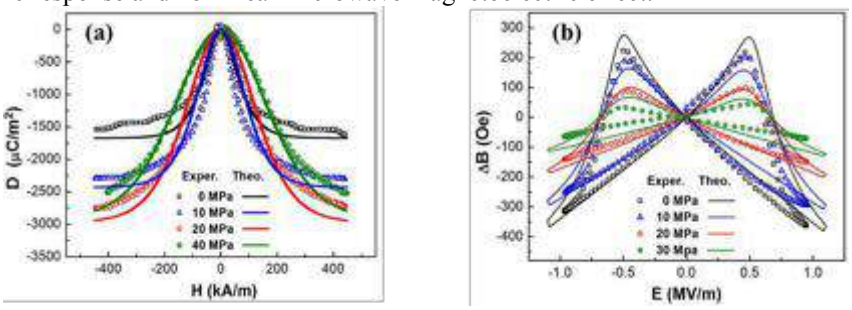

Fig. 2. Comparisons of theoretical results with experimental data: (a) The magnetic-field tuning of polarization. (b) The electric-filed control of magnetization.

References

[1] Bibes M. and Barthelemy A., Multiferroics: Towards a magnetoelectric memory, *Nature Materials*, **7**, 425-426, 2008.

[2] Dagdeviren C., Yang B.D., Su Y., Tran P.L., Joe P., Anderson E., and Rogers J.A.. Conformal piezoelectric energy harvesting and storage from motions of the heart, lung, and diaphragm, *Proceedings of the National Academy of Sciences*, **111**, 1927-1932, 2014.

[3] Zhou H., Pei Y., Huang H., Zhao H., Li F., and Fang D., Multi-field nanoindentation apparatus for measuring local mechanical properties of materials in external magnetic and electric fields. *Review of Scientific Instruments*, **84**, 063906, 2013.

[4] Zhou H., Pei Y., and Fang D., Magnetic field tunable small-scale mechanical properties of nickel single crystals measured by nanoindention technique. *Scientific Reports*, **4**, 4583, 2014.

[5] Zhou H., Zhang H.L., Pei Y., Chen H., Zhao H., and Fang D., Scaling relationship among indention properties of electromagnetic materials at micro- and nanoscale. *Applied Physics Letters*, **106**, 081904, 2015.

[6] Yu, Z.J., Mao, W.G., Li, F.X., Feng, X., Pei, Y.M., and Fang, D.N., Magnetic and electric bulge-test instrument for the determination of coupling mechanical properties of functional free-standing films and flexible electronics, *Review of Scientific Instruments*, **85**, 065117, 2014.

[7] Xu, H., Pei, Y.M., and Fang, D.N. A size-dependent nonlinear constitutive model for the layered piezoelectric-magnetostrictive composites. Unpublished.

CONCEPTS IN MECHANICS FOR 3D, BIO-INTEGRATED ELECTRONICS

John Rogers[1a)]
[1]*Department of Materials Science and Engineering, University of Illinois, Urbana, IL, USA*

Summary New concepts in mechanics provide routes to high performance electronics with physical characteristics matched to those of vital organs of the human body. The resulting opportunities for integration of sensors, actuators, radios and computing capabilities directly on the surfaces or into the depths of targeted tissues have strong potential to improve current practices in clinical care and physiological monitoring. This paper outlines some of the key ideas, and describes their use in skin-mounted systems and 3D open-mesh networks.

INTRODUCTION

Biology is soft, curvilinear and transient; modern semiconductor technologies are rigid, planar and everlasting. Electronic and optoelectronic systems that eliminate this profound mismatch in properties create opportunities for devices that can intimately integrate with the body, for diagnostic, therapeutic or surgical function with important, unique capabilities in biomedical research and clinical healthcare. A convergence of concepts in mechanics, materials science, electrical engineering and advanced manufacturing has led to the emergence of diverse, novel classes of 'biocompatible' electronic platforms, with capabilities in intimate, persistent physical interfaces with the surfaces of biological tissues, and recent work that foreshadows possibilities in full 3D integration. This paper describes the core ideas, with examples ranging from wireless, skin-like electronic 'tattoos' for continuous monitoring of physiological health to 3D mesoscale electronic networks as active cellular scaffolds.

RESULTS

When mounted on the skin, advanced sensors, circuits, radios and power supply systems have the potential to provide clinical-quality health monitoring capabilities for continuous use, outside of traditional hospital settings or laboratory facilities. The most well-developed component technologies are, however, currently available only in hard, planar

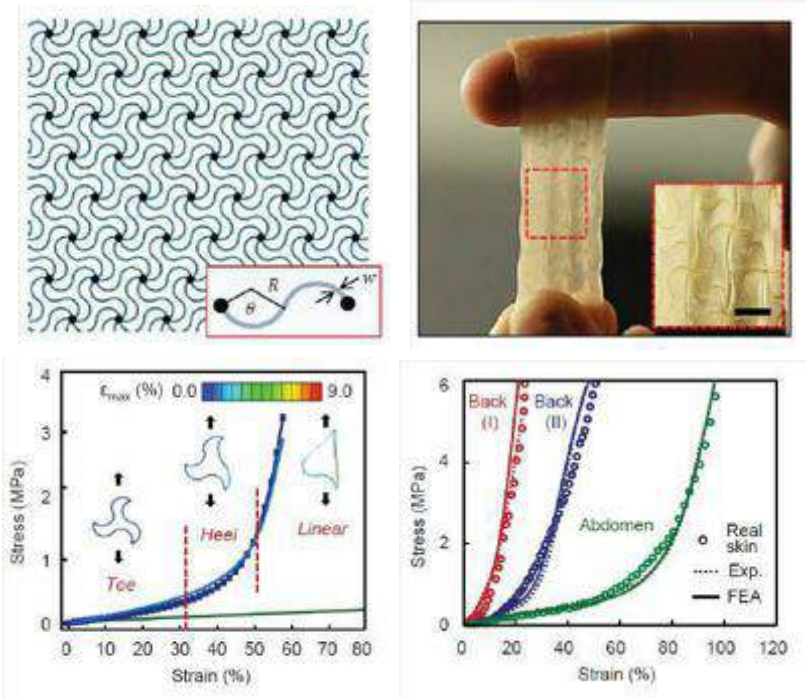

Figure 1. Upper left: Serpentine filamentary network of hard materials in a soft, surrounding elastomeric matrix, as a deterministic composite. Lower left: The mechanical responses exhibit stress/strain relationships with characteristic J-shaped behavior similar to that of biological tissues. Upper right: Image of a composite designed to match the properties of the epidermis. Bottom right: Stress/strain relationships of composites engineered with mechanical responses that match those of the skin from different regions of the body.

a) Corresponding author. Email: jrogers@illinois.edu.

formats. As a result, existing options in system design are unable to effectively accommodate integration with the soft, textured, curvilinear and time-dynamic surfaces of the skin, without irritation or interface failures. Recent work establishes experimental and theoretical approaches for using soft materials, ultrathin micro/nanostructures, and controlled processes of mechanical buckling to achieve ultralow modulus, thin and highly stretchable, systems of state-of-the-art semiconductor devices, with options in quantitatively matching the effective non-linear stress/strain relationships of the epidermis. The result is a 'skin-like' technology with measurement fidelity that can match that of large-scale tools currently used in clinical medicine. Figure 1 shows an example[1].

The essential 3D character of biological systems motivates the development of approaches to 3D electronics that adopt bio-inspired, mesoscale open network designs. Of the many methods for fabricating such structures, few are compatible with the highest performance classes of electronic materials, such as monocrystalline inorganic semiconductors, and only a subset of these can operate at high speeds, across length scales, from centimeters to nanometers. New strategies avoid these limitations, via the use of controlled compressive forces imparted by a pres-strained elastomeric substrates with the effect of transforming 2D micro/nanostructures with lithographically defined geometries and points of adhesion into 3D structures, with levels of complexity and control that significantly exceed those that can be achieved with alternative methods[2]. Examples include a diverse set of examples formed using silicon nanomembranes, plates and ribbons and heterogeneous combinations of them with micro/nanopatterned metal films and dielectrics. Quantitatively accurate theoretical modelling of the solid mechanics of the transformation process provides a design tool to create targeted geometries that offer adaptable shapes and desired modes of operation.

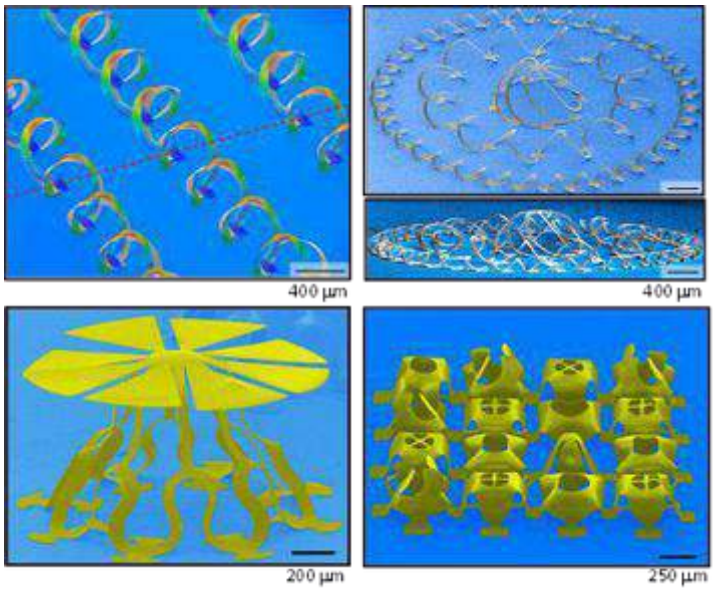

Figure 2. Colorized scanning electron micrographs of 3D mesoscale networks formed by mechanical assembly from corresponding 2D precursors. The top two frames show helical coils (left: overlaid modeling results for the distributions of strain for a pair of anti-Helmholtz coils, where the chirality undergoes an abrupt change at the dashed red line) and nested toroids with a central, open-mesh basket (right), all formed in monocrystalline, device-grade silicon. The bottom two frames show architectures that incorporate ribbons and membranes in complex architectures: left: sunflower-inspired structure; right: array of chiral and achiral features.

CONCLUSIONS

Advanced concepts in mechanics create new opportunities in the construction of 2D and 3D electronic systems with unmatched capabilities in bio-integration. Research in these areas now ranges from the study of the foundational mechanical science to the development of clinically relevant biomedical devices.

References

[1] Jang K.I., et al: Soft Network Composite Materials With Deterministic and Bio-inspired Designs. *Nat. Comm.* **6**:6566, 2015.

[2] Shu, X. et al: Assembly of Micro/nanomaterials into Complex, Three-Dimensional Architectures by Compressive Buckling. *Science* **347**, 154-159, 2015.

SOFT MACHINES

Zhigang Suo [a)]
School of Engineering and Applied Sciences, Kavli Institute for Bionano Science and Technology
Harvard University, Cambridge, MA 02138, USA

Summary Machines in engineering use mostly hard materials, whereas machines in nature are often soft. This difference has been an inspiration for the nascent field of soft machines. What does softness impart to the life of animals and plants? Softness enables deformation, and deformation provides functions. Familiar examples include the beating of the heart, the sound shaped by the vocal folds, and the flapping of the wing. In soft machines, the large deformation enable soft materials to behave as transducers, connecting multiple stimuli to multiple functions. How do molecular processes enable new classes of actuators and sensors? How efficiently can materials convert information from one form to another? These questions are stimulating new and exciting developments at the interface between science and engineering. This talk highlights the behavior of soft materials that enables the creation of soft machines. Examples include highly stretchable and transparent devices that mimic the functions of muscles, skins and axons.

LARGE DEFORMATION ENABLE MANY FUNCTIONS

A conspicuous feature of life is to receive and process information from the environment, and then move. The movements are responsible for diverse functions. Consider the accommodation of the eye, the beating of the heart, the sound shaped by the vocal folds, and the sound in the ear. Abstracting these biological soft machines, we may say that a stimulus causes a material to deform, and the deformation provides a function. Connecting the stimulus and the function is the material capable of large deformation in response to a stimulus.

An exciting field of engineering is emerging that uses soft materials to create soft machines. Soft materials in engineering are indeed apt in mimicking the salient feature of life: movements in response to stimuli. An electric field can cause an elastomer to stretch several times its length. A change in pH can cause a hydrogel to swell many times its volume. These soft active materials are being developed for diverse applications, including soft robots, adaptive optics, self-regulating fluidics, programmable haptic surfaces, and oilfield management [1,2].

TOUGH WATER

What can we do if water is a tough solid? A hydrogel aggregates water and a polymer network. The polymer network makes the hydrogel a stretchable solid, but water retains its exceptional physical and chemical properties. Several recent findings show that hydrogels can achieve properties and applications well beyond previously imagined. Most existing hydrogels, like Jell-O and tofu, are fragile and dry out in open air. We make hydrogels as tough as rubber, and retain water in low-humidity environment [3,4]. We show that hydrogels outperform existing fire-retarding materials [5]. We also demonstrate fiber-reinforced hydrogels [6].

ARTIFICIAL MUSCLES

Existing stretchable, transparent conductors are mostly electronic conductors. They limit the performance of interconnects, sensors and actuators as components of stretchable electronics and soft machines. We describe a class of devices enabled by ionic conductors that are highly stretchable and fully transparent to light of all colors [7], capable of operation at frequencies beyond 10 kHz and voltages above 10 kV. We demonstrate a transparent actuator that can generate large strains, and a transparent loudspeaker that produces sound over the entire audible range. The electromechanical transduction is achieved without electrochemical reaction. The ionic conductors have higher resistivity than many electronic conductors; however, when large stretchability and high transmittance are required, the ionic conductors have lower sheet resistance than all existing electronic conductors.

ARTIFICIAL SKIN

Our skin is a stretchable, large-area sheet of distributed sensors. These properties of skin have inspired the development of mimics, with differing levels of sophistication, to enable wearable or implantable electronics for entertainment and healthcare. We explore the potential of ionic conductors in the development of a new type of sensory sheet, which we call "ionic skin" [8]. The sensory sheet is highly stretchable, transparent, and biocompatible. It readily monitors large deformation, such as that generated by the bending of a finger. It detects stimuli with wide dynamic range

[a)] Corresponding author. Email: suo@seas.harvard.edu.

(strains from 1% to 500%). It measures pressure as low as 1 kPa, with small drift over many cycles. A sheet of distributed sensors covering a large area can report the location and pressure of touch. High transparency allows the sensory sheet to transmit electrical signals without impeding optical signals.

ARTIFICIAL AXON

We demonstrate a new type of interconnects to fulfill the primary function of axons: transmitting electrical signals over long distances and at high speeds [9]. The interconnect, which we call "ionic cable", uses ions to transmit signals, and is built entirely with soft, elastic materials—elastomers and gels. The ionic cable is highly transparent, and remains functioning after being stretched nearly eight times its original length. We describe the design, theory and experiment of the ionic cable. We show that the diffusivity of signals in the ionic cable is about 16 orders of magnitude higher than the diffusivity of ions. We demonstrate that the ionic cable transmits signals up to 100 MHz over 10 cm, and transmits music signals over meters. The ionic cable transmits enough power to turn on light-emitting diodes. Our theory shows that the ionic cables scale well, suggesting tremendous opportunities to create miniaturized ionic circuit. Furthermore, we use the ionic conductors to demonstrate electroluminescence of giant stretchability [10].

CONCLUSIONS

A large number of examples in plants and animals demonstrate that deformation of soft materials connect diverse stimuli to many functions essential to the life. An exciting field of engineering is emerging that uses soft materials to create soft machines. To participate in advancing the field of soft active materials and soft machines effectively, mechanicians must retool our laboratories and our software, as well as adapt our theories. This talk highlights this theme using recent advances in materials, devices, and theories.

References

[1] Suo Z.G.: Theory of Dielectric Elastomers. *Acta Mechanica Solida* **23**:549-578, 2010.

[2] Suo Z.G.: Mechanics of Stretchable Electronics and Soft Machines. *MRS Bulletin* **37**, 218-225, 2012.

[3] Sun J.Y., Zhao X.H., Illeperuma W.R.K., Oh K.H., Mooney D.J., Vlassak J.J., Suo Z.G.: Highly Stretchable and Tough Hydrogels. *Nature* **489**, 133-136, 2012.

[4] Bai Y.Y, Chen B.H., Xiang F., Zhou, J.X., Wang H., Suo Z.G: Transparent Hydrogel with Enhanced Water Retention Capacity by Introducing Highly Hydratable Salt. *Applied Physics Letters* **105**, 191903, 2014.

[5] Illeperuma W.R.K., Rothemund P., Suo Z.G., Vlassak J.J.: Fire-Resistant Hydrogel-Fabric Laminates: a Simple Concept That May Save Lives. *ACS Applied Materials and Interfaces*. Accepted manuscript, DOI: 10.1021/acsami.5b10538

[6] Illeperuma W.R.K., Sun J.Y., Suo Z.G., Vlassak J.J.: Fiber-Reinforced Tough Hydrogels. *Extreme Mechanics Letters* **1**, 90-96, 2014.

[7] Keplinger C., Sun J.Y., Foo, C.C., Rothemund P., Whitesides G.M., Suo Z.G.: Stretchable, Transparent, Ionic Conductors. *Science* **341**, 984-987, 2013.

[8] Sun J.Y., Keplinger C., Whitesides G.M., Suo Z.G.: Ionic Skin. *Advanced Materials* **26**, 7608-7614, 2014.

[9] Yang C.H., Chen B.H., Lu J.J., Yang J.H., Zhou J.X., Chen Y.M., Suo Z.G. Ionic Cable. *Extreme Mechanics Letters* **3**, 59-65, 2015.

[10] Yang C.H., Chen B.H., Zhou J.X., Chen Y.M., Suo Z.G. Electroluminescence of giant stretchability. *Advanced Materials*. Accepted manuscript, DOI: 10.1002/adma.201504031

THE MICROMORPHIC APPROACH TO GRADIENT CRYSTAL PLASTICITY AND DAMAGE

Samuel Forest *[1]

[1]*Mines ParisTech, Centre des Matériaux, CNRS UMR 7633, Evry, France*

Summary The micromorphic method is recalled and applied to continuum crystal plasticity in order to model size effects in the mechanical behavior of single and polycrystals. The constitutive equations are discussed with respect to the prediction of scaling laws. The regularization power of the model is illustrated in the case of crack propagation simulation in single crystals.

INTRODUCTION TO THE MICROMORPHIC APPROACH

The micromorphic approach consists in enhancing the continuum mechanical framework by introducing deformation–like independent degrees of freedom [1]. The set of constitutive variables is then extended to the gradient of these additional degrees of freedom. It originates from Eringen and Mindlin's proposal to endow each material point with a second order generally nonsymmetric microdeformation tensor representing the rotation and stretch of a triad or directors related to the microstructure, in addition to the classical displacement degrees of freedom [2]. A whole hierarchy of generalized continua is built in the micromorphic theory, including the celebrated Cosserat model when the microdeformation reduces to a microrotation [3]. The micromorphic approach was applied to crystal plasticity by [4, 5, 6] using the Cosserat framework and by [7] where a generally nonsymmetric plastic microdeformation tensor is introduced. The latter model reduces to strain gradient plasticity based on the disclocation density tensor when the microdeformation coincides with the plastic deformation itself [8]. These models involve intrinsic characteristic lengths, in contrast to the conventional Cauchy continuum, which makes it possible to describe size effects in the mechanical responses of elastic–plastic polycrystals, including Orowan and Hall–Petch effects associated with the interaction of dislocations with precipitates and grain boundaries. The method can be extended to strain–like scalar degrees of freedom related to elastic or plastic strain or damage [1]. The new scalar degree of freedom must be constitutively related to some strain or internal variable of the original model. In the case of crystal plasticity, a micromorphic variable was associated to an equivalent plastic slip measure by [9] and a microdamage variable was introduced related microcrack opening along cleavage planes in [10]. Close links exist between the micromorphic approach and phase field modeling as discussed by [11], with the difference that the phase field parameter is not necessarily related to a mechanical variable.

SIZE EFFECTS IN THE CYCLIC BEHAVIOUR OF SINGLE CRYSTALS

Strain gradient plasticity theory represents a continuum model of dislocation plasticity. It can be used to represent dislocation pile–up formation at interfaces in single crystals [12]. The *microcurl* model was shown in [7] to predict channel–size effects in the stress–plastic strain response of laminate microstructures made of alternating elastic and plastic layers. The choice of the constitutive functional related to the gradient terms is essential to the quantitative description of such effects. In particular, the quadratic ansatz in the gradient terms, widely used in strain gradient plasticity and phase field models, was shown to predict physically unrealistic scaling laws. Alternative potentials were proposed by [13]. The concept of reversible plasticity is put forward in the latter contribution leading to unusual cyclic stress–strain loops with inflection points. It represents a continuum model of the first–in last–out concept in dislocation pile–ups initially proposed in the seminal paper [14]. A remarkable effect was predicted by the *microcurl* model in the plasticity of polycrystals. Sub–micron grain sizes were shown to promote plastic slip localization in the form of intense slip bands interconnecting grains of the polycrystals whereas more diffuse slip is observed at larger grain sizes. This is due to the high energy cost associated with lattice curvature, as illustrated in Fig. 1.

SIMULATION OF CRACK INITIATION AND PROPAGATION IN SINGLE CRYSTALS

Accumulated plastic slip is known to be responsible for crack initiation, especially under fatigue loading conditions. A coupled plasticity–damage criterion was proposed allowing for damage strain associated with opening of crystallographic planes as the result of a combination of normal stress and accumulated slip [16]. A micromorphic microdamage variable is introduced akin to the cumulated damage variable. The introduction of microdamage gradient into the constitutive model provides a regularization of damage localization into cracks of finite thickness. The regularization properties of the micromorphic approach to damage were used first by [17, 18]. Thermodynamical foundations of this class of regularized models

*Corresponding author. Email: samuel.forest@mines-paristech.fr

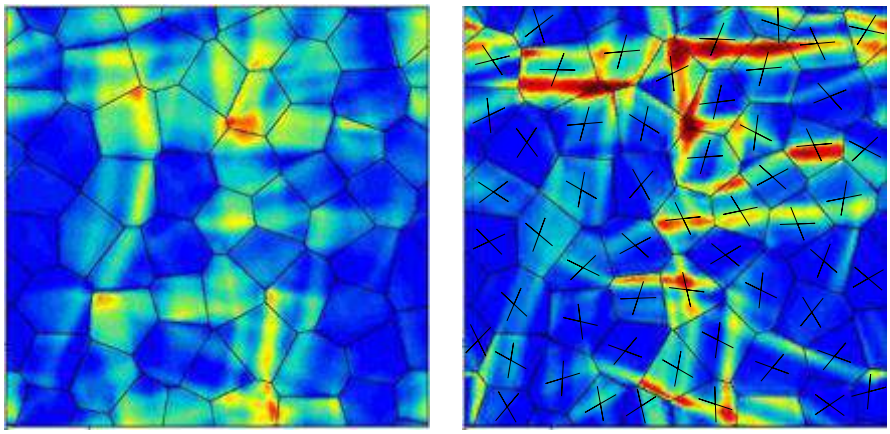

Figure 1: Field of accumulated plastic slip in two idealized polycrystals with the same microstructure (grain shape and orientations) but different grain sizes: 100 μm and 4 μm (right). The formation of intense slip bands crossing grain boundaries is observed in the right picture where the traces of the slip planes are represented, after [15].

were provided by [1]. The simulations of crack initiation and propagation in single and polycrystals will be related to recent experiments of 3D observations of short fatigue cracks combining microtomography and diffraction at the ESRF synchrotron in Grenoble [19, 20]. The role of grain boundaries as barriers to short crack growth will be illustrated.

References

[1] S. Forest. The micromorphic approach for gradient elasticity, viscoplasticity and damage. *ASCE Journal of Engineering Mechanics*, 135:117–131, 2009.

[2] A.C. Eringen and E.S. Suhubi. Nonlinear theory of simple microelastic solids. *Int. J. Engng Sci.*, 2:189–203, 389–404, 1964.

[3] S. Forest and R. Sievert. Nonlinear microstrain theories. *International Journal of Solids and Structures*, 43:7224–7245, 2006.

[4] S. Forest, G. Cailletaud, and R. Sievert. A Cosserat theory for elastoviscoplastic single crystals at finite deformation. *Archives of Mechanics*, 49(4):705–736, 1997.

[5] S. Forest, F. Barbe, and G. Cailletaud. Cosserat modelling of size effects in the mechanical behaviour of polycrystals and multiphase materials. *International Journal of Solids and Structures*, 37:7105–7126, 2000.

[6] J.R. Mayeur, D.L. McDowell, and D.J. Bammann. Dislocation–based micropolar single crystal plasticity: Comparison of multi– and single criterion theories. *Journal of the Mechanics and Physics of Solids*, 59:398–422, 2011.

[7] N. M. Cordero, A. Gaubert, S. Forest, E. Busso, F. Gallerneau, and S. Kruch. Size effects in generalised continuum crystal plasticity for two–phase laminates. *Journal of the Mechanics and Physics of Solids*, 58:1963–1994, 2010.

[8] M.E. Gurtin. A gradient theory of single–crystal viscoplasticity that accounts for geometrically necessary dislocations. *Journal of the Mechanics and Physics of Solids*, 50:5–32, 2002.

[9] S. Wulfinghoff and T. Böhlke. Equivalent plastic strain gradient enhancement of single crystal plasticity: theory and numerics. *Proceedings of the Royal Society A*, 468:2682–2703, 2012.

[10] O. Aslan and S. Forest. Crack growth modelling in single crystals based on higher order continua. *Computational Materials Science*, 45:756–761, 2009.

[11] O. Aslan and S. Forest. The micromorphic versus phase field approach to gradient plasticity and damage with application to cracking in metal single crystals. In R. de Borst and E. Ramm, editors, *Multiscale Methods in Computational Mechanics*, pages 135–154. Lecture Notes in Applied and Computational Mechanics 55, Springer, 2011.

[12] S.D. Mesarovic, R. Baskaran, and A. Panchenko. Thermodynamic coarsening of dislocation mechanics and the size-dependent continuum crystal plasticity. *Journal of the Mechanics and Physics of Solids*, 58:311–329, 2010.

[13] S. Wulfinghoff, S. Forest, and T. Böhlke. Strain gradient plasticity modeling of the cyclic behavior of laminate microstructures. *Journal of the Mechanics and Physics of Solids*, 79:1–20, 2015.

[14] R. J. Asaro. Elastic–plastic memory and kinematic hardening. *Acta Metallurgica*, 23:1255–1265, 1975.

[15] N. M. Cordero, S. Forest, E. P. Busso, S. Berbenni, and M. Cherkaoui. Grain size effects on plastic strain and dislocation density tensor fields in metal polycrystals. *Computational Materials Science*, 52:7–13, 2012.

[16] O. Aslan, N. M. Cordero, A. Gaubert, and S. Forest. Micromorphic approach to single crystal plasticity and damage. *International Journal of Engineering Science*, 49:1311–1325, 2011.

[17] R.H.J. Peerlings, W.A.M. Brekelmans, R. de Borst, and J. H. P. de Vree. Gradient–enhanced damage for quasi–brittle materials. *Int. J. for Numerical Methods in Engineering*, 39:3391–3403, 1996.

[18] M.G.D. Geers, R. de Borst, W.A.M. Brekelmans, and R.H.J. Peerling. Strain–based transient–gradient damage model for failure analysis. *Comput. Methods Appl. Mech. Engrg.*, 160:133–153, 1998.

[19] J. Li, H. Proudhon, A. Roos, V. Chiaruttini, and S. Forest. Crystal plasticity finite element simulation of crack growth in single crystals. *Computational Materials Science*, 90:191–197, 2014.

[20] H. Proudhon, J. Li, F. Wang, A. Roos, V. Chiaruttini, and S. Forest. 3d simulation of short fatigue crack propagation by finite element crystal plasticity and remeshing. *International Journal of Fatigue*, 82:238–246, 2016.

PROTEIN MECHANICS: FROM AMINO ACID TO SWIMMING CELLS

Patrick R. Onck
Micromechanics, Zernike Institute for Advanced Materials,
University of Groningen, Groningen, The Netherlands

Summary Proteins are long polypeptide chains of amino acids and their structure and biological function are directly related to their amino acid sequence. In this presentation I will discuss three different biological functions that are dominated by protein mechanics, each at their specific time and length scale. To relate structure to function, multiscale computational models have been developed for (i) the beating of cilia and flagella, (ii) the strain-stiffening of cross-linked cytoskeletal networks and (iii) transport through nuclear pores.

PROTEINS

Proteins are often referred to as the building blocks of life, playing critical roles in almost all structures and activities in biology. At the smallest, atomic length scale, proteins consist of amino acids. There are 20 different amino acids, each with their own atomic structure, chemical and physical properties. The amino acids form peptide bonds that form long polypeptide chains consisting of hundreds and sometimes thousands of amino acids. Depending on the specific amino-acid sequence the polypeptide chains fold into regular structures, such as α-helices and β-sheets (secondary structure). At a larger spatial level of organization, α-helices and β-sheets will fold into three-dimensional (tertiary) structures, i.e., the actual protein molecule. Finally, protein molecules can combine to form large protein complexes (quaternary structures).

In this presentation I will take you on a journey through protein state space, addressing three different biological functions, each with their own time and length scale.

MULTISCALE MODELLING OF PROTEIN MECHANICS

At the largest length scale I will focus on cilia and flagella, long hair-like projections from the surface of cells that play an important role in cell motility [1]. Cells and micro-organisms use cilia and flagella to propel themselves or to propel the fluid surrounding them. Examples are the beating tails (flagella) of sperm cells (see Fig. 1), or the cilia that line the respiratory tract to propel mucus out of the lungs. The beating of cilia and flagella is enabled by their internal microstrucure, the axoneme, a big protein complex (tens of μm long and 250 nm wide) that is powered by a dense distribution of motor proteins, called dyneins. Motor proteins constitute an important class of proteins that, powered by the hydrolysis of ATP, undergo conformational changes and as such convert chemical energy into mechanical work. We developed a computational model based on a minimal representation of the axoneme. Our results demonstrate that an overall regular beating pattern can emerge with time due to the spatial and temporal coordination of the individual dyneins [2].

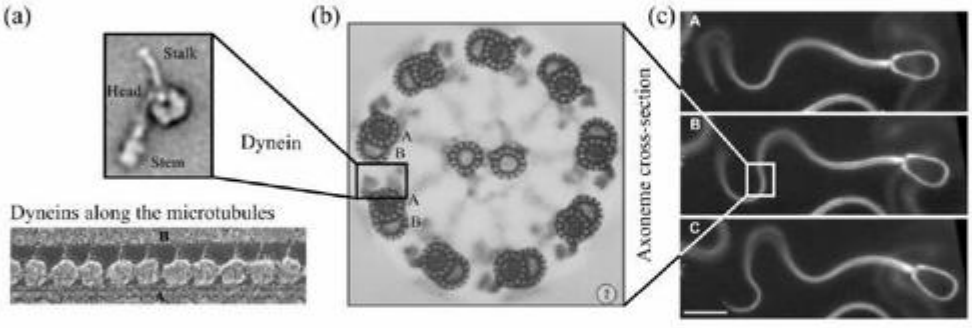

Figure 1: (a) Structure of an axonemal dynein (top). Dyneins at a regular spacing along the microtubules (bottom) [From: Goodenough and Heuser, *J. Cell Biol*. 95, 798–815 (1982)]. (b) An electron micrograph of an axoneme cross-section [From: Afzelius et al., *Tissue and Cell* 27, 241–247 (1995)]. (c) Flagellar beating of a spermatozoon. The three images (A-C) are 200 ms apart. [From: Woolley et al., *J. Exp. Biol.* 212, 18]. Figure is taken from [2].

From a biotechnology point of view, the beating of cilia and flagella are interesting examples for bio-mimicry, utilizing millions of years of biological evolution that led to optimized biological actuators at low Reynolds numbers. Here, artificial, bio-inspired cilia and flagella can be designed using light [3] or magnetic [4-7] actuation to mimic the non-reciprocal motion of their biological counter-part. Artificial cilia can effectively propel fluids in lab-on-chip microfluidic systems, resolving the scale-related problems of downsizing conventional pumping systems [8,9].

Email: P.R.Onck@rug.nl

At a somewhat smaller, subcellular length scale, living cells contain networks of cytoskeletal proteins (Fig. 2). The cytoskeleton is the key cellular component that is responsible for the mechanical behavior of the cell. The major cytoskeletal network is formed by the protein actin, which assembles into a filamentous quaternary structure, and is responsible for maintaining cell shape, stability and for cell motility. Depending on the function and location in the cell, the actin network is cross-linked by different cross-binding proteins, each with their own molecular structure. To capture the constitutive response of actin and other protein networks, we developed a discrete computational network model in two and three dimensions to study the strain stiffening of cross-linked protein networks at large strains [10-12]. Our results show that a wide range of experimental tests on in-vitro reconstituted biopolymer networks can be captured by the competition between two fundamental stiffening mechanisms.

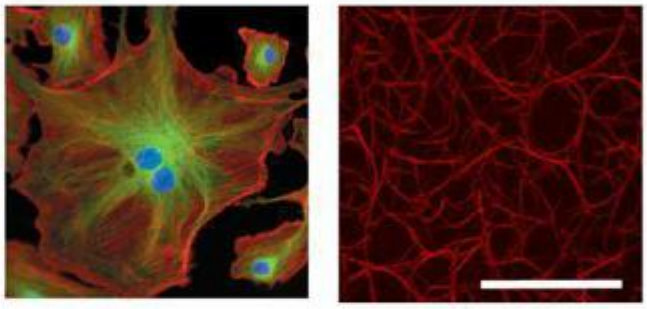

Figure 2: (left) Endothelial cells attached to a substrate, depicting the actin cytoskeleton (red), microtubuli (green) and the nucleus (blue) [from http://probes.invitrogen.com]. (right) Cross-linked actin filament networks [from: Schmoller et al., *Biophys. J.* 97, 83–89 (2009)].

It has long been thought, that proteins need to have a folded structure to perform their function, but more and more evidence is appearing that suggests that also natively unfolded proteins play an important role in many biological functions. One of these roles is in controlling the transport of proteins and nucleic acids in and out of the nucleus of living cells. This transport is mediated by a very large quaternary protein structure, the nuclear pore complex (NPC). The NPC is embedded in the membrane of the cell nucleus and features an internal structure that consists of a meshwork of natively unfolded proteins, called nucleoporins (nups), see Fig. 3. These nups are key in controlling transport, but how they exactly do that is unknown. To shed light on this we have developed a one-bead-per-amino-acid (1BPA) molecular dynamics model [13,14]. The 1BPA model distinguishes between all 20 amino acids of the nups and takes into account hydrophobic and electrostatic interactions. Our results show that these nups collectively form a high-density ring, which is encoded in the amino-acid sequence of the nups. The presence of the ring was found to be correlated with cell viability [14] and permeability [15].

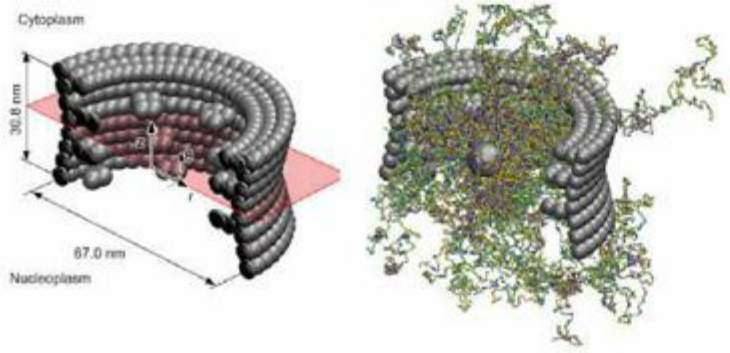

Figure 3: Structural model of the NPC featuring a rigid scaffold constructed by 5 nm-sized rigid beads (left). All natively unfolded nups are tethered to the scaffold at their anchor points (right). Figure is taken from: Ghavami et al., (under review).

References

[1] M.A. Sleigh, *Cilia and flagella*. Academic Press, London, New York, (1974).
[2] S.N. Namdeo and P.R. Onck, The emergence of flagellar beating from the collective behavior of individual ATP-powered dyneins, *under review*.
[3] D. Liu, L. Liu, P.R. Onck* and D.J. Broer*, Reverse switching of surface roughness in a self-organized polydomain liquid crystal coating. *P. Natl. Acad. Sci. USA* **112**:3880-3885 (2015). *Shared corresponding authors
[4] S.N. Khaderi, J.M.J. den Toonder and P.R. Onck, Magnetic artificial cilia for microfluidic propulsion. *Adv. Appl. Mech.* 48, 1-78 (2015).
[5] S.K. Namdeo, S.N. Khaderi and P.R. Onck, Numerical modeling of chirality-induced bi-directional swimming of artificial flagella *Proc. Royal Soc.* A 470 0130547 (2014)
[6] S.N. Khaderi and P.R. Onck (2012). Fluid-structure interaction of three-dimensional magnetic artificial cilia, *J. Fluid Mech*. 708, 303-328.
[7] S. N. Khaderi, C. B. Craus, J. Hussong, N. Schorr, J. Belardi, J. Westerweel, O. Prucker, J. Ruhe, J.M.J. den Toonder and P. R. Onck, Magnetically-actuated artificial cilia for microfluidic propulsion. *Lab Chip* 11, 2002–2010 (2011)
[8] J.M.J. den Toonder and P.R. Onck, Microfluidic manipulation with artificial/bioinspired cilia, *Trends Biotechnol.* 31, 85−91 (2013).
[9] J.M.J. den Toonder and P.R. Onck, P.R. (Eds.) *Artificial cilia*. Cambridge, RSC Publishing (2013).
[10] P.R. Onck, T. Koeman, T. van Dillen, E. Van der Giessen, An alternative explanation of stiffening in cross-linked semiflexible networks, *Phys. Rev. Lett*. 95 (17), 178102 (2005).
[11] T. van Dillen, P.R. Onck and E. Van der Giessen, Models for stiffening in cross-linked biopolymer networks: A comparative study, *J. Mech. Phys. Solids* 56 (2008) 2240–2264
[12] G. Zagar, P.R. Onck, E. Van der Giessen, Two fundamental mechanisms govern the stiffening of cross-linked networks. *Biophys. J.* 108, 1470-1479 (2015).
[13] A. Ghavami, E. Van der Giessen and P.R.Onck, Coarse-grained potentials for local interactions in unfolded proteins, *J. Chem. Theory Comp.* 9 432−440 (2013).
[14] A. Ghavami, L.M. Veenhoff, E. Van der Giessen and P.R.Onck, Probing the disordered domain of the nuclear pore complex through coarse-grained molecular dynamics simulations, *Biophys. J.* 107, 1393–1402 (2014).
[15] P. Popken, A. Ghavami, P.R. Onck, B. Poolman and L.M. Veenhoff, Size-dependent leak of soluble and membrane proteins through the yeast nuclear pore complex. *Mol. Biol. Cell*, 26(7), 1386-1394 (2015).

SOFT MACHINES: CHALLENGES TO COMPUTATIONAL DYNAMICS

Haiyan Hu[a)], Qiang Tian & Cheng Liu
School of Aerospace Engineering, Beijing Institute of Technology, Beijing, China

Summary The lecture presents the study on modeling and simulating the dynamics of soft machines from the viewpoint of rigid-soft multibody systems. The study focuses on the description of nonlinear dynamics of coupled overall motion and large deformation of a soft body made of elastic or hyper-elastic material, the modeling of frictional contacts or even entanglements of soft bodies, as well as the efficient dynamic computation algorithm of rigid-soft multibody system governed by a set of differential-algebraic equations of very high dimensions. The lecture illustrates the proposed approach through a number of case studies, including the knotting of two threads, the deployment of a mesh reflector of satellite antenna and the deployment of a spinning solar sails of spacecraft, as well as the corresponding validations via ground experiments.

INTRODUCTION

The concept of soft machine covers a wide range of advanced industrial products, such as a soft robot making surgical operations or handling fragile objects, a snake robot crawling along tunnel corners, a morphing airplane wing and a deployable solar sail. Those soft machines are mainly composed of soft bodies, which are made of soft materials, including polyamide, polyimide, silicon elastomer and electro-active polymer, in order to adapt to very complex environments or missions. Furthermore, the soft bodies are connected via various joints so that they undergo not only large deformations, but also overall motions and frictional contacts with themselves or environments. The dynamic model of a soft machine, hence, is a rigid-soft multibody system, which gives rise to numerous open and tough problems. It is essential to establish proper modeling and efficient simulating approaches for soft machines in the design phase [1,2].

DYNAMIC MODELING AND SIMULATION

Dynamic modelling of absolute nodal coordinate formulation

The finite elements of Absolute Nodal Coordinate Formulation (ANCF) have served as useful tools to describe the coupling of large deformation and overall motion of a flexible body, such as a very slender beam. The fully parameterized beam element of ANCF is able to describe the shear and cross-section deformations of the beam, but suffers from locking problems. On the contrary, the gradient deficient beam element of ANCF is suitable for describing the slender beam and shows good accuracy. Hence, the lecture presents the new spatial curved beam element and shell element of gradient deficient ANCF to model cables and membranes [3], and shows how to deal with possible slacks and wrinkles of a membrane via the integrated stiffness reduction [4].

Numerical simulation of high efficiency

The finite element of ANCF results in a constant mass matrix, and a complex expression of nonlinear restoring force vector, which requires high cost of computation. The lecture presents how to factorize the unknown generalized coordinates from the integration on a finite element level in the case of full parameters and how to reduce the model order on a soft body level so as to greatly speed up the computation. The lecture also shows how to solve the differential-algebraic equations of a soft machine in parallel on OpenMP [5].

The soft bodies in a soft machine may undergo complicated frictional contacts, such as multi-zone contacts between two surgical threads. The lecture presents a detection strategy for multi-zone contacts of two soft bodies, where the mutual penetration is a multi-peak function of the local coordinates of the soft body predicted to have a larger contact zone. It is quite efficient to locate the contact zones of two soft bodies by checking all the local minima of the function. The lecture shows how to compute the normal contact force by using the penalty method and the tangential friction force via the piecewise analytic expression of the LuGre friction model derived within an integration step [6].

CASE STUDIES

Knotting of two threads

To simulate the knotting process of threads of a surgical robot, the lecture presents the knot tightening and knot releasing of two identical threads with circular cross-sections meshed via the gradient deficient beam elements of ANCF. Figure 1a shows the initial configuration of the two straight threads placed crosswise with one end of each thread clamped at the black point. The two threads is deformed to generate three knots progressively by clamping temporarily other two internal nodes marked as smaller black points in Figure 1c and 1d, driving two chosen nodes marked as green points, to move under planning trajectories, and then freeing the temporarily clamped internal nodes. As shown in Figure 1f, at least four contact zones appear in the final configuration of knotting. Actually, the result may contain one or more contact zones separated by non-contact zones of very short lengths [6].

[a)] Corresponding author. Email: haiyan_hu@bit.edu.cn

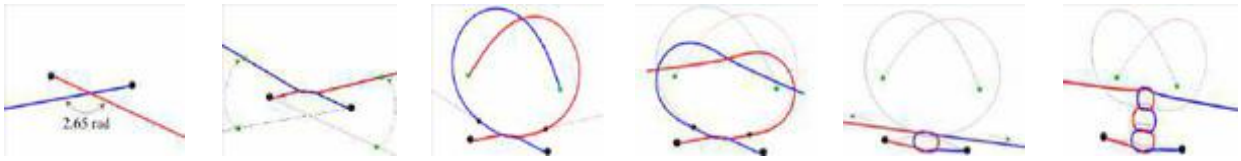

a. b. c. d. e. f.

Figure 1 Knotting of two threads

Deployment of a mesh reflector of satellite antenna

To show the feasibility of the above approach to complicated problems, the lecture presents the deployment of a satellite antenna, where the hoop truss and mesh reflector modelled via the gradient deficient beam elements of ANCF have about 200,000 degrees of freedom, as shown in Figure 2.

To speed up the dynamic simulation, the mesh reflector is decomposed into several independent subsystems by cutting its joint. Then, the Schur complement method is used to eliminate the internal generalized coordinates of subsystem and the Lagrange multipliers for joint constraint equations associated with the internal variables. With an increase of the number of subsystems, the dimension of simultaneous linear equations in the numerical solution process will inevitably increase. By using the multilevel decomposition approach, the dimension of the simultaneous linear equations can be further reduced. Figure 2 illustrates the deployment process of the mesh reflector at six specific moments.

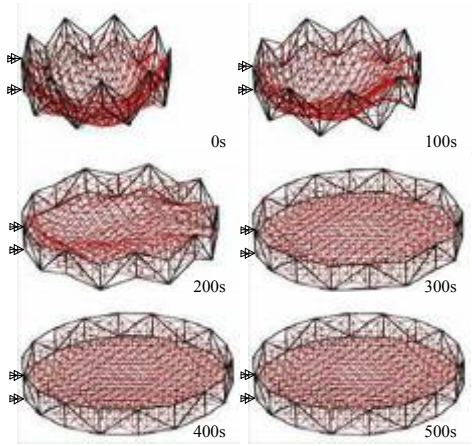

Figure 2 Deployment of a mesh reflector of satellite antenna

Deployment of a spinning solar sail of spacecraft

The spinning deployment of solar sails of spacecraft has called much attention due to their significant advantages since Japan Aerospace Exploration Agency launched IKAROS, the first spacecraft of spinning solar sail. The lecture focuses on a spinning-deployable solar sail shown in Figure 3, where the hexagonal membrane modeled via the shell elements of ANCF is wrapped around the spinning central hub at the initial moment 0s. With the rotation of central hub, the folded membrane is deployed gradually and finally stabilized by the centrifugal forces of the lumped masses at six corners of the solar sail in Figure 3a. The simulation shows the importance of proper description of wrinkle of the membrane. For example, the cyclic "deployment-shrinkage-deployment" shown in Figure 3b appears if the wrinkle is not properly modeled. In fact, the multi-scale coupling effect of small wrinkles and large rotation plays a dominant role in the deployment dynamics [4].

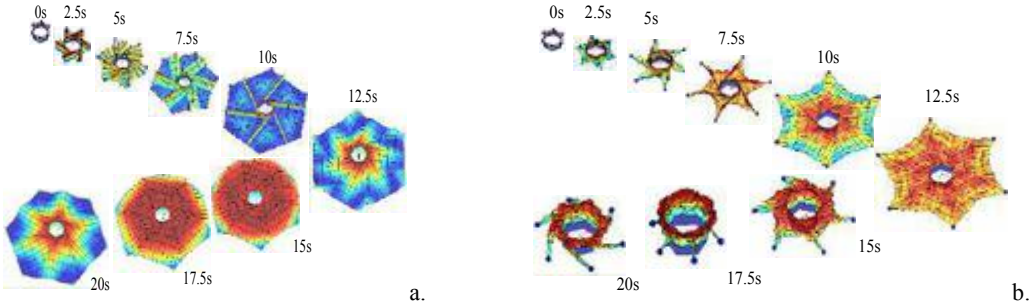

a. b.

Figure 3 Deployment of a spinning solar sail predicted when membrane wrinkles properly modelled or not.

References

[1] Iida F., Laschi C.: Soft Robotics: Challenges and Perspectives, *Procedia Computer Science*, **7**: 99-102, 2011

[2] Nurzaman S. G., Iida F., Margheri L., Laschi C.: Soft Robotics on the Move: Scientific Networks, Activities, and Future Challenges, *Soft Robotics*, **1**: 154-158, 2014.

[3] Liu C., Tian Q., Hu H. Y.: New Spatial Curved Beam and Shell Elements of Gradient Deficient Absolute Nodal Coordinate Formulation, *Nonlinear Dynamics*, **70**: 1903-1918, 2012.

[4] Liu C., Tian Q., Yan D., Hu H. Y.: Dynamic Analysis of Membrane Systems Undergoing Overall Motions, Large Deformations and Wrinkles via Thin Shell Elements of ANCF, *Computer Methods in Applied Mechanics and Engineering*, **258**(1): 81-95, 2013.

[5] Liu C., Tian Q., Hu H. Y.: Dynamics of a Large Scale Rigid-Flexible Multibody System with Composite Laminated Plates, *Multibody System Dynamics*, **26**:283-305, 2011.

[6] Wang Q. T., Tian Q., Hu H. Y.: Dynamic Simulation of Frictional Multi-Zone Contacts of Thin Beams, *Nonlinear Dynamics*, DOI 10.1007/s11071-015-2456-8 2016.

COMPUTATIONAL FRAMEWORK FOR MULTI-MATERIAL FSI, SHOCKS, TURBULENCE AND FRACTURE

Charbel Farhat *[1], Philip Avery, Arthur Morlot, Dante de Santis[2], and Zhengyu Huan[3]
[1]*Department of Aeronautics and Astronautics, Department of Mechanical Engineering, and Institute for Computational and Mathematical Engineering, Stanford University, Stanford, CA, USA*
[2]*Department of Aeronautics and Astronautics, Stanford University, Stanford, CA, USA*
[3]*Institute for Computational and Mathematical Engineering, Stanford University, Stanford, CA, USA*

Summary The FInite Volume method with Exact two-material Riemann (FIVER) problems is a robust computational framework for the solution of multi-material, Fluid-Structure Interaction (FSI) problems. It was validated for challenging applications characterized by compressible flows, shocks, turbulence, highly nonlinear structures, and dynamic fracture. It couples an Eulerian, finite volume based approach for solving flow problems, with a Lagrangian, finite element approach for solving solid mechanics problems. Most importantly, it enforces the governing fluid-fluid and fluid-structure transmission conditions by solving local, one-dimensional, exact, two-material Riemann problems at evolving interfaces that are embedded in the fluid mesh. First, this framework is reviewed with emphasis on its unique contributions to the field, and the challenging simulations it enabled. Next, recent advances pertaining to the mathematical underpinnings of this framework are presented. Finally, novel capabilities related to viscous flows, porous media, embedded constraints, and sensitivity analysis and optimization are described and demonstrated for realistic applications.

BACKGROUND

FIVER was originally developed in [1], in the context of explicit time-discretizations, for the solution of compressible, inviscid, two-phase flow problems characterized by simple equations of state (EOS) but large contact discontinuities (density jumps). In [2], it evolved into an Eulerian embedded boundary method (EBM) — or immersed boundary method — for the solution of highly nonlinear fluid and FSI problems. These include those FSI problems that cannot be handled by Arbitrary Lagrangian Eulerian (ALE) methods, because of large structural motions, finite deformations, and/or topological changes that challenge the performance of mesh motion schemes. Unlike most other EBMs which operate exclusively on Cartesian grids, FIVER can operate on arbitrary grids. This is noteworthy because even in the pure Eulerian setting, the ability of an EBM to perform on arbitrary, unstructured grids is still particularly advantageous for complex geometries and viscous flows.

For multi-material problems with complex fluid EOSs, the solution of a local, one-dimensional, exact, two-material Riemann problem may be either impossible to obtain analytically, or computationally intensive to evaluate numerically. To address this issue, a computationally efficient sparse grid tabulation technique was developed in [3] for accelerating the numerical solution of arbitrary fluid-fluid and fluid-structure Riemann problems, and thereby enabling the generalization of FIVER to multi-material problems with complex fluid EOS. In [4], the generalized FIVER method was validated for the solution of failure-induced FSI problems. Specifically, it was applied to the simulation of two experiments on the dynamic underwater implosion of cylindrical shells. In both cases, it reproduced with high-fidelity the large deformations of the collapsing structure and the compression waves emanating from it (see Figure 1-left).

FIVER was also extended to implicit time-discretizations in [5], and to viscous, multi-material fluid and FSI problems in [6]. For turbulent viscous flows, Eulerian EBMs typically suffer from the fact that they do not track the boundary layers around dynamic rigid or flexible bodies. Consequently, the application of these methods to such problems requires either high mesh resolutions in a large part of the computational fluid domain, or adaptive mesh refinement. Unfortunately, the first option is computationally inefficient, and the second one is labor intensive to implement. To address these issues, an ALE variant of FIVER that maintains all moving boundary layers resolved during turbulent FSI computations was presented in [7], and validated with the simulation of turbulent flows past a family of highly flexible flapping wings, and the prediction of the vertical tail buffeting of an F/A-18 aircraft configuration at a high angle of attack (see Figure 2).

Most recently, a generic, comprehensive, and yet effective approach for representing a fractured fluid-structure interface was developed in [8] and incorporated in FIVER. Specifically, this approach enables the coupling of FIVER with many finite element based fracture methods for the solution of multi-material FSI problems with dynamic fracture. These methods include, among others, the interelement fracture and remeshing techniques, the extended finite element method (XFEM), and the element deletion method. Equipped with this fractured fluid-structure interface representation, FIVER was further validated for highly nonlinear FSI problems with crack propagation, flow seepage through narrow cracks, and structural fragmentation [8] (see Figure 1-right).

*Corresponding author. Email: cfarhat@stanford.edu

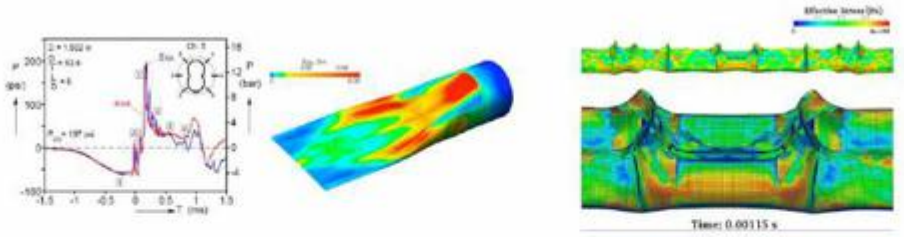

Figure 1: Left: Validated simulation of the dynamic implosion of an underwater cylindrical aluminum shell – Right: Simulation of the massive dynamic fracture of an underwater metallic structure induced by an explosive loading.

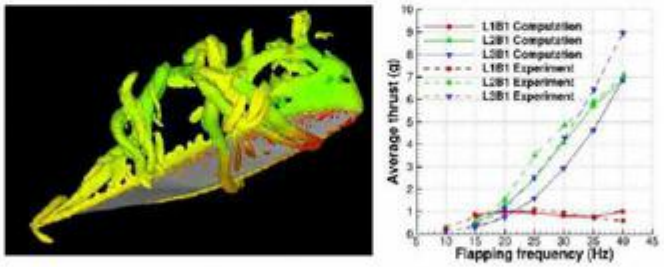

Figure 2: Validated simulation of the thrust generated by a highly flexible flapping wing.

RECENT THEORETICAL RESULTS AND NEW DEVELOPMENTS

In addition to an overview of the computational framework outlined above that emphasizes its physical and mathematical underpinnings, the scope of this "Sectional Lecture in Fluids-Solids" covers recent theoretical advances in FIVER and newly developed extensions and capabilities. Specifically, new results pertaining to numerical stability, energy conservation, and local and global order of spatial and temporal accuracy are discussed with special attention to the behavior of the solution at the material interfaces. In particular, the role of interface limiters in supporting higher-order spatial discretizations for smooth problems and their effects on nonlinear stability is elucidated. The concept of a surrogate material interface, which is ubiquitous in the context of EBMs, is revisited to guarantee the invariance of a predicted turbulent flow with respect to changes in the position of an embedded discrete surface relative to the fluid meshing lines (or simply the fluid mesh). The concept of a local, one-dimensional, exact, two-material Riemann problem is also revisited to incorporate in it a homogenization approach that dramatically enhances computational efficiency in the presence of porous media such as parachutes or porous plug nozzles, to name only a few. A new approach for enforcing *embedded constraints* in a fluid or FSI simulation based on the same concept is also presented and illustrated with several applications ranging from the preservation of symmetry boundary conditions, to the enforcement of non-trivial inlet boundary conditions on embedded discrete surfaces. Finally, an exact sensitivity analysis capability for FIVER is described, and its potential for shape optimization problems with topological changes is demonstrated for complex aeroelastic configurations.

References

[1] C. Farhat, A. Rallu, S. Shankaran, A higher-order generalized ghost fluid method for the poor for the three-dimensional two-phase flow computation of underwater implosions, Journal of Computational Physics 267:7674-7700, 2008.

[2] K. Wang, A. Rallu, J.-F. Gerbeau, C. Farhat, Algorithms for interface treatment and load computation in embedded boundary methods for fluid and fluid-structure interaction problems, International Journal for Numerical Methods in Fluids 67:1175-1206, 2011.

[3] C. Farhat, J.-F. Gerbeau, A. Rallu, FIVER: a finite volume method based on exact two-phase Riemann problems and sparse grids for multi-material flows with large density jumps, Journal of Computational Physics 231:6360-6379, 2012.

[4] C. Farhat, K. Wang, A. Main, J.S. Kyriakides, K. Ravi-Chandar, L.H. Lee, T. Belytschko, Dynamic implosion of underwater cylindrical shells: experiments and computations, International Journal of Solids and Structures 50:2943-2961, 2013.

[5] A. Main, C. Farhat, A second-order time-accurate implicit finite volume method with exact two-phase Riemann problems for compressible multi-phase fluid and fluid-structure problems, Journal of Computational Physics 258:613-633, 2014.

[6] C. Farhat, V. Lakshminarayan, An ALE formulation of embedded boundary methods for tracking boundary layers in turbulent fluid-structure interaction problems, Journal of Computational Physics 263:53-70, 2014.

[7] V. Lakshminarayan, C. Farhat, An embedded boundary framework for compressible turbulent flow and fluid-structure computations on structured and unstructured grids, International Journal for Numerical Methods in Fluids 76:366-395, 2014.

[8] K. Wang, P. Lea, C. Farhat, A computational framework for the simulation of high-speed multi-material fluid-structure interaction problems with dynamic fracture, International Journal for Numerical Methods in Engineering 104:585-623, 2015.

CAN SOLID MECHANICS HELP IN UNDERSTANDING FLUID VORTICES?

George Haller [a)]
Institute of Mechanical Systems, ETH Zürich, Switzerland

Summary Coherent vortices are the most important building blocks of complex flows, yet no universally accepted vortex definition has emerged in fluid dynamics yet. A reason is that most vortex definitions depend crucially on the frame of the observer who evaluates them, even though the significance of vortices arises from the frame-invariant material transport they induce. Recently, ideas from nonlinear dynamics and continuum mechanics have lead to new, objective notions of coherence in fluid dynamics. These reveal surprisingly coherent, previously undetected material vortices in turbulent flows. We survey these ideas and illustrate their efficacy on geophysical flow data.

BACKGROUND

Few would disagree about the intuitive statement that vortices are swirling domains of fluid. It has nevertheless proven surprisingly challenging to define coherent vortices unambiguously. Fluid mechanics has a classical focus on features of the velocity field, which indeed reveals all details of material transport in two-dimensional steady flows. Instantaneous velocity features and actual material transport, however, tend to differ vastly in unsteady flows. Still, there is a traditionally broad focus on identifying vortices in fluids from features of the velocity field or its spatial derivatives (see [1-3] for reviews).

Most such velocity features depend on the observer, and hence fail to provide firm conclusions about the material transport induced by vortices. Still, it is precisely this material transport that makes coherent vortices significant in highly incoherent or even turbulent flow fields. Figures 1a-b show examples of mesoscale (100-200km in diameter) vortices in the ocean that owe their significance entirely to the material they carry. The exact perimeter and level of coherence of such vortices, however, cannot be fully ascertained form these sporadic images: a better understanding of what the underlying flow structure is, independent of the nearly passive scalar fields it carries, is highly desirable for environmental forecasting and decision making. Figure 1c shows a smaller-scale example of an unsteady material vortex, highlighted by the volcanic steam it captures and transports. Detection of such three-dimensional structures without reliance on the material they carry, even for steady 3D flows, has long been an outstanding question.

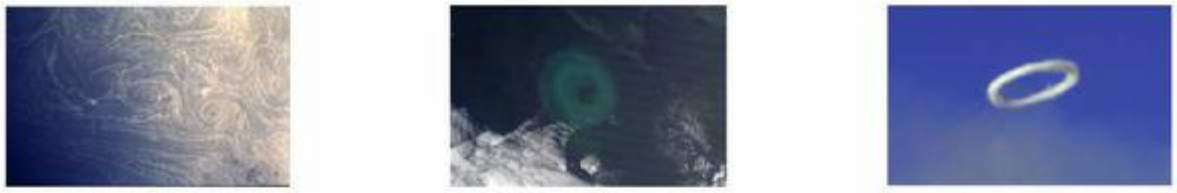

(a) (b) (c)

Figure 1. (a) Spiral eddies in the Mediterranean Sea, highlighted by biological surfactants (Paul Scully-Power/NASA) (b) Phytoplankton patch in the Agulhas leakage (Jeff Schmaltz/NASA) (c) Steam ring over Mount Etna (Tom Pfeiffer/ **www.volcanodiscovery.com**).

With its traditional focus on material behavior, as opposed to velocity features, solid mechanics is well-positioned to contribute to the understanding of coherent fluid features in a frame-independent fashion. A new challenge on the solids-side, however, is the development of objective notions of observed material coherence for large deformation fields. Over the past two decades, a number of advances have been made that address this challenge, leading to the emergence of the field of Lagrangian Coherent Structures, or LCSs [4]. Broadly speaking, LCSs are locally the most influential material surfaces in a moving continuum over a finite time interval of interest. Their unique influence is due to a special role they play in the Lagrangian stretching, shearing or rotation field of the continuum.

Specifically, coherent material vortices (elliptic LCSs) can be approached via their distinguished signatures in any of the above fields. Accordingly, material stretching-based and material rotation-based principles have been developed that identify highly coherent flow regions at a previously unseen precision. Some of these approaches are inspired by techniques from nonlinear dynamics, others by continuum mechanics. Here we give a quick overview of both types of approaches, and show their power on real-life unsteady flow data.

STRETCHING-BASED COHERENCE: AN APPROACH FROM NONLINEAR DYNAMICS

There are well-known analogues of vortex boundaries in the phase space of conservative systems of nonlinear rigid bodies. These invariant surfaces are Kolmogorov--Arnold--Moser (KAM) tori filled with quasi-periodic motions [5]. While such idealized objects do not exist in a realistic, finite-time flow of fluid particles, the coherence properties of KAM tori, notably

[a)] Corresponding author. Email: georgehaller@ethz.ch.

their complete lack of filamentation, can be expressed in a variational principle that applies under arbitrary time dependence as well. Namely, material vortex boundaries in fluids can be sought as outermost, closed stationary curves of the material-surface-averaged relative material stretching functional. The stretching in this variational problem is meant with respect to a finite time interval over which sustained coherence is required. The corresponding Euler-Lagrange equations and boundary conditions can be reformulated into the equivalent problem of finding outermost limit cycles of a two-dimensional steady vector field [6]. These limit cycles are then guaranteed to remain coherent under advection by the original unsteady fluid flow, showing no filamentation over the time interval that was used in defining the underlying stretching functional. An example of the coherent vortices extracted through this dynamical systems approach is shown in the left plot of Figure. 2.

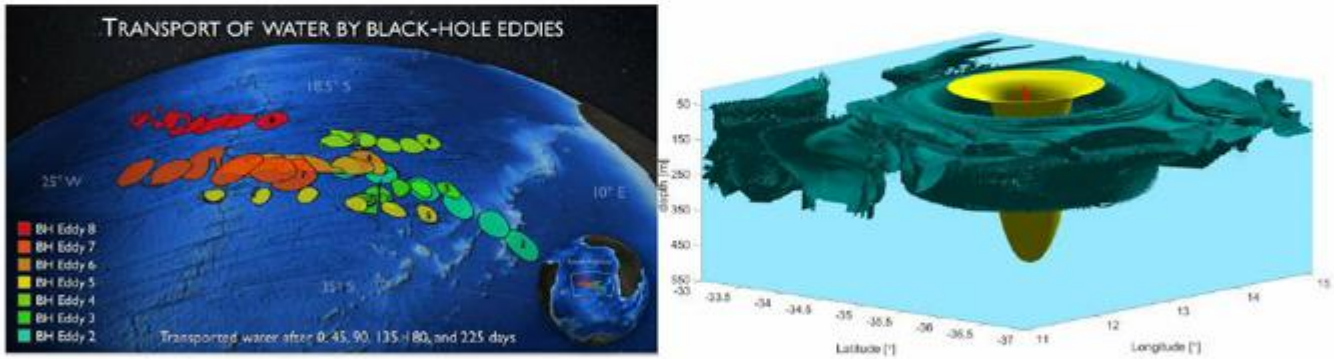

Figure 2. Left: Families of uniformly stretching coherent Lagrangian vortices (black-hole eddies) computed from satellite-detected surface velocities in the Agulhas leakage [6]. **Right:** A rotationally coherent material vortex in the Southern Ocean State Estimate (SOSE) data set [8]. Nearby level surfaces of the LAVD (green) illustrate the complexity in the incoherent water mass surrounding the extracted vortex.

ROTATIONAL COHERENCE: AN APPROACH FROM CONTINUUM MECHANICS

A recent alternative approach targets coherent vortices in terms of the coherent material rotation they exhibit. In continuum mechanics, the rotational component of the deformation is generally inferred from the polar decomposition of the deformation gradient. Rotations inferred from the classic polar decomposition, however, are neither objective nor material. A new dynamic polar decomposition developed in [7] identifies a dynamic rotation tensor that is material, i.e., serves as a self-consistently evolving rigid-body rotation component in the deformation gradient field over any finite time interval. Coherent vortex boundaries can then be identified as outermost convex level surfaces of an intrinsic dynamic rotation angle inferred from the dynamic rotation tensor. This objective material rotation angle turns out to be simply the Lagrangian-averaged deviation (LAVD) of the vorticity field from its spatial mean [8]. An application of this result is shown in Fig. 5.

References

[1] Jeung, J., and Hussein, A.K.M.F.: On the identification of a vortex. *J. Fluid Mech.* **285**:69-94, 1995.

[2] Haller, G.: An objective definition of a vortex. *J. Fluid Mech.* **525**:1-26, 2005.

[3] Chakraborthy, P., Balachandar, S., and Adrian, R.: On the relationships between local vortex identification schemes. *J. Fluid Mech.* **535**:189-214, 2005.

[4] Haller, G.: Lagrangian Coherent Structures. *Ann. Rev. Fluid Mech.* **47**:137-162, 2015.

[5] Arnold, V.I., *Mathematical Methods of Classical Mechanics*. Springer, New York, 1978

[6] Haller, G. and Beron—Vera, F.J.: Coherent Lagrangian vortices: The black holes of turbulence. *J. Fluid Mech.* **731**:R4, 2013.

[7] Haller, G.: Dynamically consistent rotation and stretch tensors from a dynamic polar decomposition. *J. Mech. Phys. Solids.* **80***:* 70-93, 2016

[8] Haller, G., Hadjighasem, A., Farazmand, M., and Huhn, F., Defining coherent vortices objectively from the vorticity. *J. Fluid Mech.* submitted, 2015; arXiv:1506.04061 [physics.flu-dyn]

MS01 - Bypass Transition

TS.MS01-1.01	Hof, Björn - Directed percolation transition to turbulence (INVITED)	42
TS.MS01-1.02	Gibson, John - Exact coherent structures in transitional flows: Dynamics and localization (INVITED)	44
TS.MS01-1.03	Gayme, Dennice - Restricted Nonlinear Roll/Streak Dynamics in Plane Couette Flow (INVITED)	46
TS.MS01-1.04	Hall, Philip - Sitting on the edge of turbulence (INVITED)	48
TS.MS01-2.01	Sano, Masaki - Universal critical behavior of the transition to turbulence in channel flow (INVITED)	50
TS.MS01-2.02	Duguet, Yohann - Localized structures on the edge in boundary layers and their traces in bypass transition	52
TS.MS01-2.03	Kushwaha, Anubhav - Temporal and spatial intermittencies within Newtonian turbulence	54
TS.MS01-2.04	Nagata, Masato - Bifurcations in rotating plane Couette flow at moderate Reynolds numbers	56
TS.MS01-2.05	Xi, Li - Effects of drag-reducing polymers on the transient development of turbulent coherent structures	58
TS.MS01-2.06	Dubief, Yves - The role of elasto-inertial turbulence on channel flow drag	60
TS.MS01-3.01	Cossu, Carlo - Exact invariant solutions for coherent turbulent motions in Couette and Poiseuille flows (INVITED)	62
TS.MS01-3.02	Lu, Jianzhou - Spatio-temporal evolution of isolated turbulent bands in channel flows	64
TS.MS01-3.03	Klotz, Lukasz - Transition to Turbulence in Plane Couette-Poiseuille Flow	65
TS.MS01-3.04	Katasonov, Mikhail - Origination of wave packets at localized streaks	67
TS.MS01-3.05	Hack, Philipp - Characterization and prediction of streak breakdown using machine learning	69

Directed percolation transition to turbulence

Gregoire Lemoult[1] , Liang Shi[1], Kerstin Avila[1], Shreyas Jalikop[1], Marc Avila[2] & Björn Hof[1]
[1]*IST Austria, Klosterneuburg, Austria*
[2] *Friedrich-Alexander-Universität Erlangen-Nürnberg, 91058 Erlangen, Germany*

Summary We report that the transition to turbulence in Couette flow corresponds to a second order phase transition and falls into the directed percolation universality class. The increase of the turbulent fraction above the critical point as well as correlation lengths and times at the transition point are described by three critical exponents, which are in excellent agreement with the exponents of the directed percolation (DP) universality class.

Introduction

The transition to turbulence in wall bounded shear flows (such as pipe, channel or Couette flow) has remained an open problem for over a century [1]. Typically here turbulence arises despite the linear stability of the laminar flow and results from perturbations of finite amplitude. At the lowest Reynolds numbers at which turbulence can be triggered it arises in the form of localised patches (e.g. puffs, spots or stripes) which coexist with laminar flow, resulting in complicated, disordered flow patterns (spatio-temporal intermittency). Individual turbulent domains can collapse or they can proliferate and seed other patches of turbulence. Balancing the growth and decay processes allows determining the critical point [2] above which turbulence first becomes sustained (in the thermodynamics limit).
As shown previously [2] the time scales on which flows evolve are extremely large and likewise the relevant length scales (the size of the turbulent domains) is comparatively large (typically 20-30 pipe diameters or wall spacings). In order to fully characterize the transition process the interaction and evolution of many such domains has to be taken into account hence requiring experiments of very large aspect ratios and extremely long observation times.
As first proposed by Pomeau [3] the transition to turbulence may be related to the universality class of directed percolation (DP), one of the simplest universality classes for non-equilibrium phase transitions. One illustration of directed percolation is that of a fluid percolating through a porous medium. Depending on the porosity the fluid will either progress through the medium or it will get stuck at a certain point. For increasing values of the connectivity of the pores (which is expressed by a single parameter, the probability P) a continuous phase transition occurs at a distinct critical point above which there is always a connected path. Figure 1a shows a model of this process (directed bond percolation). Connected bonds (open pores) are marked in blue (closed ones in black).
The transition to turbulence (like DP) is a contact process where turbulence spreads by neighbour interaction, likewise the linear stability of the laminar flow ensures that if at any point in time all turbulent sites decay the flow will afterwards remain laminar for all times. The laminar state hence corresponds to what is called the unique absorbing state in the context of DP. Determining if the transition to turbulence indeed falls into this universality class has posed a major challenge.

Results

We report [4] experiments and direct numerical simulations of Couette flow. Experiments were carried out in a circular Couette set up (a fluid layer sheared between two concentric cylinders). The aspect ratio (gap width to cylinder circumference) was 2750 while the domain height (axial direction) was 8 times the gap size. In addition direct numerical simulations were carried out for Couette flow in a domain of 960 (azimuthally) by 5h (vertically), where h is the gap width between the two cylinders. Figure 1b shows the spatio temporal evolution of turbulent domains (in blue) in the numerical simulations. Notably (like for DP) new turbulent domains branch out from existing stripes (nearest neighbour interaction). A visualisation of turbulent domains/stripes in the experiment is shown in figure 1c. Extensive experiments and simulations covering the Reynolds number regime where turbulence can first be observed, allow us to explicitly measure the critical point at which turbulence becomes sustained in Couette flow. Likewise we determine how the turbulent fraction increases as the critical point is surpassed. Like for DP the transition is continuous and follows a power law with an exponent of ~0.28 which is in excellent agreement with the universal DP value. Furthermore we determine the critical exponents describing the correlation length and correlation time close to the critical point and the respective values are again in excellent agreement with those predicted of the directed percolation universality class.

[a] Corresponding author. Email: ictam2016papers@legendconferences.com.

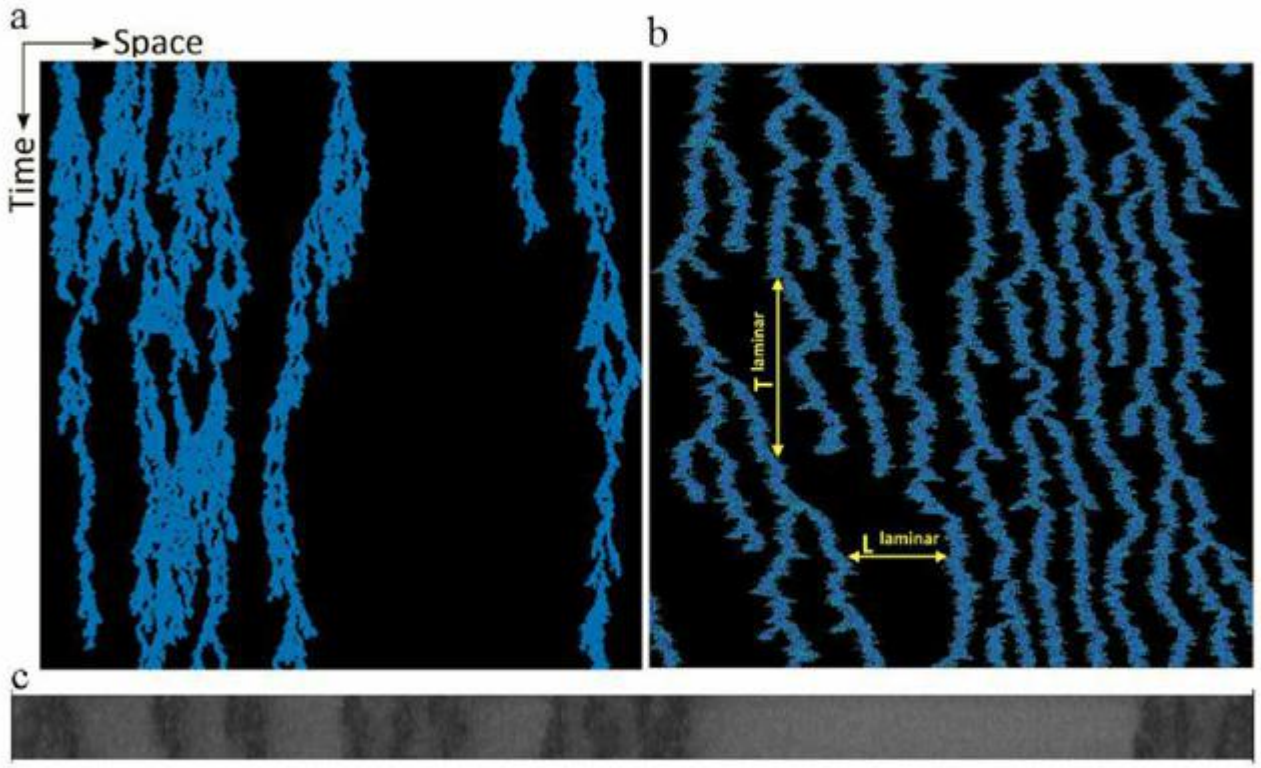

Figure 1: **a** space time plot of directed bond percolation (active sites in blue, absorbing ones in black). **b** Space time plot of turbulence in Couette simulations with turbulent domains in blue and laminar ones in black. **c** Picture of the experimental flow, where turbulent stripes appear in dark whereas the brighter regions correspond to laminar flow.

Summary

We present evidence that the transition to turbulence in Couette flow corresponds to a second order non-equilibrium phase transition and falls into the directed percolation universality class.

References

[1] Reynolds, O.: An Experimental Investigation of the Circumstances Which Determine Whether the Motion of Water Shall Be Direct or Sinuous, and of the Law of Resistance in Parallel Channels. Proc. R. Soc. London. **35**, 84–99 (1883).

[2] Avila, K. et al., The onset of turbulence in pipe flow. Science , **333**, 192–196 (2011).

[3] Pomeau, Y.: Front motion, metastability and subcritical bifurcations in hydrodynamics. Phys. D. **23**, 3–11 (1986).

[4] Shi, L. et al: The universality class of the transition to turbulence. arXiv:1504.03304

EXACT COHERENT STRUCTURES IN TRANSITIONAL FLOWS: DYNAMICS AND LOCALIZATION

John F. Gibson * [1]
[1]*Department of Mathematics and Statistics, University of New Hampshire, Durham, NH, United States*

Summary Invariant solutions of the Navier-Stokes equations provide a mathematically sound framework for the long-standing idea of coherent structures in turbulence. In recent years, computations of weakly unstable equilibria, traveling waves, and periodic orbits have shed much light on the structure and dynamics of transitional of shear flows. In this talk we present (1) a brief overview of the methodology and goals of invariant solutions or exact coherent structures as framework for analyzing transitional turbulence, and (2) recent results that extend invariant solutions from spatially periodic solutions in minimal flow units to localized solutions in extended flows. The localized solutions provide precise specifications of coherent structures long observed in turbulent shear flows and are potentially a first step towards an understanding of the spatiotemporal dynamics of turbulence as a system of self-organized, interacting coherent structures.

BACKGROUND

In the past twenty years, many equilibrium, traveling waves, and periodic orbits have been calculated for canonical shear flows as invariant solutions of the Naver-Stokes equations with appropriate boundary conditions [1, 2, 3, 4]. These solutions capture commonly observed features associated with coherent structures in transitional shear flows, such as self-sustaining wavey roll-streak structures, and dynamical processes such as bursting [5]. Moreover, numerical linear stability analysis reveals that typical invariant solutions are weakly unstable at transitional Reynolds numbers, i.e. they have only a few unstable eigenmodes, with only weakly unstable eigenvalues. Thus a turbulent trajectory of a transitional shear flow can be understood in dynamical-systems terms as a pseudo-random, chaotic walk between the flow's unstable solutions, along the low-dimensional network of their unstable manifolds. The appearance of an organized coherent structure in a turbulent flow then corresponds to the trajectory making a close pass to a weakly unstable invariant solution. Hence we call such invariant solutions *exact coherent structures*.

DYNAMICS

The dynamical-systems vision described above has been fleshed out explicitly in quantitative detail for transitional shear flows in minimal flow units [6]. For example, figure 1 shows a state-space portrait of plane Couette flow in a minimal flow unit at $Re = 400$. Equilibrium solutions are shown as solid dots and trajectories within their low-dimensional unstable manifold as solid lines. The projection is from the $O(10^5)$-dimensional state space of a DNS to a three-dimensional subspace spanning a few important equilibria, using the standard inner product associated with the L_2 energy norm of the velocity field. The unstable manifolds of the depicted solutions are clearly intertwined; in fact heteroclinic orbits can be found that describe precise dynamic connections between the nearby unstable equilibria. Farther away from laminar solution, the turbulent flow can be analyzed as shadowing a sequence of periodic orbits and transitioning between them along the orbits' low-dimensional unstable manifolds. Animations illustrating the low-dimensional state-space dynamics of heteroclinic connections and periodic orbits are available at `http://www.chaosbook.org/tutorial` and `http://www.channelflow.org/movies`.

LOCALIZATION

More recently spatially localized exact coherent structures have been computed in extended flows [7, 8, 9], with a number of interesting features. Spanwise-localized forms of the Nagata equilibria exhibit *homoclinic snaking*, a process by which additional structure is grown at the fronts of a quasi-periodic pattern through a sequence of saddle-node bifurcations [7]. This behavior in 3D solutions of Navier-Stokes is remarkably similar to that of observed for the one-dimensional Swift-Hohenberg equation, forming an intriguing connection between fluid dynamics and pattern formation theory. Spanwise-localized solutions of plane Poiseuille flow and the asymptotic suction boundary layer bear remarkable resemblance to fundamental staggered and mirror-symmetric roll-streak coherent structures observed in the high-shear region near the walls of boundary layer and channel flows [8]. Doubly-localized solutions of plane Couette flow replicate the elongated turbulent spots from which turbulence is triggered in extended systems [9].

*Corresponding author. Email: john.gibson@unh.edu

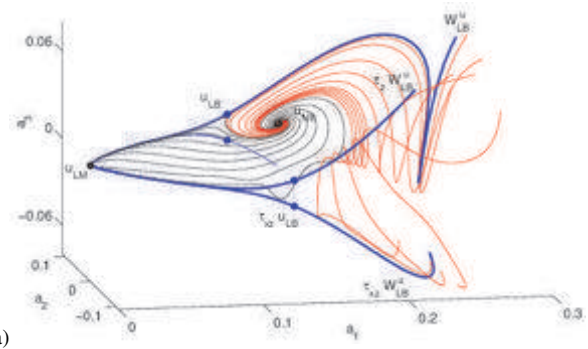

(a)

Figure 1: **A state-space portrait of transitionally turbulent plane Couette flow, in the neighborhood of laminar flow.** The origin is placed at near the laminar equilibrium (u_{LM}). Solid dots correspond to unstable equilibrium solutions of the flow; solid lines are trajectories in the low-dimensional unstable manifolds of the equilibria, computed with well-resolved DNS.

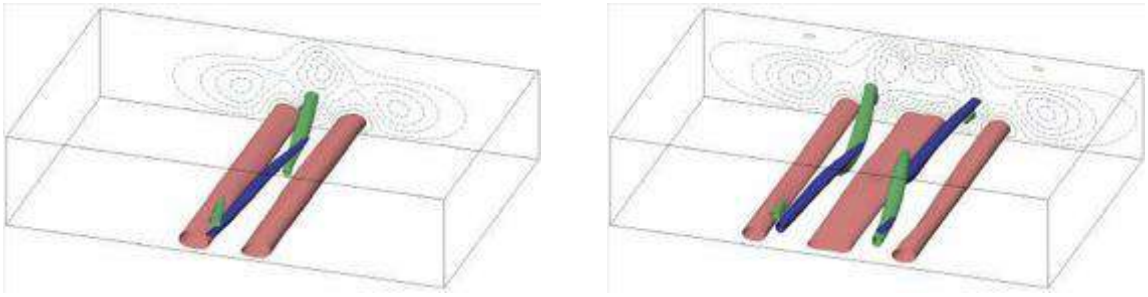

Figure 2: **Exact near-wall traveling waves of plane Poiseuille flow.** Swirling strength in blue (counterclockwise) and green (clockwise), high-speed streaks in red, and isocontours of streamwise velocity perturbation in back plane.

References

[1] NAGATA, M. Three-dimensional finite-amplitude solutions in plane Couette flow: bifurcation from infinity. *J. Fluid Mech.* **217**, 519–527, 1990.

[2] KAWAHARA, G. & KIDA, S. Periodic motion embedded in plane Couette turbulence: regeneration cycle and burst. *J. Fluid Mech.* **449**, 291–300, 2001.

[3] FAISST, H. & ECKHARDT, B. Traveling waves in pipe flow. *Phys. Rev. Lett.* **91**, 224502, 2003.

[4] VISWANATH, D. Recurrent motions within plane Couette turbulence. *J. Fluid Mech.* **580**, 339–358, 2007.

[5] HAMILTON, J.M., KIM, J. & WALEFFE, F. Regeneration mechanisms of near-wall turbulence structures. *J. Fluid Mech.* **287**, 317–348, 1995.

[6] GIBSON, J. F., HALCROW, J. & CVITANOVIĆ, P. Visualizing the geometry of state space in plane Couette flow. *J. Fluid Mech.* **611**, 107–130, 2008.

[7] SCHNEIDER, T. M., GIBSON, J. F. & BURKE, J. Snakes and ladders: Localized solutions of plane Couette flow. *Phys. Rev. Lett.* **104**, 104501, 2010.

[8] GIBSON, J. F. & BRAND, E. 2014 Spatially localized solutions of planar shear flow. *J. Fluid Mech.* **745**, 25–61, 2014.

[9] BRAND, E. & GIBSON, J. F. A doubly-localized equilibrium solution of plane Couette flow. *J. Fluid Mech.* **750** (R3), 1–12, 2014.

RESTRICTED NONLINEAR ROLL/STREAK DYNAMICS IN PLANE COUETTE FLOW

Vaughan Thomas and Dennice F. Gayme*
Department of Mechanical Engineering, Johns Hopkins University, Baltimore, Maryland, USA

Summary The recently developed restricted nonlinear (RNL) modeling framework is used to study a transitioning and turbulent plane Couette flow at moderate Reynolds numbers. The results show that the critical roll and streak structures involved in the self-sustaining process of turbulence are well represented by this model. The transitioning flow shows qualitative similarities in the development and organization of these key flow features when compared to a direct numerical simulation (DNS) of the Navier Stokes (NS) equations. However, there is greater transient energy growth in both the roll and streak structures in the RNL simulations. Further characterization of RNL transitioning flows will determine the merit of studying transition using this type of model, which is an appealing prospect due to its simplified dynamics and the order reduction that leads to significantly reduced computational requirements versus the NS equations.

Studies of disturbance energy growth in wall-bounded shear flows have identified streamwise constant disturbances as preferential in developing the types of large energy amplification associated with bypass transition. This evidence of the important role of streamwise coherent structures in linear energy growth as well as observations of their prevalence in fully developed wall-turbulence motivates the use of a streamwise constant modeling framework to study transition and turbulence in these flows. A streamwise constant projection of the Navier Stokes (NS) equations leads to a two dimensional flow field in three velocity components, a 2D/3C model. Simulations of 2D/3C systems with persistent stochastic forcing have been shown to develop turbulent flow fields that exhibit accurate turbulent velocity profiles and other structural features consistent with turbulent plane Couette flow [1].

A more comprehensive model, which can self-sustain turbulence [2], is obtained by introducing a streamwise varying perturbation field that interacts with a 2D/3C mean flow. The corresponding model is obtained by decomposing the velocity and pressure gradient fields in the NS equations into a streamwise averaged mean and perturbations from this mean, respectively $\mathbf{u_T} = \mathbf{U}(y,z,t) + \mathbf{u}(x,y,z,t) = (U,V,W) + (u,v,w)$ and $\nabla p_T(x,y,z,t) = \nabla P(y,z,t) + \nabla p(x,y,z,t)$. The nonlinear interactions between perturbations ($\mathbf{u}$) are then neglected to obtain

$$\mathbf{U}_t + \mathbf{U}\cdot\nabla\mathbf{U} + \nabla P - \frac{1}{R}\Delta\mathbf{U} = -\langle\mathbf{u}\cdot\nabla\mathbf{u}\rangle, \tag{1a}$$

$$\mathbf{u}_t + \mathbf{U}\cdot\nabla\mathbf{u} + \mathbf{u}\cdot\nabla\mathbf{U} + \nabla p - \frac{1}{R}\Delta\mathbf{u} = \mathbf{f} \tag{1b}$$

$$\nabla\cdot\mathbf{U} = 0, \quad \nabla\cdot\mathbf{u} = 0. \tag{1c}$$

Here $\mathbf{f}$ is a stochastic excitation that is used to initiate turbulence, it is removed once self-sustaining turbulence is achieved.

Previous work shows that simulations of the RNL model in (1) capture salient features of turbulent plane Couette flow at low Reynolds numbers [2]. Two particular features of interest are the roll and streak structures, whose interactions are known to play an important role in both transition and turbulence. In this work we focus on the development of these structures and their characteristics after the transient phase in turbulent flows at two Reynolds numbers, $Re_\tau \approx 65$ and $Re_\tau \approx 196$.

Simulations of the RNL system and the NS equations are out carried using the spectral solver detailed in [2]. Turbulence is initiated through the application of zero-mean delta-correlated (in y, z, and t) forcing in both the RNL simulations, through $\mathbf{f}$ in (1b), and the DNS. We characterize the streak and roll structures based on their respective RMS velocity measurements, which we define as follows.

$$U_{Streak} := \sqrt{\int_0^{L_z}\int_{-\delta}^{\delta}\left(U-[U]\right)^2\,dy\,dz}, \quad U_{Roll} := \sqrt{\int_0^{L_z}\int_{-\delta}^{\delta}V^2+W^2\,dy\,dz}, \tag{2}$$

where $[\cdot]$ indicates a spanwise average, and the spanwise and wall-normal channel extents are respectively $[0, L_z]$ and $[-\delta, \delta]$.

Figure 1 compares the development of the RMS roll and streak velocities in the RNL simulations and DNS at $Re_\tau \approx 65$ and $Re_\tau \approx 190$. These figures show that the streak and roll energies developed during the transition phase of the RNL simulations are significantly higher than those of the DNS, for an equivalent $\mathbf{f}$. One notable difference is the overshoot in the RMS velocities of the RNL structures that is not present in the DNS. Figure 1 demonstrates how the nature of $\mathbf{f}$ affects the transient behavior of the RNL systems. In particular, reducing the variance of $\mathbf{f}$ by 87.5% and 95% for the RNL simulations with $Re_\tau \approx 190$ lengthens the rise time and increases the magnitude of the overshoot. Although the energy growth of these structures shows the distinct differences discussed above, an interrogation of the instantaneous velocity fields during the transition phase uncovers qualitative similarity in both the development and organization of the roll and streak features. Once the transition phase ends, the RMS velocities of the structures arising from the DNS and RNL simulations are very similar for both Reynolds numbers, which is consistent with previous results [2].

*Corresponding author. Email: dennice@jhu.edu

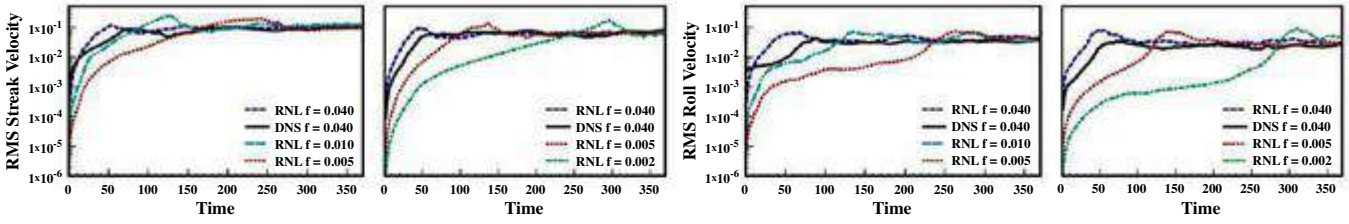

Figure 1: The evolution of the RMS streak velocities for RNL simulations and DNS at (a) $Re_\tau = 66$ and $Re_\tau = 64$ respectively and, (b) $Re_\tau = 196$ and $Re\tau = 186$ respectively. Panels (c) and (d) show the RMS roll velocities for same simulations as in (a) and (b). The variance of the zero-mean stochastic excitation $\mathbf{f}$, in (1b), is given for each simulation.

We further examine the nature of the rolls and streaks in the fully developed (self-sustaining) turbulent regime through instantaneous snapshots of the flow in the cross stream ($y - z$) plane. Figure 2 shows the $v_T - w_T$ vector field superimposed on contour plots of the streamwise component of velocity field with the laminar solution $U(y) = y$ removed, i.e. $u_T - U(y)$. Figures 2c and 2d demonstrate that the similarity in the structural features previously observed at low Reynolds numbers [2, 3] continues into this modest Reynolds number regime. The feature spacing and intensity of the roll structures also appears to be consistent in the DNS and RNL simulations at $Re_\tau \approx 190$, in accordance with the information provided in Figure 1.

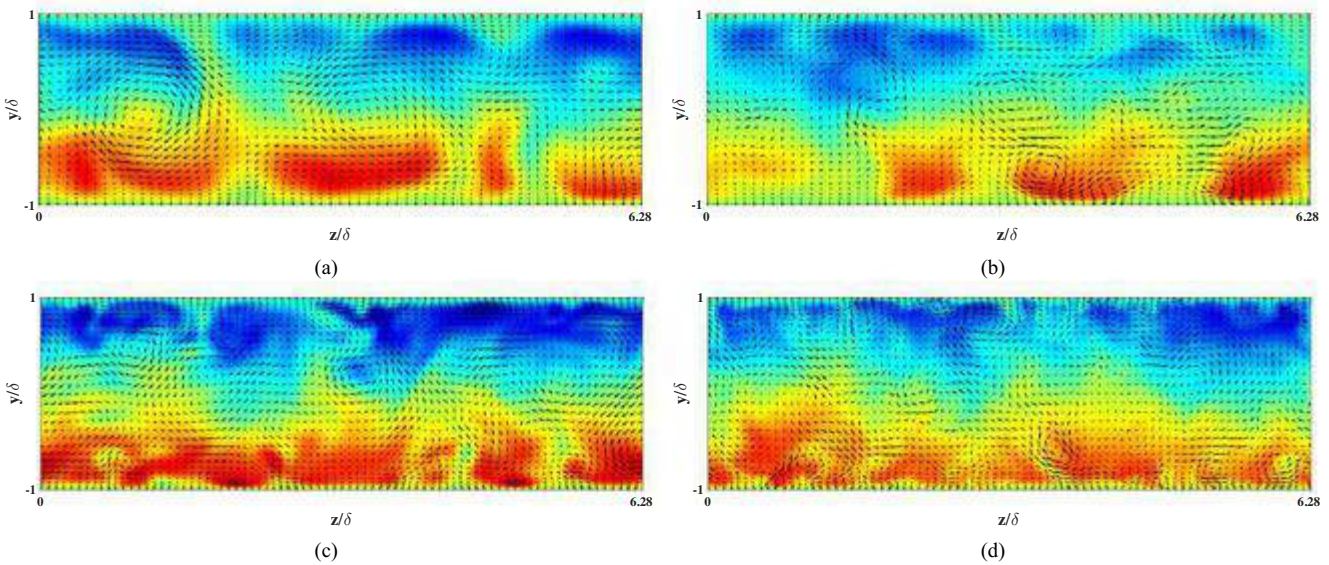

Figure 2: Cross stream ($y - z$ plane) contour plots of the streamwise velocity component with the laminar flow removed, i.e. $u_T - U(y)$ and the $v_T - w_T$ velocity vectors superimposed. (a) A RNL simulation at $Re_\tau = 66$, (b) a DNS at $Re_\tau = 64$, (c) a RNL simulation at $Re_\tau = 196$, and (d) a DNS at $Re_\tau = 186$. The time step shown ($t = 1760$) is long after the initial excitation $\mathbf{f}$ in (1b) is set to zero.

The results presented here demonstrate that the RNL framework shows promise in capturing critical features of turbulent plane Couette flow at modest Reynolds numbers. However, the energetics of the roll and streak structures in a transitioning RNL flow require further examination to better understand how this process compares to current theories regarding turbulent transition. Understanding the extent to which an RNL system can be used to study transition will help determine whether the simplified dynamics that lend to the isolation of critical interactions and the inherent order reduction that makes RNL simulations significantly less costly than DNS can be exploited in this important flow regime.

References

[1] D. F. Gayme, B. J. McKeon, A. Papachristodoulou, B. Bamieh, J. C. Doyle: Streamwise constant model of turbulence in plane Couette flow. J. Fluid Mech., 665:99-119, 2010.

[2] V. Thomas, B. K. Lieu, M. R. Jovanović, B. F. Farrell, P.J. Ioannou, D. F. Gayme: Self-sustaining turbulence in a restricted nonlinear model of plane Couette flow. Phys. of Fluids, 26:105112, 2014.

[3] B. F. Farrell, P. J. Ioannou: Dynamics of streamwise rolls and streaks in turbulent wall-bounded shear flow. J. Fluid Mech., 708:149-196, 2012.

SITTING ON THE EDGE OF TURBULENCE

Philip Hall

School of Mathematical Sciences, Monash University

Summary The properties of vortex-wave interaction states in shear high speed shear flows are investigated. In particular the relevance of these high Reynolds number solutions of the Navier Stokes equations to turbulence is discussed. It is shown that the states usually referred to as lower and upper branch states in the self-sustained process community have quite different stability properties. This explains why lower branch states can act as edge states whilst upper branch states are more closely related to fully turbulent flows. It is shown that there are three naturally occuring instabilities of VWI states and that bifurcation to the slow and fast time-periodic states found numerically by Kawahara and Kida (2001) can be predicted by the theory.

.

VORTEX-WAVE INTERACTION STATES: VWI

In recent years it has been found that exact coherent structures found by numerical or asymptotic reductions of the Navier Stokes equations play key roles in the both the process by which a flow becomes turbulent and the nature of fully developed turbulence. Non-localized structures occurring in both external and internal shear flows naturally fall into two categories at sufficiently high speed. The first kind is described by vortex-wave interaction theory, VWI for short, whilst the second canonical type of structure due to Deguchi and Hall (2014a) is referred to as a free stream coherent structure and sits at the edge of a boundary layer.

In a series of papers Hall & Smith (1989,1990,1991) gave formal asymptotic descriptions of quite general interactions involving waves and stream wise vortices. The analysis described explicitly self-sustaining processes of waves existing as instabilities of streaks and driving a roll flow through their Reynolds stresses. The process was shown to be closed because the roll driven in this way itself drives the streak. The Hall-Smith framework applies to both inviscid and viscous waves though the precise nature of the production of the rolls by the Reynolds stresses depends on the nature of the wave and whether the flow is fully-developed. At about the same time Nagata (1990) discussed numerical results for nonlinear equilibrium states in Couette flow. Subsequently, with the advent of more powerful computers, Waleffe and collaborators, see for example, Waleffe (1997) or Wang et al (2007), found a number of equilibrium states in channel flows. A numerical interrogation of the results showed that the process was a finite Reynolds number version of that described by Hall and Smith (1991). However Waleffe was unaware VWI and so described the interaction as a 'self-sustained' process. More recently such states and the vortex-wave states have been loosely referred to as exact coherent structures.

The VWI approach shows that upper and lower branch states come into existence as a saddle node bifurcation when the streamwise wavenumber of the wave is decreased. The lower branch is approached rapidly by finite Reynolds number computations of the full equations with Reynolds numbers of a few thousand being sufficient for the asymptotic theory of VWI to capture the finite Reynolds number results with remarkable accuracy. On the upper branch the approach is much more slow and significantly higher Reynolds numbers are needed for the asymptotic and finite Reynolds number results to be in excellent agreement.

Hall &Smith (2010) used the vortex-wave framework to describe equilibrium states in Couette flow and found remarkably good agreement with Waleffe et al (2007). More recently Deguchi and Hall (2014b) extended the Hall and Sherwin results to describe both upper and lower branch states. It is well-known in the exact coherent structure community that lower branch states can act as edge states which determine whether disturbances to the unperturbed state ultimately cause the flow to become laminar or turbulent. On the other hand upper branch states cannot act as edge states but are regularly visited by fully turbulent flows. The different properties of the upper and lower branch states arise from their different instability properties with the lower branch state having just a single unstable eigenvalue.

Here we will describe the stability properties of arbitrary VWI states and show how finite amplitude theory can be used to describe the initial evolutions of some neutrally stable modes found. The analysis is based on the linear theory of Deguchi and Hall (2016) who give an asymptotic description of the instabilities of both upper and lower branch states. It is shown that upper and lower branch states are potentially unstable to three types of modes. The first rather ponderous mode corresponds to a gentle oscillation in time of the vortex-wave state on the slow streak diffusion timescale. A second one is a fast Rayleigh instability of the streak. At an intermediate timescale a new mode emerges and Deguchi and Hall (2016) referred to is as the edge mode since it is the only mode of instability of lower branch states. Figure 1 is a schematic of how the instability properties of VWI states vary along the lower and upper branches. On the bulk of the lower branch there is a single unstable edge mode with growth rate $O(R^{-1/2})$ together with stable slow modes of growth rate $O(R^{-1})$. On the upper branch there are unstable fast and slow modes and an unstable edge mode. Note also that neutral periodic forms of the slow and edge

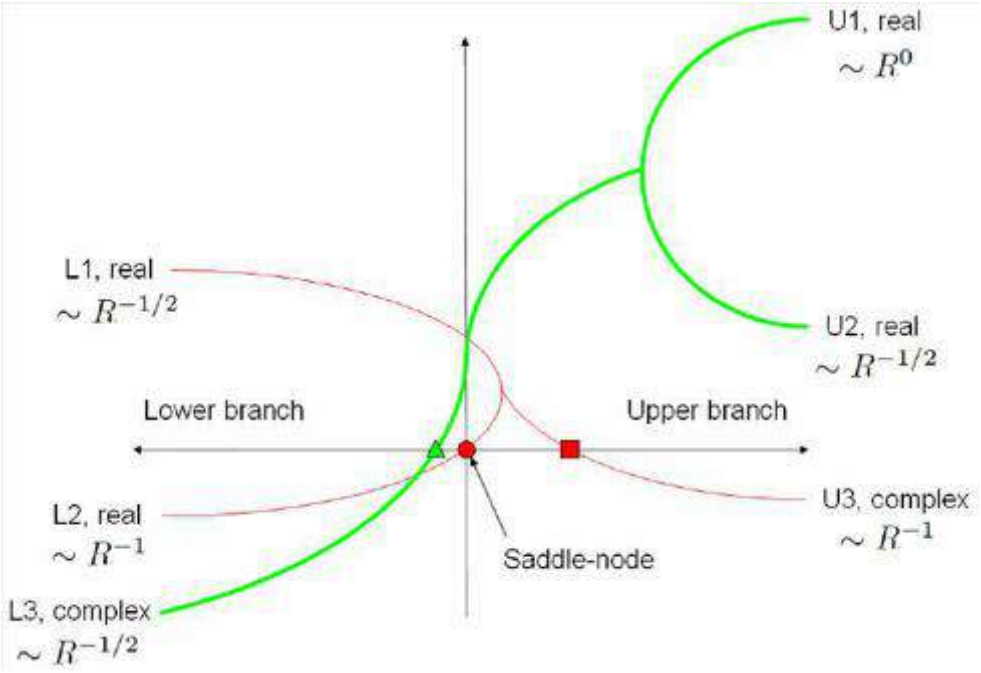

Figure 1: Schematic of the connection of the eigenvalues along the lower and upper branches. The horizontal and vertical axes represents the streamwise wavenumber α and the growth rate σ_r, respectively.

modes occur close to the saddle-node point. The stability classification found explains the results of numerical simulations of shear flows by a number of authors and points to the existence of two time periodic equilibrium states living either on the slow diffusion or edge mode timescales. The predictions of a weakly nonlinear extension of our stability calculation finds solutions closely related to those found by Kalahari and Kida (2001). Since the latter solutions have been found to capture much of the turbulent statistics of Couette flow it appears that the high Reynolds descriptions of time periodic states based on VWI problem might sensibly be used to describe high Reynolds number turbulent flows.

References

[1] DEGUCHI, K. & HALL, P. 2014a The high Reynolds number asymptotic development of nonlinear equilibrium states in plane Couette flow. *J. Fluid Mech.* **750**, 99–112.

[2] DEGUCHI, K. & HALL, P. 2014b Freestream coherent structures in parallel boundary layer flows.*J. Fluid Mech.* **752**, 602–625.

[3] DEGUCHI, K. & HALL, P. 2016 The instability of VWI states. Submitted for publication.

[4] HALL, P. & SHERWIN, S. 2010 Streamwise vortices in shear flows: harbingers of transition and the skeleton of coherent structures. *J. Fluid Mech.* **661**, 178–205.

[5] HALL, P. & SMITH, F. T. 1989 Nonlinear a Tollmien-Schlichting/vortex interaction in boundary layers. *Eur. J. Mech. B/Fluids* **8**(3), 179–205.

[6] HALL, P. & SMITH, F. T. 1990 *Near Planar TS Waves and Longitudinal Vortices in Channel Flow: Nonlinear Interaction and Focussing.* 5–39. Springer.

[7] HALL, P. & SMITH, F. T. 1991 On strongly nonlinear vortex/wave interactions in boundary-layer transition. *J. Fluid Mech.* **227**, 641–666.

[8] KAWAHARA, G. & KIDA, S. 2001 Periodic motion embedded in plane Couette turbulence: regeneration cycle and burst. *J. Fluid Mech.* **449**, 291–300.

[9] NAGATA, M. 1990 Three-dimensional finite-amplitude solutions in plane Couette flow: bifurcation from infinity. *J. Fluid Mech.* **217**, 519–527.

[10] WALEFFE, F. 1997 On a self-sustaining process in shear flows. *Phys. Fluids* **9**, 883–900.

[11] WANG, J., GIBSON, J. F. & WALEFFE, F. 2007 Lower branch coherent states: transition and control. *Phys. Rev. Lett.* **98**, 204501.

UNIVERSAL CRITICAL BEHAVIOR OF THE TRANSITION TO TURBULENCE IN CHANNEL FLOW

Masaki Sano, Keiichi Tamai
Department of Physics, The University of Tokyo, Tokyo, Japan

Summary We identified critical behavior of the transition to turbulence in channel flow. Turbulent domains continuously injected from an inlet ultimately decayed, or in contrast, spread depending on flow rates. Near a transition point, critical behavior was observed. We found that four critical exponents, a universal scaling function and a scaling relation, are all in agreement with the (2+1)-dimensional directed percolation universality class.

INTRODUCTION

Transitions from laminar to turbulent flow have been extensively studied in the past century. Among these studies, the discovery of a well-defined transition to chaos in a fluid heated from below in a small box caused the rewriting of classical textbooks on the onset of turbulence. However, this concerns only temporal disorder. When and how spatio-temporal disorder emerge remains elusive in particular, for flows under shear, such as pipe and channel flows. Is the transition abrupt or continuous? Does it depend on a particular type of perturbation? Are there universal laws in the transition? These fundamental questions have to be revisited. Recently, Hof et al. (1) conducted a series of experiments on a pipe flow and found that the transition can be regarded as a spreading process of a localized turbulent puff created by perturbations that may duplicate or die out indefinitely. Situations are similar for other wall bounded flows. In such flows, the laminar flow becomes turbulent despite its linear stability; laminar states do not break up into turbulent states unless they are invaded by turbulent neighbours due to the stability against infinitesimal perturbations. If the tendency for invasion by a turbulent state increases, the turbulent state will eventually spread over the entire space. It is this behavior that led Pomeau to conjecture that the spatio-temporal intermittency observed at the transition from the laminar flow to turbulence belongs to the directed percolation (DP) universality class (2). DP is a stochastic spreading process of an active (turbulent) state with a single absorbing state, which diverse phenomena such as spreading of epidemics, fires, synchronization, and granular flows potentially belong to. If the transition is continuous and the interaction is short-ranged, universal critical exponents are expected. However, to observe the critical behavior in a pipe flow, if it exists, an extraordinarily long pipe is required. To overcome this difficulty, we chose a quasi-two dimensional channel flow and forced the inlet boundary condition to be active (turbulent) state. It enabled us to study the transition to turbulence as a surface critical phenomena. A clear transition between decay and penetration of the injected turbulent flow was observed. Quantification of the order parameter and the correlation length revealed critical behavior of the transition in channel flow; obtained three independent critical exponents support that the transition to turbulence in channel flow belongs to the DP universality class.

EXPERIMENTAL SETUP

The flow channel has a length of 5880 mm in a streamwise (x) direction, a cross section of 5 mm in depth (the y direction) and 900 mm wide in a spanwise (z) direction. Thus the aspect ratio of the channel was $2352h \times 2h \times 360h$. The flow dynamics in the (x,z) plane were visualized and recorded using a visualization technique and three CCD cameras. Instead of triggering turbulent spots by a local perturbation for each measurement as in the previous experiments, we continuously excited turbulent flow in the buffering box using a grid and injected it at the inlet ($x = 0$).

ORDER PARAMETER

This setup enabled us to attain a steady state measurement of the area fraction of the turbulent region (the turbulent fraction ρ) as a function of x. $\rho(x)$ was estimated by measuring the time fraction occupied by turbulent flow for each of the locations averaged over a long time (about 40 min, 100 times of flow circulation time). $\rho(x)$ seemed to saturate for higher Re and for larger x. Therefore, we measured the turbulent fraction as a function of Re at several distant locations x satisfying $x/h > 1280$. The curves for different positions overlapped, implying that ρ is almost saturated for Re larger than a certain value. Order parameter increased continuously from zero as shown in Fig.1a. Thus we fit by $\rho = \rho_0 \varepsilon^{\beta}$ in the inset of Fig. 1a, where ε is the reduced Reynolds number, $\varepsilon \equiv (Re - Re^c)/Re^c$. We obtained β=0.58(3) and $Re^c = 830(4)$ as the best fit. Non-vanishing order parameter is due to finite size effect as usual.

[a] Corresponding author. Email: sano@phys.s.u-tokyo.ac.jp.

DIVERGENCE OF CORRELATION LENGTH

Critical behavior is characterized by a divergence of the correlation length at the critical point. If the transition from the laminar to turbulent state belongs to the DP universality class, the correlation length of the cluster should reflect this critical nature. In order to test this, we measured a distribution of the durations τ of the laminar state (laminar interval distribution) $N(\tau)$ at fixed downstream locations for $Re > Re^c$. For Re sufficiently close to Re^c, $N(\tau) \sim \tau^{-\mu}$ with $\mu = 1.25(5)$ is obtained. This value is close to the universal exponent in DP, $\mu_\perp^{DP} = 1.204(2)$ which characterizes the scale invariance of critical clusters. We defined the correlation length ξ, by fitting the tail of a complementary cumulative probability, $P(\tau) \equiv \int_\tau^\infty N(t)\mathrm{d}t / \int_0^\infty N(t)\mathrm{d}t$ with an exponential function, $P(\tau) \sim \exp(-\tau/\xi)$. As we approached to Re^c, ξ substantially increases. The correlation length as a function of ε showed a divergence with a power law and saturation at the smallest ε (Fig.1b). We fitted by $\xi \sim \varepsilon^{-\nu}$ with an exponent $\nu = 0.71(5)$ which agrees with $\nu_\perp^{DP} = 0.733(3)$. In addition, we obtained $\nu_\parallel$ by looking at a spatial distribution of turbulent fraction $\rho(x)$. The turbulent fraction showed an exponential decay; $\rho(x) \sim \exp(-x/L)$ for $Re<Re^c$. The decay length L increased near the critical point with a power law, $L \sim |\varepsilon|^{-\nu}$. We obtained $\nu = 1.1(3)$. This value is again close to the critical exponent for the divergence of temporal correlation length, $\nu_\parallel^{DP} = 1.295(6)$. Thus we obtained three independent critical exponents β, $\nu_\perp$, and $\nu_\parallel$ for DP together with the exponent for laminar interval distribution, $\mu_\perp$. which satisfies the universal scaling relation, $\mu_\perp = 2 - \beta/\nu_\perp$. Therefore the results strongly support that the transition belongs to (2+1)-dimensional DP universality class.

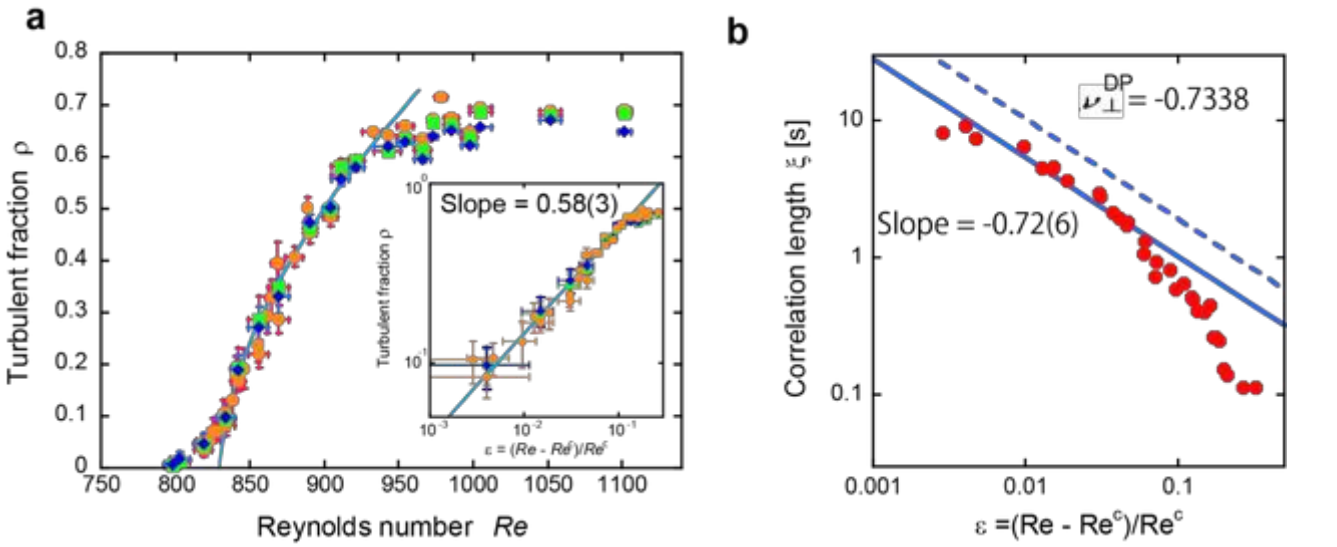

Figure 1, **a**; The turbulent fraction ρ vs. Re is plotted at different downstream locations: $x/h = 1292$ (), $x/h = 1880$ (), and $x/h = 2096$ (). Inset: A log-log plot of ρ as a function of reduced Reynolds number ε. **b**: Correlation length estimated from the tail of laminar length distributions as a function of ε.

CONCLUSIONS

Although larger scale experiments and DNSs are needed in the future, the largest channel flow experiment available at present strongly supports the idea that the transitions to turbulence in shear flows have a universal critical nature of non-equilibrium phase transition, *i.e.*, the transition belongs to the DP universality class.

References

[1] K. Avila, D. Moxey, A. de Lozar, M. Avila, D. Barkley, B. Hof, *Science* **333**, 192 (2011).
[2] Y. Pomeau, *Physica* D **23**, 3 (1986).
[3] K. A. Takeuchi, M. Kuroda, H. Chaté, M. Sano, *Phys. Rev. Lett.* **99**, 234503 (2007), *Phys. Rev.* E **80**, 051116 (2009).
[4] M. Sano, K. Tamai, to appear in *Nature Physics* (2016).

LOCALIZED STRUCTURES ON THE EDGE IN BOUNDARY LAYERS AND THEIR TRACES IN BYPASS TRANSITION

Taras Khapko[1], Tobias Kreilos[2], Philipp Schlatter[1], Yohann Duguet [*3],

Bruno Eckhardt[4,5], and Dan S. Henningson[1]

[1]*Linné FLOW Centre, KTH Mechanics, Royal Institute of Technology, Stockholm, Sweden*

[2]*Emergent Complexity in Physical Systems Laboratory, École Polytechnique Fédérale de Lausanne, Lausanne, Switzerland*

[3]*LIMSI-CNRS, Université Paris-Sud, Orsay, France*

[4]*Fachbereich Physik, Philipps-Universität Marburg, Marburg, Germany*

[5]*J.M. Burgerscentrum, Delft University of Technology, Delft, The Netherlands*

Summary Investigation of the laminar–turbulent separatrix is performed in a boundary-layer flow. Constant homogeneous suction is applied at the wall in order to prevent the spatial growth of the layer, leading to the parallel Asymptotic Suction Boundary Layer (ASBL). Edge tracking is performed in a large computational domain allowing for full spatial localization on the separatrix. The obtained localized structure experiences recurrent dynamics going through calm and bursting phases. During calm phases the structure's active core consists of a single low-speed streak which develops sinuous instabilities leading to a burst in energy. During the burst new streaks are created, with the structure growing in size and its core drifting in both planar directions. The recurrent simple structure observed during calm phases is compared with those seen in the early development of the minimal seed and during bypass transition. The implications on the dynamical systems view of the transition process are discussed.

INTRODUCTION

Lately a stimulating breakthrough occurred in transition to turbulence, when researchers started adopting tools from deterministic chaos theory and dynamical systems, supported by the on-going progress of computer simulations. One of the new concepts arising from these recent developments is the idea of "edge states": nonlinear flow structures living at the dynamical border between laminar and turbulent flow [1]. They are relative attractors within the laminar–turbulent boundary and can be simple objects, like fixed points or periodic orbits, or more complicated chaotic structures. In all cases they serve as an example of simple dynamics in the high-dimensional system. As such they can be used for understanding the mechanisms of the sustained non-trivial flow behavior. In addition, being saddles of the system, they guide the evolution of the flow going towards turbulence.

Recently, this concept was applied to the Blasius boundary-layer flow over a flat plate [2]. However due to the spatial growth of the boundary layer the proper asymptotic dynamics is inaccessible. One way to circumvent this is to apply suction at the plate which counteracts the spatial growth. If the suction is constant and homogeneous the boundary-layer thickness saturates and the associated flow is known as the Asymptotic Suction Boundary Layer (ASBL) [3].

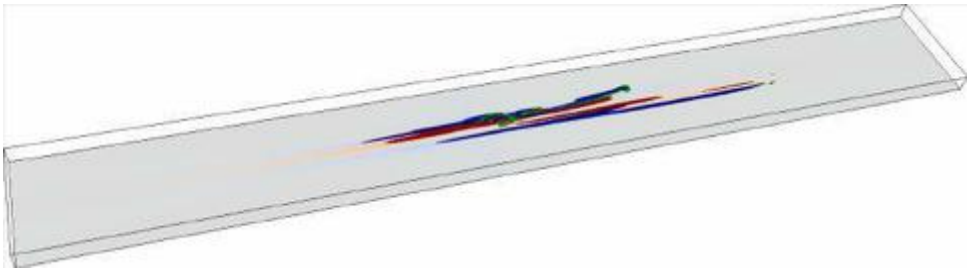

Figure 1: Three-dimensional snapshot of the edge state. Low- (blue) and high-speed (red) streaks are shown with the isosurfaces of the streamwise velocity fluctuations $u' = \pm 0.05$. The vortical structures are shown using the $\lambda_2 = -10^{-4}$ isosurfaces (green). Flow from lower left to upper right. The whole computational domain is shown.

*Corresponding author. Email: duguet@limsi.fr



Figure 2: Top views of the edge state showing the typical structure of the active core during the calm phase. Three independent events are displayed. The same color coding is used as in figure 1, however with higher isolevels ($u' = \pm 0.13$ and $\lambda_2 = -4 \times 10^{-4}$) in order to capture the most energetic parts of the structure. Flow from left to right. Only part of the computational domain is shown.

LOCALIZED EDGE STATES IN ASBL

The parameters for the current study were based on the previous results in the numerical domain of limited size [4]. We perform edge tracking in domain of size $[L_x, L_y, L_z] = [800\delta^*, 15\delta^*, 100\delta^*]$ at $Re = 500$ (defined as the ratio of the free-stream velocity U_∞ to the suction velocity V_S) using the fully spectral code with a DECI awarded allocation, as each flow field has 200 million grid points. Here δ^* is the laminar boundary-layer displacement thickness and together with U_∞ they are used for non-dimensionalization.

The obtained structure resembles a turbulent spot at the initial stages of its growth. It consists of low- and high-speed streaks and vortical structures staggered along to the streaks (see figure 1). Both visual inspection and quantitative analysis confirm the fully localized nature of the state. Its energy oscillates erratically showing no signs of regularization. Hence we conclude that the edge state is chaotic in this set-up. Still, calmer and bursting phases alternating with irregular intervals can be identified, indicating pulsating behavior with recurring dynamics.

In the calm phase the active core of the state consists of a single low-speed streak. It develops sinuous instabilities with two counter-rotating vortices flanking the streak and sustaining it through the lift-up effect. The other streaks slowly decay. The vortices above the active streak grow in strength and start leaning over it. When they cross, a region is created where the fluid is pushed down instead of being lifted up.This leads to the breakdown and to a spanwise drift of the whole structure. The vortices generated in the breakdown process create new low- and high-speed streaks and the cycle is closed.

IMPLICATIONS FOR TRANSITION TO TURBULENCE

The performed edge tracking is a way of mapping out parts of the edge manifold, where the edge can be followed for arbitrary large times. Thus it allows to identify recurrent dynamics and the regions of phase space which are repeatedly visited on the edge. The simple structure in the calm phase was identified as this recurrent structure (see figure 2). Surprisingly, very similar structures are also seen as a part of the trajectory of the minimal seed [5]. Similar structures have also been reported in many studies on transitional boundary layers [6] at the verge of the breakdown leading to creation of turbulent spots, the so-called nucleation events. Thus, it is plausible that in bypass transition (*e.g.* induced by free-stream turbulence) the secondary instability of the streaks can be associated with the approach to the stable manifold of the edge state and its linear instability.

Hence we can adopt the following dynamical systems view on the bypass transition process in boundary layers with disturbances of moderate levels. The perturbations are viewed as a cloud of initial conditions of which some are on the turbulent side of *the stable manifold of the edge state*. The corresponding trajectories approach the localized edge state for a finite time. During the approach (the receptivity process) the perturbation evolves into a low-speed streak, the structure repeatedly seen in the edge state computation. Once the sinuous instability builds up and grows, it leads to a burst of the streak. For the trajectory constrained to the edge, the burst would be followed by a decrease of the energy. However being slightly above, the burst leads to the breakdown into a turbulent spot. Thus the nucleation process of turbulent spots in bypass transition is related to appearances of the edge-type structures which can be used in the understanding and modeling of the whole process.

References

[1] Schneider T. M., Eckhardt B. and Yorke J. A.: Turbulence transition and the edge of chaos in pipe flow. Phys. Rev. Lett. 99:034502, 2007.

[2] Duguet Y., Schlatter P., Henningson D. S. and Eckhardt B.: Self-sustained localized structures in a boundary-layer flow. Phys. Rev. Lett. 108:044501, 2012.

[3] Schlichting H.: Boundary-Layer Theory. McGraw-Hill, New York, 7th edn. edition, 1987

[4] Khapko T., Kreilos T., Schlatter P., Duguet Y. , Eckhardt B., and Henningson D. S.: Localised edge states in the asymptotic suction boundary layer. J. Fluid Mech., 717:R6, 2013.

[5] Duguet Y., Monokrousos A., Brandt L. and Henningson D. S.: Minimal transition thresholds in plane Couette flow. Phys. Fluids 25:084103, 2013.

[6] Schlatter P., Brandt L., De Lange H. C. and Henningson D. S.: On streak breakdown in bypass transition. Phys. Fluids 20:101505, 2008.

TEMPORAL AND SPATIAL INTERMITTENCIES WITHIN NEWTONIAN TURBULENCE

Anubhav Kushwaha[1] and Michael D Graham *[1]
[1]*Department of Chemical and Biological Engineering, University of Wisconsin-Madison, USA*

Summary Direct numerical simulations of a pressure driven turbulent flow are performed in a large rectangular channel. Extreme and moderate drag regimes within turbulence that have earlier been found to exist temporally in minimal channels at low Reynolds numbers have been observed both spatially and temporally in full-size turbulent flows. These intermittent regimes, namely, "hyperactive", "active" and "hibernating" turbulence, display very different structural and statistical features. Using conditional sampling, we identify these intermittent intervals and present the differences between them in terms of simple quantities like mean velocity, wall shear stress and flow structures. By conditionally sampling of the low wall shear stress events in particular, we show that a Newtonian trajectory in large domains occasionally approaches some of the exact coherent states that are characteristic of very low drag in Newtonian flows.

INTRODUCTION

A way of understanding the chaotic dynamics of turbulent flows is to look at the exact coherent states (ECS) of the Navier-Stokes equations. The low-drag events in Newtonian flows resemble a recently-discovered family of ECS [1]. Similar transient behaviour at low Reynolds numbers in minimal channels has also been observed in viscoelastic flows [2]. The objective of this study is to establish whether temporal intermittency in minimal-channel Newtonian flows translates to temporal and spatial intermittencies in large-domain Newtonian flows.

RESULTS AND DISCUSSION

To detect and sample low and high drag events happening locally with time, we measure the instantaneous wall shear stress at a point on a wall. Our criteria for an event is that the wall shear stress (τ_w) at the point must surpass a threshold value and it must stay on the same side of the threshold for a specified minimum time duration. Specifically, for an event to be called hibernation, the wall shear stress must fall below the specified threshold and must last for a duration $t^* > 3$, and for an event to be hyperactive, τ_w must become higher than the corresponding threshold value and, as before, must stay high for $t^* > 3$. Figure 1(a) shows many low wall shear stress events measured at $\mathrm{Re}_\tau = 85$ that satisfy the criteria for hibernation. The beginning of each event shifted to $t^* = 0$. We are calling such low-drag events hibernating turbulence. The ensemble average of all the instantaneous hibernation events is shown as a thick green line. On average the wall shear stress during hibernation falls to a plateau in the time interval $0.7 \leq t^* \leq 2.8$ and is preceded by a sharp peak in the wall shear stress (higher than the mean, $\overline{\tau_w}$) during $-0.8 \leq t^* \leq 0$. Similarly, for hyperactive intervals we select instances when the wall shear stress becomes more than 110% and 120% of the mean and remains higher than the specified threshold for $t^* > 3$ (Figure 1(b)).

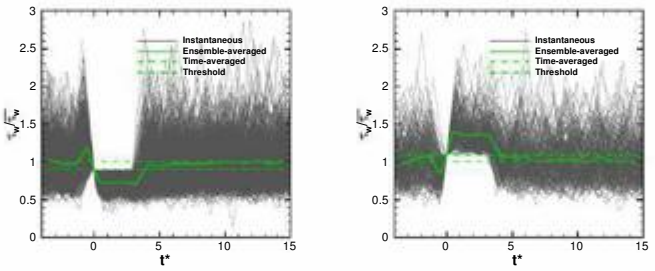

(a) Hibernation, $\tau_w \leq 90\%\overline{\tau_w}$ (b) Hyperactivity, $\tau_w \geq 110\%\overline{\tau_w}$

Figure 1: Instantaneous (thin grey lines) and ensemble-averaged (thick green solid line) wall shear stress before, during and after the intervals of hibernation and hyperactivity at $\mathrm{Re}_\tau = 85$. Here, t^* is the time measured in units of eddy turnover times.

To identify low and high drag regions spatially, we choose a detector function, which is a function of flow properties at the wall or in the fluid region. The detector function is lowpass-filtered and thresholded that results in demarcation of weakly and strongly turbulent areas. The sum of the absolute values of the streamwise wall shear stress and the spanwise derivative of the streamwise velocity is chosen as the detector function, *i.e.*, $D \equiv |\partial U/\partial y|_w + |\partial U/\partial z|_{y^+=15}$.

*Corresponding author. Email: mdgraham@wisc.edu

The filtered signal is then thresholded using Otsu's method. For a given snapshot, we divide the spatially-varying wall shear stress into three classes – low, intermediate and high – and the range for each class is determined by the thresholds obtained from Otsu's method. Note that no time-criterion has been applied to the spatial sampling technique. The result of the edge-detection algorithm is shown in Figure 2. The contours represent the wall shear stress patterns from an instantaneous flow-field at $\mathrm{Re}_\tau = 85$. Solid black line represents the demarcation line between high-drag and intermediate-drag regions and white line separates the intermediate-drag areas from the low-drag areas. A distinct difference between the three regions is observed – areas enclosed by black lines show high wall shear stress and strong fluctuations whereas the areas enclosed by white lines are smooth, local wall shear stress values are low and the variations are small. Regions between red and black lines lie in the intermediate-drag regime.

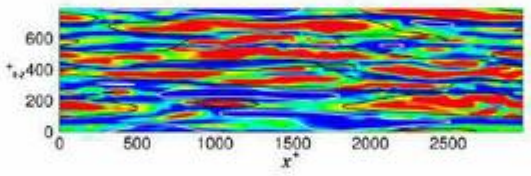

Figure 2: Edges between high- and intermediate-drag regions (black) and between intermediate- and low-drag regions (white). Flow is from left to right.

Conditional mean velocity profiles for hibernating and hyperactive turbulence at $\mathrm{Re}_\tau = 85$ occurring both in time and in space are presented in Figure 3(a). It is observed that low-stress conditional averages from edge-detection scheme (spatial) nearly matches pointwise thresholding results (temporal) – both profiles are shifted upward of the unconditional mean profile and lie close to the Virk MDR asymptote. Similarly, the mean velocity profiles during hyperactivity, both temporal and spatial, lie below the unconditional time-averaged profile. The hibernation profiles in a large domain Newtonian flow also lie close to the lower branch ECS profile near the wall (up to $y^+ \approx 25$) observed in a minimal channel (Figure 3(b)).

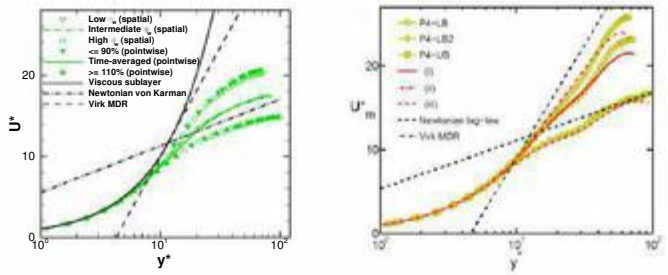

(a) (b)

Figure 3: (a) Unconditional (solid lines) and conditional (symbols) streamwise mean-velocity profiles at $\mathrm{Re}_\tau = 85$. (b) Mean velocity profiles of lower and upper branches ECS (shown in yellow) in Newtonian flows in a minimal channel [1].

CONCLUSIONS

Intermittent excursions towards low and high drag states, that have earlier been found to exist temporally in minimal channels, have also been observed to occur both temporally and spatially in large-domain Newtonian flows. Using conditional sampling and edge-detection techniques, we identified these transient intervals and it was found that the mean near-wall properties and structures of the low drag events in particular resemble some of the lower branch exact coherent states. These low drag regions in time and space can serve as potential targets for drag reduction schemes to reduce energy consumption in flow processes.

References

[1] Park J S, Graham M D: Exact coherent states and connections to turbulent dynamics in minimal channel flow. J. Fluid Mech 782:430-454, 2015.

[2] Xi L, Graham M D: Intermittent dynamics of turbulence hibernation in Newtonian and viscoelastic minimal channel flows. J. Fluid Mech 693:433-472, 2012.

BIFURCATIONS IN ROTATING PLANE COUETTE FLOW AT MODERATE REYNOLDS NUMBERS

Masato Nagata *[1]

[1]*Department of Mechanics, Tianjin University, Tianjin, P. R. China*

Summary Bifurcations in rotating plane Couette flow are investigated when the Reynolds number, R, is relatively small. We clarified the role of the second wavy vortex flow, called Ribbon, in the parameter space. In addition, a new type of tertiary flow with the symmetry classified as $\mathscr{A}_3$ in Nagata (1986) is discovered.

INTRODUCTION

During the past few decades, the problem of plane Couette flow with system rotation has served as a suitable testing ground for comparison between experiments and theories [1,2,3,4,5]. This classical problem is revisited in the current paper in order to gain a new insight into transition to turbulence.

MODEL

We analyze the bifurcation of plane Couette flow subject to a constant spanwise rotation Ω^*, which is governed by the dimensionless Navier-Stokes equations and incompressibility condition,

$$\partial_t \boldsymbol{u} + \boldsymbol{u}\cdot\nabla\boldsymbol{u} + \boldsymbol{\Omega}\times\boldsymbol{u} = -\nabla p + \frac{1}{R}\nabla^2\boldsymbol{u}, \quad \nabla\cdot\boldsymbol{u} = 0, \tag{1}$$

expressed in the rotating frame of reference, where velocity $\boldsymbol{u}$ has components (u, v, w) in the streamwise (x), spanwise (y) and wall-normal (z) directions, respectively, t denotes time and p is a modified pressure that includes the centrifugal force term. All lengths have been scaled by half the fluid depth, D^*, while velocities have been scaled by the translational wall speed V^*. The Reynolds number, $R = V^*D^*/\nu$, with ν denoting the kinematic viscosity, and the rotation number, $\Omega = 2\Omega^*D^*/V^*$, where $\boldsymbol{\Omega} = [0, \Omega, 0]$, have been introduced. The laminar basic flow satisfying no-slip at the wall, $\boldsymbol{u}(z = \pm 1) = \mp 1$, is given by $\boldsymbol{u} = (u_0(z), 0, 0)$, where $u_0(z) = -z$.

NUMERICAL METHODS

We superimpose disturbances on the laminar basic flow. The development of the disturbances is of our interest. A typical physical disturbance component, q, is expressed in the following form,

$$q(x, y, z, t) = \sum_{l=-L}^{L}\sum_{m=-M}^{M}\sum_{n=-N}^{N} q_{lmn}(t)\exp[im\alpha(x - ct) + in\beta y]T_l(z), \tag{2}$$

where m and n are integers, α and β are the wavenumbers in the streamwise and the spanwise directions, respectively, c is the wavespeed and $T_l(z)$'s denote modified Chebyshev polynomials which satisfy the no-slip condition. Upon using the orthogonality property of the Fourier series, we discretize the equations at a selected wall-normal collocation points. The resulting algebraic equations for the component amplitudes, q_{lmn}'s, and the wave speed, c, are solved by Newton method. It is found c is zero along all the solution branches presented in this paper,

RESULT

It is known that rotating plane Couette flow becomes unstable to streamwise-independent disturbances and, as a result, two streamwise-independent secondary flows, one from the first instability mode [1] and the other from the second instability mode [2], bifurcate. We call these secondary flows TV_1 and TV_2, respectively. Furthermore, it is known that the first and second tertiary flows in the form of three-dimensional wavy vortex bifurcate from TV_1 and TV_2, respectively. We call these tertiary flows WVF and Ribbon. We find that WVF, normally exists along a singly-connected branch, has a window of non-existence for some wavenumber pair (α, β) as the rotation number, Ω, varies and this non-existence window of WVF is filled by Ribbon. In this particular case, three-dimensional Ribbon bifurcates directly from the basic laminar state, as a secondary solution, with its two bifurcation points on the basic state, one at a small Ω end and the other at a larger Ω end (see Figure 1(a) and (b)). It is found that in the limit of small α, Ribbon coincides with WVF, and that, as α is increased, the bifurcation point at the small Ω moves toward a larger Ω value, until it collide with the bifurcation point of TV_2. The bifurcation point of Ribbon, then, *climb up* the TV_2 branch, so that the Ribbon is now recognised as the second tertiary flow (see Figure 1(c)).

*Corresponding author. Email: nagata@kuaero.kyoto-u.ac.jp

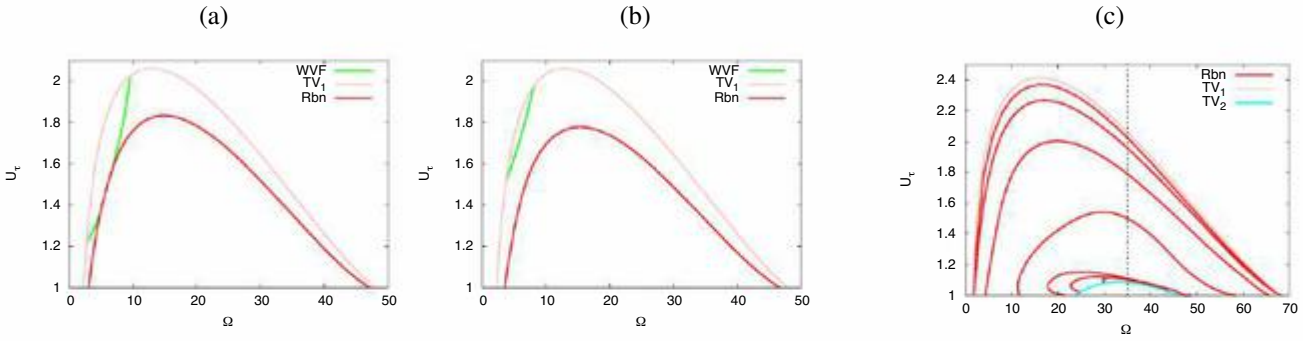

Figure 1: (a) and (b): Bifurcation diagram along the Ω-axis for TV_1 (thin pink), WVF (green) and Ribbon (red). The nonlinear τ $R = 50$ and $\beta = 1.5$. (a):The non-existence window of WVF at around $\Omega = 5$ filled by Ribbon. $\alpha = 0.20$. (b): Singly-connected WVF. $\alpha = 0.25$. (c): The branches of Ribbon as α . . $_2$ (cyaan).

Further, we investigate Ribbon for a larger R. Ribbon bifurcates from TV_2 at a smaller Ω-end as before when $R = 160$ Ω, although it is hardly seen in the figure, we confirm that it now starts from a new solution branch with the symmetry, $\mathscr{A}_3$, classified in [1]. The new solution branch of $\mathscr{A}_3$ bifurcates from

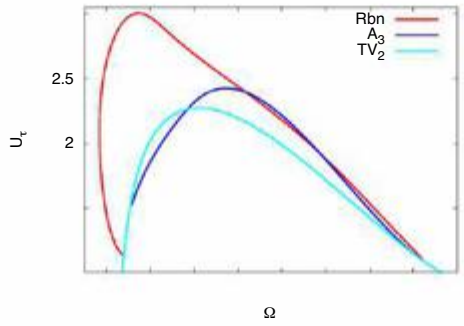

Figure 2: Bifurcation diagram along the Ω-axis for TV_2 (cyaan), $\mathscr{A}_3$ (blue) and Ribbon (red). $R = 160$. $(\alpha, \beta) = (0.8, 1.5)$.

CONCLUSIONS

In addition to the conventional two states, TV_1 and WVF, we are able to identify three flow states, TV_2, Ribbon and $\mathscr{A}_3$, at a high rotation rate. The coexistence of the total five flow states may play an important role to guide the flow into a complicated three-dimensional state, such as called Braided or Spaghetti state, which has not been resolved completely [3,4,5].

References

[1] Nagata M.: Bifurcations in Couette flow between almost corotating cylinders. J. Fluid Mech 169:229-250, 1986.

[2] Nagata M.: A note on the mirror-symmetric coherent structure in plane Couette flow. J. Fluid Mech 727:R1-8, 2013.

[3] Tsukahara T., Tillmark N., Alfredsson P. H.: Flow regimes in plane Couette flow with system rotation. J. Fluid Mech 648:5-33, 2010.

[4] Suryadi A. Tillmark N., Alfredsson P. H.: Velocity measurements of streamwise roll cells in rotating plane Couette flow. Exp. Fluids 15 (11):1617, 2013.

[5] Daly C. A., Schneider T. M., Schlatter P., Peake N.: Secondary instability and tertiary states in rotating plane Couette flow. J. Fluid Mech 781:27-61, 2014.

EFFECTS OF DRAG-REDUCING POLYMERS ON THE TRANSIENT DEVELOPMENT OF TURBULENT COHERENT STRUCTURES

Xue Bai[1] and Li Xi *[1]
[1]*Department of Chemical Engineering, McMaster University, Hamilton, Ontario, Canada*

Summary Drag-reducing polymers have profound impact on the dynamics of turbulence, not only in the statistically-converged stage but also in its transient development. Understanding of the latter is essential for solving all major remaining problems in viscoelastic turbulence. Direct numerical simulation is used to study the transient growth of the laminar-turbulent edge state into full turbulence and comparison is made between Newtonian and viscoelastic fluid flows. Polymers are found to suppress turbulence growth throughout the process. Inspection of flow fields further reveals a different pattern of turbulence development after polymers are introduced.

INTRODUCTION

Flexible long-chain polymer additives are known to cause drastic changes in flow turbulence, including significant reduction in its friction drag [1] and complex behaviors during the laminar-turbulent (L-T) transition [2]. Recent advances indicate that major unsolved problems in viscoelastic turbulence can all be linked to the dynamics in the L-T transition region [3, 4, 5, 6]. Most notably, the edge state – an asymptotic saddle state on the L-T boundary [7, 8] – was found to have invariant flow statistics with increasing polymer elasticity [4, 6], explaining the existence of a universal upper bound for polymer-induced drag reduction (DR) – the well-known puzzle of maximum drag reduction (MDR) [1]. Specific solutions responsible for MDR are yet to be identified, prompting us to shift our attention to the state-space region between the edge state and the turbulent basin. Better knowledge of the dynamics in the region, especially polymer effects thereon, is also the key to solving other important problems such as the transition mechanism of viscoelastic fluids and onset criterion of DR.

Using the edge state (perturbed by numerical errors only) as the initial condition, direct numerical simulation (DNS) is used here to track the growth of a marginal turbulent spot into full turbulence. Newtonian and viscoelastic simulations are compared to study the polymer effects. We focus on a minimal channel flow (720 and 230 wall units in streamwise and spanwise directions, respectively) and a moderate $\mathrm{Re}_\tau = 84.85$; viscoelastic simulation was performed with $\mathrm{Wi} = 40$ (Wi, Weissenberg number, is the product of polymer relaxation time and wall shear rate; $\mathrm{Wi} \gg 1$ indicates strong polymer elasticity). Details of the simulation system and numerical procedures are found in recent publications [9, 6].

RESULTS

State-space trajectories of the process is projected using various quantities of interest and shown in Fig. 1. Fig. 1(a) focuses on global statistics: bulk-average turbulent kinetic energy (TKE) and velocity (U_{bulk}). Turbulence growth in both Newtonian and viscoelastic systems starts with a spike in TKE, which is followed by a dip then a steady climb toward the magnitude of turbulent basin; U_{bulk} drastically decreases during the process. In our recent study [6], it became clear that quantities directly measuring near-wall turbulent activities – in particular, the peak value in the Reynolds shear stress (RSS) profile $|\langle v_x^* v_y^* \rangle|_{\max}$ and log-law slope $A^* \equiv y^*(dU_m^*/dy^*)$ measured at $y^* = 25$, A_{25}^* – more clearly reflects the dynamics of near-walls structures. (Here, superscript "*" indicates quantities in turbulent inner units based on instantaneous wall shear stress [3, 10]; definition of A^* comes from a log-law approximation of mean velocity profiles $U_m^* = A^* \ln y^* + B^*$.) Projections using these variables are shown in Fig. 1(b). For both Newtonian and viscoelastic cases, turbulence growth starts with a massive increase of RSS, which proceeds the growth of TKE: by the time TKE reaches the initial spike (instant B for Newtonian and instant E for viscoelastic), the RSS has already dropped down to magnitudes typical of the turbulent basin.

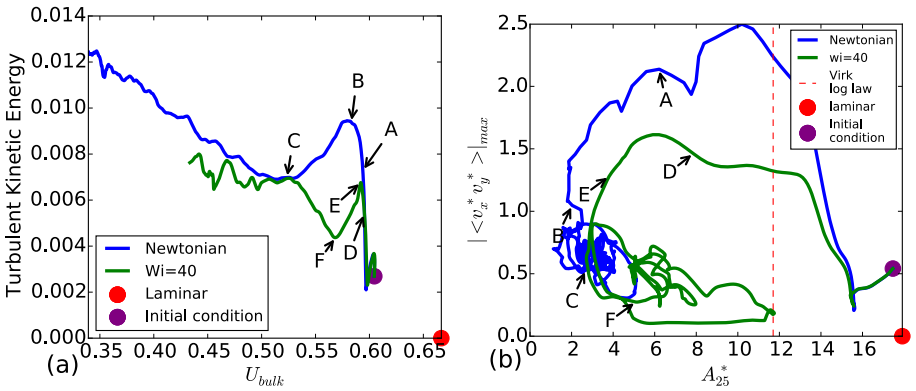

Figure 1: State-space projections of dynamic trajectories initiated from the edge state: (a) TKE vs. U_{bulk}; (b) peak value of the RSS profile vs. log-law slope at $y^* = 25$ – A_{25}^* (dashed line marks $A_{\mathrm{MDR}}^* = 11.7$).

*Corresponding author. Email: xili@mcmaster.ca

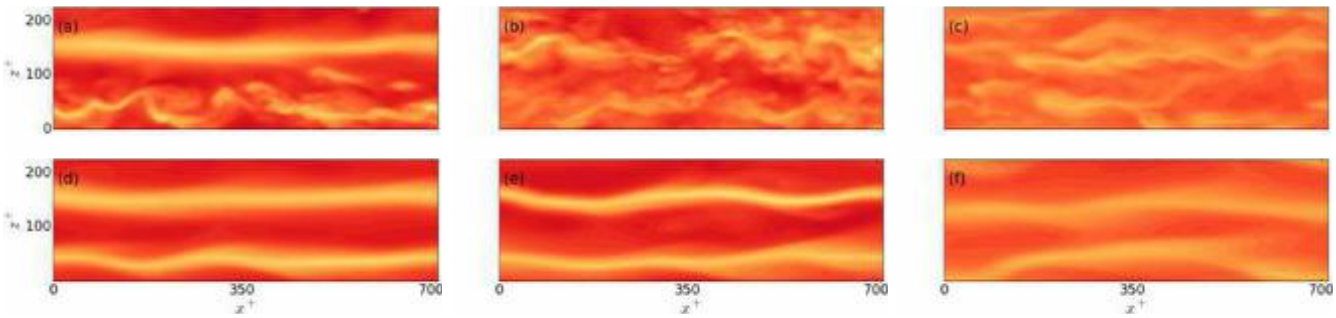

Figure 2: Distribution of v_x at $y^+ = 25$: (a)-(c) correspond to Newtonian instants A-C, and (d)-(f) correspond to viscoelastic instants D-F (instants defined in Fig 1). The color scale ranges from yellow for 0 to red for 1.

The overall picture arising from Figs 1(a)&(b) is that with a minute perturbation, the edge state, which takes form of a localized turbulent spot [6], quickly grows into a structure with much stronger turbulent activity, whose RSS is even higher than that of the turbulent basin. As RSS of this particular structure decays to typical values of the turbulent basin, its disturbance spreads across the domain, causing the spike in TKE and drop of U_{bulk}. Growth at the global scale (Fig 1(a)) takes much longer time, which does not converge in the 1500-time-unit (TU) period shown. Meanwhile, during the same time period, the initial structure has already converged to the destination state (Fig 1(b)). Fluctuations afterwards reflect the intermittent dynamics of self-sustaining turbulent cycles. In particular, for the viscoelastic case, these fluctuations lead to recurrent visits toward the direction of the edge state, with A_{25}^* occasionally approaching the magnitude of MDR. This corresponds to the so-called hibernating turbulence, a type of MDR-like states becoming more exposed as Wi increases [3, 10].

Polymer stress acts as a restraining force and inhibits the development of both the initial structure and globle turbulence, with lower TKE and RSS observed during the whole growth stage. Somewhat surprisingly, mean velocity – measured by A_{25}^* in Fig. 1(b) – of the viscoelastic case drops more rapidly despite the lower RSS. This indicates that turbulent fluctuation is no longer the only means through which energy is extracted from the mean flow. Indeed, we found that the conversion rate of mechanical energy to polymer elastic energy is positive throughout the growth stage. This energy is not returned to the flow motion until turbulent basin is reached.

Contour plots of streamwise velocity, of both Newtonian and viscoelastic cases, are shown in Fig. 2 for three representative instants: before, at, and after the TKE peak in Fig. 1. Note that the edge state flow field (not shown here) is dominated by a pair of smooth and elongated low-speed streaks [6]. In the Newtonian case, the initial perturbation first leads to the breakdown of one of the streaks (Fig. 2(a)). When TKE reaches the peak value (Fig. 2(b)), both streaks have disappeared and are replaced by high-density turbulent motions: short irregular streaks with strong streamwise variations. The final instant has similar irregular patterns with lower intensity. By contrast, the viscoelastic case retained the double-streak configuration for the whole period (Figs. 2(d)-(e)). Even at the TKE peak (Fig. 2(e)), the streaks are distorted in shape but do not break into smaller structures. Regulated and elongated coherent structures are now increasingly associated with turbulent states with weak activity and low drag [6]. Our observation here clearly indicates a qualitative change in the turbulent growth mechanism of viscoelastic fluids.

CONCLUSIONS

Starting from a marginal turbulent spot, an infinitesimal perturbation first triggers the growth of its turbulent intensity, which then propagates across the domain toward full-scale turbulence. Polymer additives suppress the growth of turbulent structures throughout the process, during which energy is extracted from the flow to the polymers. Different transition pathways are observed in Newtonian and viscoelastic flows: development of Newtonian turbulence goes through a sharp breakdown of coherent structures whereas for viscoelastic systems the changes are more continuous.

References

[1] Virk, P. S. *AIChE J.* **1975**, *21*, 625–656.
[2] Samanta, D.; Dubief, Y.; Holzner, M.; Schäfer, C.; Morozov, A. N.; Wagner, C.; Hof, B. *Proc. Natl. Acad. Sci. U. S. A.* **2013**, *110*, 10557–100562.
[3] Xi, L.; Graham, M. D. *Phys. Rev. Lett.* **2010**, *104*, 218301.
[4] Xi, L.; Graham, M. D. *Phys. Rev. Lett.* **2012**, *108*, 028301.
[5] Graham, M. D. *Phys. Fluids* **2014**, *26*, 101301.
[6] Xi, L.; Bai, X. **2015**; submitted.
[7] Skufca, J. D.; Yorke, J. A.; Eckhardt, B. *Phys. Rev. Lett.* **2006**, *96*, 174101.
[8] Schneider, T. M.; Eckhardt, B. *Chaos* **2006**, *16*, 041103.
[9] Xi, L.; Graham, M. D. *J. Fluid Mech.* **2010**, *647*, 421–452.
[10] Xi, L.; Graham, M. D. *J. Fluid Mech.* **2012**, *693*, 433–472.

THE ROLE OF ELASTO-INERTIAL TURBULENCE ON CHANNEL FLOW DRAG

Yves Dubief *[1], Samir Sid[2], and Vincent E. Terrapon[2]
[1]*Department of Mechanical Engineering, University of Vermont, Burlington, Vermont, USA*
[2]*Department of Aerospace and Mechanical Engineering, University of Liege, Liege, Belgium*

Summary The role of Elasto-Inertial Turbulence (EIT) on the bounds of friction drag is investigated in channel flows from subcritical to moderate Reynolds numbers. EIT is a newly discovered state of turbulence emerging from self-sustaining interactions between polymer dynamics and velocity perturbations in parallel shear flows. At low Reynolds numbers, EIT creates an increase in friction drag. Beyond the critical Reynolds number for Newtonian flows, EIT becomes the lower bound of the friction drag of the Maximum Drag Reduction (MDR) state. The drag reduction properties of polymer control the upper bound of MDR.

INTRODUCTION

Elasto-Inertial Turbulence (EIT) [1] is a recently discovered new state of turbulence, where interactions between inertia and elastic effects can sustain a turbulence-like state in channel and pipe flows at Reynolds numbers much lower than the critical Reynolds at which Newtonian flows undergo a transition from laminar to turbulent state. The structure of EIT[2, 3] consists of thin sheets of stretched polymers that are tilted upward by the mean shear and produce spanwise coherent flow structures by opposition to the quasi-longitudinal vortices observed in Newtonian wall turbulence (See Fig. **??**). The proposition investigated here is that EIT is the bounding state preventing a flow with polymer additives from relaminarization.

EQUATIONS

The mathematical nature of the transport equations solved in the present direct numerical simulations is of critical importance for the understanding of EIT. The momentum is transported by the Navier-Stokes equation modified to account for the viscoelastic stress:

$$\partial_t \mathbf{u} + (\mathbf{u}\cdot\boldsymbol{\nabla})\mathbf{u} = -\boldsymbol{\nabla} p + \beta Re^{-1}\nabla^2\mathbf{u} + (1-\beta)Re^{-1}\boldsymbol{\nabla}\cdot\mathbf{T}\,, \tag{1}$$

where β is the ratio of the solvent viscosity to the zero-shear viscosity of the polymer solution and $\mathbf{T}$ is the polymer stress tensor defined as:

$$\mathbf{T} = Wi^{-1}\left(f(trace(\mathbf{C}))\mathbf{C} - \mathbf{I}\right)\,. \tag{2}$$

The non dimensional Weissenberg number Wi is the ratio of the polymer solution time relaxation to a relevant flow time scale. The conformation tensor $\mathbf{C}$ is the tensorial product of the components of the end-to-end vector for a polymer molecule, phased-average over a large ensemble of molecules. The Peterlin function $f(r) = \left(1 - r/L^2\right)^{-1}$ describes the restoring spring force that polymers experience when stretched. L is the normalized polymer length. The transport equation for the conformation tensor,

$$\partial_t \mathbf{C} + (\mathbf{u}\cdot\boldsymbol{\nabla})\mathbf{C} = \mathbf{C}\cdot(\boldsymbol{\nabla}\mathbf{u}) + (\boldsymbol{\nabla}\mathbf{u})\cdot\mathbf{C}^T - \mathbf{T} + (ReSc)^{-1}\nabla^2\mathbf{C} \tag{3}$$

includes on the right hand side, the stretching of polymer molecules by the flow (first two terms), the restoring spring force (third term) and a diffusion term governed by the Schmidt number Sc. This system of equations (supplemented by $\boldsymbol{\nabla}\cdot\mathbf{u} = 0$ constitutes the FENE-P (Finite Elastic Non-linear Extensibility-Peterlin) model commonly used in the direct numerical simulation of polymer flows. Note that the derivation of the FENE-P model requires $Sc \to \infty$.

As explained in [4] (where the numerical method used here is also described), A time scale analysis of the right-hand of Eq. (3), for $Sc \to \infty$ reveals that polymer stretch on the time scale of the flow (first term) and recoil on time scale larger than the Kolmogorov scale, as stipulated by Lumley [5]. Both terms are local, with no diffusion process. On the left hand side, the nonlinear advection term, generates small scales if $Sc \to \infty$. A parallel can be made between Eq. (3) and the small scale dynamics of passive scalar [6, 7]. In the following, a numerical experiment investigates the effect of Sc on the existence of EIT.

OBSERVATION

Using direct numerical simulation in periodic 2D and 3D channel flows, the existence of EIT was established for Reynolds numbers as low as 10, based on the bulk velocity and the channel height. Here EIT was found to arise from a variety of initial perturbations including spatial variation of blowing and suction at the wall over a finite period of time and superimposition of random noise. The increase in the coefficient of drag and deviation from laminar is shown in Fig. 1a for the lowest

*Corresponding author. Email: ydubief@uvm.edu

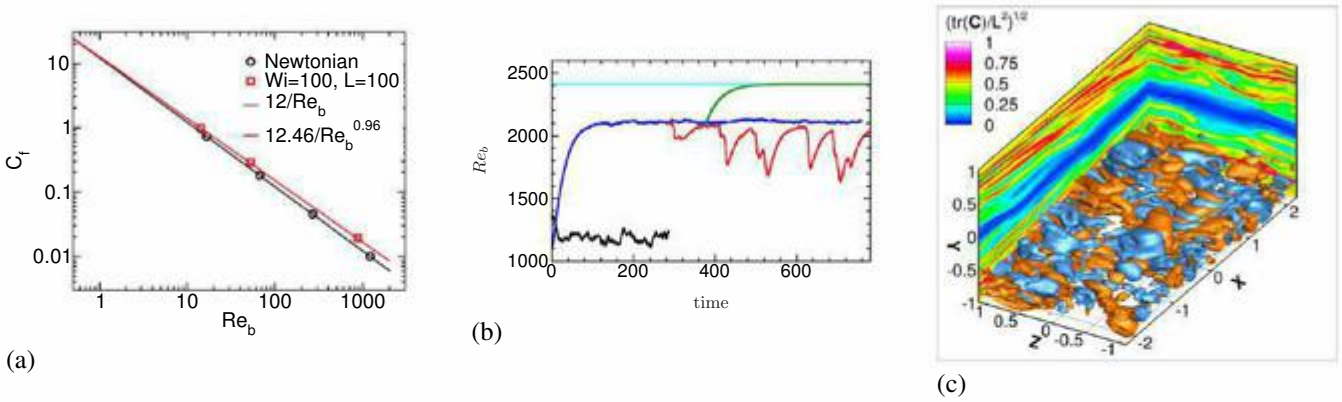

(a) (b) (c)

Figure 1: 1a: Coefficient of friction in a 2D channel as a function of the Reynolds number based on the bulk velocity and the full heigh of the channel. (1b) Time history of the bulk Reynolds number for the simulation of [8] constant pressure-gradient minimal flow unit for $Sc \to \infty$ and $Wi_\tau = 400$ (blue), $Sc \to \infty$ and $Wi_\tau = 40$ (red), $Sc = 0.3$ and $Wi_\tau = 40$ (green). The black and cyan lines show the turbulent and laminar bulk Reynolds numbers, respectively. 1c: Flow visualization of EIT at $Wi_\tau = 40$. The orange and blue isosurfaces show positive and negative regions of the second invariant of the velocity gradient tensor Q. The side panels show contours of the polymer extension. The flow is from the left lower corner to the upper right corner.

simulation. EIT was simulated for very long period of times, up to 500 flow-through time, and no decay was observed in the space-averaged turbulent kinetic energy.

In our numerical experiment, we reproduce the minimal flow unit simulation of [8], where $Sc = 0.3$ to 0.5 was used. Fig. 1b shows that small Sc leads to a relaminarization of the flow, as observed by [8] for $Wi_\tau > 31$ (here the Weissenberg number is normalized by the wall shear, equivalent to the Kolmogorov scale). Our simulations at $Sc \to \infty$ for $Wi_\tau = 40$ and 400 demonstrates that the flow does not become laminar, a snapshot of which is depicted in Fig. 1c. The spanwise, cylindrical-looking structures of the regions of positive and negative Q (second invariant of the velocity gradient tensor) are a distinct feature of EIT. As the Weissenberg number increases, the drag becomes quasi steady and the flow structure remains as shown in Fig. 1c. These simulations demonstrate that the addition of a diffusion term with low Sc number filters out the dynamics of EIT. A crucial component of EIT is therefore small scale, since EIT simulation requires $Sc \gg 1$ and numerical resolution much finer than for an equivalent Newtonian flow. Our more recent investigation (not shown here) suggest that EIT is driven by sub-Kolmogorov time scales but not necessarily sub-Kolmogorov length scales. Simulations in larger computational domains and Reynolds numbers, demonstrate that EIT is present at MDR, even in systems that are intermittent, i.e. where the drag oscillates between a low (but not laminar) and a high drag (not fully turbulent) state.

CONCLUSIONS

This abstract shows only a fraction of the body of evidence supporting that EIT is the bound on the friction drag of MDR. For any large Wi, the flow can oscillate between two states: EIT (low drag state) and the state at which the polymer drag reduction mechanism is at its peak efficiency (high drag). Even at the high drag state, we observe the present of EIT structures. In summary, MDR is not a Newtonian state as previously thought.

References

[1] Samanta D., Dubief Y., Holzner M., Schäfer C., Morozov A.N., Wagner C., Hof B.: PNAS 110(26):10557–10562, 2013.
[2] Dubief Y., Terrapon V.E., Soria J.:Phys. Fluids 25(11):110817, 2013.
[3] Terrapon V.E., Dubief Y., Soria J.: J of Turbulence 16(1):26–43,2014.
[4] Dubief Y., Terrapon V.E., White C.M., Shaqfeh E.S.G, Moin, P., Lele S.K.: Flow, Turbulence and Combustion 74(4):311–329, 2005
[5] Lumley J.L.: Ann. Rev. Fluid Mech. 1(1):367–384, 1969.
[6] Batchelor G. K.: J. Fluid Mech. 5(1):113-133, 1959.
[7] Batchelor G. K., Howells,I. D., Townsend,A. A.: J. Fluid Mech. 5(1):134-139, 1959.
[8] Xi L., Graham M.D.: Phys. Rev. Lett. 104(21):301, 2010.

EXACT INVARIANT SOLUTIONS FOR COHERENT TURBULENT MOTIONS IN COUETTE AND POISEUILLE FLOWS

Subhandu Rawat[1], Carlo Cossu *[1], and François Rincon[2]
[1]*Institut de Mécanique des Fluides de Toulouse (IMFT), Toulouse, France*
[2]*Institut de Recherche en Planétologie et Astrophysique (IRAP), Toulouse, France*

Summary The dynamical systems approach recently applied to understand subcritical transitions in wall-bounded shear flows is combined with the use of large-eddy simulations to investigate the nature of large-scale coherent motions in turbulent Couette and Poiseuille flows. Exact invariant solutions of the filtered Navier-Stokes (LES) equations are computed by using the Smagorinsky model to parametrize small-scale motions. These solutions can be continued into exact solutions of the Navier-Stokes equations therefore providing a bridge between coherent large-scale motions in wall-bounded fully developed turbulent flows and invariant solutions appearing in transitional flows.

BACKGROUND

The understanding of subcritical transition in wall-bounded shear flows has been dramatically improved by the computation and the analysis of invariant solutions of the Navier-Stokes equations. These solutions, whose existence is necessary for subcritical transition, are thought to provide the skeleton of turbulent motions, at least up to moderate transitional Reynolds numbers. When the Reynolds number is increased, however, additional invariant solutions appear and their nature can also become increasingly complex both in phase space and in physical space. It is therefore not clear that turbulent motions at high Reynolds numbers could be approximated with a reasonable number of invariant solutions of the Navier-Stokes equations.

In order to keep the number of degrees of freedom reasonable and to simplify the dynamics even at high Reynolds numbers, invariant solutions are computed for the *filtered* Navier-Stokes equations. Subgrid-scale motions are modelled by using the Smagorinsky eddy viscosity $\nu_t = D(C_s\overline{\Delta})^2\overline{\mathcal{S}}$ where C_s is the Smagorinsky constant, $\overline{\Delta}$ is the average mean grid spacing, $\overline{\mathcal{S}}$ is the norm of the the rate of strain tensor associated to the filtered velocity and $D(y^+)$ is a standard wall damping function. The reference value $C_s = 0.05$ provides the best *a posteriori* performance. Recent investigations [1, 2, 3] have shown that coherent self-sustained large-scale motions can be isolated by moderately increasing C_s above its reference value in order to artificially quench active processes at smaller scales in fully developed turbulent flows. When computing invariant solutions the Smagorinsky constant is therefore used as a continuation parameter, in addition to the Reynolds number. Furthermore, solutions of the Navier-Stokes equations can be retrieved by setting $C_s = 0$. A modified Newton-Krylov method based on time-marching integrations of the filtered equations (LES) is used to compute steady and travelling wave solutions of the filtered equations.

RESULTS

We first consider plane Couette flow in a horizontally periodic domain having the same size of turbulent large-scale motions $L_x \times L_z = 10.9h \times 5.5h$ (where h is the half-width of the channel). The edge state of coherent large-scale motions is computed, at $Re = 750$ (roughly twice the transitional Reynolds number) and $C_s = 0.14$ (overdamped simulation), by edge-tracking and is found to be a non-trivial lower branch exact steady solution of the filtered equations. By continuation to higher values of C_s it is found that the computed edge state is connected to an upper branch of solutions via a saddle-node bifurcation (see figure 1). Upper branch solutions of the filtered equations are computed up to $Re = 2150$ using specific paths in the $Re - C_s$ parameter plane (see figure 1). These solutions can be connected to Navier-Stokes solutions by continuation to $C_s = 0$, where it is found that they belong to the Nagata-Clever-Busse-Waleffe branch of solutions. We next consider plane Poiseuille flow where a recently computed [4] multi-streaks travelling-wave solution of the Navier-Stokes equations ($C_s = 0$), computed in the periodic domain $L_x \times L_z = 2\pi h \times 5.5h$, is continued from $C_s = 0$ to $C_s = 0.05$ at $Re = 2000$.

The exact solutions consist of a combination of quasi-streamwise vortices and streaks (see figure 2) which, on average, self-sustain via a coherent self-sustained process, as discussed in [1, 2, 3]. The computed 'exact' solutions of the filtered (LES) equations take into account the effect of small scales but only through their averaged effect. This approach makes possible to compute steady coherent solutions despite the fact that motions at smaller scale are unsteady and therefore focus on the relevant dynamics of the large-scale coherent solutions without the complications associated to smaller-scales motions. The spatial and *Re* dependence of the eddy viscosity associated with the averaged (residual) small-scale motions is naturally embedded in the computed solutions (see figure 2).

*Corresponding author. Email: carlo.cossu@imft.fr

References

[1] Hwang Y., Cossu C. : Self-sustained process at large scales in turbulent channel flow. *Phys. Rev. Lett.*, 105:044505, 2010.

[2] Hwang Y., Cossu C. : Self-sustained processes in the logarithmic layer of turbulent channel flows. *Phys. Fluids*, 23:061702, 2011.

[3] Rawat S., Cossu C., Hwang Y., Rincon S. : On the self-sustained nature of large-scale motions in turbulent Couette flow. *J. Fluid Mech.*, 782:515–540, 2015.

[4] Rawat S., Cossu C., Rincon S. : Travelling-wave solutions bifurcating from relative periodic orbits in plane Poiseuille flow. *ArXiv*-1601:01227v1, 2016.

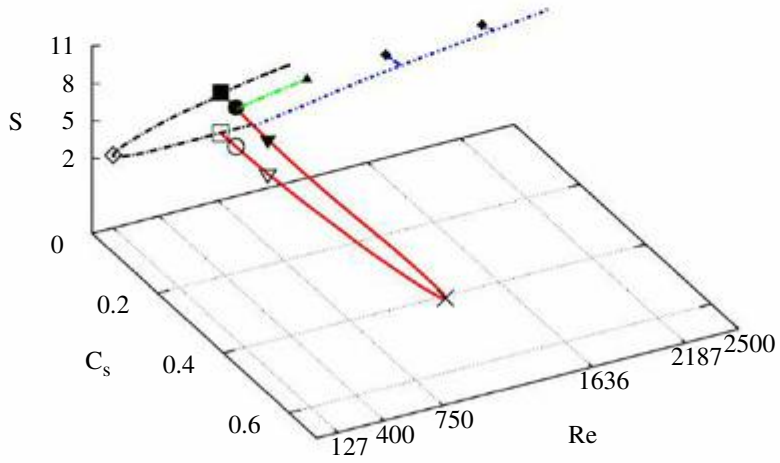

Figure 1: Continuation paths of the steady solutions of the filtered equations (LES) for plane Couette flow. The C_s continuation in C_s at $Re = 750$ (red line) shows how upper-branch solutions can be accessed in this way. Continuation to $C_s = 0$ and then in Re (black line, dashed) show that solutions continued from the turbulent case (square symbols) belong to the Nagata-Busse-Clever-Waleffe branch of Navier-Stokes solutions. Coherent steady solutions at higher Reynolds numbers are found by first continuing the solutions obtained for $C_s = 0.1$ to higher Re (blue line, dashed-dotted) and then reducing C_s.

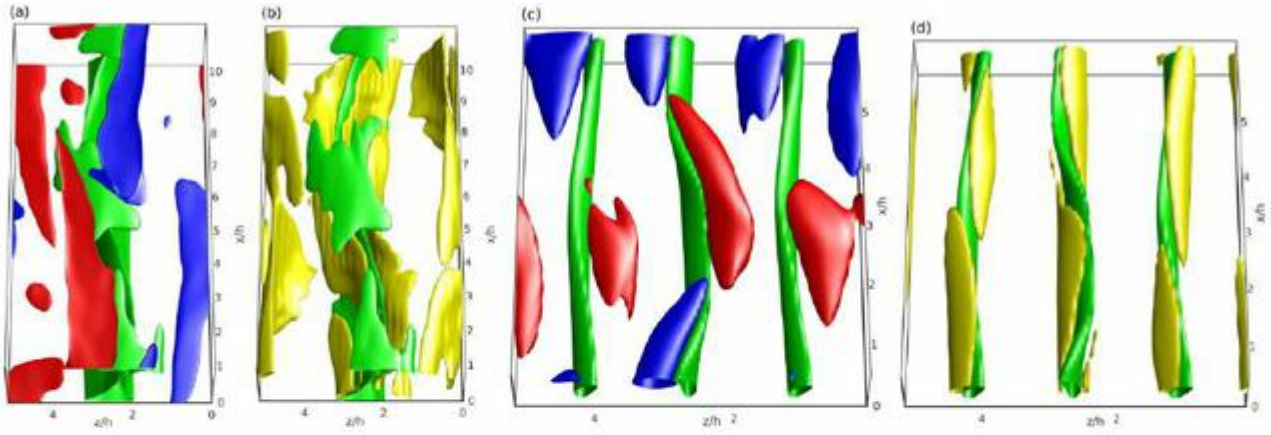

Figure 2: Visualisation of the upper branch solutions of the filtered equations (LES) obtained in plane Couette ($Re = 2150$, $C_s = 0.05$, steady solution, panels a and b) and Poiseuille ($Re = 2000$, $C_s = 0.05$, travelling-wave solution, panels c and d) flow. Panels a and c represent the large-scale coherent (i.e. filtered) streaks (green) and quasi-streamwise vorticity (blue if negative, red if positive) while panels b and d report the relative eddy-viscosity ν_t/ν associated to the residual small-scale motions.

SPATIO-TEMPORAL EVOLUTION OF ISOLATED TURBULENT BANDS IN CHANNEL FLOWS

Jianzhou Lu, Jianjun Tao[a)]
CAPT-HEDPS, SKLTCS, Department of Mechanics and Engineering Science, College of Engineering, Peking University, China

Summary In order to study the natural evolution of a turbulent band without being affected by its nearby disordered patches or domain boundaries in plane-Couette flow, an individual isolated turbulent band in a large computational domain is used as the initial disturbance. It is shown that at Re=340 the turbulent band doesn't grow remarkably in its tangential direction as the oblique extension found in plane-Poiseuille flow, but broadens in its transverse direction. With the increase of the band width, band splitting occurs.

INTRODUCTION

Transition to turbulence in linearly stable flows has remained unsolved over a century. Recent numerical and experimental investigations revealed that the splitting of localized turbulent patches plays an important role during the subcritical transition of Hagen-Poiseuille flow (HPF) [1]. Simulations in a tilted long narrow domain showed that the individual turbulent bands or stripes in plane-Couette flow (PCF) were transient as puffs in HPF, while it was found in simulations with large computational domains that the isolated turbulent band of plane-Poiseuille flow (PPF) could survive and continue to obliquely extend until the boundary influence couldn't be ignored. In simulations of PCF with a large computational domain, initial localized perturbations were found to develop to turbulent bands in a zigzag manner [4]. Due to the interactions among these bands and disturbance residues, it is difficult to examine and distinguish a clear splitting process. Considering that different tilt angles of the narrow domain may lead to different transition scenarios [5] and the artificial periodic boundaries may change the real story of the splitting behaviour, it is necessary to study the spatiotemporal evolution of a single band of PCF in a large domain at moderate Reynolds numbers. This is the motivation of this paper.

SIMULATIONS AND DISCUSSIONS

We conduct numerical simulations of PCF in a large domain of size 800 h×2 h × 712 h, where h is the half height of the channel. A spectral code [6] is employed to solve the incompressible Navier–Stokes equations, where the velocity field is expanded in a basis of Fourier modes (in the x- and z-directions) and Chebyshev polynomials (in the wall-normal direction y). The numerical resolution is 2048 spectral modes in x, 33 in y and 2048 in z, which is as fine as the previous study [4]. The boundary conditions are periodic in x and z and no-slip at the walls ($y = \pm h$).

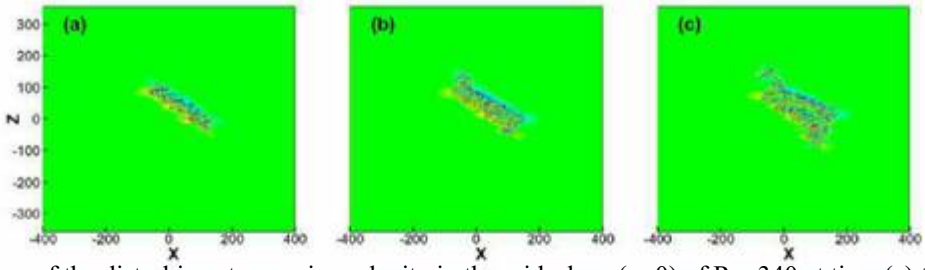

Figure 3 Iso-contours of the disturbing streamwise velocity in the mid-plane (y=0) of Re=340 at time (a) t=0, (b) t=450 and (c) t=900 (h/U), where U is the amplitude of wall velocity.

Different initial disturbances are tested at moderate Reynolds numbers, and an isolated and straight turbulent band is obtained eventually and is used as the initial perturbation for Re=340 (Fig.1a). It is shown that there are no other perturbations near the band and the domain boundaries are far enough from it. The band doesn't show a fast extension in its oblique tangential direction as what happens in PPF, instead, it grows in its transverse direction and becomes 'fat' as shown in Fig.1(b). Later on, the band splitting occurs (Fig.1c). To our knowledge, it is the first time to show the 'natural' band splitting without being interfered by other bands, disturbances or boundaries. The phenomena illustrated above are similar with the simulation results obtained with a long narrow domain.

References

[1] Avila K, Moxey D, de Lozar A, et al.: The onset of turbulence in pipe flow. Science, **333**: 192–196, 2011

[2] Liang S., Marc A.,Björn H.: Scale invariance at the onset of turbulence in Couette flow, *Phys. Rev. Lett.***110**:204502, 2013.

[3] Xiong X., Tao J., Chen S.Y., Brandt L.: Turbulent bands in plane-Poiseuille flow at moderate Reynolds numbers, *Phys. Fluids* **27**, 041702, 2015

[4] Duguet Y., Schlatter P., Henningson D.S.: Formation of turbulent patterns near the onset of transition in plane Couette flow. *J. Fluid Mech.***650**:119-129, 2010.

[5] Tuckerman L.S. and Barkley D.: Patterns and dynamics in transitional plane Couette flow, *Phys. Fluids* **23**, 041301, 2011.

[6] Chevalier M., Schlatter P., Lundbladh A., and Henningson D.S.: SIMSON a pseudo-spectral solver for incompressible boundary layer flows, Technical Report TRITA-MEK 2007:07, 2007.

[a)]Corresponding author. Email: jjtao@pku.edu.cn.

TRANSITION TO TURBULENCE IN PLANE COUETTE-POISEUILLE FLOW

Lukasz Klotz*[1], Idalia Frontczak[1,3], Grégoire Lemoult[2], Matthew Chantry[1], and José Eduardo Wesfreid[1]
[1]*Laboratoire de Physique et Mécanique des Milieux Hétérogènes (PMMH), UMR CNRS 7636 ; PSL - ESPCI; Sorbonne Université , Univ. Paris 06; Sorbonne Paris Cité - UDD, Univ. Paris 07; Paris, France*
[2]*Institute of Science and Technology; Klosterneuburg, Austria*
[3]*Institute of Aeronautics and Applied Mechanics, Warsaw University of Technology; Warsaw, Poland*

Summary We introduce an experimental set-up that enables us to create two dimensional shear flow with zero mean advection velocity. We investigate a plane Couette-Poiseuille configuration, completing the first experimental results for this flow which had only been studied theoretically to-date ([5]). Using flow visualizations we characterize subcritical transition to turbulence and we show the existence of turbulent spots in plane Couette-Poiseuille flow. Due to zero mean advection velocity of the base profile, these turbulent structures are nearly stationary (despite a non-zero pressure gradient in streamwise direction). We ascertain two characteristic wavenumbers correspond to two different inner regions of the base flow. We also determine the evolution of streamwise and spanwise dimensions of turbulent spot as a function of Reynolds number.

EXPERIMENTAL SET-UP

This new experiment is based on the classical plane Couette experimental set-up (see [2], [4]), where the base flow is generated by imposing velocity at test section walls. This is achieved using a single loop of plastic belt which imposes the opposite sign velocity at each wall. The main advantage of such an installation is the zero mean velocity of the profile, as such the generated turbulent structure is not advected ([3]) and an investigation of long time dynamics of turbulent structures is possible.

However, in our case, instead of using a single loop of belt (which can only impose the opposite sign velocity at each wall), we use two loops of belt (one for each wall of the test section). This enables us to control independently the speed at each wall. Let us assume that we set the same speed toward the right at both walls (fig.1, blue), then fluid in the vicinity of plastic belts will be driven in the same direction which in turns will increase the pressure in tank on the right side. This will result in a negative pressure gradient from right to left that will induce a reverse flow in the interior. These two factors (the same positive speed at each wall and the negative induced reverse flow at the center of the gap) will create a parabolic profile with mean advection velocity equal to zero (see the blue profile on right in the inset of fig.1).

Now we present the configuration with a single loop of plastic belt (fig.1, upper loop in red). This consists of upper moving and lower stationary walls respectively. The resulting plane Couette-Poiseuille flow (see the black profile in the inset of fig.1) can be considered as two subregions. The lower one is parabolic (Poiseuille like) and occupies approximately two-thirds of the gap. In the upper region the velocity profile can be approximated by a straight line, like in plane Couette flow. In addition the shear in the Couette region is much higher than that of the Poiseuille region.

RESULTS

We characterise the transition to turbulence with flow visualizations (fig.2). The flow is globally laminar in the test section up to Re=427 (fig.2a), where the Reynolds number is based on the half-distance of gap and the speed of the moving wall. For

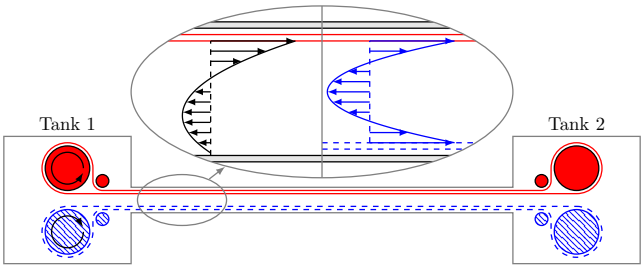

Figure 1: *Schematic of the new experimental set-up, which consists of two independent closed loops of the belt which control the speed at each wall independently. The upper loop (red lines) is used to generate the plane Couette-Poiseuille flow with zero mean advection velocity (black profile in the inset). Plane Poiseuille flow with zero mean advection velocity can be generated (blue profile on right side in the inset, [1]) if the lower loop is added (blue dashed lines).*

*Corresponding authors. Email: lukasz.klotz@espci.fr and wesfreid@pmmh.espci.fr

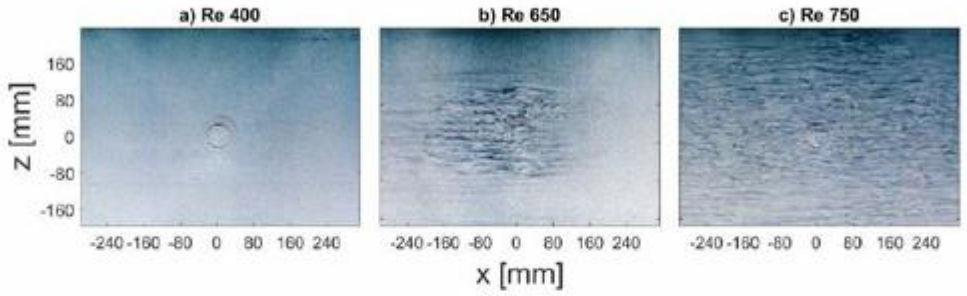

Figure 2: *Visualisations in plane Couette-Poiseuille flow: a) featureless laminar flow for low Reynolds number ($Re = 400$), b) nearly stationary v-shaped turbulent spot in transient regime ($Re = 650$), c) uniform turbulent state ($Re = *750$).*

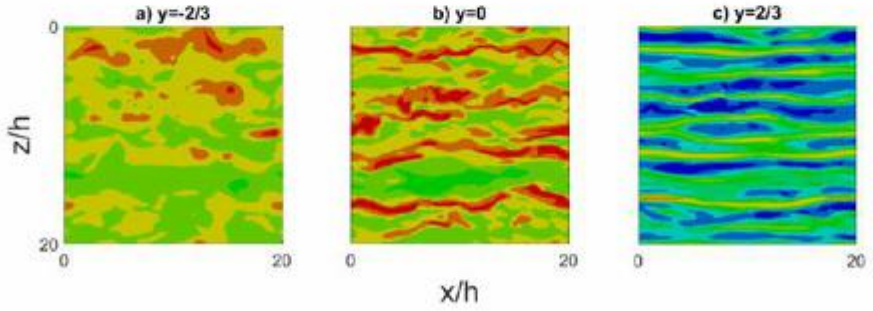

Figure 3: *Streamwise velocity fluctuations in plane Couette-Poiseuille flow in fully turbulent flow: a) near the stationary wall, b) at the center plane (plane Poiseuille region), c) near the moving wall (plane Couette region)*

higher Reynolds numbers we observe a nearly stationary v-shaped turbulent spot which is very slowly advected through the test section (fig.2b). The coexistence of laminar and turbulent phases is observed. Finally for high enough Reynolds numbers the turbulent region occupies most of the test section (fig.2c). To our knowledge this is the first time when turbulent spots in plane Couette-Poiseuille flow are observed and when the advection velocity of turbulent structures in a flow with non-zero pressure gradient is so drastically reduced.

Building on this, we also introduce a finite-size perturbation (localized in space but permanent) to investigate a forced transition to turbulence. We calculate an averaged spectrum k_z using a continuous wavelet transform. The wavenumber k_z is related to the spacing of the streamwise vortices, which dominate the turbulent region (as can be seen in fig.2a,b). We observe two different scales: $k_z = 0.68[cm^{-1}]$ for low Reynolds number ($Re = 200$) and $k_z = 0.54[cm^{-1}]$ for high Reynolds number ($Re = 520$). The former and the latter are associated with the plane Couette and Poiseuille regions respectively.

In addition we show numerical simulations in fully turbulent plane Couette-Poiseuille flow. In fig.3 we present the instantaneous streamwise velocity deviations from the base flow. Indeed the streak spacing near the moving wall (namely in Couette region, fig.3c) is different than near the center plane (Poiseuille region, fig.3b). Near the stationary wall the signature of streaks is less pronounced (fig.3a).

Finally, we determine the evolution of the spanwise and streamwise dimensions of turbulent spots as Reynolds number is varied.

References

[1] Lemoult, G. Etude expérimentale de la transition vers la turbulence dans l'écoulement de Poiseuille plan. (PhD thesis, in french, 2013).

[2] Daviaud, F., Hegseth, J., Bergé, P. Subcritical transition to turbulence in plane Couette flow. *Phys. Rev. Lett*. 69, 2511–2514 (1992).

[3] Dauchot, O. and Daviaud, F. Finite-Amplitude Perturbation in Plane Couette Flow. *EPL* 28, 225 (1994).

[4] Tillmark, N. and Alfredsson, P. H. Experiments on transition in plane Couette flow. *Journal of Fluid Mechanics* 235, 89–102 (1992).

[5] Bergström, L. B. Nonmodal growth of three-dimensional disturbances on plane Couette–Poiseuille flows. *Physics of Fluids* 17, 014105 (2005).

ORIGINATION OF WAVE PACKETS AT LOCALIZED STREAKS

Mikhail Katasonov[1a)], Victor Kozlov[12]
[1] Khristianovich Institute of Theoretical and applied Mechanics, SB RAS, Novosibirsk, Russia
[2] Novosibirsk State University, Novosibirsk, Russia

Summary Turbulence production processes in gradient boundary layer have been studied experimentally. The longitudinal localized disturbances arising in the boundary layer under the action of free-stream turbulence were artificially modeled using a blowing-suction technique. Wave packets, or forerunners, produced in the boundary layer, in the region preceding the abrupt local change of flow velocity near the longitudinal disturbance fronts, were examined. The results of the study make reason to consider the forerunners as wave packets of 3D instability (T-S) waves. It was observed that the forerunners are strongly amplified in the adverse pressure gradient flow. It was found that at downstream development of the forerunners they transform into so - called Lambda-structures.

INTRODUCTION

Researches of a bypass transition problem, whose scenario was proposed by Morkovin in 1984 [1] are still actual. Much attention has been given to the study of longitudinal localized disturbances, or localized streaks, arising in boundary layer under the action of high or enhanced level of free-stream turbulence. Such localized streaks create conditions for the development of high-frequency wave disturbances (secondary instability, wave packets) that can subsequently transform into turbulent spots; as a result, the boundary-layer flow changes its state from laminar to the turbulent [2]. At the same time, the mechanism of formation of secondary unstable oscillations is still far from complete understanding. In this study, it was shown experimentally that the longitudinal localized disturbances can be a source of localized wave packets leading to turbulence.

Experiments under natural conditions fail to give exhaustive answers to posed questions because the emergence of boundary-layer disturbances is a stochastic process, and in most cases it is almost impossible to trace the origin and subsequent evolution of a particular disturbance. For a detailed study, the localized streaks are artificially modeled in boundary layer. In [3] it has been shown that in the boundary layer it is possible to simulate the longitudinal localized disturbances with characteristics close to natural. In [4] it has been shown that the amplitude of the streamwise velocity defect due to the presence of the longitudinal localized streaks can reach about 40 percent of free stream velocity; however, it does not lead to origination of turbulent spots. As it turned out, in these experiments, sufficient conditions for the appearing of instabilities (high-frequency wave packets evolving into the turbulent spots) were not provided. In the present study we show the conditions under which the instability is formed.

WIND TUNNEL EXPERIMENTS

The experiments [5] show that in the vicinity of the leading and rear edges of localized streaks the unstable high-frequency wave packets (denoted below as forerunners) can appear. The forerunners were obtained as a consequence of an impact of a rectangular flow pulse on the boundary layer. In nature, an impact of the local disturbance from free stream on the boundary layer occurs. The rectangular pulse front consists of a continuous disturbance frequency spectrum, of which the most unstable disturbances are enhanced by the boundary layer. In previous experiments the behaviors of the artificial localized streaks and the Tollmien–Shlichting (TS) wave packets in flat plate Blasius boundary layer were studied. The localized streaks were artificially modeled from the incoming flow or wing surface using a blowing-suction technique. It was found that the magnitude of $\partial u/\partial t$ of the localized streaks, which was varied, is a critical factor in generating high-frequency wave packet near the edge of the localized streak. Damping the local streamwise velocity gradient at the edge of the localized streak prevents the formation of the forerunners.

Present investigations were carried out in the subsonic low-turbulent wind tunnels T-324 and MT-324 ITAM SB RAS. Free stream velocity was in the range $4 \le U_\infty \le 6$ m/s at the turbulence level at varied from 0.04 to 0.18 %. Test model was s straight wing (see figure 1). The blowing-suction method was used to introduce longitudinal localized structures into the boundary layer through a thin slot arranged in the surface parallel to the leading edge, or from the incoming flow using thin pipe, located at 3 mm upstream of the model nose. Measurements of the flow fields were carried out using a single-wire probe of a constant-temperature hot-wire anemometer.

Typical time traces and flow fields of localized disturbance propagation downstream are presented on figure 2 and figure 3 respectively. Those pictures are demonstrate an appearance and development of the wave packet (forerunner) near the leading and trailing front of artificial localized structure. Forerunner is clearly seen from $X/C_1=0.48$ for the leading front and from $X/C_1=0.83$ for the trailing front at figure 2; at figure 3 for $X/C_1=0.62$ at t=100 ms - leading front and for $X/C_1=0.83$ at $100<t<150$ ms - leading front and at $400<t<450$ ms - trailing front.

a) Corresponding author. Email: mikhail@itam.nsc.ru.

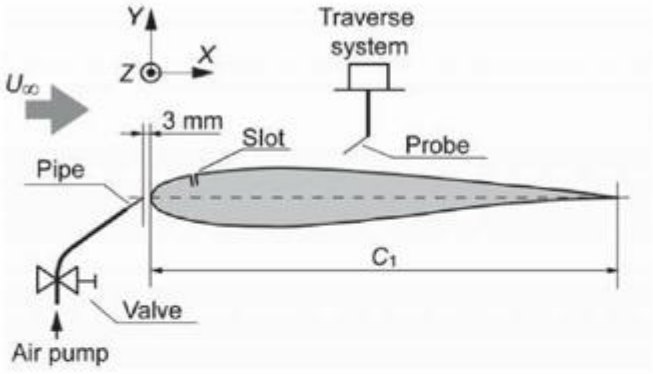

Figure 1: Experimental geometry. C_1 = 290 mm. Angle of attack, $\alpha = -1.2^0$.

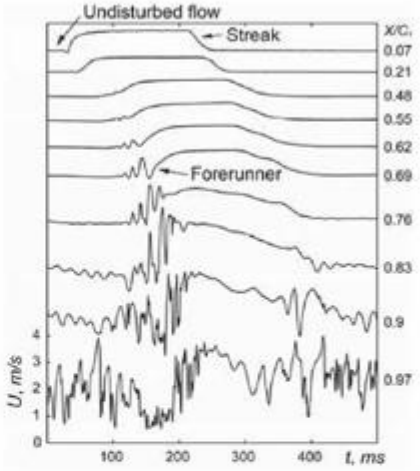

Figure 2: Time traces of the hot-wire signal inside the boundary layer at Z=40 mm. $Y=Y_{umax}$.

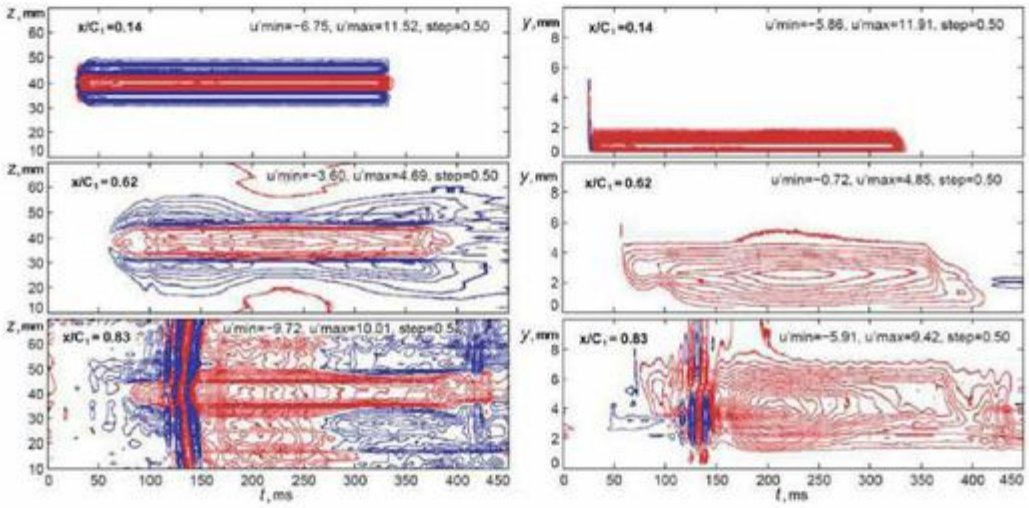

Figure 3: Space evolution of the streak; isolines of longitudinal component of velocity fluctuations. U_∞=3.2 m/s. Z-t plane is plotted at $Y_{(umax)}$ and Y-t plane at Z=40 mm.

CONCLUSIONS

The localization of longitudinal perturbations in space, namely, the presence of a large local velocity gradient near the front/rear front is a necessary condition of the occurrence of wave packets. The results of the study confirm that the forerunners are wave packets of 3D instability (T-S) waves. It was observed that the forerunners are strongly amplified in the adverse pressure gradient flow. It was found that at downstream development of the forerunners they transform into so-called Lambda-structures.

This work was supported by the project of the President of the Russian Federation for Leading Scientific Schools (NSH-НШ-8788.2016.1), RFBR 15-08-01945 and 16-19-10330.

References

[1] Morkovin M. V. Bypass Transition to Turbulence and Research Desiderata, Transition in Turbines, *NASA-CP*-**2386**, 1984
[2] Katasonov M.M., Park S.-H., Sung H.J., Kozlov V.V. Instability of streaky structures in a Blasius bound. layer *Exper. Fluids.* **V38.3**:363-371, 2005.
[3] Westin K.J.A., Bakchinov A.A., Kozlov V.V., Alfredsson P.H. Experiments on localized disturbances in a flat plate boundary layer. Pt 1. The receptivity and evolution of a localized free stream disturbances *Eur. J. Mech./Fluids*. **V17**:823-846, 1998.
[4] Alfredsson P.H., Katasonov M.M. and Kozlov V.V. Generation and development of "passive" disturbances in the Blasius boundary layer.*Thepoph. and Aeromech.* **V8.3**:337-344, 2001
[5] Katasonov M.M., Kozlov V.V., Nikitin N.V., Sboev D.S. The emergence and development of localized disturbances in a circular pipe and boundary layer. Novosib.State Univ., Novosibirsk, RIC NSU: 222, 2014 (in Russian)

CHARACTERIZATION AND PREDICTION OF STREAK BREAKDOWN USING MACHINE LEARNING

M. J. Philipp Hack[1] and Tamer A. Zaki *[2]

[1]*Center for Turbulence Research, Stanford University, Stanford, United States*
[2]*Department of Mechanical Engineering, Johns Hopkins University, Baltimore, United States*

Summary Characteristics of streaks in DNS flow fields of pre-transitional boundary layers are extracted and compared between streaks that induce the formation of turbulent spots via secondary instability and the remainder of the population. The analysis shows that the two classes of streaks differ in a variety of attributes, including their peak amplitude, distance to the wall and size. The data are used in a machine-learning approach to predict transition to turbulence. An artificial neural network identifies the streaks that will induce the formation of turbulent spots. The method is shown to achieve high prediction accuracy at low computational cost which makes the approach suitable for real-time applications.

INTRODUCTION

In bypass breakdown to turbulence, the pre-transitional boundary layer is characterized by the presence of of highly energetic streaks. By introducing inflection points in the instantaneous velocity profile, the streaks promote the amplification of secondary instabilities which ultimately trigger the formation of turbulent spots [1, 2]. Recently, it was demonstrated in Ref. [3] that linear instability analysis applied to cross-flow planes from DNS time series is able to accurately capture the properties of the instabilities such as their growth rate and phase speed. The most unstable eigenfunctions identified the specific streaks that transition to turbulence farther downstream. The work also demonstrated that while the streak amplitude is an important factor, other properties such as their shape and distance to the wall are relevant as well. A visualization of the bypass process in

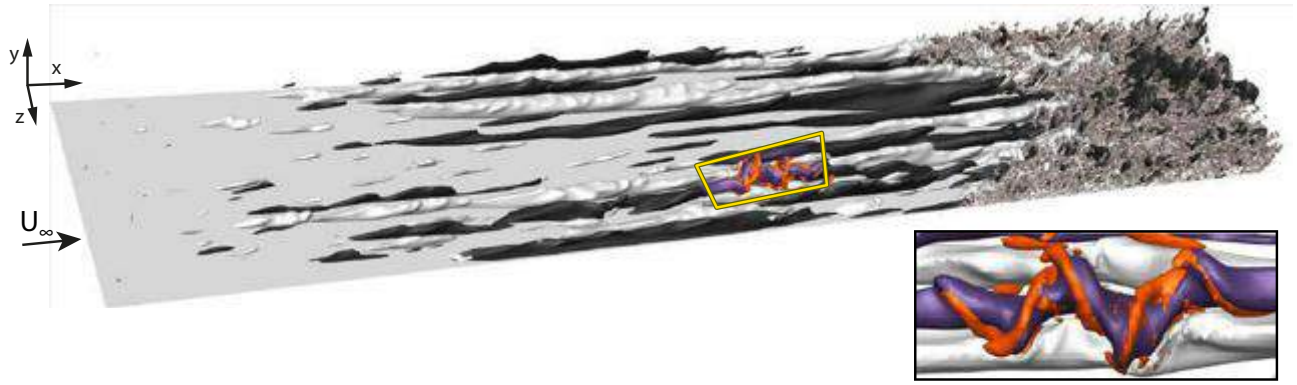

Figure 1: Transitional boundary layer with isosurfaces of low-speed and high-speed streaks and fully turbulent flow downstream with isosurfaces of the λ_2 vortex identification criterion. Enlarged detail: Low-speed streak with sinuous secondary instability.

a boundary layer is presented in figure 1. Only a small fraction of the entire streak population actively promotes the transition process by amplifying secondary instabilities that eventually spawn a turbulent spot. The present work aims to characterize the population of streaks in pre-transitional boundary layers. Streaks that break down into turbulent spots are differentiated from the remainder of the population. This information is used in a machine-learning approach to identify unstable streaks.

ATTRIBUTES OF BOUNDARY-LAYER STREAKS

The properties of the streaks are extracted in cross-planes of the DNS time series (figure 2). Features such as the peak streamwise and wall-normal velocity fluctuations, and the cross-sectional area are considered. Overall, 4,000 DNS snapshots are analyzed and provide about 30,000 data samples of individual streaks, 300 of which are unstable. Discrimination between stable and unstable streaks is achieved by tracking streaks in time and associating them with the formation of turbulent spots. PDFs of attributes of both classes are presented in figure 3. The streamwise and wall-normal velocity fluctuations show the most pronounced difference with an increase in the mean of the distribution by 80 and 155 percent, respectively.

The representation of each streak by a set of features yields a significant compression of the information contained in the DNS fields. By using these low-dimensional data as inputs to an artificial neural network (ANN), an effective and reliable classification scheme for stable and unstable streaks can be devised. In general, artificial neural networks are universal approximators which can represent any continuous, smooth function.

*Corresponding author. Email: t.zaki@jhu.edu

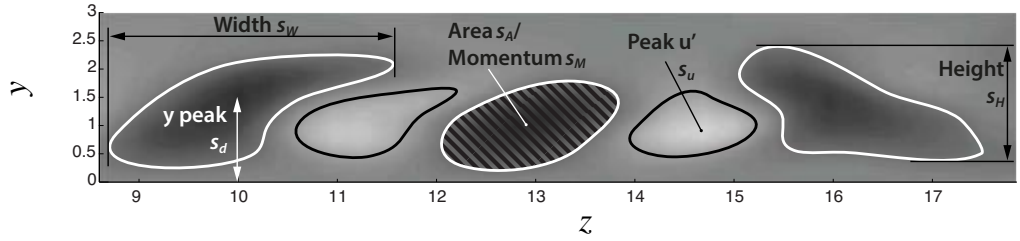

Figure 2: Streak features in cross-flow plane. Background contours give the streamwise velocity fluctuation, u'. Contour lines indicate $u' = 0.05$ (black) and $u' = -0.05$ (white).

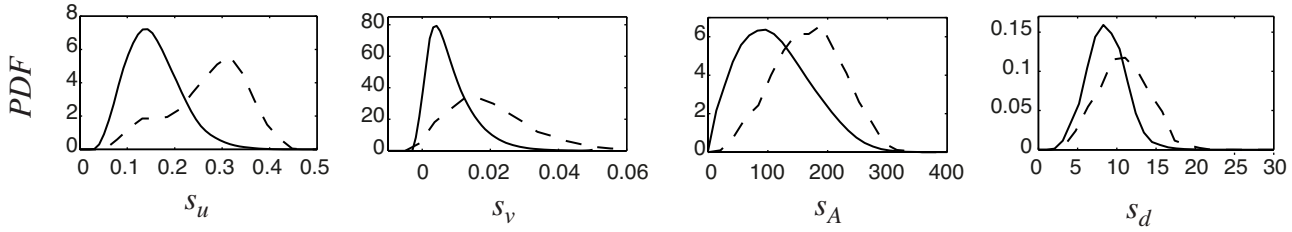

Figure 3: Probability density functions of streak features. Stable streaks (solid) and streaks inducing breakdown (dashed). Left to right: Peak streak amplitude, peak wall-normal fluctuation, cross-sectional area, wall distance of peak streak amplitude.

PREDICTION OF STREAK BREAKDOWN

Features are collected from streaks at 18 equidistant cross planes in the region $200 < Re_\theta < 350$. The performance of the neural network is evaluated using an independent test data set obtained from a second DNS time series of the same duration. The relative prediction accuracy is defined as $\mathcal{A} \equiv \frac{1}{M}\sum_{m=1}^{M} 1 - |\mathcal{P}_m - \mathcal{T}_m|$, where $\mathcal{P}_m$ is the prediction made by the neural network and $\mathcal{T}_m$ is the target value (1 for unstable streaks and 0 otherwise) of the m-th streak. Figure 4(a) shows the accuracy obtained with the ANN when using a single input feature. The peak wall-normal velocity fluctuation is the most significant indicator and leads to an identification accuracy of stable and unstable streaks of approximately 75 percent. The reliability of the approach can be further enhanced by combining inputs (figure 4b). Starting with the peak wall-normal fluctuation, other features are added in the order of their relevance when used as single input feature. The best prediction accuracy, $\mathcal{A} \approx 92\%$, is achieved when all available input features are combined.

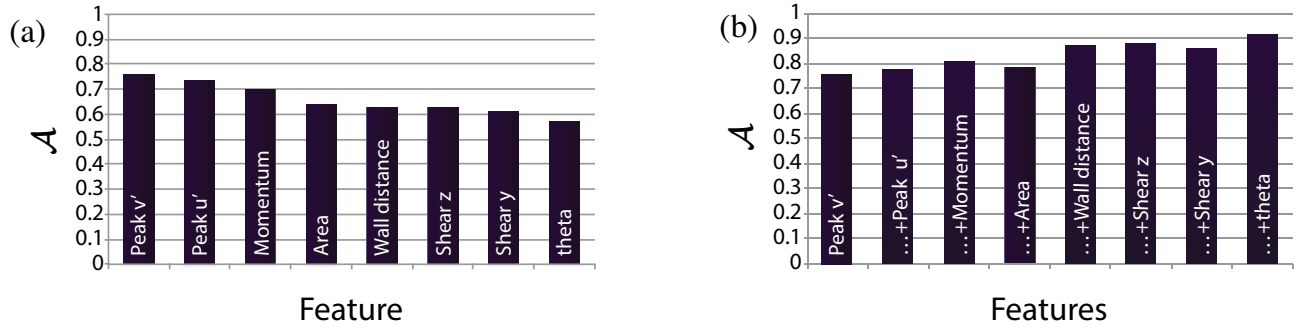

Figure 4: Prediction accuracy $\mathcal{A}$ of the neural network. (a) Single input feature. (b) Accumulated input features.

The computational cost for the classification of a single streak is several orders of magnitude lower than the solution of the eigenvalue problems which arise in classical linear stability theory. In addition to accurately identifying unstable streaks, computational efficiency is thus another significant advantage of the ANN approach. Finally, the network trained with ZPG data can be generalized to make predictions in more complex configurations, e.g. in the presence of pressure gradients.

References

[1] P. Andersson, L. Brandt, A. Bottaro, and D. S. Henningson. On the breakdown of boundary layer streaks. *J. Fluid Mech.*, 428:29–60, 2001.

[2] N. J. Vaughan and T. A. Zaki. Stability of zero-pressure-gradient boundary layer distorted by unsteady Klebanoff streaks. *J. Fluid Mech.*, 681:116–153, 2011.

[3] M. J. P. Hack and T. A. Zaki. Streak instabilities in boundary layers beneath free-stream turbulence. *J. Fluid Mech.*, 741:280–315, 2014.

MS02 - Fluid Active Matter

TS.MS02-1.01	Goldstein, Raymond - Collective Behaviour of Confined Bacterial Suspensions (INVITED)	72
TS.MS02-1.02	Pagonabarraga Mora, Ignacio - Hydrodynamic cooperativity and self-organization in active suspensions (INVITED)	73
TS.MS02-1.03	Gompper, Gerhard - Collective behaviour of active-particle suspensions (INVITED)	74
TS.MS02-1.04	Ramaswamy, Sriram - Active granular monolayers (INVITED)	76
TS.MS02-2.01	Michalec, François-Gaël - Copepod escape and relocation jumps in turbulence	77
TS.MS02-2.02	Saintillan, David - Transition to spontaneous directional flows in confined active fluids	78
TS.MS02-2.03	Popescu, Mihail - Effective interactions between chemically active colloids and surfaces	80
TS.MS02-2.04	Wan, Kirsty - Stochastic gait-switching in flagellate microalgae	82
TS.MS02-2.05	DeSimone, Antonio - Metaboly in euglenids: a model and its experimental validation	84
TS.MS02-2.06	Berti, Stefano - Effects of Discreteness on Population Persistence in an Oasis	86

COLLECTIVE DYNAMICS OF CONFINED BACTERIAL SUSPENSIONS

Raymond E. Goldstein*
Department of Applied Mathematics and Theoretical Physics, University of Cambridge, Cambridge, United Kingdom

Summary It is now well-established that laterally unbounded dense suspensions of motile bacteria can exhibit collective behaviour consisting of transient, recurring vortices and jets on scales large compared to the individual cells. Recently, through a combination of theoretical and experimental work, attention has focused on the effects of confinement on such dynamics, with the discovery that in sufficiently small circular domains there can be spontaneous circulation in the form of a spiral vortex. Subsequently it has been shown that lattices of interconnected domains can exhibit ordered patterns that are, by analogy to magnetic systems, ferro- or antiferromagnetic depending upon details of the coupling between adjacent domains. In this talk I present an overview of these systems and highlight very recent work on the role of 'edge currents' of bacteria in organizing the large-scale patterns.

Since the discovery [1] that concentrated suspensions of the aerobic bacterium *B. subtilis* exhibit collective behaviour characterized by the formation of large, transient vortices and jets, there has been intense interest in the mechanisms that create such flows. Considerable attention has been paid to the possibility that long-range hydrodynamic interactions set up by the stresslet flow fields surrounding individual swimming cells are the ultimate cause of these patterns, which constitute an intriguing form of low Reynolds number turbulence [2]. Motivated by phenomena in cytoplasmic streaming, it was conjectured [3] and then verified experimentally [4] that confining such a system in a sufficiently small, quasi-two-dimensional domain would lead to spontaneous circulation in the form of a spiral vortex. One striking and unexpected result to come from the experimental study was that there is a thin layer of cells at the domain boundary that appear to swim in a direction opposite to the interior bulk flow. A subsequent study [5] using a double-label fluorescence method to visualize separately the cell body and flagella revealed that the cells in the vortex actually swim upstream against the flows set up in the boundary layer, and computational studies of a discrete model of swimming cells revealed the crucial role of long-range hydrodynamic interactions in the phenomenon. These results led to the question of how the cells would organize if confined to two circular domains connected by a narrow neck through which edge currents might pass. Systematic study [6] of lattices of such connected domains revealed that both ferromagnetic and antiferromagnetic order are possible depending upon the lattice structure and the neck width. Returning to the simpler geometry of a channel, it is possible to see in detail [7] how the interplay between edge currents and the tendency toward vortex formation compete to determine the observed flows.

References

[1] "Self-Concentration and Large-Scale Coherence in Bacterial Dynamics", Christopher Dombrowski, Luis Cisneros, Sunita Chatkaew, John O. Kessler, and Raymond E. Goldstein, *Physical Review Letters* **93**, 098103 (2004).

[2] "Fluid Dynamics of Bacterial Turbulence", Jörn Dunkel, Sebastian Heidenreich, Knut Drescher, Henricus H. Wensink, Markus Bär, and Raymond E. Goldstein, *Physical Review Letters* **110**, 228102 (2013).

[3] "Spontaneous Circulation of Confined Active Suspensions", Francis G. Woodhouse and Raymond E. Goldstein, *Physical Review Letters* **109**, 168105 (2012).

[4] "Confinement Stabilizes a Bacterial Suspension into a Spiral Vortex", Hugo Wioland, Francis G. Woodhouse, Jörn Dunkel, John O. Kessler, and Raymond E. Goldstein, *Physical Review Letters* **110**, 268102 (2013).

[5] "Fluid Flows Created by Swimming Bacteria Drive Self-Organization in Confined Suspensions", Enkeleida Lushi, Hugo Wioland, and Raymond E. Goldstein, *Proceedings of the National Academy of Sciences USA* **111**, 9733 (2014).

[6] "Ferromagnetic and Antiferromagnetic Order in Bacterial Vortex Lattices", Hugo Wioland, Francis G. Woodhouse, Jörn Dunkel, and Raymond E. Goldstein, *Nature Physics* **12**, in press (2016).

[7] "Directed Collective Motion of Bacteria Under Channel Confinement", Hugo Wioland, Enkeleida Lush, and Raymond E. Goldstein, submitted (2016).

*Email: R.E.Goldstein@damtp.cam.ac.uk

HYDRODYNAMIC COOPERATIVITY AND SELF-ORGANIZATION IN ACTIVE SUSPENSIONS

Ignacio Pagonabarraga*[1]

[1]*Department of Fundamental Physics, University of Barcelona, Av. Diagonal, 645, 08028 Barcelona (Spain)*

Summary I will discuss the role that hydrodynamic coupling, through self propulsion and active stress generation, has in the collective motion of suspensions of self-propelled particles. I will exploit a powerful mesoscopic computational approach to reach the large length and time scales required to sample the spontaneous structures in which these suspensions self-organize. I will describe the appearance of stable cluster phases sustianed only through hydrodynamics and will describe their main features.

Active systems generate motion due to energy consumption, usually associated to their internal metabolism or to appropriate, localized, interfacial chemical reactivity. As a result, these systems are intrinsically out of equilibrium and their collective properties result as a balance between their direct interactions and the indirect coupling to the medium in which they displace. Therefore, a dynamical approach is required to analyze their evolution and quantify their selfassembly and ability to generate intermediate and large scale stable structures.

There has been significant advances in recent years to understand the basic physical mechanisms that control the collective behavior of self-propelled particles and their connection with effective, equilibrium counterparts. The role of the mobility and its coupling to the preferential direction of motion has emerged as a key player to understand how collections of self-propelled particles move and self-organize. In many circumstances self-propelled particle swim and move inside a fluid environment. The role of the medium in the collective behavior of such systems remains less well understood. In particular, the effect it may have modulating or modifying the understood mechanisms for self-assembly in their absence has not been properly addressed.

The use of computational models that couple individually-resolved self-propelling particles and the continuum solvent in which they move provides a useful means to analyze and quantify the properties of spontaneous emerging structures. I will describe how to take advantage of these coarse grained computational methods that capture the essence of activity generation and the appropriate hydrodynamic coupling when ensembles of active particles move together. I will analyze the relevant physical mechanisms underlying the specific properties of the collective behavior of model active suspensions. By focusing on simplified models, it is possible to identify the relevant parameters which control such behavior. Understanding the mechanical principles which determine the emergence of cooperativity will provide a solid basis to clarify the role of hydrodynamics in active materials and understand how to combine them with biochemical interactions to control their properties and behavior.

*Corresponding author. Email: ipagonabarraga@ub.edu

COLLECTIVE BEHAVIOR OF ACTIVE-PARTICLE SUSPENSIONS

Adam Wysocki[1], Masoud Abkenar[1], Thorsten Auth[1], Roland G. Winkler[1], and Gerhard Gompper*[1]

[1]*Theoretical Soft Matter and Biophysics, Institute of Complex Systems, Forschungszentrum Jülich, Germany*

Summary Active, self-propelled particles in suspension generically exhibit motility-induced clustering and phase-separation. A closer look reveals a pronounced dependence on particle shape and alignment interactions, hydrodynamic interactions, and noise strength. Mesoscale simulations of large ensembles of such particles help to unravel the complex dynamical behaviors of such systems. A rich variety of emergent collective behaviors is observed, ranging from motile polar clusters to jets, swirls, and travelling fronts.

ARGGREGATION AND DYNAMICS OF SELF-PROPELLED PARTICLES

Assemblies of intrinsically active objects represent an exceptional class of non-equilibrium systems. A generic phenomenon in such systems is the emergence of self-organized large-scale dynamical patterns like vortices, swarms, waves, or self-sustained turbulence. This intriguing dynamics is a consequence of the complex interplay of self-propulsion, internal or external noise, and steric and hydrodynamic interactions [1].

We have studied the collective behavior self-propelled rods [2, 3], spheres [4, 5], and beating flagella [6] or cilia [7] by mesoscale computer simulations. For rods, we investigate structure formation of bacterial carpets or motility assays, where the agents can repel and align, but also pass across each other. For spheres, we study aggregation of active colloidal particles without alignment interactions. Clustering appears in all of these different systems. However, in many other aspects, structure formation and collective dynamics strongly depend on the shapes and interactions of the active particles.

Self-Propelled Rods

Due to their excluded-volume interactions, rods align during collisions. This leads to the formation of polar motile custers, which are typically elongated in the direction of rod orientation. Depending on concentration and propulsion velocity, a disordered phase, a small-cluster phase, phase separation between a high-density polar cluster and a low-density disordered phase, and a nematic laning phase are found. However, a phase of travelling waves, as observed experimentally in motility assays, has not been found so far in simulations of self-propelled rods.

Self-Propelled Brownian Spheres

For Brownian spheres, orientation is completely decoupled from particle motion and interactions. Thus, active Brownian spheres have no obvious alignment mechanism. Simulations show that a minimal propulsion strength is required for self-propelled spheres to induce phase separation [5]. Interestingly, active Brownian spheres display the formation of large-scale swirls and jets, see Fig. 1, despite of the absence of an alignment interaction. The origin of this dynamical behavior seems to be an interfacial sorting mechanismi [5]. At the interface, particles are oriented preferentially toward the dense phase, so that they are partially blocked. They can only start to move again after orientational diffusion makes them point parallel to the interface. This implies a collection of particles with the same orientation in concave parts of the interface, which then together push in the same direction.

Mixtures of active and passive Brownian particles

Natural extensions of single-component active Brownian particle (ABP) fluids are mixtures of particles with, e.g., different activities, temperatures, or diameters. We consider mixtures of active and passive Brownian spheres. The emergent dynamics in phase-separated mixtures is studied numerically in two dimensions [8]. A novel steady-state of well-defined traveling fronts is observed, where the interface between the dense and the dilute phase propagates and the bulk of both phases is (nearly) at rest. Two kind of interfaces, advancing and receding, are formed by spontaneous symmtry breaking, induced by an instability of a planar interface due to the formation of localized vortices. Above a threshold in the fraction of active particles, necessary to induce phase separation, the interface velocity decreases linearly with increasing fraction of active particles [8].

CONCLUSIONS

Mesoscale simulations of self-propelled particles provide new insights into the emergent non-equilibrium behavior of active-particle suspensions. It becomes increasingly evident that this non-equilibrium behavior is much more complex than previousy anticipated, and many more interesting phenomena can be expected to be discovered in the near future.

*Corresponding author. Email: g.gompper@fz-juelich.de

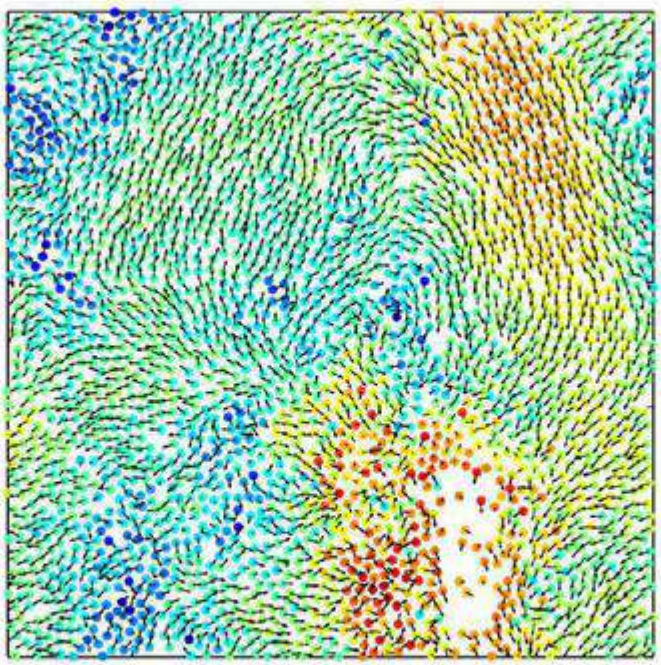

Figure 1: Self-propelled Brownian spheres display phase separation and collective swirl-like motion on large length scales. Particle displacements are shown in a cut through a three-dimensional system with periodic boundary conditions. Red (blue) color indicates large (small) displacements in a fixed time interval.

References

[1] Elgeti J., Winkler R.G., Gompper G.: Physics of Microswimmers – Single Particle Motion and Collective Behavior: a Review. Rep. Prog. Phys. 78:056601, 2015.

[2] Yang Y. , Marceau V., GompperG.: Swarm behavior of self-propelled rods and swimming flagella. Phys. Rev. E 82, 031904, 2010.

[3] Abkenar M., Marx K., Auth T., Gompper G.: Collective behavior of penetrable self-propelled rods in two dimensions. Phys. Rev. E 88:062314, 2013.

[4] Elgeti J., G. Gompper G.: Wall accumulation of self-propelled spheres. EPL 101:48003, 2013.

[5] Wysocki A., Winkler R.G., Gompper G.: Cooperative Motion of Active Brownian Spheres in Three-Dimensional Dense Suspensions. EPL 105:48004, 2014.

[6] Yang Y., Qiu F., Gompper G.: Self-organized vortices of circling self-propelled particles and curved active flagella. Phys. Rev. E 89:012720, 2014.

[7] Elgeti J., Gompper G: Emergence of Metachronal Waves in Cilia Arrays. Proc. Natl. Acad. Sci. USA 110:4470, 2013.

[8] Wysocki A., Winkler R.G., Gompper G.: Travelling fronts in active-passive particle mixtures. arXiv: 1601.00850, 2016.

ACTIVE GRANULAR MONOLAYERS

Sriram Ramaswamy[a)]
TIFR Centre for Interdisciplinary Sciences, Narsingi, Hyderabad 500 075, India

Summary Imitations of motility in nonliving systems have proved an excellent testing ground for theories of the collective behaviour of self-propelled particle systems. Shape-asymmetric macroscopic grains strewn on a horizontal surface vibrated vertically offer a simple and surprisingly faithful motility mimic. In this setting we explore the behaviour of mixtures of tapered rods and spherical beads. The former display autonomous motility, the latter do not, and the combined system presents a rich range of phenomena including flocking at low motile-particle fractions. We present results from theory, simulation and experiment on these systems, including studies of the competition between flocking and crystalline order.

BACKGROUND

It has been known for some time now [1,2] that a macroscopic particle, placed in contact with a vertically vibrating horizontally oriented substrate, say a surface or a one-dimensional track, is capable of transducing the vibration into horizontal motion. Significant lateral motion takes place only if the particle is sufficiently anisotropic: contact mechanics impels the particle when it hits the surface in a tilted orientation, and the direction of tilt sets the instantaneous direction of movement. This nature of the motion depends on the type of asymmetry carried by the particle [3]. A spherical bead will show negligible lateral motion, instead simply bouncing in place. A disc will move about randomly, an apolar, i.e., fore-aft *symmetric*, rod will move preferentially along its length without favouring either extremity [3,4], and a fore-aft *a*symmetric or *polar* rod will move with one end leading on average [4-6,1]. This elementary energy conversion property is robust enough to serve as a motor for each particle, and collections of such particles align their directions of motion spontaneously at high enough concentration, forming inanimate polar [6-8] or apolar [4,5] flocks to which, on grounds of symmetry and conservation law, equations designed to describe motile objects in general must apply.

For some time now we have been interested in mixed monolayers of grains of two types: polar rods and spherical beads or, more generally, active, motile particles in a non-motile background which nonetheless turns out to influence the dynamics rather dramatically. In the experiments of relevance to this work [6-8] the rods were made of brass and the beads of aluminium. The polarity of the rods lies in their shape: one tip is narrower than the other. The sample cell holding the particles has a base and a lid separated by a little over one particle diameter, so that the particles have room to tilt as they are agitated by the vibrating base. The asymmetry between the mechanics of contact of the two ends with the surface on which they lie results in a particle that “walks” in the direction of the narrow tip. The motion is subject to both translational and rotational noise, resulting from the statistics of which tip makes contact with the bounding surfaces and from minute asperities on all surfaces. The close confinement by the bounding surfaces means that the vibration amplitude plays no significant role. The frequency of vibration simply sets the “clock speed”. The only control parameters of relevance are the projected area fractions ϕ_r of the rods and ϕ_b of the beads. The most important result from our earlier work [6] was the observation of a spontaneous transition to a state of global alignment, i.e., a flock, even at ϕ_r of a few percent, upon increasing ϕ_b. The underlying mechanism was shown [6] to consist of two parts: flow of the spherical beads generated by the motile rods, and reorientation of the rods as a result of the bead flow.

THE PRESENT WORK

In this paper and the corresponding talk I present properties deep in the ordered phase as well as the nature of the onset of the ordered phase. The physics at high ϕ_b where the bead layer displays crystalline order is especially dramatic, with mutual exclusion between regions of collective motility and crystalline order. The findings are primarily from mechanically detailed granular dynamics simulations and analytical theory, supplemented by some experiments.

References

[1] Yamada D., Hondou T., Sano M., Phys. Rev. E **67**, 040301, 2003
[2] Neicu T., Blair D. L., Frederick E. and Kudrolli A., Phys. Rev. E **67**, 031303, 2003
[3] Narayan V. , PhD thesis, Indian Institute of Science 2008.
[4] Narayan V., Ramaswamy S., Menon N., Science **317,** 105, 2007
[5] Kumar, N., Ramaswamy, S. & Sood, A. K. Phys. Rev. Lett. **106**, 118001, 2011.
[6] Kumar, N., Soni H., Ramaswamy S., Sood A.K., Nat. Commun. **5**, 4688, 2014.
[7] Kumar, N., PhD thesis, Indian Institute of Science 2015.
[8] Soni, H., PhD thesis, Indian Institute of Science 2015.

[a)]on leave from the Indian Institute of Science, Bangalore. Email: sriram@tifrh.res.in

COPEPOD ESCAPE AND RELOCATION JUMPS IN TURBULENCE

Markus Holzner & François-Gaël Michalec
Institute of Environmental Engineering, ETH Zurich, Zurich, Switzerland

Summary We study the swimming behaviour of copepods using three-dimensional particle tracking velocimetry by tracking simultaneously the motion of many organisms and the flow surrounding them. In this work we analyse the jump reaction of the organisms in response to hydrodynamic stress, focusing on the strong escape jumps and the weaker relocation jumps. We find that the two types of jumps are influenced differently by increasing levels of turbulence and hydrodynamic stress. This may be important for their survival and mating performance in dynamic environments

INTRODUCTION

Planktonic copepods live in environments such as oceans and estuaries where they form the largest part of the zooplankton and where flows are typically turbulent. Because of their small size and relatively slow swimming speeds, zooplankton interacts very little with the large features of the flow, but at small scales swimming behaviour can overcome advective transport. Because three-dimensional observations of copepods swimming freely in turbulent flows remain scarce, most of what is known about their behaviour in energetic environments derives from extrapolation of results obtained in still water, where a local disturbance simulating turbulence is introduced [1-3]. Only recently have methods matured to enable the monitoring of many organisms in turbulent flows [4,5] and it has become possible to simultaneously measure the motion of finite sized particles [6] or organisms [7] and the flow surrounding them. In [5], an active response of copepods to background turbulence has been identified that cancels gender specific differences in motion strategy. A modification of escape reactions has been found when organisms were exposed to a contracting flow but no response has been noted in turbulence [7]. Here we focus on the response of copepods to turbulence and analyse relocation and escape jump reactions for varying turbulence intensity.

METHODS

We carried out three-dimensional particle tracking measurements using three synchronized Mikrotron EoSens high speed cameras to track the turbulent flow and one EoSens camera fitted with a four view image splitter to simultaneously track the copepods. The measurements were conducted in a water tank containing a forcing device creating quasi homogeneous and isotropic turbulence [5]. We seeded the flow with neutrally buoyant tracer particles and introduced about 1000 Eurytemora affinis parent individuals obtained from laboratory cultures at Wimereux Marine Station.

RESULTS

The intensities of turbulence produced with our set-up are comparable to characteristic values observed in coastal zones, tidal fronts and estuaries. We observed that copepods do not behave passively even at substantial turbulence intensities. Jumps and swift movements were clearly visible in all our experiments. In particular we observed that both relocation jumps and strong escape jumps are influenced by turbulence intensity.

CONCLUSIONS

This contribution will illustrate the potential of our method to characterize the behavioural response of copepods to local hydrodynamic conditions and to investigate their interactions in complex environments.

References

[1] Kiørboe T., Saiz E., Visser A.: Hydrodynamic signal perception in the copepod Acartia tonsa. *Mar. Ecol. Prog. Ser.* 179, 97–111, 1999.

[2] Fields D.M., Yen J.: The escape behavior of marine copepods in response to a quantifiable fluid mechanical disturbance. *J. Plankton Res.* 19, 1289–1304., 1997

[3] Waggett R.J., Buskey E.J.: Copepod escape behavior in non-turbulent and turbulent hydrodynamic regimes. *Mar. Ecol. Prog. Ser.* 334, 193–198, 2007.

[4] Yen J., Rasberry K.D., Webster D.R.: Quantifying copepod kinematics in a laboratory turbulence apparatus. *J. Mar. Syst.* 69, 283–294, 2008.

[5] Michalec F.G., Souissi S. & Holzner M.: Turbulence triggers vigorous swimming but hinders motion strategy in planktonic copepods. *J. Roy. Soc. Interface*, 12(106), 20150158.

[6] Saha D., Bäbler M.U., Holzner M., Soos M., Lüthi B., Liberzon A. & Kinzelbach W.: Breakup of Finite-Size Colloidal Aggregates in Turbulent Flow Investigated by Three-Dimensional (3D) Particle Tracking Velocimetry. *Langmuir*, 32 (1), 55–65, 2016.

[7] Adhikari D., Gemmell B.J., Hallberg M.P., Longmire E.K. & Buskey E.J.: Simultaneous measurement of 3D zooplankton trajectories and surrounding fluid velocity field in complex flows. J. Exp. Biol., 218(22), 3534-3540, 2015.

[a)] Corresponding author. Email: ictam2016papers@legendconferences.com.

TRANSITION TO SPONTANEOUS DIRECTIONAL FLOWS IN CONFINED ACTIVE FLUIDS

Maxime Theillard[1], Barath Ezhilan[1], and David Saintillan*[1]
[1]*Department of Mechanical and Aerospace Engineering, University of California San Diego, 9500 Gilman Drive, La Jolla, CA 92093, USA*

Summary Recent experimental, theoretical and computational studies have shown that confinement can profoundly affect self-organization in concentrated active suspensions leading to striking features such as formation of steady and spontaneous vortices in radial confinement. Motivated by these observations, we study the two-dimensional dynamics in a confined suspension of biologically active particles using a mean-field kinetic theory for which we developed a novel numerical solver. The dynamics in both circular and racetrack geometries are investigated, where we show that the interplay of confinement and activity can stabilize collective motion into spontaneous flowing states, including steady vortices, unidirectional motion, and travelling waves. Our simulation results are also shown to compare favorably with predictions from a linear stability analysis.

INTRODUCTION

Recent years have seen significant developments in the understanding of the emergence of collective motion in biologically active suspensions. There is widespread consensus that self-organization in such suspensions are driven by the stresses exerted by the active particles on the fluid as they propel themselves [1, 2]. Continuum kinetic theories,where a Smoluchowski equation for the probability distribution of the active particle positions and orientations is coupled to the Stokes equation for the flow arising from the active stresses is a powerful approach for understanding active fluids [3], in which the emergent behavior in active systems is viewed as a breakdown of stability of the various equilibrium states. While most of the mean-field based studies have focussed on unconfined systems, the interplay of confinement and activity has excited much interest recently. Experiments have shown that confinement can stabilize the collective motion into defined patterns such as a double vortex [4, 5, 6]. While various phenomenological models for active liquid crystals have focussed on the effect of confinement on collective behavior and have predicted spontaneous flow transitions, such predictions have yet to be confirmed from a hydrodynamics first-principles perspective.

Our primary motivation for this study are recent experiments [4, 5] and simulations [6] of active fluids in circular confinement. These experiments predicted that when the radius of confinement is below a critical value (or is within a critical range of values), the suspension will spontaneously form a steady single vortex encircled by a counter-rotating boundary layer closer to the wall. Their later particle simulations [6] using a simple model accounting for hydrodynamic and steric interactions reproduced these experimental observations and also clarified details about the cell orientation and swimming direction showing that the cells swim upstream against the flow. A unified picture that provides a complete characterization of the stability properties and non-linear chaotic dynamics of circularly confined active suspensions for different degrees of confinement, strength of activity and propulsion is still lacking, however, and we seek to address these questions using a continuum model and numerical simulations. A striking crucial result of our work is that several of the experimental results in the literature including the double vortex [4, 5, 6] can be captured within the mean-field theory in the complete absence of steric interactions. Hence, this double vortex could simply a result of a coupling between circular confinement and self-generated fluid flows.

KINETIC MODEL

Starting from the Smoluchowski equation for the probability density function $\Psi(\mathbf{x}, \mathbf{p}, t)$ of particle positions and orientations, hierarchical evolution equations for the concentration c, polarization $\mathbf{m}$, and nematic order parameter tensor $\mathbf{D}$ can be obtained [2], which are written in conservative form as:

$$\partial_t c = -\nabla \cdot \mathbf{F}_c, \tag{1}$$

$$\partial_t \mathbf{m} = -\nabla \cdot \mathbf{F}_m + \tfrac{3}{5}\beta \mathbf{E} \cdot \mathbf{m} - \mathbf{W} \cdot \mathbf{m} - 2\mathbf{m}, \tag{2}$$

$$\partial_t \mathbf{D} = -\nabla \cdot \mathbf{F}_D + \tfrac{2}{5}\beta c \mathbf{E} + \tfrac{6}{7}\beta \mathbf{E} \cdot \mathbf{D} + \mathbf{W} \cdot \mathbf{D} - \mathbf{D} \cdot \mathbf{W} - 6\mathbf{D}, \tag{3}$$

where the dimensionless parameter β denotes Bretherton's constant, and where the various fluxes are detailed in [2]. The source terms arise from alignment and rotation by the rate-of-strain and vorticity tensors $\mathbf{E}$ and $\mathbf{W}$ of the disturbance velocity field $\mathbf{u}$, which satisfies the incompressible Navier-Stokes equations forced by the divergence of the active stress tensor $\alpha\mathbf{D}$:

$$\nabla \cdot \mathbf{u} = 0, \quad Re\left(\partial_t \mathbf{u} + \mathbf{u} \cdot \nabla \mathbf{u}\right) = -\nabla p + \nabla^2 \mathbf{u} + \alpha \nabla \cdot \mathbf{D}. \tag{4}$$

*Corresponding author. Email: dstn@ucsd.edu

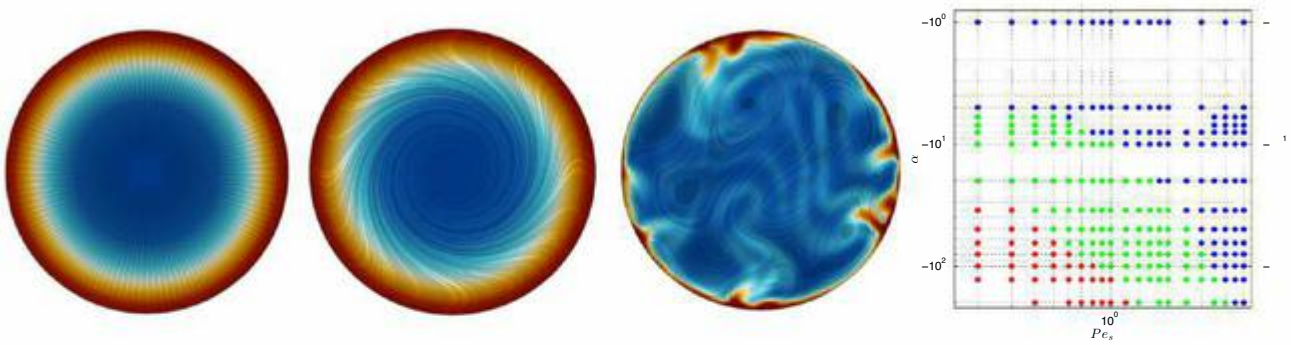

Figure 1: Left: typical simulations in circular geometries, illustrating the three observed phases: quiescent equilibrium distribution with wall accumulation; double vortex flowing state; chaotic motion. Right: phase diagram illustrating the transition between phases (blue: equilibrium; green: vortex; red: chaos).

Upon non-dimensionalization, the equations are governed by four dimensionless parameters:

$$Re = \frac{\rho H^2 d_r}{\mu}, \quad Pe = \frac{V_s}{2 d_r H}, \quad \alpha = \frac{\sigma_0 n}{\mu d_r}, \quad \Lambda = \frac{d_r d_t}{V_s^2}. \tag{5}$$

In particular, the swimming Péclet number Pe denotes the ratio of the persistence length of swimmer trajectories to the size of the domain and is a measure of confinement. The activity parameter α compares the destabilizing effects of active stresses and of concentration to dissipative processes, namely viscosity and orientation decorrelation by rotational diffusion. The equations are solved numerically using an adaptive finite-volume algorithm on quad-tree grids.

RESULTS

Typical simulation results in circular confinement are illustrated in Figure 1 and exhibit the same phenomenology as in experiments [5]. In very strong confinement (or at low activity/concentration), the distribution is axisymmetric and shows wall accumulation with wall-normal polarization and zero flow. As confinement decreases or activity increases, a transition to a double vortex state similar to that reported in experiments is observed. Finally, at very high levels of activity, the steady vortex destabilizes leading to chaotic dynamics akin to those in bulk systems [3]. Figure 1 also shows a phase diagram in terms of Pe and α.

We also simulation dynamics in periodic racetrack geometries, where a transition from equilibrium to spontaneous unidirectional flow with net pumping is observed (not shown). Upon increasing activity, the formation of traveling concentration waves is also reported in agreement with recent experiments on dense sperm suspensions [7] We further elucidate this transition to unidirectional flow by performing a linear stability analysis in a periodic channel geometry, which provides the marginal curve for the transition and compares favorably with our simulations.

References

[1] Marchetti, M. C., Joanny, J.-F., Ramaswamy, S., Liverpool, T. B., Prost, J., Rao, M. & Simha, R. A. Hydrodynamics of soft active matter, *Rev. Mod. Phys.* **85** 1143 (2013).

[2] Saintillan, D. & Shelley, M. J. Active suspensions and their nonlinear models, *C. R. Physique* **14** 497 (2013).

[3] Saintillan, D. & Shelley, M. J. Instabilities, pattern formation, and mixing in active suspensions, *Phys. Fluids* **20** 123304 (2008).

[4] Woodhouse, F. G. & Goldstein, R. E. Spontaneous circulation of confined active suspensions, *Phys. Rev. Lett.* **109** 168105 (2012).

[5] Wioland, H., Woodhouse, F. G., Dunkel, J., Kessler, J. O. & Goldstein, R. E. Confinement stabilizes a bacterial suspension into a spiral vortex, *Phys. Rev. Lett.* **110** 268102 (2013).

[6] Lushi, E., Wioland, H. & Goldstein, R. E. Fluid flows created by swimming bacteria drive self-organization in confined suspensions, *PNAS* **111** 9733 (2014).

[7] Creppy, A., Plouraboue, F., Praud, O, Druart, X. & Cazin, S. Symmetry breaking phase transitions in highly concentrated semen (submitted).

EFFECTIVE INTERACTIONS BETWEEN CHEMICALLY ACTIVE COLLOIDS AND SURFACES

Mihail N. Popescu* [1,2], William Uspal[1,2], Mykola Tasinkevych[1,2], and Siegfried Dietrich[1,2]

[1] *Max Planck Institute for Intelligent Systems, Stuttgart, D-70569, Germany*
[2] *IV. Institut für Theoretische Physik, Universität Stuttgart, Pfaffenwaldring 57, D-70569 Stuttgart, Germany*

Summary Micron-sized particles moving through solution by using self-generated chemical gradients serve as model systems for studying active matter. The self-generated hydrodynamic and chemical fields, which induce particle motion, probe and are modified by the environment, including its boundaries. We show that near a hard planar wall such a particle may exhibit motion with a steady orientation and height above the wall, or motionless, steady "hovering". Furthermore, when also chemi-osmotic hydrodynamic flow at the wall is induced, we predict that the interplay between this and the self-diffusiophoretic one can be "tuned" by chemical patterning of the wall such that one can achieve controlled motion of the active particle, e.g., the particle following a chemical stripe.

MODEL

The model system we consider is shown in Fig. 1 (left panel). A spherical particle of radius R, covered by a catalyst over a spherical cap region parametrized by ψ (black segment in Fig. 1, left panel), is suspended in a Newtonian liquid solution bounded by a planar wall. The catalytic cap releases a solute which diffuses in the solution. The particle and the wall are impenetrable to the solute and solvent. There are additional interactions, of range $\delta \ll R$, between the solute and the particle surface, as well as between the solute and the wall. In the absence of thermal fluctuations, and if the wall is chemically uniform, the particle moves only in the plane containing the wall normal and the particle's symmetry axis. In such case, the cap orientation θ and the height h of the particle's center above the wall (see Fig. 1, left panel) completely specify the particle configuration. (If the wall is chemically patterned, a situation discussed in the second part of **Results**, the position and orientation of the particle in respect to the pattern are added to the variables characterizing the configuration.) The translational and angular velocities are denoted by $\mathbf{U}$ and $\mathbf{\Omega}$, respectively. The hydrodynamic flow is assumed to have a very small (vanishing) Reynolds number, and the diffusion of the molecular solute is much faster than the transport by advection (small Péclet number). The motion of the sphere is assumed to be sufficiently slow and the diffusion of the solute to be sufficiently fast such that at each instantaneous (h, θ) a quasi-steady state of the solute number density $c(\mathbf{r})$ and of the hydrodynamic flow $\mathbf{u}(\mathbf{r})$, respectively, is established.

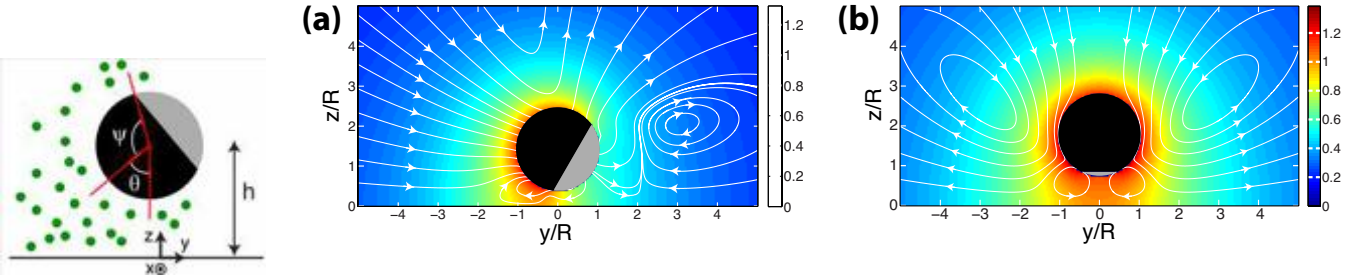

Figure 1: Schematic drawing of a chemically active Janus sphere above a planar wall located at $z = 0$ (left panel). (a) Sliding and (b) hovering steady-states for $b_i = b_w < 0$; the coverage by catalyst is given by $\psi \simeq 114°$ (a) and $\psi \simeq 154°$ (b). Streamlines (white lines) illustrate the flow field in the spatially fixed coordinate system; the color coding represents the solute number density $c(\mathbf{r})$ in units of the characteristic density $c_0 = \mathcal{K}R/D$. (Adapted from Ref. [3].)

$\mathbf{U}$ and $\mathbf{\Omega}$ are calculated within the framework of the classical theory of diffusiophoresis [1, 2]. This accounts for the solute-surface interaction via phoretic "mobilities b_k (where $k \in \{i, c, w, s\}$ indicates b can take different values at the "**i**nert" or "**c**ap"regions of the particle, as well as at the **w**all or **s**tripe), which are connecting the surface- gradients of solute density with "phoretic slip" hydrodynamic boundary condition at the corresponding surfaces: $\mathbf{v}_s(\mathbf{r}) = -b_k \nabla_{||} c(\mathbf{r})$. The signs and magnitude of b_i and b_c determine the direction of motion (catalyst- or inert-face forward). The Lorentz theorem is applied in order to reduce the complexity of the hydrodynamic problem [1, 3]. The Laplace equation with uniform particle flux $\mathcal{K}$ over the cap region of the particle (accounting for the activity), which governs the distribution of solute molecules) and the incompressible Stokes equations, governing the hydrodynamics, are solved numerically using the Boundary Element Method (BEM) (see details in Ref. [3]). For both problems (diffusion and hydrodynamics), approximate analytical expressions are obtained by employing the standard point-singularities representation of the solution [3, 4]. The rigid-body overdamped motion of the spherical colloid follows straightforwardly from the translational and angular velocities $\mathbf{U}$ and $\mathbf{\Omega}$.

*Corresponding author. Email: popescu@is.mpg.de

RESULTS

The case of a no-slip wall ($b_w \equiv 0$). In this situation, the no-slip hydrodynamic boundary condition applies at the wall. The sole role played by the wall is that of reflecting back the density and hydrodynamic fields. By analyzing the dynamics in the phase-plane (h, θ), we have established that certain steady-states of motion at fixed height h^* above the wall and with fixed orientation θ^* of the symmetry axis of the colloid, and which are stable attractor points for the dynamics in the (h, θ) plane, can emerge. The values h^* and θ^* depend on the coverage parameter ψ as well as on the phoretic mobilities b_i and b_c at the inert and catalytic regions, respectively. Figs. 1(a) and (b) illustrate the distribution of solute and the hydrodynamic flow for two examples of such steady states: (a) "sliding" (fixed height and fixed orientation $\neq$ the direction normal to the wall) and (b) "hoverer" (motionless particle at a fixed height above the wall, steadily pumping the surrounding fluid). Such states stem-out from a complex feeback-loop: the coupling of the wall-induced chemical gradients to changes in the distribution of phoretic slip on the particle surface gives rise to a hydrodynamic flow that does not rotate the particle once in configuration (h^*, θ^*).

The case of osmotic-flow response at the wall ($b_w = 0$). Here we focus on a particle with half of the surface catalytically active (i.e., $\psi = \pi/2$), "sliding" above the substrate at a fixed height h and orientation $\theta \simeq \pi/2$; i.e., the particle axis $\hat{}$ is parallel to the wall. As an example of chemically patterned wall we choose a chemical stripe (see Fig. 2), i.e., $b = b_s$ on the stripe and $b = b_w \neq b_s$ on the rest of the wall. The linearity of the Stokes equation allows to write the translational and angular velocity of the particle $\mathbf{U}$ and $\mathbf{\Omega}$, respectively, as $\mathbf{U} = \mathbf{U}^{sd} + \mathbf{U}^{w}$ and $\mathbf{\Omega} = \mathbf{\Omega}^{w}$, where the superscripts indicate the contributions from *s*elf-*d*iffusiophoresis (phoretic slip at the wall set to zero) and from the *w*all (phoretic slip on the particle set to zero), respectively. (the constraints on h and $\mathbf{d}$ imply $\mathbf{\Omega}^{sd} = 0$.) $\mathbf{U}^{sd}$ is treated as a model parameter (since it can be computed separately, following the procedure in the previous Subsection). The wall-slip contributions are calculated using the Lorentz theorem and the BEM method (similar to subsection [4]). Approximate analytical expressions for $\mathbf{U}^{w}$ and $\mathbf{\Omega}^{w}$ are obtained by using a reduced set of singularities together with their corresponding images: the monopole and dipole terms for the diffusion equation, the Stokselet or the rotlet for the hydrodynamics (auxiliary problems).

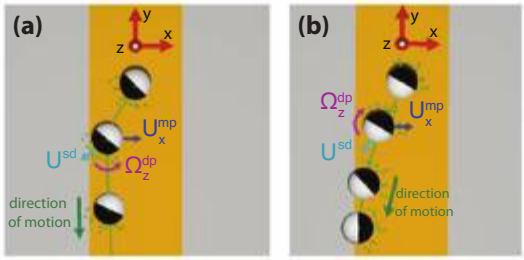

Figure 2: Mechanisms (a) stabilizing and (b) destabilizing, respectively the stripe-bound state of an (a) catalyst-forward and (b) inert-forward particle, respectively [4]. Here $b_w/b_s = 3$. Superscripts mp and dp indicate the monopole and dipole contributions, respectively, to $\mathbf{U}^{w}$ and $\mathbf{\Omega}^{w}$.

As shown in Fig. 2, a catalyst-forward moving active particle can follow a stripe: it is attracted to the center and aligns its axis parallel to the edges of the stripe. The attraction to the stripe center is driven by the contribution from the monopolar term U_x^{mp}; at the center, the contributions to U_x^{mp} from the two edges cancel. The alignment of $\mathbf{d}$ with the edges of the stripe is driven by rotations induced by the dipolar contribution U_x^{sd}, which vanish at the aligned state (Fig. 2(a)). In contrast, for an inert-forward particle, edge induced rotations of $\mathbf{d}$ towards a normal-to-the-stripe alignment are enhanced; for sufficiently small U^{sd}, the particle docks (Fig. 2(b)), while for large U^{sd} the particle escapes the stripe region.

CONCLUSIONS

We have shown that by engineering the chemistry of an active particle and that of the near-be wall one can achieve control of the motion of the particle, e.g., constrain the particle to slide along the wall and to follow a chemical stripe.

References

[1] Anderson, J. L.: Colloid Transport by Interfacial Forces. Ann. Rev. Fluid Mech. 21:61-99, 1989.

[2] Golestanian, R., Liverpool, T. B., Ajdari, A.: Designing phoretic micro- and nano-swimmers. New J. Phys. 9:126, 2007.

[3] Uspal, W. E., Popescu, M. N., Dietrich, S., Tasinkevych, M.: Self-propulsion of a catalytically active particle near a planar wall: from reflection to sliding and hovering. Soft Matter 11, 434-438, 2015.

[4] Uspal, W. E., Popescu, M. N., Dietrich, S., Tasinkevych, M.: Guiding catalytically active particles with chemically patterned surfaces. (unpublished)

STOCHASTIC GAIT-SWITCHING IN MOTILE MICROALGAE

Kirsty Y. Wan[1] and Raymond E. Goldstein *[2]

[1]*DAMTP, University of Cambridge, UK*

Summary Self-propulsion by flagella is a significant selective advantage for microorganisms which possess such capabilities. There is great diversity in the number of flagella, their beating modes, and greater still in the ultrastructure of the basal apparatus into which the flagella are inserted. For free-living unicellular eukaryotes with few flagella the question of their coordination has been receiving increasing attention from theorists and experimentalists alike. We propose that this coordination is driven intracellularly, and use select algal species to perform a comparative study of their swimming gaits. Over longer timescales, we can visualize at high spatiotemporal resolution the stochastic transitions between different gaits which produce striking manifestations of a bacteria-like run-and-tumble locomotion.

GAITS OF FREE-LIVING FLAGELLATES

Uniflagellates including many species of plant and animal sperms navigate fluidic environments by undulating a posteriorly-oriented flagellum. This single appendage can be used to effectuate directional changes, such as turning towards a source of chemoattractant. In contrast, ciliated microorganisms including the freshwater protozoan *Paramecium* and the large colonial alga *Volvox* [3] rely on a large-scale coordinated motion of large numbers of surface-attached cilia for swimming and feeding. In this case coordination is thought to be largely due to hydrodynamic interactions between the neighbouring cilia, which tend to drive pairs of cilia into in-phase synchrony, and arrays of cilia into metachrony. The generality of this phenomenon is challenged when one examines the robust in-phase breaststroke swimming of the unicellular alga *Chlamydomonas*, the physical mechanism for synchrony between its two front-mounted flagella is the subject of extensive study and some contention. The current view is that some form of intracellular coupling must be present, most likely through the contractility of connecting fibers between the basal bodies whence emanate the flagella [1].

If this were true, then a correlation must be expected between observed gaits or modes of flagellar actuation and the symmetries of the basal apparatus which not only define the configuration of flagella but also the strength and directionality of the coupling between flagella. Here we explore the morphospace of distinct modes of flagellar synchrony maintained by flagella across species of naturally-occurring quadriflagellate algae (for free-swimming or pipette-held individuals) in the context of their differing basal architectures. Unicellular flagellates possessing more than four flagella are rare, with only a few species that have either eight or sixteen flagella [1]– the selective advantage of having ever greater numbers of flagella must be eventually be outweighed by the energetic and activity costs of flagellar synthesis and coordination. By analogy with well-documented forms of locomotion in quadrupeds, we find that quadriflagellate gaits include the trot, the pronk, the gallop, and even a stand gait in which all flagella are non-moving. Species-specific symmetries existing within the basal apparatus are therefore implicated in constraining the possible phase relations between flagella.

GAIT SYMMETRIES

As in many biological systems exhibiting complex periodic behaviour, it has proved useful to consider a dimension-reduced analysis of oscillations in terms of phase. We were able to measure the phases of individual flagella in several species of quadriflagellates through a combination of micromanipulation, cell tracking, and high-speed imaging. For flagellar phases ψ_j (flagellum index j) we compute the matrix $\Delta_{ij} = \psi_i - \psi_j \quad (i, j = 1, \ldots, 4)$, where $\Delta_{ij} = \Delta_{ji}$, $\Delta_{ii} = 0$, and $\Delta_{ik} = \Delta_{ij} + \Delta_{jk}$. Each gait is then associated with a 3-tuple of phase differences: $[\Delta_{12}\, \Delta_{13}\, \Delta_{14}]$. The primitive Prasinophyte alga

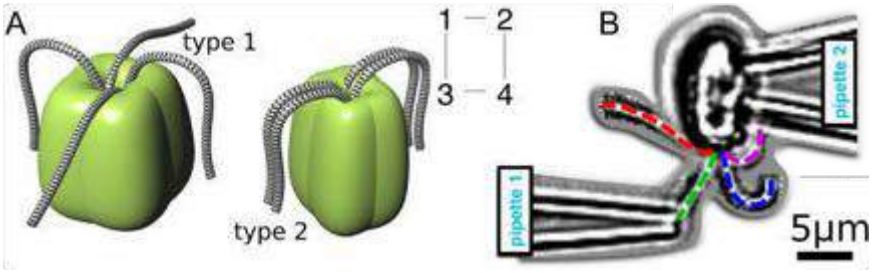

Figure 1: A) In free-living quadriflagellates, two possible configurations are possible (types 1,2). The flagella emerge from basal bodies comprising a species-specific network whose symmetries may constrain observed swimming gaits. B) In *T. suecica* (type 2) the relative phase between the remaining flagella is unchanged when beating is purposefully stalled in one flagellum.

*Corresponding author. Email: r.e.goldstein@damtp.cam.ac.uk

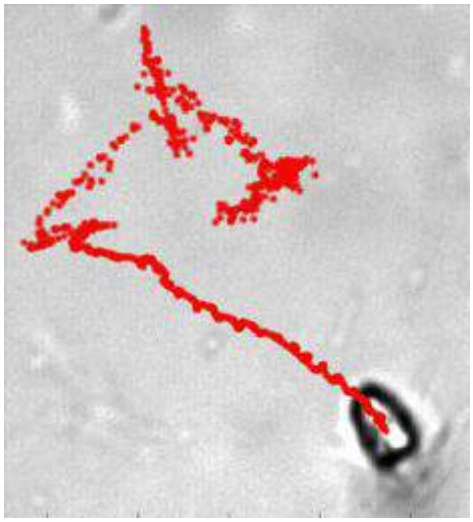

Figure 2: Flagellated eukaryote performs biased random walk by actively modulating the orientation and coordination of anteriorly-positioned flagellla.

P. parkeae swims with two pairs of precisely alternating breaststrokes akin to the 'trot' of a horse, for which $[\Delta_{12}\,\Delta_{13}\,\Delta_{14}] = [\pi\,0\,\pi]$. On the other hand the advanced green alga *C. crucifera* exhibits a rotary gallop gait ($[\Delta_{12}\,\Delta_{13}\,\Delta_{14}] = [\pi/2\,\pi\,3\pi/2]$). Inspired by studies of central pattern generators (CPGs) in the control of multilegged locomotion in vertebrates, we sought features of the basal apparatus in these species that may correlated with the spatiotemporal symmetries of observed gaits (where a spatiotemporal symmetry comprises a permutation of flagella and a temporal phase shift that fixes the dynamics). For instance the rotary gallop of four oscillators (Figure 1A) is fixed by the identity transformation, but also by interchange of diagonals with a phase shift of π, and can emerge from a square network in which the coupling between all oscillators are identical. This square symmetry is shown in electronmicrographs of sections through *C. crucifera*, in which basal bodies are inserted radially at corners of a square.

GAITS SWITCHING DURING FREE-SWIMMING

The flagellate stand gait has the most symmetries (reflection in the horizontal, in the vertical, interchange of diagonals and arbitrary phase shift) and has the symmetry group $D_2 \times S^1$, where D is a dihedral group and S the circle group. Intriguingly, bifurcation from the stand to an alternate swimming gait is observed in many species. Forward swimming can further bifurcate to a shock response in which the front-mounted flagella change from a puller-type to a pusher-type motility, and the swimming direction is dramatically reversed or altered. Such gait transitions can occur either stochastically or be induced by mechanical perturbations, but the backward-swimming phase is transient and a steady-state beating pattern is re-established within a few beats [2]. Over time (Figure 2), these episodic runs (forward-swimming) and tumbles (gait-switching) allow the cell to navigate a much larger region (effective diffusion constant of $D \propto v^2\tau \approx 10^{-4}$ cm^2/s for an alga swimming at $v = 200$ μm/s and mean run duration τ of 0.5 s, compared to passive Brownian diffusion $D_b = 10^{-9}$ cm^2/s for a 20 μm cell body).

CONCLUSIONS

Somewhat surprisingly, we find that motile algae can i) maintain precise gaits of swimming defined by specific phase relations between flagella, yet ii) also rapidly modify these gaits in response to mechanical or biochemical cues to overcome microscale diffusion barriers. Thus the propensity for a run-and-tumble like dynamics appears to be a general strategy adopted not only by peritrichously flagellated bacteria [4, 5], but many species of eukaryotic flagellates alike. In light of these results the control of flagellar coordination and synchrony must now be re-evaluated in the context of intracellular signalling.

References

[1] Wan K.Y., Goldstein R.E.:"Coordinated beating of algal flagella is mediated by basal coupling", *PNAS* 113, *in press*, 2016.

[2] Wan K.Y., Goldstein R.E.:"Spontaneous and induced gait-switching in motile microalgae", *preprint* 2016.

[3] Brumley D.R., Wan K.Y., Polin M., Goldstein R.E.:"Flagellar synchronization through direct hydrodynamic interactions", *eLife* 3 (e02750), 2014.

[4] Berg H.G.: "Random walks in biology", *Princeton University Press*, 1983.

[5] Xie L., Altindal T., Chattopadhyay S., Wu X-L.: "Bacterial flagellum as a propeller and as a rudder for efficient chemotaxis", *PNAS* 108 (6): 2246–2251, 2011.

METABOLY IN EUGLENIDS: A MODEL AND ITS EXPERIMENTAL VALIDATION

Giovanni Noselli[1], Marino Arroyo[2], Alfred Beran[3] & Antonio DeSimone[1a)]
[1]*SISSA – International School for Advanced Studies, Trieste, Italy*
[2]*UPC – Universitat Politècnica de Catalunya, Barcelona, Spain*
[3]*OGS – Istituto Nazionale di Oceanografia e di Geofisica Sperimentale, Trieste, Italy*

Summary Euglenids are unicellular aquatic organisms capable of moving either by beating a flagellum or by executing dramatic shape changes. These are accomplished thanks to a complex structure underlying the plasma membrane, made of interlocking proteinaceous strips, microtubules, and motor proteins. We study the mechanisms by which the sliding of pellicle strips leads to shape control and locomotion, by means of both theory (through the mechanics of active surfaces and its coupling to computational fluid dynamics for the surrounding fluid) and experiments. Moreover, we implement them into a new concept of surfaces with programmable shape, obtained by assembling 3d-printed strips in a construct mimicking the biological template. We show that the subtle balance between constraints and flexibility leads to a wide variety of shapes that can be obtained with relatively simple controls. This suggests that euglenids exploit the passive resistance of body parts to reduce the complexity of controlling their shape.

INTRODUCTION

Euglenids are unicellular organisms (protists) living in a wide range of aquatic environments, which are capable of moving either by beating a flagellum, or by executing dramatic shape changes (metaboly, or euglenoid movement). Beneath the plasma membrane, they exhibit a complex structure made of interlocking proteinaceous pellicle strips, with microtubules aligned with the strips and localized at the strip junctions. It is commonly believed that shape changes associated with metaboly are achieved through the relative sliding of the pellicle strips, which is in turn driven by motor proteins running along the microtubules. While a quantitative check of this hypothesis is not yet available, analyzing the mechanisms of euglenoid movement is interesting from many perspectives. One is to assess whether it provides a viable motility strategy and, if so, when and how the organism switches between flagellar-based and shape-change-driven propulsion. Another one, is that shape control by the relative sliding of pellicle strips provides a new concept to program the shape of surfaces, namely, control by active surface shears, which is unexplored.

SHAPE CONTROL BY ACTIVE SHEARS DUE TO RELATIVE SLIDING OF PELLICLE STRIPS

Pellicle structures are clearly visible in (dead) euglenids by Scanning Electron Microscopy. Fig. 1 (left) shows the correlation between local pellicle orientation and shape, with the organism thinner where the strips are parallel to the body "axis" (the mid curve), and thicker where they are at an angle. The mechanism by which the surface shears associated to relative sliding of pellicle strips determine the shape of the surface is complex. To highlight the main principles, we have implemented this mechanism in prototypes obtained by assembling 3d-printed strips, see Fig. 1 (center). This picture illustrates the mechanism quite vividly in a simple case, where a family of cylinders of increasing radius and decreasing height is obtained from a cylinder in which all the strips are initially aligned with the cylinder axis, and then a uniform relative sliding of the strips (hence a uniform surface shear) is imposed. Note that, in this way, surface area is preserved.

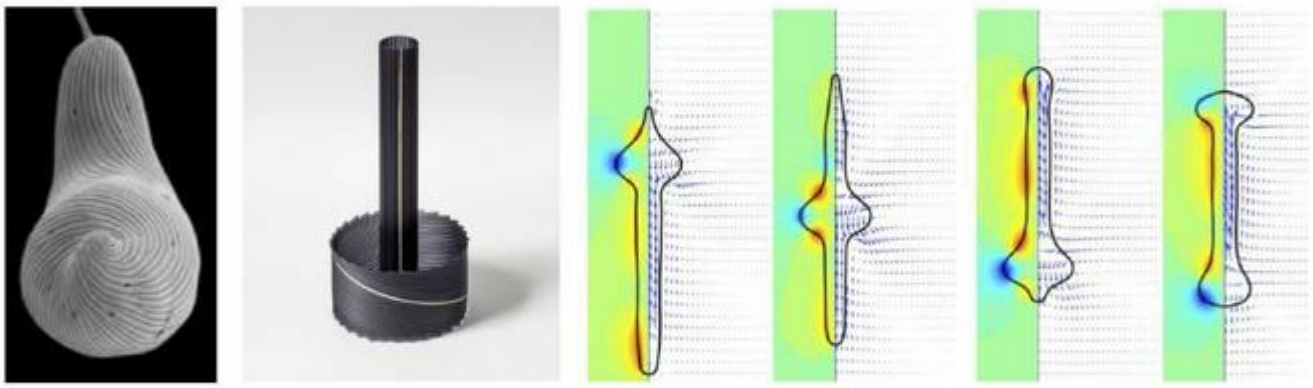

Fig. 1 Left: SEM image of the pellicle structure in Euglena sp.; center: illustration of the mechanism of shape control by relative sliding of interlocking 3d-printed strips; right: snapshots of numerical simulations to calculate displacements induced by propagating a bulge along the body in a model mimicking metaboly in Distigma.

[a)] Corresponding author. Email: desimone@sissa.it.

By allowing non-uniform relative sliding of the strips along their contour length (hence spatially variable surface shears), one can cause the propagation of a bulge along the cylinder, hence generating a propulsive force when the cylinder is immersed in a fluid. Building upon our previous work [1], we have explored this idea quantitatively. By solving numerically for the low Reynolds number flow induced by the shape changes observed in a variety of species of Euglena, and simultaneously solving the equation of motion for the swimmer subject to the forces transmitted by the surrounding fluid, we have computed the net displacements in one swimming stroke. We found that in some cases such as the one depicted in Fig.1 (right), displacements of the order of a few tenths of a body length per stroke can be attained. This suggests that metaboly can provide a viable motility strategy.

In order to validate the conclusions of our theoretical approach, we have studied the motion of euglenids executing metaboly by optical microscopy. Our preliminary observations show good agreement with the predictions of our model. In particular, Fig. 2 shows that shape changes are indeed directly correlated with the changes of orientation of the pellicle strips. An extensive campaign aimed at a quantitative comparison of theoretical predictions and experimental observations is the subject of ongoing work [2].

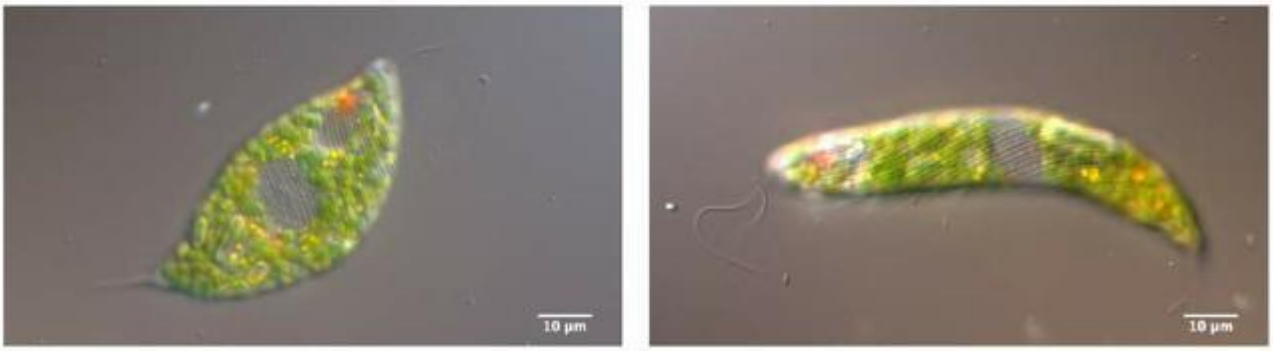

Fig. 2 Two light micrographs of the protist Euglena Ehrenbergii, showing that shape changes are correlated with changes of orientation of the pellicle strips. Images taken with an Olympus BX61 microscope equipped with a 100X/NA1.30 objective.

An interesting question arising naturally from our work is to characterize the shapes that are achievable by actuating a surface through active shears both in general (with an arbitrary continuous distribution of surface shears), and when specific discrete mechanisms (such as the interlocking 3d-printed strips of Fig. 1) are employed. The answer we find is that the range of achievable shapes is very large. For the general case, even restricting oneself to actuation by axisymmetric surface shears, we find that achievable shapes include portions of cones, spheres, pseudoshperes, or spindles [3]. By allowing non-axisymmetric shears, non-axisymmetric bent shapes can be obtained. One implication is that shape control by the relative sliding of pellicle strips provides a subtle balance between constraints and flexibility: a wide variety of shapes can be obtained with relatively simple controls. This suggests that euglenids exploit passive resistance of body parts (the stiffness of the pellicle strips, the constraints due to interlocking) to reduce the complexity of controlling their shape, in agreement with the notion of morphological computation that has been proposed for the control of soft, bio-inspired robots.

CONCLUSIONS

We have developed and validated a model of euglenoid movement based on active surface shears induced by the relative sliding of pellicle strips. Our results suggest that metaboly can provide a viable motility strategy. Moreover, we have implemented the mechanisms underlying shape changes in euglenids into a new concept of a surface with programmable shape, obtained by asssembling 3d-printed strips. We have shown that the subtle balance between constraints and flexibility leads to a wide variety of shapes that can be obtained with relatively simple controls. This suggests that euglenids exploit the passive resistance of body parts to reduce the complexity of the task of contolling their shape.

ACKNOWLEDGEMENTS

G.N., A.B., and A.D.S. gratefully acknowledge financial support from the ERC Advanced Grant 340685-MicroMotility.

References

[1] Arroyo M., Heltai L., Milan D., DeSimone A.: Reverse engineering the euglenoid movement. PNAS **109**:17874–17879, 2012.

[2] Noselli G., Arroyo M., Beran A., DeSimone A.: In preparation.

[3] Arroyo M., DeSimone A.: Shape control of active surfaces inspired by the movement of euglenids. J Mech Phys Solids **62**:99–112, 2014.

EFFECTS OF DISCRETENESS ON POPULATION PERSISTENCE IN AN OASIS

Stefano Berti *[1], Massimo Cencini[2], Davide Vergni[3], and Angelo Vulpiani[4,2]

[1]*Laboratoire de Mécanique de Lille, FRE 3723, Université Lille 1, 59650 Villeneuve d'Ascq, France*
[2]*Istituto dei Sistemi Complessi, CNR, Via dei Taurini 19, 00185, Rome, Italy*
[3]*Istituto per le Applicazioni del Calcolo, CNR, Via dei Taurini 19, 00185, Rome, Italy*
[4]*Dipartimento di Fisica, Università "La Sapienza", Piazzale Aldo Moro 2, 00185 Roma, Italy*

Summary Determining the conditions for persistence of species and populations is a question of paramount importance in population biology. The problem was first theoretically investigated adopting a continuous reaction-diffusion equation for population dynamics in a patch of finite size surrounded by a completely hostile environment, representing an oasis in a desert. The main result of this model, today known as the KiSS model (after Kierstead, Slobodkin and Skellam), is that patches need to be larger than a critical size to let the population survive. To explore the effects of discreteness and demographic stochasticity, here we propose an individual-based formulation of the KiSS model. We investigate population dynamics in our discrete model, focusing on the average time to extinction (above and below the critical patch size of the continuous model) and on the quasi-stationary distribution of the number of individuals for patch sizes larger than the critical value.

INTRODUCTION

Biological and chemical processes often involve the dynamics of discrete entities (e.g., molecules or organisms) that diffuse and interact with each other and/or with an external environment. If the number density of "particles" is very large, a macroscopic description in terms of continuous fields is typically appropriate; a well established approach to model the spatio-temporal evolution of the population density field is in terms of a reaction-diffusion equation. Conversely, if the density of particles is not very large the discrete nature of the population cannot be neglected [1], new effects arise and the continuous description becomes inaccurate. In order to account for such effects, we consider a system of particles diffusing in space and interacting when they get within a given interaction distance [2, 3]. In particular, revisiting the continuous KiSS model [4, 5], we investigate the effects induced by discreteness on the dynamics of a population inhabiting a favorable region ("an oasis") surrounded by a deadly environment ("a desert"). Accounting for such effects is important to assess the role of demographic and environmental stochasticity on extinction dynamics [6]. A peculiarity of our work with respect to previous investigations (see, e.g., [6, 7] and [8, 9] for studies respectively adopting non-spatial and spatial models) is that we fully describe the movement of individuals in space and we do not restrict the attention to steady state properties but we also deal with dynamical features of extinctions.

MODEL

The persistence/extinction problem was first ivestigated by Kierstead, Skellam and Slobodkin [4, 5] who considered a continuous population logistically growing with rate r and diffusing with diffusion coefficient D within a one-dimensional patch of size L surrounded by a deadly environment. For a given growth rate, higher diffusivities imply larger fluxes across the boundaries, so that larger patches are necessary to compensate the population loss in order to allow stable persistence. Standard eigenvalue computation for the linearized system (close to extinction the population density will be very small) gives $L_c = \pi\sqrt{D/r}$ for the minimal (critical) patch size ensuring persistence.

Among the various factors influencing extinction, demographic stochasticity, associated to the unavoidable random occurrence of birth and death events, is one of the most important ones. Here we introduce a discrete version of the KiSS model (see [2, 3] for details) to examine its role. The model is constructed with the essential feature of reproducing the FKPP (Fisher-Kolmogorov-Petrovskii-Piskunov) dynamics $\partial_t\theta = D\partial_x^2\theta + r\theta(1-\theta)$, where θ is the population density, for large numbers of particles [2]. The FKPP equation can be derived from the two coupled reaction-diffusion equations for the concentrations θ_A and θ_B of the species undergoing an autocatalytic reaction, provided the diffusion coefficients of species A and B are equal and $\theta_A + \theta_B = 1$ (i.e. local mass conservation). To discretize these equations we pass from the concentrations $\theta_{A,B}$ to a particle description in terms of N_A particles of type A and N_B of type B, with $N = N_A + N_B$ fixed. All particles undergo independent diffusive processes with the same diffusion coefficient, D, within the favorable patch $[0, L]$. A simple way to implement the interaction term $r\theta_A\theta_B$ is to impose that an A particle changes into B with a probability rate depending on the intrinsic rate, r, and on the number of B particles within an interaction distance R. Finally to reproduce the boundary conditions of the KiSS model and locally ensure mass conservation, we impose that A particles hitting the boundaries are reflected (nutrients are present only within the patch), and that if a B particle hits the boundary it is absorbed (as it cannot survive outside the favorable patch) and it is replaced in-place by an A-particle.

*Corresponding author. Email: stefano.berti@polytech-lille.fr

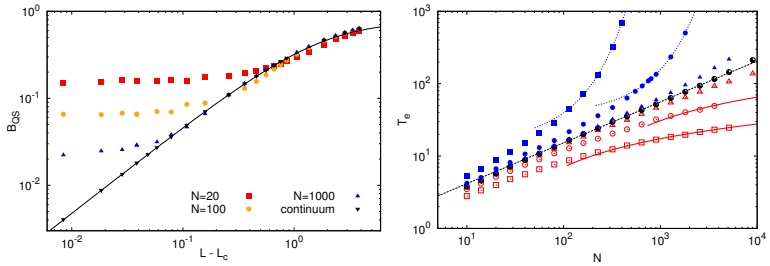

Figure 1: (Left panel) Long-time limiting biomass $\mathcal{B}_C^\infty$ in the continuous case and average biomass in the quasi-stationary state, $\mathcal{B}_{QS}$, as a function of $L - L_c$ for different values of N. The solid curve corresponds to the behavior $\mathcal{B}_C^\infty(L) \approx \lambda_1$ obtained with a mean-field-like argument, where λ_1 is the largest eigenvalue of the linearized KiSS model. (Right panel) Mean extinction time, T_e, vs population size, N, for different patch sizes $L = L_c + \delta L$: from bottom to top $\delta L = -0.3, -0.1, -0.02, 0, 0.02, 0.1, 0.3$, encompassing the extinction (empty red symbols) and persistence (blue filled symbols) regions, as well as the critical point (black half filled symbols) of the continuous model. The continuous red lines display the logarithmic prediction (see text) with b' fitted from data; the dashed blue lines correspond to the exponential behavior (see text) with a fitted. For $L = L_c$ we found a power-law behavior, $T_e \sim N^\gamma$, with best fitting exponent $\gamma = 0.565$.

RESULTS ON BIOMASS AND EXTINCTION TIMES

The main difference between the continuous model and the discrete one is that while the (continuous) stationary state $\theta = 0$ becomes unstable above the critical patch size, the (discrete) absorbing state $N_B = 0$ can always be reached due to demographic stochasticity, even when $L > L_c$. Nevertheless, the time taken by the system to be absorbed can be very long (for N and L large enough) and, in that case, the system reaches a quasi-stationary state. We have investigated the properties of this state at varying the system and population sizes by means of extensive numerical simulations. The results show that above the KiSS critical patch size the biomass in the quasi-stationary state recovers the continuum limit value only if the population is large enough (Fig. 1, left). On the other hand, when the population has a small number of individuals, the link between biomasses, defined in the continuous and particle models, ceases to exist. In particular, when the patch size tends to the critical value the number of individuals required to recover the continuum limit diverges.

We further analysed how the survival/extinction transition of the continuous KiSS model translates in the behavior of the average time to extinction T_e. Different functional dependencies of T_e on the population size N were found in the extinction ($L < L_c$), critical ($L = L_c$) and persistent ($L > L_c$) regions of the continuous model (Fig. 1, right). In the extinction region, the population density exponentially decays to zero with a rate given by the first eigenvalue $\lambda_1 = 1 - (L_c/L)^2$ (in non-dimensional units), which implies the logarithmic dependence $T_e \sim (\log N)/|\lambda_1| + b'$ (where $b' = \text{const}$). On the other hand, for $L > L_c$, T_e exponentially grows as $T_e \sim \sqrt{N} e^{aN}$ (where $a = \text{const}$), similarly to what is observed in non-spatial models. In the present case, such a behavior can be shown to be consistent, at least for L and/or N large enough, with Gaussianity of the quasi-stationary distribution. Finally, at the transition, the logarithmic and exponential behaviors are separated by the power-law $T_e \sim N^\gamma$. The value of the exponent is $\gamma = 0.565$ from a best fit, not far from the analytical prediction ($\gamma = 1/2$) obtained in the non-spatial logistic model. Despite small, the difference is clearly measurable and might be due to the spatial structure of the system under consideration.

We conclude mentioning that it would be interesting in the future to investigate the effects of population discreteness in more complex heterogeneous environments and possibly in the presence of advection.

References

[1] Durret R., Levin S.: The importance of being discrete. Theor. Popul. Biol. 46:363-394, 1994.

[2] Berti S., López C., Vergni D., Vulpiani A.: Discreteness effects in a reacting system of particles with finite interaction radius. Phys. Rev. E 76: 031139, 2007.

[3] Berti S., Cencini M., Vergni D., Vulpiani A.: Extinction dynamics of a discrete population in an oasis. Phys. Rev. E 92:012722, 2015.

[4] Skellam J.G.: Random Dispersal in Theoretical Populations. Biometrika 38:196-218, 1951.

[5] Kierstead H., Slobodkin L.B.: The size of water masses containing plankton blooms. J. Mar. Res. 12:141-147, 1953.

[6] Lande R.: Risks of population extinction from demographic and environmental stochasticity and random catastrophes. Am. Nat. 142:911-927, 1993

[7] Doering C.R., Khachik V.S., Sander L.M.: Extinction times for birth-death processes: exact results, continuum asymptotics, and the failure of the Fokker–Planck approximation. Multiscale Model. Simul. 3:283-299, 2005.

[8] Méndez V., Hortshemke W., Casas-Vázquez J., Zemskov E.: Variational principles and the effect of a cutoff on population pattern size. Eur. Phys. J. (Special Topics) 146:189-197, 2007.

[9] Escudero C., Buceta J., de La Rubia F.J., Lindenberg K.: Extinction in population dynamics. Phys. Rev. E 69:021908, 2004.

MS03 - Multiphase Flow in the Processing Industry

TS.MS03-1.01	Pillai, Krishna M. - Current challenges in upscaling multiphase flows in porous media using the volume averaging method (INVITED)	89
TS.MS03-1.02	Rao, Rekha - The fluid mechanics of polyurethane foam expansion and polymerization (INVITED)	91
TS.MS03-1.03	Sommerfeld, Martin - Modelling Requirements for Particle Agglomeration in Fluid Flows (INVITED)	93
TS.MS03-1.04	Collino, Rachel - Scaling relationships describing microfluidic acoustic nozzles for 3D-printing (INVITED)	95
PO.MS03-1.01.1	Sassi, Mohamed - Experimental Study of Flow Regimes and Empirical Correlations of the Pressure Drop in a Trickle Bed Reactor	97

CURRENT CHALLENGES IN UPSCALING MULTIPHASE FLOWS IN POROUS MEDIA USING THE VOLUME AVERAGING METHOD

Krishna M. Pillai[1a)]

[1]*Laboratory for Flow and Transport Studies in Porous Media, Department of Mechanical Engineering, University of Wisconsin-Milwaukee, Milwaukee WI, USA*

Summary The talk will start with an introduction of multiphase flows seen in industrial applications. It will be followed by the current state of theoretical development for multiphase flows as proposed using the volume averaging method. The two viscous drag tensors proposed by the theoretical developments will be discussed. Then the results of experiments and simulations done using micromodels will be presented which describe different flow regimes possible in multiphase flows including viscous fingering, capillary fingering and stable displacement. At the end, the need for a new mathematics to explain the contradictions posed by these findings.

Since any typical porous medium consists of numerous smaller particles or fibers separated by interstitial spaces, it is not practical to conduct CFD simulations in the entire domain to predict flow and transport. Hence upscaling is employed to describe the phenomena in terms of averaged quantities so that flow and transport predictions can be undertaken in porous media. The volume averaging method is a well-established method to upscale flow and transport variables in porous media. Compared to other upscaling methods such as the mixture theory or the homogenization method, the volume averaging method establishes a good connection between the larger *macroscopic* domain of volume averaged variables used to describe the porous-continuum space and the smaller *microscopic* domain of point-vise variables used to describe the pore-level (discrete) space. This allows the estimation of macroscopic properties, such as the permeability or thermal diffusivity tensors that are used in the macroscopic or upscaled governing equations, using the closure formulation on pore-level microstructures [1,2].

Displacement of one fluid by another is an example of the multiphase flow in porous media. Such multiphase flows through porous media are quite common in the processing industry where the applications range from reducing void content during processing of composites to tracking the presence of water in gas diffusion layer in fuel cells to optimizing design of person hygiene pads. Using the volume averaging method, Whitaker and co-workers [3,4,5] showed that the upscaled Stoke's equation will have the form:

$$\langle \boldsymbol{v}_\beta \rangle = -\frac{\boldsymbol{K}_\beta}{\mu_\beta} \cdot \left(\nabla \langle p_\beta \rangle^\beta - \rho_\beta \, \boldsymbol{g} \right) + \boldsymbol{K}_{\beta\gamma} \cdot \langle \boldsymbol{v}_\gamma \rangle \qquad (1)$$

$$\langle \boldsymbol{v}_\gamma \rangle = -\frac{\boldsymbol{K}_\gamma}{\mu_\gamma} \cdot \left(\nabla \langle p_\gamma \rangle^\gamma - \rho_\gamma \, \boldsymbol{g} \right) + \boldsymbol{K}_{\gamma\beta} \cdot \langle \boldsymbol{v}_\beta \rangle \qquad (2)$$

where $\boldsymbol{K}_\beta$ and $\boldsymbol{K}_\gamma$ are permeability tensors and $\boldsymbol{K}_{\beta\gamma}$ and $\boldsymbol{K}_{\gamma\beta}$ are viscous drag tensors. The proposed form was different from the usual well-accepted form of the generalized Darcy's law for the two phases, β and γ, that are identical to Eqns. (1) and (2) when the terms containing the viscous drag tensors are removed. Though this proposed form of Darcy's law is novel and based on rigorous derivation, it is yet to find acceptability due to the absence of any experimental verification of the two viscous drag tensors. We explore the possibility of conducting some accurate pore-level simulations using modern methods such as the Lattice-Boltzmann method to simulate two-phase flow in a representative elementary volume and then using the closure formulations for the two phases to upscale and estimate the two viscous-drag tensors.

In the end, the further difficulties on the path of upscaling multiphase flow in porous media will be discussed. In

[a)] Corresponding author. Email: krishna@uwm.edu

particular, the three different flow regimes of capillary fingering, stable displacement and viscous fingering, encountered during the flow of two phases through porous medium [6], will be presented. These flow regimes have been shown to be strong functions of two dimensionless groups, the Capillary number and the viscosity ratio [6]. Development of capillary fingers is quite similar to the formation of large clusters (islands of wet phase) witnessed during drying which is simulated quite accurately using the invasion-percolation algorithm in network models [7]. A common feature of these formations is that they are governed entirely by the inhomogeneities seen at the pore level and lead to a rather disconcerting result—the concept of volume averaging becomes inapplicable since the presence of such fingers lead to creation of large structures of the same size as the solution domain. (A condition of volume averaging is that the REV (representative elementary volume) used for averaging the flow and transport variables should be smaller than the solution domain but much bigger than the individual pore-level formations seen in [7].) The challenge of developing a closure formulation, that can represent these three different flow regimes, is the current obstacle facing the volume averaging method as applied to multiphase flows.

References

[1] "Estimation of Tortuosity and Effective Diffusivity Tensors using Closure Formulation in a Sintered Polymer Wick during Transport of a Nondilute, Multicomponent Liquid-Mixture", S. Beyhaghi and K.M. Pillai, *Special Topics & Reviews in Porous Media - An International Journal*, Vol. 2, issue 4, pp. 267-282, 2011.

[2] "Fast 2D Micrograph-Based Method of Permeability Estimation through Micro-Macro Coupling in Porous Media," B. Barari, S. Beyaghi and K.M. Pillai, under review with *Journal of Porous Media*.

[3] "Flow in Porous Media II: The Governing Equations for Immiscible, Two-Phase Flow," S. Whitaker, *Transport in Porous Media*, v 1, pp 105-125, 1986.

[4] "The Closure Problem for Two-Phase Flow in Homogeneous Porous Media," S. Whitaker, *Chemical Engineering Science*, v 49, n 5, pp 765-780, 1994.

[5] "Determination of Permeability Tensors for Two-Phase Flow in Homogeneous Porous Media: Theory," D. Lasseux, M. Quintard and S. Whitaker, *Transport in Porous Media*, n 24, pp 107-137, 1996.

[6] "Numerical Models and Experiments on Immiscible Displacements in Porous Media," R. Lenormand, E. Touboul and C. Zarcone, *Journal of Fluid Mechanics*, v 189, pp 165-187, 1988.

[7] "A Study on Slow Evaporation of Liquids in a Dual-Porosity Porous Medium using Square Network Model", K M. Pillai , M. Prat, M. Marcoux, *International Journal of Heat and Mass Transfer*, v 52, n 7-8, p 1643-1656, March 2009.

THE FLUID MECHANICS OF POLYURETHANE FOAM EXPANSION AND POLYMERIZATION

Rekha R. Rao[1], Lisa A. Mondy[1], Christine C. Roberts[1], Melissa M. Soehnel[1], Kevin Long[1], Victor E. Brunini[2], David Noble[1], Mathew C. Celina[3], James J. Tinsley[4]

[1]*Engineering Sciences Center, Sandia National Laboratories*, MS 0836, Albuquerque, NM USA*
[2]*Systems Engineering Center, Sandia National Laboratories, MS 9957, Livermore, CA USA*
[3]*Materials Science Center, Sandia National Laboratories, MS 01411, Albuquerque, NM USA*
[4]*Honeywell Federal Manufacturing & Technologies, 14520 Botts Road, Kansas City, MO USA*

Summary In this presentation, we discuss our new, experimentally driven, approach to foam expansion and polymerization modeling. We are working to develop high-fidelity computational models to be used to design and troubleshoot mold filling for polyurethane structural foam parts.

INTRODUCTION

We are studying PMDI polyurethane with a fast catalyst, such that filling and polymerization occur simultaneously. The foam is over-packed to twice or more of its free rise density, to reach the density of interest. Developing a relevant model to represent the expansion, filling, curing, and final foam properties is quite challenging. PMDI is chemically blown foam, where carbon dioxide is produced via the reaction of water and isocyanate. The isocyanate also reacts with polyol in a competing reaction, which produces the polymer. A new kinetic model is implemented, which follows a simplified mathematical formalism that decouples these two reactions. The model predicts the polymerization reaction via condensation chemistry, where vitrification and glass transition temperature evolution must be included to correctly predict this quantity. The foam expansion kinetics are determined by tracking the molar concentration of both water and carbon dioxide. The conservation equations, including the equations of motion, an energy balance, and three rate equations are solved via a stabilized finite element method [1]. We assume generalized-Newtonian rheology dependent on the cure, gas fraction, and temperature. The conservation equations are combined with a level set method to determine the location of the free surface over time.

RESULTS

The model is applied to a geometry similar to a flow visualization experiment we conducted of polyurethane foam expansion in a clear mold. Results from the model are compared to the experimental data (Figure 1) and post-test CT data for the density in a simpler bar geometry.

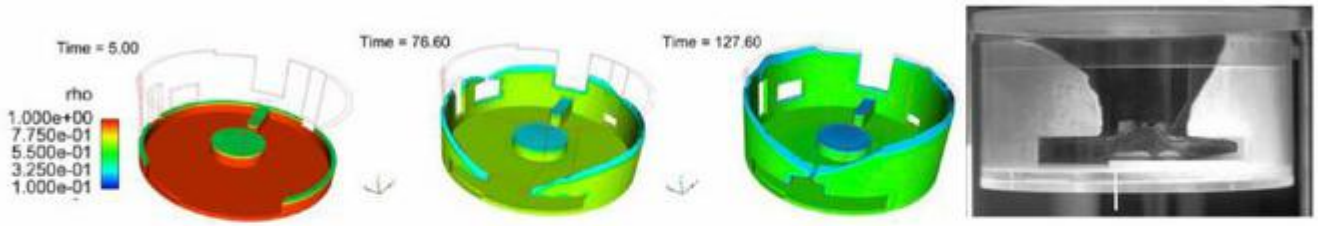

Figure 1. The left three images show the filling profile and density variations of polyurethane foam expansion as predicted by the model. The right-most image shows a flow experiment for validation of the model.

The model calculates the molar volume of carbon dioxide and uses that to predict the final density of the part. These results can be seen in Figure 2. The concentration of carbon dioxide is highest under the large circular feature and lower on the walls. The concentration is very noisy, possibly due to numerical oscillations. The density varies spatially with the lowest density seen at the bottom, including trapped gas below the largest feature. The density is higher at the walls than in the interior of the mold. The model predicts a thin skin of higher density at the walls, mostly due to temperature gradients and internal exothermic heating.

Density predictions in the bar geometry have been compared to X–Ray CT data [2]. From this comparison, we have seen that the average density was fairly representative, but that the data showed much larger density gradients than the model, even when including an ideal gas law representation of the gas bubbles. It under predicts density gradients, especially in the gravity direction and the skin is much thinner in the computational model than in the CT data. We think that some of these effect are due to bubble-scale phenomena such as foam drainage, bubble migration, and wall shear rate effects. To capture

[a] Corresponding author. Email:rrrao@sandia.gov.

this phenomenon, we plan to solve a Rayleigh-Plesset equation to determine the local bubble size over time, including both gas and liquid phase concentrations of CO_2.

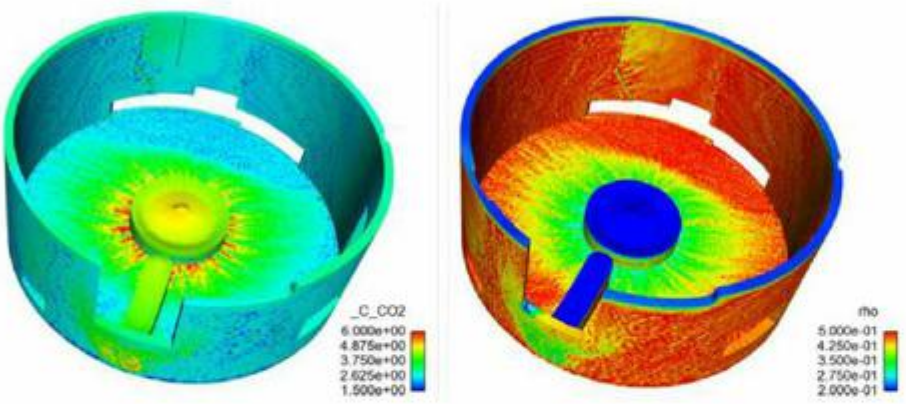

Figure 2. Carbon dioxide concentration (.01 scaling of mmol/ml) and resulting density variations (g/cm3) in pie mold showing voids under large features.

CONCLUSIONS

A numerical model has been developed for foam expansion and polymerization in complex geometries based on the finite element method and a level set method to capture the dynamic filling process. The method has been applied to various geometries and shown to capture average density and filling profiles well, though density gradients are still under predicted.

FUTURE WORK

For the next generation foam model, we will need to have an estimate of bubble size so that we can include bubble-scale effects such as foam drainage, bubble-pressurization, and coarsening. To capture this phenomenon, we need to track the carbon dioxide in both the gas and liquid phases. A Rayleigh-Plesset equation is then used to determine the local bubble size (R) over time, including both gas and liquid phase concentrations of CO_2, where ρ_{liq} is the density, $\eta_{polymer}$ is polymer viscosity, σ is the surface tension, and p is the pressure in either the bubble or the polymer.

$$\rho_{liq}\left(\frac{3}{2}\dot{R}^2 + R\ddot{R}\right) = p_{gas} - p_{liq} - 2\frac{\sigma}{R} - 4\eta_{polymer}\frac{\dot{R}}{R} \quad (1)$$

From this equation, we can see that evolving viscosity and surface tension effects will be taken into account explicitly, allowing the bubble growth to halt even if excess carbon dioxide is present. The volume fraction ϕ and the foam density can then be determined from the bubble radius and an experimentally determined bubble number density.

$$\phi(t) = N_{bubbles}\sum_{i=1}^{ng}\frac{4}{3}\pi R_i^3 \quad (2)$$

$$\rho_{foam} = (\rho_{gas} - \rho_{liq})\,\phi(t) + \rho_{liq}$$

The bubble size and number will then be used to predict the density and density gradients of the macroscopic foam, including a foam drainage model linked to bubble size. We hope this new model will be more predictive of the density gradients seen in the X-ray CT data.

ACKNOWLEDGMENTS

Sandia National Laboratories is a multi-program laboratory managed and operated by Sandia Corporation, a wholly owned subsidiary of Lockheed Martin Corporation, for the U.S. Department of Energy's National Nuclear Security Administration under contract DE-AC04-94AL85000.

References

[1] R.R. Rao, L.A. Mondy, et al., "A Level Set Method to Study Foam Processing: A Validation Study," *IJNMF*, April 2012.

[2] R.R. Rao, L.A. Mondy, et al., "A Kinetic Approach to Modeling the Manufacture of High Density Polyurethane Structural Foam: Foaming and Polymerization," September 2015, SAND2015-8282.

MODELLING REQUIREMENTS FOR PARTICLE AGGLOMERATION IN FLUID FLOWS

Martin Sommerfeld [a)]
Martin-Luther-Universität Halle-Wittenberg, Zentrum für Ingenieurwissenschaften, D-06099 Halle/Saale, Germany

Summary Particle agglomeration is important for many unit operations in process technology. A numerical calculation of such processes requires appropriate models for describing the agglomeration itself and the behaviour of the agglomerates in the flow. This implies the occurrence of collisions, the sticking probability of particles, the mapping of the agglomerate structure and the fluid dynamic drag of complex agglomerates. Models accounting for these elementary processes were developed, implemented in an in-house numerical code and tested for several flow situations, including a spray dryer.

INTRODUCTION

In the process industries agglomeration of solid particles in gas or liquid flows is relevant for many unit operations. Such an agglomeration may be a desired or undesired phenomenon and results in an effective growth of particles forming more or less complex structures. Examples for eligible particle agglomeration are particle capture in a cyclone whereby the particle size effectively grows and separation efficiency improves as well as powder production in a spray dryer wherein larger particles with desired structures may be produced through on purpose agglomeration.

Nowadays many industrial areas apply multiphase flow CFD (computational fluid dynamics) for process design and optimization. For the considered dispersed particle-laden flows, the well-known hybrid Euler/Lagrange approach is most suitable since the particle size distribution is very important to be resolved. For industrial applications the mostly turbulent fluid flow is calculated by solving the Reynolds-averaged conservation equations (RANS) in connection with an appropriate turbulence model. In the Lagrangian part a large number of particles are tracked in the before-hand calculated flow field in order to eventually obtain reliable averaged dispersed phase properties. So far such calculations consider mostly spherical particles represented as point-masses which however is a bad approximation for agglomerates. Real agglomerates consist of many primary particles which may be organized in a compact way with relatively low porosity or are made up of numerous dendritic branches yielding very high porosities. In each case however, the effective size of agglomerates is much larger than the volume equivalent diameter so that the effective size and particle density need to be accounted for in particle tracking using resistance force coefficients also accounting for porosity.

Essential for the formation of agglomerates is the occurrence of inter-particle collisions which are mainly determined by high particle concentrations and large relative velocities between particles; the latter being induced by inertial effects and/or turbulence. Agglomeration of particles will only occur if interaction forces such as Van der Waals, electrostatic and liquid binding become strong enough. Consequently these three effects, namely particle collisions, agglomerate formation and tracking of agglomerates need to be appropriately modelled in a numerical calculation.

LAGRANGIAN AGGLOMERATION MODEL

In order for appropriately conducting Euler/Lagrange calculations of agglomeration processes, a stochastic inter-particle collision model was developed, which also accounts for the impact efficiency [1, 2], i.e. a small particle might move around a larger particle with the relative flow and hence not collide. Once two particles collide it is necessary to decide whether they rebound or stick together forming an agglomerate. For dry particles, this may be done based on an energy balance, comparing the relative kinetic energy with dissipated and Van der Waals energy [1]. This yields a critical upper velocity for particle adhesion and agglomeration. If high viscous or mushy droplets collide (e.g. in a spray dryer) they may penetrate partially and form also structured agglomerates [3]. The penetration of a high viscous droplet into one with lower viscosity is calculated by considering Stokes drag and shear forces [3, 4].

Agglomeration of solid particles might be modelled in different ways depending on the degree of information expected from the two-phase flow calculations. Different modelling approaches are summarized in Figure 1. The most straight forward approach assumes that the two agglomerating particles form a new volume equivalent sphere with a velocity resulting from a momentum balance. This model does however not provide any information on the realistic structure and size of agglomerates. The second model, called sequential model, assumes that for every two particle agglomeration a new spherical particle is formed with the volume consisting of the volume of the involved two spherical particles plus the void volume resulting from the convex hull wrapped around the two particles (see Fig. 1 middle). The new particle is now tracked with a size being larger than that resulting from the volume of the two primary particles and a porosity resulting from the two particle configuration. This procedure is successively repeated for each agglomeration considering however, that the "spherical" agglomerate has already porosity. This model was applied for calculating particle separation in a gas cyclone [5]. The most sophisticated agglomeration model (Figure 1 right) allows the estimation of the complete structure of agglomerates through statistical approaches. From an initial primary particle location vectors are stored for each new primary particle being collected by the agglomerate. This information is carried throughout the flow field for every

[a)] Corresponding author. Email: martin.sommerfeld@iw.uni-halle.de.

Lagrangian agglomerate produced (Figure 1 right). Thereby it is possible to obtain a realistic agglomerate size from the convex hull volume, agglomerate porosity and effective particle density [4]. It should be noted that the agglomerate is yet treated as a point-particle.

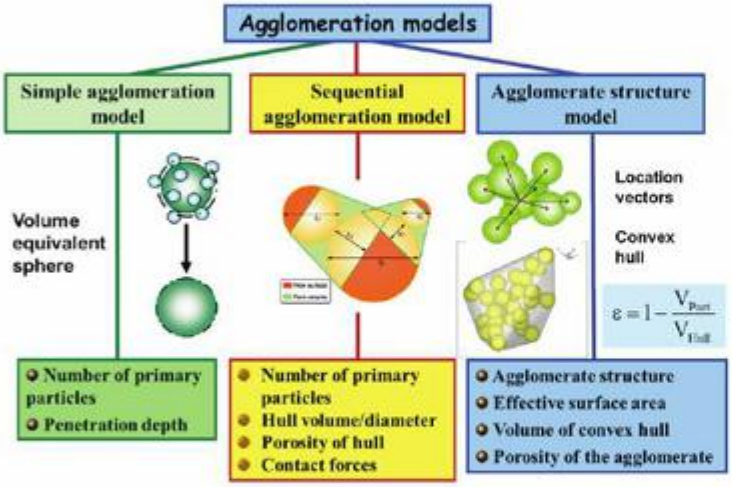

Figure 1: Overview of different approaches for modelling particle agglomeration.

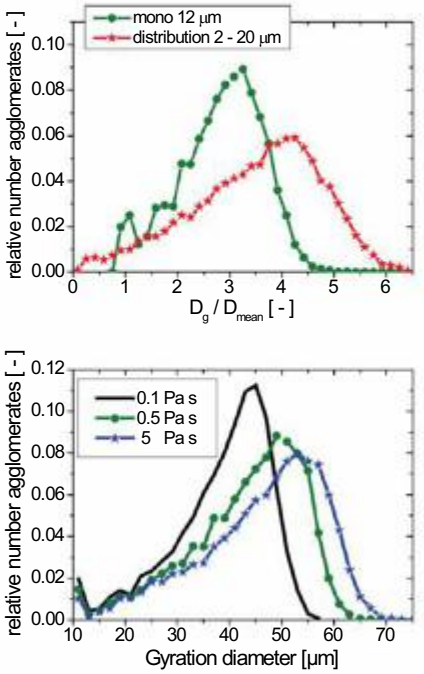

Figure 2: Simulated PDF of agglomerate sizes in homogeneous isotropic turbulence for different particle properties; a) dry particles mono-sized (12 µm) versus size distribution; b) mushy droplets with different viscosity for initially mono-sized particles (12 µm).

Having now a porous particle with an effective size and density the question arises, which drag coefficient should be used for tracking the agglomerate? It is known, that the drag coefficient decreases with increasing porosity since the flow intensity through the agglomerate increases. In order to determine the dependence of drag coefficients on porosity, Lattice-Boltzmann simulations were conducted for different randomly generated agglomerates fixed in a cubic flow domain and exposed to a laminar plug flow [6]. The results showed, that even for a compact agglomerate with a porosity of $\varepsilon = 0.8$ the drag coefficient at low Reynolds number (i.e. 0.3) is about 10 % lower than for a compact sphere.

RESULTS

For demonstrating the performance of the novel agglomerate structure model, first results obtained for particle motion in a homogeneous isotropic turbulence field are presented [4]. The results for example show that for a poly-sized population the agglomerates grow faster, have a higher porosity and become larger than for a comparable mono-sized population with the same mean diameter (Figure 2 a). Considering mushy droplets, like in a spray dryer, an increasing viscosity yields lower penetration and as a result larger Gyration diameters and more porous agglomerates (Figure 2 b).

Finally, numerical simulations for a spray dryer are being performed in order to obtain the properties of the produced agglomerates. In a spray dryer of course particle interaction is even more complex. Initially solution droplets are injected into the dryer, which, upon collision might coalesce. Due to further drying the droplet viscosity increases remarkably and the droplets become mushy yielding a penetration upon collision. The results show that the agglomerate structure obtained from the simulations is in qualitative agreement with experimental observations.

References

[1] Ho, C.A. and Sommerfeld, M.: Modelling of micro-particle agglomeration in turbulent flow. Chem. Eng. Sci. **57**: 3073 – 3084, 2002.

[2] Sommerfeld, M. and Lain, S.: From elementary processes to the numerical prediction of industrial particle-laden flows. Multiphase Science and Technology **21**: 123 – 140, 2009.

[3] Sommerfeld, M., Blei, S., Stübing, S. and Lipowsky, J.: Modelling of agglomerate structure in the Lagrangian point-particle approximation. Transport Phenomena in Multiphase Systems (Eds. Butrymowicz, D. Goscik, J. and Skiepko, T.), Proceedings of the 5th International Conference on Transport Phenomena in Multiphase Systems, June 30. to July 3. 2008, Bialystok, Poland, Vol. 1, 173-188 (2008)

[4] Sommerfeld, M. and Stübing, S.: Lagrangian modeling of agglomeration for applications to spray drying. 9th International ERCOFTAC Symposium on Engineering Turbulence Modeling and Measurements, Thessaloniki, Greece, 6. – 8. June 2012.

[5] Lipowsky, J. and Sommerfeld, M.: Influence of particle agglomeration and agglomerate porosity on the simulation of a gas cyclone. Proceedings 6th Int. Conf. on CFD in Oil & Gas, Metallurgical and Process Industries. Trondheim Norway, Paper No. CFD08-043, June 2008.

[6] Dietzel, M., Ernst, M. and Sommerfeld, M.: Application of the Lattice-Boltzmann Method for Particle-laden Flows: Point-particles and Fully Resolved Particles. Flow Turbulence Combust, DOI: 10.1007/s10494-015-9698-x.

SCALING RELATIONSHIPS DESCRIBING MICROFLUIDIC ACOUSTIC NOZZLES FOR 3D-PRINTING

Rachel Collino[1a], Tyler Ray,[1] Leanne Friedrich, [1] James Cornell [1] & Matthew Begley [1]
[1]*Materials Department, University of California, Santa Barbara, Santa Barbara, California, United States of America*

Summary: Acoustic forces are an attractive pathway to achieve directed assembly for two-phase materials *via* additive processes. On one hand, they can be used to align and consolidate particles in uncured matrices to effectively print composites in three dimensions. On the other hand, they can be used with traditional self-assembly to create hierarchical assembly techniques in which chemically-assembled 'meso-particles' (*e.g.*, each consisting of multiple nanoscale particles) are aggregated at much faster time scales than those associated with diffusion. We present key scaling relationships controlling the time for aggregation and alignment of particles, which can be used to identify acceptable levels of acoustic excitation and the required dimensions for focusing regions. The results are used to predict optimal combinations of these parameters that lead to deposition of highly packed particles without jamming.

The impact of three-dimensional printing will be enhanced considerably by developing techniques to deposit multiphase materials with controlled density and alignment of the constituents. The optical, thermal, and electrical properties of two-phase functional materials can be improved by controlling particle distributions to introduce photonic band-gaps[1], coupled electro-mechanical behaviors[2], coupled thermo-mechanical behaviors[3,4], *etc.* The control of particle aggregation and deposition within a single print stream is thus of interest for reducing the complexity and cost of multiphase printing for materials with advanced functionalities.

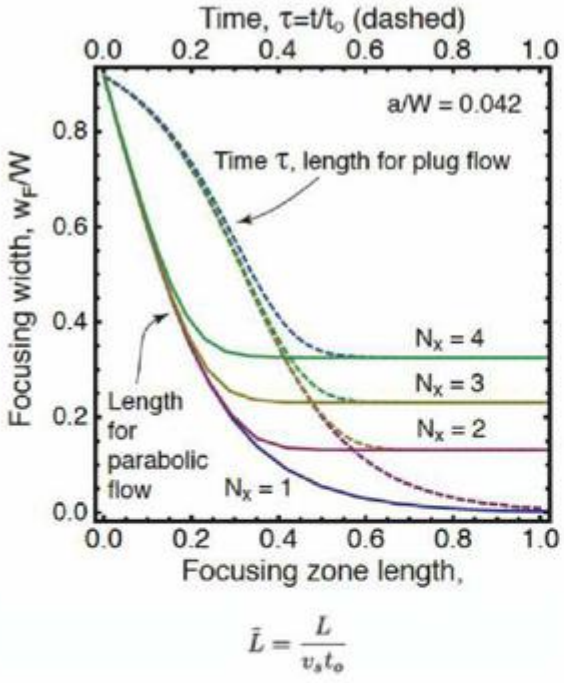

Figure 2: The predicted focusing behavior of particles experiencing primary radiation and secondary scattering forces, in parabolic and plug flows.

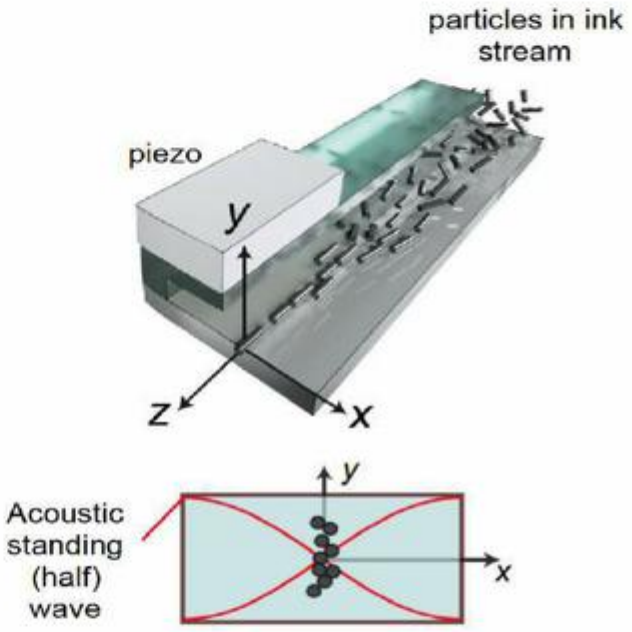

Figure 2: Microchannel print nozzle geometry and coordinate system. The piezo is excited at a frequency corresponding to a standing half-wave in pressure.

Acoustic forces created by standing pressure waves are an attractive pathway to increasing the density and alignment of particles: they are active over large distances and relatively material agnostic (*i.e.*, they do not require specific surface functionalization, solution chemistries, or electromagnetic properties). In many of the above applications, the particles are micron-sized or larger, such that the magnitude of easily achieved acoustic forces is much greater than those associated with fluid drag, implying that particles can be transported and assembled over relatively long distances on the order of seconds or less. These benefits create new opportunities to incorporate acoustic excitation in nozzles used for three-dimensional printing, to dramatically increase the density and alignment of particles relative to that of the 'ink'.

In this work, we use previously developed solutions for acoustic forces generated by standing waves in a channel[5] to identify the

[a] Corresponding author. Email: rcollino@engr.ucsb.edu

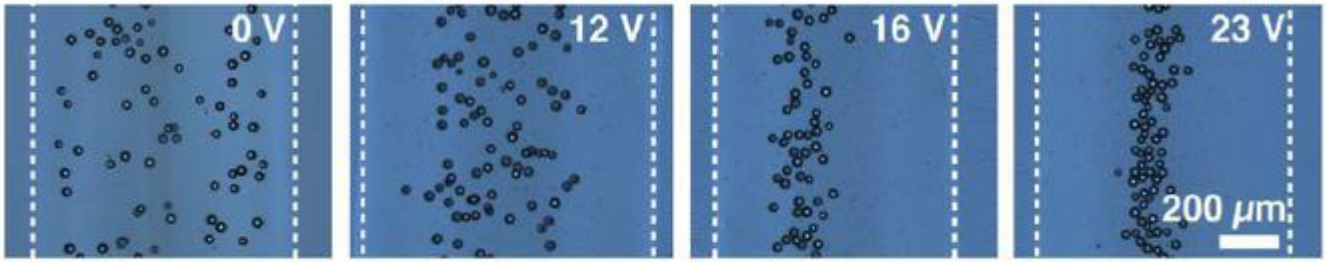

scaling relationships that control particle transport and ordering. The goal is to elucidate the connections between channel dimensions, particle dimensions, acoustic pressures, focusing zone size and flow characteristics needed to design effective

Figure 3: Microstructural variation of printed lines (outlined by dashes) of barium titanate spheres in epoxy, illustrating the effect of the excitation voltage of the piezoelectric element on the focusing width of the particles.

nozzles for material deposition. We consider a standing half-wave in pressure and particles (with radius a) that are less compressible than the fluid, which implies that particles are driven to the center of the channel, *i.e.,* there is a single focusing node at the center of the channel of width W and flow at uniform velocity v_S. The coordinate system and device geometry used in this work is shown in Fig. 1, where the direction of the wave is transverse to the channel in the $x-$direction (with $x = 0$ being the center of the channel), while the flow direction is in the positive $z-$direction. Fig. 2. Shows the normalized focusing width, w_F/W, as a function of time and as a function of the distance travelled. The effect of excitation energy of the piezoelectric element is illustrated in Fig. 3, where focusing width of particles is varied according to the applied voltage.

This analysis allows one to identify a dimensionless measure of focusing efficacy for a print nozzle, by balancing time scales for transverse focusing, and aggregation in the flow direction, as shown in Fig. 4. If the time required for axial aggregation is too small, the printed line will be have greater transverse density than axial density. Conversely, if the time for axial aggregation is too large, aggregates may form to that would lead to axial variations in printed microstructures (along the print line), critically, jamming might occur. Contours of the ratio of these time scales are shown in Fig. 4 as a function of the volume fraction of particles and the effective focusing zone length. This key result provides guidance as to the desired length of the nozzle as a function of the acoustic excitation and initial particle density.

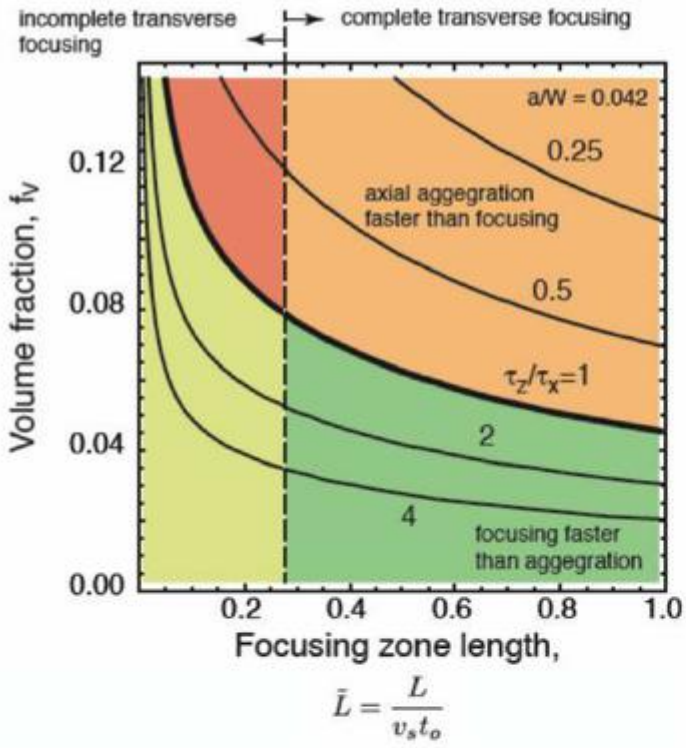

Figure 4: Contours of the aggregation parameter $P_A = \tau_Z/\tau_X$, where a value of one represents a balance of transverse focusing and axial aggregation time scales, as a function of the focusing zone length. For $P_A < 1$, axial aggregation occurs faster than focusing; the opposite is true for $P_A > 1$

References

[1] Kim, S.-H., Lee, S. Y., Yang, S.-M., Yi:, G.-R. Self-Assembled Colloidal Structures for Photonics, *NPG Asia Mater.* **3**: 25-33, 2011.

[2] O'Halloran, A., O'Malley, F., McHugh, P. A Review on Dielectric Elastomer Actuators, Technology, Applications, and Challenges. *J. Appl Phys* **104**:071101, 2008.

[3] Ge, Q., Qi, H. J., Dunn, M. L. Active Materials by Four-Dimension Printing, *Appl Phys Lett.* **103**:131901, 2013.

[4] Bakarich, S. E., Gorkin, R. Panhuis, M. i. h., Spinks, G. M. 4D Printing with Mechanically Robust, Thermally Actuating Hydrogels. *Macromol Rapid Comm* **36**:1211-1217, 2015.

[5] Collino, R. R., Ray, T.R., Fleming, R. C., Cornell, J. D., Compton, B. G., Begley, M. R. Deposition of Ordered Two-Phase Materials using Microfluidic Print Nozzles with Acoustic Focusing. *Extreme Mech Lett* **5**: 37-46, 2015.

EXPERIMENTAL STUDY OF FLOW REGIMES AND EMPIRICAL CORRELATIONS OF THE PRESSURE DROP IN A TRICKLE BED REACTOR

Imen Ben Salem[1], Humair Nadeem[1], Amna Al Maqtari[2], Mohamed Sassi[1]
[1]*Institute Center for Energy (iEnergy), Department of Mechanical and Materials Engineering, Masdar Institute of Science and Technology, Masdar City, Abu Dhabi, United Arab Emirates*
[2]*Takreer Research Center (TRC), Abu Dhabi, UAE*

Summary Trickle bed reactors (TBRs) are an important component in the refining processes. TBRs are widely popular in the hydro-treatment of the "bottom-of-the-barrel" components of medium and heavy oil fractions specifically the hydrocracking of residual oils, hydrogenation of aromatics in gasoil and the hydrocracking of lube-oils (Sie and Krishna, 1998). When such heavy oil suspensions are treated in TBRs, a residual fraction of fine particles may be deposited onto the bed surface. If continued unabated, the deposition even in small concentrations, will overtime cause pore plugging and increases the pressure drop over the TBR. The catalyst operates as a huge filter now capturing the fine particles instead of its primary role to the extent that the chemically active catalyst has to be replaced before the completion of its operating life that incurs economic costs.

METHODOLOGY

In this work, we focus on multi-scale experimental investigations of the inter-play between flow regimes and fines deposition in trickle bed reactors in pursuit of mitigation of the pressure build-up problem. The experimental work includes the visualization and characterization of flow regimes in quasi-two-dimensional porous medium with an average pore diameter close to the values encountered in trickle beds. A parametric study is done for the development of flow regimes and the transition between them when the geometry and arrangement of the particles within the porous medium are varied. Experimental observations are made to investigate the development and transition of these flow regimes over a wide range of liquid and gas velocities. Cylindrical particles are placed between two glass plates that are sealed on the sides and water and air are injected over them using an injection manifold to simulate multiphase flow in a TBR. A diffused LED light table is used to illuminate the experimental window while real time images are obtained using a high-speed camera (figure 1).

A Pilot tubular TBR was used to determine the pressure drop across the Trickle Bed Reactor with and without fine particles brought in by the liquid feed (figure 2). The pilot plant consisted tubular reactor with length 0.79 m and dia. 0.0183. Due to its similarity to the fines found commercial TBRs, kaolin particle of size 50 □m were used as fine particles. In order to prevent cake formation, Homogeneous mixing of the suspension was accomplished in the inlet tank which was equipped with a magnetic stirrer and were stirred continuously in different concentrations with LGO in the feed tank. The desired flow of LGO through the feed tank was pumped to the inlet of the reactor where it mixes with the desired flow of incoming gas and enters the Trickle Bed Reactor.

In order to record pressure drop across the reactor, two pressure transducers were installed, each at the inlet and the outlet of the reactor. After passing through the reactor, the LGO-nitrogen mixture enters the separator where gas is separated and liquid goes into the collector tank. The amount of liquid that leaves the feed tank and enters the collector tank is measured by placing the tanks at the weighing scale. The pressure of the transducers can be monitored and recorded by the electronic unit associated with the pressure transducers. The system was single pass and LGO obtained at collector end was not recycled to the feed tank to maintain concentration of fine particles in the feed.

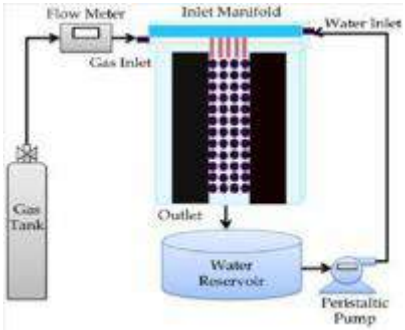

Figure 1: Schematic representation of experimental setup to visualize flow regimes in a TBR

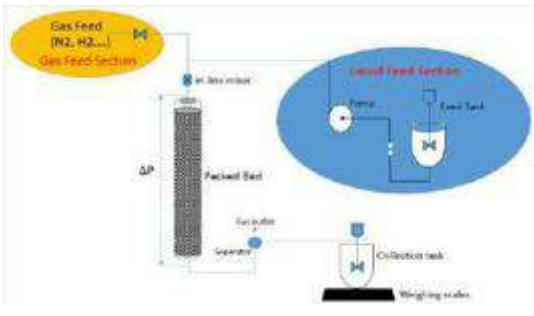

Figure 2: The pilot tubular TBR for high pressure and fine deposition study

[a)] Corresponding author. Email: msassi@masdar.ac.ae

DISCUSSION

In Figure 3, flow maps are reported depicting all four regimes and the transition regions between them. Transition regions occur where the characteristics of more than one flow regime coexist. The 2D experimental results are then compared with existing literature data of three dimensional results and found to be in good agreement. Emphasis is placed on the transition between the trickle and pulse regimes since that is the most important mode of operation in industrial trickle bed reactors. It is observed that the change in diameters of the cylindrical particles in a two dimensional trickle bed reactor has no significant effect on the transition between the flow regimes when the porosity of the bed is kept constant.

Once the dominant flow regime in the TBR has been identified, the pressure drop was investigated for different fluids with pressure varying between 10-30 bars and varying liquid and gas velocities in the ranges of 0.1-0.5 cm/s and 20-95 cm/s, respectively in a tubular TBR. Glass beads of different diameters were used instead of the catalyst in the tubular pilot reactor. Pressure drop values were plotted against superficial liquid and gas velocities, operating pressures, glass bead diameters and fluid properties. The results thus compiled were used to obtain a correlation for the pressure drop in the pilot plant reactor within a given set of operating conditions. The correlation obtained was compared with data available in literature (Giri and Majumder, 2014) and was found to be in good agreement.

It was mainly found that increases in the superficial fluid velocities, operating pressures, gas density and liquid viscosity caused a rise in the pressure drop whereas an increase in the size of the catalyst particles decreased the pressure drop in the reactor, as shown in Figure 4.

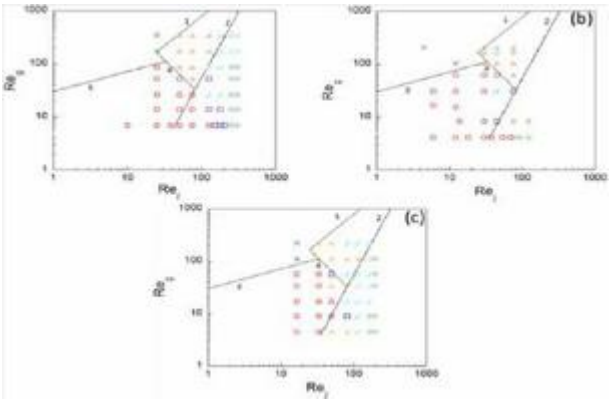

Figure 3: Boundaries between flow regimes observed for different Reynold's numbers where the lines 1-4 denote literature empirical relations (○Trickle, □Trickle-Bubble, ◇Bubble, ◢Bubble-Pulse, △Pulse and ×Spray)

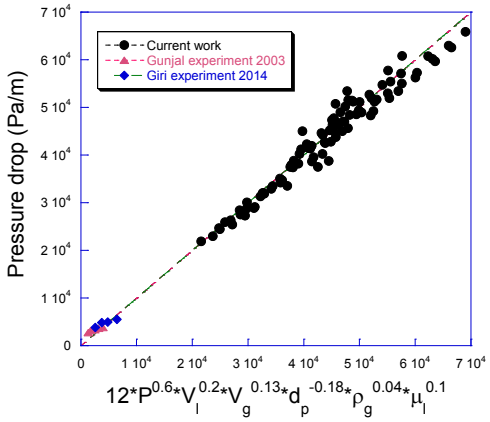

Figure 4: Pressure drop in TBR with respect to different operating and geometrical parameters compared to literature data.

The effect of fines deposition on the pressure drop is finally examined and compared with two-phase pressure drop in the absence of fine particles. It was found that with the deposition of the fine particles, the pressure drop across the reactor increases dramatically.

ACKNOWLEDGEMENTS

We would like to acknowledge Masdar Institute of Science and Technology and the Takreer Research Center (TRC) (Research Grant number 12MZZA2) for financial, material and technical support.

References

[1] Giri, Ajit Kumar, and Subrata Kumar Majumder. 2014. "Pressure Drop and Its Reduction of Gas – Non-Newtonian Liquid Flow in Downflow Trickle Bed Reactor (DTBR)." Chemical Engineering Research and Design 92(1): 34–42.

[2] Sie, S.T., and R. Krishna. 1998. 14 Process Development and Scale Up: Scale up and Scale down of Trickle Bed Processes. TU Delft: Delft University of Technology, Faculty of Chemical Technology and Materials Science.

MS04 - Nonlinear Dynamics of Engineering Systems

TS.MS04-1.01	Perkins, Noel C - Simulating nonlinear dynamical transitions of single molecule DNA (INVITED)	102
TS.MS04-1.02	Dankowicz, Harry - On the Analysis of Chatter in Mechanical Systems with Impacts (INVITED)	104
TS.MS04-1.03	Leine, Remco - Synchronization-based estimation of the maximal Lyapunov exponent of nonsmooth systems (INVITED)	106
TS.MS04-1.04	Lenci, Stefano - Nonlinear coupling between axial and transversal oscillations of shearable beams (INVITED)	108
– Rigid Body Systems		
TS.MS04-2.01	Chernousko, Felix - Optimization of locomotion for multibody systems moving along a plane	110
TS.MS04-2.02	Kelly, Scott - Entrainment and multiscale dynamics in vibrationally driven nonholonomic systems	112
TS.MS04-2.03	Pfeiffer, Friedrich - MBS Approach for a Chain Fountain	114
TS.MS04-2.04	Kirillov, Oleg - Precession on a rotating saddle: A gyro force in an inertial frame	116
TS.MS04-2.05	Shimomura, Yutaka - Freaky motion of a spinning spheroid induced by a slight break of its axial symmetry	118
TS.MS04-2.06	Naprstek, Jiri - Gibbs-Appel Formulation of Non-Holonomic Motion of a Ball on a Spherical Surface	120
– Nonlinear Phenomena in Mechanical and Structural Systems		
TS.MS04-3.01	Ross, Shane - Escape from potential wells in multi-dimensional experimental systems	122
TS.MS04-3.02	Habib, Giuseppe - Passive linearization of nonlinear system resonances	124
TS.MS04-3.03	Fidlin, Alexander - On the Strongly Nonlinear Resonance of a Rotor with a Self-balancing Device	126
TS.MS04-3.04	Steindl, Alois - Nonlinear Oscillations of a Belt Drive	128
TS.MS04-3.05	Abdel-Rahman, Eihab - Strange attractors observed in electrostatic MEMS actuators	130
TS.MS04-3.06	Shitikova, Marina - Difference combinational internal resonance in nonlinear vibrations of thin plates	132
– Systems with Time Delay and Non-Smooth Systems		
TS.MS04-4.01	Rand, Richard - On Nonlinear Differential Equations with Delayed Self-Feedback	134
TS.MS04-4.02	Radons, Günter - Analysis of systems with state-dependent delays and applications in metal cutting	136
TS.MS04-4.03	Molnar, Tamas - Higher-order estimation of limit cycle amplitude in metal cutting	138
TS.MS04-4.04	Wang, Zaihua - Delay effect on motion control of a two-wheeled inverted pendulum	140
TS.MS04-4.05	Cao, Qingjie - Dynamical Behaviours of an Archetypal Self-excited SD Oscillator	142
TS.MS04-4.06	Wiercigroch, Marian - Analysis of forward and backward whirls in drilling	144
– Nonlinear Dynamics in MEMS and NEMS		
TS.MS04-5.01	Yabuno, Hiroshi - Self-excited microcantilevers for sensing applications	146
TS.MS04-5.02	Dou, Suguang - Tailoring nonlinear dynamics of microbeam resonators with electrostatic actuation	148

TS.MS04-5.03	Park, Sangtak - Evidence of an intermittency route to chaos in electrostatic mems	150
TS.MS04-5.04	Kalafut, Devin - Multistability of a cantilever MEMS/NEMS capacitive switch model	152
TS.MS04-5.05	Ribeiro, Pedro - Non-linear Modes of Vibration of Cnts	154
TS.MS04-5.06	Lamarque, Claude Henri - Symmetry-breaking in a three-nanomechanical-resonator array for mass detection	156
– System Identification and Uncertainties		
TS.MS04-6.01	Amabili, Marco - Nonlinear identification of damping in large amplitude vibrations of plates and panels	158
TS.MS04-6.02	Moore, Keegan - Nonlinear system identification of mechanical interfaces based on wave propagation	160
TS.MS04-6.03	Bajaj, Anil - Uncertainty quantification and robustness issues in planar nonlinear resonant structures	162
TS.MS04-6.04	Agarwal, Vipin - Studies of rotor-stator system subjected to noise excitations	164
TS.MS04-6.05	Hong, Ling - Transient responses of a forced triple-well potential system with fuzzy uncertainty	166
TS.MS04-6.06	Stefanski, Andrzej - Synchronization of self-induced friction oscillators	168
– Multiphysics and Vibration Reduction		
TS.MS04-7.01	Gottlieb, Oded - Nonlinear spatio-temporal dynamics of an elastic panel in uniform laminar flow	170
TS.MS04-7.02	Pavlovskaia, Ekaterina - Nonlinear Vibrations of Elastically Supported Cylinder Moving in the Fluid Flow	172
TS.MS04-7.03	Romeo, Francesco - Nonlinear dynamics of an electro-mechanical system: Numerical and experimental study	174
TS.MS04-7.04	Rusinek, Rafal - Influence of temperature on middle ear with shape memory prosthesis	176
TS.MS04-7.05	Lacarbonara, Walter - Asymptotic approach to flutter control via hysteretic absorbers	178
TS.MS04-7.06	Benacchio, Simon - Dynamic behavior of a tunable magnetic vibration absorber	180
– Nonlinear Dynamics and Energy Harvesting		
TS.MS04-8.01	Mazzilli, Carlos - Non-synchronous free oscillations of Ziegler's column	182
TS.MS04-8.02	Chen, Li-Qun - Nonlinear Oscillation of a Circular Plate Energy Harvester	184
TS.MS04-8.03	Kecik, Krzysztof - Non-linear dynamics of a pendulum vibration absorber with a Maglev harvester	186
TS.MS04-8.04	Takahashi, Ryo - Possibility of Energy Extraction from Noise under Stochastic Resonance	188
TS.MS04-8.05	Renault, Alexandre - Hardening Softening Behavior of Antiresonance for Non Linear Torsional Vibration Absorbers	190
– Dynamical Interactions in Coupled Systems		
TS.MS04-9.01	Manevitch, Leonid - Strongly Nonlinear Resonance Dynamics of Quasi-One-Dimensional Finite Oscillatory Chains	192
TS.MS04-9.02	Gendelman, Oleg - Accelerating Oscillatory Fronts in a Sonic Vacuum with Non-local Interactions	194
TS.MS04-9.03	Charlemagne, Simon - Nonlinear Interactions Between Coupled Nonlinear Oscillators at Different Layers of Time	196

TS.MS04-9.04	Moleron, Miguel - Synchronized Frequency Conversion in Nonlinear Lattices	198
TS.MS04-9.05	Kapitaniak, Tomasz - Chimera states for coupled pendula	200
PO.MS04-1.02.4	Ario, Ichiro - Analysis of Symmetry-breaking and Multi-Bifurcation for Multi-folding Structures	202
PO.MS04-1.03.5	Biswas, Saurabh - A New Versatile Two-State Five-Parameter Hysteresis Model	204
PO.MS04-1.04.6	Ding, Jieyu - Harmonic differential quadrature method for nonlinear vibrations of transmission belts	206
PO.MS04-1.05.7	Ding, Qian - Non-linear dynamics analysis of a steering gear system with backlashes	208
PO.MS04-1.06.8	Drozdetskaya, Olga - Nonliner Dynamics of Gearboxes with Flexible Friction Clutch	210
PO.MS04-1.07.9	Hedrih, Katica (Stevanovic) - Vibro-impact dynamics in systems with trigger of couped three singular points	212
PO.MS04-1.08.10	Jiang, Jun - Switching sensitive and insensitive responses in a piecewise smooth rubbing rotor system	214
PO.MS04-1.09.11	Jiang, Shanying - Mixed-mode oscillations in a slow-fast flexible joint system with time delay	216
PO.MS04-1.11.13	Liu, Liu - Dynamic Response of Acoustically Excited Plates Resting on Elastic Foundations	218
PO.MS04-1.12.14	Naik, Shibabrat - Partial control and avoidance of escape from a potential well	220
PO.MS04-1.13.15	Perchikov, Nathan - Symmetry-induced dynamic localization in lattice structures	222
PO.MS04-1.14.16	Roy, Subhradeep - Data-based Method for Extracting Navigational Leadership Between Two Bats	224
PO.MS04-1.15.17	Singh, Harkirat - Modelling non-planar vibrations of a string in the presence of doubly curved obstacle	226
PO.MS04-1.17.19	Warminska, Anna - Nonlinear Vibrations of a Circular Plate Induced by Mechanical and Thermal Loadings	228
PO.MS04-1.18.20	Xia, Shuyan - stationary control of floating airport in waves	230
PO.MS04-1.19.21	Yan, Yao - Self-interrupted chatter in cylindrical grinding	232
PO.MS04-1.20.22	Yokoi, Yuichi - A study on variable for estimating maximum power conversion of parametric pendulums	234
PO.MS04-1.21.23	Yousefzadeh, Behrooz - Nonlinear Wave Transmission in Disordered Periodic Structures	236
PO.MS04-1.22.24	Zeidis, Igor - On the locomotion of self-propelling systems in a linear resistive environment	238
PO.MS04-1.23.25	Zhang, Shu - Mode localization in cyclic self-excited structure with symmetric delayed feedback	240

SIMULATING NONLINEAR DYNAMICAL TRANSITIONS OF SINGLE MOLECULE DNA

N. C. Perkins[1], A. Hirsh[2] & T. D. Lillian[3]
[1]*Mechanical Engineering, University of Michigan, Ann Arbor, Michigan, USA*
[2]*MathWorks, Novi, Michigan, USA*
[3]*Mechanical Engineering, Texas Tech University, Lubbock, Texas, USA*

Summary The dynamics of DNA molecules play essential roles in the life cycle of cells. Large dynamical transitions in the conformations of single DNA molecules are required for many cellular functions including, for example, DNA transcription, replication and repair. This paper summarizes how dynamical transitions of DNA can be simulated using a nonlinear rod theory that captures the nonlinear bending and twisting of the molecule on long length/time scales. The resulting numerical solutions describe conformational changes of DNA in the context of two examples; namely 1) the dynamic relaxation of DNA supercoils induced by enzymes, and 2) the dynamic ejection of DNA from viruses during host infection.

BACKGROUND AND SUMMARY

DNA is a fascinating and enormously long biopolymer molecule that encodes the genetic information to sustain life. While the chemical composition of DNA has been known for over 50 years, many unresolved questions remain regarding how the *structure* of DNA affects its cellular functions [1, 2]. By *structure*, we refer to the shape and stress of the molecule and how these control DNA's primary functions including DNA transcription, replication and repair. For example, the biomolecular motor RNA polymerase, which actively transcribes the genetic code within DNA, also mechanically twists the molecule and to a degree that frequently induces distant DNA supercoils that can hinder transcription. How supercoils and other DNA structures form, and the dynamics and energy required for their formation, are issues examined in this paper. The results contribute to our newly developing knowledge of the genome-scale dynamics of DNA.

The results in this paper follow from a nonlinear rod theory that describes the nonlinear twisting/bending dynamics of DNA on biologically relevant length/time scales [3-6]; refer to Fig. 1. This theory incorporates the physics of large twisting/bending of the DNA helical axis, DNA-protein interactions, electrostatic interactions, and the hydrodynamics of the surrounding fluid [7, 8]. These effects are present in two example systems reviewed in this paper. The first concerns the formation and the dynamical relaxation of DNA supercoils as further detailed in [7]. The second example considers the rapid ejection of DNA from viruses during host infection. In particular, we review salient results from [8] which reveal how the ejection process is initiated by a highly strained DNA supercoil that explosively straightens to prime the ejection process.

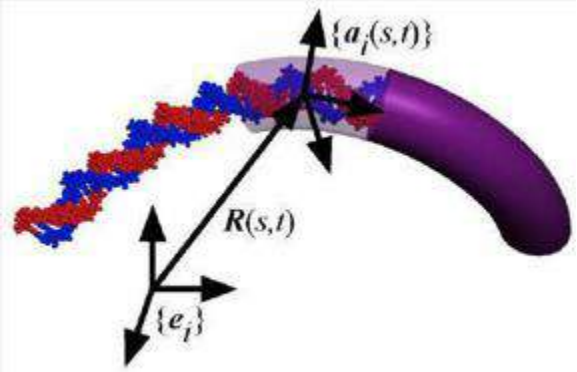

Figure 1: The DNA double-helix is approximated as a nonlinear rod that captures the nonlinear and three-dimensional bending and twisting of the helical axis, and additional forces due to DNA-bound protein/enzymes, electrostatics and hydrodynamics.

RESULTS AND DISCUSSION

Consider first the important example of DNA supercoil formation and relaxation. Note that a single DNA molecule, on the centimetre scale in length, must be compacted by four orders of magnitude to fit within the small confines of the micron-scale cell nucleus. Doing so requires that this exceedingly long but slender molecule bend and twist massively in the form of supercoils. Supercoiling is not static and it changes significantly during cellular processes including DNA transcription, replication and repair. An excellent example of this is the effect induced by the aforementioned

[a)] Corresponding author. Email: ncp@umich.edu

biomolecular motor RNA polymerase which, during transcription, locally untwists the double helix to gain access to the genetic code (base-pairs) tucked within. Sustained local untwisting during transcription alters the long-length scale supercoiling of DNA and can build strain energy that ultimately impedes further transcription. Fortunately, nature provides a means to relieve that strain energy by relaxing tight supercoils. That action derives from enzymes known as topoisomerases that chemically cut through one or both helical strands to relieve strain energy. This first example employs the nonlinear rod theory to model the dynamic relaxation of supercoils induced by the action of a particular enzyme known as human Topoisomerase IB (Topo IB) that cuts through a single DNA strand. Figure 2(A) reports the simulated relaxation of a large DNA supercoil which rapidly unwinds on the microsecond time scale. The relaxation manifests in large conformational changes of the molecule and in a cascading decrease in DNA elastic energy as signalled by the step-like decrease in the linking number Lk which describes the topology of the supercoil.

The second example concerns the packing of DNA in viruses during maturation and the subsequent ejection of the viral genome into a host during infection. The example of our study concerns the bacteriophage virus $\phi 29$ which is one of the smallest bacteriophages and it has long served as a model system to study virus structure, assembly, and ejection. Recent cyroelectron micrography [9] revealed a stunning, highly strained DNA toroidal supercoil within the so-called connector domain of the virus that connects the capsid to the tail tube through which DNA passes during infection. While the function of that highly-strained DNA is unknown, it was hypothesized to play a role during DNA ejection. That role is confirmed in the simulated results reported in Figure 2(B) which illustrate a violent straightening of this energetic supercoil at the very start of the ejection process. This large conformation change occurs on a microsecond time scale and prior to initiating the ejection of the remainder of the DNA contained in the capsid (now shown). Thus, the DNA toroid primes the ejection process through a rapid release of stored energy.

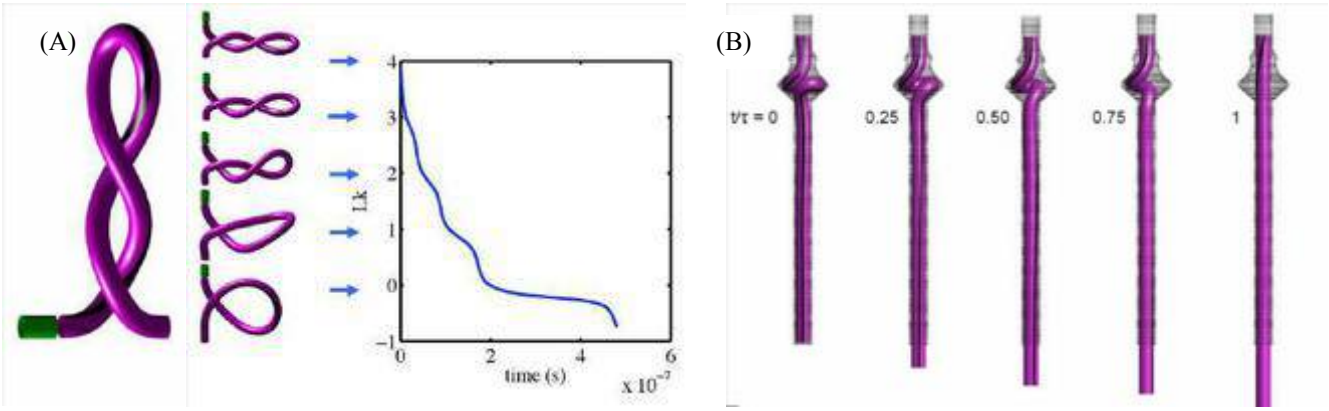

Figure 2: (A) Dynamic relaxation of a large DNA supercoil (far left) through the action of Topo IB which locally relieves strain energy (green site) and induces large and rapid conformational changes of the molecule. The strain energy (related to the linking number Lk) relaxes in a stepwise manner in a fraction of a microsecond. (B) Dynamic relaxation of a highly strained DNA supercoil confined to the connector region of the bacteriophage $\phi 29$. The explosive straightening of this constrained supercoil primes the DNA ejection process during host infection.

References

[1] Alberts B., Johnson A., Lewis J., Raff M., Roberts K., Walter P.: Molecular Biology of the Cell, (5th Ed.), Garland Science 2008.

[2] Lodish H., Berk A., Matsudaira P, Kaiser C.A., Krieger M., Scott M.P., Zipursky L., Darnell J.: Molecular Cell Biology (5th Ed.), W.H. Freeman, New York NY 2004.

[3] Schlick T.: Modeling Superhelical DNA: Recent Analytical and Dynamic Approaches. *Curr. Opinion Structural Biology* **5**:245-262, 1995.

[4] Olson W. K.: Simulating DNA at Low Resolution. *Curr. Opinion Structural Biology* **6**:242-256, 1996.

[5] Tobias I., Swigon D., Coleman B.D.: Elastic Stability of DNA Configurations. I. General Theory. *Phys. Rev. E* **61**:747-758, 2000.

[6] Goyal S., Perkins N.C., Lee C.L.: Nonlinear Dynamics and Loop Formation in Kirchhoff Rods with Implications to the Mechanics of DNA and Cables. *J. Comp. Physics* **209**:371-389, 2005.

[7] Lillian T.D., Taranova M., Wereszczynski J., Andricioaei I., Perkins, N.C.: A Multi-scale Dynamic Model of DNA Supercoil Relaxation by Topoisomerase IB. *Biophysical J.* **100**:2016-2023, 2011.

[8] Hirsh A.D, Taranova M., Lionberger T.A., Lillian T.D., Andricioaei I., Perkins N.C.: Structural Ensemble and Dynamics of Toroidal-like DNA Shapes in Bacteriophage $\phi 29$ Exit Cavity. *Biophysical J.* **104**:2058-2076, 2013.

[9] Tang J., Olson N., Jardine P.J., Girimes S., Anderson D.L., Baker T.S.: DNA Poised for Release in Bacteriophage $\phi 29$. *Structure* **16:**935-943, 2008

ON THE ANALYSIS OF CHATTER IN MECHANICAL SYSTEMS WITH IMPACTS

Harry Dankowicz *[1], Erika Fotsch[2], and Alan Champneys[3]

[1]*Mechanical Science and Engineering, University of Illinois at Urbana-Champaign, Urbana, Illinois, USA*
[2]*Mechanical Science and Engineering, University of Illinois at Urbana-Champaign, Urbana, Illinois, USA*
[3]*Department of Engineering Mathematics, University of Bristol, Bristol, United Kingdom*

Summary In rigid-body mechanics, models that capture collisional contact as an instantaneous exchange of momentum may exhibit dynamics that include infinite sequences of impacts accumulating in finite time to a state of persistent contact. In this paper, we describe recent observations of such chatter-like behavior both in forward and reverse time dynamics in several example systems. We review theoretical tools that enable a successful analysis of transient and steady-state behavior with chatter in such systems by effectively bypassing the tail end of a chatter sequence of impacts. Finally, we show how such theoretical insight informs computational implementations for forward simulation as well as parameter continuation of associated boundary-value problems.

INTRODUCTION

In models of mechanical systems that account for persistent or intermittent contact with hard and rough obstacles, a common approximation considers the limit of time-scale separation in which collisions are described as instantaneous impacts associated with sudden changes to the system velocities, and sustained contact is described in terms of the set-valued Coulomb-Amonton law of dry friction. Time histories of position and velocity coordinates are naturally partitioned into disjoint segments, governed by segment-specific force interactions, and characterized by termination conditions associated with the onset or cessation of contact, or with transitions between relative stick and slip.

Following Goebel, Sanfelice and Teel [1], we characterize a segmented time history in terms of a subset E of $R_{\geq 0} \times \mathbb{N}$ given by a sequential union of sets $([t_j, t_{j+1}], j)$ with $t_j \leq t_{j+1}$, possibly terminated by a set $([t_N, T), N)$ for some integer N and T finite or $T = \infty$. Here, the index j tracks the number of transitions, while $[t_j, t_{j+1}]$ and/or $[t_N, T)$ describe intervals of absolute continuity of the system dynamics. A time history is said to be *Zeno* if E contains an infinite union of sets $([t_j, t_{j+1}], j)$, such that the sequence $\{t_j\}$ is bounded. It follows that a Zeno time history includes infinitely many transitions in finite time and, by compactness, a finite time of accumulation of a subsequence of these transitions. We refer to the time of accumulation as the corresponding *Zeno point*.

A forward-time Zeno point occurs naturally in a mechanical system with impacts governed by a dissipative impact law, e.g., the Newtonian coefficient of restitution model for normal impacts or the Stronge energetic coefficient of restitution model for arbitrary impacts that include frictional interactions. Surprisingly, the analysis in Nordmark, Dankowicz, and Champneys [2] shows the possibility also for a reverse-time Zeno point in the Stronge impact model, even for constant free-flight acceleration. Indeed, as discussed in [2], both forward and reverse chatter is associated with one-parameter families of chatter sequences with a common Zeno point. In the case of reverse-time chatter, such a degeneracy poses a serious challenge to the description of the forward-time dynamics in terms of a unique time history past the corresponding Zeno point.

AN ANALYTICAL TREATMENT

A proper accounting of the exchange of momentum between a mechanical system and a rigid obstacle during a forward-time chatter sequence necessitates an analysis of the asymptotic behavior at the tail end of chatter. In this paper, we review the work of Nordmark & Piiroinen [3], wherein this asymptotic behavior is described in terms of dynamics along the stable manifold of a fixed point corresponding to persistent contact in a suitably defined iterated map. In particular, [3] derives an implicit equation for a *bypass* map that associates an impact late in the chatter sequence to the configuration and velocity state at the corresponding Zeno point. An explicit approximation for the bypass map, including the corresponding jump in time, is further provided in the form of a series expansion in the impact velocity.

A critical border condition occurs along a family of time histories with forward-time chatter under variations in system parameters when the Zeno point is associated with an immediate release (with zero acceleration) into sustained free flight. When the border orbit is a periodic trajectory of the dynamical system, a persistent periodic trajectory in which the chatter sequence is followed by a phase of sustained contact exists only on one side of the critical parameter value. As shown in unpublished work by Nordmark and Kisitu [4], a complex bifurcation scenario is obtained on the opposite side of the critical parameter value, including cascades of smooth saddle-node and period-doubling bifurcations, intervals of robust chaos, and grazing bifurcations. In this paper, we provide a detailed review of the analysis in [4] and illustrate the predictions on example physical applications described in Alzate and Piiroinen [5] and Fotsch [6] (cf. Fig. 1).

*Corresponding author. Email: danko@illinois.edu

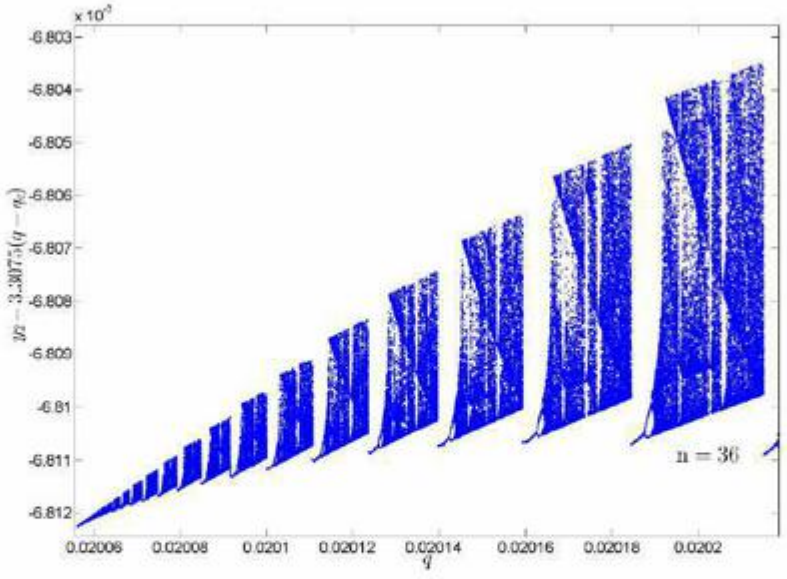

value q_c y_2 denotes a sampled velocity and

COMPUTATIONAL TOOLS

As discussed in [3], the bypass map associated with chatter may be encoded in computational tools for forward integration and parameter continuation. Here, the tail end of the chatter sequence is replaced by the application of an approximate jump

approach, [3] investigates families of periodic orbits and their bifurcations under variations in problem parameters for a sample two-degree-of-freedom mechanism.

development platform. We show how the toolbox may be embedded in a periodic orbit continuation problem for a mechanical system with impacts, and how error estimation is used to make adaptive updates to individual segment meshes, as well as to the number of segments.

advances in theoretical and computational tools. For the phenomenology associated with forward-time chatter, a relatively

the need for a better understanding of the effects of time-scale separation on the predictability of the forward-time dynamics.

References

[1] Goebel R., Sanfelice R.G., Teel A.R.: Hybrid Dynamical Systems: Modeling, Stability, and Robustness. Princeton University Press, 2012.

[2] Nordmark A., Dankowicz H., Champneys A.: Friction-Induced Reverse Chatter in Rigid-Body Mechanisms with Impacts. IMA J. Appl Math 1-35, 2011.

[3] Nordmark A.B., Piiroinen P.T.: Simulation and Stability Analysis of Impacting Systems with Complete Chatter. Nonlinear Dyn 58:85-106, 2009.

[4] Nordmark A.B., Kisitu R.E.M.:. On Chattering Bifurcations in 1 DOF Impact Oscillator Models. Unpublished, 2003.

[5] Alzate R., Piiroinen P.T., di Bernardo M.: From Complete to Incomplete Chattering: A Novel Route to Chaos in Impacting Cam-Follower Systems. Int J Bifur Chaos 22(5):1250102 1-14, 2012.

[6] Fotsch E.L.: Bifurcation Analysis Near the Cessation of Complete Chatter and Shilnikov Homoclinic Trajectories in a Pressure Relief Valve Model. MSc Thesis, University of Illinois at Urbana-Champaign, Department of Mechanical Science and Engineering, Urbana, IL, USA, 2016.

SYNCHRONIZATION-BASED ESTIMATION OF THE MAXIMAL LYAPUNOV EXPONENT OF NONSMOOTH SYSTEMS

Remco I. Leine*[1] and Michael Baumann[2]
[1]*Institute for Nonlinear Mechanics, University of Stuttgart, Germany*
[2]*Institute of Mechanical Systems, ETH Zurich, Switzerland*

Summary Lyapunov exponents of chaotic attractors are hard to estimate, especially for non-smooth systems. One method to estimate the maximal Lyapunov exponent is by using its relationship with the synchronization properties of coupled systems. The maximal Lyapunov exponent is equal to the minimal proportional feedback gain necessary to achieve full state synchronization with a replica system. In this paper, we prove this statement for the general class of nonsmooth systems in the framework of measure differential inclusions. Numerical results of a mechanical impact oscillator illustrate the effectiveness of the method for nonsmooth systems.

LYAPUNOV EXPONENT

The spectrum of Lyapunov exponents is an important characteristic of limit sets. It measures the exponential convergence or divergence of nearby trajectories, thereby capturing the sensitivity of solutions with respect to initial conditions. A chaotic attractor has at least one positive Lyapunov exponent. Estimating the maximal Lyapunov exponent using chaos synchronization has been proposed for mechanical systems with impacts and for discrete maps by the authors of [1]. In this paper, we employ this idea for the class of nonsmooth systems written in framework of measure differential inclusions [2] as

$$\frac{\mathrm{d}\boldsymbol{x}}{\mathrm{d}\mu} \in \boldsymbol{\mathcal{F}}(\boldsymbol{x},t), \tag{1}$$

where $\frac{\mathrm{d}\boldsymbol{x}}{\mathrm{d}\mu}$ is the density of the measure $\mathrm{d}\boldsymbol{x}$ with respect to a positive Radon measure $\mathrm{d}\mu$.

Consider a reference solution $\boldsymbol{x}(t)=\boldsymbol{\varphi}(t,\boldsymbol{x}_0,t_0)$ and a perturbed solution $(\boldsymbol{x}+\Delta\boldsymbol{x})(t)=\boldsymbol{\varphi}(t,\boldsymbol{x}_0+\boldsymbol{e}h,t_0)$ for the initial conditions $\boldsymbol{x}(t_0)=\boldsymbol{x}_0$ and $\Delta\boldsymbol{x}(t_0)=\boldsymbol{e}h$. We define the normalized disturbance as

$$\boldsymbol{\xi}(t,\boldsymbol{e},t_0) := \lim_{h\downarrow 0, h\notin E_h^\xi} \frac{1}{h}(\boldsymbol{\varphi}(t,\boldsymbol{x}_0+\boldsymbol{e}h,t_0)-\boldsymbol{\varphi}(t,\boldsymbol{x}_0,t_0)). \tag{2}$$

The limit exists almost everywhere, if the following assumption is fulfilled.

Assumption 1. The difference of the solutions of system (1) is in the order of the perturbation, that is, $\boldsymbol{\varphi}(t,\boldsymbol{x}_0+\boldsymbol{e}h,t_0)-\boldsymbol{\varphi}(t,\boldsymbol{x}_0,t_0)\in\mathcal{O}(h)$ a.e.

Assumption 1 implies continuous dependence on initial conditions and, consequently, uniqueness of solutions in forward time. Uniqueness of solutions implies that the density $\frac{\mathrm{d}\boldsymbol{x}}{\mathrm{d}\mu}$ is unique as well and the dynamics can be written as the measure differential equation

$$\frac{\mathrm{d}\boldsymbol{x}}{\mathrm{d}\mu} = \boldsymbol{f}(\boldsymbol{x}^-,t) \tag{3}$$

with $\boldsymbol{f}(\boldsymbol{x},t)\in\boldsymbol{\mathcal{F}}(\boldsymbol{x},t)$. The maximal Lyapunov exponent is defined using the normalized difference as

$$\lambda_{\max} := \max_{\boldsymbol{e}} \lim_{\substack{t\to\infty \\ \in E_t^\xi}} \frac{1}{t}\ln\|\boldsymbol{\xi}(t,\boldsymbol{e},t_0)\|. \tag{4}$$

CRITICAL COUPLING

We consider two coupled non-smooth systems, where (3) is accompanied by a replica extended by a proportional error feedback in the form

$$\frac{\mathrm{d}\boldsymbol{y}}{\mathrm{d}\mu} = \boldsymbol{f}(\boldsymbol{y}^-,t) - k(\boldsymbol{y}^- - \boldsymbol{x}^-)\frac{\mathrm{d}t}{\mathrm{d}\mu}, \tag{5}$$

*Corresponding author. Email: leine@inm.uni-stuttgart.de

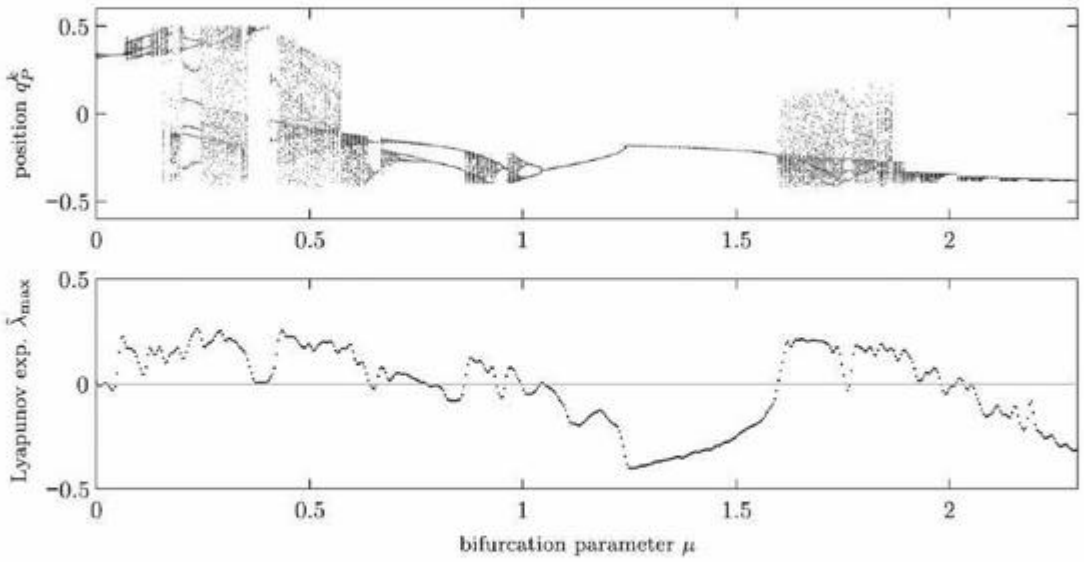

Figure 1: Brute force diagram (top) and estimation of the maximal Lyapunov exponent $\hat{}_{\max}$ (bottom) with the bifurcation parameter h. The chaotic solutions correspond to $\hat{}_{\max} > 0$, while the periodic windows correspond to $\hat{}_{\max} < 0$.

where $k \in \mathbb{R}$ is the proportional feedback gain. Let $\boldsymbol{y}(t) = \boldsymbol{\varphi}_k(t, \boldsymbol{x}_0 + \boldsymbol{e}h, t_0)$ be the solution of (5) for a given k. Therefore, local synchronization is achieved if the normalized synchronization error

$$\boldsymbol{\zeta}(t, \boldsymbol{e}, t_0) := \lim_{h \downarrow 0, h \notin E_h^\zeta} \frac{1}{h}(\boldsymbol{\varphi}_k(t, \boldsymbol{x}_0 + \boldsymbol{e}h, t_0) - \boldsymbol{\varphi}(t, \boldsymbol{x}_0, t_0)) \tag{6}$$

tends to zero. The normalized disturbance $\boldsymbol{\xi}$ in (2) and the normalized synchronization error $\boldsymbol{\zeta}$ in (6) fulfill

$$\boldsymbol{\zeta} = \boldsymbol{\xi} e^{-k(t-t_0)} \quad \text{a.e.} \tag{7}$$

if Assumption 1 is fulfilled. The statement (7) together with (4) imply that local synchronization of systems (3) and (5) is achieved if the coupling gain k is larger than the maximal Lyapunov exponent $\lambda_{\max}$. Conversely, $k < \lambda_{\max}$ implies that no local synchronization is achieved for some initial conditions. In practice, the perturbation for any initial condition will eventually turn into the direction of maximal expansion. Therefore, the maximal Lyapunov exponent can be estimated using the minimal proportional feedback gain for which synchronization is achieved.

NUMERICAL EXAMPLE

The results are illustrated using the example of a mechanical Duffing-oscillator with two geometric unilateral constraints. The impact oscillator is excited by an external, harmonic forcing and the generalized Newton's impact law is chosen. The viscous damping coefficient is chosen as bifurcation parameter. The brute force diagram in Figure 1 shows the position at the Poincaré sections for a sweep down of the bifurcation parameter. The estimated maximal Lyapunov exponent is positive for the chaotic attractors and negative ($\lambda_{\max}$ at zero is not considered) during the periodic windows.

Acknowledgment This research is supported by the Swiss National Science Foundation through the project 'Synchronization of Dynamical Systems with Impulsive Motion' (SNF 200021-144307).

References

[1] A. Stefanski and T. Kapitaniak, "Estimation of the dominant Lyapunov exponent of non-smooth systems on the basis of maps synchronization," *Chaos, Solitons & Fractals*, vol. 15, no. 2, pp. 233–244, 2003.

[2] R. I. Leine and N. van de Wouw, *Stability and Convergence of Mechanical Systems with Unilateral Constraints*, vol. 36 of *Lecture Notes in Applied and Computational Mechanics*. Berlin: Springer-Verlag, 2008.

NONLINEAR COUPLING BETWEEN AXIAL AND TRANSVERSAL OSCILLATIONS OF SHEARABLE BEAMS

Stefano Lenci[1a)], Francesco Clementi[1] & Giuseppe Rega[2]
[1]*Department of Civil and Building Engineering, and Architecture, Polytechnic University of Marche, Ancona, Italy*
[2]*Department of Structural and Geotechnical Engineering, Sapienza University of Rome, Rome, Italy*

Summary Nonlinear free oscillations of a straight planar Timoshenko beam are investigated by means of the asymptotic development method. Attention is focused on the nonlinear coupling between axial and transversal oscillations of the beam, that are decoupled in the linear regime. The existence of coupled and uncoupled motion is discussed, and the softening vs hardening behaviour of the beam is investigated in depth.

INTRODUCTION

It is known that the axial boundary conditions affect significantly the oscillation behaviour of beams. In particular, axially restrained beams exhibit hardening behaviour, while axially free beams have softening behaviour. This difference, already reported by Atluri [1], is a peculiarity of the nonlinear regime, since in the linearized framework the natural frequencies (for transverse oscillations) are unaffected by the axial restraint when the beam is initially straight. Luongo et al. [2] addressed the same problem by the Galerkin method, while Lacarbonara and Yabuno [3] applied the multiple scale method directly to the governing PDEs and also provided an experimental verification of the phenomenon.

Previous works considered slender beams, and perfectly restrained vs perfectly unrestrained boundary conditions. These limitations have been removed by the authors [4, 5]. Consistently, the (nonlinear) Timoshenko beam model has been considered, taking into account shear deformation and rotational inertia. In order to comprehensively revisit the problem, axial deformation and axial inertia have been included in the model, too. Moreover, an axial spring has been added at one hand to simulate the effect of an elastic constraint with stiffness κ. The limit cases of axially free and axially constrained boundary conditions have been obtained for $\kappa = 0$ and $\kappa \to \infty$, respectively.

In [4] the governing equations have been obtained, and the asymptotic development method, in the Poincaré-Lindstedt version, has been applied to obtain an analytical approximate solution. The expressions of the nonlinear correction coefficient ω_2 have been obtained. In [5] a detailed investigation of the effects on ω_2 of slenderness, end spring stiffness, axial and rotational inertia, and shear stiffness is reported.

To the first order of the asymptotic development, the linear regime is obtained. Here, the axial and transversal behaviour are decoupled. In [4, 5] it is assumed that to first order the axial oscillation is negligible with respect to the transversal one, which is an hypothesis commonly done in the literature. It is based on the observation that for slender beams axial natural frequencies are meaningfully larger than transversal natural frequencies. For stubby beams, however, the gap between axial and transversal frequencies reduces, and they become comparable.

To overcome the previous limitation, in this work the axial *and* transversal first order oscillations are considered simultaneously, and their (nonlinear) coupling at higher orders of the asymptotic development is investigated in depth.

NONLINEAR TIMOSHENKO BEAM MODEL AND ANALYSIS

The following kinematically exact governing equations have been obtained in [4] for the *free* oscillations of a planar, linearly elastic, initially straight Timoshenko beam:

$$\left\{EA\left[\sqrt{(1+W')^2+U'^2}-1\right]\frac{1+W'}{\sqrt{(1+W')^2+U'^2}}+GA\left[\theta-\arctan\left(\frac{U'}{1+W'}\right)\right]\frac{U'}{\sqrt{(1+W')^2+U'^2}}\right\}'=\rho A\ddot{W},$$

$$\left\{EA\left[\sqrt{(1+W')^2+U'^2}-1\right]\frac{U'}{\sqrt{(1+W')^2+U'^2}}-GA\left[\theta-\arctan\left(\frac{U'}{1+W'}\right)\right]\frac{1+W'}{\sqrt{(1+W')^2+U'^2}}\right\}'=\rho A\ddot{U},$$

$$\left[EJ\frac{\theta'}{\sqrt{(1+W')^2+U'^2}}\right]'-GA\left[\theta-\arctan\left(\frac{U'}{1+W'}\right)\right]\sqrt{(1+W')^2+U'^2}=\rho J\ddot{\theta},$$

where $W(Z,T)$, $U(Z,T)$ and $\theta(Z,T)$ are the axial and the transversal displacements of the beam axis and the rotation of the cross-section, respectively. Z is the spatial coordinate in the rest rectilinear configuration, which ranges from 0 to the length L, T is the time, prime means derivative with respect to Z and dot means derivative with respect to T.

The considered boundary conditions are (H_0 is the horizontal internal force and M is the bending moment)

$$W(0,T)=0,\quad H_0(L,T)+\kappa W(L,T)=0,\quad U(0,T)=0,\quad U(L,T)=0,\quad M(0,T)=0,\quad M(L,T)=0.$$

The beam is axially fixed at the left end (Z=0), while it has an axial linear spring, of stiffness κ, at the right end (Z=L).

a) Corresponding author. Email: lenci@univpm.it

The previous equations and boundary conditions have been solved approximately by the Poincaré-Lindstedt method, up to the third order, to obtain the linear frequency ω_0 and the nonlinear correction coefficient ω_2. The details of the computations are reported in [6], where the following dimensionless parameters (z measuring the shear stiffness) are used

$$l = L\sqrt{A/J}, \quad z = 1/[2(1+\nu)\chi] = 0.3205, \quad \kappa_h = \kappa L^3/EJ.$$

COUPLED BEHAVIOR WITHIN A REVISITED OVERALL FRAMEWORK

The main results consist of determining the region of existence of the coupled axial-transversal oscillations, and the dependence of ω_2 on the slenderness l and the end spring stiffness κ_h. The results are summarized in the behaviour chart of Fig. 1, where the meaning of the colours is the following:

1. light red: only uncoupled solutions exist and they are hardening;
2. dark red: only uncoupled solutions exist and they are softening;
3. light green: coupled and uncoupled solutions coexist and they are both hardening;
4. dark green: coupled and uncoupled solutions coexist and they are both softening;
5. light blue: coupled and uncoupled solutions coexist; the coupled is softening and the uncoupled is hardening;
6. dark blue: coupled and uncoupled solutions coexist; the coupled is hardening and the uncoupled is softening.

Light/dark colours correspond to hardening/softening of the uncoupled solutions, that always exist. Apart from the region of low values of l and κ_h, the former behaviour occurs mostly for high κ_h (i.e. toward hinged-hinged) and low slenderness, along with the coexisting, prevailingly softening (light blue), coupled oscillation. In turn, the latter occurs for very low κ_h (i.e. toward hinged-supported) and whatever slenderness, along with the coexisting, prevailingly hardening (dark blue), coupled oscillation; but the uncoupled oscillation is again hardening (light green) for not too low values of κ_h.

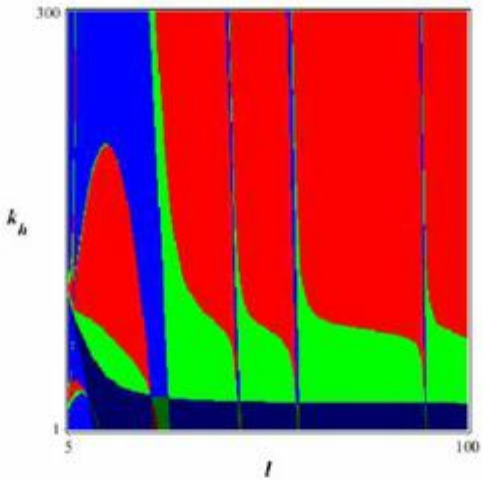

Figure 1. The behaviour chart of ω_2 in the parameters space (l,κ_h) for the first bending mode and the first axial mode.

CONCLUSIONS

An asymptotic solution of the PDEs of a planar beam with whatever slenderness and axial boundary condition has been obtained up to third order, with the aim to study the coupled axial-transversal nonlinear free oscillations. Behaviour charts show the dependence of the nonlinear behaviour upon the problem parameters and the existence of meaningfully coupled oscillations in some relevant regions. The addition of axial oscillations can meaningfully affect the character (hardening to softening or viceversa) of formerly uncoupled transverse oscillations. Numerical validation of asymptotic results is presently going on.

References

[1] Atluri S.: Nonlinear vibrations of hinged beam including nonlinear inertia effects. *ASME J. Appl. Mech.* **40**, 121-126, 1973.

[2] Luongo A., Rega G., Vestroni F.: On nonlinear dynamics of planar shear indeformable beams. *ASME J. Appl. Mech.* **53**, 619-624, 1986.

[3] Lacarbonara W., Yabuno H.: Refined models of elastic beams undergoing large in-plane motions: Theory and experiments. *Int. J. Solids Struct.* **43**, 5066-5084, 2006.

[4] Lenci S., Rega G.: Nonlinear free vibrations of planar elastic beams: A unified treatment of geometrical and mechanical effects. *IUTAM Procedia*, accepted, 2015.

[5] Lenci S., Rega G.: A comprehensive analysis of hardening/softening behaviour of shearable planar beams with whatever axial boundary constraint. *Submitted*, 2015.

[6] Lenci S., Rega G.: Asymptotic analysis of axial-transversal coupling in the free nonlinear vibrations of Timoshenko beams with arbitrary slenderness and axial boundary conditions. *In preparation*, 2016.

OPTIMIZATION OF LOCOMOTION FOR MULTIBODY SYSTEMS MOVING ALONG A PLANE

Felix Chernousko[1] and Tatiana Figurina [*2]

[1,2]*Institute for Problems in Mechanics of Russian Academy of Sciences, Moscow, Russia*

Summary Dynamics and control of multibody systems moving along a horizontal plane are considered. The bodies perform translational motions subject to friction along the plane and control forces due to the interaction between the neighboring bodies. The friction forces obey Coulomb's law. Several types of multibody systems are considered. Optimal motions are obtained that correspond to the maximum average speed or to the shortest way of translation. The obtained results are applicable to mobile robotic systems.

OPTIMIZATION OF RECTILINEAR MOTION OF TWO-BODY SYSTEM

A system consists of two interacting bodies of masses m and M, $m < M$, moving along the horizontal x axis (Fig.1a). The interaction forces acting upon masses m and M are f and $-f$, respectively. They are bounded by the constraint $f \le f_0$, where f_0 is a given constant, the inequality $f_0 > Mgk$ holds to ensure the translational motion of the system. Hereafter k is the dry friction coefficient and g is the acceleration due to gravity. Denote by x_1 and x_2 the coordinates of the bodies m and M, respectively. We find the control $f(t)$ and the corresponding motion of the system for the given interval $t \in [0, T]$ under condition $f \le f_0$ and the following assumptions:

$$x_i(0) = 0,\ \dot{x}_i(0) = \dot{x}_i(T) = 0,\ i = 1, 2, \quad x_1(T) = x_2(T), \quad 0 \le x_2(t) - x_1(t) \le L, \quad \dot{x}_2(t) \ge 0, \quad t \in [0, T], \tag{1}$$

where L is fixed. Thus, the bigger mass M does not move backwards. Also, we assume that the motion consists of several phases with constant acceleration for both masses.

For several versions of optimal control problems, optimal motions subject to conditions (1) and $f \le f_0$ are found [1]. For example, the motion having the maximum average speed is described by explicit formulas. We have

$$v = \max\{[x_2(T) - x_2(0)]/T\} = [gkLm(M - m)]^{1/2}(M + m)^{-1} \tag{2}$$

in the case where $f_0 \to \infty$. The optimal ratio m/M that provides the maximum v in the last expression is 1/3; in this case $v = (gkL)^{1/2}/4$. Similar results are obtained for a more general situation where the coefficients of friction for the bodies m and M are different [1].

If the actuator creating the interaction force rapidly brings the bodies to a state of constant relative velocity, another formulation of the locomotion control problem is reasonable. We can assume that the relative velocity of the bodies is the control bounded by certain constraints. The analysis and optimization of such motions is considered in [2].

OPTIMAL RECTILINEAR MOTION OF A CHAIN OF IDENTICAL BODIES

Let us consider a system consisting of $n \ge 3$ bodies with equal masses $m_i = m, i = 1, ..., n$, lying on a horizontal straight line with dry friction acting between the line and the masses (Fig.1b). The interaction forces between the adjacent masses are unbounded so that the velocities of the masses can change instantly. Let x_i and v_i be the coordinate and velocity of the i-th mass, and let F_i be the dry friction force acting on it. Denote by f_i the control force applied by mass i to mass $i + 1$ (we assume $f_0 = f_n = 0$). The motion of the system is governed by equations

$$\dot{x}_i = v_i, \quad m\dot{v}_i = f_{i-1} - f_i + F_i, \qquad F_i = -kmg \operatorname{sgn} v_i, \qquad i = 1, .., n. \tag{3}$$

Let at the initial and final time instants all masses be at rest and their positions be the same:

$$x_i(0) = 0, \quad v_i(0) = v_i(T) = 0, \quad i = 1, ..., n, \quad x_i(T) = x_1(T), \quad i = 2, ..., n. \tag{4}$$

The problem is to find a motion of the system obeying relations (3) and (4), which maximizes the displacement of the system, $x_1(T) \to \max$.

There exist infinite number of optimal motions with the same maximal terminal displacement [3].

Proposition 1. When optimal motion occurs, for any $t \in [0, \tau]$, $\tau = n(n - 1)^{-1}T/2$, one of the masses moves with acceleration $(n - 2)kg$, and all other masses are at rest. At the end of its movement, each moving mass stops instantly giving its momentum to another mass. At the time instant τ, all masses have the coordinate $n(n-2)(n-1)^{-2}kgT^2/8$ and acquire the

[*]Corresponding author. Email: t_figurina@mail.ru

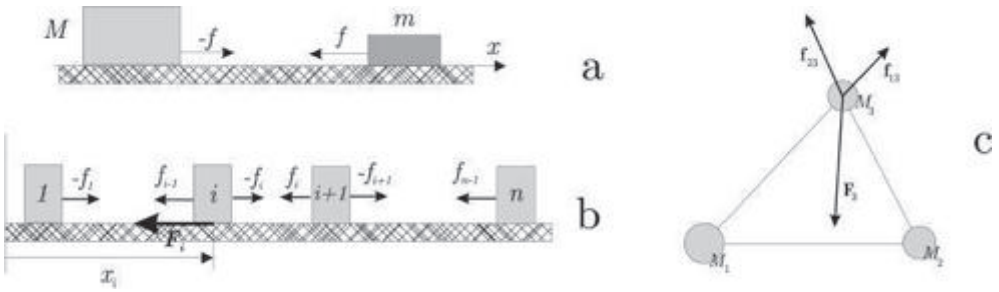

Figure 1: Multibody systems on a plane

velocity equal to $(n-2)(n-1)^{-1}kgT/2$. In the time interval $[\tau, T]$, all masses synchronously decelerate with the acceleration equal to $-kg$ until they stop at the time instant T. The maximum displacement of the system $x(T)$ subject to the optimal control is equal to $(n-2)(n-1)^{-1}kgT^2/4$. One of the possible optimal motions is defined by relations

$$v_i = \begin{cases} (n-2)kgt, & t \in [t_{i-1}, t_i], \\ 0, & t \in [0, t_n]\backslash[t_{i-1}, t_i], \\ kg(T-t), & t \in [\tau, T], \end{cases} \quad t_i = \frac{\sqrt{ni}}{2(n-1)}T, \quad i = 1, ..n, \quad t_n = \tau, \quad t_0 = 0. \tag{5}$$

OPTIMIZATION OF QUASI-STATIC MOTIONS FOR THREE-BODY SYSTEM ON A PLANE

Let us consider the system consisting of three point bodies M_i with masses m_i on a horizontal rough plane (Fig.1c). Between each pair of bodies M_i and M_j, control forces $\mathbf{f}_{ij}$ and $\mathbf{f}_{ji} = -\mathbf{f}_{ij}$ act, changing the distances between the bodies. The system moves along a plane when changing its configuration due to the dry friction forces $\mathbf{F}_i$ between the bodies and the plane. We study possible quasi-static motions of the system, i.e. the motions with infinitesimal velocities and accelerations of the bodies. In such motions, the equilibrium equations hold, $\mathbf{F}_i + \mathbf{f}_{ji} + \mathbf{f}_{ki} = 0$. We suppose that point masses satisfy triangle inequalities $m_i + m_j \geq m_k$, $\{i, j, k\} = \{1, 2, 3\}$, each of the inequalities is a necessary condition for body M_k to move [4].

Proposition 2. Quasi-static motion of body M_3 , with bodies M_1 and M_2 fixed, is possible iff the straight line containing point M_3 and parallel to its velocity intersects set D. Here, set D is the intersection of the circles with centers in points M_1 and M_2 and radii $|M_1M_2|m_2/m_3$, $|M_1M_2|m_1/m_3$, respectively.

Let it be required to move quasi-statically body M_3 from point A to point B with minimal work against friction, i.e., to construct the trajectory of quasi-static motion for body M_3 with the minimum length.

Proposition 3. If the straight line AB intersects set D, then the trajectory with the minimum length for body M_3 quasi-statically moving from point A to point B is the segment AB. If the the straight line AB does not intersect set D, then the trajectory with the minimum length is two-link broken line ACB with links AC and BC belonging to the supporting straight lines of set D. Here, point A and set D are located on different sides of straight line BC, and point B and set D are located on different sides of straight line AC.

The following algorithm for the displacement of the three–body system from any initial position to any given terminal one can be used. At any moment, only one body is moving, and each body moves only during one time interval. The bodies M_i, M_j, M_k move one after another, while two other bodies are at rest. During each time interval, the moving body follows along the shortest trajectory which is either a straight line or a two-link broken line, according to Proposition 3. Comparing six ways of displacement, with different sequences of moving body, the sequence corresponding to the minimum work easily can be chosen.

CONCLUSIONS

Optimal motions of multibody systems along a horizontal plane are considered that correspond to the maximum average speed or minimum work against friction. These results are useful for planning possible locomotion of mobile robots.

References

[1] Chernousko F.L.: The optimum rectilinear motion of a two-mass system. J. Appl. Math. Mech. 66(1): 1-7, 2002.
[2] Chernous'ko F.L.: Analysis and optimization of the rectilinear motion of a two-body system. J. Appl. Math. Mech. 75(5):493-500, 2011.
[3] Figurina T.Yu.: Optimal control of system of material points in a straight line with dry friction. J. Comput. Syst. Sci. 54(5): 671-677, 2015
[4] Borisenko I.N., Figurina T. Yu., Chernousko F.L.: The quasistatic motions of a three-body system on a plane. J. Appl. Math. Mech. 78(3):220-227, 2014

ENTRAINMENT AND MULTISCALE DYNAMICS IN VIBRATIONALLY DRIVEN NONHOLONOMIC SYSTEMS

Scott David Kelly*[1]

[1]*Mechanical Engineering and Engineering Science, UNC Charlotte, Charlotte, North Carolina, USA*

Summary Mechanical systems subject to nonholonomic constraints can exhibit surprising dynamics. A well-known system that illustrates this point is the rattleback, which can reverse its direction of spin on a horizontal platform atop which it rolls without slipping, defying the conservation of angular momentum in a dramatic way for a subtle reason. The present paper documents two new instances of unexpected behavior by nonholonomically constrained mechanical systems, one characterized by a phenomenon akin to vibrational synchronization and the other characterized by the emergence of dynamics on two distinct time scales in response to forcing on only one.

Hat trick

The left panel in Figure 1 depicts the *Chaplygin beanie*, so named in [1] because it combines features of two canonical systems in the mechanics literature, the *Chaplygin* (or *Carathéodory*) *sleigh* and *Elroy's beanie*. A balanced rotor (the "beanie") surmounts the center of mass of a cart (the "sleigh") that's supported in the front by casters and in the rear by a wheel that rolls without slipping relative to the ground. The casters and wheel are assumed to have negligible inertia. If the system is initially at rest and the rotor is induced thereafter by internal actuation to rotate relative to the cart, then the cart will translate forward. In particular, if

$$J_{LT} = m\dot{x}\cos\theta + m\dot{y}\sin\theta, \qquad J_{RW} = -m\dot{x}a\sin\theta + m\dot{y}a\cos\theta + (B+C)\dot{\theta} + B\dot{\phi}$$

represent the system's forward translational momentum and its angular momentum relative to a vertical axis passing through the center of the rear wheel, respectively, then the system's dynamics satisfy

$$\dot{J}_{LT} = \frac{ma\left(J_{RW} - B\dot{\phi}\right)^2}{\left(ma^2 + B + C\right)^2}, \qquad \dot{J}_{RW} = \frac{-a\left(J_{RW} - B\dot{\phi}\right)J_{LT}}{ma^2 + B + C}.$$

Here m, B, and C represent the system's total mass and the rotational inertias of the rotor and cart relative to their centers, respectively. The fact that m and a are necessarily positive requires that the forward momentum J_{LT} be nondecreasing. Sinusoidal oscillations of appropriate amplitude in the rotor's orientation relative to the cart will induce the cart to advance in a slaloming motion, speeding up as it goes. A movie of this is visible at `http://tinyurl.com/gm4h2nh`.

Imagine that two such devices, one with an actuator coupling the rotor to the cart and the other with a linear torsional spring in place of the actuator, are placed atop a horizontal platform. If the platform has finite mass and is free to translate in response to forces arising from its interaction with the carts, then an analogy is apparent between this system and that studied by Huygens in the 1660s [2] comprising a pair of pendulum clocks with a shared nonrigid support. In Huygens' case, the oscillations of each clock contributed to small movements of the support and thus exerted influence on the motion of the other clock, inducing the clocks to exhibit an "odd kind of sympathy" by synchronizing their oscillations. The present problem is asymmetric — one rotor will be actuated in a prescribed way while the other responds passively — but the reader familiar with Huygens' study will suppose correctly that if the actuated rotor is driven sinusoidally so that the first cart slaloms forward relative to the platform, then the platform will vibrate, inducing the second cart to pivot back and forth about its rear wheel, and the unactuated rotor will begin to oscillate, inducing the second cart to translate forward relative to the platform as well.

The number of degrees of freedom in the motion of each cart distinguishes the present system from that comprising Huygens' clocks. In principle, energy transferred through the platform from the actuated cart to the passive cart could excite any combination of translational and rotational dynamics, perhaps depending on the initial position or orientation of the one cart relative to the other. The fact that the cart with the passive rotor is biased to translate forward in response to arbitrary platform vibration suggests an analogy to the more recent experiment described in [3], in which the flexible corpse of a fish was observed to swim forward — against a background flow — when excited to undulate by vortices shed from a bluff body.

What's surprising about the present system is the way in which the relative orientation of the carts evolves. The passive cart doesn't merely begin to move forward relative to the platform when the actuated cart does. If the initial orientation of the driven cart differs substantially from that of the passive cart, then the latter will reorient as it translates — in some cases gradually, over many cycles of oscillation — in order to follow the former. This is true even if the carts are initially antiparallel, back to back. Numerical simulation with a variety of initial conditions indicates that the asymptotic average difference between the carts' orientations — "average" because both carts undulate persistently as they translate — is generally not zero, but is consistently small regardless of the initial difference in the carts' orientations. Typical results are shown in the center and right panels of Figure 1.

*Corresponding author. Email: scott@kellyfish.net

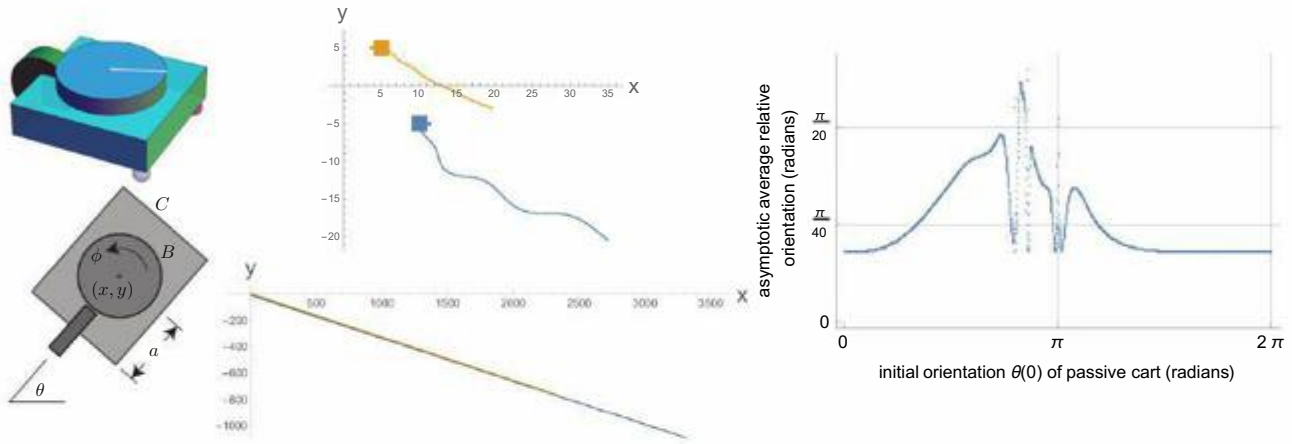

Figure 1: *Left*: Chaplygin beanie. *Center*: Trajectories of two such devices relative to a common planar support with finite mass, when the rotor atop the blue cart is driven such that $\phi = \sin t$ and the rotor atop the orange cart is coupled to the orange cart through a linear torsional spring. The carts are depicted in their initial configurations; their trajectories are shown through $t = 20$ (top) and $t = 400$ (bottom). The parameters m, B, C, and a are set to unity for both carts, as are the mass of the platform and the stiffness of the spring. *Right*: The average long-term difference in the carts' headings as a function of the initial orientation $\theta(0)$ of the passive (orange) cart, with the initial positions of the two carts as depicted in the center panel.

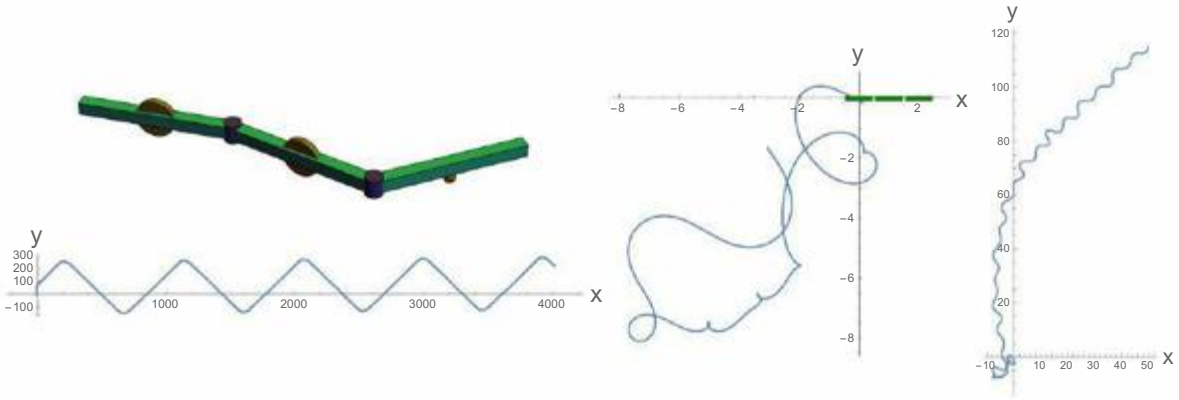

Figure 2: *Top left:* Three-link snake with spring-loaded hinges. *Remainder*: Trajectory relative to a platform induced to vibrate sinusoidally in the y direction with unit amplitude, at $t = 30$ (middle), $t = 80$ (right), and $t = 2000$ (bottom left).

Snake on a plane

The top left panel in Figure 2 depicts a mechanical system comprising three identical coplanar rigid links joined at two hinges. Two links are supported by wheels that roll without slipping, the third by a caster. With a third wheel in place of the caster, this system has been called a *kinematic snake* in the robotics literature [4]. If the hinges are fitted with linear torsional springs and the platform beneath is induced to vibrate, the system will begin to translate relative to the platform. In particular, suppose that the plane of the platform is the (x, y) plane, the three links are initially aligned at rest along the x axis, the masses and rotational inertias of the links are set to unity, and the platform is induced to accelerate perpendicular to the links from rest with $\ddot{}_{\text{platform}} = \cos t$. If the torsional springs have equal unit stiffness, the system will exhibit long-term dynamics on two distinct time scales, settling into a slaloming trajectory that corresponds in the net to translation along the y axis. If the stiffness of the spring between the center wheel and the caster is reduced to zero, the system will instead be attracted to a slaloming path along the x axis. The latter is depicted in the remaining panels of Figure 2.

References

[1] S. D. Kelly, M. J. Fairchild, P. M. Hassing, and P. Tallapragada. Proportional heading control for planar navigation: The Chaplygin beanie and fishlike robotic swimming. In *Proceedings of the American Control Conference*, pages 4885–4890, 2012.

[2] M. Bennett, M. F. Schatz, H. Rockwood, and K. Wiesenfeld. Huygens's clocks. *Proceedings of the Royal Society of London A*, 458:563–579, 2002.

[3] D. N. Beal, F. S. Hover, M. S. Triantafyllou, J. C. Liao, and G. V. Lauder. Passive propulsion in vortex wakes. *Journal of Fluid Mechanics*, 549:385–402, 2006.

[4] J. P. Ostrowski. *The Mechanics and Control of Undulatory Locomotion*. PhD thesis, California Institute of Technology, 1995.

MBS APPROACH FOR A CHAIN FOUNTAIN

Friedrich Pfeiffer, Johannes Mayet

Applied Mechanics, Mechanical Engineering, TU-Muenchen, Germany

Summary Chain fountains are known since long time, and many efforts have been taken to model and to explain the dynamics of such a chain fountain. A chain consists of many small elements starting from an inertial beaker, moving upwards by forming an arc and coming to an inertial position again after a rather long vertical distance. As the chain elements are all connected by a bearing type structure, they all have to go with the same velocity v. In the following we shall consider the stationary case and assume small chain elements (Fig. 1).

MODELING

The strange behavior of a chain leaving a beaker has interested many scientists, in the nineteenth century for example Routh [5] and Painleve [3], more recently Biggins [1] and internally Mayet [2]. Most of the contributions try a kind of a belt approach with good success. In spite of the not too complicated dynamics there remain open questions, which could not be answered completely. This paper tries a multibody approach (MBS), also with good results. Geometry and forces are depicted in Figure 2, from which we receive the following equations of motion:

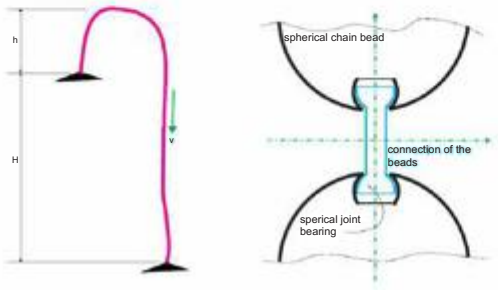

Figure 1: Chain Fountain and Chain Structure

$$\begin{aligned}\Delta m\ddot{}_i =& F_i cos\beta_i - F_{i-1}cos\beta_{i-1} + F_{Ti}sin\beta_i \\ & - F_{T,i-1}sin\beta_{i-1} \\ \Delta m\ddot{}_i =& F_i sin\beta_i - F_{i-1}sin\beta_{i-1} - F_{Ti}cos\beta_i \\ & + F_{T,i-1}cos\beta_{i-1} - \Delta mg. \end{aligned} \tag{1}$$

The frictional force writes $F_{Ti} = \mu(sign\alpha)F_i$, and the centrifugal effects with the force $F_{Ci} = \Delta m\frac{v^2}{R_i}$ and $\kappa_i = \frac{1}{R_i} = (\frac{d\alpha}{ds})_i$, are included in the acceleration terms. The initial conditions are $F_0 = k_0(\lambda v^2)$, $\alpha = \alpha_0, \beta = \beta_0$, The curvature κ_i depends on the change of the angle α with the trajectory coordinate s. The form of the chain fountain requires $\kappa_i < 0$. The factor k_0 takes uncertainties with respect to the force at the start into account. For the very small beads including their connection bars we may discretize with ($ds \approx \Delta s \approx d_i$, $dx \approx d_i cos\beta_i$, $dy \approx d_i sin\beta_i$, $\kappa_i \approx (\frac{\Delta\alpha}{\Delta s})_i \approx (\frac{\Delta\alpha}{d})_i$). Introducing the abbreviations ($f_i = \frac{F_i}{\Delta mg}$, $w_i = \frac{v^2}{gd_i}$), rearranging the eqs (1) and regarding the discretizations we come out with

$$\begin{aligned} f_i =& f_{i-1}[cos(\beta_i - \beta_{i-1}) - \mu(sign(\Delta\alpha))sin(\beta_i - \beta_{i-1})] + sin\beta_i - \kappa_i d_i w_i sin(\alpha_i - \beta_i), \\ & \kappa_i d_i w_i cos(\alpha_i - \beta_i) + \mu(sign(\Delta\alpha))(f_{i-1} + sin(\beta_i)) - \\ & f_{i-1}[sin(\beta_i - \beta_{i-1}) + \mu(sign(\Delta\alpha))cos(\beta_i - \beta_{i-1})] + cos\beta_i = 0, \end{aligned} \tag{2}$$

which within the framework of small magnitude assumptions allows the solution

$$\Delta\alpha_i \approx -\Big(\frac{cos\alpha_i + \mu_\alpha sin\alpha_i}{w_i - f_{i-1} - \frac{1}{2}sin\alpha_i + \frac{1}{2}\mu_\alpha cos\alpha_i}\Big). \tag{3}$$

Knowing $\Delta\alpha_i$ we find from the first equation (2) also f_i. Moreover, within the framework of these approximations we can write the first of the equations (2) in the reduced form ($f_i \approx f_{i-1} + sin\beta_i$). Summing up this gives the well-known result ($F_N - F_0 \approx \lambda gH$). The difference of the two ground forces F_N and F_0 is the weight of the chain part below the arc.

Considering work and energy according to Figure 2 there are several possibilities to regard the ground forces F_N and F_0. This is one of the open questions. We choose a form, where F_0 "works" along the fountain with length s_E:

$$E = \sum_{i=1}^{N}\{\frac{1}{2}\Delta mv^2 - (\Delta mg)y_i\} - F_0 s_E sin\beta_0 = \frac{1}{2}\lambda s_E v^2 + \frac{1}{2}\lambda gH^2 - \lambda k_0 v^2 s_E sin\beta_0. \tag{4}$$

The centrifugal forces over the complete fountain have to carry the whole chain together with the forces at the ground. With Figure (2) and the results above we get the balance

$$\sum_{i=1}^{N} F_{Ci}cos\alpha_i = \sum_{i=1}^{N}\Delta mg - F_N sin\alpha_E + F_0 sin\alpha_0, \qquad s_E \approx (1-k_0)(sin\alpha_0 - sin\alpha_E)(\frac{v^2}{g}) + Hsin\alpha_E. \tag{5}$$

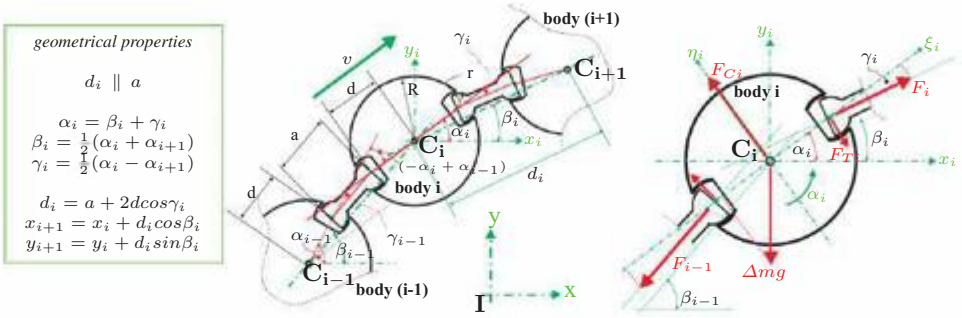

Figure 2: Chain Model - Geometry and Forces

Together with the energy equation (4) and with the property, that the fountain coordinate y can be approximated by two linear functions with respect to s, we thus can evaluate

$$(\frac{Hg}{v^2}) \approx \frac{1}{2}(1 - 2k_0 sin\beta_0)\Big\{1 - \sqrt{1 - 4\frac{(1-k_0)(1+sin\alpha_0)}{(1-2k_0 sin\beta_0)}}\Big\}, \qquad (\frac{s_E g}{v^2}) \approx -\Big[\frac{(\frac{Hg}{v^2})^2}{1 - 2k_0 sin\beta_0}\Big]. \tag{6}$$

With the above MBS structure we come out with one iteration, because a good approximation of the two magnitudes H and s_E is known. We have to iterate the empirical magnitude k_0 in dependence of the initial chain angle α_0 for meeting the height ratio $(\frac{h}{H}) \approx 0.14$, which is an experimental finding and something like a general law connected with the chain fountain. It belongs to the open questions. For $(50° \leq \alpha_0 \leq 85°)$ we get $(0.75 \leq (\frac{Hg}{v^2}) \leq 1.07)$ with a k_0 value around $k_0 \approx \frac{5}{6}$.

RESULTS AND CONCLUSIONS

In addition to the calculations some measurements have been performed. Additional calculations have been carried through for a belt approximation, which appears in literature (for example [6]) but has also developed by a co-worker to appear later [2]. The comparisons are good and confirm the model, Figure 3.

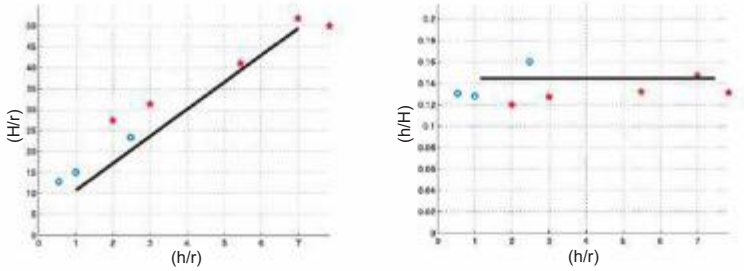

Figure 3: Results for the MBS and belt approximations compared with measurements (scaled with the arc radius r): black lines MBS approximation, blue circles belt approximation, red stars measurements (adaptation of the force F_0 by the starting coefficient k_0 to come out with a $(\frac{h}{H}) \approx 0.14$)

The dynamics of the first and the last bead in the fountain includes still open questions. The equations of motion allow a derivation of the difference of the forces connected with the first and last beads to be proportional to the weight of the chain height H ($F_N - F_0 \approx \lambda g H$). Many publications connect this result with the initial bead force only, which is not correct. On the other hand the initial force F_0 alone can be evaluated for the starting bead to be $F_0 = \lambda v^2$, which does not fit into real dynamics. Therefore we put $F_0 = k_0(\lambda v^2)$ and adapt k_0 to the ratio $\frac{h}{H} \approx 0.14$. As stated by literature the fountain process is also highly dissipative. But it is not yet clear, where dissipation takes place and if it is necessary to regard that for an analysis. First investigations indicate the ground processes, start and end.

References

[1] J.S. Biggins, M. Warner *Understanding the chain fountain*. Proceedings of the Royal Society A, March 2014
[2] J. Mayet *Chain Fountain*. Internal Communication, AM-TUM 2015
[3] P. Painleve *Cours de Mecanique I*. Ecole Polytechnique, 2eme Division, 1919-1920
[4] F. Pfeiffer, Th. Schindler *Introduction to Dynamics*. Springer Berlin Heidelberg 2015
[5] E.J. Routh *Dynamics of systems of rigid bodies, with numerous examples*. MacMillan, London, UK, 1860
[6] E. Willerding *Dynamik von Weltraumseilen - Space Elevator*. E. Willerding 2014

PRECESSION ON A ROTATING SADDLE A G RO FORCE IN AN INERTIAL FRAME

Oleg Kirillov,[1a] Mark Levi[2]

[1] ussian Academy of Sciences, Ste lov athematical Institute, 11 1 oscow, ussia
[2] athematics epartment, ennsylvania State University, University ar , State College, A 1 2

Summary Particles in rotating saddle potentials exhibit precessional motion which, up to now, has been explained by explicit computation. We show that this precession is due to a hidden gyroscopic force which, unlike the standard Coriolis force, is present in the inertial frame. We do so by finding a hodograph-like "guiding center" transformation using the method of normal form, which yields a simplified equation for the guiding center of the trajectory that coincides with the equation of the Foucault's pendulum. In this sense, a particle trapped in the symmetric rotating saddle trap is, effectively, a Foucault's pendulum, but in the inertial frame.

INTRODUCTION

The existence of Trojan asteroids in a triangular Lagrange libration point on the orbit of Jupiter is a consequence of the basic fact that a particle can be trapped in the rotating saddle potential [4,9]. Stability conditions for a heavy particle sliding without friction on a rotating saddle surface in the presence of gravity (Fig. 1) were obtained by Brouwer as early as 1918 [1,11]. Brouwer explicitly demonstrated that the saddle can be stabilized by rotation of the potential (in two dimensions) in contrast to the Paul trap for suspending charged particles in an oscillating electric field by analogy with the so-called Stephenson-Kapitsa pendulum in which the upside-down equilibrium is stabilized by vibration of the pivot [3]. Stabilization of the unstable saddle equilibrium by both rotation and vibration is well described by the concept of effective potential, which is equal to the kinetic energy of the high frequency motions of the system generated by the imposed oscillating field and affects the energy spectrum of the averaged motion [5-7]. In the case when the saddle potential is symmetric, the trajectory of the particle trapped by the rotating saddle in the non-rotating frame exhibits a slow prograde precession, Fig 1. This somewhat mysterious precession discovered first in the context of accelerator physics [2] and particle traps [8-10] is specific in that the standard averaging methods do not grasp the phenomenon [6].

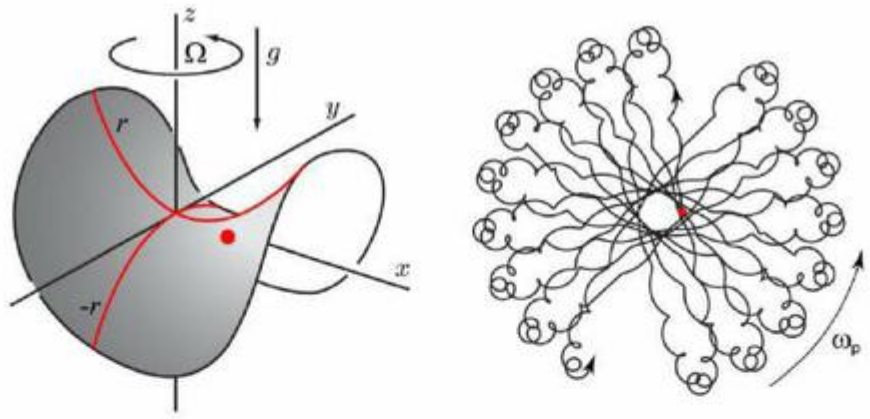

Fig. 1 (Left) A heavy particle on a symmetric rotating saddle surface and (right) prograde precession of its orbit in the non-rotating frame (figure adapted from [12])

HODOGRAPH TRANSFORMATION AND THE GUIDING CENTER E UATION

We consider a point mass sliding without friction on a saddle surface rotating about a vertical axis with the angular velocity $\omega = \varepsilon^{-1}$, $\varepsilon \ll 1$, Fig 1. Assuming the principal curvatures of the saddle at the equilibrium point to be equal, linearized equations near the equilibrium in the non-rotating frame after appropriate rescaling of time take form

$$\ddot{x} + S(\omega t)x = 0, \ x \in \mathbb{R}^2, \tag{1}$$

where

$$S(\tau) = \begin{pmatrix} \cos 2\tau & \sin 2\tau \\ \sin 2\tau & -\cos 2\tau \end{pmatrix}, \quad \tau = \omega t.$$

[a] Corresponding author. Email: kirillov@mi.ras.ru

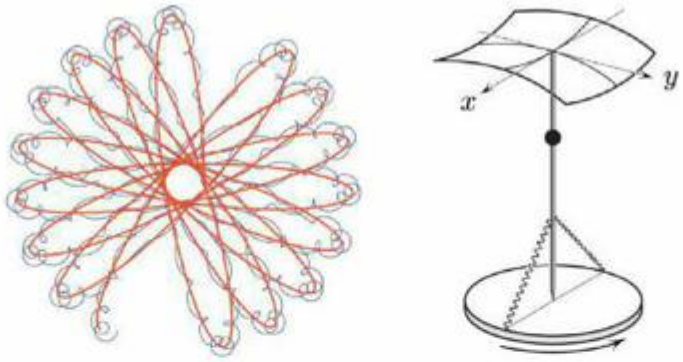

Fig. 2 (Left) Trajectory of the guiding center u (thick curve) tracking the corresponding trajectory (thin curve). The view is in the inertial frame with $\varepsilon = 0.45$. (Right) A possible mechanical realization of the rotating saddle trap. Here, and y are the angular variables of the inverted pendulum, and the graph of the potential energy is shown (figure adapted from [12]).

T e re Given a vector function $x : \mathbb{R} \to \mathbb{R}^2$, consider its "guiding center", or the "hodograph" image

$$u = x - \tfrac{\varepsilon^2}{4} S(t/\varepsilon)(x - \varepsilon J\dot{x}), \quad J = \begin{pmatrix} 0 & -1 \\ 1 & 0 \end{pmatrix}.$$

If $x(t)$ is a solution of (1), then $u(t)$ satisfies

$$\ddot{u} - \tfrac{\varepsilon^3}{4} J\dot{u} + \tfrac{\varepsilon^2}{4} u = \varepsilon^4 f(u, \dot{u}, \varepsilon),$$

where f is a function linear in u, $\dot{u}$ and analytic in ε, in a fixed neighbourhood of $\varepsilon = 0$. The guiding center therefore behaves, (ignoring the $O(\varepsilon^4)$ - terms) as a point charge of unit mass in the potential $V(u) = \frac{\varepsilon^2}{8} u^2$ in the magnetic field of constant magnitude $B = \varepsilon^3/4$ perpendicular to the u-plane.

Fig.2 illustrates a possible mechanical implementation of the rotating saddle trap as a light rod with a massive ball mounted on a turntable via a ball joint. Two springs are attached to the rod, and the height of the ball is adjustable, like in a metronome. If the ball is placed sufficiently low then the springs will stabilize the pendulum in the -direction while the y-direction remains unstable; thus, the potential acquires a saddle shape.

CONCLUSIONS

We demonstrated that the rapid rotation of the symmetric saddle potential creates a weak Lorentz-like, or a Coriolis-like force, in addition to an effective stabilizing potential - all in the inertial frame. As a result, the particle in the rotating saddle exhibits, in addition to oscillations caused by effective restoring force, a slow prograde precession in the inertial frame caused by this pseudo-Coriolis effect. By finding a hodograph-like "guiding center" transformation using the method of normal form, we found the effective equations of this precession that coincide with the equations of the Foucault's pendulum.

References

[1] Brouwer L.E.J. Beweging van een materieel punt op den bodem eener draaiende vaas onder den invloed der zwaartekracht. *N Arch v Wis* **2**: 407–419, 1918.

[2] Pearce R. M. Strong focussing in a magnetic helical quadrupole channel. *Nucl Instrum ethods* **3**(1): 101–108, 1970.

[3] Paul W. Electromagnetic traps for charged and neutral particles, *ev od hys* **2**: 531–540, 1990.

[4] Bialynicki-Birula I., Kalinski M., Eberly J. H. Lagrange equilibrium points in celestial mechanics and nonspreading wave packets for strongly driven Rydberg electrons, *hys ev ett* **3**:1777–1780, 1994.

[5] Veselic K. On the stability of rotating systems, *Angew ath ech* : 325–328, 1995.

[6] Shapiro V.E. The gyro force of high-frequency fields lost by the concept of effective potential. *hys ett A* **23** : 147–152, 1998.

[7] Levi M., Geometry of Kapitsa's potentials. *Nonlinearity* : 1365–1368, 1998.

[8] Thompson R. I., Harmon T. J., Ball M. G. The rotating-saddle trap: A mechanical analogy to RF-electric-quadrupole ion trapping? *Can J hys* : 1433–1448, 2002.

[9] Bialynicki-Birula I., Bialynicka-Birula Z., Chmura B. Trojan states of electrons guided by Bessel beams. *aser hysics* (10): 1371–1380, 2005.

[10] Hasegawa T., Bollinger J. J. Rotating-radio-frequency ion traps. *hys ev A* **2**: 043403, 2005.

[11] Kirillov O. N. *Nonconservative Stability roblems of odern hysics*, De Gruyter, Berlin/Boston, 2013.

[12] Kirillov O. N., Levi M. Rotating saddle trap as Foucault's pendulum. *Am J hys* (1): 26–31, 2016.

FREAKY MOTION OF A SPINNING SPHEROID INDUCED BY A SLIGHT BREAK OF ITS AXIAL SYMMETRY

Yutaka Shimomura
Department of Physics, Hiyoshi Campus, Keio University, Yokohama, Japan

Summary The Euler equations are derived for spinning spheroids whose mass distribution slightly loses the axial symmetry. Based on the obtained equations, the motion of a spheroid spinning on a flat surface is studied by numerical simulations, and it is found that a significant nutation is induced with a precession and it generates a beat, both by the slight break of its axial symmetry. As the initial spin rate increases, the period of nutation becomes smaller while its amplitude does larger.

INTRODUCTION

Motions of spinning bodies are so attractive, as represented by spinning tops, that many studies have been carried out up to now. However, it seems that some curious motions are left mysterious and unexplained. In fact, it was just the beginning of this century when the rising of a spinning egg was explained [1], its jumping was predicted [2] and observed [3], and the spin reversal of celt stone (or, a rattleback) was clarified [4]. Hard-boiled eggs are basically axisymmetric bodies, but the celt stones slightly lose the axial symmetry, which results in a little misalignment of the celt's principle axes of inertia and its axes of curvature at the point of contact with the table, and leads to the spin reversal.

In 2012, Cross [5] introduced to the author what he called a 'pathological egg', which shows a freaky motion. He put the "blu-tack" into the bottom of a toy egg for the axial symmetry to be lost, and spun it at a small spin rate to find its axis of geometrical symmetry oscillates between the horizontal and the vertical positions. He conjectured from his observation that spheroids with the axisymmetric structure never show such a big nutation and that it is caused by a slight break of the structure's axial symmetry.

In the present study, we derive the Euler equation for such quasi-axisymmetric spheroids to verify the Cross's conjecture by numerical simulations and study the feature of the nutation.

THE EULER EQUATIONS FOR QUASI-AXISYMMETRIC SPHEROIDS

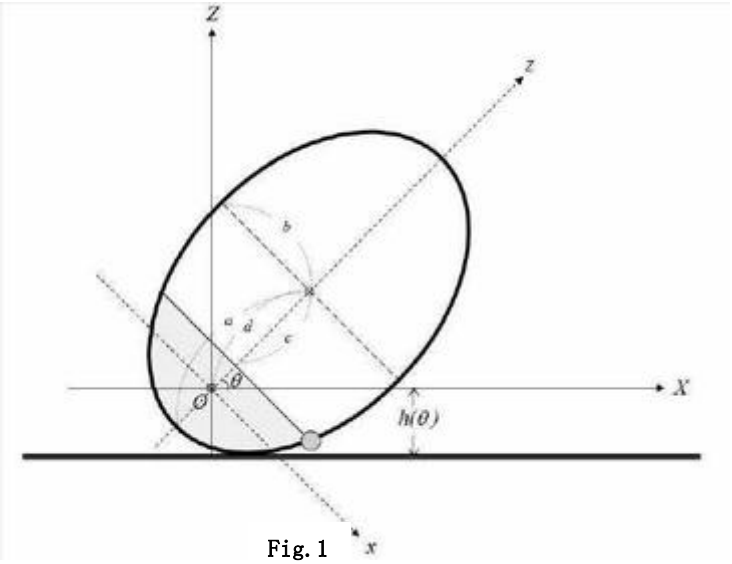

Fig. 1

As a quasi-axisymmetric spheroid, we study the kind as illustrated in Figure 1. Inside of a spheroid, there is a blunt mass M at its bottom like a weighted toy tumbler. The ellipse has the dimensions a and b, and the parameter c denotes the distance between the centre of shape and the blunt end of the mass distribution on the axis of symmetry. We add a small mass εM of point to the surface of the blunt end to make it slightly lose the original axial symmetry.

Provided the friction could be neglected, the Euler equations of order up to $O(\varepsilon)$ are derived for such quasi-axisymmetric bodies as in Figure 1, whose centre of mass is displaced a little bit off the axis of geometric symmetry and whose principle axes of inertia and its geometrical axes are misaligned generally. So, the spin angle itself comes into the Euler equations through sinusoidal functions.

The Euler equations of $O(1)$ predicts, as a result of Moffatt, Shimomura and Branicki [6] and Shimomura [7], the critical angular velocity n along z axis, over which the vertical spin state is stable. Figure 2 shows the critical angular velocity n as a function of $\gamma = -c/a$ in the case of $a/b = 3/2$. Here, we should note that the spheroids with $\gamma < -0.3$ is always stable even for zero spin.

Corresponding author. Email: yutaka@phys-h.keio.ac.jp

RESULTS OF NUMERICAL SIMULATIONS

Simulations for a spheroid with $a = 3cm, b = 2cm, \gamma = -0.5$ spinning on a frictionless flat surface are carried out by numerically solving a full system of five first order ODEs using the fourth-order Runge-Kutta method with the time step about 5μs. The initial conditions for the angle θ are $\theta = 0.01$ for $\varepsilon = 0$ and $\theta = 0.4$ for $\varepsilon = 1.0$, which mean the almost balanced states of rest for the still spheroid not spinning. After the spheroid in this almost balanced state is spun at $t = 0$ with a spin rate n (the angular velocity along the z-axis), the variations of θ in time are obtained.

First, it is confirmed that significant nutations are observed with a precession in the quasi-axisymmetric case of $\varepsilon = 1.0$, but not in the axisymmetric case of $\varepsilon = 0$. Second, as shown in Figure 3, it is also found that the nutations generate a beat, and as the initial spin rate n increases, the period of nutation becomes smaller while its amplitude does larger.

In the lecture, a demonstration will be available to observe the freaky motion of an egg-shaped body with a quasi-axisymmetric structure.

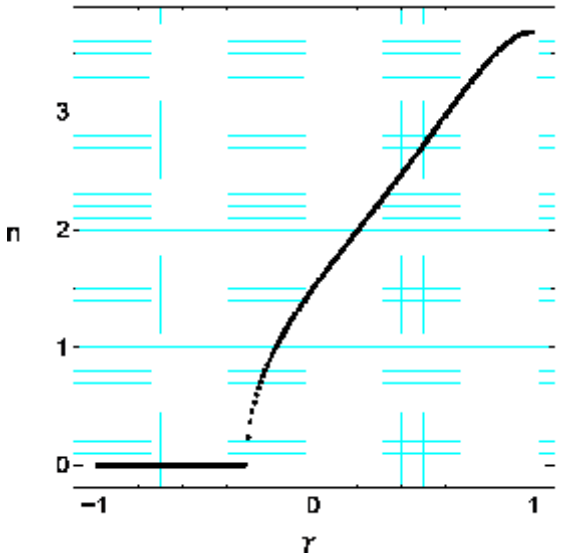

Fig. 2

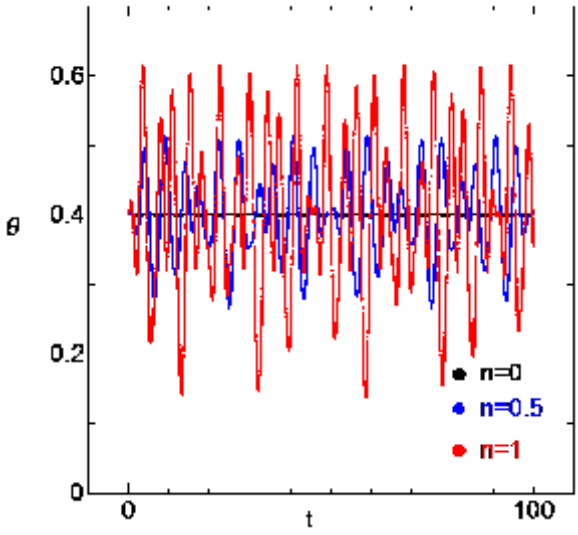

Fig. 3

CONCLUSIONS

The Cross's conjecture [5] is validated by numerical simulations of the Euler equations in the frictionless case: a slight break of the axial symmetry of a spinning spheroid gives rise to a significant nutation, which leads to its freaky motion with a precession. It is found that the nutation generates a beat, and the period of nutation becomes smaller and its amplitude does larger as the initial spin rate increases.

References

[1] Moffatt H. K., Shimomura Y.: Spinning eggs --- a paradox resolved. *Nature* **417**(2002)385 -386.

[2] Shimomura Y., Branicki M., Moffatt H. K.: Dynamics of an axisymmetric body spinning on a horizontal surface. Part II: Self-induced jumping. *Proc. Roy. Soc.* A **461**(2005)1753-1774.

[3] Mitsui T., Aihara K., Terayama C., Kobayashi H., Shimomura Y. : Can a spinning egg really jump? *Proc. Roy. Soc.* A **462**(2006)2897- 2905.

[4] Moffatt H. K., Tokieda T.: Celt reversals: a prototype of chiral dynamics. *Proc. Roy. Soc. Edinburgh* **138A**(2008)361-368.

[5] Cross R.: *Private communication* (2012).

[6] Moffatt H. K., Shimomura Y., Branicki M.: Dynamics of an axisymmetric body spinning on a horizontal surface. Part I: Stability and the gyroscopic approximation. *Proc. Roy. Soc.* A **460**(2004)3643-3672.

[7] Shimomura Y.: Effects of the air chamber and the shape on the rising motion of a spinning egg. Kyoyo－Ronso **123**(2005)39-54.

GIBBS-APPEL FORMULATION OF NON-HOLONOMIC MOTION OF A BALL ON A SPHERICAL SURFACE

Jiˇrı Náprstek*[1] and Cyril Fischer[1]

[1]*Institute of Theoretical and Applied Mechanics, Prague, Czech Republic*

Summary A new type of a passive vibration absorber is proposed and investigated as a non-linear non-holonomic system. It consists of a semi-spherical horizontal cavity in which a ball of a smaller diameter is rolling. The system of six degrees of freedom with three non-holonomic constraints is investigated. Instead of conventional way via Hamiltonian functional and Lagrangian procedure, the respective differential system is derived using the Gibbs-Appel function and related steps. Comparison of both approaches has been done. The system has an auto-parametric character and hence the semi-trivial solution and dynamic stability is investigated. Some principal post-critical regimes are outlined and qualitatively evaluated in the resonance neighborhood. Numerical experiments are performed and physically interpreted.

INTRODUCTION

Passive vibration absorbers are very widely used in engineering to suppress vibration induced by various environmental resources, e.g. wind, earthquake, technology, etc. Among many commonly used types widely discussed in literature, a non-conventional type being based on a heavy ball rolling inside a spherical cavity appeared recently. It approved many advantages over other systems in certain conditions. Schemes of pendulum and ball absorbers are outlined in Fig. 1. Dynamic character of a ball absorber is much more complicated and unlike conventional types its non-linear space character must be ever respected. It is basically an auto-parametric system with several bifurcation points of the generalized Hopf type being very prone to achieve a local or global stability limit and to fall into a post-critical state.

Authors tried in the past to formulate this problem by a classical way constructing the Hamiltonian functional with non-holonomic constraints for the planar and space problem. Then the respective Lagrangian governing system has been carried out. The planar configuration leads to the quite transparent system, see [1], which can be treated analytically. However, the full space approach provides the differential system which is too complicated and its physical interpretation can be multivalent, [2]. The system should be treated almost only numerically. Therefore it is not very suitable for further discussion. For easier analysis of a dynamic system is the problem formulated using Appel-Gibbs function. For theoretical background see, e.g., [3] and others. A similar problem related with anti-seismic protection of a building has been discussed for instance in [4]. The main advantage of the Appel-Gibbs function consists in easier problem definition and easier more transparent introduction of non-holonomic constraints.

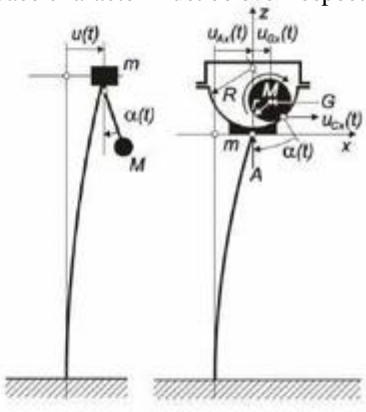

Figure 1: Tuned mass damper: a) pendulum principle; b) rolling ball principle.

GOVERNING DIFFERENTIAL SYSTEM

The Appel-Gibbs approach is used to formulate the governing non-linear differential system. The basis is the Appel function (often referred to as an energy acceleration function) defined as follows, see for instance [3]:

$$S \;=\; \frac{1}{2}M(\ddot{u}_{Gx}^2 + \ddot{u}_{Gy}^2 + \ddot{u}_{Gz}^2) + \frac{1}{2}J\;\omega_x^2 + \dot{\omega}_y^2 + \dot{\omega}_z^2), \tag{1}$$

where M - mass of the ball, J - central inertia moment of the ball with respect to point G, $\boldsymbol{\omega}$ - angular velocity of the ball with respect to the center G, $\mathbf{u}_G$ - velocity of the ball center, x, y, z - cartesian coordinates with origin in the point A.

The function S allows to write the Appel differential system:

$$\partial S^r/\partial\dot{\omega}_x \;=\; F_x, \quad \partial S^r/\partial\dot{\omega}_y \;=\; F_x, \quad \partial S^r/\partial\dot{\omega}_z \;=\; F_x, \tag{2}$$

where S^r is the reduced Appel function where only terms with 2nd time derivatives ($\mathbf{u}_G, \boldsymbol{\omega}$) are kept, $\mathbf{F}_G$ - external force vector acting in G. Vector $\mathbf{F}_G$ can be determined using the virtual displacements principle. The system (2) should be completed by three non-holonomic constraints including a conjecture of non-sliding contact between the ball and cavity:

$$u_{Gx} = \dot{u}_{Ax} - \rho(\omega_y(u_{Cx} - R) - \omega_z u_{Cy}),\; u_{Gy} = \dot{u}_{Ay} - \rho(\omega_z u_{Cx} - \omega_x(u_{Cz} - R)),\; \dot{u}_{Gz} = \;-\rho(\omega_x u_{Cy} - \omega_y u_{Cx}) \tag{3}$$

*Corresponding author. Email: naprstek@itam.cas.cz

where $\rho = 1 - r/R$, r - ball radius, R - cavity radius. Final form of the differential system reads:

$$\begin{aligned} \dot{\omega}_x &= L\,[\ \ddot{u}_{Ay}(u_{Cz} - R) - g u_{Cy} + (R-r)\omega_n(u_{Cy}\omega_z - (u_{Cz} - R)\omega_y)]\,, \\ \omega_y &= L\,[-u_{Ax}(u_{Cz} - R) + g u_{Cx} - (R-r)\omega_n(u_{Cx}\omega_z - (u_{Cz} - R)\omega_z)]\,, \\ \omega_z &= L\ u_{Ax}u_{Cy} - u_{Ay}u_{Cx} + (R-r)\omega_n(u_{Cx}\omega_y - u_{Cy}\omega_x)]\,, \\ L &= \rho/((R-r)^2 + 0.4r^2), \quad \omega_n = [\omega_x, \omega_y, \omega_z]\cdot\mathbf{n}, \end{aligned} \tag{4}$$

where $\mathbf{u}_A = [\ddot{u}_{Ax}, \ddot{}_{Ay}, 0]^T$ - vector of external acceleration, $\mathbf{u}_C$ - displacement in the contact of the ball with cavity. The system Eqs (4) should be solved simultaneously together with kinematic constraints following from non-holonomic constraints Eqs (3):

$$u_{Cx} = -\rho(\omega_y(u_{Cx} - R) - \omega_z u_{Cy}),\ u_{Cy} = -\rho(\omega_z u_{Cx} - \omega_x(u_{Cz} - R)),\ \dot{u}_{Cz} = -\rho(\omega_x u_{Cy} - \omega_y u_{Cx}) \tag{5}$$

The Eqs (4, 5) make up the system of six differential equations with six unknowns $\boldsymbol{\omega}, \mathbf{u}_C$.

NUMERICAL EXPERIMENTS

A large program of numerical experiments with Eqs (4, 5) has been performed regarding general and special configurations. A sample solution is plotted in Fig. 2. It represents free movement without external excitation and initiated by initial conditions. The ball in $t = 0$ is placed at angle $\alpha = 0.1$ above point A in the vertical plane declined from (xz) plane in $\gamma = 1.0$. Damping ratios $\delta_1 = 0.21, \delta_2 = 0.22$. Plots φ, θ, ψ are respective Euler angles evaluated as quasi-coordinates from parameters of the above solution to enable a comparison with Lagrangian approach. Coincidence was perfect. Nevertheless a number of additional configurations have been examined and compared with results obtained earlier, e.g. [2], using analytical and numerical procedures. For instance: rolling the ball on a horizontal plane ($R \to \infty$), forced movement of the ball in the cavity in a horizontal plane, spin processes ($\omega_n = 0$) and its independency on other coordinates, limit cycles, etc.

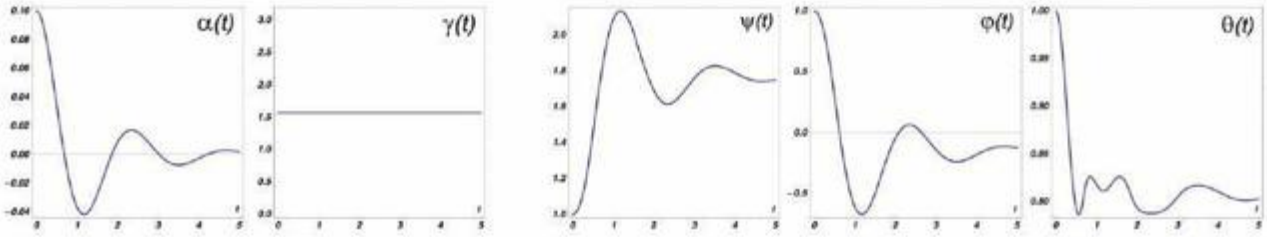

Figure 2: Sample solution of governing system in quasi-coordinates.

CONCLUSIONS

The heavy ball in a spherical cavity used as a TMD has been investigated. Unlike other systems it must be modeled in the non-linear domain. Any attempt for a linear approach failed completely. Appel-Gibbs formulation of a non-holonomic system dynamics approved excellent efficiency in comparison with a conventional way being based on Lagrangian differential system and non-holonomic constraints adjoined via indefinite Lagrange multipliers. Nevertheless, it reveals that the Lagrangian procedure can be defined as a special case of the Appel-Gibs formulation for a certain choice of quasi-coordinates, which, however, are not very convenient for detailed investigation. A simple model of the damping mechanism has been incorporated into the Appel-Gibbs system.

ACKNOWLEDGEMENT

Support of the Czech Science Foundation No. 15-01035S and of the RVO 68378297 inst. support are acknowledged.

References

[1] Náprstek J., Fischer C., Pirner M., Fischer O.: Non-linear dynamic behaviour of a ball vibration absorber. In: Proc. COMPDYN 2011 (M.Papadrakakis et al. eds). ECCOMAS - NTU Athens, Kerkyra, Corfu, 2011, CD ROM, paper 180, 14 pgs.

[2] Náprstek J., Fischer C.: Dynamic response of a heavy ball rolling inside a spherical dish under external excitation. In: Proc. Engineering Mechanics 2013 (I. Zolotarev edt.). IT ASCR Praha, Svratka, 2013, pgs 96-106, CD #46.

[3] Pars L.A.: A Treatise on Analytical Dynamics (2nd edition). Ox Bow Press, Connecticut, USA, 1972.

[4] Matta E., De Stefano A., Spencer B.F. Jr.: A new passive rolling-pendulum vibation absorber using a non-axial guide to achieve bidirectional tuning. Earthquake Engineering and Structural Dynamics, vo. 38 (2009) 1729-1750.

ESCAPE FROM POTENTIAL WELLS IN MULTI-DIMENSIONAL EXPERIMENTAL SYSTEMS

Shane D. Ross*[1], Amir E. BozorgMagham[2], Shibabrat Naik[1], and Lawrence N. Virgin[3]
[1]*Department of Biomedical Engineering and Mechanics, Virginia Tech, Blacksburg, VA, United States*
[2]*Department of Atmospheric and Oceanic Science, University of Maryland, College Park, MD, United States*
[3]*Department of Mechanical Engineering, Duke University, Durham, NC, United States*

Summary Predicting the escape from a potential energy well is a universal exercise, governing myriad engineering and natural systems, e.g., buckling phenomena, ship capsize, and human balance. Criteria and routes of escape have previously been determined for 1 degree of freedom (DOF) mechanical systems with time-varying forcing, with reasonable agreement with experiments. When there are 2 or more DOF, the situation becomes more complicated, and the theory of tube dynamics provides the criteria for which phase space states will escape. We report the validation of the tube dynamics theory for a 2 DOF experiment of a ball rolling on a surface. This experimental validation establishes a theoretical framework which can be exploited for purposes of control, e.g., avoiding or triggering escape or transition between metastable states in mechanical systems.

INTRODUCTION

Our objective is to study routes of escape from a potential well in an experimental 2 degree of freedom system. For this aim we study the chaotic motion of a rolling ball on a surface ($H(x,y)$) which has 4 potential wells, one in each quadrant of the (x,y) plane, Fig. 1(a)(b) [1]. We adopt a global geometric view of the motion analysis, using techniques which have been fruitful in other areas of mechanics, such as celestial mechanics [2] and physical chemistry [3]. The equations of motion are obtained from the Lagrangian; $\mathcal{L}(x,y,\dot{x},\dot{y}) = T(x,y,\dot{x},\dot{y}) - U(x,y)$. The kinetic energy (translational plus rotational for a ball rolling without slipping) is,

$$T(x,y,\dot{x},\dot{y}) = \frac{1}{2}\frac{7}{5}\left(\dot{x}^2 + \dot{y}^2 + (H_x x + H_y y)^2\right) \tag{1}$$

and the potential energy is $U(x,y) = gH(x,y)$, where,

$$H(x,y) = \alpha(x^2+y^2) - \beta(\sqrt{x^2+\gamma} + \sqrt{y^2+\gamma}) - \xi xy + H_0. \tag{2}$$

We use parameter values $(\alpha,\beta,\gamma,\xi) = (0.07, 1.017, 15.103, 0.00656)$ in the appropriate units, along with $H_0 = 12.065$ cm and $g = 981$ cm/s^2. The ball's mass factors out and is not included.

Small damping is present, but over short time-scales, the motion approximately conserves energy, and the conservative dynamics are the dominant contributor to transition between wells. Let $\mathcal{M}$ be the *energy manifold* given by setting the energy integral ($\mathcal{E}(x,y,v_x,v_y) = T(x,y,x,y) + U(x,y)$) equal to a constant, i.e., $\mathcal{M}(E) = \{(x,y,v_x,v_y) \subset \mathcal{R}^4 \mid \mathcal{E}(x,y,v_x,v_y) = E\}$ where E is a constant. The projection of the energy manifold onto configuration space, the (x,y) plane, is the region of

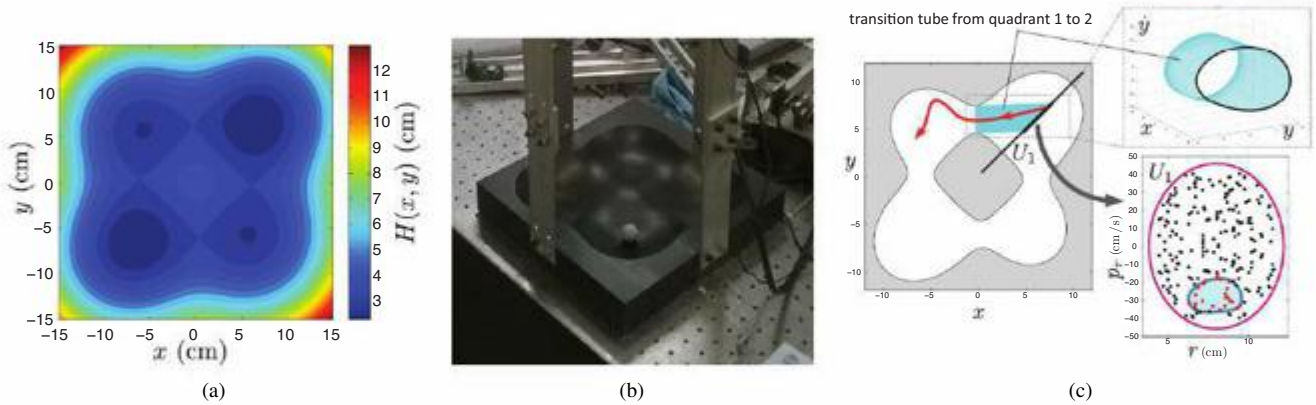

(a) (b) (c)

Figure 1: (a) Surface height $H(x,y)$. (b) Experimental apparatus. (c) For a fixed energy, E, above a critical value E_e, the permissible region (in white) has potential wells connected by necks around saddle-type equilibria. All motion from the well in quadrant 1 to quadrant 2 must occur through the interior of a stable manifold tube associated to an unstable periodic orbit in the neck between them. In the schematic of the U_1^+ Poincaré section, we the color intersecting trajectories by their near-future fate; black = no transition, red = imminent transition from quadrant 1 to 2 (an example of such a trajectory is also shown). A schematic tube boundary and interior is also shown for comparison on U_1^+. The large oval is the theoretical boundary of the energy manifold on U_1^+.

*Corresponding author. Email: sdross@vt.edu

energetically possible motion for a ball of energy E, $M(E) = \{(x, y) \mid U(x, y) \leq E\}$. The zero velocity curves are the boundary of $M(E)$ and are the locus of points in the (x, y) plane where the kinetic energy vanishes. The ball's state is only able to move on the side of this curve where the kinetic energy is positive, shown in white in Fig. 1(c). The critical energy of escape, E_e, is the same as the energy of the saddle points in each neck (which are all equal), and divides the global behavior into two cases, according to the sign of $\Delta E = E - E_e$:

Case 1, $\Delta E < 0$: the ball is safe against escape since potential wells are not energetically connected.

Case 2, $\Delta E > 0$: "necks" between all the potential wells open up around the saddle points, permitting the ball to move between the two potential wells (e.g., Fig. 1(c) shows this case).

TUBE DYNAMICS: TUBES LEADING TO ESCAPE

Within a given potential well the set of all states leading to escape to a different potential well (or having just escaped a different potential well) are within a cylindrical manifold or *tube*, as shown in Fig. 1(c). This tube bounds the set of all states for a fixed energy which will soon reach, or have just passed from, a different potential well [2, 3] (nested energy manifolds will have correspondingly nested tubes). For each E, the boundary of the tubes in phase space (or more precisely, within $\mathcal{M}(E)$) are the stable and unstable manifolds of an unstable periodic orbit of the same energy residing in the neck connecting the adjacent wells. The resulting geometric framework for understanding escape and transition we term 'tube dynamics'.

EXPERIMENTAL RESULTS

We use a Poincaré section which is selected based on the symmetry of the surface and the equations of motion, and which are best described in polar coordinates (r, p_r); $U_1^{\pm} = \{(r, p_r) \mid \theta = \frac{\pi}{2},\ \mathrm{sign}(p_\theta) = \pm 1\}$. Taking Poincaré sections of 120 experimental trajectories (e.g., the typical trial shown in Fig. 2(a)) should reveal the tube cross-sections. We first determine the instantaneous ΔE for every point on the Poincaré section U_1, so we can consider only narrow ranges of ΔE, to approximate a single energy manifold. In Fig. 2(b) we see an example of the Poincaré section U_1^+ for all intersections in the energy range $200 < \Delta E < 300\ (\mathrm{cm/s})^2$. The intersection points which are about to transition from quadrant 1 to 2, determined by following the experimental trajectory forward in time, and are marked with red circles.

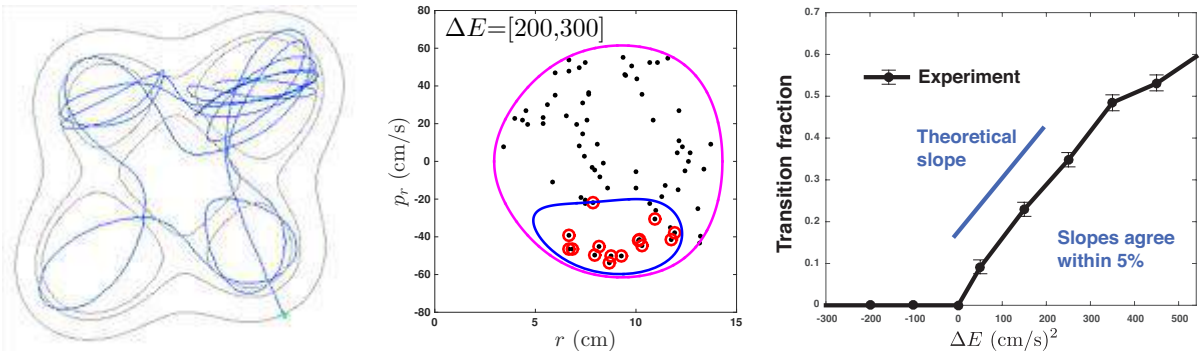

(a) (b) (c)

Figure 2: *Experimental results.* (a) A typical experimental trajectory in blue, which is released from rest at the lower right. Notice how it moves seemingly erratically between the 'wells'. Some height iso-contours are also shown, in light gray. (b) Histogram of energy for crossings of the U_1^+ Poincaré section (blue: $\Delta E < 0$, gray: $\Delta E > 0$, red: transitioning). (c) On U_1^+, we consider only a narrow range of energy ($\Delta E \in [0, 100\ (\mathrm{cm/s})^2]$) and label intersecting trajectories by their recent past or future; black: no transition, red: recent transition to quadrant 1 from quadrant 2 and magenta: imminent transition from quadrant 1 to 4. (d) Fraction of transitioning trajectories as a function of energy above the saddle.

CONCLUSIONS

The transitioning points at each energy are all found to be within the theoretical tube boundary (blue curve); as in, e.g., Fig. 2(b). Furthermore, the fraction of transitioning trajectories increases linearly with ΔE, Fig. 2(c), as expected theoretically from arguments related to the phase space flux over a saddle [4]. This experimental validation of tube dynamics establishes a theoretical framework which can be exploited for purposes of control, e.g., avoiding or triggering escape or transition between metastable states in mechanical systems. SDR thanks the NSF for partially funding this work through grant 1537349.

References

[1] Virgin, L. N., Lyman, T. C., Davis, R. B. Nonlinear dynamics of a ball rolling on a surface. *Am. J. Phys.*, 78(3):250–257, 2010.

[2] Koon, W. S., Lo, M. W., Marsden, J. E., Ross, S. D. Heteroclinic connections between periodic orbits and resonance transitions in celestial mechanics. *Chaos*, 10:427–469, 2000.

[3] Gabern, F., Koon, W. S., Marsden, J. E., Ross, S. D. Yanao, T. Application of tube dynamics to non-statistical reaction processes. *Few-Body Systems*, 38:167–172, 2006.

[4] MacKay, R. S. Flux over a saddle. *Physics Letters A*, 145:425–427, 1990.

PASSIVE LINEARIZATION OF NONLINEAR SYSTEM RESONANCES

Giuseppe Habib*[1], Chiara Grappasonni [1], and Gaetan Kerschen[1]

[1]*Space Structures and Systems Laboratory, University of Liège, Liège, Belgium*

Summary In this work we demonstrate that the addition of properly-tuned nonlinearities to a nonlinear system can increase the range over which a specific resonance responds linearly. Specifically, we seek to enforce two important properties of linear systems, namely the force-displacement proportionality and the invariance of resonance frequencies. Theoretical findings are validated through numerical simulations and experiments.

Devices used for sensing, imaging and detection are usually required to exhibit linear behavior in their dynamic range. However, nonlinearity is a frequent occurrence in physical and engineering applications. Nonlinearity may result in plethora of dynamic phenomena which can drastically limit the performance of the devices [1]. One well-established approach for enforcing linear behavior is feedback linearization, which uses feedback control to cancel the undesired nonlinearities. However, feedback linearization requires an accurate monitoring of the system's states, an actuator and an external source of energy, which complicates its practical realization.

We propose a fully passive, resonance-based approach for dealing with undesired nonlinearities in mechanical systems. Properly-tuned nonlinearities are introduced in the nonlinear system to increase the range over which a specific resonance responds linearly. Specifically, we seek to enforce two important properties of linear systems, namely the force-displacement proportionality and the invariance of resonance frequencies. Our approach relies on a principle of similarity [2] which states that the added nonlinearity should possess the same mathematical form as that of the original nonlinear system. This principle of similarity enables us to extend the linear regime over a larger range of motion amplitudes.

We consider an n-degree-of-freedom (DoF) mechanical system with concentrated nonlinearities subject to harmonic excitation:

$$\tilde{\mathbf{M}}\ddot{\mathbf{x}} + \tilde{\mathbf{C}}\dot{\mathbf{x}} + \tilde{\mathbf{K}}\mathbf{x} + \tilde{\mathbf{b}}_{nl}\left(\mathbf{x}\right) = \sqrt{\varepsilon}\tilde{\mathbf{v}} f \cos\omega t, \tag{1}$$

where ε is a small bookkeeping parameter. The vector $\tilde{\mathbf{b}}_{nl}\left(\mathbf{x}\right)$ contains both the original and additional nonlinearities, which are of polynomial nature. According to the principle of similarity [2], the additional nonlinearities should possess the same exponent as the original nonlinearity. Without loss of generality, cubic nonlinearities are considered herein.

The objective of this study is to linearize one specific resonance of system (1) through the proper design of the additional nonlinearities. To this end, the nonlinear normal mode (NNM) theory is exploited, because nonlinear resonances are known to occur in the neighborhood of NNMs [3]. First, we transform Eq. (1) into modal space through the change of variables $\mathbf{x} = \mathbf{U}\mathbf{y}$ where $\mathbf{U}$ contains the normal modes of the underlying linear system, and we define normalized modal displacements, $\mathbf{q} = \mathbf{y}/\left(\sqrt{\varepsilon}f\right)$, such that

$$\ddot{\mathbf{q}} + \mathbf{C}\dot{\mathbf{q}} + \mathbf{\Omega}\mathbf{q} + \mathbf{b}_{nl}\left(x\right) = \mathbf{v}\cos\omega t, \tag{2}$$

where $\mathbf{\Omega} = \text{diag}\left[\Omega_j^2\right]_{j=\overline{1,n}}$, $\mathbf{C} = \left[c_{ij}\right]_{i,j=\overline{1,n}}$ and $\mathbf{b}_{nl}\left(\mathbf{x}\right) = \left[\ \ldots, \quad \varepsilon f^2 \sum_{h_1+\ldots+h_n=3} b_{jh_1\ldots h_n} \prod_{i=1}^{n} q_i^{h_i}, \quad \ldots\ \right]^{\mathrm{T}}$. $\mathbf{b}_{nl}\left(\mathbf{x}\right)$ is the projection of $\tilde{\mathbf{b}}_{nl}\left(\mathbf{x}\right)$ in modal space, thus, even if $\tilde{\mathbf{b}}_{nl}\left(\mathbf{x}\right)$ is sparse, $\mathbf{b}_{nl}\left(\mathbf{x}\right)$ can be fully populated. $b_{jh_1\ldots h_n}$ are scalars, where j indicates the mode number and varies according to the rows of $\mathbf{b}_{nl}\left(\mathbf{x}\right)$, while subscripts $h_1 \ldots h_n$ are in accordance with the exponents of the modal coordinates of the corresponding terms. We assume that the system features no internal resonances, i.e., natural frequencies Ω_j are incommensurate.

The NNMs are now calculated by removing damping and forcing terms in Eq. (2). Following a standard perturbation technique and limiting the solution to the fundamental harmonic, the approximate solution has the form $\mathbf{q} = \left(\mathbf{q}_0 + \varepsilon\mathbf{q}_1 + O\left(\varepsilon^2\right)\right) \sin\left(\left(\omega_0 + \varepsilon\omega_1 + O\left(\varepsilon^2\right)\right)t\right)$, where $\mathbf{q}_0 = \left[\cdots, q_{j0}, \cdots\right]^{\mathrm{T}}$ and $\mathbf{q}_1 = \left[\cdots, q_{j1}, \cdots\right]^{\mathrm{T}}$. Imposing resonance condition at order ε^0 and solving terms of order ε^1 yields for the lth NNM

$$q_{j0} = 0,\ q_{j1} = -\frac{3}{4}\frac{b_{j0\ldots3\ldots0}q_{l0}^3}{\Omega_j^2 - \Omega_l^2} \quad \text{for } j = \overline{1,n},\ j \neq l, \quad \omega_0 = \Omega_l,\ \omega_1 = \frac{3}{4}\frac{b_{l0\ldots3\ldots0}q_{l0}^2}{2\Omega_l}. \tag{3}$$

q_{j0} and q_{j1} $(j \neq l)$ represent the influence of the nonresonant modes on the lth mode. ω_1 is the variation of the lth natural frequency with respect to the amplitude of oscillation q_{l0}. Thus, if $b_{l0\ldots3\ldots0} > 0$ (< 0), the resonance is of hardening (softening) type.

In order to relate the undamped, unforced NNM motions to the resonances of the damped, forced system, the energy balance criterion [4] is utilized:

$$\int_0^T \dot{\mathbf{x}}(t)^{\mathrm{T}}\tilde{\mathbf{C}}\dot{\mathbf{x}}(t)\mathrm{d}t = \int_0^T \dot{\mathbf{x}}(t)^{\mathrm{T}}\sqrt{\varepsilon}\tilde{\mathbf{v}} f \cos\omega t\,\mathrm{d}t, \tag{4}$$

*Corresponding author. Email: giuseppe.habib@ulg.ac.be

where T is the period of motion. Eq. (4) indicates that at resonance the energy dissipated by damping over a full period is equal to the input energy. Inserting the approximate solution for $\mathbf{q}$ in Eq. (4) gives

$$q_{l0} = \frac{v_l}{\Omega_l c_{ll}}, \quad q_{l1} = \frac{\Omega_l q_{l0} \left(\sum_{\substack{j=1 \\ j \neq l}}^{n} c_{lj} q_{j1} + \sum_{\substack{j=1 \\ j \neq l}}^{n} c_{jl} q_{j1} \right) - \sum_{\substack{j=1 \\ j \neq l}}^{n} q_{j1} v_j}{v_l - 2\Omega_l q_{l0} c_{ll}} + \frac{\omega_1 q_{l0}^2 c_{ll}}{v_l - 2\Omega_l q_{l0} c_{ll}} \tag{5}$$

and $x_k = \sqrt{\varepsilon} f \left(u_{kl} q_{l0} + \varepsilon \left(\sum_{j=1}^{n} u_{kj} q_{j1} \right) + O\left(\varepsilon^2\right) \right)$. Eqs. (3) and (5) completely define the lth resonance of system (1) and form the basis of the design procedure developed in this paper. Based on these equations, force-displacement proportionality for coordinate x_k of the lth resonance can simply be enforced through $\sum_{j=1}^{n} u_{kj} q_{j1} = 0$. Similarly, invariance of the lth resonance frequency can be enforced through $\omega_1 = 0$, such that the lth natural frequency $\omega_l \approx \omega_0$. Since these two conditions involve the n coefficients of the nonlinear terms $b_{j0\ldots3\ldots0}$, they can be used to design the additional nonlinearities in function of the original ones.

An experimental set-up is utilized to demonstrate the proposed idea. It comprises a cantilever beam made of steel to which a doubly-clamped beam is connected (Fig. 1a). A thin steel lamina located at the free end of the cantilever and the doubly-clamped beam itself generate two hardening nonlinearities, which can be modeled using cubic springs. A two-DoF reduced model of the system was identified experimentally. From this model, applying the aforementioned procedure, the nonlinearity of the doubly-clamped beam was designed, such that the second resonant peak satisfies force-displacement proportionality. In Fig. 1b, solid and dashed lines depict the envelopes of the normalized amplitude of the second resonant peak, respectively with and without the nonlinearity related to the doubly-clamped beam. The red circles depict the measured resonant peaks. These circles are almost aligned horizontally, which translates the fact that the displacement of the cantilever beam around the second resonance is proportional to the amplitude of the harmonic forcing. This condition is not verified if the additional nonlinearity is not included (dashed line).

Successively, in order to compensate the frequency shift of the first resonance, due to the hardening nonlinearities, a couple of permanent magnets was placed on the doubly-clamped beam and two others were placed symmetrically next to them on a fixed support. The two couples of magnets are mutually attractive in order to generate a softening nonlinearity. The amplitude of this nonlinearity was controllable by varying the distance between the two magnets. Choosing the appropriate distance, according to the analytical procedure proposed, we were able to linearize the frequency backbone of the first resonance, as illustrated in Fig. 1c (solid black lines). Dashed red lines in Fig. 1c show the frequency response of the system if the nonlinear magnetic force is neglected. The blue circles depict the resonance peaks measured experimentally.

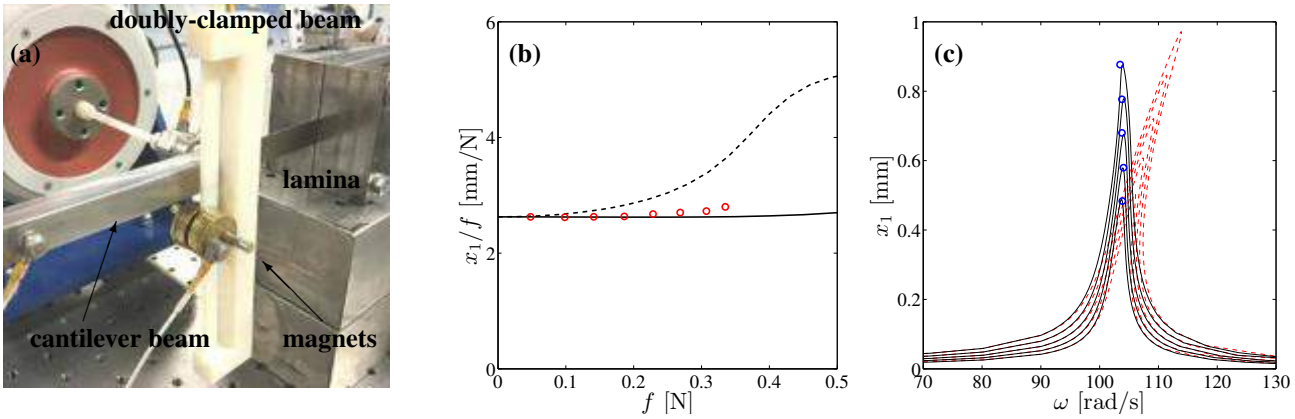

Figure 1: (a) experimental set-up. (b) first part of the experiment, envelops of resonant peak for different forcing amplitude; dashed line: nonlinearity of doubly-clamped beam neglected, solid line: nonlinearity of doubly-clamped beam included, red circles: experimental results. (c): second part of the experiment, frequency response without (dashed red lines) and with (solid black lines) magnetic nonlinear force; blue circles: experimental results.

References

[1] Postma H.C., Kozinsky I., Husain A., Roukes M.: Dynamic range of nanotube-and nanowire-based electromechanical systems. Appl Phy Lett 86:223105, 2005.

[2] Habib G., Kerschen G.: A principle of similarity for nonlinear vibration absorbers. In Proc. ASME 2015 IDETC, 2015.

[3] Vakakis A.F., Manevitch L.I., Mikhlin Y.V., Pilipchuk V.N., Zevin A.A.: Normal modes and localization in nonlinear systems, Springer, 1996.

[4] Hill T., Cammarano A., Neild S., Wagg D.: An analytical method for the optimisation of weakly nonlinear systems. Proc. EURODYN, 1981-1988, 2014.

ON THE STRONGLY NONLINEAR RESONANCE OF A ROTOR WITH A SELF-BALANCING DEVICE

Olga Drozdetskaya [1] & Alexander Fidlin[1a)]
[1]*Institute of Engineering Mechanics, Karlsruhe Institute of Technology, Karlsruhe, Germany*

Summary Passage through and capture into the resonance of a rigid rotor with the attached self-balancing device and driven by an induction engine of limited power is investigated using an averaging procedure for a partially strongly damped system. The approach is closely related to a singular perturbation technique. It is demonstrated that the system's dynamics can be reduced on the slow manifold to three first-order differential equation predicting both stationary and transient solutions of the original system. Solutions captured into the resonance differ strongly from those in the system without self-balancing devices. The velocity of the rotor oscillates slowly around a certain value while the resonant vibrations of the rotor's axis are strongly modulated in the vicinity of the resonance. The approximate results are compared with the direct numerical simulations of the full system and demonstrate very good accuracy everywhere except in the small vicinity of the bifurcation point.

INTRODUCTION

Self-balancing devices providing the perfect balancing of rigid rotors in the overcritical speed range is well known [1, 2]. However in the undercritical domain these devices maximize the overall unbalance which leads to significantly increasing amplitudes of vibrations or even to capture into the resonance while accelerating or decelerating the rotor. The last effect (also known as the Sommerfeld effect) is well analyzed and easy to understand for simple rotors [3]. Many important mathematical results on passage through and capture into the resonance have been achieved for weakly damped systems [4]. The significant complexity of this analysis even in two-frequency systems is connected to the appearance of the so-called semi-slow oscillations [5]. However, a rotor with a self-balancing device has at least four frequencies, which makes the appropriate analysis extremely elaborate [6]. On the other hand, damping in technical systems is usually not too small. The corresponding asymptotic approach suggested in [7] enables efficient analysis of strongly damped systems.

In the present paper the last approach is applied to investigation of the strongly nonlinear interaction between the rotor with self-balancing device mounted on a linear carrier system and the induction motor while passing through the main resonance. Especial attention is payed to the slowly modulated solutions arising in case of capturing resonance.

MINIMAL MODEL OF A ROTOR WITH A SELF-BALANCING DEVICE DRIVEN BY AN INDUCTION MOTOR

The simplest model of the rotor with the attached self-balancing device is shown in figure 1a.

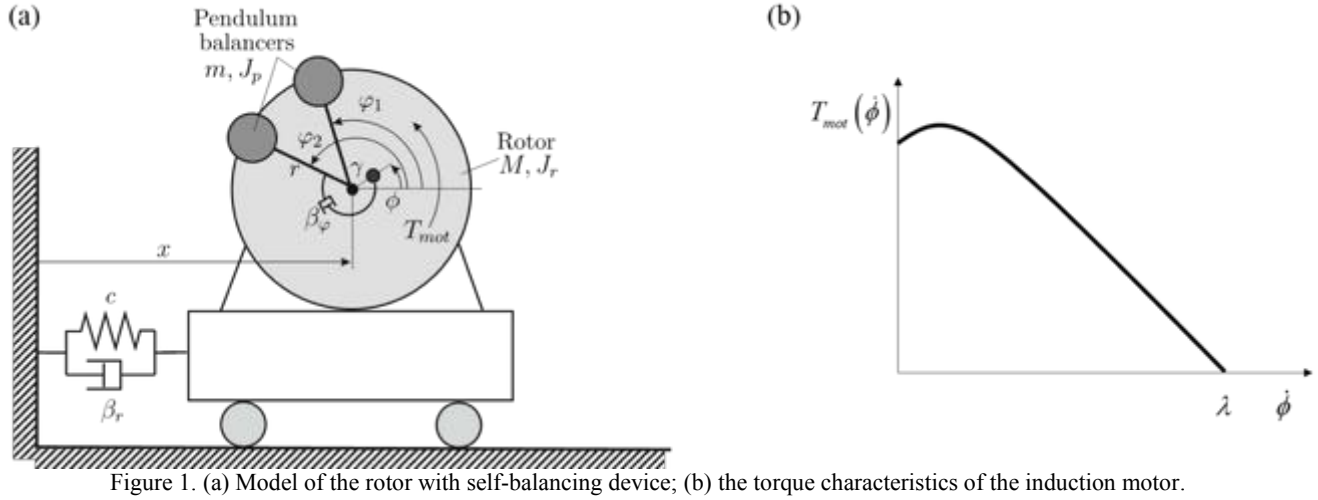

Figure 1. (a) Model of the rotor with self-balancing device; (b) the torque characteristics of the induction motor.

The rotor of mass M and mass moment of inertia J_r is elastically suspended by a spring-damper of a certain stiffness c and damping β_r. Its center of mass has an offset γ relative to the rotation axis. Two pendulum balancers of mass m, mass moment of inertia J_p and length r are placed on the axis of rotation of the rotor. A rotational damping β_φ is applied between the rotor and each of the balancers. The rotor is excited by an induction motor of limited power which static characteristics is displayed in figure 1b.

[a)] Corresponding author. Email: alexander.fidlin@kit.edu.

Equations of motion of the system are as follows:

$$\begin{aligned}
&(M+2m)\ddot{x}+\beta_r\dot{x}+cx = M\gamma\left(\dot{\phi}^2\cos\phi+\ddot{\varphi}\sin\varphi\right)+mr\sum_{i=1}^{2}\left(\dot{\varphi}_i^{\,2}\cos\varphi_i+\ddot{\varphi}_i\sin\varphi_i\right)\\
&\left(M\gamma^2+J_r\right)\ddot{\phi}+\beta_\varphi\left(\dot{\phi}-\dot{\varphi}_1-\dot{\varphi}_2\right)=T_{mot}+M\gamma\ddot{x}\sin\phi\\
&\left(J_p+mr^2\right)\ddot{\varphi}_i+\beta_\varphi\left(\dot{\varphi}_i-\dot{\phi}\right)=mr\ddot{x}\sin\varphi_i;\ \ i=1,2.
\end{aligned} \tag{1}$$

ASYMPTOTIC ANALYSIS OF THE PASSAGE THROUGH THE RESONANCE AND COMPARISON WITH NUMERIC SIMULATIONS

Approximate asymptotic solutions for these equations have been obtained using averaging technique for strongly damped systems [7] under the assumption that the unbalance of the rotor $M\gamma^2/J_r$ and the mass ratio m/M are small parameters of the same magnitude order. Dimensionless damping coefficients are assumed to be not small. The whole dynamics of the system can be reduced to three first order differential equations for the velocity of the rotor and two phase differences between the pendulum balancers and the rotor. Two examples of the transient solutions obtained by solving the averaged equations are shown in comparison to the numerical simulations of the full system (1) are presented in figure 2.

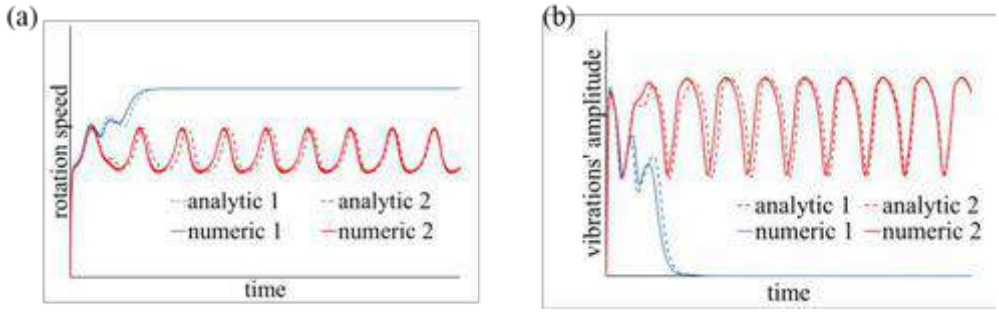

Figure 2. (a) Rotation speed of the rotor while passing through resonance (blue lines) and for capture into the resonance (red lines) (b) amplitude of the vibrations of the rotor's axis; numerical results – solid lines, analytical results – dashed lines.

Stationary capture into the resonance is not possible in a wide range of the system's parameters although the rotor speed does not reach the objected value (figure 1, red curves). Instead of the stationary solutions usual for Sommerfeld effect, periodic oscillations of the rotor speed are taking place accompanied by the slowly modulated resonance vibrations of the rotor axis attached to the carrier system (figure 2, red curves). In case of the successful passage through the resonance (blue curves) vibration of the system can be also slowly modulated. The attraction basin for the captured solutions depends strongly on the initial orientation of the pendulum balancers. The qualitative and quantitative discrepancies between the analytical and the numerical results are quite small.

CONCLUSIONS

Passage through and capture into the resonance are investigated for the unbalanced rotor with the attached self-balancing device. The system is driven by an induction engine and mounted on a linear carrier. Averaging for strongly damped systems appears to be a very efficient analytical method enabling to identify the slow manifold of the system and to obtain accurate analytical approximations. This method can be used for analysing a wide class of strongly nonlinear systems operating close to resonance in presence of significant dissipation.

References

[1] Blekhman I. *Synchronisation in Science and Technology*, ASME Press, New York, 1988.

[2] Sperling L, Ryzhik B, Duckstein H. Single-Plane Auto-Balancing of Rigid Rotors. *Technische Mechanik* **24, 1**: 1 – 24, 2004.

[3] Blekhman I. *Vibrational mechanics*. World Scientific, Singapore, 2000.

[4] Neishtadt A. Capture into resonance and scattering on resonances in two-frequency systems. *Proceedings of the Steklov Institute of Mathematics* **250**: 183 – 203, 2005.

[5] Pechenev A, Fidlin A. Hierarchy of resonant motions excited in a vibroimpact system with contact zones by an inertial source of limited power. *Izw. AN SSSR Mechanika Tverdogo Tela* **27**: 46 – 53, 1992.

[6] Ryzhik B., Amer T., Duckstein H., Sperling L. Zum Sommerfeldeffekt beim selbsttätigen Auswuchten in einer Ebene. *Technische Mechanik* **21, 4:** 297- 312, 2001.

[7] Fidlin A, Thomsen J.J. Non-trivial effects of high-frequency excitation for strongly damped mechanical systems. *Int. J. of Non-Linear Mechanics* **43**: 569 – 578, 2008.

NONLINEAR OSCILLATIONS OF A BELT DRIVE

Alois Steindl* and Yury Vetyukov
Institute for Mechanics and Mechatronics, Vienna University of Technology, Vienna, Austria

Summary The dynamics of a visco-elastic belt drive is investigated after loss of stability of its steady configuration. It is well known, that for sufficiently large drive speeds the steady configuration generically loses stability by either a zero eigenvalue or a pair of purely imaginary eigenvalues. Using bifurcation theory we investigate the branching behaviour and stability of the bifurcating solution. Special attention will be paid to the influence of viscous material damping on the stability boundary and the postcritical branching behaviour.

INTRODUCTION

A stable steady configuration of a belt drive is an important operating requirement in many industrial applications. The stability of the steady state of a stretched cable with bending stiffness and different boundary conditions at the endpoints has already been derived in [1]. It is shown, that after the transport speed exceeds the wave speed, either a zero eigenvalue occurs or two pairs of purely imaginary eigenvalues collide and leave the imaginary axis. This scenario is well known as "Hamiltonian Hopf Bifurcation" or as "Trojan Bifurcation" ([2, 3]). By calculating the Normal Form equations at the bifurcation point, one can determine whether the bifurcating periodic solution branches are stable or unstable.

Since the Hamiltonian Hopf bifurcation applies only to conservative systems, but in real world applications there will always occur non-conservative forces like damping, we either have to include non-conservative perturbation terms in the nonlinear analysis of the double imaginary eigenvalues, or introduce these perturbations already in the initial setup.

Frequently it has been observed, that small viscous damping forces may considerably influence the stability properties of oscillatory systems. Although it leads to a decay of the kinetic energy, it sometimes destabilizes the equilibrium state, especially, if two pairs of eigenvalues close to the imaginary axis approach each other.

Usually the tension forces for belt drives are assumed sufficiently large, such that the belt moves along a straight line during normal operation. If for some reason the tension force is considerably smaller, the belt may display a considerable sag. In this case the oscillations around the steady configuration contain also axial components and it becomes necessary to study two-dimensional motions of the system.

MODELLING AND TREATMENT OF THE BELT DRIVE

We investigate an inextensible, unshearable visco-elastic cable with bending stiffness, which travels with constant speed V between the eyelets. First we present the equations of planar motion in an Eulerian frame using the fundamental equations of Kirchhoff rods. Assuming a constant velocity of the belt, we first calculate the equilibrium configuration.

Stability boundaries of the equilibrium configuration

Starting with the known results for the straight, undamped configuration we study the influence of viscous damping and gravity on the equilibrium state and on the distribution of eigenvalues and stability boundaries. It should be noted, that in this case also the equilibrium configuration depends on the damping, because the belt's particles are not at rest in the equlibrium configuration, but move along the center line with constant speed. Therefore also a steady sagged configuration causes damping forces. Since the damping coefficient is usually very small, the governing equations for the steady state and the eigenmodes are singularly perturbed boundary value problems.

Preliminary results indicate, that already the introduction of a very small viscous damping changes the spectral properties considerably: Without damping most eigenvalues lie on the imaginary axis. Variation of the drive speed into the critical range causes some eigenvalues to move into the right half plane. As soon as some tiny amount of damping is added to the model, almost all eigenvalues reside in the left half plane, far away from the imaginary axis. A few eigenvalues, corresponding to low mode numbers, may still cross the imaginary axis at some critical values of the drive speed.

Bifurcations of the equilibrium configuration

Depending on the critical eigenvalues at the stability boundaries, we investigate 3 different bifurcation problems:

1. For a zero eigenvalue we calculate the bifurcating branch of steady solutions. Since in the undamped problem this zero eigenvalue occurs, when a pair of imaginary eigenvalues approaches the origin, the bifurcation point is actually a Bogdanov-Takes bifurcation with a non-semisimple pair of zero eigenvalues. In the absence of dissipative forces the investigation of that bifurcation reduces to the treatment of the ordinary steady state bifurcation.

*Corresponding author. Email: Alois Steindl@tuwien.ac.at

2. For a double pair of purely imaginary eigenvalues a Hamiltonian Hopf bifurcation has to be investigated. Proceeding as in [3], we calculate the Normal Form equation and derive the branching conditions and stability properties of a family of periodic solutions. In the conservative case the bifurcating oscillations are either elliptic or hyperbolic, depending on a certain coefficient, which is calculated in the Normal Form procedure.

   At this stage it is also possible to consider a small perturbation by non-conservative forces. This perturbation usually destroys almost all periodic solutions and leaves distinct periodic orbits, which are either stable or unstable. The situation is quite similar to the Van der Pol equation, where for $\epsilon \neq 0$ only the trivial state and the periodic orbit of radius 2 survive.

3. The generic Hopf bifurcations occur at the stability boundary of the damped system. Due to the sag of the equilibrium configuration the periodic oscillations have vertical and horizontal components.

CONCLUSIONS

In this talk we extend the available results about instabilities of a driven belt in two directions: We consider the influence of viscous damping on the equilibrium configuration and its spectral properties. Second we allow a moderate sag of the equilibrium state.

References

[1] Wickert J. A., Mote Jr. C. D.: Classical Vibration Analysis of Axially Moving Continua, J. Appl. Mech., 57(3), 1990.

[2] Van der Meer, J. C.: The Hamiltonian Hopf bifurcation. Lecture Notes in Mathematics 1160, Springer-Verlag, 1986.

[3] Meyer K. R., Hall G. R.: *Introduction to Hamiltonian Dynamical Systems and the N-Body Problem*. Number 90 in Applied Mathematical Sciences. Springer-Verlag, 1992.

[4] Chen Li-Qun: Analysis and Control of Transverse Vibrations of Axially Moving Strings, Appl. Mechanics Reviews, 58, 2005.

[5] Sandilo S.H., van Horssen, W. T.: On a cascade of autoresonances in an elevator cable system. Nonlinear Dynamics, 80(3), 2015.

[6] Eliseev V., Vetyukov Yu.: Effects of deformation in the dynamics of belt drive. Acta Mechanica 223, (2012).

STRANGE ATTRACTORS OBSERVED IN ELECTROSTATIC MEMS ACTUATORS

Sangtak Park[1a)], Mahmoud Khater[2], Ahmed Abdel Aziz[3], Eihab M. Abdel-Rahman[1]
[1] *Systems Design Eng.,* [3] *Electrical and Computer Eng., University of Waterloo, Waterloo, Ontario, Canada*
[2]*Mechanical Engineering, KFUPM, Dhahran, Saudi Arabia*

Summary We present an electrostatic MEMS actuator exhibiting superharmonic resonances as well as chaotic behaviour in soft vacuum, 500 mTorr. The displacement and velocity of the electrostatic actuator are measured with a laser vibrometer. These responses are analysed and presented in the time and frequency domains.

INTRODUTION

Electrostatic actuator have been reported to exhibits diverse nonlinear behaviors, such as superharmonic resonances [3] and aperiodic motions [1, 2, 4]. In this paper, we demonstrate a strange attractor that is experimentally observed when an electrostatic microplate actuator is excited by a biased harmonic signal in vacuum.

FABRICATION

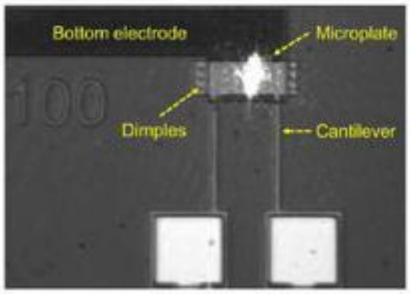

FIG. 1-(a) Top view of the actuator

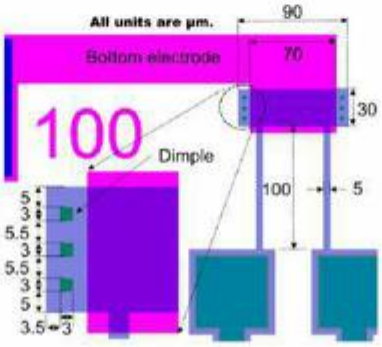

FIG. 1-(b) Magnified view of the plate

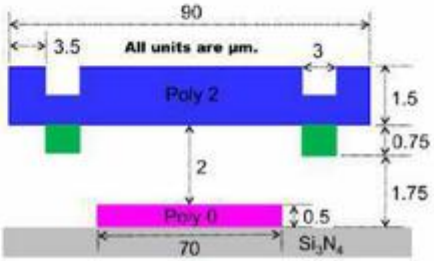

FIG. 1-(c) Cross-sectional view

The actuator is fabricated in the PolyMUMPs process, FIG. 1-(a). It consists of two cantilever beams (100×5×1.5 μm) supporting a microplate (90×30×1.5 μm) equipped with three dimples (3×3×0.75 μm), green colored in the top and fronts views of FIG 1-(b) and (c), on each side of the microplate. The bottom electrode, made in the Poly 0 layer, is narrower than the microplate, so that the dimples can land on the insulating Si_3N_4 layer. This design is adopted to prevent dielectric charging and electrical short between the microplate and the bottom electrode when the microplate lands on the substrate.

EXPERIMENT

To reduce squeeze film damping and increase the quality factor of the actuator, we perform all experiment inside a vacuum chamber at soft vacuum, 500 mTorr. The bottom electrode is electrically connected to a function generator, while the microplate is grounded. This test set-up minimizes charge leakage from the microplate to the Si_3N_4 layer during contact. The velocity and displacement of the microplate mid-point are measured using a laser Doppler vibrometer.

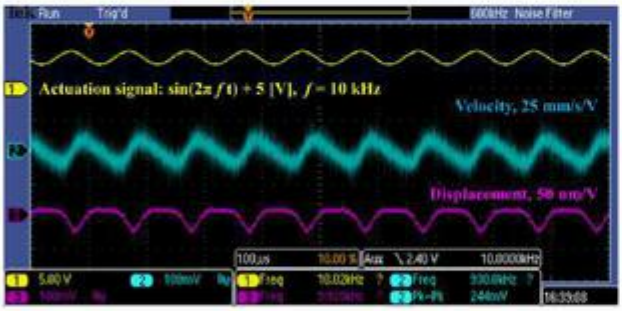

FIG. 2. Forced response of the actuator at 10 kHz

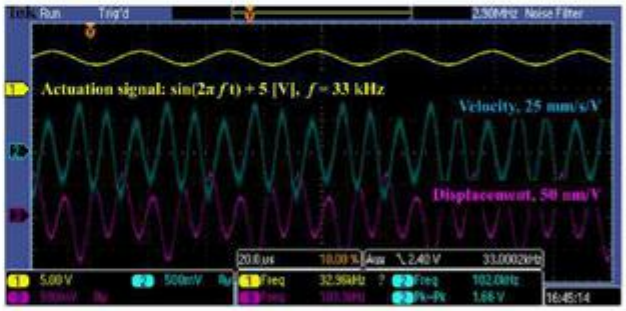

FIG.3. Superharmonic resonance at 33 kHz

When excited by a harmonic signal, 5 V_{dc}, and 2 V_{pp} (peak-to-peak) at f = 10 kHz, the actuator exhibits a forced harmonic response as seen in FIG. 2. However, when the actuator is excited by the same waveform at f = 33 kHz, superharmonic

a) Corresponding author. Email: sangtak@uwaterloo.ca.

resonance of order three is observed in FIG. 3. Superharmonic resonances of order four and five were also observed at 25 kHz and 20 kHz as well as the superharmonic resonance of order two at 46 kHz and 50 kHz.

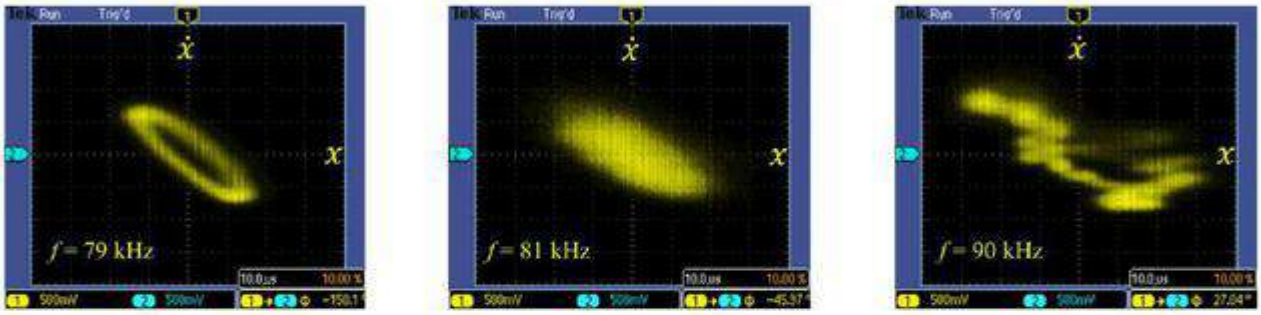

(a) (b) (c)

FIG. 4. Phase portraits of the actuator response to the harmonic signal, sin ($2\pi f$ t) + 5 [V], at the frequencies: (a) f = 79 kHz, (b) f = 81 kHz, and (c) f = 90 kHz. The negative slope of the phase portraits is due to phase delay in the vibrometer's velocity decoder with respect to the displacement decoder.

The phase portrait of the actuator excited with the same waveform shows a stable period-one periodic orbit in the vicinity of primary resonance, FIG. 4-(a), at 79 kHz. The phase portraits at 81 kHz and 90 kHz, FIGs. 4-(b) and (c), respectively, show that periodicity is lost to be replaced with an aperiodic chaotic attractor [2, 4]. The resulting strange attractor evolves from filling a limited area in the phase-space to a banded structure, as the excitation frequency increases from 81 kHz to 90 kHz.

The FFTs of the stable periodic orbit at f = 79 kHz are, FIG. 5, show a typical electrostatic response with peaks at the excitation frequency, 79 kHz, and its second harmonic, 158 kHz. The FFTs of the attractor at f = 81 kHz show elevated noise floors [2, 4] over a wide frequency range (wide-based peaks) as opposed to the flat noise floors of the stable orbit. Phase portraits that fill (wander in) areas of phase-space as well as wide-based peaks are typical characteristics of chaos.

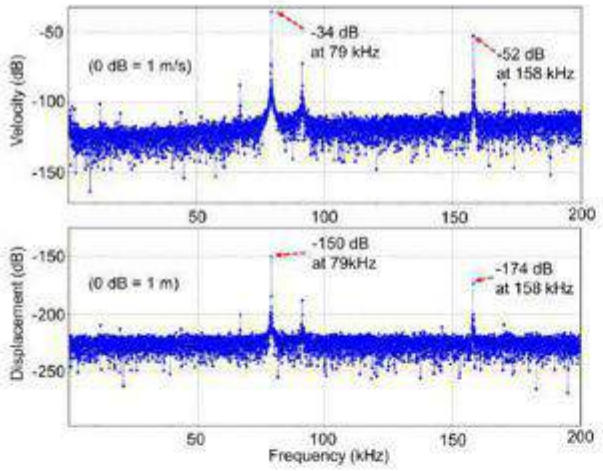

FIG. 5. FFTs of the measured velocity and displacement of the microplate at f = 79 kHz show flat noise floors.

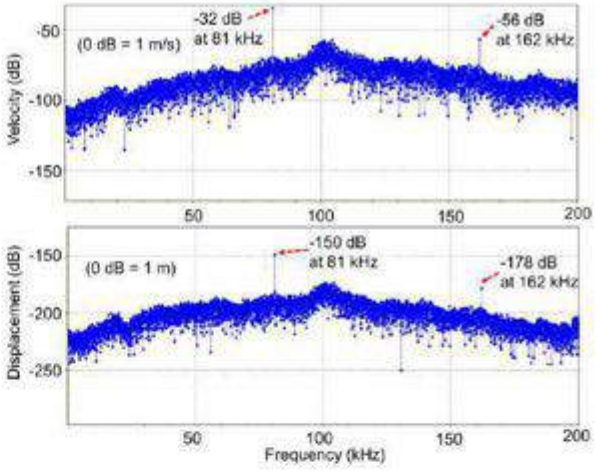

FIG. 6. FFTs of the microplate excited at f = 81 kHz show elevated noise floors over a wide frequency range.

CONCLUSIONS

We experimentally observed four superharmonic resonances as well as strange attractors, aperiodic motion confined to closed regions of phase-space, in the response of an electrostatic actuator in soft vacuum. The actuator demonstrates a softening nonlinearity and the attractors appear to belong to its primary resonance. The FFTs corresponding to the aperiodic attractors display wide-based peaks confirming that those attractors are chaotic.

References

[1] J. Stulemeijer, R.W. Herfst, J.A. Bielen, IEEE 22nd International Conference on MEMS, pp. 920-922, 2009.
[2] T. Carmon, M.C. Cross, K.J. Vahala, IEEE/LEOS International conference on Optical MEMS and their applications, pp.56-57, 2006.
[3] S.K. De, N.R. Aluru, Journal of Microelectromechanical Systems, vol.15, no.2, pp.355-369, 2006.
[4] B.E. DeMartini, H.E. Butterfield, J. Moehlis, K.L. Turner, Journal of Microelectromechanical Systems, vol.16, no.6, pp.1314-1323, 2007.

DIFFERENCE COMBINATIONAL INTERNAL RESONANCE IN NONLINEAR VIBRATIONS OF THIN PLATES

Marina Shitikova*[1], Yury Rossikhin[1], and Jean Claude Ngenzi[2]

[1]*Research Center on Dynamics of Solids and Structures, Voronezh State University of Architecture and Civil Engineering, Voronezh, Russia*
[2]*École Normale Supérieure, ENS Burundi*

Summary In the present paper, the dynamic response of a nonlinear plate embedded into a fractional derivative viscoelastic medium is studied by the method of multiple time scales under the condition of the combinational internal resonances of difference type using a newly developed approach resulting in uncoupling the linear parts of equations of motion of the plate. The influence of viscosity on the energy exchange mechanism between interacting nonlinear modes has been analyzed.

PROBLEM FORMULATION

It is well known that the nonlinear vibrations of plates are an important area of applied mechanics, since plates are used as structural elements in many fields of industry and technology [1]. Moreover, nonlinear vibrations could be accompanied by such a phenomenon as the internal resonance, resulting in multimode response with a strong interaction of the modes involved [2] accompanied by the energy exchange phenomenon.

Nonlinear free vibrations of a thin plate embedded into a fractional derivative viscoelastic medium have been considered recently [3] for the case when the plate motion is described by three coupled nonlinear differential equations. It has been shown that the occurrence of the internal resonance results in the interaction of modes corresponding to the mutually orthogonal displacements. As this takes place, the displacement functions are determined in terms of eigenfunctions of linear vibrations. The procedure resulting in decoupling linear parts of equations has been proposed with the further utilization of the method of multiple scales for solving nonlinear governing equations of motion, in so doing the amplitude functions are expanded into power series in terms of the small parameter and depend on different time scales. It has been shown that the type of the resonance depends on the order of smallness of the fractional derivative entering in the equations of motion of the plate.

In the recent paper [3] it has been shown that the following three combinational resonances could occur during vibrations of a free supported non-linear thin rectangular plate:

$$\omega_1 + \omega_2 = 2\omega_3, \tag{1}$$

$$\omega_1 - \omega_2 = 2\omega_3, \tag{2}$$

$$\omega_2 - \omega_1 = 2\omega_3, \tag{3}$$

where ω_1 and ω_2 are some particular natural frequencies of in-plane vibrations, and ω_3 is one of the natural frequencies of the out-of-plane modes.

Reference to (1)-(3) shows that the combinational resonance (1) is of the additive type, while combinational resonances (2) and (3) are of the difference type. In the present paper, we will focus our attention on the qualitative analysis of the case of the difference $\omega_1 - \omega_2 = 2\omega_3$ combinational internal resonance, when two different modes of in-plane vibrations are coupled with a certain mode of out-of-plane vibrations.

Difference combinational resonance $\omega_1 - \omega_2 = 2\omega_3$

Now let us consider the case of the difference combinational resonance (2), when $\omega_1 - \omega_2 = 2\omega_3$. Then the set of equations describing the modulations of amplitudes a_i and phases φ_i $(i = 1, 2, 3)$ has the following form:

$$\left(a_1^2\right)^{\cdot} + s_1 a_1^2 = -2\omega_1^{-1}\zeta_1 k_6 a_1 a_2 a_3^2 \sin\delta, \tag{4}$$

$$\left(a_2^2\right)^{\cdot} + s_2 a_2^2 = 2\omega_2^{-1}\zeta_2 k_7 a_1 a_2 a_3^2 \sin\delta, \tag{5}$$

$$\left(a_3^2\right)^{\cdot} + s_3 a_3^2 = \omega_3^{-1}(\zeta_{13} k_6 + \zeta_{23} k_7) a_1 a_2 a_3^2 \sin\delta, \tag{6}$$

$$\dot{\varphi}_1 = \frac{1}{2}\,\sigma_1 + \omega_1^{-1}\zeta_1 k_5\, a_3^2 + \omega_1^{-1}\zeta_1 k_6 a_1^{-1} a_2 a_3^2 \cos\delta, \tag{7}$$

*Corresponding author. Email: shitikova@vmail.ru

$$\dot{\varphi}_2 = \frac{1}{2}\,\sigma_2 + \omega_2^{-1}\zeta_2 k_6\, a_3^2 + \omega_2^{-1}\zeta_2 k_7 a_1 a_2^{-1} a_3^2 \cos\delta, \tag{8}$$

$$\dot{\varphi}_3 = \frac{1}{2}\,\sigma_3 + \frac{1}{2}\,\omega_3{}^{-1}\zeta_{13} k_7 a_1^2 + \frac{1}{2}\,\omega_3{}^{-1}\zeta_{23} k_8 a_2^2 + \frac{1}{2}\,\omega_3{}^{-1}\left(\zeta_{13} k_2 + \zeta_{23} k_4\right) a_3^2 + \frac{1}{2}\,\omega_3{}^{-1}\left(\zeta_{13} k_6 + \zeta_{23} k_7\right) a_1 a_2 \cos\delta, \tag{9}$$

where the phase difference has the form $\delta = 2\varphi_3 + \varphi_2 - \varphi_1$, and

$$s_i = \mu_i \tau_i^{\gamma} \omega_i^{\gamma-1} \sin\psi, \qquad \sigma_i = \mu_i \tau_i^{\gamma} \omega_i^{\gamma-1} \cos\psi, \quad \psi = \frac{1}{2}\,\pi\gamma \;\; (i = 1, 2, 3). \tag{10}$$

Reference to (10) shows that damping coefficients s_i depend of natural frequencies of the coupled modes ω_i and the fractional parameter γ, i.e., the order of the fractional derivative.

Thus, during free vibrations of the plate with internal resonances three regimes can be observed: stationary (absence of damping at $\gamma = 0$), quasi-stationary (damping is defined by an ordinary derivative at $\gamma = 1$), and transient (damping is defined by a fractional derivative at $0 < \gamma < 1$).

For a particular case at $\Sigma = 0$ and $s_1 = s_2 = s_3 = s$, introducing a new function representing a relative displacement $\xi(T_2)$, it is possible to obtain two first integrals of nonlinear set of Eqs. (4)-(9), one of which gives the energy distribution, while the other results in the stream function

$$G(\xi, \delta) = (c_3 + \xi)\sqrt{(c_1 - \xi)(c_2 + \xi)}\,\cos\delta - \frac{1}{2}\,K_1 b^{-1}(c_1 - \xi)^2 + \frac{1}{2}\,K_2 b^{-1}(c_2 + \xi)^2 + \frac{1}{2}\,K_3 b^{-1}(c_3 + \xi)^2 = G_0(\xi_0, \delta_0), \tag{11}$$

where c_1, c_2, and c_3 are constants of integration such that $4c_1 + 2c_2 + 2c_3 = 1$, and K_i are certain coefficients.

The stream-function allows us to construct phase portraits in terms of two functions, ξ and δ. The phenomenological analysis carried out for the combinational internal resonance of the difference type with the help of the phase portraits constructed for different magnitudes of the plate parameters reveals the great variety of vibrational motions: stationary vibrations, two-sided energy exchange between two subsystems under consideration, and onesided energy interchange resulting in the complete one-sided energy transfer. Under the presence of small viscosity all regimes attenuate with time.

CONCLUSIONS

The proposed analytical approach for investigating the damped vibrations of a nonlinear plate in a fractional derivative viscoelastic medium subjected to the combinational internal resonances of the difference type has been possible owing to the new procedure suggested recently in [3], resulting in decoupling linear parts of equations with further utilization of the method of multiple scales for solving nonlinear governing equations of motion.

The phenomenological analysis carried out for the difference combinational internal resonance using the phase portraits constructed for different magnitudes of the plate parameters reveals the great variety of vibrational motions: stationary vibrations, two-sided energy exchange between two subsystems, and complete one-sided energy transfer. The analysis of the phase portraits for various oscillatory regimes shows that they contain closed and non-closed streamlines separated by the rectilinear and curvilinear separatrixes, along which analytic solutions have been found, which define the irreversible energy transfer from one subsystem into another and are inherently soliton-like solutions in the theory of vibrations.

Acknowledgment

This research was made possible by the Grant No. 7.22.2014/K as a Government task from the Ministry of Education and Science of the Russian Federation.

References

[1] Breslavsky I.D., Amabili M., Legrand M.: Physically and geometrically non-linear vibrations of thin rectangular plates. Int. J. Non-Linear Mech. 58:30-40, 2014.

[2] Nayfeh A.H.: Nonlinear Interaction: Analytical, Computational, and Experimental Methods. Wiley, New York, USA 2000.

[3] Rossikhin Yu.A., Shitikova M.V., Ngenzi J. Cl.: A new approach for studying nonlinear dynamic response of a thin plate with internal resonance in a fractional viscoelastic medium. Shock Vibr. 2015, 2015, Article ID 795606, 28 pages, http://dx.doi.org/10.1155/2015/795606.

ON NONLINEAR DIFFERENTIAL EQUATIONS WITH DELAYED SELF-FEEDBACK

Si Mohamed Sah[1] and Richard Rand*[2]

[1]*Nanostructure Physics, KTH Royal Institute of Technology, Stockholm, Sweden.*
[2]*Dept. of Mathematics, Dept. of Mechanical & Aerospace Engineering, Cornell University. Ithaca, NY, USA.*

Summary This work concerns the dynamics of nonlinear systems that are subjected to delayed self-feedback. Perturbation methods applied to such systems give rise to slow flows which characteristically contain delayed variables. We consider two approaches to analyzing Hopf bifurcations in such slow flows. In one approach, which we refer to as approach **I**, we follow many researchers in replacing the delayed variables in the slow flow with non-delayed variables, thereby reducing the differential-delay equation (DDE) slow flow to an ordinary differential equation (ODE). In a second approach, which we refer to as approach **II**, we keep the delayed variables in the slow flow. By comparing these two approaches we are able to assess the accuracy of making the simplifying assumption which replaces the DDE slow flow by an ODE.

INTRODUCTION

When investigating a differential-delay equation (DDE) by use of a perturbation method, one is often confronted with a slow flow which contains delay terms. It is usually argued that since the parameter of perturbation, call it ϵ, is small, $\epsilon << 1$, the delay terms which appear in the slow flow may be replaced by the same term without delay, see e.g. [1, 2, 3]. The purpose of the present paper is to analyze the slow flow with the delay terms left in it, and to compare the resulting approximation with the usual one in which the delay terms have been replaced by terms without delay.

EXAMPLE 1: DUFFING EQUATION

For example take the following version of the Duffing equation with delayed self-feedback.

$$\ddot{x} + x = \epsilon \, \left[-\alpha \dot{x} - \gamma x^3 + k \, x_d \right] \tag{1}$$

where $x_d = x(t - T)$, where $T =$ delay. We treat eq.(1) with the two variable perturbation method, where $x(\xi, \eta)$, where $\xi = t$ and $\eta = \epsilon t$. We expand $x = x_0 + \epsilon x_1 + O(\epsilon^2)$ and obtain the following equation on x_0:

$$L x_0 \equiv x_{0\xi\xi} + x_0 = 0 \quad \Rightarrow \quad x_0(\xi, \eta) = A(\eta) \cos \xi + B(\eta) \sin \xi \tag{2}$$

Eliminating secular terms in the x_1 equation gives the following slow flow:

$$\frac{dA}{d\eta} = -\alpha \, \frac{A}{2} + \frac{3 \, \gamma \, B^3}{8} + \frac{\gamma \, A^2 B}{8} - \frac{k}{2} A_d \sin T - \frac{k}{2} B_d \cos T \tag{3}$$

$$\frac{dB}{d\eta} = -\alpha \, \frac{B}{2} - \frac{3 \, \gamma \, A^3}{8} - \frac{\gamma \, A B^2}{8} - \frac{k}{2} B_d \sin T + \frac{k}{2} A_d \cos T \tag{4}$$

where $A_d = A(\eta - \epsilon T)$ and $B_d = B(\eta - \epsilon T)$ are delay terms in the slow flow.

Method I involves replacing the delay terms A_d, B_d in the slow flow (3),(4) respectively by undelayed terms A, B, resulting in a slow flow of ODEs. It is argued that such a step is justified if the product ϵT is small:

$$A_d = A(\eta - \epsilon T) \approx A(\eta) + O(\epsilon), \qquad B_d = B(\eta - \epsilon T) \approx B(\eta) + O(\epsilon). \tag{5}$$

Method II involves studying the slow flow (3),(4) as it is.

Figure 1 (left side) shows a comparison, in the case of the Duffing equation (1), between the analytical Hopf conditions obtained via the two approaches and the numerical Hopf curves. The approach **II** plotted by red/dashed curves gives a better result than the approach **I** (black/dashdot curves). Therefore in the case of Duffing equation, treating the slow flow as a DDE gives better results than approximating the DDE slow flow by an ODE.

*Corresponding author. Email: rrand@cornell.edu

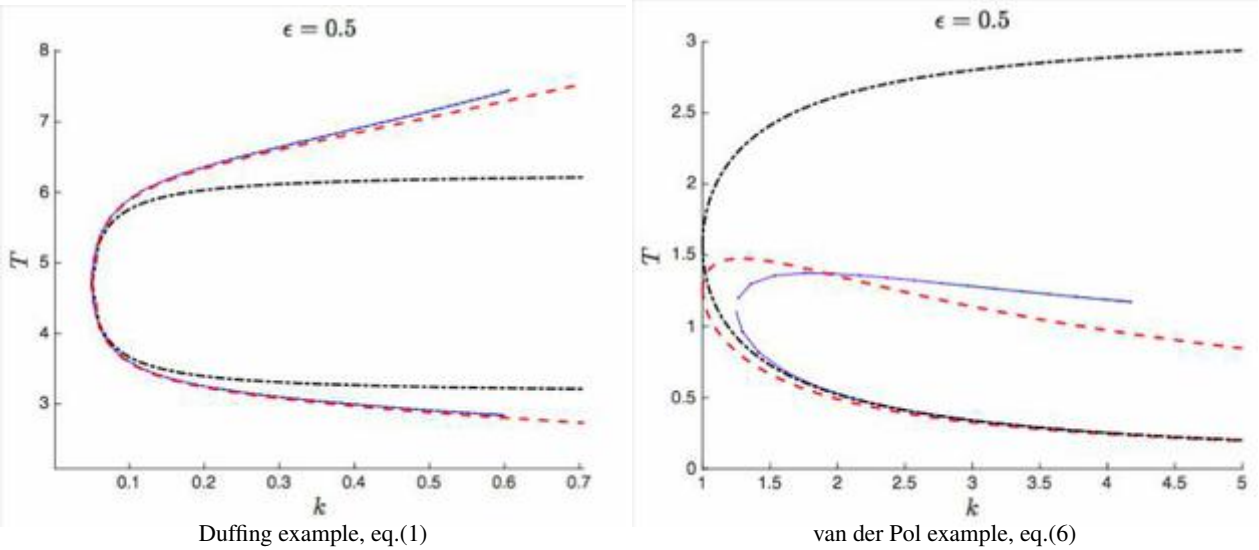

Duffing example, eq.(1) van der Pol example, eq.(6)

Figure 1: Numerical Hopf bifurcation curves (blue/solid). Also shown are the results of approach **I** (black/dashdot), and the results of approach **II** (red/dashed)

EXAMPLE 2: VAN DER POL EQUATION

As a second example, we consider a version of the van der Pol equation with delayed self-feedback [4]:

$$\ddot{x} + x = \epsilon \, \left[\dot{x}(1 - x^2) + k \, x_d - k \, x\right] \tag{6}$$

We apply the same procedure here as we did for the Duffing equation (1) and show the results in Figure 1 (right). Figure 1 (right) shows that approach **II** gives better results than approach **I**. However approach **I** still gives a good fit for the lower Hopf curve.

CONCLUSIONS

When a DDE with delayed self-feedack is treated using a perturbation method (such as the two variable expansion method, multiple scales, or averaging), the resulting slow flow typically involves delayed variables. In this work we compared the behavior of the resulting DDE slow flow with a related ODE slow flow obtained by replacing the delayed variables in the slow flow with non-delayed variables. We studied sample systems based on the Duffing equation with delayed self-feedback, eq.(1), and on the van der Pol equation with delayed self-feedback, eq.(6). In both cases we found that replacing the delayed variables in the slow flow by non-delayed variables (approach **I**) gave better results on the lower Hopf curve than on the upper Hopf curve.

Our conclusion is therefore that the researcher is advised to perform the more lengthy approach **II** analysis on the DDE slow flow in situations where values of the product ϵT is relatively large, as in the upper Hopf curves in Figures 1.

References

[1] Atay, F.M., Van der Pol's oscillator under delayed feedback. J. Sound Vib. 218(2), 333-339 (1998)
[2] Wirkus, S., Rand, R.H., The dynamics of two coupled van der Pol oscillators with delay coupling. Nonlinear Dyn. 30, 205-221 (2002)
[3] Morrison, T.M., Rand, R.H., 2:1 Resonance in the delayed nonlinear Mathieu equation. Nonlinear Dyn. 50, 341-352 (2007)
[4] T. Erneux, J. Grasman, Limit-cycle oscillators subject to a delayed feedback, Phys. Rev. E 78 (2) (2008) 026209.

ANALYSIS OF SYSTEMS WITH STATE-DEPENDENT DELAYS AND APPLICATIONS IN METAL CUTTING

Andreas Otto *[1] and Günter Radons[1]
[1]*Institute of Physics, Chemnitz University of Technology, Chemnitz, Germany*

Summary The equivalence between systems with state-dependent delays and systems with constant delays is studied. Systems with state-dependent delays appear when the dynamics of the system does not only depend on the instantaneous configuration but also on a delayed configuration of the system, and the size of the delay depends on the state of the system. It is shown that, indeed, the condition for a transformation to a constant delay is related to the mechanism that generates the state-dependent delay. With an example for the cutting force in turning it is demonstrated that variable and state-dependent delays in metal cutting vibrations can be transformed to constant delays.

INTRODUCTION

Time delay systems can be found in many engineering applications. They range from metal cutting vibrations and laser dynamics to traffic models and teleoperation of mobile robots (see [1] and Refs. therein). In some systems, as for example in laser dynamics, the assumption of time-invariant delays is quite reasonable. However, in many applications, the delays are actually time-varying or state-dependent. For example, in metal cutting the vibrations of the tool directly affect the time delay and lead to a state-dependent delay [2]. Moreover, variable delays are used for a better control of the system. Indeed, metal cutting vibrations can be suppressed by an active variation of the spindle speed, which is equivalent to a time-varying delay [3]. Thus, the analysis of systems with time- or state-dependent delays is relevant in many research areas.

Here, we focus on the analysis of systems with state-dependent delays because time-varying delays can be put in the framework of state-dependent delays. However, in contrast to the well-established theory for systems with constant delays there are many open problems in systems with state-dependent delays [4]. In this contribution we shown how a system with state-dependent delay can be transformed to a system with constant delay. It turns out that, indeed, the mathematical condition for the existence of such a transformation is fulfilled in many real word examples.

TRANSFORMATION FROM STATE-DEPENDENT DELAYS TO CONSTANT DELAYS

In general, a system with state-dependent delay $\tau(\boldsymbol{x}_t)$ can be described by the delay differential equation (DDE)

$$\dot{\boldsymbol{x}}(t) = \boldsymbol{f}\left(\boldsymbol{x}(t), \boldsymbol{x}(t-\tau(\boldsymbol{x}_t))\right), \tag{1}$$

where $\boldsymbol{x}(t)$ is the configuration of the system at time t. The state of the DDE can be specified by the vector function $\boldsymbol{x}_t = \boldsymbol{x}(t-\theta), \theta \in [0, \tau_{\max}]$, where the constant $\tau_{\max}$ is the maximum delay [4]. A nonlinear time scale transformation $\varphi = \Phi(t)$ can be used to change the delayed argument $t - \tau(\boldsymbol{x}_t)$ of the DDE Eq. (1). The function $\Phi(t)$ is assumed to be bijective, which means that there is a one-to-one mapping between the time t and the new independent variable φ. The configuration in terms of the new variable φ is given by $\boldsymbol{y}(\Phi(t)) = \boldsymbol{x}(t)$. We demand for a constant delay δ in the new representation, $\boldsymbol{x}(t-\tau(\boldsymbol{x}_t)) = \boldsymbol{y}(\varphi - \delta)$, which is equivalent to the condition

$$\Phi(t) - \delta = \Phi(t - \tau(\boldsymbol{x}_t)) \quad \leftrightarrow \quad \delta = \int_{t-\tau(\boldsymbol{x}_t)}^{t} \dot{\Phi}(t')dt'. \tag{2}$$

Eq. (2) can be interpreted as follows. The state-dependent delay $\tau(\boldsymbol{x}_t)$ is the traveling time for a transport of a particle over the constant distance δ with the velocity $\dot{\Phi}(t)$. The absolute distance covered by the particle at time t is given by the function $\Phi(t)$. A graphical illustration of the condition is presented in Fig. 1 a). The function $\Phi(t)$ defines a mapping between time t (horizontal) and space φ (vertical). A vertical shift of the function $\Phi(t)$ by the constant distance δ leads to a variable horizontal displacement (red lines), which is equal to the time delay $\tau(\boldsymbol{x}_t)$. In particular, a state-dependent delay occurs if the absolute distance $\Phi(t)$ covered by the particles is a component of the configuration $\boldsymbol{x}(t)$ or affected by the configuration $\boldsymbol{x}(t)$ of the system. In the spatial domain the system can be described by the DDE

$$\boldsymbol{y}'(\phi) = \left(\Phi^{-1}\right)'(\varphi)\boldsymbol{f}\left(\boldsymbol{y}(\varphi), \boldsymbol{y}(\varphi - \delta)\right). \tag{3}$$

Thus, a DDE with state-dependent delay $\tau(\boldsymbol{x}_t)$ Eq. (1), whose time delay is specified by the condition Eq. (2), is equivalent to the DDE Eq. (3) with constant delay δ. In other words, every delay that can be interpreted as a variable transport over a constant distance can be transformed to a constant delay. These delays are sometimes called variable transport delays and occur in many applications [5]. On the other hand, it is also possible that variable delays are generated by a transport over a variable distance. In this case it is not clear a priori if the delay is a variable transport delay or not.

*Corresponding author. Email: otto.a@mail.de

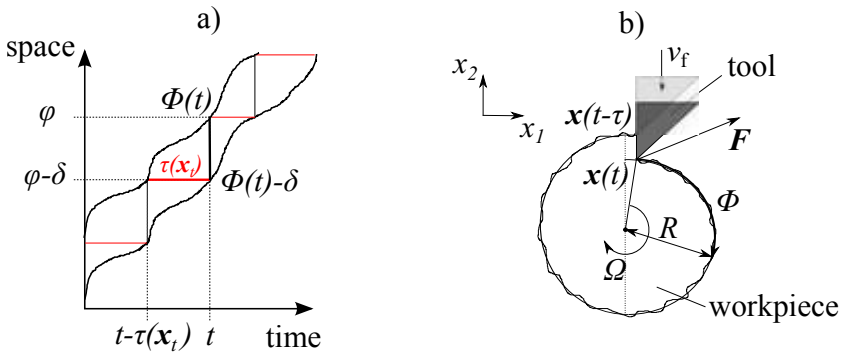

Figure 1: a) Illustration of the condition Eq. (2) between the constant delay δ (vertical shift) and the state-dependent delay $\tau(\boldsymbol{x}_t)$ (red horizontal displacement). b) State-dependent delay in turning (see text for explanations).

STATE-DEPENDENT DELAYS IN METAL CUTTING APPLICATIONS

The occurrence of undesired large vibrations at machine tools is still a significant problem in metal cutting applications. These so-called chatter vibrations are not acceptable in manufacturing industry because they cause noise, bad surface finish and increased tool wear. As a consequence the prediction of machine tool vibrations and the stability of metal cutting processes is an important field in research and industry.

An example of a turning process is shown in Fig. 1 b). Small fluctuations of the cutting force $\boldsymbol{F}(t)$ lead to dynamic displacements $\boldsymbol{x}(t) = \text{col}\,(x_1(t), x_2(t))$ of the turning tool and a wavy surface of the workpiece. The instantaneous and time-delayed vertical displacements $x_2(t)$ and $x_2(t-\tau(\boldsymbol{x}_t))$ determine the inner and the outer surface of the chip, respectively, and lead to dynamic variations of the chip thickness and the cutting force. In particular, the time delay $\tau(\boldsymbol{x}_t)$ between the present and the previous cut at the same location of the workpiece is equivalent to the time for one revolution of the workpiece. Hence, the delay in turning is defined by a variable transport delay similar to Eq. (2) with the constant distance $\delta = 2\pi R$, where R is the radius of the workpiece. In this case, the spatial variable $\Phi(t)$ can be interpreted as the absolute machined distance given by $\Phi(t) = \Omega t R - x_1(t)$, where Ω is the angular velocity of the workpiece and $x_1(t)$ are the horizontal dynamic displacements of the tool. This mechanism of self-excitation of the vibrations in machining is called regenerative effect (see [2], [3]). If the closed-loop of the regeneration is unstable, chatter vibrations occur. In many other cutting processes the time delay is similarly defined by a constant distance between two subsequent cuts.

Since the structural dynamics can be described by ordinary differential equations, metal cutting processes, in general, can be described either in time domain by Eq. (1) with state-dependent delay or by a system similar to Eq. (3) with constant delay. For Eq. (3) the linearization of the system is much simpler, whereas for systems with state-dependent delay similar to Eq. (1) the linearization is not straight forward [2], [3]. In addition, many methods for the stability analysis of linear non-autonomous DDEs can be only applied to systems with constant delay, which follow from the linearization of Eq. (3), whereas the equivalent linear system of Eq. (1) is a DDE with time-varying delay.

CONCLUSIONS

The transformation of a system with state-dependent delay to a system with constant delay is studied, which can be used to simplify the analysis in many applications. It is shown that the transformation is possible if the state-dependent delay is generated by a variable transport over a constant distance. Using the example of a turning process it is demonstrated that the time-varying and state-dependent delays in metal cutting applications belong to the class of variable transport delays and can be transformed to constant delays.

References

[1] Kyrychko Y.N., Hogan S.J.: On the Use of Delay Equations in Engineering Applications. J. Vibr. Control 16:943960, 2010.

[2] Insperger T., Stepan G., Turi J.: State-dependent delay in regenerative turning processes. Nonlin. Dyn. 47:275-283, 2007.

[3] Otto A., Radons G.: Application of spindle speed variation for chatter suppression in turning. CIRP J. Manuf. Sci. Technol. 6:102-109, 2013.

[4] Hartung F., Krisztin T., Walther H.-O., Wu J.: Functional Differential Equations with State-Dependent Delays: Theory and Applications. In: Canada A., Drabek P., Fonda A. (editors): Handbook of Differential Equations: Ordinary Differential Equations 3:435-545, North-Holland, 2006.

[5] Zhang F., Yeddanapudi M.: Modeling and simulation of time-varying delays. Proc. TMS/DEVS 34:1-8, San Diego, CA, USA, 2012.

HIGHER-ORDER ESTIMATION OF LIMIT CYCLE AMPLITUDE IN METAL CUTTING

Tamás G. Molnár *[1], Tamás Insperger[1], and Gábor Stépán[1]
[1]*Department of Applied Mechanics, Budapest University of Technology and Economics, Budapest, Hungary*

Summary Global dynamics of an orthogonal cutting model is discussed, which is governed by a nonsmooth delay differential equation (DDE), namely, the delayed term intermittently disappears if the amplitude of the vibrations exceeds some critical value. Along the linear stability boundaries of the fixed point of the DDE, subcritical Hopf bifurcation occurs and consequently, a parameter domain of bistability can be identified where the stable fixed point, an unstable periodic orbit, and a large-amplitude stable bounded motion (chatter) coexist. The first approximation of the amplitude of the unstable periodic orbit is the standard square-root function of the bifurcation parameter that is the chip width. A non-standard higher-order approximation is proposed that takes into account that the periodic solution disappears as the chip width approaches zero. This allows the construction of a more accurate still simple formula for the size of the bistable region, which is highly important for the real-world application of regenerative cutting theory.

MECHANICAL MODEL

Consider the single-degree-of-freedom mechanical model of orthogonal cutting where the tool's motion is governed by

$$\ddot{x}(t) + 2\zeta\omega_{\mathrm{n}}\dot{x}(t) + \omega_{\mathrm{n}}^2 x(t) = \frac{1}{m} F_x\left(h(t)\right) . \tag{1}$$

Here, ω_{n} is the undamped natural angular frequency, ζ is the damping ratio, and m is the modal mass of the machining system corresponding to vibrations in the feed direction x. The x-component F_x of the cutting force acting on the tool is proportional to the chip width w and can be given as a cubic polynomial of the chip thickness h according to [1]:

$$F_x(h) = w\left(\rho_1 h + \rho_2 h^2 + \rho_3 h^3\right) \quad \text{if } h > 0\,, \tag{2}$$

where $\rho_1 = 6.1096 \times 10^9\ \mathrm{N/m^2}$, $\rho_2 = -5.41416 \times 10^{13}\ \mathrm{N/m^3}$, and $\rho_3 = 2.03769 \times 10^{17}\ \mathrm{N/m^4}$ were identified in [1] for a milling tool of four teeth. Note that for non-positive chip thickness ($h \le 0$), loss of contact takes place between the tool and the workpiece and the cutting force is zero. The instantaneous chip thickness can be calculated from the feed h_0 per revolution according to the theory of regenerative machine tool vibrations:

$$h(t) = h_0 + x(t-\tau) - x(t)\,, \tag{3}$$

where $\tau = 2\pi/\Omega$ is the regenerative delay related to the angular velocity Ω of the workpiece.

Transforming Eq. (1) to shift its equilibrium to zero, scaling the tool position by h_0 and the time by ω_{n}, one obtains the dimensionless equation of motion in the form

$$\xi''(t) + 2\zeta\xi'(t) + \xi(t) = p\Big(\left(\xi(t-\tau) - \xi(t)\right) + \eta_2 \left(\xi(t-\tau) - \xi(t)\right)^2 + \eta_3 \left(\xi(t-\tau) - \xi(t)\right)^3 \Big) . \tag{4}$$

Here, p is the dimensionless chip width, η_2 and η_3 denote dimensionless cutting-force coefficients:

$$p = \frac{w\left(\rho_1 + 2\rho_2 h_0 + 3\rho_3 h_0^2\right)}{m\omega_{\mathrm{n}}^2}\,, \quad \eta_2 = \frac{\rho_2 h_0 + 3\rho_3 h_0^2}{\rho_1 + 2\rho_2 h_0 + 3\rho_3 h_0^2}\,, \quad \eta_3 = \frac{\rho_3 h_0^2}{\rho_1 + 2\rho_2 h_0 + 3\rho_3 h_0^2}\,. \tag{5}$$

ANALYSIS OF THE HOPF BIFURCATION AND REGION OF BISTABILITY

Analyzing the stability of Eq. (4) by the D-subdivision method, one obtains the linear stability boundaries in the form

$$p_{\mathrm{st}}(\omega) = \frac{\left(\omega^2 - 1\right)^2 + 4\zeta^2\omega^2}{2\left(\omega^2 - 1\right)}\,, \quad \tau_{\mathrm{st}}(\omega) = \frac{2}{\omega}\left(j\pi - \arctan\left(\frac{\omega^2 - 1}{2\zeta\omega}\right)\right)\,, \quad \Omega_{\mathrm{st}}(\omega) = \frac{2\pi}{\tau_{\mathrm{st}}(\omega)}\,, \quad j \in \mathbb{N}^+\,. \tag{6}$$

The linear stability boundaries are shown by solid line in the left panels of Fig. 1 for $\zeta = 0.02$. Along these boundaries, a subcritical Hopf bifurcation occurs [2, 3], which gives rise to an unstable limit cycle of approximate angular frequency ω.

The standard approximation [4, 5] of the amplitude $r(\omega, p)$ of the unstable limit cycle is given by a square-root function of the bifurcation parameter p:

$$r(\omega, p) \approx \sqrt{-\frac{\gamma(\omega)}{\Delta_{\mathrm{cr}}(\omega)}\left(p - p_{\mathrm{st}}(\omega)\right)}\,, \tag{7}$$

*Corresponding author. Email: molnar@mm.bme.hu

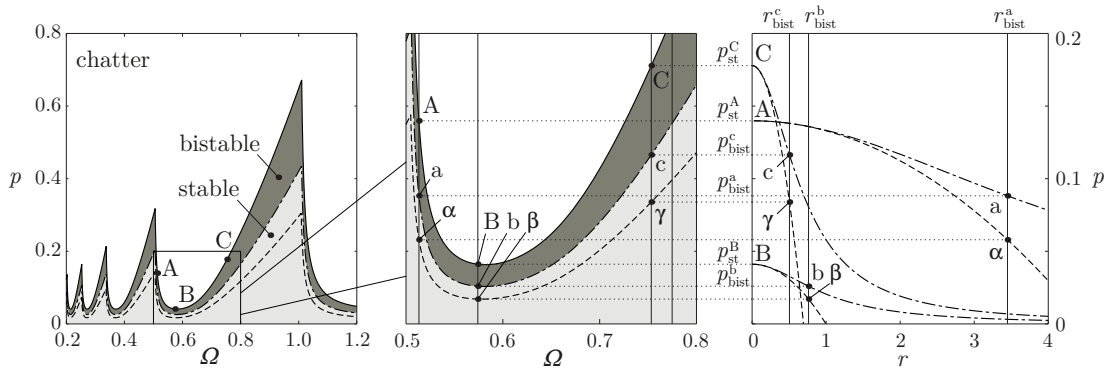

Figure 1: Left and middle panels: stability charts of the cutting process. Right panel: the corresponding bifurcation diagrams.

where $\gamma(\omega)$ is the crossing speed (root tendency) of the critical pair of imaginary eigenvalues and $\Delta_{\mathrm{cr}}(\omega)$ is the Poincaré-Lyapunov constant, which can be obtained by center manifold reduction and normal form calculations [2, 3]. A non-standard higher-order approximation of the amplitude can also be obtained by taking into account that for $p = 0$ the right-hand side of Eq. (4) vanishes and the system reduces to a damped free oscillator with no periodic solution. That is, the unstable limit cycle disappears as the bifurcation parameter p tends to zero, and it happens so that its amplitude tends to infinity: $\lim_{p\to 0} r(\omega, p) = \infty$. Accordingly, the proposed approximation of the amplitude of the unstable limit cycle becomes

$$r(\omega, p) \approx \sqrt{-\frac{\gamma(\omega)}{\Delta_{\mathrm{cr}}(\omega)} \frac{p - p_{\mathrm{st}}(\omega)}{1 + \dfrac{p - p_{\mathrm{st}}(\omega)}{p_{\mathrm{st}}(\omega)}}}\,. \tag{8}$$

The estimations (7) and (8) of the amplitude of periodic solutions bifurcating from points A, B, and C indicated in the left and middle panels of Fig. 1 are shown for $h_0 = 250\ \mu m$ in the right panel by dashed and dash-dot line, respectively. The results obtained by the proposed approximation (8) overlap with numerical results computed using DDE-BIFTOOL [6].

Due to the existence of an unstable periodic solution, the basin of attraction of the linearly stable equilibrium is bounded. Consequently, a parameter domain of bistability exists where the linearly stable equilibrium associated with stationary cutting coexists with large-amplitude stable solutions (chatter), which involve intermittent loss of contact between the tool and the workpiece [7]. The boundary $p_{\mathrm{bist}}(\omega)$ of the bistable region is located where the amplitude of the unstable limit cycle reaches the critical value $r_{\mathrm{bist}}(\omega)$ for which loss of contact ($h \le 0$) occurs [7] (see points a,b,c, and α, β, γ in Fig. 1). The boundary of the bistable region computed from Eqs. (7) and (8) is indicated in the left panels of Fig. 1 by dashed and dash-dot lines, respectively. The bistable region obtained from Eq. (8) is shaded with dark grey, the globally stable region is light grey. Using the proposed approximation (8), the relative width of the bistable region can be approximated by a simple formula

$$R_{\mathrm{bist}}(\omega) = \frac{p_{\mathrm{st}}(\omega) - p_{\mathrm{bist}}(\omega)}{p_{\mathrm{st}}(\omega)} \approx \frac{3\rho_3 h_0^2}{4\rho_1 + 8\rho_2 h_0 + 15\rho_3 h_0^2}\,, \tag{9}$$

which allows engineers to select the technological parameters needed for a globally stable chatter-free cutting process.

Acknowledgements

This work was supported by the Hungarian National Science Foundation under grant OTKA-K105433. The research leading to these results has received funding from the European Research Council under the European Union's Seventh Framework Programme (FP/2007-2013) / ERC Advanced Grant Agreement n. 340889.

References

[1] Shi H. M., Tobias S. A.: Theory of finite amplitude machine tool instability, Int J Mach Tool D R 24(1):45-69, 1984.

[2] Stépán G., Kalmár-Nagy T.: Nonlinear regenerative machine tool vibrations. Proc of DETC97, ASME Design and Technical Conferences, Sacramento, CA, USA, 1-11, 1997.

[3] Dombóvári Z., Wilson R. E., Stépán G.: Estimates of the bistable region in metal cutting, P Roy Soc A - Math Phy 464:3255-3271, 2008.

[4] Hassard B. D., Kazarinoff N. D., Wan Y.-H.: Theory and Applications of Hopf Bifurcation, London Mathematical Society Lecture Note Series 41, Cambridge, 1981.

[5] Guckenheimer J., Holmes P.: Nonlinear Oscillations, Dynamical Systems, and Bifurcations of Vector Fields, Springer, New York, 1983.

[6] Engelborghs K., Luzyanina T., Roose D.: Numerical bifurcation analysis of delay differential equations using DDE-BIFTOOL, ACM T Math Software 28(1):1-21, 2002.

[7] Dombóvári Z., Barton D. A., Wilson R. E., Stépán G.: On the global dynamics of chatter in the orthogonal cutting model, Int J Nonlin Mech 46(1):330-338, 2011.

DELAY EFFECT ON MOTION CONTROL OF A TWO-WHEELED INVERTED PENDULUM

Yusheng Zhou[1] and Zaihua Wang *[1]

[1]*State Key Laboratory of Mechanics and Control of Mechanical Structures, Nanjing University of Aeronautics and Astronautics, Nanjing, China*

Summary Two-wheeled inverted pendulum (TWIP, for short) is an open-loop unstable nonlinear system, the delay effect arising in the feedback loop has not been reported in the literature. This paper designs a delayed robust control for controlling the back-and-forth motion of a TWIP against the influence of uncertainties, and shows that the delay effect cannot be neglected in control design.

INTRODUCTION

Two-wheeled inverted pendulum, an inverted pendulum mounted on two parallel wheels, is a common mechanical model of two-wheeled robots. A TWIP is an essential nonlinear and under-actuated system, subjected to nonholonomic constraints. It is a system of open-loop unstable, different control strategies are required for different control tasks under different environment [1]. If the stabilization of the inverted pendulum is addressed only and uncertainty is not considered, a proportional feedback of the acceleration signal can be used to stabilize the inverted pendulum. Analysis shows that the inevitable time delay in the controller has a substantial influence on the stability of the closed-loop [2]. When uncertainties must be considered, more delicate control strategies are usually used, such as H_∞ control, adaptive control, disturbance observer, and especially the sliding mode control that is the mostly used strategy in controlling TWIPs. No results about delay effect on the control of TWIPs with delayed feedback have been reported in the literature [1]. This paper shows that the delay has an important influence on the robust motion control and the delay effect must be taken into account in controlling a TWIP.

DYNAMIC MODEL AND CONTROL DESIGN OF THE TWIP

Let us consider a basic motion of a TWIP, Back-and-Forth motion, for which the TWIP is required to move forward to pass a prefixed point and return back to the starting point, keeping the inverted pendulum stabilized during the whole process. Figure 1(a) shows a 2-DOF model of the TWIP, without considering the turning motion. Let $L = T_w + T_b - P$ be the Lagrangian function, where $T_w,\ T_b$ are the kinetic energies of the wheels and the intermediate body respectively, and P is the gravitational potential energy of the system. Then the Euler-Lagrange equation gives the dynamic equation of the TWIP

$$\begin{cases} (Ml^2 + I_B\ \varphi + Ml\cos\varphi x - Mgl\sin\varphi = -T, \\ Ml\varphi\cos\varphi + (M_w + M + \frac{I_w}{r^2}\ x - Ml\varphi^2\sin\varphi = \frac{T}{r}, \end{cases} \tag{1}$$

where T is the control. With the delay in control taken into consideration, T can be written as $T = u(t-\tau)$, where $\tau > 0$ is the time delay. Let $\mathbf{X} = [x_1, x_2, x_3, x_4]^{\mathrm{T}} = [\varphi, \varphi, x, x]^{\mathrm{T}}$, let $\boldsymbol{\omega}(t)$ stand for the integrated effect of the linearization error and bounded system uncertainties, then the dynamic equation can be rewritten on the basis of the linearized system $\mathbf{X}(t) = \mathbf{A}\mathbf{X}(t) + \mathbf{B}u(t-\tau) + \boldsymbol{\omega}(t)$. The control takes place only when $t \geq \tau$. Let $\mathbf{X} = [\bar{x}_1,\ ^-_2,\ ^-_3,\ ^-_4]^{\mathrm{T}} = [\bar{\varphi}(t), \varphi(t), x(t), x(t)]^{\mathrm{T}}$ be the trajectory tracking target vector depending on the control task, and let $\mathbf{Y}(t) := \mathbf{X}(t) - \ ^-(t)$, $\boldsymbol{\sigma}(t) := \mathbf{A}\ ^- - \ ^-$, then

$$\dot{\mathbf{Y}}(t) = \mathbf{A}\mathbf{Y}(t) + \mathbf{B}u(t-\tau) + \boldsymbol{\omega}(t) + \boldsymbol{\sigma}(t). \tag{2}$$

To reduce the linearization error, a quadratic performance criterion with large weight of tilt angle error is introduced

$$J = \frac{1}{2}\mathbf{Y}^{\mathrm{T}}(t_f)\mathbf{M}\mathbf{Y}(t_f) + \frac{1}{2}\int_0^{t_f} \left[\mathbf{Y}^{\mathrm{T}}(t)\mathbf{Q}\mathbf{Y}(t) + u^{\mathrm{T}}(t-\tau)\mathbf{R}u(t-\tau)\right] \mathrm{d}t, \tag{3}$$

where $\mathbf{M}, \mathbf{Q}$ are nonnegative definite symmetric matrices, $\mathbf{R}$ is a positive definite matrix, and $t_f\ (> 2\tau)$ is the terminal time of the control. With a large weight of the tilt angle error in J, the tilt angle error can be "forced" to be small when an optimal control is applied. Thus, the linearization error is small enough and can be considered as bounded, and thus the integrated disturbance $\boldsymbol{\omega}(t)$ can be assumed bounded. A robust controller can be designed in two parts: $u(t-\tau) = u_0(t-\tau) + u_1(t-\tau),\ t \in [\tau, t_f]$, where $u_0(t-\tau)$ is an optimal controller for the nominal error system (2) that minimizes the performance criterion J in (3), and $u_1(t-\tau)$ is a switched control based on an integral sliding manifold for compensating the effect of the integrated disturbance significantly. In designing the optimal delayed control $u_0(t-\tau)$, it is usually required to convert (2) into a delay-free one and then to design the controller in terms of the state of the reduced system, while in [3] the optimal controller $u_0(t-\tau)$ can be represented directly in terms of the state $\mathbf{Y}(t)$. In constructing the switch control $u_1(t-\tau)$, the optimal state of the nominal error system can be chosen as the integral sliding mode manifold. In this way, the controller not only works well in implementing the control task, but also has strong robustness against the integrated disturbance.

*Corresponding author. Email: zhwang@nuaa.edu.cn

NUMERICAL SIMULATION ON THE CONTROL PERFORMANCE

For the Back-and-Forth motion, the trajectory tracking target can be chosen in different form, for example, $\varphi(t), x(t)]^{\mathrm{T}} = [0, (at - t^2)\mathrm{e}^{-\alpha t}]^{\mathrm{T}}$, where $\varphi(t) = 0$ means that the inverted pendulum should be kept stable, the numbers a and α are to be determined by the distance s and the weight matrices in J. The terminal time is $t_f = +\infty$ for simplicity. To addresses the special feature of this paper that uses linear optimal control theory to design a robust controller for systems with strong nonlinearity and an input delay, $\boldsymbol{\omega}(t)$ is assumed for simplicity to be $\boldsymbol{\omega}(t) = [0, \omega_2, 0, \omega_4]^{\mathrm{T}}$, where $\omega_2,\ \omega_4$ are linear combination of φ^2, φ^2 and $\varphi\dot{\varphi}$, with the coefficients assumed in the form of $f_i \sin(\Omega t),\ (i = 1, 2, 3)$. Case studies are made for a given parameter comination with $\tau = 0.01$ and $\Omega = 200\,\mathrm{Hz}$ or $\Omega = 0.02\,\mathrm{Hz}$ respectively. Figs.(b)-(d) and Figs.(g)-(i) show the time-histories of the inverted pendulum and the TWIP respectively, which imply that the control task has been well implemented; While Figs.(e)(f) and Figs.(j)(k) show the corresponding time histories by neglecting the delay in the controller, and Fig.(l) is the plots of the performance criterion with respect to time, which mean that the time delay, although very small in quantity, has a significant influence on the control performance and cannot be neglected in control design.

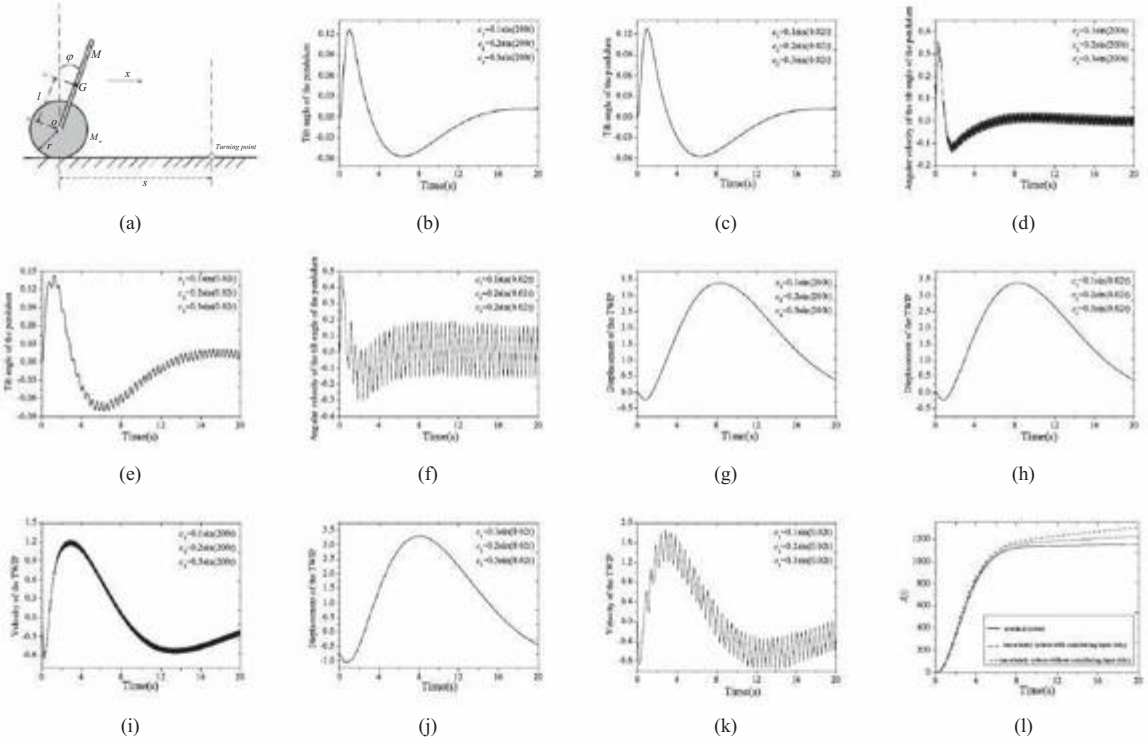

(a) (b) (c) (d)

(e) (f) (g) (h)

(i) (j) (k) (l)

Figure 1: The model of the TWIP and its control performance.

CONCLUSIONS

The designed controller based on the linearized model works well for the TWIP with strong nonlinearity, by introducting a quadratic peformance criterion with large weight to make the linearization error small enough, and by using integral sliding mode control to make the controller very robust against the integrated effect of disturbance. The results show that in the applications of the widely used sliding mode control to TWIPs, the delay effect cannot be neglected in control design.

References

[1] Chan, R.P.M., Stol, K.A., Halkyard, C.R.: Review of modelling and control of two-wheeled robots. *Annual Reviews in Control*, **37**(1): 89-103, 2013.

[2] Xu, Q., Stepan, G., Wang, Z.H.: Balancing a wheeled inverted pendulum with a single accelerometer in the presence of time delay. *Journal of Vibration and Control*, doi:10.1177/1077546315583400, 2015.

[3] Zhou, Y.S., Wang, Z.H.: Motion controller design of wheeled inverted pendulum with an input delay via optimal control theory. *Journal of Optimization Theory and Applications*, 10.1007/s10957-015-0759-z, 2015.

DYNAMICAl BEHAVIOURS OF AN ARCHETYPAL SELF-EXCITED SD OSCILLATOR

Qingjie Cao*[1], Zhixin Li[1], and Marian Wiercigroch[2]

[1]*School of Astronautics, Harbin Institute of Technology, Harbin, 150001, China*
[2]*Centre for Applied Dynamics Research, Department of Engineering, University of Aberdeen, King's College, Aberdeen AB24 3UE, Scotland, UK*

Summary In this paper, we propose an archetypal self-excited smooth and discontinuous oscillator, which is constructed with the smooth and discontinuous (SD) oscillator and the classical moving belt. Phase portraits are depicted to present the hyperbolic structure transition, multiple stick regions and the friction-induced asymmetry phenomena. Chaotic thresholds of the perturbed self-excited SD oscillator are derived by using the Melnikov's method. The numerical simulations are carried out to demonstrate the friction-induced vibration of multiple stick-slip phenomena and the stick-slip chaos for the perturbed self-excited system.

INTRODUCTION

Much attention has been paid on self-excited vibration induced by friction in mechanical engineering system, i.e. brake[1], drill string[2] and others. In this paper, we propose an archetypal self-excited smooth and discontinuous oscillator[3] based upon the SD oscillator[4] and classical moving blet, which comprises a block of mass M, supported by a moving belt, connected to a fixed support by a inclined linear spring of stiffness coefficient K, as shown in Fig. 1. The mass vibrates under the influence of dry friction F_S modeled as Coulomb friction existing in the contact zone created by the mass 's surface and the outer belt's surfaces that moves with a constant velocity V_0.

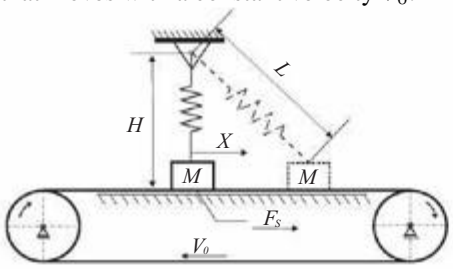

Fig. 1. The dynamical model of a self-excited oscillator.

The dimensionless equation of motion in the sense of differential inclusion of Filippov type is given by

$$x+x\Big(1-\frac{1}{\sqrt{x^2+\alpha^2}}\Big) \in \mu\Big(g_1-\alpha+\frac{\alpha}{\sqrt{x^2+\alpha^2}}\Big)Sign(v_0-x), \quad (1)$$

where μ is the friction coefficient of contacting surfaces and assumed to be constant in this friction model and $Sign(\cdot)$ denotes the set-valued sign function $Sign(p)$=$p|p|^{-1}$ for $p = 0$, and $Sign(0) = [-1, 1]$.

EQUILIBRIUM BIFURCATION AND MULTIPLE STICK REGIONS

In this section, we discuss the complex phase portraits by investigating the equilibrium and the bifurcation of this system. The transition set $\mathcal{H}$ of the equilibrium surface in a parameter space (α, μ) can be obtained and plotted in Fig. 2, where

$$\mathcal{H} = \{(\alpha,\mu)|F(x,\alpha,\mu) = F_x(x,\alpha,\mu) = 0, \alpha,\mu > 0\},$$
$$F(x,\alpha,\mu) = x\Big(1-\frac{1}{\sqrt{x^2+\alpha^2}}\Big) - \mu\Big[g_1-\alpha\Big(1-\frac{1}{\sqrt{x^2+\alpha^2}}\Big)\Big].$$

The bifurcation diagram is constructed and depicted in Fig. 2. In the parameter space (α, μ), the surface M can be divided into two persistence regions by $\mathcal{H}$, marked by I and II, as shown in Fig. 2(M). Suppose that a point $Q(\alpha, \mu)$ in the parameter plane (α, μ) starts from region II into region I, the stationary $(x_1, 0)$ state exhibits the transition from hyperbolic structure to non-hyperbolic at $\mathcal{H}$. All the corresponding phase portraits of system (1) are presented in Figs. 2(a)-2(j).

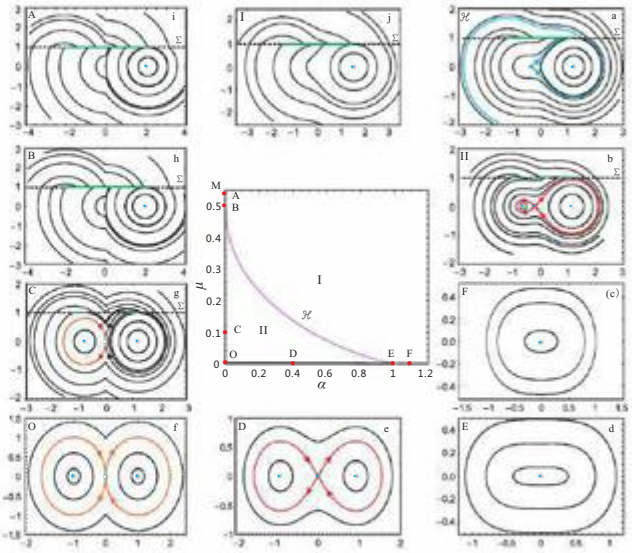

Fig. 2. Bifurcation diagram and corresponding phase portraits.

*Corresponding author. Email: qingjiecao@hotmail.com

The blue dots denote the centers and the saddle points connecting the corresponding homoclinic orbits, marked by red, see Figs. 2(b) and 2(e). While small cycles indicate non-standard or saddle-like equilibria[4] connecting the corresponding homoclinic-like orbits, marked by pink, as shown in Figs. 2(f) and 2(g). Especially, Fig. 2(a) shows a orbit, marked by blue, connecting with a non-hyperbolic equilibrium called the center-saddle point. In all the phase portraits, the symbol Σ denotes the discontinuous boundary $y = v_0$ for this self-excited system, in which, the stick regions marked by green indicate the mass have a same velocity with the belt. Hence, the difference between the SD oscillator and the self-excited SD oscillator can be seen from Fig. 2. For $\mu = 0$, the system (1) becomes the SD oscillator shown in Figs. 2(c)-2(f). For $\mu \neq 0$, Figs. 2(a)-2(b) and 2(g)-2(j) present the phase portraits of the self-excited SD oscillator. Obviously, the moving belt friction destroys the symmetry of the original SD oscillator. In conclusion, the self-excited SD oscillator with dry friction is characterized by friction-induced asymmetry and multiple stick regions in the phase plane.

PERTURBED DYNAMICS

It is assumed that the system (1) is perturbed by a viscous damping of coefficient c and an external harmonic excitation of amplitude f an frequency ω, the equation of motion can be written as

$$\ddot{} + c\dot{x} + x\Big(1 - \frac{1}{\sqrt{x^2+\alpha^2}}\Big) \in f\cos\omega t - \mu\Big[g_1 + \alpha\Big(1 - \frac{1}{\sqrt{x^2+\alpha^2}}\Big)\Big] Sign(v_0 - x), \tag{2}$$

The chaotic boundary obtained by using the Melnikov's method for this system is shown in Fig. 3. This criterion predicts that above this curve chaos can appear. In Fig. 4(a)-4(d), the short horizontal parts marked with green lines in phase portraits correspond to the sticking during the motions. A pair of asymmetric stick-slip period 1 solutions coexist $f = 0.2$, as shown in Fig. 4(a), the system dynamic responses are regular motions. With an increase of amplitude f, the regular motion vanishes and the multiple stick-slip chaotic motion follows when $f = 0.474$, as depicted in Fig. 4(b). These results are in good agreement with the Melnikov's criterion. When $f = 0.5125$, a period-3 solution with three stick-slip motions is shown in Fig. 4(c). when f increases to $f = 0.85$, chaotic motion occurs and the chaotic attractor is depicted in Fig. 4(d).

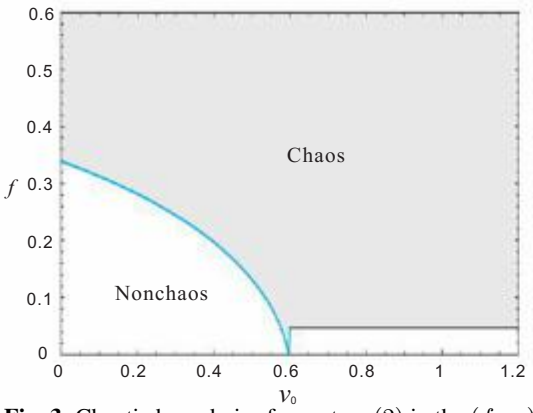

Fig. 3. Chaotic boundaries for system (2) in the (f, v_0) plane for $\alpha = 0.4$.

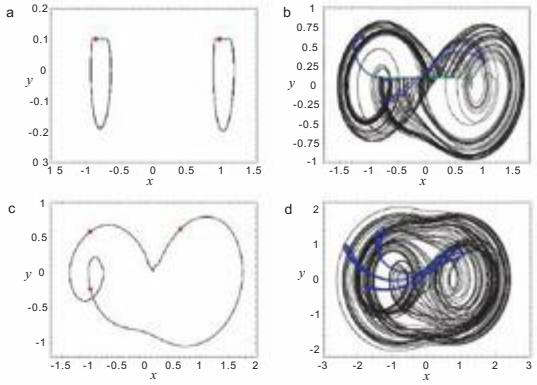

Fig. 4. The periodic motion and chaotic attractors of system (2) for $\alpha = 0.4$. (a) $f = 0.2$, (b)$f = 0.474$, (c) $f = 0.5125$, (d) $f = 0.85$.

CONCLUSIONS

In this paper, we have proposed a novel self-excited SD oscillator driven by moving belt friction. The self-excited system is characterized by the existence of multiple stick regions in the phase portraits which exhibit the hyperbolic structure transition and friction-induced asymmetry phenomena. The obtained results characterized the existence of the multiple stick-slip chaos in a range of the excitation force amplitudes as predicted by the Melnikov's criterion.

Acknowledgements. This work is upported by NSFC Granted 11372082, 11572096 and NBRP Granted 2015CB057405.

References

[1] Rhee S. K., Tsang P. H. S., Wang Y. S.: Wear 133: 39-45, 1989.
[2] Mihajlović N., Van de Wouw N., Hendriks M. P. M., Nijmeijer H.: Non. Dyn. 46: 273-291, 2006.
[3] Li Z. X., Cao, Q. J., Léger, A.: Chin. Phys. B, 2016, 25(1), 010502(1-9).
[4] Cao Q. J., Wiercigroch M., Pavlovskaia E. E., Grebogi C., Thompson J. M. T.: Phys. Rev. E 74: 046218, 2006.

ANALYSIS OF FORWARD AND BACKWARD WHIRLS IN DRILLING

Marcin Kapitaniak[1], Vahid Vaziri Hamaneh[1], Joseph Páez Chávez[2,3], and Marian Wiercigroch *[1]
[1]*Centre for Applied Dynamics Research, School of Engineering, University of Aberdeen, UK*
[2]*Center for Dynamics, Department of Mathematics, TU Dresden, D-01062 Dresden, Germany*
[3]*Facultad de Ciencias Naturales y Matemáticas, Escuela Superior Politécnica del Litoral, Guayaquil, Ecuador*

Summary In this paper we discuss whirling motion of the Bottom Hole Assembly (BHA) that occurs in downhole drilling, with particular attention to the co-existence of forward and backward whirls. First we present experimental results obtained on the unique drilling rig developed in Aberdeen and described in [2, 3], which are then used to calibrate a non-smooth low-dimensional model to investigate complex dynamics of the whirling motion.

INTRODUCTION

During a downhole drilling process, excessive vibrations can occur, which in most cases have a negative effect on the effectiveness of the process and the drilling equipment. Such vibrations may lead to an accelerated wear and a premature damage of the expensive drilling equipment. Often different dynamic effects such as bit-bounce, stick–slip, forward and backward whirl may appear simultaneously. In this work we focus on the whirling of the BHA inside the borehole, which nature is still not well understood and can lead to a catastrophic failure of the the drill-sting. .

EXPERIMENTAL OBSERVATIONS

In this section we present examples of experimental results showing co-existing forward and backward whirls, which have been observed on the unique experimental rig [2, 3]. The most important feature of the experimental apparatus is its versatility, which means that depending on chosen configuration, different type of drilling associated phenomena could be analyzed including stick-slip, bit-bounce and whirling. Here we concentrate on the whirling motion only to get further inside into its dynamics. Therefore, the experimental configuration depicted in Fig. 1(a) is used, where the main part is the loose bearing, that holds the BHA in place. A radial clearance between the BHA and the holding bush is 1 mm, what allows us to observe different types of whirling motion. The BHA is driven from the top using a flexible shaft and at its other end there is a drill-bit, that drills in a sandstone sample.

Interestingly, it has been possible to capture for the first time experimentally co-existence of forward and backward whirling, which can be seen in Figs. 1(c)-(d). Both of these phenomena can be observed for the same set of parameters (WOB=2.59 kN and angular velocity at the top, $\varphi_t = 9.36\,\mathrm{rad/s}$). Type of whirling motion is determined by comparing the angular displacements at the top, φ_t with the angular displacement of the BHA inside the bearing, θ, which are depicted in panels (e) and (f) for backward and forward whirling motion respectively. When comparing the phase portraits shown in panels (c) and (d), we notice that the qualitative responses are different, but both cases can be characterized as periodic whirling.

The top angular speed φ_t is constant (marked as black curve in panels (g) and (h)), whereas there is a considerable difference in amplitude between the angular velocity of the BHA, φ_b for the backward and forward whirls. In the case of the forward whirling, the amplitude of the BHA's angular velocity oscillations is considerably smaller than for the backward whirling . This demonstrates the fact that the backward whirling is more dangerous for the drill-string than the forward one due to a higher amplitude of torsional vibrations, which in turn result in higher stresses in the drill-string.

MATHEMATICAL MODELING

In order to understand the physics behind whirling phenomenon we introduce a simplified model of the analyzed experimental setup. Thereby, the model is similar to a Jeffcott rotor with a snubber ring, which has been studied extensively in the literature, e.g. [4]. We introduce a simplified rotor model depicted in Fig. 1(b), which consists of a disc having mass m and radius r, which spins inside the borehole with a constant angular velocity Ω. The position of the disc inside the borehole is described using polar coordinates r and θ, that constitute a two degree-of-freedom model. We assume a small imbalance of the disc. The disc is assumed to be supported by a radial bearing having a stiffness k_1 and a viscous damping c in the radial direction. The model does not include damping due to the rotation of the disc. The radial clearance between the disc and the borehole is γ. Due to the fact that two modes of operation are present, contact and non-contact, there are two sets of equations which need to be switched. We model contact of the BHA with the borehole using a spring of stiffness k_2, and dry friction

*Corresponding author. Email: m.wiercigroch@abdn.ac.uk

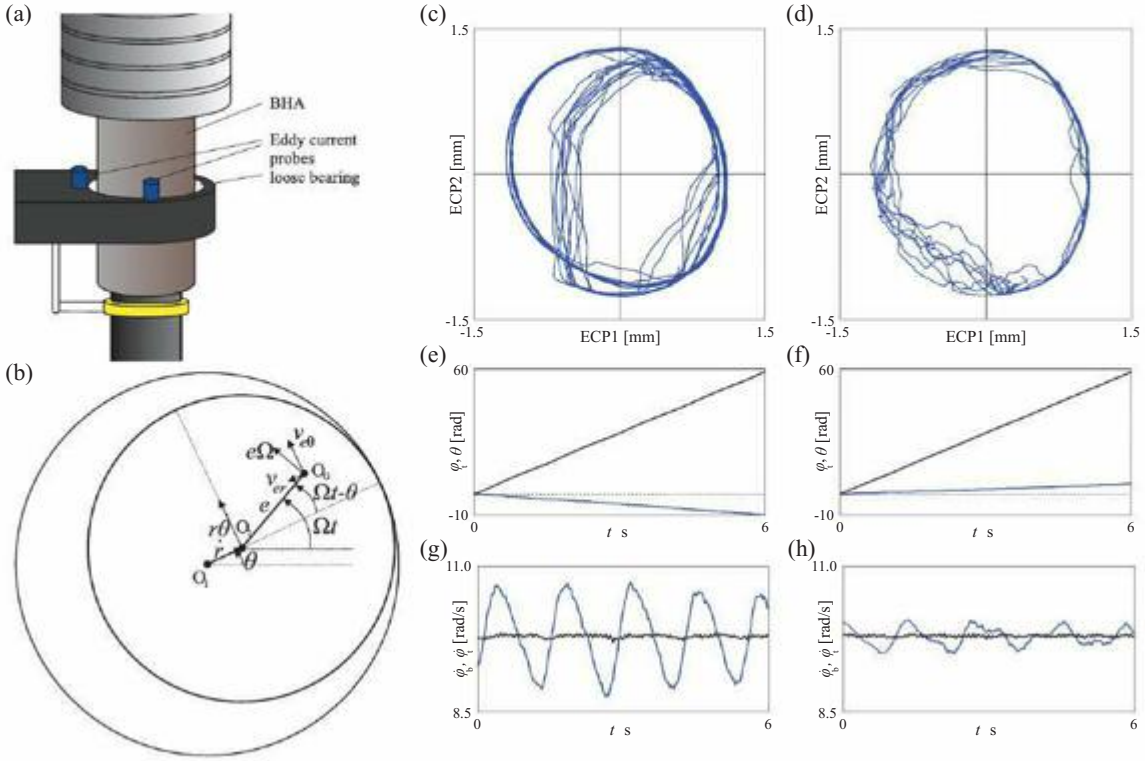

Figure 1: (a) A part of the drilling rig, showing the BHA and the bearing to simulate whirling motion; (b) schematic of the rotor model; (c)-(h) comparisons between co-existing periodic backward and forward whirling observed for $\mathrm{WOB} = 2.59\,\mathrm{kN}$; panels (c)-(d) show phase portraits, where panels (e)-(f) compare angular displacement of top φ_t vs. angular displacement inside the borehole θ and panels (g)-(h) show the angular velocity of top, $\dot{\varphi}_t$ and bottom, φ_b for backward and forward whirl respectively.

friction μ between the disc and the borehole in tangential direction. Therefore, the system can be described by following set of equations:

$$\begin{cases} M\ddot{} - Mr\dot{\theta}^2 + k_1 r + c\dot{r} = M\Omega^2\rho\cos(\Omega t - \theta) - k_2(r-\gamma)H(r-\gamma), \\ Mr\theta + 2M\dot{r}\theta + cr\theta = M\Omega^2\rho\sin(\Omega t - \theta) - \mu k_2(r-\gamma)H(r-\gamma)sgn(v_c), \end{cases} \tag{1}$$

where $H(\,)$ stands for a Heaviside function switching between contact and non-contact states [1]. In other words this means that the disc can be in contact (C) or noncontact (N) state, depending on the value $r-\gamma$. There are other modes of operation for the model, including the condition when the disc sticks to the wall [3].

CONCLUSIONS

In this paper first we have shown experimentally the co-existence of forward and backward whirling. Then a low dimensional non-smooth model to study the complexity of the whirling behaviour is introduced. After a careful calibration of the proposed model, one is able to analyze conditions that trigger forward and backward whirls [3] and ultimately to control the BHA dynamic behaviour.

References

[1] Páez Chávez J., Vaziri Hamaneh V. and Wiercigroch M.: Modelling and Experimental Verification of an Asymmetric Jeffcott Rotor with Radial Clearance. Journal of Sound and Vibration 334: 86-97, 2014.

[2] Kapitaniak M., Vaziri Hamaneh V., Páez Chávez J., Nandakumar K. and Wiercigroch M.: Unveiling complexity of drillstring vibrations: Experiments and modelling. International Journal of Mechanical Sciences 101-102: 324-337, 2015.

[3] Kapitaniak M.: Nonlinear Dynamics of Drill-Strings. PhD Thesis, University of Aberdeen, UK, 2015.

[4] Karpenko E. V., Wiercigroch M., Pavlovskaia E. E. and Neilson R. D.: Experimental verification of Jeffcott rotor model with preloaded snubber ring. Journal of Sound and Vibration 298: 907-917, 2006.

SELF-EXCITED MICROCANTILEVERS FOR SENSING APPLICATIONS

Hiroshi Yabuno*[1], Daichi ENDO*[1], Ekiichi Higashino[2], Yasuyuki Yamamoto[3], and Sohei Matsumoto[3]

[1]*Graduate School of Systems and Information Engineering, University of Tsukuba, Tsukuba, Ibaraki, Japan*
[2]*Faculty of Science and Technology, Keio University, Yokohama, Japan*
[3]*National Institute of Advanced Industrial Science and Technology (AIST), Tsukuba, Ibaraki, Japan*

Summary In the measurement procedure of vibrating-type sensing systems, the frequency response curve under external or forced excitation has been conventionally used. For instance, viscosity measurement and mass sensing are preformed from the estimation of difference in the Q-value related to the resonance amplitude and of shift in the resonance frequency, respectively. However, in the high viscosity range, it is very difficult to accurately measure these values. To overcome such difficulties, we propose the utilization of self-excited oscillation without relying on the frequency response curve; the positive velocity feedback is applied to compensate the damping force and to produce the self-excited oscillation. In the presentation, we introduce some measurement systems using self-excited microcantilevers as ultra-sensitive mass sensor, viscometer for high viscosity sensing, and AFM.

INTRODUCTION

Vibrating-type sensing devices allow for instantaneous and continuous measurements of changes in the viscosity and the mass of the sample occurring with time, i.e., on-line monitoring. In the measurement procedure of vibrating-type viscometers, the frequency response curve under external or forced excitation is employed. The viscosity is estimated by the Q-value related to the resonance amplitude (for example, see Ref. [1]) and in the mass sensing, the shift of the resonance frequency is utilized (for example, Ref. [2]). However, in the high viscosity range, it is very difficult to accurately estimate differences in Q-values and the shifting of the resonance frequency. To overcome such difficulties, we have proposed the utilization of self-excited oscillation without relying on the frequency response curve; the positive velocity feedback is applied to compensate the damping force and to produce the self-excited oscillation. First, merits of the use of self-excited oscillation are indicated using an application to the viscometer for high viscosity sensing. Next, the concept is implemented to micro-cantilevers which is widely used as a resonator for high sensitive measurement. In particular, non-contact AFM using van der Pol-type self-excited microcantilever beams are proposed and the performance of ultra-sensitive mass sensor using self-excited coupled cantilevers are experimentally shown.

SELF-EXCITED OSCILLATION BY POSITIVE VELOCITY FEEDBACK AND HIGH-VISCOSITY SENSING

We consider a resonator expressed as spring-mass-damper system with external force whose equation of motion is

$$m\frac{d^2y}{dt^2} + c\frac{dy}{dt} + ky = f, \tag{1}$$

where m and k are the equivalent mass and stiffness of the resonator, respectively. c expresses the viscous environment for the resonator and the viscosity sensing corresponds to the measurement of c [3]. In conventional viscometers, f is set to be sinusoidal force as $a\cos\nu t$. However, in the case of high viscosity, the frequency response curve has no peak and there is no Q value and the identification of c is impossible from the frequency response curve. To overcome the difficulty, f is set based on the following positive velocity feedback as $f = c_{cont}dx/dt$, where c_{cont} is positive feedback gain. Then, the critical feedback gain to produce the self-excited oscillation $c_{cont-cr}$ is equal to c and c can be estimated from the critical feedback gain which can be experimentally obtained. This method can be applicable regardless of the magnitude of viscosity [4].

AFM USING VAN DER POL-TYPE POL-TYPE SELF-EXCITED MICROCANTILEVER

FM-AFM carries out the imaging of the surface of sample in nano-meter accuracy by detecting the natural frequency shift of the cantilever due to the variation of the atomic force. The compensation of viscosity based on the above positive velocity feedback makes the eigenstate of the resonator emerge. The response frequency of the self-excited oscillation produced under the positive velocity feedback gain near the critical one corresponds to the natural frequency and the detection is easy even in liquid environments. The equation of motion of the cantilever is expressed as follows:

$$\rho A\frac{\partial^2(y+\Delta y)}{\partial t^2} + EI\frac{\partial^4 y}{\partial t^4} = 0, \tag{2}$$

where y is the deflection of the beam and Δy is displacement of the supporting point which is applied to produce the self-excited oscillation in the cantilever. In the actuation accoridng to the feedback as

$$\Delta y = c_{lin}\int y dt + c_{non}\int y^3 dt, \tag{3}$$

*Corresponding author. Email: yabuno@esys.tsukuba.ac.jp

the linear term produces the above mentioned self-excited oscillation. Furthermore, the additional nonlinear feedback of the second term can avoid the monotonically increasing response amplitude and realizes the self-excited oscillation with small steady state amplitude under high gain nonlinear feedback. Then, the non-contact imaging in AFM is achieved [5].

MASS SENSING USING SELF-EXCITED COUPLED MICROCANTILEVERS

Mass sensing by a resonator has been also based on the shift of the natural frequency, i.e., eigenvalue of the resonator system, depending on the mass. In contrast with this method, it is clarified that the utilization of the shift of an eigenmode in weakly coupled oscillators realizes more accuracy mass detection [6]. The frequency response curve under the external excitation is used to detect the eignemode. Similar to the above measurement, it is impossible in a viscous environment. Accordingly, we propose the self-excited coupled cantilevers which is modeled to two-degrees-of freedom systems as Fig. 1, where m is equivalent mass of the resonator and Δm is a measured mass. The base excitation of Δy is established by the displacement of one of cantilevers to produce the self-excited oscillation [7]. The detection of the displacements of

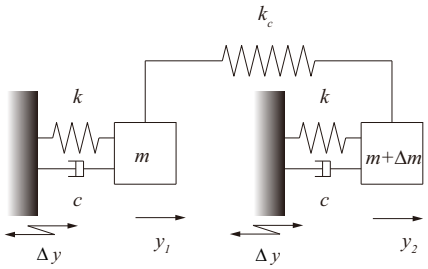

Figure 1: Sprin-mass-damper model for self-excited coupled microcantilevers.

the coupled cantilevers is carried out two laser Dopper vibrometers by the experimental apparatus as shown in Fig. 2. The experiment demonstrated mass sensing of the order of ng [8].

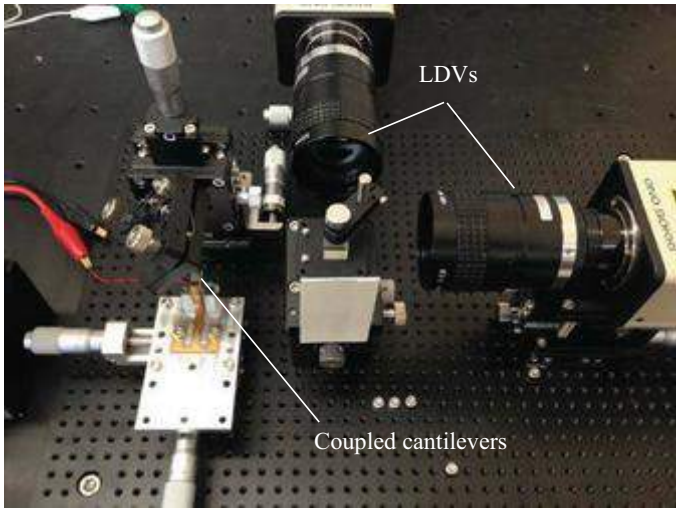

Figure 2: Experimental apparatus of self-excited coupled microcantilevers.

References

[1] Gupta, A., Akin, D., and Bashir, R.: Single virus particle mass detection using microresonators with nanoscale thickness. Physics Letters. Vol 84, pp. 19761978, 2004.

[2] Lee, I., Park, K., and Lee, J.:Precision viscosity measurement using suspended microchannel resonaors. Review of Scientific Instruments, Vol 83, 116106, 2012.

[3] Woodward, J. G., J. Acoust. Soc. Am. Vol 25, pp. 147151, 1953.

[4] Yabuno, H., Higashino, K., Kuroda, M., and Yamamoto, Y.: Self-excited vibrational viscometer for high-viscosity sensing. Journal of Applied Physics. Vol 116, 124305, 2014.

[5] Yabuno, H., Kuroda M., Someya, T., Nishimura, K., Hayashi, K., Ashida, K.: Japanese Journal of Applied Physics. Vol 50, 076601, 2011.

[6] M. Spletzer, A. Raman, A. Q. Wu, X. Xu, and R. Reifenberger, Appl. Phys. Lett., 88: 254102, 2006.

[7] H. Yabuno, Y. Seo, and M. Kuroda, Appl. Phys. Lett., 103: 063104, 2013.

[8] D. Endo, H. Yabuno, K. Higashino, Y. Yamamoto, and S. Matsumoto, Appl. Phys. Lett., 106: 223105, 2015.

TAILORING NONLINEAR DYNAMICS OF MICROBEAM RESONATORS WITH ELECTROSTATIC ACTUATION

Jakob S. Jensen*[1], Suguang Dou[1], and Steven W. Shaw[2,3]

[1]*Dept. of Elec. Eng., Technical University of Denmark, Kgs. Lyngby, Denmark*
[2]*Dept. of Mech. and Aerospace Eng., Florida Institute of Technology, Melbourne, Florida, USA*
[3]*Depts. of Mech. Eng. and Phys. and Astronomy, Michigan State University, East Lansing, Michigan, USA*

Summary We have developed an efficient shape optimization procedure for tailoring the nonlinear dynamic performance of microbeam resonators with electrostatic excitation. By relatively simple modifications of the cross-sectional dimensions along the length of the beam we demonstrate a considerable degree of control over the characteristic cubic nonlinear coefficient, allowing e.g. for extending the linear range of operation for resonant MEMS devices, which is important for improving signal-to-noise and other performance metrics.

INTRODUCTION

Recently, we demonstrated in a numerical study [1] the possibility to significantly alter the nonlinear dynamic behavior of beams and frames by employing shape optimization of the cross-sectional beam dimensions based on direct finite element calculations of the cubic nonlinear coefficient. This was later supported by experimental observations for microbeams for MEMS applications [2]. Both an increase of more than a factor 3 and a decrease of almost a factor 3 in the characteristic cubic nonlinear coefficient was demonstrated for beams with optimized height profiles.

In the present paper the design procedure is extended to cover electrostatic excitation which is of major relevance for MEMS applications. Furthermore, it introduces an additional nonlinearity in the problem due to the electrostatic force that depends on the transverse displacements. In addition to the added complexity in modelling, the extra nonlinearity offers increased possibility for tailoring the behavior since two nonlinear effects counteract: the structural hardening nonlinearity (due to midplane stretching) and the electrostatic nonlinearity which is softening. Examples of shape optimization of electrostatically actuated microbeams have recently appeared (eg. [3]), however, with focus on control of pull-in voltage and stability. To the authors' best knowledge we here present the first study on structural optimization with the aim to control the nonlinear dynamics of electrostatically actuated microbeams.

COMPUTATIONAL MODEL

The basis for the optimization procedure is a model of a clamped-clamped beam including nonlinear effects from midplane stretching and from electrostatic actuation caused by a symmetric set of fixed actuators located at distance d from the undeformed beam midplane (Figure 1 left). The basic beam equation with a variable beam height $h = h(x)$ reads:

$$\rho h b \ddot{w} + \frac{Eb}{12}(h^3 w'')'' - \frac{Eb}{2L} w'' \int_0^L h(w')^2 dx = \frac{\varepsilon b V_{\mathrm{DC}}^2}{2}\left(\frac{1}{(d - w - \frac{h}{2})^2} - \frac{1}{(d + w - \frac{h}{2})^2}\right) \tag{1}$$

here, w is the transverse beam displacement, ρ is the mass density, E is Young's modulus, b is the out-of-plane thickness, L is the beam length, ε is the permittivity of air and V_{DC} is the constant DC voltage applied to both fixed electrodes (the time-dependent actuation part is here omitted). The r.h.s. represents a simplification of the electrostatic actuation force but has

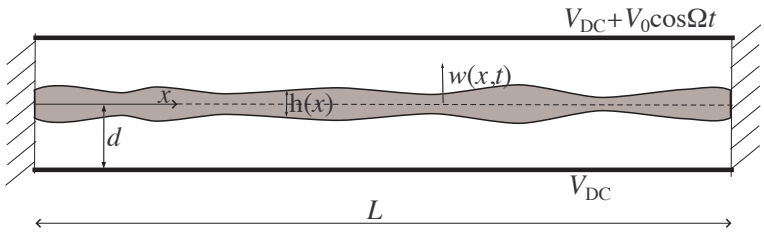

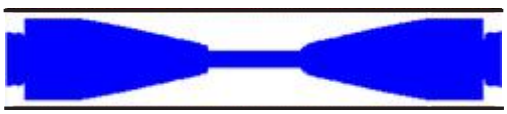

Figure 1: Left: Microbeam with variable height $h(x)$ with two fixed electrodes on each side at the nominal distance of d from the beam centerline. Deflections of the beam are given as $w(x,t)$. Right: Example of optimized beam profile.

*Corresponding author. Email: json@elektro.dtu.dk

recently been experimentally supported for a similar configuration [5]. The model is discretized using Bernoulii-Euler beam finite elements as outlined in [1].

As the first step in the analysis the corresponding linear FE eigenvalue problem is solved and based on the fundamental linear mode $\mathbf{\Phi}_1$ we directly compute the cubic nonlinear coefficient using normal forms [1, 4] as

$$\alpha = \sum_{e=1}^{ne} \frac{Ebh_e}{8l} (\mathbf{\Phi}_1^T \mathbf{K}_g \mathbf{\Phi}_1)^2 - \sum_{e=1}^{ne} \frac{\varepsilon V_{dc}^2 b}{d_e^5} \int_0^l (\mathbf{N}^T \mathbf{\Phi}_1)^4 dx \tag{2}$$

where $\mathbf{N}^T$ is the shape function matrix and $\mathbf{K}_g$ the geometric stiffness matrix.

PARAMETRIZATION AND OPTIMIZATION PROCEDURE

We choose the height of each beam element to be our design variables, i.e. we set

$$h_{\min} < h_e < h_{\min} \tag{3}$$

where the minimum and maximum values of the beam height are chosen from fabrication tolerance (min) and minimum allowable distance to the electrodes (max).

The optimization problem is now defined as a minimization problem wrt. the cubic nonlinear coefficient:

$$\begin{array}{ll} \min\limits_{\mathbf{h}}: & \alpha(h_e) \\ \text{s.t.} & \omega_1(h_e) \leq \omega^* \\ & f(h_e, \mathbf{\Phi}_1(h_e)) \geq f^* \end{array} \tag{4}$$

where we have introduced constraints in form of the maximum value of the first eigenfrequency ω^* and on the minimum value of the modal excitation force f^*. To solve the optimization problem we apply an iterative gradient-based approach with analytically computed sensitivities and use the robust mathematical programming tool MMA [6] to obtain design updates.

RESULTS

A preliminary beam design is shown in Figure 1 (right). The initial configuration has a softening nonlinearity due to the dominating electrostatic effect. However, by modifying the shape of the beam the magnitude of the nonlinear coefficient has been reduced by a factor of approximately 5. At the same time both the fundamental eigenfrequency as well as the modal excitation force is unchanged compared to the initial straight beam.

CONCLUSION

We have demonstrated that it is possible, by simple variations of the beam cross-sectional geometry along the beam, to significantly reduce out the effective nonlinearity while keeping the actuation level and linear dynamic unchanged. The results shows promising perspectives for enhancing the linear operation range for electrostatically actuated microbeams and also more complex microsized structures and devices. Further work include modifying also the shape of the electrostatic actuators as well as experimental validation of the results.

References

[1] Dou S., Strachan B.S., Shaw S.W., Jensen J.S.: Structural Optimization for Nonlinear Dynamic Response. Phil Trans R Soc A 373:20140408, 2015.

[2] Li L.L., Polunin P.M., Dou S., Shoshani O., Strachan B.S., Jensen J.S., Shaw S.W., Turner K.L.: Systematic Design of MEMS Resonators for Optimal Nonlinear Dynamic Response. Abstract for Hilton Head Conference, 2016.

[3] Trivedi R.R., Bhushan A., Joglekar M.M., Pawaskar D.N., Shimpi R.P.: Enhancement of Static and Dynamic Travel Range of Electrostatically Actuated Microbeams using Hybrid Simulated Annealing. Int J Mech Sci 98:93-110, 2015.

[4] Touze C., Vidrascu M., Chapelle D.: Direct finite element computation of non-linear modal coupling coefficients for reduced-order shell models. Comp Mech 54:567-580, 2014.

[5] Hajjaj A.Z., Ramini A., Younis M.I.: Experimental and Analytical Study of Highly Tunable Electrostatically Actuated Resonant Beams. J Micromech Microeng 25:125015, 2015.

[6] Svanberg K.: The method of moving asymptotes a new method for structural. Int J Num Meth Engng 24:359373, 1987.

EVIDENCE OF AN INTERMITTENCY ROUTE TO CHOAS IN ELECTROSTATIC MEMS

Sangtak Park [1a)], Mahmoud Khater [2], Beichen Li [3], Majed Al-Ghamdi [1],
Ahmed Abdel Aziz [4], Eihab M. Abdel-Rahman [1], Ali H. Nayfeh [5], Mustafa Yavuz [3]
[1]*Systems Design Engineering,* [3]*Mechanical and Mechatronics Engineering,* [4]*Electrical and Computer Engineering, University of Waterloo, Waterloo, Ontario, Canada*
[2]*Mechanical Engineering, KFUPM, Dhahran, Saudi Arabia*
[5]*Engineering Science and Mechanics, Virginia Tech, Blacksburg, VA, USA*

Summary We provide experimental evidence for an intermittency route to chaos in an electrostatic MEMS actuator. To our knowledge, this is the first time that an intermittency route to chaos has been observed in an electrostatic MEMS actuator. We present our experiment results obtained by a laser vibrometer that measures the displacement and the velocity of the actuator in both of the time and frequency domains.

INTRODUTION

Chaos has, thus far, been experimentally observed in the response of three MEMS/NEMS devices: a non-interdigitated comb actuator [1, 2], a nano-resonator [3], and an RF MEMS switch [4]. Chaos occurs along different routes including a homoclinic tangle [1, 2], multi-frequency excitation following the Ruelle-Takens criteria [3], or a cascade of period-doubling bifurcations [4]. Intermittency is another route to chaos, having not been experimentally observed to date in electrostatic MEMS devices.

This article reports on experimental observations for an intermittency-type III route to chaos subsequent to a subcritical period-doubling bifurcation in the motions of an electrostatic MEMS actuator.

EXPERIMENT

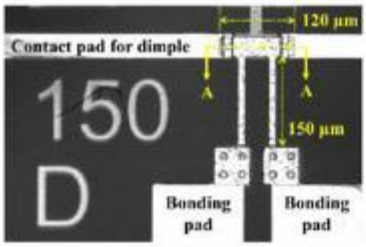

FIG. 1. Top view of the actuator

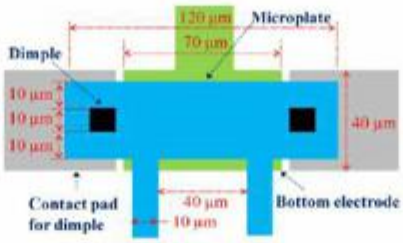

FIG. 2. Top view of the micro-plate

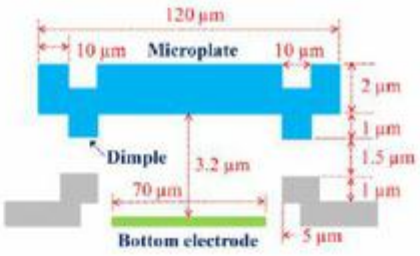

FIG. 3. A cross-sectional view

The electrostatic actuator is made of a micro-plate supported by two micro-cantilever beams presented in Fig. 1, and it is fabricated out of an electroplated gold structural layer in the UW-MEMS process [5]. A bottom electrode below the micro-plate provides the actuation voltage

$$V(t) = V_{dc} + V_{ac}\cos(2\pi f t) \tag{1}$$

Two dimples are fabricated onto both sides of the micro-plate, in Fig. 3, so as to act as stoppers in case of pull-in in conjunction with two contact pads in Fig. 2. The actuator is held close to its pull-in point by applying a DC bias voltage close to but less than the pull-in voltage that is measured to be 12 V. It is actuated by a DC biased AC signal throughout the experiments reported below. A laser vibrometer is used to measure the displacement and velocity of the micro-plate in both of the time and frequency domains. The screenshot in the upper panel of Fig. 4 shows the actuator superimposed with a grid of the measurement points used by the vibrometer.

RESULTS

The lower panel in Fig. 4 shows the frequency spectrum of the micro-plate velocity averaged over of all 85 measurement grid points, when excited by the sinusoidal signal: V_{dc} = 8.0 V, V_{pp} = 1 V at f = 10 kHz. Period-doubling is indicated in Fig. 5-(a) by the peaks appearing at half of the excitation frequency and its integer multiples. However, the measured velocity and displacement signals of the micro-plate centre point in the time domain, Fig. 5-(b), show aperiodic responses characterized by bursts occurring at irregular periods, typical of intermittent behaviours. The bursts occur over long time intervals; for example, three bursts are observed in Fig. 5-(b) within 40 seconds.

[a)] Corresponding author. Email: sangtak@uwaterloo.ca.

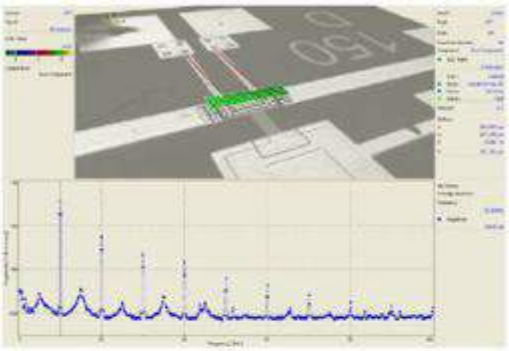

FIG. 4. Screenshot of a vibrometer interface with the actuator post-processed with the measured velocity (top panel) and its FFT (bottom panel), when actuated by the signal, 8 V_{dc} and 1 V_{pp} at 10 kHz. Peaks observed at $\frac{nf}{2}$ indicate a period-doubling bifurcation.

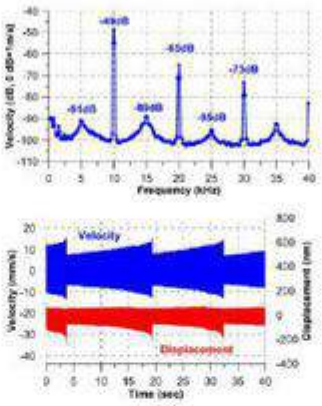

FIG. 5-(a) Measured velocity in the frequency domain indicates a period-doubling (top), (b) Measured velocity and displacement in the time domain show evidence of intermittency.

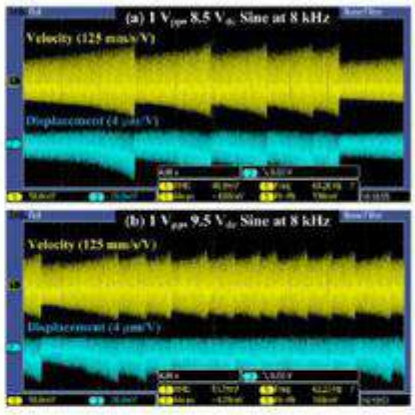

FIG. 6. Bursts occur more frequently as the intermittency approaches towards fully developed chaos with the DC bias voltage increasing from (a) V_{dc} = 8.5V to (b) V_{dc} = 9.5V.

Intermittency was observed over a wide frequency range, f = [8-10] kHz, and for the waveforms characterized by a combination of large DC bias 8 V and small AC 1 V_{pp}. Furthermore, as the DC bias voltage increases from V_{dc} = 8.5 V to V_{dc} = 9.5 V, while the AC excitation amplitude and frequency are held constant at V_{pp} = 1 V and 8 kHz in Fig. 6, we found that the bursts occurred more frequently and took less time to develop. This is also a typical characteristic of intermittent behaviours, as it approaches toward fully developed chaos with bursts interrupting shorter intervals of almost periodic (laminar) response more frequently.

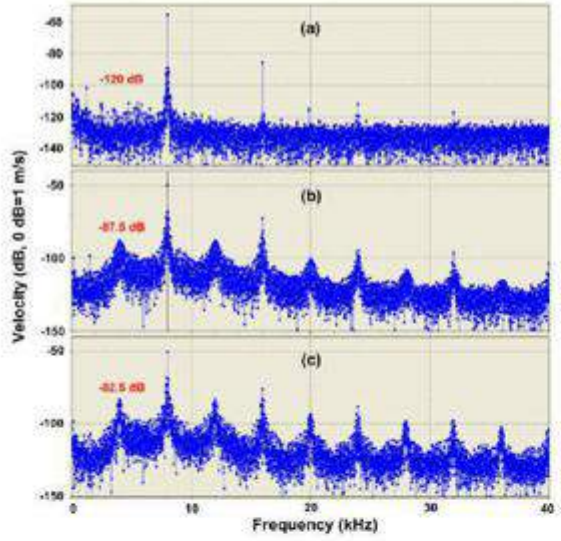

FIG. 7. Peaks in the measured velocity appear at $\frac{nf}{2}$ and grow, as laminar flow develops towards a burst; a sinusoidal waveform is used as an excitation signal, V_{dc} = 8.5 V, V_{pp} = 1 V at f = 8 kHz.

To examine the mechanism driving the intermittency, we present the FFT of the measured velocity in Fig. 7 for three subsequent intervals during a laminar build-up to a burst similar to those shown in Fig. 6. As the laminar interval develops, the power in the peaks at integer multiples $\frac{f}{2}$ increases from -120 dB to -82.5 dB, indicating unstable period-doubled oscillations leading to pull-in (the burst). Upon pull-in, the dimples come into contact and the actuator rebounds back to flight (i.e., it is re-injected into the basin of safe motions) to start another laminar interval.

CONCLUSIONS

In this experiment, we observe the period-doubling and the intermittency route to chaos in electrostatic MEMS actuators for the first time, while exciting the electrostatic actuator with a simple harmonic signal with a DC bias. Due to the aperiodic nature and low frequency components of the intermittency, we observe the intermittency mainly in the time domain at a slow time scale. However, we observe the period-doubling bifurcation mainly in the frequency domain at a fast time scale because the period-doubling bifurcation cannot be distinguished from the measured velocity signal in the time domain.

References

[1] Y. C. Wang, S. G. Adams, J. S. Thorp, N. C. MacDonald, P. Hartwell, and F. Bertsch, IEEE transactions on circuits and systems. 1, Fundamental theory and applications 45, 1013, 1998.

[2] B. E. DeMartini, H. E. Butterfield, J. Moehlis, and K. L. Turner, Journal of Microelectromechanical Systems, 16, 1314, 2007.

[3] D. V. Scheible, A. Erbe, R. H. Blick, and G. Corso, Applied physics letters, 81, 1884, 2002.

[4] J. Stulemeijer, R. Herfst, and J. Bielen, IEEE 22nd International Conference on in Micro Electro Mechanical Systems, pp. 920-922, 2009.

[5] K. Y. Chan, M. Daneshmand, R. R. Mansour, and R. Ramer, IEEE Transactions on Microwave Theory and Techniques, 57, 1612, 2009.

MULTISTABILITY OF A CANTILEVER MEMS/NEMS CAPACITIVE SWITCH MODEL

Devin Kalafut*, Anil Bajaj, and Arvind Raman
School of Mechanical Engineering, Purdue University, West Lafayette, Indiana, USA

Summary In order to fully understand nonlinear dynamics of cantilever beam micro- and nanoelectromechanical capacitive switches, thorough knowledge of static behavior is vital. Presented herein is the analysis for equilibrium positions of a generalization of such devices. The representative system model employs multiphysics features based on Euler-Bernoulli beam theory, parallel plate capacitance for electrostatics, and a form of surface interaction with both attractive and repulsive regions. The geometry, material properties, and surface features of a device are condensed into just a few dimensionless quantities, creating a parameter space of low enough dimensionality to provide accessible representations of all system equilibria within physically relevant ranges. The results offer insight into the breadth of obtainable multistability as well as sensitivity to parametric uncertainty, which is crucial for informing studies on switching dynamics and various device performance metrics.

INTRODUCTION

Micro- and nanoelectromechanical systems (MEMS/NEMS) based switches are of great interest in low-power, portable electronics and RF telecommunications devices due to their favorable operating voltages, low-insertion loss, switching time, and size [1]. Mathematical models of electrostatically actuated MEMS and NEMS switches have been key to understanding the dynamic behavior of such systems [2]. Toward this end, a first goal is to explore the eventual states of an electrostatically actuated cantilever and understand the connection between the various physical properties and the occurrence of bi- and tristability in these switches.

Many past works have focused on multistability without explicit inclusion of surface forces [3, 4, 5]. Broadly speaking, these tend to be interested in the relationship between the electrostatic forces and equilibrium positions. Conversely, varius studies have analyzed surface forces relevant to MEMS/NEMS switches without directly extending results to the breadth of multistability that may be present [6, 7]. Finally, there are a couple examples of research groups assessing both concepts for specific purposes. Stulemeijer, Bielen, Steeneken, and van den Berg analytically and experimentally identified equilibrium positions of a rectangular plate capacitive MEMS switch suspended by for spring-like supports[8], while Ouakad and Younis looked specifically at the influence of capillary forces on instabilities of a cantilever beam [9]. A void exists in discussing the basic relationship between surface forces and equilibrium positions of a cantilever capacitive switch in its most simple representation.

MODEL FORMULATION

Cantilever MEMS/NEMS capacitive switches are manufactured with a small air gap between the beam and the dielectric-coated substrate, as shown in Fig. 1 (a). Device operation is controlled by the electric potential applied between the metallic beam and underlying electrode beneath the dielectric. When a high enough potential is applied for a given configuration, it is possible for the deflecting beam to come into contact with the dielectric. Thus, surface forces between the two materials play a key role in determining final resting states and shapes of the cantilever, and, in turn, the overall capacitance of the component.

For each contributing multiphysics interaction in the model, a simple formulation is chosen to capture the most basic behavior relevant to the analysis. Bernoulli-Euler beam theory is assumed to be sufficient for deformations, as is parallel plate capacitance for the electrostatic actuation. For surface interactions, a model based on the Lennard-Jones potential is incorporated. This is physically appropriate when assuming flat surfaces approaching contact, but could also be extended as a fit to imperfect scenarios. When combined, nondimensionalized, and assessed at rest, the resulting form studied is shown in Eqn. (1). The left side is the remaining static term from beam theory, and the right side terms are from electrostatics and surface interactions, in order, where all symbols are dimensionless. Here, w is related to the deflection of the beam at a point x along the beam length, as in Fig. 1 (a), while the parameters V, g, H, and z_0 come from applied voltage, dielectric effects, surface force strength, and zero-pressure gap, respectively. It is helpful to note that the nondimensionalization of w, g, and z_0 are all done by simply dividing by the manufactured air gap, but that of V and H are more intricate, involving beam stiffness, geometry, and material properties.

$$\frac{\partial^4 w}{\partial x^4} \;/\; \frac{V^2}{1 \quad g - w^{\,2}} - \frac{H}{1 - w^{\,3}} \left[\left(\frac{z_0}{1 - w} \right)^6 - 1 \right] \tag{1}$$

*Corresponding author. Email: kalafut@purdue.edu

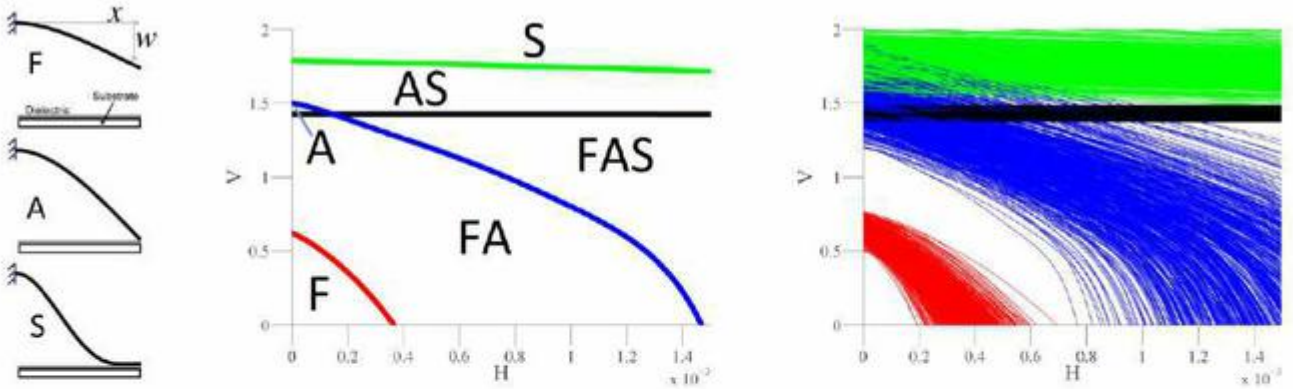

Figure 1: (a) Equilibrium shapes: floating (top), arc-shaped (middle), s-shaped (bottom). (b) Multistability diagram for $g = 0.0.066667$, $z_0 = 0.005$. (c) Parameter uncertainty with nominal values $g = 0.0.066667$, $z_0 = 0.005$.

ANALYSIS

Investigation methodology is composed of 1-parameter continuation in V of nonlinear Eqn. (1), followed by successive distillations of key outcomes toward a final depiction of multistability behavior. Continuation itself is implemented in the AUTO bifurcation software using the boundary value problem structure, while stability is inferred from direct time integration about equilibrium solutions. These solution branches can be identified as three different static equilibrium shapes: floating (freestanding, no contact), arc-shaped (point-contact), and s-shaped (line-contact), as depicted in Fig. 1 (a). Furthermore, they can be collected into various multistability categories by determining locations of turning points, as shown for one set of dimensionless parameters in Fig. 1 (b). While slices in parameter space reveal underlying behavior, the parametric sensitivity of the multistability regions is investigated using a Monte Carlo scheme. Per chosen physically-reasonable parameter distributions, the outcome provides indication of high sensitivity to the given parametric uncertainty, shown in Fig. 1 (c).

Results are relevant to the design and performance of cantilever capacitive switches, as their intended operation between capacitive states depends on what configurations are possible. Knowledge of anticipated mono-, bi-, and tristability is critical to investigations on switching dynamics, while the simplicity of the proposed model serves to inform a basic understanding of the relationship between surface interactions and multistability in the context of an ideal case.

ACKNOWLEDGMENT

This material is based upon work supported by the National Science Foundation Graduate Research Fellowship under Grant No. DGE-1333468. Any opinion, findings, and conclusions or recommendations expressed in this material are those of the authors and do not necessarily reflect the views of the National Science Foundation.

References

[1] Gabriel M. Rebeiz, 2003. *RF MEMS : theory, design, and technology*. JWiley, Hoboken, NJ.

[2] Abdel-Rahman, E. M., Younis, M. I., and Nayfeh, A. H., 2002. "Characterization of the mechanical behavior of an electrically actuated microbeam". *Journal of Micromechanics and Microengineering,* ***12***(6), Nov., p. 759.

[3] Gorthi, S., Mohanty, A., and Chatterjee, A., 2006. "Cantilever beam electrostatic MEMS actuators beyond pull-in". *Journal of Micromechanics and Microengineering,* ***16***(9), Sept., pp. 1800–1810.

[4] Snow, M. G., and Bajaj, A. K., 2010. "Comprehensive Reduced-Order Models of Electrostatically Actuated MEMS Switches and Their Dynamics Including Impact and Bounce". pp. 579–588.

[5] Krylov, S., 2007. "Lyapunov exponents as a criterion for the dynamic pull-in instability of electrostatically actuated microstructures". *International Journal of Non-Linear Mechanics,* ***42***(4), May, pp. 626–642.

[6] Kim, H., Shaik, N. H., Xu, X., Raman, A., and Strachan, A., 2013. "Multiscale contact mechanics model for RFMEMS switches with quantified uncertainties". *Modelling and Simulation in Materials Science and Engineering,* ***21***(8), Dec., p. 085002.

[7] Knapp, J., and de Boer, M., 2002. "Mechanics of microcantilever beams subject to combined electrostatic and adhesive forces". *Journal of Microelectromechanical Systems,* ***11***(6), Dec., pp. 754–764.

[8] Stulemeijer, J., Bielen, J., Steeneken, P., and van den Berg, J., 2009. "Numerical Path Following as an Analysis Method for Electrostatic MEMS". *Journal of Microelectromechanical Systems,* ***18***(2), Apr., pp. 488–499.

[9] Ouakad, H. M., and Younis, M. I., 2009. "Modeling and Simulations of Collapse Instabilities of Microbeams due to Capillary Forces". *MATHEMATICAL PROBLEMS IN ENGINEERING*.

NON-LINEAR MODES OF VIBRATION OF CNTs

Pedro Ribeiro[1 a)] & Olivier Thomas[2]
[1] *DEMec/INEGI, Faculdade de Engenharia da Universidade do Porto, Porto, Portugal*
[2] *Arts et Métiers Paris Tech, LSIS UMR CNRS 7296, Lille, France*

Summary The non-linear modes of vibration of carbon nanotubes are investigated. For that purpose, a *p* version finite element is implemented; it takes into account geometrically non-linear and non-local effects. For the first time in this problem, the free, steady-state, oscillations - which occur when the conservative system is vibrating in one of its modes of vibration – are not enforced to be harmonic by the solution procedure. Furthermore, not only the first, but also higher order modes are analysed. Modal interactions are found and it is shown that they are fundamental in some oscillations. Non-local effects are known to be influential in carbon nanotubes of very small length. However, it is demonstrated here that, because of modal interactions, non-local effects influence the non-linear oscillations of CNTs with longer lengths than what was previously believed.

INTRODUCTION

Vibrating carbon nanotubes (CNT) can be used as sensors, based on changes in the natural frequency or on alterations of the response to excitations [1]. If CNTs experience oscillations with amplitudes above about 10%-20% of their very small diameter, one should take geometrical non-linear effects into account. Furthermore, one can take advantage of geometrical non-linearity to enhance the properties of nanodevices [2, 3]. Studying the non-linear modes of vibration of CNTs is important, because these modes define essential vibratory properties.

This communication is devoted to the study of the modes of vibration of CNTs oscillating in the geometrically non-linear regime. To carry out the study, a beam *p*-version finite element for CNTs is implemented. In order to take the small scale effects into account, the non-local elasticity theory of Eringen is followed [4,5]. The equations of motion are solved by the harmonic balance method (HBM), in conjunction with an arc-length continuation method. For the first time in this problem, several harmonics are considered in the HBM, allowing us to describe modal interactions on CNTs, and to find previously undetected impacts of non-local effects on the non-linear modes of vibration of CNTs.

FORMULATION OUTLINE

In a non-local Euler-Bernoulli beam, the constitutive equation is [5]:

$$\sigma_x(x,y,t) - \mu \frac{\partial^2 \sigma_x(x,y,t)}{\partial x^2} = E\varepsilon_x(x,y,t) \tag{1}$$

where $\sigma_x(x,t)$ and $\varepsilon_x(x,t)$ represent, respectively, the axial stress and the axial strain, E the Young modulus and μ a non-local parameter. The non-local parameter is defined as $\mu=(e_0 a)^2$, with a representing an internal characteristic length and e_0 a constant that depends on the material; it is determined via comparisons with experiments or with molecular mechanics/dynamics simulations [4-6].

The geometrically non-linear relation between the axial strain and the displacement components $u(x,t)$ and $v(x,t)$ is:

$$\varepsilon_x(x,y,t) = \frac{\partial u(x,t)}{\partial x} + \frac{1}{2}\left(\frac{\partial v(x,t)}{\partial x}\right)^2 - y\frac{\partial^2 v(x,t)}{\partial x^2}. \tag{2}$$

In this work, a *p*-version finite element method (*p*FEM) approach is followed; this is characterized by the fact that, when more detailed FE models are required, the number of shape functions and generalized coordinates in the finite elements is increased, but the mesh is not altered. The *p*FEM equations of motion have the following form

$$\begin{aligned}&\left[\mathbf{M}_v + \mathbf{M}_{\mu v}\right]\ddot{\mathbf{q}}_v(t) + \mathbf{K}_v^0\mathbf{q}_v(t) - \left[2\mathbf{K}_{uv}^{1\,T}\left(\mathbf{q}_v(t)\right) + \mathbf{K}_{\mu uv}^1\left(\mathbf{q}_v(t)\right)\right]\mathbf{K}_u^{0\,-1}\,\mathbf{K}_{uv}^1\left(\mathbf{q}_v(t)\right)\mathbf{q}_v(t)\\ &+\left[\mathbf{K}_v^2\left(\mathbf{q}_v(t)\right) + \mathbf{K}_{\mu v}^2\left(\mathbf{q}_v(t)\right)\right]\mathbf{q}_v(t) = \mathbf{0}\,.\end{aligned} \tag{3}$$

There are two mass matrices in equation (3), $\mathbf{M}_v$ and $\mathbf{M}_{\mu v}$; the former is the local mass matrix, the latter represents the effects of transverse inertia on the non-local part of the bending moment. In the stiffness matrices $\mathbf{K}$, numbers in superscript specify the dependence of the matrices on the transverse generalised displacements $\mathbf{q}_v(t)$ in the following way: number 0 indicates that the matrix is constant; number 1 indicates that the matrix is a linear function of $\mathbf{q}_v(t)$ and number 2 indicates a quadratic dependence. The letters in subscript identify the displacement components or non-local effects that are related with the matrix. The influence of non-local effects on the stiffness of CNTs only transpires when the geometrical non-linearity is taken into account.

We are specifically interested in periodic solutions of equations of motion (3) and, therefore, the generalised displacements $\mathbf{q}_v(t)$ can be written as a Fourier series. Applying the harmonic balance method, a system of non-linear algebraic equations is obtained. This system is solved by an arc-length continuation method.

[a)] Corresponding author. Email: pmleal@fe.up.pt.

SAMPLE RESULTS

Several tests were carried out, of which only a small ample is given in this short text. Figure 1(a) shows the variation of the amplitude of the first harmonic with the vibration frequency when CNTs oscillate in their first mode of vibration; Figure 1(b) when CNTs oscillates in the second mode of vibration. The local and one non-local case are compared. The non-dimensional non-local parameter $\zeta=\frac{e_0 a}{L}$, where L represents the length of the CNT, is equal to 0.04. The horizontal axes provides the natural frequency of vibration in the non-linear regime, represented by ω, divided by the natural frequency of vibration in the linear regime, represented by ω_n.

Analysing Figure 1(a), one sees that the influence of non-local effects on the main branch of the backbone curve of the first mode of vibration is not large: it changes slightly the hardening spring effect, showing that non-locality has a stiffening effect at larger displacement amplitudes. Both when $\zeta=0$ and $\zeta=0.04$, a 1:5 internal resonance due to an interaction between the first and third modes of vibration is found. But the non-dimensional frequency and vibration amplitude at which this internal resonance occurs is strongly affected by the non-locality. Furthermore, close to $\omega/\omega_{\ell 1}=1.84$ a second bifurcation occurs if $\zeta=0.04$. It is due to the excitation of the 4th mode of vibration and higher harmonics, where the fifth harmonic outstands. This bifurcation is not visible if non-local effects are neglected.

Proceeding to the second mode, Figure 1 (b), the backbone curves are initially similar, with non-local effects inducing a small increase in hardening. However, the non-local effects have a major influence on bifurcations. Plots of shapes assumed by the CNTs along a vibration cycle, as well as plots of time histories and projections of trajectories on phase planes– not shown here due to space limitations – complete the demonstration that, due to bifurcations and modal couplings, non-local effects can have an influence on the dynamics of CNTs that is stronger thatwhat has been previously found.

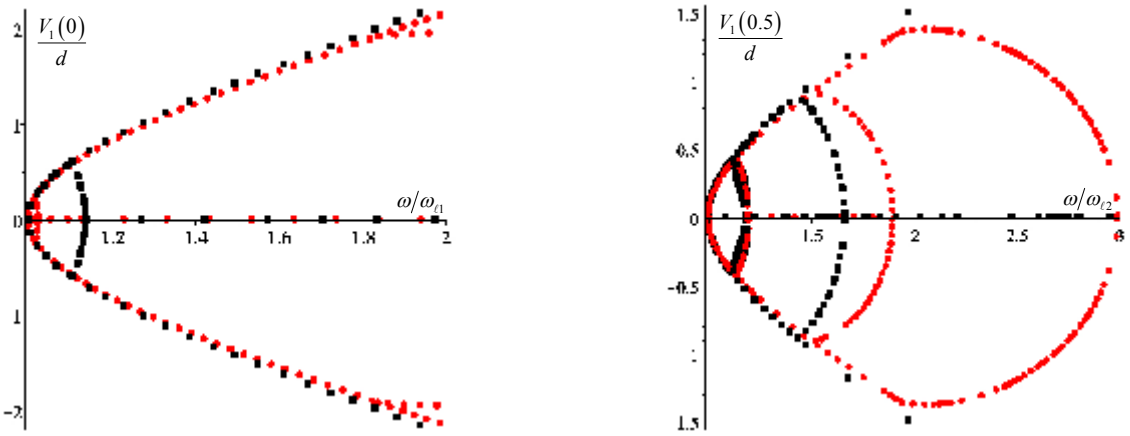

(a) First non-linear mode and bifurcations (b) Second non-linear mode and bifurcations

Figure 1. Amplitudes of first harmonic of the transverse vibration displacement of CNT, when $\zeta=0$ ■ and when $\zeta=0.04$ ●.

CONCLUDING COMMENTS

A *p*FEM, non-local, formulation is applied to investigate the modes of vibration of CNTs vibrating in the geometrical non-linear regime. It is shown that the modes of vibration of non-local CNTs can be very different from the modes of local CNTs, chiefly due to the alterations that non-local effects cause on internal resonances promoted by the non-linearity. Internal resonances result in rich vibrations, with contributions of more than one harmonic and with significant variation of the shape assumed along a vibration period. It is also found that, because of internal resonances, the non-local effects are still noticeable at lengths that are longer than what has been previously detected.

References

[1] Li, C., Thostenson, E.T., Chou, T.W.: Sensors and actuators based on carbon nanotubes and their composites: A review. Compos Sci. Technol. **68**(6): 1227-1249, 2008.

[2] Karabalin, R.B., Masmanidis, S.C., Roukes, M.L.: Efficient parametric amplification in high and very high frequency piezoelectric nanoelectromechanical systems. Appl. Phys. Lett. **97**(18): 183101, 2010.

[3] Lazarus, A., Thomas, O., Deü, J.F.: Finite element reduced order models for nonlinear vibrations of piezoelectric layered beams with applications to NEMS. Finite Elem. Anal. Des. **49**(1): 35-51, 2012.

[4] Eringen, A.: On differential equations of nonlocal elasticity and solutions of screw dislocation and surface waves. J. Appl. Phys. **54**: 8, 1983.

[5] Simsek, M.: Large amplitude free vibration of nanobeams with various boundary conditions based on the nonlocal elasticity theory Compos: Part B **56** 621–628 (2014).

[6] Arash, B., Wang, Q.: A review on the application of nonlocal elastic models in modeling of carbon nanotubes and graphenes.Comput. Mater. Sci **51**, 303-313 (2012).

SYMMETRY-BREAKING IN A THREE-NANOMECHANICAL-RESONATOR ARRAY FOR MASS DETECTION

C. GRENAT*[1], V-N. NGUYEN[1], S. BAGUET †[1], R. DUFOUR ‡[1], and C-H. LAMARQUE §[2]

[1]*Université de Lyon, CNRS, INSA-Lyon, LaMCoS UMR5259, F-69621, Villeurbanne, France*
[2]*Université de Lyon, CNRS, ENTPE, LTDS UMR5513, F-69518, Vaulx-en-Velin, France*

Summary Due to their accuracy and their size, M/NEMS resonant sensors are present in a lot of domain such as automotive, aerospace and biotechnology. They are used as accelerometers, gyroscopes for inertial navigation and also mass detection which is the target application of this investigation. The literature essentially focus on improving the sensitivity of a single resonator. Mass sensors are now able to detect a mass around a few zeptograms. This work presents a three-nanomechanical-resonator array analysis. The original contribution lies in the use of the array symmetry-breaking for mass detection.

ARRAY OF THREE NANOMECHANICAL RESONATORS

An array of three clamped-clamped beams is considered, as sketched in Fig. 1. All beams are assumed to have identical dimensions (length l, width b, height h, moment of inertia I, gap g between two adjacent beams) and identical material properties (Young's modulus E and material density ρ). Each beam is subjected to the electrostatic forces due to its two adjacent beams. The two beams at both ends of the array (beam 0 and $n+1$) are clamped and non-deformable.

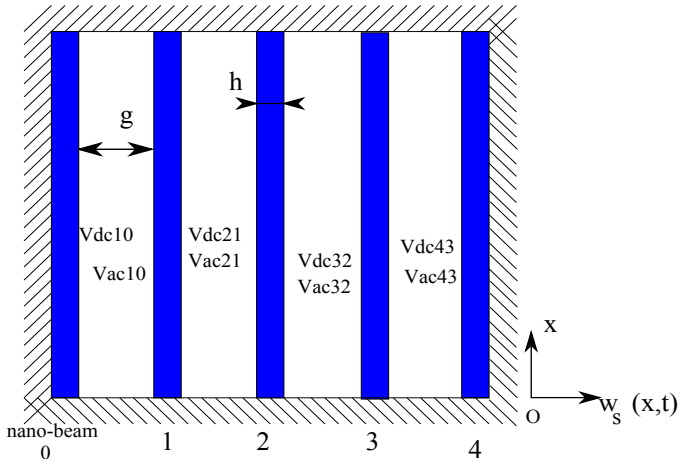

Figure 1: Array of three clamped-clamped M/NEMS beams.

Let $\tilde{w}_s$ be the lateral displacement in the plane $x-z$ along the z-axis of the s-th beam and $V_{s,s+1} = Vdc_{s,s+1} + Vac_{s,s+1}\cos(\Omega t)$ the voltage between s-th and s+1-th beams. The s-th resonator motion equation can be written as [1, 2]:

$$EI\frac{\partial^4\tilde{w}_s(\tilde{x},\tilde{t})}{\partial\tilde{x}^4} + \rho bh\frac{\partial^2\tilde{w}_s(\tilde{x},\tilde{t})}{\partial\tilde{t}^2} - \left[\tilde{N} + \frac{Ebh}{2l}\int_0^l \left(\frac{\partial\tilde{w}_s(\tilde{x},\tilde{t})}{\partial\tilde{x}}\right)^2 \mathrm{d}\tilde{x}\right]\frac{\partial^2\tilde{w}_s(\tilde{x},\tilde{t})}{\partial\tilde{x}^2} = \frac{\epsilon_0 bC_n}{2}\left[\frac{V_{s,s+1}^2}{\left(g+\tilde{w}_{s+1}-\tilde{w}_s\right)^2} - \frac{V_{s-1,s}^2}{\left(g+\tilde{w}_s-\tilde{w}_{s-1}\right)^2}\right] \quad (1)$$

where $s = 1,..,3$ and $\tilde{N}_s$ is the axial force acting on the s-th beam and resulting from an externally applied load or from residual manufacturing stress. ϵ_0, C_N are the dielectric constant and fringing field coefficient respectively. First and last resonators are clamped, therefore the following conditions apply:

$$\tilde{w}_0(\tilde{x},\tilde{t}) = \tilde{w}_{N+1}(\tilde{x},\tilde{t}) = 0. \quad (2)$$

*Email: clement.grenat@insa-lyon.fr
†Email: sebastien.baguet@insa-lyon.fr
‡Corresponding author. Email: regis.dufour@insa-lyon.fr
§Email: claude.lamarque@entpe.fr

By assumption the three identical beams have the same eigenmodes. First, a Galerkin expansion is used to eliminate the spatial dependence of the lateral displacement. Then the electrostatic forces in Eq. (1) are treated by either multiplying by the denominator or either using Taylor series expansions. Then the Harmonic Balance Method associated with the Asymptotic Numerical Method (HBM+ANM) [3] is used to solve Eq. (1). The ANM is preferred to a more conventional Newton- Raphson method because of the robustness of the ANM-based continuation and its ability to follow very complicated solution branches.

MASS DETECTION USING SYMMETRY-BREAKING OF NANOMECHANICAL RESONATOR ARRAYS

In order to use the symmetry-breaking of the resonator array for mass detection, a symmetric configuration is considered, with symmetric voltages as defined in Table 1. The electrostatic forces acting on both sides of the central beam are therefore compensating each others. Consequently, the central resonator will not vibrate. The symmetry-breaking appears when a mass fall on either the first or the third resonator. The symmetry is then broken and the central resonator starts to vibrate. The presence of a mass is thus detected.

Depending on the value of the added mass, different responses are obtained. The corresponding curves are plotted in Fig. 2. The central figure represents the response of the central beam. Without added mass ($m = 0$) the central beam does not vibrate. As soon as a mass is added on the first or the third beam, the symmetry is broken and the vibration amplitude of the central beam is not null anymore and increases with the value of the added mass.

Vdc_{10}	Vac_{10}	Vdc_{21}	Vac_{21}	Vdc_{32}	Vac_{32}	Vdc_{43}	Vac_{43}
0	0	5.3	1	5.3	1	0	0

Table 1: Voltage configuration of the three array beams.

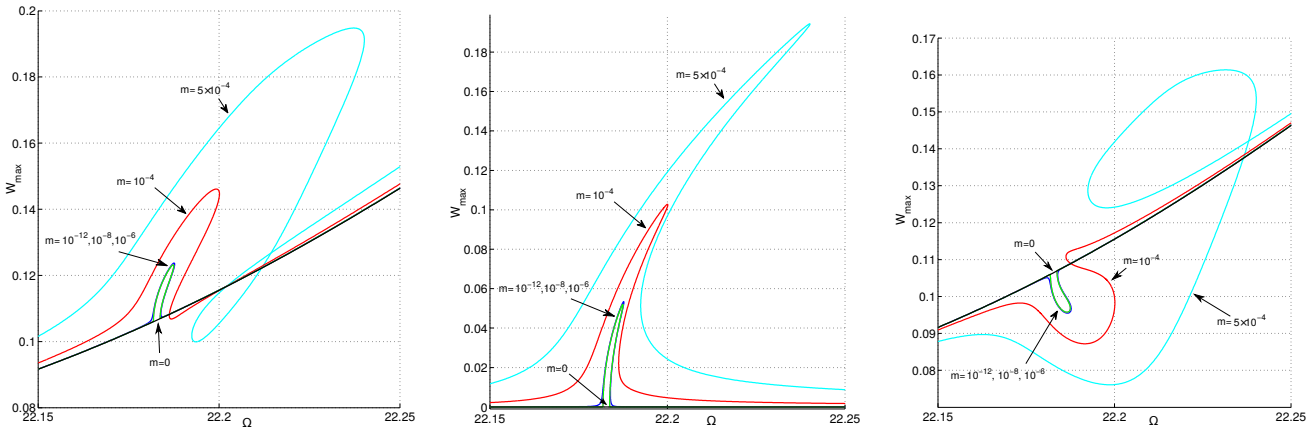

Figure 2: Array of three clamped-clamped M/NEMS beams.

CONCLUSIONS

A new mass detection method using symmetry-breaking of a M/NEMS array has been proposed. This method gives an original way to detect particles and to determine their mass. This work is a first step towards MEMS-based mass spectrometry via the implementation of thousands resonators in parallel.

References

[1] S. Gutschmidt and O. Gottlieb. Nonlinear dynamic behavior of a microbeam array subject to parametric actuation at low, medium and large dc-voltages. Nonlinear Dynamics 67(1):136, 2012.

[2] Van Nghi Nguyen, Sbastien Baguet, Claude-Henri Lamarque, Rgis Dufour: Bifurcation-based micro-/nanoelectromechanical mass detection. Nonlinear Dynamics 79(1):647-662, 2014.

[3] N. Kacem, S. Baguet, S. Hentz, and R. Dufour: Computational and quasi-analytical models for non-linear vibrations of resonant MEMS and NEMS sensors. International Journal of Non-Linear Mechanics 46(3):532-542, 2011.

NONLINEAR IDENTIFICATION OF DAMPING IN LARGE AMPLITUDE VIBRATIONS OF PLATES AND PANELS

Marco Amabili[1,a], Farbod Alijani[2], Giovanni Ferrari[1], Joachim Delannoy[1], Prabakaran Balasubramanian[1]
[1]*Department of Mechanical Engineering, McGill University, Montreal, Quebec, Canada*
[2]*Faculty of Mechanical, Maritime and Materials Engineering, Delft University of Technology, Delft, Netherlands*

Summary A nonlinear identification technique is presented to obtain the damping of isotropic and laminated sandwich rectangular plates and curved panels subjected to harmonic excitation as a function of the vibration amplitude. The response of the structures is approximated by (i) reduced-order models with 10 to 100 degrees of freedom and (ii) a single-degree of freedom Duffing oscillator. The method uses experimental frequency-amplitude data and the least-squares technique to identify parameters and reconstruct frequency-response curves by spanning the excitation frequency in the neighbourhood of the lowest natural frequencies. In order to obtain the experimental data, a sophisticated measuring technique has been used. The results reveal a strongly nonlinear correlation between the damping and the vibration amplitude.

Introduction

A challenging concept in nonlinear system identification is the characterization of damping from experimental data. Dissipation is intrinsically a nonlinear phenomenon. The modal damping assumption is a convenient tool that has been extensively used to model dissipation. However, this model generally does not take into account that damping changes with the vibration amplitude. Different nonlinear damping mechanisms have been proposed, the most common being the quadratic damping [1]. Other forms of nonlinear damping include quadratic and cubic powers of relative velocity [2]. Another damping model that is quite often used is the viscoelastic model [3]. Although there have been numerous studies about nonlinear damping, so far none has discussed the change of damping with the vibration amplitude. Therefore, different from previous studies, we propose a nonlinear identification technique to examine the damping behavior of plates and panels during large amplitude vibrations. In order to perform the identification technique, first nonlinear experiments are conducted on isotropic and laminated sandwich plates and curved panels with (i) free edges and (ii) clamped boundary conditions by using a Laser Doppler Vibrometer and a LMS signal processing system to obtain nonlinear experimental frequency-response curves. Then, the frequency-amplitude data obtained from experiments are used as the inputs for the identification scheme and the least squares method is utilized to minimize the error between the measured response and the identified model. It is observed that damping grows very significantly with the vibration amplitude.

Experimental procedure

The non-linear vibration tests have been performed by increasing and decreasing the excitation frequency in very small steps in the frequency neighbourhood of the fundamental mode by using a stepped-sine testing technique [4]. The excitation has been provided by an electro-dynamic shaker, driven by a power amplifier, via a stinger connecting the shaker to the piezoelectric miniature force transducer (B&K type 8203) attached to the structure. The response is then measured by using a very accurate Polytec single point Laser Doppler Vibrometer (sensor head OFV-505 and controller OFV-5000) in order to have non-contact displacement measurement with no introduction of added mass. The time responses have been measured by using a SCADAS III front-end connected to a workstation and the LMS Test.Lab software has been used for signal processing, data analysis and excitation control. In particular, the MIMO Sweep & Stepped Sine Testing application of the LMS system has been utilized to generate the excitation signal and its closed loop control has been used to keep the force constant while the excitation frequency is varied in the neighbourhood of the fundamental frequency.

Modelling and identification method

In order to identify the damping for the experimental data, two procedures are used and their results are compared. First, a very accurate reduced order model with a number of degrees of freedom of the order of 10 to 100 is built and the equations of motions are integrated numerically by using a pseudo-arclength continuation and collocation scheme and the damping is varied until the experimental results are matched. The details on the reduced-order models are given in [4]. In the second procedure, the response of the tested structures is approximated by a single dimensionless nonlinear oscillator with viscous damping, quadratic and cubic non-linearities as follows:

$$r^2\ddot{x} + \zeta\dot{x} + x + \eta_2 x^2 + \eta_3 x^3 = \lambda\cos(t)\,, \tag{1}$$

where x and t are made dimensionless with respect to the structure's thickness and the excitation frequency, respectively. Moreover, ζ is the damping ratio, λ is the dimensionless force, r is the frequency ratio (the ratio between the excitation frequency and the fundamental frequency), and η_2 and η_3 are the dimensionless quadratic and cubic non-linear terms, respectively. Next, the harmonic balance method is applied and the solution of equation (1) is approximated by

$$x \approx x_N = x_0 + \sum_{k=1}^{N}\left[x_{2k-1}\sin kt + x_{2k}\cos kt\right], \tag{2}$$

where N is the chosen order of truncation and x_N is the truncated Fourier series representation of x. A system of algebraic equations is obtained that relates the frequency ratio r to the amplitudes x_N. Next, the identification is conducted by assuming that the vibration amplitude x_N, the frequency ratio r and the harmonic force amplitude are already known for every frequency step from experiments. Therefore, in order to obtain the damping and the non-linear parameters, the

[a] Corresponding author: marco.amabili@mcgill.ca.

following system should be solved for every j-th frequency step, $r^{(j)}$:

$$\left[2r^{j}\mathrm{DS}_{x^{j}} \quad \mathrm{P}_{x^{j}} \quad \mathrm{Q}_{x^{j}}\right]\cdot\begin{Bmatrix}\zeta\\ \eta_2\\ \eta_3\end{Bmatrix}=\left[-\mathrm{S}_{x^{j}}-r^{j}\,\mathrm{D}\,\mathrm{S}_{x^{j}}+\mathrm{S}_{f^{j}}\right],\quad \mathrm{D}=\begin{pmatrix}0 & 0 & \cdots & 0\\ 0 & \mathrm{D}_1 & \cdots & 0\\ \vdots & \vdots & \ddots & \vdots\\ 0 & 0 & \cdots & \mathrm{D}_N\end{pmatrix},\ \mathrm{D}_k=\begin{pmatrix}-k\\ 0\end{pmatrix}\ k=\quad N\quad j=[\![\quad m]\!] \tag{3}$$

where m is the number of excitation frequency steps for which the experimental data was obtained at a specific excitation level. $\mathrm{S_x}$, $\mathrm{P_x}$ and $\mathrm{Q_x}$ are vectors comprising truncated Fourier coefficients of x, x^2 and x^3, respectively, and S_f is the dimensionless force vector. System (3) is over-constrained, since it contains $(2N+1)\times m$ equations. Therefore, in order to obtain the damping ratio and the non-linear parameters the least squares technique has been applied.

Non-linear identification results

The procedure outlined in the previous section has been applied to (i) AISI 304 stainless steel plate with 0.25×0.24×0.0005m dimensions bolted to a AISI 410 stainless steel rectangular frame exhibiting clamped boundary conditions; (ii) AISI 304 stainless steel circular cylindrical panel (0.199×0.132×0.0003m) inserted in a heavy rectangular steel frame made having V-grooves designed to hold the panel and to avoid displacement of the edges; (iii) a stainless steel rectangular plate (0.3×0.45×0.0008m) with free-edge boundary conditions; (iv) a free-edge sandwich plate (0.46×0.9×0.0033m) with Carbon/Epoxy skins having (0/90) stacking sequence and a DIAB® Divinycell foam core; (v) a second free-edge sandwich plate (0.46×0.9×0.0036m) with Carbon/Epoxy skins having (0/90) lay-up and a PLASCORE® PN2 aramid fiber honeycomb paper core. For the clamped cases the response is measured at the center while for free edges the response is measured at one of the corners. Figures 1(a), 1(b) and 1(c) compare the experimental frequency response curves for different excitation levels and the identified ones for three cases: the free edge rectangular plate, the clamped plate and the curved panel, respectively. It can be observed that the identification (red *) is reasonably accurate and the identified amplitudes are perfectly following the experimental data (blue •) predicting hardening response in case of the flat plates and softening for the curved panel. Figure 1(d) depicts the evolution of damping (normalized with respect to the small-amplitude linear damping) with the normalized peak amplitude for all studied cases (including the two sandwich plates). It is interesting to see that the damping ratio varies nonlinearly with the increase of the peak vibration amplitude. It is evident that for the supported plate and sandwich free-edge plates, the damping could increase more than 250% for vibration amplitudes greater than 1.5 times the thickness. This increase is about 50% for the curved panel and for the same vibration amplitude. However, for the completely free steel plate the increase in damping is around 280% for vibrations greater than 3 times the thickness. This behavior confirms the presence of large dissipation during large-amplitude vibrations.

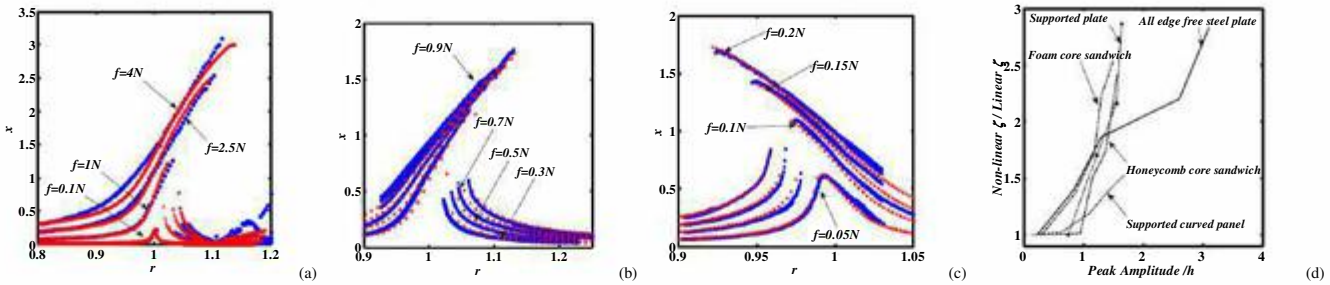

Fig. 1. (a) Comparison between the experimental and identified curves for the tested free-edge isotropic rectangular plate; (b) comparison between the experimental and identified frequency-amplitude curves for the tested clamped rectangular plate; (c) comparison between the experimental and identified curves for the tested clamped curved panel; (d) nonlinear variation of damping (normalized with respect to the linear damping) versus the peak vibration amplitude (normalized with respect to the thickness) for all the studied cases. In (a), (b) and (c) red * denote harmonic balance identification while blue • indicate experimental results.

Conclusions

A nonlinear identification technique is presented to track the evolution of damping during large-amplitude vibrations. The identified damping parameters confirm the presence of a strongly nonlinear correlation between damping and vibration amplitude in plates and curved panels. Particularly, it was found that plates and panels exhibit much larger dissipation during large-amplitude vibrations than in case of small-amplitude vibrations. Specifically, the damping increases with the vibration amplitude well over twice the linear damping ratio for the isotropic and sandwich plates experimentally investigated, and over 50 % for the circular cylindrical panel.

References

[1] Worden K., Tomlinson G.R.: Nonlinearity in structural dynamics: detection, identification and modeling, Institute of Physics Publishing, Bristol, 2001.

[2] Ozcelik O., Attar P.: Effect of non-linear damping on the structural dynamics of flapping beam. *Int. J. Non-linear Mech* **65**:148-163, 2014.

[3] Amabili M.: Nonlinear vibrations of viscoelastic rectangular plates. *J Sound Vib* **362**:142-156, 2016.

[4] Amabili M.: Nonlinear vibrations and stability of shells and plates, Cambridge University Press, New York, 2008.

NONLINEAR SYSTEM IDENTIFICATION OF MECHANICAL INTERFACES BASED ON WAVE PROPAGATION

Keegan J. Moore[1], Mehmet Kurt[2], Melih Eriten[3], D. Michael McFarland[4], Lawrence A. Bergman[4], Alexander F. Vakakis[1]
[1]*Department of Mechanical Science and Engineering, University of Illinois, Urbana, IL, USA*
[2]*Department of Bioengineering, Stanford University, Stanford, CA, USA*
[3]*Department of Mechanical Engineering, University of Wisconsin at Madison, Madison, WI, USA*
[4]*Department of Aerospace Engineering, University of Illinois, Urbana, IL, USA*

Abstract We study stress wave propagation in an impulsively forced split Hopkinson bar system with a frictional interface. By first considering only the primary-wave transmission and reflection, we reduced the problem to a first-order, strongly nonlinear ordinary differential equation. An Iwan element is chosen to model the frictional interface. The primary-wave propagation model is used to identify the Iwan parameters by maximizing the R-squared value between the experiment and simulation results. Using the optimized Iwan parameters, a high-order finite element model is used to simulate multiple transmissions and reflections across the interface. The results demonstrate that the primary-wave propagation model can be used for nonlinear system identification at a lower computational cost compared to higher-order models.

INTRODUCTION

High-order finite element (FE) models are often employed to identify system parameters, leading to high computational costs. As such, it is often desirable to develop low-cost reduced order models (ROMs) that can be used to identify accurately system parameters. One area where this proves difficult is in the prediction of mechanical wave propagation across a nonlinear interface in a waveguide due to an impulsive load. A conventional waveguide is the split Hopkinson pressure bar (SHPB) [1]. Recently, an SHPB system has been used to study the effects of threaded interfaces [2]. This work presents a new nonlinear system identification method based on the primary-wave propagation (PP) model proposed in [3]. We show that the PP model can accurately identify the parameters in an Iwan element used to model the nonlinear interface studied in [2] at a reduced computational cost.

PROBLEM FORMULATION

We consider the system depicted in Figure 1, composed of two linear elastic layers coupled by a nonlinear interface. The equation of motion governing the longitudinal waves in each layer is

$$\partial^2 u_i / \partial t^2 - \partial^2 u_i / \partial x^2 = 0, \quad i = 1,2, \tag{1}$$

where $u_i = u_i(x,t)$ is the ith longitudinal displacement. Additionally, all variables are normalized such that $0 \le x \le 1$. The layers are assumed to start with zero initial conditions, with $t = 0$ defined as the time when the primary pulse reaches the left boundary $x = 0$ of the layer. The boundary conditions for the layers are

$$\partial u_1 / \partial x\big|_{x=0} = F_{in}(t), \quad \partial u_1 / \partial x\big|_{x=1} = K(z,\dot{z}), \quad \partial u_2 / \partial x\big|_{x=0} = K(z,\dot{z}) = F_2, \quad \partial u_2 / \partial x\big|_{x=1} = 0, \tag{2}$$

where the relative displacement is $z(t) = u_2(t,0) - u_1(t,1)$. With the system defined, we turn to the method developed by Pilipchuk in [3], which reduces the problem to a single first-order, nonlinear, ordinary differential equation (ODE) by considering only the primary transmission and reflection. Pilipchuck provides a full derivation in [3]; here only the resulting equations are presented:

$$(1/2)\dot{z} + K(z,\dot{z}) = F_{in}(t), \quad z\big|_{t=0} = 0, \tag{3}$$

$$F_2(t) = F_{in}(t) - (1/2)\dot{z}, \tag{4}$$

where F_2 is the transmitted force. Additionally, the reflection into the first layer is

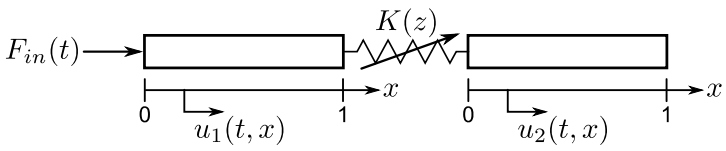

Fig. 1 Impulsively forced dual-layer system with nonlinear interface

[a] Keegan J. Moore. Email: **kmoore14@illinois.edu.**

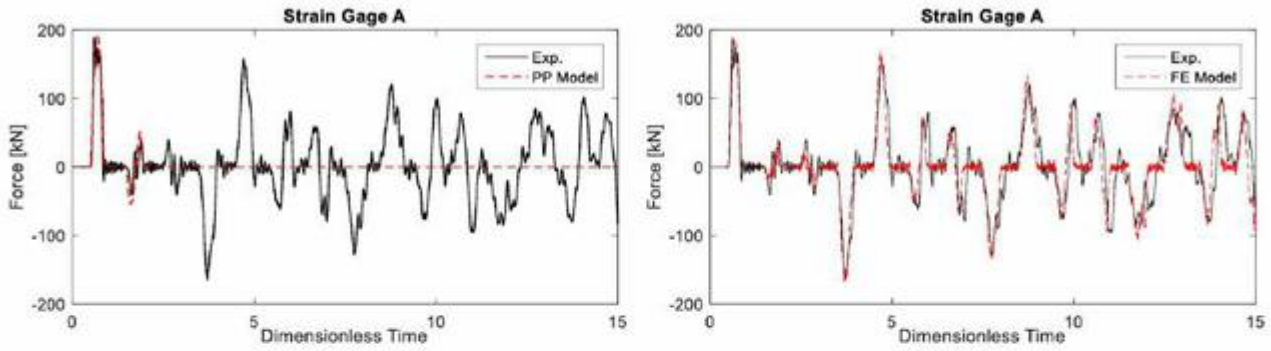

Fig. 2 Resulting waves for a preload of 25 ft-lbf and a striker velocity of 44.3 ft/s predicted using PP model and FE model.

$$\Phi_1(\ ) = -\ _{in}(\ -2) + \quad (\ -1\ , \tag{5}$$

where Φ_1 is the reflection in the first layer based on the D'Alembert representation of the solution. Thus, by solving for $\dot{z}$ in (3), the transmitted and reflected forces are calculated using (5). By matching the predicted forces with the experimentally measured strains (converted into forces), the system parameters can be identified.

NONLINEAR SYSTEM IDENTIFICATION

We study an SHPB system composed of two hardened AISI 1566 steel bars with a threaded interface. Both the incident and transmission bars had a length of 48 in. and a diameter of 1.5 in. The threaded interface was made using 1"-8 UNC threads with male threads on the incident bar and female threads on the transmission bar. An initial static torque preload, applied by hand (near zero torque) or by using a handle-less strap wrench, ranged from 25 ft-lbf to 40 ft-lbf. The incident bar was dynamically excited by a 6 in. long striker, propelled by an air gun, at velocities ranging from 23.0 to 44.9 ft/s. Strains were measured at two locations before and two locations after the interface using uniaxial semiconductor strain gages. The Air Force Research Laboratory at Eglin Air Force Base, FL conducted all experiments and documented them fully in [2].

The frictional interface is modeled using an Iwan element [4], which contains an infinite distribution of Jenkins elements in parallel, where each Jenkins element consists of a linear spring in series with a Coulomb friction slider. All springs are chosen to have equivalent stiffness, but the slip forces vary in the form of a band-limited distribution as used by Iwan in [4]. Due to the lack of striker force measurements, the input force was modeled using a half-sine impulse in the simulations. The Iwan and forcing parameters are identified using MATLAB's patternsearch optimization algorithm with the objective of maximizing the R-squared value between the experimental data and the PP model results. The PP model simulations were computed up to a dimensionless time of 2.5 before any secondary transmissions and reflections. Using the optimized Iwan parameters, a high-order FE model was used to predict the secondary transmissions and reflections. Figure 2 presents the results for a static torque of 25 ft-lbf and a velocity of 44.3 ft/s.

CONCLUDING REMARKS

This paper presented a nonlinear system identification method for identifying nonlinear interfaces in waveguides based only on primary transmissions and reflections. In this way, the problem was reduced to a first-order, nonlinear ODE, resulting in a reduced order model, the PP model, without sacrificing the interface nonlinearity. Using the PP model, Iwan parameters were identified to model a threaded interface in an SHPB system. The PP model accurately captured the primary transmission and reflection across the interface, allowing accurate identification of the Iwan parameters. Additionally, multiple transmissions and reflections were computed using a high-order FE model with the Iwan parameters identified from the PP model and the results compared to those from the ROM.

References

[1] Hopkinson, B., "A Method of Measuring the Pressure Produced in the Detonation of High Explosives or by the Impact of Bullets," Philos. Trans. R. Soc. (London) A, 213, pp. 437-456, 1914.

[2] Dodson, J. C., Lowe, R. D., Foley, J. R., Mougeotte, C., Geissler, D., and Cordes, J., "Dynamics of Interfaces with Static Initial Loading", Dynamic Behavior of Materials, vol 1. In: Song B (ed) Conference Proceedings of SEM Series, Springer, New York, pp. 37-50, 2014.

[3] Pilipchuck VN, Azeez, MAF, and Vakakis AF, "Primary-pulse Transmission in Strongly Nonlinear Periodic System." Nonl. Dyn., *11*, pp. 61-81, 1996.

[4] Iwan WD, A Distributed-Element Model for Hysteresis and Its Steady-State Dynamic Response. In: ASME Journal of Applied Mechanics, *33*, pp. 839-900, 1996.

UNCERTAINITY QUANTIFICATION AND ROBUSTNESS ISSUES IN PLANAR NONLINEAR RESONANT STRUCTURES

Astitva Tripathi[1] and Anil K. Bajaj [*1]

[1]*School of Mechanical Engineering, Purdue University, West Lafayette, IN, USA*

Summary Nonlinear resonators employing 1:2 internal resonance have been proposed as sensing elements in some Micro-Electro Mechanical Systems (MEMS). A critical aspect of their performance is their robustness of performance with respect to variations resulting from fabrication uncertainties. In this study, an uncertainty quantification analysis is performed on several candidate designs for 1:2 internal resonances obtained via a computational synthesis method, and the interplay of geometric fabrication errors and robustness is illustrated.

INTRODUCTION

MEMS Devices operating on the principal of resonant behavior under 1:2 internal resonance have been proposed in applications such as mass and chemical sensors [1]. Additionally, new synthesis methods have been developed [2] which can generate several candidate designs for such resonators. Resonators based on 1:2 internal resonances are often designed so as to have their first two natural frequencies in the ratio of 1:2. In the computational synthesis method in [2], structures composed of beams having constant cross section joined orthogonally to each other are linearly designed as candidate structures for 1:2 internal resonance by varying the shape and size of structural elements. The intended properties of 1:2 frequency ratio are achieved by optimizing topology of the linear structure and dimensions of individual beams. As manufacturing processes have some inbuilt variability in the dimensions they can produce, it is critical to analyze the candidate resonators for their ability to provide sufficient performance in the face of dimensions achieved in actual fabrication compared to the nominal structure. While applicable for linear resonators as well, such uncertainty quantification and robustness considerations are especially important for nonlinear systems as the resonators are quite sensitive to variations in the frequency ratio from nominal value. In this work, four resonators synthesized using the method described in [2] are compared for robustness of their nonlinear resonant performance in face of uncertainties induced in dimensions due to manufacturing tolerances.

STRUCTURE SYNTHESIS AND NONLINEAR REDUCED ORDER MODEL

As stated in the introduction, the candidate resonators for 1:2 internal resonances consist of constant cross-section beams joined orthogonally to each other and undergoing planar vibrations. A hierarchical optimization method described in detail in [2] is used to synthesize these structures so that their first and second natural frequencies are in the ratio 1:2. Figure 1 shows four of these candidate structures for 1:2 internal resonance obtained using the hierarchical optimization method. Note that when the structures are fabricated using MEMS fabrication techniques, the structures deviate from nominal designs.

To obtain the nonlinear equations of motion for the candidate structures, Euler-Lagrange conditions coupled with the method of averaging are used. It is assumed that the overall nonlinear structural response of these systems consists predominantly of the lowest two modes. The transverse deflection of the ith beam of the structure can be written as:

$$v_i = \epsilon(A_1\phi_{i1} + A_2\phi_{i2}) \ , \tag{1}$$

where A_1 and A_2 are the modal amplitudes that are only functions of time, and ϕ_{i1} and ϕ_{i2} are the first and second linear modes of the ith beam, respectively. Following the standard averaged Lagrangian approach [3], the two-mode nonlinear resonant dynamics with quadratic (inertial) nonlinearity is reduced to four first-order equations describing the slow evolution of the amplitudes A_1 and A_2 in Eq. (1) and the frequency response is obtained using these first-order equations. It is well-known [1, 2, 3]that when the second mode is excited near its natural frequency, under the 2:1 internal resonance, the first mode is excited due to its nonlinear modal coupling with the second mode. The strongest coupling is when the two modal frequencies have a ratio of 2. In the presence of frequency mistuning, the response of the first mode goes down significantly.

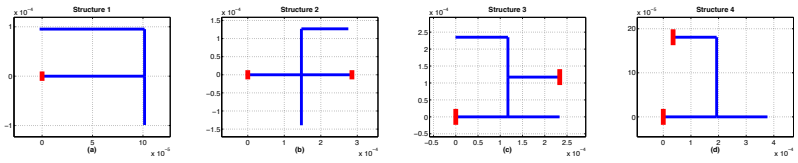

Figure 1: Optimized structures obtained for 1:2 frequency ratio as obtained in [2]. The planar structures are clamped at the red ground. The ratio of the first two natural frequencies for each of the structures is 2.0000.

*Corresponding author. Email: bajaj@purdue.edu

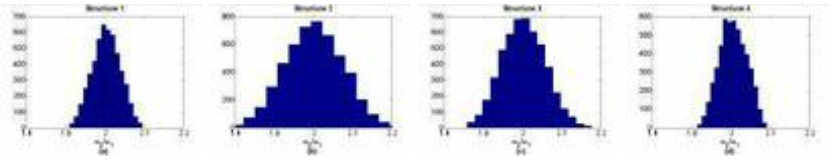

Figure 2: Histograms of the frequency ratio $\frac{\omega_2}{\omega_1}$ of the structures shown in Fig 1.

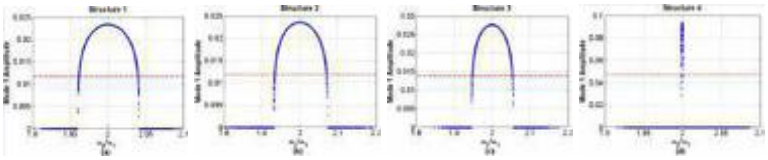

Figure 3: Mode 1 amplitude at zero external mistuning (excitation frequency equal to ω_2) of the structures shown in Fig. 1. The red line indicates the failure criterion amplitude.

UNCERTAINITY QUANTIFICATION

Variations in structural dimensions of the optimized structures result in the natural frequency ratios of the structures to deviate from 2 and thus, a degradation in device performance. To study the effects of variations in the beam lengths on the nonlinear response of the structure, consider the variations in lengths to be governed by a uniform distribution. Thus, beam length variations are assumed to be $\pm 10\%$ from the nominal. Samples generated using the Latin Hypercube Sampling technique are then used to compute the variation in natural frequencies with respect to the beam lengths. This relationship is expressed in the form of a response surface using the Multiadaptive Regression Splines (MARS) [4] which can be sampled to study the effect of dimensional uncertainties on nonlinear response of the first mode, and thus the device performance.

To compare the four candidate structures shown in Fig. 1 from the point of view of robustness of the nonlinear response, a test is defined to quantify each resonator's operational success or failure. This test can be stated as,"If for a given set of parameters along with a fixed value of forcing at the second natural frequency, the amplitude of the first mode response is more than or equal to 50% of the first mode amplitude for the nominal case, the device is said to be successful". This is based on the expectation that when a certain number of devices (or structures) are fabricated using identical manufacturing process, a certain fraction will not exhibit strong internal resonance, and thus the coupled mode nonlinear response. Figure 2 shows the histogram of the frequency ratios for the four structures. Figure 3 shows the mode 1 amplitudes of the four candidate structures at exact external resonance. Mode 1 amplitude is highest when the design is at its nominal point (i.e., the frequency ratio is equal to 2), and deviations from a frequency ratio of 2 cause a gradual drop in efficacy of modal coupling finally leading to the mode 1 amplitude becoming zero. The device failure rates for the respective structures are 28.98%, 34.62%, 35.30% and 97.14%. Thus, it is clear that among the four structures Structure 1 from Fig. 1 is the most robust to fabrication errors.

DISCUSSION AND CONCLUSIONS

Several candidate structures were compared for resonant coupled mode dynamics with regards to their ability to provide functionality in face of dimensional variability. The study brings forth the added aspect of nonlinear resonator design for internal resonances as some optimal designs, such as structure 4, may not be robust enough to handle uncertainties in device fabrication.

References

[1] Vyas A., Bajaj A. K., Raman A., Peroulis D. (2009) A Microresonator Design Based on Nonlinear 1 : 2 Internal Resonance in Flexural Structural Modes. *Journal of Microelectromechanical Systems* **18**:744-762.

[2] Tripathi A., Bajaj A. K. (2013) Computational Synthesis for Nonlinear Dynamics Based Design of Planar Resonant Structures. *Journal of Vibration and Acoustics* **135**: 051031:1-13

[3] Balachandran B., Nayfeh A. H. (1999) Nonlinear Motions of Beam-Mass Structure. *Nonlinear Dynamics* **1**:39-61

[4] Friedman J. H. (1991) Multivariate Adaptive Regression Splines. *Annals of Applied Statistics* **19**:1-67

STUDIES OF ROTOR-STATOR SYSTEM SUBJECTED TO NOISE EXCITATIONS

Vipin Agarwal*[1] and Balakumar Balachandran[1]

[1]*Department of Mechanical Engineering, University of Maryland, College Park, Maryland, 20742, USA*

Summary In this work, the authors present stochastic averaging studies conducted to examine torsional vibrations of a Jeffcott rotor subjected to continuous stator contact. The rotor drive input includes a deterministic input and white noise. The influence of noise on both forward and backward whirling motions is considered. In the experimental arrangement, noise is introduced through the drive motor signal. The experimental results are presented along with the results of the analytical-numerical studies and discussed.

INTRODUCTION

Noise is unavoidable and present is a range of engineering systems, and it can play a significant role in influencing system dynamics. In the current study, a combination of experimental and analytical-numerical studies are undertaken to understand the response of a rotor-stator system subjected to noise. The authors make use of the stochastic averaging method [1] to determine the response of the rotor-stator system. This averaging method has been used quite effectively to study the response of linear and nonlinear systems subjected to a combination of deterministic and noise inputs (e.g., [2, 3]). The physical system of interest here is a drill-string system, a representative illustration of which is provided in Fig. 1. Drill strings are long, tubular structures that are used for boring holes in the ground. These systems can undergo large torsional deformations as well as lateral displacements.. In general, noise is considered undesirable for the performance of an engineering system. However, noise may have beneficial effects on the dynamical behavior of systems and it can have a significant influence on the system dynamics (e.g., [4]). As an extension of their prior study, the authors consider the influence of noise on the dynamics of a flexible rotor with continuous stator contact.

EXPERIMENTAL ARRANGEMENT

The experimental arrangement consists of a rotor disc attached to a rotating rod. The rotating rod is made of aluminium and referred as a string due to its slenderness. In the experiments, this structure has a diameter of 3.2 mm and spans a length of approximately 2.0 m. The rotor is made of aluminium and has a diameter of 15.2 cm, and this rotor is enclosed within a circular stator with an inner diameter of 20.3 cm. A small mass is attached to the rotor in order to create an imbalance and eccentricity in the string-rotor system. The complete assembly is shown in Fig. 2.

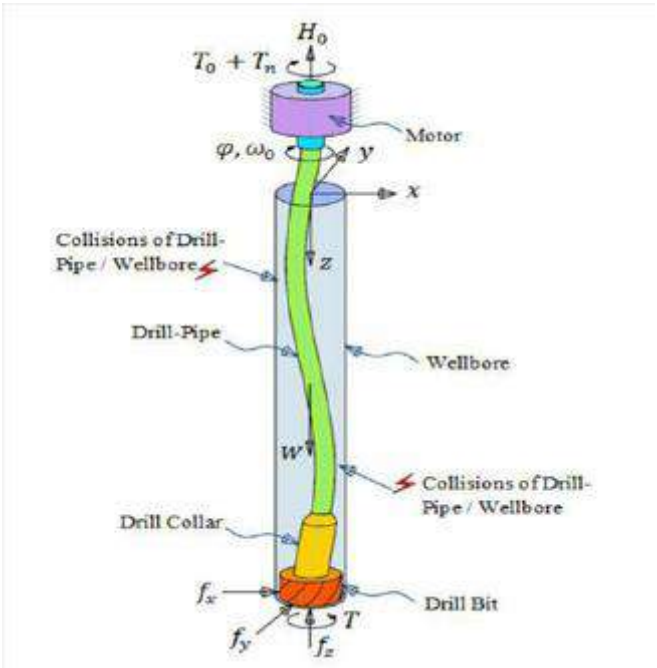

Figure 1: Representative drill-string system [5].

*Corresponding author. Email: vagarwal@umd.edu

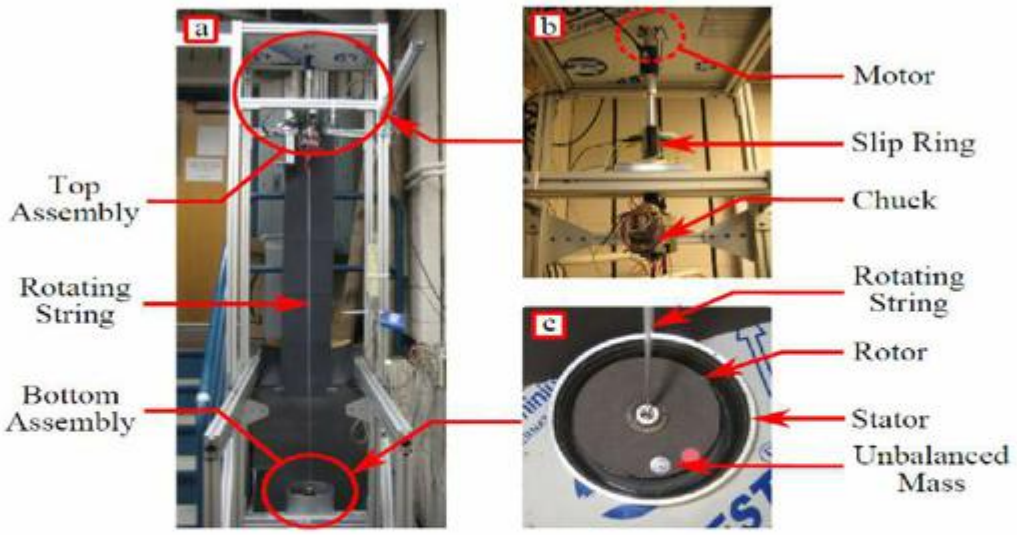

Figure 2: Experimental Arrangement. (a) Complete Experimental Arrangement, (b) Top Assembly, (c) Bottom Assembly

The entire string-rotor assembly is driven by a three-jaw self centering chuck that is connected to a stiff stainless steel driven shaft and motor. Additionally, a slip ring placed along the drive shaft allows for strain gages to be secured to the string. The strain due to bending and torsional vibrations may be measured depending upon the configuration of strain gages. For certain drive speeds, the rotor comes into contact with the stator and is subjected to frictional forces. The rotor may either stay in continuous contact in stator while it experiences different types of whirling motions or return back to the center of the stator. In the present study, the authors consider the constant contact cases in the experiments.

MODELING AND ANALYTICAL-NUMERICAL STUDIES

To complement the experiments, analytical-numerical studies based on the stochastic averaging method is carried out. The rotor-stator system is nonlinear in nature. The torsional and lateral vibrations are coupled by the eccentricity of the unbalanced mass through the inertial terms and rotor is also subjected to discontinuous forces that arise from the contact with the stator. A reduced-order model, in the form of a modified Jeffcott rotor model, is used for the averaging and numerical studies when noise is present in the system input. As part of the studies, the averaged Fokker-Planck-Kolmogrov equation is solved by using the path integration method. Numerical results are obtained for making comparisons with the experimental observations.

CONCLUDING REMARKS

The stochastic averaging method has been used to study the response of a flexible rotor system in continuous stator contact. Experiments are conducted with a laboratory scale arrangement of a portion of a drill-string system. The effectiveness of noise in influencing backward and forward whirling motions is examined through the analytical-numerical and experimental studies and discussed.

ACKNOWLEDGMENT

Support received for this work through NSF Grant No. CMMI1436141 is gratefully acknowledged.

References

[1] Stratonovich, R. L., 1967. *Topics in the theory of random noise*, Vol. 2. CRC Press.
[2] Huang, Z., Zhu, W., Ni, Y., and Ko, J., 2002. "Stochastic averaging of strongly non-linear oscillators under bounded noise excitation". *Journal of Sound and Vibration,* ***254***(2), pp. 245–267.
[3] Chen, L., and Zhu, W., 2009. "Stochastic averaging of strongly nonlinear oscillators with small fractional derivative damping under combined harmonic and white noise excitations". *Nonlinear Dynamics,* ***56***(3), pp. 231–241.
[4] Agarwal, V., and Balachandran, B., 2015. "Noise-influenced response of duffing oscillator". In ASME 2015 International Mechanical Engineering Congress and Exposition, American Society of Mechanical Engineers.
[5] Liu, X., Vlajic, N., Long, X., Meng, G., and Balachandran, B., 2013. "Nonlinear motions of a flexible rotor with a drill bit: stick-slip and delay effects". *Nonlinear Dynamics,* ***72***(1-2), pp. 61–77.

TRANSIENT RESPONSES OF A FORCED TRIPLE WELL POTENTIAL SYSTEM WITH FUZZY UNCERTAINTY

Ling Hong[1a)], Jun Jiang[1] & Jian-Qiao Sun[2]
[1] *State Key Lab for Strength and Vibration, Xi'an Jiaotong University, Xi'an, 710049, China*
[2] *School of Engineering, University of California at Merced, Merced, CA 95344, USA*

Summary Transient responses of a forced triple-well potential system with fuzzy uncertainty are studied by means of the Fuzzy Generalized Cell Mapping (FGCM) Method. The FGCM method is first introduced. A rigorous mathematical foundation of the FGCM is established as a discrete representation of the fuzzy master equation for the possibility transition of continuous fuzzy processes. The FGCM offers a very effective approach for solutions to the fuzzy master equation based on the min-max operator of fuzzy logic. A fuzzy response is characterized by its topology in the state space and its possibility measure of membership distribution functions (MDFs). This paper focuses on the evolution of transient MDFs of the fuzzy response. It is found that as the time goes on, transient MDFs spread around three potential wells. The evolutionary orientation of transient MDFs aligns with unstable invariant manifolds leading to stable invariant sets.

FUZZY GENERALIZED CELL MAPPING

Consider a dynamical system with fuzzy uncertainty,

$$\dot{\mathbf{x}} = \mathbf{f}(\mathbf{x}, t, S), \quad x \in \mathbf{D} \tag{1}$$

where $\mathbf{x}$ is the state vector, t the time variable, S a fuzzy set with a membership function $\mu_S(s) \in (0,1]$ where $s \in S$, and $\mathbf{f}$ is a vector-valued nonlinear function of its arguments. $\mathbf{D}$ is a bounded domain of interest in the state space. When the system parameter S is a fuzzy number, Equation (1) is a fuzzy differential equation. The equation of the FGCM system is given as follows by discretizing the time t, state variables $\mathbf{x}$ and the fuzzy set S in Equation (1)

$$\mathbf{p}(n+1) = \mathbf{P} \circ \mathbf{p}(n), \;\; \mathbf{p}(n) = \mathbf{P}^n \circ \mathbf{p}(0), \quad p_i(n+1) = \max_j \min[p_{ij}, p_j(n)] \tag{2}$$

where $\mathbf{P}^{n+1} = \mathbf{P} \circ \mathbf{P}^n$ and $\mathbf{P}^0 = \mathbf{I}$. $\circ$ denotes the min-max operation. The matrix $\mathbf{P}$ denotes the one-step transition possibility matrix, $\mathbf{P}^n$ denotes the n-step transition possibility matrix. The vector $\mathbf{p}(n)$ is called the n-step membership distribution vector and $\mathbf{p}(0)$ the initial membership distribution vector. The (i, j)th element p_{ij} of the matrix $\mathbf{P}$ is called the one-step transition possibility from cell j to cell i. Equation (2) describes the evolution of a fuzzy response process and its MDFs.

Consider the fuzzy master equation for the possibility transition of continuous fuzzy process [1],

$$p(\mathbf{x}, t) = \sup_{\mathbf{x}_0 \in \mathbf{D}} [\min\{p(\mathbf{x}, t | \mathbf{x}_0, t_0), p(\mathbf{x}_0, t_0)\}], \quad \mathbf{x} \in \mathbf{D}. \tag{3}$$

where $\mathbf{x}$ is a fuzzy process, $p(\mathbf{x}, t)$ is the membership distribution function of $\mathbf{x}$ at t, and $p(\mathrm{x}, t, \mathbf{x}_0, t_0)$ is the transition possibility function. Equation (2) of the FGCM can be viewed as a discrete representation of fuzzy master equation (3). The solution to this equation is in general very difficult to obtain analytically. The FGCM offers a very effective method for solutions to this equation, particularly, for fuzzy nonlinear dynamical systems [2]

TRANSIENT ANALYSIS OF MDFS

Consider a forced Duffing oscillator with a triple-well potential driven by additive fuzzy noise,

$$\begin{cases} \dot{x} = y \\ \dot{y} = -0.35y - x + 0.5x^3 - 0.05x^5 + 0.2\cos t + S \end{cases} \tag{4}$$

where S is a fuzzy parameter with a triangular MDF,

$$\mu_S(s) = \begin{cases} [s - (s_0 - \varepsilon)]/\varepsilon, & s_0 - \varepsilon \le s < s_0 \\ -[s - (s_0 + \varepsilon)]/\varepsilon, & s_0 \le s < s_0 + \varepsilon \\ 0, \quad otherwise \end{cases} \tag{5}$$

where $\varepsilon > 0$ is a parameter characterizing the intensity of fuzziness of S and is called fuzzy noise intensity. s_0 is the nominal value of S with membership grade $\mu_S(s_0) = 1$. We take s_0=0, ε =0.4.

[a)] Corresponding author. Email: hongling@mail.xjtu.edu.cn

The domain $\mathbf{D}=\{-3.5 \le x \le 3.5; -2.0 \le y \le 2.0\}$ is discretized into 141×141 cells. The 5×5 sampling points are used within each cell. S is discretized into 401 segments. Hence, out of each cell, there are 10,025 trajectories with varying membership grades. Transient MDFs are shown in Figures 1 and 2. T is one step mapping step.

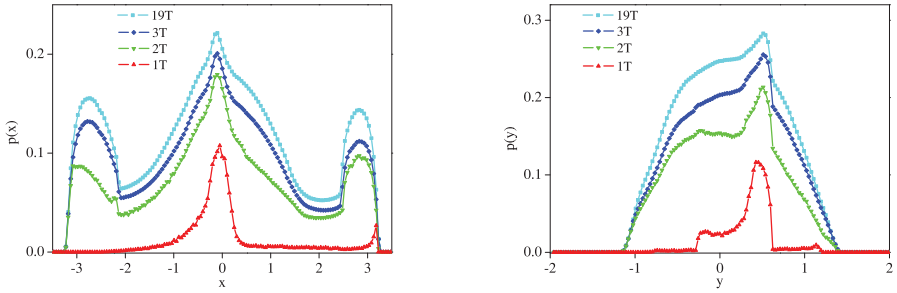

Figure 1. Transient marginal MDFs of displacement x and velocity y for the fuzzy Duffing equation (4) with the intensity of fuzzy noise ε =0.4 at different times 1T, 2T, 3T and 19T.

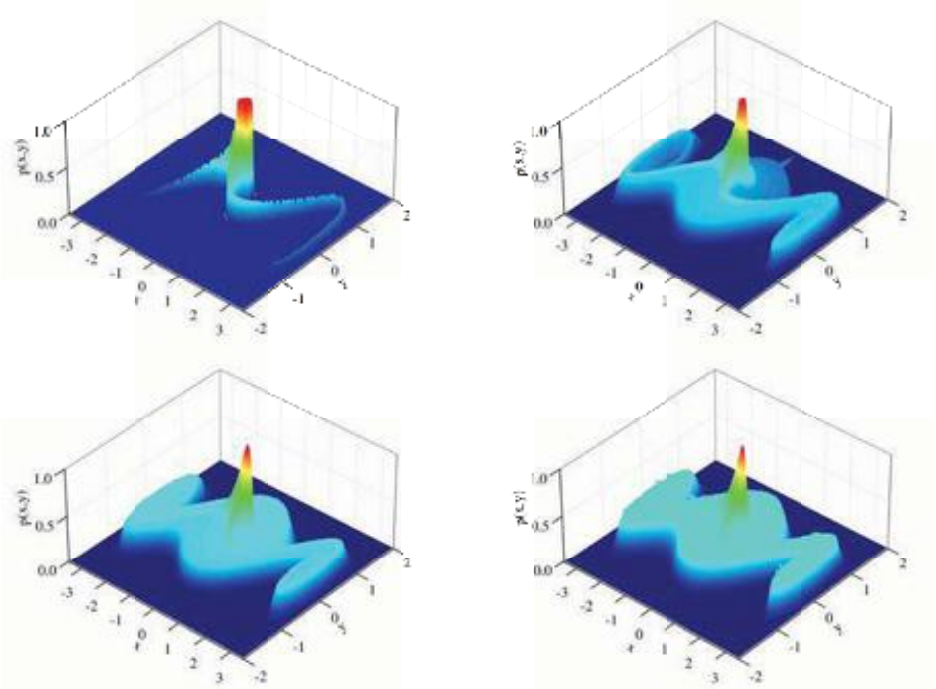

Figure 2. Transient MDFs of displacement x and velocity y for the fuzzy Duffing equation (4) with the intensity of fuzzy noise ε =0.4 at different times 1T, 2T, 3T and 19T.

CONCLUDING REMARKS

This paper investigates the evolution of transient MDFs of the fuzzy response. It is found that the evolutionary orientation of transient MDFs aligns with unstable invariant manifolds leading to stable invariant sets. As the time goes on, the mean values of transient MDFs increase moving towards to form three possibility peaks around three potential wells. The results obtained herein are of value to real engineering problems. Especially, the evolution of transient state MDFs may be difficult to obtain with other conventional methods.

Acknowledgments

This work is supported by the National Natural Science Foundation of China (NSFC) under the grant No. 11332008

References

[1] Friedman Y., Sandler U.: Evolution of Systems under Fuzzy Dynamic Laws. *Fuzzy Sets and Systems* **84**:61-74, 1996.

[2] Hong L., Jiang J., Sun J.Q.: Response Analysis of Fuzzy Nonlinear Dynamical Systems. *Nonlinear Dynamics* **78**:1221-1232, 2014.

SYNCHRONIZATION OF SELF-INDUCED FRICTION OSCILLATORS

Michal Marszal & Andrzej Stefański
Division of Dynamics, Lodz University of Technology, Lodz, Poland

Summary In this paper, the synchronization properties of self-induced dry friction oscillators coupled in array are investigated. As a research tool which allows one to predict the synchronization thresholds, the method called master stability function is applied. It is realized in the form of the reference probe of two coupled oscillators. Our results demonstrate that this technique can be successfully applied for such strongly non-smooth systems with discontinuities.

INTRODUCTION

Phenomenon of synchronization can be defined as a correlation (adjustment) in time of two or more different processes. Collective motion of dynamical systems has been known for a long time, i.e., since the second half of 17th century, when Christian Huygens observed that two pendulum clocks hanging at the same beam can synchronize in phase [1]. Next, this phenomenon has been observed and investigated in various types of mechanical or electrical systems [2]. Recently, the idea of synchronization has taken a more interdisciplinary character as a powerful basic concept in nature regulating a large variety of complex processes [3].

A concept called master stability function (MSF) is a useful tool to determine the complete synchronization (CS) thresholds for different coupling configuration of identical oscillators [4]. In general, we can define the MSF as a surface of the largest transversal Lyapunov exponent (TLE) over the complex numbers plane (α, β) representing arbitrary eigenvalue γ of the connectivity matrix $\mathbf{G}_n$ (see Sec. II), where $\alpha = \sigma\mathrm{Re}(\gamma)$ and $\beta = \sigma\mathrm{Im}(\gamma)$. In mechanical oscillators one has mutual and symmetrical interaction yielding to real coupling, i.e. $\beta = 0$. Then the MSF is a function of the real number α, such that

$$\alpha = \sigma\gamma \tag{1}$$

If all the eigenmodes corresponding to discrete spectrum of eigenvalues $\sigma\gamma_i$ (i = 1, ..., n) of the can be found in the ranges of negative TLE then the synchronous state is stable. According to the idea of two oscillators probe these synchronous ranges of α are approximated (via relation (1)) by corresponding σ-intervals of zero synchronization error [5]. Concluding, results obtained for a pair of oscillators allow us to approach possible synchronization ranges for any configuration of coupled oscillators.

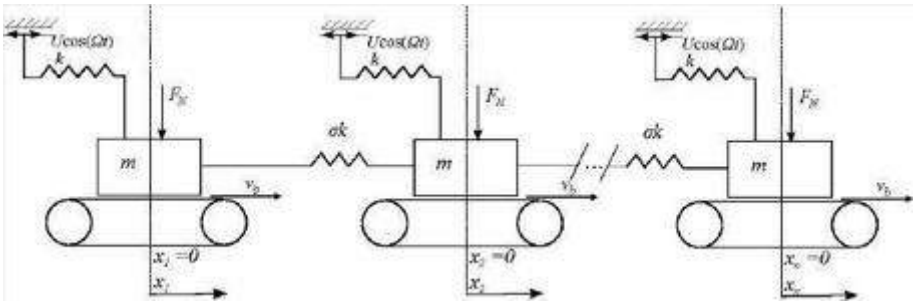

Figure 1. Array of friction oscillators coupled by springs

MODEL

Consider an array composed of forced stick-slip friction oscillators shown in Fig. 1. A single oscillator is described by the following equation

$$m\ddot{x} = -k(x - U\cos\Omega t) + F_N f(v_r), \tag{2}$$

where k is the stiffness constant, U amplitude of kinematic excitation, Ω forcing frequency, F_N normal load force, $v_r = v_b - \dot{x}$ is a relative velocity between the contact surfaces and $f(v_r) = \left(\mu_k + (\mu_s - \mu_k)\exp(-a|\vartheta|)\right)\mathrm{sgn}\,\vartheta$ represent assumed friction characteristic. Introducing $\omega_0 = \sqrt{k/m}$, static deflection $x_0 = g/\omega_0^2$, dimensionless time $\tau = \omega_0 t$ and the following substitutions: $\omega = \Omega/\omega_0$, $u = U/x_0$, $\varepsilon = F_N/mg$, $\vartheta_b = \vartheta_b/x_0\omega_0$, $\vartheta = \vartheta_b - \dot{y}$ we obtain dimensionless equations of friction oscillators array in form

[a] Corresponding author. Email: steve@p.lodz.pl.

$$\begin{Bmatrix} \ddot{y}_1 \\ \vdots \\ \ddot{y}_n \end{Bmatrix} = -\begin{Bmatrix} y_1 \\ \vdots \\ y_n \end{Bmatrix} + \sigma \mathbf{G}_n \begin{Bmatrix} y_1 \\ \vdots \\ y_n \end{Bmatrix} + \begin{Bmatrix} \varepsilon f(\vartheta_1) + u\cos\omega\tau \\ \vdots \\ \varepsilon f(\vartheta_n) + u\cos\omega\tau \end{Bmatrix}, \quad \text{where} \quad \mathbf{G}_n = \begin{pmatrix} -1 & 1 & \dots & 0 \\ 1 & -2 & \dots & 0 \\ \vdots & \vdots & \ddots & \vdots \\ 0 & 0 & \dots & -1 \end{pmatrix} \tag{3}$$

is a the connectivity matrix defining the structure of array connections. Coupling coefficient σ defines the overall strength of the coupling.

RESULTS

Let us consider the array composed of four coupled oscillators. For the assumed driving frequency ω = 1.40 the single oscillator operates in chaotic regime. Other parameters are: ϑ=0.1, μ_s=0.3, μ_k=0.15, a=2.5, ε=2.0, u=0.1. In Fig. 2 the MSF, represented by synchronization error $e_{II}(\alpha)$ calculated from two oscillators probe, is projected via eigenvalues of connectivity matrix $\mathbf{G}_4$ on the bifurcation diagram of average synchronization error e_{IV} evaluated for four coupled oscillators. Synchronization error $e_{II}(\sigma)$ is scaled according to Eq.(1) by absolute value of non-zero eigenvalue of connectivity matrix $\mathbf{G}_2$ (i.e $|\gamma_1| = 2$) in order to obtain $e_{II}(\alpha)$ function. This function is plotted vertically on top left part of Fig. 2, whereas eigenvalues spectrum $|\sigma\gamma_i|$ on top right. At the bottom, average synchronization error for four coupled oscillators as a function of coupling strength σ is presented. The synchronization occurs if all eigenmodes corresponding to the discrete spectrum of eigenvalues are found in the ranges of zero synchronization error for two oscillators test probe (horizontal grey regions in Fig. 1). As one can see in Fig. 2, synchronization of four oscillators occurs only in very narrow interval of σ, i.e. $0.153 \geq \sigma \geq 0.177$, where all three eigenvalues are located in the α-region of zero error $e_{II}(\alpha)$. Thus, knowing beforehand the synchronization thresholds for two oscillators probe, we are able to predict synchronization thresholds for longed chains of oscillators.

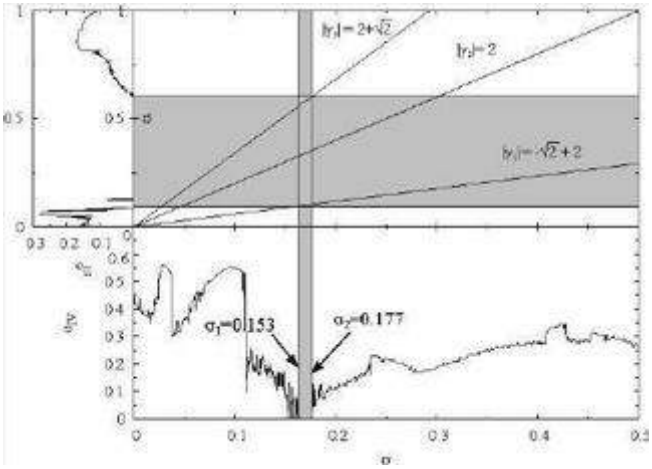

Figure 2. The MSF $e_{II}(\alpha)$ projected onto average synchronization error for three coupled self-induced dry friction oscillators via eigenvalues of connectivity matrix, for excitation angular frequency ω = 1.40. Synchronous regions are depicted with grey.

CONCLUSIONS

We investigated the synchronization properties of coupled self-induced dry friction oscillators. The array of four oscillators coupled by linear springs was analyzed in order to determine the synchronization thresholds using the MSF approach, basing on synchronization error of two oscillators probe. Our results confirmed that this technique can be successfully applied for the networks of strongly non-smooth dynamical systems.

This study has been supported by the Polish National Centre of Science (NCN) under Project no. 2012/06/A/ST8/00356.

References

[1] C. Huygens, Horologium Oscillatorium (Apud F. Muquet, Parisiis, 1673).
[2] B. van der Pol, Radio Rev. 1, 701 (1920).
[3] A. Pikovsky, M. Rosenblum J. Kurths, Synchronization: a Universal Concept in Nonlinear Science (Cambridge University Press, Cambridge, 2010).
[4] L.M. Pecora, T.L. Carroll, Phys. Rev. Lett. 80, 2109 (1998).
[5] K.S. Fink, G. Johnson, T. Carroll, D. Mar, L. Pecora, Phys. Rev. E 61, 5080 (2000).

NONLINEAR SPATIO-TEMPORAL DYNAMICS OF AN ELASTIC PANEL IN UNIFORM LAMINAR FLOW

Alex Kleiman & Oded Gottlieb[1a)]
[1]*Department of Mechanical Engineering, Technion-Israel Institute of Technology, Haifa, Israel*

Summary We formulate an initial-boundary-value problem that consistently couples an elastic field for a panel immersed in a two-dimensional viscous compressible fluid field. A finite-difference numerical solver is formulated to investigate strongly nonlinear spatio-temporal fluid-structure interaction in uniform compressible laminar flow (100<Re<1000). The investigation reveals a complex bifurcation structure that includes quasiperiodic and chaotic-like non-stationary limit-cycles that evolve from stability loss of periodic ultra-sub-harmonic solutions. These bifurcations correspond to transitions in wake formations and transitions between two distinct fluctuation modes.

The field of fluid-structure interaction (FSI) incorporates a wide range of phenomena that are of great scientific and engineering interest in various disciplines, including aerospace and ocean engineering, biology, energy harvesting, heat removal and acoustics. The essence of this interaction is in the information transfer between the structure and the surrounding fluid, where the fluid exerts a load on the structure, which in turn complies and disturbs the flow in its vicinity. One of the highly investigated FSI problems is the complex motion of an elastic rectangular panel immersed in a uniform stream parallel to the longitudinal panel direction [1]. In spite of the comprehensive research done to-date, there are large discrepancies between documented experiments and the outcome of proposed simplistic analytical models [2]. Moreover, the existing numerical analytical and computational studies lack the full insight of the complex physical bifurcation structure which includes non-stationary dynamics and culminating with a possible chaotic spatio-temporal complexity.

We thus consistently formulate an initial-boundary-value problem that incorporates a two-dimensional viscous compressible fluid field described by the Navier-Stokes equations and an extensible Euler-Bernoulli elastic panel truncated to cubic order (Fig.1-left). Following [3] we implement a first-order loose coupling where the structure and fluid are solved alternatively by a fluid and structural solvers respectively. The fluid filed is solved via a Beam-Warming finite-difference scheme whereas the structure is solved using a fourth-order Runge-Kutta method [4]. Validation of the FSI solver is done by comparison to results obtained for an elastic panel both the flutter (Hopf) and a secondary bifurcation thresholds (Fig.1-middle) where periodic limit-cycle solutions become aperiodic, is consistent with the curve-fitting thresholds obtained in [5] as a function of both Reynolds number (100<Re<1000) and mass ratio (0<m*<0.3). A characteristic bifurcation diagram (Fig.1-right) depicts the free-edge amplitude ($A_{w)}$ vs. the mass ratio for Re=750 which includes steady solutions (region I), periodic limit-cycles (region II), quasiperiodic (region III) and non-stationary chaotic-like (region V) solutions that are separated by an ultra-sub-harmonic (m/n=5/3) solution (region IV).

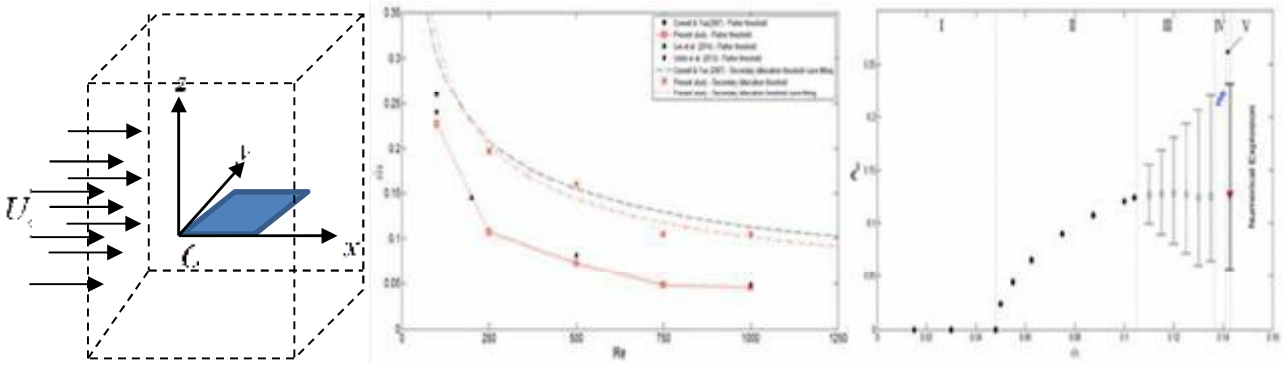

Figure 1: Elastic panel definition sketch (left), stability map (middle), bifurcation diagram (right).

The panel position snapshots for constant time-stepping intervals (Fig.2) reveals for Re=1000 a growing spatio-temporal complexity for increasing mass ratios. The periodic solution (m*=0.1) reveal an organized multi-mode spatial motion (Fig.2-left) whereas the quasiperiodic (m*=0.125) and non-stationary (m*=0.131) solutions reveal an irregularity with alternating spatio-temporal complexity which is more extensive for the chaotic-like oscillations (Fig.2-right).

a) Corresponding author. Email: oded@technion.ac.il

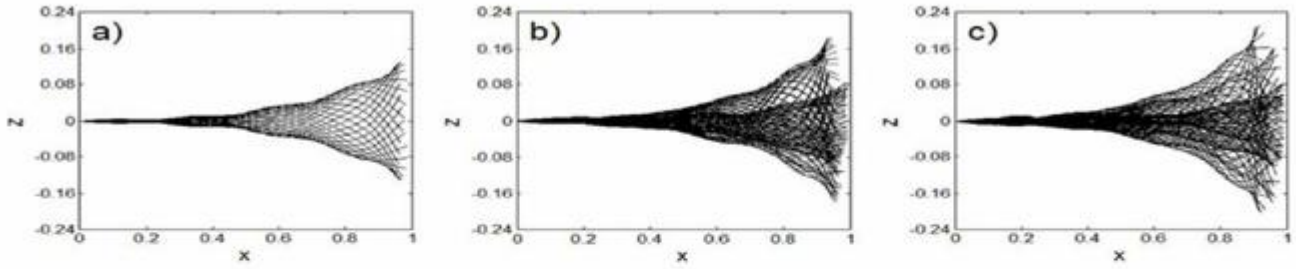

Figure 2: Panel position: periodic (left), quasiperiodic (middle), non-stationary (right).

.

The non-stationary temporal behaviour (Fig.3) is demonstrated for Re=1000 and m*=0.131 via the panel edge time-series (Fig3-left), its wide-banded power spectra (Fig.3-middle) and irregular state-space overlaid with a stroboscopic sampled Poincare' map (Fig.3-right) that is the outcome of torus breakdown.

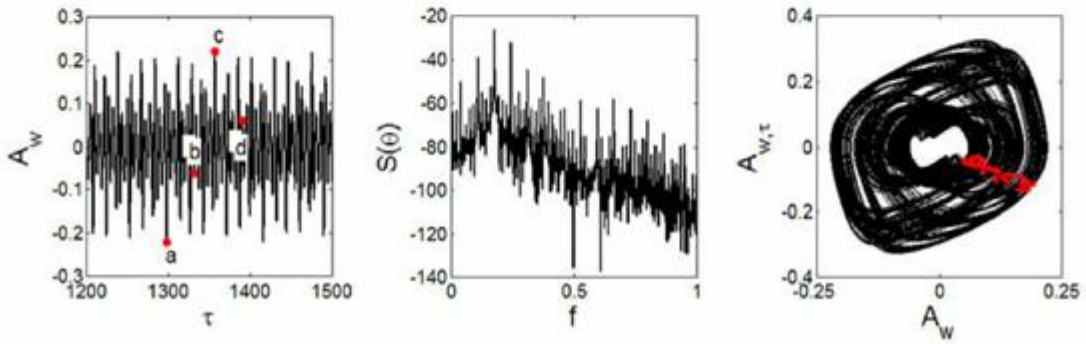

Figure 3: Chaotic time-series (left), power spectra (middle), overlaid state-space and Poincare' map (right).

The vorticity field snapshots (Fig.4) of the non-stationary solution (Re=1000, m*=0.131) reveal that the fluid dynamics is governed by an intermittent "2P" vortex shedding formation. This behaviour includes interplay between primary and secondary vortices which are governed by different distinct frequencies.

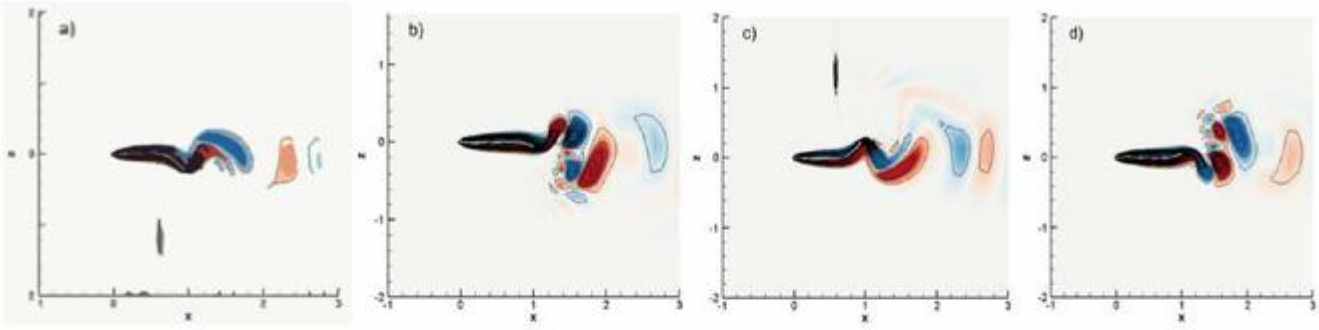

Figure 4: Snapshots of vorticity (corresponding to selected times denoted in Fig.3 left).

The results of this investigation reveal a complex bifurcation structure that includes quasiperiodic and non-stationary chaotic-like limit-cycles that are foliated with periodic ultra-sub-harmonic solutions. These bifurcations correspond to transitions in wake formations, and transitions between two distinct fluctuation modes.

References

[1] Alben, S.: Physics of Fluids, 27, 033603, 2015.

[2] Gibs C.S., Wang, I., Dowell, E.H.: Journal of Fluids and Structures, 34, 68-83, 2012.

[3] Aginsky Z., Gottlieb, O.: Physics of Fluids, 25, 076104, 2013.

[4] Gendel S., Gottlieb O., Degani D.: AIAA Journal, 53, 5, 1309-1318, 2015.

[5] Connell B.S.H. , Yue, D.K.P.: Journal of Fluid Mechanics, 581, 33-67, 2007.

NONLINEAR VIBRATIONS OF ELASTICALLY SUPPORTED CYLINDER MOVING IN THE FLUID FLOW

Ekaterina Pavlovskaia *[1], Andrey Postnikov[1], and Marian Wiercigroch[1]
[1]*Centre for Applied Dynamics Research, School of Engineering, Aberdeen University, King's College, Aberdeen, AB24 3UE, Scotland, UK*

Summary In this paper nonlinearities in the fluid-structure interactions of an elastically supported cylinder moving in the uniform fluid flow are discussed. A new two degrees-of-freedom wake oscillator model [1, 2] is utilised to describe vortex-induced vibrations of elastically supported cylinders capable of moving in cross-flow and in-line directions. Total hydrodynamic force acting on the cylinder is obtained here as a sum of lift and drag forces, which are defined as being proportional to the square of the magnitude of the relative flow velocity around the cylinder. The two van der Pol type oscillators are then used to model fluctuating drag and lift coefficients. The resulting equations of motions of the cylinder in cross-flow and in-line directions are coupled through the fluid forces. Experimental data and Computational Fluid Dynamics (CFD) results are used to calibrate the proposed model and to verify the obtained predictions of complex fluid-structure interactions for different mass ratios.

INTRODUCTION

As offshore oil and gas fields are moving into deeper waters, the nonlinearities in the slender marine structures such as risers, mooring cables and umbilicals, and the fluid-structure interaction phenomena such as vortex induced vibrations (VIVs) become more and more important. Many of VIV aspects still require further advanced modelling to investigate the impact of the phenomenon which significantly affects the service life of marine structures. This work is motivated by the need of industry to predict loads and fatigue damage on riser systems, especially most common Top Tensioned Risers (TTRs) and Steel Catenary Risers (SCRs). Accurate prediction of VIVs can help to produce more robust structural design and lead to substantial savings in the offshore applications. Although the problem of vortex-induced vibrations could be addressed by different approaches, which include experimental studies, computational fluid dynamics modelling and analytical models, in present work, we focus on analytical model known as wake oscillator model.

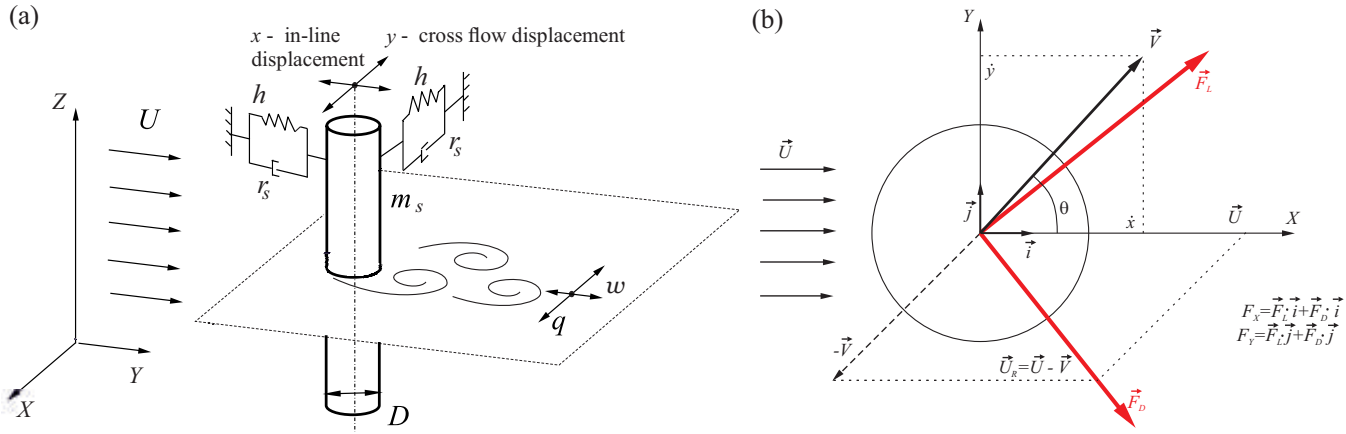

Figure 1: (a) Wake oscillator model for the cylinder moving in transversal and in-line directions; (b) Fluid forces acting on the structure [3]. Drag force $\vec{F}_D$ acts in line with relative stream velocity $\vec{U}_R$ and lift force $\vec{F}_L$ acts in perpendicular direction.

MATHEMATICAL MODELLING

In this work we consider an elastically supported cylinder experiencing VIV shown in figure 1(a), that is free to vibrate in cross-flow and in-line directions. As discussed in [1, 2], for a cylinder capable of oscillating in both directions, the equations of motion on an XY plane in terms of the displacements in in-line and cross-flow directions, x and y, are

$$m^\star \ddot{x} + r_s \dot{x} + hx = F_X, \tag{1}$$

$$m^\star \ddot{y} + r_s \dot{y} + hy = F_Y, \tag{2}$$

where the total hydrodynamic force components in X and Y directions are F_X and F_Y. Here $m^\star$ is mass per unit length including an added mass $m^\star = m_s + \frac{1}{4}\pi C_M \rho_f D^2$, r_s is structural damping, and h is stiffness of the support.

*Corresponding author. Email: e.pavlovskaia@abdn.ac.uk

This total hydrodynamic force, $\vec{F} = F_X\vec{i} + F_Y\vec{j}$, is the result of the actions of the sectional vortex-induced drag $\vec{F}_D$ and lift $\vec{F}_L$ forces which are shown in figure 1(b). As can be seen from this figure, the drag force $\vec{F}_D$ is acting along the velocity, $\vec{U}_R = \vec{U} - \vec{V}$ which is the fluid velocity relative to the cylinder ($\vec{V}$ is velocity of the cylinder and $\vec{U} = U\vec{i}$ is the velocity of the flow). The lift force $\vec{F}_L$ is then acting in the perpendicular directions and the magnitudes of lift and drag forces depends on the magnitude of relative velocity $\vec{U}_R$ $\left(|\vec{U}_R| = \sqrt{(U-\dot{x})^2 + \dot{y}^2}\right)$:

$$\vec{F}_D = \frac{1}{2}\rho_f C_D D|\vec{U}_R|^2 \frac{\vec{U}_R}{|\vec{U}_R|}, \qquad \vec{F}_L = \frac{1}{2}\rho_f C_L D|\vec{U}_R|^2 \frac{\dot{y}\,\vec{i} + (U-\dot{x})\vec{j}}{|\vec{U}_R|}. \tag{3}$$

Here the parameters are ρ_f, the fluid density, C_L, lift coefficient, and $C_D = C_{D_0} + C_D^{fl}$, total drag, which can be represented as a sum of constant mean sectional drag C_{D_0} and fluctuating drag, C_D^{fl}. Following the approach employing nonlinear oscillator equations of the van der Pol type (see for example [4]), the fluctuating lift C_L and drag C_D^{fl} coefficients could be modeled by two wake oscillators using q and w variables ($q = 2C_L/C_{L_0}$ and $w = 2C_D^{fl}/C_{D_0}^{fl}$). Thus the system can be described by the following set of the equations where the acceleration coupling recommended by Facchinetti *et. al* [5] was adopted in the wake oscillator equations:

$$(m_s + \frac{1}{4}\pi C_M \rho_f D^2)\ddot{x} + r_s\dot{x} + hx = \sqrt{(U-\dot{x})^2 + \dot{y}^2}\Big(\frac{1}{4}\rho_f C_{L_0} qD\dot{y} + \frac{1}{2}\rho_f (C_{D_0} + \frac{1}{2}C_{D_0}^{fl} w)D(U-\dot{x})\Big), \tag{4}$$

$$(m_s + \frac{1}{4}\pi C_M \rho_f D^2)\ddot{y} + r_s\dot{y} + hy = \sqrt{(U-\dot{x})^2 + \dot{y}^2}\Big(\frac{1}{4}\rho_f C_{L_0} qD(U-\dot{x}) - \frac{1}{2}\rho_f (C_{D_0} + \frac{1}{2}C_{D_0}^{fl} w)D\dot{y}\Big), \tag{5}$$

$$\ddot{w} + 2\Omega_F \varepsilon_x (w^2 - 1)\dot{w} + 4\Omega_F^2 w = (A_x/D)\ddot{x}, \tag{6}$$

$$\ddot{q} + \varepsilon_y \Omega_F (q^2 - 1)\dot{q} + \Omega_F^2 q = (A_y/D)\ddot{y}. \tag{7}$$

The developed equations of motion (4)-(7) describe the vibrations of the cylinder in the fluid flow. However, a careful calibration of the model is required and specifically empirical wake oscillators equations parameters A_x, A_y, ε_x and ε_y need to be found. In case of a single degree-of-freedom system, numerical results by Facchinetti [5] where fitted against experimental data, with A_y and ε_y estimated as 12 and 0.3 respectively. However, further investigation and calibration for 2DOF models are essential. It should be noted that in general these coefficients may be a function of various parameters of the system such as mass ratio, damping ratio, reduced velocity, added mass coefficient, Reynolds number, etc.

In this study, first, the published experimental results were utilised to calibrate the proposed wake oscillator model. Three sets of experimental data [6, 7, 8] were considered, and comparisons are made for different mass-damping ratio parameters. Then, CFD model has been created in ANSYS Fluent 12.0.16 utilizing User Defined Functions (UDFs) in order to compute the displacement of the cylinder on each time step based on the forces obtained from the dynamic pressure. Relatively low Reynolds numbers (600 to 2000) were considered for the sake of simplicity. However, even for these low Reynolds numbers ($Re > 300$) the vortex street is turbulent, and a high quality grid is required for solution to converge. The results of the simulations and comparisons with both experimental data and CFD calculations will be presented in this paper.

CONCLUSIONS

In this paper nonlinearities in the fluid structure-interactions of an elastically supported cylinder moving in the uniform fluid flow are discussed utilising new two degrees-of-freedom wake oscillator model. Equations of motion of the cylinder in cross-flow and in-line directions are coupled through the fluid forces calculated from the instantaneous relative flow velocity around the cylinder. This description of the fluid forces allows one to generalise the problem statement for the flexible structure and conduct the analysis similar to transversal vibration case considered in [3].

References

[1] Postnikov, A.: Wake Oscillator and CFD in Modelling of VIVs. PhD Thesis, School of Engineering, University of Aberdeen, UK, 2015.

[2] Postnikov, A., Pavlovskaia, E., and Wiercigroch, M.: 2DOF CFD Calibrated Wake Oscillator Model to Investigate Vortex-Induced Vibrations, submitted 2015.

[3] Pavlovskaia, E., Keber, M., Postnikov, A., Reddington, K. and Wiercigroch, M.: Multi-Mode Modelling of Vortex-Induced Vibration, International Journal of Nonlinear Mechanics, in press 2015.

[4] Bishop, R.E.D., Hassan, A.Y.: The Lift and Drag Fores on a Circular Cylinder in a Flowing Field, Proc. Roy. Soc. (London) Ser. A 277:51-75, 1964.

[5] Facchinetti M.L., de Langre E., Biolley F.: Coupling of Structure and Wake Oscillators in Vortex-Induced Vibrations, Journal of Fluids and Structures 19:123-140, 2004.

[6] Williamson, C.H.K., Jauvtis, N.: A Hight-Amplitude 2T Mode of Vortex-Induced Vibration for a Light Body in XY Motion, European Journal of Mechanics B/Fluids 23:107-114, 2004.

[7] Stappenbelt, B., Lalji, F., Tan, G.: Low Mass Ratio Vortex-Induced Motion:, The 16th Australian Fluid Mechanics Conference, Gold Coast, Australia, 1491-1497, 2007.

[8] Williamson, C.H.K., Jauvtis, N.: The Effect of Two Degrees of Freedom on Vortex-Induced Vibration at Low Mass and Damping", J. Fluid Mech. 509:23–62, 2004.

NONLINEAR DYNAMICS OF AN ELECTRO-MECHANICAL SYSTEM: NUMERICAL AND EXPERIMENTAL STUDY

Francesco Romeo [*1] and Ioannis Georgiou[2]
[1]*Department of Structural and Geotechnical Engineering, SAPIENZA University of Rome, Rome, Italy*
[2]*Naval Architecture and Marine Engineering School, National Technical University of Athens, Athens, Greece*

Summary The dynamic behavior of an electro-mechanical coupled system excited by harmonic voltage is numerically and experimentally studied. The system governing equations involve coupling quadratic nonlinearity; as a result, the obtained numerical and experimental results show the occurrence of the non-linear resonance related to the current quadratic nonlinearity and a jump, after which the mass of the mechanical oscillator undergoes large amplitude oscillations and coexisting attractors appear.

INTRODUCTION

The dynamic experimental response of a system in which a mechanical linear oscillator is nonlinearly coupled to a linear electric circuit through an electromagnet is studied. Previous analytical and numerical studies were carried out by the authors on this type of multi-physics system [1]. According to these studies, when the mechanical oscillator is excited via harmonic voltage applied to the electric circuit, interesting nonlinear phenomena arise such as the non-linear resonance related to the current quadratic nonlinearity which imposes a natural linear resonance at half the frequency of the linear oscillator, jump phenomena and transitions to complex chaotic interaction dynamics. The experimental investigations here presented aims at validating these theoretical findings.

ELECTRO-MECHANICAL MODEL

The system consists of a linear oscillator coupled nonlinearly through an electromagnet to a linear electric circuit. The motion is governed by the following two coupled differential equations:

$$\begin{array}{c} x + 2\zeta_m\omega_m x + \omega_m^2 x = \epsilon\alpha\dot{q}^2 + f \\ (1 + \alpha x\ q + (2\zeta_e\omega_e + \alpha x\ q + \omega_e^2 q = \ \hat{} \end{array} \tag{1}$$

in which m, c, k denote mass, dissipation and stiffness parameters of the linear oscillator and L, C, R denote the inductance, capacitance, and resistance of the electrical circuit. The variables x and q denote the mechanical and electrical displacement (charge), respectively. The velocity of the mass and the electric current are $v \equiv \dot{x}, i \equiv \dot{q}$, respectively; f and e denote external mechanical forcing and voltage excitation. The inductance is approximated by $L(x) = L_0 + L_1 x$. The remaining parameters are defined as: $\omega_m^2 \equiv \frac{k}{m}$, $\omega_e^2 \equiv \frac{1}{L_0 C}$, $\zeta_m \equiv \frac{c}{2\sqrt{km}}$, $\zeta_e \equiv \frac{R\sqrt{C}}{2\sqrt{L_0}}$, $\epsilon \equiv \frac{L_0}{2m}$, $\alpha \equiv \frac{L_1}{L_0}$, $f \equiv \frac{f}{m}$, $\hat{} \equiv \frac{e}{L_0}$,$\mu \equiv \omega_m/\omega_e$. Therefore the considered multi-physics coupled system is a nonlinear dynamical system with its coupling nonlinearity stemming from the dependence of the inductance on the metallic mass displacement. The interest lies in investigating how the mechanical

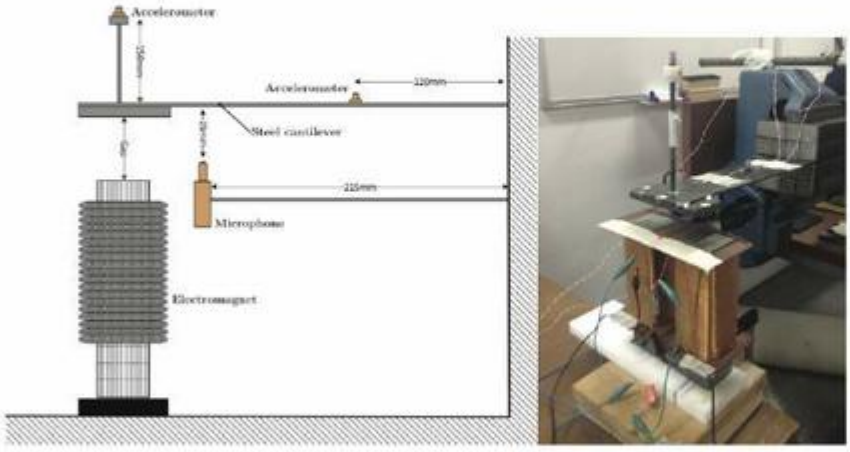

Parameter	Symbol	Num.	Exp.
Singular parameter	μ	0.2	0.021
Mechanical dissipation factor	ζ_m	0.01	0.01
Electrical dissipation factor	ζ_e	0.1	0.0011
Electro-mechanical coupling	ϵ	5.0	0.34
Inductance nonlinearity	α	10.0	-

Figure 1: Experimental setup of the electro-mechanical system and parameters of the numerical and experimental tests.

*Corresponding author. Email: francesco.romeo@uniroma1.it

part will respond when it is actuated by the electrical part. Previous Slow Invariant Manifold analytic approximations and numerical investigations [1] have shown that the system has a slow periodic response over a well-defined region of the forcing parameters. This region starts from low frequencies and includes the frequency at which the linear system undergoes a resonance due to the presence of the quadratic nonlinear dependence on the current. At some critical value depending on μ the amplitude-frequency response loses its smoothness via bifurcation mechanism that creates a finite jump.

NUMERICAL AND EXPERIMENTAL RESULTS

In Figure 1 the experimental realization of the above described coupled dynamical system is shown through a sketch and a picture. The experimental setup located in the Nonlinear Dynamics Lab at N.T.U.A. consists of the following components: electromagnet, steel cantilever beam, two acceleration sensors, sound measurement sensor, electric current recording sensor, frequency generator, power and sensor signal amplifiers. The experimental tests have been carried out by applying a constant voltage amplitude of 25 V and performing quasi-static forward and backward frequency sweeps. Different values of gap between the surface of the electromagnet and the cantilever tip were investigated in order to tune the strength of the nonlinear coupling. In the numerical and experimental investigations the system parameters are set as reported in Figure 1.

Figure 2a shows the numerical frequency-mechanical response amplitude plot. The different branches corresponding to forward and backward sweeps show how the coupling nonlinearity affects the dynamics. As shown in [1], starting from $\Omega = 2.5$, as the frequency decreases the upper branch of the period-1 attractor grows until an instability is reached around $\Omega = 1.55$. At the critical frequency $\Omega = 0.966$ (dashed red line) the period-1 attractor suffers an abrupt downwards finite jump; afterwards, the lower branch shows the resonance around $\Omega = 0.5$ (dashed blue line). The experimental results are

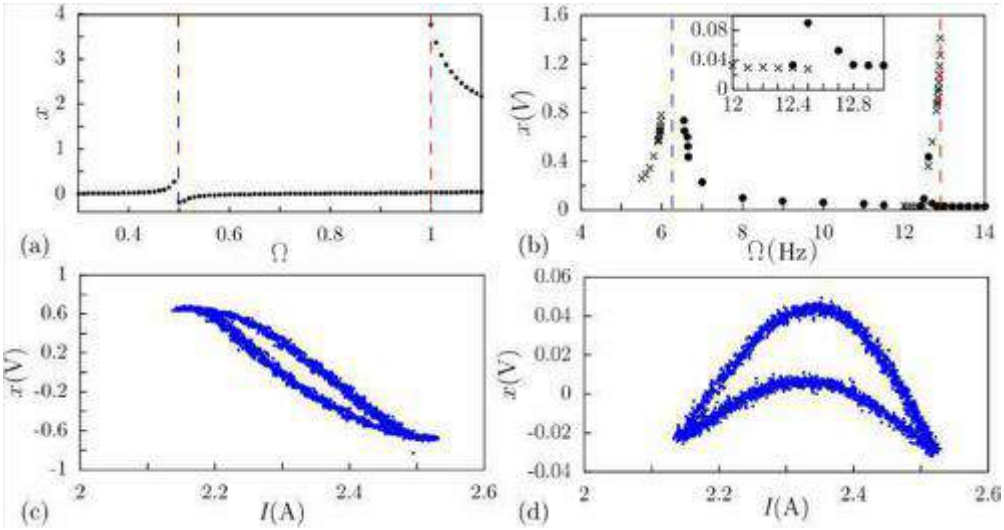

Figure 2: Numerical (a) and experimental (b) oscillator frequency-amplitude plots (forward (x) and backward (•) frequency sweep). (c)-(d) Experimental coexisting attractors on the current-mechanical displacement plane (I-x).

shown in Figure 2b; the qualitative agreement with the numerical results obtained by direct numerical integration of (1) can be seen in terms of both, the non-linear resonance related to the current quadratic nonlinearity, which imposes a natural linear resonance at half the frequency of the linear oscillator given by $\Omega = 6.4$ Hz (dashed blu line) and a jump at the cantilever natural frequency occurring at $\Omega = 12.86$ Hz (dashed red line). The coexistence of (at least) two periodic attractors can be seen by the experimental phase portraits reported in Figures 2c,d for $\Omega = 12.7$ Hz.

CONCLUSIONS

The dynamics of a coupled nonlinear electro-magneto-mechanical system was addressed by means of numerical and experimental approaches. The numerical predictions obtained via Poincaré mappings were qualitatively validated experimentally in a cantilever steel beam coupled to an electromagnet driven by harmonic voltage.

References

[1] Georgiou, I. T., Romeo, F.: Multi-physics Dynamics of a Mechanical Oscillator Coupled to an Electro-magnetic Circuit. Int. J. Nonl. Mech. 70, 153-164, 2015.

INFLUENCE OF TEMPERATURE ON MIDDLE EAR WITH SHAPE MEMORY PROSTHESIS

Rafal Rusinek[1], Jerzy Warminski[1], Marcin Szymanski [2]
[1]*Department of Applied Mechanics, Mechanical Engineering Faculty, Lublin University of Technology, Nadbystrzycka 36, 20-618 Lublin, Poland*
[2]*Department of Otolaryngology Head and Neck Surgery, Medical University of Lublin Jaczewskiego 8, 20-854 Lublin, Poland*

Summary The paper presents some dynamical aspects of dynamics of a human middle ear reconstructed by means of a prosthesis made of shape memory alloy. A two degrees of freedom nonlinear model is developed. On the base of the model a bifurcation analysis is performed and an influence of external excitation and temperature on system dynamics is presented.

INTRODUCTION

The human middle ear contains three ossicles: malleus, incus and stapes. The ossicles form a sound conduction system which transmits sound from the external ear to the fluids of the inner ear. The ossicles are connected to each other by incudomallear and incudostapedial joint. Such a complex bio-system is modelled in the literature from the last half century. The first study in this field was published in 1961 by Mőller [1] where also the first scheme of middle ear mechanism was proposed. Next, a similar model was investigated by Zwislocki [2]. In both publications, authors used an electrical circuit to analyse middle ear system. In the last decades mechanical models are developed where ossicles are represented by lumped masses, connected with springs and dashpots. In the literature, one can find three or four degrees of freedom (dof) model and sometimes even six dof but always they are linear. Usually these models focus only on kinematics of an intact middle ear however hardly ever, dynamics models are built.

Moreover, in medicine practice middle ear can be damaged e.g. by chronic otitis media. In this case usually middle ear prostheses is applied to reconstruct connection between stapes and malleus or tympanic membrane. Therefore, here a nonlinear model of reconstructed middle ear with shape memory prosthesis is proposed. Next, an influence of temperature on a reconstructed middle ear behaviour is analysed.

MIDDLE EAR MODEL

Adjustment of the prosthesis size and location is one of the main problem occurring during surgery operation. Therefore, a new concept of shape memory prosthesis (AMP) is proposed here to improve a process of implementation in a human body. The SMP can be made of shape memory alloy (SMA) which characteristic is given by the stress (σ) polynomial of the strain (ε) [3]:

$$\sigma = a_1\ T - T_M)\varepsilon - a_2\varepsilon^3 + a_5\varepsilon^5 \qquad (1)$$

where, a_1, a_2, a_3 are the material constants, T is temperature and T_M is phase temperature where martensite is stable.

Since, in most cases the incus is damaged and should be removed from ossicluar chain, the proposed model is nonlinear with 2dof presented in Fig.1

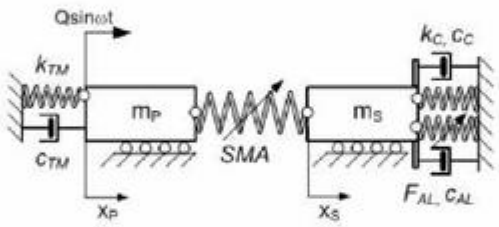

Fig.1: Two degrees of freedom model of middle ear with shape memory prosthesis.

The differential equations of motion, governing the model presented in Fig.1 is presented in the form

[a] Corresponding author. Email: r.rusinek@pollub.pl

$$m\ \ddot{x}\ +k\quad x_P+c\quad \dot{x}_P+\ _{SMA}=Q\sin\omega\tau$$
$$m\ \ddot{x}\ +\qquad +k\quad x\ +k_2\quad x^{\ 2}+k_3\quad x^{\ 3}+\quad \cdot\ +\quad \cdot\ -\ _{SMA}=0 \tag{2}$$

where, the spring force F_{SMA} *is* given as

$$F_{SMA}=a_1\ T-T_M\quad x_p-\ _s)-\ _2\quad _p-\ _s)^3+a_3\ x_p-\ _s)^5 \tag{3}$$

Dynamical behaviour of the stapes tested in the normal temperature of human body (36.6°C) is presented as a bifurcation diagram in Fig.2 showing different kind of possible solutions.

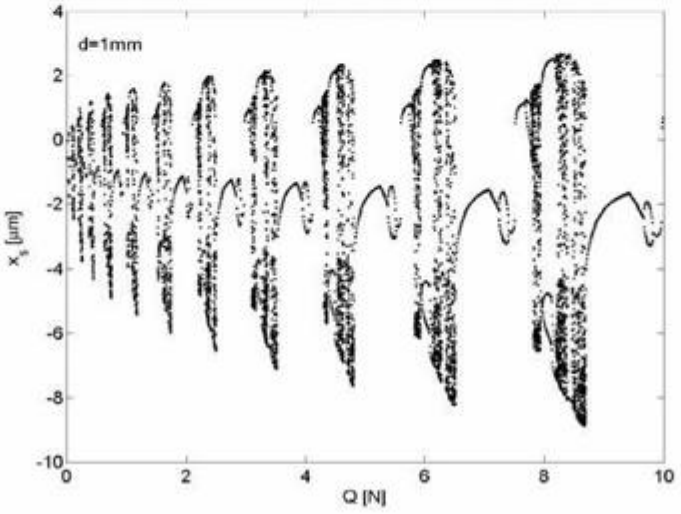

Fig.2: Bifurcation diagram of stapes vibrations versus excitation amplitude

More, examples will be given in a full paper (presentation).

CONCLUSIONS

- Smart prosthesis of human middle ear, made of shape memory alloy is an interesting alternative for classical prosthesis for the sake of possibility of easy adjustment its length and shape to individual medical case.
- Strong external excitation of middle ear system with the smart prosthesis generates irregular vibrations which lead to deterministic chaos.
- Behaviour of the SM prosthesis depends also on temperature and system nonlinearities.

Acknowledgement
The work is financially supported under the project of National Science Centre (Poland) no. 2014/13/B/ST8/04047.

References

[1] Moller A. R.: Network Model of the Middle Ear. *Journal of the Acoustical Society of America* **33:** 168–76, 1961
[2] Zwislocki J.: Analysis of the Middle-Ear Function. Part I: Input Impedance. *Journal of the Acoustical Society of America* **34:** 1514–23, 1962
[3] Paiva A., Savi M. A.: An overview of constitutive models for shape memory alloys. *Mathematical Problems in Engineering* **43:** 1–31, 2006

ASYMPTOTIC APPROACH TO FLUTTER CONTROL VIA HYSTERETIC ABSORBERS

Arnaldo Casalotti and Walter Lacarbonara *

Department of Structural and Geotechnical Engineering, Sapienza University of Rome, Rome, Italy

Summary The flutter control problem in long-span suspension bridges is discussed. A reduced-order bridge model (see Fig. 1) is augmented by the degree of freedom of a hysteretic mass nonlinearly tuned to mitigate the limit cycle oscillations (LCO) when the wind speed is above the flutter speed. The model comprises the plunge (vertical) and pitch (torsional) motions while the aerodynamic lift and moment are governed by a quasi-steady formulation. The restoring force of the absorber is characterized by linear and cubic elastic terms together with a hysteretic part governed by the Bouc-Wen model. The method of multiple scales is adopted to obtain an asymptotic approximation of the LCO behavior. An optimization procedure based on the Differential Evolutionary Algorithm is employed to obtain the set of constitutive parameters that lead to an optimal mitigation of the wind-induced oscillations.

INTRODUCTION

Flutter is an aerodynamic instability that affects real structures such as civil and military aircraft wings or long-span suspension bridges. A study on a lifting airfoil [1] revealed that the installation of a hysteretic vibration absorber allows to enhance the pre- and post-flutter behavior of the structure. In [2] the wind-induced oscillation problem was tackled in the context of long-span suspension bridges showing that the Hopf bifurcation due to the aerodynamic effects can be considerably shifted towards higher wind speeds by the introduction of multiple arrays of hysteretic mass dampers tuned to the lowest two flexural-torsional flutter modes.

Here, an asymptotic approach based on the method of multiple scales is applied to a bridge sectional model [3] and an additional hysteretic vibration absorber is added to provide proper control force and moment. The Bouc-Wen hysteresis flux law is solved analitically [4] and an optimization procedure based on the Differential Evolutionary Algorithm [5] is developed to obtain the set of absorber design parameters that lead to optimal flutter control.

EQUATIONS OF MOTION

The equations of motion for the sectional bridge model coupled with the hysteretic absorber can be expressed in nondimensional form as

$$\begin{aligned} &\mathbf{q} - \mathbf{p} \;/\; \mathbf{0}, \\ &\mathbf{M}_{\mathrm{a}}\mathbf{p} \quad \mathbf{C}_{\mathrm{a}}\mathbf{p} \quad \mathbf{K}_{\mathrm{a}}\mathbf{q} \quad \mathbf{n}_{\mathrm{k}} \;/\; -\epsilon^2\sigma_{\mathrm{u}}\,\bar{\mathbf{C}}_{\mathrm{a}}\mathbf{p} \quad \bar{\mathbf{K}}_{\mathrm{a}}\mathbf{q} \end{aligned} \tag{1}$$

where the vector $\mathbf{q} \;/\; h,\, \alpha,\, x$ lists the plunge h, the pitch angle α of the cross section and the absorber displacement x, and $\mathbf{p} \;/\; \mathbf{q}$ represents the velocities. To study the Hopf bifurcation and the associated LCOs, the wind speed is expressed as a perturbation of the critical speed according to $U \;/\; U_{\mathrm{c}} \quad \epsilon^2\sigma_{\mathrm{u}}$, where U_{c} is the flutter speed and ϵ is a small nondimensional ordering parameter. The subscript a denotes the fact that the aeroelastic effects were absorbed into $\mathbf{M}_{\mathrm{a}}$, $\mathbf{C}_{\mathrm{a}}$ and $\mathbf{K}_{\mathrm{a}}$ which thus represent the modified mass, damping and stiffness matrices, respectively, whereas $\bar{\mathbf{C}}_{\mathrm{a}}$ and $\bar{\mathbf{K}}_{\mathrm{a}}$ denote the perturbed damping and stiffness aerodynamic matrices. On the other hand, the vector $\mathbf{n}_{\mathrm{k}}$ collects the nonlinear terms due to the bridge structural quadratic and cubic nonlinearities and also to the VA hysteresis. According to [4], the hysteresis evolution law is solved analytically, and a Taylor series expansion yields the hysteretic force as a summation of linear, quadratic and cubic terms. These hysteretic terms are piece-wise continuous along the hysteresis cycle and the subscript k denotes the branch index (see the hysteresis loop in Fig. 1).

ASYMPTOTIC APPROACH AND OPTIMIZATION

The state-space coordinates are expressed according to the method of multiple scales as $\mathbf{q} \;/\; \sum_{i=1}^{3} \epsilon^i \mathbf{q}_{\mathrm{i}}\; t_0, t_2$ and $\mathbf{p} \;/\; \sum_{i=1}^{3} \epsilon^i \mathbf{p}_{\mathrm{i}}\; t_0, t_2$, where $t_0 \;/\; t$ and $t_2 \;/\; \epsilon^2 t$ are the fast and slow time scales, respectively. Under these assumptions, by collecting terms of like powers of ϵ, the typical hierarchy of perturbation problems is obtained. The unique aspect of the associated perturbation problems is the piece-wise nature of the inhomogeneous terms.

The linear problem coincides with the eigenvalue problem, which gives the critical flutter speed and the associated mode shape. The quadratic problem does not contain resonant terms, but only the terms due to the structural and hysteretic nonlinearities. The linear and quadratic solutions, substituted into the cubic problem, give rise to the resonant terms which are

*Corresponding author. Email: walter.lacarbonara@uniroma1.it

removed by the solvability conditions. Since the problem is piece-wise across the four branches of the hysteresis loop, the solvability conditions are enforced via the following integrals:

$$\sum_{k=1}^{4}\int_{\tau_k}^{\tau_{k+1}} \mathbf{w}^{\top}\mathbf{r}_3^{(k)}dt_0 = 0 \quad \text{and} \quad \sum_{k=1}^{4}\int_{\tau_k}^{\tau_{k+1}} \mathbf{w}^{\top}\bar{\mathbf{r}}_3^{(k)}dt_0 = 0 \tag{2}$$

where $\mathbf{r}_3^{(k)}$ represents the right-hand-side vector of the cubic problem on the kth branch; $\mathbf{w}$ is the solution of the adjoint problem and $\bar{}$ its complex conjugate; τ_k denotes the time instant within the linear oscillation period across the cycle which is associated with the characteristic displacements where velocity reversal or full unloading take place. Equations (2) represent the modulation equations governing the slow modulation of the amplitude and phase of the critical mode when the wind speed is in the neighborhood of the flutter condition. The modulation equations provide the bifurcation diagrams for the LCO.

An optimization procedure, based on the differential evolutionary algorithm [5], is employed to determine the optimal design parameters for the hysteretic absorber that shift the flutter condition to higher speeds and further minimize the LCO amplitude. The results on the flutter response shown in Fig. 1 demonstrate that the introduction of hysteresis has the ability to shift the flutter bifurcation to higher speeds and reduce the LCO amplitude. In particular, the linear VA shifts the critical speed by as much as 10% and reduces the LCO amplitudes by 33%, whereas the hysteretic VA has the ability to shift the flutter speed by at least 16% and reduce the LCO amplitudes by 50%.

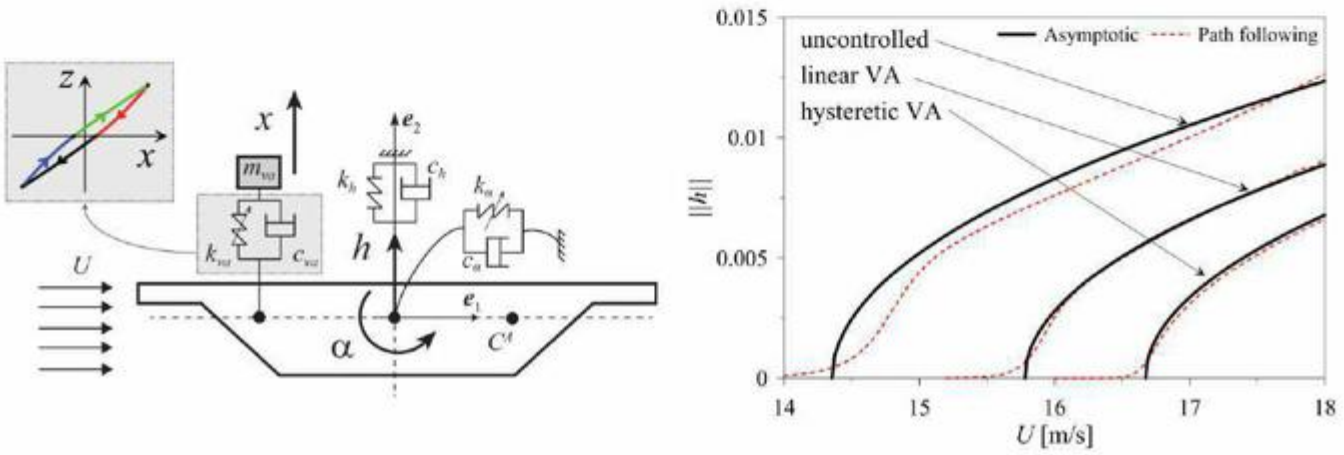

Figure 1: Left part: sectional bridge model endowed with the hysteretic vibration absorber. Inset (top left): hysteretic loop of the absorber where z represents the hysteretic part of the restoring force, the four branches are denoted by the red, black, blue and green lines. Right part: LCO bifurcation diagram of the uncontrolled system, system endowed with the linear VA or with the hysteretic VA. The red dashed lines represent the solution obtained numerically via path following, the black lines indicate the asymptotic solution.

CONCLUSIONS

The asymptotic procedure proposed here was proved to describe the response of the bridge sectional model in good agreement with the fully numerical solution, but the extreme rapidity and low cost associated with the use of the asymptotic solution in computing the objective function were critical to enhance the multi-parameter optimization procedure. Moreover, the results of such procedure allow also to show that the use of nonlinear hysteretic vibration absorbers lead to a considerable enhancement in the flutter oscillation mitigation task compared to the linear control systems performance.

References

[1] Lacarbonara W. and Cetraro M.: Flutter Control of a Lifting Surface via Visco-Hysteretic Vibration Absorbers. Int. J. of Aeronautical & Space Sci. 12:331-345, 2011.

[2] Casalotti A., Arena A., Lacarbonara W.: Mitigation of Post-Flutter Oscillations in Suspension Bridges by Hysteretic Tuned Mass Dampers. Eng. Struct. 69:62-71, 2014.

[3] Abdelkefi A., Vasconcellos R., Nayfeh A.H., Hajj M.R.: An Analytical and Experimental Investigation into Limit-Cycle Oscillations of an Aeroelastic System. Nonlinear Dyn. 71:159-173, 2013.

[4] Casalotti A. and Lacarbonara W.: Nonlinear Vibration Absorber Optimal Design via Asymptotic Approach. IUTAM 2015, in press.

[5] Storn R. and Price K.: Differential evolution - A Simple and Efficient Heuristic for Global Optimization over Continuous Spaces. J. Global Optim. 11:341-359.

DYNAMIC BEHAVIOR OF A TUNABLE MAGNETIC VIBRATION ABSORBER

Simon Benacchio[1], Arnaud Malher[1], Stefania Lo Feudo[1], Jean Boisson *[1], and C. Touzé[1]
[1]*IMSIA (Institute of Mechanical Sciences and Industrial Applications), ENSTA ParisTech - CNRS - EDF - CEA, 828 Bd des maréchaux, 91762 Palaiseau Cedex*

Summary A magnetic vibration absorber (MVA), completely relying on magnetic forces, is used to reduce the displacement of a vibrating structure. The distinctive feature of this absorber is the ability of tuning its linear stiffness together with its nonlinear cubic and quintic stiffnesses. Repulsive and corrective magnets are used to finely tune the values of these stiffness coefficients. A modelisation, relying on a multipolar expansion of the magnetic fields of each magnets, is used to predict the values of the stiffnesses from the geometry. Using only three geometrical parameters the MVA can be passively designed either as a nonlinear tuned vibration absorber (NLTVA), a nonlinear energy sink (NES), or a bi-stable absorber with negative linear stiffness.

INTRODUCTION

Due to its passive feature, the vibration mitigation of mechanical structures using vibration absorbers is an important solution for engineering issues. Linear vibration absorbers like the well-known Tuned-Mass Damper (TMD) [1, 2] have been studied for the vibration reduction of both linear undamped [3] and damped [4] primary structures (PS). However, the main drawback of the TMD is related to its narrow bandwidth of optimal control. To overcome this limitation a Nonlinear Energy Sink (NES) with an essentially nonlinear restoring force can be used. Having no natural frequency, the NES can thus adapt itself to the frequency of the PS [5, 6]. Another idea is to use the nonlinearity of the absorber in order to control the nonlinearity of the PS and has led to the concept of the nonlinear tuned vibration absorber (NLTVA). Recently, bi-stable vibration absorber devices have been investigated to make smaller the energy barrier required to activate the energy transfer between the PS and a NES [7]. If numerous experimental devices have been proposed to experiment these absorbers they are often designed for a specific application [8, 9, 10].

The proposed magnetic vibration absorber (MVA) has the ability of properly tuning its linear and nonlinear characteristics. Thus, this flexible device can be used either as an NES, an NLTVA, or a bi-stable vibration absorber, all these tunings being realized passively with a simple change in the geometry of the system. The experimental realisation of the MVA is presented in this paper. Then, preliminary results of the reduction of the PS vibration are presented when the MVA is tuned as an NLTVA, an NES and a bi-stable absorber.

THE MAGNETIC VIBRATION ABSORBER

The magnetic vibration absorber is shown in Fig. 1. It is composed of 7 permanent ring magnets. Their length, internal

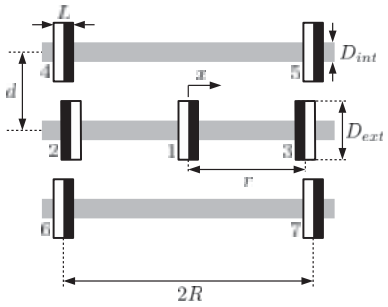

Figure 1: Diagram of the magnetic vibration absorber (MVA).

and external diameters are denoted L, D_{int} and D_{ext} respectively. Oscillating around the central position $x = 0$, the magnet 1 plays the role of the vibrating mass of the absorber. The other magnets (2, 3, 4, 5, 6 and 7) are fixed on plastic rods. The black and white parts of each magnet give the direction of their axial magnetisation. Magnets 2 and 3 are named the repulsive magnets since their magnetisation is the opposite of the magnetisation of the magnet 1. The amplitude of the repulsive force is tuned by modifying the geometric parameter r. Magnets 4, 5, 6 and 7 are named the corrective magnets since their magnetisation is the same that the magnetisation of the magnet 1. The amplitude of the corrective force is tuned by modifying

*Corresponding author. Email: jean.boisson@ensta-paristech.fr

the geometric parameters R and d. Therefore, the total force $\boldsymbol{F}_{\text{Tot}}$ applied on the mass of the MVA is tuned by the independent modifications of the geometric parameters r, R and d. Modeling the MVA using a multipolar expansion, this force can be written as

$$\boldsymbol{F}_{\text{Tot}}(x) \approx -K_1\, x - K_3\, x^3 - K_5\, x^5.$$

Modifying the geometric parameters r, R, and d, the linear, cubic and quintic stiffness terms can be tuned to change the properties of the MVA designing it as an NLTVA, an NES or a bi-stable absorber. More details about the design of the MVA can be found in [11].

VIBRATION MITIGATION

The MVA is then used to reduce the displacement of a plate selected as a PS vibrating with a large amplitude around one of its modal frequencies. Two opposite sides of the rectangular plate are clamped, whereas the other two are free. The device is attached to the PS and tuned successively as an NLTVA, an NES and a bi-stable absorber. Figure 2 shows the measured maximum displacement of the PS in each case and when the MVA is removed from the plate. These results present the effects of the linear stiffness coefficient tuning.

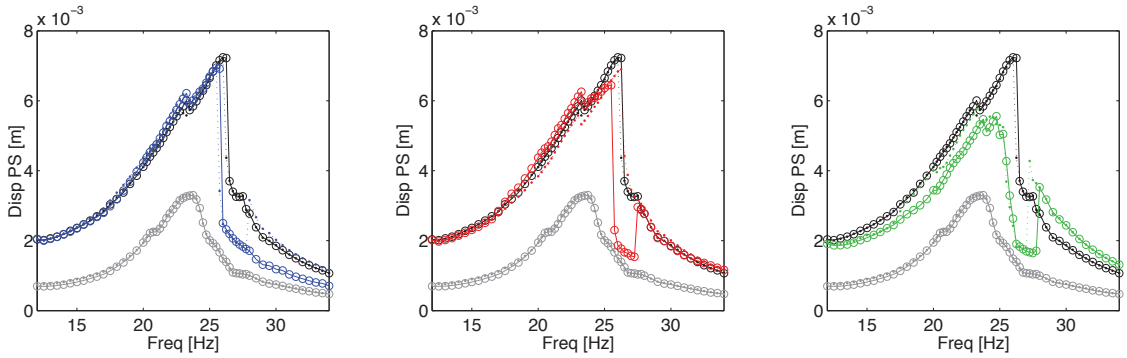

Figure 2: Maximum displacement of the primary structure without the MVA [ooo] and with the MVA tuned as an NLTVA [ooo] ($K_1 > 0$), an NES [ooo] ($K_1 \approx 0$) and a bi-stable absorber [ooo] ($K_1 < 0$). The gray circles [ooo] indicate the linear displacement of the primary structure for a lower excitation force. Circles and dots correspond to forward and backward sweeps respectively.

The measurements first show undoubtedly the effect of the vibration absorber on the nonlinear dynamics of the plate. Depending on the tuning, one can expect to control different parameters area in the frequency response curve. Current measurements are realised in order to analyze more deeply the advantages of each configurations as well as showing the best tuning that can be expected.

References

[1] Frahm H.: Device for Damping Vibrations of Bodies. US No. Patent 989958, 1909.

[2] Den Hartog J.P.: Mechanical Vibrations. McGraw-Hill, New-York, 1934.

[3] Ormondroyd J., Den Hartog J.P.: The Theory of the Dynamic Vibration Absorber. Transactions of ASME, 50:9-22, 1928.

[4] Asami T., Nishihara O., Baz A.M.: Analytical solutions to H∞ and H_2 optimization of dynamic vibration absorbers attached to damped linear systems. Journal of Vibration and Acoustics, 124:284-295, 2002.

[5] Gendelman o., Manevitch L.I., Vakakis A.F., Closkey R.M.: Energy pumping in nonlinear mechanical oscillators, I: dynamics of the underlying Hamiltonian systems, Journal of Applied Mechanics, 68(1):34-41, 2001.

[6] Vakakis A.F., Gendelman O.: Energy pumping in nonlinear mechanical oscillators, II: resonance capture, Journal of Applied Mechanics, 68(1):42-48, 2001.

[7] Manevitch L.I., Sigalov G., Romeo F., Bergman L.A., Vakakis A.F.: Dynamics of a Linear Oscillator Coupled to a Bistable Light Attachment: Analytical Study, J. Appl. Mech., 81(4):041011, 2013.

[8] AL-Shudeifat M.A., Wierschem N., Dane Quinn D., Vakakis A.F., Bergman L.A., Spencer Jr. B.F.: Numerical and experimental investigation of a highly effective single-sided vibro-impact non-linear energy sink for shock mitigation, International Journal of Non-Linear Mechanics, 52:96-109, 2013.

[9] Grappasonni C., Habib G., Detroux T., FengWen W., Kerschen G., Jensen J.S.: Practical design of a nonlinear tuned vibration absorber, Proceedings of the ISMA 2014 conference, 2014.

[10] Yamakawa I., Takeda S., Kojima H.: Behavior of a new type dynamic vibration absorber, Bulletin of the JSME, 20(146):947-954:, 1977.

[11] Benacchio S., Malher A., Boisson J., Touzé C.: Design of a Magnetic Vibration Absorber with Tunable Stiffnesses, Submitted to Nonlinear Dynamics.

NON-SYNCHRONOUS FREE OSCILLATIONS OF ZIEGLER'S COLUMN

Carlos Eduardo Nigro Mazzilli[1] & Stefano Lenci[2]
[1]*Escola Politécnica, University of São Paulo, São Paulo, Brazil*
[2]*Università Politecnica delle Marche, Ancona, Italy*

Summary A condition for non-synchronous free oscillations is addressed, which can be satisfied by systems with non-symmetric stiffness matrix. The dynamical response of a previously buckled Ziegler's column subjected to a follower force is looked at, leading to a high-frequency motion of the tip mass and a low-frequency motion of the mid span mass. Localization phenomenon can also take place, depending on the system initial conditions.

PROBLEM STATEMENT

In structural dynamics, the linear normal modes play a fundamental role. For such motions, all physical coordinates oscillate with the same frequency and phase, so that they simultaneously attain their maximum (minimum) values. Hence, by definition, they are synchronous modes and, for undamped systems, they are periodic too. This concept has been extended by Rosenberg [1] to nonlinear systems, through the definition of the "nonlinear normal modes" as vibrations in "unison". Shaw and Pierre [2] enlarged the meaning of nonlinear modes, defining them as motions restricted to an invariant manifold of the phase space tangent to the respective eigenplanes and containing an equilibrium point. In the general case, Shaw and Pierre's nonlinear modes are potentially non-synchronous, since they are influenced by both the displacements and the velocities, and phase differences between these two fields can happen. The consequence is that the vibration modes are not necessarily a standing wave. By the way, even linear systems with non-proportional damping can behave like that.

Yet, it is neither necessary, nor essential, to evoke the nonlinear modes to address non-synchronicity at this very moment. Indeed, it suffices focusing the linearized undamped free-vibration equation of a discrete system about an equilibrium configuration (which may, of course, require nonlinear analysis to be assessed)

$$\mathbf{M\ddot{u} + Ku = 0}\,. \tag{1}$$

In (1), both $\mathbf{M}$ (mass matrix) and $\mathbf{K}$ (stiffness matrix) are typically symmetric and positive definite. Yet, at times, this latter can be non-symmetric (for circulatory systems, such as those with follower forces, caused by internal/external fluid flow or friction) and even non-positive definite (static instability caused by conservative non-gyroscopic or centrifugal forces, for example). Of course, $\mathbf{u}$ and $\ddot{\mathbf{u}}$ stand for the displacement and acceleration vectors with respect to the equilibrium configuration. For undamped 2DOF systems, the so-called isolated non-synchronous vibration modes are connected to its possible non-conservativity, although this is not mandatory. A necessary condition for non-synchronous harmonic response $_i = {}^0_i \sin \omega_i t$ of a system described by (1) states that there should co-exist at least two generalized coordinates u_j and u_k, oscillating with distinct frequencies ω_j and ω_k [3]. Suppose that these frequencies are non-null

$$\omega_j^2 = \frac{K_{1j}}{M_{1j}} = \ldots = \frac{K_{jj}}{M_{jj}} = \ldots = \frac{K_{kj}}{M_{kj}} = \ldots = \frac{K_{Nj}}{M_{Nj}} \text{ and } \omega_k^2 = \frac{K_{1k}}{M_{1k}} = \ldots = \frac{K_{jk}}{M_{jk}} = \ldots = \frac{K_{kk}}{M_{kk}} = \ldots = \frac{K_{Nk}}{M_{Nk}}\,. \tag{2}$$

Hence, the condition $\omega_j \neq \omega_k$ implies that the stiffness matrix cannot be symmetric ($K_{jk} \neq K_{kj}$), assuming that the mass matrix is symmetric.

The study of Ziegler's column under follower force loading is an iconic problem to start with, since it is a simple model, yet displaying a rich dynamical behaviour. Moreover, it is a natural introduction to vibration problems in pipes carrying fluid flows. Other than flutter instability, it is seen that it can also display non-synchronous free oscillations, with characteristics of the localization phenomenon which may eventually be explored in energy harvesting applications or vibration control.

BUCKLED ZIEGLER'S COLUMN ACTED UPON BY A FOLLOWER FORCE

It is considered the Ziegler's column of Figure 1, subjected to both a conservative loading (weights mg and αmg plus the compressive vertical force F applied at the middle hinge) and a non-conservative loading (follower compressive force P applied at the free end) that supposedly causes it to buckle and a stable post-critical equilibrium configuration $\left(\hat{\theta}_1\ \hat{}_2\right)$ is then attained. Forces F and P are calibrated so that the system oscillates synchronously/non-synchronously about the post-critical equilibrium configuration. The post-critical equilibrium configuration must comply with

$$\hat{}_1 - \delta\left[\Lambda_F - 1 - \alpha\right]\sin\hat{}_1 - \frac{1}{\beta}\hat{\theta}_2 = -\Lambda_P \sin\hat{}_2 \qquad \text{and} \qquad \hat{}_2 = -\delta\alpha\beta\sin\left(\hat{}_1 + \hat{\theta}_2\right) \tag{3}$$

[a] Corresponding author. Email: cenmazzi@usp.br.

where $\delta = \dfrac{mg\ell}{\beta k}$ and $\Lambda_F = \dfrac{F}{mg}$. The necessary condition for non-synchronicity (2) requires that:

$$\left(1+cos\hat{\theta}_2\right)\left[1-\delta(\Lambda_F-1-\alpha)cos\hat{\theta}_1+\alpha\delta cos\left(\hat{\theta}_1+\hat{\theta}_2\right)\right]-\delta cos\left(\hat{\theta}_1+\hat{\theta}_2\right)\left[1+2\alpha\left(1+cos\hat{\theta}_2\right)\right]=0 \tag{4}$$

$$\Lambda_P=\frac{\left(1+cos\hat{\theta}_2\right)}{cos\hat{\theta}_2}\left[\frac{1}{\beta}+\alpha\delta cos\left(\hat{\theta}_1+\hat{\theta}_2\right)\right]-\alpha\delta\frac{cos\left(\hat{\theta}_1+\hat{\theta}_2\right)}{cos\hat{\theta}_2}$$

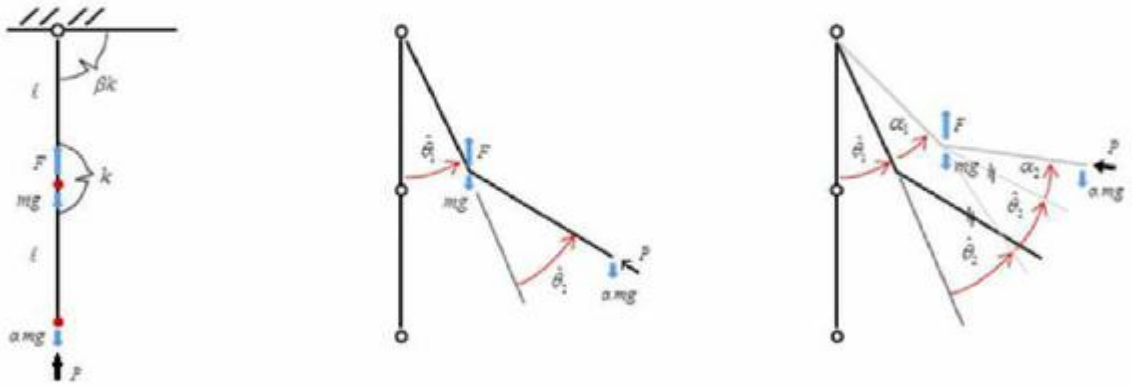

Figure 1: Buckled Ziegler's column acted upon by a follower force

For a convenient choice of parameters, such as: $m=$ kg, $k=100Nm\,rad^{-1}$, $\ell=1m$, $\alpha=1$, $\beta=1$, $\delta=0.5$, $\Lambda_F=3.26615$ and $\Lambda_P=2.450234$, the post-critical equilibrium solution is $\hat{\theta}_1=-0.91431$, $\hat{\theta}_2=0.291614$, fulfilling simultaneously conditions (3) and (4). Figure 2 displays a typical dynamical response for the system with such parameters, for a particular choice of initial conditions.

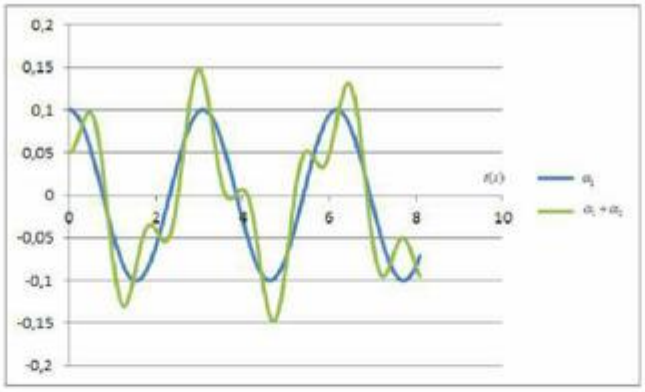

Figure 2: Example of non-synchronous motion of the masses at mid span and column tip (see Fig. 1 for the definition of α_i)

CONCLUSIONS

The tip mass can be excited by both the first (ω_1=2.03694$rads^{-1}$) and the second (ω_2=5.30312$rads^{-1}$) modes, whereas the one at mid span will not be excited by the second mode. Hence, depending on the initial conditions, the motion can be practically localized and the system energy would be concentrated in just a part of the system (possibly with large amplitude and high frequency). Both conditions can be of interest in the design of energy harvesting and vibration control systems.

References

[1] Rosenberg R. M.: The normal modes of nonlinear n-degree-of freedom systems, *J. Appl Mech* 29:7-14, 1962.

[2] Shaw S.W., Pierre C.: Non-linear normal modes and invariant manifolds, *J. Sound Vibr*, 150 (1):170-173, 1991.

[3] Lenci S., Mazzilli C.E.N.: On non-synchronous oscillations (*in preparation*), 2015.

NONLINEAR OSCILLATION OF A CIRCULAR PLATE ENERGY HARVESTER

Li-Qun Chen[1,2 a)] & Tianchen Yuan[2]
[1]*Department of Mechanics, Shanghai University, Shanghai 200444, China*
[2] *Shanghai Institute of Applied Mathematics and Mechanics, Shanghai University, Shanghai 200072, China*

Summary Nonlinear oscillation is treated for a piezoelectric vibratory energy harvester. The harvester consists of a circular composite plate with the clamped boundary, a proof mass and two steel rings. The harvesting system is analytically modeled, numerically simulated, and experimentally tested. A lumped parameter model of the harvester is established with its parameters identified from the experimental data. The equivalent capacitance and the electromechanical coupling coefficient are analytically determined. A technique is proposed to identify the electrical parameter. A fifth polynomial is employed to approximate the nonlinear restoring force. The measured response can be approximately described by the nonlinear lumped model. Both the experimental and the numerical results demonstrate that the circular plate harvester has soft characteristics under low excitation and both hard characteristics and soft characteristics under high excitation. The characteristics can be used to broaden the working bandwidth of the harvester and thus to enhance the energy harvesting.

INTRODUCTION

Vibratory energy harvesting from the environment is now an active and promising research field. Nonlinearities can be employed to broaden working frequency bandwidth of harvesters [1,2]. The circular plate structure has an axial symmetric structure which is easy to be processed and thus attracts more and more attentions.

MODELING AND PARAMETER IDENTIFICATION

As shown in Fig.1, the piezoelectric composite plate is fabricated from a brass plate (R_b=25 mm and h_b=0.2 mm) and two piezoelectric plates (R_p=25 mm and h_p=0.2 mm). The brass plate (2.5 mm) is clamped by 2 steel rings (R_s=22.5).

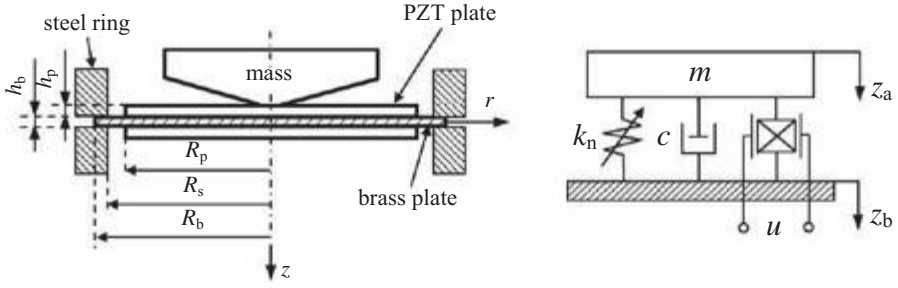

Figure 1 (a) Cutaway view of the circular plate harvester. (b) Lumped-parameter model.

The lumped-parameter model is governed by a set of equation with respect to $z(t)=z_a(t)-z_b(t)$ and u as

$$\ddot{\ } + \dot{\ } + {}_1 + {}_2 + {}_3 + {}_4 + {}_5{}^5) + \eta u = - \ddot{\ }_b, -\eta {}_L \dot{\ } + \dot{\ } + = 0 \tag{1}$$

where R_L is the load resistance, and the fifth polynomial approximates the restoring force. Damping coefficient c and k_i (i=1,…,5) can be identified from measured accelerations and its integration filtered by the empirical mode decomposition. The electromechanical coupling coefficient and the equivalent capacitance can be derived from the elasticity solution as

$$\eta = \frac{4\pi R_p^2 d_{zr}\ h_p + {}_b)\gamma^2\left(\ln R_p - \ln R_s\right)}{R_s^2 s_{rr}^E(1-\mu)}, C_p = \pi R_p^2 \frac{\varepsilon_{zz}^T s_{rr}^E(1-\mu) - 2d_{zr}^2}{s_{rr}^E(1-\mu)h_p} \tag{2}$$

where μ is PZT Poisson's ratio, ε^T_{zz} is the permittivity, ε^T_{zz} is the elastic compliances constant, and d_{zr} is the piezoelectric constant. Based on the jth experiment with excitation frequency ω_j, load resistance R_{Lj}, mass acceleration amplitude A_j, and output voltage amplitude U_{ej}, N times of experiments yield the parameter identification via the least square method

$$\min \sum_{j=1}^{N}\left[U_j \quad U_{ej}\right]^2, U_j = \frac{\eta R_L A}{\omega_j\sqrt{\left(C\ R_j\omega_j\right)^2 + 1}} \tag{3}$$

The theoretical and the identification results as well as the theoretical results of a beam [18] are listed in table 1.

Table 1. Electromechanical coupling coefficient and equivalent capacitance

parameter	unit	experimental results	theoretical results	cantilevered beam [3]
η	N/V	0.0108	0.0115	0.0037
C_p	nF	65.5	62.98	58.14

a) Corresponding author. Email: lqchen@staff.shu.edu.cn.

The beam is with larger area of piezoelectric bimorph and thicker piezoelectric layers than the plate, where the electromechanical coupling coefficient of the beam is much smaller than that of the plate. Thus a circular plate has the much high electromechanical coupling coefficient than a beam in similar sizes, which is beneficial to energy harvesting.

AMPLITUDE-FREQUENCY RESPONSE

The amplitude-frequency responses are determined by the experiment and the simulations. Figures 2 and 3 show the voltage response under 1.5 g and 2 g excitation, respectively. The results show softening characteristic in Fig. 2 and both softening and hardening nonlinearities in Fig. 3. In Fig. 3 the curve bends to the right with the jumping both in the experiment and the simulation, and at the left side of the resonance peak, a slight jump resulted from the softening can be found. The possible reason for coexistence of the soft and the hard characteristics lies in the expression of the restoring force, in which the coefficient of the quintic term is positive, and that of the cubic term is negative.

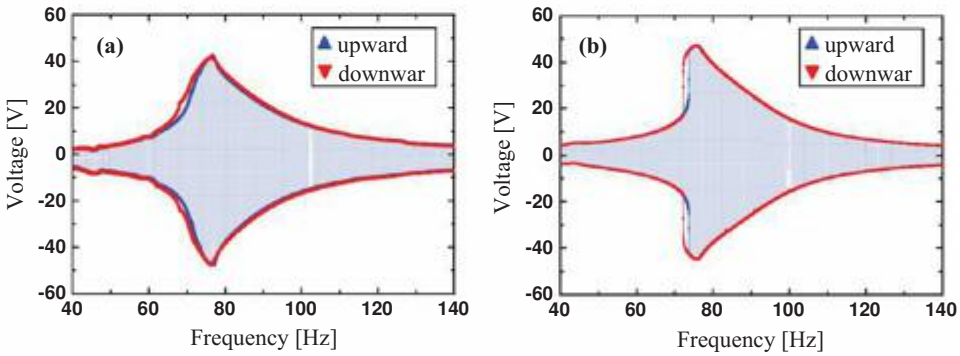

Figure 2 Voltage responses under 1.5g excitation: (a) Experiment and (b) Simulation.

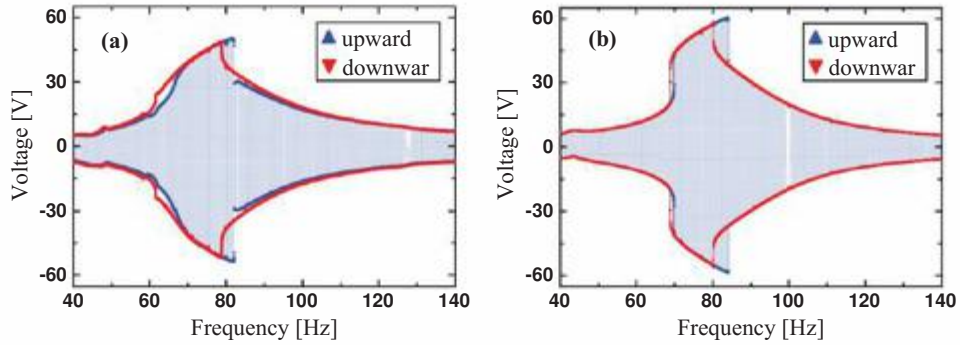

Figure 3 Voltage responses under 2g excitation: (a) Experiment and (b) Simulation.

CONCLUSIONS

The experimental and the numerical investigations yield the following conclusions: (1) the circular plate harvester has a higher electromechanical coupling coefficient than the cantilevered beam system, which is beneficial to energy harvesting; (2) the proposed technique to identify the electrical parameter is effective; (3) the experiment and the simulation show that the harvester has softening nonlinearity under small excitation, which may be caused by the negative cubic term in the nonlinear restoring force function; (4) both hardening nonlinearity and softening nonlinearity are discovered when the harvester is subjected to sufficient large excitation, which can be used to broaden the bandwidth of the harvester.

Acknowledgments

The work was supported by the National Natural Science Foundation of China (Project Nos. 11232009 and 51575334).

References

[1] Daqaq M. F., Masana R., Erturk A., Quinn D. D.: On the Role of Nonlinearities in Vibratory Energy Harvesting. *Appl. Mech. Rev.* **66**: 040801, 2014.

[2] Chen L. Q., Jiang W. A.: Internal Resonance Energy Harvesting. *J. Appl. Mech.* **82**: 031004, 2015.

[3] Erturk G., Inman D. J.: A Distributed Parameter Electromechanical Model for Cantilevered Piezoelectric Energy Harvesters. *J. Vib. Acoust.* **130**: 041002, 2008.

NON-LINEAR DYNAMICS OF A PENDULUM VIBRATION ABSORBER WITH A MAGLEV HARVESTER

Krzysztof Kecik *[1], Andrzej Mitura[1], Jerzy Warminski[1], and Stefano Lenci[2]

[1]*Department of Applied Mechanics , Lublin University of Technology, Lublin, Poland*
[2]*Department of Civil and Building Engineering and Architecture , Polytechnic University of Marche, Ancona, Italy*

Summary This paper describes and analyse a novel harvester-absorber device that uses magnetic levitation (maglev) in order to recover energy. The energy harvester is mounted in a pendulum which plays a dynamic absorber role. The non-linearity of the magnetic field suspension exhibits a hardening Duffing's characteristics. We propose a new model of an electromechanical coupling which depends on a magnet position in a coil. Theoretical investigations are followed by a series of experimental tests that validate the theoretical predictions and allow us to obtain a final model of optimized harvester.

INTRODUCTION

Energy harvesting is promising research area as demands for renewable energy sources increase. Electromagnetic energy harvesters (EEH) are based on Faradays law of induction - the property that a change in the magnetic flux of a circuit will result in the induction of an electromotive force. Maglev systems are electromechanical devices that suspend ferromagnetic materials using electromagnetism, and are characterized by non-linear dynamics, instability and are described by highly non-linear differential equations.

HARVESTER-ABSORBER MODEL

Energy harvesting under investigation is based on motion of the autoparametric vibration absorber. The model of a harvester-absorber system (HAS) consists of the main mass (oscillator) with the attached the pendulum vibration absorber. The pendulum is made of nonmagnetic tube with two magnets fixed on the ends, which ensure the levitation of a third moving magnet (Fig.1c). A coil of wire is wrapped around the outside of the pendulum tube (Fig.1d). While, the moving magnet oscillate it induces the electromotive force. The view of the laboratory rig is presented in Fig.1b. The system works as the dynamical vibration absorber with the energy recovery at the same time.

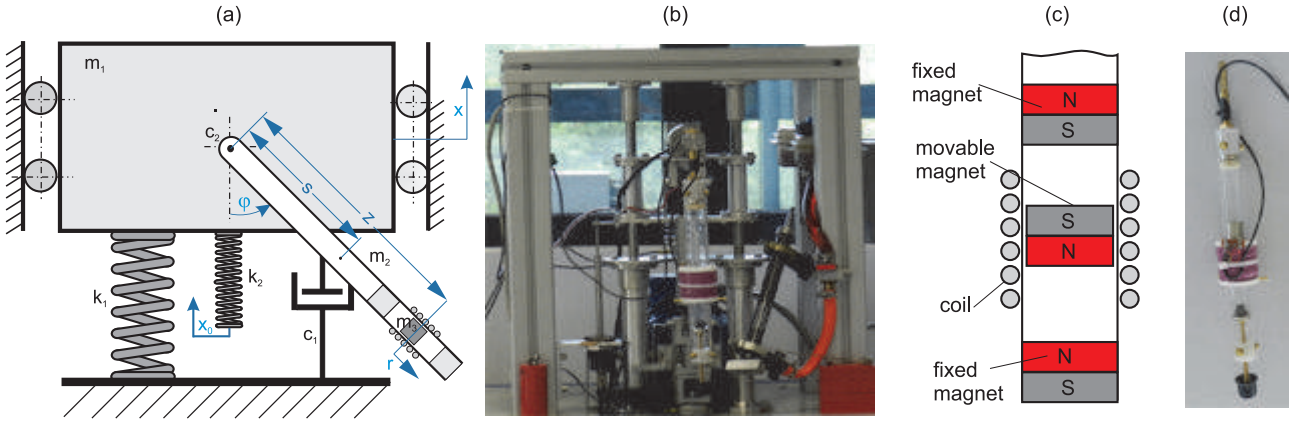

Figure 1: Model of harvester absorption system: a physical model (a), laboratory rig (b), scheme (c) and experimental device of the maglev system (d)

A schematic diagram of the proposed model is shown in Fig.1a. This is a coupled three mechanical and one electrical degrees of freedom system. The mass m_1, spring k_1 and damping component c_1, are connected to the base. The pendulum m_2 with magnet m_3 creates the vibration absorber engaged with oscillator motion, which is kinematically excited by the spring k_2 in the vertical direction. If the pendulum swings, then amplitude of the oscillator can be reduced.

*Corresponding author. Email: k.kecik@pollub.pl

EQUATION OF MOTION AND MAGLEV CHARACTERISTICS

The governing equations of the non-linear harvester-absorber system derived from the Lagrange's equations of the second kind have the form

$$(m_1 + m_2 + m_3)\ddot{x} + (m_2 s + m_3(z+r))[\ddot{\varphi} sin(\varphi) + \dot{\varphi}^2 cos(\varphi)] + m_3(2\dot{r}\dot{\varphi} sin(\varphi) - \ddot{r} cos(\varphi)) + c_1\dot{x} + k_1 x = k_2 x_0, \quad (1)$$

$$(I_0 + m_3(z+r)^2)\ddot{\varphi} + (\ddot{x} + g)[m_2 s + m_3(z+r)]sin(\varphi) + 2m_3\dot{\varphi}\dot{r}(z+r) + c_2\dot{\varphi} = 0, \quad (2)$$

$$m_3\ddot{r} - m_3[\ddot{x} cos(\varphi) + \dot{\varphi}^2(z+r)] - m_3 g cos(\varphi) + F(r) + \alpha(r)i = 0, \quad (3)$$

$$L\dot{i} + R_T i - \alpha(r)\dot{r} = 0. \quad (4)$$

The first three equation (1)-(3) describe motion of mechanical parts (i.e. oscillator, pendulum and magnet), while the last equation (4) characterizes electrical circuit obtained by applying Kirchoffs law. The i is the electrical current, R_T is the total resistance (internal coil and external load resistances), and $\alpha(r)$ means the electromechanical coupling coefficient.

The magnetic restoring levitation force $F(r)$, given by the sum of the repulsive forces acting on the top and bottom magnets, leads to the the form of hardening Duffing's characteristic $F(r) = k_3 r + k_4 r^3$, where k_3 and k_4 are estimated experimentally (see Fig.2a). The changes in the magnets separation cause alter stiffness leading to resonance [1]. For small values of relative displacements r of the moving magnet, the levitation suspension can be reduced to a linear problem.

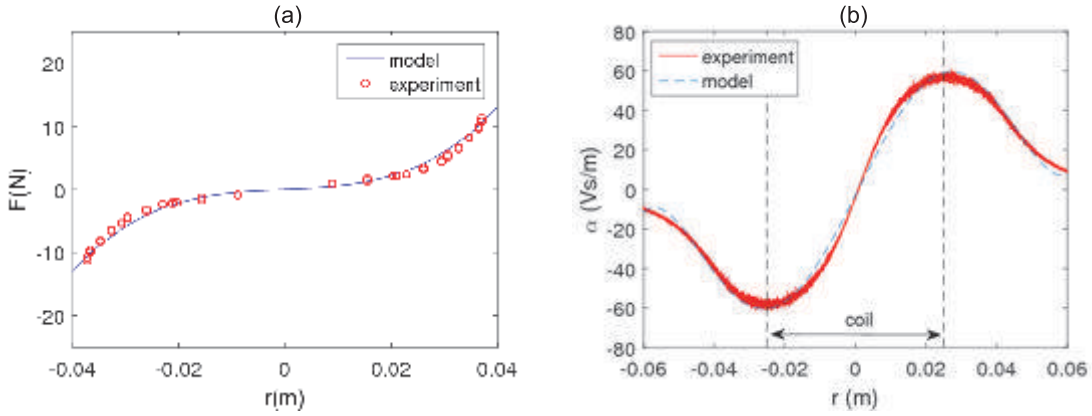

Figure 2: The force displacement characteristic (a), and electromechanical coupling coefficient vs. magnet's position for the magnet velocity $v = 0.7m/min$ (b).

Usually, in literature, the coupling coefficient (α) is constant [1, 2], assuming the magnetic flux density as uniform. The experimental investigations show that α strongly depends on the magnet position in the coil (Fig.2b). This is due to the fact, that magnetic flux density depends on the separation distance between the magnet and the coil. We propose a five-degree polynomial function to describe coupling coefficient $\alpha(r) = \sum_{n=0}^{5} \alpha_n r^n$, where α_n are coefficients computed in order to fit the experimentally determined characteristic.

CONCLUSIONS

The design and analysis of a novel energy harvesting device that uses maglev to produce energy is presented in the paper. The magnetic suspension leads to the Duffing's type equation. The coupling coefficient strongly depends on the magnet's position (but does depend on velocity) and has sinusoidal form. The highest values of α occurs at the coil ends. The system is strongly non-linear producing several interesting phenomena, including regions of multiple solutions and chaotic behavior.

*Acknowledgements: This work was financially supported under the project of National Science Centre according to decision no. DEC-2013/11/D/ST8/03311.

References

[1] Mann B. P., Sims N. D.: Energy harvesting from the nonlinear oscillations of magnetic levitation. J. Sound Vib 319:515530, 2009.

[2] Olaru R., Gherca R., Petrescu C.: Analysis and design of a vibration energy Harvester using permanent magnet. Rev. Roum. Sci. Techn. Electrotechn. et Energ.:59(2):131140, 2014.

POSSIBILITY OF ENERGY EXTRACTION FROM NOISE UNDER STOCHASTIC RESONANCE

Madoka Kubota, Ryo Takahashi*, and Takashi Hikihara

Department of Electrical Engineering, Kyoto University, Katsura, Nishikyo, Kyoto 615-8510, Japan

Summary Noise must be restrained at sensing and data processing. However, in nature, noise inevitably appears through energy spread surrounding us. From a viewpoint of energy harvesting, it has been shown that resonators can absorb energy from the excitation around each resonant frequency. In the sinusoidal vibration, the energy exchange depends on the on-site resonance and inter-cite phase between resonators and exciters. The simple noise with finite number of frequencies causes the difficulty of energy extraction. This paper discusses the stochastic resonance, when unidirectional energy flow works for energy harvesting.

STOCHASTIC RESONANCE AND EFFECT OF NOISE

Stochastic Resonance (SR) is known as a phenomenon in which a signal is enhanced by noise of moderate strength. As an example, here consider the following system,

$$m\ddot{x} = -m\gamma\dot{x} - \frac{\mathrm{d}U}{\mathrm{d}x} + h\cos\Omega t + R(t), \quad U(x) = \frac{1}{4}x^4 - \frac{1}{2}x^2. \tag{1}$$

Where m denotes mass of a particle, x displacement of the free particle, γ damping constant, $h\cos\Omega t$ sinusoidal external force, and $U(x)$ bistable potential. $\dot{(\ )}$ is time differential $\mathrm{d}/\mathrm{d}t$. Assuming the sinusoidal external force $h\cos\Omega t$ changes relatively slow to noise $R(t)$, which is the zero-mean white Gaussian noise of auto-correlation function:

$$\langle R(t)R(t+\Delta t)\rangle = 2\gamma mkT\delta(\Delta t). \tag{2}$$

Where k denotes Boltzmann constant and T noise temperature. $\langle\ \rangle$ shows the operation of ensemble average. The effect of noise with sinusoidal external forcing is given by the following potential:

$$V(x) = \frac{1}{4}x^4 - \frac{1}{2}x^2 - xh\cos\Omega t. \tag{3}$$

Depending on the frequency of sinusoidal excitation, the noise response shows various features. The faster frequency than a certain frequency Ω_0, the lower probability of the stochastic switching. (see Fig.1). Ω_0 is obtained by Kramers rate [1]:

$$\Omega_0/\pi = W/2. \tag{4}$$

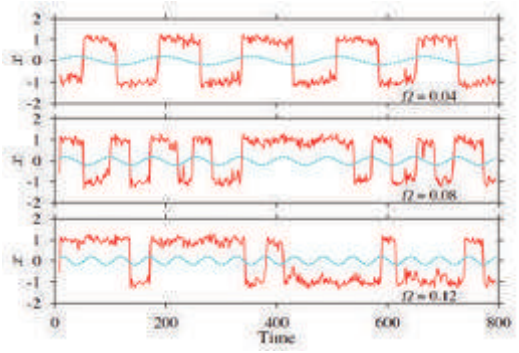

Figure 1: Response depending on Ω with $kT = 0.07$ and $h = 0.20$ kept constant; 0.04 (upper), 0.08 (middle), and 0.12 (bottom). Blue broken curve draws the sinusoidal force $h\cos\Omega t$.

The rate implies the duration required for transition from one state to the other in the bistable potential wells. The rate increases with the noise intensity kT and decreases with the potential barrier U [1]. It corresponds to the mechanical transition probability depending on kT [2].

*Corresponding author. Email: takahashi.ryo.2n@kyoto-u.ac.jp

EXTRACTION OF ENERGY FROM NOISE

The amplitude of displacement x, the velocity of displacement $\dot{x}$ and their power spectrum are direct input to the transducer from mechanical energy to electrical energy at harvesting. Electrically potential will not generate the energy flow between resonators, so that the velocity is focused. In the sinusoidal vibrations, the velocity keeps the phase shift at $\pi/2$ to the displacement. Figure 2 is the displacement of resonator and the power spectrum. It shows the clear enhancement of power from input because of stochastic resonance. However, under the long-term free vibration with noise, the power will finally converge one of balanced states between resonators. Therefore it is inevitable to push the range of power spectrum narrower for producing the energy flow from the displacement [3]. This requests the resonator and the attached transducer to match the mechanical to electrical impedances and vice versa.

The energy exchange between resonators is

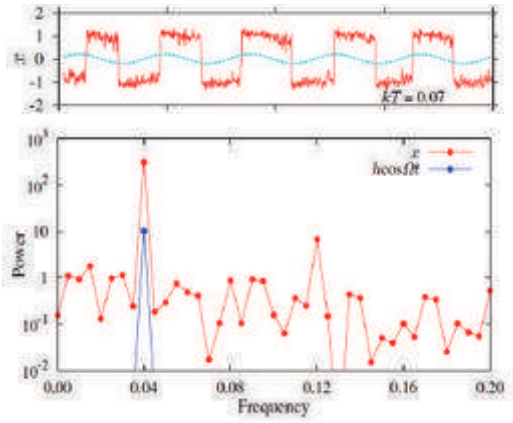

Figure 2: Displacement x and the power spectrum with sinusoidal force $h\cos\Omega t$ (blue broken line) under the noise intensity $kT = 0.07$, $h = 0.20$, and $\Omega = 0.04$.

CONCLUSIONS

This paper began to discuss the possibility of energy extraction from noise through stochastic resonance. The concept is not established but includes the general directions of research including power exchange between harmonic generators like a synchronous generator. The research on energy extractions form noise will be a rich research seed not only in nonlinear dynamics but also in applications of nonlinear characteristics [4].

References

[1] P. Hänggi, P. Talkner, and M. Borkovec, Reaction-rate theory: fifty years after Kramers, Reviews of Modern Physics, 62 (2), 251 (1990).

[2] M. Kubota, R. Takahashi, and T. Hikihara, Active and Reactive Power in Stochastic Resonance for Energy Harvesting. IEICE Transactions 98-A(7): 1537-1539 (2015).

[3] Madoka Kubota, Energy Harvesting Characteristics of Nonlinear Oscillators under Excitation, PhD dissertation, Kyoto University (2015).

[4] B. Kim, V. Putkaradze, and T. Hikihara, Manipulation of single atoms by atomic force microscope as a resonance effect, Phys. Rev. Lett. 102, 215502 (2009).

HARDENING SOFTENING BEHAVIOR OF ANTIRESONANCE FOR NON LINEAR TORSIONAL VIBRATION ABSORBERS

Alexandre Renault[1,2], Olivier Thomas [*1], Hervé Mahé[2], and Yannick Lefebvre[2]

[1]*Arts et Métiers ParisTech, LSIS UMR CNRS 7296, 8 bd. Louis XIV 59046 Lille, France*
[2] *Valeo Transmissions, Centre d'Étude des Produits Nouveaux Espace Industriel Nord, Route de Poulainville, 80009 Amiens Cedex 1, France*

Summary We address non linear torsional vibration absorbers (TVA), used in rotating machinery to counteract irregularities of rotation at a some order of the engine speed of rotation. The TVA is analogous to a tuned mass damper (TMD), tuned on the desired order. It exhibits non-linearities of various natures which affect resonance and antiresonance frequencies at large amplitude of motion, which consequently causes the detuning of the system from the targetted order. This study focuses on some non linear systems (several TVA designs and a more general Duffing like system) to study the impact of non-linearities on the hardening / softening behavior of antiresonances. Non linear solutions are obtained by a numerical continuation procedure coupled with the harmonic balance method to follow periodic solutions in forced steady-state. Moreover, we propose an original direct antiresonance continuation method for undamped systems.

INTRODUCTION

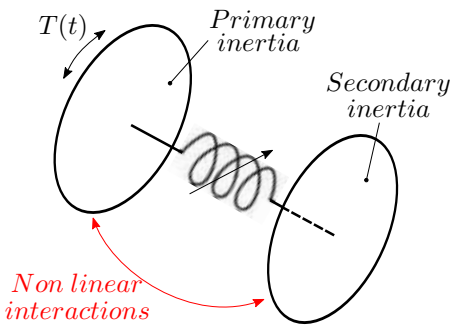

Figure 1: TVA scheme

Non linear torsional vibration absorber (TVA) is used in rotating machinery to counteract irregularities of rotation, called "acyclisms", at a some order of the engine speed of rotation. It is compose of a primary and secondary inertia and acts as the classical tuned mass damper (TMD). It is tuned on the desired engine order. In practice, the secondary inertia represents a mass subjected to move in a particular path on the primary inertia which is linked to the rotating assembly. However the TVA includes strong non-linearities. Geometric non-linearities and those due to Coriolis effect, intrinsic to rotating articulated systems. They cause the detuning of the TVA and the shifting of the operating order of TVA (an antiresonance of the whole system) from the targeted engine order. Knowledge of operating point behavior of the device is therefore essential to ensure optimal acyclisms filtering. This study focuses on tow points. First, several non linear systems, including torsional and translational systems, are studied to highlight how the hardening / softening behavior is modified by non-linearities. Non linear frequency responses in steady state are obtained by numerical continuation procedure, the harmonic balance method (HBM) [3] coupled with the asymptotic numerical method (ANM) [1], which leads to a fast and robust algorithm. Secondly, we propose an original direct antiresonance continuation method for undamped systems.

MODELLING

The equations of motion of the TVA can be written in general following form :

$$\boldsymbol{M}(\boldsymbol{x})\ddot{\boldsymbol{x}} + \boldsymbol{f_{in}}(\boldsymbol{x},\dot{\boldsymbol{x}}) + \boldsymbol{C}\dot{\boldsymbol{x}} + \boldsymbol{f_{int}}(\boldsymbol{x}) = \boldsymbol{F}\cos(\omega t)\,, \tag{1}$$

where $\boldsymbol{x}$ is the vector of unknowns. $\boldsymbol{M}(\boldsymbol{x})$ is the mass matrix and depends on $\boldsymbol{x}$. $\boldsymbol{C}$ is the damping matrix. $\boldsymbol{f_{in}}(\boldsymbol{x},\dot{\boldsymbol{x}})$ is the inertial forces vector, including Coriolis terms, and depends on $\boldsymbol{x}$ and $\dot{\boldsymbol{x}}$. $\boldsymbol{f_{int}}(\boldsymbol{x})$ is the internal forces vector and depends on $\boldsymbol{x}$. Here, because only one oscillator is forced, the external forces vector is $\boldsymbol{F} = [0\ \cdots\ f\ \cdots\ 0]$ where f is the amplitude of excitation of the forced oscillator. Assuming a periodic solution of (1), the vector of unknowns is expanded in truncated Fourier series :

$$\boldsymbol{x}(t) = \boldsymbol{x_0} + \sum_{i=0}^{H} \boldsymbol{x_{ci}}\cos(i\omega t) + \boldsymbol{x_{si}}\sin(i\omega t). \tag{2}$$

Then substituting (2) into (1) and applying HBM, we obtain a system of algebraic equations relating $\boldsymbol{x_0}$, $\boldsymbol{x_{ci}}$, $\boldsymbol{x_{si}}$, ω and f. The accuracy of the periodic solution depends on H, the number of harmonics retains on (2). The final system to solve can be written :

$$\boldsymbol{R}(\boldsymbol{U}, w, f) = 0. \tag{3}$$

*Corresponding author. Email: olivier.thomas@ensam.eu

Where $\boldsymbol{U} = [\boldsymbol{x_0}\ \boldsymbol{x_{ci}}\ \boldsymbol{x_{si}}\ ...\ \boldsymbol{x_{cH}}\ \boldsymbol{x_{sH}}]$. Finally, (3) is solved by an asymptotic numerical method, for which a quadratic recast of $\boldsymbol{R}(\boldsymbol{U}, \omega, f)$ is convenient [2]. In practice, the software Manlab 2.0 is used [4]. Unlike to predictor-corrector algorithms, where the solution is computed point by point, ANM adopts a piecewise continuous representation of the solution using a power series expansion of the pseudo arc length along the branch of solution.

ANTIRESONANCE CONTINUATION

Standard continuation procedure consist in considering ω and f as continuation parameters and compute the solutions with respect to one of them in forced vibration [2]. In free vibration ($f = 0$), the oscillation frequency can also be computed as a function of the amplitude, obtaining so-called backbone curves. In this case, the system has to be conservative so that periodic solutions are obtained and damping must be cancelled ($\boldsymbol{C} = \boldsymbol{0}$)[5]. Here, we propose an original method to perform non linear antiresonance continuation, i.e. the computation of the antiresonance frequency as a function of the amplitude of forcing. Unlike free oscillations continuation, the system has to be forced. For a linear system, an antiresonance occurs only for undamped systems, for which the response of one of the unknowns is strictly zero, $x_i(t) = 0\ \forall t$ at a given frequency, x_i being the i-th component of $\boldsymbol{x}$. If the system shows non-linearities, the antiresonance is not strict and only some harmonics of $x_i(t)$ can be set to zero, whereas the others are non zero. The antiresonance continuation is obtained by solving (3) with $\omega\ and\ f$ left free and by adding an additional condition: here the first harmonic of a given unknown is set to zero.

RESULTS

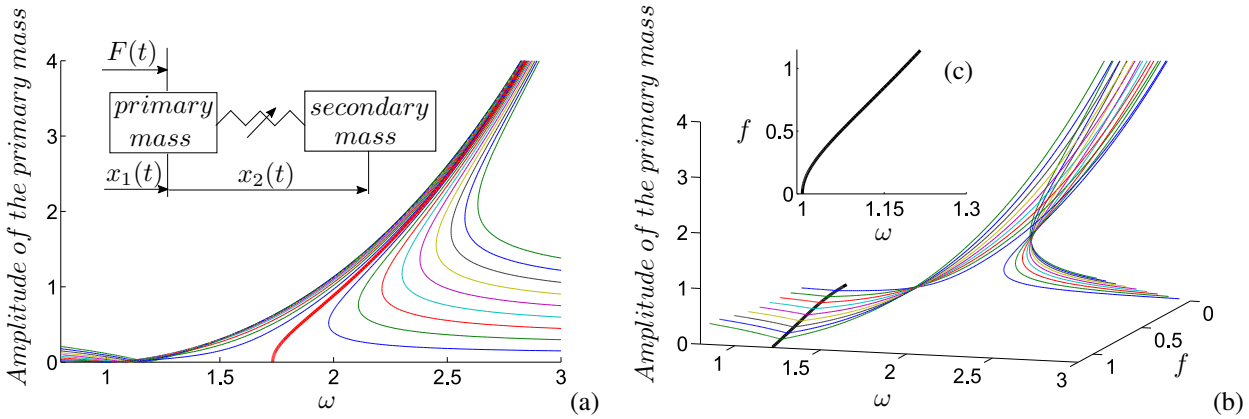

Figure 2: Frequency responses of the non linear TMD for several amplitudes of excitation (a) and antiresonance continuation (black bold line) (b)

Here, we consider a free-free non linear TMD. The equations of motion can be written :

$$\begin{cases} \ddot{x}_1 (m_1 + m_2) + \ddot{x}_2 m_2 = f \cos(\omega t), & \text{(4a)} \\ \ddot{x}_1 m_2 + \ddot{x}_2 m_2 + k x_2 + \gamma x_2^3 = 0, & \text{(4b)} \end{cases}$$

where γ and k are the non linear and linear stiffness constants, respectively. Figure 2(a) shows the frequency responses of the first harmonic of the primary mass, subjected to an harmonic forcing, for several amplitudes of excitation f. The system exhibits a hardening behavior due to the positive non linear stiffness constant. The backbone curve (red bold line), represents the oscillation frequency in free vibration. The antiresonance continuation can be viewed on the three dimensions representation, on the figure 2(b), and also on the plane (ω,f), on the figure 2(c). This procedure is very useful to accurately predict the detuning with respect to the amplitude of excitation. Moreover, it avoids redundant frequency responses simulations.

References

[1] Cochelin B. A path-following technique via an asymptotic-numerical method. *Computers & Structures*, 53(5):1181 – 1192, 1994.

[2] Cochelin B. and Vergez C. A high order purely frequency-based harmonic balance formulation for continuation of periodic solutions. *Journal of Sound and Vibration*, 324(12):243 – 262, 2009.

[3] Ali H Nayfeh and Dean T Mook. *Nonlinear oscillations*. John Wiley & Sons, 1979.

[4] Arquier R., Karkar S., Lazarus A., Thomas O., Vergez C., and Cochelin B. Manlab2.0 : an interactive path-following and bifurcation analysis software. *Tech. rep., Laboratoire de Mécanique et d'Acoustique, CNRS*.

[5] Karkar S., Cochelin B., and Vergez C. A comparative study of the harmonic balance method and the orthogonal collocation method on stiff nonlinear systems. *Journal of Sound and Vibration*, 333(12):2554 – 2567, 2014.

STRONGLY NONLINEAR RESONANCE DYNAMICS OF QUASI-ONE-DIMENSIONAL FINITE OSCILLATORY CHAINS

Leonid Manevitch[1a)], Irina Koroleva (Kikot')[1], Valeri Smirnov[1]
[1]*Semenov Institute of Chemical Physics of Russian Academy of Sciences, Moscow, Russia*

Summary We present an extension of recently developed approach to stationary and non-stationary resonance dynamics of strongly nonlinear two degree of freedom (2DoF) systems to finite strongly nonlinear oscillatory chains (strong nonlinearity implies impossibility to use the linearized equations of motion even as a starting point of dynamic analysis). The proposed extension allows revealing new nonlinear effects in series of widely used mechanical and physical systems. There are in particular: i) breaking the symmetry caused by instability of almost all nonlinear normal modes (NNMs) and appearance of stable elliptic modes (EMs) in the initially un-stretched strings and membranes carrying discrete masses; ii) mobile breathers excitation by localized initial pulse in the un-stretched membrane; iii) efficient inter-cluster energy exchange and transition to energy localization in the un-stretched membrane and in the finite system of weakly coupled pendulums. The applications of revealed strongly nonlinear effects to solution of significant mechanical and physical problems are discussed.

NONLINEAR EFFECTS

The resonance processes are responsible for energy exchange, localization and transfer in many significant mechanical and physical systems. Among them, there are un-stretched strings and membranes carrying discrete masses; arrays of Josephson junctions, ferromagnetic chains and oligomer crystals (all three latter ones can be modelled by the finite system of weakly coupled pendulums). We consider the case of strong nonlinearity when the equations of motion may not be linearized even as a starting point of dynamic analysis. Our new approach which was examined in the case of 2DoF models implies a closeness of the system to 1:1 internal resonance only. We describe briefly the revealed strongly nonlinear effects which include such phenomena as symmetry breaking because of instability and bifurcation of almost all NNMs, formation of mobile transversal breathers, transition from intense energy exchange to energy localization, and appearance of a chaos accompanying such transition.

The symmetry breaking caused by instability of NNMs in un-stretched string and membrane. The simplest model of such system is presented in Fig.1.

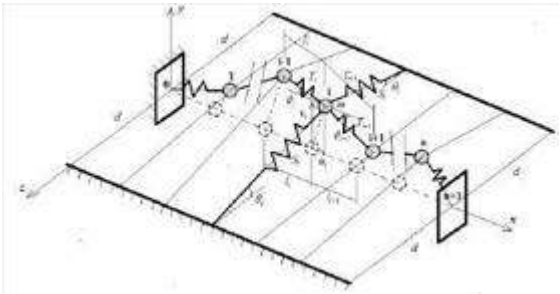

Fig. 1. The model of grounded unstretched string (symplest model of unstretched membrane) carrying n particles and possessing linear interchain and lateral stiffneseses (for the sake of clarity only the lateral spring supporting the $i-th$ particle is depicted). If the lateral springs are absent one deals with un-stretched string.

As it is shown by us recently ([1],[2],[4]) the asymptotic equations of motion in the case of dominating transversal motion can be written as

$$\frac{d^2v_j}{d\tau^2}+\frac{1}{\mu}v_j^3+\frac{1}{2(N+1)}\left(2v_j-v_{j-1}-v_{j+1}\right)\sum_{s=0}^{N}(v_{s+1}-v_s)^2=0, j=1,N, v_0=v_{N+1}=0,$$

where v_j is normalized transversal displacement of *j*-th oscillator, *N* is a number of the oscillators. These equations admit *N* exact solutions for NNMs: $v_j(t)=A_k(t)\sin\frac{\pi kj}{N+1}$ for *k*-th NNM, *k=1,...,N*. The direct analytical study reveals instability of all NNMs except the mode with highest wave number. The result of this instability can be identified as uni-directional energy flow from given NNM to those with larger wave numbers (an inverse energy flow is not observed) (fig. 2). This strongly nonlinear effect is illustrated below on the example of non-grounded un-stretched string carrying 10 particles.

The highly non-stationary dynamics of the system can be adequately described in terms of Limiting Phase Trajectories (LPTs) corresponding to maximum possible energy exchange between different parts (clusters) of the string. This process is shown in Fig.3 for the same system. For grounded string (membrane) a threshold from complete inter-cluster energy exchange to energy localization on the initially excited cluster is (Fig.4) revealed.

a)Corresponding author. Email: manevitchleonid3@gmail.com

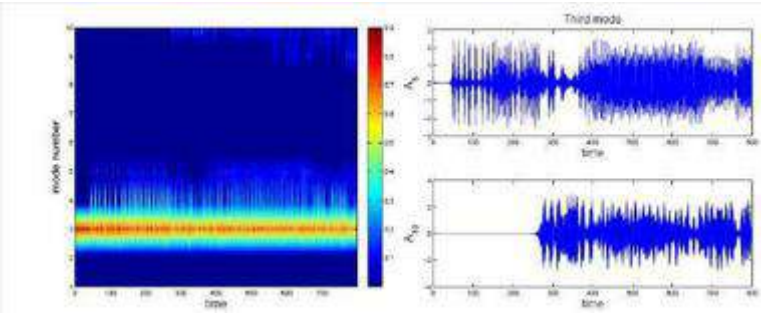

Fig. 2. Instability of third NNMs and uni-directional energy flow to fifth and tenth NNMs.

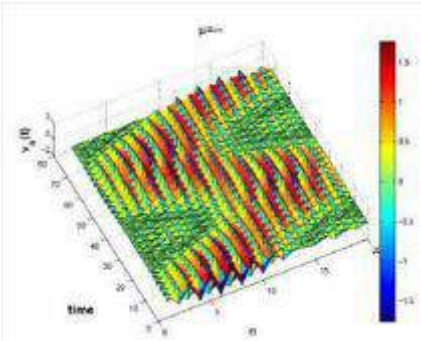

Fig. 3. Energy exchange between two parts of oscillatory chain.

System of weakly coupled pendulums

Similar transition can be observed in other significant strongly nonlinear model which is a finite system of N weakly coupled pendulums (without any restrictions on the amplitudes of oscillation). Behavior of this system in the vicinity of internal 1:1 resonance in terms of cluster variables $\{\chi_1, \chi_2\}$ can be described by complex equations (derived for parricular case of 2DoF model in [3]):

$$i\partial_{\tau_1}\chi_j - \mu\frac{\omega}{2}\chi_j + \frac{\beta}{\omega}\sin^2\kappa\left(\chi_j - \chi_{3-j}\right) + \mu\Sigma\left(\frac{\psi_k f_{j,k}}{\sqrt{2\omega}|\psi_k|}J_1\left[\sqrt{\frac{2}{\omega}}|\psi_k|\right]\right) = 0, j = 1,2$$

where ω is a resonant frequency, β is a coupling parameter, $k=\pi/N$, J_1 – modified Bessel function of 1st kind, $\psi_k = \chi_1 f_{1,k} + \chi_2 f_{2,k};\ f_{j,k} = 1 + (-1)^{3-j}(\sin\kappa k + \cos\kappa k)$. The inter-cluster energy exchange is similar to that presented in Fig.3. The transition to energy localization is illustrated in Fig.5.

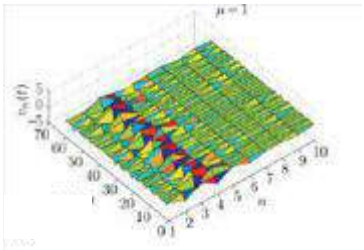

Fig. 4. Localization of the displacement (leading to energy localization) on the initially excited part of the grounded string in the presence of grounding supports.

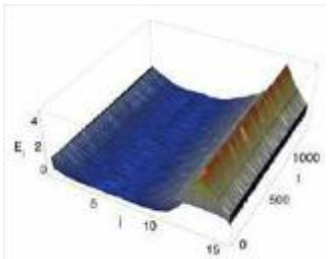

Fig. 5. Energy distribution along the chain of pendulums after transition to energy localization. Amplitude of the pendula oscillation $Q=\pi/2$.

CONCLUDING NOTES

The analysis of considered strongly nonlinear systems reveals instability of NNMs and abrupt transition from intensive inter-cluster energy exchange to energy localization on the initially excited cluster. The analytical prediction of this transition is confirmed by the results of computer simulation. The analytical results for grounded string as well as for weakly coupled pendulums were obtained in the framework of resonance asymptotics.

The above described strongly nonlinear effects can be directly applied for solution of targeted energy transfer problem and the series of physical problems mentioned in Introduction.

ACKNOWLEDGEMENTS

Authors are grateful to RFBR (grant 14-01-00284 A) for financial support.

References

[1] Manevitch L.I., Vakakis A.F.:Nonlinear Oscillatory Acoustic Vacuum. *SIAM Journal of Applied Mathematics* **74**(6): 1742-1762, 2014.

[2] Koroleva (Kikot) I.P., Manevitch L.I., Vakais A.F.: Non-stationary resonance dynamics of a nonlinear sonic vacuum with grounding supports. *Journal of Sound and Vibration* **357**:349-364, 2015.

[3] Manevitch L.I., Romeo F.: Non-stationary resonance dynamics of weakly coupled pendula. *EPL*, **112**(3): 30005, 2014.

[4] Koroleva (Kikot) I.P., Manevitch L.I.: Oscillatory chain with grounding support in conditions of acoustic vacuum. *Rus. J. Nonlin. Dyn.*, **11**(3): 487–502 (Russian), 2015.

ACCELERATING OSCILLATORY FRONTS IN A SONIC VACUUM WITH NON-LOCAL INTERACTIONS

Oleg Gendelman[1a)], Vadim Zolotarevskiy [1)], Alexander V. Savin[2)], Lawrence Bergman[3)] & Alexander F. Vakakis [4)]
[1]*Faculty of Mechanical Engineering, Technion -- Israel Institute of Technology, Haifa 32000, Israel*
[2]*Semenov Institute of Chemical Physics, Russian Academy of Sciences, Moscow 119991, Russia*
[3]*Department of Aerospace Engineering, University of Illinois in Urbana-Champaign, USA*
[4] *Department of Mechanical Science and Engineering, University of Illinois in Urbana-Champaign, USA*

Summary We describe a novel class of dynamical excitations -- accelerating oscillatory fronts in nonlinear sonic vacua with strongly non-local effects. Such models naturally arise in dynamics of common and popular lattices. In this study, we consider a chain of particles oscillating in the plane and coupled by linear springs, with fixed ends. When one end of this system is harmonically excited in the transverse direction, one observes accelerated propagation of the excitation front, accompanied by an almost monochromatic oscillatory tail. The front propagation obeys the scaling law $l \sim t^{4/3}$. This scaling law results from the nonlocal effects; we derive it analytically (including the scaling coefficients) from a continuum approximation. Moreover, a certain threshold excitation amplitude is required in order to initiate the front propagation. The initiation threshold is explained on the basis of a simplified discrete model, further reduced to a new completely integrable nonlinear system.

We start with simple numeric experiment: a fragment of common straight linear mass-and-spring chain without pre-tension is allowed to move in plane. One end of the chain is fixed, and the other is forced to move in the direction transversal to the chain axis, in accordance with harmonic law: $y_1 = A\sin\omega t$. Energy distribution in the chain is presented in Figure 1.

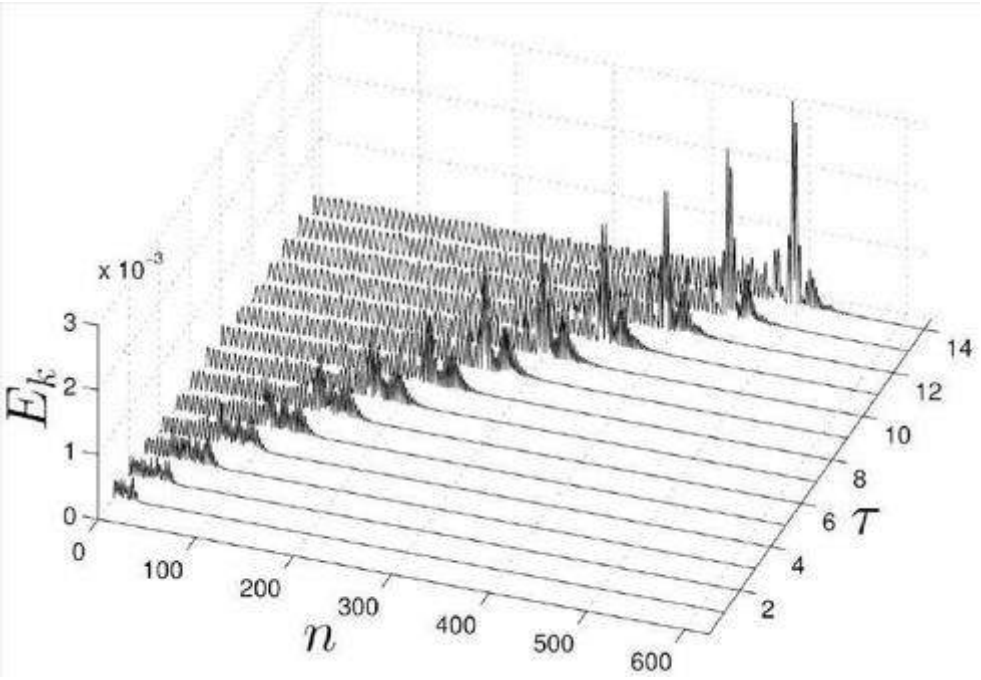

Figure 1. Propagation of the oscillatory front.

One can observe the propagation of the excitation front, accompanied by an apparently monochromatic oscillatory tail. Propagating fronts with oscillatory tails are well-known in models of phase transitions in solid state and similar problems. However, the solution presented here has very interesting new feature, not known in the settings mentioned above. It follows from Figure 1 that this front accelerates in the course of propagation.

In order to explain this finding analytically, we use continuum approximation of the transversal dynamics of the chain. It is described by the following well-known equation [1,2]:

$$y_{tt} - \frac{y_{xx}}{2L}\int_0^L y'^2 dx = 0 \qquad (1)$$

Here $y(x,t)$ is continuous field of transversal displacements of the chain. Density and stiffness characteristics of the chain are set to unity without effecting the generality, L is the chain length. Equation (1) exemplifies the concept of the sonic vacuum, since it has no linear sound velocity. Moreover, due to integral term the nonlinear interactions turn out to be

[a)] Corresponding author. Email: ovgend@tx.technion.ac.il.

non-local. Besides modal characteristics, the nonlinear dynamics and wave propagation in such systems were almost not addressed in previous studies.

We then consider a simplified model of the oscillatory region in the chain and suppose a monochromatic wave in the oscillatory tail after the front:

$$y(x,t)=\begin{cases} A\sin(\omega t-kx), 0\le x\le l(t) \\ 0, x\ge l(t) \end{cases} \quad (2)$$

Here $l(t)$ is the instantaneous coordinate of the front, and k is the wavenumber. It is also assumed at this stage that the front propagation is slow enough compared to the frequency of transverse oscillations of the particles. An additional condition can be obtained from the assumed stationary character of the front propagation. To this end, the phase velocity of the oscillatory tail should be equal to the front velocity. Substituting (1) into (2), keeping principal terms and applying the condition of the phase velocity, one obtains the following explicit expression for the front propagation dynamics:

$$l(t)=Kt^{4/3}, K=\left(\frac{81A^2\omega^2}{1024L}\right)^{1/3} \quad (3)$$

Quality of approximation (3) is illustrated in Figure 2 for three different sets of parameters, with the curves depicting the front position versus time (shifted by ln K). One can observe that the curves perfectly collapse, proving the self-similar nature of the observed regime.

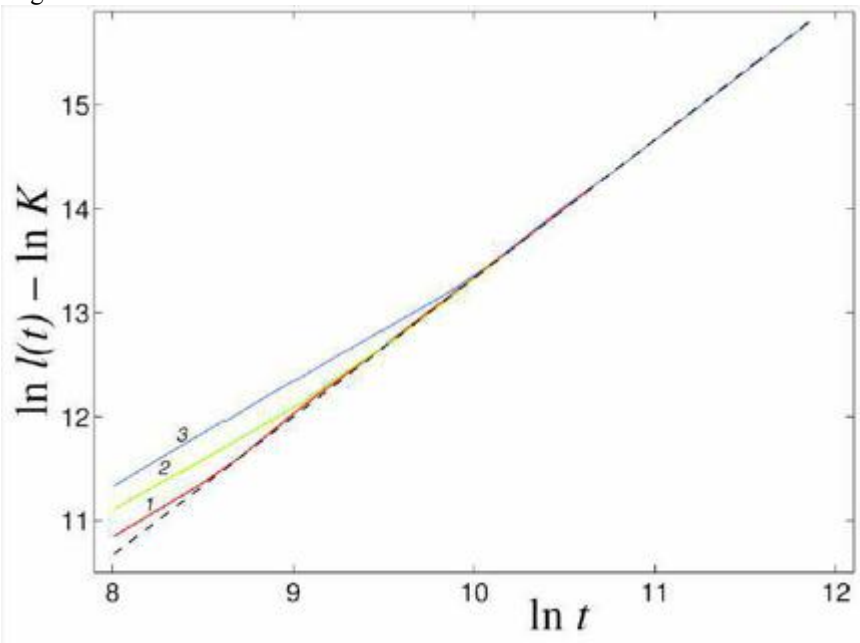

Figure 2. Numeric simulation: position of the oscillatory front versus time for different parameter values (double logarithmic scale). Line slope is 4/3.

The front formation and propagation is observed for given excitation frequency, if the amplitude overcomes certain threshold value. This value can be evaluated from discrete counterpart of Equation (1), derived recently in paper [3]. This estimation yields:

$$A_{cr}=a\omega\sqrt{2L} \quad (4)$$

Numeric simulations completely confirm scaling predictions for critical excitation amplitude (4). Numeric value of coefficient a is also predicted with accuracy of about 15%.

To conclude, we revealed a new type of excitations in a lattice representing a nonlinear sonic vacuum with strong nonlocal dynamical interactions (despite only next-neighbour physical coupling). Such fronts reveal themselves in most well-known and popular models, such as the suspended string without pre-tension and the chain of linear springs and masses with fixed ends. Simple analytic considerations allow derivation of all main parameters of the front, including the scaling characteristics and the excitation threshold.

References

[1] L. D. Landau and E. M. Lifshitz , Theory of Elasticity, Pergamon Press, 1970

[2] A. H. Nayfeh, Nonlinear Interactions, Wiley, 2000

[3] L. I. Manevitch and A. F. Vakakis, Nonlinear Oscillatory Acoustic Vacuum, *SIAM Journal of Applied Mathematics*, **74**, 1742-1762, 2014.

NONLINEAR INTERACTIONS BETWEEN COUPLED NONLINEAR OSCILLATORS AT DIFFERENT LAYERS OF TIME

Claude-Henri Lamarque[1], Simon Charlemagne[1], and Alireza Ture Savadkoohi [*1]

[1]*Univ Lyon, ENTPE, LTDS UMR CNRS 5513, Vaulx en Velin, France*

Summary The energy exchanges between two coupled systems during extreme nonlinear interactions between them around a $1:1$ resonance is studied. The auxiliary nonlinear oscillator, named as nonlinear energy sink (NES) [1, 2, 3, 4, 5], which is used for controlling the main one and/or to harvest its energy, possesses both global and local potentials and can be under external forcing terms. Slow invariant of the system and detected equilibrium and singular points provide design tools for tuning parameters of the NES for the aim of its usage.

MATHEMATICAL MODEL OF THE SYSTEM

The main forced oscillator with scaled displacement, damping and natural frequency as y, a and ω_0 is coupled to a forced NES with scaled displacement and local potential x and $\tilde{g}(x)$, respectively. Its global potential is split in linear (ω_c^2) and nonlinear (W) parts. The two nonlinear potentials W and $\tilde{g}$ are supposed to be odd functions. We can summarize governing equations of the system as it follows:

$$\begin{cases} \ddot{y} + a\dot{y} + \omega_0^2 y + c(\dot{y} - \dot{x}) + \omega_c^2(y - x) + W(y - x) = \epsilon f^0 \sin(\omega t) \\ \\ \epsilon\ddot{x} - c(\dot{y} - \dot{x}) - \omega_c^2(y - x) - W(y - x) + \tilde{g}(x) = \epsilon f_{NES}^0 \sin(\omega_N t) \end{cases} \tag{1}$$

The ϵ parameter is the mass ratio of the NES and the main oscillator. We assume that $1 < \epsilon \ll 1$.

TREATMENTS OF THE SYSTEM AND ITS BEHAVIORS AT DIFFERENT TIME SCALES

- The system is shifted to the center of masses ($v = \dfrac{y + \epsilon x}{1 + \epsilon}$) and relative displacement ($w = x - y$). Then complex variables of Manevitch [6] as $\psi e^{i\omega t} = \dot{v} + i\omega v$ and $\varphi e^{i\omega t} = \dot{w} + i\omega w$ are introduced to the system ($i^2 = -1$).
- A Galerkin technique is endowed: first harmonics are kept and higher ones are truncated. This technique for an arbitrary function Γ reads:

$$S = \frac{\omega}{2\pi} \int_0^{\frac{2\pi}{\omega}} \Gamma(t) e^{-i\omega t} dt \tag{2}$$

  We assume that ψ, φ are independent of fast $\tau_0 = t$ time scale, but could depend on slow $\tau_1 = \epsilon\tau_0$, $\tau_2 = \epsilon^2\tau_0$,... scales.
- System equations at fast time scale provide its slow invariant while at slow time scale around its invariant we can detect its equilibrium and singular points. These points correspond to potential periodic and strongly modulated responses.

Moreover, following assumptions are made:

- We investigate 1:1:1 resonance of the main system: $\omega = \omega_0(1 + \sigma\epsilon)$ and $\omega_N = \omega_0(1 + \sigma_N\epsilon)$.
- Damping coefficients are at ϵ^1 order: $c = \epsilon d$ and $a = \epsilon a_0$.
- Linear part of the global potential is at the order of ϵ^1: $\omega_c^2 = \epsilon\Omega^2$. Nonlinear part of global potential and local potential are assumed to be at the ϵ^1 order: $\tilde{g}(z) = \epsilon\mathcal{A}^0 z^3$ and $W(z) = \epsilon\mathcal{B}^0 z^3$.
- We introduce polar coordinates $\psi = N_1 e^{\delta_1}$ and $\varphi = N_2 e^{\delta_2}$.

In following sections we present two examples corresponding to two cases: the NES without external excitation and forced NES. All analytical predictions are compared with results obtained from direct numerical integration of equation (1).

The NES without external excitation: $f_{NES}^0 = 0$

Slow invariant of the system possesses three branches namely, branch l, $l = 1, 2, 3$. At slow time scale we can trace two levels of N_2 which prepare the system for bifurcations. We name them as N_{21} and N_{22} which are called as fold lines. Meanwhile, for each branch l two functions $Hjl = 0$, $j = 1, 2$ are defined. Intersections of Hjl out of fold lines are equilibrium points of the system while their intersections on fold lines are singular points of the system. Figure 1 illustrates prediction of all possible regimes (periodic and strongly modulated regimes) of the system for given parameters. It can been seen that due to the existence of singular point no. 2 (see Figure 1(a)), the system presents strongly modulated response (see Figures 1(d) and 1(e)).

[*]Corresponding author. Email: alireza.turesavadkoohi@entpe.fr

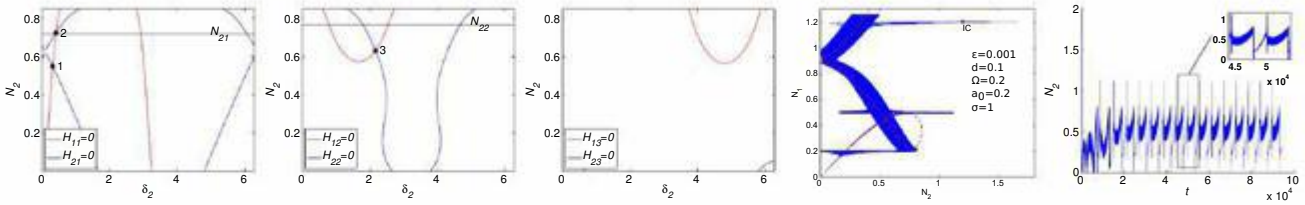

(a) (b) (c) (d) (e)

Figure 1: $\mathcal{A} = 0.25$, $\mathcal{B} = 0.6$, $\omega_0 = 1$ and $f^0 = 0.81$: (a), (b), (c) Positions of equilibrium points and fold singularities on branch 1, 2 and 3 of the slow invariant, respectively. The system has two equilibrium points (no. 1 and no. 3) and one fold singularity on fold line N_{21} (no. 2)- (d) Slow invariant (in red, dashed line) and corresponding numerical results (in blue, solid line) - (e) Numerical results of the evolution of the energy of the NES N_2 - IC stands for "Initial Conditions"

The NES with external excitation: $f^0_{NES} = 0$

Here, we consider the system with forced NES. Analytically predicted results and corresponding numerical ones are depicted in Figure 2. The system finally is attracted by an equilibrium point (see green line in Figure 2(b)) which is predicted by analytical techniques that has not been presented in this paper.

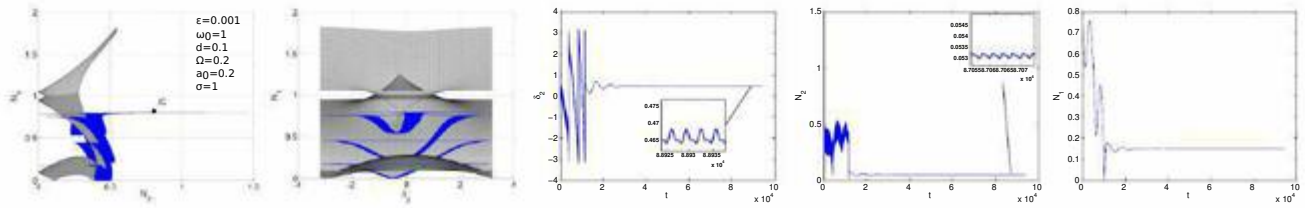

(a) (b) (c) (d) (e)

Figure 2: Slow invariant of the system and corresponding numerical results in blue - $\mathcal{A} = 2$, $\mathcal{B} = 0.5$, $f^0_{NES} = 0.1$ and $f^0 = 0.3$ - (a) N_1 vs N_2; (b) N_1 vs δ_2 - "IC" stands for initial conditions - Behavior of the system around the equilibrium point predicted via analytic technique at slow time scale is plotted in green. (c) δ_2 vs t; (d) N_2 vs t; (e) N_1 vs t.

CONCLUSIONS

Time multi-level energy exchanges and nonlinear interactions between a main forced oscillator and an auxiliary forced nonlinear system with local and global potentials are studied. Detected slow invariant and equilibrium and singular points at slow time scale provide design tools for tuning parameters of the auxiliary system for the goal of its implementations which can be passive control and/or energy harvesting of the main oscillator. Same method will be applied for an oscillator coupled to a chain of light nonlinear oscillators for localization of its vibratory energy.

References

[1] Gendelman O., Manevitch L. I., Vakakis A. F., MCloskey R.: Energy pumping in nonlinear mechanical oscillators: part i - dynamics of the underlying hamiltonian systems. J. Appl. Mech. 68: 34–41, 2001.

[2] Vakakis A. F.: Inducing passive nonlinear energy sinks in vibrating systems. J. Vib. Acoust 123: 324–332, 2001.

[3] Lamarque C.-H., Ture Savadkoohi A.: Dynamical behavior of a Bouc-Wen type oscillator coupled to a nonlinear energy sink. Meccanica 49: 1917–1928, 2014.

[4] Lamarque C.-H., Thouverez F., Rozier B., Dimitrijevic Z.: Targeted energy transfer in a 2-DOF mechanical system coupled to a non-linear energy sink with varying stiffness. J. Vib. Control, doi: 10.1177/1077546315618540, 2016.

[5] Ture Savadkoohi A., Lamarque C.-H., Contessa M. V.: Trapping vibratory energy of main linear structures by coupling light systems with geometrical and material non-linearities.Int. J. Nonlinear Mech., doi:10.1016/j.ijnonlinmec.2015.11.011, 2016.

[6] Manevitch L. I.: The description of localized normal modes in a chain of nonlinear coupled oscillators using complex variables. Nonlinear Dyn. 25: 95–109, 2001.

SYNCHRONIZED FREQUENCY CONVERSION IN NONLINEAR LATTICES

Miguel Molerón[1], Marc Serra-Garcia[1], André Foehr[1], Joseph Lydon[1], Christopher Chong[2] & Chiara Daraio [1,3a)]
[1]*Department of Mechanical and Process Engineering, Swiss Federal Institute of Technology, ETH Zurich CH-8092, Zurich, Switzerland*
[2]*Department of Mathematics, Bowdoin College, Brunswick, ME 04011, United States*
[3]*Division of Engineering and Applied Science, California Institute of Technology, Pasadena, CA, 91125, United States*

Summary We investigate energy transfer between frequencies in lattices of interacting magnets with defects. The nonlinear coupling between localized and extended lattice modes enables to convert energy between arbitrary frequencies (i.e., non related by integer ratios). In addition, in systems with multiple defects, this frequency conversion mechanism allows harvesting energy from several input frequencies in a synchronized manner. These results may inform the design of new vibration energy harvesting systems.

Vibration energy harvesting systems are able to convert ambient vibrations into electric power and are receiving a lot of interest in recent years [1]. Regardless of the transduction mechanism (e.g., piezoelectric, electromechanic), these systems operate optimally at or close to resonance. However, ambient vibrations are in general broadband or composed of multiple frequencies, which render these devices unsuited in most practical situations. A possible way to solve this issue is to introduce a frequency conversion mechanism in the system in order to match the spectrum of the excitation with the resonance frequency of the transducer. Typical uses of nonlinearity for frequency conversion are based on the phenomena of harmonic generation [2] and parametric down conversion [3]. In these mechanisms, the energy transfer occurs at a frequency that is an integer multiple or submultiple of the excitation frequency, limiting the applicability of these techniques. In this work, we demonstrate a frequency conversion mechanism in lattices of interacting magnets with mass defects that transfers energy between arbitrary frequencies, i.e., without being necessarily related by integer ratios.

To illustrate this behavior we consider two cases: a lattice with a single defect [Fig. 1(a)] and a lattice containing two defects [Fig. 1(b)]. The linear spectrum of these lattices is composed of two types of modes: extended modes, which are responsible for the propagation of energy in the lattice; and defect modes, which are localized around the defect. Localized and extended modes represent respectively the inputs and outputs of our system. Due to the hardening nonlinearity of the magnetic potential [5], when the defect mode is excited harmonically at a frequency close to its resonance frequency, the mode undergoes hysteretic cycles in which the mode pumps the input energy to the chain [5]. This results in a modulation of the localized mode amplitude that creates an energy transfer from the localized modes to the extended modes.

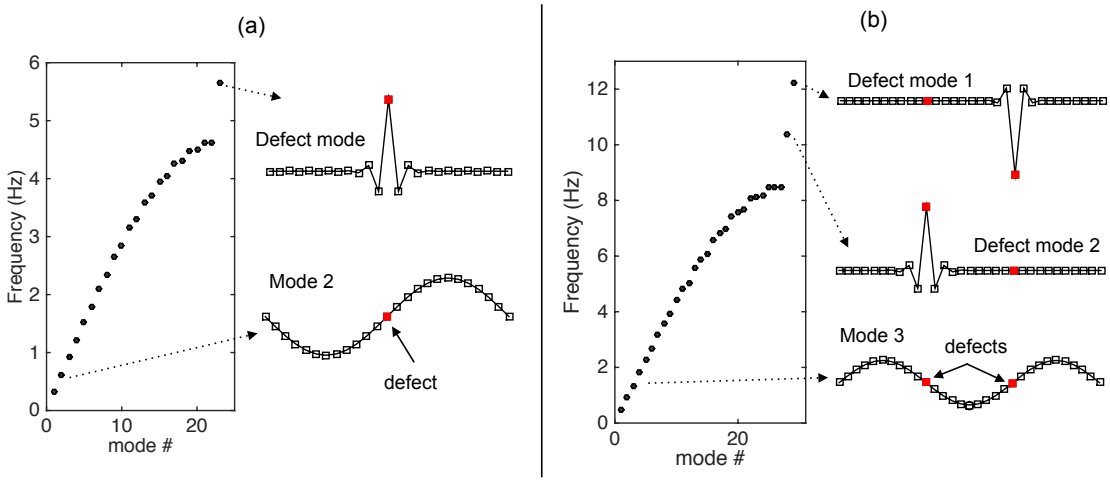

Figure 1. (a) *Linear spectrum of the single-defect lattice. (b) Linear spectrum of the double-defect lattice*.

We first illustrate this frequency conversion mechanism in the single defect lattice. The defect is excited harmonically at frequency $f_{in} = f_d + f_2$where f_2 and f_d are, respectively, the resonance frequencies of the second extended mode and the defect mode, see Fig. 1(a). The left panel in Fig. 2(a) shows the amplitudes of mode 2 (A_2, black line) and the defect mode (A_d, red line) as a function of time. After the transient regime ($t \approx 15s$) we observe that the amplitude A_d becomes modulated by A_2, which indicates a transfer of energy from the input frequency f_{in} to the frequency of the extended mode

[a)] Corresponding author. Email: daraio@ethz.ch.

f_2. This modulation can be clearly observed in the right panels of Fig. 2(a), which zooms in the modal amplitudes A_2 and A_d in the time window $[32-40]$s.

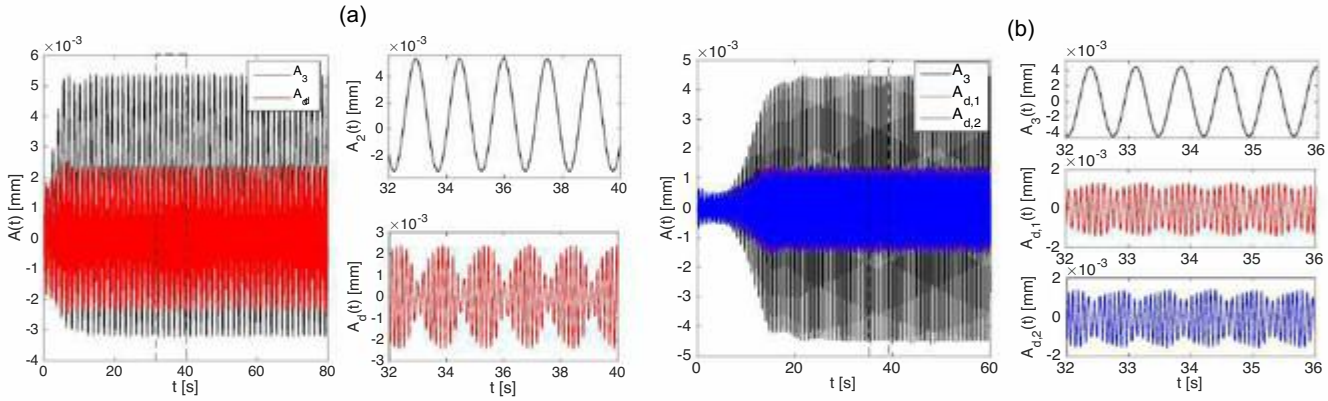

Figure 2. (a) Left panel, A_2 (black line) and A_d (red line) as a function of time for the single defect lattice. Right panels, zoom in on the region 32-40 s. (b) Right panel, A_3 (black line), $A_{d,1}$ (red line) $A_{d,2}$ (blue line) and as a function of time for the lattice with two defects. Right panels, zoom in on the region 32-36 s.

An interesting aspect of this frequency conversion mechanism is that in systems with multiple inputs (defects) the energy extracted from each input is added up in phase to the output signal. This is because the amplitude of the extended mode synchronizes the modulation of each defect mode. To illustrate this phenomenon, we show in Fig. (b) the modal amplitude of the two defect modes and the third extended mode in the double defect lattice [see Fig. 1(b)], respectively denoted respectively by $A_{d,1}$, $A_{d,2}$, A_3. In this case, the input frequencies are $f_{in,1} = f_{d,1} + f_3$ and $f_{in,2} = f_{d,2} + f_3$, where $f_{d,1}$, $f_{d,2}$, and f_3 are the resonance frequencies of the two defect modes and the third extended mode. Again, passing the transient regime the amplitude of the defect modes $A_{d,1}$ and $A_{d,2}$ become modulated by the amplitude of the extended mode A_3, showing a synchronized energy transfer from the two input frequencies $f_{in,1}$ and $f_{in,2}$ to the output frequency f_2.

The results shown in this work were obtained integrating numerically the equations of motion of the system. We are currently developing an analytical model containing a reduced number of modes in order to gain physical insight on the underlying phenomena. In addition, an experimental validation of this frequency conversion mechanism is in progress. Additional results coming out from this ongoing work will be presented.

References

[1] R. L. Harne and K W Wang, *Smart Materials and Structures*, **22**, 023001, 2014

[2] M. M. Fejer, G. A. Magel, D. H. Jundt, and R. L. Byer, *IEEE Journal of Quantum Electronics* **28**, 2631, 1904 (2010)

[3] N. C. Wong, *Opt. Lett*, **15**, 1129, (1990)

[4] M. Molerón, A. Leonard and C. Daraio, *J. Appl. Phys*, **115**, 184901, (2014)

[5] M. Serra-Garcia, J. Lydon and C. Daraio, Phys. Rev. E, **93**, 010901, (2016)

CHIMERA STATES FOR COUPLED PENDULA

Tomasz Kapitaniak[a]
Division of Dynamics, Lodz University of Technology, Lodz, Poland

Summary The phenomenon of chimera states in the systems of coupled, identical oscillators has attracted a great deal of recent theoretical and experimental interest. In such a state, different groups of oscillators can exhibit coexisting synchronous and incoherent behaviors despite homogeneous coupling. Here, considering the coupled pendula, we find another pattern, the so-called imperfect chimera state, which is characterized by a certain number of oscillators which escape from the synchronized chimera's cluster or behave differently than most of uncorrelated pendula. The escaped elements oscillate with different average frequencies (Poincare rotation number). We show that imperfect chimera can be realized in simple experiments with mechanical oscillators, namely metronomes. The mathematical model of our experiment shows that the observed chimera states are controlled by elementary dynamical equations derived from Newton's laws that are ubiquitous in many physical and engineering systems.

MODEL OF COUPLED PENDULA

Chimera states correspond to the spatiotemporal patterns in which synchronized and phase locked oscillators coexist with desynchronized and incoherent ones[1-2]. Dynamically, it represents a sort of spatially extended symmetry breaking which develops in networks of identical oscillators, surprisingly without any evidence of asymmetry or external perturbation. Furthermore, this surprising hybrid behavior obeys a substantial reserve of robustness surviving at different kind of perturbations. The experimental proof of chimeras' existence has only recently been provided for optical, chemical, mechanical and electronic systems.

Here, we show that other pattern, the so-called *imperfect chimera state*, which is characterized by a certain, small number of oscillators (solitary states) which escape from the synchronized chimera's cluster or behave differently than the most of uncorrelated pendula can be observed in the networks of identical oscillators. As a proof of concept we use the network of coupled metronomess, i.e., the system of coupled pendula which are excited by the escapement clock's mechanism.

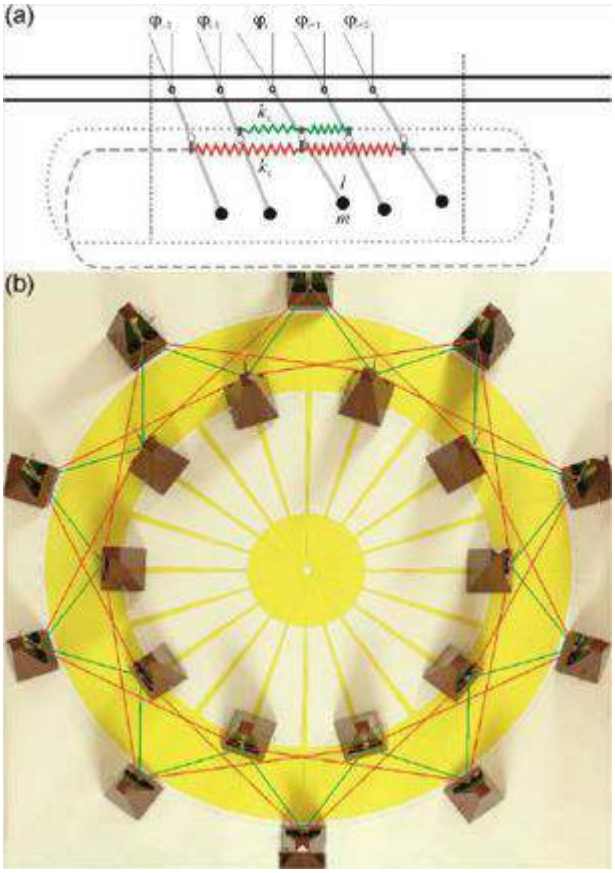

Figure 1:(a). *n* pendula coupled on the ring through springs and dampers, (b) Experimental implementation of the system of Figure 1(a) with *n*=20 metronomes which pendula are coupled by spring elements

[a] Corresponding author. Email: tomaszka@p.lodz.pl.

We consider the system of n pendula which hung from the unmovable disc as shown in Figure 1(a). Pendula of length l and mass m are coupled through the linear spring with stiffness coefficient k_x and linear dampers with damping coefficient c_x. Pendula's displacements are given by the angles φ_i. Springs and dampers are connected to each pendulum at distance l_s from the pivot. Each pendulum is connected with the nearest neighbor (green spring) and the second nearest neighbor (red springs). Additionally, the motion of each pendulum is damped by the linear damper characterized by damping coefficient c_φ. The pendula are excited by the escapement mechanism which for $\varphi_i<\gamma_N$ generate excitation torque M_N. This system can be implemented experimentally using the metronomes with the pendula connected by the spring elements as shown in Figure 1(b).

The dynamics of the system of Figure 1(a) can be analyzed using the equations of motion which are derived from Newton's laws of dynamics. We present the results for two different coupling schemes, (i) each pendulum is coupled with the nearest neighbor (local coupling), (ii) each pendulum is coupled with two nearest neighbors (nonlocal coupling).

RESULTS

Numerical simulations show that the state of complete synchronization of all pendula co-exists with the state of phase synchronization in which there exists the constant phase shift between neighboring pendula and various chimera states (including imperfect chimeras). These results have been confirmed experimentally.

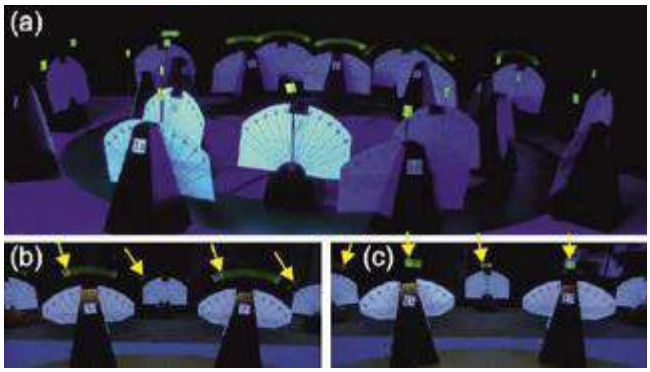

Figure 2: Experimentally observed imperfect chimera state.

The example of experimentally observed imperfect chimera is shown in Figure 2(a-c). The group of metronomes at the background of Figure 2(a) is synchronized. Their escapement mechanisms are switched on and they oscillate with the frequency equal to the nominal frequency of 200 tics per minute . The metronomes on the first plane of Figure 2(a) are either at rest or oscillate with smaller amplitudes. The escapement mechanisms of most of them are permanently switched off but metronome 15 (see Figure 2(c)) oscillates with larger amplitude and different frequency (approximately 23 tics per minute). Its escapement mechanism is intermittently switched on. The yellow arrows in Figure 2(b,c) indicate the actual positions of the pendula (snapshot). The imperfect chimera states coexist with the state of complete and phase synchronization and perfect chimeras. Imperfect chimera states are easily observed for both local and nonlocal coupling and the wide range of initial conditions (moreover, in our experiment it is easier to observe imperfect chimera states than the perfect ones).

CONCLUSIONS

We have constructed the simple experimental setup to explore the spatio-temporal dynamics of the network of the coupled pendula. The nodes in the network are locally and nonlocally coupled pendula (Huygens' clocks realized by metronomes). We observe the formation of coexisting coherent and incoherent domains in which the newly discovered patterns of imperfect chimera or multi-headed chimera are the most typical one. This behavior is observed experimentally and confirmed in numerical simulations.

References

[1] Kuramoto, Y.: Chemical Oscillations, Waves and Turbulence, Springer, New York, 1984.

[2] Kuramoto, Y. & Battogtokh, D.: Coexistence of coherence and incoherence in nonlocally coupled phase oscillators, *Nonlinear Phen. Complex Syst.* **5**, 380-385, 2002.

[3] Kapitaniak, T., Kuzma, P., Wojewoda, J., Czolczynski, K., & Maistrenko, Yu.: Imperfect chimeras for coupled pendula, Scientific Reports, **4**, 6379, 2014.

[4] Jaros, P., Borkowski, L., Witkowski, B., Czolczynski, K., & Kapitaniak, T.: Multi-headed chimera states in coupled pendula, EPJ ST, **224**, 1605, 2015.

ANALYSIS OF SYMMETRY-BREAKING AND MULTI-BIFURCATION FOR MULTI-FOLDING STRUCTURES

Ichiro Ario[1 a)]
[1]*Department of Civil Engineering, Hiroshima University, Higashi-Hiroshima, Japan*

Summary Recently, it is well-known as the symmetry-breaking phenomena in the field of physics, the block-diagonalization method (BDM) based on *representation theory of group* with the utilization of symmetry has come to be utilized to exploit structural analysis of the symmetric structure. According to the fact that topological factor is unclear in the homogeneous structures, in this paper, we present the mechanism of the breaking-down from high-symmetry of the stratified symmetry which is developed by the translation law of group theory. We propose that there is the finite element mesh issue of numeric error of computing analysis which it is confirmed *hidden symmetry* and its *symmetry-breaking* on the dynamic simulation problem by using group representation. It is possible to trace the dynamic nonlinear process from symmetric structures with strange behavior. It is found that there are different solution on dynamic process without the issue of the numeric method, it depends on the number of divided elements on symmetric structure.

THEORY OF MFM FOR A DESCRETE CYLINDRICAL STRUCTURES

We review the interesting eigenvalues problem of a folding truss allowing for the deformation using both analytical and numerical approaches. An experimental approach by Holnicki [1] showed an active shock-absorber based on the truss system. From these approaches the authors developed the concept of a pantograph truss to model the multi-folding of microstructures [2]. The paper [2] presents the theoretical basis for both static and dynamic numerical approaches to the elastic stability of a folding multi-layered truss. Both analyses are based on bifurcation theory and include geometrical nonlinearity. Comparisons are made between published experimental folding patterns and the patterns obtained from both numerical methods in which bifurcations are demonstrated as having elastic unstable snap-through behaviour. The authors suggest that understanding this behaviour will be very useful for the development of lightweight structures subject to dynamic loading based on the bifurcation static analysis and dynamic analysis.

In this paper, we investigate the mechanism of several folding patterns for the numerical work to trace the folding patterns of the system shown in Fig.1. This structure is similar to the carbon nano-tube, and inside this cage sets up the membrain structure. We consider the folding mechanisms for the cylindrical (pantographic) truss structure subject to a vertical load at the top node of the system. The system is a pin-jointed elastic truss and all nodes of the system displace vertically only. No allowance is made for friction or gravity for this geometrically nonlinear problem.

THEORETICAL APPROACH FOR A FOLDING DIAMOND TRUSS [2]

We focus a diamond truss with right-left symmetry in MFM system. Hence in this paper the theoretical bifurcation analysis, is limited to considering a collapse with symmetric deformation.

Now let's consider a theoretical estimation for a folding diamond truss model. We assume a periodic height for each layer of $h_j = \gamma_j L$ where the width L of the truss is fixed. Therefore, the initial length for each bar in geometry of the figure is expressed as

$$\ell_{ij} = \sqrt{L^2 + h_j^2} = L\sqrt{1 + r_j^2}, \quad i, j = 1, 2 \tag{1}$$

The deformed length of each bar denoted as $\hat{\ell}_{ij}$, is a function of the height and the nodal displacement variables

$$\hat{\ell}_{ij} = L\sqrt{1 + (\gamma_j - q_{ij}(\bar{v}_{ij}, \bar{v}_{i2}))^2}, \tag{2}$$

where $\gamma_j = h_j/L > 0, \quad q_{i1}(\bar{v}_{11}, \bar{v}_{i2}) = \bar{v}_{11} - \bar{v}_{i2}, q_{i2}(\bar{v}_{i2}, 0) = \bar{v}_{i2}, \ \bar{v}_{ij} = v_{ij}/L, \quad (i, j = 1, 2).$

Using Green's expression for strain, the total energy of half of the system is given by

HILL-TOP BIFURCATION EQUILIBRIUM PATHS [3]

By allowing for symmetric model, we can therefore consider nonlinear equilibrium equations based on the total strain energy theoretically.

For the 1st and 2nd equilibrium equations chained

[a)] Corresponding author. Email: mario@hiroshima-u.ac.jp

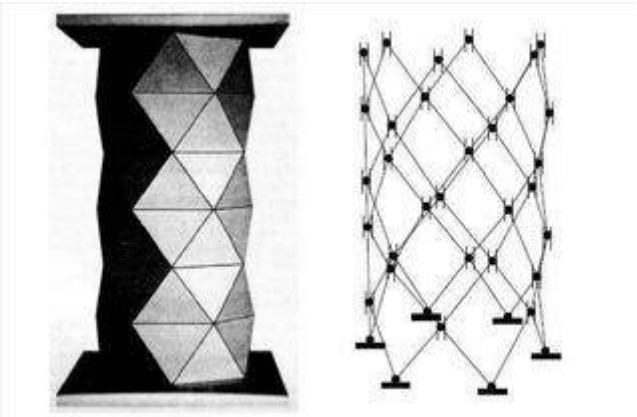

Figure 3: D_6-invariant axes-symmetric structure with MFM

$$F_{11} = \frac{\partial \mathcal{V}}{\partial v_{11}} = \sum_{i=1}^{2} \frac{\partial \mathcal{V}}{\partial q_{i1}} \frac{\partial q_{i1}}{\partial \bar{v}_{11}} \frac{1}{L} = \frac{\beta}{2} \sum_{i=1}^{2} \prod_{k=0}^{2} (\bar{v}_{11} - \bar{v}_{i2} - k\gamma) - f = 0, \tag{3}$$

$$F_{i2} = \frac{\partial \mathcal{V}}{\partial v_{i2}} = \sum_{j=1}^{2} \frac{\partial \mathcal{V}}{\partial q_{ij}} \frac{\partial q_{ij}}{\partial \bar{v}_{i2}} \frac{1}{L} = \beta \left\{ \prod_{k=0}^{2} (\bar{v}_{11} - \bar{v}_{i2} - k\gamma) + \prod_{k=0}^{2} (\bar{v}_{i2} - k\gamma) \right\} = 0,$$

These equations equal 0 in the limit value problem of total potential energy. It is possible to solve all variables $\bar{v}_{ij}$ by substituting the obtained solutions into the next limited condition using the theorem of implicit function.

$$F_{i2}(\bar{v}_{11}, \bar{v}_{i2}) = 0 \rightarrow \bar{v}_{i2} = \mathcal{F}_{i2}(\bar{v}_{11}) \tag{4}$$

$$F_{11}(\bar{v}_{11}, \bar{v}_{i2}) = F_{11}(\bar{v}_{11}, \mathcal{F}_{i2}(\bar{v}_{11})) = 0\,, \tag{5}$$

where ***F***(.) denotes a function of the nonlinear solutions. Finally, we obtain all solutions completely as equilibrium paths and it is shown the nonlinear kinetic equation in the following;

$$M\ddot{\bar{v}}_{11}(t) + C\dot{\bar{v}}_{11}(t) + K(\bar{v}_{11}(t)) = 0. \tag{6}$$

We can consider this differential equation with nonlinear stiffness for dynamic problem. Here, *M* is mass, *C* is damping and *K* is nonlinear stiffness matrices.

References

[1] I. Ario and A. Watson: Structural Stability of Multi-Folding Structures with Contact Problem: Int. J. Non-Linear Mechanics, Vol.324 (1-2), pp.263-282.

[2] I. Ario and M. Nakazawa: Nonlinear Dynamics behavior of Multi-Folding Microstructure Systems based on Origami Skill: Int. J. Non-Linear Mechanics, Vol. 45(4), pp. 337-347, 2010.

[3] I. Ario: Structure with the expanding and folding equipment as a patent (No.2006-037668), 2006.

A NEW VERSATILE TWO-STATE FIVE-PARAMETER HYSTERESIS MODEL

Saurabh Biswas[a] & Anindya Chatterjee
Mechanical Engineering, IIT Kanpur, Kanpur, Uttar Pradesh, India

Summary: We present a new five-parameter two-state hysteresis model, derived from a high dimensional frictional system. The model captures a useful range of hysteretic behaviours, including minor loops. Several examples are presented to show the versatility of the model.

INTRODUCTION

Hysteresis is a rate-independent, irreversible phenomenon observed in material stress-strain relations, damping, magnetism, and other areas. For mechanical systems with elasticity and friction, a model due to Iwan [1] seems promising, but is high dimensional. In contrast, the Bouc-Wen model [2,3] is one-dimensional, but is unrealistic under small reversals within larger load paths (minor loops are not captured, leading to unrealistic dissipation estimates). With this motivation, we have recently studied [4] a high dimensional frictional hysteretic system given by

$$\mu\,\mathrm{sgn}(\dot{x}) + Kx = bf(t), \tag{1}$$

where μ is diagonal, K is symmetric and positive definite, b is a column matrix, and $f(t)$ is scalar and differentiable. From Eq. 1, in [4] we developed a reduced order model with 6 states based on a new simple approximation for the frictional dissipation. However, some shortcomings remained in [4]. The choice of basis vectors was non-intuitive; order reductions below 6 gave poor results; and there were too many free parameters for practical use. Here, we report further on subsequent developments reported by us in [5]. A new high-dimensional model has now been studied, motivated by the Iwan model. The basis vectors are intuitively more pleasing. A model with just 2 states shows usefully rich behavior. The number of fitted parameters is 5, which is usefully small. Numerical solution is simplified, requiring solution of a 4 × 4 eigenvalue at each step. Use of the model by many analysts is now practical.

HIGH DIMENSIONAL FRICTIONAL SYSTEM

Figure 1(a) shows the underlying high dimensional frictional system [5]. In this system, each spring has stiffness $1/n$, and frictional coefficients are linearly varying $\mu_1 = \mu_0/n$, $\mu_2 = 2\mu_0/n$,..., $\mu_2 = n\mu_0/n$. As indicated in the figure, $u(t)$ is a displacement input, for which a force $f(t)$ is needed. Friction forces at the slip sites are $F_1 = -\mu_1\mathrm{sgn}(\dot{\xi}_1)$, $F_2 = -\mu_2\mathrm{sgn}(\dot{\xi}_2)$,..., $F_n = -\mu_n\mathrm{sgn}(\dot{\xi}_n)$.

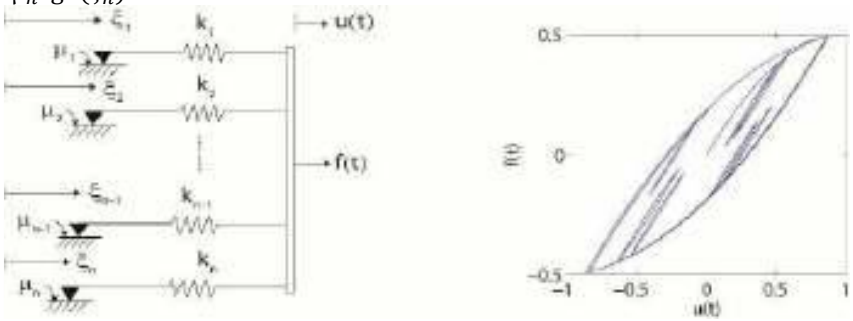

Figure 1. (a) A high dimensional frictional system. (b) Hysteresis curve obtained for the 500 dimensional system.

The governing equation of the system is

$$\mu\,\mathrm{sgn}(\dot{\xi}) + K\xi = bu(t), \tag{2}$$

Equation (2) resembles Eq. (1) but is in fact has simpler structure. Equation (2) is first incrementally solved *via* an LCP [6]. For our numerical simulation, we use $n = 500$, $\mu_0 = 0.002$, $u(t) = 0.554\sin(t) + 0.317\sin(4.858\,t)$. The solution shows hysteresis with minor loops (see Figure 1(b)). Such minor loops are not predicted by the Bouc-Wen model.

REDUCED-ORDER MODEL

Singular value decomposition of high dimensional data from the solution suggests that a two-state reduced order model is feasible (details omitted). From graphical inspection of the singular vectors, we chose basis vectors $\phi_k = \exp(-\alpha x^{1.5})(x^{1.5})^{k-1}$, where $k = 1, 2$ and the power of 1.5 is based on heuristic observations (omitted). The free parameter α gives some flexibility. We orthonormalize the ϕ_k's for analytical convenience. We then derive a reduced order model based on a

[a]Corresponding author. Email:**s.biswas90@gmail.com.**

slip-and-work criterion. Slip cannot occur if the associated frictional dissipation exceeds the external work input minus the internal increase in potential energy. Let $\xi = \Phi q$, and $\dot{\xi} = \Phi\eta$. The criterion yields

$$\eta^T \Phi^T \mu \, \mathrm{sgn}(\Phi\eta) + \eta^T (\Phi^T K \Phi) q - \eta^T (\Phi^T b) u \leq 0. \tag{3}$$

Thus, if the minimum value of the above is positive, then slip cannot occur; and the minimizing η gives the direction of potential slip. We minimize the left hand side of Eq. (3) at each time step to find η. Here, though the first term of Eq. (3) is complicated, we have found a useful approximation [4]

$$\eta^T \Phi^T \mu \, \mathrm{sgn}(\Phi\eta) \approx \frac{(\eta^T A \eta)^\beta}{(\eta^T \eta)^{\beta - 0.5}} \tag{4}$$

where $\beta = 0.5$ gives convenient yet near-optimal results, and the fitted A is symmetric and positive definite. Let $\Phi^T K \Phi = \bar{K}$, $\Phi^T b = \bar{b}$, $\sqrt{\eta^T A \eta} + \eta^T \left(\bar{K} q - \bar{b}\right) = y$. Based on Eqs. (3) and (4), we develop the following reduced order model

$$\dot{s} = \left[\frac{\eta^T \bar{b}}{\eta^T \bar{K} \eta} \dot{u} - M y |\dot{u}|\right] . \{y \leq 0\},$$

$$\dot{q} = \eta \dot{s} \, \{\dot{s} > 0\},$$

where $\dot{s}$ is the slip rate, and M is a user-defined positive number (like unity), and η can be found by solving a 4×4 eigenvalue problem (details in [5]).

FITTING PARAMETERS TO GIVEN DATA

Our reduced order model has three system matrices, namely A, $\bar{K}$, and $\bar{b}$. The model has $2 + 1 + 2 = 5$ parameters. Figure 2 shows several loop shapes that can be captured by changing the five fitted parameters.

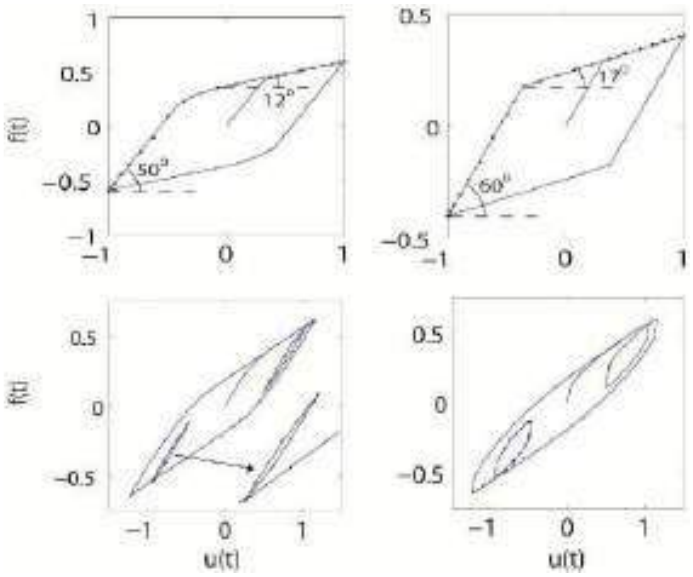

Figure 2. Various behaviours and loop shapes, to match application requirements, can be captured by the model.

CONCLUSIONS

The two-state hysteresis model has several advantages over many hysteresis models in the literature. These advantages include a minimal number of states for capturing minor loops (see [4]), a small number of fitted parameters, and the ability to match a reasonable range of hysteretic behaviors. It can now be easily used for modelling various phenomena.

References

[1] Iwan, W. D: A distributed-element model for hysteresis and its steady-state dynamic response. *J. Appl. Mech.*, **33**:4, 893-900. 1966.

[2] Bouc R: Forced vibrations of mechanical systems with hysteresis. *Proc. the Fourth Conf. on Nonlinear Oscillation*, Prague. p. 315. 1967.

[3] Wen Y. K: Method for random vibration of hysteretic systems. *J. Eng. Mech. Div.,* ASCE, **102**:2, 249-263. 1976.

[4] Biswas S. & Chatterjee A: A reduced-order model from high-dimensional frictional hysteresis. *Proc. R. Soc. A*. **470**: 20130817. 2014.

[5] Biswas S. & Chatterjee A: A two-state hysteresis model from high-dimensional friction. *R. Soc. Open Sci*. **2**: 150188. 2015.

[6] Cottle R. W., Pang, J. S. & Stone, R. E.: *The Linear Complementarity Problem*. New York, NY: Academic Press. 1992.

HARMONIC DIFFERENTIAL QUADRATURE METHOD FOR NONLINEAR VIBRATIONS OF TRANSMISSION BELTS

Jieyu Ding[1,2a)], Wei Zhang[3,2]
[1]*College of Computer Science & Technology, Qingdao University, Qingdao, China*
[2] *Beijing Center for Scientific and Engineering Computing, Beijing University of Technology, Beijing, China*
[3]*College of Mechanical Engineering, Beijing University of Technology, Beijing, China*

Summary Harmonic differential quadrature method (HDQ) is developed for the nonlinear vibration of axially moving viscoelastic belts. Different types of quadrature nodes such as Chebyshev-Gauss-Lobatto, Gauss-Legendre points, and triangle basis functions are used to discrete the partial differential vibration equations to ordinary differential equations with respect to the time. Hadamard product and SJT product are used to improve the computational efficiency of the discretized nonlinear equations. Numerical results show that the HDQ method has advantages both in efficiency and stability.

INTRODUCTION

Differential quadrature method (DQ) is a popular approach used in the area of engineering and mechanics because of its advantages of less computation, simple form and convenience. The DQ method was firstly introduced by Bellman and Casti[1], in which the partial derivatives of a function in one direction is expressed as a linear combination of the function values at all mesh points along that direction. The following studies of the DQ method were focused on the choice of mesh points, the treatment of boundary conditions, the choice of basis function, the property of weight coefficients and the convergence of solution. In the Harmonic differential quadrature (HDQ) method, the researchers chose the trigonometric functions to determine the weight coefficients, which is appropriate to the periodic solutions and is applied to structural and vibration area [2,3].

In this paper, the HDQ method is applied to the analysis on the nonlinear vibrations of two-pulley belt-drive system which is obtained in paper [4]. The different types of the quadrature nodes, such as Chebyshev-Gauss-Lobatto, Gauss-Legendre points, Hadamard product and SJT product [5], are used to discuss the nonlinear vibrations of two-pulley belt-drive system, the efficiency and stability of the algorithm.

HARMONIC DIFFERENTIAL QUADRATURE METHOD

The basis function in the DQ method can be chosen as Legendre polynomial, Lagrange interpolation polynomial, spline function, radial basis function, etc. Striz et al. developed the DQ method by using the following trigonometric functions to determine the weight coefficients, which is called harmonic differential quadrature method (HDQ). In the recent study, the basis function of the HDQ method can be chosen as

$$l_j(x)=\frac{\sin\frac{\pi}{4}(x-x_1)\cdots\sin\frac{\pi}{4}(x-x_{j-1})\sin\frac{\pi}{4}(x-x_{j+1})\cdots\sin\frac{\pi}{4}(x-x_N)}{\sin\frac{\pi}{4}(x_j-x_1)\cdots\sin\frac{\pi}{4}(x_j-x_{j-1})\sin\frac{\pi}{4}(x_j-x_{j+1})\cdots\sin\frac{\pi}{4}(x_j-x_N)}, \tag{1}$$

where $j=1,\cdots,N$, and N is the number of grid points which is normally an odd number, and $0\le x\le 1$. The corresponding explicit forms of weight coefficients for each order derivatives can be calculated by equation (1) and easy programed.

The grid points can be chosen as Chebyshev-Gauss-Lobatto, Gauss-Legendre points etc. The different types of quadrature nodes have different influences on the solutions.

NONLINEAR VIBRATIONS OF AXIALLY MOVING VISCOELASTIC BELTS

The two-pulley belt-drive system, in which the accessory shaft and the driven pulley are coupled by a wrap spring with stiffness K_d as illustrated schematically in Figure 1, where c and P_0, respectively, are the axial speed and the initial axial static tension of the translating belt and are assumed to be constant and uniform, l is the length of the belt spans, x_1, x_2 are the neutral axis coordinates of the belt span, $\omega_1(x_1,t)$, $\omega_2(x_2,t)$ are the transverse vibration displacements of the belt span at x and time t, $\theta_1(t)$ and $\theta_2(t)$, respectively, are the angular vibration displacements of the driven pulley and the driving pulley, M_1 is the preload between the accessory shaft and the driven pulley, J_a and $\theta_a(t)$ are the rotational inertia and the angular displacements of the accessory, respectively.

a) Corresponding author. Email: qdudjy@126.com.

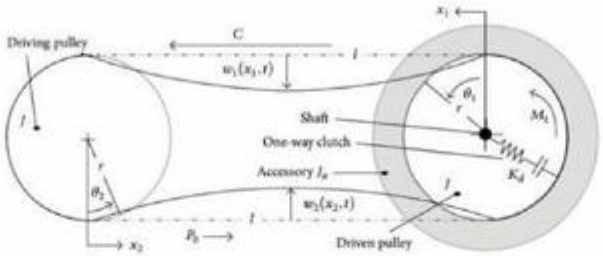

FIGURE 1: Schematic representation of a two-pulley belt-drive dynamical system coupled with a one-way clutch.

Considering the bending stiffness of the belt, the two spans of the translating belt are both modelled as Euler Bernoulli beams. The equation of transverse motion of the belt spans is nondimensionalized as

$$
\begin{aligned}
& w_{i\ tt} + c\, w_{i\ x_i t} + \left(c^2 - \right) w_{i\ xx} + k_f w_{i\ xxxx} + \alpha w_{i\ xxxxt} = T_i w_{i\ xx} \\
& J\ddot{\theta}_2 = -c_b\dot{\theta}_2 + T_2 \quad T_1, \\
& J\ddot{}_1 = -c_b\dot{\theta}_1 + T_1 \quad T_2 \quad M_1 - \frac{r_a}{r_1} f\left({}_1 - \theta_a\right)\left[k_d\left({}_1 - \theta_a\right) + \mu_c \ \dot{\theta}_1 - \dot{\theta}_a\right)\right], \\
& J_a\ddot{}_a = -c_a\dot{\theta}_a - \frac{rM_1}{r_a} + f\ \ \theta_1 - \theta_a\right)\left[k_d\ \ \theta_1 - \theta_a\right) + \mu_d \quad \dot{}_1 - \dot{\theta}_a\right)\Big]
\end{aligned}
\tag{3}
$$

The boundary conditions are $w_i\left(\quad t = \quad w_i \quad t = 0, w_{i,xx} \quad 0, \quad = \quad {}_{i,xx} \quad 1, \quad = \ / \ .$

Using the HDQ method, we discrete the equation (3) to an ordinary differential equation set with respect to the time. Hadamard product and SJT product are used to reduce the computational complexity of the nonlinear equations. The results of different types of quadrature nodes are compared to show the influences of the grid points on the solutions.

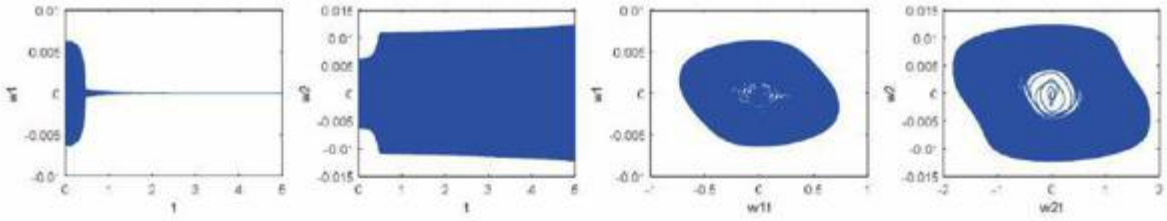

FIGURE 2: The time history and phase portrait of belt span 1 and belt span 2

CONCLUSIONS

The HDQ method is an efficient approach which can be used to solve the equations on the nonlinear vibrations of the axially moving viscoelastic belts. The HDQ method with Guass quadrature nodes illustrates the better convergence. Using Hadamard product and SJT product can reduce the computational complexity of the nonlinear equations. For the further study, localized harmonic differential quadrature method can be developed to avoid the illness of the coefficient matrices when the number of grid points reaches a certain value.

ACKNOWLEDGEMENTS

The authors gratefully acknowledge the support of the National Natural Science Foundation of China (NNSFC) through grants Nos. 11272166 and 11472143.

References

[1] Bellman R., Casti J.: Differential Quadrature and Long-Term Integration. Journal of Mechanical Analysis and Applications 34:235-238, 1971.

[2] Striz A. G., Wang X., Bert C. W.: Harmonic Differential Quadrature Method and Applications to Analysis of Structural Components. Acta Mechanica 111:85-94, 1995.

[3] Lal R., Rani R.: On the Radially Symmetric Vibrations of Circular Sandwich Plates with Polar Orthotropic Facings and Isotropic Core of Quadratically Varying Thickness by Harmonic Differential Quadrature Method. Meccanica 2015:1-24, 2015.

[4] Ding H., Zu J.: Effect of One-way Clutch on the Nonlinear Vibration of Belt-drive Systems with a Continuous Belt Model. *J. Sound Vib* **332**:6472–6487, 2013.

[5] Chen W.: Differential Quadrature Method and its Applications in Engineering − Applying Special Matrix Product to Nonlinear Computations and Analysis. *PhD Thesis*, Shanghai Jiao Tong University, Department of Mechanical Engineering, Shanghai, 1996.

NON-LINEAR DYNAMIC ANALYSIS OF A STEERING GEAR SYSTEM WITH BACKLASHES

Qian Ding [a)], Yuxin Fang &Wei Zhang
Department of Mechanics, Tianjin University, Tianjin, China
Tianjin Key Laboratory of Nonlinear Dynamics and Chaos Control, Tianjin, China

Summary Steering Gear transmission plays an important role in various transmission systems. This paper investigates the dynamic behaviour of a steering system with several backlashes. First, the motion equations of a 3-DOF system about relative movements were established. Then the modal analysis was used to analyse the natural frequencies and amplitude-frequency curves of the system using the harmonic balance method. Second. the system was numerically simulated by Runge-Kutta method. Bifurcation, chaos and other complex dynamic phenomena were presented. Finally, influences of rotational speed ratio, gear backlashes, load force and damping coefficients on dynamics of the system were analysed. The result of the paper indicates that both the operating conditions and the structural parameters of the steering gear system can be designed properly to avoid undesirable dynamic motion and realize better mechanical properties.

INTRODUCTION

Transmission systems are widely used in automotive, aerospace and other industrial machinery. Based on dynamic analysis of the steering gear parts, a transmission system can be designed with high stability, durability and efficiency. Ozguven and Hourser [1] presented a review on gear dynamics with 188 references, which also gives a summary of the mathematical models. Another review by Wang [2] presents the gear dynamic behaviours under the influence of nonlinear factors. Basic concepts, mathematical models and the solving methods were also summarized. Backlashes between the meshed gears can influence heavily on the system vibration behaviour, as described in more theoretical researches recently [3-5]. Though the electric steering gear system is an important type of transmission system, which often contains several gears and a feed screw-nut structure, the dynamics of this type of gear system has been seldom investigated. Therefore, the dynamics of a 3 degree-of-freedom steering gear system with backlashes is analysed in this paper by using of the harmonic balance method. Influences of the operating conditions and structural parameters on the system dynamics are also presented.

EQUATION OF MOTION AND MODAL ANALYSIS

The steering gear system considered is shown in Fig.1. Three gear wheels and one feed screw-nut structure, acted by the external torque T_1 on gear 1 and concentrating force T_4 on the feed screw-nut structure respectively. The displacement excitations $e(t)$, acting on each gear, are resulted from the relative gear errors of the meshing teeth. Due to the backlashes, the restoring force generated during gears meshing can be modeled by piecewise linear function in Fig 2. Considering the relative movement of the meshed gears and screw-nut, the steering gear system can be reduced as a 3 degree-of-freedom system without rigid displacements. Then dynamic equations can be established and non-dimensionalized by introducing b_0 and $\bar{t}$ as the nominal size and nominal time. The harmonic balance method based on discrete Fourier transform is adopted to modal analysis of the transmission system with backlashes. Natural frequencies and amplitude-frequency curves are presented, as an example shown in Fig 3. They indicate that the resonances occur at the nondimensional frequencies 0.67, 1.01 and 1.85 respectively. All relative vibrations are intense at the first natural frequency. Whereas at the second and third natural frequencies, only one or two relative vibrations are quite intense.

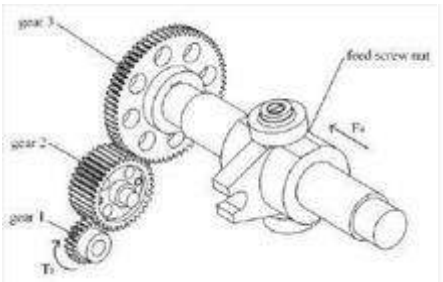

Fig. 1 The structure of a steering gear system

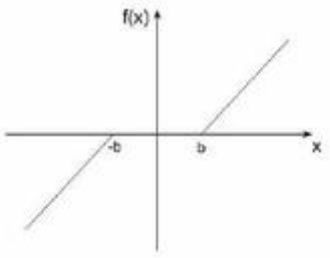

Fig. 2 Piecewise linear function of backlash

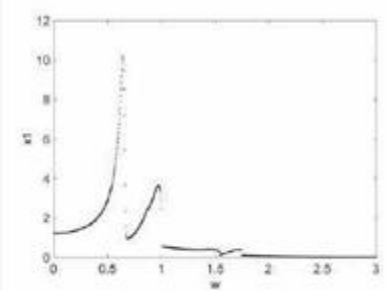

Fig. 3 A /F diagrams (b=1.2e^{-4} m)

DYNAMIC TRANSMISSION ERROR AND COMPLEX DYNAMIC PHENOMENA

The dynamical behaviors of the steering gear system are numerically solved and illustrated by bifurcation diagrams, mean value, mesh state ratio, root-mean-square (RMS) of dynamic transmission error (DTE), and so on. Results of one gear

[a)] Corresponding author. Email: qding@tju.edu.cn.

pair are shown in Fig 4-6 over the dimensionless rotating frequency Ω range of 0 to 4. In the range of 0-0.4, the mean value of DTE changes slightly and the RMS value is small, which means that the gears engage with each other only in one side and there is no collision between them at all. That is the gear engagement state is steady. In the Ω range of 0.4-0.6, the RMS value rises significantly while the mean value jumps down, and mesh state ratio of the front side is reduced by about 50%, which reflect the occurrence of double sides' collisions between the gears under the resonant conditions. As Ω increases and the mean value, RMS value and mesh state ratio value fluctuate extensively, which reflect intense gear collisions. Further increase of Ω brings the system returns back to steady movement.

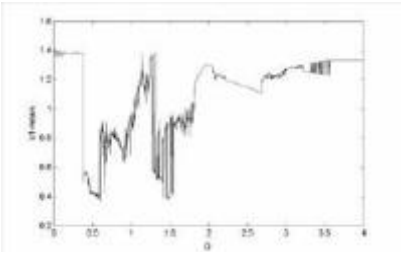

Fig 4. Mean value of DTE

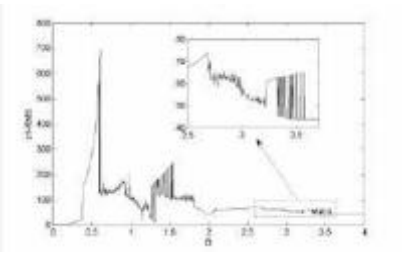

Fig 5. RMS value of DTE

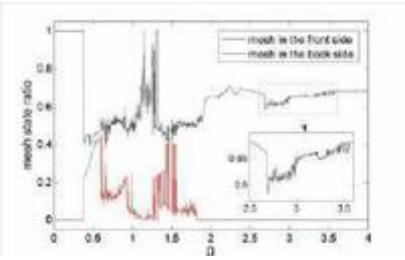

Fig 6. Mesh state ratio

INFLUENCES OF THE PARAMETERS

In general, the gear backlash is the cause of nonlinearity and has a significant effect upon the system dynamics. The research shows that every single backlash in the system can cause complex motion and the sensitive frequency areas of each backlash are different. Fig 7-9 presents the bifurcation diagrams of the system using gear backlash, dimensionless load force and damping coefficient as the bifurcation parameter, respectively. The results demonstrate the reinforce power of the complex motions when backlashes increase and the effectiveness of the higher load force and damping coefficient in suppressing non-periodic motions of the spur gear system. What is more realistic is that the parameters could be used as control parameter to avoid chaotic responses.

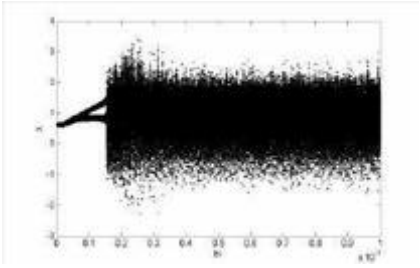

Fig 7. Bifurcation with increase of backlashes

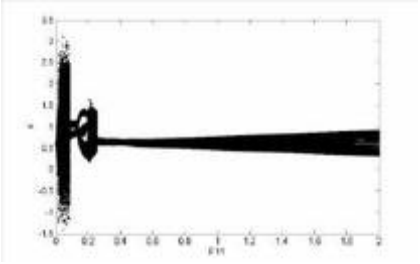

Fig 8. Bifurcation with increase of load force

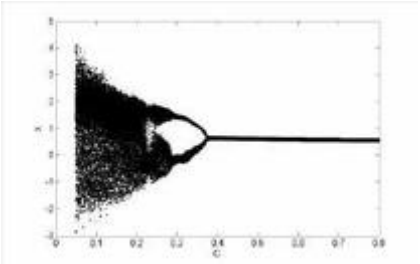

Fig 9. Bifurcation with increase of damping

CONCLUSIONS

Dynamics of a steering gear system with gear backlash nonlinearities and transmission error excitation are investigated by harmonic balance method and numerical simulations in this paper. The result shows that gear backlash is a significant factor to the bifurcations and chaos phenomenon in the steering gear system which cannot be ignored. According to the diagrams of mean value of dynamic transmission error, mesh state ratio and RMS value, bifurcations and chaos can cause gear collisions and unstable transmission to the system. Variations of the rotational speed ratio, gear backlash, dimensionless load force and damping coefficients can influence the state of the system response. The unexpected chaotic behavior, collisions within parts of the system as a result, can be avoided by designing the parameters with suitable values.

References

[1] H. Ozguven, D. Houser: Mathematical models used in gear dynamics—a review. *Journal of Sound and Vibration* **121**:383-411, 1988.

[2] Wang Jianjun, Li Runfang: A survey to nonlinear vibration of gear transmission system. *Applied Mechanics Reviews* **56**:309-329, 2003.

[3] Al-shyyab A, Kahraman A: Non-linear dynamic analysis of a multi-mesh gear train using multi-term harmonic balance method: period-one motions. *Journal of Sound and Vibration* **284**:151-172, 2005.

[4] Cai Wan, Chang Jian: Bifurcation and chaos analysis of spur gear pair with and without nonlinear suspension. *Nonlinear Analysis: Real World Applications* **12**:979–989, 2011.

[5] Chen, G. Y., Chen, G. D: Dynamic analysis of a face gear drive with spur involute pinion with backlash considered. *Mechanical Science and Technology for Aerospace Engineering* **28**:1244–1251, 2009.

NONLINER DYNAMICS OF GEARBOXES WITH FLEXIBLE FRICTION CLUTCH

Georg Jehle[1], Olga Drozdetskaya[1a)] & Alexander Fidlin[1]
[1]*Institute of Engineering Mechanics, Karlsruhe Institute of Technology, Karlsruhe, Germany*

Summary Two dynamic phenomena in automotive transmissions are investigated, which both arise while shifting. The first one is the radial displacement between the rotation axes of the clutch's discs. The second one is friction induced flutter provoking vibrations, noise and sometimes significant durability problems. The interaction between the sliding clutch and the helical gearing in the transmission is of crucial importance for both phenomena. A minimal model of a gearbox incorporating a flexible clutch disc is presented and the relevant instability mechanisms are discussed. The stability analysis based on linearization is compared to transient simulations of the complete nonlinear system, which enable to identify the main mechanisms limiting the vibration amplitude: stick-slip transitions within the clutch due to strong rotational vibrations, contact losses between the clutch discs and between the gears due to axial vibrations. It is shown that complex sequences of these events can take place within one limit cycle.

INTRODUCTION

Shifting gearboxes are common elements of mechanical transmissions, which are used both in industrial and automotive drivetrains. Combined with friction clutches they enable to operate the motor under optimal conditions and cover a wide range of operation speeds and torques. A great variety of gearboxes established itself especially in the automotive area. Manual and automatic transmissions combined with dry or wet operated clutch systems have to be mentioned here alongside with double clutch systems, which became very popular because of its fast and comfortable shifting without interruption of drive power. Friction induced phenomena are of principal importance for all these systems, because sliding within friction clutches is an inevitable part of each gear shifting. Two of the phenomena have attracted high interest of the research in the last years. The first one is the radial displacement between the engine side (primary side) disc and the gearbox side (secondary side) disc of the clutch [1, 2]. The second one is eek-noise (also called squeal) accompanied by strong vibrations of the transmission components. Different models describing particular mechanisms of the eek-noise' excitation have been suggested in the literature [3 – 5]. However, they were mainly concentrated on the modelling of the friction clutch itself (except [5]) and primarily limited to the linear stability analysis.

In the present paper, the depth of detail of the gearbox model is significantly increased concerning clutch and gears. Besides the identification of new instability mechanisms and the recognition of the governing parameters, the full nonlinear dynamics is simulated in order to distinguish between effects of different nonlinearities limiting the amplitudes of vibrations.

MINIMAL MODEL OF A HELICAL GEARBOX WITH ELASTIC LAMELLA

In the studied model, the complex structure of a real gearbox is reduced to its main components. The clutch primary side is taken to be a flexible lamella (L, cf. Figure 1), which is attached to the flywheel, mounted on the crankshaft and rotating with the constant rotational velocity Ω. The lamella is modelled using Kirchhoff's plate theory in a rotating frame.



(a) (b)

Figure 1. (*a*) Model of the shifting gearbox with a flexible lamella L; (*b*) contact between the lamella and the eccentric friction disc.

The clutch disc CD is attached to the gearbox' input shaft G1. It has four degrees of freedom $\boldsymbol{u}^{(1)} = \left[u_x^{(1)}, u_y^{(1)}, u_z^{(1)}\right]$ and $\boldsymbol{\omega}^{(1)} = \left[0,0,\dot{\varphi}^{(1)}\right]$. The compound is elastically supported by springs representing the rolling bearings. Bending or tilting of the input shaft is not taken into account, because the corresponding effects have been elaborately discussed in [3, 4]. The teeth on the input shaft contact with those placed on the secondary shaft G2. In the stationary case, this contact can be modelled as a non-holonomic constraint. For transient simulations, the unilateral tooth contact is not necessarily closed. An alternative tooth force model is needed here which is obtained through regularization of the line tension at both front and rear of the

a) Corresponding author. Email: olga.drozdetskaya@kit.edu.

flanks. The contact between the elastic lamella and the clutch disc occurs along the contact circle (cf. Figure 1b). The gear normal force shifts the input shaft away from the engine's axis, leading to a radial displacement which depends strongly on the transmitted torque. In this context, non-symmetrical deformation of the lamella arises which requires taking the corresponding elastic modes into account.

FRICTION INDUCED FUTTER AND NONLINEARITIES LIMITING VIBRATION AMPLITUDES

Depending on design parameters and operating conditions, different instability mechanisms can occur in the described system, which are all of the type friction induced flutter due to mode coupling. However, depending on the dominant oscillation modes, the instabilities can be split into several groups:

- radial-torsional instability of the input shaft
- wobbling instability of the lamella alongside with torsional vibrations of the input shaft
- combination of both

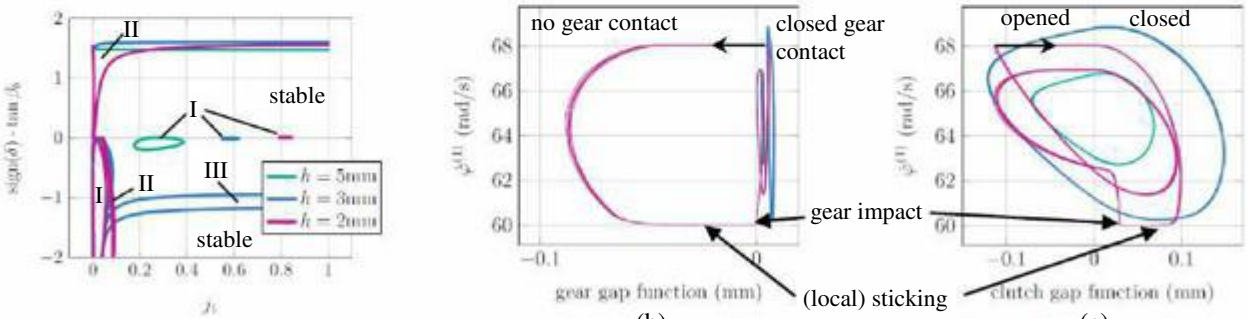

Figure 2. (a) Instability domains in the parameter space for different values of the lamella's thickness h: I –radial-torsional flutter, II – wobbling instability of the lamella, III – combination of I and II; (b) and (c) steady state oscillation: green – opening in the clutch, blue – opening and partial sticking in the clutch, magenta – opening and sticking in the clutch, impacts between the gears.

The existence domains for each type of instability are calculated in the parameter space (cf. Figure 2a). Here $j_1 = \frac{J_1}{m_1 R^2}$ is the ratio between the gear unit input shaft's rotational inertia and its mass times square of the friction radius, β_b is the gear helical angle and sign(δ) is the slip direction within the clutch.

The amplitudes of the self-excited vibrations can be limited by different nonlinearities. Contact losses between the lamella and the clutch disc (gap function < 0) alongside with the impacts within the gears are of main importance at low clamping force in the clutch which results in the low transmitted torque. At a high level of the clamping force, temporal (local) sticking along the friction circle becomes the most important nonlinearity. Complex behaviour can be observed in the intermediate range of the clamping forces, where all these mechanisms can contribute to the occurrence of the limit cycle (cf. Figure 2 (b) and (c)).

CONCLUSIONS

A wide variety of friction induced effects exists in a gearbox with attached dry friction clutch, such as radial displacement and several types of instabilities. The suggested minimal model enables the parameter value- and operation dependant description of both effects. The influence of different nonlinearities on the amplitude of the transient oscillation demonstrates the principally non-smooth character of the system, making the numerical analysis extremely difficult. Nevertheless, some approaches could be identified, which enable to capture the principal behaviour of a gearbox with a more complex structure.

References

[1] Fidlin A., Stamm W.: On the radial dynamics of friction discs. Eur. J. Mech. – A/Solids *28*:526-534, 2009.

[2] Weiss C., Morlock M.M., Hoffmann N.P.: Friciton induced dynamics of ball joints: Instability and post bifurcation behavior. Eur. J. Mech. – A/Solids *45*:161-173, 2014.

[3] Herve B., Sinou J.-J., Mahe H., Jezequel L.: Analysis of squeal noise and mode coupling instabilities including damping and gyroscopic effects. Eur. J. Mech. – A/Solids *27*:141-160, 2008.

[4] Fidlin A., Drozdetskaya O., Waltersberger B.: On the minimal model for the low frequency wobbling instability of friction discs. Eur. J. Mech. – A/Solids *30*:665-672, 2011.

[5] Jehle G., Fidlin A.: Friction induced vibrations in shift gearboxes. ZAMM, Z. Angew. Math. Mech. *94:* 911- 916, 2014.

VIBRO-IMPACT DYNAMICS IN SYSTEMS WITH TRIGGER OF COUPED THREE SINGULAR POINTS: COLLISION OF TWO ROLLING BODIES

Katica R. (Stevanović) Hedrih[1,2]
[1]*Department of Mechanics, Mathematical Institute Serbian Academy of Sciences and Arts, Belgrade, Serbia*
[2]*Faculty of Mechanical Engineering, University of Niš, Serbia*

Summary Under the author's use Petrović's elements of mathematical phenomenology, especially mathematical analogy, new expressions of post-collision outgoing angular velocities of two rolling rigid bodies are determined. Advances to theory of collision between two bodies are generalized to collision of two rolling rigid bodies. Using these results, nonlinear dynamics in the vbro-impact system with trigger of coupled singular points and homoclinic trajectory in phase trajectory portraits is study. Use phase portraits of two nonlinear dynamical systems in which appear central collision of thin rolling different size disks are studied. In first vibro-impact system disks is in rolling along straight line and coupled by springs, and in second rolling disks are moving along a circle line rotate with constant angular velocity around vertical central axis. In both considers system dynamics exist a trigger of coupled singular points.

ADWANCES TO THEORY OF COLLISION OF TWO RIGID ROLLING BODIES

Advances to theory of collision between two bodies are generalized to collision of two rolling rigid bodies. Under the authors' use Petrović's elements of mathematical phenomenology [1,2,3,4], especially mathematical analogy, new expressions of post-collision outgoing angular velocities of two rolling rigid bodies are determined in following forms (see Figure 1.a*):.

$$\omega_{P1}(t_0+\tau)=\omega_{P1}(t_0)-\frac{1+k}{1+\frac{\mathbf{J}_{P1}}{\mathbf{J}_{P2}}}(\omega_{P1}(t_0)-\omega_{P2}(t_0))$$

$$\omega_{P2}(t_0+\tau)=\omega_{P2}(t_0)+\frac{1+k}{1+\frac{\mathbf{J}_{P2}}{\mathbf{J}_{P1}}}(\omega_{P1}(t_0)-\omega_{P2}(t_0))$$

where $k=\frac{\omega_r(t_0+\tau)}{\omega_r(t_0)}=\frac{\omega_{P2}(t_0+\tau)-\omega_{P1}(t_0+\tau)}{\omega_{P1}(t_0)-\omega_{P2}(t_0)}$

$$\mathbf{J}_{P1}\bar{\omega}_{P1}(t_0)+\mathbf{J}_{P2}\bar{\omega}_{P2}(t_0)=\mathbf{J}_{P1}\bar{\omega}_{P1}(t_0+\tau)+\mathbf{J}_{P2}\bar{\omega}_{P2}(t_0+\tau)$$

Kinematical plans of pre- and post-collision angular velocities are composed for different cases of collisions.

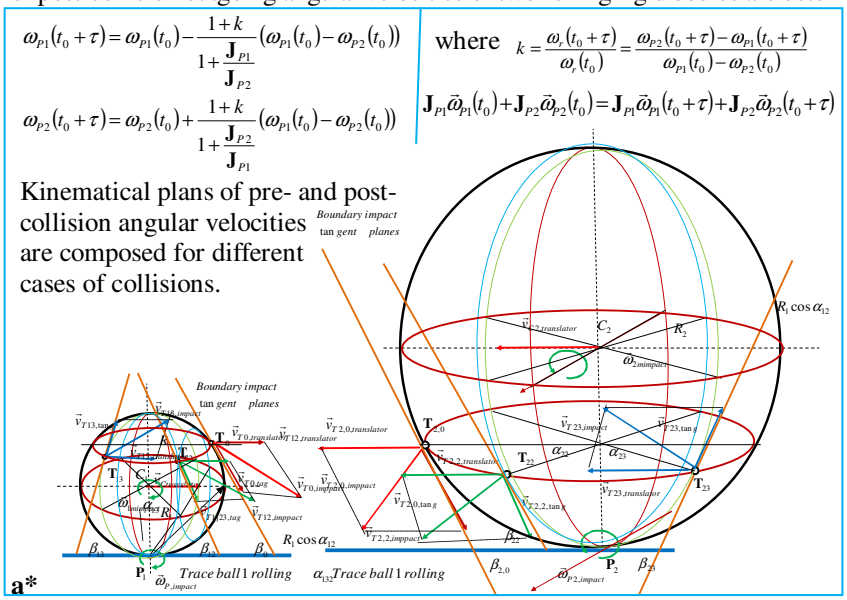

$$\ddot{x}_i+2\delta_i\dot{x}_i^2+\omega_{0i}^2x_i\left(\frac{\sqrt{b_{0i}^2+x_i^2}-l_{0i}}{\sqrt{b_{0i}^2+x_i^2}}\right)=0,\ i=1,2;\ \omega_{0i}^2=\frac{c_i r_i^2}{\mathbf{J}_{\mathbf{P}_i}}$$

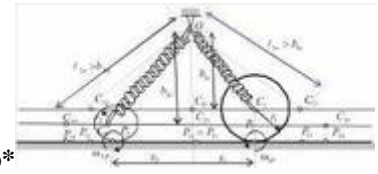

$$\ddot{\varphi}_i+2\delta_i\dot{\varphi}_i^2+\frac{\Omega^2}{\kappa_i}\langle\lambda_i-\cos\varphi_i\rangle\sin\varphi_i=0,\ i=1,2;\ \kappa_i=\left(\frac{\mathbf{J}_{Ci}}{Mr_i^2}+1\right)$$

$$\lambda_i=\frac{g}{(R-r_i)\Omega^2}$$

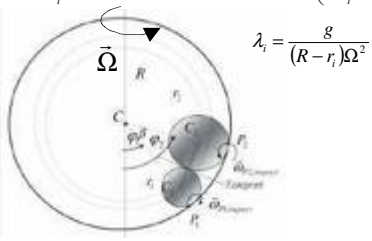

Figure 1. a* Plans of the impact velocities of possible points at corresponding circles at same height of balls in central a nd skew collisions of two rolling heavy balls different radiuses: left for first smaller ball and right for second bigger ball. b* and c* Two vibro-impact systems each containing two rolling thin different radiuses disks in central successive collisions.

NON-LINEAR DYNAMICS OF TJE VIBROIMPACT SYSTEMS WITH T RIGGESR OF COUPLED SINGULAR POINTS AND HOMOCLINIC ORBITS IN FORM NUMBER EIGHTIN PHASE PORTRAITS

In Figure 1.b* and c* two mechanical vibro-impact syst ems containing two rolling thin different size disks are presented. Each disks, in both considered systems dynamic s, a corresponding trigger [5,6] of coupled three singular po ints and homocclinic orbit in the form of number "eight" pos ses in corresponding phase portraits for corresponding rel ation of parameters of system, In both system exists a bifurcati on parameter and with its variation in the phase portrait s layering of phase trajectories appear, as well as appearance and disappe arance of trigger of coupled singular points. Kinetic para meters and phase portraits of each vibro-impact system (in Figu re 1. b* and c*) in ideal constraints as conservative and, also, in the field of turbulent damping as no conservative, an d of each of the rolling disks are determined and graphic ally presented. in Figure 2 a* and b* phase trajectory branches in phase portraits of two rolling disks for motion in interval be tween configurations of the initial condition configurations and configurations of pre-first-collision and post-first-co llision between two rolling disks for corresponding conservativ e systems are presented. On the phase portraits alterna tions of the pre-collision impact velocities of the disks into post-col lision corresponding translator or angular velocities are visible.

[a)] Corresponding author. Email: khedrih@sbb.rs,khedrih@eunet.rs.

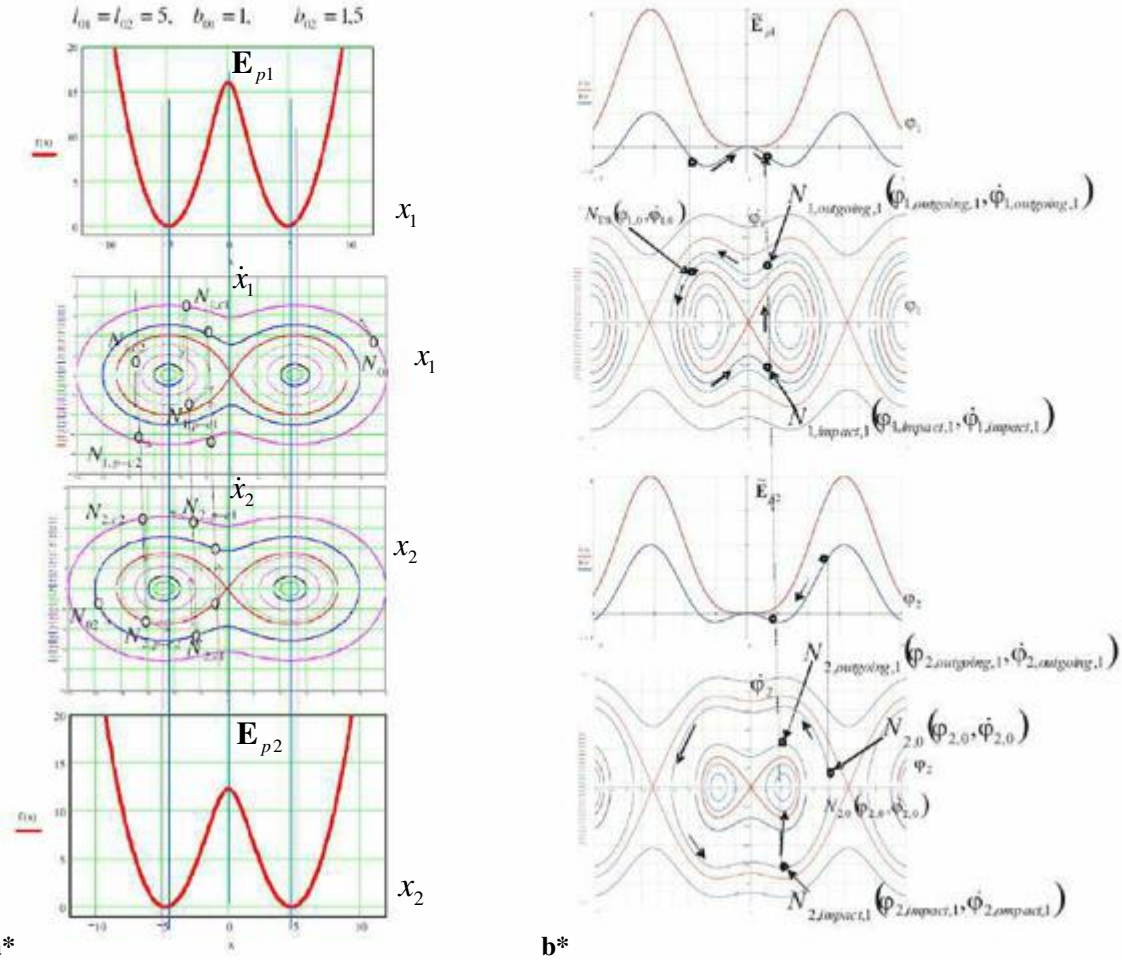

Figure 2. Phase trajectory branches in phase portraits and total mechanical energy branches of two rolling disks for motion in interval between initial condition configuration and configurations of pre-first-collision and post-first-collision between two rolling disks with vibro-impact dynamics (a*) along a line and (b*) on rotate circle trace with constant angular velocity around vertical central axis for the conservative systems presented in Figure 1,b* and 1.c*.

CONCLUDING REMARKS

Advances to theory of collision of two rolling rigid bodies open new possibilities for progress in knowledge of vibroimpact system dynamics. Obtained results are related to different ceases of conservative as well as no conservative vibro-impact dynamics. Emery analysis for turbulent damping with generalized function of energy dissipation $\Phi = b\dot{x}^3/3$ gives rate of total mechanical energy degradation in the form: $d\left(E_k + E_p\right)/dt = -3\Phi$.

Acknowledgment: Parts of this research were supported by the Ministry of Sciences and Technology of Republic of Serbia through Mathematical Institute SANU Belgrade Grant ON174001 "Dynamics of hybrid systems with complex structures. Mechanics of materials.". and through Faculty of Mechanical Engineering University of Niš.

References

[1] Petrović M., Elementi matematičke fenomenologije (Elements of mathematical phenomenology), Srpska kraljevska akademija, Beograd, 1911. str. 389.. http://elibrary.matf.bg.ac.rs/handle/123456789/476?locale-attribute=sr

[2] Petrović M., Mecanismes communs aux phenomenes disparates, Paris 1921.

[3] Preface:Elements of mathematical phenomenology and phenomenological mapping in non-linear dynamics, Edited by Katica R. (Stevanovic) Hedrih, Ivan Kosenko, Pavel Krasilnikov and Pol D. Spanos, Special Issue of International Journal of Non-Linear Mechanics, Volume 73, Pages 1-128 (July 2015)

[4] Hedrih (Stevanović) K.R. , (2015), Elements of mathematical phenomenology: I. Mathematical and qualitative analogies,. Труды МАИ Выпуск №84, pp. 42 (1-42); II. Phenomenological approximate mappings, №84, pp. 29 (1- 29) www.mai.ru/science/trudy/ , http://www.mai.ru/upload/iblock/5f6/hedrih_eng_1.pdf, Эл № ФС77-58560, ISSN: 1727-6942

[5] Hedrih (Stevanović) R. K., (2004), A Trigger of Coupled Singularities, MECCANICA, Vol.39, No. 3, 2004., pp. 295-314. , DOI: 10.1023/B:MECC.0000022994.81090.5f,

[6] Andronov A. A., Vitt A. A., Haykin S., (1981), Teoriya kolebaniy, Nauka, Moskva., pp. 568.

SWITCHING SENSITIVE AND INSENSITIVE RESPONSES IN A PIECEWISE SMOOTH RUBBING ROTOR SYSTEM

Jun Jiang[a)], Ling Hong
State Key Laboratory for Strength and Vibration, Xi'an Jiaotong University, Xi'an 710049, China

Summary In this work the response characteristics of a two-degree-of-freedom piecewise smooth nonlinear isotropic rubbing rotor system, which consists of a linear subsystem and a nonlinear subsystem controlled by a switching surface that gives the rubbing condition, are investigated. It is found that the parameters of the piecewise smooth system can be classified into the switching sensitive and insensitive regions. We show that the responses of the full non-smooth system *in the switching insensitive regions* can be well determined through the analysis of the responses both the linear and the nonlinear subsystems by the theory of nonlinear dynamics. *In the switching sensitive regions*, some responses of the full non-smooth system, although unpredictable theoretically, can still be explained from the response characteristics of the subsystems, and some other responses cannot be well understood from our current knowledge.

PIECEWISE SMOOTH MODEL FOR A RUBBING ROTOR

Rotor/stator rubbing is a malfunction in rotating machinery that degrades the machine performance and may lead to the catastrophic failure of a whole machine through dry whip in the worst case [1]. A rubbing rotor system (see Fig.1) can be modeled by a piecewise smooth system [2]:

$$\begin{aligned} &m\ddot{x}+c\dot{x}+k_s x+\Theta k_b\left(1-\frac{r_0}{r}\right)(x-\mu y)=me\omega^2\cos\omega t \\ &m\ddot{y}+c\dot{y}+k_s y+\Theta k_b\left(1-\frac{r_0}{r}\right)(\mu x+y)=me\omega^2\sin\omega t \end{aligned} \qquad \text{deflection magnitude } r=\sqrt{x^2+y^2} \tag{1}$$

where x,y are the deflections of the rotor in the horizontal and vertical directions, and m,c,k_s are mass, damping and stiffness of the rotor. e is mass eccentricity and ω the rotating speed of the rotor. k_b is the stiffness of the stator. r_0 and μ are clearance and friction coefficient between the rotor and the stator.

Θ is Heaveside function with $\Theta=0$ when the deflection amplitude $r<r_0$, that is, there is no rubbing in the rotor and the system is govern by linear equations. $\Theta=1$ when $r\geq r_0$ is the rubbing case whereby the system is governed by the nonlinear equations. Therefore, the rubbing condition is governed by the switching surface by

$$\sigma=\{(x,\dot{x},y,\dot{y})\,|\,\sqrt{x^2+y^2}-r_0=0\} \tag{2}$$

The piecewise smooth system possesses some specific features: (1) the switching surface is defined as a deflection magnitude of two displacement coordinates of the system; (2) when a periodic trajectory of the system begins to touch the switching surface, it touches switching surface at all points to make it different from gazing in the usual non-smooth systems; (3) there is no periodic motion formed by crossing the switching surface between the two subsystems.

DYNAMICS OF LINEAR AND NONLINEAR SUBSYSTEMS

By solving the equations of the linear subsystem of (1) when $\Theta=0$, the existence boundaries of the periodic solution of linear subsystem are obtained by considering the switching condition (2), which are shown by the red dashed lines marked respectively by Ω_L and Ω_U in Fig.1(left). Here Ω is the non-dimensional rotating speed defined by ω over the natural frequency of the coupled rotor/stator system. These two lines also give the rotating speeds at which the piecewise smooth system (1) is in the grazing state.

The periodic solutions of the nonlinear subsystem of (1) when $\Theta=1$ can be also solved analytically. There are two branches periodic solutions of the nonlinear subsystem, one is stable and the other is unstable. The existence ranges of the periodic solutions are decided by three saddle-node bifurcation points denoted by the black solid curves in Fig.1(left). However, when the switching condition (2) is taken into account, the periodic solutions are meaningless in the ranges between SN_1 and Ω_L as well as in right side of SN_3 because the amplitudes of the periodic solutions are smaller than the clearance r_0. The boundaries of Hopf bifurcation for each of the two periodic solutions are also derived analytically and shown by the green solid curves in Fig.1(left). It is found that the meaningful stable periodic solution of the nonlinear subsystem exists only in the range between Ω_L and SN_2 and under the green curve (+). So a meaningful quasi-periodic solution with amplitude fluctuating around r_0 exists after Hopf bifurcation in the corresponding region but above the green curve (+). Through numerical simulations, the nonlinear subsystem possesses only a pair of meaningless periodic solutions in the range between SN_1 and Ω_L, but there are meaningful chaotic and quasi-periodic responses in the ranges between SN_2 and SN_3, or in the region in the right side of SN_3, where another pair of meaningless periodic solutions exist. The dynamical characteristics of subsystems have significant influence on the behavior of the full piecewise smooth system.

[a)] Corresponding author. Email: jun.jiang@mail.xjtu.edu.cn.

SWITCHING INSENSITIVE AND SENSITIVE RESPONSE REGIONS

It is found that the response characteristics of the full piecewise smooth in the region corresponding to the regions I, II and III in Fig.1(left) can be well determine by using the dynamic information derived from the linear and the nonlinear subsystems, as shown in Fig.1(right) as given by [2]. These regions are thus defined as *switching insensitive regions* of the full piecewise smooth system (1). The features of these regions are quite different. In region I, the only meaningful solution is the periodic solution of the linear subsystem. In region II, the only meaningful response is the periodic or the quasi-periodic response of the nonlinear subsystem. In region III below green curve (+), periodic solutions of both linear and nonlinear subsystems are meaningful but they do not interference each other and can coexist. In region III above green curve (+), the meaningful quasiperiodic response loses stability due to the response at the nonlinear normal mode [3].

However, the response characteristics of the full piecewise smooth system (1) in the region in the right side of SN_2, marked by IV and V in Fig.1(left), cannot be well predicted or even understood from the responses of the linear and nonlinear subsystems. These regions are thus defined as *switching sensitive regions* of the full piecewise smooth system (1). The features of these two regions are as follows: the linear subsystem has a periodic solution with amplitude almost touch the switching surface, and on the other hand, the nonlinear subsystem has a meaningful chaotic or quasi-periodic response with the amplitude fluctuating around the switching surface and the meaningless periodic solutions with amplitudes less than the clearance r_0.

CONCLUSIONS

The responses of piecewise smooth rotor system are investigated from the point view to find the relationship between the response characteristics of the subsystems and those of the whole system. It is demonstrated that the responses of the whole system can be well predicted from those of subsystems in the switching insensitive regions. On the other hand, it is still a challenge to understand and predict the responses in the switching sensitive regions.

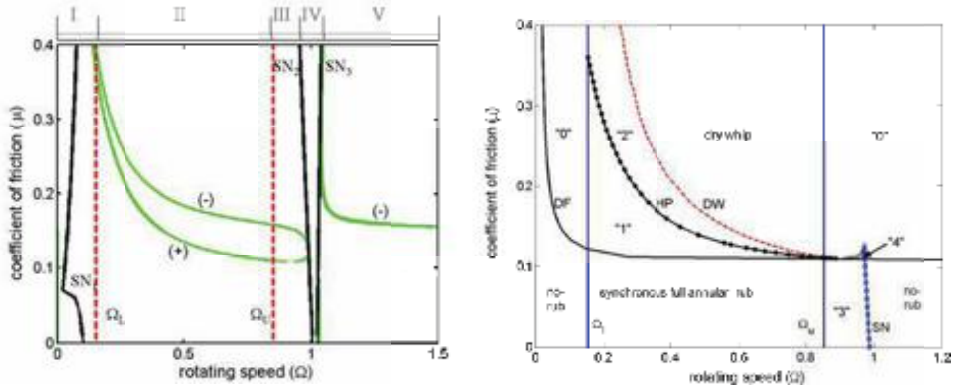

Fig.1 (Left)The existence and bifurcation boundaries of periodic solutions of the linear and nonlinear sub-systems.(Right) Response characteristics of system (1) with the boundaries of no-rub are denoted by Ω_l and Ω_u, synchronous full annular rub by curves of Ω_l, SN and HP, partial rub by HP and DW, and dry whip marked by DF. The multi-stable sub-regions are denoted by "0", "1", "2"and "3".

Acknowledgements

This work was supported by the National Natural Science Foundation of China (Grant No. 11332008).

References

[1] Yu J. J., Goldman P., Bently D.E., Muszynska A.: Rotor/seal experimental and analytical study on full annular rub. *ASME Journal of Engineering for Gas Turbines and Power* **124**: 340–350, 2002.

[2] Jiang J.: Determination of the Global Responses Characteristics of A Piecewise Smooth Dynamical System with Contact. *Nonlinear Dynamics* **57**: 351-361, 2009.

[3] Chen Y. H., Jiang J.: Determination of nonlinear normal modes of a planar nonlinear system with a constraint condition. *Journal of Sound and Vibration* **332**: 5151–5161, 2013.

MIXED-MODE OSCILLATIONS IN A SLOW-FAST FLEXIBLE JOINT SYSTEM WITH TIME DELAY

Shanying Jiang[1a)], Jian Xu[2]
[1]*School of Mechanical Engineering, Shanghai Institute of Technology, Shanghai, China*
[2]*School of Aerospace Engineering and Applied Mechanics, Tongji University, Shanghai, China*

Summary Mixed-mode oscillations (MMOs) are observed in a delay-coupled flexible joint system with multiple time scales, which behaves as a complex oscillatory pattern consisting of small amplitude oscillations followed by large excursions of relaxation type in a period. The existence of homoclinic orbits induced by Bogdanov-Takens bifurcation of the fast subsystem is proposed to explain the mechanisms of the occurrence of MMOs. It is numerically proved that the small parameter in a slow-fast system influences the convergence rate of oscillatory trajectories and thus leads to the transitions of mixed-mode oscillations.

THE SLOW-FAST FLEXIBLE JOINT SYSTEM

A delay-coupled flexible joint robot manipulator is remodelled and transformed into a typical slow-fast system in [1] as

$$\begin{cases} \varepsilon\dot{\theta}_1 = {}_1 , \\ \varepsilon\dot{p}_1\ t = \alpha_1\left(\varepsilon\ {}_2 - {}_1 - \tau\right) + \left(\theta_2\ t - \theta_1(t-\tau)\right) - \beta\sin\theta_1\ t , \\ \dot{\theta}_2 = {}_2 , \\ \dot{p}_2\ t = -\alpha_1\left(\varepsilon\ {}_2 - {}_1 - \tau\right) - \left(\theta_2\ t - \theta_1(t-\tau)\right) - \alpha_2\ {}_2 + , \end{cases} \tag{1}$$

where θ_1 and p_1 are defined as fast variables, θ_2 and p_2 are fast variables and the parameter ε is usually called as the small parameter. It is obtained that the small parameter multiplies the highest derivative of the state variables in Eq. (1), which leads to the fact that the order of the system for $\varepsilon = 0$ becomes lower than that for $\varepsilon \neq 0$. This is just why the singularity comes up in a slow-fast problem. According to geometric singular perturbation theory [2], the limit of the original full system as $\varepsilon \to 0$ is defined as the reduced slow subsystem while the limit of the rescaled full system with $= \varepsilon$ and $\varepsilon \to 0$ is the reduced fast subsystem.

EXISTENCE OF HOMOCLINIC ORBITS

Projecting the 4-dimensional fast subsystem onto the 2-dimensional plane p_1-θ_1 and regarding the state variable $\theta_2\ t$ as a constant, the fast subsystem on the p_1-θ_1 plane is obtained as

$$\begin{cases} \theta_1' = {}_1 , \\ p_1'\ t = -\alpha\ p\ \ t-\tau\right) + \left(\theta_{20} - \theta_1(t-\tau)\right) - \beta\sin\theta_1\ t . \end{cases} \tag{2}$$

After a translation of the equilibrium to the origin, the corresponding characteristic equation is derived as

$$F\ \lambda = \lambda^2 + e^{-\lambda\tau}\alpha_1\lambda + e^{-\lambda\tau} + \beta\cos\left(\theta_{10}\right) = 0. \tag{3}$$

It tells that $\lambda = 0$ is a double zero root of the characteristic equation $F\ \lambda = 0$ when the condition $\alpha_1 - = 0$ holds. Namely, the characteristic equation (3) has a zero eigenvalue with multiplicity two. Bifurcation theory in dynamical system [3] says that when the characteristic equation of a linearized system has a zero eigenvalue with multiplicity two, a BT bifurcation may occur in the original nonlinear system. Fig. 1 illustrates a series of boundary curves dividing the parameter plane $\tau\ \theta_1$ into nine areas, where the boundary curves H_i and S_i correspond to the pure imaginary eigenvalues

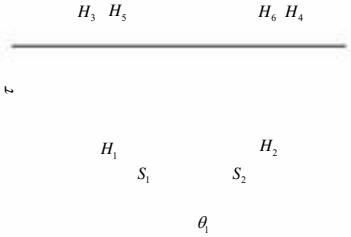

Fig. 1 The stability boundaries near the BT point.

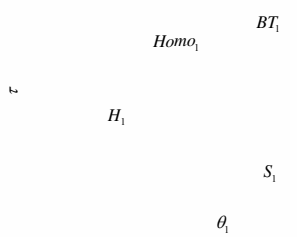

Fig. 2 The critical boundary of homoclinic bifurcation.

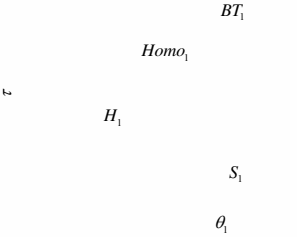

Fig. 3 The BT bifurcation diagram on the parameter plane $\tau\ \theta_1$

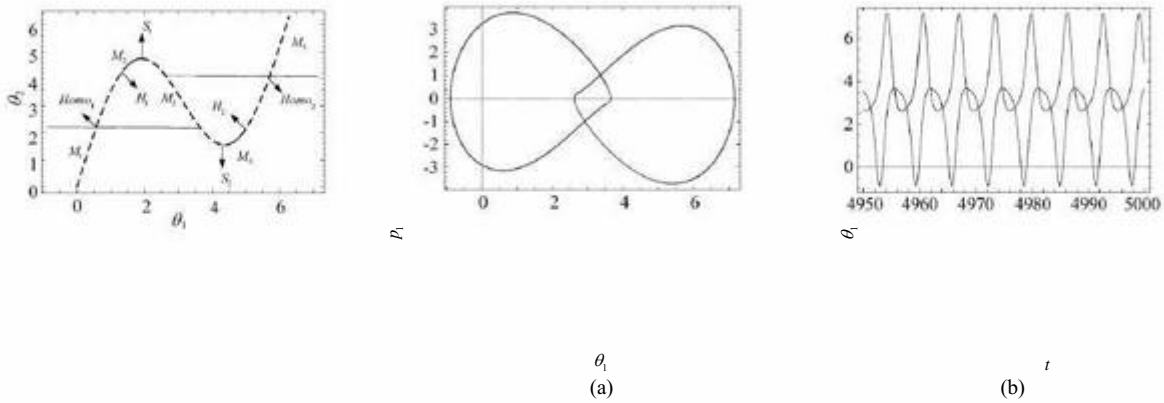

(a) (b)

Fig. 4 Structure and stability of the slow manifold with $\tau = 0.653$.

Fig. 5 Limit cycles and corresponding time-history plots, (a) limit cycles, (b) time-history plots.

and the zero eigenvalue respectively. Fig. 3 illustrates the corresponding phase diagrams in each region separated by critical bifurcation curves shown in Fig. 2. Fig. 4 explains the structure of the slow manifold with two limit cycles near the homoclinic points $Homo_1$ and $Homo_2$. The corresponding phase portraits and time histories of two limit cycles starting from different initial points are presented in Fig. 5. Numerical results show that with the variation of time delay, these two limit cycles could be infinitely close to the homoclinic orbits. So far, the existence of homoclinic orbits is identified.

OSCILLATION ANALYSIS AND EFFECTS OF SMALL PARAMETER

Once the fast manifold fails to intersect with the stable segments or the stable limit cycles bifurcated from unstable segments of the slow manifold, the flows in the phase space would not be attracted to any of the stable attractors and they would have to wander in the space. In fact, it is just these wandering flows that result in the mixed-mode oscillations. The phase portraits and the time-history plots corresponding to ε=0.05 and ε=0.01 are displayed in Fig. 6. From the comparison of Fig. 6(a) to (d), one may easily figure out that with the reduction of the small parameter ε, the convergence rate of flows being attracted to the stable segment M_4 is slowed down. Based on the results obtained above, it can be seen that with the same time delay, the mixed-mode oscillations can be transferred via adjusting the small parameter ε. Besides, the scales of the small parameter influence the attraction rate of flows to the stable segments.

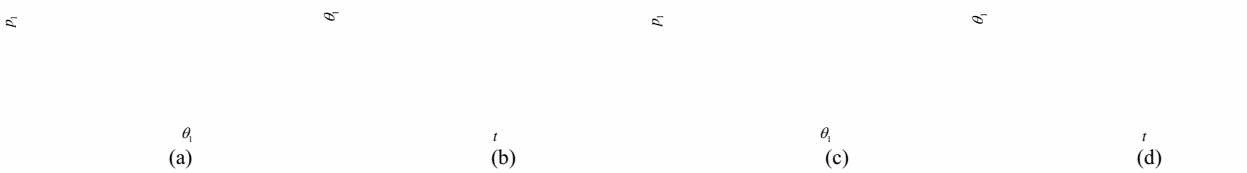

(a) (b) (c) (d)

Fig. 6 Mixed-mode oscillations, (a) phase portraits with ε=0.05, (b) time series with ε=0.05, (c) phase portraits with ε=0.01, (d) time series with ε=0.01.

CONCLUSIONS

A slow-fast flexible joint system is investigated in this paper to explain the mechanism of mixed-mode oscillations. The eigenvalue analysis of the fast subsystem achieved the condition of BT bifurcation and then confirmed the existence of homoclinic orbits around the slow manifold. Numerical results reveal that the mixed-mode oscillations can be transferred from one to another through the scale variation of the small parameter. The smaller the parameter is, the slower the convergence rate of the flows to the stable homoclinic orbit and the stable segment of the slow manifold are.

Acknowledgments

The authors would like to gratefully acknowledge the support from the National Natural Science Foundation of China under Grant No. 11502147 and 11572224.

References

[1] Jiang, S., Xu, J. & Yan, Y.: Stability and oscillations in a slow-fast flexible joint system with transformation delay. *Acta Mech. Sinica,* **30**: 727-738, 2014.

[2] Jones, C.: Geometric singular perturbation theory. *Lect. Notes Math,* **1609**: 45-118, 1994.

DYNAMIC RESPONSE OF ACOUSTICALLY EXCITED PANELS RESTING ON ELASTIC FOUNDATIONS IN THERMAL ENVIRONMENTS

Liu Liu[1], Bingyang Lv[1]&Tiren He[1]
[1]School of Aerospace Engineering, Department of Mechanics
Beijing Institute of Technology, Beijing, China

Summary In order to ensure integrity of thermal protection system for hypersonic vehicles, the stochastic dynamic response induced by the combination of thermal and acoustic loadings has been investigated for a thin panel resting on a two-parameter elastic foundation. A theoretical model is developed based on the Kirchhoff thin-plate assumptions and general von Kármán-type equation through Galerkin method. A dynamic response evolution parameter deduced from the primary-mode modal equation and the Fokker-Planck distribution function is proposed to characterize a transition from linear vibration to fully nonlinear dynamic snap-through for a thermally-buckled panel. The study demonstrates the combination of acoustic excitation, thermal effect and structural stiffness including elastic foundation stiffness governs the dynamic response evolution. As the elastic foundation stiffness increases, the buckling temperature increases and the postbuckling deflection decreases, which promote the nonlinear dynamic snap-through response remarkably for the postbuckled panel with reducing snap-through amplitude.

INTRODUCTION

In order to protect the substructure of a hypersonic flight vehicle, a multi-layered structure with a plain-woven C/SiC composite thin skin panel adhesively bonded to a very thick and light Si-C-O aerogel thermal insulator is used as a typical thermal protection system (TPS) structure. However the ceramic based composite thin skin panel is structurally weak and can fail easily. Under the overall sound pressure level (OASPL) of 140-170 dB, an erratic fully nonlinear large amplitude snap-through behavior has been observed experimentally for the thin panel at elevated temperature, which might lead to the so-called thermal–acoustic fatigue damage. In order to ensure structural integrity, it is desired to have a computationally efficient methodology to predict the dynamic response of the thin skin panel subjected to a combined loading. Few investigations have been conducted to characterize the dynamic response of the top facesheet panel for the multi-layer TPS. Current methods can neither characterize and predict occurrence of the snap-through response for the examined structure under a certain combination of thermal and acoustic loadings, nor provide an efficient way to understand the effects of the model parameters, such as elastic foundation stiffness, loadings, boundary conditions, and material properties on the stochastic dynamic response due to high computational expenses.

THEORETICAL MODEL

The top facesheet panel of the multi-layer TPS can be modeled as a thin composite plate resting on a Pasternak-type elastic foundation, where the thick thermal insulator has been considered as an elastic foundation. The theoretical model is developed based on the Kirchhoff thin-plate assumptions and general von Kármán-type equation that includes the plate-foundation interaction and the contribution of the membrane load on the transverse deflection. The governing equation has been derived using the first four symmetric modes through Galerkin method and a set of higher order coupled nonlinear ordinary differential modal equations (ODEs) have been given. It is noteworthy that three contributions to the linear stiffness term include the usual structural linear stiffness, the elastic foundation stiffness and the temperature variation, which are not related to the nonlinear stiffness terms. The modal equations can be expressed with the primary mode only and the stationary density function of the oscillator is given by the Fokker-Planck distribution:

$$f(q) = N_0 \, exp\left\{-(2\xi\omega/D_0)[\tfrac{1}{2}k_o(1-s)q^2 + \tfrac{1}{4}\alpha q^4]\right\} \tag{1}$$

Hamiltonian of the oscillator is:

$$H = \tfrac{1}{2}\dot{q}^2 + \tfrac{1}{2}k_o(1-s)q^2 + \tfrac{1}{4}\alpha q^4 \tag{2}$$

and the depth of the potential energy well h can be determined by substituting the static postbuckling displacement amplitude into the Hamiltonian. The parameter Δ is proposed to characterize the gradual evolution from no snap-through to persistent snap-through by the ratio between the density of zero-crossing and the density of reaching the static postbuckling equilibrium positions.

$$\Delta = \frac{f(q)_{q=0}}{f(q)_{q=Q}} = e^{\left[-\left(\frac{\xi\sqrt{k_o}}{D_0}\frac{k_o^2(s-1)^2}{2\alpha}\right)\right]} \tag{3}$$

where the combination effect of the acoustic sound pressure level, the strength of the thermal effect and the structural stiffness including the elastic foundation stiffness on the dynamic response evolution have been taken into account in one parameter. Three distinct cases can be identified. As $\Delta \to 0$, it represents the motion characteristic of the oscillator with high potential energy well depth or low energy input level. The oscillator is confined entirely in one of the double potential

[a)]Corresponding author. Email:liuliu@bit.edu.cn.

energy wells and no snap-through occurs; As $\Delta \to 1$, it represents the motion characteristic of the oscillator with low potential energy well depth or high energy input level. The oscillator is driven out the potential energy well constantly and the persistent dynamic snap-through appears. As $0 < \Delta < 1$, it represents the intermittent snap-through and can be expected that the snap-through motion is more frequent with higher value of Δ. The parameter clarifies the competition mechanism among the excitation energy, the strength of the thermal effect, the structural stiffness including the foundation stiffness and the nonlinear cubic stiffness, and can predict the characteristic of the dynamic response of the postbuckled panel with system parameters.

RESULTS AND DISCUSSIONS

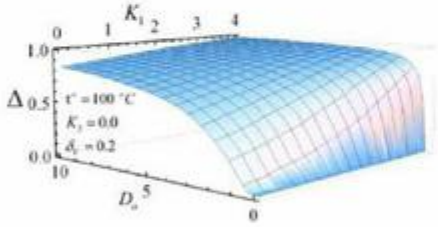

Figure 1. The surface plot of Δ for K_1 = (0, 5) and D_0= (0.1, 10)

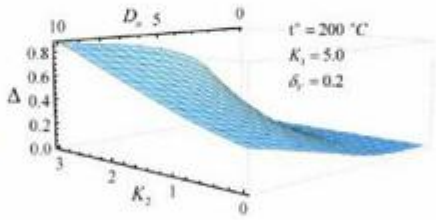

Figure 2. The surface plot of Δ for K_2 = (0, 3) and D_0 = (0.1, 10)

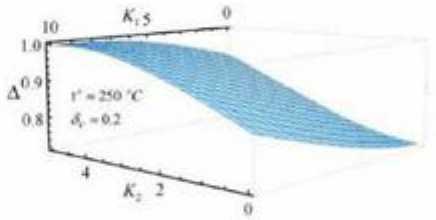

Figure 3. The surface plot of Δ for for K_1 = (0, 10) and K_2= (0.0, 5.0).

The variations of the parameter Δ with the excitation energy level and the foundation stiffness for the post-buckled panel have been given in Fig. 1 - 3. The results demonstrate some significant finds the first of which is the contribution of the stiffness to the dynamic response for the panel. Higher elastic foundation stiffness can promote the nonlinear snap-through response significantly. As the excitation energy level decreases, the dynamic response evolution parameter Δ is more sensitive to the elastic foundation stiffness. The evolution parameter is more sensitive to the shear layer stiffness compared with the Winkler foundation stiffness.

The remarkable contribution of the foundation stiffness to the dynamic response evolution can be explained through its effects to the buckling and post-buckling behavior of the panel. The thermal buckling temperature increases and the postbuckling deflection decreases significantly for the panel resting on the two-parameter elastic foundation. Hence the depth of the potential energy well reduces by increasing the elastic foundation stiffness, which can promote the nonlinear snap-through response with reducing the snap-through amplitude. However, from the point of view of acoustic fatigue damage to the panel, although the dynamic snap-through motion between two symmetric post-buckling equilibrium positions with zero mean is activated more easily by increasing the elastic foundation stiffness, the amplitude of the dynamic snap-through vibration decreases significantly with increasing the foundation stiffness. For the panel without the elastic foundation subjected to the same combination of loadings, it might exhibit small-amplitude linear vibration around large static postbuckling deflection. Thus the comparison of acoustic fatigue damage induced by a persistent nonlinear dynamic response around zero mean and a linear dynamic vibration around large thermal induced static postbuckling deformation needs to be investigated further.

CONCLUDING REMARKS

The stochastic nonlinear dynamic response of a thermally buckled composite panel resting on a two-parameter elastic foundation, where the uniform temperature rising with in-plane thermal gradient has been considered has been studied using based on Galerkin procedure. The transverse displacement *w* time history, the histogram and the accompanying pseudo-phase plane have been provided to demonstrate the global dynamic behavior. A dynamic response evolution parameter deduced from the primary-mode modal equation and Fokker-Planck distribution function can be used to characterize the transition from a persistent snap-through to no snap-through for the postbuckled panel. The contribution of the foundation stiffness to the nonlinear dynamic snap-through response has been clarified by the depth of the potential energy well, which decreases by increasing the elastic foundation stiffness and can lead to a transition from no snap-through to persistent snap-through.

References

[1] Liu L, Bing Y. L., Ti R. H.: The stochastic dynamic snap-through response of thermally buckled composite panels. *Compos Struct* 131:344-355, 2015.

[2] Jon L.: Large amplitude plate vibration in an elevated thermal environment. *Applied Mechanics Reviews* 46(2): 242-254, 1993.

[3] Jon L.: Topology of the four-mode strain energy of thermally buckling plates. *J. of Thermal Stresses* 25:813-857. 2002.

[4] Adam P., Stephen R.: Nonlinear reduced-order analysis with time-varying spatial loading distributions. *J. of Aircraft* 46(4): 1395-1402, 2009.

PARTIAL CONTROL AND AVOIDANCE OF ESCAPE FROM A POTENTIAL WELL

Shibabrat Naik*[1] and Shane D. Ross[2]

[1,2]*Engineering Science and Mechanics program, Dept. of Biomedical Engineering and Mechanics, Virginia Tech, Blacksburg, VA-24061, USA*

Summary In this work, we present application of geometric and topological approaches of phase space transport to dynamical systems which exhibit transition out of a potential well or escape from the realm of bounded motion. This phenomena is observed in problems of celestial mechanics, chemical kinetics and ship dynamics where by transition and escape may be beneficial or detrimental. We present results in the context of mechanical systems that can be geometrically reduced to two-dimensional maps using invariant manifolds of unstable periodic orbits and suitable Poincaré surfaces-of-section. We apply a recently developed notion of controlling a dynamical system, in the presence of a random bounded disturbance while applying a smaller control, to avoid transition and escape into an undesirable realm of phase space.

PROBLEM DESCRIPTION

In a myriad of natural and engineering systems, there are instants of critical motion when the trajectory *escapes* from a (or *transitions* into another) metastable state, often characterized by a potential well. This phenomenon may be undesirable if it implies a catastrophic event or could be desirable from a control and design perspective. In any case, it is of paramount interest to understand the mechanisms underlying such critical motion, providing in essence a reduced order model of transitions. The discovery of such mechanisms will also lead us to propose strategies to avoid or trigger escape/transition and make better predictions.

We will illustrate our results in the context of a ship dynamics problem. Consider a model of ship dynamics that has nonlinear coupling of roll and pitch degrees of freedom (DOF) and is of interest in naval engineering for ship safety against capsize in the presence of wave forcing. The dynamical system of interest can be expressed by the Lagrangian $\mathcal{L}(x, y, \mathring{x}, \mathring{y})$ given by

$$\left.\begin{aligned} \mathcal{L}(x,y,\mathring{x},\mathring{y}) &= T(\mathring{x},\mathring{y}) - V(x,y) \\ &= \frac{1}{2}\mathring{x}^2 + \frac{1}{2}\left(\frac{2}{R^2}\right)\mathring{y}^2 - \left(\frac{1}{2}x^2 + y^2 - x^2 y\right) \end{aligned}\right\} \qquad \left.\begin{aligned} \mathring{x} &= v_x \\ \mathring{y} &= v_y \\ \mathring{v}_x &= -x + 2xy + f_x(t) \\ \mathring{v}_y &= -R^2 y + \frac{1}{2}R^2 x^2 + f_y(t) \end{aligned}\right\} \tag{1}$$

with $V(x, y) = \frac{1}{2}x^2 + y^2 - x^2 y$ as the corresponding effective potential energy, x, y denotes the roll and pitch degrees of freedom which is non-dimensionalized using the roll and pitch angle of vanishing stability, $R = \omega_\theta/\omega_\phi$, ratio of the pitch to roll natural frequencies. In what follows, $R = 1.6$ is chosen so as to lessen the effects of parametric resonance. The equations of motion can be expressed in first order ODE form given by (1), where time is non-dimensionalized using the natural roll frequency and the non-conservative time-varying generalized forces, $f_x(t)$, $f_y(t)$, which denote rescaled angular accelerations due to wave moments. Our objective is to apply a geometrically motivated approach of identifying trajectories that lead to capsize and find if a control smaller than a disturbance can be used to avoid such event.

TUBE DYNAMICS AND PARTIAL CONTROL

When the system is autonomous i.e., ($f_x(t) = f_y(t) = 0$), Eqn. (1) conserves the energy, $E(x, y, v_x, v_y) = \frac{1}{2}v_x^2 + \frac{1}{2}\left(\frac{2}{R^2}\right)v_y^2 + \frac{1}{2}x^2 + y^2 - x^2 y$ since damping isn't considered and which represents a hypersurface in $\mathbb{R}^4$. However, by using a suitable geometric reduction technique we can classify orbits with varied fates for a given instantaneous energy, e. This is typically done by using a Poincaré surface-of-section (S-O-S), in this case a plane $\mathbb{R}^2$, that captures motion leading to escape from the potential well i.e., capsize. We consider a Poincaré S-O-S that is intersected by trajectories with motion to the right and given by $\Sigma_{U_1} = \{(y, v_y) | x = 0; v_x > 0\}$ (where $v_x > 0$ captures motion to the right) and shown in Fig. 1(a) and Fig. 1(b). Furthermore, the regions of energetically accessible motion for a ship of given energy, e, is defined by considering the projection of energy surface onto the configuration space, (x, y) plane, given by $\mathcal{M}(e) = \{(x, y) | V(x, y) \leqslant e\}$ which is historically known as *Hill's Region* (see [1]). Using basic dynamical systems theory, we obtain the critical points for the conservative system at $(\pm 1, 0.5, 0, 0)$ which is a rank-1 saddle (with eigenvalues $\pm\lambda, \pm i\omega$). The energy of saddle equilibrium points is defined as *critical energy* given by $E(\pm 1, 0.5, 0, 0) = E_{critical} = 0.25$ and all motions leading to escape from the potential well occur above this value i.e., a ship rolling and pitching with instantaneous energy e will capsize when $e > E_{critical}$.

This can be systematically explained by considering the invariant manifolds of the rank-1 saddles (this theory goes by the name of *tube dynamics* and is applied to celestial mechanics in [1]) to organize trajectories exhibiting ship's safe and capsize configuration. For a 2-DOF system (phase space is $\mathbb{R}^4$) the globalized manifolds are topologically a cylinder or *tubes* (hypersurface in $\mathbb{R}^4$ and co-dimension 1) and forms a boundary between capsize and non-capsize trajectories i.e., escape

*Corresponding author. Email:shiba@vt.edu

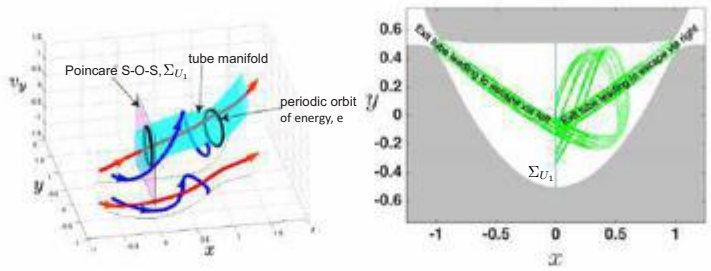

(a) (b)

Figure 1: Fig. 1(a) shows a schematic of escape (red) and non-escape (blue) trajectory, while tubes form the boundary for such critical motion and Poincaré S-O-S reduces the analysis to a study of map on $\mathbb{R}^2$. The boundary of Hills region i.e., zero velocity curve (kinetic energy vanishes) is shown in the (x, y) plane. Fig. 1(b) shows the Hill's region as shaded (where kinetic energy is negative) and the white regions are energetically accessible for $e > E_{critical}$. The stable tubes of the rank-1 saddle equilibrium points are shown in green which act as the boundary for escape and non-escape trajectories.

beyond the saddles of potential well as shown schematically in Fig. 1(a). Therefore dimension of *tubes* for a 2 DOF system is given by $\mathbb{S}^1 \times \mathbb{R}^1$ and thus its intersection with a Poincaré S-O-S, Σ_{U_1}, is $\mathbb{S}^1$ or 1-sphere in $\mathbb{R}^2$. On the plane, Σ_{U_1} the closed curves represent *forbibben* region (shown as white inside the blue in Fig. 2(a)) and trajectory entering this region will lead to imminent escape from the potential well. When the systems is non-autonomous, this geometric picture still forms the skeleton on which the escape manifests itself.

In presence of any disturbance, e.g., wave forcing or unmodeled fluid-vessel interaction, escape from the potential well becomes more prominent and our objective is to ask if it is possible to avoid escaping i.e., not entering the forbidden regions by exploiting the topology of *tubes* of the rank-1 saddles. This can be answered using a recently developed approach of *partial control* which is based on the notion of a safe set (see [2]). A safe set, say S, is a subset of the set we want to stay in, say Q, such that for every point $\mathbf{q} \in S$, we have $\max_{\mathbf{q}\in S, ||\boldsymbol{\xi}|| \leqslant \boldsymbol{\xi}_0} dist(f(\boldsymbol{q}) + \boldsymbol{\xi}, S) = \boldsymbol{u}_0 < \boldsymbol{\xi}_0$. When the safe set exists, we can find

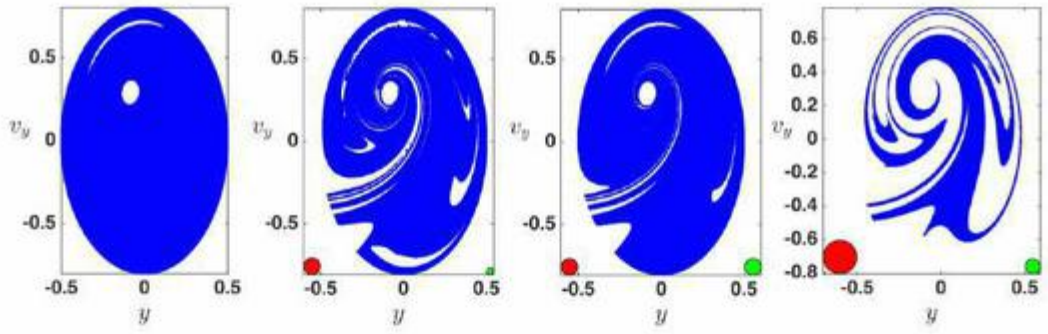

(a) (b) (c) (d)

Figure 2: Fig. 2(a) shows the initial set in blue on the Poincaré S-O-S, Σ_{U_1} with white regions inside the blue denoting intersection of tube manifolds. Fig. 2(b), 2(c) and 2(d) show the safe sets in blue for $\xi_0 = 0.05, 0.05, 0.1$ for $u_0 = 0.405\xi_0, \xi_0, 0.445\xi_0$ respectively. The red and green disks denote the disturbance and control magnitudes that are applied on the map.

safety by using a control that is smaller than the disturbance. This is illustrated for an arbitrary disturbance, ξ_0, acting on the return map $\Sigma_{U_1} \to \Sigma_{U_1}$ in Fig. 2 and computed using the sculpting algorithm in [3].

CONCLUSION

We considered two arbitrary disturbance magnitudes, for illustration here, $\xi_0 = 0.05, 0.1$ and show that the safe sets exist for a minimum control magnitudes of $u_0 = 0.405\xi_0, 0.445\xi_0$ for an instantaneous energy, $e = 0.25307$. Thus, a ship's safety can be ensured by controlling the trajectories from entering the stable tubes that lead to imminent escape from the potential well. However, from a ship's motion stand point, the magnitude of a disturbance needs to be related to the wave forcing that acts in a rough/regular sea environment while interpreting the applied control magnitude in the form of a algorithmic control law.

References

[1] Koon W. S., Lo M. W., Marsden J. E., Ross S.D.: Dynamical Systems, the Three-Body Problem and Space Mission Design. Book, 2011.

[2] Sabuco J., Zambrano S., Sanjuán M. A. F., Yorke J.A.: Dynamics of partial control. Chaos (Woodbury, N.Y.) 22:4 047507, 2012.

[3] Sabuco J., Zambrano S., Sanjuán M. A. F., Yorke J.A.: Finding safety in partially controllable chaotic systems. Communications in Nonlinear Science and Numerical Simulation (Elsevier B.V.) 11:17, 4274–4280, 2012.

SYMMETRY-INDUCED DYNAMIC LOCALIZATION IN LATTICE STRUCTURES

Nathan Perchikov * and O.V. Gendelman
Faculty of Mechanical Engineering, Technion, Haifa 32000, Israel

Summary The existence of internal symmetry in lattice structures may give rise to stationary compact solutions, even in the absence of disorder or nonlinearity. These compact solutions are related to the existence of flat dispersion curves (bands). Nonlinearity can be a destabilizing factor for such compactons. This can be illustrated by a simple one-site model, in which the compacton corresponds to a single hidden antisymmetric mode. This antisymmetric mode can lose its stability through parametric resonance, when accounting for nonlinear interactions.

SETTING AND LINEAR ANALYSIS

A chain of linearly coupled elements with symmetric internal structure is considered, as presented in Figure 1.

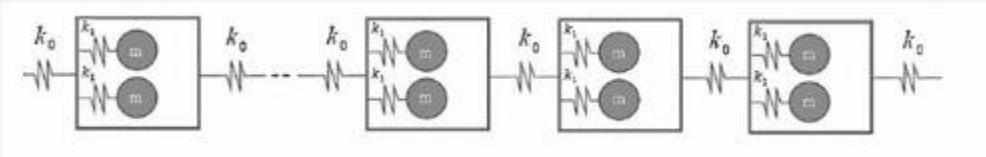

Figure 1: Schematic plot of the basic setting.

The boxes are considered to be massless. Evidently, due to internal symmetry, the antisymmetric mode in each box will not interact with the other modes in the system. Thus in the considered case, one obtains a completely localized solution (compacton). This localized solution emerges already in a linear homogeneous system. Therefore, in addition to two well-known origins of localization in lattices − disorder [1] and nonlinearity [2] − there appears to be a third possible source of localization: internal symmetry. Due to lack of direct interaction with external excitation, the aforementioned compactons may also be referred to as "hidden modes". The dispersion curves for the system depicted in Figure 1 are presented in Figure 2.

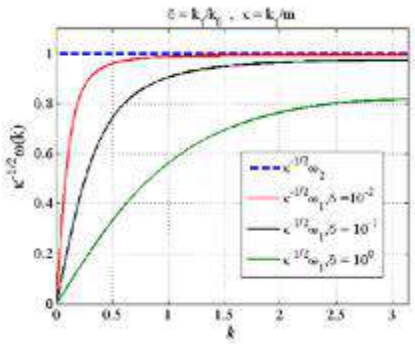

Figure 2: Oscillatory spectra for the system described in Figure 1.

One of the dispersion curves (bands) is flat, i.e. independent of the wavenumber, k. Its frequency corresponds to the frequency of compactons. In the specific system depicted in Figure 1, this flat band always lies above "regular" dispersion bands. However, for more complicated structures (for instance, for the case when internal transverse motion of particles is permitted), the emerging flat bands may also intersect other dispersion bands. In such cases, the regular "intersection avoidance" of dispersion curves is absent (due to lack of linear coupling between the modes). The existence of compactons in the model system described above depends only on the symmetry in the considered system. For a single site of such lattice, we demonstrate that slight perturbation to the symmetry can reveal the "hidden mode" under external excitation, with an additional, thin, resonance peak emerging. However, small damping (proportional to the asymmetry) can efficiently destroy this additional resonance peak, restoring the mode "hiding" effect.

*Corresponding author. Email: perchico@gmail.com

NONLINEAR DYNAMICS

The inclusion of (symmetric) nonlinearities does not affect the existence of compacton solutions. In the same time, in the nonlinear case, the compacton mode becomes coupled to the other modes of the system. Such nonlinear coupling can be destructive for compacton existence – stability can be lost through the mechanism of parametric resonance. To explore this scenario, we consider the same single-site (sub)system, only with the addition of internal cubic nonlinearity. The emerging system can represented by the following equations:

$$\begin{aligned} m\ddot{x}_1 + k_1(x_1 - x_0) + p(x_1 - x_0)^3 = 0 \\ m\ddot{x}_2 + k_1(x_2 - x_0) + p(x_2 - x_0)^3 = 0 \\ k_0 x_0 - k_1(x_1 - x_0) - p(x_1 - x_0)^3 - k_1(x_2 - x_0) - p(x_2 - x_0)^3 = 0 \end{aligned} \tag{1}$$

In Eqs. (1), x_1 and x_2 denote the displacements of the masses, and x_0 – the displacement of the external box. The last equation in the system is algebraic, as arising due to the zero box mass assumption. Evidently, system (1) admits symmetric and antisymmetric nonlinear normal mode (NNM) solutions. The antisymmetric mode is "hidden" and corresponds to the compacton solution. Partial results of numerical Floquet analysis for the NNMs of Eqs. (1) are presented in Figure 3.

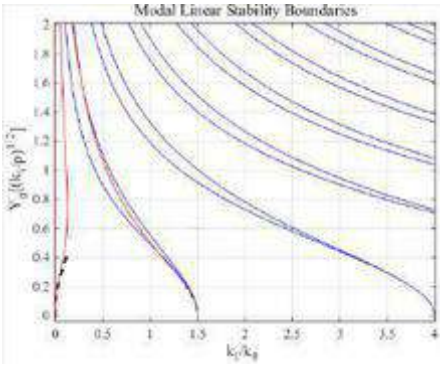

Figure 3: 1st (finite-width) and 2nd (degenerate) instability tongues of the purely antisymmetric mode (in solid red) with asymptotic expansions for tongue boundaries (dashed black), and multiple (finite-width) instability tongues of the symmetric mode (in solid blue). Y_0 denotes the (normalized) amplitude of $(x_1 + x_2)/2 - x_0$.

In addition to a finite-width instability tongue for small k_1/k_0 ratios, there exists a 2nd narrow region of instability, characterized by emerging resonance-related KAM islands, around the rightmost red curve in Figure 3, as shown in Figure 4.

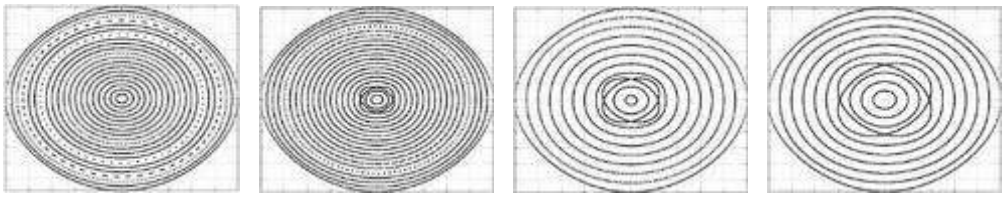

Figure 4: Poincaré sections at $x_1 = x_2$ for $k_1/k_0 = 1.25$ for (rightwards) increasing amplitudes $Y_0 = 0.31, 0.313, 0.316, 0.325$

CONCLUSIONS

In view of the above, one finds that in the presence of internal symmetry, a localized solution (a "hidden" mode, or, a compacton) exists even with no nonlinearity or disorder, and can either remain stable, when accounting for nonlinear interactions, or be destroyed by them, depending on the parameters.

References

[1] Ludlam J. J., Taraskin S.N., Elliott S.R.: Phys. Rev. B 67(13), 2003.

[2] Perchikov N., Gendelman O.V.: $Physica$ D 292-293:8-28, 2015.

DATA-BASED METHOD FOR EXTRACTING NAVIGATIONAL LEADERSHIP BETWEEN TWO BATS

Subhradeep Roy and Nicole Abaid *

Department of Biomedical Engineering and Mechanics, Virginia Tech, USA

Summary We study the navigational leadership roles in bats by implementing a recently developed dynamical systems tool, convergent cross mapping, to detect the information transfer between two bats. Small groups of bat paths are continuously tracked, from which 3D path points are extracted and converted to 1D curvature-based time series data to perform convergent cross mapping analysis. This work seeks to answer the question of whether individuals fly independently of each other or interact to plan flight paths.

NAVIGATIONAL INFORMATION TRANSFER BETWEEN A PAIR OF BATS

Collective behavior in groups of social animals is the interaction and negotiation of individuals to reach an agreement, examples of which are coordinated motion and synchronous migration. Bats are unique among such social animals in that they use active sensory echolocation or "bio-sonar", wherein they emit ultrasonic waves and sense echoes to detect and navigate surroundings. Jamming occurs when multiple bats are using echolocation and each individual's calls become difficult to distinguish, which may lead to misinterpretation of echoes and thus their environment. In the biological literature, there is evidence of such jamming happening in bats and of their different strategies to avoid misinterpretation, like frequency modulation or vocalization cessation. Also, there are instances where bats purposefully jam conspecifics during competition for food. Hence, it is clear that bats act differently in groups than alone and, in many situations, this can benefit their survival.

In real bat swarms, understanding the navigational leadership roles is a challenge and quantitative assessment of leadership appears to be an entirely untouched area of study. Given the broadcast nature of bio-sonar, the active sensing of one individual can directly influence the motion of others, making the directionality of leadership unclear. Here, we seek to understand navigational leadership in bats from direct observation of bat swarms in flight. The exploration of this area is refined by focusing efforts on pairs of bats and pursuing a method of analysis involving the evaluation of directional information transfer.

Real-world leader-follower interactions can be studied as information transfer by the use of the concepts of Granger causality (GC) [1], transfer entropy (TE) [2], and convergent cross mapping (CCM) [3]. These different tools measure the directional information transfer between two random processes. We focus on CCM which is a recently developed method for determining causality between two time series [3]. We choose this method because of the following reasons. First, it can be extended to nonlinear, non-separable dynamical systems, involving weakly coupled variables and in the presence of a third driving variable, in each of which GC does not apply [3]. Secondly, the principal difficulty to calculate TE from experimental data is in estimating probability distributions which are computed using binning methods such as histograms [4]; such challenges can be overcome with CCM.

We seek to understand the navigational leadership in a pair of bats, for which we perform CCM analysis to detect the information transfer which is assumed to flow from leader to follower. For each bat in the pair, we compute a curvature-based time series from 3D trajectories that are captured in a field experiment in a mountain cave in Jinan, China.

Convergent cross mapping (CCM)

CCM was first introduced in [3], in which it has been reported as a necessary condition for causation. This method is based on an algorithm that compares the ability of lagged components of one process to estimate the dynamics of another.

Given two time series, $X(t)$ and $Y(t)$ are causally linked if they share a common attractor manifold, M, where t denotes time index. From Taken's theorem, generically a shadow version of the original manifold M can be reconstructed from the projection of any of this time series. The time series data $X(t)$ and its delayed components, $X(t-\tau)$ and $X(t-2\tau)$, where τ is the time delay, can be used as variables to construct the shadow version of the original manifold called M_X. The reconstructed manifold preserves the properties of the original system, such as the topology and the Lyapunov exponents. This method represents a one-to-one mapping of the original manifold M and the reconstructed manifold, M_X, and similarly maps one-to-one to the reconstructed manifold, M_Y, built from the time series Y. The next step is to find the nearest neighbors in M_Y, and use the time indices to find the corresponding points in M_X. If these points are also nearest neighbors in M_X, then X and Y are causally related. This allows the historical records in Y to estimate states in X, and vice-versa. This method is used to find an estimate of Y, labeled as $\hat{Y(t)}|M_X$. Finally, a correlation coefficient is calculated between the original time series and an estimate of Y. For a pair of time series, we will have two correlation coefficients corresponding to considering each bat as a leader in turn; these are then compared to determine the CCM causality and its directionality. A more detailed description of the algorithm can be found in the supplementary materials of [3].

*Corresponding author. Email: nabaid@vt.edu

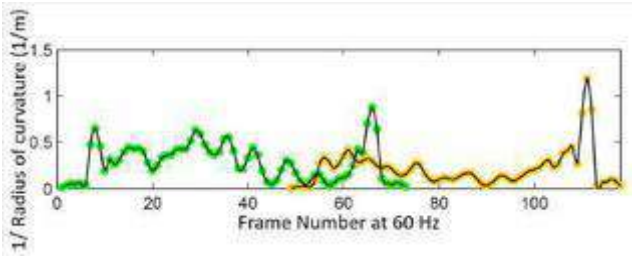

Figure 1: Inverse radius of curvature plotted for a pair of bats. Green and yellow represent front and rear bat, respectively [8].

The CCM technique requires the knowledge of the two parameters, namely embedding dimension and the time delay. To determine the minimum embedding dimension, we use the method as described in [5] because of the following advantages. First, it depends on time delay only, and does not depend on any other system parameters, unlike the method of false neighbors [6]. Second, this method is computationally very efficient.

Time delay is a required parameter for both the methods to calculate embedding dimension and CCM. If the time delay, τ is chosen to be very small, for a two dimensional construction of the state-space, $X(t)$ and $X(t+\tau)$ will be indistinguishable and all the trajectories will appear to lie on the line, $X(t) = X(t+\tau)$. This can be avoided by the choice of τ that makes $X(t)$ and $X(t+\tau)$ independent. Linear independence can be achieved by choosing the corresponding τ for which the autocorrelation function first passes through zero. However, we choose mutual information since it measures the general dependence of two variables.

CURVATURE TIME SERIES

The 3D path points of each bat were extracted from the video data collected in a mountain cave in Jinan, China, where small groups of bat paths were continuously tracked. In order to perform CCM analysis of pairs of bats, it is necessary to generate 1D time series from 3D path data. We choose an inverse radius of curvature metric for representing 1D time series for the following reasons. First, a curvature-based time series is a reflective of a bat's steering and hence provides a good depiction of the 3D navigation of the bat pairs. Secondly, an absolute inverse radius of curvature formulation ensures the data remains positive and close to zero, resulting a logarithmic binning strategy possible to calculate the minimum embedding dimension. Finally, curvature-based metrics are frequently used to assess the motion of interacting agents, such as in the study of laboratory insects [7]. Figure 1 presents an exemplary 1D time series plot for a pair of bats. In a previous study, we have seen that information flows from bats which are positionally in front to those behind as measured using TE [8]. These results are compared to the analogous analysis with CCM in this work.

CONCLUSIONS

Here we study the navigational leadership roles in bats who use active sensing making it a challenge to understand the directionality of leadership. We implement the above mentioned tools to detect the navigational information transfer between a pair of the bats, in terms of a curvature-based time series that are captured in a field experiment in a mountain cave in Jinan, China. We observe that the front bat in particular plays a leadership role for the pair and the rear bat displays path coupling behavior with the leading bat using TE, and we compare these results to those measured with CCM.

References

[1] C.W.J. Granger. Investigating causal relations by econometric models and cross-spectral methods. *Econometrica: Journal of the Econometric Society*, pages 424–438, 1969.

[2] T. Schreiber. Measuring information transfer. *Physical Review Letters*, 85(2):461, 2000.

[3] G. Sugihara, R. May, H. Ye, C. Hsieh, E. Deyle, M. Fogarty, and S. Munch. Detecting causality in complex ecosystems. *Science*, 338(6106):496–500, 2012.

[4] M. Vejmelka and M. Palus. Inferring the directionality of coupling with conditional mutual information. *Physical Review E*, 77(2):026214, 2008.

[5] L. Cao. Practical method for determining the minimum embedding dimension of a scalar time series. *Physica D: Nonlinear Phenomena*, 110(1):43–50, 1997.

[6] M. B. Kennel, R. Brown, and H. Abarbanel. Determining embedding dimension for phase-space reconstruction using a geometrical construction. *Physical Review A*, 45(6):3403, 1992.

[7] J. G. Puckett, D. H. Kelley, and N. T. Ouellette. Searching for effective forces in laboratory insect swarms. *Scientific Reports*, 4, 2014.

[8] N. Orange and N. Abaid. A transfer entropy analysis of leader-follower interactions in flying bats. *European Physical Journal: Special Topics*, 224(17):3279–3293, 2015.

MODELLING NON-PLANAR VIBRATIONS OF A STRING IN THE PRESENCE OF A DOUBLY CURVED OBSTACLE

Harkirat Singh[1] and Pankaj Wahi *[2]

[1,2]*Department of Mechanical Engineering, Indian Institute of Technology Kanpur, Kanpur, India*

Summary The present paper investigates the characteristics of a string vibrating against a smooth unilateral obstacle pertaining to the Indian stringed musical instruments. In particular, we have studied the effect of coupling due to the variable tension and the geometry of the obstacle. The mathematical model has been developed using Hamilton's principle followed by system discretization using the Galerkin approach and numerical investigations using runge-kutta algorithm. Numerical simulations have divulged the transition in characteristics of a string beyond a certain amplitude.

BRIEF BACKGROUND

Theoretically, the problem of a string vibrations against a parabolic obstacle, considering the inelastic impacts, was first studied by the Burridge et al[1]. Subsequently equations of motions were derived, assuming smooth wrapping and unwrapping and a conservative model, in the literature [2, 3]. However, all these analysis were carried out for planar motions of a string. In the present paper, we have developed a mathematical model, assuming the conservative system, for non-planar vibrations of a string vibrating against a obstacle with known geometry. The model is relevant to the Indian musical stringed instruments, since the motion of a string in such case is non-planar and quite complicated.

FORMULATION

The schematic representation of the physical system under consideration is shown in figure 1. It consists of a ideal string(no bending stiffness) vibrating against a smooth unilateral obstacle which is assumed to be fixed and rigid in our model. The tension in the string is assumed to be variable, giving rise to stretching non-linearity(σ in our case) which introduces coupling between the mutually perpendicular modes. We further assume that the string remains tangent to the bridge surface

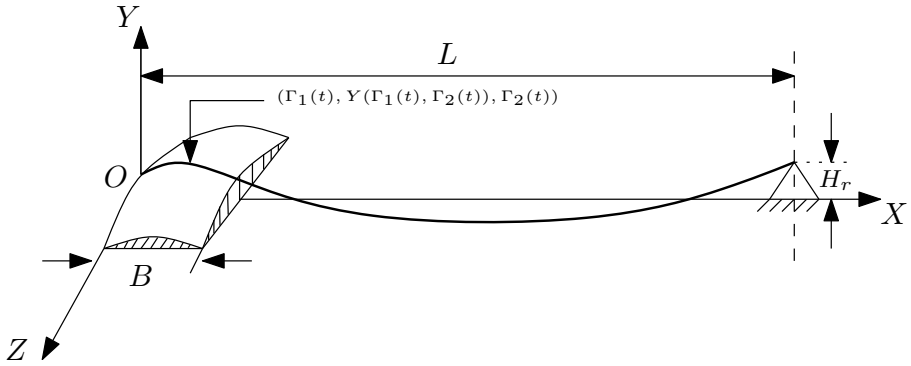

Figure 1: Simplified model for the string vibrations in musical instruments like tanpura and sitar.

at the point of separation ($X = \Gamma_1(t)$ and $Z = \Gamma_2(t)$) in figure 1. The continuity of string along with slope continuity implies zero velocity at the point of separation and thus a conservative system. The geometry of the obstacle is defined, in non-dimensionalized form, by the following surface:

$$Y_B(x,z) = ax(b-x) + c\left(\frac{d}{2} - z\right)\left(\frac{d}{2} + z\right). \tag{1}$$

Using Hamilton's principle and calculus of variation, the governing equations for the wrapped portion comes out to be:

$$y_{tt} = \frac{2cz}{1+4c^2z^2}\left(\sigma\left(2cz\frac{\partial}{\partial x}\,y_x\left(y_x^2+z_x^2\right) + \frac{\partial}{\partial x}\,z_x\left(y_x^2+z_x^2\right)\right) + 2czy_{xx} + z_{xx}\right), \quad 0 \le x \le \gamma_1^- \tag{2}$$

$$z_{tt} = \frac{1}{1+4c^2z^2}\left(\sigma\left(2cz\frac{\partial}{\partial x}\,y_x\left(y_x^2+z_x^2\right) + \frac{\partial}{\partial x}\,z_x\left(y_x^2+z_x^2\right)\right) + 2czy_{xx} + z_{xx}\right), \quad 0 \le x \le \gamma_1^- \tag{3}$$

$$\lambda(x,z) = -\frac{1}{1+4c^2z^2}\left(\sigma\left(\frac{\partial}{\partial x}\,y_x\left(y_x^2+z_x^2\right) - 2cz\frac{\partial}{\partial x}\,z_x\left(y_x^2+z_x^2\right)\right) - 2czz_{xx} + y_{xx}\right). \tag{4}$$

*Corresponding author. Email: harkirat@iitk.ac.in

Here, $\lambda(x,z)$ represents the constraint force between the string and the obstacle. For the free portion of a string the governing equations(non-dimensional form) are:

$$-y_{tt} + y_{xx} + \sigma \frac{\partial}{\partial x}\left(y_x\left(y_x^2 + z_x^2\right)\right) = 0, \qquad \gamma_1^+ \leq x \leq 1 \tag{5}$$

$$-z_{tt} + z_{xx} + \sigma \frac{\partial}{\partial x}\left(z_x\left(y_x^2 + z_x^2\right)\right) = 0, \qquad \gamma_1^+ \leq x \leq 1. \tag{6}$$

Discretization

We discretize the system using Galerkin projection approach. The functional form of the modes are assumed as:

$$z = \alpha(t)\sin(\pi x), \qquad 0 \leq x \leq 1 \tag{7}$$

$$y = a\gamma_1\left(b - \gamma_1\right) + c\left(\frac{d}{2} - \alpha(t)\sin(\pi x)\right)\left(\frac{d}{2} + \alpha(t)\sin(\pi x)\right), \qquad 0 \leq x \leq \gamma_1^- \tag{8}$$

$$y = \frac{a\gamma_1\left(b - \gamma_1\right) + c\left(\frac{d}{2} - \gamma_2\right)\left(\frac{d}{2} + \gamma_2\right)}{1 - \gamma_1}(1 - x) + \beta(t)\,\sin\left(\frac{\pi(x - \gamma_1)}{1 - \gamma_1}\right), \qquad \gamma_1^+ \leq x \leq 1. \tag{9}$$

Here, γ_1 and γ_2 are the non-dimensional forms of $\Gamma_1(t)$ and $\Gamma_2(t)$. For clarity, γ_1^- and γ_1^+ are the positions just before and after the separation point respectively. To begin with, the above representation is restricted to unimodal analysis, since that alone can capture the underlying fascinating characteristics. Besides this, unit tangent vector continuity engender the following condition:

$$a\gamma_1^2 - 2a\gamma_1 + ab + \frac{cd^2}{4} - c\gamma_2^2 - 2c\pi\gamma_2\alpha(t)\cos(\pi\gamma_1) + 2c\pi\gamma_2\gamma_1\alpha(t)\cos(\pi\gamma_1) - \pi\beta(t) \;=\; 0. \tag{10}$$

KEY RESULTS

The resultant ODEs are numerically investigated using runge-kutta algorithm. Numerical simulations unearth the peculiar features of string dynamics, i.e, the behavior of a string changes qualitatively beyond the certain amplitude of vibrations. The results in figure 2 are reported for chosen obstacle parameters, i.e, $b = 0.05$, $a = 1440$, $c = 0.1$, $d = 2$ and $\sigma = 0.001$. The

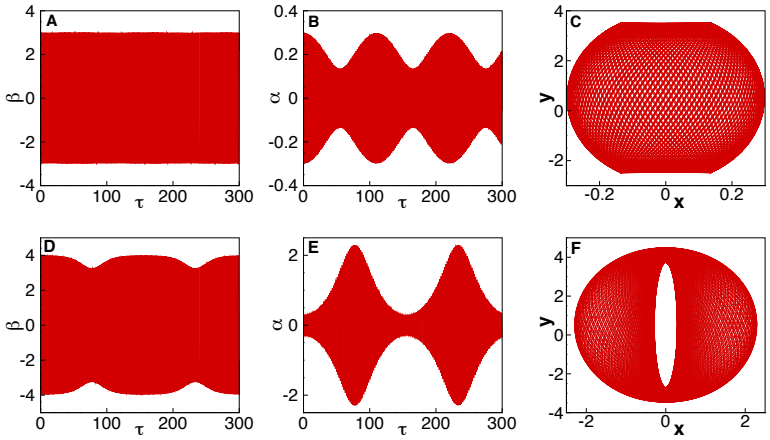

Figure 2: Fig (A),(B),(C) corresponds to the initial condition $\beta(0) = 3$, and $\dot{\alpha}(0) = 1$ and fig (D),(E),(F) corresponds to $\beta(0) = 4$ and $\dot{\alpha}(0) = 1$. Fig (A) and fig (D) represents the variation of β with non-dimensional time, and fig (D) and fig (E) represents the variation of α with non-dimensional time. Fig (C) and fig (F) represents the trajectories of a point on a string at $x = 1/2$ for corresponding initial conditions.

transition in the characteristics of the string beyond a certain amplitude indicates onset of unstable solutions, which can be checked using floquet theory. Numerical study also suggests that number of planar motions reduced to one unlike infinitely many in the absence of obstacle.

References

[1] Burridge R., Kappraff J., and Morshedi C.: The sitar string, a vibrating string with a one-sided inelastic constraint. J. Applied Mathematics,42(6):1231-1251, 1982.

[2] Vyasarayani C.P.,Birkett S., and McPhee J. :Modeling the dynamics of a vibrating string with a finite distributed unilateral constraint. JASA, 125(6):3673-3682, 2009.

[3] Mandal A.K., Wahi P. :Natural frequencies, modeshapes and modal interactions for strings vibrating against an obstacle. JSV, 338:42-59, 2015.

NONLINEAR VIBRATIONS OF A CIRCULAR PLATE INDUCED BY MECHANICAL AND THERMAL LOADINGS

Anna Warminska*[1], Emil Manoach[2], and Jerzy Warminski[3]

[1]*Department of Thermodynamics, Fluid Mechanics and Aviation Propulsion Systems, Lublin University of Technology, Lublin, Poland*
[2]*Institute of Mechanics, Bulgarian Academy of Sciences, Sofia, Bulgaria*
[3]*Department of Applied Mechanics, Lublin University of Technology, Lublin, Poland*

Summary An effect of thermal loading on vibration of a nonlinear circular plate considered as extended Mindlin model with nonlinear terms due to large deflections is analysed in the paper. The coupled thermal and mechanical model is derived first in the form of nonlinear partial differential equations and then the problem is reduced by modal projection. The importance of the elevated temperature around the main resonance for varied temperature is shown and the nonlinear characteristics with bifurcation points have been computed for selected thermal and mechanical loadings.

INTRODUCTION AND A NONLINEAR THERMO-ELASTIC MODEL OF A CIRCULAR PLATE

The structural elements like beams, shells or plates which are used in many branches of engineering often are subjected to mechanical and thermal loadings leading to large amplitude vibrations [1]. The temperature may change transient dynamics of the structure or even may shift the response to a new dynamic state [2]. In many cases, especially when structures are not very thin and they are subjected to an intensive and short heat flux or even convective heating, the consideration of the propagation of the temperature along the structure is important and then the coupled thermoelastic problem should be considered [3, 4]. These problems are quite complicated from a computational point of view, therefore, simplified techniques which allow reducing the governing partial differential equations into a reduced number of modal coordinates are applied. Such an approach is very effective for nonlinear models due to the fact that it enables the advanced bifurcation analysis as well as a detection of chaotic oscillations [5, 6].

The considered in this paper thermo-elastic model of a circular plate of radius R and thickness h is based on Midlin model. It takes into account large deflections, linear curvatures, shear deformation and rotary inertia. The derived PDEs subjected to mechanical and thermal loadings take the form:

$$\begin{aligned}
Ah\left[\frac{\partial^2 u}{\partial r^2}+\frac{\partial w}{\partial r}\frac{\partial^2 w}{\partial r^2}+\frac{1}{r}\frac{\partial u}{\partial r}-\frac{u}{r^2}+\frac{1}{2r}(1-\nu)\left(\frac{\partial w}{\partial r}\right)^2\right] &= A(1+\nu)\alpha_T\frac{\partial \gamma_T}{\partial r},\\
D\left[\frac{\partial^2 \psi}{\partial r^2}+\frac{1}{r}\frac{\partial \psi}{\partial r}-\frac{\psi}{r^2}\right]-k^2Gh\left(\frac{\partial w}{\partial r}+\psi\right)-c_2\frac{\partial \psi}{\partial t}-\frac{\rho h^3}{12}\frac{\partial^2 \psi}{\partial t^2} &= A(1+\nu)\alpha_T\frac{\partial \kappa^T}{\partial r},\\
k^2Gh\left(\frac{\partial^2 w}{\partial r^2}+\frac{1}{r}\frac{\partial w}{\partial r}+\frac{\partial \psi}{\partial r}+\frac{\psi}{r}\right)+Ah\left[\frac{\partial u}{\partial r}+\frac{1}{2}\left(\frac{\partial w}{\partial r}\right)^2+\frac{\nu}{r}u-\frac{1+\nu}{h}\alpha_T\gamma_T\right]\left(\frac{\partial^2 w}{\partial r^2}+\frac{1}{r}\frac{\partial w}{\partial r}\right)&\\
+Ah\left(\frac{\partial^2 u}{\partial r^2}+\frac{\nu}{r}\frac{\partial u}{\partial r}-\frac{\nu}{r^2}u+\frac{\partial w}{\partial r}\frac{\partial^2 w}{\partial r^2}-\frac{1+\nu}{h}\alpha_T\frac{\partial \gamma_T}{\partial r}\right)\frac{\partial w}{\partial r}+c_1\frac{\partial w}{\partial t}-\rho h\frac{\partial^2 w}{\partial t^2} &= -p(r,t)
\end{aligned}\tag{1}$$

where $u(r,t)$ is the in-plane displacement, $w(r,t)$ is the transverse displacement, r and ψ are polar coordinates and E is the Young modulus, G is the shear modulus, ν is Poison's ratio, α_T is the coefficient of thermal expansion, c_1 and c_2 denote the damping coefficients and mechanical load intensity is $p(r,t)$. The heat flow acting on the plate is included in functions γ_T and κ_T and is not reported here. The model has been studied for a particular case for fixed elevated temperature uniformly distributed through the plate span. The PDEs have been reduced to ODEs by modal projection for a clamped plate, taking just one mode projection, defined by Bessel functions obtained from the eigenvalue problem. After the reduction the nonlinear ODE take the dimensionless form

$$q_1(t)+2\xi_1\omega_1 q_1+\omega_1^2 q_1+C_L q_1^3+C_T\Delta T q_1=p_1\sin(\Omega t)\tag{2}$$

where ω_1 is the first natural frequency, ξ_1 a modal damping coefficient, p_1 and Ω are the amplitude and frequency of mechanical excitation, C_T and C_L are constant coefficients, and ΔT is the temperature difference.

PLATE DYNAMICS AT ELEVATED TEMPERATURE

The numerical example aims to illustrate the impact of the thermal and mechanical loadings on the structure's response. The results are obtained for the clamped circular plate and uniformly distributed elevated temperature. The plate of radius $R=0.1$ m, thickness $h=0.0025$ m is assumed to have the material parameters: $\rho=2778kg/m^3$, $E=0.7\times10^{11}\ N/m^2$, $G=2.612\times10^{10}N/m^2, \nu=0.34$, $\alpha_T=2.39\times10^{-5}K^{-1}$. For the assumed structural parameters

*Corresponding author. Email: a.warminska@pollub.pl

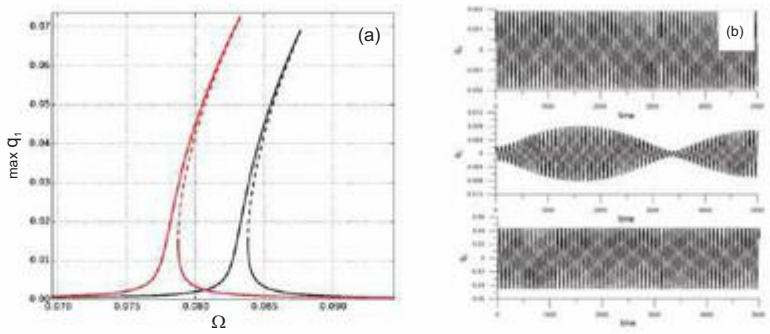

Figure 1: Resonance curves (a) for $\Delta T = 0$ (black) and $\Delta T = 0.5$ (red) and time histories (b) for $\Omega = 0.08$: $\Delta T = 0$ – steady state (upper plot), $\Delta T = 0.5$ – transient state (middle plot), $\Delta T = 0.5$ – new steady state (lower plot).

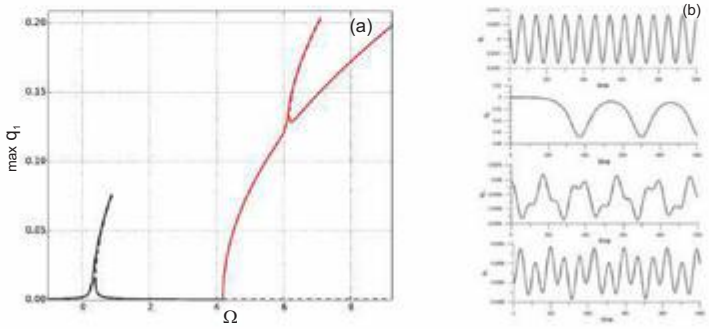

Figure 2: Bifurcation diagram (a) amplitude versus ΔT and fixed mechanical loading $p_1 = 1 \times 10^{-6}$, $\Omega = 0.08$, and time histories (b) for $\Delta T = 4.0$ (upper plot) and below for $\Delta T = 4.5$ – transient states.

the coefficients of Eq.(2) take values: $\omega_1 = 0.08321077$, $C_L = 0.21319$, $C_T = -0.0016501$. The resonance curves presented in Fig.1(a) exhibit nonlinear stiffening effect. The small increase of temperature $\Delta T = 0.5$ makes an essential shift of the resonance zone (red curve). The sensitivity of the system to the temperature is demonstrated on time histories in Fig.1(b); the first plot corresponds to a steady state for $\Omega = 0.08$ and $\Delta T = 0$. Below, due to the change of the temperature to $\Delta T = 0.5$ transient beating phenomena is observed, which finally goes to a new steady state (lower plot). The influence of the elevated temperature for fixed mechanical loading is presented in Fig.2. There are two possible situations. For ΔT up to 4.2 (black line) we observe one region of vibrations increase reminding rezonanse zone. But above the critical point $\Delta T = 4.2$ (red line) the plate loses stability and after buckling, new post-buckling oscillations around shifted vibration centre take place. The steady state for $\Delta T = 4.0$ and then transient states for $\Delta T = 4.5$ are presented in Fig.2(b).

CONCLUSIONS

The nonlinear resonance curves with hardening characteristic of Duffing type have been obtained for the extended nonlinear Mindlin plate model. The elevated temperature influenced the resonance zone and an occurrence of the bifurcation points and new solutions with different amplitudes and periods have been observed. The small temperature difference resulted in large shift of resonance curves and above a certain threshold new post-buckling dynamics has been observed. The transition between states is followed by complex transient dynamics.

References

[1] Dhainaut J.M., Duan B., Mei C., Spottswood C.S.M , Wolfe H.: Non-linear Response of Composite Panels to Random Excitations at Elevated Temperatures. Proc. of 7th Int. Conf. Recent Advances in Str. Dynamics, Vol.2, 769–784, Southampton 2000.

[2] Amabili M., Carra S.: Thermal Effects on Geometrically Nonlinear Vibrations of Rectangular Plates with Fixed Edges. J. of Sound Vib: 321, 936-954, 2009.

[3] Manoach E., Ribeiro P.: Coupled, Thermoelastic, Large Amplitude Vibrations of Timoshenko Beams. Int. J. Mech. Sci: 46,1589–1606, 2004.

[4] Ribeiro P., Manoach E.: The Effect of Temperature on the Large Amplitude Vibrations of Curved Beams. J. Sound Vibr 285: 1093–1107, 2005.

[5] Warminska A., Manoach E., Warminski J.: Nonlinear Dynamics of a Reduced Multimodal Timoshenko Beam Subjected to Thermal and Mechanical Loadings. Meccanica 49: 1775–1793, 2014.

[6] Warminska A., Manoach E., Warminski J., Samborski S.: Regular and Chaotic Oscillations of a Timoshenko Beam Subjected to Mechanical and Thermal Loadings. Continuum Mech. Thermodyn 27:719-737, 2014.

*Corresponding author. Email: a.warminska@pollub.pl

STATIONARY CONTROL OF A FLOATING AIRPORT IN WAVES

Shuyan Xia[1], Daolin Xu[1a)] & Haicheng Zhang[1]
[1]*State Key Laboratory of Advanced Design and Manufacturing for Vehicle Body, Hunan University, Changsha, 410082, P.R. China*

Summary This paper presents a nonlinear feedback control to suppress the surge motion of a serially connected multi-module floating airport in order to improve its operating condition in rough sea environment. An auxiliary system for dealing with the output saturation of actuators is introduced to design a series of the control laws based on Lyapunov stability. Numerical simulations indicate the effectiveness of the control method.

CONTROL MODEL FOR FLOATING AIRPORT

The concept of floating airports has been proposed [1] for land reclamation from sea and to avoid noise contamination on crowded cities. A floating structure with multi-modules may swing badly in wave, sensitive to the wave height and frequency. Since the operation condition of the floating airport requires for stringent tolerances on instability, it therefore seems natural to consider a control method to keep the floating structure stable [2]. This paper will use the backstepping approach [3] with considering the output saturation of actuators.

The floating airport with multi-modules is illustrated in Fig. 1 where adjacent modules are connected by elastic connectors in addition with actuators for control. The two ends of the floating airport are constrained by anchor chains to resist drift. Since each module acts as an oscillator, the connected modules can be viewed as a network where the network theory [4] can be applied.

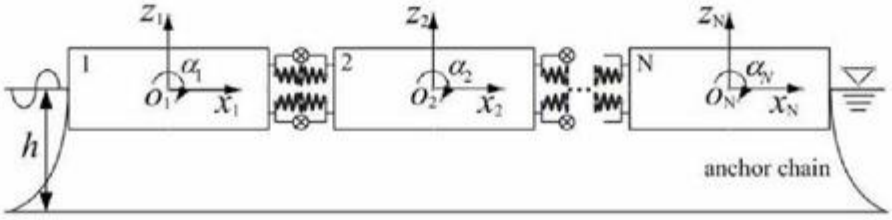

Fig. 1. Sketch for a floating airport with multi-modules connected by connectors and actuators

The network model of the floating airport [5] together with control can be in general written as

$$(\mathbf{M}_i+\boldsymbol{\mu}_i)\ddot{\mathbf{X}}_i+\boldsymbol{\lambda}_i\dot{\mathbf{X}}_i \quad \mathbf{S}_i \quad \mathbf{K}_i \ \mathbf{X}_i \quad \bar{\mathbf{f}}_i \exp[-(\omega t+\theta_i)]+\sum_{j=1}^{N}\Big(\varepsilon\Phi_{ij}G\ \mathbf{X}_i\ \mathbf{X}_j\Big)+u_j\ v_j\Big)\Gamma_{ij}\Psi_i\ \mathbf{X}_i\ \mathbf{X}_j\Big)\Big),\ \ i=1,2,\cdots N \tag{1}$$

By considering a two-dimensional problem, the vector $\mathbf{X}_i = x\ \ z\ \ \alpha_i\ ^T$ denotes the surge, heave and pitch motions of the *i*th floating module respectively. Symbols $\mathbf{M}_i$, $\boldsymbol{\mu}_i$, $\boldsymbol{\lambda}_i$ denote the matrices of the mass, additional mass and damping, $\mathbf{S}_i$ and $\mathbf{K}_i$ the matrices of buoyancy and mooring, $\bar{\mathbf{f}}_i$, ω, θ_i are the force, frequency and phase angle of regular wave, ε, Φ_{ij}, $\mathbf{G}\ \mathbf{X}_i,\mathbf{X}_j\Big)$ are the stiffness of connector, topology matrix and coupling function [5]. Symbol Γ_{ij} denotes the topological matrix of actuators and $\Psi_i\left(\mathbf{X}_i\ \mathbf{X}_j\right)$ is the control gain matrix, $u_j\ v_j\Big)$ the output force of the *j*th actuator where v_j is the control law to be designed. Without control, the floating airport excited by waves may encounter large oscillations induced by resonances and strong nonlinearity.

CONTROL LAW WITH OUTPUT SATURATION

Since the surge motion is most significant, the aim here is to suppress the surge motions, which may reduce the other motions as well due to the synergetic effect of the network [5]. To halt the surge motions of N number of modules, N actuators are required. A propeller-type actuator is mounted at the first module, and the rest actuators are installed at the same positions of connectors between adjoining modules. The actuator force of $u_i\ v_i\ t\ \Big)$ is bounded by a maximum actuation force u_{iM}. Thus the output of an actuator is defined by

$$u_i\ \ v_i\ \ t\ \Big)=\mathrm{sat}\left(v_i\ \ t\ \right)=\begin{cases}\mathrm{sign}\left(v_i\ \ t\ \right)u_{iM}, & \left|v_i\ \ t\ \right|\ge u_{iM}\\ v_i\ \ t\ , & \left|v_i\ \ t\ \right|<u_{iM}\end{cases}\qquad i=1,2,\cdots,N \tag{2}$$

a) Corresponding author. Email: dlxu@hnu.edu.cn.

where $v_i\ t$ is the *i*th control law. For the *i*th module, the coordination is converted by backstepping approach, let error variables $z_{1i}\quad x_i\quad z_{2i}\quad \dot{x}_i-\kappa_{1i}$ where κ_{1i} is a virtual control. Taking κ_{1i} in the form of $\kappa_{1i}=-k_{1i}z_{1i}$ where k_{1i} is a positive design parameter. Differentiate z_{2i} with respect to time and get

$$\dot{z}_{2i}=\ddot{}_i-\dot{\kappa}_{1i},\qquad i=1,2,\cdots N \tag{3}$$

where $\ddot{}_i$ is defined by Eq.(1). Because the outputs of actuators are in saturation, to keep the control system globally stable, an auxiliary system is introduced for the *i*th module, defined by

$$\dot{\chi}_i=-c_i\chi_i-\frac{1}{\chi_i}\left(|z_{2i}\Theta_1|+\frac{1}{2}\sum_{j=1}^{N}\left(\left(u_j\ \ v_j\right)-\ _j\right)^2\Gamma_{ij}\right)+\sum_{j=1}^{N}\left(\left(u_j\ \ v_j\right)-\ _j\right)\Gamma_{ij}\qquad i=1,2,\cdots N \tag{4}$$

where $\boldsymbol{\Theta}=(\mathbf{M}_i+\boldsymbol{\mu}_i)^{-1}\sum_{j=1}^{N}\left(\left(u_j\ \ v_j\right)-\ _j\right)\Gamma\ \Psi_i\left(\mathbf{X}_i\ \ \mathbf{X}_j\right)$ and Θ_i represents the *i*th element of the vector $\boldsymbol{\Theta}$. By solving the simultaneous equations (1) (2), (3),and (4), leads to $\dot{z}_{2i}=-z_{1i}-k_{2i}\ \ z_{2i}-\chi_i\big)$ and the design criterion of the control law $c_i-0.5\sum_{j=1}^{N}\left(\Gamma_{ij}\right)-0.5k_{2i}\geq 0$, where symbols k_{2i} and c_i are positive parameters to be designed in order to satisfy Lyapunov stability. By choosing proper design parameters, the outputs of actuators can be determined.

NUMERICAL SIMULATIONS

The data of the floating airport [2] is used for this numerical simulation. Fig.2(a) shows the significant suppression of the surge motion of the third floating module under control. The heave and pitch motions also appear relatively regular and mild. Owing to the coupling effect among the modules, the controlled motions of the rest modules are similar not presented here. Fig1(b) shows the variation of the control forces actuated on the third module. It can be seen from the first few truncated peaks that the output forces of the actuators are bounded by an assigned limitation of -200kN.

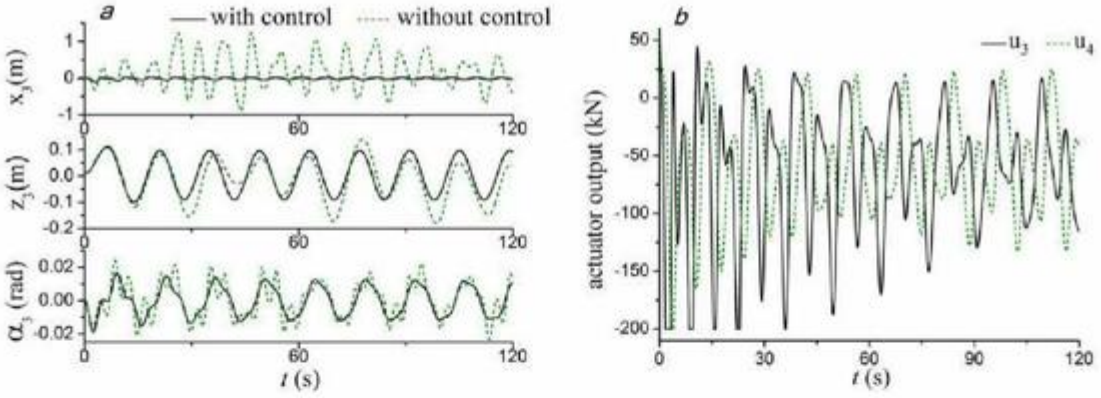

Fig.2 a) the responses of the floating airport with/without control, b) the actuator forces acted on the third floating module.

CONCLUSIONS

A nonlinear control strategy is proposed for suppressing the surge motion of a floating airport excited by waves. An auxiliary system is devised to deal with the output saturation of actuators. The numerical simulation illustrates that the stability of the floating airport is greatly improved, and the control method is effective. Thanks for the support of National Natural Science Foundation of China (11472100), the 973 research grant (2013CB036104).

References

[1] S. Ohmatsu, "Overview: Research on wave loading and responses of VLFS," *Mar. Struct.*, vol. 18, no. 2, pp. 149–168, 2005.Icer D.F., Adams J.A.: Mathematical Elements for Computer Simulation. Montreal, Canada 1977.

[2] S.Y. Xia;D.L. Xu, "On Retaining a Multi-Module Floating Structure in an Amplitude Death State," *Ocean Eng.*, 2015. (in review process)

[3] A. Boucheta, I. K. Bousserhane, a. Hazzab, B. Mazari, and M. K. Fellah, "Adaptive backstepping controller for linear induction motor position control," *COMPEL - Int. J. Comput. Math. Electr. Electron. Eng.*, vol. 29, no. 3, pp. 789–810, May 2010.

[4] D. L. Xu, H. C. Zhang, C. Lu, E. R. Qi, C. Tian, and Y. S. Wu, "Analytical criterion for amplitude death in nonautonomous systems with piecewise nonlinear coupling," Phys. Rev. E, vol. 89, no. 4, p. 042906, Apr. 2014.

[5] H. C. Zhang, D. L. Xu, C. Lu, S. Y. Xia, E. R. Qi, J. J. Hu, and Y. S. Wu, "Network dynamic stability of floating airport based on amplitude death," Ocean Eng., vol. 104, pp. 129–139, Aug. 2015.

SELF-INTERRUPTED CHATTER IN CYLINDRICAL GRINDING

Yao Yan*[1] and Jian Xu[2]

[1]*School of Astronautics and Aeronautics, University of Electronic Science and Technology of China, Chengdu, Sichuan, China*

[2]*School of Aerospace Engineering and Applied Mechanics, Tongji University, Shanghai, China*

Summary As a self-excited vibration, chatter in cylindrical grinding is mainly incurred by subcritical Hopf bifurcation and is of large amplitude, which forces grinding wheel to leave workpiece and interrupts the grinding. Normally, interactive wheel-workpiece force is described by regenerative theory and fixed time delays. However, for the self-interrupted, the theory requires modification as the regeneration can be absent. Therefore, instead of using delayed differential equations (DDEs), a model with partial differential equations (PDEs) is proposed for monitoring the regeneration. Results of the PDEs illustrate a smaller amplitude of the chatter compared with the DDEs.

CYLINDRICAL GRINDING

Cylindrical grinding uses a rotating wheel to rub a rotating workpiece, removing workpiece material and regenerating its surface. Besides, as seen in Figure 1(a), the wheel also has a translational motion for feed, which is plunge[1, 2] for wheel moving toward the workpiece and transverse[3] for that along the workpiece. When only the first mode of the workpiece is considered, the continuous model is discretized, which yields the equivalent model in Figure 1(b). Moreover, the interactive grinding force between the wheel and the workpiece is proportional to the instantaneous grinding depth determined by the doubly regenerative effect depicted in Figure 1(c), introducing time delays into the governing equation of the grinding. The grinding force repels the wheel and the workpiece, exciting the system to vibrate when system damping is insufficient.

LARGE-AMPLITUDE GRINDING CHATTER OBTAINED BY DDE

Regarding the dynamical model in Figure 1, the grinding dynamics is governed by

$$\frac{\mathrm{d}\mathbf{y}(\tau)}{\mathrm{d}\tau} = \mathbf{A}\mathbf{y}(\tau) + \mathbf{F}_{\mathrm{dde}} = (\mathbf{A}+\mathbf{D})\mathbf{y}(\tau) + \mathbf{D}_{\mathrm{w}}\mathbf{y}(\tau-\tau_{\mathrm{w}}) + \mathbf{D}_{\mathrm{g}}\mathbf{y}(\tau-\tau_{\mathrm{g}}) + \mathbf{f}, \tag{1}$$

where $\mathbf{y}(\tau)$ is the state vector of the grinding, $\mathbf{A}$ is the coefficient matrix of the system, $\mathbf{D}$, $\mathbf{D}_{\mathrm{w}}$ and $\mathbf{D}_{\mathrm{g}}$ are coefficient matrices from the grinding force, and $\mathbf{f}$ includes all the nonlinear terms. Using Eq. 1 and eigenvalue analysis, the stability boundary for the grinding is obtained, which is also a critical value for the Hopf bifurcation. Near the boundary, performing bifurcation analysis yields the subcritical Hopf bifurcation illustrated in Figure 2(a). As seen, the branch of periodic motions folds and introduces large-amplitude chatter coexisting with the stable grinding in the linearly chatter-free region. To illustrate, Points I and II have the same parameter value, but presents different time series in Figures 2(b) and (c). Specially, Figure 2(b) shows the grinding chatter accompanied by loss-of-contact effect, and thus the grinding is self-interrupted.

In the transverse grinding, as seen in Figure 2(d), the wheel is slowly moving along the workpiece, introducing a time-varying parameter into the system, and thus the grinding process is quasi-static. Thus, for each fixed wheel position P, the grinding dynamics is investigated by bifurcation analysis. Then, letting P varies between 0 and L and borrowing the idea of fast-slow system, one can construct the chatter of the transverse. Two typical cases are displayed in Figures 2(e) and (f), which are intermittent and of losing contact ($d_{\mathrm{g}} < 0$) as well.

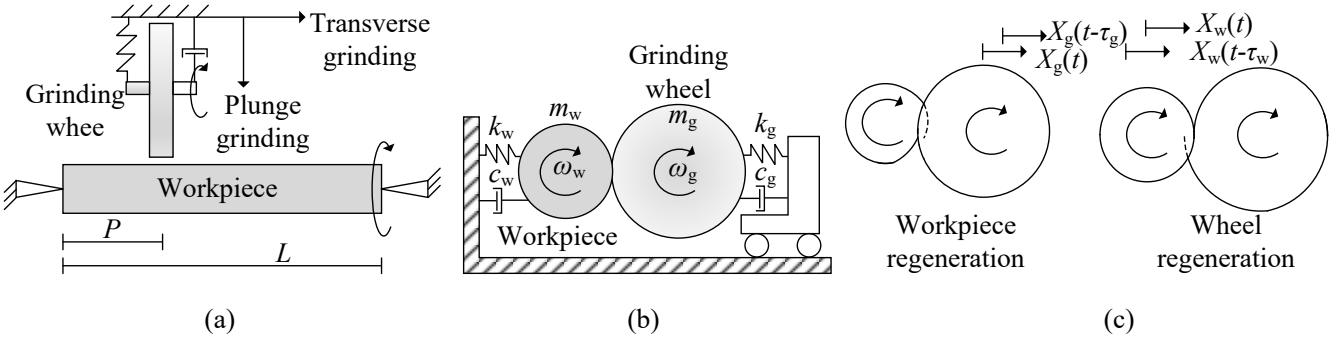

Figure 1: Schematics of the (a) plunge and transverse grinding process, (b) equivalent discrete model of the grinding with respect to the first workpiece mode, and (c) doubly regenerative effect in the wheel and workpiece surfaces.

*Corresponding author. Email: y.yan@uestc.edu.cn

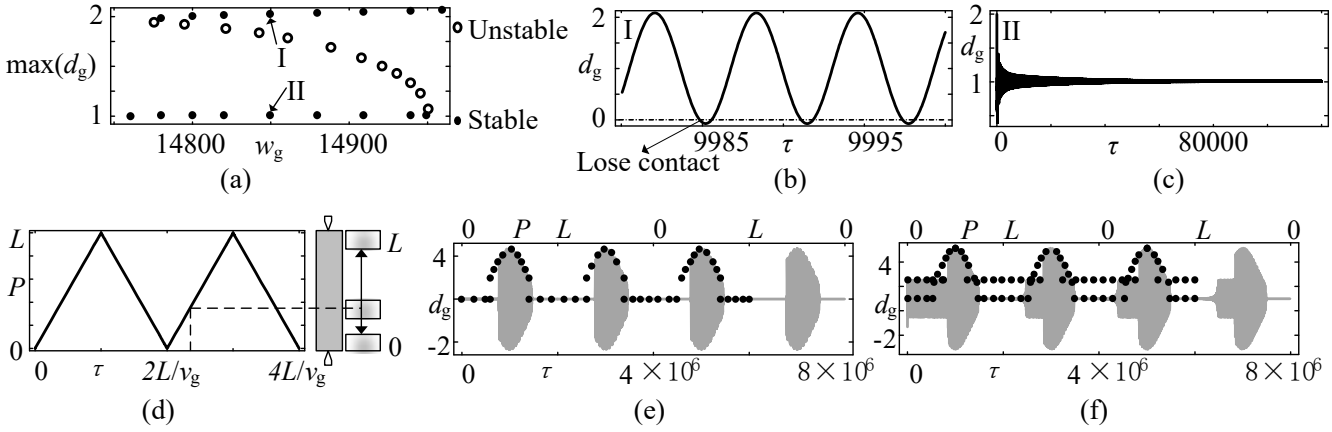

Figure 2: (a) Bifurcation diagram, (b) large-amplitude chatter, and (c) stable grinding in the plunge. (d) Wheel motion, (e) intermittent chatter, and (f) another typical chatter in the transverse.

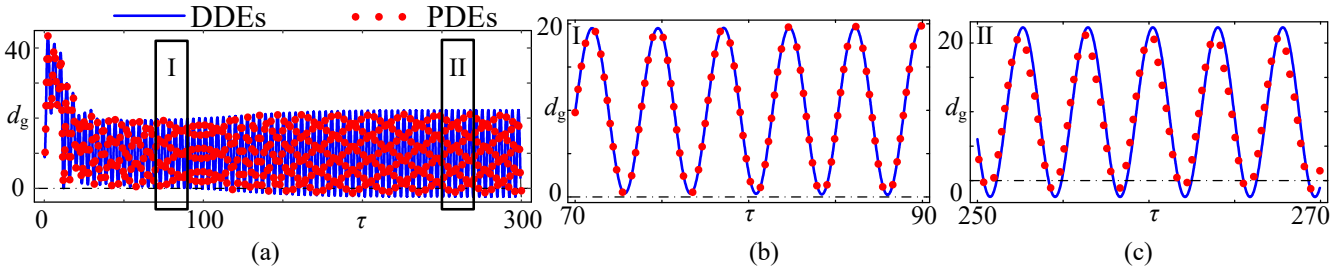

Figure 3: (a) Grinding chatter obtained by PDEs, with Regions I and II blown up and replotted in panels (b) and (c).

LARGE-AMPLITUDE GRINDING CHATTER OBTAINED BY PDE

Instead of the DDEs, PDEs can also be used to monitor the regeneration of workpiece surface by using [4]

$$\frac{\mathrm{d}\mathbf{y}(\tau)}{\mathrm{d}\tau} = \mathbf{A}\mathbf{y}(\tau) + \mathbf{F}_{\mathrm{pde}} \quad \text{and} \quad \frac{\partial\tilde{r}(\tau,\theta)}{\partial\tau} + \frac{2\pi}{\tau_{\mathrm{w}}}\frac{\partial\tilde{r}(\tau,\theta)}{\partial\theta} = 0, \tag{2}$$

where $\tilde{r}$ is the workpiece radius. Employing Galerkin Projection transforms Eq. (2) into ODEs, and solving it directory yields the grinding dynamics, which is illustrated in Figure 3. As seen in Figure 3(b), the solutions obtained from the DDEs and the PDEs are the same when the wheel keeps grinding the workpiece ($d_g > 0$). By contrast, the time series plotted in Figure 3(c) are different, where the result of the PDEs presents a smaller chatter amplitude when multiple-delay effect shows up.

CONCLUSIONS

Grinding chatter is of large amplitude and accompanied by loss-of-contact effect, making the grinding self-interrupted and introduce multi-regeneration. In this situation, the DDEs cannot describe the multi-delay effect with fixed delays. Therefore, PDEs is employed to record the workpiece profile, obtaining chatter with smaller amplitude.

References

[1] Yan Y., Xu J., Wang W.: Nonlinear Chatter With Large Amplitude in a Cylindrical Plunge Grinding Process. NONLINEAR DYNAM 69(4):1781-1793, 2012.

[2] Yan Y., Xu J.: Suppression of Regenerative Chatter in a Plunge-Grinding Process by Spindle Speed. J MANUF SCI E-T ASME 135:041019, 2013.

[3] Yan Y., Xu J., Wiercigroch M.: Chatter in a Transverse Grinding Process. J SOUND VIB 333:937-953, 2014.

[4] Wahi P., Chatterjee A.: Self-interrupted regenerative metal cutting in turning. INT J NONLINEAR MECH 43:111-123, 2008.

Acknowledgment: *This research is support by National Natural Science of China under Grant No.11502048 and 11572224, and Fundamental Research Funds for the Central Universities under Grant No. ZYGX2015KYQD033.*

A STUDY ON VARIABLE FOR ESTIMATING MAXIMUM POWER CONVERSION OF PARAMETRIC PENDULUMS

Yuichi Yokoi*[1] and Tsuyoshi Higuchi[1]

[1]*Division of Electrical Engineering and Computer Science, Nagasaki University, Nagasaki, Japan*

Summary The rotational motion of the parametric pendulum can be applied to energy harvesting from vibrations and movements of nature. In the pendulum system for the power conversion, the output power depends on the load resistance. For this reason, the output power can be controlled by regulating the load through a power converter on the basis of the Maximum Power Point Tracking (MPPT). The characteristic power curve implies that the maximum power point cannot be directly tracked by measured power. This paper finds out another variable to estimate the maximum power point for a MPPT method of the converting pendulum system.

INTRODUCTION

The parametrically excited pendulum inherently exhibits a conversion from a vertical vibration into its rotational motion. The converting motion, which can directly drive a rotational generator, is associated with energy harvesting from vibrations and movements of nature such as sea wave. The concept of the power conversion through the parametric pendulum is originated from a series of studies [1, 2, 3]. Among a variety of motions of the pendulum, the periodic rotation is suited for the application with respect to the amount of converted power. The system considered for the power conversion consists of a mechanical pendulum excited vertically or a so-called parametric pendulum, and a DC generator connected with the rotational shaft of the pendulum, and an electrical resistance as the load of the generator, as shown in Figure 1. For a vertical vibration, the output power depends on the load resistance. For this reason, the output power can be controlled by regulating the load through a power converter. The technique to maximize output power is used for wind turbines and photovoltaic systems as Maximum Power Point Tracking (MPPT) [4, 5]. A variety of control methods have been proposed for the MPPT of the systems [4, 5]. However, these methods cannot be applied to the MPPT of the converting pendulum system because the characteristic power curve of this system is different from the conventional ones. The power characteristic is described by a hysteresis curve including a jump phenomenon at the maximum point. This implies that the maximum power point cannot be directly tracked by measured power. This paper finds out another variable to estimate the maximum power point for a MPPT method of the converting pendulum system.

MATHEMATICAL MODEL

For the converting pendulum system as shown in Figure 1, a non-dimensional mathematical model is derived as

$$\frac{\mathrm{d}^2\theta}{\mathrm{d}t^2} + \gamma\frac{\mathrm{d}\theta}{\mathrm{d}t} + (1 + p\cos\omega t)\sin\theta = 0, \tag{1}$$

where θ denotes the angular displacement of the pendulum from the downward position, γ is a non-dimensional parameter governed by the load resistance, and $p\cos\omega t$ corresponds to the vertical excitation with amplitude of p and angular frequency of ω. The parameter γ is called the load coefficient. Without any losses, the input power P_{in} and the output power P_{out} are respectively expressed as follows:

$$P_{\mathrm{in}} = -\frac{1}{2}\left(\frac{\mathrm{d}\theta}{\mathrm{d}t}\right)\omega\cos\omega t\sin\theta \qquad \text{and} \qquad P_{\mathrm{out}} = \gamma\left(\frac{\mathrm{d}\theta}{\mathrm{d}t}\right)^2. \tag{2}$$

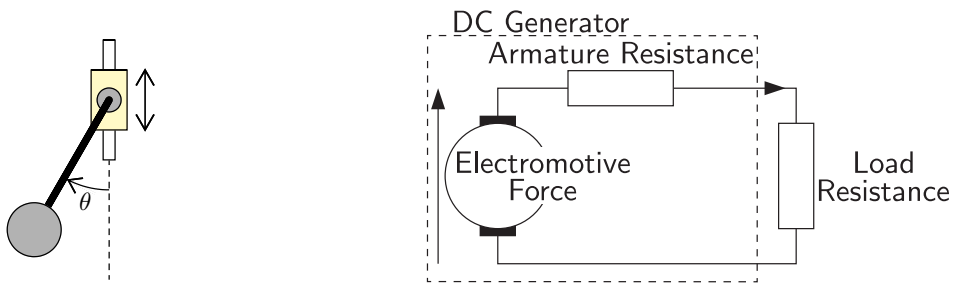

(a) Parametric pendulum. (b) Electrical circuit.

Figure 1: System for the power conversion through a pendulum.

*Corresponding author. Email: yyokoi@nagasaki-u.ac.jp

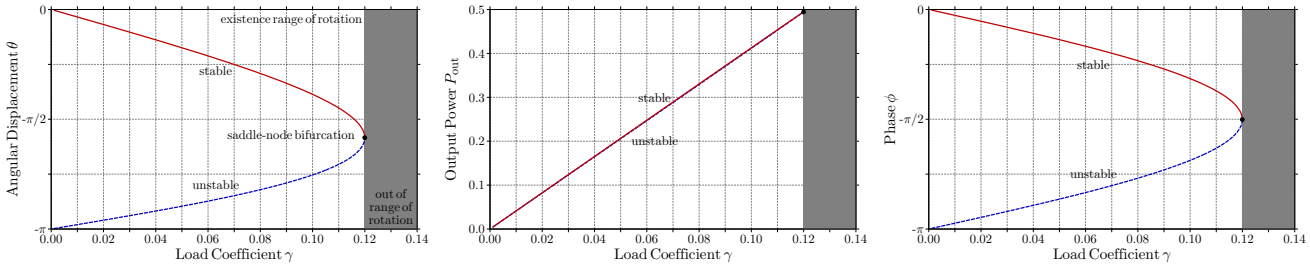

(a) Angular displacement θ. (b) Output power $P_{\rm out}$. (c) Phase ϕ.

Figure 2: Bifurcation diagram of periodic rotation with respect to the load coefficient γ.

MAXIMUM POWER CONVERSION

The load coefficient γ is regulated to control the amount of the output power $P_{\rm out}$. Figure 2 shows the bifurcation diagrams of periodic rotation with respect to γ at $p = 0.5$ and $\omega = 2$. These diagrams indicate the existence range of periodic rotation in the load coefficient γ. This implies that the load coefficient γ has to be regulated with the pendulum rotating for the power conversion. The output power $P_{\rm out}$ increases in almost proportion to γ, as shown in Figure 2(b). The power $P_{\rm out}$ is maximized at the maximum limit of γ in the range. Therefore, the load coefficient γ should be carefully regulated to establish the maximum power conversion because the coefficient γ beyond the limit prevents the periodic rotation for the power conversion. For this reason, this control previously requires the information of the maximum limit of γ. The maximum limit of γ is estimated with a variable that is less influenced by the parameters because it is difficult to directly predict the limit that severely depends on the system parameters,

A variable is found to estimate the maximum limit of γ or the maximum value of $P_{\rm out}$ from an analytical approach. The solution for periodic rotation can be written as $\theta = \omega t + \phi + \alpha(t)$, where ϕ corresponds to the phase and $\alpha(t)$ is a periodic function with period $2\pi/\omega$. In the analysis, it is assumed that the function $\alpha(t)$ is negligibly small. The averaging with the solution transforms the input power $P_{\rm in}$ into the averaged input power $\langle P_{\rm in} \rangle = -(\omega p/2)\sin\phi$. This expression indicates that the input power, which is equal to the output power, is maximized at $\phi = -\pi/2$. The phase ϕ is not dependent on the system parameters on the assumption. Thus, the output power is maximized at $\phi = -\pi/2$ regardless of the system parameters. From the stability analysis of the solution, it is found that the phase ϕ within $-\pi/2$ and 0 corresponds to stable periodic rotations. The phase ϕ is employed as the variable to estimate the maximum limit of the load coefficient γ. The efficacy of the phase ϕ is confirmed numerically, as shown in Figure 2(c). The phase ϕ converges from 0 to the vicinity of $-\pi/2$ as the increased load coefficient γ. On a control method for the MPPT, the load coefficient γ is regulated on the basis of the feedback variable ϕ to control the output power $P_{\rm out}$.

CONCLUDING REMARKS

This paper finds out a variable to estimate the maximum output power for a MPPT method of the converting pendulum system. The analytical and numerical studies verify that the phase component of periodic rotation performs as the feedback variable. In the presentation, we will show experimental evidences for the estimation through the phase and a feedback control for the MPPT.

ACKNOWLEDGMENTS

The author (Y. Yokoi) would like to thank Professor Marian Wiercigroch of the University of Aberdeen for his research visit at the Centre for Applied Dynamics Research and motivating this research. He would like to express his gratitude to Professor Takashi Hikihara of Kyoto University for fruitful discussion and continuous support with experimental systems. This work was partially supported by the Global COE Program of Kyoto University.

References

[1] Xu X. and Wiercigroch M.: Approximate Analytical Solutions for Oscillatory and Rotational Motion of a Parametric Pendulum. Nonliear Dyn 47:311–320, 2007.
[2] Lenci S., et al.: Rotating Solutions and Stability of Parametric Pendulum by Perturbation Method. J Sound Vib 310:243–259, 2008.
[3] Horton B., et al.: Transient Tumbling Chaos and Damping Identification for Parametric Pendulum. Phil Trans R Soc A 366:767–784, 2008.
[4] Baroudi J. A., Dinavahi V., Knight A. M.: A Review of Power Converter Topologies for Wind Generators. Renew Energ 32:2369–2385, 2007.
[5] Esram T., Chapman P. L.: Comparison of Photovoltaic Array Maximum Power Point Tracking Techniques. IEEE T Energy Conver 22:439–449, 2008.

NONLINEAR WAVE TRANSMISSION IN DISORDERED PERIODIC STRUCTURES

Behrooz Yousefzadeh*[1] and A. Srikantha Phani[2]
[1,2]*Department of Mechanical Engineering, University of British Columbia, Vancouver, BC, Canada*

Summary We study wave transmission through a damped nonlinear periodic structure of finite length, subjected to continuous harmonic excitation at one end. Nonlinearity leads to supratransmission phenomenon by which enhanced wave transmission occurs within the stop band of the periodic structure when forced at an amplitude exceeding a threshold. Here, we study supratransmission in the presence of deviations from periodicity (disorder), introduced as small variations in stiffness parameters throughout the structure. We find that disorder does not influence the supratransmission force threshold in the ensemble-average sense, but it reduces the average transmitted wave energy.

INTRODUCTION

A linear periodic structure exhibits filtering characteristics, whereby wave transmission is prohibited within certain frequency intervals known as stop bands. The presence of nonlinear forces provides a route to achieve enhanced transmission within a stop band, known as *supratransmission* [1]. This phenomenon occurs when the periodic structure is harmonically driven with a frequency within its linear stop band. In this case, energy transmission may become possible if the driving amplitude is larger than a certain threshold. The frequency components of the nonlinearly transmitted waves lie within the linear pass band of the structure. This has significant consequences for the transmitted energies if the periodic structure is disordered. The reason is that disorder results in localization of energy near the source of excitation (Anderson localization), particularly for frequencies within the linear pass band [2]. Thus, it is natural to expect a competition between nonlinearity and disorder with regards to transmitted energies above the supratransmission threshold. Our goal is to study this interaction.

MAIN RESULTS

We use a macro-mechanical nonlinear periodic structure that consists of coupled suspended cantilevers beams, shown in Fig. 1. See [3] for the corresponding mathematical models. The supratransmission phenomenon is explained in Fig. 2 for a periodic structure with $N = 10$ units. A key feature for supratransmission is that the motion is no longer periodic beyond the onset of transmission. As a result, the average transmitted energy (E_N) increases by orders of magnitude, where we define

$$E_N \equiv \frac{1}{(m_2 - m_1)T} \int_{m_1 T}^{m_2 T} \left(\frac{u_N(t)}{F} \right)^2 dt \quad \text{where} \quad T = 2\pi/\Omega, m_1 = 500, m_2 = 2500. \tag{1}$$

We introduce disorder throughout the structure by small variations in the stiffness parameter of each unit, drawn from a uniform statistical distribution. The strength of disorder is characterized by the ratio D/C, where D is a relative measure of the deviations in stiffness parameters and C is a measure of the strength of coupling between units [2].

We found that supratransmission persists in the presence of disorder. The change in threshold force amplitude, and whether it occurs or not, depends on the particular realization that is being considered. Nevertheless, when averaged over an ensemble of different realizations of disorder at a fixed D/C, the average onset of supratransmission remains unchanged; see Fig. 2(b).

When excitation is within the linear stop band, increasing the strength of disorder has negligible influence on transmitted energies below the onset of supratransmission, Fig. 3(a). In contrast, the average transmitted energies decrease with disorder above the transmission threshold, Fig. 3(b). This happens because the average frequency spectrum of transmitted waves lies within the linear pass band of the structure, where disorder localizes the response to the driven unit (Anderson localization).

CONCLUSIONS

Disorder does not influence the supratransmission force threshold in the ensemble-average sense, but it reduces the average transmitted wave energy. Generally, the influence of disorder decreases as forcing frequency moves away from the pass band edge, reminiscent of dispersion effects subsuming disorder effects in linear periodic structures. These results are generic to nonlinear disordered periodic structures and may be exploited for design of phononic crystals and acoustic metamaterials[4, 5].

References

[1] Geniet F., Leon J.: Energy transmission in the forbidden band gap of a nonlinear chain. Phys. Rev. Lett. 89:134102, 2002.
[2] Hodges C.: Confinement of vibration by structural irregularities. J. Sound Vib. 82:411-424, 1982.
[3] Yousefzadeh B., Phani A.S.: Energy transmission in finite nonlinear periodic structures from excitations within the stop band. J. Sound Vib. 354, 2015.
[4] Fleck N.A., Deshpande V.S., Ashby M.F.: Micro-architectured materials: Past, present and future. Proc. R. Soc. A 466:2495-2516, 2010.
[5] Liu Z., et al.:Locally resonant sonic materials. Science 289:1734-1736, 2000.

*a) Corresponding author. Email: behroozy@alumni.ubc.ca

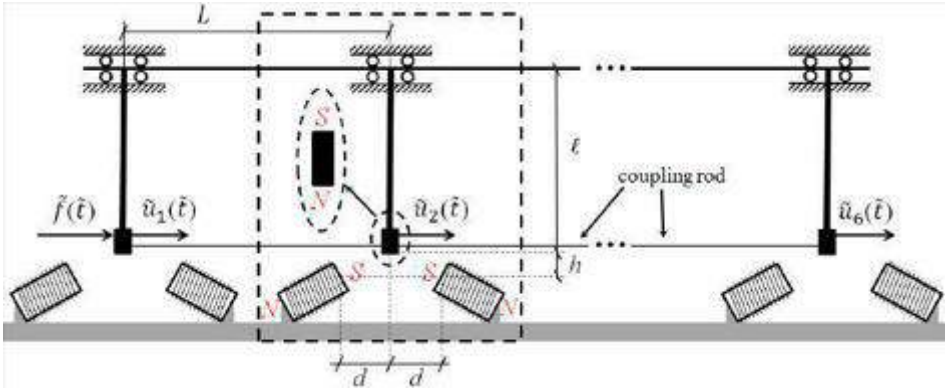

Figure 1: The schematic of the periodic structure made of N repeating units. The unit cell is indicated by the dashed box. An external harmonic force, $f(t) = F\cos(\Omega t)$, is applied to the first unit only. Two electromagnets, operated by direct currents, are fixed under the beam in each unit, such that the electromagnets have the same polarity facing the beam. Thus, the linear restoring force of each beam is combined with a strong nonlinear magnetic force to produce on-site nonlinearity. The magnetic force can be tuned, providing control over the strength of nonlinearity, as well as its type (softening or hardening).

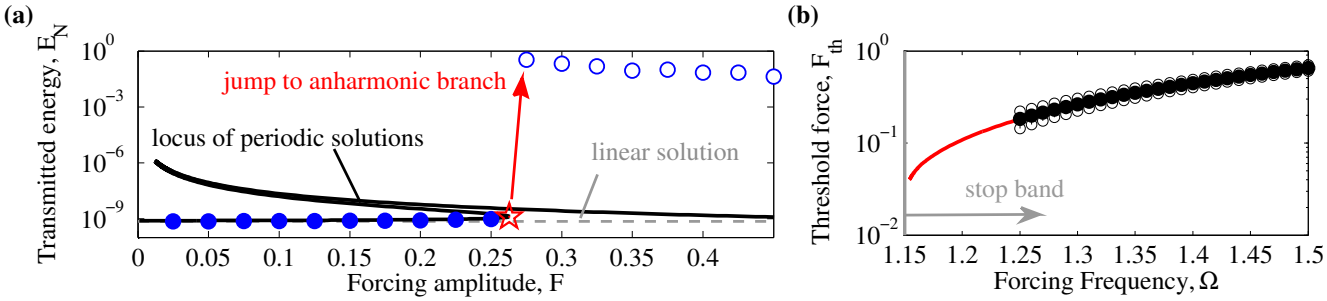

Figure 2: (a) Energy transmitted to the end of the exactly periodic structure (E_N) as a function of driving amplitude (F) at a forcing frequency above the linear pass band ($\Omega = 1.30$). The dashed grey line corresponds to the linear response of the system. The black curve indicates the evolution of periodic solutions. Circle markers indicates results from direct numerical integration of the governing equations, with filled markers indicating harmonic response and empty markers indicating non-periodic response. The periodic solutions lose their linear stability through a saddle-node bifurcation, which is depicted by the red star. (b) The red solid curve depicts the threshold curve for a periodic structure: locus of supratransmission force threshold (F_{th}) as a function of Ω. The filled circles indicate the average value of F_{th} for a disordered structure with $D/C = 2$. The corresponding standard deviations are shown using the empty circles. An ensemble of 1500 realizations is used here.

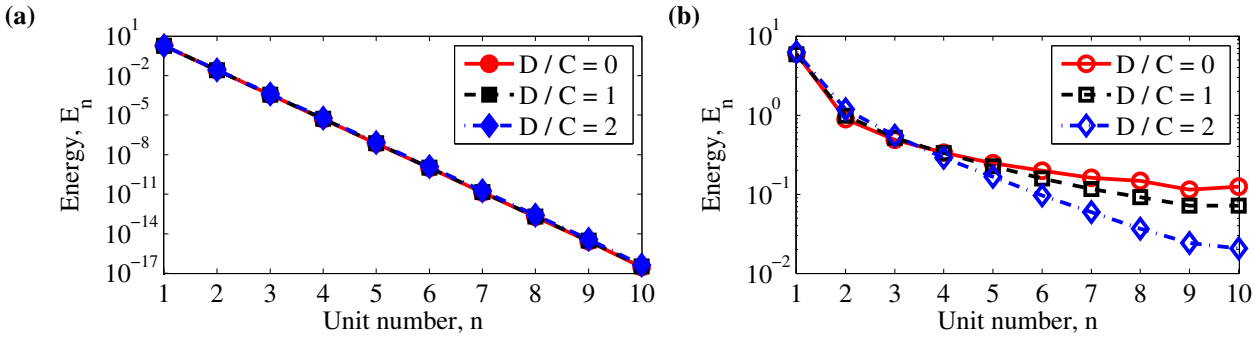

Figure 3: Average energy profiles for (a) the linear system, (b) the nonlinear system above the onset of transmission. Note the difference between the scales for the vertical axes in (a) & (b). Above the threshold, disorder results in localization of energy to the driven unit. An ensemble of 1500 realizations is used for each disordered system.

ON THE LOCOMOTION OF SELF-PROPELLING SYSTEMS IN A LINEAR RESISTIVE ENVIRONMENT

Nikolai Bolotnik[1], Igor Zeidis[2a)] & Klaus Zimmermann[2]
[1]*Institute for Problems in Mechanics of the Russian Academy of Sciences, Moscow, Russia*
[2]*Department of Technical Mechanics, Technische Univesitaet Ilmenau, Germany*

Summary The motion of self-propelling limbless locomotion systems in a linear viscous environment is considered. The resistance force acting on an element of the systems is assumed to be proportional to the velocity of this element relative to the environment. Two models of interaction of the locomotor with the environment are distinguished. In the first model, the coefficient of friction is constant for a mass element, whereas in the second model, this coefficient is constant for a length element. It is shown that progressive locomotion is impossible for the first model and is possible for the second model. This is explained by the fact that in the second model, the coefficient of friction for a mass element is in fact controlled by changing the length of this element due to deformation of the locomotor's body.

INTRODUCTION

This paper relates to mechanics of limbless locomotion. The limbless locomotion systems move without special propelling devices, such as wheels, legs, fins, or caterpillars, due to change in their shape and interaction with the environment. In a number of studies [1-2], the motion of particular systems of lumped masses (particles) along a straight line in a resistive environment was investigated. The motion of the systems was excited by a periodic change in the distances between the adjacent particles. The authors of the cited papers were interested mostly in the steady-state motion, in which the entire system moves with a periodically changing velocity. It was shown that if the resistance forces applied to each of the lumped masses are linear functions of the velocities of these masses relative to the environment, then progressive steady-state motion is impossible for the respective system. In [3], for a particular model, it was shown that a one-dimensional worm-like distributed-mass locomotor can move progressively in a viscous medium with linear rheology in a quasi-static approximation.

We investigate the specific features of the interaction of limbless locomotion systems with the environments possessing a linear rheology that allow or prevent self-propulsion of such systems in these environments. We consider both lumped-mass and distributed-mass systems. We assume that the resistance (friction) force applied by the environment to each element is a linear function of the velocity of the respective element relative to the environment with constant coefficient of friction. Unlike [3], we do not confine ourselves to a quasi-static approximation and proceed from the full dynamic equation of motion.

LUMPED MASS LOCOMOTION SYSTEMS

Consider a set of n particles (point masses) that can move along a horizontal straight line (Figure l).

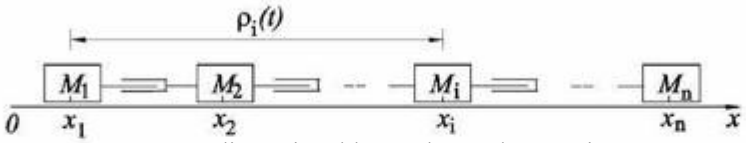

Figure 1. A one-dimensional lumped mass locomotion system.

Let x_i denote the coordinate of the ith particle measured along the line of the motion from a point O fixed in an unmovable (inertial) reference frame; M_i the mass of the ith particle; $m_i = M_i / M$, $M = \sum_{i=1}^{n} M_i$; the coordinate of the ith particle measured relative to point 1 is $\rho_i = x_i - x_1$. Each particle interacts with the other particles of the system and with the environment. We assume that the environmental forces are linear functions of the velocity: $F_i(\dot{x}_i) = -\mu_i \dot{x}_i$, where μ_i is the coefficient of friction. The motion of the center of mass X of the system is governed by the equation

$$\dot{V} = -kV - \dot{\xi}, \quad \dot{X} = V, \quad X(0) = X_0, \quad V(0) = V_0, \quad \xi = \sum_{j=1}^{n} (km_j - k_j)\rho_j, \quad k_i = \mu_i / M, \quad k = \sum_{j=1}^{n} k_j, \quad i = 1,\ldots,n. \qquad (1)$$

[a)] Corresponding author. Email: igor.zeidis@tu-ilmenau.de.

If the function $\xi(t)$ is bounded, i.e., $|\xi(t)| \le C$, where C is a constant, then the solution $X(t)$ of system (1) is estimated by $|X(t) - X_0| < \left(|V_0| + |\xi(0)| + C\right)/k$. Hence, the center of mass of a lumped mass locomotion system on a straight line cannot move by an arbitrary prescribed distance in a linear resistive environment, irrespective of the control law, provided that the change in the distances between the system's particles is constrained. Assume that (i) the system starts moving from a state of rest and, hence, $V_0 = 0$, (ii) the relative position of the system's particles changes during a finite time T, i.e., $\dot{\xi}(t) \equiv 0$ and $\xi(t) \equiv \xi(T)$ for $t > T$ and, in addition, (iii) $\xi(0) = \xi(T)$. Then $\lim_{t\to\infty} X(t) = X_0$. Therefore, if the system starts moving from a state of rest, and the configuration of the system at the terminal instant of the excitation coincides with the initial configuration, then the system eventually returns to its initial position after the excitation has been terminated.

DISTRIBUTED MASS LOCOMOTION SYSTEM

Consider a worm-like locomotion system the body of which has a shape of a thin circular cylinder (Figure 2). The system moves along the axis of the cylinder. The locomotion occurs due to the longitudinal deformation of the cylinder and its interaction with the environment. The motion of the system is excited and controlled by internal forces that act between the parts of the worm's body. We assume that in the reference (undeformed) configuration, the cylinder has length L and mass density per unit length $\rho(x)$; the total mass of the system is M. Introduce the notation: x_0 is the coordinate of the left edge of the cylinder measured from a point O fixed in the inertial reference frame; x, $0 \le$ $\le$, is the coordinate of a current section of the cylinder measured for the undeformed configuration from the left edge; $u(x,t)$ is the displacement of the section identified by the coordinate x at the time t from its position in the reference configuration.

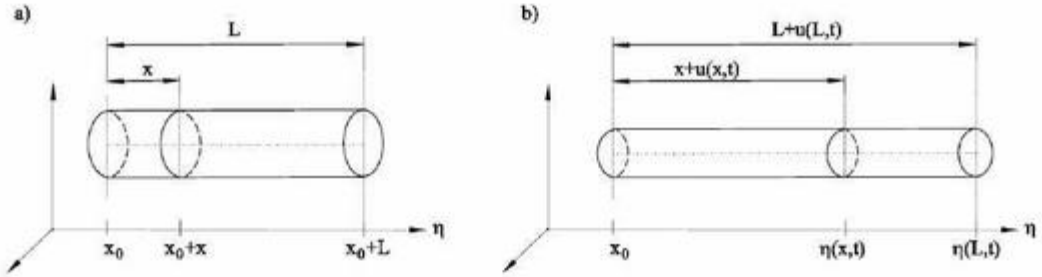

Figure 2. A distributed mass worm-like system: a) undeformed, b) deformed.

The position η of section x of the deformed cylinder with respect to point O is defined by $\eta(x,t) = x_0 + x + u(x,t)$, $u(0,t) = 0$. We assume that the resistance (friction) force acting on an element of the system is proportional to the velocity $\dot{\eta}(x,t)$ of this element relative to the environment, with the coefficient of proportionality (coefficient of friction) being constant. Two models of the interaction between the system and the environment are considered; the coefficient of friction is constant per unit mass for the first model and per unit length for the second model. The motion of the center of mass of the system to an arbitrary position is proved to be impossible for the first model and possible for the second model. It is explained by the fact that for the second model, the coefficient of friction related to a mass element changes, since the length of this element changes due to deformation of the system. The locomotion of the distributed mass system is studied in detail for the case where a periodic deformation wave runs with a constant velocity along the system. It is shown that if the length of the undeformed system is a multiple of the deformation wave length, then for the steady-state mode of motion, at which the system arrives from any initial state, the system's center of mass moves at a constant velocity in the direction of the propagation of the wave, irrespective of the wave shape. For a sinusoidal wave the length of which is incommensurable with the length of the undeformed system, the center of mass of the system moves on the average in the direction of the propagation of the wave with a velocity periodically changing in time.

Acknowledgement. This research was financed by the German Research Society (DFG) (projects ZI 540/19-1) and the Russian Foundation for Basic Research (projects 14-01-00061 and 15-51-12381).

References

[1] Chernousko F.L: Analysis and optimization of the motion of a body controlled by means of a movable mass. J. Appl Math Mech **70**:819–842, 2006
[2] Bolotnik N., Pivovarov M., Zeidis I., Zimmermann K.: The undulatory motion of a chain of particles in a resistive medium. ZAMM **91**:259–275, 2011
[3] DeSimone A., Tatone A.: Crawling mobility through the analysis of model locomotors: Two case studies. Eur J. Phys E **35**: 2–8, 2012

MODE LOCALIZATION IN CYCLIC SELF-EXCITED STRUCTURE WITH SYMMETRIC DELAYED FEEDBACK

Shu Zhang[1], Jian Xu[1a)] & Kwok-wai Chung[2]
[1]*School of Aerospace Engineering and Applied Mechanics, Tongji University, Shanghai, P.R.C.*
[2]*Department of Mathematics, City University of Hongkong, Hongkong, P.R.C.*

Summary We employ the theory of equivariant bifurcation to investigate the mode localization in a cyclic self-excited structure with symmetric delayed feedback. The method of multiple scales is applied to obtain the equation of amplitude based on which the condition for the existence mode localization is given. Our result shows that in the presence of time delays, strong nonlinearity may induce mode localization in the cyclic self-excited structure without imperfections in parameters.

INTRODUCTION

Mode localization is commonly interpreted as a dynamic phenomenon induced by mistuned parameters of a symmetric structure. Namely, the irregularities of the structure will trap the energy in a substructure while it is believed that in the absence of imperfections the energy will be uniformly distributed. The theory of equivariant bifurcation [1] provides another perspective to study this problem, i.e., the symmetry is the reason that induces non-symmetric (asynchronous) oscillation, including localization. This group-theoretic based method has been employed to investigate mode bifurcations [2] and localization of some forced vibration system [3]. However, from the view point of nonlinear dynamics, the mechanism of localization is still not quite clear especially for the self-excited structure which can be found in dry-friction-induced oscillation, the interaction between fluid and structure and so on. Van der Pol-Duffing system is one of the standard models of self-excited structures and will be used in the present paper to investigate the mode localization. The equilibrium of such system is unstable and thus people usually introduce feedback control which brings the time delay. With the aid of equivariant bifurcation theory, we show that in the presence of time delay, the symmetry of the structure can induce mode localization and the nonlinear stiffness has a strong impact on it.

MODEL SETUP AND STABILITY SWITCH BOUNDARIES

In this paper, we consider the following self-excited system of Van der Pol-Duffing type to study the mode localization phenomenon induced by the nonlinearity and delays [4]:

$$\begin{aligned}&\ddot{x}_j+\mu(x_j^2-1)\dot{x}_j+\ _j+\kappa x_j^3\\&=\alpha\ x_{j-1}\ t-\tau_2)+x_{j+1}\ t-\tau_2\ -\ x_j\ t-\tau_1))+\beta\ \dot{x}_{j-1}\ t-\tau_2)+\dot{x}_{j+1}\ t-\tau_2\ -\ \dot{x}_j\ t-\tau_1)),\end{aligned}\tag{1}$$

where $x_0\equiv\ _3$, $x_4\equiv\ _1$, μ is the damping coefficient, κ the nonlinear stiffness, α, β are the gain parameters for position and velocity feedback, respectively, τ_1, τ_2 the time lag of self-connection and mutual-connection, respectively. From the point of view of nonlinear dynamics, oscillations can be thought of as bifurcated from the equilibrium. In order to investigate the localization phenomenon, we need to analyze the stability of the equilibrium first. The characteristic equation of the linearized system of (1) around the trivial equilibrium is

$$\left(\lambda^2-\mu\lambda+\ \ +\ \ \alpha+\beta\lambda)(\mathrm{e}^{-\lambda\tau_1}-\mathrm{e}^{-\lambda\tau}\ )\right)\left(\lambda^2-\mu\lambda+\ \ +\ \alpha+\beta\lambda)(2\mathrm{e}^{-\lambda\tau_1}+\mathrm{e}^{-\lambda\tau}\ )\right)^2=0\tag{2}$$

where λ is the eigenvalue. The curves representing roots of (2) in the plane consisting of τ_1 and τ_2 are plotted in Fig. 1. The expression in the first pair of parentheses is the condition for switching to synchronous oscillation (red curve) while the one in the second pair (blue curve) is the condition for switching to asynchronous state, which may correspond to the localization. In region III, there exists the asynchronous oscillation induced by equivariant Hopf bifurcation. The asynchronous oscillation and its stability will be studied by means of the method of multiple scales, as shown in next section.

MODE LOCALIZATION ANALYSIS

In order to investigate the oscillator behaviour of (1), the method of multiple scales is employed to obtain the equation that the amplitudes of x_1, x_2 and x_3 have to satisfy. It follows from the standard procedure of equivariant Hopf bifurcation analysis that the solution can be assumed as

$$x_j=\mathrm{i}\,\omega\chi_1^{j-1}A\ T_1\ T\ \ \ ^{\mathrm{i}\omega T_0}+\mathrm{i}\,\omega\chi_2^{j-1}B\ T_1\ T\ \ \ ^{\mathrm{i}\omega T_0}+\ \ \ +\ \ \ \varepsilon\ \ \ \ \ j=1,2,3,$$

where $\chi_1=\mathrm{e}^{\ \pi}$, $\chi_2=\mathrm{e}^{\ \pi}$, $T_0=$, $T_1=\varepsilon t$, $T_2=\varepsilon^2 t$. Up to $o\ \varepsilon$, the equation of amplitude is obtained as

[a)] Corresponding author. Email: xujian@tongji.edu.cn.

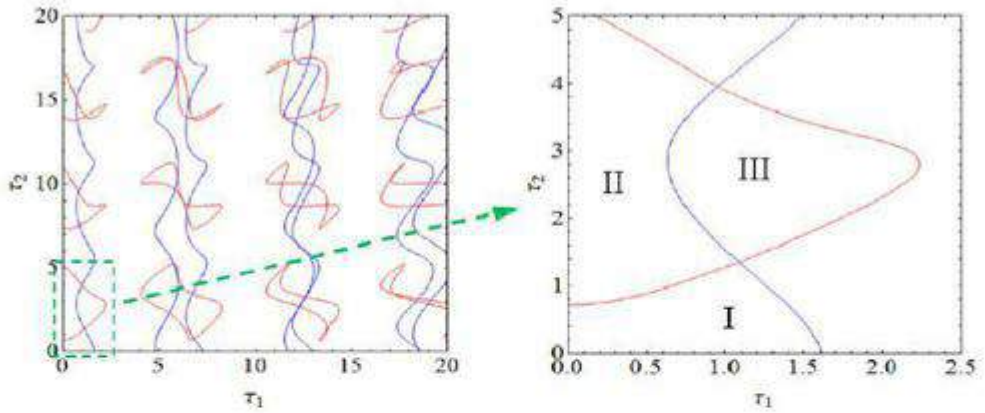

Figure 1: Stability switch boundaries for $\mu = 0.05, \alpha = 0.005, \beta = 0.1, \kappa = 1$, where the equilibrium is stable in Region I.

$$A^{(1,0)} = A\ \ p_0 + p_1\ \ A\bar{A} + \ \ B\bar{B} \qquad B^{(1,0)} = B\ \ p_0 + p_1 \quad A\bar{A} + B\bar{B})\ ,$$

where p_0 and p_1 are (complex) functions of the parameters. $A^{(0,1)}$ and $B^{(0,1)}$ can be obtained in the similar way and then the final equation of amplitude follows by combining $A^{(1,0)}$, $B^{(1,0)}$, $A^{(0,1)}$ and $B^{(0,1)}$. To provide an example, for $\mu = 0.05$, $\alpha = 0.005$, $\beta = 0.1$, $\tau_1 = 0.7$, $\tau_2 = 3$ (Region III in Fig. 1), we find that $p_0 =$ $+$, $p_1 = -$ $+$ κ $+$ $+$ κ . Based on the results of [1] (Theorem 3.1, pp. 382), we claim that when $\kappa < 0.73$, the travelling wave (non-localization) is stable, as shown in Fig. 2(a); when $\kappa > 0.73$ the standing wave (mode localization) is stable and thus the mode localization can be observed, as shown in Fig. 2(b).

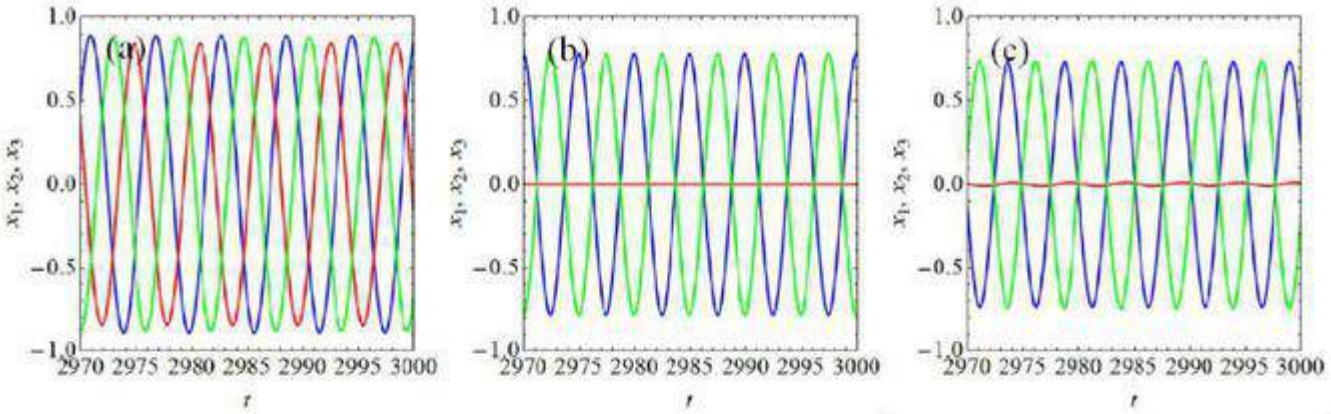

Figure 2: Numerical simulations for (1): (a) $\kappa = 0$; (b)(c) $\kappa = 1$, all integrated from $x_1\ x\ \ x\ =$ $-$ $-$.

DISCUSSIONS

It should be noticed that the mode localization studied in the present paper persists when the structure symmetry breaks, as shown in Fig.2(c) where the damping coefficients are 0.045, 0.052, 0.05, respectively. This implies that the present result provides another possible explanation for mode localization in self-excited cyclic structure.

References

[1] Golubitsky, M., et al: Singularities and Groups in Bifurcation Theory II. Springer-Verlag, New York 1988.

[2] Vakakis, A. F., et al: Normal Modes and Localization in Nonlinear Systems. Wiley Interscience, New York 1996.

[3] Folley C. N..: Bifurcation and Symmetry in Cyclic Structures *PhD Thesis*, Purdue University School of Mechanical Engineering, Lagos, 1999.

[4] Song Y. L., et al.: Bifurcation, Amplitude Death and Oscillation Patterns in A System of Three Coupled Van der Pol Oscillators with Diffusively Delayed Velocity Coupling. Chaos 21: 023111, 2011.

Acknowledgement: This research is supported by the National Natural Science Foundation of China (11572224, 11502168), the Fundamental Research Funds for the Central Universities, the Program for Young Excellent Talents at Tongji University and the Strategic Research of the City University of Hong Kong.

MS05 - Soft Solid Active Matter

TS.MS05-1.01	Huang, Yonggang - Mechanically Guided, Deterministic Three-Dimensional Assembly (INVITED)	244
TS.MS05-1.02	Mazza, Edoardo - The intriguing deformation behavior of soft biomembranes (INVITED)	246
TS.MS05-1.03	Saif, Taher - Soft neurons actively maintain strong tension for synaptic functions (INVITED)	248
TS.MS05-1.04	Zhao, Xuanhe - Mechanochemically Responsive Elastomers: Fundamental and Applications (INVITED)	250
TS.MS05-2.01	Safran, Samuel - Mechanical synchronization of active beating within and between cardiomyocytes	252
TS.MS05-2.02	McGarry, Patrick - On the Free Energy of Cells Spread on Micropatterned Substrates	254
TS.MS05-2.03	Vernerey, Franck - Catch bonds and mechano-sensitivity of acto-myosin filament networks	256
TS.MS05-2.04	Feng, Xi-Qiao - Biochemomechanical poroelastic theory of tumor growth	258
TS.MS05-2.05	Noselli, Giovanni - Hydraulic fracture and toughening of epithelial cell monolayers	260
TS.MS05-2.06	Holmes, Douglas - Geometry and Mechanics of Shell Growth	262
TS.MS05-3.01	Govindjee, Sanjay - Microsphere modeling with full relaxation and internal evolutionary mechanisms	264
TS.MS05-3.02	Purohit, Prashant - Membrane Tension Controls Kinetics of Neuron Growth	266
TS.MS05-3.03	Zhang, Yihui - Soft network materials with deterministic and bio-inspired designs	268
TS.MS05-3.04	Hu, Yuhang - Dynamic indentation: A simple method to characterize poroelasticity of gels in micron scale	270
TS.MS05-3.05	Xu, Feng - Cell alignment fabrication using stretchable hydrogels with programmable strain gradients	272
TS.MS05-3.06	Li, Tiefeng - Mechanical instabilities and multi-functions of soft active structures in soft robots	274
TS.MS05-4.01	Huang, Rui - Ion-induced swelling and volume phase transition of polyelectrolyte gels	276
TS.MS05-4.02	Chester, Shawn - Combined Modeling and Experiments Polymeric Gels	278
TS.MS05-4.03	Nardinocchi, Paola - On the effects of cavitation in hydrogel-based structures	280
TS.MS05-4.04	Duda, Fernando - On pressure-driven flow through a gel-filled channel	282
TS.MS05-4.05	Brun, Pierre-Thomas - Elastocapillary swelling: When coalesced structures curl apart	284
TS.MS05-4.06	Feng, Xiangchao - Highly stretchable double-network composite	286
TS.MS05-5.01	Liu, Ling - Computational Modelling of Light-switchable Surface Topograhies Using Liquid Crystal Polymers	288
TS.MS05-5.02	Neukirch, Sebastien - Coiling a fiber inside a drop provides a highly stretchable device	290
TS.MS05-5.03	Lu, Tongqing - Nonlinear characteristics of dielectric elastomers under electromechanical coupling loading	292
TS.MS05-5.04	Zhu, Jian - Voltage-induced buckling and wrinkling in a dielectric elastomer	294
TS.MS05-5.05	Jandron, Michael - Exploring band gap tunability in phononic crystals using dielectric elastomers	296
TS.MS05-5.06	Liu, Taixiang - Research on the microstructure and the property of magnetorheological elastomer	298

TS.MS05-6.01	Lu, Nanshu - Thickness and d33 effects on the energy conversion and actuation of piezoelectric unimorphs	300
TS.MS05-6.02	Lucantonio, Alessandro - Poroelastic toughening in polymer gels: A theoretical and numerical study	302
TS.MS05-6.03	Ma, Zhuo - Fracture of soft elastic foam	304
TS.MS05-6.04	Qi, H. Jerry - Reversible shape changing components by 3D printing	306
TS.MS05-6.05	Silberstein, Meredith - Constitutive theory for mechanochemically-based energy dissipating elastomer	308
TS.MS05-6.06	Wang, Shuolun - Modeling the effect of inelasticity on instabilities in soft dielectrics	310
PO.MS05-1.01.27	Cai, Shengqiang - Active motion and deformation of liquid crystal elastomers	312
PO.MS05-1.02.28	Jiang, Liying - Optimizing the energy harvesting performance of viscoelastic dielectric elastomer generators	314
PO.MS05-1.03.29	Li, Ying - Multiscale constitutive modeling on finite strain viscoelasticity of elastomers	316
PO.MS05-1.04.30	Liu, Liwu - Thermodynamics and instability of dielectric elastomers	318
PO.MS05-1.05.31	Liu, Zishun - A New Viscoelastic Constitutive Model of Shape Memory Polymers	320
PO.MS05-1.06.32	Manav, Manav - Mechanics of thermoresponsive polymer brush based soft materials: theory and experiments	322
PO.MS05-1.07.33	Mandre, Shreyas - Curvature of the transverse arch governs stiffness of the human foot	324
PO.MS05-1.08.34	Wang, Pengfei - Coupling kinetics of reactively ionic gels	326
PO.MS05-1.09.35	Yang, Xuxu - Mechanical instability build in hydrogel structure achieving fast actuation	328
PO.MS05-1.10.36	Zhang, Teng - Tough Adhesion of Hydrogels	330
PO.MS05-1.11.37	Zhang, Yanhang - Contributions of ECM Constituents to Arterial Wall Mechanics	332

MECHANICALLY GUIDED, DETERMINISTIC THREE-DIMENSIONAL ASSEMBLY

Yonggang Huang[1], Yihui Zhang[2] & John A. Rogers[3]
[1]*Department of Civil and Environmental Engineering, Department of Mechanical Engineering, Department of Materials Science and Engineering, and Skin Disease Research Center, Northwestern University, Evanston, IL, USA*
[2]*Center for Mechanics and Materials, and Applied Mechanics Laboratory, Tsinghua University, Beijing, P.R. China*
[3]*Department of Materials Science and Engineering and Frederick Seitz Materials Research Laboratory, University of Illinois at Urbana-Champaign, Urbana, IL, USA*

Summary: Complex three-dimensional (3D) structures in biology (e.g., cytoskeletal webs, neural circuits, and vasculature networks) form naturally to provide essential functions in even the most basic forms of life. Compelling opportunities exist for analogous 3D architectures in human-made devices, but design options are constrained by existing capabilities in materials growth and assembly. We report routes to previously inaccessible classes of 3D constructs in advanced materials, including device-grade silicon. The schemes involve geometric transformation of 2D micro/nanostructures into extended 3D layouts by compressive buckling. Demonstrations include experimental and theoretical studies of more than 40 representative geometries, from single and multiple helices, toroids, and conical spirals to structures that resemble spherical baskets, cuboid cages, starbursts, flowers, scaffolds, fences, and frameworks, each with single- and/or multiple-level configurations.

Controlled formation of 3D functional mesostructures is a topic of broad and increasing interest, particularly in the last decade, due to important envisioned uses in nearly every type of micro/nanosystem technology, from biomedical devices to microelectromechanical components, photonics and optoelectronics, metamaterials, electronics, energy storage and others. Although volumetric optical exposures, fluidic self-assembly, residual stress-induced bending and bio-templated/guided growth can be used to realize certain classes of structures in certain types of materials, techniques that rely on rastering of fluid nozzles or focused beams of light provide the greatest versatility in design. Applicability of these latter methods, however, only extends directly to materials that can be formulated as inks or patterned by exposure to light/energetic particles, and indirectly to those that can be deposited onto or into sacrificial 3D structures formed with these materials. Integration of more than one type of any material into a single structure can be challenging. Furthermore, the serial nature of these processes sets practical constraints on operating speeds and overall addressable areas. These and other limitations stand in stark contrast with the exceptional fabrication capabilities that exist for the types of planar micro/nanodevices that are ubiquitous in state-of-the-art semiconductor technologies. Routes to 3D mesostructures that exploit this existing base of competencies can naturally provide options in high performance function that would otherwise be unobtainable. Methods based on residual stress induced bending are naturally compatible with modern planar technologies and they offer yields and throughputs necessary for practical applications. Such schemes provide access to only certain classes of geometries, through either rotations of rigid plates to yield tilted panels, rectangular cuboids, pyramids or other hollow polyhedra, or rolling motions of flexible films to form tubes, scrolls or related shapes with cylindrical symmetry. Here, we present a different set of concepts in which strain relaxation in an elastomeric substrate simultaneously imparts forces at a collection of lithographically controlled locations on the surfaces of planar precursor structures (1). The resulting processes of controlled, compressive buckling induce rapid, large area geometric extension into the third dimension, capable of transforming the most advanced functional materials and planar microsystems into mechanically tunable, 3D forms with broad geometric diversity.

We also introduce ideas for a form of Kirigami that allows precise, mechanically driven assembly of 3D mesostructures of diverse materials from 2D micro/nanomembranes with strategically designed geometries and patterns of cuts (2). Theoretical and experimental studies demonstrate applicability of the methods across length scales from macro to nano, in materials ranging from monocrystalline silicon to plastic, with levels of topographical complexity that significantly exceed those that can be achieved in any other way. A broad set of examples includes 3D silicon mesostructures and hybrid nanomembrane-nanoribbon systems, including heterogeneous combinations with polymers and metals, with critical dimensions that range from 100 nm to 30 mm. A 3D mechanically tunable optical transmission window provides an application example of this Kirigami process, enabled by theoretically guided design.

Finally, Origami is a topic of rapidly growing interest in both the scientific and engineering research communities due to its promising potential in a broad range of applications. Previous assembly approaches of origami structures at the micro/nanoscale are constrained by the applicable classes of materials, topologies and/or capability of control over the transformation. Here, we introduce an approach that exploits controlled mechanical buckling for autonomic origami

[a)] Corresponding author. Email: y-huang@northwestern.edu

assembly of 3D structures across material classes from soft polymers to brittle inorganic semiconductors, and length scales from nanometers to centimeters (3). This approach relies on a spatial variation of thickness in the initial 2D structures as an effective strategy to produce engineered folding creases during the compressive buckling process. The elastic nature of the assembly scheme enables active, deterministic control over intermediate states in the 2D to 3D transformation in a continuous and reversible manner. Demonstrations include a broad set of 3D structures formed through unidirectional, bidirectional, and even hierarchical folding, with examples ranging from half cylindrical columns and fish scales, to cubic boxes, pyramids, starfish, paper fans, skew tooth structures, and to amusing system-level examples of soccer balls, model houses, cars, and multi-floor textured buildings.

References

[1] Xu S, Yan Z, Jang K I, et al. Assembly of micro/nanomaterials into complex, three-dimensional architectures by compressive buckling[J]. Science, 2015, 347(6218): 154-159.

[2] Zhang Y, Yan Z, Nan K, et al. A mechanically driven form of Kirigami as a route to 3D mesostructures in micro/nanomembranes[J]. Proceedings of the National Academy of Sciences, 2015, 112(38): 11757-11764.

[3] Yan Z, Zhang F, Wang JC, Liu F, Guo XL, Nan KW, Lin Q, Gao MY, Xiao DQ, Shi Y, Qiu YT, Luan HW, Kim JH, Wang YQ, Luo HY, Han MD, Huang Y, Zhang YH, and Rogers JA, "Controlled mechanical buckling for origami-inspired construction of 3D microstructures in advanced materials," Advanced Functional Materials (in press).

THE INTRIGUING DEFORMATION BEHAVIOR OF SOFT BIOMEMBRANES

Edoardo Mazza[1, 2,a], Alexander E. Ehret[1, 2] & Kevin Bircher[1]
[1]*Departement of Mechanical and Process Engineering, ETH Zurich, Switzerland*
[2]*Empa Materials Science and Technology, Dübendorf, Switzerland*

Summary Extensive experimental investigations revealed unexpected features of the mechanical behaviour of soft biomembranes. A comprehensive protocol including mechanical measurements in different stress states and history of loading was applied to human amnion and Glisson's capsule. Highly repeatable mechanical parameters were determined and mechanisms of deformation were identified based on in situ experiments in a multiphoton microscope. This allowed formulating simple model equations able to represent the main features of the observed mechanical response. Liquid phase influx and efflux from the collagenous membrane were shown to play an important role during deformation, and this points at osmotic processes as a mechanism for active control of stress state and membranes deformation.

INTRODUCTION

Examples of highly deformable biological membranes are leaflets of aortic valves, tympanic membrane, connective tissues layers forming skin or arteries, or the capsules covering internal organs. The mechanical behavior of these layers is important for fulfilling their function. We have recently organized a Euromech Colloquium on this topic and part of the contributions were presented in a special issue of the Journal of the Mechanical Behavior of Biomedical Materials [1]. Characterizing and modelling the deformation behaviour of soft biomembranes is relevant for medical applications, such as tissue engineering, surgery planning, car accident simulation, or elastography.

Our interest for soft biomembranes began with the investigation of fetal membranes (FM), i.e. the compliant membranes surrounding the developing fetus inside the uterus. In normal pregnancy FM are progressively deformed due to the increased intrauterine pressure and are further stretched when the fetus moves and pushes against the uterine wall. Thus, the life of the fetus depends on the integrity of a thin biological layer (few hundred μm thick) exposed to severe mechanical loads. Premature rupture of FM represents a devastating complication of pregnancy that accounts for 30 to 40% of preterm deliveries and is associated with a high risk of fetal morbidity and mortality. In order to understand conditions favouring premature rupture of FM, we have developed a comprehensive protocol for characterization of their deformation behaviour. On samples from the same human FM (in particular on the amnion layer) we performed mechanical measurements in different stress states (uniaxial, strip biaxial, equibiaxial), and history of loading (slow and fast monotonic loading, relaxation, creep, low and high number of loading cycles). We also performed the mechanical measurements in situ in a microscope for multiphoton non-linear laser scanning imaging, and thereby could visualize FM tissue through its full thickness, in quasi-physiologic conditions [2]. We thus measured local in-plane stretches based on the relative position of epithelial cell nuclei, local thickness changes during loading, and quantified the orientation and alignment of collagen fibre bundles when stretched. We recently applied the same experimental protocol to other collagenous membranes: bovine Glisson's capsule (GC, the connective tissue layer covering the liver), skin and pericardium. In particular, for GC we applied the whole set of experimental configurations that were used for the characterization of FM. The experimental findings and corresponding model predictions will be presented, illustrating unexpected features and striking similarities in the mechanical behaviour of soft collagenous membranes.

EXPERIMENTS

Details of the loading protocols for investigation of the monotonic, time and history dependence of the mechanical response in different stress states were described in [2-5] and reference therein. Local deformations were quantified using image analysis and correlation algorithms. Biomembrane samples were tested within few hours after extraction from the body and most experiments were performed with test pieces submerged in physiological saline solution. Figure 1 illustrates the set-up used for in situ measurements in the multiphoton microscope, with examples of collagen fiber orientation analysis, full-thickness visualization and cell nuclei staining for local strain measurements [2,4]. Common to all biomembranes is the fact that the uniaxial compliance is much larger than the biaxial one. The analysis of the in-plane behavior in uniaxial tension tests showed that the kinematic response is highly reproducible and that the incremental in-plane and out-of plane Poisson's ratios are very large (of up to 8). Elongation was associated with substantial volume reduction (water efflux), down to about 30% of the initial value for 20% elongation. This behavior was rationalized by mechanisms of rotation, stretching and buckling of the thin fibers which constitute the collagen network of the biomembranes. FM (amnion) and GC showed a large tension reduction during relaxation and a small inelastic strain accumulation in creep. Data indicated that the dissipative behavior is related to two mechanisms: (i) short term volume reduction due to water outflow and (ii) long-term relaxation of collagen fibers without macroscopic deformation and no global reorientation. Recoverable water efflux and influx was evident from the stabilized response in cyclic experiments. The importance of liquid motion was demonstrated also through comparison of experiments using liquids of different osmolarity.

[a)] Corresponding author. Email: emazza@ethz.ch.

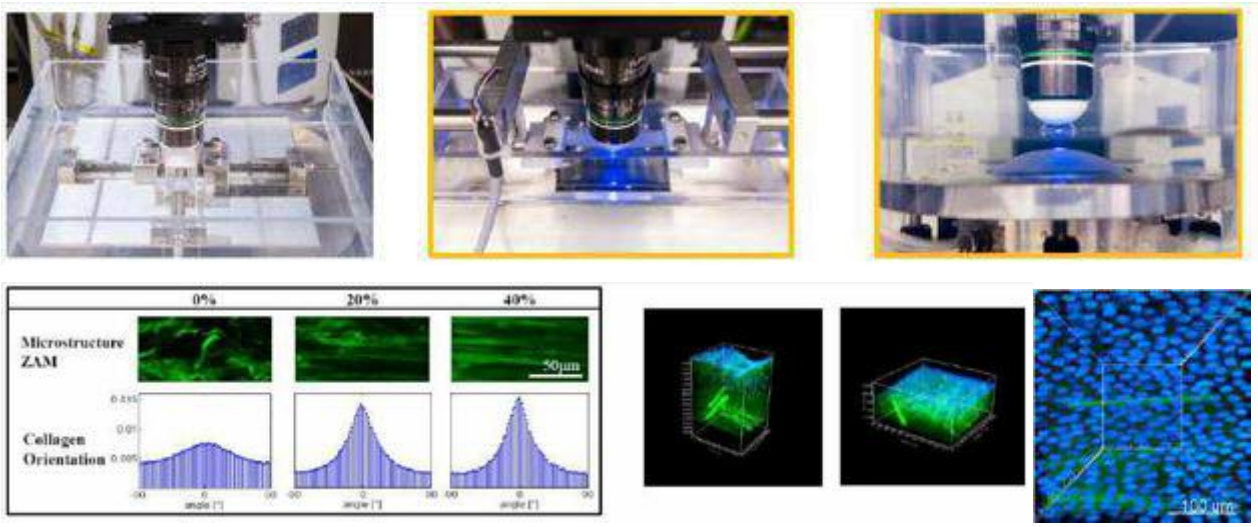

Figure 1 (from [2-6]): top row: in situ tensile devices, two axis, uniaxial and inflation. Bottom row: extraction of collagen fibers' orientation and 3D stack for measurement of thickness changes during loading (showing very large thickness reduction upon in-plane stretching). Right: images of the nuclei of epithelial cells are used to determine in-plane deformation during loading.

MODELING

A large strain viscoelastic continuum model was formulated able to represent the observed deformation mechanisms. The collagen network is phenomenologically represented by *N* representative and mechanically equivalent fiber families that are uniformly distributed in the membrane plane (quasi-isotropic) but slightly inclined out of plane, and embedded in a compressible matrix. The dissipative behavior is represented through the evolution of internal variables, in a way equivalent to a time dependent bulk modulus of the ground matrix (water efflux and influx) and to a viscoelastic deformation of the fibers. The model accurately captures the uniaxial and biaxial monotonic response, as well as the time history of tension in relaxation and strain in creep experiments, and the same formulation can be successfully applied to both, FM and GC [4,5]. While the model include a large number of parameters associated with the different terms in the strain energy function and the evolution equations of the internal variables, it was possible to fix the values of all but 1 of these parameters (for GC and FM respectively) out of one single experimental configuration and predict the response in all other tests by changing one single parameter (addressing sample to sample variability). Next to this continuum model, we developed a discrete fiber network model able to represent the main features of the multiaxial deformation behavior of the biomembranes [6]. Importantly, the discrete model represents non-affine deformations of collagen fibers and this allowed rationalizing differences in the mechanical response of GC and FM based on characteristics of their microstructure.

CONCLUSIONS

The wide range of experimental data provided evidence of unique features of the deformation behavior of these biomembranes. Correspondingly, several biomechanical parameters were highly repeatable among different samples. Based on a simple interpretation of the microstructural observations, it was possible to rationalize the complex mechanical behavior of FM and GC using continuum equations as well as a discrete fibre network model. Application of the experimental protocol to other biomembranes will allow "*comparative biomechanics*", i.e. identifying commonalities and differences in the deformation mechanisms and their relation to the function of each membrane. In particular, our current investigations focus on osmotic mechanisms for active control of stress state and membranes deformation .

References

[1] Mazza E., Ganghoffer J-F., Ehret A.E: Mechanics of biological membranes. J. Mech. Beh. Biomed. Mat., 2016

[2] Mauri A., Perrini M., Mateos J. M., Maake C., Ochsenbein-Koelble N., Zimmermann R., Ehrbar M., Mazza E.: Second Harmonic Generation Microscopy of Fetal Membranes under Deformation: Normal and Altered Morphology, Placenta, 34, 1020-1026, 2013

[3] Mauri, A., Perrini, M.; Ehret, A.E.; de Focatiis, D.; Mazza, E.: Time-dependent mechanical behavior of human amnion. Macroscopic and microscopic characterization. Acta biomaterialia, 11, 314-323, 2015.

[4] Mauri, A., Ehret, A.E.; de Focatiis, D.; Mazza, E.: A model for the compressible, viscoelastic behavior of human amnion addressing tissue variability through a single parameter. Biomechanics and Modeling in Mechanobiology, in press.

[5] Bircher K., Ehret, A.E.; Mazza, E.: Mechanical characteristics of bovine Glisson's capsule as a model tissue for soft collagenous membranes, submitted.

[6] Mauri, A., Hopf, R.; Ehret, A.E.; Picu, C.; Mazza, E.: A discrete network model to represent the deformation behavior of human amnion. J. Mech. Beh. Biomed. Mat., 2016

SOFT NEURONS ACTIVELY MAINTAIN STRONG TENSION FOR SYNAPTIC FUNCTIONS

M. Taher A. Saif [1)]
[1]*Mechanical Science and Engineering Department, University of Illinois Urbana-Champaign, Illinois, USA*

Summary *In-vitro* studies over the last three decades revealed that neurons generate tension on culture dishes. But the physiological significance of this tension remained unclear. Here we show, using embryonic fruit flies (*Drosophila*), that (1) *in vivo* neurons actively maintain a rest tension, (2) neurons employ actomyosin machinery to maintain and regulate the tension, (3) this tension is critical for accumulation of neurotransmitor vesicles at the synaptic terminals (junction with muscle or another neuron), i.e., without tension the accumulation disappears, but reappears with the supply of tension, (4) this tension regulates transport of vesicles along the axon of the neurons. Neurotransmission is the single most function of neurons, and it mediates memory and learning in animals. Since neuronal force regulates transport and accumulation of neurotransmitter vesicles, it follows that the neuronal forces are fundamentally linked with memory and learning, and they offer a new and untapped paradigm in understanding neurological diseases. **(150 words)**

BACKGROUND

Most neurons have a long axon that innervates muscles or other neurons to form neuro-muscular or neuron-neuron junctions. Neurotransmitters are packed in small vesicles and are clustered at the presynaptic terminal of the junction. Upon arrival of an action potential or a voltage spike at the presynaptic terminal travelling through the axon, synaptic vesicles exocytose releasing the neurotransmitters, which activate the post synaptic terminal. Thus the signal is transmitted from one neuron to the next, or the muscle is stimulated. The more a synapse is used, the higher is the transmission efficiency, i.e., higher is the post synaptic current due to the same action potential. This usage dependence of efficiency, known as plasticity, forms the basis of memory and learning. Vesicle clustering had long been believed to result from biochemical signaling processes that require the connectivity of the presynaptic terminal with the cell body, the central nervous system, and the postsynaptic cell. Mechanics had no role to play. During late last century, it was realized that neurons cultured on perti dishes adhere to the substrate and apply contractile traction [1]. It was hypothesized that in vivo neurons generate tension as well, which results in folding in the epical cortex of the brains. However, the evidence of tension in *in vivo* neurons was missing, and the role of tension in neuronal function remained elusive.

FRUITFLY (DOSOPHILA) EMBRYO AND NEUROMUSCULAR JUNCTIONS AS MODEL TEST BEDS

Embryonic fruit flies have extensively been used in Neuroscience for decades to develop fundamental insights on neuronal functions. We chose to study embryonic motor neurons of transgenic flies in which all neurons emit green light when shined with blue light (Fig. 1, [2]). This allows us to visualize the neurons. The cell body of the motor neurons reside at the central nervous system (CNS), but the axons, about 100 µm long and 500 nm in diameter, emanate from the CNS and innervate the muscles at the end forming neuro-muscular junctions. We asked the following questions: (1) are the axons are in tension, and if so (2) what is the origin of tension, (3) does this tension influence neurotransmitter vesicle accumulation at the junction, and their transport through the axon [3]. The significance of these questions is that if indeed tension is found to be related to vesicle accumulation at the junction, then neuro-mechanics becomes a critical component in understanding neuroscience.

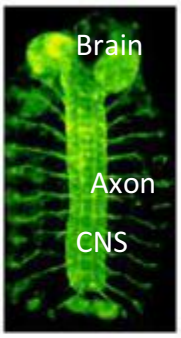

Figure 1. Embryonic fruit fly. Neurons glow green when blue light is shined on the embryo. The axons of motor neurons emanate laterally from the central nervous system (CNS). They are about 100 µm long and 500 nm in diameter. Each forms a neuromuscular junction at the end (muscle not shown).

EXPERIMENTAL RESULTS

In vivo axons are under tension: We measure tension in the axons of the motor neurons by dissecting live embryos and pulling single axons holding at the middle using a nano scale force sensor (Fig. 2). From the force-deformation relation of the axons we quantify that the axons are at a rest tension of about 2 nN [2]. If the stretch of the axons is held fixed, they relax with time reaching a steady tension with a value higher than the unperturbed tension. If the stretched axons are released, the slackned axons shorten to regain the rest tension. If the axons are slackened significantly by bringing the neuro-muscular junction close to the CNS, the axons shorten, by as high as 40%, to regain the tension (Fig. 3). Thus, axons actively maintain a steady rest tension. (2) Actomyosin machinery maintains the tension: We apply a series of drugs to the embryo independently. These drugs selectively inactivate specific cytoskeletal components. We find, slackned axons fail to

[1)] Corresponding author. Email: saif@illinois.edu

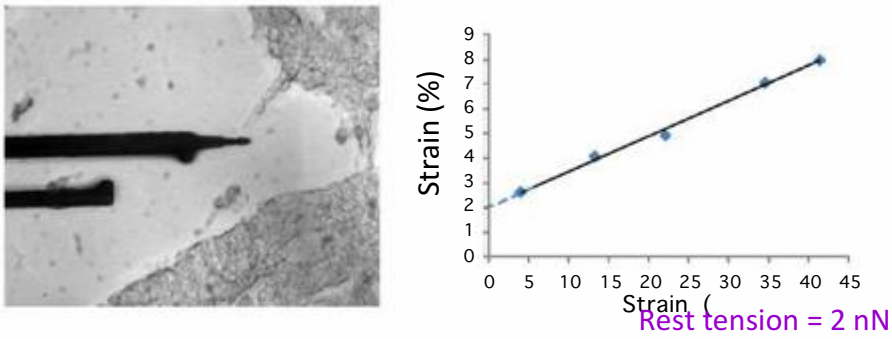

shorten if myosin II is inactivated, or cortical actin is disrupted, but the axons shorten faster if microtubules are depolymerized. (3) Axonal tension regulates neurotransmitter vesicle accumulation at NMJ and transport [3] through axons: We dissected an axon using a laser beam at mid length. This relieves the axon accumulation at the NMJ disappears. However, when the cut end of the axon is pulled by a micropipette, vesicle accumulation reappears (Fig 4), implying that tension alone is

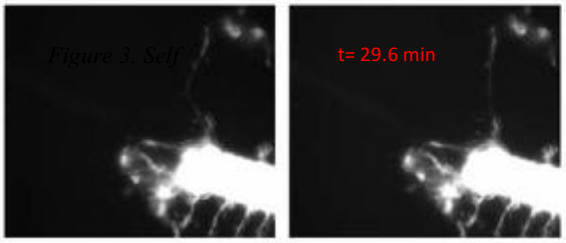

Figure 2. Measurement of axonal tension using a nano mechanical force sensor.

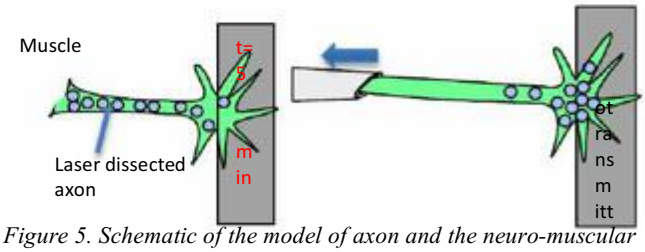

Figure 5. Schematic of the model of axon and the neuro-muscular junction.

network at the NMJ serves as a scaffold neurotransmitter vesicles allowing them to accumulate. This actin network is mechanically linked with the cortical actin and the rest of the cytoskeleton. Its stability of maintained by the tension it is subjected to due to the acto-myosin activity of the cortical actin. If tension is disrupted, the actin scaffold disappears, and hence the vesicle accumulation (Fig 5).

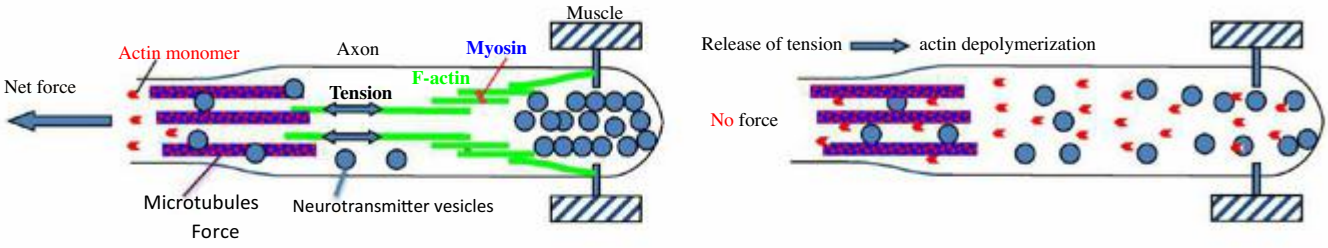

References

[1] Bray, D. Mechanical Tension Produced By Nerve Cells In Tissue Culture. *J. Cell Sci*. 37, 391-410 (1979).
[2] Siechen, S., S. Yang, A. Chiba, and T. Saif, "Mechanical Tension Contributes to Clustering of Neurotransmitter Vesicles at Presynaptic Terminals," Proceedings of the National Academy of Science, 106:31, 12611-12616, August 4, 2009.
[3] Ahmed, W. and T. A. Saif. Active transport of vesicles in neurons is modulated by mechanical tension. Scientific Reports 4, Article number: 4481 doi:10.1038/srep04481, 27 March 2014.

MECHANOCHEMICALLY RESPONSIVE ELASTOMERS: FUNDAMENTAL AND APPLICATIONS

Xuanhe Zhao[1,2 a)]
[1]*Department of Mechanical Engineering, MIT, Cambridge, MA, US*
[2]*Department of Civil and Environmental Engineering, MIT, Cambridge, MA, US*

Summary Mechanochemically responsive (MCR) elastomers have been synthesized by incorporating mechanophores – molecules whose chemical reactions are triggered by mechanical force – into conventional polymer networks. Deformation of the MCR elastomers applies force on the mechanophores and triggers their reactions, which manifest as phenomena such as changing colors, varying fluorescence and releasing molecules. In this talk, we first present a microphysical model of MCR elastomers, which quantitatively captures the interplay between the macroscopic viscoelastic deformation of the MCR elastomers and the reversible activation of mechanophores on polymer chains. Our model consistently predicts both the time-dependent stress-strain behaviours and the color or fluorescence variation of the MCR elastomers under large deformations. We then discuss model-guided design of structures and devices with extraordinary functions and applications enabled by MCR elastomers such as synthetic squid skin capable of dynamically varying colours and surface textures on demand.

Introduction

A novel strategy for fabricating mechanochemically responsive (MCR) polymers has been developed by covalently incorporating molecules capable of force-triggered chemical reactions, or so-called mechanophores, into polymer networks[2-5]. Deformation of MCR polymers stretches polymer chains which apply forces on the mechanophores and triggers their reactions, leading to phenomena such as changing colors, varying fluorescence and releasing molecules of the MCR polymers. During the design of MCR devices, it is highly desirable that the MCR polymers can be reversibly and repeatedly activated and deactivated. However, most existing MCR polymers are in glassy or semicrystalline states, whose activation requires irreversible plastic deformation or fracture of the polymers. As a result, these MCR polymers cannot fully recover their initial shapes after the first activation, and therefore cannot be activated reversibly or repeatedly [6-13]. While mechanophores have been incorporated into thermoplastic elastomers[7, 11, 12, 14-16], little success has yet been achieved to activate the MCR polymer repeatedly to fully recover its initial shape at the room temperature.

Recently, we developed new MCR elastomers by covalently coupling spiropyrans [7] – mechanophores that can change color and emit florescence under sufficiently high forces – into the backbone chains of a highly stretchable elastomer network, polydimethylsiloxane (PDMS) Sylgard 184 [17, 18]. The MCR elastomers can recover their initial shapes under multiple cycles of large deformation, allowing for reversible and repeated variations of the color and fluorescence of the elastomers on demand. The MCR elastomers can also be assembled into devices such as a display that is remotely controlled by external physical stimuli (e.g., electric fields) to generate on-demand fluorescent and color patterns (**Fig. 1A**). These MCR elastomer systems open promising venues for creating flexible MCR devices with diverse applications in flexible displays, optoelectronics, biomedical luminescent devices and dynamics camouflage skins [17]. Despite the potential, the microscopic mechanical details underlying the performance of the MCR elastomers have yet to be investigated, and those mechanistic insights might enable the optimization of MCR elastomer response. For example, the relationship between the macroscopic viscoelastic deformation of the MCR elastomers and the extent of activation of mechanophores embedded along those polymer chains is not understood. This understanding, if achieved, can help guide the development of MCR elastomers, and improve the design of various MCR-elastomer devices.

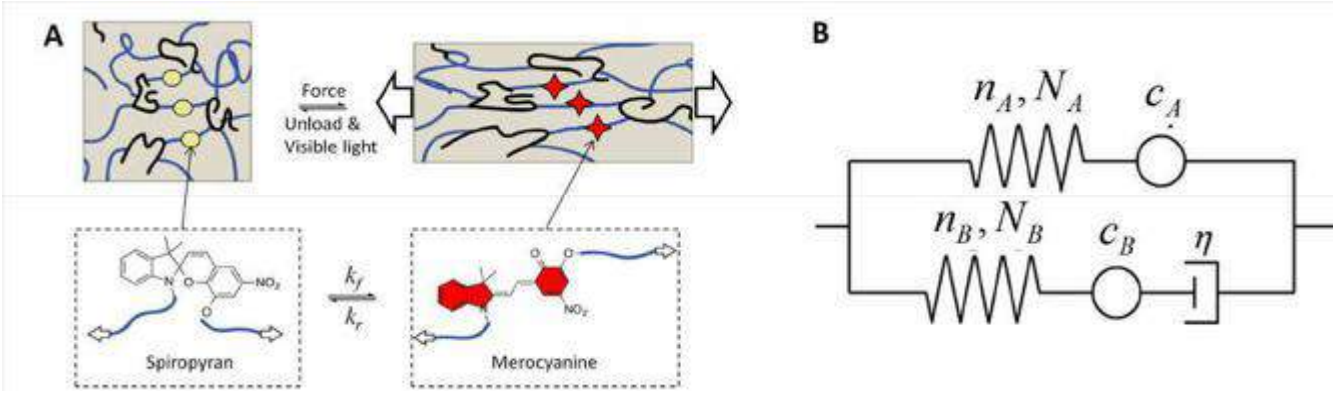

Figure 1. Schematics of the mechanochemically responsive elastomer with mechanophores spiropyran/merocyanine covalently coupled on the network (**A**), and the double-network model to account for the coupling of viscoelastic deformation and mechanochemical reactions in the elastomer (**B**).

a) Corresponding author. Email: zhaox@mit.edu

2. Model formulation

We aim to develop a simple thermodynamic-based model for mechanochemically responsive viscoelastic elastomers to account for the interactions between viscoelasticity and mechanochemical reactions in the elastomers. Adopting the generalized Maxwell model, we assume the viscoelastic behaviour of the elastomer can be attributed to two polymer networks acting in parallel as illustrated in **Fig 1B**. The first network (i.e., network A) characterizes the time-independent mechanical behavior of the elastomer using a non-linear spring, and the second network (i.e., network B) accounts for the time-dependent mechanical behavior of the elastomer using a non-linear spring and a dashpot in series. To account the mechanochemical reactions in the elastomers, we further couple modules of mechanophores in series with the non-linear springs in both networks (**Fig. 1B**).

Assuming Langevin chains in both networks that undergoes affine deformation, the chain forces can be calculated

$$f_A = \frac{k_B T}{l} L^{-1}\left(\frac{\Lambda}{\sqrt{n_A}}\right), \quad f_B = \frac{k_B T}{l} L^{-1}\left(\frac{\Lambda/\Lambda^v}{\sqrt{n_B}}\right) \tag{1}$$

where k_B is the Boltzman constant, T is the absolute temperature, l is the length of a Kuhn monomer; Λ is the stretch in polymer chains of both networks; Λ^v the viscous component of the stretch in network B; and Λ/Λ^v the elastic component of the stretch in network B. The chemical kinetics between spiropyrans and merocyanines on both networks of the MCR elastomer can be expressed as (Hänggi et al., 1990)

$$\frac{dc_A^M}{dt} = k_A^f c_A^S - k_A^r c_A^M, \quad \frac{dc_B^M}{dt} = k_B^f c_B^S - k_B^r c_B^M \tag{2}$$

where c^M and c^S are the concentrations of merocyanin and spiropiran in either network, and k^f and k^r are the forward and reverse reaction rates in either network, as indicated by the subscripts. The reaction rates can be further expressed as

$$k_A^f = k^{f0}\exp\left(\frac{f_A \Delta x}{k_B T}\right), \quad k_A^r = k^{r0}\exp\left(-\frac{f_A \Delta x}{k_B T}\right), \quad k_B^f = k^{f0}\exp\left(\frac{f_B \Delta x}{k_B T}\right), \quad k_B^r = k^{r0}\exp\left(-\frac{f_B \Delta x}{k_B T}\right) \tag{3}$$

where k^{f0} and k^{r0} are forward and reverse reaction rates of the mechanophore under no force, and Δx is a length scale the applied chain forces that affect the reaction rates.

Further adopting the standard nonlinear viscoelastic model, the chain forces in the elastomer can be quantitatively related to the viscoelastic deformation of the elastomer, which therefore affects the chemical reaction of the elastomer through Eqs. (1)-(3).

3. Summary and applications

In summary, we present a theoretical model for mechanochemically responsive elastomers to quantitatively reveal how the macroscopic viscoelastic deformation of the elastomer translates to the molecular forces in polymer networks, and how the chain forces subsequently affect chemical reactions of mechanophores coupled to the networks. We further program the constitutive model into finite-element models, through which we demonstrate the MCR elastomers' potential applications for strain imaging and color/fluorescence displays. These models can further facilitate the design of MCR polymers in the macro/micro structure level to create MCR devices for diverse applications, such as sensors, memories, flexible displays, optoelectronics, biomedical luminescent devices and dynamics camouflage skins.

References

[1] Y. Sagara, T. Kato, Nature Chemistry 2009, 1, 605.
[2] M. K. Beyer, H. Clausen-Schaumann, Chemical reviews 2005, 105, 2921.
[3] M. M. Caruso, D. A. Davis, Q. Shen, S. A. Odom, N. R. Sottos, S. R. White, J. S. Moore, Chemical reviews 2009, 109, 5755.
[4] A. L. Black, J. M. Lenhardt, S. L. Craig, Journal of Materials Chemistry 2011, 21, 1655.
[5] Z. S. Kean, S. L. Craig, Polymer 2012, 53, 1035.
[6] C. K. Lee, B. A. Beiermann, M. N. Silberstein, J. Wang, J. S. Moore, N. R. Sottos, P. V. Braun, Macromolecules 2013, 46, 3746.
[7] D. A. Davis et al , Nature 2009, 459, 68.
[8] A. L. Black, J. A. Orlicki, S. L. Craig, Journal of Materials Chemistry 2011, 21, 8460.
[9] J. M. Lenhardt et al, Journal of Materials Chemistry 2011, 21, 8454.
[10] G. O'Bryan, B. M. Wong, J. R. McElhanon, ACS applied materials & interfaces 2010, 2, 1594.
[11] C. K. Lee, D. A. Davis, S. R. White, J. S. Moore, N. R. Sottos, P. V. Braun, Journal of the American Chemical Society 2010, 132, 16107.
[12] Y. Chen, H. Zhang, X. Fang, Y. Lin, Y. Xu, W. Weng, ACS Macro Letters 2014, 3, 141.
[13] E. Ducrot, Y. Chen, M. Bulters, R. P. Sijbesma, C. Creton, Science 2014, 344, 186.
[14] M. B. Larsen, A. J. Boydston, Journal of the American Chemical Society 2014, 136, 1276.
[15] B. A. Beiermann, S. L. B. Kramer, P. A. May, J. S. Moore, S. R. White, N. R. Sottos, Advanced Functional Materials 2014, 24, 1529.
[16] H. Zhang, Y. Chen, Y. Lin, X. Fang, Y. Xu, Y. Ruan, W. Weng, Macromolecules 2014, 47, 6783.
[17] Q. Wang, G. R. Gossweiler, S. L. Craig, X. Zhao, Nature Communications 2014, 5, 4899.
[18] G. R. Gossweiler, G. B. Hewage, G. Soriano, Q. Wang, G. W. Welshofer, X. Zhao, S. L. Craig, ACS Macro Letters 2014, 3, 216.

MECHANICAL SYNCHRONIZATION OF ACTIVE BEATING WITHIN AND BETWEEN CARDIOMYOCYTES

Ohad Cohen, Kinjal Dasbiswas and Samuel Safran [a)]
Department of Materials and Interfaces, Weizmann Institute of Science, Rehovot, Israel

Summary We present theoretical models and predictions of how mechanics due to elastic interactions in actively beating heart cells can lead to synchronization of beating both within single cells and between nearby cells. Our research is motivated by recent experiments that show a correlation between the registry of adjacent muscle fibers and the beating strain of a single, embryonic cardiomyocyte and others that show how a mechanical probe can "pace" the phase and frequency of a nearby heart cell. The theory is generic and analytical in nature and focuses on the role of elastically mediated interactions of oscillating, active force dipoles in these cells. For the single cell, the theory successfully maps the registry data to the strain data. Similar ideas are used to predict the conditions under which an oscillating mechanical probe will or will not "pace" the beating of a nearby heart cell.

Experiments on single, embryonic cardiomyocytes [1] show that both striation, an indication of the structural registry in muscle fibers, as well as the contractile strains produced by beating cardiac muscle cells, can be optimized by substrate stiffness. We show theoretically how the substrate rigidity dependence of the registry data can be mapped onto that of the strain measurements. The elasticity-mediated structural registry is determined [2] including both the elastic interactions of neighboring, actively contractile acto-myosin units as well as the noise inherent in biological systems. By assuming that structurally registered myofibrils also tend to beat in phase, we explain the observed dependence of both structural striation and beating strain measurements of embryonic heart muscle cells on substrate stiffness in a unified manner. The agreement of our ideas with experiment suggests that the correlated beating of heart cells may be limited by the structural registry of the myofibrils which in turn is regulated by their elastic environment.

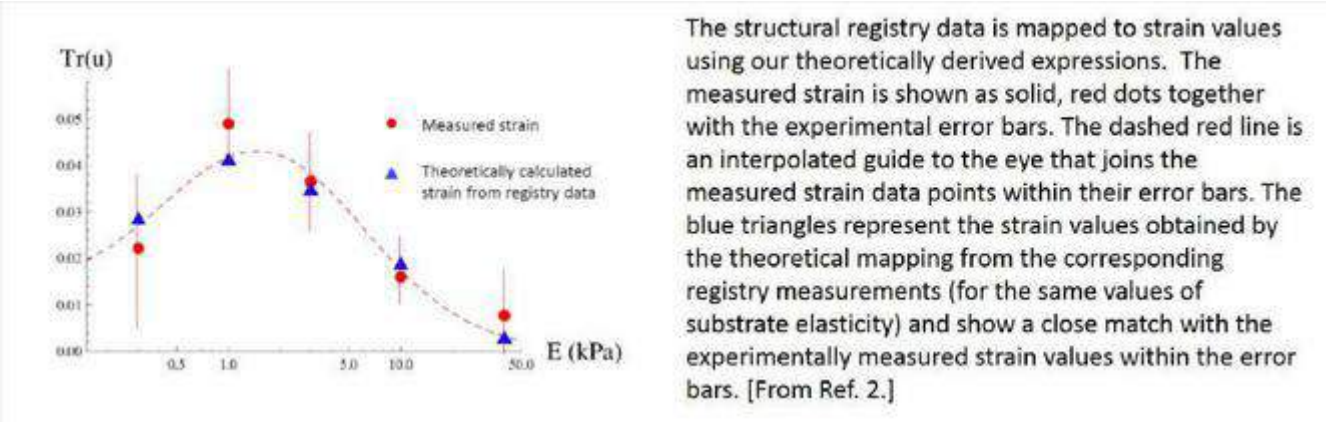

The structural registry data is mapped to strain values using our theoretically derived expressions. The measured strain is shown as solid, red dots together with the experimental error bars. The dashed red line is an interpolated guide to the eye that joins the measured strain data points within their error bars. The blue triangles represent the strain values obtained by the theoretical mapping from the corresponding registry measurements (for the same values of substrate elasticity) and show a close match with the experimentally measured strain values within the error bars. [From Ref. 2.]

Very recent experiments [3] on the synchronization of beating of two nearby neonatal cardiomyocytes has shown that a mechanical probe can "pace" a beating cell to within about twice or a quarter of its natural beating frequency. This is expected to be indicative of how nearby cardiomyocytes embedded in the extracellular matrix or on an elastic substrate can regulate their mutual beating. We predict theoretically [4] the synchronization of the beating phase and frequency of two nearby cardiomyocyte cells or a cell and a mechanical probe. Each cell is represented as an oscillating force dipole in an infinite viscoelastic medium that allows us to predict the propagation of the elastic signal within the medium. We then show that based on elastic interactions alone, two nearby cells can synchronize their phase and frequency in a manner that depends on their mutual orientation. The theory predicts both in-phase and anti-phase synchronization depending on the relative cell orientations and also shows how mechanics can predict the conditions for frequency synchronization of nearby cells. These results may be relevant for the design of cardiomyocyte-based micro devices and other biomedical applications.

[a)] Corresponding author. Email: sam.safran@weizmann.ac.il

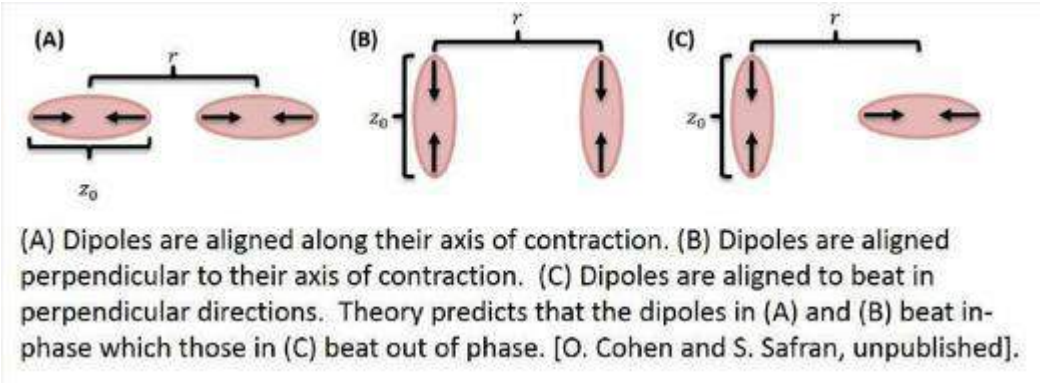

(A) Dipoles are aligned along their axis of contraction. (B) Dipoles are aligned perpendicular to their axis of contraction. (C) Dipoles are aligned to beat in perpendicular directions. Theory predicts that the dipoles in (A) and (B) beat in-phase which those in (C) beat out of phase. [O. Cohen and S. Safran, unpublished].

The authors gratefully acknowledge collaborations with experimental groups: Stephanie Majkut and Dennis Discher (University of Pennsylvania, USA) and Shelly Tzlil (Technion, Israel).

References

[1] S. Majkut *et al*., Current Biology, **23**, 2323 (2013).
[2] K. Dasbiswas, S. Majkut, D. Discher and S. A. Safran, Nature Comm., **6**, 7085 (2015).
[3] I. Nitsan, S. Drori, Y. Lewis, S. Cohen and S. Tzlil, Nature Physics, in press.
[4] O. Cohen and S. A. Safran, unpublished.

ON THE THE FREE ENERGY OF CELLS SPREAD ON MICROPATTERNED SUBSTRATES

Patrick McGarry[1], Eoin McEvoy[1], Tommaso Ristori[2], Sandra Loerakker[2], Vikram S. Deshpande[3]
[1]*National University of Ireland Galway, Galway, Ireland*
[2]*Eindhoven University of Technology, Eindhoven, The Netherlands*
[3]*University of Cambridge, Cambridge, United Kingdom*

Summary A new approach to the analysis of the spreading of cells on micro-patterned substrates is presented. A thermodynamically consistent active cell model with non-local conservation of the total number of cell cytoskeletal proteins is used to simulate a range of spread states. The minimum free energy of the system is identified and corresponding stress fibre distributions are found to match experimental observations.

INTRODUCTION

Several experimental studies demonstrate that control of cell spreading using substrate micro-patterning has a significant impact on cell behaviour. A study by McBeath et al. [1] reveals that stem cell differentiation can be controlled by limiting cell spread area. It has also been shown that the contractility of smooth muscle cells increases with increasing cell area (Tan et al. [2]). Lamers et al. [3] show the spread geometry and stress-fibre (SF) distribution of osteoblasts on grooved surfaces is highly dependent on groove spacing. Wide grooves result in polarized cells with SFs aligned along the grooves. Narrow groove spacing leads to randomly oriented cells and SFs. Finally, a study by Théry et al. [4] has shown that cells spread on V-shaped fibronectin patches exhibit SFs align along the free edge of the cell.

The bio-mechanisms underlying such experimental observations are not fully understood. In the current study we propose a new approach to the analysis of the spreading of cells on micro-patterned substrates. We demonstrate that a non-local thermodynamically consistent active cell model explains several of the key phenomena observed experimentally.

MODEL DEVELOPMENT

The thermodynamically consistent kinetic equation for SF formation/dissociation proposed by Vigliotti *et al.* (2015) [5] reduces to

$$\hat{\eta} = \widehat{\ }_V / V\hat{n}\big) exp[\hat{n}(\mu_V - \mu_b)/kT] \tag{1}$$

under steady state conditions in a representative volume element (RVE) within a cell. $\hat{\eta}$ is the SF concentration per unit surface area of the RVE, $\hat{n}$ is the number of actin-myosin contractile units along the length of the RVE, μ_b is the free energy of the bound contractile units in a stress fibre, μ_V is the free energy of unbound SF proteins, while k and T are the Boltzmann constant and absolute temperature. $\widehat{\ }_V$ is the number of unbound SF proteins. Here we implement non-local conservation of the total number of SF proteins within the cell, $\widehat{\ }_T$, under the assumption that the diffusion of unbound proteins through the cytoplasm is infinitely fast relative to the timescale of SF remodeling. The number of unbound proteins in the whole cell is therefore given as

$$\widehat{\ }_V = \widehat{\ }_T - \int_{V_c} \int \ ^{/}_{/} \ \hat{\eta}\,\hat{n}\,d\phi\,dV \tag{2}$$

where the inner integral computes the number of bound proteins in a RVE, and the outer integral provides a summation over all the RVEs in the entire cell volume V_c. At steady state, $\hat{n}$ in a SF at orientation ϕ is given as

$$\hat{n} = \big(1 + \varepsilon_n(\phi)\big)/(1 + \tilde{\varepsilon}_{ss}) \tag{3}$$

where ε_n is the SF nominal axial strain. When a SF is extended, contractile units are added, with the effect that the internal strain in the SF is reduced until a steady state value $\tilde{\varepsilon}_{ss}$ is achieved. Conversely, when a SF shortens, functional units are removed. In both cases, the internal fibre steady state strain is different from the axial material strain in the direction of the fibre, $\varepsilon_n(\phi)$. The formulation is completed by the addition of a non-linear hyperelastic formulation (Ogden, N=8) in parallel with the SF model in order to represent the passive components of the cell.

SIMULATIONS AND RESULTS

The model described above is used to simulate two separate cell spreading experiments:

Experiment 1: As shown in Fig. 1, cells spreading across a series of parallel grooves and fibronectin adhesion patches, both of width L_r , is simulated. In order to spread on N grooves the cell must deform from its reference configuration in the x-direction by a stretch λ_x, after which it may spread along the groves by deforming in the y-direction by a stretch λ_y. A parametric study is conducted for a range of spread states (λ_x and λ_y). For each spread state the free energy of the system $\bar{G}$ is computed from

$$\bar{G} = W_{Vlas} + (\rho kT)\mathrm{Vh}\big(\widehat{N}_V\big) \tag{4}$$

where W_{Vlas} is the elastic free energy due to deformation of the passive components of the cytoplasm during cell spreading. The second term is the cytoskeleton free energy, where ρ is the density of cytoskeletal proteins. Eqn.(4) can be interpreted as a competition between the elastic free energy, which increases with cell spreading, and the cytoskeleton free energy, which decreases with cell spreading (in accordance with eqns.(1-3)).

[a] Corresponding author. Email: patrick.mcgarry@nuigalway.ie.

As shown in Fig. 2(a), results reveal that when the groove spacing is wide (L_c/L_r=3) $\bar{G}$ is minimized when the cell extends along the grooves in the y-direction ($\lambda_y = 1.5$) while spanning only one grove (N=2 and $\lambda_x = 0$). Such spreading in the y-direction, coupled with the global conservation of cytoskeletal proteins, dictates that SFs align primarily in the direction of the grooves. Spreading in the x-direction is discouraged by the high elastic penalty, as shown for the case of N=4. Fig.2(b) considers the case of a small groove spacing (L_c/L_r=12). Here $\bar{G}$ is minimized when $\lambda_x \approx \lambda_y \approx 1.55$ and an isotropic distribution of stress fibres is obtained. Notably, global conservation of cytoskeletal proteins dictates that the SF concentration in any given direction, $\eta(\phi)$, in Fig.2(b) is lower than the concentration of SFs along the grooves in Fig.2(a).

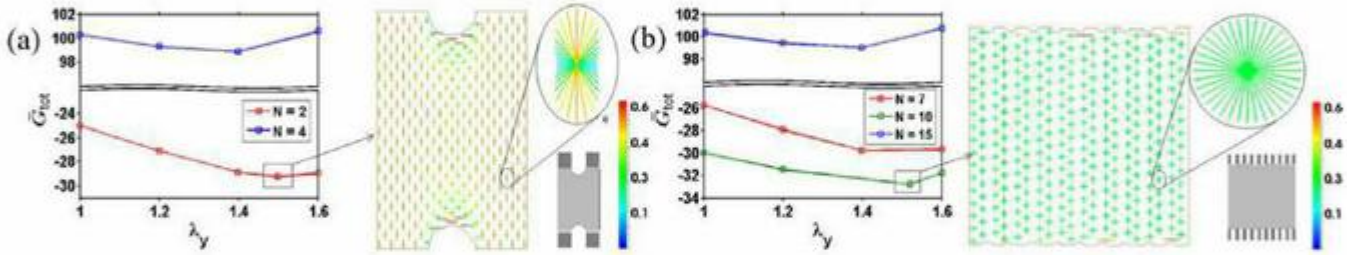

Figure 2: Free energy of the system ($\bar{G}$) and vector plot of SF concentration ($\hat{\eta}$) for: (a) Cell is spread on wide (L_c/L_r=3) grooves; (b) Cell spread on narrow (L_c/L_r=12) grooves.

Experiment 2: In a second series of simulations, a circular unadhered cell spreads on a V-shaped adhesion patch of length L_a, as shown in Fig. 3. For a cell of radius r_c , the spreading process is parameterized in terms of the proportion of the cell perimeter ωr_c that adheres to the patch. The stretch along the patch is therefore given as $\lambda_p = L_a/\omega r_c$. The influence of the ratio of initial cell size to groove length is also considered.

For the longest adhesion patch ($r_c/L_a = 0.38$) $\bar{G}$ is high due to high levels of elastic deformation required for spreading. For the shortest adhesion patch ($r_c/L_a = 0.44$), $\bar{G}$ is high due to the low levels of SF formation associated with limited cell spreading. The minimum free energy spread state, characterized by λ_p, is dependent on the length of the adhesion patch. The lowest value of $\bar{G}$ is computed for $r_c/L_a = 0.40$, with $\lambda_p = 1.24$. In this configuration highest strains occur in the region of the free unadhered edge of the cell. Global conservation of cytoskeletal proteins therefore dictates that the SFs form predominantly parallel to the free edge.

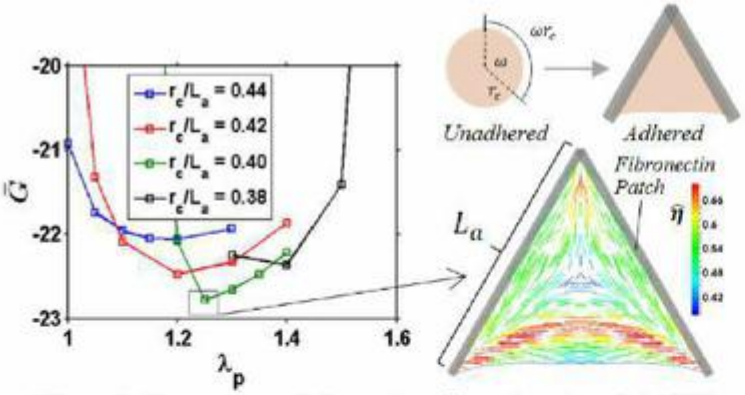

Figure 3: Free energy of the system ($\bar{G}$) and vector plot of SF concentration ($\hat{\eta}$) for cell spreading over V-shaped adhesion patch.

DISCUSSION

The modelling framework presented here captures the key trends reported in the studies by Lamers *et al.* [3] and Théry *et al.*[4], suggesting that cells tend to assume a minimum free energy ($\bar{G}$) spread state. This minimum free energy state is determined by competition between the elastic free energy due to deformation of the passive cytoplasm and the cytoskeleton free energy, subject to a non-local conservation of cytoskeletal proteins throughout the cell. Simulations suggest that the evolving strain distribution during spreading is a critical determinant of the SF distribution. This model represents a significant advance on recent phenomenological approaches to the analysis of cell spreading and SF remodeling [6, 7].

ACKNOWLEDGEMENTS: Science Foundation Ireland (SFI-12/IP/1723); Irish Research Council (RCS1434).

REFERENCES [1] McBeath, R *et al. Developmental Cell*, 6:483-95, 2004; [2] Tan, J *et al. PNAS*, 100(4):1484-89, 2003; [3] Lamers, E *et al.*, *Biomaterials*, 31(12):3307-16, 2010; [4] Théry, M et al., *Cell Motil Cytoskeleton,* 63(6):341-55, 2006; [5] Vigliotti, A *et al.*, *Biomech Model Mechanobiol*, [Epub ahead print], 2015; [6] Ronan, W *et al.*, *J Mech Behav Biomed Mater,* 14:143-57, 2012; [7]. Reynolds, N *et al.*, *Biomaterials,* 35(13):4015-25, 2014.

CATCH BONDS AND MECHANO-SENSITIVITY OF ACTO-MYOSIN FILAMENT NETWORKS

Franck Vernerey *[1] and Umut Akalp[1]
[1]*Mechanical Engineering, University of Colorado, Boulder, USA*

Summary A number of biological filament network are able to generate contratile forces and deformation over large regions with the help of motor proteins, allowing filament to slide along one-another. A particularity of such networks, such as the acto-myosin network in adherent cells, is that the assembly display a mechano-sensitive behavior, that is, contraction can be tuned by the effect of external forces and stiffness. This paper presents a mechanistic model, based on the concept of catch bond, that explains how such responses can be observed at fairly large scales. Particular examples pertaining to the contractile mechanics of adherent cells are presented.

INTRODUCTION

The contraction of adherent cells is a phenomenon that plays a large role in many biological events such as morphogenesis, wound contraction, stem cell differentiation and cell migration. These phenomena particularly rely on contractile filaments, or stress fibers, that anchor to the cell substrate and are capable of sustaining appreciable levels of contraction thanks to their underlying acto-myosin machinery powered by ATP. In the past decade, numbers of studies have shown that the architecture and contraction of the stress fiber cytoskeleton are highly responsive to the cells mechanical environment; the origin of which remains poorly understood. This paper discusses how this mechano-sensitive response can be explained by invoking an ubiquitous element used by biological systems known as the catch bond. We here investigate its role by deriving a model based on an energetic approach and complemented by numerical simulations. The latter show that the catch-bond hypothesis can explain the dependency of cell contraction on substrate stiffness, adhesion or the application of external forces on the cell boundary. The agreements between model predictions and experimental observations not only confirm that catch bonds may play a significant role in the mechano-sensitivity of adherent cells but also pinpoint the importance of the hierarchical structure of acto-myosin filaments across the scales.

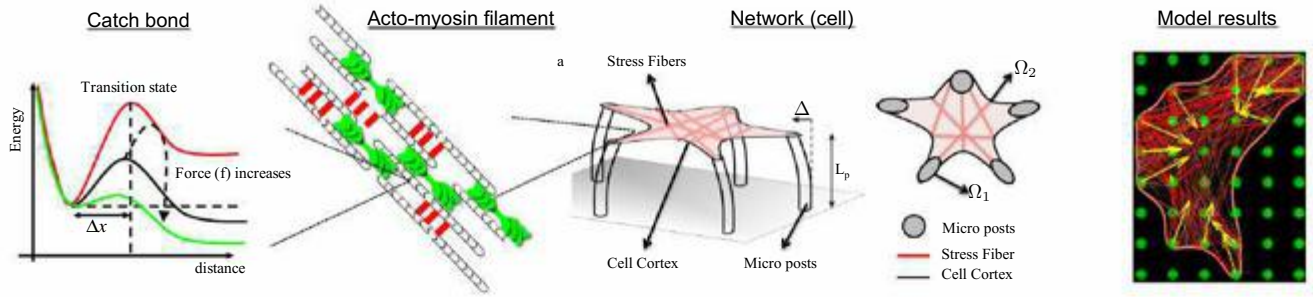

Figure 1: *Summary of the approach depicting, from left to right, the energy landscape of a catch bond, the simplified structure of an acto-myosin filament and the cytoskeleton of a cell lying on a bed of micro-pillars and finally, simulation results of the acto-myosin network and contractility of an adherent cell.*

MODEL

In this paper, we investigate the mechanical response of an acto-myosin segment segment by considering its internal structure made of a mixture of actin and myosin filaments that can slide on one-another thanks to the energy provided by ATP hydrolysis (Fig. 1). Because actin filaments are polarized, these sliding motions generate an overall shortening of the unit, and depending on the mechanical environment, the application of a more or less pronounced contractile force. The mechanics of this assembly was captured by considering an energetic approach for an acto-myosin segment that comprises: (a) the entropic contribution of the large number of acto-myosin bonds within the unit, (b) the stored elastic energy arising from the deformation of acto-myosin bonds, (c) the potential energy E_b stored in the acto-myosin bonds, (d) the work done by external forces F applied on the extremities of the filament, (e) the active power generated by ATP hydrolysis and finally (f) the energy dissipation associated with the sliding motion of myosin on actin. Using energetic principles, this approach allowed

*Corresponding author. Email: franck.vernerey@colorado.edu

us to obtain three Euler-Lagrange equations that govern the ratio η of activated acto-myosin bonds, the sliding velocity v_s of myosin on actin and the elastic deformation d_e of acto-myosin bonds:

$$\eta N k \quad d_e \ / \ F \ ; \qquad E_b \quad k_B T \ln \ \eta / \ 1-\eta \quad / \quad ; \qquad v_s \ / \ v_s^0 \ \ 1 - f/\zeta \tag{1}$$

where v_s^0 is the sliding velocity in the stress-free state, ζ is the active force generated by myosin on actin and N is the total number of available acto-myosin bond in the segment. The first equation is interpreted as the mechanical equilibrium of the control segment, while the second denotes its chemical equilibrium (equality of the chemical potentials) of bonds in attached and detached states. The last equation describes how the cross-bridge velocity is affected by the balance between the active force ζ and passive force $f \ / \ k \quad d_e$. In the range $\quad < f < \zeta$, this relation may be thought of as a simplified (bi-linear) form of the velocity-tension relationship that describes how the sliding velocity decreases if an opposing force f is applied to the acto-myosin unit. To complete the model, we then expressed the fact that the actin-myosin complex displays a catch-bond behavior by considering the energy landscape of a single bond shown in Fig. 1 (in which $\quad E$ is the energy barrier separating the bound and unbound states). Typically, the larger the energy barrier, the longer a bond can live under thermal fluctuations. When subjected to a tensile force f, the energy barrier of a conventional "slip bond" typically decreases according to Bell's law as $E_b \ f \quad / \ E_b^0 - f \quad x$ where E_b^0 is the reference energy of the bond and $\quad x \approx 3nm$ is the width of the barrier. Since acto-myosin complexes are known to be temporarily stabilized when moderate pulling forces are applied, a response that can be interpreted as an temporary increase in the energy barrier $\quad E_d$ with forces. This response is well captured by the following two-parameter function:

$$E_b \ f \quad / \ E_b^0 \quad \alpha \left[1 - e^{-f/f_0}\right] - f \quad x \tag{2}$$

where α measures the catchiness of the bond and f_0 is used to scale the force at which the bond stabilizes. We note that when $\alpha \ / \quad$, the above expression degenerates to that of a slip bond following Bell's law. Based on this model, we then constructed a simplified model of the stress fiber cytoskeleton of adherent cells, made of a random assembly of force-sensitive acto-myosin filaments (Fig. 1). This computational procedure was then used to investigate the contractile behavior and cytoskeleton architecture of adherent cells laying on beds of micro-posts, for which a variety of experimental data have been documented.

RESULTS AND SUMMARY

We investigated how the mechano-sensitive response of a stress fiber segment as described by the above equations can give rise to a complex architecture of the actin cytoskeleton observed in most adherent cells. In this context, we simulate the contraction of an adherent cell on soft circular pillars (Fig. 1, right) as presented in various experimental studies. Numerical simulations allow us to predict the evolution of the stress fiber activation, cortex deformation and the corresponding overall force per pillar for different values of the bond catchiness α. Overall results show that at stady state, the cytoskeleton is able to better activate and generate stronger contractile forces as the external environment becomes stiffer. Temporally, we observe a sharp increase in stress fiber density and micropost forces and a steady increase of the average pillar force in time. From a local viewpoint, we note that the unbalanced forces on the cell boundaries are responsible for the cortex deformation into curved arches and the large micropost deflection on the edge of the cell. In contrast, interior pillars, being subjected to more isotropic forces, tend to marginally deform. This restricted deformation in turn, makes interior posts effectively stiffer and prone to adhere to a higher number of stress fibers. Eventually, the final cytoskeleton organization is strongly dependent on the adhesion pattern, micropost stiffness as well as the overall morphology of the cell. The effect of bond catchiness is significant is these processes; a strong catch bond leads to a fairly high level of stress fiber activation and force generation while a slip bond only yields a marginal contraction and a quasi-nonexistent stress fiber cytoskeleton.

In summary, we presented a model of acto-myosin interactions within filament structures that shows that the presence of a catch-bond behavior can explain the activation of the cytoskeleton of adherent cells in response to force and stiffness. The model importantly shows that the consideration of catch bond iss enough to explain a number of experimental measurements of cell contractility with stiffness and size, in both the static and dynamic regimes. These results may therefore enable a better understanding of important biological processes and the development of active and mechano-sensitive polymeric materials.

References

[1] Vernerey F.J, Akalp, U.: The role of catch-bonds in acto-myosin mechanics and cell mechano-sensitivity. Under review

[2] Vernerey F.J, Farsad, M.: A constrained mixture approach to mechano-sensing and force generation in contractile cells. J. Mech. Behav. Biomed 4(8): 1683-1699, 2011

[3] Vernerey F.J, Farsad, M.: A mathematical model of the coupled mechanisms of cell adhesion, contraction and spreading. J. Math. Biol. 68(4): 989-1022, 2014

[4] Foucard L, Vernerey, F.J.: A thermodynamical model for stress-fiber organization in contractile cells, Appl. Phys. Let., 100, 013702 (2012)

BIOCHEMOMECHANICAL POROELASTIC THEORY OF TUMOR GROWTH

Xi-Qiao Feng[a)], Shi-Lei Xue & Bo Li
Institute of Biomechanics and Medical Engineering, Department of Engineering Mechanics, Tsinghua University, Beijing 100084, P. R. China

Summary Tumor growth is a complicated process involving genetic mutation, biochemical regulation, and mechanical deformation. In this paper, a thermodynamics-based nonlinear poroelastic model is established to interrogate the coupling among the mechanical, chemical, and biological mechanisms underpinning the growth of avascular tumors. A volumetric growth law accounting for mechano-chemo-biological coupling is proposed to describe the development of solid tumors. The regulating roles of stresses and nutrient transport in the growth of tumor spheroids are revealed under different surrounding environments. We show that the mechano-chemo-biological coupling triggers anisotropic and heterogeneous growth, responsible for the formation of layered structures in growing tumors. There exists a steady state, in which tumor growth is balanced by resorption. A phase diagram is constructed to illustrate how the elastic modulus and thickness of the confinements jointly dictate the volume of tumors at the steady state. The results are in consistency with relevant experimental results.

INTRODUCTION

Solid tumors account for more than 85% of cancer mortality [1]. Examples of solid tumors are sarcomas, carcinomas, and lymphomas, which often originate from the transformation of small nodes of normal cells into tumor cells that either lose or cease to respond to the normal physiological regulations. The development of solid tumors is a biological process involving multifactorial determinants, e.g. cell molecular and genetic abnormalities, cell–cell and cell–extracellular matrix interactions, and the supply of oxygen and nutrients.

It has been recognized that, besides genetic alterations and biochemical factors, mechanical cues sensed by or transduced to tumor cells also play a vital role in the expansion, invasion, and metastasis of tumors [2]. The mechanical stresses in solid tumors mainly arise from two ways: the heterogeneous growth of tumor itself and the confinement of host tissues. Experiments evidence that tumors respond to stresses through actively altering biochemical pathways and through passively impeding fluid transport. Therefore, the coupling among the mechanical stresses, biological factors, and the reaction–diffusion of chemical species is of paramount importance in tumor pathology [3]. In the present paper, we establish a biochemomechanical theory incorporating the mechano-chemo-biological coupling mechanisms to investigate avascular tumor growth. The tumor tissue is treated as a poroelastic material, which is capable of mass addition and resorption regulated by mechanical, chemical, and biological factors. The system is open and thermodynamic continuous, permitting the transport of mass, momentum, and energy across its boundaries. A growth law that accounts for the interplay among mechanical stresses, biochemical homeostasis, and nutrient transport within tumors is proposed. Furthermore, we also examine the regulatory role which the stiffness of the surrounding host tissues plays in tumor growth.

THEORETICAL MODEL

An avascular tumor is a mixture of cellular elements, ECM constituents, and interstitial space. It corresponds to the primary stage of tumors development before angiogenesis. The cells and ECM in a tumor provide the structural and mechanical integrity and can be considered as a solid skeleton, while the interstitial space is filled with fluid consisting of solvent, generally, water, and solutes such as nutrient, oxygen, and waste. Therefore, a solid avascular tumor is here modelled as a porous medium at the tissue level, and the theory of poroelasticity is applied to characterize its mechanical behavior. To incorporate its volumetric growth, we decompose the geometric deformation gradient tensor $\mathbf{F}$ as $\mathbf{F}=\mathbf{A}\cdot\mathbf{G}$, where $\mathbf{A}$ denotes the elastic deformation tensor and $\mathbf{G}$ is the growth tensor describing the change in mass. On the basis of thermodynamics, we establish the growth evolution law of a tumor

$$\dot{\mathbf{G}}=\sum_{\alpha} f_{\alpha}\left(c_{\alpha}^{\mathrm{g}}\right)\left[\mathbf{A}^{\mathrm{T}}\cdot\frac{\partial W}{\partial \mathbf{A}}-\left(W-W_{\mathrm{h}}\right)\mathbf{I}+\mathbf{b}_{\mathrm{H}}\right]\cdot\mathbf{G}$$

where c_{α}^{g} denotes the concentration of the α-th constituent. $f_{\alpha}\left(c_{\alpha}^{\mathrm{g}}\right)$ is a positive definite scalar function describing chemical kinetics of the α-th constituent. Furthermore, it satisfies $f_{\alpha}\left(c_{\alpha}^{\mathrm{g}}\right)\to 0$ when c_{α}^{g} approaches the threshold for cell survival. W and W_{h} are the Helmholtz free energy of the solid skeleton and the incoming mass per unit volume in the intermediate configuration, respectively. $\mathbf{I}$ is a unit tensor. $\mathbf{b}_{\mathrm{H}}$ stands for the homeostatic stress tensor, that is, the mechanical representation of the biochemical and cellular activity in the steady state of tissues.

NUMERICAL RESULTS

[a)] Corresponding author. Email: fengxq@tsinghua.edu.cn.

The proposed theory is validated by experimental data in the literature [4]. Recently, microfluidic experiments were performed to examine the morphogenesis of multicellular spheroid in response to external forces or confinements [4]. In the experiments, the spheroid of CT26 mouse colon carcinoma cells underwent free growth (Case I) or confined growth within alginate microcapsules of different radii and thicknesses (Cases II-IV), as shown in Fig. 1(a). The microcapsules were permeable and, hence, enabled outer nutrient and oxygen to flow into interior freely, providing a standard environment for cell proliferation. The following four typical cases were studied: (i) in Case I, the freely growing spheroid exhibited an initial exponential expansion followed by a power-law volume increase, and further growth led to the formation of a necrotic core (the dark region in the image) and a rim occupied by the proliferative cells. (ii) in Case II, the microcapsule was large and thick and, thus, the spheroid initially underwent a free growth. After the spheroid reached the microcapsule, its growth was almost leveled off. (iii) in Case III, the microcapsule was small and thick. The expansion of the spheroid was completely inhibited by the confinement of the microcapsule. (iv) in Case IV, the microcapsule was small and thin. The expansion of the spheroid drove the deformation of the microcapsule until the latter burst. After microcapsule ruptured, the spheroid can resumed the exponential growth observed in the free spheroid (Case I). To simulate the transition from confined growth to free growth in Case IV, we remove the boundary constraint applied on the tumor when the microcapsule bursts. The numerical results show that the proposed theoretical model can well reproduce the experimental observations at different situations, confirming the efficacy and robustness of our theory (Fig. 1(b)).

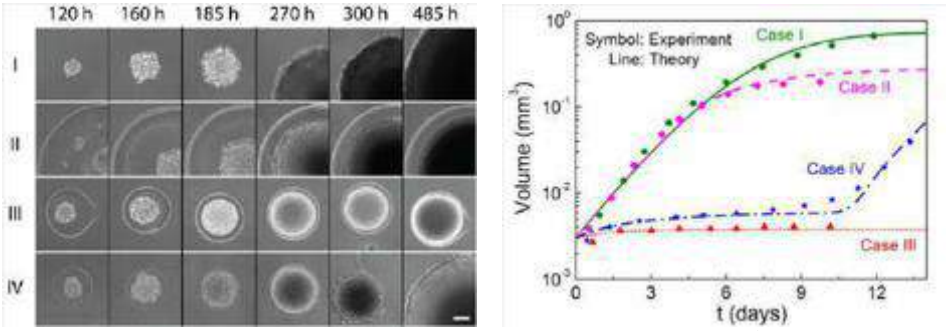

(a) (b)

Fig. 1 (a) Microfluidic experiment of in vitro tumor growth under four typical environments [4]; (b) Comparison between theoretical predictions and experimental data.

CONCLUSIONS

Based on thermodynamical compatibility, we develop a nonlinear elastic theory to investigate the interplay among stresses, nutrients, and growth in a solid tumor. The tumor is treated as a porous growing medium allowing for nutrient transport modulated by stresses. As an example, the proposed theory is applied to decipher the MCB coupling in a spheroid avascular tumor under various growing environments such as free growth, compressed growth, confined growth, and the transitions between them. Our model can predict typical features of tumor growth, in agreement with a number of pervious experiments. Although we focus on growth of an avascular tumor, the theory and the results may provide important information for understanding development of a vascular one. The method of present study can also be extended to examine embryogenesis and the development of normal tissues, e.g. hearts, brains, lungs, and blood vessels.

References

[1] Jain R. K.: Normalization of Tumor Vasculature: An Emerging Concept in Antiangiogenic Therapy. *Science* **307**: 58–62, 2005.

[2] Ambrosi, D., Ateshian, G. A., Arruda, E. M., Cowin, S. C., Dumais, J., et al.: Perspectives on Biological Growth and Remodeling. *J. Mech. Phys. Solids* **59**: 863–883, 2011.

[3] Tracqui, P.: Biophysical Models of Tumour Growth. *Rep. Prog. Phys.* **72**: 056701, 2009.

[4] Alessandri, K., Sarangi, B. R., Gurchenkov, V. V., Sinha, B., Kießling, T. R., et al.: Cellular Capsules as a Tool for Multicellular Spheroid Production and for Investigating the Mechanics of Tumor Progression in Vitro. *Proc. Natl. Acad. Sci. USA* **110**: 14843–14848, 2013.

HYDRAULIC FRACTURE AND TOUGHENING OF EPITHELIAL CELL MONOLAYERS

Giovanni Noselli[1a)], Alessandro Lucantonio[1], Xavier Trepat[2], Antonio DeSimone[1] & Marino Arroyo[3]
[1]*SISSA – International School for Advanced Studies, Trieste, Italy*
[2]*IBEC – Institute for Bioengineering of Catalonia, Barcelona, Spain*
[3]*UPC – Universitat Politècnica de Catalunya, Barcelona, Spain*

Summary Brittle materials propagate cracks under tensile or shear stresses. When these increase beyond a critical magnitude, then quasi-static crack propagation becomes unstable. In the presence of several pre-cracks, a brittle material always propagates only the weakest crack, leading to catastrophic failure. We show that all these features of brittle fracture are modified when the material susceptible to cracking is bonded to a hydrogel, a common situation in biological tissues. In the presence of the hydrogel, the brittle material can fracture in compression and can hydraulically resist cracking in tension. Furthermore, the poroelastic coupling regularizes crack tip dynamics and enhances material toughness by promoting multiple-cracking.

INTRODUCTION

Epithelial cell layers are two-dimensional, active materials capable of performing a variety of functions (e.g., morphogenesis, wound healing, protection against environmental pathogens) and routinely operating in the presence of significant levels of stretch, such as those arising from breathing manoeuvres or peristaltic contractions. Failure to withstand stretch causes epithelial fracture, leading to developmental defects and severe clinical conditions.

In vitro experiments that resemble the natural environment of epithelial layers have been recently performed [1] on cell clusters adhered to a hydrogel substrate, showing that i) failure of the monolayer can take place under compression, and that ii) this is typically accompanied by the simultaneous growth of multiple, intercellular cracks. The interest for this phenomenology stems from the fact that brittle materials typically fracture under tensile stresses. When these attain a critical magnitude, then quasi-static crack growth becomes unstable and, in the presence of several pre-cracks, catastrophic failure occurs by the propagation of the weakest crack only [2].

In this study, fracture of epithelial layers adhered to a hydrogel substrate is extensively explored by means of a mathematical model [3]. The hydraulic coupling between the fractures and the gel substrate is accounted for, revealing its key role in regularizing crack tip dynamics and in promoting material toughening by multiple-cracking.

SINGLE CRACK DYNAMICS WITH HYDRAULIC COUPLING

We first develop a simplified model [3] to examine the problem of a pre-cracked, elastic solid adhered to a hydrogel substrate, see Fig. 1(a) for a sketch of the geometry. Solutions from Linear Elastic Fracture Mechanics are employed to set the model, while accounting for the hydraulic coupling between the fracture and the gel substrate. Specifically, this requires the time rate of crack area $\dot{A}$ to equal the solvent flux q from the hydrogel into the edge crack. The flux q is approximated by means of Darcy's law, whereas the solvent pressure p acts on the crack faces. Additionally, the geometry is subject to a uniform, remote strain ε that can be either positive (tensile) or negative (compressive).

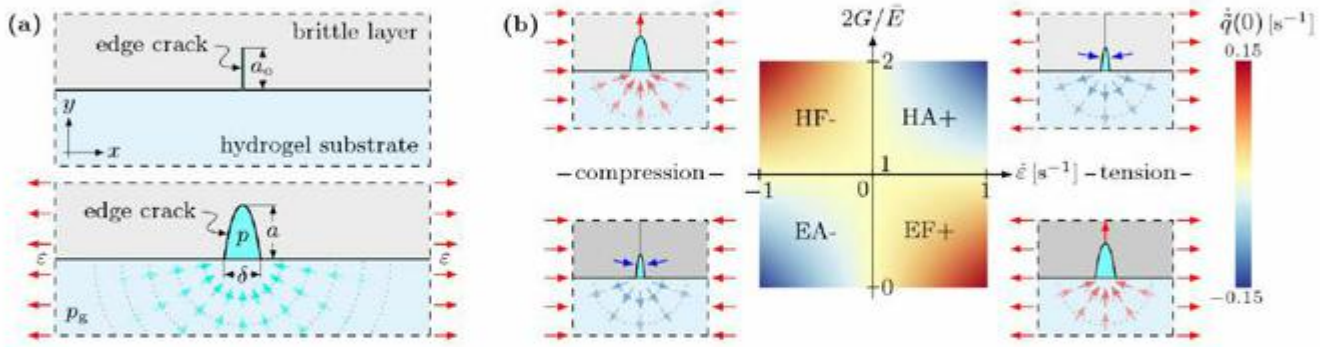

Fig. 1 Sketch of the model system at rest and under stretch (a). Distinct crack opening or closing scenarios (b), depending on the strain rate $\dot{\varepsilon}$ and on the ratio of the shear modulus G of the hydrogel to the effective Young's modulus $\bar{E}$ of the brittle material. The color map represents the time rate of the solvent flux towards the crack cavity immediately after strain application. The labels in (b) describe the dominant driving force at the crack, hydraulic (H) or elastic (E); the phenomenology, fracture (F) or crack arrest (A); and the nature of the imposed deformation, tensile (+) or compressive (−). For instance, HA+ stands for hydraulic (H) arrest (A) under tension (+). (figure adapted from [3])

[a)] Corresponding author. Email: giovanni.noselli@sissa.it.

It is found that, thanks to the hydraulic coupling, distinct fracture scenarios become possible depending upon the material parameters (specifically, the ratio of the shear modulus G of the hydrogel to the effective Young's modulus $\bar{E}$ of the brittle layer) and the loading sign, such that, for instance, the brittle material can fracture in compression (HF-) and can hydraulically resist cracking in tension (HA+), see the representation in Fig. 1(b). Remarkably, it is also shown that the hydraulic coupling regularizes crack tip dynamics allowing for quasi-static crack growth: Irrespective of the failure mode (tensile or compressive), crack tip velocity is dictated by the solvent diffusivity k and the loading rate $\dot{\varepsilon}$.

TOUGHENING BY MULTIPLE CRACKING

We now extend our study to the problem of multiple, competing edge cracks. To this purpose, we consider a detailed nonlinear Finite Element model, coupling large deformations of a neo-Hookean elastic solid with cohesive surfaces along predefined vertical paths, a finite deformation model for the mechanics and fluid transport in the hydrogel [4], and a one-dimensional hydrodynamic model for flow within the crack invoking lubrication theory. For the sake of simplicity, we restrict our computations to the ideal case of two edge cracks, see Fig. 2(b)-(d), and explore the role of solvent diffusivity.

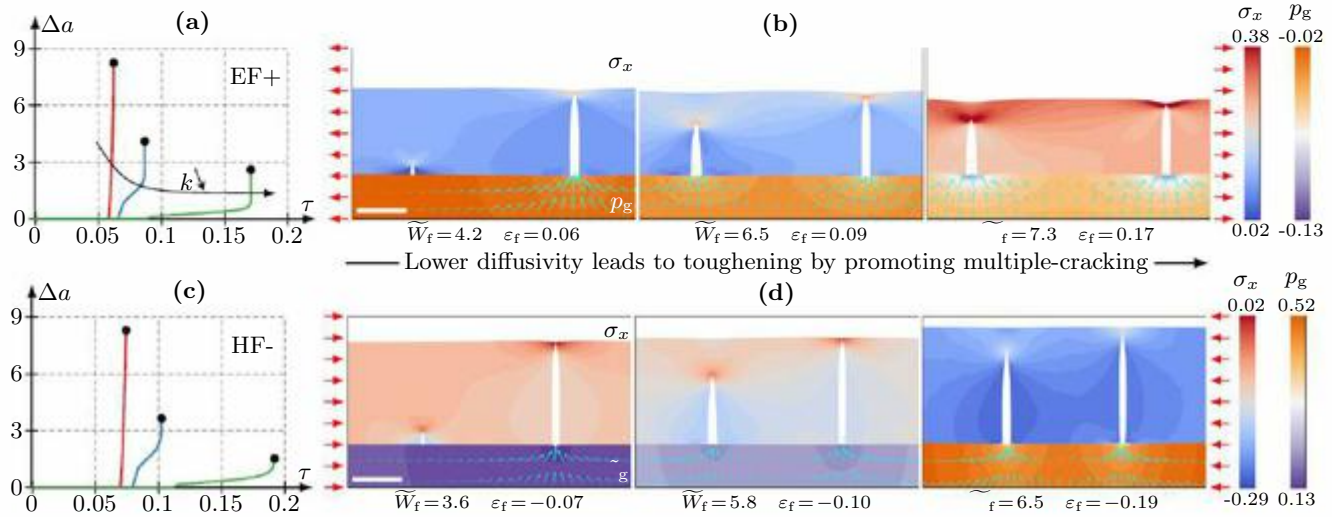

Fig. 2 Dynamics of two competing cracks at different solvent diffusivities k, in tension (a)-(b) and in compression (c)-(d). The plots in (a) and (c) show the relative crack length difference Δa for decreasing values of k. The contour plots in (b) and (d) show the longitudinal stress in the brittle layer and the solvent pressure in the hydrogel immediately prior to failure. The solvent flux in the hydrogel is depicted by means of arrows. (figure adapted from [3])

It turns out that, at high diffusivities, the cracks elastically compete in such a way that localized fracture prevails. This behaviour is similar to that exhibited by a brittle solid in the absence of the poroelastic coupling [2]. In sharp contrast, decreased diffusivity conveys material toughening by promoting multiple-cracking.

CONCLUSIONS

We have shown that the hydraulic coupling between a brittle solid and a poroelastic medium significantly modifies fracture physics. Depending on the sign of strain and the relative stiffness of the two materials, the system can exhibit unexpected fracture modes. We have also shown that, at low diffusivities, the bilayer system develops a toughening mechanism by promoting the simultaneous growth of multiple cracks. We believe that our results may contribute to the understanding of fracture in biological tissues and provide inspiration for the design of tough, biomimetic materials.

ACKNOWLEDGEMENTS

G.N., A.L. and A.D.S. gratefully acknowledge financial support from the ERC Advanced Grant 340685-MicroMotility.

References

[1] Casares L., Vincent R., Zalvidea D. *et al*.: Hydraulic fracture during epithelial stretching. Nat Mater **14**:343–351, 2015.

[2] Noselli G., Deshpande V.S., Fleck N.A.: An analysis of competing toughening mechanisms in layered and particulate solids. Int J Fract **183**:241–258, 2013.

[3] Lucantonio A., Noselli G., Trepat X. *et al*.: Hydraulic fracture and toughening of a brittle layer bonded to a hydrogel. Phys Rev Lett **115**:188105-1–5, 2015.

[4] Lucantonio A., Nardinocchi P., Teresi, L.: Transient analysis of swelling-induced large deformations in polymer gels. J Mech Phys Solids **61**:205–218, 2013.

GEOMETRY AND MECHANICS OF SHELL GROWTH

Douglas P. Holmes*[1], Matteo Pezzulla[1], and Paola Nardinocchi[2]

[1]*Department of Mechanical Engineering, Boston University, Boston, MA, USA*
[2]*Sapienza Università di Roma, via Eudossiana 18, I-00184 Roma, Italy*

Summary Understanding and controlling the shape of thin, soft objects has been the focus of significant research efforts among physicists, biologists, and mechanicians over the last decade. These studies aim to utilize advanced materials in novel, adaptive ways to fabricate smart actuators or mimic living tissues. Our recent work investigates how the underlying geometry of thin sheets will morph into shells when exposed to a local isotropic expansion, which may represent several stimuli such as nonuniform heating, local swelling, and differential growth. We present an analytical model built on a framework of differential geometry and mechanics to predict the mean and Gaussian curvatures of the growing shells. We confirm our results through both numerical analysis, and an experimental technique that relies on the residual swelling of soft, geometric composites.

GROWING SHEETS AND SHELLS

The continuous shape change during the growth and decay of biological structures is a constant presence within the natural world. Structures morph to accommodate an in flux of new material, either growing from an external nutrient source, or swelling from the absorption of water. Often, these morphological changes result in shapes that enhance the biological structure's functionality, for instance the Venus flytrap's leaves snap closed after osmotically swelling – a structural reconfiguration that is essential for its nutrition. Some of the most dramatic growth–induced deformations occur with slender structures, such as growing leaves, wrinkling skin, and the writhing of tendril–bearing climbers. Thin structures like these significantly deform to adopt nontrivial three dimensional shapes because they must bend to release their stretching energy. The coupling between growth and large deformations presents an interesting opportunity for the morphing of synthetic structures, whereby if specific regions within a thin material can be prescribed to stretch the overall structure will adopt a new shape.

In this work, we considered the programmatic shaping of 3D structures by residual swelling. The general concept is straightforward: we prepared a thin structure (beam, plate, shell) with a local excess of free monomer chains, and as this residual solvent diffused it induced a strain in the plate, causing it to morph into a 3D shape. Since the free chains equilibrate within the entire structure, the final shape is permanent. To accomplish this controlled morphing, we prepared geometric composites – structures whose geometries would be incompatible following this material diffusion – and placed the excess

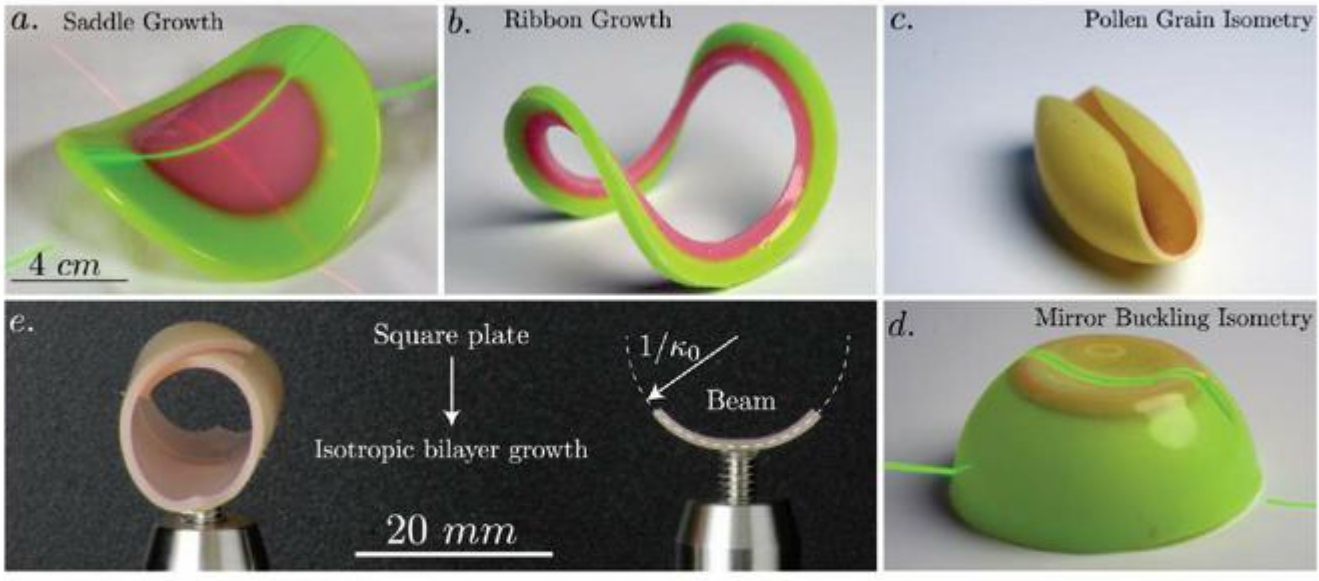

Figure 1: a. Flat sheet grows into a saddle as the green annular gets larger while the pink disk gets smaller due to residual swelling. b. Buckling of a flat ribbon due to residual swelling. c. Growth of a bilayer spherical cap mimicking the pollen grain isometry. d. Partial bilayer shell exhibiting a mirror buckling isometry. e. The cylindrical isometry of growing thin plates. The mean curvature of this shell can be predicted analytically from the curvature of a similar growing bilayer beam.

*Corresponding author. Email: dpholmes@bu.edu

monomer in one region. A diffusive–like "growth" of the thin shell followed, forming shapes that can be predicted by minimizing the structure's energy. A comparison of the energies for stretching and bending suggests that, if possible, a thin sheet exposed to such stimuli should adopt an isometric deformation in the limit of large stretch. We analytically describe the realization of this asymptotic isometry, corresponding to a zero Gaussian curvature K and a nearly stretch-free sheet. However, when an isometry cannot be realized, a structure will bend as much possible to avoid stretching. An example of this can be seen in Fig. 1a. & 1b., where an initially flat disk and ribbon grew into a saddle as material migrated from the inner disk (pink) to the outer annular ring (green) [1].

When an isometric, or nearly isometric, deformation is available to the growing structure, its morphing becomes quite straightforward as stretching will be avoided entirely, and the structure's shape will be determined by a minimization of its bending energy. This presents a direct approach to identify and exploit near isometries for growing plates and shells with or without topological constraints, *i.e.* a plate versus a cylinder. One such example is the "pollen grain" isometry of a spherical cap [2], where a growing bilayer shell breaks symmetry and adopts a folded structure which conserves the original shell's Gaussian curvature (Fig. 1c.). Growth of a partial bilayer shell accesses a more subtle isometry – the mirror buckling of a cap wherein the apex of the shell everts to a curvature with an opposite sign (Fig. 1d.). By recognizing the structures search for isometric deformations, it is evident that these shells morph in predictable ways in response to residual swelling. This controlled morphing provides a direct way to use the governing underlying geometry as a means for inducing minimally energetic shape changes.

Finally, to fully characterize this class of near–isometries, we investigate the simplest shell growth – growth of a flat sheet into a cylindrical shell. Cylindrically curved thin structures result from the nano-scale fabrication of semiconductor nanotubes, and the nonuniform heating, local swelling, and differential growth of thin sheets. For laminated composites, electrolytic thin film deposition, and concrete slabs, this cylindrical curling presents an engineering challenge, while recent work has utilized it as a mechanism for stimuli responsive self-assembly. The length scales of these examples range from the nanometer to the meter, suggesting that geometry dominates the deformation processes. Mechanically, these structures are bilayer disks in which one layer isotropically expands relative to the other. By coupling geometry and mechanics, we show that in the asymptotic limit of large bilayer growth, any arbitrarily shaped disk will adopt a cylindrical shape whose mean curvature is three-fourth's the natural curvature (Fig. 1e.). We developed an analytical model that captures both the bifurcation from spherical to cylindrical curvature and the isometric limit, verified by numerics and experiments [3]. To predict and explain the transition that turns a spherical growth into a flat state, we compare the energies of the spherical and isometric states, without any *a priori* assumptions of a stress state or displacement. These assumptions usually rely on the consideration of an Airy stress function, which is known only for a very small number of sheet's shapes, and on the account of a linearized version of the Gauss's theorem. Away from large stretches, the two principal curvatures are equal to each other and homogeneous throughout the sheet. However, the morphing into a spherical cap becomes too costly for the sheet when the stretch, or the natural curvature, reaches a critical value. While for small amounts of growth, it is convenient for the sheet to stretch and increase its Gaussian curvature, above a critical threshold it is cheaper to morph isometrically. Thus, we fully characterize the growth of a bilayer with any arbitrary shape from its flat state, through a spherical shell, and finally into a cylindrical isometry by use of an analytical, geometric model.

CONCLUSIONS

We present a novel means to grow thin sheets into shells while analytically predicting their resulting shape. In plane growth, as demonstrated through residual swelling, presents a way to take flat sheets and prescribe a non–zero Gaussian curvature. These results generalize Timoshenko's formula for beams into 2D by expressing how the dimensionless Gaussian curvature varies with material and geometric ratios. We have demonstrated how bilayer disks subjected to dome-like natural curvatures, regardless of their shape, will morph into cylindrical shells with a predictable mean curvature and orientation. We also showed how this simple experimental framework can identify near–isometries in thin shells containing arbitrary topological constraints. The capability to morph 2D shapes into 3D shells by in-plane and transverse residual swelling opens intriguing avenues towards the precise design of soft structures.

References

[1] M. Pezzulla, S. Shillig, P. Nardinocchi, and D.P. Holmes, "Morphing of Geometric Composites via Residual Swelling." Soft Matter, 11, (2015): 5812–5820.

[2] E. Katifori, S. Alben, E. Cerda, D. R. Nelson, and J. Dumais. "Foldable structures and the natural design of pollen grains." Proceedings of the National Academy of Sciences, 107(17), (2010): 7635–7639.

[3] M. Pezzulla, P. Nardinocchi, and D.P. Holmes, "Geometry and Mechanics of Thin Growing Bilayers," arXiv 1509.05259, (2015).

MICROSPHERE MODELING WITH FULL RELAXATION AND INTERNAL EVOLUTIONARY MECHANISMS

Sanjay Govindjee*[1], Miklos J. Zoller[1], and Klaus Hackl[2]

[1]*Structural Engineering, Mechanics, and Materials; Department of Civil and Environmental Engineering; University of California, Berkeley; Berkeley CA, USA*

[2]*Lehrstuhl für Mechanik – Materialtheorie; Ruhr-Universität Bochum; Bochum, Germany*

Summary The popular microsphere model, used for creating fully three-dimensional constitutive equations from single polymer chain models, relies upon an energetic relaxation argument. This formulation presents an improvement to the earlier microplane model that is predicated upon an affine, Taylor-like, assumption. While the microsphere framework has been previously applied to a wide variety of phenomena, its application has always involved relaxation only as it relates to quasi-incompressible mechanical motions *but* affine with respect to all other phenomena. In this presentation, we show how to lift these restrictions, thereby permitting the development of fully relaxed constitutive equations based on well characterized one-dimensional micromechanical models even in the presence of other evolutionary microstructural phenomena – such as strain induced crystallization, viscous flow, and other active phenomena.

OVERVIEW

A great deal of experimental and theoretical effort has been expended upon carefully characterizing the behavior of polymeric materials at the chain level. Crowning achievements in this realm include the Gaussian chain model, suitable for long chain polymers stretched to moderate degrees relative to their end-to-end length, and the Langevin chain model for large deformations of chains. These models have been successfully validated experimentally and are thus ubiquitously present in many theories of polymer-system mechanics. Despite these major achievements, among others in polymer chain mechanics, it is still quite challenging to develop mechanical models for networks of polymer chains, say, continuum level constitutive laws, even though good models are available at the chain level. The two primary hinderances that give arise to this situation are: (1) chain-chain interactions are difficult to model and (2) these networks are topologically complex and insufficiently characterized. Despite these complexities, the need for a scheme to transition from one-dimensional mechanical response to three-dimensional behavior is still present.

The original network models for achieving this are the well-known 3-, 4-, and 8-chain models; see e.g. Treloar (1958), Flory (1977), and Arruda and Boyce (1993) or the more general Wu and van der Giessen (1993) and Puso (1994) frameworks. These models are fully affine in nature or quasi-affine. More recently Miehe et al. (2004) proposed an improvement in the mathematical framework that encompasses all of these models by formulating the development of a macroscopic free energy for a network as a constrained relaxation problem – akin to a classical homogenization problem. This further permitted the incorporation of constraint effects as well as internal evolutionary processes, albeit affinely (see e.g. Miehe and Göktepe (2005) or Mistry and Govindjee (2014)). Separately, the line of papers that developed the microplane model (Bazant and Gambarova, 1984) should be noted as intermediate to the earlier cited works and Miehe et al. (2004). The microplane model is in the spirit of the microsphere model, excepting that it is fully affine. Notwithstanding, the developments under this line of thinking provide important discoveries that relevant to a properly formulated relaxed model; see e.g. Carol et al. (2004).

In our proposal, we postulate at the microstructural level that the chain stretch is described by a *tensor* $\boldsymbol{U}_m = \lambda \boldsymbol{n} \otimes \boldsymbol{n} + \nu(\boldsymbol{1} - \boldsymbol{n} \otimes \boldsymbol{n})$, where λ is the chain stretch, $\boldsymbol{n}$ is the unit chain orientation vector, and ν is the transverse constraint stretch. The connection to the macroscopic right-stretch tensor is given in terms of Hencky measures by

$$\ln \boldsymbol{U} = \frac{1}{S} \int_S \ln \boldsymbol{U}_m \, dS \,, \tag{1}$$

where S is the microsphere. Following the microplane developments as outlined in Carol et al. (2004), we advocate that in the finite deformation case that the microscopic motion be described by a microstructural Jacobian $j = \lambda \nu^2$ and a microstructural deviatoric stretch $\xi = (\lambda/\nu)^{1/3}$. This permits us to postulate a relaxed macroscopic free-energy

$$\Psi(\ln \boldsymbol{U}) = \inf_{\ln j, \ln \xi} \frac{1}{S} \int_S \psi_{mv}(\ln j) + \psi_{md}(\ln \xi) \, dS \quad \text{subject to (1)} \tag{2}$$

where ψ_{mv} and ψ_{md} are chain level energy functions emanating from microstructural polymer mechanics. The macroscopic constitutive relation follows as the gradient of the free energy, $\boldsymbol{\tau} = \partial_{\ln \boldsymbol{U}} \Psi$.

*Corresponding author. Email: s_g@berkeley.edu

The extension to the case of evolutionary processes leverages the evolutionary formulation of Biot (1955). This framework formulates inelastic evolutionary equations utilizing a dissipation potential, a concept valid for a wide variety of internal evolutionary processes. The primary postulate is that the evolution of any internal material parameters $\boldsymbol{z}$ is given by the variational problem:

$$\inf_{\dot{\boldsymbol{z}}} \left\{ \dot{\Psi} + \Delta \right\} , \tag{3}$$

where Δ is the dissipation potential for the phenomena characterized by $\boldsymbol{z}$ and Ψ now additionally depends upon $\boldsymbol{z}$. In the present context, the macroscopic dissipation potential Δ is constructed from an additional relaxation process on the microscopic dissipation potential Δ_m:

$$\Delta(\boldsymbol{z}, \dot{\boldsymbol{z}}) = \inf_{\boldsymbol{z}_m, \dot{\boldsymbol{z}}_m} \frac{1}{S} \int_S \Delta_m(\boldsymbol{z}_m, \dot{\boldsymbol{z}}_m)\, dS \tag{4}$$

subject to the constraint $\boldsymbol{z} = (1/S) \int_S \boldsymbol{z}_m \, dS$. Additionally, the free energy relaxation must now include a relaxation with respect to $\boldsymbol{z}_m$ the microscopic internal variables as ψ_{mv} and ψ_{md} will necessarily depend on the new microscopic internal variables.

Combined together, this formulation permits the modeling of a wide variety of phenomena encountered in polymer systems where single (non-interacting) chain mechanics dominates. The elemental ingredients are chain energy relations and micro-state dissipation potentials. The mathematical framework produces sensible macroscopic constitutive laws that are computable and energetically fully relaxed with respect to stretching, transverse constraints, and internal evolutionary processes. Examples will be shown for a variety of systems and compared to prior non-fully relaxed proposals.

REFERENCES

References

Arruda, E. M., Boyce, M. C., 1993. A three-dimensional constitutive model for the large stretch behavior of rubber elastic materials. Journal of the Mechanics and Physics of Solids 41, 389–412.

Bazant, Z., Gambarova, P., 1984. Crack shear in concrete: Crack band microplane model. ASCE Journal of Structural Engineering 100, 2015–2035.

Biot, M., 1955. Variational principles in irreversible thermodynamics with application to viscoelasticity. The Physical Review, 1463–1469.

Carol, I., Jirásek, M., Bažant, Z., 2004. A framework for microplane models at large strain, with application to hyperelasticity. International Journal of Solids and Structures 41, 511–557.

Flory, P. J., 1977. Theory of elasticity of polymer networks. the effect of local constraints on junctions. Journal of Chemical Physics 66, 5720–5729.

Miehe, C., Göktepe, S., 2005. A micromacro approach to rubber-like materials. Part II: The micro-sphere model of finite rubber viscoelasticity. Journal of the Mechanics and Physics of Solids 53, 2231 – 2258.

Miehe, C., Göktepe, S., Lulei, F., 2004. A micro-macro approach to rubber-like materials – Part I: the non-affine micro-sphere model of rubber elasticity. Journal of the Mechanics and Physics of Solids, 2617–2660.

Mistry, S., Govindjee, S., 2014. A micro-mechanically based continuum model for strain-induced crystallization in natural rubber. International Journal of Solids and Structures 51, 530–539.

Puso, M. A., 1994. Mechanistic constitutive models for rubber elasticity and viscoelasticity. Dissertation, University of California, Davis.

Treloar, L. R. G., 1958. The Physics of Rubber Elasticiy. Oxford University Press.

Wu, P. D., van der Giessen, E., 1993. On improved network models for rubber elasticity and their applications to orientationing hardening in glassy polymers. Journal of the Mechanics and Physics of Solids 41, 427–456.

MEMBRANE TENSION CONTROLS KINETICS OF NEURON GROWTH

Prashant K. Purohit*[1] and Douglas H. Smith[2]

[1]*Department of Mechanical Engineering and Applied Mechnaics, University of Pennsylvania, Philadelphia, Pennsylvania, USA*

[2]*Department of Bioengineering, University of Pennsylvania, Philadelphia, Pennsylvania, USA*

Summary In the first phase of axon growth, axons sprout from neuron bodies and are extended by the pull of the migrating growth cones towards their targets. Thereafter, a second phase of axon growth, called stretch growth, ensues as the mechanical forces from the growth of the animal induce rapid extension of the nerves. Here we propose a mathematical model for stretch growth of axon tracts in which the rate of production of proteins required for growth is dependent on the membrane tension. We show that there is a length dependent maximum stretching rate that an axon can sustain without disconnection, and that axon length is increased near the cell body. Our model also predicts that the diameter of an axon subjected to stretch growth must increase. Our results could inform better design of stretch growth protocols to create transplantable axon tracts to repair the nervous system.

INTRODUCTION

Smith and colleagues [1] have previously developed tissue-engineering techniques that exploit a natural "second phase" of axon growth creating long tracts of axons spanning two populations of neurons. In the well known "first phase" of axon growth, axons sprout from neurons guided by chemotactic and haptotactic factors and typically extend only up to a few millimeters to reach their targets. Thereafter, the second phase of purely mechanically stimulated, "stretch growth of integrated axon tracts," begins as the animal's body grows. Here, integrated axons spanning body regions that progressively move further apart undergo continuous mechanical tension. These forces appear to trigger growth somewhere along the center lengths of the axons, otherwise they would be stretched to the point of disconnection. To explore the cellular dynamics and boundaries of axon extension during the first phase of axon growth, several groups have developed computational models, with a focus on polymerization of microtubules as axon cytoskeleton building blocks. In most of these models, as the growth cone is guided forward, tensile forces are induced at the axon terminal or tip, just behind the growth cone. In turn, it is assumed that these forces trigger building of the microtubule selectively in this region. However, once the target is reached typically not more than a few millimeters away, integration and synapse formation essentially abolish the growth cone. Therefore, current mathematical models do not appear to account for mechanical influences during the extreme second phase of axon growth and expansion of tracts over tens of centimeters for humans and even many meters for very large animals. Furthermore, the specific role of membrane tension and stretch activated ion channels in axon stretch growth have not been explored. Here, we propose a model for stretch growth of integrated axon tracts based on overall mechanical stimulation resulting in very regional microtubule polymerization and relative contribution of stretch activated channels in the process.

Growth modeled as a polymerization process

A summary of the equations describing stretch-growth, assuming polymerization occurs at the soma (see figure 1(a)), is [2, 3]:

$$\frac{dL}{dt} \;/\; \alpha Q_s - \beta, \qquad \frac{dQ_t}{dt} \;/\; \frac{DA}{V_t L}\, Q_s - Q_t \;, \qquad \frac{dQ_s}{dt} \;/\; \frac{I}{V_s} - \frac{DA}{V_s L}\, Q_s - Q_t \qquad \frac{G}{V_s}\frac{dL}{dt}, \tag{1}$$

where L is the length of the axon, $\alpha \;/\; ek_{on}$ is related to the on-rate k_{on} for polymerization with e the monomer size, $\beta \;/\; ek_{off}$ is related to the off-rate k_{off} for polymerization, Q_s is the concentraton of monomers in the soma, Q_t is the concentration of monomers at the tip of the axon, D is a diffusion constant, A is the axon cross-sectional area, V_t is a small volume at the tip of the axon, I is the rate (in units of number of monomers per unit time) of production of tubulin monomers in the soma, V_s is a small volume in the soma where the polymerization reaction occurs and G is a constant. The steady state solution to these equations is:

$$L \;/\; L_0 \quad Ut, \qquad Q_s \;/\; Q_t \;/\; Q \;/\; \frac{\beta}{\alpha} \quad \frac{U}{\alpha}, \tag{2}$$

where $U \;/\; I/G$ is the speed of growth. We believe that the rate of monomer production I depends on the membrane tension τ. As a cell is stretched it must 'sense' the increasing membrane tension and increase the rate of production so that growth keeps up with the stretching. A potential source of this cell signaling during stretch growth is likely mechanosensitive channels in cell membranes that have been shown to open in other circumstances when the tension increases. Opening of these channels can cause an influx of ions such as Na^+ and Ca^{2+} that can influence monomer production in the soma by various means. While the exact mechanism may not be known it is reasonable to assume that I depends linearly on the probability p_{open}

*Corresponding author. Email: purohit@seas.upenn.edu

of the mechanosensitive channels being open, which in turn depends on τ in a known way [4]. Using those expressions we assume that the monomer production rate I is a monotonic function of the tension τ and is given by:

$$I(\tau) = C\left[\frac{1}{1+\exp(-\frac{\Delta G+\tau\Delta A}{k_BT})} - \frac{1}{1+\exp(-\frac{\Delta G+\tau_0\Delta A}{k_BT})}\right], \tag{3}$$

where C is a constant, k_BT is the thermal energy scale, $\Delta G = G_{closed} - G_{open} < 0$, the free energy difference between the closed and open states of the channel is several k_BT, $\Delta A = A_{open} - A_{closed} > 0$, the cross-sectional area difference between the open and closed states is on the order of tens of square nanometers, and τ_0 is the rest tension of the axonal membrane. When $\tau = \tau_L$, the lytic tension of the membrane, $I(\tau_L)$ is at its maximum and this corresponds to $U \approx 30\mu$m/hour.

RESULT

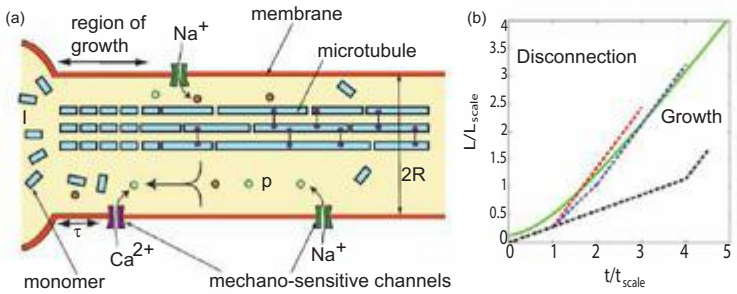

Figure 1: (a) Schematic of the axon with microtubules polymerizing at the junction between the axon and the soma. Mechanosensitive channels in the axonal membrane open in response to increased tension due to stretching causing an influx of ions. This sends a signal to the soma to increase the rate of production of monomers. (b) A limiting $L(t)$ curve is shown as the green line. Growth programs (blue and red dashed lines) that cross this line from below cause disconnection of the neurons.

The major result of the model above is a limiting growth trajectory which when crossed from below will cause the axons to disconnect. Suppose during initial stretching of a neuron the lytic tension is reached, and the cell responds by increasing the monomer production to its maximum value $I(\tau_L)$. As a result the axon grows by the addition of new material and eventually settles into a steady state with $\tau < \tau_L$, and constant growth rate U. Hence, the limit on the growth program is set by the requirement that $\tau = \tau_L$ at all times. Since, I and A are functions of τ only, they remain fixed for this $L(t)$. With these assumptions we can integrate eqns. (1) to find the limiting growth trajectory $L(t)$. This limiting growth trajectory is plotted as the green curve in figure 1(b) in terms of non-dimensional length and time variables. A comparison of the x- and y-axis of this figure to figure 4A of Smith [1](who arrived at the limiting trajectory through experiment) suggests that t_{scale} is about 1 day and L_{scale} is about 0.2mm for axons in stretch growth. In contrast, Wisnner-Gross *et al.* [5] fitted the ODE model of Samuels *et al.* [2] to their experiments on growth of neurons without stretch and concluded that t_{scale} was about 6.4 hours and L_{scale} was about 51 microns. The reason for a lower k_{on} in stretch growth can be that polymerization occurs against a compressive load that the microtubules are experiencing due to increased tension in the membrane caused by stretching.

CONCLUSIONS

We have presented a microscopically based model in which membrane tension modulates the production rate of materials required for neuron growth. We obtain a limiting growth trajectory that is similar to one obtained from experimentss [1].

References

[1] Smith, D. H., "Stretch growth of integrated axon tracts: Extremes and exploitations", *Progress in Neurobiology* **89**, 231-239, 2009.

[2] Samuels, D. C., Hentschel, H. G. E. and Fine, A., "The origin of neuronal polarization: a model of axon formation", *Phil. Trans. Roy. Soc. Series B* **351**, 1147-1156, 1996.

[3] Nguyen, T. D., Hogue, I. B., Cung, K., Purohit, P. K. and McAlpine, M. C., "Tension induced neurite growth in microfluidic channels", *Lab on Chip* **13**(18), 3735-3740, (2013).

[4] Haselwandter, C. A. and Phillips, R., "Connection between oliomeric state and gating characteristics of mechanosensitive channels", *PLoS Computational Biology* **9**(5), e1003055, 2013.

[5] Wissner-Gross, Z. D., Scott, M. A., Ku, D., Ramaswamy, P. and Yanik, M. F., "Large scale analysis of neurite growth dynamics on micropatterned substrates", *Integrative Biology*, (2010).

SOFT NETWORK MATERIALS WITH DETERMINISTIC AND BIO-INSPIRED DESIGNS

Yihui Zhang[1a)], Qiang Ma[1], Yonggang Huang[2], John A. Rogers[3]
[1]*Department of Engineering Mechanics, AML, Tsinghua University, Beijing, China*
[2]*Department of Civil and Environmental Engineering and Mechanical Engineering, Northwestern University, Evanston, IL, USA*
[3]*Department of Materials Science and Engineering, University of Illinois at Urbana-Champaign, Urbana, IL, USA*

ABSTRACT

Hard and soft structural composites found in biology provide inspiration for the design of advanced synthetic materials. Many examples of bio-inspired hard materials can be found in the literature; far less attention has been devoted to soft systems. Here we introduce deterministic routes to low-modulus thin film materials with stress/strain responses that can be tailored precisely to match the non-linear properties of biological tissues, with application opportunities that range from constructs for tissue engineering to stretchable biomedical electronics. The approach combines a low-modulus matrix with an open, stretchable network as a structural reinforcement that can yield classes of composites with a wide range of desired mechanical responses, including anisotropic, spatially heterogeneous, hierarchical and self-similar designs. A finite-deformation model of such network materials is developed, enabling accurate predictions of stress-strain curves and Poisson ratios. Demonstrative application examples include thin, skin-mounted electrophysiological sensors with mechanics precisely matched to the human epidermis.

MAIN TEXT

Concepts in materials science that draw inspiration from the natural world have yielded an impressive collection of important advances in recent years. Structural materials are of particular interest, due to their essential roles in nearly every engineered system. Biology provides examples of two general classes of such materials: (1) mineralized hard (~ GPa) materials, mainly in the form of hierarchically assembled composites that combine minerals with organic polymer additives; and 2) non-mineralized soft (~ MPa) materials, typically constructed with wavy, fibrous constituents that are embedded in extracellular matrices. Although the non-mineralized, soft biological structures offer great potential in areas ranging from artificial tissue constructs to bio-integrated devices, they have received far less attention compared to the mineralized counterparts.

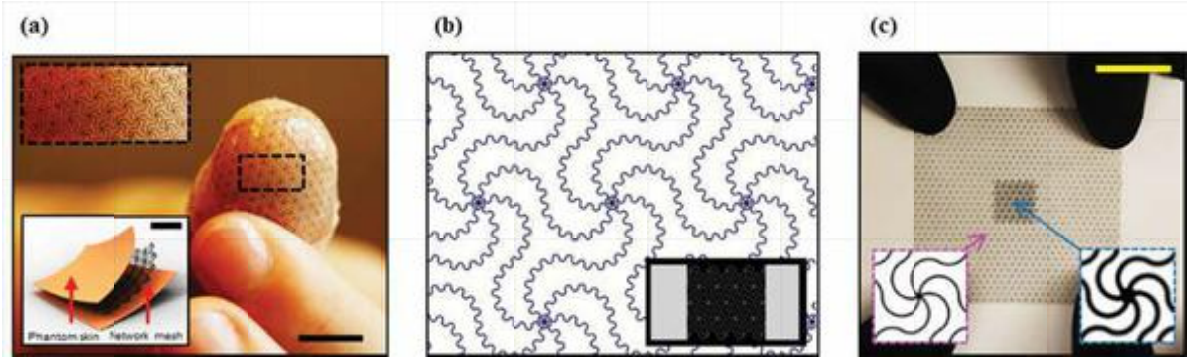

Fig. 1. (a) Optical images and an exploded view schematic illustration (lower left inset) of a skin-like composite with bio-inspired soft network. The scale bar is 1 cm. (b) Schematic illustration of a wavy network with a 2nd order self-similar architecture consisting of horseshoe building blocks. (c) An image of spatially heterogeneous designed soft composite. The scale bar is 2 cm.

Here we introduce deterministic routes to a class of soft, bio-inspired network materials with precisely tailored stress/strain responses to match the non-linear properties of biological tissues, with broad application opportunities that range from constructs for tissue engineering to stretchable biomedical electronics [1]. The concepts combine planar networks of different two-dimensional (2D) lattice topologies, with horseshoe microstructures originally developed for interconnects in stretchable electronics. A low-modulus elastomer or hydrogel serves as a supporting matrix. Such network materials exhibit 'J-shaped' stress/strain curves that offer large levels of stretchability, as well as a huge modulus

[a)] Corresponding author. Email: yihuizhang@tsinghua.edu.cn.

enhancement at large strain to yield a relatively high mechanical strength. With a computational mechanics model to serve as the design tool, the mechanical responses of the network materials can be precisely tailored by optimizing their key parameters, including the material type, the network topology, the filament dimensions and the microstructure geometry, to meet requirements of interest. Fig. 1(a) presents a schematic illustration of the strategy in the context of an artificial skin construct, as an application example of the soft network materials. Hierarchical, self-similar designs of the interconnects and spatially heterogeneous designs, as shown in Fig. 1(b) and (c), can further expand their range of mechanical properties, such as stress/strain responses with multiple hardening and gradient mechanical properties. The proposed network materials also offer a new insight into the structural design of stretchable electronics that focused more on the design of hard functional devices and/or interconnects previously [2-5]. Successful experimental demonstrations of these soft network materials integrated with electrophysiological sensors and drug release vehicles indicate their potential for practical applications in biomedical devices.

To provide theoretical guidelines for designs of such soft network materials, a nonlinear mechanics model is developed by combining a finite-deformation constitutive relation of the building block (i.e., horseshoe microstructures), with the analyses of equilibrium and deformation compatibility in the periodical lattices [6]. This model, as validated by FEA and experimental results, can predict precisely the nonlinear stress-strain curves and Poisson ratios, as well as the deformed configurations under uniaxial stretching. Analytic solutions of their key mechanical properties, including elastic modulus, critical strain, peak modulus and the associated strain, were obtained, which can characterize well their dependences on the microstructure geometry. Moreover, a demonstrative example shows that the developed model can be employed to enable rapid optimization of microstructure geometry for matching precisely the stress-strain curves of human skins, as shown in Fig. 2.

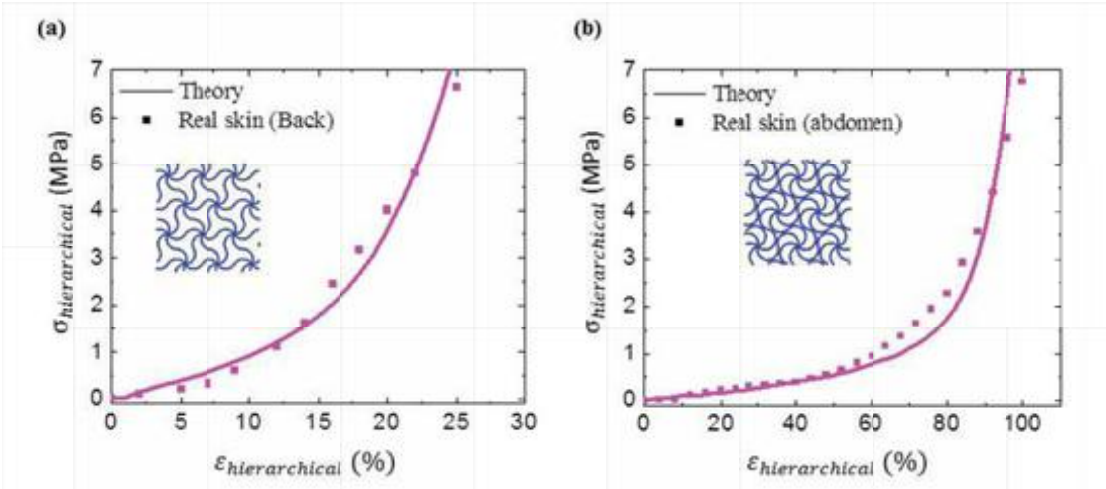

Fig. 2. Stress-strain curves of human skin for two different locations ((a) for back area and (b) for abdomen area) on different individuals and optimized skin-like network materials with triangular lattices.

References

[1] Jang K.-I., Chung H.U., Xu S., Lee C.H., Luan H., Jeong J., Cheng H., Kim G.-T., Han S.Y., Lee J.W., Kim J., Cho M., Miao F., Yang Y., Jung H.N., Flavin M., Liu H., Kong G.W., Yu K.J., Rhee S.I., Chung J., Kim B., Kwak J.W., Yun M.H., Kim J.Y., Song Y.M., Paik U., Zhang Y., Huang Y., Rogers J.A.,: Soft network composite materials with deterministic and bio-inspired designs. *Nature communications* 6, 6566 (2015).

[2] Rogers J.A., Someya T., Huang Y.G.: Materials and Mechanics for Stretchable Electronics, *Science* 327, 1603-1607 (2010).

[3] Xu S., Zhang Y.H., Cho J., Lee J., Huang X., Jia L., Fan J.A., Su Y.W., Su J., Zhang H.G., Cheng H.Y., Lu B.W., Yu C.J., Chuang C., Kim T.-I., Song T., Shigeta K., Kang S., Dagdeviren C., Petrov I., Braun P.V., Huang Y.G., Paik U., Rogers J.A.: Stretchable Batteries with Self-Similar Serpentine Interconnects and Integrated Wireless Recharging Systems. *Nature Communications* 4: 1543 (2013)

[4] Zhang Y.H., Wang S.D., Li X.T., Fan J.A., Xu S., Song Y.M., Choi K.J., Yeo W.H., Lee W., Nazaar S.N., Lu B.W., Yin L., Hwang K.C., Rogers J.A., Huang Y.G.: Experimental and Theoretical Studies of Serpentine Microstructures Bonded To Prestrained Elastomers for Stretchable Electronics. *Advanced Functional Materials* 24: 2028-2037 (2014)

[5] Zhang Y.H., Fu H.R., Xu S., Fan J.A., Hwang K.C., Jiang J.Q., Rogers J.A., Huang Y.G.: A hierarchical computational model for stretchable interconnects with fractal-inspired designs. *Journal of the Mechanics and Physics of Solids* 72: 115-130 (2014)

[6] Ma Q., Cheng H., Jang K.-I., Luan H., Hwang K.C., Rogers J.A., Huang Y.G., Zhang Y.H.: A nonlinear mechanics model of bio-inspired hierarchical lattice materials consisting of horseshoe microstructures. *Journal of the Mechanics and Physics of Solids*. (Submitted)

DYNAMIC INDENTATION: A SIMPLE METHOD TO CHARACTERIZE POROELASTICITY OF GELS IN MICRON SCALE

Yang Lai[1], Yuhang Hu[1a)]

[1]*Department of Mechanical Science and Engineering, University of Illinois Urbana Champaign, Urbana, Illinois, US*

Summary In this study, we use the characteristic phase lag between the applied oscillation indentation displacement and the force on the indenter due to the energy dissipation from solvent flow in the gel to characterize the poroelasticity of gels. We will show that the phase lag degree is a function of two parameters, Poisson's ratio and normalized angular frequency. The solutions are derived for several shapes of indenters. The maximum value of the phase lag over a spectrum of actuation frequencies can be used to characterize the Poisson's ratio of the gel, and the characteristic frequency corresponding to the maximum phase lag can be used to characterize its diffusivity.

INTRODUCTION

Gels composed of crosslinked polymeric network and solvent molecules, can swell or contract in response to external stimuli, such as relative humidity, temperature, pH, electric field and light. Gels are almost everywhere in nature, from cells, tissues, to organs. Gels are also important engineering materials, which have been widely used as cell culture scaffold, drug carrier, microfluidic device, sensors, actuators, soft robots, fuel cell membrane, transparent loudspeaker, swellable packers for sealing oil well, etc. Most gels are soft, with a typical modulus of $1\sim10^2$ kPa. Some gels are also saggy, brittle, and slippery. Most bio-gels are often inhomogeneous, degradable as time and of gradient properties. These characters of gels raise many practical difficulties in mechanical testing. Traditional techniques such as tension, compression, bending, torsion and shearing are very difficult to apply. Recently there is a growing interest in indentation on soft materials, but most previous works focus on characterizing the elastic modulus of gels. In the PI's pervious work, a poroelastic relaxation indentation method has been developed allowing the poroelastic properties of gels including shear modulus, drained Poisson's ratio and diffusivity to be measured all from one test.[1] While this method is applicable in large scales (mm), it remains challenging to be applied in small scale (1~10 μm), when inhomogeneous and local properties are of interests. In the relaxation indentation technique, identifying the contact point on soft materials and accurately measuring the initial force right after a rapid ramping of displacement are very difficult to realize in small scale. Alternatively, most commercial instruments for small scale testing, such as Atomic Force Microscope and Instrumented Nanoindenter, can perform accurate dynamic measurement with high resolution. Motivated by this fact, we develop a dynamic indentation method to characterize poroelasticity of gels for micro-scale measurement.

METHODOLOGY AND RESULTS

To define quantities of interest, we use the theory of poroelasticity to describe the diffusion-coupled-deformation of gels.[2] The initial gel is taken to be in a homogeneous state, subject to no mechanical load, with C_0 being the number of solvent molecules per unit volume of the gel, and μ0 being the chemical potential of solvent in the gel. When the gel deforms, the displacement is a time-dependent field, $u_i(x_1,x_2,x_3,t)$, and the strain is $\varepsilon_{ij} = (\partial u_i/\partial x_j+\partial u_j/\partial x_i)/2$. The conservation of solvent molecules requires that $\partial C/\partial t=-\partial J_k/\partial x_k$, where C is the concentration of the solvent in the gel, and J_k the flux which is driven by chemical potential gradient $J_k=-(k/\eta\Omega^2)\partial\mu/\partial x_k$, where k is the permeability, η the viscosity of the solvent, and Ω the volume per solvent molecule. The stress in the gel is given by $\sigma_{ij}=2G[\varepsilon_{ij}+\varepsilon_{kk}\delta_{ij}\nu/(1-2\nu)]-\delta_{ij}(\mu-\mu_0)/\Omega$, where G is the shear modulus, ν Poisson's ratio. The gel is in mechanical equilibrium, so that the field of stress satisfies $\partial\sigma_{ij}/\partial x_j=0$. A combination of the above equations leads to a familiar diffusion equation $\partial C/\partial t=D\nabla^2 C$, with the diffusivity being $D=[2(1-\nu)/(1-2\nu)]Gk/\eta$. Summarily, the material is fully described by three parameters G, ν and D.

To characterize these three parameters, we develop a dynamic indentation method. As shown in Figure 1, a depth of indentation h_o is applied on a swollen gel with a constant velocity, and then is held

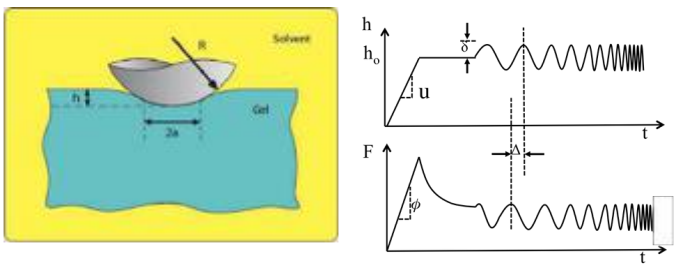

Fig.1: Schemetic of the dynamic indentation method. A depth of indentation h0 is pressed into the swollen gel and held for a period of time. After this period of holding, an oscillation displacement is applied with different frequencies. Meanwhile, the force is measured as a function of time, and the phase lag between force spectrum and displacement spectrum is recorded as actuation frequency.

a) Corresponding author. Email: yuhanghu@illinois.edu

for a period of time. Following this period of stress relaxation, an oscillatory displacement $\delta e^{-i\omega t}$ ($\delta << h_o$) is applied. Meanwhile the force on the indenter is measured as a function of time. The poroelastic gel is characterized by three parameters: shear modulus G, drained Poison's ratio ν, and diffusivity D. During the loading period, solvent molecules in the gel do not have time to migrate, so the gel is incompressible, and the slope of the measured force ϕ can be used to obtain shear modulus G through elastic solutions,

$$G=3\phi/16R^{1/2}u^{3/2}. \quad (1)$$

The real difficulty lies in how to get ν and D. The phase lag between the displacement and force spectrum characterizes the time-dependent behavior of gels. As the oscillatory displacement sweeps through a spectrum of frequencies, a peak value of the phase lag Δ_c between oscillatory displacement and the force measurement is obtained. The angular frequency ω_c corresponding to the peak is a characteristic value with respect to diffusion that scales with D/a^2 with a being the contact radius. The oscillation indentation problem is solved and the characteristic curve $\Delta=f(D\omega/a^2, \nu)$ is obtained (Fig. 2). The solution derived here is for spherical indenter.

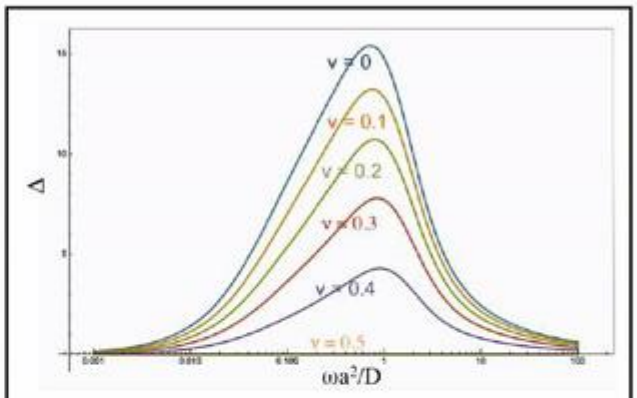

Fig.2: Phase lag is plotted as a function of normalized angular frequency for materials of different Poisson's ratio.

As is shown in Figure 2, the phase lag is plotted as a function of normalized angular frequency. It reaches a peak at a particular value of the actuation frequency. The value of the peak highly depends on the Poisson's ratio of the material. When Poisson's ratio is small, the amount of liquid that can be squeezed out of the gel is larger. Consequently, more energy is dissipated due to flow of solvent, which corresponds to a larger value of the phase lag. When Poisson's ratio is close to 0.5, liquid does not diffuse in or out of the material, no energy is dissipated, and the phase lag is zero. For ease for extraction of material properties from experimental data, the relation between peak phase lag Δ_c and Poisson's ratio ν is fitted with a continuous function as

$$\nu = 0.5\text{-}0.02\Delta_c\,, \quad (2)$$

and the relation between the normalized critical angular frequency and Poisson's ration ν is also fitted with a function as

$$D = a^2\omega_c/(0.72+0.29\nu+0.48\nu^2) \quad (3)$$

Therefore, equations (1)-(3) can be used to extract the three material parameters from dynamic indentation measurement.

CONCLUSIONS

A dynamic indentation method has been developed that is suitable for characterizing the mechanical and transport properteis of polymer gels. In this technique, a spherical indenter is used to probe the response of gels under oscillatory loading conditions. Solvent transport within the gel is driven by chemical potential gradient. The flow of solvent defines the time-dependent behavior of gels and energy dissipation due to flowof solvent through the network. In dynamic response, a lag of phase appears between the spectrum of responsive force and actuation displacement. Theoretical caculation shows that the peak value of the phase lag can be used to extract Poisson's ratio of the material, and the corresponding critical angular frequency can be used to extract the diffusivity of solvent in polymeric network of gels.

References

[1]. Hu Y., Zhao X., Vlassak J.J., Suo Z.: Using indentation to characterize the poroelasticity of gels. Appl. Phys. Lett. 96: 121904, 2010.

[2]. Biot M.A.: General theory of three-dimensional consolidation. J. Appl. Phys. 12:155-164, 1941.

CELL ALIGNMENT FABRICATION USING STRETCHABLE HYDROGELS WITH PROGRAMMABLE STRAIN GRADIENTS

Yuhui Li[1,2], Lin Wang[1.2] , Moxiao Li[2], Tian Jian Lu[2] & Feng Xu [1,2]

[1] *MOE Key Laboratory of Biomedical Information Engineering, School of Life Science and Technology, Xi'an Jiaotong University, China*

[2] *Bioinspired Engineering and Biomechanics Center (BEBC), Xi'an Jiaotong University, China*

Abstract: The mechanical gradients (e.g., stiffness and stress/strain gradients) of extracellular matrix play an important role in guiding cellular alignment, especially in tendons and muscles. Though various methods have been developed to engineer graded mechanical environment to study its effect on cellular behaviours, most of them failed to distinguish stiffness effect from stress/strain effect during mechanical loading. Here, we construct a mechanical environment with strain gradients by using a hydrogel of a linear elastic property. We demonstrate that the pattern of cellular alignment can be rather precisely tailored by substrate strains. The experiment is in consistency with a theoretical prediction when assuming that focal adhesions would drive cell to reorient to the directions where they are most stable. This work not only provides important insights into the cellular response to local mechanical microenvironment, but can also be utilized to engineer patterned cellular alignment that can be critical in tissue remodelling applications.

MAIN TEXT

Mechanical gradient microenvironment has been found to widely exist in native tissues and play an important role in regulating cell behaviors including alignment, migration, proliferation and differentiation in vitro for tissue remolding and regenerative medicine applications[1-2]. Up to now, a variety of methods based on hydrogels have been developed to engineer mechanical gradient microenvironment of cells in vitro[3-4]. However, mostly of these studies were focused on stiffness gradient construction and with less effort for engineering stress/strain gradient microenvironment, which are also associated with normal physiologic processes such as gut peristalsis and heart contraction. Recently, several approaches have been developed to simulate in vitro 3D cell environment with mechanical loading and investigated cell response to varying stress/strain conditions, which are discontinuous and lack of controllability to form gradient environment. Besides, the effects of stiffness and stress/strain are intertwined. Therefore, there is still an unmet need for a simple and controllable method to engineer hydrogels with stress/strain gradients for cells. Here, we developed a simple and facile method based on molding and photolithography approaches to fabricate methacrylate gelatin (GelMA) hydrogels with strain gradients ranging from 0~20%, which covers the muscle and heart contraction in vivo (**Figure 1**). The separation of the effects of stiffness and stress/strain has been achieved through the hydrogels with linear elastic properties in the testing strain range. Hydrogels with programmable strain gradients were formed by UV crosslinking reaction with designed shapes and then applied by static stretch loading. (**Figure 2**) The orientation of C2C12 cells seeded on gradient hydrogels was assessed under static stretch loading conditions (**Figure 3**). The analysis results of cellular stress fiber orientation have shown that cell alignment gradients will formed under strain gradients on hydrogels. For large strain region (17.0 ± 0.5%~19.7 ± 1.0%) on gradient hydrogels, cells aligned predominantly perpendicular to stretching direction whereas cells randomly oriented in control group (non-strech loading). With decreasing strain from 15.4 ± 0.4% to 13.5 ± 0.7%, stress fibers gradually oriented towards the stretching direction. Stress gradient generated on hydrogels also ranged from 1.9 ± 0.3 kPa to 3.2 ± 0.1 kPa. These results indicated that cellular response to gradient hydrogels supports the principle that cells orient in the direction of minimal substrate deformation, known as strain-avoidance or stretch-avoidance, and is in agreement with the existing findings from corresponding model systems. The gradient hydrogel fabrication approach we developed here holds great potential to impact a wide range of fields, such as cell mechanics, tissue engineering and regenerative medicine.

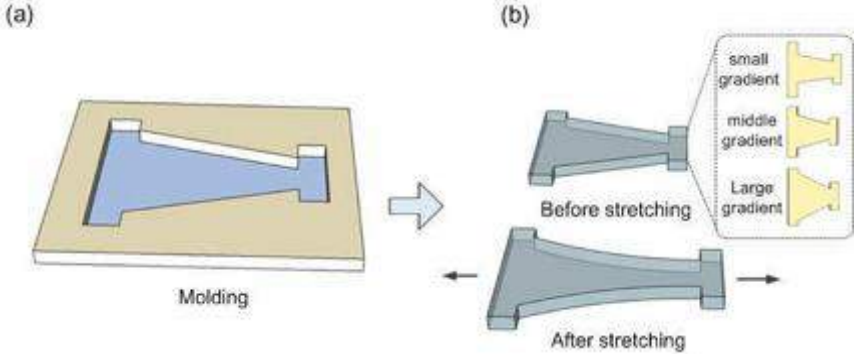

Figure 1. Schematics of fabrication method for hydrogels with stress/strain gradients. (a) Hydrogels with designed trapezoidal shape are fabricated with PMMA mold through an UV crosslinking reaction; (b) Hydrogels with programmable gradients including three levels of strain gradients under stretching.

[a] Corresponding author. Email: fengxu@mail.xjtu.edu.cn.

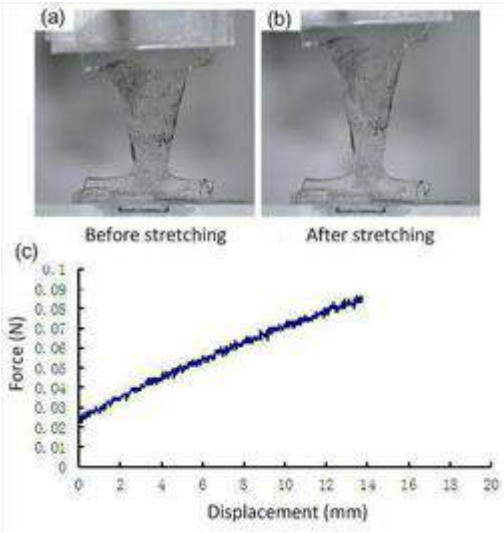

Figure 2. Characterization of strain/stress of different hydrogels. (a) Representative images depict the microbeads used in the texture correlation algorithm before (left) and after (right) stretch to determine strain distribution. (b) Stress/strain curve of hydrogels.

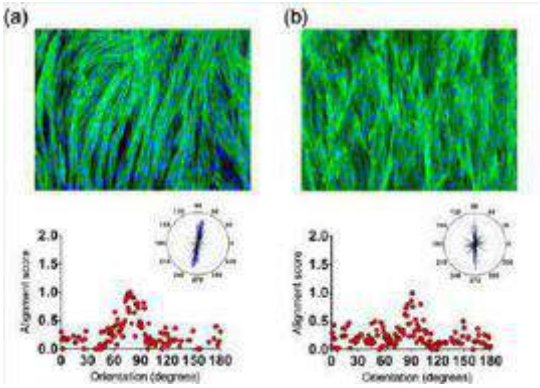

Figure 3. Analysis of cellular alignment generated on gradient hydrogels. (a-b) florescent images and quantification of cell orientation on gradient hydrogels with stretch loading after 3 days culture (cellular F-actin fibers were stained by phalloidin (green) and nuclei by DAPI (blue)).

In conclusion, we here developed a simple and feasible method to engineer patterned cellular alignment in vitro. Programmable stress/strain gradients on GelMA hydrogels are realized by stretching hydrogels with linear elastic property. When seeding cells on such hydrogels subjected to static stretches, we find that cells on hydrogels align almost perpendicularly to stretch direction in regions of large strains, and gradually align towards to stretch direction in regions of relatively small strains, whereas cells orient randomly in control group. The effect of substrate strains on cellular alignment is explained with the theory by assuming that focal adhesions would drive cell to reorient to the directions where they are most stable. The current work not only provides important insights into the cellular response to local mechanical microenvironment for understanding cellular mechanosensitivity, but can also be utilized to engineer patterned cellular alignments that can be critical in tissue remodelling and regeneration.

References

[1] Li, Y., Huang, G., Zhang, X., Wang, L., Du, Y., Lu, T. J., Xu, F. *Biotechnol Adv*, 347−365, 2014.
[2] Etemad-Moghadam, B., Guo, S., Kemphues, K. J. *Cell*, 743−752, 1995.
[3] Berthier, E., Beebe, D. J. *Lab Chip*, 3241− 3247, 2014.
[4] Du, Y., Hancock, M. J., He, J., Villa-Uribe, J. L., Wang, B.; Cropek, D. M., Khademhosseini. *Biomaterials*, 2686−2694, 2010.

MECHANICAL INSTABILITIES AND MULTI-FUNCTIONS OF SOFT ACTIVE STRUCTURES IN SOFT ROBOTS

Tiefeng Li[1,2,3a)], Yiming Liang [1],Yongbin Jin[1], Yuhan Xie [1], Tingyu Cheng[1] & Xuxu Yang [1]
[1]*Institute of Applied Mechanics, Zhejiang University, 38 Zheda Road, Hangzhou, Zhejiang 310027, China*
[2]*Soft Matter Research Center (SMRC), Zhejiang University, Hangzhou 310027, China*
[3]*Key Laboratory of Soft Machines and Smart Devices of Zhejiang Province, Hangzhou 310027, China*

Summary The natural animals and insects integrate muscles and skins providing excellent actuating and sensing functions. Inspired by the natural structure, we present various structures of dielectric elastomer (DE) elastomer with various characteristics such as integrated actuating and sensing, bi-stable actuation, and anisotropic actuation. The structure can deform when subjected to high voltage loading and generate corresponding output signal in return. We investigate the mechanical instabilities of the soft active structure of dielectric elastomer both theoretically and experimentally. It is noted that when applying high voltage, the actuating dielectric elastomer membrane deforms and the sensing dielectric elastomer membrane changes the capacitance in return. Based on the concept, finite element method (FEM) simulation has been conducted to further investigate the electromechanical behaviours and guide the structural design of the soft robot.

INTRODUCTION

Electro-active polymer (EAP) actuators have recently attracted increasing research interests due to their various performances. As a typical EAP, dielectric elastomer (DE) is one of the most promising electro-active polymer actuators because of its large deformation, light weight, high energy density, and rust free. When an electric field is applied through the thickness direction, a DE membrane expands its area and reduces its thickness. This electromechanical behaviour of DE material has been widely studied into various application including actuators, sensors and generators [1-5]. Specially, basing on the fact that electric properties such as resistance, capacitance change in accordance with the external forces, the ability to sense its position, deformation or force of dielectric elastomer has also been investigated [6-9]. Recently, numerous works have been done, including the dynamic response of the dielectric elastomer for capacitive sensing [6], a method to monitor capacitance change of the dielectric elastomer actuator during its operation [7], the resistance of electrode changes when actuating [8] and a dielectric elastomer actuator with self-sensing capability [9]. Various methods to actuate and sense the deformation or the displacement of the dielectric elastomer actuator can be applied into the smart structures. Mechanical investigations may further guide the design and optimization of the soft active material and structures [10-13].

SENSING AND ACTUATING

This paper presents a dielectric elastomer structure with integrated function of actuating and sensing Fig.1. Working principal is established to explain the experimental results. And the numerical simulation is also conducted, which corresponds well with the experimental results. This work provides a new method to design and fabricate the dielectric elastomer structure with both actuating and sensing performances, which has a variety of potential applications such as prosthetic sensing and physical monitoring. There are 10 layers of dielectric elastomer in the structure. The layers which are black, blue, yellow represent electrode, VHB4905 membrane, VHB9473 membrane respectively. VHB4905 membrane is worked as driven muscles, whereas VHB9473 membrane is employed to protect electrode and to avoid direct contact with high voltage. Fibers which are tightly sandwiched between elastomer membrane and electrode are shown as the white circles in the schematic. The right part that contains fibers is the actuating module of the structure, and the left part is sensing module correspondingly. Since VHB membrane is extremely sticky, actuating module and sensing module can tightly laminated.

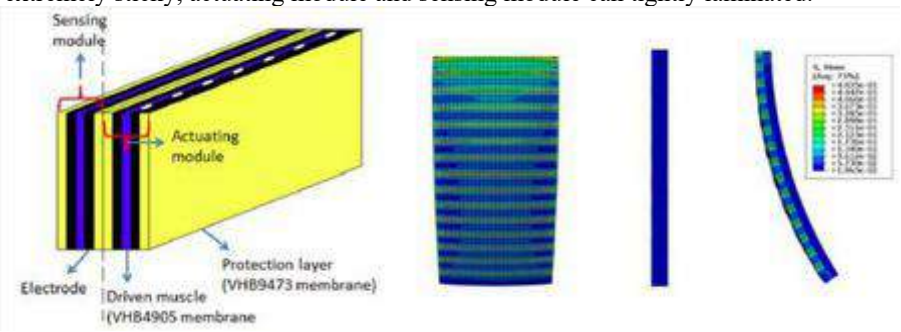

Figure 1. Images of the snap-through deformation process of the hydrogel structure

a) Corresponding author. Email: litiefeng@zju.edu.cn

ELECTRO-MECHANICAL INSTABILITY

The DE active structures such as inflated elastomeric balloon and bi-stable beam are quite promising in the application of soft robot as elastomeric actuators and artificial muscles. We carry out both experiment and modelling, focusing on the pre-stretch effect on non-linear behaviours of inflated elastomeric balloons. In the experiment, the pre-stretched elastomeric balloon is subjected to air pressure while the ends are fixed with rigid ring. The shape evolutions of the telastomeric balloons are illustrated. An analytical model based on continuum mechanics is developed to investigate the inflation behaviour of the tubular balloons, and the analytical results agree well with the experimental observation. Analysis shows that snap-through instabilities may happen during the inflation of t. Pre-stretch along the axis of the balloon can suppress instability during inflation and regulate the reaction force along the axial direction. In the buckled structure of DE membrane integrated with rigid frame, fibers can be embedded into the DE membrane and integrate together with the soft active structure to enhance the performances of the soft active device. We demonstrate the effects of fibers in the planar actuator. The long fibers are parallel distributed with fixed spacing in the perpendicular direction. We use nylon fishing lines as the fibers with 80 mm in length and 0.3 mm in diameter. We attach several fibers on one side of the pre-stretched membrane and then put another pre-stretched membrane on the fiber and make the fiber sandwiched between two membranes, and then exclude the air between the two membranes. The DE structure with multi-functions and electromechanical instabilities can be applied in the soft robot..

CONCLUSIONS

We have investigated soft active structures driven by dielectric elastomer possessing characteristics of snap-through actuation, integrated actuating and sensing. The performances of the smart structures are explored with both experiments and FEM simulations. Pre-stretch and structural stiffness play important role before the smart structure is applied with voltage. The buckling curvature will increase while the pre-stretch increases or the structural stiffness decreases. Fiber-reinforced dielectric elastomer structure with integrated function of actuating and sensing can also be combined in to the soft active structure as a functional device.The sensing module deforms by the bending of the DE structure and changes its capacitance. By measuring capacitance variation, we can monitor the deformation of the DE laminates in return. Experiments and FEM simulation have been conducted to investigate the electro-mechanical behaviours of the structure.

ACKNOWLEDGMENTS

This work is supported by the National Natural Science Foundation of China (Nos.11302190, 11572280, 11321202), Doctoral Fund of Ministry of Education of China, Qianjiang Talent Program D of Zhejiang Province, Research Foundation of Educational Commission of Zhejiang Province, and the Fundamental Research Funds for the Central Universities.

References

[1] Yoseph Bar-Cohen, "Electroactive Polymer (EAP) Actuators as Artificial Muscle: Reality, Potential and Challenges", *SPIE Press monograph*, 482, 2001.

[2] R. Pelrine, R. Kornbluh, Q. B. Pei, and J. Joseph, "High-speed electrically actuated elastomers with strain greater than 100%", *Science*, 287, 836, 2000.

[3] F. Carpi and D. De Rossi, "Contractile dielectric elastomer actuator with folded shape", *IEEE Trans. Dielectr. Electr. Insul.* 12, 835, 2005.

[4] G. Kofod, M. Paajanen, and S. Bauer, "Self-organized minimum-energy structures for dielectric elastomer actuators", *Applied Physics A: Materials Science & Processing*, 85,141, 2006.

[5] F. Carpi, G. Gallone, F. Galantini, and D. Rossi, "Silicone–poly(hexylthiophene) blends as elastomers with enhanced electromechanical transduction properties", *Adv. Funct. Mater.*, 18, 235–241, 2008.

[6] P. Sommer–larsen, J. Hooker, G. Kofod, K. West, M. Benslimane, P. Gravesen, "Response of dielectric elastomer actuators", *Proc. Smart Structures and Materials 2001: Electroactive Polymer Actuators and Devices(EAPAD)*, Vol. 4329, pp.157-163, 2001.

[7] K. M. Jung, K. J. Kim, H. R. Choi, "A Self-sensing Dielectric Elastomer Actuator", *Sensor and Actuator A*, published in electronic version, 2007.

[8] B. O'Brien, J. Thode, I.A. Anderson, E.P. Calius, E. Haemmerle and S. Xie, "Integrated extension sensor based on resistance and voltage measurement for a dielectric elastomer", *Proc. Smart Structures and Materials 2007: Electroactive Polymer Actuators and Devices(EAPAD)*, Vol. 6524, pp.6524-1–6524-15, 2007.

[9] Nguyen Huu Chuc, Doan Vu Thuy, Jonggil Park, Duksang Kim, Jachoon Koo, Youngkwan Lee, Jae-Do Namc and Hyouk Ryeol Choi, "A dielectric elastomer actuator with self-sensing capability ", *Proc. SPIE* Vol. 6927, 69270V, 2008.

[10] Xuanhe Zhao, Zhigang Suo, Method to analyze programmable deformation of dielectric elastomer layers. *Applied Physics Letters*, 93, 251902, 2008.

[11] T. Li, C. Keplinger, R. Baumgartner, S. Bauer, W. Yang, and Z. Suo, Giant voltage-induced deformation in dielectric elastomers near the verge of snap-through instability, J. *Mech. Phys. Solids* 61 2013, pp. 611–628.

[12] T. Li, Z. Zou, G. Mao, S. Qu, and M. Shi, Electromechanical bistable behavior of a novel dielectric elastomer actuator, *J. Appl. Mech.* 81 2014, 0410191.

[13] T. Li, W. Li, Z. Zou, Z. Hong, and S. Qu, Effects of stretching rate and size on the rupture of acrylic dielectric elastomer, *Int. J. Appl. Mech.* 2014.

ION-INDUCED SWELLING AND VOLUME PHASE TRANSITION OF POLYELECTROLYTE GELS

Yalin Yu, Chad M. Landis & Rui Huang[a]
Department of Aerospace Engineering & Engineering Mechanics, University of Texas, Austin, TX 78712, USA

Summary This paper presents a theoretical model for equilibrium swelling of polyelectrolyte gels immersed in ionic solutions. By varying the ion concentrations in the external solution, the polyelectrolyte gel may undergo a smooth transition in the swelling ratio or a discontinuous volume phase transition. The theoretical model is further extended for the cases with mixed solvents and compared closely with experiments.

INTRODUCTION

Polyelectrolytes are polymers that contain ionizable groups on the polymer chains. Immersed in an aqueous solution (e.g., water), the polymer network imbibes a significant amount of solvent and those ionizable groups dissociate into mobile charges (counter-ions) in the solvent and fixed charges on the polymer chains. As a result, a polyelectrolyte gel forms. Polyelectrolyte gels are sensitive to many stimuli, such as pH, temperature, ionic strength, electric field, and light. One of the most interesting phenomena is the volume phase transition of polyelectrolyte gels induced by various external stimuli. Instead of a smooth, continuous change of volume in response to a varying stimulus, a discontinuous, abrupt change of volume may occur at a critical condition, similar to the first-order phase transition. While the volume phase transition due to temperature change has been studied extensively, fewer studies have considered volume phase transition induced by the effect of salinity or ion concentration in the external solutions. Ohmine and Tanaka [1] observed in experiments that an ionized acrylamide gel underwent a discrete phase transition in equilibrium volume upon varying the salt concentration in an external solution. In this paper, we present a theoretical model that is capable of predicting equilibrium swelling of polyelectrolyte gels with both smooth and discrete transitions upon changing the ion concentration in external solutions.

THEORETICAL MODEL

Following Hong et al. [2], we write the free energy density of a polyelectrolyte gel as a function of the deformation gradient, the nominal electric displacement, and the nominal concentrations of the solvent and ions, including four parts due to stretching of the polymer network, mixing of the polymer and the solvent, mixing of the solvent and ions, and polarizing of the gel, respectively. It is assumed that the polymer network and the mobile particles (solvent molecules and ions) are incompressible at the molecular level, which is imposed as a kinematic constraint by using a Lagrange multiplier. The nominal electric field and the electrochemical potentials are then obtained from the free energy density function. To simplify calculations, we assume relatively low ion concentrations in the gel so that $J \approx 1 + vC^s$. The nominal concentrations of the ions in the gel can then be obtained explicitly as a function of the electrochemical potential and the volume swelling ratio J.

Next, by a Legendre transform, the free energy density of the gel is rewritten as a function of the deformation gradient, the nominal electric field, and the electrochemical potentials. The nominal stress in the gel is then obtained as the derivative of the free energy density function with respect to the deformation gradient, which includes an elastic part, an electrical part (Maxwell stress), and osmotic pressures of the solvent and ions. For homogeneous free swelling, the stress vanishes and the volume swelling ratio can be solved as a function of the chemical and electrochemical potentials.

When the gel reaches equilibrium with the external solution, the chemical potential of the solvent and electrochemical potentials of the ions in the gel equal to those in the external solution. We treat the external solution as an ionic liquid with a mixture of neutral solvent molecules (e.g., water) and positive/negative ions. The treatment is similar to that for polyelectrolyte gels, but the free energy density function contains only two parts, due to ion/solvent mixing and polarization. Assume an infinitely large reservoir such that the concentrations of the ions are fixed deep in the external solution (far away from the gel), where the electric potential is set to be zero and the solution is assumed to be electrically neutral and stress free. Under these conditions, the electrochemical potential for the ions is obtained as: $\mu^b = v\Pi_0 + kT\ln(vc_0^b)$, where c_0^b is the ion concentration in the external solution and $\Pi_0 = -kT\sum_b c_0^b$ is the osmotic pressure. Correspondingly, the chemical potential of the solvent is: $\mu^s = v\Pi_0$. Therefore, by changing the ion concentrations in the external solution, the chemical potential of solvent and the electrochemical potential of the ions change simultaneously, which leads to change of the equilibrium swelling of the gel.

RESULTS AND DISCUSSION

First consider a simple polyelectrolyte gel with two monovalent ions of opposite charges. The valence of the fixed charge is set to be -1. Let c_0 be the true concentration of the ions deep in the external solution. In this case, the electrical potential of

[a] Corresponding author. Email: ruihuang@mail.utexas.edu.

the gel (far away from the interface) can be obtained explicitly as a function of the volume swelling ratio (J) and the ion concentration. The equilibrium swelling ratio can then be solved by setting the stress to zero for free swelling. The result depends on two key parameters: the Flory-Huggins parameter χ and the nominal concentration of the fixed charge C_{fix}. Figure 1a shows the effect of χ for gels with $vC_{fix} = 0.02$ and $Nv = 0.001$. As the ion concentration changes in the external solution, three distinctive swelling behaviours of the polyelectrolyte gels can be identified: (i) a smooth transition when $\chi = 0.5$ or smaller (good solvents); (ii) a discontinuous volume phase transition when $\chi = 0.7$; and (iii) nearly no transition when $\chi = 0.9$ or larger (poor solvents). A phase diagram is constructed in Fig. 1b, showing that the discontinuous volume phase transition from the highly swollen phase to the collapsed phase occurs only within a narrow range of χ (around 0.7). This range depends on the fixed charge as shown in Fig. 1c. Interestingly, a minimum value of vC_{fix} is required for the discontinuous volume phase transition.

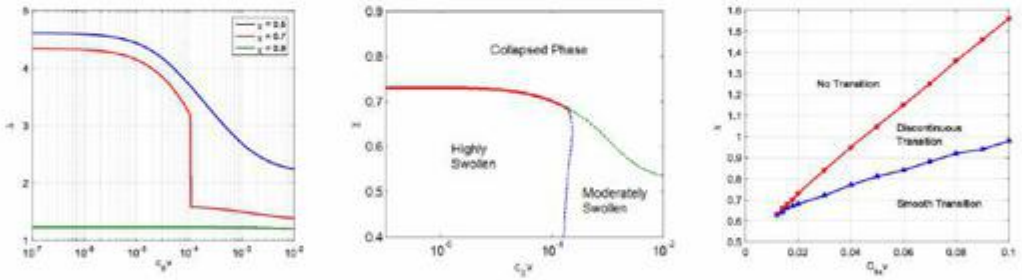

Figure 1. (a) Equilibrium swelling ratio as a function of ion concentration in the external solution; (b) A phase diagram; (c) Different transition behaviours in the two-parameter panel.

Next we take into account the effect of composition on the parameter χ by assuming $\chi = \chi_0 + \chi_1/J$. By varying the two parameters, χ_0 and χ_1, the equilibrium swelling of the gel may undergo a smooth or a discontinuous transition. In the experiments by Ohmine and Tanaka [1], partially ionized acrylamide gels with acrylic acid groups (–COOH) were immersed in a mixed solution of water, acetone, and salt with varying compositions. To compare with the experiments, we extend the model for a mixed solvent with two components (water and acetone) by using an effective interaction parameter that depends on the acetone concentration as: $\chi = \chi^a\varphi^a + \chi^b\varphi^b$. For the polyelectrolyte gel immersed in the mixed solution with NaCl, there are four types of mobile ions: H^+, OH^-, Na^+ and Cl^-. Deep in the external solution, the concentrations of Na^+ and Cl^- are identical and set by the salt concentration c_0. The concentrations of H^+ and OH^- are determined by pH, which is set to be 7. Under these conditions, the chemical and electrochemical potentials are all determined as a function of the salt concentration. Figure 2a shows the equilibrium swelling ratio of the gel as a function of NaCl concentration in the mixed solutions with different acetone concentrations. When the acetone concentration is low (0-40%), the equilibrium swelling ratio undergoes a smooth transition as the salt concentration changes. With relatively high acetone concentration (50-60%), a discontinuous volume phase transition occurs, whereas no swelling transition is observable for 70% acetone concentration. These results agree remarkably well with the experiments. To further test the model, we consider mixed solutions with $MgCl_2$ where the positive Mg^{2+} ions are not monovalent. In this case, the condition of electroneutrality leads to a more complicated relation between the ion concentrations in the gel and the electrical potential. Nevertheless, the equilibrium swelling ratio can be determined numerically by solving two coupled nonlinear algebraic equations. As shown in Fig. 2b, the result is qualitatively similar to Fig. 2a, but the discontinuous transition occurs at lower acetone concentrations (40-50%). In particular, for 50% acetone concentration, the critical salt concentration for the volume phase transition is about three orders of magnitude lower than that for the monovalent salt NaCl. This again agrees with the experiments.

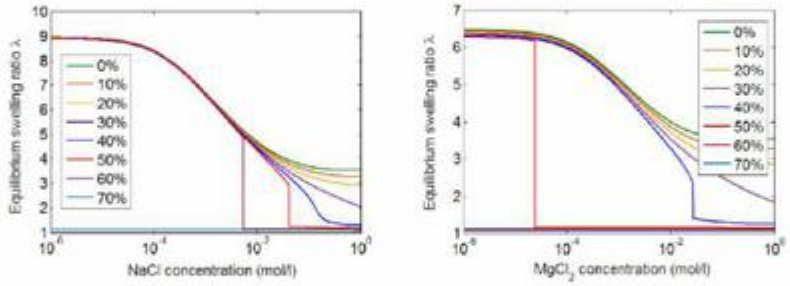

Figure 2. Equilibrium swelling ratio as a function of salt concentration in a mixed solution with (a) NaCl and (b) $MgCl_2$.

References

[1] Ohmine, I., Tanaka, T. , J. Chem. Phys. **77**, 5725-5729 (1982).

[2] Hong, W., Zhao, X., Suo, Z., Journal of the Mechanics and Physics of Solids **58**, 558-577 (2010).

COMBINED MODELING AND EXPERIMENTS OF POLYMERIC GELS

Claudio V. Di Leo[1] and Shawn A. Chester*[2]

[1]*School of Aerospace Engineering, Georgia Institute of Technology, Atlanta, Georgia, USA*
[2]*Mechanical Engineering, New Jersey Institute of Technology, Newark, New Jersey, USA*

Summary The literature on polymeric gels is burgeoning at a remarkable pace. However, the majority of the mechanics work has been directed toward modeling and computational aspects, and not nearly as much on validation. This work overviews recent research on a combined experimental and modeling effort on polymeric gels, from a mechanics based framework. This integrated approach leads to a data set useful to mechanicians to further refine those models found in the literature. Most importantly, it shows some serious faults in current modeling efforts.

INTRODUCTION

An elastomeric gel is no more than a polymer network swollen with a suitable solvent. Many gels can absorb large quantities of solvent, leading to a volumetric swelling far beyond its initial volume. This swelling allows for gels to be exploited in a variety of applications, including actuation and sensing in microfluidics, drug delivery and tissue engineering, and packers for sealing in oilfields. Correspondingly the literature has seen an explosion of interest in recent years for this class of materials (for brevity, see [2] and references therein). However, recent evidence indicates that current constitutive models may not be adequate in describing the real coupled deformation-diffusion behavior of gels [4].

The purpose of this work is to develop an integrated research approach that includes combined modeling and experiments of polymeric gels. This combined approach is used in order to fully characterize the coupled deformation-diffusion behavior of polymeric gels and understand the mechanisms that drive the material behavior.

MODELING AND EXPERIMENTS

For the modeling portion we closely follow our recently published work [1, 2] which is summarized here. We denote the solvent concentration per unit reference volume by c_R, and per unit current volume by c. We employ the decomposition

$$\mathbf{F} = \mathbf{F}^e\mathbf{F}^s, \tag{1}$$

of the deformation gradient into elastic and swelling parts, where $\mathbf{F}^s = (J^s)^{1/3}\,\mathbf{1}$, with $J^s = 1 + \Omega c_R$, is the swelling distortion, and Ω the molar volume of the solvent. Further, we define the polymer volume fraction $\phi = (1+\Omega c_R)^{-1}$, such that $\phi = 1$ is a fully dry polymer, and $\phi < 1$ is a swollen gel. We note that due to the decomposition (1), we have $\mathbf{B} = \phi^{-2/3}\mathbf{B}^e$ so that the state of stretch is composed of both swelling and elastic deformation. The final form of the Cauchy stress is given by

$$\mathbf{T} = J^{-1}\left[G\mathbf{B} - P\mathbf{1}\right], \tag{2}$$

where the shear modulus G is stretch dependent and of the form $G = G_0\zeta$. With $\zeta = \left(\frac{\lambda_L}{3\bar{\lambda}}\right)\mathcal{L}^{-1}\left(\frac{\bar{\lambda}}{\lambda_L}\right)$, and $\bar{\lambda} = \sqrt{\mathrm{Tr}\,\mathbf{B}/3}$, a scalar measure of the three-dimensional state of stretch, which includes both swelling and elastic stretching. Here $\mathcal{L}^{-1}$ is the inverse of the Langevin function given by $\mathcal{L}(\bullet) = \coth(\bullet) - 1/(\bullet)$. Also, G_0 is the initial shear modulus, and λ_L is the locking stretch. These two parameters are the only parameters required to fully characterize the "dry" mechanical response of the material.

Turning attention to the diffusion, the fluid flux is assumed isotropic and proportional to the gradient in chemical potential,

$$\mathbf{j} = -m\,\mathrm{grad}\mu, \quad \text{with} \quad m = \frac{Dc}{R\theta}, \quad \text{and} \quad \mu = \mu^0 + R\theta\left(\ln(1-\phi) + \phi + \chi\phi^2\right) - \Omega G_0\phi + \Omega P\phi. \tag{3}$$

Here, R is the gas constant, θ the absolute temperature, D the diffusivity which may be constitutively prescribed, and μ is the chemical potential. The key parameter in the chemical potential is χ, the interaction parameter (sometimes called the Flory parameter), which represents the dis-affinity between the solvent and the polymer network. The final form of diffusion of the fluid flux takes the form $\dot{\phi} = J\Omega\phi^2\mathrm{div}\mathbf{j}$.

To verify the constitutive forms, and obtain the material parameters appearing in the theory an experimental program was undertaken. Summarizing, the set of material properties to be determined are $\{G_0, \lambda_L, D, \chi\}$.

Dry tension

Dry tension tests, including loading and unloading, were carried out to determine the baseline "dry" material behavior. The tests were carried out quasi-statically at room temperature on flat dog-bone samples with a gauge section 0.25 in wide and 0.22 in thick. The axial deformation was measured using a non-contact digital image correlation system.

*Corresponding author. Email: shawn.a.chester@njit.edu

Figure 1a shows a few snapshots of the specimen in the virgin state, as well as the fully stretched ($\lambda = l/l_0 \approx 2.4$) state. Also, Figure 1b shows the measured behavior. Clearly from Figure 1b we can see that this material is essentially hyper-elastic with very little hysteresis or time dependence (not all results are shown here). Using the model described above, with $G_0 = 0.056$ MPa and $\lambda_L = 3.9$, the corresponding fit shown Figure 1b.

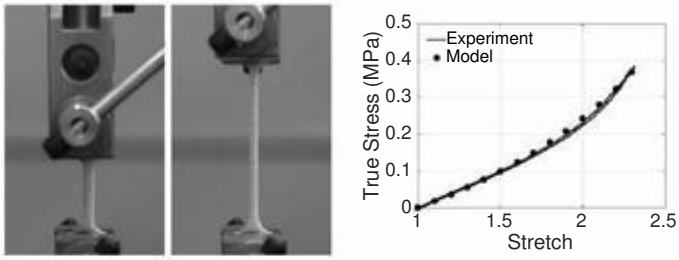

a) b)

Figure 1: Dry tension tests on vinylpolysiloxane. a) Virgin state and $\lambda = 2.4$. b) Measured true stress stretch response.

Free swelling

Free swelling experiments were performed to obtain the parameters associated with the equilibrium chemistry. Specifically, with the elastic parameters known, after equilibrium stress free swelling, we have $\mu = \mu^0$ everywhere in the body, which we may exploit to find χ. Assuming equilibrium conditions, we have $0 = \ln(1-\phi_e) + \phi_e + \chi\phi_e^2 + \frac{\Omega G_0}{R\theta}\left(\zeta\phi_e^{1/3} - \phi_e\right)$. Then, upon measuring the initial and swollen shapes, we may determine ϕ_e in this freely swollen equilibrium state. Figure 2a,b show the initial and swollen specimen, respectivly. Based on the change in geometry we find the dry volume is 7912.2 mm^3, the swollen volume 34050 mm^3, so that $J_e = 4.3035$, and $\phi_e = 1/J_e = 0.2324$, and correspondingly compute $\chi = 0.5682$ using $\Omega = 1.3162 \times 10^{-4}$ mol/m^3 for hexane.

Further experiments were performed on various compositions of PDMS swollen in Pentane. Fig. 2c shows the mechanical locking stretch λ_L, determined through dry tension tests, as well as the steady-state swelling stretch λ_{ss} determined from free swelling experiments as a function of PDSM composition. It is clear that a major discrepancy exists in these results as the measured swelling stretch is larger than the measured locking stretch, an unphysical condition.



a) b) c)

Figure 2: Free-swelling of vinylpolysiloxane in hexane: a) Initial dry body, and b) swollen body after 48 hours in hexane. c) Locking and swelling stretches for PDMS in pentane vs. gel composition.

Constrained Swelling

Obtaining repeatable data to measure the diffusivity is difficult, and still an open area of research. One method of obtaining data regarding the transient behavior of the polymer consists of swelling a gel against a platen and measuring the resulting force as a function of time. Results from such experiments are shown in Fig. 3 for PDMS of various compositions swollen in Pentane along with finite-element simulation results replicating the experiments. Clearly the currently used functional form for the diffusivity is incapable of capturing the correct, experimentally measured, transient and furthter consideration needs to be given to the constitutive form of the diffusivity D.

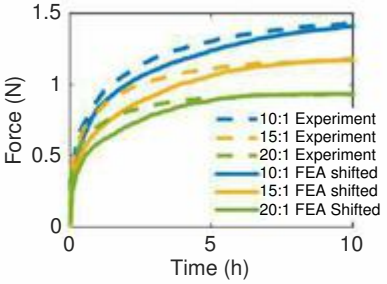

Figure 3: Constrained swelling force vs. time for PDMS swollen in pentane at various compositions.

CONCLUSIONS

We have initiated a combined experimental and modeling effort toward better understanding the behavior of polymer gels. Our results to date show that current constitutive models are in need of improvement. Work is underway to resolve the discrepancies between the experiments and models, and also examine other polymer/solvent systems.

References

[1] Chester, S. A., and Anand, L.: A coupled theory of fluid permeation and large deformations for elastomeric materials. Journal of the Mechanics and Physics of Solids 58:1879-1906, 2010.

[2] Chester, S. A., Di Leo, C. V., and Anand, L.: A finite element implementation of a coupled diffusion-deformation theory for elastomeric gels. International Journal of Solids and Structures 52:1-18, 2015.

[3] Doi, M. Introduction to Polymer Physics. Clarendon Press, 1996.

[4] Lou, Y., Robisson, A., Cai, S., and Suo, Z.: Swellable elastomers under constraint. Journal of Applied Physics 112:034906, 2012.

On the effects of cavitation in hydrogel–based structures

Paola Nardinocchi*[1] and Luciano Teresi[2]
[1]*Dipartimento di Ingegneria Strutturale e Geotecnica, Sapienza Università di Roma, 00184 Roma, ITALY*
[2]*Dipartimento di Matematica e Fisica, Università Roma Tre, 00146, Roma, ITALY*

Summary Cavitation is often observed in soft materials. Many studies focused on cavitation in elastomers, and more recently also in hydrogels, where drying–induced cavitation can determine fractures. In this paper, we investigate cavitation in hydrogel–based structures with the aim to highlight the physical principles which drive a few unique mechanisms in Nature world, which view cavitation as a tool to generate fast movements.

INTRODUCTION

Soft active materials are largely employed in Nature to realise mechanisms whose specific function is triggered by specific stimuli [1, 2]; they are also used to realize man–made devices (*actuators*), where deformations and displacements are triggered by a wide range of external stimuli such as electric field, pH, temperature, and solvent absorption [3, 4, 5, 6]. The effectiveness of these actuators critically depends on the capability of achieving prescribed changes in their shape and size and on the rate of changes. In particular, in gel–based actuators, the shape of the structures can be related to the spatial distribution of the solvent inside the gel, to the magnitude of the solvent uptake (refusal), and to the rate of solvent uptake (refusal) rate. Currently, several approaches to the shape control of swellable materials are being pursued, which involve materials in the form of thin non–homogeneous sheets realized through a controlled assembly of different gels which may be isotropic or anisotropic [10, 11, 12, 13].

The present study focus on cavitation in hydrogels as a tool to generate fast movements in hydrogel–based structures. The starting point is the observation of the cavitation–triggered catapult of fern sporangia, whose function is the realisation of a perfect dispersal mechanism. Therein, the key structural element is the *annulus*, which can be viewed as a curved beam composed by soft material organized in cells separated by stiffer walls. We start by modelling and implementing via a finite element code the mechano–chemical processes occurring in a mechanical analog of a single cell of the anulus: swelling, de–hydration, and building up of water tension up to a critical value corresponding to cavitation; and illustrates in the following the key idea behind our modelling through a simple toy problem.

A MECHANICAL ANALOG

The first step of our work, illustrated in the present abstract, refers to a mechano–chemical toy problem which can be easily solved, and is useful to illustrate the key idea behind our model. Our starting point is the multiphysics model presented and discussed in [14], where three different states of a gel body were introduced: the dry state $\mathcal{B}_d$, a swollen and stress–free state $\mathcal{B}_o$, and the actual state $\mathcal{B}_e$. Within a classical Flory–Rehner thermodynamic contex, the constitutive equation for the stress $\mathbf{S}_d$ at the dry configuration $\mathcal{B}_d$, from now on denoted as dry–reference stress, and the chemical potential μ are:

$$\mathbf{S}_d \;/\; G\mathbf{F}_d - p\mathbf{F}_d^{\star} \quad \text{and} \quad \mu \;/\; \mu\; J_d \qquad \Omega p\,, \text{ with } \mu\; J_d \;/\; RT\Big(\log\frac{J_d-1}{J_d} \quad \frac{1}{J_d} \quad \frac{\chi}{J_d^2}\Big)\,, \tag{.1}$$

being $\mathbf{F}_d$ the deformation gradient from $\mathcal{B}_d$ to $\mathcal{B}_e$ and $J_d \;/\; \det\mathbf{F}_d$; moreover, G (G / J/m^3), Ω (Ω / mol/m^3), R (R / J/Kmol), T (T / K), and χ are the shear modulus of the gel, the solvent molar volume, the universal gas constant, the temperature, and the Flory parameter, respectively. The swollen and stress–free state $\mathcal{B}_o$ is attained from $\mathcal{B}_d$ for $\mathbf{F}_d \;/\; \lambda_o\mathbf{I}$; in this case, it holds $G\mathbf{F}_o - p\mathbf{F}_o^{\star} \;/\; \mathbf{0}$ and $\mu \;/\; \mu\; J_o \qquad \Omega p \;/\; \mu_o$, with μ_o the value of the bath's chemical potential which completely determines the corresponding swelling ratio λ_o.

We consider a cubic gel whose freely swollen state $\mathcal{B}_o$ is a cube with sides of length L_o and faces anchored through linear elastic springs at a solid and permeable container (see figure 1 (left panel)); at $\mathcal{B}_o$ springs are relaxed. Due to a change in the chemical potential of the bath, from μ_o to μ_e, a further deformation process arises; the corresponding deformation gradient $\mathbf{F}$ from $\mathcal{B}_o$ to the actual state $\mathcal{B}_e$ is determined by $\mathbf{F} \;/\; \mathbf{F}_d\mathbf{F}_o^{-1}$. Depending on the boundary constraints, the latter deformation process can have different characteristics. In our toy problem, due to the uniformity of the elastic springs over the boundary, we assume that $\mathbf{F}$ can be represented as an isotropic deformation process of homogeneous intensity λ: $\mathbf{F} \;/\; \lambda\mathbf{I}$; we also assume that it is controlled by the chemical potential μ_e of the solvent's bath and by the stiffness κ_o of the boundary springs. The swollen–reference stress $\mathbf{S}$ corresponding to $\mathbf{F}$, the *push–forward* of the dry–reference stress $\mathbf{S}_d$,

$$\mathbf{S} \;/\; \frac{G}{J_o}\mathbf{F}\mathbf{F}_o\mathbf{F}_o^T - p\mathbf{F}^{\star}\,, \tag{.2}$$

*Corresponding author. Email: paola.nardinocchi@uniroma1.it

is homogeneous and the corresponding balance equations of forces prescribe that $\mathbf{S} \;/\; \sigma_e \mathbf{F}^\star$. The corresponding equation of chemical equilibrium prescribes that

$$\mu \;\lambda_o^3 \lambda^3 \qquad \Omega p \;/\; \mu_e \,. \tag{.3}$$

When the chemical potential is reduced, that is $\mu_e < \mu_o$, the gel expels solvent and shrinks, so reducing its volume (see figure 1 (left panel)); springs elongate, thus generating an uniform tension $\sigma_e \;/\; -k_o\,\varepsilon$ on the faces, being $/\; \varepsilon \;/\; \lambda - 1$.

With this, the hydrogel goes from a stress–free swollen state $\mathcal{B}_o$ (blue dot in figure 1 (right panel)) to a shrunken and under tension state $\mathcal{B}_e$, determined by the intersection between the coloured iso–chemical potential lines and the black straight line in figure 1 (right panel). The final state and the uniform tension'value depend on the new value μ_e of the chemical potential through the equations (.2)–(.3) which involve λ, and on the stiffness κ_o of the springs. When $\sigma \;/\; \sigma_{cr}$ (red dot on the critical iso–chemical potential line) the solvent inside the gel begins cavitation, hydrogel volume increases, and the spring shorten releasing the elastic energy previously stored.

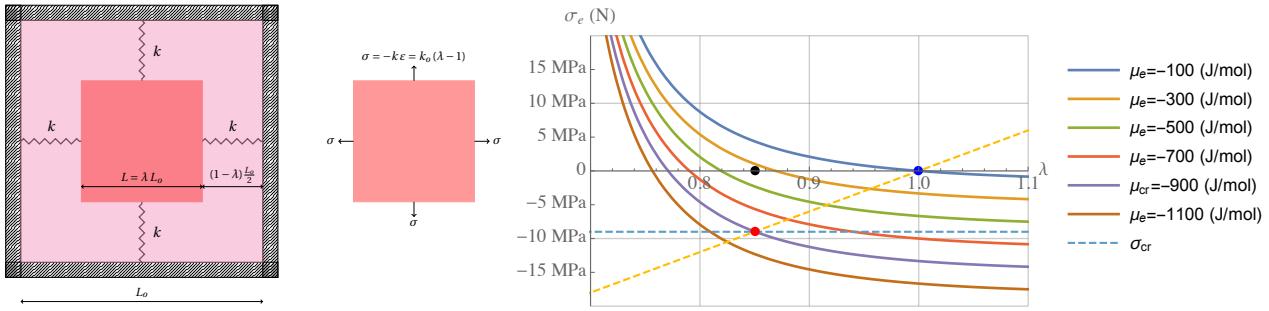

Figure 1: Left: We consider a cubic gel in a free swollen state (light red) whose faces are anchored through linear springs at a solid container (shaded frame). When the chemical potential is reduced, the gel expels solvent, reduces its volume (red square), and the springs elongate, thus generating a tension on the faces. Center: The de-swollen cube is under uniform tension whose value depends on the new value of the chemical potential through λ, and the stiffness of the spring. Right: Pressure-strain curves for different values of the external chemical potential μ_e. We consider a case for which the free-swollen reference (blue point) is realized with $\mu_e \;/\; -1$ (J/mol). By decreasing μ_e, the cube shrinks following the line $p \;/\; -k_o\,\varepsilon \;/\; k_o\;\lambda - 1$. When $\sigma \;/\; \sigma_{cr}$ (red point) the solvent inside the gel begins cavitation.

CONCLUSIONS

The toy problem illustrated above contains the key idea which is behind our investigation about the effects of cavitation on hydrogel–based systems. More complex deformation processes may occur when a series of units as the one shown in figure 1 is shown, and the contribution of the elastic walls surrounding the gel is not uniform.

References

[1] Burgert I., Fratzl P.: Actuation systems in plants as prototypes for bioinspired devices. Philos. Trans. R. Soc. A, 367:1541–1557, 2009.

[2] Noblin X., Rojas N.O., Westbrook J., Llorens C., Argentina M., Dumais J.: The Fern Sporangium: A Unique Catapult. Science 335, 1322, 2012.

[3] Dai S., Ravi P., Tam K.C.: Thermo– and photo–responsive polymeric systems. Soft Matter 5:2513–2533, 2009.

[4] Wallmersperger T., Keller K., Krplin B., Guenther M., Gerlach G.: Modeling and simulation of pH–sensitive hydrogels. Colloid Polym. Sci. 289:535–544, 2011.

[5] Kim J., Hanna J.A., Hayward R.C., Santangelo C.D.: Designing Responsive Buckled Surfaces by Halftone Gel Lithography. Soft Matter 8:2375–2381, 2012.

[6] Nardinocchi P., Pezzulla M.: Curled actuated shapes of ionic polymer metal composites strips. J. Appl. Phys. 113:22906, 2013.

[7] Wheeler T.D. and Stroock A.D.: Stability Limit of Liquid Water in Metastable Equilibrium with Subsaturated Vapors. Langmuir 25(13):7609–7622, 2009.

[8] Wang H., Cai S.: Drying-induced cavitation in a constrained hydrogel. Soft Matter 11(6):1058–1061, 2015.

[9] Wang H., Cai S.: Cavitation in a swollen elastomer constrained by a non–swellable shell. Journal of Applied Physics 117, 154901, 2015.

[10] Lucantonio A., Nardinocchi P., Pezzulla M.: Swelling-induced and controlled curving in layered gel beams. Proc. R. Soc. A 470:20140467, 2014.

[11] Nardinocchi P., Pezzulla M., Teresi L.: Anisotropic swelling of thin gel sheets. Soft Matter 11:1492, 2015.

[12] Nardinocchi P., Pezzulla M., Teresi L.: Steady and transient analysis of anisotropic swelling in fibered gels. Journal of Applied Physics 118:244904, 2015.

[13] Pezzulla M., Shillig S.A., Nardinocchi P., Holmes D.P.: Morphing of geometric composites via residual swelling. Soft Matter 11:5812, 2015.

[14] Lucantonio A., Nardinocchi P., Teresi L.: Transient analysis of swelling-induced large deformations in polymer gels. Journal of the Mechanics and Physics of Solids 61:205–218, 2013.

ON PRESSURE-DRIVEN FLOW THROUGH A GEL-FILLED CHANNEL

Fernando P. Duda *[1], Angela C. Souza[2], and Eliot Fried[3]
[1]*Programa de Engenharia Mecanica - COPPE, Universidade Federal do Rio de Janeiro, Rio de Janeiro, Brasil*
[2]*Programa de Engenharia Mecanica - TEM, Universidade Federal Fluminense, Niteroi, Brasil*
[3]*Mathematical Soft Matter Unit, Okinawa Institute of Science and Technology Graduate University, Okinawa, Japan*

Summary In this paper, we consider the problem of pressure-driven fluid flow through a gel-filled channel. This subject, which is relevant to many areas, has been addressed by several authors. Our interest here is to investigate how the network elastic response affects the solvent flow profile under steady-state conditions. We show that there is a class of elastic materials for which the flow profile is not affected by the applied pressure gradient. This class includes both neo-Hookean and Mooney materials but excludes Gent materials.

INTRODUCTION

A polymer gel is a two-component material composed of a cross-linked polymer network, which is usually described as an elastic, isotropic and incompressible solid, and an incompressible fluid, solvent for short, that permeates the interstices of the network. Such materials exhibit unusual and complex phenomena as a result of the coupling between large deformation and fluid permeation. In this paper, we study the problem of pressure-driven fluid flow through a gel-filled channel. This problem has been investigated by several authors to investigate, for instance, the phenomenon of pressure-induced channel formation (Cogan & Keener (2005)) . This work builds upon Duda, Souza & Fried (2010). Due to lack of space, details will be omitted.

PRELIMINARIES

Solvent permeation in polymer gels is governed by a set of equations comprised by the constraint of local volume preservation, which represents the conventional assumption that the solid and solvent are both incompressible, and a pair of field equations that describe the mechanical force and solvent content balances. These equations are conveniently organized as follows:

$$\det \mathbf{F} = \phi_0/\phi, \quad \operatorname{div} \mathbf{T} = \mathbf{0}, \quad \operatorname{div} (\upsilon \boldsymbol{\jmath} + \mathbf{v}) = 0. \tag{1}$$

Here and henceforth, $\mathbf{F}$ is the deformation gradient, ϕ_0 and ϕ are the polymer volume fractions in the reference and actual configurations, υ is the volume occupied by an individual solvent molecule, $\mathbf{T}$ is the Cauchy stress tensor, $\boldsymbol{\jmath}$ is the solvent flux per unit spatial area, and $\mathbf{v}$ is the network velocity field. External body forces, inertial effects, and solvent supply are neglected here.

From the constitutive point of view, the theory is fully specified by the response functions $\hat{\psi}$ and $\hat{\mathbf{M}}_s$ determining the free energy density ψ and the mobility tensor $\mathbf{M}_s$. Hereafter we suppose that $\hat{\psi}$ incorporates three contributions: the energy of the "unmixed" pure solvent; the isotropic elastic energy due to network deformation; and the energy of mixing. Invoking the Frenkel–Flory–Rehner hypothesis, we assume that the latter two contributions are additive and separable. As for the mobility, we assume a concentration-depedent isotropic response. It then follows that

$$\hat{\psi}(\mathbf{F}, c) = \mu_0 c + \hat{\psi}_e(I_1, I_2) + \hat{\psi}_m(c), \quad \mathbf{M}_s = \hat{m}(c)\mathbf{I}, \quad \hat{m}(c) > 0, \tag{2}$$

where μ_0 is a reference chemical potential, $c = (\det \mathbf{F} - \phi_0)/\upsilon$ is the number of solvent molecules per unit reference volume, and $I_1 = \operatorname{tr} \mathbf{B}$ and $I_2 = (I_1^2 - \operatorname{tr} \mathbf{B}^2)/2$ are the first and second principal invariants of the left Cauchy-Green tensor $\mathbf{B} = \mathbf{F}\mathbf{F}^\top$. Notice that both $\hat{\psi}_m$ and $\hat{m}$ can be viewed as a function of ϕ or $I_3 = \det \mathbf{B}$, the third invariant of $\mathbf{B}$. With these constitutive choices, it can be shown that $\mathbf{T}$ and $\boldsymbol{\jmath}$ can be written as

$$\mathbf{T} = \mathbf{T}_{\mathrm{n}} - p\mathbf{I}, \quad \boldsymbol{\jmath} = -\upsilon \hat{m}(c) \operatorname{grad} p \tag{3}$$

where

$$\mathbf{T}_{\mathrm{n}} = \beta_0 \mathbf{I} + \beta_1 \mathbf{B} + \beta_{-1} \mathbf{B}^{-1} - \pi \mathbf{I}, \quad \pi = -(\partial \hat{\psi}_m / \partial c)/v, \tag{4}$$

and

$$\beta_0 = 2I_2\alpha_2/\sqrt{I_3}, \quad \beta_1 = 2\alpha_1/\sqrt{I_3}, \quad \beta_{-1} = -2\sqrt{I_3}\alpha_2, \tag{5}$$

with $\alpha_1 = \partial \hat{\psi}_e / \partial I_1$ and $\alpha_2 = \partial \hat{\psi}_e / \partial I_2$. The quantities p and π are often called the fluid and osmotic pressures (e.g. Doi (2013)). Thus, the total Cauchy stress $\mathbf{T}$ results from two contributions, one due to the network, $\mathbf{T}_{\mathrm{n}}$, and other due to the solvent, $-p\mathbf{I}$. By its turn, the network stress arises from network elasticity and the osmotic pressure.

*Corresponding author. Email: duda@mecanica.coppe.ufrj.br

PRESSURE-DRIVEN FLOW THROUGH A GEL-FILLED CHANNEL

Consider the space between two infinitely long parallel plates separated by a gap $2d$ and completely filled by a gel which is fixed to and impermeable at the plates. We introduce a Cartesian coordinate system with the x-axis chosen parallel to the flow, the y-axis orthogonal to the plates, and z-axis orthogonal to the (x, y)-plane. We take the plates to be located at $y = 0$ and $y = 2d$. Suppose that the gel is in a stress-free state with polymer volume fraction constant and equal to ϕ_0. Then, a pressure gradient a is applied causing the solvent to flow through the gel. Our interest here is to investigate the influence of the gel properties on the characteristics this flow under steady-state conditions.

Specifically, we suppose that the pressure p is given up to an arbitrary and constant pressure p_0, that is,

$$p(x, y) = -ax + p_0, \tag{6}$$

with the constant a given. Taking $(1)_3$ into account, this implies that the x-component of the solvent flux $\boldsymbol{\jmath}$ is given by $j_x = \hat{m}(\phi)a$, whereas the remaining components vanish. Since the the solvent flux is fully characterized by j_x, its characteristics depend on the material function $\hat{m}$ and the polymer fraction distribution ϕ, which needs to be determined by invoking the interaction between mechanics and permeation. This issue is discussed in what follows.

We begin by assuming the gel undergoes a special time-independent deformation in which the spatial (x, y, z) and referential (X, Y, Z) coordinates of a gel particle are related by $X = x + f(y)$, with f symmetric with respect to the central line between the two plates, $Y = g(y)$, and $Z = z$. Since the gel is fixed to the plates, the functions f and g must obey the boundary conditions $f(0) = f(2d) = 0$, $g(0) = 0$, and $g(2d) = 2d$. A simple calculation shows that the deformation gradient $\mathbf{F}$ can be viewed as the result of the superimposition of an uniaxial extension with stretch $\eta = 1/g'$ on a simple shear with amount $\gamma := -f'/g'$. In this case, the incompressibility constraint imposes that $\phi = \phi_0/\eta$ which in turn yields that ϕ can depend on y only. This implies, along with the fact that $\mathbf{v} = \mathbf{0}$ and that j_x is the only non-null component of $\boldsymbol{\jmath}$, that the solvent content balance $(1)_3$ is trivially satisfied in the case under consideration. Further, as a consequence of the boundary condition on g, it is easy to see that η must satisfy the condition

$$2d = \int_0^{2d} (1/\eta(y))\,\mathrm{d}y. \tag{7}$$

We now observe that the mechanical force balance $(1)_2$ can be written as $\operatorname{div}\mathbf{T}_{\mathrm{n}} = \operatorname{grad} p$ which, under the conditions discussed in this section, implies the following equations for the network shear and normal stresses τ^{n}_{xy} and σ^{n}_{y}:

$$\tau^{\mathrm{n}}_{xy}(\gamma(y), \eta(y)) = -a(y - d), \quad \sigma^{\mathrm{n}}_{y}(\gamma(y), \eta(y)) = k, \tag{8}$$

where k is constant,

$$\tau^{\mathrm{n}}_{xy}(\gamma, \eta) = 2\gamma(\alpha_1(I_1, I_2) + \alpha_2(I_1, I_2)), \quad \sigma^{\mathrm{n}}_{y}(\gamma, \eta) = 2\eta(\alpha_1(I_1, I_2) + 2\alpha_2(I_1, I_2)) - \pi(\eta), \tag{9}$$

$I_1 = 2 + \gamma^2 + \eta^2$, and $I_2 = 1 + \gamma^2 + 2\eta^2$.

The problem under investigation here consists in solving (7) and (8) for $\gamma(y)$, $\eta(y)$ and k. Once this problem is solved, ϕ is obtained via the relation $\phi = \phi_0/\eta$ and the solvent flow via $j_x = \hat{m}(\phi)a$. The main results are as follows. When a pressure gradient is applied, the shear stress τ^{n}_{xy} is developed in the network to ensure mechanical equilibrium. This stress is accompanied by the amount of shear γ, the determination of which requires the knowledge of the"shear modulus" $2(\alpha_1 + \alpha_2)$. This in turn is a function of γ and η through I_1 and I_2. On the other hand, the polymer volume fraction ϕ is obtained by using $\phi = \phi_0/\eta$, with η being obtained by solving $(8)_2$. This equation does not involve γ wherever $\alpha_1 + 2\alpha_2$ is constant. For this class of materials, it is immediate to see that the polymer volume fraction ϕ, and hence the flow profile, is not affected by the pressure gradient a. A simple calculation shows that both neo-Hookean and Mooney elastic materials belong to this class of materials, whereas Gent elastic materials do not.

CONCLUSIONS

We have shown that the shear stress τ^{n}_{xy} is a function of the pressure gradient a. Whether the same conclusion applies or not to the normal stress σ^{n}_{y} depends on the elastic response. When it does not apply, the polymer volume fraction, and hence the flow profile, is not affected by the pressure gradient. This is the case for both neo-Hookean and Mooney elastic materials.

References

[1] Duda F.P., Souza A.C., Fried E.: A theory for species migration in a finitely strained solid with application to polymer network swelling. J. Mech Phy Sol 58:515-529, 2010.

[2] Cogan N.G., Keener J.P.: Channel formation in gels. SIAM J.Appl Math 65:1839-1854, 2005.

[3] Doi M.: Soft Matter Physics. Oxford University Press, 2013.

ELASTOCAPILLARY SWELLING: WHEN COALESCED STRUCTURES CURL APART

P.-T. Brun*[1], Douglas P. Homes [2], Anupam Pandey[3], and Suzie Protière[4]
[1]*Department of Mathematics, Massachusetts Institute of Technology, Cambridge, Massachusetts, USA*
[2]*Department of Mechanical Engineering, Boston University, Massachusetts, USA*
[3]*Physics of Fluids Group, University of Twente, Enschede, NL*
[4]*IJLRA-CNRS, Université Pierre et Marie Curie, Paris, FR*

Summary We consider the elastocapillary rise between swellable structures using a favorable solvent. We study the elastocapillary rise and subsequent swelling–induced bending, and characterize the dynamic deformations and resulting equilibrium configurations for various beam geometries. Our analysis highlights the importance of two characteristic length scales, and uses these lengths to predict both the elastocapillary rise and the critical curvature for peeling. We predict the transition between coalescence dominated beams and bending dominated beams using a balance of bending, stretching, and surface energies, and use a relaxed constraint on Euler's elastica to describe the fluid ratcheting.

INTRODUCTION

Fluid-structure interactions occur across many length scales within synthetic and biological systems. At large scales, inertial flows and fluid weight can cause substantial structural deformations, while at small length scales, surface forces may dominate a material's deformation. In addition to the forces that a fluid exerts externally onto a flexible structure, the diffusion of a favorable solvent into the material's elastic network can cause substantial swelling-induced deformations. Balancing the relevant energies in each problem leads to an elastocapillary length scale [1, 2], beyond which the fluid's surface tension will dramatically deform it, and an elastoswelling length scale, beyond which swelling by the fluid will cause significant bending. Capillary rise is a classical problem dating back to Leonardo da Vinci, and the description of the diffusive dynamics of the wetting front is attributed to Bell & Cameron, Lucas, and Washburn. The coupled problem of capillary rise between flexible sheets has received attention rather recently [1], with consideration given to the static equilibrium shapes [3] and dynamic imbibition [4, 5, 6] from a fluid bath and fluid droplets. Study of the equilibrium swelling of rubber has classical ties to polymer physics, and its theoretical and experimental origins begin with Flory & Rehner and Treloar. Recent work has focused on the dynamic, swelling-induced deformations that occur when a fluid swells a structure in a non-uniform manner, causing bending [7]. The coupled problem of capillary rise between swellable, flexible structures is new to our knowledge, yet is relevant due to the flexibility and porosity of biological tissues, microfabricated structures, and permeable membranes. In this work, we will study the elastocapillary rise between flexible, swellable sheets to study the dynamic deformations that result from these competing phenomena.

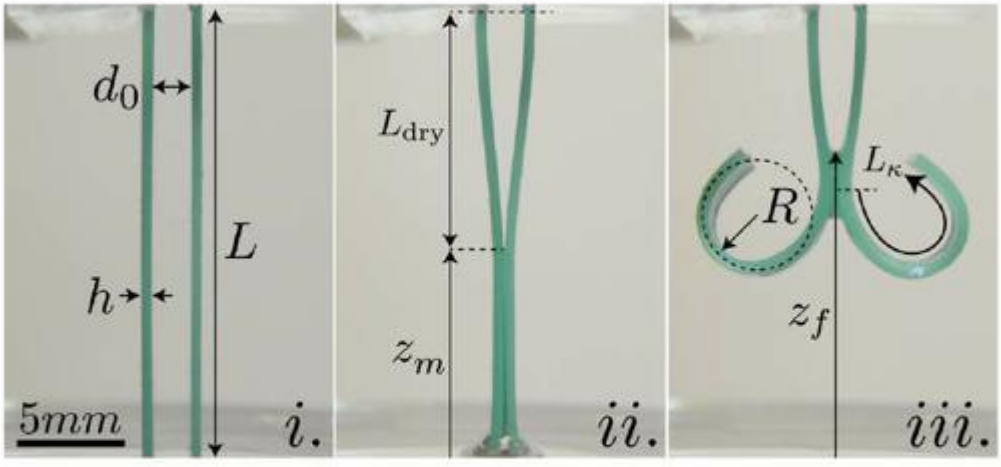

Figure 1: Images of two flexible beams deforming initially due to capillary rise (ii), and then subsequently due to swelling–induced bending (iii).

*Corresponding author. Email: ptbrun@mit.edu

EXPERIMENTS

Two polyvinylsiloxane (PVS, Zhermack Elite Double 22) elastic beams with a Young's modulus E=0.884 MPa, and rectangular cross sections of length L, width b, and thickness h are separated by a distance d_0, clamped at the top, and hung vertically in a gravitational field. We varied the length L from 15mm-24 mm, the initial gap d_0 from 1.2mm-4.9 mm, kept the width constant at b=3.5 mm for all experiments, and studied two thicknesses h=0.5 mm and h=0.8 mm. The beams are then lowered until the tips contact a bath of silicone oil (ν / 5 cSt, Sigma Aldrich). Capillary action causes the fluid to rise between the two beams, and the flexibility of the elastic beams enable the capillary pressure from the silicone oil to bend the structures until they coalesce. Silicone oil is a favorable solvent for these silicone rubber beams, so the fluid diffuses through the beam's thickness and swells the elastic network in a nonhomogenous manner. This nonhomogenous swelling causes the beams to bend away from each other [7]. Once the beam's curvature increases beyond some critical point, the deformation is enough to cause separation with the fluid bath, and the swelling-induced bending continues until fluid has permeated through half the beam's thickness. Over the course of this process a volume of fluid is transporting upwards in a ratcheting fashion (Fig1-iii). At long times the beams relax back to their initially straight configuration, and this process repeats itself.

DISCUSSION

In our experiments, E, ν and the surface tension γ are constant, leaving the geometric parameters L, h, and d_0 as our independent variables. By rescaling some of our experimental results by the characteristic length scales in this problem, we gain some insight into the underlying mechanics. First, we can split the elastocapillary rise between swellable beams into two parts by recognizing that the predominant forces act in opposing ways to deform the beam - elastocapillarity bends the beams together, and swelling curls the beams away from each other. The elastocapillary deformation is dominant until the beams peel from the surface of the fluid.

Capillary rise between flexible beams comes from a competition between the force per unit area required to bend the structure and the capillary pressure exerted by the wetting fluid. In this context, minimizing the total energy of this system with respect to the dry length gives [1]: L_{dry} / $\left(\frac{9}{2}\right)^{1/4}\sqrt[4]{d_0\ell_{ec}}$, where a characteristic elastocapillary length scale ℓ_{ec} / $\sqrt{B/\gamma}$ is introduced. The elastocapillary characteristic length scale also arises in the case of a naturally flat flexible sheet in contact with a wetted cylinder [2]. Here, the situation is reversed as the fluid's surface tension exerts a force that tries to flatten a beam with a swelling–induced natural curvature κ_b / R^{-1}. The result is the same – the coalesced beams will curl apart when the natural curvature reaches a critical value $R_c \propto \ell_{ec}$.

The short time dynamics of our experiments are dominated by capillary rise. At longer times, the swelling–induced bending becomes the main form of deformation. If capillary rise occurs, two general modes of deformation are observed: 1.) elastocapillary coalescence is dominant, and bending is localized near the bottom of beams, or 2.) swelling–induced bending is dominant, and the beams peel apart. We measured the maximum radius of curvature R_c that the beams reached while completely in contact the fluid bath, and observed that above a critical curvature the beams spontaneously peeled away from the fluid surface. The corresponding critical radius of curvature is on the order of ℓ_{ec}. Finally, we rationalize the ratcheting of the fluid integrating using Euler's Elastica equations with the appropriate set of boundary conditions, thereby revealing the energy landscape underpinning the fluid's motion.

In conclusion, we note that the deformations are dramatically different from those observed during traditional elastocapillary rise, and present a rich framework for studying coupled problems with multiple characteristic length and time scales. Our scaling analysis appears to capture some of the underlying mechanics, but we expect that a more robust theoretical approach will be necessary to capture the interplay between wetting, adhesion, and swelling. There is much to be done experimentally as well – in this work the silicone oil swells at a fairly slow rate, and both the solvent and elastomer can be changed to see enhancements in the swelling dynamics and the magnitude of deformation. Preliminary results on increasing the beam's width indicate that out–of–plane twisting can occur, in addition to the in–plane deformations discussed here. It is likely that swelling occurs in various elastocapillary environments, and while similar deformations may not be observed, confinement could lead to unexpected residual stresses, and localized deformations.

References

[1] J. Bico, B. Roman, L Moulin, and A Boudaoud. Elastocapillary coalescence in wet hair. *Nature*, page 690, 2004.

[2] B. Roman and J. Bico. Elasto-capillarity: deforming an elastic structure with a liquid droplet. *Journal of Physics: Condensed Matter*, 22(49):493101, 2010.

[3] H.-Y. Kim and L. Mahadevan. Capillary rise between elastic sheets. *Journal of Fluid Mechanics*, 548:141–150, February 2006.

[4] C. Duprat, J M Aristoff, and H.A. Stone. Dynamics of elastocapillary rise. *Journal of Fluid Mechanics*, 679:641–654, 2011.

[5] J. M. Aristoff, Camille Duprat, and H. A. Stone. Elastocapillary Imbibition. *International Journal of Non-Linear Mechanics*, 46(4):648–656, May 2011.

[6] C. Duprat, S. Protière, A. Y. Beebe, and H.A. Stone. Wetting of flexible fibre arrays. *Nature*, 482(7386):510–513, 2012.

[7] D. P. Holmes, M. Roché, T. Sinha, and H.A. Stone. Bending and twisting of soft materials by non-homogenous swelling. *Soft Matter*, 7(11):5188, 2011.

HIGHLY STRETCHABLE DOUBLE-NETWORK COMPOSITE

Xiangchao Feng, Zhuo Ma, Jonathan V. MacArthur & Wei Hong [a)]
Department of Aerospace Engineering, Iowa State University, Ames, Iowa

Summary This paper presents the manufacturing and testing results of a soft composite film, consisting of stacked layers of fabric mesh and 3M VHB tapes. The mechanical testing results show that the strength and toughness of the composite is highly dependent on the composition, and in certain range, the composite exhibits much higher mechanical strength and toughness compared with the base materials. The toughening mechanism of the composite is believed to be similar to that in the well-known double-network hydrogels [1]. A 1D shear-lag model is developed to illustrate the damage-distribution toughening mechanism of the composite. The prediction of the model agrees well with the measured properties of the composite in different compositions.

INTRODUCTION

Double-network (DN) hydrogels have drawn much attention as a soft material having both high mechanical strength and toughness, while containing up to 90% of water [1]. It consists of two interpenetrating polymer networks: one consisting of relatively short and stiff chains (the 1st network) and the other with much longer and initially coiled chains (the 2nd network). The origin of strength and toughness has been attributed to the energy dissipation in the irreversible structural change during deformation, induced by the partial damage of the 1st network [2, 3]. Inspired by the structure and working mechanism of DN gels, a highly stretchable soft composite was designed and fabricated. The experimental samples were made by stacking VHB acrylic tapes and layers of fabric mesh. The two constituents serve the same purpose as the two networks in a DN gel: the stiff but brittle mesh provides the high strength as the 1st network of a DN gel, and the soft but stretchable VHB tape serves as the ductile substrate, just like the 2nd network. The two materials were well-bonded initially, but exhibit significant sliding after the fracture and fragmentation of the mesh, which enables distributed partial damage in the mesh. After optimization, the DN composite is as strong as the mesh, and at the same time as stretchable as the VHB tape. With the energy dissipation mechanism similar to that in the DN gels, the DN composite has a toughness at least one order of magnitude higher than either of the base materials.

EXPERIMENTATION

The samples were prepared by stacking nylon fabric mesh with hexagonal grids alternatingly with VHB acrylic tape 4910 (3M Co.). The interlayer bonding is due entirely to the adhesion of the VHB tape. Unless otherwise stated, each sample was cut into rectangular shapes of width 25mm and height 30mm (gauge length between grips). As the mesh has negligible thickness compared to the tapes (~1mm thick), the sample thickness is approximately the total thickness of the VHB tapes. The mechanical tests were carried out over an Instron 5960 dual column testing system. The nominal stress was calculated by dividing the force data by the original cross-sectional area of the sample (i.e. that of the VHB tapes).

RESULTS AND DISCUSSION

As shown by the snapshots C-F in Fig.1a, the DN composite exhibits stable necking during uniaxial tension, just as DN hydrogels [1]. The necking zone corresponds to the area of partially damaged fabric mesh, as shown by the enlarged picture in Fig.1b. After partial damage in the mesh, the load is carried locally by the much softer tape with large deformation. Due to the ductility of the tape, the subsequent step is the fracture of the mesh in other areas, instead of the rupture of the tape. Similar as in a DN gel [3], the propagation of the partial damage zone (necking) corresponds to the stress plateau on the loading curve, as shown by Fig.1a. It is believed that such a damage-distribution mechanism is the key to the toughness of the DN composite as well as the DN gels [2]. This toughening mechanism and the stress-strain behavior are rationalized by the following 1D model.

Experimental observations suggested significant sliding between the mesh and the VHB tape in the partially damaged area, as shown by Fig. 1b. Due to the sliding, a shear stress is present between the mesh and the tape, which transfers the axial load gradually between the two layers. For simplicity, we approximate this interaction by a shear-lag model with constant shear stress τ. Using the shear lag model, the effective stress-stretch curve of the composite is reconstructed theoretically, as in Fig. 2b, with the material parameters extracted from independent experiments on the base materials. The deformation and damage process of the DN composite can be divided into three stages. In stage I, prior to any damage, the behavior of the composite is close to linear elastic, with the stiffness mainly given by the mesh. At a critical stretch, the damage in the mesh initiates, and the stress plateaus at the value

$$s \approx \frac{f^*}{H}\left(1+\frac{3\mu H}{k}\right), \tag{1}$$

[a)] Corresponding author. Email: whong@iastate.edu

where k is the effective tensile stiffness of the mesh, H the original thickness of the tape, μ the initial shear modulus of the VHB tape, and f^* the tensile strength of the mesh layer. The monotonic increasing curve in stage III is governed by the behavior of the tape layer, and the stress is bounded by a value set by the strength of the tape.

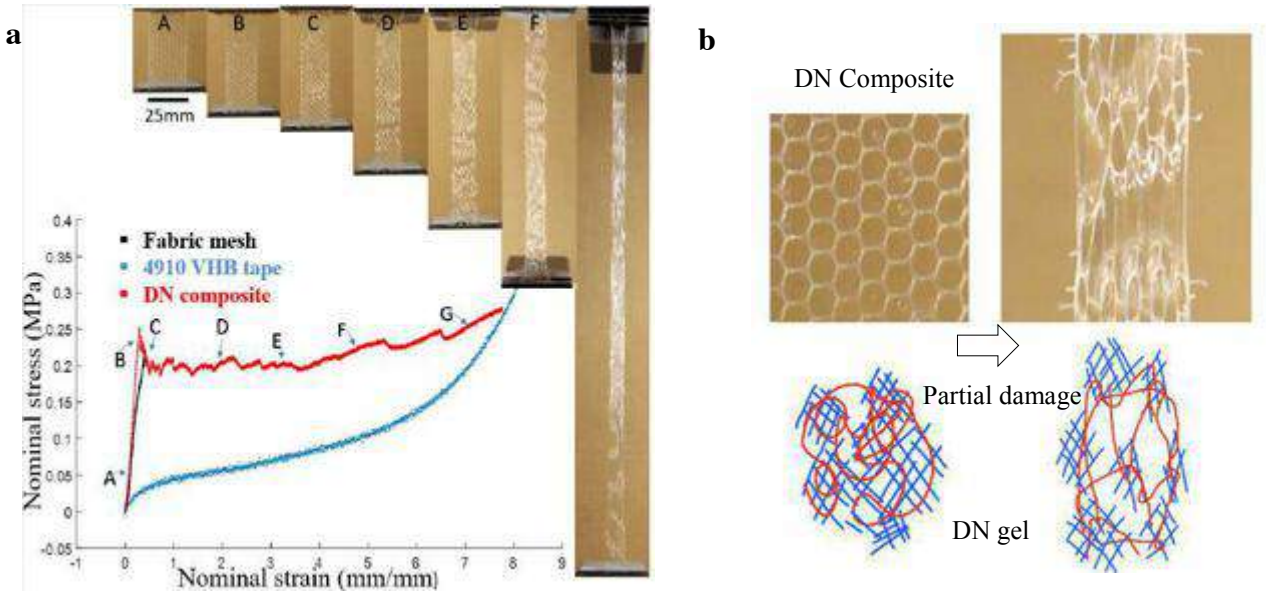

Fig 1. (a) Stress-strain curves of a VHB tape, a fabric mesh, and the DN composite with 1 layer of mesh and 2 layers of tape. For comparison, the nominal stress of the mesh is normalized by the same cross-sectional area as the DN composite. The insets (A-F) are snapshots of the sample correspond to the specific points along the loading curves. (b) Comparison between the undamaged and partially damage zones in the DN composite, and a similar mechanism in DN gels, after Ref. [2].

Comparing to the experiment results in Fig. 2a, the agreement between the shear lag model and experiments is reasonably well.

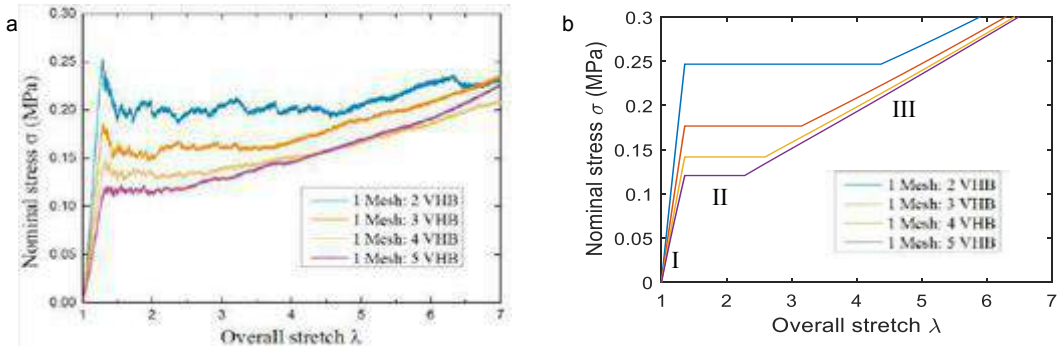

Fig 2. (a) Nominal stress-stretch curve of the DN composite at various compositions. (b) Theoretical prediction by considering the interaction in the sliding zone with a shear-lag model. The four curves have the same composition as the corresponding ones on (a). Material parameters are extracted from independent experiments on base materials.

CONCLUSIONS

Using a fabric mesh and a VHB acrylic tape, a soft but highly stretchable DN composite is manufactured. The DN composite follows the same damage-distribution and toughening mechanisms as in the well-known DN hydrogels. The DN composite is as strong as the mesh, as stretchable as the tape, and much tougher than both materials. The DN composite exhibit stable necking as the DN gels. By using a simple shear lag model to capture the finite interlayer sliding, a theory is developed and its prediction in the stress-strain behaviour agrees well with the experiments. On the other hand, the DN composite itself may be regarded as a macroscopic model for the study of DN hydrogels.

References

[1] Gong, J.P., Katsuyama, Y., Kurokawa, T. and Osada, Y., 2003. Double-network hydrogels with extremely high mechanical strength. *Advanced Materials*, *15*(14), pp.1155-1158.

[2] Gong, J.P., 2010. Why are double network hydrogels so tough? *Soft Matter*, *6*(12), pp.2583-2590.

[3] Wang, X. and Hong, W., 2011. Pseudo-elasticity of a double network gel. *Soft Matter*, *7*(18), pp.8576-8581.

COMPUTATIONAL MODELLING OF LIGHT-SWITCHABLE SURFACE TOPOGRAHIES USING LIQUID CRYSTAL POLYMERS

Ling Liu & Patrick R. Onck*
Zernike Institute for Advanced Materials, University of Groningen, Groningen, The Netherlands

Summary Liquid crystal (LC) glassy polymers co-polymerized with azobenzenes respond to ultra-violet (UV) light by undergoing anisotropic dimensional changes. Such a light-induced mechanical response can be used to generate topographical deformations when LC films are fixed to rigid substrates. Various topographical changes, dynamically controlled by light, can be produced by controlling the internal distribution of the average orientation of the liquid crystal molecules. In this presentation, we review our recent simulation results of light responsive topographical transformations of LC polydomain coatings [1].

LIGHT RESPONSIVE SURFACES

Switchable surface topographies enable many potential applications in manipulating friction and adhesion in the design of robotics and human-interactive haptics. In addition, the control of small-scale surface roughness can alter the effective hydrophobicity and thus the wetting properties. Light-driven actuations are preferable over thermal and electrically stimulations, because there is no need to build surrounding heating devices or electrodes. Photo-responsive systems are particularly advantageous in cases where remote control and localized actuation are desired.

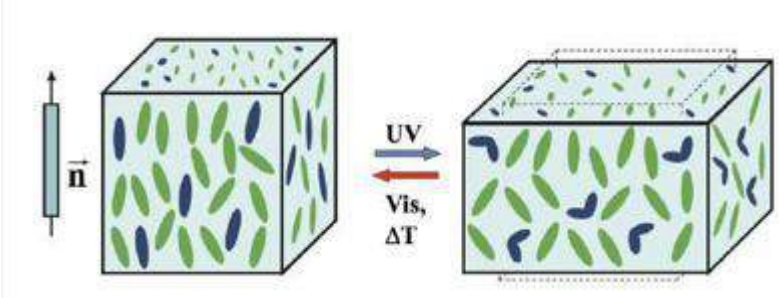

Figure 1: A 3D schematic representing the photo-physics and opto-mechanical response of azo-LC polymers under UV illumination. UV-triggered isomerizations of the embedded azobenzene molecules (blue) decrease the orientational order of the neighboring LC molecules (green) and results in a contraction along the director ($\vec{n}$) and expansions along the two perpendicular directions. Isomerization from trans (straight) to cis (bent) is driven by UV-light and the back-isomerization is driven by visible light and temperature.

Liquid crystal (LC) polymers can respond to ultra-violet (UV) light in the presence of co-polymerized azobenzene molecules [2]. As schematically shown in Fig. 1, triggered by UV-light, conformational changes from the natural trans state azobenzene (rod-like) to the bent-like metastable cis state decreases the orientational order of the liquid crystal network. These changes lead to a density decrease and a spontaneous contraction along the common direction of the LC moieties, i.e., the director, and expansions along the two perpendicular directions [3]. If LC films are fixed to rigid substrates they are able to produce surface topographical changes because their in-plane deformations are suppressed and the density changes manifest themselves as height variations. LC coatings with a spatially pre-designed patterning of the director distribution were recently constructed, which generates reversible protrusions and corrugations under UV illumination [4]. This switchable surface topography can be utilized to dynamically control the coating's friction properties [5].

CMPUTATIONAL MODEL AND RESULTS

In order to understand the underlying actuation mechanisms and to build a tool for design and optimization, a numerical model has been developed to simulate the light-induced surface topography changes of various LC coatings. Using the model, we study the dependencies of the generated surface roughness on the material properties and geometric features. A nonlinear light absorption model was developed to calculate the UV light attenuation through the thickness of the coating. With the absorption model, the corresponding isomerization process of the embedded azobenzenes can be described as a function of the director distribution and the type of the incoming light, i.e., diffuse light or polarized light. The light-triggered spontaneous deformation of the azo-LC polymer was incorporated through an anisotropic eigenstrain which is directly proportional to the relative fraction of azobenzene molecules in the cis state. An anisotropic linear-elastic constitutive relationship was adopted since the glassy LC polymers remain in the elastic regimes under UV illumination.

* Corresponding author. Email: P.R.Onck@rug.nl.

The key to generate a surface transformation from a flat to a corrugated coating is to create a non-uniform director distribution. For regions where the directors are parallel to the electric field of the incoming light, the azobenzenes inside have maximal absorbance and thus a higher trans-to-cis conversion level is triggered, leading to a large opto-mechanical response. In regions where the directors are perpendicular to the electric field, a much lower deformation is expected due to the low cis fraction. Creating a non-uniform director distribution thus produces switchable corrugations. Various types of liquid crystalline structures were tested. One of the tested cases is a polydomain film (see Fig. 2), in which the director distribution is randomly distributed over different domains and the corresponding photo-induced topographical textures feature domain-wise corrugations. The resulting topographical changes of this type of LC glassy films lead to surface profiles that are found to be in close agreement with the experimental measurements [1]. Roughness parameters were used to quantify the generated surface corrugations. The dependencies of these parameters on the structure's dimensions, illumination conditions and opto-mechanical properties of the LC polymer were studied.

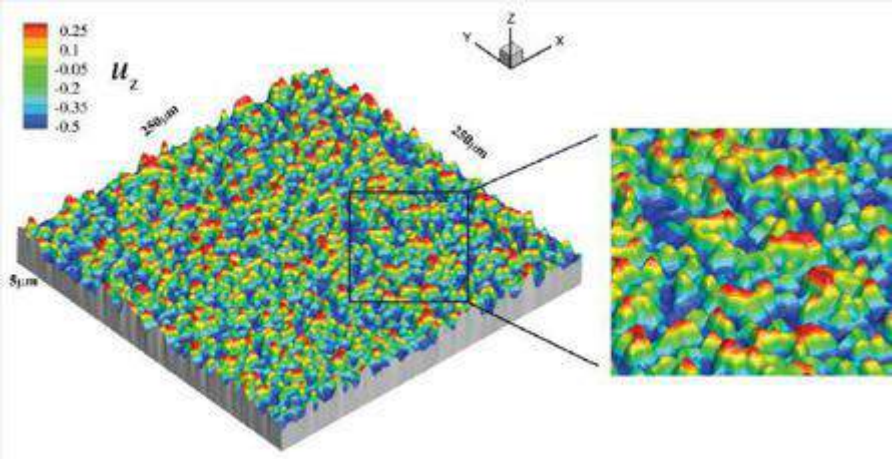

Figure 2: Simulation results of the light-triggered topographical transformation of a liquid crystal polydomain coating and a detailed texture for the boxed region. The polydomain film features domain-wise corrugations [1].

CONCLUSIONS

A computational tool was developed to simulate UV-triggered surface transformations based on azobenzene-modified liquid crystal glassy coatings. Combined with experiments, we show three-dimensional surface topographical changes that can be switched by light. Various optimized topographical textures can be produced depending on the specific director distribution.

ACKNOWLEDGMENT

This research forms part of the research programme of the Dutch Polymer Institute (DPI), project #775 TOPSWITCH.

References

[1] Liu*, D., Liu*, L., Onck, P. R., and Broer, D. J.: Reverse switching of surface roughness in a self-organized polydomain liquid crystal coating. *P. Natl. Acad. Sci. USA* **112**:3880-3885, 2015. *Shared first authorship

[2] Yu, Y., Nakano, M., and Ikeda, T.: Photomechanics: directed bending of a polymer film by light. *Nature* **425**:145, 2003.

[3] Warner, M., and Terentjev, E.M.: Liquid crystal elastomers. Oxford University Press, Oxford, 2003.

[4] Liu, D., Bastiaansen, C.W.M., Den Toonder, J.M.J. and Broer, D.J.: Light-Induced Formation of Dynamic and Permanent Surface Topologies in Chiral–Nematic Polymer Networks. *Macromolecules* **45**:8005-8012, 2013.

[5] Liu, D. and Broer, D.J.: Self-assembled Dynamic 3D Fingerprints in Liquid-Crystal Coatings Towards Controllable Friction and Adhesion. *Angew. Chem. Int. Edit.* **53**:4542-4546, 2014.

COILING A FIBER INSIDE A DROP PROVIDES A HIGHLY STRETCHABLE DEVICE

Sébastien Neukirch *[1], Arnaud Antkowiak[1], Hervé Elettro[1], and Paul Grandgeorge[1]
[1]*Sorbonne Universités, UPMC Univ Paris 06, CNRS, UMR 7190, Institut Jean Le Rond d'Alembert*

Summary Capillary forces acting at the surface of a liquid drop can be strong enough to deform small objects and recent studies have provided several examples of elastic instabilities induced by surface tension. We present such an example where a liquid drop sits on a straight fiber and we show that the liquid attracts the fiber which thereby coils inside the drop. We model the system behavior as a phase transition between a stretched phase, where the drop sits on a straight fiber, and a condensed phase, where the fiber is coiled inside the drop. The force-plateau regime during the transition between the two phases is seen as a Maxwell line, reminiscent of the Martensite-Austenite transition in Shape Memory Alloys.

PACKING OF ELASTIC WIRES

A large variety of physical phenomena can be modeled with elastic filaments packaged in cavities [10], see for example the ejection of DNA from viral capsids [6, 5], or the windlass mechanism in spider capture threads [12]. In the case of a mechanical wire spooled in a sphere, or DNA in a capsid, the presence of a motor is necessary for the packing process, the energy to bend the filament being provided by this external actuator. In the case the cavity is a liquid drop (or a bubble in a liquid medium) surface tension may provide the actuation energy: if the affinity of the filament for the liquid is stronger than that of the filament for the surrounding gas, then the bending energy required for packing could be provided by the difference of surface energies. As always, surface energy prevails at small scale and for millimeter-sized drop-on-fiber systems [7],

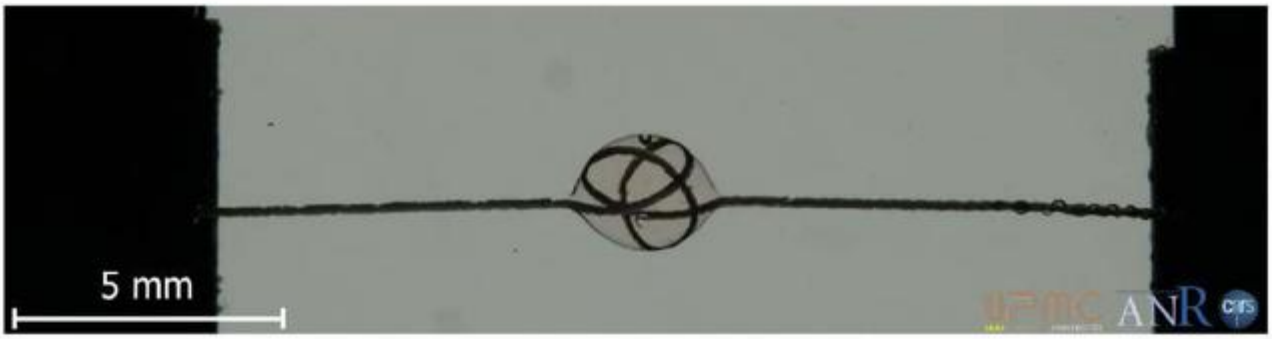

Figure 1: Elastomer beam of 140 μm section bent in a silicone oil drop (diameter $\sim$ 2.7 mm). The system is immersed in a water tank to provide buoyancy.

the competition between capillary and elastic forces is not automatically won by the former: a threshold length emerges and separates systems in which packaging is possible from those in which the fiber remains straight. This threshold length, called elastocapillary length [9], plays a central role in problems in which surface tension bends or buckles slender rods or thin elastic sheets [8]. Computations of configurations of a filament packaged in spherical cavities have been performed using finite elements [11], molecular mechanics [3], or statistical physics [1] approaches. Here we study the buckling and coiling of an elastic rod in a sphere. The rod is held in tension at its extremities and we record this tension as a function of the length of the rod packed in the sphere, while monitoring the different configurations the systems adopts.

RESULTS

We model the system of Figure 1 as an elastic rod in interaction with a rigid sphere. The rod is flexible but inextensible and unshearable, yielding a deformation energy of the form

$$E_{\text{strain}} = \int_0^L (1/2) \left[K_1 \, U_1^2(S) + K_2 \, U_2^2(S) + K_3 \, U_3^2(S) \right] \mathrm{d}S \tag{1}$$

where K_1 and K_2 are the bending rigidities, K_3 is the twist rigidity, U_1 and U_2 are the curvature strains, and U_3 is the twist strain [2, 4]. A liquid spherical drop of radius R is attached to the rod. The rod enters (exits) the drop at meniscus point A (B). The rod is then divided in three regions: (I) where $S \in (0; S_A)$, (II) where $S \in (S_A; S_B)$, and (III) where $S \in (S_B; L)$,

*Corresponding author. Email: sebastien.neukirch@upmc.fr

with region (II) lying inside the liquid drop. In regions (I) and (III) the solid-vapor interface has an energy $\gamma_{\rm SV}$ per unit area. In region (II) the solid-liquid interface has energy $\gamma_{\rm SL}$ per unit area. The total surface energy then scales linearly with the contour length:

$$E_{\rm surface} = P\left[\gamma_{\rm SV} S_A + \gamma_{\rm SL}(S_B - S_A) + \gamma_{\rm SV}(L - S_B)\right] \tag{2}$$

where P is the perimeter of the cross-section of the rod. We minimize this energy under geometrical constraints (encapsulation in the drop, fixed end-to-end distance, etc) and find the different equilibrium configurations of the system as more and more fiber length is spooled inside the drop, see Figure 2.

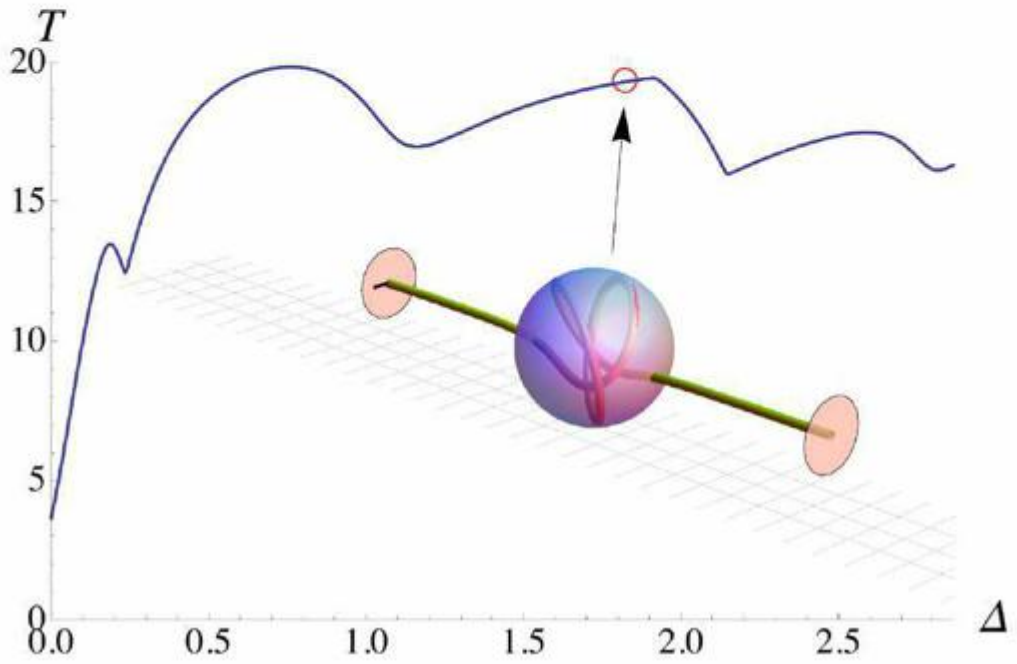

Figure 2: Bifurcation curve showing the end tension T as function of the end-shortening Δ.

ACKNOWLEDGEMENTS

The present work was supported by ANR grant ANR-09-JCJC-0022-01, ANR-14-CE07-0023-01, and ANR-13-JS09-0009. Financial support from 'La Ville de Paris - Programme Emergence' and CNRS, through a PEPS-PTI grant, is also gratefully acknowledged.

References

[1] Adda-Bedia, M., Boudaoud, A., Boué, L., Debœuf, S.: Statistical distributions in the folding of elastic structures. Journal of Statistical Mechanics: Theory and Experiment **2010**(11), P11 027 (2010)

[2] Antman, S.S.: Nonlinear problems of elasticity, 2nd edn. Springer-Verlag, New York (2004)

[3] Arsuaga, J., Tan, R.K.Z., Vazquez, M., Sumners, D.W., Harvey, S.C.: Investigation of viral DNA packaging using molecular mechanics models. Biophysical Chemistry **101-102**, 475–484 (2002)

[4] Audoly, B., Pomeau, Y.: Elasticity and Geometry: From hair curls to the non-linear response of shells. Oxford University Press (2010)

[5] LaMarque, J.C., vy L. Le, T., Harvey, S.C.: Packaging double-helical DNA into viral capsids. Biopolymers **73**(3), 348–355 (2004)

[6] Leforestier, A., Livolant, F.: Structure of toroidal DNA collapsed inside the phage capsid. Proceedings of the National Academy of Sciences of the USA **106**(23), 9157–9162 (2009)

[7] Lorenceau, E., Clanet, C., Quéré, D.: Capturing drops with a thin fiber. Journal of Colloid and Interface Science **279**(1), 192 – 197 (2004)

[8] Py, C., Reverdy, P., Doppler, L., Bico, J., Roman, B., Baroud, C.N.: Capillary origami: Spontaneous wrapping of a droplet with an elastic sheet. Physical Review Letters **98**(15), 156 103 (2007)

[9] Roman, B., Bico, J.: Elasto-capillarity: deforming an elastic structure with a liquid droplet. Journal of Physics: Condensed Matter **22**(49), 493 101 (2010)

[10] Stoop, N., Najafi, J., Wittel, F.K., Habibi, M., Herrmann, H.J.: Packing of elastic wires in spherical cavities. Phys. Rev. Lett. **106**, 214 102 (2011)

[11] Vetter, R., Wittel, F., Stoop, N., Herrmann, H.: Finite element simulation of dense wire packings. European Journal of Mechanics - A/Solids **37**, 160–171 (2013)

[12] Vollrath, F., Edmonds, D.T.: Modulation of the mechanical properties of spider silk by coating with water. Nature **340**, 305–307 (1989)

NONLINEAR CHARACTERISTICS OF DIELECTIC ELASTOMERS UNDER ELECTROMECHANICAL COUPLING LOADING

Tongqing Lu[1], Le An[1], Jianguo Li[1] & Tiejun Wang[1a)]
[1]*State Key Laboratory for Strength and Vibration of Mechanical Structures, Xi'an Jiaotong University, China*

*Summary*A membrane of a dielectric elastomer deforms subject to a voltage through the thickness. The voltage induced deformation is highly nonlinear and even non-monotonic, inducing the pull-in instability. A cylindrical elastomeric tube subject to an internal pressure exhibits quite similar instability behavior. We study the deformation behavior a dielectric elastomer tube subject to electromechanical coupling loading. Explicit expressions for the critical conditions of electro-mechanical bifurcation are derived. The post-bifurcation path and the steady state propagation is comprehensively investigated.

A BRIEF INTRODUCTION TO PULL-IN INSTABILITY

From our common experience, when a rubber balloon is inflated to a certain size it will cost less strength to blow it larger. The characteristic of transition from a stiffer balloon to a softer balloon defines a peak pressure on the pressure-stretch curve. The presence of the peak pressure is due to the strong coupling of the true stress with deformation and high nonlinearity of the material. A pressure inflates the balloon and in turn the true stresses increases such that a mechanism of positive feedback exists, inducing the so-called pull-in instability. Another characteristic of inflating a rubber balloon is the stiffening effect at large stretch due to the limiting length of polymer chains. These two characteristics give the well known N-shaped pressure-stretch curve. A membrane of a dielectric elastomer sandwiched between two compliant electrodes undergoes large deformation subject to a voltage across the thickness. The voltage induced deformation is due to Columbic force and thus the electric field determines the intensity. Like the coupling between the true stress and stretch in inflating a rubber balloon, the electric field couples strongly with deformation. The Columbic force squeezes the membrane and the decreased thickness amplifies the electric field. The positive feedback competes with the elasticity of membrane, inducing the electrical instability. Similarly, the electrical instability defines a peak voltage on the voltage-stretch curve. The curve eventually becomes N-shaped due to strain stiffening.

INSTABILITY OF A DIELECTRIC ELASTOMER TUBE UNDER ELECTROMECHANICAL LOADING

When inflating an initially flat membrane clamped at the boundary from one side, the snap-through behaviour at the peak pressure is usually observed. And the snap-back occurs in deflation. On inflating a purely spherical membrane, refined stability analysis and experiments show that the spherical configuration in inflation is unstable. The spherical membrane may bifurcate into a pear-shaped configuration through a localized thinning near one of the poles. When inflating a tubular balloon, the localized bulging instability is usually observed at a critical pressure. As more fluid is pumped into the tube, the localized aneurysm develops until its radius reaches a critical value. With continuous pumping, the pressure stays unchanged and the aneurysm shifts along the tube with more and more sections bulging up at the expense of unbulged sections. Consider an infinitely long cylindrical DE tube subjected to an internal pressure p, an axial load F at two ends and a voltage Φ through the thickness. We first establish the governing equations of the tube as

$$\frac{d}{dZ}\left(Hs_2 \sin\theta\right) = \lambda_1\lambda_2 p\cos\theta,$$

$$\frac{H}{R}s_1 - \frac{d}{dZ}\left(Hs_2\cos\theta\right) = \lambda_1\lambda_2 p\sin\quad,$$

$$\frac{\partial W\quad \lambda_1\ \lambda_2\ D\right)}{\partial D} = E,$$

The first two equations represent the force balance along longitudinal and hoop directions respectively, while the last equation represents the electric balance. By using a simplified mathematical approach, we can analytically obtain the critical conditions for bifurcation.

[a)]Corresponding author. Email: wangtj@mail.xjtu.edu.cn.

POST BIFURCATION PATH AND STEADY PROPAGATION

In the bifurcation diagram, a 45 degree straight line represents the homogenous deformation while coloured curves show the bifurcated solutions. The dashed lines represent solutions which are either periodic or unbounded. The blue and red lines represent the solutions at different levels of constant voltage or pressure. A pre-stretched membrane by pressure becomes stiffer while a pre-stretched membrane by voltage becomes more compliant. We can also analyze the bifurcation behavior from the loading-state diagram. The black curve represents the homogeneous deformation while coloured curves represent the inhomogeneous bifurcated deformation. Consider the pressure induced bifurcation under a constant voltage. The bifurcation path can be clearly traced from the bifurcation diagram. The original state is marked as O, which derivates from the undeformed state a little due to the presence of a constant voltage. Upon inflation, the deformation follows a homogenous path until the bifurcation point A. After bifurcation, the bulging solution becomes larger, following the red curve. Meanwhile, the solution at infinity becomes smaller, going back from A to O, which means that the infinite parts undergo unloading and remain uniform. Correspondingly, as shown in loading-state diagram, the black curve represents homogeneous deformation. The bifurcation point coincides with the peak of curve. When reaching the bifurcation condition, the peak of the curve, the homogenous deformation becomes unstable and bulging occurs. After bifurcation the pressure drops down and stretches bifurcate into two paths at point A, one to the right as indicated by the red curve representing the bulging section and the other to the left as indicated by the blue curve representing the unbulged section. When the pressure drops to the coexistent pressure (the dashed line), corresponding to the turning point B. Subsequently the steady propagation starts. The unbulged part gradually bulges up and the inhomogeneous transition zone shifts with its shape unchanged. The propagation continues from B to B until the whole tube bulges up. For an infinitely long tube the propagation will not terminate by itself as long as the gas continues to be pumped in. In the steady propagation the stretches remain unchanged so that points B and C coincide. After the whole tube bulges up, if we continue to pump in gas the pressure and homogeneous stretches will increase again following C to D. If we deflate the tube, necking occurs following D to E and then to F.

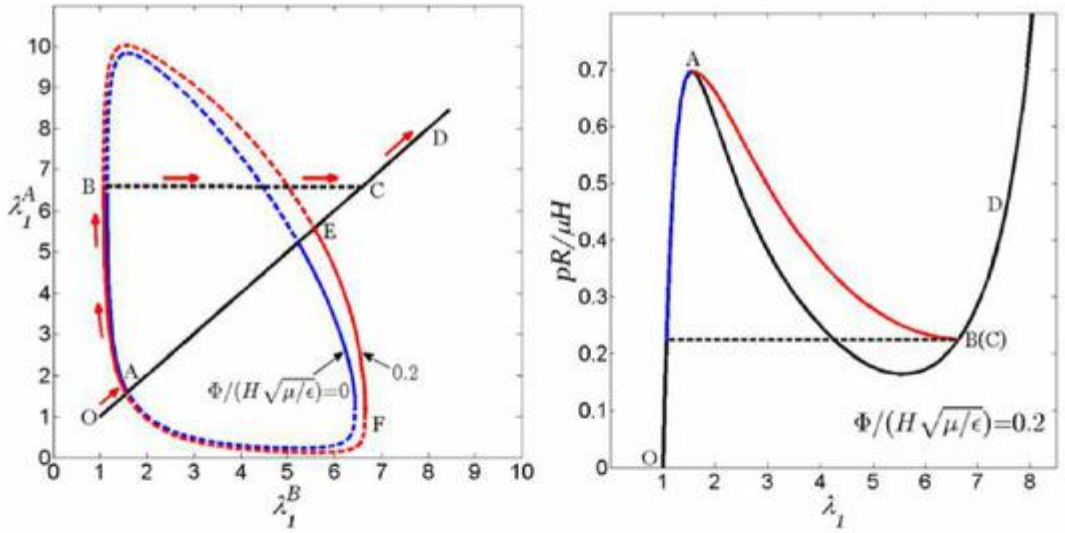

CONCLUSIONS

A cylindrical dielectric elastomer tube under an internal pressure, an axial force, and a voltage across the thickness is considered. The bifurcation condition is analytically established. The post bifurcation path and the steady propagation are analyzed in details. This work characterizes the bifurcation mechanism of rubber-like materials under complex coupling loading. The analogy between charging a dielectric elastomer and inflating a rubber balloon helps to better understand the inherent mechanisms.

References

[1] Lu T.Q., An L., Li J.G., Yuan C., Wang T.J.: Electromechanical coupling bifurcation and bulging propagation in a cylindrical dielectic elastomer tube. J. Mech. Phys. Solids ***85***:160-175, 2015.

[2] Fu Y.B., Xie Y.X.: Stability of pear shaped configurations bifurcated from a pressurized spherical balloon. J. Mech. Phys. Solids **68**: 33-44, 2014

[3] Li T.F., Keplinger C., Baumgartner R., Bauer S., Yang W., Suo Z. : Giant voltage induced deformation in dielectric elastomers near the verge of snap through instability. J. Mech. Phys. Solids **61**: 611-628, 2013

VOLTAGE-INDUCED BUCKLING AND WRINKLING IN A DIELECTRIC ELASTOMER

Hareesh Godaba, Ujjaval Gupta, Jian Zhu[a]
Department of Mechanical Engineering, National University of Singapore
9 Engineering Drive 1, Singapore, 117575

Summary This paper investigates instability and phase transition in a membrane of a dielectric elastomer. It is found that prestretches play a significant role in determining its instability modes. In the absence of prestretches, the membrane buckles without forming local wrinkles. When the applied prestretches are intermediate, the membrane exhibits discontinuous phase transition from the flat to wrinkled states. The flat and wrinkled regions not only coexist, but also keep moving with the respective areas changing (depending on the variation of the charges). When the prestretches are large, the membrane exhibits continuous phase transition, and the membrane forms wrinkles simultaneously throughout the surface.

INTRODUCTION

A dielectric elastomer actuator, one class of soft actuators, consists of a thin layer of elastomer sandwiched between two compliant electrodes. This soft actuator can deform in response to voltage and can exhibit interesting attributes including large deformation, high energy density and fast response [1]. The dielectric elastomer actuators are being extensively explored as artificial muscles for soft robots [2].

The dielectric elastomer may suffer loss of tension and form wrinkles when the applied voltage reaches a critical value. Plante and Dubowsky observed the coexistence of the flat and wrinkled regions in a circular membrane (Fig. 1), when the membrane suffers electromechanical instability [3]. Zhou et al. simulated the propagation of the instability, using a meshfree method [4]. Huang and Suo theoretically analyzed the phase transition from the flat to wrinkled states in a dielectric elastomer subject to an uniaxial load [5]. Kollosche et al. studied a membrane which is subject to a deadload vertically but is clamped horizontally. The experiments showed three types of phase transitions, including the discontinuous transition from the flat to wrinkled states, continuous transition from the flat to wrinkled states, and discontinuous transition from the wrinkled to wrinkled states [6].

This paper investigates instability and phase transition in a circular membrane of a dielectric elastomer, which is subject to equal-axial prestretches (Fig. 1). It is found that the membrane may buckle or wrinkle, dependent on the applied prestretches (λ_{pre}, Fig. 1b).

EXPERIMENTS

Figure 1 shows the schematic of the experimental setup. At the reference state (Fig. 1a), a circular membrane is subject to no mechanical and electrical loads, and has a radius B and a thickness H (= 1mm). The active part (which will be smeared with the electrodes later) has a radius A. At the prestretched state (Fig. 1b), the membrane is subject to a radial prestretch λ_{pre} and has a radius $B\lambda_{pre}$ (= 6cm), and its boundary is fixed to a rigid circular frame. The active part is brushed with the compliant electrodes and has a radius $A\lambda_{pre}$ (= 3cm). At the current state (Fig. 1c), the membrane is subject to voltage, the active part expands its area and reduces its thickness, and the point R at the reference state moves to a position with a radius r at the current state.

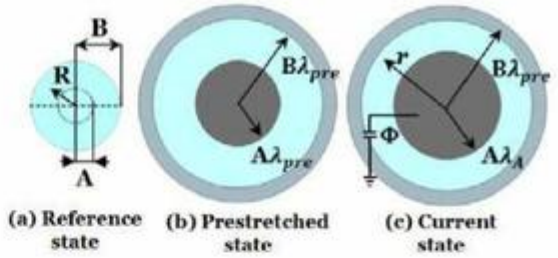

Fig. 1 A schematic of a circular membrane of a dielectric elasotmer

We employ VHB 4910 (3M) as the elastomer, and carbon grease as the compliant electrodes. Voltage is programmed through Labview (BNC-2120, NI) and is amplifed by a high voltage amplifier (FR30P10, Glassman). We then investigate the electromechanical behaviour of the membranes with different prestretches.

Buckling

In the absence of prestretches (λ_{pre} = 1), the experiments show that the actuator buckles without forming any wrinkles on the surface, when voltage reaches a critical value (Φ = 6kV). Figure 2a shows the state at Φ = 0, and Figure 2b show the buckling of the membrane when the voltage is larger than the critical value. This experimental observation can be interpreted as follows. The active part of the membrane expands when subject to voltage, which will compress the passive part. Consequently, the passive part also applies a compressive force to the active one. In the absence of any prestretches, the thickness of the membrane is large. Meanwhile, at λ_{pre} = 1 (or when the



(a) Voltage off (b) When Φ = 21kV

Fig. 2 Buckling of the membrane with λ_{re} = 1

[a] Corresponding author. Email: mpezhuj@nus.edu.sg.

stretch is close to the stretch limit), the stiffness of the membrane is generally large. As a result, the membrane is too stiff to form local wrinkles. However, the compressive stress may make the membrane buckle globally without forming local wrinkles, as shown in Fig. 2b.

Discontinuous transition from the flat to wrinkled states

When the membrane is subject to intermediate prestretches (λ_{pre} = 3), the membrane exhibits a discontinuous phase transition from the flat to wrinkled states. When the voltage is small, the active part expands. When the voltage reaches a critical value (Φ = 7.38kV), the flat and wrinkled regions coexist. Different from [6], in the current experiments we fix the voltage at the critical value (i.e. 7.38kV). It is observed that both the flat and wrinkled regions keep moving with the flat and wrinkled areas changing. Finally the membrane fails by electrical breakdown. Figure 3 show a sequence of still images of the membrane at the fixed voltage. Theoretical analysis shows that the voltage-stretch curve may have a shape of going up, down and up again. When the voltage reaches a critical value, the flat and wrinkled states have the same free energy densities. As a result, the flat and wrinkled states coexist. Since we do not control the charges on the electrodes, the flat and wrinkled regions may move as the charges vary.



Fig. 3 The membrane of a dielectric elastomer exhibits discontinuous phase transition from the flat to wrinkled states, when voltage reaches a critical value. (a) – (j), the state of the membrane at the fixed voltage (Φ = 7.38kV).

Continuous transition from the flat to wrinkled states

When the membrane is subject to larger prestretches (λ_{pre} = 4.5), the membrane may form wrinkles simultaneously throughout the surface, when the voltage reaches a critical value (Φ = 6.4kV). Theoretical analysis shows that the voltage increases monotonically with the stretch. When the voltage reaches the critical value, the active part of the membrane suffers loss of tension, and the membrane forms wrinkles. After loss of tension, the voltage still increases with the stretch.

When the membrane is subject to intermediate or even larger prestretches (but not close to the stretch limit), say λ_{pre} = 3 or 4.5, both its thickness and stiffness are small. Consequently, the membrane may form wrinkles locally, but may not buckle globally.

CONCLUSIONS

This paper investigates instability and phase transition in a circular membrane of a dielectric elastomer. Prestretches are found to play a significant role in determining instability modes of the membrane. In the absence of prestretches (λ_{pre} = 1), the membrane buckles without forming local wrinkles. When the prestretches are intermediate (λ_{pre} = 3), the membrane exhibits discontinuous phase transition from the flat the wrinkled states. The flat and wrinkled regions not only coexist but also move on the surface of the membrane. When the prestretches are large (λ_{pre} = 4.5), the membrane exhibits continuous phase transition, and the membrane form wrinkles simultaneously throughout the surface.

References

[1] Pelrine R., Kornbluh R., Pei Q.B., and Joseph J.: High-speed electrically actuated elastomers with strain greater than 100%. *Science* **287**: 836–839, 2000.

[2] Wang Y.Z., Zhu J.: Artificial muscles for jaw movements. *Extreme Mech. Lett.* **6**: 88-95, 2016.

[3] Plante J.S., Dubowsky S.: Large-scale failure modes of dielectric elastomer actuators. *Int. J. Solids Struct*. **43**: 7727-7751, 2006.

[4] Zhou J.X., Hong W., Zhao X.H., Zhang Z.Q., and Suo Z.G.: Propagation of instability in dielectric elastomers. *Int. J. Solids Struct.* **45**: 3739–3750, 2008.

[5] Huang R., Suo Z.G.: Electromechanical phase transition in dielectric elastomers. *Proc. R. Soc. A* **468**: 1014–1040, 2012.

[6] Kollosche M., Kofod G., Suo Z.G., Zhu J.: Temporal evolution and instability in a viscoelastic dielectric elastomer, *J. Mech. Phys. Solids* **76**: 47-64, 2015.

EXPLORING BAND GAP TUNABILITY IN PHONONIC CRYSTALS USING DIELECTRIC ELASTOMERS

Michael Jandron*[1,2] and David Henann[2]
[1]*Naval Undersea Warfare Center Division Newport, Newport, RI*
[2]*School of Engineering, Brown University, Providence, RI*

Summary Phononic crystals are periodic, composite materials that exhibit phononic band gaps – frequency ranges in which elastic waves are prohibited. When the periodic structure is deformed, these frequency ranges may be manipulated. Hence, frequency band gaps in phononic crystals made from elastomers may be reversibly tuned through large deformation. Furthermore, dielectric elastomers – materials in which deformation is induced through the application of an electric field – may be used in phononic crystals, opening the door for electrically actuated tunability. In order to realize this exciting capability, robust simulation and design tools are needed. We have developed finite-element technology to address this problem and have applied these tools to designing phononic crystals with band gaps tuned through electrical actuation. We present an application of our simulation capability to the design of a phononic crystal consisting of a square array of circular-cross-section threads embedded in a dielectric elastomeric matrix.

BACKGROUND

A solid phononic crystal utilizes constructive interference through Bragg scattering (see e.g., [1]) to create phononic band gaps – frequency ranges in which elastic waves cannot propagate. These materials have attracted a good deal of research attention in recent years and small-strain (e.g., metallic) phononic crystals have been extensively studied. Tunability of small-strain phononic crystals has been explored using piezoelectrics [2] and magneto-elastics [3,4], but because of the high wave speeds in stiff materials, the physical dimension of the required unit cells tend to be large. Soft materials offer the advantage of slower shear wave speeds which do not require very large unit cell dimensions. Since elasticity of elastomers is nonlinear, it is straightforward to change the stiffness properties of the unit cell through large deformation – thereby changing the speed of wave propagation. Achieving tunability through soft materials is just beginning to be explored. For instance, Bertoldi and Boyce [5] demonstrated significant tunability of band gaps through finite pre-deformations in soft elastomeric phononic crystals containing voids. Moreover, they showed that pre-deformation was not only capable of shifting band gaps but also that new band gaps could be created.

Dielectric elastomers (DEs) offer a unique way to achieve the large reversible deformations required for tunability through an externally applied electric field. These materials – which began appearing in the literature in the late 1990s [6,7] – are characterized by the ability to deform significantly when an electric field is applied. DEs are distinct from piezoelectric materials in that DEs are capable of large, reversible deformations, possess a quadratic relation between electric field and stress, and are non-polar, amorphous materials, while – on the other hand – piezoelectric materials typically only undergo small deformations, possess a linear relation of electric field to stress, and are polar, crystalline materials. The use of DEs in phononic crystals was first discussed by Shmuel [8] who developed analytical solutions for elastic wave propagation in a one-dimensional periodic laminate undergoing large homogeneous deformations in response to an electric field. Shmuel [9] expanded on this work by deriving analytical solutions for a DE phononic crystal composite made up of an array of cylindrical fibers in a matrix, but this was again limited to homogeneous deformations.

Numerical simulation is certainly required in order to study tunability induced by inhomogeneous deformations, but these simulation techniques are largely new to DEs [10,11]. Here, we utilize the finite-element approach of Henann et al. [11] through an Abaqus user-element (UEL) subroutine. This – in conjunction with a Representative Volume Element (RVE) and Bloch-Floquet boundary conditions (see e.g. [5]) – allows us to explore band-gap dependence on electric field magnitude and direction without restriction.

RESULTS

Our simulation approach – consisting of the finite-element implementation [11], the RVE (shown in Fig. 1), and Bloch-Floquet boundary conditions [5] – has been verified by reproducing the analytical work of Shmuel [9] for homogenous deformation of a phononic crystal consisting of cylindrical inclusions arranged in a square matrix. However, for brevity, we do not show that result here, instead focusing on the more interesting case of inhomogeneous, electrically-actuated pre-deformation. Representative simulation results for one set of material properties and volume fraction (50/50) is shown in Fig. 1. An electric field is applied along the diagonal of the unit cell with increasing magnitude, as shown in Figs. 1 (a)-(c). The frequency as a function of wave vector for several electric field magnitudes is shown along the top of the figure, demonstrating that phononic band gaps (depicted as blue bars) can be manipulated.

* Corresponding author. Email: michael.jandron@navy.mil.

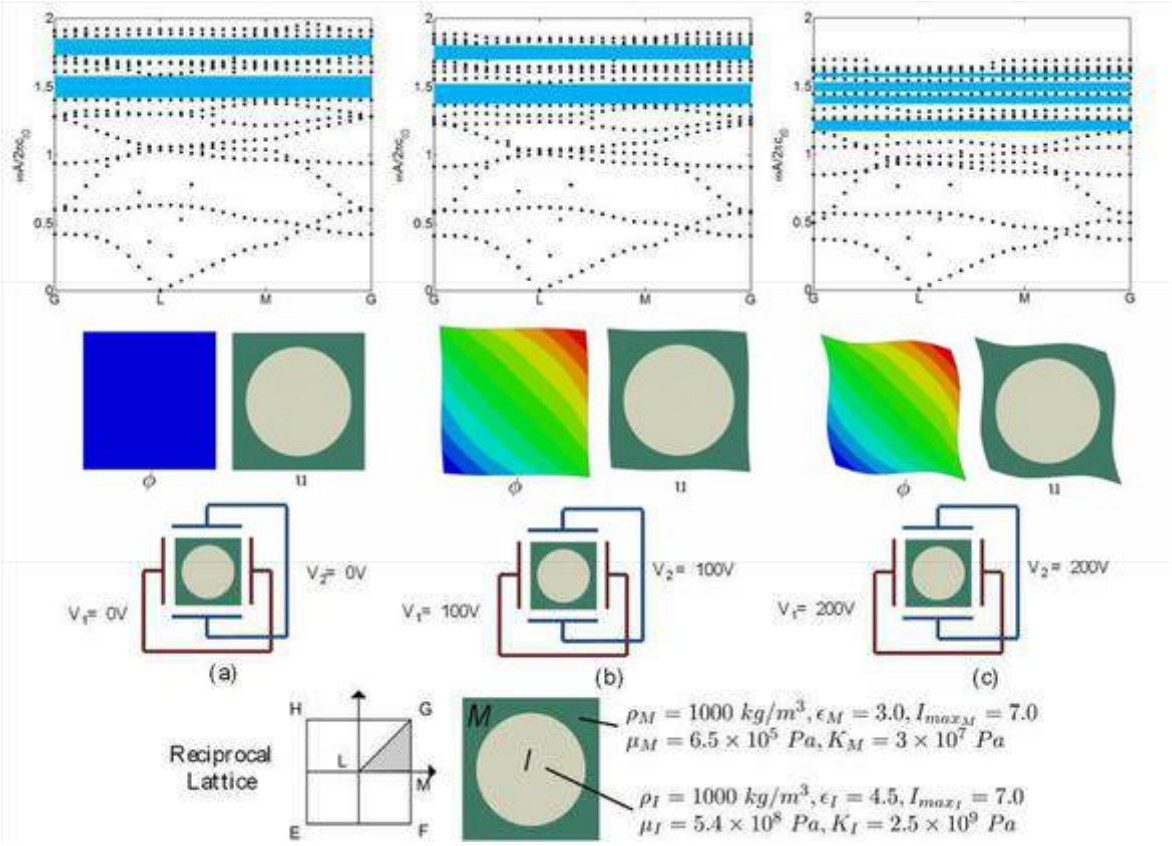

Figure 1. Effect of an external electric field on deformation and phononic band gaps in the composite DE. From left, (a) no electric field, (b) an electric field of 100V/unit cell in both the horizontal and vertical directions lowers the band gaps, and (c) an electric field of 200V/unit cell in each direction lowers the band gaps further and also opens new ones. Note that the voltage is per unit cell, and hence, in a phononic crystal of 20x20 unit cells, the actual applied voltage will be 2kV and 4kV for (b) and (c) respectively. In the figure, φ represents the voltage field, u represents the deformed shape of the unit cell, and the blue bars represent the band gaps. The band gap angular frequencies, ω, are normalized by the unit cell dimension, A, and the composite unit cell shear wave speed, $c_{t0} = c_{tM}c_{tI}/(0.5c_{tM} + 0.5c_{tI})$. The unit cell is composed of a matrix M and an inclusion, I, both modelled using the Gent hyperelasticity model. For material properties: ρ is the mass density, ϵ is the dielectric permittivity, I_{max} is a material parameter for the Gent hyperelasticity model, μ is the ground-state elastic shear modulus, and K is the elastic bulk modulus – taken to approximately enforce incompressibility. The properties used are representative of 3M VHB 4910 DE for the matrix and nylon for the inclusion material.

In this talk, we will further demonstrate the dependence of phononic band gaps on the direction of the applied electric field, shear modulus contrast, density contrast, electric permittivity contrast, volume fraction, as well as unit cell geometry (i.e., hexagonal instead of square lattice). In summary, phononic crystals made from dielectric elastomers provide an attractive strategy for achieving electrically tunable band gaps, and our work demonstrates a robust numerical simulation capability for the design of these electrically tunable phononic crystals.

References

[1] Lai, Y., Zhang, X., Zhang, Z-Q, Appl. Phys. Lett. 79, Number 20 (2011).
[2] Oh, Lee, Ma and Kim., Appl. Phys. Lett. 99, 083505 (2011)
[3] Vasseur, Matar, Robillard, Hladky-Hennion, Deymier, AIP Advances 1, 041904 (2011)
[4] Matar, Robillard, Vasseur, Jladky-Hennion, Deymier, Pernod, Preobrazhensky, Appl. Phys. 111, 054901 (2012)
[5] Bertoldi, K., Boyce, M., Physical Review B 77 (5), 052105, 2008
[6] Pelrine, R., Kornbluh, R., and Joseph, J., Sens. Act. A 64, 77-85, 1998.
[7] Pelrine, R., Kornbluh, R., Pei, Q., and Joseph J., Science 287, 836-839, 2000.
[8] Shmuel, G., deBotton, G., JMPS, 2012.
[9] Shmuel, G., Int. J. Solids Struct., 50:680-686, 2013
[10] Vu, D., Steinmann, P., Possart, G., Int. J. Numer. Meth. Engng 2007; 70:685–704
[11] Henann, D., Chester, S., Bertoldi, K., JMPS 61, 2013.

RESEARCH ON THE MICROSTRUCTURE AND THE PROPERTY OF MAGNETORHEOLOGICAL ELASTOMER

Taixiang Liu[1], Yangguang Xu[2], Ke Yang[1], Hongwei Yan[1], Xinglong Gong[3] & Xiaodong Yuan[1a)]
[1]*Research Center of Laser Fusion, China Academy of Engineering Physics, Mianyang, P. R. China*
[2]*Institute of Systems Engineering, China Academy of Engineering Physics, Mianyang, P. R. China*
[3]*Department of Modern Mechanics, University of Science and Technology of China, Hefei, P. R. China*

Summary Magnetorheological elastomer (MRE) is a kind of soft solid magnetic field-responsive material composing of micron-sized magneto-sensitive particles and non-magnetic hyper-elastic matrix. The mechanical or physical behaviour of MRE can be adjusted by using external magnetic field, and the behaviour is strongly correlated with the underlying particle-aggregated microstructures of MRE. This work aimed to find the relation between the microstructure and the property of MRE, and studied the particle aggregation of MRE in curing process and predicted the microstructure-dependent property of cured MRE using particle-level dynamics simulation and finite element analysis, respectively. It is suggested that combining particle-level dynamics with finite element analysis is a preferred way to reveal the dominating mechanism giving rise to the macroscopic performance of MRE.

INTRODUCTION

Magnetorheological elastomer (MRE) is a kind of smart magnetic field-responsive composite material. Usually, MRE is prepared by embedding micron-sized magneto-sensitive particle into magnetically insensitive polymer or rubber matrix. Attractively, the mechanical or physical property of MRE can be altered by using external magnetic field, making MRE be widely developed in vibration absorbers, vibration isolators, sensing devices, etc.[1] When preparing MRE, the composite material behaves as a high-viscosity fluid-like mixture in the curing process. Thus, an external magnetic field is usually applied to control the particle-aggregate microstructure and go further the post-curing property of MRE. Though it is clear that the macroscopic property of MRE is strongly correlated with its underlying microstructures, the microstructure-based dominating mechanism giving rise to the macroscopic property has never been identified clearly [2]. Therefore, it is imperative to reveal the dominating mechanism. As for an analogue to the high-viscosity fluid-like mixture (i.e. MRE in curing process), the microstructure-based mechanism of the performance of magnetorheological plastomer has been well studied by using particle-level dynamics simulation [3,4]. Given this, in this work, particle-level dynamics combining with finite element analysis is developed to study the particle-aggregating mechanism in the curing process and the effect of particle-aggregated microstructure on the post-curing property of MRE.

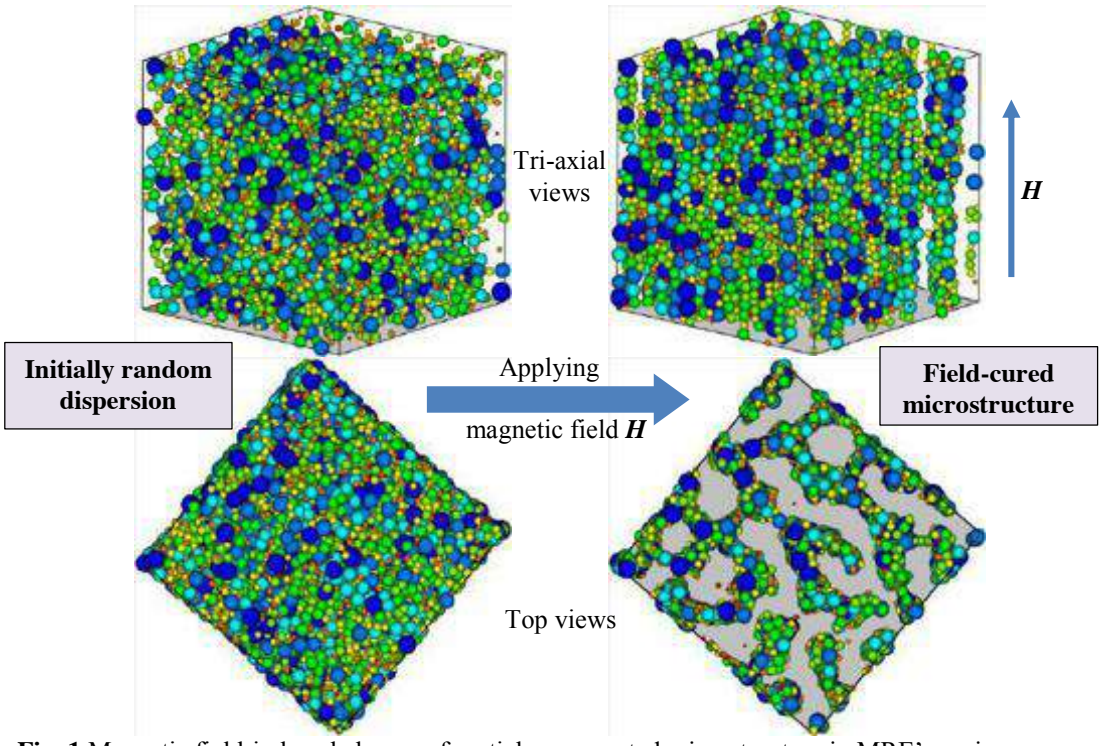

Fig. 1 Magnetic field-induced change of particle-aggregated microstructure in MRE's curing process.

[a)] Corresponding author. Email: yxd66my@163.com.

MODELING AND SIMULATION

MRE composes of magneto-sensitive particles and non-magnetic matrix with a small quantity of dispersing agent, surfactant, vulcanizing agent, etc. The particle and the matrix are the dominating components of MRE and thus the primary factors considered to model MRE. To the particle, it is vital to take its magnetic property and size distribution into consideration. The particle used here is a soft magnetic material and has a log-normal size distribution. To the matrix, its pre-curing, in-curing and post-curing states, as well as their mechanically analytical models, need to be identified clearly. The pre-curing or post-curing matrix affects little on the particle-aggregating structure comparing to the in-curing state. The matrix in curing process behaves as a high-viscosity fluid-like medium, while behaves as an elastic material after curing process. After the models of particle and matrix are identified, the particle-particle interaction and particle-matrix interaction can be constructed accordingly. In this work, a cubic cell with the edge length of 200 μm and the particle volume fraction of 20% is considered for modelling MRE. Then particle-level dynamics simulation is implemented to study the particle aggregation in curing process, and finite element analysis is applied to predict the performance of cured MRE.

RESULTS AND DISCUSSION

Fig. 1 gives the magnetic field-induced microstructural evolution of MRE in curing process. As the top-left subfigure and the bottom-left subfigure show, the particles initially and randomly disperse in the cubic cell before magnetically curing process proceeding. After applying an external magnetic field, the particles gradually aggregate to form chain-like and go further column-like microstructures, as the right subfigures show. In addition, the porous microstructure is formed by magnetic particles from the view of a top point. With the change of particle-aggregated microstructure, the microstructure-based macroscopic properties of MRE, such as storage modulus, damping, thermal conductivity, permeability, electricity, etc., will change a lot. As an example of microstructure-dependent properties in two-dimensional case, **Fig. 2** shows that the thermal conductivity of MRE is strongly microstructure dependent. That is to say, the isotropic particle dispersion leads to isotropic thermal conductivity, while the anisotropic conductivity results from anisotropic particle-aggregation, as a result of that the thermal conductivities of particle and matrix are not the same and they differ much to each other.

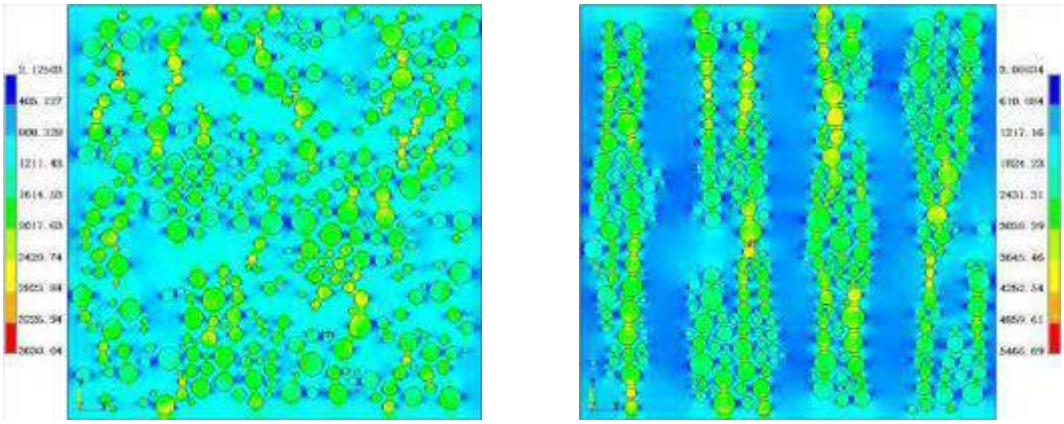

Fig. 2 The microstructure-based isotropic (left) and anisotropic (right) thermal conductivity of cured MRE.

CONCLUSIONS

1) Particle-level dynamics simulation can be developed to study the magnetic field-induced particle aggregation of MRE in curing process. Finite element method can be utilized for analysing the microstructure-based property of cured MRE.

2) Combining particle dynamics with finite element analysis is a suggested way to reveal the microstructure-based dominating mechanism giving rise to the macroscopic property of MRE.

Financial support from the National Natural Science Foundation of China (Grant No.: 11502256) is gratefully acknowledged.

References

[1] Li Y. C., Li J. C., Li W. H., Du H. P.: A State-of-the-art Review on Magnetorheological Elastomer Devices. *Smart Mater. Struct.* **23**: 123001, 2014.

[2] Han Y., Hong W., Faidley L. E.: Field-stiffening Effect of Magneto-rheological Elastomers. *Int. J. Solids Struct.* **50**: 2281-2288, 2013.

[3] Xu Y. G., Gong X. L., Xuan S. H., Zhang W., Fan Y. C.: A High-performance Magnetorheological Material: Preparation, Characterization and Magnetic-mechanic Coupling Properties, *Soft Matter* **7**: 5246-5254, 2011.

[4] Liu T. X., Gong X. L., Xu Y. G., Xuan S. H., Jiang W. Q.: Simulation of Magneto-induced Rearrrangeable Microstructures of Magnetorheological Plastomers. *Soft Matter* **9**: 10069-10081, 2013.

THICKNESS AND D33 EFFECTS ON THE ENERGY CONVERSION AND ACTUATION OF PIEZOELECTRIC UNIMORPHS

Nanshu Lu[1], Taewoo Ha[1]
[1]*Center for Mechanics of Solids, Structures, and Materials, Department of Aerospace Engineering and Engineering Mechanics, Department of Biomedical Engineering, Texas Materials Institute, The University of Texas at Austin, Austin, TX 78712, United States*

Summary Piezoelectric unimorph is composed of a piezo-layer (with top and bottom electrodes) uniformly laminated on an inactive flexible substrate. Because of their simple construction and flexibility, unimorphs are widely used as flexible sensors and actuators. Here we report a comprehensive theoretical framework to investigate the effects of the film-to-substrate thickness ratio on voltage, charge, and energy outputs when the unimorph is subjected to eight different boundary/loading conditions. For not so thin unimorphs, there is non-zero normal stress in the thickness direction (σ_3), in which case d_{33} can play a significant role. Non-monotonic voltage and energy generation versus thickness ratio relations have been found in some cases and optimum thickness ratio for unimorph generator can be predicted. When the unimorph is actuated by voltage applied across the piezo-layer, non-monotonic actuated deflection versus thickness ratio relation is also found.

INTRODUCTION

Piezoelectric materials have found wide applications in energy harvesting as well as actuation because of their unique combination of mechanical form factors and energy transduction capabilities. Existing unimorph models [1-3] are mostly limited to cantilever configurations and the d_{33} contribution has been neglected because σ_3 is always assumed to be zero. However, unimorphs can also operate under the boundary conditions of pure bending or simple-simple support and can be subjected to variety types of load or displacement excitations. Moreover, σ_3 is non-zero for thick unimorphs and may have significant contributions to the outputs. To find a remedy for aforementioned deficiencies, we derive closed-form solutions for unimorphs subjected to eight different boundary/loading conditions [4]. To validate our theory, finite element modeling (FEM) was performed using COMSOL Multiphysics. Non-monotonic electrical outputs versus thickness ratio curves are found for several boundary value problems (BVP). To resolve the discrepancy between theoretical and FEM results for some scenarios, the d_{33} effect had to be taken into consideration. Simple models to determine average σ_3 along beam length has been proposed and turn out to be very effective in accounting for the d_{33} contribution.

METHOD AND RESULTS

Suppose the piezoelectric layer and the substrate have thicknesses of h_1 and h_2 and Young's moduli of Y_1 and Y_2, as labeled in Fig. 1(a), calculating the voltage, charge, and power output of such a unimorph first requires the determination of the neutral axis and the effective second moment of inertia of the bilayer. The distance from the neutral axis to the bottom surface of the substrate is represented by Δh_1, as labeled in Fig. 1(a), where Δ has been given by [5]

$$\Delta = \frac{1 + 2\Sigma\eta + \Sigma\eta^2}{2\eta(1 + \Sigma\eta)} \tag{1}$$

where $\Sigma = \bar{Y}_1 \; \bar{}_2$ is the film-to-substrate modulus ratio with $\bar{} = Y/(1-\nu^2)$ being the plane strain modulus, Y being the Young's modulus, ν being the Poisson's ratio, and $\eta = h_1/h_2$ is the film-to-substrate thickness ratio.

The effective second moment of inertia of the bilayer is given by [4]

$$I = h_2^3 \left\{ \Sigma \left[\eta(\Delta\eta - 1)^2 - \eta^2(\Delta\eta - 1) + \frac{\eta^3}{3} \right] + \Delta\eta(\Delta\eta - 1) + \frac{1}{3} \right\} = h_2^3 \, \bar{} \tag{2}$$

where $\bar{}$ represents the non-dimensional second moment of inertia and hence the bending stiffness of the unimorph can be written as $\bar{}_2 I$. For given piezoelectric and substrate materials (i.e., Σ fixed), the only dimensionless variable in the problem is the thickness ratio η, whose effect is the focus of this study.

Based on Euler- Bernoulli beam theory, the bending induced normal stress in x direction and its vertical distribution of the unimorph is given by $\sigma_1 = (z - \Delta h_1)\Sigma M/I$. When the beam is thick, non-zero σ_3 may also exist. By the linear piezoelectric effect [6], deformation induced polarization density is proportional to stress through the piezoelectric coefficient, i.e. $P_i = d_{ij}\sigma_j$ ($i = 1,2,3,\ j = 1,2,\ldots,6$), therefore z direction polarization is given by

$$P_3 = d_{31}\sigma_1 + d_{33}\sigma_3 \tag{3}$$

Since charges are only collected from the top and bottom surface electrodes of the piezo-layer, only top ($z = h_1 + h_2$) and bottom ($z = h_2$) surface polarization density will be considered to calculate the total amount of charges. Therefore surface charge density can be calculated as the total charge from the surface polarization density divided by the surface area:

[a] Corresponding author. Email: ictam2016papers@legendconferences.com.

$$\rho = \frac{Q}{S} = \frac{-\int_S a_n \cdot P_3 \, dS}{S}. \quad (4)$$

where a_n stands for the surface normal vector and S stands for the overall surface area. Subsequently, the voltage derived through the definition of capacitance, $V=Q/C$, where $C = \varepsilon_p' L/h_1$, with ε_p' being the effective permittivity of the piezoelectric material [2]. Lastly, the generated energy density can also be calculated by $U=\rho V/2$. Following this procedure, the unimorph electric outputs versus thickness ratio has been analysed for different boundary/loading conditions. As an example, Figs. 1(b)-(e) offers the results of simply supported unimorph subjected to central point load. The analytical results (curves) show excellent agreement with finite element modelling (FEM) results (markers) if the effect of d_{33} (or σ_3) is considered. Non-monotonic outputs also suggest that optimal thickness ratio exists.

Thickness ratio also affects the actuated displacement of a unimorph subjected to applied electric field $E = V_0/h_1$ across the thickness of the piezo-layer [7]. As a result, a uniform stress $\sigma_1 = d_{31}\overline{Y}_1 V_0/h_1$ is generated in the piezo-layer, while stress in the substrate remains zero. The resultant moment will therefore bend the unimorph and the actuated displacement is again found to be non-monotonic with respect to the thickness ratio, as displayed in Figs. 1(f) & (g).

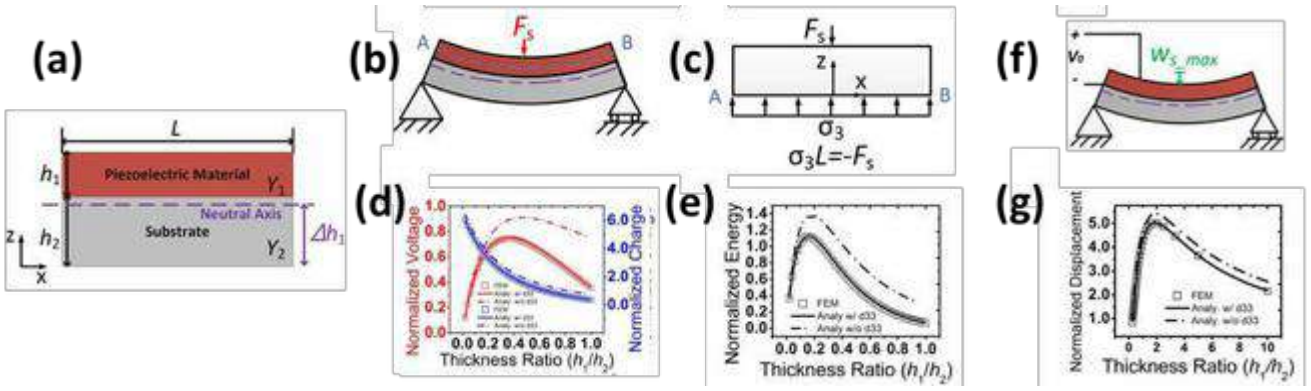

Fig. 1 (a) Illustration of basic variables of the unimorph. (b) A schematic for the simply supported unimorph subjected to central point load. (c) Free body diagram used to calculate average σ_3. (d, e) The analytical and FEM results of normalized voltage, charge density, and energy density as functions of the thickness ratio. (f) A schematic of a simply supported unimorph actuator subjected to constant electric potential. (g) The analytical and FEM results of normalized actuated displacement of the unimorph as a function of the thickness ratio.

CONCLUSIONS

We investigate the electromechanical behaviors of flexible unimorph power generators and actuators. Analytical and numerical models are built to unveil the effects of piezo-layer-to-substrate thickness ratio and piezoelectric material constants on energy conversion under eight different boundary/loading conditions. Our theory reveals that when the unimorph is subjected to displacement-controlled loading conditions, the charge, voltage, and energy outputs are monotonic functions of the thickness ratio whereas when the unimorph is subjected to load-controlled conditions, optimal thickness ratios for maximum voltage and energy outputs exist. Our linear piezoelectric theory has been fully validated by FEM. We have also found that except pure bending conditions, all cantilever and simply supported unimorphs should care about the d_{33} (i.e. σ_3) contribution when the unimorph length is not much larger than the thickness. A simplified average stress model is proven effective in accounting for the d_{33} effect. d_{33} effect may also change the outputs of displacement controlled problems from monotonic to non-monotonic. The effects of elastic mismatch and thickness-to-length ratio have been discussed and analytical solutions for unimorph based actuators are also offered. This work provides a comprehensive and accurate solution for the design and optimization of unimorph based power generators and actuators.

References

[1] Wang Q. M., Du X. H., Xu B. M., Cross L. E.: Theoretical analysis of the sensor effect of cantilever piezoelectric benders. *J Appl Phys* 85:1702-12, 1999.
[2] Smits J. G., Choi W. S.: The constituent equations of piezoelectric heterogeneous bimorphs. *IEEE Trans Ultrason Ferroelectr Freq Control* 38:256-70, 1991.
[3] Park J. K., Moon W. K.: Constitutive relations for piezoelectric benders under various boundary conditions. *Sensor Actuat a-Phys* 117:159-67, 2005.
[4] Ha T. W., Zhang J., Lu N.: Thickness ratio and d33 effects on flexible piezoelectric unimorph energy conversion. *Smart Materials and Structures*, accepted, 2016.
[5] Hutchinson J. W., Suo Z.: Mixed-mode cracking in layered materials. *Adv Appl Mech* 29:63-191, 1992.
[6] Rogacheva N. N.: The theory of piezoelectric shells and plates. Boca Raton: CRC Press; 1994.
[7] Li X. P., Shih W. Y., Aksay I. A., Shih W. H.: Electromechanical behavior of PZT-brass unimorphs. *J Am Ceram Soc* 82:1733-40, 1999.

POROELASTIC TOUGHENING IN POLYMER GELS: A THEORETICAL AND NUMERICAL STUDY

Alessandro Lucantonio*[1], Giovanni Noselli[1], Robert M. McMeeking[2,3], and Antonio DeSimone[1]
[1]*SISSA - International School for Advanced Studies, Trieste, Italy.*
[2]*Department of Mechanical Engineering and Materials Department, UCSB, Santa Barbara, USA.*
[3]*School of Engineering, University of Aberdeen - King's College, Aberdeen, UK.*

Summary We explore the fracture toughness of a polymer gel containing a Mode I growing crack. First, an expression is derived for the energy release rate within the linearized, small-strain setting. This expression reveals a velocity independent toughening that stems from the poroelastic nature of polymer gels. Then, we establish a poroelastic cohesive zone model that allows us to describe the micromechanics of fracture in gels by identifying the role of solvent pressure in promoting poroelastic toughening. We confirm our theoretical findings by means of numerical simulations.

INTRODUCTION

Soft biological tissues, such as cartilage, epithelium and muscles, can withstand relatively high levels of strain without fracturing. Since hydrogels are commonly considered as proxies for soft biological tissues, their fracture behavior is the subject of intense theoretical and experimental investigations.

In general, toughening of hydrogels relies on the energy dissipation that takes place in the process zone around the crack tip [1]. Building upon such a principle, much research currently focuses on the development of experimental techniques for the synthesis of high-toughness hydrogels, where dissipation mechanisms [2, 3] are introduced at the material scale. At the same time, a theoretical effort is needed in modeling diverse fracture modes and sources of toughening in soft materials, starting with the basic, classical fracture mechanics problems.

In this spirit, here [4] we study the propagation of a semi-infinite crack in an infinite polymer gel that is loaded in Mode I conditions and immersed in a solvent. We present a detailed energy analysis that evidences the existence of a velocity-independent toughening, which is innate in the poroelastic nature of polymer gels. Further, we establish a poroelastic cohesive zone model that provides a framework to describe the micromechanics of fracture processes in polymer gels.

ENERGY ANALYSIS FOR A PROPAGATING CRACK IN A POLYMER GEL

We consider a gel consisting of an infinite polymer network immersed in a solvent. The gel contains a semi-infinite crack propagating with velocity v along the $\mathbf{e}_1$ direction. The crack faces are traction-free and in chemical equilibrium with the surrounding solvent. At infinity, the Mode I stress field is applied with intensity factor K_v^∞, and the material responds as an incompressible elastic solid, under the assumption that fluid flow is confined to a small process zone surrounding the crack tip. We develop our theory in the linearized, plane-strain setting.

Manipulations of the energy balance statement appropriate for gels [6] lead to the following definition of the energy release rate $\mathcal{G}$, in a coordinate system $(\hat{x}_1, \hat{x}_2)$ centered at crack tip [4, 5]:

$$\mathcal{G} = \int_{\mathcal{C}} \left(\psi \mathbf{n} \cdot \mathbf{e}_1 - \mathbf{T}\mathbf{n} \cdot \frac{\partial \mathbf{u}}{\partial \hat{x}_1} \right) \mathrm{d}S - \int_{\mathcal{R}} p \frac{\partial \varepsilon}{\partial \hat{x}_1} \, \mathrm{d}A \,, \quad \psi(\mathbf{E}) = G\mathbf{E} \cdot \mathbf{E} + \frac{1}{2} \left(\kappa - \frac{2}{3} G \right) \varepsilon^2 \,, \tag{1}$$

where ψ is the free energy of the gel in the linearized poroelasticity framework [7], $\mathbf{T}$ is the Cauchy stress, $\mathbf{n}$ is the outer normal to the (arbitrary) contour $\mathcal{C}$ encircling the domain $\mathcal{R}$ and containing the crack tip, $\mathbf{u}$ is the displacement field, p is the solvent pressure within the gel, G and κ are the poroelastic moduli of the gel, and ε is the trace of the small-strain tensor $\mathbf{E}$. The first integral on the right hand side evaluated on a contour $\mathcal{C}^\infty$ far away from the tip provides the far-field energy release rate $\mathcal{G}_v^\infty = (K_v^\infty)^2 / \bar{E}_u$, where $\bar{E}_u = 4G$ is the undrained plane strain modulus. Then, we rewrite eq. (1) as

$$\mathcal{G}_v^\infty = \Gamma + \int_{\mathcal{R}^\infty} p \frac{\partial \varepsilon}{\partial \hat{x}_1} \, \mathrm{d}A \,, \tag{2}$$

where we have enforced the criterion $\mathcal{G} = \Gamma$ for crack propagation. The area integral may be estimated using the near-tip fields obtained through an asymptotic analysis of the governing equations for crack propagation, thus providing an analytical estimate for the degree of toughening, which is reported in Fig. 1(*Left*) and is confirmed by numerical simulations [4]. This result shows that the applied stress intensity factor needed for crack propagation at a certain velocity $v \neq 0$, which represents

*Corresponding author. Email: alucanto@sissa.it

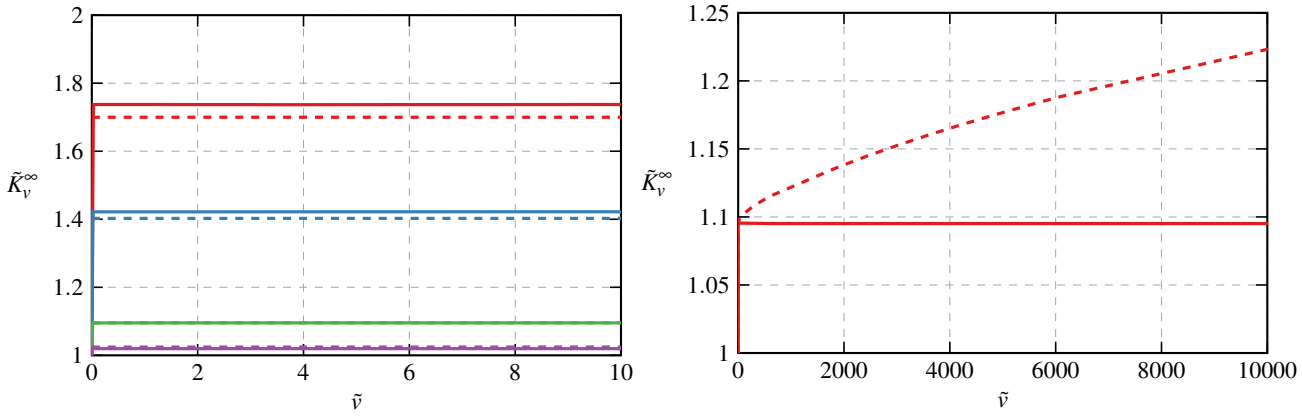

Figure 1: (*Left*) Degree of toughening $\tilde{K}_v^\infty = K_v^\infty / K_\mathrm{o}^\infty$ as a function of the dimensionless crack tip velocity $\tilde{v} = v\Gamma / D_c G$, for a Mode I crack, with D_c the effective diffusivity [4] of the solvent. Numerical results (solid lines) and analytical estimates (dashed lines) obtained from eq. (3) using the asymptotic crack tip fields. Blue line corresponds to $\kappa/G = 1$, cyan line to $\kappa/G = 2$, red line to $\kappa/G = 10$ and green line to $\kappa/G = 50$. (*Right*) Degree of toughening as a function of the dimensionless crack tip velocity, for a Mode I crack. The dashed line is the numerical result for the cohesive zone model, with $\kappa/G = 10$. The continuous line is the result obtained computing eq. $(1)_1$ from the numerical solution, without the cohesive zone model (see Fig. 1-*Left*).

the effective toughness of the system, is greater than the critical stress intensity factor needed to initiate propagation of a stationary crack in a purely elastic material, *i.e.* the intrinsic fracture toughness $K_\mathrm{o}^\infty = \sqrt{\bar{E}\Gamma}$ of the polymer network. Here, $\bar{E} = E/(1-\nu^2)$ is the effective plane-strain modulus, where E and ν are computed from G and κ through standard relations of isotropic linear elasticity. Physically, this toughening effect may be explained as follows. The stress concentration in front of the crack tip causes the material to expand. Since expansion requires an increase in solvent volume fraction, a reduction of solvent pressure develops in the process zone to draw solvent towards the crack tip. This solvent flow implies viscous dissipation that is quantified by the area integral in eq. (2). We note that toughening depends on the ratio κ/G (Fig. 1-*Left*).

Next we introduce a poroelastic cohesive zone model [4]. In this case, energy balance arguments similar to those leading to the previous equation provide the following expression for the remotely applied energy release rate

$$\mathcal{G}_v^\infty = \Gamma - \int_{\delta_f}^{0} p_c \, \mathrm{d}\delta + \int_{\mathcal{R}^\infty} p \frac{\partial \varepsilon}{\partial \hat{x}_1} \, \mathrm{d}A \,, \tag{3}$$

where p_c is the solvent pressure within the cohesive zone and δ_f is the crack opening at failure. We observe that p_c will be negative in the cohesive zone due to the pressure gradient required to draw solvent into it. Therefore, we conclude that the second term on the right hand side of eq. (3) contributes a positive increment to the toughness of the gel (Fig. 1-*Right*), in addition to toughening contribution provided by the third term on the right hand side.

CONCLUSIONS

We have demonstrated the existence of a velocity-independent toughening in a Mode I-loaded polymer gel specimen containing a semi-infinite, propagating crack. Physically, this toughening derives from the work performed by the solvent pressure against volume expansion within the process zone. For the cohesive zone case, we have shown that the applied stress intensity factor needed for propagation increases with crack tip velocity, thanks to the resistance to crack opening offered by the negative solvent pressure within the cohesive zone. Our results highlight the importance of poroelasticity to reveal and quantify possible toughening mechanisms.

References

[1] Zhao X.: Multi-scale multi-mechanism design of tough hydrogels: building dissipation into stretchy networks. Soft Matter, 10:672-687, 2014.
[2] Gong J. et al.:Double-Network Hydrogels with Extremely High Mechanical Strength, Adv. Mater., 15:1155-1158, 2003.
[3] Sun J.-Y. et al.: Highly stretchable and tough hydrogels. Nature, 489:133-136, 2012.
[4] Noselli G. et al.: Poroelastic toughening in polymer gels: A theoretical and numerical study. Submitted, 2016.
[5] Bouklas N. et al.: Effect of Solvent Diffusion on Crack-Tip Fields and Driving Force for Fracture of Hydrogels. J Appl Mech, 82:081007-081007, 2015.
[6] Lucantonio A. et al.: Transient analysis of swelling-induced large deformations in polymer gels. J. Mech. Phys. Solids, 61:205-218, 2013.
[7] Lucantonio A. et al.: Reduced models of swelling-induced bending of gel bars. Int. J. Solids Struct., 49:1399-1405, 2012.

FRACTURE OF SOFT ELASTIC FOAM

Zhuo Ma, Xiangchao Feng & Wei Hong[a)]
Department of Aerospace Engineering, Iowa State University, Ames, Iowa, USA

Summary Soft elastic foams, which consist of flexible and stretchable ligaments, exhibit extremely high fracture toughness. Comparing the cellular structure of elastic foams with the network structure of rubbery polymers, this paper proposes a scaling law for the fracture energy of soft elastic foam. A phase-field model for the fracture processes in soft elastic structures is developed to verify the scaling law. The numerical simulations in 2D foam structures of different unit-cell geometries agree with the scaling law very well. In addition, the dependences of the macroscopic fracture energy on geometric parameters such as the network connectivity and spatial orientation have also been revealed by the numerical results. To further enhance the fracture toughness, a type of soft foam structures with folded ligaments has been proposed and its effective fracture energy is one order of magnitude higher than the base material can be reached by using the soft foam structure.

INTRODUCTION

Solid foam, a state of highly porous cellular structure, is commonly found in nature and in daily life. Scaling laws between fracture properties and porosity have been proposed and widely accepted [1]. However, most existing theories are based on linear elastic fracture mechanics, their applicability becomes questionable to those consisting of soft and highly stretchable materials, such as elastomers. The major difference between stiff brittle foam and soft elastic foam lies in the slenderness of ligaments. In contrast to the cell walls of rigid foam which partially shares the load after rupture, a fractured cell wall of soft foam merely dangles over the rest of the structure.

Let us start from the fracture process of a rubber, in which the crosslinked network of long polymer chains could be regarded as an extreme case of soft foam when each slender ligament shrinks down to a molecular size. The classic Lake-Thomas model suggests that the fracture energy of a rubber scales with the number of chains per unit cross-sectional area [2]. Analogously, we deduce that the scaling relation for the fracture energy of a soft foam is

$$\Gamma \approx \alpha W_c \psi l \,. \tag{1}$$

Here, we use W_c to represent the critical energy density of cell wall at rupture, ψ for the volume fraction of the solid phase, and l for the characteristic size of the foam. Even though the scaling law (1) seems natural and plausible, it could be hard to verify directly through experiments. Alternatively, we seeks to verify the scaling law numerically through the following phase-field model.

PHASE FIELD MODEL OF FRACTURE

The phase-field model for fracture, which is capable of calculating the crack growth according to the energy criterion without a predetermined crack path, is very suitable for structures with complex geometries such as soft elastic foams. To describe the state of material damage and to avoid tracking the crack front and faces, a phase field $\phi(\mathbf{X}, t)$ varying continuously between the intact region ($\phi = 1$) and a fully damaged region ($\phi = 0$) is introduced. Following Karma et al. [3], we write the free energy density function as:

$$W(\phi, \nabla\phi, \mathbf{F}) = g\ \phi\ W_s^0\ \mathbf{F}\ + 1 - g\ \phi\ ]W_c + \frac{\kappa}{2}|\nabla\phi|^2 , \tag{2}$$

where W_s^0 is the strain-energy density of undamaged material, $g(\phi)$ an interpolation function between $g(0) = 0$ and $g(1) = 1$, and κ the coefficient of the gradient energy term. W_c is the critical strain-energy density beyond which the material will degrade spontaneously to lower the total free energy. For the evolution of the phase field variable ϕ, we assume a linear kinetic law with isotropic mobility, so that the rate of change in ϕ is proportional to the variation of the system free energy with respect to ϕ.

The system has an intrinsic length scale $r = \sqrt{\kappa/W_c}$, which represents the characteristic length of the fracture process zone. The intrinsic fracture energy of the solid described by this model is approximately $2rW_c$.

RESULTS AND DISCUSSION

The scaling relation (1) is verified through the simulation on the fracture processes of hexagonal soft foams. A set of 2D hexagonal foams of the same volume fraction but different ligament lengths are modelled first. For the hexagonal foams in both orientations, the dimensionless fracture energy Γ/rW_c is approximately linear in the ligament length l/r, as shown by Fig. 1c. Similarly, we fix the ligament length and vary the solid volume fraction ψ. The results are plotted in Fig. 1d. At relatively small volume fraction, the fracture energy is approximately proportional to the volume fraction just as predicted by (1).

[a)] Corresponding author. Email: whong@iastate.edu.

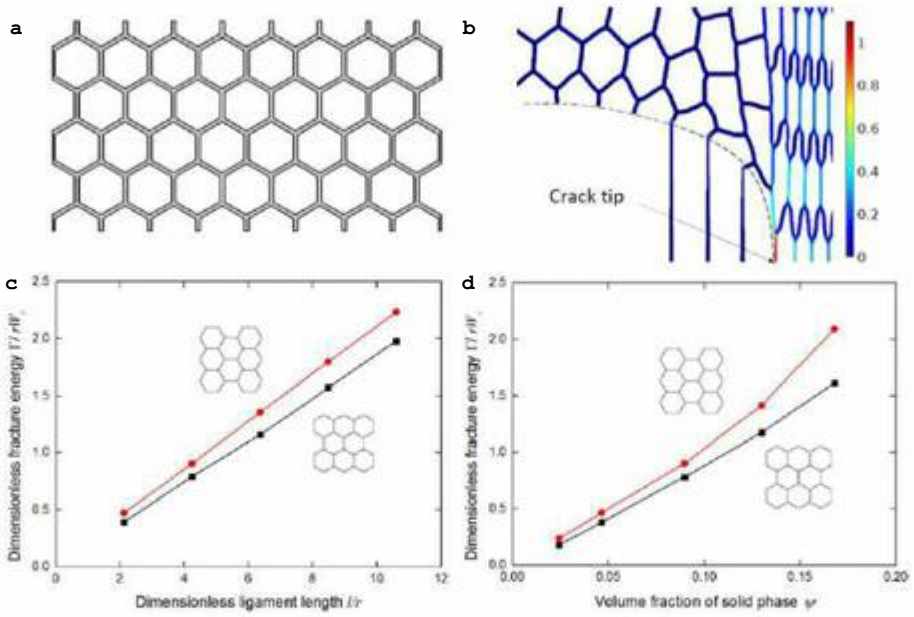

Fig 1. (a) Part of a 2D hexagonal foam structure. (b) Strain energy density of a hexagonal foam near a propagating crack tip. (c) Fracture energy as a function of the ligament length. (d) Fracture energy as a function of the volume fraction of the solid phase.

To further enhance the fracture toughness, a new kind of soft elastic foams with non-straight ligaments is proposed. As an example, the numerical model is constructed by repeating the unit cell sketched in Fig. 2a. By varying the width of the serpentine ligaments, we evaluate the fracture energy of several structures with different solid volume fraction. As plotted in Fig. 2c, the scaling law (1) still holds for the foam structures with serpentine ligaments. However, the dimensionless fracture energy has been significantly improved to $\Gamma/rW_c \approx 25$, more than one order of magnitude higher than the foam structures with straight ligaments or the same bulk material.

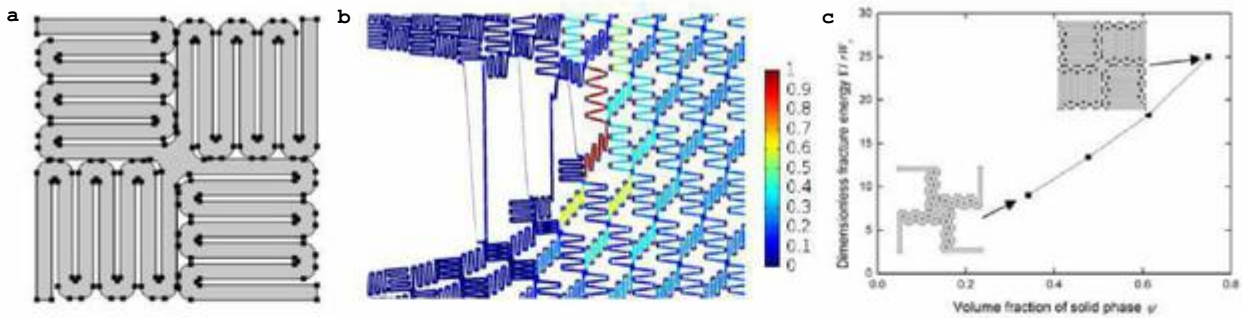

Fig 2. (a) Unit cell of a soft elastic foam containing serpentine ligaments. (b) Calculated dimensionless strain energy density of the soft elastic foam. (c) Calculated fracture energy of soft foam structures with serpentine ligaments, as a function of the solid volume fraction ψ.

CONCLUSIONS

The scaling relation between fracture energy and structural properties of soft foam structures is proposed by making an analogy between compliant ligaments in a soft elastic foam and the polymer chains in an elastomer. Through a phase-field model developed specifically for the fracture of elastomers, the scaling law is verified on soft foam structures of various geometries. Finally, a type of soft foam structures with serpentine ligaments is introduced and numerical study shows such structures may achieve an effective fracture energy much higher than that of the corresponding base material.

References

[1] Gibson L. J., Ashby M. F.: Cellular solids: structure and properties. Cambridge university press, Cambridge, UK 1999.

[2] Lake G. J., Thomas A. G.: The strength of highly elastic materials. Proceedings of the Royal Society of London, Series A, Mathematical and Physical Sciences 300(1460): 108-119, 1967.

[3] Karma A., Kessler D. A., Levine H.: Phase-field model of mode III dynamic fracture. Physical Review Letters 87(4): 045501, 2001.

REVERSIBLE SHAPE CHANGING COMPONENTS BY 3D PRINTING

Yiqi Mao[1], Zhen Ding[2], Martin L. Dunn[2 a)], H. Jerry Qi[1 a)]
[1]*The School of Mechanical Engineering, Georgia Institute of Technology, Atlanta, GA 30332, USA*
[2]*Singapore University of Technology and Design, Singapore 138682, Singapore*

Summary The availability of reversible components that can alter their shapes in response to environmental changes is crucial for active materials. The rapid development of 3D/4D printing technologies also enables the fast implementation of sophisticated designs for sensors and actuators. This paper demonstrates a new reversible component that is 3D printed to combine shape memory polymers and hydrogels. This new method uses the swelling of hydrogel as the driving force for the shape alternation and the change of the modulus of shape memory polymers as a function of temperature to regulate the time of such shape alternation. The component can be activated by changing temperature and aqueous environment, without any other further mechanical loading and unloading. The obtained structure is stiff in two different configurations. Several 2D and 3D shape changing actuators are demonstrated to illustrate the broad application potentials of the proposed design.

INTRODUCTION

Structures and devices that can change its shape in response to environmental stimuli are highly desirable in a wide range of applications [1]. Shape memory materials, such as shape memory alloys (SMAs) and shape memory polymers (SMPs), are candidates that have been widely explored. However, both materials have limitations: SMAs exhibit reversible actuations with sufficient stiffness, but the amount of actuation is low[2]; SMPs have been studied as an alternative with large shape change, but most SMPs can only achieve one-way actuation[3]. Although some new developments in SMPs can achieve reversible actuation, but they either involve complicated fabrication[4] or sophisticated chemistry[5]. One exception is environmentally responsive hydrogels[6], whose capability to hold aqueous solution can be tuned by temperature and thus to generate a large volume change. However, hydrogels have low stiffness, with the typical Young's modulus in the range of a few tens to hundreds of kPas.

3D printing allows materials to be deposited in a layer-by-layer manner to form a 3D component. In addition, the recent development of multi-material 3D printing enables digital materials, whose properties can vary almost continuously. Such capabilities, i.e. printing complicated geometries and digital materials, empower 3D printing to create components with unprecedented properties [7-10]. More interestingly, 4D printing concept was developed where active materials are used to create shape changing components[11-13], which added the 4th dimension (or time) to the 3D printing process.

In this work we achieve reversible actuations through a composite where SMPs and hydrogels are spatially distributed through a careful design, which can be easily implemented by a multi-material 3D printer[14]. We use mechanical constrains to transform an isotropic hydraulic pressure from equiaxial swelling to a uniaxial driving force that powers the shape change of the component; we also utilize the shape memory effect in the SMP to regulate the time of such shape changes. In addition, the SMP provides the stiffness to the component that is much higher than one would achieve in purely hydrogel-based component. Finally, by applying the basic design concept, we demonstrate a folding origami structure.

METHODS AND RESULTS

Design concepts

The two key concepts to our design are to convert the hydrogel swelling force from equiaxial to a linear force that can drive the shape change in one particular direction or in one particular plane, and to use the sensitivity of the SMP properties to temperature to regulate the time for actuation. To achieve this, the hydrogels and the elastomer columns are sandwiched between a layer of the SMP (top) and a layer of the elastomer (bottom). Small holes are placed in the elastomer layer to allow water flowing in and out. During a reversible actuation cycle, the printed component is straight after printing. It is then immersed into water at a temperature ~0°C for a certain amount of time to allow the hydrogel to absorb water; in addition, due to the low temperature, the stiffness of the SMP is high; therefore the volume swelling of hydrogel is highly constrained and the strip does not show significant shape change. Next, the strip is brought into a high temperature environment (such as water bath) where the SMP softens significantly, which allows the hydrogel swelling to induce large shape change. In addition, the elastomer columns that connect the top and bottom layers impose constraints on hydrogel swelling in the z-direction, thus converting the swelling force into the x-y plane, which drives the strip bending. After actuation at high temperature, we cool the strip to a temperature below the T_g of the SMP; due to the increase of the SMP stiffness, the strip is stiff. In the ambient environment, the hydrogel will lose water and dry. After the hydrogel is fully dry, immersing the strip into a high temperature environment will recover the straight shape of the strip. At low temperature, the strip becomes stiff again. This finishes one cycle of reversible actuation, which can be repeated multiple times.

[a)] Corresponding authors. Email: martin_dunn@sutd.edu.sg; qih@me.gatech.edu.

Design Demonstration

This design concept is demonstrated in Fig.1 The printed strip is shown in Fig.1a. It was firstly immersed in cold water (3°C) for 12hrs and showed a small amount of bending (Fig 1b). The strip was then immersed in water (temperature of 75°C) and bent into the shape showing in Fig. 1c in ~10 sec. The strip was then removed from the water and is cooled down to the RT (Fig. 1d). The strip maintained the bending shape (Fig. 1e). At the low temperature, the strip was stiff. Fig. 1f also shows the bent strip can support the deadweight of 25g. After drying at low temperature, the strip was immersed in high temperature water again and it recovered to the flat shape.

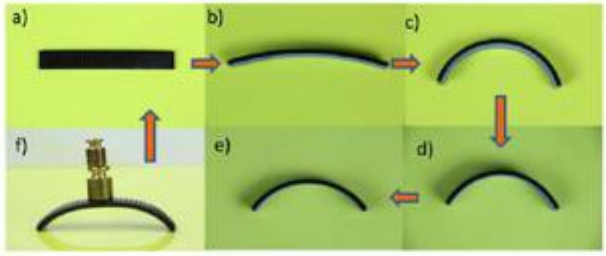

Figure 1. The bending angle of two activated shape memory strip in the desired shape memory cycle. a) The printed strip is straight; b) it bends slightly after immersing in cold water for 12hrs; c) it bends quickly when immersing in hot water; d) it is then taken out of water to the room temperature air; e) it is then air dried; f) the strip is stiff and can carry a load of 25g. If it is heated, it returns to the straight shape.

3D Reversible Structure

As an example for 3D structure, we demonstrate a flower that is capable for reversible folding and unfolding. First, we designed and printed a flower-shaped 3D structure composed of three groups of petals, which had different thickness ratios of layers of the elastomer, the hydrogel, and the SMP to allow different folding speeds. The printed structure is shown in Fig. 2a. After being put in low temperature water for 12hrs, then being immersed in high temperature water, all the layers bent immediately, forming a flower-like shape (Fig. 2b). Taking the structure out and let it dry, the structure maintained the flower shape and was stiff. As shown in Fig. 2d, it can carry a load of 25g. The flower-like structure was then put into hot water and the structure became flat again (Fig. 2c). This process could be repeated many times.



Figure 2. A self-folding/unfolding flower. a) The printed structure; b) After immersing in water then being transferred to hot water, the structure folds; c) After dry, it becomes flat again when being put into hot water. g) The structure in b) is stiff after it is dried. It can carry a load of 25g.

CONCLUSIONS

Components with large reversible shape change are highly desirable for many engineering and biomedical applications. However, the materials available for large and reversible shape change are rare. In this paper, by combining shape memory polymers with hydrogels, we demonstrated components with reversible shape changes by using 3D printing. The concept in this paper can be applied to design actuators with faster response and with other actuation method, such as electromagnetic field.

References

[1] Gandhi, M.V. and B.S. Thompson, *Smart materials and structures*. 1st ed. 1992, London ; New York: Chapman & Hall. xii, 309 p.
[2] Lexcellent, C., *Shape-memory alloys handbook*. Materials science series. 2013, London, UK; Hoboken, NJ: ISTE; Wiley.
[3] Liu, C., H. Qin, and P.T. Mather, *Review of progress in shape-memory polymers.* Journal of Materials Chemistry, 2007. **17**(16): p. 1543-1558.
[4] Westbrook, K.K., et al., *Two-way reversible shape memory effects in a free-standing polymer composite.* Smart Materials & Structures, 2011. **20**(6).
[5] Yakacki, C.M., et al., *Tailorable and programmable liquid-crystalline elastomers using a two-stage thiol-acrylate reaction.* Rsc Advances, 2015. **5**(25): p. 18997-19001.
[6] White, E.M., et al., *Advances in smart materials: Stimuli-responsive hydrogel thin films.* Journal of Polymer Science Part B-Polymer Physics, 2013. **51**(14): p. 1084-1099.
[7] Babaee, S., et al., *3D Soft Metamaterials with Negative Poisson's Ratio.* Adv Mater, 2013. **25**(36): p. 5044-9.
[8] Zheng, X.Y., et al., *Ultralight, Ultrastiff Mechanical Metamaterials.* Science, 2014. **344**(6190): p. 1373-1377.
[9] Pandey, S., B. Gupta, and A. Nahata, *Terahertz plasmonic waveguides created via 3D printing.* Optics Express, 2013. **21**(21): p. 24422-24430.
[10] Sanchis, L., et al., *Three-Dimensional Axisymmetric Cloak Based on the Cancellation of Acoustic Scattering from a Sphere.* Physical Review Letters, 2013. **110**(12): p. 124301.
[11] Ge, Q., H.J. Qi, and M.L. Dunn, *Active materials by four-dimension printing.* Applied Physics Letters, 2013. **103**(13).
[12] Ge, Q., et al., *Active Origami by 4D Printing.* Smart Materials & Structures, 2014. **23**: p. 094007-15.
[13] Raviv, D., et al., *Active Printed Materials for Complex Self- Evolving Deformations.* Scientific Reports, 2014. **4**.
[14] Mao, Y., et al., *3D Printed Reversible Shape Changing Component with Stimuli Responsive Materials.* submitted, 2015.

CONSTITUTIVE THEORY FOR MECHANOCHEMICALLY-BASED ENERGY DISSIPATING ELASTOMER

Meredith N. Silberstein*[1]
[1]*Sibley School of Mechanical and Aerospace Engineering Engineering, Cornell University, Ithaca, NY, USE*

Summary Mechanochemically responsive polymers can be designed through the incorporation of mechanophores, molecular groups with a tailored productive response to applied force. Here we present the design and corresponding constitutive theory for an elastomer that dissipates mechanical energy through the incorporation of length unveiling mechanophores. These mechanophores activate as the elastomer approaches its finite extensibility, but prior to chain scission. The reversible release of contour length temporarily increases the failure strain of the polymer chains subjected to the largest local force. The behavior of the model will be presented for monotonic, cyclic, and stress relaxation loading. Required mechanophore energetics and characteristic recovery times will be discussed.

INTRODUCTION

Mechanochemically responsive (MCR) polymers can be realized through the covalent incorporation of mechanophores chemical units that undergo a specific chemical transformation in response to applied force. While most of the demonstrated MCR to date have shown optical responses to mechanical loading, these systems have potential to adapt mechanical properties in response to mechanical load. Here we propose a synthetic analog to an approach often utilized in biological systems - length release at a critical force. Stress relief by mechanophore-based length extension has been experimentally demonstrated in single polymer chains, but not in polymer networks[1]. Here, we present a constitutive theory for an elastomer with length extending mechanophores.

THEORY

The constitutive theory for the MCR elastomer combines transition state theory for force-biased chemical reactions with polymer mechanics and builds on our prior work for an optically responsive elastomer based on covalently linked mechanophores[2]. Polymer chain segments between cross-links are assumed to follow the freely jointed chain model. The parameters governing the highly non-linear response of a single chain segment are the Kuhn segment length that sets the initial chain stiffness and the number of segments between crosslinks that sets the locking stretch. The mechanophore state is determined using transition state theory. The energy barrier between the closed (initial length) and open (extra length) states is assumed to depend linearly on force (Figure 1). When the mechanophore opens the number of segments between crosslinks increases thereby decreasing the force on the polymer chain segment. In addition to mechanophore opening, mechanochemically-driven polymer chain scission is also included. These equations are analogous to those governing the mechanophore state except that the reverse reaction (healing of the chain) is prohibited. A chain that is broken supports no force. A single polymer chain segment can occupy any one of four states: closed and intact, closed and broken, extended and intact, extended and broken. The polymer chain segments then act in concert to form the polymer network with the same force that drives the mechanophore transition and chain scission summing to give the overall network stress.

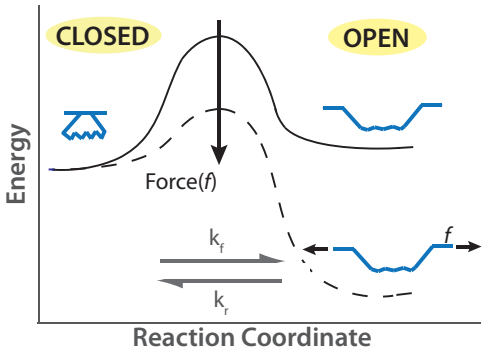

Figure 1: The application of force across a mechanophore reduces the barrier for mechanophore opening.

*Corresponding author. Email: ms2682@cornell.edu

RESULTS AND DISCUSSION

The average force-stretch behavior of an ensemble of aligned polymer chains stretched at a strain rate of $0.01s^{-}1$ is shown in Figure 2a. The polymer chain with no mechanophore behaves hyperelastically breaking at a stretch of 1.77, which corresponds to the the prescribed number of Kuhn segments along the length of the chain $N = 3$. The ensemble of polymer chains with the mechanophores incorporated initially behaves identically to those without, however at a force of 0.55 nN per chain the mechanophores start to activate, N increases to 3.6, and the force drops rapidly. Because of the highly nonlinear force response, all the chains in the ensemble have their mechanophores open over a relatively narrow stretch range. The chains are extended further the force again increases until it reaches a value that causes chain scission. This force is the same as that which causes scission in the chains without mechanophores, however the stretch is significantly larger (1.94 vs 1.77 for these particular chain and mechanophore parameters).

The polymer behavior is qualitatively quite similar to that of the ensemble of aligned chains. The polymer is initially compliant and hardens nonlinearly as the most oriented chains approach the single chain locking stretch. Under monotonic loading the work to when the first damage occurs is nearly twice as large with the mechanophore than without. Further, this model assumes that all mechanophores in a given chain segment activate at once. The energy dissipation performance could be significantly improved by a more gradual length extension that would maintain the chain closer to its present locking stretch. Under cyclic loading (Figure 2b) the difference between the elastomer with and without mechanophores is most apparent in the reloading behavior. The polymer without mechanophores reloads along the unloading curve representing the damaged polymer; the polymer with mechanophores reloads nearly along the initial loading curve since most of the open mechanophores closed during unloading.

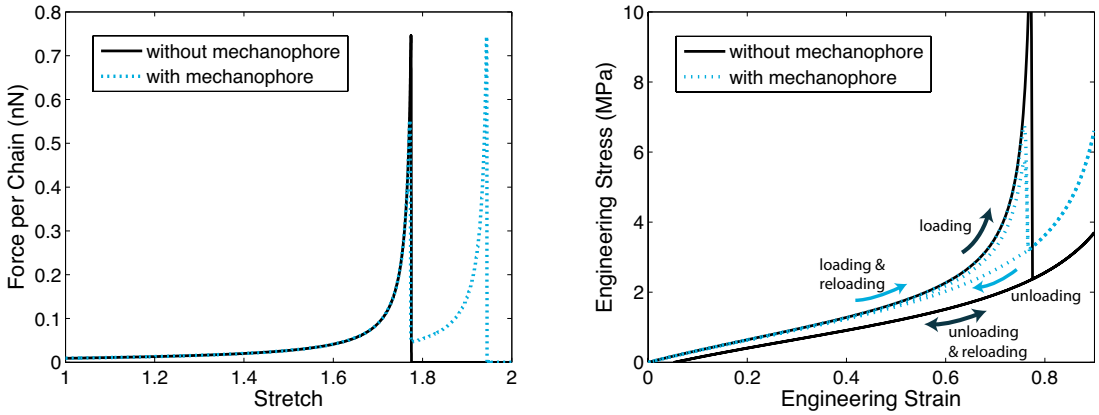

Figure 2: Simulation results for numerically implemented length-extending mechanophore constitutive theory compared to behavior without mechanophores. (a) Force-stretch response of an ensemble of single chains undergoing monotonic extension at a constant strain rate (b) Stress-strain response of a polymer subjected to load-unload-reload to a strain of 0.75 at a constant strain rate magnitude.

CONCLUSIONS

A constitutive model has been presented for an MCR elastomer with repeat energy dissipation capabilities. This model will guide the design and testing of such a material in subsequent work. *Acknowledgements: This work was funded in part by the National Science Foundation under Grant DMR-1307354.*

References

[1] Wu, D., Lenhardt, J. M., Black, A. L., Akhremitchev, B. B., Craig, S. L. : Molecular stress relief through a force-induced irreversible extension in polymer contour length. JACS 132:15936-15938, 2010.

[2] Silberstein, M. N., Cremar, L. D., Beiermann, B. A., Kramer, S. B., Martinez, T. J., White, S. R., Sottos, N. R. : Modeling mechanophore activation within a viscous rubbery network. JMPS 63:141-153.

MODELING THE EFFECT OF INELASTICITY ON INSTABILITIES IN SOFT DIELECTRICS

Shuolun Wang[1], David L. Henann[2], and Shawn A. Chester*[1]
[1]*Mechanical Engineering, New Jersey Institute of Technology, Newark, New Jersey, USA*
[2]*School of Engineering, Brown University, Providence, Rhode Island, USA*

Summary Soft dielectrics undergo large deformations in response to an electric field and consequently have attracted a lot of interest as smart active materials with a wide range of applications. The literature on this topic has historically been split between either theoretical studies or device level experiments, with limited communication. In this paper we report on our modeling capability calibrated to VHB 4910, a widely studied soft dielectric material in the literature, which exhibits a significant level of dissipation. We use specially developed finite elements to study the role of visco-elasticity on instabilities in soft dielectrics. Our results show that viscoelastic effects tend to suppress instabilities under cyclic loading.

INTRODUCTION

As soft dielectrics deform under the action of an applied electric field, it is not uncommon to encounter various instabilities. Instabilities of soft dielectrics – a heavily studied topic in the recent literature – are well known under idealized conditions, however work still remains for non-ideal conditions. Using the terminology in [6], instabilities in soft dielectrics may be categorized into three generic modes: i) pull-in, ii) electro-creasing, and iii) electro-cavitation, with the incurred instability based on the boundary conditions. Realizing that such instabilities may be harmful, the mechanics for suppressing an instability and enhancing the performance of soft dielectrics has also been investigated. Some of the proposed methods include applying a mechanical pre-stretch, using materials with "stiffening" properties, and constructing soft dielectric composites to suppress instabilities ([6, 2, 1]).

Motivated by experimental data, and the trend of the literature, the objective of this work is to produce a numerical simulation capability for the broader community that takes the real material behavior into account for more realistic simulation, including the working limits of devices that are susceptible to instability.

CONSTITUTIVE EQUATIONS

Guided by the experimental data for VHB shown in Figure 1, we assume the deformation is accommodated by a combination of one equilibrium mechanism, and N non-equilibrium mechanisms denoted by $\alpha = 1, 2, \ldots, N$. The equilibrium mechanism provides the "long-time" response of the material using the total deformation gradient, whereas the remaining N mechanisms capture the inelastic response of the material using internal variables. Based on the work of [5], we introduce a set of symmetric stretch-like tensorial internal variables $\mathbf{A}^{(\alpha)}$ for the N viscoelastic mechanisms. Although not discussed directly in this paper, thermodynamics and any restrictions required to satisfy the second law are discussed in both [3] and [5] for this class of materials and for brevity are not repeated here. In this work, the Cauchy stress is given by

$$\mathbf{T} = J^{-1}G(\mathbf{B}_{\text{dis}})_0 + K(J-1)\mathbf{1} + \epsilon\left[\mathbf{E}\otimes\mathbf{E} - \frac{1}{2}(\mathbf{E}\cdot\mathbf{E})\,\mathbf{1}\right] + \sum_{\alpha}\left\{J^{-1}G^{(\alpha)}_{\text{neq}}\mathbf{F}\left(J^{-2/3}\mathbb{P} : \mathbf{A}^{(\alpha)}\right)\mathbf{F}^{T}\right\}, \tag{1}$$

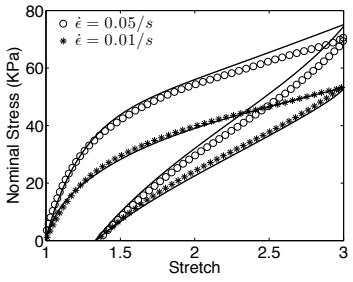

Figure 1: Comparison of the experimental data (shown as points) to our model (shown as lines) in simple tension. The experimental data is taken from [4].

where we have used the notation $G = G_{\text{eq}}\begin{pmatrix}\lambda_L\\ \bar{\lambda}\end{pmatrix}\mathcal{L}^{-1}\begin{pmatrix}\bar{\lambda}\\ \lambda_L\end{pmatrix}$ for a stretch dependent shear modulus. Also, $\mathbb{P}$ is a fourth order projection tensor $\mathbb{P} = \mathbb{I} - \frac{1}{3}\mathbf{C}^{-1}\otimes\mathbf{C}$ such that the viscous mechanisms have no volumetric contribution. Furthermore, the referential and spatial electric displacements, respectively, are given by

$$\mathbf{D}_R = \epsilon J\mathbf{C}^{-1}\mathbf{E}_R, \qquad \mathbf{D} = \epsilon\mathbf{E}, \tag{2}$$

where ϵ is the permittivity, and we denote the electric potential by φ, such that the spatial electric field $\mathbf{E} = -\text{grad}\,\varphi$.

The calibration of material parameters is straightforward process. First, we calibrate the pure mechanical parameters appearing in our model by fitting to the experimental stress-stretch data found in the literature. Then the electrical parameters are estimated based on values appearing in the literature. Our model fit to the experimental data of [4] is shown in Figure 1.

*Corresponding author. Email: shawn.a.chester@njit.edu

NUMERICAL SIMULATIONS

Now that the material parameters of our theory are calibrated for VHB, in this section we demonstrate our numerical simulation capability in a variety of interesting applications where instabilities in soft dielectrics are prone to arise. We hope to simulate such electro-mechanical instabilities in order to gain deeper understanding of the mechanisms and conditions for the onset of instability. Following the recent work of [6], we consider the following list of simulations; pull in and thinning, and creasing.

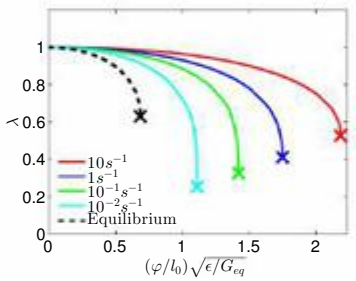

Figure 2: Simulation results for pull-in, the instability is indicated by the $\times$ symbols.

The deformation of an unconstrained soft dielectric film coated with compliant electrodes on both surfaces is prone to pull in and thinning under electro-mechanical loading. As the film thickness reduces, a constant applied voltage will induce a higher true electric field, resulting in a higher stress that further deforms the film. At a critical point, the positive feedback may cause the elastomer to thin down abruptly, resulting in the pull-in instability. Figure 2 shows the stretch (λ) corresponding to monotonic loading for multiple rates, for both equilibrium and visco-elastic material responses. It is clear that the addition of visco-elasticity acts to stabilize the instability, delaying the onset of instability with increased loading rates. Also, as reported in [6], in the equilibrium case, the onset of pull-in would occur at a critical stretch of $\lambda_{cr} = 0.63$, which agrees well with our finite element simulations.

Also, in many situations one surface of a soft dielectric is attached to a rigid electrode and another surface free from constraint. In such cases lateral motion is constrained by the rigid electrode, a condition very prone to creasing, and experimental evidence has shown this to be the case [6]. Creasing generally occurs during the application of an applied electric potential, as the soft dielectric begins to attempt to thin down, the potential eventually reaches a critical value where regions of surface on the unconstrained face will form a creasing pattern. Figure 3 shows a few snapshots of a typical plane-strain creasing simulation for cyclic loading as well as a summary of the results for this suite of simulations. Also, as reported in the literature [6], in the equilibrium case, the onset of creasing occurs at a critical electric field of $E_c \approx 1.03\sqrt{G_{eq}/\epsilon}$, which agrees well with our finite element simulations at the slowest loading rate.

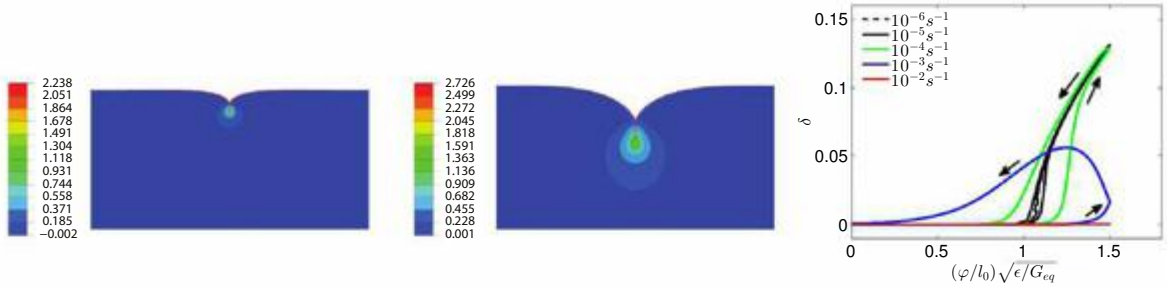

Figure 3: (Left and center) Simulation of a two-dimensional plane-strain crease at a single loading rate showing the maximum log strain. (Right) The relative normalized displacement $\delta = (u_{\text{tip}} - u_{\text{edge}})/l_0$ as a function of the applied potential for a cyclic load and unload at a constant rate. Here the arrows indicate the direction of loading and unloading.

CONCLUSIONS

Using our finite element capability we are able to show how viscoelasticity provides stabilization that may fully suppress instabilities under certain conditions, specifically under cyclic electrical loadings, which may be desirable for many applications. However, much research work yet remains, from both numerical and experimental points of view.

References

[1] Bertoldi, K., Gei, M., 2011. Instabilities in multilayered soft dielectrics. Journal of the Mechanics and Physics of Solids 59, 18–42.

[2] Dorfmann, A., and Ogden, R.W., 2014. Instabilities of an electroelastic plate. International Journal of Engineering Science 77, 79–101.

[3] Henann, D.L., Chester, S.A., Bertoldi, K., 2013. Modeling ofdielectric elastomers:Design of actuators and energy harvesting devices. Journal of the Mechanics and Physics of Solids 61, 2047-2066.

[4] Hossain, M., Vu, D.K., Steinmann, P., 2012. Experimental study and numerical modelling of VHB 4910 polymer. Computational Materials Science 59, 65–74.

[5] Linder, C., Mykola, T., Miehe, C., 2011. A micro mechanically motivated diffusion-based transient network model and its incorporation into finite rubber viscoelasticity. Journal of the Mechanics and Physics of Solids 59, 2134–2156.

[6] Zhao, X., Wang, Q., 2014. Harnessing large deformation and instabilities of soft dielectrics: Theory, experiment, and application. Applied Physics Reviews 1, 021304.

ACTIVE MOTION AND DEFORMATION OF LIQUID CRYSTAL ELASTOMERS

Shengqiang Cai[a], Chihyung Ahn
Department of Mechanical and Aerospace Engineering, University of California, San Diego, La Jolla, CA 92093, USA

Summary In the talk, I will present our recent research progress on the optically/ thermally actuated motion and deformation in liquid crystal elastomer structures.

INTRODUCTION

A combination of liquid crystal and polymer network can form a new material—liquid crystal elastomer (LCE). The special molecular combination endows LCE with many unique properties such as soft or semi-soft elasticity and multi-responsiveness, which have led to myriad applications ranging from artificial muscle to stretchable optical devices. Recently, several biological materials such as actin filament network and fibrillar collagens have also been found to have similar molecular structure and behaviors as man-made LCEs. In this talk, I will discuss some recent progresses made in our group for the active motion and deformation of LCE structures driven by light or heat.

Experiments

- Material synthesis

We adopt the chemical reaction recently developed by Yakacki et al [1] to synthesize LCEs. The synthetic process is briefly summarized as follows. First, RM257 (liquid crystal monomer), PETMP (crosslinker) and EDDET (spacer) and multiwall carbon nanotubes are dissolved in toluene by heating and vigorous mixing. The molar functionality composition of thiol monomers from PETMP and EDDET is fixed as 20:80 while that between thiol monomers and acrylate monomer from RM 257 is fixed as 1:1.15 so that there is 15% excess molar functional group of RM257 to that of PETMP and EDDET. A value of 0.5 wt% of HHMP to total monomers and 1.1 wt% of DPA to thiol monomers are added in the solution. After the solution is homogeneously mixed, it is placed in the vacuum chamber to remove bubbles trapped inside the solution. The solution is then transferred to the mold and left overnight at room temperature for the first step reaction. During the first-step reaction, RM257 reacts with PETMP and EDDET through thiol-acrylate Michael addition to form a lightly-crosslinked polydomain LCE film which are ready for applying mechanical stress and second-step reaction after the complete evaporation of toluene at 80℃. In the second-step reaction, LCE film can be completely cured by the photo-polymerization of unreacted LC monomers under the UV light exposure.

- Different active motion and deformation modes in LCE structures induced by light and heat

1. Omnidirectional bending of a LCE cylinder induced by light

As shown in Figure 1, a LCE cylinder is fabricated. With the illumination of light from one side, the LCE cylinder can quickly bend toward the light. The bending is caused by the inhomogeneous contraction of the LCE cylinder induced by the light. There is an optimized diameter of the LCE cylinder which can have the largest light-induced bending curvature.



Fig. 1 A LCE cylinder bends toward a light source

2. Light-driven rolling of a LCE cylindrical tube

As shown in Figure 2, a LCE cylindrical tube can roll in a flat surface with the light illumination from on direction. When the tube is exposed to light from one side, the tube deforms inhomogenously which will shift the gravity center of the tube. Therefore the gravity of the tube can generate a moment to roll the cylindrical tube forward.



Fig. 2 Rolling of a LCE tube driven by light illumination.



Fig. 3 Rolling of a LCE tube driven by heating.

[a] Corresponding author. Email: shqcai@ucsd.edu

3. Heat-driven rolling of a LCE cylindrical tube

As shown in Figure 3, the same LCE tube can also roll in a fat surface when it is heated from the bottom. The mechanism is still under investigation.

CONCLUSIONS

The active motion and deformation mode discussed in the presentation can be potentially useful for designing and fabricating various soft structures and devices.

References

[1] C. M. Yakacki, M. Saed, D. P. Nair, T. Gong, S. M. Reed, and C. N. Bowman: Tailorable and programmable liquid-crystalline elastomers using a two-stage thiol-acrylate reaction. *Rsc Advances*, **5**:18997-19001, 2015.

OPTIMIZING THE ENERGY HARVESTING PERFORMANCE OF VISCOELASTIC DIELECTRIC ELASTOMER GENERATORS

Jianyou Zhou, Liying Jiang[a] & Roger E. Khayat
Department of Mechanical and Materials Engineering, The University of Western Ontario, London, Ontario, Canada

Summary As a promising technology for renewable energy harvesting, dielectric elastomer generators (DEGs) have drawn much attention from the research community due to their flexibility, light weigh, low cost, large deformation capacity, and most importantly, high energy density. However, their energy harvesting schemes are relatively complex and can be affected by various material properties and failure modes. Based on a particular harvesting scheme, this work presents a theoretical study on the performance of DEGs under equi-biaxial loading. From the simulation results, it is found that the material viscoelasticity exerts a strong effect on the harvested energy. The general framework developed in this paper is expected to provide guidance for the optimal design of DEGs.

INTRODUCTION

Dielectric elastomers (DEs), as a category of soft electroactive materials, can convert energy from one form to another. Due to their large deformation capability and high energy density, DEs are desirable materials for power generators that transduce mechanical energy to electrical energy. In fact, much effort has been devoted to studying the energy harvesting performance of dielectric elastomer generators (DEGs). At the early stage, Pelrine *et al*. proposed a "rectangular" electromechanical harvesting scheme for DEGs, which is relatively easy to manage [1]. Later, various prototypes of DEG have been developed based on this "rectangular" energy harvesting scheme [2-5]. According to these studies, the achieved energy density of DEGs is already more than one order of magnitude higher than that of the piezoelectric and electromagnetic generators, while it is still far less than the predicted maximum energy density [6].

As discussed in the earlier studies, the performance of DEGs can be affected by various factors such as electrical breakdown (EB), loss-of-tension, current leakage, loading configurations and material viscoelasticity. Particularly, it is reported that the efficiency of DEGs is strongly affected by the material viscoelasticity that may lead to high energy dissipation and loss-of-tension [5, 7]. Moreover, to gain a better understanding on the influence of the material viscoelasticity, it is essential to investigate the finite-deformation viscoelastic behavior of DEs since they commonly undergo large deformation during the operation of DEGs. Based on the finite-deformation viscoelasticity model by Hong [8], this work investigates the influence of the material viscoelasticity on a "triangular" harvesting scheme and the harvested energy, aiming to provide an increased understanding on the harvesting mechanisms of DEGs

THE ENERGY HAVESTING MECHANISM AND SCHEME OF DEGS

Regardless of the electromechanical energy harvesting scheme, the energy harvesting principle of a DEG always lies in the cyclic change of the capacitance of the embedded DE, which is realized by its electromechanical deformation. In addition, the electromechanical deformation of a DE is limited by the electrical breakdown (EB) failure and its material extensibility. Figure 1(a) illustrates the electrical breakdown curve on the dimensionless voltage-charge (Φ -Q) plane of a DE. The operation of the DEG is safe when voltage level of the DE is below the EB curve, otherwise it fails by electrical breakdown. Also, the deformation of the DE is commonly restricted within a prescribed range from λ_{min} to λ_{max}, where λ_{min} and λ_{max} are the minimum stretch ratio and the maximum stretch ratio, respectively. Therefore, the maximum achievable energy for such a DEG can be indicated by the area enclosed by the λ_{min}, λ_{max} and EB curves in figure 1(a).

According to this enclosed area, a desirable scheme to maximize the harvested energy should be a triangle as denoted by A-B-C in figure 1(a), which was recently proposed by Shian *et al* [9]. Figure 1(b) shows the energy harvesting circuit of this "triangular" harvesting scheme. At state A, a DE coated with compliant electrodes on both surfaces is stretch to λ_{max} by an equi-biaxial force P (figure 1(c)). Then switch 1 is closed, which connects the DE and the transfer capacitor to the power supply. Thus, charges flow from the power supply to the DE and the transfer capacitor until the voltage of the DE (Φ) increases to the level of the power supply (Φ_L) at state B. The diode between the DE and the transfer capacitor only allow charges flow from the DE to the transfer capacitor when $\Phi > \Phi_C$ (Φ_C is the voltage of the transfer capacitor). After state B is reached, switch 1 is opened and force P is gradually decreased, which allows the DE to shrink back. When the DE shrinks back, its capacitance C decreases ($C=C_0\lambda^4$, where C_0 the capacitance of the undeformed DE and λ is the stretch ratio) and voltage increases, which forces some charges to flow to the transfer capacitor and increases its voltage. The slope of B-C line is proportional to $-1/C_p$, where C_p is the capacitance of the transfer capacitor. At state C, the DE shrinks back to λ_{min} and most of the charges on the DE have been transferred to the transfer capacitor. After state C is reached, switch 2 is closed and the charges from both the DE and the transfer capacitor flow to the harvesting circuit since they are at the highest level of voltage. After switch 2 is closed, the DE membrane is stretched again, which causes its capacitance to increase and its

[a] Corresponding author. Email: **lyjiang@eng.uwo.ca**.

voltage to further decrease (the decrease of its voltage is partly due to the discharging). When the deformation of the DE is back to λ_{max} (at state A), switch 2 is opened and the harvesting cycle is finished.

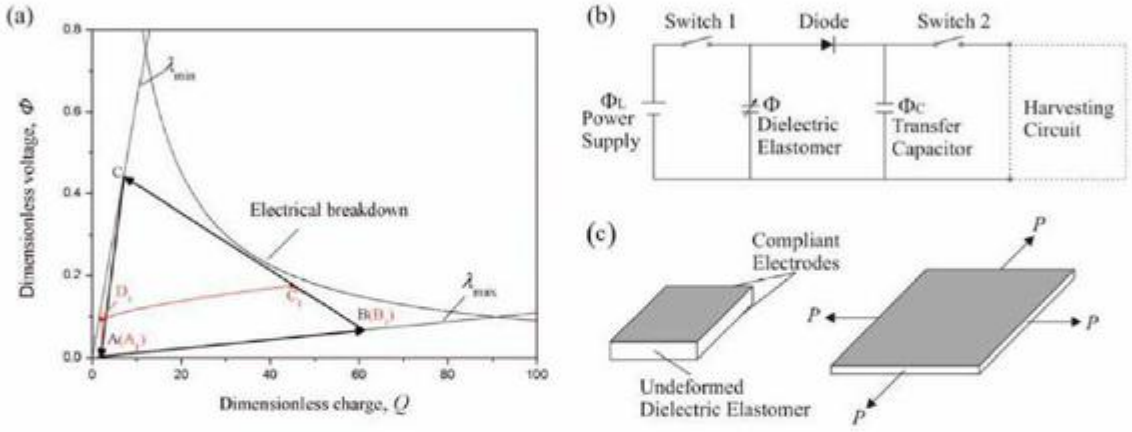

Figure 1. Schematics of a dielectric elastomer generator: (a) energy harvesting scheme and simulation results; (b) energy harvesting circuit diagram; (c) a dielectric elastomer under equi-biaxial loading.

Simulation results and discussion

Based on the finite-deformation viscoelasticity model [8], figure 1(a) shows the simulation result of the energy harvesting cycle of the DEG denoted by A_1-B_1-C_1-D_1-A_1. Due to the material viscoelasticity, loss-of tension occurs before the DE can reach state C in our simulation. This phenomenon is also in agreement with the experimental results by Shian et a1 [9]. Therefore, another state (state C_1 in the simulation) has to be prescribed to determine the time for closing switch 2. In addition, from state B_1 to state C_1 (the DE shrinks back), only a small amount of charges on the DE have been transferred to the transfer capacitor. After state C_1 is reached, switch 2 is closed and the DE continues to shrink back until it reaches a loss-of-tension condition at state D_1, during which time the charges on both the DE and the transfer capacitor flow to the harvesting circuit. After state D_1 is reached, DE is stretched again. When the DE is stretched back to λ_{max} (at state A_1), switch 2 is reopened and the harvesting cycle is complete. Although the area enclosed by A_1-B_1-C_1-D_1 is much smaller than that enclosed by A-B-C, a DEG adopting this harvesting scheme has experimentally demonstrated the highest energy density so far [9].

Since the harvested energy is still significantly less than the maximum achievable value, there is much room for the improvement of the performance of DEGS. Based on the "triangular" harvesting scheme, our simulation results suggest that the harvested energy of DEGs could be improved by some approaches such as increasing the rate of the deformation of the DE (which weakens the viscoelastic effect of the material), optimizing the position of state B_1 and C_1 (the position of state B_1 is determined by the voltage level of the power supply), and choosing an appropriate transfer capacitor (the slope of line B_1-C_1 is determined by the capacitance of the transfer capacitor).

ACKNOWLEDGEMENTS

This work is supported by the Natural Sciences and Engineering Research Council of Canada (NSERC).

References

[1] Pelrine R., Kornbluh R. D., Eckerle J., Jeuck P., Oh S., Pei Q., Stanford S.: Dielectric Elastomers: Generator Mode Fundamentals and Applications. Proc. SPIE **4329**. 148-156, 2001.

[2] McKay T. G., O'Brien B. M., Calius E. P., Anderson I. A.: Soft Generators Using Dielectric Elastomers. Appl. Phys. Lett. **98**. 142903, 2011.

[3] Kornbluh R. D., Pelrine R., Prahlad H., Wong-Foy A., McCoy B., Kim S., Eckerle J., Low T.: Dielectric Elastomers: Stretching the Capabilities of Energy Harvesting. MRS Bull. **37**. 246-253, 2012.

[4] Kaltseis R., Keplinger C., Baumgartner R., Kaltenbrunner M., Li T., Machler P., Schwodiauer R., Suo Z., Bauer S.: Method for Measuring Energy Generation and Efficiency of Dielectric Elastomer Generators. Appl. Phys. Lett. **99**. 162904, 2011.

[5] Huang J., Shian S., Suo Z., Clarke R.: Maximizing the Energy Density of Dielectric Elastomer Generators Using Equi-Biaxial Loading. Adv. Funct. Mater. **19**. 5056-5061, 2013.

[6] Koh S. J. A., Keplinger C., Li T., Bauer S., Suo Z.: Dielectric Elastomer Generators: How Much Energy Can Be Converted? IEEE/ASME Trans. Mechatron. **16**. 33-41, 2011.

[7] Zhou J., Jiang L., Khayat R. E.: Investigation on the performance of a viscoelastic dielectric elastomer membrane generator. Soft Matter **11**. 2983-2992, 2015.

[8] Hong W.: Modeling Viscoelastic Dielectrics. J. Mech. Phys. Solids **59**. 637-650, 2011.

[9] Shian S., Huang J., Zhu S., Clarke D. R.: Optimizing the Electrical Energy Conversion Cycle of Dielectric Elastomer Generators. Adv. Mater. **26**. 6617-6621, 2014.

MULTISCALE CONSTITUTIVE MODELING ON FINITE STRAIN VISCOELASTICITY OF ELASTOMERS

Ying Li *[1], Shan Tang[2], Martin Kröger[3], and Wing Kam Liu[4]
[1]*Department of Mechanical Engineering, University of Connecticut, Storrs, CT 06269, USA.*
[2]*Department of Engineering Mechanics, Chongqing University, Shapingba, Chongqing, 400017, China*
[3]*Department of Materials, Polymer Physics, ETH Zurich, CH-8093 Zurich, Switzerland*
[4]*Department of Mechanical Engineering, Northwestern University, Evanston, IL 60208, USA.*

Summary In this work, we present a mechanistic and physics-based constitutive model to describe and design the finite strain viscoelastic behavior of elastomers. Mathematically, the viscoelasticity of elastomers has been decomposed into hyperelastic and viscous parts, which are attributed to the nonlinear deformation of the cross-linked polymer network and the diffusion of free chains, respectively. Combing the non-affine network model for hyperelasticity and modified tube model for viscosity, both understood by molecular simulations, we develop a mechanism-based constitutive model for finite strain viscoelasticity of elastomers. All the parameters in the proposed constitutive model have physical meanings, which are signatures of polymer chemistry, physics or dynamics. The finite strain viscoelasticity obtained from our simulations agrees qualitatively with experimental data on both un-vulcanized and vulcanized rubbers, which captures the effects of cross-linking density, the molecular weight of the polymer chain and the strain rate.

INTRODUCTION

Elastomers consist of long polymer chains joined together by chemical bonds through cross-linkers. They are usually capable of recovering their original shapes after finite deformation due to covalent cross-linkages. Under equilibrium conditions, long polymer chains making up an elastomer are irregularly coiled together. However, when the elastomer is under tension, polymer chains tend to stretch out and straighten along the pulling direction. Upon unloading, the chains return to their original compact and random arrangement. During such a loading-unloading process, energy dissipates due to friction between polymer chains and the elastomer exhibits viscoelastic behavior (cf. Fig. 1). Examples of elastomers include polyisoprene (natural rubber), polybutadiene (butadiene rubber), polychloroprene (chloropene rubber) and the copolymer comprised of butadiene and acrylonitrile (nitrile rubber). These materials have a broad range of applications in engineering and industry.

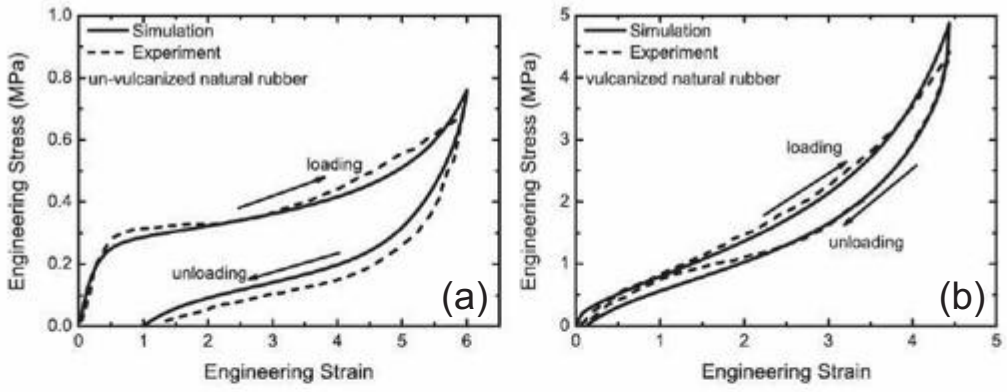

Figure 1: Experimental and computational results on uniaxial stress-strain curves during loading and subsequent un-loading of (a) un-vulcanized and (b) vulcanized natural rubber (NR) with strain rate 0.003 s^{-1} at room temperature. Experimental results are taken from [1].

Due to differences in the degree of cross-linking, the viscoelastic behavior of un-vulcanized natural rubber (NR) can be very distinct from that of vulcanized NR. For un-vulcanized NR under uniaxial tension, the stress initially increases linearly with strain during the elastic deformation stage, followed by a strain-softening stage with a stress plateau, depicted in Fig. 1(a). Upon increasing the strain further, the stress starts to increase rapidly, reminiscent of strain-hardening behavior. When the applied tension is released, the stress drops rather quickly and the polymer chains tend to return to a coiled equilibrium state that might be very different from the initial state. Therefore, the stress-strain curve of un-vulcanized NR exhibits pronounced hysteretic behavior, representing large energy dissipation. Contrary to the behavior of un-vulcanized NR, the vulcanized NR

*Corresponding author. Email: yingli@engr.uconn.edu

exhibits only the strain-hardening behavior without showing strain-softening, as given in Fig. 1(b). During the unloading stage, the stress slowly reduces with decreasing strain, signaling a much smaller hysteresis with less energy dissipation, because of the constraints applied through the cross-linkages. Moreover, the elastic modulus of vulcanized NR is about 20-30 times larger than that of un-vulcanized NR due to large differences in cross-linking densities. The above stress-strain curves for un-vulcanized and vulcanized NRs characterize the most important mechanical behavior of elastomers, which can greatly affect their performance in applications. However, a reliable constitutive model that is able to capture these qualitative differences in mechanical behavior for un-vulcanized and vulcanized NRs simultaneously does not presently exist.

DEVELOPMENT OF CONSTITUTIVE MODEL

To better understand the viscoelastic behaviors of elastomers, they have been decomposed into a cross-linked network with superimposed free chains. Mathematically, the viscoelasticity of elastomers has been decomposed into hyperelastic and viscous parts, which are attributed to the nonlinear deformation of the cross-linked polymer network and the diffusion of free chains, respectively. The hyperelastic deformation of a cross-linked polymer network is governed by the cross-linking density, the molecular weight of the polymer strands between cross-linkages, and the amount of entanglements between different chains, which we observe through large scale molecular dynamics (MD) simulations. Moreover, a recently developed non-affine network model [2] is confirmed in the current work to be able to capture these key physical mechanisms using MD simulation. The energy dissipation during a loading and unloading process of elastomers is governed by the diffusion of free chains, which can be understood through their reptation dynamics. The viscous stress can be formulated using the classical tube model [3]; however, it cannot be used to capture the energy dissipation during finite deformation. By considering the tube deformation during this process, as observed from the MD simulations, we propose a modified tube model to account for the finite deformation behavior of free chains. Combing the non-affine network model for hyperelasticity and modified tube model for viscosity, both understood by molecular simulations, we develop a mechanism-based constitutive model for finite strain viscoelasticity of elastomers. All the parameters in the proposed constitutive model have physical meanings, which are signatures of polymer chemistry, physics or dynamics. More importantly, the finite strain viscoelasticity obtained from our simulations agrees qualitatively with experimental data on both un-vulcanized and vulcanized rubbers (see Fig.1), which captures the effects of cross-linking density, the molecular weight of the polymer chain and the strain rate.

CONCLUSIONS

The hyperelastic and viscous behaviors of elastomers are attributed to the nonlinear deformation of a cross-linked network and diffusion of free chains, respectively. Large scale molecular simulations were performed to reveal the detailed physical mechanisms of the cross-linked network and free chains under uniaxial tension, simple shear and equal-biaxial tension. For the cross-linked network, its stress response is attributed to the cross-linking and entanglement. Therefore, the classical Arruda-Boyce model [4] is not applicable as it does not include the effect of entanglements. The recently developed non-affine network model [2], simultaneously considering the contributions of cross-linking and entanglement, is identified as the most proper continuum model to describe the hyperelastic behaviors of elastomers. For the free chains, the primitive chain length and tube diameter are found to be dependent on the applied deformations in the molecular simulations [5, 6], which can be captured by our theoretical formulations based on an affine deformation assumption. Based on these observations, the viscous contribution of free chains can be reformulated according to the classical tube model proposed by Doi and Edwards [3], which is named as the updated tube model. Combining the non-affine network model with the updated tube model, a new constitutive model has been proposed for studying the finite strain viscoelastic behavior of elastomers. This new model is found to be able to capture the mechanical responses of un-vulcanized and vulcanized rubber under uniaxial loading and unloading with different strain rates. Moreover, parametric studies have been performed based on the proposed constitutive model, which demonstrate that different viscoelastic behaviors can be achieved through tuning these physical parameters.

References

[1] Amnuaypornsri S., Toki S., Hsiao B.S., Sakdapipanich J.: The effects of endlinking network and entanglement to stressstrain relation and strain-induced crystallization of un-vulcanized and vulcanized natural rubber. Polymer 53: 3325-3330, 2012.

[2] Davidson J.D., Goulbourne N.: A nonaffine network model for elastomers undergoing finite deformations. J. Mech. Phys. Solids. 61: 1784-1797, 2013.

[3] Doi M., Edwards S.F.: The Theory of Polymer Dynamics. Clarendon Press, Oxford 1986.

[4] Arruda E.M., Boyce M.C.: A three-dimensional constitutive model for the large stretch behavior of rubber elastic materials. J. Mech. Phys. Solids, 41:389-412, 1993.

[5] Li Y., Abberton B.C., Kröger M., Liu W.K.: Challenges in multiscale modeling of polymer dynamics. Polymers, 5: 751-832, 2013.

[6] Li Y., Tang S., Kröger M., Liu W.K.: Molecular simulation guided constitutive modeling on finite strain viscoelasticity of elastomers. J. Mech. Phys. Solids. 2015, DOI:10.1016/j.jmps.2015.12.007.

THERMODYNAMICS AND INSTABILITY OF DIELECTRIC ELASTOMERS

Liwu Liu[1a)], Yanju[1] and Jinsong Leng[2]
[1]*Department of Astronautical Science and Mechanics, Harbin Institute of Technology, Harbin, Heilongjiang, China*
[2]*Centre for Composite Materials, Harbin Institute of Technology, Harbin, Heilongjiang, China*

Summary Dielectric elastomer is a kind of typical soft active material. It can deform obviously when subjected to an external voltage. Here, we develop a thermodynamic constitutive model of dielectric elastomers undergoing polarization saturation and strain-stiffening, and then investigate the stability (electromechanical stability, snap-through stability) and voltage induced deformation of dielectric elastomers. Analytical solution has been obtained and it reveals the marked influence of the extension limit and polarization saturation limit on its instability. The developed thermodynamic constitutive model and simulation results would be helpful in future to the research of dielectric elastomer based high-performance transducers.

INTRODUCTION

Dielectric elastomer is a kind of typical soft active material. It can deform obviously when subjected to an external voltage. When a dielectric elastomer with randomly oriented dipoles is subject to an electric field, the dipoles will rotate to and align with the electric field. The polarization of the dielectric elastomer may be saturated when the voltage is high enough. When subjected to a mechanical force, the end-to-end distance of each polymer chain, which has a finite contour length, will approach the finite value, reaching a limiting stretch. On approaching the limiting stretch, the elastomer stiffens steeply. The schematic diagram of voltage-driven dielectric elastomers can be depicted as Fig.1 [1]:

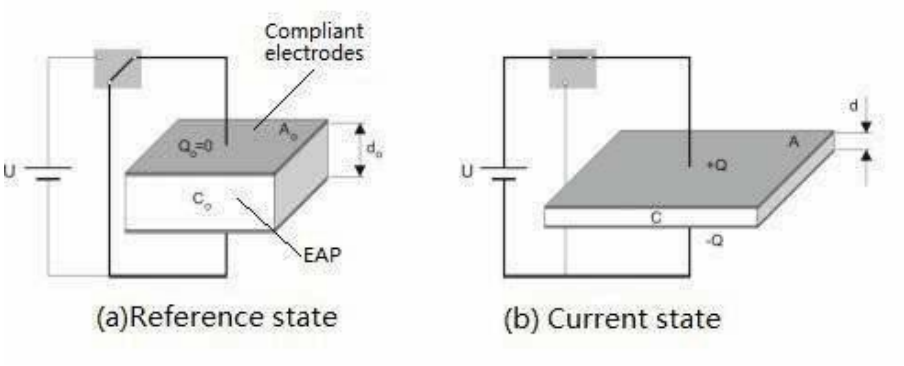

Fig.1 Schematic diagram of voltage-driven dielectric elastomers [1]

THERMODYNAMIC CONSTITUTIVE MODEL OF DIELECTRIC ELASTOMERS

In the paper, a thermodynamic constitutive model of dielectric elastomers undergoing polarization saturation and strain-stiffening is investigated. The constitutive relation of dielectric elastomer undergoing large deformation can be described as the following equations:

$$\sigma_1 = \lambda_2^{-1}\lambda_3^{-1}\frac{\partial U(\lambda_1,\lambda_2,\lambda_3)}{\partial \lambda_1} - \frac{\varepsilon}{2}E^2 - \frac{1}{2}\frac{\partial \varepsilon}{\partial \lambda_1}\lambda_1 E^2 \tag{1-a}$$

$$\sigma_2 = \lambda_1^{-1}\lambda_3^{-1}\frac{\partial U(\lambda_1,\lambda_2,\lambda_3)}{\partial \lambda_2} - \frac{\varepsilon}{2}E^2 - \frac{1}{2}\frac{\partial \varepsilon}{\partial \lambda_2}\lambda_2 E^2 \tag{1-b}$$

$$\sigma_3 = \lambda_1^{-1}\lambda_2^{-1}\frac{\partial U(\lambda_1,\lambda_2,\lambda_3)}{\partial \lambda_3} + \frac{\varepsilon}{2}E^2 - \frac{1}{2}\frac{\partial \varepsilon}{\partial \lambda_3}\lambda_3 E^2 \tag{1-c}$$

where the first parts of the equations represent elastic forces, the second parts mean Maxwell stress, and the third parts are depended on dielectric constant.

STABILITY OF POLARIZATION SATURATION DIELECTRIC ELASTOMERS

The real dielectric elastomer always undergoes a polarization saturation progress. The paper studied the stability of dielectric elastomer considering polarization saturation. An expression is utilized describing the polarization saturation.

$$E = \frac{D_s}{2\varepsilon}\log\left(\frac{1+D/D_s}{1-D/D_s}\right) \tag{2}$$

a) Corresponding author. Email: liuliwu_006@163.com.

For the uncompressible dielectric elastomer, the true stress and electric field are as follows:

$$\sigma_1-\sigma_3=\lambda_1\frac{\partial U\left(\lambda_1,\lambda_2,\lambda_1^{-1}\lambda_2^{-1}\right)}{\partial\lambda_1}-\frac{D_sD^{\sim}\lambda_1^{-1}\lambda_2^{-1}}{2\varepsilon}\log\left(\frac{1+D^{\sim}\lambda_1^{-1}\lambda_2^{-1}/D_s}{1-D^{\sim}\lambda_1^{-1}\lambda_2^{-1}/D_s}\right) \tag{3}$$

$$\sigma_2-\sigma_3=\lambda_2\frac{\partial U\left(\lambda_1,\lambda_2,\lambda_1^{-1}\lambda_2^{-1}\right)}{\partial\lambda_2}-\frac{D_sD^{\sim}\lambda_1^{-1}\lambda_2^{-1}}{2\varepsilon}\log\left(\frac{1+D^{\sim}\lambda_1^{-1}\lambda_2^{-1}/D_s}{1-D^{\sim}\lambda_1^{-1}\lambda_2^{-1}/D_s}\right) \tag{4}$$

ELECTROMECHANICAL AND SNAP-THROUGH STABILITY

The electromechanical and snap-through stability of dielectric elastomer undergoing polarization saturation are investigated. When subjected biaxial stretch ($F_1=F_2=F$), the dielectric elastomer film will obtain a deformation along two directions equally ($\lambda_1=\lambda_2=\lambda$). The free energy can be described as the following equation:

$$W\left(\lambda,D^{\sim}\right)=\frac{C_1}{2}\left(2\lambda^2+\lambda^{-4}-3\right)+\frac{kC_1}{2}\left(2\lambda^{-2}+\lambda^4-3\right)+\frac{D_sD^{\sim}\lambda^{-2}}{2\varepsilon}\log\left(\frac{1+D^{\sim}\lambda^{-2}/D_s}{1-D^{\sim}\lambda^{-2}/D_s}\right)+\frac{D_s^2}{2\varepsilon}\log\left(1-\frac{D^{-2}\lambda^{-4}}{D_s^2}\right) \tag{5}$$

For convenience, the relation between the dimensionless nominal stress and the dimensionless nominal electric field can be expressed as the following equation:

$$\frac{s}{C_1}=2\left(\lambda-\lambda^{-5}\right)+2k\left(\lambda^3-\lambda^{-3}\right)-\mathbf{2}\frac{D_s}{\sqrt{C_1\varepsilon}}\left[\frac{\exp(2\frac{E^{\sim}}{\sqrt{C_1/\varepsilon}}\lambda^2\Big/\frac{D_s}{\sqrt{C_1\varepsilon}})-1}{\exp(2\frac{E^{\sim}}{\sqrt{C_1/\varepsilon}}\lambda^2\Big/\frac{D_s}{\sqrt{C_1\varepsilon}})+1}\right]\frac{E^{\sim}}{\sqrt{C_1/\varepsilon}}\lambda \tag{6}$$

The calculation results are shown as Fig. 2.

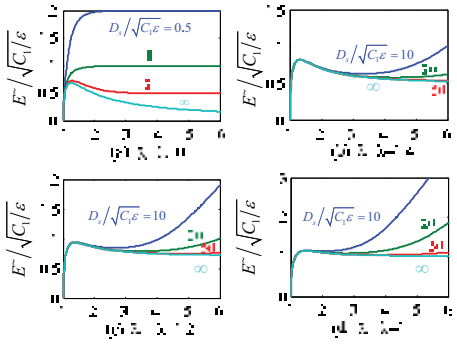

(a) Nominal electric field and stretch of dielectric elastomer undergoing polarization saturation

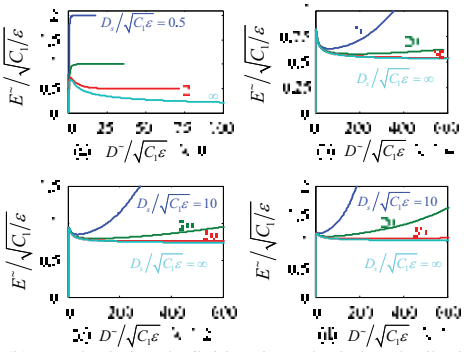

(b) Nominal electric field and nominal electric displacement of dielectric elastomer undergoing polarization saturation

Fig.2 Calculation results of dielectric elastomer undergoing polarization saturation under the loading condition $\lambda_1=\lambda_2=\lambda$

CONCLUSIONS

The paper presents the constitutive theory, stability, electromechanical and snap-through stability as well as the simulation results. It would be helpful in future to the research of dielectric elastomer based high-performance transducers.

References

[1] R. Pelrine, R. Kornbluh, Q. Pei: High-speed electrically actuated elastomers with strain greater than 100%. *Science* **287(28):** 836~839, 2000.

A NEW VISCOELASTIC CONSTITUTIVE MODEL OF SHAPE MEMORY POLYMERS

Yunxin Li[1] & Zishun Liu[a1]
[1]*International Center for Applied Mechanics, State Key Laboratory for Strength and Vibration of Mechanical Structures, Xi'an Jiaotong University, Xi'an, China*

Summary In this work, we propose a new viscoelastic model for shape memory polymers (SMPs) based on phase transition, which has clear physical significance and includes the time history. To describe the phase transition phenomenon of SMPs, our new model has different constitutive structures above and below transformation temperature. As the proposed viscoelastic model is based on phase transition, it can be used both for different types of SMP materials and to treat large strain problems. To validate the model accuracy and show the model's capability in reproducing the shape memory effect, two test examples are predicted using the new constitutive model. The simulated and predicted results are compared with available experimental results and good agreement can be observed.

INTRODUCTION

Shape memory polymers (SMPs), a kind of soft and smart material, have been widely used in aerospace structures, biomedical devices, functional textiles and other soft machines/devices. Increasing usefulness of SMPs motivates us to further understand its thermomechanical properties and deformation behavior. With that in mind, the development of more suitable constitutive models for SMPs is imperative. To develop new macro constitutive models for SMPs, two general approaches have been adopted: viscoelastic modeling and phenomenological modeling. The existing viscoelastic models may be able to describe the behavior of SMPs, but they lack a clear physical meaning. The phenomenological models based on phase transition have a clear physical meaning, but do not include the time factor and cannot describe the creep and stress relaxation of rubber. In order to overcome the shortcomings of these two types of models, we propose a new viscoelastic model based on phase transition, which has physical significance and includes the time factor. In previous research work, there is still a lack of unified constitutive model with shape memory effect. At the same time, most studies of SMPs are only based on a specific material. These factors narrow the application of models. Many models are limited to small strain (within 10%). The proposed new viscoelastic model not only can be used for different materials, but can also be used to treat large strain problems. In order to validate the model, simulated and predicted results are compared with the available experimental results. Good agreement between predict values and experimental data can be observed.

CONSTITUTIVE MODEL

With the phenomenological approach, the shape memory effect of SMPs is described by a phase transition at transformation temperature. Normally, SMPs have different microstructures at different temperature ranges. To depict the phase transition phenomenon, we propose a new viscoelastic model for SMPs. The biggest difference between the ordinary viscoelastic model and the proposed model is that the proposed model has different constitutive structures (as shown in Fig. 1) above and below transformation temperature. When the temperature is higher than the transition temperature T_r, the SMPs are in the rubbery state. Rubber is often treated as isotropic incompressible hyperelastic materials in a short time period of loading, but from the point of view of a long time period of loading, the materials in the rubbery state still exhibit stress relaxation and creep viscosity effect. Thus a simple model for SMPs at rubbery state is proposed, as shown in Fig. 1(a). This model is composed of two incompressible hyperelastic element and a viscous damping element. It represents the rubber phase which is responsible for the permanent shape at a temperature higher than transition temperature. It can be called the rubber phase element. As the temperature decreases below T_r, the material enters the glass state. In the glass state, a kind of reversible phase, the second crosslinking chain may be formed in the local area of reticular structure of SMPs, which act as small locks. The second crosslinking chain lock the material's reticular structure to fix the temporal shape at a temperature lower than transition temperature. When the temperature increases above T_r, the second crosslinking chain disappear and permanent shape is recovered. The second crosslinking chain can be considered as small springs with viscous effects. As such, two spring elements and a viscous damping element are introduced to the model to simulate the reversible phase – the second crosslinking chain (as shown in reversible phase of Fig. 1(b)). It can be called the reversible phase element. The constitutive model for SMPs consists of a rubber phase element and a reversible phase element placed in parallel at $T \le T_r$, as shown in Fig. 1(b). In the model, the effect of thermal expansion, which is assumed to be independent of the mechanical behavior, is also considered (as depicted in Fig. 1(a) and Fig. 1(b)).

The advantages of the new viscoelastic model are that it has good physical significance and includes the time factor essential to describe the creep and stress relaxation of rubber. From the corresponding experimental results, the parameters of the model can be determined for different SMP materials.

[a)] Corresponding author. Email: zishunliu@mail.xjtu.edu.cn

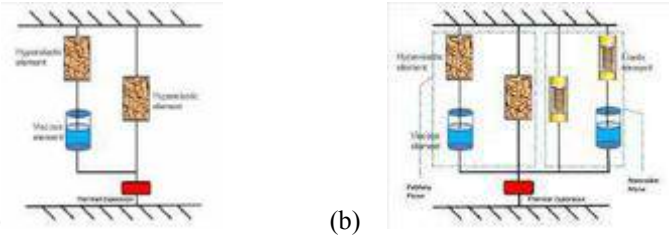

(a) (b)

Fig. 1. (a) Constitutive model for SMPs at $T>T_r$ (rubbery state); (b) Constitutive model for SMPs at $T\leq T_r$ (glass state).

VERIFICATION OF THE CONSTITUTIVE MODEL

In order to validate the acuracy of our proposed new model, two examples of uniaxial tests with two different types of SMP materials are simulated. The constitutive model is implemented and the simulated results are compared with available experimental results.

Example one considers the unconstrained free strain recovery experimental test that had been performed by Tobushi et al [1, 2]. First, Tobushi et al [1] had developed a linear viscoelastic model and performed a series of experiments on polyurethane-SMP. Then, Tobushi et al [2] further modified the linear model to a nonlinear model which can treat the behavior of larger strains. Their work can describe the shape memory behavior qualitatively, but it does not have a clear physical meaning. We use the newly proposed constitutive model and corresponding material parameters extracted from experiment results [1, 2] to simulate the uniaxial tests. The stress-strain relationship, the stress-temperature relationship and strain-temperature relationship in an unconstrained free strain recovery cycle are shown in Fig. 2. From Fig. 2, it can be observed that the proposed new constitutive model can successfully predict the shape memory behavior of SMPs. In order to compare model predictions, Tobushi's predicted results are also illustrated in Fig. 2. Better agreement can be observed between the new model and experimental data.

The second example is to predict experimental test done by McClung et al [3] for large strain recovery test. To verify the ability of the new model in large strain and show the validity for different materials, the experiments of the Veriflex E epoxy-SMP reported by McClung et al [3] are simulated. As shown in Fig. 3, the simulation results match quite well with the experimental data in describing the loading procedure as well as the following strain recovery process.

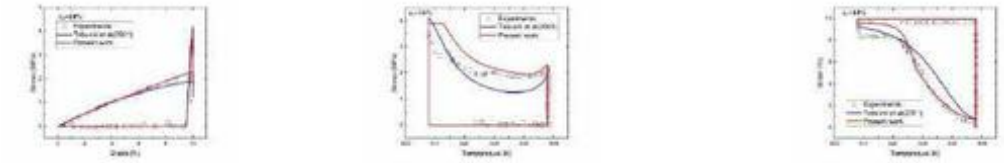

(a) Stress-strain curves (b) Stress-temperature curves (c) Strain-temperature curves

Fig. 2. Predicting the shape memory behavior of polyurethane-SMP. Experiments reported by Tobushi et al [2, 3].

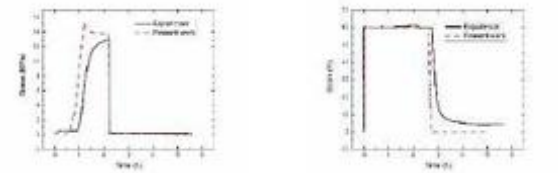

(a) Stress-time curves (b) Strain-time curves

Fig. 3. Predicting the shape memory behavior of Veriflex E epoxy-SMP, Experiments reported by McClung et al [4].

CONCLUSIONS

Proposed constitutive model of SMPs combines the advantages of phase transition constitutive and viscoelastic constitutive. It has a good physical meaning and also includes the influence of loading time. As we did not make more special assumptions for different materials and the viscoelastic model is based on phase transition, the new model can be used for modeling different materials and large strain problems.

References

[1] Tobushi, H., Hashimoto, T., Hayashi, S. and Yamada, E. *Mater. Syst. Struct.* 8, 711–718, 1977.

[2] Tobushi, H., Okumura, K., Hayashi, S. and Ito, N., *Mech. Mater.* 33, 545–554, 2001.

[3] McClung, A., Tandon, G., Baur, J.W. Mech. *Time-Depend. Mater.* 17(1), 39–52, 2013.

MECHANICS OF THERMORESPONSIVE POLYMER BRUSH BASED SOFT MATERIALS: THEORY AND EXPERIMENTS

Manav*[1], M. P. Bajgai[2], A. S. Phani[1], and J. N. Kizhakkedathu[2]
[1]*Mechanical Engineering, University of British Columbia, Vancouver, BC, Canada*
[2]*Centre for Blood Research, University of British Columbia, Vancouver, BC, Canada*

Summary Stimuli responsive soft nanomaterials are of growing scientific and technological interest. Polymer brushes are densely packed, surface tethered polymer chains. A brush behaves like an elastic surface layer with residual surface stress which produces deformation of the substrate. In a thermoresponsive brush, temperature reversibly changes the residual surface stress as well as the elastic modulus of the surface layer due to coil-globule phase transition in the brush. A mechanics model incorporating Young-Laplace effect is developed for high grafting density brush (graft density $> \ 0.2$) which produces large surface stress. The model is then applied to experiments on a poly(N-isopropylacrylamide)-co-Poly(N,N-Dimethylacrylamide) (PNIPAm-co-PDMA) polymer brush grafted on a plasticized poly(vinyl chloride) (pPVC) film using surface-initiated atom transfer radical polymerization (SI-ATRP). The model estimates effective surface stress due to the brush to be ~ -10 N/m which can be halved by applying temperature.

THERMORESPONSIVE POLYMER BRUSH

Long polymer chains grafted to a surface arrange themselves into a brush like structure when the grafting density exceeds a threshold value [1] (see Fig. $1(a)$). This structure arises due to the competition between entropic spring force associated with each polymer chain and inter chain repulsive forces. The entropic spring force tries to keep the two ends of a polymer chain together. Repulsive force between monomers, arising due to steric effects, is relieved by chain extension, resulting in brush like shape. Significantly, these interactions make a brush behave like an elastic surface layer with reversible residual surface stress which may cause deformation in the substrate [2, 3]. Establishing relationship between the molecular scale parameters of the brush with its continuum level properties is an ongoing work [2, 4]. Furthermore, polymer brush made of thermoresponsive polymers show conformation change when temperature is applied to it. This conformation change leads to a change in the residual surface stress as well as the elastic modulus of the surface layer [2]. This behaviour can be utilized in sensing and actuation applications [5].

MECHANICS MODEL OF A POLYMER COATED BEAM

We have developed a mechanics model for a thin flexible beam coated with a polymer brush layer on its top surface (see Fig. $1(c)$)). The polymer brush has been treated as an elastic surface layer with a residual stress, causing deflection in the beam. Mechanical equilibrium for the surface layer introduces correction in stress in the substrate through Young-Laplace relation. For a rectangular cross section of a substrate with thickness t, the correction is considerable if $t \sim \frac{\nu\sigma_s}{E}$, where E and ν are the Young's modulus and the Poisson's ratio of the substrate, and σ_s is surface stress in the surface layer. For a pPVC substrate $E \sim 10^7$ Pa and $\nu \sim 10^{-1}$. For surface stress, $\sigma_s \sim -10$ N/m, correction due to Young-Laplace relation is considerable if $t \sim 10^{-7}$ m. The mechanics model incorporates this effect. Assuming small strain in the beam, the following relation between the surface stress due to polymer brush and the curvature of the beam is derived:

$$\sigma_s = \sigma_s^0 + \epsilon_s E_s = \frac{E}{1-\nu^2}\left(\frac{t^2\kappa}{6+\frac{\nu}{1-\nu}t\kappa}\right), \tag{1}$$

where σ_s^0 is the residual surface stress in the undeformed substrate, and ϵ_s and E_s are strain and elastic modulus of the surface layer. (1) is akin to Stoney's equation with a correction term in the denominator $(\nu(1-\nu)^{-1}t\kappa)$ arising due to Young-Laplace effect. Surface stress due to polymer brush can be estimated by measuring curvature of a polymer coated beam experimentally, and applying the above formula.

EXPERIMENTAL ESTIMATION OF SURFACE STRESS

To estimate surface stress due to polymer brush, Poly(N- isopropylacrylamide)-co-Poly(N,N-Dimethylacrylamide) (PNIPAm-co-PDMA) polymer brush was grafted on one side of a part of a plasticized poly(vinyl chloride) (pPVC) film using surface-initiated atom transfer radical polymerization (SI-ATRP). Note that by varying polymerization time, molecular level properties of the brush can be varied. For this experiment, it was fixed to six hours. The grafting procedure ensures very high graft densities (number of polymer chains attached to unit area of the substrate) and ultrahigh molecular weight of the polymer chains

*Corresponding author. (graduate student, UBC) Email: manav@alumni.ubc.ca

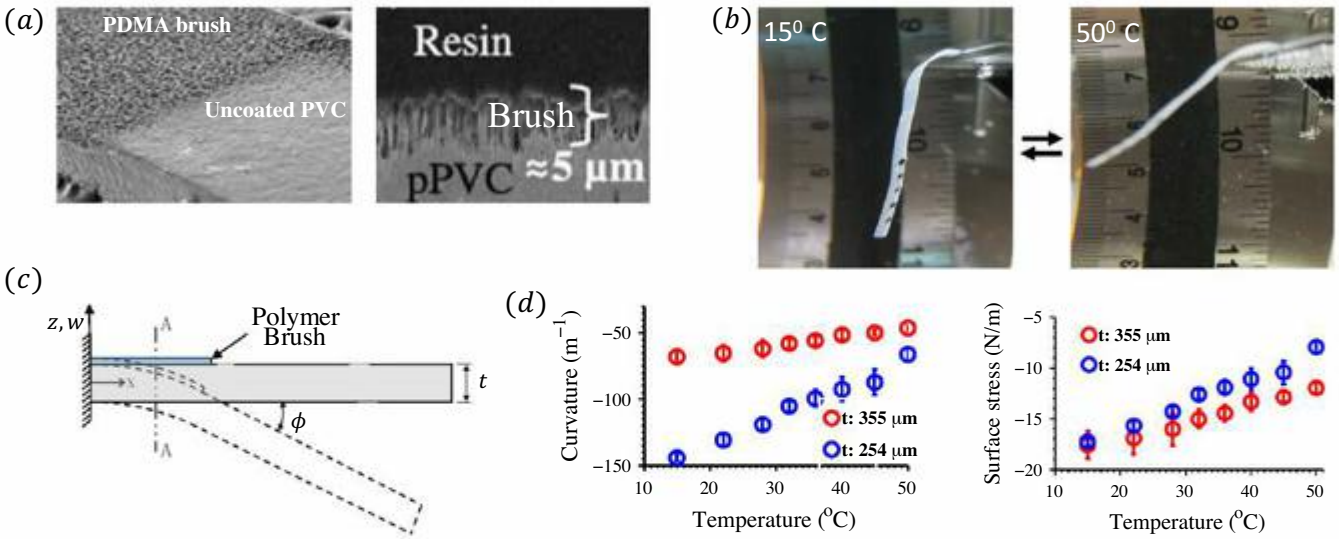

Figure 1: (a) SEM images of pPVC substrate partially coated with polymer brush [5]. (b) Partially coated pPVC beam in a water bath. Rise in temperature leads to decrease in curvature of the coated part of the beam and it is reversible. (c) Schematic of a partially coated beam. 1 cm of the 3 cm long beam is coated with polymer brush. (d) Variation of curvature and surface stress with temperature for polymer brush coated beams of thicknesses (t) 355 μm and 254 μm.

($\sim 10^6$ g/mol) leading to high surface stresses. The pPVC beams used in the experiment are 3 cm long, 5 mm wide, and 254 μm and 355 μm thick. Only 1 cm of the beam near its fixed edge is coated with polymer brush. Young's modulus and Poisson's ratio for the pPVC film are 12 MPa and 0.3 respectively. Bending rigidities of the beams are 8.19×10^{-8} N $-$ m^2 and 2.24×10^{-7} N $-$ m^2 respectively.

PNIPAm-co-PDMA is a temperature sensitive polymer. To measure curvature of a beam coated with the temperature sensitive polymer brush, the beam was placed in a water bath with temperature control. After reaching the desired temperature, we waited for a minute for the brush to reach steady state before proceeding with measurement at the temperature. At different temperatures of the bath, curvature of the beam changes (see Fig. 1(b)) due to change in effective surface stress. The beam was photographed at different temperatures by a fixed camera. Using image processing in MATLAB, the shape of the cantilever beam was traced. Using circle fitting on the part of the traced curve where brush is present, curvature of the coated part is determined, which is in turn used to find effective surface stress in the beam (Fig. 1(d)). It can be observed from Fig. 1(d) that surface stress is of the order of -10 N/m and it can be halved by increasing temperature. The change in temperature produces change in surface stress through conformation change in the brush. However, the transition is not sharp and happens over a range of temperature near lower critical solution temperature (LCST) ($\sim 32^0$ C) for the polymer. Furthermore, small difference between surface stresses for the two thicknesses, even though curvatures (and hence ϵ_s) at a particular temperature are widely different, suggests that the elastic modulus of the surface layer is very small.

CONCLUSIONS

Equation governing finite deformation of a beam with a coating of a polymer brush on its top surface has been derived including the Young-Laplace term needed to satisfy surface equilibrium. The modified stress-curvature relation was then used to extract surface stress due to polymer brush grafted on a pPVC substrate. The surface stress is found to be on the order of -10 N/m and it can be halved by applying temperature. The ability to control surface stress by varying temperature permits the design and development of soft actuators based on polymer brush material system.

References

[1] Milner S.: Polymer brushes. Science 251 (4996):905–914, 1991.

[2] Utz M. and Begley M. R.: Scaling theory of adsorption-induced stresses in polymer brushes grafted onto compliant structures. J. Mech. Phys. Solids 56:801–814, 2008.

[3] Begley M. R., Utz M. and Komaragiri U.: Chemo-mechanical interactions between adsorbed molecules and thin elastic films. J. Mech. Phys. Solids 53:2119–2140, 2005.

[4] Lei Z., Yang S. and Chen E. Q.: Membrane rigidity induced by grafted polymer brush. Soft matter 11:1376–1385, 2015.

[5] Zou Y., Lam A., Brooks D. E., Phani A. S. and Kizhakkedathu J. N.: Bending and Stretching Actuation of Soft Materials through Surface-Initiated Polymerization. Angewandte Chemie International Edition 50:5116–5119, 2011.

CURVATURE OF THE TRANSVERSE ARCH GOVERNS STIFFNESS OF THE HUMAN FOOT

Madhusudhan Venkadesan*[1], Marcelo Dias[2], Dhiraj Singh[3], Mahesh M. Bandi†[3], and Shreyas Mandre‡[4]
[1]*Department of Mechanical Engineering & Materials Science, Yale University, New Haven, Connecticut, USA*
[2]*School of Science, Aalto University, Espoo, Finland*
[3]*Collective Interactions Unit, OIST Graduate University, Okinawa, Japan*
[4]*School of Engineering, Brown University, Providence, Rhode Island, USA*

Summary Humans are unique among primates in having arched feet that provide a stiff propulsive lever for locomotion. Using mathematical and physical models of the foot as a curved elastic shell, we show that the transverse curvature is the primary determinant of foot stiffness. The stiffness of shallow thin shells has two asymptotic regimes, one that resembles a soft thin plate, and the other that shows a power-law dependence of stiffness with an exponent of $3/2$. Curvature induced coupling between bending and in-plane stretching underlies the power-law dependence. Analysis of discrete realizations of a shell also show a similar transition, but with an exponent of 2. We present implications of our work to understanding the mechanical origins of stiff human feet, and to the evolution of human feet through an analysis of extant and fossil feet.



Figure 1: Observations on the effect of curvature on stiffness. **A**. The human foot has two distinct arches in the longitudinal and transverse directions. **B**. Common experience and simple experiments show that curvature in the transverse direction significantly increases the longitudinal bending stiffness of thin continuum shells. **C**. Discrete realizations of a shell, namely, rigid bars connected by soft elastic "ligaments" also shows a similar large increase in stiffness upon increasing curvature in the transverse direction.

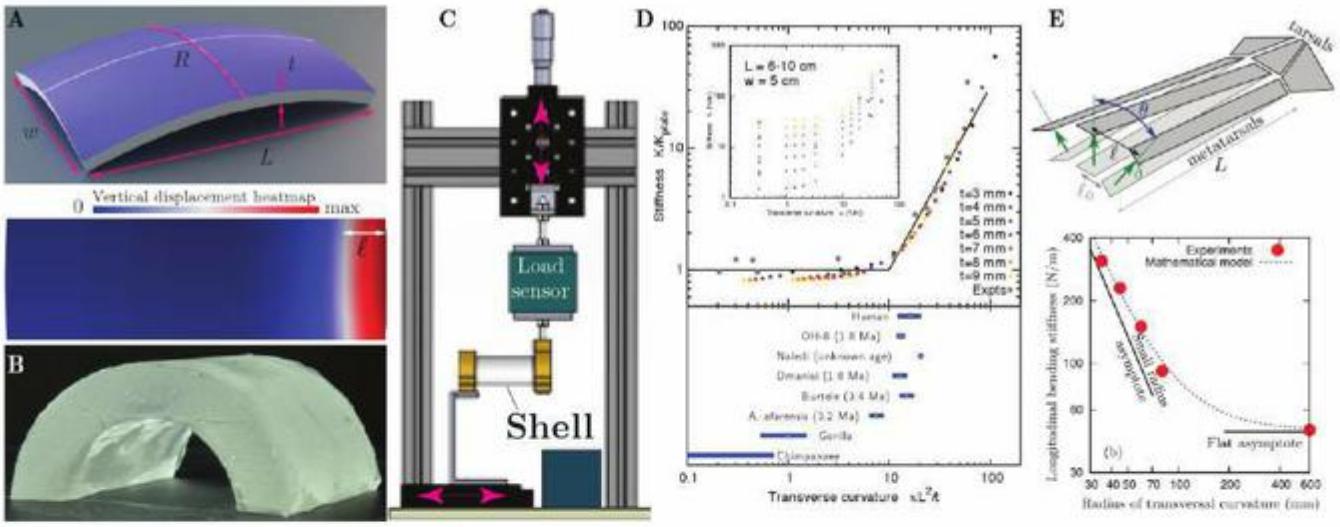

Figure 2: Mathematical and physical analyses of shells, and their implications to human evolution. **A**. Numerical model of curved elastic shells. **B,C**. Experimental fabrication and measurement of stiffness of transversally curved shells. **D**. The inset shows dimensional data, that collapse according to the asymptotic predictions. Comparing the dimensionless curvature of various biological feet, relative to the crossover point of the asymptotes, predicts that a human-like stiff foot might have emerged at least 3.4 million years ago. **E**. Ongoing work to address the mechanics of discrete mimics of the foot, with stiff "bones" and softer interconnecting "ligaments".

Just as a drooping dollar bill stiffens upon curling it in the transverse direction (figure 1B), we hypothesize that the transverse arch of the foot plays a central role in longitudinal bending stiffness. We observe a similar increase in stiffness for physical mimics of the foot, which resemble a discrete realization of the dollar bill (figure 1C).

*m.venkadesan@yale.edu
†bandi@oist.jp
‡shreyas_mandre@brown.edu

MODELS OF THE FOOT

Mathematical models: We modeled the foot computationally (using COMSOL) and experimentally (static loading experiments) as a continuum elastic shell of length L, width w, and thickness t. The shell has radii of curvature R_L and R_T in the longitudinal and transverse directions respectively (figure 2A,B). To isolate the dependence of the stiffness K of the shell on the geometrical parameters L, w, t, R_L, and R_T, but eliminate material nonlinearities, the shell is assumed to be made of a uniform linear elastic solid with Young's modulus E and Poisson ratio ν.

For flat thin plates, it is well known that stretching can be neglected and is decoupled from bending if the deflection of the end is much smaller than the thickness [Landau and Lifshitz(1959)]. For curved shells, however, stretching with bending could be a dominant effect even for small out-of-plane deflections. For a radial displacement by an amount w, the strain scales as $\sim w/R$, where R is the typical radius of curvature. The elastic stretching energy therefore scales as $\mathcal{E}_\mathrm{s} \sim EtA(w/R)^2$. When deformations are uniform, pure bending energy scales as $\mathcal{E}_\mathrm{b} \sim Et^3A(w/R^2)^2$, always resulting in a large stretching-to-bending ratio, $\mathrm{r} = \mathcal{E}_\mathrm{s}/\mathcal{E}_\mathrm{b} \sim (R/t)^2 \gg 1$.

When the deformation is caused by an external normal force applied to the shell and the characteristic length scale of the range of this deformation is ℓ, bending energy will scale as $\mathcal{E}_\mathrm{b} \sim Et^3lW(w/\ell^2)^2$, where W is the projected width of the shell. Numerical experiments indeed show the localization of the deformation for curved shells (figure 2A). Hence, by balancing the stretching and bending energies (equivalent to minimizing the total elastic energy), we derive a scaling law for the deformation depth, namely $\ell \sim \sqrt{Rt}$. Therefore, for some function f depending on the precise loading of the shell, dimensional analysis implies $\frac{K}{Bw/L^3} = f(R_Tt/L^2, R_Lt/L^2)$, where the bending rigidity of the cross section of the shell is $B = Et^3/(12(1-\nu^2))$.
Physical models: Experimental realization of this shell was made using the soft elastomer polydimethylsiloxane (PDMS) (figure 2B). The shell was clamped at one edge, and an external force was exerted on the other, to mimic the loading experienced by the foot during toe-off (figure 2C). The ratio of the applied force to the relative displacement between the edges of the shell in the limit of small displacements gives stiffness K.

RESULTS

The inset of figure 2D shows the calculated and measured stiffness K of the foot for shells with different geometries. Using the dimensionless forms of stiffness and curvature cause these data to collapse, in agreement with the asymptotic predictions. There was no such effect on longitudinal bending stiffness because of longitudinal curvature. We also plot the curvature of human, gorilla, chimpanzee and several fossil feet [Harcourt-Smith and Aiello(2004), Pontzer et al.(2010)], shown in the lower half of figure 2D. Among living primates, humans are the only feet that belong to the 3/2 power-law regime, i.e. correctly predicted to exhibit a stiff shell-like behavior [Ker et al.(1987)]. On the other hand, the gorilla and chimpanzee are flat, and correctly predicted to be soft like a thin plate [Bennett et al.(1989)]. The fossil feet show a clear increase in curvature at least 1 million years (Ma) before the emergence of the genus *Homo*. The ~ 3.4 Ma foot (Burtele, Ethiopia), which was previously thought to resemble the gorilla, has a human-like arch even if we assume its proportions to be that of a gorilla.

CONCLUSION

The curvature of the transverse arch in humans is expected to contribute to a 200% increase in stiffness, all else held the same. Human feet are approximately 220% stiffer than chimpanzee feet [Bennett et al.(1989)], after adjusting for size differences and assuming equal Young's modulus (using our dimensionless stiffness). In contrast, the elastic tissue that constitute the longitudinal arch account for less than 30% of the human foot stiffness [Ker et al.(1987)].

Measurements of stiffness as a function of curvature using the discrete foot shown in figure 1C are in agreement with theoretical predictions (with two fitting parameters). However, the power-law now exhibits an exponent of 2, different from the continuum model. We are continuing to investigate the origins of this difference in the exponent.

Our results aid in the study of fossil feet, to infer function from form. There are also implications for flatfoot disorders, and for the the design of lightweight, yet stiff, robotic or prosthetic feet. Finally, we propose that control of the transverse curvature is an attractive method to modulate foot stiffness because of the strong dependence of stiffness on curvature.

References

[Bennett et al.(1989)] M. B. Bennett, R. F. Ker, and R. M. Alexander. *J. Zool*, 217:469–475, 1989.

[Harcourt-Smith and Aiello(2004)] W. E. H. Harcourt-Smith and L. C. Aiello. *J. Anat*, 204(5):403–416, 2004.

[Ker et al.(1987)] R. F. Ker, M. B. Bennett, S. R. Bibby, R. C. Kester, and R. M. Alexander. *Nature*, 325(7000):147–9, 1987.

[Landau and Lifshitz(1959)] L. D. Landau and E. M. Lifshitz. Pergamon Press, 1959.

[Pontzer et al.(2010)] H. Pontzer, C. Rolian, G. P. Rightmire, T. Jashashvili, M. S. Ponce de León, D. Lordkipanidze, and C. P. E. Zollikofer. *J. Hum Evol*, 58(6):492–504, 2010.

COUPLING KINETICS OF REACTIVELY IONIC GELS

Pengfei Wang[1a)], Yingze Cao[1] , Yan Zhang[1] & Fangming Cui[1]
[1]*Qian Xuesen Laboratory of Space Technology, China Academy of Space Technology, Beijing, China*

Summary As typical smart soft materials, ionic gels can present a large deformation induced by environmental temperature, electric field and chemicals, which maintain great potentials in soft actuator, environmental sensor, drug delivery, etc. In this paper, the coupling mechanism of reaction kinetics, deformation of polymer network, mass diffusion and polyelectrolyte effect in the gels will be uncovered, and a general dynamic electro-chemo-mechanical model will be proposed for common ionic gels. Further investigations showed that the dynamic deformation and response time of an ionic gel are dependent on the concentration of reactive and non-reactive ions, the time of exposure to external stimuli, the initial state and the density of ionizable groups on the polymer chains. At the end, a brief introduction will be additionally given on the application of smart soft materials, especially for the space technology.

INTRODUCTION

Ionic gels consist of ionic polymers and a solution. These gels exhibit large amounts of deformation in response to mechanical forces, temperature, pH, light and electrical fields. Natural ionic gels in the periphery of plant and animal cells have important roles in the regulation of water and in stabilizing the shape of cells. Synthetic ionic gels have been widely used in engineering as environmental sensors, biomimetic actuators, autonomous flow controller and drug delivery systems. In these applications, the dynamic characteristics of ionic gels are important in device performance and improvements in the response time of devices based on ionic gels has become a critical parameter in their design. However, ionic gels usually undergo large dynamic deformations accompanied by the migration of ions in and out of the gel as a result of a nonequilibrium ionic chemical reaction. There is therefore a need to develop theoretical models for the design and optimization of devices based on ionic gels. The exploration of the dynamic behavior of ionic gels in response to chemical stimuli is of particular interest.

We consider here the system of a block ionic gel immersed in a dilute solution of reactive and non-reactive ions. The gel has a dynamic behavior (swelling or shrinking) as the result of a nonequilibrium chemical reaction within the gel. By coupling the theories of large deformation, the Donnan effect and the nonequilibrium kinetics of chemical reactions, a chemomechanical theory has been developed to describe the dynamic behavior of the gel. We validated the predictions from the proposed theory using existing experimental and theoretical results. As examples, we report here the oscillation deformation of an actuator changing with the period of externally applied chemical stimuli and the response time of a sensor affected by the initial state, the density of ionizable groups on the polymer and the measured concentration.

When immersed in a solution containing several reactive ions, a polymer network with fixed ionizable groups begins to swell or shrink as a result of the ionic reactions between the fixed and mobile species. This results in a non-equilibrium ionic gel. We focused on a specific system, but without a loss of generality, *i.e.*, a non-equilibrium process for the dissociation and association of ionizable groups

$$\mathrm{AB} \underset{k_2}{\overset{k_1}{\leftrightarrow}} \mathrm{A}^- + \mathrm{B}^+$$

where k_1 and k_2 represent the rate constants of the forward and reverse processes, respectively. When the network imbibes a number of solvent molecules, the ionisable groups AB, chemically bonded on the polymer chains, dissociate into mobile ions B^+ in the solvent and conjugate bases A^- fixed on the polymer chains. During the reversible reaction, the network of polymer chains charges and discharges. For example, the increasing number of conjugate bases A^- gives rise to the fixed electrical charges of the polymer chains and consequently induces the deformation of the reactive ionic gels (forward reaction). The opposite process occurs during the backward reaction. In addition to the mobile ions B^+ and the water molecules, the solution also contains non-reactive counter ions (+) and co-ions (–). This reaction-deformation system represents the basic working mechanism of a broad range of applications, such as hydrogel-based testing devices and drug-delivery systems.

RESULTS AND DISCUSSIONS

We validated the theoretical model by comparing the steady solutions of a previously reported pH-sensitive gel (a familiar ionic gel: A^- are carboxylic acids groups, B^+ is H^+) with the long time-limited solutions of our model (approximating to a steady-state). The solutions of our theoretical model at longer dimensionless times agreed well with the steady-state solutions[1] (Fig. 1a and 1b). We then compared the swelling ratio of our theoretical predictions at longer dimensionless times ($\tau = 100$) with previously reported steady-state experimental results with different concentrations of B^+ ($\bar{c}^{B^+}/N_A$). Here A^- is the methacrylic acid-co-acrylic acid group and B^+ is H^+. The solutions of our theoretical model at longer dimensionless times agreed well with the previous experimental results[2] (Fig. 1c).

[a)] Corresponding author. Email: wangpengfei@qxslab.cn

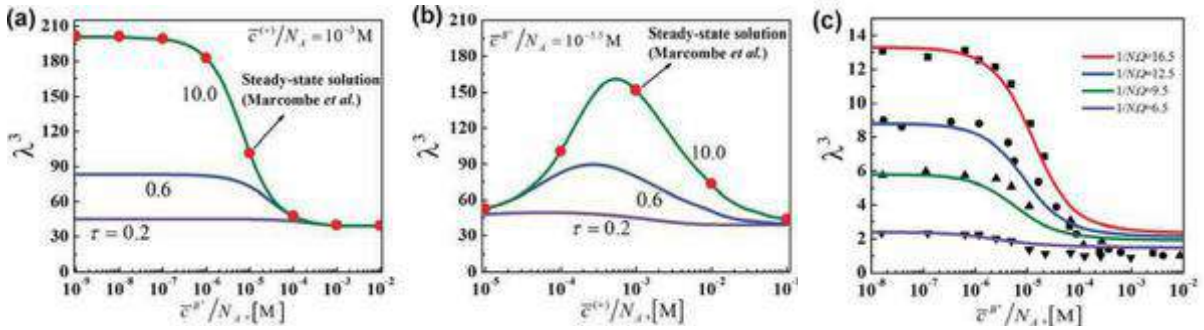

Fig. 1 The swelling ratio of a pH-sensitive gel changes (a) as a function of the concentration of B^+ ($\overline{c}^{B^+}/N_A$) and (b) as a function of salt concentration ($\overline{c}^{(+)}/N_A$) at different dimensionless time points. The red dots are the steady solution from Marcombe et al.[1] The molar fraction of the ionizable group f = 0.05 and the dissociation constant $k_1/N_A k_2 = 10^{-4.3}$. (c) Comparison between the swelling ratio of our theoretical predictions at a longer dimensionless time ($\tau = 100$) and the experimental results at steady-state with different concentration of B^+. The scattered dots are experimental data from Eichenbaum et al.[2] and the solid lines are the simulated results from our theoretical model.

CONCLUSIONS

A chemomechanical theory has been proposed to describe the dynamic behavior of ionic gels under non-equilibrium processes. We found that the dynamic behavior of an ionic gel depends not only on the dissociation constant of the ionisable groups on the polymer chains, but also on the concentration of the reactive and non-reactive ions in the external solution. When the ionic gel undergoes alternating stimuli from reactive ions in the external solution, the corresponding behavior is significantly affected by the frequency of the stimulus. The response time of an ionic gel for different measured concentrations of reactive ions is correlated with the initial state and the density of the ionizable groups on the polymer chains.

References

[1] Marcombe, R., et al: A Theory of Constrained Swelling of a pH-Sensitive Hydrogel. *Soft Matter* **6**: 784-793, 2010.

[2] Eichenbaum, G. M., et al: Investigation of The Swelling Response and Loading of Ionic Microgels with Drugs and Proteins: The Dependence on Cross-Link Density. *Macromolecules* **32**: 4867-4878, 1999.

[3] Liu, S. B., et al: Reaction-Induced Swelling of Ionic Gels. *Soft Matter* **11**: 449-455, 2015.

[4] Wang, P.F., et al: Reactive Swelling of Elastomeric Gels. Unpublished.

FAST ACTUATION ACHIEVED BY HYDROGEL STRUCTURES WITH BUILT-IN MECHANICAL INSTABILITY

Xuxu Yang [1], Guorui Li[1], Tingyu Cheng [1], Yongbing Jin[1], Tiefeng Li[1,2,3a)] & Wei Yang[1a)]
[1]Institute of Applied Mechanics, Zhejiang University, 38 Zheda Road, Hangzhou, Zhejiang 310027, China
[2]Soft Matter Research Center (SMRC), Zhejiang University, Hangzhou 310027, China
[3]Key Laboratory of Soft Machines and Smart Devices of Zhejiang Province, Hangzhou 310027, China

Abstract Stimuli-Responding structures can be actuated by the swelling/shrinking of hydrogels. The response process is slow, due to its strong dependence on the diffusion rate of the inward/outward creeps of solvent within the polymer networks of hydrogel. Inspired by plants like Venus flytrap, which enables "snapping" action with prompt actuation, mechanical instability may be built in a multilayer hydrogel structure. Tough thermo-responsive hydrogel is used to assemble the structure. The shape changing behaviour of the structures can be significantly increased by building blocks with a thermo-responsive layer. At a critical point, a small actuation may tip the structure to undergo a large deformation by fast snap-through mechanism. Finite element simulation is performed to guide the design and to illustrate the versatile responses of the hydrogel structures.

INTRODUCTION

Stimuli-responding hydrogels, with characteristics such as adaptability, biocompatibility, tuneable mechanical properties, and low cost, have broad applications in fields such as actuators, tissue engineering, drug delivery, soft biomimetic robotics and microfluidic control systems [1,2]. Similar to the movements in plants, hydrogels are driven mainly by swelling and shrinking of water. Mechanical motion with large deformations was achieved in those hydrogels by stimuli under pH, light, temperature, magnetic and/or electric fields [3,4]. Conventional structures made of stimuli-responsive hydrogels are actuated directly by the volume change of hydrogels. The size reduction of specimen may speed up the actuation of hydrogel structures. The response time, nevertheless, strongly depends on the diffusion rate of the inward/outward creeps of solvent within the polymer networks of the hydrogel. Attributed to the snap-buckling instability of the structure, plants like Venus flytrap and bladderwort exhibit "snapping" action with ultrashort response time (<1ms) [5-7]. Recent experiments demonstrate bio-inspired structures made of soft materials with various geometry and material properties for the fast, stimuli-responding motion assisted by a snap-through instability [8-10]. However, developing stimuli-responsive hydrogel structure with rapid response remains a challenge.

In this work, we synthesise thermo-responding and non-responding hydrogels with reasonable toughness, by the method of double-network hydrogel [11]. The two hydrogels are assembled into a multilayer structure to harness mechanical instabilities with rapid actuation. The hydrogel structure operates in two steps. In the first step, a temperature raise changes the hydrophilicity of the material, resulting in slow shrinking of the thermo-responding hydrogel. This step is relatively slow due to the limited diffusion rate. As the hydrogel keeps shrinking, the elastic energy of the hydrogel structure accumulates. When the structure deformation reaches the critical condition to trigger a snap-through action, the second step intervenes. The structure snaps from one state to another with fast actuation, while the stored mechanical energy in the first step is quickly released into kinetic energy.

A HYDROGEL STRUCUTRE ENABLING FAST ACTUATION

Built-in mechanical instability

By triggering snap-buckling instability, the Venus flytrap undergoes ultra-fast movement. To design a structure with built-in mechanical instability, one starts with a thin hydrogel plate under circumferential stress. The circumferential stress drives the thin plate to bend upward or downward and to transform into a spherical shell. When the buckled thin plate to deform and to snap from one stable state to another stable state, the sudden fast actuation is manifested. The structure may be accomplished by a tri-layer hydrogel. The first layer is composed of thermo-responding hydrogel, which provides the driven force for the structure deformation. The second layer is a pre-stretched non-responding hydrogel ring, which provides a constant circumferential stress on the structure. The third layer is a balancing layer of non-responding hydrogel, which also maintains the structure symmetry.

Actuated motion of the structure

Experiments are carried out in 0.0025wt% $CaCl_2$ solution. The solution is initially transparent and maintained at 22℃. We put the structure into the solution as the initial state, shown as in Fig. 1(a). The temperature of the solution is then raised to trigger the snap-through action of the structure. As the solution warms up, the thermo-responding hydrogel undergoes phase transition and turns write. The solution turns milk-like simultaneously by the spread of polymers squeezed from the

[a)] Corresponding author. Email: Yangw@zju.edu.cn, litiefeng@zju.edu.cn

hydrogel. The transparency of the solution could indicate the degree of phase transition of the thermo-responding hydrogel. During the test, the thermo-responding hydrogel in the structure slowly pumps water out and shrinks. The volume change of the thermo-responding hydrogel induces an inverse bending moment on the structure, flattening the structure curvature. It takes 350 seconds for the structure to be flattened counting from the moment of the temperature raise (Fig. 1(a-c)). At the critical point of the structure inversion, the structure instability is triggered. The structure suddenly snaps-through into another stable state with the inversely buckled shape. It only takes less than one second for the structure to snap. Furthermore, the impact force of this snap-through process drives the structure to jump up from the vessel base (Fig. 1(d-f)).

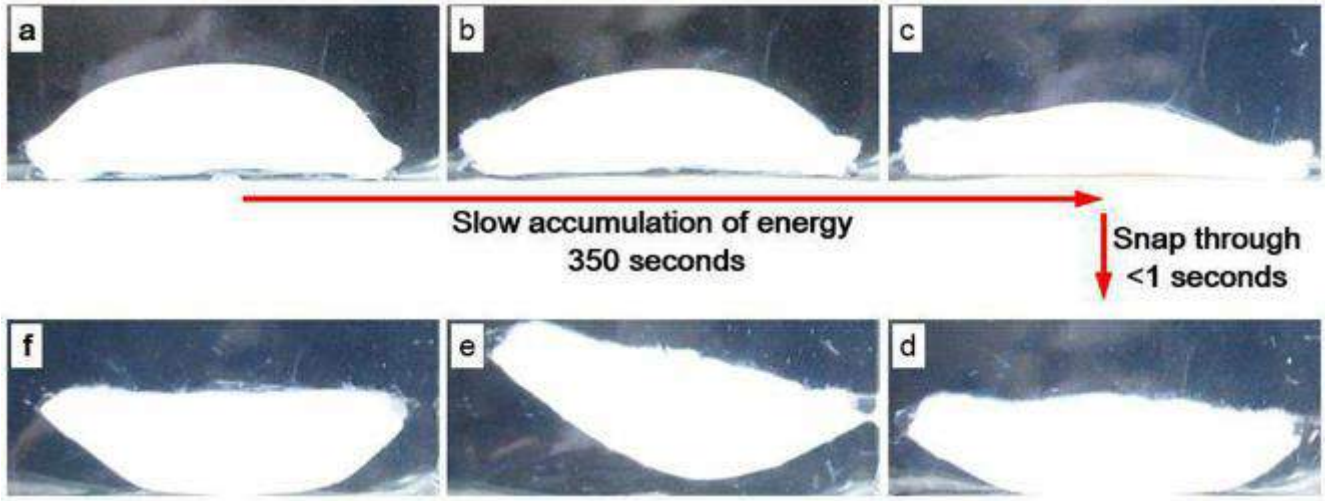

Figure 1. Images of the snap-through deformation of the hydrogel structure.

CONCLUDING REMARKS

In summary, the mechanical instability is induced by a multi-layer hydrogel structure, and fast actuation speed is achieved. A variety of snapping behaviours may be presented when pursued along this avenue. Further mechanics analyses for the snapping procedure are desirable. In addition, the mechanical principle of built-in mechanical instability in stimuli-responding hydrogel may open a door for enabling snapping behaviour of other stimuli-responding materials such as liquid crystal elastomers and shape memory polymers.

References

[1] Ionov L.: Biomimetic Hydrogel-Based Actuating Systems. *Adv. Funct. Mater.* **23**: 4555–4570, 2013.
[2] Kempaiah R., Nie Z.: From nature to synthetic systems: shape transformation in soft materials. *J. Mater. Chem. B* **2**: 2357–2368, 2014.
[3] Stuart M. A. C.: Emerging applications of stimuli-responsive polymer materials. *Nat. Mater.* **9**:101-103, 2010.
[4] Zhang J.: Multi-stimuli responsive macromolecules and their assemblies. *Chem. Soc. Rev.* **42**: 7421--7435, 2013.
[5] Hodick D., Sievers A.: On the mechanism of trap closure of Venus flytrap. *Planta* **179**:32-42, 1989.
[6] Forterre Y.: How the Venus flytrap snaps. *Nature* **433**:421-425, 2005.
[7] Vincent O.: Ultra-fast underwater suction traps. *Proc. R. Soc. B* **278**:2909-2914, 2011.
[8] Xia C.: Solvent-driven polymeric micro beam. *J. Micromech. Microeng.* **20**:085030, 2010
[9] Lee H.: First jump of microgel: actuation speed enhancement by elastic instability. *Soft Matter* **6**:4342-4345, 2010.
[10] Holmes D. P., Crosby A. J.: Snapping Sufaces. *Adv. Mater.* **19**:3589-3593, 2007.
[11] Sun J.: Highly stretchable and tough hydrogels. *Nature* **489**:133-136, 2012.

TOUGH ADHESION OF HYDROGELS

Teng Zhang[1a)], Hyunwoo Yuk[2] & Xuanhe Zhao[2]
[1]*Department of Mechanical and Aerospace Engineering, Syracuse University, Syracuse, New York, United States*
[2]*Department of Mechanical Engineering, Massachusetts Institute of Technology, Cambridge, Massachusetts, United States*

Summary Tough adhesion for synthetic hydrogels is challenging and only achieved very recently by chemically anchoring long-chain polymer networks of tough hydrogels on solid surfaces. Here we provide a quantitative understanding of the mechanism for the tough adhesion of hydrogels on solid materials by using a coupled cohesive-zone and Mullins-effect model. Numerical simulations reveal the toughening mechanism of the energy dissipation and the importance of the high intrinsic work of adhesion as well as the interfacial strength. These findings shed light on the reported strong bonding of tough hydrogels that the chemical anchoring gives high interfacial strength and large intrinsic work of adhesion to trigger significant energy dissipation and further enhance the interfacial toughness.

INTRODUCTION

Adhesion plays an essential role in applying hydrogels to biological load-bearing materials and structures; for example, tough bonding of tendons and cartilages on bones in animals and tough adhesion of mussel's plaque on rocks. Furthermore, tough interfaces between hydrogels and various solids, such as metal, ceramic, silicon and polymers, have been the foundations of the well integration and function in devices and systems in the engineering applications of hydrogels as diverse as biomedicine, biocompatible stretchable electronics, actuators for optics and fluidics, soft robotics and machines. Although the tough hydrogel adhesion is extremely important in both biological and engineering application, it is very challenging to achieve strong adhesion between hydrogels and non-porous solids, as the presence of water complicates the interfaces interaction. Most of reported hydrogel adhesions are not very strong.

Great progress was recently made by Hyunwoo and colleagues [1], who developed a strategy for designing tough hydrogel bonding on various nonporous solid surfaces via chemically anchoring the stretchy polymer networks of tough hydrogels to the solid surface. Through the standard 90-degree-peeling test, the bonding was found to be very strong with an interfacial toughness over 1,500 J/m2 and robust in the wet environment, i.e., stable during constrained swelling under water. Although the real detachment process was complicated and involved finger instabilities, viscoelasticity and possible cavitation, it has been experimentally and numerically demonstrated the strong chemical anchors and energy dissipation were the key factors to achieve the tough bonding of hydrogels. The design methodology is expected to benefit the adhesion of various tough hydrogels for diverse engineering applications and thus calls for more in-depth theoretical understanding of the mechanisms of tough interfaces to guide the rational design of tough bonding and hydrogels. Furthermore, the fundamental toughening mechanisms of the synthetic tough hydrogel interfaces can also shed light on the orders magnitude difference between the work of adhesion of the DOPA molecular interfaces and macroscale mussel's plagues [2].

Here we systemically examine the fundamental mechanisms of strong adhesion of the tough hydrogels due to chemical anchors and energy dissipations e.g., Mullins effect, with the coupled cohesive zone and Mullins effect model. We will present the validation of the simulation model and comparison between simulations and previous experiments and conducts parameter studies of the adhesion enhancement by varying the key materials parameters, such as interfacial strength and maximum energy dissipation ratio.

THEORETICAL MODEL

We developed a 2D finite-element model to simulate the 90-degree-peeling test of soft materials bonded on solid substrates. A stiff backing film (i.e., Young's modulus on the order of GPa) was attached on the top of the soft material film to reduce the elastic energy stored in the detached part so that the work of adhesion can be directly converted from the measured peeling force. The deformation of the system was assumed to be under plane-strain condition. The thickness of the soft material film and stiff backing are denoted as t and b, respectively.

To describe the intrinsic failure of the interface, we adopt the cohesive zone model. The specific model used in the current study is characterized by a triangular cohesive law with interface strength $S_{\text{interface}}$ and maximum separation distance $\delta_{\max}$. The damage of the cohesive interface follows the quadratic nominal stress criterion,

[a)] Corresponding author. Email: **tzhang48@syr.edu.**

$$\left\{\frac{t_n}{S_{\text{interface}}}\right\}^2+\left\{\frac{t_s}{S_{\text{interface}}}\right\}^2=1 \tag{1}$$

where $t_{(\bullet)}$ represents the nominal surface tractions on the crack surface, and the subscripts n and s indicate normal and tangential directions, respectively. The elastic properties and energy dissipation of the soft materials are modeled as the Ogden hyperelastic material [3] and Mullins effect [4], respectively.

CONCLUSIONS

We conduct extensive numerical simulations of tough hydrogel adhesion and show that the total work of adhesion linearly scales with the intrinsic work of adhesion of the interface and the contribution form the energy dissipation to the work of adhesion can be much larger than the intrinsic value. In addition, the simulations can capture the nontrivial thickness dependent work of adhesion observed in the experiments. We then explored the fundamental principles to design tough and adhesive soft materials by systematically varying the key bulk and interface material properties. For a material with given shear modulus and intrinsic work of adhesion, it is found that high interfacial strength and large energy dissipation (high value of $h_{\max}$ and small value of m) are the key of the strong bonding.

References

[1] Hyunwoo, Y., et al.: *Nat*. *Mater*., 2015.
[2] Desmond, K.W., et al.: Soft matter **11**: 6832-6839, 2015.
[3] Ogden, R.W., Non-linear elastic deformations. Courier Corporation 1997.
[4] Ogden, R., D. Roxburgh.: Proc. R. Soc. A**. 455** 2861-2877 1999.

[a)] Corresponding author. Email: **tzhang48@syr.edu.**

CONTRIBUTIONS OF ECM CONSTITUENTS TO ARTERIAL WALL MECHANICS

Yunjie Wang[1], Shahrokh Zeinali-Davarani[1] & Yanhang Zhang [1,2,a)]
[1]*Department of Mechanical Engineering, Boston University, Boston, MA, USA*
[2]*Department of Biomedical Engineering, Boston University, Boston, MA, USA*

Summary Considering the organization and engagement behavior of extracellular matrix (ECM) constituents in the arterial wall, here we proposed a new constitutive model of ECM mechanics that consists of medial elastin, medial collagen, and adventitial collagen, to incorporate the layer-specific distribution of elastin and collagen fiber orientations and the sequential fiber engagement in arterial mechanics. Planar biaxial tensile testing method was used to characterize the orthotropic and hyperelastic behavior of porcine thoracic aorta. Fiber distribution functions obtained previously [1] were incorporated into the constitutive model. Considering the sequential engagement of ECM constituents in arterial mechanics, a collagen recruitment function was incorporated into the model to capture the delayed engagement of adventitial collagen. A freely jointed chain model was used to capture the mechanical behavior of elastin and collagen at the fiber level. The tissue-level ECM mechanics was obtained by incorporating fiber distribution, engagement, and elastin and collagen content.

INTRODUCTION

With a goal to understand how elastin and collagen fibers interrelate and modify the dynamic behavior of the arterial wall, we previously studied the ECM fiber organization, realignment, and recruitment by coupling mechanical loading and multi-photon imaging [1]. Our study provides quantitative evidence on the sequential engagement of ECM constituents in response to mechanical loading. We found that the adventitial collagen exists as large wavy bundles of fibers that exhibit delayed fiber engagement after about 1.15-1.2 tissue stretch. The medial collagen is engaged throughout the stretching process, and prominent elastin fiber engagement is observed up to 1.2 tissue stretch after which the engagement plateaus. These findings suggest that there are intrinsic interrelations between the major ECM constituents, medial elastin, medial collagen, and adventitial collagen fibers, which determines the mechanics of arteries and may carry important implications to vascular homeostasis and mechanobiology. In this study, a new constitutive model is proposed that considers the structural and mechanical interrelations of the three major ECM constituents. The medial elastin, medial collagen, and adventitial collagen each play unique structural and mechanical roles, and their distinct contributions to arterial mechanics are considered. Material parameters in the constitutive model resemble key structural and biological information in the arterial ECM. The layer-specific structural and biological information from quantitative multi-photon imaging and analysis, and biochemical assay is incorporated into the model to study the fitting and predicting capability of the model.

MATERIALS AND METHODS

Biaxial tensile testing

Porcine thoracic aortas from 12-24 month-old pigs were harvested from a local slaughter house and cleaned of adherent tissues. Square aortic samples of about 20 mm × 20 mm were prepared for biaxial tensile testing (n=7). Equi- and nonequi-biaxial tensile tests were performed to characterize the mechanical behavior of the aortic tissue. Following the preconditioning cycles, a preload of 2 ± 0.050 N/m was applied in order to ensure tautness of the sutures. Equi-biaxial and two nonequi-biaxial tensions were applied to each aortic sample according to the following protocols: f_l:f_c = 2:3, 1:1, 3:2. Where f_l:f_c is the ratio of tension applied in the longitudinal and circumferential directions, respectively.

Constitutive Modeling

A constitutive model of ECM mechanics is developed that considers the contribution from medial elastin ($i = E$), medial collagen ($i = M$), and adventitial collagen ($i = A$) constituents, to incorporate their layer-specific distribution orientations $R_i(\theta)$ and the sequential fiber engagement in the hyperplastic and anisotropic arterial behavior. The total strain energy function of the arterial wall is the sum of the constituent strain energy, W_i, and can be represented as $W=\sum_{i=E,M,A} W_i$. A fiber distribution network model is used to incorporate the experimentally measured fiber distribution function $R_i(\theta)$, and the elastin and collagen content n_i. The ECM constituent strain energy function, W_i, is assumed to be the sum of the individual fiber strain energies and can be expressed as: $W_i = n_i \int_{-\pi/2}^{\pi/2} w_i(\rho_i) R_i(\theta) \mathrm{d}\theta$, where $w_i(\rho_i)$ is the strain energy function at the fiber level and is characterized by a freely-jointed chain model [2].

Considering the sequential recruitment of ECM constituents in response to mechanical loading, a normal recruitment function [3] is included to capture the delayed adventitial collagen engagement. The fiber orientation distribution of the ECM constituents, $R_i(\theta)$, were incorporated in two ways: A) the distributions of fiber orientation of each constituent are incorporated directly based on the analysis of multi-photon images [1]; and B) the measured distribution functions of each constituent were fitted with a three-term von Mises distribution (Figure 1). Parameter n_i is related to the content of ECM constituents. These parameters were allowed to vary within a physiological meaningful range considering the elastin and

a) Corresponding author. Email: yanhang@bu.edu.

collagen content in the arterial tissue [4]. The material parameters were determined by minimizing the objective function using the Nelder-Mead direct search method implemented in the *fminsearch* subroutine in Matlab.

RESULTS AND DISCUSSION

The fiber orientation distribution function (Figure 1a) shows remarkably different structural characteristics in ECM constituents. The elastic fibers are relatively more uniformly distributed compared to collagen. The medial collagen shows a preferred circumferential distribution, however the multi-fiber family distribution is evident in adventitial collagen. For all three ECM constituents, the three-term von Mises fittings were able to capture the fiber distributions in the arterial wall. The collagen recruitment function was determined based on the straightness parameter analysis of adventitial collagen fibers from our previous study by Chow et al. [1]. Adventitial collagen was shown to exist as large wavy bundles of fibers that exhibit delayed fiber engagement. The values of the mean and standard deviation of the normal distribution were fixed as 1.25 and 0.05, respectively, which captures a peak recruitment at about 1.25 stretch and an overall collagen engagement between 1.15-1.35 stretch (Figure 1b). Considering the structural characteristics and contributions of elastin, medial collagen, and adventitial collagen, the measured fiber orientation distributions were directly incorporated into the structurally motivated constitutive models and, hence, reduce the number of estimated parameters to only intrinsic fiber properties and fiber content. The model predicts the biaxial mechanical behavior of arteries reasonably well, while requiring less mechanical datasets for reliable estimation. With this constitutive model, we can study the mechanical contributions from the major load-bearing ECM constituents in the arterial wall (Figure 1c). Understanding the mechanical contributions of ECM constituents in the arterial wall may shed light on the underlying mechanisms of vascular remodeling and disease progressions. The small load bearing of adventitial collagen at lower stretches is consistent with its role in preventing the artery from overstretch and rupture. However contributions from the ECM constituents to the mechanical behavior of the arterial wall are highly dependent on the mechanical loading conditions. It is important to understand the interactions between elastin and collagen in arterial wall, which are currently unclear. The coexistence of multiple ECM constituents and their interrelations may be important in maintaining the fiber distributions in the arterial wall and contributing to the anisotropic tissue behavior.

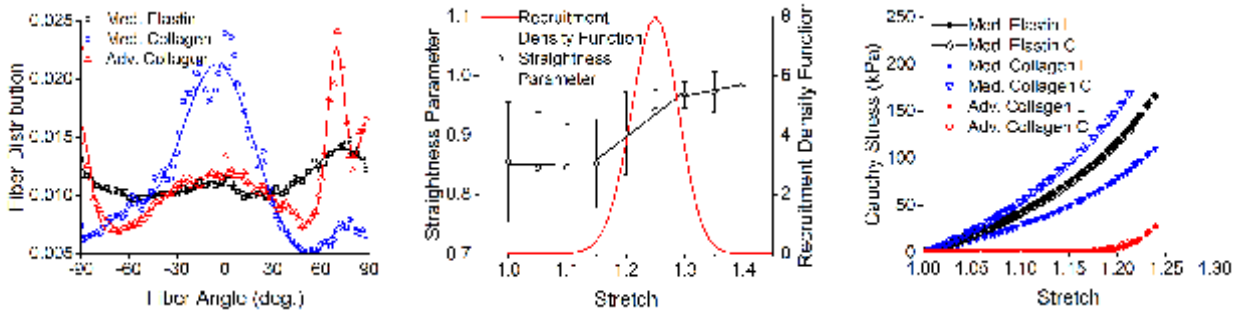

Figure 1: (a) Fiber orientation distributions of medial elastin, medial collagen, and adventitial collagen under 140% equi-biaxial tissue stretch. Symbols represent measured distribution [1] and lines represent the corresponding three-term von Mises distribution function fitting; (b) Straightness parameter of adventitial collagen fibers [1], and the recruitment distribution density function that captures the delayed adventitial collagen engagement in response to mechanical loading; and (c) stress-stretch relationship of the ECM constituents, medial elastin, medial collagen, and adventitial collagen, when the arterial tissue is under equibiaxial tension.

CONCLUSIONS

In this study, we developed a new multi-scale structure-based model of ECM mechanics from a fundamental mechanics perspective coupled with critical biophysical input. The model uniquely integrates the ECM microstructural information, such as fiber distribution, recruitment, elastin and collagen content, and fiber properties, for tissue-level biomechanical function. Contributions from layer-specific ECM structural constituents, medial elastin, medial collagen, and adventitial collagen were considered in the model to reflect the different mechanical and structural role of each individual ECM component. Moreover, the integrated model shows promises in fitting and predicting with a small set of material parameters, which has physical meanings and can be related to the structure and properties of the ECM constituents.

ACKNOWLEDGEMENT

The authors would like to acknowledge the funding support from National Institute of Health (1R01 HL098028).

References

[1] Chow, M.J., Turcotte, R., Lin, C.P., Zhang, Y. *Biophys. J.* 106(12):2684-2692, 2014.
[2] Kuhn, W., Grün, F. *Kolloid-Zeitschrift* 101(3):248–271, 1942.
[3] Lanir, Y. *J. Biomech.* 12(6):423–436, 1979.
[4] Chow, M.J., Mondonedo, J.R., Johnson, V.M., Zhang, Y. *Biomech. Model. Mechanobiol.* 12(2):361–372, 2013.

MS06 - Topology Optimization

TS.MS06-1.01	Allaire, Grégoire - Deterministic approaches for shape optimization under random uncertainties (INVITED)	336
TS.MS06-1.02	Guest, James - Projection-based topology optimization algorithms for advanced manufacturing (INVITED)	338
TS.MS06-1.03	Sigmund, Ole - On convergence speedup in topology optimization (INVITED)	340
TS.MS06-1.04	Tortorelli, Daniel - Topology optimization under uncertainty via non-intrusive polynomial chaos expansions (INVITED)	342
– micro, nano and multiscale applications		
TS.MS06-2.01	Cheng, Gengdong - Two-scale topology optimization based on Moving Morphable Components (MMC)	344
TS.MS06-2.02	Benard, Andre - Topology optimization and design of solid particles in suspension	346
TS.MS06-2.03	Cherkaev, Andrej - Optimal multimaterial composite structures and optimal designs	348
TS.MS06-2.04	Burczynski, Tadeusz - Topology Optimization in Nano-Scale for Generation of New Graphene-Like Materials	350
TS.MS06-2.05	Andreasen, Casper - On topology optimization of inertia driven dosing units	352
TS.MS06-2.06	Duysinx, Pierre - Generalized SFP parameterization for topology optimization including lattice structures	354
– transient and stability problems		
TS.MS06-3.01	Van Keulen, Fred - Topology optimization for transient thermo-mechanical problems	356
TS.MS06-3.02	Van Der Kolk, Max - Multi-material topology optimization of viscoelastically damped structures.	358
TS.MS06-3.03	Blasques, José Pedro - Design of beam cross sections with extreme structural properties using topology optimization	360
TS.MS06-3.04	Pedersen, Niels - On bifurcation sensitivities and stability optimization based on local sub-domain eigenvalues	362
TS.MS06-3.05	Aage, Niels - Efficient transient topology optimization through dynamic substructuring	364
TS.MS06-3.06	Wallin, Mathias - Topology optimization for finite strain plasticity	366
– Formulations and emerging problems		
TS.MS06-4.01	Fernandez-Perez, Miguel - Structural topology optimization of wind turbine blades fabricated by additive manufacturing	368
TS.MS06-4.02	Noël, Lise - Structural design under damage constraints with XFEM and level sets.	370
TS.MS06-4.03	Vié, Jean-Léopold - A second-order method for structural shape optimization with the level-set method	372
TS.MS06-4.04	Wadbro, Eddie - On nonlinear filters in topology optimization	374
TS.MS06-4.05	Rojas Labanda, Susana - On slowly moving boundaries in density based structural topology optimization	376
TS.MS06-4.06	Qian, Xiaoping - Topology Optimization for Additive Manufacturing: Considering Support Structures	378
PO.MS06-1.01.39	Bauduin, Simon - Overhanging constraints in additive manufacturing using three different tools	380

PO.MS06-1.02.40	Chedrik, Vasily - Topology/sizing optimization of aicraft structural components	382
PO.MS06-1.03.41	Collet, Maxime - Design of homogenized microstructures using stress-based topology optimization	384
PO.MS06-1.04.42	Gao, Jie - A novel topology optimization method for periodical cellular materials	386
PO.MS06-1.05.43	Lambe, Andrew - Topology optimization using Bernstein basis polynomials	388
PO.MS06-1.06.44	Li, Chih-Hung - Strength-based evolutionary structural optimization	390
PO.MS06-1.07.45	Myśliński, Andrzej - Topology optimization of contact problems using Cahn-Hilliard regularization	392
PO.MS06-1.08.46	Niu, Bin - On objective functions in topology optimization for vibration and wave propagation problems	394
PO.MS06-1.09.47	Paquette-Rufiange, Antonin - Adaptive design process of lattices produced by additive manufacturing	396
PO.MS06-1.11.49	Wang, Bo - Multiple Designs Approach for Continuum Topology Optimization	398
PO.MS06-1.12.50	Wang, Yingjun - Lattice hip implant design by multi-scale multi-constraint topology optimization	400
PO.MS06-1.13.51	Yamada, Takayuki - Estimates of Upper and Lower Bounds of Dispersive Effect in the Homogenized Wave Equation	402
PO.MS06-1.14.52	Yan, Jun - Global multiscale optimization design of composite laminated frame structure	404

DETERMINISTIC APPROACHES FOR SHAPE OPTIMIZATION UNDER RANDOM UNCERTAINTIES

Grégoire Allaire*[1] and Charles Dapogny[2]

[1]*Centre de Mathématiques Appliquées (UMR 7641), Ecole Polytechnique 91128 Palaiseau, France*
[2]*Laboratoire Jean Kuntzmann, CNRS, Université Joseph Fourier, Grenoble INP, Université Pierre Mendès France, BP 53, 38041 Grenoble Cedex 9, France*

Summary We consider shape and topology optimization problems with uncertainties in the loadings, the material properties or the geometry. In view of minimizing the CPU cost of solving such problems, we propose two deterministic approximation methods, based on the assumption of small uncertainties. The first one solves the so-called worst-case design scenario for a linearized approximation. The computational cost is at most twice that of the unperturbed case since it involves three adjoint equations on top of the state equation. The second one minimizes averaged objective functions (mean value, variance) of second-order Taylor expansions of standard cost functions, under the additional assumption that the (small) uncertainties are generated by a finite number N of random variables. The computational cost is now similar to that of a multiple load problems where the number of loads is N. We demonstrate the effectiveness of our approach on various geometric optimization problems in 2-d linearized elasticity. We rely on a gradient algorithm with shape derivatives in a level set framework.

GEOMETRIC OPTIMIZATION SETTING

We consider geometric optimization in the context of linear elastic structures. A shape is a bounded, Lipschitz domain $\Omega \subset \mathbb{R}^d$ $(d = 2, 3)$, filled with a linear isotropic elastic material with Hooke's law A. Every such shape is clamped on a part Γ_D of its boundary, submitted to given body forces f and surface loads g, applied on a subset $\Gamma_N \subset \partial\Omega$ disjoint from Γ_D, and only its free boundary $\Gamma := \partial\Omega \setminus (\Gamma_D \cup \Gamma_N)$ is subject to optimization. The displacement u_Ω of a shape Ω is the unique solution of the linear elasticity system:

$$\left\{ \begin{array}{cl} -\mathrm{div}(Ae(u)) = f & \text{in } \Omega \\ u = 0 & \text{on } \Gamma_D \\ Ae(u)n = g & \text{on } \Gamma_N \\ Ae(u)n = 0 & \text{on } \Gamma \end{array} \right. . \tag{1}$$

For some integrand functions $j(u)$ and $k(u)$, we consider the optimization problem

$$\inf_{\Omega \in \mathcal{U}_{ad}} \left\{ J(\Omega) = \int_\Omega j(u)\, dx + \int_{\Gamma_N} k(u)\, ds \right\}, \tag{2}$$

with the set of admissible shapes $\mathcal{U}_{ad} := \left\{ \Omega \subset \mathbb{R}^d \text{ is open, bounded and Lipschitz, } \Gamma_D \cup \Gamma_N \subset \partial\Omega \right\}$. When it comes to evaluating the sensitivity of such functionals, we rely on Hadamard's boundary variation method. Namely, variations of a shape Ω are of the form

$$\Omega_\theta := (I + \theta)(\Omega), \;\; \theta \in C^1(\mathbb{R}^d, \mathbb{R}^d), \;\; \|\theta\|_{C^1(\mathbf{R}^d, \mathbf{R}^d)} < 1$$

and shape derivatives are just usual functional derivatives with respect to the vector field θ.

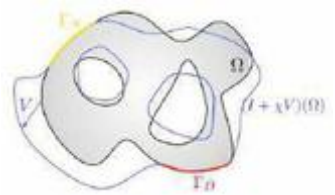

Figure 1: *Uncertainty, parametrized by a vector field V, of the geometry of the shape Ω.*

The same Hadamard setting is useful to define uncertainties with respect to the geometry. Denoting now by V a vector field, a perturbation of a given shape is defined as Ω_V (see Figure 1). It is assumed to be small in the continuous norm, $\|V\|_{C^0(\mathbf{R}^d, \mathbf{R}^d)} \ll 1$. Uncertainties or perturbations of the forces or material properties are defined in a standard way [1], [2] (many more references can be found in the bibliography of these papers).

*Corresponding author. Email: gregoire.allaire@polytechnique.fr

A LINEARIZED APPROACH TO WORST-CASE DESIGN

For a given level of uncertainty $m > 0$, we choose to optimize the worst-case scenario, namely

$$\inf_{\Omega \in \mathcal{U}_{ad}} \left\{ \mathcal{J}(\Omega) = \sup_{V \in C^1(\mathbf{R}^d, \mathbf{R}^d),\, \|V\|_{C^0(\mathbf{R}^d, \mathbf{R}^d)} < m} J(\Omega_V) \right\}.$$

In order to simplify the inner maximization, assuming that m is small, we linearize the objective function $J(\Omega_V)$ with respect to V. Linearizing the state equation (1) requires a standard ajoint state p. Then, the linearized worst-case design problem can be written as

$$\inf_{\Omega \in \mathcal{U}_{ad}} \left\{ \mathcal{J}^{\text{lin}}(\Omega) = J(\Omega) + m \int_\Gamma h(u,p)\, ds \right\}, \tag{3}$$

where the integrand h depends on both u and p and is integrated on the free boundary Γ only (like a shape derivative). Then, it is a standard matter to compute the shape derivative of (3) and to implement a gradient descent algorithm. Note that this shape derivative requires two additional adjoint (see [1] for details). A similar (albeit simpler) method applies to other types of uncertainties in the forces or material properties. In Figure 2, one can see the effect of geometry uncertainties for a gripping mechanism: the small joints are thickened by considering the linearized worst-case approach.



Figure 2: *Gripping mechanism: loadings (left), unperturbed optimal design (middle), linearized worst-case design (right).*

A SECOND-ORDER APPROACH TO AVERAGED OPTIMIZATION

We now switch to the optimization of an average of the objective function, with respect to to the probability distribution of the uncertainties. Still for small uncertainties, we further assume that they are generated by N uncorrelated and normalized random variables. We now perform a second-order Taylor expansion of the cost function (2) with respect to these small uncertainties and we optimize its mean (or combination of mean and variance). It turns out that, for compliance minimization, this expansion is exact and leads to a problem equivalent to N multiple loads optimization [2]. In any case, the only used informations on the random distribution are its mean and variance. In Figure 3 one can see the effect of (vertical) force uncertainties generated by two random variables in the blue region). The optimal design for the mean is clearly more robust than the unperturbed one. This approach extends to other type of uncertainties, including geometrical ones.



Figure 3: *Minimal compliance bridge: loadings (left), unperturbed optimal design (middle), second-order averaged optimal design (right).*

References

[1] Allaire G., Dapogny C.: A linearized approach to worst-case design in parametric and geometric shape optimization, M3AS Vol. 24, No. 11 (2014) 2199-2257.

[2] Allaire G., Dapogny C.: A deterministic approximation method in shape optimization under random uncertainties, to appear in SMAI J. Comput. Math. HAL preprint: hal-01160256v1 (June 2015).

PROJECTION-BASED TOPOLOGY OPTIMIZATION ALGORITHMS FOR ADVANCED MANUFACTURING

Andrew T. Gaynor[1] & James K. Guest[1a]
[1]*Department of Civil Engineering, Johns Hopkins University, Baltimore, Maryland, USA*

Summary The recent and rapid advancement of additive manufacturing technologies has provided engineers the capability to fabricate tailored structures with significant complexity at unprecedented length scales. In order to fully leverage these technologies, the associated new capabilities and limitations must be integrated into the design process. Herein, we extend projection-based topology optimization algorithms to address a number of advanced manufacturing methods including both polymer and metal additive manufacturing, and three-dimensional weaving. Fundamentally, all algorithms draw upon and extend the Heaviside Projection Method in order to impose manufacturing constraints, essentially utilizing tailored geometric and functional relationships between the independent design variables and the physical (and analysis) space. Specifically, we present new topology optimization algorithms for designing with multiple materials, considering support anchors for overhang regions, and respecting various geometric restrictions associated with 3D weaving. Through this, the end goal is to eliminate solution post-processing such that the optimized topologies are directly manufacturable.

DESIGN FOR ADDITIVE MANUFACTURING

With the surge of industry interest in additive manufacturing (AM) comes the increasingy need to properly design components for this truly game-changing manufacturing technology. Topology optimization and AM are a natural design-manufacture pair, with both being capable of addressing and leveraging complexity when such complexity leads to enhanced performance. While manufacturing constraints may be considered reduced for AM as compared to traditional manufacturing technologies, they are of course still present and must be considered in the design process. In this paper, several projection-based topology optimization algorithms are highlighted, which design for a number of advanced manufacturing methods including direct metal laser sintering (DMLS), material jetting, and 3D weaving. All algorithms are derived from the Heaviside Projection Method (HPM) to topology optimization [1].

MAXIMUM OVERHANG ANGLES AND APPLICATION TO DIRECT METAL LASER SINTERING (DMLS)

Direct Metal Laser Sintering (DMLS) is a powder bed additive manufacturing technology in which metal powder is selectively sintered or melted in a layer-wise fashion. After one layer is selectively sintered/melted, the machine sweeps another thin layer of powder across the build plate. While possessing the capability of making truly novel metal parts, this energy-intense process is susceptible to processing errors including curling and shrinkage due to development of large residual stresses. These stresses develop when the heat of the weld-like process cannot dissipate from the point of melting.

To mitigate this deleterious effect, designers often introduce support structures to help anchor the part to the build plate. Not only is the curling from residual stresses counteracted, but these stresses are reduced as the heat can more effectively dissipate from the point of melting. That said, there are signficant advantages to eliminating these material using, sacrificial support materials during the additive manufacturing build process. As such, by stipulating that the built part not possess an overhang angle greater than the maximum observed printable overhang, the need for support material is completely eliminated, thus ensuring that all material used is for an efficient, structural purpose. Here are shown some solutions designing for various overhang angles and printing directions.

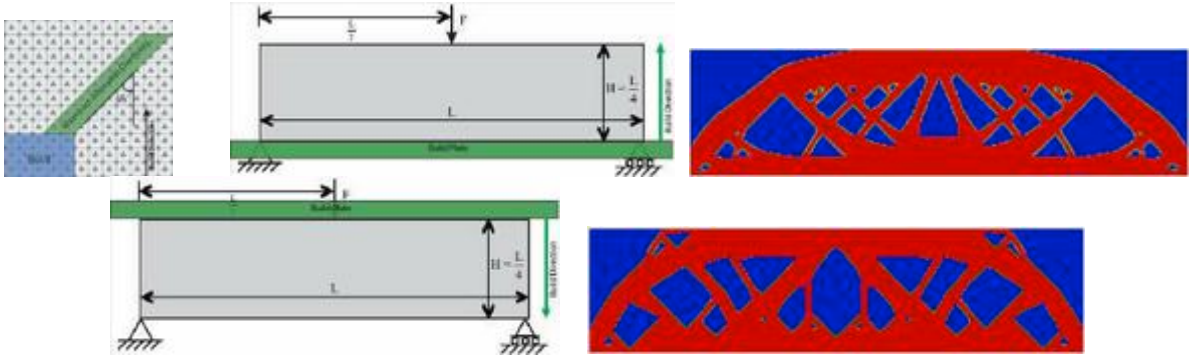

Figure 1: Topology optimization under a 45° overhang angle constraint building from bottom-up and top-down.

[a] Corresponding author. Email: jkguest@jhu.edu

As expected, the build directly significantly influences the optimized topology. Building in the bottom-up direction, the topology optimization algorithm designs up to the 45° overhang, creating 45° peaks in the design. Conversely, in the top-to-bottom build, the algorithm creates 45° "wells".

As in the case of imposing the minimum length scale constraint [1], the maximum overhang constraint is imposed through a projection of independent design variables onto the finite element space. The key difference here is the introduction of an additional projection operation from the support material zone onto an element [2]. This leads to a series of two projections, one from the support material region and one from the local region, leading to overhang angle and minimum length scale constraints being observed.

MULTI-MATERIAL TOPOLOGY OPTIMIZATION AND APPLICATION TO MATERIAL JETTING

Multi-material additive manufacturing processes, such as Stratasys PolyJet [3] and 3D Systems MultiJet [4] technologies possess the ability to print multiple materials during the same build. In this material jetting process, the printer extrudes liquid photopolymeric material in a drop-by-drop manner, which is "instantaneously" solidified by ultraviolet light. This technology is clearly unique in its ability to place up to 10+ materials on a pixel-by-pixel basis. To design for this capability, a new projection based topology optimization algorithm is introduced in which a single design variable is capable of not only determining topology, but critically, the material selection.

Recently the authors demonstrated the use of topology optimization to design compliant mechanisms with multiple materials [5]. The algorithm chose to place stiff material where load transfer was critical and compliant material in hinge-like regions to maximize motion (Figure 2). In this approach, the overall Young's modulus E of a particular finite element in the design domain was expressed as a summation of the Young's modulus contribution ΔE of the material placement variable, ϕ, as follows:

$$E^e = \sum_i^n \rho_i^e(\phi_i)\,\Delta E_i$$

Herein, we introduce a thresholding Heaviside function to allow the independent design variables to specify whether a particular material phase is actively projecting material. Just as in the overhang algorithm, there are two levels of projection. The first level determines which material phase contributions are active, while the next level projection imposes typical minimum length scale control.



Figure 2: Compliant mechanism designed for E=0,1,2. Mechanical testing seen on right [5]

CONCLUSIONS

In order to fully leverage the capabilities of advanced manufacturing processes, design engineers and optimization algorithms must properly account for the process capabilities and limitations, even if such limitations are significantly reduced over traditional manufacturing processes. This paper presents advancements in projection-based topology optimization algorithms towards this goal, including addressing overhang angles and multiple materials in AM, with extensions to lattice-like materials manufactured through 3D weaving [6] also being achievable.

References

[1] Guest JK, Prévost JH, Belytschko T. Achieving minimum length scale in topology optimization using nodal design variables and projection functions. *International Journal for Numerical Methods in Engineering* 61(2):238–254, 2004.

[2] Gaynor AT, Guest JK. (2014). Topology Optimization for Additive Manufacturing Considering Maximum Overhang Constraint. *Proceedings of the 15th AIAA/ISSMO Multidisciplinary Analysis and Optimization Conference*, Atlanta, GA, p. 1-8, 2014.

[3] "PolyJet Technology." Stratasys. Web. 15 Jan. 2016. <http://www.stratasys.com/3d-printers/technologies/polyjet-technology>.

[4] "MultiJet Printing." 3D Systems. Web. 15 Jan. 2016. <http://www.3dsystems.com/quickparts/prototyping-pre-production/multijet-printing-mjp>.

[5] Gaynor AT, Meisel NA, Williams CB, Guest JK. Multiple-Material Topology Optimization of Compliant Mechanisms Created Via PolyJet Three-Dimensional Printing. *ASME Journal Manufacturing Science and Engineering* 136(6):061015-061015-10, 2014.

[6] Zhao L, Ha S, Sharp KW, Geltmacher AB, Fonda RW, Kinsey AH, Zhang Y, Ryan SM, Erdeniz D, Dunand DC, Hemker KJ, Guest JK, Weihs TP. Permeability measurements and modeling of topology-optimized metallic 3-D woven lattices, *Acta Materialia*, 81: 326-336, 2014.

ON CONVERGENCE SPEEDUP IN TOPOLOGY OPTIMIZATION

Ole Sigmund*
Department of Mechanical Engineering, Solid Mechanics, Technical University of Denmark

Summary This paper introduces a simple-to-implement, multiscale-inspired approach to improve convergence speed in topology optimization. To ensure convergence toward globally optimal Michell-like structures, topology optimization approaches often apply continuation schemes where e.g. the penalization exponent is increased gradually. In this way, one nudges the process by going from an initially convex problem (variable thickness sheet) to a penalized, black and white solution. Iteration counts for such continuation approaches are usually counted in many hundreds or up to thousands. By introducing an extra constraint that limits the p-norm of the difference between the local density field and a smoothed (homogenized) one, the continuation scheme can be eliminated. It is demonstrated that this approach systematically creates extremely detailed and highly optimized Michell-like structures within at most 200 iterations.

THEORY AND METHOD

The standard density-based minimum compliance topology optimization problem reads

$$\begin{aligned} \min_{\boldsymbol{\rho}} \quad &: \quad C(\boldsymbol{\rho}) \\ \text{s.t.} \quad &: \quad \mathbf{K}(\hat{\boldsymbol{\rho}}(\boldsymbol{\rho}))\mathbf{D} = \mathbf{F} \\ &: \quad V(\hat{\boldsymbol{\rho}}(\boldsymbol{\rho})) \leq V^* \\ &: \quad \mathbf{0} \leq \boldsymbol{\rho} \leq \mathbf{1} \end{aligned} \tag{1}$$

where $\boldsymbol{\rho}$ is the vector of element-based design variables, $\hat{\boldsymbol{\rho}}(\boldsymbol{\rho})$ are the (density) filtered, physical design variables using a filter size r_{min}, $C(\boldsymbol{\rho})$ is compliance, $\mathbf{K}$, $\mathbf{F}$ and $\mathbf{D}$ are global stiffness matrix, load and displacement vectors, respectively, and V and V^* are volume and volume bound, respectively. The optimization problem (1) is set up for a density filtering approach, however, it can easily be simplified to a sensitivity filtering approach by substituting $\hat{\boldsymbol{\rho}}(\boldsymbol{\rho})$ with $\boldsymbol{\rho}$ or applied with PDE-based filtering [1]. The relation between density design variables and local (isotropic) stiffness is modelled by the SIMP interpolation scheme

$$E(\rho) = E_{min} + \hat{\rho}^q(E_0 - E_{min}), \quad E_{min} \ll E_0 \tag{2}$$

where E_0 and E_{min} are Young's modulus of solid and void material, respectively, and q is the penalization factor.

In its standard form, the optimization problem (1) is solved by selecting appropriate penalization factors (c.f. $q = 3$) and filter radii and is then run until convergence. However, this usually results in convergence towards suboptimal topologies, where design features tend to agglomerate, resulting in suboptimal objective values and feature sizes much bigger than those allowed by the filter size. In order to circumvent this, researchers often use continuation approaches where e.g. the (SIMP) filter factor is increased from 1 to 3 in steps of 0.2, c.f. [2]. The increase in penalization factor is performed upon convergence or every say 100 iterations. Although this scheme probably can be tuned, e.g. by a recent constrained approach [3], total iteration counts are often reported to exceed a thousand.

To reduce the iteration count, the original optimization formulation (1) is appended with an extra constraint

$$\begin{aligned} \min_{\boldsymbol{\rho}} \quad &: \quad C(\boldsymbol{\rho}) \\ \text{s.t.} \quad &: \quad \mathbf{K}(\hat{\boldsymbol{\rho}}(\boldsymbol{\rho}))\mathbf{D} = \mathbf{F} \\ &: \quad V(\hat{\boldsymbol{\rho}}(\boldsymbol{\rho})) \leq V^* \\ &: \quad \frac{||\bar{\boldsymbol{\rho}}(\hat{\boldsymbol{\rho}}(\boldsymbol{\rho})) - \boldsymbol{\rho}_c||_p}{||\boldsymbol{\rho}_c||_p} \leq \epsilon, \qquad (V(\boldsymbol{\rho}_c) = V^*) \\ &: \quad \mathbf{0} \leq \boldsymbol{\rho} \leq \mathbf{1} \end{aligned} \tag{3}$$

where $||\cdot||_p$ indicates p-norm, ϵ is a small number that sets the allowed error, $\bar{\boldsymbol{\rho}}$ is a smoothed version of the physical density field using a large filter radius R_{min} and $\boldsymbol{\rho}_c$ is an auxiliary smoothed density field with subscript c for "coarse" to make the association to multiscale approaches, although its meaning and function can be seen in several different perspectives. The basic requirement to the coarse field $\boldsymbol{\rho}_c$ is that it satisfies the volume constraint. If this is fulfilled and ϵ is small enough, this implies that the volume constraint on the physical density field (third line of (3)) is automatically satisfied. However, the volume constraint is maintained in the optimization problem since it tends to stabilize convergence and allows some freedom

*Email: sigmund@mek.dtu.dk

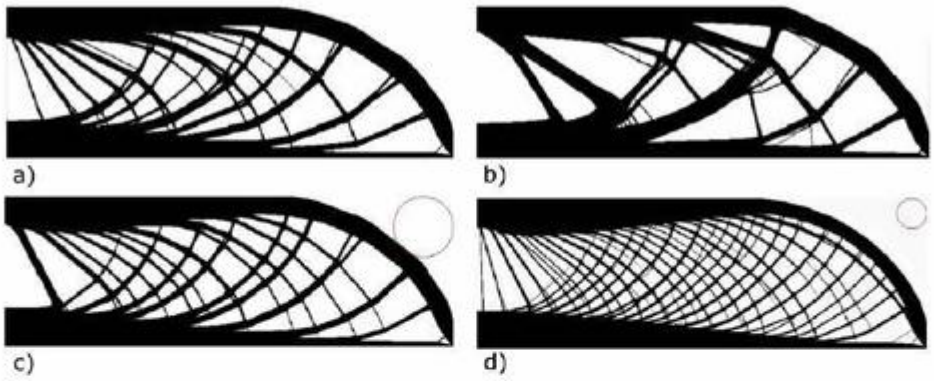

Figure 1: a) Optimized Michell-like half-cantilever structure based on continuation approach. b) Result without continuation. c) Result with proposed scheme and large coarse scale filter radius (radius indicated with circle). d) Result with proposed scheme and small coarse scale filter radius (radius indicated with circle) and finer mesh.

in selecting ϵ. The choice of coarse scale filter radius R_{min} for the ρ constraint influences the distance between local features, i.e. it introduces a weakly enforced maximum length scale both on solid and on void regions of the optimized designs.

The added p-norm constraint in (3) effectively introduces a local smoothed density constraint everywhere in the design domain. Hence, choosing different properties of the coarse field ρ_c allows a range of interesting features and effects to be controlled. Here we discuss and apply a concept where ρ_c is obtained as the optimized solution from the variable thickness sheet problem. Here one first solves the convex $q = 1$ SIMP problem (i.e. the variable thickness sheet problem in 2d), possibly on a coarse mesh which afterwards can be smoothed and projected to the fine mesh. This added local density constraint hinders design features in agglomerating and hence ensures convergence to very detailed and highly optimal Michell-like solutions.

RESULTS

Preliminary results are presented in Fig. 1. Subfigure a) shows an optimized half beam obtained through the continuation approach using 1472 iterations. Subfigure b) shows the optimized half beam obtained without continuation approach after 273 iterations. Neither the visual resemblance to an analytical Michell structure nor a quantitative comparison to subfigure a) in terms of objective function speak in favour of subfigure b). Subfigures c) and d) are obtained using the following strategy: A) ρ_c is obtained from running (1) on a coarse mesh. B) Based on A), (3) is run with $q = 2$ and a minimum filter size of $r_{min} = 1.2$ times the element size, either up to 100 iterations or a certain measure of non-discreteness, whichever comes first. Then the added constraint is turned off. After 150 iterations the local filter is switched off and the optimization is continued up to a maximum of 200 iterations. This makes for a fair comparison of approaches and settings if the goal is to provide an efficient algorithm that can converge to excellent designs in less than 200 iterations. Clearly there may be settings that can speed up convergence even further. Usually, one would not remove the local filter entirely, however, it is necessary here in order not to penalize fine detail structures in terms of optimized compliance values. Fine featured structures have large perimeters and hence have more intermediate density elements than coarse scaled structures. The resulting designs in subfigures c) and d) are obtained using two different coarse scale filter sizes R_{min} as indicated with circles. Both visual comparison to the analytical Michell solution as well as objective function values compare favourably to those of subfigure a) that were obtained with the inefficient standard continuation approach.

References

[1] B. Lazarov and O. Sigmund. Filters in topology optimization as a solution to Helmholtz type differential equation. *International Journal for Numerical Methods in Engineering*, 86(6):765–781, 2011.

[2] O. Sigmund, N. Aage, and E. Andreassen. On the (non-)optimality of Michell structures. *Submitted*, 2016.

[3] S. Rojas-Labanda and M. Stolpe. Automatic penalty continuation in structural topology optimization. *Structural and Multidisciplinary Optimization*, 52(6):1205–1221, 2015.

TOPOLOGY OPTIMIZATION UNDER UNCERTAINTY VIA NON-INTRUSIVE POLYNOMIAL CHAOS EXPANSIONS

Daniel A. Tortorelli*[1] and Vahid Keshavarzzadeh[1]

[1]*Department of Mechanical Science and Engineering, University of Illinois at Urbana-Champaign, Urbana, Illinois, USA*

Summary This paper presents a systematic approach for topology optimization under uncertainty. The approach integrates an efficient non-intrusive polynomial chaos expansion with design sensitivities for reliability-based and robust topology optimization. Uncertainty is introduced in the loading and elemental densities to address the manufacturing variability. The manufacturing variability is represented via a random process with a Karhunen Loeve expansion on underlying uncertain parameters. To demonstrate the effect of uncertainty, the results of the optimization under uncertainty are compared with deterministic optimization results.

TOPOLOGY OPTIMIZATION UNDER UNCERTAINTY

The subject of topology optimization has received considerable attention in the past two decades [1]. A majority of these works assume deterministic material distribution parameters and boundary and load conditions in the optimization process. However, the performance of a structure varies due to the inherent uncertainty in these quantities. More recently researchers have developed robust and reliable designs by incorporating the effects of uncertainty into their optimization studies.

In robust design optimization (RDO) researchers minimize the effect of variations on their designs by including higher-order statistics such as variance in the cost and constraint functions. Typically, the statistical moments are obtained via a Monte Carlo approach which requires numerous realizations or a perturbation technique that uses Taylor expansions which requires the computation of higher-order sensitivities with respect to the random variables [2, 3]. Alternatively, in reliability based design optimization (RBDO) researchers constrain the probability of failure. The probability of failure is often approximated via First-Order Reliability Methods (FORM) or Second-Order Reliability Methods (SORM) [4, 5]. The FORM and SORM require the solution of a constrained optimization problem, and hence the RBDO requires the solution of a nested, i.e. two-level, optimization problem. It is evident that the Monte Carlo approach is computationally intractable particularly in conjunction with an optimization process for large scale problems. Moreover, while numerical techniques based on Taylor expansions are efficient, they may not yield enough accuracy when there is a significant variation in uncertain parameters.

POLYNOMIAL CHAOS BASED DESIGN OPTIMIZATION UNDER UNCERTAINTY

In the present study, we adopt a different perspective and pursue a methodology based on polynomial chaos expansion (PCE) for uncertainty propagation[6, 7]. PCE provides a systematic approach to characterize the random response and is an attractive approach due to its fast convergence property and its ability to provide a mapping between the random response and random model parameters.

The PCE greatly facilitates the calculation of statistical moments and their design sensitivities. And for this reason the majority of existing design optimization efforts that utilize PCE concentrate on RDO [8, 9]. Insofar as RBDO is concerned, the PCE can be used to evaluate the probability of failure by integrating the probability of the random variables over the failure region. Indeed, this integral is easily evaluated via Monte Carlo, but bear in mind that the realizations in this Monte Carlo computation are based on the PCE, and thus the computational burden is minimal. The probability of failure design sensitivity computation is another story however. It requires knowledge on the failure region's boundary, and more importantly, how the boundary varies as the design parameters vary. This information is not explicitly available and thus RBDO is problematic, even with PCE.

We provide a systematic framework for design optimization under uncertainty that addresses both RDO and RBDO via the PCE. Uncertainty is introduced in the loading and geometry to address the load and manufacturing variability. The geometry variability is represented via a random process with a truncated Karhunen Loeve expansion that maps the assumed low dimensional underlying uncertainty to correlated random variables in the random field. Accordingly, the PCE of quantities of interest such as volume and compliance are developed on the basis of the low dimensional underlying uncertainty.

We demonstrate the easily implemented non-intrusive PCE in the topology optimization of benchmark problems such as Messerschmitt-Blkow-Blohm (MBB) beam and cantilever beam. To show the significance of uncertainty, the response of designs which considered uncertainty are compared to those that do not, i.e. deterministic designs. Not surprisingly deterministic designs do not necessarily satisfy the probabilistic RDO and RBDO constraints.

*Corresponding author. Email: dtortore@illinois.edu

References

[1] Bendsoe MP, Sigmund O. Topology Optimization: Theory, Methods, and Applications Springer-Verlag Berlin Heidelberg. 2004;.

[2] Fu M. Optimization for Simulation: Theory vs. Practice. Informs Journal on Computing. 2002;14(3):192–215.

[3] Sundaresan S, Ishii K, Houser D. A Robust Optimization Procedure with Variations on Design Variables and Constraints. Engineering Optimization. 1995;24(2):101–117.

[4] Haldar A, Mahadevan S. Probability, Reliability, and Statistical Methods in Engineering Design. Wiley, New York. 2000;.

[5] Rackwitz R. Reliability analysisa review and some perspectives. Structural Safety. 2001;23(4):365–395.

[6] Ghanem R, Spanos P. Stochastic Finite Elements: A Spectral Approach. Dover publications. 2002;.

[7] Xiu D, Karniadakis GE. The Wiener–Askey Polynomial Chaos for Stochastic Differential Equations. SIAM Journal on Scientific Computing. 2002;24(2):619–644.

[8] Maute K, Weickum G, Eldred M. A reduced-order stochastic finite element approach for design optimization under uncertainty. Structural Safety. 2009;31(6):450 – 459.

[9] Tootkaboni M, Asadpoure A, Guest JK. Topology optimization of continuum structures under uncertainty A Polynomial Chaos approach. Computer Methods in Applied Mechanics and Engineering. 2012;201204(0):263 – 275.

TWO-SCALE TOPOLOGY OPTIMIZATION BASED ON MOVING MORPHABLE COMPONENTS (MMC)

Gengdong Cheng[1], Liang Xu[2a)]
[1]*State Key Laboratory of Structural Analysis for Industrial Equipment, Dalian University of Technology, Dalian, Liaoning, China*
[2]*Department of Engineering Mechanics, Dalian University of Technology, Dalian, Liaoning, China*

Summary This paper studies concurrent topology optimization with multi micro material design. Unlike traditional concurrent topology optimization presented by Liu et al. [1], where a uniform micro material is used, the macro structure in this research is composed of sub domains, each with a different micro material design. This gives more flexibility to industrial use and is more reasonable as materials in different domains may experience different stress states. In micro material design, in order to overcome the zig-zag boundaries and grey elements in SIMP interpolation scheme, the Moving Morphable Component (MMC) approach is used to get a clear and smooth topology in favour of manufacturing applications, like the 3-D printing techniques. A numerical example is given to show the validity of this method. Issues of manufacturability related to 3-D printing techniques are discussed.

INTRODUCTION

Structures with periodic porous material are widely used in engineering applications due to their high specific stiffness, strength and other good performances. In the design of this kind of structures, two-scale concurrent topology optimization is an effective approach. However, there are still some disadvantages of this approach. First, the macro structure is assumed to be composed of a uniform micro material, whereas, in practical applications, micro materials in different areas of the structure may be subject to different stress states, which makes a uniform micro material design not efficient. The second disadvantage is due to the limitation of SIMP interpolation scheme in the micro material design. With the development of 3-D printing technique, porous material with complex geometric micro-structures could be made in industrial applications. However, optimal micro materials with SIMP method may suffer from zig-zag boundaries and grey elements, which make 3-D printing of these materials difficult to implement. In order to overcome this problem, we try the Moving Morphable Component approach, the distinctive feature of which is that a set of morphable components are used as building blocks of topology optimization and the optimal topology is found by optimizing sizes and layout of these components, to obtain a smooth and clear boundary of micro materials in favour of manufacturing perspectives.

In this paper, we consider plane stress continuum with a number of sub domains and each domain is assigned a micro material. The MMC approach is used in the micro scale design to get a clear topology of the micro material.

PROBLEM FORMUILATION AND A NUMERICAL EXAMPLE

Consider a periodic porous structure subject to plane stress in Figure 1(a), where the design domain Ω of the porous structure is divided into s sub domains, denoted as Ω_1, Ω_2 ,……, Ω_S respectively. Each sub domain composed of porous material with different micro structure is homogenized as an equivalent anisotropic continuum in the macro scale. The effective modulus matrix of the equivalent anisotropic continuum is assumed as $\mathbf{D}^{H1}$, $\mathbf{D}^{H2}$,……,$\mathbf{D}^{HS}$ for sub domains Ω_1, Ω_2 ,……, Ω_s respectively.

For topology optimization of macro structure, the design domain Ω is meshed into N finite elements. An artificial density is assigned to each element P_i, which is the design variable in macro-scale structural topology optimization. The modulus matrix of ith macro element with density P_i is expressed in the PAMP approach, which is the abbreviation for Porous Anisotropic Material with Penalty [1]:

$$P_i^{MA} = P_i^3 \mathbf{D}^H \ \left(i = 1, 2, \cdots, N\right) \tag{1}$$

Where $\mathbf{D}^H$ could be $\mathbf{D}^{H1}$, $\mathbf{D}^{H2}$,……,$\mathbf{D}^{HS}$ depending on which sub domain ith element belongs to.

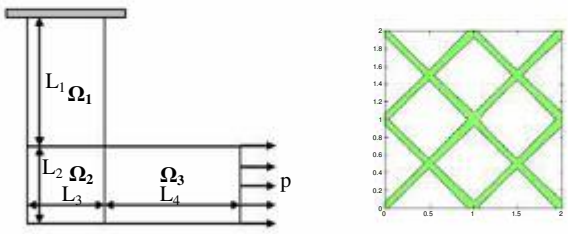

(a) (b)

Figure1. (a). A periodic porous structure subject to plane stress; (b). Initial micro design

a) Corresponding author. Email: xuliangdagong@163.com.

With MMC approach, the unit cell of micro material is composed of n components and each component has a number of design parameters. The effective property $\mathbf{D}^{\mathrm{H}}$ is calculated by the asymptotic homogenization through MMC approach and the ersatz material model. Thus, $\mathbf{D}^{\mathrm{H}}$ is a function of parameters of components in the unit cell of the micro material, denoted as $\omega_1, \omega_2, \ldots, \omega_S$ respectively. For the example shown in Fig.1, sub domain Ω_1 has components 1 to n, sub domain Ω_2 n+1 to 2n and sub domain Ω_3 2n+1 to 3n. The design variable of jth component is written as

$$\mathbf{D}^j = \left[x_0 \;\; y_0 \;\; L \; t_1 \;\; t_2 \;\; t_3 \;\; \sin\theta\right]^T \;\; \left(j = 1, 2, \cdots, 3n\right) \tag{2}$$

The design variables of the two scale optimization problem should be

$$\mathbf{d} = \left\{P_1, P_2, \cdots, P_N, \left(\mathbf{D}^1\right)^T, \left(\mathbf{D}^2\right)^T, \cdots, \left(\mathbf{D}^{3n}\right)^T\right\}^T \tag{3}$$

The optimization problem is to minimize the compliance subject to volume constraints on both the macro beam and micro material. The optimization problem can be written as

$$\begin{aligned} &\text{find} && \mathbf{d} \\ &\text{minimize} && C = \mathbf{F}^T\mathbf{U} \\ &s.t. && \mathbf{K}\left(\mathbf{d}\right) = \mathbf{F} \\ & && \frac{\sum_{i=1}^{N} P_i V_i}{\sum_{i=1}^{N} V_i} \le \overline{V}, \frac{\int_{\omega_1} H\left(\phi^s\left(\mathbf{D}\right)\right) dV}{\int_{\omega_1} dV} \le \overline{v}_1, \frac{\int_{\omega_2} H\left(\phi^s\left(\mathbf{D}\right)\right) dV}{\int_{\omega_2} dV} \le \overline{v}_1, \frac{\int_{\omega_3} H\left(\phi^s\left(\mathbf{D}\right)\right) dV}{\int_{\omega_3} dV} \le \overline{v}_3 \end{aligned} \tag{4}$$

Where $\overline{V}, \overline{v}_1, \overline{v}_2, \overline{v}_3$ denote prescribed volume fraction for macro beam, micro material ω_1, ω_2 and ω_3 respectively.

For the example structure in Fig.1, the size parameters of the L-shaped beam are L_1=2, L_2=1, L_3=1 and L_4=2. The beam is discretized with 4-node plane stress element of size 0.1×0.1 and into N=500 elements. The distributed force of the macro beam is p=1. The three units in micro materials scale are of size 2×2 and discretized into 400 elements. The properties of the base material are E=10, ν=0.3.

The prescribed volume fractions for both macro beam and micro materials are 50%. The initial design of the macro plate is uniform and the initial design of the micro material is n=8 components for each sub domain, as plotted in Figure 1(b). During optimization, the calculation of effective property $\mathbf{D}^{\mathrm{H}}$, the macro beam analysis, and sensitivities is done in Matlab through proper modification of 188-line MMC Matlab code in Zhang et al. 2016 [2]. The MMA optimizer is used.

The optimal topologies are plotted in Figure 2 with minimum compliance C=4.19.

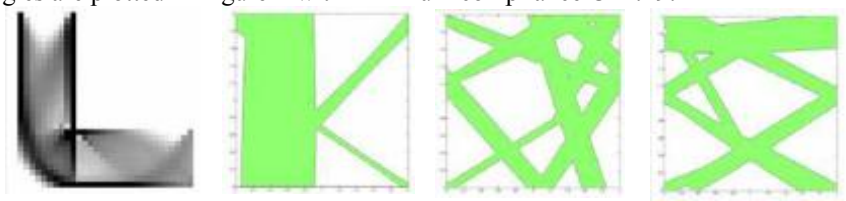

macro beam | micro material in Ω_1 | micro material in Ω_2 | micro material in Ω_3

Figure 2. Optimal topologies

CONCLUSIONS

In this paper, a two-scale concurrent optimization is carried out. The macro design domain is divided into three sub domains where micro materials differ from each other. This gives more design flexibility than the traditional concurrent optimization procedure as different parts of the macro structure are subject to different stress state. A trial application of the MMC approach to the micro scale design is given, which achieves smooth boundaries of micro materials, and is more appealing to manufacturing applications. There are also some minor problems with this method. For example, some oscillation may occur during optimization process and the iteration number needed to converge is comparatively large, which will be amended in our future work.

References

[1] Liu L, Yan J, Cheng GD. Optimum Strucutre with Homogeneous Optimum Truss-like Material. Comput Struct 86(13-14): 1417-1425,2008.

[2] Zhang WS, Yuan J, Zhang J, Guo X. A New Topology Optimization Approach Based On Moving Morphable Components (MMC) and the Ersatz Material Model. Struct Multidisc Optim 2016(accepted).

TOPOLOGY OPTIMIZATION AND DESIGN OF SOLID PARTICLES IN SUSPENSION

André Bénard[1], Tong Gao[1,2], & Alejandro R. Diaz[1]
[1]*Department of Mechanical Engineering, East Lansing, Michigan, USA*
[2]*Department of Computational Mathematics, Science, and Engineering, East Lansing, MI, USA*

Summary A methodology for the design of solid particles in suspension is presented as an extension of the material design problem in topology optimization. The tensor describing the interactions of the particles with the surrounding fluid is provided as a target and shapes of particles matching this mobility tensor are identified. The theoretical framework describing the motion of single and ensemble of particles is introduced and discussed in the context of its application to topology optimization.

INTRODUCTION

Nanoparticles and colloids with exotic shapes and functionality are engineered today at the nanometer and micrometer scales and can exhibit interesting flow-induced patterns and result in unusual assembled systems [1,2]. Novel synthesis and fabrication techniques allow the production of particles with various degrees of asymmetry, and a wide range of shapes (fibers, rings, cubes, prisms), and anisotropic interactions. Such shapes include "nano-acorns", "nano-centipedes", "nano-guitars", "nano-squids" and "nano-whiskers" [1]. It is now clear that the shape of particles plays a crucial role, especially at the small scale, in determining many of the interesting physical properties observed. In this work a framework for the design of particles based on topology optimization is presented to identify possible particle shapes allowing the realization of desired orientation states. The design problem is posed as a material distribution problem as in [3,4,5] in which the goal is to find an actual distribution of a material in the fluid that matches the prescribed mobility or fluid interaction tensor for a desired orientation state. The proposed approach is outlined below, beginning with an overview of suspension hydrodynamics.

SINGLE PARTICLE DYNAMICS

The dynamics of neutrally buoyant, rigid ellipsoidal particles in Newtonian fluid flow was first studied theoretically by Jeffrey [6] and he showed that the time-rate-change of the unit vector $\mathbf{p}$ parallel to particle' symmetry-axis can be expressed as $\dot{\mathbf{p}} = \mathbf{W}\cdot\mathbf{p} + \left(\lambda_e^2 - 1\right)/\left(\lambda_e^2 + 1\right)\left(\mathbf{E}\cdot\mathbf{p} - \mathbf{E}:\mathbf{ppp}\right)$. **E** and **W** are the symmetric and asymmetric components of the velocity gradient. The scalar parameter λ_e represents the fiber-fluid coupling coefficient for particles with certain axisymmetric shapes. This theory has been generalized by Bretherton [7] where a third rank tensor **B** is employed to describe the coupling between the shape of a particle and its rate of rotation. For a single particle of arbitrary shape, a formulation based on a "grand resistance matrix" is sometimes employed, which relates exerted force ($\mathbf{F}$), torque ($\mathbf{L}$) and stresslet ($\mathbf{S}$) to particle motion and which can be expressed as

$$\begin{pmatrix} \mathbf{F} \\ \mathbf{L} \\ \mathbf{S} \end{pmatrix} = \begin{pmatrix} \mathbf{X} & \mathbf{P} & \mathbb{Q} \\ \mathbf{P}' & \mathbf{Y} & \mathbb{R} \\ \mathbb{Q}' & \mathbb{R}' & \mathbb{Z} \end{pmatrix} \begin{pmatrix} \mathbf{u} - \mathbf{U} \\ \boldsymbol{\omega} - \boldsymbol{\Omega} \\ \mathbf{E} \end{pmatrix} \tag{1}$$

where $\mathbf{X}, \mathbf{Y}, \mathbf{P}$ are second order tensors while $\mathbb{Q}, \mathbb{R}, \mathbb{Z}$ are third order tensors. $\mathbf{B}$ can be solved for a force-free particle as $\mathbb{B} = -2\left(\mathbf{Y} - \mathbf{P}'\cdot\mathbf{X}^{-1}\cdot\mathbf{P}\right)^{-1}\cdot\left(\mathbb{R} - \mathbf{P}'\cdot\mathbf{X}^{-1}\cdot\mathbb{Q}\right)$. Simple cases for which all entries of the tensors are known include ellipsoids and various special cases e.g. the sphere. Such cases can be used for validation purposes. In addition, Bretherton [7] proposed a configuration of arrays of ellipsoids connected with a sphere, which won't tumble but only migrate in the shear flow. Figure 1 below shows a possible candidate of a complex particle. This particle design greatly reduces the particle-particle interaction and facilitates particle aggregation and alignment. If such shapes could be produced and aerosolized, they could deliver, for example, a much larger amount of drugs deep in the lungs when compared to a spherical particle with similar frontal area (a fibrous particles would rotate, thus increasing its propensity at being captured by a sticky surface).

[a] Corresponding author. Email: diaz@egr.msu.edu

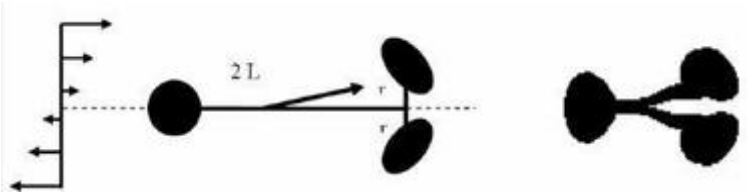

Figure 1. Illustration of a non-axisymmetric particle of finite length that will not rotate in simple shear flow but will migrate laterally toward a center of a channel (adapted from [4]).

ENSEMBLE OF PARTICLES

The flow-induced alignment of ensemble of particles can be described by an orientation distribution function. For rod-like particles it satisfies the following continuity equation in orientation space [8]:

$$\frac{D\Psi}{Dt} = -\nabla_{\mathbf{p}} \cdot \left(\dot{\mathbf{p}}\Psi\right) \tag{2}$$

In the above, $\dot{\mathbf{p}}$ represents the angular velocity of a particle. $D\Psi / Dt$ is the material derivative of the orientation distribution function. The differential operator $\nabla_{\mathbf{p}}$ is defined as $(\mathbf{I}-\mathbf{pp})\cdot\nabla$ on a surface of a unit sphere. The microstructure of spheroidal suspension is characterized by the second and fourth moments of Ψ:

$$<\mathbf{pp}> = \int_0^{2\pi}\int_0^{\pi} \mathbf{pp}\Psi \sin\theta d\theta d\varphi, \; <\mathbf{pppp}> = \int_0^{2\pi}\int_0^{\pi} \mathbf{pppp}\Psi \sin\theta d\theta d\varphi, \tag{3}$$

where $\Psi(\mathbf{x},\mathbf{p},t)\sin\theta d\theta d\varphi$ represents the fraction of particles with orientation vectors between $\mathbf{p}$ and $\mathbf{p}+\delta\mathbf{p}$. The well-known evolution equation for the second moment $<\mathbf{pp}>$ must be solved to identify the orientation states for a given flow field [8]. The theory has been extend by our group based on a formulation introduced by Rallison [9] involving a rotation tensor **R** which include all three Euler angles.

PARTICLE DESIGN PROBLEM

In the material design problem as described in [3,4,5], a target tensor is given and the goal is to find the vector of design variables that result in an effective tensor that matches the target as closely as possible. The problem can be cast as an optimization problem where a prescribed amount of material is provided and the weighted mean square deviation from the target tensor is minimized. The same approach is employed here. We first estimate the shape tensor $\mathbb{B}$ that characterizes the hydrodynamic interactions. The problem is formulated as in [10] for estimating the relevant entries of the mobility tensor of a specific realization. For simple cases where the steady-state solutions of the orientation tensor can be achieved, it is straightforward to solve $\mathbb{B}$ directly by setting the equations to a steady state. For simplicity the rotational diffusion is assumed small, i.e., $D_R \approx 0$, and the concentration of particles Φ are approximately uniform.

SUMMARY AND CONCLUSION

Preliminary work on a methodology for the design of particles is introduced in the work that allows to identify shapes of particles with desired motion. The problem can be cast as a material design problem. Extension of this work is possible for large ensemble of interacting particles in which the target would be specific rheological properties.

References

[1] Glotzer, S.C. and Solomon, M.J., "Anisotropy of building blocks and their assembly into complex structures", Nature Materials, 6 (8), 557-562, 2007.
[2] Bricard, A., Caussin, J.B., Desreumaux, N., Dauchot, O., Bartolo,D. "Emergence of macroscopic directed motion in populations of motile colloids". Nature **503**, 95–98, 2013.
[3] Bendsøe, M.P. and Sigmund, O. *Topology Optimization-Theory, Methods and Applications*. Berlin: Springer, 2003.
[4] Sigmund, O. "Tailoring materials with prescribed constitutive parameters." Mechanics of Materials, 20: 351-368, 1995.
[5] Diaz, A.R. and Benard, A., "Designing materials with prescribed elastic properties using polygonal cells," Int. J. Numer. Meth. in Engng, 57: 301-314, 2003.
[6] Jeffrey, G.B., "The Motion of Ellipsoidal Particles Immersed in Viscous Fluid", *Proc. R. Soc. Lond. A*, **102**, 161-179, 1922.
[7] Bretherton, F. P., "The Motion of Rigid Particles in a Shear Flow at Low Reynolds Number", *J. Fluid Mech.*, **14**,284-304, 1962.
[8] Doi, M. and Edwards, S.F. *Theory of Polymer Dynamics*, Oxford University Press, 1986.
[9] Rallison, J.M., "The Effects of Brownian Rotations in Dilute Suspension of Rigid Particles of Arbitrary Shape", J. of Fluid Mechanics, V. 84, pp. 237-263, 1978.
[10] Borrvall, T. and Petersson, J. (2003 January). Topology optimization of fluids in stokes flow, *International Journal for Numerical Methods in Fluids*: 41,77-107.

OPTIMAL MULTIMATERIAL COMPOSITE STRUCTURES AND OPTIMAL DESIGNS

Andrej Cherkaev [*1] and Gzegorz Dzierźanowski[2]

[1]*Department of Mathematics, University of Utah, Salt Lake City, Utah, U.S.A.*
[2]*Department of Structural Mechanics and Computer Aided Engineering, Politechnika Warszawska, Warsaw, Poland*

Summary Technological capabilities, such are 3d printing and microfabrication, allow a huge variety of structures to be manufactured for roughly the same price, and one wants to know "the best" structure, or how composite microstructures can be optimized. There is no gap between optimal designs and the optimal composites that are structures at at the micro level. So far, the vast majority of related results deals with two-material composites because of theoretical limitations. Meanwhile, numerous applications call for the optimal design of multimaterial composites, or of porous composites made of two materials and void. The paper describes various structures of optimal multi-material composites, the bounds of their effective properties that are achievable by these structures, and optimal designs from several materials. We show designs from two elastic materials and void.

BOUNDS AND OPTIMAL MULTIMATERIAL STRUCTURES

The bounds show the range of improvement that can be achieved for overall composite properties by varying the structure. In particular, we study the bounds of the stored energy, find the exact bounds and the set of matching structures, and use these structures to compose an optimal design. In the past few years (2009-2012), [2, 3, 4, 5] a new approach for optimal bounds of multimaterial mixtures was suggested and tested on several examples. Calculating the lower bound, we also determine sufficient conditions on the fields in materials (wells) in an optimal structure [1, 8, 2]. The bound also provides a hint for optimal structures such as high-rank laminates [1, 8], wheel-type structures [4], or other structures.

Optimal microstructures of multimaterial composites differ drastically from two-material ones. The latter have a steady and intuitively expected topology: a strong material always surrounds weak inclusions, as in Hashin-Shtrikman coated circles and second-rank laminates. In contrast, optimal three-material structures [3, 5, 4], see Figure 1 show a large variety of patterns and the optimal topology depends on the volume fractions.

Optimal structures are diverse; they may or may not contain a strong envelope, and they may contain "hubs" of intermediate material connected by anisotropic "pathways" - laminates from the strong and weak materials, envelopes, and other configurations that reveal a geometrical essence of optimality. The parameters of the A-E of the optimal structures (Figure 1) depend on the volume fractions and the ratio of eigenvalues of the applied external stress σ_0. It is observed that the strongest material is always placed in the most stressed parts, the field in the intermediate material stays isotropic if passible and in the strongest material it is anisotropic.

Testing optimal structures, we stay in the class of structures with explicitly computable effective properties. These structures are obtained by hierarchical modeling, and they are interesting objects for study. These structures may or may not be optimal, but they all provide convenient and realistic models for the various sophisticated geometries; acting like LEGO pieces that are used in the process of modeling to create metamaterial hybrids between composites and machanisms.

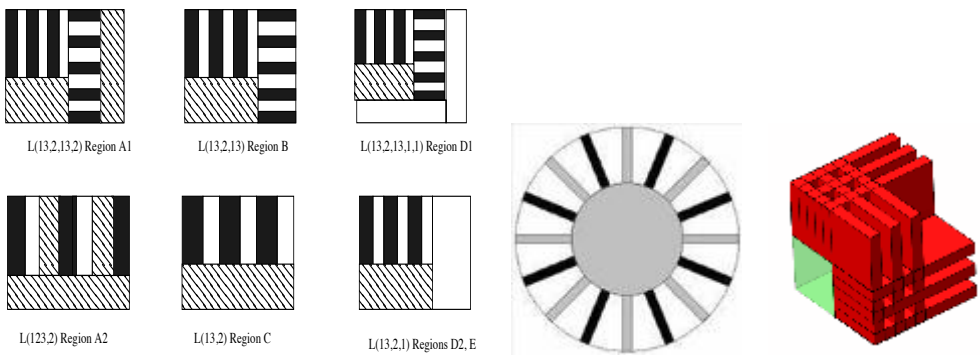

Figure 1: *Left*: Cartoon of optimal multi-rank laminates that minimize elastic energy (compliance) of a three-material composite [3, 5]. Black fields denote void (an infinite compliance), striped fields denote a material of intermediate compliance and white fields denote the stiffest material. *Center*: The wheel assemblage resembles the Hashin?Sthrikman coated spheres. *Right*: The cuboudal structure in a 3d development of Gibiansky-Sigmund 2d structure [7].

*Corresponding author. Email: cherk@math.utah.edu

OPTIMAL DESIGN

The most popular problem in structural optimization today, called “topology optimization”, is a problem of optimal layout of a material and void. The optimal structural designs are commonly known as “black-and-white” or “grey” designs. Optimal multilateral composites allow us to instead deal with with “multi-colored” designs, see Figure .

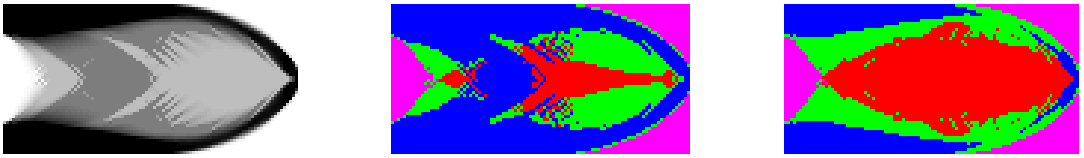

The first obtained optimal designs from three materials are shown in Figure The designs are made from an expensive strong material, a cheap weak material, and void. This design shows that the strong material tends to form elongated beam-like ligaments at the contour of the design, the weaker material is concentrated in the areas where the stress is moderate and close to isotropy.

CONCLUSIONS

1. Investigation of the range of fields in optimal multimaterial structures will allow for prediction of their microstructues and for for computing of optimal design from several materials. The presented examples prove that the problem can be solved.

2. The optimal structures are in fact fractal minimizing sequences of alternating materials. To make the theory usable for practitioners, these structures need to be transformed to a coarse scale designs for suboptimal projects.

References

[1] A. Cherkaev. Variational methods for structural optimization. Springer Verlag NY 2000.
[2] A. Cherkaev. 2009. . Mechanics of Materials 41, 411-433.
[3] A. Cherkaev and Y. Zhang. 2011. . Int. J, of Solids and Structures 48 (20), pp. 2800-2813.
[4] A. Cherkaev. 2012. Int. J. of Eng. Science, 59, 27-39.
[5] A. Cherkaev and G. Dzierżanowski 2013. Int. J. of Solids and Structures, 50, pp. 4145-4160.
[6] A. Cherkaev. 2014. Int. J of Eng. Sc., 83, 162-173.
[7] L. V. Gibiansky, O. Sigmund 2000. JMPS, 48, 3, 461-498.
[8] G. W. Milton 2001. The Theory of Composites. Cambridge University Press.

TOPOLOGY OPTIMIZATION IN NANO-SCALE FOR GENERATION OF NEW GRAPHENE-LIKE MATERIALS

Tadeusz Burczyński[1a], Wacław Kuś[2] and Adam Mrozek[3]
[1]*Institute of Fundamental Technological Research, Polish Academy of Sciences, Warsaw, Poland*
[2]*Institute of Computational Mechanics and Engineering, University of Technology, Gliwice, Poland*
[3]*AGH University of Science and Technology, Cracow, Poland*

Summary. The paper describes an application of a hybrid algorithm to optimal searching for new, stable atomic arrangements of two-dimensional graphene-like carbon lattices. The proposed approach combines the parallel evolutionary algorithm and the conjugated-gradient optimization technique. The main goal of the topology optimization is to find stable arrangements of carbon atoms under certain imposed conditions such as density, shape and size of the unit cell. The objective function is formulated as the total potential energy of an atomic carbon system. The optimized structure is considered as a discrete atomic model and interactions between atoms are modeled using the AIREBO potential, especially developed for carbon and hydrocarbon materials. The parallel approach used in computations allows significant reduction of computation time. Validation of the obtained results and examples of the models of the new grapheme-like materials are presented.

INTRODUCTION

Carbon atoms form various types of bondings and spatial configurations. This ability is determined by the atoms' hybridization states, which depend on their particular electronic configuration. This phenomenon is responsible for the existence of many different allotropes of the carbon. This is due to unique electronic, thermal and mechanical properties of such structures. Additionally, 2D graphene-like materials can be used to create another, more complex class of nanostructures, such as nanotubes. Graphene-like materials can be classified as periodic, flat atomic networks, made of stable configurations of carbon atoms in certain hybridization states. Since the stable configurations of atoms correspond to the global minima on the Potential Energy Surface (PES), such a task can be considered as a special topology optimization problem in which optimal material layout is searched on the nano-scale. However, the number of local minima increases almost exponentially with the number of atoms in the considered structure, thus searching for the global minimum on a PES became a non-trivial, NP-hard problem.

HYBRID EVOLUTIONARY-GRADIENT OPTIMIZATION METHOD

The hybrid algorithm, proposed and presented in this work, combines the parallel **E**volutionary **A**lgorithm (EA) prepared by the authors, and the classical **C**onjugated-**G**radient (CG) minimization of the total potential energy of the optimized atomic system. Since the processed structure is considered as a discrete atomic model, the behavior and the potential energy of carbon atoms are determined using the **A**daptive **I**ntermolecular **R**eactive **E**mpirical **B**ond **O**rder (AIREBO) potential developed for molecular dynamics simulations of hydrocarbons [2].
Chromosomes represent design variables in the form of real-valued Cartesian coordinates of each atom in the considered unit cell of the newly created atomic lattice. Each chromosome represents a certain spatial arrangement of atoms. In the initial population, atoms have randomly generated coordinates and are placed in the area of the unit cell with periodic boundaries. Dimensions, the rectangular or triclinic type of the unit cell, as well as the number of atoms, are part of a set of parameters of the simulation. Such an approach allows to control the value of atomic density of the newly-created structure. The periodicity of the atomic structure significantly reduces the number of design variables.
The fitness function is formulated as the total potential energy of the considered atomic system, i.e., the total sum of all potential energies of particular atomic interactions. The AIREBO potential in the following form is used in computation:

$$FF = \sum_{i} \sum_{j \neq i} \left(E_{ij}^{REBO} + E_{ij}^{LJ} + \sum_{\neq} \sum_{\neq} E_{kijl}^{TORSION} \right) \tag{1}$$

where: E^{REBO} corresponds to the short range interactions between covalently bonded pair of atoms, E^{LJ} is responsible for the long range interactions and is computed in a simplified way, using the Lennard-Jones-like function with additional distance-dependent switching functions and $E^{TORSIONAL}$ is torsional potential which depends on the neighboring atom's dihedral angles.
In order to avoid the situation when distances between atoms are very small, the initial and offspring populations have to be equilibrated, i.e., the potential energy has to be minimized by correction of the positions of atoms. The CG algorithm is used for this purpose. This routine is invoked in each iteration of EA for all individuals in the processed population and

[a)] Corresponding author. Email: tburczynski@ippt.pan.pl

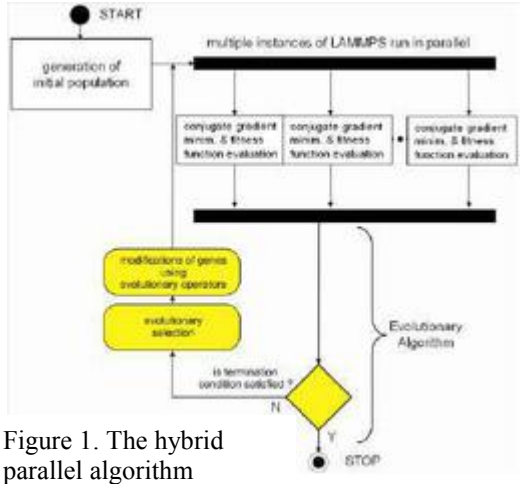

Figure 1. The hybrid parallel algorithm

temporarily pushes solutions into the local minima. Such an approach assists in forming of the new, real carbon-based molecular structure, i.e., during the CG minimization, each individual – a certain spatial configuration of atoms, starts to form a unique, hybridization-dependent, geometry of flat carbon networks. This step ensures that EA does not process the sets of randomly placed atoms, but operates on fragments of properly bonded carbon structures. Additionally, this method ensures that the optimized structure of atoms is properly equilibrated. The coordinates of atoms are exchanged between EA and the LAMMPS software and the equilibration process is performed using the minimization method based on the Polak-Ribiere algorithm. The periodicity of the newly-created structure is also achieved in this step by proper boundary conditions, imposed on the unit cell. After the CG minimization of the potential energy, the objective function is computed for each individual in the population. The CG optimization is the most time-consuming part of the algorithm. To overcome this problem, the authors decided to parallelize the proposed algorithm and make it suitable for running on multiprocessor computers. Thus, the population is scattered into certain number of parts using the MPI library. In the next step, each part is further processed in the parallel way using the dedicated instance of LAMMPS running on a separate core or node of the computer (Figure 1).

VALIDATION AND RESULTS FOR KNOWN GRAPHENE-LIKE MATERIALS

In order to validate the accuracy of the results, certain arrangements of carbon atoms already known from literature have been examined, e.g. the supergraphene (triclinic unit cell containing 8 carbon atoms) and the graphyne (triclinic unit cell containing 12 carbon atoms). Since all the tests yield promising results, the proposed optimization algorithm has been applied to search for new stable configurations of a given number of carbon atoms in a unit cell of given size and periodic boundaries [1]. For eight carbon atoms placed in the 4 Å ×7 Å rectangular unit cell obtained a stable flat network named X (Figure 2A) and for the same number of carbon atoms placed in the rectangular unit cell 4 Å ×6 Å obtained a stable flat network named Y (Figure 2B).

A)

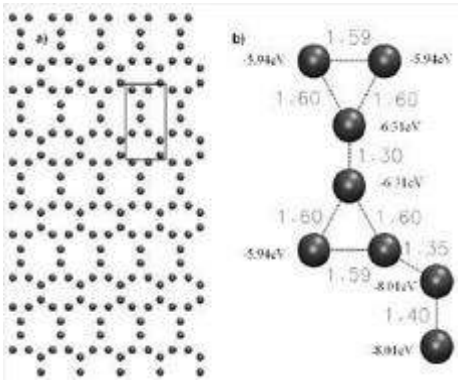

B)

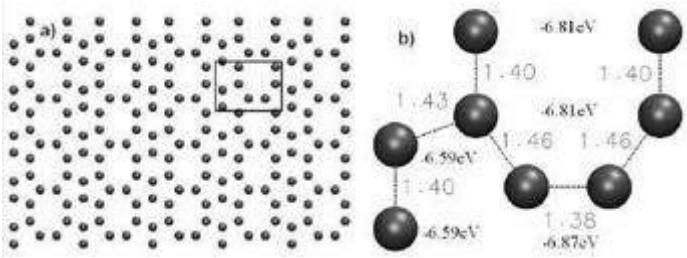

Figure 2. Layout of new stable carbon networks X (A) and Y (B) found by the hybrid algorithm

CONCLUSIONS

The main purpose of this paper was to present the hybrid parallel algorithm, applied to searching for new 2D graphene-like materials. The proposed method is able to find already-known structures like supergraphene and graphyne as well as new stable ones, named X and Y. Examples performed for new carbon networks clearly show that the final form and properties of optimized structures depend on the assumed size, type and atomic density of the unit cell. Thus, the considered topology optimization problem can be reformulated and applied to searching for a molecular structure with predefined material properties, not only in the case of carbon-based structures.

References

[1] Mrozek A., Kuś W., Burczyński T.: Nano level optimization of graphene allotropes by means of hybrid parallel evolutionary algorithm, *Computer Material Science* **106**: 161-1, 2015.

[2] Stuart S.J., Tutein J.A., Harsison A.: A reactive potential for hydracarbons with intermolecular interactions. *J. Chemical Physics* **112**: 6472-6486, 2000.

ON TOPOLOGY OPTIMIZATION OF INERTIA DRIVEN DOSING UNITS

Casper Schousboe Andreasen[1]

[1]*Department of Mechanical Engineering, Section for Solid Mechanics, Technical University of Denmark*

Summary This paper describes how topology optimization can be used to design inertia driven dosing units for the continuous dosage of one fluid into another. These components often referred to as eductors, utilize the low static pressure in a venturi-type nozzle to drive the dosing flow. The fluids are modeled using the steady state incompressible Navier-Stokes equations and the two fluids are considered having the same properties. A Brinkman penalization term is added to the governing equations such that a control problem of the flow topology is obtained. Optimized component geometries for a range of flow conditions are obtained efficiently by using a gradient based numerical optimization scheme in order to investigate the performance limit.

INTRODUCTION

The engineering problem of continuous dosage of one fluid into another has multiple solutions. One easy, but also expensive solution is to use a pump for each fluid and by means of adjusting the flow rate ensure a proper dosage. A more elegant solution is one where a single pump is driving the primary fluid and the secondary fluid is dosed by elaborating on the *venturi principle*. Figure 1 show a sketch of such a unit where the primary inflow is the one driven by the pump. Assuming that the fluid is inviscid and following the Bernoulli principle the dynamic pressure is increasing as the valve contracts and the static pressure is therefore decreasing. The low static pressure at the throat (minimum cross sectional area of the nozzle) will allow fluid to enter through the secondary inlet and mix with the primary fluid and eventually leave at the outlet. The principle is well known and has been used for e.g. ground water pumps, spray paint guns and firefighting foam proportioners.

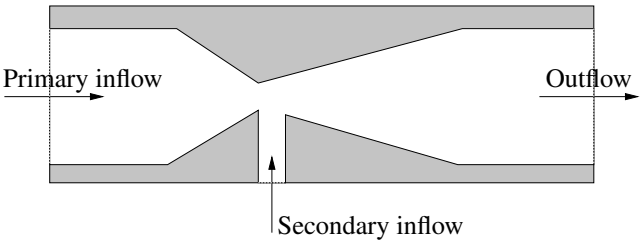

Figure 1: Sketch of an eductor, an inertia driven dosing unit. Left boundary is primary inflow. Right boundary is outlet. The secondary dosed fluid enters from the lower port and is driven by the lower static pressure right after nozzle.

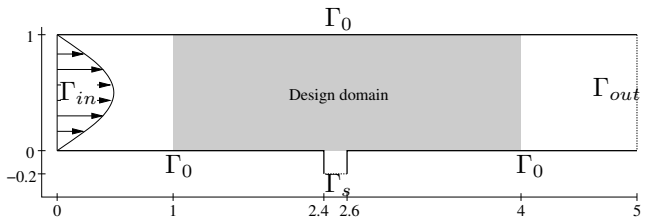

Figure 2: Physical conditions for the optimization problem. Left boundary (Γ_{in}) is a fully developed laminar profile with mean flow rate U. Right boundary (Γ_{out}) is modeled as stress free outlet with $p = 0$. Secondary flow port (Γ_s) has a stress free condition. The remaining thick solid line boundaries (Γ_0) have no-slip condition.

The optimization of such devices, primarily operating at high speed conditions, has previously been studied in the context of shape optimization c.f. [1]. This paper investigates the performance limit at low to moderate flow speeds for such devices by applying topology optimization to the design of the nozzle geometry. The method used in this paper relies on the work published in the seminal paper on topology optimization in Stokes flow[2] and the extension to Navier-Stokes flow[3]. The design problem is shown in Figure 2 where the gray design domain is subject to change controlled by the gradient based optimization algorithm MMA[4]. The objective of the optimization is to maximize the amount of incoming secondary fluid in order to investigate the upper limit for such devices.

Modeling

The flow is modeled by the steady-state incompressible Navier-Stokes equations with an additional Brinkman penalization term yielding

$$-\nabla \cdot (\mu(\nabla \mathbf{u} + (\nabla \mathbf{u})^T) - \mathbf{I}p) + \mathbf{u} \cdot \rho \nabla \mathbf{u} + \alpha(\xi)\mathbf{u} = 0 \tag{1}$$

$$\nabla \cdot \mathbf{u} = 0 \tag{2}$$

where $\mathbf{u}$ is the velocity, p the pressure, μ the dynamic viscosity and ρ the mass density. The α parameter (inverse permeability) is interpolated using the scheme from [2]

$$\alpha(\xi_i) = \overline{\alpha} + (\underline{\alpha} - \overline{\alpha})\xi_i \frac{1+q}{\xi_i + q} \tag{3}$$

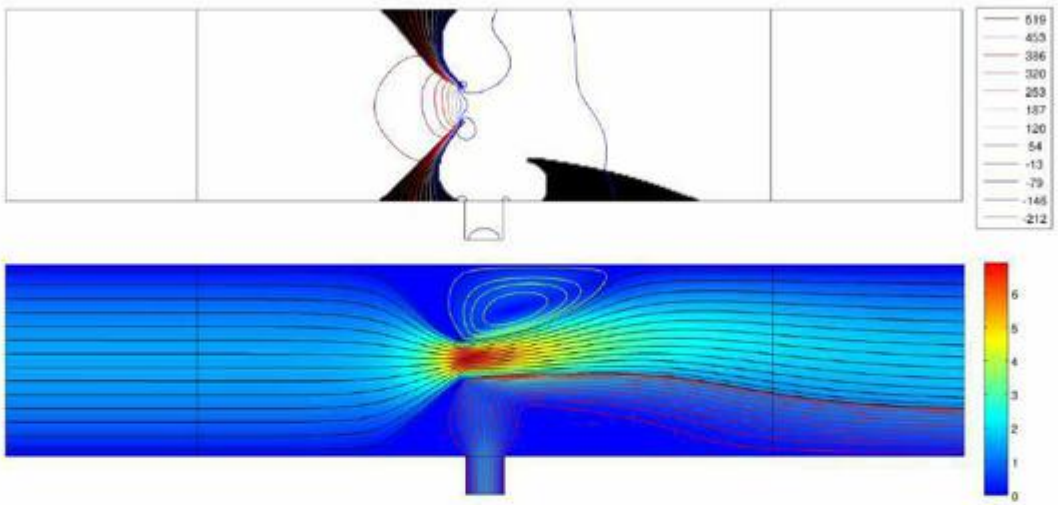

Figure 3: Optimized flow geometry for $Re = 20$ and $\gamma = 10$. Upper: Component design with pressure contours (outlet is $p = 0$). Lower: Flow speed, inflow has mean speed 1, and streamlines seeded at the inlet port (black), secondary port (red) and the recirculation opposite the secondary port (yellow). Mesh has a uniform element size with 100×300 elements in the design domain.

which is dependent on the spatial design field $\xi \in [0; 1]$ where 0 represents solid material (black) and 1 represents fluid (white). The inverse permeability is limited by $(\underline{\alpha}, \overline{\alpha}) = (0, 10^6)$ and the parameter q determines the non-linearity of the interpolation.

The gradients needed for the optimization procedure is obtained using the adjoint method that for this problem is a linear problem of the same size as the original, thus much less computationally demanding. The numerical solution is obtained by discretizing the problem using stabilized finite elements. The implementation is done in a framework of Comsol Mutiphysics used for the modeling and Matlab for the optimization.

RESULTS

The optimized designs depend on the operating conditions. In order to compare the results the Reynolds number is introduced as $Re = \frac{\rho U H}{\mu}$, where U mean flow rate and H is the channel height. The design also depends on the allowed pressure drop over the component why this is unified in terms of relative pressure drop over the component (primary inlet to outlet) in comparison to an empty channel i.e. $\gamma = \Delta p / \Delta p_{empty}$. The study investigates the performance limit and resulting component designs for flow conditions with low to moderate Reynolds numbers. Here only a single design case is presented.

Figure 3 shows the result of an optimization for $Re = 20$ and $\gamma = 10$. From the upper figure it is clear that the design consists of a contracting nozzle that speeds up the fluid flow thus lowers the static pressure right after the nozzle throat. This is also evident from the printed pressure contours that are relative to the condition $p = 0$ at the outlet. After the throat the flow area is suddenly expanded however, at the lower boundary a structure is formed that could be seen as half a diverging nozzle. This structure creates a semi open cavity near the secondary inlet port.

The color surface of the lower figure shows that fluid speed at the throat is increased with almost a factor 7 in comparison to the incoming mean flow rate. After the throat the flow expands and the interface between the diverging fast flow from the nozzle and the surrounding fluid creates a vortex at the upper boundary while fluid is dragged into the component at the lower boundary. This is also illustrated by the colored streamlines that are black if the fluid is entering through the primary inlet and red if it enters from the secondary inlet. The streamlines that illustrates the recirculating vortex opposite the secondary inlet are colored yellow.

References

[1] Dvorák V.: Shape optimization of axisymmetric ejector. In *ECCOMAS CFD 2006: Proceedings of the European Conference on Computational Fluid Dynamics*, Delft University of Technology; European Community on Computational Methods in Applied Sciences (ECCOMAS), 2006.

[2] Borrvall T., Petersson J.:Topology optimization of fluids in Stokes flow. International Journal for Numerical Methods in Fluids, 41(1):77–107, 2003.

[3] Gersborg-Hansen A., Sigmund O., Haber R.B.: Topology optimization of channel flow problems. Structural and Multidisciplinary Optimization, 30(3):181–192, 2005.

[4] Svanberg K.: The method of moving asymptotes - a new method for structural optimization. International Journal for Numerical Methods in Engineering, 24(2):359–373, 1987.

GENERALIZED SFP PARAMETERIZATION FOR TOPOLOGY OPTIMIZATION INCLUDING LATTICE STRUCTURES

Pierre Duysinx[1], Maxime Collet[1], Simon Bauduin[1], Emmanuel Tromme[2] & Michael Bruyneel [1,3]
[1]*Department of Aerospace and Mechanical Engineering, University of Liege, Liege, Belgium*
[2]*Department of Civil Engineering, The Johns Hopkins University, Baltimore, Maryland, USA*
[3]*GDTECH SA, Liege, Belgium*

Summary Laminate selection in composite structure optimization can be formulated as a topology optimization problem with N materials. To interpolate the material properties of the candidate materials, we extend the Shape Function with Penalization (SFP) parameterization introduced by Bruyneel (2011). With the SFP parameterization and Lagrange shape functions, the number of possible materials is limited to the number of nodes found in classical finite elements (N=3, 4, 8…). We show here that is possible to consider any number of materials by resorting to Wachspress functions, which have been used to define finite elements with an arbitrary number of nodes. The generalized parametrization is presented before being validated by solving academic test problems. Then the new parametrization scheme is illustrated in solving composite structures and topology optimization of structures fabricated by additive manufacturing making use of lattice structures subdomains.

INTRODUCTION

High performance structures take advantage of composite materials or cellular materials with superior physical properties per unit of mass. The component layout can be optimized to take benefit of the full capabilities of the porous composite materials to sustain efficiently the applied loads. To this end, topology optimization [1] is an efficient design tool to suggest the best material distribution to maximize the component performance. While black and white designs have been searched for a long while, now availability of additive manufacturing techniques makes possible to fabricate structures including regions of intermediate density made of porous cellular materials. In particular the lattice microstructures have received quite a long of attention in the literature (e.g. Ref [2]). However other microstructural configurations of porous microstructures should be investigated in order to have better material usage under given loading conditions. Some recent pieces of work have focused in optimizing simultaneously the macrostructural material distribution and the local microstructural layouts in all points of the design domain (see Ref [3, 4]).

In this work we adopt a rather practical approach based on the selection of porous cellular materials out of a given catalogue. To this end, we follow along the idea inspired by Stegmann and Lund [5] with the so-called Discrete Material Optimization (DMO). The fundamental items of the approach are 1/ to formulate the design optimization problem as an optimal material selection problem in which the different kinds of cellular porous solids as well as their orientations if orthotropic are considered as different materials, 2/ to solve the selection problem using the topology optimization with multiple materials, 3/ to solve efficiently the optimization problem using continuous existence variables. To transform the discrete problem into a continuous one, one introduces a suitable parametrization identifying each material by a unique set of continuous design variables while the material properties are expressed as a weighted sum of all candidate materials.

The first contribution of this work consists in proposing a novel efficient formulation of the parameterization scheme. For composite structures, Bruyneel [6] has proposed an efficient interpolation scheme based for the Finite Element functions namely the Shape Function Parameterization (SFP), but the extension to any number of plies is still difficult. To this end, the Binary Coded Parametrization (BCP) was proposed by Gao et al. [7]. However the procedure can deal with a catalogue of 2^N materials. Here we show that it is possible to build shape function for an arbitrary number of materials by resorting to the Wachpress rationale functions [8,9] used in polygonal finite elements [10]. The interpolation schemes are compared with the particular perspective of solving large-scale applications. The influences of the penalization factor and initial design variables are studied and discussed.

As a second contribution, we also apply the generalized SFP approach to design components made of void / solid but also different patterns of porous microstructures including lattice microstructures. In order to evaluate the advantages of including subdomains made of porous microstructures, we revisit some of the classical examples of topology optimization. The influence of the types of the porous pattern is investigated for single and multiple load cases applications.

The developments are illustrated by several numerical applications including academic examples and benchmarks inspired by industrial applications.

INTERPOLATION SCHEME OF MATERIAL PROPERTIES USING WACHPRESS FUNCTIONS

The discrete optimal orientation design of the laminate can be treated as an optimization material selection problem with multiple materials. Following the idea by Stegmann and Lund [5], the material stiffness of the local material is a linear

[a)] Corresponding author. Email: p.duysinx@ulg.ac.be

anisotropic material stiffness matrix C_i of a composite ply/ material noted 'i' as a weighted sum over the stiffness of some candidate materials {j}:

$$\mathbf{C}_i = \sum_{j=1}^{m} w_{ij} \mathbf{C}_i^{(j)} \qquad \text{with} \qquad 0 \le w_{ij} \le 1 \qquad \sum_{j=1}^{m} w_{ij} \le 1 \qquad w_{ik} = 0 \left(k \ne j\right) \text{ when } w_{ij} = 1 \tag{1}$$

The weighting function w_{ij} are associated with the jth material phase. From the last conditions of (1), it comes that one ends up with a 0/1 design satisfying the constraints. This is achieved by using a penalization of the intermediate densities.

When dealing with the classical balanced composite aerospace structures based on laminates made of plies of the four discrete orientations 0°/90°/45°/-45°, Bruyneel [6] proposed a parameterization model named SFP (Shape Function with Penalization) based on the four node finite element shape functions that, obviously, satisfies the conditions (2):

$$w_{i1,2,3,4} = \left[\frac{1}{4} \left(1 \pm x_{i1}\right)\left(1 \pm x_{i2}\right) \right]^p \qquad -1 \le x_{ij} \le 1, \quad j = 1,2,3,4 \tag{2}$$

As in the SIMP method, the penalization factor p is applied to push the design variables to their extreme values +/-1. SFP introduces only two variables for four materials, which is an advantage to reduce the size of the optimization problem. The presence of one material phase is characterized by a specific combination of design variables taking values of +1 and/or -1.

Extending the SFP scheme to more than four materials by building complex shape functions related to 'N' node finite elements satisfying the conditions (1) is not straight forward using Lagrange interpolation functions. To account for a variable number of material candidates in the catalogue, the original idea is to use the Wachspress rationale functions [8,9] used in a N-node polygonal reference finite element [10]. As depicted in Figure 1, the shape functions of a regular N-node finite element are used as interpolation schemes between the mechanical properties of the candidate materials.

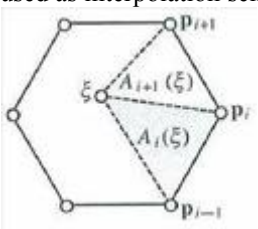

Figure 1: N-Polygonal reference element

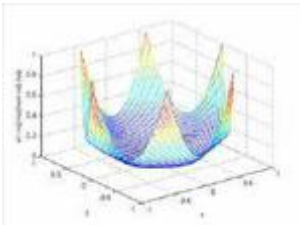

Figure 2: 6-Polygonal interpolation functions

Ref [11] provides a simple expression for Wachpress basis functions:

$$w_i^{PSF} = \frac{\alpha_i(\xi)}{\sum_{j=1}^{n} \alpha_j(\xi)} \quad \textit{where} \quad \alpha_i(\xi) = \frac{A(p_{i-1}, p_i, p_{i+1})}{A(p_{i-1}, p_i, \xi)\, A(p_i, \xi, p_{i-1})} \tag{4}$$

Where $A(p_{i-1}, p_i, p_{i+1})$ denotes the area of the triangle with the three vertices p_{i-1}, p_i, p_{i+1}. This expression can be further simplified since the reference element is a regular polygon so that $A(p_{i-1}, p_i, p_{i+1})$ is the same for all i. Figure 2 shows the interpolation function after applying a power law penalization with p=3

Acknowledgment

The author, Maxime Collet would like to acknowledge the Belgian National Fund for Scientific research (FRIA) for its financial support. Part of this work has been supported by the Walloon Region of Belgium and SKYWIN (Aerospace Cluster of Wallonia), through the project AERO+ (contract RW 7445).

References

[1] Bendsøe M.P. & Sigmund O. Topology Optimization - Theory, Methods and Applications. Springer Verlag.

[2] Chua C., Grafa G. & Rosen D. W. Design for Additive Manufacturing of Cellular Structures. Computer-Aided Design and Applications. 5 (5), 686-696, 2008

[3] Rodrigues H.C., Guedes J. & Bendsøe M.P. Hierarchical optimization of material and structure. Struct. Multidisc. Optim. 24: 1-10, 2002.

[4] Xia L. Towards Optimal Design of Multiscale Nonlinear Structures. PhD Thesis, Université de Technologie de Campiègne. Novembre 2015.

[5] Stegmann J. & E. Lund. Discrete material optimization of general composite shell structures. IJNME, 62: 2009-2027, 2005

[6] Bruyneel, M. SFP - a new parameterization based on shape functions for optimal material selection: application to conventional composite plies. Structural and Multidisciplinary Optimization 43 (1), 17-27, 2011.

[7] Gao T., W. Zhang & P. Duysinx. A bi-value coding parameterization scheme for the discrete optimal orientation design of the composite laminate. IJNME, 91 (1), 98-114, 2012

[8] Wachspress E.L. A Rational Finite Element Basis. New York: Academic Press, 1975.

[9] Dasgupta G. Interpolants within convex polygons: Wachspress' shape functions. Journal of Aerospace Engineering, 16, 1, pp. 1-8, 2003.

[10] Talischi C., G.H. Paulino, A. Pereira & I.F.M. Menezes. Polygonal finite elements for topology optimization: a unifying paradigm. International Journal for Numerical Methods in Engineering, 82, 6, pp. 671-698, 2010.

[11] Meyer M., Lee H., Barr A.-H., and Desburn M. Generalized barycentric coordinates for irregular n-gons. Journal of Graphic Tools. 1 (1), 13-22. 2002.

TOPOLOGY OPTIMIZATION FOR TRANSIENT THERMO-MECHANICAL PROBLEMS

Evert Hooijkamp[1] and Fred van Keulen [*1]
[1]*Department for Precision and Microsystems Engineering, Mekelweg 2, 2628CD Delft, The Netherlands*

Summary Thermo-mechanical transient problems impose major design challenges for a wide range of applications. This paper focuses on topology optimization for transient thermo-mechanical problems with extreme precision requirements. The transient nature causes standard adjoint sensitivity formulations to suffer from backward time integrations, leading to computational inefficiency. To overcome this obstacle, reduced-order models are used to evaluate the transient thermo-mechanical responses and the associated adjoint sensitivities. Aspects of investigation include the construction of reduced-order models, application of mode acceleration, accuracy of the transient response and associated adjoint sensitivities and their use in topology optimization. It is shown, that good topological designs are obtained, whereas costly adjoint sensitivities are replaced by relatively inexpensive counterparts involving simple backward convolutions.

INTRODUCTION

Transient thermo-mechanical problems emerge in a wide range of applications, for example, energy conversion, combustion processes, but also instrumentation and tooling. The present paper aims at problems with relatively small temperature fluctuations, but with major impact on ultimate performance. Examples are instruments operating at the nanometer scale and precision (manufacturing) tools. For these applications, transient thermal effects cause thermal drift of instruments or thermally induced errors in manufacturing processes [1].

Designing advanced thermo-mechanical systems is very challenging as multiple physics domains are interacting, the transient nature of the problems at hand, complex layouts are required and active thermal management systems might be integrated. Given this complexity, application of topology optimization is an obvious choice. Topology optimization relies on adjoint sensitivities to deal with a large number of design variables. The transient nature however, is severely hindering adjoint sensitivity analysis, as it requires a backward time integration for transient problems.

In the present paper, reduced-order models are investigated to overcome the difficulties caused by the backward time integration. Reduced-order models are based upon so-called thermal modes. Herewith, the tedious backward time integrations can be replaced by simple backward time convolutions. The latter rigorously eliminates the need for huge memory storage and associated computational costs. Different schemes for model reduction are investigated and their effects on sensitivities and application in topology optimization is investigated.

THERMAL MODES

A discretized linear thermal problem can be described by

$$\mathbf{C}_{\mathrm{T}}\dot{\boldsymbol{\theta}}(t) + \mathbf{K}_{\mathrm{T}}\boldsymbol{\theta}(t) = \mathbf{q}(t), \tag{1}$$

here $\boldsymbol{\theta}(t)$ denotes the temperature difference with respect to a reference temperature, $\mathbf{C}_{\mathrm{T}}$ denotes the heat capacity matrix, $\mathbf{K}_{\mathrm{T}}$ the heat conductivity matrix and $\mathbf{q}$ the thermal load. The thermal modes $(\boldsymbol{\phi}_k)$, see [2], and associated thermal time constants (τ_k) follow from the eigenvalue problem defined by setting the thermal load to zero and substituting $\boldsymbol{\theta}(t) = e^{-t/\tau_k}\boldsymbol{\phi}_k$ into (1). Like in structural dynamics, the thermal problem can be represented on the modal basis.

Reduced models may be formulated by selecting only the most relevant modes. Effective mode selection is however paramount and should account for (i) thermal excitation, (ii) observability and (iii) time relevance. Thus, the thermal problem is modeled using a limited number of carefully selected modes. The efficiency and accuracy of these reduced-order models can be improved significantly if a static correction is added, a so-called mode acceleration technique [3]. It is important to emphasize, that the transient behavior is now determined by simple time convolutions which provide the modal coordinates as functions of time.

For the applications mentioned in the Introduction, the relevant thermal time constants are orders of magnitude larger than their mechanical counterparts. This allows for a one-way coupling between the thermal and mechanical domain. Hence, the thermo-mechanical effects are modeled using equivalent loads which enter the equations of motions. If inertia and damping effects can be neglected, then the transient thermo-mechanical solution is determined by

$$\mathbf{K}_{\mathrm{u}}\mathbf{u}(t) = \mathbf{f}(t) + \mathbf{f}_{\theta}(t), \tag{2}$$

here $\mathbf{u}$ denotes the nodal degrees of freedom and $\mathbf{K}_{\mathrm{u}}$ the constant mechanical stiffness matrix. The load is divided into a mechanical load $(\mathbf{f})$ and an equivalent thermal load $(\mathbf{f}_{\theta})$. The latter is evaluated via a reduced-order transient model as summarized above.

*Corresponding author. Email: A.vanKeulen@tudelft.nl

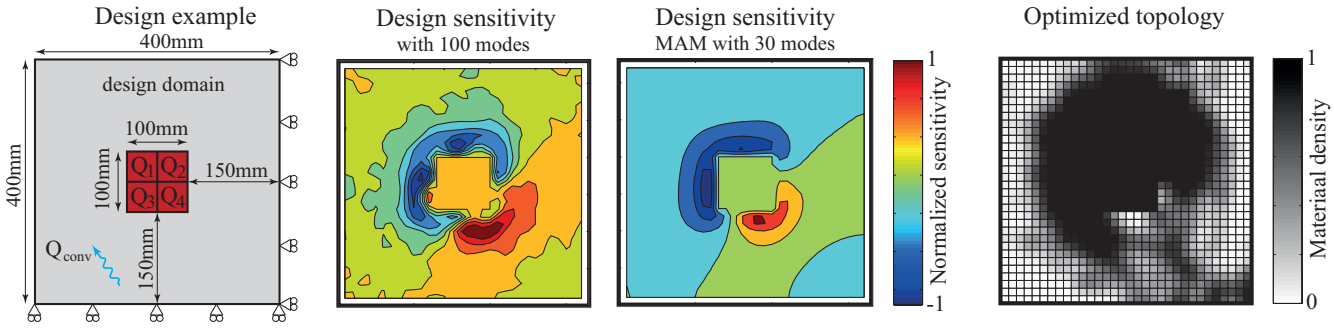

Figure 1: Left, thermo-mechanica topology optimization problem. Heat sources Q1–Q4 switch on alternatingly, whereas the center of the heat exposed area should exhibit minimal displacement once the heat load is activated. Sensitivities obtained with a reduced-order model without and with mode acceleration (MAM) are depicted. Right, the resulting topology.

ADJOINT SENSITIVITIES

For transient problems, adjoint sensitivities require backward time integrations. The latter implies that many intermediate results obtained during the forward response evaluations must be kept, thus, severely hindering topology optimization of transient problems [4].

The adopted reduced modal basis is used as a staring point for the adjoint sensitivity analysis as well. Since for the reduced modal basis the transient thermal behavior is described by decoupled ordinary differential equations, the adjoint sensitvity formulation can be formulated in such a manner that exhaustive memory requirements are avoided and ultimately results in simple backward convolutions. This adjoint sensitivity formulation can be easily adapted to also accommodate a static correction as used in the mode acceleration method.

APPLICATION TO TOPOLOGY OPTIMIZATION

Figure 1 shows a typical test case of a system subjected to convection and alternating heat loads (Q1–Q4). The objective is to obtain minimal center displacement of the area which is exposed to an active heat load. The figure provides results for the sensitivities based on 100 modes and 30 modes but with mode acceleration. It is clearly seen, that the sensitivities with fewer modes, but with mode acceleration are significantly more accurate. The resulting topology design is also provided.

CONCLUSIONS

The proposed topology optimization scheme for transient thermo-mechanical problems makes efficient use of a reduced modal basis. The fact that the transient thermal analysis reduces to a set of ordinary differential equations provides an excellent starting point for an efficient adjoint sensitivity analysis. The best efficiency and accuracy of both response evaluations and adjoint sensitivities are obtained if the modal reduction is combined with a mode acceleration scheme. The advocated method turns out to be effective for topology optimization problems with transient thermo-mechanical responses.

References

[1] Mayr J. *et al.*: Thermal issues in machine tools, CIRP Ann.-Manuf. Techn. 61, 771 (2012).

[2] Biot M.A.: New methods in heat flow analysis with application to flight structures, J. Aeronautical Sciences 24, 857 (1957).

[3] Besselink B. *et al.*: A comparison of model reduction techniques from structural dynamics, numerical mathematics and systems and control, J. Sound Vibration 332, 4403 (2013).

[4] Choi K.K. and Kim N.H.: Structural Sensitivity Analysis and Optimization, Springer (2005).

MULTI-MATERIAL TOPOLOGY OPTIMIZATION OF VISCOELASTICALLY DAMPED STRUCTURES

Max van der Kolk *[1,2], Gijs J van der Veen[1], Jan de Vreugd[2], and Matthijs Langelaar[1]
[1]*Department of Precision and Microsystems Engineering, Delft University of Technology, Delft, The Netherlands*
[2]*Optomechatronics, Netherlands Organisation for Applied Scientific Research, Delft, The Netherlands*

Summary The design of high performance instruments often involves the attenuation of poorly damped resonant modes. Current design methods typically rely on informed trial and error based modifications to improve dynamic performance. In this contribution, we present a multi-material topology optimization as an alternative, systematic methodology to design structures with optimized damping characteristics. A parametric, level set-based topology optimization is employed to simultaneously distribute structural and viscoelastic material to optimize the structure's damping characteristics. To model the viscoelastic behavior a complex-valued material modulus is applied. The structural loss factor is determined from the complex-valued eigensolutions and its value is maximized during the optimization. We demonstrate the performance of the optimization by maximizing the damping of a cantilever beam.

INTRODUCTION

In this contribution we address the optimization of components containing both viscoelastic and structural material to achieve optimized damping characteristics. The design of high-performance instruments often involves the attenuation of poorly damped resonant modes, as has been encountered in the design of optomechatronic instruments at the Netherlands Organisation for Applied Scientific Research (TNO) [1]. Current design methods typically start from a baseline design and introduce stiffening or damping reinforcements to modify these modes. Difficulties in predicting the influence of these reinforcements leads to a time-consuming, trial and error based design proces. To overcome this, we propose a multi-material topology optimization routine as a systematic method for the design of these structures.

Multi-material designs containing viscoelastic material are known to provide high structural damping [2]. These type of materials dissipate energy during deformation. To increase the structural damping, we can therefore introduce viscoelastic materials at locations that undergo deformation. Moreover, the geometrical design could be modified to promote deformations in the regions of viscoelastic material. This provides a challenging optimization problem, where to goal is to achieve optimal structural damping: both the location and the geometry of the viscoelastic regions are determined during the optimization. In previous works these two aspects have been investigated separately: by shape optimization of (un)constrained layer damping [3] and by topology optimization of the material distribution within predefined damping configurations [4, 5]. These methods are limited by the initial design configuration of the viscoelastic material.

To overcome these restrictions, we present a multi-material topology optimization routine to simultaneously distribute the viscoelastic and structural material throughout the design to optimize the damping characteristics. The proposed method is able to achieve freeform material distributions, resulting in higher structural damping. Moreover, the method does not require the designer to specify any initial (un)constrained layer configuration for the viscoelastic material.

TOPOLOGY OPTIMIZATION OF VISCOELASTIC AND STRUCTURAL MATERIAL

In this work we aim to optimize the damping characteristics for structures subjected to harmonic excitations. This allows to represent the viscoelastic material behavior using a complex-valued material modulus [6]. Either a complex-valued shear, bulk or Young's modulus can be applied. In the remainder of this work, it is assumed that only shear deformation dissipates energy and therefore a complex-valued shear modulus is implemented. The structural loss factor is applied to quantify the damping of these designs [7]. However, compared to the referred implementation the complete complex-valued eigensolutions are used for the formulation of the structural loss factor to achieve better prediction of the structure's Q-factor.

A multi-material, parametric level set method allows to describe multiple material regions within the design domain [8]. We have opted for a level set-based approach, in order to obtain clearly distinct material regions. Trials using density-based multi-material topology optimization often resulted in designs containing mixture of materials that are difficult to interpret. For each material a level set function is defined, which are parameterized using radial basis functions [9]. The numerical implementation applies four-node square quadrilateral (Q4), plane stress elements to discretize the domain. The material properties of any elements near the boundaries of the level set functions are scaled by the ersatz material model. Also, the discrete Heaviside and its derivative are implemented with continuous approximations. Finally, the Method of Moving Asymptotes (MMA) solves the gradient-based optimization problem [10].

The optimization aims to maximize the structural loss factor corresponding to the specified number of eigenmodes. Constraints are applied to limit the volume of viscoelastic material and enforce a minimum eigenfrequency. An exact formulation

*Corresponding author. Email: M.vanderKolk@tudelft.nl

of the structural loss factor are found by an adjoint sensitivity analysis. The complex-valued eigenvalue problem encountered in the adjoint sensitivity analysis is dealt with similarly as presented in [11].

To illustrate the performance of the optimization routine the maximization of the damping of a cantilever beam is presented. Figure 1a shows the initial design domain with L = 70 and H = 20 elements.. The average damping of the first and second resonant modes is maximized during the optimization. The volume of viscoelastic material is constrained to 40% of the domain volume and a minimum eigenfrequency for the first resonant mode is imposed. The materials have the following properties: structural $E = 200\,\mathrm{GPa}, \nu = 0.3, \rho = 7.85 \times 10^3\,\mathrm{kg/m^3}$ and viscoelastic: $E = 1\,\mathrm{GPa}, \nu = 0.3, \rho = 1 \times 10^3\,\mathrm{kg/m^3}$ and a material loss factor equal to 1. Figure 1b shows the final converged design after 35 iterations. All constraints are satisfied and an objective value of 0.5057 is obtained. The design shows a freeform distribution of viscoelastic material and achieves higher structural loss factors compared to conventional CLD configurations which vary between 0.26 and 0.39 for the analyzed domain. Since a complex-valued shear modulus was assumed, the dissipated energy is directly related to the shear strains during resonance. Figure 1c and 1d present the shear strain distribution and illustrate that almost all viscoelastic material contributes to the total energy dissipation for the optimized modeshapes.

CONCLUSIONS

A well-performing topology optimization approach has been presented which is able to generate multi-material designs with optimized damping properties. The level-set based formulation provides a clear separation between the different material phases compared with previous investigations using density-based approaches. With the presented example, we have demonstrated that the optimized designs achieve significantly higher structural loss factors compared to conventional constrained layer damping configurations by applying a freeform distributions of the viscoelastic and structural material. This offers new potential for applications where high structural damping is an important design aspect, e.g. high precision equipment and satellite instruments.

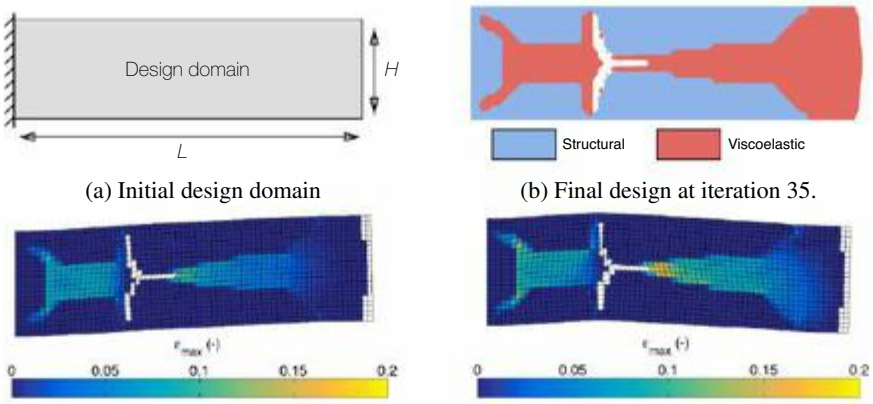

(a) Initial design domain

(b) Final design at iteration 35.

(c) Shear strain for eigenmode 1.

(d) Shear strain for eigenmode 2.

Figure 1: Example of loss factor maximization of a cantilever beam. (a) design domain, (b) obtained distribution of viscoelastic and structural material after 35 iterations, (c) shear strain in first resonant mode and (d) shear strain in second resonant mode.

References

[1] de Vreugd J., de Lange D., Winters J., et al.: Damping in space constructions, Proceedings of ECSSMET, 2014.
[2] Johnson C.D.: Design of passive damping systems. Journal of Vibration and Acoustics, 117:171, 1995.
[3] Plunkett R., Lee C.: Length optimization for constrained viscoelastic layer damping. J. Acoustic Society of America, 48:150-161, 1970.
[4] El-Sabbagh A., Baz A.: Topology optimization of unconstrained damping treatments for plates. Engineering Optimization, 49:1153-1168, 2013.
[5] Zheng W., Lei Y., Li S., et al.: Topology optimization of passive constrained layer damping with partial coverage on plate. J. Shock and Vibration 20:199-211, 2013.
[6] Tschoegl N.W.: The phenomenological theory of linear viscoelastic behavior. Springer-Verlag, Berlin, 1989.
[7] Johnson C.D., Kienholz D.A.: Finite element prediction of damping in structures with constrained viscoelastic layers. J. AIAA, 20:1284:1290, 1982.
[8] Wang Y., Luo Z., Kang Z., et al.: A multi-material level set-based topology and shape optimization method. J. CMAME, 283:1570-1586, 2015.
[9] Wendland H.: Piecewise polynomial, positive definite and compactly supported radial basis functions of minimal degree. Advances in Computational Mathematics 4:389-396, 1995.
[10] Svanberg K.: The method of moving asymptotes - A new method for structural optimization. Numerical Methods in Engineering, 24:359-373, 1987.
[11] van der Veen. G., Langelaar M., van Keulen, F.: Integrated topology and controller optimization of motion systems in the frequency domain. Structural and Multidisciplinary Optimization, 51:673-685, 2014.

DESIGN OF BEAM CROSS SECTIONS WITH EXTREME STRUCTURAL PROPERTIES USING TOPOLOGY OPTIMIZATION

José Pedro Blasques[1] and Miguel Fernandez-Perez[2]

[1]*Department of Wind Energy, Technical University of Denmark, jpbl@dtu.dl*
[2]*Vestas Wind Systems A/S, Hedeager 42, 8200 Aarhus, Denmark, mifpe@vestas.com*

Summary Optimal topologies and material distributions are presented which minimize the individual components of the beam cross section compliance matrix (e.g., transverse shear stiffness, shear-torsion coupling, among other). The entries of the compliance matrix are determined using a finite element based cross section analysis tool. A multimaterial topology optimization framework is employed which accommodates any number of isotropic and anisotropic materials. Results are presented for minimization of the individual entries of the cross section compliance matrix subjected to a volume constraint. Some non-intuitive cross section designs are obtained which help shed light on the role of different topological features and material combinations for design of beam structures with non-trivial static and dynamic behaviour. This approach will be used in the future for large scale structural topology optimization of wind turbine blades with nonlinear aeroelastic constraints.

INTRODUCTION

A beam is a type of structure whose length dimension is much larger than its cross section width and height. Beam type structures include wind turbine, helicopter, and airplane rotor blades, among other. The structural response of beam structures can be correctly analysed using beam finite elements. The analysis of the beam response is split in two steps. Firstly the stiffness properties of the beam cross section are analysed. Secondly, these properties are integrated along the length to build the beam finite element stiffness matrix. The author has previously presented results in which structural topology optimization techniques are used to design beam cross sections to control the static and dynamic properties of beam structures ([1, 2]). This paper follows the same approach to focus on the identification of cross section designs - topology and material distribution - which minimize the entries of the cross section compliance matrix (e.g., transverse shear stiffness, shear-torsion coupling, etc.). The work is analogous to design of microstructures to tailor the material properties whereas here the cross section is designed to tailor the beam properties.

METHODOLOGY

For a linear elastic beam there exists a linear relation between the cross section generalized forces $\boldsymbol{T}$ and moments $\boldsymbol{M}$ in $\boldsymbol{\theta} = \left[\boldsymbol{T}^T \boldsymbol{M}^T\right]^T$, and the resulting strains $\boldsymbol{\tau}$ and curvatures $\boldsymbol{\kappa}$ in $\boldsymbol{\psi} = \left[\boldsymbol{\tau}^T \boldsymbol{\kappa}^T\right]^T$ (see Figure 1). This relation is given in its compliance form as $\boldsymbol{F}_s\boldsymbol{\theta} = \boldsymbol{\psi}$, where $\boldsymbol{F}_s$ is the 6×6 cross section compliance matrix. In the most general case, considering material anisotropy and inhomogeneity, all the 21 compliance parameters in $\boldsymbol{F}_s$ may be required to describe the deformation of the cross section. The entries of $\boldsymbol{F}_{s,ij}$ are determined here following the description and nomenclature in [1] of the theory in [3]. The formulation relies on a finite element discretization of the cross section to approximate the three-dimensional cross section deformation or warping. The cross section compliance matrix $\boldsymbol{F}_s$ is obtained as

$$\boldsymbol{F}_s = \boldsymbol{W}^T \boldsymbol{G} \boldsymbol{W}, \text{ where } \boldsymbol{W} \text{ is the solution to } \boldsymbol{K}\boldsymbol{W} = \boldsymbol{F} \tag{1}$$

where the coefficient matrix $\boldsymbol{K}$ and $\boldsymbol{G}$ are associated with the stiffness of the cross section. Furthermore, the solution matrix $\boldsymbol{W}$ contains the cross section rigid body motions $\boldsymbol{\psi}$ and the three dimensional warping displacements $\boldsymbol{u}$. Finally, the load array $\boldsymbol{F}$ is associated with a series of unit load vectors $\boldsymbol{\theta}$.

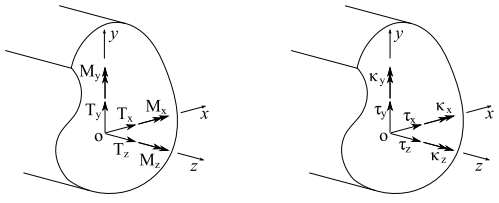

(a) Forces and moments (b) Strains and curvatures

Figure 1: Cross section coordinate system, foces and moments (a), and corresponding strains and curvatures (b).

The optimal design problem is formulated within a multi-material topology optimization context as

$$\begin{aligned} \underset{\boldsymbol{\rho}\in\mathbb{R}^{n_e\times n_c}}{\text{minimize}} \quad & \boldsymbol{F}_{s,ij}(\boldsymbol{\rho}) \\ \text{subject to} \quad & V(\boldsymbol{\rho}) \leq \overline{V} \\ & \sum_{m=1}^{n_c} \rho_{em}(\boldsymbol{\rho}) < 1 \ , \ \forall e = 1, ..., n_e \\ & 0 \leq \rho_{em} \leq 1, \ \forall e = 1, ..., n_e \ , \ \forall m = 1, ..., n_c \end{aligned} \tag{P1}$$

where $V(\boldsymbol{\rho})$ is the total volume of the beam occupied with material. The design variable ρ_{em} represent the volume fraction of candidate material m at element e of the cross section finite element mesh, where n_c and n_e are the number of candidate materials and finite elements, respectively. The sensitivities of the cross section compliance matrix $\boldsymbol{F}_s(\boldsymbol{\rho})$ are analytically determined as described in [1]

NUMERICAL RESULTS

A few illustrative results are presented in Figure 2. The design domain defining the beam cross section is 1×1 m and is meshed using 120×120 elements with three degrees of freedom per node. In view of future plans to manufacture and test the resulting beam designs, results are obtained using Polylactic Acid (PLA), an isotropic material typically used in additive manufacturing. The designs presented in Figure 2 refer to the cross sections of the beam. A three-dimensional beam structure with constant cross section can be obtained by simply extruding these cross sections.



(a) min $F_{s,11}$ (b) min $F_{s,22}$ (c) min $F_{s,12}$ (d) min $F_{s,16}$ (e) min $F_{s,44}$ (f) min $F_{s,55}$ (g) min $F_{s,45}$ (h) min $F_{s,66}$

Figure 2: Optimized beam cross section topologies (a) minimizing $F_{s,11}$ (transverse shear compliance in x direction); (b) minimizing $F_{s,11}$ (transverse shear compliance in x direction); (c) minimizing $F_{s,12}$ (transverse shear-shear coupling); (d) minimizing $F_{s,16}$ (transverse shear-twist coupling); (e) minimizing $F_{s,44}$ (bending compliance around x); (f) minimizing $F_{s,55}$ (bending compliance around y); (g) minimizing $F_{s,45}$ (bending-bending coupling); (h) minimizing $F_{s,66}$ (torsion compliance). The topology minimizing $F_{s,26}$ is the same as in (c) rotated 90 degrees with respect to the z axis. The remaining coupling terms (e.g., $F_{s,46}$) cannot be activated using isotropic materials.

CONCLUSION

Initial results are presented for the optimal design of beam cross sections with extreme stiffness properties using isotropic materials. Further results show that including material anisotropy it is possible to activate the remaining coupling terms which were not active using a single isotropic material. Future work will utilize the solutions presented here to establish the bounds on the entries of the cross section compliance matrix to formulate a new class of Free Beam Section Optimization (FBSO) problems, an approach identical to Free Material Optimization applicable to beam structures. The aim is to use this approach to develop a computationally very efficient framework for large scale structural topology optimization of wind turbine blades with nonlinear aeroelastic constraints.

References

[1] Blasques, J. P., Stolpe, M.: Multi-material topology optimization of laminated composite beam cross sections. Composite Structures, 94(11), 32783289, 2012.

[2] Blasques, J. P.: Multi-material topology optimization of laminated composite beams with eigenfrequency constraints. Composite Structures, 111, 4555, 2014.

[3] Giavotto, V., Borri, M., Mantegazza, P., Ghiringhelli, G., Carmaschi, V., Maffioli, G., Mussi, F.: Anisotropic beam theory and applications. Computers & Structures, 16(1-4), 403413, 1983.

ON BIFURCATION SENSITIVITIES AND STABILITY OPTIMIZATION BASED ON LOCAL SUB-DOMAIN EIGENVALUES

Niels L. Pedersen and Pauli Pedersen

Department of Mechanical Engineering, Solid Mechanics, Technical University of Denmark, Nils Koppels Allé, Building 404, DK-2800 Kgs. Lyngby, Denmark

Summary The engineering approach of fully stressed design is a practical tool with a theoretical foundation. The analog approach to structural bifurcation instability optimization is presented with its theoretical foundation. A numerical redesign procedure is proposed and illustrated with examples. For the ideal case, an optimality criterion is fulfilled if the design have the same sub-domain "critical load" (local Rayleigh quotient). Sensitivity analysis results in a simple relation between system critical load and local "critical load" for a given bifurcation mode.

For a general continuum subjected to loads and boundary conditions, the stability analysis is rather complicated and is normally based on non-linear finite element (FE) analysis. In the present work focus is on bifurcation instability that after non-linear displacement analysis involve an eigenvalue problem to determine a critical load factor at which bifurcation take place. The design problem of maximizing such a load factor by optimized distribution of a given amount of material within a specified design space is the the subject of our work. With analysis being complicated, this synthesis problem seems to relay on pure numerical procedures, but theoretical results are obtained. Due to recent experience on optimal design of eigenfrequencies in [1], simplified results are expected also for the bifurcation eigenvalue problem. This holds for the sensitivity analysis that is necessary for optimizing a design. A simple optimality criterion is derived from the obtained sensitivities..

DIFFERENT STIFFNESS MATRICES FOR ANALYSIS

The static equations of equilibrium for an elastic problem, including reversible non-linear elastic problems, is for a model with a finite number of degrees of freedom written as $[S_s]\{D\} = \{A\}$ where the stiffness matrix $[S_s]$ is the system secant stiffness matrix that directly relate the resulting displacement vector $\{D\}$ and the corresponding force vector $\{A\}$ and may express equilibrium for a total model (system) or for a single element. For the differential of the displacement vector $\{dD\}$ and the differential of the corresponding force vector $\{dA\}$ the relation is described by the tangent stiffness matrix $[S_t]$ by $[S_t]\{dD\} = \{dA\}$

System stiffness matrices may be obtained by accumulating (FE assembled) over all the element stiffness matrices $[S_s] = \sum_e [S_s]_e$ and $[S_t] = \sum_e [S_t]_e$. For non-linear models different stiffness matrices are involved

- $[S_0]$, symmetric stiffness matrix for a non-displaced model,
- $[S_s]$, non-symmetric secant stiffness matrix for a displaced model,
- $[S_\gamma]$, symmetric displacement gradient stiffness matrix for a displaced model,
- $[S_\sigma]$, symmetric stress stiffness matrix for a displaced model and
- $[S_t] = [S_\gamma] + [S_\sigma]$, symmetric tangent stiffness matrix for a displaced model.

For a simple triangular 2D plane element analytical expressions for all these different stiffness matrices are available. These results are derived in [2] and important information follows from these analytical results.

Analysis for bifurcation buckling

With the tangential stiffness matrix available for a FE model, buckling may be determined as described in [3], Chapter 18. In bifurcation buckling two close equilibrium states are possible for the same load. The procedure is here based on an already solved non-linear elastic equilibrium. A such solution is given the index n to indicate a step of a possible incremental load $\{A\}_n = \sum_{\tilde{n}=1}^{\tilde{n}=n} \{\Delta A\}_{\tilde{n}}$. The determined solution gives a determined stress stiffness matrix $[S_\sigma]$ by

$$[S_s]_n\{D\}_n = \{A\}_n \;\Rightarrow\; \{D\}_n \;\Rightarrow\; [S_\gamma]_n \text{ and } \sigma_n \;\Rightarrow\; [S_\sigma]_n \tag{1}$$

with assumed linearity between $\lambda\{\Delta A\}_{n+1}$ and $\lambda[S_\sigma]_n$ giving

$$\begin{aligned} &([S_\gamma]_n + \lambda[S_\sigma]_n)\,\{\Delta D\}_{n+1} = \lambda\{\Delta A\}_{n+1} \\ &([S_\gamma]_n + \lambda[S_\sigma]_n)\,(\{\Delta D\}_{n+1} + \{\Delta\}) = \lambda\{\Delta A\}_{n+1} \end{aligned} \tag{2}$$

where $\{\Delta\}$ is the bifurcation mode from $\{\Delta D\}_{n+1}$. The difference of these two equations give an eigenvalue problem

$$([S_\gamma]_n + \lambda_C[S_\sigma]_n)\{\Delta\} = \{0\} \quad \Rightarrow \quad \text{the eigen pair } \lambda_C, \{\Delta\} \tag{3}$$

The critical load $\{A\}_C$ corresponding to the bifurcation displacement $\{\Delta\}$ is

$$\{A\}_C = \{A\}_n + \lambda_C\{\Delta A\}_{n+1} \tag{4}$$

BIFURCATION LOAD SENSITIVITIES

The eigenvalue problem (3) presented without index n and C is

$$([S_\gamma] + \lambda[S_\sigma])\{\Delta\} = \{0\} \tag{5}$$

This is pre multiplied by the transposed bifurcation eigenmode $\{\Delta\}^T$ to

$$U_\gamma + \lambda U_\sigma = 0 \text{ with } U_\gamma := \{\Delta\}^T[S_\gamma]\{\Delta\} \text{ and } U_\sigma := \{\Delta\}^T[S_\sigma]\{\Delta\} \tag{6}$$

with the Rayleigh quotient $\lambda = -\frac{U_\gamma}{U_\sigma}$.

The sensitivity of the bifurcation eigenvalue with respect to the density ρ_e is

$$\frac{\partial\lambda}{\partial\rho_e} = -\frac{\partial\widehat{\frac{U_\gamma}{U_\sigma}}}{\partial\rho_e} - \frac{\partial\frac{U_\gamma}{U_\sigma}}{\partial\Delta}\frac{\partial\Delta}{\partial\rho_e} = -\frac{\partial\widehat{\frac{U_\gamma}{U_\sigma}}}{\partial\rho_e} \tag{7}$$

simplified by the stationarity of the Rayleigh quotient with respect to change of eigenmode and applying a hat notation for gradients with unchanged eigenmode, see [4]. Expanding the final term in (7) give

$$\frac{\partial\lambda}{\partial\rho_e} = -\frac{\partial\widehat{U}_\gamma}{\partial\rho_e}\frac{1}{U_\sigma} + \frac{\partial\widehat{U}_\sigma}{\partial\rho_e}\frac{U_\gamma}{U_\sigma^2} = -\frac{1}{U_\sigma}\left(\frac{\partial\widehat{U}_\gamma}{\partial\rho_e} + \lambda\frac{\partial\widehat{U}_\sigma}{\partial\rho_e}\right) \tag{8}$$

where the energies are accumulated from element energies

$$U_\gamma = \sum_e (U_\gamma)_e \text{ and } U_\sigma = \sum_e (U_\sigma)_e \tag{9}$$

The stiffness matrices are here assumed to depend explicitly only on the local element density ρ_e and this dependence is assumed to be linear proportionality, that give

$$\frac{\partial\lambda}{\partial\rho_e} = -\frac{1}{U_\sigma}\left(\frac{\partial(\widehat{U}_\gamma)_e}{\partial\rho_e} + \lambda\frac{\partial(\widehat{U}_\sigma)_e}{\partial\rho_e}\right) = -\frac{1}{U_\sigma\rho_e}\left((U_\gamma)_e + \lambda(U_\sigma)_e\right) = \frac{(U_\sigma)_e}{U_\sigma}\frac{1}{\rho_e}(\lambda_e - \lambda) \tag{10}$$

Optimality criterion

With the objective of maximizing the bifurcation load $\{A\}_n + \lambda\{\Delta A\}_n$, i.e., of maximizing λ subject to a constant of unchanged total mass/volume

$$\text{Maximize } \lambda \text{ for } g = \sum_e \rho_e V_e - V = 0 \tag{11}$$

the necessary optimization criterion with a constant C is

$$\frac{\partial\lambda}{\partial\rho_e} = C\frac{\partial g}{\partial\rho_e} = CV_e \quad \Rightarrow \quad \frac{\partial\lambda}{\partial\rho_e}\frac{1}{V_e} = -\frac{1}{U_\sigma}\frac{1}{\rho_e V_e}\left((U_\gamma)_e + \lambda(U_\sigma)_e\right) = \frac{(U_\sigma)_e}{U_\sigma}\frac{1}{\rho_e V_e}(\lambda_e - \lambda) = C \tag{12}$$

where U_σ may be normalized to 1 by normalizing the bifurcation mode $\{\Delta\}$.

References

[1] P. Pedersen and N. L. Pedersen. A note on eigenfrequency sensitivities and structural eigenfrequency optimization based on local sub-domain frequencies. *Struct. Multidisc. Optim.*, 49(4):559–568, 2014.

[2] P. Pedersen. Analytical stiffness matrices with Green-Lagrange strain measure. *Int. J. Numer. Meth. Engng.*, 62:334–352, 2005.

[3] R. D. Cook, D. S. Malkus, M. E. Plesha, and R. J. Witt. *Concepts and Applications of Finite Element Analysis*. Wiley, New York, USA, fourth edition, 2002. 719 pages.

[4] P. Pedersen and N. L. Pedersen. Eigenfrequency optimized 3D continua, with possibility for cavities. *Journal of Sound and Vibration*, 341:100–115, 2015.

EFFICIENT TRANSIENT TOPOLOGY OPTIMIZATION THROUGH DYNAMIC SUBSTRUCTURING

Niels Aage*[1]

[1]*Technical University of Denmark, Department of Mechanical Engineering, Centre for acoustic-mechanical micro systems, Denmark*

Summary This paper presents an efficient topology optimization methodology for dynamic structural design problems. The key to the method is to utilize dynamic substructering, or component mode synthesis, i.e. the Craig-Bampton reduction method to speed up the transient analysis. The dynamic substructuring concept is used for both the forward (the state equation) and the backward (adjoint equation). The developed optimization scheme is demonstrated on design problems for linear elastic Mindlin plates subject to impact loads, where the goal is to minimize the deflection in a specified region.

INTRODUCTION AND MOTIVATION

Structural shape and topology optimization for transient problem is known to be computionally expensive and thus less attractive than its steady state counterparts. This is partly due to the fact that a transient analysis is more expensive than a static analysis - especially for implicit time integration schemes - and partly because the sensitivity analysis requires the solution to a terminal value problem. To illustrate the extra computional efforst required one may use an example from non-linear static optimization. Here one have to solve a non-linear problem for the state equation, bu the adjoint problem turns out to be linear and thus much cheaper than the state problem [1]. Despite this obvious drawback several works on transient structural topology optimization have been presented and studied in the past decade. The approach has, among others, been used for 1D pulse modulators and filter design in [2], material microstructure design in [3] and design of composites in [4].

The focus of this work is to develop a methodology which is capable of speeding up the computations by orders of magnitude. To realize this goal the dynamic substructering method, namely the Craig-Bampton method, is applied [5], [6]. The main idea of dynamic substructuring, or component mode synthesis, is to partition the computational domain into a set of smaller substructures. The finite element equations on each substructure is then reduced in size by its normal modes while retaining the interface, or boundary degrees of freedom, by so-called constraint modes. The reduced substructure stiffness, mass and damping matrices (also known as super elements) are then assemblied into a reduced global system which can be orders of magnitude smaller than the original, full finite element system. Based on the reduced system, it is now possible to perform the transient analysis very fast which paves the way for a fast transient topology optimization methodology.

THEORY

The mechanical problem considered in this work is based on Mindlin plate theory for which the unknowns are the out of plane displacement w and the two rotations $\boldsymbol{\theta} = \{\theta_x, \theta_y\}$. The governing equations can be stated compactly as follows

$$\nabla^T \boldsymbol{G} \left(\nabla w - \boldsymbol{\theta}\right) = \rho h \frac{\partial^2 w}{\partial t^2} \tag{1}$$

$$\left(\boldsymbol{\alpha}_1 \frac{\partial}{\partial x} + \boldsymbol{\alpha}_2 \frac{\partial}{\partial y}\right)^T \boldsymbol{D} \left(\boldsymbol{\alpha}_1 \frac{\partial}{\partial x} + \boldsymbol{\alpha}_2 \frac{\partial}{\partial y}\right) + \boldsymbol{G} \left(\nabla w - \boldsymbol{\theta}\right) = \frac{\rho h^3}{12} \frac{\partial^2 \boldsymbol{\theta}}{\partial t^2} \tag{2}$$

where h is the thickness, $\boldsymbol{G}$ and $\boldsymbol{D}$ are constitutive matrices and $\boldsymbol{\alpha}_1$ and $\boldsymbol{\alpha}_2$ are appropriate 3×2 matrices.

When discretized by the standard Galerkin finite element method and including proportional damping, i.e. $\boldsymbol{C} = \alpha \boldsymbol{M} + \beta \boldsymbol{K}$ the matrix equations becomes as follows

$$\boldsymbol{M}\ddot{\boldsymbol{u}} + \boldsymbol{C}\dot{\boldsymbol{u}} + \boldsymbol{K}\boldsymbol{u} = \boldsymbol{F}(t), \quad t \in [0; T] \tag{3}$$

where $\boldsymbol{u} \equiv \boldsymbol{u}(t)$ is a vector collecting both displacement and rotational degrees of freedom and $\boldsymbol{M}$, $\boldsymbol{C}$, $\boldsymbol{K}$ and $\boldsymbol{F}(t)$ are the mass-, damping-, stiffness-matrices and load vector, respectively. The system, together with appropriate boundary and initial conditions, can now be solved by a time integration scheme from 0 to time T. In this work the unconditionally stable Newmark algorithm is used [5].

*Corresponding author. Email: naage@mek.dtu.dk

Solving Eq. (3) will lead to the aforementioned issues with computional time and we will therefore study a reduced system obtained by the Craig-Bampton method first. For each substructure i in the domain the following reduction is performed

$$\boldsymbol{R}_j = \begin{bmatrix} \boldsymbol{\Phi}_j & \boldsymbol{\Psi}_j \\ \boldsymbol{0} & \boldsymbol{I} \end{bmatrix} \tag{4}$$

where $\boldsymbol{I}$ is the identity matrix, $\boldsymbol{\Phi}_j$ is the matrix with n normal modes computed on the interior i of substructure j, i.e. the solution to the eigenvalue problem $(\boldsymbol{K}_j^{ii} - \omega^2 \boldsymbol{M}_j^{ii})\boldsymbol{\Phi}_j = \boldsymbol{0}$ and $\boldsymbol{\Psi}_j$ is the static correction matrix for the interface b degrees of freedom , i.e. $\boldsymbol{\Psi}_j = -\left(\boldsymbol{K}_j^{ii}\right)^{-1} \boldsymbol{K}_j^{ib}$. The super elements are then obtained by

$$\boldsymbol{M}_j^r = \boldsymbol{R}_j^T \boldsymbol{M}_j \boldsymbol{R}_j, \quad \boldsymbol{C}_j^r = \boldsymbol{R}_j^T \boldsymbol{C}_j \boldsymbol{R}_j, \quad \boldsymbol{K}_j^r = \boldsymbol{R}_j^T \boldsymbol{K}_j \boldsymbol{R}_j \ \boldsymbol{F}_j^r \text{and } \boldsymbol{R}_j^T \boldsymbol{F}_j \tag{5}$$

Once assemblied into a system equivalent to Eq. (3), the time response is obtained effeciently by the Newmark algorithm.

The optimization problem investigated in this work can be posed in discrete form as a standard mathematical programme.

$$\begin{aligned} \min_{x \in \mathbb{R}^n} \quad & \phi = \textstyle\int_{t_1}^{t_2} \boldsymbol{w}(t)^T \boldsymbol{w}(t) \, \mathrm{d}t \\ \text{s.t.} \quad & \boldsymbol{M}\ddot{\boldsymbol{u}} + \boldsymbol{C}\dot{\boldsymbol{u}} + \boldsymbol{K}\boldsymbol{u} = \boldsymbol{F}(t) \\ & V(\boldsymbol{x})/V^* - 1 \leq 0 \\ & 0 \leq x_i \leq 1, \ \ i = 1, n \end{aligned} \tag{6}$$

where the objective function is the out of plane displacement evaluated in a specified region from time t_1 to t_2. The first constraint refers to the state equation, the second to a volume constraint and the last to a box constraint on the design variables denoted by $\boldsymbol{x}$. The optimization problem is solved using the Method of Moving Asymptotes [7] and the sensitivities are determined using the adjoint method obtained purely from the discretized state equation and objective. This leads to the solution of a terminal value problem for the Lagrange multiplier $\boldsymbol{\lambda}$.

$$\boldsymbol{M}\ddot{\hat{\boldsymbol{\lambda}}} + \boldsymbol{C}\dot{\hat{\boldsymbol{\lambda}}} + \boldsymbol{K}\hat{\boldsymbol{\lambda}} = \left.\frac{\partial \phi}{\partial \boldsymbol{u}}^T\right|_{T-\tau}, \quad \hat{\boldsymbol{\lambda}} = \boldsymbol{\lambda}(T - \tau) \tag{7}$$

here formulated as an initial value problem by a change in variables. The sensitivity can then be obtained from the following

$$\frac{\partial \phi}{\partial x_e} = \int_0^T \frac{\partial (\boldsymbol{w}^T \boldsymbol{w})}{\partial x_e} + \boldsymbol{\lambda}^T \left(-\frac{\partial \boldsymbol{M}}{\partial x_e}\ddot{\boldsymbol{u}} - \frac{\partial \boldsymbol{C}}{\partial x_e}\dot{\boldsymbol{u}} - \frac{\partial \boldsymbol{K}}{\partial x_e}\boldsymbol{u} \right) \, \mathrm{d}t \tag{8}$$

To reduce memory requirements, the developed implementation uses a check pointing scheme to avoid storing all displacements, velocities and acceleration from the forward problem.

DISCUSSION

The presented study shows that it is possible to reduce the computational effort of transient topology optimization by order(s) of magnitude by use of dynamic substructering. As expected, the price for the obtained speed up is the more involved sensitivity analysis and the bookkeeping associated with the substructuring (i.e. a domain decomposition). The findings presented here can, with some modifications, be applied to e.g. acoustic-structural interaction problems and thus pave the way for new, interesting multi-physical transient topology optimization problems.

References

[1] Bendsøe, M. P. and O. Sigmund (2003). *Topology Optimization: Theory, Methods and Applications*. Engineering online library. Springer.

[2] Dahl, J., J. S. Jensen, and O. Sigmund (2008). Topology optimization for transient wave propagation problems in one dimension : Design of filters and pulse modulators. *Structural and Multidisciplinary Optimization 36*, 585–595.

[3] Le, C., T. E. Bruns, and D. a. Tortorelli (2012). Material microstructure optimization for linear elastodynamic energy wave management. *Journal of the Mechanics and Physics of Solids 60*(2), 351–378.

[4] Tavakoli, R. (2016). Optimal design of multiphase composites under elastodynamic loading. *Computer Methods in Applied Mechanics and Engineering 300*, 265–293.

[5] Cook, R. D., D. S. Malkus, M. E. Plesha, and R. J. W. Witt (2002). Concept and Applications of Finite Element Analysis.

[6] Craig, R.R. and Bampton, M.C.C. (1968), Coupling of substructures for dynamic analysis. *AIAA Journal*, Vol. 6 No. 7, pp. 1313-19.

[7] Svanberg, K. (1987). The method of moving asymptotes - a new method for structural optimization. *International Journal for Numerical Methods in Engineering 24*(June 1986), 359–373.

TOPOLOGY OPTIMIZATION FOR FINITE STRAIN PLASTICITY

Mathias Wallin[1]*, Viktor Jönsson[1] and Eric Wingren[1]

[1]*Division of Solid Mechanics, Lund University, Sweden*

Summary In this work finite strain rate-independent plasticity is combined with topology optimization. The employed constitutive model is based on rate-independent isotropic hardening plasticity and to separate the elastic deformation from the plastic deformation, use is made of the multiplicative split of the deformation gradient. The mechanical balance laws are solved using the finite element method and the optimization problem is solved using the method of moving asymptotes. The sensitivity is derived using a coupled transient adjoint strategy. A boundary value problem where the plastic work is maximized is used to demonstrate the capability of the presented model.

INTRODUCTION

Most research related to topology optimization has been concerned with linear problems and only a small fraction of the published research has been concerned with non-linear elasticity. Although topology optimization formulations combined with plasticity are rare they do exist and an early example of topology optimization combined with a path-dependent material is provided by [1]. So far, topology optimization combined with plasticity has, however, been restricted to the assumption of small strains.

One application of topology optimization of path-dependent materials is design of energy absorbing structures and materials where finite strain plasticity evidently is highly relevant. In the present work an isotropic finite strain elasto-plastic model is implemented in a finite element environment and combined with topology optimization.

For path-dependent problems the sensitivity is also path-dependent and as a consequence the sensitivity will be obtained by the solution to a terminal value problem. In the present paper the adjoint procedure for calculating the sensitivity for transient coupled problems proposed in [3] will be utilized. The resulting optimization problem is solved using the method of moving asymptotes (MMA), cf. [4]. The presented formulation will be used to find topologies that generates maximum plastic work when subject to a prescribed displacement.

ELASTO-PLASTIC BOUNDARY VALUE PROBLEM

The employed constitutive model is an isothermal version of the model presented in [2] and it is based on the multiplicative split of the deformation gradient. The strain energy governing the elastic response is a Neo-hookean potential function defined in terms of the elastic Finger tensor. The non-dimensional density, c, reduces the strain energy, or stiffness, using the canonical scaling c^p where the penalty exponent is chosen as $p = 3$.

To distinguish plastic response from elastic response, use is made of the von-Mises yield function formulated in terms of the Kirchhoff stress tensor. Similar to elasticity, the initial threshold to plasticity is scaled with the non-dimensional density, however, for the yield stress the penaly exponent $q = 2$ is employed. The plastic evolution laws are based on the postulate of maximum dissipation, i.e. associated plasticity is utilized. In each integration point throghout the structure, the evolution laws for the plastic deformation and the internal variables are integrated using the implicit backward Euler scheme.

The mechanical balance laws are formulated in the reference configuration and discretized using a total Lagrangian finite element formulation. The set of non-linear equations govering the equilibrium is solved using the Newton-Raphson scheme. Since the problem is path-dependent, the load is applied in a number of load steps and for each step the non-linear mechanical balance laws are solved together with the non-liner constitutive equations.

OPTIMIZATION

The objective of the optimization is to maximize the total plastic work for given prescribed displacements. Based on the spatial and temporal discretization, the plastic work can be expressed as a function of the internal variables in all gauss points and all time steps. The optimization problem will be solved by using the method of moving asymptotes (MMA), cf. [4] and consequently the gradients of the constraints and the objective function with respect to the design variables are required. In contrast to elasticity, plasticity is path-dependent which requires that the entire load path needs to be included in the sensitivity analysis. In this work, the adjoint method for coupled transient problems presented in [3] will be exploited. In this approach the discrete constitutive equations and mechanical balance laws are enforced via Lagrangian multipliers in each load step. The Lagrangian multipliers are then obtained from the solution to a sequence of adjoint problems. To avoid mesh sensitivity, use is made of a PDE based filter strategy.

*Corresponding author. Email: Mathias.Wallin@solid.lth.se

NUMERICAL RESULTS

The finite strain plasticity model has been used to simulate the response of the simple boundary value problem depicted

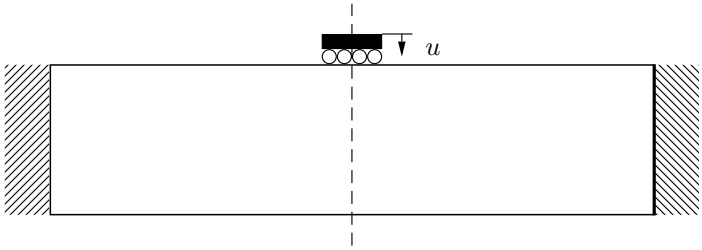

Figure 1: Illustration of geometry of the design domain and boundary conditions used in the numerical example. Due to symmetry only the right hand side of the structure is included in the numerical model.

in Fig. 1. Initially, the design domain is filled with 50% material and after the optimization procedure the optimal design is shown in Fig. 2.

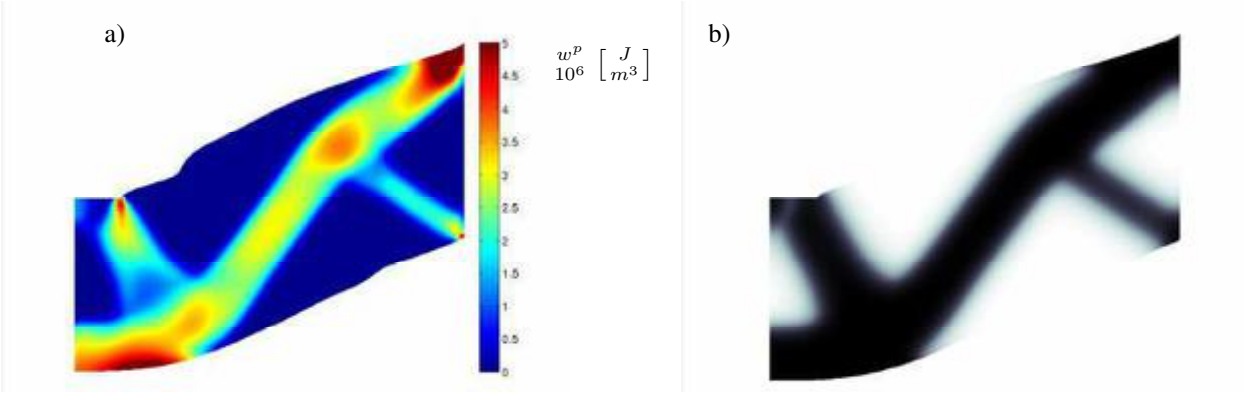

Figure 2: a) Distribution of plastic work, w^p, throughout the design in the deformed state. b) Optimal design.

From Fig. 2a it can be concluded that the plastic work is at maximum where the load is applied and where the structure is attached to the wall. The peak of the plastic work is located at the upper right corner of the structure. In Fig. 2b, the optimal design is plotted and a comparison to simulations using the assumption of small strains reveals that the optimal design will be highly influenced by the load level.

References

[1] Maute, K., Schwarz, S., Ramm, E.: Adaptive topology optimization of elastoplastic structures. Structural Optimization **15**(2), 81–91 (1998)

[2] Simo, J.C., Miehe, C.: Associative coupled thermoplasticity at finite strains: Formulation, numerical analysis and implementation. Comput. Methods Appl. Mech. Engng. **98**, 41–104 (1992)

[3] Michaleris, P., Tortorelli, D.A., Vidal, C.A.: Tangent operators and design sensitivity formulations for transient non-linear coupled problems with applications to elastoplasticity. International Journal for Numerical Methods in Engineering **37**(14), 2471–2499 (1994)

[4] Svanberg, K.: The method of moving asymptotes- a new method for structural optimization. Int. J. Numer. Meth. Engng. **24**, 359–373 (1987)

STRUCTURAL TOPOLOGY OPTIMIZATION OF WIND TURBINE BLADES FABRICATED BY ADDITIVE MANUFACTURING

Miguel Fernandez-Perez[1a)], José Pedro Blasques[2]
[1]*Vestas Wind Systems A/S, Aarhus, Denmark*
[2]*Department of Wind Energy, Technical University of Denmark, Roskilde, Denmark*

Summary This article proposes a method to identify optimal wind turbine blade structures fabricated by additive manufacturing based on topology optimization techniques. The structural model is based on the beam cross-sections through a 2D finite element representation. The optimization problems are formulated through the blade properties and response at the cross-section level. The numerical experiments performed challenge the topology optimization method proposed against several problem formulations, geometries and candidate materials.

INTRODUCTION

Large scale wind turbine blade designs are heavily influenced by the manufacturing constraints currently inherent in their production using fiber-reinforced composites. The emergence of industrial-scale additive manufacturing techniques has the potential to release most manufacturing constraints from design, thus enable novel blade structures which are more efficient in the use of material in order to withstand loads and capture wind power. Topology optimization techniques allow the highest degree of design freedom for the optimal allocation of structural mass inside an available design space. Therefore, it is considered here as the methodology for conceptual design of wind turbine blades built by additive manufacturing.

METHODOLOGY

The optimization problems are based on the structural model of a blade by Timoshenko beam finite elements. These are defined from the stiffness and mass matrices at the beam cross-section level. Through a 2D solid finite element discretization of a beam slice, its cross-section stiffness matrix is obtained using the cross-section analysis tool BECAS [1]. The formulated problems use the 2D FE discretization of the beam cross-sections as design variables through the SIMP parameterization extended for multiple materials. The objective is to minimize the overall structural mass of the blade with constraints formulated in terms of the cross section deformations described by the in- and out-of-plane strains and curvatures, due to the forces and moments along the blade. The restrictions on the deformations along the blade are set attending to structural and aero-elastic criteria. The loads and deformations are pre-processed from the DTU-10MW-RWT [2] benchmark blade, from nonlinear time-domain wind turbine simulations using the aero-elastic code Hawc2 [3]. The optimization is solved by the interior point solver IPOPT [4], using the analytical solutions of the objective and constraint functions and their sensitivities.

RESULTS AND DISCUSSION

The results presented demonstrate the ability of the proposed methodology to generate optimal topologies of a set of cross-sections along a wind turbine blade, by achieving the lowest mass possible while ensuring that it withstands multiple extreme load cases. The topologies for each cross-section are obtained from a very fine discretization of the design space available inside a predefined aero-foil surface. The computational expense of these problems is orders of magnitude lower than the full blade discretization with solid 3D finite elements. This level of refinement can reflect the low volume fraction that characterizes modern wind turbine blade structures. The solutions for multiple material topology optimization problems reflect the influence of combining orthotropic materials in the topology to optimally carry loads inside a blade. The topologies obtained are reproduced as small-scale prototypes through additive manufacturing.

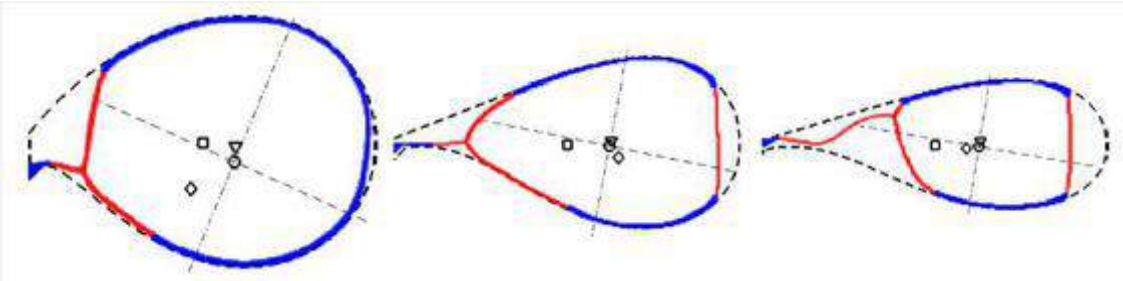

Figure 1 Topologies with minimum mass that comply with deformation restrictions on the cross-sections of the 10MW-RWT blade at 15m, 21m and 28m, respectively. Each topology is composed of unidirectional (blue) and bidirectional (red) glass fiber composite laminates. The design space is the area enclosed by the dashed line.

[a)] Corresponding author. Email: mifpe@vestas.com.

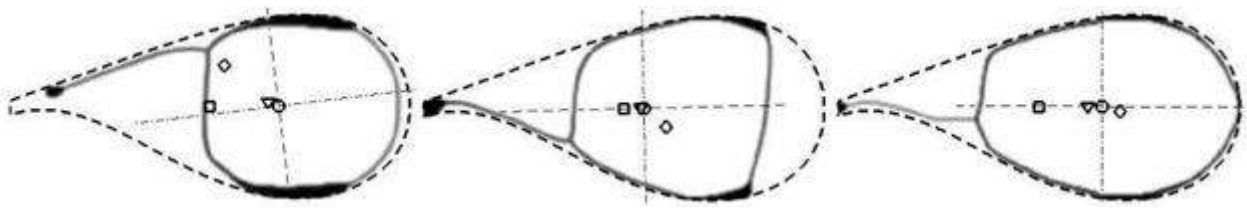

Figure 2 Topologies with minimum isotropic material that comply with deformation restrictions on each strain and curvature component set by the benchmark 10MW-RWT blade at 21m. The topology on the left fulfills a more restrictive constraint for the curvature around the in-plane horizontal axis (higher flapwise stiffness). The central topology allows a lower curvature around the in-plane vertical axis (higher edgewise stiffness). The topology on the right is restricted to a lower twist (higher torsional stiffness).

References

[1] Blasques, J. P.; Stolpe, M.: Multi-material topology optimization of laminated composite beam cross sections. *Composite Structures*, 2012, vol. 94, no 11, p. 3278-3289.

[2] Bak, C. et al.: "Light Rotor: The 10-MW reference wind turbine." *EWEA 2012-European Wind Energy Conference & Exhibition*. 2012.

[3] Larsen, T. J.; Hansen, A. M.: *How 2 HAWC2, the user's manual*. Risø National Laboratory, 2007.

[4] Wächter, A.; Biegler, L. T.: On the implementation of an interior-point filter line-search algorithm for large-scale nonlinear programming.*Mathematical programming*, 2006, vol. 106, no 1, p. 25-57.

STRUCTURAL DESIGN UNDER DAMAGE CONSTRAINTS WITH XFEM AND LEVEL SETS.

Lise Noël [*1], Pierre Duysinx[2], and Kurt Maute[3]
[1,2]*Department of Aerospace and Mechanics, University of Liège, Liège, Belgium*
[3]*Center for Aerospace Structures, University of Colorado, Boulder, Colorado, USA*

Summary This work aims at developing tools to design structures that can sustain a certain level of degradation, i.e. structures that present a low sensitivity to damage. To achieve this goal, an optimization approach is chosen. The analysis of the structures is performed resorting to an XFEM-level set framework. The damage propagation is represented through a non-local model and solved resorting to a non-linear analysis controlled by prescribed displacement. To optimize structures considering a potential degradation, a sensitivity analysis of the damage process is required. The latter is carried out through a fully analytical approach and considering both the direct and the adjoint formulations. Finally, the developed methodology is applied to design 2D structures undergoing damage constraints. The influence of the degradation of the materials constituting the structures can be observed on the optimized designs.

INTRODUCTION

Composite materials exhibits extremely interesting properties as they combine a high stiffness and a very light weight. However, their integration in structures is made difficult because of their high damage sensibility. The latter is scarcely taken into account while designing structures. Therefore, this work aims at developing a systematic methodology to design structures exhibiting a certain resistance to degradation. An optimization approach is chosen. To represent complex geometries and deal with large shape modifications, a level set representation of the geometry advantageously combined with the extended finite element method (XFEM) is used. The degradation of the material is represented using a non-local damage model, which reduces the material stiffness by a scalar damage value D. To solve optimization problem with damage constraints, a sensitivity analysis of the damage process is required. As damage growth is an irreversible process, the history of the structural response has to be taken into account. A fully analytical approach is developed to perform the sensitivity analysis accurately and efficiently. Finally, ongoing work aims at applying the developed tools to design structures with damage constraints.

FRAMEWORK

The structural response is obtained combining the XFEM and a level set representation of the geometries. The XFEM allows representing discontinuities, such as material interfaces, within finite elements. A fixed mesh can be used through the optimization process and costly remeshing operations are avoided. The level set description of the geometries enables to represent discontinuities, interfaces ... implicitly. It allows an easy handling of moving boundaries.

DAMAGE MODEL

The degradation of the materials is represented using a non-local damage model. The damage is given by a scalar value D evaluated at each Gauss point of the structure. The stiffness of the materials are directly reduced by these damage values. The damage growth is characterized by an evolution law depending on the displacement $\mathbf{u}$: $\mathbf{D} = g(\mathbf{u})$. The obtained damage variables $\mathbf{D}$ are then smoothed using a smoothing function f^S to avoid abrupt change from zero to non-trivial values. Finally, a damage filter is applied to the smoothed damage values $\mathbf{D}^S$ to prevent the localization of the degradation in a thin strip of elements.

DAMAGE PROCESS ANALYSIS

The damage process is non-linear and presents a limit point in its force-displacement curve. Classical iterative solvers, as Newton-Raphson, can no longer be used except if dealing with low damage values. A displacement controlled solver, based on imposed incremental displacements at each iteration, is then implemented to be able to reach high degradation in the materials. The problem is solved simultaneously on the displacement $\mathbf{u}$ and the damage $\mathbf{D}$ state variables, collected in a global one $\mathbf{y}$. The damage propagation is an irreversible process and the damage growth history has to be taken into account. This path dependence shows through the residuals, given as functions of the current (k) and the previous $(k-1)$ iterations and the design parameters $\mathbf{s}$:

$$\mathbf{R}^{(k)} = \mathbf{R}(\mathbf{y}^{(k)}, \mathbf{y}^{(k-1)}, \mathbf{s}). \tag{1}$$

*Lise.Noel@ulg.ac.be

DAMAGE PROCESS SENSITIVITY ANALYSIS

To perform the sensitivity analysis, a fully analytical approach, inspired from Michaleris et al. [3] is developed. The evaluation of the derivatives is following and extending the basic methodology explained in Noël et al. [2]. The derivatives of an objective/constraint function $\mathcal{F}$ with respect to a particular design parameter s_i is given as:

$$\mathcal{F}^{(k)} = \mathcal{F}(\mathbf{y}^{(k)}, \mathbf{s}), \qquad \frac{d\mathcal{F}^{(k)}}{ds_i} = \frac{\partial \mathcal{F}^{(k)}}{\partial s_i} + \frac{\partial \mathcal{F}^{(k)}}{\partial \mathbf{y}^{(k)}} \frac{d\mathbf{y}^{(k)}}{ds_i}. \tag{2}$$

To evaluate this expression, the derivatives of the state variables $\mathbf{y}$ with respect to the considered design parameter s_i are required. They can be obtained through the computation of the derivatives of the residuals $\mathbf{R}$:

$$\frac{d\mathbf{R}^{(k)}}{ds_i} = \frac{\partial \mathbf{R}^{(k)}}{\partial s_i} + \frac{\partial \mathbf{R}^{(k)}}{\partial \mathbf{y}^{(k)}} \frac{d\mathbf{y}^{(k)}}{ds_i} + \frac{\partial \mathbf{R}^{(k)}}{\partial \mathbf{y}^{(k-1)}} \frac{d\mathbf{y}^{(k-1)}}{ds_i}. \tag{3}$$

Using the direct (resp. adjoint) approach and proceeding from the first (resp. last) to the last (resp. first) iterations, the derivatives of the objective/constraint function can be recovered provided that $\frac{\partial \mathbf{R}^{(k)}}{\partial s_i}$, $\frac{\partial \mathbf{R}^{(k)}}{\partial \mathbf{y}^{(k)}}$ and $\frac{\partial \mathbf{R}^{(k)}}{\partial \mathbf{y}^{(k-1)}}$ are known.

VALIDATION

The accuracy of the developed sensitivity analysis is illustrated on a simple benchmark example: a plate with a hole. The considered problem is illustrated in Figure 1 and all the used parameters are given in Table 1. The derivative of the compliance with respect to the four design parameters a, b, ξ, η is shown in Figure 2. One can see that the sensitivity results using finite difference (FD) are in very good agreement with the analytical ones either resorting to the direct (A Direct) or the adjoint (A adjoint) formulations.

Figure 1: Plate with a hole: description.

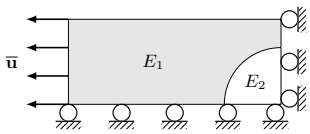

Table 1: Plate with a hole: parameters.

Dimensions	$[m]$	$L = 7.5,\ l = 3$
Elastic moduli	$[N/m^2]$	$E_1 = 3 * 10^{10},\ E_2 = 3 * 10^4$
Displacement	$[m]$	$\overline{u} = 10^{-4}$
Level set function		$\phi(x, s) = (\frac{x}{a})^{\xi} + (\frac{y}{b})^{\eta} - 1$
Gauss points per subelement		$n_{gp} = 7$
Strain threshold		$\varepsilon_{th} = 10^{-4}$
Smoothing parameter		$\eta_S = 7$

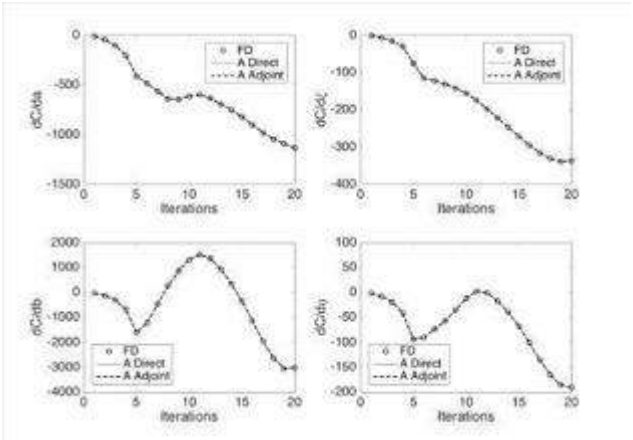

Figure 2: Plate with a hole: sensitivity analysis.

CONCLUSIONS

An optimization approach to design structures resistant to degradation is developed. The analysis is performed within an XFEM-level set framework and resorting to a displacement controlled iterative solver. The sensitivity analysis of the damage process is carried out through a fully analytical approach. Finally, the optimization procedure will be applied to design structures under damage constraints.

The first author, Lise Noël, is supported by a grant from the Belgian National Fund for Scientific Research (F.R.S.- FNRS) which is gratefully acknowledged.

References

[1] James K. A., Waisman H.: Failure mitigation in optimal topology design using a coupled nonlinear continuum damage model. Comp. Methods Appl. Mech. Engrg 268:614-631, 2013.

[2] Noël L., Van Miegroet L., Duysinx P.: Analytical sensitivity analysis using the extended finite element method in shape optimization of bimaterial structures. Int. J. Numer. Meth. Engng DOI: 10.1002/nme.5181, 2015.

[3] Michaleris P., Tortorelli D., Vidal C. A.: Tangent operators and design sensitivity formulations for transient non-linear coupled problems with applications to elastoplasticity. Int. J. Numer. Meth. Engng 37:2471-2499, 1994.

A SECOND-ORDER METHOD FOR STRUCTURAL SHAPE OPTIMIZATION WITH THE LEVEL-SET METHOD.

Jean-Léopold Vié *[1,2], Éric Cancès[1], and Grégoire Allaire[2]

[1]*CERMICS, École des Ponts Paristech, Champs-sur-Marne, France*
[2]*CMAP, École Polytechnique, Palaiseau, France*

Summary In topology optimization, there are two formalisms for computing derivatives : one where the variations of the shape are given by a transformation by a diffeomorphism, and another one where they are described by the flow of a regular vector field. In the level-set approach, a shape is represented by the negative domain of a scalar function, and its variations are performed trough a transport equation, namely the Hamilton-Jacobi equation. The present work focuses on computing derivatives in that context. The knowledge of the second order shape derivatives gives also different indications on numerical aspects, that we illustrate with a few examples at the end.

SHAPE DERIVATIVES

The derivation with respect to a shape - a variable subset of $\mathbb{R}^d$ - is a crucial tool in shape optimization. It was widely developed by many authors [5], [6], [12] (and references therein). Here we follow the approach and notations of Murat and Simon [6, 11]. Given a bounded open set Ω_0 of $\mathbb{R}^d$, a variation of the domain is a perturbation by a regular mapping : any domain Ω "close" to Ω_0 can be seen as $\Omega = \big(\mathrm{Id} + \theta\big)(\Omega_0)$, where θ is a small displacement field and Id the identity operator on $\mathbb{R}^d$. Following this idea, one can define Fréchet derivatives of functions depending on Ω. Zolésio and co-workers [3, 12], proposed another point of view which consits in considering a moving domain

$$[0, \tau[\ni t \mapsto \Omega_t,$$

with $\Omega_t = X_V(t, \Omega_0)$, where $X_V : [0, \tau[\times \mathbb{R}^d \to \mathbb{R}^d$ is the maximal flow of a regular vector field $V \in C^k\big(\mathbb{R}_+ \times \mathbb{R}^d; \mathbb{R}^d\big)$: $\partial_t X_V(t, x) = V\big(t, X_V(t, x)\big)$ with $X_V(0, x) = x$. This allows one to derive a function of the shape with respect to the time parameter t. The structure of the second order shape derivatives is also known in this context.

DERIVATION WITH RESPECT TO NORMAL EVOLUTION

The goal of this work is to derive along time trajectories, in the framework of the level-set method [1], when the vector field is aligned with the outer normal to the shape at every point of its boundary. Let ϕ_0 be a level-set function representing Ω_0 :

$$\begin{cases} x \in \Omega_0 & \text{if } \phi_0(x) < 0, \\ x \in \partial\Omega_0 & \text{if } \phi_0(x) = 0, \\ x \in \mathbb{R}^d \backslash \Omega_0 & \text{if } \phi_0(x) > 0. \end{cases} \tag{1}$$

The boundary of Ω_0 is given by the level set $\{x \in \mathbb{R}^d \mid \phi_0(x) = 0\}$. Given a regular vector field $v \in C^k\big(\mathbb{R}_+ \times \mathbb{R}^d; \mathbb{R}\big)$, let $\phi_v \in C^k\big([0, \tau[\times \mathbb{R}^d\big)$ be a classical solution of the following Hamilton-Jacobi equation (with t small enough) :

$$\begin{cases} \partial_t \phi_v(t, x) + v(t, x) \left|\nabla_x \phi_v(t, x)\right| = 0, \\ \phi_v(0, x) = \phi_0(x). \end{cases} \tag{2}$$

For $0 \leq t < \tau$ we define Ω_t as being the set of negative values of $\phi_v(t, \cdot) : \Omega_t = \{x \in \mathbb{R}^d \mid \phi_v(t, x) < 0\}$. The perturbation by the Hamitlon-Jacobi equation corresponds to a normal evolution of the shape. Thanks to the bicharacteristics method for solving the Hamilton-Jacobi equation [10], we can compute shape derivatives in this framework. It appears that the first derivatives are all the same, and that the second derivatives are all different.

EXTENSION OF A SCALAR FIELD - APPROXIMATION OF THE SHAPE HESSIAN.

The first shape derivatives only depends on the trace of the field v on $\partial\Omega$. It is then necessary to extend v to $\mathbb{R}^d$. This question has already been studied in [2, 4]. As a result, v being a descent direction we may choose any extension method from $\partial\Omega$ to $\mathbb{R}^d$. On the first hand, the structure of the second order shape derivatives allows to find an extension method that may be efficient. On the other hand, it helps to approximate the shape Hessian, which is the basic idea of a quasi-Newton method [7].

*Corresponding author. Email: viej@cermics.enpc.fr

NUMERICAL EXPERIMENTS

At the end we show some numerical comparison between the presented quasi-Newton, the Newton method and the gradient method. For example, we consider the case of a bridge, and try to minimize the compliance with a fixed penalization on the volume. We consider three algorithms : the gradient method (`GExt0`, `GExt1` in Figure 2), the Newton method (`NExt0`, `NExt1`) and a Quasi-Newton method (`QExt0`, `QExt1`). We also try on each algorithm two extension method. Below we plot the evolution of the objective L, where $L(\Omega_\infty)$ is the minimum of each method.

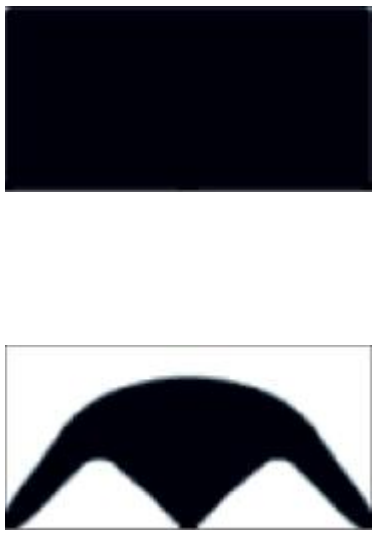

Figure 1: Initial and Optimal domains.

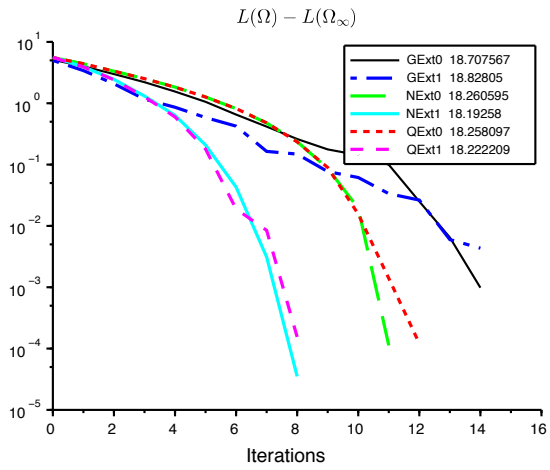

Figure 2: Evolution of the error with each optimal value $L(\Omega_\infty)$. The value of $L(\Omega_\infty)$ is different for each method; it is given in the legend.

CONCLUSION

The computation of the second order shape derivatives in the level-set framework and the knowledge of their structures allowed us to propose some extension method coupled to a gradient, a Newton and a Quasi-Newton algorithms. This combination seems at first to be efficient in some basics numerical examples.

References

[1] G. ALLAIRE, F. JOUVE, A-M. TOADER, *Structural optimization using sensitivity analysis and a level-set method*, J. Comp. Phys., Vol 194/1, pp.363-393, 2004.

[2] M. BURGER, *A Framework for the Construction of Level Set Methods for Shape Optimization and Reconstruction*, Interfaces and Free Boundaries, 2002, 5, 301-329

[3] M-C. DELFOUR AND J-P. ZOLÉSIO, *Velocity method and lagrangian formulation for the computation of the shape Hessian*, SIAM Journal on Control and Optimization, 29(6):14141442, 1991.

[4] F. DE GOURNAY, *Velocity Extension for the Level-set Method and Multiple Eigenvalues*, Shape Optimization SIAM Journal on Control and Optimization, 2006, 45, 343-367

[5] A. HENROT, M. PIERRE, *Variation et optimisation de formes*, Springer, 2005.

[6] F. MURAT AND J. SIMON, *Sur le contrôle par un domaine géométrique*. Rapport du l.a., Université Paris VI, 1976.

[7] J. NOCEDAL, S-J. WRIGHT, *Numerical Optimization*, Springer, 1999.

[8] A. NOVRUZI, J-R. ROCHE, *Second order derivatives, Newton method, application to shape optimization*, INRIA, 1995.

[9] S. OSHER, J-A. SETHIAN, *Fronts propagating with curvature-dependent speed : Algorithms based on Hamilton-Jacobi formulations*, Journal of Computational Physics , 1988, Vol 79, pp 12-49.

[10] J. RAUCH, *Hyperbolic partial differential equations and geometrics optics*, volume 133 of Graduate Studies in Mathematics. American Mathematical Society, 2012.

[11] J. SIMON, *Differentiation with respect to the domain in boundary value problems*, Numer. Funct. Anal. Optim., 2:649687, 1980.

[12] J. SOKOLOWSKI AND J-P. ZOLESIO, *Introduction to Shape Optimization*, volume 16 of Springer Series in Computational Mathematics. Springer Berlin Heidelberg, 1992.

ON NONLINEAR FILTERS IN TOPOLOGY OPTIMIZATION

Eddie Wadbro*[1] and Linus Hägg[1]
[1]*Department of Computing Science, Umeå University, SE–901 87 Umeå, Sweden.*

Summary It is well known that material distribution topology optimization problems often are ill-posed if no restriction or regularization method is used. A drawback with the standard linear density filter is that the resulting designs have large areas of intermediate densities, so-called gray areas, especially when large filter radii are used. To produce final designs with less gray areas, several different methods have been proposed; for example, projecting the densities after the filtering or using a nonlinear filtering procedure. In a recent paper, we presented a framework that encompasses a vast majority of currently available density filters. In this talk, we present that these nonlinear filters ensure existence of solutions to a continuous version of the minimal compliance problem. Moreover, we show numerical experiments that illustrates that cascades of these nonlinear filters can be used to efficiently solve large-scale topology optimization problems.

INTRODUCTION—THE fW-MEAN FILTERED CONTINUOUS MINIMAL COMPLIANCE PROBLEM

Since the seminal paper by Bendsøe and Kikuchi [2] regarding topology optimization of linearly elastic continuum structures, the field of topology optimization has been subject to intense research. It is well known that material distribution topology optimization problems often are ill-posed if no restriction or regularization method is used. Amongst the most popular techniques to achieve mesh-independent designs is to use a filtering procedure. In a classic paper, Bourdin [4] established existence of solutions to a continuous version of the linearly filtered minimal compliance problem. Since the introduction of the linear density filter by Bruns and Tororelli [5], a whole range of *nonlinear* filters developed to produce final designs with less gray areas has been presented [6, 8, 9]. We have recently introduced the class of generalized fW-mean filters that include the vast majority of filters used in topology optimization [10] and provide a common framework for analyzing and evaluating various filters.

Here, we consider a standard test problem, namely the problem of designing a linearly elastic structure with minimal compliance given a certain load-case and an upper bound V on the availiable volume. Let $\Omega \subset \mathbb{R}^d$ be a bounded and connected domain in which we want to place our structure. We describe the design by using the material distribution approach to topology optimization and define the spatially varying forth order elasticity tensor $E(\rho) = (\underline{\rho} + (1-\underline{\rho})P(F(\rho)))E_0$, where $\underline{\rho} > 0$, $F(\rho)$ is a continuous version of the fW-mean filter, $P : [0,1] \to [0,1]$ is a smooth and invertible penalty function, and E_0 is a constant forth order elasticity tensor. The above formulation includes the case when the problem is penalized using SIMP [3], that is the case when $P(x) = x^p$ for some $p > 1$. The continuous fW-mean filtered density is, for $x \in \Omega$, given by

$$\big(F(\rho)\big)(x) = f^{-1}\left(\int_\Omega w(x,y)(f \circ \rho)(y)\,\mathrm{d}y\right), \tag{1}$$

where $f : [0,1] \to [f_{\min}, f_{\max}] \subset \mathbb{R}$ is a smooth and invertible function and $w(x,\cdot)$ is a non-negative normalized weight function. We let $\mathcal{A} = \big\{\rho \mid 0 \le \rho \le 1 \text{ a.e. on } \Omega,\ \|F(\rho)\|_{L^1(\Omega)} \le V\big\} \subset L^\infty(\Omega)$ denote the set of admissible designs and assume that the boundary $\partial\Omega$ is Lipschitz and that the structure is fixed at a non-empty open boundary portion $\Gamma_D \subset \partial\Omega$. The displacement of the structure u solves the problem, find $u \in \mathcal{U}$ such that $a(\rho; u, v) = \ell(v)\ \forall v \in \mathcal{U}$, where $\mathcal{U} = \big\{u \in H^1(\Omega)^d \mid u|_{\Gamma_D} \equiv 0\big\}$ is the set of kinematically admissible displacements, a is the energy bilinear form, and ℓ denotes the load linear form. In this setting, the minimal compliance problem admits solutions, that is, we can formulate and prove the following theorem.

Theorem 1. *There exists a solution to the following variation of the minimal compliance problem. Find $u^* \in \mathcal{U}^*$ such that $\ell(u^*) = \inf_{u \in \mathcal{U}^*} \ell(u)$, where $\mathcal{U}^* = \big\{u \in \mathcal{U} \mid \exists \rho \in \mathcal{A}$ such that $a(\rho; u, v) = \ell(v)\ \forall v \in \mathcal{U}\big\}$.*

Remark 1. *Theorem 1 also holds true for a cascade of fW-mean filters of the form* (1) *with different filter functions f.*

NUMERICAL EXPERIMENTS

Figure 1 shows the final physical designs (not post processed nor sharpened!) of cantilever beams optimized with aim of minimizing their compliance when a load is uniformly distributed over the middle 10 % of the beam's right side; a standard test problem in topology optimization. Here, we use an open–close filtering strategy (comprising a cascade of four fW-mean filters) over octagonal shaped neighborhoods as suggested by Sigmund [8]. However, instead of using exponential averaging, we use harmonic averaging as introduced in topology optimization by Svanberg and Svärd [9]. Remark that even though the open–close filtering strategy in general does not guarantee minimal size control for both structure and void [7], our

*Corresponding author. Email: eddiew@cs.umu.se

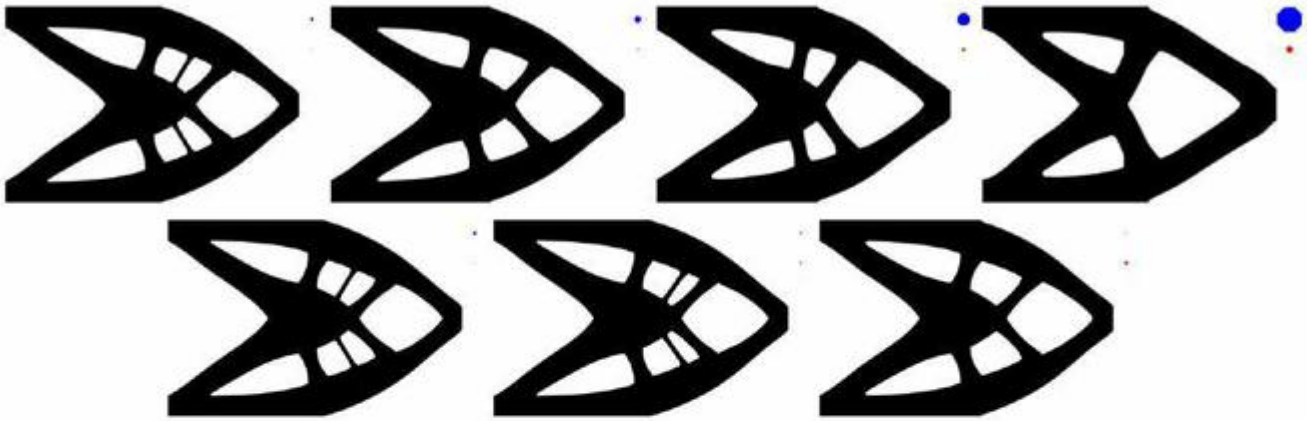

Figure 1: Optimized cantilever beams using 1536×1024 elements, and different harmonic open–close filters. The filter neighborhoods are indicated in the upper-right corner of each sub-figure, and the upper neighborhood corresponds to the open step while the lower corresponds to the close step. Top row, the relative ratio between the filter radius used in the open and closed step is 4 for all experiments, filter radii increases toward the right. Bottom row, the relative ratio between the filter radius used in the open and close step is from left to right, 4, 1, and 1/4, respectively.

numerical experiments for the minimal compliance problems suggest that this strategy in combination with a gradient based optimization method guides the design into a desirable configuration. The volume fraction used was 0.5 and the final measure of non discreteness (of the physical design) is at most 0.3 %. To the best of our knowledge, previously no contribution has used an open–close or close–open filtering strategy to solve problems with more than a few tens of thousands degrees of freedom. Here, we capitalize on our fast filtering strategy [10] and use a modified version of the 2D multigrid-CG topology optimization code by Amir et al. [1] to solve design problem with approximately 1.5 million degrees of freedom. In each sub-figure in Figure 1, the upper neighborhood corresponds to the open step that should impose a minimum size on the material regions while the lower neighborhood corresponds to the close step that should impose a minimum size on the void regions. The beams in the top row are optimized with increasing filter radii from left to right while the beams in the bottom row are optimized by using a different ratio between the filter radii in the open and close step. As reference, the leftmost figures on both rows shows the same design.

For the cantilever beam in the third subfigure from the left in the top row in Figure 1, the size of the filter neighborhoods are $3,465$ elements for the *open step* and 249 elements for the *close step*. The solution process required 182 iterations and took 3 hours, the filtering and modification of sensitivities accounted for around 20 % of this time, on a desktop equipped with an Intel Xeon E5-1650 v3 CPU and 32 GB RAM. It should be noted that the fast summation algorithm was executed almost $40,000$ times and that the elementwise evaluation of the nonlinear functions, corresponding to f in equation (1), dominated the time required for the filtering and evaluation of the sensitivities.

References

[1] O. Amir, N. Aage, and B. S. Lazarov. On multigrid-CG for efficient topology optimization. *Struct. Multidiscip. Optim.*, 49(5):815–829, 2014.

[2] M. P. Bendsøe and N. Kikuchi. Generating optimal topologies in structural design using a homogenization method. *Comput. Methods Appl. Mech. Engrg.*, 71:197–224, 1988.

[3] M. P. Bendsøe and O. Sigmund. *Topology Optimization. Theory, Methods, and Applications*. Springer, 2003.

[4] B. Bourdin. Filters in topology optimization. *Internat. J. Numer. Methods Engrg.*, 50:2143–2158, 2001.

[5] T. E. Bruns and D. A. Tortorelli. Topology optimization of non-linear elastic structures and compliant mechanisms. *Comput. Methods Appl. Mech. Engrg.*, 190:3443–3459, 2001.

[6] J. K. Guest, J. H. Provost, and T. Belytschko. Achieving minimum length scale in topology optimization using nodal design variables and projection functions. *Internat. J. Numer. Methods Engrg.*, 61(2):238–254, 2004.

[7] M. Schevenels and O. Sigmund. On the implementation and effectiveness of morphological close-open and open-close filters for topology optimization. *Struct. Multidiscip. Optim.*, In press:1–7, 2016.

[8] O. Sigmund. Morphology-based black and white filters for topology optimization. *Struct. Multidiscip. Optim.*, 33(4–5):401–424, 2007.

[9] K. Svanberg and H. Svärd. Density filters for topology optimization based on the pythagorean means. *Struct. Multidiscip. Optim.*, 48(5):859–875, 2013.

[10] E. Wadbro and L. Hägg. On quasi-arithmetic mean based filters and their fast evaluation for large-scale topology optimization. *Struct. Multidiscip. Optim.*, 52(5):879–888, 2015.

ON SLOWLY MOVING BOUNDARIES IN DENSITY BASED STRUCTURAL TOPOLOGY OPTIMIZATION

Susana Rojas-Labanda[1] and Mathias Stolpe *[1]

[1]*Technical University of Denmark, DTU Wind Energy Department, Roskilde, Denmark*

Summary Structural topology optimization problems are commonly defined using material interpolation schemes. One of the challenges observed in the review article [3] for this density based topology optimization is the slow convergence of the solvers when an almost solid-and-void design is found. In this work, we numerically investigate the reasons for slowly moving boundaries, which are often encountered in practice, and attempt to indicate how this problem can be remedied.

INTRODUCTION

The recent review article [3] studies, among many other topics, the way optimization algorithms generate the designs in structural topology optimization. The design parametrization is based on density based topology optimization combined with the SIMP approach [2]. The review article [3] reports that "the optimization rapidly finds a fairly good design but requires a very large number of iterations for just slight improvements in objective function but rather large changes in geometry". Thus, the final geometry is found by slowly moving the boundaries. This behaviour is illustrated in [3] by two different examples, namely the inverter mechanism design and a minimum compliance problem resulting in a two-bar truss like structure.

The authors of [3] suggest that the underlying reasons for the slowly moving boundaries is the use of the SIMP approach. However, other reasons could be the choice of problem formulation, the choice of optimization algorithms, the choice of regularization technique, a combination of several of these issues, or even something completely different.

The problems presented in [3] are only formulated in the nested approach. In contrast, this note shows the results using also the Simultaneous Analysis and Design (SAND) formulation of the problem. Furthermore, only two numerical optimization algorithms were tested in [3], the Method of Moving Asymptotes (MMA) method [5] and the Optimality Criteria (OC) method [6]. These two algorithms are first-order methods developed for structural optimization. However, none of the general purpose state-of-the-art nonlinear methods have been tested. The benchmarking study in [1] suggests that interior point methods, such as IPOPT [4], work particularly well for structural topology optimization problems. In fact, since they are second-order methods, the number of iterations is considerably reduced. Furthermore, special purpose second-order optimization methods have been successfully implemented in [1] for the minimum compliance problem, such as TopSQP (Sequential Quadratic Programming solver) and TopIP (interior point method).

We expect that the issue of slowly moving boundaries in topology optimization problems can be avoided, or at least decreased, by using different optimization solvers. The numerical results in this work support our hypothesis and suggest that this issue can potentially be reduced or even remedied by changing optimization methods.

PROBLEM FORMULATION

The structural topology optimization problem which is considered throughout is the classical single load minimum compliance problem

$$\begin{aligned} \underset{\mathbf{t}}{\text{minimize}} \quad & \mathbf{u}^T(\mathbf{t})\mathbf{K}(\mathbf{t})\mathbf{u}(\mathbf{t}) \\ \text{subject to} \quad & v(\mathbf{t}) \leq V \\ & \mathbf{0} \leq \mathbf{t} \leq \mathbf{1}, \end{aligned} \tag{1}$$

where $v(\mathbf{t})$ is the volume of the structure described by the design variables $\mathbf{t}$ and $V > 0$ is the volume limit. The nodal displacements $\mathbf{u}(\mathbf{t})$ are obtained from the equilibrium equations $\mathbf{K}(\mathbf{t})\mathbf{u} = \mathbf{f}$. The stiffness matrix is described with $\mathbf{K}(\mathbf{t})$. More details about the formulation of the problem (in both nested and SAND formulation) can be found in e.g. [2] and [1].

NUMERICAL EXPERIMENTS

In [3] a simple minimum compliance problem, namely 2-bar (see Figure 1), is used to illustrate the slowly moving boundaries issue. The design domain is discretized using 50 by 20 elements, with a volume fraction equal to 0.2. A density filter is used to avoid checkerboards and mesh-dependency problems. The SIMP penalization parameter is set to $p = 3$. Finally, the contrast gap between the Young's modulus of the void and solid material is set to $E_0/E_{\min} = 10^3$ as in [1].

Two different initial designs are considered to compare and study the slowly moving boundaries behaviour as in [3]; an uniform density (of 0.2) and a solid bar in the middle of the domain satisfying the volume constraint, see Figure 1.

*Corresponding author. Email: srla@dtu.dk

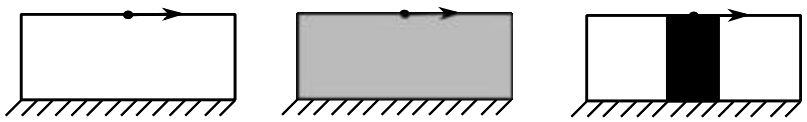

Figure 1: Design domain of the studied minimum compliance benchmarked problem (left), uniform density starting point (middle) and solid bar starting point (right).

Table 1: The table contains the objective function value and the number of iterations when the benchmarked problem is solved with MMA, TopSQP, TopIP, IPOPT-N and IPOPT-S. The table shows the results using two different starting points; the uniform design (U) and the solid band (S B).

Solver	MMA		TopSQP		TopIP		IPOPT-N		IPOPT-N*		IPOPT-S	
Initial point	U	S B	U	S B	U	S B	U	S B	U	S B	U	S B
Compliance	11.18	11.47	11.23	11.47	11.19	11.22	11.72	11.37	11.81	11.80	11.18	11.22
Iterations	40	173	34	108	58	48	60	266	74	111	50	85

Different optimization algorithms, such as MMA, TopSQP, TopIP (monotone approach), and IPOPT, are used to conduct the numerical experiments. In particular, the interior point solver in IPOPT is used to solve both the nested (IPOPT-N) and the SAND (IPOPT-S) formulation. All details of the parameter selection and implementation can be found in [1].

Table 1 shows the number of iterations and the objective function value at the local minima obtained by the solvers for the two different starting points. All the executions are run until some first-order necessary optimality conditions are numerically satisfied (norm of the KKT conditions is less than or equal to 10^{-4} for MMA and 10^{-6} for the rest).

For this particular problem, the slowly moving boundaries cannot be visually observed in most of the interior point methods presented, such as TopIP, IPOPT-S, and IPOPT-N* (monotone barrier parameter strategy selected with an initial barrier parameter value equal to 10). IPOPT-N uses a BFGS approximation while TopIP and IPOPT-S use the exact Hessian of the Lagrangian. Thus, the two latter solvers requires fewer iterations. In contrast, TopSQP behaves similar to MMA even if second-order information is used.

The reason of this performance is the ability of the interior point method to take advantage of the barrier function. Within few iterations, interior point methods modify the starting point to a "grey" design.

Nevertheless, further investigations are needed to avoid the slow moving boundaries when it is produced close to the optimal design, as in the inverter example. Since this effect occurs at the end of the optimization process, the barrier penalty parameter is very small and it will have very little effect in the solver.

CONCLUSIONS

The numerical results presented in Table 1 suggest (but by no means prove) that the choice of the optimization method might affect the slowly moving boundaries behaviour observed in the review article [3]. The remedy to this issue is thus to switch to second-order interior point solvers. However, this suggestion is only supported by a small and specific numerical experiment and must therefore be confirmed (or refuted) by additional and extensive numerical and theoretical surveys.

References

[1] Rojas-Labanda, S., Stolpe, M.: Mathematical programming methods for large-scale topology optimization problems. PhD Thesis, Technical University of Denmark, DTU Wind Energy PhD-0057, 2015.

[2] Bendsøe, M. P. and Sigmund, O.: Topology optimization: Theory, methods and applications. Springer, 2003.

[3] Sigmund, O. and Maute, K.: Topology optimization approaches. Structural and Multidisciplinary Optimization, 48(6):1031–1055, 2013.

[4] Wächter, A. and Biegler, L. T.: On the implementation of an interior point filter line-search algorithm for large-scale nonlinear programming. Mathematical Programming, 1(106):25–57. 2006.

[5] Svanberg, K.: The method of moving asymptotes - A new method for structural optimization. International Journal for Numerical Methods in Engineering, 24(2):359–373, 1987.

[6] Andreassen, E., Clausen, A., Schevenels, M., Lazarov, B.S. and Sigmund, O.: Efficient topology optimization in MATLAB using 88 lines of code. Structural and Multidisciplinary Optimization, 43(1):1–16, 2011.

TOPOLOGY OPTIMIZATION FOR ADDITIVE MANUFACTURING: CONSIDERING SUPPORT STRUCTURES THROUGH PROJECTED UNDERCUT PERIMETER

Xiaoping Qian *[1]

[1]*Department of Mechanical Engineering, University of Wisconsin-Madison, Madison, WI, USA*

Summary Additive manufacturing can build parts of complex shape through support structures. The fabrication of such support structures leads to the waste of the materials, build time and energy. This paper presents an approach for incorporating support structure consideration into topology optimization for additive manufacturing. A new measure based on the perimeter length of boundary with undercut, projected along the build direction, is developed to characterize the support volume. By constraining this projected undercut perimeter in topology optimization, the amount of support structures in the resulting designs can be effectively controlled. Our study has also revealed one interesting finding, that is, accounting for support structures in topology optimization can, in some cases, lead to designs with better performance, in addition to the reduction of support volume.

INTRODUCTION

Additive manufacturing builds part by depositing materials layer-by-layer under computer control. For part shapes with undercuts, sacrificial support structures are usually used to hold the subsequent layers. The fabrication of such support structures leads to the waste of the materials, build time and energy. Topology optimization [1] is a computational design tool that can generate optimal topology and shape under physical constraints. As a design tool, it has been become the method of choice for exploiting shape freedom of additive manufacturing. However, thus far, limited research [2] has been done in reducing support structures during the part design stage.

In order to consider support structures in topology optimization, a new measure based on the perimeter length of boundary with undercut, projected along the build direction, is developed in this paper to characterize the support volume. By constraining this projected undercut perimeter (PUP) in topology optimization, the amount of support structures in the resulting designs can be effectively controlled.

CONSIDERING PROJECTED UNDERCUT PERIMETER IN TOPOLOGY OPTIMIZATION

Our topology optimization formulation for considering support structures via PUP is as follows

$$\min_{\mathbf{u}\in U,\gamma} \quad C(\mathbf{u}) \qquad \text{Compliance} \tag{1a}$$

$$\text{s.t.} \quad a_E(\mathbf{u},\mathbf{v}) = l(\mathbf{v}), \forall \mathbf{v} \in U_0 \qquad \text{Equilibrium} \tag{1b}$$

$$\frac{\int_\Omega \gamma \ \mathrm{d}\Omega}{V_0} \leq \theta_0, \gamma[0,1] \qquad \text{Volume fraction constraint} \tag{1c}$$

$$\int_\Omega H(\mathbf{b}\cdot\nabla\gamma)\mathbf{b}\cdot\nabla\gamma \ \mathrm{d}\Omega \leq P_0 \qquad \text{Projected undercut perimeter constraint} \tag{1d}$$

$$\frac{\int_\Omega 4\gamma(1-\gamma) \ \mathrm{d}\Omega}{V_0} \leq \varepsilon_0 \qquad \text{Density grayness constraint,} \tag{1e}$$

where V_0 represents the volume of the design domain, θ_0 represents the allowed volume fraction of the material, P_0 represents the allowed projected undercut perimeter, and ε_0 the specified grayness measure [3]. In this formulation, equations (1a), (1b), (1c) form the standard formulation of density based topology optimization of a minimal compliance problem under an equilibrium equation and the volume constraint. In order to take into account the support structures, we here add two additional constraints with (1d) constraining the projected undercut perimeter and (1e) constraining the grayness in the resulting design.

For a density field γ, its spatial gradient $\nabla\gamma$ and directional gradient $\mathbf{b}\cdot\nabla\gamma$ along build direction $\mathbf{b}$, the LHS of (1d) represents the integration of the directional gradient multiplied with the Heaviside function $H(\mathbf{b}\cdot\nabla\gamma)$ over the design domain to obtain. Therefore, when the directional gradient $\mathbf{b}\cdot\nabla\gamma$ is negative, i.e. there is no undercut, this term does nothing. When it has undercut, i.e. the directional gradient is positive, it has contribution to the term in (1d). By constraining this term within a pre-specified value, we constraint the amount of support needed in a design.

*Email: xiaoping.qian@wisc.edu

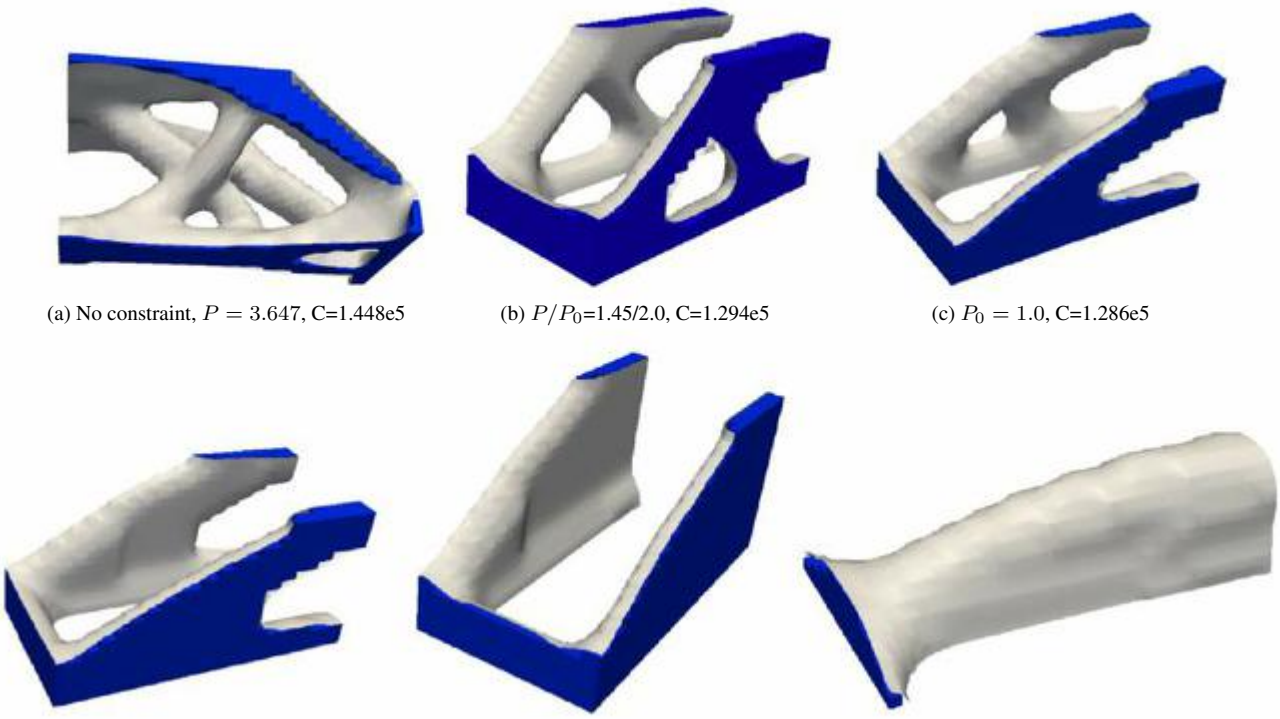

(a) No constraint, $P = 3.647$, C=1.448e5 (b) P/P_0=1.45/2.0, C=1.294e5 (c) $P_0 = 1.0$, C=1.286e5

(d) $P_0 = 0.5$, C=1.400e5 (e) $P_0 = 1.0$e-3, C=1.656e5 (f) P/P_0 =-0.02/1.0e-4, C=3.583e5

Figure 1: 3D minimal compliance optimization under different undercut perimeter constraint.

NUMERICAL RESULTS

Figure 1 shows optimized 3D designs under different projected undercut perimeter area. The domain is of size $4 \times 2 \times 2$ and is divided into 9,600 linear tetrahedral elements, consisting of 18,081 nodes. The volume fraction θ_0 is 15% of the design domain. The Young's modulus is 1 for solid and 10^{-9} for the void. The r in the PDE filter is 0.087. All designs are obtained with $\varepsilon_0 = 0.2$, except the last two designs. The last two designs are obtained with $\varepsilon_0 = 0.15$. Figure 1(a) shows two views of the optimized design without the PUP constraint and the compliance is 1.448e5. Optimized design under various PUP constraints and the corresponding compliance are shown in the figure. It can be seen that, as the PUP becomes smaller, the resulting designs have less support volume. In the end, when the PUP becomes close to zero, the resulting designs, Fig. 1(e) and (f), have no undercut. This suggests that the proposed PUP is an effective measure for controlling the support structures. Also, an optimized 3D design with PUP constraint does not necessarily lead to worse compliance since the design in Fig. 1(b), (c), and (d) are all have smaller compliance than the design in Fig. 1(a). This can be ascribed to the fact that multiple local minimums exist for the non-convex optimization problem.

CONCLUSIONS

This paper presents a formulation in topology optimization to take into account support structures via PUP and grayness constraints. Our numerical results demonstrate that PUP is an effective in controlling the amount of support in the optimized design. Accounting for support structures in 3D topology optimization for additive manufacturing may lead to designs with better performance, in additive to the reduction of support structures. This PUP formulation is also computationally efficient and involves just one extra constraint, without the need for solving any state equation.

References

[1] M.P. Bendsøe and O. Sigmund. *Topology Optimization: Theory, Methods, and Applications*. Springer Verlag, 2003.

[2] Andrew T Gaynor and James K Guest. Topology optimization for additive manufacturing: considering maximum overhang constraint. In *15th AIAA/ISSMO multidisciplinary analysis and optimization conference*, pages 16–20, 2014.

[3] Ole Sigmund. Morphology-based black and white filters for topology optimization. *Structural and Multidisciplinary Optimization*, 33(4-5):401–424, 2007.

OVERHANGING CONSTRAINTS IN ADDITIVE MANUFACTURING USING THREE DIFFERENT TOOLS

Simon Bauduin*[1], Maxime Collet[1], and Pierre Duysinx[1]
[1]*Aerospace and Mechanical engineering departement, University of Liege Liege, Belgium*

Summary As manufacturing methods undergo huge evolution thanks to the emergence of additive manufacturing techniques, the interest of a coupling with the topology optimization design tool is highly demanded by industries (such as automotive and aerospace). The challenges are still numerous around such coupling and this work focuses on the overhanging problem related to the metalic additive manufacturing technics (LBM and EBM). To tackle the problem, various research directions are investigated and compared to another.

INTRODUCTION

Topology optimization is widely used as a design tool for advanced application in mechanical, aerospace and automotive industries. This technique offers an optimal distribution of a predetermined amount of material in a given design space. In the last years, a lot of efforts has been invested into the development of high performance methods such as homogenization, SIMP or BESO. However as the state of the art in manufacturing experiences evolution, a coupling between topology optimization and additive manufacturing is needed.

Additive manufacturing has numerous advantages that fits the characteristics of topology optimized designs. It can manufacture highly complex design without high cost increase and furthermore continuous density material of the SIMP method could be manufactured by lattice structures. With all the opportunities given by the additive manufacturing the urge to bind the last one to topology optimization is heavily required.

Specific constraints related to manufacturing issues have to be taken into account [1] such as the need of supports structures to ensure a good heat evacuation during the manufacturing process, as well as to hold up overhanging section as shown in Figure 1. Some researches have been done to try to include this constraint in the optimization problem such as Leary and al [2] or Andrew T. Gaynor [3]. However this work focuses on 3 different methods (projection scheme, computer vision techniques and mechanical approach) to tackle the overhanging problem and compare them .

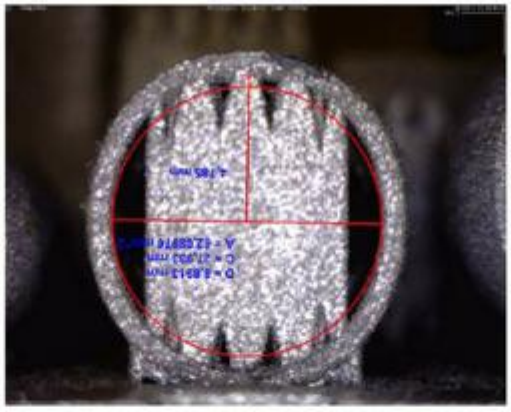

Figure 1: Overhanging problem

METHODS TO TACKLE THE OVEHANGING PROBLEM

Projection scheme Approach

The first approach to be investigated is similar to the idea proposed by Gaynor [3] in his work. A projection scheme [4] with particular shape has to ensure a self supported design. The choice of the shapes are guided by the need to have a big library of different shapes and the superformula of Geilis [5] offers us this diversity of the projective domain. The optimization problem can be expressed as fellows for the projection scheme:

*Corresponding author. Email: S.Bauduin@ulg.ac.be

$$\mathbf{min}_{\rho_n,u} \quad \mathbf{f^T u} \tag{1}$$

$$s.t. \quad \mathbf{K}\ \boldsymbol{\rho_n}\ \mathbf{u}\ /\ \mathbf{f} \tag{2}$$

$$\sum_{e\in\Omega} \rho^e\ \boldsymbol{\rho_n}\ v^e \leq V \tag{3}$$

$$\rho_n^{min} \leq \rho_n \leq 1\ \ \forall \mathbf{n} \in \boldsymbol{\Omega} \tag{4}$$

In the expression, the nodal densities n_i are linearly projected onto the element e if

$$dist_{n_ie} \leq r\ \theta_{n_ie}\ \ /\ \ \frac{1}{|\frac{1}{a}cos\ \theta_{n_ie}\frac{m}{4}\ |^{\ n_2}\quad |\frac{1}{b}sin\ \theta_{n_ie}\frac{m}{4}\ |^{\ n_3\ \frac{1}{n1}}} \tag{5}$$

Computer Visison Approach

The second approach tends to use the work done in computer vision researchers to construct the skeleton of the design and check if the latest does not show overhanging problem. This view of using computer vision technics in topology optimization problem was initially introduce by Sigmund [6] and opens up lots of new possibilities.

Body load Approach

The last approach relies more on a mechanical approach by adding body load cases [7] during the manufacturing process. Hence the optimization problem is formulated by introducing multiple body load cases to simulate the printing process and thus tackling the overhanging problem.

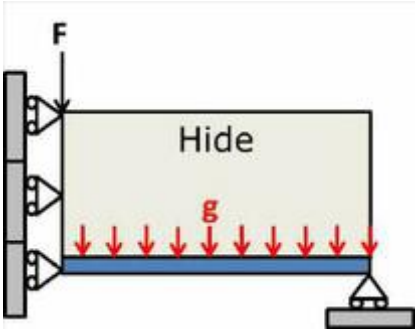

Figure 2: Body load approach

References

[1] B. Meunier : Perspectives de dveloppement pour le couplage optimisation topologique et fabrication additive de composants mecaniques. Master thesis, University of Liege, Liege, Belgium, 2014.

[2] M. Leary, L. Merli, F. Torti, M. Mazur, Milan Brandt : Optimal topology for additive manufacture: A method for enabling additive manufacture of support-free optimal structures. Materials & Design 63:678-690, 2014.

[3] Andrew T. Gaynor : TOPOLOGY OPTIMIZATION ALGORITHMS FOR ADDITIVE MANUFATURING. PhD Thesis, The Johns Hoptkins University, Baltimor, Maryland, USA, 2015.

[4] J. K. Guest, J. H. Prevost, T. Belytschko : Achieving minimum length scale in topology optimization using nodal design variables and projection functions. Int. J. Numer. Meth. Engng 61:238-254, 2004.

[5] J. Geilis : A GENERIC GEOMETRIC TRANSFORMATION THAT UNIFIES A WIDE RANGE OF NATURAL AND ABSTRACT SHAPES. Amercian Journal of Botany 90(3):333-338, 2003.

[6] O. Sigmund : Morphology-based black and white filters for topology optimization. Struct Multidisc Optim 33:401-424, 2007.

[7] M. Bruyneel, P. Duysinx : Note on topology optimization of continuum structure including self weight. Struct Multidisc Optim 29:245-256, 2005.

TOPOLOGY/SIZING OPTIMIZATION OF AICRAFT STRUCTURAL COMPONENTS

Vasily Chedrik[1a)], Sergey Tuktarov[1]
[1]*Central Aerohydrodynamic Institute (TsAGI), Zhukovsky, 140180, Russia*

Summary The application of energy-based topology optimization methods together with two-level design method for determination of structural sizes is considered. Main stages of such evolutionary approach to synthesis structural layouts of aircraft components are described. The approach is demonstrated on the example of structural optimization of helicopter wing and tail boom. It is shown that sizing optimization with including strength/buckling/aeroelasticity constraints results in to the design with significantly less weight compared with the one obtained by conventional approach.

INTRODUCTION

Nowadays, leading aviation companies often use topology optimization methods as an efficient tool for obtaining new and lighter structural component designs. Most of such researches are related with design of small structural parts such as ribs, spars, door intercostals, etc. [1]. The application of topology optimization for determination of reasonable structural layout was proven to result in advanced designs. Significant weight reducing is achieved after the sizing optimization of the obtained structural layout. The purpose of this research is to develop novel approach which combines modern topology optimization methods with two-level sizing optimization technique for design of larger aircraft components such as wing, tail and fuselage. Some approaches to design of wing structures with using topology optimization were demonstrated in the papers [2, 3]. The proposed method is based on the integration of the global-local method for sizing optimization described in [4] together with topology optimization in the unified cycle of multidisciplinary design which includes aerodynamic and aeroelasticity analyses.

METHODOLOGY OF TOPOLOGY/SIZING OPTIMIZATION

The general flow-chart of the developed approach is presented in Figure 1 on example of wing design. The first step of the procedure is to build solid topology optimization model and aerodynamic model which are specified by geometric outlines from CAD system. The specified geometric outlines of mechanical body define the place of load-bearing structure or design domain. Some part of the domain is supposed to be fixed and another part is subjected by external loads. The design domain is subdivided in detail on 3D finite elements for analysis of displacements and stresses.

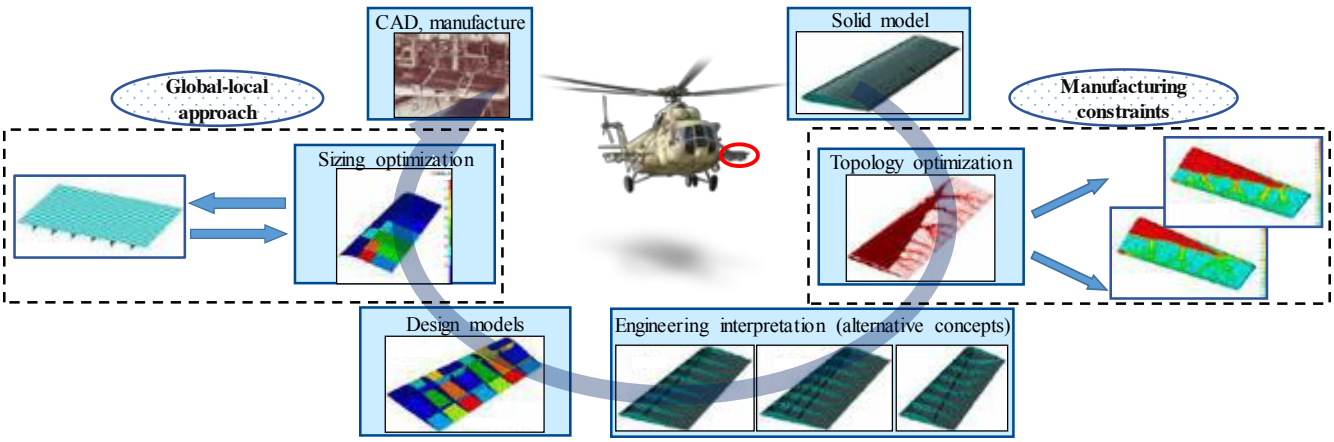

Fig. 1 – Flowchart of topology/sizing optimization

The second step is to perform a set of topology optimizations with different control parameters. The topology optimization results can be slightly different for these parameters. For example, manufacturing constraints with extrusion in vertical direction can give pattern with more explicit place for wing box. The obtained topology patterns allow us to reveal where load-bearing material should be located in global sense. Location of ribs is specified by intuition and then it can be determined by sizing optimization taking into account buckling constraints.

[a)] Corresponding author. Email: chedrik@yandex.ru.

The third step is most complicated and it implies engineering interpretation of the obtained topology results. It is difficult to determine one optimal structure. So we should imagine several alternative structural layouts to choose one of them as optimal. The forth step is generation of finite element models for the alternative structures. These structures we consider as shell/beam ones which usually include skins, ribs and spars. At generation of the models it is necessary to take into consideration various manufacturing constraints such location of control surfaces, fuel tanks and technology factors. The fifth step is accomplishment of design optimization for determination of sizes of structural elements with satisfying stress/buckling/aeroelasticity constraints. Stress and aeroelasticity constraints are involved into the optimization process on the global level model while the buckling constraints are engaged on the local level models of structural panels. The final step is ranking of obtained structural layouts based on comparison of optimal weights.

NUMERICAL RESULTS

The proposed method is demonstrated on the example of helicopter wing design. An aerodynamic model of the wing was developed to determine aerodynamic forces in extreme load cases and to perform aeroelasticity analyses. It was important for this problem to correctly transfer pressure loads from aerodynamic model to FE model. It was performed by interpolation of the obtained pressures with using polynomial function of nodal coordinates on outer surfaces of the FE model. Topology optimization was performed with the aim to minimize compliance at saving 50 percent of initial solid model weight in the final design. The obtained patterns where the load-bearing material should be distributed are shown in Figure 1 (right). Seven alternative structural layouts based on these results and engineering intuition were proposed. The structural optimization under strength/buckling/aeroelasticity requirements for the layouts leads to the final optimal design with different weight values. Comparison of the chosen alternative structural layouts with optimal distribution of material showed that the weight benefit was about 10 percent owing to the choice of location of the primary elements. The best structural layout is two-spar wing with additional sloped ribs at the wing end rear part. Note that this design is lighter by 60% than the design obtained by traditional methods used in design companies. The second example is a helicopter tail boom. The optimization procedure and topology and sizing results are presented in pictures in Figure 2.

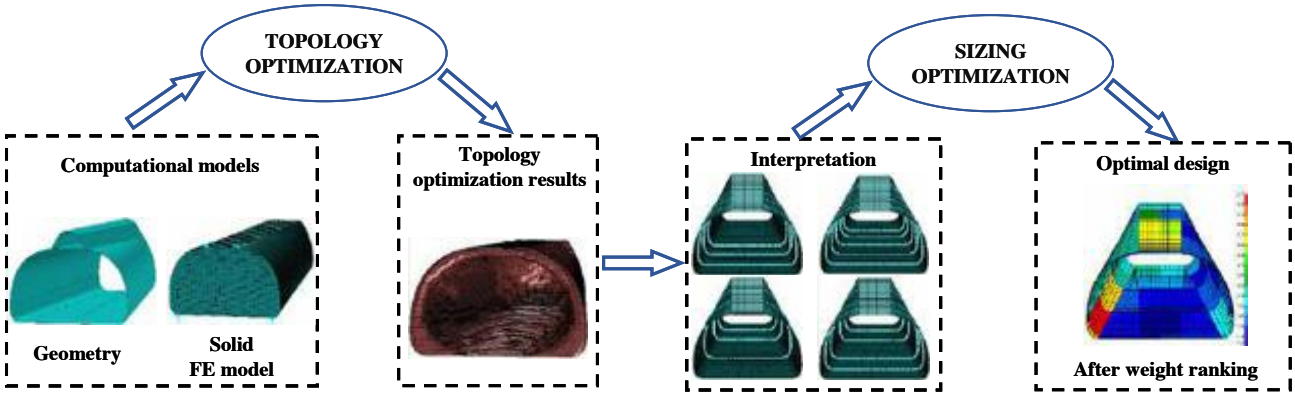

Fig. 2 – Optimization results for helicopter tail boom structure

The solid finite element model was generated based on CAD drawing and the nodes of its larger section were fixed. Forces which modelled vertical/horizontal bending and torsion were applied to the nodes on the opposite section. Two extreme load cases were considered. Topology optimization was performed at saving 30 percent of initial weight in the final design. It can be seen that the obtained design can be treated as a semi-monocoque, namely a structure including stiffened shell. Such structure is traditional for aircraft fuselages. In this example the topology optimization results show some regions which can be considered as design variables for sizing optimization. Four alternative structural layouts were proposed based on the topology pattern. Strength/buckling optimization identified optimal design which had three frames separating the regions of different panel thicknesses.

References

[1] Krog L., Tucker A., Kemp M. and Boyd R.: Topology optimization of aircraft wing box ribs. 10th AIAA/ISSMO Multidisciplinary Analysis and Optimization Conference, 2004, Albany, New York, USA.

[2] Eves J., Toropov V.V., Thompson H.M., Gaskell P.H., Doherty J.J., Harris J.C.: Topology Optimization of Aircraft with Non-Conventional Configurations. 8th World Congress on Structural and Multidisciplinary Optimization, 2009, Lisbon, Portugal, WCSMO-8.

[3] Chedrik V.V., Tuktarov S.A.: Structural design of aircraft wing based on topology and global-local optimization. 11th World Congress on Structural and Multidisciplinary Optimization, 2015, Sydney, Australia, WCSMO-11.

[4] Chedrik V.V., Tuktarov S.A.: Optimization of Composite Structures Based on Global-Local Approach. International Conference on Engineering and Applied Sciences Optimization, 2014, Kos, Greece, ISBN:978-960-99994-5-8, OPT-*i*.

DESIGN OF HOMOGENIZED MICROSTRUCTURES USING STRESS-BASED TOPOLOGY OPTIMIZATION

Maxime Collet *[1], Matteo Bruggi[2], Lise Noël[3], Simon Bauduin[4], and Pierre Duysinx[5]
[1,3,4,5]*Aerospace and Mechanical Engineering Department, University of Liège, Liège, Belgium*
[2]*Department of Civil and Environmental Engineering, Politecnico di Milano, Milan, Italy*

Summary This paper aims at designing microstructures using stress-based topology optimization. Most of the developments so far have been made for compliance design in various field of applications as reflected in the literature. The emergence of the new additive manufacturing techniques allows to consider porous material, such as lattice structures for instance, which ca be used for the design of structural components subject to various solicitations. Those components must account for the stress level to prevent failure everywhere in the microstructures and by extension the whole structure itself. This work proposes to design such microstructures using topology optimization with limitation on the stress level within the microstructures before printing the result. The homogenization technique is used to determine the equivalent material properties. The issues and perspectives are also discussed.

ABSTRACT

Topology optimization aims at giving the optimal distribution of the material within a design domain, enabling to place the material where it is the most efficient while staying with void in less effective regions. Problems based on the discrete valued approach (0-1) of the optimal distribution of material are difficult to solve numerically but they are also ill-posed exhibiting convergence issues. To overcome this difficulty, Bendsøe and Kikuchi [2] proposed to relax the problem by introducing porous material, made of an infinite number of holes, whose effective properties can be computed thanks to the homogenization techniques, see e.g. Hassani and Hinton [4, 5, 6]. Even if the numerical solution of the problems is tractable, the manufacturability of the optimized design based on classic machine tooling techniques is not straightforward. Thus clear designs, i.e. nearly black-and-white designs, can be enforced by introducing a penalization of intermediate densities. To this end, a successful approach is the famous SIMP approach as proposed in Bendsøe. [3]. However nowadays, thanks to the emergence and the effectiveness of the novel additive manufacturing techniques, structures including regions made of porous microstructures are now becoming possible to fabricate and topology optimization using homogenization methods receive a revived interest as attested by recent works of Andreassen et al [1] and Xia [8]. The practical applications of these designs including microstructures is motivated by the great performances that can be achieved compared to classical solutions of topology optimization.

In this work, a stress based–topology optimization procedure is considered along with the homogenization technique for the computation of the equivalent material properties of the porous material. Most of the contributions dealing with the design of porous material are indeed focused on compliance minimization in a wide variety of applications. The design using stress–based topology optimization is however gaining in interest, as pointed out by Le et al [7], and it has become critically important to account for the strength of the microstrucutres and not only their stiffness. To this end, we investigate here the problem of bounding the stress level within microstructures, problem that has not been much considered so far, to the author knowledge. The design problem is to find the optimal material distribution within the periodic base cell subject to prescribed macro strains and bounded stress criterion everywhere in the microstructure and *de facto* ensure the structural intregrity of the whole component.

The adopted approach continues along the work developed by the authors. The SIMP approach is adopted while a sequential convex programming approach using MMA is used to solve the optimization problems. The paper discusses the design problem formulation as well as the choice of the considered failure criterion (von Mises, principal stresses, etc) while solving numerical applications. The numerical procedure is at first validated against some analytical results proposed by Vigdergauz [9, 10] for a single inclusion before investigating more complex loading conditions. Design obtained with pure stress–based topology optimization is compared to a formulation embedding both stress constraints and a global compliance constraint. The former method has proven to exhibit better numerical performances, i.e. reduced CPU time . The work focuses also on an efficient and accurate way to measure the stress field coming from the solution of the adopted finite element procedure. Numerical issues and perspectives for further works are also discussed.

Finally the optimized designs are fabricated using a multimaterial inkjet polymer printer (Connex by Stratasys) to assess the actual performance of the optimized designs compared to more conventional results such as compliance–based designs.

ACKNOWLEDGMENTS

The first author, Maxime Collet and author Lise Noël, would like to acknowledge the Belgian National Fund for Scientific research (FRIA and FNRS) for their financial support. Part of this work has been supported by the Walloon Region of Belgium and SKYWIN (Aerospace Cluster of Wallonia), through the project AERO+(contract RW 7445)

*Corresponding author. Email: maxime.collet@ulg.ac.be

References

[1] Andreassen, E., Jensen, J. S., Sigmund, O., & Thomsen, J. J. (2015). Optimal Design of Porous Materials. DTU Mechanical Engineering. (DCAMM Special Report; No. S172).

[2] Bendse, M.P. and Kikuchi N. (1988). Generating Optimal Topologies in Structural Design Using a Homogenization Method. Comp. Meth. in Appl. Mech Engng. 71, 197-224

[3] Bendsoe M.P. (1989) Optimal shape design as a material distribution problem. Structural Optimization 1, 193-202.

[4] Hassani B., Hinton E. (1998) A review of homogenization and topology optimization I- homogenization theory for media with periodic structure. Computers and Structures 69:707-717

[5] Hassani B., Hinton E. (1998) A review of homogenization and topology optimization II -homogenization theory for media with periodic structure. Computers and Structures 69:719-738

[6]] Hassani B., Hinton E. (1998) A review of homogenization and topology optimization III- homogenization theory for media with periodic structure. Computers and Structures 69:739-756

[7] Le C., Norato J., Bruns T., Ha C., Tortorelli D.(2010) Stress-based topology optimization for continua. Struct Multidisc Optim 41:605-620.

[8] Xia L. (2015) Towards Optimal Design of Multiscale Nonlinear Structures. PhD Thesis, Universit de Technologie de Campigne. Novembre 2015.

[9] Vigdergauz S. (1994). Two dimensional grained composites of extreme rigidity J. of Applied Mechanics 61(2), 390-394.

[10] Grabovsky Y and Kohn R. (1995). Microstructures minimizing the energy of a two phase elastic composite in two space dimensions. II: The vigdergauz microstructure. Journal of the Mechanics and Physics of Solids. 43 (6), 949972

A NOVEL TOPOLOGY OPTIMIZATION METHOD FOR PERIODICAL CELLULAR MATERIALS

Jie Gao[1], Liang Gao[1a)] & Mi Xiao [1] & Hao Li [1]& Zhen Luo[2]
[1]*The State Key Laboratory of Digital Manufacturing Equipment and Technology, School of Mechanical Science and Engineering, Huazhong University of Science and Technology, Wuhan, China*
[2]*School of Mechanical and Mechatronic Engineering, The University of Technology Sydney, Sydney, Australia*

Summary The design of periodic microstructural composite materials to attain specific properties has been carried out by a new combination method of the parametric level set method (PLSM) and the energy-based homogenization method (EBHM) in this article. The PLSM is utilized to determine microstructural architecture of the representative volume element (RVE) in composites. And its objective function is defined by the EBHM which is employed to predict specific material properties. The key characteristic of the PLSM is that the implicit level set function is interpolated by a series of compactly support radial basis functions (CSRBF). Besides, the EBHM eliminates the bound of macro structure and material microstructure design based on the energy principle and has an easier numerical implementation compared with the numerical homogenization method. Finally, some optimal microstructures are achieved by the proposed method, and which validate the design capability and favourable features compared with the other design method.

PARAMETRIC LEVEL SET METHOD

The level set method has become popular recently for tracking and modelling the motion of a dynamic interface. Because many favourable characteristics of the PLSM [1] are quite benefit to numerical implementation, it is chosen as the basis of the microstructural optimization formulation, and which is to determine the layout of materials with a specified volume fraction in the RVE. The mathematical formulation could be approximately divided into four key parts. The first part is that the structural design boundary is implicitly described by the zero level set of a higher dimension scalar function, the dynamic evolution of design boundary is equivalent to propagating the LSF. The second part is that the dynamic evolution process of structural boundary is formulated by the rigorous mathematical function. The structural design domain is modeled as the zero level set and updated with the merging and splitting of the design boundary. By introducing a pseudo-time t into zero level set function and then differentiating on both sides with respect to time, the motion of the structure boundary is modelled by a first-order H-J PDE. It is shown at Eq (1).

$$\frac{\partial \Phi(\mathbf{x},t)}{\partial t} + \mathbf{v}\cdot\nabla\Phi(\mathbf{x},t) = 0 \tag{1}$$

The intention of the third part is to eliminate these poor numerical features of the standard LSM based on above two parts. The LSF is interpolated by a series of compactly supported radial basis functions (CSRBF) and unknown expansion coefficients, so that the time and space have been decoupled in LSF. It is shown as follows:

$$\Phi(\mathbf{x},t) = \left(\boldsymbol{\varphi}(\mathbf{x})\right)^T \boldsymbol{\alpha}(t) = \sum_{i=1}^{N} \phi_i(x)\alpha_i(t) \tag{2}$$

The Eq (2) has shown that the LSF have been completely transformed into a linear algebraic system equation based on the discretized design domain. The final part is that the velocity function is computed by the shape derivative analysis.

ENERGY-BASED HOMOGENIZATION METHOD

The homogenization theory [2] is built on the small asymptotic expansion theory, and which is utilized to evaluate the homogenized effective properties of the periodical composites from directly analysing its periodic RVE. The homogenized effective elasticity tensor and the subjected elasticity equilibrium function are reflected at Eq (3).

$$\begin{cases} E^H_{ijkl} = \dfrac{1}{|\mathrm{Y}|}\displaystyle\int_\Omega \left(\varepsilon^{0(ij)}_{pq} - \varepsilon^{*(ij)}_{pq}\right)^T E_{pqrs}\left(\varepsilon^{0(kl)}_{rs} - \varepsilon^{*(kl)}_{rs}\right) d\Omega \quad (i,j,k,l = 1,2,\cdots,d) \\ \displaystyle\int_\Omega E_{ijpq}\varepsilon^{*(kl)}_{rs}\frac{\partial v_i}{\partial y_j} d\Omega = \int_\Omega E_{ijpq}\varepsilon^{0(kl)}_{rs}\frac{\partial v_i}{\partial y_j} d\Omega \quad \forall v_i \in H_{per}\left(\Omega, \mathbf{R}^3\right) \end{cases} \tag{3}$$

The Eq (3) could be transformed into the sum of the integration of the finite-element based on the FEA.

$$E^H_{ijkl} = \sum_{e=1}^{NE}\left\{\frac{1}{|\mathrm{Y}_e|}\left(\int_{\Omega_e}\left(\varepsilon^{0e(ij)}_{pq} - \varepsilon^{*e(ij)}_{pq}\right)^T E_{pqrs}\left(\varepsilon^{0e(kl)}_{rs} - \varepsilon^{*e(kl)}_{rs}\right) d\Omega_e\right)\right\} \tag{4}$$

Observing the marked Eq (4), the part surrounded by the dotted red line could be interpreted as the average strain energy of each finite-element, and which is named by the element mutual energy densities [3]. Hence, it is important to note that the elasticity tensor is calculated by the summation of the element mutual energy densities. It is necessary to build appropriate boundary conditions in order to evaluate element mutual energy based on the FEA.

a) Corresponding author. Email: gaoliang@mail.hust.edu.cn.

MICROSTRUCTURAL DESIGN MODEL AND SENSITIVITY ANALYSIS

The intention of material design [4] is defined by seeking optimal configuration of the RVE in order to obtain the improved homogenized properties. In this article, a new systematic design method is constructed by integrating the PLSM with the EBHM. The material microstructural optimization formulation is defined as follows:

$$\begin{aligned} &\underset{\left(\mathbf{u}^*,\Phi\right)}{Minimize}: J\left(\mathbf{u}^*,\Phi\right)=\sum_{i,j,k,l=1}^{d}\eta_{ijkl}E_{ijkl}^{H} \\ &Subject\ to: \begin{cases} V\left(\Phi\right)=\int_{\Omega}H\left(\Phi\right)d\Omega-V_{max}\le 0 \\ a\left(\mathbf{u}^*,\mathbf{v},\Phi\right)=l\left(\mathbf{v},\Phi\right)\quad \forall\,\mathbf{v}\in H_{per}\left(\Omega,\mathbf{R}^3\right) \\ \alpha^L\le\alpha_i\le\alpha^U\quad \left(i=1,2,\cdots,NE\right) \end{cases} \end{aligned} \tag{5}$$

The OC method is employed to update design variables in the proposed method, and which requires first-order derivatives of the objective function and volume constraint function with respect to design variables. as follows:

$$\frac{\partial J}{\partial\boldsymbol{\alpha}}=\sum_{i,j,k,l=1}^{d}\left(\eta_{ijkl}\frac{\partial E_{ijkl}^{H}}{\partial\boldsymbol{\alpha}}\right)=\frac{1}{\left|\mathrm{Y}\right|}\left(\sum_{i,j,k,l=1}^{d}\left(\eta_{ijkl}\int_{D}\left(\varepsilon_{pq}^{0(ij)}-\varepsilon_{pq}^{*(ij)}\right)^{T}E_{pqrs}\left(\varepsilon_{rs}^{0(kl)}-\varepsilon_{rs}^{*(kl)}\right)\boldsymbol{\varphi}\left(\mathbf{x}\right)^{T}\delta\left(\Phi\right)d\Omega\right)\right) \tag{6}$$

NUMERICAL EXAMPLES

In all examples, the Young's modulus are defined $E_0^S=1$ of the solid phase, and $E_0^V=0.001$ of the void phase. The Possion's ratio are equal 0.3. The lower and upper bounds of design variables $\boldsymbol{\alpha}$ are defined as $\alpha^L=2\times min\left\{\alpha_i\right\}$ and $\alpha^U=2\times max\left\{\alpha_i\right\}\left(i=1,2,\cdots,NE\right)$ in OC method. Finally, the optimization will be terminated when the difference of objective functions between two successive steps is less than 10-4.

Parameters	PLSM + EBHM	3*3 Repetitive RVE	PLSM + NHM	J
0.40 120×120 Bulk modulus $J=K=\sum_{i,j=1}^{2}E_{iijj}^{H}$	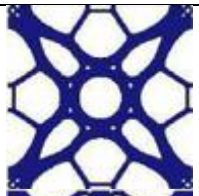	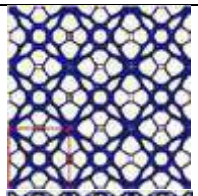		0.136
0.50 100×100 Shear modulus $J=G=E_{1212}^{H}$		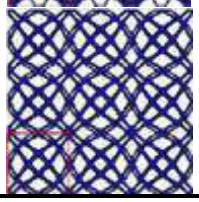		0.130

Tab 1: the optimal configuration of the RVE in different parameters

CONCLUSIONS

In conclusion, a new systematic, scientific and efficient computation design method is proposed to design the cellular material microstructure, and which optimize the shape and topology of the RVE by the PLSM subjected to the objective function defined by the EBHM. Based on above results, it is summarized that the optimized results have the distinct and smooth structure boundary and the optimal microstructures derived by two different homogenization methods are mostly identical.

Acknowledgments

This work was supported by the National Basic Research Plan of China under Grant [number JCKY2016110C012].

References

[1] Luo, Z., et al.: A level set-based parameterization method for structural shape and topology optimization. Int. J. Numer. Methods Eng. 76:1-26, 2008.

[2] Sigmund, O.: Materials with prescribed constitutive parameters: an inverse homogenization problem. Int. J. Solids Struct. 31:2313-2329, 1994.

[3] Xia L., et al.: Design of materials using topology optimization and energy-based homogenization approach in Matlab. Struct. Multidiscip. Optim. 52: 1229-1241. 2015.

[4] Cadman, J.E., et al.: On design of multi-functional microstructural materials. J. Mater. Sci. 48: 51-66. 2012.

TOPOLOGY OPTIMIZATION USING BERNSTEIN BASIS POLYNOMIALS

Andrew Lambe*[1] and Aleksander Czekanski[1]
[1]*Department of Mechanical Engineering, York University, Toronto, Ontario, Canada*

Summary A new method for density-based topology optimization is presented in which the density field is parametrized using Bernstein polynomial basis functions on a finite-element mesh. This parametrization permits a continuous variation of the density between mesh elements to suppress checkerboards without a filter. In addition, rather than refining the design variable mesh, the material boundary is more accurately captured by elevating the order of the basis functions. Standard meshing techniques may be used to define the design variable mesh, even with complex domain shapes, and different meshes may be used to define the design variables and the finite element analysis. Results are presented for two structural topology design problems.

DENSITY FIELD PARAMETRIZATION

In density-based topology optimization with element-based design variables, each finite element is assigned a design variable to indicate whether that element is solid material or void. Important issues with optimal solutions computed using element-based design variables include checkerboards of solid and void elements, ragged edges of features not aligned with the design mesh, and mesh-dependence of the optimal topology. Typically, these issues are mitigated using a filter. In a filter, the density value of a given element is computed using a weighted average of the density variables in a small neighborhood of that element. This approach leads to a "gray" transition between solid and void regions whose size depends on the filter size. Material boundaries are then identified using a projection method.

Several alternative density-field parametrizations also exist to mitigate the issues identified above without using filters. Matsui and Terada [1] assign design variables to linear shape functions to define a continuous distribution of the density field. Ngyuen et al. [2] define a multiresolution topology optimization scheme (MTOP) in which each element contains many constant-density regions with corresponding design variables. Kang and Wang [3] assign density design variables to points in the domain and use Shepard interpolation to compute the density at any other point in the domain. Qian [4] embeds the design domain in a tensor-product B-spline mesh and assigns design variables to the B-spline basis functions.

We propose a density field parametrization based on Bernstein polynomial basis functions. The degree-n basis functions are given by

$$b_{k,n}(x) = \binom{n}{k} x^k (1-x)^{n-k} \quad k = 0, ..., n. \tag{1}$$

Over the interval $x \in [0, 1]$, these $n + 1$ functions are nonnegative and sum to one regardless of the choice of n. These properties make the Bernstein polynomials ideal for parametrizing a density field whose values must stay between zero and one. Figure 1 shows the cubic Bernstein polynomials as basis functions for two adjacent one-dimensional elements, compared to the cubic Lagrange polynomials over the same interval. Figure 2 shows two example basis functions for adjacent square elements.

This particular parametrization has several attractive features. First, we are not restricted to using linear basis functions, so more detailed features of the density field may be revealed with fewer elements. Second, the support size of the basis

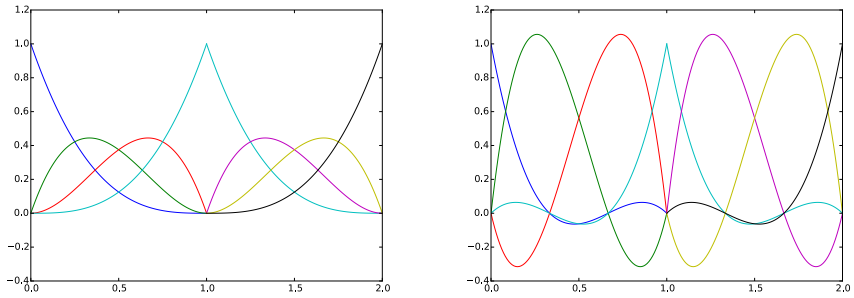

Figure 1: The cubic Bernstein polynomials (left), unlike the cubic Lagrange polynomials (right), never take values greater than one or less than zero.

*Corresponding author. Email: alambe@yorku.ca

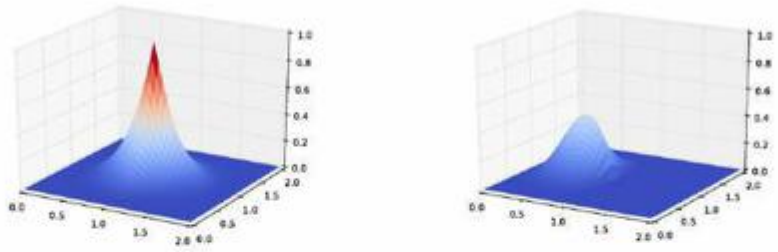

Figure 2: Bicubic Bernstein basis functions for square Q16 elements. The left image shows a nodal basis function while the right shows a basis function on the edge between elements.

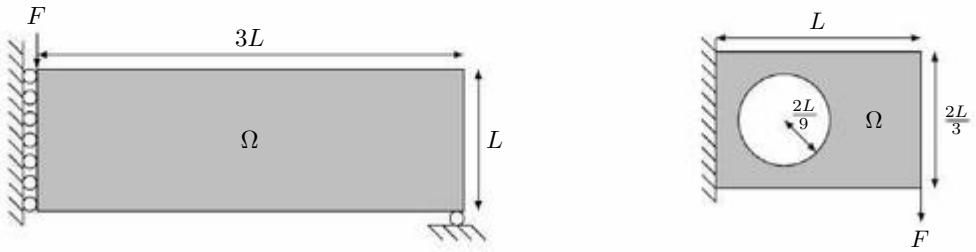

Figure 3: Design domains of (left) the MBB beam and (right) the cantilever beam with a circular hole.

functions is restricted to adjacent elements, so feature size control is naturally integrated into mesh generation and refinement. Third, the parametrization may be applied to domains with complex geometry and may use a different mesh than that used in the finite element analysis. Finally, analogous to an h-p finite element method, the design variable mesh may be refined using both element size reduction and order elevation.

TEST PROBLEMS

We study two example problems from the literature: the classical MBB beam problem and a cantilever beam with a circular hole. Figure 3 shows the geometry and boundary conditions for these problems. The objective of both optimization problems is to minimize the compliance of the loaded structure subject to a volume fraction constraint of 0.5. We use deal.ii [5] for the design variable parametrization and finite element analysis and IPOPT [6] for the optimization.

Our results demonstrate the absence of checkerboard patterns in our optimized designs and the recovery of well-known topologies. We also show the effect of using higher-order basis functions on the optimal designs, especially on the identification of the material boundary with a coarse design variable mesh. Finally, we conduct a preliminary study of refining the design variable mesh using both element size reduction and order elevation.

References

[1] Matsui, K., Terada, K.: Continuous approximation of material distribution for topology optimization. Int. J. Numer. Meth. Engng. 59:1925–1944, 2004.

[2] Ngyuen, T.H., Paulino, G.H., Song, J., Le C.H.: A computational paradigm for multiresolution topology optimization (MTOP). Struct. Multidisc. Opt. 41:525–539, 2010.

[3] Kang, Z., Wang, Y.: Structural topology optimization based on non-local Shepard interpolation of density field. Comput. Methods Appl. Mech. Engrg. 200:3515–3525, 2011.

[4] Qian, X.: Topology optimization in B-spline space. Comput. Methods Appl. Mech. Engrg. 265:15–35, 2013.

[5] Bangerth, W., Hartmann, R., Kanschat, G.: deal.II – a general purpose object oriented finite element library. ACM Trans. Math. Softw. 33:24/1–24/27, 2007.

[6] Wachter, A., Biegler, L.: On the implementation of a primal-dual interior point filter line search algorithm for large-scale nonlinear programming, Mathematical Programming 106:25–57, 2006.

STRENGTH-BASED EVOLUTIONARY STRUCTURAL OPTIMIZATION

Chih-Hung G. Li
Department of Mechanical Engineering, Ming-Hsin University of Science and Technology, Hsinchu, Taiwan, ROC

Summary Here the author reports a novel structural design optimization method that deals with the orthotropic strength properties of Fused Deposition Modelling (FDM) structures. The proposed Strength-Based Evolutionary Structural Optimization (SBESO) method inherits the concept of the traditional ESO with a new severeness index to evaluate the stresses in all directions based on the orthotropic strengths. Material rejection in the finite element analyses and the topology evolution is performed based on the proposed severeness index.

INTRODUCTION TO THE PROBLEM

Fused Deposition Modelling (FDM) is a popular type of 3D printing technology, where molten material is ejected through a nozzle and deposited layer by layer to form a 3D object. Various thermoplastic polymers such as acrylonitrile butadiene styrene (ABS), polycarbonate (PC), or the others in the form of a filament are used as the raw material. It has been discovered that the structures fabricated using the FDM method exhibit significant anisotropy in the ultimate strength [1]. In the preliminary testing performed by the author for the properties of the FDM structures, similar results were observed. The ultimate strengths were found to be 26.5MPa along the filament direction, 11.98MPa in the direction normal to the filament, and 18.67MPa for shear. When forming a design guide for the designer aiming at achieving mass optimized FDM structures, such anisotropy should be considered for better accuracy. In this research, the author adopted the concept of the Evolutionary Structural Optimization (ESO) method for its simplicity and ease of implementation [2], noting that other sophisticated methods for topology optimization exist [3]. A Strength-Based ESO (SBESO) was devised to reflect the orthotropic strength characteristics of the FDM structures. A severeness index was defined to evaluate the stresses, instead of the von Mises stress commonly used for isotropic materials. The ultimate strengths mentioned above were used as the reference for calculating the severeness index of each stress component of each finite element. In this study, the SBESO was demonstrated with a short cantilever problem. A strategy of direct incrementing and fixed material removal rate was also adopted [4].

OPTIMIZATION PROCESS

The optimization process is detailed in Figure 1. A finite element model of the design envelop was first created with boundary conditions applied. The calculated stress components of each finite element were used to compute the severeness indices by taking the ratio of the stress to the strength. For each finite element, the maximum severeness index among the six components would be taken as the representative index of that element. All the elements would then be ranked based on the representative index, and the lowest 1% of the elements would be rejected for the next finite element calculation until a desired percentage of total material removal has been achieved.

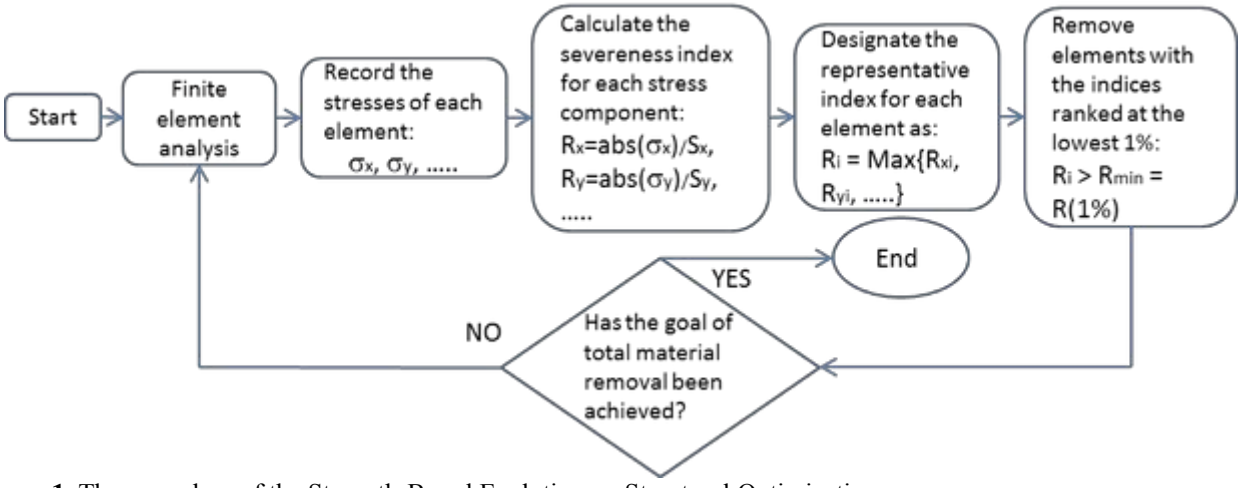

Figure 1. The procedure of the Strength-Based Evolutionary Structural Optimization.

RESULTS AND DISCUSSIONS

A plane stress short cantilever problem was attempted using the proposed SBESO. The length of the beam is twice as much as the height; line constraints were applied at the right side of the beam, and a point load was applied at the bottom

[a] Corresponding author. Email: cL4e@must.edu.tw.

left corner (Figure 2 (a)). The optimized topology of the three cases calculated was shown in Figure 2. For the isotropic case, von Mises stress was used for evaluation. In the horizontal case, the filament direction was assumed to be horizontal; in the vertical case, the filament was vertical. The finite element model has 5000 elements in total. For each calculation increment, 1% of the total elements that have the lowest severeness indices were rejected. Thus, the volume fraction was controlled to be steadily decreasing until 20% as shown in Figure 3(a). The conventional rejection rate and evolutionary rate were not adopted [2]. However, for comparison reason, equivalent rejection rates were calculated by taking the ratio of the rejected severeness index to the maximum severeness index for every increment. The results were also shown in Figure 3(a). Note that although the evolutionary process of the topology was not driven by the rejection ratio, the history of the rejection ratio exhibits a similar increasing trend with progressing evolution. As a rough confirmation of the effectiveness in topology optimization, the collective representative severeness indices of the final models were compared with each other, along with some arbitrary topology (see Figures 2(e)&(f) and 3(b)&(c)). The optimized topology appears to have the lowest deviation from the average severeness index, indicating the highest efficiency in material usage in terms of stress distribution.

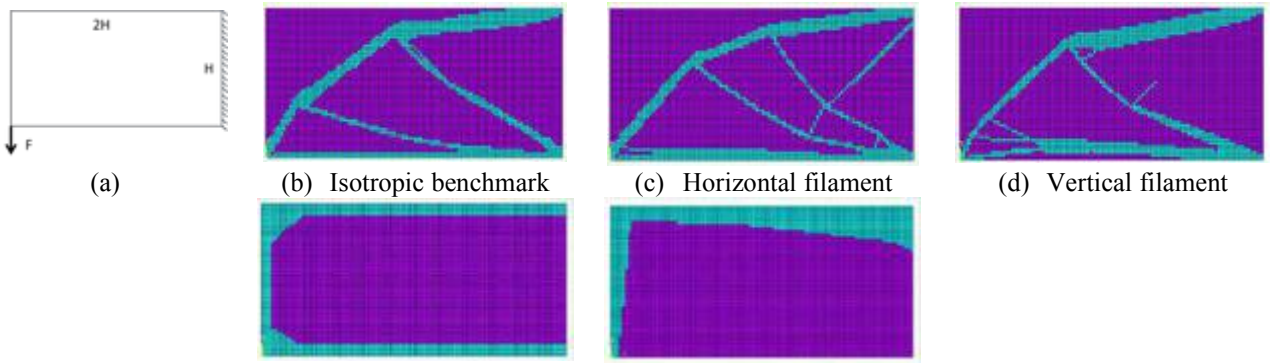

(a) (b) Isotropic benchmark (c) Horizontal filament (d) Vertical filament

(e) Arbitrary design 1 (f) Arbitrary design 2

Figure 2. The problem of a short cantilever beam: (a), and the results of the optimized topology: (b), (c), & (d). Arbitrary designs for comparison: (e) & (f).

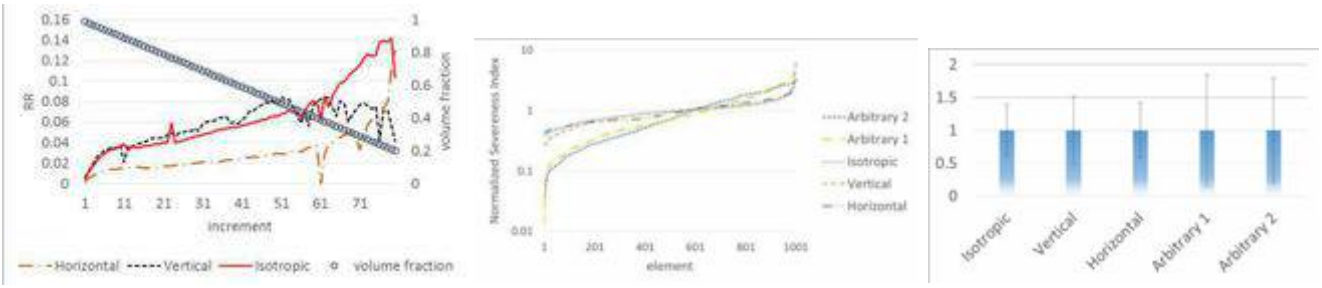

(a) (b) (c)

Figure 3. (a) Evolutionary histories of the equivalent rejection ratio and the volume fraction; (b) Distributions of the normalised severeness indices of the final models; (c) Averages and standard deviations of the normalized severeness indices.

CONCLUSIONS

A Strength-Based Evolutionary Structural Optimization method was proposed for the structures of the Fused Deposition Modelling, which exhibits significant orthotropy in the ultimate strength. Instead of using the von Mises stress as the rejection index, a severeness index for each stress component was defined, and the maximum value among the six components was taken as the representative index of every finite element. A strategy of direct incrementing and fixed material removal rate was also adopted. Results of a short cantilever problem showed that the optimized topology exhibited the highest efficiency in material usage in terms of stress distribution while compared with some arbitrary designs.

References

[1] Ahn S.H., Montero M., Odell D., Roundy S., Wright P.K.: Anisotropic Material Properties of Fused Deposition Modeling ABS. *Rapid Prototyping J*. 8(4):248-257, 2002.

[2] Xie Y.M., Steven G.P.: Evolutionary Structural Optimization. Springer, London 1997.

[3] Bendsøe M.P., Sigmund O.: Topology Optimization: Theory, Methods, and Applications. Springer, Berlin 2004.

[4] Li C. G.: Design of the Lower Chassis of a Monorail Personal Rapid Transit (MPRT) Car Using the Evolutionary Structural Optimization (ESO) Method. *Struct Multidisc Optim* (in press).

TOPOLOGY OPTIMIZATION of CONTACT PROBLEMS using CAHN-HILLIARD REGULARIZATION

Andrzej Myśliński*[1]

[1]*Systems Research Institute, Warsaw, Poland and Faculty of Manufacturing Engineering, Warsaw University of Technology, Warsaw, Poland*

Summary The paper is concerned with the topology optimization of elastic bodies in unilateral contact with a given friction. The aim of the optimization problem is to find such distribution of the material density function to minimize the normal contact stress. The phase field approach is used to analyze and solve numerically this optimization problem. The original cost functional is regularized using Ginzburg-Landau free energy functional including the surface and bulk energy terms. These terms allow to control global perimeter constraint and the occurrence of the intermediate solution values. The Lagrangian approach is used to calculate the derivative of the regularized cost functional and to formulate a necessary optimality condition. The optimal topology is obtained as the steady state of the phase transition governed by modified Cahn-Hilliard equation. The finite difference and finite element methods are used as the discretization methods. Numerical examples are provided and discussed.

TOPOLOGY OPTIMIZATION PROBLEM

Consider deformations of an elastic body occupying two–dimensional domain Ω with the smooth boundary Γ [6]. The body is subject to body forces $f(x) = (f_1(x),\ f_2(x)),\ x \in \Omega$. The boundary Γ of domain Ω is split into three mutually disjoint parts such that $\Gamma = \bar{\Gamma}_0 \cup \bar{\Gamma}_1 \cup \bar{\Gamma}_2, \Gamma_i \cap \Gamma_j = \emptyset, i \neq j,\ i,j = 0,1,2$. The body is clamped along the portion Γ_0 of the boundary Γ. The surface tractions $p(x) = (p_1(x), p_2(x)), x \in \Gamma$, are applied on a portion Γ_1 of the boundary Γ. The contact conditions with Tresca friction are prescribed on the portion Γ_2 of the boundary Γ. Let $\rho = \rho(x) : \Omega \to R$ denote the material density function at any generic point x in a design domain Ω. It is a phase field variable taking value close to 1 in the presence of material, while $\rho = 0$ corresponds to regions of Ω where the material is absent, i.e. there is a void or weak material. In the phase field approach the interface between material and void is described by a diffusive interfacial layer of a thickness proportional to a small lenght scale parameter $\epsilon > 0$ and at the interface the phase field ρ rapidly but smoothly changes its value [1, 2, 3, 5]. We require that $0 \leq \rho \leq 1$. The ρ values outside this range do not seem to correspond to admissible material distributions. The elastic tensor $\mathcal{A}$ of the material body is assumed to be a function depending on density function ρ:

$$\mathcal{A} = g(\rho)\mathcal{A}_0,\ \ \mathcal{A}_0 = \{a_{ijkl}\}_{i,j,k,l=1}^{2} \tag{1}$$

and $g(\rho) > 0$ is a suitable chosen function [5, 7]. It is assumed, that elements $a_{ijkl}(x), i,j,k,l = 1,2$, of the elasticity tensor $\mathcal{A}_0$ satisfy [1, 6] usual symmetry, boundedness and ellipticity conditions. We denote by $u = (u_1, u_2), u = u(x), x \in \Omega$, the displacement of the body and by $\sigma(x) = \{\sigma_{ij}(u(x))\}, i,j = 1,2$, the stress field in the body. Consider elastic bodies obeying Hooke's law, i.e., for $x \in \Omega$ and $i,j,k,l = 1,2$

$$\sigma_{ij}(u(x)) = g(\rho)a_{ijkl}(x)e_{kl}(u(x)) \ \text{ where } \ e_{kl}(u(x)) = \frac{1}{2}(u_{k,l}(x) + u_{l,k}(x)),\ \ u_{k,l}(x) \stackrel{def}{=} \frac{\partial u_k(x)}{\partial x_l}. \tag{2}$$

We use here and throughout the paper the summation convention over repeated indices. The stress field σ satisfies the system of equations in the domain Ω [6]

$$-\sigma_{ij}(x)_{,j} = f_i(x) \quad x \in \Omega, i,j = 1,2, \ \text{ where } \ \sigma_{ij}(x)_{,j} = \frac{\partial \sigma_{ij}(x)}{\partial x_j}. \tag{3}$$

The following boundary conditions are imposed on the boundary $\partial\Omega$

$$u_i(x) = 0 \ \ \text{on} \ \ \Gamma_0,\ \ i = 1,2, \ \text{ and } \ \sigma_{ij}(x)n_j = p_i \ \ \text{on} \ \ \Gamma_1,\ \ i,j = 1,2, \tag{4}$$

$$u_N \leq 0,\ \ \sigma_N \leq 0,\ \ u_N\sigma_N = 0 \ \text{ and } \ \mid \sigma_T \mid \leq 1, \quad u_T\sigma_T + \mid u_T \mid = 0 \ \text{ on } \Gamma_2, \tag{5}$$

where $n = (n_1, n_2)$ is the unit outward versor to the boundary Γ. Let us introduce the set U_{ad} of admissible domains. This set has the form: $U_{ad} = \{\Omega \ : \Omega \subset D \subset R^2 \ : \ \Omega \text{ is suitable regular, } Vol(\Omega) - Vol^{giv} \leq 0,\ P_D(\Omega) \leq const_1\}$ where $Vol(\Omega) = \int_\Omega dx$ and $P_D(\Omega) = \int_\Gamma dx$. The subset D as well as constants $Vol^{giv}, const_1 > 0$ are given. The set U_{ad} is assumed to be nonempty. Consider the following structural optimization problem: *for a given function $\eta \in M^{st}$, find a domain $\Omega^\star \in U_{ad}$ such that*

$$J_\eta(u(\Omega^\star)) = \min_{\Omega \in U_{ad}} J_\eta(u(\Omega)) \ \text{ where } \ J_\eta(u(\Omega)) = \int_{\Gamma_2} \sigma_N(u)\eta_N(x)ds. \tag{6}$$

The set $M^{st} = \{\eta = (\eta_1, \eta_2) \in [H^1(D)]^2 : \eta_i \leq 0 \ \text{ on } D,\ i = 1,2, \quad \| \eta \|_{[H^1(D)]^2} \leq 1\}$ and the functional $J_\eta(\cdot)$ approximates the normal contact stress.

*Corresponding author. Email: myslinsk@ibspan.waw.pl

Phase field based topology optimization problem

We apply phase field approach to formulate a necessary optimality condition and to solve numerically the optimization problem (6). We shall consider domain Ω as a two phase domain. We use Ginzburg-Landau energy functional [3] as a regularization term rather than standard perimeter term. Material density function ρ describes the concentration of one of the phases in the domain Ω. The other phase is obtained as $(1-\rho)$. This variable is used to describe the phase transition. In order to indicate the evolution of the material density function ρ let us assume this function depends not only on $x \in \Omega$ but also on the artificial time variable $t \in [0,T), T > 0$ given, i.e. $\rho = \rho(t,x)$. Let us introduce the regularized cost functional $J(\rho,u)$ in the form:

$$J(\rho,u) = J_\eta(u) + E(\rho), \quad E(\rho) = \int_\Omega \psi(\rho) d\Omega, \quad \psi(\rho) = \frac{\gamma\epsilon}{2} \mid \nabla\rho \mid^2 + \frac{\gamma}{\epsilon}\psi_B(\rho), \tag{7}$$

where the functional $J_\eta(u)$ is given by (6) and $\epsilon > 0$ is a constant, $\gamma > 0$ is a parameter related to the interfacial energy density, $\psi_B(\rho)$ is a double-well potential which characterizes the two phases [3] usually taken as an even-order polynomial of the form $\psi_B(\rho) = \rho^2(1-\rho^2)$. The structural optimization problem (6) takes the form: *find* $\rho^\star \in U^\rho_{ad}$ *such that*

$$J(\rho^\star, u^\star) = \min_{\rho \in U^\rho_{ad}} J(\rho,u), \tag{8}$$

where $u^\star = u(\rho^\star)$ denotes a solution to the state system (3)-(5) depending on $\rho^\star$ and $U^\rho_{ad} = \{\rho : Vol(\Omega) = Vol^{giv}\}$ denotes the set of admissible material density functions.

NUMERICAL IMPLEMENTATION AND RESULTS

Necessary optimality condition for the optimization problem (8) in the form of the gradient flow generalized Cahn-Hilliard equation has been formulated. Finite difference and finite element methods have been used as approximation methods. Primal-dual active set method has been used to solve state and adjoint systems. Biconjugate gradient method has been used to solve generalized Cahn-Hilliard system. Fig. 1 presents the optimal domain obtained by solving structural optimization problem (8) in the computational domain D using the optimality condition. The areas with low values of density function appear in the central part of the body and near the fixed edges. The obtained normal contact stress is almost constant along the optimal shape boundary and has been significantly reduced comparing to the initial one (see Fig. 2).

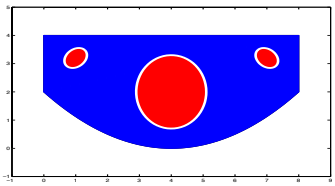

Figure 1: Optimal material density distribution in domain $\Omega^\star$.

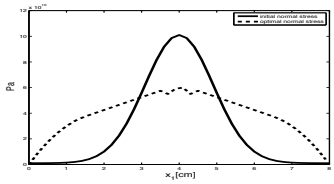

Figure 2: Initial and optimal normal contact stress.

CONCLUSION

The obtained numerical results indicate that the proposed numerical algorithm allows for significant improvements of the structure and reduction of the normal contact stress. Phase field approach based on the Cahn-Hilliard equation is flexible and can be easily combined with material density field. In this sense this approach follows SIMP method.

References

[1] Blank L., Garcke H., Sarbu L., Srisupattarawanit T., Styles V., Voigt A.: Phase-field approaches to structural topology optimization. *Constrained Optimization and Optimal Control for Partial Differential Equations*, G. Leugering, S. Engell, A. Griewank, M. Hinze, R. Rannacher, V. Schulz, M. Ulbrich, S. Ulbrich (Eds.), International Series of Numerical Mathematics, Birkhäuser, Basel, 160:245-256, 2012.

[2] Burger M., Stainko R.: Phase-field relaxation of topology optimization with local stress constraints. SIAM J. Control. Optim. 45:1447-1466, 2006.

[3] Dede L., Boroden M.J., Hughes T.J.R: Isogeometric analysis for topology optimization with a phase field model. Archives of Computational Methods in Engineering 19(3):427-465, 2012.

[4] van Dijk N.P., Maute K., Langlaar M., van Keulen F.: Level-set methods for structural topology optimization: a review. Struct. Multidisc Optim. 48: 437-472, 2013.

[5] Gain A.L., Paulino G.H.: Phase-field based topology optimization with polygonal elements: a finite volume approach for the evolution equation. Struct. Multidisc Optim. 46:327-342, 2012.

[6] Myśliński A.: Piecewise Constant Level Set Method for Topology Optimization of Unilateral Contact Problems. Advances in Engineering Software, 80:25-32, 2015.

[7] Wallin M., Ristinmaa M., Askfelt H.: Optimal topologies derived from a phase-field method. Struct. Multidisc Optim. 45:171-183, 2012.

ON OBJECTIVE FUNCTIONS IN TOPOLOGY OPTIMIZATION FOR VIBRATION AND WAVE PROPAGATION PROBLEMS

Bin Niu [1,a)], Xiaomeng He [1] & Rui Yang [1]
[1] *School of Mechanical Engineering, Dalian University of Technology, 116024 Dalian, China*

Summary This paper deals with the topological design of continuum structures for vibration and wave propagation problems. Different definitions of objective functions for minimizing vibration response and transmission are compared, and a new optimization model is proposed for minimizing the vibration response and the material used. The minimization of vibration transmission is also related with the bandgap design of wave propagation. Plane and plate structures are optimized using different optimization formulations in numerical examples. The influence of excitation frequencies, the eigenfrequencies of the structure, and damping are discussed in the numerical examples.

INTRODUCTION

Topology optimization on vibration and wave propagation problems has been widely studied. In comparison with well-known static compliance minimization, various objective functions are proposed in literature to minimize the response of vibrating structures, such as power flow, sound radiation, vibration transmission, and dynamic compliances, etc. Even for the dynamic compliance, different definitions are found in literature, which have quite different formulations and great influences on the optimization results. It has been found that the minimization of vibration transmission is also related with the bandgap design of wave propagation. The bandgap design may be realized by the maximization of the frequency gap of the free vibration of a structure, maximization of the frequency gap of wave propagation in a periodic microstructure, or maximization of the wave attenuation in a structure. The aim of this paper is to provide a comparison of these different objective functions for design optimization of vibrating and wave propagation problems. A more appropriate optimization model will be proposed based on the comparison results.

PROBLEM DEFINITION AND OPTIMIZATION FORMULATIONS FOR VIBRATING

An objective function termed as dynamic compliance is proposed to minimize the global response of vibrating structures by Olhoff and Du [1], where the objective function is calculated by the square of the product of force vector and displacement vector. By introducing damping, the optimization problem is reformulated as:

$$\begin{aligned} \min_{x_e, e=1,\ldots,N_E} \quad & \left(\mathbf{P}^{\mathrm{T}}\mathbf{U} \quad \overline{\mathbf{P}^{\mathrm{T}}\mathbf{U}}\right) \\ s.t.: \quad & (\mathbf{K} + \omega_p \mathbf{C} - \omega_p{}^2 \mathbf{M})\mathbf{U} = \mathbf{P}, \\ & \sum_{e=1}^{N_E} x_e V_e - V^* \le 0 \ , \quad \left(V^* = \alpha V_0\right), \\ & 0 < x_{\min} \le x_e \le 1 \ , \quad \left(e = 1,\ldots,N_E\right). \end{aligned} \tag{1}$$

where $\mathbf{P}$ and ω_p are the prescribed amplitude and the frequency of the time-harmonic external mechanical loading $\mathbf{p}\ t\ = \mathbf{P}e^{\omega_p}$ respectively, and $\mathbf{U}$ is the amplitude of related displacement vector $\mathbf{a}\ t\ = \mathbf{U}e^{\omega_p}$. The problem will reduce to the well-known compliance minimization in static topology optimization when $\omega_p = 0$. $\mathbf{K}$ and $\mathbf{M}$ are the stiffness matrix and mass matrix, $\mathbf{C}$ is the damping matrix, x_e denotes the design variable of the *e*-th element, and N_E is the total number of finite elements. $V^* = \alpha V_0$ is the given volume of material, and α is the volume fraction. Overbar denotes the conjugate of a complex quantity.

Jog [2] has introduced a new measure for the dynamic compliance, which is computed as the average input power over a cycle of the excitation. Minimization of the average input power $-1/2\,\omega_p \mathbf{P}^{\mathrm{T}}\mathbf{U}_{\mathbf{s}}$ is chosen as the design objective, where $\mathbf{U}_{\mathbf{s}}$ is the imaginary part of the displacement amplitude vector $\mathbf{U}$.

The minimizing the vibrating magnitude at a point, a line, or an area of a structure subjected to periodic loading was studied by Sigmund [3]. Olhoff and Niu [4] proposed an optimization formulation for vibration transmission in a lightweight building from vibrating machinery by simultaneous minimization of the power flow and the material used for the base plate design of the machinery. The minimization of vibration transmission is found to be related with the bandgap design of wave propagation. The optimization formulations for realizing bandgap structure are compared and discussed next.

PROBLEM DEFINITION AND OPTIMIZATION FORMULATIONS FOR WAVE PROPAGATION

[a)] Corresponding author. Email: **niubin@dlut.edu.cn**

By designing a periodic structure with band gap, it is effective to prevent the wave in the range of the band gap from propagating. The classical formulation for maximizing the bandgap is rewritten as, ref. Sigmund [3]:

$$\begin{aligned} \max_{x_e\ \beta\ \beta} \quad & c\ x\ = \frac{\Delta\omega^2\ x}{\omega_0^2\ x} = 2\frac{\beta_2-\beta_1}{\beta_2+\beta_1} \\ s.t. \quad & \beta_1 \ge \max_{\mathbf{k}} \omega_j\ \mathbf{k}\ x \\ & \beta_2 \le \min_{\mathbf{k}} \omega_{j+1}^2\ \mathbf{k}\ x \\ & \mathbf{K}\ \mathbf{k}\ -\omega^2\mathbf{M})\mathbf{U}\quad \mathbf{0} \\ & 0 \le x_e \le \quad e = \quad \dots\ N_E \end{aligned} \tag{2}$$

where ω_j is the *j*th order frequency, **K** and **M** are stiffness matrix and mass matrix of the unit cell, **k** is the wave vector, and β_1 β_2 are two scalar variables that denote the upper and lower bound parameters in the constraint equations, respectively.

The maximization of a frequency gap of the free vibration of a structure can result into a periodic structure, which has been demonstrated by Olhoff et al.[5] for a beam band gap design for travelling wave. The results demonstrate that there is almost perfect correlation between the bandgap size/location of the emerging band structure and the size/location of the corresponding natural frequencygap in the finite structure. The optimization formulation is written as:

$$\begin{aligned} & \max_{\beta_2\ \beta\ x_e} \quad \beta_2-\beta_1\} \\ & s\,t\quad \beta_2-\omega_j^2 \le 0, \qquad j \quad n,n\quad 1, \quad ,J, \\ & \omega_j^2-\beta_1 \le 0, \qquad j= \qquad n \\ & (\mathbf{K}-\omega^2\mathbf{M})\mathbf{U}\quad \mathbf{0} \\ & 0 < x_{\min} \le x_e, \qquad e=1, \quad ,N_E \end{aligned} \tag{3}$$

Bandgap design can also be realized by maximizing the loss/attenuation of propagating waves as in Søe-Knudsen [6], Andreasen and Jensen [7]

$$\begin{aligned} & \max_{c\ x_e} \quad c \\ & s.t. \quad (\mathbf{K}-\ \mathbf{M})\mathbf{U}\quad \mathbf{0} \\ & \eta=\frac{k''}{k'} \le c \end{aligned} \tag{4}$$

where the complex wave number = + , and *c* is a bound variable.

CONCLUSIONS

The topology optimization of continuum structures for vibrating and the wave propagation problems is studied in this paper. Different objective functions are presented and compared by numerical examples of plane and plate structures. The validity and efficiency of the objective functions are discussed for realizing the minimization of vibration response and transmission.

Acknowledgement

This work was partially supported by the National Natural Science Foundation of China (no. 51505064), Natural Science Foundation of Liaoning Province (2015020154), and the Fundamental Research Funds for the Central Universities. These supports are gratefully appreciated.

References

[1] Olhoff N., Du J.: Topological Design for Minimum Dynamic Compliance of Structures under Forced Vibration. G. Rozvany, T. Lewinski (Eds.), Topology Optimization in Structural and Continuum Mechanics, CISM International Centre for Mechanical Sciences, Springer, Vienna, 325-339, 2014.

[2] Jog CS.: Topology Design of Structures Subjected to Periodic Loading. *J Sound Vib* 253(3):687–709, 2002.

[3] Sigmund O., Jensen J.: Systematic Design Of Phononic Band–Gap Materials and Structures by Topology Optimization. *Philos T Roy Soc A* 361:1001-19, 2003.

[4] Olhoff N., Niu B.: Minimizing the vibrational response of a lightweight building by topology and volume optimization of a base plate for excitatory machinery. *Struct Multidiscip O* DOI 10.1007/s00158-015-1345-6, 2016.

[5] Olhoff N., Niu B., Cheng G.: Optimum Design of Band-Gap Beam Structures. *Int J Solids Struct* 49:3158-69, 2012.

[6] Søe-Knudsen A.: Design of stop-band filter by use of curved pipe segments and shape optimization. *Struct Multidiscip O* 44: 863-874, 2011

[7] Andreassen E., Jensen J.: Topology Optimization of Periodic Microstructures for Enhanced Dynamic Properties of Viscoelastic Composite Materials. *Struct Multidiscip O* 49:695-705, 2014.

ADAPTIVE DESIGN PROCESS OF LATTICES PRODUCED BY ADDITIVE MANUFACTURING

Antonin Paquette-Rufiange[1], Serge Prudhomme *[1], Marc Laforest[1], and Augustin Schmidt[1]

[1]*Département de mathématiques et génie industriel, École Polytechnique Montréal, Montreal, Quebec, Canada*

Summary Recent developments in additive manufacturing now allow one to contemplate the fabrication of lightweight parts by the use of lattice structures. Most lattices to date are designed with a structured configuration (with repeated truss cells), while the freedom provided by additive manufacturing technologies does not impose this restriction on the design. We propose here a numerical methodology to design unstructured lattices such that material is only placed where it is needed. Lattices are described in terms of bar, beam and torsion models in order to handle the simulation of the lattice, even if they possess a large amount of trusses. For given operational constraints, we search for the truss configuration that minimizes the energy of deformation to weight ratio. The optimization is performed adaptively using a succession of increasingly complex models. This design process is finally tested on several numerical examples to demonstrate its performance.

INTRODUCTION

Additive manufacturing technologies, such as stereolithography and electron beam melting, now allow for the creation of complex structural parts using various materials like plastic and titanium alloy. In particular, one could replace solid parts by lattice structures with the main advantage of being lightweight while respecting geometrical and mechanical requirements. Lattices are therefore attractive to the aerospace and automobile industries because lighter parts lead to significant savings. Researches have been made in order to describe the mechanical strength of structured and/or conformal lattices. Also, published works have investigated the optimization of some parameters (e.g. the truss diameter) in order to obtain a homogeneous distribution of mechanical stresses within the lattice [1, 2].

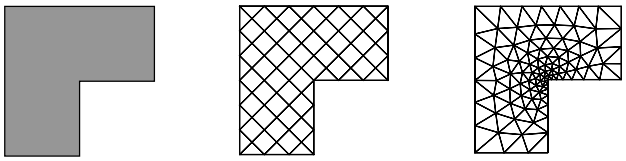

Structural system | Structured lattice | Unstructured lattice

However, one faces several challenges when trying to optimize the design of an unstructured lattice. First, the entire lattice must be analyzed in a "discrete" way, meaning that each truss member must be represented. Hence, the number of degrees of freedom rapidly increases as the lattice becomes denser. Second, obtaining a somewhat optimized configuration of the truss with respect to loads applied to the system is computationally hard because the position and the size of each truss correspond to parameters of the optimization problem. We now briefly explain the novel strategies we employ to tackle some of these challenges.

DESCRIPTION OF THE LATTICE MODEL

We address the first challenge by modeling each truss member as unidimensional single bar, beam and torsion elements. This allows us to significantly reduce the number of degrees of freedom. For example, if one takes a cubic lattice of 15cm of length filled with truss members of minimal length of 5mm, one obtains approximatively 230 000 truss members connected by 30 000 nodes. Thus, using for example the bar model to describe each truss member, one would have about 90 000 degrees of freedom compared to millions of degrees of freedom if one was to discretize each bar solving for the 3D continuum linear elasticity equations by the finite element method. This approach can therefore considerably reduce the complexity and computational cost of simulating the mechanical behavior of the lattice.

*Corresponding author. Email: serge.prudhomme@polymtl.ca

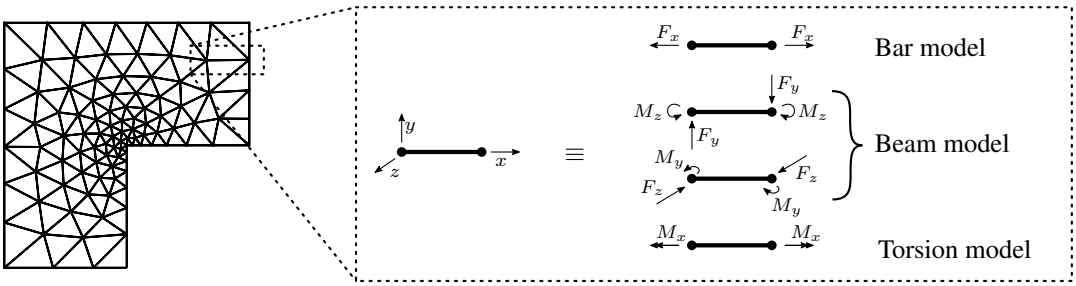

ADAPTIVE DESIGN PROCESS

The simple models presented in above section to simulate the mechanical response of a lattice can be used for design in such a way that the quantity of material involved be minimized while satisfying the specific operational requirements of the lattice. The design variables of the lattice are for example the number of truss members, their diameters, and their position within the computational domain. The following diagram describes the methodology of the adaptive design process.

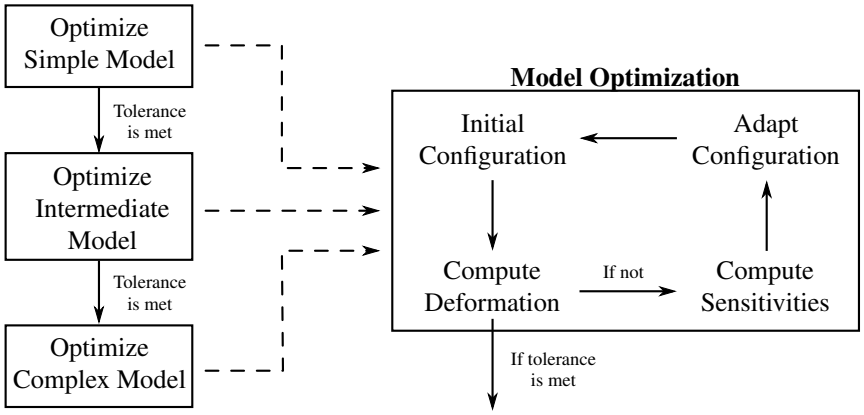

The adaptive process, with the objective of minimizing the computational cost, consists of two stages: 1) one is to start with a coarse lattice and refining it with truss members until mechanical tolerance is met, 2) the second is concerned with adaptive modeling in the sense that each lattice is first described with the simple bar model, which can be locally adapted with finer models, e.g. beam and torsion models, in order to reduce the modeling errors.

References

[1] Jason Nguyen, Sang-In Park, David W. Rosen, Luis Folgar, and James Williams. Conformal lattice structure design and fabrication. In *Solid Freeform Fabrication Symposium*, 2012

[2] S. Teufelhart and G. Reinhart. Optimization of strut diameters in lattice structures. In *Solid Freeform Fabrication Symposium*, 2012.

MULTIPLE DESIGNS APPROACH FOR CONTINUUM TOPOLOGY OPTIMIZATION

Bo Wang[1a)], Yan Zhou[2] & Yiming Zhou[3]

[1] *State Key Laboratory of Structural Analysis for Industrial Equipment*, *Department of Engineering Mechanics, Dalian University of Technology*, *Dalian 116024*, *China*

Summary Topology optimization can provide creative conceptual designs for industry design in the preliminary design stage. However, the traditional topology optimization approaches focus on searching for one optimal solution which may be invalid due to the refinements of models or the additional design requirements. This paper presents the Multiple Designs Approach (MDA) to get several diverse topology designs, which can reduce the risk of lacking full knowledge of the designs by providing multiple designs. Weighting function is used as the objective function to evaluate the performances of multiple solutions. Diversity function is used as constraint to measure the diversity between different topology solutions.

MOTIVATION

Many researchers are focused on finding an optimal topology design since Bendsøe and Kikuchi[1] first applied homogenization technique for generating optimal topology designs. In fact, topology optimization plays an important role in obtaining conceptual designs in the preliminary design stage[2]. These conceptual designs from topology optimization can give researchers the insights for shape and sizing optimization in detailed design stage. However, preliminary design stage lacks of full knowledge of all the constraints and objectives. In detailed design stage, more latent structural and multidisciplinary performances like strength, structural stability, thermal property, etc., need to be taken into consideration. Furthermore, it is a common practice to use coarse discretization and simpler models in simulations. This occasionally results in rendering the optimum design deficient or useless when checked with a refined model. Moreover, objectives and constraints may change in detailed design stage. If a tight constraint changes, the optimal solution may be out of the new feasible region. Hence designers would like to have multiple design alternatives to single optimal solution in the preliminary design stage.

In order to reduce design risks in detailed design stage, Villanueva[3] used k-means clustering algorithm in sub-regions surrogate-based optimization to find all global and local optimal solution. However, the local optima sometimes are not worth finding because they are not competitive. Also it is difficult to find all the optimal solutions for high-dimensional problems. Later, Zhou, Haftka[4] introduced several surrogate based algorithms to get two diverse competitive solutions in the design domain.

In topology optimization, it is usually a single objective problem to obtain material distribution under material volume constraint and other functional constraints. This paper presents a Multiple Designs Approach (MDA) for topology optimization with diversity constraint to get multiple designs. Thus it is not necessarily required to obtain global optimal solution in this paper.

MULTIPLE DESIGNS APPROACH

General topology optimization formula for MDA

$$
\begin{aligned}
&\min_{\rho_1,\rho_2} : F = \sum_{i=1}^{n} \alpha F, \quad \sum_{i=1}^{n} \alpha_i = 1 \\
&s\,t \quad G_0^i \ \rho_i \ \leq \\
&\qquad G_j^i \ \rho_i \ \leq \\
&\qquad \rho_i \ \mathrm{x} \ \in \qquad \forall \mathrm{x} \in \Omega \ i \qquad n \ j \qquad m \\
&\qquad G(\rho_p, \rho_q \ \leq \eta \ p \ q = \qquad n \, and \ p \neq q
\end{aligned}
\tag{1}
$$

Where n represents the number of topology configurations, m represents the number of functional constraint. Topology optimization problem applied to find optimal material distribution $\rho_i(\mathbf{x})$ in design domain Ω to minimize the objective function F_i with material volume constraint $G_0{}^i$ and other functional constraint G_j. In the formula, V is volume of design domain, V_f is material volume fraction.

Here, MDA uses a multi-objective problem to get multiple solutions simultaneously and tries to use the weighting function to solve this problem. $\alpha_i \in [0,1]$ is weighting coefficient. Furthermore, we add diversity constraint to obtain different topology configurations. G is the diversity constraint and η is the upper bound for diversity constraint.

Diversity constraint and similarity/difference functions

To obtain two topology configurations in MDA, we need to define a diversity constraint in equation (3). Diversity constraint is a function of ρ_1 and ρ_2 which can measure the difference between topology configurations. The function should be continuous, smooth and bounded for gradient algorithm.

a) Corresponding author. Email: wangbo@dlut.edu.cn.

In graphics, there are many approaches to measure difference or similarity between two images, including Cross-Correlation(CC), Sum of Squared Differences(SSD), Sum of Absolute Differences(SAD) and their derivative algorithm. Here, we give a simple Similarity Function as the diversity constraint.

$$= \quad (\rho_1,\rho_2) = \frac{\int_\Omega s\ \rho_1\ \mathbf{x}\ ,\rho_2\ \mathbf{x}\ \ dv}{\int_\Omega dv} \tag{2}$$

$$s\ \rho_1\ \mathbf{x}\ ,\rho_2\ \mathbf{x}\ \ = \rho_1\ \mathbf{x}\ \rho_2\ \mathbf{x}\ \ \forall \mathbf{x} \in \Omega$$

For multiple design problems, all the objective and constraints as well as the material volume fraction for the designs are the same. In this case, the codomain of SF is related to V_f for binary configurations as follow:

$$\mathrm{SF} \in [\max(0,2V_f - 1), V_f] \tag{3}$$

It is worth noting that upper bound for diversity constraint must be larger than the low bound of SF.

As the codomains of SF are not uniform in different V_f, this paper presents a uniform metric for description of the diversity between topology configurations. Here, the difference function is defined by normalizing SF in the range of SF.

$$DF = 1 - \frac{SF - \max(0, 2V_f - 1)}{V_f - \max(0, 2V_f - 1)} \tag{4}$$

In this case, DF represents the relationship between non-overlap volume and material volume. DF is used as diversity measurement in the rest of the paper.

NUMERICAL EXAMPLE

In this paper, we give an example of L beam for minimization compliance topology problem. Design domain and dimensions of L beam are shown in figure 1 left. Its volume is 4800 and it is discretized into 4800 bi-linear elements. Design variables are element densities. Upper edge of model is clamped and unit load is applied on up-right vertex in figure 1 left. The upper bound of elastic modulus E_0 is 1, and the lower bound of elastic modulus E_{min} is 10^{-6}. Poisson's ratio of material ν is 0.3. Penalty of SIMP is 3, filter radius of sensitivity filtering is 1.5. Volume fraction of material V_f is 50%. Weighting factor $\alpha_1 = \alpha_2 = 0.5$. To get two configurations and ensure DF is equal to 0.2, η can be calculated by equation (5). Hence η are 0.4. The result is shown in figure 1 middle and right, which the middle one is Configuration I, and the right one is Configuration II. It is very different between the two configurations.

$$\eta = max(0,2V_f - 1) + (1 - DF)[V_f - max(0,2V_f - 1)] \tag{5}$$



Figure 1 Domain of L beam (Left) Configuration I (middle) Configuration II (right)
DF=0.2, F_1=83.08, F_2=82.82, F=82.95

CONCLUSIONS

This paper introduces multiple designs approach (MDA) for topology optimization to get diverse designs and presents the similarity and difference function as the diversity constraint. Compliance minimization examples based on SIMP method are tested in MDA algorithm framework to verify the validity of MDA.

References

[1] Bendsøe, M.P. and N. Kikuchi, Generating Optimal Topologies In Structural Design Using a Homogenization Method. Computer Methods In Applied Mechanics And Engineering, 1988. 71(2): p. 197-224.Icer D.F., Adams J.A.: Mathematical Elements for Computer Simulation. Montreal, Canada 1977.

[2] Olhoff, N., M.P. Bendsoe, and J. Rasmussen, On Cad-Integrated Structural Topology And Design Optimization. Computer Methods In Applied Mechanics And Engineering, 1991. 89(1-3): p. 259-279.

[3] Villanueva, D., R. Le Riche, G. Picard, et al. Dynamic design space partitioning for optimization of an integrated thermal protection system. in The 54th AIAA/ASME/ASCE/AHS/ASC Structures, Structural Dynamics, and Materials Conference, Boston, Massachusetts, USA. 2013.

[4] Zhou, Y., A. Chaudhuri, R.T. Haftka, et al., Global Search for Diverse Competitive Designs, in 15th AIAA Multidisciplinary Design Optimization Specialist Conference. 2014: Atlanta, Georgia, USA.

LATTICE HIP IMPLANT DESIGN BY MULTI-SCALE MULTI-CONSTRAINT TOPOLOGY OPTIMIZATION

Yingjun Wang & Damiano Pasini[a)]
Department of Mechanical Engineering, McGill University, Montreal, Quebec, Canada

Summary Bone resorption is one of the main issues that lead to aseptic loosening and revision surgery after total hip arthroplasty. One of the reasons for bone resorption is stress shielding caused by the prosthesis stiffness usually much higher than that of the bone tissue. To address this problem, we present a mechanically biocompatible hip implant that consists of a graded-density lattice material obtained via multi-scale multi-constraint topology optimization (TO). Asymptotic homogenization is used to deal with the multi-scale mechanics of the implant and a modified proportional TO is used to obtain the relative density distribution of the implant. The result shows that bone resorption for the optimized implant is only 9% of that of a fully solid titanium implant that is commonly used in current total hip arthroplasty.

INTRODUCTION

Total hip arthroplasty (THA) is an effective treatment for osteoarthritis and has been successfully performed on over 1 million patients every year worldwide [1]. Current orthopedic prostheses are generally made of metals, such as 316L stainless steel, cobalt chromium alloys, titanium-based alloys and tantalum [2]. These materials, however, are much stiffer than the surrounding bone tissue, thereby yielding to stress shielding [3], one of the reasons for bone resorption. Currently, 13% of hip prostheses require revision surgeries as a result of bone resorption [4]. Khanoki and Pasini [2] introduced a hip replacement implant made of a lattice material with graded relative density capable to simultaneously reduce bone resorption and bone-implant interface stress. To solve the multi-objective optimization problem, they resorted to an evolutionary scheme, which was time consuming and applied to a planar domain only. In this paper, we focus on the minimization of bone resorption in a 3D lattice hip implant via a multi-scale multi-constraint topology optimization scheme, which is gradient free, more accurate and more efficient than the approach previously used [2].

METHODS

Figure 1 shows the scheme proposed in this paper to design a graded lattice implant with minimal bone resorption. The main steps are briefly described below.

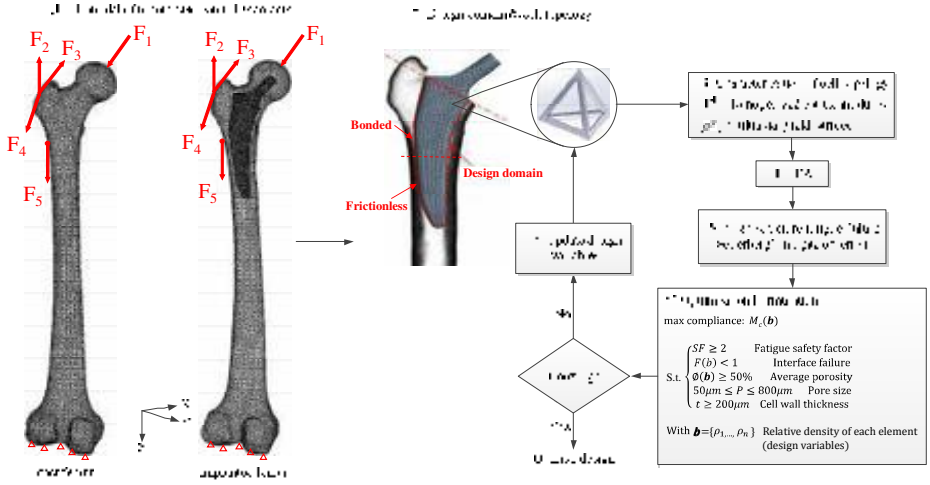

Figure 1. Design flow chart to obtain the optimal density distribution for the hip implant.

(1) A finite element (FE) model is created by processing the CT-scan data from the femur of a 38-year old patient. Two FE models are generated, one for the intact femur and the other for implanted femur; the difference in strain energy between them is used as proxy to quantify bone resorption [3]. The distal end and condyle are fixed and the loads, written in the (X, Y, Z) coordinate system, are F1 (-486, -295, 2063), F2 (75, 6, -111), F3 (9, 15, -111), F4 (-1, -1, 24) and F5 (-1, 19, 93).

(2) The macrogeometry of the implant is a minimally invasive design clinically relevant to current THA, whereas the microgeometry of the unit cell is a tetrahedron, which is used to aperiodically tessellate the implant domain. This unit cell is selected for its smooth mapping relationship to the tetrahedral solid element.

[a)] Corresponding authors: Email: damiano.pasini@mcgill.ca

(3) The properties of the unit cell are obtained via asymptotic homogenization (AH), e.g., the homogenized elastic modulus and the yield surfaces of the cell topology under multi-axial loading conditions. More details about the AH procedure can be found in [5].

(4, 5) The full strain and stress regimes for both the intact femur and the implanted femur are obtained via FEA. The mean and alternating stresses are used in the Soderberg's fatigue criterion to obtain the implant safety factor (SF).

(6, 7) A multi-constraint topology optimization (TO) scheme modified from the proportional TO [6] is used to optimize the relative density distribution of all elements associated to the 3D design domain. In particular, the maximal compliance problem is solved by using a density-continuous optimization approach modified from the proportional TO. In addition, the constraints of average porosity, pore size and cell wall thickness are directly taken into account during the optimization process by converting them into lower and upper bounds of relative density. Failure and fatigue analyses are performed at each iteration, and the design variables are updated to satisfy the failure and fatigue requirements. The optimal density distribution is obtained upon convergence of the modified TO.

RESULTS

Figure 2 (a), shows the optimal relative density distribution, and Figure 2 (b) the graded lattice obtained with an in-house code that can create the geometric model of the lattice ready for manufacturing. The performance of the optimized lattice implant is compared with a fully solid implant in Figure 2 (c), which shows that the former can greatly reduce bone resorption (1.4% vs 15.7%). Bone loss for the porous implant is only 9% of that for a benchmark implant with solid material. Comparing to our previous work [2], where the optimization time required to design a 2D implant was almost 3 days, the method presented in this paper for a more realistic 3D implant needs 10 minutes only, a factor that proves the superior efficiency of the scheme here proposed.

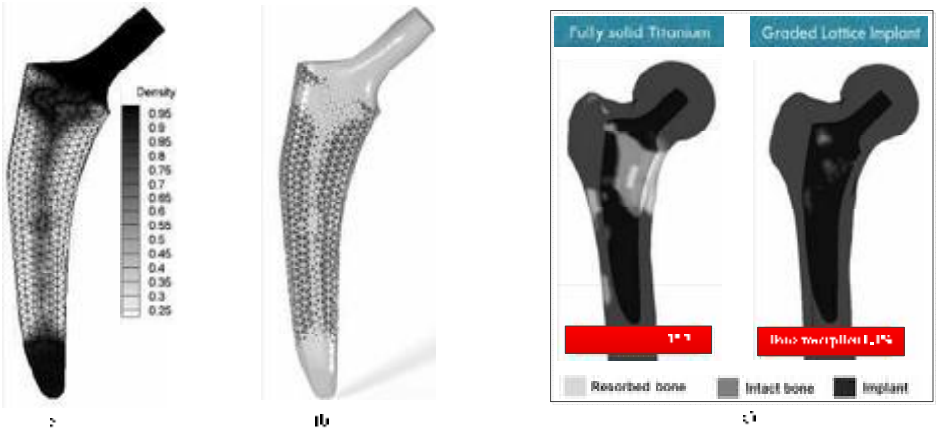

Figure 2. Results of optimized 3D lattice implant: (a) relative density distribution, (b) CAD model of the lattice implant and (c) bone resorption comparison with a fully solid implant.

CONCLUSIONS

In this paper, a multi-scale multi-constraint topology optimization method is proposed to optimize the relative density distribution of a 3D hip implant made of graded lattice material. Compared to a fully solid implant, the optimized implant here presented can reduce bone resorption of more than 90%.

References

[1] Pivec R., Johnson A.J., Mears S.C., Mont M.A.: Hip arthroplasty. *The Lancet* **380**:1768-1777, 2012.

[2] Khanoki S.A., Pasini D.: Multiscale design and multiobjective optimization of orthopedic hip implants with functionally graded cellular material. *Journal of biomechanical engineering* **134**:031004, 2012.

[3] Ridzwan M., Shuib S., Hassan A., Shokri A., Ibrahim M.M.: Problem of stress shielding and improvement to the hip implant designs: a review. *J Med Sci* **7**:460-467, 2007.

[4] Kurtz S., Ong K., Lau E., Mowat F., Halpern M.: Projections of primary and revision hip and knee arthroplasty in the United States from 2005 to 2030. *The Journal of Bone & Joint Surgery* **89**:780-785, 2007.

[5] Khanoki S.A., Pasini D.: Fatigue design of a mechanically biocompatible lattice for a proof-of-concept femoral stem. *Journal of the mechanical behavior of biomedical materials* **22**:65-83, 2013.

[6] Biyikli E., To A.C.: Proportional Topology Optimization: A New Non-Sensitivity Method for Solving Stress Constrained and Minimum Compliance Problems and Its Implementation in MATLAB. *PloS one* **10**, 2015.

ESTIMATES OF UPPER AND LOWER BOUNDS OF DISPERSIVE EFFECT IN THE HOMOGENIZED WAVE EQUATION

Takayuki Yamada[1 a)] & Grégoire Allaire[2)]
[1]*Department of Mechanical Engineering and Science, Kyoto University, Kyoto, Japan*
[2]*Centre de Mathématiques Appliquées, École Polytechnique, Palaiseau, France*

Summary Waves in periodic media undergo dispersion, namely the propagation velocity depends on the frequency. This effect can be modeled by an additional term in the homogenized wave equation. This paper presents the estimation of upper and lower bound of the dispersive effect in the two-dimensional wave equation in the case of an 8-fold symmetric periodic microstructure with constraints of volume, perimeter and homogenized properties.

INTRODUCTION

Dispersive effect is observed on wave propagation in inhomogeneous media. It is well known that the dispersive effect is modelled as a higher order terms (namely a fourth order term) in the homogenized wave equation. The fourth order term can be obtained by the method of two-scale asymptotic expansions or by the Bloch wave method. That is, wave propagation in periodic inhomogeneous media considering dispersive effect is modelled by the following equation.

$$\begin{cases} \dfrac{\partial^2 u_\epsilon}{\partial t^2} - \mathrm{div}(a^*\nabla u_\epsilon) + \epsilon^2 \mathbb{D}^*\nabla^4 u_\epsilon = f + \epsilon^2 \mathrm{div}(d^*\nabla f) \\ u_\epsilon(0,x) = u^{init}(x) \\ \dfrac{\partial u_\epsilon}{\partial t}(0,x) = v^{init}(x) \end{cases} \tag{1}$$

where ϵ is the ratio between the period size and a characteristic length scale, a^* is homogenized material property $\mathbb{D}^*$ is a fourth-order tensor, called Burnnet tensor studied in [1,2,3], f is a source term and d^* is second-order tensor. The Burnnet tensor satisfies for any $\eta \in \mathbb{R}^d$ [2]

$$\mathbb{D}^*(\eta\otimes\eta):(\eta\otimes\eta) = -\int_Y a\nabla_y\left(\chi_\eta^{(1)} - \frac{1}{2}\left(\chi_\eta^{(1)}\right)^2\right)\cdot\nabla_y\left(\chi_\eta^{(2)} - \frac{1}{2}\left(\chi_\eta^{(1)}\right)^2\right)dy \le 0, \tag{2}$$

where $\chi_\eta^{(1)}$ and $\chi_\eta^{(2)}$ are defined as follows:

$$-\mathrm{div}_y\left(a\nabla_y\chi_\eta^{\ 1}\right) = -\mathrm{div}_y(a\eta), \qquad \text{for } \eta\in\mathbb{R}^d \tag{3}$$

$$-\mathrm{div}_y\left(a\nabla_y\chi_\eta^{(2)}\right) = b\eta\cdot\eta - a^*\eta\cdot\eta, \qquad \text{for } \eta\in\mathbb{R}^d \tag{4}$$
$$\mathrm{b_{ij}} := a_{ij} - a\nabla_y\chi_i\cdot e_j - \mathrm{div}_y(\chi_i a e_j)$$

The dispersive effect is very important in engineering standpoint, because the periodic size of microstructure is finite. This work presents numerical estimates of upper and lower bounds of the dispersive effect in the two-dimensional wave equation. We assume that the microstructure is imposed an 8-fold symmetric configuration and consist of two isotropic phases. Under this assumption, the Burnett tensor is characterized by two scalar parameters as follows:

$$\mathbb{D}^*(\eta\otimes\eta):(\eta\otimes\eta) = -\alpha\eta_1^4 - \beta\eta_1^2\eta_2^2 - \alpha\eta_2^4 \tag{5}$$

where is $\alpha,\beta\in\mathbb{R}_+^d$ defined as follows:

$$\alpha := \int_Y a(\nabla\chi_{11} - \chi_1\nabla\chi_1)^2 dy \tag{6}$$

a) Corresponding author. Email: takayuki@me.kyoto-u.ac.jp

$$\beta := \int_Y a(\nabla\chi_{12} + \nabla\chi_{21} - \chi_1\nabla\chi_2 - \chi_2\nabla\chi_1)^2 dy \tag{7}$$

FORMULATION OF THE OPTIMIZATION PROBLEM

We introduce an additional assumption that the microstructure is made of two phases with boundary Γ and imposed constraints of phase proportions, interface perimeter and prescribed homogenized tensor. In order to estimate the upper and lower bound of the dispersive effect, we consider the multi-objective problems

$$\min_{\Gamma} \quad \text{or} \quad \max_{\Gamma} \qquad \alpha(\Gamma), \beta(\Gamma) \tag{8}$$

subject to:
- Volume constraint
- Perimeter constraint
- Prescribed homogenized tensor

(9)

That is, we compute the upper and lower curve in $\alpha - \beta$ coordinate system. In this work, the curve is estimated as a set of optimal solutions respect to a parameter θ_i utilizing level set-based shape optimization method [4]:.

$$\max_{\Gamma} \qquad J_i(\Gamma) = \alpha_{\theta_i} - c_p\beta_{\theta_i}^2 \tag{10}$$

where c_p is a parameter and

$$\begin{pmatrix}\alpha_{\theta_i}\\ \beta_{\theta_i}\end{pmatrix} := \begin{pmatrix}\cos\theta_i & \sin\theta_i\\ -\sin\theta_i & \cos\theta_i\end{pmatrix}\begin{pmatrix}\alpha_N\\ \beta_N\end{pmatrix}, \qquad \begin{pmatrix}\alpha_N\\ \beta_N\end{pmatrix} := \begin{pmatrix}\frac{\alpha(\Gamma)-\alpha_{\min}}{\alpha_{\max}-\alpha_{\min}} - c_\alpha\\ \frac{\beta(\Gamma)-\beta_{\min}}{\beta_{\max}-\beta_{\min}} - c_\beta\end{pmatrix}, \qquad 0 \le \theta_i \le 2\,\pi \tag{11}$$

where $\alpha_{\max}$, $\alpha_{\min}$, $\beta_{\max}$, $\beta_{\min}$ are maximum and minimum value of α, maximum and minimum value of β, respectively. That is, the Pareto optimal solutions are obtained by optimizing the interface Γ in the microstructure based on the optimization problem (10) and (11).

CONCLUSIONS

This works presents an optimization problem for the estimates of upper and lower bounds of the dispersive effect for wave propagation in two-phase periodic media.

References

[1] Santosa F., Symes, W.W.: A Dispersive Effective Medium for Wave Propagation in Periodic Composites, *SIAM Journal on Applied Mathmatics* **51**: 984-1005, 1991.

[2] Conca C. Orive R. Vanninatha, M.: On Burnett Coefficient in Periodic Media, *Journal of Mathematics Physics*, **47**: 032902, 2006.

[3] Lamacz A.: Dispersive Effective Models for Waves in Heterogeneous Media, *Math. Models Methods Appl. Sci.*, **21**:1871-1899, 2011.

[4] Allaire G., Jouve F., Toader A.M.: Structural Optimization Using Sensitivity Analysis and a Level Set Method, *Journal of Computational Physics*, **194**: 363-393, 2004.

GLOBAL MULTISCALE OPTIMIZATION DESIGN OF COMPOSITE LAMINATED FRAME STRUCTURE WITH MINIMUM STRUCTURAL COMPLIANCE

Zunyi Duan[1], Jun Yan[1, a)], Jingyuan Wang[1], Tao Yu[1], Erik Lund[2] & Guozhong Zhao[1]
[1]*State Key Laboratory of Structural Analysis for Industrial Equipment, Department of Engineering Mechanics, Dalian University of Technology, Liaoning, Dalian, 116024, China*
[2]*Department of Mechanical and Manufacturing Engineering, Aalborg University, Fibigerstraede 16, DK-9220 Aalborg East, Denmark*

Summary The concurrent multiscale optimization design of composite frames is investigated with gradient-based optimization algorithms. The winding angle in micro-material scale and the geometrical parameter of components of the frame in macro-structural scale are introduced as the independent variables on the two geometrical scales. The coupling effect of macro- and micro-scale design variables can be fully considered in the established multiscale optimization model to probe the potential of composite structures. The feasible domain is found to be non-convexity with the fiber winding angle as micro-material design variable. Then a new two-step optimization scheme is proposed to investigate the optimization design of the composite frame with minimum structural compliance, which increases the possibilities to find the global optimum with the gradient based algorithm.

INTRODUCTION

Fiber-reinforced composite frame structure is considered to be an ideal load carrying structure for aerospace structures. The composite frame can be considered as a geometrical multiscale structure, since the fiber-reinforced composite is characterized by its microstructure. With the point view of multiscale structure [1-3], the composite frame can be optimized concurrently at the macro-structural scale of geometrical parameters of components of the frame and at the micro-material scale of fiber winding angle. Significantly, filament winding parameters (filament winding angle, winding thickness and stacking sequence) can be considered as micro-material design variables which greatly influence the mechanical performance of the composite frame. However, one of the major difficulties using the filament winding angle as design variables is that the feasible domain of the optimization problem is non-convexity. This leads classical gradient-based optimization algorithms may be not effective, which is difficult to ensure the optimization converges to the global optimum [4]. The present paper presents a new two-step optimization scheme and investigates the optimization of composite frame with minimum structural compliance. It should be pointed out specially that the feasible domain is convex when the structural stiffness parameters (tension stiffness, bending stiffness, torsional stiffness) are considered as the design variables. The global optimum can be found in this case. Then adopting layer-wise constant shear beam theory, the equivalent structural stiffness parameters of composite beam can be explicitly integrally expressed as functions of filament winding angle. With ensuring the filament winding angle invariance of physical quantities, the sub-optimization problem between structural filament winding angle and equivalent structural stiffness parameter has been presented. Then implement the independent sub-optimization problems in the non-convex filament winding angle space and the convex structural stiffness parameter space iteratively. The objective sensitivity information with respect to design variables has been solved with the semi-analytical method [5] for the two kinds of design variables, i.e., the optimizations in the filament winding angle space and the equivalent structural stiffness parameter space. Numerical examples show that the proposed two-step optimization scheme can effectively improve the quality of optimization solution of the composite frame, which provides an effective method to approach a global optimum for the composite frame structure.

CONCURRENT OPTIMIZATION OF COMPOSITE FRAME

The schematic figure of concurrent multi-scale optimization of composite frame structure is shown in Fig. 1. For easy of deduction and no loss of generality, we assume the composite frame structure studied in this paper is composed with circular tubes. In macro-scale, the radius of cross-section (r_i) is recognized as macro design variable. As in classical topology optimization of frame structure, the tube's radius can be recognized as the size and topology variables at the same time. When the radius reaches its lower limit, the tube can be regarded to be deleted from the ground structure to realize the structural topology optimization. In micro-scale, the fiber winding angle (the continue fiber winding angles $\theta_{i,j}$) is recognized as the micro design variable.

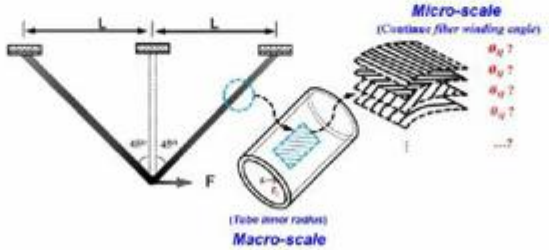

Fig. 1 Schematic of two-scale optimization of the composite frame structure

THE TWO-STEP OPTIMIZATION SCHEME FOR COMPOSITE FRAME

To cope with the non-convexity problem using the fiber winding angle as design variable, we propose a new two-step optimization scheme for composite frame optimization. The schematic diagram of the two-step optimization scheme is shown in Fig.2. Where x-axis represents the angle and the stiffness parameter space, y-axis is the value of optimized objective function. The solid black line represents the non-convex domain of fiber winding angle space. In the diagram, point A represents the local optimum, and point E is the global optimum. The black dashed line represents the convex domains of the stiffness parameter space.

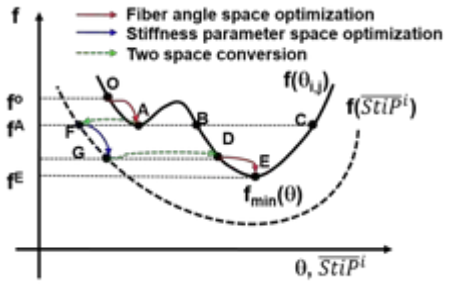

Fig. 2 Schematic diagram of the two space optimization

A two-step optimization scheme is established to lead the design domain to switch from a non-convex domain to a convex domain. Firstly, we generate a set of random or specified initial filament winding angle ${}^{SP}_{s}\theta_{i,j}$ as shown in Fig.2 with corresponding to the point O. Secondly, carry out the minimize optimization to obtain the local optimum point A with filament winding angle ${}^{OPT}_{s}\theta_{i,j}$ in fiber winding angle space. Thirdly, converse the filament winding angle ${}^{OPT}_{s}\theta_{i,j}$ to stiffness parameter space, then obtain the local optimum stiffness parameter $\left({}^{OPT}_{s}\overline{StiP^k}\right)$s corresponding to point A. Finally, with the local optimum stiffness parameters $\left({}^{OPT}_{s}\overline{StiP^k}\right)$ obtained by the previous step, we can obtain its corresponding objective function point F in the stiffness parameter space. Then set up the multi-objective minimized optimization problem in the parameter spaces $\min_{\theta_{i,j}} I$, where $I = \{4f_1 + f_2\}$, and following the constraints as $f\left\{\left({}^{SP}_{s}\theta_{i,j}\right)^{k+1}\right\} \le f\left\{\left({}^{SP}_{s}\theta_{i,j}\right)^{k}\right\} \cap \left({}^{SP}_{s}\theta_{i,j}\right)^{k+1} \neq \left({}^{OPT}_{s}\theta_{i,j}\right)^{k}$. By this minimize optimization problem, we can get point G in stiffness space which is corresponding to point D in fiber winding angle space as the new starting point of design variables $\left({}^{SP}_{s}\theta_{i,j}\right)^{k+1}$ in fiber winding angle space. Using the value of $\left({}^{SP}_{s}\theta_{i,j}\right)^{k+1}$ as the new start point to optimize iteratively to approach point E. Repeat the third step and last step in this process until the $\min_{\theta_{i,j}} I$ can not determine a new start point for the optimization. Thus f^E will be regarded as the global optimum for the optimization of composite frame.

CONCLUSIONS

The present paper investigates the concurrent multiscale optimization design of composite frame with global optimization problem. With the layer-wise constant shear beam theory, we get the equivalent structural stiffness parameter by explicitly integrally expressed with respecting to the filament winding angle. To overcome the difficult of local optimum problem in case of the fiber winding angle as design variable, a new two-step optimization scheme is proposed. The multi-objective minimize optimization problem is established between the fiber winding angle space and stiffness parameter space, which can obtain a new optimized starting point in the fiber winding angle space and greatly increase the probability to approach the global optimal solution.

References

[1] Duan Z.Y., Yan J., Zhao G.Z.: Integrated optimization of the material and structure of composites based on the Heaviside penalization of discrete material model. Structural and Multidisciplinary Optimization, 2015 51, 721-732.

[2] Ferreira R.T.L, Rodrigues H.C., Guedes J.M., et al: Hierarchical optimization of laminated fiber reinforced composites. Composite Structures, 2014, 107: 246-259.

[3] Yan J, Duan Z.Y., Lund E., Zhao G.Z.: Concurrent multi-scale design optimization of composite frame structures using the heaviside panealization of discrete material model. Acta Mechanica Sinica, 2015, 1-12.

[4] Foldager J., Hansen J. S., Olhoff N.: A general approach forcing convexity of ply angle optimization in composite laminates. Structural Optimization, 1998. 16(2-3):201-211.

[5] Lund E: Buckling topology optimization of laminated multi-material composite shell structures. Composite Structures, 2009. 91(2):158-167

[a)] Corresponding author. Email: yanjun@dlut.edu.cn

FM01 - Biological Fluid Mechanics

TS.FM01-1.01	Freund, Jonathan - The stability of flowing trains of confined red blood cells (INVITED)	408
TS.FM01-1.02	Atwell, Scott - Microcirculation of red blood cells for two major genetic diseases	410
TS.FM01-1.03	Balogh, Peter - Flow of blood cells in complex geometry	412
TS.FM01-1.04	Coupier, Gwennou - Inversion of hematocrit partition at microfluidic bifurcations	414
TS.FM01-1.05	Graham, Michael - Theory of margination in blood and other multicomponent suspensions	416
TS.FM01-1.06	Qi, Qin - A coarse-grained theory to predict particle margination and migration in blood suspensions	418
TS.FM01-2.01	Niazi, Erfan - Development of an Experimental Correlation for Red Blood Cells Aggregation Rate	420
TS.FM01-2.02	Wang, Zhen - Motion of a spherical capsule in branched tube flow with finite inertia	422
TS.FM01-2.03	Salsac, Anne-Virginie - Motion of an oblate capsule in simple shear flow	424
TS.FM01-2.04	Vejdani, Hamid - The dynamical reasons for maneuverability of bats	426
TS.FM01-2.05	Kolomenskiy, Dmitry - Dynamics of bumblebees flying in a vortex street	428
TS.FM01-2.06	Darakananda, Darwin - Minimally low order vortex modeling of bio-inspired locomotory flows	430
TS.FM01-3.01	M, M. Jimreeves - Vortex formation and transport from a rotating plate in still fluid	432
TS.FM01-3.02	Wong, Jaime - How animals use spanwise flexibility for extreme manoeuvrability	434
TS.FM01-3.03	Xin, Zhiqiang - Vorticity dynamics of maneuver locomotions of the three dimensional bionic fish	436
TS.FM01-3.04	Yeaton, Isaac - The stability of flying snakes during transient glides	438
TS.FM01-3.05	Socha, John - A new understanding of aerial undulation in flying snakes	440
TS.FM01-4.01	Tam, Daniel - Hydrodynamic vs. intracellular coupling in synchronization of eukaryotic flagella (INVITED)	442
TS.FM01-4.02	Chateau, Sylvain - Emergence of metachronal waves in cilia arrays: A hydrodynamic mechanism	444
TS.FM01-4.03	Lee, Tet Chuan - Modelling the endothelial glycocalyx layer in the microcirculation	446
TS.FM01-4.04	Leontini, Justin - Enhanced gas transport during high-frequency ventilation	448
TS.FM01-4.05	Viallat, Annie - Physics of the mucociliary clearance in airways and the application to severe asthma (INVITED)	450
TS.FM01-4.06	Pak, On Shun - Propulsive thrust of a driven filament at low Reynolds number with non-uniform flexibility	452
PO.FM01-1.01.54	DeGroot, Christopher - Development of a porous media model for flow in alveolated ducts within the human lung	454
PO.FM01-1.02.55	Ghigo, Arthur R. - A 2D multiring simulation of blood flow in arteries	456
PO.FM01-1.03.56	Goto, Tomonobu - A Discrete Biased Random Walk Model Based on Bacterial Chemotaxis	458
PO.FM01-1.04.57	Hu, Wen - Hydrodynamics of tadpole swimming in the wake of a cylinder	460
PO.FM01-1.05.58	Iima, Makoto - Hierarchical structure of spatially localized bioconvection of photosensitive microorganism	462

PO.FM01-1.06.59	Prahl Wittberg, Lisa - Flow and blood clot detection in the ECMO system	464
PO.FM01-1.07.60	Qian, Qin - Drug Transport in Anterior Human Eye after Subconjunctival and Episcleral Implants	466
PO.FM01-1.08.61	Rival, David - The influence of hematocrit on the decaying shear turbulence of blood flow in large arteries	468
PO.FM01-1.09.62	Staples, Anne - A model for tracheolar flow in insects	470
PO.FM01-1.10.63	Wu, Wei-Tao - Numerical simulation of thrombosis in a blood vessel	472
PO.FM01-1.11.64	Yeh, Han Hung - FSI analysis of artificial heart valves using Newtonian and non-Newtonian models	474
PO.FM01-1.12.65	Zayko, Julia - Effect of the flow regime on flutter in collapsible tubes	476

THE STABILITY OF FLOWING TRAINS OF CONFINED RED BLOOD CELLS

Jonathan B. Freund*[1] and Spencer H. Bryngelson[2]

[1]*Mechanical Science & Engineering and Aerospace Engineering, University of Illinois at Urbana-Champaign, Urbana, Illinois, USA*

[2]*Mechanical Science & Engineering, University of Illinois at Urbana-Champaign, Urbana, Illinois, USA*

Summary The asymptotic and transient stability of single-file trains of fluid-filled elastic capsules flowing in narrow channels is analyzed as a model for the lines of red blood cells commonly observed in small tubes or vessels. The most amplified disturbances in larger channels are found to have a rich variety of characteristics depending upon the details of the particular configuration. Transient growth mechanisms are found to be significant, even for relatively small perturbations, and are shown to precipitate nonlinear saturation and chaotic flow many times more quickly than the $t \to \infty$ asymptotic stability would predict even for nominally small perturbations.

INTRODUCTION

Red blood cells or similar elastic capsules in sufficiently small vessels or tubes are well-known to flow in a regular single-file formation down the center of the vessel. In wider tubes or vessels, seemingly chaotic flow is observed (*e.g.* figure 1), presumably because such capsule trains are unstable. The source of this instability is unclear yet fundamentally important, particularly how it might be affected by geometric and capsule mechanical properties to avoid line disruption in microfluidic devices to process blood. We consider the character of the most amplifying perturbations that might lead to chaotic flow.

The model system we analyze is a two-dimensional flow of capsules, which empirically displays both stable and chaotic behaviors. We assume that the transition between these regimes arises due to the growth of small perturbations via linear mechanisms. There is no expectation that linearization of this coupled fluid–structure system leads to a diagonalizable system, so we also consider transient linear amplification of disturbances in addition to the eigensystem that governs long-time linear amplification. These methods[1], as well as the transient non-modal behavior they expose, have been used to study, for example, boundary layer stability. Here they are adapted to the complete fluid–structure coupled flow in the viscous limit. Direct numerical simulations for specific cases confirm both the predicted transient and asymptotic amplification rates, and are used to track the subsequent nonlinear evolution of the system to a chaotic behavior. Of particular interest are the most amplified disturbances and what perturbation amplitudes are needed for transient disturbances to achieve nonlinear saturation significantly before corresponding eigenmodes might lead to finite-amplitude effects at long times, as they must if any eigenvalues are amplifying.

METHODS

The cells are modeled as finite-deformation elastic shells, each containing a Newtonian fluid of area πr_o^2, which for this study matches that of the suspending fluid.[2,3] A boundary integral method[4] is used to evaluate their surface velocities $\mathbf{u}$, which are nonlinear functions of cell surface positions $\mathbf{x}$ due to geometric factors. The full nonlinear system evolves as

$$\frac{\mathrm{d}\mathbf{x}}{\mathrm{d}t} = \mathbf{u}(\mathbf{x}). \tag{1}$$

From this numerical model, with M spectral collocation points $\vec{\mathbf{x}}$ representing the cell surfaces, a perturbation method is used to construct the $2M \times 2M$ matrix $\mathbf{A}$ that governs the temporal behavior of perturbations $\vec{\boldsymbol{\varepsilon}}$ to $\vec{\mathbf{x}}$:

$$\frac{\mathrm{d}\vec{\boldsymbol{\varepsilon}}}{\mathrm{d}t} = \mathbf{A}\vec{\boldsymbol{\varepsilon}}. \tag{2}$$



Figure 1: Simulation results for cell shapes and locations for a stable case (left) and an unstable case (right).

*Corresponding author. Email: jbfreund@illinois.edu

To assess the linear evolution of perturbations governed by (2), we consider both the $t \to \infty$ behavior, dictated by its eigenvalue with the largest positive real component $\alpha = \mathrm{Re}(\lambda_\alpha)$ with corresponding eigenvector $\mathbf{s}_\alpha$, and transient growth, which corresponds to the maximum singular value of the singular-value decomposition of $\exp \mathbf{A}t$. The $t \to 0^+$ transient growth rate is η, with corresponding singular vector $\mathbf{v}_\eta$. These perturbations, amplification rates, and subsequent transition to nonlinear chaotic motion are considered.

RESULTS

Figure 2 (a) shows the disturbance growth in time for five different initial perturbations for flow of 20 cells in $W = 10r_o$ wide streamwise-periodic channel. The initial disturbances are determined by the linear analysis of $\mathbf{A}$ as outlined and their evolution is computed by direct numerical solution of (1). For initial perturbation amplitudes $\varepsilon = 0.001r_o$, the initial transient linear growth rate η is significantly faster than the long-time eigenvalue-based growth rate α. (Direct simulations with small-amplitude initial conditions verify the numerical procedures in the linear limit.) However, for this small initial perturbation, the cumulative amplification of this transiently amplified disturbance is insufficient to lead to significant nonlinear behavior before the eigenvector growth dominates behavior at later times. Increasing the initial perturbation to a still small value of $\varepsilon = 0.01r_o$ allows the transient amplification to saturate nonlinearly and develop rapidly to a chaotic flow (see figures 2 b to h). This occurs about 100 times faster than growth at the asymptotically most amplified rate. An ad hoc disturbance for the same amplitude, formed by randomly perturbing cell centroids by the same ε is less amplified still.

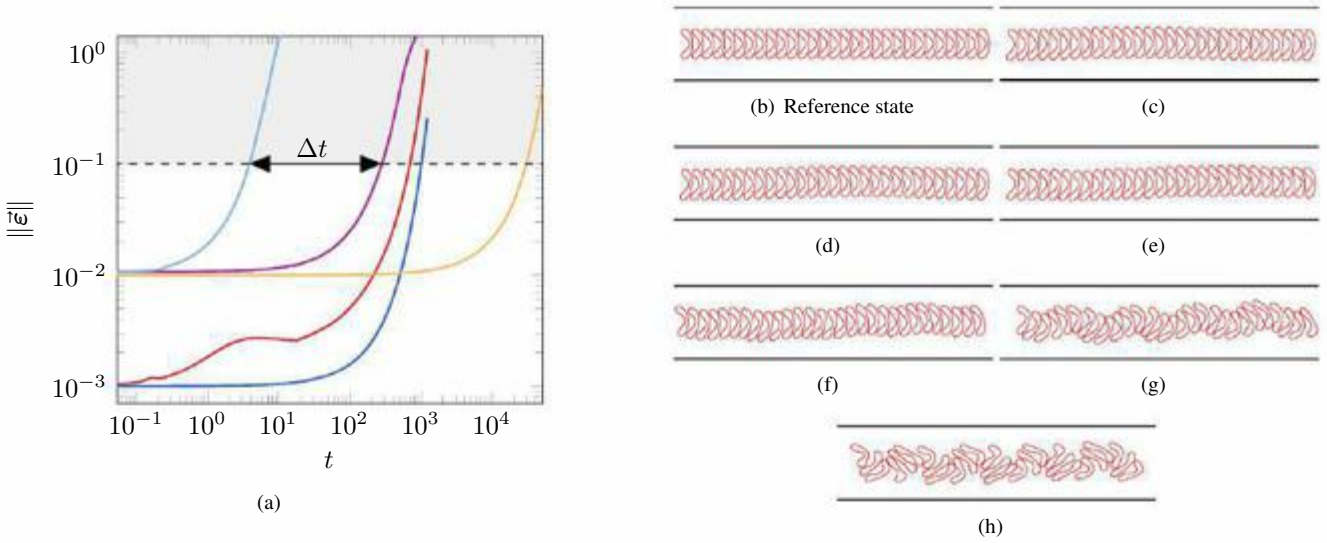

Figure 2: (a) Amplification 5 different initial perturbations for a channel with packing $Nr_o/L = 0.7$ and width $W = 40r_o$: — most amplified $t \to 0^+$ disturbance for $\varepsilon = 0.001$, — most amplified $t \to \infty$ for $\varepsilon = 0.001$; — most amplified $t \to 0^+$ for $\varepsilon = 0.01$; — most amplified $t \to \infty$ for with $\varepsilon = 0.01$; and — *ad hoc* disturbance $\varepsilon = 0.01$. (b) Visualization of the base flow state. (c–h) Evolution of the most unstable eigenvector perturbation to a chaotic flow condition.

The most amplified transient and eigenvector disturbances change qualitatively for different configurations, showing longitudinal displacements, rotations, transverse displacements, and symmetric and asymmetric distortions of the membranes. The corresponding eigenvectors (not shown) are typically different in character from the most amplified transient disturbances.

This work was supported in part by the National Science Foundation under Grant No. CBET 13-36972.

References

[1] P. J. Schmid, "Nonmodal stability analysis," Annu. Rev. Fluid Mech. **39**, 129 (2007).
[2] J. B. Freund, "Leukocyte margination in a model microvessel," Phys. Fluids **19**, 023301 (2007).
[3] H. Zhao, A. H. G. Isfahani, L. N. Olson and J. B. Freund, "A spectral boundary integral method for flowing blood cells," J. Comp. Phys. **229**, 3726 (2010).
[4] C. Pozrikidis, *Boundary integral and singularity methods for linearized viscous flow* (Cambridge University Press, Cambridge) (1992).

MICROCIRCULATION OF RED BLOOD CELLS FOR TWO MAJOR GENETIC DISEASES

Scott Atwell[1], Priya Gambhire[1], Emmanuèle Helfer[1], Catherine Badens[2], Anne Charrier[1] & Annie Viallat[1 a)]
[1]*Université Aix-Marseille, CNRS, CINaM UMR 7325, 13288 Marseille, France*
[2]*Medical Genetics Department, Timone Children Hospital, Marseille, France*

Summary Sickle Cell Anaemia and Hereditary Spherocytosis are genetic hematological disorders in which red blood cell rigidity is increased. These changes result in problems of RBC circulation in narrow capillaries and through the thin slits of splenic sinusoids - both situations where the RBCs may be subject to very strong deformations. Here, we first show that even in presence of oxygen most RBCs from sickle cell anemia patients have an impaired motion when submitted to a shear flow at low shear rate. We then observe the passage of sickle RBCs, spherocytes and healthy RBCs through slits mimicking interendothelial slits within the spleen. Their difference in terms of transit time, trapped cell ratio, lysis ratio and RBC recovery time are quantitatively determined.

INTRODUCTION

Two of the most important genetic diseases of red blood cells (RBCs), namely sickle cell anaemia - a very handicapping and the most prevalent genetic disease in the world - and hereditary spherocytosis are both characterized by an increase in the cell rigidity [1], [2]. In hereditary spherocytosis, the lack of deformability occurs via changes in membrane proteins which in turn alter the cytoskeleton resulting in a spherical cell shape whereas in sickle cell anaemia the mutated haemoglobin S able to form rigid fibers in conditions of deoxygenation is the cause. Moreover, sickle cell RBCs have been shown to be more rigid than healthy ones even in conditions of oxygenation [2]. Surprisingly, the effect of this increased rigidity of oxygenated RBCs on their flow behaviour has not been studied. Here, we quantitatively characterize the impact of the rigidity of sickle oxygenated RBCs on their orientation under shear flow. We then address the question of the passage of RBCs through the interendothelial slits within the spleen. Indeed, both diseases severely affect the spleen albeit leading to different conditions. In the case of spherocytosis, the spleen enlarges leading to splenomegaly and anaemia while the sickle cell disease leads to the condition of hyposplenism. We developed a technique that enabled us to mimic submicronic interendothelial slits in-vitro and we report the first quantitative description of the deformation and the dynamics of RBCs passing through submicronic slits in sickle cell anaemia, spherocytosis and healthy conditions.

OXYGENATED RBC DYNAMICS UNDER SHEAR FLOW IN SICKLE CELL DISEASE

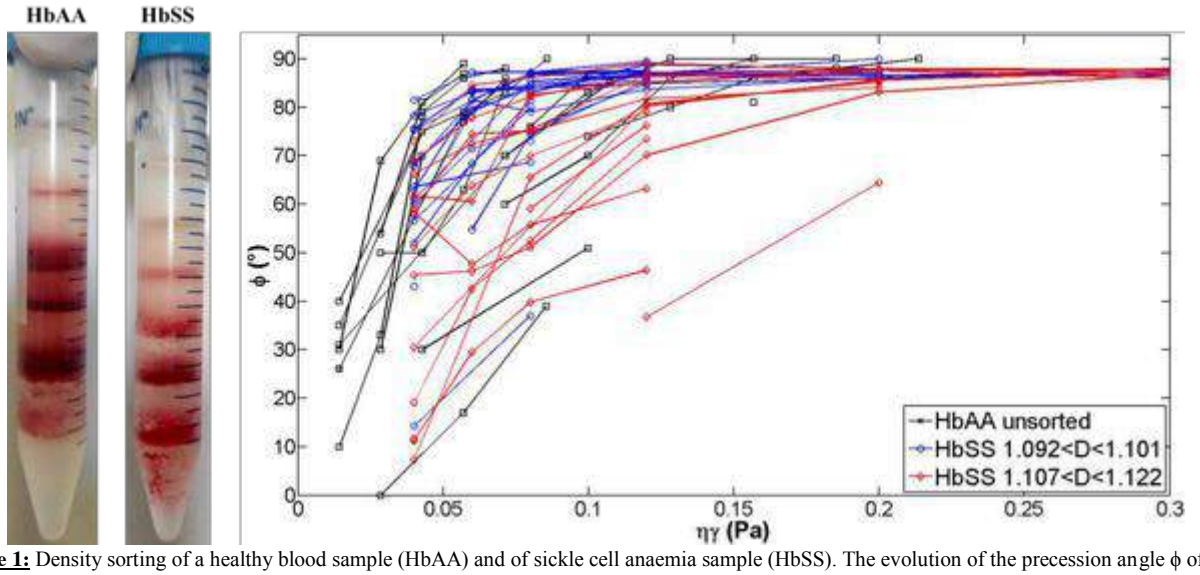

Figure 1: Density sorting of a healthy blood sample (HbAA) and of sickle cell anaemia sample (HbSS). The evolution of the precession angle ϕ of RBCs with regards to the applied shear stress is shown for unsorted healthy blood samples and two density subpopulation of a sickle anaemia sample.

In a simple shear flow at low shear rates, RBCs may display a variety of motion regimes such as steady tank-treading/swinging, unsteady tumbling, and chaotic motion. In the tumbling-flipping motion, it has been shown that the orientation of the RBC axis of symmetry with the flow direction is determined by the shear stress as a way to minimize energetically costly deformations [3]. As such the transition from tumbling to rolling undergone by RBCs as the shear rate is increased is a true signature of their elasticity. Oxygenated RBCs from 15 sickle cell patients were suspended in 9% Dextran

a) Corresponding author. Email: viallat@cinam.univ-mrs.fr

2M. RBCs with a regular biconcave shape were selected and submitted to a controlled shear flow. In order to reduce variability, the blood samples have been separated in four different subpopulations based on their densities by using five Percoll density solution with densities of respectively 1.085, 1.092, 1.101, 1.107 and 1.122 as described in [4]. As expected, sickle RBCs were found to be overall denser than healthy ones (**Fig.1 left**). The evolution of RBC orientation with the shear rate for RBCs belonging to the main dense layer is shifted towards higher shear rates compared to healthy cells. The tank-treading regime appears for higher shear rates too. This result shows that the enhanced rigidity of dense oxygenated RBCs from sickle cell anaemia patients induces a specific flow behaviour. However, RBCs from sickle cell anaemia patients and for controls that all belong to the main (less dense) layer of healthy cells present the same flow behaviour (**Fig. 1 right**). The alteration of the flow dynamics of RBCs from sickle cell anaemia seems therefore to be closely related to their density, i.e. to the haemoglobin concentration. We finally exploit these results to characterize the average rigidity of a blood samples of patients from the automatic detection of the orientation of a large population of RBCs in shear flow.

BIOMIMETIC SPLEEN SLITS

We then studied how the passage of the sickle RBCs and the spherocytes differ within the spleen and to compare them to healthy RBCs. To enable this, an on-chip biomimetic spleen is developed. The novelty of this device is the presence of submicron sized channels (0.5 µm) which have been obtained by the standard procedures of photolithography and wet chemical etching. Moreover, the submicron channels are prepared on a silicon master, which enables obtaining reproducible, transparent and disposable biomimetic spleen devices in PDMS.

Using this device, the passage of sickle cells, spherocytes and healthy RBCs is studied. A difference in the behaviours of spherocyte RBCs and sickle RBCs is readily observed. A majority of the spherocyte RBCs are observed to be entrapped within the channels compared to the healthy RBCs (**Fig. 2**). The entrapment is effected by the flow rate of the passage. In certain cases, haemolysis of the cells is also observed. In contrast, most of the sickle RBCs are observed to pass through the channels but have higher shape recovery times compared to the healthy cells. In addition, the post-deformation shapes of the sickle and spherocyte RBCs are seen to be different from each other.

The present work can therefore answer important questions such as how a difference in the cause of RBC rigidity can significantly influence its behaviour in microcirculation. To our knowledge, RBC deformation through channels of submicron size has not been studied and this opens up plethora of interesting experiments to be explored using this device.

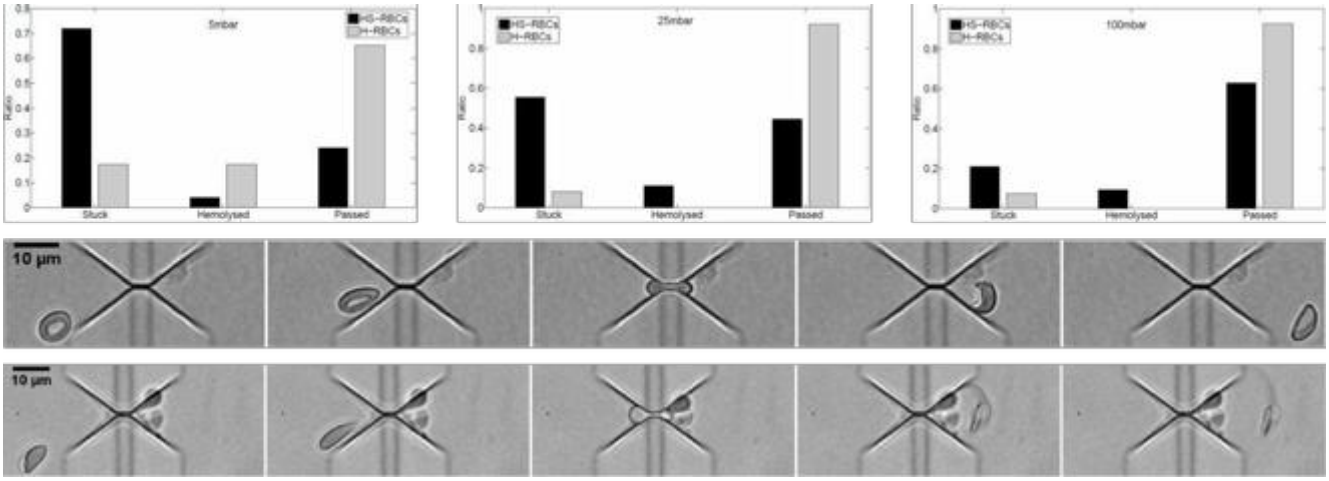

Figure 2: Ratio of healthy RBCs (H-RBCs) and hereditary spherocytosis (HS-RBCs) passing through, haemolysing or getting stuck within the sub-micronic PDMS slits (Width*Length*Depth=1.08±0.09*2.28±0.16*10µm) studied at 5mbar, 25mbar and 100mbar pressure drops. Time lapses of a RBC passing through the slit and of a haemolysed RBC are shown.

References

[1] I. Dulińska, M. Targosz, W. Strojny, M. Lekka, P. Czuba, W. Balwierz, and M. Szymoński, "Stiffness of normal and pathological erythrocytes studied by means of atomic force microscopy," *J. Biochem. Biophys. Methods*, vol. 66, no. 1–3, pp. 1–11, 2006.

[2] J. L. Maciaszek and G. Lykotrafitis, "Sickle cell trait human erythrocytes are significantly stiffer than normal.," *J. Biomech.*, vol. 44, no. 4, pp. 657–61, Feb. 2011.

[3] J. Dupire, M. Socol, and A. Viallat, "Full dynamics of a red blood cell in shear flow," *Proc. Natl. Acad. Sci. U. S. A.*, vol. 109, no. 51, pp. 20808–20813, Dec. 2012.

[4] J. D. Corbett, W. E. Mickols, and M. F. Maestre, "Effect of Hemoglobin Concentration on Nucleation and Polymer Formation in Sickle Red Blood Cells," *J. Biol. Chem.*, vol. 270, no. 6, pp. 2708–2715, Feb. 1995.

FLOW OF BLOOD CELLS IN COMPLEX GEOMETRY

Peter Balogh & Prosenjit Bagchi [(a)]
Mechanical and Aerospace Engineering, Rutgers University, Piscataway, NJ 08854, USA

Abstract A three-dimensional computational tool for simulating the flow of blood cells through geometries of arbitrary complexity is presented. Examples of complex geometries include, but are not limited to, micro-fluidic channels and networks, stenosed blood vessels, cell and particulate sorting devices, and complex micro-vascular networks. The computational tool is designed to span the entire spectrum of scales typically encountered in microcirculatory blood flow, thus enabling the direct simulation of physiologically realistic problems. The three-dimensional unsteady Stokes equations are solved numerically in conjunction with two separate types of immersed boundary methods; a sharp-interface method is used to simulate stationary and moving rigid boundaries, while a front-tracking method is used to simulation the motion of highly deformable blood cells. The resulting tool provides a fast, stable, and accurate platform for simulating highly complex problems involving cellular motion in a wide range of complex geometries.

BACKGROUND AND INTRODUCTION

High-fidelity computational modelling of blood flow in a microvascular network remains a major challenge due to a lack of a model that can consider the entire spectrum of lengths scales, from an entire network comprised of many vessels with bifurcations and mergers, to deformation of every single cell, to the nano-scale receptor-ligand interaction. Microvascular blood flow modelling, to date, falls under two broad categories: (i) Continuum modelling, and (ii) cellular-scale modelling. The continuum approach is often utilized for capturing macroscale effects. As applied to large networks, for example, each vessel is treated as a one-dimensional conduit, and the pressure-flow relationship is specified by Poiseuille's law, while the rheological effects are added using empirical relations for non-Newtonian blood viscosity. Individual blood cells are not explicitly considered in such models. Although these models have been useful in understanding the network-scale hemodynamics, they lack the ability to address multiscale and realistic pathophysiological processes. In the cellular scale modelling, each blood cell is treated as a finite-size particle, and its deformation in flow is sufficiently resolved. While such an approach provides a very rich understanding of the cellular-scale processes, it is computationally demanding when a large number of cells are present. Moreover, most cellular-scale studies have considered blood flow in simple geometry, such as unbranched, straight conduits of uniform cross-section. In contrast, the architecture of a vascular network is highly complex, and is characterized by frequently bifurcating, merging, and tortuous vessels. The extent to which the existing knowledge of the cellular-scale flow in simple conduits can be applied to a complex microvascular network remains unknown.

To bridge this knowledge gap, we follow a bottom-up approach that has been recently taken in modelling whole-body circulation. Our broad objective is to scale the cellular-level modelling up to a network level, while coarse-graining the nano-scale receptor-ligand interactions. This allows us to address pathophysiological processes at realistic network scales yet resolving cellular-scale details and essential molecular interactions.

NUMERICAL METHOD AND RESULTS

We have developed a fully 3D, multiscale direct simulation technique for flow of deformable polydisperse cell suspension through microvascular network and geometrically complex conduits. The major challenge in the numerical development is that it involves highly deformable cell surfaces that are governed by complex physical laws, and non-moving boundaries that are characterized by the network architecture. A ghost-node immersed-boundary (GNIBM) method is used to model the vascular network. 3D network topology can be obtained from in vivo images of the microvasculature, and rendered to be used in a GNIBM-based flow solver. The methodology also allows us to simulate flow of perfectly rigid particles. A finite-element method is used to resolve large deformation of every blood cell with high fidelity. A front-tracking method is used to obtain a two-way coupling between the cell deformation and fluid flow. A coarse-grain technique using stochastic Monte-Carlo method is used to model the molecular interactions between the cells and the vascular wall.

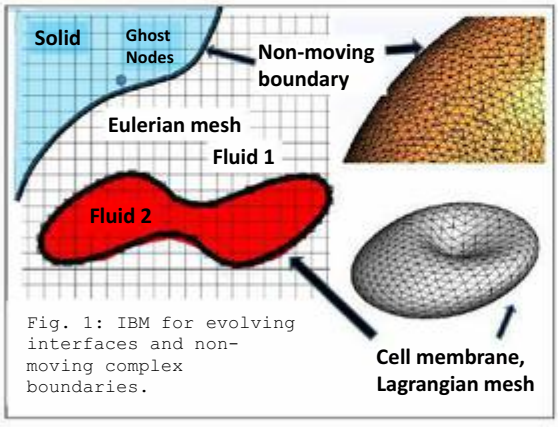

Fig. 1: IBM for evolving interfaces and non-moving complex boundaries.

Physiologically realistic microvascular network is considered in our modeling based on published high-resolution imaging data. Digital reconstruction is performed segment-by-segment by tracing the centerline path of each vessel, and manual demarcation of the vessel boundary. A 3D solid model is then created by sweeping a circular cross section through these paths, with radius varying in accordance

[a)] Corresponding author. Email: pbagchi@jove.rutgers.edu.

with that of the image. Once the solid model is completed, a finite element mesh is generated on the surface of each vessel (Fig 2) which defines the non-moving solid-fluid boundary. The basic premise of any IBM is to provide a means of simulating flows in presence of complex boundaries, such as the vascular network, without requiring a boundary-conforming mesh. The entire domain, including the fluid and solid, can be discretized using a rectangular Cartesian mesh (Fig 1). The main idea is to impose certain velocity at the solid nodes (i.e. ghost nodes) nearest to the boundary such that the desired velocity at the boundary is achieved. We have developed an interpolation scheme using the image points of the ghost nodes inside the fluid domain, which resulted in a linear system that can be solved to obtain the ghost-node unknowns in an accurate and self-consistent manner for both stationary and moving rigid boundaries.

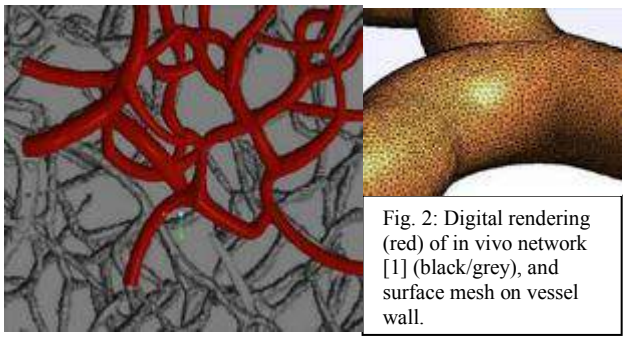

Fig. 2: Digital rendering (red) of in vivo network [1] (black/grey), and surface mesh on vessel wall.

As for the cell deformation, we previously had developed a 3D numerical model for deformable blood cells that is most comprehensive [2-4]. We model the cells as viscous liquid drops enclosed by zero-thickness hyper-viscoelastic membranes whose mechanical properties include resistance against shear deformation, area dilatation, bending, and membrane viscosity. The cell membrane is made of a lipid bilayer and an underlying viscoelastic cortex. The bilayer is modeled following Helfrich formulation for bending energy, and a finite-strain viscoelastic model is used to obtain the cortical tension. The membrane force is transferred to the fluid using a finite-span Delta function. The fluid flow is obtained by solving the three-dimensional Stokes equations on the fixed rectangular Cartesian grid using a staggered-grid discretization of the primitive variables. Overall, a single set of equations is solved using a combined finite difference and spectral method to obtain flow fields inside and outside of each deformable cell, with the surfaces of rigid boundaries represented using constraints placed on Eulerian mesh points identified as ghost nodes.

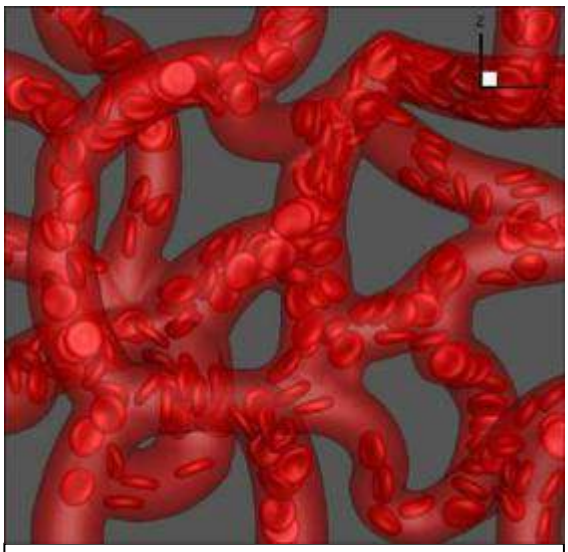

Fig 3. Simulation of flow of blood cells in a microvascular network.

Various validation cases have been performed to assess the accuracy of the simulation tool, such as the motion of deformable capsules flowing through constricted microchannels, and red blood cells moving through a micro-fluidic bifurcation. The later example has been used to predict the so-called Zweifach-Fung effect. As a further demonstration of the capability of the tool, Fig 3 presents a snapshot from a simulation on the flow of blood cells through a microvascular network.

CONCLUSIONS

We have developed an IBM-based multiscale direct simulation technique to simulate flow of blood cells in complex geometry. The technique allows us to consider cellular motion in microvascular network comprised of bifurcating, merging, and tortuous vessels, while retaining the cellular-scale details, and essential molecular-scale information. This multiscale tool would enhance our ability to consider pathophysiological problems in microcirculation under realistic geometric conditions. Problems that can be readily addressed are the influence of vascular network architecture on the heterogeneity of the blood cell distribution in microcirculation, and on the platelet margination and leukocyte adhesion. It could also serve as a virtual test bed for optimizing the physical characteristics of engineered drug particles for rapid segregation and deposition in the microvasculature.

References

[1] Lorthois, S., Cassot, F.: Fractal analysis of vascular networks: Insights from morphogenesis. *J. Theor. Biol.* **262**:614-633, 2010.

[2] Yazdani, A., Bagchi, P.: Influence of membrane viscosity on capsule dynamics in shear flow. *J. Fluid Mech.* **718**: 569-595, 2013.

[3] Vahidkhah, K., Bagchi, P.: Microparticle shape effects on margination, near-wall dynamics, and adhesion in a three-dimensional simulation of red blood cell suspension. *Soft Matter*. **11**: 2097-2109, 2015.

[4] Cordasco, D., Bagchi, P.: Intermittency and synchronized motion of red blood cell dynamics in shear flow. *J. Fluid Mech.* **759**: 472-488, 2014.

INVERSION OF HEMATOCRIT PARTITION AT MICROFLUIDIC BIFURCATIONS

Z. Shen[1], G. Coupier [*1], B. Kaoui[2], B. Polack[3], J. Harting[4], C. Misbah[1], and T. Podgorski[1]

[1]*Laboratoire Interdisciplinaire de Physique (LIPhy) CNRS-Université Grenoble Alpes, Grenoble, France*
[2]*CNRS-Sorbonne University, Université de Technologie de Compiègne, UMR7338 Biomechanics and Bioengineering, 60203 Compiègne, France; TP1, University of Bayreuth, D-95447 Bayreuth, Germany*
[3]*Laboratoire d'Hématologie, CHU, Grenoble, France; TIMC-IMAG/TheREx, CNRS-Université Grenoble Alpes, Grenoble, France;*
[4]*Department of Applied Physics, Eindhoven University of Technology, P.O. Box 513, 5600MB Eindhoven, The Netherlands; Faculty of Science and Technology, Mesa+ Institute, University of Twente, 7500 AE Enschede, The Netherlands*

Summary Partitioning of red blood cells (RBCs) at the level of bifurcations in the microcirculatory system affects many physiological functions yet it remains poorly understood. We address this problem by using T-shaped microfluidic bifurcations as a model. Our computer simulations and *in vitro* experiments reveal that the hematocrit (ϕ_0) partition depends strongly on RBC deformability, as long as $\phi_0 < 20\%$. Furthermore, we discover a deviation from the Zweifach-Fung effect which states that the child branch with lower flow rate recruits less RBCs than the higher flow rate child branch. At small enough ϕ_0, we get the inverse scenario, and the hematocrit in the lower flow rate child branch is even higher than in the parent vessel.

INTRODUCTION

Blood flows through a complex network of the circulatory system – from large arteries to very tiny capillaries – in order to ensure oxygen delivery and to remove metabolic waste. This task is mainly carried out by red blood cells (RBCs) that are remarkably deformable, in healthy conditions, and therefore able to squeeze into tiny capillaries. A major open problem in blood circulation is to understand the perfusion in the vasculature networks, especially in the microvasculature where RBCs accomplish their vital functions. In such a network, cell distribution is essentially heterogeneous, a phenomenon that is mainly dictated by hematocrit partition at the level of bifurcations, where RBCs do not behave as passive tracers. Their shape flexibility and dynamics have a decisive role because their size is comparable to that of blood capillaries. A well known phenomenon in microcirculation is the Zweifach-Fung effect [Pries (1989)]: If we consider a bifurcation (as in Figure 1), the child branch with the lower flow rate is depleted in RBCs as compared to the parent vessel, while the other, higher flow rate child branch is enriched. That is, if in the parent vessel the total volumetric flow rate is Q_0 and the RBC volumetric flux is N_0, and in the child branch with the lower flow rate this flow rate is Q_1 and the RBC flux N_1, then $N_1/N_0 < Q_1/Q_0$.

The Zweifach-Fung effect results from the existence of a cell free layer (CFL) close to the walls, which is only occupied by plasma [Doyeux (2011)]. The feeding flow is divided by a separating streamline into two parts, one feeding the low flow rate branch and the other feeding the high flow rate branch. Due to the CFL, the RBC fraction entering the low flow rate branch is smaller compared to the original RBC fraction in the total feeding flow.

In the present work, we study the hematocrit partition at bifurcations using two-dimensional lattice Boltzmann simulations, whose outcomes are validated and supported by microfluidic experiments.

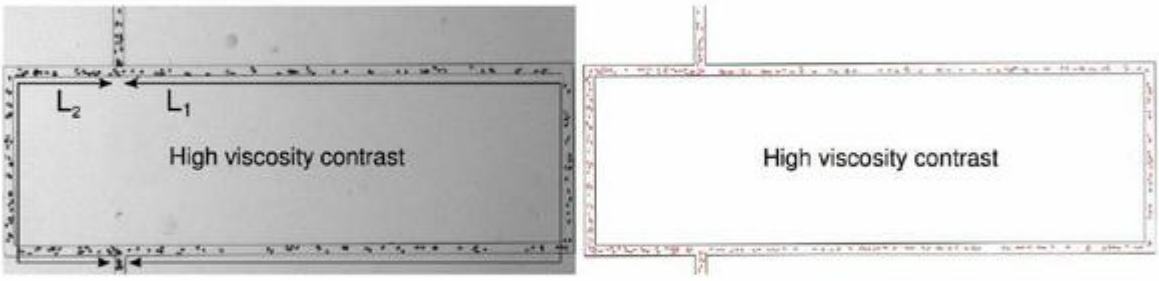

Figure 1: Snapshots of the RBCs partition, in both experiments and simulations, when the hematocrit of the feeding flow is around $\phi_0 = 10\%$. The length ratio between the two child branches is set to 3. The channels width is 20μm and the height is 8 μm. Only the high viscosity contrast (physiological conditions) is shown.

*Corresponding author. Email: gwennou.coupier@univ-grenoble-alpes.fr

MAIN RESULTS

Our main results are summarized in Fig 2. We first show that RBCs deformability strongly impacts partition when the hematocrit is below 20%. RBC deformability is governed by several parameters such as membrane stiffness and viscosity, swelling degree, and the viscosity contrast between the hemoglobin and the suspending fluid. Here we tune the deformability through the viscosity contrast, that controls the RBC dynamics then all the migration mechanisms at the origin of the CFL.

The CFL is the result a balance between lift forces due to hydrodynamic interaction between the cells and the wall and interactions between cells, that tends to widen the cell distribution. Both interactions depend on cell deformability. At low concentration, interactions between cells play a minor role compared to lift phenomenon and the resulting CFL mainly depends on lift forces intensity, therefore on deformability. So does the splitting law at the level of the bifurcation (Fig 2, middle panel). At higher concentration, interactions between cells come into play, and our result show that they probably depend on deformability the same way lift forces do, so that those dependencies cancel out. Therefore the CFL and the splitting do not depend any more on cell deformability (Fig 2, left panel).

At lower hematocrit (below 5%), a peculiar effect arises due to the prevalence of the discrete nature of blood at that scale. For all hematocrits, the distribution of RBCs in the feeding channel is not homogeneous, but rather exhibits two lateral peaks. This become more pronounced at low hematocrit, where a two-file distribution of RBCs is observed.The central part is depleted in RBCs, but it is escorted by two enriched layers, which themselves are surrounded by two depleted layers at the periphery (close to the channel walls). This 5-layer configuration (fluid-cell-fluid-cell-fluid) has an extremely interesting impact on the partition (Fig 2, right panel): at low Q_1/Q_0, the peripheral CFL in the parent vessel is recruited by the branch 1 so ϕ_1 starts at 0 and increases when Q_1 increases. Then, in some intermediate range for Q_1/Q_0, the low flow rate branch recruits the lateral CFL layer plus the adjacent RBC-rich layer among the five layers. By contrast, the high flow rate branch recruits the CFL layer close to the opposite wall plus its adjacent RBC-rich layer (exactly as the low flow rate branch) as well as the central (and depleted) layer. This implies that the hematocrit is increased in the low flow rate branch, which is the reverse behavior of the Zweifach-Fung effect.

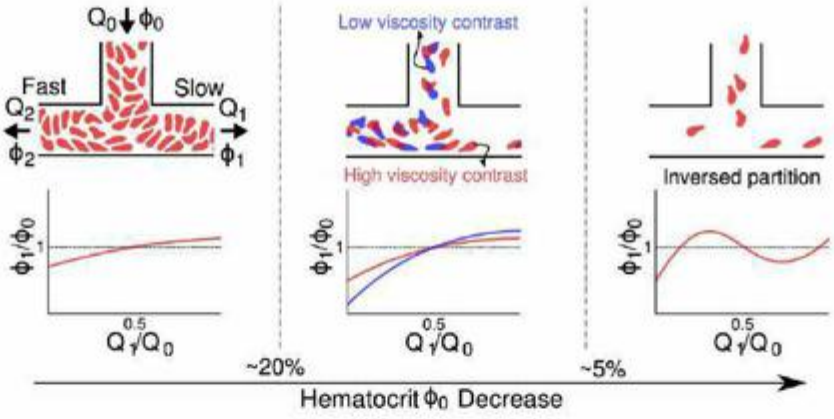

Figure 2: Summary of the main results. See also [Shen (2016)].

CONCLUSION

The hematocrit in microcirculation can reach values as low as 10-20% compared to the average hematocrit in human body (45%). At such a low hematocrit, our simulations and *in vitro* microfluidic experiments have revealed that RBCs partition at the level of bifurcations depends strongly on cell deformability. In the extreme hemodilution, our results exhibit a newly reported phenomenon: The low flow rate branch may receive higher hematocrit than the high flow rate branch. This phenomenon is observed under moderate confinement and is the result of a peculiar structuring of the cell suspension.

References

[Pries (1989)] A. R. Pries, K. Ley, M. Claassen, and P. Gaethgens. Red cell distribution at microvascular bifurcations. *Microvasc. Res.*, 38:81–101, 1989.

[Doyeux (2011)] V. Doyeux, T. Podgorski, S. Peponas, M. Ismail, and G. Coupier. Spheres in the vicinity of a bifurcation: elucidating the Zweifach-Fung effect. *J. Fluid Mech.*, 674:359, 2011.

[Shen (2016)] Z. Shen, G. Coupier, B. Kaoui, B. Polack, J. Harting, C. Misbah, and T. Podgorski. Inversion of hematocrit partition at microfluidic bifurcations. *Microvasc. Res.*, 105:40, 2016.

Theory of margination in blood and other multicomponent suspensions

Rafael G. Henriquez Rivera[1], Xiao Zhang[1], and Michael D. Graham [*1]
[1]*Department of Chemical and Biological Engineering, University of Wisconsin-Madison, Madison WI 53706 USA*

Summary A mechanistic theory is developed to describe segregation in confined multicomponent suspensions such as blood. It incorporates the two key phenomena arising in these systems at low Reynolds number: hydrodynamic pair collisions and wall-induced migration. In simple shear flow, several regimes of segregation arise, depending on the value of a "margination parameter" M. Most importantly, there is a critical value of M below which a sharp "drainage transition" occurs: one component is completely depleted from the bulk flow to the vicinity of the walls. Direct simulations also exhibit this transition as the size or flexibility ratio of the components changes. Results are presented for both Couette and plane Poiseuille flow.

Using kinetic theory a mechanistic theory is developed to describe segregation in multicomponent suspensions in confined flow. It incorporates the two key phenomena arising in these systems at low Reynolds number: hydrodynamic pair collisions (see a schematic in Fig. 1b) and wall-induced migration. We consider a binary suspension of deformable particles in a slit geometry in Couette and Poiseuille flows. A simple drift-diffusion model is obtained by taking several approximations such as considering the important case of a binary suspension composed of a "primary" component ('p') and a "trace" component ('t') such that $\phi_p \gg \phi_t$, where ϕ_p and ϕ_t are the volume fractions of p and t. Fig. 1a shows an illustration of the binary suspension in confined simple shear flow with the walls located at $y = 0$ and $y = 2H$.

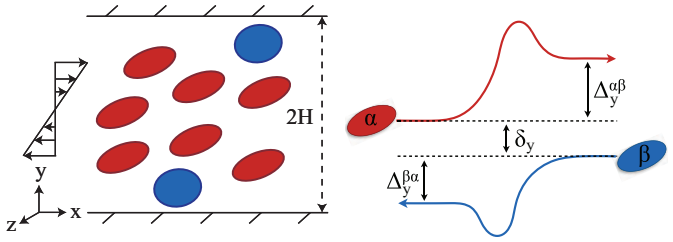

(a) (b)

Figure 1: (a) Suspension of particles in a slit under simple shear flow. (b) Pair collision trajectories of particles of species α and β under simple shear flow, where $\alpha = p$ or t and $\beta = p$.

In simple shear flow, several regimes of segregation arise, depending on the value of a "margination parameter" M. Remarkably, this single quantity determines the qualitative nature of the concentration profile. The sign of M is determined by the competition between the ratio of the migration velocities of the two components and the ratio of the collisional terms.
(1) $M > 1$: the trace component is displaced further from the wall than the primary component: it *demarginates*.

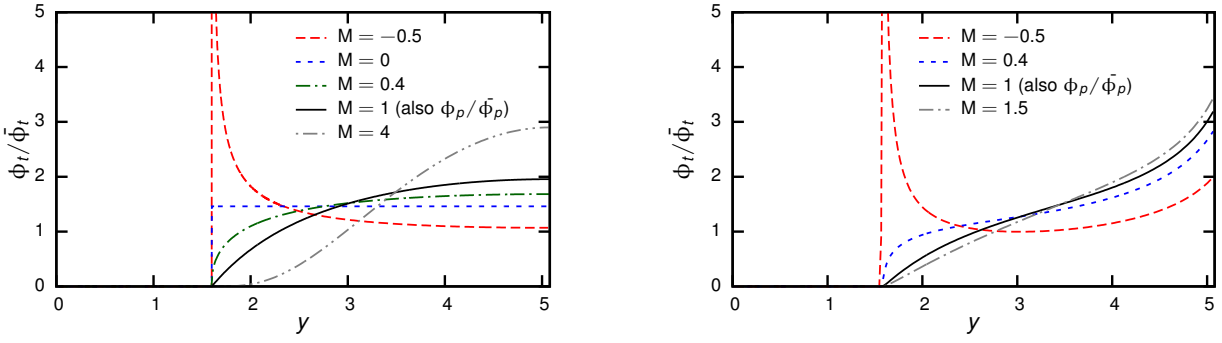

(a) (b)

Figure 2: Steady state volume fraction profiles of $\phi_p/\bar{\phi}_p$ (black solid line) and $\phi_t/\bar{\phi}_t$ for various values of M for (a) Couette flow and (b) Poiseuille flow. (The curves coincide when $M = 1$.)

(2) $0 < M < 1$: the relative concentration of the trace component is higher near the wall than the primary component but does not display a peak: it *weakly marginates*.
(3) $-1 < M < 0$: the trace component displays a peak at $y = l_d$, corresponding to an integrably singular concentration profile: it *moderately marginates*. l_d is the so-called cell-free layer or depletion layer thickness.

*Corresponding author. Email: mdgraham@wisc.edu

(4) $M \leq -1$: the solution for the trace component displays a nonintegrable singularity at $y = l_d$. This steady state is physically unrealizable as it corresponds to an infinite amount of material in a finite region. In this regime collisional transport overwhelms migration, and the trace component accumulates indefinitely at $y = l_d$, indicating *strong margination*.
$M = -1$ is a critical value of M below which a sharp "drainage transition" occurs: one component is completely depleted from the bulk flow to the vicinity of the walls. Direct simulations also exhibit this transition as the size or flexibility ratio of the components changes. Fig. 2a shows the volume fraction profiles of the trace component for different M values. Similar results from the theory are observed for Poiseuille flow, as shown in Fig. 2b.

The mechanistic nature of the theory leads to substantial and systematic insight into the origins of margination; this will complement detailed simulations and experiments in guiding development of technologies involving blood and other multicomponent suspensions at small scales.

References

[1] Henriquez Rivera, R. G., Sinha, K. & Graham, M. D. Margination regimes and drainage transition in confined multicomponent suspensions. *Phys. Rev. Lett.* 114, 188101 (2015).

A COARSE-GRAINED THEORY TO PREDICT PARTICLE MARGINATION AND MIGRATION IN BLOOD SUSPENSIONS

Qin M. Qi *[1] and Eric S.G. Shaqfeh[1,2,3]
[1]*Department of Chemical Engineering, Stanford University*
[2]*Department of Mechanical Engineering, Stanford University*
[3]*Institute for Computational and Mathematical Engineering, Stanford University*

Summary The inhomogeneous distribution of red blood cells and platelets normal to the flow direction plays a significant role in hemostasis, drug delivery and microfluidics. In this paper, we develop a coarse-grained theory to predict these distributions in pressure-driven channel flow at zero Reynolds number and compare them to experiments and simulations. We demonstrate that the balance between the deformability-induced lift force and shear-induced diffusion results in a red blood cells' peak concentration at the channel center and leaves a cell-free or "Fahraeus-Lindqvist" layer near the walls. On the other hand, in the absence of a lift force, platelets have excess concentration in the cell-free layer due to cell-platelet collisions. We also include in the model the process of platelets forming bonds with VWF-coated surfaces, linking cell migration and platelet margination to bleeding events. We thus describe the role of hematocrit in platelet activity as found in our associated experimental results.

INTRODUCTION

Blood is a multicomponent suspension consisting of many species including red blood cells, platelets *etc*. Under pressure-driven flow in channels, each species exhibits a unique inhomogeneous center-of-mass distribution due to differences in deformability, size and concentration. Red blood cells' migration behavior, characterized by a concentration peak at the channel center and a cell-free layer or "Fahraeus-Lindqvist" layer near the wall, results from a deformability-induced lift force created by wall interactions. Platelets, however, "marginate" and thus develop an excess concentration in the cell-free layer, primarily due to the lack of such a lift force. Experimental results show that bleeding time is influenced by red blood cell volume fraction, or hematocrit, suggesting a direct influence of erythrocyte concentration distribution (and thus migration) on platelet margination. The inhomogeneous concentration distribution is also important in applications such as drug delivery and microfluidic diagonostics. In this paper, we propose a theory that determines both erythrocyte and platelet distributions in the cross-flow direction using a semi-analytical approach as well as numerically calculated inputs from fast small-scale simulations. Our method is similar to those used in simple shear flow[1, 2], and the novelty of our work lies in:(1) resolving issues unique to shear rate gradients in pressure-driven flow (2) modeling the membrane properties and asperity of red blood cells instead of treating them as capsules in an idealized fashion (3) comparing with simulation and experimental results for verification and (4) introducing the platelet adhesion to a "wall trauma" as well as platelet margination.

METHODOLOGY

Our work focuses on flow through rectangular channels with the smallest dimension(height) being $O(10\mu m)$. This size matches capillary-sized blood vessels as well as many microfluidic devices. We assume the Reynolds number is zero so that inertial effects can be ignored. As mentioned above, our theory does rely on output functions from computer simulations. To determine the latter, we utilize an existing boundary integral simulation method[3] that solves Stokes flow including red blood cell (RBC) deformation, plasma flow, and platelet dynamics. The properties of the RBC membrane are modeled using the Skalak law with a reduced volume of 0.65. Platelets are treated as rigid oblates. We consider a capillary number($Ca = \frac{\mu\dot{\gamma}_c a}{E_s}$)between 0.5 and 2, corresponding to those characteristic of arteriole flow. Steady platelet and RBC distributions are determined from flux balances. Three types of fluxes normal to the flow direction appear in these two balances: hydrodynamic collisions, hydrodynamic lift and platelet adhesion (at the wall). We begin by examining the flow-induced "collision" of two particles (e.g. cell-cell, cell-platelet), which results in irreversible cross-stream displacements due to cell deformation. These changes in trajectories result in shear-induced diffusion and we use two particle collision simulations to obtain displacement values. Red blood cells experience a lift force away from the wall due to their deformability and curvature of the flow. This lift force creates a convective flux $N_{lift} = u_{lift}n$ which is the fundamental cause of RBC migration. We also use single cell simulations to determine the lift velocity u_{lift} numerically. Finally, platelets begin the process of thrombosis upon vascular trauma via multi-step reactions and we consider the initial step of platelets forming GPIb bonds with VWF factors on a damaged channel surface. This reaction produces a flux of platelets exiting the flow at the associated adhesion rate.

*Corresponding author. Email: qinq@stanford.edu

[a] 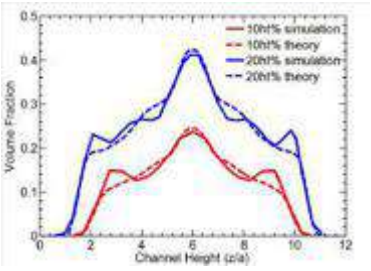

[b] 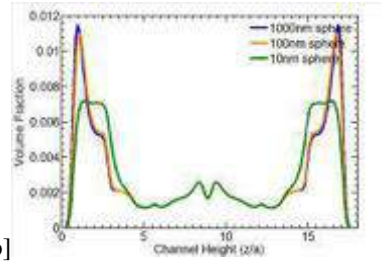

Figure 1: Red blood cell(a) and platelet concentration(b) profile

RESULTS AND DISCUSSIONS

Red blood cell distributions are thus determined from the balance between lift force and shear-induced diffusion. From simulation, the correlation for lift velocity is $u_{lift} = \frac{0.0095\dot{\gamma}(z)}{z^{1.05}}$, and the fitted values are similar to those reported from vesicle experiments. The scaling of the lift velocity associated with the wall distance z differs from the usual wall-induced migration velocity scaling $\frac{S_{zz}}{z^2}$ in shear flow because the variation of the shear rate in the cross stream direction creates an additional contribution to the lift velocity. As discussed by various researchers, a flux balance continuum model has a singularity issue at the centerline due to vanishing fluxes from both lift and collision. We thus add a non-local shear rate correction term: $\bar{\dot{\gamma}}(z) = \dot{\gamma}(z) + \epsilon\frac{u_{max}}{H/2}$. Our shear-induced diffusion flux includes only cell-cell collisions for the RBCs because of the relative paucity and size of RBC displacements in cell-platelet collisions. With a usual hematocrit between 10% and 20% in the microcirculation, red blood cells are, in fact, in the dilute to semi-dilute regime, and thus multiple particle interactions are important. We therefore lump higher-order collision processes into a second diffusivity term $D\frac{\partial n}{\partial z}$. The diffusivity D is used as a fitting parameter and it increases with hematocrit nearly linearly as expected but is uniformly smaller than the two particle effects. Figure 1(a) shows the comparison between our theoretical results and those from simulation. Both methods predict a reduction in the cell-free layer thickness with increasing hematocrit as a result of increased shear-induced diffusion.

In the absence of the deformation-induced lift force, platelet margination can be treated almost exclusively as a consequence of RBC migration and collisions. We thus solve for the platelet distribution by balancing the cell-platelet collision flux and platelet-platelet collision flux. The former drives platelets toward the cell-free layer and the latter controls the platelets' distribution within the layer. We compare our model results to *platelet-sized* sphere margination experiments and demonstrate that our model successfully captures the margination behavior. For *platelet-sized* particles, we assume $Pe = \frac{\rho\dot{\gamma}_c a^3}{kT} \rightarrow \infty$ and ignore Brownian motion. However, for smaller particles used in drug delivery applications, Brownian motion may be indeed significant. We therefore expand our model to study nanoparticle margination by adding a thermal diffusion flux. As in Figure 1(b), margination by RBC collisions is predicted to still be significant for particles as small as $O(10nm)$.

In the final stage of model development, we take platelet adhesion into consideration in the event of bleeding trauma. VWF factors have an average size of $200nm$ and therefore only platelets within such a wall normal length are able to form bonds with the surface. From the difference in cell-free layer thickness due to hematocrit (i.e. as a result of migration), we find that the near-wall concentration of platelets changes and thus affects the adhesion rate. We then compare our results to platelet adhesion experiments completed at different channel hematocrits.

CONCLUSIONS

By balancing the dominant mass fluxes normal to the flow direction calculated by a Boltzmann-collision approach, we solve for RBC and platelet distributions in pressure-driven flow through a channel. Our theory predicts cell migration and platelet margination and explains how hematocrit affects platelet adhesion in the case of a wall trauma. During the development of our model, we also address important questions in regard to determining the red blood cell lift velocity in Poiseuille flow as well as how particle size affects channel margination in blood flow. We compare our data to experimental and simulation results to confirm the validity of theory and suggest it is a good alternative to large-scale simulation.

References

[1] Narsimhan, V., Zhao, H., and Shaqfeh, E. S. (2013). Coarse-grained theory to predict the concentration distribution of red blood cells in wall-bounded Couette flow at zero Reynolds number. Physics of Fluids (1994-present), 25(6), 061901.

[2] Rivera, R. G. H., Sinha, K., and Graham, M. D. (2015). Margination regimes and drainage transition in confined multicomponent suspensions. Physical review letters, 114(18), 188101.

[3] Zhao, H., Shaqfeh, E. S., and Narsimhan, V. (2012). Shear-induced particle migration and margination in a cellular suspension. Physics of Fluids (1994-present), 24(1), 011902.

DEVELOPMENT OF AN EXPERIMENTAL CORRELATION FOR RED BLOOD CELLS AGGREGATION RATE

Erfan Niazi[1] & Marianne Fenech [1]
[1]*Department of Mechanical Engineering, University of Ottawa, Ottawa, Ontario, Canada*

Summary Red Blood Cells (RBCs) aggregation depends on the shear rate of the flow, under low shear rate rouleaux (aggregated RBCs) are formed and formed rouleaux disaggregate under high shear rates in the flow. Population Balance Modeling (PBM) is used to find the aggregation rate in a dynamic situation of RBCs sedimentation. In this configuration, disaggregation can be neglected due to low shear rate. The sizes of the aggregates are extracted using an image processing techniques and by using these data the aggregation rate is found.

INTRODUCTION

Blood shows a non-Newtonian characteristics in microcirculation where low shear rates (lower than $100s^{-1}$) are present. This behavior is related to the particular nature of the blood component; as it is composed of a Newtonian base fluid (plasma) with suspended particles (RBCs, white blood cells, platelets, etc.). RBCs are the most abundant cell in blood and hence are responsible of the changes in blood behavior. However white blood cells, platelets and other component of blood have a negligible effect on blood rheology [1].

RBCs tend to clump together and form regular stacks called rouleaux. This phenomenon is defined as red blood cells aggregation. These stacks are not static, and constantly move and break apart. This is a healthy part of the blood function, and can be viewed as a natural function preserving a more constant set of properties in the human body. There is evidence that aggregation of red blood cells plays a crucial role in regulating blood viscosity [2]. Recently, Owens [3] proposed a model for blood viscosity as a function of rouleaux size. His model is based on Population Balance Equation (PBE) to find rouleaux size. The population balance equation is based on an experimental expression as it ignores microscopic interactions. Therefore, in order to use this equation, it is crucial to develop these experimental expressions. As mentioned in [3], due to lack of information on aggregation and disaggregation rates, a linear relation between disaggregation and aggregation rates with shear rate was assumed. Equation (1) shows the averaged PBE developed by Owens [3]:

$$\frac{d(\boldsymbol{AAS})}{dt} = \frac{1}{2}\Omega_A n_0 - \frac{1}{2}\Omega_D(\boldsymbol{AAS})^{\boldsymbol{2}} + \frac{1}{2}\Omega_D(\boldsymbol{AAS}) \qquad (1)$$

where AAS denote the average aggregate size and n_0 is the total number of red blood cells per unit volume. The aim of this study is to experimentally estimate coefficients for aggregation rate Ω_A and disaggregation rate Ω_D in order to be implemented in PBE to predict the aggregate size and the viscosity of the flow [3].

EXPERIMENTAL PROCEDURE

The Experimental set-up is shown in Fig. 1. It consists of a high speed camera controlled using the LabVIEW software, 10x lens magnification and a white light source. Images are recorded at the rate of one frame per second. Via a program developed in LabVIEW, the exposure time of the camera, the frame rate and the field of view can be varied to obtain the highest image quality for proper post processing. To study the sedimentation of RBCs in plasma, a U shaped channel with 100μm height is used. This channel is similar to the channel proposed in [4] to study the sedimentation of RBCs. The dimensions of this channel are shown in Fig. 1. Poly-Di-Methyl-Siloxane (PDMS) is used for the fabrication of the channel. Human Blood is collected from 5 healthy individuals (Ethical clearance, University of Ottawa, H11-13-06). RBCs are suspended in their own native plasma at hematocrits (H_t) of 5%.

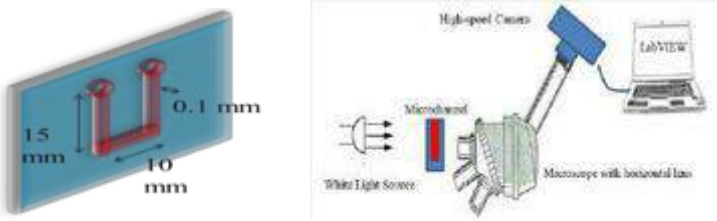

Fig. 1 RBCs sedimentation test microchannel and video microscopic system

ImageJ software is used to detect the aggregation sizes in the domain. Each image is cropped to remove the additional information in the picture. The background is subtracted and bandpass FFT filtering is applied to the pictures to get a clearer picture of the RBCs. Images are then converted to a binary image and then aggregate sizes are automatically estimated. Resulted images are shown in Fig. 2.

[a] Corresponding author. Email: eniazi@uottawa.ca.

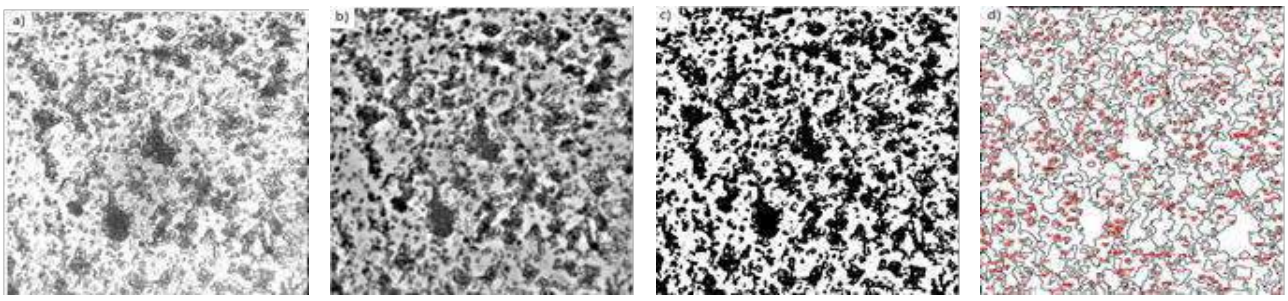

Fig. 2. a) Cropped image b) Removing the background and filtering c) Binary image d) Analyzed picture

RESULTS AND DISCUSSION

It is assumed that there is no disaggregation due to low shear rate in this set-up, therefore Equation (1) further simplifies to $\frac{d(\boldsymbol{AAS})}{dt} = \frac{1}{2}\Omega_A n_0$. Fig. 3 shows$AAS$ and number of particles in each size found using image processing results for the first 140 seconds. Particle size measurements in this study is done according to Table I.

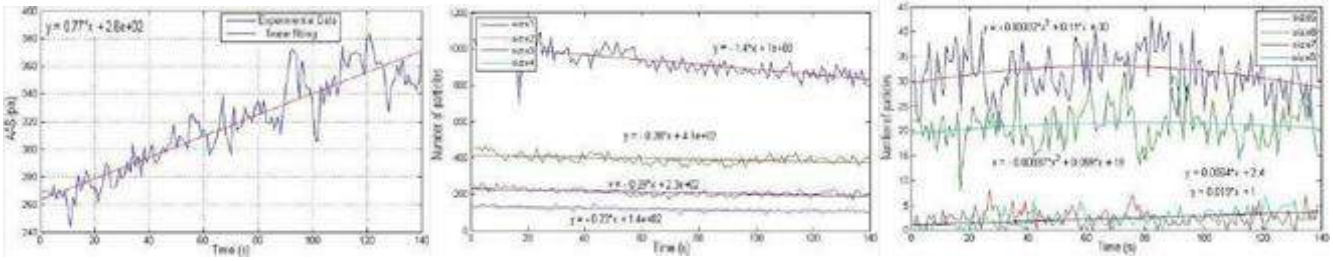

Fig. 3 Sample EU08A (a) Change of average aggregate size with time (b and c) Change of number of aggregates in different sizes with time

The aggregation rate of $\Omega_A = 2.7 \times 10^3\ {}^{1}/_{S}\ (\pm 0.3 \times 10^3)$ is estimated from dividing the rate of change of AAS $(0.75 \pm 0.09\ {}^{\mu m^3}/_{S}$, obtained from the five samples) by ${}^{n_{0S}}/_{2}$.

As is shown in Fig 3 (b and c), the number of aggregated RBCs in small classes decrease whereas the number of aggregates in larger class increase. The reduction of the number of the smaller aggregates are due to the aggregation of RBCs and thus the number of the larger size aggregates increases. The initial increases in the number of the sizes 5 and 6, is due to the formation of new classes from the aggregation of the smaller size aggregates. Furthermore, these newly formed classes tend to aggregate to produce bigger size aggregates resulting in a drop in the number of the aggregates in sizes 5 and 6.

TABLE I
PARTICLE SIZES AND VOLUMES

Class i	Estimated Number of RBCs	Pixel size range	Pictures (not on scale)
1	1	25-60	
2	2	60-120	
3	4	120-360	
4	8	360-675	
5	16	675-1500	
6	32	1500-2600	
7	64	2600-5600	
8	128 and more	5600 >	

CONCLUSION

Ponder [5] suggested that there is a linear relation between the aggregation rate and the hematocrit (constant Ω_A). This relationship can be seen in our experimental data. The aggregation rate found in this study can be called a macroscopic aggregation rate and can be used in the Owens' model [3]. However, this is not taking into account the aggregate sizes distribution. Furthermore, the distribution of the number of aggregates in the different classes collected in this study will be used for the development of a more comprehensive population balance model.

References

[1] Baskurt O., Neu B. and Meiselman H. J.: Red Blood Cell Aggregation, Boca Raton, FL: CRC Press Taylor & Francis Group, 2012.

[2] Popel A. and Johnson P.: Microcirculation and hemorheology, Annual Review of Fluid, pp. 37(1):43-69, 2005.

[3] Owens R.G.:A new microstructure-based constitutive model for human blood, J. Non-Newtonian Fluid Mech., vol. 140, pp. 57-70, 2006.

[4] Jayavanth S. and Singh M.: Computerized analysis of erythrocyte aggregation from sequential video-microscopic images under gravitational sedimentation, ITBM-RBM, vol. 25, no. 2, pp. 67-74, 2004.

[5] Ponder E.: On sedimentation and rouleaux formation, Q. J. Exp. Physiol., vol. 16, p. 173–194, 1924.

MOTION OF A SPHERICAL CAPSULE IN BRANCHED TUBE FLOW WITH FINITE INERTIA

Z. Wang[1], Y. Sui *[1], A.-V. Salsac[2], D. Barthès-Biesel[2], and W. Wang[1]

[1]*School of Engineering and Materials Science, Queen Mary University of London, London, UK*
[2]*Biomechanics & Bioengineering Laboratory (UMR CNRS 7338), Université de Technologie de Compiègne - Sorbonne Universités, Compiègne, France*

Summary We study computationally the transient motion of an initially spherical capsule flowing through a tube with a right-angled side branch, using an immersed-boundary lattice Boltzmann method. We focus on path selection of the capsule at the bifurcation as a function of a range of parameters, including the flow split ratio, the Reynolds number, the capillary number, and the capsule-to-tube size ratio. We find that the capsule trajectory is strongly influenced by the Reynolds and capillary numbers which play opposite role. Through its significant effect on the background flow, inertia increases the likelihood of the capsule to flow into the downstream main tube. On the contrary, the deformation of the capsule promotes its cross-stream migration towards the side branch. When the flow strength is increased, both the fluid inertia and capsule deformation increase: we summarize their effects in a phase diagram, which provides information on path selection depending on the parameters.

INTRODUCTION

A capsule is a liquid droplet enclosed by a thin membrane which can resist shear deformation. Capsules are widely found in nature in the forms of red blood cells (RBCs), eggs, etc. Artificial capsules have a vast range of applications in food, cosmetic, biomedical and pharmaceutical industries [1]. In many situations, capsules are suspended in a fluid and flow through a complicated network of tubes or channels. Central to these flows is the path selection of capsules at bifurcations.

Extensive in-vivo and in-vitro experiments have been conducted on blood flows in branched capillaries or microchannels [2]. It has been well established that the daughter branch with a higher flow rate receives a larger number of RBCs than the other branch; furthermore, it is possible that a daughter branch receives no RBC when its flow rate is very low (Zweifach-Fung effect [3, 4, 5]). For capsules flowing in a branched tube, most previous studies have considered dense suspensions. In the dilute limit, the problem has not been thoroughly studied experimentally, possibly due to the difficulty of manipulating individual cells. On the numerical side, the problem has been studied mostly by means of 2D models [6]. To the best of our knowledge, there is no systematic and in-depth 3D numerical study of a deformable capsule in a branched tube. In particular, how results obtained from previous 2D simulations can be applied to 3D flows remains unclear. Furthermore, almost all previous studies have considered low-Reynolds-number flows. The effect of inertia on path selection of a capsule at a bifurcation remains unknown. The present study aims at addressing these open questions.

PROBLEM STATEMENT AND NUMERICAL METHOD

We consider the flow of an initially spherical capsule in a right-angled bifurcation, composed of cylindrical tubes with the same diameter $2R$ (figure 1a). The capsule is initially spherical with a diameter of $2a$. It is enclosed by a hyperelastic membrane which obeys the Skalak's (SK) law [7] and has a small bending stiffness. The fluids inside and outside the capsule have identical viscosity μ and density ρ. The mass center of the capsule is initially positioned on the centerline of the parent tube in the cross-section S_c. The fluid motion in the branched tube is governed by the Navier-Stokes equations. At the tube wall a no-slip boundary condition is imposed; at the upstream inlet S_0 and the two downstream outlets S_1 and S_2, we set the velocity profiles to be the fully developed Poiseuille flows with corresponding flow rates of Q_0, Q_1 and Q_2 respectively. The problem parameters are the branch flow ratio $q = Q_2/(Q_1 + Q_2)$, the flow Reynolds number $Re = 2\rho VR/\mu$, V being the mean flow velocity in the parent tube, the size ratio a/R and the capillary number $Ca = \mu V/G_s$, G_s being the surface shear elastic modulus of the capsule membrane. The capillary number measures the ratio between viscous and elastic forces. The ratio between the area dilatation modulus and the shear modulus in the SK law is equal to 3. In the present study, the fluid flow and the fluid-capsule interactions are solved using the lattice Boltzmann method and the immersed boundary method [8], respectively.

*Corresponding author. Email: y.sui@qmul.ac.uk

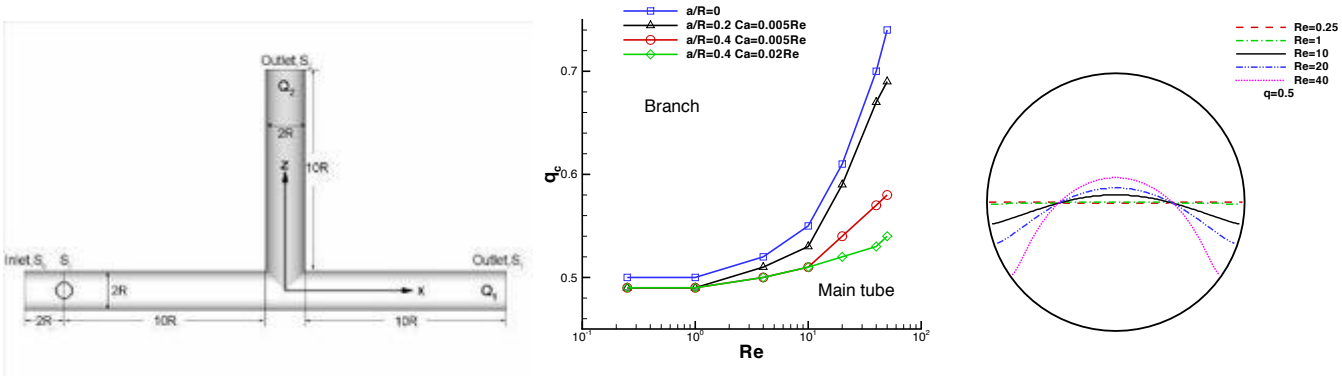

(a) (b) (c)

Figure 1: (a) Geometry of a branched tube; (b) Phase diagram: the critical branch flow ratio q_c as a function of the flow Reynolds number for capsules with different sizes and membrane shear elasticity; (c) Unperturbed flow separation lines in the cross-section S_c for $q = 0.5$ at different flow Reynolds numbers. The fluid elements above the separation line enter the side branch and those below the line remain in the main tube.

RESULTS

We define a critical branch flow ratio q_c, above which the capsule enters the side branch. Thus the branch flow ratio q must be higher than q_c for an initially centred capsule to choose the lateral flow. A phase diagram of q_c as a function of Reynolds number Re is shown in figure 1b for capsules with different membrane properties and sizes. Note that, for a given capsule with fixed membrane properties, increasing the mean flow speed simultaneously increases Re and Ca. In the extreme case of an infinitely small capsule ($a/R = 0$), the capsule will follow the streamline of the unperturbed background flow.

As shown in figure 1b, q_c increases significantly with Re. This could be due to the bending of the fluid separation line (in S_c) towards the side branch, as shown in figure 1c for $q = 0.5$. Comparing q_c for two capsules with the same size $a/R = 0.4$ but different membrane shear elasticity (different Ca), we note that the capsule with a lower membrane shear elasticity is easier to flow into the side branch, in general. This is mainly because a more deformable capsule has an enhanced capability of cross-stream migration towards the side branch. The capsule deformation can also be affected by the size ratio between the capsule and the tube: a smaller capsule with the same membrane is less deformable than a larger one in the same tube flow. Indeed, as shown in figure 1b, it is more difficult to deviate a capsule with $a/R = 0.2$ into the side branch than a capsule with $a/R = 0.4$, and the effect is more obvious at high Reynolds numbers.

DISCUSSION

The present results suggest that the trajectory of a capsule in a branched tube can be controlled by adjusting a range of parameters such as the capsule size, membrane elasticity, tube flow rate. One potential application of the results is to guide the development of microfluidic devices, using a bifurcation geometry, to separate capsules from a suspension or to sort capsules with different size or membrane elasticity. In this application, it could be important for a branch to capture the capsule without receiving too much matrix fluid. The present study suggests that this can be achieved by using the downstream main tube as the capturing branch and flowing the suspension at a high rate when inertia becomes important. For using a branched tube as a capsule sorter, the present results show that the capsule trajectory is sensitive to the capsule size and membrane elasticity, in particular when inertial effect is significant (i.e., in figure 1b, the value of q_c for capsules with different sizes and membrane elasticity are very different at higher Re).

References

[1] Barthès-Biesel, D.: Modeling the motion of capsules in flow. Curr. Opin. Colloid Interface Sci. 16, 3-12, 2011.

[2] Popel, A. S. and Johnson, P. C.: Microcirculation and hemorheology. Annu. Rev. Fluid Mech. 37, 43, 2005

[3] Svanes, K. and Zweifach, B. W.: Variations in small blood vessel hematocrits produced in hypothermic rats by micro-occlusion. Microvasc. Res. 1, 210-220, 1968

[4] Fung, Y. C.: Stochastic flow in capillary blood vessels. Microvasc. Res. 5, 34-48, 1973

[5] Shen, Z. et al.: Inversion of hematocrit partition at microfluidic bifurcations. Microvasc. Res. 105, 40-46, 2016.

[6] Woolfenden, H. C. and Blyth, M. G.: Motion of a two-dimensional elastic capsule in a branching channel flow. J. Fluid Mech. 669, 3-31, 2011

[7] Skalak, R. et al.: Strain energy function of red blood cell membranes. Biophys. J. 13 (3), 245-264, 1973

[8] Sui, Y. et al.: A hybrid method to study flow-induced deformation of three-dimensional capsules. J. Comput. Phys. 227 (12), 6351-6371, 2008

MOTION OF AN OBLATE CAPSULE IN SIMPLE SHEAR FLOW

Anne-Virginie Salsac[1 a)], Claire Dupont[1] & Dominique Barthès-Biesel[1]
[1]*BMBI Laboratory, CNRS - Université de technologie de Compiègne, Sorbonne universités, Compiègne, France*

Summary The present study is focused on the dynamics of non-spherical liquid-core capsules in simple shear flow. The objective is to determine the stability of the equilibrium configurations of oblate capsules. To solve the fluid-structure interaction problem, we use a numerical model coupling a finite element method for the capsule deformation with a boundary integral method for the internal and external flows. The equilibrium motions are found to be independent of the capsule initial inclination and to depend only on the capillary number *Ca* and inner-to-outer viscosity ratio λ. For λ =1, the tumbling and swinging regimes are found to be stable only until $Ca \sim 0.9$. Above, the capsule follows an out of plane motion which converges towards the rolling motion for $Ca > 1.2$. For $\lambda > 4$, only tumbling is stable at low *Ca* and rolling at higher *Ca*.

INTRODUCTION

Microcapsules consist of a liquid internal medium enclosed within a thin elastic membrane. The dynamics of an oblate capsule in simple shear flow has recently received great attention [1,2,3], owing to its relevance to model a red blood cell (RBC). Most studies have modelled the motion of a capsule with its revolution axis in the shear plane, which is a special case, as it is an equilibrium configuration in Stokes flow conditions. It has been shown that the capillary number *Ca*, ratio of the viscous to elastic forces, strongly influences the capsule motion. At low *Ca*, the capsule has a tumbling motion and rotates like a solid particle. As *Ca* is increased, the capsule experiences a transition and takes a swinging motion where it oscillates about the straining direction, while the capsule membrane tank-treads around the deformed shape (fluid-like motion). As *Ca* is further increased, the oscillation amplitude decreases and a tank-treading motion is recovered.

We have recently studied the motion of an initially off-plane prolate capsule in shear flow and shown that tumbling is mechanically unstable as the capsule revolution axis moves to become normal to the shear plane (rolling regime) [4]. At high *Ca*, the swinging regime is stable. In the intermediate range of capillary numbers, the capsule precesses around the vorticity axis. We have shown that the stable equilibrium states do not depend on the initial orientation of the capsule revolution axis. Dupire et al. [5] found experimentally that a RBC orbit is unstable in simple shear flow near the tumbling-to-swinging transition. This shows that the dynamics of oblate capsules is still not well understood, particularly at low *Ca*. The present objective is to investigate the influence of the capillary number, viscosity ratio and initial orientation on the equilibrium configurations of an oblate capsule.

PROBLEM FORMULATION AND NUMERICAL METHOD

We consider an oblate capsule of long-to-short axis ratio equal to 0.5 (volume $4\pi l^3/3$) suspended in a simple shear flow (shear rate $\dot{\gamma}$, fluid viscosity μ) with inner-to-outer viscosity ratio λ. The capsule wall (surface shear modulus G_s and area-dilatation modulus $K_s = 3G_s$) is described as an elastic surface obeying a strain-hardening Skalak type law [6]. The capsule revolution axis is initially positioned with an angle ζ_0 with respect to the vorticity axis. The fluid-structure interaction problem governing the deformation of the capsule is thus a function of three main parameters: the capillary number $Ca = \mu\dot{\gamma}l/G_s$, the viscosity ratio λ and the initial orientation ζ_0. We use a numerical model, that couples a finite element method for the capsule deformation with a boundary integral method for the internal and external flows [7]. Knowing the initial position of the capsule membrane, we compute the stretch ratios and tension tensor using the membrane constitutive law. The membrane equilibrium equation is solved using a finite element method to deduce the load on the membrane. The velocity of the membrane nodes is obtained from the boundary integral formulation. The new position of the capsule membrane points is calculated integrating the velocity with an explicit second-order Runge-Kutta scheme.

RESULTS AND DISCUSSION

The capsule mechanical equilibrium configurations have been determined by initially positioning the capsule revolution axis off the shear plane and by following the capsule dynamics. The capsule equilibrium motion is found to be independent of the capsule initial inclination ζ_0 and to depend only on *Ca* and λ.

For viscosity ratios $\lambda \leqslant 1$ and very low *Ca* ($Ca \leqslant 0.02$), the oblate capsule rotates around the vorticity axis and eventually places its revolution axis in the shear plane (see results for $\lambda = 1$ in Figure 1). The tumbling motion observed when the revolution axis is initially in the shear plane is recovered and is therefore mechanically stable. As *Ca* is increased ($0.05 < Ca \leqslant 0.9$), the oblate capsule places the smallest and longest deformed axes in the shear plane and assumes a swinging motion. The swinging regime is stable only until $Ca \sim 0.9$. Above this threshold, the capsule experiences a

[a)] Corresponding author. Email: a.salsac@utc.fr.

transition towards an out-of-plane motion characterized by precession around the vorticity axis until $Ca \sim 1.2$. Above this value, the capsule stabilizes into a rolling motion with the revolution axis normal to the shear plane.

When $\lambda < 3$, the mechanical equilibrium configurations correspond to the ones observed for $\lambda = 1$ (Figure 1). The viscosity ratio, however, influences the capillary number at which the tumbling–to–swinging and swinging–to–rolling transitions occur. The tumbling-to-swinging transition takes place at higher Ca, since the increase in internal viscosity reduces the capsule deformability. On the contrary, the swinging-to-rolling transition tends to occur at lower values of Ca, as λ increases. As a consequence, the swinging motion disappears for $\lambda \sim 3$: the stable mechanical equilibrium states, for $\lambda > 4$, are thus only the tumbling and the rolling regimes. The capillary number of the tumbling-to-rolling transition decreases with λ: at high λ, the rolling regime thus becomes the most likely mechanical equilibrium configuration.

We finally show that a capsule initially placed off the shear plane takes a finite time to reach its stable equilibrium configuration depending on its initial orientation, flow strength and viscosity ratio. For a capsule initially inclined by 45° off the shear plane, the non-dimensional convergence time varies between 50 and 400 for $Ca \leq 0.5$, and is about 600 for $Ca > 2$ ($\lambda = 1$). Long computational times are thus required to study the equilibrium configurations of oblate microcapsules or cells.

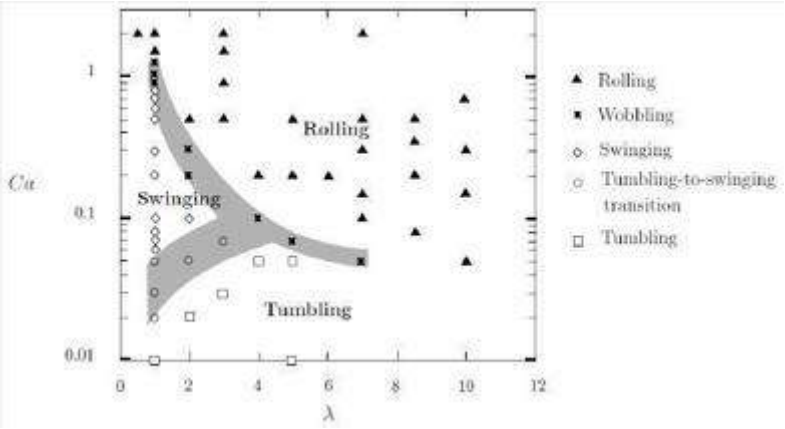

Figure 1: Phase diagram of the mechanical equilibrium configurations of an oblate capsule as a function of the capillary number Ca and viscosity ratio λ. The grey zones represent the tumbling–to–swinging and swinging–to–rolling transitions. From Dupont *et al.* [8].

CONCLUSIONS

By simulating oblate capsules initially placed out of the shear plane numerically, we have studied their stable equilibrium configurations [8]. For the first time, the complete phase diagram of the stable steady-state regimes has been derived as a function of the capillary number and viscosity ratio. Experimentally the external viscosity is indeed rarely matched with the viscosity of the internal fluid. In particular we have shown that the final equilibrium motion of an oblate capsule does not depend on its initial orientation, in contrast with previous conclusions.

Another important result is the time required for an oblate capsule initially placed off the shear plane to reach its mechanical equilibrium state. Such information is crucial when setting up experiments to observe the behaviour of oblate capsules, or when choosing the computational times in numerical models. Specifically, it is important to distinguish whether the observed motion is transitory or at steady state. For experiments, it is interesting to translate the non-dimensional times into dimensional ones. If one considers the case of a RBC subjected to simple shear flow, one finds that the stable tumbling equilibrium regime is reached after ~50 s, stable swinging after ~10 s and stable rolling after ~2 s. Since the typical experimental window time for observation is of the order of 1 minute, one must be careful to check that equilibrium conditions have indeed been reached when the measurements are recorded, especially for low Ca experiments.

References

[1] Sui Y., Low H., Chew Y., Roy P.: Tank-treading, swinging, and tumbling of liquid filled elastic capsules in shear flow. *PRE*. **77**:016310, 2008.

[2] Walter J., Salsac A.-V., Barthès-Biesel D.: Ellipsoidal capsules in simple shear flow: prolate versus oblate initial shapes. *J. Fluid Mech* **676**:318-347, 2011.

[3] Omori T., Imai Y., Yamaguchi T., Ishikawa T.: Reorientation of a nonspherical capsule in creeping shear flow. *PRL* **108**:138102(5), 2012.

[4] Dupont C., Salsac A.-V., Barthès-Biesel D.: Off plane motion of a prolate capsule in shear flow. *J. Fluid Mech* **721**:180-198, 2013.

[5] Dupire J., Socol M., Viallat A.: Full dynamics of a red blood cell in shear flow. *PNAS*. **109**:81-88, 2012.

[6] Skalak R., Tozeren A., Zarda R.P., Chien S.: Strain energy function of red blood cell membranes. *Biophys. J.* **13**:245-264, 1973.

[7] Foessel E., Walter J., Salsac A.-V., Barthès-Biesel D.: Influence of internal viscosity on the large deformation and buckling of a spherical capsule in a simple shear flow. *J. Fluid Mech* **672**:477-486, 2011.

[8] Dupont C., Delahaye F., Barthès-Biesel D., Salsac A.-V.: Stable equilibrium configurations of an oblate capsule in shear flow. *J. Fluid Mech* In Press, 2015.

The dynamical reasons for maneuverability of bats

Hamid Vejdani*[1], David Boerma[2], Sharon M. Swartz[2,1], and Kenneth S. Breuer[1,2]

[1]*School of Engineering, Brown University, Providence, RI, USA*
[2]*Department of Ecology and Evolutionary Biology, Brown University, Providence, RI, USA*

Summary In this paper we study the dynamical reasons for bats' maneuverability. We developed a model similar to bats' dynamical characteristics and used a quasi-steady method for modeling aerodynamic forces. After validating the model with hovering motion, we investigated the contribution of aerodynamic forces and inertial forces in creating roll and pitch maneuver. The results show that while the effect of aerodynamic forces is negligible on roll motion, it has a substantial effect comparable to inertial forces on pitch maneuvers.

INTRODUCTION

Bats' agility during flight, takeoff and landing is unique among flying animals and is achieved through a combination of aerodynamic and inertial control afforded by use of their highly articulated membrane wings [1]. We seek to understand the physical basis for such agile behavior, and to achieve this goal we have developed a dynamical model that mimics several characteristics of bats including the inertial effects of the articulation and folding of their heavy wings as well as a detailed aerodynamic model. The current model greatly extends our previous work, incorporating a more sophisticated aerodyamic model as well as allowing for completely untethered motion (translation and rotation). In this paper, we use this model to explore several characteristic modes of flight, including straight and level flight, climbing, descending and hovering, as well as roll and pitch maneuvers necessary for flight stability and landing.

METHODS AND RESULTS

A 3D dynamical model is derived using a Lagrangian formulation. The model consists of a rigid body with 6 degrees of freedom (3 rotational and 3 translational DoFs) and two rectangular wings. Each wing has mass and rotational inertia with 4 degrees of actuation (sweeping angle, flapping angle, wing pronation/supination angle, and half wingspan extension/flexion) that allow the wings to move relative to the body. Figure 1 shows these degrees of freedom with respect to the body and the order of the wing rotations for the dynamical modeling.

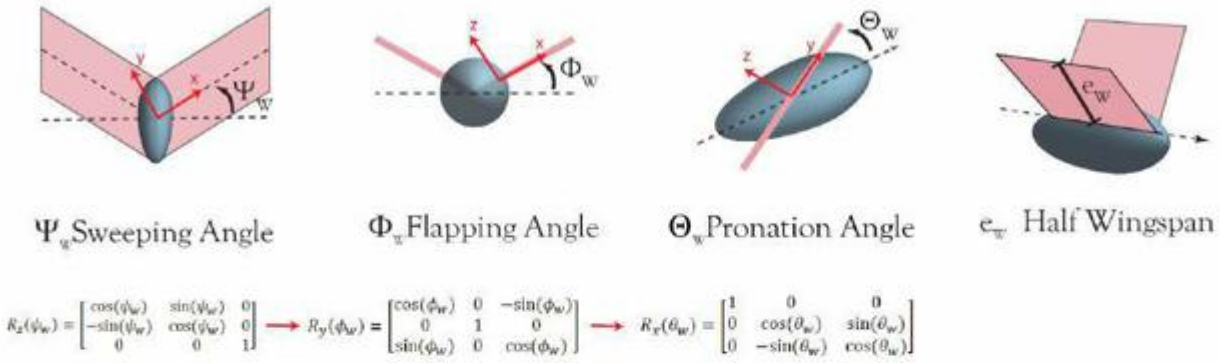

Figure 1: Wing degrees of freedom and the sequence of rotation matrices.

The aerodynamic forces are calculated using a quasi-steady model in conjunction with a blade element method (e.g. [2]), which divides the wing into finite narrow strips along the wing span and applies the drag and lift forces on each strip independently based on its motion and geometry (Figure 2). We have validated our model for gliding flight, and for a hovering condition typical of insects and hummingbirds [2, 3]. The results compare very well with a Newton-Euler solution of the system using quasi-steady aerodynamic modeling.

*Corresponding author. Email: hamid@brown.edu

To achieve a rolling motion, we apply asymmetric extension to the wings during the wingbeat. Figure 3 shows the sequence of time stamps during one wingbeat both with and without the application of aerodynamic forces. It is performed here with parameters typical of a moderate-sized bat, *Carollia perspicillata*, which has relatively heavy wings. As can be seen, the effect of the aerodynamic forces is negligible in achieving a roll maneuver using wingspan asymmetry.

To achieve a pitching motion, we apply additional symmetric sweeping angle to each wing during a wingbeat. Figure 4 shows the behavior of the system, again with and without aerodynamic forces. This time, the results show that the effect of aerodynamic forces for pitching motion is comparable to the effect of inertial forces.

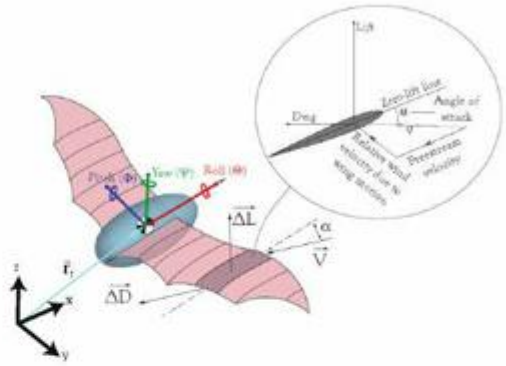

Figure 2: Aerodynamic modeling.

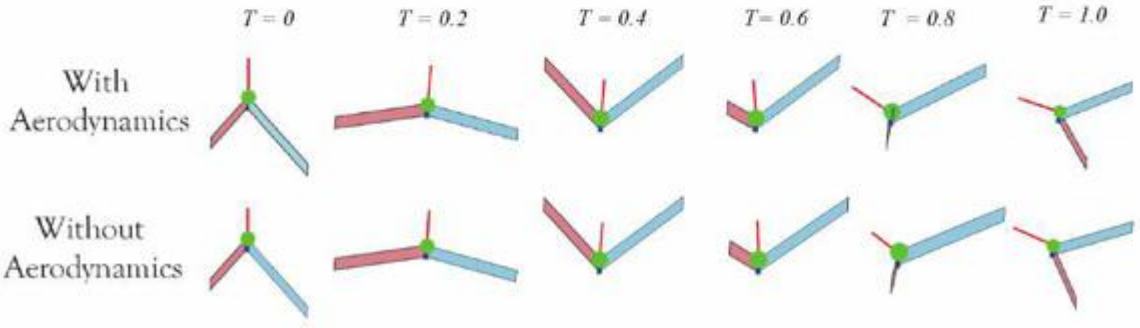

Figure 3: Simulation of roll motion with and without aerodynamics.

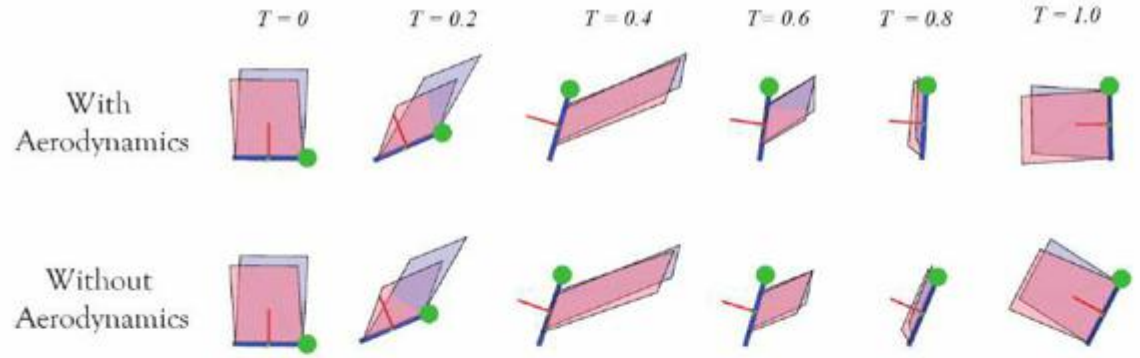

Figure 4: Simulation of pitch motion with and without aerodynamics.

CONCLUSIONS

The full paper will include a more detailed parametric study of these maneuvers, varying wing mass, geometry and kinematic parameters. We will also explore the effect of wing mass in hovering motion, and provide the dynamical reasons for the differences that have evolved among hovering kinematics of insects, hummingbirds and bats.

References

[1] Bergou A.J., Swartz S.M., Vejdani H., Riskin D.K., Reimnitz L., Taubin G., Breuer K.S. : Falling with style: Bats perform complex aerial rotations by adjusting wing inertia. PLoS Biology, 13(11), 2015.

[2] Ellington C.P. : The aerodynamics of hovering insect flight. I. the quasi-steady analysis. Philos. Trans. R. Soc. Lond. B Biol. Sci. 305(1122), 1984.

[3] Byl K. : A passive dynamic approach for flapping-wing micro-aerial vehicle control. ASME-DSCC , 2010.

DYNAMICS OF BUMBLEBEES FLYING IN A VORTEX STREET

Sridhar Ravi[1,2], Dmitry Kolomenskiy[*1], Thomas Engels[3,4],

Kai Schneider[4], Chun Wang[2], Jörn Sesterhenn[3], and Hao Liu[1]

[1]*Graduate School of Engineering, Chiba University, Chiba, Japan*

[2]*RMIT University, Melbourne, Australia*

[3]*ISTA, Technische Universität Berlin, Berlin, Germany*

[4]*M2P2-CNRS & Aix-Marseille Université, Marseille, France*

Summary We analyze the flight dynamics of bumblebees using a combination of experiments and high fidelity numerical simulations. We focus on unsteady inflow conditions generated by placing a vertical cylinder at the inlet of the wind tunnel test section, resulting in the formation of a von Kármán vortex street in the wake. Flight trajectories of bumblebees flying upwind in unsteady winds towards an artificial flower were measured using high speed videography. Then we performed high fidelity numerical simulations of an insect model with similar anatomical features, flying in similar unsteady wind, with no flight control, to investigate the passive dynamic interactions. By comparing the experiment and the numerical simulation, we reveal that bumblebees use a combination of active and passive strategies to mitigate the challenges imposed by the inflow unsteadiness.

INTRODUCTION

Bumblebees are relentless foragers capable of flying in a wide range of weather conditions. Flight in unsteady wind is of particular interest as it presents a complex dynamical interaction between the fluid and the insect. To interpret the observed behavior and identify the control strategies employed, it is essential to disentangle the voluntary maneuvering performed by the insect from the passive mechanical response of the flight apparatus in unsteady winds. Earlier work has shown that bumblebees are most sensitive to lateral perturbations and roll rotations along the longitudinal body axis [1]. Rolling motion and lateral translation are also critical components of voluntary maneuvering. In this study, we generate a von Kármán vortex street behind a vertical cylinder in a wind tunnel. We compare the rolling and lateral flight dynamics of bumblebees flying in the vortex street to their flight in a steady uniform inflow. In addition to the wind tunnel experiment, we develop a model of a flapping bumblebee flying through a von Kármán vortex street that is nominally identical to the one utilized in experiments. The model accounts for flow properties at all length scales in the oncoming flow [2, 3]. Such high fidelity simulations require extensive computational resources, and over 8192 cores were used in this study, the highest number that has been used to resolve flapping flight to date. We compare the body motions of live insects to those of the model bee in similar flow conditions with no active control, to parsimoniously estimate the control strategies being implemented by bumblebees.

MATERIALS AND METHODS

Wind tunnel experiments

All experiments were conducted in a 6 meter-long wind tunnel with a $0.9 \times 0.5 \times 0.5$ m working section. Bumblebees (*Bombus impatiens*) from a commercial breeder (BioBest) were used in this study. Once sufficiently starved, each bee was placed in the wind tunnel where it was trained to feed from an artificial flower. After consistent behavior was established, the wind speed was set to 2.55 m/s and the bees flew upstream. Each bee was flown in two airflow conditions, steady and unsteady. With a 25-mm cylinder positioned vertically at the inlet of the test section, a von Kármán street developed in the wake, shedding at approximately 23 Hz. The bees were filmed within an interrogation 100-mm cube volume located 100 mm downstream from the cylinder. A total of 13 bees were subjected to this assay. Paired trials in steady and unsteady inflow conditions were obtained for each individual.

Numerical simulation

The bumblebee was approximated by three rigid elements: the body and two wings, which moved with respect to each other. We modeled the wings as flat plates, which followed a prescribed periodic flapping motion with frequency $f = 152$ Hz. Two degrees of freedom of the insect motion were taken into account: lateral displacement and roll rotation about the longitudinal axis of the body. We developed a numerical wind tunnel and placed the insect model in a virtual rectangular test section of width $8R$, height $4R$ and length $10R$, where $R = 13.2$ mm is the wing length of the bee. The cylinder of diameter $2R$ was placed in front of the insect, at $6R$ from the insect's center of mass. The computational domain was discretized with a uniform Cartesian grid consisting of $960 \times 768 \times 384$ points. The three-dimensional Navier–Stokes equations were solved by direct numerical simulation on a massively parallel computer, using a Fourier pseudo-spectral method. The volume penalization method was used to handle the no-slip boundary conditions on the time-varying geometry [3].

*Corresponding author. Email: dkolom@chiba-u.jp

DISCUSSION

In the unsteady flow condition, we observed high-frequency rolling motions and lateral accelerations superimposed on top of slow casting motions, with a clear separation between these two types of oscillations in terms of their temporal scale (see figure 1). The high-frequency oscillations occurred primarily at the vortex-shedding frequency associated with the wake of the cylinder. They could be purely passive motions induced by the external airflow, as in the numerical simulation (see figure 2), or they could represent a combination of passive, externally-induced motions and active, corrective maneuvers. Our results showed that bees do not actively respond to the flow perturbations on a wingbeat-by-wingbeat basis [4].

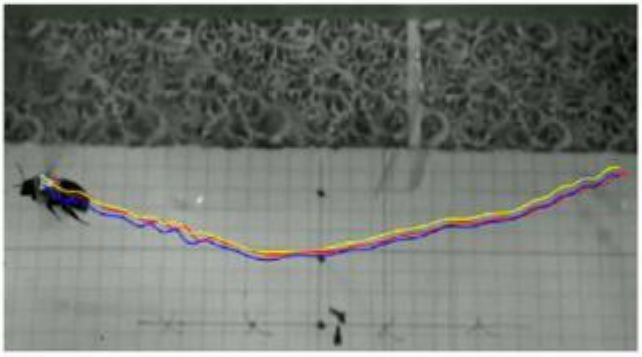

Figure 1: Flight path of a bee in the wake of a cylinder. The red, blue and yellow lines track the position of the triangular marker over the time.

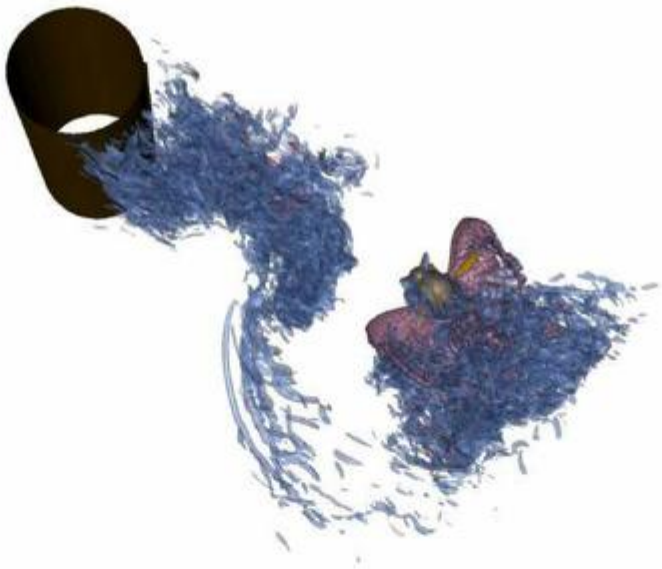

Figure 2: Visualization of the flow field obtained from numerical simulation. Blue iso-surface shows the dimensionless vorticity magnitude $|\omega| = 5$, red shows $|\omega| = 40$. The insect is colored in orange. The cylinder placed upstream from the insect produces a vortex street with a characteristic length scale comparable to the insect wing span, that makes the insect roll and drift laterally.

References

[1] Ravi S., Crall J. D., Fisher A. and Combes S. A.: Rolling with the flow: bumblebees flying in unsteady wakes. J. Exp. Biol. 216, 4299-309, 2013.

[2] Engels T., Kolomenskiy D., Schneider K., Lehmann F. O. and Sesterhenn, J.: Bumblebee flight in heavy turbulence. Phys. Rev. Lett. 116, 028103, 2016.

[3] Engels T., Kolomenskiy D., Schneider K. and Sesterhenn J.: FluSI: A novel parallel simulation tool for flapping insect flight using a Fourier method with volume penalization. arXiv 1506.06513, to be published in SIAM J. Sci. Comput.

[4] Ravi S., Kolomenskiy D., Engels T., Schneider K., Wang C., Sesterhenn J. and Liu H.: Bumblebees minimize control challenges by combining active and passive modes in unsteady winds. Manuscript submitted for publication.

MINIMALLY LOW ORDER VORTEX MODELING OF BIO-INSPIRED LOCOMOTORY FLOWS

Darwin Darakananda[1] and Jeff D. Eldredge*[1]

[1]*Department of Mechanical and Aerospace Engineering, University of California, Los Angeles, CA 90095, USA*

Summary A novel vortex model is presented for the unsteady flows developed in biological or biologically-inspired locomotion at moderate to high Reynolds number. The model preserves, with a minimal number of degrees of freedom, the essential physics of sustained vortex shedding in such flows. The fluid dynamics are modeled with a hybrid of a vortex sheet and variable-strength point vortices. While the vortex sheet is allowed to undergo the instability dynamics inherent to a wake or separated flow, its length is strategically limited by continuously siphoning its strength into a point vortex. The overall number of degrees of freedom is thereby kept orders of magnitude smaller than in a full vortex sheet solution, and much smaller still than in a high-fidelity simulation, while still capturing the physics of sustained vortex shedding. The model's accuracy is assessed with representative problems, including impulsive start of a wing at very high angle of attack.

MOTIVATION

At moderate to high Reynolds number, aerial and aquatic forms of locomotion in nature—or in vehicles inspired by nature—are generally characterized by propulsors that undergo large amplitude motions, generating flows dominated by vortices shed directly into the wake or into a separated flow. These unsteady vortical flows resist description by simple models that efficiently capture their essential physics. By 'efficient', we mean computationally tractable in a manner required for design and real-time control purposes; by 'essential', we hypothesize that the large spectrum of phenomena in these flows can be distilled into a small number of basic (but still non-linear) interactions between vortex elements.

In previous work [1], we developed a planar model for the separated flow past a flat plate in which vorticity shed from the edges of plate was collected in a small number of point vortices of variable strength. This model was adequate for the early development of the flow, when it consists only of two coherent vortices: one associated with each edge. However, the model was not sufficiently rich to capture the effects of vortex shedding (i.e. the detachment of a vortex from the plate into the wake, and its replacement by a new vortex). The objective of the present work is to enrich the model with vortex sheets that capture the emergence of new vortex structures through their intrinsic instability.

METHODOLOGY

The model uses a plate of infinitesimal thickness to represent a propulsive surface (e.g. wing, fin) and a collection of free vortex sheets and point vortices to represent the flow. Each vortex sheet is rooted at the edge of the plate and is discretized by a finite number of connected control points whose motions are tracked with the usual Kirchhoff velocity. However, rather than letting the sheet's length grow indefinitely, the strength (and therefore, its length) is continuously siphoned, with a specified rate of vorticity flux $\dot{\Gamma}$, into an accompanying variable-strength point vortex. The dynamics of this point vortex are amended in order to cancel the spurious rate of change of linear impulse due to the transfer of circulation from the sheet to the vortex. This also ensures that the force exerted on the plate is unaffected by discontinuous changes in $\dot{\Gamma}$.

RESULTS

The model is applied here to the impulsive start of a flat plate at 60 degrees angle of attack. Figure 1 depicts a comparison between high-fidelity simulations of this flow (at Reynolds number 1000), a vortex sheet model of the flow (in which the sheet is allowed to grow indefinitely, and control points are inserted into the sheet where stretching is severe), and the current hybrid model. All results capture the early development of the starting vortex from the trailing edge, the leading-edge vortex, and the emergence of a new vortex due to roll-up of the shear layer near the trailing edge. The number of control points required for the hybrid model remains around 500, an order of magnitude smaller than that of the sheet. This difference becomes more stark at later times, as illustrated in the right panel in Figure 2. The normal force exerted on the plate, depicted in the left panel Figure 2, is generally predicted well by the hybrid model, though there is some disagreement after 3 convective time units, when the new vortex emerges from the trailing edge. Results from other representative biologically-inspired problems will also be presented.

*Corresponding author. Email: eldredge@seas.ucla.edu

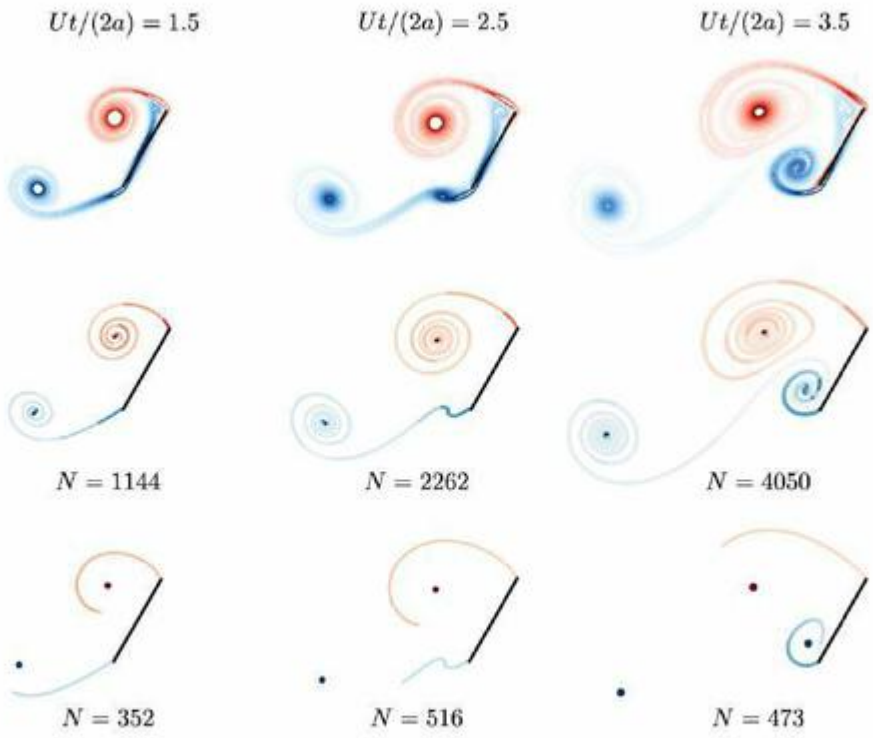

Figure 1: Comparison of the predicted large scale structures around the plate using high fidelity CFD at Re $= 1000$ (top row), a vortex sheet model (middle row), and the hybrid point/sheet model (bottom row). The CFD results show the vorticity contours. The vortex models show the strength and positions of the vortex sheets and point vortices, as well as the number of control points used to resolve the vortex sheet.

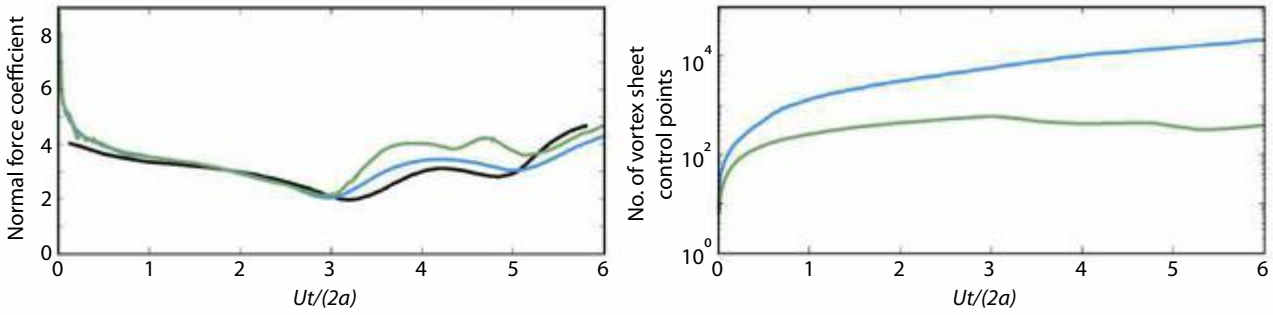

Figure 2: (Left) Comparison of the force response predicted by high fidelity CFD (black), vortex sheet model (blue), and the hybrid model (green). (Right) Number of computational elements over time in the vortex sheet model with point insertion (blue) and the hybrid model (green).

ACKNOWLEDGMENTS

This work was funded by AFOSR award number FA9550-14-1-0328, monitored by Dr Ivett Leyva.

References

[1] C. Wang and J. D. Eldredge. Low-order phenomenological modeling of leading-edge vortex formation. *Theor. Comput. Fluid Dyn.*, 27(5):577–598, 2013.

VORTEX FORMATION AND TRANSPORT FROM A ROTATING PLATE IN STILL FLUID

[1,3,4] M. Jimreeves David *[1], Manikandan Mathur[2], R N Govardhan[3], and J H Arakeri[4]
[1,3,4] *Department of Mechanical Engineering, Indian Institute of Science, Bangalore, India.*
[2] *Department of Aerospace Engineering, Indian Institute of Technology Madras, Chennai, India.*

Summary We investigate, using the framework of Lagrangian Coherent Structures (LCS), the vortex pair formation in an idealized model of a fish turning manoeuvre called C-start. The two-dimensional flow, generated by a thin plate performing a large angle rotation in still fluid, comprises the formation of a starting vortex during the plate rotation and the formation of a stopping vortex after the plate stops, thus resulting in a vortex pair which travels in a direction closely aligned with the final stopping angle of the plate. LCS are shown to objectively extract the boundaries of various transport entities in the flow, thus alowing us to map the long-term fate of various regions in the fluid at the initial time. We conclude by demonstrating the correlation between the momentum associated with the material parcel that is advected away from the plate and the impulse experienced by the plate.

Introduction Flapping foils in a freestream and the associated forces have often been investigated to provide insights on the development of biomimetic underwater vehicles. An important characteristic of any bio-mimetic mechanism is its manoeuvrability. Some fishes use a mechanism called C-start [1], which involves the fish contracting its muscles to assume a C-shape and then beating the tail through a large angle to propel itself from rest in the direction of the final stopping angle of the tail. Here, we study an idealized model of the C-start, as described in fig-1 A, where we see a bulk flow that is pushed back in the direction of the final stopping angle of the plate (fig-1, C-F). Previous related works have focused on formation time calculation by tracking vortex circulation on a rotating 3D plate [2] and direct force measurements on a 2D plate [3].

Temporally and spatially well-resolved velocity fields for the low Reynolds number flow are obtained using a finite-volume solver in which the two-dimensional, incompressible Navier-Stokes equations are solved in the rotating plate frame, and are validated by comparisons with experimental data. Results are presented for the case where the plate undergoes a rotation of $\theta_{max} = 90^o$ in a time $t_o = 10s$ and with an angular velocity $\dot{\theta}(t) = A\sin^2(\omega t)$, leading to a Reynolds number of around 800.

Lagrangian Coherent Structures (LCS) have recently been shown to be a powerful tool to understand advective transport and mixing in a wide range of flows ([4], [5]). Applications to vortex-dominated flows have resulted in an objective identification of vortices and related coherent patterns (see [6], [7]). To extract the LCS in our simulated flow, we adopt techniques based on the forward- and backward- finite-time Lyapunov exponents, described in detail in [8]. We implement the recently proposed variational theory of LCS to extract the elliptic and hyperbolic LCS in the flow.

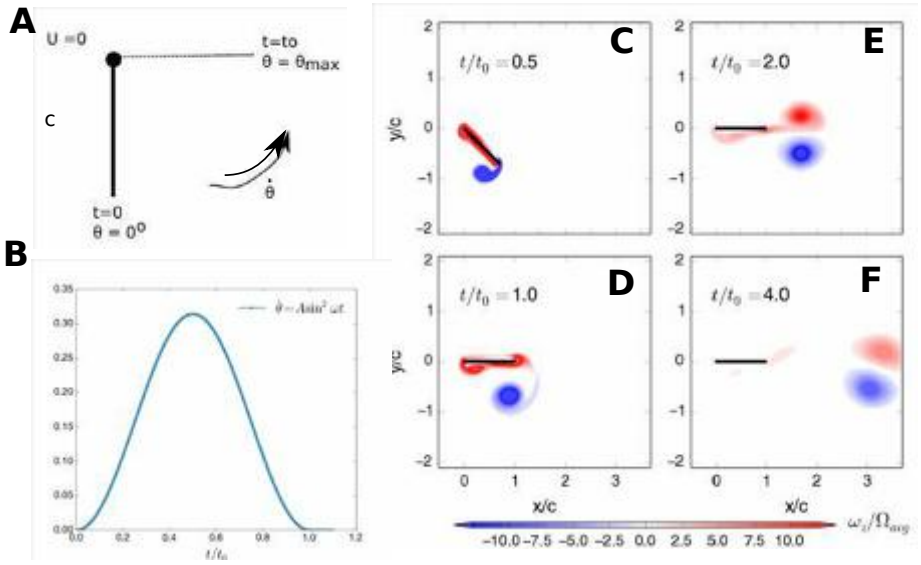

Figure 1: **A**: Schematic of the plate rotation, **B**: The angular velocity $\dot{\theta}$ of the plate as a function of non-dimensional time t/t_o, Vorticity (non-dimensionalized by the average plate angular velocity Ω_{avg}) contours at times **C**: t/t_o = 0.5, **D**: t/t_o = 1, **E**: t/t_o = 2, **F**: t/t_o = 4.

*Corresponding author. Email: jimme@mecheng.iisc.ernet.in

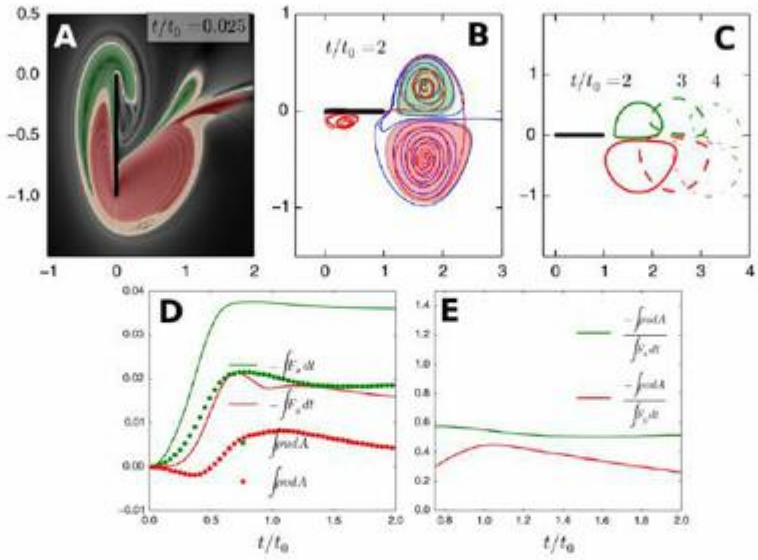

Figure 2: **A**: The red, green and brown regions represent the fluid regions at $t = 0.025$ that will ultimately comprise the starting vortex, stopping vortex and the white region inside the material bulk shown in fig-2 B, respectively. The forward FTLE field is shown in the background, **B**: Attracting, repelling and elliptic LCS at $t/t_o = 2$, **C**: Elliptic LCS at times $t/t_o = 2, 3, 4$, **D**: Horizontal (green) and vertical (red) impulse experienced by the plate (solid lines) and the corresponding linear momentum acquired by the bulk of fluid (dotted lines) as a function of t/t_o. **E**: Ratio between the momentum acquired by the bulk of the fluid advected away from the plate and the corresponding impulse experienced by the plate.

Results and Discussion The plate accelerates from zero velocity at $t/t_o = 0$ and decelerates to rest at $t/t_o = 1$. The attracting (red lines) and repelling (blue lines) LCS at $t/t_0 = 2$ are shown in fig-2 B. The region encompassed by these LCS represent the material bulk of the fluid that is pushed away from the plate in the direction of the final stopping angle of the plate. Within this bulk are the elliptic LCS (red and green shaded regions, see fig-2 B)[9], whose material boundaries travel forward with no-streching (fig-2 C). Most of the vorticity lies within these elliptic LCS. The regions that are outside the elliptic LCS but inside the attracting and repelling lines at $t/t_o = 2$ travel forward with the bulk but get streched and folded, which is unlike the fluid inside the ellipic LCS that travel forward without any filamenting. Furthermore, computing fluid trajectories backward in time, we find that the regions encompassed by the repelling LCS at $t/t_o = 0$ ultimately form the material bulk of the fluid that is advected away from the plate (Fig-2 A). Fig-2 D shows how the bulk of the fluid that moves away from the plate as one coherent unit acquires momentum as the plate rotates. We see that the total momentum of this bulk represents only a fraction of the total impulse felt by the plate, with the remaining impulse presumably generating the potential flow around this main bulk fluid. More specifically, roughly half of the x-force-impulse ($\int_0^t F_x dt$) felt by the plate goes into creating the x-momentum of the fluid bulk ($\oint_A \rho u dA$)(fig-2 E).

References

[1] Triantafyllou, Michael S., Gabriel D. Weymouth, and Jainmin Miao. Biomimetic survival hydrodynamics and flow sensing. Annual Review of Fluid Mechanics 48.1 (2016).

[2] DeVoria, Adam C & Ringuette, Matthew J 2012 Vortex formation and saturation for low-aspect-ratio rotating flat-plate fins. *Experiments in fluids* **52** (2), 441–462.

[3] Ahlborn, B, Chapman, Stafford, Stafford, R & Harper, R 1997 Experimental simulation of the thrust phases of fast-start swimming of fish. *Journal of Experimental Biology* **200** (17), 2301–2312.

[4] Mathur, Manikandan, Haller, George, Peacock, Thomas, Ruppert-Felsot, Jori E & Swinney, Harry L 2007 Uncovering the lagrangian skeleton of turbulence. *Physical review letters* **98** (14), 144502.

[5] Green, M. A., C. W. Rowley, and George Haller. Detection of Lagrangian coherent structures in three-dimensional turbulence. Journal of Fluid Mechanics 572 (2007): 111-120.

[6] Shadden, Shawn C., John O. Dabiri, and Jerrold E. Marsden. Lagrangian analysis of fluid transport in empirical vortex ring flows. Physics of Fluids (1994-present) 18.4 (2006): 047105.

[7] Huhn, F, van Rees, WM, Gazzola, M, Rossinelli, D, Haller, G & Koumoutsakos, P 2015 Quantitative flow analysis of swimming dynamics with coherent lagrangian vortices .

[8] Haller, George 2015 Lagrangian coherent structures. Annual Review of Fluid Mechanics. Vol. 47.137-162.

[9] Haller, George & Beron-Vera, FJ 2013 Coherent lagrangian vortices: The black holes of turbulence. *Journal of Fluid Mechanics* **731**, R4.

HOW ANIMALS USE SPANWISE FLEXIBILITY FOR EXTREME MANOEUVRABILITY

Jaime G. Wong* and David E. Rival

Department of Mechanical and Materials Engineering, Queen's University, Kingston, Ontario, Canada

Summary Similar bending rules are observed on the wings and fins of animals across the entire domain of swimming and flight. The purpose of this study is to investigate why they pursue similar strategies, in terms of how profile deformation affects the growth and convection of the leading-edge vortex (LEV). To this end, three-component velocimetry measurements capturing the LEV has been conducted in order to determine how the choice of profile bending shapes can be used to control LEV strength and convection. Preliminary results suggest tip-lagging kinematics reduce LEV circulation, while tip-leading kinematics increase circulation.

A harmonically plunging profile is a common abstraction of flapping wings and undulating fins, and is used to investigate the formation of the leading-edge vortex (LEV) ubiquitous to animal locomotion. Of particular interest is how appendage kinematics of swimming and flying animals are used to manipulate the strength and streamwise convection of the LEV, as the LEV is the dominant source of circulation in such flows [1]. The distribution of circulation along a wing can be manipulated by transporting vorticity, as described by the spanwise-component of the vorticity transport equation:

$$\frac{\partial \omega_z}{\partial t} + u\frac{\partial \omega_z}{\partial x} + v\frac{\partial \omega_z}{\partial y} + w\frac{\partial \omega_z}{\partial z} = \omega_x\frac{\partial w}{\partial x} + \omega_y\frac{\partial w}{\partial y} + \omega_z\frac{\partial w}{\partial z}\,, \tag{1}$$

where the terms from left-to-right represent the rate of change of vorticity due to unsteadiness, convection of vorticity in the streamwise (x), wall-normal (y), and spanwise (z) directions, vortex tilting in the streamwise and wall-normal directions, and vortex stretching, respectively. Recently, it has been shown that spanwise-vorticity transport, specifically spanwise convection and stretching, reduces streamwise LEV convection speed [2]. This allows the LEV to continue producing lift on a wing or fin for longer periods of time. Moreover, when a root-fixed spanwise-flexible wing is impulsively towed from rest, it has been shown that the circulation distribution along the wing will dynamically redistribute itself, implying that the deformed wing shape must produce spanwise vorticity transport [3]. However, neither has the vorticity transport along a spanwise-flexible wing been measured, nor has it been directly related to the resulting LEV strength and streamwise LEV convection. The purpose of this study is to elucidate whether the above hypothesis holds and thus shed light on how animals use spanwise flexibility for extreme manoeuvrability.

In animal locomotion, flexible appendages have been observed to curve both into and away from the direction of motion [4]. This observation can be visualized with the aid of Figure 1, which on the left shows the magnitude of plunging amplitude at the tip of a flexible profile relative to the root $h(R)/h_0$, where the motion is forced from the root, for a wide range of dimensionless stiffnesses Π_1 and density ratios ρ^*. On the right, three arbitrary animal-like sets of dimensionless stiffness Π_1 and density ratio ρ^* have been selected to be illustrated in time, to show the possible phase relationship as well. Here, the kinematics of the profile tip may lead (dashed green line, Figure 1) or lag (dashed red line) the profile root (solid black line), despite several orders of magnitude variation in the aforementioned dimensionless parameters. Indeed, animals exploit similar profile-bending strategies across the entire domain of swimming and flight [5].

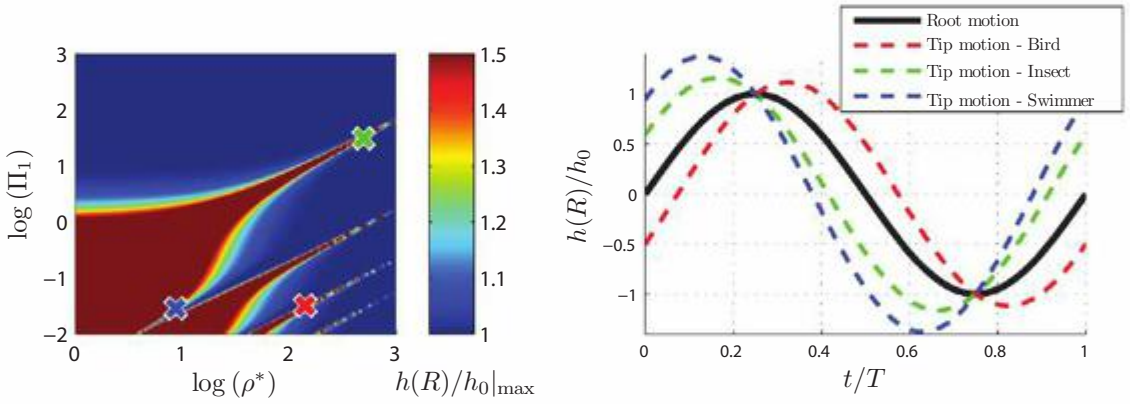

Figure 1: (left) A qualitative visualization of the magnitude of tip deflection of a plunging, spanwise flexible profile normalized by the root. (right) This tip deflection results in a phase-lead or phase-lag of the tip with respect to the root.

*Corresponding author. Email: jaime.wong@queensu.ca

The tip-lead or tip-lag described above generates spanwise vorticity transport, as illustrated in Figure 2. Due to the phase-lead or lag of the profile tip, there is a spanwise variation in plunge velocity v, and therefore also a spanwise variation in vorticity feeding rate and vorticity magnitude $\partial\omega_z/\partial z = 0$. Meanwhile, through either the curvature of the profile or through profile sweep, a spanwise flow w is generated. Together with the gradient in vorticity, these terms serve to convect vorticity along the profile span. As tip-leading versus tip-lagging kinematics should have opposite signs of vorticity transport, such cases will be investigated experimentally in order to determine how these profile kinematics influence LEV growth, in addition to a nominally two-dimensional reference case.

Emulating realistic wing kinematics as described above in an experimental setup poses a number of challenges, especially considering the possibility that animals actively deform their wings or fins. Therefore, as the principle goal of this work concerns the influence of vorticity transport on vortex evolution and not the biology which inspires it, a pitch-flap analogue was developed to reproduce the variation in effective incidence and spanwise flow of a wing or fin in a simple reproducible way. The pitching degree of freedom reproduces the same effective incidence as the plunging motion at a wing root, while the superimposed flapping motion produces a gradient of effective incidence similar to the profile deflection, producing similar vorticity-transport behaviour in the resulting LEV.

A pitching-flapping mechanism was developed for use in an optical towing-tank at Queen's University. The wing span was chosen to closely fit into the 1m×1m cross-section of the towing tank, in order to minimize the effect of tip vortices near the mid-span where measurements would take place. Preliminary results are shown in Figure 3, where the tip-leading and tip-lagging kinematics are directly compared. Whereas the tip-leading kinematics on the left show a strong and coherent LEV, the tip-lagging kinematics on the right show a completely suppressed LEV at the same effective incidence. As the two cases have very similar effective-incidence histories, this preliminary result supports the hypothesis that strong vorticity transport is affecting circulation distribution. Specifically, it appears that outboard-directed vorticity transport from tip-lagging kinematics reduces LEV circulation, while inboard-directed transport from tip-leading kinematics increases circulation. Currently, 4D-PTV data has been acquired to resolve all elements of the velocity-gradient tensor. This will allow direct measurements of vorticity transport within the LEV, facilitating the remainder of the proposed analysis.

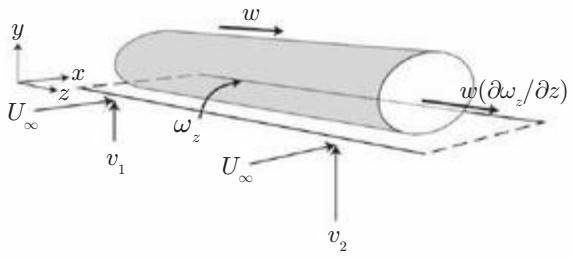

Figure 2: Vorticity ω_z fed into the LEV is convected along the span of the wing by spanwise flow w, given that there exists a gradient in effective incidence along the span, $v_2 > v_1$. This convection $w\partial\omega_z/\partial z$ acts to reduce the streamwise LEV convection.

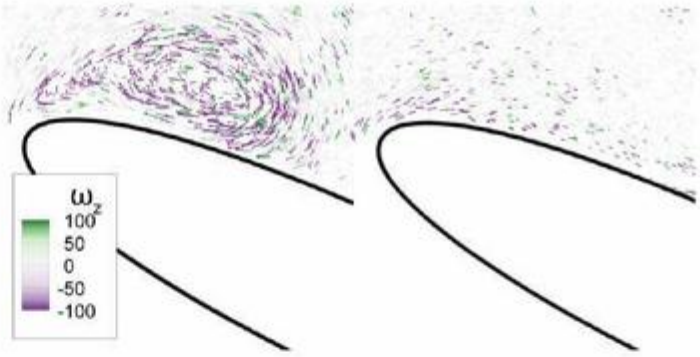

Figure 3: Preliminary vector fields are visualized here coloured by spanwise vorticity magnitude for tip-leading (left) and tip-lagging (right) cases with wing locations illustrated. The tip-lagging case exhibits a completely suppressed LEV, compared to the pronounced LEV in the tip-leading case.

References

[1] Pitt Ford C.W., Babinsky H.: Lift and the leading edge vortex. J. Fluid Mech. 720:280-313, 2013.

[2] Wong J.G., Rival D.E.: Determining the relative stability of leading-edge vortices on nominally two-dimensional flapping profiles. J. Fluid Mech. 766:611-625, 2015.

[3] Jain M.V., Wong J.G., Rival D.E.: A model of fluid-structure-interaction for impulsively started spanwise-flexible wings. J. Fluid Struct. 54:466-478, 2015.

[4] Flammang B.E., Alben S., Madden P.G.A., Lauder G.V.: Functional morphology of the fin rays of teleost fishes. J. Morphol. 274:1044-1059, 2013.

[5] Lucas K.N., Johnson N., Beaulieu W.T., Cathcard E., Tirrell G., Colin S.P., Gemmell B.J., Dabiri J.O., Costello J.H.: Bending rules for animal propulsion. Nat. Commun. 5:3293, 2014.

VORTICITY DYNAMICS OF MANEUVER LOCOMOTION OF THE THREE DIMENSIONAL BIONIC FISH*

Zhiqiang XIN[1,a)] & Chuijie WU[2]
[1]*College of Mechanics and Materials, Hohai University, Nanjing, China*
[2]*State Key Laboratory of Structural Analysis for Industrial Equipment & School of Aeronautics and Astronautics, Dalian University of Technology，Dalian, China*

Summary Numerical simulations of unsteady maneuvering of the 3D bionic fish in a viscous flow are investigated in the present study, using a 3D computational fluid dynamics package, which includes the adaptive multigrid finite volume method, the immersed boundary method and the control strategy of fish swimming. With the direction control strategy of the swing of the head mainly, the 3D bionic fish can turn quickly and swim in a given semicircle path. The analysis of fluid mechanism of maneuver locomotion reveals that the rotation moment in favor of turning motion is yielded by the pressure around the fish body, which are induced by the wake vortex, and the swing of the fish can manipulate the location and strength of the vortices shedding from the fish body.

RAPID TURN OF THE 3D BIONIC FISH

Fast starting and maneuvering of fish are used for catching prey or avoiding predators. The unsteady movement modes are crucial to swimming performance of the fish. Although the knowledge of maneuvering control of swimming fish has made considerable advances, most studies are basically limited in the 'C' types or 'S' types, which fast starts and turns are classically characterized as. Therefore, no systematic theories and exact formulas can define the changes of the fish geometry during the maneuvers at present. Distinguished from the predecessors, in this paper the 3D bionic fish achieves rapid turns and swimming in a given circle trajectories, using the direction control strategy of the swing of the head mainly, in which the impact of the swing of the fish body and the caudal fin on the direction control are also taken into account.
When the 3D bionic fish swims with steady high undulation frequency during the maneuvering, the impact of the swing of the fish body and the caudal fin on the directional control of head swing cannot be ignored. In the process of fast turn, the fish need excellent maneuver features rather than high power. Therefore, the undulation frequency of the 3D bionic fish is not necessarily as high as straight-line cruising. The undulation frequency of the 3D bionic fish is not constant during rapid turn. Fig. 1(a) and (b) presents the angular velocity and the angle of attack of 3D bionic fish swimming during the rapid turning motion with the directional control strategy of the swing of the head. It can be seen from Fig. 1(a) that the angular velocity of the 3D bionic fish induced by the positive moment exerted on the fish body continuously increases. Accordingly, the angle of attack of 3D bionic fish also increases steadily, and finally reaches up to $\theta_z = \pi/2$ at time $t = 3.0$, as shown in Fig. 1(b).. It shows that the 3D bionic fish executes a 90° rapid turn using this directional control strategy.

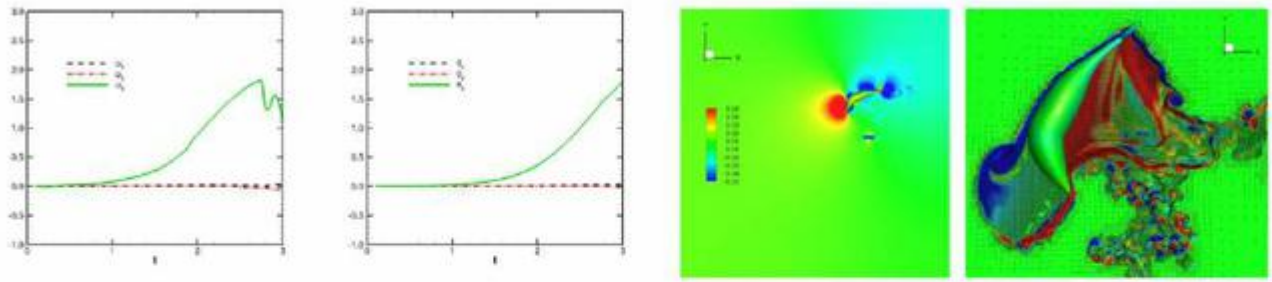

(a) Angular velocity (b) Angle of attack (c) Pressure fields (d) Vorticity fields

Fig. 1: Analyses of the kinematic data and the flow field of 3D bionic fish during the rapid turn

Fig. 1(c) shows that a high pressure region is formed on the right side of the fish head, and the region on the left side of the head is a low pressure region. At the same time, a high pressure and low pressure region occur on the left side and the right side of the posterior parts of the fish body, respectively. It is the common characteristic of the pressure fields during the rapid turn. Thus, favorable rotational moments forms near the head and around the posterior parts of the fish body. The pressure distributions around the fish body in favor of the rapid turn are induced by the vortices generated on the fish body and the caudal fin, and released into the wake. The vortex shedding successively before time t = 1.5 generates a downward jet in the inner side of the fish body, only the strength of the jet varies at different times. Fig. 1(d) presents the vorticity fields near the fish body at the time t = 2.5. The vortex pair on the outside of the fish head forms a strong jet, which is also favor for turning towards its inner side, as shown in Fig. 1(d).

* Project supported by National Natural Science Foundation of China(Grant No. 11302071) and the Fundamental Research Funds for the Central Universities of China (Grant No. 2015B01814)
a) Corresponding author. Email: **xinzhiqiang@hhu.edu.cn**

TURNING IN A PRESCRIBED SEMICIRCLE LINE

In the previous section, the 3D bionic fish achieves rapid turning motion with the directional control strategy of the head swing. The 3D bionic fish is only required to spend short time achieving substantial changes of the angle of attack within the smaller region during the turning process. In order to test deeply the accuracy and validity of the directional control strategy of the head swing, the 3D bionic fish completes swimming in a given semicircle path on the basis of the above study.

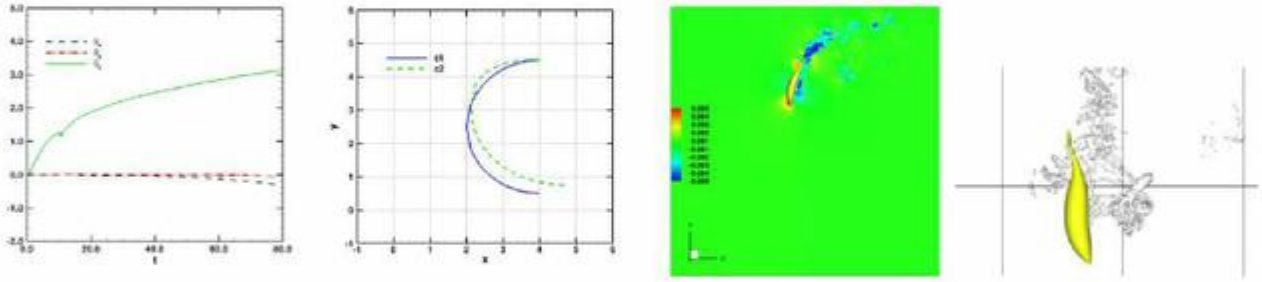

(a) Angle of attack (b) Moving path (c) Pressure fields (d) 3D vortex structure

Fig. 2: Analyses of the kinematic data and the flow field of 3D bionic fish swimming in a given semicircle.

In Fig. 2(b), the curve c1 and c2 is the target trajectory and the swimming trajectory, respectively. Fig. 2(b) shows that the trajectory of the 3D bionic fish is approximately a semicircle with centre coordinates (4.5, 2.5), of which the radius is 2. Namely, the 3D bionic fish succeeds in swimming around a predetermined circular trajectory, with the directional control strategy of the head swing. Fig. 2(a) shows the changes of the fish posture with time. Using this control strategy, the attack angle of 3D bionic fish gradually increases, the direction of which is basically the same as tangent direction of a prescribed circular trajectory. The angle of attack of the 3D bionic fish finally reaches up to $\theta_z = \pi$, due to the positive angular velocity. The 3D bionic fish just reaches at the bottom of a given semicircle when the angle of attack is $\theta_z = \pi$. It is evident that not only the trajectory of the 3D bionic fish is a semicircle, but also the body posture is adjusted accordingly. The fish body is basically tangent to the swimming trajectory circle. This further illustrates the accuracy and effect of the directional control strategy of head swing.

Fig. 2(c) shows the pressure fields of the 3D bionic fish swimming in a semicircle line, which features are the same as rapid turning movement. A high pressure region is formed on the outside of the fish head, and the region which the head sweeps to is always a low pressure area. At the same time, a region with high pressure occurs on its inner side, as the region on the outer side of the posterior parts of the fish body is a low pressure region. Thus, favorable rotational moments forms near the head and the posterior parts of the fish body, respectively. Only the strength of pressure distribution in favor of turning varies with different amplitudes of head swing.

The λ_2 criterion suggested by Jeong and Hussain is employed for identifying the 3D vortical structure of fish swimming in the study. The favorable rotation moment is yielded by the pressure around the fish body, which are induced by the wake vortex, as shown in Fig. 2(d). The swing of the fish can manipulate the location and strength of the vortex shedding from the fish body. The vortex shedding is asymmetric in the process of swimming in a given semicircle path. The asymmetric vorticity distributions generate the moments in favor of turn on the fish body, and the vorticity strengths are not bigger, compared with that of rapid turn. Thus the 3D bionic fish would not rotate too fast, and the accurate swimming around a given path is achieved.

CONCLUSIONS

During the maneuvering motion, the fish can manipulates the vortices shed from the fish body to form the pressure fileds around the fish head and the posterior parts of fish body, which are in favor of rapid turning movement, using the directional control strategy of head swing. The biggest advantage of directional control strategy of head swing is that the directional control and swimming propulsion is relatively independent during the self-propelled swimming. It is easier to implement the control of swimming with this directional control strategies. This study provides new ideas for the direction control of fish swimming and has great significance for the development of the bionic Robot fish.

References

[1] Wu C. J., Wang L.: Numerical simulations of self-propelled swimming of 3D bionic fish school, Sci. China Ser. E-Tech. Sci., 52(3):658–669,2009.

[2] Xin Z. Q., Wu C. J.: Topology Optimization of the Caudal Fin of the Three-Dimensional Self-Propelled Swimming Fish, Adv. Appl. Math. Mech., 6(6): 732-763, 2014.

[3] Wu J. Z. , Ma H. Y., Zhou M. D.: Vorticity and Vortex Dynamics, Springer-Verlag, Berlin 2006.

THE STABILITY OF FLYING SNAKES DURING TRANSIENT GLIDES

Isaac J. Yeaton *[1], John J. Socha[2], and Shane D. Ross[2]
[1]*Mechanical Engineering, Virginia Tech, Blacksburg, Virginia, USA*
[2]*Biomedical Engineering and Mechanics, Virginia Tech, Blacksburg, Virginia, USA*

Summary Arboreal snakes of the genus *Chrysopelea* are the only known snakes to glide. These snakes use large amplitude three-dimensional body undulations in a controlled and stable glide to the ground. We use recently acquired glide data (provided in a complimentary presentation) and a variable-geometry rigid-body model to address the passive stability properties of this system. By varying the spatial and temporal characteristics of the undulation in simulated glides, we find that flying snakes are likely unstable in pitch and moderately unstable in roll.

INTRODUCTION

Powered flight confers great advantage to species that can fly, yet has evolved only four times in the history of life. Additionally, the evolutionary pathway to active powered flight is unknown. One possible explanation is the transition from passive gliding of arboreal species to active flapping, necessitating increased control authority to compensate for time-varying aerodynamic and inertial forcing during flapping flight. Therefore, studying the stability properties of gliding animals may provide insights into how animals evolved flight.

Possibly the most unique gliders are flying snakes of the genus *Chrysopelea*. To execute aerial locomotion, a snake jumps from a tree into the air while simultaneously flattening its body into an aerodynamically favorable shape. Snake gliding is distinguished by complex, three-dimensional body undulations resulting in a stable glide. Flying snakes are highly dynamic gliders that cannot truly fly, and therefore provide a unique opportunity to study how animals compensate for varying forces distributed over their body.

VARIABLE-GEOMETRY RIGID-BODY MODEL OF SNAKE GLIDING

Our objective is to understand glide performance, as well as translational and rotational stability properties, of snake flight. To address this, we formulate a reduced-order model for the dynamics of snake gliding and use experimentally determined aerodynamic force coefficients. The model is comprised of three components: 1) kinematics of the snake's body, 2) a variable-geometry rigid-body model for the equations of motion, and 3) the aerodynamics model based on simple sweep theory.

The simulated kinematics are based on a prescribed planar undulation given by the serpenoid curve for the body curvature $\kappa(s,t)$ as a function of position along the body s and time t,

$$\kappa(s,t) = -\frac{2\pi A}{\lambda_k}\sin\left(\frac{2\pi}{\lambda_k}x - 2\pi f t + \phi\right) \tag{1}$$

where the parameters A and λ_k affect the spatial compactness and wavelength, respectively, and f is the undulation frequency. The $(x(s,t), y(s,t))$ coordinates of the body are found by integrating the tangent angle $\theta(s,t)$ using $\partial_s\theta = \kappa$, $\partial_s x = \cos\theta$, and $\partial_s y = \sin\theta$. Recently acquired body kinematics of short glides indicate a serpenoid curve with $A = 1.6$, $\lambda_k = 0.6$, and $f = 1.4$ Hz is a good approximation of the snake's body [1].

We derive the dynamical equations in discrete form, using a variable-geometry rigid-body formulation, which includes all inertial terms associated with the changing configuration of the body. The body kinematics are described in a co-moving

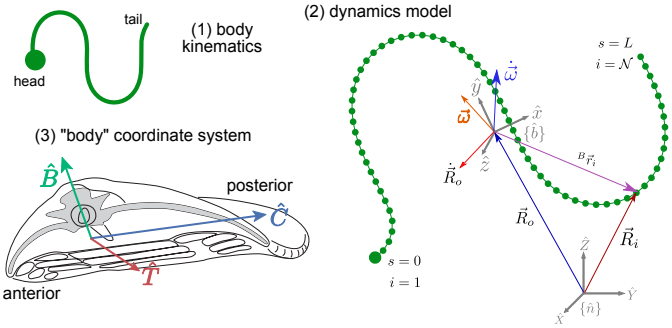

Figure 1: Components of snake simulation: body kinematics, variable-geometry rigid-body formulation, and body coordinate system to define the airfoil cross section. The equations of motion are written for the co-moving snake frame $\{\hat{b}\}$ as it translates and rotates in the inertial frame $\{\hat{n}\}$. The body kinematics are defined in the $\hat{x}$–$\hat{y}$ plane of the co-moving frame. Sketch (3) is a modified version from ref. [2], originally adapted from an illustration by Tara Dalton Bensen and Jake Socha.

*Corresponding author. Email: iyeaton@vt.edu

plane that is free to translate and rotate in the full six degrees of freedom. We write the equations of motion for the location and orientation of this plane, where the origin does not have to be coincident with the center of mass of the body. We discretize the body into $\mathcal{N}$ point masses and write Newton's and Euler's equations, summing the contribution from each piece of mass (figure 1). The equations read in general form as,

$$\begin{aligned}\sum \vec{F}_{i,\text{grav}} + \sum \vec{F}_{i,\text{aero}} = \sum m_i \ddot{\vec{R}}_o + \sum -m_i \vec{r}_i \times \dot{\vec{\omega}} + \sum \vec{\omega} \times (\vec{\omega} \times m_i \vec{r}_i) \\ + 2 \sum \vec{\omega} \times m_i [\dot{\vec{r}}_i] + \sum m_i [\ddot{\vec{r}}_i]\end{aligned} \tag{2}$$

$$\begin{aligned}\sum \vec{r}_i \times (\vec{F}_{i,\text{grav}} + \vec{F}_{i,\text{aero}}) = \sum m_i \vec{r}_i \times \ddot{\vec{R}}_o + \sum \vec{r}_i \times (\dot{\vec{\omega}} \times m_i \vec{r}_i) + \sum \vec{r}_i \times (\vec{\omega} \times (\vec{\omega} \times m_i \vec{r}_i)) \\ + 2 \sum \vec{r}_i \times \left(\vec{\omega} \times m_i [\dot{\vec{r}}_i]\right) + \sum \vec{r}_i \times m_i [\ddot{\vec{r}}_i]\end{aligned} \tag{3}$$

where the square bracket denotes body derivatives expressed in the inertial frame. The last two terms in each equation constitute the inertial contributions.

As the simulated snake translates and rotates, each mass element along the body will experience a different three-dimensional flow velocity. Because the full aerodynamics of snake flight are unknown, we make the simplifying assumptions of local aerodynamic interactions and of simple sweep theory, i.e. only the velocity component locally normal to the body contributes useful aerodynamic work. This allows us to use previously measured lift and drag coefficients (C_L, C_D) as model inputs [3]. We define the chord-line $\hat{C}(s,t)$ and backbone $\hat{B}(s,t)$ unit vectors using a Darboux-like frame, such that $\hat{C}$ is within the co-moving plane and is perpendicular to the local tangent vector $\hat{T}(s,t)$. Each local velocity vector is projected into the $\hat{C}$–$\hat{B}$ plane and lift and drag are calculated using the high Reynolds number formulae, $F_L = {}^1\!/_2 \rho U^2 S C_L(\alpha, \text{Re})$ and $F_D = {}^1\!/_2 \rho U^2 S C_D(\alpha, \text{Re})$, where the angle of attack α is measured between $\hat{C}$ and the projected flow velocity vector U.

RESULTS AND CONCLUSIONS

Because the simulated snake never satisfies an equilibrium condition, we define stability by viewing trajectories through phase portrait projections of key dynamic variables, for varying undulation parameters A, λ_k, and f. Examples of pitch – pitch rate and roll – roll rate phase portrait trajectories are shown in figure 2. For these initial conditions, undulation slows the manifestation of a pitch instability (pitch angles are negative and becoming more negative) as shown in the left plot. We see cyclic dynamics in roll (right plot), and that without undulation, the animal simply rolls to one side. Additionally, velocity phase portrait movies indicate that pitch strongly affects the translational motion of the animal. These results suggest that flying snakes may require active control to mitigate an inherent pitch instability, and that a roll instability cannot manifest fully during transient glides because of cyclic roll dynamics. Supported by NSF 1351322 to JJS and NSF 1150456 to SDR.

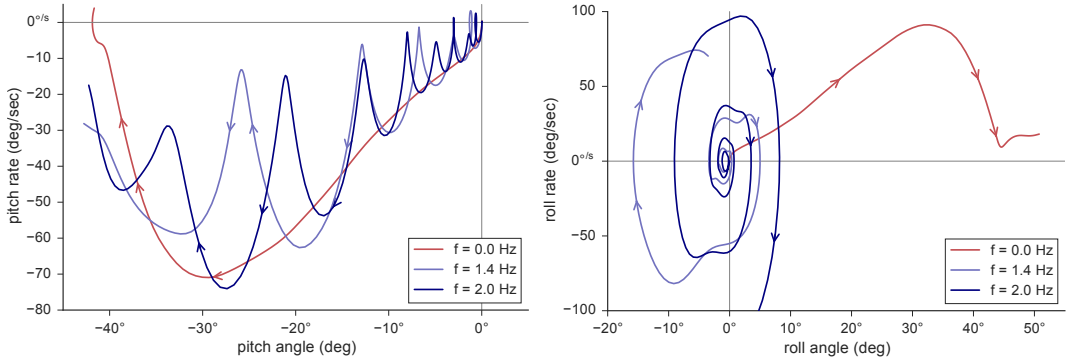

Figure 2: Transient glide stability is viewed as phase portrait projections of key dynamic variables, in this case pitch and roll for simulated glides for three different undulation frequencies.

References

[1] Socha J. J., Baumgardner G. A., Ross S. D., Yeaton I. J.: A new understanding of Aerial Undulation in Flying Snakes. XXIV ICTAM submission, 2016.

[2] Krishnan A., Socha J. J., Vlachos P. P., Barba L. A.: Lift and wakes of flying snakes. Phys. Fluids 26, 2014.

[3] Holden D., Socha J. J., Cardwell N. D., Vlachos, P. P.: Aerodynamics of the flying snake *Chrysopelea paradisi*: how a bluff body cross-sectional shape contributes to gliding performance. J. Exp. Biol. 217:382-394, 2014.

A NEW UNDERSTANDING OF AERIAL UNDULATION IN FLYING SNAKES

John J. Socha*[1], Grant A. Baumgardner[2], Shane D. Ross[1], Isaac J. Yeaton[2]
[1]*Department of Biomedical Engineering & Mechanics, Virginia Tech, Blacksburg, VA 24061, USA*
[2]*Department of Mechanical Engineering, Virginia Tech, Blacksburg, VA 24061, USA*

SUMMARY
Flying snakes are perhaps the world's most unconventional gliders, turning their whole body into a wing and undulating in the air. Understanding the snake's inertial mechanics and aerodynamics requires detailed knowledge of its kinematics, but previous data are under-resolved for such analyses. Here, we describe a new experiment of live flying snakes using a unique indoor arena at Virginia Tech, adapted for motion-capture recordings of gliders. The results provide the first comprehensive description of the snake's body throughout its trajectory, enabling new modeling of the snake's mechanics (provided in a complimentary presentation).

MOTIVATION
'Flying' snakes glide like no other animal: with no conventional wings or other membranes for flight surfaces, they flatten their entire body and send traveling waves from head to tail, giving the appearance of a ribbon swimming through the air [1]. Although highly unconventional, these snakes glide well for an animal, display surprising control, and in some species, can even maneuver [1-5]. In a developed glide, flying snakes move downward at a shallow angle (typically reaching ~30° from the horizon, but as little as 13° has been observed) and cover significant horizontal distance. Their glides are stable—the snake is under control, and it can even recover from induced instabilities such as a forced tumble.



Fig. 1. A view from the launch site in The Cube at Virginia Tech, showing the target landing tree and floor covered with padding to protect the snakes upon impact. Dimensions, 13x15x9 m.

A thorough understanding of animal flight requires knowledge of a flyer's body posture, shape, and orientation to the oncoming airflow, and how these factors change through time. These features can be used to find speed and acceleration, lift and drag coefficients (C_L and C_D), center of mass (CoM), center of pressure (CoP, the location of net aerodynamic force), and moment of inertia. Together, these kinematic and geometric factors form the core parameters used to understand how a flyer produces aerodynamic forces and how it maintains stability. However, we currently lack sufficient information on the snake's complex body kinematics to perform such analyses with confidence. Here, we address this issue by performing new experimental measurements of flying snakes tracked with high fidelity using a large motion-capture system.

BACKGROUND
A recent study [5] tracked five markers on the flying snake's body using four cameras (for 3D reconstruction of position), representing our best understanding of the snake's kinematics during a glide. Although the study provided valuable information on the snake's body movements, the data are insufficient for conducting inertial and aerodynamic modeling, for the following reasons: 1) There were too few markers to identify the location and curvature of curves on the body, and the precise spacing of the body segments. Without this information, the exact posture of the aerial snake remains unknown, which is a key piece of information for determining the snake's aerodynamics. 2) The tail was not marked, and so its patterns of movement have not been described. Although the tail does not flatten, it represents ~25% of the total length of the snake, and its apparent whip-like motion may create vortices that contribute to force production and therefore play a role in balance. 3) The five landmarks alone cannot provide information on the local orientation to air flow, meaning that the angles of attack along the body could not be determined. Angle of attack is a critical variable, because lift and drag coefficients are highly sensitive to airfoil orientation [6]. The angles of attack of local 'airfoils' along the snake's body may in fact vary with position on the body and phase of the undulation cycle. 4) Accelerations were calculated from noisy spatial data, a process that amplifies error [7] and resulted in a high uncertainty in understanding the forces on the snake.

*Corresponding author. Email: jjsocha@vt.edu

MOTION CAPTURE OF FLYING SNAKES IN THE CUBE AT VIRGINIA TECH

Recently, we conducted glide experiments using two species of the flying snake *Chrysopelea.* Our aim was to improve the temporal (6X) and spatial (4X) resolutions of the body of the snake during aerial undulation, as compared to previous studies, and to provide the first measurements of tail motion. We recorded a total of 97 glides from 7 individuals of *C. paradisi* and 34 glides from 5 individuals of *C. ornata* in a large indoor arena, "The Cube" at Virginia Tech. Snakes were tagged with 12 to 17 infrared-reflective markers along the trunk and tail, and allowed to jump and glide from a height of 8.5 m. Markers were tracked using a 23-camera motion-capture system (179 fps, Qualisys Oqus 500) and two high-speed cameras (500 fps, Photron APX-RS). We reconstructed body posture throughout the glide by fitting global cubic splines to the measured points and estimated the airfoil orientation through local rotations of a torsion-minimizing frame.. Separately from the live animal recordings, we sectioned a snake (which had previously died of natural causes) into one centimeters segments for weighing, enabling us to determine its mass distribution.

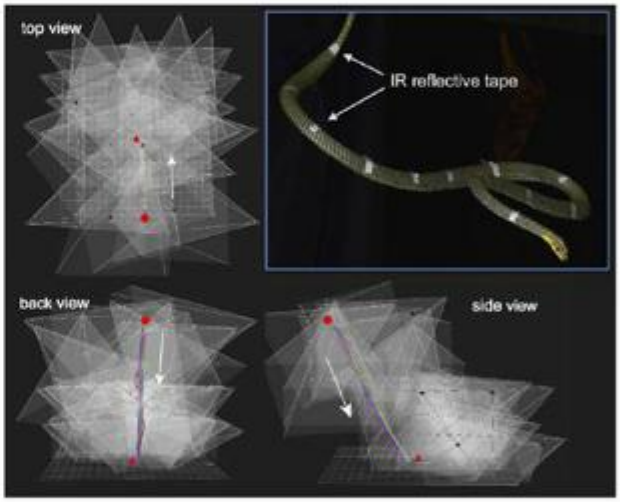

Fig. 2. The recorded volume, represented by the overlapping fields of view of the 23 motion-capture cameras. Inset: the marked snake in the air.

RESULTS AND CONCLUSION

The results from this new experiment using live flying snakes provide the first full description of the snake's body kinematics through a full glide trajectory. In contrast to all other animal gliders, the snake is highly dynamic, and can be considered as a morphing wing whose kinematic characteristics continuously change. Along with velocity and acceleration, these data enable the calculation of time-varying variables including body spacing, curvature, angle of attack, and center of mass. We find that sections of the snake are highly swept, and that angles of attack are higher than expected, with typical values in the range of 40-50° but with parts of the body reaching up to 90°. Such values mean that the aerodynamic forces on the body can vary dramatically, and that at times parts of the body may act as drag-producing bluff bodies. We will use the results from this study to accurately model the snake's inertial and aerodynamic mechanics for the first time, which will be presented in a complimentary presentation [8]. Supported by NSF 1351322 to JJS.

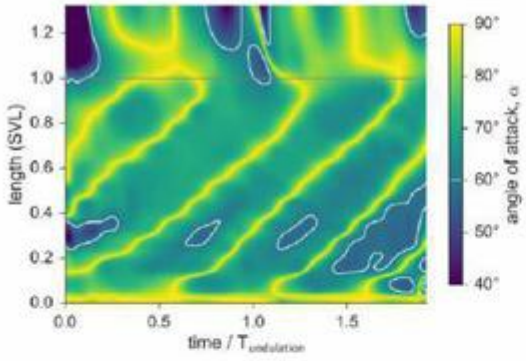

Fig. 3. Angle of attack along the body (in snout-vent lengths) vs. time for one snake in a single glide.

References

1. Socha, J.J., *Gliding flight in the paradise tree snake.* Nature, 2002. **418**: p. 603-604.
2. Socha, J.J. and M. LaBarbera, *Effects of size and behavior on aerial performance of two species of flying snakes (Chrysopelea).* Journal of Experimental Biology, 2005. **208**(10): p. 1835-1847.
3. Socha, J.J., T. O'Dempsey, and M. LaBarbera, *A 3-D kinematic analysis of gliding in a flying snake, Chrysopelea paradisi.* Journal of Experimental Biology, 2005. **208**(10): p. 1817-1833.
4. Socha, J.J., *Gliding flight in Chrysopelea: Turning a snake into a wing.* Integrative and Comparative Biology, 2011. **51**(6): p. 969-982.
5. Socha, J.J., et al., *Non-equilibrium trajectory dynamics and the kinematics of gliding in a flying snake.* Bioinspiration & Biomimetics, 2010. **5**(4): p. 045002.
6. Abbott, I.H. and A.E. Von Doenhoff, *Theory of Wing Sections*. 1959, New York: Dover Publications, Inc. 693.
7. Walker, J.A., *Estimating velocities and accelerations of animal locomotion: a simulation experiment comparing numerical differentiation algorithms.* Journal of Experimental Biology, 1998. **201**: p. 981-995.
8. Yeaton, I.J., J.J. Socha, and S.D. Ross, *The stability of flying snakes during transient glides.* XXIV ICTAM submission, 2016.

SYNCHRONIZATION OF EUKARYOTIC FLAGELLA: HYDRODYNAMIC VS. INTRACELLULAR COUPLING

Greta Quaranta[1], Marie-Eve Aubin-Tam[2], and Daniel Tam*[3]
[1]*Laboratory for Aero and Hydrodynamics, Delft University of Technology, 2628CD Delft, Netherlands*
[2]*Department of Bionanoscience, Delft University of Technology, 2628CJ Delft, Netherlands*
[3]*Laboratory for Aero and Hydrodynamics, Delft University of Technology, 2628CD Delft, Netherlands*

Summary We investigate the influence of hydrodynamic forces on the synchronization of two eukaryotic flagella by triggering phase-locking between a controlled external flow and the flagella of *C. reinhardtii* cells. We directly measure the hydrodynamic forces required for synchronization between the controlled hydrodynamic forcing and beating flagella. We find these forces to be over an order of magnitude larger than hydrodynamic forces experienced by *C. reinhardtii* in physiological conditions. Our results suggest that synchronization is due instead to coupling through cell internal fibers connecting the flagella inside the cell body. This conclusion is confirmed by observations of the *vfl3* mutant, with impaired mechanical connection between the flagella. For these mutants, we do not observe consistent flagellar synchronization.

MOTIVATIONS

The emergence of coherent behaviour is ubiquitous in the natural world and has long captivated physicists and biologists alike. Phase transitions leading to synchronization are observed between and within biological organisms. Recently, the organized dynamics of micron sized hair-like cell projections called cilia has attracted high levels of interest. The synchronization between the two flagella of *C. reinhardtii* has been investigated as a model system for flagellar synchronization and several mechanisms have been proposed. The dominant view has been that synchronization occurs through hydrodynamic interactions [1, 2] and another recent view suggests that the cell rocking motion causes synchronization by creating synchrony-restoring hydrodynamic drag on the flagella [3] . Both mechanisms rely on the eukaryotic flagellum responding to hydrodynamic feedback forces. In this study, we investigate experimentally how eukaryotic flagella respond to external hydrodynamic forces and quantify the coupling strength between flagella and flow. We also investigate the role of intracellular coupling of the flagella through direct mechanical interactions [4]. We do this by studying *Chlamydomonas vfl3* mutants, with impaired mechanical connection between the flagella.

EXPERIMENTAL SET UP

Our experimental set up allows us to apply a periodic external flow with a controlled amplitude and frequency. The flow is generated around a single biflagellated *C. reinhardtii* cell. The beating of the flagella is imaged through an inverted microscope and recorded with a sCMOS camera at 838.4 frames per seconds. The flow is generated as follow. A micropipette is inserted in an open flow chamber through an air-water interface, without direct contact with the walls of the chamber. A single *C. reinhardtii* cell is held fixed at the end of the micropipette. The flow chamber itself rests on a piezo-stage which can be translated. The motion of the piezo generates a relative translation of the flow chamber with respect to the cell, which remains fixed in the laboratory frame of reference. This is akin to creating a background flow with respect to the cell. We impose periodic flows of frequency $f_{\mathrm{F}} = 48 - 63$Hz and amplitude varying from $A_{\mathrm{F}} = 0 - 10\mu$m, corresponding to flow velocities $U_{\mathrm{F}} = 0 - 1360\mu\mathrm{m.s}^{-1}$. The largest flows imposed are an order of magnitude higher than flows typically experienced by a swimming cell, whose free swimming velocity has been measured to be $U_0 = 110 \pm 12\mu\mathrm{m.s}^{-1}$, in agreement with previous studies. Movies of beating flagella are processed and analyzed to extract the phase dynamics of the flagella. In this study, we track the phase difference between the flagella and the external forcing in order to investigate under which conditions beating flagella synchronize with the external flow.

RESULTS

Our experiments reveal that Eukaryotic flagella are able to synchronize with an exterior background flow, however the hydrodynamic forces required to reach synchronization are significantly larger than the forces experienced by flagella in physiological conditions.

For a given flow amplitude, the frequency of the periodic motion of the piezo-stage was varied around the intrinsic beating frequency of the flagella f_0 recorded in the absence of forcing. For forcing frequencies far from the intrinsic beating frequency f_0, the flagella beat at their own intrinsic frequency and do not phase lock with the external flow. For forcing frequencies within

*Corresponding author. Email: d.s.w.tam@tudelft.nl

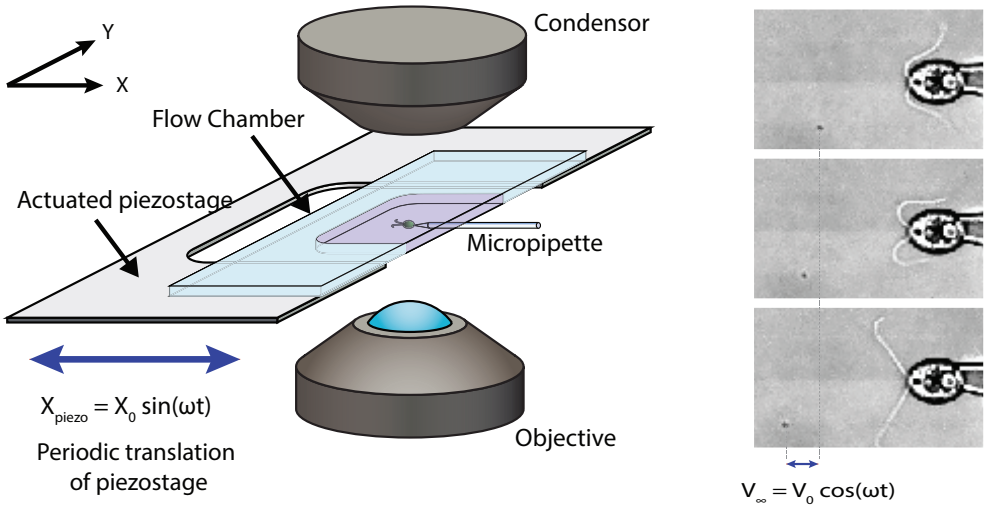

Figure 1: (left) Experimental setup. (right) Snapshots representing beating *C. reinhardtii*. The motion of a particle is due to the periodic background flow of amplitude 5μm

a small frequency interval centered around f_0, we observe that the power and recovery strokes of the flagella perfectly follow the back and forth motion of the background flow and the flagella phase lock with the external flow. The size of the frequency interval for which synchronization is triggered increases for larger amplitudes of the piezo-motion.

The synchronization between the external flow and the beating flagella is very well represented by the stochastic Adler equation, which corresponds to a classic first order model for the dynamics of the phase difference[5]. Fitting our experimental data with this simple model allows us to quantify the coupling strength ϵ. We find that the coupling strength linearly increases with the velocity of the forcing flow $\epsilon = \mu U_F/U_0$. Here U_F is the velocity of the forcing flow $U_F = 2A_F f_F$ and $\mu = 0.51$ s^{-1}.

CONCLUSIONS

Our results show that the coupling between external flows and the eukaryotic flagella of *C. reinhardtii* is weak. For external flows $U_F \approx 1\mathrm{mm.s}^{-1}$, which are one order of magnitude larger than the free swimming velocity, the coupling strength is $\epsilon \approx 5$Hz. Hence, the flagella will synchronize with a background flow, only when the frequency f_F is within 5 Hz of their intrinsic frequency. For forcing frequencies outside of this frequency range, the eukaryotic flagella of *C. reinhardtii* will beat at their own intrinsic frequency despite strong hydrodynamic forcing. We find that the flagella of *C. reinhardtii* are weakly coupled with hydrodynamic forces. This suggests that flagellar synchronization in *C. reinhardtii* does not primarily rely on hydrodynamic forces and points towards the role of direct mechanical forces transmitted through the cell cortex. To test this hypothesis we performed experiments with *Chlamydomonas vfl3* mutants. In this mutant, the mechanical connection through the distal striated fiber, between the two basal bodies from which the flagella emerge, is impaired. We recorded movies for over 20 biflagellated *vfl3* cells and investigated the phase dynamics between the two flagella. We never observed consistent phase-locking between the flagella except for one cell. We measured the average beating frequency of both flagella and find a difference in intrinsic beating frequency of ~ 15 Hz with the slower one beating at 48.6 ± 8.8 Hz and the faster one at 63.1 ± 6.9 Hz. These results indicate that the mechanical connection between the two flagella plays an important role in the synchronization of the two flagella of *C. reinhardtii*.

References

[1] T. Niedermayer, B. Eckhardt, and P. Lenz, Chaos 18, 037128 (2008)

[2] D. R. Brumley, K. Y. Wan, M. Polin, and R. E. Goldstein, Elife 3, e02750 (2014).

[3] V. F. Geyer, F. Jülicher, J. Howard, and B. M. Friedrich, Proc. Natl. Acad. Sci. U.S.A. 110, 18058 (2013)

[4] K. C. Leptos, K. Y. Wan, M. Polin, I. Tuval, A. I. Pesci, and R. E. Goldstein, Phys. Rev. Lett. 111, 158101 (2013)

[5] A. Pikovsky, M. Rosenblum, and J. Kurths, Synchronization: a universal concept in nonlinear sciences, Vol. 12 (Cambridge university press, 2003)

EMERGENCE OF METACHRONAL WAVES IN CILIA ARRAYS: A HYDRODYNAMIC MECHANISM

Sylvain Chateau*[1,2], Jean Mercat[1], Zhe Li[3], Sébastien Poncet[1,2], Julien Favier[1], and Umberto d'Ortona[1]

[1]*Aix-Marseille Université, CNRS, Centrale Marseille, M2P2 UMR 7340, 13451, Marseille, France*
[2]*Mechanical Engineering Department, Université de Sherbrooke, Sherbrooke, Québec, Canada*
[3]*École Centrale de Nantes, LHEEA, ECN/CNRS, Nantes, France*

Summary The present work reports the emergence of metachronal waves in cilia arrays immersed in a two-fluid environment using a coupled lattice Boltzmann - Immersed Boundary method. The periciliary layer (PCL) is confined between the wall and the mucus layer. Its depth is chosen in such a way that the tips of the cilia can penetrate the mucus layer. The cilia are initially set in a random state but quickly synchronize with their immediate neighbors with a phase shift giving birth to sympleptic or antipleptic metachronal waves, depending on the strength of the fluid retroaction onto the cilia. Antiplectic waves are found to be the most efficient to transport mucus compared to other random or synchronised cilia motions.

INTRODUCTION

Fluid propulsion by moving cilia is an universal phenomenon that can be found everywhere in Nature from the locomotion of micro-organisms to multiple processes in biological organisms at the cellular scale. For examples, in the early human embryonic development, cilia are responsible for the heart placement on the left side of the chest. Cilia move also the ovules in the Fallopian tubes, or the nutriments in the brain. In the specific problem of mucociliary clearance, cilia are responsible for transporting the mucus outside the lungs. In severe respiratory diseases, such as cystic fibrosis or asthma, the number of cilia clusters is decreased compared to the case of a healthy patient, and many cilia may beat in an abnormal way resulting in a less efficient transport of mucus. It has been experimentally observed [1] that cilia beat in a synchronised way with a phase shift between two neighboring cilia, forming a metachronal wave which appears to greatly enhance the transport of mucus. Then, it is of great importance to understand how this wave emerges and which type of waves provides the most efficient transport. This work could result in a better understanding of the mucociliary clearance process.

NUMERICAL METHOD

The fluid part is solved on a Cartesian grid using the lattice Boltzmann method with a D3Q19 scheme. The model of Porter et al. [2] is used to model the fluid-fluid repulsion forces. The cilia are modeled with a set of 20 Lagrangian points, and the immersed boundary method is used to ensure the no-slip condition along the cilia [5]. The equations of motion for the cilia are taken from Chatelin [3] and the motion of each cilium is decomposed into a finite number of steps during a period. If needed, an interpolation between two steps can be done in order to have the right velocity values along the cilia. The code is suitable for High Performance Calculation using a MPI parallelization. Cilia are set in arrays in a two-fluid layer, with PCL at the bottom and mucus above it. The PCL depth is set in such a way that the tips of the cilia emerge into the mucus layer. Periodic boundary conditions are used in the X and Y directions. A Bounce-Back Rule condition is imposed at the bottom of the domain and a free-slip velocity condition at the top using the "mirror method". The fluid retroaction onto the cilia is evaluated by projecting the immersed boundary forces calculated at each time step for every Lagrangian points onto the corresponding velocity vectors, and then the torques are computed. By doing so, only the norm of the velocity vector, but not its direction, is modified. A new parameter α controls then the intensity of the retroaction: $||\vec{V}|| = ||\vec{V}|| \pm \alpha||d\vec{V}||$

RESULTS

Starting from an initially random state, cilia quickly synchronize with their immediate neighbors with a phase shift. With time, metachronal waves -antipleptic or sympleptic- emerge. The sign of the parameter α, and the ratio h/L_{cil} of the PCL depth with regards to the cilia length are two key parameters that determine the kind of emerging waves. Positive (resp. negative) α-values correspond to sympleptic (resp. antipleptic) waves. A proper value of h_{PCL}/L_{cil} is needed for the metachronal waves to emerge. As it can be seen on figures 1(a) and 1(b), cilia move along a plane and so can be subjected to collisions. But, since a 3D configuration is considered, one can suppose that cilia would actually slip onto each other in reality. Figure 2 shows the mean mucus velocity evolving with time. It can be seen that, for the same set of parameters, antipleptic metachronal coordination appears to greatly enhance the transport of mucus compared to random or other synchronized

*Corresponding author. Email: sylvain.chateau@USherbrooke.ca

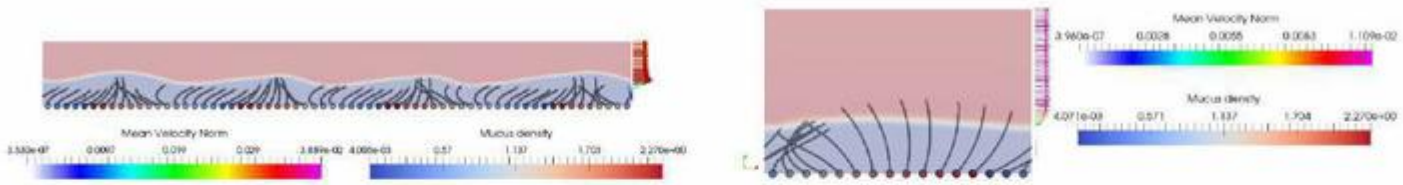

(a) (b)

Figure 1: (a) Sympleptic metachronal wave emerging from an array of 64 cilia disposed along the X direction, with $\alpha = 3$. Spacing between two cilia is 7 lattice units, and $h_{PCL}/L_{cil} = 0.9$. Size of the domain in X, Y, Z is 449, 8, 50. (b) Antipleptic metachronal wave emerging from an array of 16 cilia disposed along the X direction, with $\alpha = -3.5$. Spacing between two cilia is 5 lattice units, and $h_{PCL}/L_{cil} = 0.6$. Size of the domain in X, Y, Z is 81, 6, 50. In both cases (a) and (b), $L_{cil} = 22$ lattice units and the viscosity ratio is set to 15.

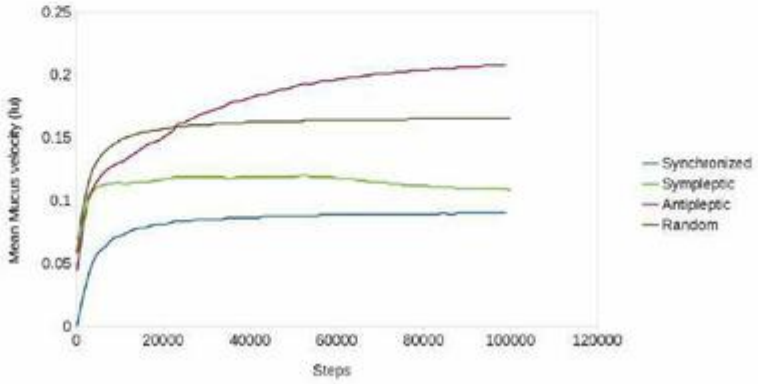

Figure 2: Mean mucus velocity for different kind of coordinations.

collective motions. As for sympleptic metachronal coordination, the mean mucus transport is weaker that in the case of cilia beating randomly. We explain this by the fact that this kind of synchronization induces large recirculations in the mucus phase. Moreover, the cilia tips are always in the PCL phase and never emerge into the mucus. Confirming the simulations of Ding et al. [4] using the regularized Stokeslet method, antiplectic waves are the most efficient for mucus transport.

CONCLUSIONS

An efficient and validated 3D lattice Boltzmann solver coupled to the immersed boundary method has been applied for the first time to investigate the emergence of metachronal waves and their superiority to transport mucus in a two-phase flow environment. A simple and efficient method has been applied successfully to take into account the fluid retroaction onto the cilia. Metachronal waves emerge quickly before the flow reaches a steady state. The efficiency of the metachronal waves for the mucus transport has been calculated, and antipleptic waves are found to be the most efficient ones compared to other random or synchronised motions.

The authors acknowledge the support of the Physio-Assist company. The PhD of Sylvain Chateau is funded through the NSERC discovery grant program.

References

[1] M.A. Sleigh. The biology of Cilia and Flagella. *Pergamon Press*, Oxford, 1962.

[2] M.L. Porter, E.T. Coon, Q. Kang, J.D. Moulton, and J.W. Carey. Multicomponent interparticle-potential lattice Boltzmann model for fluids with large viscosity ratios. *Physical Review E*, vol.86, 036701, 2012.

[3] R. Chatelin. Méthodes numériques pour l'écoulement de Stokes 3D : fluides à viscosité variable en géométrie complexe mobile; application aux fluides biologiques. *PhD thesis*, Institut de Mathématiques de Toulouse, 2013.

[4] Y. Ding, J.C. Nawroth, M. McFall-Ngai and E. Kanso. Mixing and transport by ciliary carpets: a numerical study. *Journal of Fluid Mechanics*, vol.743, p.124-140, 2014.

[5] Z. Li, J. Favier, U. d'Ortona, and S. Poncet. An improved explicit immersed boundary method to couple with Lattice Boltzmann model for single- and multi-component fluid flows. *Journal of Computational Physics*, vol.304, p.424-440, 2015.

MODELLING THE ENDOTHELIAL GLYCOCALYX LAYER IN THE MICROCIRCULATION

Tet Chuan Lee[1], Richard J. Clarke *[1], and David S. Long[1,2]
[1]*Department of Engineering Science, University of Auckland, Auckland, New Zealand*
[2]*Auckland Bioengineering Institute, University of Auckland, Auckland, New Zealand*

Summary The Endothelial Glycocalyx Layer (EGL) is a porous layer that lines the inside of blood vessels. It is of interest as it is believed to fulfil a number of roles important for vessel health including regulating vessel permeability and as a transducer of mechanical stress from flowing blood. In order to simulate a physiologically realistic microvessel, we derive an asymptotic treatment of the equations governing fluid flow and solid deformation in the EGL based on the low permeability limit. We perform simulations on a physiologically realistic microvessel that has been reconstructed from confocal microscopy data. By comparing results from the full governing equations against the asymptotic treatment, we show that a physiological microvessel is within the asymptotic regime. We also show that redistribution of the EGL away from cell peaks can reduce the shear stress experienced by the endothelium. Finally, we consider a more sophisticated EGL model based on homogenisation.

INTRODUCTION

The Endothelial Glycocalyx Layer (EGL) is a porous macromolecular layer that lines the luminal surfaces of blood vessels.The EGL as it lies at the important interface between flowing blood and the endothelium. The EGL consists of a complex network of glycoproteins, proteoglycans and glycoaminoglycans and exists in a dynamics equilibrium with blood. In this paper, we are particularly interested in modelling the EGL in the microvasculature. In microvessels, it is commonly accepted to be approximately $0.5\,\mu\mathrm{m}$ thick, although some recent studies have found a thicker layer ($1.5\,\mu\mathrm{m}$ [1]).

The EGL is hypothesised to be serve a range of functions including as a molecular sieve which regulates trans-endothelial mass transport, as a barrier that protect vessel walls from harmful levels of fluid shear stress and as a transducer of mechanical stress from blood flow. The EGL is difficult to study experimentally in the microcirculation not only due to the small scales involved, but also because of its dynamic nature which makes it sensitive to changes in its environment. As such, we are interested in modelling the EGL both to gain better understanding of it as well as to potentially inform future experiments.

FORMULATION

Current models of the EGL generally treat microvessels as a coupled system involving the lumen (which can be modelled as a Stokes flow) and the EGL which is modelled using Biphasic Mixture Theory [2] as shown in figure 1. The endothelium is treated as an impermeable wall. Based on the typical physical parameters involved in the microcirculation, the fluid flow model for the EGL reduces to a Brinkman equation. The solid deformation reduces to a linear elasticity problem with additional fluid pressure gradient and a fluid velocity forcing terms. Previous work in modelling the EGL has used Biphasic Mixture Theory. However, it has only be considered under simplified geometries (axisymmetric) or in two dimensions. As such, we were interested in modelling the EGL in a more physiologically realistic microvessel in three dimensions.

The EGL is highly impermeable and this results in a large Brinkman parameter ($\sim 10^3$) in the fluid model. This makes performing simulations on a complex geometry computationally challenging. As such, we developed an asymptotic treatment around this low permeability limit. In this asymptotic treatment, we find that at leading order, the fluid flow in the lumen

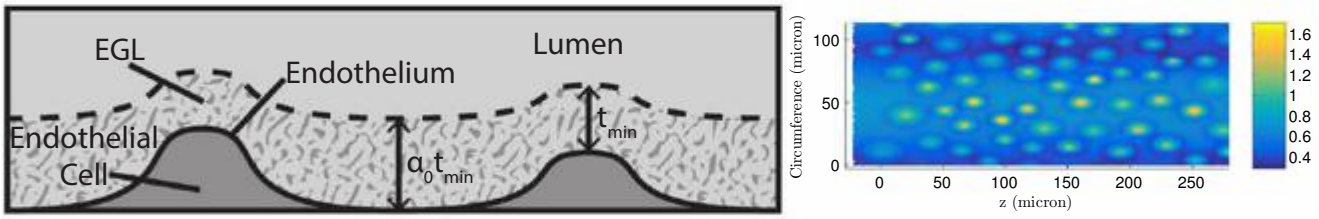

Figure 1: (Left) A microvessel is modelled as a tube with a non-uniform wall shape. The vessel consists of two regions, the lumen and the EGL. We consider two distributions of the EGL. One where the EGL that has redistributed to the relatively flat regions between cell nuclei ($\alpha_0 = 1.8$) and a non-redistributed EGL, which has constant thickness, $t_{\min}$ ($\alpha_0 = 1$). (Right) An example section of the elastic shear stress results obtained from the asymptotic treatment for a non-redistributed EGL.

*Corresponding author. Email: rj.clarke@auckland.ac.nz

Elastic Stress

EGL Type	α_0	$t_{\min} = 0.25$	$t_{\min} = 0.5$	$t_{\min} = 1$	$t_{\min} = 1.5$
Non-Redistributed EGL	1	0.84	0.89	0.97	1.00
Redistributed EGL	1.8	0.79	0.80	0.79	0.76

Fluid Stress (10^{-3})

EGL Type	α_0	$t_{\min} = 0.25$	$t_{\min} = 0.5$	$t_{\min} = 1$	$t_{\min} = 1.5$
Non-Redistributed EGL	1	1.25	1.16	0.99	0.88
Redistributed EGL	1.8	1.11	0.92	0.65	0.48

Table 1: The maximum magnitude of longitudinal shear stress for (Top) elastic and (Bottom) fluid stress. Both tables are normalised on the solid stress value for a non-redistributed EGL with $t_{\min} = 1.5\,\mu\text{m}$ which has a non-dimensional stress value of 1.708. The values given for the fluid stress are 10^{-3} smaller than the solid stress.

decouples from the EGL. The fluid flow in the EGL reduces to a core D'Arcy flow with two thin viscous layers. One thin viscous region adjacent to the lumen-EGL interface allows continuity of traction to be enforced while another at the endothelium ensures that no-slip is satisfied. The slip velocities that appear at the endothelium of the core D'Arcy flow give us the fluid shear stress experienced by the endothelium. The modelling of the solid deformation also simplifies as the fluid velocity is equivalent to a fluid pressure gradient in the D'Arcy flow, allowing the forcing term to be combined.

However, modelling the EGL using a volume averaged approach has some disadvantages. Experiments suggest that the inner layer of the EGL consists of a periodic hexagonal structure of interlinked filaments that are anchored to the endothelium in a regular pattern. This suggests that the elastic stress that results from the deformation of the EGL will likely be concentrated at certain points rather than smeared out over the whole surface as is the case for the Biphasic Mixture Theory treatment. As such, we are also pursuing a more sophisticated model for the EGL which using homogenisation theory to better represent that structure details in modelling the EGL.

Numerical Method and Geometry

A bespoke computational program was created using the Boundary Element Method in order to perform the required simulations. This program allowed the simulation of a microvessel with arbitrary three-dimensional geometry. The microvessel used in the simulations was reconstructed from a confocal microscopy image of mouse cremaster muscle which was generously provided by Dr Jennifer Bodkin and Professor Sussan Nourshargh, Queen Mary University of London.

RESULTS

By comparing predictions from the full model against its asymptotic treatment, we find that the microvessel has reached the asymptotic regime for parameters that lie within the physiological range. Furthermore, we find that the elastic shear stresses on the endothelium are up to a thousand times greater than the fluid shear stresses, which leads further support to the hypothesis that the majority of mechanotransduction across the EGL occurs through solid deformation of the EGL.

We also use consider another hypothesis that has been proposed in the literature where it has been suggested that the EGL redistributes away from the peaks of cells into order to reduce the shear stress experienced by the endothelium. In order to investigate this, we considered two different distributions of the EGL as shown in figure 1, one where the EGL redistributes ($\alpha_0 = 1.8$) and one where the EGL has a constant thickness ($\alpha_0 = 1$). An example of these results are shown in figure 1. We find that redistribution does reduce the shear stress experienced by the endothelium. These results are summarised in table 1 for different values of $t_{\min}$.

CONCLUSIONS

We show for physiological parameters, microvessels are within the asymptotic regime of low permeability in the EGL. We also find that our simulations support the hypothesis that the majority of mechanotransduction occurs through the solid phase. Finally, our simulations show that the redistribution of the EGL does indeed reduce the the shear stress experienced by the endothelium, especially for a thicker EGL.

References

[1] Yen, Wan-Yi, Cai, Bin, Zeng, Min, Tarbell, John M. and Fu, Bingmei M.: Quantification of the endothelial surface glycocalyx on rat and mouse blood vessels. Microvasc Res 83:337-346, 2012.

[2] Damiano, E.R.: The effect of the endothelial-cell glycocalyx on the motion of red blood cells through capillaries. Microvasc Res 55:77-91, 1998.

ENHANCED GAS TRANSPORT DURING HIGH-FREQUENCY VENTILATION

Justin S. Leontini*[1], Md. Kamrul Hasan[1], Rachel Swain[1], and Richard Manasseh[1]
[1]*Faculty of Science, Engineering and Technology, Swinburne University of Technology, Hawthorn, Victoria, Australia*

Summary This study focuses on the potential for nonlinear mean streaming to enhance the gas transport during high-frequency ventilation, a ventilation strategy used in intensive care wards. Direct numerical simulations of the reciprocating flow in a pipe are conducted, as this basic flow serves as a model of the flow in various sections of the human airway. In particular, the impact of modifying the end conditions of the pipe, so that there is some asymmetry from one end to the other, is investigated. Preliminary results show that the streaming flow, which progresses in one direction in the middle of the pipe, and the opposite direction at the sides, is reasonably insensitive to the frequency of oscillation, but it is heavily dependent on the amplitude.

PROBLEM DESCRIPTION

High-frequency ventilation (HFV) is a ventilation technique used in intensive care wards, particularly for neonatal patients. It is an invasive process, requiring the use of an endotracheal tube (a tube inserted down the throat of the patient into the trachea). It completely controls the breathing process, and therefore patients are generally heavily sedated whilst undergoing HFV.

The defining feature of HFV is the use of very small, but very fast "breaths" - the breathing rate is usually of the order of 10Hz, and because of this the volume of gas that flows into and out of the airway in one breath is much less than the volume of the airway. This avoids large peak pressures in the airway and lungs, and therefore reduces the risk of lung tissue damage. However, the transport of Oxygen into the lungs, and Carbon Dioxide out, is not achieved by simply emptying and filling the lungs each breath. More subtle fluid mechanics phenomena are involved.

A number of candidate phenomena have been proposed, including the Pendeluft effect, Taylor dispersion, turbulent diffusion and nonlinear mean streaming. Basic descriptions of these mechanisms are provided in the reviews of [1, 5, 3].

An obvious candidate for the study of the fundamental flow phenomena in the airways is the reciprocating flow in a straight pipe. The focus of this study is the potential for mean streaming to occur. In a reciprocating pipe flow, this is a mean flow that has a net zero mean flux through the pipe, but the mean flow is non-zero. One such mean flow is one that progresses in one direction in the middle of the pipe, and in the other direction along the sides. In this way, gases can be transported both up and down the pipe. [2] showed that such a flow can occur if a straight pipe is slightly tapered, i.e, the symmetry from one end of the pipe to the other is broken. It is clear that the difference in end conditions will influence the strength of this streaming flow.

Here, a simple end condition is studied, that of a straight pipe with an entry/exit into a large reservoir. The impact of the presence of the free end on the flow regimes present, and in turn their effect on the mean streaming flow are investigated using direct numerical simulations and Floquet stability analysis. While the reciprocating flow in a straight pipe appears not to be well predicted with stability analysis, the vortical flow structures expected to be produced by the free end may be unstable.

METHODOLOGY

The simulations and stability analysis have been run using a well-validated spectral-element method solving the incompressible Navier-Stokes equations [6, 4]. The setup of the problem is a straight circular cross-section pipe that connects two large reservoirs. Time-dependent Dirichlet boundary boundary conditions are used to control the flow rate into and out of the reservoirs. The flow rate into one is always equal and opposite to the flow into the other, so that the flow rate at any instant through the connecting pipe is controlled. The magnitude of the peak flow rate, and the frequency of oscillation of the flow rate are the parameters of interest. These are expressed non-dimensionally as the Keulegan-Carpenter number $KC = \overline{U}_{\max}/(2\pi f D)$, and the Wommersley number $\alpha = fD^2/\nu$ where $\overline{U}_{\max}$ is the maximum cross-sectional mean velocity in the pipe, f is the frequency of oscillation, D is the pipe diameter, and ν is the kinematic viscosity of the fluid. A no-slip boundary condition is applied at the pipe wall. Neumann boundary conditions, specifying a zero-normal-gradient, are applied for the pressure at all boundaries. Initially the simulations are restricted to a two-dimensional, axisymmetric setup.

*Corresponding author. Email: justin.leontini@gmail.com

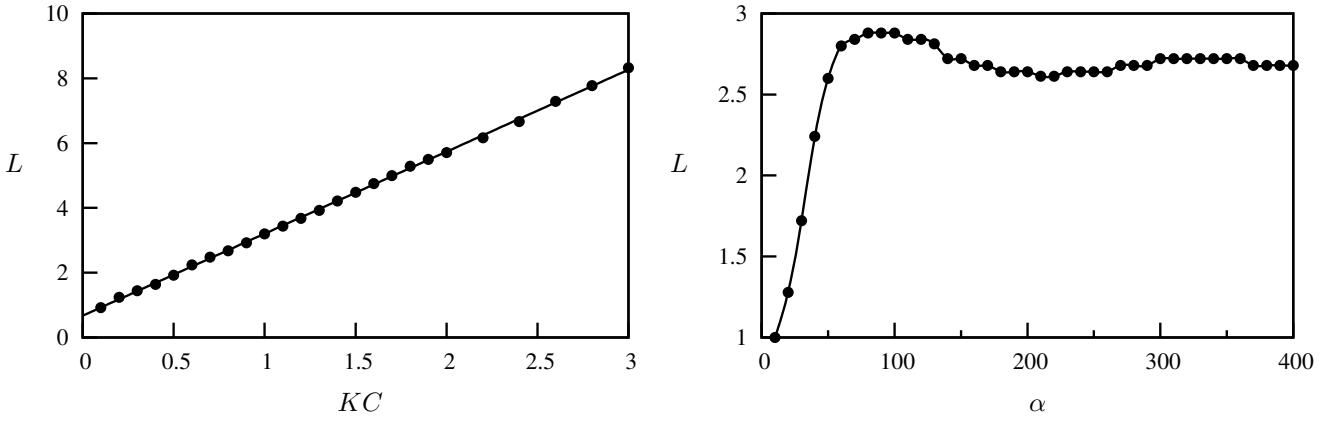

Figure 1: Development length as a function of KC, $\alpha = 400$ and as a function of α, $KC = 0.85$. Points are measurements, lines are best fits. It is clear that for the majority of the range of α tested, KC has a much stronger effect on the development length.

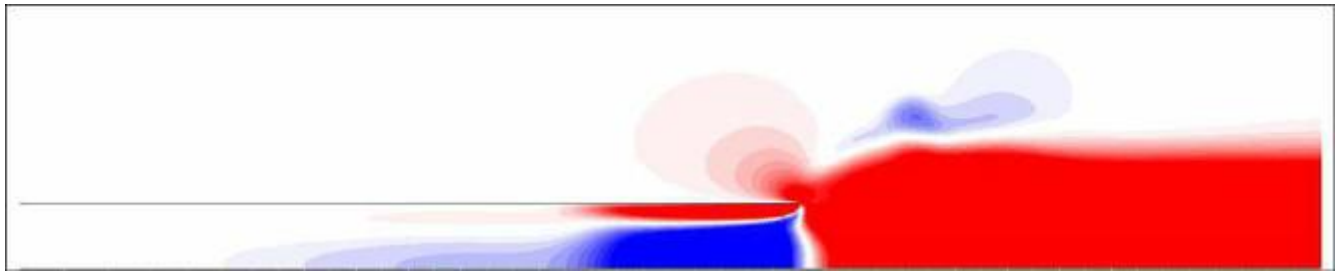

Figure 2: Colour contours of the mean axial velocity field in one half of the pipe for a case where $KC = 2$, $\alpha = 400$. White is zero, blue (red) is negative (positive). The image shows there is a mean axial velocity to at least $4.5D$ from the end of the pipe.

RESULTS AND DISCUSSION

A first indication of the impact of the free end is the measurement of the development length of the flow, L. To ascertain this, the shear stress on the pipe wall was measured. The fully developed flow does not vary along the pipe, so that $\partial(\partial u/\partial r)/\partial x = 0$ in the fully developed section, where u is the velocity in the axial direction, r is the distance in the radial direction, and x is the distance in the axial direction. Therefore, the distance from the end of the pipe where $\partial(\partial u/\partial r)/\partial x$ deviates from zero provides a measure of the distance where there is some impact from the free end, and therefore the distance at which there is some potential impact of mean streaming.

Figure 1 plots this length for a constant $\alpha = 400$ as a function of KC, and for a constant $KC = 0.85$ as a function of α. It is clear that there is a strong, linear relationship between KC and L of the form $L = 2.53KC + 0.67$. The development length L initially increases quickly with increasing α, but is practically independent of α for $\alpha > 200$. Figure 2 shows contours of the mean axial velocity of $KC = 2$, $\alpha = 400$. The image shows that there is a non-zero mean axial velocity, and therefore a streaming flow, to at least $4.5D$ from the end of the pipe.

References

[1] H. K. Chang. Mechanisms of gas transport during ventilation by high-frequency ventilation. *Journal of Applied Physiology*, 56(3):553–563, 1984.

[2] J.B. Grotberg. Volume-cycled oscillatory flow in a tapered channel. *Journal of Fluid Mechanics*, 141:249–264, 1984.

[3] J.B. Grotberg. Pulmonary flow and transport phenomena. *Annual Review of Fluid Mechanics*, 26:529–571, 1994.

[4] J. S. Leontini, D. Lo Jacono, and M. C. Thompson. Stability analysis of the elliptic cylinder wake. *Journal of Fluid Mechanics*, 763:302–321, 2015.

[5] T.J. Standiford and M.L. Morganroth. High-frequency ventilation. *Chest*, 96(6):1380–1389, 1989.

[6] M. C. Thompson, K. Hourigan, and J. Sheridan. Three-dimensional instabilities in the wake of a circular cylinder. *Exp. Therm. Fluid Sci.*, 12(2):190–196, 1996.

PHYSICS OF THE MUCOCILIARY CLEARANCE IN AIRWAYS. APPLICATION TO SEVERE ASTHMA

Kamel Khelloufi[1], Delphine Gras[2], Pascal Chanez[2] & Annie Viallat[1a)]
[1]*Université Aix Marseille, CNRS, CINaM UMR 7325,13288, Marseille, France*
[1]*Université Aix Marseille, CNRS, LAI UMR 7333,Inserm UMR1067, 13288, Marseille, France*

Summary Mucociliary clearance is the transport of a mucus layer in the airways, induced by beating cilia present on the epithelial surface. We present a physical analysis on the density and dynamics of cilia required to transport the mucus at a macroscopic scale. We used cultures of human bronchial epithelium obtained by biopsies from controls and asthmatic patients. A power law shows that the ciliated cell density controls the distance over which a fluid can be transported. The fluid rotates at a constant angular velocity on localized circular domains thanks to a local force density that linearly increases with the distance to the domain center, through a local control of cilia density and beat directions. subcritical ciliated cell density may explain the impaired clearance in severe asthma, while the mucus rheological properties remain unchanged.

INTRODUCTION

Mucociliary clearance is an essential innate mechanism of lung protection. Chronic respiratory diseases such as severe asthma are associated with impaired mucociliary clearance and a dramatic increased susceptibility to infection and inflammation. The mucociliary clearance mechanism consists in the circulation of a protective mucus layer at the surface of the airways epithelium. Mucus is transported along the airways and out of the lungs whereupon it is swallowed. Mucus is propelled by the asymmetric beating of microscopic cilia located on epithelial cells. During its forward motion, a cilium performs a fast effective stroke and its tip immersed in mucus propels it forward. The slow recovery stroke of a cilium occurs below the mucus layer, within the periciliary layer (2). The mucus velocity is determined by the density and the activity of cilia (frequencies, directions, phase synchronization of cilia beats), by their hydrodynamic interactions and by the mucus rheological properties. The physics of the integrated mucociliary coupled system has been little studied because quantitative *in vivo* measurements are difficult. Fundamental questions remain open. What density and spatial repartition of ciliated cells, what degree of coordination in cilia beat directions, phases and frequencies are required to enable mucus transport at the macroscopic scale? We report a detailed physical analysis of ciliary activity, fluid transport and mucociliary coupling on human bronchial cultures of primary airway epithelial cells at air–liquid interface (ALI), obtained by biopsies from controls and patients with asthma and chronic obstructive pulmonary disease (3).

RESULTS

We used ALI cultures for 17 controls, 7 patients with mild asthma, 18 patients with severe asthma and 7 patients with chronic obstructive pulmonary disease (COPD). Cultures are circular with a diameter of 1.2 cm. By optical microscopy, we characterized the density of active ciliated cells (ACCD) and the cilia beat frequency (CBF). We analyzed local and macroscopic transport of 1μm-beads and mucus and we correlated the transport to the forces exerted by cilia at the epithelium's surface. Our approach is finally applied to severe asthma and COPD.

Cilia activity

ACCD was determined by measuring the fraction of epithelial surface covered by beating ciliated cells. It ranges from 0% to 70%, with a large variability among different donors and a significant decrease for patients with COPD and severe asthma. Removal of the mucus layer on the epithelium surface did not affect the ACCD. The mean value of CBF measured at 37°C on healthy donors is 18.2 Hz. We qualitatively explored phase and directional correlation of beats between cilia located on a same cell and between cilia located on distant cells. Steric interactions between neighboring cilia impose a directional order and a partial phase synchronization of individual cilia on a same cell. Metachronal waves over several cells were observed only in zones of high ACCD, where mucus transport was observed over several hundreds of micrometers.

Transport

We visualized the motion of native mucus and that of 1μm-beads diluted in PBS and placed on the culture's surface immediately after mucus removal. In several culture chambers we observed a macroscopic rigid-like rotational motion of both native viscoelastic mucus and beads/buffer Newtonian fluid over the whole chamber (Fig. 1) (4). In the other culture chambers mucus remained still. However, local motions of beads were observed after mucus removal (trajectories shown in Fig. 1). In particular circular bead motion was observed on local domains ranging from 10 μm to hundreds of microns. The size of the largest circular domain of each culture displays a scaling law over more than 3 orders of magnitude with ACCD,

[a)] Corresponding author. Email: viallat@cinam.univ-mrs.fr

thus showing that the ciliated cell density governs the distance over which fluid transport is possible. The law is valid both for native mucus and Newtonian fluid.

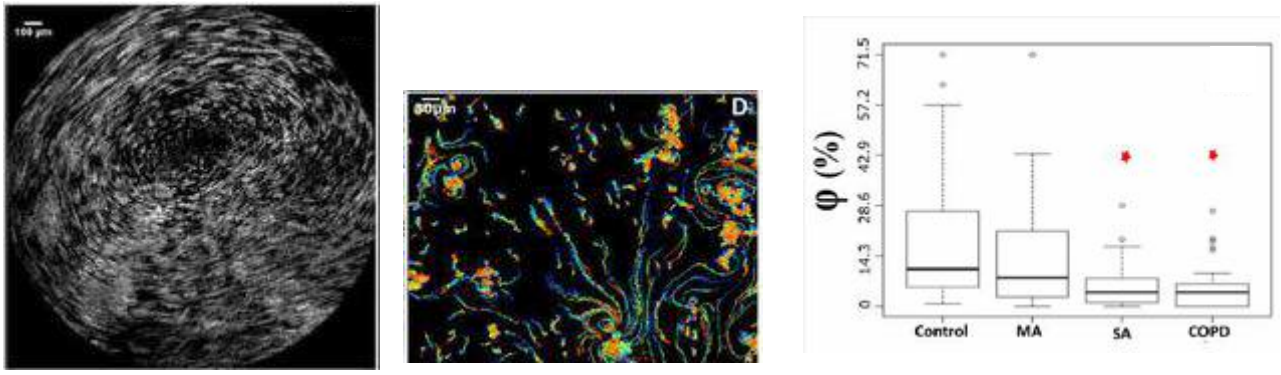

Figure 1. Left: stacks of images showing the rotational motion of mucus over the hole culture chamber ; center:trajectories of latex beads in buffer during localized motions; Right: ACCD for contols, patients ith mild asthma (MA), severe astma (SA) and COPD.

Force

We have analyzed the ciliary dynamics and circular transport within 6 domains in 5 different culture chambers. Each active cilium exerts a force on the surface fluid layer. This force has the direction of the cilium beat and its tangential component propels the surface layer circularly. We assumed that the force per unit area exerted by cilia at distance r from a circular domain center is proportional to $\nu_r < \sin\alpha >_r$, where α is the angle of the beat direction with the radial direction of the circular domain, ν_r. We indeed found that $\nu_r . < \sin\alpha >_r$ varies linearly with r. It shows that the epithelium regulates cilia orientations and cell differentiation along the radial position of a circular domain to provide a linear variation of the force per unit area with r. An affine relationship of the curvilinear velocity of the surface fluid with the force is obtained and a tentative interpretation is proposed, based on the balance between the propulsion of mucus during the effective cilia stroke and the friction exerted by periciliary layer friction during cilia recovery. During ciliogenesis these local domains grow and merge to form a single macroscopic domain extended to the whole sample on which the viscoelastic mucus is transported. The merging of these domains requires a gradual spatial reorganization of ciliary beat directions and ACCD. This only occurs when the viscoelastic mucus is constantly present on the epithelium's surface, thus inducing strong shear stresses. This suggests that these stresses experienced by cilia are transmitted to the cells that respond actively.

Diseases

Our approach is applied to ALI cultures from patients with mild and severe asthma and with COPD. Patients with severe asthma and COPD present a low ACCD, far beyond the critical value required to transport a surface fluid at the macroscopic scale (Fig, 2). No alteration of the rheological properties of mucus is observed. We therefore suggest that the origin of the impaired clearance in asthma and COPD comes from a lack of active ciliated cells and no from impaired rheological properties of mucus (5).

SUMMARY

A low-viscosity Newtonian fluid can be transported at the epithelium's surface on domains whose size obeys a power law with ACCD. The Newtonian fluid has a solid-like rotational motion on circular domains. This motion results from the linear increase of the tangential force exerted by cilia with their distance to the domain center. The force's profile is provided by a fine spatial regulation of ciliary beat directions and ACCD. A subcritical ACCD may explain the impaired mucociliary clearance observed in severe asthma and COPD, while the rheological properties of mucus remain unchanged.

References

[1] Button B, et al.: A periciliary brush promotes the lung health by separating the mucus layer from airway epithelia. *Science* 337(6097):937–41, 2012 D.F., Adams J.A.: Mathematical Elements for Computer Simulation. Montreal, Canada 1977.

[2] Gras D, et al.: An ex vivo model of severe asthma using reconstituted human bronchial epithelium. *J Allergy Clin Immunol* 129(5):1259–1266.e1, 2012 Nygus G.: Numerical Analysis Using Finite Element Method. *PhD Thesis*, NTU Mech. Eng. Dept., Lagos, 1983.

[3] Matsui H, Randell SH, Peretti SW, Davis CW, Boucher RC: Coordinated clearance of periciliary liquid and mucus from airway surfaces. *J Clin Invest* 102(6):1125–31I, 1998.

[4] Khelloufi K. : Physics of mucociliary dynamics / Device for 3D migration. Application to severe asthma and COPD, PhD Thesis Aix %arseille Université France, 2015

PROPULSIVE THRUST OF A DRIVEN FILAMENT AT LOW REYNOLDS NUMBER WITH NON-UNIFORM FLEXIBILITY

Zhiwei Peng[1], Gwynn J. Elfring [*1], and On Shun Pak [†2]
[1]*Department of Mechanical Engineering, The University of British Columbia, Vancouver, BC, Canada*
[2]*Department of Mechanical Engineering, Santa Clara University, Santa Clara, CA, USA*

Summary In the low Reynolds number regime, actuating a rigid filament periodically at one end leads to a reciprocal motion and hence produces no propulsive force. Instead if the filament is flexible viscous forces lead to a deformation of the filament and the generation of a net propulsive force (thrust). For a given actuation frequency and filament length, an optimal bending modulus of the filament can be determined to produce the largest propulsive force. Here we explore the possibility of further improving the propulsive performance by allowing variable flexibility along the filament. We demonstrate that by simply dividing a filament into two segments with different bending rigidity a higher propulsive force can be obtained compared with the case of uniform stiffness. The results suggest the possibility of exploiting this new degree of freedom for enhancing propulsion at low Reynolds numbers.

INTRODUCTION

Locomotion of microorganisms in fluids is ubiquitous and crucial to many biological processes. In low-Reynolds-number environments, where inertia effects are negligible and viscous forces dominate, microorganisms have to break time-reversal symmetry in order to move, because any reciprocal motion results in zero net motion as dictated by the "scallop theorem". Some microorganisms propel by rotating rigid helical flagella while others propagate flagellar waves by coordination of dynein motion proteins. Advances in fabrication technologies at small scales allow the recent rapid development of synthetic micro-propellers capable of swimming at velocities comparable with microorganisms. In particular, slender flexible filaments have been employed to enable locomotion at small-scales [1, 2].

A rigid filament driven at one end cannot propel itself because the motion is reciprocal. By introducing flexibility in the filament, the coupling between the viscous and elastic forces produces deformation along the filament that can lead to propulsion [4]. For a given actuation frequency and filament length, an optimal bending modulus of the filament can be determined to produce the largest propulsive force. However, the possibility of further improving the propulsion performance by allowing variable flexibility along the filament remains largely unexplored. At high Reynolds numbers, flying animals such as hoverflies and hummingbirds exhibit non-uniform flexibility distribution along their wings, which provides optimal performance. In this work, we consider the propulsive force generated by a boundary-driven passive filament at low Reynolds number. The mathematical formulation allows variable bending flexibility, and we consider here arguably one the simplest case of non-uniform flexibility distribution with two segments of different bending rigidities connected serially together. Asymptotic analysis in the limit of small actuation amplitudes reveals the advantage of this simple non-uniform flexibility arrangement over the uniform case.

MATHEMATICAL FORMULATION

We consider an inextensible cylindrical filament of length L and uniform radius a such that $a \ll L$, and describe the elasticity of the filament by the Euler-Bernoulli beam theory. In order to describe the dynamics of the filament, we start from an energy functional $\mathcal{E} = \frac{1}{2}\int_0^L \left(A\mathbf{x}_{ss}^2 + \sigma\mathbf{x}_s^2\right)\,\mathrm{d}s$, where $\mathbf{x}(s,t)$ is the filament shape parametrized by the arclength s at time t, $A(s)$ is the bending rigidity allowed to vary along the filament, and $\sigma(s,t)$ is a Lagrange multiplier introduced to satisfy the local inextensibility condition [5]. The elastic force density along the filament can then be obtained by taking a variational derivative, $\mathbf{f}_{\text{elastic}} = -\delta\mathcal{E}/\delta\mathbf{x} = -\partial_s\left[\partial_s(A\kappa)\mathrm{n} - (\sigma + A\kappa^2)\mathbf{t}\right]$, where the subscript s denotes derivative with respect to the arclength, $\kappa = ||\mathbf{x}_{ss}||$ is the local curvature, and $\mathbf{t}$ and $\mathbf{n}$ are the local tangent and normal vectors respectively. We remark that we have kept bending rigidity generally as a function of s instead of a uniform value as usually done in previous studies.

At low Reynolds numbers, the force acting on a slender filament can be related to its velocity relative to the fluid, and to leading-order in small filament aspect ratio, results in a purely local theory called the resistive force theory, which states that the viscous force per unit length on the body at a point is related linearly to the local filament velocity, $\mathbf{f}_{\text{vis}} = -\left(\xi_\perp\mathbf{nn} + \xi_\parallel\mathbf{tt}\right)\cdot\mathbf{x}_t$, where the hydrodynamics at this order is characterized by the tangential $\xi_\parallel$ and normal $\xi_\perp$ resistive coefficients.

The local force balance between the viscous and elastic forces together with the local inextensibility condition

$$\mathbf{f}_{\text{vis}} + \mathbf{f}_{\text{elastic}} = \mathbf{0}, \tag{1}$$

$$\mathbf{x}_{ts}\cdot\mathbf{x}_s = 0, \tag{2}$$

[*]Email: gelfring@mech.ubc.ca
[†]Email: opak@scu.edu

result in a set of coupled nonlinear partial differential equations governing the evolution of the filament shape $\mathbf{x}(s,t)$ and Lagrange multiplier $\sigma(s,t)$.

We consider a torque-free harmonic oscillation at one end of the filament ($s = 0$): $y(0,t) = y_0 \sin \omega t$ and leave the other end ($s = L$) force-free and torque-free. To make analytical progress, we perform asymptotic analysis in the small-amplitude oscillation limit, $\epsilon = y_0/L \ll 1$, to determine order by order the filament shape, and the propulsive force generated by the actuation can be obtained by integrating the viscous force along the filament averaged over a period of actuation, $F_{\mathrm{p}} = -\left\langle \mathbf{e}_x \cdot \int_0^L \mathbf{f}_{\mathrm{vis}}\, \mathrm{d}s \right\rangle$.

RESULTS AND DISCUSSION

The dimensionless propulsive force occurs at $O(\epsilon^2)$: $F_p/(L^2\xi_\perp\omega) \sim \epsilon^2 F_2$. For the classical case of uniform bending rigidity ($A =$ constant) along the filament, the variation of propulsive force as a function of a dimensionless number comparing the magnitude of viscous and elastic forces, the sperm number $\mathrm{Sp} = L(\xi_\perp\omega/A)^{1/4}$, is shown in Fig. 1(a). As indicated by the two blue dots in the proximity of the maximum propulsive force in Fig. 1(a), one can have deforming filaments of two different sperm numbers generating the same propulsive force. In other words, for a given actuation frequency and filament length one can generate the same propulsive thrust with filaments of two different bending rigidities (A_1 and A_2).

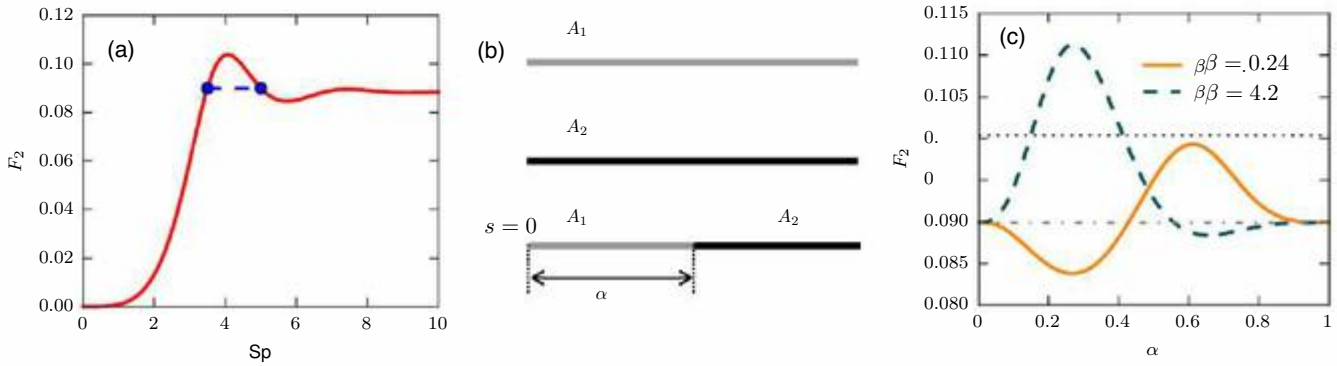

Figure 1: (a) Propulsive thrust generated by a filament of uniform bending rigidity actuated at one end [3]. (b) Schematic of a filament consisting of two segments of different bending rigidities ($A1$ and A_2) connected serially and $\beta = A_2/A_1$. (c) α at different values of bending rigidity ratio β. For $\beta = 0.24$ (more flexible materials at the actuation end), the maximum propulsive force generated is greater than the maximum achievable thrust with a filament of uniform flexibility (see figure 1(a); also indicated by horizontal dotted line in figure 1(c)).

We probe the potential advantages of non-uniform flexibility by connecting the filaments with bending rigidities A_1 and A_2 serially as shown in Fig. 1(b). For a given ratio of bending flexibility $\beta = A_2/A_1$, by varying the relative portion α of the two segments, a non-monotonic variation of the propulsive force is observed (Fig. 1(c), $\beta = 0.24$, orange solid line). The limits $\alpha = 0, 1$ reduce to the case of uniform flexibility (with a propulsive force $F_2 = 0.09$), and it is interesting to notice that the propulsive force generated by a two-component filament can be greater than the case of uniform one when $\alpha \gtrsim 0.4$. Furthermore, by putting a more flexible material at the actuation end *i.e.* $\beta > 1$ (e.g. $\beta = 4.2$, dashed line, Fig. 1(c)), the propulsive force generated by such an arrangement can be greater than the maximum possible propulsive thrust achievable by a filament with uniform bending rigidity (see Fig. 1(a) and dotted line in Fig. 1(c)). The two-segment arrangement considered here is arguably one of the simplest scenario of non-uniform flexibility, and it already demonstrates an enhancement in the propulsive force compared with the uniform case. This points to an optimization of this new degree of freedom for the design of synthetic flexible micro-propellers.

References

[1] Dreyfus R, Baudry J., Roper M. L., Fermigier M., Stone H. A., Bibette J.: Microscopic artificial swimmers. Nature 437: 862-865, 2005

[2] Pak, O. S., Gao W., Wang J., Lauga E.: High-speed propulsion of flexible nanowire motors: Theory and experiments. Soft Matter 7: 8169-8181, 2011

[3] Pak O. S., Lauga E.: Theoretical models in low-Reynolds-number locomotion, in *Fluid-Structure Interactions in Low-Reynolds-Number Flows*, edited by Duprat C. and Stone H. A., Royal Society of Chemistry, 2014.

[4] Wiggins C. H., Riveline D., Ott A., Goldstein R. E.: Trapping and wiggling: elastohydrodynamics of driven microfilaments. Biophys. J. 74: 1043-1060, 1997

[5] Camalet E., Julicher F.: Generic aspects of axonemal beating. New J. Phys. 2:1-2423, 2000.

DEVELOPMENT OF A POROUS MEDIA MODEL FOR FLOW IN ALVEOLATED DUCTS WITHIN THE HUMAN LUNG

C.T. DeGroot*[1] and A.G. Straatman[1]
[1]*Department of Mechanical and Materials Engineering, University of Western Ontario, London, Ontario, Canada*

Summary The flow of air in an alveolated duct, which is the main porous structure found within the human lung, has been considered. A model is developed based on the method of volume-averaging, which is used to derive macroscopic governing equations for a large number of alveolated ducts. In order to close the volume-averaged equations, a set of partial equations is derived in terms of transformed variables and is solved over a unit-cell of the duct to obtain the relevant effective flow parameter, namely the duct permeability. One-dimensional analytical solutions have then been derived to verify the model in comparison to direct computational fluid dynamics.

INTRODUCTION

Simulation of flow in the human lung is of interest because it can provide details of the flow that cannot be measured *in vivo*. Knowledge of the flow patterns within the lung are of practical importance because of the potential impacts on respiratory drug delivery, particle deposition, and our general understanding of the relationship between lung structure and function [1]. The internal structure of the lung consists of a network of bifurcating airways that become smaller in both length and diameter with each subsequent bifurcation. Each level of bifurcation is referred to as an airway generation. The first sixteen generations are known as the conducting airways which take no part in the gas exchange process, but lead the air to the respiratory region of the lung [2]. Gas exchange occurs by passive diffusion through the thin walls of small sacs, known as alveoli, which line the airways in the respiratory region (17th generation and beyond) [3, 2]. The ducts surrounded with alveoli are known as alveolated ducts.

Simulating flow in the lung is particularly challenging due to the large number of flow paths and the wide range of length scales spanned by the various components of its structure. The zeroth generation of the airway tree is the trachea, which has a typical diameter of about two centimetres [3]. At each of the approximately 23 bifurcations, the diameter of the subsequent generation is reduced by a factor of approximately $2^{1/3}$, leading to diameters as small as a fraction of a millimetre [3]. There are approximately 300 million alveolar sacs in the human lung, each of which are about 0.3 mm in diameter [3].

Given the porous nature of the lung, it is the goal of this work to develop a porous media model for air flow in the lung parenchyma using the method of volume-averaging [4], which yields a general model that is applicable to three-dimensional flows and is readily coupled with models for the upper airways. Closure of the resulting volume-averaged momentum equation is considered theoretically, which results in a closure problem that can be solved numerically on a periodic unit-cell of the parenchyma to determine the relevant effective properties, shown in this case to be solely the permeability, or the resistance to flow. As the majority of the lung parenchyma is made up of alveolated ducts, this is taken as the pore geometry of interest. Results for the permeability are obtained using a realistic geometric idealization of an alveolated duct, shown in Fig. 1a. The resulting volume-averaged model is then compared to direct pore-level simulations of an alveolated duct with moving walls and some one-dimensional results are presented which are also compared to direct CFD calculations.

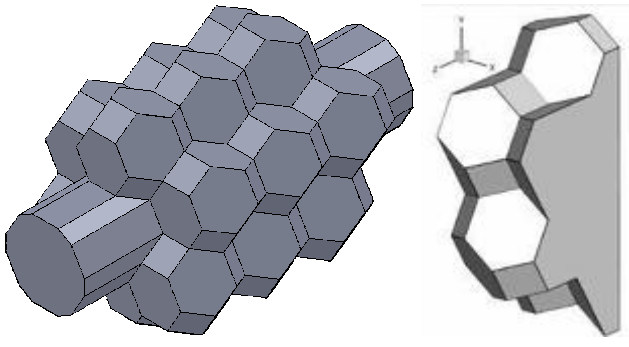

(a) (b)

Figure 1: A schematic diagram of (a) an idealized geometric model of an alveolated duct and (b) a periodic unit-cell of the idealized geometric model of an alveolated duct.

*Corresponding author. Email: cdegroo5@uwo.ca

THEORETICAL MODEL

The theoretical model is based on the volume-averaged form of the governing continuity and Navier-Stokes equations, given respectively as

$$\nabla \cdot \langle \mathbf{u} \rangle = -\frac{1}{V} \int_{A_{fs}(t)} \mathbf{u} \cdot \mathbf{n}_{fs} dA \tag{1}$$

and

$$\rho_f \left[\frac{\partial \langle \mathbf{u} \rangle}{\partial t} + \nabla \cdot \left(\frac{1}{\varepsilon} \langle \mathbf{u} \rangle \langle \mathbf{u} \rangle \right) \right] = -\varepsilon \nabla \langle p \rangle^f + \mu_f \nabla^2 \langle \mathbf{u} \rangle + \frac{1}{V} \int_{A_{fs}(t)} \left(-\tilde{p} \mathbf{n}_{fs} + \mu_f \nabla \tilde{\mathbf{u}} \cdot \mathbf{n}_{fs} \right) dA - \rho_f \nabla \cdot \langle \tilde{\mathbf{u}} \tilde{\mathbf{u}} \rangle, \tag{2}$$

respectively, where $\mathbf{u}$ is the fluid velocity vector, p is the pressure, ρ_f is the fluid density, t is time, and μ_f is the fluid dynamic viscosity, $A_{fs}(t)$ is the area of intersection between the fluid and solid volumes, V_f and V_s. The unit-normal vector directed from the fluid to solid phase on $A_{fs}(t)$ is denoted $\mathbf{n}_{fs}$. Spatial deviations are denoted, for a generic scalar ϕ, as $\tilde{\phi} = \phi - \langle \phi \rangle^f$.

In this study we treat in detail the integral terms appearing on the right sides of Eqs. 1 and 2 by deriving transport equations for the spatial deviation terms and, based on dimensional analysis and appropriate transformations, deriving a set of "closure" partial differential equations that can be solved over a unit cell of the porous material to put the integral terms in a closed from, in terms of the duct permeability.

RESULTS

Based on a one-dimensional form of the closed-form governing equations, an analytical solution is derived and compared with direct computational simulations of an alveolated duct with walls oscillating periodically in order to expand and contract the domain in a breathing motion. Results show agreement within 2% for all cases, with the error increasing with the amplitude of wall motion. For amplitudes typical of actual lung motions, agreement was well within 1%. Plots of the one-dimensional solutions for dimensionless velocity and pressure are shown in Fig. 2.

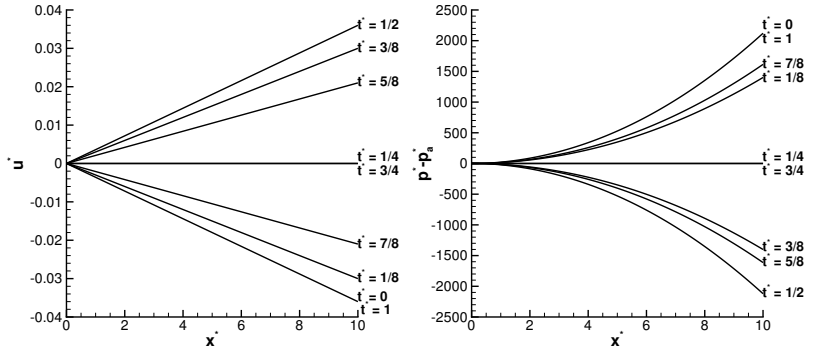

(a) (b)

Figure 2: A plot of (a) the dimensionless velocity and (b) the difference between the dimensionless pressure and the dimensionless alveolar pressure, $p^* - p_a^*$, as functions of the dimensionless coordinate x^* for initial Womersley and Reynolds numbers (at $t^* = 0$) of $Wo = Re_{D_H} = 0.01$.

CONCLUSIONS

A porous media model for flow in alveolated ducts within the human lung has been developed using the theory of volume averaging. A set of closure partial differential equations has been derived and solved within a unit cell representing an alveolated duct to obtain the duct permeability. Based on analytical one-dimensional solutions, compared with direct computational fluid dynamics simulations, the model has been verified.

References

[1] Tawhai, M. H. and Lin, C.-L., 2010, Image-based modeling of lung structure and function, J. Magn. Reson. Imaging, **32**, pp. 1421–1431.

[2] West, J. B., 2008, Respiratory Physiology: The Essentials, Lippincott Wiliams & Wilkins, Baltimore.

[3] Weibel, E. R., 1963, Morphometry of the human lung, Springer-Verlag, New York.

[4] Whitaker, S., 1967, Diffusion and dispersion in porous media, A.I.Ch.E. J., **13**, pp. 420–427.

A 2D MULTIRING SIMULATION OF BLOOD FLOW IN ARTERIES

Arthur R. Ghigo *[1], Jose-Maria Fullana[2], and Pierre-Yves Lagrée[3]

[1,2,3]*Sorbonne Universités, UPMC Univ Paris 06, CNRS, UMR 7190, Institut Jean Le Rond ∂'Alembert, Paris, France*

Summary We propose a novel 2D multiring numerical model to compute blood flow in arteries, inspired from the multilayer shallow water theory. This model is based on a long wave approximation of the Navier-Stokes equations and requires no *a priori* estimation, contrary to classical 1D models. The wall shear stress (WSS), the axial velocity profiles and the flow rate computed with the multiring model are in good agreement with the linear Womersley solution whereas classical 1D models' solutions are much less accurate.

INTRODUCTION

In recent years, the numerical simulation of the propagation of the pressure pulse in the human systemic network has been intensively studied to help doctors and medical practitioners better understand and predict the hemodynamics of the human body. However, it is difficult and costly to compute accurate numerical solutions due to the complexity of the equations, the size of the network and the strong interactions between the flow and the mechanics of the arterial wall. Using simplifying assumptions (axisymmetric artery, long wavelength compared to the radius of the artery, incompressible Newtonian fluid) Womersley [1] obtained the following simplified boundary-layer-like system of equations describing the conservation of mass and momentum of blood flow in an artery:

$$\begin{cases} \dfrac{\partial u_r}{\partial r} + \dfrac{u_r}{r} + \dfrac{\partial u_z}{\partial z} = 0 \\ \dfrac{\partial u_z}{\partial t} + u_r \dfrac{\partial u_z}{\partial r} + u_z \dfrac{\partial u_z}{\partial z} = -\dfrac{1}{\rho}\dfrac{\partial p}{\partial z} + \nu \left(\dfrac{\partial^2 u_z}{\partial r^2} + \dfrac{1}{r}\dfrac{\partial u_z}{\partial r} \right) \\ p\left(z,t\right) = p_0 + K\left(R\left(x,t\right) - R_0\left(x\right)\right) \end{cases} , \quad \begin{cases} u_r(r=R,z,t) = \dfrac{\partial R}{\partial t} \\ u_z(r=R,z,t) = 0 \\ \dfrac{\partial u_r}{\partial r}\left(r=0,z,t\right) = 0 \, , \end{cases} \tag{1}$$

where R_0, R and K are respectively the radius at rest, the instantaneous radius and the rigidity of the artery. By integrating (1) over the cross-section of the artery, Hughes and Lubliner [3] obtained a simple conservative one-dimensional (1D) system of equations. This 1D system can be solve using efficient and robust numerical methods that allow to compute accurate pressure and flow waveforms in large networks with minimal costs [6]. Unfortunately, information on the axial velocity profile is lost in the integration process and additional assumptions are required to estimate the friction and advection coefficients of the 1D model [3, 6]. To overcome those difficulties, we solve (1) with a novel two-dimensional (2D) axisymmetric method taking into account fluid-structure interactions and requiring no approximation contrary to previously existing 2D methods [2, 4]. We show that we correctly compute, up to the degree of approximation, the axial velocity profile and the wall shear stress (WSS) of the classical Womersley solution [1].

METHODS

We decompose each artery in a series of concentric rings (see figure (1)), inspired by the multilayer theory introduced by Audusse [5] in the framework of shallow water equations. We integrate (1) over each ring and obtain the following equations of mass and momentum conservation in the ring j, similar to those of the 1D theory, with additional source terms $G_{j\pm\frac{1}{2}}$ representing the mass exchanges between the neighboring rings $j-1$ and $j+1$:

$$\begin{cases} \dfrac{\partial A_j}{\partial t} + \dfrac{\partial Q_j}{\partial z} = G_{j+\frac{1}{2}} - G_{j-\frac{1}{2}} \ , \ G_{j\pm\frac{1}{2}} = \dfrac{\partial A_{j\pm\frac{1}{2}}}{\partial t} + u_{z\, j\pm\frac{1}{2}} \dfrac{\partial A_{j\pm\frac{1}{2}}}{\partial z} - 2\pi r_{j\pm\frac{1}{2}} u_{r,j\pm\frac{1}{2}} \\ \dfrac{\partial Q_j}{\partial t} + \dfrac{\partial}{\partial z}\left(\dfrac{Q_j^2}{A_j}\right) = u_{z\, j+\frac{1}{2}} G_{j+\frac{1}{2}} - u_{z\, j-\frac{1}{2}} G_{j-\frac{1}{2}} - \dfrac{A_j}{\rho}\dfrac{\partial p}{\partial z} + 2\pi\nu \left(\left[r \dfrac{\partial u_z}{\partial r} \right]_{r_{j+\frac{1}{2}}} - \left[r \dfrac{\partial u_z}{\partial r} \right]_{r_{j-\frac{1}{2}}} \right) , \end{cases} \tag{2}$$

where Q_j and A_j are respectively the flow rate and the cross section of the ring j. This system of equations is a natural discretization of (1) in the radial direction. Indeed, while preserving the dependence in the axial (z) and radial (r) variables, this approach does not require any *a priori* estimation, contrary to usual 1D approaches, and benefits from the simplicity and robustness of the 1D theory, for which stable shock capturing numerical schemes exist.

*Corresponding author. Email: arthur.ghigo@dalembert.upmc.fr

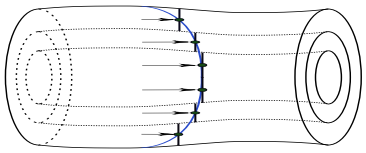

Figure 1: Sketch of the discretization of an artery in a series of concentric rings and a shape of an axial velocity profile (blue).

RESULTS

We compared our multiring numerical results to the linear Womersley analytic solution [1] for different Womersley numbers α ($0.1 < \alpha < 20$) and found good agreement between both solutions for every α. As an example, we compare on figure (2) the results obtained for $\alpha = 10$ with the analytic Womersley solution (black line), the multiring model (blue line) and two 1D models for which the advection coefficient was set to 1 and two classical values of the 1D friction coefficient $C_f = \gamma\pi\nu$ were used: $\gamma_1 = 8$ (red line) and $\gamma_2 = 22$ (green line). The multiring solutions for the WSS (figure (2) left) and the flow rate (figure (2) right) at $t = 6$ s almost perfectly coincide with the analytic Womersley solutions, whereas both 1D models' solutions are less accurate for both the amplitude and propagation speed of the wave forms. In figure (2) center, we also show a good agreement between the multiring and the analytic solutions for the axial velocity profiles at different times.

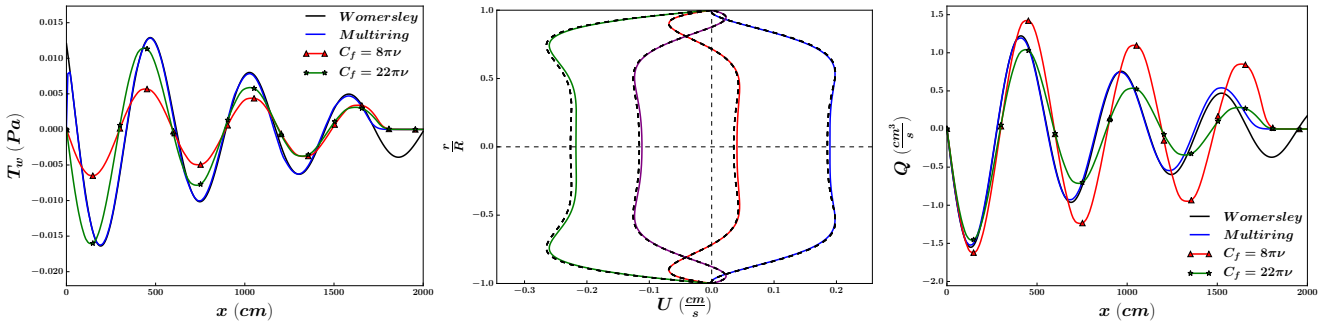

Figure 2: Comparison between the Womersley (black), the multiring (blue) (100 layers, 500 cells) and two 1D model solutions (500 cells, $C_f = 8\pi\nu$ (red) and $C_f = 22\pi\nu$ (green)) for $\alpha = 10$: (Left) Wall shear stress $\tau_w\,(z, t = 6\text{ s})$ Pa; (Center) Velocity profiles $U\,(r, z = 1000\text{ cm}, t)$ cm.s^{-1} for $t \in \{8.4\text{ s}, 8.6\text{ s}, 8.96\text{ s}, 9.5\text{ s}\}$; (Right) Flow rate $Q\,(z, t = 6\text{ s})$ cm^3.s^{-1}.

CONCLUSIONS AND PERSPECTIVES

We have presented a novel 2D axisymmetric multiring method to solve blood flow in arteries, taking into account fluid-structure interactions. This model is a correct discretization of (1), in comparison to 1D models and other 2D approaches that are biased by the required estimation of the shape of the velocity profile. The numerical results are in good agreement with the linear Womersley solution of (1). Furthermore, due to its similarity with the 1D models, it can be easily inserted inside a large 1D network computation, to locally obtain an accurate description of the blood flow in stenoses or aneurysms. This model can therefore provide valuable information to doctors and medical practitioners and can also be used to give an *a posteriori* estimation of the coefficients required by the 1D model. These last points are the subject of future works.

References

[1] Womersley J. R.: Oscillatory motion of a viscous fluid in a thin-walled elastic tube: I: the linear approximation for long waves, Phil. Mag 46:199-221, 1955.

[2] Ling S. C., Atabek H. B.: A nonlinear analysis of pulsatile flow in arteries, J. Fluid Mech 55:493-511, 1972.

[3] Hughes T. J. R., Lubliner J.: On the One-Dimensional Theory of Blood Flow in the Larger Vessels, Mathematical Biosciences 18:161-170, 1973.

[4] Lagrée P.-Y.: An inverse technique to deduce the elasticity of a large artery, Eur. Phys. J. AP 9:153-163, 2000.

[5] Audusse E., Bristeau M.-O., Perthame B., Sainte-Maire J.: A Multilayer Saint-Venant System With Mass Exchanges For Shallow Water Flows. Derivation and Numerical Validation. ESAIM: M2AN 45:169-200, 2011.

[6] Wang X., Fullana J.-M., Lagrée P.-Y.: Verification and comparison of four numerical schemes for a 1D viscoelastic blood flow model. Computer Methods in Biomechanics and Biomedical Engineering 18(15):1704-1725, 2014.

A DISCRETE BIASED RANDOM WALK MODEL BASED ON BACTERIAL CHEMOTAXIS

Tomonobu Goto[1 a)] & Tonau Nakai[1]
[1]*Department of Mechanical and Aerospace Engineering, Tottori University, Tottori, Tottori, Japan*

Summary A bacterial cell moves in a ballistic manner for a certain time period (run), and then changes its direction randomly (tumble). When a cell senses that it has moved to higher attractant chemical concentration, it reduces the frequency of the direction change. Collectively, this modulation produces bacterial chemotactic response, in which the cells accumulate around the chemoattractant source.
In this study, a discrete biased random walk model based on bacterial chemotaxis was investigated. A steady distribution of cells was analytically obtained in one dimensional model. In this model, the cells move along a uniformly spaced number line at the rate of one interval per time step. A chemical attractant source is placed at the origin. The probability mass function of cells decays with the distance from the source as a geometric sequence. We confirmed the distribution by Monte Carlo simulations.

INTRODUCTION

Bacterial chemotaxis occurs via a sequence of runs and tumbles (e.g. [1], [2]). A "run" refers to a smooth swimming motion, and a "tumble" indicates a directional change. In aqueous media, run and tumble motions are randomized. However, near a chemical attractant, a cell reduces the frequency of its tumbles [3], which biases its motion toward the source.

A bacterial cell is too small to sense the spatial distribution of the chemical attractant at a given time using two or more sensors [4]. Thus, bacterial chemotactic behavior results from three distinct mechanisms.

First, by moving a certain distance, the bacterium can detect whether it is approaching or receding from the chemoattractant source. The cell senses and compares the chemical concentration at two consecutive times. If the concentration has increased or decreased at the later time, the cell has approached or receded from the source, respectively. Second, the cell randomly determines its direction after a tumble. The direction is changed by fluid dynamic interactions between the deforming flagella and the cell body. Although the process of tumbling is well understood [5], the prediction of tumbling remains a complex fluid dynamics problem [6]. A bacterial cell cannot choose a proper posture relative to the source. Third, the cell does not stop when it detects the maximal concentration. Because the cell might be smaller than the spatial variability of the concentration distribution, continued motion is a suitable strategy to avoid trapping in local concentration maxima.

We proposed a one-dimensional discrete model of bacterial chemotaxis [7]. A cell moves along a number line, as in the classical random walk model [8]. The model applies two simple rules based on real chemotactic behavior: if a cell approaches the origin in one time step, it moves in the same direction in the next time step, and if a cell recedes from the origin in one time step, it randomly moves right or left with a probability of 1/2. When many cells initially reside at the origin, their biased random motions following these rules eventually lead to a steady distribution.

In the present study, we introduce a parameter α, denoting the intensity of the bias, into our discrete model. The previous model corresponds to the most intense bias (α=1).

DISCRETE BIASED RANDOM WALK

One dimensional model

Bacterial cells move along a number line sectioned at uniform intervals, at a rate of one interval per time step. The chemical attractant is sourced from the origin.

The direction of cell movement in each time step is dictated by two rules (see Fig. 1): (a) If a cell has receded from the origin in the previous time step, it moves to the left or right with the same probability (1/2). (b) If the cell has approached the origin in the previous time step, it either continues in the same direction with probability α or randomly selects a new direction with probability 1/2. The total probability that a cell will maintain or reverse its direction is $(1+\alpha)/2$ and $(1-\alpha)/2$, respectively. When α=0, this model reduces to the classical random walk.

Rule (a) corresponds to a tumbling motion, wherein the cell randomly changes its swimming direction. Rule (b) corresponds to the reduction in tumbling frequency when the cell senses a higher concentration of attractant chemical.

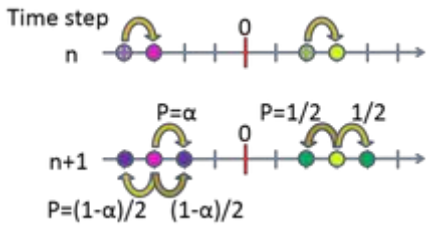

Fig. 1. One-dimensional discrete biased random model. In each time step, the cell moves along a number line by one interval to the left or right.

Steady distribution

[a)] Corresponding author. Email: goto@damp.tottori-u.ac.jp.

Figure 2 indicates the probability propagation along the positive region of the number line. L and R denote that the probability propagates from the left and right sides, respectively. L_i^{n+1} depends on the probability at position $i-1$ at time n. The probability L_{i-1}^n corresponds to the cell's motion from the left side, wherein the cell previously receded from the origin. Therefore, the cell will tumble and L_{i-1}^n propagates to R_{i-2}^{n+1} or L_i^{n+1} with equal probability (1/2). The probability R_{i-1}^n corresponds to the cell's motion from the right side, wherein the cell previously approached the origin. The cell will continue toward the origin with probability α and will tumble with probability 1-α. R_{i-1}^{n-1} propagates to the left or right with probabilities of (1+ α)/2 or (1-α)/2, respectively (see Fig. 2). Thus we have

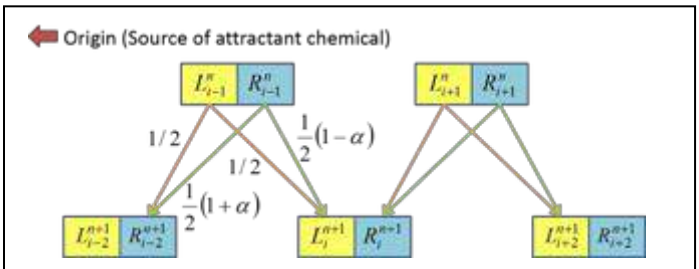

Fig. 2. Time-position diagram of probability mass function along the right half of the number line. The chemo-attractant is sourced from the left of this diagram.

$$L_i^{n+1} = \frac{1}{2}L_{i-1}^n + \frac{1}{2}(1-\alpha)R_{i-1}^n, \quad R_i^{n+1} = \frac{1}{2}L_{i+1}^n + \frac{1}{2}(1+\alpha)R_{i+1}^n.$$

From these relations, we get the probability mass function at position $p_i (= L_i + R_i)$ in steady state as

$$p_i \propto \frac{1}{(1+\alpha)^i},$$

assuming that p_i is a geometric sequence.

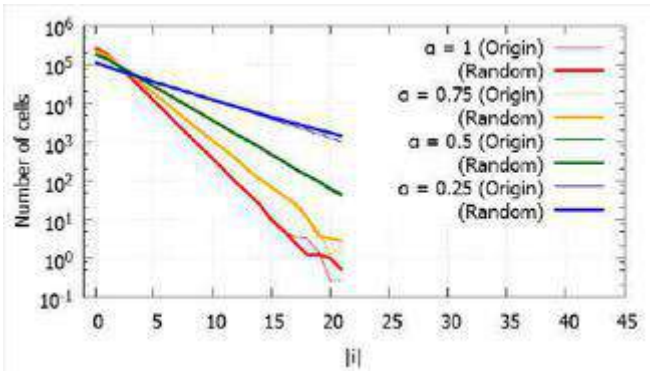

Fig. 3. Spatial distribution of cells calculated by Monte Carlo simulation.

Monte Carlo simulation

The previous rules were implemented in a simulation of 10^6 cells. Two initial distributions were adopted: (i) all cells were gathered at the origin, (ii) cells were randomly distributed in the region $|i| \le 30$ .Figure 3 plots the spatial distributions of the cells at approximately 300 time steps. Under initial condition (i), two converged distributions at even and odd time steps alternate as time elapses. Therefore, the average of the two distributions is plotted in Fig. 3. Both the initial distributions appear to converge to a single distribution. Each distribution is a geometric sequence whose common ratio is 1/(1+α).

CONCLUSIONS

A discrete biased random walk model based on bacterial chemotaxis was proposed. The bias intensity α introduced into this model may indicate the strength of bacterial chemotaxis. To verify this idea, we need to compare our present results with experimental data of bacterial cell distributions around a chemoattractant.

This work was supported by JSPS KAKENHI Grant Number 15K05796.

References

[1] Adler, J., Chemotaxis in bacteria, Science, Vol. 153 (1966), pp. 708–716.
[2] Rubik, B. A. and Koshland, D. E., Jr., Potentiation, desensitization, and inversion of response in bacterial sensing of chemical stimuli, Proceedings of the National Academy of Sciences of the United States of America, Vol. 75, No. 6 (1978), pp. 2820–2824.
[3] Macnab, R. M. and Koshland, D. E., Jr., The Gradient-Sensing Mechanism in Bacterial Chemotaxis, Proceedings of the National Academy of Sciences of the United States of America, Vol. 69, No. 9 (1972), pp. 2509–2512.
[4] Berg, H. C., E. coli in motion (2004), Chapter 4, Springer.
[5] Turner, L., Ryu, W. S. and Berg, H. C., Real-Time Imaging of Fluorescent Flagellar Filaments, Journal of Bacteriology, Vol. 182, No. 10 (2000), pp. 2793–2801.
[6] Kanehl, P. and Ishikawa, T., Fluid mechanics of swimming bacteria with multiple flagella, Physical Review E, Vol. 89 (2014), 042704.
[7] Goto, T. and Nakai, T., A one-dimensional discrete model of biased random walk relating to bacterial chemotaxis, J. Aero Aqua Biomechanisms, Vol. 4, No. 1 (2015), pp.853–858.
[8] Berg, H. C., Random walks in biology (1993), Chapter 1, Princeton University Press.

HYDRODYNAMICS OF TADPOLE SWIMMING IN THE WAKE OF A CYLINDER

Wenrong Hu[1,2a)], Haotian Yuan[1,2]
[1] *Department of Engineering Mechanics, Shanghai Jiaotong University, China(200240)*
[2] *Shanghai Jiaotong University and Chiba University International Cooperative Research Center, Shanghai Jiaotong University, China(200240)*

Summary The vortex structures and hydrodynamic performance of a tadpole undulating in the wake of a D-section cylinder are studied by solving the Navier-Stokes equations for the unsteady incompressible viscous flow. It is found that three factors can contribute to thrust of the tadpole behind a D-cylinder. Tadpole's relative undulating frequency and the distance between the D-cylinder and the tadpole have a great influence on both vortex structure and hydrodynamic performance. At different undulating frequency, a tadpole may break or dodge vortices from the D-cylinder, corresponding to the performance of the tadpole. As the tadpole is located behind the D-cylinder at different distances, three typical kinds of wake are observed.

INTRODUCTION

Unsteady water flows are common in nature. There are always vortices in the living environment of aquatic animals. According to the researches, aquatic animals are usually expert in taking advantages of the surrounding vortices. By adjusting the body to control the flow around, aquatic animals are able to improve swimming abilities.

Understanding how fish extract energy from environmental vortices is a topic of considerable interest. Studies on the interaction between fish and vortices shedding from a cylinder have provided a focused way to begin to understand how fish swim in complex flows. Previous studies[1,2] revealed that the vortex wakes may lead to a passive propulsion to the dead fish in the wake. Liao et al.[3-5] compared fish swimming in the wake of a D-cylinder to those swimming in free stream. It was shown that fish behind a D-cylinder adopts novel body kinematics behind a cylinder, termed the Kármán gait. The fish changes its undulating frequency and wavelength to synchronize the vortices shedding from the D-cylinder, slaloming between vortices shedding from the D-cylinder rather than swimming through them. On the other hand, numerical simulations on fish interacting with the environmental vortices have also been carried out. Shao and Pan[6] investigated the hydrodynamic performance of an undulating foil in vortex wakes of D-cylinder. The wake area can be divided into three domains: suction domain, thrust enhancing domain, and weak influence domain.

There are many experimental and numerical researches about how fish extract energy from environmental vortices. However, much less is known about the interaction between the tadpole and its surroundings. As the larva of the frogs and toads, the abrupt transition from their globose bodies to the laterally compressed tails make them seem less 'streamlined'[15]. In fact, the undulating mode of a tadpole is different from that of fish because of its blunt body[7,8]. The interaction between the tadpole and its surroundings would be more complicated than that of fish.

The aim of this paper is to numerically study the vortex structure and hydrodynamic performance of a tadpole undulating in the wake of a D-section cylinder. In addition, the effects of various controlling parameters on hydrodynamic performance of an actively undulating tadpole model with no forward motion are also investigated.

METHODS

According to the observed data[9], the tadpole model is built. Just like other studies, a tadpole undulates actively without forward motion in the wake of a stationary D-section cylinder.

The finite volume method is used to solve the Navier-Stokes equations for the unsteady incompressible viscous flow. The PIMPLE method is specially introduced to solve the unsteady flow. A special dynamic mesh fitting deforming body surface at each time step is employed to match tadpole's high-amplitude periodic motion.

RESULTS AND DISCUSSION

Propulsive mechanism

Here we compare the tadpole swimming in different motions, such as a non-undulating tadpole gliding in the cylinder wake, an undulating tadpole swimming either in free stream or in vortex wakes. The undulating tadpole in the cylinder wake can gain the highest thrust. Besides, as the non-undulating tadpole glides in the wake of a cylinder, the tadpole is also subject to a weak thrust. It is found that three main factors can contribute to thrust of the tadpole behind a D-cylinder: the backward jet in the wake, the local reverse flows on the tadpole surface and the suction force caused by the passing vortices.

[a)] Corresponding author. Email: wrhu@sjtu.edu.cn.

Effect of relative undulating frequency

Table.1 Parameters and hydrodynamic performance of the cases with different frequencies

Cases	*Re*	*fL/U*	*S/L*	*D/L*	$\overline{C_T}$	$\overline{C_P}$
UW1	2000	0.3	1	0.3	0.1386	0.0049
UW2	2000	0.6410	1	0.3	-0.0124	0.0002
UW3	2000	0.7	1	0.3	0.2219	0.0144
UW	2000	2	1	0.3	0.7329	0.1572

From Table.1, mean thrust coeffecient $\overline{C_T}$ and mean power coeffecient $\overline{C_P}$ vary in large range with different undulating frequency. Among all the cases in Table.1, the case UW2, in which the tadpole undulates at the frequency just as same as the vortex shedding frequency of D-cylinder, is quite different from the others. There are no thrust produced and little swimming cost in the case UW2. While in the other cases, both thrust and power consumption increase with the relative frequency increasing. In fact, different hydrodynamic performances are caused by different vortex structures in flow field. In this study, it is found that when the vortices shedding from the D-cylinder reach the area around tadpole's tail tip, the tadpole may dodge vortices or break them. According to this, the motion of the tadpole can be divided into three types: the dodging mode(Fig.1), the breaking mode(Fig.2) and the dodging mode alternates with the breaking mode. With a breaking mode, tadpole has higher mean thrust coefficient and mean power thrust coefficient, which means the tadpole generates larger thrust but also does more work to maintain the undulating swimming. On the contrary, with a dodging mode, the tadpole is subject to low thrust or even drag. However, it can maintain undulating swimming in the wake with very little energy consumption.

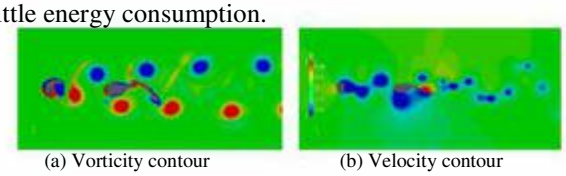

(a) Vorticity contour (b) Velocity contour

Fig.1 Flow field of the dodging mode

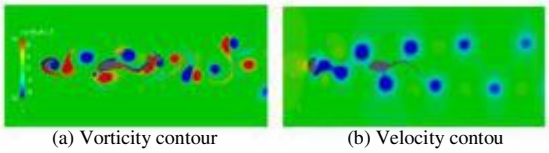

(a) Vorticity contour (b) Velocity contou

Fig.2 Flow field of the breaking mode

Effect of the distance between D-cylinder and the tadpole

Three kinds of the wake are observed at different distances between the D-cylinder and the tadpole. When undulating in a relative high frequency, a tadpole has higher mean thrust coefficients and mean power coefficients behind a D-cylinder than that in free stream. When the distance meets the requirement that vortices shed from the D-cylinder and form an incomplete Kármán vortex street, the vorticity magnitude of vortices is the highest, resulting in the strongest local reverse flows, the highest suction force and the strongest local high-speed jet stream in the wake. All these contribute to the highest thrust. In the study, when the distance between the D-cylinder and the tadpole is 0.6 tadpole's length, the tadpole has the highest mean thrust coefficient and mean power coefficient.

CONCLUSIONS

In this study, two-dimensional simulations have been performed to investigate the tadpole undulating swimming in the wake of a D-sector cylinder. The vortex structure of the flow filed and the hydrodynamic performance of the tadpole is studied.

When the tadpole undulates in the wake of the D-cylinder, three main reasons contribute to the increase of the thrust. They are the backward jet in the wake, the local reverse flows on the tadpole surface and the suction force caused by pressure difference between the head and the tail tip of the tadpole.

The relative undulating frequency of the tadpole has great influences on the hydrodynamic performance. At different undulating frequency, the tadpole breaks or dodges the vortices from the D-cylinder. In general, the breaking mode provides great thrust and the dodging mode save energy for tadpole undulating swimming.

When the tadpole is located at different distances behind the D-cylinder, three typical kinds of wake are observed, which are classified by the vortex structures behind the D-cylinder. When an incomplete Kármán vortex street forms between the D-cylinder and the tadpole, the tadpole is subject to the highest thrust.

Acknowledgement

This work was supported by the National Science Fund of People's Republic of China grant no. 11472173.

References

[1] Beal D N, Hover F S, Triantafyllou M S, et al. *Journal of Fluid Mechanics*, 2006, 549: 385-402.

[2] Fish F E, Lauder G V. *Annu. Rev. Fluid Mech.*, 2006, 38: 193-224.

[3] Liao J C.. Philosophical Transactions of the Royal Society B: Biological Sciences, 2007, 362(1487): 1973-1993.

[4] Liao J C, Beal D N, Lauder G V, et al. Science, 2003, 302(5650): 1566-1569.

[5] Liao J C, Beal D N, Lauder G V, et al.. Journal of experimental biology, 2003, 206(6): 1059-1073.

[6] Shao X, Pan D, Deng J, et al. Physics of Fluids, 2010, 22(11): 111903.

[7] Wassersug R J. American Zoologist, 1989, 29(1): 65-84.

[8] Wassersug R J, Hoff K. Journal of Experimental Biology, 1985, 119(1): 1-30.

[9] Köhler G, Lehr E, McCranie J R. Journal of Herpetology, 2000: 303-306.

HIEARCHICAL STRUCTURE OF SPATIALLY LOCALIZED BIOCONVECTION OF PHOTOSENSITIVE MICROORGANISM

Makoto Iima * [1], Takayuki Yamaguchi[2], Takuma Ogawa[1], Nobuhiko Suematsu[3], Hiraku Nishimori[1], Akinori Awazu[1], and Shunsuke Izumi[1]

[1]*Graduate School of Science, Hiroshima University, Higashi-Hiroshima, Japan*

[2]*Graduate School of BioMedical & Health Science, Hiroshima University, Hiroshima, Japan*

[3]*Meiji Institute for Advanced Study of Mathematical Sciences, Meiji University, Tokyo, Japan*

Summary It is known that the suspension of *Euglena gracilis* exhibits macroscopic spatially localized patterns when it is illuminated from below with strong light. Such structure is hierarchical ranging from μm scale of microorganism to cm scale of the convection cells. We discuss the localization mechanism in terms of the photosensitive behavior of *Euglena gracilis* in both scales. Individual's response to light gradient is analyzed experimentally, and the result is related to the flux of the number density in macroscopic scale to construct a hydrodynamic model. The model has spatially localized steady solutions, and the bifurcation structure has a bistable region, which often observed in spatially localized structures in dissipative systems.

INTRODUCTION

Euglena gracilis is a photosensitive microorganism with flagella; the body is approximately 10 μm wide and 50-100 μm long(Fig.1(a)). They can swim by the flagellum, and the statistical property of the motion depends on the surrounding light environment. In particular, they swim away from the light source if the light intensity is stronger than a critical value (negative phototaxis), while forward to the light source if the light intensity is less than the critical value (positive phototaxis).

When a suspension of *Euglena gracilis* is illuminated from the bottom with strong light, they form ordered convection patterns called bioconvection (Fig.1(b)). Unlike other bioconvection patterns known so far, the bioconvection pattern of *Euglena gracilis* is peculiar because it is spatially localized[1]. Shoji et al.[2] succeeded in obtaining the elementary structures of the localized bioconvection. The aim of this paper is to investigate the hierarchical structure of the localized bioconvection pattern and its dynamical property to understand the localization mechanism.

EXPERIMENTS

A key mechanism of the localization is the photomovement of *Euglena gracilis* due to the light intensity gradient. We will show experimental results of the characteristics in both microscopic and macroscopic scales. In microscopic motion, we track the orbit of individuals in the light gradient environment to construct a statistical model. A simple Markov model is constructed to explain the response to the light gradient, and the equilibrium state of the model agrees with the observation. In macroscopic motion, number density flux of the suspension of the microorganism has been measured for light intensity gradient .

For experiments of the macroscopic convection pattern, we prepared an annular container to suppress the complex patterns in the radial direction and to exclude the wall effect in the azimuthal direction. So far, two types of localized convection patterns were observed[2]. One pattern consists of a single region of high microorganism density sandwiched with two counter-rotating convection rolls ('bioconvection unit'). Another pattern is a spatially localized traveling wave, a wave of high density region in confined region. These two typical patterns are similar to those observed in thermal convection of binary fluid mixtures (e.g., mixtures of water and alcohol): so-called "convecton" and "localized traveling wave", respectively[3], although physical mechanisms of the binary fluid convection is the (positive) buoyancy and the Soret effect, which are different from the bioconvection. For the bioconvection unit, several bound states are observed. In particular, two (or three) bioconvection units exists for a long time before disappearing one by one. Such interaction of bioconvection units will be discussed.

NUMERICAL MODEL

Based on the experimental results, we construct a hydrodynamic model in which the number density flux depends on the light intensity gradient. The model reproduces a localized bioconvection pattern similar to the bioconvection unit. Linear stability analysis indicates that the effect of the light gradient on the number density flux greatly shifts the critical value of the onset of the convection. The bifurcation analysis using a branch-tracking technique reveals that a bistability region is observed when the aspect ratio Γ is large ($\Gamma = 8$), while such region is not obtained when Γ is small ($\Gamma = 2$).

*Corresponding author. Email: makoto@mis.hiroshima-u.ac.jp

CONCLUDING REMARKS

The experimental results of the localized convection patterns suggests that the localized patterns are similar to those in the binary fluid convection. The bioconvection unit, a minimal localized structure, and their dynamics are similar to those in the reaction-diffusion systems. Such similarities are not directly owing to the similarities of the physical mechanism. However, the mathematical similarities are suggested to explain the similarities. Bistability is the first evidence of the conjecture and the further research is needed. Interaction between the localized bioconvections is an interesting topic and a theoretical approach based on the dynamical system theory may be useful[4, 5].

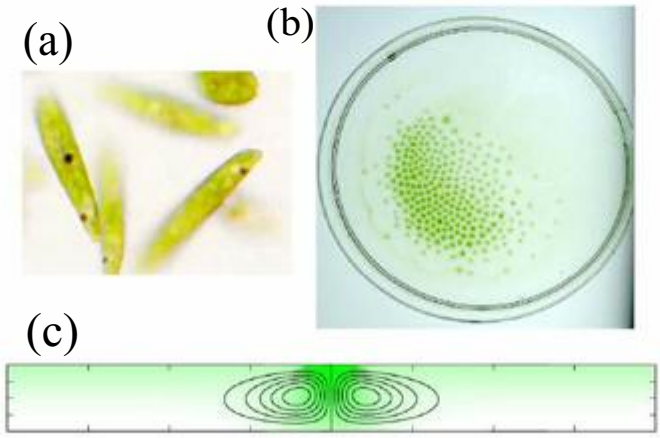

Figure 1: (a) *Euglena gracilis*. (b) Localized convection pattern of suspension of *Euglena gracilis* illuminated below. (c) Steady solution representing bioconvection unit.

References

[1] Suematsu N.J., Awazu A., Izumi S., Noda S., Nakata S. and Nishimori H.: Localized Bioconvection of Euglena Caused by Phototaxis in the Lateral Direction. J. Phys. Soc. Jpn. 80: 064003, 2011.

[2] Shoji E., Nishimori H., Awazu A., Izumi S. and Iima M.: Localized Bioconvection Patterns and Their Initial State Dependency in *Euglena gracilis* Suspensions in an Annular Container. J. Phys. Soc. Jpn 83:043001, 2014.

[3] Watanabe T., Iima M. and Nishiura Y.: Spontaneous formation of traveling localized structures and their asymptotic behaviour in binary fluid convection. J. Fluid Mech 712: 219–243, 2012.

[4] Yamaguchi T. and Iima M.: Numerical analysis of transient orbits by the pullback method for covariant Lyapunov vector. Theor. Appl. Mech. Jpn 63:91–96, 2015.

[5] Iima M., Yamaguchi T., Watanabe T., Kawaharada A., Tasaka Y. and Shoji E.: Towards understanding global flow structure. Proc. Int. Conf. on Mathematical Fluid Dynamics, Present and Future, 2016 (*in press*)

FLOW AND BLOOD CLOT DETECTION IN THE ECMO SYSTEM

Niclas Berg[1], Gabriel Fuchs[2], and Lisa Prahl Wittberg *[1]

[1]*Linné FLOW Center, Department of Mechanics, Royal Institute of Technology (KTH), Stockholm, Sweden*
[2]*Umeå University Medical School, Umeå, Sweden*

Summary During certain severe medical situations, the only option for treatment is to use a heart and lung machine. This is carried out by temporarily relieve the heart and lungs to allow for recovery. One of the main issues associated with the treatment is the possible risk of blood clot formation within the machine. During such an event, the entire system needs to be changed. In this study, the flow in the pump, cannula as well as tubing of such a system is investigated. The main motivation is to understand the reason for the formation of blood clots as well as identify possible sites where blood coagulation may be initiated.

INTRODUCTION

Generally, all critical organs in the human body have an excessive capacity to manage severe situations. However, during certain operations or serious illnesses, extra support may be needed to maintain life. When organ failure is temporary and no other options exist, artificial replacements may be used during the time needed for recovery. During the last decades, the so-called ”heart and lung machines” have been developed in which a mechanical system manages the blood pumping of the heart and the oxygenating function of the lungs. The Extra Corporal Membrane Oxygenator (ECMO) system belongs to this group of mechanical life support systems. Introduced by Bartlett *et* al [1] in 1976, the function of the heart and lung is replaced by a pump and a membrane oxygenator, respectively.

Although known to enable treatment in situations where no other alternatives are available, there are complications associated with ECMO. Hemolysis, i.e. destruction of Red Blood Cell due to shear, as well as blood clot formation (thrombogenesis) are the most common side effects of ECMO. Figure 1 shows coagulation of blood in the pump (middle) and a tubing connector (right) of an ECMO system. Besides the direct formation of clots, hemolysis is as well associated with an enhanced tendency for blood coagulation due to increased platelet activation [2, 3]. However, the mechanisms contributing to hemolysis-associated platelet activation are not well understood. Platelets may be activated as a result of biochemical reactions started by ambient substances or due to fluid mechanical forces acting on the platelet itself. The activation leads to a change of platelet morphological structure along with the release of chemical substances promoting clot formation. Once activated, other platelets are allowed to attach to the activated platelet, in turn activating these attaching platelets. This chain reaction leads to a quick release of coagulation factors advancing the formation of clots. Thus, the role of platelets and their activation is essential for the understanding of why and where clotting may occur in patients receiving ECMO treatment.

In this study, the focus is on thrombogenesis, investigating the flow characteristics within the ECMO system as well as the reason for platelet activation along with the location associated with activation of platelets. The main purpose is to understand the fluid mechanical processes contributing to the initiation of blood coagulation in the ECMO system.

Components of the ECMO system

The ECMO system consists of pumps, oxygenators, cannula, tubing and heat exchangers. The pump and oxygenator with accompanying control units for flow, blood oxygenation and anticoagulation are the most vital parts of the system. The pump is either a roller or a centrifugal pump, where the latter is used at the ECMO unit at Karolinska Hospital in Stockholm, Sweden, Fig. 1 (left). The blood enters and leaves the pump through the central and side tube, respectively. The role of blood oxygenation within the ECMO system can be carried out by different types of oxygenators, all with the purpose of providing an efficient oxygenation along with a simple, safe and reliable operation as well as sterilization. Another important component is the cannula coupling the system to the patient. The side connected to the patient (venous side) ends with multiple holes to enable quick suction of blood without risking attaching the tip to the wall. The arterial side, i.e connected to the tubing of the extracorporeal parts of the ECMO system, has a single hole through which the resistance is lower to avoid blocking the flow.



Figure 1: The centrifugal pump used in ECMO (left). Blood coagulation in the pump (middle) and the connector (right).

*Corresponding author. Email: prahl@mech.kth.se

NUMERICAL METHOD AND GEOMETRICAL SET-UP

The flow of an incompressible, isothermal fluid is represented by the Navier-Stokes equations:

$$\frac{\partial \rho}{\partial t} + \frac{\partial}{\partial x_i}(\rho u_i) = 0, \tag{1}$$

$$\rho \frac{\partial}{\partial t}(u_i) + \rho \frac{\partial}{\partial x_j}(u_i u_j) = -\frac{\partial p}{\partial x_i} + \frac{\partial}{\partial x_j}\left(\mu \frac{\partial u_i}{\partial x_j}\right) \tag{2}$$

The flow is resolved using implicit LES. The fluid, i.e. blood, is considered to be single phase and Newtonian, having a viscosity equal to that of water. The platelets are modelled using Lagrangian Particle Tracking applying the platelet activation model according to Nobili *et* al [4].

Three parts of the ECMO system is investigated; the pump, the cannula and the connector. As for boundary conditions for the pump, velocity inflow with 5% synthetic turbulence is applied at the inlet and constant a pressure is used at the outlet. No slip is considered at all walls and the impeller is rotated using sliding mesh. For the connector and cannula, constant velocity is applied at the inlet, pressure boundary condition is used at outlet and no slip is applied at the walls.

RESULTS / DISCUSSION

The main motivation for this study is the fact that the actual location of initial clot formation in the ECMO system is unknown. Considering the characteristic speed of the pump, if taken to be the speed of the blade tip, the velocity is approximately 1.3 m/s when running the pump at 3600 rpm. A similar velocity magnitude is found in the pipe, which has a diameter of 1 cm. A typical length scale of the pump could be the height of the tip, corresponding to 2 mm. This leads to a Reynolds number that is less than a number in-between the range of $1000 - 10000$, in turn depending on the viscosity chosen for the fluid (water or blood analogue). Thus, the flow is less likely to be turbulent in the lower Reynolds number range and could display transitional or turbulent behavior at the larger Reynolds numbers.

Figure 2 (left) shows the isosurfaces of the $\lambda 2$-criterion in the pump, clearly showing the vortical structures forming around and behind the trailing edge of the blades as well as from the tongue region near the outlet. Moreover, the velocity field in a cross-section of the pump also displays the vortical structures. Especially, the vortices found in the bottom parts of the pump are interesting since these vortices, under certain conditions, could enhance platelet aggregation [5], possibly explaining the line of platelets found in this area, Fig. 2 (mid). This could indicate a possible site of platelet activation within the ECMO system.

Blood clots are often found on the cannulas. Thus this component is suspected to be another site prone to blood coagulation. Moreover, these catheters are also associated with strong unsteady shear-layers that may lead to damaging of the RBCs as well as activation of the platelets. This, however, is still to be evaluated through the simulations carried out in this study.



Figure 2: Vortical structures found in the pump, visualized by $\lambda 2$-criterion (left). The trace of activated platelets in the lower parts of the pump (middle) and the velocity vectors in the gap in the lower parts of the pump (right).

References

[1] Bartlett R.H., Gazzaniga, A.B., Jefferies, M.R., Huxtable, R.F., Haiduc, N.J., Fong, S.W.: Extracorporeal membrane oxygenation (ECMO) cardiopulmonary support in infancy. Trans Am Soc Artif Intern Organs, 22:80-93, 1976.

[2] Gladwin, M.T., Kato, G.J.: Hemolysis-associated hypercoagulability in sickle cell disease: the plot (and blood) thickens!. Haematologica, 93:13, 2008.

[3] Villagra J., Shiva S., Hunter L.A., Machado R.F., Gladwin M.T., Kato G.J.: Platelet activation in patients with sickle disease, hemolysis-associated pulmonary hypertension, and nitric oxide scavenging by cell-free hemoglobin. Blood, 110: 216672, 2007.

[4] Nobili, M., Sheriff, J., Morbiducci, U., Redaelli, A., Bluestein, D.: Platelet activation due to hemodynamic shear stresses: damage accumulation model and comparison to in vitro measurements. SAIO J., 54(1):6472, 2008.

[5] Ijzermans, R.H.A., Hagmeijer, R., van Langen, P.J.: Accumulation of heavy particles around a helical vortex filament. Phys Fluids, 19:107102, 2007.

DRUG TRANSPORT IN ANTERIOR HUMAN EYE AFTER SUBCONJUNCTIVAL AND EPISCLERAL IMPLANTS

Feng Zhang[1a)], Han Chen[1], Qin Qian[1] & Yukan Huang[2]

[1]*Department of Mechanics, Huazhong University of Science & Technology, Wuhan, China*

[2]*Department of Ophthalmology, Union Hospital, Tongji Medical College, Huazhong University of Science & Technology, Wuhan, China*

Summary This paper numerically investigates the diffusive and convective transport of subconjunctivally and episclerally implanted drugs in the anterior segment of human eyes. Effects of implant location and orientation of the eye are analyzed. The results can help to understand drug transport processes in the anterior human eye, and improve the drug delivery efficacy in clinical treatment of anterior eye diseases.

INTRODUCTION

Currently, bioavailability of topically applied drugs in the treatment of anterior eye diseases is mainly limited by the anatomical and physiological barriers in the anterior eye, which includes nasolacrimal drainage, corneal epithelium, clearance from the blood vessels in the conjunctiva, and the protection against the entry of xenobiotics [1]. Recently, anterior segment implants in subconjunctiva [2] were adopted to treat primary open angle glaucoma and ocular hypertension, and episcleral implants [3,4] were found to be effictive with long duration in the treatment of keratoconjunctivitis in animal preclinical studies. To make the implant treatment more effective, understanding of the drug delivery process becomes crucial. Due to the difficulty of experimental measurement of drug distribution in the eye, numerical modelling has been a useful tool to comprehensively describe drug delivery process in the eye. In our previous work [5], transport processes of topically applied drugs were investigated numerically, and suggestions of clinical applications were proposed. The goal of this work is to investigate the transport process of subconjunctivally and episclerally implanted drugs in the anterior segment of human eyes.

METHODOLOGY

A 3D numerical model of the eye (Fig. 1) is developed, which includes the cornea, sclera, anterior chamber, posterior chamber, lens, vitreous, iris, trabecular meshwork (TM), ciliary body (CB) and the subconjunctival/ episcleral implant which is modeled as a drug source. Temperature distribution is governed by the transient bioheat equation, with heat loss due to convection, radiation and tear evaporation on the corneal surface and a heat flux boundary condition specified on the sclera surface. Steady 3D incompressible Navier-Stokes equations are solved to obtain the AH flow in the anterior and posterior chamber, in which the buoyancy force due to temperature gradients across the eye is considered. Inlet and outlet of the AH flow are specified at CB and TM, respectively, and no-slip conditions are specified on other boundaries. Finally, evolution of drug concentration is obtained by solving a transient convection diffusion equation, with a time-dependent concentration flux (calculated from the experimental results in [3]) on the bottom surface of the episcleral/subconjunctival implant. The coupled heat transfer, fluid flow and mass transfer problem is solved numerically in COMSOL Multiphysics.

RESULTS AND DISCUSSIONS

Since the corneal temperature increases from its center to the periphery, warmer fluids with lower densities tend to rise along the corneal surface, resulting in the AH natural convection in the anterior chamber of an up-facing eye (Fig. 2). Fig. 3 and 4 plot the top-view and side-view AH flow in a horizontally-facing eye, respectively, and velocity components in the horizontal plane (Fig. 3) are about one order of magnitude smaller than those in the vertical plane (Fig. 4). In Fig. 4, a clockwise AH circulation is present in the anterior chamber, also due to natural convection effects.

[a)] Corresponding author. Email: zhangfenghust@foxmail.com.

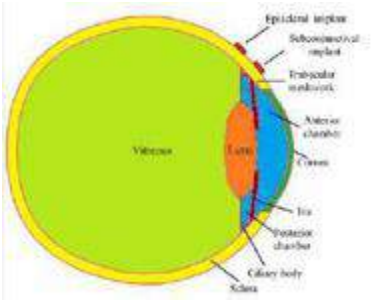

Fig. 1

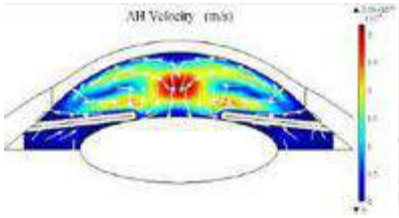

Fig. 2

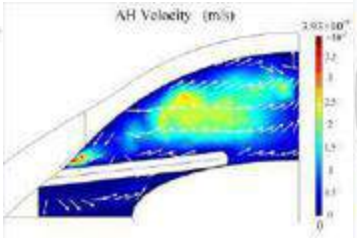

Fig. 3

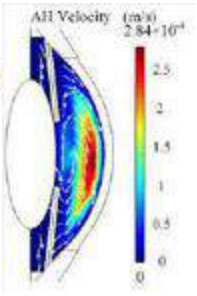

Fig. 4

Time-dependent evolution of accumulative amount of the drug at iris, lens, and TM in a horizontally-facing eye (Fig. 5) shows that subconjunctival implant is more effective in drug delivery to all the three targets than episcleral implant, due to the shorter delivery path, and more drug is delivered to iris and lens than TM, due to their greater surface areas. Our numerical results also demonstrate that drug delivery to all the three targets is more effective in the horizontally-facing eye than in the up-facing eye (Fig. 6), and drug distribution in the anterior eye is more uniform, 2 days after subconjunctival implant, in the horizontally-facing eye than in the up-facing eye (Fig. 7). However, it is seen from Fig. 7 that most of the drug released from the implant is lost in the vitreous. Circumferential position of the implant is also investigated, and Fig. 8 demonstrates that drug implant at 12 o'clock position (looking from the outside) is the most effective for drug delivery to iris and lens, and implant at 3 o'clock position is the most effective for drug delivery to TM.

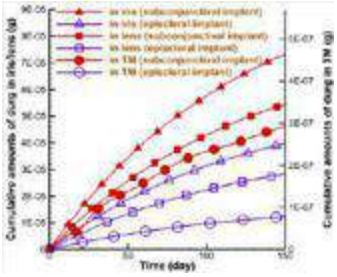

Fig. 5

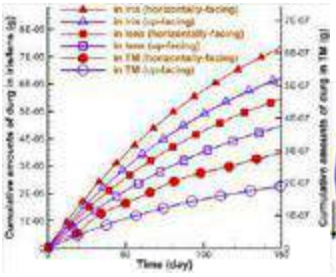

Fig. 6

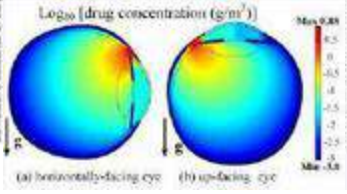

Fig. 7

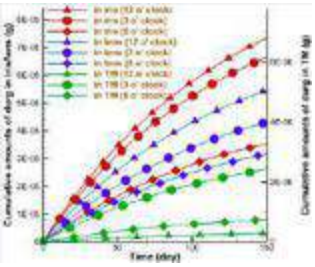

Fig. 8

CONCLUSIONS

In this study, a coupled numerical model of heat transfer, AH flow and drug transport is developed to investigate the transport process of subconjunctival and episcleral implants in the anterior human eye. Our numerical results show that subconjunctival implant is more effective in drug delivery than episcleral implant; drug delivery to iris, lens and TM is more effective in the horizontally-facing eye than in the up-facing eye; implant at 12 o'clock position is the most effective for drug delivery to iris and lens, and drug implant at 3 o'clock position is the most effective for drug delivery to TM. These results can help to understand drug transport processes in the anterior human eye, and improve the drug delivery efficacy in clinical treatment of anterior eye diseases.

References

[1] Weiner A.L., Gilger B.C.: Advancements in Ocular Drug Delivery. *Vet. Ophthalmol.* **6**: 395-406, 2010.

[2] Safety Study of Latanoprost Slow Release Insert (Latanoprost SR). Available online: http://clinicaltrials.gov/ct2/show/NCT01180062.

[3] Kim H., Csaky K.G., Gilger B.C.: Preclinical Evaluation of a Novel Episcleral Cyclosporine Implant for Ocular Graft-versus-Host Disease. *Invest. Ophthalmol. Vis. Sci.* **46**: 655-662, 2005.

[4] Gilger B.C., Moore C.P., Narfstrom K.: Preclinical Acute Toxicity and Pharmacokinetics of Episcleral LX201 Implants in Rabbits. In Proceedings of ARVO 2008 Annual Meeting, Jersey City, NJ, USA, Program number 1964, 27 April–May 2008.

[5] Chen, H., Zhang F., Huang Y.K., Wu J.K.: Numerical Investigation of Topical Drug Transport in the Anterior Human Eye. *Int. J. Heat Mass Tran.* **85**: 356-366, 2015.

THE INFLUENCE OF HEMATOCRIT ON THE DECAYING SHEAR TURBULENCE OF BLOOD FLOW IN LARGE ARTERIES

David E. Rival*, Saeed Rahgozar, and Lucas Serafini
Department of Mechanical and Materials Engineering, Queen's University, Kingston, Ontario, Canada

Summary A novel experimental approach, consisting of scaled hydrogel beads representing red blood cells, is used to model pulsatile turbulent flow in large arteries. The large optical facility uses a boundary-free, uniformly-sheared flow that decays in time, in which the velocity fields are acquired via particle image velocimetry on streamwise/cross-stream and streamwise/spanwise planes for Newtonian and non-Newtonian single-phase blood analogues, as well as for the two-phase case representing varying levels of hematocrit. Changes in the decay rate are observed when moving from the Newtonian to non-Newtonian and finally two-phase (varying hematocrit) blood analogues.

BACKGROUND AND MOTIVATION

A proper characterization of local flow separation in large artery hemodynamics, as represented in Figure 1, is crucial to advancing biomedical devices, and for our diagnosis, prevention and treatment of cardiovascular disease. Despite the general assumption that blood flow remains laminar throughout most arteries, several exceptions have been reported in the literature including instances of transitional flow in the ascending aorta, at branch points in large arteries, in stenotic arteries and in unhealthy or mechanical heart valves [1-2]. The occurrence of transition to turbulence in the cardiovascular system has been of hemodynamic interest over the past decades since it is generally agreed that this localized turbulence may be responsible for a number of cardiovascular diseases and abnormalities such as cardiac murmurs, thrombus formation, hemolysis, platelet activation and atherosclerosis [1,3-6]. Despite the growing awareness of the importance of turbulence in hemodynamics, our knowledge about characteristics, scales and structures of turbulence in blood flow is still rudimentary. Beyond the inherent challenge of characterizing turbulence, blood flow is particularly complex because of its pulsatile, multi-phase and viscoelastic characteristics as well as its irregular deforming boundaries. Moreover, due to the limitation of instrumentation and access, very little *in vivo* information exists about the turbulent statistics and structures in the cardiovascular system. While the early *in vivo* investigations were limited to invasive point measurements [1,7], the modern non-invasive techniques such as magnetic resonance imaging (MRI) suffer from lower signal-to-noise ratios and lower spatial and temporal resolutions [8-9]. Thus these limitations in characterizing this flow hinders not only our progress towards understanding of turbulence in large arteries but also our ability to develop realistic models for future simulations.

In the present work, we endeavour to characterize the influence of hematocrit on turbulence decay in the inherent pulsatile environment of blood flow in large arteries. By keeping the geometry as simple as possible, i.e. boundary-free shear, and allowing the turbulent characteristics of the flow to be representative of the turbulent motion in real arteries based on the relevant dimensionless parameters and available *in vivo* data, we expect to identify where classic single-phase, Newtonian assumptions of blood break down. Our optically-matched, scaled up experimental setup allows us to employ particle image velocimetry (PIV) in order to accurately measure velocity fields and consequently to investigate the details of turbulence scales, parameters and structures for the various blood analogues tested. The specific methodology is described next.

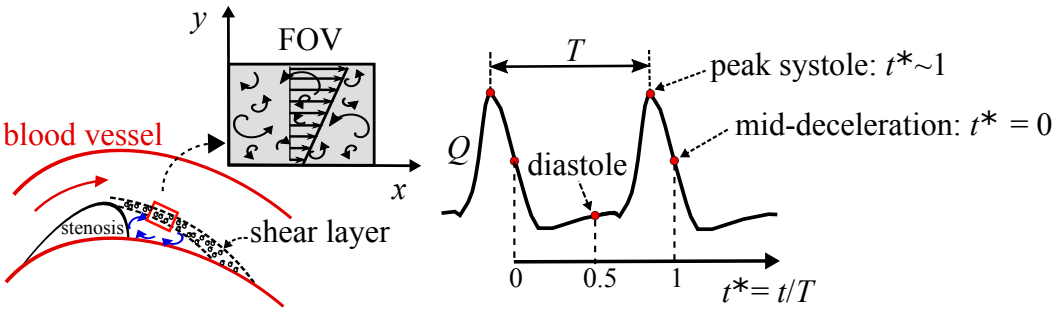

Figure 1: Cross section of a generic artery showing the generation of a shear layer downstream of a stenosis. On the right-hand side, three representative times in the cardiac cycle are denoted. Note t^* is dimensionless time, which is normalized by the cycle period T.

*Corresponding author. Email: d.e.rival@queensu.ca

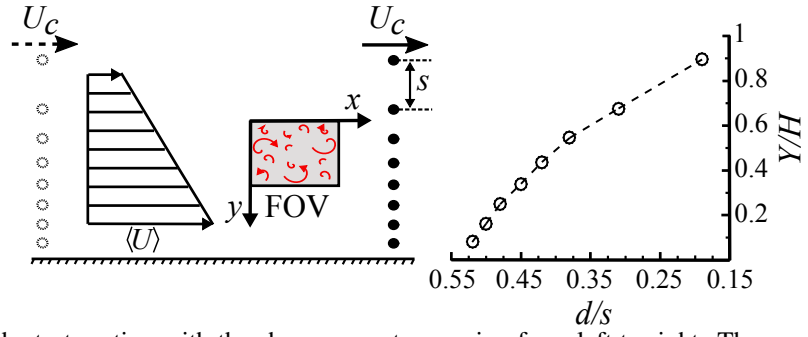

Figure 2: Side view of the test section with the shear generator passing from left to right. The curve on the right shows the solidity distribution of the grid generator. Y is the cross-stream coordinate and H is the overall cross-sectional height of the tank.

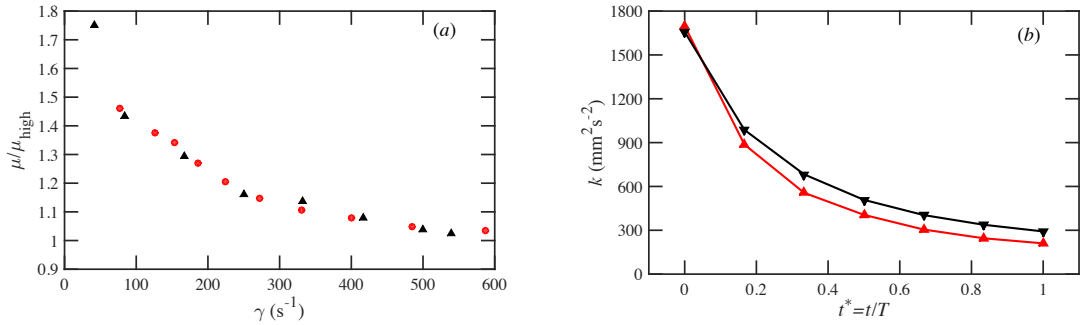

Figure 3: (a) Bulk viscosity characterization for the non-Newtonian, single-phase blood analogue (red) compared to literature (black) [10]; and (b) initial findings of turbulent kinetic energy (k) decay indicate increased dampening for non-Newtonian analogue (red curve) when compared to the Newtonian case (black curve).

METHODS AND PRELIMINARY RESULTS

The experiment is performed in a large optical towing tank with approximate dimensions of $8 \times 1 \times 1$ m^3. The test section is located in the middle of the tank to ensure negligible end wall effects. A high-speed traverse system tows a shear generator in the center of the towing tank at speeds up to 1 m/s over a maximum distance of 4 m. An approximately uniform mean shear is generated in the tank by towing the shear generator consisting of a plane parallel-rod grid of uniform rod diameter (d) with non-uniform spacing (s). Figure 2 shows a schematic of the shear generator passing through the field of view. In the present experiments the towing speed (U_c) was 0.2 m/s and the diameter of the rods was 42 mm. The right-hand curve in this figure shows the solidity distribution of the grid. The blockage necessary for generating shear is kept minimal (i.e. about 30% of the area of the cross section) in order to minimize potential large-scale secondary flows. High-speed planar PIV measurements are performed using a Photron SA-4 camera at 125 Hz with full resolution of 1024×1024 pixels. In Figure 3, the single-phase, non-Newtonian analogue is compared to literature to ensure consistency (left). Subsequently this non-Newtonian analogue demonstrates an increased dampening to turbulent kinetic energy relative to the Newtonian case. Data for the two-phase analogue with scaled hydrogel beads - representing red blood cells - has since been collected and is currently being processed. Here the influence of hematocrit will determine at what critical level attenuation in decaying turbulence becomes apparent.

References

[1] Stein, P. D., Sabbah, H. N.: Turbulent blood flow in the ascending aorta of humans with normal and diseased aortic valves. Circ. Res. 39 (1) 1976.

[2] Steinman, D. A.: Assumptions in modelling of large artery hemodynamics. In Modeling of Physiological Flows, Springer, 2012.

[3] Coulter, N. A., Pappenheimer, J. R.: Development of turbulence in flowing blood. Am. J. Physiol. Legacy Content 159 (2), 1949.

[4] Sutera, S. P., Mehrjardi, M. H.: Deformation and fragmentation of human red blood cells in turbulent shear flow. Biophys. J. 15 (1), 1975.

[5] Dyverfeldt, P., Gardhagen, R., Sigfridsson, A., Karlsson, M., Ebbers, T.: On MRI turbulence quantification. Magn. Reson. Imaging 27 (7), 2009.

[6] Fortini, S., Espa, S., Querzoli, G., Cenedese, A.: Turbulence investigation in a laboratory model of the ascending aorta. J. Turbul. 16 (3), 2015.

[7] Nerem, R. M., Seed, W. A.: An in vivo study of aortic flow disturbances. Cardiovasc. Res. 6 (1), 1972.

[8] Gulan, U., Luthi, B., Holzner, M., Liberzon, A., Tsinober, A., Kinzelbach, W.: Experimental study of aortic flow in the ascending aorta via particle tracking velocimetry. Exp. Fluids 53 (5), 2012.

[9] Petersson, S., Dyverfeldt, P., Ebbers, T.: Assessment of the accuracy of MRI wall shear stress estimation using numerical simulations. J. Magn. Reson. Imaging 36 (1), 2012.

[10] Li, L., Walker, A., Rival, D.: The characterization of a non-Newtonian blood analog in natural-and shear-layer-induced transitional flow. Biorheology 51 (4), 2014.

A MODEL FOR TRACHEOLAR FLOW IN INSECTS

Anne Staples*[1] and Krishnashis Chatterjee[2]
[1,2]*Department of Biomedical Engineering and Mechanics, Virginia Tech, Blacksburg, Virginia, USA*

Summary Inspired by some of the fundamental features of insect respiratory systems, we investigate the effects of rarefaction on low-Reynolds number, collapse-driven flow through a microtube. The Navier-Stokes equations are linearized, a periodic wall collapse motion is prescribed at two sites along the tube, and physiologically realistic pressure boundary conditions are applied along with first-order slip boundary conditions. The axial and radial velocities, axial pressure gradient, and time averaged flow rate in the tube are found as a function of the phase lag between the two contraction sites, with and without slip. Unlike for purely pressure- or collapse-driven flows, when slip is added, this flow is highly sensitive to the phase lag parameter, and the flow can be accelerated, decelerated, or reversed, depending on its value, resulting in a multi-functional microfluidic system that can acccelerate or decelerate flow as needed with slight changes in the timing of its wall collapses.

INTRODUCTION

Insect tracheal tubes collapse periodically as a result of the animal's regular abdomenal contractions in the rhythmic tracheal contraction (RTC) respiration regime [1]. Furthermore, the diameter of typical insect tracheal tubes is from 1 to several hundred micrometers, and the working fluid is air at close to atmospheric pressures, resulting in flow in the slip regime in a significant portion of the tracheal system. Additionally, the flow in the respiratory system, which is comprised of a complex network of tracheal tubes that begin at the body openings called spiracles (typically $100 - 500$ μm diameter) and terminate at the tissue (typically ≤ 1 μm diameter), delivering freshly oxygenated air directly to the cells, is creeping flow with Reynolds numbers typically less than 1.

Here, we build on one author's previous work modeling the insect respiratory flow transport mechanism as low-Reynolds number flow through a periodically collapsing microtube [3, 4] by adding first-order slip boundary conditions to the model, as well as physiologically accurate pressure boundary conditions at the ends of the tube. The pressure boundary conditions are adapted from the intratracheal pressure measurements taken in blowfly respiratory systems by Wasserthal [2].

METHODS

Referring to the schematic in Figure 1, assuming the tube length to be much greater than its diameter, the tube wall profile including its two collapse sites is governed by the spatio-temporal function $H(x,t)$, which is periodic in time, with x parameterizing the axial direction. Using the boundary conditions (i) at $r = H(x,t)$, $u = \beta\frac{\partial u}{\partial r}, v = \frac{\partial H}{\partial t}$, (ii) at $x = 0$, $p = p_o(t)$, and (iii) at $x = L$, $p = p_L(t)$, where β is the slip parameter (slip length), we derive the following expressions for the axial and radial velocities, and the instantaneous volumetric flow rate [3]:

$$\mathrm{u}_x = \tfrac{1}{4}\tfrac{dp}{dx}(r^2 - H^2 + 2\beta H)$$

$$u_r = \tfrac{r}{4}\tfrac{dp}{dx}\tfrac{dH}{dx}(H - \beta) + \tfrac{r}{4}\tfrac{d^2p}{dx^2}(\tfrac{H^2}{2} - \tfrac{r^2}{2} - \beta H)$$

$$Q(x,t) = \textstyle\int_0^{H(x,t)} u_x(x,r,t) r dr.$$

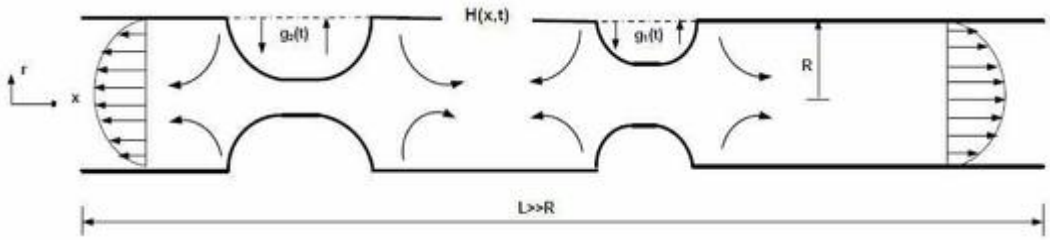

Figure 1: Schematic of collapsing microtube with two collapse sites, wall position function $H(x,t)$, and phase lag between collapse times θ.

*Corresponding author. Email: aestaples@vt.edu

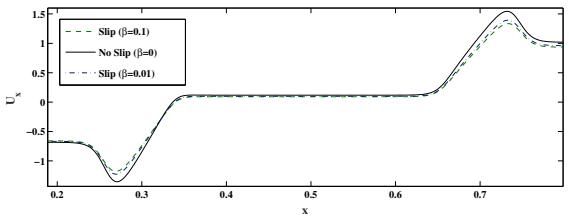

Figure 2: Axial velocity: $\theta = 30°$, $t = 0.3s$.

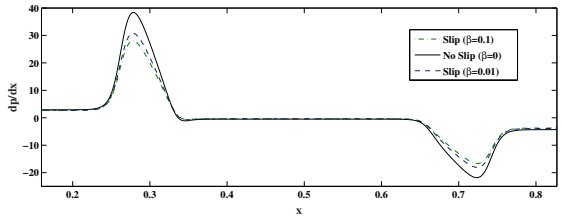

Figure 3: Axial pressure gradient: $\theta = 30°$, $t = 0.3s$.

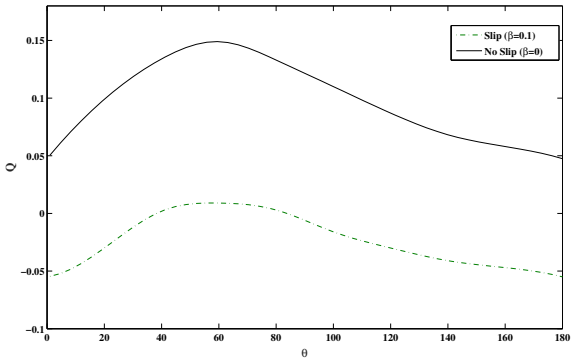

Figure 4: Average volumetric flow rate over one period versus phase lag.

RESULTS

Using slip parameter values of $\beta = 0, 0.001$, and 0.1, which correspond to no slip, low slip, and high slip conditions, respectively, we calculated the axial and radial velocities, axial pressure gradient, and average volumetric flow rate over one cycle as functions of x and θ, the phase lag parameter, which specifies the fraction of a period between the time when the first collapse site is actuated and the time when the second collapse site is actuated. When θ is zero, there is no net flow. The spatial or temporal symmetry needs to be broken to produce unidirectional flow. We found that the effect of adding slip was to reduce the magnitude of axial and radial velocities, the pressure gradients, and the flow rates. Figure 2 show the axial velocity along the tube for the three different slip parameter values at time $t = 0.3$ and phase lag $\theta = 30°$. Figure 3 shows the axial pressure gradient along the tube under the same conditions. Finally, in Figure 4, the cycle-averaged volumetric flow rate is plotted versus the phase lag parameter, θ. We see that the flow rate is reduced when slip is added, but we also see a surprising new feature – for certain values of θ, the flow reverses. This does not occur for purely pressure-driven flow through a microtube, or for purely collapse-driven flow, nor does it occur without the addition of slip boundary conditions.

CONCLUSIONS

In this work we derived an analytical model for Stokes flow through a periodically collpasing microtube with slip, as a simplifed model for the nexus of specialized fluid flow regimes that can occur in insect respiratory systems. We find that the combination of creeping flow in a microtube with slip that is both pressure- and collapse-driven constitues a highly sensitive, tunable microfluidic device that can accelerate, decelerate, or reverse its flow with slight variations in the phase lag parameter, θ. We conjecture that an insect could change its phase lag parameter easily by varying its rate of abdominal pumping.

References

[1] Socha, J. J., Lee, W. K., Harrison, J. F., Waters, J. S., Fezzaa, K., Westneat, M. W.: Correlated patterns of tracheal compression and convective gas exchange in a carabid beetle. J. Exp. Biol. 211:3409-3420, 2008.

[2] Wasserthal, L. T.: Influence of periodic heartbeat reversal and abdominal movements on hemocoelic and tracheal pressure in resting blowflies Calliphora vicina. J. Exp. Biol. 215:362-37, 2012.

[3] Aboelkassem Y., Staples, A. E.: Selective pumping in a network: insect-style microscale flow transport. Bioinspiration Biomimetics, 8(2):026004, 2013.

[4] Aboelkassem Y., Staples, A. E.: A bioinspired pumping model for flow in a microtube with rhythmic wall contractions. Journal of Fluids and Structures 42:187-204, 2013.

NUMERICAL SIMULATION OF THROMBOSIS IN A BLOOD VESSEL

Wei-Tao Wu [1], Nadine Aubry [2a)], Mehrdad Massoudi[3] & James F. Antaki[1]
[1] *Department of Biomedical Engineering, Carnegie Mellon University, Pittsburgh, PA, 15213, USA*
[2] *Department of Mechanical and Industrial Engineering, Northeastern University, Boston, MA, 02115, USA*
[3] *U. S. Department of Energy, National Energy Technology Laboratory (NETL), Pittsburgh, PA, 15236, USA*

Summary Based on Sorenson *et al.*'s model of platelet deposition on to artificial surfaces [1, 2], an improved mathematical model describing the process of thrombus growth in-vivo is developed. The new model is comprised of two parts: the equations of fluid motion and a set of convection-reaction-diffusion equations representing the transport and reactions of chemical and biological species. The model is then applied to the rapid thrombus growth in an injured blood vessel with Adenosine Diphosphate (ADP) injection, for which a good agreement between our numerical results and available experimental data is demonstrated.

INTRODUCTION

A thrombus is commonly known as a "blood clot," or cluster of deposited platelets, anchored to a surface. The normal function of thrombosis is to prevent bleeding. However, pathological thrombosis in the coronary artery can lead to a heart attack; if transported to the brain it is likely to cause a cardiogenic stroke. Decades of basic scientific studies have revealed complex biological reactions involved thrombus formation, which have enabled the possibility of quantitatively describing thrombus formation by means of mathematical models [3]. Our current work capitalizes on recent findings to improve a previously published model of thrombosis by Sorenson et al. [1, 2]. Specifically, it offers three improvements: (1) shear-induced platelet activation, (2) thrombus embolization due to shear, and (3) fluid-solid interaction of the growing thrombus with the flow field.

METHODS: MATHEMATICAL MODEL

Equations of Motion

Blood is treated as a multi-constituent mixture comprised of (1) a fluid phase which is modeled as a linear fluid and (2) a thrombus phase. The fluid phase which consists of red blood cells (RBCs) suspended in plasma is governed by:

$$\frac{\partial \rho_f}{\partial t} + div\left(\rho_f \boldsymbol{v}_f\right) = 0 \tag{1}$$

$$\rho_f \frac{D\boldsymbol{v}_f}{Dt} = div\left(\boldsymbol{T}_f\right) + \rho_f \boldsymbol{b}_f - C_2 f(\phi)\left(\boldsymbol{v}_f - \boldsymbol{v}_T\right), \tag{2}$$

where $\boldsymbol{T}_f = [-p(1-\phi)]\boldsymbol{I} + 2\mu_f(1-\phi)\boldsymbol{D}_f$ is the stress tensor of the fluid, p is the pressure, and μ_f is the asymptotic dynamic viscosity (whose value is 3.5cP). A scalar field ϕ is introduced to represent the volume fraction of deposited platelets (thrombus). The density of the fluid phase is defined in terms of the volume fraction according to $\rho_f = (1-\phi)\rho_{f0}$, where ρ_{f0} is the density of the fluid phase (1060 kg/m^3), $\boldsymbol{b}_f$ is the body force, $\boldsymbol{v}_f$ and $\boldsymbol{v}_T$ are the velocities of the fluid and thrombus phases, respectively. The term $C_2 f(\phi)\left(\boldsymbol{v}_f - \boldsymbol{v}_T\right)$ is the resistance force on the fluid from the thrombus, where C_2 is computed by assuming that the deposited platelets behave like densely compact particles of 2.78μm in diameter (see Johnson *et al.* [4] and Wu *et al.* [5, 6]), and $f(\phi) = \phi(1 + 6.5\phi)$ is the hindrance function.

Convection-Diffusion-Reaction Equations

The process of thrombosis is represented by a set of coupled convection-diffusion-reaction equations. The current model includes ten (10) chemical and biological species, illustrated in Figure 1. These include five categories (states) of platelets: (i) **RP**: resting platelets (in the flow field); (ii) **AP**: activated platelets (in the flow field, and more reactive); (iii) $\mathbf{RP_d}$: deposited (trapped) resting platelets; (iv) $\mathbf{AP_d}$: deposited active platelets; and (v) $\mathbf{AP_s}$: deposited and stabilized platelets. Additional five biochemical species include: (1) $\mathbf{a_{pr}}$: platelet-released agonists (ADP); (2) $\mathbf{a_{ps}}$: platelet-synthesized agonist (thromboxane A2); (3) **PT:** prothrombin; (4) **TB:** thrombin, synthesized from prothrombin on the platelet phospholipid membrane; and (5) **AT:** anti-thrombin III, which inhibits thrombin and whose action is catalyzed by heparin via the kinetic model of Griffith [1]. Figure 1 also depicts the fundamental mechanisms represented in the thrombosis model, including: *Platelet Activation, Platelet Deposition, Thrombus Propagation, Thrombus Dissolution or Erosion, Thrombus Stabilization, Thrombus Inhibition,* and *Thrombus-fluid interaction*. The transport of the above species in the flow field is described by a corresponding set of convection-diffusion-reaction equations [1, 2] of the form:

$$\frac{\partial [C_i]}{\partial t} + div\left(\boldsymbol{v}_f \cdot [C_i]\right) = div(D_i \cdot \nabla [C_i]) + S_i, \tag{3}$$

where $[C_i]$ is the concentration of species *i*, D_i refers to the diffusivity of species *i* in blood, and S_i is a reaction source term for species *i*, with the time dependency of the concentration of deposited platelets (RP_d, AP_d, and AP_s) governed by:

$$\frac{\partial [C_i]}{\partial t} = S_i. \tag{4}$$

[a)] Corresponding author. Email: n.aubry@neu.edu.

For details on the source terms S_i, species concentration $[C_i]$, boundary conditions and detailed computational methods, see Reference [7]. For all general parameters, as well as the case-specific parameters (3) which were adjusted to best fit the experiment, we refer the reader to References [1, 2, 7].

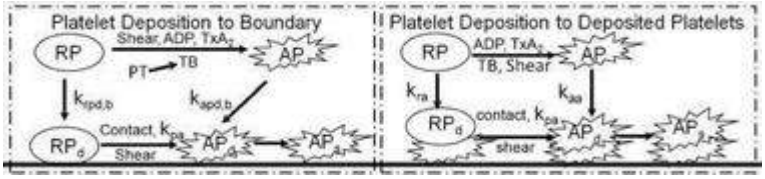

Figure 1. Schematic of the thrombosis model, comprised of platelet deposition, aggregation, and stabilization.

RESULTS AND DISCUSSION

Begent and Born [8, 9] experimentally studied thrombosis induced by the iontophoresis of Adenosine Diphosphate (ADP) in a hamster's blood vessel *in vivo*. The schematic of the simulated blood vessel flow is shown in Figure 2 (Left), where the inlet velocity was chosen to be $800\mu m/s$ to match the experimental value. From the experimental observation [8] [see Figure 2 (Right)], it is clear that the thrombus grows both upstream and downstream of the location of the pipette, in agreement with our numerical results shown in Figure 3 (Left). According to Reference [8], the thrombus took approximately 100s to reach a size of 1/3 height of the blood vessel in the experiment while the same size was obtained after about 150s in our simulation. Figure 3 (Right) shows that the height versus length curves of the expanding thrombus in obtained numerically and experimentally [9] are in good agreement. In the future, the current model will be applied to further investigate thrombosis in practical medical devices such as artificial hearts and lungs.

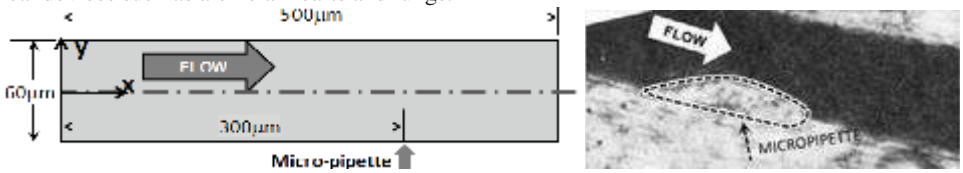

Figure 2 (Left) Schematic of the simulated blood vessel. The ADP is injected by a micro-pipette locating at the bottom vessel wall. (Right) Thrombus in blood vessel observed by Begent and Born [8] after approximately 100s of ADP injection through a micropipette. (The experimental data is reused with permission.)

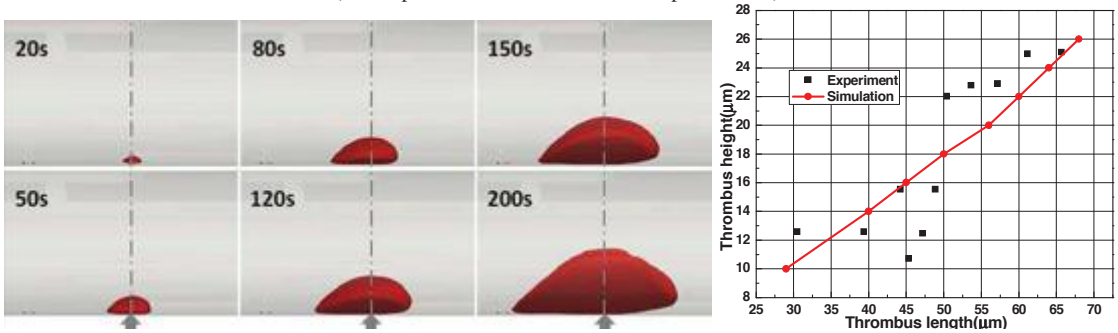

Figure 3 (Left) Progression of thrombosis obtained with the current model; The arrow indicates the position of the micro-pipette. (Right) Comparison of the thrombus' height versus length by numerical simulations (current work) and experiments in [9].

REFERENCES

[1] E.N. Sorensen, G.W. Burgreen, W.R. Wagner, J.F. Antaki, Computational simulation of platelet deposition and activation: I. Model development and properties, Ann Biomed Eng, 27 (1999) 436-448.

[2] E.N. Sorensen, G.W. Burgreen, W.R. Wagner, J.F. Antaki, Computational simulation of platelet deposition and activation: II. Results for Poiseuille flow over collagen, Ann Biomed Eng, 27 (1999) 449-458.

[3] D.M. Wootton, D.N. Ku, Fluid mechanics of vascular systems, diseases, and thrombosis, Annu Rev Biomed Eng, 1 (1999) 299-329.

[4] G. Johnson, M. Massoudi, K. Rajagopal, Flow of a fluid—solid mixture between flat plates, Chem Eng Sci, 46 (1991) 1713-1723.

[5] W.-T. Wu, F. Yang, J.F. Antaki, N. Aubry, M. Massoudi, Study of blood flow in several benchmark micro-channels using a two-fluid approach, Int J Eng Sci, 95 (2015) 49-59.

[6] W.-T. Wu, N. Aubry, M. Massoudi, J. Kim, J.F. Antaki, A numerical study of blood flow using mixture theory, Int J Eng Sci, 76 (2014) 56-72.

[7] W.-T. Wu, Theoretical and Computational Studies on Thrombus Formation and Multiphase Characteristics of Blood Flow, in: Mechanical Engineering, Carnegie Mellon University, Pittsburgh, 2015.

[8] N. Begent, G. Born, Growth rate in vivo of platelet thrombi, produced by iontophoresis of ADP, as a function of mean blood flow velocity, Nature, 227 (1970) 926-930.

[9] G. Born, P. Richardson, Activation time of blood platelets, J Membr Biol, 57 (1980) 87-90.

FSI ANALYSIS OF ARTIFICIAL HEART VALVES USING NEWTONIAN AND NON-NEWTONIAN MODELS

Han Hung Yeh [1,2] & Dana Grecov[1,2(a)]
[1]*Department of Mechanical Engineering, University of British Columbia, Vancouver, BC, Canada.*
[2]*Biomedical Engineering Program, University of British Columbia, Vancouver, BC, Canada.*

Summary Hemodynamics studies on artificial heart valve has been conducted since the first available valve on market. However, better and more accurate prediction in the hemodynamic performance that an artificial heart valve could offer is still needed. Current advance computational technique, such as FSI (fluid-structure interaction), integrated with proper rheological properties of human blood could provide further insight for optimal hemodynamics in an artificial heart valve implantation. The presented hemodynamics studies demonstrates an accurate numerical modelling with the Newtonian and non-Newtonian rheological implementation using FSI approach for analysis of the variance of different hemodynamic parameters between the two models. Minimum difference in leaflet motion was found with noticeable variations in wall shear stress distribution throughout different phases of one cardiac cycle.

INTRODUCTION

Among of all people who deceased in Canada in 2012, 19.7% of them were caused by the disease of heart[1]. For those who has a diseased heart valve, mitral and aortic valves are the most commonly affected valves, which account for 34% and 44% morbidity, respectively[2][3]. With the increase of popularity in adopting computational methods for the investigations and modeling of hemodynamics for cardiovascular diseases, the use of fluid-structure interaction (FSI) method for simulating the hydrodynamics of heart valves and other cardiac vasculatures has gain significant insight[4]-[8]. Although the rheological properties of blood in large arteries are typically assumed as Newtonian fluid, blood behaves as non-Newtonian fluid with shear thinning and thixotropic properties. By integrating the non-Newtonian relationship, the locations with concentrated high and low shear stress can be identified for further hemodynamics investigate and assessments for blood cell damage. Therefore, this paper presents a generalized FSI model for the hemodynamics investigation of artificial heart valve using both Newtonian and non-Newtonian rheological models for predicting leaflet motion, velocity profiles and shear stress distribution under physiological conditions and geometry.

METHODOLOGY

The numerical models presented in this paper were constructed using COMSOL Multiphysics (V5.2). The geometrical parameters for the artificial heart valve model and the surrounding aortic root were gathered from experimental setup by ViVitro Lab Inc. The artificial valve modelled represented a bileaflet mechanical heart valve with an approximate aortic diameter of 23.4 mm. Valve leaflets were assumed to behave as isotropic material with a Young's modulus of 30 GPa, Poisson ratio of 0.3, and density of 2116 $kg \cdot m^{-3}$. Laminar flow region was assumed with a density of 1060 $kg \cdot m^{-3}$ and a Newtonian dynamic viscosity of 0.0035 Pa·s. The non-Newtonian rheological model for blood was constructed using Carreau equation using parameters with η_∞ = 0.0035 Pa·s, η_0 = 0.056 Pa·s, λ = 3.313, and n = 0.3568, based on study published by Karimi et al[9]. Inlet and outlet boundary conductions were applied with normal physiological pulsatile blood pressure profiles, which are identical to the experiments, at the ventricular and aortic position. Pressure pulses have a period of 0.86 s that represent a nominal heart rate of 70 beats per minute. The arterial wall boundaries were assumed to be rigid with no-slip condition. Free rotation condition was applied to the hinge of artificial heart valve with conditionally prescribed counter moment added only when the leaflets reached either minimum or maximum allowable angular position, which was 25 and 85 degree, respectively. The numerical models were conducted using fully coupled direct solve technique with a multifrontal massively parallel sparse direct solver (MUMPS). Deformation and displacement of the valve leaflet in the simulation was handled with arbitrary Lagrangian-Eulerian (ALE) formulation and require domain-wide remesh based on mesh quality or relative mesh volume. Relative tolerance for the simulation was set to be 0.01. Mesh independence study was conducted on the Newtonian model and concluded with a change in solution less than 5%. The flow experiments, used for numerical validation, were conducted using a cardiovascular testing system at ViVitro Lab.

RESULTS

In general, the variation in leaflet dynamics between the Newtonian model and non-Newtonian model was insignificant and the motion of the leaflets was in agreement with [7]. The approximate duration for open leaflet was 230 ms from leaflet opening to closing. The leaflets remained fully opened for approximately 100 ms. Maximum Von Mises stress was also processed for both leaflet and found to be below 100 MPa, which is less than the yield strength of the leaflet material. In terms of wall shear stress (WSS), both Newtonian and non-Newtonian models had similar WSS magnitude. However, with

[a)] Corresponding author. Email: dgrecov@mail.ubc.ca.

higher flow velocity magnitude during peak systole forward flow and diastole leakage flow, the variance in WSS between the two models could be differentiated more since the distribution of high WSS region in non-Newtonian model was larger. Similar observation and conclusion was made by [10]. There are minor velocity distribution difference between the Newtonian and non-Newtonian models. Shown below in Figure 1 is the flow velocity field during peak systole with Newtonian viscosity. Recirculation of blood within aortic sinuses as well as forward blood jet around valve leaflet, identified with forward red arrows, can be seen during fully opened leaflets.

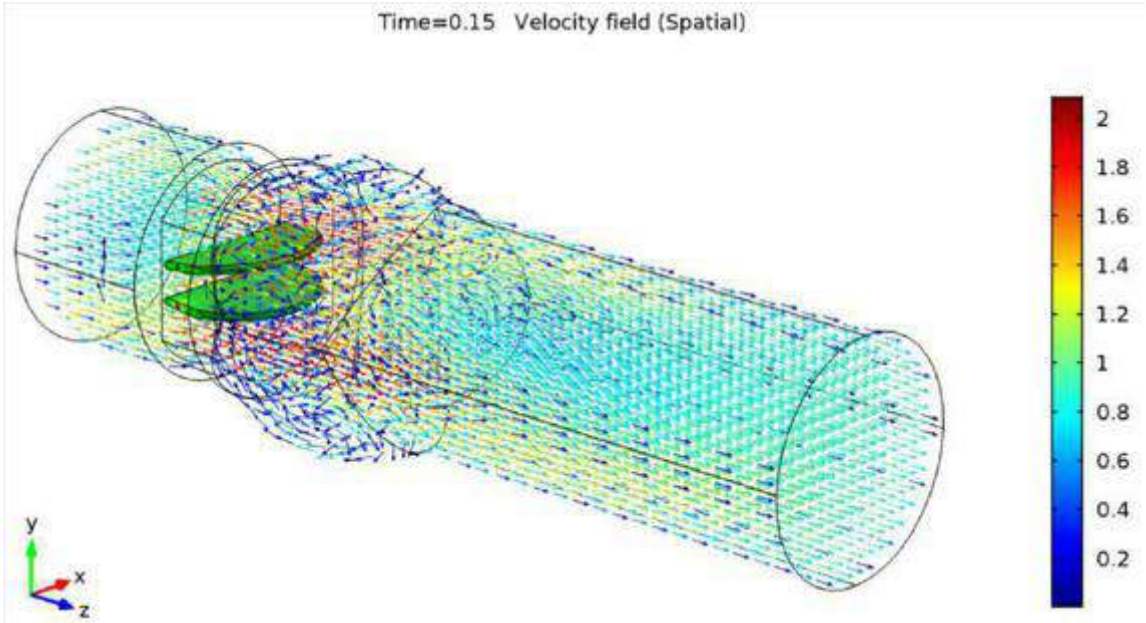

Figure 1: 3D Velocity Arrow Field for Bileaflet Mechanical Valve with Newtonian properties at Peak Systole

CONCLUSION

The presented FSI model demonstrated an accurate prediction of leaflet dynamics and the hemodynamic performance for the mechanical valve, which was validated experimentally. Between the Newtonian and non-Newtonian model, difference in velocity profile was found; however, there was only minor velocity distribution difference between the two computational models. Similarly, the leaflet dynamics was slightly affected by different viscosity models. WSS analysis, on the other hand, has identified regions close to arterial wall and valve leaflet with larger WSS distribution for the case of non-Newtonian model. Since the non-Newtonian model used in current study only depend on shear rate, a more complex rheological fluid model that considers either haematocrit or viscoelasticity will be used for further improvement.

References

[1] Leading Causes of Death, 2012, web site: http://www.statcan.gc.ca/daily-quotidien/151210/t001f-eng.htm.

[2] Iung B., et al.: A prospective survey of patients with valvular heart disease in Europe: the Euro heart survey on valvular heart disease. *Eur Heart J*., **24**: 1231-1243, 2003.

[3] Yoganathan A., et al.: Fluid mechanics of heart valves. *Annu Rev Biomed Eng*., **6**: 331-362, 2004.

[4] Guivier C., et al.: New insights into the assessment of the prosthetic valve performance in the presence of subaortic stenosis through a fluid-structure interaction model. *J Biomech*, **40**: 2283-2290, 2007.

[5] Dumont K., et al.: Validation of a Fluid–Structure Interaction Model of a Heart Valve using the Dynamic Mesh Method in Fluent. *Comput Method Biomec*., **7**: 139-146, 2004.

[6] De Tullio, M. D., et al. Direct numerical simulation of the pulsatile flow through an aortic bileaflet mechanical heart valve. *Journal of Fluid Mechanics* **622**: 259-290, 2009.

[7] Choi, C. R., et al.: Numerical analysis on the hemodynamics and leaflet dynamics in a bileaflet mechanical heart valve using a fluid-structure interaction method. *ASAIO Journal* **55**.5: 428-437, 2009.

[8] Redaelli A., et al.: 3-D Simulation of the St. Jude medical bileaflet valve opening process: fluid-structure interaction study and experimental validation. *J Heart Valve Dis*., **13**: 804-813, 2004.

[9] Karimi, S., et al.: Effect of rheological models on the hemodynamics within human aorta: CFD study on CT image-based geometry. *J Non-Newton Fluid*, **207**, 42-52, 2014.

[10] Pohl, Manfred, et al.: In Vitro Testing of Artificial Heart Valves: Comparison Between Newtonian and Non-Newtonian Fluids. *Artificial organs* **20**.1: 37-46, 1996.

EFFECT OF THE FLOW REGIME ON FLUTTER IN COLLAPSIBLE TUBES

Julia Zayko*[1], Vladimir Yushutin[2]&Vasily Vedeneev[1]
[1]*Faculty of Mechanics and Mathematics, Lomonosov Moscow State University, Moscow, Russia*
[2]*Institute of Mechanics, Lomonosov Moscow State University, Moscow, Russia*

Summary We study the stability of elastic tubes conveying fluids. An apparatus for investigations of self-exciting oscillations of the elastic Penrose tubes was created. The effect of the flow regime (laminar vs turbulent) on the limit cycle oscillations and the stability boundary is experimentally analyzed. The influence of the fluid viscosity on the limit cycle oscillations is studied. Maps of regimes are obtained.

INTRODUCTION

Self-exciting oscillations of elastic tubes conveying fluid have been extensively studied during last 50 years in the context of biological applications, including blood vessel vibrations [1 – 4]. Although biofluid flows are generally laminar, most experimental studies deal with turbulent flows. In this investigation we find the stability boundary for different regimes, analyze the effect of the flow rate limitation and the influence of the fluid viscosity on these characteristics at the turbulent regimes.

EXPERIMENTAL APPARATUS

The apparatus used is shown in the Fig. 1. An elastic Penrose tube is attached at each end to a rigid tube of the same diameter. The external pressure p_e in the chamber is constant. The fluid flows through the elastic tube under the pressure drop $\Delta p = p_1 - p_2$, where p_1 and p_2 are the upstream and downstream pressures. The pressure drop is changed by the flow rate Q or downstream pressure p_2. The flow rate Q may by controlled by the adjustable resistance and is measured by flowmeter, p_2 may by controlled by the position of draining hose.

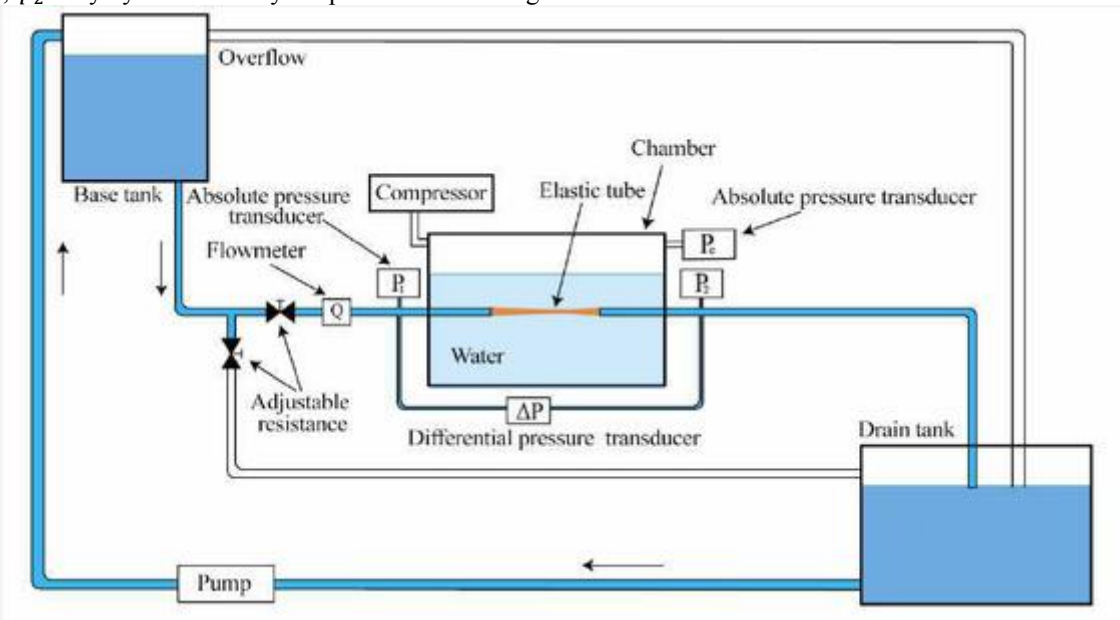

Figure 1: An apparatus for investigations of self-exciting oscillations of elastic tubes conveying fluid.

RESULTS OF EXPERIMENTS

Glycerin solutions of different concentrations and water were used at the experiments. Viscosities of the solutions provided laminar or turbulent flow regimes with the same pressure drops.

The first series of experiments was conducted for fluids with various viscosities corresponding to turbulent regimes. Reynolds number based on the Penrose tube diameter was varied in the range 2500<Re<16000. Results showed that the stability boundary and the character of limit cycle oscillations do not significantly depend on the fluid viscosity. This is explained by the fact that the molecular viscosity is negligible compared to the turbulent viscosity. When the stability was lost while keeping $p_1 - p_e$ constant and increasing $\Delta p = p_1 - p_2$, the tube first oscillates in the following manner: two

*Corresponding author. Email:juliazaiko@yandex.ru.

collapses followed by a delay in the stable state, then again two collapses, etc. For higher Δp, the tube collapsed three times followed by a delay; then four, five, and up to eleven times. As a rule, for higher Δp single-frequency oscillations were finally established and locked the tube, i.e. neither frequency nor flow rate are changed when Δp is increased more. The map of the regimes is shown in the Fig. 2a. In all the regimes the frequency representing consecutive collapses was not changed much when changing Δp.

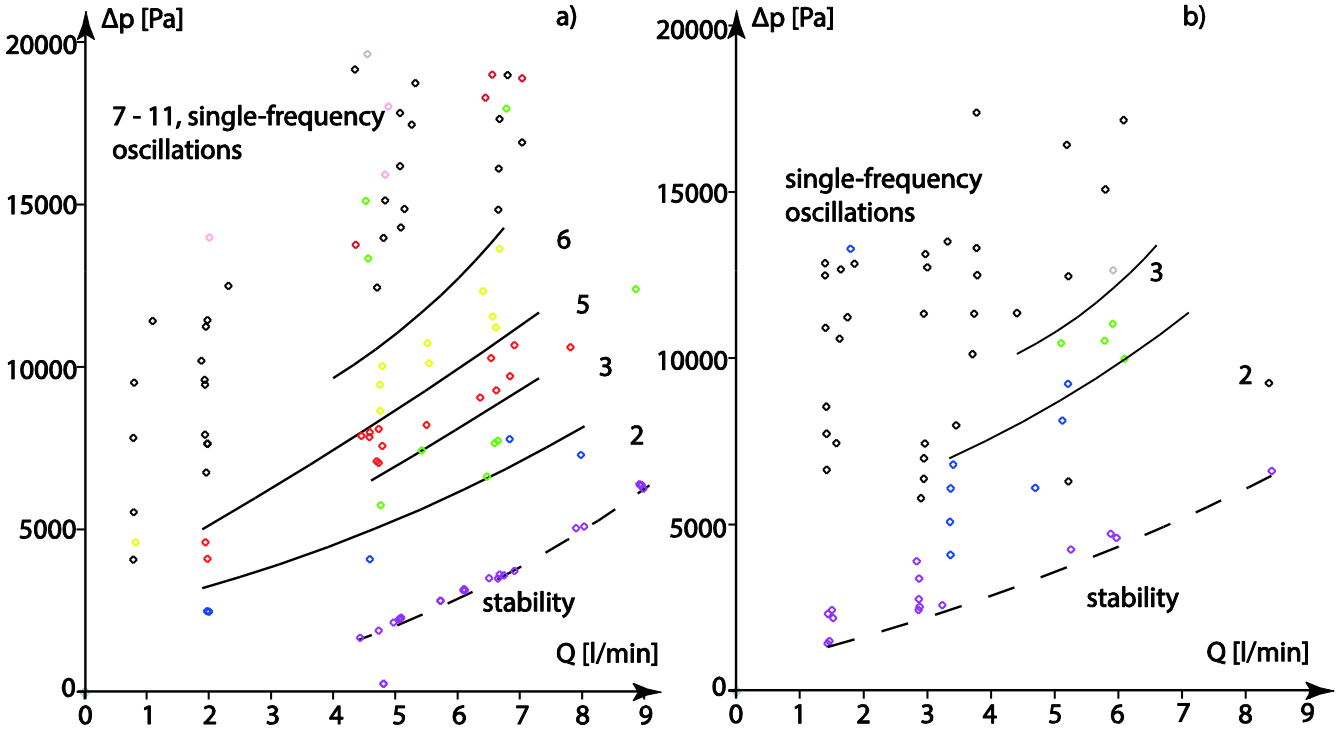

Figure 2: Map of the limit cycle oscillations for turbulent (a) and laminar (b) flow regimes. Number of consecutive tube collapses followed by a delay for each limit cycle type is marked by number and color. Dashed lines show the stability boundaries.

At the second series of tests a more viscous glycerine solution was used, which provides laminar flow at the unstable regimes with 100<Re<1000 with similar pressure drop along the Penrose tube. Unstable behaviour is quite different. For most flow rates, single-frequency oscillations developed almost immediately after the loss of stability (Fig. 2b). When increasing Δp, the regime does not change.

Oscillation amplitude at the laminar regime is essentially lower than at turbulent, so that the oscillations do not fully block the tube, that is why the oscillation frequency is more significantly affected by the pressure drop than at turbulent regimes.

The work is supported by grant MD-4544.2015.1.

References

[1] C.D. Bertram, C.J. Raymond, T.J. Pedley. Mapping of instabilities for flow through collapsed tubes of different length. Journal of Fluids and Structures. 1990. 4. P. 125 – 153.

[2] C.D. Bertram, J. Tscherry. The onset of flow-rate limitation and flow-induced oscillations in collapsible tubes. Journal of Fluids and Structures. 2006. 22. P. 1029 – 1045.

[3] James B. Grotberg, Oliver E. Jensen. Biofluid mechanics in flexible tubes. Annu. Rev. Fluid Mech. 2004. 36. P. 121 – 147.

[4] T.J. Pedley, X.Y. Luo. Modelling flow and oscillations in collapsible tubes. Theoret. Comput. Fluid Dynamics. 1998. 10. P. 277 – 294.

FM02 - Boundary Layers

TS.FM02-1.01	Morrison, Jonathan - The inertial subrange in turbulent pipe flow (INVITED)	480
TS.FM02-1.02	Tardu, Sedat - Fine structure of near wall dissipation	482
TS.FM02-1.03	Monkewitz, Peter - How comparable are the three “canonical” turbulent flows?	484
TS.FM02-1.04	De Giovanetti, Matteo - Skin friction generation by attached eddies in a turbulent channel	486
TS.FM02-1.05	Diaz Daniel, Carlos - A conceptual model for the filtered wall-shear stress statistics in turbulent boundary layers	488
TS.FM02-1.06	Byers, Clayton - Turbulent temperature measurements in water	490
TS.FM02-2.01	Bretheim, Joel - A restricted nonlinear large-eddy simulation model for wall-bounded turbulence	492
TS.FM02-2.02	Rosenberg, Kevin - Data-driven optimization of forcing in the resolvent analysis of wall turbulence	494
TS.FM02-2.03	Lee, Jin - Turbulent/non-turbulent Interface in Transitional and Turbulent Boundary Layers	496
TS.FM02-2.04	Saxton-Fox, Theresa - Scale interactions and 3D critical layers in wall-bounded turbulent flows	498
TS.FM02-2.05	Chini, Greg - Coupled uniform momentum zones and internal layers in turbulent wall flows	500
TS.FM02-2.06	Han, Guowen - Experimental investigation of space-time correlation in the atmospheric surface layer	502
TS.FM02-3.01	Flack, Karen - Prediction of frictional drag in the transitionally rough regime (INVITED)	504
TS.FM02-3.02	Pathikonda, Gokul - Inner-Outer Interactions in a Turbulent Boundary Layer Overlying Complex Roughness	506
TS.FM02-3.03	Klaas, Michael - Frequency dependence of drag reduction in a wavy surface turbulent boundary layer	508
TS.FM02-3.04	Maciel, Yvan - Sweeps and ejections in ZPG and strong APG turbulent boundary layers	510
TS.FM02-3.05	Örlü, Ramis - History effects in adverse pressure gradient turbulent boundary layers	512
TS.FM02-3.06	Le Floch, Arnaud - Effect of boundary-layer superstructures on separation bubble unsteadiness	514
TS.FM02-4.01	Reed, Helen - Hypersonic boundary layer instabilities (INVITED)	516
TS.FM02-4.02	Wu, Xuesong - Response and receptivity of a hypersonic boundary layer to free-stream disturbances	518
TS.FM02-4.03	Paredes, Pedro - Interaction of supersonic boundary layer instabilities with stationary streamwise streaks	520
TS.FM02-4.04	Marensi, Elena - Effect of medium-intensity free-stream vorticity on a compressible boundary layer	522
TS.FM02-4.05	Bodony, Daniel - Instability and Transition of a Mach 5.8 ZPGBL Over a Thermomechanically Compliant Panel	524
TS.FM02-4.06	Denier, Jim - The post-collisional boundary layer on an impulsively rotated sphere	526
TS.FM02-5.01	Gaster, Michael - Boundary layer transition initiated by a random excitation	528
TS.FM02-5.02	Walton, Andrew - Localized self-sustaining processes in the asymptotic suction	530

	boundary layer	
TS.FM02-5.03	Mao, Xuerui - Nonlinear optimal streaks induced by free-stream disturbances in flow over a thin flat plate	532
TS.FM02-5.04	Wang, Zhefu - Control of crossflow instability using plasma actuators	534
TS.FM02-5.05	White, Christopher - Transition to turbulence in reciprocating channel flow	536
TS.FM02-5.06	Munsi, Monalisa - Magnetohydrodynamic flow in channels with cross-channel pressure interaction	538
TS.FM02-6.01	Ruban, Anatoly - Viscous-inviscid interaction and boundary-layer separation in transonic flows (INVITED)	540
TS.FM02-6.02	Cassel, Kevin - Unsteady boundary-layer separation at finite and infinite Reynolds numbers	542
TS.FM02-6.03	Vétel, Jérôme - Investigation of fixed and moving separation in a viscous flow	544
TS.FM02-6.04	Braun, Stefan - On the Triple Deck Stage of Marginally Separated Flows	546
TS.FM02-6.05	Ben-Gida, Hadar - Leading-edge vortices as a high-lift mechanism for large aspect ratio wings	548
TS.FM02-6.06	Choi, Kwing-So - Leading edge separation control with DBD plasma actuators	550
PO.FM02-1.01.67	Azanov, Georgii - The Efficiency of One Method of Machineless Energy Stratification in a Gas Flow	552
PO.FM02-1.02.68	Bernots, Tomass - Boundary layer receptivity to acoustic noise in transonic flows	554
PO.FM02-1.03.69	Chamorro, Leonardo - On the turbulence dynamics over geophysical-scale topography	556
PO.FM02-1.04.70	Chimetta, Henrique - Experiments on a closed-conduit flow perturbed by a two-dimensional hill of low aspect ratio	558
PO.FM02-1.05.71	Couliou, Marie - Experimental study of interactions between turbulent structures and poro-elastic surfaces	560
PO.FM02-1.06.72	Cui, Kai - Study of shock wave/boundary layer interactions on high-pressure capturing wings	562
PO.FM02-1.07.73	Dong, Ming - Effects of local suction on boundary-layer instability and acoustic radiation	564
PO.FM02-1.08.74	Fang, Yihong - Analysis of mach radiation in an axisymmetric supersonic jet	566
PO.FM02-1.09.75	Han, Yufeng - Non-parallel effects on mode characteristics in hypersonic boundary layers	568
PO.FM02-1.10.76	Hutchinson, Ashleigh - A new model for the two-fluid laminar classical wake	570
PO.FM02-1.11.77	Jing, Zhenrong - Effect of crossflow vortex on TS wave in a Falkner-Skan-Cooke boundary layer	572
PO.FM02-1.12.78	Liu, Jianxin - Multiple families of solutions of secondary instabilities in hypersonic flows	574
PO.FM02-1.13.79	Su, Caihong - Tentative explanation of the mechanism of noise reduction for trailing edge with chevron	576
PO.FM02-1.14.80	Xu, Hui - Effect of a 3D surface indentation on boundary layer stability	578
PO.FM02-1.15.81	Zhang, Chi - Reynolds-number universality of quasi-steady quasi-homogeneous theory	579
PO.FM02-1.16.82	Zhang, Cunbo - Nonlinear interaction of the first mode with the second mode	581

THE INERTIAL SUBRANGE IN TURBULENT PIPE FLOW

Jonathan Morrison*[1], Margit Vallikivi [2], and Alexander Smits[3]
[1]*Department of Aeronautics, Imperial College, London*
[2]*GE Global Research turbomachinery, Garching b., Munich*
[3]*MAE, Princeton University; Department of Mechanical & Aerospace Engineering, Monash University*

Summary A dual space-spectral description of energy flux is presented for the axial velocity component at the centreline and in the log region of turbulent pipe flow at large Re_λ.

OUTLINE

We have previously examined[1] the inertial subrange scaling of the axial velocity component for the centreline of turbulent pipe flow for Reynolds numbers in the range $249 \leq Re_\lambda \leq 986$, where λ is the Taylor length scale. Measurements were performed in the Princeton/ONR Superpipe using NSTAP probes of length, $\ell = 30$ μm or 60 μm, with temporal resolution up to 300 kHz. Estimates of the dissipation rate, ϵ, are made by both integration of the one-dimensional dissipation spectra and the third-order moment of the structure function, where the separation $r = -U\delta t$. Figure 1 shows A plotted as a function of Re_λ, where $\epsilon = v_\epsilon^3/\eta = Au_\tau^3/R$. In the case of the "$4/5$ths" law, the estimate of ϵ is taken to be the maximum over a range of r/η — this is made necessary by the nature of the third-order moments which do not show a pronounced plateau.

It is noticeable that neither dissipation estimate provides values of A that asymptote to a constant: rather A increases almost linearly with Re_λ. The ordinate is proportional to ϵ: therefore the increase in A at higher Reynolds numbers cannot be attributed to poor spatial resolution. Furthermore, there is a remarkable consistency between estimates of A using the 30 μm and 60 μm probes. Hence this scaling does not fully account for the effects of the outer boundary condition. This important result is not the same as that shown, for example, by [2], in which the influence of the large scales appears as $C_\epsilon \equiv A$ **decreasing** with Re_λ. Both viscous and turbulent transport at the centreline contribute to a non-conservative spectral flux, the effect of which is clearly evident in both the corresponding spectra and in the dimensionless dissipation rate. Turbulent transport is clearly the dominant mechanism in determining global effects on spectral flux, where the principal effects of the boundary conditions appear through finite turbulent transport which constitutes a source or a sink at each wavenumber. Moreover, these effects cannot be described well by Kolmogorov's "extended similarity hypothesis", K62, in which the dissipation rate retains its self-similar form.

In this paper, we extend the analysis to examine the scaling of the inertial subrange in the local-equilibrium region, $y/R = 0.052$. With the assumption of "wall" (u_τ, y) scaling, we expect the log-law and local-equilibrium regions to be approximately coincident. With the assumption of local equilibrium, and using the momentum equation,

$$-\overline{uv}^+ = 1 - \frac{y}{R} - \frac{1}{\kappa y^+}, \tag{1}$$

we estimate the dissipation rate as $\epsilon^+ = (-\overline{uv}^+)/\kappa y^+$. However, the spectral flux is much more spatially intermittent than either the production or dissipation spectra, and since the energy balance at any point in space is an integration over all wavenumbers, local equilibrium will only ever be an approximation. Figure 2 shows that A in the local-equilibrium region is closer to a constant value than at the centreline over a similar range of Re_λ. This could be attributed to the fact that the turbulent transport in the local-equilibrium region is a somewhat smaller fraction of production and dissipation there. Estimates of dissipation rates are compared with locally-isotropic estimates available from integration of the one-dimensional dissipation spectra and the "$4/5$ths" law.

References

[1] Morrison J. F., Vallikivi M. and Smits A. J.: The inertial subrange in turbulent pipe flow: centreline. J. Fluid Mech 788:602-613, 2016.
[2] Sreenivasan, K. R.: On the universality of the Kolmogorov constant. Phys. Fluids 7, 27782784, 1995.

*Corresponding author. Email: j.morrison@imperial.ac.uk

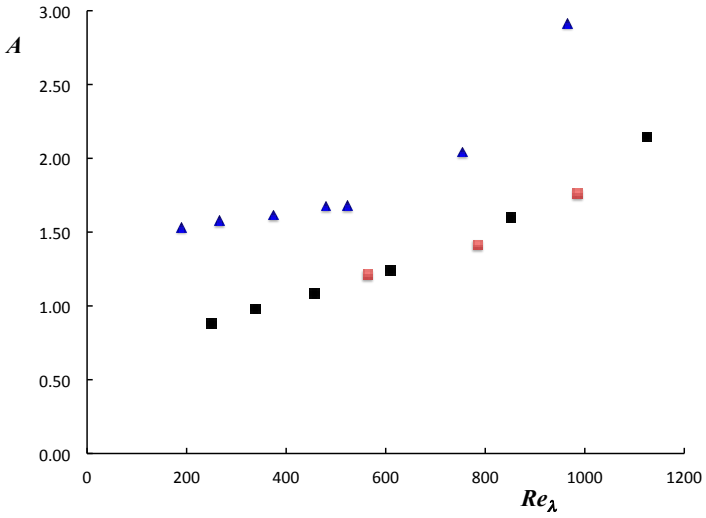

Figure 1: Nondimensional dissipation rate at centreline, $A = \epsilon R/u_\tau^3$. ▲, isotropic estimate; ■, "$4/5$ths" law.

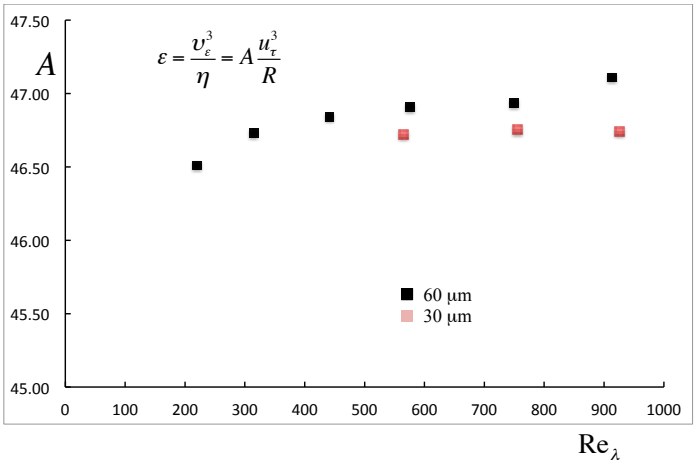

Figure 2: Nondimensional dissipation rate at $y/R = 0.052$, $A = \epsilon R/u_\tau^3$.

FINE STRUCTURE OF NEAR WALL DISSIPATION

Sedat Tardu[a)]
Laboratoire des Ecoulements Géophysiques et Industriels, Grenoble Alpes University, France

Summary Direct numerical simulations of a turbulent channel flow performed in large computational domains up to the Karman number 1100 are analyzed in order to clarify the near wall behaviour of the dissipation. It is shown that the axisymmetric homogeneous distribution predicts well the dissipation in the whole layer, and that the local isotropy is only valid towards the end of the log-layer. The dissipation characteristics conditioned by fixed amplitudes of the velocity fluctuations show that the level-crossings of the wall normal velocity in the spanwise direction contribute most significantly to the dissipation next to the wall.

INTRODUCTION

Zero-crossings of fluctuating velocity time series provide a simple way to access to Taylor scales in wall-bounded flows (see Kailasnath & Sreenivasan [1] and references within). Experiments have shown that the time scale related to the velocity zero-crossings (the Liepmann scale) is roughly equal to the Taylor scale in wall-bounded flows. We revisit the problem here by considering the zero-crossings of fluctuating velocity fields in space, at a given time. Direct numerical simulations (DNS) performed in large computational domains of a turbulent channel flow up to the Karman number of 1100 are used for this purpose (Bauer et al., [2]; Tardu [3]). The fine characteristics of the dissipation are further analyzed by investigating the related statistics at fixed amplitudes of the velocity fluctuations.

RESULTS

Fig. 1 shows the distribution of the mean dissipation $\bar{\varepsilon} = \nu \overline{u_{i,j}\left(u_{i,j} + u_{j,i}\right)}$, (where $u_{i,j} = \partial u_i / \partial x_j$) versus the wall normal distance in wall units at four Karman numbers $Re_\tau = h\bar{u}_\tau / \nu$ in the range 180 to 1100 (wall units are the shear velocity $\bar{u}_\tau$ and the viscosity ν; h is the half channel width). It is seen that the Reynolds number dependence are particularly significant below the low buffer layer in agreement with [4]. We will first show that the axisymmetric homogeneous distributions (form 2) proposed by George&Hussein [5] provide a good approximation to the dissipation at all the Reynolds numbers across the whole layer, in agreement with the earlier analysis of Antonia et al. [6] performed at lower Reynolds numbers. The local isotropy is never exactly reached but can be supposed to approximately hold only towards the end of the log-layer (precisely at wall distances larger than 300 wall units (wall units are the shear velocity $\bar{u}_\tau$ and the viscosity ν). The Taylors and Liepmann scales collapse also well at all the Reynolds numbers.

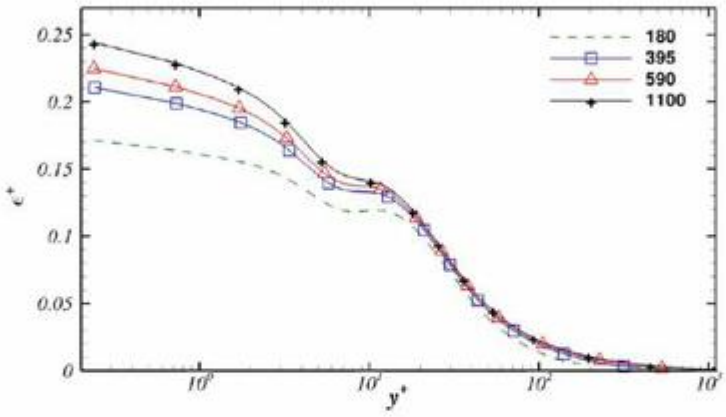

Figure 1 Mean dissipation versus the wall normal distance in wall units.

The data is further analyzed by exploring the dissipation characteristics for fixed amplitudes of fluctuating velocity components in the same way as in [3] and [7]. It has been argued for a while that the zero-crossings of the streamwise velocity fluctuations should largely contribute to the dissipation [1]. That the zero-crossing frequency of u is related to

[a)] Corresponding author. Email: Sedat.Tardu@legi.grenoble-inp.fr.

$\overline{(\partial u/\partial x)^2}$, does obviously not imply that the dissipation is locally important during the zero-crossings, and this point has not been entirely elucidated. Furthermore, there is no reason for u zero crossings to mostly contribute to ε near the wall. One has to be careful in determining the statistics conditioned by level crossings of a stochastic signal. Using a suitably defined Dirac function at the $\ell\sigma_{u_i}$ level crossings, where σ_{u_i} is the rms of u_i, it can be rigorously shown that the ensemble-averaged dissipation $\overline{\varepsilon}_\ell$ conditioned by level crossings is the normalized mean of the dissipation times the absolute velocity derivative along the assigned direction, and not simply the ensemble averaged dissipation when the level-crossings occur (for details see Tardu&Bauer, [7]). In return, the correct definition of the contribution c_ε of the level crossings to the dissipation poses no particular problems. Fig. 2 shows the distribution of c_ε at the zero-crossings of the streamwise u, wall normal v and spanwise w velocity components versus the wall normal distance in wall units y^+. Contrarily to what has been suggested before, the zero crossings of the *wall normal velocity* v (predominantly in in the *spanwise* direction z *contribute mostly to the dissipation* instead of longitudinal x crossings of the streamwise velocity u [1]. It is seen in Fig. 2 that in the viscous sublayer wherein the dissipation reaches its maximum and where the Reynolds number dependences are much prominent, the contribution of the spanwise zero crossings of v is about 30 %, while the contribution of u hardly exceeds 5 %.

One of the most striking results we obtained concerns the mean dissipation conditioned by fixed amplitudes of the spanwise velocity fluctuations w. The mean dissipation condition by fixed w is remarkably constant beyond the viscous sublayer independently of the threshold ℓ. This last result indicates different roads to model the dissipation in wall bounded turbulent flows, as it will be discussed in detail during the talk.

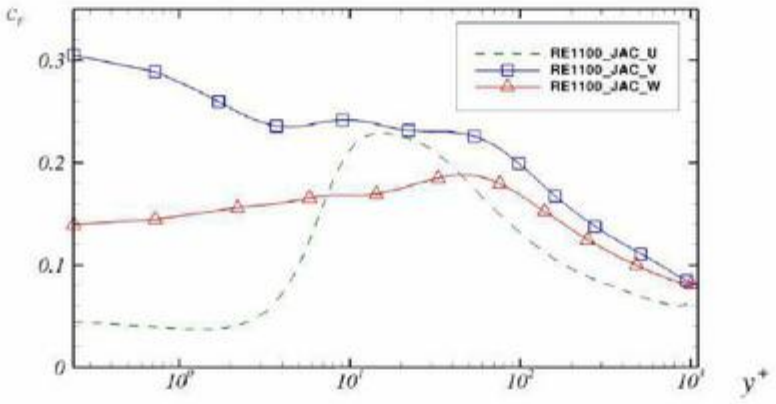

Figure 2 Contribution to the dissipation of the zero-crossings of fluctuating velocity components at $Re_\tau = 1100$.

References

[1] Kailasnath P., Sreenivasan K.R., Phys. Fluids, A5(11), 2879, 1993.
[2] Bauer F., Tardu S, Doche O., Computers and Fluids, 107, 123, 2015.
[3] Tardu S., Phys. Fluids, 28, 015108, 2016.
[4] Hoyas S., Jiménez, Phys. Fluids, 20, 101511, 2008.
[5] George W.K., Hussein J.H., J. Fluid Mech., 233, 1, 1991
[6] Antonia R.A., Kim J., Browne L.W.B., J. Fluid Mech., 233, 369, 1991
[7] Tardu S., F. Bauer, J. Turbulence, 16(9), 2015.

HOW COMPARABLE ARE THE THREE "CANONICAL" TURBULENT FLOWS ?

Peter A. Monkewitz*[1] and Hassan M. Nagib[2]
[1]*Engineering Science, Swiss Federal Institute of Technology, Lausanne, Switzerland*
[2]*Armour College of Engineering, Illinois Institute of Technology, Chicago, USA*

Summary The three canonical turbulent flows, the zero pressure-gradient turbulent boundary layer (abbreviated ZPG TBL), turbulent channel (TCh) and turbulent pipe flow (TP), have often been compared and their similarities analysed. Focussing on the three mean velocity profiles obtained from some of the best available experiments and computations, the consequences of assuming a unique Kármán constant on the large Reynolds number asymptotic expansion of the free stream and the centerline velocities, respectively, are explored.

Introduction

The quest of unifying the description of the three "canonical" wall-bounded turbulent flows, ZPG TBL, TCh and TP, has a long history (see e.g. [1]) and is principally rooted in the belief that at very high Reynolds numbers the near-wall flow becomes independent of the outer flow. Concentrating on the mean velocity profile $U(y)$, this implies that all three inner velocity profiles approach the same logarithmic law $\kappa^{-1}\ln(y^+)+B$, where $y^+\equiv yu_\tau/\nu\to\infty$. This view has been challenged in [2] where different Kármán coefficients κ are derived for the three flows by fitting composite expansions to the complete profiles up to the highest Re data available.

It is nevertheless worthwhile to explore the consequences of assuming that the inner expansions of U^+ in all three flows, in particular the log-law constants κ, are identical. Whatever the log-law-κ's are, the standard asymptotic matching between inner and outer profiles requires that the outer expansions have a leading term equal to $\ln(\mathrm{Re})/\kappa$, with $\mathrm{Re}=\mathrm{Re}_{\delta_*}$, H^+ or R^+. Hence, the outer expansions of all three "canonical" flows must be of the general form

$$U^+ \sim \kappa^{-1}\ln(\mathrm{Re})+\sum_{n=0} f_n(\eta)\,[\ln(\mathrm{Re})]^{-n}+\mathcal{O}(\mathrm{Re})^{-1} \qquad (1)$$

$$\text{with}\quad \eta \equiv y^+/\mathrm{Re}_{\delta_*},\ y/H \text{ or } y/R \quad\text{and}\quad f_0(\eta\to 0)\sim\kappa^{-1}\ln(\eta)+B\,.$$

with the *same* κ as in the respective inner log-laws $\kappa^{-1}\ln(y^+)+B$.

The zero-pressure gradient turbulent boundary layer

The mean velocity data in the ZPG TBL are the most abundant and come from the largest diversity of facilities. Since the advent of independent wall shear stress measurements, most estimates of κ have converged to the interval $[0.38, 0.39]$. In the following we will use $\kappa=0.384$, which has been found in [3], and propose a new outer fit

$$U^+_{\mathrm{out}}(\eta)=\frac{1}{0.384}\ln\left\{3.50\,\mathrm{Re}_{\delta_*}\,\tanh^{1/2}\left[\left(\frac{5.05\,\eta}{3.50}\right)^2\,\frac{1+(10.8\,\eta)^4+(12.7\,\eta)^5+(11.2\,\eta)^8}{1+(12.7\,\eta)^5}\right]\right\} \qquad (2)$$

The quality of this outer fit (2) is evident from figure 1 which shows in particular, that $U^+_\infty=\ln(3.50\,\mathrm{Re}_{\delta_*})/0.384$ with the κ of the log-law. Note also that for the ZPG TBL the $f_n(\eta)$ in (1) appear to be zero for $n\geq 1$ or buried in the experimental scatter.

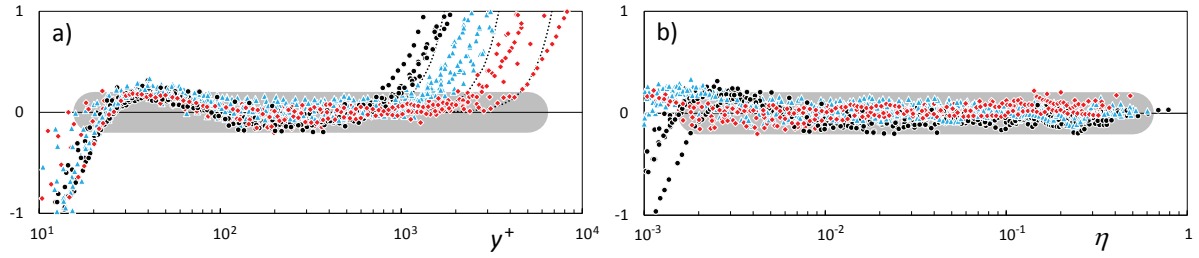

Figure 1: (a) 19 ZPG TBL U^+-profiles used in [4] and 6 profiles of [5] minus the log-law $U^+_{\log}=\ln(5.05\,y^+)/0.384$ corresponding to (2). • (black), $\mathrm{Re}_{\delta_*}\leq 2\times10^4$; ▲ (blue), $2\times10^4<\mathrm{Re}_{\delta_*}\leq 4\times10^4$; ♦ (red), $\mathrm{Re}_{\delta_*}>4\times10^4$. $\cdots$, leading term $(10.6\,\eta)^4$ of the small-η departure from the log-law for $\mathrm{Re}_{\delta_*}=2\times10^4$, 4×10^4 and 7.84×10^4 (last red profile). The grey band indicates deviations of up to ±0.2 from the log-law. (b) Same profiles minus outer expansion (2) versus $\eta=y^+/\mathrm{Re}_{\delta_*}$.

*Corresponding author. Email: peter.monkewitz@epfl.ch

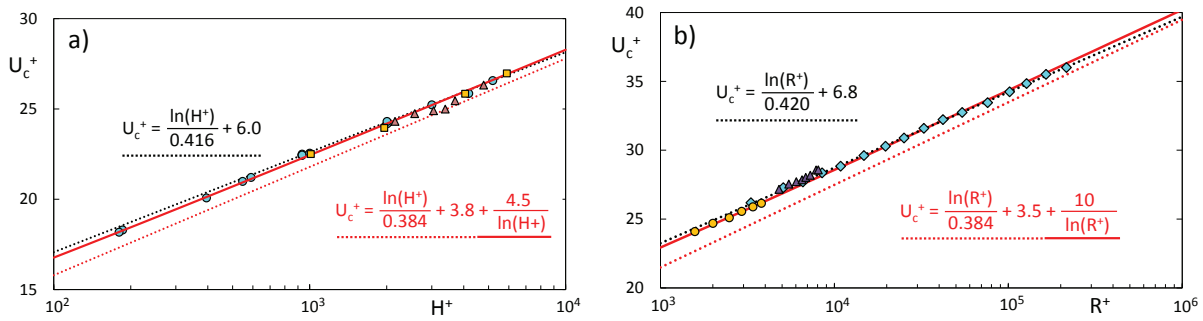

Figure 2: (a) Centerline velocity U_c^+ in turbulent channel flow versus H^+. ∘, CFD data from [6], [7] and [8]; △, experimental data from [9]; □, data from [10]. (b) Centerline velocity U_c^+ in turbulent pipe flow versus R^+. ∘, "superpipe" Pitot data from [4]; △, experimental data from [11]; □, data from [12]. Fits as indicated on the figures.

Centerline velocity in turbulent channel and pipe flows

In channel and pipe flows, the κ_c obtained by fitting the centerline velocity with $U_c^+ = \ln(\mathrm{Re})/\kappa_c + C$ is clearly different from 0.384. As seen in fig. 2a for the channel, $\kappa_c = 0.416$, resulting from the best fit of the CFD data for $H^+ \geq 10^3$, is far from 0.384 and even further from the value deduced in [2]. However, when allowing for a non-zero f_1 in (1) with $f_1(\eta \equiv H^+ = 1) = 4.5$ and $f_1(\eta \to 0) = 0$, the centerline data can be perfectly reconciled (see the solid red line in fig. 1a) with a log-law-κ of 0.384, found in [8], for instance.

For pipe flow, the situation is similar to the channel, as the fit of a simple log-law to the Pitot data in the Princeton "superpipe" yields a $\kappa_c = 0.42$. Again, a three-term asymptotic series (1) with $f_1(\eta \equiv R^+ = 1) = 10$ and $f_1(\eta \to 0) = 0$, shown as solid red line in fig. 1b, fits the data nicely.

Conclusions

In this contribution, we are pointing out the fact that in turbulent channel and pipe flows the κ_c obtained from fitting the centerline velocity U_c^+ is significantly larger than the log-law-κ in [8], [1], etc. and the κ deduced from both log-law and free-stream velocity in the ZPG TBL. This has received very little attention so far, despite the incompatibility of $\kappa_c \neq \kappa$ with the asymptotic matching of inner and outer U^+-expansions across a logarithmic overlap. Here we propose a way out of this dilemma by generalizing the outer expansion to equation (1).

One may think that the dilemma only exists if one believes in a unique log-law-κ dictated by the widely scrutinized TBL data, but the requirement $\kappa_c = \kappa$ remains valid if the log-law-κ's in the three flows are different. As the centerline data in figure 2 are thought to be reliable, at least for TP where there are no issues related to side-walls and span-wise variation of Uc^+ (see e.g. [13]) or span-wise periodicity, the question is whether log-law-κ's of 0.416 and 0.42 are compatible with TC and TP data. Given the history of κ deduced from the "superpipe" data and the limited Reynolds number range of channel/duct data, it appears difficult to settle the question without further theoretical work.

References

[1] Marusic M., Monty J.P., Hultmark M., Smits A.J.: On the logarithmic region in wall turbulence. J. Fluid Mech. 716:R3, 2013.

[2] Nagib H.M., Chauhan K.A.: Variations of von Kármán coefficient in canonical flows. Phys. Fluids 20:101518, 2008.

[3] Monkewitz P.A., Chauhan K.A., Nagib H.M.: Self-consistent high-Reynolds-number asymptotics for zero-pressure-gradient turbulent boundary layers. Phys. Fluids 19:115101, 2007.

[4] Bailey S.C.C., Hultmark M., Monty J.P., Alfredsson P.H., Chong M.S., Duncan R.D., Fransson J.H.M., Hutchins N., Marusic I., McKeon B.J., Nagib H.M., Örlü R., Segalini A., Smits A.J., Vinuesa R.: Obtaining accurate mean velocity measurements in high Reynolds number turbulent boundary layers using Pitot tubes. J. Fluid Mech. 715:642-670, 2013.

[5] Kulandaivelu V.: Evolution and structure of zero pressure gradient turbulent boundary layer. PhD thesis, Univ. Melbourne, 2011.

[6] Lozano-Durán A., Jiménez J.: Effect of the computational domain on direct simulations of turbulent channels up to Re=4200. Phys. Fluids 26:011702, 2014.

[7] Thais L., Mompean G., Gatski T.: Spectral analysis of turbulent viscoelastic and Newtonian channel flows. J. of Non-Newtonian Fluid Mech. 200:165-176, 2013.

[8] Lee M., Moser R.D.: Direct numerical simulation of turbulent channel flow up to Re_τ = 5200. J. Fluid Mech. 774:395-415, 2015.

[9] Zanoun E.-S., Durst F., Nagib H.: Evaluating the law of the wall in two-dimensional fully developed turbulent channel flows. Phys. Fluids 15:3079-3089, 2003.

[10] Schultz M.P., Flack K.A.: Reynolds-number scaling of turbulent channel flow. Phys. Fluids 25:025104, 2013.

[11] Zanoun E.-S., Durst F., Bayoumy O., Al-Salaymeh A.: Wall skin friction and mean velocity profiles of fully developed turbulent pipe flows. Exp. Thermal Fluid Sci. 32:249-261, 2007.

[12] Perry A.E., Abell C.J.: Asymptotic similarity of turbulence structures in smooth- and rough-walled pipes. J. Fluid Mech. 79:785-799, 1977.

[13] Vinuesa R., Schlatter Ph., Nagib H.M.: On minimum aspect ratio for experimental duct-flow facilities. J. Turb. 16:588-606, 2015.

SKIN FRICTION GENERATION BY ATTACHED EDDIES IN A TURBULENT CHANNEL

Matteo de Giovanetti *[1], Yongyun Hwang[1], and Haecheon Choi[2]
[1]*Department of Aeronautics, Imperial College London, United Kingdom*
[2]*Department of Mechanical & Aerospace Engineering, Seoul National University, South Korea*

Summary The role of different scales in skin friction generation is investigated in a turbulent channel, at moderately high Reynolds numbers. Three different methods are used: the FIK identity, and two sets of LESs using minimal boxes and selective flow damping respectively. We show that the self-similar coherent motions in the form of Townsend's attached eddies in the logarithmic layer are the dominant contributors to wall shear stress at sufficiently high Reynolds numbers, whereas the near-wall and outer coherent structures are of limited importance.

INTRODUCTION

Background

The near-wall region has often been understood as the largest contributor to wall shear stress. At low Reynolds number, coherent structures in this region have been shown to dictate drag production with the major role played by the streamwise-aligned vortices [1]. However, for the last decade, the measurements at high Reynolds numbers significantly challenged this early view, revealing the significance of the regions above the near-wall region. Indeed, the structures in the logarithmic and outer regions have been shown to be very energetic and to influence the near-wall region with significant generation of turbulent skin-friction drag [2, 3]. Furthermore, a growing body of very recent evidence suggests that the coherent structures in wall-bounded turbulent flows are organized in a hierarchical form throughout the entire wall-normal layers with a self-similar energy-carrying eddy entity, as in the attached eddy hypothesis by Townsend [4, 5]. It is, however, almost completely unknown how these self-similar structures (i.e. attached eddies), populating mainly the logarithmic region, are involved in turbulent momentum transport, particularly, to the wall (i.e. turbulent skin-friction generation). The purpose of this study is to explore this issue by quantifying turbulent skin-friction generation by these structures at moderately high Reynolds numbers.

Methodology

Based on recent finding that the size of the attached eddies is characterized by the spanwise length scale [5], in this study, we introduce three approaches in order to quantify turbulent skin-friction generation by the motions, the spanwise size of which λ_z is smaller than a given cut-off wavelength $\lambda_{z,c}$: 1) the FIK identity [6] combined with the spanwise wavenumber spectra from existing DNS database [7]; 2) selective damping of the motions at $\lambda_z > \lambda_{z,c}$ in a sufficiently large computational domain; 3) 'minimal-box' simulation, which means that the motions, and relative coherent structures, at $\lambda_z > \lambda_{z,c}$ are physically limited by the spanwise size L_z such that $\lambda_{z,c} = L_z$ [8] ('minimal' is here used with this particular implication). For the latter two approaches, a set of near-wall resolved large-eddy simulations are performed in a turbulent channel of the half height h with the Vreman model. The simulations have been carefully validated with the existing DNS database at the bulk Reynolds numbers varying from $Re_m = 38 \times 10^3$ to $Re_m = 193 \times 10^3$, resulting in the friction Reynolds numbers from $Re_\tau \simeq 1000$ to $Re_\tau \simeq 4000$.

RESULTS

Figure 1 shows that variation of the skin friction coefficient C_f with the cut-off spanwise wavelength $\lambda_{z,c}$ obtained with the three approaches introduced. Note that, in turbulent channel flow, the spanwise wavelength of the outer structures, namely very-large-scale and large-scale motions, is $\lambda_z \simeq 1.5h$ [5]. All the three different approaches clearly show drastic decrease of C_f on decreasing $\lambda_{z,c}$. The drop in C_f is particularly severe for $\lambda_{z,c}/h < 1$. The spanwise size of the self-similar coherent motions in the logarithmic region is given in the range of $0.05 < \lambda_z/h < 1.5$ at this Re: this suggests that the largest amount of turbulent skin-friction generation comes from the self-similar coherent motions, which belong to the logarithmic region given their length scale. We also mention that the FIK-identity-based approach, which applies only to the relevant portion of the λ_z spectra, exhibits remarkable discrepancy from the other two approaches which artificially remove the motions at $\lambda_z > \lambda_{z,c}$. This implies that the remainder of the flow is affected by the removal of the motions at $\lambda_z > \lambda_{z,c}$ and it undergoes non-negligible changes that partially recover the lost skin friction. Inspection of the spectra (not shown) revealed that this is due to the lack of proper scale interaction of the motions near the cutoff wavelength $\lambda_{z,c}$ (i.e. the largest permitted structures in the given flow) with the removed motions, resulting in a non-negligible amount of Reynolds-stress generation in the wall-normal location supposed to be emptied by the removal. We also underline that the statistics and C_f, obtained based on selective damping and minimal boxes, show remarkable agreement, meaning that the manner of the removal has little effect on the flow and skin friction.

*Corresponding author. Email: m.de-giovanetti14@imperial.ac.uk

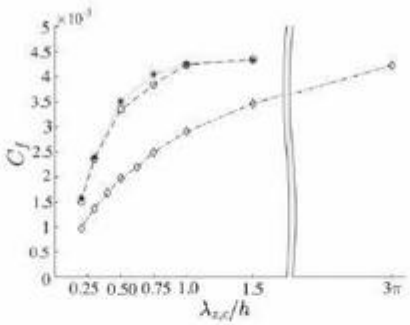

Figure 1: Variation of C_f on the cut-off spanwise wavelength $\lambda_{z,c}$ at $Re_\tau \approx 2000$: $\diamond$, FIK; $\circ$, selective damping; $*$, minimal boxes.

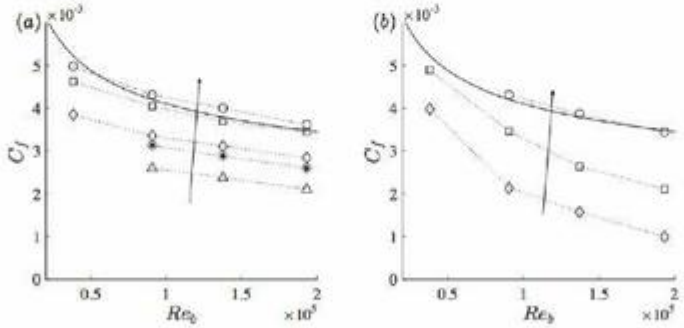

Figure 2: Dependence of C_f on Re_b with minimal-box approach (i.e. $\lambda_{z,c} = L_z$): (*a*) $L_z/h = 0.25, 0.4, 0.5, 0.75, 1.5$; (*b*) $L_z^+ \approx 400, 1000, 3000$. Solid line shows the empirical fit by Dean, $C_f = 0.073 Re_m^{-0.25}$. Arrows represent increasing values of L_z and L_z^+.

The relative contributions of the motions at $\lambda_z < \lambda_{z,c}$ to C_f on increasing Re_m are shown in figure 2 using the minimal-box approach (i.e. $\lambda_{z,c} = L_z$). The lines in figure 2(*a*) indicate C_f when L_z is chosen to be scaled with the outer unit. On the other hand, those in figure 2(*b*) are C_f when L_z is scaled with the inner unit. Figure 2(*a*) suggests that the relative contribution of the motions at $\lambda_z > L_z$ is almost unchanged with Re_m when L_z is scaled in the outer unit. In contrast, the relative contribution of the motions at $\lambda_z > L_z$ decays with Re, when L_z is scaled in the inner unit (figure 2*b*). This implies that the motions, the size of which are larger than a certain outer length scale, generate the almost same relative contribution, whereas those smaller than a certain inner length scale progressively reduce their importance on growing Re. This trend implies an increasing contribution of the self-similar motions in the logarithmic layer to total turbulent skin-friction drag with Re, thereby dominating in overall skin-friction generation at sufficiently high Re. It is worth noting that outer structures at $\lambda_z > 1h$ are found to bear only a small amount of drag (figures 1 and 2), indicating that their removal would be only marginally beneficial.

CONCLUSIONS

Turbulent skin-friction generation by the motions at different length scale has been quantified by taking three independent approaches in the range of Re_τ from 1000 to 4000. All the three approaches indicate that turbulent skin friction at sufficiently high Reynolds numbers is collectively generated by the self-similar coherent motions given in the form of Townsend's attached eddies in the logarithmic region. This finding may explain the failure of many drag-reducing techniques, targeting the near-wall motions, at moderate and high Re.

References

[1] Choi, H., Moin, P. & Kim, J. Active turbulence control for drag reduction in wall- bounded flows. J. Fluid Mech. 262:75-110, 1994.

[2] Mathis, R., Hutchins, N. & Marusic, I. Large-scale amplitude modulation of the small-scale structures in turbulent boundary layers. J. Fluid Mech. 628-311:337, 2009.

[3] Hwang Y.: Near-wall turbulent fluctuations in the absence of wide outer motions. J. Fluid Mech. 723:264-288, 2013.

[4] Townsend, A. A. The structure of turbulent shear flow, 1st edn. Cambridge University Press, 1976.

[5] Hwang, Y. Statistical structure of self-sustaining attached eddies in turbulent channel flow. J. Fluid Mech. 767:254-289, 2015.

[6] Fukagata, K., Iwamoto, K. & Kasagi, N. Contribution of Reynolds stress distribution to the skin friction in wall-bounded flows. Phys. Fluids 14(11), 13-17, 2002.

[7] Hoyas, S. & Jiménez, J. Scaling of the velocity fluctuations in turbulent channels up to $Re_\tau = 2003$. Phys. Fluids 18(1), 1-4, 2006.

[8] Hwang, Y. & Cossu, C. Self-sustained processes in the logarithmic layer of turbulent channel flows. Phys. Fluids 23(6), 061702, 2011.

A CONCEPTUAL MODEL FOR THE FILTERED WALL-SHEAR STRESS STATISTICS IN TURBULENT BOUNDARY LAYERS

Carlos Diaz Daniel *, Sylvain Laizet, and Christos Vassilicos
Department of Aeronautics, Imperial College London, United Kingdom

Summary We present near-wall results from zero-pressure gradient boundary layer DNS, at Reynolds numbers up to $Re_\theta = 2000$ based on momentum thickness θ and free-stream velocity U_∞. Statistics and probability distributions of fluctuating skin friction suggest increasing standard deviation and higher moments with increasing Re_θ. An algebraic correlation for wall dissipation is proposed, fitting current and previous data. The wall-shear stress angle appears correlated with the streamwise vortex structures which are responsible for rare negative shear stress events. A conceptual model is presented, relating statistics of filtered skin friction fluctuations with velocity structure function in $\delta_\nu \ll y \ll \delta$ (δ_ν and δ are wall viscous length and boundary layer thickness). According to the model, the fluctuating shear stress influences velocity spectra in the Townsend-Perry attached-eddy range $1/\delta < k < 1/y$, inducing a higher slope than the classical result $E(k) \propto k^{-1}$.

INTRODUCTION

Estimating wall-shear stress fluctuations in turbulent boundary layers is very important, as they play a fundamental role in noise and drag generation in wall bounded flows. Accurate numerical studies are especially useful, since experiments usually have limited resolution to measure skin friction fluctuations, due to wall thermal effects on hot-wire and hot-film probes. Moreover, understanding the dynamics of wall shear stress is also very interesting from a fundamental point of view, since it is linked to velocity fluctuations along the boundary layer by attached eddies, as explained by the model of Townsend-Perry [5]. A comprehensive computational study of shear stress fluctuations is summarised here, confirming an empirical correlation for wall dissipation with Reynolds number and presenting an algebraic model relation between skin friction and velocity statistics, in order to account for the fluctuating skin friction in the classical theory of Townsend-Perry.

Computational method

Results have been obtained from a high resolution Direct Numerical Simulation of a zero-pressure gradient boundary layer. The computational solver is Incompact3d [1], a 6th-order finite difference code, with a spectral treatment for the pressure equation and a semi-implicit time advancement for the viscous terms. The simulation has been performed with $4097 \times 513 \times 256$ cells, and size $480 \times 40 \times 15$ $\delta_{99,0}$, based on boundary layer thickness at the inlet. The computational domain is only stretched in the wall normal direction and the resolution, in wall viscous units (at $Re_\theta = \theta U_\infty/\nu = 1470$, based on the momentum thickness θ and free-stream velocity U_∞), is: $\Delta x^+ = 10.2$, $\Delta z^+ = 5.1$, $\Delta y^+ = 0.42$ at the wall and $\Delta y^+ = 108.8$ at the top of the domain. Periodic boundary conditions are specified in the spanwise direction and a homogeneous Neumann condition is imposed at the top boundary. The Reynolds number range of the simulation, based on momentum thickness, is $Re_\theta = 270 - 2100$. A laminar Blasius profile is prescribed at the inlet and transition to turbulent state is triggered, $15\delta_{99,0}$ downstream, via a random-forcing method as in [2]. After an initial period of $T \approx 2000\delta_{99,0}/U_\infty$ mean quantities and statistics have been averaged over $T = 3000\delta_{99,0}/U_\infty$ ($T^+ = 11000$).

RESULTS

The standard deviation dependence on Re_τ of both streamwise and spanwise shear stress fluctuations fits a logarithmic trend (as in [2]), and this can be used to formulate an empirical correlation for the wall dissipation dependence. The proposed correlation is in good agreement not only with current simulation results but also with other published numerical data (Figure 1). The Reynolds dependence of τ_x must come from the influence of large scale wall-attached eddies, and Townsend-Perry theory predicts that turbulence kinetic energy in the inertial region also increases logarithmically with Re_τ. This correlation can be important, for instance, in turbulence modelling, since it allows to extrapolate the wall dissipation value for Reynolds numbers at which DNS simulations do not exist.

The p.d.f. of streamwise shear stress follows a quasi log-normal distribution but there are extreme events with negative values for τ_x. The instantaneous shear stress vector $\boldsymbol{\tau} = \{\tau_x, \tau_z\}$ forms an angle with the x direction which follows a symmetric, high kurtosis distribution. The probability of events with $\pm 90^\circ$ angle is much higher than greater angle events, showing that the negative τ_x events correspond to high values of spanwise shear stress τ_z. The spatial location of turbulence structures alongside angle contours (Figure 3) suggests a correlation between the near wall quasi-streamwise vortices and the high values of the shear stress angle, and both often come in opposite pairs.

*Corresponding author. Email: c.diaz-daniel13@imperial.ac.uk

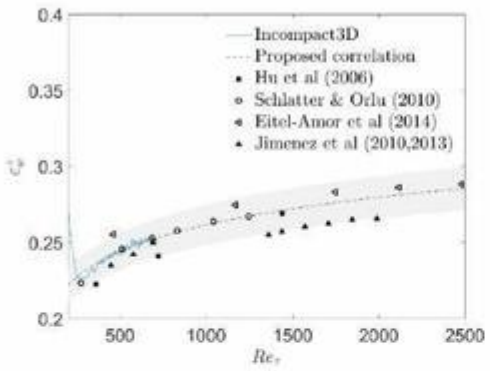

Figure 1: Empirical correlation for dissipation rate along different simulation data. Shadowed region represents an error of $\pm 5\%$.

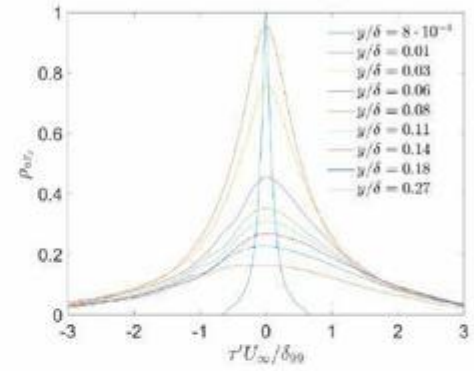

Figure 2: Cross-correlation between shear-stress and streamwise velocity. The peak is centred using a constant delay angle $\alpha \approx 15°$, $\tau' = \tau - y/(\tan(\alpha)u(y))$.

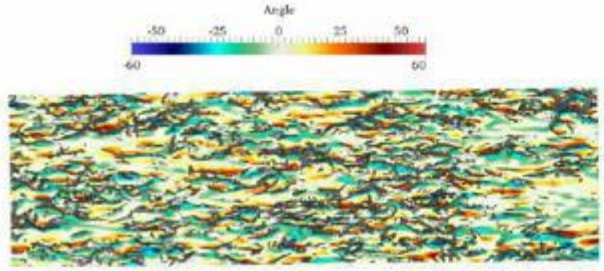

Figure 3: Vortex structures visualised with λ_2 criterion superimposed on contours of shear-stress angle. High angle values locations are correlated with the vortex positions.

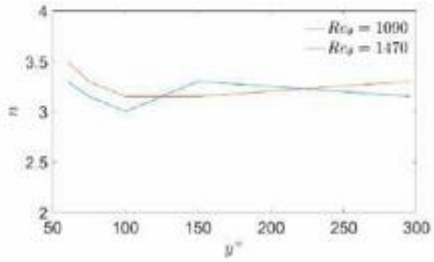

Figure 4: Model parameter n, showing a consistent value around 3-3.5 for several y^+ and two different Reynolds numbers.

A conceptual model for the filtered shear stress fluctuations

An algebraic model is proposed to relate the statistics of shear stress filtered fluctuations, $u_*^2(x,r,t)$ (r is the filter scale), and the structure function of streamwise velocity at y positions along the boundary layer, within $\delta_\nu \ll y \ll \delta$ (where δ_ν and δ are the wall viscous length and boundary layer thickness). The range of scales $y < r < \delta$ is dominated by attached eddies, linking the wall shear stress and velocity fluctuations at y. In a general way, following the ideas proposed by Kolmogorov in 1962 [3,4], the relation can be formulated as $\langle (u'(x+r,y) - u'(x,y))^2 \rangle \sim u_\tau^2 f\left(\langle \left[\frac{u_*^2(x,r,t)}{u_\tau^2} \right]^n \rangle \right)$, where n is the model parameter, assumed constant, and u_τ is the mean friction velocity. Statistical moments with $n > 2$ decrease with the filter scale r while the structure function increases with this variable, so we chose $f(x) \sim 1/x$, keeping a simple formulation for the model. Numerical results from time collecting probes were used to validate this model, using Taylor hypothesis to transform between temporal (τ) and spatial streamwise structure functions. A relation between streamwise and wall-normal scales r is suggested by cross-correlations of u along y, as $\tan\alpha = \frac{y}{\overline{u}(y)\tau}$, which shows a constant delay angle α around $15°$ (Figure 2). Simulation results confirmed a consistent value for the model parameter n between 3 and 3.5, for several y and Re_τ (Figure 4), which provides a good correlation along the wall-attached eddy range $y < \tan\alpha \overline{u}(y)\tau < \delta$. The influence of shear stress fluctuations on the structure function in the wall-attached range, $1/\delta < k < 1/y$, predicts an increase of the energy spectra slope, $E(k) \propto k^{-1-\mu}$, with small $\mu \approx 0.1$ which is determined by n and the decay rate of the variance with r.

References

[1] Laizet S. and Lamballais E., High-order compact schemes for incompressible flows: a simple and efficient method with the quasi-spectral accuracy, J. Comp. Phys., vol 228-15, pp 5989-6015, 2009

[2] Orlu, R. and Schlatter, P., On the fluctuating wall-shear stress in zero pressure-gradient turbulent boundary layer flows. Physics of Fluids, 23:021704, 2011

[3] Kolmogorov, A. N., A refinement of previous hypotheses concerning the local structure of turbulence in a viscous incompressible fluid at high reynolds number. Journal of Fluid Mechanics, 13(01):8285, 1962

[4] Vassilicos, J., Laval, J., Foucaut, J., and Stanislas, M., The streamwise turbulence intensity in the intermediate layer of turbulent pipe flow. Journal of Fluid Mechanics, 774:324-341, 2015

[5] Perry A.E., Henbest S.M., Chong M.S., A theoretical and experimental study of wall turbulence, Journal of Fluid Mechanics, 165:163199, 1986

TURBULENT TEMPERATURE MEASUREMENTS IN WATER

Clayton Byers*[1], Matthew Fu[1], Yuyang Fan[1], and Marcus Hultmark[1]
[1]*Mechanical and Aerospace Engineering, Princeton University, Princeton, New Jersey, USA*

Summary The fluctuating temperature field in a heated turbulent boundary layer is investigated. The working fluid is water, which is shown to have implications on the measurement devices, which typically are optimized for operation in air. A novel nano-scale temperature sensor, previously utilized in air, is redesigned for water measurements with a bandwidth of up to 1 MHz and spatial resolution more than an order of magnitude better than conventional sensors. The new sensor enables a detailed study of both mean and fluctuating temperature profiles in the boundary layer, as well as the turbulent heat fluxes when combined with velocity measurements.

BACKGROUND

Even though there have been tremendous improvements in flow measurement techniques over the last couple of decades, instrumentation for measuring turbulent temperatures have not advanced at the same pace. The need for miniature probes to avoid spatial filtering has been shown in several studies (see for example Ligrani *et al.* [1]). A common rule of thumb is that the size of the sensing element should not exceed 20 viscous units, which is typically challenging to satisfy, especially at high Reynolds numbers. Cold-wires are still the preferred technique for obtaining turbulent statistics for temperature, even though they have been shown to have inadequate bandwidth [2]. This results in temporal filtering, while the long length of conventional cold wires (typically 0.5-1 mm) leads to the spatial filtering as described in [1]. The inadequacy of the instrumentation has resulted in a lack of high-quality temperature data, especially in wall-bounded turbulent flows where the resolution requirements typically are high. Modern semiconductor manufacturing techniques have enabled miniaturized sensors to be developed and manufactured (Bailey *et al.* [3] and Fan *et al.* [4]), which have been utilized successfully. However, these sensors have only been used in gaseous media, and they have consequently been optimized for such environments.

By using water as the test fluid, scaling parameters for the temperature field can be better evaluated. Most previous thermal boundary layer data have been acquired in air flows, where the Prandtl number (ratio of viscous to thermal diffusion) is 0.7, meaning that temperature and velocity fields develop in a similar fashion. Therefore, many data sets for the temperature field utilize identical scaling parameters as those for the velocity field. With a Prandtl number of 7 in water (and adjustable from 3 to 9 depending on the free stream temperature), both classical and newly developed scaling relations can be tested. However, testing in water implies that the length scales are even smaller, and spatial resolution even more critical.

One of the main concerns when miniaturizing temperature sensors is to reduce any end-conduction effects, since the timescales associated with the supports of the sensing element are much larger than those associated with the sensing element itself. Conventional cold wires are subject to severe attenuation even at low to moderate frequencies, due to end-conduction, resulting in large discrepancies in measured versus actual temperature in turbulent flows [2]. A cold wire model based on the lumped capacitance approach was developed and validated experimentally with multiple cold wire geometries. The results and the model lead to the development of the TNSTAP sensor, a nano-scale temperature probe modified from the NSTAP velocity sensor developed at Princeton [3, 4]. These modifications reduce the influence of the probe support and enable high bandwidth temperature measurements, reduced low frequency attenuation and an increased roll-off frequency both compared to conventional cold-wires and NSTAPs when used as a constant current cold wire. The advantage of the TNSTAP over regular cold wires was shown by Arwatz *et al.* [5], and the cold wire model accurately accounted for the cold wire attenuation.

TEMPERATURE MEASUREMENTS IN WATER

By utilizing the cold wire model developed by Arwatz *et al.*, the frequency response for different wire geometries and flow conditions can be predicted. The response for a conventional cold-wire is compared to an NSTAP and a TNSTAP, operating in air at 10 m/s, in figure 1. The four wires simulated (a Wollaston 2.5 μm (90% Pt and 10% Rh) conventional cold-wire with $l/d = 500$, a 30 μm and a 60 μm long NSTAP, and a 200 μm long TNSTAP) have radically different response curves. As can be seen, the two NSTAPs have improved low frequency behavior compared to the conventional cold-wire, but suffer from severe attenuation above 100 Hz. This is perhaps not surprising, since the NSTAPs were designed to be hot-wires, where end conduction effects are less critical. The TNSTAP, which was specifically designed to eliminate the attenuation observed in the NSTAPs and the conventional cold-wires, exhibits an order of magnitude increase in roll-off frequency and significantly improved low frequency attenuation.

However, a cold-wire operates on the principle of adjusting to the ambient flow temperature, thus the heat transfer characteristics to the flow is of great significance to the dynamics of its response. In this study we are particularly interested in temperature measurements in a heated water channel. The heat transfer coefficient is significantly higher in water, at an

*Author. Email: claytonb@princeton.edu

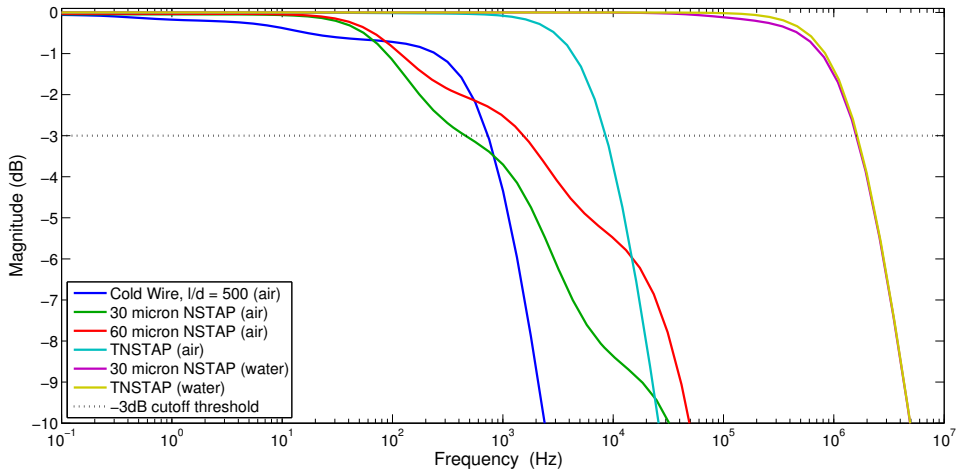

Figure 1: Comparison of wire response utilizing lumped capacitance model of Arwatz *et al.* [2].

otherwise similar configuration, compared to air. It can therefore be expected that all of these sensors will perform better in water, since they can adapt faster to a change in the ambient temperature. The model used above allows investigation of this effect, and figure 1 also shows the response of the 30 μm NSTAP and the TNSTAP in water at 2 m/s. The roll-off frequency is nearly identical for both sensors with a bandwidth greater than 1 MHz, and low frequency attenuation is nearly non-existent. This is almost two orders of magnitude faster than what the model predicts for a conventional cold-wire in water. Furthermore, in order for a sensor to respond fast enough to changes in the ambient flow, the internal accumulation of heat in the sensor itself must be small. This is characterized by the Biot number (ratio of external to internal heat conduction), which must be less than 0.1 for the lumped capacitance method to work. The cold wire studied in figure 1 has a Biot number much smaller than 0.1 in air, but in water it becomes greater than 0.1, especially for the larger geometries. This implies that the model will over predict the bandwidth of a conventional cold-wire in water. In contrast, the nano-scale probes all have Biot numbers less than 0.1 both in air and water, implying that the lumped capacitance model is valid and the above predictions accurate.

DISCUSSION

The results of the modeling above indicate that a wire with poor frequency response in air may have exceptional response in water. It further indicates that there is no advantage of utilizing the TNSTAP over the 30 μm NSTAP for temperature measurements in water since both have nearly identical temporal response. However, with the 30 μm NSTAP being 7 times shorter than the TNSTAP, the spatial resolution is almost an order of magnitude better. In the planned water channel boundary layer experiment, the thermal length scale can approach 2.5 μm, thus the NSTAP has an length of 12 thermal units versus 80 for the 200 μm long TNSTAP. Therefore, the 30 μm NSTAP will be able to accurately capture the temperature fluctuations in the innermost regions of the thermal boundary layer. In addition to capturing the temperature variance more accurately, this small wire can also be utilized as a constant current hot wire in water. With the modified end conduction requirement developed by Hultmark et al. [6], the 30 μm NSTAP can be shown to still satisfy end conduction criteria for use as a hot wire in water. Therefore, in addition to a significantly improved response to temperature fluctuations over a standard cold wire, the 30 μm NSTAP can be utilized for velocity measurements. This comes as a significant savings in experimental complexity, since only one sensor is required for two different measurements. Furthermore, combined temperature and velocity measurements will enable measurements of the turbulent heat fluxes, one of the more difficult parameters to measure.

References

[1] Ligrani P.M., Bradshaw P.: Spatial resolution and measurement of turbulence in the viscous sublayer using subminiature hot-wire probes. Experiments in Fluids 5, 407-417, 1987.

[2] Arwatz G., Bahri C., Smits A. J., Hultmark M.: Dynamic calibration and modeling of a cold wire for temperature measurement. Meas. Sci. Technol. 125301, 2013.

[3] Bailey S.C., Kunkel G.J., Hultmark M., Vallikivi M., Hill J.P., Meyer K.A., Tsay C., Arnold C.B., Smits A.J.: turbulence measurements using a nanoscale thermal anemometry probe. J. Fluid Mech., vol 663, 2010.

[4] Fan Y., Arwatz G., Van Buren T.W., Hoffman D.E., Hultmark M.: Nanoscale sensing devices for turbulence measurements. Exp Fluids 56:138, 2015.

[5] Arwatz G., Fan Y., Bahri C., Hultmark M.: Development and characterization of a nano-scale temperature sensor (T-NSTAP) for turbulent temperature measurements. Meas. Sci. Technol. 035103, 2015.

[6] Hultmark M., Ashok A., Smits A.J.: A new criterion for end-conduction effects in hot-wire anemometry. Meas. Sci. Technol. 055401, 2011.

A RESTRICTED NONLINEAR LARGE-EDDY SIMULATION MODEL FOR WALL-BOUNDED TURBULENCE

Joel U. Bretheim*[1], Charles Meneveau[1], and Dennice F. Gayme[1]
[1]*Department of Mechanical Engineering, Johns Hopkins University, Baltimore, Maryland, USA*

Summary Recent direct numerical simulations (DNS) of the restricted nonlinear (RNL) model have demonstrated its ability to reproduce important features of wall-bounded turbulent flows despite the system's simplified dynamics. The computational effort required by DNS has limited these studies to relatively low Reynolds numbers. In order to investigate the RNL system in the very high Reynolds number regime, we develop a new large-eddy simulation (LES) framework for the model to facilitate studies at effectively "infinite" Reynolds number. Early results confirm that the RNL-LES at "infinite" Reynolds number is successful in reproducing some of the same important statistical features captured in previous low Reynolds number simulations. The RNL-LES framework offers a new and useful tool to aid in understanding the connection between coherent structures and critical momentum transfer mechanisms of wall-bounded turbulent flows.

BACKGROUND

The streamwise-coherent structures often observed in wall-bounded turbulent shear flows have, in recent years, motivated the study of reduced-order models with simplified streamwise dynamics. One example is the two-dimensional, three-velocity-component (2D/3C) model which consists of 2D fields for all three velocity components and the pressure gradient. Studies of the 2D/3C dynamics have elucidated important mechanisms in turbulent plane Couette [1] and pipe [2] flows.

The related restricted nonlinear (RNL) model builds on the 2D/3C system by coupling its dynamics with those of a streamwise-varying perturbation field. The RNL system is straightforwardly derived from the Navier-Stokes equations by decomposing the velocity field into a streamwise mean flow, $U_i(y,z,t)$, and perturbations about that mean, $u_i(x,y,z,t)$. The perturbation field is associated with streamwise-varying wavenumbers (i.e., non-zero streamwise wavenumbers) while the mean flow only includes the zeroth streamwise wavenumber. The total velocity is thus: $(u_T, v_T, w_T) = (U+u, V+v, W+w)$. The same decomposition is employed for the pressure field. The nonlinear term associated with the interactions between perturbations is then eliminated to obtain the RNL system:

$$\partial_i U_i = 0, \qquad \partial_t U_i + U_j \partial_j U_i + \partial_i P - \nu \partial_j \partial_j U_i = -\langle u_j \partial_j u_i \rangle - \partial_x p_\infty \hat{\mathbf{i}} \tag{1}$$

$$\partial_i u_i = 0, \qquad \partial_t u_i + U_j \partial_j u_i + u_j \partial_j U_i + \partial_i p - \nu \partial_j \partial_j u_i = 0. \tag{2}$$

The angle brackets in equation (1) indicate the streamwise-averaging operation. Direct numerical simulations (DNS) of the RNL system have highlighted that its dynamics are supported by a reduced set (compared to the Navier-Stokes system) of streamwise-varying wavenumber modes [3]. Studies have also indicated that the streamwise-varying wavenumbers involved in the dynamics can be changed, e.g. by shifting and/or band-limiting these modes, while still maintaining a turbulent flow [4, 5]. Additionally, the particular streamwise-varying wavenumbers involved have a strong effect on the turbulence statistics.

The RNL studies carried out to date have focused on friction Reynolds numbers (Re_τ) below 1000. In order to investigate the behavior of the RNL system at very high Reynolds numbers, such as those encountered in the atmospheric boundary layer and various engineering applications, we propose a version of the RNL model suitable for large-eddy simulations (LES). This RNL-LES model requires a sub-grid scale model as well as a wall model to circumvent the high-cost associated with resolving the near-wall region. We present results using a standard Smagorinsky model, τ_{ij}^{sgs}, which is desirable for its simplicity and appropriate for an initial, proof-of-concept step. Thus, in the LES version, equations (1) and (2) contain the additional sub-grid stress terms $\partial_j \langle \tau_{ij}^{\mathrm{sgs}} \rangle$ and $\partial_j [\tau_{ij}^{\mathrm{sgs}} - \langle \tau_{ij}^{\mathrm{sgs}} \rangle]$, respectively. The wall region is modelled by imposing stresses at the first gridpoints above the wall which assume the standard rough wall log law.

NUMERICAL TECHNIQUE

The spatial discretization is pseudospectral in the horizontal directions (streamwise x, spanwise y) with second-order finite differencing in the wall-normal (z) direction. We use 3/2-rule dealiasing and integrate forward in time with the second-order Adams-Bashforth method. The horizontal boundary conditions are periodic while the wall-normal direction has a stress-free condition at the top boundary and the aforementioned wall model at the bottom boundary. For all simulations we have uniform mesh spacing with 128^2 grid points in the y-z cross-plane with a box size of $[L_x, L_y, L_z]/H = [2\pi, 2\pi, 1]$. For the LES case we also have 128 grid points in the x-direction while the RNL-LES cases require fewer streamwise grid points (depending upon the particular streamwise wavenumbers retained in the restricted dynamics).

RESULTS

The natural RNL-LES dynamics, which we refer to here as the "baseline" scenario, over-predicts the mean velocity profile in a way that is consistent with earlier DNS of the RNL system. The profile does not exhibit the standard logarithmic dependence on wall-normal height as the RNL system over-predicts the velocity in the bulk of the flow and is too flat in the upper region of the domain. The spanwise (not shown) and wall-normal Reynolds stresses, respectively $[v'_T v'_T]/u_*^2$ and $[w'_T w'_T]/u_*^2$, are under-predicted (square brackets indicate horizontal- and time-averaged quantities, the prime symbol indicates the deviation from the time-averaged total velocity), while the streamwise Reynolds stress, $[u'_T u'_T]/u_*^2$, is strongly over-predicted, also consistent with prior work [4].

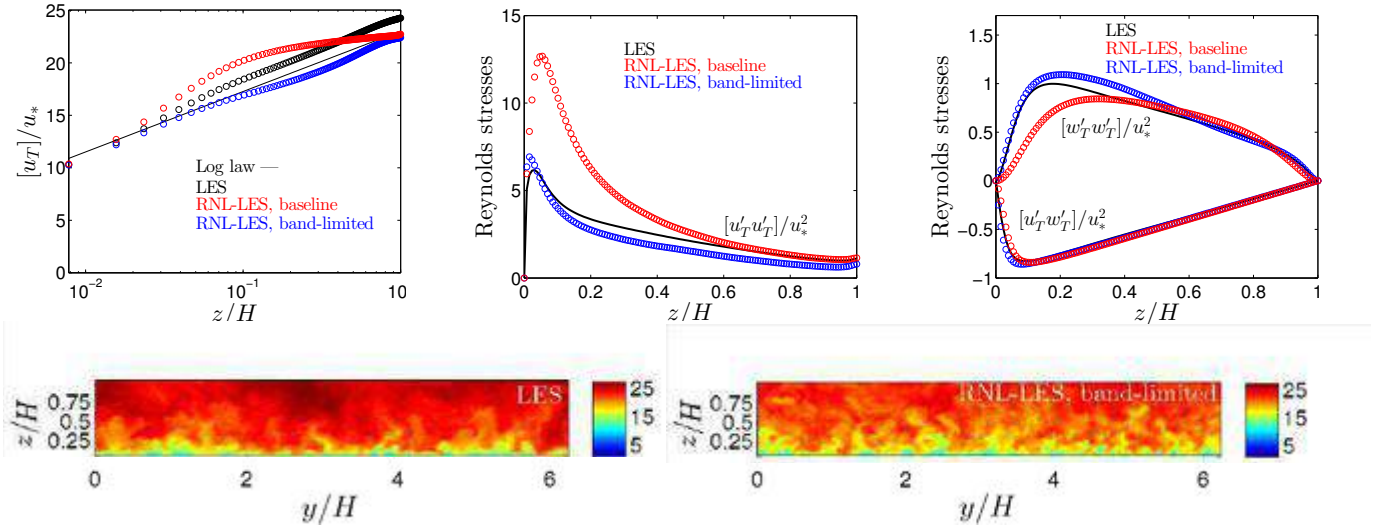

Figure 1: Mean velocity (top left) and Reynolds stress (top middle, right) profiles; streamwise velocity, u_T/u_*, cross-plane snapshots (LES: bottom left, RNL-LES: bottom right).

By forcing the perturbation dynamics (i.e., the non-zero streamwise wavenumbers present in equation (2)) to operate over a different set of non-zero streamwise wavenumbers, which we refer to as the "band-limited" scenario, we observe marked improvement in all of the turbulence statistics, aside from the $[u'_T w'_T]/u_*^2$ Reynolds stress, which is accurate in all scenarios due to the required momentum balance which must hold in all cases in the statistical steady state. While earlier DNS studies of the RNL system showed that one streamwise-varying wavenumber is sufficient to accurately reproduce the mean velocity profile at low Reynolds numbers, these new results indicate that a more complex wavenumber set may be required at very high Reynolds numbers. In this band-limited instance, the selected streamwise-varying wavenumbers are chosen to be the 8th and 16th streamwise modes, based on some initial insights, but another more optimal set (and number) of modes may exist. Ongoing work is targeted at precisely characterizing the relationship between the streamwise wavenumber support and the turbulence statistics, which is still not fully understood even in the low Reynolds number regime.

CONCLUSIONS

Our results provide evidence that further study of the RNL system could aid in the development of reduced-order models of wall-turbulence. The extreme computational expense associated with high-fidelity turbulence simulations is well-known. By investigating and manipulating the spatial structures embedded in turbulent wall-bounded flows, we can gain insights into some key mechanisms of wall-turbulence and exploit that knowledge in the development of less-expensive, reduced-order models. LES of the RNL system provide another angle of attack to further understand the structures and mechanisms involved in wall-turbulence by allowing one to approach the problem from the very high Reynolds number regime.

This work is supported by the US NSF (Nos. ECCS-1230788, and IIA-1243482, the WINDINSPIRE project).

References

[1] D. F. Gayme, B. J. McKeon, A. Papachristodoulou, B. Bamieh, and J. C. Doyle, A streamwise constant model of turbulence in plane Couette flow, J. Fluid Mech. 665, 99 - 119 (2010).

[2] J.-L. Bourguignon and B. J. McKeon, A streamwise-constant model of turbulent pipe flow, Phys. Fluids 23, 095111 (2011).

[3] N. C. Constantinou, A. Lozano-Durn, M.-A. Nikolaidis, B. F. Farrell, P. J. Ioannou, and J. Jimnez, Turbulence in the highly restricted dynamics of a closure at second order: Comparison with DNS, J. Phys.: Conf. Ser. 506, 118 (2014).

[4] V. L. Thomas, B. K. Lieu, M. R. Jovanović, B. F. Farrell, P. J. Ioannou, and D. F. Gayme, "Self-sustaining turbulence in a restricted nonlinear model of plane Couette flow," Phys. Fluids **26**, 105112 (2014).

[5] J. U. Bretheim, C. Meneveau, and D. F. Gayme, "Standard logarithmic mean velocity distribution in a band-limited restricted nonlinear model of turbulent flow in a half-channel," Phys. Fluids **27**, 011702 (2015).

DATA-DRIVEN OPTIMIZATION OF THE FORCING IN THE RESOLVENT ANALYSIS OF WALL TURBULENCE

Kevin Rosenberg*[1] and Beverley J. McKeon[1]

[1]*Graduate Aerospace Laboratories, California Institute of Technology, Pasadena, California, U.S.*

Summary The resolvent framework developed by McKeon & Sharma [1] for wall turbulence is a systems-level model that treats the nonlinear term of the Navier-Stokes equations as a forcing that acts upon the linear dynamics to output a velocity and pressure response across wavenumber-frequency space. An optimization scheme was developed to determine a full spectral representation of the unknown nonlinear forcing such that the resulting velocity spectra optimally matched those of DNS for turbulent channel flow. Results show that this optimization not only determines a forcing field that leads to excellent reproduction of the DNS velocity spectra but also highlights the potential of this framework to make predictions about statistical quantities not explicitly constrained in the optimization scheme. This study represents continued progress in the development of the resolvent model as a systematic pathway towards both understanding the dynamics of wall turbulence and control objectives such as turbulent drag reduction.

INTRODUCTION

Turbulent drag reduction continues to be an important engineering challenge, and the potential economic and environmental impact is well-documented [2]. A model of turbulence amenable to the rich tools of controls and system theory would provide a practical means of achieving this desired drag reduction. In this context, we seek to develop a low-order model of turbulence at a systems-level that captures the key statistical and structural features observed in experiments and simulations, and that can be scaled with Reynolds number. The resolvent framework has shown promise in possessing these characteristics [3, 4] and admitting linear control laws via modification of the boundary conditions [5, 6]. The framework formulates the Navier-Stokes equations as a input/output system across (streamwise and spanwise) wavenumber-frequency space in which the nonlinear term is treated as a forcing that acts upon the linear dynamics (resolvent operator) to yield a velocity and pressure response.

In previous work, Moarref et. al. [7] employed a singular value decomposition of the resolvent operator and used optimization and DNS data to identify a finite number of resolvent modes which contributed directly to the velocity spectra. Most notably, this formulation failed to accurately match the $\langle uv \rangle$ Reynolds stress, which is needed to sustain the assumed mean profile. Since it is not known *a priori* how many resolvent modes are needed to fully represent the velocity/forcing fields, a new approach has been developed that does not decompose the operator and instead attempts to solve for the nonlinear forcing directly. In this study, turbulent channel flow DNS data is combined with optimization techniques to determine and characterize the unknown nonlinear forcing that yields a velocity/pressure field whose spectral and statistical features optimally match, and ultimately predict, those of DNS.

METHODOLOGY

A schematic of the optimization procedure is shown in figure 1. The scheme used an iterative approach within MATLAB to determine the nonlinear forcing such that the resulting time-averaged velocity spectra matches the DNS data of del Alamo and Jiménez [8]. As this DNS database did not have pressure spectra data available, in addition to matching velocity spectra

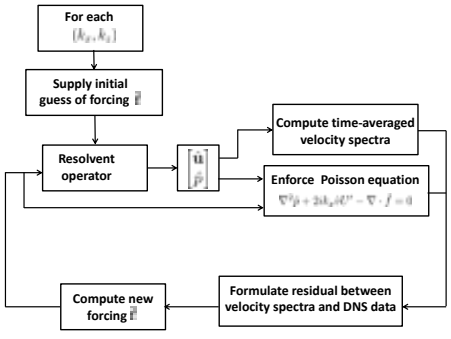

Figure 1: Optimization algorithm used to iteratively solve for the nonlinear forcing

*Corresponding author. Email: krosenbe@caltech.edu

the optimization framework enforced the Poisson equation in an attempt to further constrain the forcing (see figure 1). The optimization was run for a pair of streamwise and spanwise wavenumbers (k_x, k_z) and over a range of frequencies to obtain time-averaged spectra. The first singular forcing mode of the resolvent operator was used to provide an initial guess of the forcing shape and was found to be a robust choice for the range of wavenumbers considered. Optimization results were obtained on a grid of 30 streamwise wavenumbers, 30 spanwise wavenumbers, and 50 wall-normal points, which is a significant reduction in degrees of freedom from the corresponding DNS.

RESULTS

Optimization results in the form of intensity profiles are shown in figure 2 for $Re_\tau = 186$. The velocity plots indicate the success of the optimization scheme to match the DNS data it was explicitly enforced to match. Moreover, the pressure intensity profile reveals that without providing any information about the pressure spectrum and by simply enforcing the Poisson equation within the optimization scheme, the framework was able to closely match the results from DNS. This helps to lend support to the notion that the forcing obtained from the optimization is unique, though further validation of this claim is the subject of ongoing work. The 1-D pre-multiplied spectrum of the v-component of the forcing ($\hat{f}_v$), also shown in figure 2, clearly shows a defined spectral signature and thus may provide insight into the spatio-temporal scales that drive the linear dynamics of the flow. The other two forcing components, not reported here, also showed similar discernible signatures. These results are encouraging and suggest a complete characterization of the nonlinear forcing via this optimization framework is possible and has the potential to elucidate the complex dynamics of wall-bounded turbulent flows.

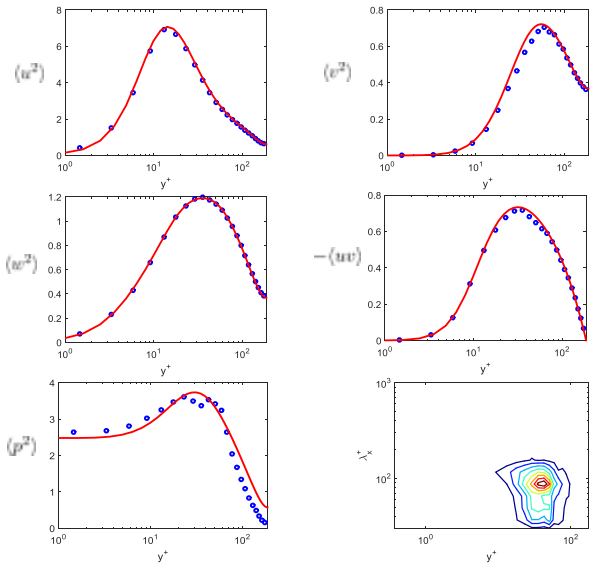

Figure 2: Intensity profiles for velocity and pressure components (DNS- red line, resolvent optimization- blue circles) for $Re_\tau = 186$ and the 1-D pre-multiplied spectrum of $\hat{f}_v$ obtained using the algorithm outlined in Figure 1.

References

[1] McKeon, B. J. and Sharma, A. S. (2010) A critical-layer framework for turbulent pipe flow. Journal of Fluid Mechanics, 658, pp. 336-382

[2] J. Alonso, H. Balakrishnan, I. Kroo, and C. Tomlin, Energy-efficient air transportation, in *The Impact of Control Technology*, edited by T. Samad and A. M. Annaswamy (IEEE Control Systems Society, 2011).

[3] Moarref, Rashad and Sharma, Ati S. and Tropp, Joel A. et al. (2013) Model-based scaling of the streamwise energy density in high-Reynolds-number turbulent channels. Journal of Fluid Mechanics, 734 . pp. 275-316.

[4] McKeon, B. J. and Sharma, A. S. and Jacobi, I. (2013) Experimental manipulation of wall turbulence: A systems approach. Physics of Fluids, 25 (3). Art. No. 031301.

[5] Luhar, M., Sharma, A. S. and McKeon, B. J. (2014) Opposition control within the resolvent analysis framework. Journal of Fluid Mechanics, 749, pp. 597-626.

[6] Luhar, M., Sharma, A. S. and McKeon, B. J. (2015) A framework for studying the effect of compliant surfaces on wall turbulence. Journal of Fluid Mechanics, 768, pp. 415-441; also arXiv 1411.6690.

[7] Moarref, R. and Jovanovi, M. R. and Tropp, J. A. et al. (2014) A low-order decomposition of turbulent channel flow via resolvent analysis and convex optimization. Physics of Fluids, 26 (5). Art. No. 051701.

[8] Juan C. del Alamo, Javier Jimenez, Paulo Zandonade and Robert D. Moser (2004) "Scaling of the energy spectra of turbulent channels", J. Fluid Mech. vol 500, pp 135-144

TURBULENT/NON-TURBULENT INTERFACE IN TRANSITIONAL AND TURBULENT BOUNDARY LAYERS

Jin Lee and Tamer A. Zaki*
Department of Mechanical Engineering, Johns Hopkins University, Baltimore, MD 21218, USA

Summary The turbulent/non-turbulent (T/NT) interface in a transitional boundary layer is examined using direct numerical simulation (DNS) flow field. The interface is identified using the local vorticity, and its statistical properties are reported. Similarities between the turbulence spots and fully turbulent region are evaluated using conditional sampling. In addition, the modulation of the interface by large-scale motion (LSM) is investigated with the aid of a streak detection algorithm.

BACKGROUND

The turbulent/non-turbulent (T/NT) interface is an important region in the study of mass and scalar transport [1]. In the wall-bounded flow, especially the transitional boundary layer, the mechanics of the flow in the vicinity of the T/NT interface are complex because of the sharp gradients in the local intermittency and propagation of the turbulence into the surrounded laminar region. Recently, it has been revealed that the T/NT interface in fully turbulent boundary layers has similarity with the internal layer, of the edge of large-scale motion (LSM) [2]. However, this similarity has not been explored in the context of turbulence spots in transitional boundary layers. In the current study, propagation of the turbulence at the T/NT interface and modulation of the interface by large-scale motion (LSM) in transitional and early turbulent boundary layers are examined using conditional sampling techniques.

SIMULATION DETAILS AND STRUCTURE IDENTIFICATION

Direct numerical simulation (DNS) of a transitional boundary layer is performed for flow over a semi-infinite flat plate. The leading edge of the flat plate is a super ellipse (aspect ratio $AR = 20$). Laminar-to-turbulence transition takes place due to forcing by inflow free-stream turbulence. Zero pressure gradient is ensured by applying the appropriate suction velocity at the top and bottom boundaries, which is based on the continuity equation and active control to maintain a constant mean free-stream speed. The domain size is $1050R$, $40R$ and $240R$ in the streamwise (x), wall-normal (y) and spanwise (z) directions, where R is the plate half thickness (see figure 1). The Reynolds number at the exit plane is $Re_\theta \equiv U_\infty \theta/\nu = 1{,}400$. By storing a time-series of the flow field in a crossflow plane, we can perform a subsequent simulation to higher Reynolds number ($Re_\tau > \mathcal{O}(10^3)$); for this purpose, the width of the current simulation is very large in the spanwise direction.

For the main statistical analysis, the T/NT interface and the large-scale motions are identified and tracked within the 3-D velocity fields. The T/NT interface is detected using the vorticity magnitude excluding the spanwise component since it is large even in the laminar region. Large-scale motions (LSM), on the other hand, are identified using a streak detection algorithm

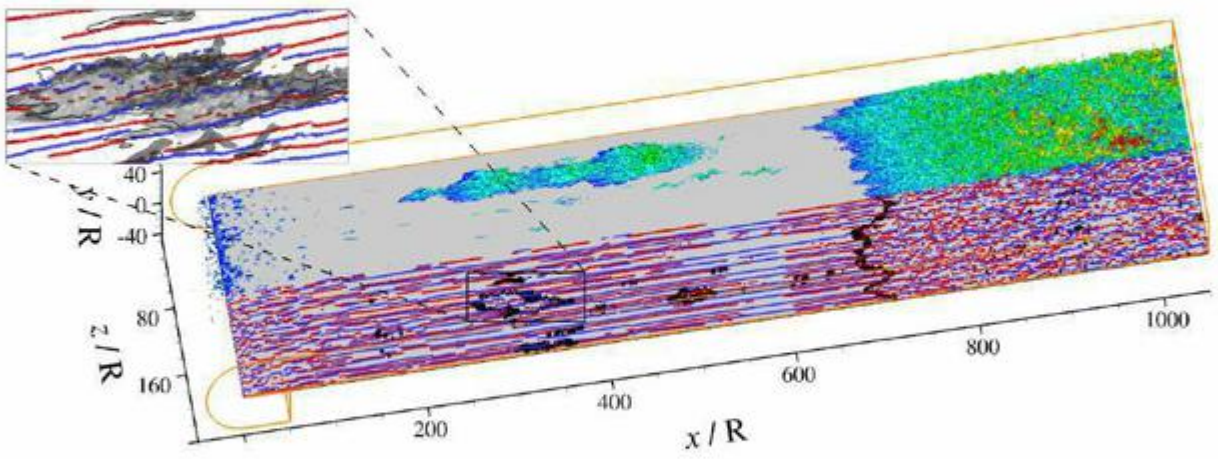

Figure 1: Computational domain (orange) and detected structures. Upper region ($z/R < 120$): Isosurface of the turbulent/non-turbulent interface. Lower region ($z/R > 120$): Cores of low- and high-speed streaks.

*Corresponding author. Email: t.zaki@jhu.edu

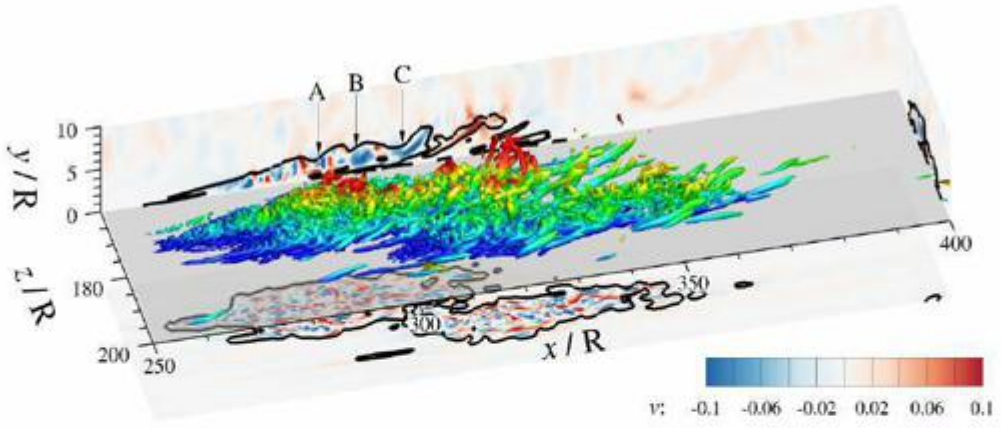

Figure 2: Instantaneous visualization of vortical structures within a spot ($\lambda_2 = -0.005$) colored by the wall-normal location, and the turbulent/non-turbulent interface ($|\omega_x| + |\omega_y| = 0.1$). The side, end and top views are extracted at $z/R = 180$, $x/R = 310$ and $y/R = 1$, and show contours of the wall-normal velocity.

[3]. In order to eliminate the small-scale feature, a Gaussian filter is applied to the streamwise velocity with a filter size that represents the characteristic dimension of the turbulent streak [4]. Figure 1 shows an example of the structure identification within the instantaneous flow field of the transitional and turbulent boundary layers. The T/NT interface is accurately captured and the LSM are correctly identified within the laminar region, the turbulent flow, and also across the interface.

RESULTS

In the transitional boundary layer, the T/NT interface marks (i) turbulence spots within the laminar region and (ii) the most upstream position of the fully-turbulent flow [5]. First, we examine the relationship between the T/NT interface and the turbulence within the interface statistically. Analysis of the instantaneous flow field within the spot (figure 2) can correlate depressions of the interface (marked 'A' to 'C') with sweep motions. The joint probability density function of the interface height and positions of the underlying streaks confirms that the low- and high-speed streaks promote locally thicker and thinner interfaces, respectively. Because the detected streaks represent large-scale motions in wall-turbulence, the shape of the interface also undergoes large-scale deformations. These deformations induce the engulfing process, and ultimately result in a rapid entrainment of the outer laminar fluid into the turbulent zone. Although the spatial dimensions of young turbulence spots are too small to enclose large-scale structures, mature turbulence spots exhibit similar trends to those observed in the fully turbulent zone. Furthermore, the mechanism of spot spreading is investigated in terms of (i) the growth of the enclosed turbulence structures or (ii) the genesis of new turbulence structures in the vicinity of the interface.

Characteristics of the T/NT interface are computed using conditional sampling. Turbulence quantities such as the mean velocities and the turbulent kinetic energy are conditionally averaged in the vicinity of the interface. The velocity jump at the interface, which is found in the fully turbulent regime [2], is also observed at the sides of the spot in the transitional regime. Both turbulence spots and the fully turbulent region include a back edge of the interface, which is the most upstream position of the turbulent zone. The conditional spatial-temporal correlation of the edge position shows that the propagation speed of the turbulent interface at the back of the spot is faster than the back edge of the fully turbulent region [6]. Although the advection velocities of these edges differ for the spot and the fully turbulent region, both interfaces mark a sharp variation in mean-flow and turbulence quantities. The faster propagation of the spot in comparison to the fully turbulent region results in their continual merging, which sustains the upstream edge of the fully turbulent boundary layer.

References

[1] da Silva, C. B., Hunt, J. C. R., Eames, I., Westerweel, J.: Interfacial layers between regions of different turbulence intensity. Annu. Rev. Fluid Mech. 46:567-590, 2014.

[2] Eisma, J., Westerweel, J., Ooms, G., Elsinga, G. E.: Interfaces and internal layers in a turbulent boundary layer. Phys. Fluids 27:055103, 2015.

[3] Nolan, K. P., Zaki, T. A.: Conditional sampling of transitional boundary layers in pressure gradient. J. Fluid Mech. 728:306-339, 2013.

[4] Lee, J., Lee, J. H., Choi, J.-I., Sung, H. J.: Spatial organization of large- and very-large-scale motions in a turbulent channel flow. J. Fluid Mech. 749:818-840, 2014.

[5] Zaki, T. A.: From streaks to spot and on to turbulence: Exploring the dynamics of boundary layer transition. Flow Turbul. Combust. 91:451-473, 2013.

[6] Lee, J., Zaki, T. A.: Characteristics of the laminar-turbulent edge in transitional boundary layers. In proceedings of 68th Annual Meeting of the APS Division of Fluids Dynamics, Boston, MA, November 22-24, 2015.

SCALE INTERACTIONS AND 3D CRITICAL LAYERS IN WALL-BOUNDED TURBULENT FLOWS

Theresa Saxton-Fox*[1] and Beverley McKeon[2]
[1]*Department of Mechanical and Civil Engineering, California Institute of Technology, Pasadena, California, USA*
[2]*Graduate Aerospace Laboratories, California Institute of Technology, Pasadena, California, USA*

Summary Phenomena related to scale interaction in wall-bounded turbulent flows were considered through the lens of critical layer analysis. A 3D critical layer formulation was used, with the 3D critical layer associated with a particular structure defined as the height where the instantaneous velocity field composed of the large scales and the mean velocity matched the convection velocity of that structure. Characterization of the velocity field surrounding the 3D critical layer in wall-bounded turbulent flows led to conclusions consistent with previously observed phenomena including the shape of the interface defining uniform momentum zones (UMZs) [1] [2] and amplitude modulation of the small scales by the large scales [5]. The use of a 3D critical layer formulation in wall-bounded turbulent flows may lead to improved modeling of small scale activity in reduced order models and LES.

The 3D critical layer has previously been considered in wall-bounded turbulent flows in the context of self-sustaining, exact solutions to the Navier-Stokes equations [3]. The present work links phenomena related to a critical layer and current observations of scale interaction in wall-bounded turbulent flows. The shape of the interface outlining UMZs in instantaneous snapshots of turbulent boundary layers has been observed to lie along an isocontour of velocity [1] [2], which can be considered to constitute an instantaneous 3D critical layer. Additionally, observations that large scales in the flow can modify the local wall shear stress [4] and the amplitude of the local small scales [5], can be considered through the perspective of the 3D critical layer analysis. Considering physical and statistical features of wall-bounded turbulent flow through a critical layer framework allows for improved understanding of scale interactions and may lead to improved modeling of these phenomena.

Figure 1 offers an illustration of a 3D critical layer identified in PIV data. 2D Gaussian filters were used to identify distinct scales in the PIV velocity data, and Taylor's hypothesis was used to visualize a larger field of view than is available in the data. Large-scale velocity structures corresponding to instantaneous velocity higher than the mean velocity are shown to correspond to depressions in the 3D critical layer towards the wall (relative to the 2D critical layer corresponding to the location where the *mean* velocity is equal to the structure convective velocity) and are correlated (both visually and statistically) with energetic small scales at lower heights in the flow, while those leading to instantaneous velocities slower than the mean velocity are shown to correspond to raised regions of the 3D critical layer and are associated with energetic small scale activity at higher heights in the flow.

The resolvent analysis of McKeon and Sharma [6] has been used to model this simplified definition of the 3D critical layer in wall-bounded turbulent flows. A single velocity response mode from resolvent analysis superimposed with the mean velocity profile leads to a 3D critical layer signature that qualitatively matches observations of 2D PIV data.

In summary, the utility of the 3D critical layer to describe a range of phenomena that have been observed in the literature is demonstrated and exploited.

The support of an NDSEG fellowship (TSF) and AFOSR (grant FA9550-12-1-0060) is gratefully acknowledged.

References

[1] C. de Silva, N. Hutchins, and I. Marusic. Uniform momentum zones in turbulent boundary layers. *Journal of Fluid Mechanics*, 786:309–331, 2015.
[2] J. Eisma, J. Westerweel, G. Ooms, and G. E. Elsinga. Interfaces and internal layers in a turbulent boundary layer. *Physics of Fluids*, 27(055103), 2015.
[3] P. Hall and S. Sherwin. Streamwise vortices in shear flows: harbingers of transition and the skeleton of coherent structures. *Journal of Fluid Mechanics*, 661:178–205, 2010.
[4] N. Hutchins, J. Monty, B. Ganapathisubramani, H. Ng, and I. Marusic. Three-dimensional conditional structure of a high-Reynolds-number turbulent boundary layer. *Journal of Fluid Mechanics*, 673:255–285, 2011.
[5] R. Mathis, N. Hutchins, and I. Marusic. Large-scale amplitude modulation of small-scale structures in turbulent boundary layers. *Journal of Fluid Mechanics*, 628:311–337, 2009.
[6] B. McKeon and A. S. Sharma. A critical-layer framework for turbulent pipe flow. *Journal of Fluid Mechanics*, 658:336–382, 2010.

*Corresponding author. Email: tsaxtonf@caltech.edu

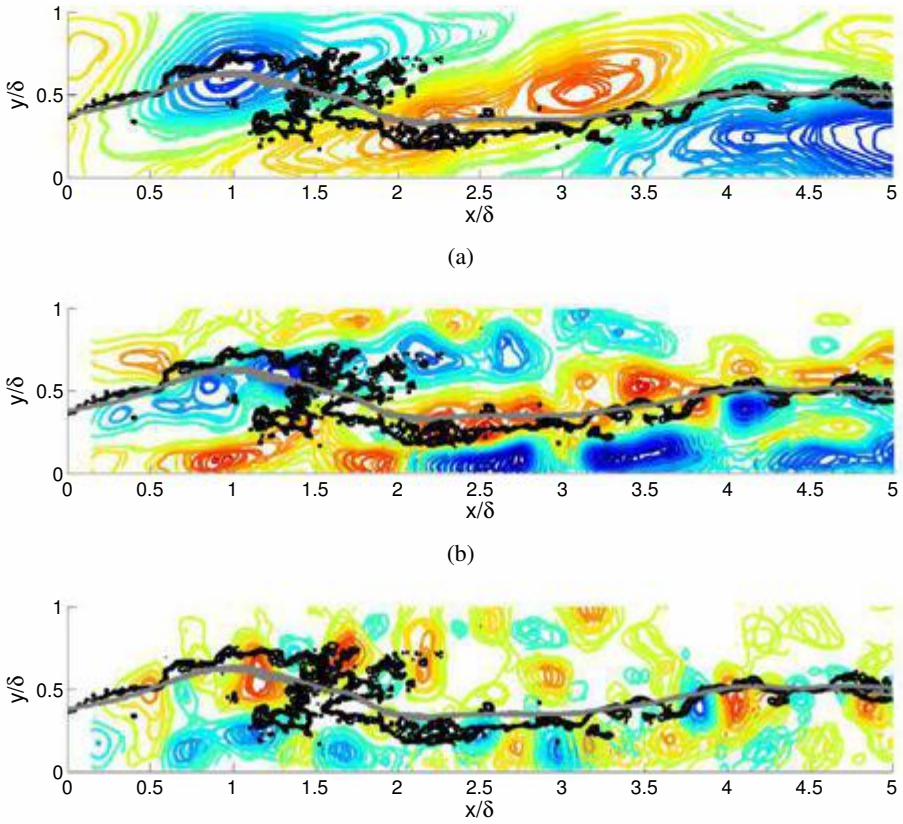

(a)

(b)

(c)

Figure 1: A visualization of a 3D critical layer is shown using PIV observations of a turbulent boundary layer. The streamwise large-scale (a), streamwise small-scale (b), and wall-normal small-scale (c) fluctuating velocity structures are identified from PIV velocity data using 2D Gaussian filters. The black contour line in each figure is an instantaneous contour of $u = 0.83U_\infty$ in the full, unfiltered flow field. The grey contour line is the same velocity isocontour identified from the velocity field of the superposition of only the mean and the large scales, and represents a 2D cut through the 3D critical layer corresponding to the large scale structure. The similarity of the black and grey contour lines suggests that the large-scale streamwise velocity structure identified in (a) is largely responsible for the shape of the full velocity isocontour. The small scales in (b) and (c) are seen to follow the black and grey contour lines closely, potentially identifying the source of the well-characterized amplitude modulation effect. Note that Taylor's hypothesis has been applied to all velocity contours using a convection velocity of $0.83U_\infty$ to show a larger field of view than is available in the data. Adjacent images are overlapped to visualize the accuracy of Taylor's hypothesis.

COUPLED UNIFORM MOMENTUM ZONES AND INTERNAL LAYERS IN TURBULENT WALL FLOWS

Greg Chini*[1,2], Brandon Montemuro[1], Chris White[2], and Joe Klewicki[2,3]

[1]*Program in Integrated Applied Mathematics, University of New Hampshire, Durham, NH 03824, USA*
[2]*Department of Mechanical Engineering, University of New Hampshire, Durham, NH 03824, USA*
[3]*Department of Mechanical Engineering, University of Melbourne, Parkville, VIC 3010, Australia*

Summary A candidate flow configuration is identified that has the potential to generate a self-sustaining interaction between a single vortical fissure and adjacent uniform momentum zones, i.e. the primal coherent structures and interactions observed in the outer part of turbulent wall flows at asymptotically large Reynolds number Re. Matched asymptotic analysis is used to derive a reduced set of PDEs governing the coupled dynamics of the fissure and uniform momentum zones in the limit $Re \to \infty$. The analysis clarifies the nature of the hypothesized interaction and provides an equation set that is suitable for efficient multiscale numerical simulations.

INTRODUCTION

Both field observations and laboratory experiments suggest that at extremely large Reynolds numbers $Re \equiv u_\tau h/\nu$, where u_τ is the friction velocity, h an appropriate integral length scale and ν the kinematic viscosity, fluid motions in the outer part of turbulent wall flows self-organize into interacting vortical fissures (VF) and uniform momentum zones (UMZ). The fissures are essentially internal shear layers across which the instantaneous streamwise (x directed) velocity changes sharply, thereby separating adjacent UMZ in the wall-normal (y) direction (see Fig. 1, left). Experiments reveal that the dimensionless thickness of the VF (normalized by h) is $O(1/\sqrt{Re})$, while the dimensionless streamwise velocity jump across the fissures (normalized by u_τ) is $O(1)$ [1]. These scalings, which are consistent with the conceptual notion that the turbulent boundary layer comprises logarithmically many viscous internal layers containing most of the vorticity and, hence, dissipation, must be respected by any credible predictive asymptotic theory.

A CANDIDATE FLOW CONFIGURATION

The UMZ are colocated with very large-scale motions (VLSM) or super-structures, elongated regions of spanwise (z) alternating, relatively uniform, low and high streamwise-momentum fluid. Observations confirm that the low-momentum regions are separated by the vortex cores of nearly inviscid streamwise roll modes [2]. Here, we suggest that these observations are consistent with the notion that the super-structures and UMZ are driven by a *variant* of the self-sustaining process (SSP) first proposed by Waleffe [3] for plane parallel shear flows and subsequently described in the large-Re limit by Hall & Sherwin [4] and Beaume *et al.* [5]. According to this theory, comparably weak [$O(Re^{-1})$] streamwise vortices drive an $O(1)$ redistribution of the background streamwise shear; the resulting spanwise inflections in the streamwise velocity are the sites of x-varying shear instabilities that nonlinearly interact to reinforce the (weak) streamwise vortices, thereby comprising a SSP. Until recently, Waleffe's SSP and the associated "exact coherent states" (ECS) – unstable 3D equilibrium, traveling-wave or periodic-orbit solutions of the Navier–Stokes (NS) equations – had been thought to be relevant only to the near-wall dynamics of the turbulent boundary layer (if at all). However, it is conceivable that a *similar* mechanism partially sustains the UMZ much farther from the wall. One crucial difference concerns the dynamics of the streamwise-averaged flow: in the SSP articulated by Waleffe and Hall, the effective Reynolds number for this x-mean flow is $O(1)$; in contrast, our scaling analysis confirms that the streamwise-averaged dynamics within the UMZ are essentially *inviscid*. This is significant, since the x-averaged streamwise flow (the 'streaks') associated with Waleffe's lower- and upper-branch ECS is not uniform. In contrast, at sufficiently large *effective* Reynolds number, a counter-rotating cellular flow in the y–z plane is expected to *homogenize* the (x-mean) streamwise velocity component, consistent with the defining property of UMZ.

ASYMPTOTIC DEDUCTION AND REDUCTION

Consider the incompressible Navier–Stokes (NS) equations normalized using u_τ, ρu_τ^2 (where ρ is the fluid density), h and h/u_τ as scales for the velocity, pressure, length and time, respectively. Letting $\epsilon \equiv 1/\sqrt{Re}$, we require the (emergent) internal shear-layer thickness $\Delta \sim \epsilon$ in accord with the observed scalings of VF in turbulent wall flows at large Re. As $\epsilon \to 0$, the shear layer thins to a sheet and the dynamics is expected to be largely inviscid except within a thin $O(\epsilon)$ region centered on the shear layer. Thus, this configuration is amenable to analysis using the method of *matched asymptotic expansions*, with an outer region in which $y = O(1)$ and an inner region in which $y = O(\epsilon)$ and, hence, $Y \equiv y/\epsilon = O(1)$.

*Corresponding author. Email: greg.chini@unh.edu

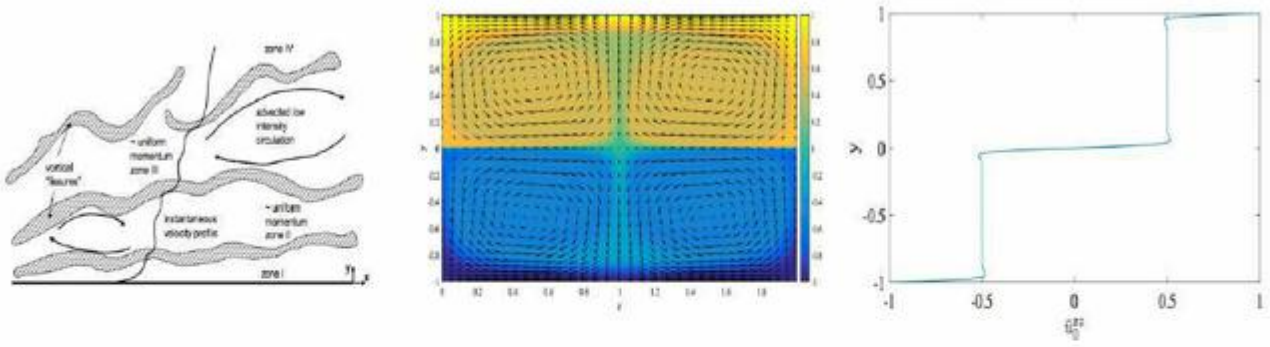

Figure 1: Left: Schematic of the flow structure in the outer part of turbulent wall flows at large Re [1]. Middle: Snapshot of the streamwise-averaged streamwise (i.e. 'streak') velocity, with the roll velocity field overlaid, taken from a numerical simulation of the 2D advection-diffusion equation governing $\bar{}_0(y,z,T)$ in the weak-diffusion limit. Right: The horizontally (x and z) averaged streamwise velocity profile u_0^{xz} obtained by averaging in z the 2D field shown in the middle panel. Note the emergence of uniform momentum zones (UMZ) and an internal shear layer (vortical fissure).

Within the UMZ (i.e. the outer regions), the field variables are expanded in the following asymptotic series:

$$u(x,y,z,t;\epsilon) \sim \bar{}_0(y,z,T) + \epsilon\ u_1(y,z,T) + u_1'(x,y,z,t,T)]\,; \quad \mathbf{v}_\perp(x,y,z,t;\epsilon) \sim \epsilon\ \mathbf{v}_{1\perp}(y,z,T) + \mathbf{v}_{1\perp}'(x,y,z,t,T)]\,,$$

where $\mathbf{v}_\perp = (v,w)$, and u, v and w are the x, y and z velocity components. A slow time scale $T \equiv \epsilon t$ has been introduced, and the fields have been decomposed into a streamwise/fast-time mean and a fluctuation. The form of these expansions is identical to that employed by Beaume *et al.* [5], but the scaling of ϵ with Re differs. Consequently, weak rolls drive $O(1)$ streaks, as in Waleffe's ECS, but the scalings employed here ensure that $u_0(y,z,T)$ satisfies a 2D advection equation with subdominant diffusion that nevertheless must be retained: a shear-dispersion mechanism enhances diffusion as the roll motion twists iso-surfaces of and thereby homogenizes u_0 (Fig. 1) [6]. Also unlike Waleffe's SSP, the streamwise-averaged flow is driven by the fluctuation dynamics within the shear layer; i.e. *exterior* to the rolls. Within the VF (i.e. the inner region), the field variables are again expanded in appropriate asymptotic series. In particular, the magnitude of the streamwise velocity fluctuation (u_1') is amplified by a factor $1/\epsilon$ within the internal shear layer, as can be verified by analysis of the Orr-Sommerfeld equation with a mixing layer shear-flow profile having an $O(\epsilon)$ thick region of strong shear. For obliquely-oriented disturbances on the shear layer, incompressibility implies the spanwise velocity fluctuation w_1' experiences the same amplification. The wall-normal velocity fluctuation remains $O(\epsilon)$, but experiences a jump in value across the VF. Using these deductions, the NS equations within the VF reduce to a variant of the laminar boundary-layer equations.

DISCUSSION

Our matched asymptotic analysis yields reduced equations that are less computationally expensive to time-integrate than the NS equations in the large-Re limit of interest. More significantly, the analysis makes clear one possible mechanism for the self-sustenance of coexisting uniform momentum zones and internal shear layers (vortical fissures) in the outer part of turbulent wall flows. Our preliminary results indicate that the large-scale roll modes act as a homogenizing agent that leads to the formation and sustenance of the UMZ while simultaneously producing concentrated regions of spanwise vorticity (i.e. VF). Owing to this homogenization, the fluctuations (streamwise-varying fields) are largely irrotational within the UMZ, implying that the primary mechanism for driving the roll modes necessarily arises from the nonlinear fluctuation dynamics within the fissure. The analysis also reveals the precise scaling properties of the roll modes and internal fissure structure that are required to self-consistently generate internal shear layers with the experimentally observed $O(1/\sqrt{Re})$ thickness.

References

[1] Priyadarshana P., Klewicki J., Treat S., Foss J.: Statistical Structure of Turbulent Boundary-Layer Velocity-Vorticity Products at High and Low Reynolds Numbers. J. Fluid Mech. 570: 307-346, 2007.

[2] Papavassiliou D., Hanratty T.: Interpretation of Large-Scale Structures Observed in Turbulent Plane Couette Flow. Int. J. Heat Fluid Fl. 18: 55-69, 1997.

[3] Wang J., Gibson J., Waleffe F.: Lower Branch Coherent States in Shear Flows: Transition and Control. Phys. Rev. Lett. 98:204501, 2007.

[4] Hall P., Sherwin S.: Streamwise Vortices in Shear Flows. J. Fluid Mech. 661:178-205, 2010.

[5] Beaume C., Chini G., Julien K., Knobloch E.: Reduced Description of Exact Coherent States in Parallel Shear Flows. Phys. Rev. E 91: 043010, 2015.

[6] Rhines P., Young W.: How Rapidly is a Passive Scalar Mixed within Closed Streamlines? J. Fluid Mech. 133:135-145, 1983.

EXPERIMENTAL INVESTIGATION OF SPACE-TIME CORRELATION IN THE ATMOSPHERIC SURFACE LAYER

Guowen Han [1,2], Tian-Li Bo [1,2] & Xiao-Jing Zheng [3a)]

[1]*Key Laboratory of Mechanics on Western Disaster and Environment,Lanzhou University, Lanzhou, China*

[2]*Department of Mechanics, Lanzhou University, Lanzhou, China*

[3]*School of Electronical and Machanical Engineering, Xidian University, Xi'an, China*

Summary We investigated the space-time correlation of streamwise velocity in the high Reynolds number atmospheric surface layer (ASL) using multipoint synchronous field observation array. The experimental results show that the iso-correlation contours of space-time correlations have an elliptical shapes rather than straight lines, which suggests that, instead of Taylor hypothesis, the elliptic model [1] is more suitable for describing the space-time correlation for the streamwise velocity in the ASL. It relates the space-time correlation to the space correlation via convection velocity U and sweeping velocity V. The further experimental results suggest that U is basically equal to local mean streamwise velocity and V is approximately twice as large as the root-mean-square of the streamwise velocity.

INTRODUCTION

Turbulence contains eddies with various scales which is characterized by the fluctuating velocity field $v\ \mathbf{x}\ \tau$ at position $\mathbf{x}$ and time τ. The space–time correlation function of fluctuating velocities, defined as eq (1) is a fundamental description on fluctuating velocity field.

$$C\ \mathbf{r}\ \tau = \frac{\langle v(\mathbf{x}\ \ \mathbf{r}\ t+\tau\ v\ \mathbf{x}\ \tau\ \rangle}{v_{rms}(\mathbf{x}\ \ \mathbf{r})v_{rms}(\mathbf{x})} \tag{1}$$

For simplicity, we just analyzed the space–time correlation of streamwise velocity $C_u\ r\ \tau$ and r is the spatially streamwise separation. The space–time correlation function $C\ \mathbf{r}\ \tau$ provides more information on turbulent structures than time autocorrelation or spatial cross correlation. However, there is little research on $C\ \mathbf{r}\ \tau$ in the ASL. Understanding the relationship between space and time in $C\ \mathbf{r}\ \tau$ of fluctuating velocities is one of the important scientific issues in turbulence research. For example, $C\ \mathbf{r}\ \tau$ can characterize the cascade processes in turbulence which can describe the transportation of energy between eddies. It is also important in subgrid scale (SGS) modeling for large eddy simulation (LES) in the closure theory of turbulence[2].

EXPERIMENTAL SET-UP

The field experimental observations were conducted at a dry and flat lake bed of the Qingtu Lake which is located between Tenger Desert and Badain Jaran Desert in the western area of China ($E\ \ ^\circ\ '\ ''\ N\ \ ^\circ\ '\ ''$; 1300m elevation) during the period of 26 March to 06 May 2014.This area has strong steady northwest and southeast winds in spring and the variation of the surface topography within 10 km in northwest and southeast is less than 2m. The observation array consist a streamwise array of 9 movable towers with the spacing were: 0, 1, 5, 10, 15, 20, 30, 40, 50m respectively. In order to get more experimental data, the direction of the array is adjusted in the direction of the streamwise velocity before every strong wind. There were 9 three component sonic anemometers (Gill Instruments R3-50) settled on the movable towers at the height of 2.5m.The anemometers measure wind velocities as well as temperature at a sampled rate of 50Hz, all 9 anemometers are sampled simultaneously and calibrated by GPS every hour.

[a)] Corresponding author. Email: hangw2014@lzu.edu.cn

CONCLUSIONS

We studied the space-time correlations for streamwise velocity. It can be obviously seen from the figure 1(left) that the 2D plot of the contours of $C_u\ r\ \tau$ have an elliptic shape. If Taylor frozen hypothesis is hold in the ASL, the iso-correlation contours of $C_u\ r\ \tau$ should be straight lines [4]. The fact that the shape of the $C_u\ r\ \tau$ is different from Taylor frozen hypothesis reveals that that elliptic model is more suitable to describe $C_u\ r\ \tau$ than Taylor frozen hypothesis in the ASL.

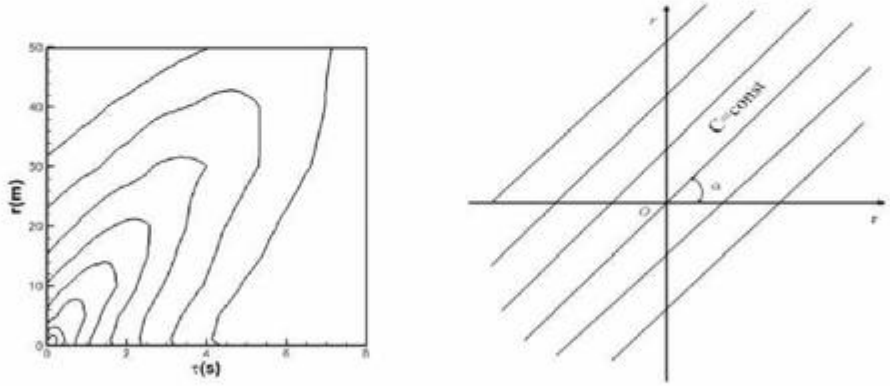

Figure 1. (left) 2D contours of the space-time correlation function in time and space plane; (right)The schematic diagram for the 2D contours in Taylor's frozen flow.

The elliptic model relates the $C_u\ r\ \tau$ to $C_u\ r_E$ via $r_E^2 = (\ -\ \tau\ + V\tau\ ^2$, the convection velocity U can be calculated from the condition, $\partial r_E\ \partial r\ _{r=0}$;while the sweeping velocity V which is determined by $\partial r_E\ \partial \tau\ _{r=0}$ as mentioned by He et al [3] and Zhou et al [4].The comparison between the magnitudes of U and V is made in figure 2. The further experimental results suggest that U is basically equal to the local mean streamwise velocity and V is approximately twice as large as the root-mean-square of the streamwise velocity.

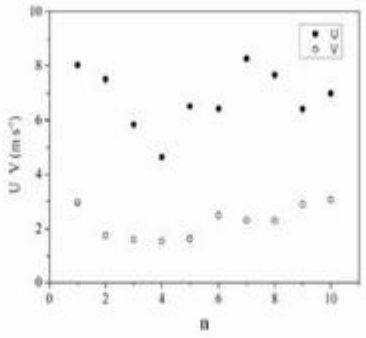

.

Figure 2. Comparison of the magnitudes of the convection velocity U (solid circles) and sweeping velocity V (hollow circles) for $C_u\ r\ \tau$ in 10 groups of independent experiments.

References

[1] He GW, Zhang JB.: Elliptic model for space-time correlations in turbulent shear flows. Physical Review E, 73(5), 055303, 2006.

[2] Sagaut P.: Large eddy simulation for incompressible flows: an introduction. Springer Science and Business Media, 2006.

[3] He X, He G, Tong P.: Small-scale turbulent fluctuations beyond Taylor's frozen-flow hypothesis. Physical Review E, 81(6), 065303,2010.

[4] Zhou Q, Li CM, Lu ZM, Liu YL.: Experimental investigation of longitudinal space–time correlations of the velocity field in turbulent Rayleigh–Bénard convection. Journal of Fluid Mechanics, 683, 94-111,2011.

PREDICTION OF FRICTIONAL DRAG IN THE TRANSITIONALLY ROUGH REGIME

Karen Flack[1], Julio Barros[1] & Michael Schultz[2]
[1]*Department of Mechanical Engineering, U. S. Naval Academy, Annapolis, Maryland, USA*
[2] *Department of Ocean Engineering and Naval Architecture, U. S. Naval Academy, Annapolis, Maryland, USA*

Summary The goal of the study is to determine the scales that define the shape and extent of the transitionally rough regime. This is accomplished by testing rough surfaces with systematically altered surface statistics. Preliminary results are presented for a rough surface with scales that follow a power law spectrum.

INTRODUCTION

Understanding the relationship between a surface's topography and its hydraulic resistance is an important, yet illusive, goal in fluids engineering. Particularly poorly understood are the flow conditions at which a given surface will begin to show the effects of roughness in the form of increased wall shear stress above that of the hydraulically smooth wall and the behaviour of frictional drag in the transitionally rough regime. The goal of the research is to develop engineering correlations for the prediction of frictional drag for all roughness regimes. Ideally, the correlations should be based on information that can be obtained solely from the surface topography, thus excluding any information that requires hydrodynamic testing. Previous results (Flack & Schultz 2010) showed that the root-mean-square roughness height (k_{rms}) and the skewness (Sk) of the probability density function are the roughness scales that best predict frictional drag in the fully rough regime. These statistics will be tested as predictive scales for determining the frictional drag in the transitionally rough regime. In order to accomplish this, the roughness function must be mapped throughout the entire transitionally rough regime from hydraulically smooth to fully rough using roughness where surface statistics are parametrically altered. The extent and shape of the transitionally rough regime are then related to appropriate scales.

EXPERIMENTAL METHODS

Experiments on rough surfaces are conducted in the high Reynolds number turbulent channel flow facility at the United States Naval Academy (figure 1). The test section is 25 mm in height (H), 200 mm in width (W), and 3.1 m in length (L). The bulk mean velocity in the test section ranges from 0.4 – 11.0 m/s, resulting in a Reynolds number based on the channel height and bulk mean velocity (Re_m) range from 10,000 – 300,000. The wall shear stress, τ_w, is determined via measurement of the streamwise pressure gradient, dp/dx. A similarity-law procedure is employed to determine the roughness function, ΔU^+. The flow develops over smooth walls for a distance of $60H$ in the upstream portion of the channel. The roughness-covered plates form the top and bottom walls for the remainder of the test section. There is a roughness fetch of $30H$ before the first tap used in the determination of dp/dx. Fully-developed flow was confirmed with velocity profiles located $90H$ and $110H$ downstream of the trip.

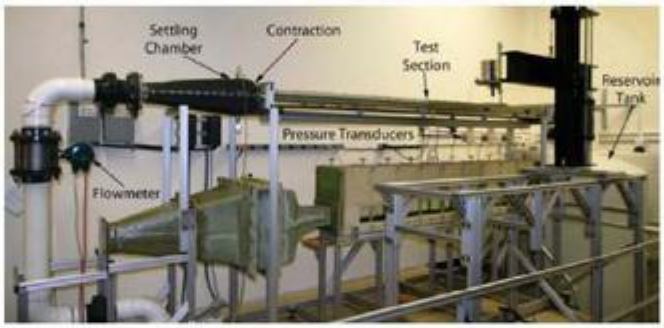

Figure 1. High Reynolds number channel flow facility

The rough surfaces are generated mathematically so the surface statistics can be systematically changed and controlled to identify the roughness scales that contribute the most to frictional drag. The current surfaces have a range of scales that follow a power law spectrum $E(k) \sim k^P$. The slope of the power law is changed while holding k_{rms} constant. Three sample test surfaces with power law slopes of P = -0.5, -1.0 and -1.5 are shown in figure 2. The generated surfaces are reproduced using a high-resolution 3D printer (lateral resolution 34μm, elevation resolution 16μm). Silicon rubber molds are made to replicate the printed surfaces and the surfaces are batch duplicated using cast resin. The cast surfaces are randomly arranged across the test plates, as shown in figure 3.

[a] Corresponding author. Email: flack@usna.edu

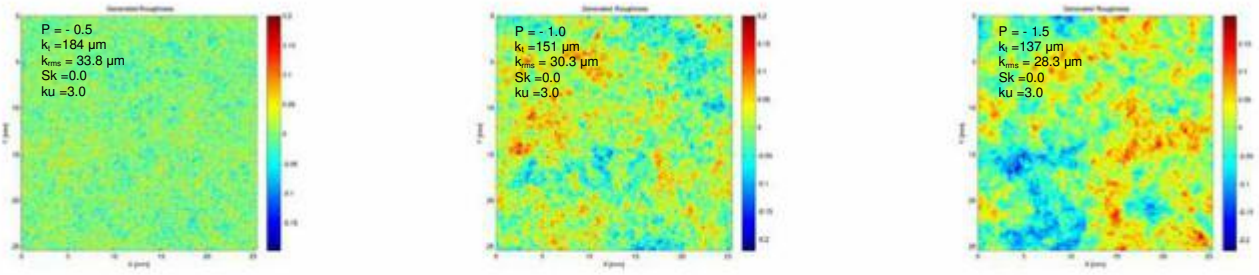

Figure 2. Mathematically generated rough surfaces with power law slopes P = -0.5, -1.0 and -1.5.

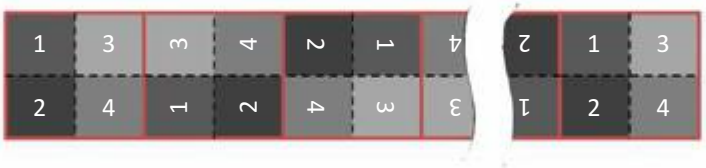

Figure 3. Tiling of surface with roughness coupons

RESULTS AND DISCUSSION

Sample skin friction results for the P = -0.5 case are shown on Figure 4. Also shown are the smooth wall results of Schultz & Flack (2013). At low Reynolds number the surface is hydraulically smooth. At higher Reynolds number the surface exhibits fully rough behaviour where the skin friction is independent of Reynolds number. The roughness function (ΔU^+) for a range of roughness Reynolds number (k_s^+), where k_s is the equivalent sand grain roughness height, is shown on figure 5. Roughness effects are evident at $k_s^+ \sim 2$ and the onset of the fully rough regime occurs at $k_s^+ \sim 15$. The shape of the roughness function in the transitionally rough regime does not follow the Nikuradse (1933) roughness function for uniform sand grain or the Colebrook (1939) roughness function that is used in the Moody Diagram (1944).

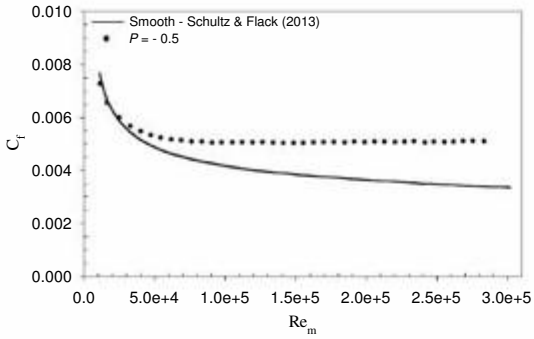

Figure 5. Skin-friction coefficient

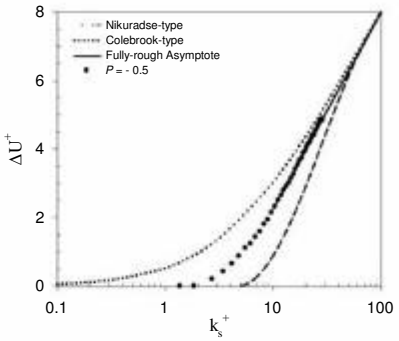

Figure 6. Roughness function

CONCLUSIONS

Results are presented for a rough surface with a range of scales following a power law slope of P = - 0.5. The entire roughness function is mapped to determine the extent and shape of ΔU^+ in the transitionally rough regime. Additional surfaces that have parametrically altered surface statistics will be presented to determine the roughness scales that define the transitionally rough regime.

References

[1] Flack, K.A., Schultz, M.P., "Review of Hydraulic Roughness Scales in the Fully Rough Regime," ASME J. Fluids Engr, 132(4), 041203, 2010.

[2] Schultz, M.P., Flack, K.A. "Reynolds-number Scaling of Turbulent Channel Flow," Physics of Fluids, 25, 025104, 2013.

[3] Nikuradse, J., 1933, "Laws of Flow in Rough Pipes," NACA Technical Memorandum 1292.

[4] Colebrook, C. F., 1939, "Turbulent Flow in Pipes, With Particular Reference to the Transitional Region between Smooth and Rough Wall Laws," J. Inst Civ. Eng., 11, pp. 133–156.

[5] Moody, L. F., 1944, "Friction Factors for Pipe Flow," Trans. ASME, 66, pp. 671–684.

INNER–OUTER INTERACTIONS IN A TURBULENT BOUNDARY LAYER OVERLYING COMPLEX ROUGHNESS

Gokul Pathikonda[1,2] and Kenneth T. Christensen *[2]

[1]*Department of Mechanical Science and Engineering, University of Illinois, Urbana-Champaign, USA*
[2]*Department of Aerospace and Mechanical Engineering, University of Notre Dame, Notre Dame, USA*

Summary Experiments were performed to investigate the modulating influences of the inertial-region large-scale structures, on the small scales near the wall in a turbulent boundary layer. Hot-wire measurements were made in flow over a smooth- and a rough-wall (a multi-scale topography), in light of recent studies establishing the phenomena in flows over smooth walls. One-probe measurements capture the streamwise turbulent kinetic energy distribution among various scales and local large-scale–small-scale interactions across the flow. Two-probe measurements, measuring the large scales in the inertial region and small scales in the near-wall region simultaneously, were then performed to investigate the modulation influences. Amplitude (AM) and frequency modulation (FM) were observed in rough-wall flow, similar in structure to that of the smooth-wall flow. Further, among different spanwise locations investigated in flow over the roughness, it was found that the subtle differences in interactions exist between regions of low-momentum pathways (LMPs) and high-momentum counter parts (HMPs).

INTRODUCTION

Recent studies on high Reynolds number (Re) smooth-wall turbulent boundary layers have shown strong modulation influences of the outer layer on the near-wall, small-scale turbulence. Particularly, the small scales close to the wall were found to be amplitude- and frequency- modulated by the large- and very large-scale motions (LSMs and VLSMs) in the inertial layer. Since the latter grow stronger with Re, these influences on the 'autonomous' (and Re-independent) near-wall production cycle could gain significance at high-Re flows. More details and analyses can be found in earlier experiments ([1, 2] etc.) and DNS simulations ([3] etc.) for smooth-wall flows.

While these phenomena are well observed in smooth-wall turbulent flows, it is of interest to investigate the same in rough-wall turbulent boundary layers. A fully-rough turbulent boundary layer is expected to have an outer-layer structure similar to that of smooth-wall flows (outer-layer similarity). The near-wall turbulence production cycle of the smooth-wall flow is substituted, in this case, with a roughness sublayer, to which the outer-layer merely 'adjusts'. Thus, it would be interesting to investigate if such interactions exist across the 'outer' region and the roughness sublayer. The current work investigates these influences on a complex roughness reproduced from a damaged turbine blade [4]. With the outer-layer similarity established in earlier studies [5], we aim to understand the amplitude and frequency modulating influences across the boundary layer using 1- and 2- hot-wire probe measurements.

EXPERIMENTS

All experiments were performed in open-circuit wind tunnel ([4] for details). Two types of streamwise velocity time series measurements were taken employing the hot-wire CTA technique. The first set, *1-probe* measurements, were made using a single-component hot-wire probe, traversing across the boundary layer in the wall-normal direction. Amplitude and frequency modulation analyses were then performed using this 1-probe data by assuming that large scales locally measured with the probe are representative of the outer-layer structure owing to a superposition of large scales in the logarithmic region. A second set of measurements, *2-probe* measurements, were performed using two hot-wire probes. While the first-, *outer-* probe was fixed in the logarithmic region to directly measure the large scales of the flow, a second-, *inner-* probe simultaneously measured the small scales close to the wall. These latter 2-probe measurements eliminate the aforementioned 1-probe analysis assumption regarding the large scales.

The roughness and flow characteristics can be found in earlier studies [4, 5, 6]. Particularly, Barros and Christensen [6] reported spanwise alternating high- and low-momentum pathways (HMPs and LMPs) in the mean flow, bounded by streamwise-oriented roll cells, associated with roughness-induced turbulent secondary flows driven by the heterogeneity of the roughness under consideration. 1- and 2-probe measurements and analyses were performed at two spanwise locations corresponding to one HMP-LMP pair, centered at the HMP and LMP. For the sake of brevity, only 1-probe results are presented here.

RESULTS

A single-probe **amplitude modulation** analysis is performed using the Hilbert transform method described in [1]. As mentioned before, this method assumes that the large-scale velocity fluctuations measured (close to the wall) are a superimposed imprint of the LSMs and VLSMs in the logarithmic region. The Hilbert transform can then be used only on the small scales, and large-scale variations in amplitude of small scales can be correlated with the large scales to compute 1-probe amplitude modulation correlation coefficients (R_a^1). Figure 1(a-c) shows the contours of time-delayed R_a^1 at various wall-normal positions corresponding to the smooth-wall, rough-wall LMP and rough-wall HMP cases. It can be seen that the contours

*Corresponding author. Email: christensen.33@nd.edu

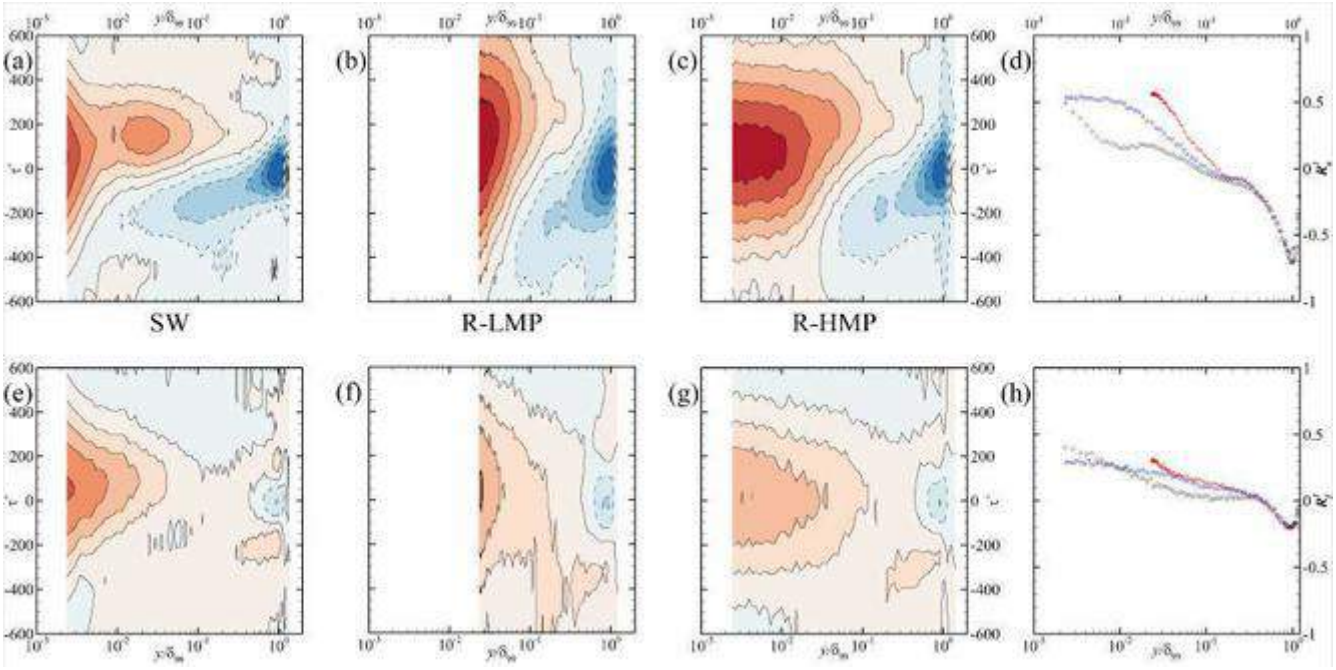

Figure 1: (a-c) Contours of AM correlation coefficient (R_a^1) for smooth-wall (SW), rough-wall LMP (R-LMP) and rough-wall HMP (R-HMP) cases. (e-g) Corresponding FM correlation coefficients (R_f^1). Contour levels are from -0.5 to 0.5 in steps of 0.1; dashed contour lines are negative levels. (d,h) AM and FM coefficients, respectively, at zero time delay ($R_{a;\tau=0}^1$ and $R_{f;\tau=0}^1$). black, circles: SW; red, triangles: R-LMP; blue, squares: R-HMP.

of R_a^1 of rough-wall flow are anatomically similar to the smooth-wall case, with the interactions reflected in high correlation values near the wall. Further, the zero-time delay correlation coefficients [$R_{a;\tau=0}^1$; Figure 1(d)] show clearly that the amplitude modulation as measured by this technique also persists in the rough-wall cases as well. However, the correlation coefficient appears to behave differently in the HMP and LMP regions.

Frequency modulation analysis can also be performed using 1-probe measurements using wavelet transforms instead of the Hilbert transform [7], where the velocity time series are decomposed into time-frequency wavelet power spectrum (WPS). By choosing an 'instantaneous frequency' per time instant, one can obtain the small-scale frequency time series which can be correlated with the large-scale signal to obtain frequency modulation correlation coefficients (R_f^1), and investigate the FM influences of large scales on the small scales. Figure 1(e-g) shows contours of R_f^1, akin to the AM counterparts. The near-wall modulation effect is readily apparent close to the wall, much more so than the AM analysis, since the effects measured in FM do not overlap with scale arrangement in the inertial region (that is captured in R_a^1). Further, it can be seen from the zero-time correlation [$R_{f;\tau=0}^1$; Figure 1(h)] that the frequency modulation effects also exist alongside the amplitude modulation in both the HMP and LMP regions, and in a similar fashion.

The 2-probe simultaneous measurements and analyses (not shown here) enable direct correlation of roughness sublayer dynamics with the inertial region structures. Work is being done to examine the similarities and differences, if any, with the smooth-wall flow dynamics. We expect this analysis to shed additional light on the interaction mechanisms in both smooth- and rough-wall turbulent flows.

References

[1] Mathis, R., N. Hutchins and I. Marusic. Large-scale amplitude modulation of the small-scale structures in turbulent boundary layers. *J. Fluid Mech.*, 628:311-337, 2009.

[2] Mathis, R., N. Hutchins and I. Marusic. A predictive inner–outer model for streamwise turbulence statistics in wall-bounded flows. *J. Fluid Mech.* 681:537-566, 2011.

[3] Bernardini, M. and S. Pirozzoli. Inner/outer layer interactions in turbulent boundary layers: a refined measure for the large-scale amplitude modulation mechanism. *Phys. Fluids* 23, 2011.

[4] Mejia Alvarez, R. Experimental study of low-order models of highly-irregular roughness and their impact on turbulent boundary layers. PhD thesis, University of Illinois at Urbana-Champaign, 2011.

[5] Wu, Y., and K. T. Christensen. Outer-layer similarity in the presence of a practical rough-wall topography. *Phys. Fluids* 19, no. 8: 85108-85108, 2007.

[6] Barros, J. and K. T. Christensen. Observations of Turbulent Secondary Flows in a Rough-Wall Boundary Layer. *J. Fluid Mech.*, 748:R1, 2014.

[7] Baars, W. J., K. M. Talluru, N. Hutchins, and I. Marusic. Wavelet analysis of wall turbulence to study large-scale modulation of small scales. *Exp. Fluids* 56, no. 10: 1-15, 2015.

FREQUENCY DEPENDENCE OF DRAG REDUCTION IN A WAVY SURFACE TURBULENT BOUNDARY LAYER

Wenfeng Li[1a)] , Dorothee Roggenkamp[1], Wilhelm Jessen[1], Michael Klaas[1] & Wolfgang Schröder[1]
[1]*Institute of Aerodynamics, RWTH Aachen University, Aachen, Germany*

Summary Drag reduction effects by spanwise traveling surface waves with wall deformation in a fully turbulent flat plate boundary layer are investigated by PIV and μ-PTV. A parametric study is performed in a low speed wind tunnel by varying the wave frequency, the amplitude, and the Reynolds number. Several parameters, e.g., wave amplitude, frequency, and Reynolds number are found to be relevant factors of the drag reduction effect. In this study, we focus on the wave frequency dependence of the drag reduction. Within the range of the parameters investigated, the maximum drag reduction ratio is 3.4 % at $A^+ = 9$ and $T^+ = 110$. Furthermore, the turbulence statistics above the moving surface are investigated in detail and the drag reduction mechanism is related to a damping of the turbulent flow structures with the induced spanwise velocity component.

Introduction

Due to the high energy consumption and the need of reducing pollutant emissions in the environment, friction drag reduction of turbulent wall-bounded flow is increasingly drawing attention from the fluid mechanics research community. In the past two decades, many control strategies have been developed for drag reduction, such as micro-structured surfaces [1], MEMS-based closed-loop feedback control [2], and open-loop wall motions [3]. Amongst these methods, the in-plane wall motions with which large scale flow control is feasible have been reviewed by Quadrio [4]. Tamano and Itoh [5] analyzed the effect of spanwise traveling waves with surface deflection in the wall-normal direction using a flexible sheet. A maximum drag reduction ratio (*DR*) of 13% was obtained in a turbulent boundary layer, which agrees well with the numerical simulation by Klumpp et al. [6]. A similar approach by Tomiyama and Fukagata [7] with direct numerical simulation achieved a drag reduction of 13.4% in a channel flow. Recently, the impact of the amplitude and pressure gradient were investigated by Koh et al. [8] and Meysonnat et al. [9], respectively. These investigations suggest that the traveling wave-like wall deformation is an effective control method for drag reduction. However, the drag reduction mechanism and how the wave parameters dominate the drag reduction effect by spanwise traveling wave motion in turbulent boundary layers are not fully understood, yet. In this study, the experimental investigations focus on the influence of the wave frequency on the drag reduction with a transversal surface wave, i.e., a spanwise traveling wave with surface deformation in the wall-normal direction. Particle-image velocimetry (PIV) and micro-particle tracking velocimetry (μ-PTV) measurements in the near-wall region of a fully turbulent flat plate boundary layer are conducted at the position above and downstream of a moving surface to investigate the impact of the wave-like surface deformation. The experiments are performed under several sets of wave conditions, i.e., frequency, amplitude, and Reynolds number to analyze the impact of the wave parameters on the wall-shear stress distribution.

Experimental setup and methods

The experiments are performed in a low speed wind tunnel. A flat plate with a tripping wire downstream of an elliptical leading edge is used to generate a fully developed zero pressure gradient turbulent boundary layer. The center of the flat plate is equipped with a flush-mounted insert, in which an aluminum surface of 0.3 mm thickness is actuated creating a spanwise traveling sinusoidal wave with wall-normal deflection. The transversal wave is imposed on the aluminum surface by an electromagnetic actuator system developed by the Central Institute for Electronics (ZEL) of the Forschungszentrum Jülich. It consists of 10 bars with a lateral spacing of 20 mm aligned in the streamwise direction which are glued to the lower surface of the aluminum sheet. Each bar is equipped with a copper coil of 200 windings and is located between permanent magnets. The actuator system is operated by a control unit that allows the generation of transversal surface waves with an amplitude up to $A = 0.5$ mm and frequencies in the range 0 Hz $< f <$ 160 Hz. To obtain the flow field in the boundary layer, several measurement techniques are applied including standard 2D-2C PIV, high resolution μ-PTV, and multi-camera 2D-2C/3C PIV. The velocity profiles in the *x*-*y* plane are measured by a standard 2D-2C PIV setup and the near-wall region is obtained using a μ-PTV system. The local wall-shear stress τ_w is determined by the velocity gradient in the viscous sublayer ($y^+ \leq 3.5$) which yields $\tau_w = \mu \partial u/\partial y \cong \mu du/dy$. Furthermore, the spanwise velocity distribution over the moving surface in the *x*-*z* plane is determined by a multi-camera 2D-2C/3C PIV setup. To investigate the impact of the wave phase, the measurement systems are triggered by the wave signal such that the flow fields over the wave crest and trough can be analyzed.

Results and discussion

The experiments were conducted at three Reynolds numbers of $Re_\Theta = 1200$, 1660, and 2080 based on the momentum thickness Θ. The wavelength of the surface wave was kept at a constant value of $\lambda = 160$ mm, whereas three amplitudes $A = 0.26$, 0.315, 0.375 mm were analyzed. Additionally, three frequencies of $f = 27$, 54, 81 Hz were investigated. However, only those parameter combinations of Reynolds number, frequency, and amplitude that are listed in Table 1 were investigated. These values corresponded to dimensionless periods of $T^+ = u_\tau^2 / (f\,\nu) = 330$, 165, 110 and amplitudes of $A^+ =$

a) Corresponding author. Email: w.li@aia.rwth-aachen.de

$A\,u_\tau / \nu = 6, 7, 9$ at $Re_\Theta = 1200$. Figure 1 shows the results of the local drag reduction (DR) defined as the relative wall-shear stress difference between the modified and the non-impacted flow 3 mm (75 wall units for $Re_\Theta = 1200$) downstream of the actuated surface. The comparison of the results of $f = 27$, 54, 81 Hz at $Re_\Theta = 1200$ shows that the drag reduction effect depends strongly on the wave frequency. At a lower T^+ value a higher drag reduction is achieved while at higher T^+ the drag reduction effect decreases. The PIV and μ-PTV results in the x-y plane show that the velocity gradient and turbulence intensity are reduced by the traveling surface wave motion in the drag reduction cases. A phase-averaging measurement over the moving surface in the x-z plane is conducted at $Re_\Theta = 1200$ with the frequency of 81 Hz and amplitude of 0.375 mm which shows the maximum drag reduction of 3.4%. The results in Figure 2 show that a velocity component in the spanwise direction is induced by the wave motion. Above the wave trough a spanwise flow is induced in the same direction as the traveling wave, while above the wave crest a weaker flow is induced in the opposite direction. The quasi-streamwise vortices are weakened and shifted away from the wall by the induced spanwise flow. These experimental results confirm the findings of Tomiyama and Fukagata [7] on the mechanisms of spanwise traveling surface waves.

Table 1. Experimental parameter combinations of Reynolds number, frequency, and amplitude

Re_Θ	A = 0.26 mm	A = 0.315 mm	A = 0.375 mm
1200	27/54/81 Hz	27/54/81 Hz	27/54/81 Hz
1660	81 Hz	81 Hz	81 Hz
2080	81 Hz	81 Hz	81 Hz

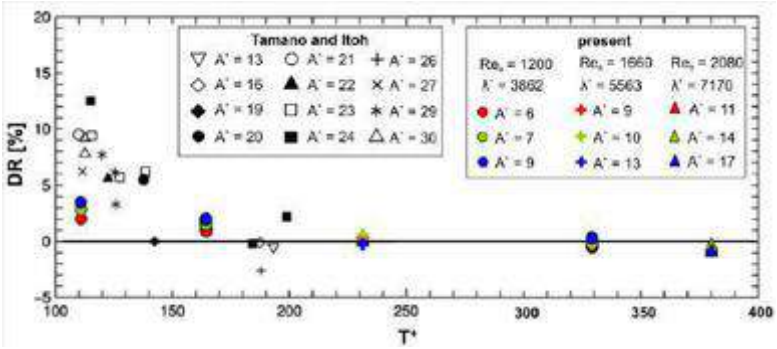

Figure 1. DR versus T^+ showing the comparison of present results and the findings of Tamano and Itoh [5]

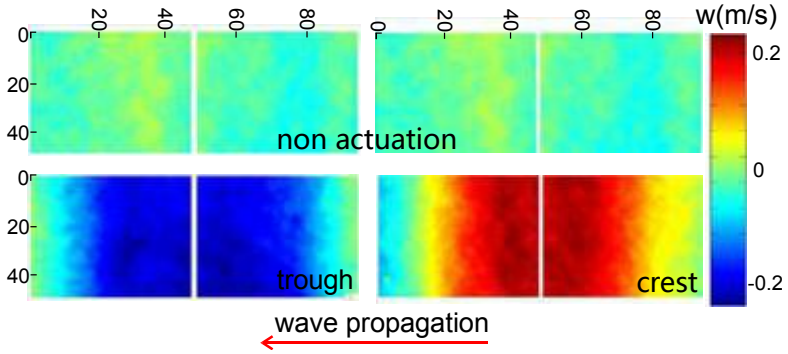

Figure 2. Comparison of the phase-averaged spanwise velocity distributions over the nonactuated surface, wave trough and crest, x-z plane, $y^+ = 25$, $A^+ = 9$, $T^+ = 110$

Reference

[1] Bechert, D. *et al*. 1997 *Journal of Fluid Mechanics*, **338**(5), pp. 59-87.
[2] Kasagi, N. *et al*. 2009 *Annual review of fluid mechanics*, **41**, pp. 231-251.
[3] Du, Y. & G.E. Karniadakis 2000 *Science*, **288**(5469), pp. 1230-1234.
[4] Quadrio, M. 2011 *Philosophical Transactions of the Royal Society of London A: Mathematical, Physical and Engineering Sciences*, **369**(1940), pp. 1428-1442.
[5] Tamano, S. & M. Itoh 2012 *Journal of Turbulence*, **13**(13).
[6] Klumpp, S. *et al*. 2010 *Journal of Turbulence*, **11**(11), pp. 1-13.
[7] Tomiyama, N. & K. Fukagata 2013 *Physics of Fluids (1994-present)*, **25**(10), pp. 105-115.
[8] Koh, S. *et al*. 2015 *Computers & Fluids*, **119**, pp. 261-275.
[9] Meysonnat, P.S. *et al*. 2016 *Applied Mathematics and Computation*, **272**, pp. 498-507.

SWEEPS AND EJECTIONS IN ZPG AND STRONG APG TURBULENT BOUNDARY LAYERS

Yvan Maciel[1], Ayse Gungor *[2], and Mark P. Simens[3]
[1]*Department of Mechanical Engineering, Laval University, Quebec City, Quebec, Canada*
[2]*Faculty of Aeronautics and Astronautics, Istanbul Technical University, Istanbul, Turkey*
[3]*School of Aeronautics, Universidad Politécnica de Madrid, Madrid, Spain*

Summary We analyse the properties of three-dimensional sweeps and ejections in two zones of a zero-pressure-gradient turbulent boundary layer (ZPG TBL), corresponding to two ranges of Reynolds number, and three zones of a strongly decelerated TBL, corresponding to three ranges of mean velocity defect. In the case of the APG TBL, the last zone includes a very thin separation bubble. The ZPG TBL results show that the properties of sweeps and ejections are only minimally affected by the Reynolds number for the Reynolds number range considered. The effect of increasing mean velocity defect in the adverse pressure gradient (APG) TBL is however significant. The near-wall sweeps and ejections and the taller ones that reach the wall (important in the log layer of the ZPG TBL) become progressively less numerous, less intense and less streamwise elongated. They lose their role as the main contributors to the Reynolds shear stress.

A turbulent boundary layer subjected to a strong or prolonged adverse pressure gradient develops a large mean velocity defect. Consequently, turbulence activity and production is small near the wall and important in the outer region, in contrast to canonical turbulent wall flows. Various studies suggest that the physical mechanisms and coherent structures responsible for the production and transport of turbulence might be different in APG TBLs, but information on the coherent structures found in APG TBLs is sparse (see [1]). Recently, we investigated the three-dimensional properties of the u and uv structures (Qs) found in the two flows of the present study by focusing on one zone in each flow [1]. In the APG TBL, it was found that near-wall streaks, ejections and sweeps are less numerous in the large-defect zone of the flow. Large sweeps and ejections that reach the wall region (wall-attached) were also found to be much less predominant. The present study pushes further the analysis of the three-dimensional Q structures by investigating their streamwise evolution in a ZPG TBL (effect of the Reynolds number) and in an APG TBL with a progressive increase of its mean velocity defect (effects of the pressure gradient, principally, and of the Reynolds number).

The two direct numerical simulations have been performed with the same code. The ZPG TBL was simulated by Sillero et al. [2] while the APG TBL simulation was carried out recently by the present authors [1]. The ZPG DNS covers the Reynolds number range $Re_\theta = 2780-6680$. For the APG DNS, the inflow boundary conditions are those of a ZPG TBL at $Re_\theta = 1003$ provided by an auxiliary ZPG TBL simulation running concurrently. The flow at the edge of the boundary layer decelerates over most of the domain but reaccelerates at the end. It results in a turbulent boundary layer with a steadily increasing mean velocity defect. At the wall, the flow separates near the exit of the domain in the form of a very thin separation bubble (the height of the zone of negative U never exceeds 0.02δ). The reacceleration of the flow at the end reattaches the boundary layer.

The three-dimensional Qs are identified with a method similar to that of [3]. They are defined as regions of connected points that satisfy simultaneously two conditions. The first condition is $|uv| > H^*\sigma_u\sigma_v$, where $H^* = 1.75$ is the threshold constant determined via a percolation analysis [1] and σ_u, σ_v are the local standard deviations of u and v. The second condition is that all points within a Q structure are in the same quadrant of the u, v space. Following the notation of [3], Q2 and Q4 structures will be referred to as Q^-s, and Q1s and Q3s as Q^+s. Table 1 describes the 5 extraction volumes chosen in the two flows. $Re_m = U_m\delta/\nu$ is the outer region Reynolds number expressed with a mixing-layer-type outer-velocity scale $U_m = 2(U_e - U(y = 0.5\delta))$ [1]. B_x, B_y and B_z are the box dimensions along the three axes and δ_a is the average boundary layer thickness inside the box. The extraction volumes are chosen long enough to ensure that the longest Qs are detected. The APG2 box ends at the position of mean flow separation and APG3 includes the thin separation bubble.

Before discussing the Q results, the Reynolds shear stress and its quadrant decomposition are presented. Figure 1 shows the rapid evolution of the Reynolds shear stress in the APG TBL whereas changes with Reynolds number in the case of the ZPG TBL are relatively small. In the APG flow, its maximum is in the outer region and it shifts further away from the wall with increasing velocity defect. The trend just described is common to all Reynolds stress components. The fact that Reynolds

Table 1: Parameters of the Q extraction zones and number and volume proportions (in %) of the Q^-s

Case	Re_θ	Re_m	H	$(B_x, B_y, B_z)/\delta_a$	N_a	V_a	N_w	V_w	N_{wa}	V_{wa}
ZPG1	4544-5801	10195-10811	1.38-1.37	4.5, 2.0, 10.6	58	88	72	86	42	2.2
ZPG2	6270-6600	14126-14931	1.37-1.36	4.5, 2.0, 7.7	57	89	68	84	46	2.0
APG1	1506-2577	3708-9181	1.54-1.97	6.5, 2.0, 7.6	62	86	81	85	14	1.2
APG2	2577-3916	9204-27889	1.97-3.42	5.0, 2.0, 4.1	52	83	58	62	12	1.1
APG3	3635-4409	21894-32700	2.98-3.75	3.8, 2.0, 2.9	51	78	48	49	8	1.2

*Corresponding author. Email: yvan.maciel@gmc.ulaval.ca

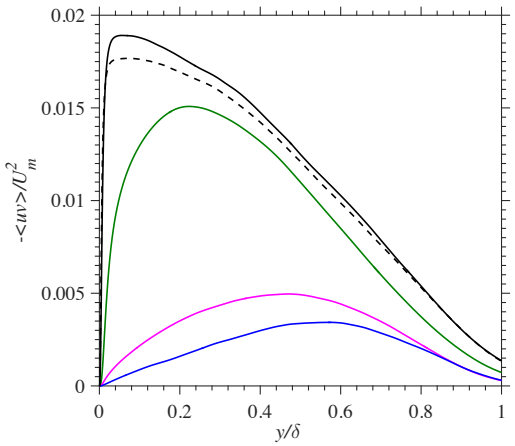

Figure 1: Reynolds shear stress normalized with U_m at the center of each zone: ZPG1 (solid black), ZPG2 (dashed black), APG1 (green), APG2 (magenta), APG3 (blue)

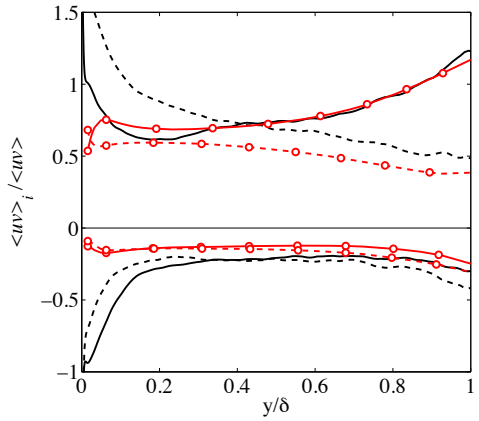

Figure 2: Quadrant contribution to the Reynolds stress. Positive: solid, Q2; dashed, Q4. Negative: solid, Q1; dashed, Q3. Black: APG TBL at $H = 3.43$, red with circles: ZPG

stresses normalized with U_m decrease with velocity defect throughout the outer region implies that large-defect TBLs are less efficient in transferring energy from the mean flow to turbulence. Figure 2 presents the fractional contributions from the four quadrants to the Reynolds shear stress (data at position of mean flow separation for the APG TBL). The pressure gradient increases the fractional contribution of all quadrants, except for Q2 in the outer region. The differences between the two flows are more pronounced near the wall. The crossing between the sweep-dominated region and the ejection-dominated region takes place much further from the wall in the APG case. This point is close to the local maximum of the Reynolds shear stress.

The following results come from the examination of several joint pdfs of parameters of individual Qs: linear dimensions and volume, wall-normal position, volumetric average of u, v and uv. In Table 1, N_a and V_a are respectively the number and volume percentage of Q$^-$s (sweeps and ejections) with respect to all Qs, for the whole boundary layer. As in channel flows [3], Q$^-$s are more frequent than Q$^+$s in both TBLs, and they occupy a larger fraction of the space. However, the predominance of the Q$^-$s diminishes as the defect increases in the APG TBL. But sweeps and ejections remain bigger than Q1s and Q3s. In the logarithmic region of the ZPG TBL, streaky wall-attached sweeps and ejections are bigger and stronger than wall-detached ones as in channel flow [3]. They are the ones that contribute significantly to the Reynolds shear stress. In the outer region of the APG TBL, as the velocity defect increases, the wall-attached Q$^-$s progressively become less numerous and voluminous than the detached ones. The stronger Q$^-$s are always in the region of maximum Reynolds shear stress and very big ones regularly reach the wall, especially sweeps.

N_w and V_w in Table 1 are respectively the number and volume percentage of near-wall Q$^-$s with respect to all near-wall Qs (near-wall Qs are defined here as structures whose center is below 0.05δ). Again, for the small defect cases, near-wall Q$^-$s tend to be more numerous and bigger than near-wall Q$^+$s. Moreover, Q2s are stronger than the other Qs. In the case of the ZPG TBL, as expected, most of the sweeps are found very close to the wall, below the strong ejections. The near-wall sweeps divide in two groups: flattened sweeps very close to the wall and streaky sweeps, like the streaky ejections, that tend to be taller than wider. In the APG TBL, the organisation of the near-wall Qs changes as the velocity defect increases. The predominance in terms of number and size of the near-wall Q$^-$s over Q$^+$s has completely disappeared in zone APG3. In that zone, near-wall Q4s and Q1s are the strongest events, with higher u values. They however have comparable size, wall-normal distributions and shapes as Q2s and Q3s. All near-wall Qs tend to be flattened. They lose their streamwise elongation and become as wide as they are long, with the most probable aspect ratios being roughly $\Delta_x \approx \Delta_z \approx 2\Delta_y$. The biggest near-wall Qs tend to be wider than longer. N_{wa} and V_{wa} in Table 1 are respectively the number and volume percentage of near-wall Q$^-$s with respect to all Q$^-$s. The proportion of near-wall ejections and sweeps in the large defect APG TBL is considerably smaller than in the ZPG TBL, and it diminishes as the velocity defect increases.

References

[1] Simens M. P., Gungor A. G., Maciel Y.: Coherent structures in a zero-pressure-gradient and a strongly decelerated boundary layer. J. of Physics: Conf. Series (in press), 2016.

[2] Sillero J., Jiménez J., Moser R: One-point statistics for turbulent wall-bounded flows at Reynolds numbers up to $\delta^+ \approx 2000$. Phys. Fluids 25, 2013.

[3] Lozano-Durán A., Flores O., Jiménez J.: The three-dimensional structure of momentum transfer in turbulent channels. J. Fluid Mech. 694, 2012.

HISTORY EFFECTS IN ADVERSE PRESSURE GRADIENT TURBULENT BOUNDARY LAYERS – SIMULATIONS & EXPERIMENTS

Ramis Örlü *[1], Alexandra Bobke[1], Carlos Sanmiguel Vila[2],
Ricardo Vinuesa[1], Stefano Discetti[2], Andrea Ianiro[2], and Philipp Schlatter[1]

[1] *Linné FLOW Centre, KTH Mechanics, Stockholm, Sweden,*
[2] *Aerospace Engineering Group, University Carlos III of Madrid, Leganés, Spain*

Summary The present investigation focusses on the concerted investigation of pressure gradient and streamwise curvature effects on turbulent boundary layers. In particular, a number of direct and large-eddy simulations covering a wide range of pressure gradient parameters and streamwise histories on flat and curved surfaces is performed and will be compared with wind tunnel experiments that overlap and extend the Reynolds number range. Results are aimed at isolating the effects of pressure gradients, streamwise curvature and streamwise (pressure gradient) histories, which have traditionally inhibited to draw firm conclusions from the available data.

MOTIVATION

The quest for more efficient airplanes, trains and other ground vehicles is directly coupled to reducing the form and/or friction drag without compromising the other. A prototype of a canonical flow on which our understanding of friction drag has been developed is the zero-pressure gradient (ZPG) turbulent boundary layer (TBL). Despite its importance for fundamental research, most flows of relevance in technical applications are exposed to various pressure gradients and surface curvature which instead may lead to changes (increase) of the form drag. The applicability of knowledge from canonical wall-bounded flows is hence limited when it comes to these complex flows and geometries (see e.g. Ref. [4]). While the effect of pressure gradient and surface curvature has been the focus of much attention, their combined effect is not a simple superposition and therefore deserves special attention [8]. Although a number of simulations and experiments on e.g. adverse pressure gradients (APG) were performed in the past (spanning a wide range of Reynolds numbers Re and the values of the Clauser pressure gradient parameter β), it is hard to draw firm conclusions from the available data due to the differently varying streamwise gradients of β, i.e. different upstream histories leading to a particular pressure gradient condition. The present contribution aims therefore at establishing different upstream histories on curved and flat surfaces, and in particular to maintain a region of constant β, in order to study the genuine effect of the imposed pressure gradient and its upstream history separately.

METHODS AND OUTLOOK

A number of direct numerical and large-eddy simulations (DNS and LES) have been performed in flat plate ZPG [5, 6] and APG [1] TBLs with different power-law free-stream parameters m. Additionally, the results of a DNS of the flow around a wing section represented by a NACA4412 profile are at hand (Fig. 1), which complement the numerical data base and already indicate clear dependencies on pressure gradient and upstream histories as evident from Fig. 2: By comparing the wing and the flat plate at a matched Re_τ and β, it is possible to assess the effect of history, i.e. of $\beta(x)$, on the state of the TBL. As apparent, the wake region in the mean velocity as well as the outer peak in the variance profile are significantly affected by the history of the pressure gradient; a manifestation of the interaction between the large-scale motions, which are more energetic due to the APG, and the outer flow. Further simulations are being performed in which a sufficiently long constant β range is established. To extend the Re-range and cross-validate numerical and physical experiments, wind tunnel experiments are currently ongoing in the Minimum Turbulence Level (MTL) wind tunnel at KTH Royal Institute of Technology in which the desired pressure gradient conditions and histories will be established by means of wall inserts. Besides oil-film interferometry, hot-wire anemometry and particle image velocimetry will be employed to measure the wall shear stress and study the flow kinematics and dynamics, respectively.

The results from these concerted efforts will be presented at the congress.

*Corresponding author. Email: ramis@mech.kth.se

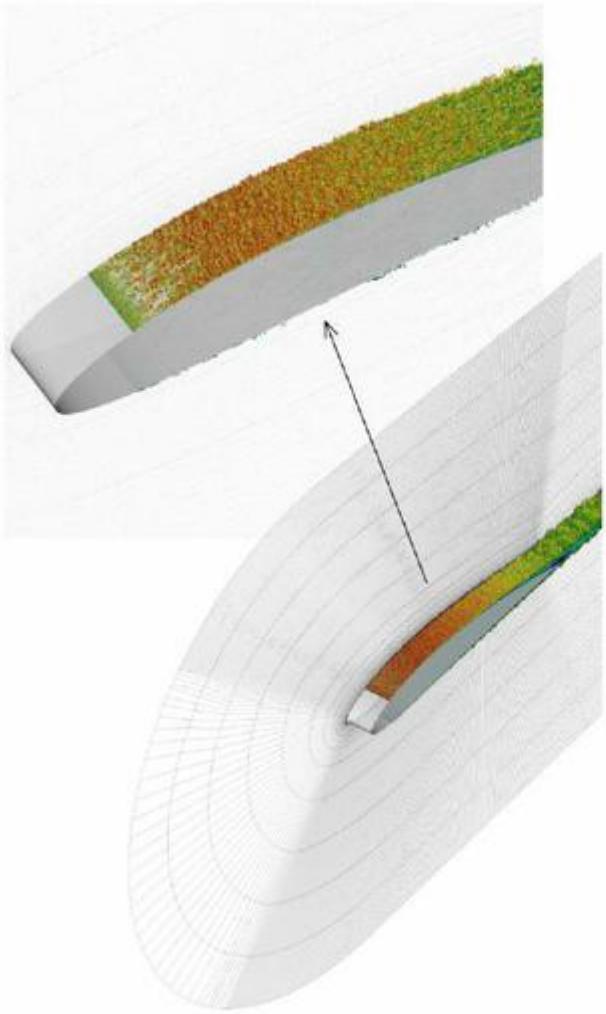

Figure 1: Instantaneous visualization of the flow around the NACA-4412 airfoil, with $Re_c = 400000$ and angle of attack of 5 degrees. The figure shows coherent vortices identified by means of the λ_2 criterion [2]. The spectral element mesh is also shown, but not the individual grid points within elements. Note that the flow is tripped at a distance 10% of the chord length downstream of the leading edge, both on the pressure and suction sides. For full details, see Ref. [7].

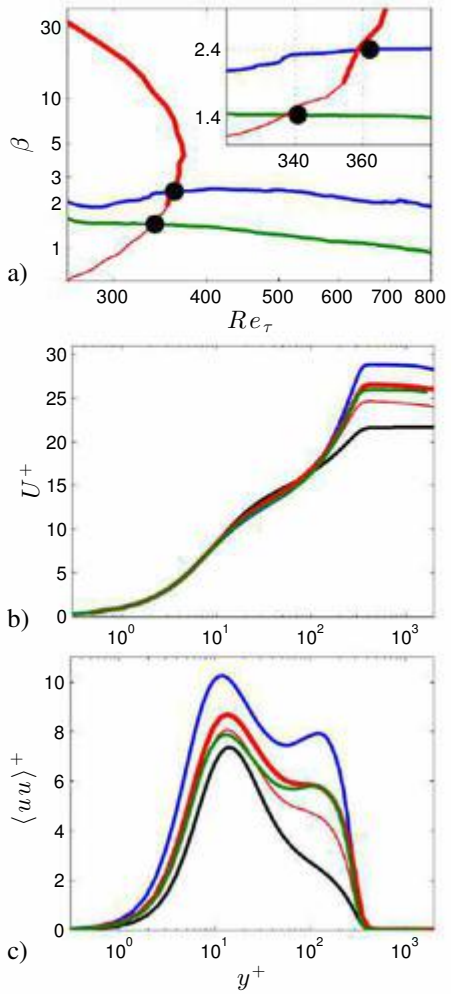

Figure 2: a) Clauser pressure gradient parameter β as function of friction Reynolds number Re_τ for the boundary layer on the wing (red), and the flat plate ($m = -0.13$: green, $m = -0.16$: blue). Inset indicates the matched $\beta - Re_\tau$ values. Inner-scaled b) mean and c) variance profiles for the matched conditions (filled circles) shown in a) compared with a ZPG TBL on a flat plate [5] at comparable Re_τ (black).

References

[1] Bobke, A., Vinuesa, R., Orlü, R., Schlatter, P.: Large-eddy simulations of adverse pressure gradient turbulent boundary layers. J. Phys.: Conf. Ser. (In Press), 2016.

[2] Jeong, J., Hussain, F.: On the identification of a vortex. J. Fluid Mech. 285:69–94, 1995.

[3] Marusic I., Mckeon B. J., Monkewitz P. A., Nagib H. M., Smits A. J., Sreenivasan K. R.: Wall-bounded turbulent flows at high Reynolds numbers: Recent advances and key issues. Phys. Fluids 22:065103, 2010

[4] Patel V.C., Sotiropoulos F.: Longitudinal curvature effects in turbulent boundary layers. Prog. Aerosp. Sci. 33:1–70, 1997.

[5] Schlatter, P., Orlü, R.: Assessment of direct numerical simulation data of turbulent boundary layers. J. Fluid Mech. 659:116–126, 2010.

[6] Schlatter, P. and Orlü, R.: Turbulent boundary layers at moderate Reynolds numbers: inflow length and tripping effects. J. Fluid Mech. 710:5–34, 2012.

[7] Vinuesa R., Hosseini S. M., Hanifi A., Henningson D. S., Schlatter P.: Direct numerical simulation of the flow around a wing section using high-order parallel spectral methods. Proc. 9th Int. Symp. Turbulence & Shear Flow Phenomena, Melbourne, Australia. 2015

[8] Webster D. R., DeGraaf D. B., Eaton J.K.: Turbulence characteristics of a boundary layer over a two-dimensional bump. J. Fluid Mech. 320:53–69, 1996.

EFFECT OF BOUNDARY-LAYER SUPERSTRUCTURES ON SEPARATION BUBBLE UNSTEADINESS

Arnaud Le Floch[1], Abdelouahab Mohammed-Taifour[1], Julien Weiss[1a)], Louis Dufresne[1], Jérôme Vétel[2], Emmanuel Jondeau[3]

[1]*TFT - Thermo-Fluid for Transport Laboratory, École de technologie supérieure, Montréal, Québec, Canada*

[2]*LADYF - Fluid Dynamics Laboratory, École Polytechnique Montréal, Montréal, Québec, Canada*

[3]*LMFA - Fluid Mechanics and Acoustics Laboratory, École Centrale Lyon, France*

Summary: In order to investigate the cause of the low-frequency unsteadiness of a pressure-induced turbulent separation bubble (TSB), long meandering superstructures are observed in the zero-pressure-gradient turbulent boundary layer well upstream of the TSB. The characteristic frequency associated with the superstructures is compared to that of the low-frequency breathing motion previously documented in the TSB. The large difference between the two characteristic frequencies indicates that the superstructures are not the cause of the unsteadiness.

INTRODUCTION

Turbulent separating and reattaching flows are often characterized by unsteady motions in a wide range of time scales. Recently, Weiss *et al* [1] investigated the unsteady behavior of an incompressible, pressure-gradient-induced, turbulent separation bubble (TSB) formed on a flat test surface by a combination of adverse and favorable pressure gradients. Using single-point instrumentation including unsteady pressure transducers and thermal-tuft probes, they showed that the TSB is characterized by two unsteady modes: a low-frequency mode, with a Strouhal number $St_1 = f \cdot L_b/U_{ref} \approx 0.01$, which is related to a global "breathing" motion (i.e., contraction/expansion) of the separation bubble, and a medium-frequency mode, with a Strouhal number $St_2 \approx 0.35$, which occurs because of the vortex shedding associated with the shear-layer instability. In both cases the Strouhal number is constructed with the average length L_b of the TSB and the velocity U_{ref} in the potential region of the incoming flow. The medium-frequency shedding mode was shown to be consistent with the mechanism already observed in flows were separation is fixed by a geometric singularity: vortices are created through a Kelvin-Helmholtz instability and subsequently merge to form larger coherent structures that are shed downstream [2]. On the other hand, the mechanism responsible for the breathing mode remains unexplained.

In the present contribution we investigate if the long, meandering superstructures detected in turbulent boundary layers by several researchers (*e.g.* [3]) may be the cause of the low-frequency breathing motion. This hypothesis is motivated by the results of Ganapathisubramani *et al* [4] and Pearson *et al* [5], who suggested that those superstructures might be responsible for the low-frequency unsteadiness observed in a shock-induced separated flow and a forward-facing step flow, respectively. In a first step, we attempt to visualize the superstructures and compare their size with those reported by Hutchins and Marusic [3]. Then, in a second step, we compare the characteristic frequencies of these superstructures with that of the breathing motion documented in our TSB.

EXPERIMENTAL SETUP

Measurements are performed in the TFT Boundary-Layer Wind Tunnel at a reference velocity $U_{ref} = 25$ m/s, as in Weiss *et al* [1]. A 2D-2C high-speed Particle Image Velocimetry (PIV) system is used to measure the velocity field in a streamwise / spanwise plane (*x*-*z*) upstream of the TSB. The laser sheet of 1 mm thickness is positioned 4 mm away from the wall ($y^+ = y \cdot u_\tau/\nu = 250$). The streamwise dimension of the field-of-view (FOV) is $\Delta x_{PIV} = 76.4$ mm and the spanwise dimension is $\Delta z_{PIV} = 216.7$ mm. The upstream side of the FOV is positioned at $x_u = -1.17 L_b$ from the mean detachment line, where $L_b = 0.4$m is the average length of the TSB on the test-section centerline [1]. The pressure gradient within the FOV is essentially zero, the boundary-layer thickness in the midpoint of the FOV is $\delta = 30$ mm, and the friction velocity is $u_\tau = 0.98$ m/s. Images are recorded by two Phantom V9.1 CMOS cameras that are positioned side by side. The frame rate is $f_{PIV} = 900$ Hz and the resolution of the vector field is approximately 1.1 mm in the *x* and *z* directions. The images are processed by the LaVision DaVis software (v.8.2). More details about the PIV setup are provided in [6].

RESULTS AND CONCLUSION

Figure 1 shows a contour plot of the streamwise velocity fluctuations $u(x,z)$. The streamwise domain is reconstructed using Taylor's hypothesis in a manner similar to [3] and [4]. The convection velocity U_c is assumed to be equal to the average local velocity: $U_c = \overline{U} \approx 18.7$ m/s. Without the use of Taylor's hypothesis, the extent of the streamwise plane would be limited by the cameras FOV to about 2.5δ. The figure reveals the presence of elongated meandering structures whose length can be in excess of 20δ. This is consistent with the results of [3] and [4]. Figures 2 and 3 show the streamwise correlation $R_{uu}(\Delta x, z_{ref})$ and the spanwise correlation $R_{uu}(x_{ref}, \Delta z)$ respectively, where x_{ref} and z_{ref} are the FOV central coordinates. Here also, the data compares reasonably well with the values provided by Hutchins and Marusic (H&M) [3] but our longitudinal correlation appears slightly larger. A possible explanation might be that our structures have not yet "relaxed" from their travel through the wind-tunnel nozzle. There is also a difference in Reynolds number ($Re_\tau = \delta \cdot u_\tau/\nu \approx 2000$ for the

a) Corresponding author. Email: **julien.weiss@etsmtl.ca**

present case and $Re_\tau = 7610$ for H&M). Nevertheless, based on these comparisons, we conclude that the elongated structures observed in Fig. 1 are indeed consistent with the notion of "superstructures" identified by Hutchins and Marusic [3].

Following [4] and [5], we now attempt to relate these superstructures to the unsteady breathing motion of the TSB. Recall that the breathing motion is a contraction/expansion of the TSB with a characteristic Strouhal number $St_1 = f \cdot L_b/U_{ref} \approx 0.01$ [1,6]. Assuming that the superstructures have an average length of 20δ [3], their characteristic frequency f_s is equal to: $U_c/(20\,\delta)$. The Strouhal number St_s associated with the superstructures is then:

$$St_s = f_s \cdot \frac{L_b}{U_{ref}} = \frac{U_c}{20\delta} \cdot \frac{L_b}{U_{ref}} \approx 0.50$$

Hence the Strouhal number associated with the convected superstructures is fifty times larger than the characteristic Strouhal number of the breathing mode. We therefore conclude that the unsteady breathing mode is not likely to be related to the presence of the superstructures upstream of the TSB. This is in contrast with the shock-induced TSB investigated in [4], where the superstructures documented upstream of the separated zone were correlated with the low-frequency unsteadiness at $St = f \cdot L_b/U_{ref} = 0.03$. The large difference in characteristic frequencies observed in our flow also contrasts with the forward-facing step investigated in [5], in which the time scale corresponding to the separation region fluctuations was shown to be consistent with the superstructures. Clearly, further work is required to understand the causes of the low-frequency breathing motion and, more generally, the effect of the superstructures on separated flow regions.

References

[1] Weiss J., Mohammed-Taifour A., and Schwaab Q.: Unsteady Behavior of a Pressure-Induced Turbulent Separation Bubble. *AIAA J*. Vol. 53, No. 9, 2015.

[2] Simpson, R. L.: Turbulent Boundary-Layer Separation. *Ann. Rev. Fluid Mech*. Vol. 21, pp. 205-232, 1989.

[3] Hutchins N. and Marusic I.: Evidence of very long meandering features in the logarithmic region of turbulent boundary layers. *J. Fluid Mech*. vol. 579, pp. 1–28, 2007.

[4] Ganapathisubramani B., Clemens N. T., and Dolling D. S.: Low-frequency dynamics of shock-induced separation in a compression ramp interaction. *J. Fluid Mech*. vol. 636, pp. 397–425, 2009.

[5] Pearson D., Goulart P. J., and Ganapathisubramani B.: Turbulent separation upstream of a forward-facing step. *J. Fluid Mech*. vol. 724, pp. 284-304, 2013.

[6] Mohammed-Taifour A. and Weiss J.: PIV Investigations in the Centerline Plane of a Pressure-Induced Turbulent Separation Bubble, AIAA 2016-2078.

FIGURES

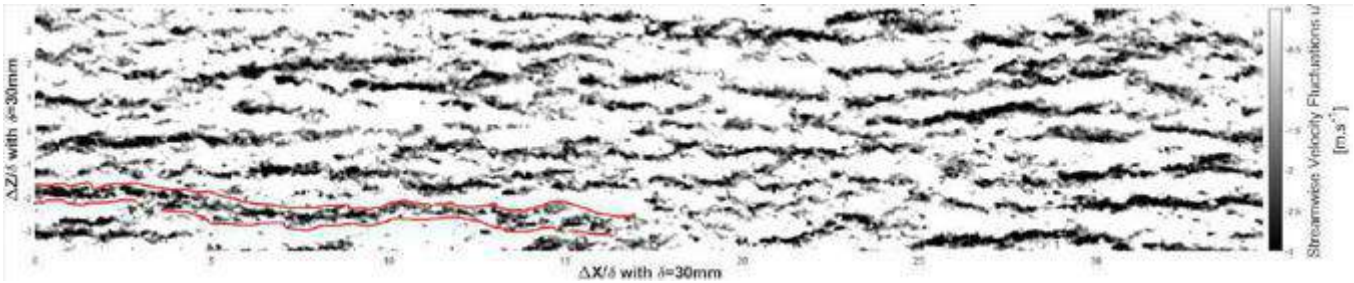

Figure 1: Example of Taylor reconstruction from PIV data. The convection velocity is 18.7 m/s. A part of a meandering superstructure is circled in red. Only negative values are shaded for illustration.

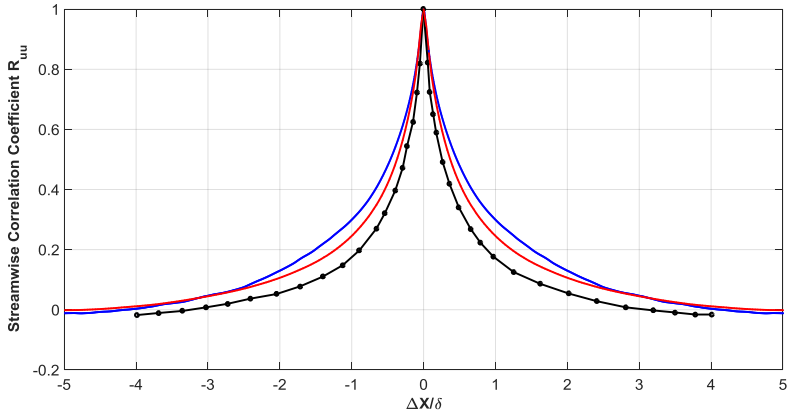

Figure 2: Streamwise Correlation coefficients $R_{uu}(\Delta x, z_{ref})$
In black, results from Hutchins and Marusic [3] ($\delta_{H\&M} = 0.336$m); In red, the streamwise autocorrelations from the Taylor reconstruction of the PIV field, averaged on the spanwise values ($\delta = 0.030$m); In blue, the autocorrelations from a single hot wire, built from its own Taylor reconstruction with a sampling rate of 102.4kHz.

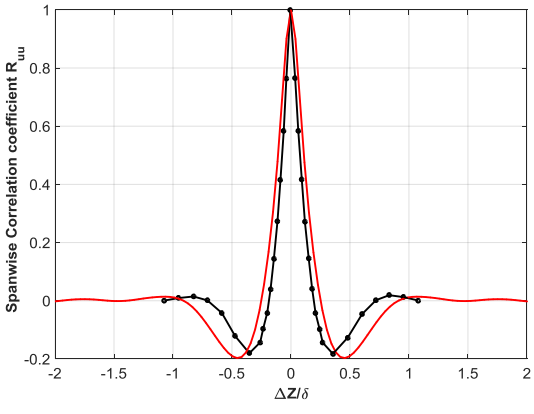

Figure 3: Spanwise Correlation coefficients $R_{uu}(x_{ref}, \Delta z)$
In black, results from Hutchins and Marusic [3] ($\delta_{H\&M} = 0.336$ m); In red, the spanwise autocorrelations from the Taylor reconstruction of the PIV field, averaged on the streamwise values ($\delta = 0.030$m).

HYPERSONIC BOUNDARY LAYER INSTABILITIES

Helen Reed[1a)], Alexander Moyes[1] & Travis Kocian [1]
[1]*Aerospace Engineering, Texas A&M University, College Station, Texas, United States of America*

Summary Our current activities focus on nonlinear parabolized stability equation (NPSE) and bi-global stability analysis of the crossflow, second-mode, and secondary instabilities associated with hypersonic geometries such as the yawed straight cone and the elliptic cone. A predictive NPSE formulation (EPIC) has been developed in-house for modeling of the evolution of instabilities, including the stationary-crossflow-vortex path and the variation of the spanwise wavenumber in the streamwise direction. Multiple instabilities and secondary instabilities are mapped, and these studies are extensively verified and validated with lessons learned provided.

BACKGROUND

The ability to accurately predict and control the transition process from laminar to turbulent flow will provide significant advances in air-vehicle design, with applications ranging from high-altitude long-endurance unmanned aerial vehicles, to energy-efficient transports, to hypersonic systems. The development, validation, and introduction of physics-based approaches for stability and transition prediction will lead to smaller and more manageable uncertainties in the design of vehicles. Moreover, control may be applied for two different reasons. First there is the desire to delay transition, which contributes to aerodynamic heating load reduction and range and/or endurance. A second desire is to encourage transition for enhanced mixing or separation delay, such as over control surfaces and the inlet of a scramjet engine. The most effective strategy for control is to capitalize on the flow physics, identify the relevant instability mechanisms and what affects them, and modulate the most unstable disturbances as they are just beginning to grow. Our team has successfully applied linear and nonlinear parabolized stability equation and global methods to these problems, and also considered the effects of 2-D surface excrescences and formulated a physics-based correlation for forward-facing steps (in subsonic flow) in 3-D boundary layers. Through mechanism identification, verification, and validation activities, several lessons have been learned in applying stability formulations.[1]

There is much information available concerning low-speed fundamental stability mechanisms leading to transition. Mack[2] describes three major differences between supersonic and subsonic flow: the presence of a generalized inflection-point, the dominance of 3-D viscous disturbances called 'first modes' (as compared with 2-D viscous disturbances for subsonic), and the presence of high-frequency acoustic modes. For a 2-D adiabatic flat-plate boundary layer at edge Mach number greater than approximately 4, a 2-D inviscid acoustic mode is generally found to be the dominant instability. This is termed the 'second mode', or 'Mack mode', and is tuned to and influenced by the thermal boundary layer. Mack modes become slightly oblique in a 3-D boundary layer.[3]

Three-dimensional geometry and non-zero angle-of-attack can result in curved streamlines and 3-D basic-state velocity profiles which can be highly inflectional, and thus unstable, and lead to the crossflow instability. Concerning crossflow, the past decades have seen an international effort with close collaboration among theory, computation, experiment, and flight tests, resulting in the identification of important factors for subsonic, transonic, and low supersonic flows.[4,5] First, linear theories predict that traveling crossflow waves are more amplified than stationary waves. In addition, crossflow is ultra sensitive to leading-edge roughness and freestream disturbances and leads to important nonlinear effects across much of the transition zone (necessitating a nonlinear approach such as a nonlinear parabolized stability equation (NPSE) or direct numerical simulation (DNS) approach). Nonlinear effects and modal interaction play an early and important role in transition because of the presence of stationary co-rotating vortices. These vortices distort the mean flow to include inflection points which destabilize the high-frequency secondary instabilities that rapidly breakdown to turbulence.

PROBLEM FORMULATION

Recently, simple 3-D geometries (yawed straight circular cones and elliptic cones) have been studied to provide insight into the stability and transition of hypersonic vehicles, and these are the configurations considered here. (References are provided in Moyes et al.[6]). To model disturbance growth within the boundary layer, different methods may be applied. This work utilizes linear stability theory (LST), NPSE, and 2-D partial-differential-equations (PDE)-based LST, aka spatial bi-global (SBG) theory, for secondary stability analysis.[6,7] In each case, each flow variable is decomposed into a basic state quantity, upon which a disturbance is to be superposed, and the disturbance itself. This superposition is substituted into the governing equations to yield the disturbance equations, which describe the evolution of the disturbance. Each method considers a different solution form of the disturbance.

[a)] Corresponding author. Email: helen.reed@tamu.edu.

RESULTS AND CONCLUSIONS

Focusing on the stationary crossflow instability, our in-house developed NPSE capability, called EPIC[7], predicts nonlinear disturbance evolution that has been verified with DNS of Balakumar & Owens[8] and validated with the quiet-tunnel experiments of Craig & Saric[9]. See Moyes et al.[6] for details and figures. The direction of the crossflow vortex paths and the variation of the spanwise wavenumber are well predicted solely from the basic state.[7]

As the next step, considering the resulting nonlinearly distorted basic state (due to the presence of the stationary crossflow) with low momentum fluid over high momentum fluid and the appearance of new inflection points in the streamwise profile, we apply a bi-global analysis to it. Multiple instabilities are found, including traveling crossflow, secondary instabilities, and second modes. The traveling crossflow begins concentrated near the wall and then as it is more modulated by the stationary crossflow waves, it concentrates in the trough and upwelling of the wave. The secondary instabilities fall into two categories, type-I and type-II. Type-I appear in the shoulder and type-II appear in the crest. The second mode appears near the wall and extends through the boundary layer, with a concentration slightly above the critical layer as well. There is qualitative and quantitative agreement with the experiment of Craig & Saric.[9] Finally, there are similarities between the secondary instabilities associated with the nonlinear evolution of both hypersonic and incompressible-swept-wing stationary crossflow.[10] Further details are found in Reference [6].

ACKNOWLEDGMENTS

This work is supported by Program Manager Rengasamy Ponnappan under AFOSR grant FA9550-14-1-0365. The authors are grateful to Pointwise for providing the gridding software, to NASA for providing DPLR, and to Megan Heard and Lindsay Kirk for running this basic state for us.

References

[1] Reed H., Perez E., Kuehl J., Kocian T., Oliviero N.: Verification and Validation Issues in Hypersonic Stability and Transition Prediction. *Special Section on Numerical Simulation of Hypersonic Flow*. *Journal of Spacecraft and Rockets* **52/1**:29-37, 2015.

[2] Mack L.: *Boundary Layer Stability Theory: In AGARD Special Course on Stability and Transition of Laminar Flow*, AGARD Report 709, 3.1-3.81, 1984.

[3] Balakumar P., Reed H.: Stability of Three-Dimensional Supersonic Boundary Layers. *Physics of Fluids* **3/4**: 617-632, 1991.

[4] Reed H., Saric W.: Stability of 3-D Boundary Layers. *Annual Review of Fluid Mechanics* **21**: 235-284, 1998.

[5] Saric W., Reed H., White E.: Stability and Transition of Three-Dimensional Boundary Layers. *Annual Review of Fluid Mechanics* 413-442, 2003.

[6] Moyes A., Paredes P., Kocian T., Reed H.: Secondary Instability Analysis of Crossflow on a Hypersonic Yawed Circular Cone. *AIAA Paper No*. *2016-0848*, 2015.

[7] Oliviero N., Kocian T., Moyes A., Reed H.: EPIC: NPSE Analysis of Hypersonic Crossflow Instability on Yawed Straight Circular Cone. *AIAA Paper No*. *2015-2772*, 2015.

[8] Balakumar P., Owens L.: Stability of Hypersonic Boundary Layers on a Cone at Angle of Attack. *AIAA Paper No*. *2010-4718*, 2010.

[9] Craig A., Saric W.: Experimental Study of Crossflow Instability on a Mach 6 Yawed Cone. *AIAA Paper No*. *2015-2774*, 2015.

[10] White E., Saric W.: Secondary Instability of Crossflow Vortices, *Journal of Spacecraft and Rockets* **525**: 275-308, 2005.

RESPONSE AND RECEPTIVITY OF A HYPERSONIC BOUNDARY LAYER TO FREE-STREAM DISTURBANCES

Xuesong Wu *[1,2] and Fufeng Qin[2]

[1]*Department of Mathematics, Imperial College London, SW7 2AZ, UK*
[2]*Department of Mechanics, Tianjin University, Tianjin 300072, China*

Summary This paper analyses the response and receptivity of the hypersonic boundary layer over a wedge to free-stream acoustic, vortical and entropy disturbances. In the presence of a shock, the boundary layer supports viscous Tollmien-Schlichting (T-S) instability modes, whose eigenfunctions are oscillatory in the far field. Any of three elementary types of disturbances interacts with the shock to generate a slow acoustic wave, which is reflected between the shock and the wall. Through this induced acoustic wave, vortical and entropy disturbances drive significant fluctuations in the boundary layer, which is impossible without a shock. A quasi-resonance occurs for high frequencies leading to a strong response to a continuum of disturbances. In the vicinity of the lower-branch neutral curve the slow acoustic wave of suitable frequency and wavenumbers is in exact resonance with a neutral eigen mode. As a result, the latter can be generated directly by each of three types of free-stream disturbances without involving any surface roughness element.

INTRODUCTION

Laminar-turbulent transition in super- and hyper-sonic boundary layers evolves, similar to its subsonic counterpart, through a sequence of stages, the first of which is the receptivity, i.e. the process in which ambient disturbances excite instability modes. Several receptivity mechanisms have been identified, and they can be classified into two types. The first involves interactions of two external perturbations, including: free-stream acoustic/vortical disturbances interacting with local or distributed roughness [1]-[4] and interaction between acoustic and vortical perturbations [5]. Such an interaction produces an equivalent forcing that is resonance with, and hence excites, an instability mode. The second type is the leading-edge adjustment, where an acoustic wave is diffracted by the strongly non-parallel flow near the leading edge to generate an so-called asymptotic eigen mode of the boundary-layer equations, which then develops into an unstable mode downstream [6]-[7]. In the subsonic regime, the acoustics/vorticity-roughness interaction provides a more efficient mechanism than the leading-edge adjustment since the asymptotic mode in the latter experiences severer decay before amplifying. In contrast, the leading-edge mechanism is of primary importance in the supersonic regime as the asymptotic mode amplifies from the outset. Surface roughness, on the other hand, does not appear to play a significant role.

None of existing receptivity theories has considered the effects of shocks, which are usually present in super- and hypersonic flows. Cowley & Hall [8] showed that when a shock is close to the outer edge of the boundary layer, additional viscous instability modes on the triple-deck scales arise. In this paper, we investigate how such modes are excited by, as well as the boundary-layer response to, free-stream disturbances. A shock is found to be instrumental in both processes.

THEORETICAL ANALYSIS

The boundary layer due to a uniform U_∞ flow past a wedge is considered. We assume that the half angle $\theta \ll 1$, and the Mach number $M \gg 1$ so that the shock is close to the wedge surface. The Cartesian coordinates (x, y, z) are used with x and y being in the directions along and normal to the wedge surface respectively; they are normalized by L, the distance of the location of interest to the apex of the wedge. The Reynolds number $R = U_\infty L/\nu_\infty \gg 1$.

The velocity, pressure and density of a free-stream disturbance with a small amplitude ϵa_∞ are represented by

$$\mathbf{u}, p, \rho) = \epsilon a_\infty(\mathbf{u}, p, \rho)\, \mathrm{e}^{\mathrm{i}(\alpha x+\gamma y+\beta z-\omega t)}, \tag{1}$$

where the wavenumbers α and β, and the frequency ω satisfy the corresponding dispersion relations for acoustic, vortical/entropy waves. They are assume to be on the triple-deck scales. Each disturbance interacts with a shock to generate all three types downstream of the shock. In the presence of a surface, the disturbance downstream also consists of reflected waves as well as the signature associated with instability modes of the boundary layer; the latter may be modulated. A general shock condition, which allows for these complications, is derived first.

Broad-brand Response At an arbitrary streamwise location, the response to the free-stream disturbance has an $O(\epsilon)$ pressure, $p = \epsilon(a_I\, \mathrm{e}^{\mathrm{i}\,\gamma_a y} + a_R\, \mathrm{e}^{-\mathrm{i}\,\gamma_a y})\, \mathrm{e}^{\mathrm{i}(\alpha_a x+\beta_a z-\omega t)}$, where a_I and a_R represent the waves propagating towards and away from the wall respectively. They must, together with the velocity fluctuations, be determined by considering the boundary layer. The response may be measured by a_I. Solving a triple-deck system governing the response, we obtain

$$a_I = a_\infty F/\Delta(\alpha_a, \beta_a, \omega; x), \tag{2}$$

*Corresponding author. Email: x.wu@ic.ac.uk

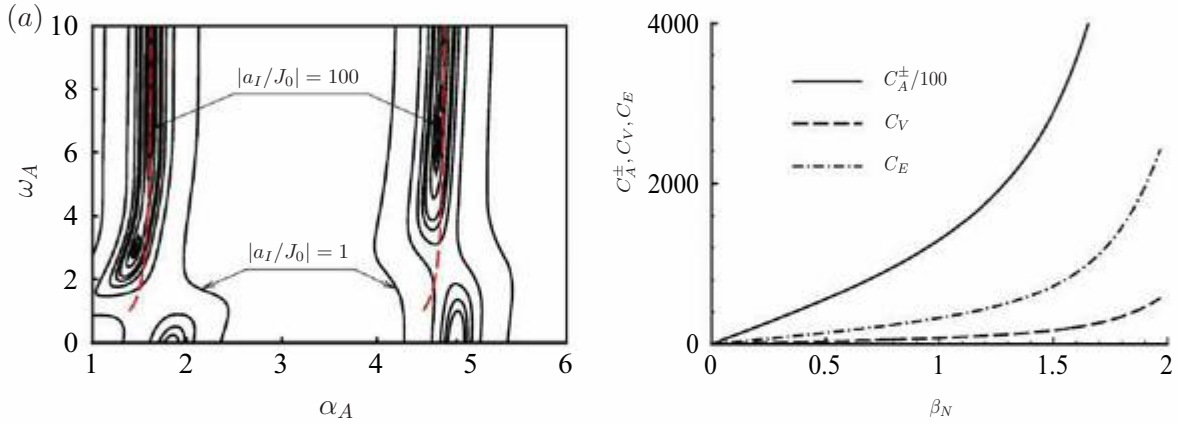

Figure 1: Left: contours of the response $|a_I/a_\infty|$ in the $\omega - \alpha_a$ for $\beta_N = 0.5$. Right: variation of the coupling coefficients $C_A^{\pm}$, C_V and C_E with β_N. The wedge half angle $\theta = 20^o$, $M = 20$ and $R = 5.0 \times 10^6$. The parameters ω_A, α_A, β_N and J_0 represent the rescaled ω, α_a, β_a and a_∞ respectively.

where $\Delta(\alpha_a, \beta_a, \omega : x)$ denotes the local dispersion function of T-S waves and the effective forcing, respectively.

Receptivity Among all disturbances with a frequency ω, there exist α_a and β_a such that the dispersion relation of a neutral T-S mode is satisfied, i.e. $\Delta(\alpha_a, \beta_a, \omega; x_0) = 0$. Such a disturbance resonantes with, and thereby excites, the T-S mode in the vicinity of x_0. The pressure and streamwise velocity in the lower deck are

$$(p_{TS}, u_{TS}) = \epsilon R^{3/16} M^{-15/8} A(^-)(1, M^{11/4} u_{TS})\, \mathrm{e}^{\mathrm{i}(\alpha_a x + \beta_a z - \omega t)} \quad \text{with} \quad x = R^{-3/16} M^{15/8}(x - x_0), \tag{3}$$

where the amplitude function $A\ x)$ describes the evolution from the upstream response to a T-S mode, and is found to satisfy the equation, $A' = \sigma x A + \mathcal{F}$, where σ and $\mathcal{F}$ can be determined numerically. As $x \to \infty$, $A \to A_0 \exp\{\frac{1}{2}\sigma^{-2}\}$ with $A_0 = \mathcal{F}(2\pi/\sigma)^{1/2}$ representing the scaled initial amplitude of the T-S mode excited. The streamwise velocity u_{TS} of the T-S mode is of $O(R^{5/16} M^{7/8} A_0)$. We may define the coupling coefficient

$$C = \max_y |u_{TS}|/(\epsilon a_\infty). \tag{4}$$

A SAMPLE OF RESULTS

The plot on the left-hand side of figure 1 shows the contours of a_I in the $\omega - \alpha_a$ parameter plane. There is an extremely strong response to a broadband of high-frequency disturbances within a narrow band of α_a, represented by the two narrow and almost vertical strips in the figure. Examination of (2) shows that this occurs because $\Delta \ll 1$ but remains non-zero as $\omega \gg 1$ and α_a approaches a particular value α_c. This is referred to as 'quasi-resonance'.

The plot on the right-hand side of figure 1 shows typical coupling coefficients for acoustic (C_A), vortical (C_V) and entropy (C_E) disturbances respectively. They are very large, ranging from $O(10^5)$ for acoustic waves to $O(10^2)$ for vortical disturbances. This is in striking contrast to typically $O(1)$ coupling coefficients in known receptivity mechanisms. The large coupling is due to the resonant nature of excitation and the well-known amplification effect of a strong shock. Moreover, excitation at the neutral position means that the mode excited grows immediately without undergoing any decay, or missing any portion of the unstable region. All these indicate that this new mechanism is particularly efficient.

References

[1] Goldstein, M.E. 1985 Scattering of acoustic waves into T-S waves by small streamwise variations in surface geometry. *J. Fluid Mech.* **154**, 509-529.

[2] Ruban, A.I. 1984 On Tollmien-Schlichting wave generation by sound. *Fluid Dyn.* **19**, 709-716.

[3] Duck, P.W., Ruban, A.I. & Zhikharev, C.N. 1996 The generation of Tollmien-Schlichting waves by free-stream turbulence. *J. Fluid Mech.* **312**, 341-371.

[4] Wu, X. 2001 Receptivity of boundary layers with distributed roughness to vortical and acoustic disturbances. *J. Fluid Mech.* **431**, 91-133.

[5] Wu, X. 1999 Generation of Tollmien-Schlichting waves by convecting gust interacting with sound. *J. Fluid Mech.* **397**, 285-316.

[6] Goldstein, M.E. 1983 The evolution of Tollmien-Schlichting waves near a leading edge. *J. Fluid Mech.* **127**, 59-81.

[7] Fedorov, A.V. & Khokhlov, A.P. 1991 Excitation of unstable modes in a supersonic boundary layer by acoustic waves. *Fluid Dyn.*, **9**, 456-467.

[8] Cowley, S. J. & Hall, P. 1990 On the instability of hypersonic flow past a wedge. *J. Fluid Mech.* **214**, 17-42.

INTERACTION OF SUPERSONIC BOUNDARY LAYER INSTABILITIES WITH STATIONARY STREAMWISE STREAKS

Pedro Paredes,* Meelan M. Choudhari, and Fei Li
Computational AeroSciences Branch, NASA Langley Research Center, Hampton, VA 23681, USA

Summary The nonlinear evolution of the linearly optimal stationary perturbations in a Mach 3 flat plate boundary layer is computed using the nonlinear, perturbation form of parabolized Navier-Stokes equations. As noted in previous works, the optimal initial disturbances correspond to steady counter-rotating streamwise vortices, which subsequently lead to the formation of streamwise-elongated structures, i.e., streaks, via a lift-up effect. To assess the effect of the finite-amplitude streaks on boundary layer instabilities, the plane-marching PSE are used to investigate the instability of the boundary layer flow modified by spanwise periodic streaks. Finite-amplitude streaks are known to stabilize Tollmien-Schlichting waves in the incompressible regime. Here, subcritical streaks are observed to destabilize first mode instabilities with two spanwise wavelengths of the streak while they stabilize those with three and four spanwise wavelengths. These results support the passive flow control strategy of using micro-vortex-generators for delaying transition due to oblique first mode instabilities in supersonic boundary layers.

EXTENDED SUMMARY

Under low levels of background disturbances, transition is initiated by the exponential amplification of linearly unstable eigenmodes, i.e., modal instabilities of the laminar boundary layer. In two-dimensional boundary layers, different instability mechanisms dominate the exponential growth phase depending on the flight speed. Planar, i.e., two-dimensional Tollmien-Schlichting (TS) waves are the most unstable in the incompressible regime, whereas oblique first mode instabilities correspond to the most amplified disturbances in the supersonic regime. The hypersonic regime is again dominated by the growth of planar waves of the second mode type [1]. In the presence of sufficiently strong external disturbances in the form of either freestream turbulence (FST) or three-dimensional wall roughness, streamwise streaks involving alternately low and high streamwise velocity have been observed to appear in incompressible boundary layers [2]. Further research in the incompressible regime has shown that high amplitude streaks can become unstable to shear layer instabilities that lead to a form of "bypass transition" [3]. When the streak amplitudes are low enough to avoid these instabilities, i.e., when the background disturbance level is moderate, the streaks can actually reduce the growth of the TS waves [4]. The stabilizing effect of stationary streaks has been utilized to demonstrate delayed laminar-turbulent transition via micro vortex generators (MVG) along the body surface [5].

The onset of streak instabilities at supersonic speeds has been addressed in recent work [6]; however, the effect of lower amplitude, i.e., stable or at most weakly unstable streaks (referenced as subcritical streaks in this paper) on the growth of oblique first mode instabilities has not been studied as yet. The present work seeks to bridge this gap in order to expand the range of available techniques for transition control at supersonic edge Mach numbers, as well as to provide insights that will contribute to more robust transition prediction in such flows.

To that end, we first consider the nonlinear evolution of finite-amplitude linearly optimal disturbances in a Mach 3, zero pressure-gradient, flat plate boundary layer, and on the effect of subcritical streaks on the first mode boundary layer instability. Transient growth analysis is performed using the linear parabolized stability equations (PSE). For illustration, we consider a final optimization location ($x = x_1$) corresponding to a length Reynolds number of $Re_{x_1} = 10^6$ and set the initial disturbance location to $x_0/x_1 = 0.0004$, i.e., very close to the leading edge. The optimal stationary perturbation that leads to maximum energy gain at x_1 has a spanwise wavenumber of $\beta_{TG} = 0.25$ relative to similarity length scale at $x = x_1$ and the associated energy gain is $G_{max}/Re_{x_1} = 0.002525$. For the flow conditions of interest, the optimal initial perturbation is influenced by the Mach wave emanating from the leading edge, resulting in a reduction of the maximum gain by a factor of 9% with respect to results based on the self-similar basic state [7]. Subsequently, the nonlinear development of the above linearly optimal disturbances is computed for selected initial amplitudes by solving the nonlinear form of the plane-marching PSE [8] in a fully implicit manner. Figure 1(a) shows the downstream evolution of the streak amplitude, which is defined as $As_u(x) = [\max_{y,z}(\tilde{u}) \circ \min_{y,z}(\tilde{u})]/2$, where $\tilde{u}$ is the streamwise velocity perturbation, for selected initial disturbance amplitudes, defined as $A_0 = \sqrt{E_0} = A/\sqrt{G_{max}}$. A three-dimensional view of the boundary layer flow across four spanwise wavelengths of the $A = 1$ streak is also shown in figure 1(b).

Finally, the amplification of first mode instabilities in the boundary layer flow modified by the presence of the streaks has been computed using the linear plane-marching PSE, which account for the three-dimensionality of the perturbed basic state. Figure 2 compares the N-factor evolution for the first mode instability in the unperturbed case ($A = 0$) with three perturbed cases ($A = 0.1$, 0.5, and 1.0). The three separate subfigures correspond to different values of the spanwise wavenumbers, with the frequency parameter corresponding to the most amplified frequency for that wavenumber when $A = 0$. Results show that the first mode disturbances with a relatively large spanwise wavenumber ($\beta = \beta_{TG}/2$), are destabilized by the presence

*Corresponding author. Email: pedro.paredes@nasa.gov. Position: NASA Postdoctoral Program Fellow

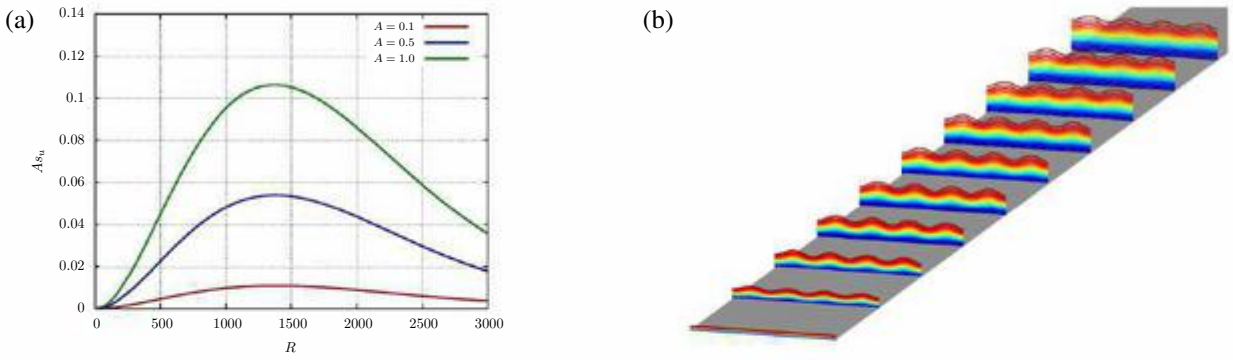

Figure 1: (a) Streak amplitude evolution of the optimal linear perturbations initialized with selected amplitudes in a Mach 3 flat plate boundary layer with $Re_{x_1} = 10^6$ and $x_0/x_1 = 0.0004$. (b) Iso-lines of streamwise velocity at streamwise locations up to $x/x_1 = 9$ for four spanwise wavelengths of the $A = 1$ streak. The color map varies from $u = 0.05$ (dark blue) to $u = 0.95$ (dark red).

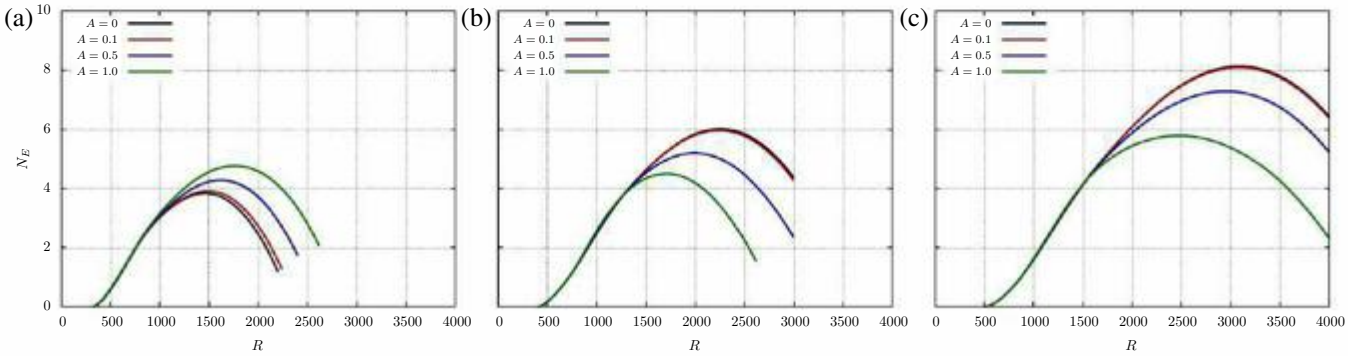

Figure 2: Evolution of logarithmic amplification ratio (i.e., N-factor) of first mode instabilities in Mach 3 flat plate boundary layer perturbed by linearly optimal perturbations with initial amplitudes from Fig. 1. The spanwise wavenumber scaled by similarity length scale at $x = x_1$ ($Re_{x_1} = 10^6$) corresponds to $\beta_{TG} = 0.25$, which yields the maximum energy gain from $x_0/x_1 = 0.0004$ to x_1. From left to right, the selected spanwise wavenumbers and the associated circular frequencies are (a) $\beta = \beta_{TG}/2$ and $\omega = 0.040$, (b) $\beta = \beta_{TG}/3$ and $\omega = 0.024$, and (c) $\beta = \beta_{TG}/4$ and $\omega = 0.016$.

of the streak. However, these disturbances correspond to lower N-factors, and hence, are unlikely to initiate transition in the low disturbance environment characteristics of flight. In contrast, a reverse effect is observed at the smaller spanwise wavenumbers, which are likely to play an important role in causing transition by virtue of their enhanced linear growth potential. The implication of these findings is that the presence of subcritical streaks leads to a flattening of the N-factor envelope and, consequently, to a reduction of the maximum N-factor values within the parameter range examined herein. These results provide the basis for the development of a passive flow control strategy to delay transition due to first mode instabilities in the supersonic boundary layer.

This work is supported by the Transformational Tools & Technologies (TTT) subproject of the National Aeronautics and Space Administration (NASA).

References

[1] L.M. Mack. Boundary layer linear stability theory. In *AGARD–R–709 Special course on stability and transition of laminar flow*, pages 3.1–3.81, 1984.

[2] P.S. Klebanoff. Effect of free-stream turbulence on the laminar boundary layer. *Bull. Am. Phys. Soc.*, 10:1323, 1971.

[3] P. Andersson, L. Brandt, A. Bottaro, and D.S. Henningson. On the breakdown of boundary layer streaks. *J. Fluid Mech.*, 428:29–60, 2001.

[4] A.V. Boiko, K.J.A. Westin, B.G.B. Klingmann, V.V. Kozlov, and P.H. Alfredsson. Experiments in a boundary layer subjected to free stream turbulence. Part 2. The rhole of TS-waves in the transition process. *J. Fluid Mech.*, 281:219–245, 1994.

[5] F.H. Fransson, A. Talamelli, L. Brandt, and C. Cossu. Delaying transition to turbulence by a passive mechanism. *Phys. Rev. Lett.*, 96:064501, 2006.

[6] P. Paredes, M.M. Choudhari, and F. Li. Nonlinear transient growth and boundary layer transition. AIAA Paper, submitted, 2016.

[7] P. Paredes, M.M. Choudhari, F. Li, and C.-L. Chang. Optimal growth in hypersonic boundary layers. *AIAA J.*, submitted, 2016.

[8] P. Paredes, A. Hanifi, V. Theofilis, and D. Henningson. The nonlinear PSE-3D concept for transition prediction in flows with a single slowly-varying spatial direction. *Procedia IUTAM*, 14C:35–44, 2015.

EFFECT OF MEDIUM-INTENSITY FREE-STREAM VORTICITY ON A COMPRESSIBLE BOUNDARY LAYER

Elena Marensi [*1,2], Pierre Ricco[2], and Xuesong Wu[3]
[1]*Department of Fluid Dynamics, A*Star Institute of High Performance Computing, Singapore*
[2]*Department of Mechanical Engineering, The University of Sheffield, Sheffield, United Kingdom*
[3]*Department of Mathematics, Imperial College London, London, United Kingdom*

Summary The nonlinear response of a compressible boundary layer to unsteady free-stream vortical fluctuations is investigated theoretically and numerically. The amplitude of the disturbances is strong enough for nonlinear interactions to arise within the boundary layer. Compressibility is taken into account through aerodynamic heating effects due to the free-stream Mach number being $\mathcal{O}(1)$ and through heat transfer at the wall. The free-stream flow is studied by including the boundary-layer displacement effect and is found to assume different forms depending on the regime being subsonic or supersonic. Even in a low-disturbance environment such as flight conditions, nonlinearity is found to play a significant stabilizing role on the velocity and temperature streaks, the latter being more markedly attenuated than the former at supersonic speeds. The effect of different parameters, which are relevant to the study of the nonlinear compressible streaks, is also investigated.

INTRODUCTION

Laminar-to-turbulent boundary-layer transition is known to be strongly affected by disturbances present in the free stream, which are characterised by their intensity Tu, length scales and spectra. In boundary layers with $Tu{>}1\%$, transition occurs rapidly, bypassing the so-called orderly route via Tollmien-Schlichting (T-S) waves. In this scenario, referred to as bypass transition, the laminar boundary-layer breakdown is preceded and caused by unsteady streamwise-elongated regions of high and low streamwise velocity, known as Klebanoff modes or laminar streaks. The focus of our work is on the nonlinear evolution of the streaks in the compressible regime because in high-speed flows transition occurs more frequently through the bypass route than via the T-S wave growth described by classical stability theory. The streaks are studied using the mathematical framework of the boundary-region equations, i.e. the asymptotic limit of the Navier-Stokes equations for low-frequency disturbances, developed by Leib *et al.*[1] and extended by Ricco & Wu [2] and Ricco *et al.*[3] to linear perturbations in compressible boundary layers, and nonlinear disturbances in incompressible boundary layers, respectively.

SCALING AND GOVERNING EQUATIONS

An air flow with mean uniform velocity U^*_∞ and constant temperature T^*_∞ passing over a semi-infinite flat plate is considered. The symbol * is used to indicate dimensional quantities. The oncoming perturbation consists of a pair of vortical modes with the same frequency (and hence streamwise wavenumber k^*_x) but opposite spanwise wavenumbers $\pm k^*_z$. The free-stream Mach number is $M_\infty{=}U^*_\infty/c^*_\infty{=}\mathcal{O}(1)$, where c^*_∞ is the speed of sound. The space coordinates are non-dimensionalised by $\lambda^*{=}1/k^*_z$ and the other variables are scaled by their respective constant values in the free stream. Spanwise-diffusion effects become important at a downstream location $\bar{x}{=}k^*_x x^*{=}\mathcal{O}(1)$, where the boundary layer thickness $\delta^*{=}\,\mathcal{O}(\lambda^*)$.

The boundary-layer flow is decomposed as the sum of the Blasius flow and the unsteady perturbation induced by the free-stream disturbance. The perturbation is expressed as a Fourier series in time and in the spanwise direction z. By taking the limits of the continuity, Navier-Stokes and energy equations for low frequency disturbances, $k^*_x{\ll}k^*_z$, and large Reynolds number, $R_\lambda{=}U^*_\infty\lambda^*/\nu^*_\infty{\gg}1$, with $k_x R_\lambda{=}\mathcal{O}(1)$, the nonlinear unsteady compressible boundary region equations are derived.

The boundary-layer displacement effect influences the free-stream flow at leading order. The irrotational part of the outer perturbation assumes different forms depending on the regime being subsonic or supersonic. A close analogy with the flow over a thin oscillating airfoil is exploited to find analytical solutions of the Helmholtz and Klein-Gordon equations which arise in the subsonic and supersonic cases. This analogy is used here for the first time to study unsteady boundary layers.

RESULTS

The parameters for the numerical results inside the boundary-layer are selected to be representative of two possible industrial and aerospace applications, i.e. subsonic turbomachinery and supersonic flight conditions, and of typical high-speed wind-tunnel experiments. For brevity, the first two cases are shortly discussed in the following paragraph, while the latter is further analyzed thereafter.

The turbomachinery case is characterized by a low Mach number ($M_\infty{=}0.7$) and an intense turbulence level ($Tu{=}1\circ\ 2\%$),

*Corresponding author. Email: e.marensi@sheffield.ac.uk

while the flight case features a higher Mach number (M_∞=$2-6$) and a quieter disturbance environment (Tu=$0.1-0.3\%$). The relevant parameter for the study of the nonlinear effects is the turbulence Reynolds number, $r_t \equiv \epsilon R_\lambda = \mathcal{O}(1)$, where ϵ is a measure of the turbulence level. Ricco *et al.*[3] already observed a stabilizing effect of nonlinearity on the streamwise velocity fluctuations in the incompressible regime for high turbulence levels. Here, it is shown that in the compressible case the nonlinear effects play the same role on the temperature streaks and that nonlinearity needs to be taken into account even for low turbulence levels, such as in flight conditions. Increasing the free-stream Mach number attenuates the velocity fluctuations while enhancing the thermal streaks, relative to U^*_∞ and T^*_∞, and the overall effect of nonlinearity becomes weaker.

The idealized case of a supersonic (M_∞=3) wind tunnel with no acoustic modes is now considered. An abrupt deviation of the nonlinear solution from the linear approximation is observed for the highest turbulence Reynolds number considered, r_t=6 (Tu=0.3%), as shown in figure 1(a). Only the signature of the streamwise velocity is presented, as that of the temperature is qualitatively very similar. This sharp deviation was not reported in the incompressible work of Ricco *et al.*[3]. A parametric study shows that this phenomenon occurs at supersonic speeds when a sufficiently small streamwise wavenumber is employed, $k_x \leq 1.5 \cdot 10^{-3}$, together with a high turbulence Reynolds number, $r_t \geq 6$.

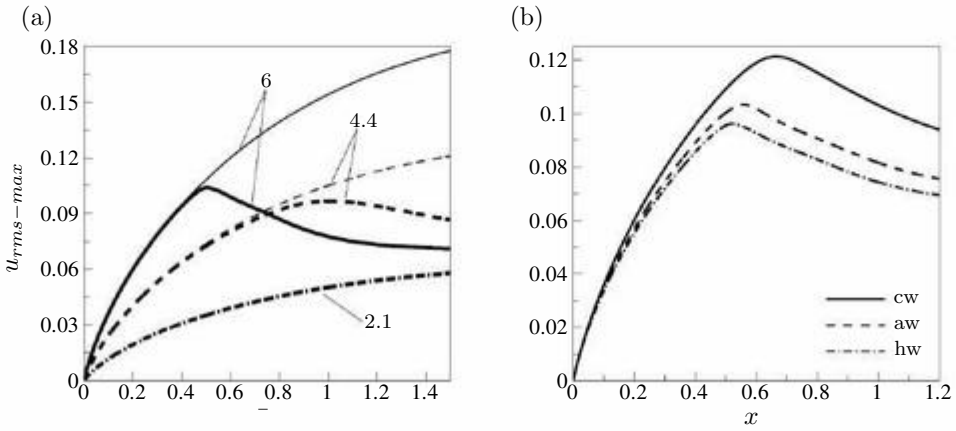

Figure 1: Evolution of the maximum root mean square (r.m.s.) of the streamwise velocity for different r_t (a) at M_∞=3, and for different wall-temperature conditions (b): hot wall (hw), adiabatic wall (aw) and cold wall (cw) at M_∞=3 and r_t=6. In (a): thick lines: nonlinear solutions, thin lines: linearized solutions.

In figure 1(b) three different wall-temperature conditions are considered: hot, adiabatic and cold wall. The wall-heat flux is found to influence the position where the onset of the strong stabilizing effect occurs. This suggests that the employment of the adiabatic-wall condition in wind-tunnel experiments may lead to an inaccurate prediction of the transition location for flight conditions, which are instead characterized by a cold-wall condition due to the radiative-cooling effect.

The numerical results for the outer flow show that in the subsonic regime the disturbance propagates in all directions from the plate, while at supersonic speeds the fluid ahead of the body remains undisturbed and the perturbation is confined to within the Mach dihedron defined by the Mach line.

CONCLUSIONS

The boundary region equations are employed to describe the nonlinear unsteady streaks generated by medium-intensity free-stream vorticity within a compressible laminar boundary layer. The results show that, even for a low-disturbance environment such as free flight, the nonlinear effects play a significant role in attenuating the velocity and temperature streaks inside the boundary layer. For a sufficiently high free-stream turbulence level and a sufficiently long streamwise wavelength an abrupt deviation of the nonlinear solution from the linear one is observed, which is a new feature of the compressible analysis. The present study provides the accurate description of the compressible boundary-layer streaks, which is indispensable for the secondary instability analysis of the unsteady nonlinear boundary-layer flow. This paper also includes numerical evidence of the effect of nonlinearity on the T-S waves found by Ricco & Wu [2] for vortical disturbances with a relatively large λ^*.

References

[1] Leib S.J., Wundrow D.W., Goldstein M.E.: Effect of free-stream turbulence and other vortical disturbances on a laminar boundary layer. J. Fluid Mech. 380: 169-203, 1999.

[2] Ricco P., Wu X.: Response of a compressible laminar boundary layer to free-stream vortical disturbances. J. Fluid Mech. 587: 97-138, 2007.

[3] Ricco P., Luo J., Wu X.: Evolution and instability of unsteady nonlinear streaks generated by free-stream vortical disturbances. J. Fluid Mech. 677: 1-38, 2007.

INSTABILITY AND TRANSITION OF A MACH 5.8 ZERO PRESSURE GRADIENT BOUNDARY LAYER OVER A THERMOMECHANICALLY COMPLIANT PANEL

Daniel J. Bodony* and Fabian S. Dettenrieder
Department of Aerospace Engineering, University of Illinois at Urbana-Champaign, Urbana, Illinois, USA

Summary Boundary layer instability and transition are fundamental design considerations in hypersonic flight vehicles. Recent results have shown that the fluid-thermal-structural interaction between the structure and grazing boundary layer can affect the turbulence and that transient growth mechanisms appear to be important in amplifying structural motion-induced disturbances. In this paper we use convective and global stability descriptions to identify and characterize the stability properties of a Mach 5.8 flat plate zero pressure gradient boundary layer grazing a thermo-mechanically compliant panel. The new coupled stability modes are verified using direct numerical simulation and their impact on transition is demonstrated.

BACKGROUND

Sustained hypersonic flight, with $M_\infty \geq 5$ occuring for periods of time of up-to 100 minutes, is accompanied by severe thermal and fluid dynamic loads on the vehicle structure. Conservative air vehicle design methodologies that separately treat the fluid, structural, and thermal dynamics make "worse case" assumptions that are not long-term viable for future designs. Instead, more radical procedures are needed where all three disciplines are treated simultaneously to yield equally safe, but less conservative and thus lighter, vehicle concepts. Perhaps the most uncertain feature of hypersonic flight is predicting over which portion of the body does the boundary layer transition from laminar to turbulent. Developing the new design methods will require a critical reexamination of the interaction of compressible wall-bounded flows with mechanically- and thermally-compliant surfaces. Preliminary results from a temporally-developing Mach 2.25 turbulent boundary layer over a metallic panel (see Fig. 1) suggest that under certain scenarios, turbulence-induced surface motion can reduce turbulence production and bring current RANS-based design methods into question [1]. It is thus necessary to understand how mass, momentum, and energy are exchanged between the flow and the dynamic underlying surface from a fundamental perspective. Our recent investigation into the behavior of compliance-induced disturbances strongly suggests that they can use transient growth mechanisms to amplify and modify the otherwise-canonical turbulent flow [2]. Computation-based methods are thus well positioned to examine the fluid-thermal-structure interaction (FTSI).

APPROACH

We examine the hypothesis that fluid and structural waves can couple to modify the canonical natural transition mechanisms of zero pressure gradient laminar boundary layers. Support for this hypothesis can be seen in Fig. 2 where the phase velocity of several fluid- and solid-borne waves are given for a Mach 5.8 boundary layer grazing a steel-like panel, such as shown in Fig. 1. The waves in the freestream are either convective or compressive, with phase velocities U_∞ and $U_\infty \pm c_\infty$, respectively, with c_∞ being the fluid sound speed. In the solid, shear and compressive waves exist and travel at phase velocities proportional to $\sqrt{E/\rho_s}$ where E is the material Young's modulus and ρ_s is the material density. Rayleigh waves travel near the solid surface, being evanescent away from it, and travel at a speed of slightly more than 92% of the shear wave speed. For thin panels of thickness h dispersive bending waves exist with phase speed $\sqrt{E(\alpha h)^2/(3\rho_s(1 \circ \nu^2))}$ for streamwise wavenumber α and Poisson's ratio ν.

As Fig. 2 makes apparent the wavespeeds are of a similar order of magnitude except for the very smallest values of αh and several direct couplings between the waves are feasible. In addition, under suitable boundary conditions resonance conditions may exist where solid waves are trapped between the upstream and downstream boundaries and extract energy from the mean flow during each cycle, similar to what we found earlier [1]. It is thus conceivable that both convective and absolute instabilities may exist in the coupled system.

Convective stability analysis for FTSI

Referring to the coordinate directions shown in Fig. 1, a traveling wave-type solution of the form $q'(\boldsymbol{x},t) = \hat{q}(y)e^{\mathrm{i}(\alpha x+\beta z-\omega t)}+$ c.c. is assumed for any disturbance q' taken about an appropriate mean value of $\overline{q}$ within the fluid domain. In the usual manner by assuming ω and β to be real-valued and specified, an eigenvalue problem for α is obtained once the boundary conditions are specified. We treat the structure as a simple flat plate whose transverse deflection $\eta(x,z,t)$ satisfies the equation

$$m_s\frac{\partial^2\eta}{\partial t^2} + B\left[\frac{\partial^4\eta}{\partial x^4} + 2\frac{\partial^4\eta}{\partial x^2\partial z^2} + \frac{\partial^4\eta}{\partial z^4}\right] + p'(x,0,z,t) = 0 \tag{1}$$

*Corresponding author. Email: bodony@illinois.edu

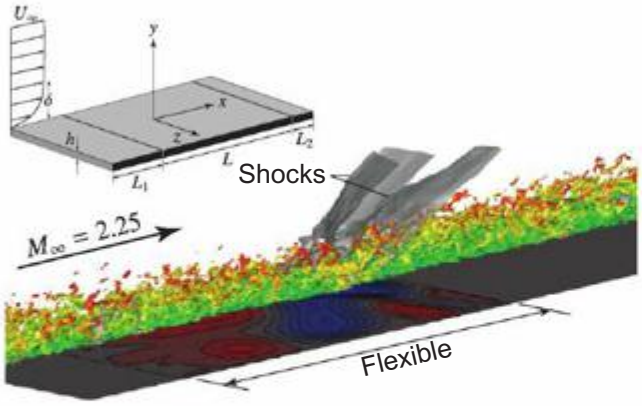

Figure 1: Visualization of the boundary layer vorticity (color), pressure iso surfaces (gray), and panel deformation (contour) caused by a Mach 2.25 turbulent boundary layer grazing a deformable panel. Inset shows problem definition.

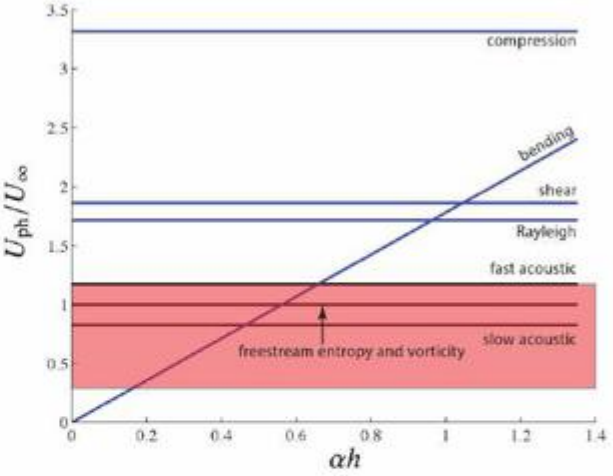

Figure 2: Phase velocities of several fluid and solid waves for a Mach 5.8 boundary layer grazing a steel-like panel of thickness h. Shaded region gives phase velocity range of boundary layer instability waves.

for a plate of mass per unit area $m_s = \rho_s h$, bending stiffness B, and exposed to an unsteady pressure field p' directed in the $-y$-direction. Apply the ansatz and requiring the panel deformation and fluid velocity to be compatible yields an impedance boundary condition relating the pressure and wall normal velocity, namely

$$\hat{p}(0) = Z^{-1}\hat{}(0) \quad \text{where} \quad Z = \frac{\mathrm{i}\omega}{-m_s\omega^2 + B(\alpha^2+\beta^2)^2}. \tag{2}$$

The thermal fluctuations can be shown to satisfy the heat equation whose solution can be analytically determined such that a Robin boundary condition for the fluid temperature exists.

Global stability analysis for FTSI

The global stability analysis begins by discretizing the linearized form of the equations of mass, momentum, and energy density with the plate equation (Eq. (1)) using summation-by-parts finite difference operators [3] and the simultaneous-approximation-term [4] boundary condition enforcement to yield the linear system

$$\frac{\mathrm{d}\boldsymbol{q}'}{\mathrm{d}t} = \mathsf{L}(\boldsymbol{q}_e)\boldsymbol{q}', \tag{3}$$

where $\mathsf{L}(\boldsymbol{q}_e)$ is the discrete operator, including boundary terms, linearized about the equilibrium solution $\boldsymbol{q}_e$. The eigenvalue problem we consider is based on a modal decomposition of the form $\boldsymbol{q}'(\boldsymbol{x},t) = \widehat{\ }(\boldsymbol{x})e^{\sigma t}$ so that Eq. (3) becomes

$$\sigma\widehat{\boldsymbol{q}} = \mathsf{L}(\boldsymbol{q}_e)\widehat{\boldsymbol{q}} \quad \text{with adjoint} \quad \mathsf{L}^\dagger\widehat{\boldsymbol{q}}^\dagger = \sigma\widehat{\boldsymbol{q}}^\dagger \quad \text{where} \quad \mathsf{L}^\dagger = \mathsf{V}^{-1}\mathsf{L}^T\mathsf{V}, \tag{4}$$

with σ as the eigenvalue and $\widehat{\ }$ and $\widehat{\ }^\dagger$ as the forward and adjoint eigenvectors. The matrix $\mathsf{V} = \mathrm{diag}(v_1/V, v_2/V, \ldots, v_n/V)$, with V, the volume of the fluid domain and v_i, the volume of the cell associated with grid point i is a norm.

DNS-predicted transition

Using both the convective instability and global stability FTSI tools as a guide, we will present cases for which the FTSI system is expected to be measurably different from the traditional, rigid, non-FTSI cases.

References

[1] C. Ostoich, D. J. Bodony, and P. H. Geubelle. Aerothermoelastic response of a panel under a high speed turbulent boundary layer using direct numerical simulation. AIAA Paper 2013-1662, Presented at the 54nd AIAA/ASME/ASCE/AHS/ASC Structures, Structural Dynamics, and Materials Conference, April 2013.

[2] D. J. Bodony. Structural changes to a turbulent boundary layer grazing a compliant panel. In *Proceedings of the Summer Program*, pages 285–293, Stanford, California 94035, 2014. Center for Turbulence Research, Stanford University.

[3] B. Strand. Summation by parts for finite difference approximations for d/dx. *Journal of Computational Physics*, 110:47–67, 1994.

[4] M. H. Carpenter, D. Gottlieb, and S. Abarbenel. Time-stable boundary conditions for finite difference schemes involving hyperbolic systems: Methodology and application for high-order compact schemes. *Journal of Computational Physics*, 111:220–236, 1994.

THE POST-COLLISIONAL BOUNDARY-LAYER ON AN IMPULSIVELY ROTATED SPHERE

James P. Denier*[1], Sophie A.W. Calabretto[2], Benjamin Levy[3], and Trent Mattner[4]

[1]*Department of Mathematics, Macquarie University, Sydney, Australia*
[2]*Institute for Mechanical Systems, ETH Zürich, Switzerland*
[3]*Auckland Bioengineering Institute, University of Auckland, Auckland, New Zealand*
[4]*School of Mathematical Sciences, University of Adelaide, Adelaide, Australia*

Summary The unsteady flow generated due to the impulsive motion of a sphere is a paradigm for the study of many temporally developing boundary layers. The boundary layer is known to exhibit a finite-time singularity at the equator. We present results of a new study that focuses upon the behaviour of the flow after the onset of this singularity. Our new computational results demonstrate that the singularity in the boundary layer manifests as the ejection of a radial jet. This radial jet is preceded by a toroidal starting vortex pair which detaches and propagates away from the sphere. The radial jet subsequently develops an absolute instability, which propagates upstream towards the sphere surface. New experimental results will also be presented confirming the fundamental stages of flow evolution post the development of the finite-time singularity in the unsteady boundary-layer equations.

INTRODUCTION

The flow induced by a rotating sphere provides a paradigm for the study of many fundamental questions in fluid mechanics, in particular the phenomena of boundary-layer collisions and unsteady boundary-layer separation. If a sphere immersed in a body of fluid, and initially at rest, is imparted with angular momentum, fluid is advected around the sphere from the poles, within a boundary layer, to collide at the equator. The study of this boundary-layer development process, and subsequent collision, has a long history, [6, 1]. The latter study demonstrated that the boundary-layer collision is manifest in the boundary-layer equations through the development of a finite-time singularity. The structure of this singularity was first considered by [8] and later by [4, 9]. Van Dommelen [9] used a Lagrangian approach to obtain the most accurate prediction of the time for the onset of the finite-time singularity.

A number of other studies of the boundary-layer on a rotating sphere have demonstrated that the flow undergoes a transition to turbulence as a result of an absolute instability within the boundary layer. Theoretical results by [5] suggest that the absolute instability occurs well away from the equator (typically 60-70 degrees towards the sphere's pole), providing good confirmation with experimental results of [7]. Here we explore the boundary-layer development, its breakdown through a finite-time singularity and the subsequent development of a radial jet through a combined computational and experimental approach.

COMPUTATIONAL RESULTS

The flow around an impulsively rotated sphere was determined numerically exploiting a spectral element discretisation of the axisymmetric Navier-Stokes equations; full details of the computational scheme, domain and grid has been described in [2]. The flow was taken to be axisymmetric in order to focus on the development of the singularity/eruption process and the subsequent development, and instability, of the radial jet. Representative results are shown in fig. 1 for a flow Reynolds number (based upon the sphere radius) of 16000 and a variety of times post-spin-up (the sphere is spun up from rest at time $t = 0$). Here we can clearly (top image) see the radial jet (preceded by a starting toroidal vortex pair) emanating from the equator, a consequence of the ejection of fluid at the equator due to the boundary-layer collision. The incipient detachment of the toroidal vortex pair coincides with the onset of an absolute instability in the jet (middle image) which grows in amplitude and propagates back towards the sphere surface (bottom image).

EXPERIMENTAL RESULTS

A solid sphere (an "8-ball") of diameter 57.15 ± 0.127 mm was mounted on a 4 mm metal rod. This was achieved by drilling a hole through the (approximate) centre of the sphere, then gluing the rod into the hole. With the rod mounted through the sphere, the tolerance of this sphere/rod system was accurate to within 0.1 mm. The rod was placed in a perspex tank, with a depth and width of 600 mm and height of 300 mm, and held in place at the top and bottom of the tank with small, circular perspex brackets. The rod was attached to a variable speed DC motor using a pulley system which was designed to minimise any vibrational effects from the motor being transferred to the rod/sphere. A laser sheet was generated perpendicular to the sphere and Time Resolved Particle Image Velocimetry of the flow was conducted.

Figure 2 shows false streamlines of the flow from which we observe the thickening of the boundary layer at the equator and the radial jet that results from the collision of fluid which has been transported from the poles to the equator as a result of the

*Corresponding author. Email: jim.denier@mq.edu.au

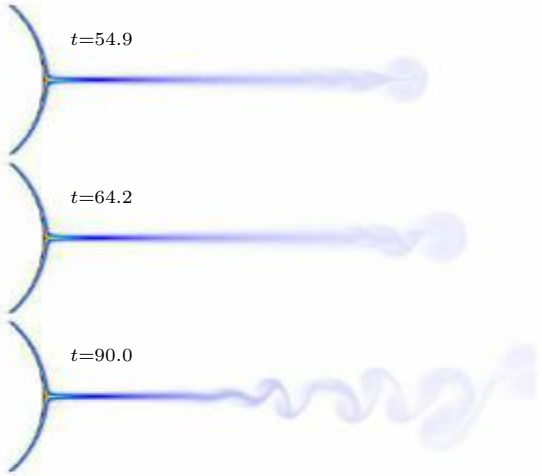

Figure 1: Contour plots of the azimuthal velocity ($Re = 16000$).

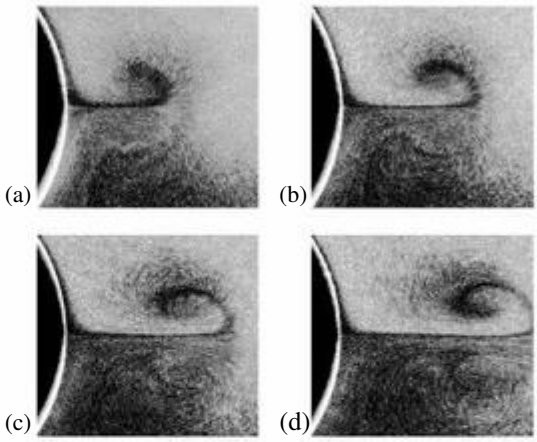

Figure 2: False streamlines (obtained from 5 images) of the flow showing the starting vortex for four different times post spin-up. The flow Reynolds number in this case is 388.

centrifugal forces arising from the rotation of the sphere. The development of the absolute instability, for a flow with Reynolds number 15000, is seen in the false streamline images of the flow presented in figure 3a. The thin radial jet can clearly be seen in the first image, together with the finite amplitude, Kelvin-Helmholtz-like, "billows" resulting from the absolute instability. At later times, the absolute instability has propagated back towards the sphere, as can be seen in fig. 3b, and will ultimately serve to drive a transition to turbulence in the boundary layer in the vicinity of the equator.

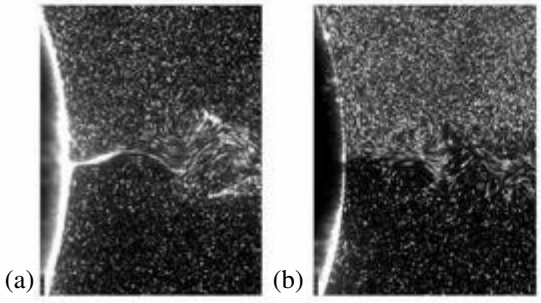

Figure 3: False streamlines showing the instability and its development with time.

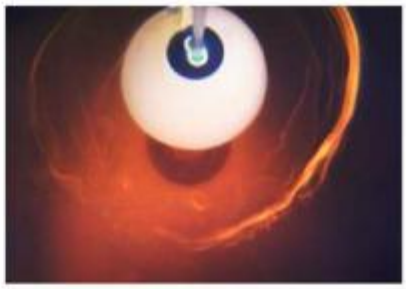

Figure 4: Top-down flow visualisation showing the absolute instability in the radial jet; see [2] for more details

.

CONCLUSIONS

Through a mix of computational and experimental techniques we have elucidated the dynamics of the flow around an impulsively rotated sphere. This flow is known to develop a finite-time singularity in the boundary layer near the sphere's equator. Our results demonstrate that this singularity results in an eruption of fluid at the equator which propagates outwards as a radial jet. This radial jet is preceded by a toroidal starting vortex pair and the jet is susceptible, at sufficiently high Reynolds numbers, to an absolute instability which in turn can propagate back towards the sphere, and so impacting up the flow stability within the boundary layer. The effects of three-dimensionality on this flow remain to be explored. Preliminary results suggest that the radial jet is highly susceptible to three-dimensional disturbances; see fig. 4.

References

[1] Banks W.H.H., Zaturska, M.B. The collision of unsteady laminar boundary layers. J. Eng. Math., 13:193–212, 1979
[2] Calabretto S.A.W., Levy, B., Denier J.P., Mattner T.W. The unsteady flow due to an impulsively rotated sphere. Proc. R. Soc. A, 471:20150299, 2015.
[3] Cowley S.J., van Dommelen L.L., Lam S.T. On the use of Lagrangian variables in descriptions of unsteady boundary-layer separation. Phil. Trans. Roy. Soc. A, 333:343–378, 1990
[4] Dennis S.C.R., Duck P.W. 1988 Unsteady flow due to an impulsively started rotating sphere. Comp. Fluids, 16:291–310, 1988
[5] Garret S.J., Peake N. The stability and transition of the boundary layer on a rotating sphere. J. Fluid Mech., 456:199–218, 2002.
[6] Howarth L. Note on the boundary layer on a rotating sphere. Philos. Mag., 42: 1308–1315, 1951.
[7] Kohama Y, Kobayashi R.: Boundary-layer transition and the behaviour of spiral vortices on rotating spheres. J. Fluid Mech., 37:153–164, 1983
[8] Simpson C.J., Stewartson K.: A note on a boundary-layer collision on a rotating sphere. ZAMP, 33:370–378, 1982
[9] van Dommelen L.L.: On the Lagrangian description of unsteady boundary-layer separation. Part 2. The spinning sphere. J. Fluid Mech., 210:627–645, 1990.

BOUNDARY LAYER TRANSITION INITIATED BY A RANDOM EXCITATION

Michael Gaster
School of Engineering, Mathematics and Computer Science, City University, London, U. K

Summary Laminar boundary layers subjected to weak random excitations break down into turbulent motion through a succession of turbulent spots. The late stage of transition is therefore different from that observed when excitation is periodic, as is common in many investigations. The spot occurrence is not necessarily where the magnitudes of the perturbation time series are at a maximum. A series of experiments mapping out the flow oscillations that arise downstream from a pseudo-random driven point source are discussed. It would seem that the breakdown process obtained in these experiments mimics the naturally occurring behaviour observed when background system noise creates the disturbances.

INTRODUCTION

The prediction of the state of a boundary layer on an aircraft wing has been a necessary design requirement for almost one hundred years. The transition from a laminar state to a turbulent one has been known to influence the characteristic of a flying surface. In particular, a turbulent boundary layer has higher skin friction drag than a laminar one and thus the position of transition will influence performance. Generally transition increases drag and reduces flight performance, but there are situations where a turbulent boundary layer can prevent local separations and therefore be beneficial. The transition process is complex and prediction methods have had to rely, to an extent, on empirical data derived from experimental measurements. As more understanding of the complex phases of the transition are formed the degree of empiricism employed has been reduced with a consequent improvement in the ability to correctly estimate the occurrence of transition. Over the years a great deal of understanding of boundary layer transition has been obtained from analytical, experimental and, more recently, from computational studies. We now have some understanding of how the environment can excite small perturbations in the flow that grow into large amplitude distortions to the flow and eventually into turbulent motion. Unfortunately nearly all these studies deal with over-simplified scenarios involving time periodic excitations. This may have seemed reasonable as the early stages of excitation and amplification involve very weak perturbations that can quite properly be described by linearized theory. However it turns out that naturally occurring random excitations generate narrow band modulated disturbances that evolve very differently during the nonlinear phase of growth.

In a flat plate boundary layer a periodic excitation from a point source produces clean wedge shaped zones of travelling waves that grow spatially downstream. The same physical set up involving a pulsed excitation will generate a downstream travelling wave packet. Both of these flows can be described by linear theory when the amplitudes are sufficiently weak. But, it turns out that the wave packet becomes highly distorted and deviates from the linear model at a fraction of the amplitude that the periodic wave train exhibits any non-linear effects [1]. In any real situation the excitation will inevitably be broad band and the subsequent break down will be influenced by the myriad of rich wave-wave interactions as observed in experiment [2].

EXPERIMENTAL SETUP

The evolution of an irregular train of waves emanating from a randomly excited point source and monitored by a traversable hot-wire element is considered. The work builds on previous studies [3] & [4]. The experiment was carried out in the laminar boundary layer that formed on a flat plate mounted in a wind tunnel that had a background turbulence intensity of 0.007% at 10 m/s free-stream velocity. This type of investigation can only be carried out in a very low noise environment if the data is too be free from corruption by system noise. The controlled excitation was provided by a computational derived deterministic pseudo-random signal driving a miniature acoustic driver buried in the plate that coupled to the flow through a 0.5 mm dia. hole. The experiment was fully computer controlled so that position of the probe, the tunnel unit Reynolds number and the sampling rate were all set, taking account of the temperature and atmospheric pressure variations during the acquisition period. This was necessary because many of the data sets were recorded over periods of up to a week of continuous running.

RESULTS

The random time series was stored on the controlling computer and could be used repetitively. Each signal realisation generated by the excitation time series created a slightly different outcome because of additional weak system noise. In this experiment 50 realisations were recorded at each measuring station so as form an ensemble mean and the deviation from that mean. A set of records at 600mm from the leading edge taken directly downstream from the source at various distances from the wall show the ensemble mean and, drawn in red, the deviation together with the mean profile. In the initial stages of development the records were very repeatable and show irregular quasi-periodic ripples arising from a narrow band response to a broad-band excitation. Further downstream at 860mm we see a short period within the record

Michael.gaster.1@city.ac.uk

where the deviation is significant. Subsequent analysis focuses on these secondary oscillations as they rapidly growth with downstream position, until a third somewhat higher frequency appears before true chaotic motion occurs as an embryo spot.

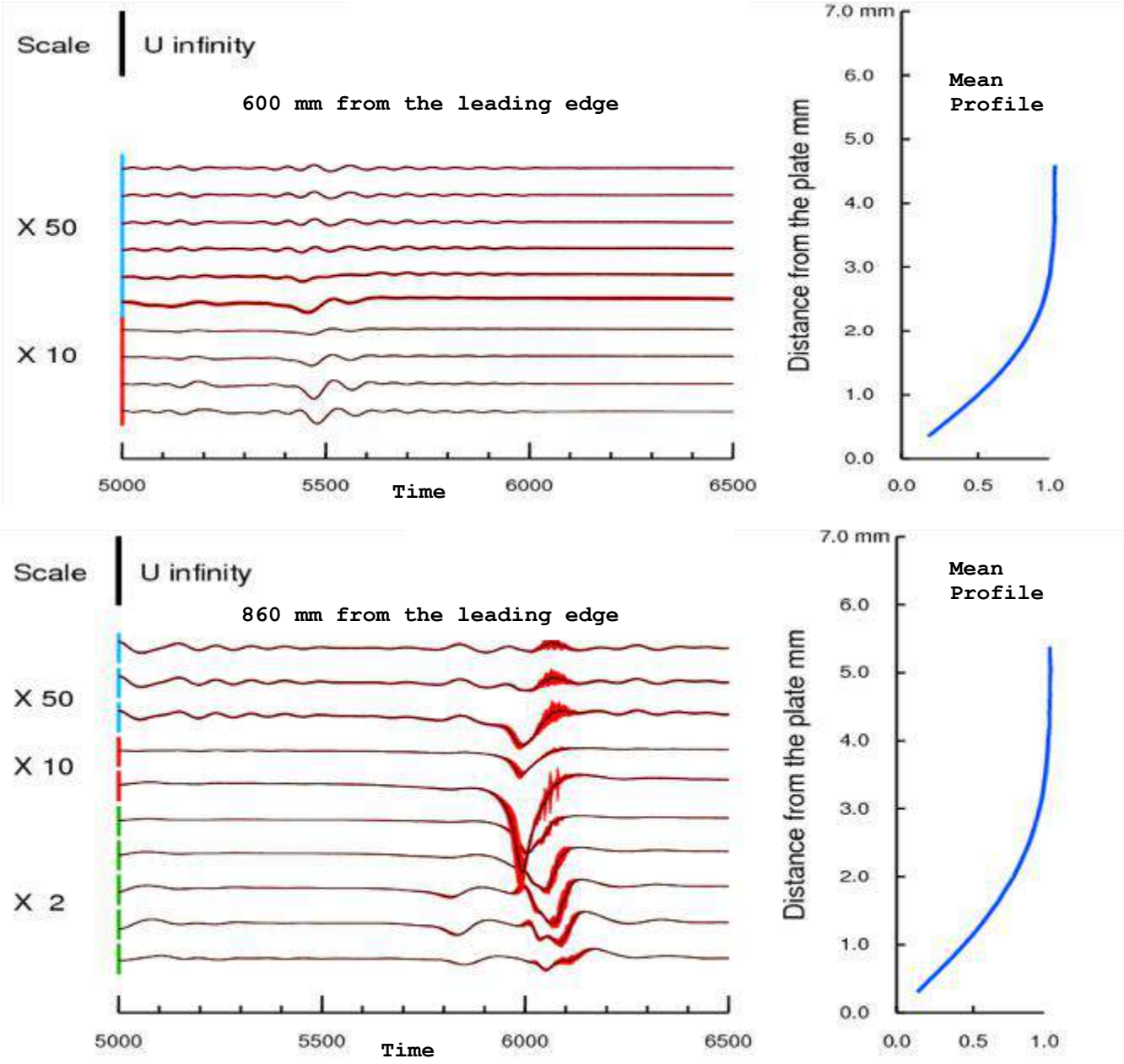

CONCLUSIONS

Highly modulated oscillations arising from a random excitation evolve different from purely periodic waves when the nonlinear effects become important. Secondary ripples appear and grow rapidly to form small bursts of oscillations that evolve through even higher frequency disturbances that evolve into spots of chaotic turbulence.

References

[1] Gaster M., Grant I.: An experimental investigation of the formation and development of a wave packet in a laminar boundary layer. *Proc. Roy. Soc.*, A., 347, pp 253. 1975.

[2] Gaster M.: The Origins of Turbulence, 'New Approaches and Concepts in Turbulence', Ed. Th. Dracos & A.Tsinober, Birkhauser Verlag 1993.

[3] Shaikh F, N.:'Turbulent spots in a transitional boundary layer', *PhD Thesis*, Cambridge University, 1994.

[4] Shaikh F.N., Gaster M.: The nonlinear evolution of modulated waves in a boundary layer, *J.Eng Maths,* 28, pp 55-77. 1994.

LOCALIZED SELF-SUSTAINING PROCESSES IN THE ASYMPTOTIC SUCTION BOUNDARY LAYER

Andrew Walton *[1] and Liam Dempsey[1]
[1]*Department of Mathematics, Imperial College London, South Kensington Campus, London SW7 2AZ, UK*

Summary Strongly nonlinear three-dimensional interactions between a roll/streak structure and a Tollmien-Schlichting wave are considered at high Reynolds number in the asymptotic suction boundary layer. A brief derivation of the interaction equations will be given, followed by the presentation of the results of numerical computations corresponding to nonlinear travelling-wave states bifurcating from the lower branch linear neutral point. The states are observed to localize in the spanwise direction with increasing amplitude due to the formation of a singularity which slowly develops in the governing interaction equations.

In recent years a dynamical systems picture of transition to turbulence has emerged in which equilibrium solutions of the Navier-Stokes equations have been shown to play a key role in transitional and turbulent dynamics. These equilibrium solutions consist of three crucial components: a roll flow in the cross-stream plane, a streamwise streak and a finite amplitude three-dimensional travelling wave. These three components interact in a mutually sustaining manner in which the roll flow drives a spanwise-modulated streak which is itself unstable to the wave. The wave then self-interacts nonlinearly to reinforce and re-energize the roll flow. This interaction can be described approximately at finite Reynolds number, e.g. [1], and exactly at asymptotically large Reynolds number, where it is known as vortex-wave interaction (VWI) [2]. In the latter formulation the wave can either be governed predominantly by inviscid Rayleigh instability of the streak profile away from the wall or viscous TS wave instability of the near-wall form of the streak. For the former Rayleigh-type interaction it has been demonstrated that the states computed are directly related to finite Reynolds number solutions. In contrast the numerical study of the interaction involving viscous TS waves has received far less attention. We aim to redress this balance here by considering the important problem of roll/streak/TS wave interactions at high Reynolds number within the asymptotic suction boundary layer (ASBL) and demonstrate the existence of alternative three-dimensional solutions to the well-known exact Navier-Stokes solution.

The linear stability properties of ASBL are well-known: there are distinct upper and lower branches along which neutral solutions exist and the streamwise wavenumber tends to zero as the Reynolds number R tends to infinity. Here the Reynolds number is defined as the ratio of the uniform external velocity to the wall suction speed. The solutions we are interested in bifurcate from the lower branch at high Reynolds number and are generated through the interaction of a pair of neutral oblique TS waves. On the lower branch at large R, the linear instability of ASBL is described by a triple deck structure in which the instability wavenumber and wavespeed are both of $O(R^{-1/4})$. Since this framework can also describe the nonlinear development of the instability we can use it as our starting point for the formulation of the relevant governing interaction equations.

After some asymptotic modelling (with brief details to be given in the talk) and matching between the three layers of the triple-deck structure, the final governing interaction equations can be written down as follows.

In the main part of the boundary layer the roll/streak flow dominates over the wave and to leading order the velocity components are

$$(U(y,z), R^{-1}V(y,z), R^{-3/4}W(y,z)),$$

where $U(y,z)$ is the spanwise-modulated streak flow, (V,W) are the scaled normal and spanwise components of the roll flow, with (y,z) the scaled coordinates in the normal and spanwise directions. From substitution into the governing Navier-stokes equations it is found that the roll/streak flow satisfies the balances

$$\frac{\partial V}{\partial y}+\frac{\partial W}{\partial z}=0, \qquad V\frac{\partial W}{\partial y}+W\frac{\partial W}{\partial z}=\frac{\partial^2 W}{\partial y^2}, \qquad V\frac{\partial U}{\partial y}+W\frac{\partial U}{\partial z}=\frac{\partial^2 U}{\partial y^2}. \tag{1}$$

It is notable that there is no contribution from the pressure gradient in these equations: the asymptotic modelling shows that the roll pressure exerts only a higher order effect. Also absent from these equations is any direct effect from the three-dimensional wave. In fact the wave exerts its most prominent effects within the lower deck and transmits its influence to the roll/streak flow via an azimuthal slip condition. This forms one of the boundary conditions for the system (1), together with the usual suction condition for ASBL, and the decay of the spanwise roll component in the far-field:

$$W(0,z)=q(z), \;\; V(0,z)=\circ\, 1, \;\; W\to 0 \text{ as } y\to\infty. \tag{2}$$

From these equations we can see the roll/streak/wave interplay explicitly. Firstly the roll satisfies nonlinear boundary-layer-type equations (1a,b) and the resulting roll-field then provides coefficients for equation (1c) which describes the development

*Corresponding author. Email: a.walton@imperial.ac.uk

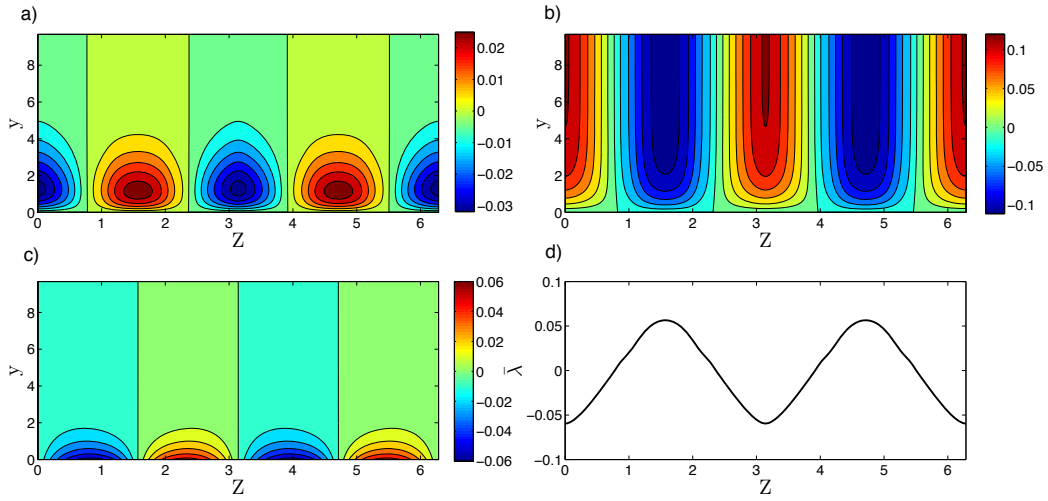

Figure 1: Numerical solution of the ASBL roll/streak/wave interaction equations for a moderate wave amplitude. (a) The perturbation $U(y,z) \circ U_B(y)$ to the streak basic state; (b) normal roll perturbation $V(y,z) \circ V_B$; (c) spanwise roll component $W(y,z)$; (d) perturbation to wall shear stress $U_y(0,z) \circ U_B'(0)$.

of the streak. However, in the absence of any wave forcing, a suitable roll flow cannot be sustained (all such solutions would decay in time) and the equations would then only admit the familiar undisturbed ASBL flow:

$$U \equiv U_B = 1 \circ \mathrm{e}^{-y}, \quad V \equiv V_B = \circ\, 1. \tag{3}$$

The spanwise slip condition (2a), representing the effect of the wave on the roll, is therefore absolutely crucial in setting up a self-sustaining process and generating nonlinear three-dimensional alternative solutions to (3). For a given spanwise slip profile $q(z)$ it indeed proves possible to generate non-trivial solutions to the system (1), (2). However calculating this profile for a given wave amplitude is a complicated numerical process involving the determination, for a given near-wall streak shear, of the wavenumber and frequency of the corresponding 3D TS wave. This calculation is also responsible for introducing an element of spanwise ellipticity into the interaction equations which are otherwise parabolic in z in view of the lack of spanwise diffusion in the roll/streak equations (1). More details of this process and the numerical treatment used will be given in the talk.

Once the slip profile $q(z)$ is identified the roll/streak problem consisting of (1), (2) also needs to be solved numerically. Periodic boundary conditions are applied in the spanwise direction. A spectral approach is adopted in which the spanwise variations are expressed in terms of Fourier series while suitably-mapped Chebyshev polynomials are used over the semi-infinite domain in y. A solution is then obtained by a Newton-Raphson approach. A suitable initial guess for the solution is obtained in the first instance by starting at small wave amplitudes and using the linear neutral TS solution to generate an analytic small amplitude solution for the roll and streak. The solution can then be found at higher amplitudes by a continuation strategy.

A typical solution for a moderate wave amplitude is given in Figure 1 where the departures from the undisturbed flow (3) are given. A feature of the solution is an apparent localization which develops in which various flow properties at particular spanwise locations adjust over increasingly short lengthscales as the wave amplitude is increased. It will be shown that this localization is due to the existence of an eigenfunction perturbation to the solution of the spanwise-local version of (1). This perturbation is responsible for an increasing lack of regularity in the flow solution at various spanwise locations with increasing nonlinearity of the fluid motion. Eventually a critical amplitude is reached beyond which spanwise derivatives of the key flow quantities are no longer continuous. The breakdown of the solution can also be attributed in part to the lack of spanwise ellipticity in (1), as mentioned earlier. At such large amplitudes the VWI formulation described here is no longer valid and a new interactive structure in which spanwise diffusion is more prominent must come into play. Possible replacement structures will be discussed briefly if time allows.

References

[1] Waleffe F.: On a self-sustaining process in shear flows. Phys. Fluids 9:883-900, 1997.

[2] Hall P., Smith F. T.: On strongly nonlinear vortex/wave interactions in boundary-layer transition. J. Fluid Mech 227:641-666, 1991.

Nonlinear optimal streaks induced by free-stream disturbances in flow over a thin flat plate

Xuerui Mao [*1] and Tamer A. Zaki [2]

[1] *School of Engineering and Computer Sciences, Durham University, Durham, DH1 3LE, UK*
[2] *Department of Mechanical Engineering, Johns Hopkins University, Baltimore, MD 21218, USA*

Summary The nonlinear optimal inflow disturbance to the flow over a flat plate with a slender leading edge is calculated. At a prescribed frequency ω and a given magnitude, the optimal inflow disturbance is the one which induces the maximum disturbance energy within the computational domain. The Reynolds number based on free-stream velocity and half thickness of the plate is $Re = 800$. The optimal is a combination of streamwise vorticity and streamwise velocity, where the second part can be attributed to the leading edge effect. The flow response to the optimal inflow disturbance has the form of high- and low-speed streaks, whose amplitude increases as the frequency of the inlet disturbance is reduced. The steady inflow rolls and streaks response are therefore the global nonlinear optimal for a monochromatic inflow forcing.

INTRODUCTION

Previous studies have computed the nonlinear optimal initial condition in pipe flow and boundary layers [1, 2]. By comparison, few efforts have been devoted to the optimal inflow disturbance, which is most relevant to the bypass transition [3]. In linear investigations, the optimal inflow disturbance to a boundary layer flow downstream of a leading edge is streamwise vorticity whose spanwise wavelength is on the order of the boundary-layer thickness [4]. In the present work, the methodology by Mao et al. (2015) [5] is extended to compute three-dimensional nonlinear optimal inflow disturbances in a boundary layer flow. A flat plate with a slender leading edge is adopted, and the Reynolds number based on the free-stream velocity and half thickness of the plate is $Re = 800$.

METHODOLOGY

The flow is decomposed into an undisturbed (base) flow and a superposed disturbance, $(\boldsymbol{u}, p) = (\boldsymbol{U}, P) + (\boldsymbol{u}', p')$, where $\boldsymbol{u}$, $\boldsymbol{U}$ and $\boldsymbol{u}'$ denote the total, base and disturbance velocity vectors, respectively, and p, P and p' represent the total, base and disturbance pressure terms, respectively. Substituting this decomposition into the Navier-Stokes equations, the following disturbance equations are derived,

$$\partial_t \boldsymbol{u}' + \boldsymbol{U}\cdot\boldsymbol{\nabla}\boldsymbol{u}' + \boldsymbol{u}'\cdot\boldsymbol{\nabla}\boldsymbol{U} + \boldsymbol{u}'\cdot\boldsymbol{\nabla}\boldsymbol{u}' + \boldsymbol{\nabla}p' \circ\ Re^{-1}\nabla^2\boldsymbol{u}' = 0 \ \text{ with } \ \boldsymbol{\nabla}\cdot\boldsymbol{u}' = 0. \tag{1}$$

The initial condition of the disturbance velocity is set to zero while the inflow boundary condition is given by

$$\boldsymbol{u}'(\boldsymbol{B}, t) = G(t)\boldsymbol{u}'_B(\boldsymbol{B}) \ \text{ with } \ G(t) = (1 \circ\ \mathrm{e}^{-\sigma t^2})(1 \circ\ \mathrm{e}^{-\sigma(T-t)^2})\mathrm{e}^{\mathrm{i}\omega t}, \tag{2}$$

where the temporal and spatial dependences of the inflow disturbance are separated. $\boldsymbol{B}$ denotes the inflow boundary, ω represents the frequency of the inflow disturbance, and the definition of G ensures that the boundary disturbance is zero at $t = 0$ so as to be compatible with the zero initial condition of the disturbance. The term $\boldsymbol{u}'_B(\boldsymbol{B})$ is the spatial distribution of the inflow disturbance. This distribution will be optimized in order to maximise the disturbance energy $E = \int \boldsymbol{u}'_T \cdot \boldsymbol{u}'_T \mathrm{d}\Omega$, where $\boldsymbol{u}'_T$ is the disturbance velocity at $t = T$ and Ω denotes the computational domain. In each optimisation calculation, the final time T, the frequency ω and the boundary norm of the inflow disturbance, $||\boldsymbol{u}'_B||_b = (\int \boldsymbol{u}'_B \cdot \boldsymbol{u}'_B \mathrm{d}\boldsymbol{B})^{1/2}$, are prescribed.

The gradient of the disturbance energy within the domain with respect to the inflow disturbance can be computed as,

$$\boldsymbol{\nabla}_{\boldsymbol{u}'_B} E = T^{-1}\int_0^T (p^*\boldsymbol{n} \circ\ Re^{-1}\boldsymbol{\nabla}_{\boldsymbol{n}}\boldsymbol{u}^*) G\,\mathrm{d}t,$$

where $\boldsymbol{u}^*$ and p^* are adjoint variables that are computed by integrating the adjoint equations

$$\partial_t \boldsymbol{u}^* + \boldsymbol{u}\cdot\boldsymbol{\nabla}\boldsymbol{u}^* \circ\ \boldsymbol{\nabla}\boldsymbol{u}\cdot\boldsymbol{u}^* \circ\ \boldsymbol{\nabla}p^* + Re^{-1}\nabla^2\boldsymbol{u}^* = 0, \quad \text{with} \quad \boldsymbol{\nabla}\cdot\boldsymbol{u}^* = 0.$$

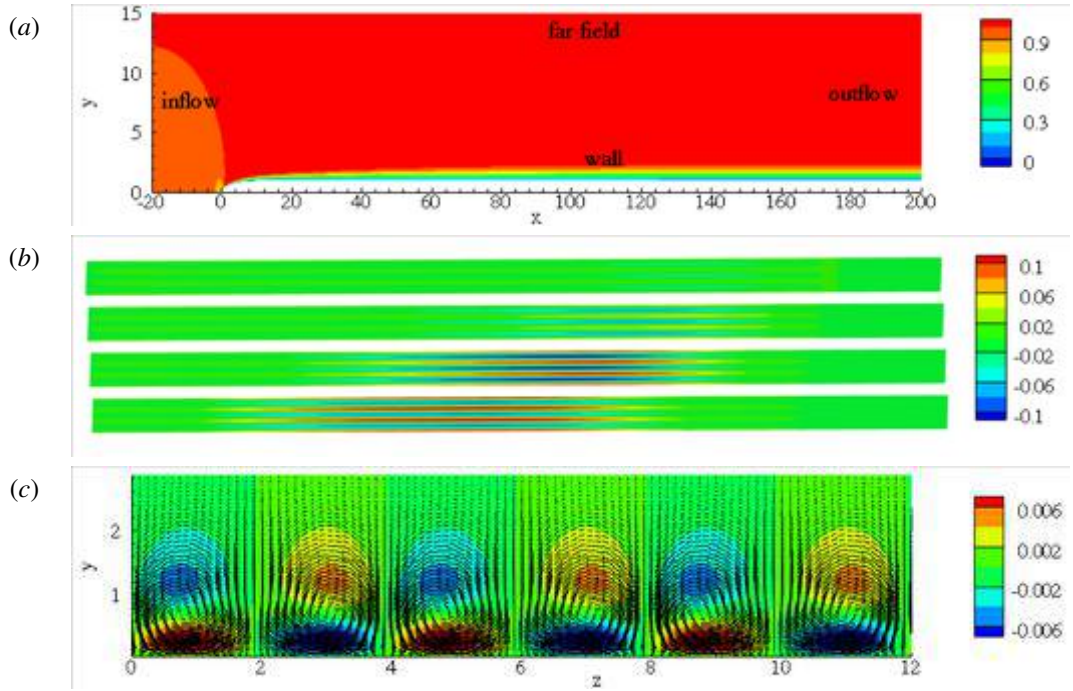

Figure 1: (a) Contours of the base-flow streamwise velocity. (b) Plane view (top to bottom) on the $x \circ z$ plane at y= $\{3, 2.5, 2, 1.5\}$, colored by streamwise disturbance velocity induced by the optimal inflow disturbance. (c) Optimal inflow velocity; the arrows denote the in-plane spanwise and wall-normal velocities; the contours represent the out-of-plane, streamwise velocity. The target time is $T = 180$ and the inflow parameters are $\omega = 0$ and $||\boldsymbol{u}'_B||_b = 0.01$.

RESULTS

A Cartesian system is adopted and x, y and z denote the streamwise, vertical and spanwise directions, respectively. The inflow and outflow boundaries are located at $x = \circ 20$ and $x = 200$; the leading edge of the plate is at $(x, y) = (0, 0)$; the spanwise domain length is 12 and 48 Fourier modes are used in the spanwise direction.

The two-dimensional base flow is shown in figure 1(a). The flow response to the optimal inflow disturbance at $T = 180$, $\omega = 0$ and $||\boldsymbol{u}'_B||_b = 0.01$ is shown in figure 1(b). This response clearly has the form of high- and low-speed velocity streaks, which are commonly observed in bypass transition.

The corresponding optimal inflow disturbance is illustrated in figure 1(c). This disturbance consists of a streamwise velocity and a streamwise vorticity. The maximum magnitude of the streamwise, vertical and spanwise velocities are 0.023, 0.009 and 0.008, respectively. Clearly this nonlinear optimal is dominated by the streamwise component which arises only in the presence of the leading edge boundary layer.

CONCLUSIONS

Three-dimensional nonlinear optimal inflow disturbances are calculated in flow over a thin flat plate with a slender leading edge. The optimal disturbance is the combination of streamwise velocity and streamwise vorticity, and the flow responses have the form of high- and low-speed streaks. The form of the optimal disturbance differs from earlier results that do not simulate the effect of the leading-edge region.

References

[1] Monokrousos A., Bottaro A., Brandt L., Vita A. and Henningson D.: Physical Review Letter,106: 134502, 2011.
[2] Pringle C. and Kerswell R.: Physical Review Letter,105: 154502, 2010.
[3] Jacobs, R. and Durbin P.: J. Fluid Mech., 428: 185-212, 2001.
[4] Monokrousos A., Åkervik E., Brandt L. and Henningson D.: J. Fluid Mech., 650: 181-214, 2010.
[5] Mao X., Blackburn H. and Sherwin S.: J. Fluid Mech., 775: 241-265, 2015.

*Corresponding author. Email: maoxuerui@sina.com

CONTROL OF CROSSFLOW INSTABILITY USING PLASMA ACTUATORS

Zhefu Wang[1], Song Fu[1a)]
[1]*School of Aerospace Enginering, Tsinghua University, Beijing, P.R.China*

ABSTRACT

Nonlinear parabolized stability equations are used to provide a computational assessment of potential use of plasma actuators for transition control on flow dominated by crossflow instability. The disturbance evolution is resolved with the plasma effect modelled by a distributed body force. Numerical study of crossflow instability in swept Hiemenz flow shows that plasma actuators which are posited just beneath the crossflow vortices reduce the growth rate of primary instability disturbance and weaken the crossflow vortices. Three operating voltages of plasma actuators are tested as well and the moderate voltage performs best. This control approach works even better in infinity swept wing flow and decreases the energy of disturbance nearly two orders of magnitude. The result demonstrates that plasma control offers great potential for transition delay.

INTRODUCTION

Laminar flow technology plays an important role in the development of future aerospace vehicles and it would reduce not only aerodynamic drag but also thermal loads on the structure. Recently, many researchers focus on transition delay of the boundary layer attached on the upper surface of a swept wing. This kind of boundary layer is susceptible to crossflow instability. Crossflow instability often results in the formation of crossflow vortices that modify the mean velocity field and hence the stability characteristics of the boundary layer. Breakdown is caused by the secondary instability ride on the new distorted mean flow. The key to control the crossflow instability is to control crossflow vortices. Inducing body force near wall with the opposite direction of the flow in the crossflow vortices is considered a potential approach. The relative position of crossflow vortices and the body force is shown in Fig 1. Here, x,y,z-direction is the streamwise direction, wall-normal direction and spanwise direction, respectively. Lines in Fig 1 are the isolines of the streamwise velocity and the colour indicates the body force strength. Crossflow vortices convect low-momentum fluid away from the wall at the left side and high-momentum fluid toward the wall at the right. The figure is viewed facing downstream. The electrodes are mounted parallel to vortices' axis. Thus the body force is distributed in a strip regions that aligned to crossflow vortices and the resultant force direction is just perpendicular to the vortex's axis. The body force distribution used in this work came from Kriegseis et al.[1] and it is induced by a dielectric barrier discharges (DBDs) plasma actuator.

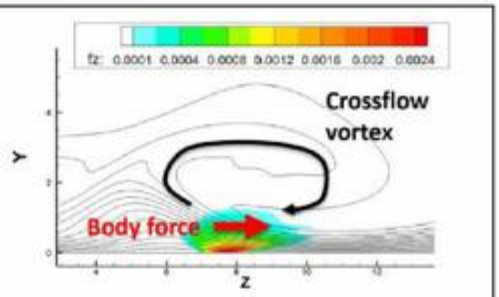

Fig 1 relative position of crossflow vortices and induced body force in y-z plane

RESULTS AND DISCUSSIONS

Linear stability theory is used to find the most unstable mode in swept Hiemenz flow and then the mode is treated as the target mode. The target mode is imposed at the inlet of computational domain and the control region is from X=500 to 550. To find the best spanwise position to put the plasma actuator, 10 different positions were tested. Here, z0 is used to denote the relative position of the plasma actuator in different test cases. z0=0.1 means that in this test case the plasma actuator is 0.1 wave length away from the origin point of z axis. All the electrode in the plasma actuator are parallel to the crossflow vortices. Fig 2 gives the evolution of primary stationary crossflow maximum streamwise disturbance velocity component with and without control. The calculation with an actuator was put at z0=0.7,0.8,0.9 were also performed but the disturbance grew too fast such the computation crashed when it just marched into the control region. The evolution of modes' energy and the body force relative position in the best case is shown in Fig 3. It can be seen plasma actuators which

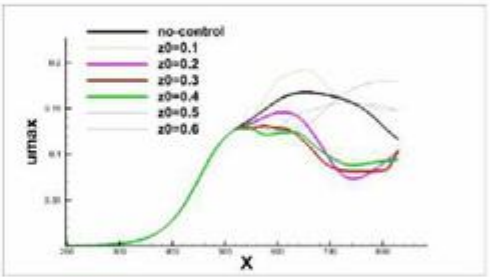

Fig 2 Evolution of primary stationary crossflow mode's maximum streamwise disturbance velocity component with and without control

[a)] Corresponding author. Email: fs-dem@tsinghua.edu.cn.

are posited just beneath the crossflow vortices reduces the growth rate of primary instability disturbance and weakens the crossflow vortices. Three operating voltages of plasma actuators are tested as well and the moderate voltage performs best.

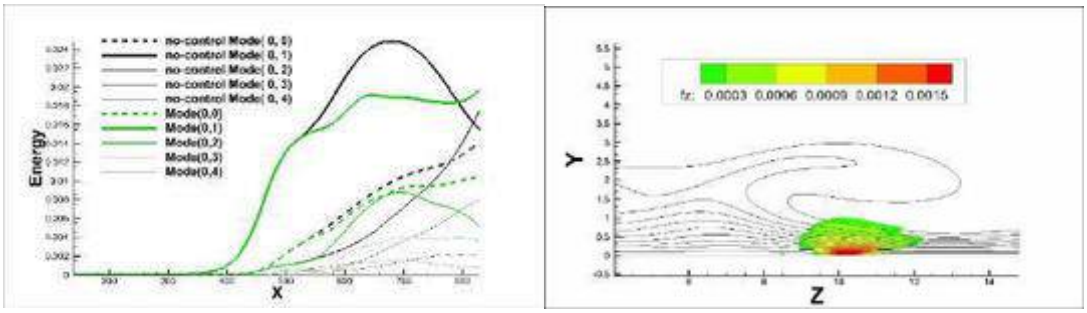

Fig 3 Comparison of modes' energy with and without control (left) and the body force relative position (right) (z0=0.4)

The infinity swept wing flow whose configure conforms to Reibert's experiment[2] is used here to test the plasma control approach. Evolution of modes' energy is shown in Fig 4. The control region is between the two red points. The harmonic (0,2) mode grow fast in the control region, but dies out soon when it comes out of the region due to its decreasing stability feature. Combined with the (0,2) mode which suppresses the fundamental mode through nonlinear effect, plasma actuators attenuate the fundamental mode and decreases its nearly two orders of magnitude. So, even though the mode keeps growing from X/C=0.46 to 0.7, it would never recover back. From the energy evolution, we can see that disturbances is totally suppressed when the plasma control approach is used and then transition is delayed.

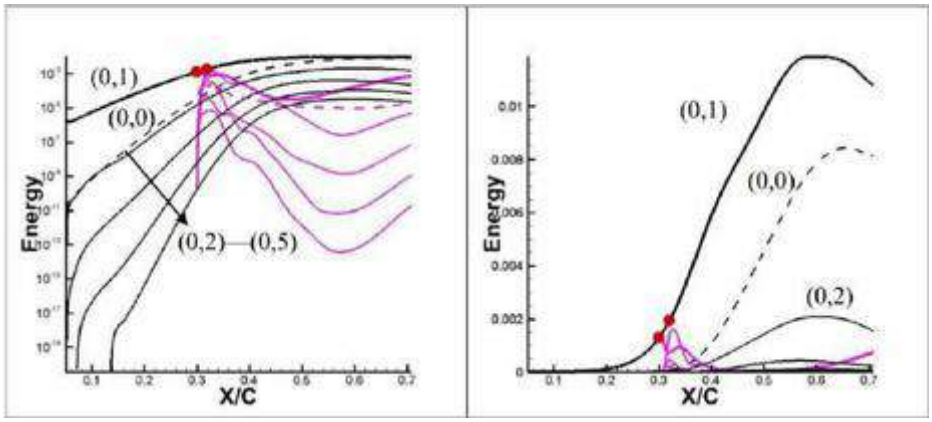

Fig 4 Evolution of modes' energy with (red) and without (black) control

CONCLUSIONS

This paper numerically studied the use of plasma actuators for transition control on boundary-layer flows dominated by crossflow instability. With a wall-paralleled body force assumption for plasma actuators, the disturbance evolution was resolved using parabolic stability equations in swept Hiemenz flow and infinity swept wing flow. In the swept Hiemenz flow, it was found that plasma actuators which were posited just beneath the crossflow vortices reduced the growth rate of primary instability disturbance and weakened the crossflow vortices. Otherwise, if the plasma actuators was put in a wrong position, it won't work. Three operating voltages of the plasma actuator were tested and the moderate voltage performs best. Too strong forcing would cause formation of nocent vortices which promoted disturbance growth. In the swept wing flow, the instability almost totally suppressed since the harmonic (0,2) which excited by plasma actuators has the decreasing feature and it helped to control the primary mode through nonlinear effect. The result demonstrated that the elaborately designed plasma actuators would delay the transition dominated by crossflow instability and it offered great potential for application on airplane with swept-wings.

References

[1] J. Kriegseis, C. Schwarz, C. Tropea, S. Grundmann, Velocity-information-based force-term estimation of dielectric-barrier discharge plasma actuators, Journal of Physics D: Applied Physics, 46 (2013) 055202.

[2] M.S. Reibert, Nonlinear stability, saturation, and transition in crossflow-dominated boundary layers, 1996.

TRANSITION TO TURBULENCE IN RECIPROCATING CHANNEL FLOW

Alireza Ebadi[1], Christopher M. White *[1], Ian Pond[2], and Yves Dubief[2]

[1]*Department of Mechanical Engineering, University of New Hampshire, Durham, NH, USA*
[2]*Department of Mechanical Engineering, University of Vermont, Burlington, VT, USA*

Summary The mean dynamics in reciprocating channel flow is studied to better understand transition to turbulence in periodic flows. The balance of the leading order terms in the phase-averaged mean momentum equation confirms that fully-developed turbulence first emerges at the early phases in the decelerating portion of the cycle. The underlying mechanism of this transition is the emergence of an internal shear layer that first develops during the late phases of the accelerating portion of the cycle. In the absence of this internal shear layer, the flow remains transitional over the entire cycle.

INTRODUCTION

Reciprocating channel flow is a periodic flow that oscillates at a fixed angular frequency, ω, with a cycle-averaged zero mean velocity. The mean flow over a half-period first accelerates to maximum velocity, next decelerates to zero velocity, then reverses direction. The process is then repeated indefinitely. The important similarity variable is the Stokes Reynolds number, $Re_s = \frac{U_m l_s}{\nu}$, where U_m is the amplitude of the cross-sectional average velocity, $l_s \equiv \sqrt{2\frac{\nu}{\omega}}$ is the Stokes layer thickness, and ν is the kinematic viscosity of the fluid. Based on Re_s, reciprocating flow is typically categorized into five flow regime types: I (laminar), II (disturbed laminar), III (self-sustaining transition), IV (intermittently turbulent), V (fully-developed turbulent) [1, 2]. Understanding the mechanisms of transition between flow regime types is important to understand and predict the transport mechanisms in many biological and engineered flow systems. In the present study, the balance of the leading order terms in the phase-averaged mean momentum equation are used to define the onset of turbulence in type IV flows. At this onset condition, mean flow properties are investigated to understand the underlying mechanisms of transition to turblence.

METHODOLOGY

Direct numerical simulations (DNS) of a reciprocating channel flow is used to study transition to turbulence in periodic flows. The simulations are performed for $Re_s = 648$ and 1019, representing type III (self-sustaining transition) and type IV (intermittently turbulent) flow regimes, respectively. The phase-averaged mean momentum balance is analyzed to determine the leading order terms as a function of phase angle. Turbulence is defined when the magnitude ordering of the leading order terms in the mean momentum equation matches with the four layer structure first introduced by Wei *et al.* [3] for fully-developed wall-bounded turbulent flows. Mean flow properties such as the turbulent inertia and the temporal acceleration are investigated prior to and during the onset of turbulence to understand the underlying mechanisms of transition.

RESULTS AND DISCUSSION

In fully-developed channel flow with a periodic pressure gradient, the phase-averaged momentum equation is

$$\underbrace{\circ\ \frac{\partial U}{\partial t}}_{\text{i}} + \underbrace{\frac{1}{\rho} cos(\omega t)}_{\text{ii}} + \underbrace{\nu \frac{\partial^2 U}{\partial y^2}}_{\text{iii}} + \underbrace{\frac{\partial(\circ\ \overline{u'v'})}{\partial y}}_{\text{iv}} = 0, \tag{1}$$

where t is time, x and y are streamwise and wall-normal directions, U is the phase-averaged velocity in the x direction, u' and v' are fluctuating velocities in x and y directions, and ρ is the density of the fluid. The ratio of term iii and term iv in Eq. 1 as a function of wall-normal position is shown in Fig. 1a and 1d for $Re_s = 648$ and 1019, respectively. A four-layer structure similar to that first described by Wei *et al.* [3] for canonical wall-bounded flow emerges at $\frac{9\pi}{16} \leq \phi \leq \frac{11\pi}{16}$ for $Re_s = 1019$. Similarly, the phase-averaged velocity and temperature profiles shown in Fig. 1e at the same phases agree reasonably well with the expected profiles for canonical wall-bounded turbulent flow. Conversely, the profiles for $Re_s = 648$ do not exhibit behaviors similar to canonical wall-bounded flow at any phase. In summary, fully-developed turbulent channel flow behaviors are observed for $Re_s = 1019$ (during the early phases in the decelerating portion of the cycle) but not for $Re_s = 648$. It follows that $Re_s = 1019$ is a type IV flow while $Re_s = 648$ is a type III flow. To investigate the mechanisms of transition from type III to IV, the temporal acceleration (term i in Eq. 1) for each phase angle in a half-cycle is shown Fig. 1c and 1f, for $Re_s = 648$ and 1019, respectively. For $Re_s = 1019$, inspection of the phases prior to and after $\phi = \frac{\pi}{2}$, when the bulk flow

*Corresponding author. Email: Chris.White@unh.edu

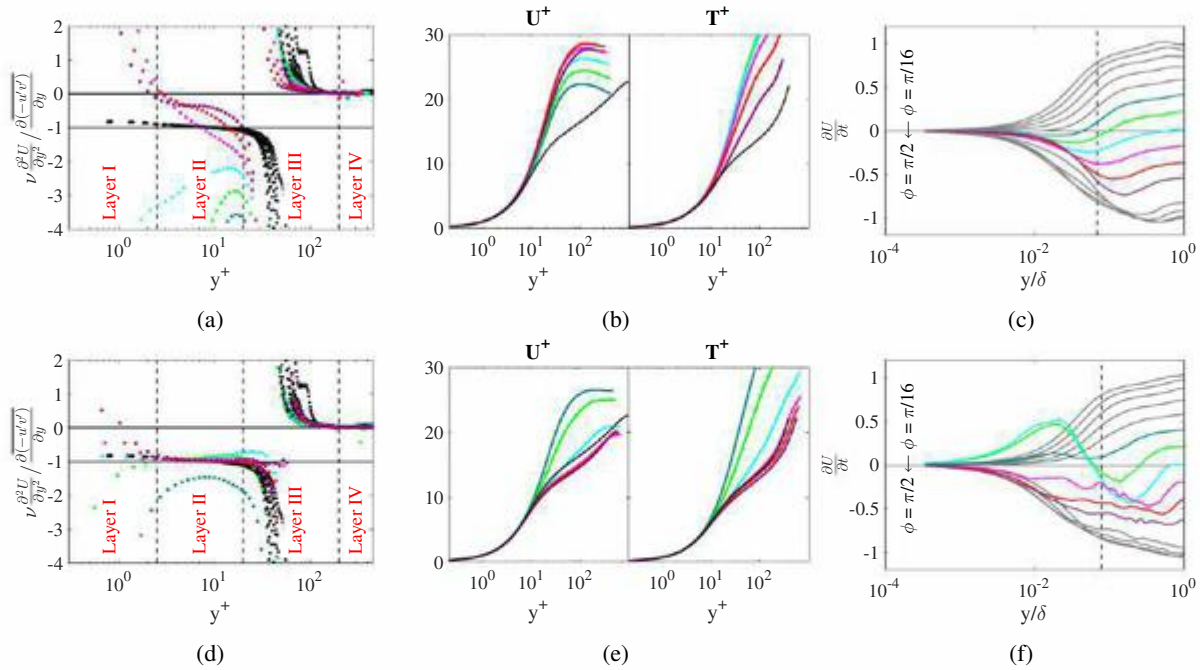

Figure 1: (a) The ratio of term iii and term iv in Eq. 1 as a function of wall-normal position for $Re_s = 648$. Black circles represent fully-developed zero pressure gradient turbulent boundary layer at different Reynolds numbers. Vertical dashed lines mark the approximate boundary between the four layers introduced by Wei *et al.*. Dark green, light green and cyan are $\phi = \frac{6\pi}{16}, \frac{7\pi}{16}, \frac{8\pi}{16}$, respectively. Magna, red and purple are $\phi = \frac{9\pi}{16}, \frac{10\pi}{16}, \frac{11\pi}{16}$, respectively. (b) Phase-averaged profiles of velocity and temperature in wall-units for $Re_s = 648$. Black lines represent ensemble-averaged profiles of fully-developed turbulent channel flow. (c) Phase-averaged profiles of $\frac{\partial U}{\partial t}$ for $Re_s = 648$. Grey lines are the rest of the phases with phase increasing from top-to-bottom. Vertical dashed line marks the laminar Stokes layer. (d), (e) and (f) are the same profiles as (a), (b) and (c) for $Re_s = 1019$. Colored line identifiers are the same in all six figures.

transitions from an accelerating flow to a decelerating flow, reveals the emergence of an internal shear layer that decelerates at a phase-lead compared to the near-wall and core regions. The emergence of the internal shear layer coincides with the spatially coincident strong sink-like behavior of the turbulent inertia. With increasing phase (i.e., bulk flow deceleration), the internal shear layer likely rolls-up triggering further flow instabilities that transition the flow to a fully-developed turbulent channel. The eventual acceleration of the flow suppresses the turbulence and the flow transitions back to a transitional flow. The cycle is then repeated indefinitely. For $Re_s = 648$, an internal shear layer does not emerge and the flow never transitions to a fully-developed turbulent channel. It follows that the key mechanism of transition from a type III to type IV flow is the emergence of an internal shear layer.

CONCLUSIONS

The mean dynamics in reciprocating channel flow is studied to better understand transition to turbulence. When the Stokes Reynolds number is large enough ($Re_s > 750$), the turbulent inertia is large enough to create an internal shear layer that phase-leads both the near wall and the core regions of the flow. The development of this shear layer transitions the flow to a fully developed turbulent channel flow in the early phases of the deceleration portion of the cycle.

References

[1] Ozdemir, Celalettin E., Tian-Jian Hsu, and S. Balachandar, Direct numerical simulations of transition and turbulence in smooth-walled Stokes boundary layer, Phys. Fluids, 26 (4), 045108, 2014.

[2] Akhavan, R., R. D. Kamm, and A. H. Shapiro, An investigation of transition to turbulence in bounded oscillatory Stokes flows Part 1. Experiments, J. Fluid Mech., 225, 395-422, 1991.

[3] Wei, T., P. Fife, J. Klewicki, and P. McMurtry, Properties of the mean momentum balance in turbulent boundary layer, pipe and channel flows, J. Fluid Mech., 522, 303-327, 2005.

MAGNETOHYDRODYNAMIC FLOW IN CHANNELS WITH CROSS-CHANNEL PRESSURE INTERACTION

Monalisa Munsi[1], Alric P. Rothmayer *[2], and Paul Sacks[3]
[1]*Department of Mathematics, Iowa State University, Ames, Iowa, USA*
[2]*Department of Aerospace Engineering, Iowa State University, Ames, Iowa, USA*
[3]*Department of Mathematics, Iowa State University, Ames, Iowa, USA*

Summary A transverse magnetic field of finite and large strength is applied to a hydrodynamic channel flow that has asymmetric channel wall distortions and a cross-channel pressure interaction. As the magnetic field strength is gradually increased, the basic character of the hydrodynamic interaction is preserved but on a shorter stream-wise length scale. At a sufficiently large value of the magnetic field strength, a new flow structure emerges, where the stream-wise length of the interaction is comparable to the channel width. Linear free interactions are used to investigate the properties of these structures.

Flow of a steady, incompressible, electrically conducting fluid through a plane channel in the presence of a transverse magnetic field is considered. The fluid flow is governed by the continuity and Navier-Stokes equations, coupled with the magnetic induction equations [4]. The nature of the hydrodynamic flow is controlled by a competition between viscous and inertial terms in the Navier-Stokes equations, often resulting in flow separation from the channel walls, especially for large Reynolds number, Re, flows. For very long stream-wise length scales, Smith [1, 2] showed that the hydrodynamic flow is controlled by a prescribed displacement, which is the average of the wall shapes. As the stream-wise length decreases to $O(Re^{1/7})$ [3], a cross-channel pressure gradient develops in the channel core which is sustained by the displacement of the viscous wall layers. On longer length scales that correspond to the hydrodynamic solution of Smith [1, 2], the transverse magnetic field tends to suppress flow separation [4]. In this study, we address how increasing magnetic field strength alters the properties of the flow of [3].

We start with flow at finite Hartmann number Ha, where the flow upstream in a straight channel is given by the Hartmann solution [4]. A gradual increase in Ha leads to a suppression of the leading order core velocity, which affects the pressure-displacement interaction of [3] through

$$P_{upper} = P_{lower} + \kappa(Ha)A''(X) \tag{1}$$

where

$$\kappa(Ha) = \int_0^1 U_0^2\, ds = \operatorname{csch}^2(\frac{Ha}{2}) \left[\frac{Ha(2+\cosh(Ha)) \circ 3\sinh(Ha)}{8Ha^3}\right], \tag{2}$$

$U_0(y, Ha)$ is the Hartmann solution in the straight channel [4], $\kappa(Ha)$ has the limits $\lim_{Ha\to 0} \kappa = 1/120$ (same as Smith's [3]) and $\lim_{Ha\to\infty} \kappa \sim 1/(4Ha^2)$.

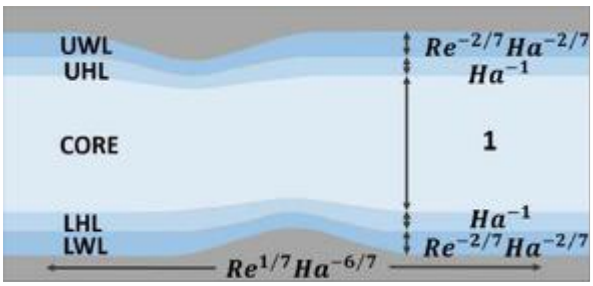

(a) $1 << Ha << Re^{1/6}$

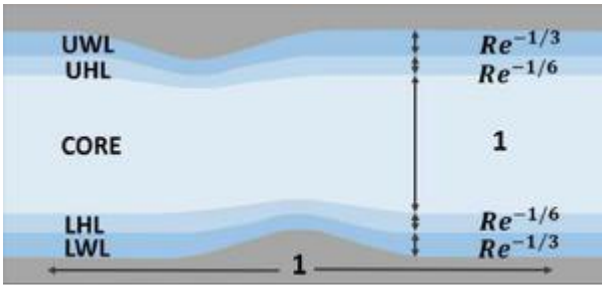

(b) $Ha \sim O(Re^{1/6})$

Figure 1: **Flow Structures**

When $1 << Ha << Re^{1/6}$ this interaction and the near-wall viscous layers are maintained through shortening of the channel wall distortion length scale, i.e., $x \sim Re^{1/7}Ha^{-6/7}$. As a result, a five-deck structure (see Fig.1(a) above) develops, which has two wall layers (LWL, UWL) similar to Smith's [3] structure, two Hartmann layers (LHL, UHL) and a core. The wall layers are connected through a linearly varying core pressure. The decreasing x-scale and core velocity lead to a decrease

*Corresponding author. Email: roth@iastate.edu

in the core perturbation velocity scales. Hence the convective term uu_x in the x-momentum equation will eventually fall to the level of the stream-wise pressure p_x, the largest neglected term of the stream-wise momentum equation. This balance leads to a breakdown of the structure when $Ha = Re^{1/6}H$, where H is the scaled Hartmann number.

In the new structure (Fig. 1(b)) where $Ha = Re^{1/6}H$, the core is governed by

$$P_{XX} + P_{yy} = 0, \tag{3}$$

$$A + B = 4H^2 \int_0^1 P(X, s)\, ds \tag{4}$$

where $U_{lower} \to \lambda(Y + A(X))$ and $U_{upper} \to \lambda(Y + B(X))$ as $Y \to \infty$ are the U-matching conditions for the LWL and UWL, respectively. For $H = 0$, the displacement equation (4) reduces to Smith's [3] where $B = \circ A$.

To further assess the properties of the structures, we examine the linear free interactions through a perturbation of the displacement function, i.e., $A(X) = \pm\epsilon e^{\theta X}$, where $x = Re^{1/7}X$ and $\epsilon \ll 1$. The solution of the resulting linear problem yields the growth rate, $\theta = [\circ\, 3Ai'(0)/2^{2/3}\kappa(Ha)]^{3/7}$ where $\kappa(Ha)$ is given by (2) and $Ai'(0) \simeq \circ\, 0.2588$. For $Ha \to 0$, $\theta = 2[\circ\, 45Ai'(0)]^{3/7}$ and the hydrodynamic value of [3] is recovered. For $1 << Ha << Re^{1/6}$, the dispersion relation between θ and Ha is given by $\theta = [\circ\, 12Ai'(0)/2^{2/3}]^{3/7}Ha^{6/7}$ (Fig. 2(a)). Therefore, the pressure interaction (1) of the hydrodynamic solution [3], as well as the linear free-interactions, are preserved, but on a shorter stream-wise length scale. When Ha increases to the level of $Ha = Re^{1/6}H$, we obtain a dispersion relation between the scaled growth rate θ and H, given by

$$2^{2/3}\theta^{8/3} + 12H^2Ai'(0)\theta^{4/3}\cot(\theta) = \frac{36}{2^{2/3}}H^4(Ai'(0))^2, \tag{5}$$

shown in (Fig. 2(b)) where θ is the growth rate on the $O(1)$ stream-wise length scale.

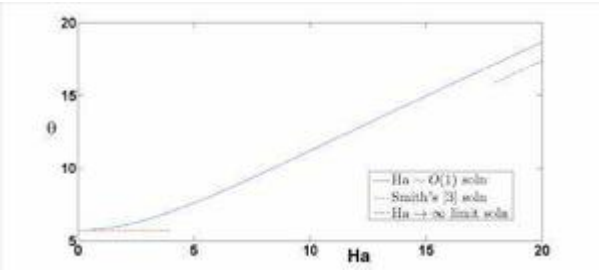

(a) $1 << Ha << Re^{1/6}$

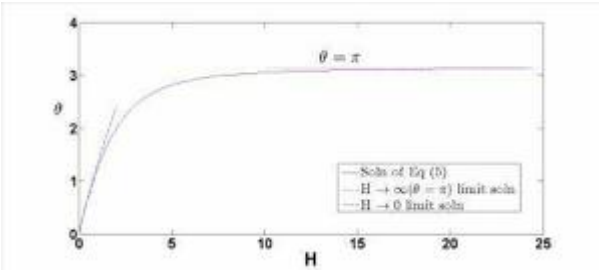

(b) $Ha = Re^{1/6}H$

Figure 2: **Free interaction**

As $H \to 0$, we can recover the $1 << Ha << Re^{1/6}$ solution. On the other hand, the $H \to \infty$ limit shows that the linear free interaction is preserved but approaches a constant stream-wise length scale that is proportional to the channel width.

In summary, a large Reynolds number asymptotic structure for steady, two dimensional laminar MHD flow in channels with wall shapes of stream-wise length $O(Re^{1/7})$ has been examined. The hydrodynamic wall layer solution can be recovered at very small Ha. Smith's interaction [3] can also be preserved as $Ha \to \infty$ but on a shorter stream-wise length scale. A new structure develops when $Ha \sim O(Re^{1/6})$. The authors believe that the $Ha \sim O(Re^{1/6})$ structure of this study likely has a direct correspondence to the entry flow structure originally examined by Smith [5], and that there is also a likely connection between the progression from finite to large Ha and the movement of the Smith [3] interaction into an entry flow region.

References

[1] Smith F.T.: Flow through constricted or dilated pipes and channels I. Q. J. Mech. Appl. Math 29:343-364, 1976.

[2] Smith F.T.: Flow through constricted or dilated pipes and channels II. Q. J. Mech. Appl. Math 29:365-376, 1976.

[3] Smith F. T.: Upstream Interactions in Channel Flows. J. Fluid Mech 79:631-655, 1977.

[4] Rothmayer A.P.: Magnetohydrodynamic Channel Flows with Weak Transverse Magnetic Fields. Phil. Trans. R. Soc. A 372:20130344, 2014.

[5] Smith F. T.: On entry-flow effects in bifurcating, blocked or constricted tubes. J. Fluid Mech 78:709-736, 1976.

VISCOUS-INVISCID INTERACTION AND BOUNDARY-LAYER SEPARATION IN TRANSONIC FLOWS

Anatoly Ruban *[1]

[1]*Department of Mathematics, Imperial College London, London, UK*

Summary This paper is concerned with the behaviour of boundary-layers in transonic flows. When the Reynolds number is large, the interaction between the boundary layer and inviscid flow outside the boundary layer becomes important in many flow situations. These include the flows in a vicinity of the separation point and near body surface irregularities. Even a simple discontinuity in the surface curvature proves to be capable of creating a pressure gradient that is strong enough to cause the boundary-layer separation. Alternatively, small surface imperfections may be arranged in such a way that they would produce a strong favourable pressure gradient, which allows to accelerate the flow in the boundary layer making it more resistant to separation and laminar-turbulent transition. We use asymptotic (large Reynolds number) analysis of the Navier–Stokes equations to describe this flow behaviour.

Historic background

As the aerospace industry is now in pursuit of laminar wing design for passenger aircraft, a better understanding of the behaviour of laminar boundary layer in transonic flows at large values of the Reynolds number is required. Of particular interest is theoretical prediction of possible separation of the boundary layer and of the laminar-turbulent transition.

It is well known that the classical boundary-layer theory, as formulated by Prandtl (1904), is not applicable near the separation point, where the displacement effect of the boundary layer becomes strong enough to cause a significant redistribution of the pressure outside the boundary layer. This phenomenon, known as the viscous-inviscid interaction, was initially discovered experimentally. A large number of experimental studies were perform during 1940s and 1950s concentrating mainly on the boundary-layer separation in supersonic flows (a review of these studies was given by Chapman *et al*, 1958). Among the first was a work of Ferri (1940) devoted to supersonic and transonic flows.

A formal theory of viscous-inviscid interaction was developed independently by Neiland (1969) and Stewartson & Williams (1969) in application to the boundary-layer separation in supersonic flows. Using the asymptotic analysis of the Navier–Stokes equations they found that the flow near the point of separation can be described in the framework of the so-called triple-deck model (see Figure 1). The flow in region 1 is governed by Ptrandtl's boundary-layer equations. However, the pressure acting on the boundary layer is not known in advance, and has to be found by analysing the interaction with region 3 that lies outside the boundary layer. The interaction process consists of the following. Being exposed to perturbations of the pressure, the flow in region 1 produces the displacement of the streamlines from the body surface. These are then transported through region 2 to the upper tier (region 3), where the deformation of the streamlines are 'converted' into the pressure perturbations, and these are then transported back to region 1. Region 2 plays a passive role in the interaction process; it does not contribute into the displacement effect of region 1, nor it changes the pressure produced in region 3. If this flow is supersonic, then the Ackeret theory holds in region 3.

Later the theory was shown to be applicable to wide variety of flows, both supersonic and subsonic (see, for example, Sychev *et al*, 1999).

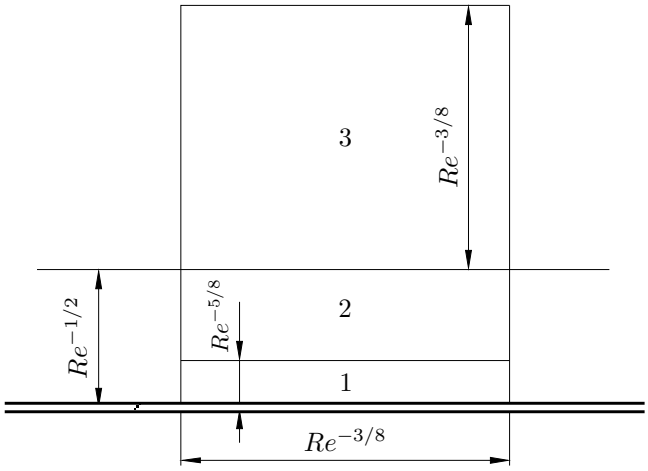

Figure 1: Three-tiered structure of the interaction region.

TRANSONIC VISCOUS-INVISCID INTERACTION

The triple-deck theory was first applied to transonic flows by Bodonyi & Kluwick (1977, 1998), who analysed, among other flows, the flow near the trailing edge of a flat place. In this problem the flow is only perturbed near the trailing edge where the viscous-inviscid region is situated. The process of viscous-inviscid interaction proceed in the same way as in supersonic and subsonic flows, that is the middle deck (region 2) remains passive, and the interaction takes place between the lower deck (region 1) and the upper deck (region 3). Of course, in transonic flow one has to use the Kármán-Guderley equation for region 3. This changes the size of the interaction region from $\Delta x \sim Re^{-3/8}$ to $\Delta x \sim Re^{-3/10}$, and also some changes of the flow properties have been observed.

However, the true nature of the transonic flows has been revealed in analysis of the transonic flow separation from a corner point (see Ruban & Turkyilmaz, 2000) and of the transonic Prandtl–Meyer flow (see Ruban *et al*, 2006). In both problems, the transonic flow outside the interaction region develops a strong singularity with an 'extremely favourable' pressure gradient acting on the boundary layer. As a result the nature of the interaction changes completely. Instead of viscous-inviscid interaction it becomes inviscid-inviscid interaction taking place between the middle tier (region 2) and the upper tier (region 3).

In the present paper we will also discuss the transonic flow near a point of discontinuity of the body surface curvature, which may be expressed by the equation

$$y = \begin{cases} \varkappa_1 x^2 & x < 0, \\ \varkappa_2 x^2 & x > 0. \end{cases}$$

Depending on $\varkappa_1$ and $\varkappa_2$ the flow might display a deceleration and separation from the body surface or strong acceleration. An example of the latter is shown in Figure 2 which demonstrates how the skin friction increases in the interaction region. Obviously, instead of using suction for the flow control, it is much easier to accelerate the flow in the boundary layer by introducing a simple discontinuity in the surface curvature.

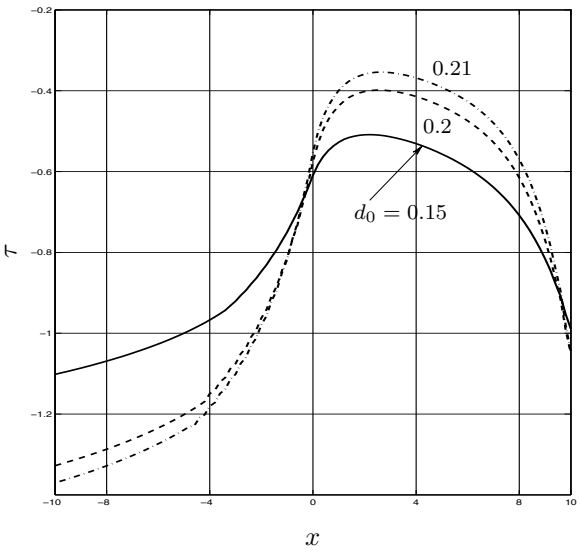

Figure 2: Skin friction $\tau(x)$.

References

[1] Prandtl L.: Über Flüssigkeitsbewegung bei sehr kleiner Reibung, Verh. III. Intern. Math. Kongr., Heidelberg, pp. 484–491, 1904.

[2] Chapman D. R., Kuehn D. M., Larson H. K.: Investigation of separated flows in supersonic and subsonic streams with emphasis on the effect of transition, *NACA Rep. No. 1356*, 1956.

[3] Ferri A.: Esperienze su di un biplano iperacustic. *Atti di Guidonia*, No. 37-38, 1940.

[4] Neiland, V. Ya: Theory of laminar boundary layer separation in supersonic flow, *Izv. Akad. Nauk SSSR, Mech. Zhidk. Gaza*, no. 4, pp. 53–57, 1969.

[5] Stewartson K., Williams P. G.: Self-Induced Separation, *Proc. Roy. Soc. London*, **A 312**, pp. 181–206, 1969.

[6] Sychev V. V., Ruban A. I., Sychev Vic. V., Korolev G. L. *Asymptotic Theory of Separated Flows*, CUP, 1999.

[7] Bodonyi R. J., Kluwick, A. Freely interacting transonic boundary layers. *Phys. Fluids*, **20**, pp 1432–1437, 1977.

[8] Bodonyi R. J., Kluwick, A. Transonic trailing-edge flow. *Q. J. Mech. Appl. Maths*, **51**, pp 297–310.

[9] Ruban A. I., Turkyilmaz. On laminar separation at a corner point in transonic flow. *J Fluid Mech*., **423**, pp 345–380.

[10] Ruban A. I., Wu X., Pereira R. M. S. Viscous-inviscid interaction in transonic Prandtl–Meyer flow. *J Fluid Mech*., **568**, pp 387–424.

UNSTEADY BOUNDARY-LAYER SEPARATION AT FINITE AND INFINITE REYNOLDS NUMBERS

Kevin Cassel [*1] and Michael Boghosian[1]
[1]*Department of Mechanical, Materials, and Aerospace Engineering, Illinois Institute of Technology, Chicago, IL, USA*

Summary Unsteady boundary-layer separation in the limit as Reynolds number goes to infinity is marked by the onset of the Van Dommelen singularity, which signals a sudden, small-scale eruption of vorticity from the boundary layer. A more complete and comprehensive picture of the unsteady separation process has been sought for some time, including how the limiting process based on asymptotic methods is adjusted for finite Reynolds numbers of practical interest. Here, an alternative mechanism is described that also leads to an ejection of near-wall vorticity, *i.e.* unsteady separation. It is predicated on the splitting of a recirculation region or vortex within the boundary layer owing to the Vortex-Shedding Mechanism (VSM). However, it is not found to be permissible in the boundary-layer limit. Therefore, it is an alternative to the Van Dommelen singularity-based unsteady separation mechanism that may occur at finite Reynolds numbers.

UNSTEADY SEPARATION

Unsteady separation marks a turning point in a wide variety of high Reynolds-number, surface-bounded flows. Instigated by an adverse pressure gradient acting upon a boundary layer, it is characterized by a sudden ejection of near-wall vorticity into the outer flow. Such an event leads to significant and abrupt changes in aerodynamic forces and/or mixing, for example. Although isolated in space and time, it typically has significant consequences for the global flow field in flows for which it occurs.

In general, unsteady separation is defined as a sudden ejection of near-wall vorticity on small spatial scales. In the context of the unsteady boundary-layer equations, which apply in the limit as Reynolds number goes to infinity, unsteady separation has a clear and definitive criterion. First articulated as the Moore, Rott, and Sears (MRS) criterion in Eulerian coordinates, an adverse pressure gradient acting on the boundary layer produces the Van Dommelen singularity[1], which consists of a narrow region in space within the boundary layer erupting suddenly away from the surface. Subsequent asymptotic stages also have been identified that involve interaction between the viscous boundary layer and inviscid outer flow followed by the influence of normal pressure gradients, which are neglected in leading-order boundary-layer theory.

Attempts have been made to delineate these initial three stages of the unsteady separation process within the context of the full Navier-Stokes equations at large, but finite, Reynolds numbers[2, 3]. Although broadly in agreement, there are important differences that call into question the validity of the limiting, infinite-Reynolds-number picture of unsteady separation. In particular, there is evidence that the scales at which viscous-inviscid interaction arises are only valid at extremely high Reynolds numbers, even beyond those that are of practical relevance.

In addition to the prospect of their being severe limits on the extensibility of the boundary-layer theory to Reynolds numbers of practical interest, the question arises as to the possibility that additional mechanisms may lead to unsteady separation as defined generally above. In particular, is the Van Dommelen singularity-induced eruption the only mechanism that may lead to an ejection of vorticity from within a boundary layer?

VORTEX-SHEDDING MECHANISM

There is growing evidence that an unsteady separation mechanism exists at finite Reynolds numbers that is triggered by the splitting of an existing recirculation region or vortex within a boundary layer[4]. After summarizing this mechanism, we then consider whether such a mechanism is permissible in the unsteady boundary-layer equations that govern at infinite Reynolds numbers.

Assume we have a two-dimensional, incompressible finite Reynolds-number flow such as the flow past a circular cylinder or a vortex above a plane wall. These flows are known to have vortices or recirculation regions that undergo splitting and subsequent shedding. Recent investigations have shown that the Vortex Shedding Mechanism (VSM) predicts if a vortex or recirculation region will undergo a splitting event in any two-dimensional, incompressible flow. The VSM is based upon the second invariant of the velocity gradient tensor or Q-criterion given by

$$|\nabla \mathbf{v}| = Q = \frac{\partial u}{\partial x}\frac{\partial v}{\partial y} \circ \frac{\partial u}{\partial y}\frac{\partial v}{\partial x}, \tag{1}$$

[*]Corresponding author. Email: cassel@iit.edu

and the divergence of the net forces of the Navier-Stokes equations, $\nabla \cdot \mathbf{f}_{net}$, defined as

$$\nabla \cdot \mathbf{f}_{net} = \circ \nabla^2 p + \nabla \cdot \mathbf{f}_b, \tag{2}$$

where $\mathbf{f}_b$ is the body force. Note that for an incompressible fluid, the divergence of the viscous terms is identically zero by continuity; therefore, only pressure gradient and body force terms appear. It can be shown that the Q-criterion is related to both the determinant of the Hessian matrix of the streamfunction and to the divergence of the net forces according to

$$Q = |\mathbf{H}(\psi)| = \circ \frac{1}{2} \nabla \cdot \mathbf{f}_{net}. \tag{3}$$

As a result, if the divergence of the net forces is positive, then by the Second Partial Derivative Test, the vortex or recirculation region experiences a splitting via a saddle-node. Formally, the VSM states that given a two-dimensional, incompressible flow, an existing vortex or recirculation region, having positive Q, will undergo a splitting event at a location, if and only if, (1) there is a critical point in the streamfunction (zero momentum), and (2) the Q-criterion is less than zero which occurs if there is a positive divergence of the net forces.

Recently, splitting and shedding of the "parent" recirculation region or vortex via the VSM has been found to play a critical role in determining if an ejection of near-wall secondary vorticity will occur. From numerical simulations of the flow about a circular cylinder and that induced by a thick-core vortex above a wall, we have observed that the ejection event is *always* preceded by a splitting of the parent recirculation region or vortex via the VSM. This occurs because the zero-vorticity "front" of the ejection cannot pass through a region where $Q > 0$. Moreover, we have shown suppression of an ejection event by mitigating the VSM. Thus, the ejection phenomenon appears to require the VSM as a prerequisite in these problems. This may be viewed as follows. The parent recirculation region splits via the VSM creating a corridor or pathway for escape of the near-wall vorticity. Not only can the VSM be proven to be a necessary and sufficient condition for splitting of a recirculation region or vortex, but the ejection phenomenon appears to require the VSM as a prerequisite.

Given this mechanism leading to a vorticity ejection in finite Reynolds-number flows, *i.e.* unsteady separation, it raises the question as to whether the VSM-induced ejection is in any way related to the Van Dommelen singularity or if it is an alternative mechanism altogether. In order to decipher which is the case, let us determine whether the VSM is permissible within the context of the unsteady boundary-layer equations.

The $O(Re^{-1/2})$ thick boundary layer gives rise to the boundary-layer scalings $y = Re^{-1/2}Y$ and $v = Re^{-1/2}V$ for the normal coordinate and velocity, respectively. According to these scalings, the force-divergence criterion (2) takes the form

$$\nabla \cdot \mathbf{f}_{net} = \circ \frac{\partial^2 p}{\partial x^2} + \nu \frac{\partial}{\partial x} \left(\frac{\partial^2 u}{\partial Y^2} \right). \tag{4}$$

As this form does not admit the Q-criterion inherent to the VSM, it is concluded that the VSM-based ejection mechanism is not permitted by the unsteady boundary-layer equations. Consequently, the VSM is therefore found to be a distinct mechanism from the Van Dommelen singularity.

CONCLUSIONS

Whereas unsteady separation is clearly defined by the Van Dommelen singularity within the context of the unsteady boundary-layer equations, which formally govern in the limit as Reynolds number goes to infinity, finite Reynolds-number flows are found to admit an alternative mechanism leading to unsteady separation. This mechanism requires the splitting of a recirculation region or vortex within the boundary layer that provides a pathway for the ejection of near-wall secondary vorticity from deep within the boundary layer. Whereas the Van Dommelen singularity occurs when the MRS criteria are satisfied, or equivalently when a stationary point forms in the continuity equation, the criteria for the VSM requires a positive force divergence at a location of zero momentum. Anecdotal numerical evidence suggests that this mechanism may be more common than a finite Reynolds-number version of the Van Dommelen singularity.

References

[1] Van Dommelen L.L., Shen S.F.: The Spontaneous Generation of the Singularity in a Separating Laminar Boundary Layer. *J. Comput. Phys.* **38**, 1980.

[2] Brinckman K.W., Walker J.D.A.: Instability in a Viscous Flow Driven by Streamwise Vortices. *J. Fluid Mech.* **432**, 2001

[3] Obabko A.V., Cassel K.W.: Navier-Stokes Solutions of Unsteady Separation Induced by a Vortex. *J. Fluid Mech.* **465**, 2002.

[4] Boghosian M.E., Cassel K.W.: A Pressure-gradient Mechanism for Vortex Shedding in Constricted Channels. *Phys. Fluids* **25**, 2013.

INVESTIGATION OF FIXED AND MOVING SEPARATION IN A VISCOUS FLOW

Pauline Beaudoux[1] and Jérôme Vétel*[2]
[1,2]*Fluid Dynamics Laboratory (LADYF), Polytechnique Montréal, Québec, Canada*

Summary The rotor-oscillator flow consists in rotating a cylinder parallel to a wall in a viscous fluid to generate a separation. If in addition the cylinder is translated along the wall with a given velocity profile, the separation profile becomes unsteady and can be easily manipulated. Particle image velocimetry is used to study different scenario of two-dimensional fixed and moving separation. For the fixed case, existing formulae to compute the profile of the on-wall separation are validated. For the moving case, the separation point coincides with a Lagrangian saddle-point moving inside the flow and a method is proposed to compute the stable and unstable manifolds to which it belongs.

INTRODUCTION

In 2004, G. Haller [1] extended the conditions proposed by L. Prandtl to capture separation in two-dimensional steady flows to the unsteady case, thus unifying prior works into a single theory and extending them to cases not covered before. This new approach showed that the key point to capture separation is to use a Lagrangian approach where the separation profile can be described by a material line that first attracts, then ejects fluid particles initially located in the vicinity of the boundary. Two types of separation were considered. A *fixed* separation occurs when the flow has a well-defined mean value, such as in periodic flows. In this case, the boundary point of separation is fixed at a location where the backward-time average of the skin friction vanishes, but the shape of the separation profile is time-dependent. A *moving* separation occurs when the flow does not have a mean value, such as in a boundary layer where the external velocity changes constantly. In this case, the separation point may move, and is defined at the location where the time-varying mean component of the skin friction vanishes.

A very few studies have focused on the experimental validation of the new theory. The reason is that the computation of the time-dependent separation profile requires to measure instantaneous spatial gradients of the two velocity components. To the authors knowledge, only one study has been reported in the literature. In [2], a cylinder whose axis can be oscillated parallel to a wall is simultaneously rotated in a viscous liquid to manipulate an unsteady separation. Under periodic, quasi-periodic and random forcing, observations reveal that separation emanates from a fixed location on the surface, its position and orientation over time being accurately predicted by the theory. However, experiments were used only to provide visualisations, since quantitative data were extracted from a numerical simulation of the experimental flow. In this study, an experimental set-up similar to the one used in [2] was designed and particle image velocimetry (PIV) was used to explore diverse two-dimensional separation phenomena thanks to different combinations of rotation and translation of the cylinder.

METHODS

A cylinder of diameter 2.54 cm is inserted vertically in a rectangular acrylic tank. The stepper motor used to rotate the cylinder is mounted on a motorized linear stage that is parallel to the longest side of the tank. The tank is filled with a water-glycerin mixture of 95% glycerin by weight. This mixture was chosen because the density of the fluid is very close to that of fluorescent tracer particles (Rhodamin B, mean diameter of $\sim$10 µm) used for PIV measurements. The laser light sheet is positioned horizontally and a camera is placed vertically below the tank to obtain the two components of velocity vectors in the whole area between the cylinder and the vertical wall. The particle images are processed by the LaVision DaVis software to obtain the velocity fields, and are also averaged in different ways depending on the type of separation that is investigated.

RESULTS

The rotation speed of the cylinder is Ω and its translation speed is $U_c = U_0 + \beta \cos \omega t$, where U_0 is a constant translating velocity on which an oscillating movement of angular frequency ω and amplitude β is superimposed. In the case of a periodic flow, i.e. when $U_0 = 0$, the separation profile $\mathscr{S}(t)$ at time t corresponds to a material line (an unstable manifold) anchored to a point s fixed to the wall, as schematically presented in figure 1(*a*). In this case, formulae to obtain the shape of the unsteady separation profile are provided in [1] for any desired approximation order, i.e. the first order gives the separation angle, the second order the curvature and so on. As an example, figure 1(*b*) superimposes the second order theoretical profile (yellow line) to particule images averaged over a long time for the steady case ($U_c = 0$). As can be observed, the theory perfectly predicts the particle trajectories in the vicinity of the boundary.

For the general case, the flow is no longer periodic ($U_0 \neq 0$), and the separation point is considered to be moving but should still be captured from on-wall signatures according to [1] and [3]. In these studies, separation occurs at a point on

*Corresponding author. Email: jerome.vetel@polymtl.ca

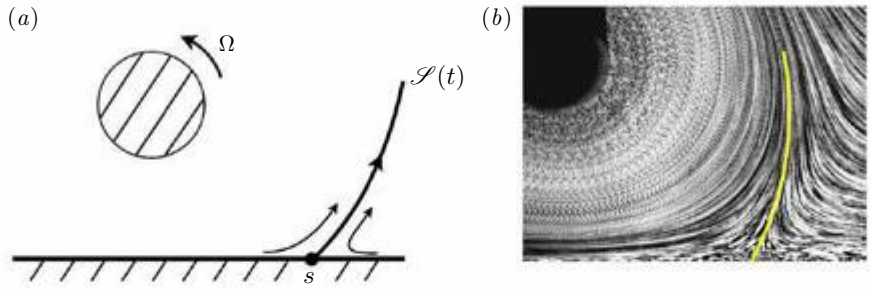

Figure 1. Description (*a*) and validation (*b*) of the fixed separation for the steady case ($U_c = 0$).

the wall where an adequate temporal filtering of the shear signal vanishes. However, here, measurements do not show any point on the wall where the skin friction vanishes. Instead, it is proposed in [4] that the separation point may on the contrary be represented by a moving point off the wall without any connection to on-wall quantities, as schematically presented in figure 2(*a*). This point corresponds to a Lagrangian saddle point defined by an attracting material line $\mathscr{S}(t)$ (the unstable manifold), that coincides with the separation profile, and a repelling material line $\mathscr{L}(t)$ (the stable manifold).

To verify experimentally if the curves $\mathscr{S}(t)$ and $\mathscr{L}(t)$ exist, we first need to capture the separation point. This point should follow the cylinder motion, and since the flow is periodic in a reference frame moving with the cylinder, we first seek a Lagrangian point whose position relative to the cylinder is the same at t and $t + T$, where T is the flow period. Then, we seek the attracting and repelling lines in the form of a time-dependent material line defined by a second order Taylor series around the separation point of coordinates $(x_s(t), y_s(t))$ previously obtained:

$$a_1(x - x_s) + a_2(x - x_s)^2 + b_1(y - y_s) + b_2(y - y_s)^2 + c(x - x_s)(y - y_s) = 0. \tag{1}$$

By differentiating (1) with respect to time, we obtain a first equation where velocity components of particles belonging to the material line appear. Then, by differentiating this new equation with respect to the curvilinear coordinate and set $(x, y) = (x_s, y_s)$, we obtain a linear differential equation for the slope m of the material line. By repeating the procedure for the second derivative, we obtain an equation for the curvature γ of the material line. By numerically integrating in time the equation for m over T, it is possible to find two initial guess $m_0 = m(t_0)$ for which $m(t_0 + T) = m(t_0)$, which therefore correspond to the tangent to $\mathscr{S}(t_0)$ and $\mathscr{L}(t_0)$. Finally, by integrating in time the equation for γ, we obtain the initial curvature γ_0 of both material lines.

To validate these results, the average of five consecutive particle images acquired at an arbitrary time is shown in figure 2(*b*) for a given set of non-zero parameters (U_0, β, ω). Before the averaging process, images have first been shifted to follow the trajectory of the separation point, thus revealing the organization of the flow pattern around s. The computed profiles for $\mathscr{S}(t_0)$ and $\mathscr{L}(t_0)$ are superimposed in yellow, and a good agreement is obtained, thus confirming that the separation point is indeed not anchored to the wall.

Further investigations on the periodic case ($U_0 = 0$) have finally shown that depending on the value of the velocity amplitude β, it is possible to obtain two separation points, one fixed and the other mobile.

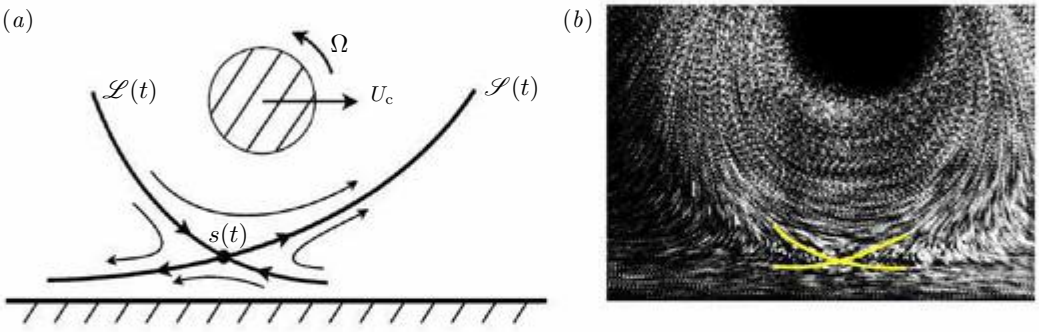

Figure 2. Description (*a*) and validation (*b*) of the moving separation for the case where $U_c = U_0 + \beta \cos \omega t$.

References

[1] HALLER, G. 2004 Exact theory of unsteady separation for two-dimensional flows. *J. Fluid Mech.* **512**, 257–311.

[2] WELDON, M., PEACOCK, T., JACOBS, G. B., HELU, M. & HALLER, G. 2008 Experimental and numerical investigation of the kinematic theory of unsteady separation. *J. Fluid Mech.* **611**, 1–11.

[3] SURANA, A. & HALLER, G. 2008 Ghost manifolds in slow-fast systems, with applications to unsteady fluid flow separation. *Physica D* **237**, 1507–1529.

[4] MIRON, P., VETEL, J. 2015 Towards the detection of moving separation in unsteady flows. *J. Fluid Mech.* **779**, 819–841.

ON THE TRIPLE DECK STAGE OF MARGINALLY SEPARATED FLOWS

Stefan Braun*[1] and Stefan Scheichl[1]
[1]*TU Wien, Institute of Fluid Mechanics and Heat Transfer, Vienna, Austria*

Summary A Chebyshev collocation method is applied to the triple deck equations governing the transient flow regime which ensues finite time blow-up events occurring in the solution of the fundamental equation of marginal separation theory under certain conditions.

MOTIVATION

The present investigation of marginally separated boundary layer flows (so-called laminar or alternatively transitional separation bubbles) is based on a high Reynolds number asymptotic approach first published in [5] and [8]. Typical situations featuring laminar separation bubbles include, among others, the flow past the suction side of slender airfoils at small to moderate angels of attack and channel flows with suction or (smooth) wall distortion. As is well-known, classical (hierarchical) boundary layer computations usually break down under the action of an adverse pressure gradient on the flow, a scenario associated with the appearance of the Goldstein separation singularity. If, however, the parameter controlling the strength of the pressure gradient (the angle of attack, the relative suction rate or distortion magnitude in the examples mentioned above) is adjusted accordingly, the application of a local viscous-inviscid interaction strategy by using triple deck arguments is capable of describing localized boundary layer separation (*marginal separation*, dashed lines regions indicated in Fig. 1). Moreover, taking into account unsteady effects and flow control devices allows the investigation of the conditions leading to forced or self-sustained vortex generation and the subsequent evolution process culminating in separation bubble bursting, [7], [2]. Within the asymptotic formulation of this stage bubble bursting is associated with the formation of finite time singularities in the solution and a corresponding break down of the underlying equations. The distinct blow-up structure gives rise to a fully non-linear, interacting *triple deck stage* featuring shorter spatio-temporal scales characteristic of the successive vortex evolution process, Fig. 1, [7]. Although the Cauchy problem associated with this stage has been extensively studied in [4], it still lacks a satisfactory numerical treatment. Following the achievements of [3], we aim at numerical solutions of the triple deck stage bridging the gap between proper initial conditions and the formation of yet another finite time blow-up, whose terminal structure has been computed in [6].

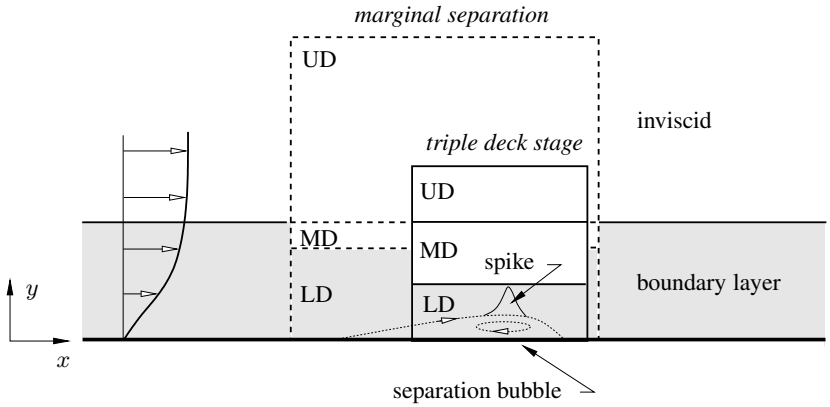

Figure 1: Asymptotic layer structure of laminar marginally separated flows including bubble bursting (schematic). Spike formation initiated by a finite time blow-up event, modeled up to the triple deck stage. Inviscid, irrotational upper decks UD, predominantly inviscid, rotational main decks MD, viscous boundary layer and lower deck regions LD (highlighted in gray).

SHORT OUTLINE

Specifically, we consider laminar, two-dimensional incompressible flows, the LD problem of the triple deck stage then reads

$$\frac{\partial^2\Psi}{\partial Y\partial T}+\frac{\partial\Psi}{\partial Y}\frac{\partial^2\Psi}{\partial Y\partial X}-\frac{\partial\Psi}{\partial X}\frac{\partial^2\Psi}{\partial Y^2}=-\left(1+\frac{\partial P}{\partial X}\right)+\frac{\partial^3\Psi}{\partial Y^3}\,,\qquad P=\frac{1}{\pi}\int_{-\infty}^{\infty}\frac{\partial A/\partial\xi}{X-\xi}\,\mathrm{d}\xi\,. \tag{1}$$

Here $\Psi(X,Y,T)$, $P(X,T)$, $A(X,T)$ denote the stream function, the induced pressure and the displacement function to be determined and X, Y, and T the stream-wise, wall-normal coordinates and the time. All quantities are non-dimensionalized

*Corresponding author. Email: stefan.braun@tuwien.ac.at

and suitably scaled. Equations (1) represent the boundary layer equation with both, prescribed adverse and induced pressure gradients and the interaction law (Hilbert integral). They are subject to the no-slip conditions $\Psi = \partial\Psi/\partial Y = 0$ at $Y = 0$, and the far field conditions $\Psi \sim (Y + A)^3/6 + \cdots$ as $Y \to \infty$ and $\Psi \to Y^3/6$, $A, P \to 0$ as $|X| \to \infty$. A connection to the self-similar blow-up structure of the previous stage is ensured by means of the initial - or equivalently matching - condition

$$\begin{aligned}
\Psi &\sim |T|^{1/3}\left[\frac{\hat{y}^3}{6} + |T|^{-7/9}\frac{\hat{y}^2}{2}\hat{A}_1(\hat{x}) + |T|^{-11/9}\frac{\hat{y}^2}{2}\hat{e}_1(\hat{x}) + |T|^{-14/9}\hat{\psi}_2(\hat{x},\hat{y}) + |T|^{-16/9}\frac{\hat{y}^2}{2}\hat{e}_2(\hat{x}) + \cdots\right],\\
P &\sim |T|^{-10/9}\hat{p}_1(\hat{x}) + |T|^{-14/9}\hat{p}_{e1}(\hat{x}) + |T|^{-17/9}\hat{p}_2(\hat{x}) + |T|^{-19/9}\hat{p}_{e2}(\hat{x}) + \cdots,\\
A &\sim |T|^{-6/9}\hat{A}_1 + |T|^{-10/9}\hat{e}_1 + |T|^{-13/9}\hat{A}_2(\hat{x}) + |T|^{-15/9}\hat{e}_2 + \cdots
\end{aligned} \tag{2}$$

as $T \to -\infty$ with the appropriate scalings $X = |T|^{4/9}\hat{x}$ and $Y = |T|^{1/9}\hat{y}$. The leading term $\hat{y}^3/6$ represents the separation profile and $(\hat{p}_1, \hat{A}_1)$, $(\hat{p}_2, \hat{A}_2)$, $(\hat{p}_{e1}, \hat{e}_1)$, etc. form Hilbert pairs according to (1). Whereas $\hat{A}_1$, $\hat{A}_2$, $\hat{\psi}_2$, etc. are uniquely determined, the eigenfunctions $\hat{e}_1 \propto \hat{A}_1'$ and $\hat{e}_2 \propto (\hat{A}_1 + 2/3\hat{x}\hat{A}_1')$ with indeterminate amplitudes carry the 'history' of the flow, Fig. 2. The *numerical approach* to solve the initial value problem (1), (2) in essence is as follows. As a starting basis,

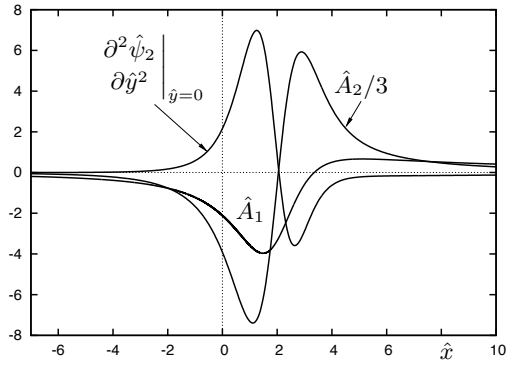

Figure 2: Various quantities which constitute the blow-up structure (2) and are used to initialize the triple deck computations.

the stream function is split into two parts: one part is introduced to capture the singular far field behaviour and the second is treated as the intrinsic unknown of $O(1)$. Furthermore, for the problem to be discretized in bounded computational domains, transformations are applied, which map the (semi-) infinite X-, Y- and T-domains to $[-1, 1]$. Finite differences with adaptive time stepping are used for temporal derivatives and the spatial derivatives are realized via a differentiation matrices approach based on Chebyshev polynomials. To this end each unknown quantity u is represented by a polynomial interpolant of degree n in barycentric Lagrange form (here demonstrated for one spatial coordinate $s \in [-1, 1]$ only), [1]

$$u(s) = \sum_{j=0}^{n} u_j \ell_j(s)\,, \quad u(s_j) = u_j\,, \quad \ell_j(s) = \frac{w_j}{s - s_j}\left[\sum_{k=0}^{n}\frac{w_k}{s - s_k}\right]^{-1}. \tag{3}$$

For the polynomial interpolation to be a well-conditioned process, Gauss-Lobatto grid point sets $s_j = -\cos(j\pi/n)$, $j = 0, \cdots, n$ that are clustered at the endpoints of the interval are used. This choice yields the weights $w_j = (-1)^j\delta_j$ with $\delta_j = 1/2$ for $j = 0, n$ and $\delta_j = 1$ otherwise. E.g., the first order differentiation matrix then is given by $D^{(1)}_{ij} = \ell_j'(s_i)$. Special treatment is required for the occurring integrals, e.g. for the Hilbert transform we obtain, using integration by parts and (3)

$$g(X_i) = g_i = \frac{1}{\pi}\int_{-\infty}^{\infty}\frac{f(\xi)}{X_i - \xi}\,\mathrm{d}\xi = \sum_{j=1}^{n-1} H_{ij} f_j\,, \quad H_{ij} = \frac{1}{\pi}\int_{-1}^{1}\ln|X_i - \xi(s)|\,\ell_j'(s)\,\mathrm{d}s\,, \quad H_{n-i,n-j} = -H_{ij}\,. \tag{4}$$

References

[1] Berrut J.-P., Trefethen L.N.: Barycentric Lagrange Interpolation. SIAM Rev. 46(3):501-517, 2004.

[2] Braun S., Kluwick A.: Blow-up and control of marginally separated boundary layers. Phil. Trans. R. Soc. A 363:1057-1067, 2005.

[3] Braun S., Scheichl S.: On recent developments in marginal separation theory. Phil. Trans. R. Soc. A 372:1-16, 2014.

[4] Elliott J.W., Smith F.T.: Dynamic stall due to unsteady marginal separation. J. Fluid Mech. 179:489-512, 1987.

[5] Ruban A.I.: Asymptotic theory of short separation regions on the leading edge of a slender airfoil. Izv. Akad. Nauk SSSR: Mekh. Zhidk. Gaza 1:42-51 (Engl. Transl.: Fluid Dyn. 17:33-41), 1982.

[6] Scheichl S., Braun S.: On blow-up solutions in marginally separated triple-deck flows. AIP Conf. Proc. 1558:285-288, 2013.

[7] Smith F.T.: Concerning dynamic stall. Aero. Q. 33:331-352, 1982.

[8] Stewartson K., Smith F.T., Kaups K.: Marginal separation. Stud. Appl. Maths. 67:45-61, 1982.

LEADING-EDGE VORTICES AS A HIGH-LIFT MECHANISM FOR LARGE ASPECT RATIO WINGS

Hadar Ben-Gida[1a)], Roi Gurka[2] & Daniel Weihs [1]
[1]*Faculty of Aerospace Engineering, Technion – Israel Institute of Technology, Haifa 32000, Israel*
[2]*School of Coastal and Marine Systems Science, Coastal Carolina University, Conway, SC 29528, USA*

Summary The Leading-Edge Vortex (LEV) is one of the primary mechanisms to achieve high lift forces on wings. Theoretical and experimental studies suggest the spanwise flow along a wing has a major role in the stabilization of LEVs over the upper wing surface. While this is well known for low aspect ratio (delta) wings we show that continuous spanwise flow is achievable for high aspect ratio wings, depending on on the wing planform. A two-dimensional potential flow model is developed here for Joukowski type airfoils with a LEV and a sink element at the vortex core representing the spanwise flow. The results reported provide significant insight for developing a full three-dimensional potential flow model of the LEV phenomenon about a varying sweep, large aspect ratio wing at post-stall angles.

INTRODUCTION

Most designs of high lift wings require attached flow over the wing. Yet, separating the flow and forming a leading-edge vortex (LEV) offers much higher lift as well known for low aspect ratio wings. Over the years, two-dimensional potential flow studies have investigated the mechanism attributed to localizing LEVs about high aspect ratio airfoils as they offer a convenient and efficient way to predict aerodynamic performances. The first potential flow studies modeled the LEV as a point vortex element trapped about a flat plate (Saffman and Sheffield, 1977) and a Joukowski airfoil (Huang and Chow, 1982). A different approach was proposed by Rossow (1978), who suggested attaching a vertical flap to the leading-edge region in order to generate the LEV while stabilizing it through suction applied at the vortex axis, in the spanwise direction. He reasoned that the LEV phenomenon is strongly coupled with a spanwise gradient of momentum that convects excess vorticity from the vortex core, thus preventing it from growing in strength and shedding. As a result, conically shaped vortices are formed, similar to those observed on delta wings (Brown and Michael, 1954). Rossow modeled the spanwise flow with a sink element and found it has a major role in positioning the LEV above the wing. However, the implementation of the flap concept to imitate the spanwise flow might be mechanically complicated for practical applications.

We suggest that by varying the wing shape, airfoil sections and the sweep and twist angles along the wingspan, one can control the spanwise flow, and thereby the localization and fixing of the LEV on a high aspect ratio wing. Here we present a steady, incompressible potential flow analysis, including computation of the forces and moments, for various Joukowski airfoils with a vortex-sink pair fixed over the leading-edge region. The results reported provide significant insight for developing a full three-dimensional potential flow model of the LEV phenomenon about a varying sweep, large aspect ratio wing at post-stall angles.

FLOW MODEL

We consider a steady, inviscid, incompressible and irrotational flow with a free stream velocity U_∞ around a Joukowski airfoil section with an angle of attack α, taken as part of a large aspect ratio wing with chord c. The potential around the airfoil is obtained by applying the Joukowski transformation ($2z=\zeta+\lambda^2/\zeta^2$) on a circle. A LEVSP (Leading-Edge Vortex-Sink Pair) is defined by a stationary clockwise vortex Γ_{LEV} and a sink Q located at the vortex core. A bound circulation Γ is generated by the airfoil providing the linear lift component.

Two boundary conditions are applied: a stationary LEVSP and the Kutta condition at the trailing-edge. A family of LEVSP equilibrium locations is computed for different combinations of angle of attack, airfoil shape and sink strength. Furthermore, forces on the airfoil, and moments about the airfoil center are calculated using the Blasius theorem.

RESULTS

Our model for a Joukowski airfoil was first validated for the limiting case of a flat plate with no sink from Saffman and Sheffield (1977). Introducing the sink element at the vortex core resulted with two equilibrium branches, originating from the leading-edge, on which a LEV can be trapped about the plate. This resembles the results reported by Mourtos and Brooks (1996) and Xia and Mohseni (2012). The equilibrium curves reported in the papers above are valid for any value of the bound circulation Γ. Yet, a LEV is only relevant at a positive angle of attack; i.e. a positive bound circulation value. Thus, equilibrium locations having negative bound circulations are not valid for trapping the LEVSP for practical cases. Allowing only positive bound circulation values causes the range in which the stationary LEVSP can exist to be much more narrow, in the leading-edge region.

[a)] Corresponding author. Email: bengida@campus.technion.ac.il

Increasing the suction inside the LEVSP core resulted equilibrium locations that appear further away from the airfoil leading-edge and in smaller region (see Fig. 1a), where they are accompanied by a stronger LEV strength. This indicates that strong vortices need high amount of suction in order to be positioned about the airfoil, as is intuitively obvious. Yet, increasing the suction is also accompanied with higher drag, since the streamwise momentum of the fluid is further removed into the spanwise direction. Thus, the lift to drag ratio is reduced and the aerodynamic performance is degraded. Adding thickness t to the Joukowski airfoil was found to have negligible effect on the LEVSP equilibrium locations and the forces and moments generated about the airfoil. In contrast, adding camber σ extended the region of LEVSP equilibrium locations in the streamwise direction and gave a higher lift to drag ratio (see Fig. 1c-d), accompanied with higher pitching moment. Increasing the angle of attack resulted the LEVSP equilibrium curves to move closer to the upper surface of the airfoil, and towards the leading-edge (see Fig. 1b), similar as reducing the suction in the LEVSP core. Higher angles of attack also resulted in higher lift to drag ratio, similar as adding camber or reducing the sink strength. Yet, higher pitching moment also accompanied when increasing the angle of attack, similar as increasing the camber or the sink strength.

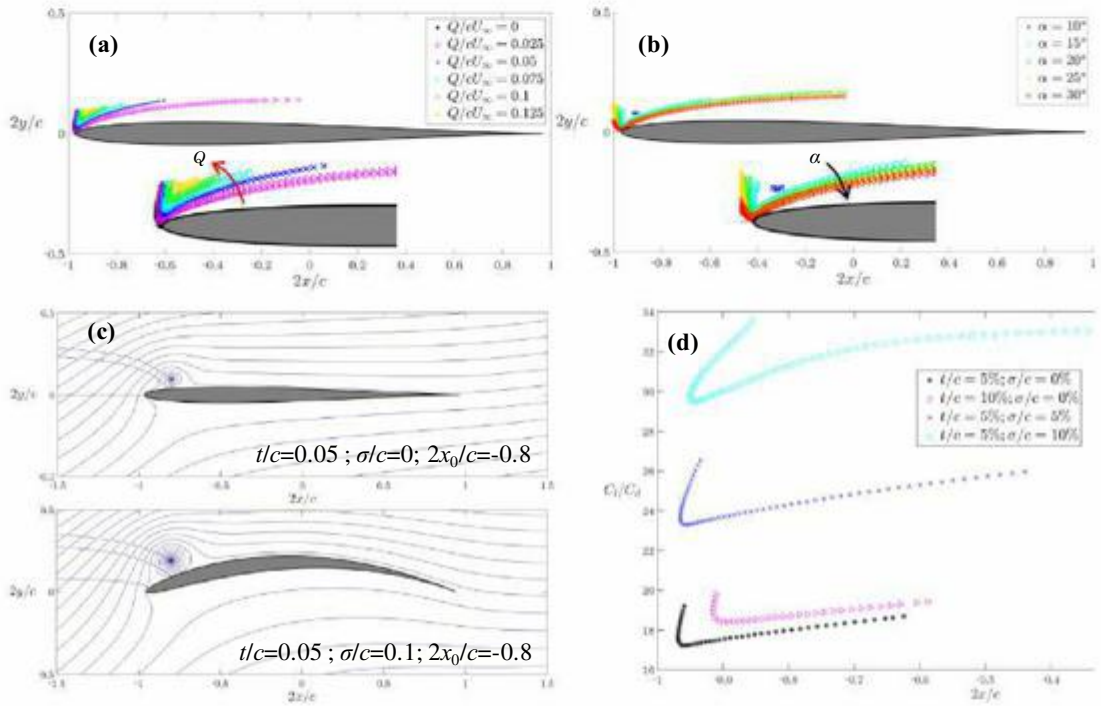

*Figure 1: (a) LEVSP equilibrium locations for various sink strengths, including a closer view of the leading-edge region; (b) LEVSP equilibrium locations for various angles of attack; (c) Flow field about an uncambered (σ=0) and a cambered (σ=0.1**c**) airfoil, each with 0.05**c** thickness and a LEVSP located 10% from the leading-edge; (d) Lift to drag ratio along the LEVSP streamwise equilibrium locations for various airfoil shapes*

CONCLUSIONS

We investigated the possibility of fixing an LEV over various Joukowski airfoils by using a potential model with a vortex-sink pair about the leading-edge region. Results show two equilibrium branches, both exist around the leading-edge region, on which the LEV can be stationary. We found the equilibrium locations with high suction were correlated with strong LEVs; in order to convect the excess vorticity produced by the viscous flow into the spanwise direction. Moreover, increasing the angle of attack, adding camber or reducing the suction in the LEVSP core have all found to increase the lift to drag ratio. The results herein can serve as the basis for a three-dimensional potential flow model for designing an efficient large aspect ratio wing with lift enhancement through LEV.

References

[1] Brown C. E. and Michael Jr. W. H.: Effect of Leading-edge Separation On the Lift of a Delta Wing. J. Aeronautical Sciences *21(10)*:690-694, 1954.

[2] Mourtos N. J. and Brooks M.: Flow Past a Flat Plate with a Vortex/Sink Combination. J. Applied Mechanics *63*:543-550, 1996.

[3] Rossow V. J.: Lift Enhancement by an Externally Trapped Vortex. Journal of Aircraft *15(9)*:618-625, 1978.

[4] Saffman P. G. and Sheffield J. S.: Flow Over a Wing with an Attached Free Vortex. Studies in Applied Mathematics *57*:107-117, 1977.

[5] Xia X. and Mohseni K.: Trapped Vortex on a Flat Plate: Equilibrium and Stability. 42nd AIAA Fluid Dynamics Conference and Exhibit, New Orleans, Louisiana, USA, AIAA *3156*, 2012.

LEADING-EDGE FLOW SEPARATION CONTROL WITH PLASMA ACTUATORS

Longfei Song[1], Kwing-So Choi[1a)], Xin Zhang[2] and Wanbo Wang[2]
[1]*Faculty of Engineering, University of Nottingham, NG7 2RD, Nottingham, UK*
[2]*China Aerodynamics Research and Development Center, Mianyang 621000, China*

Summary An experimental study into a use of a vectored wall-normal jet from dielectric-barrier-discharge (DBD) plasma actuator was carried out to control leading-edge flow separation over a NACA 0012 aerofoil at the chord Reynolds number of 20,000. Here the plasma jet with a momentum coefficient of C_μ = 0.25% was issued against the freestream along the aerofoil chord line, generating vortices which help reattach the separated flow. PIV results also suggest that the plasma jet has a virtual shaping effect in flow separation control.

Experiments were conducted in an open-return low-speed wind tunnel at the University of Nottingham, whose test section is 1.5m x 0.3m x 0.3m with the turbulence intensity of 0.3%. The freestream velocity was U_∞ = 3m/s, corresponding to the chord Reynolds number of 20,000. A NACA 0012 aerofoil of the chord length c = 100 mm and the span s = 250 mm was mounted in the wind tunnel through a rod at 25% chord.

The dielectric-barrier-discharge (DBD) plasma actuator used in this study is composed of two exposed electrodes with a common ground electrode of 0.06 mm thick and 10 mm long, which are separated by a 0.14 mm thick Cirlex dielectric layer. This was placed at the leading edge of the aerofoil as shown in Fig. 1. A high-voltage power supply (PSI-MCPG2503C) from KI Tech Ltd. was used to drive the plasma actuator at 5.5 kV peak-to-peak voltage at a frequency of 34 kHz. The direction of the plasma jet could be changed by adjusting the voltages applied to each of the two exposed electrodes.

A time-resolved PIV system from Dantec was used to investigate the flow around the aerofoil. This consists of a Litron LDY 302 PIV 100W Nd: YLF laser, two SpeedSense 9060 high-speed cameras and a computer. Olive oil particles with diameter of 1 μm were produced via a TSI seeder, which were uniformly spread across the test section. The cameras were set at a frequency of 2000 to capture 1000 image pairs without plasma, followed by 2000 image pairs with plasma and another 1000 image pairs without plasma. This allowed us to carry out a transient analysis of leading-edge flow separation control using plasma actuator. Image analysis was conducted with Dantec DynamicStudio 4.10 using Adaptive PIV method, which automatically adjusts the interrogation area according to local seeding densities.

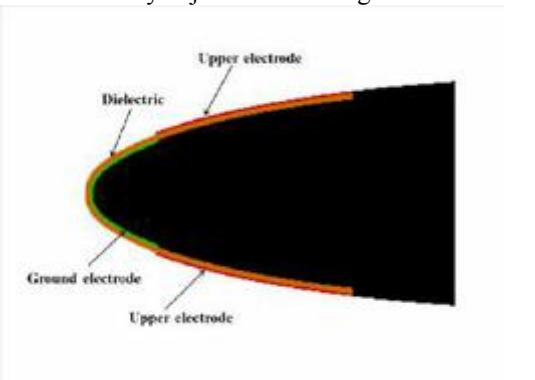

Figure 1 Schematic of the DBD plasma actuator placed at the aerofoil leading edge. The red parts denote exposed upper electrodes while the green part represents the common ground electrode.

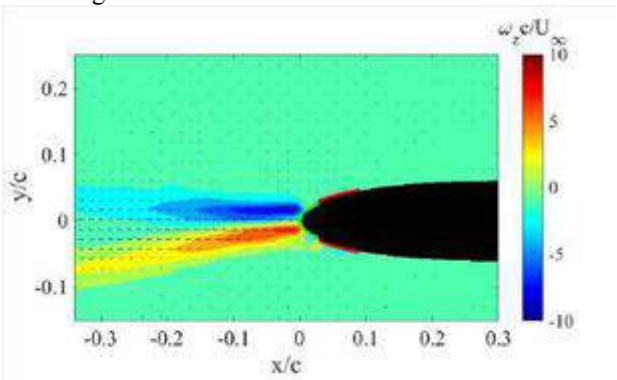

Figure 2 Time-averaged velocity field with superimposed vorticity field of the plasma wall-normal jet in quiescent air.

PIV measurements of flow around the aerofoil with plasma actuator were initially conducted in quiescent air to characterize the induced plasma jet. Figure 2 shows the distribution of time-averaged velocity vectors superimposed by vorticity contour of the plasma jet, demonstrating that a wall-normal jet is created in front of the aerofoil leading edge. Here, the wall-normal flow was produced when the wall jets from a pair of asymmetric plasma actuators collided with each other to give rise to a wall-normal flow [1]. Here, the momentum coefficient of the plasma jet $C_\mu = F_p/(0.5\rho U_\infty{}^2 c)$ is 0.25%, where ρ is the air density, U_∞ is the freestream velocity and c is the aerofoil chord length. The plasma jet momentum is given by $F_p = \int \rho U_j{}^2 \, dl$, where U_j is the plasma jet velocity.

Figure 3(a) shows the streamlines around the aerofoil for the base flow, showing that there is a leading-edge flow separation at the angle of attack of 10°. This flow separation behavior agrees very well with the results in our previous test [2]. When plasma is activated, the separated flow is reattached as shown in Fig. 3(b). The corresponding vorticity maps are

[a)] Corresponding author: Professor Kwing-So Choi Email: kwing-so.choi@nottingham.ac.uk

given in Figs 3(c) and 3(d) for the base flow and with plasma, respectively. With plasma, the vorticity field is moved closer to the aerofoil surface as expected from the reattachment of leading-edge flow separation, see Fig 3(d). What is interesting to observe in Fig. 3(d) is a shift of the vorticity region away from the leading edge, suggesting that there may be virtual shaping of the aerofoil by the plasma jet, reducing the leading-edge curvature.

Figure 4(a) shows that the change in vorticity flux with time per unit span, indicating that the vortex flux is increased by nearly 65% when plasma is activated. The increase in the momentum flux was only 40%, however. Here, the vorticity flux $\int \omega U \mathrm{d}y$ and the momentum flux $\int \rho U^2 \, \mathrm{d}y$ were obtained by integrating the measured vorticity and momentum from y/c = 0 to 0.15 at x/c = 0.065 in the upstream of the natural flow separation point (x/c ≈ 0.13) at this angle of attack.

An increase in the turbulent kinetic energy over the aerofoil in the downstream of x/c = 0.1 is evident (not shown here) when plasma is activated, suggesting that a mixing of the separated flow by vortices generated by plasma (see Fig. 3(d)) helped reattach the separated flow at the leading edge.

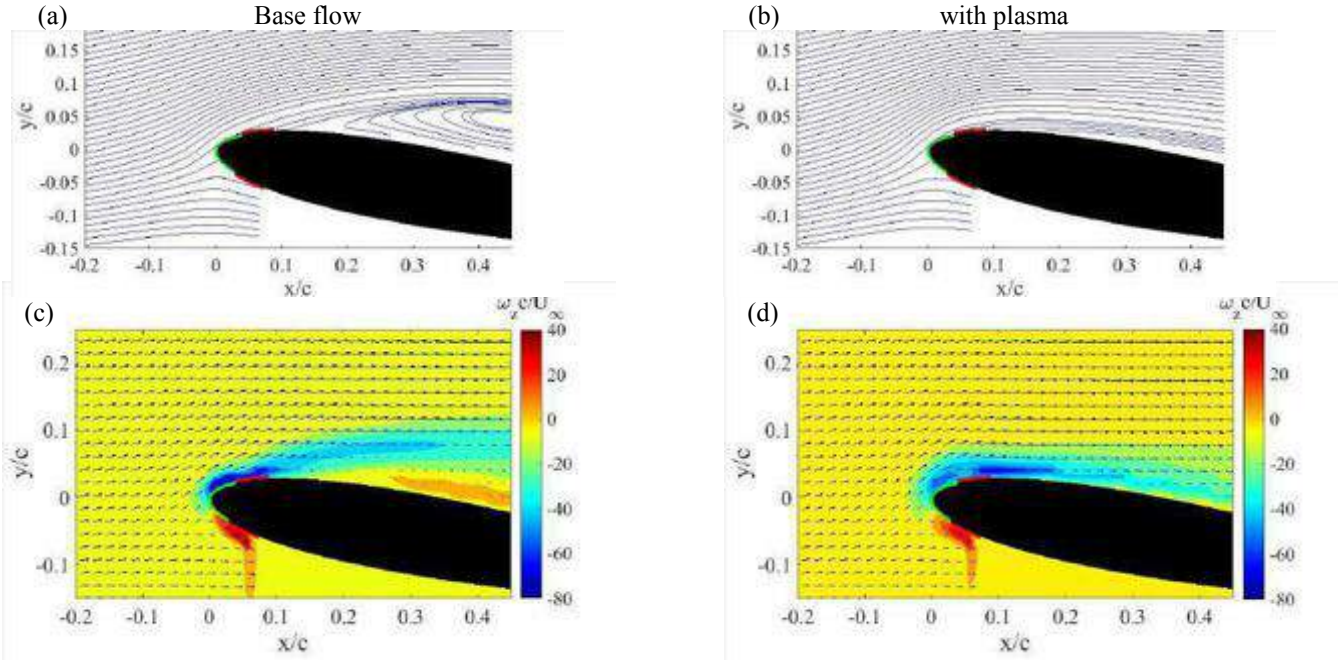

Figure 3 Time-averaged flow field around NACA 0012 aerofoil for base flow (a and c) and with plasma (b and d) at the angle of attack of 10°.

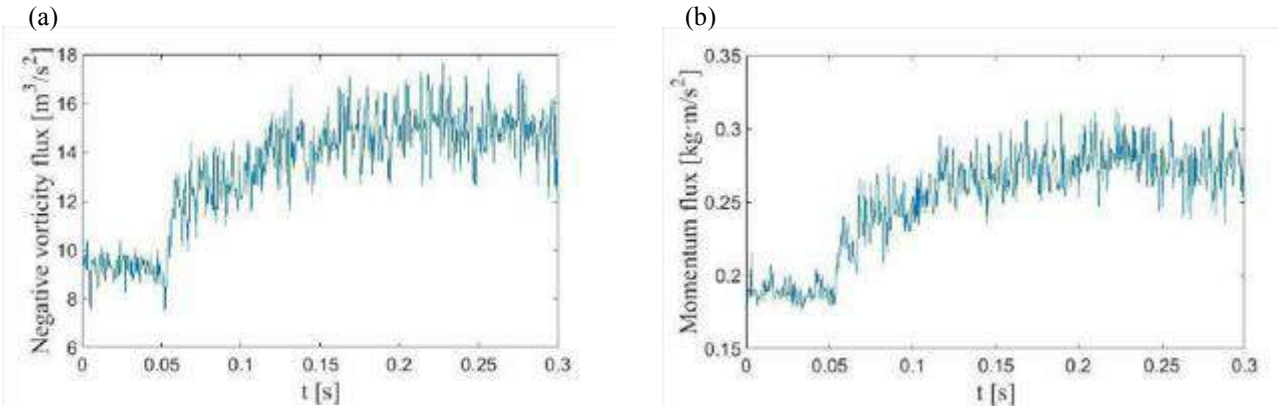

Figure 4 Transient profiles at x/c = 0.065: (a) vorticity flux; (b) momentum flux. Activation of plasma took place at t = 0.05s.

References

[1] M. Bolitho and J.D. Jacob, "Thrust vectoring flow control using plasma synthetic jet actuators," AIAA 2008-1368, 2008.

[2] L. Feng, K.-S. Choi and J. Wang, "Flow control over an airfoil using virtual Gurney flaps," *J. Fluid Mech.*, 767, 595–626, 2015.

THE EFFICIENCY OF ONE METHOD OF MACHINELESS ENERGY STRATIFICATION IN A GAS FLOW

Georgii M. Azanov[1a)] and Alexander N. Osiptsov[2]
[1]*Faculty of Mechanics and Mathematics, Lomonosov Moscow State University, Moscow, Russia*
[2]*Institute of Mechanics, Lomonosov Moscow State University, Moscow, Russia*

Summary: The efficiency of a method for machineless gasdynamic energy stratification based on heat transfer between sub- and supersonic flows separated by a thin wall is studied numerically. A model flow consisting of two sub- and supersonic laminar boundary layers separated by a thin heat-conductive plate is considered. In the first part, pure-gas flows with different Mach and Prandtl numbers are investigated and, in the second part, the effect of an admixture of small evaporating droplets presenting in the supersonic boundary layer on the efficiency of the considered energy stratification scheme is examined. The Saffman force acting on the droplets in shear flow is taken into account.

DESCRIPTION OF THE MODEL

In [1], a new method for machineless energy separation in a gas stream, alternative to the well-known Ranque-Hilsch vortex tube, is proposed. The scheme is based on heat transfer between steady sub- and supersonic gas flows (with identical inlet stagnation parameters), separated by a thin heat-conductive wall. The effect of noticeable heat transfer between sub- and supersonic boundary layers, resulting in energy stratification, is attributable to the fact that, in case of adiabatic wall, the difference between the recovery temperatures on both sides of the wall can reach large values. The energy separation efficiency is defined as the difference between the average values of the stagnation temperature in the outlet streams passed through the boundary layers. The main aim of the present work is a parametric numerical study of possible ways to increase this efficiency.

As the basis for numerical simulation, we use a model of two interacting sub- and supersonic compressible boundary layers with the same stagnation parameters in the outer streams. In case of gas-droplet supersonic boundary layer, considered in the second part, we use a two-fluid model in which the phases are treated as interpenetrating continua [2]. It is assumed that the droplets are spheres with a variable radius. The wall temperature is greater than the droplet evaporation point, and the heat flux to the droplet surface is totally spent on the evaporation. This results in the fact that the droplet temperature in the boundary layer is constant and equal to that of the outer flow. In addition to the Stokes drag, the Saffman lifting force, exerted on the droplets in shear flows, is also included in the model. The equations of compressible two-phase and single-phase boundary layers are solved numerically using an implicit finite-difference scheme on a Cartesian grid. As the boundary conditions, we assume that both the temperatures and heat fluxes on both sides of the heat-conductive wall coincide.

RESULTS AND CONCLUSIONS

Our numerical calculations show that in the pure-gas flow the stagnation temperature profiles in the boundary layers depend strongly on the Prandtl number (Fig. 1). The efficiency of energy separation may increase up to 7% for gases with low Prandtl numbers, but for air (Pr = 0.72) the efficiency turns out to be small (less than 1%). The calculated equilibrium wall temperature in the pure-gas flow agrees well with the approximate self-similar solution considered in [3]. The model of two-phase boundary layer contains additional dimensionless parameters, the most important of which are the free-stream droplet mass concentration α, droplet evaporation rate $a = 2c_pT_\infty/3H\mathrm{Pr}$, coefficient in the Saffman force κ, and ratio of specific heats of the phases c_s/c_p. In case of fine evaporating droplets, when the Saffman force can be dropped, the droplets do not deposit on the wall and are completely evaporated in the supersonic boundary layer (Fig. 2). The stagnation temperature in the supersonic stream decreases significantly with increase in the ratio α/a (Fig. 3). For coarser droplets, the effect of the Saffman force is significant. Such droplets start to deposit on the wall surface (Fig. 4) and result in a stronger reduction of the wall temperature even when the free-stream droplet mass concentration is less than 1%. Numerical calculations demonstrated the formation of a near-wall pure-gas region inside the supersonic boundary layer, where the droplets are completely evaporated. The leading edge of this region on the plate surface is shifted downstream with increase in κ (Figs. 2, 4). Far from the leading edge of the plate, where the thickness of the pure-gas region is sufficiently large and the phase velocity relaxation process is completed, the solution becomes almost self-similar. Parametric study of the energy separation effect shows that, far from the leading edge of the plate where the flow is almost self-similar, the difference between the average stagnation temperatures in the streams on both sides of the wall increases with increase in the ratio α/a. Our calculations demonstrated that the use of an admixture of evaporating droplets in the supersonic boundary layer is a promising way to improve substantially the efficiency of machineless energy separation method [1].

The work was supported by the Russian Science Foundation (project 14-19-00699).

a)Corresponding author. Email:azanovgm@gmail.com.

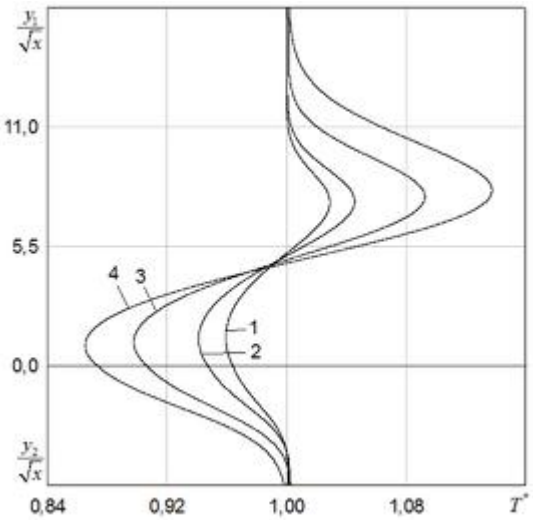

Fig. 1. Self-similar stagnation temperature profiles in pure-gas flow for different Prandtl numbers: Pr=0.72, 0.6, 0.35, 0.2 (curves 1-4). Supersonic upper boundary layer (M_1=3), subsonic lower boundary layer (M_2=0.7).

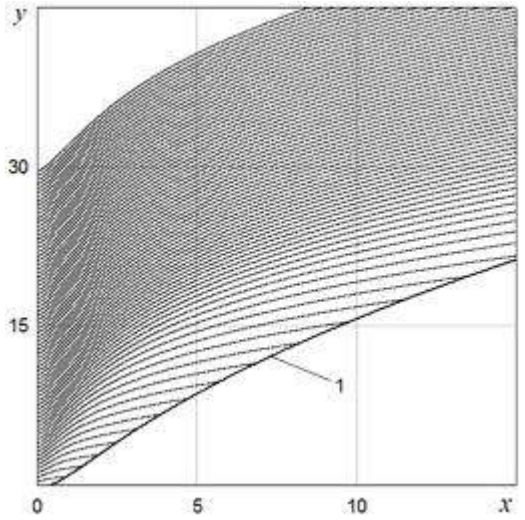

Fig. 2. Boundary of the pure-gas region (curve 1) and the droplet trajectories in a supersonic boundary layer with negligibly small influence of Saffman force ($\kappa=0$); x is scaled to the Stokes droplet velocity relaxation length.

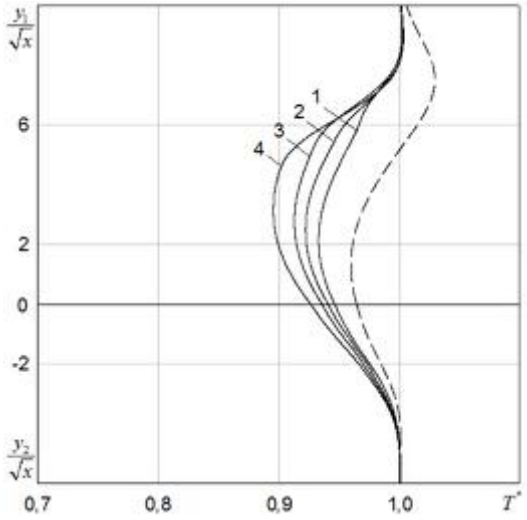

Fig. 3. Self-similar stagnation temperature profiles 'in the two-phase flow for a = 0.1,0.075,0.06,0.045 (curves 1-4). Broken curve - stagnation temperature profiles in pure-gas flow. M_1=3, M_2=0.7, Pr = 0.72, α=0.03.

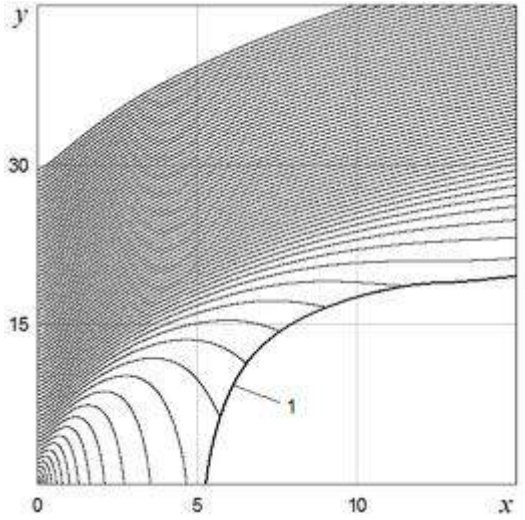

Fig. 4. Boundary of the pure-gas region (curve 1) and the droplet trajectories in a supersonic boundary layer with significant influence of Saffman force (κ =300), x is scaled to the Stokes droplet velocity relaxation length.

Nomenclature

Pr, M_1, M_2	Prandtl and Mach numbers in super- and subsonic flow
α, a	Particles mass concentration ($\alpha = m_\infty n_{s\infty}/\rho_\infty$) and vaporization rate ($a = 2c_pT_\infty/3H\mathrm{Pr}$)
T^*	Dimensionless stagnation temperature ($T^* = [T+((\gamma-1)M^2/2)u^2]/[1+((\gamma-1)M^2/2)]$)
H	Latent heat of vaporization [kJ kg^{-1}]
m_∞, $n_{s\infty}$, ρ_∞	Particle mass [kg], particle number concentration [1/m^3], gas density [kg/m^3] in outer stream
$y_{1,2}/x^{1/2}$	Dimensionless self-similar coordinates in boundary layers
κ	Dimensionless coefficient in the Saffman force

References

[1] Leont'ev A.I.: Gas-dynamic method of energy separation of gas flows. High Temperature, 35(1): 155-157. 1997

[2] Osiptsov A.N., Shapiro Ye.G.: Heat transfer in the boundary layer of a "gas-evaporating drops" two-phase mixture. Int. J. Heat Mass Transfer 36(1): 71-78. 1993

[3] Vigdorovich I.I., Leont'ev A.I., Theory of the energy separation of a compressible gas flow. Fluid Dynamics 45(3): 434-440. 2010

BOUNDARY LAYER RECEPTIVITY TO ACOUSTIC NOISE IN TRANSONIC FLOWS

Tomass Bernots* and Anatoly I. Ruban

Department of Mathematics, Imperial College London,180 Queen's Gate, London SW7 2AZ, UK

Summary In this study we analyse the process of the generation of Tollmien-Schlichting waves in a laminar boundary layer on an aircraft wing in the transonic flow regime. We assume that the boundary layer is exposed to a weak acoustic noise. We develop the receptivity theory, assuming that the Reynolds number is large. In this case we were able to deduce an analytic formula for the amplitude of the generated Tollmien-Schlichting wave.

INTRODUCTION

Reduction of the vehicle drag has been under a close attention of researchers for many years, and still remains one of the central problems of aerodynamics. It is well established that a significant fraction of aircraft fuel consumption come from the drag, which in consequence increases the cost of air travel and the impact on the environment. For today's commercial aircrafts, half of the total drag corresponds to skin-friction drag. And as laminar skin friction, in comparison to the turbulent skin friction, is much lower, flow control through delaying boundary-layer transition has a potential to provide desired reductions. However, to achieve this, one has to predict the position of the transition on the aerodynamic surfaces. This in consequence is impossible without an accurate description of the receptivity process.

In aerodynamic flows, the laminar-turbulent transition, follows a scenario with a succession of well defined stages. At first, the external perturbation, such as acoustic noise, penetrate the boundary layer and turn into the boundary-layer instability modes: Tollmien-Schlichting waves and cross-flow vortices. In real flight conditions, the external perturbations are very weak, and therefore, the initial amplitude of instability modes generated is small, and cannot cause the transition. Propagating further downstream instability modes are amplified until the amplitude reaches a certain level. Then nonlinear effects come into play, and a rapid transition to a turbulent state is observed.

The receptivity theory aims to establish a link between the external perturbations and the laminar-turbulent transition, and serves the following purposes: to identify the perturbations that turn into instability modes, to calculate the initial amplitude of the instability modes, and to devise the means to control of the transition process. The second of these tasks can be performed using various mathematical tools, however, it is the asymptotic approach that proves to be instrumental in performing the first and the third tasks.

The boundary-layer receptivity to acoustic noise in subsonic flows was first analysed by Ruban [2] and Goldstein [1], where they highlighted importance of the "double-resonance" principle. It suggests that in order to observe the resonance in fluid flows, not only the frequency of the external forcing should be close to the neutral frequency of the boundary layer, but also wavenumber. Both authors demonstrated that the interaction of an acoustic wave with a wall roughness produces Tollmien-Schlichting waves in the boundary layer, and deduced an explicit formula for the amplitude of the generated Tollmien-Schlichting wave.

In the present work, our attention is with the receptivity of the boundary layer to acoustic noise in transonic flows; the latter represent the cruise flight conditions of modern passenger aircrafts. In our study we rely on the asymptotic description of the Tollmien-Schlichting waves in transonic flow, given by [3].

PROBLEM FORMULATION

We start by considering a flow of a prefect gas past a two-dimensional aerofoil with uniform flow upstream. We assume that there is a plane acoustic wave travelling parallel to the airfoil surface. The flow analysis is conducted using the compressible Navier-Stokes equations, in the limit of large Reynolds number, Re. It is also assumed that the free-stream Mach number differs little from one and is given as

$$M_\infty^2 = 1 + Re^{-1/9} Q_\infty \,,$$

where Q_∞ is an order one quantity and is referred to as the transonic similarity parameter. In this situation the resonance conditions are achieved when the frequency of the acoustic wave is $O(Re^{2/9})$ and the characteristic length of the wall roughness is $O(Re^{-1/3})$.

When acoustic waves penetrate the boundary layer, the Stokes layer forms on the wing surface. However, the Stokes layer on it own is incapable to generate Tollmien-Schlichting waves. Therefore the acoustic wave has to come into interaction with wall roughnesses, which are plentiful on a real aircraft wing. To satisfy the resonance conditions we shall assume that longitudinal size of the roughness is estimated as $\Delta x = O(LRe^{-1/3})$ i.e. is comparable with the wavelength of the Tollmien-Schlichting wave.

*Corresponding author. Email: t.bernots@imperial.ac.uk

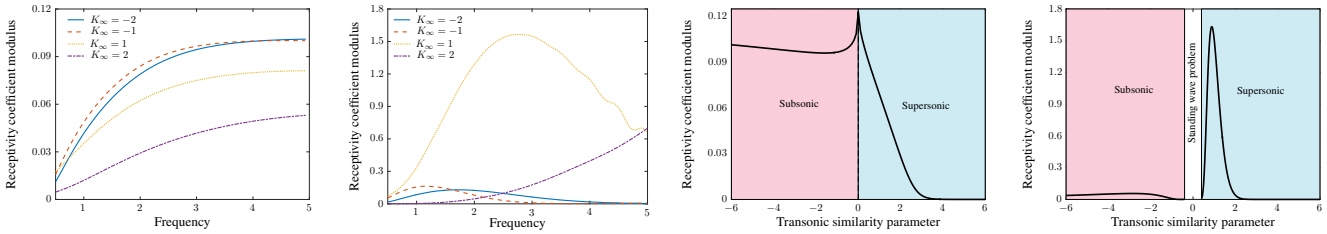

(a) "Fast wave" (b) "Slow wave" (c) "Fast wave" (d) "Slow wave"

Figure 1: Receptivity coefficient dependance on the frequency (a, b) and on the transonic similarity parameter (c, d).

Form this follows that the triple-deck region forms in the vicinity of the roughness and is composed of three tiers: the viscous sublayer (Lower deck), the main part of the boundary layer (Main deck) and the potential flow region that lies outside the boundary layer (Upper deck). All the three layers have the same longitudinal extent.

THE VISCOUS-INVISCID INTERACTION PROBLEM

Analysis begins with a region situated outside the boundary layer, where solution of the Navier-Stokes equations is sought in the form of asymptotic expansions. One can show that the Navier-Stokes equations, in transonic limit, reduce to the wave equation equivalent, that is, the Transonic Small Perturbation equation,

$$2\frac{\partial^2 p}{\partial x \partial t} + Q_\infty \frac{\partial^2 p}{\partial x^2} - \frac{\partial^2 p}{\partial y^2} = 0.$$

This equation admits two traveling wave solutions with different phase velocities. The first wave has $O(1)$ phase velocity while the second $O(Re^{-2/9})$ which is comparable with the phase speed of the the Tollmien-Schlichting wave in transonic flow.

Pressure perturbations caused by the acoustic waves do not influence the main deck of the boundary layer and are merely transmitted from the upper to the lower deck. In the lower deck flow is described by unsteady Prandtl boundary layer equations. Here pressure perturbations perturb the flow field, which manifest itself as a displacement of the flow. This displacement creates an additional pressure perturbations in the upper deck, which in consequence changes the displacement. This continues until certain equilibrium is achieved. In order to find the relation describing this interaction, it is necessary to solve the lower and upper deck equations simultaneously. Solution of this viscous-inviscid interaction problem leads to an expression describing the Tollmien-Schlichting wave, which amplitude is proportional to the so-called receptivity coefficient.

CONCLUSIONS

The results of the analysis confirm that an effective generation of the Tollmien-Schlichting waves takes place when the "double-resonance" principle is observed. This condition required that the frequency of the acoustic wave is tuned to the frequency of the Tollmien-Schlichting wave, and in the Fourier spectrum of the steady perturbations produced by the wall roughness there is a harmonic with the wavenumber that coincides with the wave number of the Tollmien-Schlichting wave.

In the case of small amplitude of the acoustic wave and the roughness height, the governing equations are solved in an analytic form, and, as a result, an explicit formula for the amplitude of the generated Tollmien-Schlichting wave is deduced. It can be expressed as the product of the receptivity coefficient and the Fourier Transform of the roughness shape calculated for wavenumber of the Tollmien-Schlichting wave. The former does not depend on the roughness shape, and reaches maximum when transonic similarity parameter Q_∞ becomes zero or, equivalently, the free-stream Mach number is one.

The asymptotic approach used in this work is primarily intended to uncover the fundamental physical processes involved in the first stage of the laminar-turbulent flow transition phenomena. From a number of comparisons of the triple-deck theory with the Navier-Stokes simulations of the boundary-layer receptivity in subsonic flows we know that the triple-deck predictions are rather accurate. Therefore the results of the work can be used as the initial conditions in the further studies of the boundary-layer transition on aircraft wings.

References

[1] GOLDSTEIN, M. E. 1985 Scattering of acoustic-waves into Tollmien-Schlichting waves by small streamwise variations in surface geometry. *JFM* **154** 509-529.

[2] RUBAN, A. I. 1984 On generation of Tollmien-Schlichting waves by sound. *Fluid Dyn.* **19** (5) 709-717.

[3] TIMOSHIN, S. N. 1990 Asymptotic form of the lower branch of the neutral curve in transonic boundary layer. *Uch. Zap. TsAGI* **21** 50-57.

ON THE TURBULENCE DYNAMICS OVER GEOPHYSICAL-SCALE TOPOGRAPHY

Leonardo P. Chamorro*[1,2], Ali M. Hamed [1], and Luciano Castillo[3]
[1]*Department of Mechanical Science and Engineering, University of Illinois, Urbana, IL, USA*
[2]*Department of Civil and Environmental Engineering, University of Illinois, Urbana, IL, USA*
[3]*Department of Mechanical Engineering, Texas Tech University, Lubbock, TX, USA*

Summary Laboratory experiments were performed to quantify the spatial and temporal features of the turbulence over geophysical-scale topography defined by large-scale wavy walls. High-resolution and high-frame-rate particle image velocimetry in a refractive-index-matching channel was used to infer the distinctive dynamics of the flows in terms of the topography and Reynolds number. We place the attention on the cases with 2D and 3D walls, where the 2D topography is defined by a sinusoidal wave in the streamwise direction with amplitude to wavelength ratio $a/\lambda_x = 0.05$, while the 3D wall has an additional wave superimposed on the 2D wall in the spanwise direction with $a/\lambda_y = 0.1$. The flow over these walls is characterized at Reynolds numbers $Re \sim 4\times10^3$ and 4×10^4, based on the bulk velocity and the channel half height. Turbulence statistics, flow decomposition via POD and LES-like and compensated spectra are used to gain insights into the topography modulation on the flow.

GENERAL

Flow over large-scale complex topography exhibits a rich dynamics strongly modulated by the characteristics of the terrain, where multiscale processes control the scalar transport, momentum and energy exchange between the inner and outer layers. From an environmental stand point, large-scale topographic features can even impact local weather and precipitation patterns [1]. The flow over low-order large-scale wavy walls resembles that over natural terrains and, therefore, has been the subject of numerous experimental [e.g., 2, 3], numerical [e.g., 4, 5] and theoretical [e.g., 6] studies.

The effect of increasing the topography complexity on the inner and outer flow is still far from being well understood and characterized. Multiple studies have investigated the flow over organized roughness similar to a complex wavy wall with superimposed waves [7, 8, 9]; however, the effect of incremental complexity has not yet been fully addressed and remains as an outstanding subject of interest in turbulent boundary layer as well as geophysical-flow research [10]. This investigation points towards addressing such gap that we aim to fulfill by using a RIM facility at the University of Illinois.

EXPERIMENTAL SETUP

The developing and developed flows over 2D and 3D wavy walls was experimentally studied using high-resolution and high-frame-rate particle image velocimetry (PIV) in a 2.5 m long refractive index matching (RIM) channel with a 112.5 mm $\times$ 112.5 mm cross section. A schematics of the setup is shown in figure 1. The 2D wall is characterized by a sinusoidal wave in the streamwise direction x with a wavelength λ_x = 100 mm and an amplitude to wavelength ratio a/λ_x = 0.05. The 3D wall has an additional wave superimposed in the spanwise direction y with a wavelength λ_y= 50 mm and the same amplitude as the streamwise wave resulting in a/λ_y = 0.1. The geometry of both walls $\sigma(x, y)$ is also shown in figures 1. For the purpose of refractive index matching, the wavy walls were casted from urethane resins using hydrodynamically smooth molds. The refractive index of the working fluid (NaI aqueous solution, 63% by weight) was carefully matched to that of the walls rendering them nearly invisible, allowing for measurements to be made near the surface and within the geometry.

A planar PIV system from TSI consisting of an 11 MP (4000 $\times$ 2672 pixels), 12 bit, frame-straddle, CCD camera and a 150 mJ/pulse, double pulsed laser (Quntel) was used for the flow field characterization. A high-frame-rate PIV system will is used to resolve the temporal structure of the turbulence. The system consists on two Phantom Miro 340 cameras with 12 GB onboard memory, 2560 1600 pixes at 800 fps, and a dual cavity YLF laser with 25 mj per pulse at 1kHz pulse rate per cavity; 80 W. The flow was seeded with 14 μm silver-coated, hollow glass spheres.

REMARKS

We will discuss the impact of topographic changes on the statistics and structure of the turbulence in both developing and developed regions. This information is being used to define flow control strategies at geophysical scale to modulate scalar transport in natural environments.

*Corresponding author. Email: lpchamo@illinois.edu

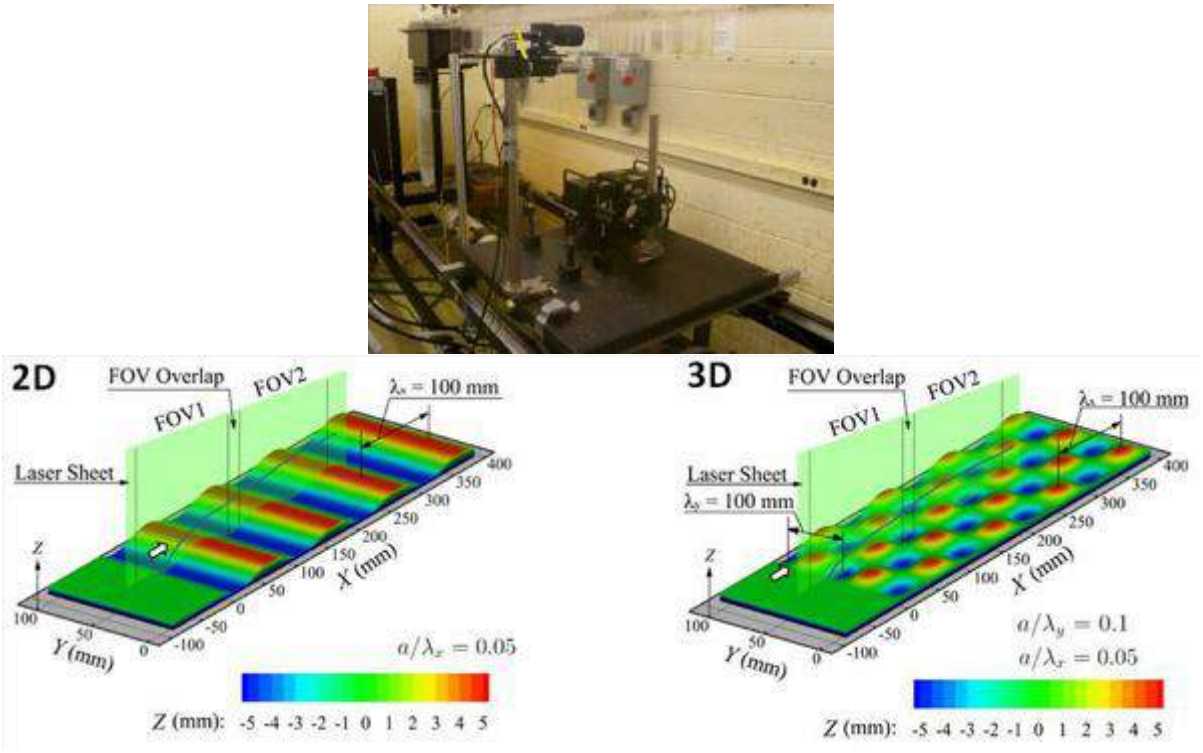

Figure 1: Schematics of the experimental setup: (top) photograph of the flumewith the basic PIV components; (bottom) a section of the 2D and 3D wavy wall with wall-normal planes.

References

[1] Wood N.: Flow over complex terrain: a historical perspective and the prospect for large eddy modelling," Boundary-Layer Meteorol. 96, 11-32 (2000).

[2] Gunther A., von Rohr P. R.: Large-scale structures in a developed flow over a wavy wall, J. Fluid Mech. 478, 257-285 (2003)

[3] Kruse N., Kuhn S., von Rohr P. R.: Wavy wall effects on turbulence production and large-scale modes, J. Turbulence 7 (2006), no. 31.

[4] Henn D. S., Sykes R.: Large-eddy simulation of flow over wavy surfaces, J. Fluid Mech. 383, 75-112 (1999).

[5] Choi S., Suzuki K.: Large eddy simulation of turbulent flow and heat transfer in a channel with one wavy wall, Intl J. Heat Fluid Flow 26, 681-694 (2005).

[6] Thorsness C. B.: Transport phenomena associated with flow over a solid wavy surface. (1975), ph.D. thesis, Department of Chemical Engineering, University of Illinois, Urbana.

[7] Orlandi P., Leonardi S.: DNS of turbulent channel flows with two-and three dimensional roughness, J. Turbulence 7 (2006).

[8] Sen M., Bhaganagar K., Juttijudata V.: Application of proper orthogonal decomposition (pod) to investigate a turbulent boundary layer in a channel with rough walls, J. Turbulence 8 (2007), no. 41.

[9] Volino R. J., Schultz M. P., Flack K. A.: Turbulence structure in boundary layers over periodic two-and three-dimensional roughness, J. Fluid Mech. 676, 172-190 (2011).

[10] Hamed A.M., Kamdar, A. Castillo L., Chamorro L.P.: Turbulent boundary layer over 2D and 3D large-scale wavy walls. Phys Fluids. 27, 106601 (2015).

EXPERIMENTS ON A CLOSED-CONDUIT FLOW PERTURBED BY A TWO-DIMENSIONAL HILL OF LOW ASPECT RATIO

Henrique Pelisson Chimetta*[1] and Erick de Moraes Franklin[1]

[1] *Faculty of Mechanical Engineering, University of Campinas - UNICAMP, Campinas, São Paulo, Brazil*

Summary We present here some preliminary results of an experimental study on the perturbation of a fully developed turbulent boundary layer by a two-dimensional hill of low aspect ratio. Water flows were imposed over an asymmetric hill, with a relatively small curvature, fixed on the bottom wall of a closed conduit. Particle image velocimetry (PIV) was used to measure the flow fields. For the flow upstream of the hill, we found some usual characteristics of a turbulent channel flow, such as logarithmic regions and typical profiles of the xy component of the Reynolds stress. Over the ripple, the maximum of the vertical component of the mean velocity is restrict to a narrow band, above the ripple surface, for every longitudinal position toward the crest. We also found the region where the Reynolds stress is perturbed, and the turbulent kinetic energy production was computed.

INTRODUCTION

Perturbations in boundary layers are frequently encountered in nature and industry. Some examples are airflows over hills, water flows over river dunes, and liquid flows over sand ripples and dunes in closed conduits such as petroleum pipelines. With the boundary layer perturbed, the distributions of velocities and stresses change along the flow. These new distributions are important to understand the bed instabilities associated with sediment transport [1, 2], for example.

Many studies were made on the perturbation of a turbulent boundary layer by a low hill. Some of these studies are based on asymptotic methods, where the turbulent boundary layer over a hill of small aspect ratio (height to length ratio of $O(0.1)$) is divided into two regions, which can be used to determined the perturbed flow [3, 4]. In the case of high Reynolds numbers, the outer region, distant from the bed, is not in local equilibrium because the timescale for the dissipation of the energy-containing eddies is much larger than the timescale for their advection. In the inner region, close to the bed, the timescale for the dissipation of the energy-containing eddies is considered much smaller than the timescale for their advection, so this region is in local equilibrium, allowing the use of turbulent model stress. For the case of moderate Reynolds numbers ($\sim 10^4$), Franklin and Ayek [5] showed that the inner regions of the perturbed closed-conduit flow are not in local equilibrium, a least for a two-dimensional hill with triangular shape. This happens because of the relatively large ratio between the vertical and longitudinal flow scales (when compared with the aeolian case). This means that the asymptotic expressions for the perturbed boundary layer based on local equilibrium conditions must be used with care in case of aquatic ripples of triangular shape.

This study presents the preliminary results of an experimental study on the perturbation of a turbulent boundary layer by a two-dimensional hill. Closed-conduit water flows were imposed over an asymmetric hill with aspect ratio of $O(0.1)$, and the flow was measured by particle image velocimetry (PIV). The mean velocities and fluctuations were computed from the acquired images, and the shear stress over the ripple could be determined.

EXPERIMENTAL SETUP

We used PVC plates of 7-mm thickness to cover the entire bottom of the channel in order to reduce the height and facilitate the handling of the hill. To model the two-dimensional hill, a small bedform of wavy shape was fixed on a PVC plate in the test section. The wavy bedform had the same scales as the aquatic ripples [1, 2, 6]. The bedform, of PVC, was painted in black to minimize undesirable reflections. The employed flow rates were 8 and 10 m^3/h. These flow rates corresponded to cross-sectional mean velocities $\bar{U}$ of 0.32 and 0.40 m/s and to Reynolds numbers Re = $\bar{U}2H_{eff}/\nu$ of 2.75×10^4 and 3.5×10^4, where H_{eff} is the distance from the surface of the PVC plates to the top wall of the channel.

To obtain the instantaneous velocity fields of the flow we used PIV. The employed light source was a dual cavity Nd:YAG Q-Switched laser, capable of emitting 2×130 mJ at 15-Hz. The power of the laser was fixed at 66 % of the maximum power to assure a good balance between the image contrasts and undesirable reflection from the channel walls. 10-μm hollow glass beads (S.G. = 1.05) were employed as seeding particles. To capture the images, we used a 7.4-μm $\times$ 7.4-μm (px^2) CCD (charge coupled device) camera with a spatial resolution of 2,048 px $\times$ 2,048 px and acquiring pairs of images at 4 Hz. The total field employed was of 140 mm $\times$ 140 mm, with a magnification of 0.1, and the employed interrogation area was of 16 px $\times$ 16 px, corresponding to 1.09 mm $\times$ 1.09 mm. The computations were made with 50 % of overlap, corresponding to 256 interrogation areas. The test section was divided in five parts, for each part were acquired 3,000 pairs of images for both flow rates, from which the fields of instantaneous velocity were computed in fixed Cartesian grids by the PIV controller software.

*Corresponding author. Email: henriquepc@fem.unicamp.br

RESULTS

The flow was measured in five different parts, the first one was upstream of the bedform. In this part, the flow corresponded to a fully-developed turbulent channel flow. Using Matlab, the instantaneous fields were time averaged and the second-order moments (fluctuation fields) were computed and time averaged. The time-averaged fields were then space averaged in the longitudinal direction because the flow was fully developed. We encountered the typical characteristics of a fully-developed turbulent channel flow, such as the logarithmic region for both walls ($70 < y^+ < 200$, where y^+ is the dimensionless vertical coordinate, $y^+ = yu_*/\nu$, with u_* being the shear velocity, and ν the kinematic viscosity) by considering a hydraulic smooth regime [7], and the typical profiles of the xy component of the Reynolds stress. The same flow rates were used for the flow over the ripple. The water stream is deflected by the ripple, and, close to the surface, the vertical component of the mean flow v is no longer negligible. We observe in this region an increase of the longitudinal component of the mean velocity, u, as the flow approaches the ripple crest, what is expected from the mass conservation. The vertical component, v, increases from zero at the ripple surface, reaches a maximum and decrease to zero as we approach the upper wall. For every longitudinal position the maximum occurs between 0.9 and 1.6 mm above the ripple surface. Franklin and Ayek [5] found, for a bedform of triangular shape, that toward the crest the maximum of the vertical component becomes closer to the ripple surface ($y_d \approx 2$ mm, where y_d is the distance between the ripple surface and the upper wall). The explanation for the difference in the position of the maximum, for the vertical component, lies in the relatively small curvature of our bedform. Approximately 30 mm downstream the crest, the flow begin to detaches and a thin layer with small velocities starts to form.

We found that the Reynolds stress is perturbed in the $50 < y_d^+ < 250$ region, where $y_d^+ = y_d u_{*,0}/\nu$, with $u_{*,0}$ being the shear velocity upstream the bedform. This region corresponds to the overlap sublayer of the unperturbed boundary layer [7]. We also found that, longitudinally, the perturbation of the Reynolds stress decreases near the crest. Fig. 1a shows some profiles of the xy component of the Reynolds stress, for Re = 2.75×10^4, in seven different longitudinal positions. We computed the turbulent kinetic energy production ($\circ\ \overline{u'v'}\partial u/\partial y$) for this region as indicated in Fig. 1b. Here u' and v' represents the longitudinal and vertical components of the velocity fluctuation, respectively. Most of the production occurs downstream the crest and it is confined to small region, what is expected due the relatively small curvature of the bedform.

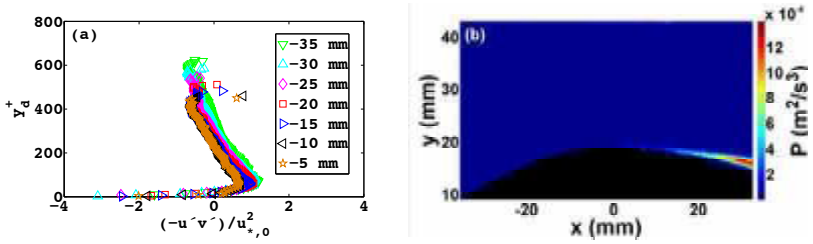

Figure 1: **a** Some profile of the xy component of the Reynolds stress in dimensionless form upstream of the ripple crest: y_d^+ versus $-\overline{u'v'}/(u_{*,0}^2)$.; **b** Turbulent kinetic energy production.

CONCLUSIONS

We presented preliminary results of an experimental study on the perturbation of a liquid turbulent boundary layer by a two-dimensional ripple in the hydraulic smooth regime. Upstream of the bedform, the usual turbulent closed-conduit profiles were found. Over the ripple, we obtained different results for the maxima of the vertical component of the mean velocities, when compared with previous studies. This can be explained by the small curvature of our bedform. For the xy component of the Reynolds stress upstream of the ripple crest, the profile is perturbed in the region that corresponds to the overlap of the unperturbed boundary layer. Owing to the relatively small curvature of the hill, the turbulent kinetic energy production is confined to a small region downstream the crest.

References

[1] Franklin E. M.: Initial instabilities of a granular bed sheared by a turbulent liquid flow: length-scale determination. J. Braz. Soc. Mech. Sci. Eng. 32(4):460-467, 2010.

[2] Franklin E. M.: Nonlinear instabilities on a granular bed sheared by a turbulent liquid flow. J. Braz. Soc. Mech. Sci. Eng. 33(3):265-271, 2011.

[3] Belcher S. E., Hunt J. C. R.: Turbulent flow over hills and waves. Ann. Rev. Fluid Mech. 30:507-538, 1998.

[4] Jackson P. S., Hunt J. C. R.: Turbulent wind flow over a low hill. Quart. J. R. Met. Soc. 101:929-955, 1975.

[5] Franklin E. M., Ayek G. A.: The perturbation of a turbulent boundary layer by a two-dimensional hill. J. Braz. Soc. Mech. Sci. Eng. 35:337-346, 2013.

[6] Franklin E. M., Charru F.: Morphology and displacement of dunes in a closed-conduit flow. Powder Technol. 190:247-251, 2009.

[7] Schlichting H.: Boundary-layer theory, Berlin, Germany, 2000.

EXPERIMENTAL STUDY OF INTERACTIONS BETWEEN TURBULENT STRUCTURES AND PORO-ELASTIC SURFACES

Marie Couliou *[1], Fredrik Lundell[1], Jonas Hansson[2], Carl Fredrik Carlborg[2], and Shervin Bagheri[1]
[1]*Department of Mechanics, KTH, Stockholm, Sweden*
[2]*Micro and Nanosystems, KTH, Stockholm, Sweden*

Summary This work aims to study experimentally the interaction of fibrous poro-elastic surfaces with wall-bounded turbulent flows. We fabricate the coatings using Off-Stoichiometry-Thiolene-Epoxy (OSTE+) polymers and multidirectional UV-lithography. We assess the effects of these coatings on an overlying low-Reynolds number turbulent flow using a water-table facility and PIV measurements. In particular, we focus on the modification of near wall turbulent structures in both space and time due to the presence of the poroelastic coatings. The overall goal is to classify stabilizing and destabilizing fluid-structure interaction mechanisms of turbulent flows over poroelastic surfaces.

INTRODUCTION

Flows over slender, deformable and dense structures are ubiquitous in both nature and technological applications, ranging from the flow over canopies and forests to the flow over the over the skin of organisms. In particular, surfaces found on organisms are often filamentous and dense, inducing effectively a poroelastic surface. Although, increasing number of reports [1, 5, 8] indicate that these surfaces interact with overlying flowing fluid in a favorable manner, the physical fluid-structure mechanisms are not well understood. One particular interesting application of non-smooth, soft, permeable surfaces is to reduce turbulent skin-friction drag. The most successful coatings for this purpose are inspired from the scales of the shark's skin [1, 2, 3] and from the surface of the lotus leaf [4] which has motivated the development of riblets for the former and super-hydrophobic surfaces for the latter. In order to create a fundamental understanding of how poroelatic surface can be used for flow control purposes, in this talk, we report on the interaction of complex anisotropic materials with wall-bounded turbulent flows; especially, how the small features of complex surfaces affect global turbulence characteristics evolving on a larger scale and vice versa. In this perspective, we fabricate a selected number of surface textures and characterize the flow over them in an open channel flow facility.

EXPETIMENTAL SET-UP

The experimental setup consists of a water-table with an inclined glass plate as is sketched in figure 1. The water is pumped from a downstream reservoir to an upstream reservoir, allowing the water to flow down the inclined glass plate. The flow down the inclined glass plate is driven by gravity alone which allows one to calculate the wall shear stress τ_w as:

$$\tau_w = \rho g h sin\alpha \tag{1}$$

where ρ is the density of water, g is the gravitational acceleration, h is the height of the water layer and α is the inclination angle of the glass plate. The test section of the water table is made of a glass plate with length 230 cm over the streamwise direction and width 56 cm and the height of the water layer is typically around 10 mm. Depending of the flow rate imposed by the pump and of the inclination angle, the range of achievable friction Reynolds Number is between $Re_\tau = 50$ and $Re_\tau = 350$.

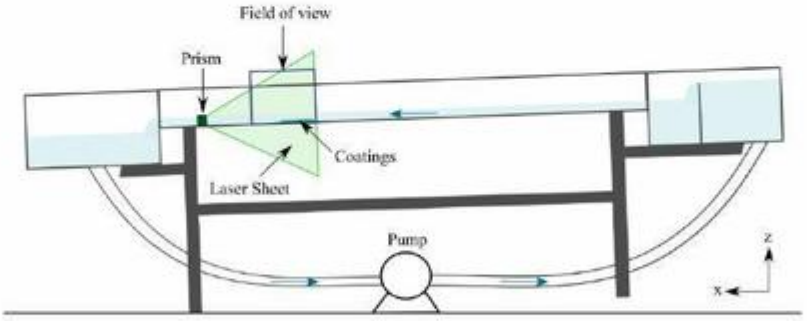

Figure 1: Sketch of the water table set-up.

*Corresponding author. Email: marie.couliou@mech.kth.se

Velocity measurements are achieved by Particle Image Velocimetry (PIV). The used LaVision system consists of a ND:YLF laser (Litron Lasers, double-exposure, 30 mJ, 527 nm) which is mounted on a linear traverse to allows us to measure 2D velocity fields (U_x,U_z) over several spanwise plans. The flow is seeded by Glass Hollow Spheres with a mean size of 8-11 μm as tracer particles. A single camera (Imager Pro HS 4M; double-frame 12 bit CMOS with resolution of 2016×2016 pixels^2 with a pixel size of 11×11 μm^2) is placed in front of the water table. The 2016×387 pixels^2 observation window corresponds to physical sizes of 52×10 mm^2. An adaptive cross-correlation processing is applied to an initial interrogation area of 64×64 pixels^2 followed by a second interrogation area of 32×32 pixels^2 with a 50% overlap. Image pairs are acquired in a range of rate between 200 Hz and 600 Hz.

MATERIALS

In order to fabricate surfaces with elastic high-aspect-ratio microstructures, a soft-lithography technique using elastomers (e.g. PDMS) is appropriate, since it allows materials with adjustable elasticity. We use multidirectional UV lithography to create filamentous structures with certain connectivity. In particular, we construct slanted filaments and 3D interlocked filaments in Off-Stoichiometry-Thionele-Epoxy (OSTE+) polymer developed by the KTH Micro and Nanosystems group [6]. In order to fabricate the filaments, the OSTE+ polymer is squeezed by the photomask and then exposed to a UV-lamp for curing as illustrated in figure . The use of mirrors and blockage effects enable to create fibers anchored and interlocked at different angles with a single single mask. The described fabrication is realized at the KTH Microsystem Technology Laboratory.

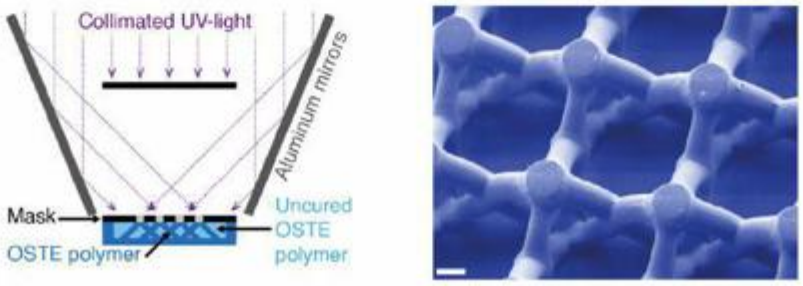

Figure 2: (Left) Setup to manufacture the OSTE polymer filaments using multidirectional UV-lithography (Right) Example of a manufactured slanted interlocked filaments (Scale bar is 30 μm)

APPROACH AND ONGOING WORK

For both the turbulent flow and the coating materials, we can define characteristic timescales. For the flow τ_f is related to the frequency of the quasi-streamwise streaks, whereas for the poro-elastic material, τ_p is related to the time it takes for the flow inside the material to reach an equilibrium due to an external forcing. By fabricating a selected number of coatings using UV-lithography and exposing them to different turbulent flow conditions, we can vary these two timescales. This allows us to compare the effect of the coatings on the flow and vice versa in each configuration e.g when $\tau_p << \tau_f$ or when $\tau_p >> \tau_f$. These investigations are ongoing and the results will be reported at the conference. This new understand of interaction between turbulent flow structures and poro-elastic coatings will allow the design of filaments in order to reduce turbulent skin-friction drag.

References

[1] Bechert D.W., Bruse M., Hage W., Meyer R.: Fluid mechanics of biological surfaces and their technological application. Naturewissenschaften 87:157-171, 2000.

[2] Oeffner J., Lauder G.V.: The hydrodynamic function of shark skin and two biomimetic applications. J. Exp. Biol. 215: 785-795, 2012.

[3] Wen L., Weaver J.C., Lauder G.V. : Biomimetic shark skin: design, fabrication and hydrodynamic function. J. Exp. Biol 217:1656-1666, 2014.

[4] Bhushan B.: Biomimetics inspired surfaces for drag reduction and oleophobicity/philicity. Bellstein J. Nanotechnolol 2:66-84, 2011.

[5] Bushnell D.M., Moore K.J. . Drag reduction in nature. Ann. Rev.of Fluid Mech, 23:65-79, 1991.

[6] Carlborg C., Haraldsson T., berg K., Malkoch M. , van der Vijngaart W.: Beyond PDMS: off-stoichiometry thiol–ene (OSTE) based soft lithography for rapid prototyping of microfluidic devices. Lab on Chip 11:3136-3147, 2011.

[7] Skotheim, Jan M., and L. Mahadevan: Physical Limits and Design Principles for Plant and Fungal Movements. Science 5726:1308-1310, 2005.

[8] Bullen R.D., McKenzie N.L.: The pelage of bats and the presence of aerodynamic riblets. Zoology, 111:279-286, 2008.

STUDY OF SHOCK WAVE/BOUNDARY LAYER INTERACTIONS ON HIGH- PRESSURE CAPTURING WINGS

Kai Cui [a], Guangli Li, Yao Xiao, & Yingzhou Xu
LHD of Institute of Mechanics, Chinese of Academy of Sciences, Beijing China

Summary To evaluate the heating load of high-pressure capturing wings (HCW) at various design conditions, a series of numerical cases were carried out to study the shock wave/boundary layer interactions between the inclined shock wave compressed by the airframe and the HCW. The results show that the maximal value of the heat-flux on the lower surface of the HCW decreases with the increase of the blunt radius of the HCW, the backward position of the inclined shock wave, and the decrease of the Reynolds number. While it increases with the increase of both the Mach number and the half cone angle. Besides, the maximal value of the heat-flux on the lower surface of the HCW is significantly lower than the value on the stagnation point. The present results show that the HCW configuration should have a good application prospect.

INTRODUCTION

A high-pressure capturing wing (HCW) is a kind of lift device, which can effectively improve the lift-to-drag ratio (L/D) of a high-speed flight vehicle with large volume [1]. A two-dimensional illustration for elaborating the principle of lift enhancement for a HCW configuration is sketched in Fig. 1. Here the body is the main part of the vehicle, the upper surface of the body is a wedge or a cone-shape typically. In according with the positions of the shock and the expansion waves, the whole flowfield can be divided into five regions that labeled from 1 to 5. The air pressure in region 1 is the freestream pressure, and the pressure in region 2 is higher than that in region 1 since the airflow is compressed by the body. When the airflow arrives in region 3, the pressure continues to increase because the HCW compresses the airflow once again. As the airflow leaves region 3 and enters in region 4, the pressure gradually decreases due to the existence the expansion fan. The pressure in region 5 is approximately equal to the freestream pressure because the HCW is parallel to the direction of the freestream flow.

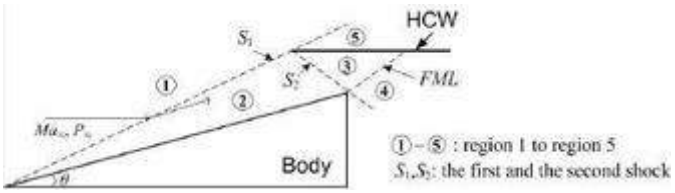

Fig. 1 Illustration of design principle of the HCW

On the basis of the above analysis, we know that the pressure on the lower surface must be much higher than that on the upper surface of a HCW. Therefore, the HCW configuration can get a considerable lift augmentation, which benefits from the pressure difference on the lower and the upper surfaces. However, it is well known that the aerothermal problem must be well studied for any high-speed configurations. This is the motivation of this paper. In order to evaluate the heating load of high-pressure capturing wings (HCW) at various design parameters and freestream conditions, a series of numerical cases were carried out to study the shock wave/boundary layer interactions (SBLI) [2-4] between the inclined shock wave compressed by the airframe and the HCW.

NUMERICAL RESULTS

To a HCW configuration, this problem presents that a conical shock acts on a cylinder wall. A typical flow structure is shown in Fig. 2. The conical shock compressed by the body crosses over the bow shock compressed by the HCW, and interacts with boundary layer on the lower surface of the HCW. Then a separation bubble emerges and induces an impinging shock. Accordingly, the distribution of both the wall pressure and the wall heat-flux present complex variation.

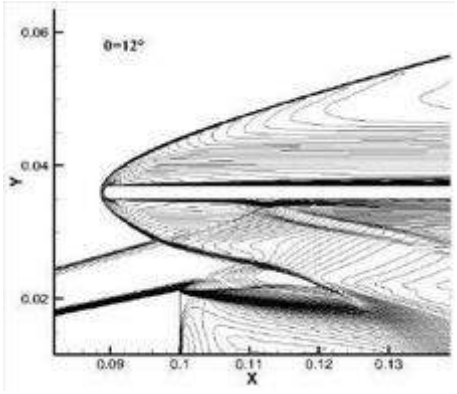

Fig. 2 A typical flow structure of the flowfield (pressure distribution)

To aim at studying the effect of design parameters and freestream flow parameters to the heat flux distribution, a series of two-dimensional and axisymmetric cases were carried out numerically. A full three-dimensional structural grid was used to discretize the computational domain for each of above three configurations, in which algebraic transfinite interpolation methods with elliptic interior point refinement were utilized. Numerical solutions were obtained by solving the three dimensional compressible Navier-Stokes equations, with the use of a second order TVD finite-volume scheme for spatial discretization and a second order implicit time marching scheme, a realizable k-ε model was used in the computations. The results of the heat flux are presented in the dimensionless form:

[a] Corresponding author. Email: kcui@imech.ac.cn.

$$St = \frac{q}{\rho_\infty U_\infty c_p \left(T_t - T_w\right)} \qquad (1)$$

where q is a heat flux, ρ_∞ and U_∞ are gas density and velocity in the unperturbed flow, respectively, c_p is a specific heat of gas at a constant pressure, T_t is a total temperature of gas, and T_w is the wall temperature.

Fig. 3 shows the heat flux distributions on the lower surface of the HCW at different conditions. Note from these figures that the S_t presents different distributions with variation of each parameter. In general, the peak value of the heat flux is directly proportional to the cong angle. While it is inversely proportional to the Mach number, the blunt radius of the leading edge of the HCW, and the Reynolds number. In addition, it should be noted that the starting points in all curves are at the end of blunt arc. Compared with the value of the heat flux at the standing point, the peak value on the surface is lower by about an order of magnitude. This means that the aerothermal load of a HCW is acceptable under normal circumstances.

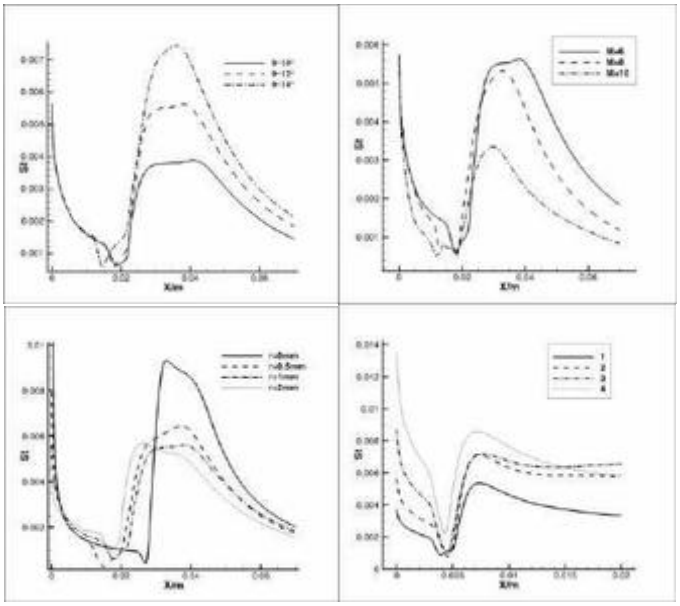

Fig. 3 Variation of St with different conditions (top-left: different cone-angles; top-right: different Mach numbers; bottom-left: different blunt radiuses; bottom-right: different Reynolds numbers)

CONCLUSIONS

In this paper, a preliminary study for aerothermal analysis of HCW was carried out. When the incident oblique shock directly acts on the HCW, a SBLI phenomenon appears. Thus, the value of the heat-flux on a HCW increases. Moreover, the peak value of the heat-flux varies with the cone-angle of the body, the freestream Mach number, the blunt radius of the HCW, and the Raynolds number. However, the maximal value of the heat flux induced by the SBLI is much lower than the value on the standing point. Thus, the present results show that the HCW should have a good application prospect.

ACKNOWLEDGEMENTS

This research was funded by the National Natural Science Foundation of China (NSFC) under grant number 11372324 and 11572333.

References

[1] Cui, K., Li, G. L., and Xiao, Y.: Aerodynamic Performance Study of High Pressure Zone Capture Wing Configurations. AIAA Paper 2015-3388

[2] Gaitonde, D. V.:Progress in Shock Wave/ Boundary Layer Interactions,. Progress in Aerospace Sciences, 72, 2015, 80–99

[3] Borovoy, V. Y., Egorov, I. V., Skuratov, A. S., and Struminskaya, I. V.:Two-Dimensional Interaction of the Oblique Shock Wave with the Boundary and High-Entropy Layers of the Blunt Plate. AIAA Paper 2011-731

[4] Marvin, J. G., Brown, J. L., and Gnoffo, P. A.: Experimental Database with Baseline CFD Solutions: 2-D and Axisymmetric Hypersonic Shock-Wave/Turbulent-Boundary-Layer Inter- actions. NASA/TM–2013–216604

[5] Murray N., Hillier R., Williams S.: Experimental investigation of axisymmetric hypersonic shock-wave/turbulent-boundary-layer interactions. Journal of Fluid Mechanics, 2013, 714: 152-189.

EFFECTS OF LOCAL SUCTION ON BOUNDARY-LAYER INSTABILITY AND ACOUSTIC RADIATION

Ming Dong*[1,2] and Xuesong Wu [1,2]

[1]*Department of Mechanics, Tianjin University, Tianjin, China*
[2]*Department of Mathematics, Imperial College London, UK*

Summary When a boundary-layer instability mode propagates through a region of rapid distortion, its amplitude changes substantially while at the same time a sound wave is radiated, both due to the ensuing scattering. This paper focuses particularly on the impact of a local suction on an incident T-S wave by employing a Local Scattering Theory. The central idea is to introduce a transmission coefficient, defined as the ratio of the T-S wave amplitude downstream of the scatter to that upstream. The mathematical description is based on the triple-deck formulism, but in order to accommodate the acoustic field, the unsteady terms in the upper deck are retained. It is found that a suction slot would suppress the oncoming T-S wave. The intensity of the radiated sound increases with the mass flux if the latter is not too large, but is suppressed when the flux exceeds a critical value.

INTRODUCTION

The natural route of laminar-turbulent transition in boundary layer flows involves four successive stages: receptivity, linear instability, nonlinear interaction and breakdown into turbulence. This process is affected significantly by surface imperfections, which may appear at different locations and in different forms. The presence of an abrupt change induces a region of rapid distortion on the mean flow, causing mainly three consequences of physical interest: (I) at the receptivity stage, the distortion could interact with the free-stream disturbances to generate T-S waves; (II) in the linear instability region, the distortion could interact with the oncoming T-S waves, thereby altering the amplitude of the latter and further affecting transition location [1]; (III) acoustic waves are radiated to the far field if the flow is compressible [2]. These three issues can mathematically be described by a recently-proposed framework, Local Scattering Theory.

The central idea of this framework is to treat the abrupt change as a scatter, and the wave activities in its vicinity as a scattering problem, while in the relatively smooth regions away from the abrupt change, the disturbances evolve as instability modes. Since the mean flow in the smooth regions varies slowly along the streamwise direction, the evolution of the disturbances can be described by the classical linear stability theory or parabolized stability equations (PSE). These approaches however cease to be valid when the perturbations propagate through a rapidly distorting mean flow that occurs over a length scale comparable with the characteristic wavelength of the instability modes. A rational means to address this issue is to formulate a local scattering theory, which can be done by employing the triple-deck formalism [1].

MATHEMATICAL DESCRIPTION

This paper focuses particularly on the application of the Local Scattering Theory to the scattering of T-S waves by the mean-flow distortion induced by a local steady surface suction. The characteristic suction velocity is expressed as $Re^{-3/8}U_\infty V_s(X)$, where Re is the Reynolds number based on the free-stream velocity U_∞ and the distance of the suction slot to the leading edge, and X is the scaled variable in the triple deck theory. For illustration purpose, the suction velocity is taken in calculations to be Gaussian, $V_s(X) = V_{s0}\exp(-X^2/d^2)$, where V_{s0} is the suction velocity at the slot center and d characterizes the slot width. We introduce the transmission coefficient $\mathcal{T}$, defined as the ratio of the amplitude of the disturbance downstream of the slot to that upstream. The disturbance in the lower deck takes the form $\tilde{}(X,Y)\,\mathrm{e}^{\mathrm{i}\,\omega T}+c.c.$, where ω is the frequency, and ϕ is a function of the streamwise variable X and the transverse variable Y in the lower deck.

Far upstream, the disturbance corresponds to an incoming T-S mode, and so $\phi \sim \mathrm{e}^{\mathrm{i}\,\alpha X}$ as $X \to -\infty$ with α being the wavenumber. Far downstream, the perturbation relaxes back to a local T-S mode with a different amplitude, and so it behaves like $\tilde{} \sim \mathcal{T}\,\mathrm{e}^{\mathrm{i}\,\alpha\mathcal{X}}$ as $X \to \infty$. In order to accommodate the acoustic field, we retain the unsteady second-order terms in the upper deck, which play a leading-order role for acoustic radiation, as well as the influence of the radiated sound on the near-wall perturbation [3]. The governing equation for the pressure then reduces to a Helmholtz equation, which leads to a modified displacement-pressure relation. The latter is coupled with the linearized boundary-layer equations governing the disturbance in the lower deck. Discretization of these equations and the modified pressure-displacement relation in a chosen computational domain leads to a generalized eigenvalue problem,

$$\mathbf{A}\,\tilde{} = \mathcal{T}\mathbf{B}\,\tilde{} \tag{1}$$

where $\mathcal{T}$ is the eigenvalue of the system, $\mathbf{A}$ and $\mathbf{B}$ are coefficient matrices, and $\tilde{}$ is the unknown vectors representing the velocities and pressure of the unsteady perturbation at each grid. As well as predicting the transmission coefficient, the solution of the eigenvalue problem provides an adequate description of the near-wall hydrodynamic motion.

*Corresponding author. Email: dongmin@tju.edu.cn

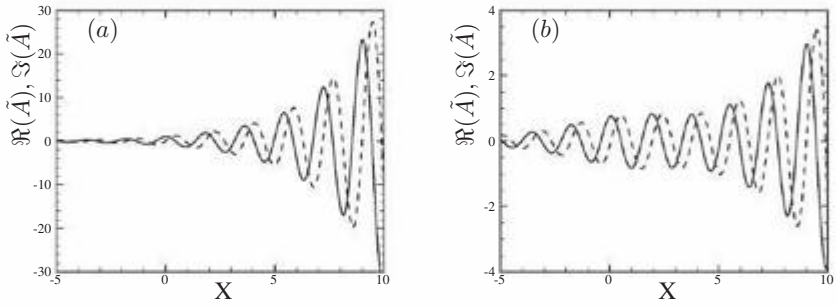

Figure 1: The real (solid line) and imaginary (dashed line) parts of the disturbance amplitude for $V_{s0} = 0$ (a) and $V_{s0} = -0.4$ (b) with $(\omega, M, Re, d) = (0.8, 0.2, 10^6, 1.0)$.

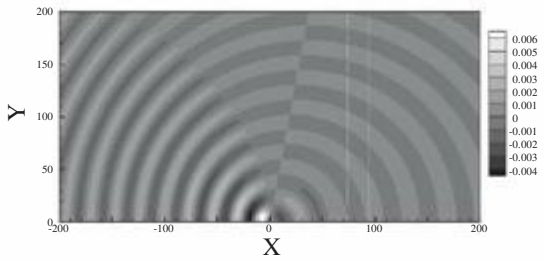

Figure 2: Acoustic pressure $\Re(p_s)$ for $\omega = 8.0$, $V_{s0} = -0.4$ and $(M, Re, d) = (0.2, 10^6, 1.0)$.

NUMERICAL RESULTS

While the disturbance evolves exponentially in the regions far upstream and downstream, i.e. as $X \to \pm\infty$, it undergoes a sudden change in the vicinity of the suction slot. A typical result is shown in Fig. 1 for Mach number $M = 0.2$. Suction turns out to produce a suppressing effect on the oncoming T-S waves. Correspondingly, the transmission coefficients are less than unity. Further calculations show that the transmission coefficient $\mathcal{T}$ decreases with the suction velocity or the slot width. For $V_{s0} = O(1)$, $\mathcal{T}$ can be smaller than 0.1, implying a significant delay on transition. Note that the physical suction velocity normalized by U_∞, is rather small for a large Reynolds number, and the mass flux of suction is also moderate.

The far-field sound can be computed by using the stationary-phase method. Fig.2 shows the far-field acoustic pressure for $M = 0.2$. The dominant radiation is in the upstream direction, and an angle of silence of 77° is observed. This directivity is found to be independent of the frequency and other parameters, however, the intensity increases remarkably with the frequency and the width of the slot. It increases first with the suction velocity. Interestingly and significantly, a further increase of the suction velocity suppresses radiation, and for the case with $V_{s0} = O(1)$, the radiated sound is very weak, indicating that the gain of stabilizing effect does not cause an aeroacoustic penalty.

CONCLUSIONS

The Local Scattering Theory is applied to solve the scattering of the incident T-S wave by a local steady suction in a subsonic boundary layer, and quantitative results for both the T-S wave amplitude and the radiated sound are obtained.

References

[1] Wu X., Dong M.: A local scattering theory for the effects of isolated roughness on boundary-layer instability and transition: transmission coefficient as an eigenvalue. J. Fluid Mech. Submitted.

[2] Dong M., Wu X.: Acoustic radiation due to scattering of a T-S wave by nonlinear roughness in a subsonic boundary layer. AIAA P. AIAA-2015-2626.

[3] Wu, X. 2011 On generation of sound in wall-bounded shear flows: mean-flow refraction, back action of sound and global acoustic coupling. *J. Fluid Mech.* **689**, 279-316.

ANALYSIS OF MACH RADIATION IN AN AXISYMMETRIC SUPERSONIC JET

Meixiang Zhang, Na Guo & Yihong Fang
Department of Mechanics, School of Mechanical Engineering, Tianjin University, Tianjin, China

Summary The Mach wave radiation give rise by the instability waves in a supersonic axisymmetric jet with Ma=2.1 is investigated. Near field of supersonic axisymmetric jet is computed by nonlinear disturbance equations ,while sound radiation in far field is computed by Wu method. The results are in good agreement with experiment data and DNS. Present study can analysis the Mach wave radiation both quantitative and qualitative.

INTRODUCTION AND MOTIVATION

The study of sound radiated from supersonic jet has a long history and received renewed interest in recent years, for numerous technology application, in particular for the aviation industry. Recent theoretical investigations have described that instability waves, or in a broader sense large-scale orderly structures, constitute a dominant source of shear flow noise. In the supersonic jets, the role of supersonic modes in radiating Mach waves was confirmed by a series of experiments. Tam and Burton[1] applied the linear stability theory on relates the far-field sound to the growth and decay of instability waves in the jet flow. In predicting supersonic mixing noise, two prevalent approaches are Lighthill's equation and the Kirchhoff surface method.

Wu[3] present an analysis for nonlinear evolution of supersonic modes and the associated Mach wave radiation, based on asymptotic expansion in conjunction with the multiple-scale method. The goal of present study is the quantitative description of the radiated sound field, its prediction and its link to sound-generating structures in the supersonic jet flow. In this effort, we use nonlinear disturbance equations to simulate the instability waves of a supersonic axisymmetric jet and analyse the associated Mach wave radiation by using Wu's Integration. This study aims at underlying mechanisms contained in the growth and decay of instability waves that give rise to intense Mach wave radiation quality as well as quantity.

NUMERICAL SIMULATION

The governing equations are nonlinear, compressible, axisymmetric disturbance equations with the assumption of constant viscosity. Spatial derivative are discretized with 5th-order upwind finite-difference scheme for convective terms and 6th-order finite-difference scheme. Time advancement is with the three-order Rung-Kutta algorithm.

A steady base flow is first computed from experimental fitting function in [1], for a Reynolds number Re = 70000, Mach number Ma =2.1, Prandtl number Pr = 1. In a second step, nonlinear disturbance equations simulations are performed using the base flow above. To this end, non-reflecting boundary condition[2] is employeed at lateral boundary. The inflow condition is given by linear stability theory and extrapolation boundary condition is used for outflow. The evolution of only axisymmetric perturbations (m = 0) are computed, and symmetry conditions on the jet axis are imposed accordingly.

To predict the Mach wave radiated by supersonic instability waves, the numerical method used in the currently study is nearly identical to the method used in [3], it is summarized only briefly. The Mach wave radiation wave is divided two asymptotic region: a near field and a far field. Using the asymptotic expansion and multiple-scale techniques in a supersonic jet, the acoustic pressure was expressed explicitly in terms of the amplitude function of the instability waves, which are calculated above, in each field. With analytical result, we known that a Mach wave propagates along the characteristics ζ=constant, while its envelope propagates along the characteristics ξ=constant.

In order to compare with the experiment data in [1], the parameters of inflow instability wave are summarized in table 1.

Table 1 The parameters of inflow instability wave

St	ω_0	α_r	$-\alpha_i$	A_0
0.4	1.2560	1.6478	0.4985	0.0001

RESULTS

Fig. 1 show us the numerical results of pressure contour in near field by using nonlinear disturbance equation. For a weak disturbance, its radiated Mach wave is obviously along the fixed line and energy concentrates in a region, here refer to as Mach beam. So that the Mach wave beam is perpendicular to the Mach wave front, and as if to emanate from the streamwise location where the amplitude of the instability mode is maximum. Fig. 2 is the pressure contours of Mach waves radiation by instability

[a] Corresponding author. Email: yhfang@tju.edu.cn.

waves in far-field, which computed by Wu method. Mach wave beam could be seen clearly in Fig. 2. It also indicated that a Mach wave propagates along the characteristics ζ, while its envelope propagates along the characteristics ξ.

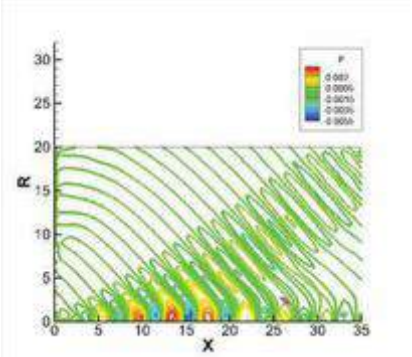

Figure 1 Pressure contour of Mach waves radiated in near-field.

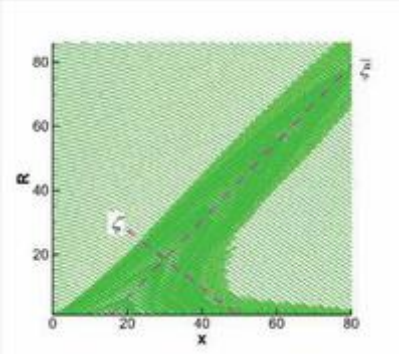

Figure 2 Pressure contour of Mach waves radiated in far-field.

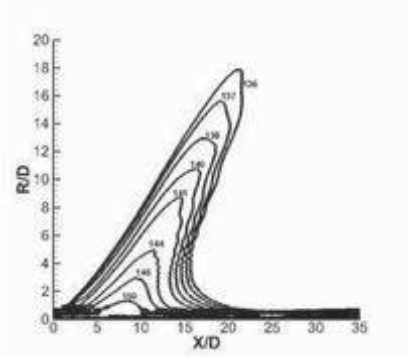

Figure 3 SPL calculation by Wu method.

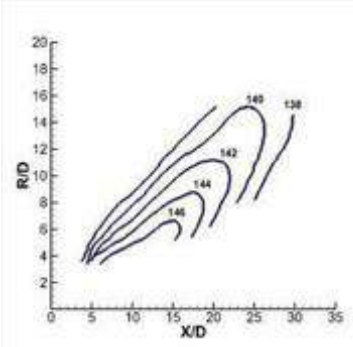

Figure 4 SPL from experiment (Tam & Burtun)

Comparisons of with present results and relevant experimental data are show in Fig. 3 and Fig. 4. The two are in a good degree of quantitative agreement.

It can be note that the present analysis and solution can successfully predict the quantitative as well as qualitative features of the Mach wave radiation associated with supersonic instability waves. It must be pointed out that the analysis for the Mach waves are also valid for an instability wave packet. A more complete analysis of the wave packet will be presented at the Congress.

References

[1] Tam, C. K. W.; Burton, D. E.: Sound generated by instability waves of supersonic flows. Part 1: Two dimensional mixing layers. J. Fluids Mech. 138:249-271, 1984. Part 2: Axisymmetric jets. J. Fluids Mech. 138: 273-295, 1984.

[2] Poinsot, T. J, Lele, S.K.: Boundary conditions for direct simulations of compressible viscous flows. J. Comp. Phys., 101(1): 104-129, 1992.

[3] Mitchell, B.E , Lele, S.K., Moin P.: Direct computation of Mach wave radiation in a axisymmetric supersonic jet. AIAA Journal, 35(10): 1574-1580, 1997

[4] Wu, X.: Mach wave radiation of nonlinear evolving supersonic instability modes in shear layers. J. Fluids Mech. 523: 289-313, 2005.

[5] Ladeinde, F., Alsbi, K., Colonius, T., et al. An integrated RANS-PSE-Wave packet tool for the prediction of subsonic and supersonic jet noise. 16th AIAA/CEAS Aeroacoustics Conference. 2010: 4021

.

NON-PARALLEL EFFECTS ON MODE CHARACTERISTICS IN HYPERSONIC BOUNDARY LAYERS

Yufeng Han, Jianxin Liu & Jisheng Luo[a)]
Department of Mechanics, Tianjin University, Tianjin, China

Summary The discrete modes and continuous spectra are essential to receptivity and instability of the hypersonic boundary layers. The coalescence between discrete modes and continuous spectra was studied with the non-parallel flow effects taken into account. Investigations were performed in Mach=4.5 flat plate boundary layers by solving the expansion of parabolized stability equations (EPSE). The stability analysis indicates that fast mode can cross the branch cuts of vorticity/entropy waves continuously, i.e., the fast mode is a normal mode of discrete spectrum. The unstable supersonic mode can also cross the branch cuts of slow acoustic waves continuously. It suggests that the coalescence between discrete modes and continuous spectra can be avoided by including non-parallel effects.

INTRODUCTION

Stability of hypersonic boundary layer has been studied for many years. Fedorov & Khokhlov (2001) [1] revealed following three synchronization of the receptivity process in hypersonic boundary layers: 1) in the leading-edge region, fast mode and slow mode are synchronized with the fast and slow acoustic waves of the continuous spectrum, respectively. 2) Further downstream, the fast discrete mode is synchronized with the entropy and vorticity waves of the continuous spectrum. 3) The fast mode is synchronized with the slow mode near the lower neutral branch of the Mack second mode. In region 2, based on the linear stability theory (LST), the fast mode coalesces with vorticity/entropy waves of the continuous spectrum. The fast mode is treated as two different normal modes of discrete spectrum on two sides of the vorticity/entropy waves branch cuts. Detailed discussion of the characteristics of these spectra and the receptivity to entropy disturbance were given by Fedorov & Tumin (2003) [2]. Recently, the influence of high levels of wall cooling on the stability of hypersonic boundary layers was investigated by Bitter & Shepherd (2015) [3], in which the unstable supersonic mode synchronized with free-stream acoustic waves was identified. It is similar to the synchronization between fast mode and vorticity/entropy waves.

However, it is difficult for discrete modes to get through these branch cuts caused by continuous spectra using traditional stability analysis method. Fedorov (2011) [4] also proposed the question: "How should PSE and LST codes be modified to handle the coalescence of discrete modes with waves of continuous spectra?". For this aim, accounting for the non-parallel flow effects, stability analysis is performed to investigate the coalescence between discrete modes and continuous spectra. The coalescence between fast mode and vorticity/entropy waves, and the coalescence between unstable supersonic mode and acoustic waves are studied by solving the expansion of parabolized stability equations (EPSE).

MAIN RESULTS

In this paper, the non-parallel flows effects are taken into account by the EPSE. Details on the problem formulation and the governing equations are given by Yu et al. [5]. Considering the first order expansion, two different eigenvalues are obtained in the eigenvalue problem. The spatial growth rate of disturbance is defined as

$$\sigma = -\alpha_i + (\partial\hat{\phi}/\partial x)/\hat{\phi}$$

Where α_i is the eigenvalue of EPSE, and $(\partial\hat{\phi}/\partial x)/\hat{\phi}$ stands for the distortion of the shape function $\hat{\phi}$.

The stability analysis is performed in a flat plate boundary layer and the flow parameters are chosen from Ref. 3 as: $Ma = 4.5$, $Re = \sqrt{U_e^* x^*/v_e^*} = 2000$, $Te = 1500K$, $Tw = 300K$.

The variation of growth rates σ with the frequency ω is shown in Fig. 1(a). It can be seen that there are three branches (labelled F^-, F^+, and F^N) of the LST curves which were analyzed by Bitter & Shepherd (2015)[3] . For the same frequency, two growth rates curves labelled U and L can be obtained by EPSE, which are shown in Fig. 1(a). We define the branch with larger $-\alpha_i$ as 'upper branch' and the smaller one as 'lower branch'. In the region $c_r \sim 1$, the lower branch of EPSE is discontinuous (labelled L^- and L^+), which is similar to the behavior of fast mode in LST. A new phenomenon can be seen that the upper branch of EPSE is continuous from $c_r > 1$ to $c_r < 1$ as frequency increases. To further investigate this new feature in EPSE, the real and imaginary parts of the complex phase speeds are plotted in Fig. 1(b). Two thick black lines are also shown in the figure which represent the branch cuts of continuous spectrum: the vertical branch near $c_r = 1$ is the vorticity/entropy branch cuts while the nearly horizontal one corresponds to slow acoustic branch cut at $\omega = 0.47$. It can be seen that the LST branch and the lower EPSE branch both cross the branch cuts of vorticity/entropy waves, i.e. they are discontinuous. However, the upper branch of EPSE bypasses the branch cut of vorticity/entropy with the imaginary part of phase speed $c_i > 0$ in the vicinity $c_r = 1$. It makes the growth rate of this upper branch keep continuous near $c_r = 1$. It suggests that the fast mode can cross the branch cuts of vorticity/entropy waves continuously by the EPSE method.

In Fig. 1(a), a sharp change in slope of LST and EPSE curves can be observed at $\omega \sim 0.47 (c_r \sim 1 - 1/Ma)$, owing to the unstable modes of LST and EPSE travel supersonically with respect to the free stream. Additional analysis of the supersonic

[a)] Corresponding author. Email: jsluo@tju.edu.cn.

mode characteristics is available in Ref. 3. A new feature in the region $c_r < 1 - 1/Ma$ is that there is a significant gap between growth rate curves of upper and lower EPSE branches. The upper EPSE branch's $c_i > 0$ while the lower one's $c_i < 0$, as shown in Fig.1 (b). These two branches correspond to the unstable supersonic mode and the damped supersonic mode, respectively, which have different growth rates and are discussed by Mack (1987) [6]. It can be seen in Fig.1 (a) that in the vicinity of point S^-, the unstable supersonic mode of LST ceases to be a discrete mode, and a new mode emerges from the vicinity of point S^+. These two points are synchronization points of supersonic mode and acoustic waves [3]. However, the upper and the lower branches of EPSE both exist when they pass through the synchronization points. Comparing $c_r - c_i$ curves between EPSE and LST in Fig. 1(b), it can be clearly observed that the upper branch of EPSE crosses the slow acoustic branch cut at the point E^-, which is far away from S^-. The lower branch of EPSE passes below the slow acoustic branch point in the complex plane. Therefore, the growth rates of these two EPSE branches are continuous through the synchronization points, which indicates that the unstable supersonic mode can cross the branch cut of slow acoustic waves continuously.

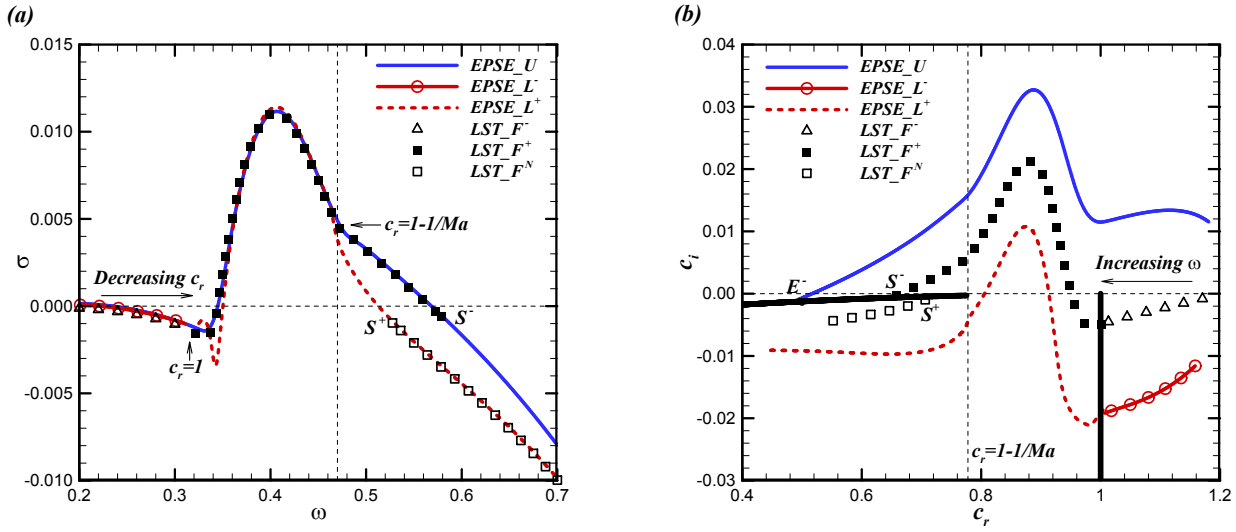

Figure 1. (a) Spatial growth rates. (b) Map of real and imaginary parts of phase speeds in the complex plane, Solid black lines correspond to the continuous spectra.

CONCLUSIONS

The synchronism of discrete mode with continuous spectrum leads to a discontinuity in discrete modes, and this causes difficulties in stability analyses using the traditional local stability analysis method, based on the quasi-parallel flow assumption. In this study, non-parallel effects on the coalescence between discrete mode and continuous spectrum was investigated by EPSE method. The results indicate that fast mode can keep continuous when it crosses the branch cuts of vorticity/entropy waves of the continuous spectrum, i.e., the fast mode is a normal mode of discrete spectrum. In highly cooled hypervelocity boundary layers, the unstable supersonic mode can cross the branch cuts of slow acoustic waves continuously. The coalescence between discrete modes and continuous spectra can be avoided accounting for the non-parallel effects of the boundary layers. This may be helpful for the stability analyses and receptivity studies.

Acknowledgement

This work was supported by the National Natural Science Foundation of China (11332007), the Tianjin Natural Science Foundation (15JCYBJC19500).

References

[1] Fedorov A V., Khokhlov A P.: Prehistory of instability in a hypersonic boundary layer. *Theoret. Comput. Fluid Dynamics* **14**: 359~375, 2001.

[2] Fedorov A, Tumin A.: Initial-value problem for hypersonic boundary-layer flows. *AIAA journal* **41(3)**: 379-389, 2003.

[3] Bitter N P, Shepherd J E.: Stability of highly cooled hypervelocity boundary layers. *Journal of Fluid Mechanics* **778**: 586-620, 2015.

[4] Fedorov A V.: Transition and stability of high-speed boundary layers. *Annu. Rev. Fluid Mech* **43**: 79~95, 2011.

[5] Yu G, Gao J, Luo J.: Stability analysis method considering non-parallelism: EPSE method and its application. *Applied Mathematics and Mechanics* **37(1)**: 27-36, 2016.

[6] Mack L M.: Review of linear compressible stability theory. Stability of time dependent and spatially varying flows. Springer New York, 164-187, 1987.

A NEW MODEL FOR THE TWO-FLUID LAMINAR CLASSICAL WAKE

Ashleigh Jane Hutchinson*[1]

[1]*School of Computer Science and Applied Mathematics, University of the Witwatersrand, Johannesburg, South Africa*

Summary Existing models for two-fluid laminar wakes fail to incorporate the effect of the boundary layer that is formed between parallel streams with different velocities in their analysis. In this work, the impact of the boundary layer formed by two parallel streams flowing at different velocities past a fixed obstruction is considered. The presence of the body perturbs the boundary layer flow. A model detailing this scenario is developed and the results are compared with existing models. In particular, the limit in which a lighter fluid flows on top of another stationary fluid with a much higher density so that the no-slip condition is approximately satisfied, is studied. This important case is related to wall-wake flows which have been thoroughly researched thus providing a reasonably sound platform for comparative observation.

INTRODUCTION

A study on laminar two-fluid wake flows has been undertaken by Herczynski, Weidman and Burde [1]. In this inspiring work, similarity solutions are derived for both the two-fluid classical wake and the wake of a self-propelled body for laminar flows. The formation of a boundary layer between the two streams of fluid was not incorporated in this model because it was assumed that the streams have the same mainstream speed. Generally, a boundary layer forms between parallel streams of different densities and viscosities as described in the work by Lock [2]. Hunt developed a model for laminar wakes behind obstacles in a boundary layer [3]. These wakes, which are called 'wall-wakes', are formed by an obstruction situated on a boundary wall. The wall occupies the entire lower half of the plane and the fluid sticks to its boundary. The obstruction perturbs the flow in the boundary layer.

The purpose of this work is to modify the existing model for the two-fluid laminar classical wake by including the effects of the boundary layer formed by the two fluids flowing at different speeds. In the limit where the lower fluid is stationary and has a significantly larger density, the no-slip condition is satisfied and a wall-wake develops. This special case is then compared to the wall-wake model formulated by Hunt [3]. The situation where the two-fluids are flowing at the same speed will also be investigated and compared to the work in [1].

MATHEMATICAL MODEL

Consider a planar two-dimensional two-fluid classical wake as illustrated in Figure 1. A fluid with density ρ_1 and viscosity μ_1 initially occupies the top half of the plane. A fluid of density ρ_2 and viscosity μ_2 initially occupies the bottom half of the plane. The two fluids are immiscible and have mainstream speeds of U_{10} and U_{20} respectively. The fluids flow past a thin symmetric planar body aligned with the mainstream flow. The origin of the Cartesian coordinate system (x, y) is located at a point on the trailing edge of the body. Define δ_1 and δ_2 to be the outer boundary layer widths of the top and bottom fluids respectively in the undisturbed boundary layer flow. The effective half-widths of the top and bottom halves of the wake are denoted by h_1 and h_2. We assume that $max(h_1, h_2) \ll max(\delta_1, \delta_2)$ so that the wake is confined within a small region in the outer boundary layer. The position of the unknown interface is at $y = \phi(x)$. The far-wake is divided into three regions: the wake region (C) in which viscosity effects are important; the external flow or disturbed flow region (B) where viscosity effects are negligible; and the mainstream flow region (A) where the disturbed flow returns to its upstream flow configuration. The equations in the wake region will be derived. Matching conditions with region (B) will be required. The suffix $i = 1$ will refer to the top fluid and the suffix $i = 2$ will refer to the bottom fluid.

The variables (U_i, V_i, P_i) denote the velocities and pressure in the undisturbed boundary layer flow upstream of the body. Because the wake is confined within a small region in the outer boundary, the following simple shear flow assumption can be implemented:

$$U_i = \alpha_i(y + \beta_i), \quad V_i = 0, \quad i = 1,\ 2. \tag{1}$$

A similar assumption was made in [3] where $\beta_1 = 0$. In this current work the constants β_i will be related to the expression obtained in [2] for the flow speed at the interface of the fluids. In the wake region the flow variables are denoted by (u_i, v_i, p_i). The velocity deficit w_i is defined as follows:

$$u_i = U_i \circ\ w_i, \quad v_i = v_i, \quad i = 1,\ 2. \tag{2}$$

*Corresponding author. Email: hutchinson.ash@gmail.com

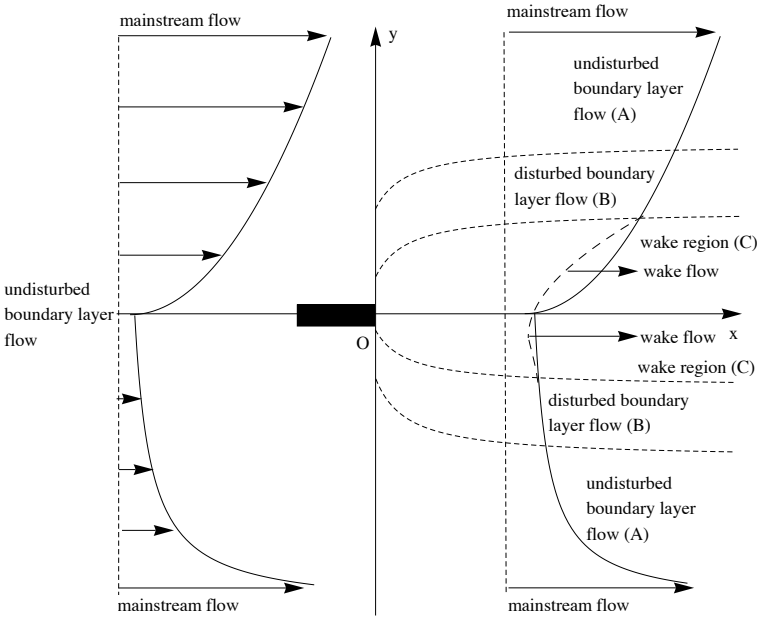

Figure 1: Two-fluid classical wake behind a thin symmetric planar body.

The pressure in the wake is determined by the flow in the disturbed flow region [3]. The dimensionless governing equations in the wake region are (for convenience the original notation is kept)

$$\left(\frac{\alpha_i}{\alpha_1}(y+\beta_i)\right)\frac{\partial w_i}{\partial x} \circ\ v_i\frac{\alpha_i}{\alpha_1} = \frac{\rho_1}{\rho_i}\frac{\partial p_i}{\partial x} + \frac{\nu_i}{\nu_1}\frac{\partial^2 w_i}{\partial y^2}, \qquad \frac{\rho_1}{\rho_i}\frac{\partial p_i}{\partial y} = 0, \qquad \circ\ \frac{\partial w_i}{\partial x} + \frac{\partial v_i}{\partial y} = 0, \quad i = 1,\ 2. \tag{3}$$

At the interface $y = \phi(x)$ the velocity components and the tangential and normal stresses must be continuous. In the wake region, the velocity deficit and its y derivative tend to zero as y approaches infinity. Any addition assumptions implemented by Lock [2] and Hunt [3] will be used if required. A conserved quantity can be obtained in each region.

RESULTS

The Lie symmetry associated with the conservation law that generates the conserved quantity will be derived and the invariant solution will be obtained. The results of this new model will be compared with existing models to establish its validity.

CONCLUSIONS

The model developed in this work generalises two-fluid wake flows to allow for fluids that are travelling at different speeds. It is consistent with existing models in certain limiting cases.

References

[1] Herczynski A, Weidman P D, Burde G I.: Two-fluid jets and wakes. Phys. Fluids 16 (2004) 1037-1048.

[2] Lock R C.: The velocity distribution in the laminar boundary layer between parallel streams. Quart. J. Mech. Appl. Math., Vol. IV, Pt. 1 (1951).

[3] Hunt J C R.: A theory for the laminar wake of a two-dimensional body in a boundary layer. J. Fluid Mech. 49 (1971) 159-178.

EFFECT OF CROSSFLOW VORTEX ON TS WAVE IN A FALKNER-SKAN-COOKE BOUNDARY LAYER

Zhenrong Jing[1], Lei Zhao[1] & Zhangfeng Huang [1, 2, a)]
[1] *Department of Mechanics, Tianjin University, Tianjin, China*
[2] *State Key Laboratory of Aerodynamics, CARDC, Mianyang Sichuan, China*

Summary Nonlinear Parabolic Stability Equation (NPSE) was applied to study the effect of Cross-Flow (CF) vortex on the evolution of Tollmien-Schlichting (TS) wave in a Falkner-Skan-Cooke (FSC) boundary layer. The basic flow is chosen such that unstable CF waves and unstable TS waves coexist. The growth of a relatively small TS wave ($A=10^{-5}$) is studied with the presence of CF vortices. Both the stationary CF vortices and travelling CF vortices have been investigated. It is found that the TS wave can be greatly boosted by CF vortices through Mean Flow Distortion (MFD) and nonlinear interaction.

MOTIVATION

Understanding the laminar-turbulent transition is crucial to the design of Natural Laminar Flow (NLF) wing. Four mechanisms leading to transition can occur on a typical swept wing, namely, attachment line stability, CF instability, TS instability and Görtler instability, among which CF instability and TS instability are the most commonly observed ones. Although each of the four mechanisms has been studied extensively for the last few decades, the study on interaction between each other is rather limited. Mueller et al (1981) [1] observed that both CF vortices and TS waves superimposed simultaneously on a spinning axisymmetric body. Runyan L J et al (1984) [2] calculated the N factors for swept wing boundary layer based on the flight test data obtained from F-111. Utilising Herbert's concept of secondary instability, Reed H L (1985) [2] showed that the growth of oblique TS waves can be magnified by the presence of CF vortices. Bassom A P and Hall P (1985) [4] found that the mean flow modification played the primary role in the influence of stationary CF vortices on TS waves using asymptotic theory. This paper aims to provide some the numerical results for the CF-TS interaction. Since CF instability is always amplified firstly on a swept wing, we focus on the influence of CF vortices on TS waves' evolution.

RESULTS

Mean flow used in present calculation is FSC similar solution, which is a prototype for swept wing boundary layer flow. Length and velocity are made dimensionless by displacement thickness and x-direction freestream velocity at reference station $x_0=200$, respectively. The swept angle at x_0 is 45 degrees and Reynolds number based on the displacement thickness at the inlet is equal to 4000. The Hartree parameter β_H describing the pressure gradient along the plate is set to 0.113 in order to ensure that both CF instability and TS instability occur simultaneously. It should be noted that the velocity is decomposed into potential flow and cross-flow direction at the reference station (referred as streamwise and spanwise hereafter) throughout the calculation.

Figure 1(a) shows the amplitude evolution of the CF stationary vertex, Mean Flow Distortion (MFD), and TS wave when both CF vortex and TS wave are introduced to the NPSE inlet, the evolution of a single TS wave in FSC boundary layer and the distorted mean flow. The spanwise wave number of the stationary CF vortices is 1.5 and the TS wave's frequency is 0.25. The MFD grows as the CF vortex is amplified and finally reaches as large as 0.1 at the outlet. In the presence of CF wave, the initial growth of the TS wave is unaffected until x=650, where MDF reaches an amplitude about 0.01, and the TS wave begins growing much stronger than a single TS evolving in FSC boundary layer. The final amplitude of the TS wave is two orders higher than that of the single TS case. The unstable range for the given TS wave is extended downstream from x=800 to x=850. The single TS wave evolves much closer to the CF and TS case in distorted mean flow than in FSC flow, but there is still a noticeable difference in the final amplitude, suggesting the nonlinear interaction between each other might also play a role in boosting the TS wave. Figure 1(b) gives the growth rate contour in β-ω plane for the FSC profile and distorted mean flow at x=750. The region around β=0 denotes TS instability and the region around ω=0 denotes CF instability. The unstable TS region is greatly expanded by MFD while the unstable CF region is narrowed.

Figure 2 is the same as Figure 1 except that a travelling CF vortex is introduced at the same time with the TS wave. The frequency of the CF vortex is 0.15. The growth of TS wave diverges from a single TS wave near x=850 where the MFD reaches the same amplitude 0.01. A new phenomenon is that the amplitude of TS wave finally overtakes that of CF vortices and maintains for a long distance, implying that TS wave might dominate the final transition stage. The effect of MFD on TS wave evolution shows the same trend as that of stationary CF vortex. However, unlike previous case, the unstable TS wave region and unstable CF wave region separate with each other when MFD is taken into account, and the unstable CF region is partly extended toward higher wave number region.

[a)] Corresponding author. Email: hzf@tju.edu.cn

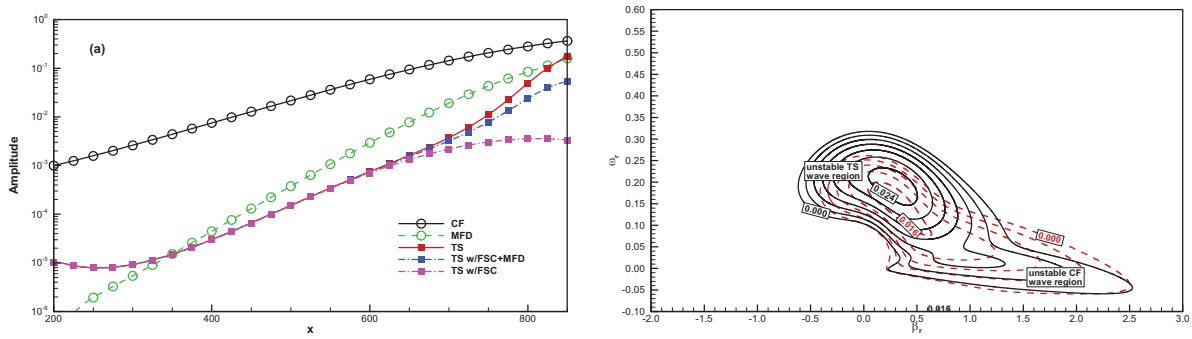

Figure 1 (a) Amplitude evolution curve for stationary CF vortex and TS wave. (b) Growth rates contour on β-ω plane at x=750 with a step size 0.004

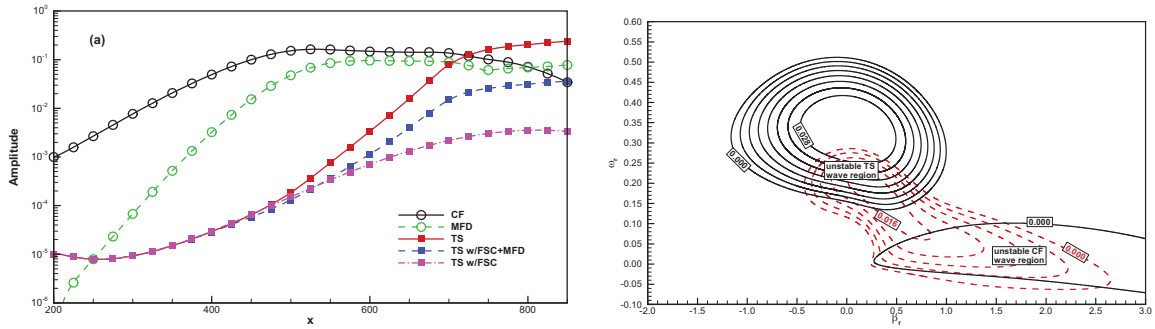

Figure 2 (a) Amplitude evolution curve for travelling CF vortex and TS wave. (b) Growth rates contour on β-ω plane at x=650 with a step size 0.004

CONCLUSIONS

This study provides some numerical results concerning the effect of CF vortices on the TS wave evolution. It is shown that the TS waves grow independently when CF vortices are small, but it can be greatly boosted by both stationary and travelling CF vortices once the mean flow distortion reaching an amplitude about 0.01. The TS waves' amplitude can overtake that of CF vortices in the travelling CF wave case, suggesting nonlinear interactions between them can play a role in transition. The interaction between them is mainly accomplished through the base flow modification, which changes the stability characteristic of TS waves. However, the nonlinear interaction between each other also increases the TS wave's growth rate and could not be neglected.

Acknowledgments This work was supported by the National Natural Science Foundation of China (11332007), the Tianjin Natural Science Foundation (15JCYBJC19500) and an open fund from the State Key Laboratory of Aerodynamics (SKLA201401).

References

[1] Mueller T J, Nelson R C, Kegelman J T, et al. Smoke visualization of boundary-layer transition on a spinning axisymmetric body. *AIAA Journal*, 1981, 19(12): 1607-1608.

[2] Runyan L J, Navran B H, Rozendaal R A. F-111 natural laminar flow glove flight test data analysis and boundary layer stability analysis. *NASA Contractor Report.* 1984.

[3] Reed H L. An analysis of wave interactions in swept-wing flows. *Laminar-Turbulent Transition*. Springer Berlin Heidelberg, 1985: 471-478.

[4] Bassom A P, Hall P. On the interaction of stationary crossflow vortices and Tollmien-Schlichting waves in the boundary layer on a rotating disc. *Proceedings of the Royal Society of London A: Mathematical, Physical and Engineering Sciences*. The Royal Society, 1990, 430(1878): 25-55.

MULTIPLE FAMILIES OF SOLUTIONS OF SECONDARY INSTABILITIES IN HYPERSONIC FLOWS

Jianxin Liu[1] and Jisheng Luo *[1]
[1]*Department of Mechanics, Tianjin University, Tianjin, China*

Summary The secondary instability was investigated in a Mach 4 flat-plate boundary layer with second mode primary disturbances by numerical methodology. A new family called fundamental family of solutions was found which is the least stable secondary instability when the amplitude of the primary mode instability reaches a threshold value such as 0.1. It is help for us to understand the fundamental breakdown in hypersonic boundary layers.

MOTIVATION

The secondary instability mechanism is very important to the natural transition process dominated by streamwise instabilities in boundary layers. Generally, the subharmonic secondary instability is considered as the least stable disturbance. Herbert's results[1] in an incompressible and Ng's[2] in an compressible flow support this viewpoint. However, recent work [3][4] observed that the fundamental secondary mode is the least stable one in boundary layers, such as . And the fundamental (K-type) breakdown also was observed by the DNS[5]. It means that there is a gap between the recent results and the traditional viewpoint. For this aim, the secondary instability was investigated with a second mode primary instability in a Mach=4 flat-plate boundary layer.

RESULTS

The base flow can be written as $U(x,y,z) = U_b(y) + A\hat{u}(y)e^{i(\alpha x-\omega t)}$. With introducing a new coordinate system $\tilde{x} = x - c_r t, \tilde{y} = y, \tilde{z} = z$, the secondary disturbance can be written as $\tilde{q}_2 = e^{\sigma t}e^{i\beta\tilde{z}}e^{i\epsilon\tilde{\alpha}\tilde{x}}\sum_{j=-\infty}^{\infty}\hat{q}_{2,j}(y)e^{ij\tilde{\alpha}x}$. Here, ϵ is a detuning parameter. When $\epsilon = 0.5$, the secondary waves are called subharmonic modes; when $\epsilon = 0$, they are called fundamental modes. The equations are a complex eigenvalue problem $L\phi = 0$. For a given spanwise wavenumber β, the unknown complex eigenvalue σ describes the instability of the secondary disturbance. More detailed description of the secondary instability theory can be found in Ref. [2].

The investigations were performed in a Mach=4.5 flat-plate boundary layer. The parameters can be found in Ref. [2]. The primary mode is the Mack mode; the amplitude A is defined by the temperature perturbance and it is called A_T. The secondary instability is the subharmonic mode. The secondary stability analysis tool was validated by comparing to the results in Ref. [2].

Figure 1 and Fig. 2 show the detuning parameter ϵ versus the secondary growth rates σ_r and the frequency shifts σ_i of the secondary disturbance respectively. It can be seen that: (1) the least stable secondary disturbance is subharmonic. (2) there is a new unstable fundamental solution which is not found in Ref. [2].(3) the family of solutions of the least stable subharmonic secondary disturbance is different from the one of fundamental mode. (4) the frequency shifts of the least stable subharmonic and fundamental secondary disturbance are both zero, i.e. the phase velocity of these least stable subharmonic and fundamental modes are equal to the one of the second mode primary instability.

The new fundamental mode was investigated with different parameters. Figure 3 plots the spanwise wavenumber versus the secondary growth rates with different amplitudes of the second mode primary instability. It can be seen that the range of the unstable fundamental mode disturbances also becomes wider and wider with the amplitude of the primary mode instability increasing. However, it is very different from the subharmonic mode discussed above that the spanwise wavenumbers of the least stable fundamental mode instabilities also become larger. It should, however, be noted that the nonlinear effect is ignored in our analysis when the amplitude A is large enough. It will make the growth rate a little different from the real value.

Then, the secondary instability was also investigated accounting for the nonlinear effect. For this aim, the base flows of the secondary instability here were obtained by the nonlinear parabolic stability equations(NPSE). The amplitude here called A_u is defined by the amplitude of the streamwise velocity perturbance. Figure 4 plots the detuning parameter ϵ versus secondary growth rates at $A = 0.1$. It can be seen that the least stable secondary instability is the fundamental one rather than the subharmonic one as the amplitude of the primary mode instability is large enough. It means that the fundamental secondary mode instability may have a larger amplitude in some case and will lead to a "fundamental breakdown" as Fasel's results**??**. In addition, the least harmonic secondary mode instability is also another family.

*Corresponding author. Email: jsluo@tju.edu.cn

DISCUSSION AND CONCLUSION

The secondary instability was investigated with a second mode primary mode instability in a Ma=4.5 flat-plate boundary layer. The results suggest that there are two families of solutions in the boundary layers which lead to the unstable secondary instability. One of them was not found in the past research. The least stable fundamental secondary mode instability is from this new family of solutions (called fundamental family). On the contrary, the least stable subharmonic secondary mode instability is another family of solutions (subharmonic family). This feature is very different from that in a incompressible boundary layer. The amplitude of the second mode primary instability is a important to the secondary instability in a hypersonic boundary. When it is small, the least stable secondary instability in the flow is from the subharmonic family. However, when the amplitude is large enough, the fundamental secondary mode instability becomes the least unstable one. This work fill the gap of the past research.

In conclusion, the dominant family of solutions has a very direct relationship with the amplitude of the primary mode. Future work will concentrate on the primary mode effect on the secondary instability accounting for the nonlinear process in a real hypersonic boundary layer.

Acknowledgements This study is supported by the National Natural Science Foundation of China (Nos. 11332007 and 11402167)

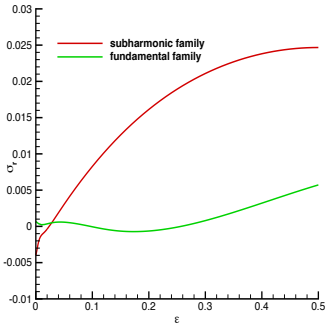

Figure 1: the detuning parameter ϵ vs. the secondary growth rates σ_r at $A_T = 0.06$.

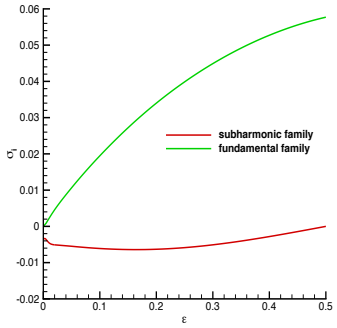

Figure 2: the detuning parameter ϵ vs. the frequency shifts σ_i at $A_T = 0.06$.

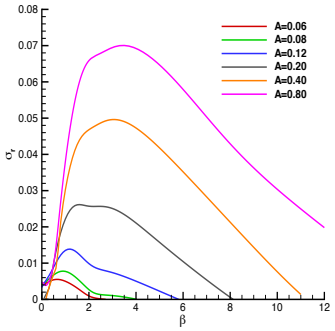

Figure 3: β vs. σ_r with different amplitude A_T of the primary mode, fundamental family.

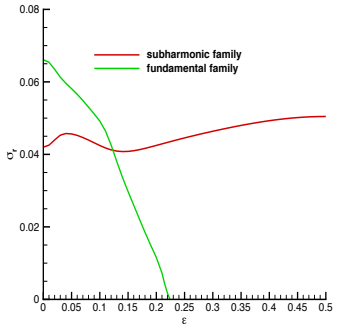

Figure 4: the detuning parameter ϵ versus secondary growth rates at $A_u = 0.1$.

References

[1] Herbert T.: Secondary Instability of Boundary layers. Annual Review of Fluid Mechanics 20(1):487-526, 1988.
[2] Ng L. L., Erlebacher G.: Secondary Instabilities in Compressible Boundary layers. Physic of Fluids A 4:710-726, 1992.
[3] Li F., Choudhari M., Chang C-L., et al.: Secondary Instability of Second Mode Disturbances in Hypersonic Boundary layers. NASA report: NF1676L-13407.
[4] Yu M., Luo J-S.:Nonlineawr evolution of Klebanoff type second mode disturbances in supersonic flat-plate boundary layer. Appl. Math. Mech. -Engl. Ed. 35(3):359-368, 2014
[5] Sivasubramanian J., Fesel H.F.: Direct numerical simulation of transition in sharp cone boundary layer at Mach 6: fundamental breakdown. J. Fluid Mech. 768: 175-218, 2015.

TENTATIVE EXPLANATION OF THE MECHANISM OF NOISE REDUCTION FOR TRAILING EDGE WITH CHEVRON

Caihong Su
Department of Mechanics, Tianjin University, Tianjin, China

Summary Recently, chevron appears at the trailing edge of commercial aircraft jet engines, for example, jet engine of Boeing 787. It is believed to be for the noise reduction. So far, there is no theoretical explanations for its mechanism in published literatures, though there were papers for this purpose for the serration appeared at the jet exit. In this paper, a simplified model is proposed, to explore the possible cause of the noise reduction by chevron at the trailing edge of commercial aircraft jet engines.

INTRODUCTION

Aircraft noise is an important issue, especially for commercial aircraft. Jet engine exhaust is one of the main sources during airplane take-off. One of the measure for noise reduction appears very recently is the use of chevron at the downstream end of the engine housing. According to experimental measurements, nearly 3dB of noise reduction during take-off can be achieved while only less than 0.5% thrust could be lost during cruise[1]. The first attention has been received on application level in mid 1990s. However, the understanding of the physical mechanism behind and the impact of chevrons on noise reduction still remains incomplete[2]. To date, the most popular explanation of its cause is that chevrons generate stream-wise vortices which enhance jet mixing, leading to the reduction of the amplitude of large scale structures in the flow field, and thus reducing the noise. However, they were mostly aiming at the case of chevron with sharp saw-tooth. For smooth chevron as appeared on engines of Boeing 787, there could be another different mechanism. We believe that the existence of chevron may well change the stability characteristics of the mean flow downstream of the engine, so that the amplification rate of large scale vortices, which plays the dominant role of generating noise, may be significantly reduced. In this paper, a simplified model is proposed to show how it works.

COMPUTATIONAL MODEL AND METHODS

For a real engine, the shear layer downstream of the engine is axis-symmetric. To simplify the computation and analysis, we consider a plane shear layer instead, which is formed downstream of an infinitely thin flat plate splitting two oncoming streams with Mach numbers 0.3 and 0.35 respectively. The length of the flat plate is assumed to be 2m, the average of the two oncoming flow velocities and other oncoming flow quantities are used to nondimensionalize the respective quantities. The Reynolds number so defined is 1.8×10^4. The oncoming temperture is 281.7K. The flow is assumed to be an ideal gas and the viscosity coefficient is comupted using Sutherland's law.

The governing equations are compressible unsteady Navier-Stokes equations. A 5th order upwind and a 6th order central scheme are used to discretize the split nonlinear term and viscous term respectively. The 3rd order Runge-Kutta scheme is used for the time advancing. The computational domain starts from the trailing edge of the flat plate and extends far downstream. Grid points are clustered in the vicinity of trailing edge to make sure the required resolution can be achieved. In the wall-normal direction, mesh grids are stretched gradually from the wall towards the upper and lower boundaries. The wall is non-slip and isothermal whose temperatures on both sides are set to be 284K. The Blasius profiles are maintained at the inlet of the computational domain and sponge zones combined with characteristic boundary conditions are used for the top, bottom and outflow boundaries. For 3D cases periodic condition is used in the spanwise direction.

RESULTS AND DISCUSSIONS

1. DNS: Generation of unsteady vortex

Unsteady vortex is found to appear starting from some distance downstream of the trailing edge as shown in Fig.1. Fourier analysis is performed for time squences of transverse velocities at three locations at the centerline. As shown in Fig.2(a), at x=0.002, very close to the trailing edge which locates at (0,0), the component with frequency 6~7Hz dominates. Downstream at x=0.06, another peak with frequency 23~24Hz emerges. This component overtakes the one with lower frequency and then plays a dominant role throughout the downstream region. The harmonic wave can also be observed.

2. Linear stability analysis: wake mode and shear layer mode

Spatial linear stability analysis is performed to search for the most unstable modes. In reality the flow is turbulence. However, since the profile of the basic flow has inflection points, so at least at the initial stage, inviscid instability plays the major role while the turbulence plays only a secondary role. So here we can ignore the turbulence as the first step. Two types of unstable modes, that is, wake mode and shear layer mode are identified as shown in Fig.3. Fig.4(a), (b) shows the variations of frequency and the growth rate respectively for the most unstable modes along x. We can see that at x=0.06 the

Corresponding author. Email: su_ch@tju.edu.cn.

frequencies for the most unstable wave mode and shear layer mode are 6.67 and 23.4 respectively, which are in very good agreement with what we observed in DNS. And the shear layer mode has much bigger growth rate so that it overtakes the wake mode and plays a dominant role further downstream.

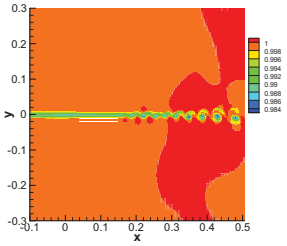

Fig.1. Density contour at t=24.

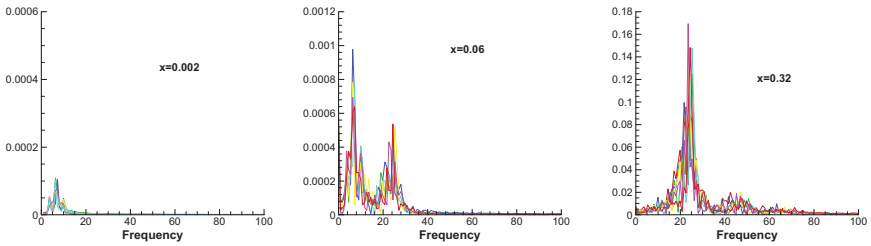

Fig.2 Amplitude of Fourier components versus frequency (different colored lines refer to different time periods Fourier tranform performed): (a)x=0.002, (b) x=0.06, (c) x=0.49.

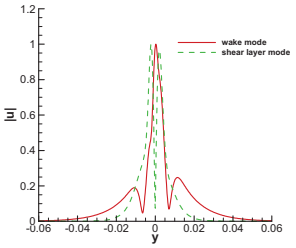

Fig.3 Eigenfunctions of streamwise velocity at x=0.06.

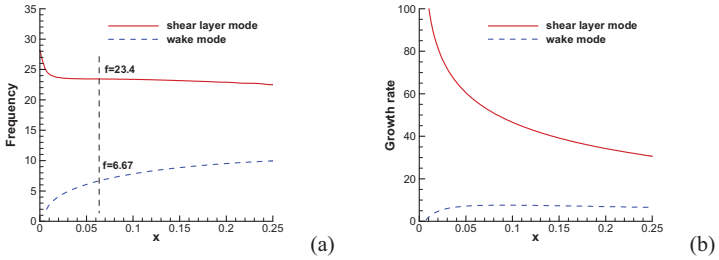

Fig.4 The most unstable wave. (a) frequency, (b) growth rate.

3. Preliminary results with chevron

We consider one chevron with a sinuous shape shown in Fig.5. Since the streamwise velocity is much bigger than the other velocity components, the initial baseflow is approximated by the mean flow we have got without chevron, but with its origin shifted in x direction according to the curve of the chevron. The inlet of the computational domain is shown in Fig.5 and its profiles are maintained during computation. Similarly, we performed Fourier transform for time sequencs of transverse velocity at (0.1,0) for several spanwise positions. And compare the result with the 2D case as shown in Fig.7. It can be seen that the existence of chevron reduces the amplitude of the dominant component. Also a temporal DNS at a given x is performed to search for the most unstable mode to compare its growth rate with its 2D counterpart. It shows that the growth rate also drops. More in-depth work is under way.

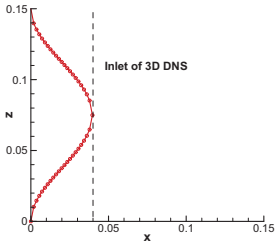

Fig.5 Shape of chevron

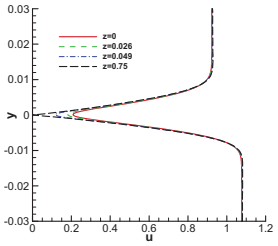

Fig.6 Profiles at inlet

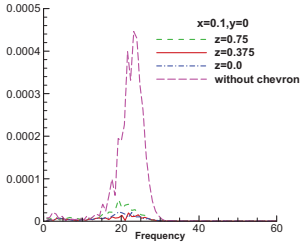

Fig.7 Fourier components for cases with/without chevron

CONCLUSIONS

Vortex roll-up appears whose frequency is actually chosen by the stability characteristics of the mean flow. For the case with chevron, the dominant unstable mode is found to be less unstable compared with the case without chevron, which may just be the cause of noise reduction.

References

[1] Xia H., Tucker P.G. and Eastwood S.: Large-eddy simulations of chevron jet flows with noise predictions. *International Journal of Heat and Fluid Flow*, 30(6):1067-1079, 2009.

[2] Bridges J., Brown C.A.: Parametric testing of chevrons on single flow hot jets. *AIAA paper 2824*, 2004.

EFFECT OF A 3D SURFACE INDENTATION ON BOUNDARY LAYER STABILITY

Hui Xu*[1], Shahid Mughal[1], and Spencer J. Sherwin[2]
[1]*Department of Mathematics, Imperial College London, 180 Queens gate, London, SW7 2AZ, UK*
[2]*Department of Aeronautics, Imperial College London, 180 Queens gate, London, SW7 2AZ, UK*

Summary Effect of a three-dimensional (3D) surface indentation on boundary layer stability is studied in a high Reynolds number (Re) regime. Once the Tollmien-Schlichting (TS) wave undergoes a base flow (with/without a separation flow bubble) distorted by a 3D surface indentation, the growth rate of the TS wave can be changed downstream and some interesting properties from the 3D indentation distortion are observed. It is also found that under suitable indentation geometry parameters, it is observed that a global instability can be triggered, which has a strong impact on boundary layer transition. In this paper, these instabilities are investigated and effect of a 3D surface indentation is elucidated.

In a boundary layer, the primary unstable mode is a Tollmien-Schlichting (TS) wave which is a viscous instability. The TS wave is receptive to surface roughness interacting with free stream disturbances and/or surface vibrations. Once the excited TS wave propagates downstream and experiences a base flow distortion which is generated by a surface indentation, the growth properties (energizing or weakening) of the TS wave can be changed. These properties are significantly influenced by 3D effect of a base flow distortion. When a 3D separation flow bubble appears, 3D effect of the separation flow bubble on the TS wave varies with respect to indentation geometry parameters, which is remarkably different from that of a 2D separation flow bubble. This difference has a strong impact on the growth properties of the TS wave. Generally, the boundary layer transition onset is prompted. Meanwhile, under suitable indentation geometry parameters, it is observed that a global instability can be triggered, which also has a strong impact on boundary layer stability. In this paper, these instabilities are conducted and effect of a 3D surface indentation is elucidated. The linear analyses of the TS wave growth properties are investigated by the parabolic stability equations (PSE) and the triglobal stability is done by the time-stepper-based Arnoldi algorithm. Finally, a DNS calculation is implemented to simulate the boundary layer transition.

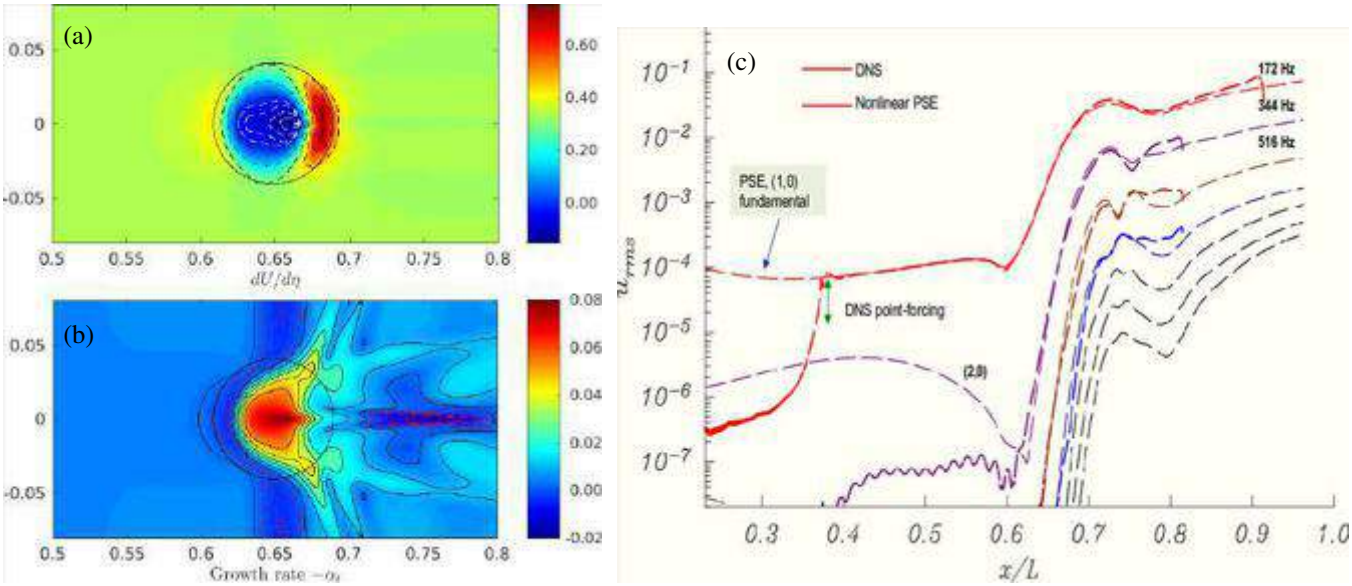

Figure 1: Wall shear (a), the growth rate (b) of the TollmienSchlichting wave and harmonics calculated by nonlinear PSE (c).

References

[1] Herbert T.: Parabolized stability equations. Annu. Rev. Fluid Mech. 29: 245-283, 1997.
[2] Theofilis V.: Global linear instability. Annu. Rev. Fluid Mech. 43: 319-52, 2011.
[3] Xu H., Sherwin. S. J., Hall P., Wu X.: The behaviour of Tollmien-Schlichting waves undergoing small-scale localised distortions, J. Fluid Mech., to appear, 2016.
[4] Wu X. S., Hogg Linda W.: Acoustic radiation of Tollmien-Schlichting waves as they undergo rapid distortion. J. Fluid Mech. 550: 307347, 2006.
[5] Newman D. J., Karniadakis G.: A direct numerical simulation study of flow past a freely vibrating cable. J. Fluid Mech. 344: 95-136, 1997.
[6] Darekar R., Sherwin S. J.: Flow past a square-section cylinder with a wavy stagnation face. J. Fluid. Mech. 426: 263-295, 2001.
[7] Gao B., Park D. H., Park S. O.: Stability analysis of a boundary layer over a hump using parabolized stability equations. Fluid Dyn. Res. 43: 055503, 2011.

*Corresponding author. Email: hui.xu@imperial.ac.uk

REYNOLDS-NUMBER UNIVERSALITY OF QUASI-STEADY QUASI-HOMOGENEOUS THEORY

Chi Zhang [*1] and Sergei Chernyshenko[1]

[1]*Department of Aeronautics, Imperial College London, London, UK*

Summary A rigorous formal statement of the hypothesis of quasi-steady and quasi-homogeneous (QSQH) nature of the scale interaction in the near-wall part of a turbulent boundary layer is proposed. This makes the corresponding derivations easier. Multi-objective optimisation is applied to determine the cut-offs for the large-scale filter, which gave better results than the filters based on the known suggestions for the cut-offs. Comparisons for a set of statistical characteristics obtained from the databases of direct numerical simulations of a plane channel flow were performed. It was observed that the accuracy of the predictions based on the QSQH hypothesis improve as the Reynolds number increases. The next step will be testing extrapolation from medium to high Reynolds numbers based on the QSQH approach.

Obtaining the flow properties in a near-wall turbulent boundary layer at high-Re is always a challenge due to insufficient computing power and imprecise experimental devices. Recently, distinctive alterations to near-wall turbulence by outer large-scale structures have been observed and confirmed in many experimental and numerical studies, see for example [1] and references therein. Marusic *et al.* [1] proposed an empirical model, described by the expression:

$$u'^{+}(y^{+}) = \alpha_u(y^{+})u'_{OL} + \left(1 + \beta_u(y^{+})u'_{OL}\right) u^{*}_{\mathrm{MHM}}(t^{+}, x^{+}, y^{+}, z^{+}), \tag{1}$$

where $\alpha_u(y^+)$ and $\beta_u(y^+)$ are universal Re-independent functions found empirically, prime denotes fluctuations, and the subscript OL marks the large-scale filtered velocity measured by a second probe located further away from the wall, as illustrated by Fig. 1(a). One can measure (or calculate) $u'^{+}(y^+)$ and u'_{OL} at a moderate Re and determine the statistical properties of $u^{*}_{\mathrm{MHM}}(t^+, x^+, y^+, z^+)$, which are expected to be Re-independent. This makes it possible to measure only u'_{OL} in the high-Re regime and determine the statistical properties of $u'^{+}(y^+)$ from (1). However, since the statistical properties of u'_{OL} depend on Re, (1) with Re-independent α_u, β_u and u^{*}_{MHM} is not compatible with the classical idea of universality of near-wall turbulence, according to which

$$u = \bar{u}_\tau u^{*}(t^{+}, x^{+}, y^{+}, z^{+}) \tag{2}$$

with Re-independent statistical properties of u^*. To resolve this, Chernyshenko *et al.* [2] proposed to replace (2) with

$$u = u_{\tau_L}(t, x, z)\tilde{u}\left(\frac{tu^2_{\tau_L}}{\nu}, \frac{xu_{\tau_L}}{\nu}, \frac{yu_{\tau_L}}{\nu}, \frac{zu_{\tau_L}}{\nu}\right), \tag{3}$$

where $u_{\tau_L}(t, x, z)$ is the large-scale-filtered friction velocity. This amounts to replacing the friction velocity $\bar{u}_\tau$ with $u_{\tau_L}(t, x, z)$ in the definition of wall units. This can be justified by the the assumption that the effect of the large scales on the small scales is quasi-steady and quasi-homogeneous. Chernyshenko *et al.* [2] showed that (1) can be derived from (3) with an additional assumption that $u'_{\tau_L} \ll u_{\tau_L}$.

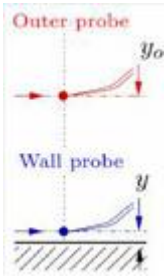

(a)

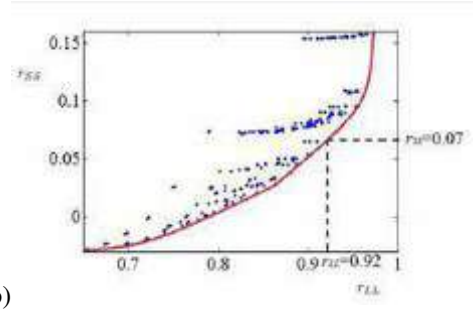

(b)

Figure 1: (a) Probe setup; (b) Pareto front of large-large and small-small correlation coefficients, where each point represent a combination of cut-off frequency and wave-numbers.

In fact, the QSQH hypothesis is a combination of two hypotheses, the first being that $u_{\tau_L}(t, x, z)$ and $\tilde{u}$ are statistically independent for a fixed Re, and the second hypothesis being that $\tilde{u}$ is independent of Re. We tested the first hypothesis by the comparisons between various statistical properties and their QSQH predictions for one value of Re. The cut-off parameters of the large-scale Fourier cut-off filter in the wave-number and/or frequency space were selected by multi-objective optimisation, with one objective being the correlation coefficient between the large-scale velocity at the outer probe placed at $y^+ = 100$

*Corresponding author. Email: c.zhang13@imperial.ac.uk

and the large scale velocity at the probe in close vicinity to the wall, and another objective being the correlation coefficient between the small-scale velocities at the same probes. Fig. 1(b) shows the Pareto front and the point we selected. We also extended the analysis for the $u'_{\tau_L} \ll u_{\tau_L}$ case by calculating the higher-order terms of the expansions. As a result, the first hypothesis was found to be satisfactory within 100 wall units from the wall. A paper describing the test of the first hypothesis is now under consideration.

An attempt to examine the second hypothesis was made on the basis of the data on $u_{\rm rms}$ available in the literature [3]. Extrapolating u_{rms} requires the value of $\langle {u'}^{+\,2}_{\tau_L} \rangle$, which is not available from [3]. Fortunately, the QSQH theory predicts that for $u'_{\tau_L} \ll u_{\tau_L}$ in the main term of the expansion

$$D = \frac{d}{dy} \log \left(u^2_{\rm rms}\big|_{\rm Re_1} - u^2_{\rm rms}\big|_{\rm Re_2} \right) \approx \frac{d}{dy} \log \left(U(y) + y \frac{dU}{dy} \right)^2 , \tag{4}$$

where $U(y)$ is the mean velocity. The comparison is given in Fig. 2(a). For the pair of higher Re values the agreement is quite satisfactory, but for the pair of smaller values it is not, even though the qualitative behavior is similar. This might be in line with the general idea that the applicability of the QSQH theory improves with Re increasing.

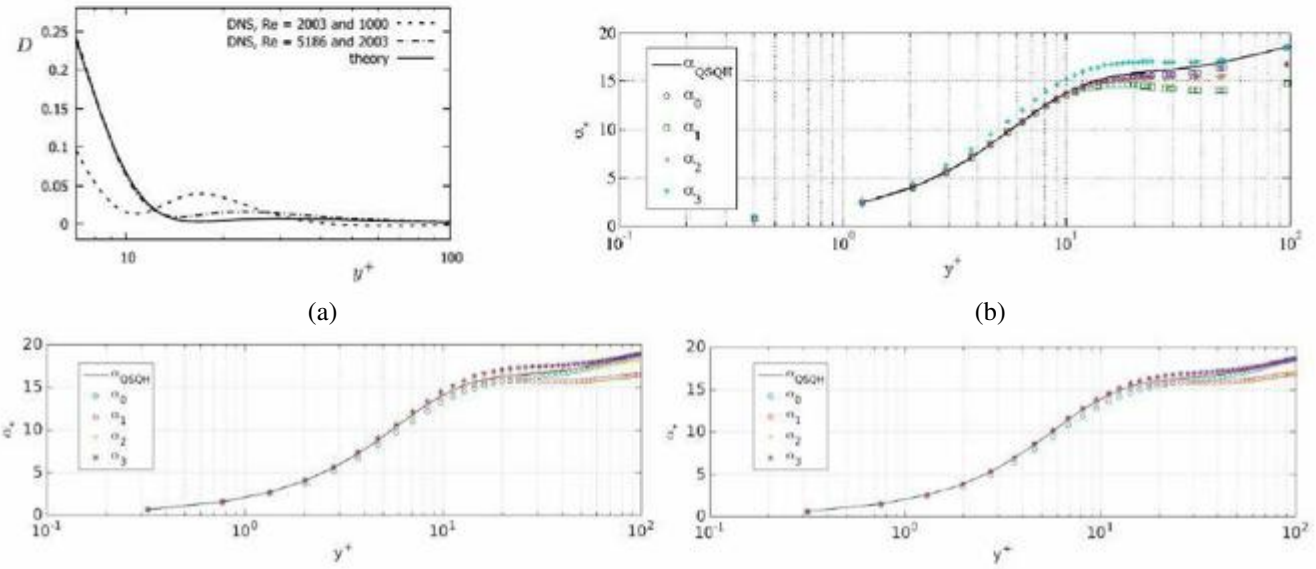

(a) (b) (c) (d)

Figure 2: Comparisons: (a) the logarithmic derivative of the increment with Re of the rms fluctuation velocity, the QSQH prediction (solid), the numerical data [3] for Re increasing from 1000 to 2003 (dashed) and from 2003 to 5186 (dot-dashed); (b–d) curves are the theory (5), points are α_0 (circle), α_1 (square), α_2 (plus), and α_3 (star), DNS data for $\mathrm{Re}_\tau = 1000$ (b), [4], and 2000 (c) and 4000 (d), [5].

Another examination on the second hypothesis was based on the DNS channel flow databases [4, 5] with Re_τ equal to 1000, 2000 and 4000. We derived that for four functions, $\alpha_0(y) = \langle {u'}_L(y) u'_L(y_{\rm o}) \rangle / \langle {u'}^2_L(y^2_{\rm o}) \rangle \left(U(y_{\rm o}) + y_{\rm o} \frac{dU}{dy_{\rm o}} \right)$, $\alpha_1(y) = \langle {u'}^+_{\tau_L} u'_L(y) \rangle / \langle {u'}^{+\,2}_{\tau_L} \rangle$, $\alpha_2(y) = \sqrt{\langle {u'_L}^2(y) \rangle / \langle {u'}^{+\,2}_{\tau_L} \rangle}$, and $\alpha_3(y) = \sqrt{\langle {u'_L}^2(y) \rangle / \langle {u'_L}^2(y_{\rm o}) \rangle} \left(U(y_{\rm o}) + y_{\rm o} \frac{dU}{dy_{\rm o}} \right)$ the higher-order terms of the expansion in ${u'}^+_{\tau_L}$ are negligible, and the linearized QSQH theory gives the same expression

$$\alpha_0(y) \approx \alpha_1(y) \approx \alpha_2(y) \approx \alpha_3(y) \approx U(y) + y \frac{dU}{dy}. \tag{5}$$

As shown in Fig. 2, the accuracy of QSQH predictions improves with increasing Re.

In a reasonably short term we hope to provide the procedure of extrapolating arbitrary statistical characteristics of near-wall turbulence from medium to higher Re using the QSQH theory. This procedure will also be reported.

[1] I. Marusic, R. Mathis, and N. Hutchins. Predictive model for wall-bounded turbulent flow. *Science*, 329 (5988):193–196, 2010.

[2] S. Chernyshenko, I. Marusic, and R. Mathis. Quasi-steady description of modulation effects in wall turbulence, 2012. arXiv:1203.3714.

[3] M. Lee and R. D. Moser. Direct numerical simulation of turbulent channel flow up to Re$_\tau$=5200. *J. Fluid Mech.*, 774:395–415, 2015.

[4] L. Agostini, E. Touber, and M.A. Leschziner. Spanwise oscillatory wall motion in channel flow: drag-reduction mechanisms inferred from DNS-predicted phase-wise property variations at Re-tau=1000. *J. Fluid Mech.*, 743:606–635, 2014.

[5] A. Lozano-Durán and J. Jiménez. Effect of the computational domain on direct simulations of turbulent channels up to Reτ= 4200. *Physics of Fluids (1994-present)*, 26(1):011702, 2014.

NONLINEAR INTERACTION OF THE FIRST MODE WITH THE SECOND MODE

Cunbo Zhang and Jisheng Luo *
Department of Mechanics, Tianjin University, Tianjin, China

Summary The evolution of the second mode and the first mode was investigated using Parabolized Stability Equations (PSE) in Ma=6.0 flat-plate boundary layers. It is found that the growth of the first mode disturbance is significantly promoted by the nonlinear interaction of the first mode disturbance, the second mode disturbance and a forced wave with the difference frequency. Enhanced by the nonlinear interaction, the first mode is likely to play an important role in the transition of hypersonic boundary layers.

INTRODUCTION

Boundary layer transition has import implications for the aerodynamic design of hypersonic flight vehicles. According to Linear Stability Theory (LST), there are multiple instability modes in hypersonic boundary layers. In recent years, many researches has focused on the second mode (Mack mode) for its higher amplification rates. Sivasubramanian&Fasel (2014) [1] numerically simulated a sharp cone boundary layer at Mach 6. They attributed the transition to fundamental breakdown and oblique breakdown of the second mode instability. However, results from experiments (2003, 2008)[2, 3]suggested that the first mode may also play an import role. Hotwire data was analyzed by the bispectal analysis method, and the nonlinear interaction of the first and the second mode was identified in the hypersonic cone boundary layer transition process. Unfortunately the experimental results were very limited, and few numerical results are available accounting for the interaction of the first and the second mode instability. In this paper, a numerical simulation was performed in a Ma=6.0 flat-plate boundary layer to study the interaction of the first and the second mode instability, hoping to clarify the role of the first mode instability in the hypersonic boundary-layer transition.

MAIN RESULTS

The research was carried out in a Ma=6.0 flat-plate boundary layer using PSE. The free stream temperature is 80K and the wall temperature is 520K. The Reynolds Number based on the boundary layer displacement thickness is 2.0×10^4. At the inlet a 2D second mode disturbance $(3, 0)$ and a pair of first mode disturbances $(1, \pm 1)$ were introduced. Here mode (h, k) is defined with h as the multiple of the fundamental frequency ($\omega = 0.5$) and k as the multiple of fundamental spanwise wave number ($\beta = 1.0$) . DNS was also performed to validate the results, and perfect agreement was achieved, as shown in Fig. 1.

At first, both the second (3,0) and first mode (1,1) disturbance evolve linearly. At about $x = 200$, near the second mode disturbance's neutral point, the second mode reaches its peak amplitude(about 7% of the freestream velocity) and then decays. In this area, the amplification of the first mode is firstly suppressed, and then significantly promoted by nonlinear effects. As a result, the first mode disturbance overtakes the second mode. Further downstream, the stationary vortex (0,2) grows to be the dominate mode, a characteristic of the first mode oblique breakdown[4]. At $x = 330$ the skin friction coefficient rises steeply and reaches the turbulent estimate value close to the end of the computational domains, suggesting that the boundary layer transition is triggered.

It is different from the previous research that both the second mode and first mode participate in the nonlinear process. The crucial part in the process is that the first mode is promoted by its nonlinear interaction with the second mode. This is confirmed by conducting an extra calculation, in which only the first mode, the second mode, and a forced wave with the difference frequency were reserved and the second mode was forced according to the previous results. As shown in Fig. 2,the interaction of the wave triad promotes the first mode disturbance $(1, 1)$ significantly. The nonlinear process includes two steps and is illustrated bellow by equation 1. It is noted that the nonlinear process is similar to the interaction of phase-locked modes theoretically derived by Wu et al.[5] in incompressible boundary layers.

$$(3, 1) - (1, 1) \rightarrow (2, -1); (3, 0) - (2, -1) \rightarrow (1, 1) \tag{1}$$

Two additional calculations were performed which corresponded to the fundamental resonance (FR) and subharmonic resonance (SR) of the second mode respectively. In these simulations, the 2D second mode disturbance is the same as the above case and the spanwise wave number of the oblique waves corresponding the largest secondary growth rate was selected. Based to skin friction coefficient shown in Fig. 3, for the subharmonic resonance (SR) case $x = 460$ is the possible transition location, and for the fundamental resonance (FR) case the possible transition location is $x = 320$. For nonlinear interaction of the first and the second mode discussed above in this paper, the transition location is $x = 330$, much earlier than the subharmonic resonance case and almost the same as the fundamental resonance case. This indicates that the nonlinear interaction of the first mode and the second is likely to play a role in the process of hypersonic boundary layers.

*Corresponding author. Email: jsluo@tju.edu.cn

CONCLUSIONS

The interaction of the first mode and the second mode was studied in this paper. It is identified that the amplification of the first mode will be greatly enhanced by the nonlinear interaction of a wave triad consisting of a second mode disturbance, a first mode disturbance and a forced wave with the difference frequency. The nonlinear interaction makes the first mode more likely to play an important role in hypersonic boundary-layer transition.

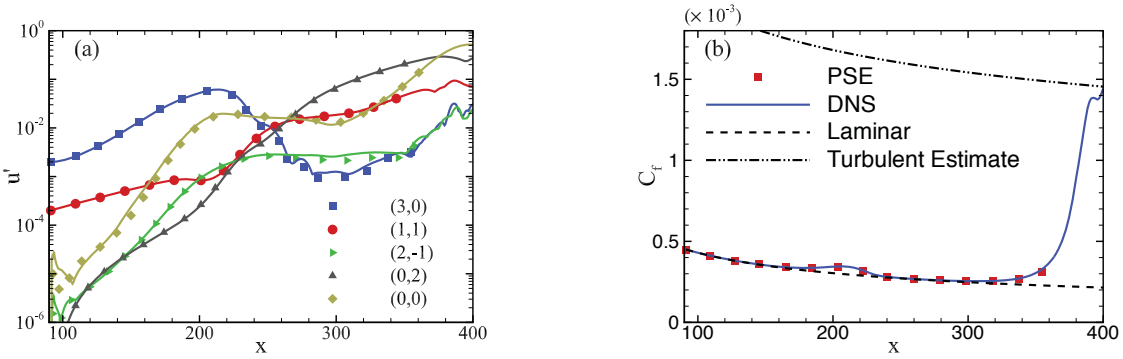

Figure 1: Streamwise development of (a) the maximum u-velocity disturbance (b) skin friction coefficient. Solid Lines: DNS results. Symbols: PSE results

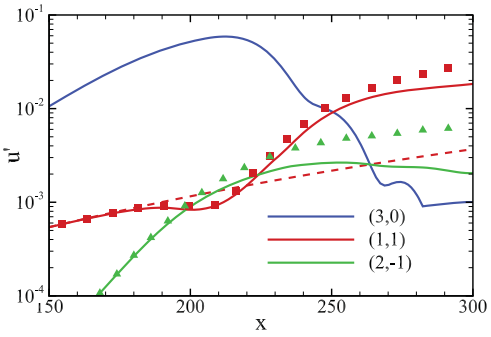

Figure 2: Evolution of the wave triad. Dashed Line: Linear result. Solid Lines: All modes reserved. Symbols: Only the wave triad reserved

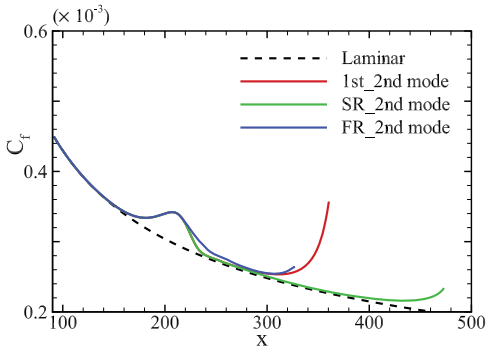

Figure 3: Streamwise development of skin friction coefficient of different transition routes.

Acknowlegement

This work was supported by the National Natural Science Foundation of China (11332007), the Tianjin Natural Science Foundation (15JCYBJC19500).

References

[1] Sivasubramanian J., Fasel H. F.: Numerical investigation of the development of three-dimensional wavepackets in a sharp cone boundary layer at Mach 6. J. Fluid Mech 756:600-649, 2014.

[2] Shiplyuk A. N., Maslov A. A., Chokani N. D.: Nonlinear interactions of second mode instability with natural and artificial disturbances. AIAA paper 787,2003.

[3] Bountin D., Shiplyuk A., Maslov A.: Evolution of nonlinear processes in a hypersonic boundary layer on a sharp cone. J. Fluid Mech 611:427-442,2008.

[4] Chang C. L., Malik M. R.: Oblique-mode breakdown and secondary instability in supersonic boundary layers. J. Fluid Mech 273:323-360,1994.

[5] Wu X., Stewart P. A., Cowley S. J.: On the catalytic role of the phase-locked interaction of TollmienCSchlichting waves in boundary-layer transition. J. Fluid Mech 590:265-294,2007.

FM03 - Combustion and Flames

TS.FM03-1.01	Higgins, Andrew - Percolating reactive waves: Flames in the discrete regime (INVITED)	585
TS.FM03-1.02	Oran, Elaine - Shock-Flame Complexes: Transitional and Steady States	587
TS.FM03-1.03	Jin, Tai - Direct numerical simulation of turbulence-detonation interaction: Parametric study	589
TS.FM03-1.04	Radulescu, Matei - Dynamics of gaseous detonations with global mass divergence	591
TS.FM03-1.05	Palecka, Jan - Coupling and quenching in dual-front flames	593
TS.FM03-1.06	Lam, Fredric - Front roughening of a flame in a discrete source system	595
TS.FM03-2.01	Oefelein, Joseph - Dynamics of gas-liquid interfaces in high-pressure systems (INVITED)	597
TS.FM03-2.02	Attili, Antonio - Turbulent premixed Bunsen flames over a wide range of Reynolds number	599
TS.FM03-2.03	Capecelatro, Jesse - Adjoint-informed ignition characterization	601
TS.FM03-2.04	Semenov, Ilya - Modeling of detonation processes in H2-air mixtures with concentration gradients	603
TS.FM03-2.05	Dunnmon, Jared - 3D Flame Characterization via X-ray Computed Tomography	605
TS.FM03-2.06	Osborne, Jeffrey - Particle dynamics through turbulent premixed flames using 10 kHz TPIV, OH PLIF, and CH2O PLIF	607
TS.FM03-3.01	Carder, Daniel - Emission control challenges for compression ignition engines (INVITED)	609
TS.FM03-3.02	Candel, Sebastien - The Describing Function of Swirled Spray Flames	611
TS.FM03-3.03	Chatterjee, Sandipan - Swirl-stabilized non-premixed propane/air flames in a gas turbine model combustor	613
TS.FM03-3.04	Kheirkhah, Sina - Heat release rate and pressure phase differences inside an aeronautical gas turbine combustor	615
TS.FM03-3.05	Coenen, Wilfried - Global stability analysis of line-fire flickering	617
TS.FM03-3.06	Boujo, Edouard - Quantifying stochastic limit-cycle parameters from the adjoint Fokker-Planck equation	619
PO.FM03-1.01.84	Al Sarraf, Elias - Premixed flame instability in a Hele-Shaw burner	621
PO.FM03-1.02.85	Almarcha, Christophe - Modelisation and Forecast of Premixed Flames	623
PO.FM03-1.03.86	Grek Genrich - Visualization of conventional and combusting subsonic jet instabilities	625
PO.FM03-1.04.87	Lau-Chapdelaine, She-Ming - Stability characteristics of pulsating one-dimensional detonations using a simple analogue	627
PO.FM03-1.05.88	Lutsenko, Nickolay - On Numerical Modeling of Combustion and Other Energy Release in Porous Objects	629
PO.FM03-1.06.89	Merk, Malte - On hydrodynamic effects during self-excited thermoacoustic oscillations	631
PO.FM03-2.01.1	Mi, Xiaocheng - Propagation of Gaseous Detonation Waves in a Spatially Heterogeneous Reactive Medium	633
PO.FM03-2.02.2	Moreno-Boza, Daniel - The Frank-Kamenetskii vortex	635
PO.FM03-2.03.3	Paquet, Frederick - Experimental determination of the height of propellant flames	637
PO.FM03-2.04.4	Ren, Zhaoxin - Ignition and Flame Stabilization in Supersonic Evaporating Fuel	639

	Sprays	
PO.FM03-2.05.5	Scholle, Markus - A Variational Framework for Reactive Flows and Shock Waves	641
PO.FM03-2.06.6	Teng, Honghui - Initiation characteristics of oblique detonation waves in hydrogen-air mixture	643

PERCOLATING REACTIVE WAVES: FLAMES IN THE DISCRETE REGIME

Andrew J. Higgins [a)]
Department of Mechanical Engineering, McGill University, Montreal, Quebec, Canada

Summary An overview of investigations into flame propagation in discrete systems is given. Discrete effects become pronounced when the heat release time scale of a source is much less than the characteristic time of diffusion between sources. Under these conditions, flame propagation becomes dominated by local fluctuations in particle concentration, sharing many characteristics with directed percolation. Attempts to model such systems using traditional, continuum models that assume a homogeneous media would result in erroneous predictions of flame dynamics. Attempts to experimentally realize such systems are discussed, and the need for a microgravity platform with duration on the order of minutes is articulated. Key experimental features of flames in the discrete source propagation regime are identified, and planning for an upcoming sounding rocket experiment is discussed.

OVERVIEW

Historically, combustion is the first field in which solutions for self-sustained waves that propagate by activated release of an agent (i.e., heat, chemical species) that diffuses forward were identified. The propagation of an advantageous gene [1] and spread of disease [2] through populations are further examples. Classical models are continuum-based, assuming the excitable media to be spatially homogeneous. However, a great many systems of interest have spatially discrete sources. A forest fire, wherein the flame front must jump from tree to tree is an obvious example. The spiral arms of galaxies have been conjectured to be self-propagating waves of star formation, wherein the shock wave from a newly ignited star results in the collapse of interstellar gas necessary to trigger star formation, which is an example of a medium with highly disparate scales.[3] Calcium waves, a mechanism of intracellular signaling, are diffusive waves that propagate via activating discrete sources of Ca(2+) within a cell.[4] All of these examples feature media wherein the spatial randomness of the media is likely to profoundly influence the propagation dynamics that any spatial averaging technique (necessary for a continuum-level description) will likely fail to capture. Recently, the recognition that discrete effects in the combustion of spatially random media can result in unique flame behavior, separate from more traditional heterogeneous media, has been articulated by Mukasyan and Rogachev.[5] Development of this field has been motivated by flames in Self-Propagating High Temperature Synthesis (SHS or "Solid Flame") and in low volatile fuel particulates suspended in a gaseous oxidizer.

The existence of a clean experimental system that exhibits source-to-source propagation is an outstanding challenge.[6] Ideally, such a system would use a large particle size (20 μm or larger) so that individual particles can be visualized using digital photography. The creation of a suspension of large particles of this size is not feasible in the normal gravity environment. In addition, in the discrete regime, flame speeds are limited by particle to particle diffusion, resulting in flame speeds that are on the order of cm/s. Flame speeds less than about 20 cm/s are not feasible in the normal gravity environment due to the disruption of the flame by the buoyancy of the combustion products. Thus, there exist two strong rationales for the necessity of utilizing the microgravity environment to examine flame propagation in particulate suspensions. McGill University has led a 20 year investigation into the fundamental properties of flame propagation in dust suspensions utilizing the approximately 25 second duration of microgravity available onboard parabolic flight aircraft. The majority of the work performed over this period falls into a regime that is amenable to classical thermal flame theory, and including the discrete source effects is not necessary.[7] Only recently has experimental investigation into the discrete regime been attempted.[8-10] A study using a fuel that burns entirely heterogeneously (iron) in suspension in xenon-oxygen mixtures exhibited a near independence of flame speed upon the oxygen concentration. The ratio of the combustion time to the timescale of interparticle diffusion, giving the so-called discreteness parameter $\tau_c = t_r/t_d = t_r/(l^2/\alpha)$, where l is the interparticle spacing and α is thermal diffusivity, was estimated to be less than unity due to the low thermal diffusivity of the inert xenon component of the mixture.[9] In effect, the flame speed becomes entirely bottlenecked by the interparticle diffusion time, such that even an infinitely fast burning fuel will yield a finite flame speed. Use of helium (replacing the xenon) resulted in the discreteness ratio greater than unity, and the results confirmed that using an inert component with a large thermal diffusivity resulted in the expected square-root dependence of flame speed upon oxygen concentration.[9] A more recent experimental investigation by Wright et al. [11] using a faster burning fuel (aluminum) in the normal gravity environment also confirmed the predicted independence of flame speed on oxygen concentration. Both of these studies were severely limited in the range of particle sizes, concentrations, and flame speeds that could be explored due to the limited duration and poor quality of microgravity onboard parabolic flight aircraft.

[a)] Corresponding author. Email: andrew.higgins@mcgill.ca.

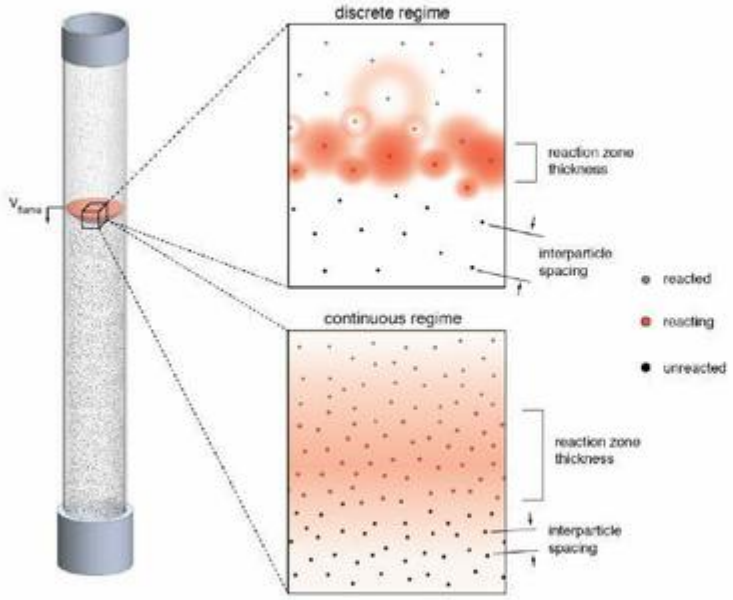

Fig. 1 Schematic of flame propagation in discrete and continuum regimes. [11]



Fig. 2 Photograph of flame propagating (from top to bottom) through a suspension of iron particles in gaseous oxidizer (20% oxygen/80% xenon), taken on board Canadian Falcon-20 parabolic flight aircraft.

The scientific rationale for better understanding of reactive wave propagation in the discrete regime has led the European Space Agency to select this investigation for a sounding rocket flight that will provide 12 to 14 minutes of extremely high quality microgravity, during which time approximately 36 separate flame propagation experiments will be conducted using iron particulate suspensions in microgravity. Cameras onboard the payload will record the iron particulate concentration suspended in oxygen/xenon, the flame front structure, and the flame propagation speed.[12]

The definitive experimental validation of flame propagation in the discrete regime would firmly establish a third branch of combustion, distinct from homogenous (gas-phase) and heterogeneous (multi-phase) combustion. This new regime is inherently statistical, such that local fluctuations in particle concentration can significantly influence flame front propagation, requiring concepts from statistical mechanics be adopted in modeling such flames.

References

[1] Fisher, R.A.: The wave of advance of advantageous genes. *Annals of Eugenics* 7:355-369, 1937.

[2] Sander, L.M., Warren, C.P., Sokolov, I.M., Simon, C., Koopman, J.: Percolation on heterogeneous networks as a model for epidemics. *Mathematical Biosciences* 180:293-305, 2002.

[3] Schulman, L. S., Seiden, P. E.: Percolation and galaxies. *Science* 233(4762):425-431, 1986.

[4] Bar, M., Falcke, M., Levine, H., Tsimring L.S.: Discrete stochastic modeling of calcium channel dynamics. *Physical Review Letters* 84:5664, 2000.

[5] Mukasyan A., Rogachev, A.: Discrete reaction waves: Gasless combustion of solid powder mixtures. *Prog. Energy Combust. Sci.* 34:377–416, 2008.

[6] Hinrichsen, H.: On possible experimental realizations of directed percolation. *Brazilian Journal of Physics* 30(1):69-82, 2000.

[7] Goroshin, S., Tang, F. D., Higgins, A. J., Lee, J. H.: Laminar dust flames in a reduced-gravity environment. *Acta Astronautica* 68(7):656-666, 2011.

[8] Tang, F. D., Higgins, A. J., Goroshin, S.: Effect of discreteness on heterogeneous flames: propagation limits in regular and random particle arrays. *Combustion Theory and Modelling* 13(2), 319-341, 2009.

[9] Goroshin, S., Tang, F. D., Higgins, A. J.: Reaction-diffusion fronts in media with spatially discrete sources. *Physical Review E* 84(2), 027301, 2011.

[10] Tang, F. D., Higgins, A. J., and Goroshin, S.: Propagation limits and velocity of reaction-diffusion fronts in a system of discrete random sources. *Physical Review E* 85(3), 036311, 2012.

[11] Wright, A., Higgins, A.J., Goroshin, S.: The Discrete Regime of Flame Propagation in Metal Particulate Clouds. *Combust. Sci. Technol.* (submitted) 2015.

[12] Higgins, A.J. Wright, A., Goroshin, S., Tang, F.D., Verga, A., Schütte, A., Schmitz, B., PERWAVES: Towards a Spaceflight Experiment to Realize Discrete Combustion Waves. 65th International Astronautical Congress, Toronto, Canada, September 29-October 3, 2014.

SHOCK-FLAME COMPLEXES: TRANSITIONAL AND STEADY STATES

Elaine S. Oran *

Department of Aerospace Engineering, University of Maryland, College Park, Maryland

Summary A *shock-flame complex* describes a combustion state involving the continuous interactions of a shock and a flame. These are often but not always transient phenomena, and they often provide an environment that allows transition to detonation. Three types of shock-flame complexes are described here: (1) a turbulent flame coupled to a leading shock; (2) a marginal detonation with an extended reaction-zone structure; and (3) a dust-driven shock in a multiphase flow. These are contrasted and general features are described.

INTRODUCTION

The term *shock-flame complex* has been used to describe a range of combustion configurations describing continuous interactions of a shock and a flame. This is often a transient state [1, 2, 3], but not always. Sometimes, after the complex has developed, it exists for a substantial time or until the fuel is consumed. This paper briefly describes a subset of shock-flame complexes which involve the coupled propagation of a shock and a flame. The first state arises when a turbulent flame couples to a leading shock. The second is the close coupling that occurs in a detonation, but here we talk about the case of a marginal detonation with an broad reaction zone structure. Finally, we describe a type of complex that can occur in a multiphase dust flow that creates volatile gases and char.

EXAMPLES OF SHOCK-FLAME COMPLEXES

Turbulent Flames and Shock

Figure 1 is an illustration of a shock-flame complex consisting of a leading shock, followed by a turbulent, shock-laden region of heated and compressed gas, followed by a turbulent flame [4]. The figure was taken from a simulation of the evolution of a flame in a lean methane-air mixture. In the simulation, the final state if a shock-flame complex that travels down the channel at about a velocity of approximately $0.5D_{CJ}$. It oscillates about this velocity somewhat, but does not undergo a transition to detonation, either in the simulations or in comparable experiments. This complex is maintained by a combination of the energy released from the turbulent flame, which is enhanced by shock-flame interactions, and a series of "explosions" resulting from shock reflections from the obstacles in the channel. None of these explosions is strong enough to create a spontaneous wave strong enough to transition to a detonation. They do, however, create a shock that is strong enough to perturb the flame further and increase its energy release.

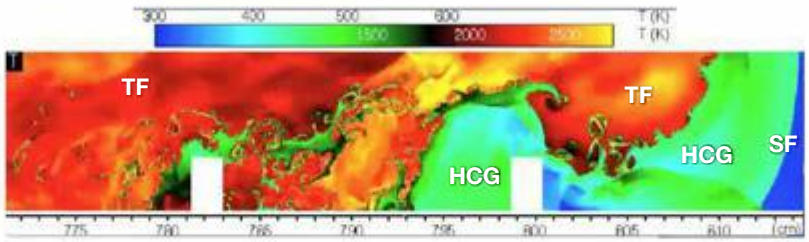

Figure 1: Frame from a simulation of a turbulent flame generated in a mixture of lean methane and air at atmospheric conditions in an obstacle-laded channel [4]. The complex is traveling from left to right. SF: shock front. HCG: region of heated and compressed gas. TF: region of turbulent flame. Symmetry conditions on the upper boundary. Two temperature scales: upper for unreacted fas and lower for reacted gas.

Marginal Detonations

The limiting case of a gas-phase detonation is the tightest form of coupling. In this case, the complex consists of a leading shock, which heats and compresses material behind it in an reaction zone. An actual gas-phase detonation is comprised of multidimensional, continuously changing and interacting shock and reaction-zone structures behind a leading shock front that varies continuously and often cyclically in strength. The energy release behind the reaction zone is an autoignition process. The "flame" is at a limit in which physical diffusion effects, such as thermal conduction and molecular diffusion, are of at

*Corresponding author. Email: eoran@umd.edu

most secondary importance. For low-pressure stoichiometric mixtures of gases diluted with inert gas, these structures repeat in very regular fashions, creating the beautiful detonation cells that have been a scientific obsession for fifty years.

When the gas mixture is near the detonation limit, the shock-flame complex becomes even more complicated. Gamezo et al. [5] reports experiments and simulations that show that the flame-shock structure consists of an overlay of the more usual detonation structure of leading and transverse shocks, but now the reaction zones can become so large so that complex interactions can occur in these zones. The are simultaneously three three kinds of detonation structure. The primary structure causes the usual cells structure. The overdriven sections of the leading shock create secondary detonation cells that coexist with primary cells. Finally, the transverse detonations produce a fine structure called transverse detonation cells.

Dust Explosions

Recent simulations of explosions created when a shock traverses a layer of coal dust show a different sort of shock-flame complex that could, for example, develop in a coal mine [6]. Consider the case in which there is an initial natural-gas explosion that eventually runs out of fuel. It then decays into a shock that propagates down a long tunnel. The tunnel floor is covered with coal dust that accumulates from the mining operation. This shock lifts the dust, heats and compresses the air behind it, and after a time, combustible material volatilize from the dust and begin to react. This can result in ignition centers behind the shock, and these centers merge to form a turbulent flame behind the shock front. Figure 2 shows the results of a simulation for a coal dust layer with a packing fraction of 47%. For this packing fraction and dust size, the leading shock and the turbulent flame reach a state in which the distance between them levels off and remains essentially constant. For lower packing fractions, (e.g., $\alpha = 1\%$ in Fig. 2b) and therefore more easily dispersed dust, the dust flame contributes more substantially to the explosion and continues to accelerate the shock. This could lead to a dust-driven detonation.

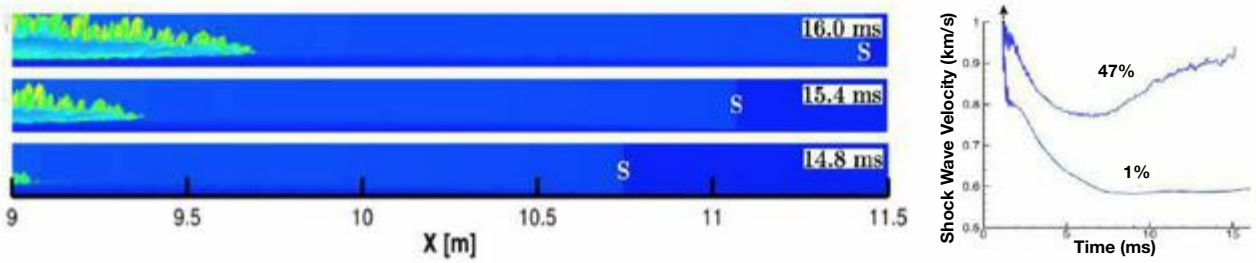

Figure 2: Left panels: Three frames showing temperature and location of shock (white S) at three times. X-axis in in meters, vertical axis is 5 cm. Dust packing is 47%. Right figure: Profiles of shock velocity as a function of time (ms) for two packing fractions, upper curve 1%, lower curve 47%. See [6].

OBSERVATIONS AND CONCLUSIONS

A *shock-flame complex* describes a combustion state involving the continuous interactions of a shock and a flame. These are often but not always transient phenomena, and they often it provide an environment that allows transition to detonation. The three types of complexes described here cover a range of phenomena. One was the more standard example of a turbulent flame and a leading shock, a situation which often produces conditions that lead to a detonation. At the opposite extreme, there is what seems like a rather loose or distant connection (meters) between dust burning and a leading shock. In some cases, such as high packing fraction of dust, this too will lead to a detonation after the complex travels far enough. The marginal detonation structure is a complex overlay of what we already know about detonation cell structures. The important point in that case is that very local over-pressures due to the secondary detonations in near-limit mixtures of natural gas can be extremely high (greater than 150 MPa) and therefore damaging, as was actually observed in experiments in natural gas [7].

References

[1] Urtiew, P.A., Oppenheim, A.K.: Transverse Flame-Shock Interactions in an Explosive Gas. Proc. Roy. Soc. A 304:379-385, 1968.

[2] Thomas, G., Bambrey, R., Brown, C.: Experimental Observations of Flame Acceleration and Transition to Detonation following Shock-Flame Interaction. Combust. Theory Mod. 5:573-594, 2001.

[3] Gamezo, V.N., Khohlov, A.M., Oran, E.S.: Shock Bifurcations and Shock-Flame Interactions. Combust. Flame 126:1810-1826, 2001.

[4] Kessler, D.A., Gamezo, V.N., Oran, E.S.: Simulations of Flame Acceleration and deflagration-to-Detonation transitions in Methane-Air Systems. Combust. Flame 157:2063-2077, 2010.

[5] Gamezo, V.N., Vasil'ev, A.M., Khokhlov, A.M., Oran, E.S.: Fine Cellular Structures in Marginal Detonations. Proc. Combust. Inst. 28:611617, 2000.

[6] Houim, R. W., Oran, E.S.: Numerical Simulation of Dilute and Dense Layered Coal-Dust Explosions. Proc. Combust. Inst. 25:2083-2090, 2015.

[7] Gamezo, V.N., Zipf, R.K., Jr., Sapko, M.J., et al.: Detonability of Natural Gas-Air Mixtures. Combust. Flame 159:870-881, 2012.

DIRECT NUMERICAL SIMULATION OF TURBULENCE-DETONATION INTERACTION: PARAMETRIC STUDY

Tai Jin, Kun Luo & Jianren Fan
State key laboratory of clean energy utilization, Zhejiang University, Hangzhou, China

Summary Direct numerical simulations of three dimensional isotropic turbulence-detonation interactions are conducted, based on Navier-Stokes equations and global one-step chemical reaction model. High-resolution bandwidth-optimized WENO scheme spatial discretization and total variation diminishing temporal integration are adopted for shock capturing. Comparative studies of turbulent inflow vertical and entropic forcing effects on the three dimensional detonation front and cellular structures are first conducted. It has been found that the turbulence field imposed has created small scale wrinkles embedded in the detonation front, apart from the large scale features of detonation without turbulence. The periodical movement of the triple points has been delayed and the length of the regular cellular structure increase under turbulent forcing. Effects of different inflow turbulence intensity and detonation strength on turbulence-detonation interactions are investigated in detail.

INTRODUCTION

Renewed interests in advanced propulsion concepts have remarkably rekindled the research activities in detonation waves. Detonations are supersonic flow phenomena with leading shock waves that ignite premixed gas. The interaction of detonation waves with nonuniform flows is of interest for different applications in the technological and scientific areas including aerodynamics, propulsion, and astrophysics. Although the detailed structures and properties of the detonation have been extensively studied through experimental and numerical methods as well as theoretical approach, the detonation interacting with nonuniform flows has received considerably less attention.

The simplest circumstance in which turbulence interacts with a detonation wave is concerned with the case of homogeneous, isotropic turbulence interacting with a detonation wave. Understandings of this problem have been greatly improved through the continuously developed theoretical studies based on the linear analysis[1-3], however with its limits about the involved simplifications, such as the infinitesimally thin detonation neglecting of detonation reaction length scales, et al.. Furthermore, the detonation wave is known to be sustained by multi-dimensional interactions with the transverse waves, thus, the detonation wave front structure presents to be three-dimensional and complex, which needs further analysis. Predictive numerical simulations of detonations could be an alternative approach to deep insight into the detonation turbulence interaction, especially for the detonation wave structure and dynamics[4].

In the present study, a high resolution weighted essentially non-oscillatory (WENO) numerical method, with low numerical dissipation, high-order shock-capturing, has been developed for the direct numerical simulation (DNS) of turbulence-detonation interactions. Comparative studies of turbulent inflow vertical and entropic forcing effects on the three dimensional detonation front and cellular structures are first conducted. Effects of different inflow turbulence intensity and detonation strength on turbulence-detonation interactions are compared in detail.

DNS SIMULATION

The simulations are performed in the reference frame of the steady ZND (Zeldovich, von Neumann, and Doering) wave. The mean flow is aligned with x direction, and periodic conditions are specified in the two other directions. The turbulent data superposed onto the mean flow at the inflow boundary of the computational domain corresponds to several developed turbulent fields obtained from preliminary simulations of time-decaying isotropic turbulence. The turbulent fluctuations are advected through the boundary using Taylor's hypothesis.

The detailed simulation of compressible turbulence requires numerical methods that simultaneously avoid excessive damping of spatial features over a large range of length scales and prevent spurious oscillations near shocks and shocklets through robust shock-capturing. Numerical schemes that were developed to satisfy these constraints include, among others, weighted essentially non-oscillatory (WENO) methods. In the current work, an eighth-order-accurate version of this scheme (WENO-BO4) is adopted to compute the convective terms of the governing equations. A simple eighth-order-accurate standard central difference scheme is employed to compute the viscous terms. The third order TVD Runge-Kutta multistage method is used for time integration. The detailed numerical methods and validations have been described in our previous work[5].

RESULTS ANS DISCUSSIONS

The three dimensional detonation structures under different inflow conditions are shown in Fig.1, where the snapshots of the shock front and contours plots of the vorticity along the lateral boundaries are presented. The flow front shows

Corresponding author. Email: fanjr@zju.edu.cn

alternatively “convex” and “concave” shapes, which corresponds to Mach stem and incident shock, respectively. The detonation front switches between Mach stem and incident shock during the propagation of detonation. The strong coupling in the area of triple points makes the detonation overdriven locally and sustains the detonation by the transverse motion of these zones along the front. A regular cell pattern with diamond shape is formed by the trajactories of triple points. The diamond shaped cell pattern changes little with the inflow forcing, however the length of the cell is a little larger, due to the delay of the collision of triple points by inflow forcing. The incoming turbulence perturbs the detonation front beyond its “smooth” shape. It can be found that the turbulence field imposed has created small scale wrinkles embedded in the detonation front, apart from the large scale features corresponding to Mach stem and incident shock presented in the case without turbulence (Fig.1a). The detonation front appears corrugated due to the vertical inflow fluctuations as shown in Fig.1c,d, while much weaker for the entropic fluctuations shown in Fig.1b.

Table 1 Computational parameters

case	Inflow M_0	Inflow M_t	N= $L_{1/2}/\lambda_0$	fluctuations
A (M3.0M$_t$0.0)	3.0	0.0	1.0	No forcing
B (EF3.0M$_t$0.15)	3.0	0.15	1.0	Entropy forcing
C (EF3.0M$_t$0.25)	3.0	0.25	1.0	Entropy forcing
D (M3.0M$_t$0.15)	3.0	0.15	1.0	Vertical forcing
E (M3.0M$_t$0.25)	3.0	0.25	1.0	Vertical forcing
F (M3.0M$_t$0.25)	3.0	0.25	0.2	Vertical forcing
G (M3.0M$_t$0.25)	3.0	0.25	5.0	Vertical forcing

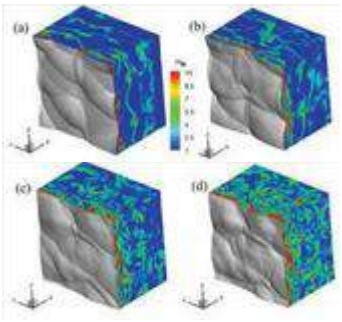

Fig.1 Instantaneous image of the detonation front and the vortex structures,(a) case A, (b) case C, (c) case D, (d) case E

The vortex structure along the lateral boundaries can well exhibit the turbulent flow field downstream the detonation. It has been indicated that the detonation produces vortex-like features and essentially all propagating detonations show a wide range of behavior from laminar unsteady periodic behavior to chaotic instability with highly turbulent behavior. For detonation without inflow fluctuations as shown in Fig.1a, vortices are only generated by the collision of triple points. The counter-rorating vortex are generated after the collision of triple points, and then convected downstream. The flow field presents to be intermitent and the distance between the two rows of vortexes is related to the collision period of triple points. For the turbulence-detonation interactions as shown in Fig.1c, the generated vortex and the convected vortex interact with each other. The generated pairs of vortex can hardly been seen. For the entropy inflow forcing, the large scale pairs of generate vortex can still be found, however with smaller scales embedded in them.

Pametric studies of different inflow turbulence intensity and detonation strength on turbulence-detonation interactions are also conducted. The detailed computational conditions are listed in Table 1, where λ_0 is the Taylor scale of the inflow homogeneous isotropic turbulence and $L_{1/2}$ is the half-reaction distance of the initial detonation.

CONCLUSIONS

Direct numerical simulations of three dimensional isotropic turbulence-detonation interactions are conducted, based on Navier-Stokes equations and global one-step chemical reaction model. High-resolution bandwidth-optimized WENO scheme spatial discretization and total variation diminishing temporal integration are adopted for shock capturing. Comparative studies of turbulent inflow vertical and entropic forcing effects on the three dimensional detonation front and cellular structures are first conducted. It has been found that the turbulence field imposed has created small scale wrinkles embedded in the detonation front, apart from the large scale features of detonation without turbulence. The periodical movement of the triple points has been delayed and the length of the regular cellular structure increase under turbulent forcing. Effects of different inflow turbulence intensity and detonation strength on turbulence-detonation interactions are also investigated in detail.

References

[1] Huete C., Sánchez A.L., and Williams F.A., Theory of interactions of thin strong detonations with turbulent gases, *Physics of Fluids*, 2013, Vol. 25, No. 7, pp.453-467

[2] Massa L., and Lu F.K., The role of the induction zone on the detonation – turbulence linear interaction, *Combustion Theory and Modelling*, 2011, Vol. 15, No. 3, pp.347-371

[3] Jackson T.L., Hussaini M.Y., and Ribner H.S., Interaction of turbulence with a detonation wave, *Physics of Fluids*, 1993, Vol. 5, No. 3, pp.745-749

[4] Massa L., Chauhan M., and Lu F.K., Detonation – turbulence interaction, *Combustion and Flame*, 2011, Vol. 158, No. 9, pp.1788-1806

[5] Jin T., Luo K., Dai Q., and Fan J., Simulations of Cellular Detonation Interaction with Turbulent Flows, *AIAA Journal*, 2015, Vol., No., pp.1-15

DYNAMICS OF GASEOUS DETONATIONS WITH GLOBAL MASS DIVERGENCE

Matei I. Radulescu *and Bijan Borzou
Mechanical Engineering, University of Ottawa, Ottawa, Ontario, Canada

Summary The dynamics of detonation waves in arbitrary geometries can be modeled by the Bdzil-Stewart DSD framework, provided a relation is known relating the shock speed dependence on geometric mass divergence behind the shock. We propose a novel test geometry which permits to establish such a dependence unambiguously for gas phase detonations. It is shown that channels with an exponentially increasing cross-section provide a constant mass divergence and a steady front speed below the CJ value. We find that predictions of the wave speed using the classical ZND model do not agree with experiment, unless much lower effective activation energies are used, consistent with previous observations in regards to the hydrodynamic structure of cellular detonations.

INTRODUCTION

The dynamics of detonation waves are intrinsically multi-scale. The reaction zone structure of detonation waves in gases is turbulent [1], and controls the overall dynamics of detonations on much larger scales. At present, Direct Numerical Simulations is restricted only to sub-components of the reaction zone structure, [2], due to the requirement of solving the complex chemistry evolution in a non-equilibrium time-varying shock structure over length and time scales spanning in excess of several orders of magnitude [3]. For this reason, large scale detonation dynamics are difficult to predict.

A generic feature of macroscopic detonation dynamics in complex geometries is the intrinsic dependence of the front speed on the local mass divergence in the reaction zone, or, equivalently, the lead front curvature - the so-called $D - \kappa$ relation. Bdzil and Stewart, for example, have extended Whitham's Geometrical Shock Dynamics theory to allow for the prediction of detonation dynamics (known as Detonation Shock Dynamics), whereby the front evolution can be reconstructed for arbitrary boundary conditions [4]. Unfortunately, the required intrinsic $D - \kappa$ curves cannot be directly obtained from first principles in a given gaseous system, due to the difficulties described above. For condensed phase detonations, the kinetics in heterogeneous systems are not known and $D - \kappa$ relations are also obtained from experiment.

In the present paper, we formulate a new experimental method for determining such a $D - k$ relation for an arbitrary reactive *gaseous* system, consisting of a diverging channel geometry that keeps the global rate of mass divergence constant. Recognizing that a quasi-1D motion of a fluid in a channel with variable cross section $A(r)$ has a source in the mass equation of the form $K = d(lnA)/dr$, we consider a channel geometry with a constant logarithmic derivative K, i.e., a channel with an exponentially shaped wall, also known as an *exponential horn* in acoustics. This provides a constant mass divergence at any cross section of the channel. In this manner, a traveling wave solution (detonation) in quasi-steady state can be achieved.

RESULTS

The dynamics of detonations in a characteristic weakly unstable unstable ($2C_2H_2 + 5O_2 + 21Ar$) and a highly unstable ($C_3H_8 + 5O_2$) mixture were monitored. The experiments were performed in a 3.5-m-long thin rectangular channel, 203-mm-tall and 19-mm-wide. The last meter of the channel was equipped with glass windows allowing to visualize the flow evolution via high-speed large scale shadowgraphy. Two different divergence sections were used, in order to correct the experimental results for boundary layer wall losses. The diverging section consisted of either a long (1m long and $K = 2.302\ m^{-1}$) or a short (0.5 m long and $K = 4.605\ m^{-1}$) exponential ramp. The mixture sensitivity was monitored by changing the

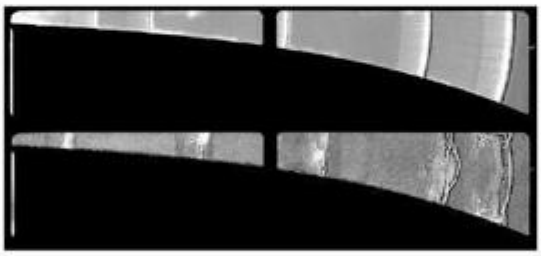

Figure 1: Evolution of the detonation front structure in an exponentially diverging 1-m-long channel in the propane mixture at 10.3 kPa intial pressure (top) and 3.45 kPa (bottom).

*Corresponding author. Email: matei@uottawa.ca

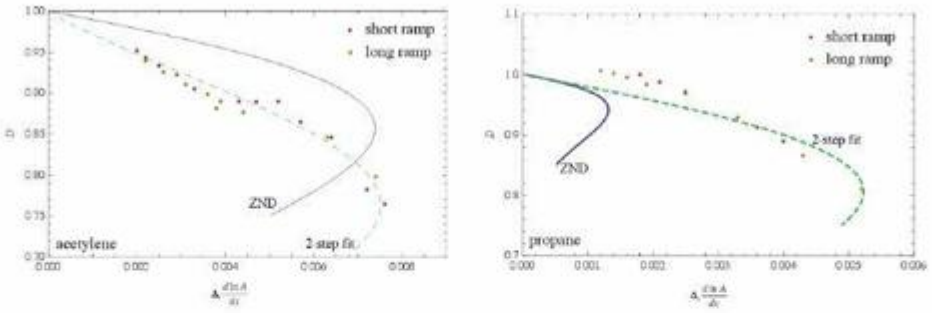

Figure 2: $D - K$ curves for the two reactive systems investigated and comparison with model prediction (see text).

initial pressure. Experiments were performed for decreasing pressures until a self-supported detonation wave can longer be established in the diverging section, marking the maximum possible divergence.

Figure 1 shows two examples of the front evolution in the propane-oxygen mixtures. The top figure shows the multi-headed curved detonation front, as it progresses in the enlarging section and acquires the expected curvature due to the geometrical divergence of the front. The bottom figure shows the detonation wave in a less sensitive mixture at a lower pressure, exhibiting a larger reaction zone structure and a higher velocity deficit. In the reaction zone, the complex cellular structure of unstable detonations can be observed [1].

The mean speed of the front recorded along the axis of the channel for all the experiments performed is shown in Figure 2 in the two tested mixtures normalized by the Chapman-Jouguet ideal speed. The abscissa is the rate of mass divergence normalized by the calculated induction length at the corresponding pressure. Both mixtures have approximately the same behavior, with maximum velocity deficits of approximately 20%. The limiting maximum mass divergence $K\Delta_i$ beyond which detonations are quenched is also similar for both mixtures, approximately 0.008 for the acetylene mixture and 0.005 for the propane mixture. The experimental results of Figure 2 were also compared with the prediction obtained for the expected steady state traveling wave solution with constant mass divergence (D-K curves). The model assumed a two-step decomposition of a perfect gas, mimicking the chain branching behavior of real fuels, whose parameters were estimated via constant volume ignition simulations using CANTERA and the SANDIEGO thermo-chemical database. The model formulation follows similar arguments for eigenvalue detonations with frontal divergence found in the literature [4], which will be communicated at the conference. The eigenvalue solution obeying the generalized CJ solution was obtained numerically.

For both mixtures, the computed $D - k$ curves differ substantially from the experiments, particularly for the more unstable detonations in the propane mixtures. Surprisingly (perhaps coincidently), the correct limit is captured in the acetylene mixtures, but clearly not the velocity deficits. This is the first successful unambiguous comparison between the ZND model prediction with mass divergence and experiment.

The experimental data, however, can be used to formulate an empirical reaction model to be calibrated to the data. In the context of the two step model considered in the present study, the model allows to adjust the global activation energy and the ratio of the induction to reaction time. The first controls principally the velocity deficit attainable, while the latter the maximum amount of loss at the limit[5]. Curve-fits obtained by calibration to the experimental data are also shown in Figure 2. The significant result obtained is that the experiments are only compatible with much lower activation energies than dictated by 1D chemical decomposition. For the acetylene the reduction is 26%, while for propane, the reduction in the activation energy is by 70%! This makes a dramatic change in the overall detonation dynamics characteristics, which we will address in future studies. The lower effective activation energies are not surprising, as it was already noted that the enhancement of burning mechanism in turbulent detonations by turbulent mixing suppresses much of the thermal character of the ignition mechanism, yielding effectively lower activation energies [1].

References

[1] M. I. Radulescu, G. J. Sharpe, C. K. Law, and J. H. S. Lee. The hydrodynamic structure of unstable cellular detonations. *Journal of Fluid Mechanics*, 580:31–81, 2007.

[2] J.L. Ziegler, R. Deiterding, J.E. Shepherd, and D. I. Pullin. An adaptive high-order hybrid scheme for compressive, viscous flows with detailed chemistry. *Journal of Computational Physics*, 230(20):7598–7630, 2011.

[3] K. Mazaheri, Y. Mahmoudi, and M.I. Radulescu. Diffusion and hydrodynamic instabilities in gaseous detonations. *Combustion and Flame*, 159(6):2138–2154, 2012.

[4] J. B. Bdzil and D. S. Stewart. The dynamics of detonation in explosive systems. *Annual Review of Fluid Mechanics*, 39:263–292, 2007.

[5] M. Short and J. B. Bdzil. Propagation laws for steady curved detonations with chain-branching kinetics. *Journal of Fluid Mechanics*, 479:39–64, 2003.

COUPLING AND QUENCHING IN DUAL-FRONT FLAMES

Jan Palecka[1], Sam Goroshin[1], Jeffrey Bergthorson[1], David Frost[1] & Andrew Higgins[1]
[1]*Department of Mechanical Engineering, McGill University, Montreal, Quebec, Canada*

Abstract The combustion of mixtures of two very different fuels sometimes leads to the formation of two-front flames with complex propagation and quenching behaviours. A simple, one-dimensional analytical model has been developed to explain previously obtained experimental results. The only interaction between the fronts considered is through the gas phase temperature. The model assumes that the reaction associated with each front starts at some ignition temperature and proceeds at a constant rate. The model predicts three different flame configurations: The fronts are either coupled, with both fuels burning within the same flame zone, de-coupled with a distinct preheat zone, or one of the fuels may not burn at all, playing the role of an inert additive. The results of the model are in very good qualitative agreement with experiments performed on hybrid aluminium-methane mixtures in narrow channels and explain the flame coupling/de-coupling through simple heat transfer considerations.

INTRODUCTION

Multistage combustion, involving two or more interacting and competing chemical reactions, appears in many fuel systems. In some systems this leads to the formation of dual-front flames as, in gas mixtures [1] or in mixtures involving solid particle suspensions, used for example in solid propellants, where combustion properties vary considerably with the size of particles as well as with the presence of combustible gases in so-called hybrid flames [2]. A closer study of the propagation of such flames [3], using quenching distance measurements in narrow channels as a probing technique, has revealed a complex interaction between the gas (methane) reaction and suspension (micron-sized aluminium) reaction fronts. Depending on the relative concentration of the fuels and the amount of heat losses to the channel wall, both fronts either couple in a unique flame zone, de-couple, burning as separated fronts, or a fuel with too low a concentration may not burn at all, becoming an inert additive to the front formed by the other fuel.

MODEL

The flame is represented as a one-dimensional steady-state structure propagating into an unburned mixture of an oxidizer and two fuels and is tracked by means of a single temperature profile. The model follows the temperature profile across the flame and as soon as the latter reaches a given ignition value, associated with each fuel, the respective reaction starts and proceeds at a constant rate for a given combustion time. The concentration of the first fuel is kept constant while the second one is varied.

In this simplified model, chemical transport is neglected and the mixture is assumed fuel-lean so that the depletion of oxidizer has no effect on the reaction rates. The system is then defined solely by the steady-state one-dimensional energy equation, which is solved analytically to obtain the temperature profile over the entire flame domain. This procedure also yields the propagation velocity of the flame as well as the distance between the two fronts. The calculations are performed for both adiabatic flames as well as for cases with heat losses, representing the heat losses to the narrow channels.

RESULTS

The equations are solved for each of the flame configurations shown in Fig. 1 for adiabatic flames as well as for flames with different amounts of heat losses. The results show the flame speed dependence for each such case on concentration of the 2nd fuel φ. For simplicity, each flame configuration is associated with a colour: one-front with blue, two-front decoupled with red, and two-front coupled with green. The simplified formulation of the model allows the equations to be solved entirely analytically, which guarantees that all solutions for all parameter ranges are identified.

For each configuration, the adiabatic case is represented by a unique bold curve. As Fig. 1 shows, at low φ, only the 1st fuel can form a front, while the 2nd acts as an inert additive, and raising its concentration φ slows the overall flame until it cannot propagate (bold blue curve). If the 2nd fuel is reactive, however, at a critical concentration, the 2nd fuel can form its own front in the wake of the 1st one, and raising φ leads to the 2nd front approach the 1st one until they merge. The 2nd front enhances the speed of the overall flame (bold red curve). Raising φ further leads to the propagation of a coupled flame (bold green curve).

The presence of heat losses leads to the possibility of multiple solutions. Each flame curve is composed of two branches, a physical (solid curves) and an unphysical one (dashed curves). Both branches meet at a bifurcation. The curve linking these meeting points for all values of heat losses represents the quenching curve for both the one-front and the two-front flame. The behaviour of each flame is described by its physical branch.

Adding the 2nd fuel, i.e., increasing φ, has very different effects on both flames. For a given amount of heat losses, as φ increases, a one-front flame (curve C_1) will slow down until it quenches whereas the two-front flame (curve C_3) will appear

[a] Jan Palecka. Email: jan.palecka@mail.mcgill.ca.

at a critical φ and its velocity will increase for higher φ. As the heat losses are increased, a lower value of φ is sufficient to quench the one-front flame (curve C_2) while a higher φ is needed for the two-front flame to appear (curve C_4).

As in the adiabatic case, for a given heat loss value, an increase in φ causes the two separated fronts in the flame to merge (transition from red to green curves). These two cases are separated by the front merging curve. As the heat losses are increased, this curve crosses the quenching curve. Thus, below a certain heat loss value, the flame quenches as two separated fronts, and above, it quenches as two merged ones.

For low ranges of heat losses, the red curves are wrapped around the blue ones which leads to three sets of bifurcations and a possibility of up to four solutions for a two-front flame for a given value of φ and the possibility of a second physical branch.

The results of Fig. 1 have been compared to the experimental findings of [3], described in the Introduction, and a very good qualitative agreement has been achieved. Despite the simplicity of its formulation, the model is able to recover all the behaviours observed in the quenching tests.

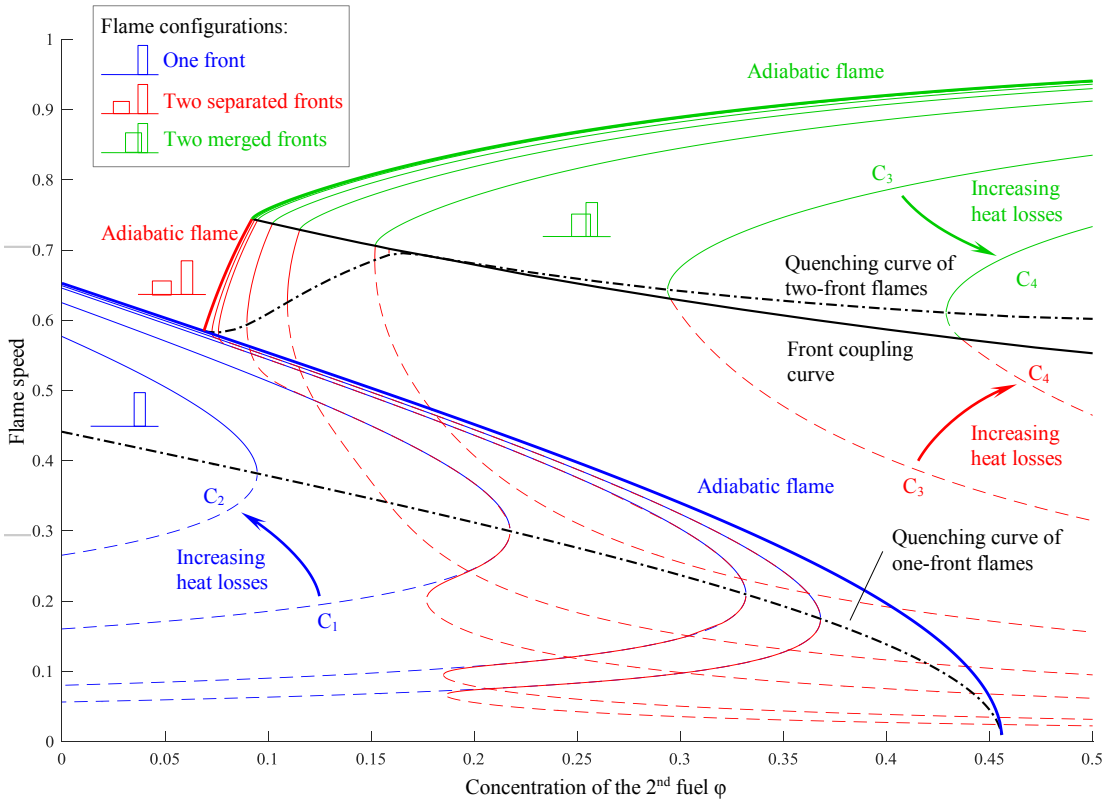

Figure 1. Flame speed of one-front and two-front flames with respect to the concentration of the second fuel

CONCLUSIONS

The complex behaviours observed in flames of some mixtures of different fuels have been qualitatively recovered by means of a simple analytical model based only on thermal considerations. In this light, the front coupling and de-coupling, observed in these systems, results mainly from the thermal interaction between the two fuels. These can either form fronts, which enhance each other, or due to low concentration and/or high heat losses, may fail to do so. In the latter case, the respective fuel hinders the propagation of the flame, increasing the heat capacity of the mixture and reinforces the effect of heat losses on the one-front flame.

References

[1] Branch M. C., Sadequ M. E., Alfarayedhi A. A., Van Tiggelen P. J.: Measurements of the structure of laminar, premixed flames of CH4/NO2/O2 and CH2O/NO2/O2 Mixtures. *Combust. Flame* **83 (3-4)**: 228–239, 1991.

[2] Julien P., Soo M., Goroshin S., Frost D., Bergthorson J., Glumac N., Zhang F.: Effect of metal concentration on aluminum reactivity in combustion products of hydrocarbons. *J. Propul. Power* **30**:1047-1054, 2014.

[3] Palecka J., Julien P., Goroshin S., Bergthorson J., Frost D., Higgins A.: Quenching distance of flames in methane-aluminum hybrid mixtures. *Proc. Combust. Inst.* **35**: 2463-2470, 2015.

FRONT ROUGHENING OF A FLAME IN A DISCRETE SOURCE SYSTEM

Fredric Lam[a)], Caroline Wagner, XiaoCheng Mi, Samuel Goroshin, & Andrew J. Higgins
Department of Mechanical Engineering, McGill University, Montreal, Quebec, Canada

Summary The front dynamics of a reactive wave in a system dominated by the spatial discreteness of the energy sources is explored via simulations in two dimensions. The system consists of randomly positioned point-like heat sources that are triggered when the temperature of a source reaches a prescribed ignition temperature, which then release heat. The width of the front (defined by deviation of the ignition temperature contour from mean position) is measured as a function of the elapsed time of propagation. While the front dynamics are complex due to the stochastic nature of the medium, by performing ensemble averaging over multiple realizations of the system, the power-law growth of the front can be measured. The results of front width exhibit a one-third power law scaling, consistent with the predictions of the Kardar-Parisi-Zhang model. This system may be an ideal experimental system to explore front roughening for flame propagation in discrete media.

INTRODUCTION

The propagation of reactive waves in systems where the spatial discreteness of the media dominates the wave propagation has now been recognized as a new branch of combustion, "discrete combustion."[1] This regime has a number of unique features that would not be predicted by classical flame theory, including the existence of a limit to propagation distinct from the thermodynamic limit and, in some cases, the ability to sustain propagation beyond the thermodynamic limit.[2,3] Experimental observation of flame speed independence upon oxygen concentration, a result that cannot be explained by classical flame theory, has provided the best evidence yet that this regime can occur in real systems.[4,5] Despite these advances, no detailed attention has been devoted to examining the dynamics of the reactive wave front structure. The closest effort to the present work is that of Provatas et al. [6], who examined kinetic roughening of flames in random media. Their work verified an approximate one-third power law growth of the flame front thickness, suggesting that their system belonged to the universality class of the Kardar-Parisi-Zhang interface equation. The system that studied, however, was a random chess-board pattern of reactive and nonreactive squares. Their system also featured Arrhenius reaction kinetics and a uniform Newtonian cooling across the entire domain. Direct experimental realization of this system would be challenging.

Point-like solid fuel particles in gaseous oxidizer suspension are a promising experimental system to observe discrete effects in the asymptotic limit of highly discrete sources.[4] This system can also be modelled via a simple analytic approach of superimposing Green's functions to represent the heat release from prior sources and then solve for the ignition time of new sources.[4] Although the solution method is entirely analytical (i.e., no finite difference approximations are required), a computer is required when the number of sources becomes large (in this study, system with up to 25,000 sources will be considered). The complete details of the model are given in Refs. [2,3].

RESULTS

The modelled system is described by two parameters: (1) The nondimensional ignition temperature $T_{\mathrm{ign}} = \tilde{}_{\mathrm{ign}} - \tilde{T}_0)/\tilde{}_{\mathrm{f}} - \tilde{T}_0)$, where subscripts "ign", "0", and "f" denote the ignition, initial and adiabatic flame temperatures, respectively, and the tilde "~" denotes dimensional properties and (2) The nondimensional combustion $\tau_{\mathrm{c}} = \tilde{}_{\mathrm{c}}/\tilde{}_{\mathrm{d}}$, where $\tilde{}_{\mathrm{c}}$ is the dimensional combustion time over which the point sources release their heat and $\tilde{}_{\mathrm{d}}$ is the inter-particle diffusion time, l^2/α, where l is interparticle spacing and α is thermal diffusivity. The preliminary results reported here only considered $\tau_{\mathrm{c}} = 0$, which is the case of a highly discrete system where inter-particle diffusion should dominate over combustion time. In this study, the average particle spacing is set to unity.

The simulations are conducted in a 2-D domain, with the width of the domain (direction perpendicular to flame propagation) equal to $W = 100$ particle spacings and the length of the domain (in direction of flame propagation) equal to $L = 250$. Periodic boundary conditions are used on the edges of the domain. The details of the initiation of the wave and visualizations of wave propagation are reported in [2,3].

[a)] Corresponding author. Email: fredric.lam@mail.mcgill.ca.

ANALYSIS

After a simulation is complete, the entire history (ignition time) of every discrete source is known. A grid is then created over the entire domain that is kept the same for the entire analysis, as shown in Fig. 1(a). For each time step, for each y position (i.e., all of the grid points along the length at a given height), the furthest grid point in the direction of propagation is found for which the temperature is greater than or equal to T_{ign}. The temperature is obtained by summing the Green's Function temperature contributions from all of the particles that have ignited at this point in time towards the temperature at that particular grid point. This point is shown as a red dot in the figure. Then, an average position is obtained by averaging the x-location of all of the red dots. This is shown as the red line. The front width is then obtained as a root mean square calculation of the distance between all of the red dots (front position at a specific height), and the actual averaged front position. This width value and front x-position value are recorded for all times considered.

The history of flame width for an individual run is quite noisy, and only via ensemble averaging can the growth rate of the front be extracted. Shown in Fig. 1(b) is the average of the front width extracted from averaging 20 simulations performed with different randomly generated sources. Note that a log-log scale is used so that power law behaviour can be identified. A linear fit to the data in Fig. 1(b) shows a power law growth rate of $\beta = 0.3255$, which is in excellent agreement with the value $\beta = 1/3 = 0.333\ldots$ predicted by the KPZ model.

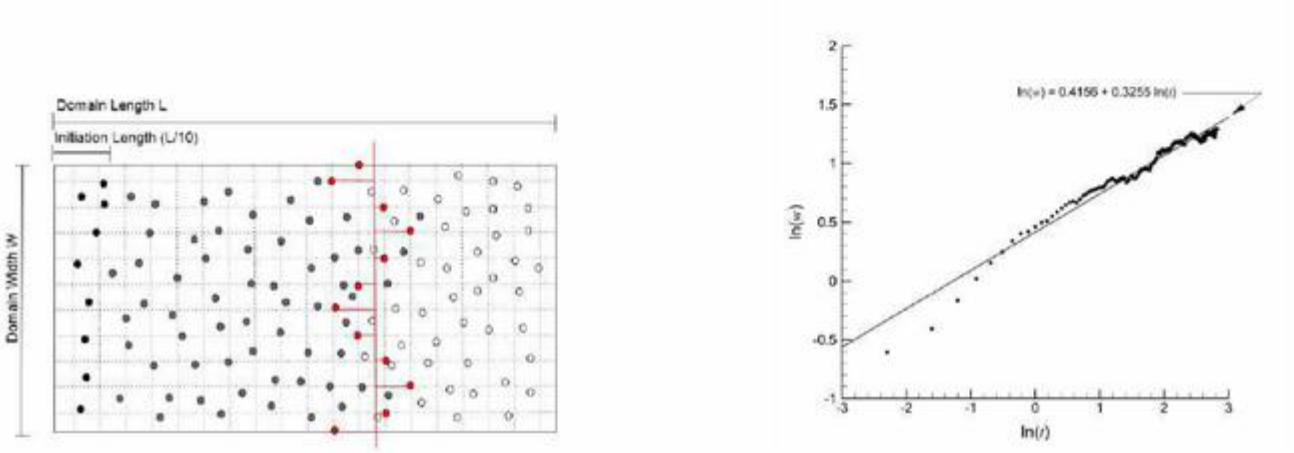

Fig. 1 (a) Method of extracting front width w from a simulation of a discrete source flame. (b) Front width as a function of time, plotted on log-log scale, for $T_{\mathrm{ign}} = 0.05$, $L = 250$, $W = 100$. Results shown are derived from an average of 20 simulations. A linear fit to the data gives the exponent β describing the roughening of the front.

CONCLUSIONS

The results presented here suggest that a reactive wave in a system of discrete, point-like sources may fall into the KPZ universality class. Such a system can be experimentally realized by using a fuel that reacts without volatilization, such as iron, in a medium with low thermal diffusivity (e.g., xenon). Such an experiment is scheduled to fly on the ESA MAXUS-9 sounding rocket in 2016 ("PERWAVES") and may provide direct experimental confirmation of kinetic roughening of a flame front in a discrete source system.

References

[1] Mukasyan A., Rogachev, A.: Discrete reaction waves: Gasless combustion of solid powder mixtures, *Prog. Energy Combust. Sci.*, 34:377–416, 2008.

[2] Tang, F.D., Higgins, A.J., Goroshin, S.: Effect of discreteness on heterogeneous flames: propagation limits in regular and random particle arrays. *Combust. Theor. Model.*, 13(2), 319-341, 2009.

[3] Tang F., Higgins, A., Goroshin, S.: Propagation limits and velocity of reaction-diffusion fronts in a system of discrete random sources, *Phys. Rev. E*, 85:036311, 2012.

[4] Goroshin, S., Tang, F., Higgins A.: Reaction-diffusion fronts in media with spatially discrete sources, *Phys. Rev. E*, 84:027301, 2011.

[5] Wright A., Higgins A.J., Goroshin S.: The Discrete Regime of Flame Propagation in Metal Particulate Clouds. *Combust. Sci. Technol.* (submitted) 2015.

[6] Provatas, N., Ala-Nissila, T., Grant, M., Elder, K.R., Piché, L.: Scaling, propagation, and kinetic roughening of flame fronts in random media. *J. Stat. Phys.*, 81:737-759, 1995.

[7] Myllys M., Maunuksela J., Alava M., Ala-Nissila T., Merikoski J., Timonen J.: Kinetic Roughening in Slow Combustion of Paper. *Phys. Rev. E*, 64:036101, 2001.

DYNAMICS OF GAS-LIQUID INTERFACES IN HIGH-PRESSURE SYSTEMS

Joseph C. Oefelein*[1]

[1]*Combustion Research Facility, Sandia National Laboratories, Livermore, California, USA*

Summary This paper summarizes recent theoretical work aimed at explaining the dynamics of gas-liquid interfaces in high-pressure systems. Imaging has long shown that at certain high-pressure conditions, the presence of discrete two-phase flow processes becomes diminished. The molecular gas-liquid interface is replaced by a diffusion dominated shear-layer that evolves in the presence of exceedingly large but continuous thermo-physical gradients. Analysis reveals that the two-phase interface breaks down not necessarily because of vanishing surface tension forces, but because of thickened interfaces in a state of nonequilibrium due to the presence of thermal gradients and an inherent reduction in the molecular mean free path.

INTRODUCTION

Research over the past decade has provided significant insights into the structure and dynamics of multiphase flows at high pressures [1–4]. There are two extremes that must be considered. At subcritical, or certain supercritical operating pressures relative to the injected liquid component, the classical situation exists where a well defined molecular interface separates the injected liquid from ambient gases due to the presence of surface tension. Interactions between dynamic shear forces and surface tension promote primary atomization and secondary breakup processes that evolve from a dense state, where the liquid exists as sheets filaments or lattices intermixed with sparse pockets of gas, to a dilute state, where drop-drop interactions are negligible and dilute spray theory can be used. When operating pressures exceed the critical pressure of the injected liquid, however, the situation can become quite different. Under these conditions, internal thermal gradients can form within the gas-liquid interface due to a combination of thickening within the interface and reduced molecular mean free path. The interfacial structure enters the continuum length scale regime and disappears as interfacial fluid temperatures rise above the critical temperature of the local mixture. Lack of inter-molecular forces, coupled with broadening interfaces, promote diffusion dominated mixing prior to atomization. As a consequence, injected jets evolve in the presence of exceedingly large but continuous thermo-physical gradients in a manner markedly different from classical assumptions.

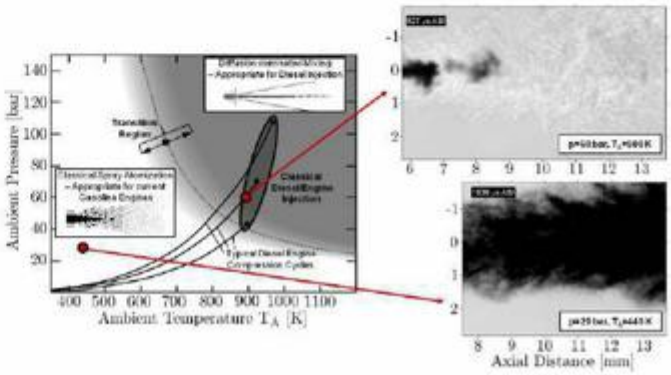

Figure 1: The regime diagram (left) describes conditions where n-dodecane injected at a temperature of 363 K into nitrogen transitions to a dense supercritical jet without drop formation. High-speed imaging of a dense supercritical jet (top right) and spray (bottom right) illustrates the change induced as a function of different ambient conditions (Images on right courtesy of L. M. Pickett, Sandia National Laboratories).

Detailed analysis suggests that the transitional changes described above are controlled by the multicomponent nature of the gas-liquid interface [5, 6]. A key output are regime diagrams for liquid injection such as the example shown in Fig. 1. This figure shows results for n-dodecane injected at a temperature of 363 K into gaseous nitrogen at varying ambient pressures and temperatures. The classical spray regime (highlighted in white) and diffusion dominated mixing regime (gray) are found using a Knudsen number criterion based on the molecular mean free path within the interface divided by the interfacial thickness (See Ref. [5]). Ambient gas pressure-temperature traces, which span a set of conditions for different Diesel engine compression cycles, are shown as follows: (a) turbo-charged (2.5 bar, 363 K), (b) medium-load (1.6 bar, 343 K), and (c) light-load (1 bar, 335 K). Fuel injection occurs at full compression conditions indicated by the three respective end points. Note that only at light-load operation does there appear to be a chance that classical fuel spray atomization takes place. These predictions have been corroborated using imaging to visualize the features of dense-fluid jets (top right image in Fig. 1) and classical spray atomization (bottom right image).

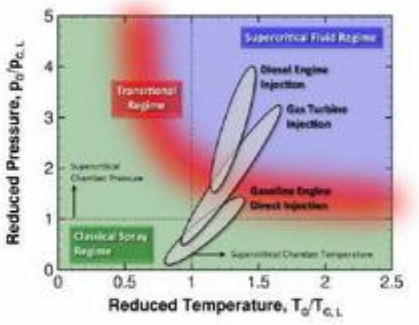

Figure 2: Typical operating envelopes in advanced Diesel, gas turbine, and gasoline direct injection systems.

*Corresponding author. Email: oefelei@sandia.gov

DISCUSSION

Applying the theory to a variety of system specific operating conditions suggests that almost all modern high-performance combustion devices operate over ranges of pressures and temperatures in the vicinity of, or across, the transitional regime [7, 8]. Figure 2 shows the typical operating envelopes associated with advanced Diesel, gas turbine, and gasoline direct injection systems using n-dodecane, n-decane, and iso-octane as respective fuel surrogates. The diagram is constructed for liquid injection temperatures from 300 to 363 K by normalizing the ambient gas pressure and temperature using the critical properties of the liquid phase. The Classical Spray Regime is highlighted in green, the Supercritical Fluid Regime in blue, and the Transitional Regime in red. Respective operating envelopes are indicated by the oval white areas. In each case the operational envelopes cross into the Transitional Regime, which highlights the need study these regimes simultaneously.

To further understand the dynamics of high-pressure injection, the large-eddy simulation technique has been applied using real-fluid thermodynamics and transport [9]. Liquid n-dodecane at 363 K is injected into a quiescent gaseous mixture at 900 K and 60 bar, which are precisely the same conditions represented by the medium-load compression trace shown in Fig. 1. Results from a high-resolution case (2 μm spacing across a 0.09 mm injector nozzle) are shown in Fig. 3 (see Lacaze et al. [9]). A three-dimensional rendering of the injected fuel jet is shown in the center. Fuel is injected from left to right. The red iso-surface marks the central liquid core where large density gradients exist. These gradients induce high shear forces through strongly coupled interactions between turbulence and nonideal multicomponent thermodynamics and transport processes. Instabilities form in these regions creating flow structures that entrain air and generate intense turbulence. These structures are highlighted by the yellow (500 m/s) to blue (50 m/s) iso-surfaces. Molecular diffusion completes the mixing, as shown by the more diffuse nature of the temperature field in the lower panel (363 K in dark blue to 900 K in red). Significant variations in the local speed of sound also occur. Scalar mixing within the shear-layer causes a strong decrease in the speed of sound, which reaches a minimum of approximately 200 m/s in the shear region of the jet between 30 and 70 diameters downstream, compared to 1008 m/s for the pure fuel jet at injection. The ambient speed of sound is approximately 600 m/s. The transonic variation generates pressure fluctuations of approximately ± 5 bar through compression-expansion effects. These pressure variations modify local turbulent flow characteristics, which further enhance transient mixing processes.

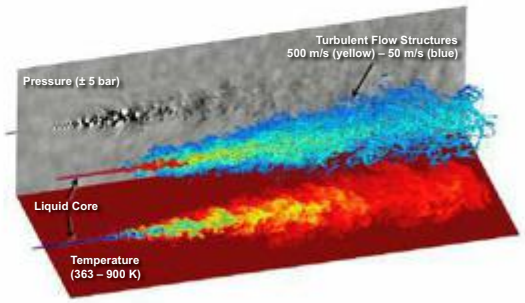

Figure 3: Three dimensional rendering liquid n-dodecane injected into nitrogen at $t = 200$ μs. The red iso-surface marks where density is 200 kg/m^3, the blue iso-surface marks a Q-criterion threshold that localizes coherent turbulent structures, the bottom panel shows the temperature and rear the pressure.

CONCLUSIONS

Recent theory aimed at explaining what causes the widely observed transition from classical spray dynamics to dense-fluid mixing in multiphase systems at high pressures suggests that it occurs due to nonequilibrium processes induced through thickening of the gas-liquid interface combined with a significant reduction of the molecular mean free path. This allows formation of temperature gradients within the interface, which ultimately leads to its disintegration. The resulting shear-layer then evolves in the presence of exceedingly large but continuous thermo-physical gradients in a manner markedly different from classical assumptions. Three regimes must be considered: (1) the Classical Spray Regime, (2) the Transitional Regime, and (3) the Supercritical Regime. Applying the theory across a variety of system specific operating conditions suggests that almost all modern high-performance combustion devices operate over ranges of pressures and temperatures in the vicinity of, or across, all of these regimes. Moreover, both drops and nonideal dense fluid mixing can exist in the transitional regime, which adds significant complexities to current modeling challenges. This highlights the need to understand both classical spray and supercritical fluid phenomena simultaneously in modern devices.

References

[1] J. C. Oefelein, V. Yang, *Combustion Science and Technology* 178 (1-3) (2006) 1–621, 20 Topical Papers.
[2] L. C. Selle, N. A. Okong'o, J. Bellan, K. G. Harstad, *Journal of Fluid Mechanics* 593 (2007) 57–91.
[3] G. Ribert, N. Zong, V. Yang, L. Pons, N. Darabiha, S. Candel, *Combustion and Flame* 154 (2008) 319–330.
[4] T. Schmitt, Y. Mery, M. Boileau, S. Candel, *Proceedings of the Combustion Institute* 33 (2011) 1383–1390.
[5] R. N. Dahms, J. C. Oefelein, *Physics of Fluids* 25 (092103) (2013) 1–24.
[6] R. N. Dahms, J. C. Oefelein, *Proceedings of the Combustion Institute* 35 (2015) 1587–1594.
[7] R. N. Dahms, J. C. Oefelein, *Journal of Propulsion and Power* 31 (5) (2015) 1221–1231.
[8] R. N. Dahms, J. C. Oefelein, *Combustion and Flame* 162 (2015) 3648–3657.
[9] G. Lacaze, A. Misdariis, A. Ruiz, J. C. Oefelein, *Proceedings of the Combustion Institute* 35 (2015) 1603–1611.

TURBULENT PREMIXED BUNSEN FLAMES OVER A WIDE RANGE OF REYNOLDS NUMBERS

Antonio Attili*[1], Stefano Luca[1], and Fabrizio Bisetti[1]
[1]*King Abdullah University of Science and Technology (KAUST), Clean Combustion Research Center (CCRC), Thuwal, Saudi Arabia*

Summary A set of turbulent premixed flames is simulated to investigate the effect of Reynolds number on the flame characteristics. Emphasis is placed on the overall characteristics of the flame and on the fractal dimension of the flame surface. It is found that the flame length decreases as the Reynolds number increases suggesting an increase of the turbulent flame speed with the Reynolds number. The fractal dimension of the flame surface is 2.6 and does not show a significant dependence on the Reynolds number.

METHODS AND FLAME CONFIGURATION

The flame configuration consists of a slot jet surrounded by a coflow of burnt gases. This arrangement is similar to piloted flames used in experiments. The jet consist of a methane/air mixture with global equivalence ratio $\phi = 0.7$ and temperature of 800 K. These conditions were chosen since they are representative of gas turbines. The temperature and species concentrations in the coflow correspond to the equilibrium state of the unburnt reactive mixture. The simulations are performed at 4 atm.

The bulk jet velocity is $U_b = 100$ m/s, while the coflow has a uniform velocity of $U_c = 15$ m/s. The jet Reynolds number based on the slot width and the jet bulk velocity $U_b H/\nu$ varies between 2800 and 22400. The variation of the Reynolds number is obtained varying the jet slot width H between 0.6 and 4.8 mm. The flow is periodic in the spanwise (z) direction, open boundary conditions are prescribed at the outlet in the streamwise (x) direction and no-slip conditions are imposed at the boundaries in the crosswise (y) direction. The jet and the coflow are separated at the inlet by walls with thickness H/10 and length 2H/3. Relevant parameters are summarized in Tab. 1.

The resolution for all the flames is set at $20\,\mu$m except for the highest Reynolds number case in which the resolution is $40\,\mu$m. The simulation at Re=11200 has been performed with a resolution of $40\,\mu$m without observing significant differences with respect to the case computed on the finer $20\,\mu$m grid. Therefore, we conclude that the results obtained for the Re=22400 case with the $40\,\mu$m grid can be used to assess the Reynolds number scaling shown in the present work.

Table 1: Parameters of the simulations.

Jet Reynolds Number, Re	2800	5600	11200	22400
Jet Bulk Velocity, U_{bulk}	100 m/s	100 m/s	100 m/s	100 m/s
Slot width, H	0.6 mm	1.2 mm	2.4 mm	4.8 mm
Grid Size	720×480×256	1440×960×256	2880×1920×512	2880×1920×512
$\Delta x = \Delta y = \Delta z$	$20\,\mu$m	$20\,\mu$m	$20\,\mu$m	$40\,\mu$m

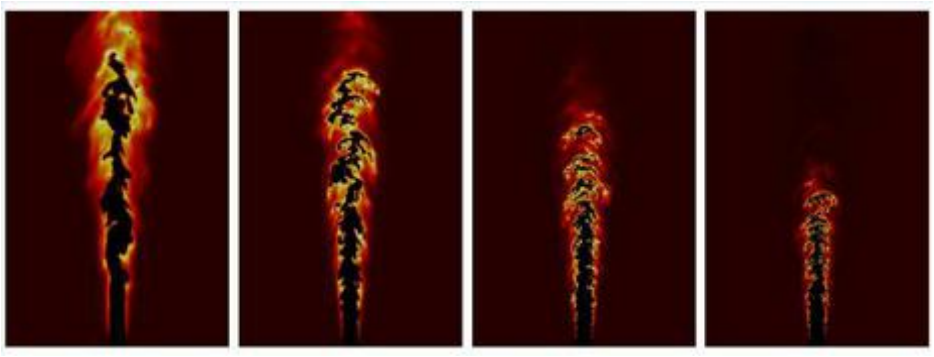

Figure 1: Two dimensional cuts of the field of the mass fraction of atomic oxygen in the four flames simulated. The domain is scaled with the slot width, H.

*Corresponding author. Email: antonio.attili@kaust.edu.sa

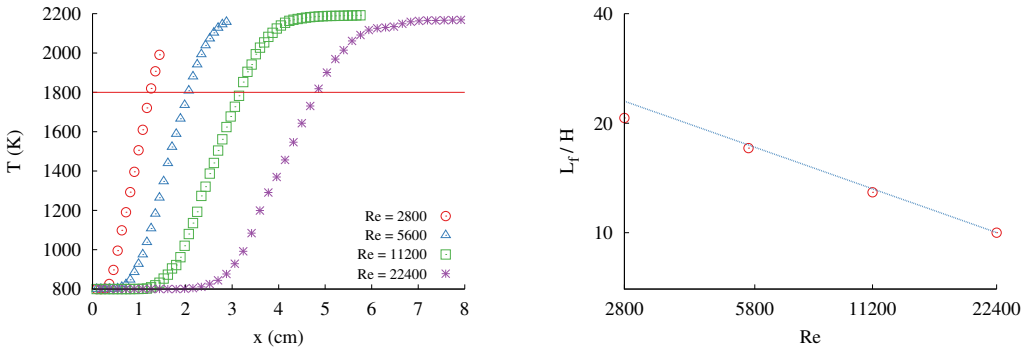

Figure 2: Left: mean temperature along the jet centerline for the four flames at different Reynolds numbers. The red horizontal line marks the temperature value used to define the flame tip and the length of the flame. Right: length of the flame for different Reynolds numbers, normalized with the slot width; the line is a power-law fit to the three cases with the highest Reynolds number with the form Re^c with $c = -0.4$.

The gas phase hydrodynamics are modeled with the reactive, unsteady Navier-Stokes equations in the low Mach number limit [1]. The species obey the ideal gas equation of state and all transport properties are computed with a mixture-average approach. Combustion is modeled using a skeletal mechanism of 16 species and 73 reactions and is treated with finite-rate chemistry.

RESULTS

Overall behavior and flame length

Figure 1 shows the mass fraction of oxygen in the four flames at different Reynolds number. As expected, it is evident that the range of scale characterizing the fields increases with the Reynolds number. In addition, the figure show that the length of the flames, measured in terms of the slot width H, decreases as the Reynolds number increases. A quantitative assessment of the dependence of flame length L_f on the jet Reynolds number is presented in Fig. 2. The flame length, normalized with the jet width H, decreases significantly as the Reynolds number increases. This is consistent with an increase of the turbulent flame speed due to the increased flame surface area caused by the larger Reynolds number.

Fractal dimension of the flame surface

The fractal dimension of the flame, identified by the temperature isosurface T=1800 K, has been computed with a box counting algorithm and it is shown in Fig.3 for the flame at Re=11200. The analysis shows a fractal dimension of the flame surface of 2.6, in agreement with recent results obtained in different turbulent premixed flames [2]. Very similar fractal dimensions have been obtained for the flames at Re=5600 and 22400.

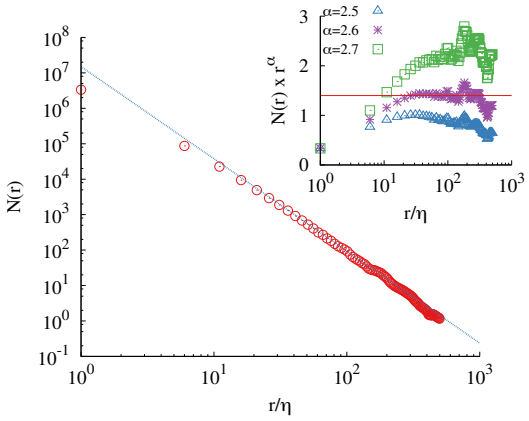

Figure 3: Application of the box counting algorithm to the flame at Re=11200. Number of boxes needed to cover the flame surface as function of the box size (red dots). The blue line has a slope in the log-log plot of -2.6, corresponding to a fractal dimension of 2.6. The inset shows the same results compensated with the scaling $r^{2.6}$ (purple star). The compensated results is shown also for a fractal dimension of 2.5 and 2.7 to assess the robustness of the results.

[1] Attili A. *et al.*: Formation, growth, and transport of soot in a three-dimensional turbulent non-premixed jet flame. Comb. Flame 161:1849-1865, 2014.
[2] Chatakonda O. *et al.*: On the fractal characteristics of low Damköhler number flames. Comb. Flame 160:2422-2433, 2013.

ADJOINT-INFORMED IGNITION CHARACTERIZATION

Jesse Capecelatro*[1], Daniel J. Bodony[2], and Jonathan B. Freund[2,3]

[1]*The Center for Exascale Simulation of Plasma-coupled Combustion (XPACC), University of Illinois at Urbana-Champaign, Urbana, Illinois, USA*

[2]*Department of Aerospace Engineering, University of Illinois at Urbana-Champaign, Urbana, Illinois, USA*

[3]*Department of Mechanical Science and Engineering, University of Illinois at Urbana-Champaign, Urbana, Illinois, USA*

Summary The adjoint of the linearized reactive compressible flow equations is used to quantify ignition sensitivity in unsteady combustion. The corresponding sensitivity gradients are used to map the boundary between successful and failed ignition. Owing to the ultimately binary outcome (i.e., it succeeds or fails after some period), care must be taken to define an appropriate cost functional that both quantifies ignition success and varies smoothly near its threshold. Such a cost functional is designed to measure early-time behavior, and an indicator function identifies successful ignition. The approach is demonstrated in a homogenous reactor and a non-premixed shear layer. The line-search algorithm is shown to automatically detect the ignition boundary from an initial set of modeling parameters within a few iterations. The gradient information is used to construct a tangent space for mapping the ignition boundary subject to specific constraints.

BACKGROUND

The repeatable and accurate control of ignition in fuel-air mixtures has remained a key challenge in the design of many practical combustion systems. In general, the initiation and propagation of a flame from a cold (non-reacting) mixture is sensitive to the instantaneous flow conditions, local mixture fraction, and position, extent, and intensity of the ignition source. Due to the large number of modeling parameters required to simulate unsteady combustion, detecting the source of uncertainty in large-scale simulations is tedious and computationally intensive. Ignition probability maps of canonical flows (e.g., turbulent jets and counterflow diffusion flames) generated experimentally are reported. Unfortunately, such a brute-force search is both time consuming and expensive, problem specific, and does not illuminate underlying mechanisms. In recent years, adjoint methods have been used to calculate sensitivity to an arbitrarily large number of parameters in turbulent flows, with a computational cost that is only marginally greater than the primal solution [1]. Due to the binary outcome of ignition, sensitivity gradients near its threshold are ill-defined, and thus special care needs to be taken to formulate a useful adjoint method in this context.

APPROACH

In the present study, a space-time discrete-adjoint method recently developed for high-fidelity compressible turbulence simulations [1] is extended to chemically-reacting mixtures. The compressible Navier-Stokes equations are solved in a high-order finite-difference framework that satisfies the summation-by-parts property with the simultaneous-approximation-term boundary treatment to ensure an energy estimate. The chemistry is described by a single-step irreversible Arrhenius reaction. The thermal effect of ignition is modeled as a source term in the energy equation that is a function of position $(x_0,\ y_0)$, radius $(r_x,\ r_y)$, time of peak power t_0, duration τ_{ig}, and applied power a. Here, x and y represent the streamwise and vertical coordinates, respectively. Shock-induced vorticity at the location of the thermal deposition is modeled empirically as a source term in the momentum equation that depends on a user-defined value of the Mach number of the resulting shock, M_0.

To quantify ignition success, a burning index $\mathcal{I}$ is defined as

$$\mathcal{I} = \int_\Omega W_Z T d\mathbf{x}, \tag{1}$$

where Ω is the region occupied by the interior of the simulation domain, T is a non-dimensional temperature that varies from 0 in a cold non-reacting mixture to 1 at the adiabatic flame temperature, and W_Z localizes the functional near the stoichiometric surface. The cost functional is computed as $\mathcal{J} = \int_{t_1}^{t_2} r\mathcal{I} dt$, where t_1 and t_2 are the start and end times of the simulation, and r windows the cost functional about the ignition transient. It was found that representing r as Gaussian with a peak value at t_0 and a standard deviation τ_{ig} provides smooth gradients in $\mathcal{J}$ near the ignition boundary. However, the cost functional is unable to detect whether or not successful ignition has occurred, and thus an indicator function is defined as the instantaneous burning index at steady state, $\mathcal{I}_f \equiv \mathcal{I}(t = t_2)$. Using these two metrics, a backtracking line-search algorithm can find a set of parameters on the ignition boundary. The adjoint solution is used to form a normal vector $\hat{\mathbf{n}} = \frac{\partial \mathcal{J}}{\partial \theta} / \| \frac{\partial \mathcal{J}}{\partial \theta} \|$ that provides a direction to adjust the set of parameters. Once on the ignition boundary, the gradient obtained from the adjoint solution is used to construct a tangent space at that point. Under specific guidance, the ignition surface can be mapped out from the identified set of parameters.

*Corresponding author. Email: jcaps@illinois.edu

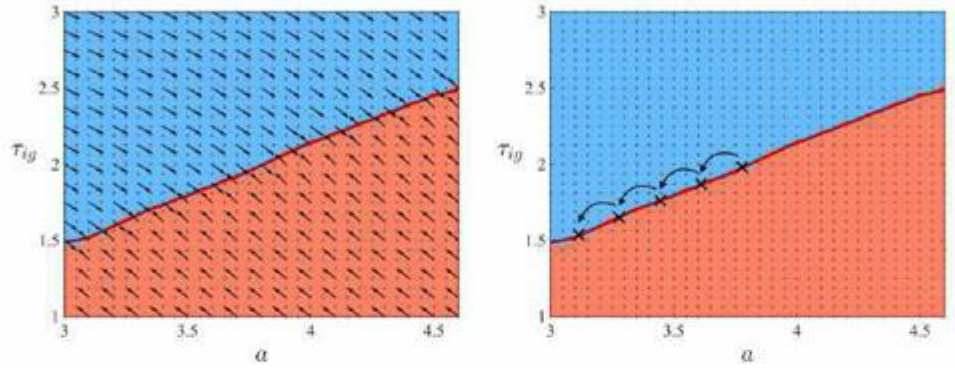

(a) Normal vectors $\hat{} = \pm \frac{\nabla \mathcal{J}}{\|\nabla \mathcal{J}\|}$.

(b) Traversing the ignition boundary.

Figure 1: Ignition maps of the WSR configuration in $\theta = [a \quad \tau_{ig}]^{\mathsf{T}}$ parameter space. Successful (red) and unsuccessful (blue) ignition.

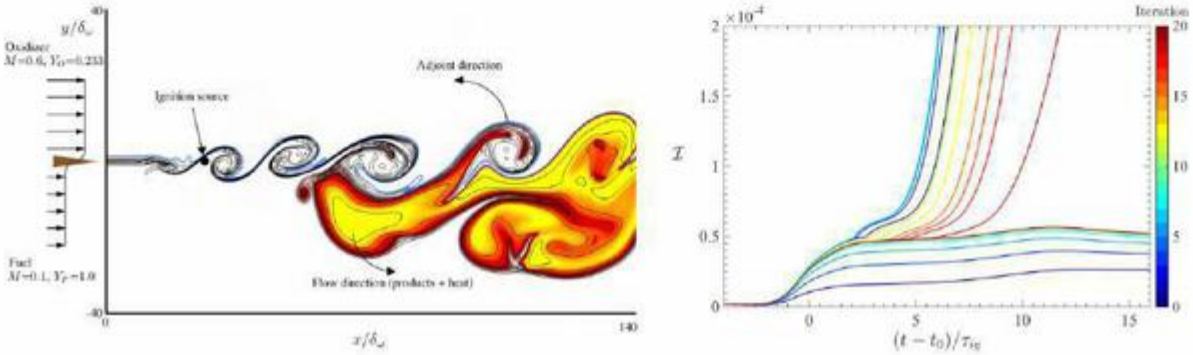

(a)

(b)

Figure 2: Localized ignition in a non-premixed spatially evolving mixing layer. (a) Mixture fraction (black lines), stoichiometric mixture (blue line), and temperature (increasing from red to yellow) shortly after ignition. (b) Convergence of the burning index towards the ignition boundary.

RESULTS

The method is demonstrated in a homogeneous (zero-dimensional) well-stirred reactor (WSR), shown in Fig. 1. For this case, 289 solutions were obtained to reveal the ignition behavior in $a-\tau_{ig}$ parameter space. Figure 1(a) shows how $\boldsymbol{n}$ obtained from the adjoint solution points to the ignition boundary at each point in parameter space. In Fig. 1(b), the tangent space is explored by updating τ_{ig} with the constraint of minimizing a. This is achieved by defining a unit tangent vector $\boldsymbol{t}$ such that $\boldsymbol{t} \cdot \boldsymbol{n} = 0$.

Identification of the ignition boundary is also demonstrated in the two-dimensional hydrogen–air mixing layer shown in Fig. 2(a). The mixing layer consists of an upper stream of pure fuel (mass fraction $Y_F = 1$) with Mach number $M = 0.6$, and lower stream of oxidizer (mass fraction $Y_O = 0.233$) with $M = 0.1$. The mixture is initially cold with a Reynolds number based on the velocity difference and vorticity thickness δ_ω of 500. Further details for a corresponding non-reacting mixing layer under similar conditions are described elsewhere [2, 1]. Figure 2(b) shows convergence of $\mathcal{I}$ towards the ignition boundary during the first 20 iterations of the line-search algorithm. It can be seen that convergence towards the ignition boundary increases the ignition delay time.

This material is based in part upon work supported by the Department of Energy, National Nuclear Security Administration, under Award Number DE-NA0002374. This research used resources of the Oak Ridge Leadership Computing Facility, which is a DOE Office of Science User Facility supported under Contract DE-AC05-00OR22725.

References

[1] Vishnampet, R., Bodony, D. J., and Freund, J. B.: A practical discrete-adjoint method for high-fidelity compressible turbulence simulations. J. Comp. Phys. 285:173–192, 2015.

[2] Wei, M. and Freund, J. B.: A noise-controlled free shear flow. J. Fluid Mech. 546:123–152, 2006.

MODELING OF DETONATION PROCESSES IN H2-AIR MIXTURES WITH CONCENTRATION GRADIENTS

Ilya Semenov[1,2a)], Roman Solomatin[1,2] & Nikita Puchkin[1,2]
[1]*Institute for Computer Aided Design, Russian Academy of Sciences, Moscow, Russia*
[2]*Moscow Institute of Physics and Technology, Dolgoprudny, Russia*

Summary The work is devoted to the numerical modeling of detonation propagation in rectangular channel filled hydrogen-air mixture with transverse concentration gradient. The statement of problem is based on experimental investigations, which were performed recently in Technical University of Munich. Modeling is implemented in two-dimensional statement with using detailed kinetics model of hydrogen combustion. The presence of deficiency propagation velocity of the detonation wave (DW) in a channel filled a mixture with transverse concentration gradient compared with one in the channel filled with a homogeneous mixture at the same average volumetric hydrogen concentration is consistent with the experimental data. The special mode of detonation propagation for channel filled hydrogen-air mixture with averaged volumetric concentration of hydrogen 40% and volumetric concentration of hydrogen 64.6% at the upper wall of the channel is revealed. In that mode, there is strong periodically arising transverse wave, which burns rich mixture at the upper part of the channel.

STATEMENT OF THE PROBLEM

There are many numerical and experimental investigations of initiation and propagation detonation in homogeneous reactive mixtures. However, in accident scenarios and in the combustion chambers of detonation engines reactive mixtures can be inhomogeneous due to mixing processes: convection and diffusion. Propagation of the detonation in channel with transverse concentration gradient can be considered as one of the example propagation of detonation in real world. There are several experimental [1], [2] and theoretical [3] [4] investigations which devoted to that problem. In [2] two different modes single- and multi-headed of detonation propagation in channel filled hydrogen-air mixture with concentration gradients were revealed. Single-headed mode with one strong transverse wave in channel was obtained for the cases with special profiles of hydrogen concentration and averaged volumetric concentration of hydrogen in channel less than 30%. For those cases volumetric concentration of hydrogen at the bottom of channel is less than 9.5%. In present work we consider the statement of problem which based on the experimental work [2]. The propagation of detonation in rectangular two-dimensional channel with height 0.06 m and length 0.5 m filled by hydrogen-air mixture with transverse concentration gradients profiles from [2] is investigated. Detonation in the channel is initiated by explosion of stoichiometric hydrogen-air mixture at the left closed end of the channel. Two profiles of volumetric concentration of hydrogen for averaged volumetric concentrations 30% and 40% is presented on fig. 1. The computational domain consist of 75 millions cells.

MATHEMATICAL MODEL AND NUMERICAL PROCEDURE

The mathematical model is based on Euler equations, which describe two-dimensional (2D) non-stationary flows of non-viscid compressible multicomponent reactive gaseous mixture, coupled with chemical kinetics model. Method of splitting with respect to physical processes, finite volume method and predictor-corrector time integration scheme are used for the numerical solution of the problem. The fluxes through the computational cells faces are calculated with Godunov's method. To enhance the accuracy of the numerical procedure the MUSCL approach with upwind-biased 3rd order scheme of interpolation and minmod limiter are used. The dependences of heat capacity and enthalpy of components from the temperature are approximated by the polynomial functions. For numerical investigations, we used high performance computing. Parallelization is performed by means of decomposition of a computational domain. The numerical investigations were implemented with the use of up to 3000 processor cores of multiprocessor systems MVS-100k (Joint Supercomputer Center RAS) and LOMONOSOV (Research Computing Center of the Moscow State University). The detailed description of the mathematical model, numerical procedure and parallelization technique can be found in [5]. The combustion of hydrogen-air mixture is modeled by detailed kinetics, which includes 22 reversible chemical reactions with 9 components [6].

RESULTS OF CALCULATIONS

On fig. 2 computed smoke-foil records for the case of averaged volumetric concentration of hydrogen in channel 40% are presented. For that case, we revealed strong periodically arising transverse wave, which burns rich mixture at the upper part of the channel. The length of the period is about 0.12 m. At the bottom wall of the channel in the lean mixture, we can observe Mach stem, that corresponds to the calculation data from [3], [4]. For the case with averaged volumetric concentration of hydrogen in channel 30% cellular structure of the DW is more regular (see fig.3). It should be noted, that detonation cell size, obtained in our calculations, is smaller than in experimental data [2]. Propagation velocity DW is lower in a gradient mixture than in a homogeneous mixture at equal average hydrogen concentration. Deficiency of detonation

[a)] Corresponding author. Email: semenov@icad.org.ru.

propagation velocity is about 2% in our calculations. The dynamics of developing strong transverse detonation wave in the upper part of the channel is presented on fig.4. At the upper part of the channel in fuel-rich mixture, a big unreacted pocket is generated before initiated strong transvers detonation due to the decoupling of leading shock wave and reaction zone. The strong transverse detonation wave propagates in the upper part of the channel where volumetric concentration of the hydrogen more than 50%.

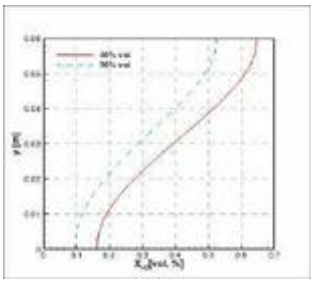

Figure 1. The initial profiles of volumetric concentration of hydrogen in channel.

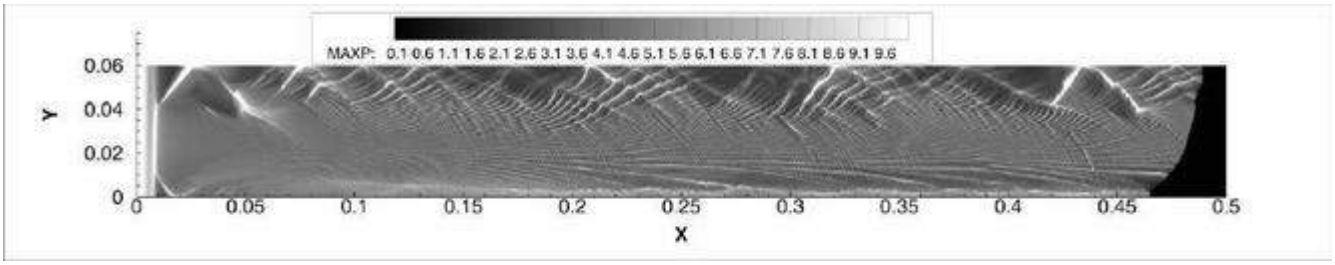

Figure 2. Cellular structure of DW for the case of averaged volumetric concentration of hydrogen in channel 40%.

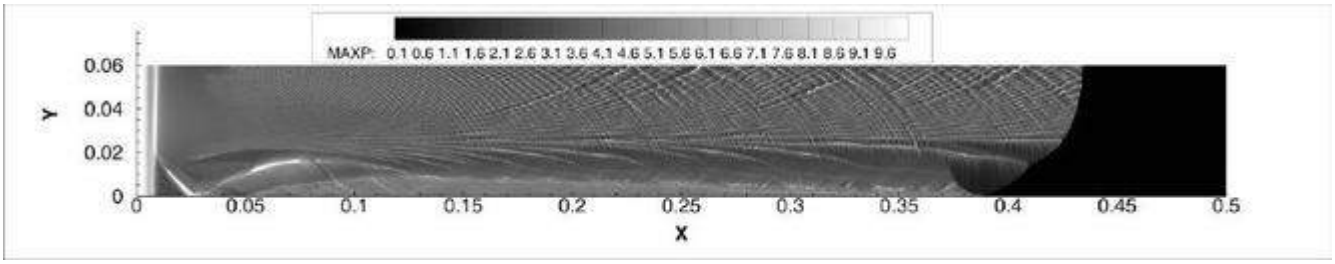

Figure 3. Cellular structure of DW for the case of averaged volumetric concentration of hydrogen in channel 30%.

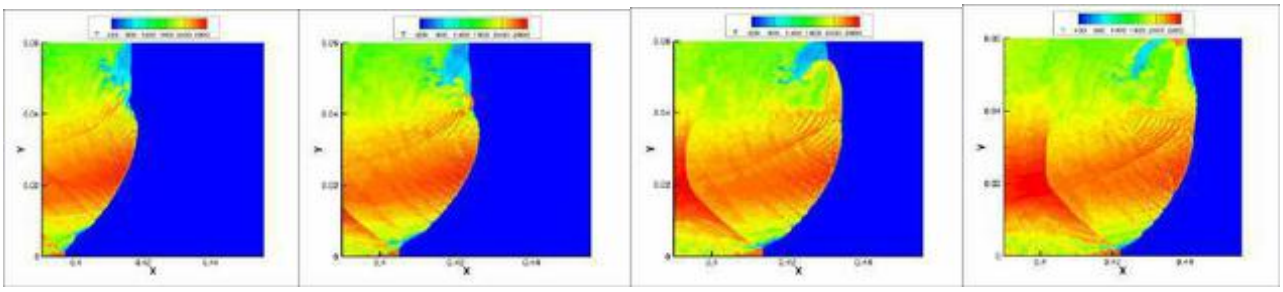

Figure 4. Gas temperature fields in Kelvin degrees at the successive time moments (time interval is 4 mcs).

References

[1] Ishii, K. and Kojima, M.: Behavior of Detonation Propagation in Mixtures with Concentration Gradients. *Shock Waves* **17**:95–102, 2007.

[2] Boeck L.R.: Deflagration-to-Detonation Transition and Detonation Propagation in H2-Air Mixtures with Transverse Concentration Gradients. *PhD Thesis*, TUM Institute of Energetic, Munich, 2015.

[3] Kessler D.A., Gamezo V.N., Oran E.S.: Gas-Phase Detonation Propagation in Mixture Composition Gradients. *Phil. Trans. R. Soc. A* **370**:567–596, 2012.

[4] Ettner, F., Vollmer, K.G. and Sattelmayer T.: Mach Reflection in Detonations Propagating Through a Gas With a Concentration Gradient. *Shock Waves* **23**:201–206, 2013.

[5] Semenov I., Akhmedyanov I., Lebedeva A., Utkin P.: Three-dimensional Numerical Simulation of Shock and Detonation Waves Propagation in Tubes with Curved Walls. *Sci. Tech. Energetic Materials* **72**:116–122, 2011.

[6] Keromnes, A., Metcalfe, W.K., Heufer, K.A. et al.: An experimental and detailed chemical kinetic modeling study of hydrogen and syngas mixture oxidation at elevated pressures. *Combustion and Flame* **160**:995–1011, 2013.

3-D FLAME CHARACTERIZATION VIA X-RAY COMPUTED TOMOGRAPHY

Jared Dunnmon* [1], Meng Wu[2], Yan Xia[2], Sadaf Sobhani[1], Rebecca Fahrig[2], and Matthias Ihme[1]
[1]*Department of Mechanical Engineering, Stanford University, Stanford, California, USA*
[2]*Department of Radiology, Stanford University, Stanford, California, USA*

Summary X-ray Computed Tomography (XCT) measurements are used to characterize a krypton-diluted methane-air Bunsen flame in three dimensions. Multiple tomographic datasets are averaged in order to reduce noise in the recorded attenuation field. Internal attenuation fields within the Bunsen cone give insight into thickening of the reaction zone as gas travels towards the top of the flame, and extraction of a thresholded isosurface via Otsu's method allows for 3-D visualization of the flame front. Results presented here reflect encouragingly on the potential of XCT to provide powerful characterization of flame structure in three dimensions regardless of optical accessibility.

INTRODUCTION AND BACKGROUND

X-ray Computed Tomography (XCT) has the potential to allow for 3-D visualization of flame structure at high spatial resolution, with short acquisition times, and without optical access. XCT is generally accomplished by measuring projections of integrated X-ray attenuation at multiple angles around a subject and reconstructing a 3-D attenuation field using an implementation of the inverse Radon transform as described in [1]. Common flat-panel detector systems can meet the 250 μm criterion introduced by [2] to define the upper limit on resolution that could be reasonably expected to visualize the primary reaction zone. Further, it would be unnecessary to estimate 3-D surface areas from 2-D images if 3-D field data on the location of a wrinkled flame front were available. While XCT methods do have lower temporal resolution than planar laser-based techniques, the potential for even time-averaged 3-D flame structure represents a potentially useful addition to the current toolset of experimental combustion. The fundamental theory behind applying XCT to flame structure is based on the fact that the number density of an inert, radiodense gaseous tracer such as krypton can be used to explicitly identify the location of the flame front via the reduction in X-ray attenuation that occurs as number density of the radiodense tracer decreases with increasing temperature. The goal of this study is to demonstrate the capacity of XCT to extract 3-D flame structure in an experimental setting. For this reason, a canonical laminar Bunsen flame is used as a test case for illustrating not only the viability of these physical concepts, but also the accessibility of associated imaging and analytic techniques.

METHODS

Experimental data for this study were obtained using the Stanford Tabletop X-ray Facility, consisting of a fluoroscopic cone-beam X-ray source (CPI), flat-panel detector (Varian), and precision motion control system (Parker). The X-ray setup was modified to allow for a steady flow of gas to be directed through an assembly that could be rotated in controlled fashion by the motor. A Bunsen burner of 152.4 mm in length and 12.5 mm in diameter with an upstream flow straightener was mounted to the motor apparatus. A premixed krypton-diluted methane-air Bunsen flame was established with mole fractions of $X_{Kr} = 0.339$, $X_{N_2} = 0.455$, $X_{O_2} = 0.121$, $X_{CH_4} = 0.085$, an overall flow rate of $u_o = 50$ cm/s, $Re = 600$, and corresponding $\Phi = 1.41$. The flame was first lit and allowed to reach steady state before visual photographs were recorded to enable comparison between the luminous visual profile and that extracted from XCT. A plastic tube of 95 mm in inner diameter and 3 mm in thickness was then placed around the burner to shield the flame from ambient drafts while also making the flame optically inaccessible. Fifteen tomographic datasets were acquired, with each set consisting of 625 projections over 360 degrees acquired in one minute of scan time. Scan parameters of 45 kVp peak tube voltage and 30 mA tube current were used to maximize Signal-to-Noise Ratio (SNR). The flame was then extinguished and fifteen background datasets were obtained to allow for subtracted attenuation measurements. Unless otherwise specified, differential attenuation data presented here defines the difference between the projection-domain average of fifteen flame scans and that of the fifteen background scans. Reconstructions were computed using the analytic Feldkamp-Davis-Kress filtered backprojection method with a Hamming-windowed ramp kernel to eliminate high-frequency noise [1]. Additional data processing steps included standard ring-artifact correction and projection-domain wavelet denoising to further reduce spurious high-frequency phenomena. The reconstruction volume is $101 \times 101 \times 332$ voxels with 0.2 mm isotropic spacing.

RESULTS AND DISCUSSION

As shown in Fig. 1, the XCT reconstruction yields a rich dataset from which a variety of conclusions can be drawn. In the XCT data in Fig. 1(a), for instance, we observe a well-visualized flame cone with a profile that is substantially more linear

*Corresponding author. Email: jdunnmon@stanford.edu

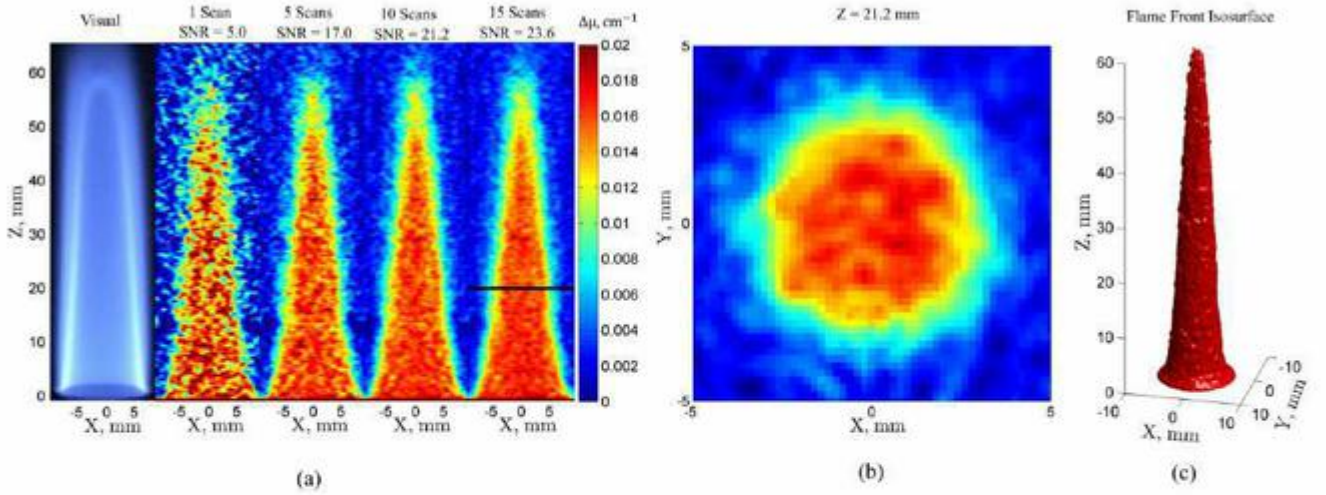

Figure 1: Bunsen flame visualization (colormap for differential attenuation $\Delta\mu$ in cm^{-1}); (a) Vertical cross sections, visual and mean XCT; (b) Axial XCT cross-section at height indicated by horizontal line in panel (a); (c) Flame front isosurface from XCT

than that of the visual contour and is relatively insensitive to the outer combustion zone characteristic of rich Bunsen flames. This sharpness in the XCT outer contour in Fig. 1(a) occurs because the X-ray signal is by definition only affected by the gas temperature and (to a small degree) krypton diffusion at the flame boundary, and thus what we are observing is a close approximation of the cold gas cone suggested by [3] as the ideal contour to use for computation of the laminar flame speed. As expected, SNR increases with the number of scans considered in the averaging procedure. Further, as one can observe from the axial cross-section of Fig. 1(b), the attenuation within the inner cone becomes lower (a light blue color) as the mixture crosses the flame front. This reaction zone region of higher temperature and lower krypton number density near the edges of the flame cone (visualized here by the light blue regions) increases in extent towards the top of the flame as the diameter of the flame cone decreases. These results also give insight into flame axisymmetry, as small deviations from axisymmetry do indeed occur and are easily diagnosed by XCT as in Fig. 1(b). Another advantage of using computed tomography is the capability to characterize results in full three dimensional space. Thus, we visualize the reaction front by thresholding the XCT data using Otsu's method to separate the burned gases from the unburned signal—extracting the attenuation isosurface at the threshold pixel value yields a 3-D realization of the flame-front contour [4]. Notably, this non-parametric thresholding technique requires no user input or modeling parameters while performing robustly over several trials. A 3-D flame front visualization of this type is shown in Fig. 1(c), after application of a $3 \times 3 \times 3$ median filter to ensure appropriate smoothness. Such isosurfaces defining the location of the flame front in three dimensions would be particularly helpful in diagnosing such critical quantities as flame structure, flame speed, and reaction zone thickness in experimental combustion studies.

CONCLUSIONS

We have demonstrated the applicability of XCT to characterization of a premixed krypton-diluted methane-air Bunsen flame in three dimensions within an optically inaccessible environment. The ability of this diagnostic to supply data on the location of the flame front and reaction zone thickness while assessing flame structure in a manner that is not confined to axisymmetric configurations gives it distinct advantages over traditional experimental combustion techniques. Further applications could include flame speed calculation via the total area method, measuring key turbulent combustion quantities such as the reaction zone thickness, and obtaining 3-D, time-averaged visualizations of spatially complex flame fronts found in a wide variety of configurations [2]. Future work should involve investigation of diluent effects on combustion chemistry and flame structure along with optimization of the reconstruction methodology for low-contrast datasets.

References

[1] Hsieh, J.: Computed Tomography: Principles, Design, Artifacts, and Recent Advances. Bellingham, WA, USA, 2009.
[2] Driscoll, J.F.: Turbulent Premixed Combustion: Flamelet Structure and its Effect on Turbulent Burning Velocities. Prog. Ener. Comb. Sci. 34:91-134, 2008.
[3] Andrews, G.E. and Bradley, D.: Determination of Burning Velocities: A Critical Review. Combust. Flame 18:133-153, 1972.
[4] Otsu, N. A Threshold Selection Method from Gray-level Histograms. Automatica 11:23-27, 1975.

PARTICLE DYNAMICS THROUGH TURBULENT PREMIXED FLAMES USING SIMULTANEOUS 10 KHZ TPIV, OH PLIF, AND CH_2O PLIF

Jeffrey R. Osborne[1], Campbell D. Carter[2], and Adam M. Steinberg *[1]

[1]*Institute for Aerospace Studies, University of Toronto, Toronto, M3H 5T6, Canada*
[2]*Air Force Research Laboratory, Wright-Patterson AFB 45433-7103, YSA*

Summary This work experimentally quantifies the relationship between local reaction rate and flame thickness for turbulent premixed flames in the corrugated flamelet and thickened preheat zone/thin reaction zone regimes using data from simultaneous 10 kHz tomographic particle image velocimetry (TPIV), hydroxyl planar laser induced fluorescence (OH PLIF), and formaldehyde (CH_2O) PLIF. Two novel reaction rate metrics are presented, which are based on tracking fluid elements in a Lagrangian manner as they traverse from the flame leading edge to the reaction zone. Results indicate that in the thickened preheat zone regime there is a reduction in residence time by nearly 20%, despite the flame being broader. A positive linear correlation is observed between a flame speed metric and flame thickness, which is attributed to their mutual relationship with turbulent diffusivity.

INTRODUCTION

Past measurements of reaction rate in turbulent flames have been achieved through measuring scalar representations of an important reaction pathway or via the local displacement speed. Scalar information can be obtained from planar laser-induced fluorescence (PLIF) of the CH or HCO radical [1, 2], or through the product of OH and CH_2O [3]. Such information however is challenging for model development because the measurements are difficult to quantify and not directly related to model inputs. Conversely, several studies have investigated the local displacement speed in turbulence premixed flames [4, 5, 6] to quantify reaction rate. This method however is highly dependent on the particular isosurface being interrogated, with negative local displacements speeds often reported despite the flame not exhibiting negative reaction rate [7]. Instead, it is more informative to consider metrics of the total reaction rate experienced by a fluid element as it traverses the flame. The use of Lagrangian paths inherently accounts for actual fluid trajectory and any changes to the flow-flame interaction.

This paper will present conditional statistics of two experimentally-derived metrics of local reaction rate in turbulent premixed flames based on the tracking of theoretical Lagrangian particles (TLPs) through two turbulent premixed flames. In doing so, this paper will describe the relation between flame structure and reaction rate in flames spanning from the laminar flamelet to the thin reaction zone regimes.

EXPERIMENTAL SETUP

Simultaneous 10 kHz TPIV, OH PLIF, and CH_2O PLIF were performed in a piloted premixed jet burner. The burner consisted of a plenum, two turbulence generating plates, and a converging/diverging nozzle. The premixed methane/air main flame issuing from the nozzle was stabilized using a non-premixed hydrogen pilot flame on a concentric grid of holes at the nozzle exit plane. The flow and flame properties were such that Case 1 was in the corrugated laminar flamelet regime and Case 2 was in the thickened preheat zone regime. Details of the experiment and diagnostics can be found in Ref. [8].

Four high-speed cameras were used to image the ca. $25 \times 15 \times 2.5$ mm^3 volume, illuminated by an Nd:YAG laser at 10 kHz repetition rate. The final vector field was calculated using an interrogation volume length of ca. 620 μm, with a ca. 155 μm spacing between vectors in all three dimensions. The temporal resolution was sufficient to capture the dynamics of the smallest resolved spatial scales [8].

Two intensified high-speed cameras were used to image the OH and CH_2O fluorescence at approximately 283.2 nm and 355 nm respectively. The formed laser heights were approximately 30 mm and 7.5 mm respectively. Mean signal-to-noise of the two systems were approximately 6-35 and 2-3, the latter owing to the low fluorescence yield of CH_2O.

RESULTS

Two metrics are proposed to characterize reaction rate. The first is based on the time required for a fluid element to traverse the local flame structure, equivalent to the residence time of fluid elements in the flame (τ_c). The second simultaneously utilizes the residence time and local flame structure to determine a flame speed metric ($S_i = d_{i,0}/\tau_c$, where $d_{i,0}$ is the fluid element initial distance to the flame) for a given particle i.

Calculation of τ_c requires tracking of theoretical Lagrangian particles from the CH_2O leading edge (equivalent to the preheat layer leading edge) until they pass a flame surface based on Mie scattering tomography, which coincides with the

*Corresponding author. Email: adam.steinberg@utoronto.ca

region of rapid OH production albeit in 3D (equivalent to the region of high heat release). An example of this tracking for Case 1 is shown in Fig. 1. Means residence times for Cases 1 and 2 are respectively 0.57 ms and 0.47 ms. Moreover, a positive linear correlation exists between S_i and d_{i0}, indicating an increase in reaction rate with flame broadening which is attributed to an increase in turbulent diffusivity, as shown in Figure 2.

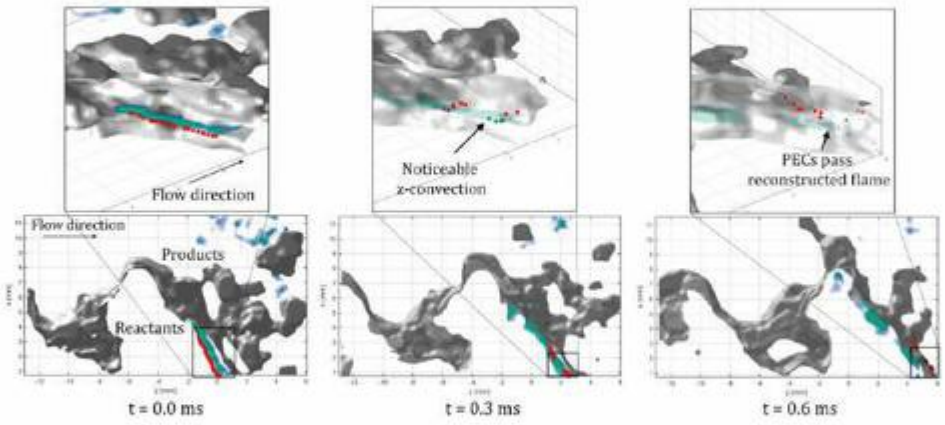

Figure 1: Example of particle tracking through the preheat layer for Case 1. Red circles denote centroid of control masses, black circles denotes control masses that have passed the flame surface, green contours is the extent of the CH_2O layer, and grey isosurface is the Mie scattering surface. Top and bottom images correspond to the same time steps. One in three particles shown for clarity

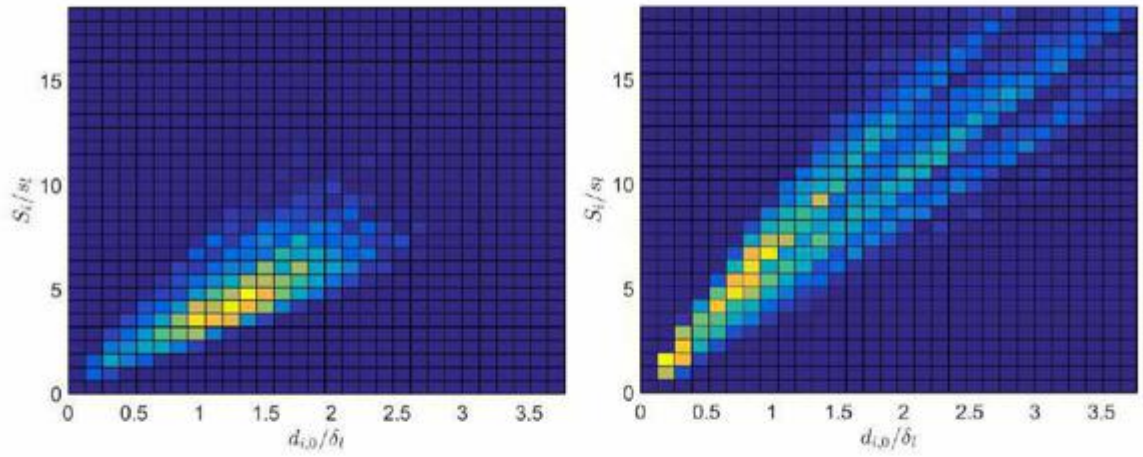

Figure 2: Joint PDF of flame speed metric S_i versus $d_{i,0}$, normalized by s_l and δ_l respectively, for (left) Case 1 and (right) Case 2.

References

[1] C. Carter, S. Hammack, T. Lee, *Applied Physics B* 116 (2014) 515–9.

[2] B. Zhou, J. Kiefer, J. Zetterberg, Z. Li, M. Aldén, *Combustion and Flame* 161 (2015) 1566–74.

[3] B. Ayoola, R. Balachandran, J. Frank, E. Mastorakos, C. Kaminski, *Combustion and Flame* 144 (2006) 1–16.

[4] G. Hartung, J. Hult, R. Balachandran, M. Mackley, C. Kaminski, *Applied Physics B* 96 (2009) 843–62.

[5] P. Trunk, I. Boxx, C. Heeger, W. Meier, B. Böhm, A. Dreizler, *Proceedings of the European Combustion Meeing* 34 (2013) 3565–72.

[6] A. Johchi, Y. Naka, M. Shimura, M. Tanahashi, T. Miyauchi, *Proceedings of the Combustion Institute* 35 (2015) 3663–71.

[7] S. Ruan, N. Swaminathan, Y. Mizobuchi, *Combustion Science and Technology* 186 (2014) 243–72.

[8] J. Osborne, S. Ramji, C. Carter, S. Peltier, S. Hammack, T. Lee, A. Steinberg, *Experiments in Fluids* Submitted.

EMISSION CONTROL CHALLENGES FOR COMPRESSION IGNITION ENGINES

Daniel Carder, Marc Besch, Arvind Thiruvengadam, & Ross Ryskamp[1]
[1]*Center for Alternative Fuels, Engines and Emissions, West Virginia University, Morgantown, WV, USA*

Summary As emission standards continue to evolve, it is clear that future control strategies will involve the integration of combustion optimization, fuel refinement and advanced exhaust after-treatment technologies. WVU CAFEE continues to engage the challenge of future regulation in a multi-pronged approach, investigating advanced combustion regimes, alternative fuels, and next-generation emission control technology. Results presented herein summarize recent results and discuss future pathways.

Modern Compression Ignition Engines, commonly referred to as diesel engines, face many challenges with respect to meeting U.S. federal- and state-mandated exhaust emissions standards. Additionally, these engines and their emissions control subsystems must comply with emissions standards for "useful life" periods of up to 435,000 miles all, while retaining the fuel efficiency and durability for which diesel engines are renowned. Since 1990, emissions standards of oxides of nitrogen (NOx) and particulate matter (PM) from heavy-duty diesel engines have decreased by approximately 97 and 98 percent, respectively [1]. To meet these standards, engine manufacturers have developed complex engine and after-treatment technologies. Diesel engines typically operate at a lean air-to-fuel ratio, one of the reasons for their superior fuel economy when compared to spark ignited engines that generally operate at stoichiometric air-to-fuel ratios. Lamentably, this lean operation is not conducive to the use of three-way catalysts for NOx abatement and requires the use of more complex technologies such as selective catalytic reduction (SCR). Additionally, diesel engines predominantly feature direct injection and stratified combustion which can result in the formation of PM, which must be controlled with technologies such as a diesel particulate filter (DPF).

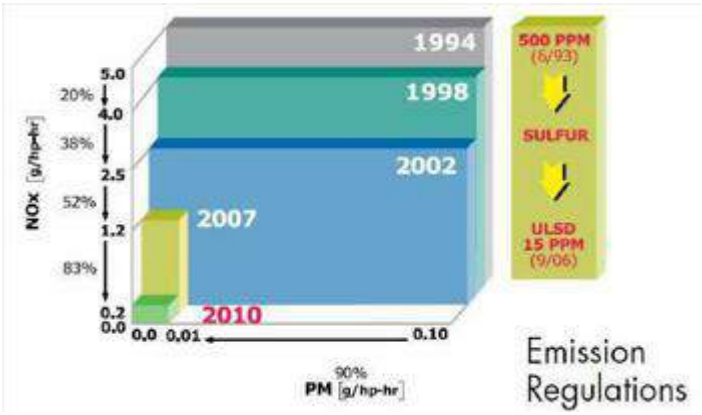

Figure 1 Historical trend of emissions standards for heavy-duty on-highway engines in the U.S. [4].

While, NOx and PM emissions have been steadily approaching near-zero levels, upcoming regulations will focus on reduction in fuel consumption and improvement of engine efficiency. Of the many pathways available for engine efficiency improvements, combustion optimization and advanced combustion strategies are one of the main focuses of next generation diesel engines. Closed loop combustion optimization techniques can benefit from improvements in miniature sensing technologies, while advanced combustion strategies can benefit from tailor made fuels that support low emissions and high efficiency pathways. One of the primary challenges of diesel engine combustion is to break the trade-off between PM and NOx. Concepts such as LTC, PCCI, and RCCI have demonstrated promise in this regard, however, fundamental understanding of fuel-air mixing, ignition delays and control of in-cylinder pressure rise rates are key in translation of such strategies to production platforms. WVU's Advanced Combustion Laboratory, with an optical engine and a single cylinder heavy-duty engine platform is conducting fundamental research in combustion visualization and the role of fuel property effects.

In August 2011 the first federally mandated greenhouse gas (GHG) and fuel consumption standards for medium and heavy-duty vehicles were adopted [2]. The GHG portion of the standard pertains to carbon dioxide (CO2), nitrous oxide (N2O), and methane (CH4) exhaust emissions. Phase 1 of these standards became applicable in 2014, with stringency increasing through Phase 2 which will cover model years 2021 through 2027. The intersection of these standards with existing pollutant standards, especially for NOx emissions, present a challenge to manufacturers. Technologies that reduce engine-out NOx emissions, such as exhaust gas recirculation (EGR), are typically associated with CO2 emission and fuel economy penalties. Placing further reliance of NOx reduction on after-treatment systems can increase the consumption of reductants such as diesel exhaust fluid (DEF) for SCR systems, and present duty-cycle challenges with respect to fatigue and warranty concerns.

Bio-derived and alternative fuels present an opportunity to simultaneously reduce CO2, NOx, and PM exhaust emissions, compared to petroleum derived diesel fuel. Although benefits in these exhaust constituents have been realized, increased carbon monoxide (CO) and hydrocarbon (HC) emissions have been observed during recent studies performed at WVU from i) biodiesel fuels investigated for the U.S. Navy and ii) dual-fuel diesel-natural gas retrofit kits for heavy-duty diesel engines. Unfortunately, in many instances bio-derived diesel fuel is more costly to produce than petroleum derived diesel. Additionally, there can be challenges related to the implementation of biodiesel in fueling systems designed for

[a] Corresponding author. Email: Daniel.Carder@mail.wvu.edu

petroleum based diesel fuel. In addition to the availability from large scale natural gas reserves in the shale gas region, the production of bio-methane from biomass has significantly increased as well. As of 2015 there were 645 operational landfill gas plants in the U.S. Waste Management estimates renewable natural gas could provide 25% lower diesel fuel consumption in the state of California. However, alternative fuel approaches, such as dual-fuel diesel-natural gas compression ignition, and dedicated natural gas engines are often associated with high levels of CH4 exhaust emissions that are not easily reduced by after-treatment based on current CH4 catalysts technologies. Current research at WVU is focused on developing after-treatment technologies aimed at reducing tailpipe emissions of methane from heavy-duty natural gas engines. Reducing the global warming potential of natural gas vehicle exhaust is the key to promoting natural gas technology over traditional diesel technology.

Perhaps adding to the challenges that lie ahead, regulations for light-duty diesel engines differ from heavy-duty in that they are certified in a vehicle on a chassis dynamometer. Consequently light-duty diesel vehicles must meet the same standards as their gasoline counterparts with the same regulatory classification (tier and bin). As emissions regulations progressed into the 21st century, the emissions reduction technologies for light-duty diesel vehicles had not commercially progressed as quickly as those for gasoline vehicles. This resulted in very few vehicles offered as shown in the figure to the right. Introduction and improvement of NOx storage catalysts, also known as lean NOx traps, and SCR technologies has helped to increase light-duty diesel vehicle market-shares today. Although, recent developments with Volkswagen may prove that NOx storage catalysts are not as efficient as claimed, leaving few options to SCR systems that typically occupy more space and require an additional fluid to be carried. These developments have also spawned regulatory agencies to announce future changes regarding future certification and compliance programs.

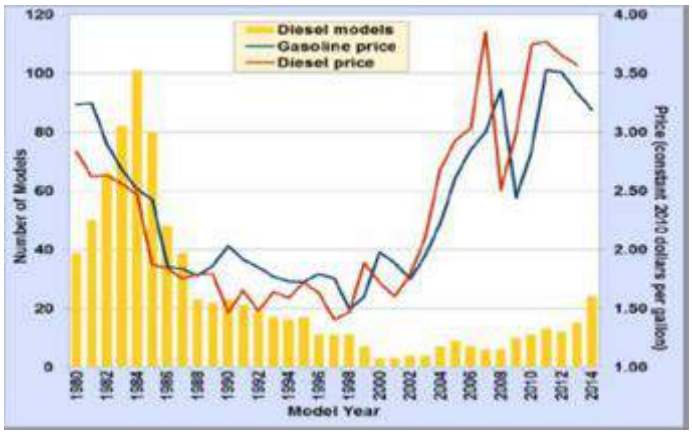

Figure 2 Diesel Engine Equipped Light-duty Vehicle Offerings by Model Year [3].

CONCLUSIONS

The compression ignition engine will remain the primary workhorse of the economy for the foreseeable future. However, currently available technology packages heavily depend on after-treatment systems to reduce regulated pollutants to the required low levels. This poses a challenge, especially for application subjected to lower engine operating loads such as drayage operation around ports, refuse hauling and urban driving, where after-treatment components experience lower than optimal thermodynamic exhaust gas conditions. In order to achieve high pollutant reduction efficiencies exhaust gas temperatures are being raised via thermal management strategies that in most cases adversely affect fuel consumption which stands in direct contrast to upcoming fuel economy requirements by the U.S. EPA. Additionally, projected improvements in thermal engine efficiencies will further escalate this problem by reducing exhaust gas temperatures. This discrepancy between improved energy efficiency and low emissions shows the need for a symbiosis between improvements in combustion strategies leading to reduced engine-out emissions rates, development of advanced fuels that enable and support advanced combustion regimes and finally, catalytic after-treatment systems that are capable of efficiently converting emissions during a broad range of exhaust temperatures.

References

[1] W. J. Charmley, "The Federal Government's Role in Reducing Heavy Duty Diesel Emissions," in SAE Commerical Vehicle Engineering Conference & Exhibition, Rosemont, 2004.

[2] ECOpoint Inc., "Heavy-Duty Vehicles: GHG Emissions & Fuel Economy," September 2011. [Online]. Available: https://www.dieselnet.com/standards/us/fe_hd.php. [Accessed 10 January 2016].

[3] S. C. Davis, S. W. Diegel, R. G. Boundy and S. Moore, "2014 VEHICLE TECHNOLOGIES MARKET REPORT," Oak Ridge, 2014.

[4] GRAINCO GS, Inc., "DEF," 2015. [Online]. Available: http://www.graincofs.com/energy/Pages/DEF.aspx. [Accessed 22 February 2016].

THE DESCRIBING FUNCTION OF SWIRLED SPRAY FLAMES

Kevin Prieur[1,2], Daniel Durox[1], Thierry Schuller[1], and Sébastien Candel [*1]
[1]*Laboratoire EM2C, CNRS, CentraleSupélec, Université Paris-Saclay, 92295 Châtenay-Malabry, France*
[2]*Safran Tech, E&P, Châteaufort, CS 80112, 78772 Magny-Les-Hameaux, France*

Summary The dynamical response of flames is of central importance in combustion instability analysis. The response of swirl spray flames considered in this article is determined experimentally in the form of a Flame Describing Function for various flames. Using a generic injector comprising a swirler, a hollow cone pressurized injection unit and a diverging end cup it is shown that flame shapes are markedly influenced by the end piece angle and that this parameter induces important changes in the describing function. This information in combination with a dynamical model is used in a second stage to infer potential bands of instability in an annular combustor.

Dynamical phenomena appear in many modern combustion systems giving rise to large amplitude oscillations driven by the unsteady flame response resonantly coupled by the acoustic eigenmodes of the system [1]. Much effort is being expanded to predict such instabilities, design systems which are less sensitive to perturbations, derive solutions to reduce or suppress oscillations [2]. One useful method has been to characterize the flame response through a transfer function (FTF) or in order to capture some of the flame nonlinearities through a describing function depending on frequency and amplitude of the incident perturbations (FDF) [2]:

$$\mathcal{F}(\omega, u') = \frac{Q'/\overline{\dot{Q}'}}{u'/\overline{u}} = G(\omega, u')\, e^{i\varphi(\omega,u')} \tag{1}$$

This information combined with an acoustic network model or a Helmholtz solver is then used to determine regions of instability and limit cycle amplitudes. While premixed flame FDFs are well documented, this is not the case for swirl spray flames despite their widespread use in applications like aircraft engines, thus motivating the present investigation. The experimental

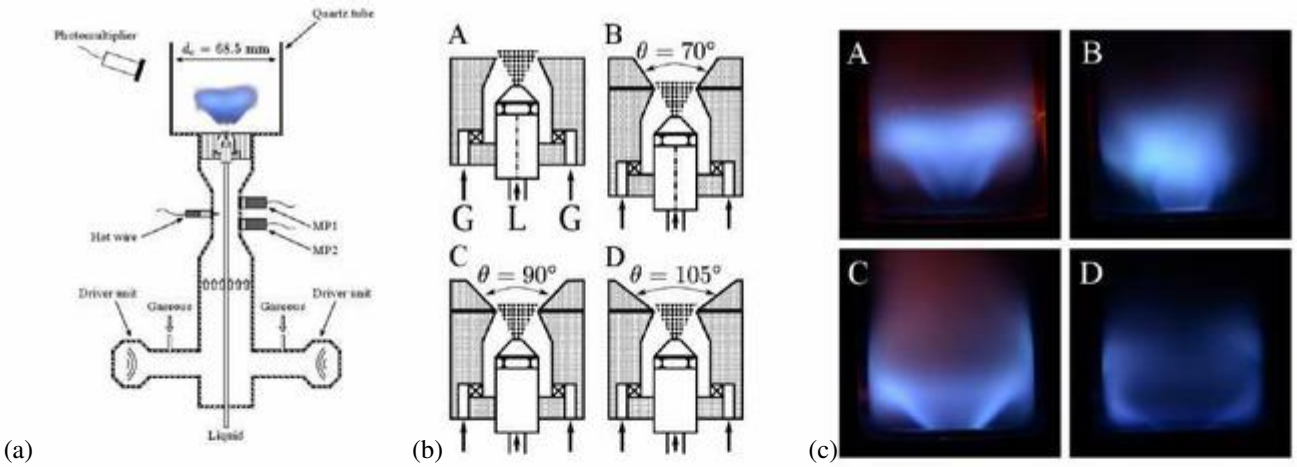

Figure 1: (a) Schematic of the burner to determine the flame response. (b) Injector configurations. Case A: No cup is installed. Case B: a $70°$ cup is installed. Case C: a $90°$ cup is installed. Case D: a $105°$ cup is installed. G stands for gas and L for liquid. (c) Flame shapes with different injector configurations. Case A: injector without cup generates an M flame. Case B: injector with $70°$ cup generates an amphora flame. Case C: injector with $90°$ cup generates a V flame. Case D: injector with $105°$ cup generates a corner flame.

configuration (Fig. 1(a)) comprises a plenum and a chamber (diameter d_c = 68.5 mm and a length l_c = 150 mm). Two driver units are plugged on the plenum formed by a cylindrical duct of 300 mm to modulate the gaseous flow. The injection system linking the plenum to the chamber comprises a swirler, a convergent section followed by a divergent cup with a variable angle. A simplex atomizer supplied with n-heptane at 9 bar generates a hollow cone spray. Detailed velocity profiles yield a swirl number of 0.68 and a droplet SMD $d_{32} \simeq 25\,\mu$m. The four different injector configurations considered in this study (see Fig. 1(b)) induce notable changes in the mean flame shape (Fig. 1(c)) an indication of possible modifications in the dynamical flame response.

*Corresponding author. Email: sebastien.candel@centralesupelec.fr

Flame dynamics

Flame Describing Functions are measured by modulating the air flow by the two driver units of 100 W RMS connected to the plenum. The amplitude u' of the modulation is measured with a hot wire placed at 100 mm from the back of the chamber. The region is chosen in order to have a nearly flat velocity profile. Two microphones (MP1 and MP2) are placed at the same position to evaluate u' using a second method. A photomultiplier (PM) with an OH* filter records the flame emission and this signal is used as a signature of the heat release rate. This sensor is tilted towards the injector position in order to capture the entire flame luminosity no matter its shape. One finds a notable difference in the gain shape and in the phase slope between the two configurations. The gain of the FDF in case A features two peaks at 600 and 1000 Hz. In case B, the gain is much flatter with a reduced peak at 600 Hz. The phase of the FDF is nearly linear indicating the presence of a time lag. The slope of the phase response changes significantly with the cup angle value. A theoretical modeling of annular combustors provides necessary conditions for instability in the form of instability bands. According to this model when $\pi < \varphi < 2\pi$ or $3\pi < \varphi < 4\pi$, the configuration is potentially unstable. These data may then be used to examine azimuthal instabilities of an annular combustor investigated at EM2C [4] which is now equipped with swirl spray injectors (MICCA-Spray).

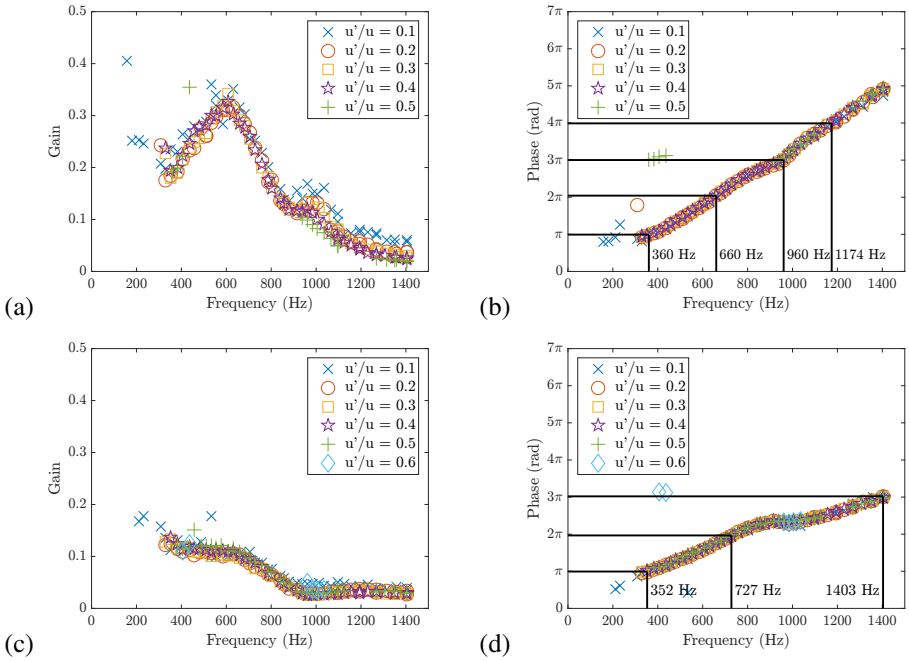

Figure 2: (a) and (b) Gain and phase of the FDF when the injector is mounted without any cup (conf. A), (c) and (d) Gain and phase of the FDF when the injector is mounted with a 70° cup (conf. B).

Conclusions

Flame Describing Functions of swirling spray flames are determined experimentally. It is found that for the particular injection system investigated, the FDF does not change significantly with the amplitude level but that the gain and phase functions notably change with the angle of the end piece divergent unit. It is found that the mean flame shape evolves with this angle and this in turn changes the dynamical flame response. Potential bands of instability are inferred from an examination of the measured phase response obtained in this single injector configuration leading to possible indications of instability in the MICCA-Spray annular system equipped with multiple injector units.

Acknowledgments Continuous support provided to this research project by Safran is gratefully acknowledged.

References

[1] Candel S. : Combustion dynamics and control- progress and challenges. Proceedings of the Combustion Institute 29:1-28, 2002.

[2] Yang, V. and Lieuwen T.C. (eds): Combustion instabilities in gas turbine engines. Progress in Astronautics and Aeronautics, vol. 210. AIAA Washington.

[3] Noiray N., Durox D., Schuller T., and Candel S. : A unified framework for nonlinear combustion instability analysis based on the flame describing function. J. of Fluid Mech. 615:139-167, 2008.

[4] Bourgouin J.F., Durox D., Moeck J.P., Schuller T., and Candel S. : Self-sustained instabilities in an annular combustor coupled by azimuthal acoustic modes. Proceedings of ASME Turbo Expo 2013, Paper GT2013-95010, San Antonio, Texas, USA, 2013.

SWIRL-STABILIZED NON-PREMIXED PROPANE/AIR FLAMES IN A GAS TURBINE MODEL COMBUSTOR

Sandipan Chatterjee [*1] and Ömer L. Gülder [1]

[1] *University of Toronto Institute for Aerospace Studies, Toronto, Ontario, Canada*

Summary Turbulent non-premixed swirl-stabilized flames were investigated in a gas turbine model combustor. Velocity and soot concentration fields for propane/air combustion at three overall fuel-air equivalence ratios were studied. Stereoscopic particle image velocimetry was used to acquire the three-dimensional velocity data in the combustor. The time-averaged soot volume fractions were obtained using the technique of laser induced incandescence. The flow field and soot measurements were conducted separately, but under identical experimental conditions. The velocity measurements depicted the inner and outer recirculation zones, the boundaries of which showed high turbulence intensity. The soot volume fractions showed a strong dependence on the overall fuel-air equivalence ratio. The combustor axis showed the peak time-averaged soot concentration at nearly all axial heights.

INTRODUCTION

The widespread use of swirl-stabilized combustion systems has motivated research on their efficiency and environmental friendliness. Turbulent non-premixed swirl combustion is predominantly used in aircraft gas turbine engine combustors. Non-premixed combustion can cause particulate (soot) formation, which are argued to have detrimental effects on engine components, human health, and the global climate. Therefore, understanding of soot processes in technically relevant combustors is vital to the design of high-performance, low-emission gas turbine engines [1, 2].

The current study focuses on swirling non-premixed turbulent propane/air combustion at atmospheric pressure. The time-averaged velocity data and soot concentration distribution were measured at three overall fuel-air equivalence ratios (ϕ or *ER*): 0.47, 0.44 and 0.41. The fuel flow rate was held constant at 91 mgs^{-1}. The experimental techniques of stereoscopic particle image velocimetry (SPIV) and laser induced incandescence (LII) were utilized to measure the flow field and soot respectively. Experiments were conducted separately but under identical conditions.

EXPERIMENTAL METHODOLOGY

Gas turbine model combustor: Combustor has dimensions of 94 mm $\times$ 94 mm $\times$ 114 mm. An axial jet of propane is injected into a swirling jet of air. The air and fuel nozzles have coplanar exit planes (axial height y = 0 mm), hence premixing of fuel and air is prevented. The combustor has 4 fused silica glass windows for optical access into the flame and to facilitate the use of laser diagnostics.

Stereoscopic Particle Image Velocimetry: The three-dimensional velocity data was acquired using SPIV [3]. A laser sheet illuminated the axial plane of the flow seeded with 1 μm titanium oxide particles. The illuminated flow was imaged using two CCD cameras. The particle image pairs from both cameras were cross-correlated for velocity vector computation, using the commercial software LaVision Davis 7.2.

Laser Induced Incandescence: A laser beam was focused and shot at the soot particles present at a point in the flame. The broadband black-body radiation from the laser heated soot is recorded using photo-multiplier tubes at two different wavelengths. Using the recorded signals, the temperature, volume fraction and primary particle diameter of soot at the measurement location were computed [4].

RESULTS

For the reason of near-axisymmetry of the velocity field, one-half of the flow field are in Figs. 1 and 2. In Figure 1, the mean axial $\overline{V_{\mathrm{y}}}$ and the mean radial $\overline{V_{\mathrm{x}}}$ velocities form the vectors, while the contour plot shows the mean tangential velocity $\overline{V_{\mathrm{z}}}$. The mean velocity distribution shows the high velocity swirled inlet flow, and the inner and outer recirculation zones. Figure 2 shows the distribution of turbulence intensity (TI), which is defined as the square root of turbulence kinetic energy k and the magnitude of local mean velocity $|\overrightarrow{V_m}|$. The boundaries of the recirculation zones, shown as dark lines in Figs. 1 and 2, experience high turbulence intensity. The high *TI* is the cause for the rapid mixing of fresh inflowing fuel and air mixture, with the hot recirculating products and chemically active species in the vicinity of the inner recirculation zone boundary (IRZB) [1, 2]. Hence, IRZB is considered as the site for majority of the combustion as well as soot formation reactions. Further, the mixing processes can transport the soot to the interior of the IRZ. Given the axisymmetry of the flow field, an axisymmetric transport of the soot agglomerates from the IRZB to the combustor axis will cause the time-averaged soot concentration (f_{v})

[*]Corresponding author. Email: sandipan.chatterjee@mail.utoronto.ca

to peak near the combustor axis. The above hypothesis is supported by Fig. 3, where the radial profiles of f_v show a peak at the combustor axis (r = 0 mm) at all axial heights of $y \geqslant 25$ mm. Furthermore, the effect of lowering the overall fuel-air equivalence ratio are shown in Figs. 4 and 5. The f_v shows a near 50% drop for a 6% increase in air flow rate. However, the general trends of the radial profiles of f_v is nearly the same across the test cases.

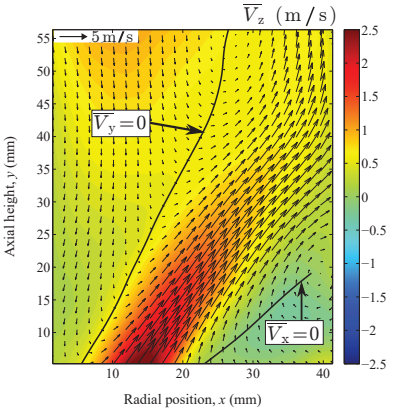

Figure 1: Mean velocity field for $\phi = 0.44$.

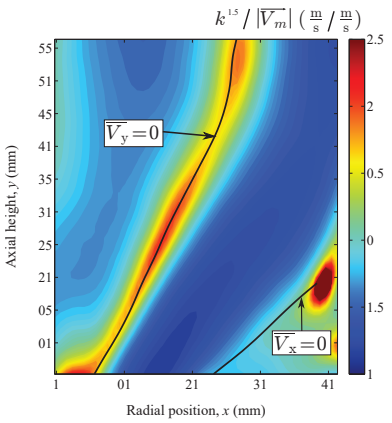

Figure 2: Turbulence intensity (*TI*) for $\phi = 0.44$.

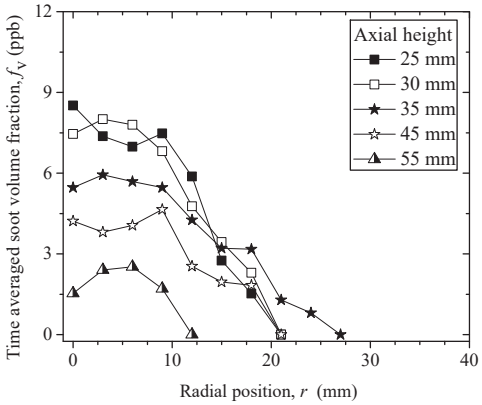

Figure 3: Time-averaged f_v for $\phi = 0.44$.

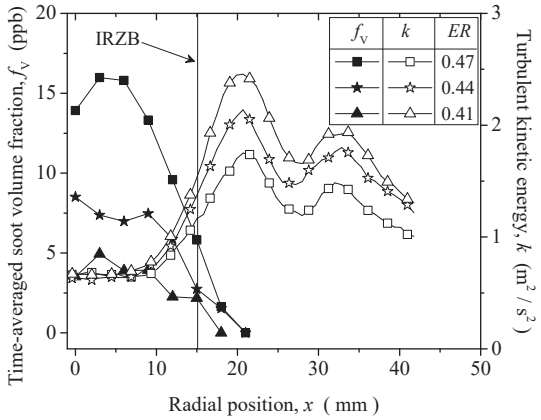

Figure 4: f_v and k profiles at y = 25 mm.

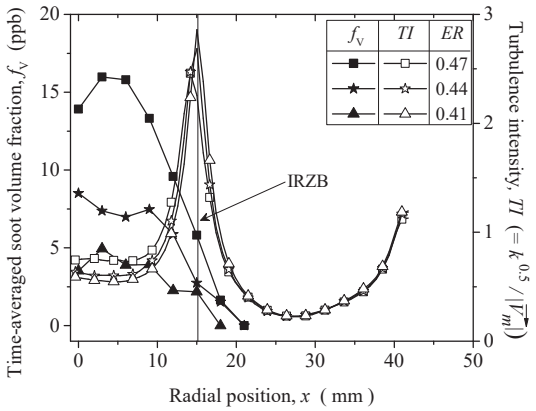

Figure 5: f_v and *TI* profiles at y = 25 mm.

CONCLUSIONS

Swirl-stabilized turbulent non-premixed propane/air flames were studied experimentally in a gas turbine model combustor for three overall fuel-air equivalence ratios. Stereoscopic particle image velocimetry and laser induced incandescence experimental techniques acquired the time-averaged velocity and the time-averaged soot concentrations, respectively. Experiments were conducted separately, but under identical conditions. The velocity field featured two recirculation zones, boundaries of which show high turbulence intensity. Majority of soot was found in the interior of the inner recirculation zone. The soot concentration showed a strong dependence on the overall fuel-air equivalence ratio.

References

[1] Geigle K. P., Zerbs J., Köhler M.m Stöhr M., Meier W.: Experimental Analysis of Soot Formation and Oxidation in a Gas Turbine Model Combustor using Laser Diagnostics. Journal of Engineering for Gas Turbines and Power, 133:121503-1–121503-9, 2011.

[2] Weigand P., Meier W., Duan X. R., Stricker W., Aigner M.: Investigation of Swirl Flames in a Gas Turbine Model Combustor I: Flow Field, Structures, Temperature and Species Distributions, Combustion and Flame, 144:205–224, 2006.

[3] Ruggles A., Kelman J.: A Gas Turbine Combustor for Instability Research and LES Validation: Methods and Mean Results, Combustion Science and Technology, 186:313-331, 2014.

[4] Snelling D. R., Smallwood G. J., Liu F., Gülder Ö. L., and Bachalo W. D.: A Calibration-Independent Laser-Induced Incandescence Technique for Soot Measurement by Detecting Absolute Light Intensity, Applied Optics, 31:6773-6785, 2005.

HEAT RELEASE RATE AND PRESSURE PHASE DIFFERENCES INSIDE AN AERONAUTICAL GAS TURBINE COMBUSTOR

Sina Kheirkhah *[1], Pankaj Saini[1], Krishna Venkatesan[2], and Adam M. Steinberg[1]
[1]*University of Toronto Institute for Aerospace Studies, Toronto, Ontario, Canada*
[2]*GE, Global Research Center, Niskayuna, USA*

Summary Spatial maps of instantaneous phase difference between heat release rate and pressure oscillations is presented during non-stationary behavior in a high-pressure, liquid-fueled gas turbine combustor. Using the Hilbert transform technique, simultaneous high-speed OH^* chemiluminescence images along with pressure oscillations data were analyzed to obtain the corresponding phase difference. The results show that, for time periods with increasing amplitude pressure fluctuations, in-phase heat release rate and pressure oscillations developed throughout the upstream portion of the combustor, which extended along the burner centerline and towards the downstream portion of the combustor. This behavior is reversed during time periods with decreasing amplitude pressure oscillations.

INTRODUCTION

The phase difference ($\Delta\phi_{p,q}$) between local pressure (p) and heat release rate ($\dot{q}$) oscillations is important for understanding why the pressure oscillation amplitudes increase, decrease, or remain constant [1, 2]. Whereas many studies have focused on constant amplitude (stationary) conditions corresponding to the thermoacoustic limit cycle, relatively few investigations have focused on non-stationary behavior [3, 4]. The present study aims at extending the experimental analysis of thermoacoustic oscillations to local non-stationary behavior in high-pressure liquid-fueled flames that are relevant for aeronautical applications. Specifically, a heat release rate marker (OH^* chemiluminescence) and the pressure are utilized to identify regions in which the thermoacoustic phase difference changes prior-to and during changes in oscillation amplitude. This framework does not require knowledge of the absolute heat release rate magnitude, and hence is robust to uncertainty in its measurement. Thus, the presented framework provides a potential means for comparison with numerical simulations based on the temporally evolving spatial distribution of in-phase and out-of-phase oscillation regions.

EXPERIMENTAL MOTHODOLOGY

The experiments were performed inside a liquid-fueled gas turbine combustor configuration. The combustor was installed inside a high pressure vessel, which is equipped with fused silica window for optical access. The combustion chamber was comprised of a single-piece of fused silica, having a square cross-section with a side length of $L = 125$ mm. The field of view spanned almost the entire combustion chamber. The nozzle studied here had a dual co-annular air swirlers and multi-point fuel injection, similar to that detailed in [5]. Simultaneous OH^* chemiluminescence images and pressure measurements were recorded at 200 kHz and 10 kHz, respectively. Signal in the emission range of the OH^* chemiluminescence was isolated using a bandpass filter with a center wavelength of 310 nm and a full-width at half-maximum of 20 nm.

RESULTS

For pressure oscillations with increasing amplitude, the $|\Delta\phi_{p,q}|$ fields transition from a relatively disorganized structure to one with distinct regions of in-phase and out-of-phase oscillations. A typical pressure oscillation with increasing amplitude along with the corresponding transition in the $|\Delta\phi_{p,q}|$ field is shown in Fig. 1(a) and Figs. 1(b-e), respectively. For this behavior, the upstream portion ($x/L < 0.4$) initially features a mixture of in-phase and out-of-phase regions, which develops into a coherent region of in-phase oscillations during the time sequence. Specifically, there exist transitions between an out-of-phase region along the centerline and regions near the nozzle. There also is evidence of dynamics in the shear layer at $y/L > 0$, which transitions between out-of-phase and in-phase p' and $\dot{q}'$ oscillations. In addition, a relatively large region of in-phase oscillations occasionally develops in the downstream region of the combustor and along $y/L \approx 0$ (Figs. 1(c)- 1(e)). Hence, this behavior is characterized by the formation of a large coherent region of in-phase p' and $\dot{q}'$ oscillations in the upstream portion of the combustor, which may extend into the downstream region.

Representative decreasing amplitude pressure oscillations as well as the corresponding sequence of $|\Delta\phi_{p,q}|$ field are presented in Fig. 2(a) and Figs. 2(b-e), respectively. As shown in the sequence of phase difference fields, out-of-phase regions are developed in the upstream portion of the combustor, which is accompanied by increasing coherence of the downstream out-of-phase region. Comparison of the results presented in Figs. 2(b-e) and those in Figs. 1(b-e) suggests that the $|\Delta\phi_{p,q}|$ field during time periods with decreasing pressure oscillation amplitude is similar to the reverse of the processes during increasing pressure oscillations amplitude.

*Corresponding author. Email: kheirkhah@utias.utoronto.ca

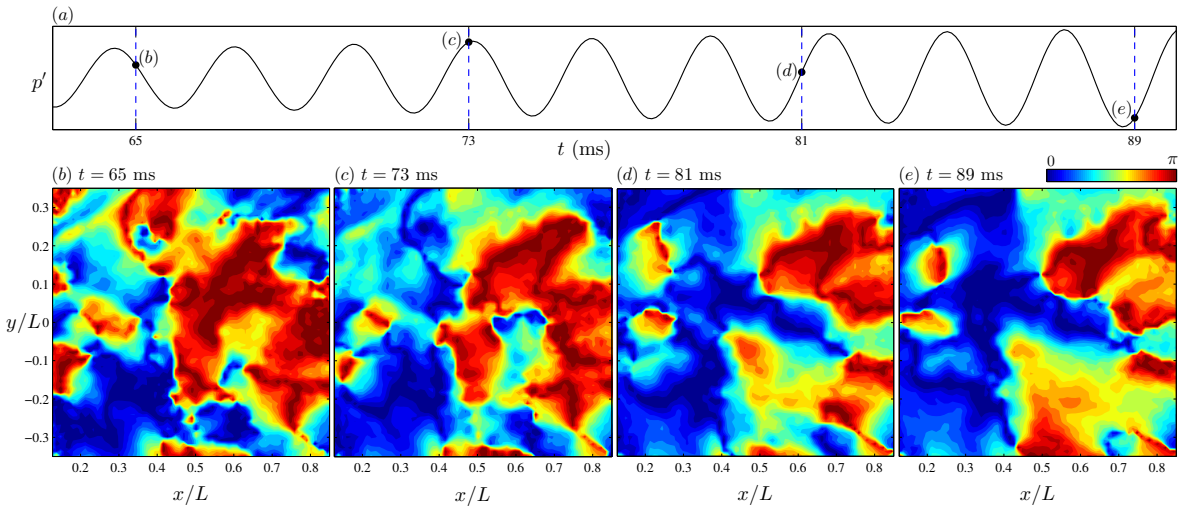

Fig. 1: Development of a coherent region of in-phase oscillations at $x/L < 0.4$, which also extends into the downstream portion of the combustor. The results pertain to pressure fluctuations with increasing amplitude.

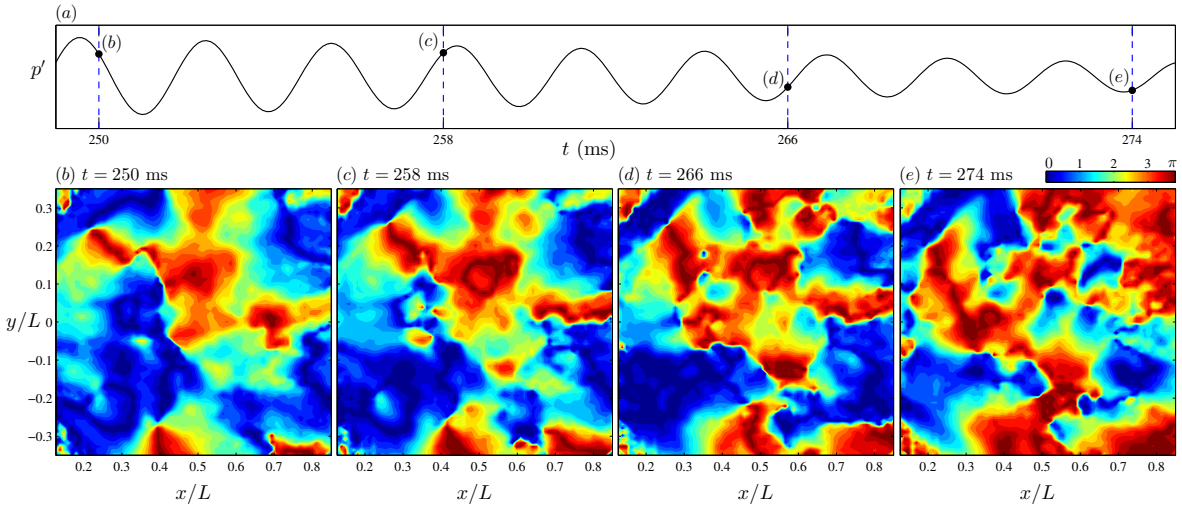

Fig. 2: Development of an out-of-phase region in the upstream portion of the combustor during a time period with decreasing oscillation amplitudes.

CONCLUSIONS

Development of local phase difference between heat release rate and pressure fluctuations inside an aeronautical gas turbine combustor was investigated experimentally. The experiments were performed using high-repetition-rate simultaneous OH* chemiluminescence images and pressure measurements. The results show that, for increasing amplitude pressure oscillations, the upstream portion of the combustor becomes dominated by in-phase oscillations between heat release rate and pressure fluctuations. This process is reversed for pressure oscillations with decreasing amplitude.

References

[1] Lieuwen T., Neumeier, Y.: Non-linear Pressure-Heat Release Transfer Function Measurements in a Premixed Combustor. Proc Combust Inst 29:99-105, 2002.

[2] Dowling A. P., Morgans, A. S.: Feedback Control of Combustion Oscillations. Annu Rev Fluid Mech 37:151-182, 2005.

[3] Boudy F., Durox D., Schuller T., Candel, S.: Nonlinear Mode Triggering in a Multiple Flame Combustor. Proc Combust Inst 33:1121-1128, 2011.

[4] Kim K. T., Hochgreb S.: Measurements of Triggering and Transient Growth in a Model Lean-Premixed Gas Turbine Combustor. Combust Flame 159:1215-1227, 2012

[5] Dhanuka S. K., Temme J. E., Driscoll J. F., Mongia, H. C.: Vortex-Shedding and Mixing Layer Effects on Periodic Flashback in a Lean Premixed Prevaporized Gas Turbine Combustor. Proc Combust Inst 32:2901-2908, 2009.

GLOBAL STABILITY ANALYSIS OF LINE-FIRE FLICKERING

Wilfried Coenen*, Daniel Moreno-Boza, and Antonio L. Sánchez
MAE Department, UCSD, USA

Summary In the present work we investigate the flickering of planar jet diffusion flames as a global instability mode. Our study attempts to give a quantitative description of the dynamics of the unsteady processes observed in line fires, which have recently been shown to play a key role in their spread rate. Because the character of the instability is purely hydrodynamic, the flame can be described in the infinitely fast reaction limit. The analysis permits the determination of the critical conditions, in terms of the Reynolds and the Froude number, for the onset of the global instability, as well as its associated frequency. The analysis is extended to include spatially periodicity in the spanwise direction. It is investigated if there is a spanwise wave number that maximizes the growth rate of the global instability mode, explaining the spanwise undulations with peaks and troughs that prevail in realistic line fires.

Non-premixed flames are characterized by large density differences which, often times, lead to the development of instabilities that are global in nature, affecting the entire flow field with a distinct frequency that scales with the macroscopic properties of the flow. This is perhaps one of the most striking features of both jet flames and pool fires, which are known to "puff" or "flicker" at a characteristic frequency [1]. The observed behavior is a result of a hydrodynamic global instability [2, 3] associated with baroclinic vorticity production, leading to self-sustained oscillations that are independent of the external flow perturbations. Despite the prevalence of this phenomenon, depicted in figure 1, there is not yet a full understanding of the mechanisms of instability [1].

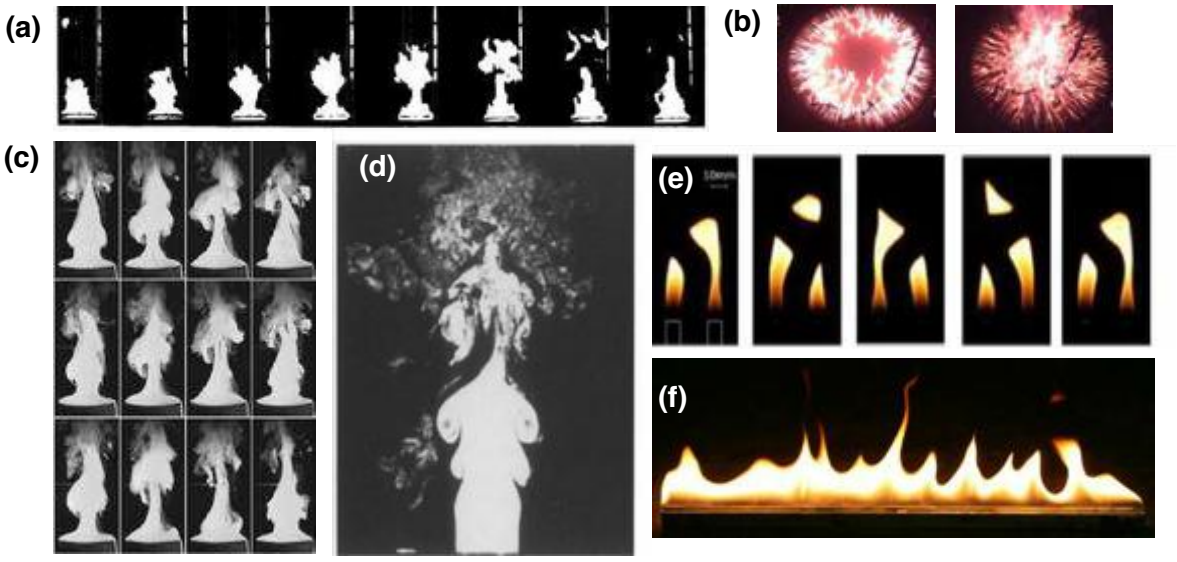

Figure 1: Images of intermittent instabilities found in (a) puffing 0.3 gas burner fires [5], (b) large-scale acetylene ring burners (c/o M. Finney, USFS), (c) cylinderical helium plumes [6], (d) non-buoyant light jets [7], (e) small interacting flames (c/o Nakamura, TUT), and (f) planar liquid fires.

Although combustion scientists have been aware of the flame-flickering phenomenon for almost seven decades [8], the first insightful stability studies are relatively recent. The role of buoyancy as the driving mechanism was recognized in the theoretical analysis of Buckmaster and Peters [9], who postulated that the flickering was associated with a modified Kelvin-Helmholtz instability of the annular flow induced by buoyancy in the envelope of hot gases surrounding the jet flame. Although this early theoretical work assumed a convective instability, later experimental observations by Maxworthy [3] suggested that the flame flickering phenomenon was associated instead with a globally excited oscillation forced by a region of absolutely unstable flow near the base of the jet exit. These findings were later supported by DNS [10] and by local linear stability analyses assuming nearly parallel flow [11, 12].

The line fire has received less attention than its axisymmetric counterpart. As can be seen figure 1(f), in these planar flames, the flickering exhibits an additional feature, in the form of spanwise undulations with peaks and troughs, with a wave length comparable to the flame height. This phenomenon is especially relevant in the context of wildfire spread, as forward flame bursts often occur at the troughs of flame fronts [4].

*Corresponding author. Email: wicoenen@ucsd.edu

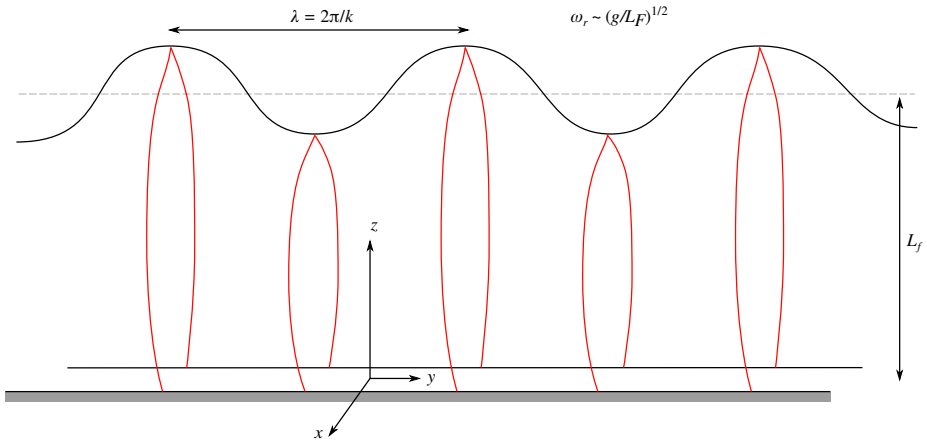

Figure 2: A model for the spanwise undulations often present in line fires.

In the present work, we investigate the flickering of laminar planar jet diffusion flames as a global instability mode. This approach has recently been taken to study axisymmetric buoyant [13] and non-buoyant [14] jet diffusion flames. Small perturbations in the form of temporal Fourier modes $\hat{\boldsymbol{q}}(x,z)\mathrm{e}^{\mathrm{i}(ky-\omega t)}$ are added to a steady basic state of the flow. Here, $\hat{\boldsymbol{q}}(x,z)$ denotes the vector containing the two-dimensional fields of the flow variables, and $k = 2\pi/\lambda$ is the wavenumber of the spanwise spatial oscillations, as sketched in figure 2. The complex angular frequency $\omega = \omega_r + \mathrm{i}\omega_i$ is obtained as an eigenvalue of the generalized eigenvalue problem formed by the linearized flow equations. The sign of the growth rate ω_i dictates whether the flow is globally stable or unstable, and ω_r gives the associated oscillation frequency. As we consider the instability to have a purely hydrodynamic character, the flame is described in the limit of infinitely fast combustion [15]. The formulation contemplates realistic cases in which the Lewis number of the fuel is nonunity. Besides the Lewis number, the Prandtl number, and the thermochemical parameters that appear in the formulation, the two fluid mechanical parameters that control the flow are the Reynolds number and the Froude number. For the numerical solution of the steady base flow, as well as the discretization of the eigenvalue problem, the finite element solver FreeFem++ is employed.

First, the scrictly planar case $k = 0$ is considered. The cricital conditions for the onset of global instability are sought in the Reynolds-Froude number parameter plane for different values of the Lewis number and different values of the fuel dilution ratio. Along the curve of the marginal stability, the spatial structure of the eigenfunctions associated with the leading eigenmode shows whether the global mode is of the symmetric (varicose) or antisymmetric (sinuous) kind.

Finally, it is investigated whether there is a value of the spanwise wavenumber $k \neq 0$ for which the growth rate of the global instability mode is maximum. This value of k would be the one prevailing in realistic conditions, explaining the spanwise undulations with peaks and troughs often encountered in line fires.

References

[1] Tieszen, S. On the Fluid Mechanics of Fires. Annu. Rev. Fluid Mech. 33:67–92, 2001.

[2] Huerre, P. & Monkewitz, P.A. Local and global instabilities in spatially developing flows. Annu. Rev. Fluid Mech. 22:473–537, 1990.

[3] Maxworthy, T. The flickering candle: transition to a global oscillation in a thermal plume. J. Fluid Mech. 390:297323, 1999.

[4] Finney, M.A., Cohen, J.D., Forthofer, J.M., McAllister, S.S., Gollner, M.J., Gorham, D.J., Saito, K., Akafuah, N.K., Adam, B.A., & English, J.D. Role of buoyant flame dynamics in wildfire spread. Proceedings of the National Academy of Sciences, 112(32):9833–9838, 2015.

[5] Heskestad, G. Dynamics of the fire plume. Phil. Trans. R. Soc. Lond. A 356:28152833, 1998.

[6] Cetegen, B., Dong, Y., & Soteriou, M. Experiments on stability and oscillatory behavior of planar buoyant plumes. Phys. Fluids 10(7):16581665, 1998.

[7] Monkewitz, P.A. & Sohn, K. Absolute instability in hot jets. AIAA journal, 26(8):911916, 1988.

[8] Chamberlin, D. & Rose, A. The flicker of luminous flames. Proc. Combust. Inst. 12:2732, 1948.

[9] Buckmaster,J. & Peters, N. The infinite candle and its stability—a paradigm for flickering diffusion flames. Proc. Combust. Inst. 21:1829–1836, 1986.

[10] Jiang, X. and Luo, K. Combustion-induced buoyancy effects of an axisymmetric reactive plume. Proc. Combust. Inst., 28:1989–1995, 2000.

[11] Lingens, A., Neemann, K., Meyer, J., and Schreiber, M. Instability of diffusion flames. Proc. Combust. Inst., 26:1053–1061, 1996.

[12] See, Y. & Ihme, M. Effects of finite-rate chemistry and detailed transport on the instability of jet diffusion flames J. Fluid Mech. 745:647–681, 2014.

[13] Moreno-Boza, D., Coenen, W., Sevilla, A., Sánchez, A.L. Diffusion-flame flickering as a hydrodynamic global mode. J. Fluid Mech. Submitted, 2016.

[14] Qadri, U.A., Chandler, G.J., & Juniper, M.P. Self-sustained hydrodynamic oscillations in lifted jet diffusion flames: origin and control. J. Fluid Mech. 775:201–222, 2015.

[15] Liñán, A., Vera V., Sánchez, A.L. Ignition, liftoff, and extinction of gaseous diffusion flames. Annu. Rev. Fluid. Mech. 47:293:314, 2015.

QUANTIFYING STOCHASTIC LIMIT-CYCLE PARAMETERS FROM THE ADJOINT FOKKER-PLANCK EQUATION

Edouard Boujo* [1] and Nicolas Noiray[1]

[1] *CAPS Lab., Mechanical and Process Engineering Dept., ETH Zürich, Switzerland*

Summary Important parameters such as linear growth/decay rates in thermoacoustic systems can be identified based on acoustic pressure signals, by taking advantage of turbulent-induced noise and making use of the Fokker-Planck equation. However, this kind of system identification technique suffers from finite-time effects, e.g. band-pass filtering or low sampling rates. A new method based on the adjoint Fokker-Planck equation is presented for identifying parameters in a robust and accurate way, even in the presence of finite-time constraints.

Gas turbines are prone to combustion instabilities that can lead to high-amplitude oscillations and reduce the lifetime of mechanical parts. A common and practical way to mitigate these instabilities is to use passive control devices such as acoustic dampers. The robust and efficient design of such dampers requires the knowledge of thermoacoustic linear growth/decay rates at different operating conditions. While the measurement of decay rates in linearly stable conditions is fairly straigthforward through the processing of pressure data, the measurement of growth rates in linearly unstable conditions is not possible using the same method because the system adapts too quickly to varying conditions. One way to circumvent this difficulty is to take advantage of the turbulent noise present in limit-cycle pressure signals and to apply system identification to the stochastic process. Indeed, starting from the acoustic wave equation, one can derive a Langevin equation for the enveloppe A of the acoustic pressure $p(t) = A(t)\cos(\omega t + \phi(t))$, and the associated Fokker-Planck equation (FPE) that describes the evolution of the probability density function (PDF) of the acoustic amplitude:

$$\dot{A} = A(\nu - \frac{\kappa}{8}A^2) + \frac{\Gamma}{4\omega^2 A} + \zeta = \mathcal{F}(A) + \zeta, \qquad \frac{\partial}{\partial t}P(A,t) = -\frac{\partial}{\partial A}(\mathcal{F}(A)P(A,t)) + \frac{\Gamma}{4\omega^2}\frac{\partial^2}{\partial A^2}P(A,t), \tag{1}$$

where ν is the linear growth/decay rate, κ is the strength of the heat release source term nonlinear (cubic) saturation, and ζ is a δ-correlated additive forcing of intensity $\Gamma/2\omega^2$. The drift coefficient $D^{(1)}(A) = \mathcal{F}(A)$ and diffusion coefficient $D^{(2)}(A) = \Gamma/4\omega^2$ of the FPE are related to the first two moments of the conditional probability $P(a, t+\tau|A, t)$:

$$D^{(n)}(A) = \lim_{\tau\to 0} D_\tau^{(n)}(A), \qquad D_\tau^{(n)}(A) = \frac{1}{n!\tau}\int_{-\infty}^{\infty}(a-A)^n P(a, t+\tau|A, t)\mathrm{d}a. \tag{2}$$

One can compute these coefficients through basic processing of pressure measurements (figure 1(b,c,d,e)), and perform model-based fitting to identify the important governing parameters ν, κ and Γ [1].

In practice, however, one cannot compute exactly the limit for infinitesimally small time shift $\tau \to 0$, either because of the finite sampling rate of measurement instruments, or because real-world noise is not strictly δ-correlated. In our case, the most important reason is the presence of secondary peaks in the pressure frequency spectrum, which requires the signal to be band-pass filtered (figure 1(a)), thus removing high-frequency contents in $A(t)$. Therefore, only finite values $\tau \geq \tau_{min} > 0$ can be used to compute the finite-time coefficients $D_\tau^{(n)}(A)$ and to estimate the exact coefficients $D^{(n)}(A)$. Such finite-time effects can significantly affect the estimation accuracy (figure 1(f)).

In this study, the method proposed in [2] is applied for the first time to real-world measurements to identify the governing parameters of a thermoacoustic system undergoing a supercritical Hopf bifurcation. The finite-time coefficients $D_\tau^{(n)}(A)$ are directly computed from the solution $P^\dagger(a,t)$ of the so-called adjoint Fokker-Planck equation (AFPE), solved in time from appropriate initial conditions $P^\dagger(a,0) = (a-A)^n$ and evaluated at the values of interest $(a,t) = (A,\tau)$. This yields exact values of $D_\tau^{(n)}(A)$ for any A and τ, provided the expression of $D^{(1)}(A)$, $D^{(2)}(A)$ that appear in the AFPE are correct. Therefore, the following procedure allows one to extract the system parameters: choose a set of amplitudes A and time shifts τ, and optimize the values of $[\nu, \kappa, \Gamma/4\omega^2]$ in the AFPE coefficients $D^{(1)}(A)$ and $D^{(2)}(A)$ so as to minimize the overall error between the finite-time coefficients $\widehat{D}_\tau^{(n)}(A)$ computed from measurements and the finite-time coefficients $D_\tau^{(n)}(A)$ obtained with the AFPE.

The method is illustrated with acoustic data from a lab-scale combustion chamber, both in linearly stable and unstable operating regimes. Band-pass filtering of the pressure signal restricts time shifts to finite values $\tau \geq \tau_{min} = 0.06$ s when evaluating conditional moments. The optimization yields an excellent agreement between the drift and diffusion coefficients estimated from data and those obtained from the AFPE (figure 1(g)), as well as between the stationary PDF constructed from data and the PDF given analytically as $P(A) \propto \exp[(4\omega^2/\Gamma)\int \mathcal{F}(A)\mathrm{d}A]$ and evaluated with the extracted optimal parameters (figure 1(h)). This new method is expected to considerably enhance the robustness and accuracy of system identification for practical, finite-time and/or filtered measurements.

*Corresponding author. Email: eboujo@ethz.ch

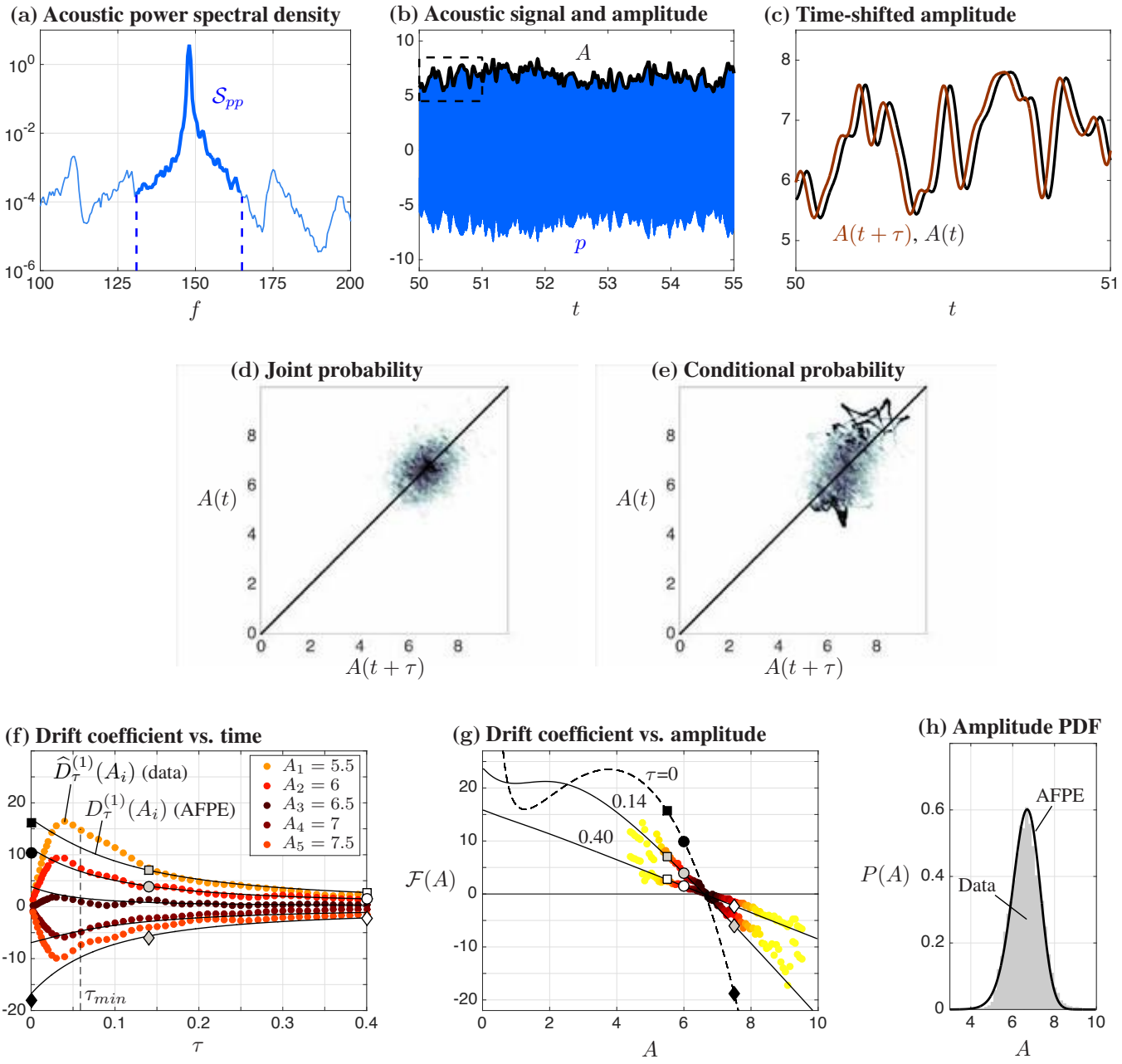

Figure 1: **(a)** Power spectral density of the acoustic pressure, before and after band-pass filtering. **(b)** Subset of a pressure signal $p(t)$ and its envelope $A(t)$. **(c, d, e)** Conditional moments are evaluated by time-shifting the amplitude by τ, and evaluating the joint probability $P(a(t+\tau), A(t))$ and conditional probability $P(a, t+\tau|A, t)$. **(f)** For small values of the time shift $\tau \leq \tau_{min}$, finite-time drift coefficients $\widehat{D}_\tau^{(1)}$ estimated from limit-cycle data (dots) diverge from the exact values $D_\tau^{(1)}$ calculated with the AFPE (lines). Here, band-pass filtering of the pressure signal restricts the time shift to finite values $\tau \geq \tau_{min} = 0.06$ s. Symbols show $D_\tau^{(1)}$ for τ=0 (black), τ=0.14 (grey) and τ=0.40 (white) (see also fig. 1(g)). **(g)** Exact drift coefficient $D^{(1)}$ (dashed line, $\tau = 0$); exact finite-time coefficients $D_\tau^{(1)}$ calculated by solving the AFPE (solid lines); finite-time coefficients $\widehat{D}_\tau^{(1)}$ estimated from data with finite time shifts $\tau \geq \tau_{min} > 0$ (dots). Symbols correspond to A=5.5, 6 and 7.5 (see also fig. 1(f)). **(h)** Stationary PDF obtained from limit-cycle data (histogram) and from the parameters identified with the AFPE (line).

References

[1] Noiray N. and Schuermans B.: Deterministic quantities characterizing noise driven Hopf bifurcations in gas turbine combustors. International Journal of Non-Linear Mechanics 50:152-163, 2013.

[2] Honisch C. and Friedrich R. Estimation of Kramers-Moyal coefficients at low sampling rates. Physical Review E 83:066701, 2011.

PREMIXED FLAME INSTABILITY IN A HELE-SHAW BURNER

E. Al-Sarraf [1], C. Almarcha [1], B. Radisson [1], J. Quinard* [1], B. Denet [1]
[1] *Aix Marseille Universite, CNRS, Centrale Marseille, IRPHE UMR 7342, 13384, Marseille, France*

Summary: Experiments were performed with propane- and methane-air mixtures in a 2D-Hele-Shaw burner to determine the characteristic scales of the premixed flame instability that can be used to define an evolution equation for the front. It is found that the most unstable wavelength, depending on the Lewis number of the mixture, and the linear rate of growth of perturbations, directly measured in the present experiments, have the same order of magnitude than those previously measured on planar flames propagating freely downwards in wide tubes.

INTRODUCTION

Combustion instabilities are of primary importance for turbulent burning in actual burners and there are some hopes so that they can be simulated using a model equation such as the Sivashinsky nonlinear equation first proposed in 1977 for the flame front propagation [1]. Large-scale flame front in a number of configurations were studied theoretically and numerically [2,3] in good qualitative agreement with the experiments [4]. However a quantitative comparison is hardly expected unless a 2D-flame can be observed.

To this end, we study a flame propagating in a Hele-Shaw burner where the flame dynamics is more easily recorded than in a cylindrical burner. The only parameters of the model are a cut-off wavelength λ_c and a characteristic growth rate σ of the most unstable perturbation with wavelength $\lambda_{max} \sim 2\lambda_c$. These parameters can be estimated knowing the unstable wavelength at the onset of instability for a planar flame propagating downwards [5], and some direct measurements of the rate of growth σ were performed as a function of the wavenumber of the flame perturbation [4,6]. But these values are not directly to be carried forward on the present configuration, since a point is to know whether the mechanism of instability can be described in the same way in a 2D configuration and for a 3D planar flame [7].

The burner consists of two glass plates 0.50 m wide and 1.5 m high, separated by a gap width of 5 or 10 mm. An acoustic damper, situated at the bottom, prevents the thermo-acoustic instabilities by damping the reflection of acoustic waves. After each run, the airflow is opened and maintained until the tube walls have cooled to ambient temperature. The flow of combustible, methane or propane, is then adjusted to the desired equivalence ratio and a 2D inverted V-flame is ignited at the top of the burner with a lighter. Closing the valve at the bottom of the burner then stops the flow and the downward flame propagation is recorded thanks to a high-speed camera (Fig. 1-2).

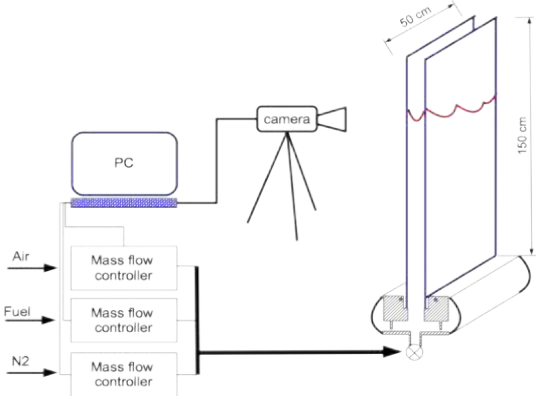

Figure 1: Experimental set-up

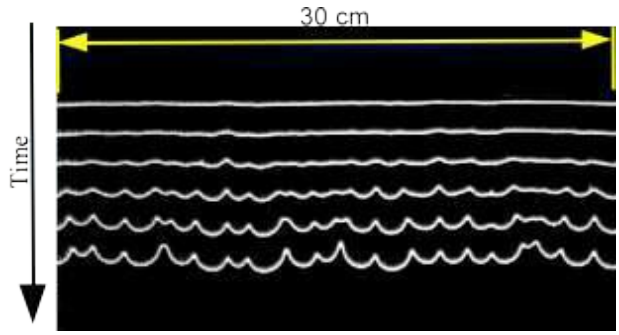

Figure 2: Flame front at successive moments separated from 16 ms (vertical scale expanded)

EXPERIMENTAL RESULTS

Experiments were performed with propane and methane-air mixtures whose dynamic properties are a priori known [5]. Near stoichiometric mixtures were diluted with nitrogen in order to reduce the growth rate of the perturbations and to improve the accuracy of the measurements. The initial flame contour appears relatively flat (Fig. 2), so Fourier analysis of the successive records of the flame contour can give access to the linear growth rate of the spontaneously excited

* Corresponding author. Email: quinard@irphe.univ-mrs.fr

perturbations of the flame (Fig. 3). Using this procedure, we only access to the growth rate of large wavelengths of perturbations (Fig. 4, colored symbols) as the information on the domain of large wavenumbers is quickly hidden by the most unstable response of the flame. Introducing a plate with periodic bights a few centimeters above the burner exit, it is possible to force the flame response at the desired wavelength, so extending the measurements of the dispersion relation to larger wavenumbers $k=2\pi/\lambda$ (Fig. 4, black symbols). A best parabolic fit through these data (blue line) compares favorably with previous measurements (large red symbol) and with the classical relation [5-7]: the slope $d\sigma/dk$ at small wavenumber is close to the one calculated by considering only the Darrieus-Landau instability, and the general trends of this curve resemble the hypotheses used in Sivashinsky's simulations. In particular, the large-scale cut-off wavelength is close to the one calculated with gravity effects, the small-scale cut-off wavelength is about half the most unstable wavelength, and its value varies with the equivalence ratio of the combustible mixture (not shown here) in relation with Lewis number effects [8].

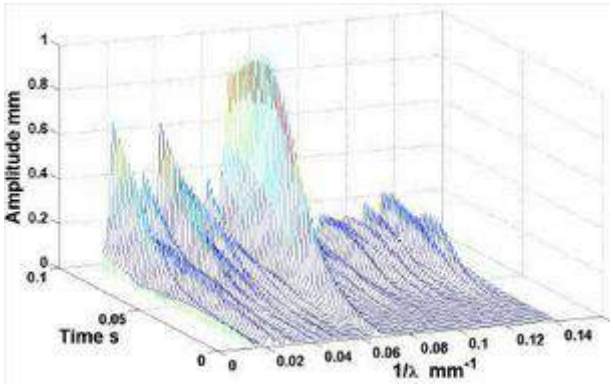

Figure 3: Spectrogram of successive flame contours with forcing at λ=15mm; propane-air, ϕ=0.7, δ= 0.21

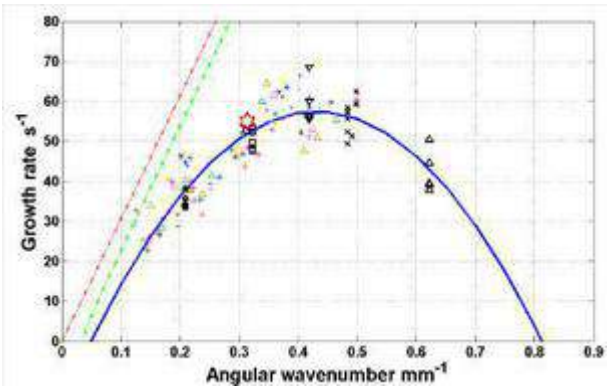

Figure 4: Measured growth rate of propane-air flame (ϕ=0.7, δ= 0.21) compared to the dispersion relation of Darrieus-Landau instability with (---) or without (---) gravity effects. See text for the meaning of the symbols.

However, these wavelengths are slightly larger than those measured at the onset of instability of planar flames propagating downwards, probably because of 3D-effects that modify the 2D flame speed and the transverse flux, inducing changes in the expansion ratio that controls the rate of growth.

CONCLUDING REMARKS

These experiments confirm that the dynamics of 2D-flame that can be observed in a Hele-Shaw burner is analogous to the dynamics of planar flames previously described, with only small changes needed to correct the cut-off wavelength and the growth rate for 3D effects. It is thus probable that these flames could be relevantly simulated using a model equation such as the Sivashinsky's equation.

Acknowledgements: This work was supported by the French National Research Agency under agreement ANR-14-CE05-0006 and it has been carried out in the framework of the Labex MEC (ANR-10-LABX-0092) and of the A*MIDEX project (ANR-11-IDEX-0001-02).

References:

1] G. Sivashinsky, Nonlinear analysis of hydrodynamic instability in laminar flames; Part 1: derivation of basic equations, Acta Astronaut. 4 (1977) 1117.
2] D.M. Michelson, G.I. Sivashinsky, Thermal expansion induced cellular flames, Combust. Flame 48 (1982) pp.211–217.
3] G. Joulin, B. Denet, H. El-Rabii, Potential-flow models for channelled twodimensional premixed flames around near-circular obstacles, Phys. Rev. E 81 (2010) 016314.
4]] J.M. Truffaut, G. Searby, Experimental Study of the Darrieus-Landau instability on an inverted-'V' flame, and measurement of the Markstein number, Comb. Sci. Techn. 149 n° 1-6 (1999) pp35-52.
5] C. Almarcha, B. Denet, J. Quinard, Premixed flames propagating freely in tubes, Combust. Flame, 162 (2015) pp1225-1233.
6] C. Clanet, G. Searby, First experimental study of the Darrieus-Landau instability, Phys. Rev. Let. 80 n°17(1998) pp.3867-3870.
7] G. Joulin; G. Sivashinsky, Influence of Momentum and Heat Losses on the Large-Scale Stability of Quasi-2D Premixed Flames, Combustion Science and Technology, 98: 1 (1994) pp.11- 23.
8] J. Wongwiwat, J. Gross, P. Ronney, Flame Propagation in Narrow Channels at Varying Lewis Number, 25th ICDERS Leeds, UK (August 2 – 7, 2015).

MODELISATION AND FORECAST OF PREMIXED FLAMES

Basile Radisson[1], Christophe Almarcha *[1], Joel Quinard[1], Elias Al-Sarraf[1], and Bruno Denet[1]

[1] *Aix-Marseille Universite, CNRS, Centrale Marseille, IRPHE, UMR 7342, 13384 Marseille, France*

Summary We demonstrate here the possibility to compare the evolution of an analytical flame corresponding to a pole solution of the Sivashinsky equation with the evolution of an experimental flame. The experiment used as a benchmark consists of the propagation of a quasi two-dimensional propane-air flame in a Hele-Shaw burner. A best approximation of the experimental flame at an initial time is first calculated by fitting with a limited series of pole-based functions. The trajectories of the poles are then integrated numerically in time and the evolution of the front they are representing is finally compared with the evolution of the experimental flame.

INTRODUCTION

Even when propagating in a medium initially at rest, premixed flames can undergo intrinsic destabilizations and folding among which the Darrieus-Landau instability. As a consequence, the surface and velocity increase up to higher values that fluctuate in time. These fluctuations result from nonlinear processes occuring on the flame surface, which can be described as a succession of local singularities, called cusps, that are created and then compete and eventually merge. A Hele-Shaw burner [1, 2, 3] appears to be an adequate apparatus for quantitative analysis of this dynamics in a quasi two dimensional configuration. It allows comparison with the Sivashinsky equation [4], which is generally used as a description of the non-linear dynamics involved in the instability. This equation can be derived in the limit of small unburnt to burnt gas expansion ratios $\theta = \frac{\rho_u}{\rho_b}$ and accounts for the evolution of the position $\phi(x,t)$ of the flame taken as a discontinuity. The extension to larger expansion ratios, proposed by Joulin and Cambray [5] is used in this study in the following non-dimensional form : $\phi_t + \frac{a}{2}\phi_x^2 = \Omega\left(\frac{\phi_{xx}}{k_c} + I\left(\phi, x\right)\right)$. In this equation with unity laminar flame-speed, lengths have been rescaled by the width of the flame front divided by 2π, k_c stands for the non-dimensional cut-off wave number, the linear operator $I\left(\phi, x\right)$ corresponds to multiplication by $|k|$ in Fourier space, $\Omega = \frac{\theta}{\theta+1}\left(\sqrt{\frac{\theta^2+\theta-1}{\theta}} \circ 1\right)$ is Darrieus-Landau coefficient and a is taken from Kazakov 2005 [6] where $A = \frac{2\Omega}{ak_c} = \frac{1}{k_c}\frac{(\theta+1)^2(\theta-1)}{4\theta^2}$.

According to Thual et al. [7] this equation admits exact, "pole-decomposable", 2π-periodic solutions in the form

$$\phi = \circ\, A\sum_{n=1}^{N}\left\{ln\left(sin\left(\frac{x \circ z_n(t)}{2}\right)\right) + ln\left(sin\left(\frac{x \circ z_n^*(t)}{2}\right)\right)\right\} \tag{1}$$

and each pole z_n evolves according to the following coupled ODE's :

$$\dot{z_n} = \circ\, \Omega\sum_{p\neq n}\frac{1}{k_c}cot\left(\frac{1}{2}\left(z_n \circ z_p\right) \circ isign\left(Im(z_n)\right)\right) \tag{2}$$

In this work we propose to compare the flame front dynamics described by this set of ODE to the dynamics observed in a real experiment.

POLE DECOMPOSITION OF AN EXPERIMENTAL FLAME FRONT

In order to compare the flame front evolution described by system (2) with an experimental flame front we should start with conditions as close as possible to the conditions from which the Sivashinsky equation is derived (i.e small slope hypothesis). A propane air flame (equivalence ratio 0.7) is thus ignited as an inverted V-flame on top of vertically oriented Hele-Shaw cell (two glass plates 50cm large and 150cm high separated by a thin gap of 5mm) then the flow is stopped by closing the valve at the bottom of the cell and a nearly planar flame starting is downward propagation. The evolution of the flame is recorded using a high-speed camera (500fps). Figure 1a extracted from this sequence is a typical frame exhibiting 7 cusps. It is used as reference front for fitting with decomposition (1) by way of Levenberg-Marquardt least-squares algorithm. The 126mm field of view is chosen so that the right and left limits are sufficiently far from cusps and with horizontal tangent in order to better satisfy the periodicity of the functions. Moreover in order to assure continuity between the right and left limits we rotated the front by 0.025 radians. For such a flame, we assumed $k_c = 19.2$ according to the linear growth rate measured from initial flat interface. The minimum number of poles for a reasonable agreement for the shape was found to be 12. The locations of these poles are represented by points under the frame, with vertical coordinate corresponding to their imaginary part. Poles with small imaginary part in the complex plane induce physical cusps visible at the same abscissa. The resulting analytical solutions are superimposed in red on the picture.

*Corresponding author. Email : almarcha@irphe.univ-mrs.fr

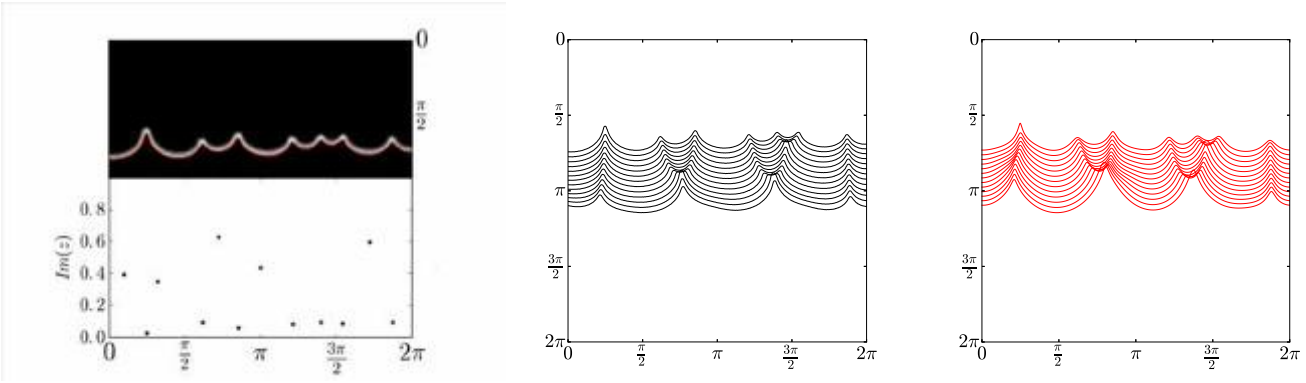

(a) (b) (c)

FIGURE 1 – (a) Fitting of the flame front (top) and associated pole positions in the complex plane (bottom). (b) Evolution of the experimental flame front. (c) Evolution of the pole solutions according to the system of ODE (2).

Evolution in time

The system of equations (2) corresponding to pole trajectories is integrated numerically in time starting from the solution obtained above. We assumed $\theta = 6.4$ and a laminar flame speed of $0.22m.s^{-1}$. These values could eventually be corrected due to the heat and momentum loss in the Hele-Shaw cell. The evolution of the simulated front reported in fig 1c exhibits three cusp mergings and favorably compares to the evolution of the experimental one reported on figure 1b at the same instants.

CONCLUSIONS

The quantitative agreement in time and length scale proves that although the Sivashinsky equation is derived in a small expansion limit, it appears to be valid for real flames with expansions around $\theta = 6$ with a good accuracy. Moreover, the complex dynamics of the front can be reduced to the calculation of the trajectory of a limited number of pole pairs in the complex plane (12 pairs for the evolution of a front with 7 cusps in our case). A perspective for this study would be to validate the ability of this method to simulate premixed flame fronts for a wider range of gas mixtures and equivalence ratio.

This work was supported by the French National Research Agency under agreement ANR-14-CE05-0006, and it has been carried out in the framework of the Labex MEC (ANR-10-LABX-0092) and of the A*MIDEX project (ANR-11-IDEX-0001-02).

Références

[1] Kang Sun Kang, Hong G. Im, Seung Wook Baek : A Computational Study of Saffman-Taylor Instability in Premixed Flames. Combustion Theory and Modelling 7 :343-363, 2003.
[2] Sharif J., Abid M., Ronney P.D. : Premixed-Gas Flame Propagation in Hele-Shaw Cells. SpringTechnical Meeting, Joint US Sections, Combustion Institute, Washington, DC, http ://ntrs.nasa.gov/archive/nasa/casi.ntrs.nasa.gov/20000005014.pdf. 1999.
[3] Almarcha C., Quinard J., Denet B., Al-Sarraf E., Laugier J.M., Villermaux E. : Experimental Two Dimensional Cellular Flames. Physics of Fluids 27 :091110. 2015.
[4] Sivashinsky, G.I. : Nonlinear Analysis of Hydrodynamic Instability in Laminar flames. I-. Derivation of Basic Equations. Acta Astronautica 4 :177-1206, 1977.
[5] Joulin G., Cambray P. : On a Tentative, Approximate Evolution Equation for Markedly Wrinkled Premixed Flames. Combustion Science and Technology 81 :243-256, 1992.
[6] Kazakov K. A. : On-Shell Description of Stationary Flames. Physics of Fluids 17 :032107, 2005.
[7] Thual O., Frisch U., Henon M. : Application of Pole Decomposition to an Equation Governing the Dynamics of Wrinkled Flame Fronts. Journal de Physique 46 : 1485-1494, 1985.

VISUALIZATION OF CONVENTIONAL AND COMBUSTING SUBSONIC JET INSTABILITIES

Victor V. Kozlov[1,2], Genrich R.Grek[1a)], Yury A. Litvinenko[1]

[1]*Institute of Theoretical and Applied Mechanics, Siberian Branch, Russian Academy of Sciences Novosibirsk, Russia*
[2]*Novosibirsk State University, Novosibirsk, Russia*

Summary Based on new information obtained for free microjets, this study is aimed to explain some phenomena of flame evolution at round and plane propane microjet combustion in the presence of transverse acoustic field. It gives an overview of recent experimental results on instability and dynamics of jets at low Reynolds numbers and provides the recent advances in jet flow stability and combustion. Some clarification of the differences between top-hat and parabolic round and plane jet instability [1] is also given.

INFLUENCE OF INITIAL CONDITIONS AT THE NOZZLE EXIT AND ACOUSTICS ON THE CHARACTERISTICS OF THE ROUND AND PLANE MACROJET EVOLUTION

A round macrojet with top-hat mean velocity profile at the nozzle exit is prone to the Kelvin–Helmholtz instability in the form of ring vortices, whereas the round macrojet with parabolic mean velocity profile at the nozzle exit results in an extended laminar flow region and suppression of the vortices (see figure 1).

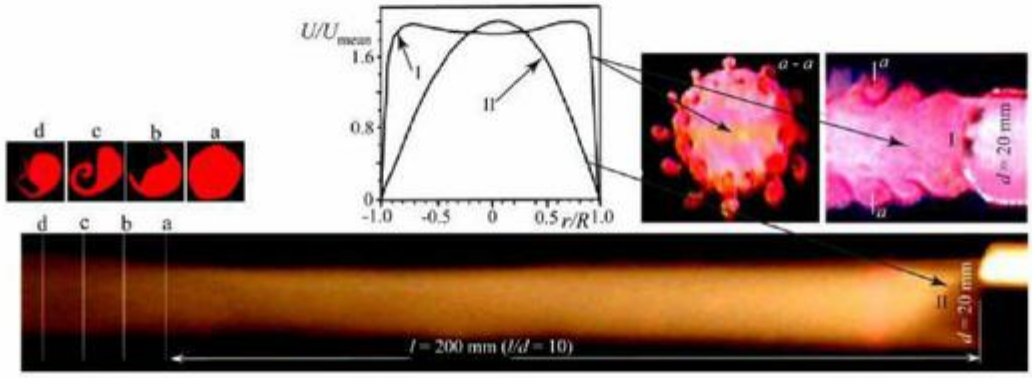

Figure 1. Influence of initial conditions at the nozzle exit on structure and characteristics of a round jet evolution: I,II - top-hat and parabolic mean velocity profiles, accordingly; a, b, c, d - macrojet cross sections, U_0= *5 m/sec (*$Re = U_0 \times d / \nu$ = 6667).

Plane macrojet with top-hat and parabolic mean velocity profile at the nozzle exit is prone to sinusoidal instability (see figure 2). The round macrojet with parabolic mean velocity profile at the nozzle exit results in an extended laminar flow region and suppression of the ring vortices.

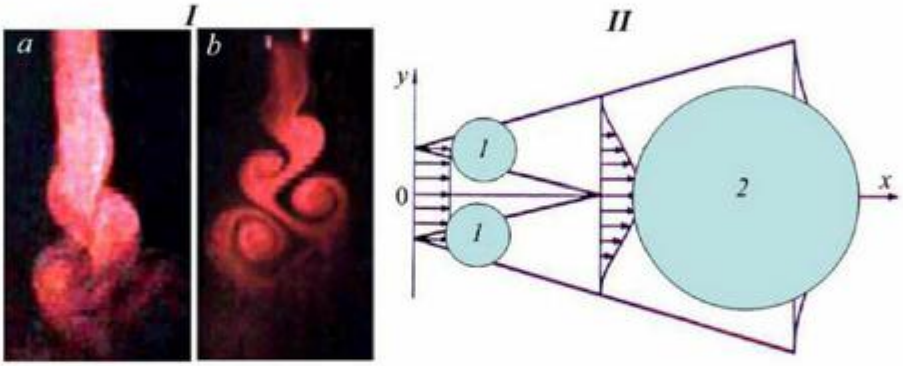

Figure 2. Sinusoidal instability of the plane macrojet with top-hat and parabolic mean velocity profile at the nozzle exit – ***I*** (*a* – under natural conditions, *b* - under external acoustic forcing at frequency *f* = 40 Hz). Plane macrojet with top – hat mean velocity profile at the nozzle exit involve three independent of each other instability regions: 1 - two independent of each other narrow regions of strong velocity gradient near nozzle, 2 - region with parabolic mean velocity profile far downstream from a nozzle – ***II.***

[a)] Corresponding author. Email: grek@itam.nsc.ru**.**

INFLUENCE OF INITIAL CONDITIONS AT THE NOZZLE EXIT AND ACOUSTICS ON THE CHARACTERISTICS OF THE ROUND AND PLANE MICROJET EVOLUTION

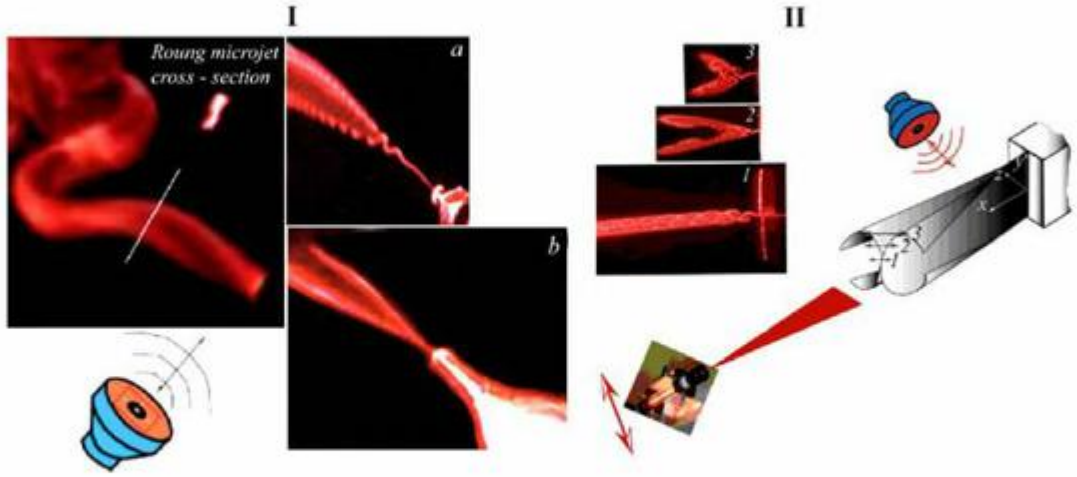

Figure 3. Round microjet flattening (f = 40 Hz) and bifurcation (a - f = 200 Hz, b – 1500 Hz) in a transverse acoustic field (nozzle diameter d = 200 mm) – ***I***. Bifurcation scheme of the plane macrojet in a transverse acoustic field (nozzle: l = 36 mm, h = 200 mm): flow patterns in x-z planes at variation of the y coordinate (1, 2, and 3 correspond to y = 0, 15, and 18 mm, respectively), f = 150 Hz, 90 dB – ***II.***

DIFFUSION COMBUSTION OF THE ROUND AND PLANE PROPANE MICROJET IN A TRANSVERSE ACOUSTIC FIELD

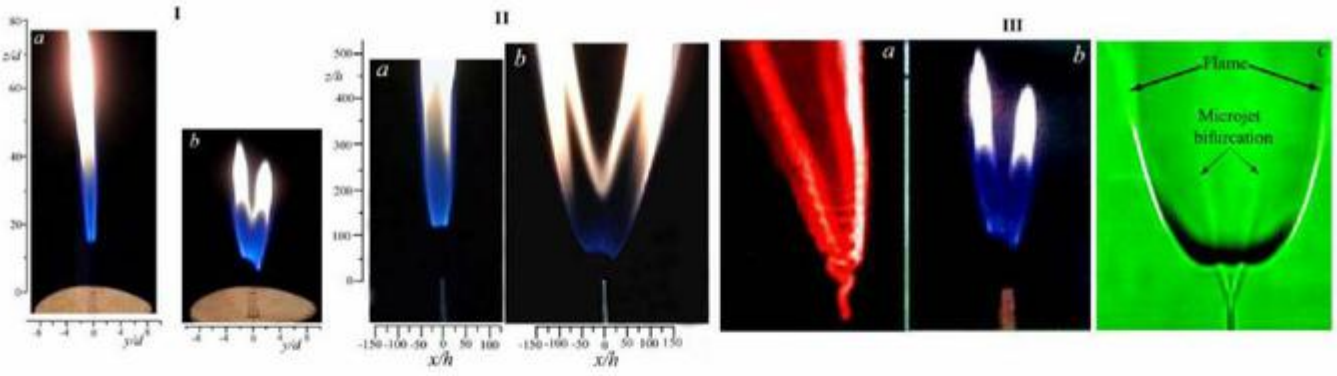

Figure 4. Round (**I**) and plane (**II**) microjet flame bifurcation in a transverse acoustic field: nozzle No. 1, d = 0.5 mm, acoustics, f = 5 - 7.5 kHz, U_0 = 12.5 m/sec (**I**); nozzle No. 2, l = 2 mm, h = 200 μm, acoustics, f = 1 – 3 kHz, U_0 = 21 m/sec (**II**); without acoustics (a), with acoustics (b), A = 90 dB. **III** - Round microjet bifurcation (a), round propane microjet flame bifurcation (b), and shadowgraph image of a round propane microjet combustion (c).

CONCLUSIONS

Visualizations of conventional and combusting subsonic jet instabilities are presented**.** Features of structure and characteristics of subsonic round and plane macro- and microjets evolution depending on initial conditions at the nozzle exit and acoustic effect are shown. It is found, that round and plane propane microjets combustion in a transverse acoustic field result in flame bifurcation.

This work was supported by the project of the President of the Russian Federation for Leading Scientific Schools (NSH-8788.2016.1), RFBR 16-07-00946, 16-08-00425 and 16-19-10330.

References

[1] Kozlov V, Grek GR, Litvinenko Y: Visualization of Conventional and Combusting Subsonic Jet Instabilities**.** Book Springer Briefs in Applied Sciences and Technology, 2016, p.126, ISBN: 978-3-319-26957-3 (Print), 978-3-319-26958-0 (Online).

STABILITY CHARACTERISTICS OF PULSATING ONE-DIMENSIONAL DETONATIONS USING A SIMPLE ANALOGUE

S. She-Ming Lau-Chapdelaine *[1], André Bellerive[1], and Matei I. Radulescu[1]

[1]*Department of Mechanical Engineering, University of Ottawa, Ottawa, Ontario, Canada*

Summary Results of asymptotic modeling of one-dimensional pulsating detonations using Fickett's model with two-step chemistry, an analogue of the reactive Euler equations, are compared to numerical simulations to better understand the stability boundary and unstable modes of propagation. Two distinct modes of instability are observed. In the limit of large reaction-to-induction lengths, evidence suggests a galloping detonation mode. At smaller reaction-to-induction lengths, increasing activation energy leads to a period-doubling bifurcation cascade into chaos.

INTRODUCTION

The dynamics of detonations predicted by the Euler equations are quite complex. Direct simulation of chemical decomposition in the framework of the one-dimensional Zel'dovich-von Neumann-Döring detonation model indicates a route to chaos via period-doubling bifurcations [1, 2].

Recently, toy models have been formulated to gain better insight into these dynamics [3, 4]. These models use an extension of Burgers' equation with an added source term to account for energy release, first introduced by Fickett [5]. The models reproduce the period-doubling bifurcation route to chaos previously predicted numerically using the Euler equations.

Such a route to chaos has never been observed experimentally. However, galloping detonations have been espied in one dimension, and cellular detonations have been observed in two dimensions, maintaining characteristic quasi-periodic dynamics. The discrepancy between the predicted chaotic dynamics and experiments may be due to the choice of reaction model, which is the topic of investigation in the present study. Previous investigations focus on extensions of the square wave model, with relatively thin reaction zones compared to the induction zone. In reality, multi-dimensional effects give rise to a reaction zone which is systematically longer than the induction zone. For cellular detonations, hydrodynamic thicknesses of the reaction zone have been reported to be approximately two orders of magnitude longer than the induction zone [6]. In galloping detonations, the turbulent flame brush following the lead shock is also much thicker than the shock-flame separation distance [7].

This study revisits the dynamics of detonations for the toy model introduced by Radulescu and Tang [3] in the limit of an induction zone that is much longer than the reaction zone, and extends the investigation to a longer reaction zone. Both numerical and asymptotic analyses have been performed, and are communicated below.

MODEL

Fickett's model $\partial_t \rho + \partial_x p = 0$ was used, where $p = \frac{1}{2}(\rho^2 + \lambda_\mathrm{r} Q_\mathrm{r})$ with reactions consisting of a neutral induction period followed by an exothermic reaction (subscripts i and r respectively) such that

$$r_\mathrm{i} = \partial_t \lambda_\mathrm{i} = \mathrm{H}(1 \circ \lambda_\mathrm{i}) k_\mathrm{i} \exp\left(E_\mathrm{a}\left(D/D_\mathrm{CJ} \circ 1\right)\right) \quad \text{and} \quad r_\mathrm{r} = \partial_t \lambda_\mathrm{r} = (1 \circ \mathrm{H}(1 \circ \lambda_\mathrm{r}))\mathrm{H}(1 \circ \lambda_\mathrm{r}) k_\mathrm{r} (1 \circ \lambda_\mathrm{r})^\nu$$

where H is the Heaviside function, $k = k_\mathrm{r}/k_\mathrm{i}$ is a reaction rate parameter which represents the reaction-to-induction length ratio, E_a is the activation energy parameter, $Q = 1$, $\nu = 1/2$, D is the detonation velocity and at steady state $D = D_\mathrm{CJ} = \sqrt{Q}$. Using the method of matched asymptotic expansions with small parameter $\epsilon = 1/E_\mathrm{a}$, a third-order-in-time evolution equation was derived, approximating the solution to Fickett's model:

$$3h_\tau \circ F_\tau + \epsilon\left(\frac{7 \circ 4\nu}{4k(\nu \circ 1)(2\nu \circ 3)}(h_{\tau\tau} + F_{\tau\tau}) \circ h_{\tau\tau} F \circ h_\tau F_\tau\right) + \epsilon^2 \Bigg\{ \left(\frac{9 \circ 4\nu}{2k^2(\circ 1 + \nu)(\circ 3 + 2\nu)(6 \circ 8\nu)} \circ \frac{1}{4k^2(\circ 1 + \nu)(\circ 3 + 4\nu)}\right)(F_{\tau\tau\tau} + h_{\tau\tau\tau}) + \frac{3}{4k(\circ 3 + 2\nu)}(F_\tau + h_\tau)(F_{\tau\tau} + h_{\tau\tau}) \Bigg\} = 0,$$

where $F = \circ \exp(\circ h_\tau)$ is the length of the induction zone, h is the lead shock position, and $\tau = \epsilon t$ is the slowed time variable. Numerically, the discretized system of equations was solved in the shock-fixed frame of reference using the first-order Godunov's method.

*Corresponding author. Email: slauc076@uottawa.ca

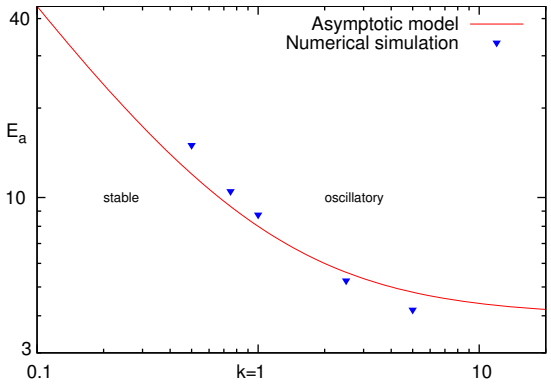

Figure 1: Stability Boundary

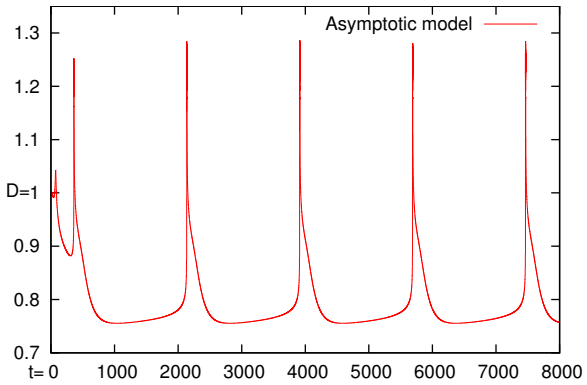

Figure 2: Detonation velocity history ($k = 0.5$, $E_\mathrm{a} = 40$)

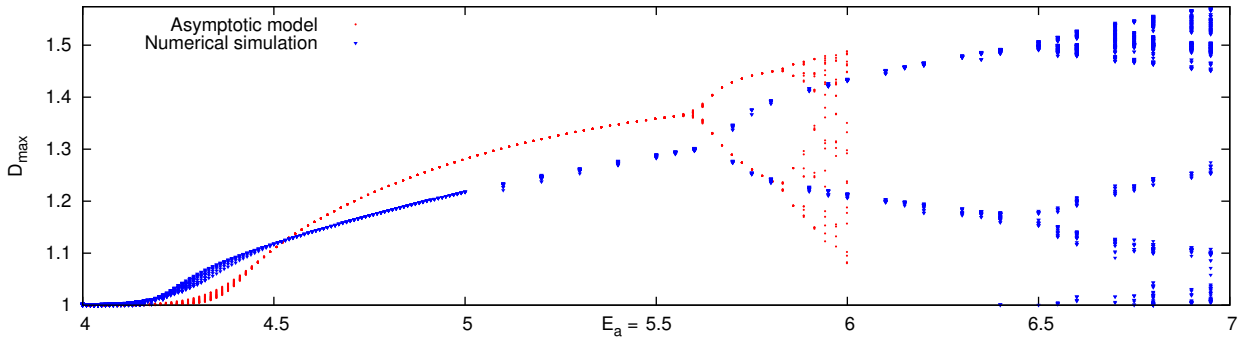

Figure 3: Period-doubling bifurcations of detonation velocity maxima ($k = 5$)

RESULTS

A parametric study was performed for different values of k and E_a comparing the asymptotic model to numerical simulations. At low values of k and E_a, the detonation propagates steadily. The detonation becomes unstable and the shock velocity oscillates when these parameters are increased. Figure 1 compares the analytical stability boundary found with the asymptotic model to results obtained with numerical simulations, which are in good agreement. For large values of k, results show that stability is controlled solely by E_a, whereas for low values of k, the stability boundary is a product of both k and E_a.

At high values of k, the asymptotic model and numerical simulations both follow the period-doubling route to chaos as E_a is increased, as shown in figure 3. The asymptotic model shows that at lower values of k and increasing E_a, a galloping-type behavior is recovered, as shown in figure 2. Long periods of slow propagation that near the quenched detonation velocity are interrupted by the sudden acceleration of the shock front, followed by a slower speed reduction.

CONCLUSION

The present study recovered the characteristics of stability for one-dimensional pulsating detonations using Fickett's model with two-step chemistry, which was completed using asymptotic modeling and numerical simulations. Two modes of instabilities were found, which are dependent on the ratio of the induction to reaction lengths. At large values, period doubling was observed, whereas smaller values yielded galloping-type detonations at sufficient activation energies.

References

[1] H Ng, A Higgins, C Kiyanda, M Radulescu, J Lee, K Bates, and N Nikiforakis. Nonlinear dynamics and chaos analysis of one-dimensional pulsating detonations. *Comb. Theory and Modelling*, 2005.

[2] A. K. Henrick, T. D. Aslam, and J. M. Powers. Simulations of pulsating one-dimensional detonations with true fifth order accuracy. *J. Comput. Phys.*, 2006.

[3] M. I. Radulescu and J. Tang. Nonlinear dynamics of self-sustained supersonic reaction waves: Fickett's detonation analogue. *Phys. Rev. Lett.*, 2011.

[4] A. R. Kasimov, L. M. Faria, and R. R. Rosales. Model for shock wave chaos. *Phys. Rev. Lett.*, 2013.

[5] W. Fickett. Detonation in miniature. *Am. J. Phys.*, 47(12):1050–1059, 1979.

[6] J.H.S. Lee. Dynamic parameters of gaseous detonations. *Ann. Rev. Fluid Mech.*, 1984.

[7] D. H. Edwards and J. M. Morgan. Instabilities in detonation waves near the limits of propagation. *J. Phys. D: Appl. Phys.*, 1977.

ON NUMERICAL MODELING OF COMBUSTION AND OTHER ENERGY RELEASE IN POROUS OBJECTS

Nickolay A. Lutsenko[1, 2a)]
[1]*Institute of Automation and Control Processes, Far Eastern Branch of the Russian Academy of Sciences, Vladivostok, Russian Federation*
[2]*Engineering School, Far Eastern Federal University, Vladivostok, Russian Federation*

Summary The work is devoted to the numerical modeling of heterogeneous combustion and other energy sources in porous objects with self-regulation of flow rate of the gas passed through the object. Such porous objects can arise from various natural or man-made disasters like self-ignition of peatlands or solid waste dumps, explosions at industrial or energy plants. Mathematical models and original numerical algorithms have been developed for the investigation of unsteady heterogeneous combustion of porous two-dimensional objects with one-step chemical kinetics and time-dependent regimes of gas flow through three-dimensional porous objects with sources of energy release without detailed chemical kinetics; some 2D and 3D time-dependent problems have been solved numerically. It has been shown that the combustion waves can move complicatedly; the gas flows inside of the porous object can be complex. When the natural convection takes place, the vortex-type gas flows can occur in the combustion zone and in its vicinity.

INTRODUCTION

Combustion and other energy sources in porous media often arise as a result of various natural or man-made disasters. Porous media in terms of mechanics are soils, peat, debris of ruined buildings, solid waste dumps, etc. Heterogeneous combustion in porous media is due to the exothermic reaction between the fuel in the porous solid medium and oxidizer contained in the gas flowing through the porous object. Such combustion can appear after spontaneous self-ignition of peat or solid waste dumps (landfills), after explosions at industrial and power plants and so on. There are a lot of publications devoted to both solid and gas combustion in the filtration mode, among which we would especially like to emphasize the review article [1]. Zones of other energy release, which differ from combustion sources, can appear in porous media after the explosions at nuclear power plants (like Chernobyl NPP). The exploded unit of the Chernobyl NPP showed that the gas (air) cooling of such heat sources can be the only available counteraction method of the disaster [2].
A distinctive feature of the combustion and other energy sources arisen in porous media after disasters is that the flow rate of gas passed through the porous object is unknown a priori, and only the gas pressure at the object boundaries is known. In other words, the self-regulation of gas flow rate passed through the porous object takes place in a self-heating object. It should be noted that knowledge of the gas pressure at the object boundaries allows to model processes under both forced filtration and natural convection. The present work is devoted to the numerical investigations of the time-dependent gas flows through porous self-heating media with self-regulation of gas flow rate.

MATHEMATICAL MODELS AND NUMERICAL METHODS

Mathematical models, which are discussed in this paper, can describe the processes of heterogeneous combustion and other energy-release process in motionless porous objects, which have some impermeable non-heat-conducting borders and some boundaries opened to the atmosphere. The cold gas can flow into the open walls of the porous object; the gas can flow through porous medium and flow out.
The mathematical models are based on the assumption of interacting interpenetrating continua [3] using the classical approaches of the theory of filtration combustion [1] and include equations of state, continuity, momentum conservation and energy for each phase (solid and gas). In the energy equation for solid component not only heat generation is taken into account but also the thermal conductivity and the intensity of the interphase heat exchange. In the energy equation for gas the homogeneous reactions are not considered. For describing the dynamics of gas, the equation of momentum conservation for porous media is used, which is more correct than the classical Darcy's equation and can be used in a greater range of Reynolds numbers [3]. The solid phase is assumed to be fixed, so the equation of motion for it degenerates. We assume that the perfect gas equation of state is valid and the dynamical viscosity of gas depends on temperature.
When investigating the combustion in porous objects, we suppose that a solid porous substance consist of combustible and inert components, and the solid combustible material transforms into a gas in the reaction with gaseous oxidizer. Combustion processes are described by one-step chemical reaction of first order with respect to both arguments. The equation for oxidizer concentration is added; the changes in volume and weight of the phases are taken into account.
When investigating the other energy-release process (for example, processes in porous objects with radioactive energy sources), the detailed chemical kinetics is not considered, and it is assumed that the heat evolution is directly proportional to the concentrations of the reagent whose rate of decay is directly proportional to the concentration itself. The volume and

[a)]Corresponding author. Email: NickL@inbox.ru

weight of the condensed phase changes insignificantly, and these changes can be neglected. Such assumptions are valid, in particular, in the modeling of processes in the exploded unit of the Chernobyl NPP [2].
A distinctive feature of the considered models is that the gas flow rate and gas velocity at the opened boundaries of the porous object are unknown and have to be found from the solution of the problem. So we assume that at the object boundaries, which are opened to the atmosphere, we know gas pressure and the conditions of heat exchange. Also at these boundaries we know either gas temperature and (if the chemical kinetics is taken into account) the oxidizer concentration or conditions for gas temperature and oxidizer concentration depending on the directions of the gas flow. At the impermeable boundaries of the object the conditions of non-heat-conductivity and impermeability are known.
The original numerical methods, which are based on a combination of explicit and implicit finite-difference schemes, have been developed for the investigation of unsteady heterogeneous combustion of porous 2D objects with one-step chemical kinetics and time-dependent regimes of gas flow through 3D porous objects with sources of energy release without detailed chemical kinetics. These methods are the development of earlier proposed numerical algorithms for modeling 1D problems of heterogeneous combustion in porous objects [4-5] and 2D problems of the other energy release in porous media [6]. According to the method the energy equations, momentum conservation equation and equation for oxidizer concentration are transformed into the explicit finite difference equations. The gas temperature, solid phase temperature, gas velocity and oxidizer concentration are determined from these equations. The continuity equation is transformed into the implicit finite difference equation. From this equation taking into account the perfect gas equation of state the gas pressure is determined using Thomas algorithm [7]. The effective gas density and the remaining unknown quantities are determined trivially from the perfect gas equation of state and other closure equations.

MAIN RESULTS

Some problems of time-dependent heterogeneous combustion and other energy release in porous objects of complex shape have been solved numerically using original algorithms for various locations of the ignition zones (for the combustion process) and various locations of the heat-releasing zones (for the process of energy release without detailed chemical kinetics). The numerical experiments have shown that the two-dimensional time-dependent waves of heterogeneous combustion in porous media propagate, as well as one-dimensional combustion waves [4-5], in two modes with different degrees of burnout of solid combustible material. At the same time, when the initial and boundary conditions in the porous object are non-one-dimensional, the combustion front can move complicatedly.
When the forced filtration takes place, the gas, moving from inlet to outlet of the porous object, tends to go around the heated part and prefers to flow in the cold part of the object both for combustion and for the process of energy release without detailed chemical kinetics. In the case of the forced filtration, the combustion wave cannot reach every part of the porous object as a rule, so the size of burned-out part of the porous object depends on the location of the ignition zone and the pressure at the object inlet. It has been shown that the partial closure of the object outlet by means of top cover can strongly affect the process of heat release and can greatly increase the maximal temperature in the porous object.
When the natural convection takes place, the combustion wave can go through the all parts of the object regardless of where the ignition zone was located as a rule, so all combustible material in each part of the object is burned, in contrast to forced filtration. In the case of the natural convection, the combustion waves can move in various directions depending of the location of the ignition zones. During the initial period of the process in the combustion zone and in its neighbourhood the vortex gas flows can occur. So, the gas can come into the porous object not only through its lower border, but through its upper border too, where gas pressure is less, as the pressure at the lower and upper boundaries of the porous objects corresponds to the atmospheric pressure at assigned heights.
The work was supported financially by the Ministry of education and science of Russian Federation (project 14.Y26.31.0003), the Russian Foundation for Basic Research (project 16-01-00103-a), the Far-Eastern Branch of the Russian Academy of Sciences (project 15-I-4-021).

References

[1] Aldushin A.P., Merzhanov A.G., in: Matros Yu. Sh. (Ed.), Heat Wave Propagation in Heterogeneous Media. Novosibirsk, Russian Federation 1988 (in Russian).

[2] Maslov V.P., Myasnikov V.P., Danilov V.G.: Mathematical modeling of the exploded unit of the Chernobyl nuclear power plant. Moscow, Russian Federation 1987 (in Russian).

[3] Nigmatulin R.I.: Principles of the mechanics of heterogeneous media. Moscow, Russian Federation 1978 (in Russian).

[4] Lutsenko N.A.: Modeling of heterogeneous combustion in porous media under free convection. *Proc. Combust. Inst.* **34**: 2289-2294, 2013.

[5] Lutsenko N.A., Levin V.A.: Effect of Gravity Field and Pressure Difference on Heterogeneous Combustion in Porous Media. *Combust. Sci. Technol.* **186**: 1410-1421, 2014.

[6] Lutsenko N.A.: Numerical modeling of unsteady gas flow through porous heat-evolutional objects with partial closure of the object's outlet. *Int. J. Heat Mass Transfer* **72**: 602-608, 2014.

[7] Tannehill J.C., Anderson D.A., Pletcher R.H.: Computational fluid mechanics and heat transfer, 2nd ed. Washington, USA 1997.

ON HYDRODYNAMIC EFFECTS DURING SELF-EXCITED THERMOACOUSTIC OSCILLATIONS

Malte Merk*[1], Stefan Jaensch[1], and Wolfgang Polifke[1]
[1]*Professur für Thermofluiddynamik, Technische Universität München, Garching, Germany*

Summary We study hydrodynamic aspects during a self-sustained thermoacoustic oscillation by means of a fully compressible CFD simulation. By coupling the CFD domain to state-space formulated impedance boundary conditions, an elongation of the plenum can easily be realized without changing the computational grid. We obtain different states of self-sustained thermoacoustic oscillations by varying the plenum length of the setup. Instantaneous flow fields reveal a vortex shedding at the burner plate of the investigated slit burner induced by large velocity fluctuations. The vortices are transported downstream by convection and interact with each other and the flame front, respectively. We observe that vortex-vortex and vortex-flame interactions influence the form of the thermoacoustic oscillations strongly.

INTRODUCTION

A profound understanding of thermoacoustic oscillations is important, as they can limit the operating range of combustion devices like gas turbines. Kabiraj et al. [3] experimentally observed various types of complex self-excited thermoacoustic oscillations in a Rijke burner by varying the flame position. A similar setup was numerically studied by Kashinath et al. [4]. In their work a G-Equation based model was used to carry out a bifurcation analysis with the flame position as a bifurcation parameter. However, the proposed model was not capable of capturing important hydrodynamic effects such as e.g. vortex shedding or vortex-flame interactions. Hence, only a qualitative agreement with experimental results can be expected. To circumvent these shortcomings, a more realistic model is used in the present work that couples a fully compressible Navier-Stokes approach with 2-step reaction scheme (AVBP, Cerfacs) to a low-order acoustic model at the boundaries. It takes the acoustics as well as hydrodynamic effects into account and permits a detailed evaluation of instantaneous flow fields and the therein resolved hydrodynamics during self-excited thermoacoustic oscillations. This coupled model was successfully cross-validated in the work of Jaensch et al. [1] against a weakly compressible model, which takes the thermoacoustic feedback into account via a coupled acoustic network model. While in [1] the focus was laid on time series analysis, in the present work we investigate observed flow structures. We find that shed vortices and their interaction with the flame exhibit distinct non-linear effects on the thermoacoustic oscillations which have to be considered in the formulation of suitable low-order models.

PROBLEM SETUP

The slit burner setup investigated is shown in Fig. 1. According to the experimental work of Kornilov et al. [5] the working conditions are chosen: An inlet velocity of $0.4\ m/s$ is imposed for a methane/air mixture with an equivalence ratio $\phi = 0.8$. The inlet temperature equals $293\ K$. A fixed temperature of $293\ K$ is set for the plenum wall while the burner plate and the combustion chamber wall have a fixed temperature of $373\ K$. On all walls no-slip conditions are applied. Only one half of the flame is resolved in the CFD domain so a symmetry boundary condition is used. The acoustics of the compressible CFD are coupled at the inlet and outlet to Characteristic Based State-space Boundary Conditions (CBSBC) [2]. These boundary conditions ensure that the CFD simulation exhibits a specified acoustic impedance and allow thus a virtual extension of the plenum length L_{P1} (no need to modify the computational grid), whose acoustical behavior is crucial for the thermoacoustic stability. Since complex flow phenomena are only present in close vicinity to the burner plate ($L_{P2}+L_S+L_C$), the impedance boundary conditions provide a computationally cheap method to take the acoustics of different plenum length into account without resolving the fully compressible Navier-Stokes equations in this part of the setup. By continuously elongating the plenum length L_{P1}, the system can be driven from stable working conditions through different states of self-sustained thermoacoustic oscillations. Two cases are shown here, see Tab. 1. Because oscillation amplitudes grow larger in experiment L700 the CFD domain is stretched in this case to capture all relevant hydrodynamic- and combustion effects.

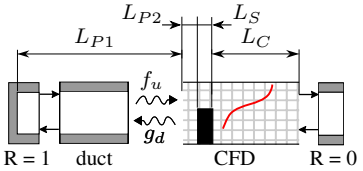

Case	L_{P1}	L_{P2}	L_S	L_C	cell size	cells
L200	195 mm	5 mm	1 mm	20 mm	0.025 mm	65700
L700	685 mm	15 mm	1 mm	40 mm	0.025 mm	122300

Figure 1 & Table 1: Sketch of the investigated setup (left) and the respective length of two conducted experiments (right).

*Corresponding author. Email: merk@tfd.mw.tum.de

RESULTS

L200: By looking at the time series of L200 (Fig. 2), we observe a period-2 oscillation for u' and a period-1 oscillation for Q'. Furthermore, u' and Q' are out of phase. u' peaks when Q' is minimal (see time instant (1)) and accordingly Q' has its maximum during an intermediate minimum of u' (4). The different types of oscillations as well as the phase between Q' and u' can be explained by the flow fields at the respective time instants. When u' peaks (1) the flame is expanded and pushed downstream, resulting in an increase of flame surface and Q' (2). At this instant a vortex is shed at the trailing edge of the plate, imposing a constricting motion behind itself and traveling downstream with the flame front (3). u' reaches here an intermediate maximum. At instant (4) pinch off occurs. Q' has its global maximum, while u' reveals an intermediate minimum similar to instant (2). Again a vortex is shed at the edge of the plate, but due to the previous pinch off the remaining flame front is moving upstream, collides with the vortex and smears it out directly. Consequently the second vortex has only a minor effect on the flame shape. In the following, the quickly shrinking flame surface yield a drastic decrease of heat release.

L700: The longer plenum in this case leads to more complex oscillations. The periodicity is gone but Q' and u' are still out of phase. The oscillating amplitude is 7 times larger as in L200 and we find a rich hydrodynamical behavior. Two occurring effects in this case are depicted. Firstly, increased oscillation magnitudes cause flashback phenomena and additionally shed vortices at the leading edge of plate (1). These vortices mix unburnt gas into the region of burnt gas downstream of the flame front, where the entrained fuel pocket is burnt in the following (not shown). Secondly, vortex-vortex interactions are observable between the instants (2)-(4). The large inlet velocity at this time results in multiple detaching vortices that are mutually interacting by "vortex leapfrogging". The upstream vortex in instant (2) overtakes the leading vortex in instant (3). Vortex-vortex interactions have a definite impact on the flame shape and thus on the behavior of the thermoacoustic oscillation.

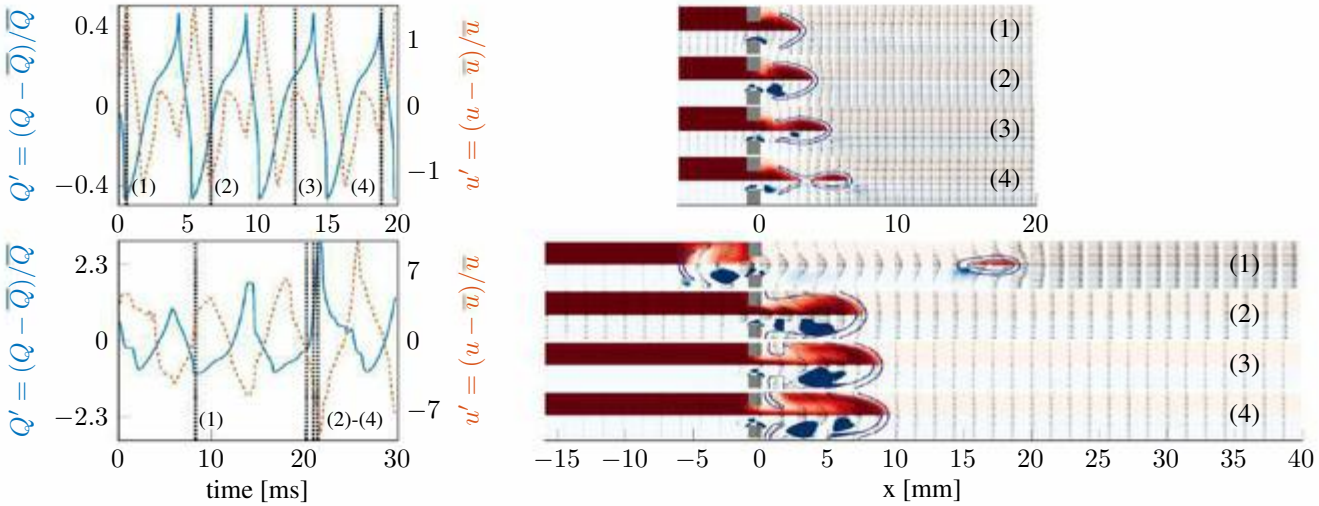

Figure 2: Top: L200; Bottom: L700; Left: Time series of global Q' and u' at the inlet; Right: Fields at 4 distinct instants (see time series) of CH4 mass fraction (upper half) and Q-Criterion (lower half); Isoline: Heat release; Arrows: Velocity.

CONCLUSIONS

Coupling a fully compressible CFD to low-order acoustic models at the boundaries allows to capture all relevant effects during self-sustained thermoacoustic oscillations. Thus a detailed study of instantaneous flow fields and the therein resolved hydrodynamics is possible with reasonable computational effort. We can show that detached vortices have a distinct non-linear impact on the flame shape and consequently on the behavior of the thermoacoustic oscillation itself. These effects have to be taken into account in the development of suitable and accurate non-linear low-order models.

References

[1] S. Jaensch, M. Merk, E. Gopalakrishnan, S. Bomberg, T. Emmert, R. I. Sujith, and W. Polifke. Hybrid CFD/ low-order modeling of nonlinear thermoacoustic oscillations. In *accepted for the 36th Symposium of the Combustion Institute*, Seoul, Korea, 2016.

[2] S. Jaensch, C. Sovardi, and W. Polifke. On the robust, flexible and consistent implementation of time domain impedance boundary conditions for compressible flow simulations. *Journal of Computational Physics*, 2015.

[3] L. Kabiraj, A. Saurabh, P. Wahi, and R. I. Sujith. Experimental study of thermoacoustic instability in ducted premixed flames: periodic, quasi-periodic and chaotic oscillations. In *n3l – Non-Normal and Nonlinear Effects in Aero- and Thermoacoustics*, Munich, Germany, 2010.

[4] K. Kashinath, I. C. Waugh, and M. P. Juniper. Nonlinear self-excited thermoacoustic oscillations of a ducted premixed flame: bifurcations and routes to chaos. *Journal of Fluid Mechanics*, 761:399–430, 2014.

[5] V. N. Kornilov, R. Rook, J. H. M. ten Thije Boonkkamp, and L. P. H. de Goey. Experimental and numerical investigation of the acoustic response of multi-slit Bunsen burners. *Combustion and Flame*, 156(10):1957 – 1970, 2009.

PROPAGATION OF GASEOUS DETONATION WAVES IN A SPATIALLY HETEROGENEOUS REACTIVE MEDIUM

XiaoCheng Mi[1], Andrew J. Higgins[1a)], Hoi Dick Ng[2], Charles B. Kiyanda[2] & Nikolaos Nikiforakis[3]
[1]*Department of Mechanical Engineering, McGill University, Montreal, Quebec, Canada*
[2]*Department of Mechanical and Industrial Engineering, Concordia University, Montreal, Quebec, Canada*
[3]*Cavendish Laboratory, Department of Physics, University of Cambridge, Cambridge, United Kingdom*

Summary The effect of both one- and two-dimensional spatial heterogeneities on the propagation of a detonation wave governed by single-step Arrhenius kinetics is computationally examined in this study. The reactive medium consists of a calorically perfect gas. The spatial heterogeneity can be introduced to the reactive medium as a piecewise-continuous distribution (e.g., Gaussian or step function) in the initial density or concentration of the reactant. In one-dimensional simulations, the resulting detonation velocity will be compared with that of an ideal Chapman-Jouguet detonation in a homogeneous medium with the same amount of energy release. The influence of the spatial heterogeneity on the detonation limits will also be computationally investigated by simulating two-dimensional detonations experiencing losses due to lateral expansion.

INTRODUCTION

Detonation waves are supersonic combustion waves which consist of a leading shock wave propagating in an energetic medium followed by a zone of exothermic chemical reactions which are triggered by shock compression. The speed at which a detonation wave propagates in a medium with known chemical energy density can be accurately predicted by the classical Chapman-Jouguet (CJ) criterion, which is based on the assumption of a steady, one-dimensional detonation structure and a homogenous reactive medium. A large amount of experimental evidence of gaseous detonations dominated by a transient, multidimensional cellular or irregular structure have, however, been found in the past half century [1]. With activated chemical reactions (i.e., Arrhenius kinetics), Short and Stewart proved that the resulting detonation would be unconditionally unstable in two-dimensions [2]. The success of the steady, one-dimensional CJ criterion in predicting the propagation speed of a detonation wave with a highly complex, transient structure seems thus contradictory. Although this paradoxical situation was first articulated by Oppenheim in 1960 [3], a fully satisfactory explanation still eludes researchers.

In this study, the applicability of the CJ criterion on a detonation wave with a transient, irregular structure resulting from a spatially heterogeneous reactive medium will first be examined via one-dimensional numerical simulations. The effect of spatial heterogeneity on detonation limits will also be computationally investigated by simulating two-dimensional detonations experiencing losses due to lateral expansion. In these two-dimensional cases, the reactive system is modelled as a planar slab of detonable gases confined by a layer of inert material, where a critical slab thickness marks the propagation limit of detonation. In both one- and two-dimensional simulations, single-step Arrhenius kinetics with values of heat release and activation energy representing a realistic mixture of detonable gases will be incorporated.

PROBLEM DESCRIPTION

The reactive system consists of an inviscid, calorically perfect gas. The gasdynamics of this system is described by the one- or two-dimensional reactive Euler equations in a lab-fixed reference frame. The reaction progress is monitored by a variable Z, which represents the normalized concentration of the product. The reaction rate is governed by single-step Arrhenius kinetics, i.e., $\dot{Z} = k(1-Z)\mathrm{Exp}(E_\mathrm{a}/\mathrm{R}T)$. The pressure, density, and flow velocity are non-dimensionalized with respect to the initial state ahead of the leading shock front. Given a reactive system with a dimensionless energy density Q, the CJ detonation velocity D_CJ can be calculated. The one-dimensional simulations are performed with $Q = 50$, activation energy $E_\mathrm{a} = 20$, and ratio of specific heats $\gamma = 1.2$. The pre-exponential factor $k = 16.45$ is arbitrarily chosen, so that the half-reaction-zone length is unity.

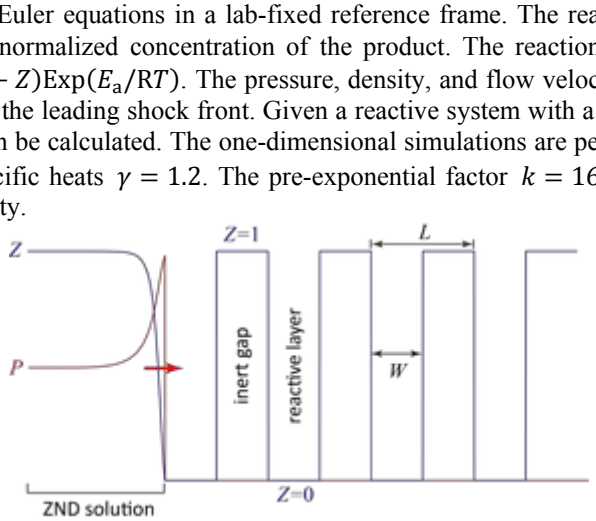

Fig.1 Schematic representation of the problem.

[a)] Corresponding author. Email: andrew.higgins@mcgill.ca

The one-dimensional reactive system is spatially discretized by concentrating the reactant into layers separated by inert gaps. The discretization is realized by initializing Z as 0 in the reactive layers and 1 in the inert gaps as shown in Fig. 1. The spatial discreteness is described by a parameter $\Gamma = W/L$, where W is the reactive layer width and L the spacing between two consecutive layers. The energy density in each reactive layer is Q/Γ, so that the average energy density of the overall medium is maintained at Q while Γ is varied. As shown in Fig. 1, the detonation wave is initialized using a ZND-structured wave propagating rightward at the ideal CJ velocity from the left end of the computational domain.

RESULTS AND DISCUSSION

The simulation results of the instantaneous detonation velocity D_{ins} are plotted as a function of the leading shock position in Fig. 2(a) and (b). As shown in Fig. 2(a), with $L = 10$, the curve of D_{ins} history for the continuous case ($\Gamma = 1.0$) and corresponds to the CJ velocity. As Γ decreases, the history of D_{ins} exhibits fluctuations with increasing amplitude around or slightly above CJ velocity. In Fig. 2(b), after an initial increase, D_{ins} relaxes to the CJ velocity with $\Gamma = 0.5$ and L equals twice the ZND half-reaction-zone length. The fluctuations in D_{ins} become increasingly pronounced as L increases. With $L = 100$, it can be identified in the velocity history shown in Fig. 2(b) that the leading shock travels at a significantly super-CJ speed in a reactive layer since the energy density there is twice the average value over the entire medium; D_{ins} gradually decays to a speed below the CJ velocity in an inert gap since there is no energy release supporting its propagation.

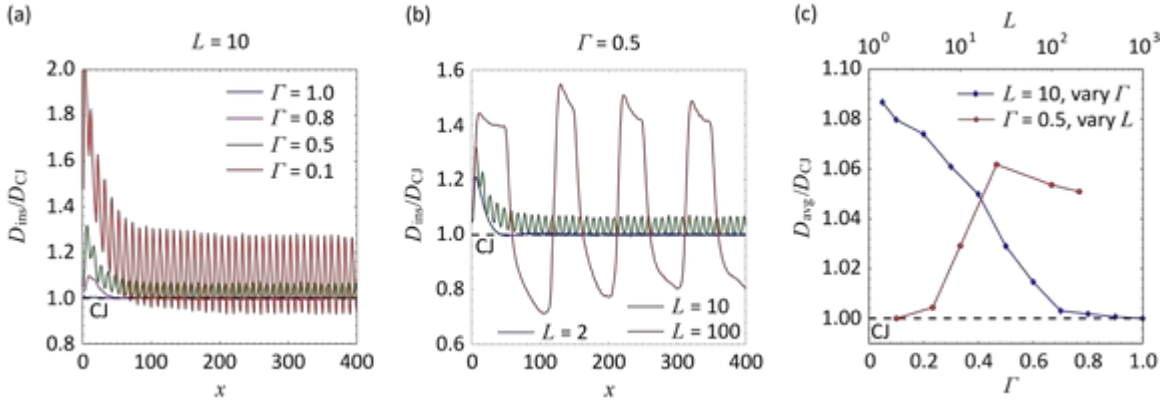

Fig. 2 History of the instantaneous detonation velocity normalized by D_{CJ} as a function of leading shock position with (a) $L = 10$ and various Γ and (b) $\Gamma = 0.5$ and various L. (c) Average detonation velocity normalized by D_{CJ} as a function of L (red circles, *vs*. top axis) and Γ (blue diamonds, *vs*. bottom axis).

In all simulations, the computational domain has to contain at least 15 reactive layers to observe quasi-steady propagation. The average detonation velocity D_{avg} is measured as the leading shock travels over the last 5 reactive layers. As shown in Fig. 2(c), with $L = 10$, D_{avg} is less than 0.3% different from D_{CJ} for $\Gamma \geq 0.7$. As Γ further decreases, D_{avg} increases significantly above D_{CJ}. Also shown in Fig. 2(c), with $\Gamma = 0.5$, D_{avg} reverts to D_{CJ} for a heterogeneity size close to its half-reaction-zone length, reaches a maximum at $L = 10$, and gradually decreases as L further increases. A similar non-monotonic effect of heterogeneity size on the detonation wave propagation is identified in the simulations of two-dimensional detonations propagating in a medium with sinusoidally distributed initial density [4].

CONCLUSIONS

A one-dimensional reactive system representing a gaseous detonable mixture was simulated in this study. Spatial heterogeneity resulted in an average wave speed up to 9% greater than the ideal CJ velocity. This enhancing effect of heterogeneity on detonation speed is expected to enable detonation waves with losses to propagate beyond the limit that would be obtained in a homogeneous medium, and will be explored via two-dimensional simulations.

References

[1] Lee J.H.S., *The Detonation Phenomenon*, Cambridge University Press, Cambridge, 2008.

[2] Short M., Stewart D.S.: Cellular Detonation Stability: A Normal Mode Linear Analysis. *J. Fluid Mech* **368**:229-262, 1998.

[3] Oppenheim A.K.: Development and Structure of Plane Detonation Waves. Milan, Italy 1960.

[4] Li J., Mi X., Higgins A.J.: Effect of Spatial Heterogeneity on Near-Limit Propagation of a Pressure-Dependent Detonation *Proc. Combust. Inst.* **35**:2025-2032, 2015.

THE FRANK-KAMENETSKII VORTEX

Daniel Moreno-Boza*[1], Immaculada Iglesias[2], Antonio L. Sánchez[1], Amable Liñán[3], and Forman A. Williams[1]
[1]*MAE Department, UCSD, USA*
[2]*Fluids Group, Universidad Carlos III of Madrid, Spain*
[3]*ETSI Aeronáuticos, Madrid, Spain*

Summary The effect of the buoyancy-driven motion on the quasi-steady "slowly-reacting" mode of combustion of a gaseous mixture enclosed in a spherical vessel with a constant wall temperature is addresed here. Following Frank-Kamenetskii's (FK) analysis, combustion is modeled by an overall Arrhenius reaction with large activation energy, resulting in a critical value of the vessel radius above which the slowly-reacting mode of combustion no longer exists. In his buoyancy-free quasi-steady analysis the critical conditions were found to depend on the value of the Damköhler number. For small values of *Ra*, temperature is given in the first approximation by the spherically symmetric FK distribution, involving an axisymmetric annular vortex determined at leading order. The analysis is extended to investigate the influence of convection on the resulting explosion limits through introduction of expansions for the flow variables in powers of *Ra*.

While the initial work of FK [1] addressed stagnant systems, for which the critical Damköhler number Da_c is obtained from the steady reaction-conduction balance, this is altered in the presence of buoyancy-driven convection, which necessarily emerges in gaseous systems under normal gravity conditions as a result of the density differences induced by the chemical reaction. The resulting characteristic velocities can be estimated to be of order $v_g = \beta^{-1} g a^2/\nu$, as follows from the balance between viscous forces and buoyancy forces, with β the nondimensional activation energy and g and ν representing the magnitude of the gravitational acceleration and the unperturbed value of the kinematic viscosity, respectively. Using v_g to scale the velocity reduces the continuity, momentum, and energy equations for the slowly reacting mode of combustion to

$$\nabla \cdot \mathbf{v} = 0, \qquad (Ra/Pr)\ \mathbf{v} \cdot \nabla \mathbf{v} = \nabla^2 \mathbf{v} \circ\ \nabla p' + \phi\ \mathbf{e}_z, \qquad \text{and} \qquad Ra\, \mathbf{v} \cdot \nabla \phi = \nabla^2 \phi + Da\, \mathrm{e}^{\phi}, \tag{1}$$

where $\mathbf{e}_z$ is the unit vector pointing upwards (against gravity) and p' represents the pressure differences from the hydrostatic value scaled with $\rho_o g a/\beta$. A Boussinesq approximation has been employed in writing (1). The influence of the buoyancy-induced motion on the associated temperature field is thus measured by the Rayleigh number, $Ra = (\beta^{-1} g a^3)/(\nu D_T)$ with the Grashof number, Ra/Pr, involving the Prandtl number $Pr = \nu/D_T$, similarly measuring convective transport in the momentum equation. The description of the quasi-steady slowly reacting state accounting for buoyancy-induced motion is obtained by integrating (1) with boundary conditions $\mathbf{v} = \phi = 0$ at the vessel walls. At leading order in the limit $Ra \ll 1$ the energy equation 1 reduces to the classical FK equation $\nabla^2 \phi + Da\, \mathrm{e}^{\phi} = 0$, with the associated motion described from the viscous-buoyancy balance $\nabla^2 \mathbf{v} \circ\ \nabla p' + \phi\ \mathbf{e}_z = 0$, stemming from the momentum conservation equation in that same limit. The small deviations from the FK solution resulting from the presence of slow fluid motion for $Ra \ll 1$ can be formally addressed by expanding the different fluid variables in powers of *Ra*. Because of the extremely slow motion found at leading order, it will be found that the resulting predictions, although formally applicable only for small values of *Ra*, remain accurate even for quite large values of *Ra*. In principle, for many values of *Da* the asymptotic solution in the limit $Ra \ll 1$ can be addressed as the problem of computing the perturbations arising for a fixed value of *Da*. Such a strategy is inadequate, however, near the turning point of the bifurcation curve giving the temperature at the center of the vessel as a function of *Da* because there is no leading-order solution that can be perturbed for $Da > Da_c$. Therefore a different perturbation scheme must be adopted to enable corrections to Da_c to be determined. For that reason, in the analysis outlined below we begin by prescribing the temperature at the center of the vessel ϕ_o, corresponding to a value $Da = Da_{\mathrm{FK}}$ of the associated FK Damköhler number in the absence of convection (i.e. for $Ra = 0$). The problem is then posed as that of finding the perturbed Damköhler number $Da \neq Da_{\mathrm{FK}}$ that, for a given value of $Ra \ll 1$, results in a temperature at the center of the vessel equal to ϕ_o. It is evident, for example from Fig. 1(a), that leading-order solutions exist for all values of ϕ_o.

Besides expansions for the different variables of the form

$$\phi \circ\ \phi_{\mathrm{FK}} = Ra\phi_1 + Ra^2\phi_2 + O(Ra^3), \quad \omega \circ\ \omega_{\mathrm{FK}} = Ra\omega_1 + Ra^2\omega_2 + O(Ra^3), \quad \psi \circ\ \psi_{\mathrm{FK}} = Ra\psi_1 + Ra^2\psi_2 + O(Ra^3), \tag{2}$$

the development requires introduction of an expansion for the Damköhler number $Da = Da_{\mathrm{FK}}[1 + Ra\delta_1 + Ra^2\delta_2 + O(Ra^3)]$, where ω is the magnitude of the vorticity and ψ is the stream function, which is introduced to facilitate the description of the motion. The terms in the above expansions are determined by solving sequentially the different problems that arise at different orders in powers of *Ra* when introducing (2) together with the Damköhler number expansion into the equation for the vorticity [obtained by taking the curl of the momentum equation in (1)] and the energy equation, with the condition $\phi_j = 0$ applying at all orders $j = 1, 2, \ldots$, for the temperature perturbations at the center $r = 0$. Although a term proportional to *Ra* is included

*Corresponding author. Email: dmorenob@ucsd.edu

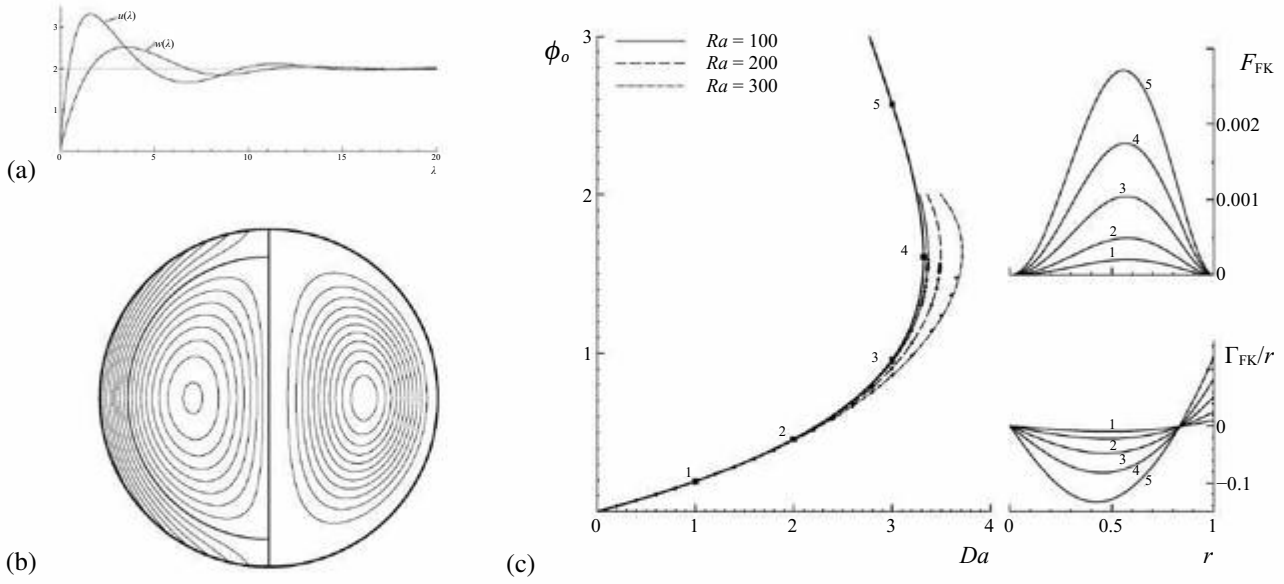

Figure 1: (a) The universal FK functions, $u(\lambda)$ and $w(\lambda)$, where $u = Da\ r^2 e^{\phi_{\rm FK}}$, $w = -r\phi'_{\rm FK}$ and $\lambda := \phi_o - \phi_{\rm FK}$ is the temperature drop variable. (b) Streamlines and isocontours of vorticity for $Da = 3.322$ for the FK vortex. (c) FK explosion curve and modified explosion curves for $Ra = 100,\ 200$ and 300, accompanied by the auxiliary functions $F_{\rm FK}$ and $\Gamma_{\rm FK}/r$.

in the expansion of *Da* for consistency with (2), it can be shown that this term is identically zero, so that the corrections to the explosion curve $\phi_o - Da$ are of order Ra^2. Introduction of spherical coordinates with origin at the vessel suggests the definition of auxiliary variables such that

$$\omega_{\rm FK} = -\sin\theta\Gamma_{\rm FK}/r,\ \ \psi_{\rm FK} = \sin^2\theta F_{\rm FK}, \tag{3}$$

$$\phi_1 = \cos\theta H_1 + \mathcal{H}_1,\ \ \omega_1 = -\sin\theta\cos\theta\Gamma_1/r,\ \ \psi_1 = \sin^2\theta\cos\theta F_1,\ \ \phi_2 = \cos^2\theta H_2 + \mathcal{H}_2, \tag{4}$$

which reduces the problem to that of integrating a set of boundary value problems in the radial coordinate with corresponding boundary conditions. To make the description universal, equidimensionality is leveraged from the resulting set of differential equations (using a similar methodology as described in [2]), allowing to further reduce the problem to integrating an autonomous system, ultimately enabling us to determine the factor δ_2 as an eigenvalue of a second-order differential problem in quasi-analytic form. The function $\delta_2(\phi_0)$ can be used to evaluate the modified explosion curves

$$Da = Da_{\rm FK}(1 + Ra^2\delta_2). \tag{5}$$

This is illustrated in Fig. 3(c), which includes comparisons of (5) with results of numerical integration of (1) for $Ra = 100, 200$ and 300.

References

[1] FRANK-KAMENETSKII, D. A. 1939 The temperature distribution in a reaction vessel and the time-independent theory of thermal explosions. *Zh. Fiz. Khim* **13**, 738–755.

[2] CHANDRASEKHAR, S. & WARES G. W. 1949 The isothermal function. *Astrhophys. J.* **109**, 551–554.

[3] FRANK-KAMENETSKII, D. A. 1969 *Diffusion and Heat Transfer in Chemical Kinetics*, Second ed., Plenum Press, New York, NY.

[4] JONES, D. R. 1973 The dynamic stability of confined, exothermically reacting fluids *Int. J. Heat Mass Transfer* **16**, 157–167.

[5] JONES, D. R. 1974 Convective effects in enclosed, exothermically reacting gases *Int. J. Heat Mass Transfer* **17**, 11–21.

[6] LIU, T.-Y., CAMPBELL, A. N., CARDOSO, S. S. S. & HAYHURST, A. N. 2008 Effects of natural convection on thermal explosion in a closed vessel *Phys. Chem. Chem. Phys.* **10**, 5521–5530.

[7] LIU, T.-Y., CAMPBELL, A. N., HAYHURST, A. N. & CARDOSO, S. S. S. 2010 On the occurrence of thermal explosion in a reacting gas: The effects of natural convection and consumption of reactant *Combust. Flame* **157**, 230–239.

[8] MERZHANOV, A. G. & SHTESSEL', E. A. 1973 Free convection and thermal explosion in reactive systems. *Acta Astronautica* **18**, 191–199.

[9] STEGGERDA, J. J. 1965 Thermal stability: an extension of Frank-Kamenetsky's theory. *J. Chem. Phys.* **43** 4446–4448.

EXPERIMENTAL DETERMINATION OF THE HEIGHT OF PROPELLANT FLAMES

Frederick Paquet *[1,2], Hoi Dick Ng[1], and Mario Paquet[2]

[1]*Department of Mechanical and Industrial Engineering, Concordia University, Montreal, Quebec, Canada*
[2]*General Dynamics - Ordnance and Tactical Systems - Canada, Valleyfield, Quebec, Canada*

Summary Propellant fires can be especially dangerous as the combusting materials are designed to liberate a large amount of energy in a relatively small timescale. In any industrial fire, the size of the event is important knowledge as it can guide in the proper design of equipments and facilities. This paper looks at the flame height of propellant fires through distance measurement of experimental tests video recordings. It is found that by properly scaling the configuration variables, a simple relationship is obtained between the horizontal and vertical dimensions of the event. The final result is coherent with the conclusions of previous studies involving a variety of other materials.

The ability to predict the size of an accidental fire is useful in planning the disposition of equipment, material and people inside industrial buildings. A proper design should limit secondary ignition sources and ensure the safety of everyone around. Because of its importance in safety problems, flame height has been studied extensively. A study published in 1961 proposes the following general expression for the height of liquid pool fires [1]:

$$H = 1.7D \tag{1}$$

In trying to obtain more general results, subsequent studies have used the power generation of the fires. One of the popular dimensionless scaling of the power generation was developed by Zukoski [2]. More recent correlations have been proposed by Quintiere et al. [3]. These last results use the chemical heat of combustion and Froude number to account for combustion efficiency, source geometry and air entrainment more precisely.

A series of large scale open air burnings were performed on propellant samples ranging from 1 kg to 1000 kg [4]. Single base (nitrocellulose) and double base (nitrocellulose and nitroglycerin) propellant formulations were used for these trials. The events were captured on a Casio Exilim camera at a rate of 256 frames per second and a reference distance marker was placed beside the sample. The footage captured for each fire was reviewed on a frame by frame basis using the Matlab Image Processing Toolbox [5]. The width at the base and top of the fire and total height were noted. A photo of the setup and a sample measurement plot of all trials are shown on Figure 1. When observing the initial and maximum base fire width, it is observed that the fire plume often extends to a lateral width greater than the original propellant stack diameter. Three main behaviors have been noted:

- Fireball generation and expansion – propellant stack engulfed by the fireball
- Steady growth with propellant grains projection – ignition by contact with projections
- Steady growth – closer to ideal surface flame spread



(a) Test setup

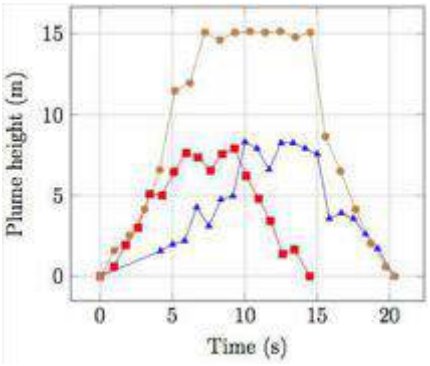

(b) Flame heights measurements for cases involving 68 kg (square marker), 136 kg (triangular marker) and 909 kg (circular marker) of single base propellant

Figure 1: Photograph of the test setup and plot of measured flame heights as a function of time for three single base fires.

*Corresponding author. Email: frede_pa@encs.concordia.ca

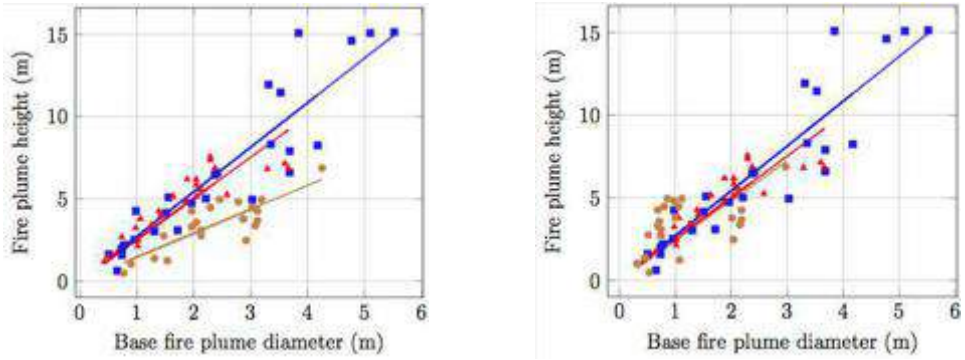

(a) (b)

Figure 2: Comparison of the measured base fire plume diameter and total height. In these plots, the double base diameter data is shown both in an unscaled (a) and scaled (b) format while the single base data is always unscaled. The triangular and square markers represent two different single base propellants. The circular markers represents a double base propellant. Note that the solid lines represent a linear regression through the corresponding data.

In the first case, the expanding fireball explains the larger values obtained. For the second case, the projected grains ultimately collect outside of the propellant stack, which result in a larger apparent diameter. The third case is only observed with slower burning propellants.

Using the recorded dimensional data for the test fires, it is possible to verify if a correlation between the fire height and diameter can be found. The flame height and base diameter are compared in Figure 2a for all tested propellant types and quantities. Note that Figure 2a contains all the data points from ignition to maximum for the test cases (as opposed to only the maximum values). Not including the points beyond the maximum base diameter is a logical choice as the diameter will vary when the fuel depletes and thus not yield reliable results.

Two families of points can be observed in Figure 2a. These families correspond to the single and double base propellants. Linear regression lines are given for each family and show the slopes to be different. The main familly cases have slopes varying from 2.41 to 2.71. The second familly has a slope of 1.45. In order to properly analyze the data, it is important to visualize the main difference between the families. Other than differences in power generation, the second family (double base case) has one important particularity: it is the only one for which the measured base diameter is larger then the actual source diameter. For the other cases, the source diameter can become larger than the original diameter due to projections. In keeping with the methodology of previous studies, it is the actual source diameter which should be considered when studying the flame height. Correcting the double base data to account for the original base diameter yields what is shown on Figure 2b. It can be observed that the diameter correction has the effect of merging the two families by increasing the double base slope from 1.45 to 2.86. By taking an average slope of 2.63, all the tested case can be by a single flame height correlation:

$$H = 2.63D \tag{2}$$

The observed variation in slope gives an indication of the error bound for this relation. With the obtained extremes, a variation of $\pm 9\%$ is expected for the flame height. Given the fact that the test cases cover power generations relevant to most propellants used, it is thus not necessary to go any further in this analysis. The simple relationship found here is precise enough to describe relevant cases provided that the correct base dimension is used.

References

[1] Blinov V.I., Khudiakov, G.N.: Certain Laws Governing Diffusive Burning of Liquids. Fire Res. Abstr. Rev. 1, 41, 1958.

[2] Zukoski E., Kubota T., Cetegen B.: Entrainment in Fire Plumes. Fire Safety Journal, 24:383-419, 1981.

[3] Quintiere J.G., Grove B.S.: Correlations for Fire Plumes. Technical Report NIST-GCR-98-744, National Institute of Standards and Technology, Gaithersburg, MD, 1998.

[4] Paquet F., Ng H.D., Paquet M.: A generalized model for propellant fire radiant heat flux output. Submitted to Fire Safety Journal (FISJ-D-15-00147), 2015.

[5] Matlab (software), The Mathworks Inc., 2012.

Ignition and Flame Stabilization in Supersonic Evaporating Fuel Sprays

Zhaoxin Ren[1], Bing Wang[1a)]&Huiqiang Zhang[1]
[1]*Department of Engineering Mechanics, Tsinghua University, Beijing, China*

Summary This paper numerically investigates ignition and combustion stabilization in supersonic droplet-laden shear flows. The spatially developing turbulent shear flow separates two hot air streams with different velocities and fuel droplets are injected at the flow inlet to form premixed reactive mixtures. Due to the high compressibility of the present supersonic shear flow, ignition occurs in the high-strain vortex-braid regions but the reactive mixtures entrained in the large eddies are difficult to be ignited at normal atmospheric pressure. Therefore, we increase ambient pressure and introduce oblique shock wave to achieve ignition enhancement and flame stabilization. The results show that the pressure perturbation in the combustion field is enhanced by combustion reaction and increase in internal pressure. The post-shock ignition kernel that is found to exist around the point of maximum temperature, depending on the profiles of the fuel concentration, temperature and Mach number across the shear layer.

INTRODUCTION

Spray combustion is utilized in many industrial devises including energy conversion devices and propulsion systems. Recently the design of combustion systems for supersonic propulsion faces difficulties associated with the high compressibility of the flow and the high flow velocity, which limits the residence time available for both fuel-oxidizer mixing and combustion. Combustion stabilization and flame anchoring in high-speed flows must depend on auto-ignition of the reactive mixture. The auto-ignition of fuel-oxidizer mixtures strongly relies on the temperature and the pressure, which affect the droplet evaporation and the chemical reaction rate. Therefore, the elevated temperature and the increasing ambient pressure in the highly strained shear layers facilitate auto-ignition in supersonic flows. The research on the effects of the ambient pressure on the droplet evaporation has shown the pressure dependence of droplet lifetime and increasing the pressure contributes to the increase of the chemical reaction rate. Local compression by shock waves impinging on shear layers promotes auto-ignition by raising the temperature and the pressure of the shocked gas, which is also the phenomenon addressed in this paper.

FORMULATION

The gas-phase is governed by the compressible Navier-Stokes equations together with species transport equations. The spray is sparsely dispersed and every single droplet is unaware of the existence of the other droplets. A finite difference methodology is used to discretize the conservative equations. An explicit third-order Runge-Kutta methodology is applied for time-integration. The non-viscous flux is evaluated via using a fifth-order adaptive central-upwind weighted essentially non-oscillatory (WENO) scheme for considering the efficiency of calculating smooth turbulent field and for resolution of shock-capturing calculation. For the calculation of droplet-phase, a fourth-order Lagragian interpolation method is employed to compute the physical quantities of gas phase at the droplet location. The position, velocity and temperature of droplets along trajectories are integrated by a third-order Adams scheme. The flow configuration is that of a spatially developing shear layer, as depicted in Figure 1, which is formed between a stream of high-speed air moving at velocity U_{A1} and a stream of low-speed air moving at velocity U_{A2}. The velocity ratio, $r_U=U_{A2}/U_{A1}$, is 0.5 and the convective Mach number (M_c) based on the initial velocity difference is 0.4. L_p is the penetration length of droplets and δ is the shear layer thickness. Pure *n*-decane spray is injected at the center of the shear layer inlet. The droplets are initially randomly seeded, with a same size. The initial droplet velocity is identical to the local gas velocity and initial droplet temperature is T_d=298.15K. Table 1 lists the inflow parameters and the cases performed in this study. The incident angle of oblique shock in Case C is 27°, hence the post-shock pressure equals with the ambient pressure in Case B.

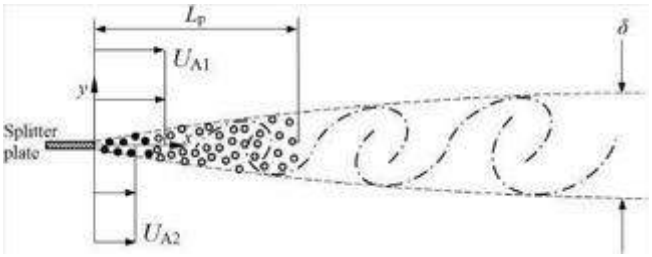

Figure 1. Schematic of a fuel spray in a two-dimensional turbulent shear layer.

Table 1. Cases and computational conditions.

Case	Pressure (MPa)	Temperature (K)	Oblique shock
A	0.1	1000	No
B	0.2	1000	No
C	0.1	1000	Yes

[a)]Corresponding author. Email: wbing@tsinghua.edu.cn.

RESULTS AND DISCUSSTION

Figure 2 shows the general features of spray combustion field. It is observed that fuel droplets evaporate in the upstream region and the increase of ambient pressure do not have significant effects on the evaporation process and the penetration depth. Flame is formed in the high-strain vortex-braid regions for Case A and fuels vapors entrained in the large eddies are not consumed. The increase of ambient pressure accelerates the ignition obviously for Case B and fuel vapors combusted in a short distance, resulting in a stable flame formed in the large eddies. Shock-wave impingement also triggers ignition in supersonic flows to lead to establishment of premixed flames by raising the temperature and the pressure of the shocked gas.

Maximum dimensionless temperatures in the flow-field and fluctuations of pressure at probe P_5 located at x/δ_0=2000 are recorded [illegible] nition ten [illegible] mum value. Ignition [illegible] e fluctuat [illegible] mperatures is much sm [illegible] fluctuations of [illegible] for Cases B and C is [illegible] is a phase [illegible] ases A & B and Case C due to the impingement of shock waves.

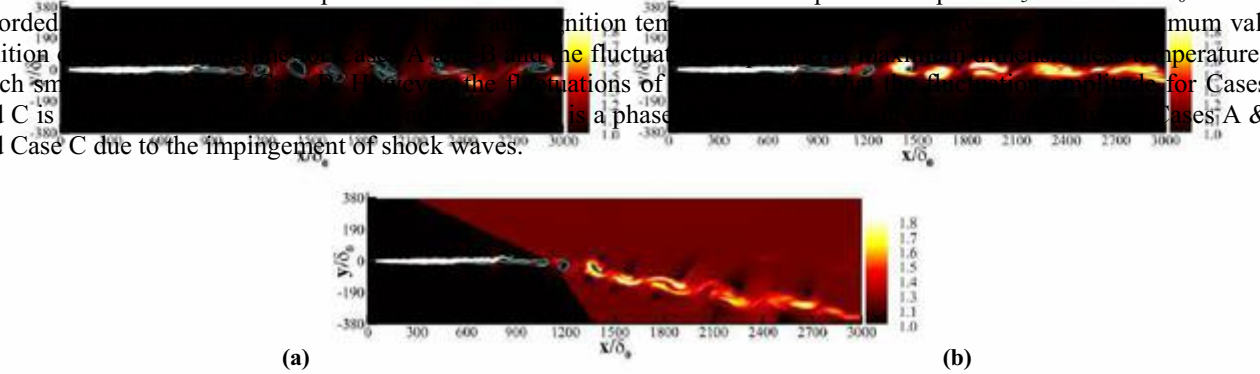

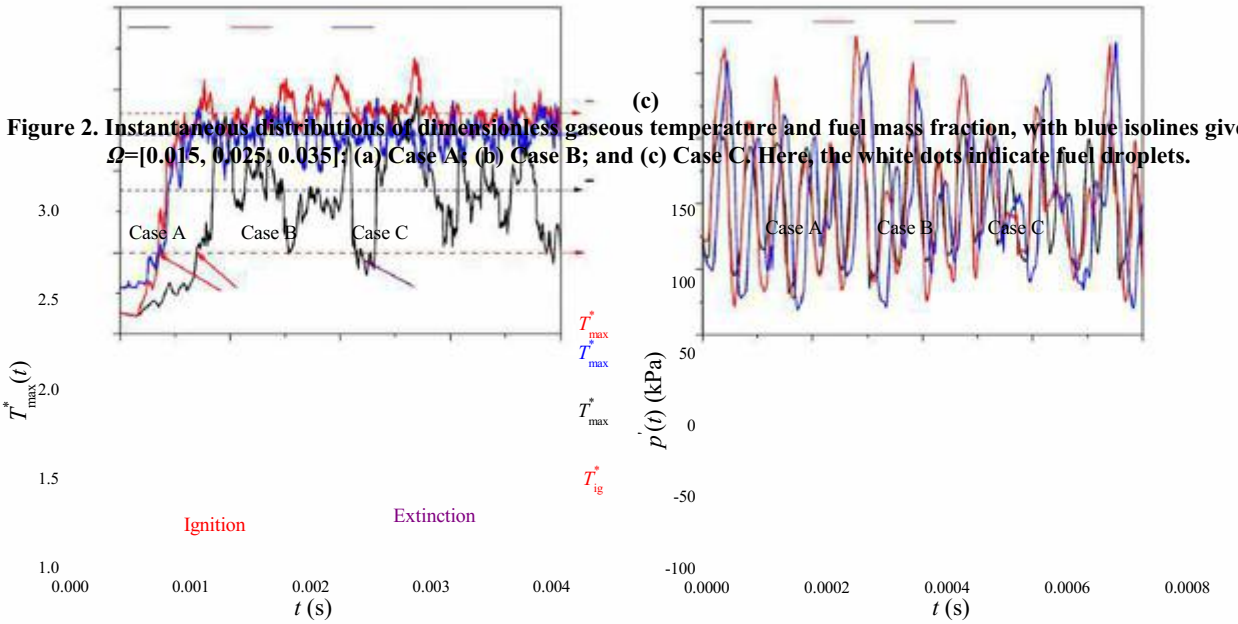

Figure 2. Instantaneous distributions of dimensionless gaseous temperature and fuel mass fraction, with blue isolines given by Ω=[0.015, 0.025, 0.035]: (a) Case A; (b) Case B; and (c) Case C. Here, the white dots indicate fuel droplets.

Figure 3. Maximum dimensionless gaseous temperatures in the flow-field during five flow circles (left) and fluctuations of pressure at probe P_5 during one flow circle (right).

CONCLUSIONS

In this study, effects of ambient pressure and shock-wave impingement on ignition and flame stabilization are investigated. Ignition in supersonic turbulent flows tends to occur around the points of peak temperature and pressure. The ignition dynamics is sensitive to intermittent fluctuations of turbulent flows. The increase of temperature and pressure contributes to stable the flame formed in large energetic eddies.

References

[1] Jenny, P., Roekaerts D., Beishuizen N.. Modeling of Turbulent Dilute Spray Combustion. *Prog. Energy Combust. Sci.*, 38: 846-887, 2010.

A VARIATIONAL FRAMEWORK FOR REACTIVE FLOWS AND SHOCK WAVES

Markus Scholle[1] and Florian Marner *[1]

[1]*Institute for Automotive Technology and Mechatronics, Heilbronn University, Heilbronn, Germany*

Summary For physical systems formulated within the framework of Lagrange formalism the dynamics is completely defined by only one function: the Lagrangian. This concept successfully applies e.g. to Newtonian mechanics, quantum mechanics, electrodynamics and nuclear physics. In continuum theories, however, many open problems remain up to date. In this paper is shown how reactive flows and shock waves are embedded into the framework of Lagrange formalism: motivated by ideas formulated by Anthony [1], an existing Lagrangian of Seliger and Whitham [2] for adiabatic baroclinic flow is extended towards flows with chemically reacting agents along the line of a systematic procedure [3].

A key feature is the use of complex fields, invoking discontinuities of the Lagrangian for irreversible processes and therefore requiring an extension of the general formalism. This allows for elaborating systems in thermofluiddynamics with discontinuities in general and with shock waves in particular.

The present state of the theory and examples are shown.

PRELIMINARY WORK

Despite the great success of Lagrange formalism in classical mechanics, a convincing formulation of fluid dynamics, especially thermofluiddynamics including irreversible processes, has not been established yet. The first contribution toward this topic, although restricted to inviscid irrotational flows, was proposed by Clebsch [4], who found a variational formulation based on the following potential representation of the velocity,

$$\vec{u} = \nabla\chi + \alpha\nabla\beta\,, \tag{1}$$

known as *Clebsch transformation* [5].

Since viscosity leads to dissipation and therefore to the irreversible transfer of mechanical energy to heat, thermal degrees of freedom have to be considered in order to remain consistent to Noether's theorem which implies conservation of energy for systems with time-translation invariance, because otherwise the time-translation invariance would have to be violated by an explicit time-dependence. Seliger and Whitham [2] made a suggestion how to embed thermal degrees of freedom in a variational formulation of fluid flow by the Lagrangian

$$\ell = \circ\,\varrho\left[\partial_t\chi + \alpha\partial_t\beta \circ\ s\partial_t\vartheta + \frac{\vec{u}^2}{2} + e(\varrho,s)\right] \tag{2}$$

$$\vec{u} = \nabla\chi + \alpha\nabla\beta \circ\ s\nabla\vartheta \tag{3}$$

where $e(\varrho,s)$ denotes the specific inner energy, given in terms of the mass density ϱ, specific entropy s, the three Clebsch potentials χ, α, β and an additional potential ϑ. The meaning of the latter one becomes apparent by calculating the Euler Lagrange equation with respect to s, giving the 'potential representation'

$$\{\partial_t + \vec{u}\cdot\nabla\}\,\vartheta = \frac{\partial e}{\partial s} = T\,, \tag{4}$$

for the temperature T, which has already been used three decades before by Van Dantzig, who termed the field ϑ as *thermasy* [6]. Although still restricted to adiabatic and therefore reversible processes, the Lagrangian (2) seems to be a momentous step forward because of the rudimentary embedding of thermodynamics.

CHEMICAL REACTIONS WITH CONVECTION

By comparing the two potential representations (3) and (1), it becomes apparent that any kind of extension of the systems, by additional degrees of freedom as well as by additional physical effects, requires an adjustment of the potential representation By Scholle [3] a general explanation for the necessity to use different potential representation of the observables for different physical systems is given along the line of a rigorous analysis of fundamental symmetries the Lagrangian has to fulfill, with particular regard to Galilean invariance. In the same paper an easily manageable symmetry criterion for verifying Galilean

*Corresponding author. Email: florian.marner@hs-heilbronn.de

invariance is derived, which finally leads to a general construction rules for Lagrangians. It is demonstrated that for fluid systems with chemical reactions this criterion is fulfilled by a Lagrangian of the form

$$\ell = \circ\, \varrho \left[\partial_t \chi + \alpha \partial_t \beta \circ\ s \partial_t \vartheta \circ \sum_i c_i \partial_t \vartheta_i + \frac{\vec{u}^2}{2} + F\left(\varrho, s, c_i, \vartheta, \vartheta_i, \cdots\right) \right] \tag{5}$$

$$\vec{u} = \nabla \chi + \alpha \nabla \beta \circ\ s \nabla \vartheta \circ \sum_i c_i \nabla \vartheta_i \tag{6}$$

containing as additional fields: (i) the concentration c_i of the i-th constituent and (ii) its conjugated field ϑ_i which by variation with respect to c_i fulfills the evolution equation

$$\left\{ \partial_t + \vec{u} \cdot \nabla \right\} \vartheta_i = \frac{\partial F}{\partial c_i} = \mu_i \,, \tag{7}$$

with the chemical potential μ_i of the i-th constituent. Since the analogy to the thermasy ϑ and its evolution equation (4) is obvious, ϑ_i is termed as *chemasy* subsequently.

DISCONTINUOUS LAGRANGIANS, IRREVERSIBLE PROCESSES AND SHOCK WAVES

The proposed Lagrangian (5) is obviously a generalization of Seliger and Whitham's Lagrangian (2), but also a generalization of another Lagrangian proposed by Anthony [1] for chemical reactions within a medium at rest, if thermasy and chemasy are substituted according to $\vartheta\omega = \circ\, T\varphi$ and $\vartheta_i\omega = \circ\, \mu_i\varphi_i$ by non-dimensional fields φ and φ_i which are interpreted as phases of respective complex fields $\chi = \sqrt{T}\exp(\mathrm{i}\varphi)$ and $\psi_i = \sqrt{\mu_i}\exp(\mathrm{i}\varphi_i)$ related to heat and to the chemical constituents. The constant frequency ω has to be introduced due to dimensional reasons. This alternative representation in terms of complex fields can be understood as the inversion of Madelung's idea [7] of reformulating the complex Schrödinger's equation into a hydrodynamic form. Depending on reversibility or irreversibility of the process the Lagrangian turns out to by continuous or discontinuous. The latter case, in particular, is outside the scope of classical Lagrange formalism and therefore requires a general analysis of variation based on a discontinuous Lagrangian as roughly sketched subsequently.

We consider in general a variational principle $\delta I = 0$ based on N independent fields ψ_i. The Lagrangian ℓ is assumed to be discontinuous with respect to $\psi_N = \varphi$ at fixed values φ_n, but continuous differentiable with respect to all other fields and also with respect to the derivatives. In three-dimensional space, the discontinuities $\varphi = \varphi_n$ become manifest along surfaces $S_n(t)$. From a physical viewpoint, these time-dependent inner boundaries are propagating *shock fronts*. By variation $\delta I = 0$,

$$\vec{n} \cdot \left[\frac{\partial \ell}{\partial \nabla \psi_i} \circ\ \vec{v}_s \frac{\partial \ell}{\partial \dot{\psi}_i} \right]_- \circ\ \vec{n} \cdot \left[\frac{\partial \ell}{\partial \nabla \psi_i} \circ\ \vec{v}_s \frac{\partial \ell}{\partial \dot{\psi}_i} \right]_+ = 0 \tag{8}$$

$$\nabla\varphi \cdot \left[\frac{\partial \ell}{\partial \nabla \varphi} \circ\ \vec{v}_s \frac{\partial \ell}{\partial \dot{\varphi}} \right]_- \circ\ \nabla\varphi \cdot \left[\frac{\partial \ell}{\partial \nabla \varphi} \circ\ \vec{v}_s \frac{\partial \ell}{\partial \dot{\varphi}} \right]_+ = [l]_- \circ\ [l]_+ \tag{9}$$

are obtained next to the usual Euler-Lagrange equations as *matching conditions* (8) and *jump condition* (9) for the fluxes at each shock front. In above formulae $\vec{n}$ denotes the normal vector of the shock front and $[\cdots]_\pm$ indicates the limit of the respective discontinuous expression by approaching from the front side or the back side of the shock.

CONCLUDING REMARKS

This methodical framework is at a early stage on the one hand but promises a high potential on the other hand. Especially the choice of the function F in the Lagrangian (5) opens many perspectives toward many different problems related to reactive flows and shock waves, also for the development of numerical codes.

References

[1] Anthony K.-H.: Hamilton's action principle and thermodynamics of irreversible processes – a unifying procedure for reversible and irreversible processes. J. Non-Newt. Fluid Mech. 96:291-339, 2001.

[2] Seliger R. L., Whitham G. B.: Variational principles in continuum mechanics. Proc. R. Soc. Lond. A 305:1-25, 1968.

[3] Scholle M.: Construction of Lagrangians in continuum theories. Proc. R. Soc. Lond. A 460:3241-3260, 2004.

[4] Clebsch A.: Ueber die Integration der Hydrodynamischen Gleichungen. J. f. d. reine u. angew. Math. 56:1-10, 1859.

[5] Lamb H.: Hydrodynamics. Cambridge University Press, 1974.

[6] Van Dantzig D.: On the phenomenological thermodynamics of moving matter. Physica 6:673-704, 1939.

[7] Madelung E.: Quantentheorie in hydrodynamischer Form. Zeitschrift für Physik 40:322-326, 1927.

INITIATION CHARACTERISTICS OF OBLIQUE DETONATION WAVES IN HYDROGEN-AIR MIXTURE

Honghui Teng[1a)], Hoi Dick Ng[2]&Zonglin Jiang[1]
[1]*State Key Laboratory of High Temperature Gas Dynamics, Institute of Mechanics, Chinese Academy of Sciences, Beijing, China*
[2]*Department of Mechanical and Industrial Engineering, Concordia University, Montreal, Quebec, Canada*

*Summary*The initiation features of two-dimensional, oblique detonations from a wedge in a stoichiometric hydrogen-air mixture are investigated via numerical simulations using the reactive Euler equations with detailed chemistry. A parametric study is performed to analyze the effect of inflow pressure P_0, and Mach number M_0 on the initiation structure and length. Quantitatively the initiation length decreases with increasing M_0, primarily due to the increase of post-shock temperature. The effect of M_0 on initiation length is independent of P_0, but given the same M_0, the length is found to be inversely proportional to P_0. Theoretical analysis based on the constant volume combustion (CVC) theory is also performed, which are close to the numerical simulations in the case of high M_0 regardless of P_0, demonstrating that temperature is the key parameter affecting the initiation. Decreasing M_0, the CVC theory breaks down, suggesting a switch from chemical kinetics-controlled to a wave-controlled gasdynamic process.

INTRODUCTION

In recent years, the idea of using oblique detonation waves (ODW) for high efficiency propulsion systems have generated great interest in the development of air-breathing hypersonic aircrafts [1]. This hypersonic propulsion concept not only has the advantages of the scramjet, but also achieves high thermal cycle efficiency through the detonation mode of combustion [3]. However, for proper design and operation of ODW engines, it is critical to predict the necessary conditions and understand the mechanism behind the ODW initiation from a wedge.

Classical theory on ODWs simplifies the structure into an oblique shock wave with a post-shock energy release zone attached to the wedge. The formation of oblique detonations was first analyzed numerically by Li et al. [2], who observed a structure composed of a nonreactive oblique shock, an induction region, a set of deflagration waves, and the oblique detonation surface. This abrupt, steady, oblique shock-to-detonation transition by a multi-wave point is confirmed experimentally, and the formation of unstable cellular structures on the established oblique detonation surface are also revealed numerically downstream of the kink-like, oblique shock-to-detonation transition [3].

In this work, numerical simulations are conducted to further investigate the initiation characteristics of ODW from a wedge. As shown from [4], both aerodynamic and mixture thermodynamic properties greatly influence the initiation of detonation. As such, a parametric study is performed here using two bifurcation parameters: the incident Mach number M_0, and inflow pressure P_0. Most of the previous studies used simplified chemical reaction models, mainly the one- or two-step irreversible Arrhenius-type, temperature dependent kinetic model. The influence of M_0 is analyzed in almost every of these investigations, but the effect of inflow pressure P_0 is seldomly discussed due to the use of simplified chemical kinetic models. To address this drawback, ODWs in a stoichiometric hydrogen-air mixture are investigated here with detailed chemistry. The effect of both M_0 and P_0 on the initiation characteristics are analyzed, by looking at the variation of a characteristic length scale describing the initiation process.

COMPUTATIONAL DETAILS

The presence of a wedge in supersonic inflow induces first an oblique shock wave (OSW). For a high inflow Mach number causing a high post-shock temperature behind the OSW, an exothermic chemical reaction begins, leading to the formation of an oblique detonation wave (ODW). For the computation, the coordinate is rotated to the direction along the wedge surface. The analysis is based on the 2D, multi-species, Euler equations, with an H_2/O_2 chemical mechanism for high-pressure combustion [5] is considered. This mechanism involves 27 reversible elementary reactions among the 8 species H_2, O_2, H_2O, H, O, OH, HO_2, and H_2O_2, with 5 non-reacting species, N_2, Ar, He, CO, and CO_2. The governing equations are discretized on Cartesian uniform grids and solved with the DCD (Dispersion-Controlled Dissipation) scheme [6] with Strang's splitting. A stoichiometric hydrogen-air mixture with $H_2:O_2:N_2 = 2:1:3.76$ is used. Because of the multi-scale nature of the phenomena, both the computational domain and mesh scale are adjusted. In this study, the numerical grid resolution used for different cases varies from a coarsest mesh of 64 μm to the finest mesh of 2 μm. The results are also examined to ensure that the ODW initiation structure is unaffected by the influence of mesh properties.

NUMERICAL RESULTS

[a)]Corresponding author. Email:hhteng@imech.ac.cn.

Twelve cases are simulated to study the initiation characteristics of oblique detonations, with incident Mach number M_0 = 10.0, 9.0, 8.0, 7.0 and inflow pressure P_0 = 1.0, 0.5, 0.2 atm. The present numerical results demonstrate that the two transition patterns, i.e., an abrupt transition from a multi-wave point connecting the oblique shock and the detonation surface and a smooth transition via a curved shock, depend strongly on the inflow Mach number, while the inflow pressure is found to have little effect on the oblique shock-to-detonation transition type. The present results also reveal a slightly more complex structure of abrupt transition type in the case of M_0 = 7.0, consisting of various ignition processes in the shocked gas mixtures

To further quantify the effect of these two parameters, a characteristic initiation length, L_c, is considered for the following analysis. The initiation length is defined along the flow stream direction, parallel with the x-axis. It starts from the oblique shock and terminates at the end of the induction zone, i.e., the location at which the temperature increases over 10%. Note that the lengths are different depending on the distance from the wedge, and thus, for convenience, the characteristic length of initiation is given by the maximum value for each case of (M_0, P_0), always located on the wedge surface. For a given P_0, L_c decreases when M_0 increases. The decrease in L_c with increasing M_0 can be explained by the increase of post-shock temperature. Moreover, we notice that L_c is almost inversely proportional to P_0. the inverse proportionality gives a relatively good zero-order characterization of the initiation length as a function of inflow pressure.

Following our previous work [7], a theoretical approach based on constant volume combustion (CVC) theory is used to estimate L_c with post-oblique-shock conditions. This theoretical approach assumes a flow structure where near the wedge, the mixture is completely burned, and pressure build-up and the formation of pressure waves are weak. The initiation is thus assumed to be kinetically-controlled. First, the post-oblique-shock specie densities and temperature are used to simulate CVC to obtain the reaction time required to attain a mixture temperature with 10% increase from its post-shock value. The initiation length L_c is then calculated by multiplying the time with the post-oblique-shock particle velocity. Despite a simple formulation, this analysis provides a predictive approach for the general structure of oblique detonations. For P_0 = 0.2 atm, both results are in good agreement. It appears more difficult to predict the initiation length in the case high P_0 using this simplified chemical kinetic approach. Overall, theoretical results are close to numerical ones in the case of high M_0 regardless of P_0. When M_0 decreases, the present theory deviates faster in the case of high P_0.

CONCLUDING REMARKS

Two-dimensional, oblique detonations induced by a wedge were simulated to study the initiation structure and length with differing inflow Mach number M_0 and pressure P_0 in a stoichiometric hydrogen-air mixture. Analysis of the characteristic initiation length, defined along the flow stream direction, parallel with the x-axis from the oblique shock and terminating at the end of induction zone, shows it to decrease with increasing M_0 primarily due to the increase in post-shock temperature, and the effect of M_0 on the initiation length is independent of P_0. The present numerical results also show that given a M_0, the initiation length is roughly inversely proportional to P_0.

Chemical kinetic calculations based on constant volume combustion (CVC) theory were performed to estimate the initiation length and compared with numerical simulations. Overall, theoretical results from chemical kinetic calculation are shown to be close to the numerical ones for all cases of high M_0 regardless of P0, demonstrating that the temperature is the key parameter and the initiation is kinetically-controlled. In contrast, at lower M_0, theoretical results for high P_0 diverge faster than those of low P_0 due to the non-monotonic behavior of the induction kinetics at elevated pressure from the explosion characteristics of hydrogen. The complex, gasdynamic structure in the case of low M_0 eventually causes the breakdown of CVC theory predictions. The onset of deviation between the theoretical estimation with the numerical results indirectly provides an indication of the transition mechanism from an ignition- (or kinetically-) controlled process to a wave-controlled gasdynamic initiation phenomenon.

References

[1] Kailasanath K.: Recent developments in the research on pulse detonation engines. *AIAA J*. **41**: 145-159, 2003.

[2] Li C., Kailasanath K., Oran E.S.: Detonation structures behind oblique shocks. *Phys*. *Fluids* **6**, 1600-1611, 1994.

[3] Teng H.H., Jiang Z.L., Ng H.D.: Numerical study on unstable surfaces of oblique detonations. *J*. *Fluid Mech*. **744**: 111-128, 2014.

[4] Teng H.H., Jiang Z.L.: On the transition pattern of the oblique detonation structure. *J*. *Fluid Mech*. **713**: 659-669, 2012.

[5] Burke M.P., Chaos M., Ju Y., et al.: Comprehensive H2/O2 Kinetic Model for High-Pressure Combustion *Int*. *J*. *Chem*. *Kinet*. **44**: 444-474, 2012.

[6] Jiang Z.: On Dispersion-Controlled Principles For Non-Oscillatory Shock-Capturing Schemes. *Acta Mech*. *Sin*. **20**: 1-15, 2004.

[7] Wang T., Zhang Y., Teng H.H., et al.: Numerical study of oblique detonation wave initiation in a stoichiometric hydrogen-air mixture. *Phys*. *Fluids* **27**: 096101, 2015.

FM04 - Compressible Flow

TS.FM04-1.01	Austin, Joanna - Hypervelocity shock-boundary layer interactions with varying freestream composition (INVITED)	647
TS.FM04-1.02	Cinnella, Paola - Direct numerical simulations of supersonic turbulent channel flows of dense gases	649
TS.FM04-1.03	Sciacovelli, Luca - Small scale dynamics of dense gas decaying turbulence	651
TS.FM04-1.04	Alferez, Nicolas - Non-ideal shock refraction properties in dense vapours	653
TS.FM04-1.05	Koren, Barry - Application of a fully compressible multiphase SPH scheme to hypervelocity impacts	655
TS.FM04-1.06	Kluwick, Alfred - Steady transonic dense gas flow past a two-dimensional compression/expansion ramp	657
TS.FM04-2.01	Pasquariello, Vito - Large-eddy simulation of strong shock-wave/turbulent boundary-layer interaction at Reθ= 14000	659
TS.FM04-2.02	Sherwin, Spencer - On the Riemann flux performance in DG-based implicit LES at very high Reynolds numbers	661
TS.FM04-2.03	Livescu, Daniel - Subgrid scale analysis of turbulence after the shock-turbulence interaction	663
TS.FM04-2.04	Sen, Oishik - Multiscale modeling using a Dynamic Kriging-based metamodeling technique	665
TS.FM04-2.05	Paolucci, Samuel - Shock structure in hypersonic flows	667
TS.FM04-2.06	De Brauer, Alexia - Compressible multimaterial flows	669
TS.FM04-3.01	Jacquin, Laurent - Transonic airfoil buffet: A decade of research at ONERA (INVITED)	671
TS.FM04-3.02	Wang, Tiejin - Experiment on nonliner growth of supersonic mixing layers	673
TS.FM04-3.03	Tenaud, Christian - Shedding Intermittency in a Shock Wave-Laminar Boundary Layer Interaction	675
TS.FM04-3.04	Timofeev, Evgeny - Regular-to-Mach reflection transition on curved surfaces	677
TS.FM04-3.05	Grogan, Kevin - Detailed simulations of shock boundary layer interaction in shock tube experiments	679
TS.FM04-4.01	Martínez-Ruiz, Daniel - On the interaction of oblique shocks and laminar mixing layer	681
TS.FM04-4.02	Arbos Torrent, Sara - Internal and external jet modes of an over-expanded tic nozzle	683
TS.FM04-4.03	Bonnet, Jean-Paul - Sonic flow control by plasma: a new pulsed jet actuator	685
TS.FM04-4.04	Zhang, Yang - Flow Visualization of High-speed Cavity Flows	687
TS.FM04-4.05	Tagawa, Yoshiyuki - Structure of a laser-induced shock wave in water	689
TS.FM04-5.01	Vanstone, Leon - Effect of upstream disturbances on the unsteadiness of swept-ramp interactions at mach 2 (INVITED)	691
TS.FM04-5.02	Karimi, Mona - Kelvin-Helmholtz instability in compressible shear flows: Effect of wavenumber	693
TS.FM04-5.03	Kosinov, Alexander - Excitation of the streaks by weak shock waves in the supersonic boundary layer	695
PO.FM04-1.01.8	Alzamora Previtali, Federico - Unsteady shock wave reflection from concave surfaces	697
PO.FM04-1.02.9	Hassanpour, Soroosh - Real-Time Solution of One-Dimensional Distributed	699

	Parameter Models with Application to DPF	
PO.FM04-1.03.10	Keblawi, Amer - A Reduced Control-Oriented Model for Quasi One-Dimensional Flow in Area Varying Channels	701
PO.FM04-1.04.11	Lu, Hongbo - Numerical investigation of wall heat transfer influence on shock train in Scramjet isolator	703
PO.FM04-1.05.12	Stern, Catalina - BOS and PSV in a supersonic jet	705

HYPERVELOCITY SHOCK-BOUNDARY LAYER INTERACTIONS WITH VARYING FREESTREAM COMPOSITION

Andrew M. Knisely[1] and Joanna M. Austin [*1]

[1]*Graduate Aerospace Laboratories, California Institute of Technology, Pasadena CA, USA*

Summary Shock-boundary layer interactions in hypervelocity flows have been demonstrated to be sensitive to nonequilibrium, with the macroscopic features of the flow responding to changes in the molecular processes. Experiments are carried out examining interactions over double-wedge and double-cone geometries while varying the freestream oxygen content from nitrogen to air. Time-resolved high speed schlieren and chemiluminescence imaging, together with vibrational temperature measurements, quantify the response of flow features as a function of the thermochemical state.

INTRODUCTION

Shock-boundary layer interaction (SBLI) can induce flow distortion, create flow separation with loss of control authority, and, particularly in high enthalpy conditions, result in severe heating rates due to flow impingement. In hypervelocity flows, SBLI predictions have been demonstrated to be very sensitive to the choice of thermochemical model. State-of-the-art simulations and experiments showed universally poor agreement in high enthalpy (>5 MJ/kg) air flows with significant thermochemical activity, in spite of good agreement at lower enthalpies [1]. For example, simulations predict a decrease in separation length with increasing freestream enthalpy, but this is not observed experimentally [2]; experiments measured three times less nitric oxide in the freestream than predicted [3]. Unraveling the fluid-thermochemical coupling in highly nonequilibrium environments is an extremely challenging problem due to the disparity in both the spatial and temporal scales, even if the flow is laminar. Shock interactions which respond on the measurable macroscale to changes in the molecular processes provide valuable diagnostic tools for studying the inter-scale energy exchange.

Experiments are carried out in the Hypervelocity Expansion Tube (HET) [4]. The facility has the flexibility to achieve a range of test gas conditions while minimizing freestream dissociation. Our approach is to vary the oxygen content in the freestream from nitrogen to air, while maintaining the other flow parameters to within 2%, with the goal of examining the response of the shock configurations and chemiluminescence in different regions of the interaction. We also measure the vibrational temperature of post-shock nitric oxide (experimental setup described in more detail in Sharma et al. [5]).

EXPERIMENTAL SETUP

A 25-55 degree double-cone and 30-55 degree double-wedge model are sting mounted in the HET. The model configurations are designed to match the cone-angles of previous studies for directly comparable measurements [1, 2, 6]. More details on the models can be found in Swantek and Austin [7]. Freestream conditions are calculated using one-dimensional gas dynamics assuming equilibrium flow through the facility operation. The chemical composition of the test gas was: nominally pure nitrogen (we note there is some residual oxygen even after the facility is evacuated, estimated at 2%), 30%, 50%, 80% percent oxygen, and air. The percent oxygen refers to the content relative to air, which corresponds to 100% using our nomenclature. Equilibrium post-shock conditions are listed in Table 1.

Schlieren images are captured using a pco.1600 Cooke camera (exposure 1 μs) and the system is illuminated by Xenon 437B nanopulse system. Chemiluminescence images are obtained using the same camera in a repeat experiment with no light source and with a 4 μs exposure. Vibrational temperature measurements of nitric oxide are made at selected points using emission spectroscopy in the experimental setup described in more detail in Sharma et al. [5].

Table 1: Calculated equilibrium post-shock conditions for HET tests. % O_2 is relative to air at 100%.

% O_2	T_∞ K	p_∞ kPa	ρ_∞ kg/m^3	N_2	N	O_2	O	NO
0	5201.8	47906.8	2.989e-02	9.268e-01	7.323e-02	0.000e+00	0.000e+00	0.000e+00
30	4840.1	48684.8	3.153e-02	8.346e-01	2.961e-02	2.457e-04	1.290e-01	6.614e-03
50	4551.0	49271.1	3.323e-02	7.778e-01	1.316e-02	1.283e-03	1.950e-01	1.269e-02
80	4136.0	50154.4	3.634e-02	7.012e-01	3.411e-03	9.148e-03	2.608e-01	2.540e-02
100	3956.9	50626.1	3.806e-02	6.595e-01	1.738e-03	2.150e-02	2.836e-01	3.357e-02

*Corresponding author. Email: jmaustin@caltech.edu

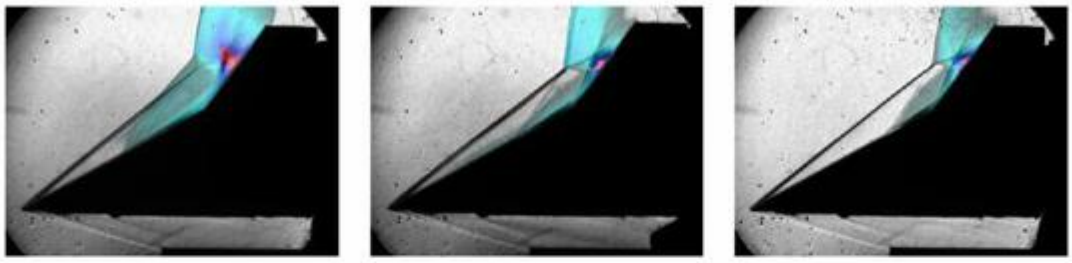

a) b) c)

Figure 1: Overlaid schlieren and chemiluminescence (false color) images of SBLI over a double-wedge geometry from two repeat experiments in a) nitrogen, b) 80% O_2 content of air, and c) air.

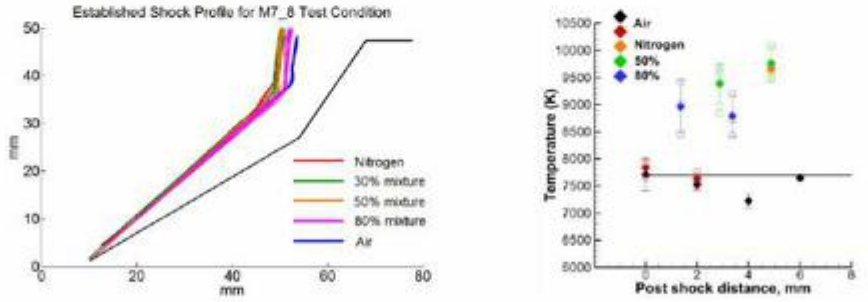

a) b)

Figure 2: a) Lead shock location. b) NO vibrational temperature measurements downstream of the bow shock.

RESULTS

Overlaid schlieren and chemiluminescence images indicate changes in extent of thermochemical reactions with varying freestream oxygen, Figure 1. In all cases, there is chemiluminescence signal behind the bow and separation shocks, but not the oblique shock, with the greatest signal in the region of flow impingement on the second wedge. In the nitrogen case, the separation shock interacts with the bow shock and the separation length is greatest. As expected, the bow shock standoff distance decreases with increasing oxygen content, and the region of greatest chemiluminescence signal is reduced.

An edge detection algorithm was applied to the schlieren images from repeat experiments, Figure 2a). The bow shock standoff distance decreases with increasing oxygen content as discussed above. An interesting feature of the data is that up to 50% O_2, the standoff distance is the same as the nitrogen case to within the experimental measurements. A transition in the location of the bow shock is apparent between 50 and 80% O_2. We compare this transition in shock location with post-shock temperature measurements obtained using emission spectroscopy, Figure 2b). The vibrational temperature in nitrogen (with 2% residual O_2) and 50% O_2 are similar, while a decrease in the temperature is measured in the 80% case towards the lower temperature in air. We are further investigating this apparent transition between 50 and 80% O_2 content.

This work was funded by AFOSR FA 9550-15-1-0288 with Dr. Ivett Leyva as program officer.

References

[1] Nompelis, I., Candler G.V., MacLean, M., Wadhams, T.P., Holden, M.S., Numerical investigation of double-cone flow experiments with high-enthalpy effects, AIAA Paper 2010-1283, 2010.

[2] Nompelis, I., Candler, G.V., Holden, M.S., Computational investigation of hypersonic viscous/inviscid interactions in high enthalpy flows, AIAA Paper 2003-3642, 2003.

[3] Parker, R., Wakeman, T., MacLean, M., Holden, M.S., Measuring nitric oxide freestream velocity using quantum cascade lasers at CUBRC, AIAA Paper 2007-1329, 2007.

[4] Dufrene, A., Sharma, M., Austin, J.M.: Design and Characterization of a Hypervelocity Expansion Tube. J. Prop. Power 23: 1185-1193, 2007.

[5] Sharma, M., Austin, J.M., Glumac, N.G., Massa, L. NO and OH spectroscopic vibrational temperature measurements in a post-shock relaxation region, AIAA J 48: 1434-1443, 2010.

[6] Davis J.-P., Sturtevant, B., Separation length in high-enthalpy shock/boundary-layer interaction, Phys. Fluids 12:2661-87, 2000.

[7] Swantek, A.B., Austin, J.M., Flowfield establishment in hypervelocity shock-wave/boundary layer interactions, AIAA J 53:311-320, 2015.

DIRECT NUMERICAL SIMULATIONS OF SUPERSONIC TURBULENT CHANNEL FLOWS OF DENSE GASES

Luca Sciacovelli *[1,2], Paola Cinnella[1], and Xavier Gloerfelt[1]
[1]*DynFluid Laboratory, Arts et Mtiers-ParisTech, Paris, France*
[2]*DMMM, Politecnico di Bari, Bari, Italy*

Summary In this work we investigate the influence of dense gas effects on compressible wall-bounded turbulence. Direct numerical simulations of supersonic turbulent channel flows are performed both for air and PP11, a heavy fluorocarbon representative of dense gases. Using different thermodynamic models, a parametric study on the bulk Mach and Reynolds numbers is carried out. In the dense-gas flow, friction heating effects are reduced due to the much smaller coupling between thermal and kinetic fields. The location of peak values for the premultiplied spectra of thermodynamic variables changes and the characteristic size of the observed turbulent structures is closer to that observed in incompressible turbulence.

Turbulent flows of dense gases represent a research field of great importance for a wide range of applications. Dense gases are usually defined as single-phase fluids with complex molecules, at pressure and temperature conditions of the same order of magnitude of their thermodynamic critical point (see, e.g., [1] and reference cited therein). In the transonic and supersonic regime, they may exhibit nonclassical phenomena, in particular for the family of Bethe–Zeldovich–Thompson (BZT) fluids, which may exhibit expansion shocks in particular thermodynamic conditions [2]. In this work we investigate the influence of dense gas effects on compressible wall-bounded turbulence. Specifically, we carry out direct numerical simulations of supersonic turbulent channel flows of a BZT heavy fluorocarbon, namely PP11 ($C_{14}F_{24}$). The results are compared with those of perfect gases.

The thermodynamic behaviour of PP11 is modelled through two different equations of state: Van der Waals (VDW), which is computationally inexpensive and provides a qualitative description of the main effects of interest, and the more accurate and complex Martin-Hou (MAH) equation. The VDW model is supplemented by a power-law for computing the transport properties, whereas the Chung-Lee equation is used in conjunction with the MAH model. For comparison, we also performed the simulations for a typical diatomic gas (air) and for a perfect gas with a specific heat ratio characteristic of heavy fluorocarbons ($\gamma = 1.0125$). The influence of dense gas effects is evaluated by means of a parametric study at various bulk Reynolds numbers ($Re_B = 3000 \div 12000$) and bulk Mach numbers ($M_B = 1.5 \div 3.$). Calculations are based on a in-house code [3] solving the compressible Navier-Stokes equations with high-order dispersion-relation preserving schemes. The code has been preliminarily validated against reference results for supersonic channel flows of a perfect gas [4]. The computational grids are chosen in order to ensure a good spatial resolution in all directions, i.e., $\delta x^+ = 10\circ\ 18$, $\delta y^+ = 0.5\circ\ 0.8$, $\delta z^+ = 4\circ\ 8$. For high Reynolds number cases, grids of $\sim 5 \times 10^8$ points are considered.

Sample results are presented in figure 1 for air and PP11 with the MAH model. Several considerations are in order. First of all, the specific heat ratio of the gas has a strong influence on the results. For the dense gas, γ is close to 1 instead of 1.4, which leads to very different average profiles of the thermodynamic quantities, due to the fact that the Eckert number for the heavier gas is much smaller and the coupling of thermal and dynamic effects weaker. This reduces the friction heating considerably. We also observe significant variations of the Prandtl number through the flow. Due to weak dynamic and thermal coupling, velocity profiles for the dense gas flow are much less sensitive to Mach variations and collapse in the logarithmic region, unlike the case of air. Figure 2 shows the spanwise premultiplied energy spectra for v and T. The spectrum of v is similar for both the PFG and the dense gas, with peak values moving towards lower wavenumbers as y^+ increases. The temperature spectra are rather different: the peak is shifted towards higher k_z^+ and lower y^+. Figure 3 shows isosurfaces of the Q-criterion coloured with the streamwise velocity in the case $M_B = 3$ and $\mathrm{Re}_B = 7000$ for the two thermodynamic models considered. Air exhibits quite large eddy structures because friction heating leads to an increase of the temperature and viscosity, and thus to a larger Kolmogorov length-scale. For the dense gas, the reduced coupling leads to much smaller structures and the behaviour is closer to the incompressible one. We will present a detailed study of the influence of dense gas effects on the evolution of kinematic and thermodynamic variables, and we will study the energy budgets and the statistical features of the turbulent structures.

References

[1] Cinnella P., Congedo P. M.: Inviscid and viscous aerodynamics of dense gases. J. Fluid Mech 580:179-217, 2007.
[2] Cramer M. S., Kluwick A.: On the propagation of waves exhibiting both positive and negative nonlinearity. J. Fluid Mech 142:9-37, 1984.
[3] Gloerfelt X., Berland J.: Turbulent boundary-layer noise: direct radiation at Mach 0.5. J. Fluid Mech 723:318-351, 2013.
[4] Coleman G. N., Kim J., Moser R. D.: A numerical study of turbulent supersonic isothermal-wall channel flow. J. Fluid Mech 305:159-183, 1995.

*Corresponding author. Email: luca.sciacovelli@ensam.eu

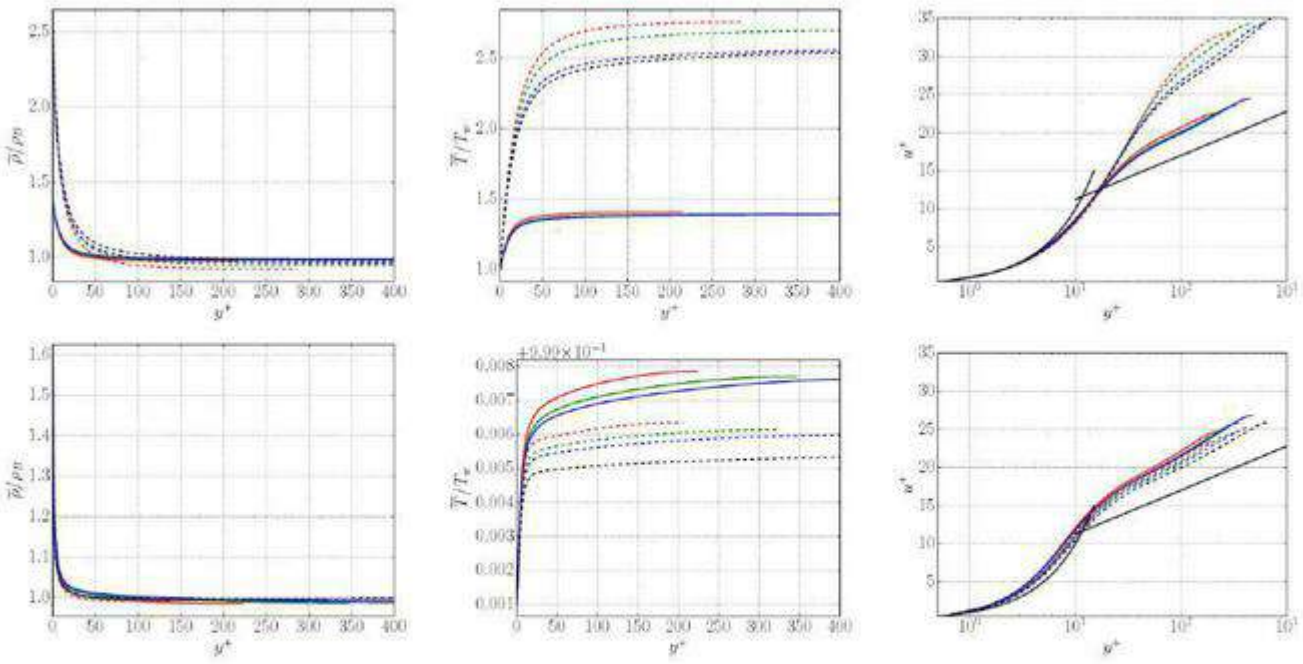

Figure 1: Velocity u^+, density ρ and temperature $\overline{T}$ profiles along the channel. Top: air. Bottom: PP11 (MAH). Solid lines: $M_B = 1.5$, Dashed lines: $M_B = 3.0$. Red: $Re_B = 3000$, green: $Re_B = 5000$, blue: $Re_B = 7000$, black: $Re_B = 12000$.

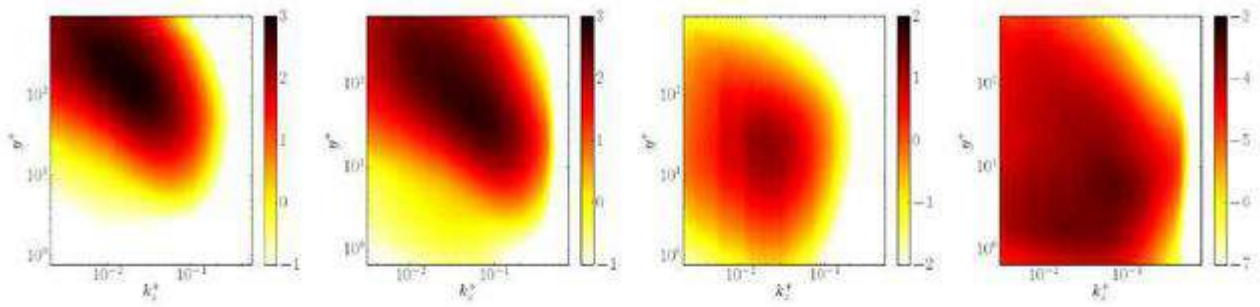

(a) $k_z^+ E_{vv}^+$ (b) $k_z^+ E_{TT}^+$

Figure 2: Spanwise premultiplied energy spectra for case $M_B = 3$, $Re_B = 12000$. Left: air, Right: PP11(MAH).

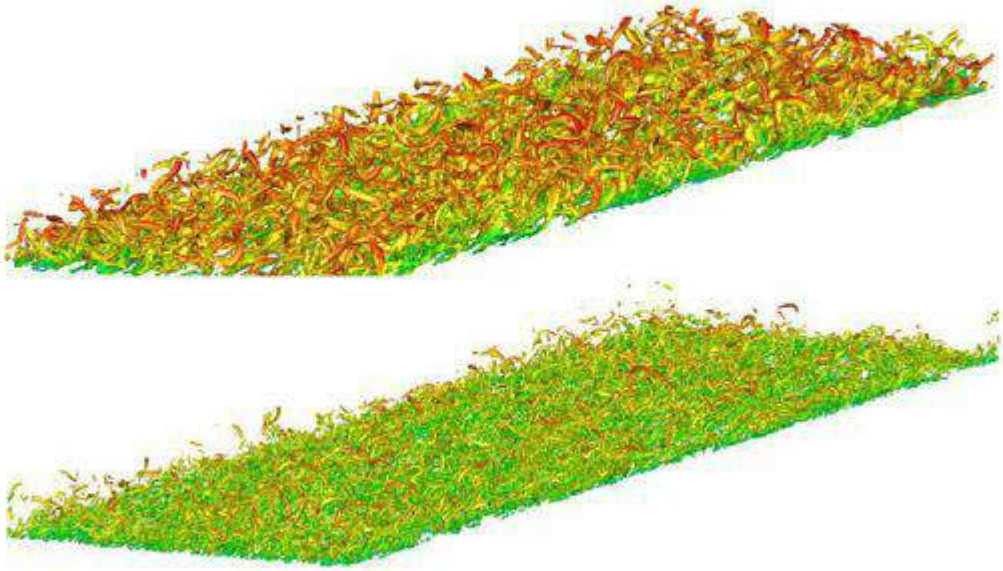

Figure 3: Isosurfaces of Q criterion coloured with the streamwise velocity in a supersonic compressible turbulent channel flow with $M_B = 3$ and $Re_B = 7000$. Top: air; bottom: PP11 (MAH).

SMALL SCALE DYNAMICS OF DENSE GAS DECAYING TURBULENCE

Luca Sciacovelli[1,2], Paola Cinnella[1], and Francesco Grasso *[1]
[1]*DynFluid Laboratory, Arts et Mtiers-ParisTech, Paris, France*
[2]*DMMM, Politecnico di Bari, Bari, Italy*

Summary The decay of compressible homogeneous isotropic turbulence for dense gases is studied by means of Direct Numerical Simulations. A family of heavy fluorocarbons, which exhibit non-classical phenomena, is considered. The thermodynamic behavior of the fluids is modeled by the politropic Van der Waals or the five-term Virial Martin-Hou equations of state, and the results are compared to those obtained for a thermally and calorically perfect gas.

Turbulent flows of dense gases, i.e. gases with high molecular complexity working at thermodynamic conditions of the general order of magnitude of the liquid/vapor critical point, are of interest for a wide range of applications, including industrial and technological processes, aerospace propulsion or energy production. An interesting family of dense gases is represented by the so-called Bethe-Zel'dovich-Thompson (BZT) fluids, heavy polyatomic compounds characterized by a region of negative values of the Fundamental Derivative of Gas Dynamics Γ [1], in which non-classical phenomena such as rarefaction shock-waves, mixed shock/fan waves and shock splitting are expected to occur (e.g., see [2] and references therein). In this work, the influence of dense gas and BZT effects on the decay of Compressible Homogeneous Isotropic Turbulence (CHIT) is analysed by means of Direct Numerical Simulation (DNS), and the results are compared with those obtained for perfect gases (PFG). The compressible Navier–Stokes equations are solved by means of a tenth-order accurate centered scheme for the discretization of the convective fluxes, supplemented by a high-order nonlinear artificial viscosity term (inspired from [3]) of 9th-order accuracy in smooth flow regions. A Ducros-type sensor [4] is used to minimize dissipation errors introduced by the artificial viscosity. The flow solver has been validated against literature results for both inviscid and viscous CHIT computations available in the litterature. To account for dense gas effects, the simple polytropic Van der Waals (VDW) equation of state (EoS) and the more complex Martin-Hou (MAH) EoS are used, in conjunction with a power law of the temperature for the specific heat at constant volume in the ideal gas limit. The VDW EoS is computationally inexpensive compared to more complex thermodynamic models, and provides a reasonable qualitative description of the main effects of interest. Transport properties are modelled via a simple power-law of the temperature when using the VDW EoS, whereas the accurate Chung-Lee-Starling model [5], which takes into account correction terms for the dense gas region, is used in conjunction with the MAH EoS. The fluid under investigation, a heavy fluorocarbon referred-to as PP11 (chemical formula $C_{14}F_{24}$) , is predicted to exhibit BZT effects for thermodynamic conditions near (but outside of) the critical region [6]. To initialize the isotropic turbulence field, divergence-free initial conditions with no density fluctuations were assumed. A Passot-Pouquet-type initial spectrum is considered and the peak wavenumber is fixed to $k_0 = 2$. Turbulent Mach numbers from 0.2 to 1.0 are investigated using mesh resolutions ranging from 128^3 to 768^3. For the chosen initial thermodynamic conditions, relatively close to the critical region, part of the flow evolves in the inversion zone and the fluid compressibility exhibits large variations throughout the flow. This leads to larger density and speed of sound fluctuations than in a perfect gas with a similar specific heat ratio. Additionally, in the dense gas the speed of sound varies non monotonically with the density, leading to remarkable differences in turbulence decay. At high turbulent Mach numbers, the occurrence of eddy shocklets is possible, which strongly modify turbulence structure. In the neighborhood of eddy shocklets, indeed, the pressure is highly correlated with dilatation, and the production of dilatational dissipation increases, leading to a conversion of kinetic energy into internal energy. However, for BZT fluids working in regions where $\Gamma < 0$, the second law of thermodynamics requires that compression shocks cannot form; hence, locally, the occurrence of compressive eddy shocklets is not physically admissible, whereas expansion shocklets are allowed. Fig. 2 shows a comparison of the ratio of the local velocity divergence to its RMS value $\theta/\theta_{\text{rms}}$ for fluid PP11 modeled with PFG, VDW and MAH EoS. This quantity has been widely used ([7, 8]) to detect regions in which eddy shocklets may occur. Isosurfaces at $\theta/\theta_{\text{rms}} = \circ\, 3$ (strong compressions) and $\theta/\theta_{\text{rms}} = 3$ (strong expansions) are plotted. In the dense gas case, extremely strong expansion regions are present, whereas compressions are shown to be weaker than in the PFG case. Both of the thermodynamic models under investigation give similar qualitative results, even if the VDW models tends to overestimate dense gas effects with respect to the more realistic MAH model. Finally, a statistical analysis of the turbulent structures is performed to show up the differences between dense and perfect gases. Precisely, a study in the plane of the second and third invariants of the deviatoric part of the velocity gradient tensor is carried out. Preliminary results show that the universal behavior found in compressible and incompressible turbulence (i.e., [9]) is globally recovered also in the dense gas regime, as shown in Fig.2. However, when conditioned on the local dilatation value, the p.d.f.s in strong expansions tend to exhibit a branch aligned along the left part of the null discriminant curve, due to the non-classical phenomena occurring in negative Γ regions.

*Corresponding author. Email: francesco.grasso@cnam.fr

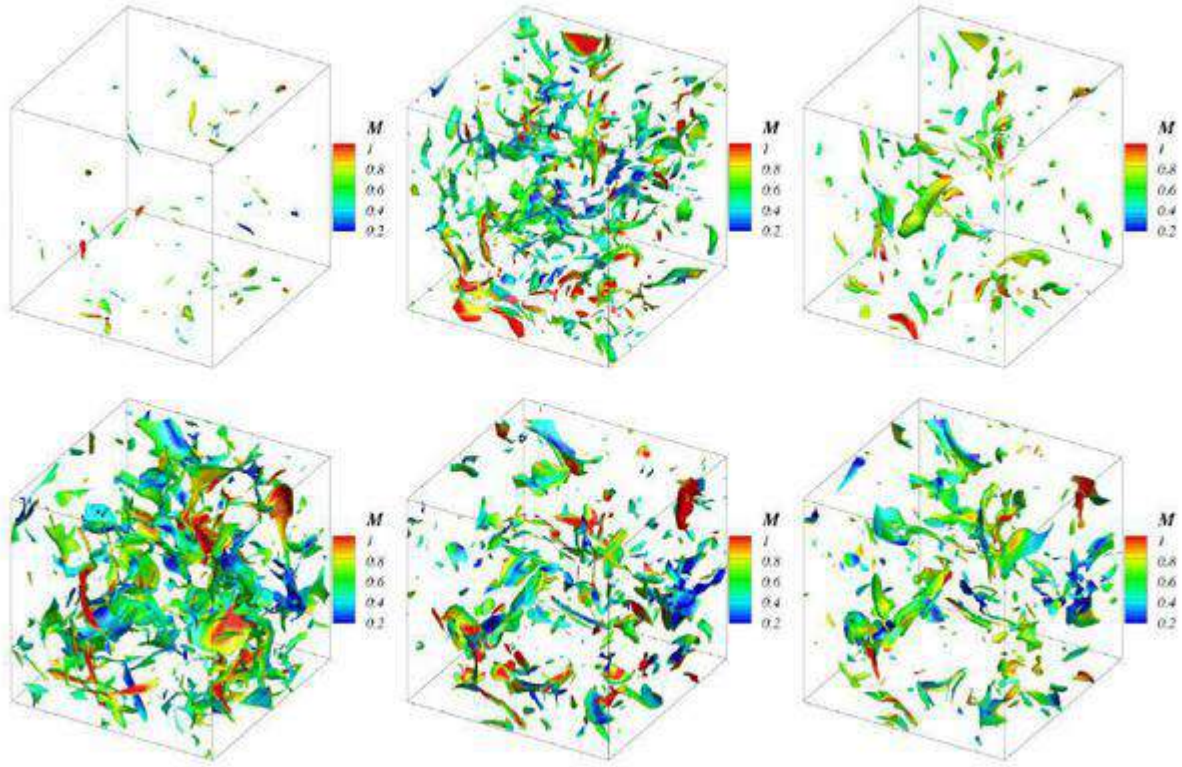

Figure 1: Ratio of dilatation to RMS dilatation for PFG (left), VDW (center) and MAH (right) EoS for fluid PP11 at $t = \tau$. Top: $\theta/\theta_{\text{rms}} = 3$ (strong expansions), bottom: $\theta/\theta_{\text{rms}} = -3$ (strong compressions).

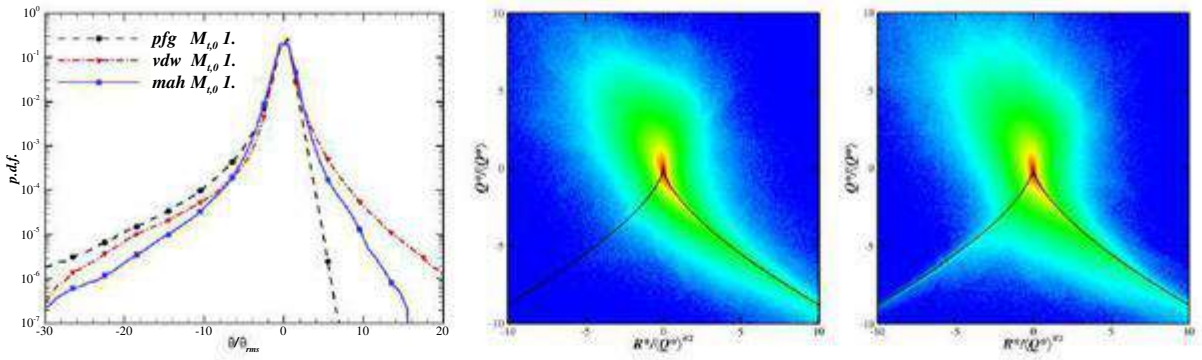

Figure 2: Left: P.d.f.s of dilatation to RMS dilatation for PP11 with PFG, VDW and MAH EoS at $t = 2\tau$ for $M_{t,0} = 1$. Right: Comparison of $\log_{10}$ pdf(R^*, Q^*) for PFG and MAH models.

References

[1] Thompson, P. A.: A fundamental derivative in gas dynamics. Physics of Fluids 14:1843-1849, 1971.

[2] Cinnella P., Congedo P. M.: Inviscid and viscous aerodynamics of dense gases. J. Fluid Mech 580:179-217, 2007.

[3] Kim J. W., Lee D. J.: Adaptive nonlinear artificial dissipation model for computational aeroacoustics. AIAA Journal 39:810-818, 2001.

[4] Ducros F., Ferrand V., Nicoud F., Weber C., Darracq D., Gacherieu C., Poinsot T.: Large-eddy simulation of the shock/turbulence interaction. J. Computational Physics 152:517-549, 1999.

[5] Chung T. H., Ajlan M., Lee L. L., Starling K. E.: Generalized multiparameter correlation for nonpolar and polar fluid transport properties. Ind. & Eng. Chem. Research 27(4):671-679, 1988.

[6] Cramer, M. S.: Negative nonlinearity in selected fluorocarbons. Physics of Fluids A 11(1):1894-1897, 1989.

[7] Samtaney R., Pullin D. I., Kosovic B.: Direct numerical simulation of decaying compressible turbulence and shocklets statistics. Physics of Fluids 13:1415-1430, 2001.

[8] Wang J., Shi Y., Wang L. P., Xiao Z., He X. T., Chen S.: Effect of compressibility on the small-scale structures in isotropic turbulence. J Fluid Mech 713:588-631, 2012.

[9] Pirozzoli S., Grasso F.: Direct numerical simulations of isotropic compressible turbulence: Influence of compressibility on dynamics and structures. Physics of Fluids 16:4386-4407, 2004.

NON-IDEAL SHOCK REFRACTION PROPERTIES IN DENSE VAPOURS

Nicolas Alferez*[1] and Emile Touber[1]
[1]*Department of Mechanical Engineering, Imperial College London, London, SW7 2AZ, UK*

Summary The linear shock-refraction response to an incoming perturbation is investigated for a fluid modelled with a non-ideal equation of state close to its thermodynamic liquid-vapour critical point. Fluids with large heat capacities (dense vapours) are shown to produce shocks with highly selective transmission properties based on the upstream Mach number. This selectivity could fundamentally modify the post-shock turbulence kinetic energy in shock/turbulence interactions.

INTRODUCTION

Dense vapours are single-phase fluids with high heat capacities with respect to their molecular mass (typically, organic compounds). They are used as working fluids in Organic Rankine Cycles (ORCs) for energy-conversion on low-temperature heat sources. Dense vapours are known to depart from the ideal-gas model in ORC expanders, where they operate near the liquid-vapour saturation curve. A typical outcome is the significant decrease of the sound speed which makes the expander flow highly supersonic [1]. Non-ideal compressible gasdynamic has been extensively studied mainly for its nonclassical shock formation process (*e.g* admissible expansion shocks) which enforces constrains on turbine blade design [1].

In most applications shocks are formed in a surrounding turbulent flow. In ideal gas, shocks interacting with weak turbulent flows have been known to generate strong thermo-acoustic waves. Ribner [2] demonstrated using a Linear Interaction Analysis (LIA) how a shock interacting with a 0.1% turbulence intensity could result in a 120 dB noise downstream of the shock. The LIA has recently been confronted favourably against expensive ideal-gas three-dimensional direct numerical simulations of shock turbulence interactions [3]. A remarkable prediction of the post-shock turbulence intensity was achieved, confirming the suitability of the linear framework in this context.

Although the linear-stability properties of shock fronts in non-ideal gases are known to produce different properties compared to that of an ideal-gas shock [4], there exists no theoretical study on the interaction of a turbulent flow field with a shock in such non-ideal media. This study is a first step in that direction. A linear analysis of a non-ideal gas shock interacting with an incoming fluctuating flow is performed and the shock-refraction properties are investigated.

METHOD AND RESULTS

Methodology

A detailed theoretical analysis of the non-classical compression shock admissibility problem, for dense vapours, is performed. It provides a family of base flow suitable for a linear perturbation analysis, in the spirit of Ribner's pioneering development. Explicit formula for the refraction coefficients of incoming linear waves are obtained for shocks modelled with an arbitrary equation of state (EoS). Detailed analyses of the effects of the near thermodynamic critical point (TCP) region are investigated when the EoS models a fluid with complex molecules (dense-gas regime).

Theoretical results are then compared with direct numerical simulations (DNS) of the compressible Euler equations for a gas modelled with a van der Waals EoS. A new solver based on high-order Dispersion Relation Preserving (DRP) finite difference centred schemes together with optimised filter shape in wave number space was developed. A shock-capturing technique based on a new artificial viscosity defined from analytical solutions of the one-dimensional viscous-shock structure was formulated. It allows for direct control of the numerical shock thickness, providing a simple way of reducing spurious-wiggles amplitude. The new approach is crucial when shocks are considered near TCP Hugoniot locus where classical approaches can fail to capture the discontinuity.

Results

Geometrical interpretations of the refraction properties in the pressure/specific-volume diagram were built based on the analytic shock-refraction coefficients derived in the linear framework. The change of curvature of the Hugoniot line is found to be a key parameter in the transmission coefficients. An asymptotic equivalence between Hugoniot lines and isotherms is demonstrated in the context of a dense gas in the limit of c_v/R going to infinity. Strong non-ideal gas effects (*e.g* local maxima and discontinuous admissible path in both the post-shock Mach number and the eigen-mode amplification coefficients) are found in this limiting case for which there exists a saddle point on the Hugoniot line at the TCP (originating from intermolecular forces). The linear response for increasing large but finite values of c_v/R (*e.g* for PP10 with $c_v/R = 78.2$) departs from the ideal-gas behaviour and approaches this limit relatively well (Figure 1).

*Corresponding author. Email: n.alferez@imperial.ac.uk

TCP effects induce large variations in the shock-refraction coefficients for small changes in the upstream Mach number (up to the appearance of jumps when the Hugoniot line is discontinuous, Figure 1b). These sharp response effects are illustrated in two-dimensional numerical simulations of shocks impinged by a low-density Gaussian pulse (Figure 2). It is possible to direct the incoming energy more into the acoustic or the vortical post-shock Euler eigen-modes with an arbitrary small change in the incoming Mach number. Such selective effects are not possible in ideal gas and should be considered in turbulent numerical modelling and/or for practical application involving non-ideal gas compressible dynamics of dense vapours close to critical conditions.

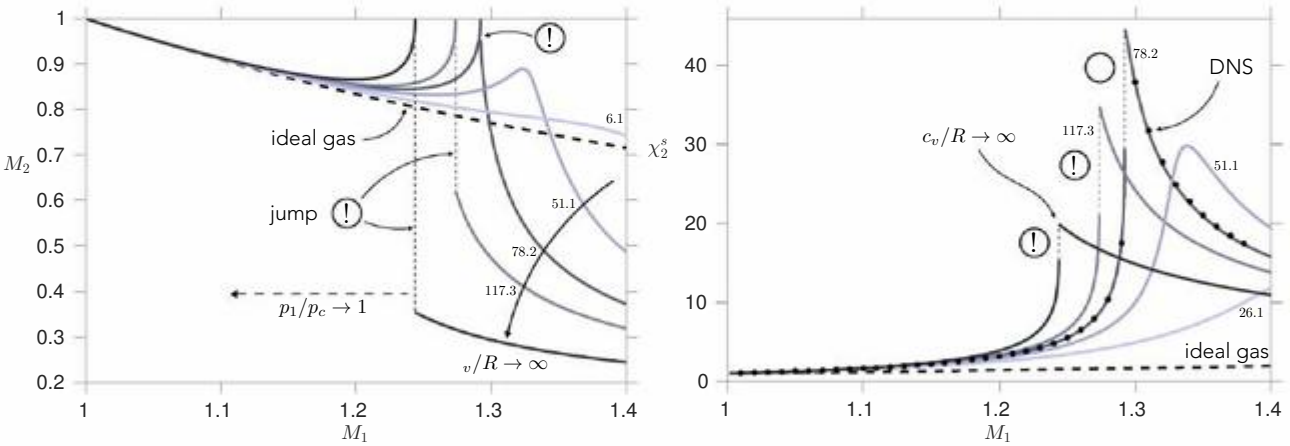

(a) Non-monotonic and discontinuous admissible post-shock Mach numbers.

(b) Selective entropy-mode amplification coefficient.

Figure 1: Typical non-ideal gas effects obtained for a van der Waals gas with increasing molecular complexities. The pre/post-shock conditions are close to the thermodynamic critical point ($p_1/p_c = 0.55$ and $T_1/T_c = 1.00$).

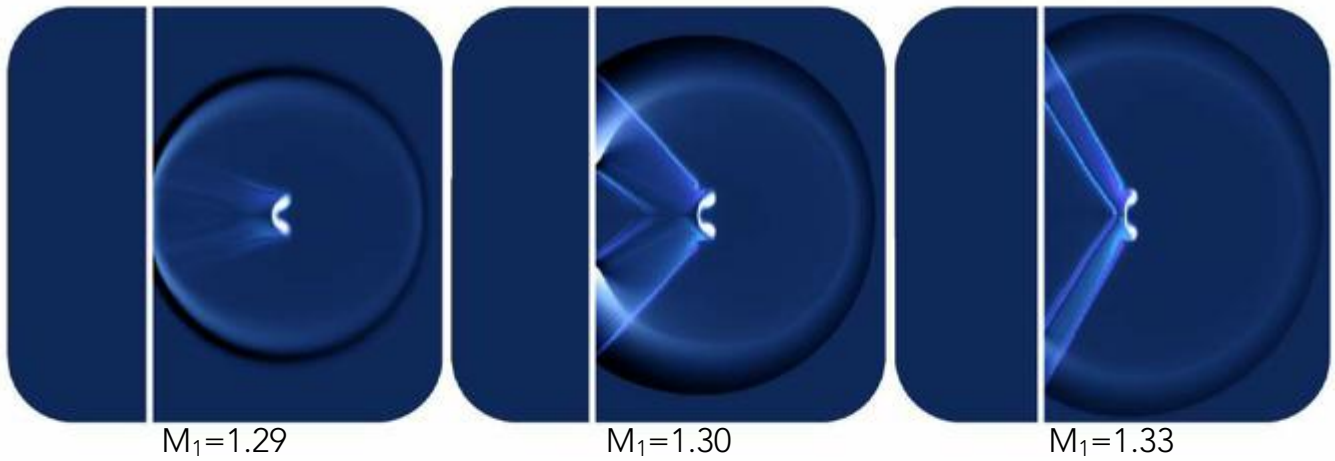

Figure 2: Refraction of a low-density pulse (in white) on a shock at $T_1/T_c = 1.00$ and $p_1/p_c = 0.55$ for PP10 modelled as a van der Waals gas ($c_v/R = 78.2$) and very small variations in the incoming Mach numbers. The colouring is such that both the dilatation rates and vorticity field are made visible. More energy goes into the acoustic modes (left) and the vortical modes (right).

References

[1] P. Colonna, E. Casati, C.Trapp, T. Mathijssen, J. Larjola, T. Turunen-Saaresti, and A. Uusitalo. Organic Rankine Cycle Power Systems: From the Concept to Current Technology, Applications, and an Outlook to the Future. *J. Eng. Gas Turbines Power*, 137(10), 100801, 2015.

[2] H. S. Ribner. Shock-turbulence interaction and the generation of noise. Technical Report 1233, NACA, 1955.

[3] J. Larsson, I. Bermejo-Moreno, and S. K. Lele. Reynolds- and Mach-number effects in canonical shock-turbulence interaction. *J. Fluid Mech.*, 717:293-321, 2 2013.

[4] S. P. D'yakov. *Zh. Erksp. Teor. Fiz.*, 27, 288 1954.

APPLICATION OF A FULLY COMPRESSIBLE MULTIPHASE SPH SCHEME TO HYPERVELOCITY IMPACTS

Iason Zisis, Bas van der Linden, and Barry Koren*
Centre for Analysis, Scientific computing and Applications, Eindhoven University of Technology, Eindhoven, The Netherlands

Summary The present study concerns a fully compressible Smoothed Particle Hydrodynamics scheme for multiphase flows. It is validated against a one-dimensional multiphase shock-tube flow, with known analytical solution, and it is applied to a hypervelocity impact experiment. It is found that the new scheme can accurately simulate the propagation of shocks and offers improved results in the simulation of hypervelocity impacts between bodies of high-density ratios.

INTRODUCTION

Various alternatives have been studied for the simulation of weakly compressible multiphase flows with Smoothed Particle Hydrodynamics (SPH) [1, 2, 3, 4]. Typically, particles of unequal masses are employed in SPH, such that the mass ratio of the particles depicts the density ratio of the phases. For the standard SPH fully compressible scheme —where the smoothing length needs to adapt to the large variations of density— particles of equal masses are advised [5]. Thus, the ratio of initial densities dictates the discretization length per phase, which implies computational and geometrical restrictions [6, 7]. Schemes based on number-density can accommodate particles of unequal masses and therefore offer a robust alternative. The present study validates a number-density scheme against a one-dimensional multiphase shock-tube problem with known analytical solution, and also applies the scheme to the simulation of a hypervelocity impact experiment. Hypervelocity impacts [8] are essentially processes of solids under extreme compression. In case of different materials the problem becomes a multiphase compressible problem.

RESULTS AND DISCUSSION

The fully compressible multiphase SPH scheme of [6] has been developed by varying the density estimate $\rho_i = m_i \sum_j W_{ij}(h_i)$, as prescribed by the variational SPH framework of [5, 9]. The variation of the smoothing function W is taken without neglecting terms attributed to the variation of the smoothing length $h_i \equiv h(n_i)$, where n_i is the local number density.

Liquid-gas shock tube

The first test is a liquid-gas shock tube of initial density and pressure ratio $1/20$ and $1/100$ respectively, with discontinuous parameters for the stiffened-gas equation of state [7]. In Fig.1, we plot the SPH results versus the exact results (red line) at $t = 2.3 \times 10^{-3}$ s. The convergence of the SPH scheme for 200, 400 and 800 particles per unit length is shown in the inset plots (blue, magenta and black dots respectively). A timestep of $\Delta t = 1 \times 10^{-8}$ s is used for the highest resolution.

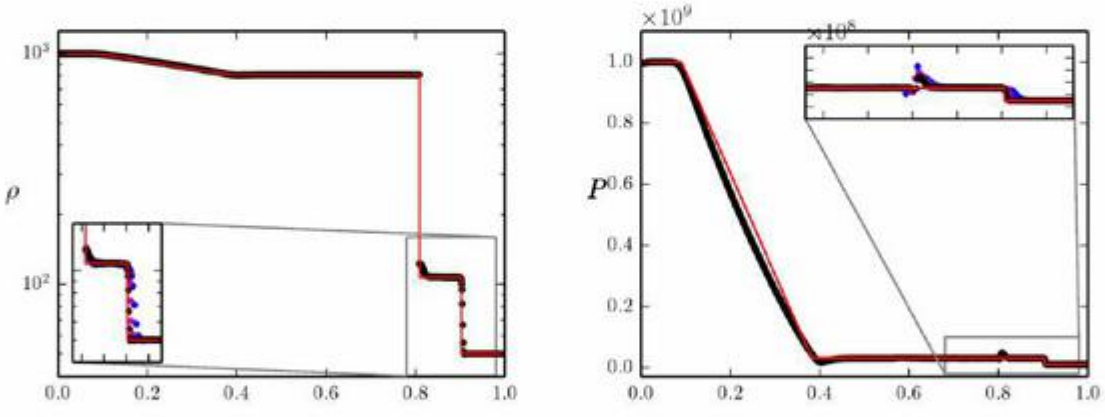

Figure 1: Density (log scale) and pressure of the liquid-gas shock-tube test at $t = 0.0023$s. Magnitudes are in SI units.

*Corresponding author. Email: b.koren@tue.nl.

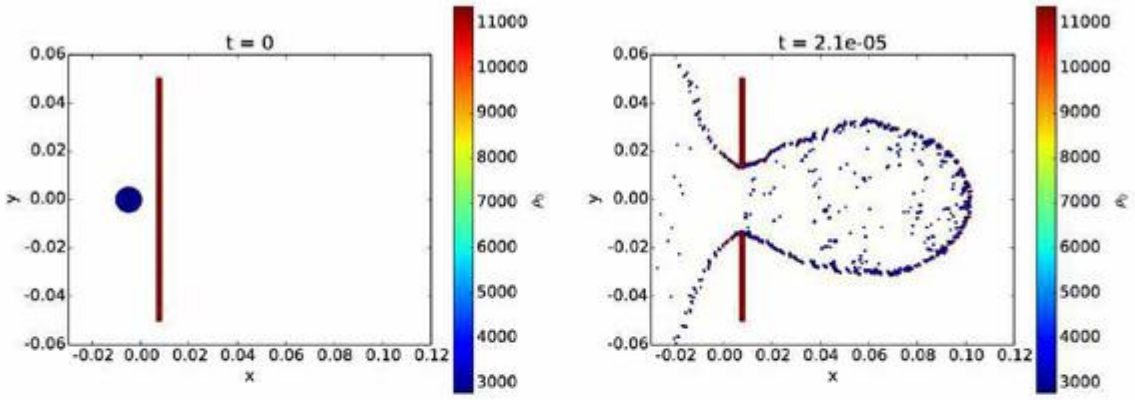

Figure 2: Density in kg/m^3 for the Al-Pb hypervelocity impact, at $t = 0$ and $t =$21 μs.

Hypervelocity impact

The second test is one of the hypervelocity impact scenarios studied —experimentally and with older SPH schemes— by [8], and concerns materials with a density ratio of approximately $1/6$. A lead (Pb) sphere of radius $R = 5$ mm impacts an aluminum 2024 (Al) plate of thickness $D = 1.5$ mm at $U = 6.85$ km/s. Our number-density scheme models the hydrodynamic response of media. For solids, which also exhibit material strength, the effect of deviatoric stresses on acceleration and internal energy has been derived from variational principles and the use of number density. An upcoming publication deals with this task and discusses the differences with the standard or other approaches (e.g. [10]). We use the Mie-Grüneisen equation of state [11] with data from [12] and [13]. For material strength we use a simple Von Mises yield criterion with data from [8]. The timestep is $\Delta t = 5 \times 10^{-5}$ μs, bounded by the CFL citerion [11]. The geometry is discretized by taking 10 particles per mm, which results in $N = 25184$ particles. The initial problem set-up is shown in Fig.2. The initial distance of the plate from the projectile is such that it is covered by the projectile in 1 μs. The material distribution 20 μs after impact is depicted in Fig.2, when the ratio of length-to-width of the debris cloud is recorded for validation by [8]. We find the latter value to be 1.48, which is in good agreement with the experimentally observed 1.56, especially compared to the computational value 1.16 of [8]. Regarding the resulting opening of the plate, we find it to be 27 mm, with the experimental value being 26 mm, and the result of [8] being 30 mm. Finally, the energy loss of the scheme is 0.002% of its initial value, in contrast to the energy loss of 3.1% mentioned in [8]. Our finding is in good agreement with the conservative system which is solved. This good agreement is attributed to the variational consistency of the scheme and the structure of the artificial dissipation terms.

References

[1] Colagrossi A., Landrini M.: Numerical simulation of interfacial flows by Smoothed Particle Hydrodynamics, J. Comp. Physics, 191:448–475, 2003.

[2] Hu X.Y., Adams N.A.: A multi-phase SPH method for macroscopic and mesoscopic flows, J. Comp. Physics 213:844–861, 2006.

[3] Grenier N., Antuono M., Colagrossi A., Le Touzé D., Alessandrini B.: An Hamiltonian interface SPH formulation for multi-fluid and free surface flows, J. Comp. Physics 228:8380–8393, 2009.

[4] Monaghan J.J., Rafiee A.: A simple SPH algorithm for multi-fluid flow with high density ratios, Int. J. Num. Meth. Fluids 5:537–561, 2013.

[5] Price D.J., Smoothed particle hydrodynamics and magnetohydrodynamics, J. Comp. Physics 231:759–794, 2012.

[6] Zisis I., van der Linden B., Giannopapa C., Koren B.: On the derivation of SPH schemes for shocks through inhomogeneous media, Int. J. Multiphysics 9:83–99, 2015.

[7] Zisis I., Messahel R., van der Linden B., Boudlal A., Koren B.: Validation of robust SPH schemes for fully compressible multiphase flows, Int. J. Multiphysics 9:225–234, 2015.

[8] Hiermaier S., Könke D., Stilp A.J., Thoma K.: Computational simulation of the hypervelocity impact of Al-spheres on thin plates of different materials, Int. J. Impact Eng: 20:363–374, 1997.

[9] Monaghan J.J.: Smoothed particle hydrodynamics, Rep. Prog. Physics 68:1703–1759, 2005.

[10] Bonet J. Kulasegaram S., Rodriguez-Paz M.X., Profit M.: Variational formulation for the Smooth Particle Hydrodynamics (SPH) simulation of fluid and solid problems, Comp. Meth. Applied Mech. and Eng. 193:1245–1256, 2004.

[11] Libersky L.D., Petschek A.G., Carney T.C., Hipp J.R., Allahdadi F.A.: High Strain Lagrangian Hydrodynamics: A Three-Dimensional SPH Code for Dynamic Material Response, J. Comp. Physics 109:67–75, 1993.

[12] Marsh S.P. (Edit.): LASL Shock Hugoniot Data, University of California Press, 1980.

[13] Hasegawat M., Young W.H.: Grüneisen parameters for simple metals, J. Phys. F: Metal Phys. 10:225-234, 1980.

STEADY TRANSONIC DENSE GAS FLOW PAST A TWO - DIMENSIONAL COMPRESSION/EXPANSION RAMP

Alfred Kluwick*[1] and Edward A. Cox[2]

[1]*Institute of Fluid Mechanics and Heat Transfer, TU Vienna, Austria*
[2]*School of Mathematics and Statistics, UCD, Dublin, Ireland*

Summary The behaviour of steady transonic dense gas flow is essentially governed by two nondimensional parameters characterising the magnitude and sign of the fundamental derivative of gas dynamics (Γ) and its derivative with respect to the density at constant entropy (Λ). The resulting response to external forcing is surprisingly rich and studied in detail for the canonical problem of 2D flow past compression/expansion ramps.

MOTIVATION

The possibility that compression as well as rarefaction shocks may form in single phase vapours was envisaged first by Bethe [1]. However his calculations based on the Van der Waals equation of state indicated that the latter type of shock is possible only if the ratio c_v/R (where c_v and R denote the specific heat at constant volume and the universal gas constant respectively) is larger than about 17.5 which he considered too large to be satisfied by real fluids. This conclusion was contested by Thompson (see Thompson [6]) and coworkers who showed that this required condition for the existence of rarefaction shocks is indeed satisfied for a large number of Fluorocarbon vapours. For these vapours the ratio c_v/R far exceeds the critical value so that the required condition for the existence of rarefaction shocks is satisfied in the general neighbourhood of the thermodynamic critical point. For a detailed review see Kluwick [5]. This finding spawned a burst of theoretical studies elaborating on the unusual and often counterintuitive behaviour of flows with rarefaction shocks present. These produced both results of a fundamentally theoretical character (addressing, among other issues, questions of admissibility and existence) but also results suggesting the practical importance of rarefaction shocks including the observation that the entropy increase and thus losses resulting from weak rarefaction shocks may be much smaller than those associated with compression shocks in perfect gases.

Expectations were high that the first experimental observation of a rarefaction shock was just around the corner providing verification of the accumulating theoretical predictions. Unfortunately, however, attempts to reach this goal by means of classical shock tube experiments have so far failed. Studies analysing the reasons for this failure have been carried out by a number of research groups resulting in a much better understanding of the thermodynamic properties of possible fluids and identifying a new family of siloxanes as testing fluids (see Colonna, Guardone & Nannan [3]). Finally, and most importantly, the properties of vapour mixtures have recently been investigated by Guardone, Colonna, Casati & Rinaldi [4] allowing for the optimisation of experimental work as well as leading to new practical applications. Therefore we think that the time is ripe for a second round of experiment efforts to settle the long standing question "do rarefaction shocks exist?" but more than this to further explore the unusual behaviour of dense gas flows theoretically. The results presented here aim to contribute to our understanding of dense gas flows for a practically realisable flow setup.

OUTLINE

Analytical studies of dense gas flows have in the past mainly concentrated on 1D unsteady flows. In contrast to such flows which are of strictly hyperbolic type 2D steady flows are of mixed type, i.e. hyperbolic or elliptic depending on whether the Mach number M is larger or smaller than one. In 1D unsteady flows it is not necessary to distinguish between the properties of shock polars and characteristics as they agree automatically as long as changes of the entropy are negligible small. In contrast, for the case of 2D steady flows, however, the construction of shock polars has to be considered separately and their connection with characteristics deserves special attention. To provide insight into the more complex flow behaviour is the aim of the present investigation. In this connection we note that 2D steady flows have been treated already in Cramer and Tarkenton [2] but as the authors approach was predominantly a numerical investigation the present analysis is considered to close a "hole" in our understanding of such flows. To make things as clear as possible it is necessary to keep the geometrical complexity as simple as possible. A generic problem which satisfies this requirement is given by supersonic flow past a compression/expansion ramp. Specifically we assume that the corner of the ramp is located at the origin of a Cartesian coordinate system (x, y), that the upstream flow $\mathbf{u}_\infty = (u_\infty, 0)$ is aligned with the x - axis and the corner geometry is: $y = 0, x < 0$; $y = \delta a x, x > 0$. Here the parameter $a = O(1)$ while the positive parameter δ with $\delta \ll 1$ ensures that the subsequent

*Corresponding author. Email: alfred.kluwick@tuwien.ac.at

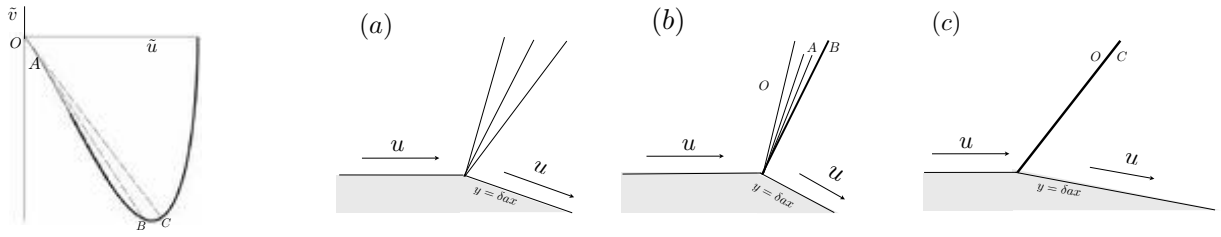

Figure 1: Fan, compound shock-fan and single shock structures for $K_1 > 0$ and $K_2 > 0$ in hodograph plane (—— characteristic, ▬ shock polar, - - - Rayleigh lines) and with the resulting flow geometry (—— wavefronts, ▬ shocks). Results are presented for $K_2 < \frac{3}{2K_1}$ and $\Gamma_\infty > 0$.

flow generated around the corner is a small perturbation of the uniform flow. Introducing suitably nondimensionalised and scaled quantities $\xi, \eta, \tilde{u}, \tilde{v}$ in place of x, y, u, v the problem under consideration can be cast into the form

$$J(\tilde{u})_\xi + \tilde{v}_\eta = 0, \quad \tilde{u}_\eta \circ \tilde{v}_\xi = 0. \tag{1}$$

The boundary conditions on $\eta = 0$ become

$$\tilde{v} = 0, \quad \xi \leq 0, \qquad \tilde{v} = a \ \mathrm{sgn}(\Gamma_\infty), \quad \xi > 0. \tag{2}$$

The function $J(\tilde{u})$ in (1) is given by

$$J(\tilde{u}) = \circ K_1 \tilde{u} \circ \tilde{u}^2 + \frac{K_2}{3}\tilde{u}^3 \tag{3}$$

and measures the perturbed mass flux where K_1, K_2 are the similarity parameters

$$K_1 = \frac{M_\infty^2 \circ 1}{(\delta\Gamma_\infty)^{\frac{2}{3}}}, \quad K_2 = \frac{\delta^{\frac{2}{3}}\Lambda_\infty}{\Gamma_\infty^{\frac{4}{3}}}. \tag{4}$$

Here $M_\infty, \Gamma_\infty, \Lambda_\infty$ denotes the freestream Mach number and the values of the thermodynamic quantities Γ, Λ evaluated in the unperturbed flow. Also we require $K_1 > 0$ (supersonic flow) while $K_2 \gtrless 0$ depending on the signs of $\Gamma_\infty, \Lambda_\infty$. Characteristics of (1) are given by the integral curves of

$$\frac{d\tilde{v}}{d\tilde{u}} = \pm\sqrt{K_1 + 2\tilde{u} \circ K_2\tilde{u}^2} = \pm\sqrt{\circ \frac{dJ}{d\tilde{u}}} \tag{5}$$

and shock polars in the hodograph $(\tilde{u}, \tilde{v})$ plane are given by

$$\frac{[\tilde{v}]}{[\tilde{u}]} = \pm\sqrt{\circ \frac{[J]}{[\tilde{u}]}}. \tag{6}$$

Equations (5), (6) provide the necessary information to construct solutions of the problem posed. Equation (3) suggests that five parameter ranges of K_2: $K_2 < \circ \frac{1}{K_1}, \circ \frac{1}{K_1} < K_2 < \circ \frac{3}{4K_1}, \circ \frac{3}{4K_1} < K_2 < 0$, $K_2 = 0$, $K_2 > 0$ have to be distinguished. This reflects the fact that, in contrast to classical gasdynamics, the perturbation mass flux $J(\tilde{u})$ is not a monotonic function of the perturbed velocity if K_2 is nonzero. As an example, Figure 1 displays results for $K_2 > 0$. In this parameter range shock solutions exist which lead to a reduction of the velocity and give qualitatively similar results to those observed in perfect gases. These shocks are not included here. In contrast to the classical case however an additional branch of the shock polar is seen to exist for $\tilde{u} > 0$ and to connect with the characteristic describing accelerated flows. Increasing values of the downstream velocity (and associated with a non-monotonic variation of the parameter a then causes a transition from a centered wave fan (a) to a wave fan terminated by a sonic rarefaction shock (b) and finally to a single rarefaction shock (c).

References

[1] H. A. Bethe (1942). The theory of shock waves for an arbitrary equation of state. Report No. 545, Office of Scientific Research and Development.

[2] M. Cramer, G. Tarkenton (1992). Transonic flows of Bethe-Zel'dovich-Thompson fluids. J. Fluid Mech., 240: pp. 197–228.

[3] P. Colonna, A. Guardone, N.R. Nannan (2007). Siloxanes: A new class of candidate Bethe-Zel'dovich-Thompson fluids. Phys. Fluids, 19(8): pp. 086102-086114.

[4] A. Guardone, P. Colonna, E. Casati, and E. Rinaldi (2014). Nonclassical gasdynamics of BZT mixtures. J. Fluid Mech., 741: pp. 681 - 701.

[5] A. Kluwick (2001). Rarefaction Shocks. in: "Handbook of Shock Waves, Vol 1", G. Ben-Dor, T. Elprin, O. Ingra (ed.); Academic Press, San Diego.

[6] P. A. Thompson (1971). A Fundamental Derivative in Gas Dynamics. Physics of Fluids 14 pp. 1843 - 1849.

LARGE-EDDY SIMULATION OF STRONG SHOCK-WAVE/TURBULENT BOUNDARY-LAYER INTERACTION AT $\mathrm{Re}_\theta = 14000$

Vito Pasquariello*[1], Stefan Hickel[2], and Nikolaus A. Adams[1]

[1]*Institute of Aerodynamics and Fluid Mechanics, Technische Universität Munchen, Garching, Germany*
[2]*Faculty of Aerospace Engineering, Technische Universiteit Delft, Delft, The Netherlands*

Summary We investigate the interaction of an oblique shock-wave with a turbulent boundary-layer at a free-stream Mach number of $\mathrm{Ma}_\infty = 3.0$ and a Reynolds number based on the incoming momentum thickness of $\mathrm{Re}_{\theta_0} = 14000$ by means of wall-resolved large-eddy simulations (LES). Previous numerical studies (both LES or DNS) mainly focused on weak interactions at rather low Reynolds numbers up to around $\mathrm{Re}_{\delta_0} \approx 50 \cdot 10^3$. We extend the numerical database to strong interactions with massive mean-flow separation at a Reynolds number of $\mathrm{Re}_{\delta_0} \approx 203 \cdot 10^3$. A direct comparison of simulation and experiment is given in terms of mean and unsteady wall-pressure measurements. The low-frequency unsteadiness is studied in more detail by linear spectral analysis (power spectral density, coherence and phase), as well as modal decomposition techniques (dynamic mode decomposition in 2D and 3D).

INTRODUCTION

Shock-wave/boundary layer interactions (SWBLI) frequently occur in flows of technical interest, such as supersonic air intakes, turbo-machine cascades, helicopter blades, supersonic nozzles, and launch vehicles. SWBLI are often critical for the vehicle or machine performance, since the interaction region is a main source of maximum mean and fluctuating pressure loads acting on the underlying structure [1]. Of particular concern is the low-frequency unsteadiness observed in SWBLI with mean boundary-layer separation, imposing additional fatigue loading on the structure and possibly exciting surface panel flutter, which endangers structural integrity.

Over decades, researchers studied SWBLI both experimentally and numerically, and confirmed the existence of such low-frequency motions associated to the separation shock. Despite the general agreement of characteristic frequency scaling [2], the exact mechanism that explains the disparity between the characteristic frequency of energetic scales associated to the incoming turbulent boundary-layer and the shock oscillation frequency, which is typically two or three orders of magnitude lower, still remains an open question.

INVESTIGATED SETUP AND NUMERICAL METHOD

The topology studied in this work is an oblique shock-wave impinging on a flat plate turbulent boundary-layer. The shock is generated by a 19.6° wedge at a freestream Mach number of $\mathrm{Ma}_\infty = 3.0$. The Reynolds number based on the inlet boundary-layer thickness is $\mathrm{Re}_{\delta_0} = 203 \cdot 10^3$. Table 1 summarizes the main flow parameters, which are consistent with recent experimental studies [3]. Experiments for this case were conducted in the trisonic wind tunnel at the German Aerospace Center (Cologne), which is a blow-down facility with a closed test section of $0.6 \times 0.6\,\mathrm{m}$.

We conduct wall-resolved LES: The compressible Navier-Stokes equations in conservative form are solved using the Adaptive Local Deconvolution Method (ALDM, [4]) for discretizing the convective fluxes, which provides a physically consistent subgrid-scale turbulence model for implicit LES. Employing a shock sensor to detect discontinuities, ALDM can capture shock waves while smooth waves and turbulence are propagated accurately without excessive numerical dissipation [4]. Diffusive fluxes are discretized using a 2nd order central difference scheme, and a 3rd order Runge Kutta scheme is used for the time integration. The high Reynolds number and the strong interaction lead to a total number of $364 \cdot 10^6$ cells. Additionally, the long integration time of approximately $246\, L_{\mathrm{sep}}/U_\infty$, which is needed to enable spectral analysis, make this study computationally expensive.

Ma_∞	T_0	p_0	ϕ	U_∞	θ_0	Re_{δ_0} [1]	Re_{θ_0} [2]
3.0	273.7 [K]	582 [kPa]	19.6 [°]	594 [m/s]	0.28 [mm]	$203 \cdot 10^3$	$14 \cdot 10^3$

[1] $\mathrm{Re}_{\delta_0} = U_\infty \delta_0 / \nu_\infty$; [2] $\mathrm{Re}_{\theta_0} = U_\infty \theta_0 / \nu_\infty$, $\theta_0 = \int_0^{\delta_0} \frac{\langle\rho\rangle\langle u\rangle}{\rho_\infty U_\infty}\left(1 - \frac{\langle u\rangle}{U_\infty}\right) \mathrm{d}y$

Table 1: Flow parameters.

*Corresponding author. Email: vito.pasquariello@tum.de

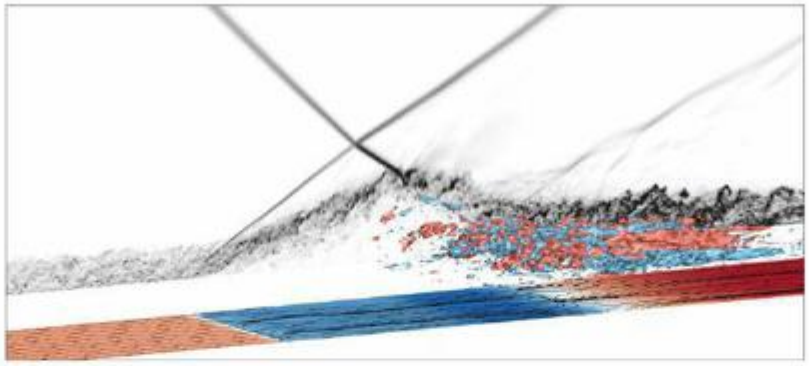

Figure 1: Schematic of the oblique SWBLI investigated in this study.

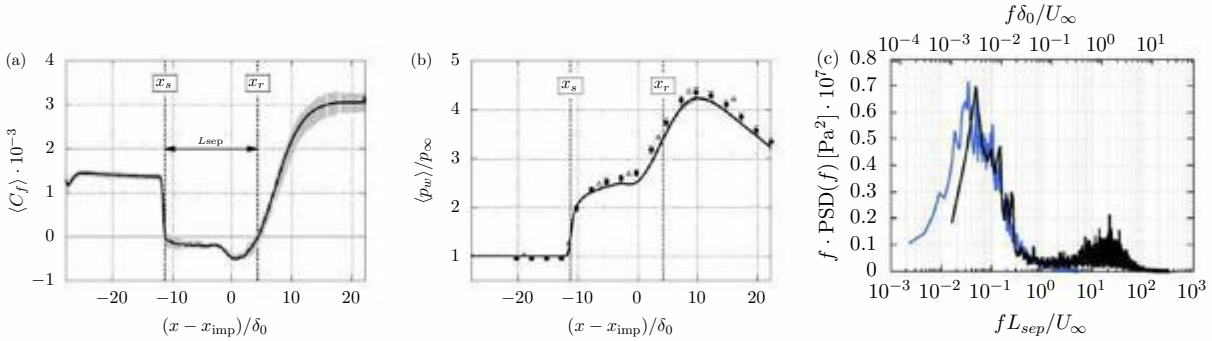

Figure 2: (a) Skin friction $\langle C_f \rangle$ (b) and wall-pressure $\langle p_w \rangle / p_\infty$ evolution. (—) LES, (•) experimental static data, (▵) mean experimental Kulite data. (c) Weighted power spectral density at x_s. (—) LES, (—) experiment.

PRELIMINARY RESULTS

Figure 1 visualizes the SWBLI by means of contours of the instantaneous density gradient magnitude on an xy-plane, indicating the strong character of the interaction and the presence of a large area of separated flow. Isosurfaces of time-averaged streamwise vorticity indicate the presence of pairs of counter-rotating Görtler-like vortices, which emerge close to the reattaching shear layer. Similar vortices are often found in compression-ramp configurations. Surface-streamlines show distinct saddle and nodal points along the reattachment line, while further downstream footprints of streamwise vortices can be identified.

A more quantitative description of the flow is given in Fig. 2. The mean skin friction evolution (Fig. 2(a)) shows a large separated flow region of $L_{\mathrm{sep}} = 15.5\,\delta_0$ length. The gray shaded area indicates time-averaged minimum and maximum values observed over the spanwise direction. It highlights an increased spanwise variation of $\langle C_f \rangle$ close to the mean separation location and a strong modulation after reattachment due to the presence of Görtler-like vortices. The mean wall-pressure evolution $\langle p_w \rangle / p_\infty$ is shown in Fig. 2(b) and validated against experimental data. The pressure increase associated with the impinging shock is felt approximately $12\,\delta_0$ upstream of the theoretical inviscid impingement location, x_{imp}. Within the initial part of the separation bubble ($x_s < x < x_{\mathrm{imp}}$), a significant pressure plateau is observed, indicating the presence of a strong interaction. Numerical and experimental data for the pressure evolution are in good agreement, confirming the ability of our LES solver to correctly predict SWBLI at high Reynolds numbers. Finally, the unsteadiness of the reflected shock is addressed in Fig. 2(c), where we show numerical and experimental power spectral densities evaluated close to the mean separation location. Both spectra agree well and predict a low-frequency unsteadiness in the range $St_{L_{sep}} = 0.03 \ldots 0.05$, which is consistent with previous findings [2].

The preliminary results show a good agreement between experiment and numerics for both mean and unsteady aspects of the SWBLI. Thus, we are confident that our LES is accurate and will enable us to gain deeper insight into the low-frequency unsteadiness once advanced post-processing techniques are applied, which is currently under investigation and will be part of the talk.

References

[1] Délery, J. M., Dussauge, J.-P.: Some physical aspects of shock wave/boundary layer interactions. Shock Waves 19:453-468, 2009.

[2] Dussauge, J.-P.,Dupont, P.,Debiève, J.-F.: Unsteadiness in shock wave boundary layer interactions with separation. Aerospace Science and Technology 10:85-91, 2006.

[3] Daub, D., Willems, S., Gülhan, A.: Experimental results on unsteady shock-wave/boundary-layer interaction induced by an impinging shock. CEAS Space Journal, 2015

[4] Hickel, S., Egerer, C. P., Larsson, J.: Subgrid-scale modeling for implicit large eddy simulation of compressible flows and shock-turbulence interaction. Physics of Fluids 26:106101, 2014.

On the Riemann flux performance in DG-based implicit LES at very high Reynolds numbers

Rodrigo Moura[(a)], Joaquim Peiró & Spencer Sherwin
Department of Aeronautics, Imperial College London, London, UK

Summary We discuss the effect of the Riemann flux in implicit large eddy simulations carried out with the discontinuous Galerkin (DG) method at very high Reynolds numbers. The study is based on a set of computations of the inviscid TGV (Taylor-Green vortex) test problem spanning different grid sizes and polynomial orders. Inviscid cases have been chosen so that the isolated effects of the Riemann solver could be assessed in a scenario that mimics that of under-resolved computations at very high Reynolds numbers. Comparisons are made mainly between the Lax-Friedrichs and Roe solvers and significant differences are found, especially for higher-order solutions. An explanation based on dispersion-diffusion (eigensolution) analysis [1] is proposed as to why Riemann solvers that take into account the complete set of physical eigenvalues consistently via upwinding are expected to display a more accurate and robust behaviour for DG-based implicit LES over a wider range of Mach numbers.

INTRODUCTION, MODEL PROBLEM AND TEST CASES CONSIDERED

Compressible flow simulations carried with the discontinuous Galerkin (DG) method over the years have indicated that the choice of the Riemann solver is not very important, especially at higher-order discretizations. As a result, nowadays the DG community uses the Lax-Friedrichs flux very often due to its simplicity and reduced computational cost. Here, we point out that for under-resolved computations, the Riemann flux choice can be quite important regarding both numerical stability and solution quality. Discussion is based on a set of simulations of the inviscid Taylor-Green vortex (TGV) problem.

The Taylor-Green vortex flow was introduced in [2] as a model problem for the analysis of transition and turbulence decay. The test problem was originally proposed for the incompressible Navier-Stokes equations in a cubic domain with triply-periodic boundary conditions. Here we adopt a modified version of the initial conditions which is suited for compressible flow solvers, as done in [3], so that the Euler equations (representing inviscid flow conditions) are solved within $[-\pi,\pi]^3$ at a baseline Mach number of 0.1. In the present study, even though the Euler equations are simulated directly, the presence of numerical dissipation is expected to make results consistent with the non-singular solution of the viscous TGV problem in the limit of zero viscosity, provided that enough small scales are captured by the DOFs employed.

The evolution of the TGV flow at high Reynolds numbers (say, higher than 10^3) can be characterized by three distinct phases, see e.g. [4]. During the first phase dissipation effects can be neglected and vortex lines begin to fold and stretch first by pressure gradients and then via three-dimensional vortex interactions, but still through a well-organized (non-chaotic) process. In the second phase transition takes place, whereby non-linear effects intensify and small-scale energy grows rapidly through the cascade mechanism leading to a peak in overall dissipation. Finally, in the third phase the TGV flow tends to a more homogeneous state of decaying turbulence, where energy decays monotonically towards zero.

The overall behaviour described above has been captured quite well by our stable computations, with minor differences being observed upon DOF refinement. The base set of test cases addressed here relied on Lax-Friedrichs and Roe fluxes (in their original form), which are arguably the most popular solvers currently used in compressible DG formulations. This base set of simulations is given in Table 1, where each column corresponds to the number of polynomial modes $M = P + 1$ used, in which P is the polynomial order, and each row corresponds to the number of degrees of freedom $N_{dof} = N_{el}M^3$ employed, N_{el} being the total number of elements. Equispaced grids (of cubic elements) have been used. The values in the core of Table 1 represent, for each test case, the number of elements per direction, namely $N_{el}^{1/3}$.

Table 1: Test cases' discretization parameters, also differentiating stable/unstable cases

$N_{dof} \setminus M$	4	5	6	7	8
113^3	28	23	19	16	14
159^3	39	32	28	23	19
227^3	56	45	39	32	28

Within Table 1, the cases in green ran successfully with both Roe and Lax-Friedrichs. The cases in orange crashed with Lax-Friedrichs, but ran successfully with Roe. The remaining ones (in red) crashed with both fluxes. Such results clearly indicate that, for the problem considered, Roe's solver yields a more robust discretization when compared to Lax-Friedrichs. This is counter-intuitive since the former is known to be less dissipative than the latter (in well resolved computations). All the cases that crashed yielded reasonable results (with no signs of numerical instability) until the time of crash, which took place consistently within the transitional phase of the TGV flow. This lack of robustness, found especially for the higher-order discretizations, has been verified not to be related to time-step restrictions or aliasing errors. Typical CFL numbers employed (based on the acoustic wave speed) are in the order of 0.1 and an increased number of quadrature points ($Q = 2M$) has been used to ensure consistent integration of the cubic non-linearities of the compressible Euler equations. Experiments conducted to rule out these factors consistently showed the time of crash to be practically insensitive to time-step reductions or to a further increase in the number of integration points. A subtle cause of crash is suggested in what follows.

[(a)] Corresponding author. Email: r.moura13@imperial.ac.uk

SOLUTION QUALITY, TRUNCATION ERRORS AND NUMERICAL INSTABILITY

Energy spectra at different phases of the flow and typical transitional/turbulent structures are shown in Figs 1a and 1b, respectively. The energy spectra on the left-hand side of Fig 1a show that near the dissipation peak (attained around t = 9) there is an inertial region following the -5/3 slope, consistent with previous DNS of the TGV at high Reynolds numbers [5]. The right-hand side plot of Fig 1a makes clear that Lax-Friedrichs allows for an unphysical build-up of small-scale energy at the final phase of the flow (which begins around t = 14), along which energy distribution is maintained. The vertical dotted line in Figs 1a,b is an estimate of the effective resolution power of the DG scheme [1], after which non-negligible numerical error (diffusion in particular) takes place. Another feature very clear in the spectra is that the large scales of Lax-Friedrichs computations are less energetic. It is believed that this results from a spurious energy drain caused by the over-energetic small scales via a more intense eddy viscosity-like mixing effect. The flow structures in Fig 1b support this reasoning. We note that Fig 1b shows flow structures near the end of the transitional phase (at t = 7) where independent eddies are more easily seen, and that large/small-scale differences between the fluxes only intensify as time progresses (Fig 1a). These results concern the cases computed with $N_{dof} = 227^3$ and M = 4, but the main features observed are common to all the test cases in Table 1.

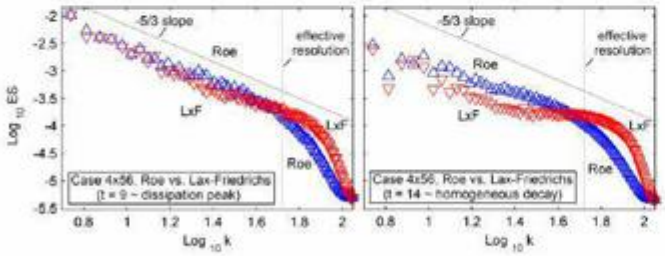

Fig 1a: Comparison of 3D energy spectra obtained using Roe and Lax-Friedrichs solvers at t = 9 (left) and t = 14 (right)

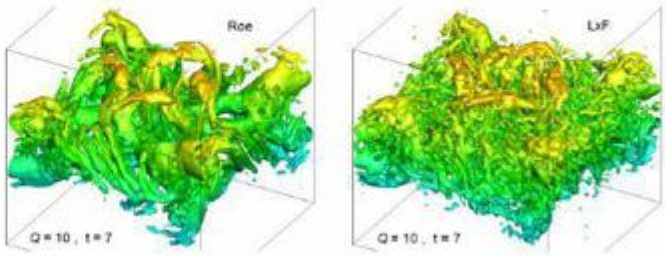

Fig 1b: Comparison of turbulent flow scales (via the Q-criterion) obtained using Roe (left) and Lax-Friedrichs (right) solvers

An explanation as to why the Lax-Friedrichs solver induces an accumulation of small-scale energy is proposed as follows. Roe's formulation uses the correct eigenvalues when upwinding (for all the equations), while Lax-Friedrichs uses instead the spectral radius alone ($|u|+c$, in 1D). This results in over-upwinding for the momentum equations due to the upwind ratio $\beta = (|u|+c) / |u| > 1$. Note that β increases as the Mach number is reduced. DG's spectral distribution of numerical diffusion (linear estimates) are given in Fig 2 for M = 4 polynomial modes and different ratios β. There is a critical ratio β^C above which non-smooth dissipation characteristics take place. For M = 4, $\beta^C \sim 2.18$ corresponding to $Mach^C \sim 1/(\beta^C-1) \sim 0.85$. Lax-Friedrichs computations below $Mach^C$ may therefore display adverse effects owing to non-smooth features in DG's truncation error. Further inspection showed that $Mach^C$ increases with the discretization order (e.g. $Mach^C \sim 2$ for M = 9). Roe's flux does not have this problem since its unit upwind ratio does not change with the flow's Mach number. This might as well be the cause of Roe's superior robustness for the inviscid TGV, since small-scale wiggles may facilitate non-positivity and thus instability.

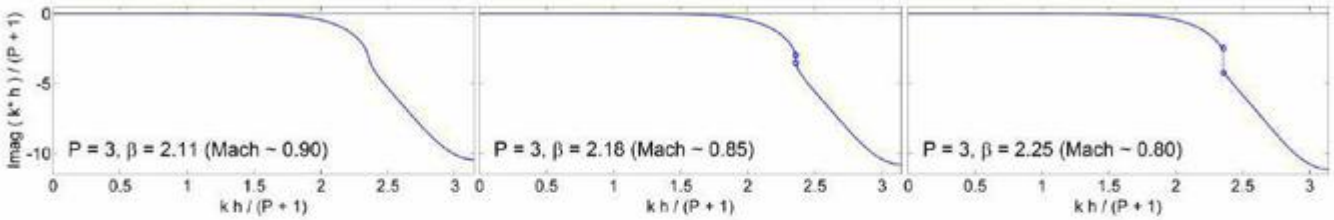

Fig 2: Numerical diffusion in wavenumber space (Lax-Friedrichs flux for M = 4) as Mach number is reduced from 0.9 to 0.8 (left to right)

CONCLUSION

An assessment of Riemann solver performance for DG-based under-resolved simulations at very high Reynolds numbers has been conducted through simulations of the inviscid Taylor-Green vortex problem. The main conclusion is that Riemann solvers that take into account the complete set of physical eigenvalues consistently via upwinding are expected to display a more accurate and robust behaviour for DG-based implicit LES over a wider range of Mach numbers.

References

[1] Moura R.C., Sherwin S.J., Peiró J.: Linear dispersion-diffusion analysis and its application to under-resolved turbulence simulations using discontinuous Galerkin spectral/hp methods. *J. Comput. Phys.* **298**: 695-710, 2015.

[2] Taylor G.I., Green A.E.: Mechanism of the production of small eddies from large ones. *Proc. R. Soc. Lon. (A)* **158 (895)**: 499-521, 1937.

[3] Shu C.W, Don W., Gottlieb D. *et al*.: Numerical convergence study of nearly incompressible, inviscid Taylor-Green vortex. *J. Sci. Comput.* **24 (1)**: 1-27, 2005.

[4] Brachet M.E., Meiron D., Orszag S. *et al*.: Small-scale structure of the Taylor-Green vortex. *J. Fluid Mech.* **130**: 411-452, 1983.

[5] Brachet M.E.: Direct simulation of three-dimensional turbulence in the Taylor-Green vortex. *Fluid Dyn. Res.* **8 (1)**: 1-8, 1991.

SUBGRID SCALE ANALYSIS OF TURBULENCE AFTER THE SHOCK-TURBULENCE INTERACTION

Daniel Livescu[1a)] and Zhaorui Li[2]
[1]*CCS-2, Los Alamos National Laboratory, Los Alamos, New Mexico, USA*
[2]*Department of Mechanical Engineering, Texas A&M University Corpus Christi, Texas, USA*

Summary Turbulence structure and statistics of the subgrid scales (SGS) in the context of Large Eddy Simulations (LES) are studied after the interaction with a shock wave. Recent high resolution shock-resolved Direct Numerical Simulations (DNS) [1] show that, when there is a large separation in scale between turbulence and the shock width, the interaction can be described by the Linear Interaction Approximation (LIA). By using LIA to alleviate the need to resolve the shock, DNS post-shock data can be generated at much higher Reynolds numbers than previously possible. Here, results with Re_λ ~180 are used to investigate the structure of post-shock turbulence. In particular, the interaction with the shock leads to a local axisymmetric flow state. In turn, this induces an M_s dependent symmetrization of the SGS dissipation PDF and a large increase in its variance. This corresponds to significant enhancement in size of the regions and magnitude of backscatter.

The interaction of shock waves with turbulence is an important aspect in many types of flows, from hypersonic flight, to supersonic combustion, to astrophysics and Inertial Confinement Fusion (ICF). In general, in practical applications, the shock width is much smaller than the turbulence scales, even at low shock Mach numbers, M_s, and it becomes comparable to the molecular mean free path at high M_s values. When there is a large-scale separation between the shock and turbulence, viscous effects become negligible during the interaction. If, in addition, the turbulent Mach number, M_t, of the upstream turbulence is small, the nonlinear effects can also be neglected during the interaction. In this case, the interaction can be treated analytically using the linearized Euler equations and Rankine-Hugoniot jump conditions. This is known as the Linear Interaction Approximation (LIA) [2]. However, due to the high cost of simulations for the parameter space close to practical applications and difficulties with accurate measurements close to the shock, previous studies have demonstrated only limited agreement with LIA. Recently, Ryu and Livescu [1], using high resolution fully resolved DNS extensively covering the parameter range, have shown that the DNS results converge to the LIA solutions as the ratio δ/η where δ is the shock width and η is the Kolmogorov microscale of the upstream turbulence, becomes small. The results reconcile a long time open question about the role of the LIA theory and establish LIA as a reliable prediction tool for low M_t turbulence-shock interaction problems. Furthermore, when there is a large separation in scale between the shock and the turbulence, the exact shock profile is no longer important for the interaction, so that LIA can be used to predict arbitrarily high M_s interaction problems, when the Navier-Stokes equations are no longer valid and fully resolved DNS are not feasible.

The shock-turbulence interaction has been traditionally studied in an open-ended domain, with the turbulence fed through the inlet plane encountering a stationary shock at some distance from the inlet. This approach is very expensive even when a shock-capturing scheme is used and limited to low Reynolds numbers. However, the range of the achievable Re values can be significantly increased if, instead, one uses the LIA theory to generate the post-shock fields. In order to generate full 3-D post-shock fields, Refs. [1,3] have extended the classical LIA formulas, which traditionally have been used to calculate second order moments only. Using this procedure, Refs. [1,3] have shown profound changes in the structure of post-shock turbulence, with significant potential implications on turbulence modelling.

High Re post-shock DNS data are generated by first performing triply periodic forced compressible isotropic turbulence (IT) simulations using the linear forcing method [4]. This forcing method has the advantage of specifying the Kolmogorov microscale and ratio of dilatational to solenoidal kinetic energies, χ, at the outset. Here, we present results from simulations with Re_λ~180, χ<0.01 (quasi-vortical turbulence) and M_t=0.05. The resulting turbulence fields are passed through the generalized LIA formulas [2,3] to obtain the post-shock turbulence data. In order to examine the properties of the subgrid scales, the post-shock data is filtered using a Gaussian filter.

The usual picture of an energy cascade typically holds in a statistically-averaged sense, it does not always describe the local behaviour of a turbulent flow. The turbulent dissipation is actually the difference between two energy fluxes, a "forwardscatter", corresponding to the classical energy cascade, and the "backscatter", a reversal of this process in which energy is transferred from the small scales back to the large scales. In LES approaches, the SGS backscatter acts as a source term in the kinetic energy equation and poses significant difficulties in maintaining stable computations [5]. Many of the simple SGS models do not account for backscatter and properly describing this phenomenon is an active area of research [5].

[a)] Corresponding author. Email: livescu@lan.gov.

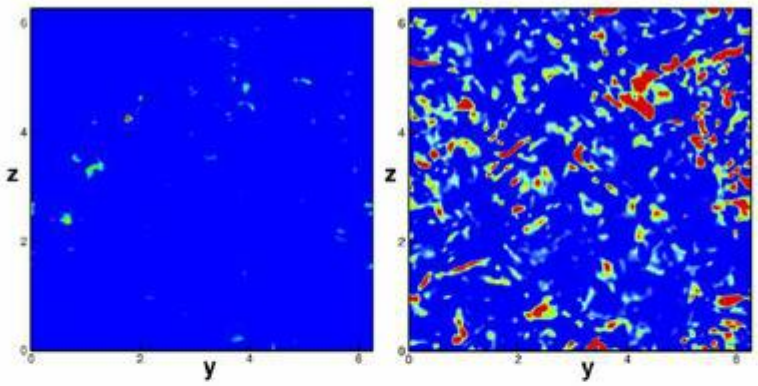

Figure1: Distribution and magnitude of backscatter in a) IT and b) after the interaction with a M_s=4 shock wave. Blue regions correspond to positive ε_{SGS}, while green to yellow to red denote regions with increasing magnitude of negative ε_{SGS}.

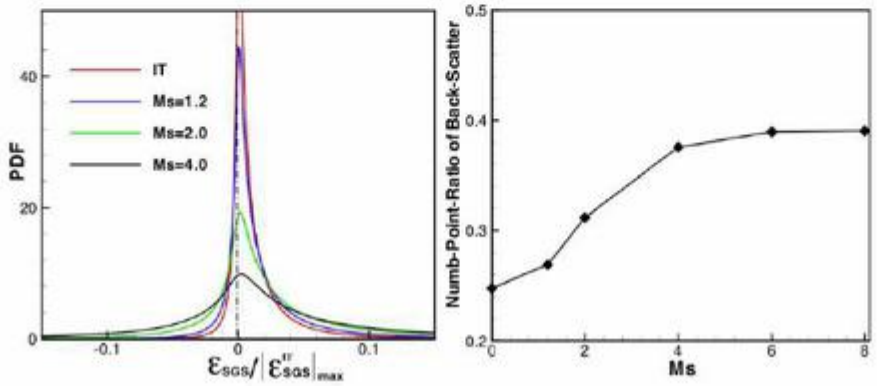

Figure 2: a) PDF of SGS dissipation (ε_{SGS}) for IT and post-shock turbulence. Negative values are associated with backscatter. b) Ratio of points with backscatter as a function of the shock Mach number.

The interaction with the shock wave preferentially amplifies the transverse components of the rotation and strain rate tensors together with an M_s dependent symmetrization of the PDF of the longitudinal derivative of the velocity components, consistent with a tendency towards a local axisymmetric state [1,3]. Thus, the strain rate tensor contribution to the subgrid dissipation is expected to become more symmetrical as M_s increases, resulting in a significant increase in regions with negative ε_{SGS} or backscatter. Indeed, Figure 1 compares the distribution of backscatter between IT (M_s=0) and after the interaction with an M_s=4 shock wave. In IT, fowardscatter dominates, but backscatter increases significantly after the interaction with the shock.

Figure 2a) compares the PDF of ε_{SGS} between IT and post-shock data at several M_s values. In IT, the regions with backscatter and the magnitude of the negative ε_{SGS} are limited and the PDF is strongly skewed towards positive values. However, post-shock turbulence exhibits a more symmetrical PDF and a strong increase in the variance at higher M_s values. This indicates that both the number of points with backscatter and the magnitude of backscatter increase, in an M_s dependent manner, after the interaction with the shock. The number of points with backscatter increases fast at small M_s values and seems to reach a plateau slightly below 40% of the total number of points at $M_s \approx 4$ (Figure 2b). These are profound changes in the structure of turbulence due to the interaction with the shock wave, which pose important challenges for subgrid modelling of this flow.

Acknowledgements: Los Alamos National Laboratory is operated by Los Alamos National Security, LLC for the US Department of Energy NNSA under Contract No. DE-AC52-06NA25396. Computational resources were provided by the LANL Institutional Computing (IC) Program and Sequoia Capability Computing Campaign.

References

[1] Ryu, J. Livescu, D.: Turbulence structure behind the shock in canonical shock-vortical turbulence interaction. J. Fluid Mech 756:R1, 2014.

[2] Mahesh, K., Lele, S.K., Moin, P.: The influence of entropy fluctuations on the interaction of turbulence with a shock wave. J. Fluid Mech 334:353-379, 1997.

[3] Livescu, D., Ryu J.: Vorticity dynamics after the shock-turbulence interaction. Shock Waves, http://dx.doi.org/10.1007/s00193-015-0580-5, 2015.

[4] Petersen, M.R., Livescu, D.: Forcing for statistically stationary compressible isotropic turbulence. Phys. Fluids, 22:116101, 2010.

[5] O'Brien, J., Urzay, J., Ihme, M., Moin, P., Saghafian, A.: Subgrid-scale backscatter in reacting and inert supersonic hydrogen-air turbulent mixing layers. J. Fluid Mech 743:554-584, 2014.

MULTISCALE MODELING USING A DYNAMIC KRIGING-BASED METAMODELLING TECHNIQUE

Oishik Sen[1,a], Nicholas J. Gaul[1], H.S. Udaykumar[1], K.K. Choi[1] & Gustaaf Jacobs[2]
[1]*Department of Mechanical Engineering, The University of Iowa, Iowa City, Iowa, USA*
[2]*Department of Aerospace Engineering, San Diego State University, San Diego, California, USA*

Summary This paper demonstrates the use of metamodeling techniques for bridging scales in a multiscale modelling framework. For the problem of the interaction of a shock wave with a cloud of particles, unknown source terms appear as momentum/energy exchange terms between the two phases in the momentum and energy equations of the respective phases in the macroscopic description of the system. In order to close the system of equations, resolved mesoscale numerical experiments are performed and the unknown momentum/energy exchange terms are explicitly computed using the Dynamic Kriging method (DKG). The metamodel may be used "on-the-fly" for computing the sources in a macroscale computation.

INTRODUCTION

The simulation of the interaction of shock waves with clouds of particles is a multiscale modelling problem. The macroscale model comprises a set of computational particles, each of which are agglomerates of real physical particles; the computational particles are modelled as points in the flow field and are coupled to the flow field via momentum and energy exchange terms which appear as source terms in the momentum and energy equations of the respective phases (for example consider the Particle Source in Cell Method [1]). The source terms are typically obtained from semi empirical experimental correlations [1]; these provide closure to the macroscopic model.

Because physical experiments are expensive and may be only conducted in a limited parameter space, an alternative to experimental correlations is to calculate the closure terms explicitly from resolved mesoscale computations. In this work, the authors demonstrate the use of metamodeling techniques to compute closure laws from numerical experiments. A metamodel, or a model of a model, is constructed from a set of resolved mesoscale computations and is shown to provide a numerical closure law as surrogates to semi-empirical models. Once the metamodel is constructed, instead of performing mesoscale computations "on-the fly" at every macroscopic time step, the metamodel may be evaluated for obtaining the closure terms in a macroscale computation at every instant of time. This method therefore also obviates performing a large number of mesoscale computations at each time instant of the macroscopic simulation as in typically done in a concurrent coupling multiscale modelling approach and therefore reduces the computational cost significantly.

In the next section, the mesoscale system is described and a procedure for constructing a metamodel for drag force using a Dynamic Kriging Method (DKG) [2] is explained. Following this, a metamodel for the momentum exchange term (i.e. the drag force on the particles) is presented as an example.

CONSTRUCTION OF METAMODELS FOR DRAG FORCE FROM MESOSCALE COMPUTATIONS

The mesoscale computational domain consists of cylinders embedded in a flow field as shown in Figure 1. The cylinders are modelled as rigid and static, while the surrounding flow field is assumed inviscid and are modelled by the unsteady compressible Euler equations. The system of equations are solved using a massively parallel in-house Eulerian flow code, SCIMITAR3D [3]. The drag on the immersed cylinders is computed by integrating the pressure on the cylinders. The average drag force is the mean drag of all the cylinders in the flow field; this mean drag force, F_D which is a function of Ma and φ is used for constructing a numerical drag law using the DKG method. The DKG method is essentially an interpolation technique, which constructs a metamodel from a given number of realizations of a numerical experiment. The convergence of the method and its suitability for metamodeling in a multiscale framework has been studied previously by the authors [4]; in the current work, the method is used to construct a drag law from a set of mesoscale computations performed using SCIMITAR3D.

In order to "train" the DKG method, numerical experiments are conducted. Each numerical experiment involves the computation of F_D for a given Ma and φ. The values of Ma and φ are varied over ranges of 1.1 to 3.5 and 5% to 20% respectively. Several such experiments are conducted and the DKG method is then used to construct a metamodel for F_D.

RESULTS AND DISCUSSIONS

Figure shows a numerical drag law constructed using the DKG method from mesoscale computations. For a given Ma, F_D increases with increasing φ. This is because the area of the cylinder increases with increasing φ and the pressure acts over larger area. Similarly for a given φ, Figure also shows that F_D increases with increasing Ma. This is because there is a higher pressure jump across the shock for a higher value of Ma; this increases the pressure difference along the cylinder and the

[a)] Corresponding author. Email: oishik-sen@uiowa.edu

pressure drag increases. The drag hypersurface may be probed at any point "on-the-fly" in course of macroscale computations to provide closure laws to macroscale systems.

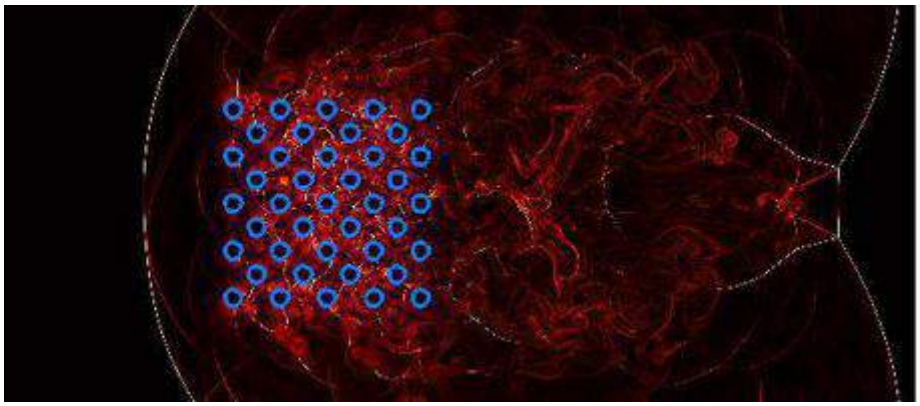

Figure 1. Description of the mesoscale computational experiment; the mesoscale experimental set up comprises 41 static cylinders each of radius, r, inscribed in a unit square. A right moving shock of strength, Ma impinges on the array of cylinders. The volume fraction, φ, of the array is given by $\varphi = 41\pi r^2$. The given plot shows the numerical Schlieren image for $Ma = 3.5$ and $\varphi = 20.6\%$.

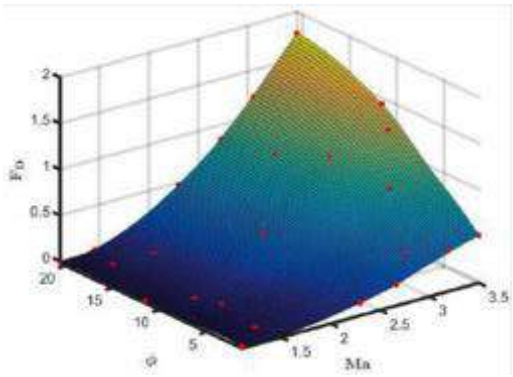

Figure 2. Metamodel of F_D as a function of Ma and φ computed from 24 mesoscale computations; the mesoscale computations are performed at the locations marked by the red dots in the parametric space.

CONCLUSIONS

The present work demonstrates the construction of numerical closure laws from mesoscale experiments using metamodeling techniques. In the macroscopic description of the interaction of shock waves with a cloud of particles, unknown terms appear as sources in the momentum and energy equations of the respective phases. Typically, semi-empirical experimental correlations are used to model the source terms to provide closure to the system. In the present work, the authors demonstrate the use of metamodels generated from resolved mesoscale computations as surrogates to semi-empirical closure laws. As an example, a numerical momentum-exchange (drag) law is constructed from mesoscale computations and is presented in the current work. This may be used in a macroscopic system to close the system of equations.

References

[1] G.B. Jacobs, W.S. Don, A high-order WENO-Z finite difference based particle-source-in-cell method for computation of particle-laden flows with shocks, J. Comput. Phys. 228 (2009) 1365–1379.

[2] H. Song, K.K. Choi, D. Lamb, A Study on Improving the Accuracy of Kriging Models by Using Correlation Model/Mean Structure Selection and Penalized Log-Likelihood Function, in: 10th World Conf. Struct. Multidiscip. Optim., 2013: pp. 1–10.

[3] A. Kapahi, J. Mousel, S. Sambasivan, H.S. Udaykumar, Parallel, sharp interface Eulerian approach to high-speed multi-material flows, Comput. Fluids. 83 (2013) 144–156.

[4] O. Sen, S. Davis, G. Jacobs, H.S. Udaykumar, Evaluation of convergence behavior of metamodeling techniques for bridging scales in multi-scale multimaterial simulation, J. Comput. Phys. 294 (2015) 585–604.

SHOCK STRUCTURE IN HYPERSONIC FLOWS

Samuel Paolucci*[1] and Christopher Paolucci[2]
[1]*Aerospace & Mechanical Engineering, University of Notre Dame, Notre Dame, Indiana, USA*
[2]*Chemical & Biomolecular Engineering, University of Notre Dame, Notre Dame, Indiana, USA*

Summary The structure of a gas-dynamic shock wave at hypersonic conditions is of great interest. The Navier–Stokes–Fourier formulation is known to yield incorrect shock profiles even at moderate Mach numbers. This is an excellent test problem for extensions of such equations for flows with large gradients since accurate experimental results are available. We present a second order formulation of the constitutive equations based solely on continuum theory. Results of the second-order theory applied to the shock structure are obtained for monatomic and diatomic gases over a large range of Mach numbers and are compared to experimental results.

INTRODUCTION

The shock wave structure [6] is important in the analysis of certain hypersonic flows. It is well-known that the Navier–Stokes–Fourier (NSF) equations do not represent the shock structure well [3], even at moderate Mach numbers, $M \geq 2$ [7]. As Fig. 1 shows, the equations predict values for shock thickness which are unrealistically small. Hence the shock structure has often been investigated both experimentally and theoretically to gain a better understanding of non-equilibrium flows.

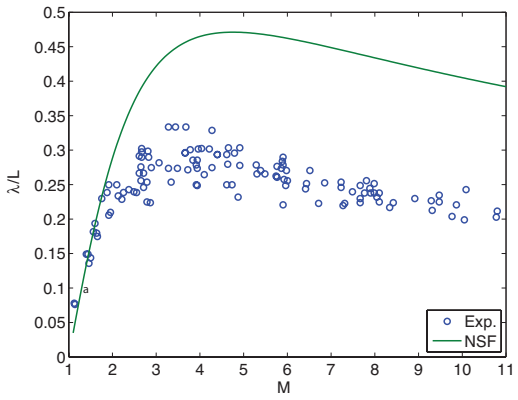

Figure 1: Experimental results [1] and NSF predictions of the reciprocal of shock thickness as a function of Mach number for Argon.

There have been many efforts to extend the theory, most of them based on perturbation expansions of the Boltzmann equation. A well-known expansion is the Chapman-Enskog expansion which yields the so-called Burnett equations [8, 9, 12, 10, 5, 7], where second order terms are retained. Grad's 13-moment theory [4] is based on an expansion based on moments. Such efforts have been largely unsuccessful for a variety of reasons. The exception has been Bird's Monte Carlo simulation [2] using a simple repulsive intermolecular force law. His results show very good agreement with Alsmeyer's experimental data [1] over a large Mach number range. Nevertheless, it is clear that Monte Carlo simulations are impractical in realistic engineering applications. We present a second order formulation of the governing constitutive equations based solely on a continuum formulation.

Results of the second-order equations applied to the shock structure are obtained for monatomic and diatomic gases over a large range of Mach numbers and are compared to experimental results.

METHODOLOGY AND RESULTS

The NSF equations represent a continuum theory based on linear relations between thermodynamic forces and fluxes. In a strong shock wave, the forces are large and the failure of the NSF equations can be attributed to deviations from the linear Newtonian and Fourier laws. Subsequently, the computation of the shock structure, particularly at the large Mach numbers encountered in hypersonic flows, has provided an excellent opportunity to find extended theories.

*Corresponding author. Email: paolucci@nd.edu

We begin by assuming that the constitutive quantities of Helmoholtz free energy, entropy, heat flux, entropy flux, and stress tensor are functions of the independent basic fields consisting of density, density gradient, stretch (or rate of strain) tensor, temperature, and temperature gradient. Subsequently, applying the principles of equipresence, frame-invariance, isotropy, and thermodynamic principles (including the 2nd law of thermodynamics), we arrive at the most general representations of the constitutive quantities of a fluid based on the 2nd order theory.

APPLICATION TO SHOCK WAVE

The general constitutive results of the second-order theory, in conjunction with the conservation equations for mass, linear momentum, and energy, are applied to the problem of the one-dimensional shock structure. The constitutive equations for the fluid, in addition to the known transport properties, also introduce one additional viscosity and two additional thermal conductivities which generally depend on density and temperature. In this case, the scalings used for the new thermophysical properties reflect Truesdell's dimensional invariance principle [11]. Results are obtained for monatomic and diatomic gases over a large range of Mach numbers and are compared to experimental results as shown in Fig. 2. More specifically, in addition to shock thickness, we also compare density and temperature distributions.

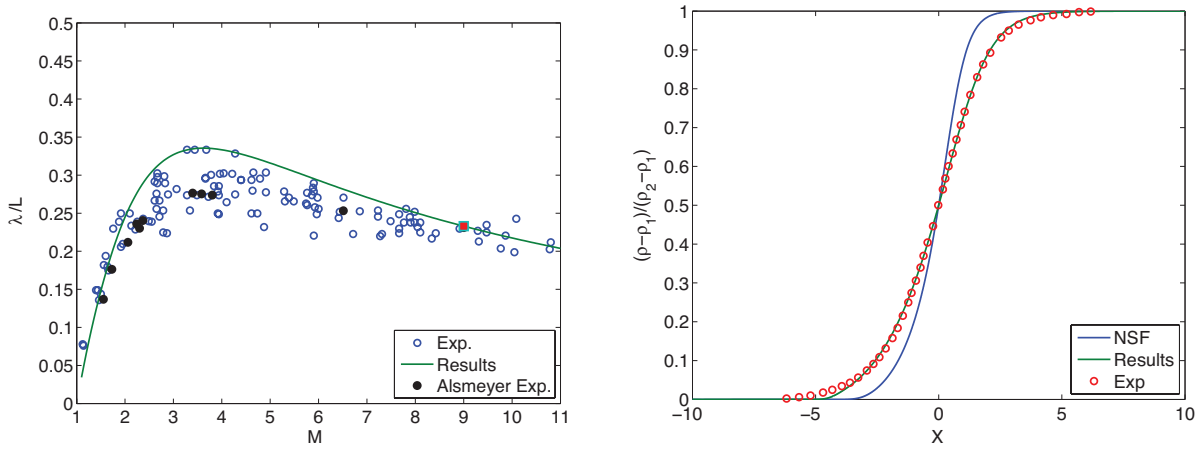

Figure 2: Experimental results and 2nd order theory predictions of the reciprocal of shock thickness as a function of Mach number and density distribution at $M = 9$ for Argon.

CONCLUSIONS

We derive general forms of constitutive equations based on 2nd order continuum theory. Such equations are generally valid and are essential for non-equilibrium flows where large gradients occur in the flow field, such as in hypersonic flows. Results of the second-order theory are applied to the solution of the shock structure at various Mach numbers where it is well-known that the NSF equations yield inaccurate results. Specific results for shock thickness, and density and temperature distributions for monatomic and diatomic gases are presented and compared with experimental data.

References

[1] Alsmeyer H.: Density Profiles in Argon and Nitrogen Shock Waves Measured by the Absorption of an Electron Beam. J. Fluid Mech. 74:497-513, 1976.

[2] Bird G.A.: Aspects of the Structure of Strong Shock Waves. Phys. Fluids 13:1172-1177, 1970.

[3] Gilbarg D., Paolucci D.: The Structure of Shock Waves in the Continuum Theory of Fluids. J. Rat. Mech. Anal. 2:617-642, 1953.

[4] Grad H.: On the Kinetic Theory of Rarefied Gases. Comm. Pure Appl. Math. 2:331-407, 1949.

[5] Grad H.: The Profile of a Steady Plane Shock Wave. Comm. Pure Appl. Math. 5:257-300, 1952.

[6] Landau L.D., Lifshitz E.M.: Fluid Mechanics. Course of Theoretical Physics, Vol. 6, Pergamon Press, Oxford, UK, 1959.

[7] Liepmann H.W., Narasimha R., Chahine M.T.: Structure of a Plane Shock Layer. Phys. Fluids 5:1313-1324, 1962.

[8] Lumpkin III F.E., Chapman D.R.: Accuracy of the Burnett Equations for Hypersonic Real Gas Flows. J. Thermophys. Heat Transfer 6:419-425, 1992.

[9] Reese J.M., Woods L.C., Thivet F.J.P., Candel S.M.: A Second-order Description of Shock Structure. J. Comp. Phys. 117:240-250, 1995.

[10] Thomas L.H.: Note on Becker's Theory of the Shock Front. J. Chem. Phys. 12:449-453, 1944.

[11] Truesdell C., Noll W.: Non-linear Field Theories of Mechanics. Handbuch der Physik, 3rd Edition, Ed. Antman, S., Springer-Verlag, 2004.

[12] Woods L.C.: An Introduction to the Kinetic Theory of Gases and Magnetoplasmas. Oxford University Press, Oxford, UK, 1993.

COMPRESSIBLE MULTIMATERIAL FLOWS

Alexia de Brauer[1], Angelo Iollo*[2], and Thomas Milcent[3]

[1]*University of Iowa, IIHR, Iowa City, Iowa 52242-1585, USA*
[2]*University of Bordeaux, IMB, UMR CNRS 5251; INRIA Memphis Team, F-33400 Talence, France*
[3]*University of Bordeaux, I2M, UMR CNRS 5295; Arts et Métiers Paristech, F-33600 Pessac, France*

Summary We simulate flow phenomena that involve both fluids and elasto-plastic solids. The numerical model is the same for all materials and can handle high-speed flows, large deformations, frictionless contacts and plasticity. Hyperbolicity of the hyperelastic neohookean model is granted thanks to an explicit computation of the characteristic speeds. The plastic model satisfies a classic entropy inequality and we prove that it leads to a decrease in norm of the stress deviator tensor. Numerical illustrations of the method include air-helium, water-air shock interactions in three dimensions. A supersonic projectile-shield impact beyond the yield limit is presented.

EULERIAN MODEL

This model was introduced in the literature thanks to several authors [4, 8, 7, 2, 3]. We follow here the formulation presented in [5] and extend it to plasticity modelling. The equations of mass, momentum, deformation and energy conservation are given by

$$\begin{cases} \partial_t \rho + \mathrm{div}_x(\rho u) = 0 \\ \partial_t(\rho u) + \mathrm{div}_x(\rho u \otimes u \circ \sigma) = 0 \\ \partial_t(\nabla_x Y) + \nabla_x(u \cdot \nabla_x Y) = 0 \\ (\rho e)_t + \mathrm{div}_x(\rho e u \circ \sigma^T u) = 0 \end{cases} \tag{1}$$

The physical variables are the density $\rho(x,t)$, the velocity $u(x,t)$, the total energy per unit mass $e(x,t)$ and the Cauchy stress tensor $\sigma(x,t)$. Here $Y(x,t)$ are the backward characteristics that for a time t and a point x in the deformed configuration, give the corresponding initial point.

We assume that the internal energy per unit mass $\varepsilon = e \circ \frac{1}{2}|u|^2$ is the sum of a term accounting for volumic deformation that depends on ρ and entropy s, and a term accounting for isochoric deformation depending on the modified left Cauchy-Green tensor $\overline{B}$ given by $\overline{B}(x,t) = [\nabla_x Y]^{-1}[\nabla_x Y]^{-T}/J^{\frac{2}{3}}(x,t)$, $J(x,t) = \det([\nabla_x Y])^{-1}$. A general constitutive law that models gas, fluids and elastic solids is given by

$$\varepsilon(\rho, s, \nabla_x Y) = \frac{\kappa(s)\rho^{\gamma-1}}{\gamma \circ 1} + \frac{p_\infty}{\rho} + \frac{\chi}{\rho_0}(\mathrm{Tr}(\overline{B}) \circ 3) \tag{2}$$

where the first term accounts for a perfect gas, the second for a stiffened gas (e.g. water) and the third for a neohookean elastic solid. According to the formula $\sigma = \rho \frac{\partial \varepsilon}{\partial F} F^T$, where $F = [\nabla_x Y]^{-1}$, we obtain the stress tensor from the constitutive law. Here $\kappa(s) = \exp(s/c_v)$ and $c_v, \gamma, p_\infty, \chi$ are positive constants that characterize a given material.

The characteristic speeds of this quasi-linear model are $\Lambda = \left\{u_1, u_1, u_1 \pm \sqrt{\frac{\alpha_1}{\rho}}, u_1 \pm \sqrt{\frac{\alpha_2}{\rho}}, u_1 \pm \sqrt{\frac{\alpha_3}{\rho}}\right\}$, where α_1, α_2 and α_3 are the roots of a given third order polynomial. It can be shown that the necessary conditions for hyperbolicity, i.e., $\alpha_1 > 0, \alpha_2 > 0$ and $\alpha_3 > 0$, are actually satisfied for the neohookean model considered.

Plasticity describes the deformation of a material undergoing non-reversible changes of shape in response to applied forces. The deformation is the composition of a plastic and an elastic deformation [6]. Introducing the backward characteristics for elastic and plastic deformations denoted by Y^e and Y^p and taking the gradient of the relation $Y(x,t) = Y^p(Y^e(x,t),t)$, we get $[\nabla_x Y] = [\nabla_x Y^p][\nabla_x Y^e]$ and the total deformation gradient F is given by $F := [\nabla_x Y]^{-1} = [\nabla_x Y^e]^{-1}[\nabla_x Y^p]^{-1} := F^e F^p$. Let us define the deviatoric part of the stress tensor $\mathrm{dev}(\sigma) = \sigma \circ \frac{\mathrm{Tr}(\sigma)}{3} I$. Experimentally plasticity occurs when the stress exceeds a critical value. The yield function of von Misses $f_{VM}(\sigma) = |\mathrm{dev}(\sigma)|^2 \circ \frac{2}{3}(\sigma_y)^2$ defines a yield surface $f_{VM}(\sigma) = 0$ where σ_y is the plastic yield limit. We restrict ourselves to the case of perfect plasticity where σ_y is a constant.

The Eulerian form of the evolution equation for the plastic deformation tensor F^p writes $\partial_t(F^p) + u \cdot \nabla_x F^p = L^p F^p$ where L^p is the constitutive law which defines the plastic deformation rate. From the deformation tensor equation we have that $[\nabla Y^e] = [F^e]^{-1} = F^p F^{-1}$ verifies $\partial_t(\nabla Y^e) + \nabla_x(u \cdot \nabla Y^e) = L^p[\nabla Y^e]$. A constitutive law for plasticity [7, 1] is defined by $L^p = \frac{1}{\chi\tau}[\nabla Y^e]\mathrm{dev}(\sigma)[\nabla Y^e]^{-1}$, where χ is the shear modulus and τ is relaxation time of the plastic process. Finally, the conservation equations with plasticity are the same except for the deformation equation that is now

$$\partial_t(\nabla_x Y^e) + \nabla_x(u \cdot \nabla_x Y^e) = \frac{1}{\chi\tau}[\nabla_x Y^e]\mathrm{dev}(\sigma) \tag{3}$$

*Corresponding author. Email: angelo.iollo@inria.fr

Beyond yield, plasticity appears as a source term in the equation of deformations and can be seen as a penalization of the deviatoric part of σ. The internal energy depends only on elastic deformations $\varepsilon = \varepsilon(F^e, s)$ and hence the stress tensor is given by $\sigma = \rho \frac{\partial \varepsilon}{\partial F^e}[F^e]^T$. When plasticity occurs, entropy is increasing according to $\rho \frac{\partial \varepsilon}{\partial s}(\partial_t s + u \cdot \nabla s) = \frac{1}{\chi^\tau}|\mathrm{dev}(\sigma)|^2 \geq 0$. Also, we can prove that the plasticity model is such that $\partial_t(|\mathrm{dev}(\sigma)|^2) \leq 0$ beyond the plasticity limit.

A NUMERICAL ILLUSTRATION

We have extended the scheme described in [5] to model elasto-plastic flows. The scheme is based on a sharp-interface locally non-conservative approximate Riemann solver that has been validated in 2D and 3D. Here we show a 2D test case where an iron circular projectile is impacting onto an aluminium flat plate fixed to the upper and lower boundaries of the computational domain. The initial horizontal velocity of the iron projectile is $1000m.s^{-1}$. The physical parameters for the different materials are found in the literature and the computational domain is $[-0.3, 0.7] \times [-0.4, 0.4]$m. The computation is performed on a 2000×1600 mesh with 144 processors. Homogeneous Neumann conditions are imposed on the left and right borders and embedded on the top and bottom.

The results are presented in Fig. 1 with a Schlieren image (bottom) and the von Mises criteria $|\mathrm{dev}(\sigma)|^2 - \frac{2}{3}(\sigma_y)^2$ (top) at a time step corresponding to an highly deformed plastified state. A longitudinal wave propagating in the plate is followed by a shear wave that causes the plasticity of the material. We can observe that the plate, initially stright, is strongly deformed and forms a long filament; the projectile, initially round, is considerably flattened. Shock waves and contact discontinuities charcterise the air flow.

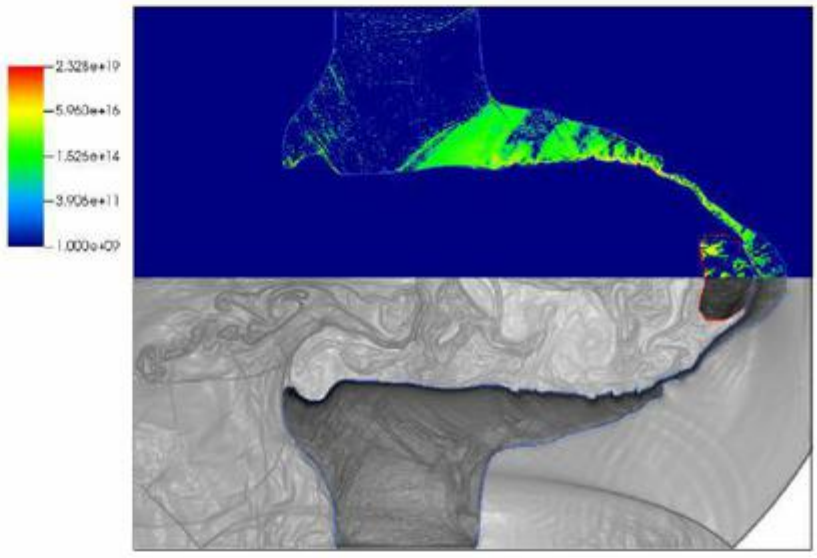

Figure 1: Iron round projectile on an aluminium shield in air. Schlieren image and von Mises criterium at $t = 1.04$ms

In the proposed presentation we plan to discuss how these numerical tools can improve the study of new and surprising phenomena that are unattainable by traditional theoretical approaches and hazardous and expensive to investigate in a laboratory.

References

[1] P.T. Barton, R. Deiterding, D. Meiron, and D. Pullin. Eulerian adaptive finite-difference method for high-velocity impact and penetration problems. Journal of Computational Physics, 240(C):76–99, 2013.

[2] G.H. Cottet, E. Maitre, and T. Milcent. Eulerian formulation and level set models for incompressible fluid-structure interaction. ESAIM: Mathematical Modelling and Numerical Analysis, 42:471–492, 2008.

[3] N. Favrie, S.L. Gavrilyuk, and R. Saurel. Solid-fluid diffuse interface model in cases of extreme deformations. Journal of Computational Physics, 228(16):6037–6077, 2009.

[4] S.K. Godunov. Elements of continuum mechanics. Nauka Moscow, 1978.

[5] Y. Gorsse, A. Iollo, T. Milcent, and H. Telib. A simple cartesian scheme for compressible multimaterials. Journal of Computational Physics, 272:772–798, 2014.

[6] E.H. Lee and D.T. Liu. Finite-strain elastic-plastic theory with application to plane-wave analysis. Journal of Applied Physics, 38(1):19–27, 1967.

[7] G.H. Miller and P. Colella. A high-order eulerian godunov method for elasticplastic flow in solids. Journal of Computational Physics, 167(1):131–176, 2001.

[8] B.J. Plohr and D.H. Sharp. A conservative eulerian formulation of the equations for elastic flow. Advances in Applied Mathematics, 9:481–499, 1988.

TRANSONIC AIRFOIL BUFFET: A DECADE OF RESEARCH AT ONERA

Vincent Brion[1], Julien Dandois[2], Sébastien Deck[2], Laurent Jacquin[3],
Pascal Molton[1], Fulvio Sartor[2] & Denis Sipp[1]

[1] *ONERA-Fundamental / Experimental Aerodynamics Dept, Meudon, France*
[2]*ONERA-Applied Aerodynamics Dept, Meudon, France*
[3]*ONERA- Fluid Mechanics & Energetics Scientific Direction, Palaiseau, France*

Summary The lecture will review the results obtained on the transonic buffet at ONERA during the past ten years by theoretical, numerical and experimental means.

Airfoil buffet is one of the most important compressibility-based problems which limit the performance of transonic and supersonic vehicles. Buffet may develop in all flow regions where shock waves are present (i.e. on airframe lifting surfaces and on rotating blades) and is a major factor limiting load capacity and efficiency of cruising civil aircrafts. Buffet control, which could enlarge flight envelopes and lead to significant energy savings, is a major goal to accomplish. Important efforts in applied and fundamental research need to be done in the future to get to this point. Relevant domains are flow stability, unsteady CFD and experiments in transonic/supersonic facilities.

We present a synthesis of the research conducted on this subject in the Fluid Mechanics and Energetics branch of ONERA over more than a decade. Experiments were conducted on two types of geometries: 2D airfoils (Jacquin et al., 2005, 2009) and swept wings (Molton et al., 2013). 2D airfoil buffet may be considered as rather academic regarding applications. However, the 2D case has revealed that the buffet mechanism coincides with the onset of a global flow instability controlled by the free stream Mach number and the angle of attack (Crouch et al., 2007). This is proved by using a combination of the stability theory based on perturbing a steady flow field obtained from the Reynolds averaged Navier-Stokes equations, see figure 1. The global mode obtained in this way mixes high frequency Kelvin-Helmholtz-type oscillations located in the separated viscous flow region downstream of the shock and low frequency oscillations of the Euler flow. The theory and experiment show good agreement for the 2D buffet onset conditions, including the critical angle of attack and the buffet-onset frequency. While 2D global stability is not sufficient to understand the nature of the mechanism, it paves the way to closed loop control strategies (Sartor et al., 2015).

In the case of 3D airfoils, experiments show that the buffet develops in a restricted region on the wing. Global stability of such 3D flows are envisaged but are not yet feasible due to the limitation of current method in terms of memory requirements. Experiments show that 2D and 3D buffets can be delayed using an open loop control based on mechanical or fluid actuators (Molton et al., 2013). Now, nearly 2D (i.e. low swept angle) wings come to the forefront when laminar transonic regimes are considered, that is when cross flow transition must be avoided as it is the case for several advanced high speed aircraft projects. Recent investigations of the laminar buffet on a 2D airfoil have been conducted at ONERA in the framework of a European-Russian project. They reveal that the 2D buffet is strongly sensitive to the incoming boundary layer state: in the case where the boundary layer is laminar, buffet is weaker and the onset frequencies are moved to larger values, see figure 2. Global stability analysis of this flow is under way and its full simulation by a LES (Large Eddy Simulation) approach becomes tractable thanks to the laminar nature of the boundary layer upstream of the shock, even if this will still require the use of the largest available computing capacities.

Overall, the talk will illustrate how challenging the understanding of the buffet physics remains.

[a)] Corresponding author. Email: laurent.jacquin @onera.fr

(a) (b)

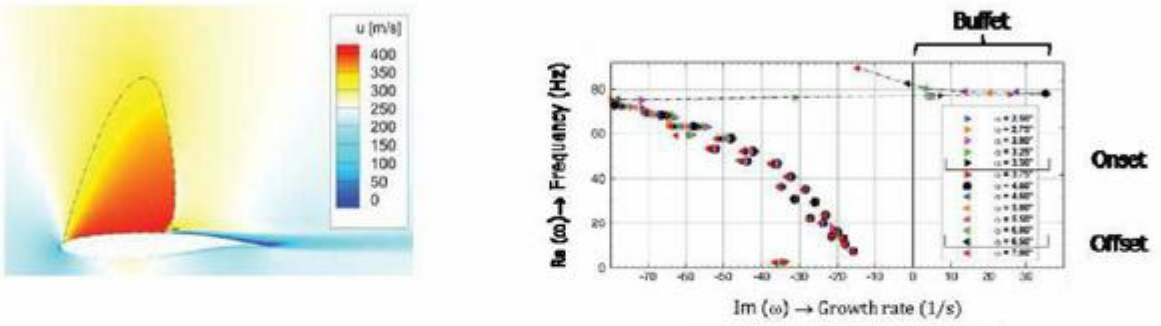

Figure 1 - Buffet onset on a turbulent profile at $M = 0.735$ in turbulent conditions: (a) base flow horizontal velocity field with RANS solution for an angle of attack $\alpha = 3.5°$, (b) eigenvalue spectra for various angles of attack and $M = 0.73$ (Sartor et al., 2015).

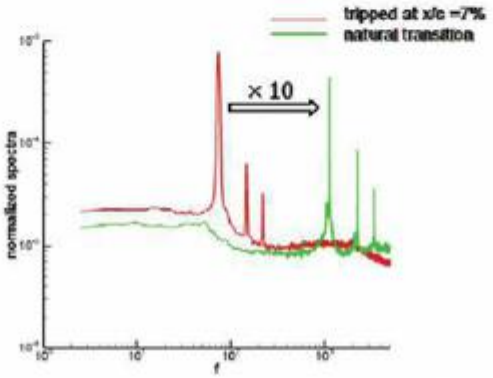

Figure 2 - Laminar / turbulent profile at $M = 0.735$, $\alpha =$ °: trailing edge pressure spectra with tripped (turbulent regime) and untripped (laminar regime) boundary layer.

References

[1] Jacquin, L., Molton, S., Deck, S., Maury, B. and Soulevant, Experimental study of shock oscillation over a transonic supercritical profile. AIAA Paper 2005-4902 (2005) and AIAA Journal (2009)

[2] Crouch, J.D., Garbaruk, A. and Magidov, D., Predicting the onset of flow unsteadiness based on global instability. J. Comput. Phys. (2007)

[3] Molton P., Dandois J., Lepage A., Brunet V. & Bur R., Control of Buffet Phenomenon on a Transonic Swept Wing, AIAA J. (2013)

[4] Sartor F., Mettot C. & Sipp D., Stability, Receptivity, and Sensitivity Analyses of BuffetingTransonic Flow over a Profile, AIAA J. (2015)

[5] Dandois J., Experimental study of transonic buffet phenomenon on a 3D swept wing, Physics of Fluids (2016)

EXPERIMENT ON NONLINER GROWTH OF SUPERSONIC MIXING LAYERS

Wang Tiejin[1], Shi Xiaotian[2,a)], Zhang Guiru1[2]
[1] *China Aerospace Academy of Aerodynamics, P.O.Box 7215, Beijing, China*
[2] *China Aerospace Academy of Aerodynamics, P.O.Box 7201, Beijing, China*

Summary It is known that large scale structures play important role in the growth of supersonic mixing layer, and a great deal of experimental works focused on the characteristics and functions of large scale structure in the past, unfortunately, little experiments have been conducted on the spatial evolution of these structures up to now, which may be helpful to solve the issues of growth rate. In the present study, the evolution of large scale structures of the planar supersonic mixing layer at convective Mach numbers of 0.25, 0.5 and 0.7, respectively formed by the streams with the responding Mach number combination of 2.0 & 1.5, 3.0 & 2.0 and 2.0 & 0.6, is visualized using a planar laser Mie scattering (PLMS) technique. The instantaneous images at convective Mach number of 0.25 are respectively obtained by seeding ethanol vapor as a marker in one stream in each experiment, and those at convective Mach numbers of 0.5 and 0.7 were obtained by seeding the ethanol vapor in the stream of Mach number 2.0. The results show that the spatial evolution of large scale structures is comprised primarily of three parts, which is in some degree consistent with the structural investigations of linear stability theory. The different growth rates of large scale structure in the three parts suggest that only one coefficient used as previous investigations is not enough to represent the growth rate of supersonic mixing layer. Specific issues regarding the description of growth rate are discussed in detail.

INTRODUCTION

The growth rate has been extensively studied for both supersonic mixing layer and subsonic mixing layer. In 1974, Brown and Roshko[1] found large scale structures in the experiments of subsonic mixing layer, and according to the feature of spatial evolution of the large scale structure, chose one coefficient to describe the growth rate of subsonic mixing layer, then deduced the equation of variance of growth rate. In 1980s, Papamoschou and Roshko[2] also found the large scale structure in the schlieren results of supersonic mixing layer experiment. Since then, great efforts[3] [4] [5]were taken to try to obtain a result of the growth rate of supersonic mixing layer similar to that of subsonic mixing layer. But, until now, there still exist some inconsistence on the variance of growth rate[6]. It is now known that large scale structures play very important role in the growth of supersonic mixing layer, and a great deal of experimental works focused on the characteristics and functions of large scale structure in the past, but a little has been conducted on the spatial evolution of these structures up to now, which may be helpful to solve the issues of growth rate.
In the present study, the evolution of large scale structures of the planar supersonic mixing layer at convective Mach numbers of 0.25, 0.5 and 0.7 will be visualized and the spatial evolution features of the structures will be discussed in details.

Experimental facility and techniques

The experimental facility is a blow-down type, two-stream, supersonic mixing wind tunnel, which is combined with a hypersonic wind tunnel by replacing its nozzle section. The overall gas flow schematic and the wind tunnel schematic are shown in Fig. 1and Fig. 2. The Mach of both streams can be supersonic or subsonic, and the maximum Mach number can reach 4.0 with run time of more than 10 minutes. For the present studies, three Mach number combinations were tested, and the Mach number of upper stream is bigger than that of lower stream.

A Cartesian coordinate system with its origin at mid-span of the tip of the nozzle plate defines the streamwise direction x, the transverse direction y and the spanwise direction z. The test section is 360×30×55mm in the streamwise (x), the transverse (y) and the spanwise (z) directions, respectively. The height for both streams at the tip of the nozzle plate is 15mm, and the thickness of the tip is 0.2mm. The flow path of the two streams is almost symmetric in structure with the same height of 80mm for perforated plate and the sections of honeycomb and nets. Optical windows on the top of the test section provides the path for the laser sheet shining from outside. The upper and lower test section walls are adjustable and allow for the setting of the streamwise pressure gradient; the upper wall of test section is converged about 0.3 degree in order to obtain constant streamwise pressure in the present study. During the run of the facility, two streams come from two air sources with total pressure values of 10.0MPa and 2.0MPa, respectively, after the regulating valves, the pressure of both streams reach the values needed for corresponding Much numbers, then passing through perforated plate and the sections of honeycomb and nets, the two streams are regulated in flow quality, and meets at the tip of nozzle plate after passing the nozzles of themselves, thus a supersonic mixing layer is formed. The specific conditions for the present study are given in Table 1.

Table 1 flow parameters of the three convective Mach numbers

Mc	0.25		0. 5		0.7	
M1,M2	2.0	1.5	3.0	2.0	2.0	0.6
T1,T2 (K)	143.3	199.3	106.43	165.56	165.56	277.99

a)Corresponding author. Email: xxtshi@163.com.

a1,a2 (m/s)	283.0	290.0	207.51	258.8	258.8	335.37
U1,U2 (m/s)	480.0	424.5	622.53	517.62	517.62	201.22
r= U2/U1	0.884		0.83		0.39	

Experimental results and discussions

The typical images at Mc=0.5, 0.7 are shown in Fig.1 and Fig.2. I t can be seen from Fig. 8 and Fig.9 that the structures in the mixing layers at Mc=0.5, 0.7 differ in scale, incline angle, number of feature structures and size increase along the streamwise direction, but both these structures have the same evolution course in the supersonic mixing layer, namely, a nonlinear evolution course of large scale structure.

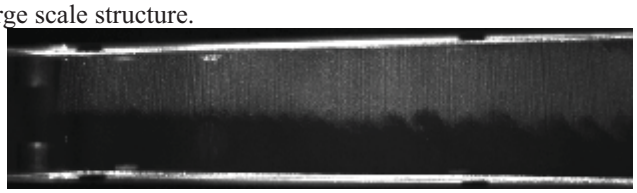

Fig. 8 Mie scattering image at Mc=0.5

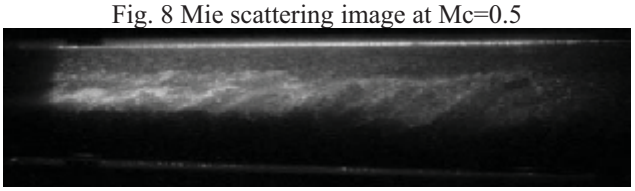

Fig. 9 Mie scattering image at Mc=0.7

The above Mie scattering images also show that with the increase of convective Mach number, the evolution course of the supersonic mixing layer become shorter, and the number of feature structures decreases.

On the basis of the height of the structures in the three sections in the stream of Ma=1.5, three fitting curves with different slopes, shown in Fig.3 are obtained for describing the growth course of the large scale structure, which, on the point of view of structure, can be used represents the growth course of the supersonic mixing layer, just as that of subsonic mixing layer.

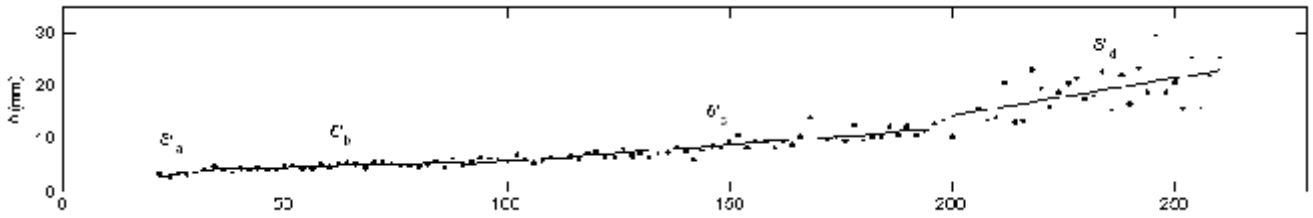

Fig.3 Fitting curves of the structures in the three sections

CONCLUSIONS

The large scale structure of the supersonic mixing layer is found to evaluate through three sections: the first section with no apparent structure growth, the second section featured by structure nonlinear growth such as breaking -up, coupling and so on, and the third section of the structure which can be seen in the schlieren image. Three fitting curves with different slopes corresponding the three sections are obtained for describing the growth course of the large scale structure. These results are helpful to understand that only one coefficient may be not enough to describe the growth rate of the supersonic mixing layer completely.

References

[1] Brown, G.L., and A. Roshko," On Density Effects and Large structure in Turbulent Mixing Layers", Journal of Fluid Mechanics Vol. 64, 1974, pp. 775-816.
[2] Papamoschou, D., and A. Roshko," The compressible turbulent shear layer: An experimental study", Journal of Fluid Mechanics Vol. 197, 1988, pp. 453-477.
[3] Bogdanoff, D.W.," Compressibility effects in turbulent shear layers", AIAA J. Vol. 21, 1983, pp. 926.
[4] Smits, A., and J.P. Dussage, Turbulent Shear Layers in Supersonic Flow, New York: Springer Verlag, 1996.
[5] Clemens, N.T., and M.G. Mungal," Two- and three-dimensional effects in the supersonic mixing layer", AIAA Journal Vol. 30, 1992, pp. 973-981
[6] Clemens, N.T., and M.G. Mungal," Journal of Fluid Mechanics Vol. 284, 1995, pp. 171-216.

SHEDDING INTERMITTENCY IN A SHOCK WAVE-LAMINAR BOUNDARY LAYER INTERACTION

Guillaume Fournier*[1], Amer Chpoun[1], and Christian Tenaud[2]
[1]*Laboratoire de Mécanique et d'Energétique d'Evry, Université d'Evry-Val-d'Essonne, Evry, France*
[2]*LIMSI-CNRS, Orsay, France*

Summary The interaction between an oblique shock wave and a laminar boundary layer has been studied using Direct Numerical Simulations at $M = 2.25$ for a shock angle $\beta = 33.1°$. For these shock conditions, the boundary separates and forms a large recirculation bubble. Unlike in the turbulent case, the vortices created in the shear layer are found not to be uniformly distributed along the spanwise direction because of a strong shedding intermittency.

INTRODUCTION

In the aeronautical and aerospace industries, the flow configurations where an incident oblique shock wave impinges upon a boundary layer are very common. Under certain circumstances (High Mach number, large shock angle…), the interaction between the incident shock wave and the boundary layer may create an unsteady separation bubble. This bubble, as well as the subsequent reflected shock, are known to oscillate in a low-frequency streamwise motion that can spread over several tenth of the boundary layer thickness [6]. The origin of those oscillations, however still unclear, has been related either to the shedding of vortices in the mixing layer downstream of the separation [1], or to the turbulent structures in the incoming boundary layer [3]. Most of the previous studies however dealt with turbulent boundary layers and only a very few of them considered the laminar case [5]. A campaign of Direct Numerical Simulations has then been performed for laminar boundary layers, in which no incoming structures are encountered. The aim of this study is to reduce the possible causes of unsteadiness to the sole vortex shedding, and see if the streamwise motion still appears.

NUMERICAL METHODS

The simulations have been performed using an in-house parallel (MPI) Finite-Volume based DNS/LES solver developed at LIMSI-CNRS [7]. A Monotonicity-Preserving shock-capturing scheme, based on the Lax- Wendroff method through a 7th order accurate coupled space and time approximation is used for the convective fluxes. The diffusive fluxes are discretized by a second order centered scheme. The freestream and shock conditions ($M = 2.25$ and $\beta = 33.1°$) have been chosen to be identical to those of Pirozzoli and Grasso [4]. The incoming boundary layer is created using a 4th order polynomial interpolation of the Blasius profile. The computational domain is discretised using $M = 840 \times 100 \times 128$ cells and extents over $D = 300\delta_0 \times 30\delta_0 \times 30\delta_0$. The subsequent resolutions in wall units are $\Delta x^+ = \Delta y^+ = 15$ in the streamwise and spanwise directions respectively. In the wall-normal direction, a 3% geometrical stretching is applied so that the first cell is located at $\Delta z^+_{wall} = 1$ and 35 points are located in the inlet boundary layer.

RESULTS

The vortical structures obtained by the DNS are represented in Fig. 1. As expected, under the influence of the oblique shock wave, the laminar boundary layer separates and creates a large separation bubble. It then undergoes transition towards turbulence in the shear layer just upstream of the reattachement point and relaxes to a fully turbulent state a few boundary layer thicknesses further. The very first simulations showed that the separation bubble is subjected to a streamwise motion even with no vortical structures in the incoming boundary layer [2]. This result tends to prove that this motion is mainly due to the vortex shedding occuring in the shear layer. On the other hand, the separation bubble has been found to only move upstream and not oscillate around an equilibrium position. One of the most interesting results concerns the vortical shedding in the shear layer. Unlike in its turbulent counterpart, where vortices are uniformly created along the spanwise direction, the laminar case paradoxically exhibits a very irregular shedding pattern. Coherent structures from two differents timesteps are represented in Figure 2. On the right-hand side, the shedding is uniform over the spanwise direction. On the other hand, the leftmost side of the figure shows the presence of a vortex-free region, in which the shedding no longer occurs, that will eventually be convected downstream. This region, which origin is still unknown, is of critical importance since it is responsible for the occurence of a very low-frequency peak on the power spectrum. A thorough investigation is currently in progress in order to find the physical explanation to that shedding intermittency.

*Corresponding author. Email: guillaume.fournier@ufrst.univ-evry.fr

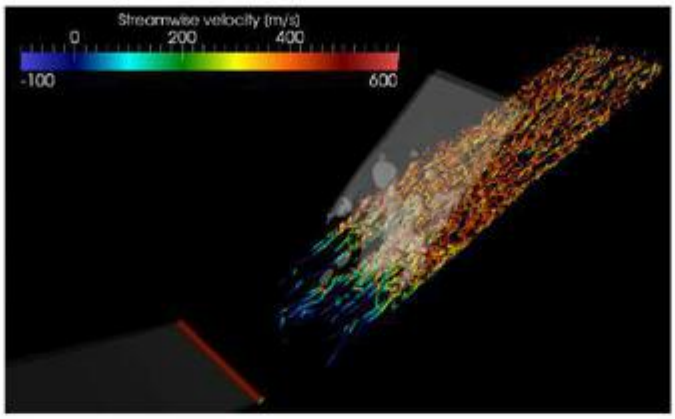

Figure 1: Vortical structures in the interaction region, represented by Q criterion isosurfaces and coloured with the streamwise velocity. The shock system (translucent gray) is made visible by isosurfaces of the divergence of the velocity.

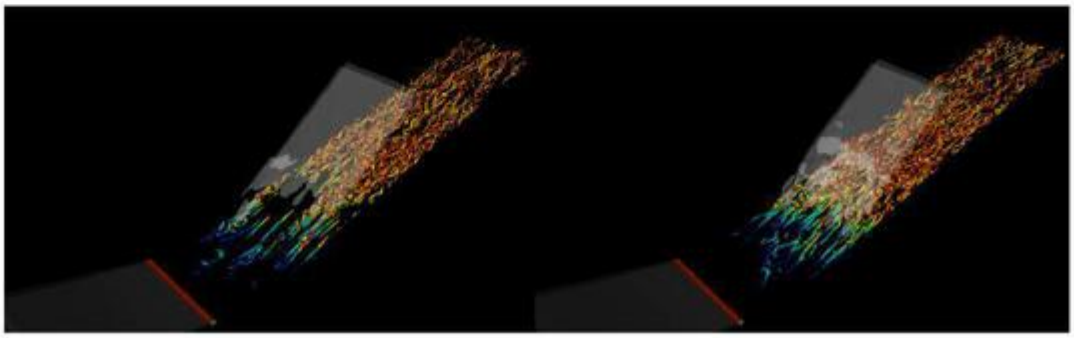

Figure 2: Isosurfaces of the Q-criterion at two differents time steps.

CONCLUSIONS

Direct Numerical Simulations have been performed for the interaction between an oblique shock wave and a laminar boundary layer developing along a flat plate. The aim of this study is to conclude with respect to the possible causes of the streamwise motion of both the recirculation bubble and the reflected shock. Previous studies linked those oscillations to either the turbulent structures in the incoming boundary layer or the vortex shedding in the shear layer. By considering a laminar boundary layer, the turbulent structures have been suppressed. It has been shown however that even if no oscillations have yet been found, the recirculation bubble is moving upstream, indicating that this motion is more likely due to the vortex shedding. Finally, a strong intermittency of the shedding has been evidenced, leading to the presence, in the flow, of large vortex-free regions responsible for very low-frequency phenomena.

References

[1] Aubard, G., and Gloerfelt, X. and Robinet, J.-C.: Large-Eddy Simulation of Broadband Unsteadiness in a Shock/Boundary-Layer Interaction. *AIAA Journal*, **51** (2013).

[2] Fournier, G., and Sellam, M., and Chpoun, A. and Fraigneau, Y. and Tenaud, C. : Direct Numerical Simulations of the Interaction between an Oblique Shock Wave and a Boundary Layer Developing Along a Flat Plate. *Proceedings of the 30th International Symposium on Shock Waves*, Tel-Aviv, Israel (2015)

[3] Ganapathisubramani, B. and Clemens, N. T. and Dolling, D. S.: Effects of Upstream Boundary Layer on the Unsteadiness of Shock-Induced Separation.*Journal of Fluid Mechanics*, **585** (2007).

[4] Pirozzoli, S. and Grasso, F.: Direct numerical simulation of impinging shock wave/turbulent boundary layer interaction at M=2.25. *Physics of Fluids*, **18** (2006).

[5] Sansica, A. and Sandham, N.D. and Hu., Z.: Forced response of a laminar shock-induced separation bubble. Phys. Fluids, **26** (2014).

[6] Selig, M. S., Andreopoulos, J., Muck, K. C., Dussauge, J.-P. and Smits, A. J.: Turbulence Structure in a Shock Wave/Turbulent Boundary-Layer Interaction, AIAA J., **27** (1989).

[7] Tenaud, C. , Fraigneau, Y. and Daru, V.: Numerical simulation of the turbulent separation reattachment flow around a thick flat plate. J. Phys. Conf. Ser., **318** (2011).

REGULAR-TO-MACH REFLECTION TRANSITION ON CURVED SURFACES

Sannu Mölder *[1] and Evgeny Timofeev [2]
[1]*Aerospace Engineering, Ryerson University, Toronto, Ontario, Canada*
[2]*Mechanical Engineering, McGill University, Montreal, Quebec, Canada*

Summary It is shown, using the curved shock theory, that the flow near the leading edge of a doubly curved wedge can choke to force the shock to detach from the wedge. It is then observed that the fluid-mechanical process involved in the detachment of an oblique shock from a plane or curved surface and the termination of regular reflection on a plane or curved surface have the same underlying causes. This leads to a new criterion for regular-to-Mach reflection transition based on this 'local choking.' Numerical experiments are carried out to explore the possibility that transition to Mach reflection can be induced by streamwise and transverse wall curvature.

Curved shock theory (CST) [1] is used to show that the flow behind attached shocks on doubly curved wedges can have either positive or negative post-shock pressure gradients depending on the freestream Mach number, the wedge angle and the two wedge curvatures. Given enough wedge length, the flow near the leading edge can choke to force the shock to detach from the wedge. This 'local choking' can pre-empt both the maximum deflection and the sonic criteria for shock detachment. Analytical predictions for detachment by local choking are supported by CFD results obtained with an adaptive unstructured Euler solver `Masterix` [2].

Figure 1a demonstrates shock detachment from a wedge caused by streamwise curvature of the wedge surface. The top and bottom wedge angles are equal, but the bottom wedge is curved. Figure 1b shows an annular ring-wedge that has no streamwise curvature. Shock detachment is caused by lateral curvature and flow contraction on the inner surface. In both cases detachment has occurred at wedge angles below the maximum flow deflection angle as well as below the sonic shock angle as proven by the attached flows on the opposing wedge surfaces.

Our investigation of shock detachment from a plane or curved wedge has led to a study of the classical, more complicated and more interesting, regular reflection termination conditions because the detachment of a shock from a wedge has, as its cause, the same limiting flow conditions (e.g. excessive flow turning; subsonic post-shock flow) as does the termination of regular reflection of an oblique shock wave. In the regular shock reflection situation the flow behind the incident shock, approaching the reflecting shock, sees the reflecting surface as a freestream flow would see a flow-deflecting wedge. This implies that the fluid-mechanical process involved in the detachment of an oblique shock from a plane or curved surface and the termination of regular reflection on a plane or curved surface have the same underlying causes. The two flow disruptions are governed by the same equations and, at their termination, have the same values of independent parameters and boundary conditions, including surface curvature.

In the study of transition, some resolution between differences in theory and experiment is required as noted by Sudani et al. [3] who state that "...transition from regular to Mach reflection occurs significantly below the maximum deflection

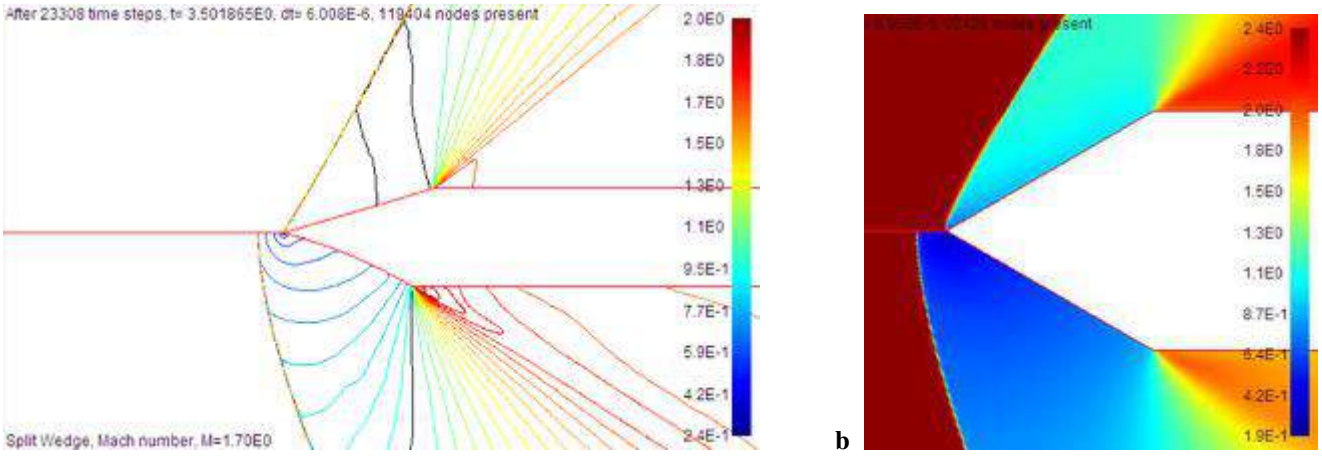

Figure 1: **(a)** Local choking caused by flow curvature in planar flow at Mach 1.7 over -16.5° wedge on lower surface with streamwise curvature of -1; shock is detached. Upper wedge, at $+16.5^\circ$ is flat and supports an attached shock; **(b)** Shock detachment on lower surface by local choking on 30° circular wedge at Mach 3. Local choking caused by lateral convergence. Shock is attached on upper 30° wedge surface.

*Corresponding author. Email: smolder@sympatico.ca

condition". Using the curved shock theory, a formula is derived for the length of curved wedge or cylindrical surface required to produce a locally choked flow at the leading edge or behind a reflected shock. CFD analysis predicts detachment if the surface exceeds this length. Thus the curvature and length of the post-reflection surface becomes a transition criterion that can pre-empt the previously posed classical criteria.

CFD studies of regular-to-Mach reflection transition on curved surfaces are carried out to examine the validity of the newly proposed transition criterion. A solid ring with the profile based on an M-flow streamline [4] is placed into supersonic stream to produce a straight converging axisymmetric shock. The shock interacts with an axial straight or curved cylinder. In the course of a computation the radius of cylinder is changed very slowly to obtain a sequence of quasi-steady states displaying transition from a regular reflection (RR) to a Mach reflection (MR). The possibility of a RR-MR hysteresis induced by the variation of cylinder radius is also explored. Similar studies are performed using the shock from a cone reflecting off a concave cylindrical surface.

These results provide an explanation for how shock detachment from a wedge and termination of RR can be caused by local choking which allows for the possibility that transition to MR can be induced by streamwise and transverse wall curvature, in turn, leading to an explanation for a long standing paradox in reconciling experiment and theory of RR termination.

References

[1] Mölder S.: Curved Shock Theory. Shock Waves J. DOI 10.1007/s00193-015-0589-9, 2015.

[2] `Masterix`, ver. 3.40, RBT Consultants, Toronto, Ontario, 2003-2015

[3] Sudani N., Saito M., Karasawa T., Noda J., Tate A., Watanabe M.: Irregular Effects on the Transition From Regular to Mach Reflection of Shock Waves in Wind Tunnel Flows. J. Fluid Mech. 459:167-185, 2000.

[4] Mölder S.: Internal, Axisymmetric, Conical Flow. AIAA Journal 5(7):12521255, 1967. DOI: 10.2514/3.4179

DETAILED SIMULATIONS OF SHOCK BOUNDARY LAYER INTERACTION IN SHOCK TUBE EXPERIMENTS

Kevin Grogan* and Matthias Ihme
Department of Mechanical Engineering, Stanford University, Stanford, CA, USA

Summary Detailed simulations of inert, multi-dimensional, viscous, shock tube experiments are undertaken. From these simulations, distinct regimes of shock boundary layer interaction are observed. These regimes show a dependence on the composition of the test gas and the Mach number of the incident shock wave. From these simulations, it is suggested that tailoring the incident shock Mach number could reduce the inhomogeneity in the flow and increase the operable range in chemical kinetic experiments.

INTRODUCTION

Shock tubes are a primary tool for chemical kinetic measurements, providing ignition delay times, species time-histories, and elementary reaction rates [1]. They replicate constant-volume reactors to high accuracy for test times up to the millisecond range, allowing for idealized zero-dimensional modeling of the combustion process.

There has been increased interest in recent years for chemical kinetics measurements in shock tubes within the negative temperature coefficient (NTC) region due to advancements in extending shock tube test times [1, 2]; the NTC region refers to a non-monotonic ignition delay time curve with respect to temperature for a given fuel. Boundary layer effects can influence the ignition properties for fuels exhibiting NTC characteristics due to an increased sensitivity to fluctuations in the test gas, which can give rise to weak ignition [3, 4]. Hence, the regimes of interaction of the shock wave with the boundary layer must be understood in order to circumvent weak ignition. Therefore, the objective of this work is to employ detailed simulations to study regimes of the shock boundary layer interaction (SBLI) relevant to reaction kinetic experiments in shock tubes.

SET-UP OF THE DETAILED SIMULATIONS

For the detailed simulations, the flow-field is described by the two-dimensional, viscous Navier-Stokes equations:

$$\frac{\partial \mathbf{U}}{\partial t} + \frac{\partial}{\partial x_j}\left(\mathbf{F}_j^c \circ \mathbf{F}_j^v\right) = 0 \,, \tag{1}$$

where $\mathbf{U}$ is the state vector, and $\mathbf{F}_j^c$ and $\mathbf{F}_j^v$ are the convective and viscous fluxes. These vectors have the following definition:

$$\mathbf{U} = [\rho u_i, \rho e_t, \rho Y_n]^T \,, \tag{2a}$$
$$\mathbf{F}_j^c = [\rho u_j u_i + p\delta_{ij}, u_j(\rho e_t + p), \rho Y_n u_j]^T \,, \tag{2b}$$
$$\mathbf{F}_j^v = [\tau_{ij}, u_i\tau_{ij} + q_j, \rho Y_n V_{jn}]^T \,, \tag{2c}$$

for $i, j \in \{1, 2\}$ and $n \in \{1, \ldots, N_S\}$, where N_S is the number of chemical species. The total internal energy is denoted by e_t, τ_{ij} is the viscous stress tensor using Stokes' hypothesis, V_{jn} is the diffusion velocity of species n, q_i is the heat-flux vector, and the mass diffusion is described by a multi-component diffusion model with thermal and pressure diffusion. The ideal gas law is used as the state equation.

The governing equations are solved using a block-structured adaptive mesh refinement (AMR) method, which is implemented in the object-oriented framework AMROC (Adaptive Mesh Refinement in Objective-oriented C++) [5, 6]. The computational domain consists of a symmetric two-dimensional planar shock tube. The computational mesh consists of stretched cells with a minimum cell height of 18.75 μm, corresponding to approximately 80 cells across the boundary layer at the end of the simulation; three levels of mesh refinement are used. The flow-field is initialized by a moving shock using normal-shock relations [7] at a sufficient distance away from the end wall to ensure boundary layer development. Cases are selected to span the SBLI regimes for an n-heptane mixture with an equivalence ratio of $\phi = 0.5$, a test temperature of $T_5 = 700$ K, and a test pressure of $p_5 = 2.7$ bar. The n-heptane mixture is diluted with either 78.3% nitrogen or argon, and for both diluents, three initial temperatures ($T_1 = 300$ K, 400 K, and 500 K) are examined; n-heptane is selected as the fuel due it's prevalent NTC characteristics.

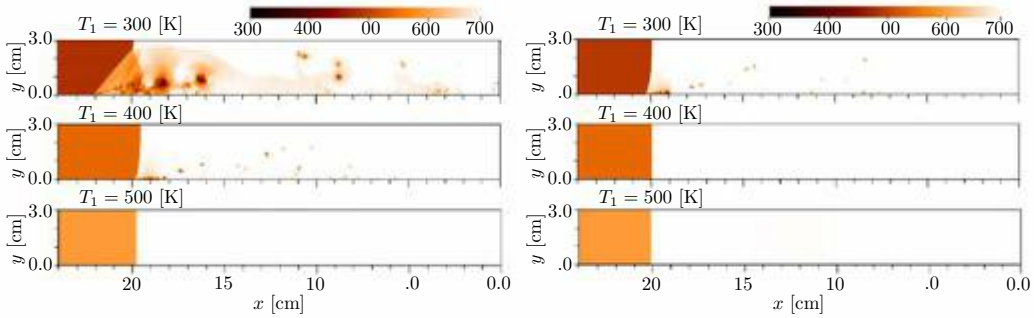

(a) N_2 Dilution. (b) Ar Dilution.

Figure 1: Comparison of different initial temperatures on the quality of the flow field. Snapshot taken after shock wave reflects from the end wall (right side).

RESULTS AND DISCUSSION

Pseudocolor plots of the temperature field for each simulation are shown in Fig. 1. The figure demonstrates that for both the nitrogen and argon diluted mixtures, the severity of the SBLI decreases as the initial temperature increases (i.e., as the strength of the incident shock decreases). Nitrogen is shown to yield a much more inhomogeneous flow for comparable conditions than argon; this is due to the lower heat capacity ratio for the nitrogen mixture.

Three different regimes of SBLI are depicted in Fig. 1. For the lowest incident shock Mach number cases (i.e., $T_1 = 500$ K in nitrogen and $T_1 = 400$ and 500 K in argon), the flow is shown to be free of large-scale structures emanating from the separated boundary layer. However, as the incident shock Mach number increases (i.e., $T_1 = 400$ K in nitrogen and $T_1 = 300$ K in argon), the periodic ejection of roller vortices is shown. This is attributed to the decreasing timescale of the hydrodynamic instability of the separated flow with increasing incident Mach number. Finally, in the highest incident Mach number case in nitrogen (i.e., $T_1 = 300$ K), a clear bifurcation structure manifests. In this scenario, the separated boundary layer cannot navigate the pressure rise and is contained within a stagnation bubble over which a triple-shock structure forms [8].

The results of the detailed simulation suggest that preheating the mixture may provide an opportunity for reducing some of the inhomogeneity in the flow field by weakening the incident shock wave. Although the feasibility in obtaining a uniformly heated test gas and chemical effects such as fuel pyrolysis may make the application of this strategy difficult, a preheated test gas could expand the operation range of shock tubes.

CONCLUSIONS

The character of the interaction of a reflected shock wave with the boundary layer requires understanding to circumvent weak ignition. Detailed simulations of a shock tube flow over a range of conditions demonstrate three regimes of SBLI, which depend primarily on the mixture and the incident shock Mach number. An intermediate regime between shock bifurcation and quiescent flow is found, which could lead to weak ignition in sensitive mixtures. Additionally, the simulations show that tailoring the Mach number of the incident shock could reduce the inhomogeneity in the test gas.

References

[1] R. K. Hanson and D. F. Davidson. Recent advances in laser absorption and shock tube methods for studies of combustion chemistry. *Prog. Energy Combust. Sci.*, 44:103–114, 2014.

[2] M. Campbell, S. Wang, C.S. Goldenstein, M. Spearrin, A. Tulgestke, L. Zaczek, D. Davidson, and R. Hanson. Constrained reaction volume shock tube study of n-heptane oxidation: Ignition delay times and time-histories of multiple species and temperature. *Proc. Combust. Inst.*, 35:231–239, 2015.

[3] J. W. Meyer and A. K. Oppenheim. On the shock-induced ignition of explosive gases. *Proc. Combust. Inst.*, 13:1153–1164, 1971.

[4] K. Grogan and M. Ihme. Weak and strong ignition of hydrogen/oxygen mixtures in shock-tube systems. *Proc. Combust. Inst.*, 35(2):2181–2189, 2015.

[5] R. Deiterding. AMROC - Blockstructured Adaptive Mesh Refinement in Object-oriented C++. Available at `http://amroc.sourceforge.net`, 2008.

[6] R. Deiterding. Detonation structure simulation with AMROC. In L. T. Yang, O. F. Rana, B. Martino, and J. Dongarra, editors, *High Performance Computing and Communications*, volume 3726 of *Lecture Notes in Computer Science*, pages 916–927. Springer Berlin Heidelberg, 2005.

[7] G. Ben-Dor, O. Igra, and T. Elpherin, editors. *Handbook of Shock Waves*. Elsevier, New York, 2001.

[8] H. Mark. The interaction of a reflected shock wave with the boundary layer in a shock tube. *J. Aeronaut. Sci.*, 24:304–306, 1957.

ON THE INTERACTION OF OBLIQUE SHOCKS AND LAMINAR MIXING LAYERS

Daniel Martínez-Ruiz[1], César Huete[2], and Antonio L. Sánchez*, Forman A. Williams[3]
[1]*IRPHE, Aix-Marseille Université, France*
[2]*Fluids Group, Universidad Carlos III of Madrid, Spain*
[3]*MAE Department, UCSD, USA*

Summary This paper examines the interaction of a mixing layer separating two supersonic streams with an oblique shock approaching from the faster stream with an incident angle sufficiently small for the resulting post-shock flow to remain everywhere supersonic. The interaction region, including the shape of the resulting curved shock, is described by integrating the Euler equations in the post-shock region formulated in characteristic form subject to the Rankine-Hugoniot jump conditions at the shock front, thereby accounting for the influence of the post-shock flow in the computation of the shock curvature. The results are used to investigate the accuracy of Whitham's rule for computing the shape of the shock wave in these scenarios.

The interaction of an oblique shock with a shear layer constitutes a fundamental problem in compressible-flow theory. These interactions occur, for instance, in combustion chambers of supersonic combustion ramjets (scramjets), where shocks generated in the air stream at wedged walls and fuel injectors impinge on the mixing layer surrounding the fuel jets downstream from the injection point [2]. Although the flow is typically turbulent in these high-Reynolds-number applications, analyses of laminar flows have been shown to be instrumental in providing insightful information pertaining to mixing augmentation [3] and enhanced chemical reaction leading to ignition [4] behind the curved shock.

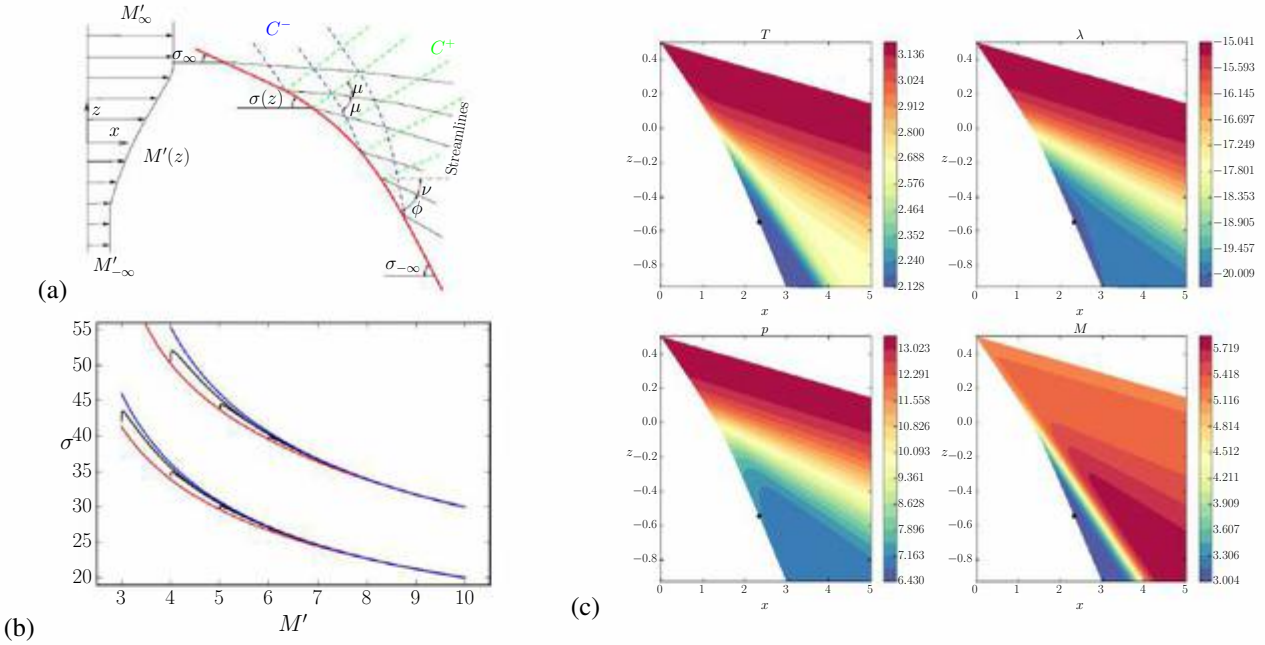

Figure 1: (a) Sketch of the model problem; (b) black curves: numerical results corresponding to $M'_\infty = 10$ with $\sigma_\infty = 20^\circ$ and $\sigma_\infty = 30^\circ$ for different values of $M'_{-\infty}$, blue curves: predictions obtained using Whitham's rule by integration of Moeckel's equation (3), red curves: incident angle for the transmitted shock $\sigma_{-\infty}$ obtained by computation of shock reflection on a contact surface; (c) results corresponding to $M'_\infty = 10$, $M'_{-\infty} = 5$, and $\sigma_\infty = 20^\circ$ including distributions of deflection angle, Mach number, and dimensionless temperature and pressure (scaled with their uniform upstream values); the inflection point of the shock front is indicated with a dot.

We consider a laminar mixing layer separating two supersonic parallel streams with Mach numbers M'_∞ and $M'_{-\infty} < M'_\infty$, as indicated in Fig. 1(a). An oblique shock generated in the faster stream, with initial incident angle σ_∞, impinges on the mixing layer at a given location. As a result of the interaction with the nonuniform flow, the shock front curves, giving a distribution of incident angle $\sigma(z)$ that varies across the mixing layer. The computation of $\sigma(z)$ constitutes a complicated free-boundary problem involving the integration of the Euler equations downstream from the shock, with the conditions immediately behind the shock determined by application of the Rankine-Hugoniot relations. If the post-shock flow remains

*Corresponding author. Email: als@ucsd.edu

supersonic everywhere, then the Euler equations can be formulated in characteristic form, with three different characteristic lines crossing any given point. The entropy is conserved along the streamlines, a condition that can be expressed in the form

$$\frac{\mathrm{d}p}{p} \circ \frac{\gamma}{2}\frac{\mathrm{d}(M^2)}{1+\frac{\gamma-1}{2}M^2} = 0, \quad \text{on} \quad \frac{\mathrm{d}z}{\mathrm{d}x} = \tan\lambda, \tag{1}$$

where p is the pressure, M is the Mach number, and λ is the (counterclockwise) local angle of deflection of the streamlines with respect to the horizontal. On the other hand, manipulation of the conservation equations of continuity and momentum provides the two additional characteristic equations [1]

$$\frac{\mathrm{d}p}{p} \pm \frac{\gamma M^2}{\sqrt{M^2 \circ 1}}\mathrm{d}\lambda = 0, \quad \text{on} \quad \frac{\mathrm{d}z}{\mathrm{d}x} = \tan(\lambda \pm \mu), \tag{2}$$

where $\mu = \sin^{-1}(1/M)$ is the angle of inclination of the two Mach lines relative to the local flow direction, as depicted in Fig. 1(a). The integration along the streamlines and along the C^+ characteristic lines $\mathrm{d}z/\mathrm{d}x = \tan(\lambda+\mu)$ starts at the shock, with corresponding initial conditions evaluated from the Rankine-Hugoniot relations, including the jump of pressure $p/p'_\infty = F_p(M',\sigma)$, the clockwise flow deflection $\nu = F_\nu(M',\sigma)$, and the post-shock Mach number $M = M(M',\sigma)$, with $\lambda = \circ\,\nu$ at the shock. On the other hand, the C^- characteristics originate in the shocked stream above the mixing layer, so that the associated uniform values of p_∞ ($> p'_\infty$) and $\lambda_\infty = \circ\,\nu_\infty$ must be used as initial conditions in the integration, which must be continued until the C^- characteristic line intersects the shock, providing the information needed at each point to determine the shock curvature $\mathrm{d}\sigma/\mathrm{d}z$.

To the best of our knowledge, the problem formulated above has never been solved. Previous computations (see e.g. [5]) incorporate instead the approximate analytic method developed by Moeckel [6] for determining the shock shape $\sigma(z)$. As explained by Whitham [7], Moeckel's method amounts to applying the relation $\mathrm{d}p/p = \gamma M^2\mathrm{d}\lambda/\sqrt{M^2 \circ 1}$, corresponding to the C^- characteristic line, along the shock front, a condition that yields

$$\frac{\mathrm{d}\sigma}{\mathrm{d}M'} = \circ\,\frac{A_p + \gamma M^2 A_\nu/(M^2 \circ 1)^{1/2}}{B_p + \gamma M^2 B_\nu/(M^2 \circ 1)^{1/2}}, \tag{3}$$

as a local expression for the shock curvature, where the factors $A_p = \frac{1}{F_p}\frac{\partial F_p}{\partial M'}$, $B_p = \frac{1}{F_p}\frac{\partial F_p}{\partial \sigma}$, $A_\nu = \frac{\partial F_\nu}{\partial M'}$, and $B_\nu = \frac{\partial F_\nu}{\partial \sigma}$ can be evaluated explicitly in terms of σ and M' from the Rankine-Hugoniot relations. In Moeckel's simplified approach, integration of (3) with initial condition $\sigma = \sigma_\infty$ at $M' = M'_\infty$ provides $\sigma(M')$, thereby determining $\sigma(z)$ for a given upstream Mach-number distribution $M'(z)$.

Sample results corresponding to the upstream Mach-number distribution $M' = M_\infty \circ \frac{1}{2}(M_\infty \circ M_{-\infty})[1 \circ \tanh(5z)]$ are shown in Fig. 1(b) and 1(c). As can be seen in Fig. 1(b), Whitham's rule, which gives the blue curves, tends to overpredict the resulting incident angles. For the specific conditions selected, the resulting overpredictions are however quantitatively small. Our computations also reveal that the variation of $\sigma(z)$ is non-monotonic, resulting in a curved shock front with an inflection point, corresponding to a local maximum of the incident angle, indicated by a dot in Fig. 1(c). The inflection point is located near the lower boundary of the mixing layer. The non-negligible deflection occurring farther down, in the region where the upstream Mach-number profile is nearly uniform, is due to the interactions of the C^- characteristics with the shock, resulting in a decrease of the incident angle. The value of σ eventually approaches the value $\sigma_{-\infty}$ corresponding to the transmitted wave, which can be determined in terms of M'_∞, $M'_{-\infty}$ and σ_∞ by considering the outer regular-reflection problem, in which the mixing-layer appears as a contact surface, giving the red curves represented in Fig. 1(c).

References

[1] Hayes W.D., Probstein R.F.: Hypersonic Inviscid Flow, Second ed., Dover, Mineola, NY, 2004.

[2] Laurence S.J., Karl S., Schramm J., Martínez, J., Hannemann, K. Transient fluid-combustion phenomena in a model scramjet. J. Fluid Mech. 722:85–120, 2013.

[3] Buttsworth D.R. Interaction of oblique shock waves and planar mixing regions. J. Fluid Mech. 306:43–57, 1996.

[4] Huete C., Sánchez A.L., Williams F.A., Urzay, J. Diffusion-flame ignition by shock-wave impingement on a supersonic mixing layer. J. Fluid Mech. 784:74–108, 2015.

[5] Collins R., Chen H-T., Propagation of a shock wave of arbitrary strength in two half planes containing a free surface. J. Comp. Phys. 5:415–442, 1970.

[6] Moeckel W.E., Interaction of oblique shock waves with regions of variable pressure, entropy, and energy. NACA Tech. Note 2725, 1952.

[7] Whitham G.B. On the propagation of shock waves through regions of non-uniform area or flow. J. Fluid Mech. 4:337–360, 1958.

INTERNAL AND EXTERNAL JET MODES OF AN OVER-EXPANDED TIC NOZZLE

Sara Arbos Torrent[1,2], Vincent Jaunet*[2], Vladimir Parezanovic[2], Steve Girard[2], and Julien Herpe[1]

[1]*Centre National D'Etudes Spatiales,CNES, Direction des Lanceurs DLA,Paris,France*
[2]*Institut Pprime, CNRS, ISAE-ENSMA, UniversitÃl' de Poitiers, F 86962 FUTUROSCOPE CHASSENEUIL, France.*

Summary Experiments at different pressure ratios are conducted on a Truncated Ideal Contour nozzle operating under over-expanded conditions. A system permitting synchronised data acquisition of internal pressure signals and external velocity fields is implemented. Preliminary results display a strong flapping motion of the external jet. This motion is seen to be maximised for a specific nozzle pressure ratio. On the other hand, internal pressure signals reveal the existence of highly organised pressure fluctuations of great amplitude in the separation region which are linked to specific azimuthal modes. Furthermore, the first azimuthal mode has been associated with the generation of side-loads. The characteristic dynamics of the external jet are linked to the dominant modes observed inside the nozzle to try to unravel its connection with the generation of side-loads.

INTRODUCTION

The nozzles operating under *over-expanded* regimes ($P_e < P_{atm}$) are characterised by oblique shocks emanating into the flow-field to adapt the exhaust flow to the ambient pressure (**?**). **?** described that depending on the nozzle geometry two flow separation regimes exist for over-expanded nozzles: *Free Separation Shock, FSS* and *Restricted Separation Shock, RSS*. Truncated Ideal Contour, TIC, nozzles only display, FSS separation regimes. During this operational regime large structural asymmetric forces referred to as *side-loads* take place. Studies by **?????** have suggested that side-loads in the FSS regime are a result of oscillations of the internal shock pattern within the nozzle. Nonetheless, the causes of the asymmetric pressure fluctuations remain unclear. This abstract suggests to explore the coupling between the internal pressures and external flow filed as a method to characterise the internal shock oscillation.

EXPERIMENTAL FACILITIES AND SET-UP

The tests presented are conducted at the S150 cold blow down supersonic wind tunnel at Pprime Institute in Poitiers. A reduced scale Truncated Ideal Contour Nozzle is utilised as it guarantees an FSS separation structure. The Mach number of the full flowing flow is 3.5. The nozzle is equipped with 18 flush-mounted pressure transducers Kulite XCQ-062. The range of the sensors is of 1.7 bar absolute. The sensitive element has a diameter of 1.7 mm which allows the acquisition of good spatial resolution. The cut-off frequency of the sensors is around 40 kHz which guarantees a good temporal resolution. In order to obtain quantitative information of the jet a 2D-2C Particle Image Velocimetry, PIV, system is utilised. The acquisition as well as the initial post-processing analysis is done in DaVis 8.1 Software from LaVision. Finally, tests are performed such that the PIV snapshots and the pressure measurements are synchronised; hence, permitting the correlation between the internal and the external jet dynamics.

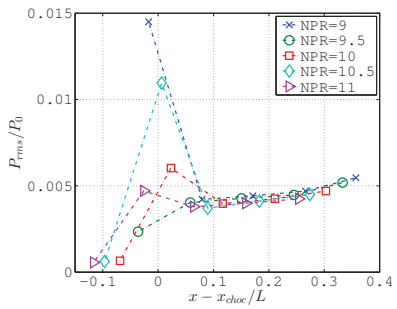

Figure 1: P_{rms} along the nozzle for several NPR. Normalised by total pressure, P_0.L is the distance between the col and the nozzle exit.

RESULTS

PIV together with pressure measurements show a large amplitude jet beating around NPR=9. These observations are in agreement with the findings by **??**.It should be recalled that the flow unsteadiness while in the FSS regime is strongly dependant on the NPR (**?**). Figure 1 depicts the evolution of the P_{rms} along the nozzle for several NPR. Despite the sparse resolution of the pressure transducers, it can be seen that the highest pressure fluctuations occur at a *nozzle pressure ratio* of 9. These results together with the PIV vector fields confirm that for the given nozzle and range of NPR tested the highest pressure fluctuations occur at NPR=9. Moreover, the data suggests that the internal shock occurs between $x/L = 0.481$ and $x/L = 0.574$.

*Corresponding author. Email: vincent.jaunet@univ-poitiers.fr

Internal Flow

To further analyse the flow inside the nozzle the azimuthal contribution of wall pressure fluctuations is studied. To do so, the time-space dependant pressure signal is firstly decomposed into azimuthal Fourier modes,

$$p(x,\theta,t) = \sum_{m=-N}^{N} p_m(x,t)e^{im\theta}, \tag{1}$$

where N is the number of pressure transducers available. Therefore, the axi-symmetric pressure fluctuation modes correspond to $m = 0$ while the asymmetric ones correspond to $m = 1$. Symmetry considerations suggest that only modes $m \pm 1$ can contribute to the generation of side-loads. Once the azimuthal Fourier modes are obtained the PSD for each $p_m(x,t)$ can be obtained. The results are displayed in figure 2 for $x/L = 0.667$.

It can be seen that for $St < 0.2$ the spectra is dominated by the axi-symmetric mode 0. This suggests that the low frequency unsteadiness comprised in the separated region contains mainly axi-symmetric pressure fluctuations. On the other end of the spectra, for $St > 2$, no dominating mode can be observed, thence, it consists of a highly disorganised pressure field; which is to be expected since high frequency fluctuations could be related to finer stochastic turbulent scales. Finally analysis of frequencies $0.2 < St < 2$ shows that the spectra is dominated by distinct peaks, each of which attributed to a specific mode number. The most energetic peak is the one corresponding to mode $m = 1$. Thereby, entailing that, for the given NPR, the pressure fluctuations within the separated region are very well organised. It can be further argued that, because the mode with the highest energy content is asymmetric, side-loads are being generated.

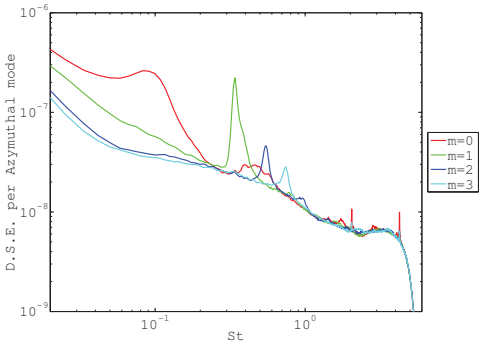

Figure 2: First 4 azimuthal modes at $x/L = 0.667$ positions.

External Flow

In order to be able to couple the dominant internal pressure modes with the dominant external modes an energy based modal decomposition is done on the PIV velocity fields. The velocity field is decomposed into temporal and spatial modes using a POD analysis,

$$u(x,t) = \sum_{n=0}^{N} \alpha^n(t)\phi^n(x), \tag{2}$$

The results of the snapshot POD analysis (**?**) are presented in figures.3(a) to 3(b). Note that the first 4 modes represent about 30% of the total fluctuating energy. The figures expose that the velocity field presents some preferred organization. Mode 1 and 2 form a pair representing some kind of vertical motion of the entire jet. Hence, both the external flow field and the internal pressure field are dominated by coherent organisation.

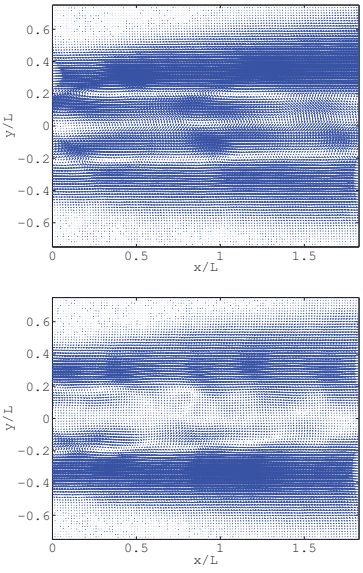

Figure 3: POD modes 1 and 2. The coordinate origin corresponds to the nozzle exit centre

CONCLUSIONS

In conclusion, the experimental measures have shown that both the internal nozzle flow and the exiting jet are dominated by well-organised structures. Moreover, a clear dominant asymmetric azimuthal mode has been found to characterise the flow and could be playing a significant role in the creation of side-loads. Finally, a survey of the effect of NPR on the anti-symetric mode is underway and will render completeness to the descriptions of the observed azimuthally organized pressure fluctuations.

SONIC FLOW CONTROL BY PLASMA: A NEW PULSED JET ACTUATOR

Jean-Paul Bonnet[1a], Gwenaël Acher[1], Nicolas Bénard[1], Anton Lebedev[1] & Eric Moreau [1]

[1] Institut PPRIME (CNRS UPR 3346, Université de Poitiers, ISAE-ENSMA),
SP2MI Téléport 2 Bd Marie et Pierre Curie BP 30179, Futuroscope, 86962 Poitiers, France

Summary: Preliminary measurements on the modulation of a sonic flow have been conducted by increasing the temperature at a sonic throat with the help of a plasma discharge. For a perfect gas, the flow rate being proportional to the inverse of the square root of the temperature at a constant settling chamber pressure, the jet flow rate should be able to be varied. In view of flow control actuator design, the frequency is then no limited by any mechanical constraint. The discharge can be either continuous or pulsed at high frequencies. The influence of the settling chamber pressure and electrode gap distance have been investigated. For an aerodynamically steady actuation, the jet flow rate can be reduced down to 70% of its nominal value (30% of flow rate reduction), the best effectiveness being obtained with a dc discharge. However, better potential efficiency is expected with a high current pulse discharge.

Introduction In most cases, active flow control requires high frequency actuators. Particularly for high velocity (eventually supersonic) flow control configurations, high frequency and high authority (in terms of flow rate) are required ([1], [2]). Usual pressurized flowing jets have a high potential but they are limited in terms of frequency (up to typically a few hundred of Hz). In this project, we developed a new flowing jet driven by a plasma discharge. The principle is to increase the temperature at a sonic throat located upstream of the jet exit with the help of a plasma discharge located at the throat (Fig. 1). For a perfect gas, the flow rate being proportional to the inverse of the square root of the temperature at a constant settling chamber pressure, the jet flow rate can be varied.

The aim of the present study is to quantify the maximum mass flow reduction that can be obtained by different types of discharges ignited in the vicinity of the sonic throat. Three different power supplies are used (Fig. 2). The first power supply is a DC one. In this case, the discharge is either switched off or switched on and both cases are compared. The second power supply is composed of the DC power supply followed by a high voltage switch transistor, allowing us to pulse the discharge with small duration high current pulses. Finally, the last study deals with a pulse discharge with long duration small current pulses. As far as the flow itself is concerned, two parameters have been varied, namely the settling chamber pressure and the distance between the electrodes. The aerodynamic effects are observed by considering the flow rate measured by a direct flow meter and the temperature of the jet measured by a thermocouple.

Actuator design. In the present configuration, a single 0.95-mm-diameter cylindrical hole is used. The settling chamber pressure can be adjusted from 1.4 up to 5 bar (the theoretical minimum pressure for sonic condition being 1.893 bar). The electrical characterization of the system is not given here, the main focus being on the discharge effect on the flow modulation. Details on the electric data can be found in [3]. Fig. 3 shows the evolution of the parameter $\Gamma = Q\sqrt{T}/P$ where T is the total temperature and P the pressure in the settling chamber. This parameter should be constant when the flow is sonic at the throat (Γ = 2.8 10^{-8} m² under the present conditions). From the figure, it can be observed that the flow rate follows the isentropic theory for the natural as well as for the plasma actuated flows [4].

Major results of the plasma activation. Figure 3 shows also the air jet temperature T and the thermal power P_{th} versus discharge power P_d for several pressure values in the DC mode. First, one can observe that both quantities increases nearly linearly with the power injected by the discharge inside the flow. Secondly, the jet temperature reaches about 650°K for P = 2 bar and P_d = 200 W.

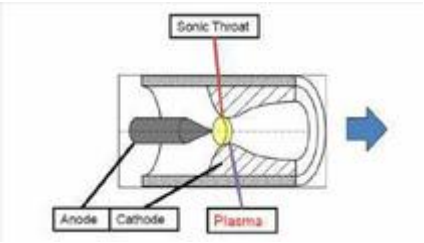

Fig.1. Schematic of the plasma pulsed jet actuator.

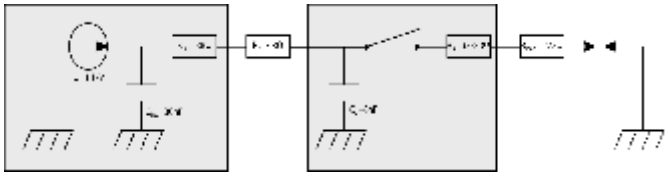

Fig. 2. Schematic of the electrical setup.

[a] Corresponding author. Email: jean-paul.bonnet@univ-poitiers.fr.

The thermal conversion efficiency η, defined as the ratio between the thermal power and the discharge electrical power, increases from 32–37% at 1.4 bar (not a sonic condition) to 48–50% at 2.8 bar, with a mean value equal to 41% for P = 2 bar. As shown on Fig. 4, the value of the gap between electrodes is important if the discharge power is considered but less in the conversion effectiveness, excepted a light effect for a gap equal to 1 mm. The reduction of the flow rate being the major goal of the study, the results are plotted in Fig. 5 in terms of discharge power and temperature ratios. The results are compared with the theoretical law corresponding to a pure thermal effect $Q/Q_0 = \sqrt{T_0/T}$. First, one can see that a flow rate reduction down to 70% can be achieved. , Moreover, it seems that a better efficiency can be expected for a high current pulse discharge.

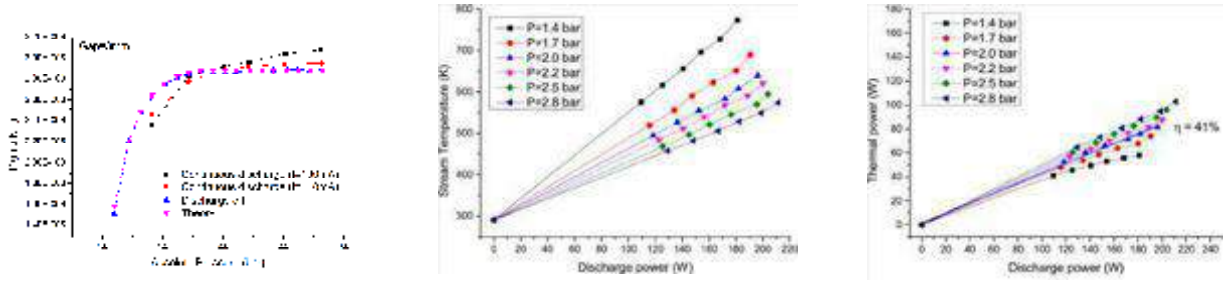

Fig. 3. Γ vs pressure (left), temp. vs discharge power (center) and thermal power vs discharge power (right). Gap = 3 mm.



Fig. 4 . Influence of the electrode gap (DC power supply) and thermal power vs electrical power (P =2 bar).



Fig. 5. Mass flow ratio versus temperature ratio (left) and mass flow ration vs discharge (right). Gap = 3 mm, P = 2 bar.

CONCLUSION

We present a new method to control a sonic flow by introducing an electric discharge at the throat. The effect of the plasma is essentially a thermal one. Reduction up to 30% of the mass flow rate can be obtained, opening new perspectives for high authority, high frequency actuators in view of active flow control without any mechanical part.

References

[1] Cattafesta III L.N., Sheplak M., Actuators for Active Flow Control, Annual Rev. Fluid. Mech., Vol. 43: 247-272, 2011.

[2] Gatski T.B., Bonnet J.P., Compressibility, Turbulence and High Speed Flows, 2nd ed., Elsevier Science Publishing Co Inc, USA, 2014.

[3] Acher G., Moreau E, Bénard N., Bonnet J.P., "A new plasma pulsed jet actuator: electrical and mechanical characteristics" , to be published in 2016

[4] Thompson P.A., Compressible Fluid Dynamics, McGraw-Hill Inc.,US 1972.

FLOW VISUALIZATION OF HIGH-SPEED CAVITY FLOWS

Yang Zhang*[1] and Lou Cattafesta[2]

[1,2]*Florida A&M University and Florida State University, Tallahassee, Florida, 32310*

Summary Experimental investigations are conducted on cavity flows at Mach 0.6. Flow visualization techniques, including surface oil flow, two- and three-component Particle Image Velocity (PIV), along with fluctuating surface pressure measurements are performed on a full-span and a finite-span cavity with a length-to-depth ratio (L/D) of 6 but different width-to-depth ratios (W/D) of 3.85 and 2, respectively. The results provide comparisons between these two kinds of cavity flows showing that they share some global flow features. However, higher velocity fluctuations and pressure fluctuations are observed in the full-span cavity.

INTRODUCTION

Flow over cavity structures can generate intense pressure fluctuations inside the cavity that can cause damage to its contents. The open-cavity flow mechanism can be briefly described as follows: a shear layer forms as the flow detaches from the cavity leading edge, the shear layer impinges on the cavity trailing edge and generates an acoustic source that radiates waves which propagate upstream. These waves initiate disturbances in the shear layer through a receptivity process. This overall feedback process can produce strong resonances, known as Rossiter modes[1], and broadband pressure fluctuations. Cavity flow oscillations encountered in practical applications, like weapons bays and landing gear wells, all have rigid sidewall boundaries. However, in wind tunnel tests, cavity models usually have full-span widths to facilitate improved flow visualization, and sidewalls with a no-slip boundary condition are neglected to reduce the computational resources needed to adequately resolve the flow near the walls. Although the mechanism of open-cavity oscillations is similar for different cavity geometries, the flow structures and pressure loads inside the cavity can be quite different. In the current study, both full- and finite-span cavity geometries are tested at Mach 0.6, and flow visualizations present similarities and differences between these two kinds of cavity flows.

EXPERIMENTAL METHODOLOGIES

The experimental investigations are carried out in the pilot wind tunnel located at the Florida Center for Advanced Aero-Propulsion at the Florida State University. The schematics of the cavity models with main dimensions and coordinate system are shown in Figure 1. Kulite unsteady pressure transducers are instrumented along the centerline of the cavity for the fluctuating surface pressure measurements. A cavity floor piece without any holes is used for the flow visualization tests. For the oil flow visualization, a mixture of mineral oil and fluorescent pigment is applied on the cavity floor surface, which forms a surface-streamline pattern that fluoresces under UV light. Two- and three-component PIV measurements are conducted at the centerline plane ($z/D = 0$) of the full- and finite-span cavities to measure the velocity fields, respectively. An Evergreen Nd:YAG laser (EVG00200) is pulsed at a repetition rate of 15 Hz. A laser sheet of approximately 1.5 mm thickness is formed through a series of optics. A two-axis scheimpflug setup enables the Imager sCMOS cameras to peer over the opaque sidewall of the finite-span cavity and focus on the seeding particles illuminated in the field of interest[3]. Approximately 1000 image pairs are acquired for each case and processed using DaVis 8.2.1 software.

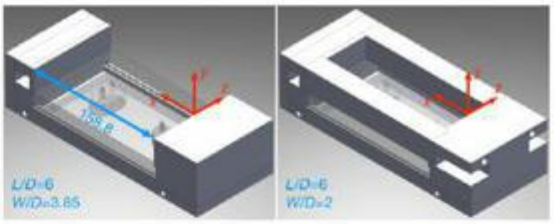

Figure 1: Cavity models. Full-span (left) and finite-span (right). Units are in mm.

RESULTS AND CONCLUSIONS

The non-dimensional power spectral densities ($PSD^* = 10\log_{10}\frac{U_\infty \times P_{xx}}{L \times q_\infty^2}$)[2] of surface pressure fluctuations are provided in Figure 2. Higher pressure fluctuations are observed towards the downstream cavity wall. Rossiter mode II is the dominant mode, and the resonance frequencies are very similar in both cases. The high level peaks (Rossiter mode II and III) in the full-span cavity are significantly reduced in the finite-span cavity, but the low level peaks at higher Strouhal number (St) are enhanced.

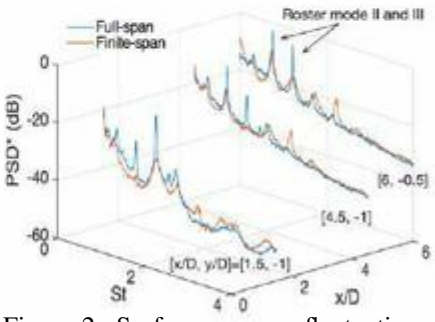

Figure 2: Surface pressure fluctuations measured along the centerline.

*yz12b@my.fsu.edu

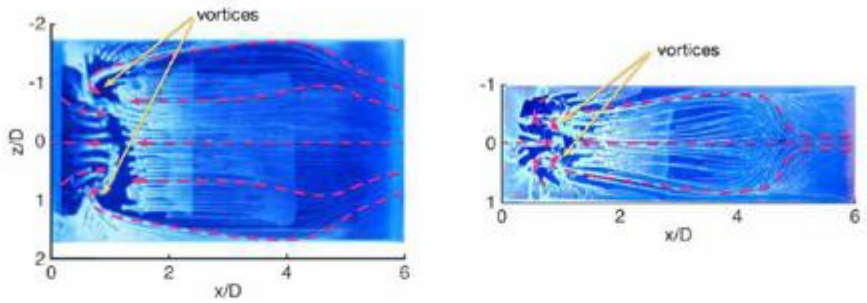

Figure 3: Surface oil flow patterns. Full-span cavity (left) and finite-span cavity (right).

Surface oil flow patterns are presented in Figure 3. The back flow induced by the main recirculation occupies the majority of the cavity floor. Two vortices on the front floor appear in both cases. A separation line is observable when the two recirculation regions meet near $x/D = 1$ in the full-span cavity. However, this separation line is less evident in the finite-span cavity. These recirculation regions agree with the PIV measurements discussed below.

In Figures 4(a) and (b), the ensemble-averaged streamlines indicate there are three recirculation regions in the full-span cavity; the primary one is in the middle of the cavity while two smaller ones are in the front and rear corners, respectively. It is quite different in the finite-span cavity case, in which the primary recirculation almost occupies the entire cavity, and a much smaller one is partially observed in the front corner. The contours of ensemble-averaged velocity components show that the flows are similar. However, the flow is clearly more three-dimensional in the finite-span cavity. The contours of turbulence kinetic energy (Figures 4(c) and (d)) and Reynolds stress (Figures 4(e) and (f)) show that the high turbulence in the mid plane of the full-span cavity is greatly reduced in the finite-span cavity.

One of the reasons to study cavity flows is to suppress the oscillations. The three-dimensionality of the cavity flow field can have great influence on the flow and on the control approach. In particular, the appropriate control strategy for the full-span cavity may not be optimal for the finite-span case. However, the full-span cavity case serves as a good starting point for implementing flow control.

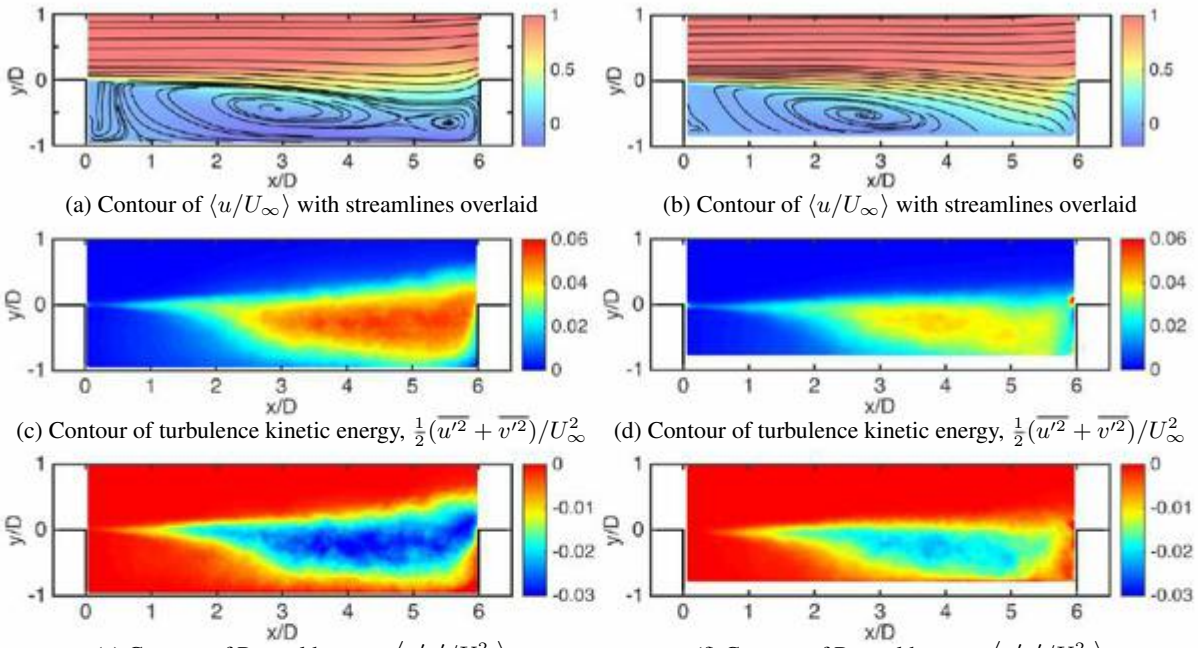

(a) Contour of $\langle u/U_\infty \rangle$ with streamlines overlaid

(b) Contour of $\langle u/U_\infty \rangle$ with streamlines overlaid

(c) Contour of turbulence kinetic energy, $\frac{1}{2}(\overline{u'^2} + \overline{v'^2})/U_\infty^2$

(d) Contour of turbulence kinetic energy, $\frac{1}{2}(\overline{u'^2} + \overline{v'^2})/U_\infty^2$

(e) Contour of Reynolds stress $\langle u'v'/U_\infty^2 \rangle$

(f) Contour of Reynolds stress $\langle u'v'/U_\infty^2 \rangle$

Figure 4: Flow properties of full-span cavity (left) and finite-span cavity (right).

References

[1] Rossiter J. E.: Wind-Tunnel Experiments on the Flow over Rectangular Cavities at Subsonic and Transonic speeds, tech. rep. No. 3438, Aeronautical Research Council Reports and Memoranda, 1964.

[2] Zhang Y., Sun Y., Arora N.,Cattafesta L., Taira K., and Ukeiley L.: Suppression of cavity oscillations via three-dimensional steady blowing, AIAA Paper 2015-3219, 2015.

[3] Walker S.: Two-Axes Scheimpflug Focusing for Particle Image Velocimetry, Measurement Science and Technology, Vol. 13, No. 1, 2002, pp. 1-12.

STRUCTURE OF A LASER-INDUCED SHOCK WAVE IN WATER

Yoshiyuki Tagawa*[1], Shota Yamamoto[1], Keisuke Hayasaka[1] & Masaharu Kameda[1]
[1]*Department of Mechanical systems engineering, Tokyo University of Agriculture and Technology, Tokyo, Japan*

Summary We experimentally investigate the structure of a laser-induced underwater shock wave, which is often modelled as spherically symmetric. We measure plasma formation, shock wave expansion, and pressure in water using a combined measurement system. The pressure measurements reveal that the distribution of peak pressure is non-spherically-symmetric while pressure impulse distributes symmetrically for a wide range of experimental parameters. With considering high-resolution nanosecond-order image sequences of plasma and shock waves, we model the structure of a laser-induced shock wave as a collection of spherical shocks originated from multiple plasmas. The model is found to rationalize both spherically-symmetric distribution of pressure impulse and non-spherically-symmetric distribution of peak pressure.

INTRODUCTION

A laser-induced underwater shock wave is of great importance in low-invasive medical treatments, such as shock wave lithotripsy[1] and drug delivery for cytoplasmic molecules[2]. The pressure distribution of the shock wave has been often regarded as spherically symmetric (so-called a spherical shock)[3]. However, there are several reports that the spherical-shock model is not applicable. Sankin et al.[4] measured pressure peaks for a shock at various positions and determined that the peak pressure at a point in the direction perpendicular to the laser beam is more than twice as high as that in the direction of the laser. Vogel et al.[5] reported that the shape of a shock wave is not spherical due to conical plasma formation. Although aforementioned results were reported, a model for the shock wave has still been under discussion.

This research investigates experimentally the structure of a laser-induced shock wave. Such an experiment is crucial but challenging since the time scale for generating the shock is very short; the time scale for plasma growth is in a few nanoseconds and the shock velocity in water is approximately 1,500 m/s. To the best of the authors' knowledge, we for the first time measure plasma growth, the expansion process of the shock, and pressure in water simultaneously.

EXPERIMENTAL SETUP

Figure 1 shows the experimental setup. A 532 nm, 6 ns laser pulse illuminates a point inside a water-filled glass tank (100×100×450 mm) through an objective lens, which results in generating an underwater shock wave. In the experiments we vary magnification of objective lens (5× [N.A. 0.1], 10× [N.A. 0.25], 20× [N.A. 0.25], MPLN series, Olympus co., Japan) and laser energy (2.6 mJ, 6.9 mJ, 12.3 mJ). The setup uses two hydrophones (Muller Platte-Gauge, Muller Co.) to measure pressure in water. Both hydrophones are placed 5 mm away from the focal point of the laser, one of which is set in the direction of the laser beam ($\theta = 0^\circ$ direction) and the other in the direction perpendicular to the laser beam ($\theta = 90^\circ$ direction). For recording plasma formation, we utilize an ultra-high-speed camera (Imacon 200, DRS Hadland Co.) with up to 200×10^6 fps (5 ns time interval) and a 1200×980 pixel array. For obtaining images of shock waves, we use another ultra-high-speed video camera (Kirana, Specialized Imaging Co.) with up to 5×10^6 fps and a 924×768 pixel array, which is synchronized with a laser stroboscope (SI- LUX 640, Specialized Imaging co., UK), the repetition rate of which is also up to 5×10^6 Hz. We use a digital delay generator (Model 575, BNC Co.) to synchronize the laser, the hydrophones, the cameras, and the stroboscope. We repeat measurements under the same experimental conditions more than three times.

RESULTS AND DISCUSSION

The measurement results with the 10× objective lens are shown in figure 2. The plasma emit lights in an elongated area, the major axis of which is in the direction of the laser beam as shown in figure 2(i). A laser-induced bubble then expands from a point where the plasma was formed (figure 2(ii)). Non-spherical shock is observed at $t = 0.4$ μs while the shock looks a single spherical shock at $t = 2.4$ μs (see Fig. 2(iii)). However, enlarged images in figure 2(iii)θ=0° and θ= 90° show two shock waves for $\theta = 0^\circ$ and the single shock wave for $\theta = 90^\circ$. The pressure in water measured at different positions are shoen in figure 2(iv). We find two peaks for $\theta = 0^\circ$ and a single large peak for $\theta = 90^\circ$, which is approximately 1.3 times higher than that for $\theta = 0^\circ$. This dependence of the peak pressure on the angle θ is consistent with the report by Sankin et al.[4]. Here, we compute the pressure impulse for $\theta = 0^\circ$, P_0, and that for $\theta = 90^\circ$, P_{90}. The definition of the pressure impulse is

$$P = \int p dt$$

where p is the shock pressure and t is the elapsed time. The pressure impulse is calculated for $t = 2.5$ to 4.5 μs, where time for plasma formation (<10 ns) is totally covered. Remarkably, as shown in figure 2(iv), P_0 reasonably agree with P_{90}. Furthermore, both pressure impulse and peak pressure are examined for all the other experimental conditions. It is found that even if peak pressure in $\theta = 0^\circ$ and 90° differ significantly, the P_0 is in good agreement with the corresponding P_{90}

* Corresponding author. Email: tagawayo@cc.tuat.ac.jp.
This work was supported by Kakenhi Grant-in-Aid (No. 26709007) from the Japan Society for the Promotion of Science (JSPS).

within the experimental uncertainty for a wide range of experimental parameters. The order of pressure impulse in this study is similar to drug delivery systems for cytoplasmic molecules[2].

In order to rationalize aforementioned results, we now propose a physical model for the structure of the laser-induced shock wave: The shock consists of multiple spherical shock waves as shown schematically in figure 3. In this model, each spherical shock wave originates from the corresponding plasma formation. In addition, we assume that the superposition principle is applicable: the net pressure produced by multiple shock waves which reach at the same position is the sum of the pressures obtained by the individual shock waves. This assumption reasonably works if the shock wave has pressure lower than approximately 100 MPa[5] where the shock behaves acoustically. Analogous phenomenon to this may be the surface wave after multiple stones are thrown into a quiescent liquid bath (the so-called Huygens–Fresnel principle).

This model successfully rationalizes both pressure peak of the shock (i.e. multiple pressure peaks for $\theta = 0^{\circ}$ and the single large peak for $\theta = 90^{\circ}$) and the pressure impulse (i.e. pressure impulse for $\theta = 0^{\circ}$ is equal to that for $\theta = 90^{\circ}$) for a wide range of experimental parameters. It should be noted that this model includes the well-known spherical-shock model. The origin of the elongated plasma is expected to be multiple spots of plasma even if just a single plasma or a bubble is observed as shown in figure 2. In addition, The model for the multiple shock structure may possibly rationalize the results reported in previous research. For instance, Sankin et al.[4] reported that a shock wave emitted from the elongated plasma has an angular variation of pressure distribution. Although the shape of the shock wave appears to be spherical, the elongated plasma shape might cause a multiple shock, as observed in the present experiments (see figure 2), which would lead to a non-spherically-symmetric pressure peak of the shock.

It is known that the nonlinear effect arises when the shock pressure is larger than 100 MPa[5], i.e. the liner superposition in this model is not applicable. However, spherically symmetric distribution of pressure impulse found in our study indicates that the nonlinear effect on the initial shock pressure is negligible or spherically symmetric in our experimental conditions. Thus the superposition model might be still applicable to rationalize results for both peak pressure and pressure impulse.

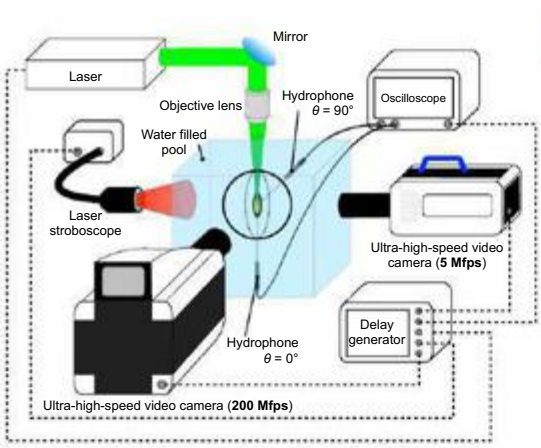

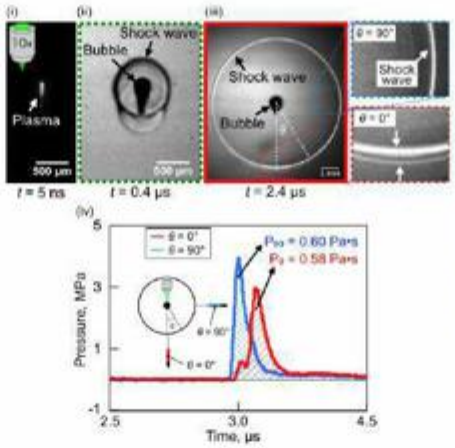

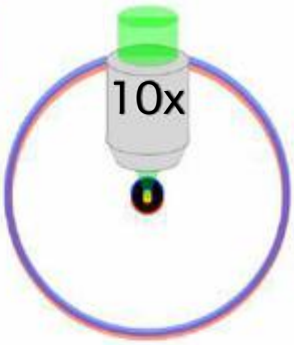

(Left) Figure 1: Measurement system consisting of two ultra-high speed cameras and two pressure sensors. An ultra-high speed video camera records laser-induced shock waves and bubbles at up to 5×10^6 fps with a synchronized laser stroboscope. Plasma luminescence is captured by another ultra-high speed video camera at up to 200×10^6 fps. Temporal pressure evolution is measured by two hydrophones. One hydrophone is arranged in the direction of the laser beam ($\theta = 0\circ$) at a stand-off distance of 5 mm from the laser focal point, while the other hydrophone is at right angles to the hydrophone ($\theta = 90\circ$) at the same stand-off distance.
(Center) Figure 2: Measurement results for a laser-induced underwater shock wave obtained with a 10× objective lens. (i) Plasma luminescence at t = 5 ns after the laser is fired. The image is captured by an ultra-high-speed video camera at 200 Mfps. (ii) Shock waves and bubbles at t = 0.4 μs imaged with an ultra-high speed video camera at 5 Mfps. (iii) Shock waves at t = 2.4 μs measured with an ultra-high-speed video camera at 5 Mfps. Enlarged images for the areas of $\theta = 0\circ$ and $\theta = 90\circ$ are also presented. (iv) Shock pressure measured by the two hydrophones arranged at $\theta = 0\circ$ (red line) and $\theta = 90\circ$ (blue line) with respect to the laser direction. Integrations for the pressure with respect to the elapsed time indicate pressure impulses.
(Right) Figure 3: Schematic of a multiple structure model for a laser induced underwater shock wave. Multiple plasmas emit multiple bubbles and spherical shock waves. In a linear system, the shock pressure at a certain point is the sum of spherical shock pressures that reach the same point.

References

[1] M. Sofer, J. Watterson, T. Wollin, L. Nott, H. Razvi, and J. Denstedt, *J. Urol.*, **167**:31, 2002.
[2] T. Kodama, M. R. Hamblin, and A. G. Doukas, *Bio-Phys. J.*, **79**:1821, 2000.
[3] K. Ando, A. Q. Liu, and C. D. Ohl, *Phys. Rev. Lett.*, **109**:044501, 2012.
[4] G. N. Sankin, Y. Zhou, and P. Zhong, *J. Acoust. Soc. Am.*, **123**: 4071, 2008.
[5] A. Vogel, S. Busch, and U. Parlitz, *J. Acoust. Soc. Am.*, **100**:148, 1996.

EFFECT OF UPSTREAM DISTURBANCES ON THE UNSTEADINESS OF SWEPT-RAMP INTERACTIONS AT MACH 2

Leon Vanstone[1], Mohammad Saleem[1], Serdar Seckin[1] & Noel Clemens [1a]
[1]Department of Aerospace Engineering and Engineering Mechanics, The University of Texas at Austin, Austin, Texas, USA

Summary This study examines the effect of upstream disturbances on the unsteadiness of a 3D shock-wave boundary-layer interaction generated by a swept-ramp in a Mach 2 flow. The disturbances studied are present in the undisturbed upstream boundary layer or imposed by a pulsed-jet actuator operating at kilohertz rates. A number of diagnostic techniques are employed, including surface flow visualization, fast-response surface pressure measurements, planar laser scattering and high resolution planar and stereo PIV. Previous work in this facility has identified a correlation between upstream disturbances and unsteadiness in 2D interactions. However, swept ramp interactions exhibit an "open" separated flow that does not recirculate. Open interactions are likely have significantly different unsteadiness mechanisms in comparison to 2D interactions. This work is part of an on-going study that seeks to better understand driving mechanisms of low-frequency unsteadiness in 3D interactions.

The Facility and Experiment

Experiments are conducted in the University of Texas at Austin blowdown supersonic Mach 2 wind tunnel. Stagnation pressure and temperature are 261±7 kPa and 292±5 K respectively with a free stream velocity of 510 ms^{-1}, a boundary layer height of 12.5 mm (based on U_{99}) and a unit Reynolds number (based on freestream conditions) of $Re_\infty=38\times10^6$ m^{-1}. Further information on the tunnel conditions can be found in [1]. The ramp has a 30° sweep and 22.5° compression angle which generates a swept interaction which grows in the spanwise direction, as shown in Figure 1. The ramp is fitted with a single fence on the upstream ramp location in order to prevent contamination with the side walls. The surface flow visualization has been conducted using mineral oil mixed with a fluorescent dye which is fluoresced with a UV lamp and recorded at 30 FPS. The PIV is high resolution, it is taken at 5Hz. The PIV plane shown in Figure 1 is at 10% the boundary layer height. High speed alcohol PLS was also conducted at 10 kHz. Surface pressure measurements are taken at 100 kHz.

The Time Averaged Structure

The time-averaged structure of the interaction is shown in Figures 1 and 2a. Figure 1a shows the surface features extracted from surface flow visualisation of the entire tunnel floor with certain features of the interaction superimposed. Figure 1b shows the same image with the PIV field of view super imposed. The interaction is clearly 3D, it shows a clear non-linear region at the most upstream location of the ramp with the interaction becoming conical and growing linearly in the spanwise direction. Significant cross flow is apparent in both the surface flow visualisation and time-averaged PIV. The time-averaged distribution gives the impression of a relatively steady interaction with features that are in good agreement with the general literature [2], [3].

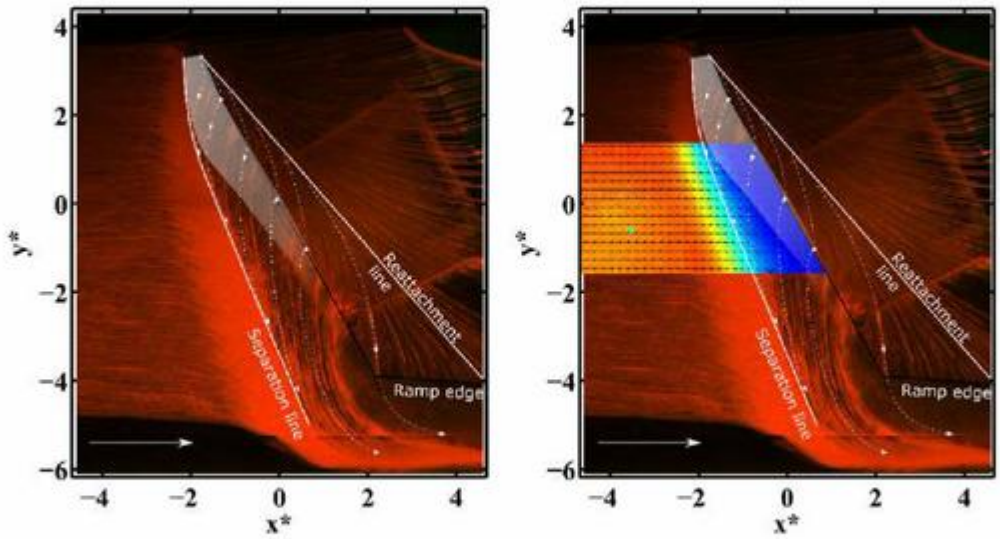

Figure 1 – Annotated surface flow visualization (left) with *u*-velocity contour overlaid (right) for comparison. White dotted lines are highlighted streak lines. Shaded white region shows region of reverse flow estimated from surface streak-lines.

[a)] Corresponding author. Email: clemens@mail.utexas.edu

The Instantaneous Structure

Figure 2 shows a comparison between the time-averaged and instantaneous surface flow visualisation. The instantaneous structure is very different to the average, showing significant local separation-line distortion and relatively weak cross-flow (three dimensionality) in the separation region relative to the average. Casual inspection of Figure 2b shows large elongated super-structures in the boundary layer of high and low velocity which appear to correlate with the separation-line position. It has been shown [1], [4] that the speed of the incoming boundary layer has a strong influence on the 3D separation line position. High speed regions survive the adverse pressure gradient longer pushing the separation line downstream, while low speed region survive it for less time moving the separation line upstream. The presence of these super-structures has been seen before [5]–[7] in this facility and in incompressible flows [8]. The distortion of the separation line caused by these superstructures is very similar in size to the unsteadiness region inferred from the RMS of the time-averaged distribution, suggesting it is a very significant mechanism.

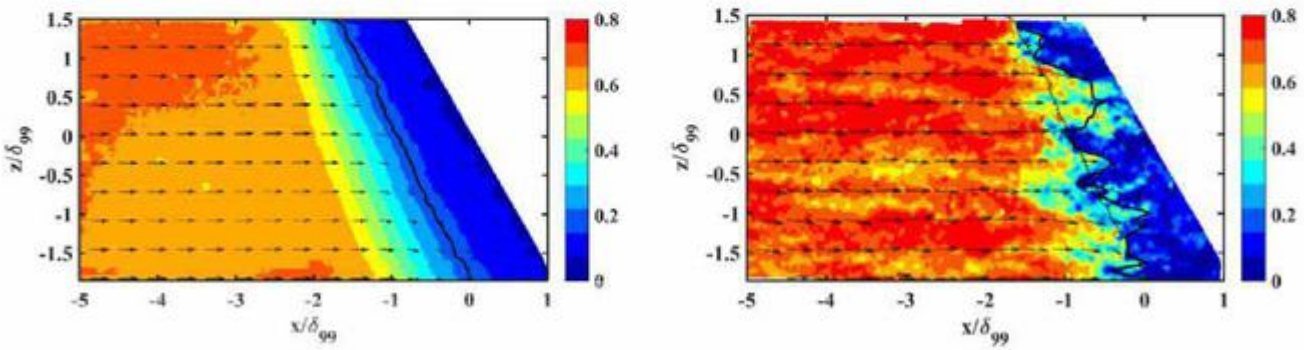

Figure 2 –*u*-velocity component in the *x*-*z* plane. (a) Time-averaged. (b) Instantaneous. Velocity has been normalised by the free stream velocity (510 ms^{-1}). Black solid line shows the surrogate separation line. Black dotted line shows the average separation line.

Conclusions

This study finds a strong correlation between the location of the separation line and the velocity of the incoming boundary-layer for a swept-ramp interaction at Mach 2. The high degree of local distortion to the separation line and the low instantaneous cross flow could be interpreted as implying that the three dimensionality is relatively diminished and that this 3D interaction might share similarity with the 2D case. However, this conclusion is speculative and requires further investigation. In future work, we will make extensive use of arrays of fast-response pressure measurements to explore the correlation among fluctuations in the upstream boundary layer, the separation shock foot, and the reattachment region. Furthermore, disturbances will be imposed in the upstream boundary layer using an array of pulsed microjets, which will be pulsed at frequencies ranging from 1 to 10 kHz. The effect of the pulsed microjets on the interaction dynamics will be explored with the fast-response pressure measurements and PIV.

[1] L. Vanstone, M. Saleem, S. Seckin, and N. T. Clemens, "Effect of Upstream Boundary Layer on Unsteadiness of Swept-Ramp Shock/Boundary Layer Interactions at Mach 2," *AIAA SciTech*, pp. 1–14, 2016.

[2] M. E. Erengil and D. S. Dolling, "Effects of Sweepback on Unsteady Separation in Mach 5 Compression Ramp Interactions," *AIAA J.*, vol. 31, no. 2, pp. 302–311, 1993.

[3] J. C. Gonsalez and D. S. Dolling, "Correlation of Interaction Sweepback Effects on the Dynamics of Shock-Induced Turbulent Separation," *AIAA*, 1993.

[4] L. Vanstone, M. Saleem, S. Seckin, and N. T. Clemens, "Experimental Investigation of Unsteadiness of Swept-Ramp Shock / Boundary Layer Interactions at Mach 2," *AIAA Aerosp. Sci. Meet.*, no. June, pp. 1–12, 2015.

[5] S. J. Beresh, N. T. Clemens, and D. S. Dolling, "Relationship Between Upstream Turbulent Boundary-Layer Velocity Fluctuations and Separation Shock Unsteadiness," *AIAA J.*, vol. 40, no. 12, pp. 2412–2422, Dec. 2002.

[6] B. Ganapathisubramani, N. T. Clemens, and D. S. Dolling, "Effects of upstream boundary layer on the unsteadiness of shock-induced separation," *J. Fluid Mech.*, vol. 585, p. 369, Aug. 2007.

[7] B. Ganapathisubramani, N. T. Clemens, and D. S. Dolling, "Low-frequency dynamics of shock-induced separation in a compression ramp interaction," *J. Fluid Mech.*, vol. 636, p. 397, Sep. 2009.

[8] N. Hutchins and I. Marusic, "Evidence of very long meandering features in the logarithmic region of turbulent boundary layers," *J. Fluid Mech.*, vol. 579, no. 2007, p. 1, 2007.

[9] N. T. Clemens and V. Narayanaswamy, "Low-Frequency Unsteadiness of Shock Wave/Turbulent Boundary Layer Interactions," *Annu. Rev. Fluid Mech.*, vol. 46, no. 1, pp. 469–492, Jan. 2014.

KELVIN-HELMHOLTZ INSTABILITY IN COMPRESSIBLE SHEAR FLOWS: EFFECT OF WAVENUMBER

Mona Karimi *[1,2] and Sharath S. Girimaji [2]

[1]*Department of Mathematics , Texas A&M University, College Station, TX, USA*
[2]*Aerospace Engineering Department, Texas A&M University, College Station, TX, USA*

Summary Kelvin-Helmholtz (KH) instability is central to shear flow mixing and is known to be suppressed in compressible flows. The objective of this work is to investigate the effect of perturbation wavenumber on the degree of suppression of the KH instability in high-speed shear flows. We demonstrate that the degree of suppression decreases with increasing the initial perturbation wavenumbers.

INTRODUCTION

Kelvin-Helmholtz (KH) instability occurs at the interface between two fluid streams of different velocities. The experimental/numerical investigations and modal analyses of the compressible KH instability clearly demonstrate significant suppression [1,2]. The physical suppression mechanism underlying the stabilizing effect of compressibility on KH instability has been explained recently [3]. We further that work to demonstrate the influence of wavenumber perturbation on the degree of suppression. In the incompressible flows, shear effects dominate the interface flow dynamics causing monotonic roll-up of vorticity and mixing between the two streams, leading to the KH instability. However, the instability mechanism in sufficiently compressible flows is fundamentally different. In high-speed flows, compressibility forces the dominance of dilatational rather than shear dynamics at the interface, leading to the segregation of the flow domain into dilatational interface layer (DIL) in the middle and the outer regions in the far-field. We utilize the results of transient stability analysis and numerical simulations to explain the degree of suppression mechanism within the DIL.

LINEAR ANALYSIS

We consider the linear stability of a steady, planar, parallel free-shear layer with the base velocity field of $\overline{\mathbf{u}} = (U_1(x_2), 0, 0)$, where x_1, x_2 and x_3 are taken to be streamwise, normal and spanwise directions. The flow and thermodynamic variables are decomposed into base and perturbation fields: $q(\rho, u_i, p)$=$\bar{q} + q'$ where $q = q(\rho, \mathbf{u}, \mathbf{p})$; density$\circ$ ρ; velocity field$\circ$ $\mathbf{u}$ and pressure$\circ$ p. Note that a planar shear layer invokes that $\partial\bar{p}/\partial x_i = 0$ and $\partial\bar{u}_i/\partial x_i$=0. We assume an inviscid, ideal gas, $p = \rho RT$ at uniform Temperature (T), where γ is the specific heat ratio. It is important to examine the evolution of the perturbation field in a reference frame advecting with the unperturbed flow. Thus, the following coordinate transform is invoked: X_1=x_1-$\int_0^t U_1 d\xi$, X_2=x_2 and X_3=x_3. To understand the suppression mechanism of KH instability by compressibility, investigating the change in the character of p' by u_2' is essential [3]. To identify the non-modal stabilization mechanism [4] of KH instability and modeling transition to turbulence in compressible flows, we explain the transient suppression mechanism by employing a linear *initial value analysis* rather than the previous eigenvalue analyses [5,6] . Hence, we examine the temporal evolution of the two-dimensional perturbation mode of the type: $q = \hat{q}(X_2, t)e^{i\kappa X_1}$, where $\hat{(.)}$ is the Fourier amplitude; κ is the wavenumber; and $\hat{q}(X_2, 0)$ satisfies the free-stream boundary conditions. The linearlized perturbation equations are rearranged in the form of wave (hyperbolic) equations with source terms [3]:

$$M_g^2 \frac{\partial^2 \hat{u}_2^*}{\partial t^{*2}} = \frac{\partial^2 \hat{u}_2^*}{\partial x_2^{*2}} + (\hat{u}_2^* S^* \circ \hat{u}_1^*) S^* + \frac{i}{\kappa} \frac{\hat{p}^*}{\gamma u^0} S, \tag{1}$$

$$M_g^2 \frac{\partial^2 \hat{p}^*}{\partial t^{*2}} = \frac{\partial^2 \hat{p}^*}{\partial x_2^{*2}} \circ \hat{p}^* + 2i \frac{u^0 \bar{\rho}}{\kappa \bar{p}} \hat{u}_2^* S, \tag{2}$$

the relevant parameter to characterize compressibility effects on perturbation field, *gradient Mach number*, M_g, is defined by

$$M_g \equiv \frac{S}{\bar{a_0}\kappa}, \tag{3}$$

where $\bar{a_0} = \sqrt{\gamma\bar{p}/\bar{\rho}}$ is the speed of sound. $S \equiv \partial_{X_2} U_1$ is the shear rate of the base velocity and $S^* \equiv \int_0^t S(X_2) d\xi$. The independent variables are normalized as follows: $t^* \equiv St$ and $x_2^* \equiv \kappa X_2$, where κ is the magnitude of the perturbation wavenumber. The normalized pressure and velocity amplitudes are: $\hat{p}^* \equiv \hat{p}/\overline{p}$ and $\hat{u}_i^* \equiv \hat{u}_i/u^0$, respectively, where u^0 is the root mean square of the initial perturbation velocity. At high speeds ($M_g > 1$), p' evolution is described by the non-homogeneous wave equation (2) and pressure propagates through the flow field at a wave speed proportional to $1/M_g$. It is

*Corresponding author. Email: mona.karimi@tamu.edu

immediately evident that u_2' is coupled as a harmonic oscillator, also attains the wave-like character in compressible flows. The changing sign of u_2' in a compressible shear layer has a profound effect on perturbation kinetic energy and spanwise vorticity. The analysis of the reduced mathematical equations demonstrate that spanwise vortex structures roll and un-roll repeatedly. Furthermore, perturbation energy production is alternately positive and negative. Such behavior will necessarily result in stabilization of the flow nearby the interface of two streams.

NUMERICAL SIMULATIONS

We test the validity of the theoretical analysis by performing a sequence of three-dimensional simulations of perturbation evolution in a temporally evolving mixing layer at different convective Mach number $M_c \equiv \Delta U/2\bar{a}$= 0.7, 1.0, and 1.2. The hyperbolic base velocity field, $\overline{u}$, and the sinusoidal perturbation velocity field are identified: $\overline{u}$=$(\Delta U/2\tanh(0.5x_2/\delta_m^0), 0, 0)$, where δ_m^0 is the initial momentum thickness of the mixing layer. To examine how the initial M_g can characterize thickness of the DIL, we examine the evolution of perturbation field at different κ and S in equation (3) at a fixed M_c.

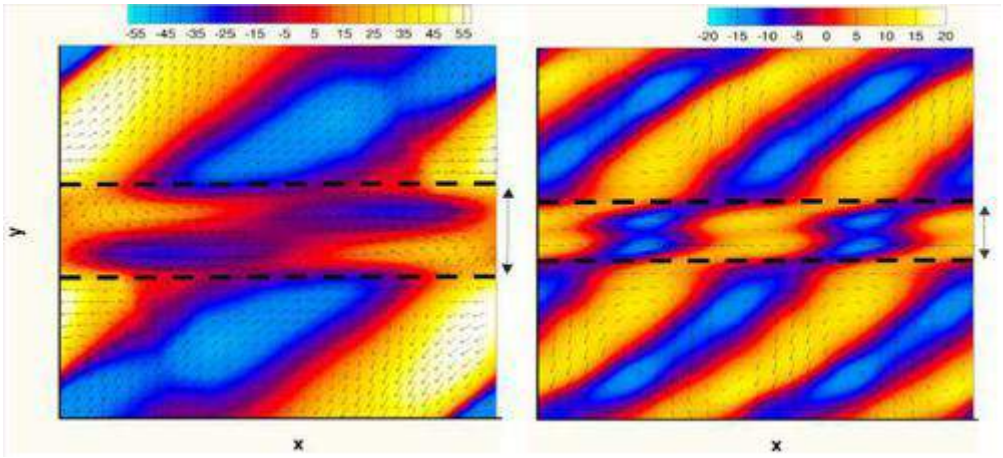

Figure 1: Contour plots of pressure perturbation of a mixing layer at the initial M_c=1.2, for (a) $\kappa = 1$ (b) $\kappa = 2$. The dilataional interface layer is indicated by the dash line.

DISCUSSION

The difference between KH instability of compressible and incompressible flows is explained through the change in the character of pressure. In the incompressible flows, shear-driven motion of pressure leads to the merging, roll-up of the vortices and more circulation at the interface of two streams. While in the compressible flows, there is a dilatation-driven oscillatory which separates the two streams. The interface layer acts as a physical structure for channelling the flow and guiding the pressure waves. There is some sort of active feedback mechanism within the DIL where the source terms, the right-hand sides of the equations (1)-(2), set up an oscillation within the DIL. The pressure gradient in the outer regions travels with the oblique to the high pressure gradients inside the interface layer. When and where the DIL starts forming are investigated through the numerical simulation and linear analysis. Dynamics of the evolution of the DIL depends on the local value of the gradient Mach number. As wavenumber of the initial perturbations increases, the thickness of the DIL decreases at a fixed convective Mach number as shown in Fig. 1. This is in agreement with the the equations (1)-(2), as the effect of compressibility diminishes, as $M_g \to 0$, resulting in the sustained growth of perturbation vorticity and kinetic energy.

References

[1] Papamoschou D., Roshko A.: The Compressible Turbulent Shear Layers: an Experimental Study. J. Fluid Mech 9:453-477, 1988.

[2] Sandham N.D., Reynolds W. C.: Three-dimensional simulations of large eddies in the compressible mixing layer. J. Fluid Mech. 224:133-158, 1991.

[3] Karimi M.: Compressibility effects on the Kelvin-Helmholtz instability and mixing layer flows. PhD Thesis, Texas A&M University, 2015.

[4] Schmid P.J.: Nonmodal Stability Theory. Annu.Rev. Fluid Mech. 29: 129-162, 2007.

[5] Blumen W.: Shear Layer Instability of an Inviscid Compressible Fluid. J. Fluid Mech. 40:769-781, 1970.

[6] Jackson T. L., Grosch C. E.: Inviscid Spatial Stability of a Compressible Mixing Layer. Phys. Fluids A 2:949-954, 1990.

EXCITATION OF THE STREAKS BY WEAK SHOCK WAVES IN THE SUPERSONIC BOUNDARY LAYER

Alexander Kosinov[1, 2a)], Nikolay Semionov[1], Gleb Kolosov[1], Yury Yermolaev[1] & Aleksey Yatskikh[1, 2]
[1]*Khristianovich Institute of Theoretical and Applied Mechanics SB RAS, Novosibirsk, Russia*
[2]*Novosibirsk State University, Novosibirsk, Russia*

Summary The occurrence of the streaks was detected in the flat plate boundary layer at Mach 2.5. They arise due to the interaction of the weak shock waves with the flow in the vicinity of blunted leading edge. The process is accompanied by increasing of the local skin friction as well as the pulsation amplitude in the boundary layer. Here this simple case is discussed in comparison to the similar results obtained before in the boundary layer of the flat delta wing.

INTRODUCTION

The transition mechanisms in a supersonic boundary layer are largely dependent on the level of disturbances in the free flow. For example, conventional supersonic wind tunnels have the measurable level of acoustic pulsations in the test section [1, 2], which leads to the early laminar-turbulent transition. The effect of acoustic pulsations on the turbulence origin in a supersonic boundary layer was mainly investigated for flat plate [3, 4]. In some cases, in addition to acoustic pulsations there are the quasi-stationary perturbations in the form of weak shock waves in the test section of the wind tunnel that can affect models too. We have detected the abnormally high levels of mass flow fluctuations in the boundary layer of the plane delta wing, which achieved up to 20% of the local value of the mass flow [5]. The cause of these high-intensity disturbances could be attributed either to the impact of external Mach's wave on the boundary layer along the attachment line of the leading edge of the delta wing, or to its interaction with bow shock. To test this, the excitation of disturbances by weak shock waves in the boundary layer of delta wing were experimentally investigated in [6] at Mach numbers 2, 2.5, 4, but the radius of the side edge was several times greater than one used in [5]. The studied cases therefore corresponded to subsonic, near sonic and supersonic leading edge. It has found out that the mass flow pulsation reached 12-15% and varied only slightly from the flow conditions. Thus, the effect of the interaction of the incident weak shock wave with the bow shock can be not very significant. The streaks occurrence was always detected in the boundary layer.

Since the results presented in [5, 6] are the only confirmation of the disturbance excitation, it is necessary to further investigate in detail other relevant cases. In experiments presented here, we used the flat plate with blunted leading edge at Mach 2.5, as the disturbance excitation is several times less for the model with a sharp leading edge.

SET-UP OF THE EXPERIMENTS

The experiments were conducted in a supersonic wind tunnel T-325 of the Institute of Theoretical and Applied Mechanics at Mach 2.5 and unit Reynolds number $Re_1 = 5\times10^6$ m^{-1}. The flat plate had a cylindrical leading edge with the bluntness radius of 2.5 mm. To create a pair of weak shock waves, 2D sticker is glued on the sidewall surface of the test section upstream of the model as it is presented in Fig. 1. Dimensions of the sticker were 0.13 or 0.26 mm in thickness, 15 mm in width and about 150 mm in length. In this case, pair weak shock waves are generated to free flow by the front and rear edges of the 2D surface irregularity, similarly to data published in [6]. To measure the flow characteristics, constant temperature anemometer (CTA) was used. Hot-wire sensors made from tungsten wire were 10 μm in diameter and about 1.6 mm in length. The overheat loading of the wire was about of 0.8, so that the measured disturbance on 95% was coincident to the mass flow pulsations (m'). To measure the pressure distribution over the model surface, a Preston tube is used.

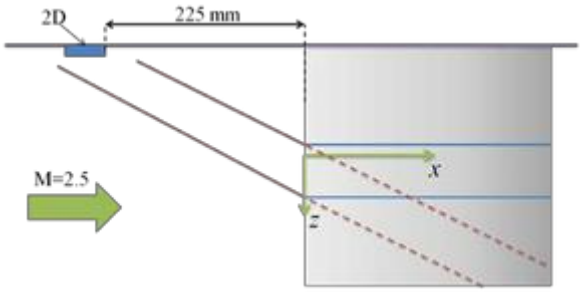

Figure 1. Experiment set-up.

RESULTS

Pulsations of the supersonic flow in the test section of the T-325 have normal distribution for the amplitude that does not correspond to their interaction in a free flow. Generated by two-dimensional sticker, the disturbance in the free flow has local non-linear properties, which are characterized by significant deviation of the amplitude distribution from the normal probability density. It was checked by the hot-wire measurements of the spanwise pulsation distribution in the free flow at x = -10 mm upstream from the leading edge. An example of the measurements for 0.13 mm sticker is shown in Fig. 2.

[a)] Corresponding author. Email: kosinov@itam.nsc.ru.

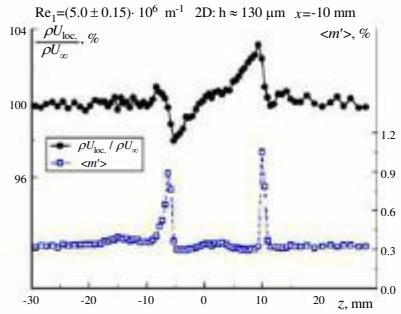

Figure 2.

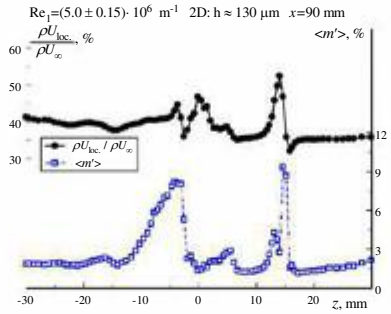

Figure 3.

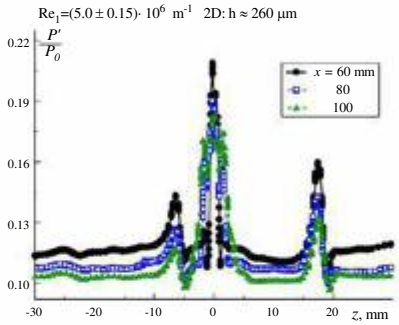

Figure 4.

Here, there are sharp peaks in the spanwise distribution of the mass flow disturbances in the neighbourhood of weak oblique shocks generated by the 2D sticker on the sidewall surface. Under the experimental conditions, the sidewall boundary layer was turbulent with thickness of about 12 mm. The maximum in the pulsation distribution at z = 10 mm corresponds to a wave from the front edge of the sticker and z = 0 is the centreline of the flat plate. As for the mass flow distribution, the relative value of ρU (z) reminds well-known N-wave, the amplitude of which is about ±3 % relative to the mean value of the mass flow in free flow.

The results of the hot-wire measurements in the flat plate boundary layer at x = 90 mm and y = 0.7 mm, where y is normal to the flat plate coordinate, are shown in Fig. 3 together with results for undisturbed artificially free flow. It is typical response of the supersonic boundary layer to these artificial disturbances, which is similar to results published in [5, 6]. Just only, the pulsation amplitude has less value and reaches approximately 8-10%. Not considering here the statistical features of the disturbances, it is necessary to mention that there was mainly the low-frequency pulsation excitation in the boundary layer. Defects of the mean flow in the spanwise direction indicates the existence of a pair of vortices in the boundary layer. It is interesting to know how they changed the skin friction.

We consider here only data obtained using the sticker of 0.26 mm in thickness on sidewall of the test section, which produces the more intensive amplitude of the weak shock waves in comparison with the data shown in Fig. 2. As an indicator of the skin friction, Preston's tube measurements over the flat plate surface are used. Relevant pressure distributions obtained for the various coordinates is shown in Fig 4. In order to have an arbitrary scale of the obtained values, the figure also includes the data on the pressure distributions of the submerged weak jet that is intentionally blown into the boundary layer through a surface aperture of 0.42 mm in diameter at z = 0 and x = 35 mm. It was found out that at the downstream distance up to 100 mm from the leading edge the boundary layer remains laminar, despite of the existence of stationary vortices and their significant influence to the skin friction. These data confirm one of the features of evolution of the perturbations mentioned in [6]. The spanwise scale of the stationary perturbations in boundary layer generated by the external weak shock waves was not almost changed downstream. Perhaps, the disturbances have "streaky structures" features downstream in the supersonic boundary layers [7].

CONCLUSIONS

The origin of the streaks were detected in the flat plate boundary layer at Mach 2.5. They arise due to the interaction of the weak shock waves with the flow in the vicinity of blunted leading edge. The process is accompanied by increasing of the local skin friction as well as the pulsation amplitude in the boundary layer. The data are similar to the results obtained before in the boundary layer of the flat delta wing [5, 6]. The results are suitable for the CFD code verification.

This work is supported by the Russian Foundation for Basic Research (grant number 16-01-00743).

References

[1] Laufer J.: Aerodynamic noise in supersonic wind tunnels. *J. Aerospace Sci*. **28**: 685-692, 1961.

[2] Kendall J.M.: Wind tunnel experiments relating to supersonic and hypersonic boundary-layer transition. *AIAA J*, **13**: 290-299, 1975.

[3] Kosinov A.D., Maslov A.A., Semionov N.V.: An experimental study of generation of unstable disturbances on the leading edge of a plate at M=2. *J. AMTP*, **38(1)**: 45-51, 1997.

[4] Schneider S.P.: Effects of high-speed tunnel noise on laminar-turbulent transition. *J. Spacecraft and Rockets* **38(3)**: 323-333, 2001.

[5] Vaganov A.V., Kosinov A.D., Semionov N.V.: The origin of turbulence in vicinity of lateral edge of blunted triangular plate in supersonic flow. *ICMAR 2012, book of Abstracts*, Kazan, Russia, **Pt. II**: 269-270, 2012.

[6] Kosinov A.D., Yermolaev Yu.G., Kolosov G.L., Panina A.V., Semionov N.V.: On the effect of the incident Mach wave on the pulsation level in boundary layer of the plane delta wing *ICMAR 2014*, Novosibirsk, Russia: Proc. http://www.itam.nsc.ru/users/libr/eLib/confer/ICMAR/2014/pdf/ Kosinov283.pdf.

[7] Matsubara M., Alfredsson P.H.: Disturbance growth in boundary layers subjected to free-stream turbulence. *J. Fluid Mech*. **430**: 149- 168, 2001.

UNSTEADY SHOCK WAVE REFLECTION FROM CONCAVE SURFACES

Evgeny Timofeev*[1], Harald Kleine [2], Federico Alzamora Previtali[3], and Ali Hakkaki-Fard[4]
[1]*Department of Mechanical Engineering, McGill University, Montreal, Quebec, Canada*
[2]*School of Engineering and Information Technology, University of New South Wales, Canberra, Australia*
[3]*Department of Mechanical Engineering, McGill University, Montreal, Quebec, Canada*
[4]*Department of Mechanical Engineering, Sharif University, Tehran, Iran*

Summary Shock wave reflection from concave surfaces including a purely cylindrical concave reflector and a composite one consisting of a concave cylindrical arc transitioning to a straight inclined surface is the subject of the present study. A combined – theoretical, numerical and experimental – approach is used. The main attention is given to the transition from a Mach reflection to a regular reflection. New theoretical predictions of the transition are based on the information on the corner signal propagation obtained from numerical simulations via an original signal tracking technique. Numerical simulations are carried out using the Euler and Navier-Stokes models. State-of-the-art time-resolved optical flow visualization is employed in shock tube experiments. The obtained results and conclusions significantly alter the current state of knowledge about the phenomena.

The paper presents work aiming at the re-examination of the current state of knowledge regarding initially planar shock reflection from concave surfaces. A concave cylindrical surface as well as a composite surface consisting of a concave cylindrical arc followed by a straight wedge are considered. The emphasis is on the transition from a Mach reflection (MR) to transitioned regular reflection (TRR). Combined – theoretical, numerical and experimental – studies are undertaken.

The recent (2007) state-of-the-art in this research area is summarized in [1]. Analytical and experimental results from [1] regarding the MRR-TRR transition on a cylindrical concave surface are shown in Fig. 1a. Our numerical results obtained with an adaptive unstructured finite-volume Euler code `Masterix` [2] are plotted in Fig. 1a as well ('CFD'). It is seen that the MR-TRR transition is predicted to happen at appreciably higher wall angles as compared to the experimental results from [1]. It is conjectured that the discrepancy between the present numerical simulation and the experimental results is primarily caused by insufficient optical resolution rather than viscous effects which manifest themselves mainly via effective modification of local wall angle due to boundary layer displacement. According to [1] and our numerical modeling, the triple point trajectory is tangential to the reflecting surface prior to transition. This results in very small Mach stems over a rather wide range of wall angles and poses significant challenges for optical diagnostics. This fact is illustrated by Fig. 1b,c showing an instant when the Mach stem height is $\sim 0.0016R$, where R is the radius of curvature of the reflecting surface. Therefore, to clarify the issue, new experimental observations are undertaken with the cylindrical concave model of larger radius and up-to-date high-resolution imaging; details of the experimental setup may be found in [3].

The previous theoretical treatment [1] is based on two main assumptions: (1) the MR-TRR transition takes place when the corner signal generated at the leading edge of the reflecting surface is no longer capable of catching up with the reflection point; (2) the corner signal velocity is evaluated using the flow parameters behind the incident shock, assuming that the reflected shock is weak. The three modifications of the theory shown in Fig. 1a differ in the additional assumption on the path which the corner signal follow. None of the three theories provide satisfactory agreement with the numerical findings for the entire range of Mach numbers. Examination of our numerical flowfields shows that the above-mentioned second assumption seems to be in significant error at later stages of the interaction, prior to transition, when the reflection shock becomes stronger.

We use the numerical signal tracking technique proposed in [4] to observe signal propagation and obtain more accurate information on the velocity and front geometry of the corner signal and its propagation path. In this technique, signals are considered as infinitesimally weak sound waves propagating with the local speed of sound relative to the flow and being carried by the flow itself as well. The tracking is done at the end of each time step as a postprocessing procedure. Since no actual disturbance is introduced to the flow, the technique is as accurate as the numerical flowfield itself. Information on the corner and other signals provides further insight into the gasdynamics of the refection process and allow us to improve the existing theories predicting the MR-TRR transition angle by more accurately accounting for physics of corner signal propagation.

In the second part of the paper, a combination of a concave cylindrical surface (an arc) and a straight wedge is considered with the aim of investigating how such a concave wedge tip may alter the resulting reflection pattern. It was numerically demonstrated in [5] that the resulting reflection pattern established far away from the wedge tip (regular or Mach reflection) may differ depending on whether the reflecting wedge has a straight or concave tip. Parametric studies in [6] showed that the effect is observed for shock Mach numbers corresponding to the dual solution domain (where both Mach and regular reflection are physically admissible) and wedge angles ranging from the sonic angle to a value slightly lower than the von Neumann angle, i.e., within the most part of the dual solution domain. The first experimental demonstration of the effect for a concave tip wedge with the radius of curvature $R = 12$ mm and a straight wedge with the same angle was published in [6].

In the present paper, experiments for the wedge tip radius as low as 4 mm are presented. It is demonstrated that even with such a small tip the above-mentioned effect is observed, i.e., minute variations in geometry may lead to different reflection

*Corresponding author. Email: evgeny.timofeev@mcgill.ca

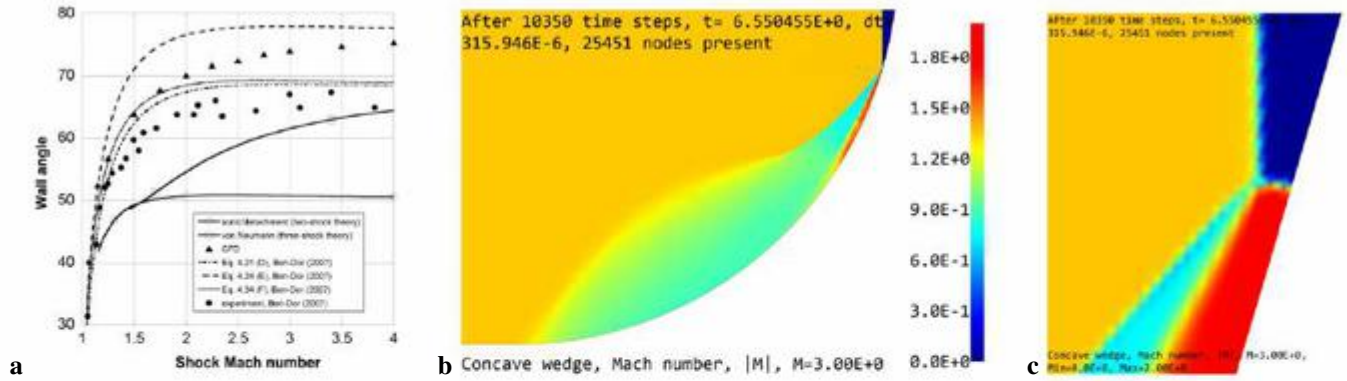

Figure 1: **a** Analytical ($\gamma = 1.4$), experimental and numerical predictions of MR-TRR transition on the concave cylindrical surface; **b, c** A CFD result for shock Mach number $M_s = 3.0$ ($\gamma = 1.4$) and an instant close to MR-TRR transition. The Mach number distribution is shown: **b** entire flowfield, the reflection seems to be regular; **c** magnified image near the reflecting surface revealing true nature of the reflection.

patterns and hence different dynamic and heat loads. The resulting reflection is of iregular type (see Fig. 1a,b) in the presence of the small concave tip while a straight wedge with the same angle produces a regular reflection. The above-mentioned signal tracking technique [4] is also used to study the propagation of the corner signal front as illustrated in Fig. 2c. Information about the velocity of the corner signal and its path is therefore obtained from numerical experiments and used in an analytical treatment to predict the regular-to-Mach reflection transition angle for wedges with concave tips. Furthermore, numerical simulations using the Navier-Stokes equations are carried out for selected cases. The study of the influence of viscous effects is essential because in most shock tube experiments high Mach numbers (> 2) can be achieved only at low pressures in the test section. As a result, the Reynolds number based on the tip radius R can be as low as 15,000 for $R = 4$ mm.

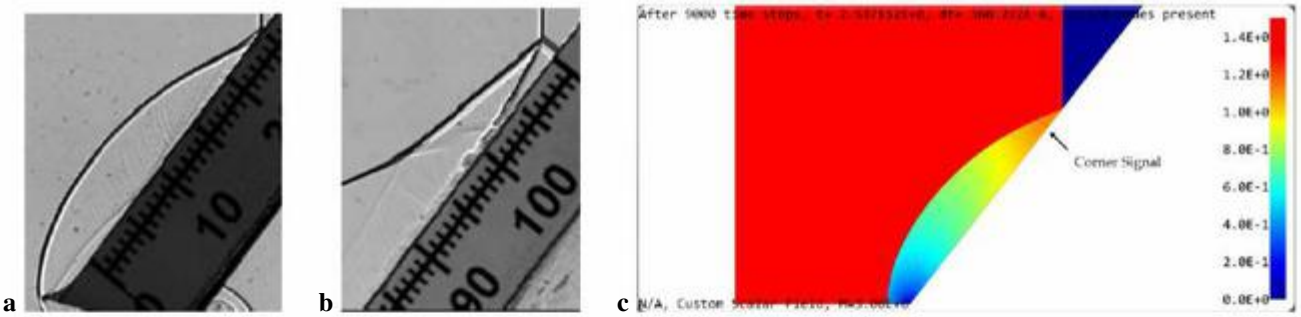

Figure 2: **a, b** Shadowgraph movie frames for the wedge angle $\theta_w = 52°$, the concave tip radius $R = 4$ mm, and the nominal shock Mach number $M_s = 3.0$. The frame **a** shows the flowfield near the tip; a small Mach stem is already discernible. The frame **b** shows a well-developed irregular reflection close to the end of the wedge; **c** Inviscid CFD simulation by an adaptive unstructured finite-volume code `Masterix` of shock wave ($M_s = 3.0$) reflection from a straight wedge with the wedge angle $\theta_w = 52°$, with corner signal tracking. The corner signal front at the displayed time moment is shown with a thin solid line running along the reflected shock and then coming to the surface well behind the reflected point, i.e., the signal is not catching up with the reflection point. This corresponds to the regular nature of the observed shock reflection.

References

[1] Ben-Dor G.: Shock Wave Reflection Phenomena. 2nd ed., Springer, 2007.

[2] `Masterix` (2003-2015), ver. 3.40, RBT Consultants, Toronto, Ontario.

[3] Kleine H., Timofeev E., Hakkaki-Fard A., Skews B.: The Influence of Reynolds Number on the Triple Point Trajectories at Shock Reflection off Cylindrical Surfaces. J. Fluid Mech. 740:47-60, 2014.

[4] Hakkaki-Fard A., Timofeev E.: On Numerical Techniques for Determination of the Sonic Point in Unsteady Inviscid Shock Reflections. Internat. J. of Aerospace Innovations 4:41-52, 2012.

[5] Lau-Chapdelaine S.S., Radulescu M.I.: Non-Uniqueness of Solutions in Asymptotically Self-Similar Shock Reflections. Shock Waves 23(6):595-602, 2013.

[6] Alzamora Previtali F., Timofeev E., Kleine H.: On Unsteady Shock Wave Reflections from Wedges with Straight and Concave Tips. AIAA Paper 2015-2642, 2015 doi: 10.2514/6.2015-2642

REAL-TIME SOLUTION OF ONE-DIMENSIONAL DISTRIBUTED-PARAMETER MODELS WITH APPLICATION TO COMPRESSIBLE FLOW IN DIESEL PARTICULATE FILTERS

Soroosh Hassanpour [*1], Amer Keblawi[1], and John McPhee[1]

[1]*Systems Design Engineering, University of Waterloo, Waterloo, Ontario, Canada*

Summary A modified orthogonal collocation method is proposed for reduction and real-time solution of one-dimensional distributed-parameter system models. The method uses Lagrange polynomials as trial functions and sets the nodal points to coincide with the collocation points. Maple™ is used to illustrate the application of the method for real-time simulation of compressible flow in a diesel particulate filter.

INTRODUCTION

Limited time and storage play a key role in computational aspects of computer simulations. Design optimization and advanced controller development require accurate but fast computer models. This is challenging to achieve with a distributed-parameter model governed by (nonlinear) partial differential equations (PDEs) with variables changing in time and space. There are several approximation schemes by which the spatial domain of such a model can be discretized and the governing PDEs can be reduced or converted into a system of ordinary differential equations (ODEs) that can be solved efficiently. The commonly-used numeric approaches, such as finite difference and finite element formulations, are computationally expensive and hide the physics of the model. Black box techniques such as look up tables and neural networks are fast but offer no access to model parameters. Neither of these methods are therefore suitable for model-based design and control. Symbolic reduction methods, such as weighted residual schemes and variational principles [1], on the other hand can both expose model parameters and be computationally efficient. Symbolic simplification algorithms of computer algebra packages, such as Maple™ and Mathematica®, can be employed along with these symbolic reduction schemes to derive very efficient models. Developed symbolic models are expected to run significantly faster than current numeric-based approaches. In addition, further reduction of these symbolic models by the use of model order reduction schemes, such as the proper orthogonal decomposition, is possible.

OBJECTIVE

The main goal is to develop the mathematical theories and computer algorithms necessary to symbolically reduce the governing PDEs of various one-dimensional (1D) distributed-parameter models to a system of symbolic ODEs. Such a tool would have a wide range of applications, *e.g.* in automotive applications for modeling engine manifolds, drive belts, and after-treatment components. The work is based on using a specific form of the method of weighted residuals (MWR) and harvesting the power of symbolic computation in Maple™ to achieve computational efficiency.

METHODOLOGY

The MWR is a general method of symbolically reducing PDEs to ODEs. It is based on expanding the unknown solution as the finite summation of a set of known trial spatial functions multiplied by unknown time-varying coefficients. The approximate solution is substituted into the PDE to form a residual. Then using a (complete) set of known weighting functions, the weighted integrals of the residual are set to zero to derive a set of ODEs from which the unknown coefficients can be computed. The weighting functions can be chosen in many ways and each choice corresponds to a different MWR. The Galerkin method is one of the best known approaches where the weighting functions are chosen to be the trial functions. The method forces the residual to be zero by making it orthogonal to each member of a complete set of functions. The method, however, is not suitable for nonlinear PDEs where the integrals of the weighted residual cannot be calculated analytically and may result in a very complex system of ODEs if a numerical integration has to be used. In the collocation method, the weighting functions are chosen to be the displaced Dirac delta functions, reducing the integration over a domain to evaluation at a point inside the domain. Thus, the method forces the residual to be zero at some specified collocation points and, since no spatial integration is required, it drastically reduces the drudgery of setting up the problem. It has proved to be suitable for nonlinear PDEs and as accurate as the Galerkin approach provided a higher-order approximation is used.

In the collocation method, the low-order approximation results depend on the choice of collocation points. There are choices of collocation points which make the calculations more dependable and accurate. The orthogonal collocation method (OCM) [1, 2] uses a set of N orthogonal polynomials, up to order $(N-1)$, as trial functions and the roots of the $(N+1)$th orthogonal polynomial (of order N) as collocation points. The residual function is therefor forced to contain the $(N+1)$th orthogonal polynomial as a factor, because its zeros are set to match the roots to the $(N+1)$th polynomial. Due to orthogonality relations, the OCM has an accuracy that is comparable to that of the Galerkin method [2].

It is interesting that the OCM approximate solution depends only on the collocation points and not on the form of trial polynomials, which can therefore be selected to expedite the reduction procedure. This work is based on applying two

[*]Corresponding author. Email: soroosh@uwaterloo.ca

adjustments on trial polynomials. First, Lagrange polynomials of order $(N-1)$, based on N nodal points, are used as trial functions to ensure that the unknown coefficients have the same physical meaning and order of magnitude (they would represent the solution at the nodal points). This helps in smoothing the behavior of the final ODEs. Second, the N nodal points of the Lagrange polynomials are set to coincide with the N collocation points. As shown in the following, this significantly simplifies the form of the final ODEs.

For illustration, consider a 1D PDE: $f(y, \dot{y}, y', x, t) = 0$ (1), where f is a general nonlinear function (boundary conditions are neglected for simplicity of description), x and t are the spatial coordinate and time, $y = y(x,t)$ is the unknown solution, and $\dot{y}$ and y' are time and spatial derivatives of y. The approximate solution is: $\bar{y}(x,t) = \sum_{i=1}^{N} Y_i(t) L_i(x)$ (2), where $Y_i(t) = Y_i$ are unknown coefficients and $L_i(x)$ are the Lagrange trial polynomials with nodal points $\hat{x}_j$: $L_i(x) = \prod_{j=1, j\neq i}^{N} \frac{x \circ \hat{x}_j}{\hat{x}_i \circ \hat{x}_j}$ (3). Note that: $L_i(\hat{x}_j) = \delta_{ij}$ (4), where δ_{ij} is the Kronecker delta. Substitution from (2) into (1) results in the residual function: $R(Y_i, \dot{Y}_i, x, t) = f(\sum_{i=1}^{N} Y_i L_i(x), \sum_{i=1}^{N} \dot{Y}_i L_i(x), \sum_{i=1}^{N} Y_i L_i{}'(x), x, t)$ (5), where $L_i{}'(x)$ is the spatial derivative of $L_i(x)$. The final ODEs are obtained by forming weighted residuals (the residual function evaluated at the collocation points $\bar{x}_j$) and setting them equal to zero: $W_j(Y_i, \dot{Y}_i, t) = R(Y_i, \dot{Y}_i, x, t)|_{x=\bar{x}_j} = f(\sum_{i=1}^{N} Y_i L_i(\bar{x}_j), \sum_{i=1}^{N} \dot{Y}_i L_i(\bar{x}_j), \sum_{i=1}^{N} Y_i L_i{}'(\bar{x}_j), \bar{x}_j, t) = 0$ (6). The ODEs in (6) are the reduced form of the PDE given in (1). Now, by recalling (4), for the case where the nodal points of the trial Lagrange polynomials are the same as the collocation points ($\hat{x}_j = \bar{x}_j$), the set of ODEs in (6) would reduce to: $W_j(Y_i, \dot{Y}_i, t) = f(Y_j, \dot{Y}_j, \sum_{i=1}^{N} Y_i L_i{}'(\hat{x}_j), (\hat{x}_j), t) = 0$ (7). A comparison between the ODEs in (7) and (6) indicates that the method results in a set of ODEs which are decoupled to a great extent and are therefore significantly less expensive to solve.

RESULTS AND CONCLUSIONS

To compare the proposed OCM against the Galerkin method and other OCMs with different trial polynomials, these methods are implemented in Maple™ as a seventh-order approximation ($N = 7$) and are used to reduce the PDEs associated with the compressible gas flow inside an unloaded wall-flow diesel particulate filter (DPF) [3]. The equations are simplified 1D Navier-Stokes equations for the DPF inlet and outlet channels, along with the pressure-drop equation for the wall-flow and the appropriate thermodynamics and ideal gas relations [3, 4]. These are combined into a set of 4 nonlinear PDEs which are then reduced to a set of 28 ODEs (including the time derivative of the boundary conditions). The DPF parameters are those given in [4]. The inlet velocity starts from zero and exponentially increases to reach its final value at $t = 10(\mathrm{s})$. The initial conditions are zero velocity and ambient pressure throughout the DPF channels. The obtained ODEs are integrated from $t = 0(\mathrm{s})$ to $t = 50(\mathrm{s})$ by employing the "Rosenbrock" procedure in Maple™. For each method the required simulation time (averaged over 5 runs on a desktop PC equipped with an Intel® Core™ i7-4790 @ 3.90 GHz CPU and 16 GB of RAM, running the 64-bit Windows 10) and the range of variations of the coefficients in the velocity and pressure extensions (*i.e.* $V_i(t)$ and $P_i(t)$ in $\bar{v}(x,t) = \sum_{i=1}^{N} V_i(t) L_i(x)$ and $\bar{p}(x,t) = \sum_{i=1}^{N} P_i(t) L_i(x)$, as a measure of ODEs well-conditionedness) are measured and reported in the following table. Clearly the proposed method gives rise to a set of ODEs which can be solved in real-time. Regardless of the employed reduction method, a very good agreement with the results in [4] is observed.

Reduction Method	**CPU Time** (s)	**Range of V_i** (m/s)	**Range of P_i** (kPa)
Proposed OCM with Lagrange polynomials and $\hat{x}_j = \bar{x}_j$	9.3	$[0, 25]$	$[101, 105]$
OCM with Lagrange polynomials and equidistant $\hat{x}_j$	44.6	$[0, 25]$	$[101, 105]$
OCM with Legendre polynomials	128.6	$[-12, 13]$	$[-0.2, 105]$
Galerkin method with Lagrange polynomials and equidistant $\hat{x}_j$	547.3	$[0, 25]$	$[101, 105]$

Acknowledgments

This work was supported by the Natural Sciences and Engineering Research Council of Canada (NSERC), Toyota, and Maplesoft Inc.

References

[1] B.A. Finlayson. *The method of weighted residuals and variational principles*, volume 73 of *Classics in applied mathematics*. Society for Industrial and Applied Mathematics, Philadelphia, PA, USA, 2013.

[2] J.V. Villadsen and W.E. Stewart. Solution of boundary-value problems by orthogonal collocation. *Chemical Engineering Science*, 22(11):1483–1501, 1967.

[3] E.J. Bissett. Mathematical model of the thermal regeneration of a wall-flow monolith diesel particulate filter. *Chemical Engineering Science*, 39(7):1233–1244, 1984.

[4] A.G. Konstandopoulos, E. Skaperdas, J. Warren, and R. Allansson. Optimized filter design and selection criteria for continuously regenerating diesel particulate traps. Technical Report 1999-01-0468, SAE Technical Paper, 1999.

A REDUCED CONTROL-ORIENTED MODEL FOR QUASI ONE DIMENSIONAL FLOW IN AREA VARYING CHANNELS

Amer Keblawi [*1], Soroosh Hassanpour[1], and John McPhee[1]
[1]*Systems Design Engineering, University of Waterloo, Waterloo, Ontario, Canada*

Summary The aim of this study is to provide a reduced control-oriented model for transient, non-isothermal, quasi one-dimensional gas flow inside channels of varying cross-sectional area. The orthogonal collocation method is applied to transform the governing system of PDEs to an equivalent system of ODEs utilizing symbolic computations; the derived ODEs are then solved using a numerical integrator. This study can be applied to the flow of ideal gases in channels, ducts, engine manifolds, etc...

INTRODUCTION

Control oriented models for internal compressible flows, for the most part, are lumped models that consider the whole spatial geometry as a single node. In the proposed model, the spatial variation is considered with an aim of making a real time simulation that has approximates a real flow in a better fashion.

THEORETICAL BACKGROUND

System of Equations

It is considered that the fluid in the system is a prefect fluid that follows the ideal gas law. The friction is included in the model by applying the friction factor. The equations are modelled in terms of the velocity u, pressure p, and temperature T. Also, the specific heat c_v, hydraulic diameter D, friction factor f, ideal gas constant R, and specific heat ratio γ are included. The independent variables are the distance along the length of the channel x, and the time t.

The system of governing partial differential equations that govern compressible internal flow in channels with varying cross-sectional area is given in equations (1–3) [2].

$$\frac{\partial p}{\partial t} = \frac{p}{T}\frac{\partial T}{\partial t} \circ p\frac{\partial u}{\partial x} \circ u\frac{\partial p}{\partial x} + \frac{up}{T}\frac{\partial T}{\partial x} \circ \frac{up}{A}\frac{dA}{dx} \tag{1}$$

$$\frac{\partial u}{\partial t} = \circ \frac{1}{2}\frac{\partial u^2}{\partial x} \circ \frac{RT}{p}\frac{\partial p}{\partial x} \circ \frac{f\rho_u u\,|u|}{2D} \tag{2}$$

$$\frac{\partial T}{\partial t} = \circ\, u\frac{\partial T}{\partial x} \circ (\gamma \circ 1)\,T\left(\frac{u}{A}\frac{dA}{dx} + \frac{\partial u}{\partial x}\right) + \frac{q}{c_v} + \frac{fu^3}{2Dc_v} \tag{3}$$

The system of equations is simplified by considering the substitution of variables $\alpha = \ln(T)$ and $\beta = \ln(p)$ after dividing equation (1) by p and equation (3) by T.

Method of Orthogonal Collocation

To be able to use orthogonal collocation effectively, the distance along the channel is normalized to vary between 0 and 1 by applying $x^* = x/L$. In the considered method of orthogonal collocation, the space derivatives are found by applying a Lagrange interpolating polynomial fit, and differentiating the polynomial with respect to space at the different collocation points. Thus, an arbitrary variable ϕ is expanded as shown in equation (4), the Lagrange interpolating polynomial is given in equation (5), and the derivative approximation is derived in equation (6) [1]. The collocation points are the roots of the corresponding Legendre polynomial of order $N+2$ considering that N is the number of internal nodes.

$$\hat{\phi}(t,x^*) = \sum_{i=1}^{N+2} l_i(x^*)\;\phi(t)|_{x^*=x_i^*} \quad (4) \qquad l_i(x^*) = \prod_{\substack{j=1\\ j\neq i}}^{N+2} \frac{x^* \circ x_j^*}{x_i^* \circ x_j^*} \quad (5) \qquad \frac{\partial\hat{\phi}(t,x^*)}{\partial x^*} = \sum_{i=1}^{N+2}\frac{dl_i(x^*)}{dx^*}\;\phi(t)|_{x^*=x_i^*} \quad (6)$$

The space derivatives in the PDE system (1–3) are evaluated symbolically using Maple™. The system of three PDEs is transformed to a system of $3(N+2)$ ODEs that is solved using a variable time step Rosenbrock solver.

CASE STUDY

A converging circular pipe with a linearly decreasing diameter is considered in this analysis. The inlet pipe diameter is 11 cm and the outlet diameter is 4 cm, the overall length of the pipe is 1 m, there is a heat loss of 150 W/m, and the friction factor is considered to be 0.03. The gas constant and specific heat ratio are 287 J/kg-K and 1.4 respectively. The flow is simulated for 10 seconds.

*Corresponding author. Email: akeblawi@uwaterloo.ca

Initially, the flow starts from rest, at a prescribed uniform boundary pressure of 100 kPa and temperature of 300 K. The boundary conditions are that the velocity at the outlet of the pipe is 60.4 m/s, and the pressure and temperature at the inlet of the pipe are 200 kPa and 450 K respectively. The changes from the initial conditions to the final boundary conditions follow an exponential smooth function in time.

RESULTS AND CONCLUSIONS

To be be able to quantify grid independence of this study for the orthogonal collocation method, the steady state spatial mean and outlet pressure and temperature are reported in table (1). For convenience, the computational time for each case is also recorded. It is noticed that the system becomes grid independent within the first decimal place at 16 nodes. The spatial variation of velocity and temperature is provided in figure (1) at time values of 0, 0.02 till 0.15 with an increment of 0.01, 0.2 till 1 with an increment of 0.2, 2, 3, 4, and 10 seconds. The flow velocity and temperature profiles in the plots move upwards as time passes. It is noticed that the spatial variation in the system varies smoothly with the variation in boundary conditions.

		Outlet Values		**Average Values**		
Number of Nodes	**CPU Time (s)**	**Temperature**	**Pressure**	**Velocity**	**Pressure**	**Temperature**
4	0.36	448.36	1.972×10^5	27.50	1.990×10^5	449.390
6	0.69	448.099	1.968×10^5	22.76	1.993×10^5	449.631
8	25	448.093	1.968×10^5	22.29	1.994×10^5	449.658
10	2.13	448.093	1.968×10^5	22.10	1.994×10^5	449.667
12	2.86	448.093	1.968×10^5	22.01	1.995×10^5	449.672
14	3.75	448.093	1.968×10^5	21.96	1.995×10^5	449.675
16	4.78	448.093	1.968×10^5	21.92	1.995×10^5	449.677
18	6.03	448.093	1.968×10^5	21.91	1.995×10^5	449.678

Table 1: Grid Independence Results

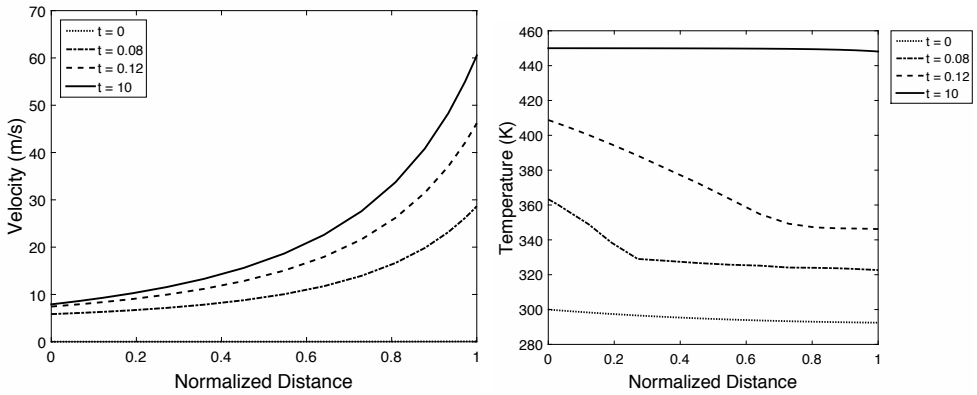

(a) Velocity versus Normalized Distance

(b) Temperature versus Normalized Distance

Figure 1: Plots of Flow Parameters at Different Time Stamps

The proposed method has an acceptable computational time of around 5 seconds for 16 nodes implying that the simulation was done faster than real time. Moreover, it is found from the grid independence study that a lumped model has a deviation in velocity computations greater than 25% from the results of a model that considers spatial variation.

Acknowledgments

This work was supported by the Natural Sciences and Engineering Research Council of Canada (NSERC), Toyota, and Maplesoft Inc.

References

[1] Ebrahimzadeh E., Shahrak M. N., Bazooyar B.: Simulation of Transient Gas Flow using the Orthogonal Collocation Method. Chemical Engineering Research and Design 90:1701-1710, 2012.

[2] Shapiro. A. H.: The Dynamics and Thermodynamics of Compressible Fluid Flow, volume II. The Ronald Press Company, 1954.

[3] Gottlieb D., Hesthaven J.S.: Spectral Methods for Hyperbolic Problems. Journal of Computational and Applied Mathematics, 2000.

NUMERICAL INVESTIGATION OF WALL HEAT TRANFER INFLUENCE ON SHOCK TRAIN IN SCRAM ET ISOLATOR

Hongbo Lu[1], Dan Wang[1], Zhan Liu[1] & Lianjie Yue[2a)]
[1] *China Academy of Aerospace Aerodynamics, Beijing, China*
[2]*Institute of Mechanics, Chinese Academy of Sciences, Beijing, China*

Summary Due to the scramjet isolator suffering from the severe aeroheating problem at a long time fly, this paper studied the influence of wall heat transfer on flow characteristics and performance of a scramjet isolator by numerical simulation. The results show that shock train is affected by the dual mechanism of isolator wall temperature and airflow total temperature. Shock train length increases with ratio of wall temperature to total temperature. To predict shock train length of practical design with more accuracy, the parameter involved wall heat transfer is introduced to improve Waltrup and Billig correlation [1].

INTRODUCTION

A scramjet isolator module with an optimal length is required to house the shock train induced by heat release in a combustor and prevent engine unstart. Various researchers [1-2] have investigated shock train behavior in constant-area rectangular and round ducts, but these results are obtained using room-temperature supply air, taking no account of wall heat transfer. At real flight conditions, a serious heat transfer exists in the isolator [3]. The few available researches [4-6] do not well elucidate this influence. This paper focuses on effects of wall heat transfer on shock train in the scramjet isolator by numerical simulation.

NUMERICAL DESCRIPTION

Numerical simulations were performed on a two dimensional domain, which includes a nozzle with the exit Mach number of 2.5 (Ma_1=2.5) and an isolator with height H of 50mm and length L of 600mm. The full N-S equations for two-dimensional turbulent flow were solved by the finite volume method. The turbulence model of k-ω SST was employed to close the governing equations. To guarantee the credibility of numerical results, a comparison between numerical and experimental results was also made at the conditions of T_t=1500K, P_t=1.0MPa, γ=1.33 and T_w=300K, shown in Fig. 1, where T_t, P_t, γ and T_w denotes total temperature, total pressure, specific heat ratio and wall temperature, respectively. It can be seen that numerical results are in agreement with the experimental data, specially the start location of shock train, in spite of some scatter being present.

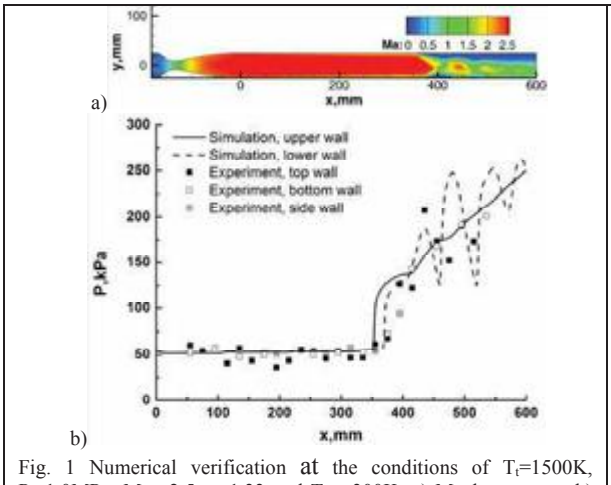

Fig. 1 Numerical verification at the conditions of T_t=1500K, P_t=1.0MPa, Ma_1=2.5, γ=1.33 and T_w= 300K; a) Mach contours, b) wall pressure distributions.

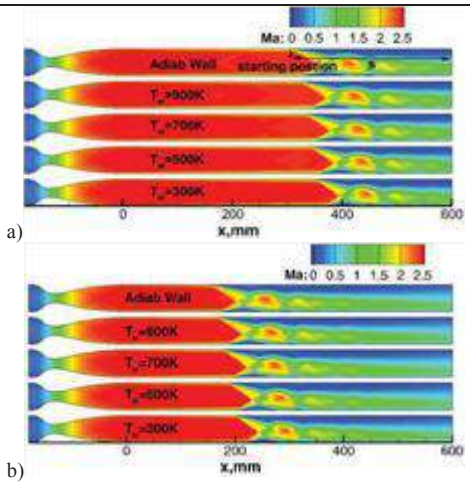

Fig. 2 Mach contours for different wall temperatures and backpressures at T_t=1500K, P_t=1.0MPa, Ma_1=2.5 and γ=1.33; a) P_b/P_1=4.8, b) P_b/P_1=6.2.

RESULTS AND DISCUSSION

Figure 2 shows Mach contours for different wall temperatures at the conditions of T_t=1500K, P_t=1.0MPa, Ma_1=2.5 and γ=1.33. A similarity exists in shock train pattern for different wall temperatures, but a remarkable difference exists in shock train length at the same back pressure. With an increase of wall temperature, the starting position of shock train moves upstream and shock train length increases. However, this tendency is contrary to the tendency given by Waltrup and Billig relationship [1] (see Eq. (1)). In Eq. (1), θ denotes the boundary layer momentum thickness expressed by Eq. (2) and reduces with an increase of wall

[a)] Corresponding author. Email: yuelj@imech.ac.cn

temperature (see Fig. 3). Consequently, wall temperature effect cannot be elucidated by the only parameter θ involved wall temperature effect in Eq. (1).

$$\frac{s\left(Ma_1^2-1\right)\mathrm{Re}_\theta^{1/4}}{H^{1/2}\theta^{1/2}}=50\left(\frac{P_b}{P_1}-1\right)+170\left(\frac{P_b}{P_1}-1\right)^2 \quad (1) \quad , \quad \theta=\int_0^\infty\frac{\rho u}{\rho_\infty u_\infty}\left(1-\frac{u}{u_\infty}\right)dy \quad (2)$$

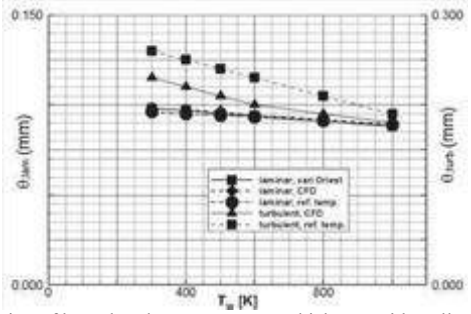

Fig. 3 Variation of boundary layer momentum thickness with wall temperature.

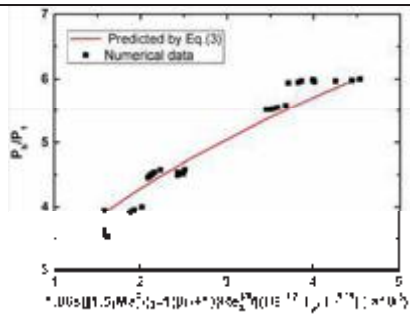

Fig. 4 A comparison of numerical data against those from Eq. (3).

Table 1 Shock train length s for different wall and total temperatures at P_t=1.0MPa, Ma_1=2.5 γ=1.33 and P_b/P_1=4.8						
	T_w(K)	300	500	700	900	Adiabatic wall
T_t=1500K	T_w/T_t	0.2	0.33	0.47	0.6	≈1
	s(mm)	250	261	270	279	296
T_t=1000K	T_w/T_t	0.3	0.5	0.7	0.9	≈1
	s(mm)	256	277	284	294	295

$$\frac{1.91s\left(\frac{1.7\gamma}{\gamma+1}Ma_1^2-\frac{2.4\gamma-1}{\gamma+1}\right)\mathrm{Re}_{\theta_1}^{1/4}}{H^{1/2}\theta_1^{1/2}\left(\frac{T_w}{T_t}\right)^{0.18}}=50\left(\frac{P_b}{P_1}-1\right)+170\left(\frac{P_b}{P_1}-1\right)^2 \quad (3)$$

To figure out the dimensionless parameter elucidating wall heat transfer effect, a further computation is performed at the conditions of T_t=1000K, P_t=1.0MPa, Ma_1=2.5 and γ=1.33, shown in Table 1. It can be observed that shock train length is almost identical for different total and wall temperatures when the ratio of wall temperature to gas total temperature is approximately the same. Additionally, shock train length increases with the ratio of wall temperature to gas total temperature, coinciding with the findings of Lin et al. [4].

To improve the accuracy of Eq. (1) in predicting shock train length of practical design, a correlation is further performed based on numerical data. Considering data correlating Eq. (1) from the cold flow experiments with γ=1.4 while our data from the high enthalpy flow tests with γ≈1.33, the proposed relationship denoted by Eq. (3) also involves specific heat ratio. The degree of success obtained in the correlation Eq. (3) is shown in Fig.4. Some scatter is present, but Equation (3) covers more physical influencing factors, not only considering wall heat transfer, but accounting for specific heat ratio. Need of special note, it needs to be further perfected by experimental data.

CONCLUSIONS

Numerical tests were performed on a two dimensional domain including a nozzle and an isolator study effects of wall heat transfer on shock train in a scramjet isolator. It is found that wall heat transfer in determining shock train behavior can be characterized by the ratio of wall temperature and gas total temperature. Furthermore, a modified correlation is proposed for predicting shock train length of practical design, which covers the more influencing factors such as the ratio of wall temperature to total temperature and specific heat ratio.

References

[1] Waltrup P. J., Billig, F. S.: Structure of Shock Waves in Cylindrical Ducts. AIAA J. 11(10): 1404-1408, 1973.

[2] Mtsuo K., Miyazato Y.: and Kim H. D.: Shock train and pseudo-shock phenomena in internal gas flows. Prog. Aerosp. Sci. 35: 33-100, 1999.

[3] Cuffel R., Back L.: Flow and heat transfer measurement in a pseudo shock region with surface cooling. AIAA J. 14(12): 1716-1722, 1976

[4] Lin K. C., Tam C. J., Jackson K..: Effects of Temperature and Heat Transfer on Shock Train structures inside Constant-Area Isolators. AIAA 2006-817.

[5] Dillmann A.: Numerical Investigation of the Isolator Flow Field of a SCRAMJET Engine with Elevated Wall Temperatures (Eds.). Numerical & Experimental Fluid Mechanics VII, NNFM 112, 415–422.

[6] Fischer C., Olivier H.: Experimental Investigation of Wall and Total Temperature Influence on a Shock Train. AIAA J. 54(4): 757-766, 2014.

BOS AND PSV IN A SUPERSONIC JET

Carlos Echeverria, David Porta & Catalina Stern
Department of Physics, Facultad de Ciencias, UNAM, Mexico City, Mexico

Summary We use Background Oriented Schlieren (BOS) and Particle Shadow Velocimetry (PSV) to study the shock structure and the flow field in a supersonic axisymmetric jet. We can visualize the regions of maximum density and those of maximum change in the density.

INTRODUCTION

We have been studying a supersonic axisymmetric air jet for several years with various techniques that give information about different aspects of the jet.
With Rayleigh scattering we visualized the shock structure and we obtained information about the local density fluctuations and the sound emission pattern inside and outside the flow. With Particle Shadow Velocimetry (PSV) we obtained the mean velocity field. With hig- speed schlieren and shadowgraph we also visualized the shock structure and part of the turbulence, and through Background Oriented Schlieren (BOS) were able to determine the index of refraction field that is proportional to the density field. In this paper we emphasize the latest results obtained through PSV and BOS.

EXPERIMENTAL SET-UP AND TECHNIQUES

The jet is produced by the discharge of compressed air at about 5.5 atm into to the atmosphere (at Mexico City's altitude it is about 0.8 atm) through a 4mm axisymmetric straight duct with a length of 8cm; that is, the nozzle is not convergent-divergent. However, we have determined the mean transverse size of the flow and there is a contraction a few millimeters outside the nozzle. The Mach number is about 1.2. We have observed an apparently stationary shock structure both with Rayleigh scattering, and with schlieren and shadowgraphs.
PSV is a novel technique (proposed by Estevadiordal 2005), that relies on the shadow cast by the seeds and not on their Mie scattering properties. It uses the same cross correlation as Particle Image Velocimetry (PIV). The width of the studied region was determined by the correlation depth instead of the width of the light sheet. This notion is very important in micro PIV; it depends on the optics of the camera and the wavelength of the light. In our experiment, the video camera recorded at 7200 fps, with a resolution of 778x776 pixels. The time interval between frames was 320 ns with an exposure time of 880 ns. We designed a device to inject the particles and were able, in spite of the speed and size of the flow, to obtain homogeneous seeding with titanium dioxide particles that have a relaxation time of 7.2×10^{-6} seconds.
BOS (proposed by Meier 1999) is used to measure the change in the index of refraction through the apparent displacement of a known background pattern with and without the flow. The change of the index of refraction and the displacement in a transparent gas are related through a Poisson equation that is obtained using principles of optics. The changes in the index of refraction and in the density are proportional, and can be related through the Gladstone Dale equation, but the required constant is not easily obtained for our experimental conditions. The BOS technique was validated in free subsonic flows of carbon dioxide and acetylene. The difference between our values and those that appear in tables was of 0.005%. For the supersonic flow, the camera recorded at 1000fps with a resolution of 1280 x 800 pixels. The resolution obtained with the BOS is of 47 pixels per millimeter.

RESULTS

With the combination of PSV and BOS we can relate the shock structure with the mean density (proportional to the index of refraction) and velocity fields. The mean values are obtained through averages of a hundred images. High-speed videos show that the shock structure is actually fluctuating but more studies have to address this question.
The first two figures show an image of the shock structure and the corresponding index of refraction field for an exit pressure of 5.4 atm. The third figure is the superposition of both. It is interesting to notice that he region of maximum change in the density is slightly above the region of maximum density.

[a] Carlos Echeverria Email: carlosea1982@ciencias.unam.mx

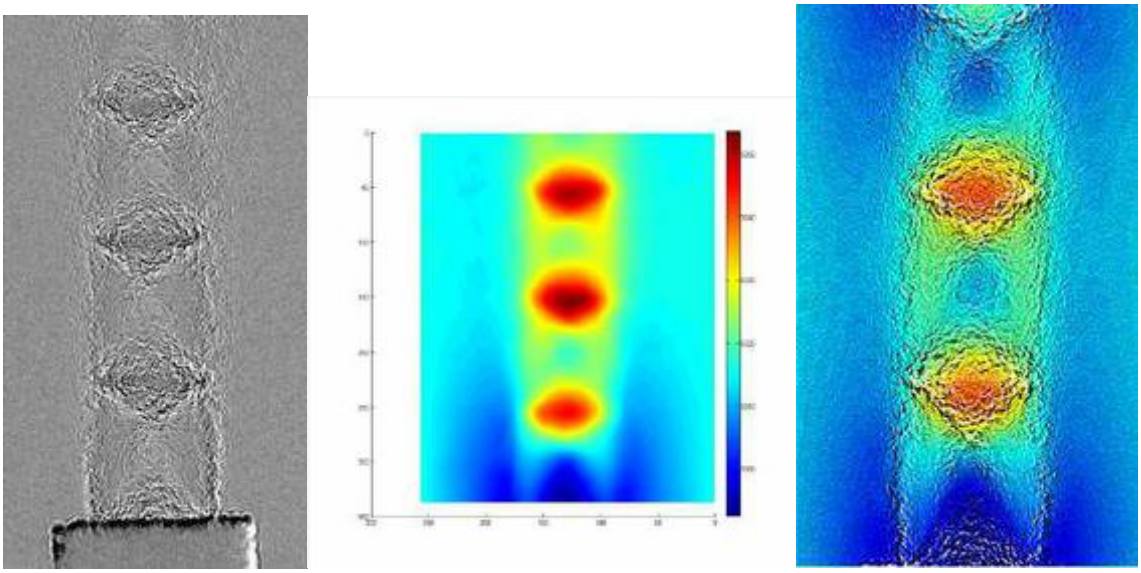

The next figure corresponds to the shock structure at an exit pressure of 4.6atm.

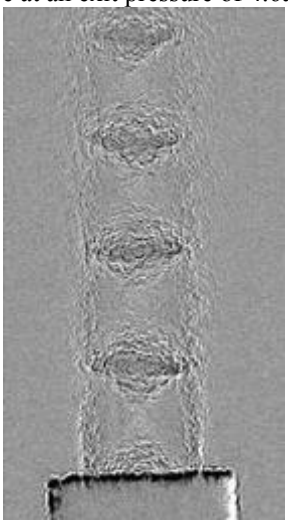

In the oral presentation these images will be compared with the velocity fields obtained with PSV.

References

[1] Echeverría C., Implementación de PIV-PSV para el estudio de las interfaces de un flujo supersónico, *ME Thesis*, UNAM, 2015

[2] Estevadeordal , J., & Goss, L., PIV with LED: Particle Shadow Velocimetry (PSV). En AIAA (Ed.), *43rd AIAA Aerospace Sciences Meeting and Exhibit*. Reno, Nevada: AIAA., 2005

[3] Porta, D., Estudio de las interfaces de un jet supersónico axisimétrico usando schlieren con un fondo como referencia, *ME Thesis*, UNAM, 2015

FM05 - Convection

TS.FM05-1.01	Chilla, Francesca - Lagrangian Measurements in Turbulent Thermal Convection (INVITED)	709
TS.FM05-1.02	Shishkina, Olga - Heat and momentum transport in horizontal convection (INVITED)	711
TS.FM05-1.03	Tasaka, Yuji - Two-dimensional oscillations in MHD Rayleigh-Benard convection (INVITED)	713
TS.FM05-1.04	Zhong, Jin-Qiang - The large-scale circulation dynamics in rotating Rayleigh-Benard convection (INVITED)	715
TS.FM05-1.05	Xia, Ke-Qing - Turbulent thermal convection over rough surfaces with varying roughness size	717
TS.FM05-1.06	Wynn, Andrew - Optimal Bounds on Energy Dissipation for Stress-driven Shear Flows	719
TS.FM05-2.01	Schmeling, Daniel - On the influence of the aspect ratio on structure formation in turbulent mixed convection	721
TS.FM05-2.02	Arakeri, Jaywant - Light propagation through axially homogeneous buoyancy driven turbulence	723
TS.FM05-2.03	Floryan, J. M. - Flow in a dual heated channel	725
TS.FM05-2.04	Tilgner, Andreas - High Rayleigh number convection with double diffusive fingers	727
TS.FM05-2.05	Tong, Penger - Boundary layer fluctuations and their effects on mean and variance temperature profiles	728
TS.FM05-3.01	Du Puits, Ronald - Boundary layers in turbulent Rayleigh-Bénard convection: The 3D velocity field	730
TS.FM05-3.02	Ching, Emily S.C. - Turbulent Rayleigh-Benard convection with polymers	732
TS.FM05-3.03	Chong, Kai Leong - Effect of confinement on global heat transfer scaling in Rayleigh-Bénard convection	734
TS.FM05-3.04	Zhang, Jun - Dynamics of a free boundary atop thermal convection	736
TS.FM05-3.05	Goluskin, David - Zonal flows in Rayleigh-Bénard convection	738
TS.FM05-4.01	Kelley, Douglas - Low-dimensional convection models from vector cylindrical harmonics	739
TS.FM05-4.02	Kunnen, Rudie - Turbulent rotating convection: A Lagrangian perspective	741
TS.FM05-4.03	Shaw, Raymond - Cloud formation through isobaric mixing in turbulent Rayleigh-Bénard convection	743
TS.FM05-4.04	Xi, Heng-Dong - The Role of Higher Order Flow Modes in Turbulent Thermal Convection	745
TS.FM05-4.05	Abtahi, Arman - On the analysis of flows in heated corrugated conduits	747
PO.FM05-1.02.15	Dichamp, Jules - Analysis of counter-flow convective exchangers using general Graetz modes	749
PO.FM05-1.03.16	Knupp, Diego - Integral transforms in convection-diffusion through convective eigenvalue problems	751
PO.FM05-1.04.17	Kozlov, Victor - Steady thermal convection in a rotating horizontal annulus	753
PO.FM05-1.05.18	Liu, Chao - Study of heat-transfer coefficient on hypersonic boundary layer flow over a flat	755
PO.FM05-1.07.20	Qu, Qi-Qi - Computation of heat flux in the stagnation point for a cold wall with high speed flow	757

PO.FM05-1.08.21	Shanmugam, Saravanan - Natural convection in a cubical enclosure with opposing active sectors	759
PO.FM05-1.09.22	Villeneuve, Thierry - Three-mode heat transfer simulations in parallelogrammic air enclosures	761
PO.FM05-1.10.23	Wan, Zhenhua - On non-Oberbeck-Boussinesq effects in cessation-led reversals in Rayleigh-Bénard convection	763
PO.FM05-1.11.24	Wetzel, Tim - Subgrid-scale modeling of relaminarizing mixed convection in a vertical channel	765
PO.FM05-1.12.25	Xiao, Yue - Large-scale circulations in an oscillating thermal convection	767
PO.FM05-1.13.26	Xu, Feng - Numerical simulation of a near field plume from a duct	769

LAGRANGIAN MEASUREMENTS IN TURBULENT THERMAL CONVECTION

Olivier Liot[1], Julien Salort[1], F. Seychelles[1], J.F. Pinton[1,2], Y. Gasteuil[2], and Francesca Chillà*[1]
[1]*Laboratoire de Physique, ENS de Lyon, Université de Lyon, CNRS, Lyon, France*
[2]*SmartInst Company Lyon, France*

Summary Turbulent thermal convection is a complex problem, the flow is forced at almost all scales, because of the presence of both large scale circulation and small scale plumes. Moreover the difference of density induced by temperature adds an ingredient in the basic equations of the flow, so that turbulence could be different from the case of pure mechanical forcing. Mixing is in principle different and probably increased because of the structure of the plumes. Moreover the entire flow is not homogeneous (at least at large scales) and the statical behavior can be influenced by the large scale flow. One way to probe all these specific effects is to use a Lagrangian point of view, measuring, for example, Lagrangian transport of velocity and temperature, or heat flux and acceleration, as we will show.

INTRODUCTION

Because of the difficulty of the problem, Lagrangian studies in turbulent thermal convection are just in their beginning. The first pioneer works are those of Gasteuil et al.[1], who first measured the Lagrangian heat flux using a smart particle at $Ra \sim 10^{10}$, and of Schumacher et al. [2] who using numerical simulations measured the Lagrangian accelerations at a Rayleigh number of 10^9. Afterwards, first measurement of Lagrangian acceleration was performed by Ni et al [3]. In the present work, we report new experimental results obtained with a highly improved smart particle capable to measure for 24 consecutive hours.

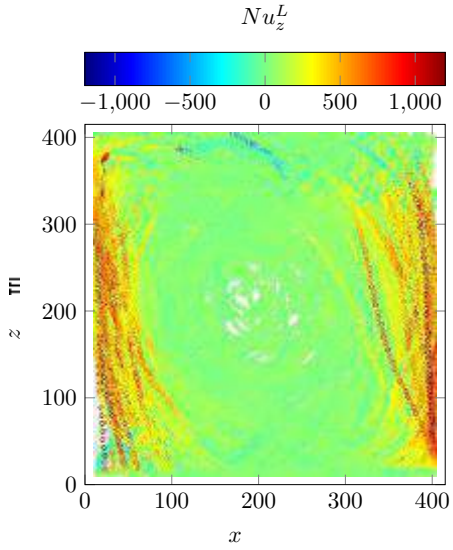

Figure 1: Lagrangian vertical Nusselt Nu_z^L for $Ra = 5 \times 10^{10}$. Trajectories are undersampled for more readability.

NUSSELT NUMBER MEASUREMENTS

The convection cell is a rectangular box of size $41.5\,\mathrm{cm}$ X $41.5\,\mathrm{cm}$ and $10.5\,\mathrm{cm}$ of width. The walls are of $2.5\,\mathrm{cm}$-thick PMMA. Both plates consist in $4\,\mathrm{cm}$-thick copper plates coated with a thin layer of nickel. The bottom plate is Joule-heated while the top plate is cooled with a temperature regulated water circulation. Plate temperatures are controlled by PT 100 temperature sensors. The working fluid is deionized water. The bulk temperature is fixed at $37.05\,^{\circ}\mathrm{C}$ and Prandtl number is 4.6. The particle is a $2.1\,\mathrm{cm}$-diameter capsule containing temperature instrumentation, a radio-frequency emitter, and two batteries. Four cylindrical thermistors ($0.8\,\mathrm{mm}$ in length, $0.4\,\mathrm{mm}$ in diameter, $230\,\mathrm{k}\Omega$, with a response time of $0.6\,\mathrm{s}$ in water) are mounted on the capsule wall protruding $0.5\,\mathrm{mm}$ into the surrounding flow. The emitter sends a signal proportional to the temperature. The temperature signal is recovered on the fly by a stationary receiver. The capsule has been redesigned

*Corresponding author. Email: francesca.chilla@ens-lyon.fr

to receive two batteries to extend the working time which can now reach up to 1000 turnover times. The particle trajectory is synchronously recorded with a digital camera placed in front of the large face of the cell. Post-processing differentiation allows for the velocity measurement.

Because of the shape of the container, the overall flow is almost 2D, meanwhile the small scale structures as plumes are 3D. The global Nusselt number is about 250 and so the boundary layers are about $800\,\mu\mathrm{m}$. So because of its size, the sensor never see the boundary layers, but it can enter and well measure the mixing zone between the boundary and the bulk or the bulk itself. Thanks to the joint measurements of velocity and temperature, it is possible to infer the Lagrangian Nusselt number which has a vertical and an horizontal component. The vertical Nusselt reads :

$$Nu_z^L = \frac{H}{\kappa \Delta T} \left(T(t) \circ \langle T(t) \rangle_t\right) v_z(t), \tag{1}$$

and its lagrangian map is shown in the figure 2.

The mean feature is that the transport is essentially organized in a sort of "vertical jet" , a gathering of plumes which flows all along the wall showing that the contribution of the bulk is very weak at this Rayleigh number.

VELOCITY AND TEMPERATURE STATISTICS

Another major result concerns Lagrangian statistics. The Lagrangian distribution function of temperature is not gaussian and exhibits exponential tails. This is different from the Eulerian PDF usually found in the bulk at similar Rayleigh number. That indicates that exponential tail are due to the large fluctuations linked to plumes that are confined near the walls and near the plates. The fluctuations of temperature exhibits also an interesting feature, their Lagrangian power spectrum exhibits a power law as $f^{-2.5}$ which do not correspond to any theoretical model. We presently do not have a quantitative explanation, also if inhomogeneity of the flow could be the fundamental ingredient of this feature and more studies are underway.

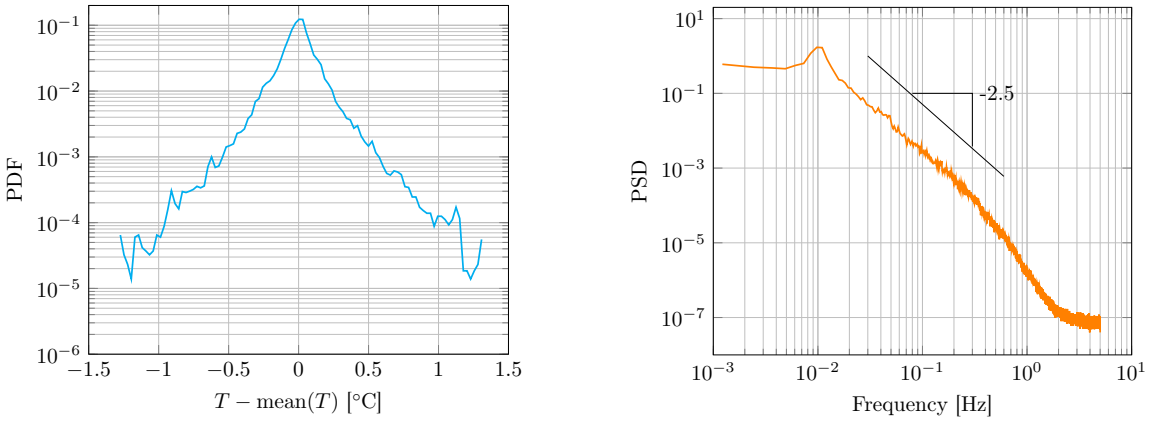

(a) (b)

Figure 2: (a) Normalized histogram of the Lagrangian temperature fluctuations and (b) Power spectrum of the temperature fluctuations at $Ra = 3.5 \times 10^{10}$.

CONCLUSIONS

Smart sensors can give new insight in turbulent thermal convection. The possibility to have a Lagrangian measurement of temperature leads to a better understanding of the structure and properties of the scalar field. Moreover, such a sensor can explore the whole bulk and make possible both the study of inhomogeneity on turbulent statistics and the interaction between large scale flow and plumes.

We thanks Smart Inst industry for collaboration in the developing of the particle.

References

[1] Y. Gasteuil, W. L. Shew, M. Gibert, F. Chillá, B. Castaing, and J.-F. Pinton, PRL 99, 234302 (2007).
[2] J. Schumacher, PRL 100, 134502 (2008).
[3] Ni, R., Huang, S.-D. and Xia, K.-Q.,JFM,693,pp. 395,(2012).

HEAT AND MOMENTUM TRANSPORT IN HORIZONTAL CONVECTION

Olga Shishkina [*1]

[1]*Max Planck Institute for Dynamics and Self-Organization, Am Fassberg 17, D-37077 Göttingen, Germany*

Summary In horizontal convection systems heat is supplied and removed through a single, top or bottom, surface of a fluid layer. For such systems we derive limiting scalings for the Reynolds number and for the convective heat transport, measured by the Nusselt number, with the input parameters, which are the Rayleigh number, Prandtl number and the aspect ratio of the convection cell. The theoretical findings are supported by Direct Numerical Simulations for a wide range of the Rayleigh and Prandtl numbers.

HORIZONTAL CONVECTION

Horizontal convection (HC) [1] is a paradigm system to study heat and momentum transport in such flow configuration systems, where heating and cooling are applied to different parts of the same horizontal surface of a fluid layer. This type of convection is relevant in many geophysical systems, in particular, in the large-scale ocean circulation, and in process engineering.

The HC flows are determined mainly by the Rayleigh number $Ra \equiv \alpha g \Delta L^3/(\kappa\nu)$, the Prandtl number $Pr \equiv \nu/\kappa$ and geometrical characteristics of the cell like the length-to-height aspect ratio $\Gamma = L/H$ and the relative areas of the heated and cooled surfaces compared to the bottom area. Here ν denotes the kinematic viscosity, κ the thermal diffusivity, α the isobaric thermal expansion coefficient of the fluid, g the acceleration due to gravity, L is the length and H the height of the convection cell and $\Delta \equiv (T_+ - T_-)$ with T_+ the temperature of the heated part of the bottom and T_- the temperature of the cooled part of the bottom, see Fig. 1.

THEORETICAL SCALINGS IN HORIZONTAL CONVECTION

The Rossby model [2] for the scaling with Ra and Pr of the mean heat flux, measured by the Nusselt number $Nu \equiv -\langle \partial T/\partial z \rangle_+/(\Delta/L)$, suggests $Nu \propto Ra^{1/5} Pr^0$, i.e. independence from Pr. Here z is the vertical coordinate, T the temperature and $\langle\cdot\rangle_+$ denotes the averaging over the heated part of the bottom and in time. The proportionality $Nu \propto Ra^{1/5}$ is supported by several numerical and laboratory experiments in non-turbulent HC, while the independence of Nu from Pr is not. The Rossby scaling is based on the assumptions of the laminarity and boundary-layer determinacy of the flow.

The universality of the Rossby scaling seems to be very questionable, since the HC flows are observed to become more turbulent with increasing Ra [3]. Thus, in [4] it was shown with variational analysis that the upper bound of the scaling exponent β in HC equals $1/3$ and this allows scalings different from that by Rossby. We refer the regime with the upper bound limiting scaling $Nu \propto Ra^{1/3}$ as the ultimate regime in HC. To date, the ultimate scaling has not been observed in experiments or simulations, probably due to the limited Ra-range of the conducted numerical and experimental investigations.

In [5] we applied to the case of HC the approach by Grossmann and Lohse [6], which originally was developed for Rayleigh–Bénard convection (RBC) [7, 8]. The resulting model suggests various known and new limiting scaling laws in HC with smooth transitions between the various regimes.

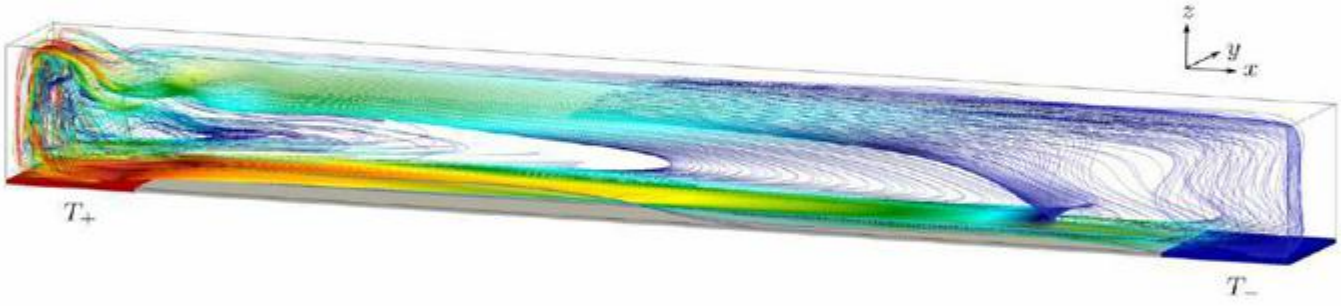

Figure 1: Scheme of a horizontal convection setup together with the streamlines for the Rayleigh number 10^{10} and Prandtl number 1, as obtained in the DNS. $1/10$ of the bottom is heated (left, $T = T_+$, red), while the other $1/10$ of the bottom is cooled (right, $T = T_- < T+$, blue). The other walls and the rest of the bottom are adiabatic. Adopted from [9].

*Corresponding author. Email: Olga.Shishkina@ds.mpg.de

RESULTS OF DIRECT NUMERICAL SIMULATIONS

In [9] we reported the Prandtl- and Rayleigh-number dependencies of the Reynolds number Re and the Nusselt number Nu for HC, based on our Direct Numerical Simulations (DNS) using the computational code GOLDFISH, as in [10]. The computational domain is of the aspect ratio $L/H = 10$ and is sketched in Fig. 1. The computational mesh resolves Kolmogorov and Batchelor scales as required in DNS [11]. For laminar HC we find that $Re \sim Ra^{2/5}Pr^{-4/5}$, $Nu \sim Ra^{1/5}Pr^{1/10}$ with a transition to $Re \sim Ra^{1/2}Pr^{-1}$, $Nu \sim Ra^{1/4}Pr^{0}$ for large Pr. In [9] the studied Ra varies from 3×10^8 to 5×10^{10} and Pr from 0.05 to 50. The obtained result were found to be in perfect agreement with the scalings, derived in [5] for laminar regimes.

DNS results for higher Rayleigh numbers, where horizontal convection becomes transitional and turbulent, show that the Nusselt number scalings with the Rayleigh number follows the theoretical scalings for turbulent regimes, as predicted in [5].

CONCLUSIONS AND ACKNOWLEDGEMENTS

A theoretical model [5] for the heat and momentum transport scalings with Rayleigh and Prandtl numbers in horizontal convection will be presented at ICTAM 2016. This is an extension of the Grossmann and Lohse approach [6] to the case of horizontal convection. The model suggests multiple scaling regimes, including in particular the Rossby scaling and the ultimate scaling proposed in [4], with smooth transitions between different regimes. Our DNS results for a wide range of the Rayleigh and and Prandtl numbers support the theoretical fundings [5] for laminar [9] and turbulent regimes.

OS is grateful to Eberhard Bodenschatz, Siegfried Grossmann, Detlef Lohse and Sebastian Wagner for the support, useful discussions and their contributions to this study.

OS gratefully acknowledges the Leibniz Supercomputing Centre (LRZ) for providing computing time and the Deutsche Forschungsgemeinschaft (DFG) for financial support under the grant Sh405/4 – Heisenberg fellowship.

References

[1] Hughes G. O., Griffiths R. W.: Horizontal convection. Ann. Rev. Fluid Mech. 40: 185–208, 2008.

[2] Rossby H. T.: On thermal convection driven by non-uniform heating from below: an experimental study. Deep Sea Res. 12: 9–16, 1965.

[3] Scotti A., White B.: Is horizontal convection really "non-turbulent?" Geophys. Res. Lett. 38: L21609, 2011.

[4] Siggers J. H., Kerswell R. R., Balmforth N. J.: Bounds on horizontal convection. J. Fluid Mech. 517: 55–70, 2004.

[5] Shishkina O., Grossmann S., Lohse D.: Heat and momentum transport scalings in horizontal convection, submitted, 2016.

[6] Grossmann S., Lohse D.: Scaling in thermal convection: A unifying view. J. Fluid Mech. 407: 27–56, 2000.

[7] Ahlers G., Grossmann S., Lohse D.: Heat transfer and large scale dynamics in turbulent Rayleigh–Bénard convection. Rev. Mod. Phys. 81: 503–537, 2009.

[8] Chillà F., Schumacher J.: New perspectives in turbulent Rayleigh–Bénard convection. Eur. Phys. J. E 35: 58, 2012.

[9] Shishkina O., Wagner S.: Prandtl number dependence of heat transport in laminar horizontal convection. Phys. Rev. Lett., accepted, 2016.

[10] Shishkina O., Horn S., Wagner S., Ching, E. S. C.: Thermal boundary layer equation for turbulent Rayleigh–Bénard convection. Phys. Rev. Lett. 114: 114302, 2015.

[11] Shishkina O, Stevens R. J. A. M., Grossmann S., Lohse D.: Boundary layer structure in turbulent thermal convection and its consequences for the required numerical resolution. New J. Phys. 12: 075022, 2010.

TWO-DIMENSIONAL OSCILLATIONS IN MHD RAYLEIGH-BENARD CONVECTION

Yuji Tasaka[1,a)], Kodai Fujita[1], Takatoshi Yanagisawa[2], Tobias Vogt[3], Ataru Sakuraba[4] & Sven Eckert[3]
[1]*Laboratory for Flow Control, Faculty of Engineering, Hokkaido University, Sapporo, Japan*
[2]*Japan Agency for Marine-earth Science and Technology, Yokosuka, Japan*
[3]*Helmholtz Zentrum Dresden-Rossendorf (HZDR), Dresden, Germany*
[4]*School of Science, The University of Tokyo, Tokyo, Japan*

Summary Short-period oscillations on convection rolls in Rayleigh-Bénard convection affected by a horizontal magnetic field confined in moderate aspect ratio box were invested experimentally. Detailed measurements of temperature and velocity fluctuations corresponding to the oscillations elucidated that the oscillation around its onset is two dimensional and may be originated in absolute instability of recirculation vortices formed flow separations due to large inertia of the main convection rolls restricted by Lorenz force.

INTRODUCTION

For Rayleigh-Bénard convection in a liquid metal layer with a moderate aspect ratio of five under a horizontal magnetic field, our research group found recently spontaneous flow reversals on quasi-two dimensional rolls, which are arranged parallel to the magnetic field, accompanied by skewed-varicose instability [1]. Here the circulation direction of the rolls changes with duration times being much longer than circulation time of the convection rolls. The appearance of the reversal is determined by Rayleigh number, Ra and Chandrasekhar number, Q [2] defined as

$$Ra = \beta g \Delta T L^3/(\nu\kappa), \quad (1) \qquad\qquad Q = \sigma B L^2/(\rho\nu), \quad (2)$$

where β, ν, κ, σ, ρ are respectively, bulk modulus, kinematic viscosity, thermal diffusivity, electric conductivity, and density of a test liquid metal, and g, ΔT, L, B are respectively, gravity acceleration, vertical temperature difference and height of the fluid layer, and intensity of the magnetic field. The fraction of Ra/Q is a measure for the ratio of the buoyancy to the Lorenz force. The flow reversals occur around $Ra/Q = 10$ as transitions between four-rolls and five-roll conditions [2, 3]. Increasing of Ra/Q also induces short-period oscillations on steady, quasi-two dimensional rolls for smaller Ra/Q conditions, where the period of the oscillation is close to the circulation time [2, 3]. Detailed velocity profile measurements using ultrasonic velocity profiling (UVP) elucidated that the flow reversals are accompanied by the short-period oscillations [2, 3].Numerical simulations revealed complex, fine vortex structures, which may induce the oscillations, surrounding the primary convection rolls [4]. Relations between the flow reversals and the short-period oscillations are still unclear. This study thus focuses on the onset and development of the short-period oscillations toward a detailed understanding of the phenomena in this system including flow reversals.

EXPERIMENTAL SETUP AND MEASUREMENTS

The experiments were performed at Hokkaido University (HU) and HZDR with different setups having common dimensions and configurations as shown in Fig. 1. The fluid layers are sandwiched by two copper plates for realising isothermal boundaries at the top and bottom, and surrounded by resin sidewalls for both thermal and electric insulation. The temperature difference ΔT was adjusted by water circulations inside the copper plats and monitored by temperature probes embedded in the plates. Size of the fluid layer is 200×200 mm^2 in sides and height $L = 40$ mm resulting in a corresponding aspect ratio of 5. The setups adopted different test fluids, liquid gallium at HU and $Ga^{67}In^{20.5}Sn^{12.5}$ at HZDR. A coil system to generate quasi-uniform magnetic field at HU has smaller intensities (120 mT) than that used at HZDR (700 mT), but a somewhat better uniformity (2 % at HU and 5 % at HZDR). We confirmed that the different test fluids and the coil systems do not cause essential difference on the flow regimes [3]. Time variations of instantaneous velocity profiles and temperature fluctuations were measured by UVP and temperature probes, respectively, in the both institutions. Multiple sensors were mounted on the vessels, but Fig. 1 shows only the specific sensor arrangement used for the flow measurements presented here.

RESULTS AND DISCUSSIONS

Typical temperature fluctuations with decreasing Q at fixed Ra around the onset of the oscillations are shown in Fig. 2, where $Ra = 2.5 \times 10^4$ and Q is varied from 4.4×10^4 to 2.7×10^4. The temperature signal shows regular oscillations at larger Q (Fig. 2 (a), $Q = 3.4\times 10^4$), where the spectral analysis on the fluctuations provides a single frequency component. The fluctuation takes a nonlinear development with appearance of an additional frequency component, whereas the amplitude of the main component becomes small (Fig. 2 (b), $Q = 4.9\times 10^3$). Fig. 3(a) shows a variation of the phase difference between

a) Corresponding author. Email: tasaka@eng.hokudai.ac.jp

the fluctuations measured by the probes T_1 and T_2 arranged parallel to the magnetic field as shown in Fig. 1(a). The difference is almost zero at larger Q values, and the fluctuations are in-phase, namely the convection rolls aligned parallel to the magnetic field show two-dimensional oscillations unlike the theoretical prediction [5]. The phase takes a difference with decreasing Q because of the appearance of an additional frequency component indicating a three-dimensional behaviour of the rolls. A similar behaviour is also observed for the velocity field. Fig. 3(b) shows a variation of the phase difference on the velocity fluctuations measured by UV1 and UV2 at x = 50 mm near the onset of oscillation. The variation also departures from zero with decreasing Q in spite of the different parameter range, $Ra = 1.5 \times 10^5$, $2.4 \times 10^4 \leq Q \leq 1.6 \times 10^5$. To explore the origin of two-dimensional oscillations, we investigate the shape of the convection rolls from the recorded velocity profiles. Fig. 4(a) shows an averaged velocity profile measured by UV1 at $Ra = 1.5 \times 10^5$ and $Q = 5.0 \times 10^4$. Alternative positive and negative curves represent individual rolls, thus there are six rolls arranged parallel to the magnetic field. The curves are not symmetric and considerably deformed, especially around the places where the flow detaches from the top and bottom boundaries, $x \sim 0$, 65, 130, and 190 mm considering that the measurement line places near the bottom. In comparison with numerical simulations shown in Fig. 4(b), where the vortices are represented by 2nd invariant of the velocity gradient [4], the deformation may represent the existence of secondary, fine vortices indicated by white arrows in the figure, and also schematically shown in Fig. 4(c). In this configuration, the three-dimensional motion of the rolls is restricted by Lorenz force, and the rolls have relatively larger rotation speed and inertia. This may provide flow separations as shown in the figure. Such a 'recirculation bubble' is unstable and provides vortex shedding like von Karman vortices behind a cylinder. The Reynolds number estimated from the size of recirculation bubble and rotation velocity of the rolls provides a reasonable value for the onset of vortex shedding.

CONCLUSIONS

We investigated short-period oscillations in MHD-Rayleigh-Bénard convection. Detailed measurements of temperature and velocity fluctuations elucidated that the oscillation is two-dimensional and originated in instability of recirculation vortices.

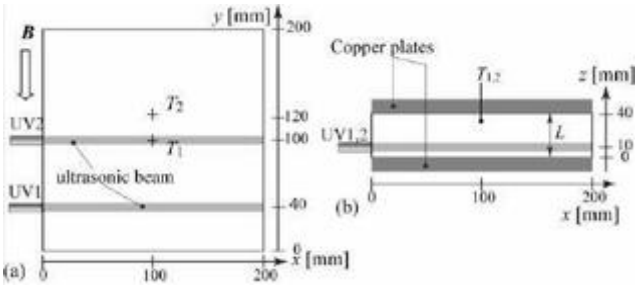

Fig. 1 (a) top and (b) side view of the schema of experimental apparatus

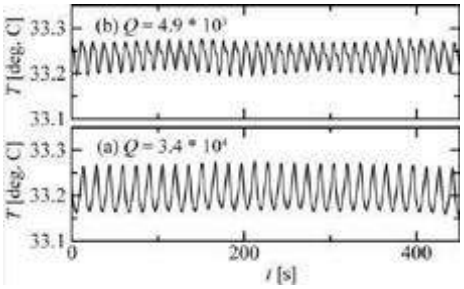

Fig. 2 Typical temperature fluctuations at $Ra = 2.5 \times 10^4$

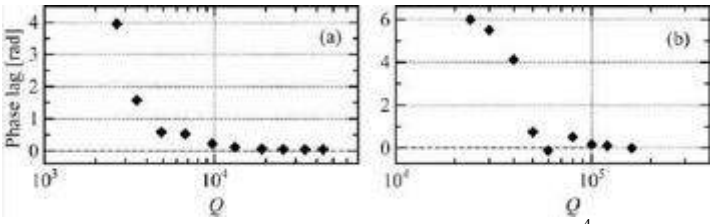

Fig. 3 Variations of the phase difference of (a) temperatures between T_1 and T_2 at $Ra = 2.5 \times 10^4$, and (b) velocity between UV1 and UV 2 at x = 50 mm for $Ra = 1.5 \times 10^5$

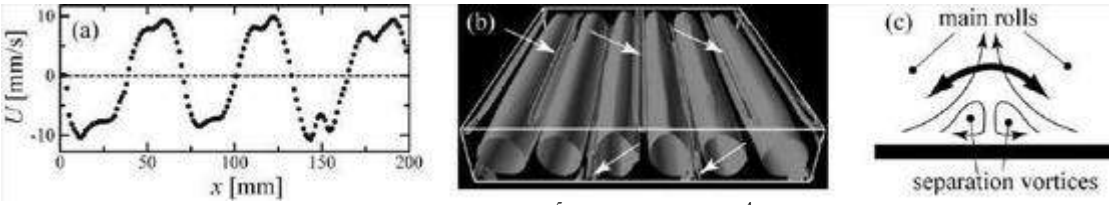

Fig. 4 (a) Mean velocity profile measured by UV1 at $Ra = 1.5 \times 10^5$ and $Q = 5.0 \times 10^4$ ($R/Q = 3.0$), (b) vortex structure represented by numerical simulation at $Ra = 1.0 \times 10^5$ and $Q = 3.2 \times 10^4$ ($R/Q = 3.1$) and, and (c) schematic illustration of vortex structures

References

[1] Yanagisawa T. *et al*., *Phys*. *Rev*. *E* **83,** 036307, 2011.

[2] Yanagisawa T. *et al*., *Phys*. *Rev*. *E* **88,** 063020, 2013.

[3] Tasaka Y. *et al*.: Regular flow reversals in Rayleigh-Bénard convection in a horizontal magnetic field, submitted.

[4] Yanagisawa T., Hamano Y. and Sakuraba A., *Phys*. *Rev*. *E* **92**: 023018, 2015

[5] Clever R. M. and Busse F. H., *J*. *Fluid Mech*. **176**, 403, 1987.

THE LARGE-SCALE CIRCULATION D NAMICS IN ROTATING RA LEIGH-BENARD CONVECTION

Jin-Qiang Zhong[1,a)], Hui-Min Li[1] & Xue-Ying Wang[1]
[1]*School of hysics Science and Engineering, Tong i University, Shanghai, China*

Summary: In this talk I will present new experimental measurements of the large-scale circulation (LSC) dynamics in rotating Rayleigh-Bénard convection. In cylindrical samples we probe the angular orientation θ and the flow strength δ of the LSC, through measurements of the azimuthal fluid temperature profile. We report linear retrograde precession of θ driven by constant Coriolis force in an unprecedented large Rossby number range ($10 \leqslant Ro \leqslant 314$). Enhanced precession speed is observed when $Ro \geqslant 70$ that is ascribed to stochastic cessation dynamics. A New oscillatory state of the LSC appears when the flow is subjected to modulated rotations. Both θ and δ exhibit periodic oscillations in the modulation frequency. We present a LSC model that predicts accurately the oscillation amplitudes and phases.

In r c n

In rotating turbulent Rayleigh-Bénard convection (RBC), the nature of the main flow structure, a large-scale circulation (LSC), is determined by the Rayleigh number $Ra=\alpha g\Delta TL^3/\kappa\nu$, the Prandtl number $Pr=\nu/\kappa$, the Rossby number $Ro=(\alpha g\Delta T/L)^{1/2}/2\Omega$, and the aspect ratio of the sample cell. Here α is the thermal expansion coefficient, g is the gravitational acceleration, κ and ν the thermal diffusivity and kinematic viscosity, respectively, ΔT is the temperature difference between the top and the bottom of the sample, Ω is the sample rotating velocity, and L is the height of the sample.

Re r r e r n f e r e-sc e c rc n r eR n ers

Figure 1a depicts the LSC flow structure in a cylindrical sample cell with an aspect ratio 1.0. We determine the orientation of the LSC plane θ by fitting the azimuthal temperature profile T_i (i=0,…,7) measured at eight points on the sidewall at the mid-height level of the cell, with a sinusoidal function: $T_i = T_0 + \delta\cos(i\pi/4-\theta)$, (i = 0, ..., 7). In doing so both the LSC temperature amplitude δ and the azimuthal orientation θ are determined. Over the entire Ro range studied ($1 \leqslant Ro \leqslant 314$), retrograde precession of the LSC circulating plane is observed. Time series $\theta(t)$ for several Ro are shown in Fig.1b for $Ra = 8.24\times10^9$ and Pr = 4.38. When Ro increased the mean rotating rate $<\dot{\theta}>$ decreases monotonically. However, the ratio of the LSC precession speed, $\gamma=-<\dot{\theta}>/\Omega$, experiences a complicated Ro-dependence in the range $1 \leqslant Ro \leqslant 10$. When Ro increases $<\dot{\theta}>$ appears to be proportional to Ω when $10 \leqslant Ro \leqslant 70$, yielding γ=0.13 independent of Ro. For $Ro \geqslant 70$, γ gradually increases with increasing Ro and reaches a value near 0.42 for Ro=314 .

Through further data analysis we find that in short time scales normal di**ff**usive motion with a constant drift velocity in the retrograde rotation presents the main dynamical feature of $\theta(t)$. The diffusivity of θ increases when the LSC amplitude δ decreases during cessation events, as predicted by a LSC dynamical model [3]. We show that it is the stochastic cessation dynamics that enhances the precession speed of the LSC at large Ro numbers.

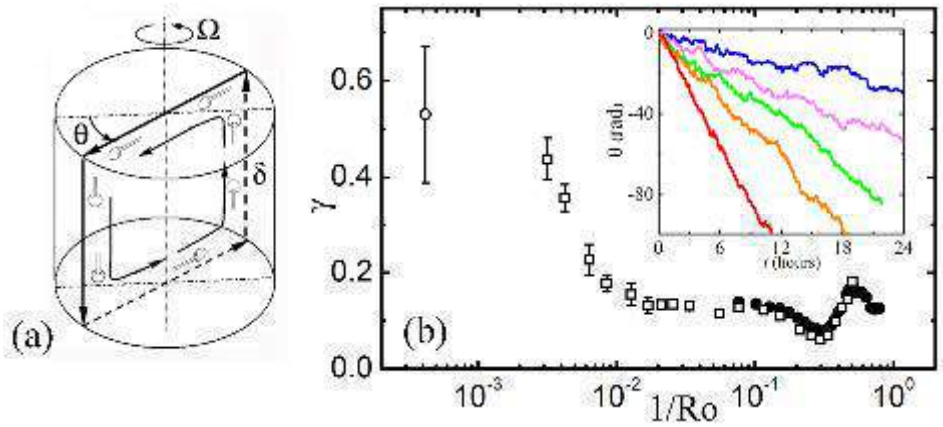

Fig. 1 (a) Sketch of the LSC structure in rotating turbulent RBC indicating the LSC angular orientation θ and and thermal amplitude δ. (b) Results for the LSC precession velocity ratio γ as a function of 1/Ro. Solid circles: data for from [1] with $Ra=8.97\times10^9$, Pr=4.38; Open circles: data adapted from [2] with $Ra= 8.9\times10^{10}$, Pr=4.38 and $\Omega=\Omega_E$ is the spinning rate of the Earth; Open squares: present data. The error bars indicate the standard deviations. Inset: Examples of the time series of θ(t) for Ro = 13.1 (red), 18.2 (orange), 39.4 (green), 59.0 (magenta) and 236 (blue).

[a)] Corresponding author. Email: jinqiang@tongji.edu.cn

Osc ns f e r e-sc e c rc n r n n

We present measurements of the LSC dynamics when the flow is subjected to librating rotations. Our studies are focus on the dynamical response of the LSC azimuthal velocity $\dot{\theta}$ when the fluid acceleration is created by oscillating Coriolis force, and the time-dependent LSC thermal amplitude δ driven by oscillatory viscous boundary layers. During these measurements the rotating velocity of the sample varies according to $\Omega = \Omega_0[1+\beta\cos(\omega t)]$, with Ω_0=0.104 rad/s and β=0.212. So Ro varies periodically in the range $0.31 \leqslant /Ro \leqslant 0.51$. The normalized modulation rate ω/Ω_0 ranges from 0.025 to 1.0.

Osc ns f e LSC r en n θ

Figure 2a shows a time series of the detrended orientation $\theta_d(t)=\theta(t)-<\dot{\theta}>*t$ for $\omega/\Omega_0 = 0.1$. $\theta_d(t)$ exhibits clear oscillations at the modulation frequency. Typical power spectra of $\theta_d(t)$, given in Fig. 2c, show a main peak at $f = \omega$ in a background spectrum falling off as f^{-2}, the latter corresponding to a diffusive meandering of the LSC in the azimuthal direction.

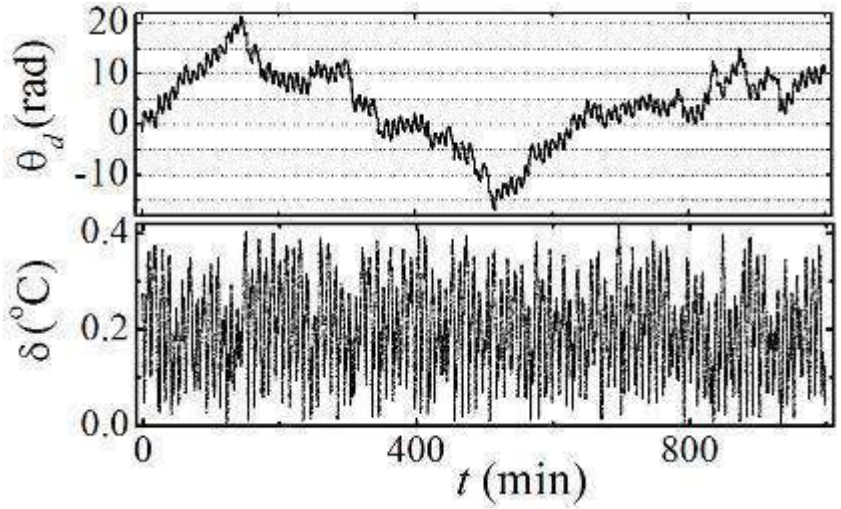

Fig. 2 Time traces for the LSC detrended orientation θ_d (a) and the thermal amplitude δ (b). Results for $\omega/\Omega_0 = 0.1$ [4].

Osc ns f e LSC er e δ

The time series of $\delta(t)$ is also found to consist of oscillations in a random-fluctuation background. An example is plotted in Fig. 2b for $\omega/\Omega_0 = 0.1$, with its power spectrum given in Fig. 2d, wherein higher harmonics appear at $f = (2\omega,\ldots,5\omega)$ in addition to the main peak at the frequency of modulation.

We determine the phases and amplitudes for both $\dot{\theta}(t)$ and $\delta(t)$ in this oscillatory state. We find that when ω increases fluid acceleration driven by oscillating Coriolis force causes an increasing phase lag in $\dot{\theta}(t)$. Oscillation of $\dot{\theta}(t)$ with maximum amplitude occurs at a finite modulation frequency. Such a resonance-like phenomenon is interpreted as a result of optimal coupling of $\delta(t)$ to the modulated rotation velocity [4].

C nc s ns

New dynamical phenomena of the LSC flow in turbulent RBC appear in the presence of Coriolis force. We study the azimuthal rotation of its circulating plane and its thermal amplitude with large or time-varying Ro. We show that a large-scale flow model provides predictions of the observed flow dynamics including the LSC linear retrograde rotation and the oscillations both in $\dot{\theta}$ and δ. Some of the observed phenomena are still unexplained and remained to be further investigated.

References

[1] J.-Q. Zhong and G. Ahlers: Heat transport and the large-scale circulation in rotating turbulent Rayleigh-Bénard convection. J. Fluid Mech., 665, 300-333, 2010.

[2] E. Brown and G. Ahlers,: Effect of the Earth's Coriolis force on the large-scale circulation of turbulent Rayleigh-Bénard convection. Phys. Fluids, 18, 125108, 2006.

[3] E. Brown and G. Ahlers,: Large-scale circulation model for turbulent Rayleigh–Bénard convection. Phys. Rev. Lett. 98, 134501, 2007.

[4] J.-Q. Zhong, Sebastian Sterl, and Hui-Min Li,: Dynamics of the Large-Scale Circulation in Turbulent Rayleigh-Bénard Convection with modulated rotation. J. Fluid Mech., 778, R4, 2015.

Turbulent thermal convection over rough surfaces with varying roughness size

Yi-Chao Xie and Ke-Qing Xia *

Department of Physics, The Chinese University of Hong Kong, Shatin, N.T., Hong Kong, China

Summary We present experimental study of turbulent thermal convection over rough surfaces with varying roughness size. It is found that the local temperature fluctuations measured at the cell center and near the sidewall change significantly with the increase of the roughness parameter λ, which is defined as the ratio of the height of the pyramid-shaped roughness element over the width of its base. The change of the local temperature fluctuations occur concomitantly with the change of the global heat transport law of the system, i.e. the Rayleigh number Ra dependence of the non-dimensional heat flux Nusselt number Nu. Detailed examinations of the local temperature time series indicate that the changes are brought into by the changes of plume dynamics which is supported by the observation that the dissipative power Q increases with the increase of λ.

INTRODUCTION

Turbulent thermal convection, which finds numerous examples in nature, such as in the atmosphere, the ocean and the mantle of the Earth. In the laboratory, turbulent thermal convection is usually studied in a simplified model system, i.e. the Rayleigh-Bénard convection where a fluid layer is confined between two horizontally parallel plates strongly heated from below and cooled from above [1, 2, 3]. As many convection phenomena in nature occur over rough surfaces, it is thus interesting to investigate turbulent thermal convection in convection cells with rough surfaces, which has been done in experiments and numerical simulations [4, 5, 6, 7, 8, 9, 10]. Although the effects of roughness have been studied extensively, the effects of roughness geometry and distribution on turbulent convection attract less attention in previous studies. To the best of our knowledge, the only experimental investigation of roughness distribution on turbulent thermal convection was done in [6] in which glass spheres with different diameter were glued to the conducting plates. Owing to the poor thermal conductivity of glass, there existed unknown and possibly significant thermal resistance between the conducting plates and the roughness elements making the situation much more complex, which prompts us to study the geometrical effects of roughness on turbulent thermal convection using directly machined roughness elements on plates.

THE EXPERIMENTS

The experiments were carried out in cylindrical convection cells with Plexiglas sidewalls. The wall-roughness was directly machined tiny pyramids arranged in a square lattice form on both the top and bottom plates. The height of the roughness elements was 8 mm. The width of the base of each pyramid was varied from 16 mm to 2 mm. Thus, the roughness parameter λ, as defined by the ratio of roughness height to the base width, was from 0.5 to 4.0. Totally for sets of plates with $\lambda = 0.5, 1.0, 1.9,$ and 4.0 were used in the study. The convection cell had a diameter D of 19.2 cm and a height H of 20.0 cm. Thus the aspect ratio Γ was nearly unity. Flourinert FC770 fluid with $Pr = 23.34$ was used in the experiment. By varying the temperature difference ΔT applied to the top and bottom plates, we achieved Ra from 4×10^9 to 2×10^{11}. The temperature of the top (bottom) plate was monitored by four (five) thermistors embedded into it. The sampling rate of those temperature measurements was 1.6 Hz. The local temperatures at the cell center and $\sim$1 cm away from the sidewall were measured using two tiny thermistors with a time constant of 0.03 s. The sampling rate of the local temperature measurements varied from 32 Hz to 128 Hz depending on Ra. To obtain sufficient statistics, measurement at different Ra lasted at least 12 hours.

RESULTS AND DISCUSSION

It is found that, surprisingly, the local temperature fluctuations change significantly with different λ, i.e. with the increase of λ, the magnitude of the local temperature fluctuations increases. The power law scaling relation of the normalized temperature fluctuations changes with the increase of λ as well. Detailed examination of the temperature time series implies that these changes come from the changes of thermal plume dynamics: With the increase of λ for a plate with fixed diameter, the number of roughness elements increases, and the increased roughness elements also means increase of the "plume emitters". Thus for larger λ, more thermal plumes will be emitted. There has been evidence that the thermal plumes emitted from nearby heat sources will form plume clusters or large plumes[11]. These large thermal plumes are more able to maintain their "heat" (or temperature difference with the background fluid) during their migration from one plate of the convection cell to another, leading to changes in both the magnitude of the temperature fluctuations and its $Ra\circ$ dependence.

*Corresponding author. Email:kxia@phy.cuhk.edu.hk

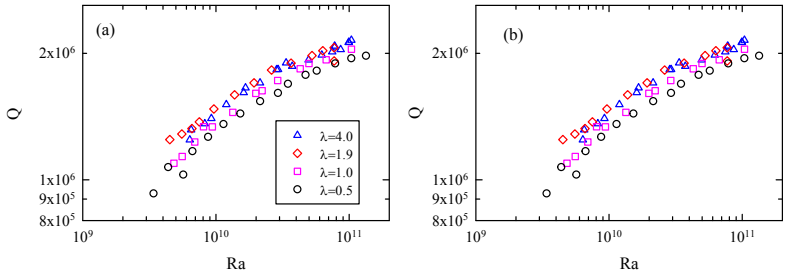

Figure 1: Dissipation power Q measured at the cell centre (a) and the sidewall (b) for different roughness parameter λ.

To quantify the change of the plume dynamics, we calculate the dissipative power Q introduced in [13]. which is defined as:

$$Q = \sigma_T/\sigma_{T'} \times H^2/\kappa \tag{1}$$

where $\sigma_T = \sqrt{(T \circ \langle T \rangle)^2}$ and $\sigma_{T'} = \sqrt{(T' \circ \langle T' \rangle)^2}$ with T' being the time derivative of the local temperature T and κ the thermal diffusivity of the convecting fluid. The measured Q as a function of Ra for different λ is shown in figure 1. It is seen that with the increase of λ, the dissipation power Q increases, suggesting that the plume dynamics has changed. Similar change of the dissipation power Q was interpreted as the change of plume dynamics [13]. As thermal plumes are the main heat carriers in turbulent thermal convection, the changes of plume dynamics will surely change the heat transport of the system, which is confirmed by the measured change of the power relation between Nu and Ra. Since thermal plumes self-organize themselves into a coherent large-scale circulation (LSC), the change of plume dynamics, should also be reflected from the LSC dynamics. The measured Ra dependence of the Reynolds number Re associated with the LSC also changes with increase of λ.

CONCLUSION

We have demonstrated that simple manipulation of the surface roughness geometry in turbulent thermal convection can significantly modify the local temperature fluctuations as well as the heat transport. The changes lie in the change of plume dynamics, reflected by the dissipative power. With the increase of roughness parameter λ, defined as the ratio between the roughness height and the roughness base width, the thermal plume emissions enhances, leading to the enhancement of the local temperature fluctuation and the heat transport.

ACKOWLEGEMENT

This work was supported by the Research Grant Council of Hong Kong SAR through grant No. 403712.

References

[1] G. Ahlers, S. Grossmann, D. Lohse. Heat transfer and large scale dynamics in turbulent Rayleigh Bénard convection. *Rev. Mod. Phys.*,**81**:503-537, 2009

[2] D. Lohse, K.-Q. Xia. Small-scale properties of turbulent Rayleigh-Bénard convection. *Annu. Rev. Fluid Mech.*,**42**: 335-364, 2010

[3] F. Chillá, J. Schumacher New perspectives in turbulent Rayleigh-Bénard convection. *Eur. Phys. J. E*,**35**: 58, 2012

[4] Y. Shen, P. Tong, and K.-Q. Xia. Turbulent convection over rough surfaces. *Phys. Rev. Lett.*, **76**:908–911, 1996.

[5] Y.-B. Du and P. Tong. Enhanced heat transport in turbulent convection over a rough surface. *Phys. Rev. Lett.*, **81**:987–990,1998.

[6] S. Ciliberto and C. Laroche. Random roughness of boundary increases the turbulent convection scaling exponent. *Phys. Rev. Lett.*, **82**:3998–4001,1999.

[7] G. Stringano, G. Pascazio, and R. Verzicco. Turbulent thermal convection over grooved plates. *J. Fluid Mech.*, **557**:307–336, 6 2006.

[8] O. Shishkina and C. Wagner. Modelling the influence of wall roughness on heat transfer in thermal convection. *J. Fluid Mech.*, **686**:568–582, 2011.

[9] J.-C. Tisserand, M. Creyssels, Y. Gasteuil, H. Pabiou, M. Gibert, B. Castaing, and F. Chillà . Comparison between rough and smooth plates within the same Rayleigh-Bénard cell. *Phys. Fluids*, **23**(1) 2011.

[10] P. Wei, T.-S. Chan, R. Ni, X.-Z. Zhao, and K.-Q. Xia. Heat transport properties of plates with smooth and rough surfaces in turbulent thermal convection. *J. Fluid Mech.*, **740**:28–46, 2014.

[11] E. Moses, G. Zocchi, A. Libchaberii, An experimental study of laminar plumes *J. Fluid Mech.*, **251**:581–601, 1993.

[12] S. Toppaladoddi, S. Succi, J. S. Wettlaufer. Tailoring boundary geometry to optimize heat transport in turbulent convection. *EPL (Europhysics Letters)*,**111**:44005, 2015.

[13] I. Procaccia, E. S. C. Ching, P. Constantin, L. P. Kadanoff, A. Libchaber and X.-Z. Wu Transitions in convective turbulence: The role of thermal plumes. *Phys. Rev. A*, **44(12)**: 8091-8102, 1991

OPTIMAL BOUNDS ON ENERGY DISSIPATION FOR STRESS-DRIVEN SHEAR FLOWS

Giovanni Fantuzzi[1] and Andrew Wynn*[1]

[1]*Department of Aeronautics, Imperial College London, London, UK, SW7 2AZ*

Summary A novel method is proposed to provide bounds on energy dissipation for stress-driven flows. The particular approach is based upon the fact that the *background method* for establishing bounds on emergent quantities for fluid flows typically requires the solution of an infinite dimensional variational problem. We show how such a problem can be rigorously relaxed so that a feasible solution can be found by instead solving an associated finite-dimensional convex optimization problem. In particular, we make use of Semidefinite-Programming methods, for which established and efficient solution methods are available. We apply this new technique to compute near-optimal upper bounds on the dissipation coefficient for stress-driven shear flows, improving previously known bounds by more than 10 times.

INTRODUCTION

Turbulent flows typically exhibit enhanced transport, mixing and/or dissipation compared to steady flows, but an accurate characterization of their properties is challenging due to their dynamic complexity. Given the computational cost of full numerical simultion in chaotic, highly turbulent regimes is prohibitively costly, a common approach is to attempt to prove rigorous *scaling laws* which attempt to express emergent flow properties such as dissipation or transport as a functions of the forcing parameters, for example, Reynolds number, boundary conditions or body forces.

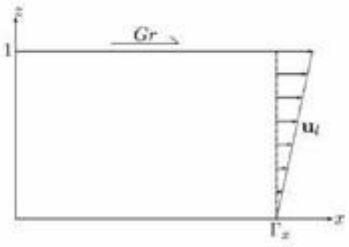

Figure 1: Stress-driven flow.

In this paper, we will consider the particular case of a flow driven by a stress on its upper surface, shown in Figure 1. It is assumed that the fluid occupies a cell $[0,\Gamma_x]\times[0,1]$, is periodic in the x direction and satisfies no-slip boundary conditions on the lower surface. Such a flow is of interest in physical oceanography as a model of the effect of wind blowing over a fluid surface. In non-dimensional variables the velocity field $\boldsymbol{u}=(u_1,u_2)$ can be shown [2] to satisfy

$$\boldsymbol{u}_t+\boldsymbol{u}\cdot\nabla\boldsymbol{u}+\nabla p=\nabla^2\boldsymbol{u},\qquad \nabla\cdot\boldsymbol{u}=0,$$

with boundary conditions $\boldsymbol{u}|_{z=0}=0$, $\frac{\partial u_1}{\partial z}\big|_{z=1}=Gr$, $u_2|_{z=1}=0$. Here, Gr is the *Grasshoff number* which acts as the control parameter determining the magnitude of the shear force driving the flow. An emergent quantity of interest [3] for this flow is the nondimensional dissipation coefficient $C_\epsilon:=Gr/\overline{u}(1)^2$ where $\overline{u}(1)$ is the space-time average of the x-velocity component u_1 over the upper surface of the flow domain.

It is known [2] that the dissipation rate is lower bounded by $C_\epsilon\geq 1/Gr$, which corresponds to the laminar solution $\boldsymbol{u}_\ell=Gr\,z\boldsymbol{e}_x$, indicated in Figure 1. The interesting case is therefore to provide an upper bound on the dissipation coefficient and this can be achieved using the background method [1]. In particular, suppose that the flow field is decomposed as $\boldsymbol{u}=\phi(z)\boldsymbol{e}_z+\boldsymbol{u}'$ where $\phi(z)$ is the *background profile*. If ϕ can be chosen to satisfy $\phi(0)=0,\phi'(1)=Gr$ and is such that the quadratic form $Q_\phi(\boldsymbol{u}'):=\int_0^1\|\nabla\boldsymbol{u}'\|^2+2\frac{d\phi}{dz}uw\,dx\,dz$ is positive for all time-independent vector fields $\boldsymbol{u}'=(u,w)$ satisfying suitable homogeneous boundary conditions, then it can be shown [3] that the dissipation coefficient is bounded from above by

$$C_\epsilon\leq Gr^3\mathcal{B}(\phi)^{-2},\qquad\text{where}\qquad \mathcal{B}(\phi):=2Gr\phi(1)-\|d\phi/dz\|_2^2. \tag{1}$$

The best dissipation bounds achievable with this method are therefore obtained by constructing $\phi(z)$ such that it maximizes $\mathcal{B}(\phi)$ while satisfying the specified boundary and integral inequality constraints. The established approach is to attempt to solve the Euler-Legrange equations [1] for the background profile. However, for the flow in question, such an approach is highly challenging due the mixed Neumann/Dirichlet boundary conditions. We therefore propose a novel method of constructing ϕ, motivated by the work of the authors in [4].

BACKGROUND PROFILE CONSTRUCTION VIA SEMIDEFINITE PROGRAMMING

Our approach is to relax the infinite dimensional positivity constraint $Q_\phi\geq 0$ by deriving a sufficient condition for it which is *finite dimensional* and can consequently be verified computationally. To this end, we perform series decompositions of the functions involved. Invoking periodicity, we first take a Fourier transform $\boldsymbol{u}'=\sum_k\boldsymbol{u}_k(z)e^{ikx}$ in the x direction. Next, in view of the need to enforce Neumann boundary conditions at the upper surface, it is convenient to perform *Legendre series*

*Corresponding author. Email: a.wynn@imperial.ac.uk

decompositions of both the background profile ϕ and the z-dependent functions $\boldsymbol{u}^{(k)}$. Consequently, Q_ϕ can be decomposed as a sum of quadratic forms, each corresponding to a particular wavenumber k, and it can be proven that each such form can be lower-bounded in the following manner

$$Q_\phi(\boldsymbol{u}') = \sum_k Q_{\phi,k}\left(\boldsymbol{u}^{(k)}\right) \geq \sum_k \underbrace{\begin{pmatrix} u_1^{(k)} \\ \vdots \\ u_N^{(k)} \end{pmatrix}^\top M_k(\phi) \begin{pmatrix} u_1^{(k)} \\ \vdots \\ u_N^{(k)} \end{pmatrix}}_{\text{finite dimensional part}} + \overbrace{c\left(1-\kappa_N\|\phi\|_1\right)\|\boldsymbol{u}^{(k)}\|_2^2}^{\text{tail terms}}.$$

Here, $(\hat{}_i^{(k)})_{i=1}^N$ are the first N *Legendre coefficients* of $\boldsymbol{u}^{(k)}$, $\boldsymbol{u}^k$ is the tail of this function relating to the (infinitely-many) remaining Legendre coefficients, each $M_k(\phi)$ is a real symmetric matrix which depends linearly on ϕ and $c > 0$. Such a decomposition makes efficient and rigorous computer-assisted verification of the lower bound possible: (i) positivity of the finite dimensional part corresponds to *positive definiteness* of the matrices $M_k(\phi)$, and due to their linear dependence on ϕ, well-established [5] and efficient methods exist to search for functions ϕ for which this is true; (ii) the tail term is positive so long as $\|\phi\|_1 \leq \kappa_N^{-1}$ and it can be shown that $\kappa_N = \mathcal{O}(N^{-3})$ for the considered shear flow, meaning that this condition can be made negligible by increasing the the size N of the finite-dimensional term; (iii) the boundary conditions upon ϕ and the term $\mathcal{B}(\phi)$ that, in view of (1), we wish to maximize are easily recast in terms of the Legendre coefficients of ϕ, which become the variables of the optimization problem; and (iv) it can be proven that only finitely many wavenumbers k need to be checked. In summary, $Q_\phi \geq 0$ can be proven by constructing a background profile which enforces positive definiteness of a finite collection of matrices while at the same ensuring that its norm $\|\phi\|_1$ is not too large. The importance of this result is that the search over such functions to find the one which maximizes $\mathcal{B}(\phi)$ (hence providing the best bound on C_ϵ) results in an optimization problem which has the general form of a Semidefinte Program (SDP), for which established solution methods [5] are available.

RESULTS AND CONCLUSIONS

Background profiles arising from the solution of the finite-dimensional SDP for $10^3 \leq Gr \leq 10^5$ are shown in Figure 2 (left) for the aspect ration $\Gamma_x = 2$. The corresponding upper bounds on C_ϵ for $\Gamma_x = 2, 3$ are shown in Figure 2 (right) together with the lower bound $C_\epsilon \geq Gr^{-1}$ corresponding to the laminar solution. In particular, as $Gr \to \infty$ the computed bound can be seen to be an order of magnitude improvement on $C_\epsilon \leq 1/16 = 0.0625$ recently proven in [3]. The form of the background profile is influenced, in view of (1), by the competing aims of maintaining ϕ close to a constant value (to minimize $\|d\phi/dz\|_2$) while simultaneously satisfying the boundary conditions. The asymmetry of the boundary conditions can be observed in the asymmetry of the background profiles. This methodology can also be applied to the 3D problem and achieves a similar order of magnitude improvement to the upper bound on C_ϵ to previously known results. In conclusion, we have proposed a novel method, based on convex optimization, to computationally assist the proof of bounds on emergent flow properties.

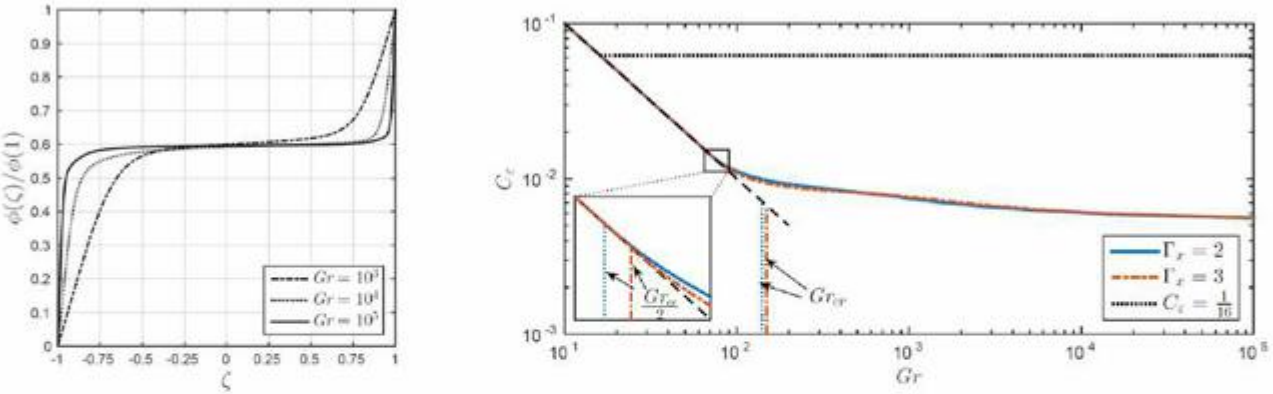

Figure 2: Background profiles (left) and associated bounds on C_ϵ (right).

References

[1] Constantin P., Doering C.R.: Phys. D Nonlinear Phenom. **82**, 221–228, 1995.
[2] Tang W., Caulfield, C.P., Young, W.R.: Journal of Fluid Mechanics, **510**, 333–352, 2004.
[3] Hagstrom, G. I., Doering, C. R.: Journal of Nonlinear Science, **24**, 185–199, 2014.
[4] Fantuzzi, G., Wynn, A.: Physics Letters A **379**, 23–32, 2015.
[5] Boyd, S., Vandenberghe L.: Convex Optimization (Cambridge University Press, Cambridge, 2004).

ON THE INFLUENCE OF THE ASPECT RATIO ON STRUCTURE FORMATION IN TURBULENT MIXED CONVECTION

Daniel Schmeling[1a], Stefan Winter[1], Johannes Bosbach[1] & Claus Wagner [1,2]
[1]*German Aerospace Center (DLR), Institute of Aerodynamics and Flow Technology, Göttingen, Germany*
[2]*Ilmenau University of Technology, Institute of Thermodynamics and Fluid Mechanics, Ilmenau, Germany*

Summary Mixed convection in a cuboidal convection cell is studied under variation of the aspect ratio Γ_{xz} = L/H in the range 0.2 ≤ Γ_{xz} ≤ 4 at Pr ≈ 0.7, Re ≈ $8.6 \cdot 10^3$, Ra ≈ $2.4 \cdot 10^8$ and Ar ≈ 4.5 by temperature measurements at certain locations. It is shown that the evaluation of dipole moments from the local temperatures leads to a quantity, which possibly indicates the formation of large-scale structures. Further it is found, that the number of convection rolls, which are formed in the sample, is less or equal in mixed convection as compared to pure thermal convection for all investigated Γ_{xz}.

INTRODUCTION

The influence of the aspect ratio Γ on the flow structures and heat transport of pure thermal convection or Rayleigh-Bénard convection in cubically shaped containers has been analysed frequently [1][2][7][8]. Van der Poel et al. [7] considered a wide range of aspect ratios (0.23 ≤ Γ ≤ 13) in two-dimensional thermal convection. They presented, among others, the number of large-scale convection rolls as a function of Γ. Chong et al. [1] as well as Wagner and Shishkina [8] studied the impact of Γ on the flow in a cuboidal container in the range from unity to very thin samples. Thereby, they found different arrangements of the large-scale structures and other phenomena like "super plumes" or pumping effects. At a fixed aspect ratio of Γ = 5, mixed convection has been studied in a cuboidal convection sample by Schmeling et al. [5][6] and Kühn et al. [4]. The current study addresses aspect ratio variations in mixed convection, which has not been studied systematically yet.

CONVECTION SAMPLE & MEASUREMENT TECHNIQUE

The cuboidal convection sample has a length L = 2.5 m, a width W = 0.5 m and a height H = 0.5 m, i.e. an aspect ratio of Γ = 5:1:1. It allows for investigation of mixed convection by superposition of pure thermal convection, induced by a temperature gradient between the cold top and warm bottom plate, and forced convection, generated by a pressure gradient between air inlet (vent) below the ceiling and air outlet above the floor of the sample. The working fluid is air at ambient pressure. Both vents span the full length of the sample, see Fig. 1 (left) and for more details [5][6].

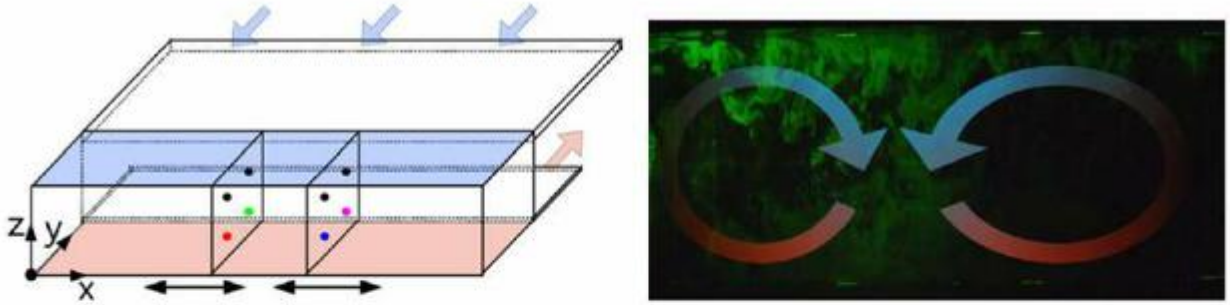

Fig. 1 Sketch of the convection sample with dots marking the positions of the temperature probes mounted to the sidewalls (left). Laser smoke visualization for Γ_{xz} = 3.5 with super imposed sketch of the large-scale convection rolls (right).

Variation of the aspect ratio was realized by installation of two separation walls within the convection sample. They are placed symmetrically to the centre of the sample and can be moved in x direction. Hence, the aspect ratio between length and height of the sample, Γ_{xz}, can be varied, while the aspect ratio between width and height, Γ_{yz} = W/H = 1, is kept constant. In addition to the geometry, three dimensionless numbers, namely the Prandtl, Reynolds and Rayleigh number, define the studied flow cases. The latter are further characterized by the Archimedes number $Ar = \frac{Ra}{Pr \cdot Re^2}$. For detailed definitions and interpretations, the reader is referred to [5][6].

Eight temperature probes are installed at the movable separation walls in a similar way as described by [3]. Additionally, more than 70 temperature probes monitor the temperature of heating and cooling plates, in- and outflowing air as well as ambient air temperature. Complementary to the temperature measurements, smoke visualizations are conducted.

RESULTS

To characterize the flow cases, resulting from different Γ, a dimensionless temperature is used. It is defined by $\Theta_i = \frac{T_i - T_{in}}{T_h - T_c}$ and calculated using the local temperature of a probe T_i as well as the global temperatures of the hot plate T_h,

[a] Corresponding author. Email: daniel.schmeling@dlr.de

the cold plate T_c and the inflowing air T_{in}. It must be noted that the colours of the markers in Fig. 2 (top left) correspond to those in Fig. 1 (left). Whenever multiple dots appear for one Γ, two measurement runs were conducted for the same settings. It is observed that for Γ = 0.2, 0.5, 3 and 3.5, almost symmetric temperatures are observed at the left and the right probes. This means that either no, or an even number of thermal convection rolls, whose rotation axis is mainly oriented in y-direction, is superimposed to the forced convection roll. In contrast, for Γ = 1, 1.5, 2, 2.5 and 4. Odd numbers of thermal convection rolls are reflected by different temperatures of the right and left probes.

To summarize this behaviour, a quantity $\vec{\chi}$ is defined by $\vec{\chi} = \sum_{i=1}^{4} \Theta_i \; \bar{}_i$, following the definition of the dipole moment in classical electrodynamics. Here, $\bar{}_i$ denotes the vector from the central position of the measurement plane to the probe. The length of $\vec{\chi}$, is only determined by the temperature gradient. Meanwhile, the orientation points towards the higher temperature. This means, for cases with no thermal convection roll or those with a single roll state (Γ < 3), this vector points in the direction of the fluid motion in the lower measurement plane. Contrarily, for Γ ≥ 3, low inclinations of the orientation of $\vec{\chi}$ with respect to the y-axis point to an even number of convection rolls, whereas high inclinations indicate an odd roll number state. Fig. 1 (right) shows the laser smoke visualization for Γ = 3.5, recorded in a vertical plane at y = 11 cm, that is, close to the front temperature probes. The cold fresh air, seeded with the smoke, descents in the centre region and separates above the heating plate. Accordingly, two convection rolls are established in the sample as depicted by the arrows. This visualization confirms the interpretation of the small inclination of $\vec{\chi}$ (Fig. 2, right) for Γ = 3.5 as an even number convection rolls.

Comparison with the pure thermal convection studies presented in [7] reveals, that in mixed convection (MC) less or equal convection rolls are established as compared to thermal convection (TC) for all investigated Γ, see Fig. 2 (bottom left). Thus, by superimposing forced convection on thermal convection states with less convection rolls are stabilized.

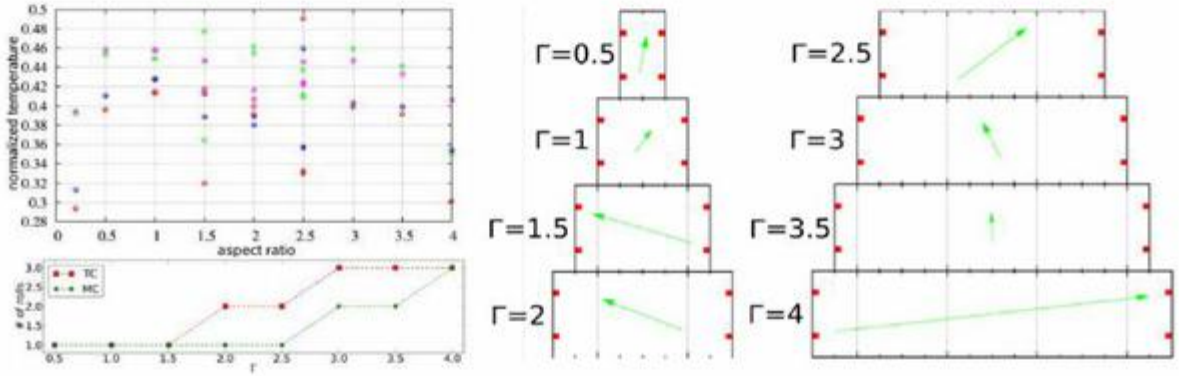

Fig. 2 Normalized temperature Θ for the lower four probes (top left) and number of convection rolls (bottom left) as a function of Γ. Arrangement of the "dipole moment" using the lower four probes depicted for nine different Γ (right).

The upper temperature probes, not shown for the sake of brevity, reveal in general a similar behaviour as the lower probes just at lower temperature levels. However, for Γ = 0.5 and Γ = 1, the orientation of the dipole moment was found to point towards the rear left probe, in contrast to the lower probes where it points to the rear right probe. This finding corresponds very well a state, which occurs as one extremum of the twisting mode of the large-scale circulation, as described by [3].

CONCLUSIONS

We presented results of an experimental study on the variation of the aspect ratio in mixed convection. A simple quantity $\vec{\chi}$ is found to serve as an indicator for the number of convection rolls in combination with smoke visualizations. It was found that the number of convection rolls is lower or equal in mixed convection as compared to pure thermal convection for all investigated aspect ratios. From this, we conclude that the superimposed forced convection stabilizes states with less convection rolls. Measurements with more temperature probes installed in the long sidewalls and for a wider Archimedes number range are in progress and will be presented at the conference.

References

[1] Chong K.L., Huang S.-D., Kaczorowski M., Xia K.-Q.: Condensation of coherent structures in turbulent flows. Phys Rev Lett 115:264503. 2015.

[2] Du Puits R., Resagk C., Thess A.: Measurements oft he instantaneous local heat flux in turbulent Rayleigh-Bénard convection. New J Phys 12:075023. 2010.

[3] Funfschilling D., Brown E., Ahlers G.: Torsional oscillations of the large-scale circulation in turbulent Rayleigh-Bénard convection. J Fluid Mech 607:119-139. 2008.

[4] Kühn M., Ehrenfried K., Bosbach J., Wagner C.: Large-scale tomographic PIV in forced and mixed convection using a parallel SMART version. Exp Fluids 53:91–103. 2012.

[5] Schmeling D., Westhoff A., Kühn M., Bosbach J., Wagner C.:Large-scale flow structures and heat transport of turbulent forced and mixed convection in a closed rectangular cavity. Int J Heat Fluid Flow 32:889–900. 2011.

[6] Schmeling D., Bosbach J., Wagner C.: Oscillations of the large-scale circulation in turbulent mixed convection in a closed rectangular cavity. Exp Fluids 54:1517. 2013.

[7] Van der Poel E.P., Stevens R.J.A.M., Sugiyama K.: Flow states in two-dimensional Rayleigh-Bénard convection as a function of aspect-ratio and Rayleigh number. Phys Fluids 24, 085104. 2012.

[8] Wagner S., Shishkina O.: Aspect-ratio dependency of Rayleigh-Bénard convection in box-shaped containers. Phys Fluids 25, 085110. 2013.

LIGHT PROPAGATION THROUGH AXIALLY HOMOGENEOUS BUOYANCY DRIVEN TURBULENCE

Shashikant S. Pawar & Jaywant H. Arakeri*
Department of Mechanical Engineering, Indian Institute of Science, Bangalore, India 560012

Summary Frequency spectra obtained from the measurements of intensity and angle of arrival (AOA), in axially homogeneous buoyancy driven turbulent flow are presented. The highest gradient based Rayleigh number (Ra_g) in the experiments is about 8×10^9, the Reynolds number based on Taylor microscale (Re_λ) is 210 and the Schmidt number (Sc) is 605. The measurement techniques used are – Shadowgraphy for intensity measurement, deflections of narrow laser beams for AOA measurements and background oriented schlieren (BOS) in obtaining the displacement fields. All these techniques jointly are used for the first time in this type of study. The spectra of the measured AOAs and intensity are compared respectively with those of displacements (from BOS) and relative intensity ($\mathcal{J}$) derived from displacement fields. The observed asymptotic scalings of the spectra are also compared with the scalings obtained from the theoretical relations from the literature.

INTRODUCTION

Refractive index (RI) inhomogeneities in the turbulent atmosphere cause the fluctuations in the propagating light waves. The effect is not desirable e.g. in ground-based astronomical observations, laser communication etc. while optical scintillation has been useful in remotely sensing the normal wind component, rain rates, drop size distributions etc. and in the measurement of fluxes of heat, momentum and humidity in the atmospheric surface layer. There are however, not many studies of light propagation in laboratory generated turbulence. In this work, we present the frequency spectra obtained from the measurements of intensity and AOA of parallel light propagating through the buoyancy driven turbulent flow, created in a long vertical tube. This flow [1, 2] has some unique features: zero mean, axial homogeneity and turbulence production solely due to buoyancy. Also, the non dimensional flux and Reynolds numbers are orders of magnitude higher than those in the classically studied Rayleigh-Benard convection for similar Rayleigh and Prandtl numbers [2, 3]. All these features make this flow suitable for the study of light propagation through turbulence. Theoretical relations for intensity and AOA spectra in the literature [5] are obtained assuming Kolmogorov-Obukhov (KO) scaling in the RI spectrum. Whether any other (e.g. Bolgiano-Obukhov, BO) scaling is observed in the buoyancy driven turbulence, is the motivation of the present study.

EXPERIMENTAL SETUP

The experimental set up used to create the turbulent flow comprised of an open ended long (L/d~10) vertical tube, interconnecting two fairly large tanks. Density difference across the tube ends was created using brine and fresh water. The Rayleigh number defined based on the linear mean density gradient is given by, $\mathrm{Ra_g} = \frac{g}{\rho_0}\frac{\left(\frac{\overline{d\rho}}{dz}\right)d^4}{\upsilon\alpha}$. At high enough Rayleigh numbers, Nusselt and Reynolds number scalings are obtained as, $\mathrm{Nu}\sim(\mathrm{Ra_g Pr})^{1/2}$ and $\mathrm{Re}\sim\mathrm{Ra_g}^{1/2}\mathrm{Pr}^{-1/2}$ respectively [2, 3], which are predicted by the mixing length model proposed by Arakeri et al. [1]. These scalings also correspond to the 'ultimate regime' of turbulent convection.

The intensity and angle of arrival measurements were carried out in the middle portion of the tube, where the flow was axially homogeneous. Three measurement techniques were used – laser shadowgraphy, deflection of the narrow laser beams and BOS to obtain respectively the instantaneous intensity, AOAs and displacement fields. Schematic of the setup used in shadowgraphy is shown in Figure 1. The setup used in the deflection of narrow laser beams was same as that used in shadowgraphy, except that the collimated laser beam was passed through an opaque mask having equispaced grid of holes, creating multiple narrow laser beams. In BOS, the mask was replaced by synthetic PIV image, backed by a diffuser plate and a halogen lamp was used as light source. It is easy to show that the displacements obtained from BOS are proportional to the AOAs.

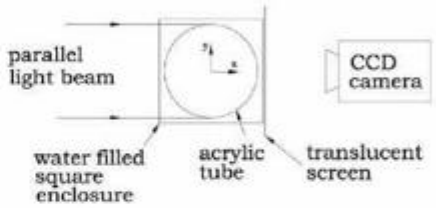

Figure 1. Schematic showing top view of the setup used in laser shadowgraphy

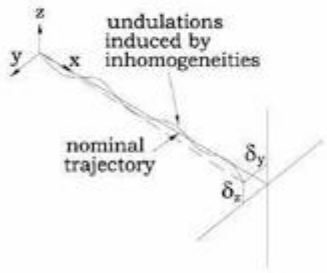

Figure 2. Displacement of the ray at the exit plane

THEORETICAL BACKGROUND

The log amplitude and the phase of the propagating wave are decomposed into the mean and the fluctuating part as, $\log A = \log \bar{A} + \chi$ and $S = \bar{S} + S'$ respectively. The log

* Corresponding author. Email:jaywant@mecheng.iisc.ernet.in.

amplitude fluctuation χ is related with the intensity (I) by [4], $\chi = \log\left(\frac{A}{\bar{A}}\right) = \frac{1}{2}\log\left(\frac{I}{\bar{I}}\right)$. For the wave propagated in the x-direction over distance L through the turbulent medium having refractive index field $n(x, y, z)$, the fluctuations of AOA in the horizontal (y) and vertical (z) directions are [5, 6], $\alpha'_y = \int_o^L \frac{\partial n'(x,y,z)}{\partial y} dx$ and $\alpha'_z = \int_o^L \frac{\partial n'(x,y,z)}{\partial z} dx$ respectively. The AOA is the net deflection of the light ray. For a light ray, the two AOAs obtained from the displacements of the ray from the nominal trajectory are, $\alpha_y = \frac{\delta_y}{L}$ and $\alpha_z = \frac{\delta_z}{L}$. For narrow laser beam images, the AOAs are calculated by replacing the two displacements by the intensity weighted centroids $(\bar{y}, \bar{z})$. A quantity proportional to the relative intensity change sensed in shadowgraphs can be obtained from the displacement fields as $\mathcal{I} = \int_0^L \frac{1}{n}\left(\frac{\partial^2 n}{\partial y^2} + \frac{\partial^2 n}{\partial z^2}\right) dx$.

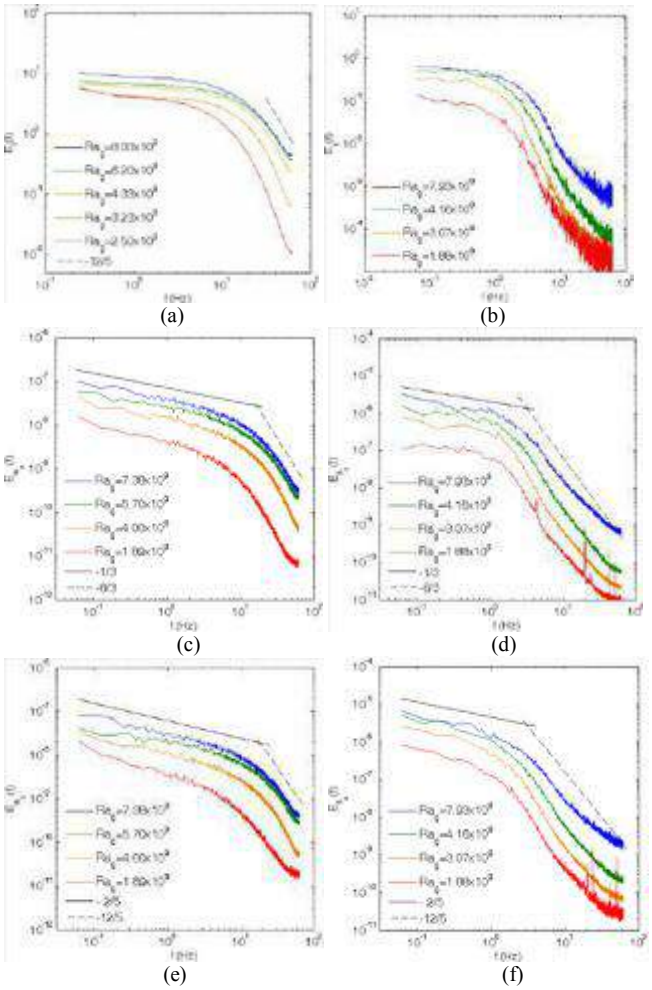

Figure 3. Frequency spectra of fluctuations of (a) intensity obtained from shadowgraphs, (b) quantity $\mathcal{I}$ derived from displacement fields of BOS, (c) horizontal AOA, (d) horizontal displacements, (e) vertical AOA and (d) vertical displacements for various Rayleigh numbers (All spectra are for the location $y = 0$).

RESULTS AND DISCUSSION

From the theoretical relations for frequency spectra of intensity and AOA for homogeneous, isotropic turbulent medium (assumed to be following KO scaling) developed by Tatarski [5], the asymptotic scalings for the low and high frequency ranges can be obtained as f^0 and $f^{-8/3}$ for intensity spectra and $f^{-2/3}$ and $f^{-8/3}$ for the AOA spectra. By modifying the theoretical relations for BO scaling, the corresponding asymptotic scalings are obtained as f^0 and $f^{-12/5}$ for the intensity and $f^{-2/5}$ and $f^{-12/5}$ for the AOA spectra.

Figure 3(a) shows the frequency spectra of intensity fluctuations, obtained from the shadowgraphs for different Rayleigh numbers. The spectra approach a constant value (f^0 scaling) for low frequencies, while they seem to follow $f^{-12/5}$ scaling in the high frequency range. They are in qualitative agreement with the spectra of the relative intensity $\mathcal{I}$, derived from displacement fields, shown in Figure 3(b).

Frequency spectra of horizontal AOA and horizontal displacement fields (obtained from BOS) for different Rayleigh numbers are shown in Figures 3(c) and (d) respectively. The asymptotic scalings in the low and high frequency ranges in this case seem to be $f^{-1/3}$ and $f^{-8/3}$ respectively. Figures 3(e) and (f) show the frequency spectra of vertical AOA and vertical displacement fields and the asymptotic scalings are $f^{-2/5}$ and $f^{-12/5}$ respectively in the low and high frequency ranges.

It was found thus that the asymptotic scalings of the intensity and vertical AOA spectra follow BO scaling more closely. The horizontal AOA scaling in the high frequency range is closer to KO scaling, while the low frequency asymptotic scaling $f^{-1/3}$, is unknown and may be associated with the inhomogeneity of the flow in lateral direction.

References

[1] Arakeri J. H., Avila F. E., Dada J. M. and Tovar R. O.: Convection in a long vertical tube due to unstable stratification-a new type of turbulent flow? Current Science, 79(6), 859–866, 2000.

[2] Cholemari M. R. and Arakeri J. H.: Axially homogeneous, zero mean flow buoyancy driven turbulence in a vertical pipe. J. Fluid Mech., 621, 69–102, 2009.

[3] Pawar S. S.: Axially homogeneous turbulent convection at high Rayleigh numbers: scaling laws for flux and spectra. PhD Thesis, Indian Institute of Science, Dept. of Mech. Engg., Bangalore, India, 2015.

[4] Tatarski V. I.: Wave propagation in a turbulent medium. McGraw Hill Book Company, Inc., 1961.

[5] Tatarski V. I.: The effects of the turbulent atmosphere on wave propagation. Israel program for scientific translations Ltd., 1971.

[6] Chandrasekhar S.: A statistical basis for the theory of stellar scintillation. Monthly notices of Royal astronomical Soc., 112(5), 475–483, 1952.

FLOW IN A DUAL HEATED CHANNEL

M. Z. Hossain[1a)] & J. M. Floryan[1]
[1]*Department of Mechanical and Materials Engineering, University of Western Ontario, London, Ontario, Canada*

*Summary*The drag reduction in a horizontal channel exposed to a spatially-periodic heating along the upper and lower walls has been analyzed. It has been shown that the drag reduction increases by up to a factor three when compared with the drag reduction achieved using one-wall heating. This increase is possible only when both heating patterns have a proper relative position.

INTRODUCTION

In a channel flow, the friction between the fluid and the bounding solid wall creates drag, and the development of techniques for its reduction attracted a lot of interest in recent years. One relatively new technique developed by Hossain and Floryan [1] is the use of spatial heating patterns which create a buoyancy field leading to the formation of a system of separation bubbles. The fluid trapped inside bubbles rotates due to the actions of horizontal density gradients and, thus, provides a propulsive force which contributed to the fluid pumping. The bubbles also isolate the stream from the direct contact with the bounding walls and, thus, reduce friction acting on the stream. The main objective of this article is to study the system response when both walls of a horizontal channel are heated and to determine positioning of the heating patterns which lead to the largest drag reduction.

PROBLEM FORMULATIONAND RESULTS

Consider steady flow of a fluid confined in a channel bounded by two parallel walls extending to $\pm\infty$ in the x-direction and placed at a distance 2h apart from each other with the gravitational acceleration g acting in the negative y-direction, as shown in Fig.1. The flow is driven in the positive x-direction by a pressure gradient. The fluid is incompressible and Newtonian. The lower and the upper walls are subject to the periodic heating patterns with the phase difference Ω between them. The resulting walls' temperatures have the forms $\theta_L(x) = \cos(\alpha x)/2$, $\theta_U(x) = \cos(\alpha x + \Omega)/2$, where subscripts L and U refer to the lower and upper walls, respectively, θ_L and θ_U denote the relative temperatures of the lower and the upper walls, respectively, and α is the wavelength of the heating.

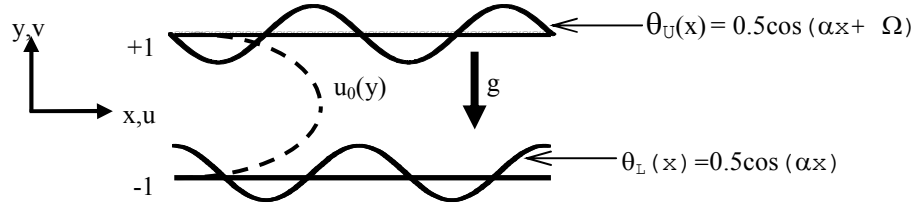

Figure 1. Sketch of the system configuration.

In the above u_0 is the reference Poiseuille flow. To denote the strength of the reference flow, the Reynolds number Re is defined based on the channel half-height. The upper and lower wall heating intensities are expressed by the periodic lower and upper Rayleigh numbers $Ra_{p,L}$ and $Ra_{p,U,}$ respectively. The relevant field equations consist of the continuity, Navier-Stokes and energy equations supplemented with the proper boundary conditions and the fixed flow rate constraint. This system is solved using a spectral discretization with Fourier series and Chebyshev collocation method [1]. The imposed heating changes the shear stress distribution which results in change in the pressure gradient, e.g. $\partial p/\partial \mathbf{x}|_{mean} = \mathrm{Re}\,(-2 + A/\mathrm{Re})$. The effectiveness of the heating is judged by comparing A with the isothermal pressure gradient -2Re (or by comparing A/Re with -2).

The flow topologies resulting from the application of the imposed dual heating are illustrated in Fig.2(a-b). It can be seen that the size of the separation bubbles as well as the intensity of the motion inside the bubble depend on the phase shift between both heating patterns; they are largest for $\Omega = 0$ and smallest for $\Omega = \pi$. This result demonstrates potential for increase of the drag reduction through the judicious selection of Ω. The flow topologies display the up/down symmetries combined with the horizontal phase shifts. $\Omega = \pi$ produces a simple symmetry without any phase shifts. Topologies with the up/down symmetries and the proper phase shifts have the same global characteristics, e.g. the same drag reduction.

[a)]Corresponding author. Email:**mhossa7**@uwo.ca**.**

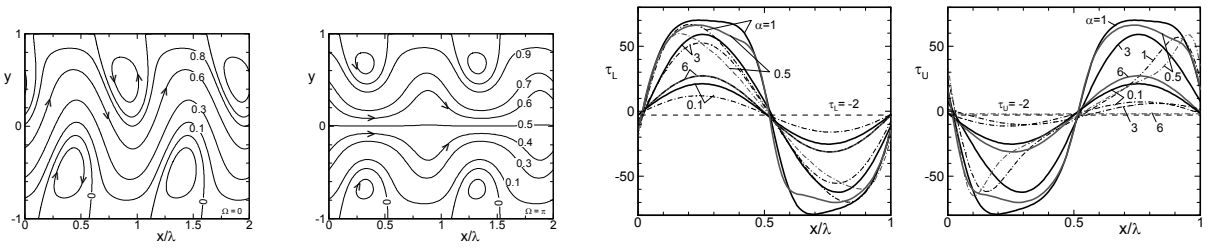

Figure 2. (a-b) Flow topology for the sinusoidal heating patterns applied at both walls with $Ra_{p,L} = Ra_{p,U} = 1000$, Re = 5, α = 2.5, Pr = 0.71, and for the phase shifts $\Omega = 0$ (Fig. 2a), π (Fig.2b).Figure 2. (c-d) Shear stress distributions at the lower (Fig.2C) and upper (Fig.2d) walls for selected values of the heating wave numbers α for $\Omega = 0$, Re = 1. The solid, dashed-dotted and dashed lines correspond to the two-wall heating, the lower-wall heating and the isothermal channel, respectively.

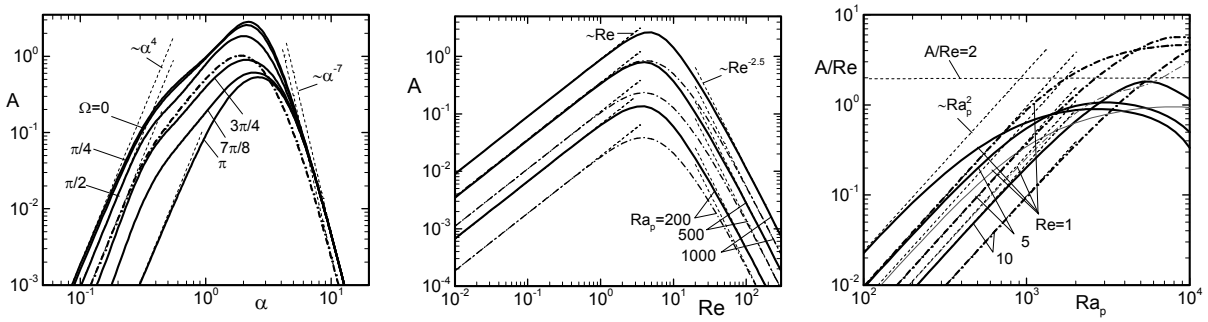

Figure 3. Variation of the pressure-gradient correction A as a function of (a) the heating wave number α for $Ra_{p,L} = Ra_{p,U} = 1000$, Re = 5and selected phase angles Ω;(b) the Reynolds number Re for selected heating intensities $Ra_p = Ra_{p,L} = Ra_{p,U}$ for α = 2.5, and $\Omega = 0$;(c) the Rayleigh number $Ra_p = Ra_{p,L} = Ra_{p,U}$ for $\Omega = 0$, and $\alpha = 2$ (thick solid lines) and $\alpha = 3$ (thick dashed-dotted lines).

Variations of the pressure gradient correction as a function of α are illustrated in Figure 3(a).The drag reduction is clearly visible but its magnitude rapidly decreases for α's which are either too large or too small. A significant increase of the drag reduction, as compared with what can be achieved using the single-wall heating, is clearly demonstrated but only if one uses proper phase difference between both heating patterns. This increase may reach up to 300%. Use of the improper phase difference significantly weakens this effect and can lead to drag reduction smaller than that which can be achieved using the one-wall heating. The effect the Reynolds number on the pressure gradient corrections are illustrated in Fig.3(b). The correction increases linearly for small Re, the growth saturates at Re $\approx$ 6 and is followed by a rapid decrease. Such variations occur for all Rayleigh numbers considered with the higher drag reduction achieved for higher values of Ra_p. The effectiveness of the heating intensity can be judged using data displayed in Fig.3(c). The pressure gradient correction initially increases proportionally to Ra_p. The growth eventually saturates and the further increase of Ra_p results in a reduction rather than any further increase of the pressure gradient correction. The reader may note that it is possible to create pressure gradient correction which is larger than the isothermal pressure gradient, i.e., it is possible to use wall heating to pump the fluid without the use of any externally applied pressure gradient.

CONCLUSIONS

The pressure-gradient-driven flow in a horizontal channel exposed to sinusoidal heating at the upper and lower walls, with a phase shift Ω between them, has been investigated for fluids with the Prandtl number Pr = 0.71. It has been found that that the intensity of convective effects strongly depends on the phase shift between the upper and lower heating patterns.

References

[1] Hossain,M. Z., Floryan,D., and Floryan, J. M.: Drag reduction due to spatial thermal modulations. *J. Fluid Mech.* **713**, 398-419, 2012.

HIGH RAYLEIGH NUMBER CONVECTION WITH DOUBLE DIFFUSIVE FINGERS

Matthias Kellner[1] and Andreas Tilgner*[1]

[1]*Institute of Geophysics, University of Göttingen, Friedrich-Hund-Platz 1, 37077 Göttingen, Germany*

Summary Rayleigh-Bénard convection experiments observe a large scale circulation up to the highest Rayleigh numbers accessible to experiments. Here, it is shown that this organization at large scales is disrupted by a relatively small perturbation in double diffusive convection. Experiments reported here show that the large scale circulation disappears in favor of double diffusive fingers even if the total density stratification is unstable and the buoyancy introduced by the stabilizing agent is two orders of magnitude smaller than the buoyancy force due to the destabilizing agent. Another spectacular change in the large scale flow pattern occurs if the flow splits into several layers stacked upon each other. This is observed in the oceans, and this effect has been reproduced in our experiments.

An electrodeposition cell is used to sustain a destabilizing concentration difference of copper ions in aqueous solution between the top and bottom boundaries of the cell [1, 2]. The resulting convecting motion is analogous to Rayleigh-Bénard convection at high Prandtl numbers. In addition, a stabilizing temperature gradient is imposed across the cell. Even for thermal buoyancy two orders of magnitude smaller than chemical buoyancy, the presence of the weak stabilizing gradient has a profound effect on the convection pattern because double diffusive fingers appear and replace the usual convection roll.

Fingers are narrow vertical columns in which fluid is moving vertically. They require a stabilizing temperature and a destabilizing salt concentration gradient. They allow convective transport even if the total density stratification is stable. Fingers form because heat diffuses more rapidly than ions. According to the commonly accepted picture for finger formation, narrow fingers should not appear if the stabilizing temperature gradient is weak enough so that density increases with height due to the destabilizing salinity gradient. In this case, a convection roll of the same form as observed in ordinary Rayleigh-Bénard convection is expected. These convection rolls have in order of magnitude the same width and height and therefore suffer less from dissipative losses as long and narrow fingers. One naively expects convection rolls to supercede fingers as long as the fluid is top heavy. However, fingers appeared in the experiments even for unstable density stratifications.

Fingers are a form of convection distinct from a convection roll and convection undergoes a genuine transition as control parameters are varied and the system switches from fingers to rolls. Remarkably, the ion transport at the transition is larger than without an opposing temperature gradient.

The experiments are compatible with two different mechanisms triggering the transition from finger to roll convection. Finger convection is replaced by an ordinary convection roll either if convection is fast enough to prevent sufficient heat diffusion between neighboring fingers, or if the thermal buoyancy force is less than 1/30 of the compositional buoyancy force.

The size of these fingers and the flow velocities are independent of the height of the cell, but they depend on the ion concentration difference between top and bottom boundaries as well as on the imposed temperature gradient. The scaling of the mass transport is compatible with previous results on double diffusive convection.

Ongoing experiments focus on another modification of the large scale circulation introduced by double diffusive effects: If the experimental cell is high enough, the flow splits into three layers, with a usual convective layer sandwiched between two finger layers. When this occurs, new scaling laws hold for the ion transport.

References

[1] E. Hage and A. Tilgner. High Rayleigh number convection with double diffusive fingers. *Phys. Fluids*, 22:076603, 2010.

[2] M. Kellner and A. Tilgner. Transition to finger convection double diffusive convection. *Phys. Fluids*, 26:094103, 2014.

*Corresponding author. Email: andreas.tilgner@physik.uni-goettingen.de

BOUNDARY LAYER FLUCTUATIONS AND THEIR EFFECTS ON MEAN AND VARIANCE TEMPERATURE PROFILES IN TURBULENT RAYLEIGH-BENARD CONVECTION

Yin Wang[1], Xiaozhou He[2], and Penger Tong*[1]

[1]*Hong Kong University of Science and Technology, Clear Water Bay, Kowloon, Hong Kong*
[2]*Shenzhen Graduate School, Harbin Institute of Technology, Shenzhen, China*

Summary We report direct measurements of the mean temperature profile $\theta(z)$ and temperature variance profile $\eta(z)$ near the lower conducting plate of a specially designed quasi-two-dimensional cell for turbulent Rayleigh-Bénard convection. Near the thermal boundary layer (BL), the measured $\theta(z)$ is found to have a universal scaling form $\theta(z/\delta)$ with varying BL thickness δ, and its functional form agrees well with the recently derived BL equation by Shishkina *et al.*. The measured $\eta(z)$, on the other hand, is found to have a scaling form $\eta(z/\delta)$ only in the near-wall region with $z/\delta \leq 2$. Based on the experimental findings, we derive a new BL equation for $\eta(z/\delta)$, which is in good agreement with the experimental data. The experiment clearly demonstrates the effect of BL fluctuations.

Recent studies of the thermal boundary layer (BL) for the Rayleigh number $Ra \leq 10^{12}$ showed that the measured (and DNS calculated) $\theta(z)$ has the classical Prandtl-Blasius-Pohlhausen (PBP) form only when the vertical distance, $\xi \equiv z/\delta$, from the conducting plate normalized by the thermal BL thickness δ is in the region $\xi \leq 0.6$. Deviations of $\theta(z)$ from the PBP form were found when $0.6 < \xi < 4$. The deviations were attributed to BL fluctuations resulting from intermittent eruption of thermal plumes from the BLs, and they still exist after a dynamical rescaling method was applied to the measured $\theta(z)$ [1]. More recently, Shishkina et al. [2] considered the effect of BL fluctuations and included the temperature-velocity correlation function, $\langle \delta v \delta T \rangle_t$, into the BL equation for $\theta(z)$, where δT and δv are, respectively, the local temperature and vertical velocity fluctuations. When the Prandtl number $Pr = \nu/\kappa > 1$, where ν and κ are, respectively, the kinematic viscosity and thermal diffusivity of the convecting fluid, Shishkina *et al.* obtained an analytical form of the mean temperature profile [2]

$$\theta(\xi; c) \equiv \frac{T_b - \langle T(\xi) \rangle}{\Delta_b} = \int_0^{\xi} (1 + a^3 \eta^3)^{-c} d\eta, \qquad (1)$$

where $\Delta_b \equiv T_b - T_0$ is the temperature difference across the BL with T_b and T_0 being, respectively, the temperature of the bottom plate and at the cell center. In the above, $c \geq 1$ is a parameter which satisfies the condition $a = \Gamma(1/3)\Gamma(c - 1/3)/[3\Gamma(c)]$ and changes with Pr. When $c \to \infty$, $\theta(\xi; \infty)$ approaches the PBP form for laminar BLs without BL fluctuations.

In this talk, we will report direct measurements of the mean temperature profile $\theta(z)$ and temperature variance profile $\eta(z) \equiv \langle [T(z,t) - \langle T(z) \rangle]^2 \rangle_t$ near the lower conducting plate in RBC. The convection cell is a specially designed vertically orientated thin circular disk, as sketched Fig. 1. The large-scale flow in the circular plane of the convection cell has a fly-wheel-like structure with a mean rotating speed U_0 along a fixed orientation. Compared to the large-scale flow in a conventional upright cylinder, this quasi-two-dimensional (2D) flow has a geometry more closely satisfying the assumption of the boundary theory for a 2D flow over an infinite horizontal plane. These simplifications allow us to have a stringent test of the theory. The convection experiment is conducted in the thin disk and its large-scale flow rotates counterclockwise with the velocity components and spacial coordinates indicated in Fig. 1. The cell has a diameter $D = 188$ mm and thickness $W = 20$ mm, and thus the corresponding aspect ratio $\Gamma \equiv L/D = 0.11$. The top (and bottom) $1/3$ of the circular sidewall is made of copper, and their temperature is controlled at an accuracy of 10 mK. Other walls of the cell are made of Plexiglas. Here the Rayleigh number is defined as $Ra \equiv \alpha g \Delta T D^3/(\nu\kappa)$, where g is the gravitational acceleration, ΔT is the temperature difference between the two copper surfaces, and α is the thermal expansion coefficient of the convecting fluid. Two working fluids are used in the experiment, one is distilled water (with $Pr = 4.4$) and the other is a 20 wt.% aqueous solution of glycerin ($Pr = 7.6$). A movable thermistor of diameter 0.3 mm and time constant 10 ms is used to measure the temperature profile $T(z)$ along the central axis of the cell. The accuracy of the temperature measurement is 5 mK and that of the spatial movement z is 50 μm. Another thermistor of the same type is placed at the cell center to measure T_0. Recent studies [3] have shown that this system possesses the key features of turbulent convection,

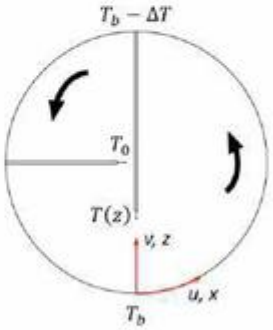

Figure 1: Sketch of the experiment setup for the measurement of the local temperature profile near the lower conducting plate. The black arrows indicate the direction of the large-scale flow in the circular plane of the cell. The red arrows indicate the velocity components and spatial coordinates used in the experiment.

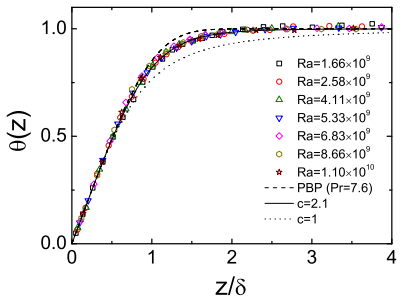

Figure 2: Normalized mean temperature profile $\theta(z)$ as a function of z/δ. The measurements are made near the lower conducting plate for different values of Ra and at fixed $Pr = 7.6$. The solid and dotted lines are, respectively, the calculated $\theta(\xi; c)$ using Eq. (1) with $c = 2.1$ and $c = 1$. The dashed line shows the PBP profile for $Pr = 7.6$.

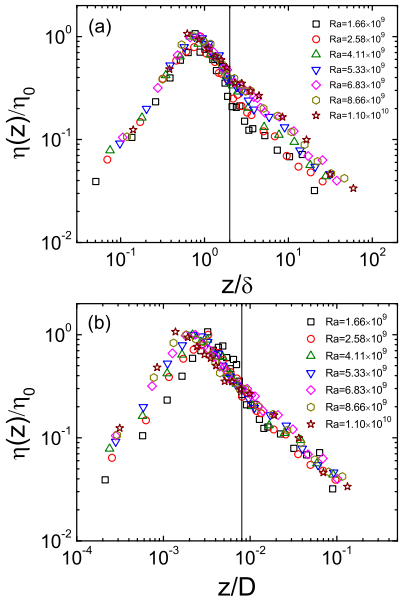

Figure 3: Normalized temperature variance profile $\eta(z)/\eta_0$ as a function of the normalized distance (a) z/δ and (b) z/D. The measurements are made near the lower conducting plate for different values of Ra and at fixed $Pr = 7.6$. The vertical lines in (a) and (b) indicate the transition distance $\xi_c = (z/\delta)_c \simeq 2$ or equivalently $z/D \simeq 0.008$.

which have been observed in the upright cylindrical cells.

Near the BL, the measured $\theta(z)$ is found to have a universal scaling form $\theta(z/\delta)$ when the values of δ are varied in the Ra range studied ($1.5 \times 10^9 \leq Ra \leq 1.5 \times 10^{10}$). Figure 2 shows the measured $\theta(z)$ near the lower conducting plate for different values of Ra and at fixed $Pr = 7.6$. All of the measured $\theta(z)$ curves collapse onto a single master curve once z is normalized by the BL thickness δ. Similar scaling was also found for the measured $\theta(z)$ in the upright cylinders [4] and rectangular cells [5] with $Ra \leq 10^{11}$. It is seen that the measured $\theta(z/\delta)$ is well described by Eq. (1) with $c = 2.1$ (solid line), which deviates from the PBP form (dashed line) in the region $0.6 \leq \xi \leq 2$. Similarly, we measure $\theta(z)$ in water ($Pr = 4.4$), which is also found to be well described by Eq. (1) with $c = 1.8$.

While the deviations of the measured $\theta(z)$ from the PBP form are clearly visible, they are nonetheless small and are only shown in the region $0.6 \leq \xi \leq 2$. The temperature variance profile $\eta(z)$, on the other hand, is a direct measure of BL fluctuations and equals to zero for laminar BLs without fluctuations. Figure 3(a) shows the measured $\eta(z)$ as a function of distance z for different values of Ra. In the plot, $\eta(z)$ is normalized by its maximal value η_0 and z is normalized by δ. In the region $\xi = z/\delta \leq 2$, all the measured $\eta(z)/\eta_0$ curves collapse onto a single master curve, which has a single peak at $\xi_0 \simeq 0.78 \pm 0.05$. A similar single-peaked $\eta(z)$ was also found in the upright cylinders [6, 7] and rectangular cells [5]. Beyond $\xi > 2$, the measured $\eta(z)/\eta_0$ does not scale with z/δ anymore. Instead, it scales with z/D, where D is the cell diameter, as shown in Fig. 3(b). It is seen that all the measured $\eta(z)/\eta_0$ curves superimpose with each other in the region $0.008 \leq z/D \leq 0.15$. Figure 3 thus reveals a sharp transition to a new scaling regime at $\xi_c = (z/\delta)_c \simeq 2$ or equivalently $z/D \simeq 0.008$.

The scaling behavior of the measured $\eta(z)/\eta_0$ is a unique property of the thermal BL in turbulent Rayleigh-Bénard convection, and one has not yet found an equation to describe the function form of $\eta(z)/\eta_0$. Based on the above experimental results, we derive a new BL equation for $\eta(\xi)$ and obtain a numerical solution of $\eta(\xi)$ for $Pr > 1$, which is found to be in an excellent agreement with the experimental data. More details about the derivation of the equation and the fitting to the experimental data will be given at the oral presentation.

We thank E. Ching for useful discussions. This work was supported in part by RGC of Hong Kong SAR under Grant No. 16305214 (P.T.). X.H. acknowledges the support through the China Thousand Young Talents Program.

References

[1] Q. Zhou and K.-Q. Xia, Measured Instantaneous Viscous Boundary Layer in Turbulent Rayleigh-Bénard Convection, Phys. Rev. Lett. **104**, 104301 (2010).

[2] O. Shishkina, S. Horn, S. Wagner, and E. S. C. Ching, Thermal Boundary Layer Equation for Turbulent Rayleigh–Bénard Convection, Phys. Rev. Lett. **114**, 114302 (2015).

[3] H. Song, E. Villermaux, and P. Tong, Coherent oscillations of turbulent Rayleigh-Bénard convection in a thin vertical disk, Phys. Rev. Lett. **106**, 184504 (2011).

[4] R. du Puits, C. Resagk, and A. Thess, Thermal boundary layers in turbulent Rayleigh–Bénard convection at aspect ratios between 1 and 9, New J. Phys. **15**, 013040 (2013).

[5] Q. Zhou and K.-Q. Xia, Thermal boundary layer structure in turbulent Rayleigh–Bénard convection in a rectangular cell, J. Fluid Mech. **721**, 199 (2013).

[6] A. Belmonte, A. Tilgner, and A. Libchaber, Temperature and velocity boundary layers in turbulent convection, Phys. Rev. E **50**, 269 (1994).

[7] Y.-B. Du and P. Tong, Turbulent thermal convection in a cell with ordered rough boundaries, J. Fluid Mech. **407**, 57 (2000).

BOUNDARY LAYERS IN TURBULENT RAYLEIGH-BÉNARD CONVECTION: A FIRST INSIGHT INTO THE 3D VELOCITY FIELD FROM EXPERIMENT

Robert Kaiser, Christian Resagk & Ronald du Puits
Institute of Thermodynamics and Fluid Mechanics, Technische Universitaet Ilmenau, Ilmenau, Germany

Summary We present the fully three-dimensional boundary layer flow field in turbulent Rayleigh-Bénard convection in air. The experiments have been performed in the large-scale convection facility 'Barrel of Ilmenau' and cover a parameter range in Rayleigh number between $Ra = 10^8$ and $Ra = 10^{12}$. The aspect ratio was kept constant at $\Gamma = 1$ and the Prandtl number is $Pr = 0.7$. Using a tomographic Particle Image Velocimetry set-up the fully three dimensional velocity field at the lower surface of the cooling plate has been measured. In our talk we will show first results of these measurements that are still being in progress. We will discuss as well statistical properties of the near-wall flow field, like profiles of all three components of the mean velocity and the fluctuations, the vorticity and the Reynolds stresses as the dynamics of the boundary layer like time series of the boundary layer thickness or the temporal evolution of the wall shear stress.

INTRODUCTION

Rayleigh-Bénard (RB) convection in an infinite fluid layer heated from below and cooled from above is a canonical problem of turbulence research [1,2,3]. It represents a great variety of heat transfer problems as diverse as atmospheric and oceanic circulation, room ventilation or convection in the outer Earth's core. Although RB convection has been comprehensively investigated over the past two decades, our knowledge of the flow field in the vicinity of both the heated bottom and the cooled top plates at very high Rayleigh numbers, $Ra = \left((\beta g \Delta T h^3)/(\upsilon\kappa)\right)$, is limited to local statistics or the two-dimensional velocity field in a single plane. This is partially due to the fact that a simultaneous measurement of all three velocity components in more than a single point is an extremely challenging task. However, data obtained from planar Particle Image Velocimetry (PIV) measurements [4] as well as recent direct numerical simulations [5] show that the near wall transport of heat and momentum cannot be fully understood without that information. In order to answer that question and to provide a set of reference data for the validation of computational results we perform a series of tomographic PIV measurements covering a wide range in Rayleigh number between $Ra = 10^8$ and $Ra = 10^{12}$. While the Rayleigh number was varied, the aspect ratio and the Prandtl number were kept constant at $\Gamma = 1$ and $Pr = 0.7$.

EXPERIMENTAL SET-UP AND MEASUREMENT TECHNIQUE

The measurements have been undertaken in a large-scale RB experiment, called the 'Barrel of Ilmenau'. This RB cell with a diameter of $D = 7.15$ m and a maximum thickness of the fluid layer of $h = 6.30$ m is filled with air and currently the only one where Ra numbers up to $Ra = 10^{12}$ can be set and the boundary layer is sufficiently large (of the order of 20 mm) to probe the flow field with commercial measurement techniques. In order to realize Ra numbers below $Ra = 10^{11}$ various insets with diameters of $D = 2.50$ m and $D = 0.90$ m can be placed between the heating and the cooling plates. A detailed description of the facility can be found in [6]. Figure 1 shows the set-up of the tomographic PIV measurement.

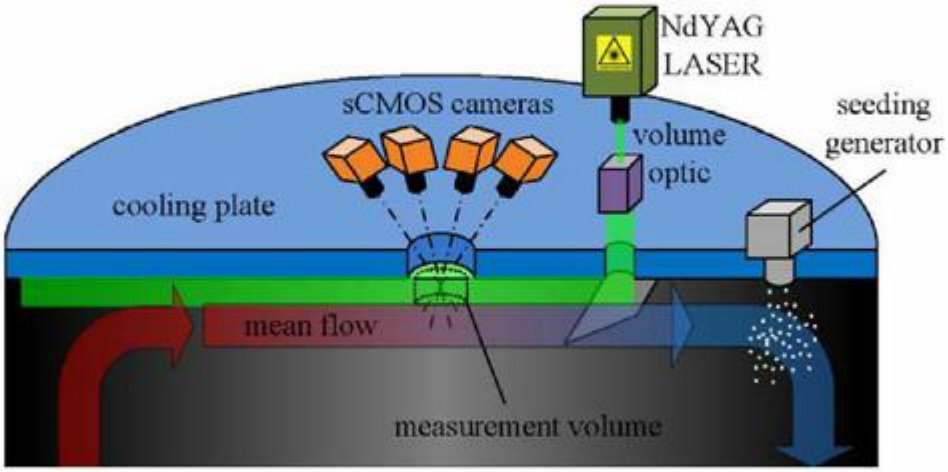

Figure 1: Set-up of the tomographic PIV system to measure the three-dimensional flow field in the boundary layer below the cooling plate.

[a] Corresponding author. ronald.dupuits@tu-ilmenau.de.

The measurements volume is located below the center of the cooling plate, where a sapphire window provides the optical access for the cameras. Due to its high thermal conductivity (about 20 times better than mineral glass) the temperature at the lower surface of the window equals the temperature of the cooling plate very well and local convection effects can be excluded. The size of the measurement volume amounts to a cuboid with a base area of 5 cm by 5 cm (parallel to the orientation of the plate surface) and a depth of about 2 cm (normal to the orientation of the plate surface). The measurement volume is illuminated by a 100 mJ double pulse Nd:YAG Laser which can fire 100 times per second. Small tracer droplets of various sizes between 0.5 µm and 5 µm will be tested to find an optimum between a good visibility (larger particles scatter more light) and a good ability to follow the flow (smaller particles better follow the flow). The camera system consists of four highly sensitive sCMOS cameras with a resolution of 2560 x 2160 pxs² and a maximum frame rate of 25 double frames per second. Series of 10.000 frame sets – each of them consists of four double frames – at a frame rate of one frame set per second has been acquired to study the long-term statistics of the flow. In order to analyse the dynamics of typical boundary layer quantities shorter time series of 1.000 frame sets with the maximum rate of 25 per second have been captured.

RESULTS

A first preliminary result of a test measurement is plotted in Figure 2. The graph shows the local vorticity $\omega_z = \partial v/\partial x - \partial u/\partial y$ along with selected streamlines of the three-dimensional velocity field. In our talk we will present final results of the tomographic PIV measurements for the entire range in Ra number between $Ra = 10^8$ and $Ra = 10^{12}$. We will discuss a selection of the statistical properties of the near-wall flow field, like e. g. profiles of all three components of the mean velocity and the fluctuations, the vorticity and the Reynolds stresses as well as the dynamics of the boundary layer like time series of the boundary layer thickness or the temporal evolution of the wall shear stress.

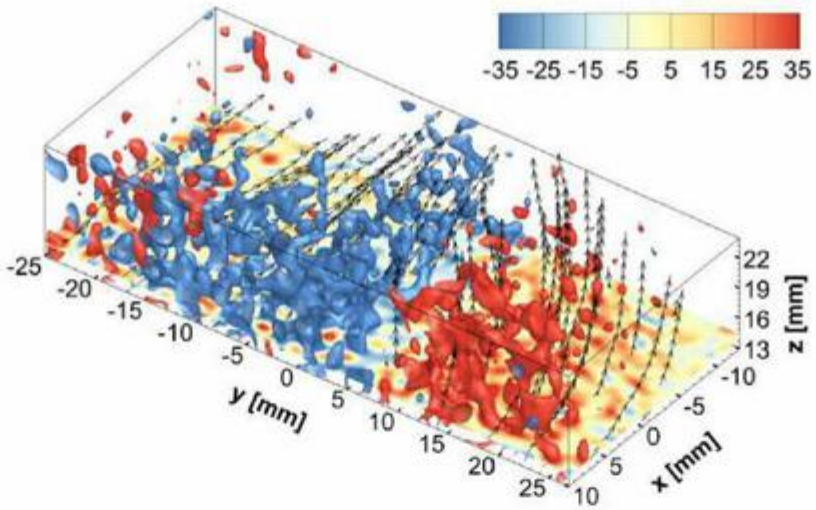

Figure 2: Instantaneous vorticity field $\omega_z = \partial v/\partial x - \partial u/\partial y$ [1/s] along with selected streamlines of the near wall velocity field.

ACKNOWLEDGEMENT

We wish to acknowledge the support of the German Research Foundation under the grant number PU436/1-2 and the European Union under the Grant Agreement number 312778. Moreover, we thank Vigimantas Mitschunas and Sabine Abawi for their valuable contribution to run the experiment and the tomographic PIV measurements.

References

[1] Castaing, B. Gunaratne, G., Heslot, B., Kadanoff, L., Libchaber, A., Thomae, S., Wu, X.-Z., Zaleski, S., Zanetti, G.: Scaling of hard thermal turbulence in Rayleigh-Bénard convection. *J . Fluid Mech.* **204**: 1-30, 1989.

[2] Siggia, E.D.: High Rayleigh number convection. *Annu. Rev. Fluid Mech.* **26**: 137-68 (1994).

[3] Lohse, D., Xia, K.-Q.: Small-Scale Properties of Turbulent Rayleigh-Bénard Convection. *Annu. Rev. Fluid Mech.* **42**:335–64, 2010.

[4] Du Puits, R., Li, L., Resagk, C., Thess, A., and Willert, C.: Turbulent Boundary Layer in High Rayleigh Number Convection in Air. *Phys. Rev. Lett*. **112**: 124301, 2014.

[5] Scheel, J. and Schumacher, J.: Local boundary layer scales in turbulent Rayleigh-Bénard convection. *J. Fluid Mech*., **758**: 344-373, 2014.

[6] du Puits, R., Resagk, C., Thess, A.: Thermal boundary layers in turbulent Rayleigh-Bénard convection at aspect ratios between 1 and 9, *New J. Phys.* **15**: 013040, 2013.

TURBULENT RAYLEIGH-BÉNARD CONVECTION WITH POLYMERS

Roberto Benzi[1], Emily S.C. Ching*[2], and Elisabetta De Angelis[3]

[1]*Dip. di Fisica and INFN, Università "Tor Vergata", Via della Ricerca Scientifica 1, I-00133 Roma, Italy*
[2]*Department of Physics, The Chinese University of Hong Kong, Shatin, Hong Kong*
[3]*School of Engineering - Cardiff University, Queen's Buildings, The Parade, Cardiff, CF24 3AA, United Kingdom*

Summary We study the effects of polymers on heat transport in turbulent Rayleigh-Bénard convection using direct numerical simulations. We find that for small Weissenberg number, which is the ratio of the polymer relaxation time to the typical time scale of the flow, heat transport is reduced but for sufficiently large Weissenberg number, heat transport is enhanced. Our generalization of the classical boundary layer theory to flows with polymers has demonstrated that polymer stretching gives rise to a space-dependent effective viscosity. By carrying out the generalized boundary layer analysis using the effective viscosity profile computed from the numerical data, we provide a theoretical explanation of the observed transition of heat reduction to heat enhancement when Weissenberg number is increased.

INTRODUCTION

In turbulent Rayleigh-Bénard (RB) convection, a fluid constrained between two horizontal plates is heated from below and cooled from above. The system is controlled by the Rayleigh and Prandtl numbers, $\mathrm{Ra} = \alpha g \Delta T H^3/(\kappa\nu_s)$ and $\mathrm{Pr} = \nu_s/\kappa$, where α, ν_s and κ are respectively the volume expansion coefficient, kinematic viscosity, and thermal diffusivity of the fluid, ΔT is the temperature difference, H is the distance between the top and bottom plates, and g is the acceleration due to gravity. The bulk flow without the boundary layers is believed to be a good approximation of the ultimate regime at large Ra. To study the effect of polymers in this case, we have performed direct numerical simulations (DNS) of homogeneous turbulent thermal convection with polymers using periodic boundary conditions [1], and found that polymers enhance heat transport. At variance with this result, experiments on turbulent RB convection at moderate Ra [2, 3] reveal that polymers reduce heat transport and the amount of reduction increases with polymer concentration. To account for these experimental findings, we have generalized the classical Prandtl-Blasius-Pohlhausen (PBP) theory to study heat transport by boundary-layer flow with polymers [4, 5]. Our work demonstrated that polymer stretching gives rise to a space-dependent effective viscosity. When the effective viscosity is non-zero only within a region very close to the plate, heat transport is reduced and the amount of reduction increases with polymer concentration as observed in the experiments. The above studies lead us to the idea that how heat transport is affected is determined by the specific details of the polymer stretching, and motivates our present DNS study.

NUMERICAL SIMULATIONS AND RESULTS

In Boussinesq approximation, the equations of motion for RB convection with polymers are

$$\partial_t u_a + \vec{u}\cdot\vec{\nabla}u_a = -\nabla_a p + \nu_s\nabla^2 u_a + \nabla_b \mathcal{T}_{ab} + \alpha g(T - T_*)\,\delta_{az} \quad (1)$$

$$\partial_t T + \vec{u}\cdot\vec{\nabla}T = \kappa\nabla^2 T \quad (2)$$

where $\vec{u}$ is the velocity field with components u_a, $a = x, y, z$, with x and y along the horizontal directions and z along the vertical direction, p is the pressure, and T is the temperature field with T_* being the mean temperature averaged over time and space. We have used the repeated indices summation convention and the density of the fluid is taken to be 1. The polymeric stress tensor $\mathcal{T}_{ab}$ depends on how much the polymer chains are stretched. For the Oldroyd-B model, $\mathcal{T}_{ab}(\vec{r}, t) = \nu_p\left[R_{ab}(\vec{r}, t) - \delta_{ab}\right]/\tau$, where ν_p is the polymer contribution to the zero-shear viscosity of the polymer solution and τ is the relaxation time of the polymers. Let $\vec{d}$ be the end-to-end distance vector of a polymer chain, the conformation tensor R_{ab} is the ensemble average of $d_a d_b$ normalized by the equilibrium value of the ensemble average of $d_a^2/3$, and is governed by

$$\partial_t R_{ab} + \vec{u}\cdot\vec{\nabla}R_{ab} = \partial_c u_a R_{cb} + R_{ac}\partial_c u_b - \left(R_{ab} - \delta_{ab}\right)/\tau\,. \quad (3)$$

Periodic boundary conditions are imposed at the lateral planes whereas fixed-temperature and no-slip boundary conditions are used at the top and bottom plates. The DNS is performed at $\mathrm{Ra} = 1.7 \times 10^5$ and $\mathrm{Pr} = 7$. The Weissenberg number is defined by $\mathrm{Wi} \equiv \tau U_c/H$, where $U_c = \sqrt{\alpha g \Delta T H}$. Heat transport is measured by the Nusselt number, which is defined by $\mathrm{Nu} \equiv (\langle u_z T - \kappa\partial_z T\rangle_A)/(\kappa\Delta T/H)$, where $\langle\cdots\rangle_A$ denotes an average over a horizontal plane and time. Nu_0 denotes the value for the case without polymers. For $\mathrm{Wi} = 2$ we observe a small reduction in heat flux with $\delta\mathrm{Nu} = \mathrm{Nu} - \mathrm{Nu}_0 < 0$ while at $\mathrm{Wi} = 5$ and $\mathrm{Wi} = 15$, $\delta\mathrm{Nu} > 0$ and the heat flux is enhanced. Thus we observe a *transition from heat reduction to enhancement* as Wi is increased.

*Corresponding author. Email: ching@phy.cuhk.edu.hk

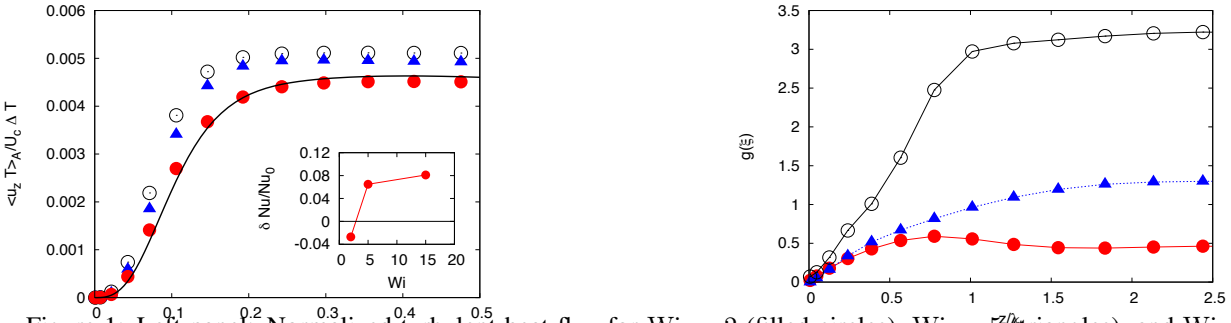

Figure 1: Left panel: Normalized turbulent heat flux for $\mathrm{Wi} = 2$ (filled circles), $\mathrm{Wi} = 5$ (triangles), and $\mathrm{Wi} = 15$ (open circles), and without polymers (solid line). The inset shows $\delta\mathrm{Nu}/\mathrm{Nu}_0$ as a function of Wi. Right panel: The function $g(\xi)$ that measures the effective viscosity of polymers for different Wi; the results for $\mathrm{Wi} = 2$ are multiplied by 2 for clarity purpose.

In the presence of Oldroyd-B polymers, the classical Prandtl-Blasius boundary layer equation for velocity becomes [4, 5]

$$u_x \partial_x u_x + u_z \partial_z u_x = \nu_s \partial_{zz}^2 u_x + \nu_p \partial_z \left(R_{xz} \right) / \tau \, . \tag{4}$$

Here x denotes the direction along the plate and z is the direction perpendicular to the plate, and $u_x \to U$ as $z \to \infty$. The mainstream velocity U plays the role of the large-scale mean flow velocity in turbulent RB convection. Introducing the stream function $\Psi(x,z) \equiv \sqrt{\nu_0 x U}\phi(\xi)$ where $\xi \equiv z\sqrt{U/(\nu_0 x)}$ and $\nu_0 = \nu_s + \nu_p$, we obtain

$$2\partial_\xi \{[1 + g(\xi)]\phi_{\xi\xi}\} + \phi\phi_{\xi\xi} = 0 \, , \tag{5}$$

where ϕ_ξ denotes $\partial_\xi \phi$, $g(\xi) \equiv \nu_{\mathrm{eff}}(\xi)/\nu_0 - 1$, and $\nu_p R_{xz}(\xi)/\tau \equiv \nu_{\mathrm{eff}}(\xi)\partial_z u_x$, together with the boundary conditions $\phi(0) = \phi_\xi(0) = 0$ and $\phi_\xi(\infty) = 1$. Writing the temperature field $T(x,z)$ as $T_0 + (T_1 - T_0)\theta(\xi)$ where T_1 and T_0 are respectively the temperatures at $z = 0$ and $z \to \infty$ (corresponding to the cell center in turbulent RB convection), then we have

$$2\theta_{\xi\xi} + \mathrm{Pr}\ \phi\theta_\xi = 0 \tag{6}$$

with the boundary conditions $\theta(0) = 1$ and $\theta(\infty) = 0$. The generalization of the PBP theory to boundary layer flows with polymers thus shows that the effect of polymer can be represented by a space-dependent effective viscosity $\nu_{\mathrm{eff}}(\xi)$ or $g(\xi)$. We can now use our DNS to get a quantitative computation of $\nu_{\mathrm{eff}}(\xi)$. The energy dissipation rate due to viscosity is $\epsilon_p(z) = \langle -u_a \nabla_b \mathcal{T}_{ab} \rangle_A$ and the rate of energy transfer to the polymers is $\epsilon_p(z) = \langle -u_a \nabla_b \mathcal{T}_{ab} \rangle_A$. Thus we define $\nu_{\mathrm{eff}}(z)/\nu_s \equiv \epsilon_p(z)/\epsilon(z)$ and obtain $g(\xi) \approx \nu_{\mathrm{eff}}(\xi)/\nu_s - 1$ with $\nu_0 \approx \nu_s$ and $\xi = z/\lambda_t$, where λ_t is the thermal boundary layer thickness. We capture the general shape of $g(\xi)$ by a simplified form: $g(\xi) = \mu\xi$ for $\xi \le \xi_m$ and $g(\xi) = \mu\xi_m \equiv A$ for $\xi \ge \xi_m$ and use Eqs. (5) and (6) with this simplified form of $g(\xi)$ to study how heat flux depends on ξ_m and A. Two clear features emerge: there is a transition from heat reduction to heat enhancement for all values of A and, most importantly, heat enhancement occurs for $\xi_m > 1$. This result beautifully matches our DNS results: for $\mathrm{Wi} = 2$ the maximum in $g(\xi)$ occurs at $\xi < 1$ and heat reduction is observed while for both $\mathrm{Wi} = 5$ and 15 the maximum occurs at $\xi > 1$ and heat enhancement is observed.

CONCLUSIONS

Using DNS we have found a transition from heat reduction to heat enhancement in turbulent RB convection with polymers when Wi is increased. We have carried out an analysis using the generalized PBP boundary-layer theory with a space-dependent effective viscosity computed from the DNS data, and provided a physical way to understand the transition.

ACKNOWLEDGEMENT

The work of ESCC was supported by the Hong Kong Research Grants Council under Grant No. CUHK-400311.

References

[1] R. Benzi, E.S.C. Ching, and E. De Angelis, Phys. Rev. Lett. **104**, 024502 (2010).
[2] G. Ahlers and A. Nikolaenko, Phys. Rev. Lett. **104**, 034503 (2010).
[3] P. Wei, R. Ni, and K.-Q. Xia, Phys. Rev. E **86**, 016325 (2012).
[4] R. Benzi, E.S.C. Ching and V.W.S. Chu, J. Fluid. Mech. **696**, 330 (2012).
[5] R. Benzi, E.S.C. Ching, W.C.K. Yu, and Y. Wang, J. Fluid Mech. **788**, 337 (2016).

EFFECT OF CONFINEMENT ON GLOBAL HEAT TRANSFER SCALING IN RAYLEIGH-BÉNARD CONVECTION

Kai Leong Chong, Shi-Di Huang, Matthias Kaczorowski, and Ke-Qing Xia *
Department of Physics, The Chinese University of Hong Kong, Shatin, N.T., Hong Kong

Summary We present the results from direct numerical simulations of Rayleigh-Bénard (RB) convection of Rayleigh number $10^6 \leq Ra \leq 10^{10}$, Prandtl number 4.38 and width-to-height aspect ratio $1/32 \leq \Gamma \leq 1$. Our results suggest that the power law is more rational to be fitted conditionally according to the three regimes classified by Chong et al.[1] as they are under different physical mechanisms on heat transfer. For instance, in regime II heat transport is accomplished by a single, or a few, system-sized plume(s), whereas in regime I it is carried out by fragmented plumes. Therefore, in contrast to RB flow at $\Gamma = 1$ (in the explored Ra range), there is no pure power-law scaling between Nusselt number Nu and Ra whenever the convective state straddles over different regimes.

INTRODUCTION

Rayleigh-Bénard (RB) convection is the classical model for studying turbulent thermal convection which is the phenomena ubiquitously existing in nature. In brief, the configuration of this model is a fluid layer heated from below and cooled from above by parallel plates (see, for example, reviews [2, 3]). The relevant input parameters in RB convection are the Rayleigh number $Ra = \alpha g \Delta T H^3/\nu\kappa$, Prandtl number ν/κ, aspect-ratio of the container Γ (here only the width-to-height aspect ratio is varied), while the relevant response parameters are the Nusselt number and Reynolds number. Here ΔT represents the imposed temperature difference over the cell height H while ν, κ, α and g represents the kinematic viscosity, thermal diffusivity, thermal expansion coefficient and gravitational acceleration. One focus on RB flow is the study of scaling properties on global heat transfer, and preferentially the power-law relation of Nu-Ra. Previously, most of the experimental or numerical results were done in cylindrical cell with Γ around one or done with very large Γ for the asymptote of planetary convection. However, a comprehensive study for $\Gamma << 1$ is lacking until the recent works by Huang et al. [4] and Chong et al. [1]. Their result can be summarized as: Three regimes are classified for RB cell with $\Gamma \leq 1$. Regime I is the classical regime in which Nu is insensitive to the change in Γ; Regime II is the plume-controlled regime in which thermal plumes condensation occurs, leading to the enhanced heat transfer efficiency; Regime III is reached when Nu starts to drop sharply beyond regime II. There are actually different underlying physical mechanism in these regimes. For instance, heat transport is carried out no longer by fragmented, individual thermal plumes but by a single, or a few, system-sized giant plumes formed through coherent structure condensation[1] when turbulent flow fully enters regime II. It implies that fitting of the power-law relation between Nu and Ra to the data should be done conditionally on each regime rather than the whole parameter range. The present study complements the previous work by investigating the global Nu-Ra relation in the three regimes separately.

NUMERICAL SET-UPS

We simulate the incompressible RB flow with dimensionless Navior-Stokes equations and heat equation within the Boussinesq approximation. The equations are expressed as:

$$\partial \mathbf{u}/\partial t + \mathbf{u} \cdot \nabla \mathbf{u} + \nabla p = \nu \nabla^2 \mathbf{u} + \theta \mathbf{z}, \tag{1}$$

$$\partial \theta/\partial t + \mathbf{u} \cdot \nabla \theta = \kappa \nabla^2 \theta, \tag{2}$$

$$\nabla \cdot \mathbf{u} = 0, \tag{3}$$

Here the non-dimensionalization is done by using the free-fall velocity, H and ΔT. After the non-dimensionalization, the cold plate is fixed at the value -0.5 while the hot plate is fixed at 0.5, and the sidewalls are adiabatic. For velocity boundary conditions, no-slip and impermeable boundary conditions are adopted. The design of meshes is based on the paper by Shishkina et al. in which non-uniform meshes are used with finer grid near the boundaries. The data were collected when the RB flow reached statistical steady state which is judged by convergence of Nu.

*Corresponding author. Email: kxia@phy.cuhk.edu.hk

RESULTS

The Nusselt number Nu against Rayleigh number Ra for three different Γ is shown in fig. 1(a). As three different regimes has been classified by Chong et al. [1] for $\Gamma < 1$, it leads us to distinguish the data under different regimes by using different symbol styles (open symbol for regime I, crossed symbol for regime II, closed symbol for regime III). In contrast to having a pure scaling at $\Gamma = 1$ with exponent 0.30, separate scaling ranges are markedly noted for $\Gamma = 1/8$ cases due to the regimes crossover. However, when Γ reaches $1/32$, it becomes apparent that a power law over two decades in Ra can be fitted by power law with the exponent 0.49 (fitted by data lying in regime III). To better distinguish the scaling exponents at $\Gamma = 1$ and $\Gamma = 1/8$, the compensated Nu is plotted against Ra as shown in fig. 1(b). Now, it is clear that the exponent for data in regime II at $\Gamma = 1/8$ is 0.28 which is different from that at $\Gamma = 1$.

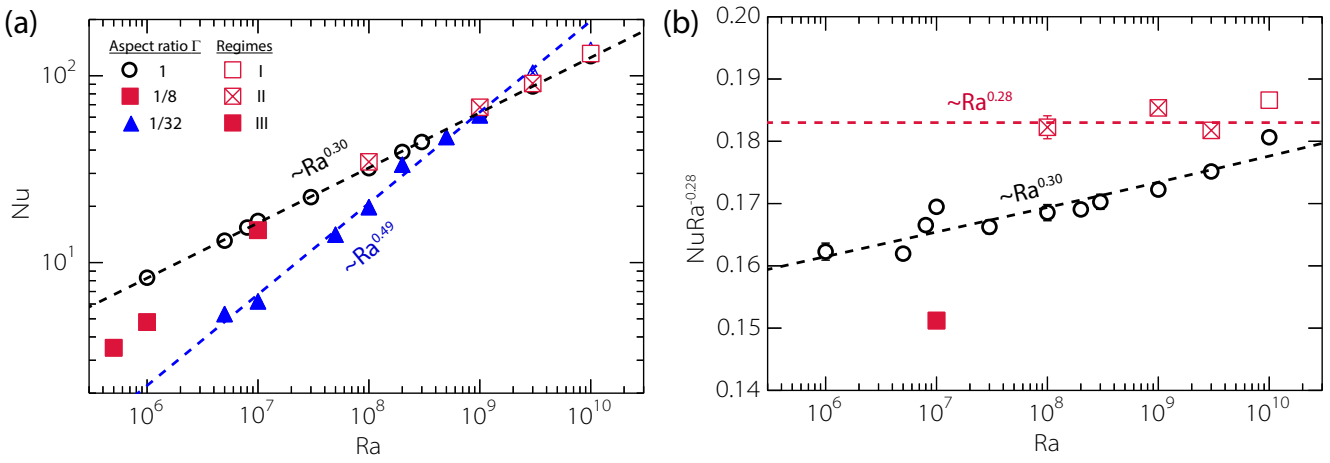

Figure 1: Nu versus Ra for $\Gamma = 1/32$, $1/8$ and 1 in (**a**). Note that the three regimes is based on Chong et al. [1]. Here the black line is the fitting of $\Gamma = 1$ data while the blue line is the fitting of $\Gamma = 1/32$ data. Compensated Nu versus Ra for $\Gamma = 1/8$ and 1 in (**b**). The red line is the fitting of $\Gamma = 1/8$ data within regime II (crossed symbol) while the black line is the fitting of $\Gamma = 1$ data

CONCLUSIONS

We have fitted the Nu-Ra scaling exponent exponents conditionally on the three regimes classified by Chong et al.[1]. Pure scaling law is found at $\Gamma = 1$ with exponent 0.30 where the data points entirely lie in regime I. But no pure scaling law can be found over the whole parameter range at $\Gamma = 1/8$, whereas power law can be fitted conditionally on regime II which gives the exponent of 0.28. When Γ becomes $1/32$, two decades of Ra lying in regime III allows us to observe the new scaling exponent 0.49.

ACKOWLEGEMENT

This work was supported by the Hong Kong Research Grants Council under Grant No. CUHK404513 and through a Hong Kong PhD Fellowship.

References

[1] Chong K.L., Huang S.-D., Kaczorowski M., Xia K.-Q.: Condensation of coherent structures in turbulent flows. Phys Rev Lett. 115:264503, 2015.

[2] Ahlers G., Grossmann S., Lohse D.: Heat transfer and large scale dynamics in turbulent Rayleigh-Bénard convection. Rev Mod Phys. 81:503-537, 2009.

[3] Lohse D., Xia, K.-Q.: Small-scale properties of turbulent Rayleigh-Bénard convection. Annu Rev Fluid Mech. 42:335-364, 2010.

[4] Huang S.-D., Kaczorowski M., Ni R., Xia K.-Q.: Confinement-induced heat-transport enhancement in turbulent thermal convection. Phys Rev Lett. 111:104501, 2013.

[5] Shishkina O., Stevens R.J.A.M., Grossmann S., Lohse D.: Boundary layer structure in turbulent thermal convection and its consequences for the required numerical resolution. New J Phys. 12:075022, 2010.

DYNAMICS OF A FREE BOUNDARY ATOP THERMAL CONVECTION

Jin-Qiang Zhong[1], Bin Liu[2] & Jun Zhang [3,a)]
[1]*School of hysics Science and Engineering, Tong i University, Shanghai, China*
[2]*School of Natural Sciences, University of California, erced, USA*
Courant Institute, New or University, New or , USA esearch Institutes, N U Shanghai, China

Summary: The theory of continental drift by Elder [1] suggests that continents exert a thermally insulating effect on the mantle convection underneath thus modify its large-scale flows, and in turn the continents are driven by the convective flows into cyclic motion [2]. We study through laboratory experiments the dynamics of a free boundary floating on top of turbulent flows that undergo thermal convection. Depending on its relative size, the free boundary either oscillates periodically or becomes locally trapped over an upwelling flow. These phenomena can be understood preliminarily by a low-dimensional model that elucidates how the large-scale flows response to, and in turn, dictate the free boundary motion.

E er en r s n e

Figure 1a presents a schematic drawing of the thermal convection apparatus. The convection tank has an aluminium bottom plate and an open surface. Its inner dimensions are 60 cm ( ) long, 7.8 cm (W) wide, and 11.3 cm ( ) in height. The container is filled with deionized water. The bottom plate is heated uniformly with a foil heater and the fluid is cooled from its open surface, which is exposed in a laminar air-hood. During our experiments, the temperature difference across the fluid is maintained at a constant $\Delta T = 12.0$ K. The convection flows are characterized by two control parameters, i.e. the Rayleigh number $Ra = 1.1\times10^9$ and the Prandtl number $Pr = 4.4$.

Introduced to the fluid surface is a floating boundary, which is free to move about along the container's long axis X, is made of a Plexiglas plate with length l. The coverage ratio, $CR = l/$, varies from 0.2 to 0.8. A shadowgraph, projected by a nearly parallel beam of light sent through the convection tank from behind, reveals the flow pattern on the translucent screen.

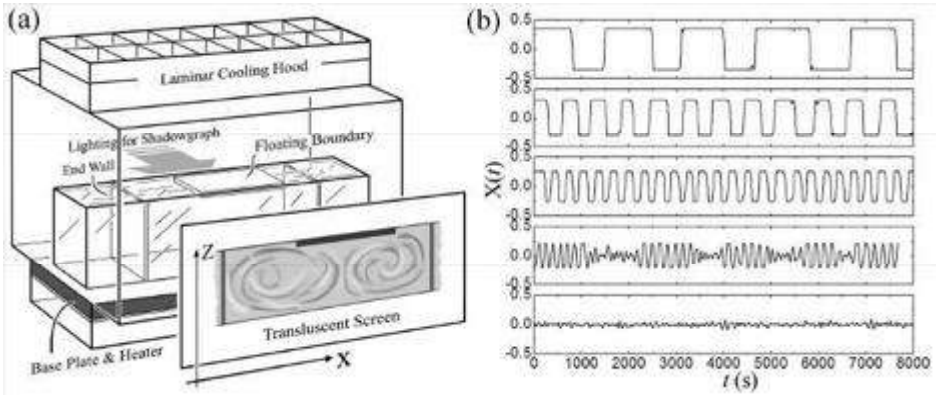

Fig. 1 (a) Schematic diagram of the apparatus. See text for details of the various components. (b) Time series of the free boundary's position. From top to bottom: results for CR = 0.3, 0.4, 0.5, 0.6 and 0.7, respectively. Results reported in [3].

D n cs f e free n r --- sc r r r e s es

When the free boundary is on top of the fluid surface, it exerts a sizeable thermal perturbation to the underlying fluid by reducing the local heat loss of the connective system. This effect is often referred to as the "thermal blanket effect." Under this effect, a two-roll flow structure typifies the main feature of the flow field, with downwelling flows on the two sides that are separated by an upwelling flow (Fig. 1a). We observe that such a free-boundary-convection coupled system is unstable for small boundaries: as the boundary lies on the top of the convective fluid, it is driven about and oscillates between the two sidewalls of the tank. The first 3 panels of Fig. 1b show the position of the boundary center X as a function of time. When the coverage ratio increases from 0.3 to 0.5, the oscillation period of X becomes progressively shorter and more regular. These results imply that larger boundaries give greater thermal perturbation to the convection flows, causing shortened periods with increased regularity.

The free-boundary-convection system presents a different dynamical state if the coverage ratio exceeds 0.6. We observe that in this state the free boundary ceases oscillating between the two sidewalls. Instead, it appears to be trapped in the central area of the convection sample, making only small excursions in both directions randomly. Flow visualization shows that when the boundary lies on top of the upwelling it is passively driven by the randomly passing hot plumes entrained by

a) Corresponding author. Email: jun@cims.nyu.edu

the large-scale flow. The exact excursion of the boundary, both in direction and amplitude, depends on the detailed position and size of the passing plumes. The last series of Fig. 1b shows the time series of the boundary in such a trapped state.

If the coverage ratio is chosen as 0.6, we observe dynamical intermittency between the two states. Boundary oscillation and localization appear alternatively as shown in panel 4 of Fig. 1b.

In er re n f e n c s es --- n er c e

The transition between the two distinct dynamical states can be well explained by a one-dimensional model [3]. The model captures the important mechanism to elucidate the interactions between the free boundary and the convective flows underneath. Through the thermal blanketing effect, the presence of the boundary modifies the flow structure below; in turn, the flow exerts a viscous drag that causes the free boundary to move. Both the oscillatory state and the trapped state are found from this model, depending on the boundary size. The model also offers details on the transition between the states, and shed insights onto this coupled system without the need for full-scale fluid dynamics simulations. Recently, this simple model is used to explain the dynamics of a free boundary interact with and driven by turbulent thermal convection in an annular tank [4]. The model provides quantitative predictions of the boundary motion in good agreement with our experimental observations.

References

[1] J. Elder, : Convective self-propulsion of continents, Nature, 214, 657, 1967.

[2] J. T. Wilson,: Did the Atlantic close and then re-open? Nature (London) 211, 676, 1966.

[3] J.-Q. Zhong and J. Zhang,: Dynamical states of a mobile heat blanket on a thermally convecting fluid. Phys. Rev. E. 75, 055301 (R), 2007.

[4] J.-Q. Zhong, B. Liu, and J. Zhang,: Coupled free-boundary-convection system offers two types of oscillations. preprint 2016.

ZONAL FLOWS IN RAYLEIGH-BENARD CONVECTION

David Goluskin*[1], Jost von Hardenberg[2], Antonello Provenzale[3], Edward A. Spiegel[4], Hans Johnston[5], and Glenn R. Flierl[6]

[1]*Mathematics Department and Center for the Study of Complex Systems, University of Michigan, Ann Arbor, Michigan, USA*

[2]*Institute of Atmospheric Sciences, National Research Council, Torino, Italy*

[3]*Institute of Geosciences and Earth Resources, National Research Council, Pisa, Italy*

[4]*Astronomy Department, Columbia University, New York, New York, USA*

[5]*Department of Mathematics and Statistics, University of Massachusetts, Amherst, Massachusetts, USA*

[6]*Department of Earth, Atmospheric, and Planetary Sciences, Massachusetts Institute of Technology, Cambridge, Massachusetts, USA*

Summary Spontaneously arising zonal flows in Rayleigh-Bénard convection are studied by direct numerical simulations of horizontally periodic flows between free-slip boundaries. The phenomenon is studied in 2D flows and in 3D flows that are rendered horizontally anisotropic by rotation about a distant horizontal axis. In the 2D case, zonal flows appear to be inevitable for sufficiently large Rayleigh number (Ra), and their portion of the total kinetic energy approaches 100% as $Ra \to \infty$. In the 3D anisotropic case, zonal flows develop at large Ra when the anisotropy is sufficiently strong. Convection in the presence of zonal flow can be either bursting or sustained depending on the Prandtl number. Zonal flow significantly suppresses vertical heat transport, causing the growth of the Nusselt number with increasing Ra to slow and sometimes to reverse.

2D SIMULATIONS

The 2D simulations that will be addressed have been reported in [1]. The qualitative differences between convection with and without spontaneously arising zonal flows are apparent in the example temperature fields of figure 1. In the talk, quantitative differences between each state will be described, including differences in the parameter-dependence of key integral quantities such as the Nusselt number.

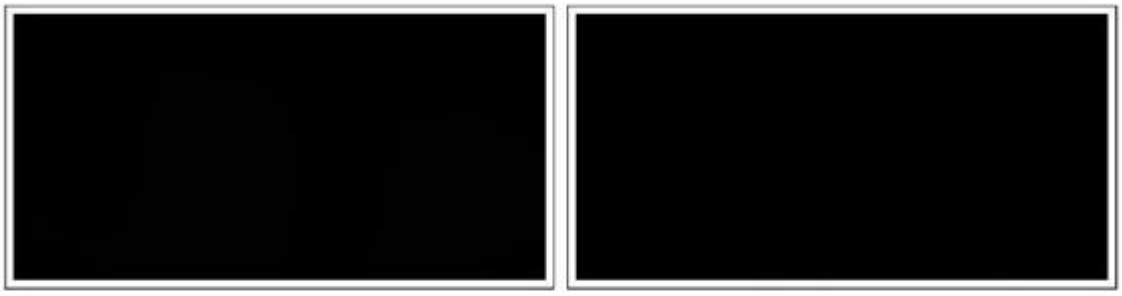

Figure 1: Instantaneous temperature fields from simulations of convection without zonal flow (left) and in which zonal flow has spontaneously developed (right). Warm fluid is light and cool fluid is dark.

3D SIMULATIONS

The 3D simulations that will be addressed have been reported in [2]. Prandtl and Rayleigh numbers are fixed while the uniform horizontal rotation rate is varied. Zonal flows arise when the rotation rate is sufficiently large. Rotation breaks the symmetry between cyclonic and anticyclonic zonal flows, both of which are observed. Zonal flow significantly reduces heat transport and increases intermittency, but not as much as in 2D convection at the same Rayleigh and Prandtl numbers.

References

[1] D. Goluskin, H. Johnston, G. R. Flierl, and E. A. Spiegel. Convectively driven shear and decreased heat flux. *J. Fluid Mech.*, 759:360–385, 2014.

[2] J. von Hardenberg, D. Goluskin, A. Provenzale, and E. A. Spiegel. Generation of large-scale winds in horizontally anisotropic convection. *Phys. Rev. Lett.*, 115:134501, 2015.

*Corresponding author. Email: goluskin@umich.edu

LOW-DIMENSIONAL CONVECTION MODELS FROM VECTOR CYLINDRICAL HARMONICS

Douglas H. Kelley*[1], Catherine A. Knox[2], and Eric G. Blackman[3]

[1]*Department of Mechanical Engineering, University of Rochester, Rochester, New York, USA*
[2]*Department of Mechanical Engineering, University of Rochester, Rochester, New York, USA*
[3]*Department of Physics & Astronomy, University of Rochester, Rochester, New York, USA*

Summary Low-dimensional models of thermal convection can allow us to study the essential dynamics of the flow in simplified form, and to produce empirical estimates using only a few parameters. Low-dimensional representations of convection can be constructed systematically by writing numerical or experimental measurements as summations of a set of appropriate basis functions. For Boussinesq convection in a cylinder, those basis functions should be defined in cylindrical coordinates, vector-valued, divergence-free, and complete. Here we present such a basis set, the vector cylindrical harmonics. We demonstrate that they have the desired characteristics, show their use for representing measurements, and point out their potential for low-dimensional convection models.

MOTIVATION: MODELING CONVECTION IN LIQUID METAL BATTERIES

Thermal convection occurs anywhere a fluid is heated from below with sufficient power, and convection plays a key role in ocean currents, climate models, astrophysical flows, combustion, chemical processing, and jet propulsion, among many other systems. We are particularly interested in convection in liquid metal batteries, a new technology capable of storing large amounts of energy on world electrical grids at very low cost. Convection occurs because the batteries are hotter than their surroundings, and convection drives mixing, which affects battery charge/discharge speed as well as battery lifetime.

We are developing low-dimensional models of convection in liquid metal batteries in order to predict mixing, and therefore battery performance, using the limited information available about an operating battery. We want to capture essential dynamics of convection with as few parameters as possible. Low-dimensional models can be built systematically from empirical measurements by representing those measurements as summations of appropriate basis functions, then truncating the summation to a desired number of modes. For convection of a nearly-incompressible fluid in a cylinder, we require basis functions that are defined in cylindrical coordinates, vector-valued, and divergence-free. We also require that the set of basis functions be complete, that is, that their sums can represent any arbitrary incompressible flow. Such basis functions could also represent magnetic fields in cylindrical coordinates, since magnetic fields always have zero divergence.

THE VECTOR CYLINDRICAL HARMONICS

We have devised a basis set that has the desired characteristics; we call them the vector cylindrical harmonics. Their construction proceeds in analogy to the construction of the vector spherical harmonics [1], which have similar characteristics

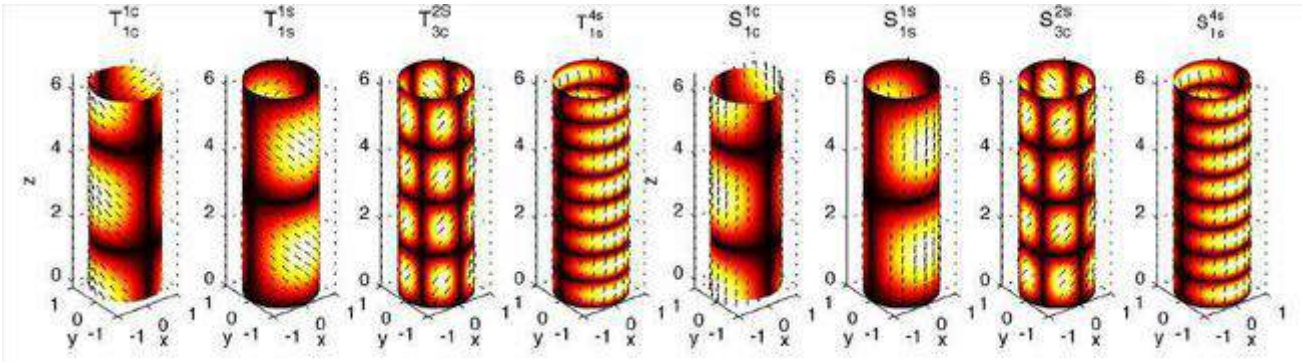

Figure 1: Examples of toroidal and poloidal vector cylindrical harmonics. Each mode is characterized by a azimuthal wavenumber n and an axial wavenumber k, both of which are positive integers. Toroidal modes are denoted $\boldsymbol{T}_n^k$ and poloidal modes are denoted $\boldsymbol{S}_n^k$. Suffixes "c" and "s" indicate sine or cosine modes, respectively. Each mode is plotted on a cylinder of radius 1, with direction indicated by arrows and speed indicated in color. Brighter colors signify higher speed.

*Corresponding author. Email: d.h.kelley@rochester.edu

but are defined in spherical coordinates. First, we seek to solve Laplace's equation $\nabla^2\Phi = 0$ in cylindrical coordinates. Its scalar solutions are necessarily complete because of the Sturm-Liouville form of the equation [2]. Using separation of variables in cylindrical coordinates, we can show that the solutions are $\Phi = \sum_{n,k} C_n^k$, where

$$C_n^k(\rho, \varphi, z) = \Re\left(J_n(\circ\, ik\rho)\cos n\varphi \cos kz\right), \tag{1}$$

written in terms of the cylindrical coordinates (ρ, φ, z), with J_n being Bessel functions of the first kind. Each mode C_n^k is identified by two positive integers, the azimuthal wavenumber n and the axial wavenumber k. Though we have written cosines in Eq. 1, sines also solve Laplace's equation, as do products of a sine and a cosine. To specify, we will denote the various possible modes with "c" and "s" suffixes, e.g., $C_{3c}^{2s} = \Re(J_3(\circ\, i2\rho)\cos 3\varphi \sin 2z)$. We call the C_n^k the *scalar* cylindrical harmonics.

We can use the C_n^k to construct incompressible vector-valued functions by appending a unit vector and calculating curls. We define the toroidal vector cylindrical harmonics as

$$\boldsymbol{T}_n^k = \Re\left(\nabla \times \hat{\boldsymbol{\rho}} J_n(\circ\, ik\rho)\cos n\varphi \cos kz\right),$$

where $\hat{\boldsymbol{\rho}}$ is the unit vector in the cylindrical radial direction. Likewise we define the poloidal vector cylindrical harmonics as

$$\boldsymbol{S}_n^k = \Re\left(\nabla \times \nabla \times \hat{\boldsymbol{\rho}} J_n(\circ\, ik\rho)\cos n\varphi \cos kz\right).$$

Again, either cosines or sines provide solutions, and we will use suffixes to specify when necessary. Together, the $\boldsymbol{T}_n^k$ and $\boldsymbol{S}_n^k$ form a basis set that can be used to represent incompressible vector fields in cylindrical coordinates. Because each $\boldsymbol{T}_n^k$ and $\boldsymbol{S}_n^k$ is constructed from a curl, its divergence is automatically zero. We expect that the $\boldsymbol{T}_n^k$ and $\boldsymbol{S}_n^k$ together form a complete vector-valued set because the C_n^k are complete for scalars, but we have not proved it rigorously. A few vector cylindrical harmonics are plotted in Fig. 1.

REPRESENTING MEASUREMENTS WITH VECTOR CYLINDRICAL HARMONICS

Having explicit forms for the vector cylindrical harmonics, we can represent numerical or experimental measurements as summations of the modes. Suppose a convection flow field $\boldsymbol{u}$ is measured at N locations $\boldsymbol{x}_j$ $(1 \le j \le N)$. Then we can write

$$\boldsymbol{u}(\boldsymbol{x}_j) = \sum_{n=1}^{N_n}\sum_{k=1}^{N_k}\left(\alpha_n^k \boldsymbol{T}_n^k(\boldsymbol{x}_j) + \beta_n^k \boldsymbol{S}_n^k(\boldsymbol{x}_j)\right), \tag{2}$$

for some coefficients α_n^k and β_n^k. If $N_n = N_k = \infty$, a suitable choice of the α_n^k and β_n^k can always satisfy Eq. 2 exactly. When the mode count is finite, the particular α_n^k and β_n^k that best fit the data can be determined via linear least-squares projection [3]. We will show examples of representing convection flow fields in terms of the vector cylindrical harmonics, and quantify the fidelity of the representation as it varies with mode count.

FUTURE WORK AND APPLICATIONS

Once convection flows can be represented as a list of coefficients $\left\{\alpha_n^k, \beta_n^k\right\}$, numerical or experimental measurements can be used to build empirical models. We will discuss strategies for constructing models and consider how their accuracy depends on mode count and on measurement resolution in both space and time. Those strategies are equally applicable to any vector-valued quantity in cylindrical geometry, including convection of fluids other than liquid metal, magnetic fields in liquid metal batteries, and magnetic fields in other cylindrical systems. We will discuss potential applications in these and other contexts.

References

[1] E. Bullard and H. Gellman. Homogeneous dynamos and terrestrial magnetism. *Phil. Trans. R. Soc. London A*, 247(928): 213–278, November 1954.

[2] G. B. Arfken and H. J. Weber. *Mathematical Methods for Physicists*. Harcourt Academic Press, San Diego, fifth edition, 2001.

[3] D. H. Kelley. *Rotating, hydromagnetic laboratory experiment modelling planetary cores*. PhD thesis, University of Maryland, 2009.

TURBULENT ROTATING CONVECTION: A LAGRANGIAN PERSPECTIVE

Hadi Rajaei[1], Kim Alards[1], Rudie Kunnen*[1], Federico Toschi[1], and Herman Clercx[1]
[1]*Fluid Dynamics Laboratory, Department of Applied Physics, Eindhoven University of Technology, Eindhoven, The Netherlands*

Summary We measure flow tracer trajectories in turbulent rotating convection using both experiments and direct numerical simulations. This Lagrangian viewpoint provides unique possibilities for diagnostics. We present tracer acceleration statistics and geometrical statistics of the trajectories, both displaying an intimate relation with the coherent structures found in this flow.

Introduction

Large-scale buoyancy-driven flows abound in nature. The rotation of celestial bodies subsequently shapes these flows. We study the interplay of buoyant forcing and rotation in a model system: rotating Rayleigh–Bénard convection (RRBC), the flow between two rotating horizontal plates driven by heating from below and cooling from above. The strength of the thermal forcing is quantified by the Rayleigh number $Ra = g\alpha\Delta T H^3/\nu\chi$, where g is the gravitational acceleration, H the vertical separation of the plates and ΔT the applied temperature difference, and α, ν and χ are the thermal expansion coefficient, kinematic viscosity and thermal diffusivity of the fluid, respectively. The Prandtl number $\sigma = \nu/\chi$ characterizes the fluid. Finally, to quantify rotation we shall use the Rossby number $Ro = \sqrt{g\alpha\Delta T/H}/2\Omega$.

It is well-known that rotation stabilizes the flow, i.e. a larger thermal forcing Ra is required to enact convection under rotation [1]. In the turbulent regime the main change in flow phenomenology is from a domain-filling large-scale circulation driven by thermal plumes at low rotation rates to an ensemble of vortical columns at high rotation rates [2]. We want to understand these changes. We employ a Lagrangian viewpoint: we go with the flow, follow individual flow tracers and monitor their trajectories. This is done with both experiments and direct numerical simulations (DNS). In this contribution we present the effect of rotation on statistics that can only be obtained using a Lagrangian viewpoint, namely tracer acceleration — indicating the force on fluid parcels — and geometrical statistics of the trajectories (curvature and torsion), expected to be related with the flow structures.

Experimental setup

The setup is displayed in figure 1. The cylindrical convection cell of equal height and diameter $H = D = 200$ mm is placed on a rotating table. The working fluid (water) is heated electrically from below. At the top, cooling water is circulated through a transparent cooling chamber, maintaining a constant temperature. Four cameras mounted above the cell are used to track the motions of tracer particles in regions within the cell. From these 3D trajectories we can calculate velocity and acceleration. The operation conditions are $Ra = 1.28 \times 10^9$, $\sigma = 6.7$ and $0.1 \leq Ro \leq \infty$.

Numerical setup

In the DNS we employ the well-known Verzicco code for convection in a cylindrical domain [3]. The positions of tracer particles are updated using local flow velocities from trilinear interpolation and third-order Runge–Kutta time-integration. The governing parameters are chosen to match the experimental conditions. In figure 2 some example trajectories are shown, revealing the vortical columns in the flow at $Ro = 0.1$.

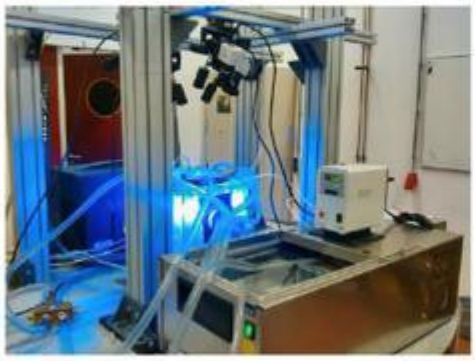

Figure 1: Experimental setup.

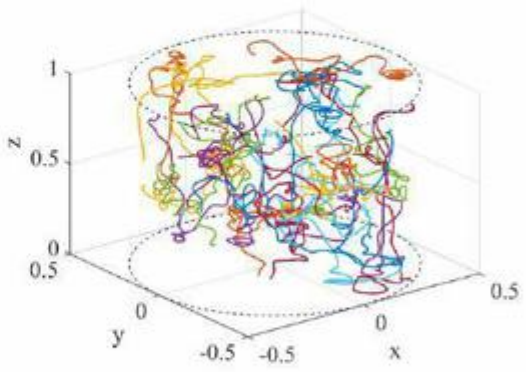

Figure 2: Tracer trajectories from DNS at $Ro = 0.1$.

*Corresponding author. Email: r.p.j.kunnen@tue.nl

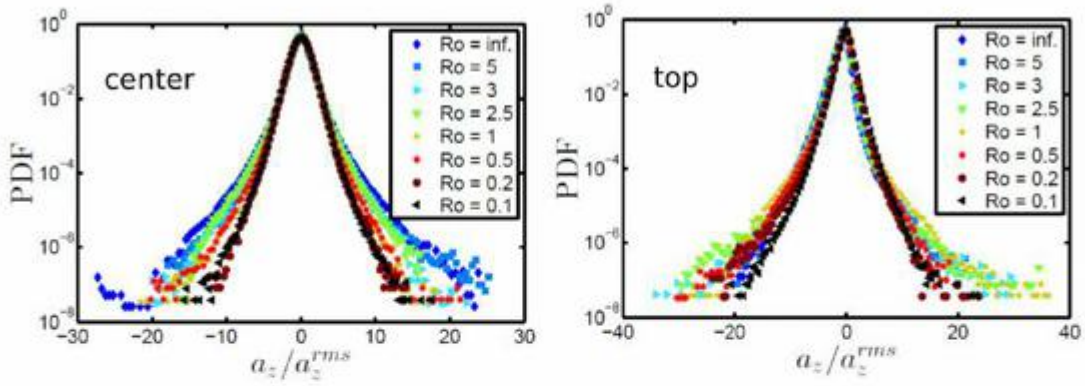

Figure 3: Vertical-acceleration PDFs at the center of the cell (left) and near the top plate (right), at several Ro.

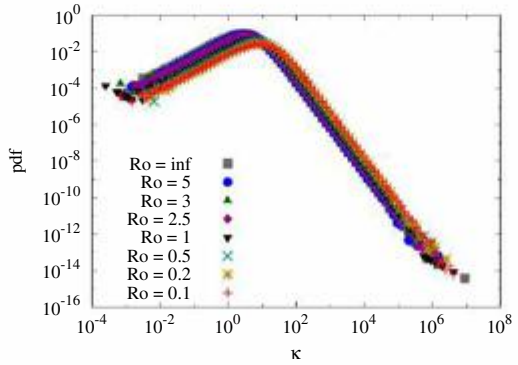

Figure 4: PDFs of curvature κ as a function of Ro.

Acceleration statistics

Tracer acceleration displays different behavior depending on the position where the data is collected. We compare vertical accelerations in a volume at the center of the cell to the same data collected in a volume close to the top plate in figure 3. The vertical-acceleration PDFs at the center display a steady reduction in width as rotation is increased (Ro is reduced) towards a nearly exponential distribution. Conversely, close to the top the width is maximal around $Ro = 2.5$, exactly the Ro at which an abrupt and major flow transition takes place from the so-called large-scale circulation, a domain-filling convection roll, to an ensemble of vertically oriented vortex tubes [4]. The cause of the transition is the activation of the so-called Ekman boundary layers, which enhance convective heat transfer by Ekman pumping.

Curvature statistics

From the tracer trajectories we can also calculate the instantaneous curvature $\kappa = |\mathbf{u} \times \mathbf{u}|/|\mathbf{u}|^3$, where $\mathbf{u}$ is the instantaneous tracer velocity. It is related to the geometry of the trajectories. In figure 4 curvature PDFs are plotted for several Ro. Remarkably, the PDF shape does not change under rotation, nor does it deviate from the shape reported for homogeneous isotropic turbulence [5]. Just the peak of the PDFs are shifted. The peak shift towards larger κ for reduced Ro indicates that the characteristic size of the flow structures (inverse curvature) is actually decreasing.

References

[1] Chandrasekhar S.: Hydrodynamic and Hydromagnetic Stability. Oxford University Press, 1961.

[2] Stevens R.J.A.M., Clercx H.J.H., Lohse D.: Heat transport and flow structure in rotating Rayleigh–Bénard convection. Eur. J. Mech. B/Fluids 40:41–49, 2013.

[3] Verzicco R., Orlandi P.: A finite-difference scheme for three-dimensional incompressible flow in cylindrical coordinates. J. Comput. Phys. 123:402–413, 1996; Verzicco R., Camussi R.: Numerical experiments on strongly turbulent thermal convection in a slender cylindrical cell. J. Fluid Mech. 477:19–49, 2003.

[4] Kunnen R.P.J., Clercx H.J.H., Geurts B.J.: Breakdown of large-scale circulation in turbulent rotating convection. EPL 84:24001, 2008.

[5] Scagliarini A.: Geometric properties of particle trajectories in turbulent flows. J. Turbul. 12:N25, 2011.

CLOUD FORMATION THROUGH ISOBARIC MIXING IN TURBULENT RAYLEIGH-BÉNARD CONVECTION

K. Chandrakar, K. Chang, D. Ciochetto, D. Niedermeier, W. Cantrell, R. A. Shaw*

Department of Physics, Michigan Technological University, Houghton, Michigan, USA

Summary Cloud formation through isobaric mixing of water vapor in turbulent Rayleigh-Bénard convection is studied in the Michigan Tech Pi Chamber (aspect ratio, diameter over height, of 2). Steady-state cloud conditions are achieved, allowing reliable sampling of turbulent time series of air velocity, temperature, water vapor concentration, and cloud droplet size distribution. The water vapor and temperature measurements allow for quantification of the turbulent fluctuations of water vapor supersaturation. For large temperature differences (high Rayleigh number), the droplet size distributions exhibit a pronounced large-drop tail reminiscent of drizzle formation. This opens the door for controlled, laboratory studies of aerosol-cloud-drizzle interactions.

THE PI CHAMBER

We have developed a laboratory facility for studying cloud formation in turbulent Rayleigh-Bénard convection: the Pi Chamber, height 1 m and diameter 2 m. It is capable of pressures ranging from 1000 to ≈ 100 mbar, and can sustain temperatures of $+40$ to $\circ\ 55$ °C. Temperature differences between the floor and ceiling of up to approximately 20 K are achievable, yielding Rayleigh numbers of order 10^9. Clouds can be generated during turbulent convection by maintaining water saturated conditions at the top and bottom boundaries. Specifically, glass fiber filter paper covers the top and bottom thermal panels and can be connected to water reservoirs to ensure long-lifetime liquid (or ice) boundaries. Due to the nonlinearity of the Clausius-Clapeyron equation, isobaric mixing between cold and warm water-saturated air results in water vapor supersaturation. When cloud condensation nuclei (CCN) are present in the chamber, clouds form in supersaturated regions, and with fixed thermodynamic conditions the cloud conditions can persist for long times (hours to days). We can thus explore how the microphysical properties respond to aerosol input, and the relative roles of growth by condensation and collision-coalescence.

Coarse turbulence in the chamber is characterized utilizing a sonic anemometer for the three air velocity components and a Lyman-alpha hygrometer for water vapor concentration fluctuations. Resistance thermometers (RTDs) with ≈ 1 second response time provide the mean temperature profile and a linear array of thermistors is used to measure fast temperature fluctuations. The cloud droplet size distribution and derived quantities like number density and liquid water content are measured with a phase-Doppler interferometer (PDI); this instrument also provides two velocity components for the sampled cloud droplets.

MIXING CLOUDS IN TURBULENT RAYLEIGH-BÉNARD CONVECTION

The experiment reported here generated steady-state cloud conditions for more than 10 hours. A three hour subset of the time series is shown in Fig. 1. The top panel is the air temperature measured by those RTDs closest to the floor and the ceiling respectively, showing that the convection is indeed stationary in time. Note that the mean temperature difference between the two sensors is about 2 K. The temperature fluctuations detected by the lower RTD are larger compared to the fluctuations measured by the upper one as the former sensor is closer to the heated floor panel. The second panel of Fig. 1 depicts the supersaturation based on the water vapor partial pressure determined from the Lyman-alpha measurements (at 20 Hz), and the saturation vapor pressure which is based on the temperature measurement closest to the Lyman-alpha instrument. Here it is clearly observed that fluctuations in temperature and especially in water vapor concentration lead to a randomly, strongly varying supersaturation. The mean supersaturation is approximately 5%, compared to typical supersaturation in atmospheric clouds not much above 1%. The third panel shows the vertical velocity component measured by the sonic anemometer at 20 Hz. From its power spectrum, averaged over a time interval of 4 minutes, the turbulent kinetic energy dissipation rate was calculated (panel 4) as a measure for the degree of turbulence inside the chamber. It is in the same range as observed in the cloudy boundary layer in the mid-latitudes (Siebert et al. 2006). The bottom panel shows the cloud droplet number density and the liquid water content, as derived from the PDI. We note that the fluctuations here are rather large, due to the limited sampling statistics over a broad size distribution, but the values are steady within that range.

Table 1 summarizes the flow properties of the turbulent mixing cloud. All properties represent averages over the three hour time interval. W represents the mean vertical velocity. The root-mean-square (rms) average of the vertical velocity fluctuations is $w' = \langle w^2 \rangle^{1/2}$. The energy dissipation rate is estimated in two ways. First, we use the relationship $\varepsilon = (S_2/C)^{3/2}/r$, where $S_2 = \langle \delta w^2(z,r) \rangle$ is the second moment of the velocity increment, $\delta w(z,r) = w(z+r) \circ\ w(z)$, $\langle \cdot \rangle$ is the spatial average, z

*Corresponding author. Email: rashaw@mtu.edu

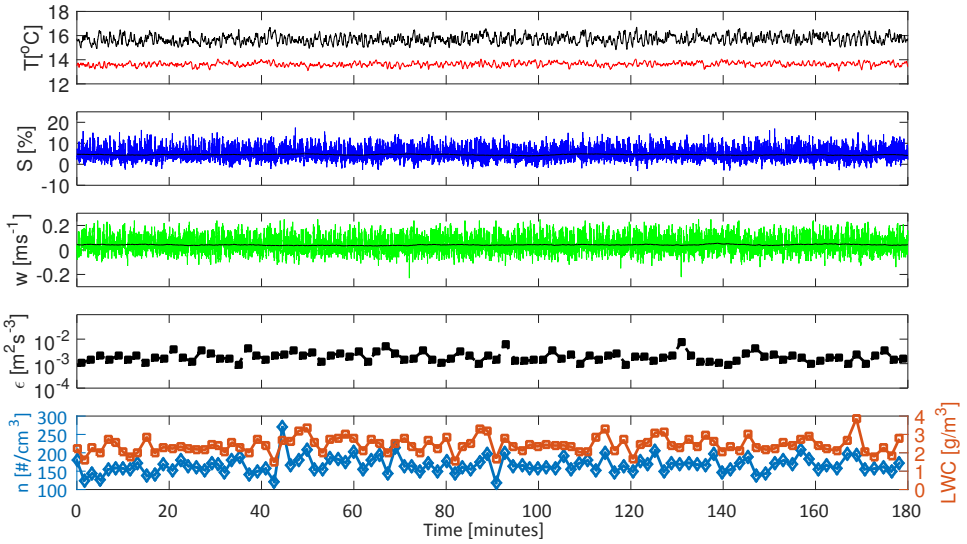

Figure 1: Time series of temperature, supersaturation, vertical velocity, turbulent kinetic energy dissipation rate, cloud droplet number density, and liquid water content for a steady-state mixing cloud.

Table 1: Turbulence parameters calculated from measurements during the steady-state turbulent mixing experiment.

Boundary condition	W (cm s^{-1})	w' (cm s^{-1})	ε_1 (m^2 s^{-3})	ε_2 (m^2 s^{-3})	L (cm)	η (mm)	τ_η (s)	λ (cm)	R_λ
wet	4.2	5.4	1.1×10^{-3}	2.7×10^{-3}	8.8	1.1	0.27	1.6	55

is the vertical position, r is the separation distance, and $C = 2.1$ is the Kolmogorov constant. Second, we obtain the integral of the dissipative spectrum $k^2\,E(k)$, which for isotropic flow must yield $\int k^2\,E(k)\,\mathrm{d}k = 2\,\varepsilon/(15\,\nu)$.

The integral length, L, is estimated by integrating the correlation function $\langle w(z+r)\,w(z)\rangle/w'^2$. The Kolmogorov length and time scales are given by $\eta = (\nu^3/\varepsilon)^{1/4}$ and $\tau_\eta = (\nu/\varepsilon)^{1/2}$. We obtain the Taylor scale through the relation $\lambda = (15\,\nu\,w'^2/\varepsilon)^{1/2}$. The Taylor Reynolds number of the flow is given by $R_\lambda = w'\,\lambda/\nu$. The latter four calculations are based on the ε value which was determined from the integral of the dissipative spectrum. The Taylor Reynolds number is in the range of values determined in other Rayleigh-Bénard convection experiments (Ni et al. 2012).

DISCUSSION

The droplet size distribution reveals a mean droplet diameter of approximately 25 μm, with a large droplet tail extending beyond 60 μm, which can be considered the drizzle range. Under these very strong gradient conditions the mean supersaturation is several percent, and based on the diffusional growth law we estimate that droplets starting with a diameter of 1 μm could grow to about 40 μm in diameter after one minute. To what extent the number of CCN together with condensation and collision-coalescence in the turbulent environment account for the determined droplet size distribution is a matter of current investigation. It is worth noting that this mode of cloud formation, allowing steady cloud microphysical conditions for times much greater than typically available in an expansion chamber, opens up a number of experimental possibilities. In particular, aerosol-cloud-drizzle interactions thought to be important for regulating low cloud amounts in the earth's boundary layer, can be explored.

The work was supported by the U.S. National Science Foundation grant. D. Niedermeier acknowledges support from the Alexander von Humboldt Foundation during the time this research was carried out.

References

[1] Ni R., Huang S.-D., Xia K.-Q.: Lagrangian acceleration measurements in convective thermal turbulence. J. Fluid Mech. 692:395-419, 2012.

[2] Siebert H., Lehmann K., Wendisch M.: Observations of small-scale turbulence and energy dissipation rates in the cloudy boundary layer. J. Atmos. Sci. 63:1451-1466, 2006.

THE ROLE OF HIGHER ORDER FLOW MODES IN TURBULENT THERMAL CONVECTION

Heng-Dong Xi [*1,2,3], Yi-Bao Zhang[1], Jian-Tao Hao[3], and Ke-Qing Xia[2]
[1]*School of Aeronautics, Northwestern Polytechnical University, Xi'an, China*
[2]*Department of Physics, The Chinese University of Hong Kong, Hong Kong, China*
[3]*Institute for Turbulence-Noise-Vibration Interaction and Control, Shenzhen Graduate School, Harbin Institute of Technology, Shenzhen, China*

Summary We present experimental studies of higher order flow modes in turbulent thermal convection in cells of aspect ratio (Γ) 1 and 0.5. We found that in both $\Gamma = 1$ and $\Gamma = 0.5$ cells the first mode, which corresponds to the large-scale circulation (LSC), dominates the flow, the remaining higher order modes are very weak . While during the cessation/reversal the second mode (quadrupole mode) dominates the flow. The experiment reveals that the second mode and the remaining higher order modes play important roles in the reversal/cessation of the LSC. In addition, it is found that the usually-referred cessation event is not the cessation of the entire flow but only the cessation of the first mode (LSC).We also show direct evidence that the first mode is more efficient for heat transfer.

INTRODUCTION

Thermal convection is ubiquitous in nature and many engineering applications. Rayleigh-Bénard convection (RBC) is a model system for the study of the thermal convection problem [1-4]. In previous studies, attentions were mostly paid to the single-roll structure (LSC), i.e. the dipole mode of the convective flow (the ascending flow and the descending are separated azimuthally by 180°). It is a natural question whether higher order modes exist? Examples of such modes are the quadrupole mode (ascending flow and descending flow appear alternately and separated azimuthally by 90 degrees, Fig. 1 (b)), the sextupole mode (ascending flow and descending flow are separated azimuthally by 60 degrees, Fig. 1 (c)) and even the octupole mode (ascending flow and descending flow are separated azimuthally by 45 degrees, Fig. 1 (d)). Recent numerical and experimental studies found that the higher order modes indeed exist [5-8]. While their dynamics, their roles in the cassation and reversal of the LSC, the relationship between different Fourier modes and heat transfer are not known.

In this paper we present an experimental study of the first and a few higher order flow modes in convection cells with aspect ratios 1 and 0.5. The convection cell is similar to those used in previous experiments [9]. The working fluid is water while Prandtl number remained to be around 5.0. We use the multi-temperature-probe method to measure the orientation and the strength of the flow [9]. Applying the Fourier transform to the azimuthal temperature profile $T(\phi)$ at any time instant would give the amplitude/strength of the first four modes: A_1, A_2, A_3 and A_4. Repeat this process to the time trace of $T(\phi)$, the time traces of amplitude/strength of the four modes $A_1(t)$, $A_2(t)$, $A_3(t)$ and $A_4(t)$ are obtained. Similarly the time traces of the orientation of the four modes are obtained.

RESULTS AND DISCUSSION

We firstly study the behaviour of the high order modes during cessation/reversal events. It is found that during a reversal/cessation the amplitude of the second mode and the remaining modes experience an increase then followed by a decrease, which is opposite to the behavior of the amplitude of the first mode — it decreases to almost zero then re-bounds. In addition, the total amplitude of the flow does not drop too much which reveals that the usually-referred cessation event is not the cessation of the entire flow but only the cessation of the first mode (LSC).

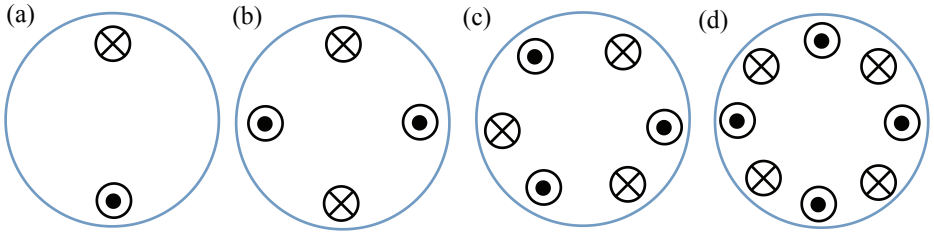

Figure 1: The cartoons show the mid-height cut of (a) the first mode (dipole mode, or LSC), (b) the second mode (quadrupole mode), (c) the third mode (sextupole mode) and (d) the fourth mode (octupole mode) of the flow in the convection cell, viewed from above. Dots represent up-going flow and crosses represent down-going flow.

*Corresponding author. Email: hengdongxi@nwpu.edu.cn

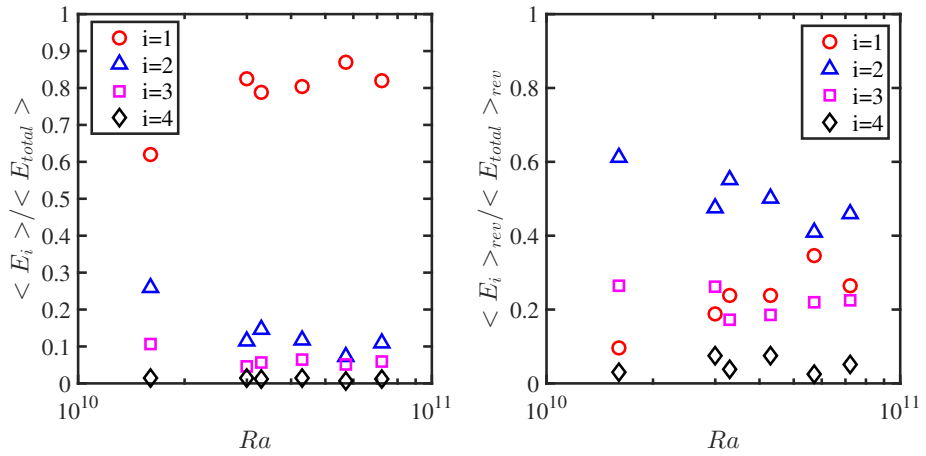

Figure 2: Left: The ratio between the time averaged energy contained in the *i*th mode $\langle E_i \rangle$ and the time averaged total energy of the flow $\langle E_{total} \rangle$ as function of Ra for $\Gamma = 0.5$. Right: the same quantity but averaged only during reversals.

We then calculate the ratio between the time averaged energy contained in the *i*th Fourier modes $\langle E_i \rangle$ and the time averaged total energy of the flow $\langle E_{total} \rangle$, where $\langle E_i \rangle = \langle {A_i}^2 \rangle$, and $\langle E_{total} \rangle = \langle E_1 \rangle + \langle E_2 \rangle + \langle E_3 \rangle + \langle E_4 \rangle$ [5,7-8]. We found that in $\Gamma = 1$ cells, overall the first mode, which corresponds to the large-scale circulation (LSC), dominates the flow. The remaining higher order modes are very weak, each contains less than 4% of the total flow energy. In $\Gamma = 0.5$ cells, as shown in Fig. 2 (a), overall the first mode is still the strongest but less dominant, the second mode becomes stronger which contains 13.67% of the total flow energy and the third and the fourth modes are also stronger. With a large number of measured cessation/reversal events in $\Gamma = 0.5$ cells, we are able to obtain the statistical properties of the higher order modes during a cessation/reversal. To study the amplitude of the different mode during reversals, we calculated the relative weight of *i*th mode's energy — $\langle E_i \rangle / \langle E_{total} \rangle$ during reversals. It is found that during the reversal of the LSC, the second mode dominates, containing about half of the total flow energy, as shown in Fig. 2 (b). This finding reveals that the second mode plays an important role in the reversal of the LSC.

We in addition measured simultaneously the instantaneous heat transfer efficiency (Nu(t)) and amplitudes of the different modes and show directly that the first mode, which is more coherent, produces higher heat transfer efficiency. It reveals that the global heat transfer is controlled by the internal flow states and a more coherent flow is able to transfer heat more efficiently. Our results show that under nominally identical control parameters (Ra, Pr and Γ) and boundary conditions, the turbulent flow can assume different internal states, and this may be detected by the global transport properties (here the instantaneous heat transfer efficiency (Nu(t)). Although the difference in Nu when the flow is in different internal states is very small, this finding may provide a way to control heat transfer by manipulating the internal flow states. It also provides an example of how the global properties of a fluid system is directly linked to its internal flow states.

We are grateful to the support by the National Natural Science Foundation of China (through grant no. 11472094), the Fundamental Research Funds for the Central Universities of China, the Research Grants Council of Hong Kong SAR (through grant no. 403712) and the Peacock Plan of Shenzhen Municipal Government (through contract no. KQCX20130627094615415).

References

[1] Ahlers, G., Grossmann, S. and Lohse, D: Heat transfer and large scale dynamics in turbulent Rayleigh-Bénard convection. Rev. Mod. Phys. 81, 503, 2009.

[2] Lohse, D. Xia, K.-Q: Small-scale properties of turbulent Rayleigh-Bénard convection. Annu. Rev. Fluid Mech. 42, 335-364, 2010.

[3] Chilla, F. Schumacher, J: New perspectives in turbulent Rayleigh-Bénard convection. Eur. Phys. J. E 35, 58, 2012.

[4] Xia, K.-Q: Current trends and future directions in turbulent thermal convection. Theor.Appl. Mech. Lett. 3, 052001, 2013.

[5] Kunnen, R. P. J., Clercx, H. J. H. and Geurts, B. J: Breakdown of large-scale circulaiton in turbulent rotating convection. EPL 84, 24001, 2008.

[6] Mishra, P. K., De, A. K., Verma, M. K. and Eswaran, V: Dynamics of reorientaiton and reveral of large-scale-flow in Reyleigh-Bénard convection. J. Fluid. Mech 668, 480-499, 2010.

[7] Stevens, R. J. A. M., Clercx, H. J. H. and Lohse, D: Effect of plumes on measuring the large scale circulation in turbulent Rayleigh-Benard convection. Phys. Fluids 23, 095110, 2011.

[8] Weiss, S. Ahlers, G: The large scale flow structure in turbulent rotating RayleighBenard convection. J. Fluid Mech. 688, 461, 2011.

[9] Xi, H.-D. and Xia, K.-Q: Flow mode transition in turbulent thermal convection. Phys. Fluids 20, 055104, 2008.

ON THE ANALYSIS OF FLOWS IN HEATED CORRUGATED CONDUITS

Arman Abtahi[*a)] & Jerzy M. Floryan[*]
[*]*Dept. of Mechanical and Materials Engineering, University of Western Ontario, London, Ontario, CANADA*

Summary It is known that the application of periodic heating along the walls results in drag reduction in pressure-gradient driven flow. The heating creates a buoyancy field that leads to the creation of separation bubbles which separate the stream from the bounding walls. The strength of this effect is of practical interest for heating with wave numbers O(1) and for flows with small Reynolds numbers [1]. This analysis is focused on the determination of the role played by surface corrugations in a heated channel. The results suggest that a significant increase of the drag reduction can be achieved by placing the grooves in a proper relative position with respect to the heating pattern.

INTRODUCTION

In the super-hydrophobic effect, gas bubbles become trapped in surface micro-pores, effectively reducing the shear stress as shear between the liquid and the solid is replaced by shear between the liquid and the trapped gas [2]. The presence of liquid and gas phases and a proper surface topography are required to create this effect. It has been shown that imposing a correct pattern of heating-cooling at the walls can create a qualitatively similar effect [3]. A proper distribution of the buoyancy force leads to the formation of separation bubbles which isolate the stream from direct contact with the bounding walls and, at the same time, fluid rotation inside the bubbles provides a propulsive force. This effect is active in single phase fluids and does not require special surface topography. In the present study, the effects of a combination of surface topography and distributed heating are studied with particular attention paid to the potential for reduction of the pressure gradient required to drive a prescribed flow rate through such a conduit.

PROBLEM FORMULATION AND RESULTS

Consider a channel formed by two horizontal corrugated plates whose geometries are illustrated in Fig. 1 where half of the mean channel opening h has been used as the length scale.

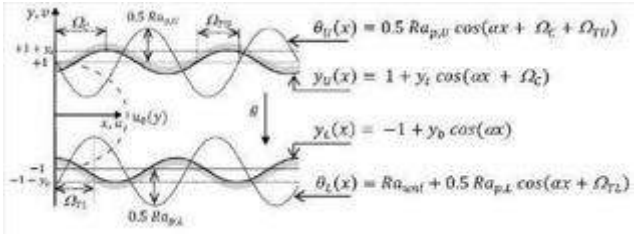

Figure 1. Schematic diagram of the flow system

In the above, y_b and y_t are the amplitudes of the corrugations at the lower and upper plates, respectively, Ω_C stands for the phase shift between the upper and lower corrugations, and α denotes the corrugation wave number which is the same as the heating wave number. The gravitational acceleration g is acting in the negative y-direction. The steady, incompressible flow of a Newtonian fluid is driven in the positive x-direction by an externally imposed pressure gradient. The fluid has thermal conductivity k, specific heat c, thermal diffusivity $\kappa = k/\rho c$, kinematic viscosity ν, dynamic viscosity μ, thermal expansion coefficient Γ and variations of the density ρ that follow the Boussinesq approximation. All material properties are evaluated at the reference temperature.

The lower and upper walls are subject to a spatially periodic heating resulting in the temperatures shown in Fig.1. The intensity of the uniform heating component is expressed in terms of the uniform Rayleigh number $Ra_{uni} = g\Gamma h^3 T_{uni}/(\kappa\nu)$, the amplitude of the lower periodic heating is expressed in terms of the lower periodic Rayleigh number $Ra_{p,L} = g\Gamma h^3 T_{p,L}/(\kappa\nu)$, the amplitude of the upper heating is expressed in terms of the upper periodic Rayleigh number $Ra_{p,U}$=$g\Gamma h^3 T_{p,U}/(\kappa\nu)$, T_{uni} is the difference between the mean temperatures of the lower and upper walls, $T_{p,L}$ and $T_{p,U}$ are the peak-to-peak amplitudes of the lower and upper periodic heating components, respectively, and $\kappa\nu/(g\Gamma h^3)$ has been used as the temperature scale. Positions of the upper and lower heatings with respect to the groove locations are expressed using the phase shifts Ω_{TL} and Ω_{TU} where the former refers to the lower wall while the latter refers to the upper wall. The relevant field equations consist of the continuity, Navier-Stokes and energy equations supplemented with the proper boundary conditions and the fixed flow rate constraint. This system is solved using a spectral discretization combined with the Immersed Boundary Conditions (IBC) method [4] to account for the irregularity of the flow domain. The pressure gradient correction A is defined as $\partial p/\partial x\,|_{mean} = Re(-2 + A/Re)$ and positive values signal drag reduction.

[a)] Corresponding author. Email: **sabtahi4@uwo.ca**

Figure 2 displays the flow and temperature fields. The buoyancy force creates separation bubbles at low Reynolds numbers. Increase of *Re* initially decreases the size of the bubbles and, eventually, eliminates them completely.

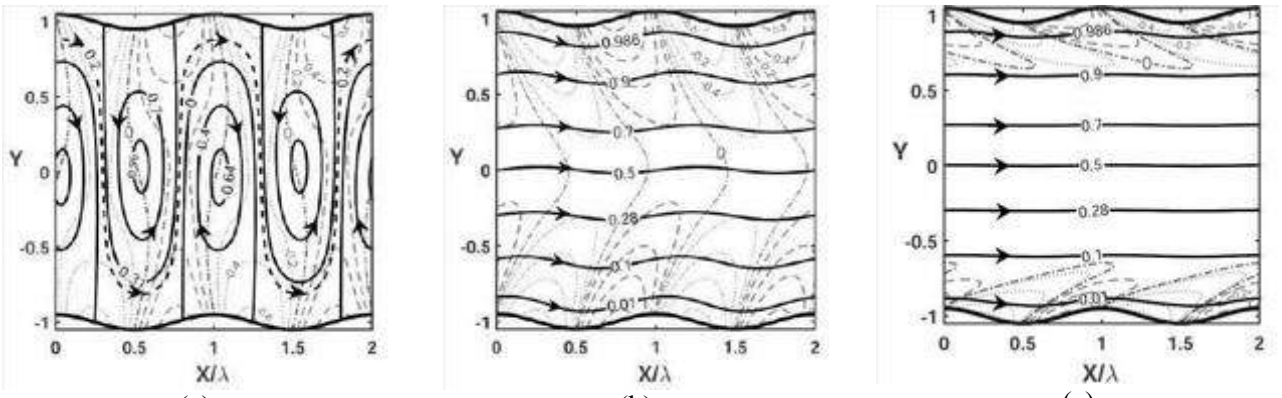

(a) (b) (c)

Figure 2. Flow and temperature fields for $\alpha = 2$, $Pr = 0.71$, $\Omega_{TL} = \pi/2$, $\Omega_{TU} = \pi/2$, $\Omega_C = 0$, $y_t = y_b = 0.05$, $Ra_{uni} = 0$, $Ra_{p,U} = Ra_{p,L} = 500$ for Re =1 (Fig.2a), Re = 20 (Fig.2b) and Re = 1000 (Fig.2c). Dashed (dashed-dotted) lines correspond to the positive (negative) isotherms. The stream function and the temperature have been normalized with their maxima.

Figure 3a illustrates variations of the pressure gradient correction as a function of the phase shift between the corrugation and the heating. It can be seen that the correction changes from positive to negative as a function of Ω_{TL}. The addition of grooves may either significantly decrease the pressure gradient required to drive the flow or increase this pressure gradient depending on the phase shift. The drag reduction may increase by a factor of 10 when compared with the smooth channel exposed to the same heating if a proper phase shift is used. Figure 3b illustrates variations of the pressure-gradient correction as a function of the wave number and demonstrates that $\alpha \approx 2$ is the most effective. Figure 3c illustrates variations of the pressure-gradient correction A as a function of Re and demonstrates the decrease of the magnitude of the drag reduction as Re increases.

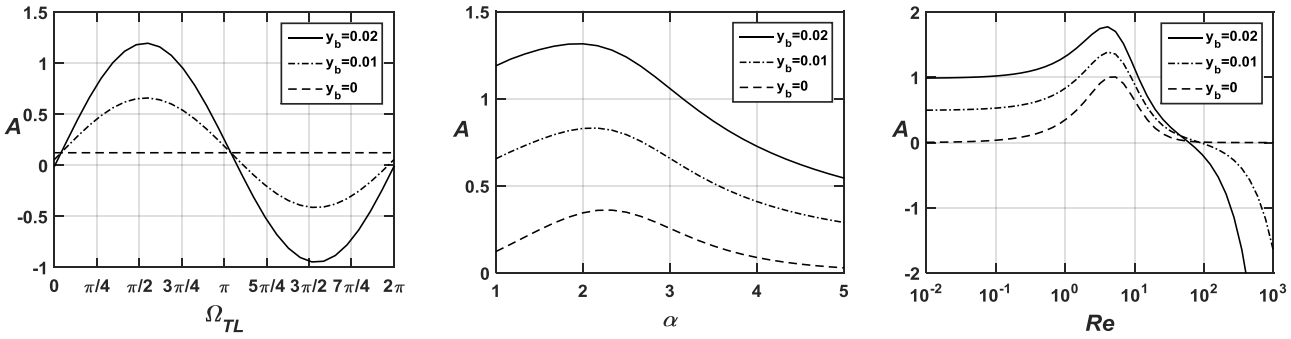

(a) (b) (c)

Figure 3. Variation of the pressure-gradient correction A as a function of a) the phase difference between the corrugation and the heating Ω_{TL} for $Re = 1$, and $\alpha = 1$; b) the heating and corrugation wave number α for $Re = 1$, and $\Omega_{TL} = \pi/2$; c) the Reynolds number Re for $\alpha = 2$, and $\Omega_{TL} = \pi/2$. Other parameters are $Ra_{p,L} = 1000$, $Ra_{p,U} = 0, Ra_{uni} = 0, y_t = 0, \Omega_{TU} = 0$, and $\Omega_C = 0$.

CONCLUSIONS

The reduction of pressure losses in a pressure-driven flow in a heated channel with wall corrugations has been analyzed. Detailed results have been presented for the Prandtl number $Pr = 0.71$ which well approximates the properties of air. It has been shown that the use of a proper phase shift between the heating pattern and the corrugation pattern results in a significant reduction of pressure losses.

References

[1] Hossain, M. Z., Floryan, D., and Floryan, J. M. : Drag reduction due to spatial thermal modulations. *J. Fluid Mech.* **713**, 398-419, 2012.

[2] Rothstein, J.P. : Slip on superhydrophobic surfaces. *Annu. Rev. Fluid Mech.* **42**, 89-109, 2010.

[3] Floryan, J.M. : The thermo-superhydrophobic effect. *Bull. Am Phys Sci* **57** (1), X50.00015, 2012.

[4] Fernandez, D.C. Del Rey, Husain, S.Z., and Floryan, J.M. : Immersed boundary conditions method for heat conduction problems in slots with time-dependent geometry. *Int. J. Numer. Meth. Fluids*. **67**, 478-500, 2010.

ANALYSIS OF COUNTER-FLOW CONVECTIVE EXCHANGERS USING GENERAL GRAETZ MODES

Jules Dichamp[1], Frédéric De Gournay [2], and Franck Plouraboué [*1]

[1]*Institut de Mcanique des Fluides de Toulouse (IMFT) - Universit de Toulouse, CNRS-INPT-UPS, Toulouse FRANCE*

[2]*Institut de Mathématiques de Toulouse, CNRS and Université Paul Sabatier, Toulouse, FRANCE*

Summary We perform a systematic analysis of heat transfer in a counter-current three dimensional convective exchanger, when the inlet/outlet influence is fully taken into account as is the longitudinal diffusion in the exchanger and the inlet/outlet tubes. The analysis, carried out for constant fluid properties and using generalized Graetz mode decomposition consider the various influence of the fluid/solid diffusivity, the imposed convection, inlet/outlet far-field conditions, and lateral boundary conditions. In all cases we found an optimal Péclet number for the cold or hot efficiency. This study open new perspectives for micro-heat exchangers where moderate convection provides the best efficiency and compactness.

Conjugate counter-flow heat-exchangers are widely used in thermal and building energy, chemical, and many other industrial applications [5]. In the recent years, efforts have been dedicated to design micro-heat exchanger for micro-cooling systems associated with high power density micro-chips.Compactness, efficiency, and performance are indeed all-together crucial in many contexts and different strategies have been proposed to search for optimal designs.

In many cases, for highly convective regimes are considered, the influence of longitudinal diffusion inside the exchanger is neglected. Similarly, a fully developed convective outlet condition [6] is generally chosen. The aim of this contribution is to revisit this problem when taking into account the full influence of inlet/outlet coupling as well as longitudinal diffusion based upon a new theoretical formulation [3, 4, 1]. Optimal transfer is obtained for moderate convective effects, which a aposteriori justifies to consider full convection/diffusion couplings.

GOVERNING PROBLEM

We consider laminar convection-diffusion arising in a fluid having constant properties. Fully developed solution of Navier-Stokes momentum equations in cylindrical tubes oriented along direction z are given by the Poiseuille longitudinal velocity $\mathbf{v}_{H,C} = v_{H,C}(r)\,\mathbf{e}_z = \pm(3V_{H,C}/2)\left(1 \circ (r/R)^2\right)\,\mathbf{e}_z$ where V_H —resp. V_C– stands for the average velocity in the hot — resp. cold — tube, where R is the tube radius and $\mathbf{e}_z$ is the unit vector along z direction. In most of the case $V_H = V_C$ (balanced configuration).

Following previous studies [6], we define the stationary flux balance in three dimensions for dimensionless temperature $T^\star = T/T_H^{-\infty}$

$$\begin{array}{rrcll} Pe_{H,C} v^\star(\xi^\star)\partial_{z^\star} T^\star \circ & (\partial^2_{x^\star} + \partial^2_{y^\star} + \partial^2_{z^\star})T^\star & = & 0, & \text{in} \quad \text{Fluid} \\ & (\partial^2_{x^\star} + \partial^2_{y^\star} + \partial^2_{z^\star})T^\star & = & 0, & \text{in} \quad \text{Solid} \end{array} \tag{1}$$

At infinity, hot/cold inlet/outlet tubes have homogeneous temperatures $T^{\pm\infty}_{H,C}$. $T_H^{-\infty}$ and $T_C^{+\infty}$ are the known imposed temperatures at hot inlet tube ($z \to \circ\,\infty$) and cold inlet tube ($z \to +\infty$). $T_H^{+\infty}$ and $T_C^{-\infty}$ are unknowns outlet conditions, standing for temperatures at hot outlet tube ($z \to \circ\,\infty$)) and cold outlet tube ($z \to +\infty$)). In most cases we study balanced configurations $T_H^{-\infty} = \circ\, T_C^{+\infty}$. Thermal conductivity in the solid is k^S whilst, in the fluid it is k^F. All inlet/outlet tubes fulfill lateral homogeneous Neumann boundary conditions, whereas the exchanger fulfills a Robin lateral boundary condition. A schematic view of a full exchanger is depicted Figure 1 **(b)**.

THEORETICAL FORMULATION AND NUMERICAL IMPLEMENTATION

Main equation (1) refers as the extended Graetz problem which is an extension of a classical class of PDE problems in which one can decompose the temperature field on a basis of eigenvalues and eigenvectors which are called in the literature Graetz modes and Graetz eigenvalues. On previous contributions [3, 4, 1] it was proven that equation (1) on general configurations can be written as an ODE $\frac{d}{dz}\phi(z) = A\,\phi(z)$ and that matrix A satisfies self-adjointness and compacity which allows a similar spectral decomposition as in classical case. Following this mathematical framework, a numerical method based on Graetz modes was developed in [2]. Since we use a generalyzed Graetz-mode decomposition, all longitudinal variations are analytically known. Then, providing proper continuity coupling conditions between hot/cold inlet/outlet tubes and the exchanger part by minimizing a functional (see [2] for the more details) and correct eigenvalues sequences and eigenvectors, one can compute the dimensionless temperature field $T^\star$ at very low computational cost.

[*]Corresponding author. Email: fplourab@imft.fr

RESULTS

Here, we mainly focused the discussion on hot and cold efficiency defined as $\epsilon_H \equiv \frac{T_H^{-\infty} - T_H^{+\infty}}{T_H^{-\infty} - T_C^{+\infty}}$ and $\epsilon_C \equiv \frac{T_C^{-\infty} - T_C^{+\infty}}{T_H^{-\infty} - T_C^{+\infty}}$. $\epsilon_H = \epsilon_C$ in balanced configurations. A systematic exploration of the problem having seven dimensionless parameter has been performed. Here, we focus on the influence of the main parameters on the efficiency. We therefore explore the influence of the Péclet number, the exchanger dimensionless length $L^\star$, the conductivity ratio k^S/k^F, and the Biot number Bi (which is related to the lateral Robin boundary condition of the exchanger). In all cases we found an optimal Péclet number Pe^o for the efficiency associated with moderate convection, i.e, $6 < Pe^o < 12$.

When the Péclet number rises, so does the transfer performances, at the cost of very low efficiency. Elongated exchangers reduce the lost of efficiency but they also result in poor compactness. Performance degradation at high Péclet number are related to convective leaks at the outlets. Figure 1 **(a)**, display the behavior of hot efficiency versus Péclet number, for various Biot numbers. One can observe an optimal efficiency at moderate Péclet which is poorly sensitive to large Bi variations. Figure 1 **(c)** is the corresponding 2D longitudinal section in (x, z) plane of the temperature field at optimal Péclet for $Bi = 10^{-1}$.

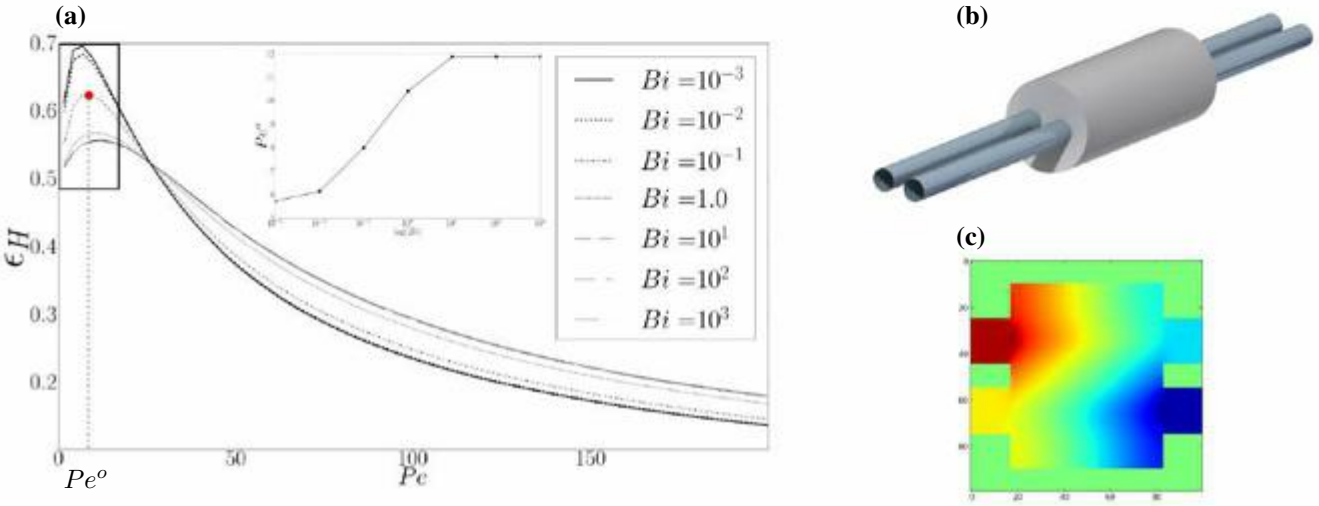

Figure 1: **(a)** Hot efficiency against Péclet for $Bi = 10^{-3}, 10^{-2}, 10^{-1}, 1, 10^1, 10^2, 10^3$. Inset figure is Péclet at maximum hot efficiency against $\log(Bi)$. **(b)** Perspective view using real size of full exchanger. **(c)** Longitudinal temperature fields at optimal Péclet on $Pe^o = 8$, $L^\star = 20$, $Bi = 10^{-1}$ (red dot in **(a)**). We have rescaled the horizontal $z^\star$ axis for the inset figures to reach a 1:1 aspect ratio.

CONCLUSIONS

We perform a systematic study of a parallel convective exchanger from analyzing the influence of physical, mechanical, and thermal parameters when properly taking into account the influence of inlet/outlet as well as longitudinal and transverse diffusion within the solid. Using a Generalized Graetz mode decomposition, we analyze the exchanger efficiency and performance, in many operating conditions. Our results show that moderate convection provides optimal efficiency. We believe these results to be of general scope for many other counter- flow exchanger geometries. We also have interesting results concerning the fully-developed regime when the convection is large and/or the exchanger is elongated. As a perspective, the use of Generalized Graetz mode decomposition could allow some systematic exploration of the exchanger geometry.

References

[1] J. Fehrenbach, F. De Gournay, C. Pierre, and F. Plouraboué. The Generalized Graetz problem in finite domains. *SIAM. J. Appl. Math*, 72:99–123, 2012.

[2] C. Pierre, J. Bouyssier, F. de Gournay, and F. Plouraboué. Numerical computation of 3D heat transfer in complex parallel heat exchangers using generalized Graetz modes. *J. Comp. Phys*, 268:84–105, 2014.

[3] C. Pierre, J. Bouyssier, and F. Plouraboué. Mathematical analysis of parallel convective exchangers. *Math. Models and Methods Appl. Sci.*, 24(4):627–667, 2013.

[4] C. Pierre and F. Plouraboué. Numerical analysis of a new mixed-formulation for eigenvalue convection-diffusion problems. *SIAM. J. Appl. Math*, 70:658–676, 2009.

[5] R. K. Shah and Dušan P. Sekulić. *Fundamentals of heat exchanger design*. John Wiley and Sons, New Jersey, 2003.

[6] M. Vera and A. Liñán. Exact solution for the conjugate fluid-fluid problem in the thermal entrance region of laminar counter-flow heat exchangers. *Int. J. Heat Mass Transfer*, 54(1-3):490–499, 2011.

INTEGRAL TRANSFORMS IN LINEAR OR NONLINEAR CONVECTION-DIFFUSION THROUGH CONVECTIVE EIGENVALUE PROBLEMS

Renato M. Cotta[1,3a)], Diego C. Knupp[2] & Carolina P. Naveira-Cotta [1]
[1]*Mechanical Eng. Dept. - PEM/COPPE, Federal University of Rio de Janeiro, UFRJ, Brazil*
[2]*Mech. Eng. Dept. – Polytechnic Institute, State University of Rio de Janeiro, UERJ, Brazil*
[3]*President – National Commission of Nuclear Energy, CNEN, Rio de Janeiro, Brazil*

Summary The Generalized Integral Transform Technique (GITT) is employed in the solution of nonlinear convection-diffusion problems by incorporating the convective effects into the chosen eigenvalue problem that forms the basis of the proposed eigenfunction expansion. The aim is to improve convergence behavior of the eigenfunction expansions, especially in the case of highly convective formulations, in comparison against the traditional approach of adopting a purely diffusive eigenvalue problem. The developed methodology is then illustrated for both linear and nonlinear, one-dimensional and multidimensional Burgers equations.

INTRODUCTION AND ANALYSIS

The present work considers the application of the Generalized Integral Transform Technique (GITT) [1-2] in the solution of a class of linear or nonlinear convection-diffusion problems, by incorporating the convective effects into the chosen eigenvalue problem that forms the basis of the proposed eigenfunction expansion. The aim is to markedly improve convergence behavior of the eigenfunction expansions, especially in the case of highly convective formulations, in comparison against the traditional approach via a purely diffusive eigenvalue problem, by directly accounting for the relative importance of convective and diffusive effects within the eigenfunctions themselves. Through a straightforward transformation of the original convection-diffusion problem, basically by redefining the coefficients associated with the transient and diffusive terms, the convective term is merged into a generalized diffusion term with a transformed space variable diffusion coefficient. The generalized diffusion problem then naturally leads to the eigenvalue problem to be adopted for deriving the eigenfunction expansion in the linear situation, as well as for the appropriate linearized version in the case of a nonlinear application. The resulting eigenvalue problem with space variable coefficients is then solved through the GITT itself, yielding the corresponding algebraic eigenvalue problem upon selection of a simple auxiliary eigenvalue problem of known analytical solution [3]. The GITT is also applied in the solution of the generalized diffusion problem, and the resulting transformed ordinary differential equations system is solved either analytically, for the linear case, or numerically for the nonlinear formulation. The developed methodology is here briefly illustrated for both linear and nonlinear applications, both in one-dimensional and multidimensional formulations, as represented by examples of Burgers equation.

The adoption of convective eigenvalue problems in the integral transforms solution of transient convection-diffusion is here analyzed first by considering a fairly general nonlinear one-dimensional formulation:

$$w(x)\frac{T(x,t)}{t}+u(x)\frac{T(x,t)}{x}=\frac{}{x}[k(x)\frac{T(x,t)}{x}]\quad d(x)T(x,t)+P(x,t,T),\quad x_0<x<x_1,t>0 \tag{1}$$

where $u(x)$ is a characteristic linear representation of the convective term coefficient, while the remaining of the nonlinear convective operator (or of any other operator) is incorporated into the nonlinear source term, $P(x,t,T)$. Problem (1) can be readily rewritten as a generalized diffusion problem, through a simple transformation of the diffusive and transient terms as:

$$\hat{w}(x)\frac{T(x,t)}{t}=\frac{}{x}[\hat{k}(x)\frac{T(x,t)}{x}]\quad \hat{d}(x)T(x,t)+P(x,t,T),\quad x_0<x<x_1,t>0 \tag{2}$$

where,

$$\hat{w}(x)=w(x)\hat{k}(x)/k(x);\ \hat{d}(x)=d(x)\hat{k}(x)/k(x);$$

$$P(x,t,T)=P(x,t,T)\hat{k}(x)/k(x);u^*(x)=\frac{1}{k(x)}\ u(x)\quad \frac{dk(x)}{dx}\ ;\ and\ \hat{k}(x)=e^{\quad u^*(x)dx} \tag{3.a-e}$$

Equation (2) is a special case of the nonlinear diffusion problems that have been extensively handled through the GITT [1-2], but are here treated through an eigenfunction expansion basis that includes convective effects through the characteristic convective term coefficient, $u(x)$. The self-adjoint eigenvalue problem with space variable coefficients to be considered would then be given by the following equation:

a) Corresponding author. Email: renato.cotta@cnen.gov.br

$$\frac{d}{dx}[\hat{k}(x)\frac{d\ (x)}{dx}]+[\ \ ^2\hat{w}(x)\quad \hat{d}(x)]\ \ (x),\ \ x_0 < x < x_1 \tag{4}$$

which can be readily solved by the GITT itself [3], yielding the corresponding algebraic eigenvalue problem. The extension of this analysis to multidimensional problems is straightforward, but is here omitted due to space restrictions.

RESULTS AND DISCUSSION

The illustration of the proposed procedure is started with the analysis of the one-dimensional Burgers equation, both in linear and nonlinear formulations [4], which allows for the analysis of the transformation procedure on the eigenfunction expansion convergence behavior. The following functional forms for the coefficients are considered: w(x)=1, k(x)=1, d(x)=0, u(x)= u_0+bT(x,t). Table 1 illustrates the convergence behaviour of the eigenfunction expansions for T(x,t), with u_0=10, b=0 (linear problem) and b=5 (nonlinear problem). Clearly, from those columns associated with the use of the convective eigenvalue problem (Conv.), one may clearly observe the marked gain in convergence rates in comparison to the diffusive alternative (Diff.), even for the nonlinear situation, when the convective eigenvalue problem does not account for the full influence of the nonlinear convection term. Table 2 provides a convergence analysis for T(x,y,t) in the two-dimensional Burgers equation, with u_0=10, v_0=1, b=0 (linear problem), again reconfirming the excellent convergence behaviour of the expansions that follow the convective basis proposal.

Table 1 – Convergence analysis of eigenfunction expansions with convective and diffusive eigenvalue problems in the solution of the one-dimensional Burgers equation in both linear and nonlinear formulations.

N	u_0=10, b=0 (linear problem)				u_0=10, b=5 (nonlinear problem)			
	T(0.5,0.05) Conv.	T(0.5,0.05) Dif.	T(0.9,0.01) Conv.	T(0.9,0.01) Dif.	T(0.5,0.05) Conv.	T(0.5,0.05) Dif.	T(0.9,0.01) Conv.	T(0.9,0.01) Dif.
2	0.386565	0.462380	-1.81418	0.430194	0.286084	0.360552	-1.43571	0.450501
4	0.379714	0.356180	0.200342	0.653885	0.276093	0.249478	0.409794	0.688207
6	0.379716	0.388818	0.704696	0.726450	0.276946	0.287617	0.762698	0.781085
8	0.379716	0.375350	0.738297	0.748564	0.276724	0.271688	0.791899	0.812893
10	0.379716	0.382043	0.738805	0.750988	0.276796	0.279440	0.794770	0.816583
12	0.379716	0.378270	0.738798	0.746579	0.276769	0.275180	0.794446	0.810758
14	0.379716	0.380596	0.738798	0.741232	0.276781	0.277753	0.793992	0.803719
16	0.379716	0.379064	0.738798	0.737306	0.276774	0.276080	0.793768	0.798590
18	0.379716	0.380126	0.738798	0.735361	0.276778	0.277236	0.793735	0.796028
20	0.379716	0.379359	0.738798	0.735074	0.276775	0.276386	0.793817	0.795626

Table 2 – Convergence analysis of eigenfunction expansions with convective and diffusive eigenvalue problems in the solution of the two-dimensional Burgers equation in linear formulation.

N	u_0=10, v_0=1, b=0 (linear problem)					
	T(0.5,0.1,0.01) Conv.	T(0.5,0.1,0.01) Diff.	T(0.1,0.1,0.01) Conv.	T(0.1,0.1,0.01) Diff.	T(0.9,0.1,0.05) Conv.	T(0.9,0.1,0.05) Diff.
10	0.516515	0.485608	0.110953	0.133233	0.108255	0.097938
20	0.491783	0.501325	0.135094	0.155057	0.108368	0.102400
30	0.493395	0.497816	0.140490	0.137969	0.108368	0.106297
40	0.493082	0.492352	0.141373	0.145203	0.108368	0.108567
50	0.493041	0.491333	0.141533	0.139425	0.108368	0.109549
60	0.493100	0.494026	0.141569	0.140748	0.108368	0.109946
70	0.493122	0.495103	0.141574	0.140942	0.108368	0.109924
80	0.493123	0.495309	0.141574	0.140974	0.108368	0.109922

References

[1] Cotta R. M.: Computational Integral Transforms in Heat and Fluid Flow, CRC Press, FL, 1993.

[2] Cotta R. M., Mikhailov M. D.: "Hybrid Methods and Symbolic Computations", in: *Handbook of Numerical Heat Transfer*, 2nd edition, Chapter 16, Eds. W.J. Minkowycz, E.M. Sparrow, and J.Y. Murthy, John Wiley, New York, pp.493-522, 2006.

[3] Naveira-Cotta C.P, Cotta R.M., Orlande H.R.B., Fudym O..: Eigenfunction Expansions for Transient Diffusion in Heterogeneous Media, *Int. J. Heat and Mass Transfer*, 52:5029-5039, 2009.

[4] Cotta R. M, Serfaty R..: Hybrid Analysis of Transient Nonlinear Convection-Diffusion Problems, *Int. J. Num. Meth. Heat & Fluid Flow*, 2:55-62, 1992.

STEADY THERMAL CONVECTION IN A ROTATING HORIZONTAL ANNULUS

Alevtina Ivanova [1], Victor Kozlov [1 a)], Ramil Siraev[2] & Aleksei Vjatkin [1]
[1] *Laboratory of vibrational hydromechanics,*
Perm State Humanitarian Pedagogical University, Perm, Russia
[2] *State National Research Polytechnical University of Perm*

Summary We study theoretically and experimentally the thermal convection of liquid in a quickly rotating horizontal annulus with isothermal boundaries of different temperatures. Experiments show that the convection manifests itself in a threshold excitation of two-dimensional vortexes parallel to the cavity axis in both cases, when heating from inside and outside. It is demonstrated that the convection is determined by two mechanisms, centrifugal and "thermovibrational". The last one appears due to a mean effect of oscillations of nonisothermal liquid in the cavity frame caused by gravity. We present the results of the linear stability analysis and nonlinear numerical simulation based on the equations of a thermovibrational convection obtained by the method of averaging. Experimental and theoretical results match up on a plane of the governing dimensionless parameters, centrifugal Rayleigh number and vibrational parameter.

Thermal convection in rotating systems is an actual problem connected with the geophysical problems, in particular with convection in the atmospheres and the cores of the planets. The fluctuations of the non-isothermal liquid can be a source of an averaged lift force - thermovibrational convection [1], along with the Rayleigh mechanism. As shown in [2], the rotation qualitatively changes the mechanism of thermovibrational convection. This is because the inertia forces, especially Coriolis force act not only on an averaged flow but also on the oscillating motion of the nonisothermal fluid. A special case is the averaged convection excited in the cavity, rotating in a static external force field orthogonal to the axis of rotation. At this the averaged convection is excited in the rotating system because of tidal oscillations of nonisothermal liquid. As shown in [3] the averaged convection could develop even in the case when the centrifugal force has a stabilizing effect. In this paper, we continue the experimental study of the stability and heat transfer in a rotating horizontal annulus, as well as solve the problem of convective stability and study the heat transfer by DNS. The theory is based on the equations of thermal vibrational convection in rotating systems, which were obtained by averaging in [2].

EXPERIMENT

Experimental studies are performed in a relatively thin layer, with the relative thickness h/R=0.2, where R is mean radius of an annulus. A special technique was elaborated to study the flow structure and the wave length of the convective structures. The threshold of convection onset and the heat transfer in the supercritical region were studied. When heating the annulus from the outside, the well known centrifugal convection manifests itself, the convective rolls diameter is close to the thickness of the layer (Fig. 1).

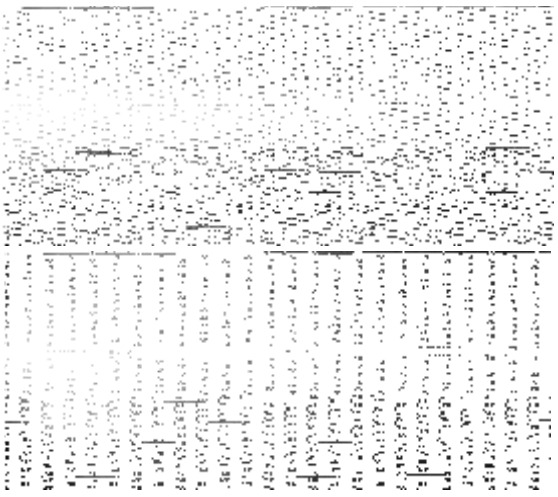

Fig.1. Convective structures (view from aside). a) – centrifugal convection (the external boundary of the annulus is hot); b) – thermovibrational convection (the internal boundary of the annulus is hot)

[a)] Corresponding author. Email: kozlov@pspu.ru

hypersonic boundary layer flow over a flat plate. Using the boundary conditions, DNS results show that wall temperature will take a long time to rise to the adiabatic temperature, during this period take isothermal or adiabatic wall condition is not appropriate. According to the results of the estimation and DNS comparison, we can infer that there must be a formula to calculate the wall temperature and heat flux by wall position, time, and any other parameters.

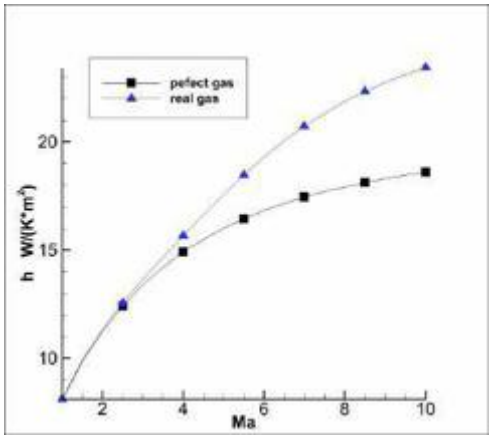

Fig. 1 Comparison of heat transfer coefficient calculated by Blasius similar solution considering the effect of real gas or not, respectively.

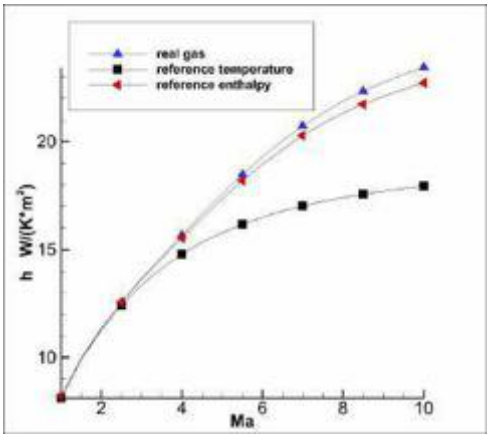

Fig. 2 Comparison of heat transfer coefficient calculated by reference enthalpy method, reference temperature method and Blasius similar solution considering effect of real gas.

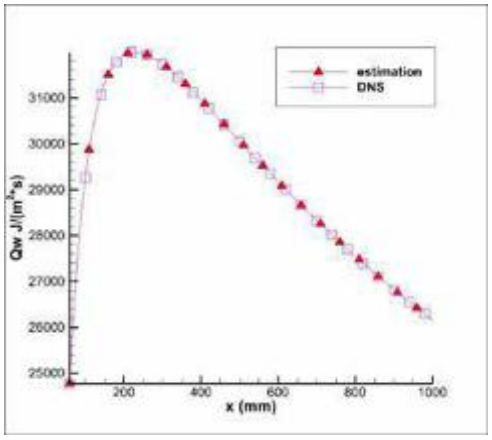

Fig.3 At time 23.9s, comparison of heat flux on the wall between estimated values and DNS results.

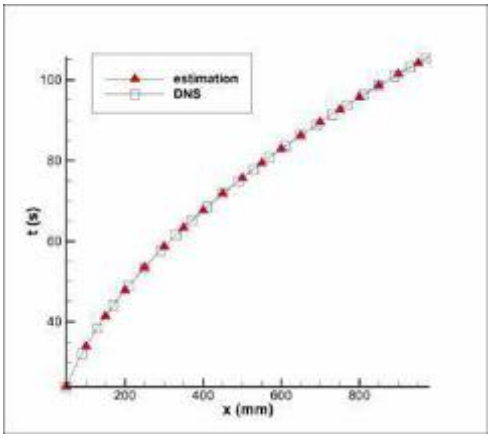

Fig.4 The comparison of time between estimated values and DNS results when the wall temperature is 4 times of the free stream temperature.

Acknowledgements:

This work was supported by the National Natural Science Foundation of China (11332007), the Tianjin Natural Science Foundation (15JCYBJC19500).

References

[1] Klopfer G H, Yee H C. Viscous hypersonic shock-on-shock interaction on blunt cowl lips[R]. AIAA paper, 1988-0233, 1988.

[2] Hoffmann K A, Siddiqui M S, Chiang S T. Difficulties associated with the heat flux computations of high speed flows by the Navier-Stokes equations[R]. AIAA paper,1991-0467,1991.

[3] Hoffmann K A, Papadakis M, Suzen Y B. Aeroheating and skin friction computations for a blunt body at high speeds[R]. AIAA paper,1994-0455,1994.

[4] Eckert, E. R., Surrey of Heat Transfer at High Speeds, WADC, TR-54-70(1954)

[5] Sommer, S.C. and Short, B.J., Free-Flight Measurements of Turbulent Boundary layer Skin Friction in the Presence of Aerodynamic Heating, J.A.S.23,6(1956)

[6] Zhang Zhicheng, military training textbook editing committee of the PLA General Armament Department, Hypersonic Aerodynamic Heating and Thermal Protection. Beijing: National Defense Industry Press, 2003 (in Chinese)

[7] Wen-li JIA, Wei CAO, The effects of variable specific heat on the stability of hypersonic boundary layer on a flat plate, Applied Mathematics and Mechanics(English Edition). 2010

[8] Li,Haiyan,Numerical Simulation of Hypersonic and High Temperature Gas Flowfields[D]. China Aerodynamics Research and Development Center, 2007.

STUDY OF HEAT-TRANSFER COEFFICIENT ON HYPERSONIC BOUNDARY LAYER FLOW OVER A FLAT

Chao LIU, Wei CAO[a)]
Department of Mechanics, Tianjin University, Tianjin, China

Summary Method of computing convective heat transfer coefficient is examined by the numerical study on hypersonic boundary layer flow over a flat plate. For the similar solutions existing in hypersonic boundary layer flow for the variable specific heat, the heat flux on isothermal wall is calculated and being served as a standard to examine the accuracy of the method. The results showed that reference enthalpy method is more applicability than reference temperature method for variable specific heat. Then, using the formula above as the wall temperature condition, the DNS is conducted from an initially given temperature to adiabatic temperature for one meter long flat with incoming flow Mach number 4.5. According to the calculation results, we found that the temperature and heat flux on the wall associated with time and distance to the flat front edge.

Motivation

In most cases, wall temperature condition is assumed to be isothermal or adiabatic condition in the computation of the location prediction of transition and turbulence of supersonic flow in the past, that is reasonable in the cases when the Mach number is not very large and gas temperature is not Significant. But when the vehicle flies with hypersonic, the gas temperature in the boundary layer will rise significantly [1-3]. For instance, in flat plate boundary layer flows, if the wall condition is adiabatic and the Mach number is 5, the gas temperature near the wall can reach 5.2 times the temperature of the coming flow. Wall temperature condition should be assumed to be convective heat transfer condition, which is more suitable for the vehicle flies with hypersonic. Boundary layer flow stability is likely to be different from the cases used isothermal or adiabatic condition. It is a new problem to be worth studying.

In this paper, the method of calculating heat transfer coefficient[4,5,6] is examined by Blasius similar solution for variable specific heat[7,8]. Then, the DNS is conducted from an initially given temperature to adiabatic temperature for one meter long flat. The wall condition is the convective heat transfer condition of the formula which has been verified.

Main Results

Lots of examples are calculated to examine the accuracy of the method computing convective heat transfer coefficient. For the cases of oncoming flow Mach 1-10, isothermal wall condition, considering the effect of real gas or not, heat transfer coefficient calculated by the Blasius similar solution is shown in Fig.1. It is found that the values calculated considering the effect of real gas should be taken as the standard to examine the applicability of the method. The heat transfer coefficient calculated by the reference enthalpy and the reference temperature method, respectively, are compared with the standard values as shown in Fig.2. It is found that the results calculated by reference enthalpy method is close to the standard values and their relative errors are small enough to be accepted. Therefore, we use the convection heat transfer formula calculated by reference enthalpy method as the wall boundary conditions for direct numerical simulation (DNS).

Using the wall conditions of convective heat transfer, DNS is used to calculate the compressible boundary layer of a flat plate during the wall temperature rises from a given temperature to the adiabatic temperature. The model is a one-meter long thin metal plate with a thickness of 2mm. Free stream parameters are taken corresponding to 5km altitude ones and Mach number is 4.5. A no-slip, convective heat transfer wall was chosen for wall boundary condition. Adopting the assumption of the thin metal flat plate that temperature distribution along normal direction tends to be uniform, ignore heat conduction along the flow direction and considering only air-to-wall convective heat transfer.

The results of DNS show that, neither the isothermal nor the adiabatic condition is the suitable wall temperature condition in most part of the heat transfer process. At the initial moment, the wall heat flux is only related to the heat transfer coefficient formula. According to the calculation results of a certain section from leading edge of the plate, we can estimate the heat flux and temperature at different locations of the wall at anytime. At 23.917 seconds, the wall heat flux of DNS and estimation is shown in Fig.3. We tried to estimate the time from the wall temperature of different location points to reach a certain temperature without the DNS results. The time of DNS and estimation that wall temperature rises to 4 times the free stream temperature is shown in Fig.4. Therefore, there must be a formula to calculate the wall temperature and heat flux through wall position, time, and any other parameters.

Conclusion

The convection heat transfer coefficient calculated by reference enthalpy method are in good agreement with the numerical results considering variable specific heat, which can be used as convective heat transfer boundary condition on hypersonic boundary layer flow over a flat plate. Using the boundary conditions, DNS results show that wall temperature will take a long time to rise to the adiabatic temperature, during this period take isothermal or adiabatic wall condition is not appropriate.

a)Corresponding author Wei CAO, Professor, E-mail: caow@tju.edu.cn

According to the results of the estimation and DNS comparison, we can infer that there must be a formula to calculate the wall temperature and heat fluxby wall position, time, and any other parameters.

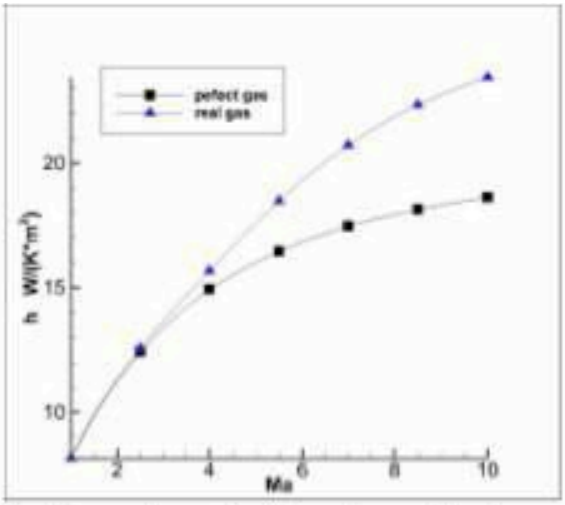

Fig.1 Comparison of heat transfer coefficient calculated by Blasius similar solution considering the effect of real gas or not, respectively.

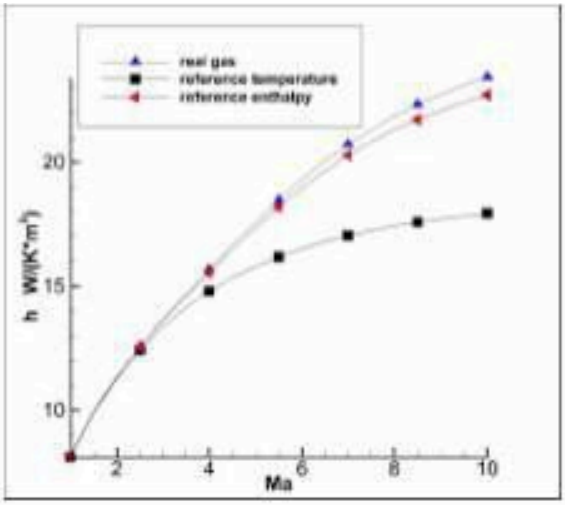

Fig.2 Comparison of heat transfer coefficient calculated by reference enthalpy method, reference temperature method and Blasius similar solution considering effect of real gas.

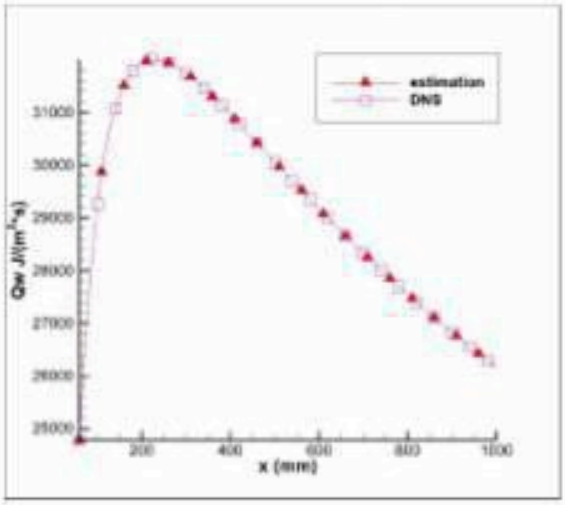

Fig.3 At time 23.9s, comparison of heat flux on the wall between estimated values and DNS results

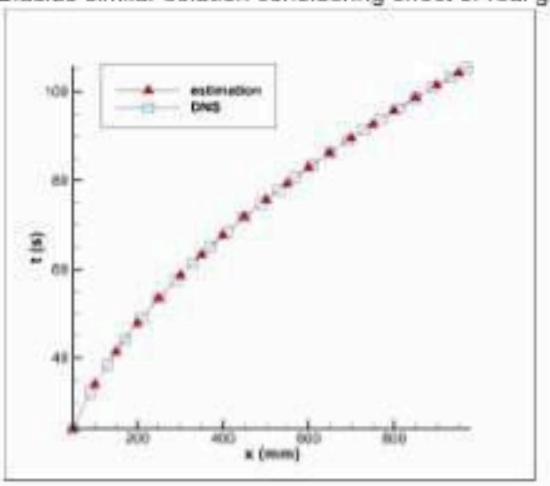

Fig.4 The comparison of time between estimated values and DNS results when the wall temperature is 4 times of the free stream temperature.

Acknowledgements:

This work was supported by the National Natural Science Foundation of China (11332007), the Tianjin Natural Science Foundation (15JCYBJC19500)

References

[1] Klopfer G H, Yee H C. Viscous hypersonic shock-on-shock interaction on blunt cowl lips[R]. AIAA paper, 1988-0233, 1988.

[2] Hoffmann K A, Siddiqui M S, Chiang S T. Difficulties associated with the heat flux computations of high speed flows by the Navier-Stokes equations[R]. AIAA paper,1991-0467,1991.

[3] Hoffmann K A, Papadakis M, Suzen Y B. Aeroheating and skin friction computations for a blunt body at high speeds[R]. AIAA paper,1994-0455,1994.

[4] Eckert, E. R., Surrey of Heat Transfer at High Speeds, WADC, TR-54-70(1954)

[5] Sommer, S.C. and Short, B.J., Free-Flight Measurements of Turbulent Boundary layer Skin Friction in the Presence of Aerodynamic Heating, J.A.S.23,6(1956)

[6] Zhang Zhicheng, military training textbook editing committee of the PLA General Armament Department, Hypersonic Aerodynamic Heating and Thermal Protection. Beijing: National Defense Industry Press, 2003 (in Chinese)

[7] Wen-li JIA, Wei CAO, The effects of variable specific heat on the stability of hypersonic boundary layer on a flat plate, Applied Mathematics and Mechanics(English Edition). 2010

[8] Li,Haiyan,Numerical Simulation of Hypersonic and High Temperature Gas Flowfields[D]. China Aerodynamics Research and Development Center, 2007.

COMPUTATION OF HEAT FLUX IN THE STAGNATION POINT FOR A COLD WALL WITH HIGH SPEED FLOW

Qi-Qi Qu[1], Wei Cao[1a)]
[1] *Department of fluid mechanics, Tianjin university, Tianjin, china*

Summary In order to get the exact heat flux in the stagnation point numerically, direct numerical simulation (DNS) is performed to solve Navier-Stokes equations for hypersonic blunt cone flow with Mach numbers 4.5, 6 and 8. The convective terms are calculated using fifth order WENO schemes. To study how the parameter properties affect the stagnation heat flux, the comparisons were given between constant and variable specific heat ratio taken respectively. The basic flow is obtained at isothermal wall condition and then the heat flux in the stagnation point by Fourier heat conduction law. We also compute and analyze the proportions of various kinds of items in the energy equation at different point on the axis. Basing on this, we manage to develop a method to get the stagnation point heat flux by virtue of calculating some item such as convective heat transfer.

INTRODUCTION

The heat flux in the stagnation point for a cold wall means that high speed flow moves to the stagnation point in very short period time, heat transfer to solid being ignored and the solid surface temperature maintained unchanged. It may be treated as a fixed temperature, while the amount of heat flux to the wall are usually so large that it was much concerned in the engineering area. Only to accurate calculating heat flux can provide us with reliable basis for the requirement in hypersonic vehicle thermal protection design. There are many researches about the calculation of stagnation point heat flux, especially, several engineering calculation formula have been put forward and widely applied in practical engineering [1-3]. There are also a lot of experiments and calculation research about the stagnation point heat flux. But the results are difference among calculation results and the experimental or actual flight case. It is key problem how to get the exact heat flux in the stagnation point.

In the paper, Direct Numerical Simulation (DNS) is performed for blunt cone flow with Mach numbers 4.5, 6 and 8, the air parameters adopted the gas corresponding to the altitude of 30km. Oncoming flow gas temperature equal to 226.7K. Air treated as perfect gas. For isothermal wall boundary conditions, the basic flow field is obtained by using DNS for constant and variable specific heat ratio taken respectively in order to study how the parameter properties affect the stagnation heat flux.

MAIN RESULTS

Figure 1 shows one meridian plane of the sphere nose cone and coordinate system. The nose radius is 0.0059m and oncoming flow Mach 4.5. The angle of attack is zero and symmetry conditions adopted along the polar axis. In order to validate the code, for adiabatic wall boundary conditions, the stagnation temperature was consistent to the theoretical results. In addition, the results are also verified by checking the grid independence to get appropriate grid size.

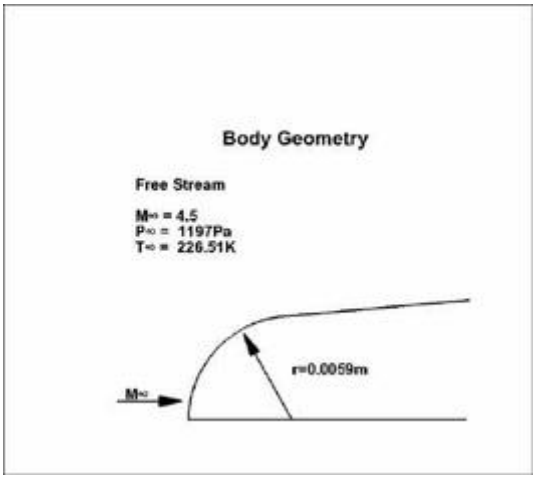

Fig.1 Schematic of the sphere nose cone and coordinate system

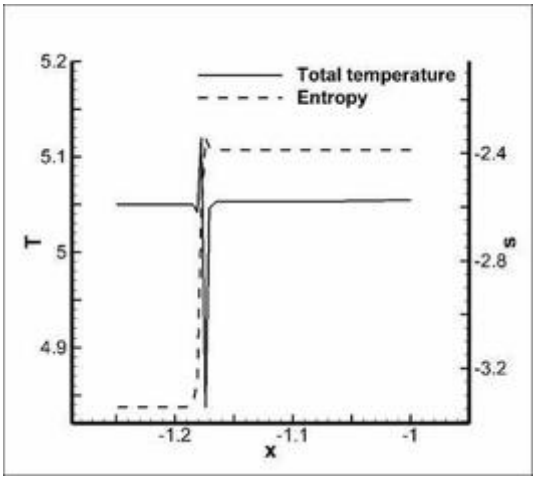

Fig.2 For adiabatic wall the total temperature entropy along polar axis

[a)]Corresponding author. Email: caow@tju.edu.cn.

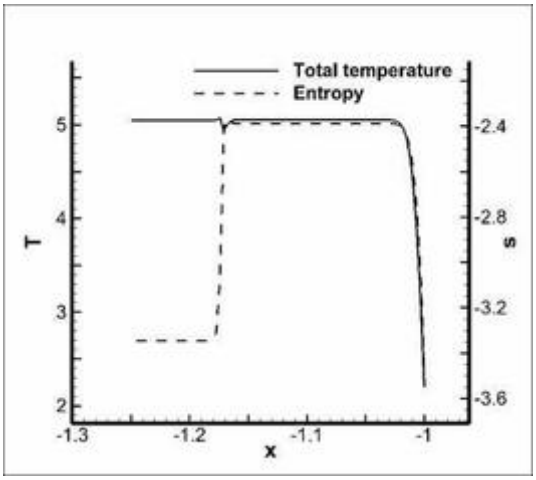

Fig.3 For isothermal wall the total temperature entropy along polar axis

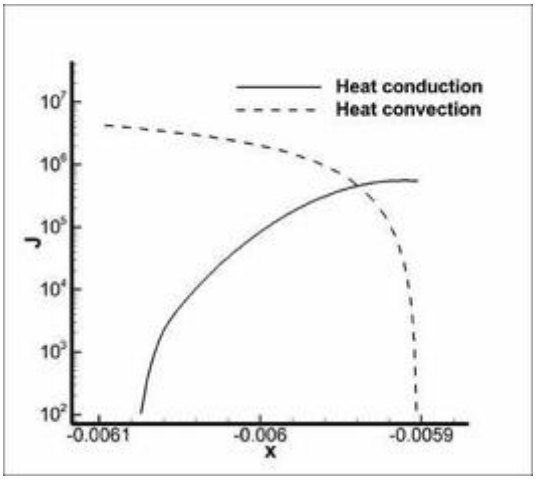

Fig.4 For isothermal wall the heat flux along polar axis

As well known that the thickness of the shock wave is a very small, and the velocity gradient and temperature gradient are high inside the shock wave. There is an assumption that when the fluid passed through the shock wave, it is an adiabatic irreversible process. For adiabatic wall condition the total temperature remains constant and the entropy remains constant before and after shock but a jump near the shock, shown in Fig.2. And the temperature computed at stagnation point is equivalent to the theoretical one. Whereas for isothermal wall conditions, the total temperature and entropy are decrease as near to the wall because of heat loss being transferred to the cold wall, shown in fig 3. It showed that the assumption is reasonable.

By analyzing the distributions of the flow field near the stagnation point, the distribution of heat flow with different rules in different boundary conditions has been found. For the adiabatic wall boundary conditions, from Figs.2 it is clear that the total temperature and entropy of gas remains constant; for isothermal wall boundary conditions, Figure 3 shows the total temperature was decreased near the stagnation point, entropy was diminished, meanwhile heat was given off, then, through comparative analysis the numerical value between total enthalpy difference and released heat we found that the error is 0.7%. After this, by comparing the numerical value of the heat flux in the stagnation point by Fourier heat conduction law between constant and variable specific heat ratio taken respectively, we found that the latter result is $5.2 \times 10^5 \mathrm{J/m^2 \cdot s}$, which lower than the former $5.5 \times 10^5 \mathrm{J/m^2 \cdot s}$. Figure 4 shows the heat flux along polar axis by Fourier heat conduction law and convective heat-transfer equation, we can see heat flux by convective heat-transfer equation have the same value at some point with the stagnation point by Fourier heat conduction law, for isothermal wall the temperature gradient is great in the stationary point, which make a difference for accurate calculation of stagnation point of heat flux, to avoid this, we manage to develop a method to get the stagnation point heat flux by virtue of calculating some item such as convective heat transfer.

CONCLUSIONS

Through numerical simulation for supersonic flow around blunt cone, and comparing the corresponding result from calculation with adiabatic wall and, the following conclusion can be made:

For isothermal wall conditions, the total temperature and entropy are decrease as near to the wall because of heat loss being transferred to the cold wall. Amount is in agreement with the decrement of total Enthalpy. The assumption that holds for an adiabatic irreversible process when the fluid through the shock wave. Considering the thermal physical properties have the impact on the stagnation point heat flux, the heat flux in the stagnation point with variable specific heats is below the value with constant specific heat.

Acknowlegement

This work was supported by the National Natural Science Foundation of China (11332007), the Tianjin Natural Science Foundation (15JCYBJC19500).

References

[1] Fay J A, Riddell F R. Theory of stagnation point heat transfer in dissociated air [J]. Journal Aero nautical Science, 1958, 25(2):73- 85.

[2] Kemp N H, Riddell F R. Heat Transfer to Satellite Vehicles Reenters the Atmosphere [J].Jet Propulsion, 1957, 27 (2).

[3] Lee JH, Rho OH .Accuracy of AUSM+ scheme in hypersonic blunt body flow calculation[R] .AIAA paper, 1998-1538, 1998.

NATURAL CONVECTION IN A CUBICAL ENCLOSURE WITH OPPOSING ACTIVE SECTORS

S Saravanan[a] & V P M Senthil Nayaki
UGC DRS Centre for Differential Equations and Fluid Dynamics, Department of Mathematics, Bharathiar University, Coimbatore 641 046, Tamil Nadu, India

Summary Natural convection in a cubical enclosure with differentially heated horizontal sectors mounted on its opposing lateral walls is investigated. We focus on the effect of different relative locations of these isothermally heated and cooled sectors. Finite volume method on a uniform staggered grid is used and the asymptotic steady state results are obtained from the transient governing equations. Among the different cases considered the highest heat transfer rate is obtained when the sectors are located in the Middle-Middle fashion. The possible mechanisms causing the three dimensional effects are highlighted.

INTRODUCTION

Buoyancy induced flows in differentially heated enclosures are of immense importance in many engineering applications such as electronic cooling devices, heat transfer through double glazed windows, etc. There has been considerable recent interest in such flows when the heating is done partially. The characteristics of heat dissipation due to partial heating are significantly different from those corresponding to complete heating. In fact the locations of the partially active regions play a crucial role in optimizing the resulting heat transfer. Several works in two dimensional differentially and partially heated cavities have been undertaken (for example see Valencia and Frederick [1]). However there is always a need of three dimensional simulations to understand the most realistic physical situation and to validate the results. Very few studies have discussed partial heating in three dimensional enclosures (see Frederick [2], Ishihara et al. [3] and Ben-Cheikh et al. [4]). In this work, we have made a numerical study of three dimensional natural convection induced by partially active sectors mounted at various locations on the opposing lateral walls of a cubical enclosure.

PROBLEM ANALYSIS

The physical configuration consists of a fluid filled cubical enclosure with sides of length L kept vertically. A Cartesian coordinate system having its origin at one of the bottom corners and aligned with the enclosure walls is used so that the gravity acts along the negative z axis. The sectors measuring half of the height of the enclosure lateral walls at y=0 and L are kept at a higher temperature T_h (heater) and a lower temperature T_c (cooler) respectively making the enclosure walls partially active. The remaining parts of the end walls and all other enclosure walls are insulated. The midheights of the heated and cooled sectors are fixed at z=L/4, L/2 and 3L/4 respectively from the bottom wall, corresponding to bottom, middle and top positions. Thus we consider an enclosure with six different heater-cooler locations, viz., (i) Bottom-Bottom (BB), (ii) Bottom-Top (BT), (iii) Top-Bottom (TB), (iv) Top-Top (TT), (v) Middle-Middle (MM) and (vi) Middle-Bottom (MB). This set up drives a convective roll, rising along the heater and sinking along the cooler and having its axis along the x direction. Hence the fluid flow at x=L/2 can be well approximated to be two dimensional.

The governing equations for the three dimensional, laminar and incompressible flow are those corresponding to conservations of mass, momentum and energy with the Boussinesq approximation. These equations were nondimensionalized suitably leading to the parameters Ra, the Raykeigh number and Pr, the Prandtl number. The appropriate boundary conditions are $\theta=1$ at the heater, $\theta=0$ at the cooler, $\partial\theta/\partial n=0$ at the insulated regions and U=V=W=0 at the enclosure walls. The average Nusselt number Nu_{av} is calculated at the surface of the heater and is defined as $(1/A_H)\iint Nu(X,Z)\,dX\,dZ$ with $Nu(X,Z)=\partial\theta/\partial Y$ and A_H representing the area of the heater.

A numerical solution was found through the finite volume method by employing a fully implicit time marching scheme. For this a staggered uniform grid was used to implement the SIMPLE algorithm [5]. The power law scheme was used to handle convective and diffusive terms. The resulting set of discretized equations was solved by the line-by-line Tri-Diagonal Matrix Algorithm (TDMA). The iterative procedure was terminated when some predefined condition was satisfied. A numerical code was written to implement the above iterative procedure. A good agreement between the results produced by this code and the earlier results was noticed. The 82^3 grid was used throughout as it produced grid independent results.

RESULTS

Computations were carried out for a wide range of parameters, viz., $10^3 \le Ra \le 10^7$ and $0.054 \le Pr \le 9$. However limited results for the BT and MM cases alone have been reported here for want of space. Figure 1(a,b) shows the isothermal surfaces within the enclosure for $Ra=10^5$ and Pr=9. One may notice the similarities between the overall isothermal surface distributions of the BT case and a fully differentially heated one. The entire enclosure is thermally more active in the MM case compared to the others. The velocity vectors are plotted in Fig. 1(c,d) at plane sections X=0.5 (midwidth) and X=0.05

[a]Corresponding author. Email:sshravan@lycos.com

(near lateral wall). Streamtraces are included in the midwidth section in order to highlight the flow pattern. A clockwise rotating flow pattern is observed, however with different strengths. In the BT case a comparatively higher contrast in velocities between the up and down flows near the active regions can be noticed. As Pr increases the simple unicellular flow pattern deforms into a stronger cell with two centers.

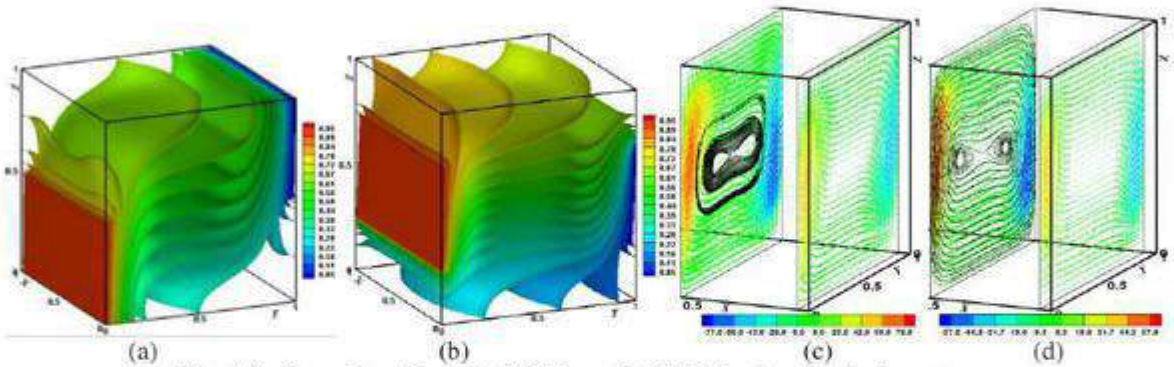

(a) (b) (c) (d)

Fig. 1 Isothermal surfaces ((a) BT Case, (b) MM Case) and velocity vectors ((c) BT Case, (d) MM Case) at $X = 0.05, 0.5$ for $Ra = 10^5$ and $Pr = 9$

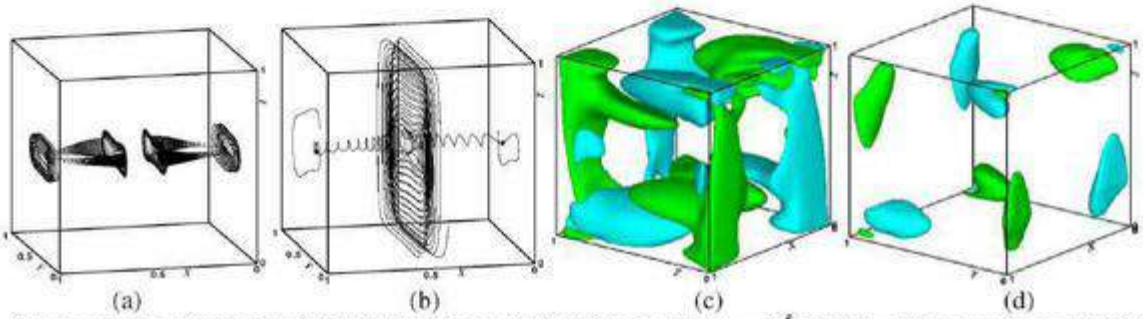

(a) (b) (c) (d)

Fig. 2 Streamtraces of velocity field ((a) BT Case, (b) MM Case) for $Ra = 10^5$ and $Pr = 9$; Iso-surfaces of U in the transverse direction ((a) BT Case, (b) MM Case) for $Ra = 10^7$ and $Pr = 0.71$ (Contour levels: -12 (blue), 12 (green))

In order to understand possible axial flows, streamtraces originating from the lateral walls are considered. They resembled toroidal patterns on both sides of the enclosure. In many cases these patterns extend well into the cavity even up to the cavity midwidth showing a high degree of penetration of disturbances (see Fig.2(a,b)). For those situations, the isosurfaces of U corresponding to the BT and MM cases are displayed in Fig. 2(c,d) when Pr=0.71 and Ra=10^7. The overall heat transfer rate across the enclosure was evaluated after the fluid flow reached a steady state. In general Nu_{av} assumed its highest value for the MM case and lowest value for the TB case. Moreover the computed average Nusselt numbers were found to obey a power law depending on the positions of the partially active sectors.

CONCLUSIONS

The study leads to the following important conclusions. Among the different cases considered the BT case exhibits highest velocities. The flow pattern of the MM case looks almost identical with that of the BT case but with weaker velocities. The enclosure is thermally more active in the MM case. The TB case makes the enclosure the most inactive one for higher Ra. Three dimensional effects come into picture only when convection is strong enough. For high Ra, the transverse component of velocity shows its presence over a larger volume in the BT case. The highest and lowest heat transfer rates are obtained for the MM and TB cases respectively.

References

[1] Valencia, A., Frederick, R.L.: Heat transfer in square cavities with partially active vertical walls. *Int. J. Heat Mass Transfer* **32**: 1567-1574,1989.

[2] Frederick, R. L.: Natural convection heat transfer in a cubical enclosure with two active sectors on one vertical wall. *Int. Comm. Heat Mass Transfer* **24**: 507-520, 1997.

[3] Ishihara, I., Fukui, T., Matsumoto, R.: Natural Convection in a vertical rectangular enclosure with symmetrically localized heating and cooling zones. *Int. J. Heat Fluid Flow* **23**: 366-372, 2002.

[4] Ben-Cheikh, N., Campo, A., Ouertatani, N., Lili, T.: Three dimensional study of heat and fluid flow of air and dielectric liquids filling containers partially heated from below and entirely cooled from above. *Int. Comm. Heat Mass Transfer* **37**: 449-456, 2010.

[5] Patankar, S. V.: Numerical Heat Transfer and Fluid Flow, New York 1980.

THREE-MODE HEAT TRANSFER SIMULATIONS IN PARALLELOGRAMMIC AIR ENCLOSURES

Thierry Villeneuve *, Matthieu Boudreau, and Guy Dumas

LMFN Laboratory, Department of Mechanical Engineering, Laval University, Quebec, Quebec, Canada

Summary The impact of the three heat transfer modes on the thermal diode potential of parallelogrammic air-filled enclosures stacked between two isothermal vertical walls is assessed for different parametric cases. Focusing on a single enclosure in this paper, it is found that the thermal diode potential significantly decreases when conduction and radiation are taken into account in comparison with the classical problem of the pure-convection cavity.

INTRODUCTION AND PHYSICAL CASE

Natural convection in closed cavities has been investigated in numerous occasions over the past decades [1, 2]. More specifically, several papers have dealt with the impact of the inclination angle of the upper and lower walls of the cavity (ϕ) which was shown to strongly affect the convection heat transfer [1, 3]. Because of the density variations resulting from the temperature distribution, the convective motion of the fluid is much more vigorous when the vertical hot wall is located *below* the cold wall (positive ϕ) while a hot wall *higher* than the cold one (negative ϕ) can even lead to stratification in the cavity (Figure 1) and, ultimately, to a purely conductive heat transfer in a stagnant fluid. The fact that the convective heat transfer may be much higher in a direction than the other has suggested that such a cavity could be used as a thermal diode. Due to this attractive behavior, the differentially heated inclined cavity became the matter of several studies [3]. However, most of these studies have treated the case of a single cavity with adiabatic upper and lower walls, considering exclusively the convection heat transfer. Only a few studies have considered radiation and conduction even if it has been shown that under certain conditions, they can be quite significant [4, 5].

The present study considers the combined convection, conduction and radiation heat transfer in an enclosure composed of an air-filled cavity between two half-partition walls located above and below the cavity, as shown in Figure 2. The energy transfer is generated by the vertical walls which are maintained isothermal at specified hot (T_H) and cold (T_C) temperatures. The upper and lower walls of the enclosures are allowed to be inclined by an angle (ϕ) ranging from $\circ\, 60°$ to $60°$ with respect to the horizontal and they are considered adiabatic when there is no conduction involved. For cases with conduction, the solid partition walls added to the cavity are allowed to have two different thicknesses (t) and two different thermal conductivities (k_s). Moreover, all four inner surfaces of the cavity may radiate and three different emissivities (ϵ) are considered. As the inclination angle varies, the height (h) of the cavity and the distance between the hot and cold walls (L) remain equal to each other, leading to an aspect ratio of 1. The Rayleigh number considered is $5 \cdot 10^5$ (which corresponds to a temperature difference of about 30°C across a 6 cm wide cavity) and the Prandtl number is 0.71. In these conditions, the convective flow may be assumed laminar.

The physics at play is studied through steady, two-dimensional numerical simulations using ANSYS FLUENT [6]. The Boussinesq approximation is used, which means that the physical properties of the fluid are taken as constant, except for density variations in the buoyancy term. To compute the radiation heat transfer, a *Surface-to-Surface* model is used, meaning that the surfaces are gray and diffuse and that the air is a nonparticipating medium.

To compare the heat flow (q'') between different parametric cases, Nusselt numbers are defined. They are evaluated using a reference heat flux which is equivalent to a conduction heat transfer in the fluid as described in Equation (1). Moreover, to quantify the thermal diode potential for the different investigated cases, the diode parameter ξ is defined in Equation (2).

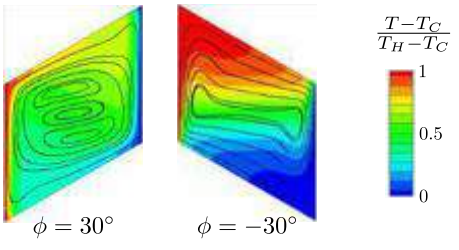

Figure 1: Isosurfaces of temperature and streamlines for air-filled cavities with adiabatic upper and lower walls and isothermal vertical walls (the hot wall is located on the left).

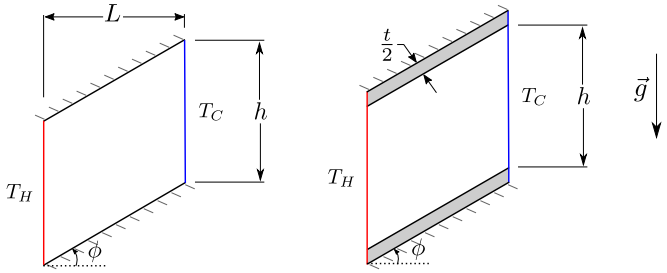

Figure 2: Adiabatic cavity without partition walls (left) and adiabatic cavity with upper and lower partition walls (right).

*Corresponding author. Email: thierry.villeneuve.2@ulaval.ca

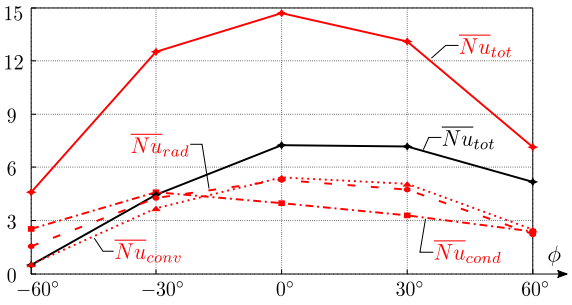

Figure 3: Nusselt numbers as a function of the inclination angle of the enclosure for a case without partition walls and without radiation (black curve) and for a case with $^{t}/_{h} = 0.1$, $^{k_s}/_{k_f} = 10$ and $\epsilon = 0.9$ (red curves).

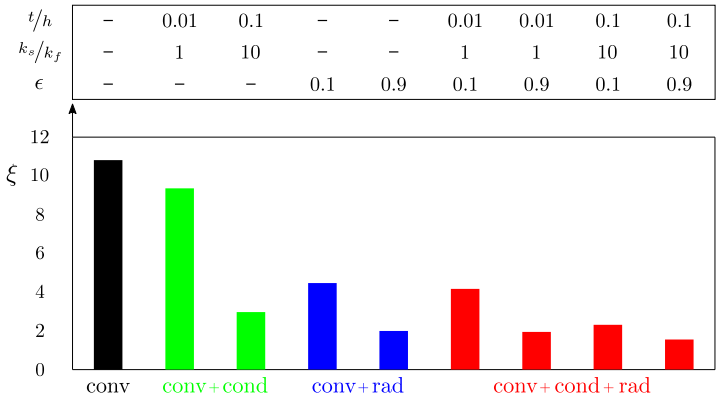

Figure 4: Diode parameter ξ for different parametric cases.

$$\overline{Nu} = \frac{q''}{q''_{ref}} = \frac{q''}{k_f \cdot (T_H - T_C)/L} \qquad (1)$$

$$\xi = \frac{\overline{Nu}_{tot}\big|_{\phi=60°}}{\overline{Nu}_{tot}\big|_{\phi=-60°}} \qquad (2)$$

RESULTS AND CONCLUSION

The reference case is the cavity with adiabatic upper and lower walls (without solid partition walls and without radiation), in which the only heat transfer mode involved is convection. As shown in Figure 3 (black curve), a negative inclination angle leads to a reduction of the heat transfer in the cavity compared to the $\phi = 0$ case. The high asymmetry of the curve qualitatively demonstrates the thermal diode potential that is discussed in other works [1, 3]. For this specific configuration, the thermal diode potential is $\xi = 10.8$.

In order to assess the impact of the conduction heat transfer, solid partition walls are added to the pure-convection cavity discussed above. Obviously, taking conduction into account results in an increase of the total Nusselt number in the enclosure. Most importantly, it is interesting to note that conduction tends to decrease the thermal diode potential, as shown in Figure 4 (green bars). For very thin partition walls having a low conductivity, the value of ξ is slightly reduced. However, for thicker, but still thin, partition walls having a higher conductivity, the effect is much more accentuated.

The impact of radiation on the thermal diode potential is considered using an adiabatic cavity without partition walls where the inner surfaces have nonzero value of emissivity. It is found that the effect of radiation is even more important than conduction. Indeed, as shown in Figure 4 (blue bars), for a surface emissivity as low as 0.1, the thermal diode potential falls from 10.8 to 4.4, with all other parameters remaining constant.

In order to observe the combined effect of the three heat transfer modes on the thermal diode potential, an enclosure with solid partition walls and with radiation is considered. As shown by the red curves in Figure 3, for a case with $^{t}/_{h} = 0.1$, $^{k_s}/_{k_f} = 10$ and $\epsilon = 0.9$, the three heat transfer modes each account approximately for the same fraction of the total Nusselt number. Since the asymmetry of the total Nusselt number curve comes mainly from the convection heat transfer, it is no surprise that the thermal diode potential is strongly reduced (from 10.8 to around 2) when the three-mode problem is considered (Figure 4).

In conclusion, the conjugate heat transfer through a parallelogrammic air-filled enclosure has been investigated. It has been shown that the thermal diode potential is significantly weakened if the three heat transfer modes are considered. Thus, in order to accurately investigate the physics of the problem, one must consider the three heat transfer modes combined since conduction and radiation are not negligible. Work in progress is devoted to the analysis of the interaction between each of the heat transfer modes and to the thermal diode potential in an infinite stack of enclosures.

References

[1] Nguyen D.N., Dumas G. & Dhatt G. Convection and conduction heat transfer in cavities-composed walls, *Proc. Fourth Int. Conf. on Num. Methods in Thermal Problems*, Vol. 1, Sect. 4.7, pp. 412-423, Swansea, U.K., July 1985.

[2] De Vahl Davis G. & Jones, I. P. Natural convection in a square cavity : a comparison exercise, *Int. J. Num. Meth. Fluids* 3 (1983) 227-248.

[3] Bairi A., Zarco-Pernia E. & Garcia de Maria J.-M. A review on natural convection in enclosures for engineering applications. The particular case of parallelogrammic cavity, *Applied Thermal Engineering* 63 (2014) 304-322.

[4] Bairi A., Laraqi n. & Garcia de Maria J.-M. Importance of radiative heat exchange in 2D closed diode cavities applied to solar collectors and building, *Int. J. Sustain. Energy* 24 (2005) 33-44.

[5] Costa V.A.F., Oliveira M.S.A. & Sousa A.C.M. Laminar natural convection in a vertical stack of parallelogrammic partial enclosures with variable geometry, *Int. J. Heat Mass Transfer* 48 (2005) 779-792.

[6] ANSYS Inc., Ansys fluent 14.5 users guide. 2013. www.ansys.com.

ON NON-OBERBECK- BOUSSINESQ EFFECTS IN CESSATION-LED REVERSALS IN RAYLEIGH-BÉNARD CONVECTION

Shu-Ning Xia, Zhen-Hua Wan[a], Shuang Liu & De-Jun Sun
Department of Modern Mechanics, University of Science and Technology of China, Hefei, 230027, China

Summary The non-Oberbeck-Boussinesq (NOB) effects on flow reversals in two-dimensional (2D) Rayleigh-Bénard convection (RBC) are studied by direct numerical simulation. The Prandtl number is fixed to 0.71. The flow reversals are triggered by NOB effects when Rayleigh number (Ra) is approximately in the range of $10^5 \leq Ra \leq 1.5 \times 10^7$. Once the NOB effects are included, the flow pattern of only one dominant roll, becomes unstable and turns into its symmetric counterpart while the flow circulates clockwise and counter-clockwise in turn, i.e. reversal. The parameter range where flow reversals occur is considerably affected by temperature differential ε. It is found the flow reversals are led by the growth in size of the single cold corner roll, and two kinds of physical mechanisms are identified to be responsible for the corner roll's growth: baroclinicity and asymmetry of buoyancy force.

INTRODUCTION

Cessation-led reversal in which the LSC sometimes stops and subsequently restarts randomly in a different direction has been exhibited by many experiments and numerical simulations [Brown & Ahlers, 2006; Sugiyama *et. al.*, 2010; Chandra & Verma, 2013; Podvin & Sergent, 2015 *and references therein*]. The influence of NOB effects on flow dynamics and heat transfer in turbulent thermal convection has been extensively studied in recent years [Ahlers *et. al*., 2008; Sameen *et. al.*, 2009; Sugiyamma *et. al.*, 2009; Horn *et. al.*, 2013 *and references therein*]. Implicitly or explicitly, all the aforementioned work shows no reversals when NOB effects are considered. In this study, considering NOB effects for a perfect gas, we show the scenario of flow reversals in a 2D RBC and corresponding physical mechanisms from the perspective of vortex dynamics are analysed as well.

GOVERNING EQUATIONS

The governing equations under low Mach number limit of compressible Navier-Stokes (NS) equations are statements of conservation of mass, momentum and internal energy added by a state equation of a prefect gas. The non-dimensional low-Mach-number NS equations are cast in the form of Cartesian tensor

$$\frac{\partial \rho}{\partial t} + \left(\rho u_j\right)_j = 0, \qquad p = \rho T$$

$$\frac{\partial \rho u_i}{\partial t} + \left(\rho u_i u_j\right)_{,j} + \pi_{,i} = \left(\frac{Pr}{Ra}\right)^{0.5} \tau_{ij,j} + \frac{1}{2\epsilon}(\rho - 1) n_i$$

$$\rho c_p \left(\frac{\partial T}{\partial t} + u_j u_{i,j}\right) = \left(\frac{1}{RaPr}\right)^{0.5} \left(kT_{,j}\right)_{,j} + \Gamma \frac{dp}{dt}$$

Here, the comma notation for spatial derivatives is adopted, for example, $\pi_{,i} = \partial_i \pi$. π is hydrodynamic pressure. $\Gamma = (\gamma - 1)/\gamma$ measures the resilience of the fluid. The flow system is governed by three dimensionless parameters which are temperature differential $\epsilon = \Delta\hat{T}/2\,\Delta\hat{T}_0$, Rayleigh number $Ra = \Delta\hat{T}\hat{c}_p\hat{\rho}^2\hat{g}\hat{L}^3\ \hat{}_0\hat{\mu}\hat{k}$ and Prandtl number $Pr = \hat{c}_p\hat{\mu}/\hat{k} = 0.71$.

RESULTS AND DISCUSSION

Figure 1 shows plots of *Nu* as a function of *Ra* for various temperature differentials. In general, two kinds of flow patterns are identified, one is P_{11} and the other is P_{12}, where the number in subscript represents the number of rolls in the (x, y) directions, respectively. For P_{11}, this flow pattern is unchanged in most of times within the range of $10^6 \leq \mathrm{Ra} \leq 10^7$. Figure 1(a) shows, under Oberbeck-Boussinesq (OB) approximation, P_{11} remains unchanged in the range of $10^5 \leq \mathrm{Ra} \leq 5 \times 10^7$ and no flow reversal is found. When ϵ is increased to 0.2, seen in figure 1(b), in the range of $10^6 < Ra \leq 9.25 \times 10^6$ P_{11} becomes unstable, in the range of $9.5 \times 10^6 \leq \mathrm{Ra} \leq 1.1 \times 10^7$ P_{11} can turn into its symmetric pattern and back, with the flow circulating clockwise and counter-clockwise in turn with long periods, i.e. flow reversals occur, represented by the symbols '+'. As shown in figure 1(b)-(d), grey dashed lines represent that the flows are unstable due to the growth of the cold corner roll and which would all turn into pattern P_{12} finally indicated by green solid symbols. It is conjectured that sometimes, in the phase space, the trajectory of a pair of P_{11} passes by the stable pattern P_{12} and then attracted by the stationary point or limiting cycle of P_{12}. Moreover, it is easy to find that multiple solutions co-exist in the most computing range and hysteresis phenomena are observed as $0.2 \leq \epsilon \leq 0.6$. In figure 1(d), it is noteworthy that with strong NOB effects two symmetric patterns P_{11} could switch back

[a] Corresponding author. Email: wanzh@ustc.edu.cn

and forth caused by the cold corner roll's growth between $\mathrm{Ra} = 3 \times 10^6$ and 4×10^6, with an unstable intermediate pattern P_{12}. In short, as $\epsilon \geq 0.2$, in a wide range of Ra, flow pattern P_{11} is unstable because of the corner roll's growth and flow reversals emerge. Interestingly, due to the co-existed flow pattern P_{12}, the flow reversal sometimes will be broken ending up with flow pattern P_{12}.

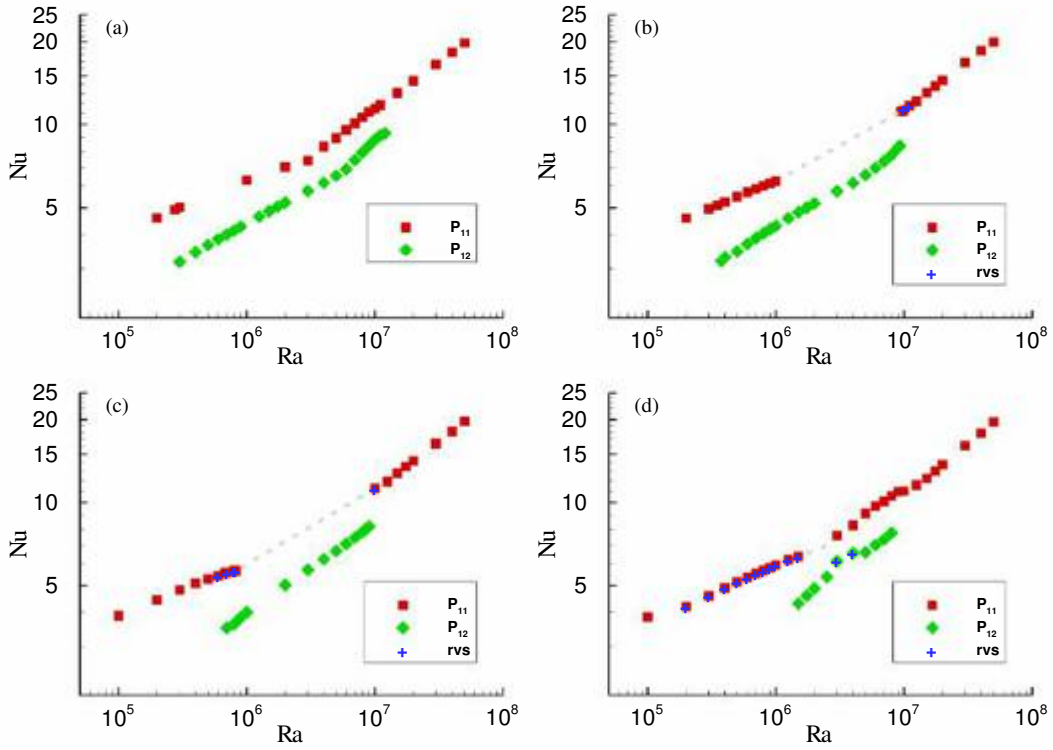

Fig 1. Log-log plots of Nu as a function of Ra for various temperature differentials. (a) under OB approximation; (b) with weak NOB effects, i.e. $\varepsilon = 0.2$; (c) with moderate NOB effects, i.e. $\varepsilon = 0.4$; (d) with strong NOB effects, i.e. $\varepsilon = 0.6$. Blue symbols '+' denote flow reversals occur continuously, while the grey dashed lines denote that there are no flow reversals whereas the growth of corner roll exists.

Intuitively, it is the single cold corner roll's growth in size that is responsible for the flow reversals. In this study, we particularly study the flow reversals from the perspective of vortex dynamics. The results show that the synergy of the baroclinicity and asymmetry of buoyancy force caused by NOB effects could reasonably explains why the single corner roll grows and eventually replaces the LSC, resulting in flow reversals.

This work is supported by National Natural Science Foundation of China (11402262, 11232011, and 11572314), the Fundamental Research Funds for the Central Universities.

References

[1] Ahlers G, Calzavarini E, Araujo FF, Funfschilling D, Grossmann S, Lohse D, Sugiyama K.: Non-Oberbeck-Boussinesq effects in turbulent thermal convection in ethane close to the critical point. Physical Review E. 77(4):046302, 2008

[2] Brown E, Ahlers G. Rotations and cessations of the large-scale circulation in turbulent Rayleigh–Bénard convection. Journal of Fluid Mechanics. 568:351-86, 2006.

[3] Chandra M, Verma MK.: Flow reversals in turbulent convection via vortex reconnections. Physical review letters. 14;110(11):114503, 2013

[4] Horn S, Shishkina O, Wagner C.: On non-Oberbeck–Boussinesq effects in three-dimensional Rayleigh–Bénard convection in glycerol. Journal of Fluid Mechanics. 724:175-202, 2013

[5] Podvin B, Sergent A.: A large-scale investigation of wind reversal in a square Rayleigh–Bénard cell. Journal of Fluid Mechanics. 766:172-201, 2015.

[6] Sameen A, Verzicco R, Sreenivasan KR.: Specific roles of fluid properties in non-Boussinesq thermal convection at the Rayleigh number of 2×10^8. Europhysics Letters. 86(1):14006, 2009.

[7] Sugiyama K, Calzavarini E, Grossmann S, Lohse D.: Flow organization in two-dimensional non-Oberbeck–Boussinesq Rayleigh–Bénard convection in water. Journal of Fluid Mechanics. 637:105-35, 2009

[8] Sugiyama K, Ni R, Stevens RJ, Chan TS, Zhou SQ, Xi HD, Sun C, Grossmann S, Xia KQ, Lohse D.: Flow reversals in thermally driven turbulence. Physical review letters. 105(3):034503, 2010.

SUBGRID-SCALE MODELING OF RELAMINARIZING MIXED CONVECTION IN A VERTICAL CHANNEL

Tim Wetzel [*1, 2] and Claus Wagner[1, 2]
[1]*Institute of Aerodynamics and Flow Technology, German Aerospace Center (DLR), Göttingen, Germany*
[2]*Institute of Thermodynamics and Fluid Mechanics, Technische Universität Ilmenau, Ilmenau, Germany*

Summary Large Eddy Simulations using an eddy-viscosity and a scale similarity subgrid-scale model are performed in comparison with Direct Numerical Simulations in order to assess the models' capabilities with respect to relaminarization effects. The considered case of mixed convection in a vertical channel is adopted from Kasagi & Nishimura [1] and shows distinct features in the flow close to the heated and cooled channel walls caused by buoyancy. An analysis of the development of coherent structures is performed in order to discern the models with regard to relaminarization effects occuring on the heated channel wall as observed in DNS.

INTRODUCTION

It is of great interest in many engineering applications to simulate turbulent mixed convection, i.e. the combination of forced and natural convection, at high Rayleigh and Reynolds numbers. Since simulations of such highly turbulent flows are still not within reach for Direct Numerical Simulations (DNS), reliable turbulence models are needed. Research on Large Eddy Simulations (LES) has yielded a variety of modeling approaches for the approximation of subgrid-scale (SGS) stresses for the momentum equation. Although, only a few of them are applicable to buoyancy driven flows. One turbulence model for the heat flux vector in the filtered Navier-Stokes equations (NSE) has been proposed by Peng & Davidson [2]. This model is formulated in analogy to an eddy-viscosity model for the SGS stresses in the momentum equation. Additionally, in [4] a dynamic scale similarity model was developed to approximate the turbulent heat transport in Rayleigh-Bènard convection. In the present study, both approaches are applied in LES of mixed convection in a vertical channel in comparison to DNS performed with the same finite-volume method and to the spectral DNS by Kasagi & Nishumura [1]. The objective is to benchmark these different dynamic modeling approaches and to analyse their potentials with respect to the prediction of flow relaminarization in mixed convection.

COMPUTATIONAL DETAILS

A vertical channel flow with differentially heated walls driven by an upwards pressure gradient at friction Reynolds number based on the channel height and the friction velocity $Re_\tau = 291$ and a Grashof number of $Gr = 9.6 \cdot 10^5$ is considered. In the LES, the filtered incompressible Navier-Stokes equations (NSE) are solved together with the Boussinesq approximation. A finite volume method based on a fourth-order spatial interpolation technique adapted from Feldmann & Wagner [3] in combination with a second-order Euler-leapfrog scheme for the temporal integration and Chorin's projection method for the velocity – pressure coupling is employed. A grid with equidistantly distributed nodes in the streamwise and spanwise directions is used. The wall-normal grid resolution is non-uniform in order to account for the high velocity and temperature gradients close to the walls. The channel domain extends $L_x = 2.5\pi\delta$ in streamwise direction and $L_y = \pi\delta$ in spanwise direction, with δ being the channel height. The grid resolution for the DNS is sufficiently high with a grid spacing in wall units of $\Delta_x^+ = 4.4639$, $\Delta_y^+ = 3.5711$ in streamwise and spanwise directions, respectively. The spacing in wall-normal direction is provided by a hyperbolic tangent function leading to $0.258 < \Delta_z^+ < 4.453$.

ANALYSIS

Figure 1 shows the mean streamwise velocity profile obtained in the DNS with the finite volume method in comparison with the data by Kasagi & Nishimura [1]. With an integral deviation of 1.288% with regard to the mean velocity, the finite volume DNS is deemed reliable as reference for the assessment of SGS models in the present study. The mean velocity profile is asymmetric about the channel centerline with a maximum close to the heated channel wall. This indicates that the friction Reynolds number at the heated wall is higher than at the cooled wall. Figure 2 shows profiles of the rms velocity fluctuations, which are generally speaking higher close to the cooled than to the heated wall. This is unexpected and in contradiction to the eddy-viscosity ansatz which assumes higher fluctuations on the side with higher gradients. This counter-intuitive behaviour is therefore interpreted as the result of buoyancy induced flow relaminarization close to the heated wall. Figure 3 shows the instantaneous streamwise velocity fluctuations u' at $z^+ = 14.5$ on the left and $z^+ = 276.5$ on the right. The velocity fluctuations are organized in streaky structures and exhibit a more uniform behaviour close to the heated wall (left picture)

*Corresponding author. Email: tim.wetzel@dlr.de

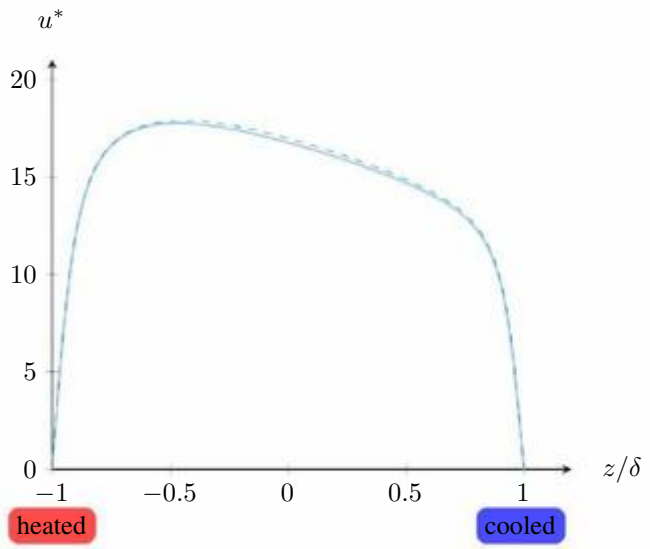

Figure 1: Mean streamwise velocity profile (solid line: DNS, dashed line: Kasagi & Nishimura [1])

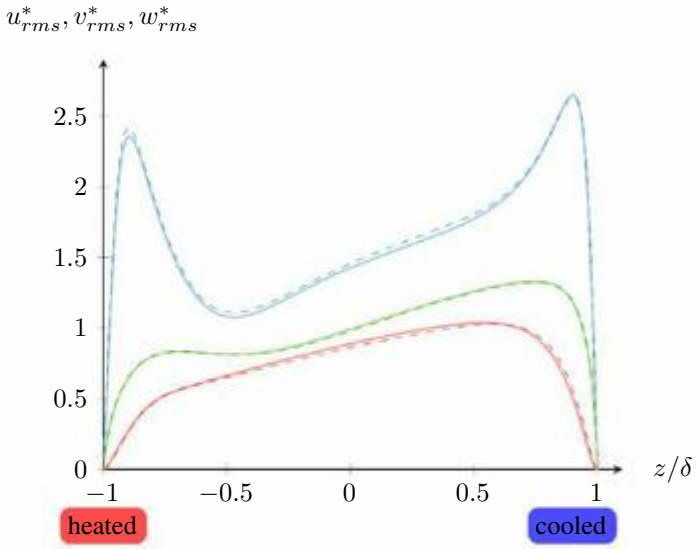

Figure 2: Profiles of rms velocity fluctuations (solid lines: DNS, dashed lines: Kasagi & Nishimura [1]; top: u_{rms}, middle: v_{rms}, bottom: w_{rms})

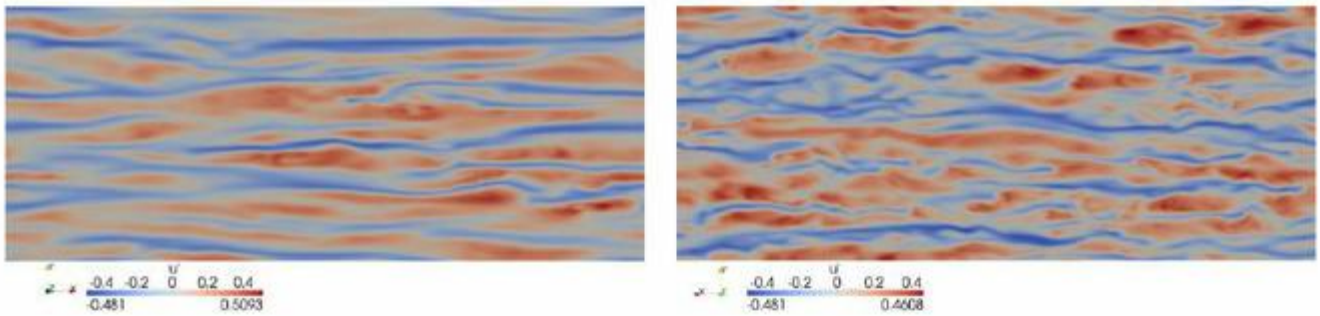

Figure 3: Coulour contours of the fluctuating streamwise velocity at $z^+ = 14.5$ (left) and $z^+ = 276.5$ (right) showing streaks.

while they are much more disrupted close to the cooled wall (right picture). This is another indication of the relaminarization effect, which is also reflected the instanteous flow field. Thus, the here considered case is perfectly suited for studying the performance of SGS models in case of flow relaminarization.

OUTLOOK

Eddy-viscosity SGS models are known to be dissipative in comparison to scale similarity models. Thus, it is expected that LES based on eddy viscosity SGS models will predict a faster decay of the aforementioned streaky structures. This hypothesis will be examined in detail and presented at the conference.

References

[1] Kasagi N., Nishimura M.: Direct numerical simulation of combined forced and natural turbulent convection in a vertical plane channel. Int. J. Heat Fluid Flow 18:88-99, 1997.

[2] Peng S.H., Davidson L.: On a subgrid-scale model for large eddy simulation of turbulent thermal flow. Int. J. Heat Mass Transfer 45:1393-1405, 2002.

[3] Feldmann D., Wagner C.: Direct numerical simulation of fully developed turbulent and oscillatory pipe flows at Re_tau = 1440. J. Turbulence 13/32:1-28, 2012.

[4] Czarnota T., Wetzel T., Wagner C.: Large eddy simulation of turbulent thermal convection using different subgrid-scale models. In print in Notes on Numerical Fluid Mechanics and Multidisciplinary Results, Contributions to the 19th STAB/DGLR Symposium in Munich, 2014.

LARGE-SCALE CIRCULATIONS IN AN OSCILLATING THERMAL CONVECTION

Yue Xiao, Jianjun Tao[a)], Xue Ma
CAPT-HEDPS, SKLTCS, Department of Mechanics and Aerospace Engineering, College of Engineering, Peking University, China

Summary The interaction between large-scale circulations and unstable thermal plumes of air in a horizontally partitioned rectangular enclosure is investigated numerically. Both a hot and a cold plume flows originated at the central vent in the partition are formed when the wall temperature difference (ΔT) of the upper and the lower parts of the enclosure keeps a constant. When ΔT is larger than a threshold value, the hot plume is unstable to a small-scale sinuous wave mode with high frequency, while the two symmetric convection circulations in the lower cavity are taken place by a large-scale circulation, whose strength varies with a low frequency. With the increase of ΔT, different spatiotemporal evolution scenarios are revealed, and it is concluded that the large-scale low-frequency circulations play important roles at high temperature differences.

INTRODUCTION

The buoyancy-induced flow through a vent in a horizontal partition between two cavities is a basic model for many applications in daily life and industries (e.g. nature ventilation, cooling of electronic units and fire dynamics). The temporal evolution of fluid with different initial temperatures confined to separate adiabatic enclosures has been extensively studied [1, 2, 3], and several flow regimes are revealed, i.e. the conduction, the counter-current, and the oscillatory flow regimes. Recently, the bidirectional flow exchange between the enclosures was simulated with a Non-Boussinesq variable density approach [4]. In most previous studies, the walls are treated as adiabatic boundaries, and hence all phenomena are transient and the convection will decay to a static state eventually.

In this paper, the enclosure walls are assumed to be isothermal except the vent, whose walls are still adiabatic. Consequently, the thermal convection always sustains and then the model becomes convenient to study the interaction among different flow structures.

PHYSICAL MODEL AND RESULTS

We consider the air convection in two square cavities with the same length of 0.2 meter, connected with a vent of 10 mm wide and 3mm high (Fig.1). The wall temperature of the upper cavity is set as 293K, which is smaller than that of the lower cavity with a constant temperature difference ΔT. Air is treated as an ideal gas, and the temperature dependences of its physical parameters follow NIST database. The two-dimensional flow field is solved with FLUENT and several evolution scenarios of flow patterns are found with the increase of the temperature difference as follows.

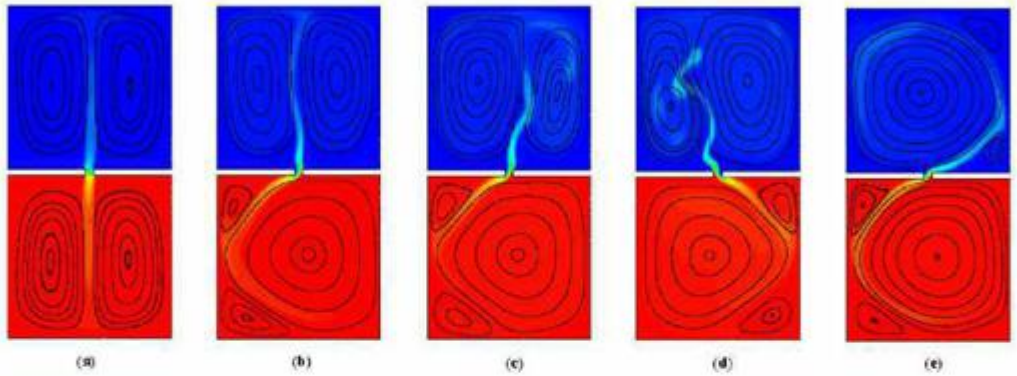

Figure 1 Transient streamlines and contour of temperature at (a) ΔT=43K, (b) ΔT=45K, (c) ΔT=50K, (d) ΔT=60K and (e) ΔT=70K.

(a)The Conduction Regime ($\Delta T \leq 43K$)

For small ΔT, there is almost no flow across the vent, as the buoyancy force is not strong enough to overcome the viscous force in the vent. All the heat is transferred solely by conduction for this regime. In another word, the vent acts like a heater plate for the upper cavity, which is similar to the Bénard convection problem (Fig. 1a). The flow is steady and each cavity has two roll cells, which are symmetric about the vertical middle line. The flow patterns in this regime are similar as those observed previously for adiabatic walls.

(b) First Symmetry Breaking and the Bi-Oscillation Convection (ΔT=45K)

[a)] Corresponding author. Email: jjtao@pku.edu.cn.

When the temperature difference is increased to 45K, the symmetric roll cells in the lower cavity are taken place by a large and asymmetric circulation, while the hot plume becomes unstable to a sinuous wave mode with a wave length about one-sixth of the circulation scale (Fig.1b). The time series of temperature measured at the vent centre is used to calculate the power spectrum as shown in Fig.2 (a), where 0.584Hz and its harmonics correspond to the oscillating hot plume. The two convection cells in the upper cavity oscillate with the plume and keep statistically symmetric. It is worth to note that there is another peak with a low frequency 0.131Hz in the spectrum, which is caused by the strength oscillation of the large-scale circulation in the lower cavity. Therefore, this flow phenomenon is called as bi-oscillation convection and to our knowledge hasn't been reported before.

(c) Second Symmetry Breaking (ΔT=50K)

As shown in Fig.1(c), the waving hot plume tilts at ΔT=50K, and the statistically symmetric cells in the upper cavity become asymmetric. In the meantime, the superharmonics of the high-frequency oscillation are strengthened (Fig.2b).

(d) Tri-Oscillation Convection (ΔT=60K)

As ΔT is increased to 60K, a new phenomenon is observed. By carefully examining the simulation movies, we find that the tilt angle of the hot plume varies very slowly and quasi-periodically, leading to the third peak with a frequency of 0.046Hz in the spectrum (Fig.2c). The flow field as shown in Fig.1(d) is governed by three oscillation mechanisms, the hot plume wave, the plume-angle oscillation and the strength oscillation of the bottom circulation, and hence is named as the tri-oscillation convection.

(e) Counter-Current Convection

When the temperature difference is increased further (ΔT=70K), the two cells in the upper cavity are replaced by a large-scale circulation rotating in the same direction as the bottom one. Consequently, counter currents occur at the vent (Fig.1e), and the oscillating manner of the whole flow field is dominated by these large-scale circulations (Fig.2d). In addition, both the high-frequency wave and the tilt-angle oscillation of the hot plume are suppressed by the circulation in the upper cavity.

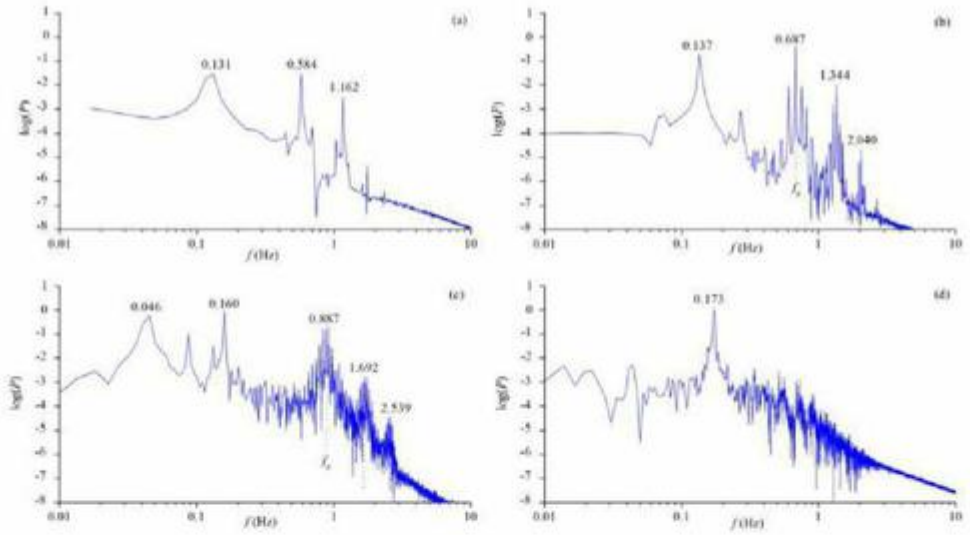

Figure 2 Power spectra of temperature measured at the vent centre for (a) ΔT=45K, (b) ΔT=50K, (c)ΔT=60K and (d)ΔT=70K.

CONCLUSIONS

By numerically simulating the thermal convection in a horizontally partitioned enclosure, a sequence of symmetry breaking is illustrated, and several new phenomena (the bi-oscillation convection and the tri-oscillation convection) are revealed. The interaction mechanisms between the small-scale plume wave and the large-scale circulations shown in this paper are expected to be helpful in the understanding of the large-scale motions in turbulent convection flows.

References

[1] Kumar R., Sleiti A. & Kapat J.: Unsteady laminar buoyant flow through rectangular vents in large enclosures. *J. Thermophys. Heat Transfer* **20**, 276,2006

[2] Mishra A.A., Hasan N., Sanghi S. & Kumar R.: Two-dimensional buoyancy driven thermal mixing in a horizontally partitioned adiabatic enclosure. *Phys. Fluid* **20**, 063601, 2008.

[3] Ahmad K.: Transient flow of air through rectangular vents in a horizontal partition. *HVAC&R Research* **15**, 1145-1163, 2009.

[4] R. Harish.: Numerical investigation of instability patterns and nonlinear buoyant exchange flow between enclosures by variable density approach. *Computers & Fluids* **96**, 276–287, 2014.

NUMERICAL SIMULATION OF A NEAR FIELD PLUME FROM A DUCT

Manman Qiao, Feng Xu[a)]
School of Civil Engineering, Beijing Jiaotong University, Beijing 100044, China

Abstract Plumes are present in nature and industry. In this study, a near field plume rising from a duct is investigated using direct numerical simulation. The results show that the development of the near field plume may be identified to three stages: a starting stage, a transitional stage and a fully developed stage. The transient features in the development of the near field plume are characterized. Further, the dependence on the Rayleigh number of heat transfer of the near filed plume is quantified.

INTRODUCTION

Buoyant plume may be easily found in nature and industry. Industrial activities often result in a great number of pollutants discharged into the atmosphere and hydrosphere such as rivers, lakes and ocean in the form of jets or plumes [1]. A plume is fluid motion which is driven purely by buoyancy derived from density inhomogeneity and supplied at its heating origin. The fact that plumes may originate from a point or a line source, can have a sustained or 'one-shot' heat input (thermals), can be steady (the stem) or starting (the cap), and can be turbulent or laminar. A great number of corresponding substantial research progresses have been reviewed in the literature [2-3].

NUMERICAL PRODECURES

The 2D numerical method was adopted to simulate the near field plume rising from a duct. Figure 1 presents the schematic of the computational domain of 12×24 and boundary conditions. The inlet boundary in the duct is defined as pressure-inlet with a temperature difference between the inlet and the environment (ΔT). The sidewalls of the duct are assumed as adiabatic and no slips. The remaining boundaries are specified as open boundaries where the normal gradients of velocity and temperature are zero.

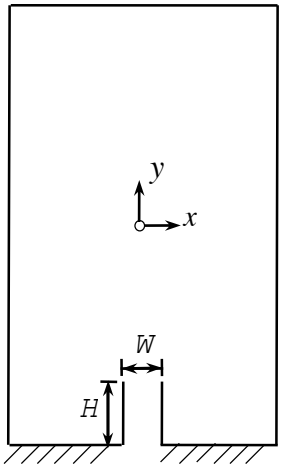

Fig. 1. Schematic of computational domain and boundary conditions

The transient flow is governed by Navier-Stokes and energy equations with the Boussinesq approximation, which were implicitly solved using a finite-volume algorithm. The convective term was discretized using the QUICK scheme and the pressure-velocity coupling was implemented using the SIMPLE algorithm. The time term was segregated using a first-order implicit scheme. Under consideration of the computing time and accuracy the grid system of 400 (H) × 700 (L) and time step of $\Delta t = 0.19$ were adopted in the subsequent calculations after the grid and time step dependence test.

TRANSIENT FEATURE OF THE NEAR FILE PLUME FROM THE DUCT

For the purpose of obtaining insights into the development and transient feature of the plume rising from the duct, a number of numerical simulations for different Rayleigh numbers were performed in this study.

[a)] Corresponding author. Email: fxu@bjtu.edu.cn.

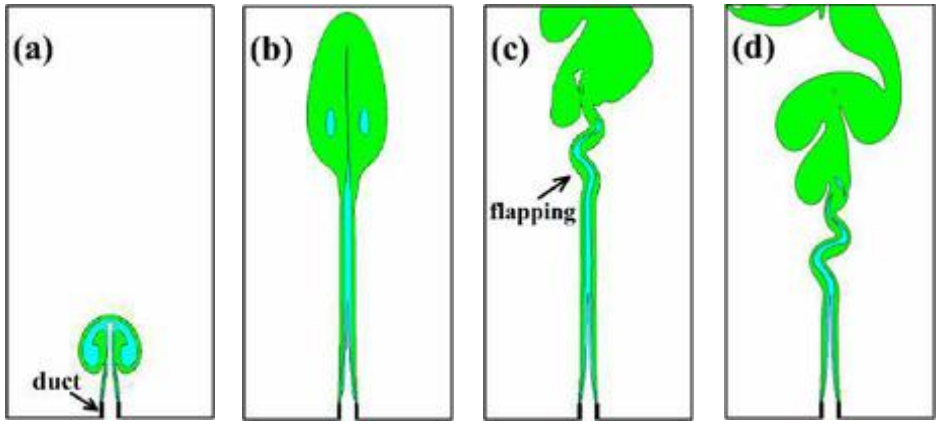

Fig. 2 Isotherms (contours from 0.05 to 0.9 with an interval of 0.5) of the plume rising from the duct for Ra = 10^5, Pr = 0.7 and A = 1. (a) at t = 72. (b) at t = 126. (c) at t = 190. (d) at t = 1000.

Figure 2 shows the development of the near field plume from the duct. The thermal boundary layer appears above the intlet boundary after start-up and then the plume forms. The plume front rises from the duct and a clearly mushroom-like cap results, as seen in Fig. 2(a). As the plume front moves downstream, the mushroom cap becomes larger and a stem or trailing plume appears (see Fig. 2b). With the increase of time, the plume front moves out of the computational domain and the starting stage ends. In the transitional stage, the plume stem displays firstly puffing and then flapping phenomena. With the development of the plume stem, the flapping becomes clear, as seen in Fig. 2(c). As time increases further, the disturbance of the plume decreases and the plume from the duct ultimately enters into the fully developed stage with regular flapping in the plume stem at the fixed height, which is shown in Fig. 2(d).

CONCLUSIONS

In this paper, a near filed plume induced by heated air from a duct is numerically investigated. The results show that the development of the near field plume may be identified to three stages: a starting stage, a transitional stage and a fully developed stage. The transient features in the development of the near field plume are characterized. The dependence on the Rayleigh number of heat transfer of the near filed plume from a duct has been on the way.

ACKNOWLEDGE

The authors would like to thank National Natural Science Foundation of China (11272045 and 11572032) and the 111 Project (B13002) for their financial support.

References

[1] List E. J.: Turbulent jets and plumes. *Ann*. *Rev*. *Fluid Mech*.**14**: 189-212, 1982.

[2] Morton B. R. Taylor G. I. & Turner J. S.: Turbulent gravitational convection from maintained and instantaneous sources. *Proc*. *R*. *Soc*. *Lond*. A **234**: 1–23, 1956.

[3] Gebhart B.: Instability, transition, and turbulence in buoyancy-induced flows. *Ann*. *Rev*. *Fluid Mech*. **5**: 213-246, 1973.

FM06 - Drops, Bubbles and Multiphase Flows

TS.FM06-1.01	Clanet, Christophe - Giant Soap Bubbles (INVITED)	774
TS.FM06-1.02	Lister, John - Bubble coalescence at any Reynolds number (INVITED)	776
TS.FM06-1.03	Barakat, Joseph - The motion of a closely fitting vesicle in a tube	778
TS.FM06-1.04	Biben, Thierry - Laser generated nano-bubbles around nano-particles	780
TS.FM06-1.05	Bird, James - The residence time of a drop on a spoked macrotexture	782
TS.FM06-1.06	Gong, Shi Wei - Bubble oscillating near a deformable sphere in water	784
TS.FM06-2.01	Jian, Zhen - Coalescence Between Two Convex Liquid Surfaces	786
TS.FM06-2.02	Moffatt, Keith - Soap film dynamics under continuous deformation	788
TS.FM06-2.03	Séon, Thomas - Size and velocity of jet drops following bursting bubbles	790
TS.FM06-2.04	Qian, Tiezheng - Onsager's variational principle and the moving contact line problem (INVITED)	792
TS.FM06-2.05	Burton, Justin - Measurements of Molecular Slip and Contact Line Motion Using a Quartz Crystal Microbalance	794
TS.FM06-2.06	Huerre, Axel - Micro-confined droplets: From lubrication film to droplet velocity	796
TS.FM06-3.01	Das, Debasish - Dynamics of leaky dielectric drops in strong electric fields: Boundary element simulations	798
TS.FM06-3.02	Xiang, Yaolei - Wetting transition of submerged structures under hydrostatic and flow conditions	800
TS.FM06-3.03	Cantat, Isabelle - Velocity measurements in draining foam films (INVITED)	802
TS.FM06-3.04	Lohse, Detlef - Role of natural convection in the dissolution of sessile droplets	804
TS.FM06-3.05	Pandey, Anupam - Elasto-capillary interaction of liquid drops	806
TS.FM06-3.06	Steen, Paul - Freezing vortex rings into shaped particles	808
TS.FM06-4.01	Ganan-Calvo, Alfonso - From the onset of electrospray and disintigration of leaky-dielectric drops to steady cone-jet	810
TS.FM06-4.02	Gerbeth, Gunter - Magnetically induced cavitation and nano-particle dispersion in liquid metals	812
TS.FM06-4.03	Zhang, Rui - The characteristics of droplets impacting on closed-cell hydrophobic surfaces	814
TS.FM06-4.04	Basu, Saikat - On Modeling Drop Impacts at Shallow Angles on Flowing Soap Films	816
TS.FM06-4.05	Bonn, Daniel - Universal rescaling of drop impact on smooth and rough surfaces	818
TS.FM06-4.06	Josserand, Christophe - Controlling crack dynamics using drop impact on cold substrates	820
TS.FM06-5.01	Kant, Pallav - Sequential droplet deposition on geometrically and chemically patterned substrates	822
TS.FM06-5.02	Colinet, Pierre - Leidenfrost drops on a liquid substrate: Theory and experiments	824
TS.FM06-5.03	Magnaudet, Jacques - Short- and long-term tailing dynamics during the settling of a sphere through an interface	826
TS.FM06-5.04	Villermaux, Emmanuel - Explosive Fragmentation	828
TS.FM06-5.05	Prosperetti, Andrea - Fully resolved simulation of fluid flow with suspended particles	830
TS.FM06-5.06	Zaleski, Stephane - 3D DNS of spray formation in gas-assisted atomization	832

TS.FM06-6.01	Sáenz, Pedro - Geometrically controlled dynamics in evaporating sessile drops	834
TS.FM06-6.02	Wu, Wen - Particle resuspension by a periodically-forced impinging jet	836
TS.FM06-6.03	De Jong, Edwin - Numerical Simulation of Droplet Transport Using Switchable Hydrophobic Surfaces ***(Paper Confidential – to be disclosed at later date)***	
TS.FM06-6.04	Fontelos, Marco - Healing capillary films	838
TS.FM06-6.05	Nore, Caroline - Tayler instability in liquid metal columns and liquid metal batteries	840
TS.FM06-6.06	Bertin, Nicolas - Bubble-based Acoustic Micropropulsion: Mixing and Advanced Swimmers	842
PO.FM06-1.07.91	Attarzadeh, Reza - A numerical study of the effect of roughness topology on surface hydrophobicity	844
PO.FM06-1.08.92	Ayati, Anis - Wave induced fluctuations in the gas-phase of a stratified air/water pipe flow	846
PO.FM06-1.09.93	Brownell, Cody - Laser heating and evaporation of a levitated water drop	848
PO.FM06-1.10.94	Das, Soumik - Electrostatic suppression of the Leidenfrost state	850
PO.FM06-1.11.95	Favelukis, Moshe - Mass transfer with slender drops in shear and extensional flows	852
PO.FM06-1.12.96	Gong, Zhaoxin - Effects of atmospheric pressure on water entry of hydrophobic spheres	854
PO.FM06-1.13.97	Gubaidullin, Damir - Influense of Oscillations on Coagulation and Sedimentation of Aerosols in Tubes	856
PO.FM06-1.14.98	Hamouda, Ouajih - Transient fluid phenomena during a rapid two-phase depressurisation	858
PO.FM06-1.15.99	Huang, Kuan-Ling - Rotational saperation in binary droplet collison	860
PO.FM06-1.16.100	Imani, Ramin - Quantitative Measurement of Acoustic Separation of Submicron Solid Aerosols	862
PO.FM06-1.17.101	Jackson, Samuel - The effect of inhomogeneous mobility on immiscible Hele-Shaw flow	864
PO.FM06-1.18.102	Kindelan, Ultano - Stability and equilibrium of charged rotating drops	866
PO.FM06-1.19.103	Kiyama, Akihito - Effects of a water hammer and cavitation on the motion of a gas-liquid interface	868
PO.FM06-1.20.104	Koga, Kazuki - Oscillation and pinchoff of axisymmetric droplets	870
PO.FM06-1.21.105	Kong, Tiantian - The coiling and whipping instability of an electrically charged liquid jet	872
PO.FM06-1.22.106	Lavrenteva, Olga - Dynamic deformation of toroidal drops in compressional stokes flow	874
PO.FM06-1.23.107	Le Bars, Michael - Fragmentation and exchanges during planetary core formation	876
PO.FM06-1.24.108	Li, Jiang - Lubrication and adhesion of bubbles/droplets in microchannels	878
PO.FM06-1.25.109	Liu, Yunqiao - Translation of two encapsulated bubbles in an ultrasound field	880
PO.FM06-1.26.110	Loureiro, Juliana - Experimental Investigation of Slug Flow in a Pipe Subjected to Fluid Injection at the Wall	882
PO.FM06-1.27.111	Mak, Sze Yi - Rapid generation of small water-water droplets at the interface of a jet flowing at high speed	884
PO.FM06-1.28.112	Pan, Shucheng - Multiscale simulation of soap bubbles rupture	886

PO.FM06-1.29.113	Rodriguez, Mauro - Non-spherical bubble collapse dynamics in viscoelastic media	888
PO.FM06-1.30.114	Sawaguchi, Erina - Pressure distribution on a levitating drop over a moving surface	890
PO.FM06-1.31.115	Semprebon, Ciro - Mesoscale modelling of multiphase flow in contact with elastic surfaces	892
PO.FM06-2.01.28	Amini, Ghobad - Instability of liquid jets in weak gaseous crossflow	894
PO.FM06-2.02.29	Shukla, Prashant - Study of path instability of a rising oil droplet using PIV	896
PO.FM06-2.03.30	Shum, Ho Cheung - Inertial and viscous forces on dripping-to-jetting transition in aqueous two-phase systems	898
PO.FM06-2.04.31	Son, Gihun - Numerical simulation of colloid evaporation in confined convective coating	900
PO.FM06-2.05.32	Tsai, Pei-Hsun - On drop induced vortex ring and its related oscillation parameter	902
PO.FM06-2.06.33	Tyatyushkin, Alexander - Steady electrorotation of a drop in a constant electric field	904
PO.FM06-2.07.34	Xia, Zhenyan - Investigation on the breakup mechanism of the liquid jet under longitudinal disturbance	906

Giant Soap Bubbles

Caroline Cohen[1], Baptiste Darbois Texier[1], Etienne Reyssat[2], Jacco Snoeijer[3], David Quéré[2], and Christophe Clanet *[1]

[1]*LadHyX, UMR 7646 du CNRS, Ecole Polytechnique, 91128 Palaiseau Cedex, France*
[3] *PMMH, UMR 7636 du CNRS, ESPCI, 75005 Paris, France*
[4]*Physics of Fluids Group and MESA+ Institute for Nanotechnology, University of Twente, P.O. Box 217, 7500 AE Enschede, The Netherlands*

Summary We study the effect of gravity on soap bubble and show that it becomes dominant above the critical size a^2/e_0, where e_0 is the mean thickness of the bubble and $a = \sqrt{\gamma/(\rho g)}$ the capillary length (γ stands for vapor-liquid surface tension and ρ for the liquid density). The shape which minimizes both surface and gravitational energies for a given volume is derived theoretically and compared to experiments. The different asymptotic regimes are discussed. Finally, the analogy with large inflatable structures is presented.

PRESENTATION OF THE PROBLEM

Soap films and soap bubbles have a long scientific history since Robert Hooke [1] first called the attention of the Royal Society and of Newton to optical phenomena [2]. Concerning the shape of soap bubbles, it is classically obtained by minimizing the surface energy for a given volume and thus reduces to a sphere. The weight is always neglected and it is the purpose of this article to discuss its effect (figure 1).

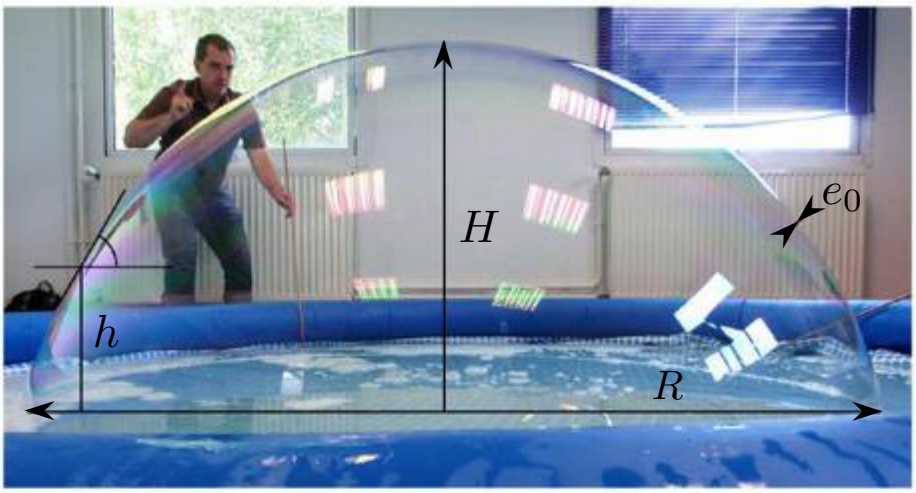

Figure 1: Presentation of a "giant" soap bubble and definition of its radius, R, and height, H. (Here, $R = 1.09\,\mathrm{m}$, $H = 0.97\,\mathrm{m}$)

For liquid drops, the transition from a spherical cap drop to a puddle occurs when the gravitational energy, $\rho g R^4$ (R is the typical size of the drop), becomes of the same order as its surface energy γR^2. That is for a drop size of the order of the capillary length $a = \sqrt{\gamma/\rho g}$ (γ is the liquid-vapor surface tension and ρ the liquid density). Typically, this transition is observed at the millimetric scale [3].

If we look for the same transition in soap bubbles, we expect the gravitational energy, $\rho R^3 e_0 g$, to become of the order of the surface energy, γR^2, at the typical size $\ell \sim a^2/e_0$ (e_0 stands for the mean thickness of the film). Thanks to the iridescence, the mean thickness can be evaluated to a few microns and the light-heavy transition is thus expected at the metric scale.

MODEL AND COMPARISON

The shape of the bubble is described by the pressure equation

$$\Delta P = -2\left[\gamma + \frac{1}{2}\rho g e_0 h\right]\kappa + \rho g e_0 \cos\theta, \tag{1}$$

*Corresponding author. Email: clanet@ladhyx.polytechnique.fr

In this equation, ΔP is the difference of pressure between the inside and the outside of the bubble, e_0 is the thickness of the bubble, h the local height, θ the local angle between the bubble surface and the horizontal direction and κ the mean curvature of the interface. The above equation is subjected to the boundary condition $\theta = \pi/2$ at $h = 0$. For small bubbles ($H/\ell \ll 1$), this equation shows that the effect of gravity is negligible and the bubble has indeed a constant curvature, $\Delta P = -2\gamma\kappa$, corresponding to a sphere of radius $R = 2\gamma/\Delta P = H$. The influence of gravity arises when the term $\rho g e_0 h$ becomes of the order of γ, that is when $H \sim \ell$. This effect flattens the bubble as shown in figure 2 where we present the reduced height of the bubble H/ℓ as a fonction of the reduced radius R/ℓ. The spherical limit ($H/\ell = R/\ell$) is plotted with a solid black line. We observe that soap bubbles remain spherical up to $R/\ell \approx 0.5$. Above this limit, the height is lowered by gravity.

Remarkably, the analysis of equation (1) also reveals that the bubble height does not saturate to a maximum value $\sim \ell$ in the limit of large volumes. While the aspect ratio H/R is found to decrease for larger bubbles, the height continues to grow indefinitely. This is in stark contrast to the case of large liquid drops, which do not reach heights beyond the capillary length.

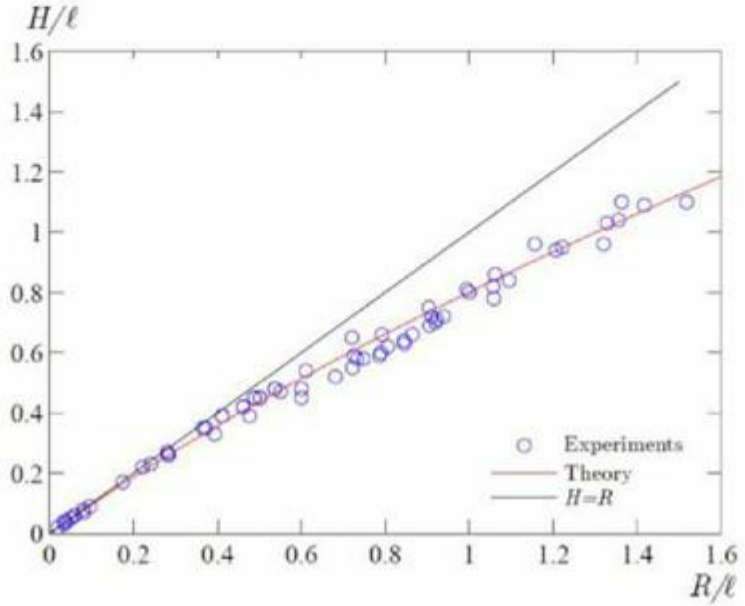

Figure 2: Comparison between the experimental shape of soap bubble (circles), the spherical limit (black solid line) and the shape derived from equation (1).

References

[1] R. Hooke. On holes (black film) in soap bubbles. *Communications to the Royal Society*, 1672 (March 28th).

[2] Sir I. NEWTON. *Opticks or, a Treatise of the Reflections, Refractions, Inflections, and Colours of Light*. Royal Society, 1730.

[3] PG de Gennes, F. Brochard-Wyart, and D. Quéré. *Capillarity and wetting phenomena*. Springer, 2004.

BUBBLE COALESCENCE AT ANY REYNOLDS NUMBER

John R. Lister*[1] and James P. Munro[1]
[1]*Department of Applied Mathematics and Theoretical Physics, Wilberforce Road, Cambridge CB3 0WA, UK*

Summary When two bubbles touch, a hole is formed in the fluid sheet between them, and surface tension acting on its tightly curved edge drives radial flow which quickly pulls the hole wider. We present similarity solutions for the thickness of the fluid sheet and the velocity profile, which show that the radius of the hole increases as $r_E \propto t^{1/2}$ for any Reynolds (Ohnesorge) number. Remarkably, the initially quadratic profile of the sheet allows for an exact solution in which inertia and viscosity have the same scalings with time and remain in fixed proportion. Numerical solution of the third-order set of ODEs determines the prefactors and profiles. Asymptotic analysis of the compressional boundary layer structure in the inviscid limit formally justifies and brings new insight to earlier ad hoc 'blob' models. There is excellent agreement with full Navier–Stokes simulations and experimental data from Paulsen et al. [1]

INTRODUCTION

Drops and bubbles are important in many industrial, environmental, biological and geophysical settings, and the processes of drop/bubble breakup and coalescence are essential to the determination of the size distributions, which is of practical interest. But breakup and coalescence are of great interest in their own right as examples of free-surface flows in which the change in topology is associated with a singularity in the curvature, which leads to the possibility of universal self-similar behaviour near the singularity.

In this paper we present solutions to the problem of coalescence, focusing on the case of two bubbles. The gas inside the bubbles can be considered to be of sufficiently low density and viscosity that it is dynamically passive. Hence the fluid dynamics is dominated by the motion in the thin sheet of fluid between the bubbles as surface tension acts on the edge of the hole in the sheet formed when the bubbles touch. The work is motivated by experimental observations by Paulsen et al. [1] and is described in more detail in Munro et al. [2]

BUBBLE COALESCENCE

Consider spherical bubbles of radius a, brought into contact in fluid of density ρ and viscosity μ. The Ohnesorge number is defined by $Oh = \mu/(\rho a \gamma)^{1/2}$, where γ is the surface tension. We assume the system is axisymmetric with coordinates (r, z) and let $r_E(t)$ be the radius of the hole in the fluid sheet between the coalescing bubbles. We analyse the early behaviour for $r_E \ll a$.

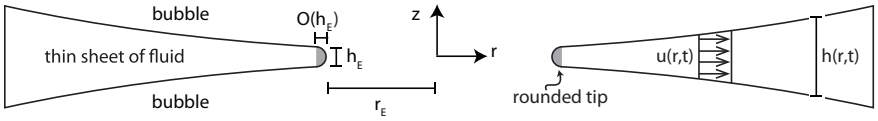

Figure 1: Schematic section through the axisymmetric problem, showing the fluid sheet of thickness $h(r,t)$ exterior to the bubbles and the velocity $u(r,t)$ in the radial direction. The edge of the sheet has radial position r_E and thickness h_E, and is rounded over a length scale $h_E \ll r_E$. Surface tension exerts a radial force 2γ on the rounded edge.

From the initial geometry, the fluid sheet has lengthscale r_E in the radial direction and $r_E^2/a \ll r_E$ in the axial direction, and so we expect the velocity to be predominantly radial. Moreover, the sheet is bounded by free surfaces, so we expect the radial velocity $u(r,t)$ to be constant over the thickness $h(r,t)$ of the sheet (see figure 1). Hence we use the radial extensional-flow equations:

$$\underbrace{\rho h \frac{\mathrm{D}u}{\mathrm{D}t}}_{\text{Inertia}} = \underbrace{\gamma h \frac{\partial \kappa}{\partial r}}_{\text{Capillary}} + \underbrace{\frac{2\mu}{r}\frac{\partial}{\partial r}\left[rh\left(\frac{u}{r}+2\frac{\partial u}{\partial r}\right)\right]}_{\text{Radial Stress}} \underbrace{\circ\ \frac{2\mu h}{r}\left(2\frac{u}{r}+\frac{\partial u}{\partial r}\right)}_{\text{Hoop Stress}}, \qquad \frac{\partial h}{\partial t} = \circ\ \frac{1}{r}\frac{\partial}{\partial r}\big(ruh\big) \qquad (1a,b)$$

with initial conditions $h(r,t) \to r^2/a$ and $u(r,t) \to 0$ as $t \to 0^+$ at fixed r, and with boundary conditions

$$2\gamma = \circ\ \gamma h \kappa\,(r_E,t) \circ\ 2\mu h \left(\frac{u}{r}+2\frac{\partial u}{\partial r}\right)\bigg|_{r_E} \quad \text{and} \quad u(r_E,t) = \frac{\mathrm{d}r_E}{\mathrm{d}t}\,. \qquad (2a,b)$$

*Corresponding author. Email: lister@damtp.cam.ac.uk

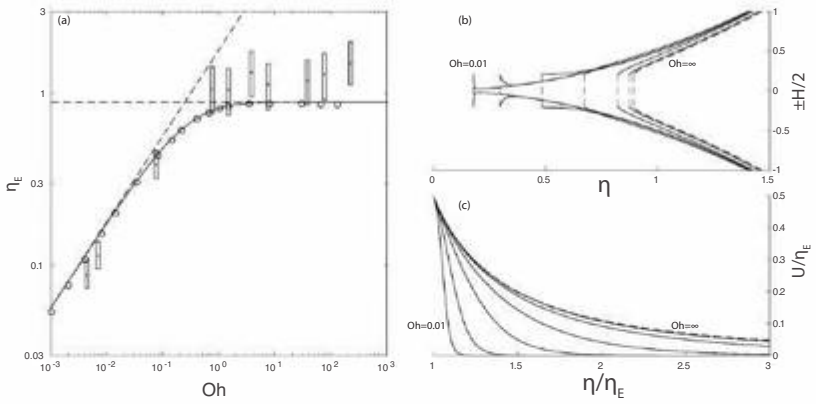

Figure 2: (a) Solution for η_E from the similarity equations (4) and (5) (solid line), from full Navier–Stokes simulations [2] (circles), and experimental data from [1] (points, boxes indicate error bars). Dashed lines: asymptotic theory for the limits $Oh \ll 1$ and $Oh \gg 1$. (b) Similarity thickness profiles $H(\eta)$ for $Oh = 0.01$, 0.03, 0.1, 0.3, 1 and 3, and for the limit $Oh = \infty$. (c) Velocity profiles $U(\eta)$ for the same values of Oh, with η and U both scaled by η_E.

Equation ($2a$) balances the capillary force 2γ from the rounded tip with the radial stress at the edge of the sheet. (The hoop stress and inertia are negligible at the edge.) The $O(2/h)$ curvature at the edge of the sheet is much larger than the curvature elsewhere, which allows us to neglect κ in $(1a, 2a)$. Perhaps surprisingly, there is then an exact similarity solution of the form

$$h = (\gamma t/\mu)H(\eta), \quad u = (a\gamma/\mu t)^{1/2}\,U(\eta), \quad r = (a\gamma t/\mu)^{1/2}\,\eta, \tag{3}$$

in which the viscous and inertial terms retain the same relative magnitude. Equations (1) and (2) become a system of ODEs:

$$\frac{1}{4Oh^2}\left(-\frac{1}{2}U - \frac{1}{2}\eta U' + UU'\right) = U'' + \frac{U'}{\eta} - \frac{U}{\eta^2} + \frac{H'}{H}\left(U' + \frac{U}{2\eta}\right), \qquad H' = H\left(\frac{1 + U' + \frac{U}{\eta}}{\frac{\eta}{2} - U}\right), \tag{4}$$

$$U = \tfrac{1}{2}\eta_E \quad \text{and} \quad H(U/\eta_E + 2U') = -1 \quad \text{at } \eta = \eta_E, \qquad H \sim \eta^2, \quad \eta U \to 0 \quad \text{as } \eta \to \infty, \tag{5}$$

where primes denote derivatives. This third-order system has two boundary conditions at the edge η_E and two boundary conditions at infinity, which also determine the edge position η_E. Numerical solutions for η_E, $H(\eta)$ and $U(\eta)$ are shown in figure 2. The similarity solution gives good agreement with experimental data from [1] and full-scale Navier–Stokes simulations in [2].

There are limiting regimes with $\eta_E \sim (32/3)^{1/4}Oh^{1/2}$ for $Oh \ll 1$ and $\eta_E \sim 0.8908$ for $Oh \gg 1$. For $Oh \ll 1$ the solution has the form of a thickened toroidal ring that is expanding and sweeping up fluid that is still at rest; all of the mass in the accumulating ring moves at essentially the speed of the edge of the sheet. Even though the ring has a short radial lengthscale in similarity variables, the dimensional solutions are still long and thin for sufficiently early times as $h \propto t$, $r \propto t^{1/2}$ by (3). The equations can be analysed asymptotically, and give a formal justification for the ad hoc 'blob' model of Keller [3].

PERSPECTIVES

We have solved the problem of bubble coalescence, and the theory agrees well with experiment. The case of drop coalescence, when the dynamics are dominated by the viscosity in the drops, has a very different flow structure and theoretical considerations [4, 5] give $r_E \propto t \ln t$ rather than $t^{1/2}$. Recent experiments [1, 6] allowed these ideas to be tested and challenged. We anticipate that the talks in this ICTAM session will demonstrate continuing interest in a fascinating field.

References

[1] PAULSEN, J. D., CARMIGNIANI, R., BURTON, A. KANNANAND J. C. & NAGEL, S. R. 2014 Coalescence of bubbles and drops in an outer fluid. *Nat. Commun.* **5**.

[2] MUNRO, J. P., ANTHONY, C. R., BASARAN, O. A. & LISTER, J. R. 2015 Thin-sheet flow between colaescing bubble. *J. Fluid Mech.* **773**.

[3] KELLER, J. B. 1983 Breaking of liquid films and threads. *Phys. Fluids* **26** (12), 3451–3453.

[4] HOPPER, R. W. 1984 Coalescence of two equal cylinders: Exact results for creeping viscous plane flow driven by capillarity. *J. Am. Ceram. Soc.* **67** (12), 262–264.

[5] EGGERS, J., LISTER, J. R. & STONE, H. A. 1999 Coalescence of liquid drops. *J. Fluid Mech.* **401**, 293–310.

[6] PAULSEN, J. D., BURTON, J. C., NAGEL, S. R., APPATHURAI, S., HARRIS, M. T. & BASARAN, O. A. 2012 The inexorable resistance of inertia determines the initial regime of drop coalescence. *Proc. Natl. Acad. Sci. U.S.A.* **109** (18), 6857–6861.

THE MOTION OF A CLOSELY FITTING VESICLE IN A TUBE

Joseph M. Barakat[1], Andrew P. Spann[2], and Eric S. G. Shaqfeh *[1]

[1]*Department of Chemical Engineering, Stanford University, Stanford, CA 94305, USA*
[2]*Department of Chemical Engineering, The University of Texas at Austin, Austin, TX 78712, USA*

Summary The motion of a lipid bilayer vesicle through a narrow, cylindrical tube is modeled theoretically. The vesicle is treated as a sac of fluid enclosed by a thin, elastic sheet that admits resistance to bending deformation. The governing equations of viscous flow are simplified in the "quasi-parallel approximation" and solved numerically. The pressure drop across the vesicle is found to increase when the reduced volume is decreased or confinement is increased. The "critical tube radius," below which the vesicle cannot pass through the tube without rupturing, is determined as a function of reduced volume. Under high confinement, bending resistance can be neglected and an asymptotic solution is developed, in the spirit of F. P. Bretherton's original work on bubble transport [1], using singular perturbation methods. In this limit, vesicles of all reduced volume approach a spherocylindrical shape and the pressure drop scales inversely with gap thickness.

INTRODUCTION

In aqueous environments, lipid bilayers self-assemble to form closed, microscopic structures – so-called "vesicles" – that can encapsulate and transport molecular cargo, *e.g.* pharmaceutical drugs [2]. Squeezing a vesicle through a narrow constriction significantly increases the internal pressure and membrane tension, which can subsequently lead to poration and rupture of the bilayer [3]. Recent work with cells has shown that mechanically-induced poration by controlled squeezing can enhance the permeability of the membrane, enabling the uptake of macromolecules for targeted delivery applications [4].

Although the role of fluid stresses in deforming a vesicle during passage through a narrow channel is understood qualitatively, a rigorous theoretical model is absent in the current literature. Such models exist for bubbles [1,5,6], rigid particles [7], elastic particles [8], and red blood cells [9] and fall under the class of "resistance problems" in which the desired output is the relationship between the pressure head Δp and particle translation speed U. Previous efforts to develop a quantitative theoretical description of the mobility of vesicles and red blood cells in tubes have yielded useful insight into the connection between hydrodynamic stresses and membrane mechanics [9,10,11]. However, in all of these studies a form for the particle shape is typically assumed *a priori*, thus neglecting the full free boundary problem.

The objective of the present work is to develop a simple but rigorous theoretical description of the motion of a neutrally buoyant vesicle in a tube of circular cross section. Symmetry about the tube axis is assumed *a priori*, thus reducing the problem to the solution of fields along the contour of the membrane. By solving the equations of viscous flow together with the equations of mechanical equilibrium for a thin shell, the shape as well as the local distribution of pressure and membrane tension can be calculated over a range of geometries and flow conditions. In particular, the critical geometry corresponding to membrane rupture can be determined.

THEORY

The problem under consideration is the translation of a neutrally buoyant vesicle at a speed U through a circular tube containing a Newtonian fluid of viscosity μ. The nominal radius R of the vesicle is defined such that the surface area of the membrane is $4\pi R^2$ and the enclosed volume is $\frac{4}{3}\pi R^3 v$, where $0 < v \leq 1$ is the vesicle's "reduced volume;" both the surface area and enclosed volume are assumed to be fixed quantities. In this work, R, μ, and U are set equal to unity, which is tantamount to rendering all variables dimensionless with respect to these characteristic scales.

In cylindrical coordinates (x, σ, ϕ), the equations of motion and continuity can be solved under the "quasi-parallel approximation" to yield differential equations for the gap pressure p along the tube axis x and the membrane tension γ along the meridional coordinate s of the membrane:

$$\frac{\mathrm{d}p}{\mathrm{d}x} = \frac{8}{a^2 \circ\ r^2}\left(2Qa \circ\ a^2 \circ\ \frac{a^2 \circ\ r^2}{2\log(r/a)}\right)\left(a^2 + r^2 + \frac{a^2 \circ\ r^2}{\log(r/a)}\right)^{-1}, \tag{1a}$$

$$\frac{\mathrm{d}\gamma}{\mathrm{d}s} = \frac{1}{4}\frac{\mathrm{d}p}{\mathrm{d}x}\left(2r + \frac{a^2 \circ\ r^2}{r\log(r/a)}\right) + \frac{1}{r\log(r/a)}, \tag{1b}$$

where a is the tube radius, $\sigma = r(s)$ is the radial position of the membrane and Q is the volume flux per unit circumference through the gap. Eq. (1) was also derived in [9] for red blood cells. Supposing the bending moment in the bilayer is $2\kappa c$, then p and γ are related by balancing normal stresses across the membrane:

$$\frac{1}{r}\frac{\mathrm{d}}{\mathrm{d}s}\left(r\frac{\mathrm{d}c}{\mathrm{d}s}\right) = \kappa^{-1}(\gamma c \circ\ \tfrac{1}{2}p) \circ\ 2c\bar{c}^2, \tag{2}$$

*Corresponding author. Email: esgs@stanford.edu

where c is the mean curvature, $\bar{c}$ is the deviatoric curvature, and κ is the bending stiffness (measured in units of $\mu U R^2$). For a given choice of v, a, and κ, Eqs. (1)-(2), together with the appropriate boundary conditions and integral constraints, may be solved numerically for the dependent variables as well as Q (an eigenvalue) and S (a free boundary).

RESULTS

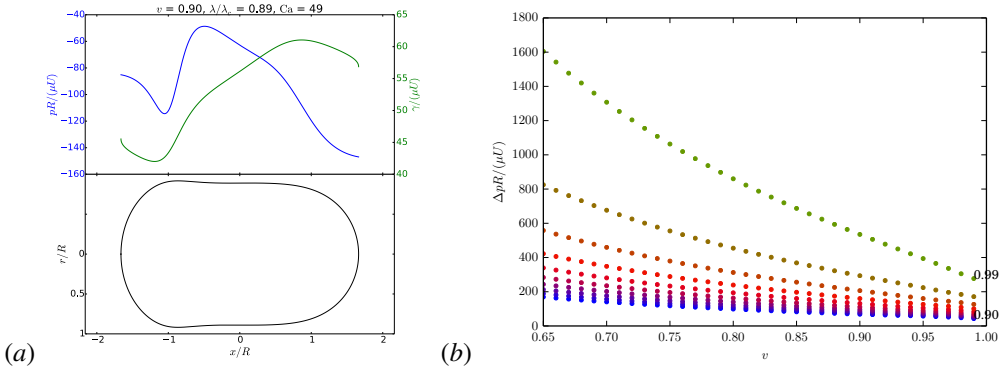

(*a*) (*b*)

Figure 1: (*a*) Representative solution for the shape contour r (black curve), gap pressure p (blue curve), and membrane tension γ (green curve) plotted against the axial coordinate x for $v = 0.9$, $a_c/a = 0.89$, and $\kappa^{-1} = 49$. (*b*) The pressure drop Δp plotted against the reduced volume v for $\kappa^{-1} = 1$ and various values of a_c/a.

Local profiles of the shape contour, gap pressure, and membrane tension are calculated over a wide range of the parameters v, a, and κ. As $\kappa \to 0$ or ∞, two asymptotic limits are reached corresponding to very strong and very weak fluid stress relative to the bending stiffness of the membrane. Decreasing the reduced volume (*i.e.* deflating the vesicle) results in higher drag for the same degree of confinement; the limit $v = 0.61$ corresponds to the reduced volume for a red blood cell.

The critical radius a_c corresponding to rupture is found to satisfy the cubic equation,

$$a_c^3 \circ \ 3a_c + 2v = 0. \tag{3}$$

The vesicle shape in the limit $a \to a_c$ approaches a spherocylinder and the membrane is well described by an isotropic tension, in agreement with recent experimental observations [11]. Asymptotic analysis in the small clearance ϵ furnishes the scaling $\Delta p \simeq 2L/(\epsilon a)$ in the limit $a \to a_c$, where $L \simeq 2(a_c^{-1} \circ \ a_c)$ is the length of the cylindrical segment.

CONCLUSIONS

A rigorous theory describing the motion of vesicles in tubes has been developed over a wider parameter space than has been reported for red blood cells. The pressure distribution along the membrane mimics that of a rigid particle of the same shape, and the corresponding tension distribution indicates the front nose as a potential site for poration. An asymptotic theory has been developed in the limit $a \to a_c$, where a_c has been shown to be a function of reduced volume.

References

[1] Bretherton F. P.: Journal of Fluid Mechanics 10, 166-188 (1961).
[2] Gregoriadis G.: FEBS Letters 36-3, 292-296 (1973).
[3] Nichol J. A., Hutter O. F.: Journal of Physiology 493.1, 187-198 (1996).
[4] Sharei A. et al: Proceedings of the National Academy of Sciences 110-6, 2082-2087 (2013).
[5] Park C. W., Homsy G. M.: Journal of Fluid Mechanics 139, 291-308 (1984).
[6] Ratulowski C., Chang H. C.: Physics of Fluids A: Fluid Dynamics 1, 1642-1655 (1989).
[7] Bungay P. M., Brenner H.: International Journal of Multiphase Flow 1, 25-56 (1973).
[8] Tözeren H., Skalak R.: Journal of Fluid Mechanics 87.1, 1-16 (1978).
[9] Secomb T. W., Skalak R., Özkaya N., Gross J. F.: Journal of Fluid Mechanics 163, 405-423 (1986).
[10] Bruinsma R.: Physica A 234, 249-270 (1996).
[11] Savin T., Bandi M. M., Mahadevan L.: Soft Matter (2015).

LASER GENERATED NANO-BUBBLES AROUND NANO-PARTICLES

Julien Lombard, Thierry Biben *, and Samy Merabia
Light and Matter Institut, UMR5306 University of Lyon 1-CNRS, Villeurbanne, France

Summary On the basis of a free-energy model coupled to compressible hydrodynamics we discuss the formation of nanobubbles around heated nano-particles. In particular, we show that nanoscale specificities like the Kapitza resistance at the particle-liquid interface or the ballistic heat transport inside the nano-bubble play a key role in the bubble formation and controls its size.

The vapor nanobubbles generated around overheated nanoparticles are very peculiar objects. They are generated in extreme conditions by intense and short duration laser pulses (femtosecond or nanosecond pulses), that may induce very localized hot spots (thousands of kelvins on few nanometer particles). These bubbles are very transient effects, they grow and collapse in few tenth of nanoseconds. However, the pressure wave generated during their production is intense enough to allow very promising medical applications (cancer diagnosis and possible therapy [1]). A control of the mechanisms that drive their production is thus an important issue for these applications. It is also an important issue from the point of view of physics since it is an example of phase transition induced in extreme out–of–equilibrium conditions where the usual nucleation-growth scenario has no time to occur, as already discussed in [2] and showed in molecular simulations [3], or using the free energy functional approach used in this paper [4]. It is however tempting to use ordinary equilibrium thermodynamics to predict the bubble formation threshold or to investigate the bubble growth and collapse kinetics. We showed in previous papers that a good criterion for the bubble production is the crossing of the spinodal line 1 or 2 nm away from the nanoparticle surface [4], a result confirmed by Molecular Dynamics (MD) simulations [3], and the possibility to use the Rayleigh-Plesset formalism to treat the growth and collapse kinetics. This good behavior is due to the very fast equilibration of water molecules at the nanometer scale: Although the fluid is globaly very far from its equilibrium state close to the nanoparticle, as illustrated by the strong temperature gradient observed in this region (hundred of Kelvins per nanometers [5]), a local equilibrium approximation is still possible, that gives the possibility of a local thermodynamic treatment of the bubble. However, due to the nanometer scale of the bubble, thermal transport inside the bubble has a particular nature. From the work of Knudsen in the early nineties it is known that below the mean-free-path of the molecules, the thermal transport is ballistic, and not diffusive because the molecules have no time to collide. For water vapor, the mean-free-path in saturation conditions at atmospheric pressure is around 86 nm, we can expect that the thermal transport in a bubble with a radius below this value is essentially ballistic. Another important feature is the existence of a thermal resistance at the particle-liquid interface, the Kapitza resistance, that produces a temperature discontinuity at the interface. This effect is usually neglected for macroscopic systems, due to the smallness of the associated Kapitza length. However, the thermal resistance becomes an important effect for nanometer scale systems, it delays the thermal transfer between the particle and the fluid. Taking into account these specificities is the goal of our model. The precise formulation has already been the subject of a publication so we shall restrict the discussion to the main ingredients here. The model is based on the conservation equations (mass, momentum and energy) and we solve the dynamics of the three important fields: density $\rho(r,t)$, velocity $\boldsymbol{v}(r,t)$ and temperature $T(r,t)$ around a spherical gold nanoparticle (GNP), as schematically represented in Fig. 1. To account for the liquid-vapor phase transition in the momentum equation, we use a density functional approach based on the van der Waals bulk free energy with an additional square gradient term to account for the finite thickness of the interface at the nanometer scale. The resulting pressure tensor is a function of the local density in the fluid, $\rho(r,t)$ and its gradient: $P_{\alpha\beta} = \left[P_{\text{vdW}} - w\rho\Delta\rho + \frac{w}{2}(\nabla\rho)^2\right]\delta_{\alpha\beta} + w\partial_\alpha\rho\partial_\beta\rho$. Here, P_{VdW} is the pressure obtained from the van der Waals theory. The parameter w fixes the interface thickness as well as the surface tension. This parameter has been adjusted to match the surface tension of water at room temperature ($T = 297$ K). $\delta_{\alpha\beta}$ is the Kronecker symbol, and ∂_α is a derivative with respect to the spatial coordinate in the direction α. Δ is the Laplace operator. The two parameters a and b of the van der Waals theory have been chosen so that the density of the liquid phase at $T = 297$ K corresponds to the density of water, and the critical temperature is $T_c = 647.3$ K.

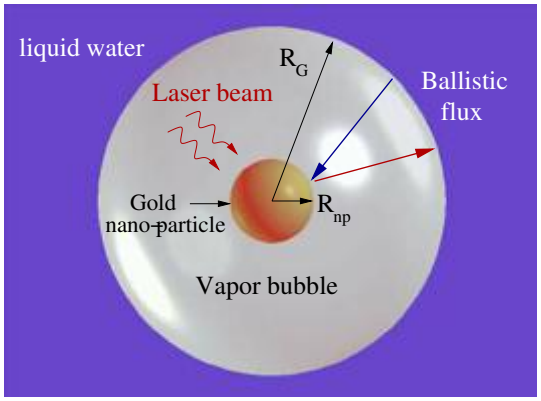

Figure 1: Schematic view of the system

*Corresponding author. Email: thierry.biben@univ-lyon1.fr

The boundary conditions at the nanoparticle interface are the key ingredients of the model. The Kaptiza resistance is introduced through the thermal conductive flux at the particle-liquid interface:

$$\phi_c = G(T_{\rm np} - T_{\rm s}), \qquad (1)$$

where G is the thermal conductance of the GNP-water interface ($G \simeq 90\,\mathrm{MWm^2K^{-1}}$for liquid water), $T_{\rm np}$ is the nanoparticle temperature and $T_{\rm s}$ is the temperature of the fluid in contact with the GNP. In the vapor phase the conductive flux becomes very small, G is divided by a factor of nearly 20 meaning that the vapor bubble is a good insulator, as expected. However, due to the small size of the bubble at the onset of vaporization it is necessary to include in the model the ballistic nature of the thermal transfer in the vapor phase at the nanometer scale by adding the ballistic flux $\phi_{\rm b}$:

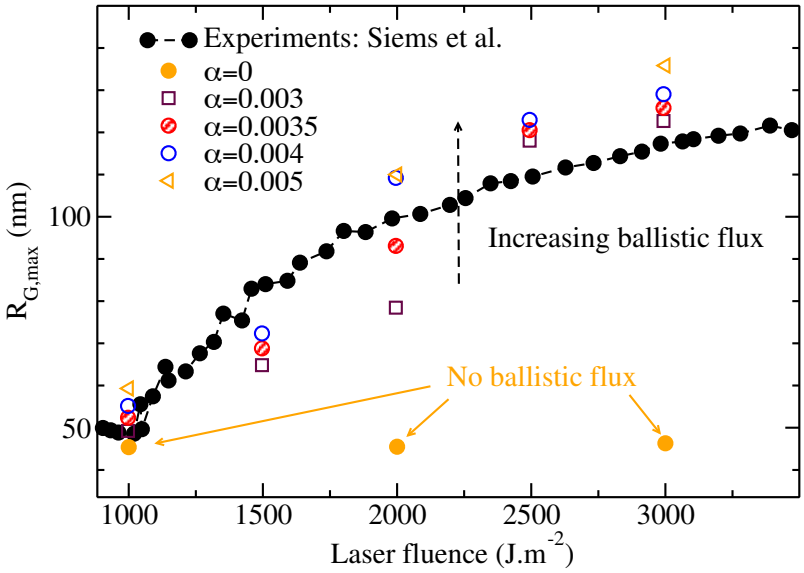

Figure 2: Maximum radius of the bubbles: comparison with experiments

$$\phi_{\rm b} = \alpha\rho_{\rm s}\sqrt{\frac{2k_B^3}{m}}\left(T_{\rm np}^{3/2} - T_G^{3/2}\right), \qquad (2)$$

where $\rho_{\rm s}$ is the vapor density in contact with the particle, m is the mass of a water molecule, k_B is the Boltzmann constant and T_G is the temperature at the surface of the bubble, defined as the Gibbs position of the liquid-vapor interface. The physical meanning of this expression is simple: in the vapor phase, molecules evaporated at the liquid-vapor interface with a temperature T_G are carying a kinetic energy proportional to k_BT_G with a velocity proportional to $\sqrt{k_BT_G}$ in the direction of the GNP. These molecules are reaching the surface of the GNP and are re-emitted in the opposite direction with a temperature $T_{\rm np}$ leading to the difference $T_{\rm np}^{3/2} - T_G^{3/2}$. This scenario is sketched in Fig. 1 by the blue and red arrows. Since $T_{\rm np}$ is much larger than T_G, the net energy flux goes from the GNP to the bubble surface, that is warmed up by this incoming ballistic flux. The prefactor is not trivial, but from dimensional analysis it is proportional to a density, we took the contact density between the vapor and the GNP as a reference ($\rho_{\rm s}$ in equation (2)). More complex is the parameter α, a dimensionless accommodation coefficient that plays a key role in the following. A kinetic theory argument shows that α should be in the range $0.002 \leq \alpha \leq 0.004$, and a direct comparison between our model and the experiments presented in [6] show that a value $\alpha = 0.0035$ gives a good estimate of the bubble sizes (see Fig. 2). It is important to note that without the ballistic flux, the bubbles remain very small (few nanometers of thichness). With the ballistic flux, they can reach more than 100nm.

It is surprising that such a low value of α is able to produce such a large effect. Our model shows that there is a threshold in the value of the ballistic flux that allows the ballistic flux to inflate the bubbles. Below this value, the bubbles remain small.

Another very important parameter is the laser pulse duration: short and intense pulses (femtoseconds) are able to produce large bubbles, but the nanoparticle does usually not survive to the experiment. Longer pulses (10 nanoseconds or more) but with lower intensities can produce a full series of small bubbles before the ballistic flux is large enough to bypass the threshold and inflate a large bubble. Finally the model gives also access to the pressure wave generated by the laser pulse, that is produced close to the onset of the bubble formation, and which intensity is of great relevance for applications.

It is our scope to discuss these non-trivial effects during the presentation.

References

[1] Lapotko D.: Plasmonic Nanobubbles as Tunable Cellular Probes for Cancer Theranostics. Cancers 3: 802, 2011.

[2] Löwen H. and Madden P. A.: A microscopic mechanism for shock-wave generation in pulsed-laser-heated colloidal suspensions. J. Chem. Phys. 97: 8760, 1992.

[3] Sasikumar K. and Keblinski P.: Molecular dynamics investigation of nanoscale cavitation dynamics. J. Chem. Phys. 141: 234508, 2014.

[4] Lombard J., Biben T. and Merabia S.: Kinetics of Nanobubble Generation Around Overheated Nanoparticles. Phys. Rev. Lett. 112: 105701, 2014.

[5] Lombard J., Biben, T. and Merabia, S.: Nanobubbles around plasmonic nanoparticles: Thermodynamic analysis. Phys. Rev. E 91: 043007, 2015.

[6] Siems A., Weber S. A. L., Boneberg J. and Plech A.: Thermodynamics of nanosecond nanobubble formation at laser-excited metal nanoparticles. New Journal of Physics 13: 043018, 2011.

THE RESIDENCE TIME OF A DROP ON A SPOKED MACROTEXTURE

James C. Bird[1] & Colin Patterson[1,2]
[1]*Department of Mechanical Engineering, Boston University, Boston, MA, USA*
[2]*General Electric, Aviation, Lynn, MA, USA*

Summary When a water drop impacts a superhydrophobic surface, it can bounce [1]. Recently, it has been shown that the contact time can be reduced by incorporating ridged macrotextures on the surface [2-4]. When non-parallel macrotextures are present, they intersect to create spoked junctions. It is expected that these junctions would affect the impact of the drop; yet existing models disagree on how many droplets might be produced and the time for these droplets to clear the surface. Here we show that the overall residence time depends on the number of spokes if there are less than 2 or more than 5. We develop a physical model that rationalizes our experimental results and also demonstrate that the phenomenon observed for macrotextured, superhydrophobic surfaces extends to macrotextured, wettable surfaces above the Leidenfrost temperature.

INTRODUCTION

When drops impact on a surface at moderate Weber numbers, they typically spread out and create a thin film. If the surface is non-wetting, the liquid film will recoil to such an extent that the drop will recoil, or bounce, from the surface. The time that the drop resides on the surface is dominated by the recoil time, which depends predominantly on the surface tension, density, and size of the drop, and only weakly on the impact velocity [1]. For macroscopically smooth and flat surfaces, drops typically maintain axisymmetry and only leave the surface once the retracting film reaches the centre of the drop. However, if the surface is macroscopically textured, the film reaction may no longer be axisymmetric providing the opportunity for the film to fragment and more rapidly detach from the surface [2]. Different mechanisms have been suggested to rationalize the reduction in contact time [2-4] and these mechanisms lead to different predictions on how the residence time might scale with macrostructure geometry. Additionally, prior studies exploring the breaking of symmetry with macrotextures have been restricted to superhydrophobic surfaces. Here we explore the dynamics when impacting drops land on a sufficiently hot surface so that they reside on a cushion of their own vapour. The addition of macrotexture spokes is explored and related to the residence time.

METHODS

An aluminium block is milled so that there are raised macrotextured spokes that radiate from a central point. These ridges are approximately 100 microns high and all other features from the milling process are less than 10 microns (Fig. 1). Blocks are made with varying number of spokes ranging from zero to six. In each experiment, the milled aluminium is heated above the Leidenfrost temperature. A drop of water is released from different heights above the surface, and the impact dynamics of the drop are recorded with a high-speed camera.

RESULTS AND DISCUSSION

We find that the residence time varies with the number of spokes on the surface. We find that the maximum extension of the film is different for the film covering the spokes than the film away from the spokes (Fig. 1, top row). Additionally we find that the film rapidly retracts into a radial array of ligaments before breaking up (Fig. 1, bottom). The overall reduction in contact time and number of fragmented drops can be related to this shape changeover. A physical model based on a centre-assisted recoil framework can be developed to rationalize the results.

[a)] Corresponding author. Email: jbird@bu.edu.

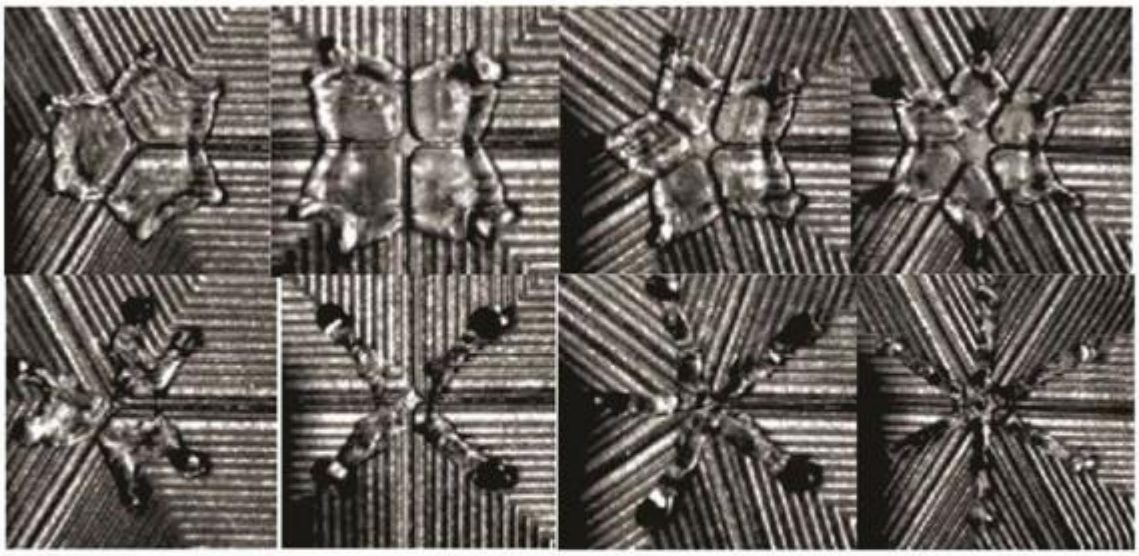

Figure 1. A drop impacting non-wetting surfaces with different number of spokes (n = 3, 4, 5, and 6, each corresponding to a column in the figure). Images at maximum spreading (top row) and initiation of breakup (bottom row) illustrate the rapid retraction along each spoke.

CONCLUSIONS

We have investigated the residence time for drops impacting a macrotextured surface with a number (n) of radial spokes that is heated above the Leidenfrost temperature. For a flat surface (n=0) and ridged surface (n=2), the results match those described in the literature for superhydrophobic surfaces [2,4]. For other numbers spokes, the residence times do not follow the existing models proposed in the literature. Instead, predicting the residence time requires a physical model – which we have developed – that accounts for the change in shape during the retraction.

ACKNOWLEDGMENTS

We thank Kripa Varanasi for helpful early-stage discussion. We also thank Robin Song for assistance with the data collection and Bob Sjostrom for milling the surfaces.

References

[1] Richard, D., Clanet, C. & Quéré, D. Contact time of a bouncing drop. Nature 417, 2002.
[2] Bird, J.C., Dhiman, R., Kwon, H.M. and Varanasi, K.K.: Reducing the contact time of a bouncing drop. *Nature*, *503,* 2013.
[3] Patterson C.: Reducing the contact time of impinging droplets on non-wetting surfaces. *MS Thesis*, Boston University Mech. Eng. Dept., USA, 2014.
[4] Gauthier, A., Symon, S., Clanet, C., & Quéré, D.: Water impacting on superhydrophobic macrotextures. *Nature Comm.*, 6, 2015.

BUBBLE OSCILLATING NEAR A DEFORMABLE SPHERE IN WATER

Shi Wei Gong[1], Bing Hui Terence Goh[2], Siew-Wan Ohl[1] & Boo Cheong Khoo[3a)]
[1]*Institute of High Performance Computing, A*STAR, 1 Fusionopolis Way, Singapore 138632, Singapore*
[2]*NUS Graduate School for Integrative Sciences and Engineering, National University of Singapore, 28 Medical Drive, Singapore 117456, Singapore*
[3]*Department of Mechanical Engineering, National University of Singapore, 9 Engineering Drive 1, Singapore 117576, Singapore*

Summary This paper investigates bubble oscillating near a deformable sphere with different materials. The boundary-element method (BEM) is used to simulate the bubble growth, contraction and collapse near the deformable sphere. The finite element method (FEM) is used to calculate the sphere response to the fluid pressure induced by the bubble oscillating. The interaction of the oscillating bubble and the deformable sphere is simulated via the coupled BEM-FEM. A good agreement between the numerical simulations and experimental observations is achieved. Parametric studies are further carried out for the oscillating bubble near the deformable sphere with different material properties. The results show the influences of the sphere stiffness, the bubble-sphere size ratio, and the relative distance of the bubble and the sphere, on the bubble collapse and the sphere deformation. From the results obtained, some insights to the problem of an oscillating bubble near a deformable sphere are deduced.

INTRODUCTION

The interaction of an oscillating bubble with an elastic membrane or a sphere is a complex phenomenon that is highly relevant to medical applications. This is because when laser, shock waves, or ultrasound in applied in clinical treatment, bubbles are often formed at the target area or around its vicinity. In view of the need to minimize the destructive effects of bubble pressure on the deformable structure or to utilize it in medical and clinical therapies, a profound understanding of the interaction between a bubble and a deformable structure with different material properties becomes a requirement.

Various coupled boundary element and finite element methods have been developed for bubble-structure interactions [1-3]. Turangan et al. [4] studied a non-equilibrium bubble placed next to a (stretched) membrane. Ohl et al. [5] conducted low-voltage spark bubble experiments and adopted a boundary-element method (BEM) model to predict the dynamics of oscillating bubbles placed near a thick layer of elastic biomaterial. Gong et al. [6] studied the physical behavior of the interaction of a spark-generated bubble and an elastic rubber beam numerically and experimentally. In their study, the scaling law for spark-generated bubbles and underwater explosion bubbles [7] was used to get the parameters for the spark-generated bubble. Although the results reported have shown good agreement with the experiments, there is no study involving 3D numerical simulations of a cavitation bubble beside a finite element representation of a deformable sphere to the best knowledge of the authors. The present work addresses this and investigates the interaction of an oscillating bubble and a deformable sphere, both numerically and experimentally. The experiments were carried out using high-speed photography for the observations of the spark-generated bubble dynamics as well as the elastic sphere deformation. The numerical simulations were accomplished by coupling a three dimensional boundary element (BE) potential flow code with an explicit finite element (FE) structural solver. Furthermore, the interaction of an oscillating bubble and a deformable viscoelastic sphere is explored with the coupled BE-FE code incorporating a viscoelastic model [8], which can be useful for potential application in biomedicine.

MODELLING OF AN OSCILLATING BUBBLE NEAR A DEFORMABLE SPHERE

In this study, the boundary-element method (BEM) is used to simulate the bubble growth, contraction and collapse near the deformable sphere, in which the scaling law for spark-generated bubble and underwater explosion bubble [7] is employed to get the initial parameters for the oscillating bubble. For a bubble with a prescribed maximum radius R_m, the small equivalent charge weight W can be determined by $W = \left[D + \left(p_{ref} - p_v\right)/\rho g\right]\left(R_m/K_R\right)^3$. Here, D is the initial distance from the bubble centre to the free surface, K_R is the charge parameter, ρ is the density of the fluid, p_{ref} and p_v are the reference pressure and the vapour pressure, respectively. On the other hand, the dynamics of the deformable sphere in response to the oscillating bubble is simulated via the finite element method (FEM). For the rubber like elastic material, the Blatz and Ko model with the simplified strain energy $W = G/2\left[\left(J_1 - 3\right) + \left(\left(1-2\upsilon\right)/\upsilon\right)\left(J_3^{-2\upsilon/(1-2\upsilon)} - 1\right)\right]$ is employed for this simulation, which had been used for a rubber beam response to sparkle-generated bubble in our previous work [6]. In strain energy equation, G is the shear modulus, and υ is the Poisson ratio. J_1 and J_3 are the invariants defined as: $J_1 = \lambda_1^2 + \lambda_2^2 + \lambda_3^2$, and $J_3 = \lambda_1\lambda_2\lambda_3$, where λ_1, λ_2 and λ_3 are the principal stretch ratios of the deformation at the point considered. For the viscoelastic material, a Zener type viscoelastic model is used [8] with the shear modulus in the form of $G(t) = G_\infty + (G_0 - G_\infty)\exp(-\beta t)$, where G_0 is the dynamic shear modulus, G_∞ is the static shear modulus and β is a decay constant. The deformable sphere

a) Corresponding author. Email: mpekbc@nus.edu.sg.

is modelled using 6912 hexahedral elements and the wet surface of the elastic sphere is modelled by 1728 triangle shell elements. The wet surface is a layer that covers the deformable sphere and contacts with the fluid.

In the numerical simulation, the pressure in the fluid domain induced by the bubble are calculated using the BE fluid code and then given as input to the FE structural solver, from which the fluid pressure is applied on the wet surface of the deformable sphere. The FE structural solver then calculates the displacements of the deformable sphere, which are then returned as input for the fluid solver with the bubble. From the complete simulation, we can obtain two sets of results: one set includes the bubble growth, contract and collapse; the other set includes the deformable sphere response to the pressure induced by the bubble oscillating. For more details on the simulation methods, readers may refer to the references [3, 6, 8, and 9].

RESULTS AND DISCUSSIONS

We first present the numerical results obtained in comparison to the empirical images from our experiments. Due to the two-paper limitation, only one of the comparison results is shown in Fig.1. The reasonable comparison results allow us to examine the effects of a stand-off distance and a size ratio between the bubble and the sphere on their interaction; and also extend our simulations for further explorations of the influence from the sphere elasticity and viscosity on the interaction between the bubble and the sphere. The simulation results show that the stand-off distance and the size ratio have significant effects on both the bubble collapse and the sphere deformation; the sphere elasticity in certain range has significant effects on the sphere deformation but has little influence on the bubble size; the sphere viscosity affects both bubble collapsing and solid deformation, and also attenuates the pressure induced by the bubble around the bubble collapse time. From the results obtained, some insights to the problem of an oscillating bubble near a deformable sphere are deduced, which can be useful for potential applications in biomedicine.

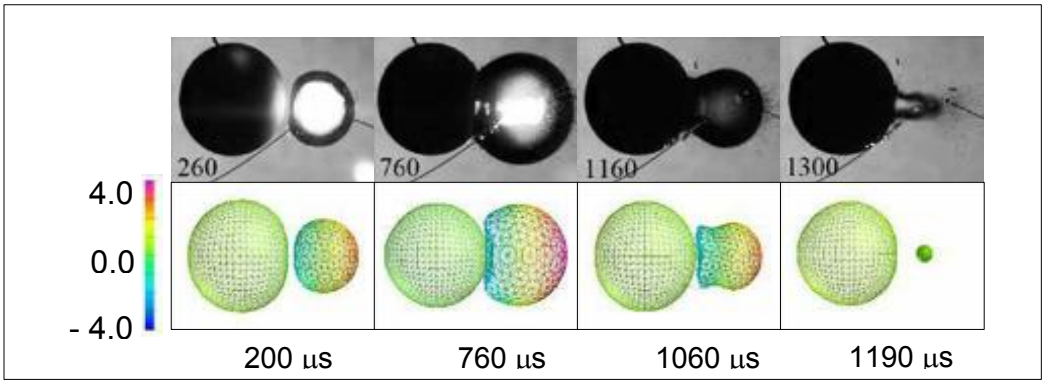

Figure 1: Comparison between the numerical simulations and the experimental images. The rubber sphere (left) has a radius of R_e = 4.30 mm, shear modulus of G = 312 *k*Pa, and density of ρ = 1170 kg/m^3. The spark-generated bubble, with the initial spark point at H = 6.71 mm away from the rubber sphere centre, expands to its maximum volume (R_{max} = 4.30) at t = 760 μs.

References

[1] Duncan J. H, Zhang S.: On the interaction of a collapsing cavity and a compliant wall. J. Fluid Mech **226**: 401-423, 1991.

[2] Chahine G. L., Kalumuck, K.M., Hsiao, C.-T.: Simulation of surface piercing body coupled response to underwater bubble dynamics utilizing 3DYNAFS, a three-dimensional BEM code. Comput Mech. **32**: 319–326, 2003.

[3] Klaseboer E., Hung K.C., Wang C., Wang C.W., Khoo B.C., Boyce P., Debono S., Charlier H.: Experimental and numerical investigation of the dynamics of an underwater explosion bubble near a resilient/rigid structure. J Fluid Mech **537**: 387-413, 2005.

[4] Turangan C. K, Ong G. P, Klaseboer E, Khoo B. C.: Experimental and numerical study of transient bubble-elastic membrane interaction. J Appl Phys **100**: 054910, 2006.

[5] Ohl S.-W., Klaseboer E, Khoo B. C.: The dynamics of a non-equilibrium bubble near bio-materials. Phys Med Biol **54**: 6313-6336, 2009.

[6] Gong, S. W., Goh, B. H. T., Ohl, S.-W., Khoo, B. C.: Interaction of a spark-generated bubble with a rubber beam: Numerical and experimental study. Phys. Rev. E, **86**: 026307, 2012.

[7] Gong, S.W., Ohl, S.-W., Klaseboer, E., Khoo, B. C.: Scaling law for bubbles induced by different external sources: Theoretical and experimental study. Phys. Rev. E **81**: 0563117, 2010.

[8] Gong, S.W., Klaseboer, E.: Interaction between collapsing bubble and viscoelastic solid: Numerical modelling and simulation, *Appl Math Model*. In Press, (doi:10.1016/j.apm.2015.11.050), 2016.

[9] Gong S.W., Khoo B.C.: Transient response of stiffened composite submersible hull to underwater explosion bubble, Compos Struct **122**: 229-238, 2015.

COALESCENCE BETWEEN TWO CONVEX LIQUID SURFACES

Zhen Jian, Fan Yang, Erqiang Li, Sigurdur T. Thoroddsen *
King Abdullah University of Science and Technology, Thuwal, Saudi Arabia

Summary Coalescence between two convex surfaces is investigated in experiments and in numerics by a code called Gerris. This problem can be determined by two dimensionless numbers: the Ohnesorge number $Oh = \mu_l/\sqrt{\rho_l \sigma D_b}$ and the size ratio between droplet and bubble $\alpha = D_d/D_b$. The fast dynamics is captured by an ultra-high-speed camera (Phantom V2511) at the recording speed 35 $kfps$ with a 896×768 resolution. Three different liquids as deionized(DI) water, glycerin 25% and glycerin 50% with different size ratios α were studied. As the droplet coalesces with the surface, two vortex rings are generated symmetrically at the tip of the liquid bridge. They grow in time and form a mushroom-like structure. A secondary droplet inside the bubble is also observed in simulations.

INTRODUCTION

Coalescence between two convex surfaces of the same liquid is investigated experimentally and numerically in this article. A gas bubble of diameter D_b, density ρ_g and viscosity μ_g is immersed in a liquid pool. A same liquid droplet of smaller diameter D_d, density ρ_l and viscosity μ_l is located inside the bubble and released from rest on the bubble. The process has no external velocity scale, as it starts from rest and it occurs in a small temporal and spatial scale. We assume that gravity does not play a significant role in the coalescence dynamics and the dynamics is due to competition between surface tension and viscous forces. The problem can be determined by two dimensionless numbers: the Ohnesorge number $Oh = \mu_l/\sqrt{\rho_l \sigma D_b}$ and the size ratio between the drop and the bubble $\alpha = D_d/D_b$. The Navier-Stokes equation considering surface tension σ is set $\rho \frac{d\mathbf{u}}{dt} = -\nabla p + \mu \triangle \mathbf{u} + \sigma \kappa \delta \mathbf{n}$. The effects of the Ohnesorge number Oh and the size ratio α were studied. Numerically, it is solved axisymmetrically by a code called Gerris, which is a partial differential equation solver for multiphase flows based on the finite-volume discretization and an adaptive tree-structured mesh as an open source software[1].

EXPERIMENTAL STUDIES

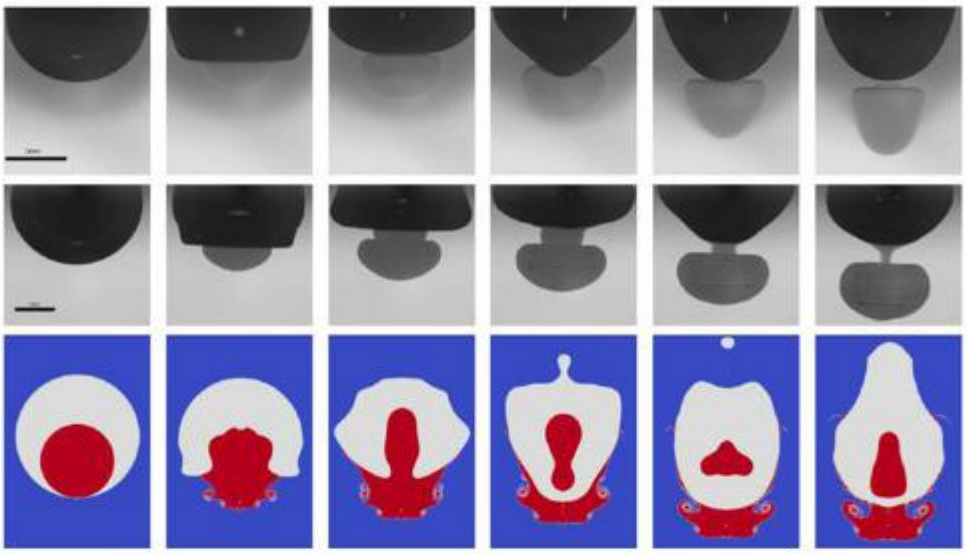

Figure 1: Snapshots of coalesced interface. Time interval between frames is $\Delta t = 0.00114286s$. Top row: glycerin $50\%, \alpha = 0.5$; middle row: DI water $\alpha = 0.6$; bottom row: snapshots of simulations, DI water $\alpha = 0.6$.

In experiments, the bubble was realized by a hemisphere convex liquid surface. To capture the fast dynamics following the liquid contact, an ultra-high-speed camera (Phantom V2511) was used, which can provide up to 25 $kfps$ recording speed at 1280×720 HD resolution and as high as 1000 $kfps$ at reduced resolution. 35 $kfps$ with 896×768 resolution was chosen in our experiments. Bubble diameter D_b was kept constant at 4.8 mm. Three different liquids as deionized(DI) water, glycerin 25% and glycerin 50% were used, which corresponds to the Ohnesorge number $Oh = 0.00241, 0.00521$ and 0.01677 respectively. The size ratio α took: 0.5, 0.6, 0.7, 0.8. A small amount of dye was added to the droplet to obtain a good illustration of the interface profile. As droplet contacts with the liquid surface, a liquid bridge between the droplet and the pool is immediately formed and grows in size against a thin air layer. Meanwhile, the droplet falls into the pool and two vortex rings are generated symmetrically at the tip of liquid bridge. They grow in time and form a mushroom-like structure (see Fig.1), which is also observed in coalescence between two concave surfaces [2].

*Corresponding author. Email: sigurdur.thoroddsen@kaust.edu.sa

NUMERICAL INVESTIGATIONS

As shown in Fig.2, the velocity of the tip of the liquid bridge decreases in time, the motion of the droplet is mainly along the coalescence axis (see Fig.3). As the size ratio increases, the velocity of the tip increases and the size of the vortex ring increases as well. From Fig. 3, we can observe that the initial droplet is not entirely coalesced into the liquid pool. Following the first contact, a hole (liquid bridge) is formed on the bubble and grows in size. After certain time, the separated thin gas layers can connect to each other again. A daughter droplet is formed inside the bubble and oscillates; the mushroom-like structure continues to develop in the pool (see Fig.3). For small size ratios, vortices are observed to be formed successively after the two primary vortices and enter into the primary one (see case of $\alpha = 0.3$ in Fig.3 (pink line)). Two small vortex rings of opposite sign are formed and expand along the bubble surface, which creates a thin liquid layer (liquid from the drop) covering the bubble surface (see case of $\alpha = 0.5$ in Fig.3 (green line)).

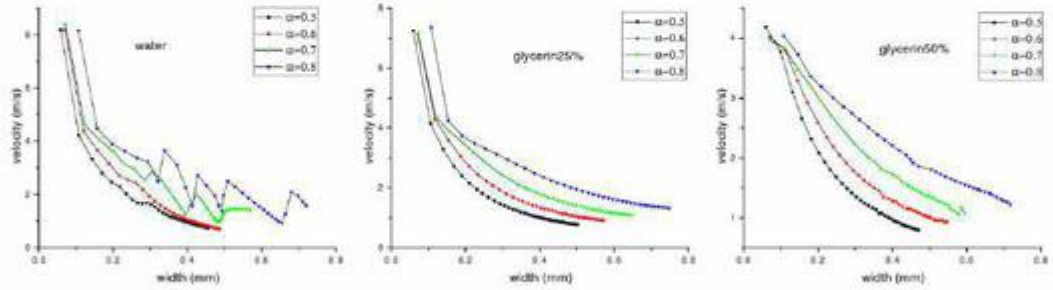

(a) water (b) glycerin 25% (c) glycerin 50%

Figure 2: Velocity of the tip of the liquid bridge vs width of the liquid bridge for different size ratios $\alpha = 0.5, 0.6, 0.7, 0.8$.

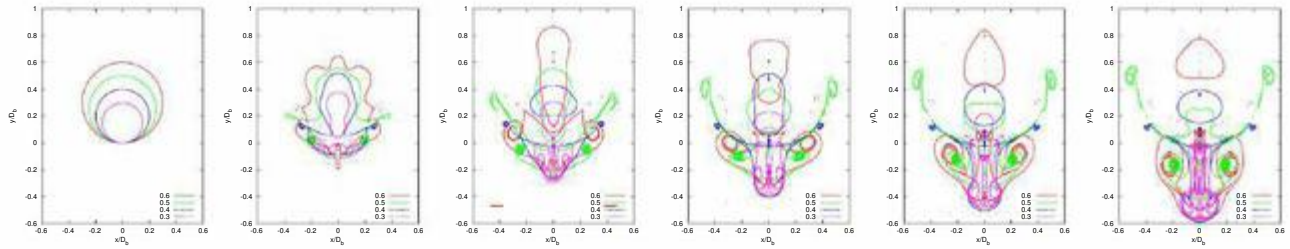

Figure 3: Evolution of droplet interface in time for different size ratios α at $Oh = 0.00246957$. Time interval between figures is $\Delta t = 0.0825614s$.

CONCLUSIONS

In this article, we investigate the coalescence between two convex liquid surfaces by experiments and numerical simulations. The system is determined by two dimensionless numbers: the Ohnesorge number and the size ratio. Different scenarios are observed on varying these two numbers. Following the contact between droplet and pool, the drop falls into the pool and two primary vortex rings with opposite sign are observed by experiments and confirmed in simulations. The two vortices are symmetric to the coalescence axis and form a mushroom-like structure. With a larger size ratio, the tip of the thin gas layer between the drop and the pool retracts faster and results a larger vortex ring. In simulations, more dynamics are found and we have a clear view of the dynamics of gas layer and inside the drop, which is not observed in experiments due to transmittance. Besides the primary vortices, a pair of vortices is also observed and expand along the bubble. The droplet is not entirely coalesced with the pool, a secondary droplet is formed and oscillates inside the bubble.

References

[1] Popinet S.: An accurate adaptive solver for surface-tension-driven interfacial flows. J. Comput. Phys. 228(16)(2009):5838-5866, 2009.

[2] Thoroddsen S. T. , Takehara K. and Etoh T. G.: The coalescence speed of a pendent and a sessile drop. J. Fluid Mechanics, 527, pp 85-114, 2005.

SOAP FILM DYNAMICS UNDER CONTINUOUS DEFORMATION

R. E. Goldstein[1], Adriana Pesci [1], and H. K. Moffatt [*1]
[1]*DAMTP, University of Cambridge, Wilberforce Road, Cambridge, CB3 0WA, UK*

Summary This paper will report on progress in our study of possible topological transitions of a soap film bounded by a deformable wire (or set of wires), with particular attention to the jump of a one-sided Möbius-strip soap film to a two-sided disc. Attention will be focussed on the nature of the boundary singularity that occurs in this case, and the manner in which this singularity is resolved.

BACKGROUND

A soap film bounded by a wire in the form of a closed curve, or a set of such wires, may be two-sided (like a disc) or one-sided (like a Möbius strip). Under static conditions, the soap film is a minimal-area surface on which the mean curvature is everywhere zero. When the wire configuration is slowly and continuously deformed, the surface may become unstable and may then jump to a topologically different configuration. The simplest example is the catenoid bounded by two circular wires, initially close to each other, which becomes unstable at a critical separation when the wires are pulled slowly apart, and which then jumps to two discs spanning the wires separately. In this case, the topological transition involves a singularity at an interior point of the surface, i.e. in the bulk of the fluid.



Figure 1: Soap film just after collapse; here, the local twist of the Plateau border on the wire and the associated local twist of the soap-film surface are revealed by optical reflection.

THE MOBIUS STRIP TRANSITION

We have studied a similar situation when the film has initially the form of a Möbius strip. This may be created by twisting a circular wire, folding it back on itself to form (nearly) the double cover of a circle, and dipping it in soap solution; if the resulting two-sided disc is removed by pricking, a one-sided Möbius-strip soap film remains. The Plateau border of this film (i.e. the curve where the projection of the soap film meets the boundary wire) is doubly linked with the center-line of the wire. If the wire is now slowly unfolded and untwisted back towards a circle, then at a critical stage the soap film surface jumps to a two-sided surface, topologically a disc. This jump occurs through a singularity on the boundary wire (Fig. 1), when the linking number of the Plateau border and the wire centre-line jumps from 2 to zero (Goldstein et al. 2010). Different aspects of this type of phenomenon have been explored in a series of recent papers (Goldstein et al. 2014a, b, Pesci et al. 2015). Collapse is in general localised near a systole (i.e. a non-contractable closed curve of minimum length on the surface) (Fig. 2), and if the systole is linked with the boundary wire, then collapse occurs to a point on the boundary. We have determined the instability threshold for the one-sided minimal surface of Meeks (1981) (Fig. 3), in good qualitative agreement with experiment; in this situation, the systole passes near the maximum of the unstable eigenmode.

*Corresponding author. Email: hkm2@cam.ac.uk

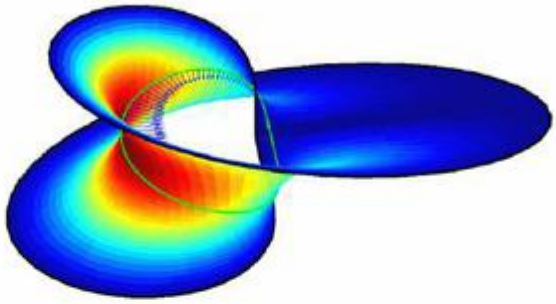

Figure 2: Systole and contours of unstable eigenmode at instability threshold for the incomplete Meeks minimal surface.

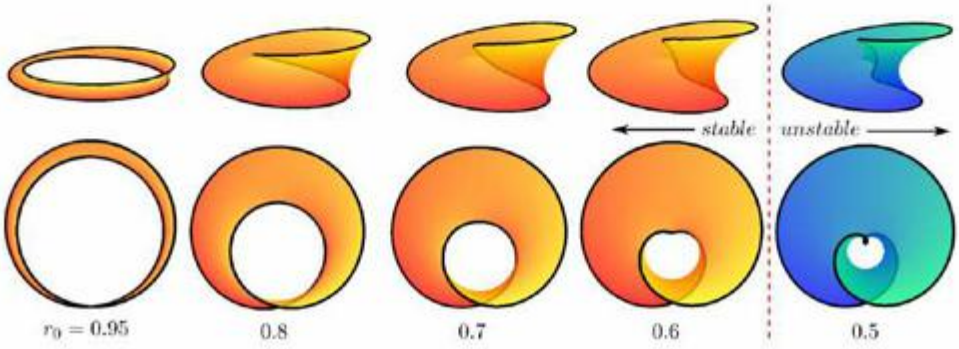

Figure 3: The incomplete Meeks minimal surface and its instability threshold; the critical value of the unfolding parameter is $r_0 \approx 0.545$.

WORK IN PROGRESS

On the assumption that the final stage of collapse of the hole of the Möbius strip is controlled by surface tension and fluid inertia, dimensional analysis shows that this collapse proceeds at speed $v \sim (\sigma/\rho)^{1/3}(t_p - t)^{-1/3}$ where t_p is the singularity time, σ is the surface tension of the film, and ρ its density. If the wire has radius a, the singularity is resolved when $t_p - t \sim (a^3\rho/\sigma)^{1/2}$. The work to be presented aims (i) to confirm the dependence on wire radius, (ii) to analyse the thin-film evolution on the wire surface, and (iii) to describe the viscous mechanism by which the singularity is resolved.

References

Goldstein, R. E., Moffatt, H. K., Pesci, A. I., and Ricca, R. L. 2010. Soap-film Möbius strip changes topology with a twist singularity. *Proc. Natl. Acad. Sci.*, **107**(51), 21979–21984.

Goldstein, R. E., McTavish, J., Moffatt, H. K., and Pesci, A. I. 2014a. Boundary singularities produced by the motion of soap films. *Proc. Natl. Acad. Sci.*, **111**, 8339–8344.

Goldstein, R. E., Huppert, H. E., Moffatt, H. K., and Pesci, A. I. 2014b. Instability of a gravity current within a soap-film. *J. Fluid Mech.*, **753**, R1.

Meeks, W. H. III. 1981. The classification of complete minimal surfaces in R^3 with total curvature greater than -8π. *Duke Math. J.*, **48**(3), 523–535. doi:10.1215/S0012-7094-81-04829-8. http://projecteuclid.org/euclid.dmj/1077314779.

Pesci, A. I., Goldstein, R.E., Alexander, G.P., and Moffatt, H. K. 2015. Instability of a Möbius strip minimal surface and a link with systolic geometry. *Phys. Rev. Lett.*, **114**, 127801.

SIZE AND VELOCITY OF JET DROPS FOLLOWING BURSTING BUBBLES

Thomas Séon*[1], Luc Deike[2], Elisabeth Ghabache[1], Stéphane Popinet[1], and Stéphane Zaleski[1]
[1]*Université Pierre et Marie Curie & CNRS, Institut Jean Le Rond d'Alembert, Paris, France*
[2]*Scripps Institution of Oceanography, University of California San Diego, La Jolla, California*

Summary Bubbles lying at a free surface usually burst and eject myriads of droplets. A quantitative description of these bursting bubble aerosols constitutes a major issue in oceanography. Indeed, this would enable to improve our knowledge of sea spray aerosols, which is crucial to better understand air–sea interactions. Focusing on the bubble bursting, from the collapsing cavity to the jet drop ejection, we show a comparison between experimental results and numerical simulations. In this context, the jet velocity and the drop size are presented as functions of the relevant dimensionless parameters. The results are then discussed in the light of both their fundamental applications in the understanding of the phenomena and their quantitative implications in air–sea interactions.

OBJECTIVE AND PRINCIPLE OF EXPERIMENTS AND SIMULATIONS

Introduction

Sea spray, which transports dissolved gases, salts, surfactants, and biological materials in the atmosphere, is largely attributed to aerosols produced by an estimated 10^{18} to 10^{20} bubbles that burst every second across the oceans [1, 2, 3]. Two distinct types of droplets are involved, based on two different mechanisms during bubble bursting [4]. When the thin liquid film – the bubble cap – separating the bubble from the atmosphere disintegrates, *film drops* are produced [5] with radius mainly less than 1 μm. The resulting opened cavity (see Fig.1) then collapses and a jet emerges producing *jet drops* by breaking up [2, 6]. This latter mechanism accounts for the majority of sea spray aerosol particles in the atmosphere with radius between 1 and 25 μm [3]. The last sixty years have witnessed a number of laboratory studies documenting jet drops properties [2, 4], but a complete comprehensive picture of the mechanisms at play in bubble bursting is still lacking and the size and velocity distributions of the jet drops for a given bubble size distribution is yet unknown.

Objectives

In this talk, experimental and numerical results on bursting bubbles will be presented together. After a brief presentation of the mechanism, we will show that the comparison of the results from these two methods is quite good up to drop detachment (see Fig.1), thus cross-validating the numerical and experimental approaches. The jet velocity and drop size measurements, along with their variations as functions of the control parameters, will allow us to reach two different objectives : improve our understanding of fundamental mechanisms at play in bubble bursting (capillary wave collapse, influence of the bubble shape, roles of liquid properties ...) and quantify the proportion of the jet drop size distribution in the general sea spray aerosol.

Experimental setup and numerical simulation

Our experiment consists in releasing a gas bubble from a submerged needle in a liquid and recording the upward jet after the bubble bursts at the free surface. Different needle diameters ($5 < \Phi$ (μm) < 1800) allow us to create bubbles with radii (R) ranging from 300 μm to 5 mm. The liquids used in this study include water-glycerol-ethanol mixtures with varying viscosity, surface tension and density. The bubble collapse, jet dynamics and drop size are analyzed through extreme close-up ultra-fast imagery. Macro lenses and extension rings allow us to record with a definition reaching 5 μm per pixel. Images are obtained between 10000 and 150000 frames per second using a digital high-speed camera.

Numerically, we solve the axisymmetric, two-dimensional, two-phase, incompressible Navier Stokes equations accounting for surface tension and viscous effects using the open source solver Gerris ([7]), based on a quad/octree adaptive spatial discretization, multilevel Poisson solver. The interface between the high density liquid (water) and the low density gas (air) is reconstructed by a Volume Of Fluid (VOF) method. We initialize the liquid-gas interface with the theoretical shape of the cavity left by a bursting bubble of radius R_b . We use the adaptive mesh of Gerris to solve the collapsing dynamics at very high resolution, with a grid size up to an equivalent of 16384^2, which is necessary to obtain numerically-converged results. The ejection velocity of the jet and the resulting droplets can then be analyzed and compared to the experimental results.

PRESENTATION OF EXPERIMENTAL AND NUMERICAL RESULTS

Figure 1 illustrates a typical jetting event following a bubble bursting at a free surface in water. The top sequence shows the free surface view while the bottom one displays the underwater dynamics. The first image of the top sequence shows a static bubble lying at the free surface. The film separating the bubble from the atmosphere then drains and bursts leaving an unstable opened cavity. The bottom sequence displays capillary waves propagating along this cavity and focusing at the

*Corresponding author. Email: thomas.seon@gmail.com

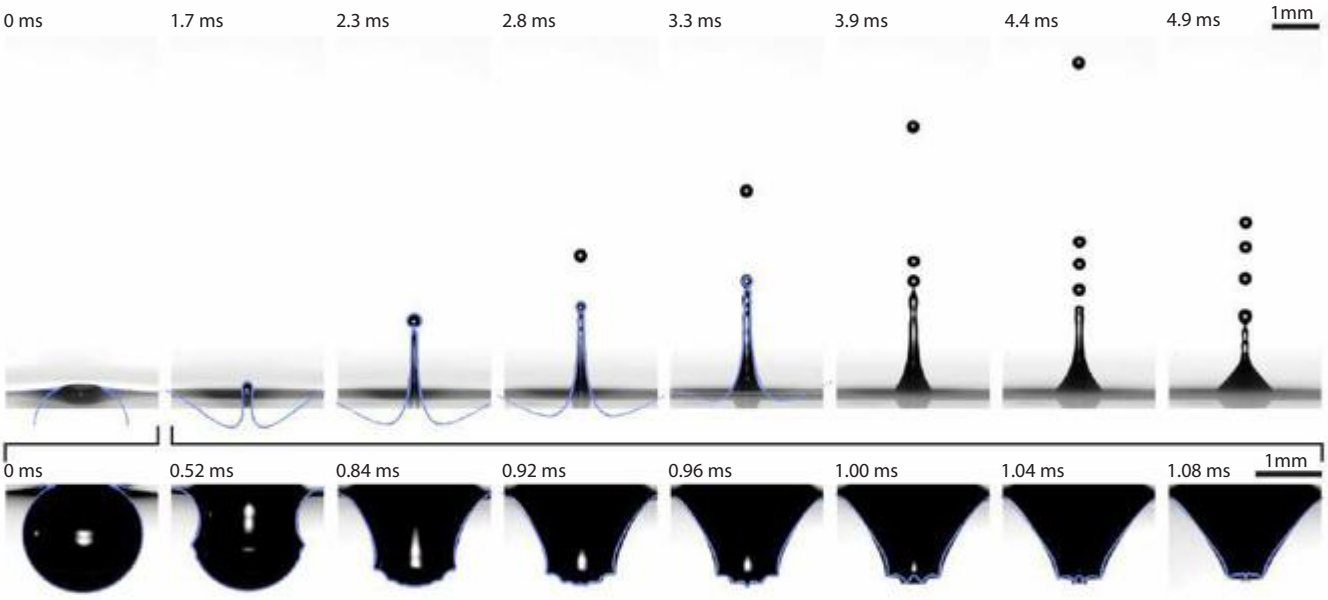

Figure 1: Experimental time sequences superposed with numerical profiles of a typical jetting event following a bubble bursting at a free surface of water. The top sequence shows the bubble bursting event above the free surface, while the bottom sequence displays the bubble under the free surface during the collapse.The bottom sequence takes place between the first two images of the top sequence. Space scale is on each sequence and times are shown on the snapshots with the same origin. Bubble radius is $R_b = 915\mu m$.

bottom. These collapsing waves give rise to a high-speed vertical jet shooting out above the free surface as observed on the top sequence. The jet then fragments into droplets due to Rayleigh-Plateau destabilization generating an aerosol of one to ten droplets [4]. On the two sequences, the cavity and jet profiles computed with numerical simulation have been added, we observe a very good superposition of the numerical profiles with the experimental images up to drop detachment. In the course of the talk we will also present very consistent quantitative comparisons of the jet velocity or drop size [8].

Armed with this new tool, we study the normalized jet velocity variation with the relevant dimensionless numbers for a much larger range than possibly reachable experimentally. In particular, this allows us to decrease continuously the Bond number (Bo = $\frac{\rho g R_b^2}{\gamma}$ with R_b the bubble radius and ρ and γ respectively the density and the surface tension of the liquid) from ~ 1 to 0 [9]. We observe that Bo=0 gives different results than even very small Bond numbers. This is because the shape of the bubble changes slightly [8], modifying somewhat the way the capillary waves propagate (lower sequence of Fig.1). This little change of capillary wave path has a strong influence on the jet dynamics. We look at the fine-scale dynamics, and in particular the collapse, of the capillary waves in order to explain this sensibility of the jet dynamics on the cavity shape. We then present the experimental and numerical data on the drop size as functions of the control parameters, in particular the bubble size. Finally, by convoluting the jet drop size as a function of the bubble radius, with the size distribution of the bubbles generated upon a wave breaking event [10, 11], we obtain the jet drop size distribution generated by bursting bubbles following wave breaking. In a typical sea spray aerosol population we are then able to determine the respective parts of the jet drops and film drops.

References

[1] Woodcock, A. H., Kientzler, C. F., Arons, A. B., Blanchard, D. C., (1953) Giant Condensation Nuclei from Bursting Bubbles. *Nature* **172** 1144

[2] Spiel, D.E., (1997) More on the births of jet drops from bubbles bursting on seawater surfaces. *J. Geophys. Res.* **102** 5815–5821

[3] Lewis, E. R., Schwartz, S. E., (2004) Sea Salt Aerosol Production.*Ed. Geophysical Monograph 152.* (American Geophysical Union, Washington, DC)

[4] Blanchard, D. C., (1963) The electrification of the atmosphere by particles from bubbles in the sea. *Progress In Oceanography* **1** 73

[5] Lhuissier, H., Villermaux, E. (2012) Bursting bubble aerosols. *J. Fluid Mech.* **696** 5–44

[6] MacIntyre, F. (1972) Flow patterns in breaking bubbles. *J. Geophys. Res.* **77** 5211–5228

[7] Popinet, S., An accurate adaptative solver for surface-tension-driven interfacial flows. (2009) *J. Comput. Phys.* **228** 5838–5866

[8] Ghabache, E., Antkowiak, A., Josserand, C., Séon, T., (2014) On the physics of fizziness *Phys. of Fluids.* **2612**

[9] Duchemin, L., Popinet, S., Josserand, C., Zaleski, S., (2002) Jet formation in bubbles bursting at a free surface. *Phys. Fluids* **14** 3000-3008

[10] Deane, Grant B and Stokes, M Dale, (2002) Scale dependence of bubble creation mechanisms in breaking waves *Nature*, **418** 6900, 839–844

[11] Deike, L., Melville, W. K. and Popinet, S. (2016) Air entrainment and bubble statistics in three-dimensional breaking waves *J. Fluid Mech.*, under rev.

ONSAGER'S VARIATIONAL PRINCIPLE AND THE MOVING CONTACT LINE PROBLEM

Tiezheng Qian *

Department of Mathematics, Hong Kong University of Science and Technology, Clear Water Bay, Kowloon, Hong Kong

Summary Onsager's variational principle gives us a general framework to describe non-equilibrium phenomena in the linear response regime. It has been used to derive the hydrodynamic boundary conditions for the moving contact line in two-phase flows. In this paper, we first discuss the moving contact line in immiscible two-phase flows, and then discuss the moving contact line in one-component van der Waals fluids.

ONSAGER'S VARIATIONAL PRINCIPLE

Onsager discovered a fundamental symmetry in the thermodynamic description of irreversible processes for which he was awarded the Nobel Prize [1, 2]. Based on Onsager's reciprocal symmetry, Onsager's variational principle can be outlined as follows. Consider an isothermal system described by a set of coarse-grained variables $\alpha \equiv \{\alpha_i\}$. The free energy is given by $F = F(\alpha)$ and the rate of change of the free energy is $\dot{F}(\alpha, \dot{\alpha})$ which is linear in the rates $\{\dot{\alpha}_i\}$. The dissipation function is half the rate of free-energy dissipation, given by $\Phi(\dot{\alpha}, \dot{\alpha})$, which is quadratic in the rates $\{\dot{\alpha}_i\}$. The action (called Rayleighian) is

$$\mathcal{R} = \frac{\partial F}{\partial \alpha_i}\dot{\alpha}_i + \frac{1}{2}\zeta_{ij}\dot{\alpha}_i\dot{\alpha}_j,$$

where the first term on the right-hand side is $\dot{F}$ and the second term is $\Phi(\dot{\alpha}, \dot{\alpha})$, which is in a quadratic form with the friction coefficients ζ_{ij} forming a *symmetric* and positive definite matrix. Minimization of $\mathcal{R}$ with respect to the rates $\{\dot{\alpha}_i\}$ gives the kinetic equations

$$-\frac{\partial F}{\partial \alpha_i} = \zeta_{ij}\dot{\alpha}_j,$$

which describe the balance between the reversible force $-\partial F/\partial \alpha_i$ and the dissipative force linear in the rates. For a closed system, the entropy shall be used instead of the free energy. In fact, the variational principle is formulated based on the entropy consideration.

THE MOVING CONTACT LINE PROBLEM

The moving contact line problem has been an unsolved classical problem in continuum hydrodynamics for decades. The contact line denotes the intersection of the fluid-fluid interface with a solid wall. When one fluid displaces the other, the contact line moves along the wall. It has been well known that the moving contact line is incompatible with the no-slip boundary condition — the latter leads to a non-integrable singularity in viscous dissipation. As shown by Dussan V. and Davis [3], under the usual hydrodynamic assumptions, namely incompressible Newtonian fluids, smooth rigid solid walls, impenetrable fluid-fluid interface, and the no-slip boundary condition, there is a velocity discontinuity at the moving contact line, and the tangential force exerted by the fluids on the solid bounding surface in the vicinity of the moving contact line is infinite. The heart of the moving contact line problem lies in the boundary condition(s) at the fluid-solid interface. In particular, molecular dynamics (MD) simulations showed that fluid slip indeed occurs at the moving contact line. Numerous models have been proposed over the years, but none have been able to give a quantitative account of the fluid slip measured in MD simulations. In fact, there has been a lasting debate over the boundary conditions for a fluid flowing past a solid surface. In recent years, the Newtonian flows in confined geometries have received much attention, and numerous research efforts have shown that fluid slip occurs at the solid boundary in many circumstances.

MOVING CONTACT LINE IN IMMISCIBLE TWO-PHASE FLOWS

MD simulations have proven to be instrumental in investigating the fluid dynamics in the molecular scale vicinity of the moving contact line. Through analysis of extensive MD data, we found that the fluid slip measured in nanoscale MD simulations is governed by the generalized Navier boundary condition (GNBC). The GNBC states that the relative slip velocity between the fluid and the solid wall is proportional to the total tangential stress — the sum of the viscous stress and the uncompensated Young stress; the latter arises from the deviation of the fluid-fluid interface from its static configuration. By combining the GNBC with the Cahn-Hilliard hydrodynamic formulation for immiscible two-phase flows, we have obtained a

*Corresponding author. Email: maqian@ust.hk

continuum model for moving contact line hydrodynamics. Its numerical implementation has produced continuum solutions in quantitative agreement with MD simulation results [4]. We have also shown that the GNBC can be derived in a variational approach based on Onsager's variational principle [5].

MOVING CONTACT LINE IN ONE-COMPONENT VAN DER WAALS FLUIDS

The moving contact line also exists in one-component two-phase fluids, i.e., liquid-vapor systems. Compared to the immiscible binary fluids, the liquid-vapor systems allow the contact line to move solely through phase transformation (evaporation/condensation), and mathematically, there is no stress singularity due to the no-slip boundary condition applied at the solid surface. There have been several studies of the moving contact line in liquid-vapor systems by the use of diffuse-interface models subject to the no-slip boundary condition. The diffuse-interface models have been developed for one-component fluids and binary fluids, with the interface intervening between the two bulk phases represented by an interfacial region of finite thickness. The order parameter, which is the density for one-component fluids or the composition for binary fluids, assumes distinct constant values in each bulk phase and undergoes rapid but smooth variation in the interfacial region. In our continuum hydrodynamic model for the moving contact line in immiscible two-phase flows, the GNBC is combined with the Cahn-Hilliard diffuse-interface modeling for binary fluids [4, 5]. The diffuse-interface modeling can also be applied to the study of contact-line motion in one-component liquid-vapor systems, with the fluid slip at the solid surface fully taken into account. The dynamic van der Waals theory has recently been presented for one-component fluids. It provides a general scheme of two-phase hydrodynamics involving liquid-vapor transition in non-uniform temperature fields [6]. We have combined the dynamic van der Waals theory for the hydrodynamic equations in the bulk region with Waldmann's method for formulating the boundary conditions at the fluid-solid interface [7, 8]. Our derivation focuses on the balance equations for various fluxes and the positive definiteness of local entropy production. We have derived the hydrodynamic boundary conditions at the fluid-solid interface, which are able to describe velocity slip, temperature slip (Kapitza resistance), and the cross coupling between mechanical and thermal processes [8]. Numerical simulations have shown that the contact line can move through both phase transition and boundary slip, with their relative contributions determined by a competition between the two coexisting mechanisms in terms of entropy production [7]. Recently numerical studies have been carried out for droplet motion driven by a thermal gradient on solid substrates [9] and bubble growth on heated substrates in pool boiling [10].

CONCLUDING REMARKS

We would like to point out that the framework presented above for modeling two-phase flows at solid surfaces, from bulk equations to boundary conditions, can be generalized for modeling other fluid-solid interfacial phenomena. In this regard, Onsager's variational principle has proved to be powerful and successful for describing coupled irreversible processes in the linear response regime.

ACKNOWLEDGEMENTS

This work is supported by Hong Kong RGC Grant No. HKUST604013.

References

[1] Onsager L.: Reciprocal relations in irreversible processes. I. Phys. Rev. 37: 405-426, 1931.
[2] Onsager L.: Reciprocal relations in irreversible processes. II. Phys. Rev. 38: 2265-2279, 1931.
[3] Dussan V. E. B., Davis S. H.: On the motion of a fluidfluid interface along a solid surface. J. Fluid Mech. 65: 71-95, 1974.
[4] Qian T. Z., Wang X. P., Sheng P.: Molecular scale contact line hydrodynamics of immiscible flows. Phys. Rev. E 68: 016306, 2003.
[5] Qian T. Z., Wang X. P., Sheng P.: A variational approach to moving contact line hydrodynamics. J. Fluid Mech. 564: 333-360, 2006.
[6] Onuki A.: Dynamic van der Waals theory. Phys. Rev. E 75: 036304, 2007.
[7] Xu X., Qian T.: Contact line motion in confined liquid-gas systems: Slip versus phase transition. J. Chem. Phys. 133: 204704, 2010.
[8] Xu X., Liu C., Qian T.: Hydrodynamic boundary conditions for one-component liquid-gas flows on non-isothermal solid substrates. Comm. Math. Sci. 10: 1027-1053, 2012.
[9] Xu X., Qian T.: Thermal singularity and droplet motion in one-component fluids on solid substrates with thermal gradients. Phys. Rev. E 85: 061603, 2012.
[10] Xu X., Qian T.: Single-bubble dynamics in pool boiling of one-component fluids. Phys. Rev. E 89: 063002, 2014.

MEASUREMENTS OF MOLECULAR SLIP AND CONTACT LINE MOTION USING A QUARTZ CRYSTAL MICROBALANCE

Justin Pye, Clay Wood, and Justin C. Burton*
Department of Physics, Emory University, Atlanta, GA, USA

Summary The liquid/solid boundary condition and the stick-slip motion of a three-phase contact line represent complex problems where our understanding is incomplete. We have performed a series of experiments that address these issues using a quartz crystal microbalance (QCM). Our first experiment focuses on the evaporation of a sessile drop. The stick-slip motion of the contact line manifests as a sharp increase in frequency of the QCM, followed by a sharp decrease, whereas the dissipation displays a single sharp peak. QCMs pre-cleaned in an oxygen plasma environment exhibited a significantly reduced occurrence and magnitude of these features. Second, a drop of liquid is grown on the QCM in the presence of a second, ambient liquid. The liquids are chosen so that their bulk effects on the QCM frequency and dissipation are identical in the presence of no-slip. Deviations from the conventional theory are identified as anomalous interfacial dynamics, such as slip.

The fluid mechanics of a drop on a solid surface is controlled by the motion of the contact line, as well as the boundary condition at the solid surface, which may vary near the contact line. We have performed a number of experiments exploring both the bulk boundary condition at the interface between a solid and liquid, as well as the stick-slip motion of a three-phase contact line. Our measurements are acquired using an ultra-sensitive technique based on a quartz crystal microbalance (QCM). A QCM is a shear-wave oscillator formed from a very thin piece of quartz crystal. Two electrodes, often made of gold, are sputtered or evaporated onto each side of the crystal. The crystals are excited by applying an AC voltage at the mechanical resonant frequency of the oscillator, where the fundamental mode is typically $f_0 \approx 5$ MHz. The amplitude of the oscillation will depend on the amplitude of the applied voltage, and is typically a few nanometers or less. Thus the speed of the surface is usually 1-10 cm/s. Due to the high quality of the quartz crystal, there is very little internal dissipation. In vacuum, QCMs can attain quality factors of 10^6 or more.

Upon immersion in a liquid, the transverse oscillations of the quartz couple to the liquid near the surface. The shear waves radiated by the crystal travel into the liquid, but are damped by the viscosity of the liquid. The characteristic decay length of the oscillations is known as the penetration depth $\delta = \sqrt{2\eta/\omega\rho}$, where ω is the angular frequency of the oscillations, η is the dynamic viscosity of the liquid, and ρ is the liquid density. For a 5 MHz crystal immersed in water, $\delta \approx 240$ nm. The local shear in the liquid occurs over this length scale, so that typical shear rate for a low viscosity liquid such as water is $\approx 10^5$ s^{-1}. This coupling to the liquid has two effects on the crystal. First, the quartz oscillator behaves as if it has been loaded with an amount of mass equal to the area of contact multiplied by the penetration depth. Second, the crystal experiences viscous dissipation in the liquid. Both the frequency and quality factor will shift, and the 1st-order shifts are predicted to be proportional, yet opposite in sign:

$$\frac{\Delta f}{f_0} = \circ \frac{f_0^{1/2}}{n^{1/2}\pi R_Q}\left(\pi\eta\rho\right)^{1/2}, \qquad \Delta Q^{-1} = \frac{2f_0^{1/2}}{n^{1/2}\pi R_Q}\left(\pi\eta\rho\right)^{1/2}. \tag{1}$$

Here n is the odd harmonic number and R_Q is the acoustic impedance of quartz.

Some of our experiments with the QCM are designed to measure bulk slip occurring at the interface between a liquid and a solid. The simplest model for molecular slip is known as Navier slip, which extends the point at which a linear velocity profile becomes zero near the solid surface to a position inside the solid. This is shown in Fig. 1. The distance below the surface at which the fluid velocity would be zero is known as the slip length s. More complicated interpretations of slip can involve non-Newtonian behavior just nanometers away from the solid surface [1], or the presence of a thin gas film smaller than the mean free path at ambient conditions [2]. In order to resolve the nature of the fluid/solid interaction and the slip length, precision experimental techniques are necessary such as total internal reflection microscopy [3] or atomic force microscopy [4], and each technique spans different ranges of stress and shear rates.

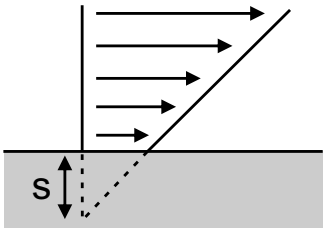

Figure 1: Linear velocity profile inside a fluid near a solid surface.

There have also been a number of studies which investigate interfacial slip using a QCM [5–10]. However, interpreting deviations from equation 1 is very difficult since the crystal frequency is sensitive to stress, temperature, and also is somewhat history dependent. If slip is occurring at the interface, it would be nearly impossible to measure with confidence by depositing a droplet directly from an ambient air environment. To overcome this limitation, we have developed a pseudo-differential measurement in order to isolate anomalous effects at the liquid/solid boundary due to slip. Upon immersion into an ambient fluid, a sessile drop of a second fluid will be grown on the QCM electrode using a small needle. According to equation 1, if the product of the viscosity and density of the fluids is constant, then each fluid should affect the crystals motion in the same way. If there is slip in either fluid, there will be deviations from the simple prediction.

*Corresponding author. Email: justin.c.burton@emory.edu

Let's first look at the response of the QCM to the evaporation of a water drop. Figure 2a shows typical data for a 10μl water drop on the gold surface of the QCM in an enclosed air environment. The change in circuit resistance, ΔR is proportional to ΔQ^{-1}, and has been scaled so that changes in frequency and resistance should lie on top of one another, according to equation 1. The change in resistance and frequency track each other almost perfectly, as predicted. The constant of proportionality is approximately $5 \times 10^{-7}\ \Omega^{-1}$, and is related to properties of the quartz, not the liquid. Upon deposition, there is a large increase in $-\Delta f/f_0$ and ΔR (note the frequency axis is inverted). Liquid has been deposited on the crystal, resulting in an increase in mass (decrease in frequency) and excess dissipation (increase in resistance). The drop first undergoes a regime of shrinkage where the contact area with the surface is mostly constant, as indicated by the plateau between $t = 15$ and 30 minutes. During this time the contact angle is decreasing. After $t = 30$ minutes, the solid contact area of the drop then begins to shrink until the liquid has completely evaporated.

There are several spikes in both the frequency and resistance which are associated with the stick-slip motion of the receding contact line. The frequency first decreases, then sharply increases, while the resistance shows a single sharp peak. QCM's which have been pre-cleaned in an oxygen plasma environment show significantly less pinning events. In principle, the size of these features allow us to quantitatively measure the pinning forces on the contact line. This requires a model for how a force applied to the surface of the QCM affects both its frequency and dissipation. Although we do not currently have such an analytical model, we note that our data is consistent with a slow build-up of tangential force on the crystal as the contact angle decreases, then a regime of high dissipation as the contact line lurches to a new position, and finally a slow relaxation back towards the equilibrium contact angle.

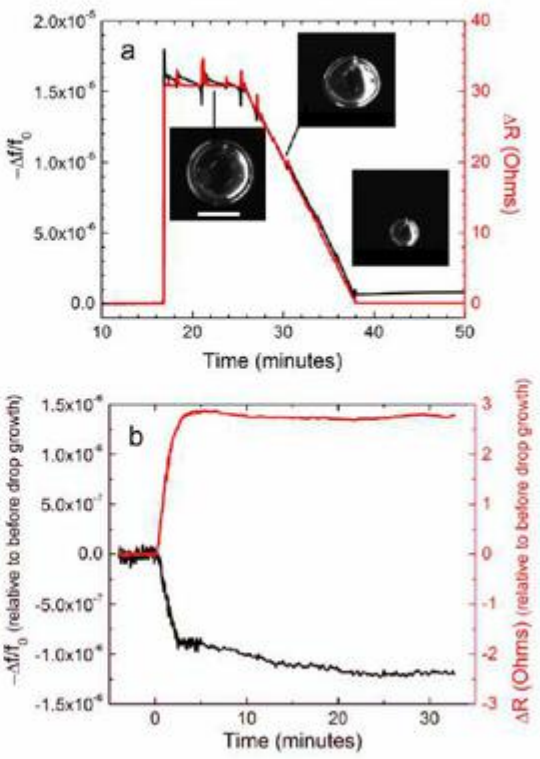

Figure 2: Changes in frequency and resistance during the deposition and evaporation of a water drop in air (a), and during the growth of a water drop surrounded by undecane. Both experiments are performed on the gold surface of a QCM.

Now we turn our attention to more sensitive, pseudo-differential measurements which are designed to measure interfacial slip. Preliminary data from the growth of a water drop in this experiment can be seen in Figure 2b. The water drop is grown in an ambient fluid, undecane, which has the same density-viscosity product as water at 48°C. There is a sharp change in the data as the drop is grown, and then both curves flatten out when growth is ceased. The data is scaled with the same constant of proportionality used in Figure 2. The technique is very sensitive, note that the changes here are ≈ 100 times smaller than Figure 2a. According to Eqn. 1, these two curves should be superimposed, yet surprisingly, both the frequency and resistance increase. Since $\eta_w \rho_w = \eta_u \rho_u$, these effects are due to anomalous behavior occurring the interface. Taken at face value, the change in frequency would suggest a slip length at the water/gold interface of ≈ 5 nm, assuming that the undecane does not experience interfacial slip since it strongly wets the gold.

References

[1] D. E. Weidner & L. W. Schwartz. "Contact-line motion of shear-thinning liquids." *Phys. Fluids*, **6**, 3535–3538 (1994). DOI: 10.1063/1.868412.

[2] P. G. de Gennes. "On fluid/wall slippage." *Langmuir*, **18**, 3413–3414 (2002). DOI: 10.1021/la0116342.

[3] P. Huang & K. S. Breuer. "Direct measurement of slip length in electrolyte solutions." *Phys. Fluids*, **19**, 028104 (2007). DOI: 10.1063/1.2539829.

[4] S. P. McBride & B. M. Law. "Viscosity-dependent liquid slip at molecularly smooth hydrophobic surfaces." *Phys. Rev. E*, **80**, 060601 (2009). DOI: 10.1103/PhysRevE.80.060601.

[5] F. Ferrante, A. L. Kipling, & M. Thompson. "Molecular slip at the solid-liquid interface of an acoustic-wave sensor." *J. Appl. Phys.*, **76**, 3448–3462 (1994). DOI: 10.1063/1.357475.

[6] J. S. Ellis & G. L. Hayward. "Interfacial slip on a transverse-shear mode acoustic wave device." *J. Appl. Phys.*, **94**, 7856–7867 (2003). DOI: 10.1063/1.1627949.

[7] F. Lu, H. Lee, & S. Lim. "Detecting solidliquid interface properties with mechanical slip modelling for quartz crystal microbalance operating in liquid." *J. Phys. D: Appl. Phys.*, **37**, 898–906 (2004). DOI: 10.1088/0022-3727/37/6/014.

[8] J. Jones & T. Coffey. "Using the quartz crystal microbalance to study macro- and nanoscale bubbles at solidliquid interfaces." *J. Phys.: Conf. Series*, **100**, 072026 (2008). DOI: 10.1088/1742-6596/100/7/072026.

[9] M. Salom'aki & J. Kankare. "Large apparent interfacial slippage at polyelectrolyteperfluorocarbon interfaces on a quartz crystal resonator." *Langmuir*, **20**, 7794–7801 (2004). DOI: 10.1021/la049107g.

[10] B. Du, I. Goubaidoulline, & D. Johannsmann. "Effects of laterally heterogeneous slip on the resonance properties of quartz crystals immersed in liquids." *Langmuir*, **20**, 10617–10624 (2004). DOI: 10.1021/la0483515.

MICRO-CONFINED DROPLETS: FROM LUBRICATION FILM TO VELOCITY

Axel Huerre*[1], Benjamin Reichert[1], Isabelle Cantat[2], Olivier Théodoly[3], and Marie-Caroline Jullien[1]

[1]*MMN, UMR CNRS Gulliver 7083, PSL research University, ESPCI ParisTech, F-75005 Paris, France*

[2]*IPR, UMR CNRS 6251, Université de Rennes 1, 35000 Rennes, France*

[3]*LAI, INSERM U600, CNRS UMR 6212, Case 937, 13009 Marseille, France*

Summary We study the motion of droplets in a confined, micrometric geometry, by focusing on the lubrication film effect on droplet velocity. When capillary forces dominate, the lubrication film thickness evolves non-linearly with the capillary number due to the viscous dissipation between the meniscus and the wall. However, this film may become thin enough (tens of nanometres) that intermolecular forces come into play and affect classical scalings. Our experiments yield highly resolved topographies of the shape of the interface and allow us to bring new insights into droplet dynamics in microfluidics. We report the novel characterization of two dynamical regimes as the capillary number increases: (i) at low capillary numbers, the film thickness is constant and set by the disjoining pressure, while (ii) above a critical capillary number, the interface behaviour is well described by a viscous scenario. Considering this, we propose a refined model to predict the droplet velocity.

DROPLET DYNAMICS

Droplet-based microfluidics is a growing field of research in both academic and industrial issues. Systems are getting more and more complex, in the perspective of integrating combined functionalities (generation, merging, sorting, breaking...) requiring an accurate synchronization for automated systems. The synchronization addresses the issue of predicting droplet velocity while it is carried by a continuous phase of, say, imposed flow rate. Up to our knowledge, despite the importance of such a question, this issue is not addressed in the literature in confined geometries at microscales. Predicting droplet velocity call for a full knowledge of the dissipation mechanisms at play, this requires determining the full 3D profile of a travelling droplet, mostly close to the walls.

Since the historical work of Taylor & Saffman, our understanding of bubbles/droplets displacement in confined geometries have been steadily refined. For example, the work of Bretherton [1] was the first to describe the influence of the lubrication film (i.e. the thin film lying between a meniscus and a wall) on the motion of a slender inviscid bubble. Far from the meniscus, in the flat region, the film reaches a uniform thickness h_∞, related to the bubble velocity through the capillary number $Ca = \mu_f U_d/\gamma$, where U_d is the bubble velocity, μ_f the viscosity of the continuous phase, and γ the surface tension. More precisely, when $Ca \ll 1$, the thickness of the film follows $h_{\mathrm{Breth}} = 1.34\, r\, Ca^{2/3}$, where r is the radius of the capillary tube. Subsequent studies refine this scaling argument [2], *e.g.* to take into account the influence of surfactants in the outer phase. In those cases, the power law is not affected, but numerical prefactors are introduced in the expression of h_∞ [3]. However, this scaling can be modified by the droplet viscosity [4] leading to thicker films than the Bretherton case.

From these laws on the lubrication film thickness, one can derive the velocity ratio β, taking into account the different sources of dissipation. Doing so, Dangla, Baroud and Gallaire derived the following expression [5] (DBG formula):

$$\beta = \frac{U_d}{U_f} = \frac{2}{(1+\lambda) + \alpha_1 h_\infty^{-1/2} + \alpha_2 h_\infty^{-1}}. \tag{1}$$

where $\lambda = \mu_d/\mu_f$ is the viscosity ratio, U_f the outer fluid velocity, α_1 and α_2 prefactors depending on geometrical parameters.

Among the literature cited above, most of the works on film thicknesses or droplet velocitites were conducted with millifluidic experiments. However, the typical velocities and lengthscales involved in droplet-based microfluidics would lead to lubrication films so thin that intermolecular forces should come into play, and the classical macroscopic predictions based on Bretherton's model are expected to fail [6].

We report an experimental characterization of h_∞ with two dynamical regimes as the capillary number increases, see Fig.1.a: (i) at low capillary numbers, the film thickness is constant and set by the disjoining pressure, *i.e.* intermolecular forces come into play, while (ii) above a critical capillary number Ca^*, the interface behaviour is well described by a Bretherton-like viscous scenario [7] in which the viscosity of the droplet strongly influences the lubrication film thickness. We also show at the transition that there is a difference between the interfacial velocity and the droplet velocity. This is possible using a micellar solution and taking advantage of the surfacic patterns emerging from the oscillating shape of the disjoining pressure (see Fig.1.b). Tracking those patterns allow recovering the interfacial velocity. The scalings obtained for h_∞ lead to a mobility β which is constant in the disjoining pressure regime and is expected to scale with the DBG formula. We show that this model in the capillary regime ($Ca > Ca^*$) does not recover the experimental results as the dissipation is overestimated. The expected

*Corresponding author. Email: axel.huerre@gmail.com

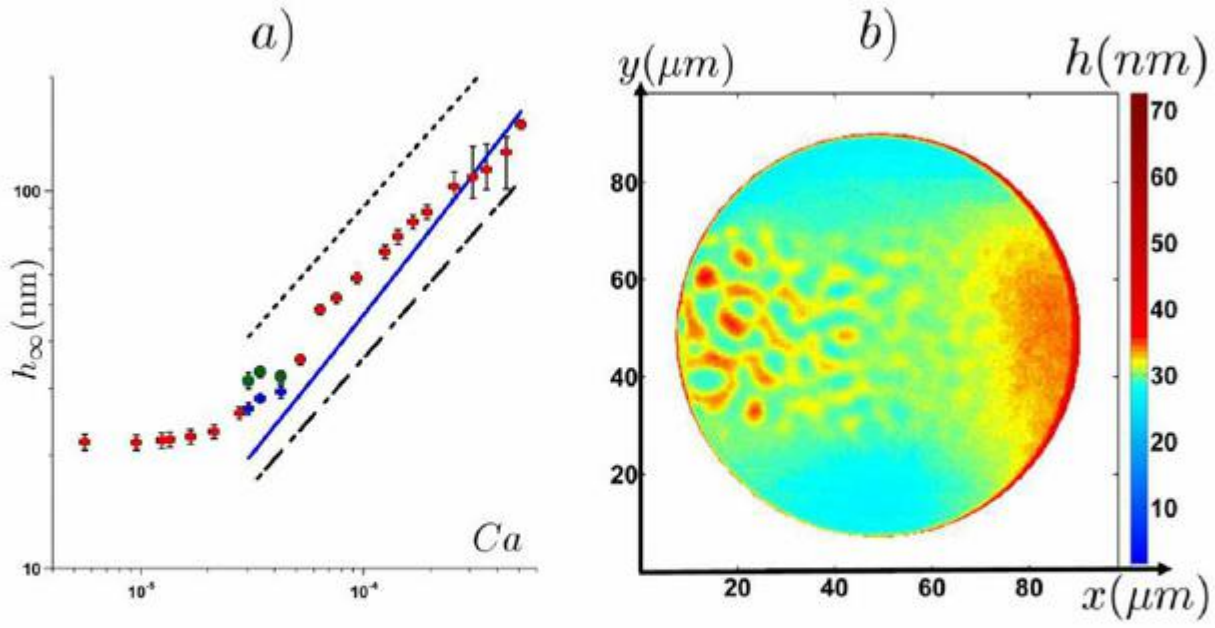

Figure 1: **a)** Local film thickness as a function of the capillary number. (•): Experimental data. For $3 \cdot 10^{-5} < Ca < 5 \cdot 10^{-5}$, two thicknesses coexist: (■) $h_{\max}$ and (⧫) $h_{\min}$.**b)** Spatial plot of the film thickness, for $Ca = 3.4 \cdot 10^{-5}$. $h_{\max}$ is coded in red and $h_{\min}$ in light blue. Note that the color scales is adjusted in order to enhance the pattern contrast.

velocity is lower than what is observed, *i.e.* the droplet goes too fast. We propose a refinement of the DBG model by taking into account both the viscosity ratio of the two phases (the importance was evidenced in the investigation of h_∞) and the interfacial velocity, evidenced for $Ca \sim Ca^*$ in the measurement of h_∞, as a boundary condition for the interface. Doing so allows building a new model with only one fitting geometrical parameter which recovers well our experiment (see Fig.2).

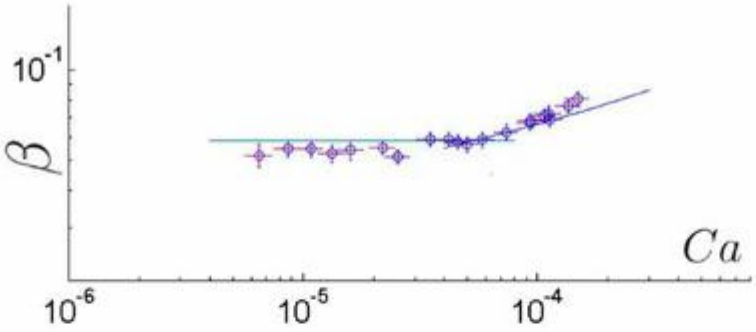

Figure 2: Velocity ratio β as a function of the capillary number. (•): Experimental data. The blue lines are obtained by fitting the data with the interfacial velocity model, with the same fitting parameter.

References

[1] F.P. Bretherton. The motion of long bubbles in tubes. *Journal of Fluid Mechanics*, 10(02):166–188, 1961.

[2] A. Huerre, V. Miralles, and M.-C. Jullien. Bubbles and foams in microfluidics. *Soft Matter*, 10(36):6888–6902, 2014.

[3] I. Cantat. Liquid meniscus friction on a wet plate: Bubbles, lamellae, and foams. *Physics of Fluids (1994-present)*, 25(3):031303–031303–21, 2013.

[4] S.R. Hodges, O.E. Jensen, and J.M. Rallison. The motion of a viscous drop through a cylindrical tube. *Journal of Fluid Mechanics*, 501:279–301, 2004.

[5] Rémi Dangla. *2D droplet microfluidics driven by confinement gradients*. PhD thesis, 2012.

[6] G.F. Teletzke, H.T. Davis, and L.E. Scriven. Wetting hydrodynamics. *Revue de Physique Appliquée*, 23(6):989–1007, 1988.

[7] A. Huerre, O. Theodoly, A. M. Leshansky, M.-P. Valignat, I. Cantat, and M.-C. Jullien. Droplets in microchannels: Dynamical properties of the lubrication film. *Physical Review Letters*, 115(6):064501, 2015.

DYNAMICS OF LEAKY DIELECTRIC DROPS IN STRONG ELECTRIC FIELDS: BOUNDARY ELEMENT SIMULATIONS

Debasish Das[1] and David Saintillan *[1]

[1]*Department of Mechanical and Aerospace Engineering, University of California, San Diego, 9500 Gilman Drive, La Jolla, California 92093-0411, USA*

Summary The deformation of leaky dielectric drops in a dielectric fluid medium when subject to a uniform electric field is a classic electrohydrodynamic phenomena best described by the well known Melcher-Taylor leaky dielectric model [1, 2]. In this work we develop a three-dimensional boundary element method for the full leaky dielectric model to systematically study the deformation and dynamics of drops in electric fields. The inclusion of charge convection in our simulations permits us to investigate dynamics in the so-called Quincke regime of strong electric fields, in which experiments have demonstrated symmetry breaking bifurcations leading to spontaneous rotation [8]. Most previous simulations have neglected charge convection or assumed axisymmetric drop shapes which prevents investigation of Quincke rotation in drops. Our numerical simulations show excellent agreement with experiments [9]. We also extend Taylor's small deformation theory [1] to include the transient shape deformation, charge relaxation and convection terms in the leaky dielectric model.

INTRODUCTION

The electrodynamics of liquid droplet subject to an electric field is a classic and rich problem governed primarily by the interplay of electric and viscous stresses at the interface between the two immiscible liquids. In his pioneering work, Taylor showed that when the drop and the suspending fluid medium are allowed to have finite conductivities, surface charges can generate on the interface which in turn can drive circulatory currents inside and outside the drop. Taylor [1] derived an expression for a discriminating function $\Phi(R, Q, \lambda)$ that predicts whether the drop attains a prolate or an oblate shape, and also calculated the drop deformation $D = (L \circ\ B)/(L + B)$ correct to first order in electric capillary number $Ca_E = a\epsilon_1 E_0/\gamma$, where L, B are the length and width of the drop, respectively, and γ is the interfacial surface tension. Taylor's deformation parameter *D* represents deviations from sphericity and the electric capillary number captures the ratio of electric to capillary forces. Here, E_0 is the applied electric field, *a* is the original drop radius, ϵ and σ are the fluid permittivity and conductivity respectively. Throughout this article, subscript 1 and superscript $+$ shall refer to the fluid medium while subscript 2 and superscript $\circ$ shall refer to the drop. $R = \sigma_1/\sigma_2$, $Q = \epsilon_2/\epsilon_1$ and $\lambda = \mu_2/\mu_1$ are the conductivity, permittivity and viscosity ratios. Melcher and Taylor [2] developed a more complete model applicable for leaky dielectric drops, in which charge conservation on the drop surface is expressed as

$$\frac{\partial q}{\partial t} + [\![\mathbf{n} \cdot \mathbf{J}]\!] + \boldsymbol{\nabla}_s \cdot (q\mathbf{u}) = 0, \quad \mathbf{x} \in S. \tag{1}$$

where, $q = \epsilon_1 E_n^+ \circ\ \epsilon_2 E_n^-$ is the interfacial charge density, $[\![\mathbf{n} \cdot \mathbf{J}]\!] = \sigma_1 E_n^+ \circ\ \sigma_2 E_n^-$ is the jump in electric current, $\mathbf{u}$ is the interfacial velocity and S is the drop-fluid interface. There have been numerous simulations [4, 7] based on this model to reproduce experimental results [5]. However, most of these simulations have either neglected charge convection or assumed axisymmetric drops shapes. Making either or both of these assumptions prevents observation of Quincke rotation of drops. The novelty of our work lies in the formulation of a boundary element method for the full Taylor-Melcher leaky dielectric model in 3D domain including transient charge relaxation and convection terms, which enables us to predict Quincke rotation.

PROBLEM FORMULATION

We consider a neutrally buoyant leaky dielectric drop suspended in a fluid medium with no net charge. The electric problem is governed by Laplace's equation while the flow problem is governed by Stokes' equation. We use standard boundary element method to solve these two equations [6]. Towards this purpose, we discretize the surface of the drop into 6-nodes curved elements using successive subdivision of an icosahedron. We briefly summarize the numerical method here. At any given point in time, we obtain the normal component of the electric field, E_n^+ and E_n^-, from the interfacial charge distribution q on the drop surface using a regularized boundary integral equation and Gauss's law. Once the electric field is known we can compute the Maxwell electric stress on the surface. The electric $\mathbf{T}^E$ and viscous stress $\mathbf{T}^H$ balance the surface tension acting on the drop.

$$[\![\left(\Delta\mathbf{T}^E + \Delta\mathbf{T}^H\right) \cdot \mathbf{n}]\!] = \frac{2\kappa_m \mathbf{n}}{Ca_E}, \quad \mathbf{x} \in S, \tag{2}$$

where κ_m is the mean curvature and $\mathbf{n}$ is the unit normal vector. The interfacial velocity is then computed from the hydrodynamic force on the surface using the boundary integral equation for Stokes flow [3]. The charge conservation equation

*Corresponding author. Email: dstn@ucsd.edu

is then advanced in time using a second order Runge-Kutta scheme. In order to validate our more complicated 3D simulations, we also perform axisymmetric simulations. Additionally, we also use small deformation theory to obtain two coupled ODEs for the shape deformation D and the interfacial charge that are integrated in time. We only present the results of the semi-analytical theory and omit the details here for brevity.

RESULTS

The electrohydrodynamics of drops is completely characterised by five dimensionless parameters namely, R, Q, λ, Ca_E and $Ma = 2\mu_1/(\epsilon_1 \tau_{mw} E_0^2)$ known as the Mason number, which denotes the ratio of viscous to electric forces and involves the Maxwell-Wagner relaxation time τ_{mw}. Our simulations show excellent agreement with the experimental results of Salipante and Vlahovska [8] and Lanauze et al. [9].

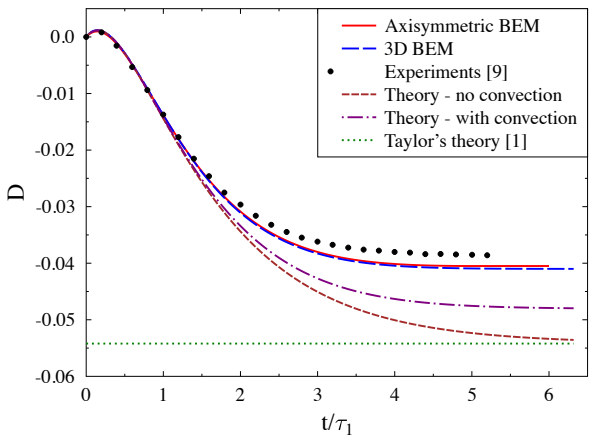

(a) Transient deformation of a silicone oil drop suspended in castor oil. The electric field strength is $E/E_c = 0.49$, $R = 29$, $Q = 0.57$, $\lambda = 0.074$, $Ca_E = 0.49$, $Ma = 1.30$. The time is non dimensionalized with the charge relaxation time of the medium τ_1.

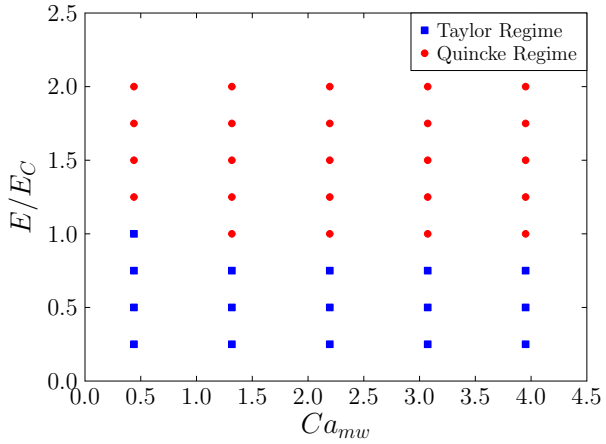

(b) Transition of silicone drop suspended in castor oil from Taylor Regime to Quincke Regime for various electric field strength and drop sizes. $Ca_{mw} = MaCa_E(1+\lambda)/2$ is independent of the electric field strength but is directly proportional to the drop size a.

Figure 1: Comparison of numerical simulations with experiments

CONCLUSIONS

We have developed a three-dimensional boundary element for studying the electrohydrodynamics of drops in strong electric fields. Our numerical simulations predicts transient drop deformations accurately when compared to experimental results. Our simulations also enabled us to predict the transition from Taylor regime characterized by oblate-shaped drops and quadrupolar flow fields to the Quincke regime characterized by titled drops and rotational flows as the electric field strength is increased. Our simulation method can be easily extended to study the electrohydrodynamics of arbitrary shaped rigid objects, deformable objects like vesicles and pair interactions as well. Our novel small deformation theory also works extremely well for small drop deformations and captures the transient behavior accurately; we are currently investigating its extension to study droplet pair interactions.

References

[1] Taylor G. I.: Studies in electrohydrodynamics I. The circulation produced in a drop by an electric field. Proc. R. Soc. A **291** 15966, 1966.
[2] Melcher J. R., Taylor G. I.: Electrohydrodynamics: a review of the role of interfacial shear stresses. Annu. Rev. Fluid Mech. **1** 111 46, 1969.
[3] Rallison J. M., Acrivos A.: A numerical study of the deformation and burst of a viscous drop in an extensional flow. J. Fluid Mech. **89** 191-200, 1978.
[4] Sherwood J. D.: Breakup of fluid droplets in electric and magnetic fields. J. Fluid Mech. **188** 13346, 1988.
[5] Ha J., Yang S.: Deformation and breakup of Newtonian and non-Newtonian conducting drops in an electric field. J. Fluid Mech **405** 131-156, 2000.
[6] Pozrikidis C.: A practical guide to boundary element methods with the software library BEMLIB. CRC Press, 2002.
[7] Lac E., Homsy G. M.: Axisymmetric deformation and stability of a viscous drop in a steady electric field. J. Fluid Mech. **590** 239-264, 2007.
[8] Salipante P. F., Vlahovska P. M.: Electrohydrodynamics of drops in strong uniform dc electric fields. Phys.Fluids **22** 112110, 2010.
[9] Lanauze J. A., Walker L. M., Khair A. S.: Nonlinear electrohydrodynamics of slightly deformed oblate drops. J. Fluid Mech. **774** 245-266, 2015.

WETTING TRANSITION OF SUBMERGED STRUCTURES UNDER H DROSTATIC AND FLOW CONDITIONS

Yaolei Xiang[1], Pengyu Lv[1], Yahui Xue[1], Huiling Duan[1, a)]
[1] *State Key Laboratory for Turbulence and Complex Systems, Department of Mechanics and Engineering Science, College of Engineering, Peking University, Beijing, P. R. China*

Summary Superhydrophobicity relies on the maintenance of air cushions on structured hydrophobic surfaces buried underwater. However, the water-air interfaces are subject to instabilities induced by various mechanisms, leading to the wetting transition from a Cassie-Baxter to Wenzel state. In this work, the wetting transition on submerged microtextures under a hydrostatic or flow condition is studied. Confocal microscopy technique is used to observe the dynamic evolution of the water-air interfaces. The whole wetting transition process is monitored, and the classic CB, Wenzel states and an intermediate metastable state are directly observed. A diffusion-based mode is developed to predict the evolution process of metastable states under both hydrostatic and flow conditions. The acceleration of air diffusion by a convection regime to is captured, which is well described by a scaling law. The current work reveals the underlying mechanism of wetting transition on submerged structures and provides a longevity prediction of underwater superhydrophobicity.

INTRODUCTION

Superhydrophobic surfaces with remarkable properties have promising applications in many fields such as self-cleaning and drag reduction [1]. The existence of air cushions on structured hydrophobic surfaces buried underwater in a Cassie-Baxter (CB) state is the key mechanism to realize superhydrophobicity. However, many factors cause the instabilities of the water-air interfaces and induce the transition from a non-wetted CB to fully wetted Wenzel state along with the loss of superhydrophobicity. Understanding the CB-to-Wenzel transition and the dynamic evolution of the metastable states is critical for the design of CB-based superhydrophobic structures.

Various experiments have investigated the CB-to-Wenzel transition and metastable states in two typical situations, i.e., hydrostatic and flow conditions. When submerged in still water, air cushions decay on superhydrophobic surfaces, as induced by air diffusion. When structured surfaces are exposed in a flow field, the longevity of the air cushions will decrease with increasing flow rate because of the promoted air diffusion. Although previous attempts have been made to capture the dynamic transition process, a controlled, sufficiently resolved measurement to establish a quantitative understanding is currently absent under both hydrostatic and flow conditions, which is the focus of the present work.

E PERIMENTAL SETUPS

Based on the confocal microscopy technique, we built up experimental setups to observe the dynamic wetting transition process on submerged microstructured surfaces in still water and channel flow field, respectively. As shown in Fig. 1, for the hydrostatic condition, the sample was mounted on the bottom of a sealed chamber. A water immersion objective right above the sample was protruded and sealed in the chamber to observe the evolution of menisci under different hydrostatic pressures. A similar setup was used for the channel flow condition, but with a rectangular channel of high aspect ratio (10: 1), through which the liquid flowed circularly. Here, only relatively low flow rate range (less than 12 mm/s) was investigated. The sample was embedded in the bottom of the channel with an optical window right above. The surrounding pressure was changed by regulating pressure in the water tank connected to the channel.

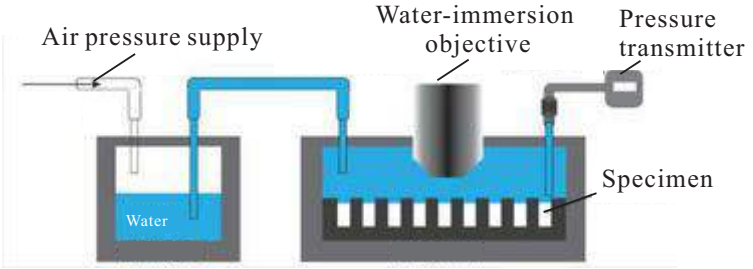

Figure 1. Schematics of the experiment setup for direct observation of the wetting transition process under a hydrostatic condition.

RESULTS

We n r ns n n er r s cc n n

[a)] Corresponding author. Email: hlduan@pku.edu.cn

In still water, the wetting transition on structured hydrophobic surfaces submerged underwater is mediated by air diffusion under different hydrostatic pressures. Due to the compressibility of entrapped air in the cavities, a depinned metastable state can be established in-between the CB and Wenzel states [2]. Especially for the metastable state, the impalement of the meniscus was monitored by recording the increase of the sagging depth over time under different hydrostatic pressures [3], as shown in Fig. 2(a). A diffusion-based theoretical model is used to interpret the evolution process of the metastable states. A similarity law along with a characteristic time scale is derived which governs the lifetime of the air pockets and can be used to predict the longevity of underwater superhydrophobicity [2],

$$\frac{h(t)}{H} = \frac{h_0}{H} + \frac{A/\pi r^2}{K_G/RT}\left(\frac{t}{t_D}\right), \tag{1}$$

where $h(t)$ is the sagging depth, A is the meniscus area, H and r are the height and the radius of the micropore, respectively, h_0 is the initial sagging depth, K_G is Henry's constant, T is the surrounding temperature, R is the universal gas constant and t_D is the characteristic time scale, equal to $[p_G/(p_G - sp_{G,0})](Hl/D_G)$ where p_G is the gas partial pressure inside the micropore, $p_{G,0}$ is the gas partial pressure at atmospheric pressure, s is the saturation degree and l is the diffusion length which is constant in still water. Fig. 2(b) shows that all the experiment data collapse on the curve predicted by the similarity law, indicating the simple model captures the main mechanism controlling the longevity of the air pockets, namely, gas diffusion under a pressure gradient across a thin boundary layer adjacent to the interface.

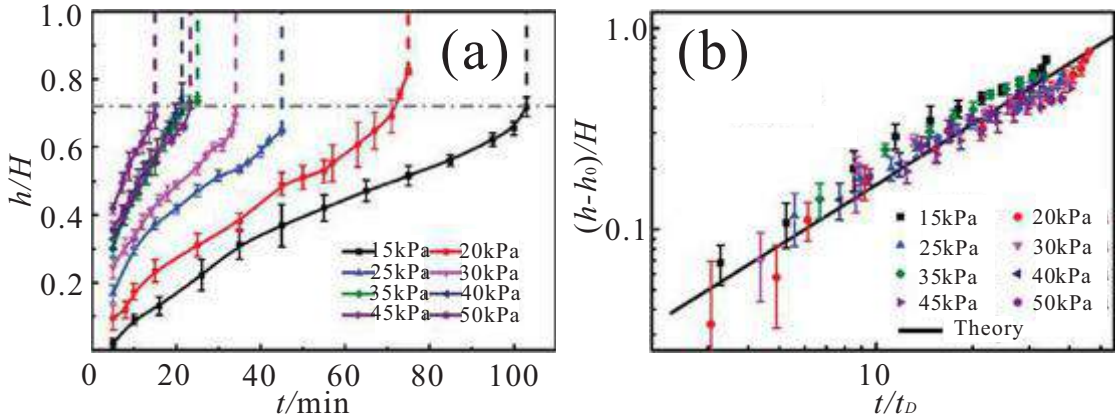

Figure 2. Experimental results and theoretical predictions under hydrostatic conditions. (a) Experimental measurement of the dynamic evolution of the normalized sagging depth under different liquid pressures. (b) Normalized sagging depth as a function of normalized time in the metastable states.

We n r ns n n er c nne f c n n

The instability of water-air interfaces is deteriorated under fluid flow conditions, as the promoted air diffusion from entrapped air cavities into bulk water in a convection regime advances the wetting transition. We directly observed the meniscus evolution in both pinning and depinned states at several low Reynolds numbers (*Re*). If the meniscus is initially pinned at the pore corners under a relatively low liquid pressure, low flow rates will not cause the wetting transition but accelerate the process from one stable state to another. If the meniscus has already depinned before it is subject to flow, the evolution rate of metastable states will increase with *Re*. This positive correlation indicates that the air diffusion is enhanced by increasing the flow rate, as reflected by the decrease of the diffusion length *l*. Consider the diffusion length *l* as a function of *Re* instead of a constant under hydrostatic conditions. Eq. 1 can also be used to predict the diffusion rate under flow conditions. Intriguingly, a 1/3-power law between *l* and *Re* was discovered experimentally, that is,

$$l(\mathrm{Re}) = k \times \mathrm{Re}^{1/3}, \tag{2}$$

where k is constant related to flow conditions. The power low agrees well with the analysis about boundary diffusion problems in flow channels [4].

References

[1] Rothstein J. P.: Slip on superhydrophobic surfaces. *Annu. Rev. Fluid Mech*. **2**: 89-109, 2010.

[2] Xue, Y., Chu, S., Lv, P., Duan, H.: Importance of hierarchical structures in wetting stability on submersed superhydrophobic surfaces. *Langmuir* **2** : 9440-9450, 2012.

[3] Lv P. Y., Xue Y. H., Shi Y. P., Lin H., Duan H. L.: Metastable states and wetting transition of submerged superhydrophobic structures. *Phys. Rev. Lett.* **2**: 196101, 2014.

[4] Levich V. G., Technica S.: Physicochemical hydrodynamics. Englewood Cliffs, NJ: Prentice-hall, 1962.

VELOCITY MEASUREMENTS IN DRAINING FOAM FILMS

J. Seiwert[1], R. Kervil[1], S. Nou[1] & I. Cantat[1a)]
[1]*Institut de Physique de Rennes, Université de Rennes 1, Rennes, France*

Summary Foam film drainage under gravity is a key ingredient controlling foams and bubbles stability. It has been shown by Mysels *et al.* in a pioneering work [1] that the drainage time is proportional to the film width, which was qualitatively explained at that time by the dominant role of the menisci at the film boundaries. This implies a complex flow within the draining film that we measure here for the first time using a tracer-free innovative velocimetry technique. Fluorescein is added in the film and a dark spot is photo-bleached. This spot then acts as a perfect passive tracer during fractions of second, before disappearing by diffusion or mixing. We evidence the lateral part of the film moving upward and the central part moving downward and we propose scaling laws for the associated velocities [2].

INTRODUCTION

Foam films are stable because surface tension gradients induce a net force on the trapped solution and balance the gravity [3]. The velocity within the film, *relatively to the interface,* is a simple Poiseuille flow, with a typical velocity given by the Reynolds prediction $v_R=\rho g h^2/\eta$, with ρ the fluid density, g the gravity, h the local film thickness and η the fluid viscosity. If h is of the order of 1 micron, this Reynolds velocity is of the order of 10 μm/s which is much lower than the measured velocities. The velocities in the film are thus controlled by the interface velocities, which are governed by much more complex physical processes, involving the rheological properties of the surfactants. The experimental and theoretical study of the gravity drainage process may thus shed a new light both on foam stability and on surfactant dynamics.

EXPERIMENTAL SET-UP

Our measurements rely on a fluorescent labeled surfactant solution (sodium dodecyl sulfat (SDS) 10 g/L, fluorescein sodium 0.1 g/L, glycerol 10 % wt). A dark spot is photo-bleached and its trajectory is recorded. This is repeated in time during the whole life time of the film, and at many location, in order to obtained the velocity field in the whole film as a function of the time. The successive positions of a dark spot are shown in the figure.

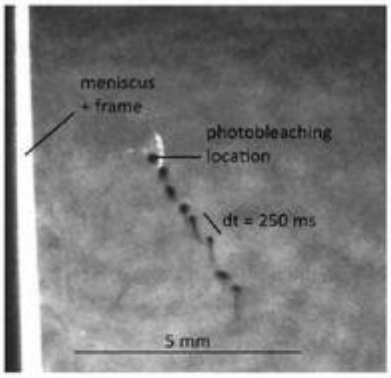

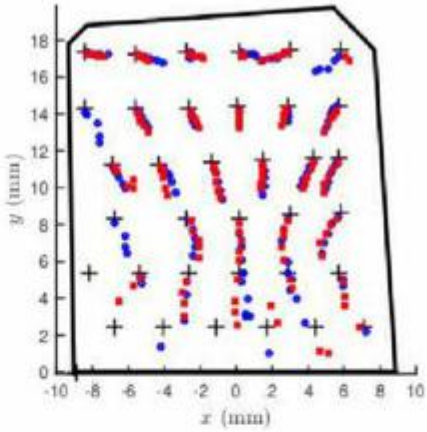

RESULTS

The velocity fields shows an downward velocity of the order of 1 mm/s in the central part of the 1 micron thick film (one second after its formation). Refine measurements in the first millimetre close to the lateral meniscus evidence an upward velocity that may reach 10 mm/s. This coincide with an observable pinching of the film, in contact with the lateral meniscus. This marginal pinching has been described theoretically by Aradian et al. [4] and arises from the capillary suction in the meniscus.

a) Corresponding author. Email: **isabelle.cantat@univ-rennes1.fr**

INTERPRETATION

The total flux of interface across an horizontal line is close to zero, thus validating the assumption of conserved interface area during the flow. With this assumption, the velocity field in the film can be deduced from the force balance on an elementary piece of foam. It is govern schematically by the following processes: the film near the meniscus get thinner because of the capillary suction, and its mass per unit area (2D density) is thus smaller than in the middle of the film. An Archimede-like force arises from this 2D-density discrepancy, based on gravity and surface tension gradient, at the origin of the upward motion. Finally the surface viscosity induces a friction between the fluid moving upward and the fluid moving downward and governs the velocity scales.

References

1. Mysels, K. J., Shinoda, K. & Frankel, S. *Soap films: Study of their thinning and a bibliography*. (Pergamon, 1959).
2. Seiwert, J. & Cantat, I. Generation of soap films with instantaneously adsorbed surfactants: Concentration-dependent film thinning. *Colloids Surf A* **473,** 2 – 10 (2015).
3. de Gennes, P. G. 'Young' Soap Films. *Langmuir* **17,** 2416–2419 (2001).
4. Aradian, A., Raphaël, E. & Gennes, P.-G. de. 'Marginal pinching' in soap films. *Europhys. Lett. EPL* **55,** 834–840 (2001).

ROLE OF NATURAL CONVECTION IN THE DISSOLUTION OF SESSILE DROPLETS

Detlef Lohse*[1], E. Dietrich[1,2], S. Wildeman[1], C. W. Visser[1], K. Hofhuis[2], E. S. Kooij[2], and H. J. W. Zandvliet[2]
[1]*Physics of Fluids Group, Mesa+ & Department of Science and Technology, University of Twente, Enschede, The Netherlands*
[2]*Physics of Interfaces and Nanomaterials Group, Mesa+ & Department of Science and Technology, University of Twente, Enschede, The Netherlands*

Summary The dissolution process of small (initial (equivalent) radius $R_0 < 1$ mm) long-chain alcohol (of various types) sessile droplets in water is studied, disentangling diffusive and convective contributions. The latter can arise for high solubilities of the alcohol, as the density of the alcohol-water mixture is then considerably less as that of pure water, giving rise to buoyancy driven convection. The convective flow around the droplets is measured, using micro-particle image velocimetry (μPIV) and the schlieren technique. When non-dimensionalizing the system, we find a universal $\mathrm{Sh} \sim \mathrm{Ra}^{1/4}$ scaling relation for all alcohols (of different solubilities) and all droplets in the convective regime. Here Sh is the Sherwood number (dimensionless mass flux) and Ra the Rayleigh number (dimensionless density difference between clean and alcohol-saturated water). This scaling implies the scaling relation $\tau_c \propto R_0^{5/4}$ of the convective dissolution time τ_c, which is found to agree with experimental data. We show that in the convective regime the plume Reynolds number (the dimensionless velocity) of the detaching alcohol-saturated plume follows $\mathrm{Re_p} \sim \mathrm{Sc}^{-1}\mathrm{Ra}^{5/8}$, which is confirmed by the μPIV data. Here, Sc is the Schmidt number. The convective regime exists when $\mathrm{Ra} > \mathrm{Ra_t}$, where $\mathrm{Ra_t} = 12$ is the transition Ra-number as extracted from the data. For $\mathrm{Ra} \leq \mathrm{Ra_t}$ and smaller, convective transport is progressively overtaken by diffusion and the above scaling relations break down.

INTRODUCTION

Conventional wisdom says that oil and water do not mix. However, some oily liquids, e.g. long-chain alcohols, are slightly soluble in water. When a droplet of such an alcohol is placed in a bath of water, it will slowly dissolve. Figure 1 shows an example of a sessile 1-hexanol droplet in water for which the dissolution time τ was about 3 hours. Considering this long dissolution time, it may seem plausible to assume that mass transport away from the droplet is governed by diffusion. Equivalent to the diffusion driven mass transport from small gas bubbles [1] or small sessile droplets [2] the relevant time-scale would in this case then be given by

$$\tau_\mathrm{d} = \frac{R_0^2 \rho_\mathrm{d}}{2D\Delta c} \sim R_0^2 \tag{1}$$

where R_0 is the initial equivalent radius of the droplet, D the diffusion constant of the alcohol in water, ρ_d is the density of the droplet material, and Δc is the difference between the saturated concentration c_s at the droplet interface and the (undersaturated) concentration $c_\infty < c_s$ far away from the drop. However, for the 1-hexanol droplet with an initial radius $R_0 = 0.7$ mm, one finds $\tau_\mathrm{d} \approx 11$ hours, which is much longer than the 3 hours observed experimentally. In this work we reveal the reason for this discrepancy. We show that above a transition solutal Rayleigh number, which corresponds to the buoyancy of the alcohol-water mixture, which is lighter than the surrounding clean water, the solute is mainly transported

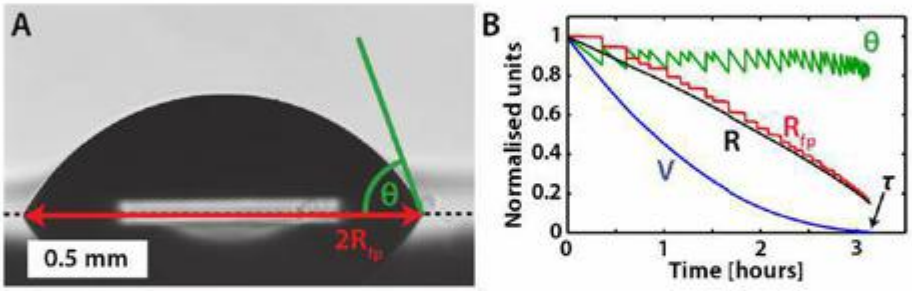

Figure 1: (a) Snapshot of a dissolving long-chain alcohol droplet (1-hexanol) in water. The dotted black line indicates the location of the silicon substrate, which mirrors part of the droplet. The footprint radius R_fp and the contact angle θ are indicated. (b) Evolution of the aforementioned parameters in time, along with the volume V of the droplet and the equivalent radius $R = (3V/2\pi)^{1/3}$. All parameters have been normalised by their initial values: $V_0 = 750$ nL, $R_{\mathrm{fp},0} = 0.825$ mm, $R_0 = 0.708$ mm, and $\theta_0 = 72°$.

*Corresponding author. Email: d.lohse@utwente.nl

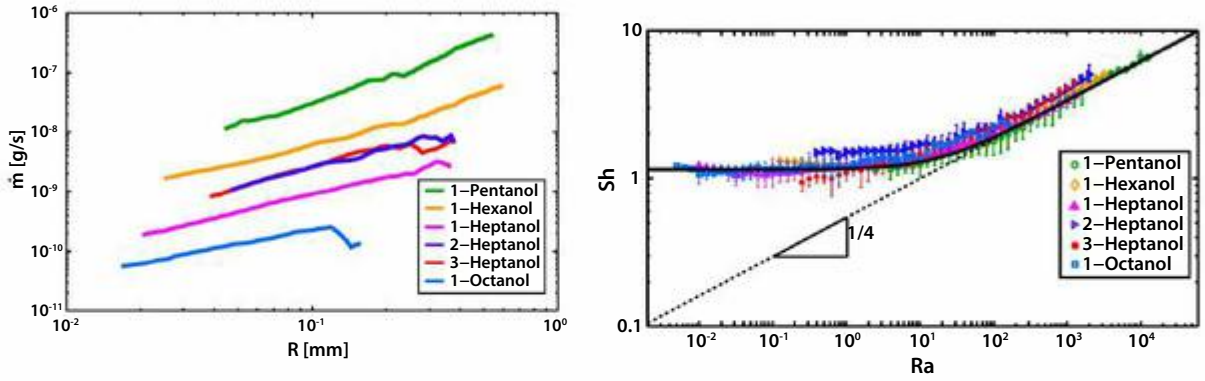

Figure 2: (a) Rate of mass loss as a function of R for droplets of different alcohols. The mass loss rates are ordered as a function of alcohol solubility, with 1-pentanol and 1-octanol being the best and least soluble alcohols, respectively. (b) Sherwood number as a function of Rayleigh number. The plot shows the mean value and the spread for a total of 70 measurements on droplets with initial volumes 2 nl $\leq V_0 \leq$ 1200 nl. Since the Ra-number depends both on the droplet size and its material properties, large Ra−number droplets are easily made using large droplets of 1-pentanol, whereas low Ra droplets are best studied using small droplets of the poorly soluble 1-heptanol and 1-octanol.

away in a single steady plume above the droplet. Knowledge of the flow structure allows us to derive scaling laws for both the dissolution rate and the plume velocity in the convective regime, which are in good agreement with experiments. Finally, as the droplet shrinks and its Rayleigh number drops below the transition value, a transition occurs in which convection dies out and is overtaken by diffusion.

METHOD AND UNIVERSALITY OF THE DISSOLUTION PROCESS

We combine imaging of the droplet to extract the droplet size and shape with qualitative schlieren imaging and quantitative micro-particle image velocimetry (μPIV) to directly visualize the concentration field and flow around slowly dissolving droplets of various types of long-chain alcohols in clean water. A snapshot of a droplet and its dissolution dynamics, which takes place in the stick-jump mode [2], is shown in figure 1. The droplet mass loss as function of droplet size is shown in figure 2a for various droplets of different liquids. Given the different solubilities of these liquids, the dissolution rate covers more than 4 orders of magnitude. Nonetheless, the dissolution process, when expresses in terms of the Rayleigh number and Sherwood number (figure 2b), is universal, showing a diffusive regime in which Sc is independent of Ra, and a convective regime $Sc \sim Ra^{1/4}$. In this convective regime the life time of the droplet can be derived to obey

$$\tau_c = \left(\frac{\nu \rho_d^4 R_0^5}{g \beta_c \Delta c^5 D^3} \right)^{1/4} \sim R_0^{5/4}, \tag{2}$$

which is found to be in excellent agreement with our data.

OUTLOOK

The observed convection and associated increase in mass transport also applies to the dynamics of a growing CO_2 bubbles in supersaturated water [3]. Presently, we are studying the dissolution of droplets consisting of *mixtures* of two liquids with different solubilities and the dissolution and growth of *arrays* of interacting droplets. In particular, growth process of competing droplets are intriguing [4].

References

[1] P. S. Epstein and M. S. Plesset, J. Chem. Phys. **18**, 1505 (1950).

[2] D. Lohse and X. Zhang, Rev. Mod. Phys. **87**, 981 (2015).

[3] O. R. Enríquez, C. Sun, D. Lohse, A. Prosperetti, D. van der Meer, J. Fluid Mech. **741**, R1 (2014).

[4] S. Peng, D. Lohse, X. Zhang, ACS-Nano **9**, 11916 (2015).

ELASTO-CAPILLARY INTERACTION OF LIQUID DROPS

Anupam Pandey[1], Stefan Karpitschka*[1], Luuk A. Lubbers[2], Jhoost H. Weijs[3], Lorenzo Botto[4], Siddhartha Das[5], Bruno Andreotti[6], and Jacco H. Snoeijer[1,7]

[1]*Physics of Fluids Group, University of Twente, P.O. Box 217, 7500 AE Enschede, The Netherlands*
[2]*Huygens-kamerlingh Lab, Universiteit Leiden, P.O. Box 9504, 2300 RA Leiden, The Netherlands*
[3]*Laboratoire de Physique de l'École Normale Supérieure de Lyon, Université de Lyon, 46, allée d'Italie, 69007 Lyon, France*
[4]*School of Engineering and Materials Science, Queen Mary University of London, London E1 4NS, UK*
[5]*Department of Mechanical Engineering, University of Maryland, College Park, MD 20742, USA*
[6]*Laboratoire de Physique et Mécanique des Milieux Hetérogènes, UMR 7636 ESPCI-CNRS, Univ. Paris-Diderot, 10 rue Vauquelin, 75005, Paris, France*
[7]*Department of Applied Physics, Eindhoven University of Technology, P.O. Box 513, 5600MB Eindhoven, The Netherlands*

Summary We study the interaction between sessile drops on a soft substrate. When millimetric liquid drops run down a soft, vertical surface under gravity, we notice deviation of their trajectories from straight line as two drops approach each other. Remarkably, if the wall is very thick drops always attract and coalesce, whereas two similar drops on a thin layer give rise to a short-ranged repulsion. We develop force-distance curves from experimentally measured drop trajectories and perform a free energy minimisation that unravels the underlying mechanism of drop-drop interaction. Importantly, we show that the interplay between capillarity and bulk elasticity of the soft substrate governs the nature of the interaction force.

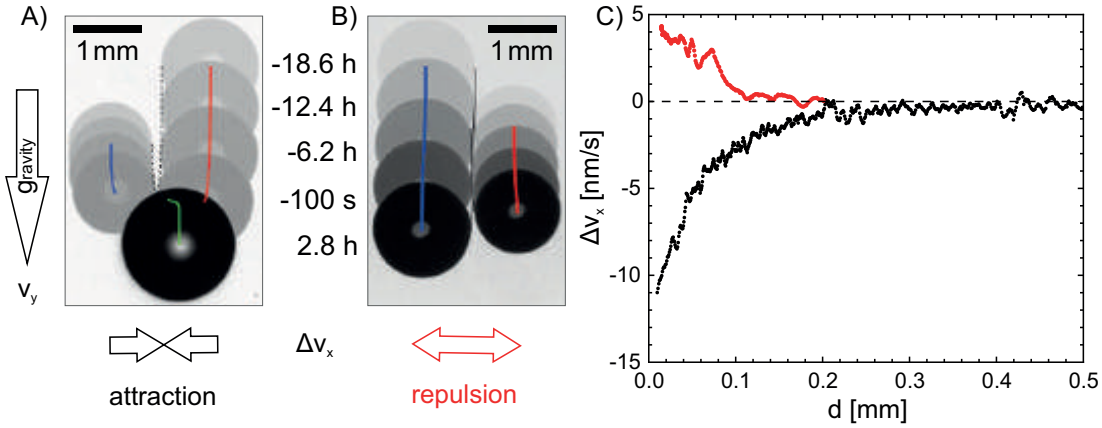

Figure 1: Drops interact as they run down a soft surface under gravity. A) Snapshots of two drops on a thick substrate as they attract and coalesce. Solid lines represent drop trajectories. B) Two similar drops on a thin substrate repel and move away from each other. Time stamps accompanying the snapshots show the slow motion of drops. Coalescence corresponds to $t = 0s$. C) Measured interaction velocity as a function of shortest distance d between contactlines. Black points represent attraction, whereas red points show repulsion.

Small objects, trapped at a liquid interface tend to form clusters: a phenomena popularly known as 'Cheerios effect' in reference to the aggregation of breakfast cereals floating on milk [1]. Deformation of the liquid interface due to the floating particles gives rise to the interaction force. Recently, this mechanism has been exploited for targeted self-assembly and patterning at the microscale [2, 3]. Here we study the opposite situation. Interaction of liquid drops sitting on a soft solid interface. Surface tension of the liquid drop causes a non-local deformation of the underneath solid: pulling the substrate up at the contactline, forming a ridge and pushing it down inside the drop due to Laplace pressure. The ratio of solid surface tension to substrate elastic modulus (γ_s/G) gives the radial extent of this deformation around the drop. Figure 1A), B) shows snapshots from experiment. Ethylene Glycol ($\gamma = 47$ mN/m) drops of different volume run vertically down a soft surface made of silicone gel (DOW Corning CY52-276, shear modulus $G = 276$ Pa) under the action of gravity. As two drops

*Corresponding author. Email: s.a.karpitschka@utwente.nl

come in close proximity, they develop a horizontal velocity component. Interestingly, this interaction velocity is attractive for very thick substrate and repulsive on thin ones. In figure 1 C) we plot the horizontal velocity as a function of shortest distance d between two contactlines. Due to dissipation inside a soft material, velocity of drops on soft substrate is orders of magnitude smaller than their rigid counterpart. Rheology of the soft material relates velocity to interaction force at the drop contactline [4]. We also develop a 2D variational formulation using linear elasticity to understand the interaction mechanism. In equilibrium, solid surface tension γ_s regularises the substrate deformation by forming a Neumann's triangle at the three phase contactline. Figure 2 shows substrate deformation due to a single drop and equilibrium contact angles. Presence of a second drop breaks the equilibrium configuration. We assume interaction between nearest contactlines only and find that the interaction force arises as the imbalance of Neumann's condition along the horizontal direction at the contactline,

$$F_{int} = \gamma \cos\theta + \gamma_{s\ell} \cos\theta_{s\ell} - \gamma_{sv} \cos\theta_{sv}. \tag{1}$$

Here θ, θ_{sv}, $\theta_{s\ell}$ are the new liquid, solid-vapor and solid-liquid contact angles simultaneously. In our experiments, $\gamma_{sv} = \gamma_{s\ell} = \gamma_s$. Equation 1 can be interpreted as the rotation of the solid ridge at the contactline from equilibrium. As we superimpose the deformation of a second drop onto the profiles shown in fig. 2, due to the nonzero slope of the already deformed substrate the ridge gets rotated. γ_s/G governs the slope of the deformed surface and hence F_{int}, whereas γ/G only affects the magnitude of the interaction force.

Finally, we address the attractive/repulsive nature of the interaction. Figure 2 shows that the substrate deformation is quite different for thick and thin case. For the thick substrate (figure 2A), the deformation decays monotonically. Whereas, thin substrate (figure 2B) shows a dimple (position of zero slope) around the drop and distance of the dimple from the contactline depends on the substrate thickness. For the thick case, a second drop always sits on a uphill (positive slope), resulting in an attractive force. Whereas in the thin limit, for large separation distance d, the second drop sits on a downhill (negative slope) and feel a repulsion. As the slope changes its sign, for very small distance the force is attractive. In short, we just need

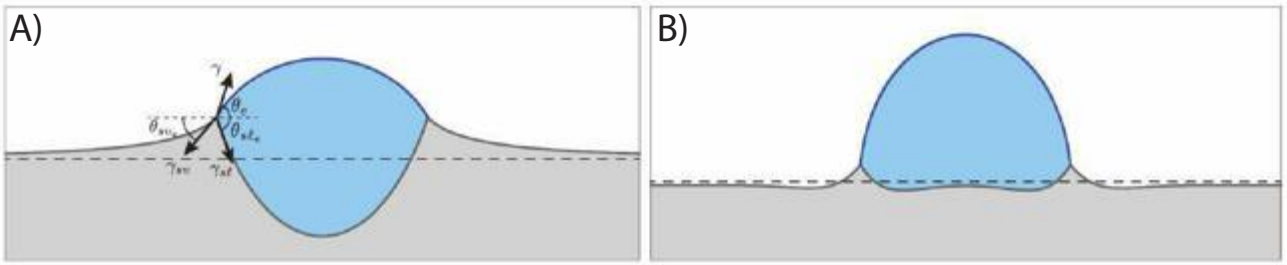

Figure 2: Deformation of the soft substrate due to a single drop. The dashed line shows the unperturbed flat surface. A) An elastic half space B) A thin substrate attached to a rigid base at the bottom.

the slope of the deformed substrate due to single drop to calculate the interaction force. This robust mechanism inspires an axisymmetric calculation of deformation around a drop of circular footprint and distribution of the interaction force along the contactline.

In the presentation, we shall discuss experimental force measurement, give physical interpretation of the equations derived from energy minimisation and compare theoretical and experimental force-distance curves. We believe this solid analogue of the 'cheerios effect' will be crucial in understanding cell-cell interaction on soft substrates and influence drop condensation on soft, thin films.

References

[1] Vella D, Mahadevan L (2005) The Cheerios effect. *Am J Phys* 73(9):817-825.

[2] Furst EM (2011) Directing colloidal assembly at fluid interfaces. *Proc Natl Acad Sci USA* 108(52):20853–20854.

[3] Cavallaro M, Botto L, Lewandowski EP, Wang M, Stebe KJ (2011) Curvature-driven capillary migration and assembly of rod-like particles. *Proc Natl Acad Sci USA* 108(52):20923–20928.

[4] Karpitschka S, Das S, van Gorcum M, Perrin H, Andreotti B, Snoeijer JH (2015) Drops move over viscoelastic substrates by surfing a ridge. *Nature Commun.* 6:7861.

FREEZING VORTEX RINGS INTO SHAPED PARTICLES

Duo An[1], Alex Warning[1], Kenneth G. Yancey[1], Chun-Ti Chang[2], Vanessa R. Kern[2], Ashim K. Datta[1], Paul H. Steen[2a], Dan Luo[1] & Minglin Ma[1]
[1]Department of Biological and Environmental Engineering, Cornell University, Ithaca, NY, USA
[2]School of Chemical and Biomolecular Engineering, Cornell University, Ithaca, NY, USA

Summary A miscible drop falling into a quiescent liquid bath forms a vortex-ring-like shape which evolves before eventually dissipating. This talk reports on controlling a crosslinking reaction that occurs upon contact of the drop with the buffer bath to 'freeze' the vortical formations into particles. Remarkably, the gelation reaction can be controlled with precision to yield a range of differently-shaped particles. The particles can be mass produced by an electrospray technique and are attractive for a number of applications, including cell-encapsulation and cell-free protein production. Reaction and mixing timescales compete during particle formation. A phase diagram is reported that shows how to tune this competition to obtain particles of a desired shape.

PARTICLE SHAPES

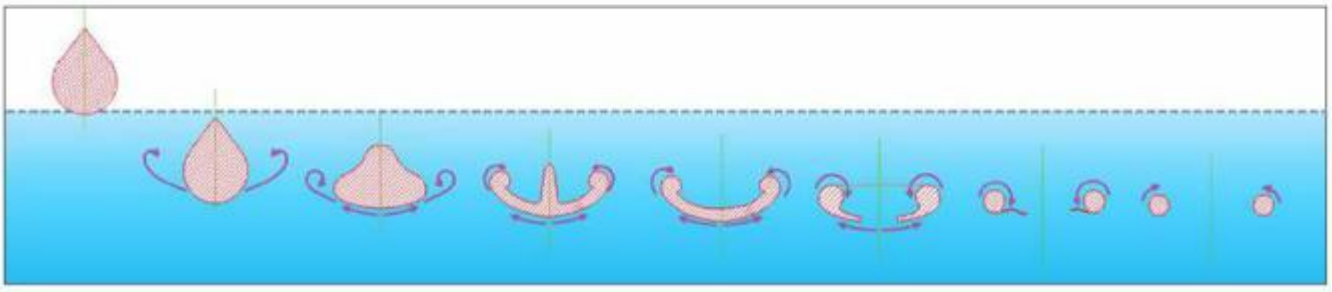

Figure 1. Schematic shapes (axis-of-revolution, dotted) that evolve after a falling drop penetrates an air/bath interface (dotted line) and during the subsequent vortex ring formation and spreading (left to right): teardrop (2nd from left) ; jellyfish (4th); cap (5th); and donut shape (7th or 8th). Gelation within bath by crosslinking reaction yields particles of similar shapes.

The size and shape of hydrogel 'particles' is primarily controlled by the electrospraying voltage. A classic scaling law, which is valid for liquids with relatively low viscosities and electrical conductivities, indicates an inverse power function relationship between droplet diameter (d) and voltage (V)[1]:

$$d \sim V^{-1/3}$$

In experiment, droplet size is observed to decrease with increasing voltage according to this scaling.

SHAPE CONTROL

To understand the controllability of particle shape, a series of experiments and simulations were conducted to study how the properties of the drop before impact and after immersion dictate the development of the vortex structure. On impact, drop deformation is resisted by interfacial tension while, after immersion, particle formation depends on a rate of mixing by invasion of vorticity into vorticity-free regions relative to the rate of reaction. Pre-impact ballistics is controlled by Weber (We) and Ohnesorge (Oh) numbers (equivalently, Weber and Reynolds) while post-impact vorticity invasion and reaction is controlled by (a different) Reynolds (Re) and Damköhler (Da) numbers,[2,3,4], defined as

$$We \equiv \frac{\rho v^2 d}{\sigma},\ Oh \equiv \frac{\mu}{\sqrt{\rho d \sigma}},\ Re \equiv \frac{\rho a \gamma}{\mu},\ Da \equiv \frac{kC}{\gamma}$$

where material parameters in We and Oh refer to the drop liquid (pre-impact) and those in Re refer to the bath liquid (post impact). Specifically, ρ is liquid density, v impact velocity, d drop radius, μ dynamic viscosity, and σ the surface tension. Also, $a\gamma$ is the rate of formation of interfacial area a between regions with and those without vorticity while k represents the reaction rate constant and C the concentration of binding sites. Rate γ is a strain rate estimated from the simulation results. In summary, We and Oh numbers characterize the strength of inertia and viscosity relative to surface tension of the impacting drops, Re characterizes the rate of area formation by vorticity invasion, $a\gamma$, relative to rate of resistance by kinematic viscosity, μ/ρ, and Da characterizes the rate of cross-linking, kC, relative to the strain rate, γ.

PHASE DIAGRAM

a) Corresponding author. Email: phs7@cornell.edu.

In the experiments the droplet fluid is a solution of clay nanoparticles in water with droplet viscosity varied over two orders of magnitude by adding glycerol. The bath liquid is a solution of water with salt of various concentrations – the viscosity of the bath liquid does not change much from that of pure water. The density of the bath solution is also close to that of the droplet liquid. Dimensionless groups *We*, *Oh*, *Re* and *Da* are controlled as described above. However, under these conditions an alternative to the bath *Re* number is the drop/bath viscosity ratio, μ_{drop}/μ_{water}[4], rationalized by the noting that the drop *We* and *Oh* numbers can be replaced by the drop *Re* and *Oh* numbers and that the drop/bath *Re* ratio controls mixing, which simplifies to the viscosity ratio. Moreover, droplet *Oh* changes for the experiments reported only by drop viscosity since the drop size is fixed.

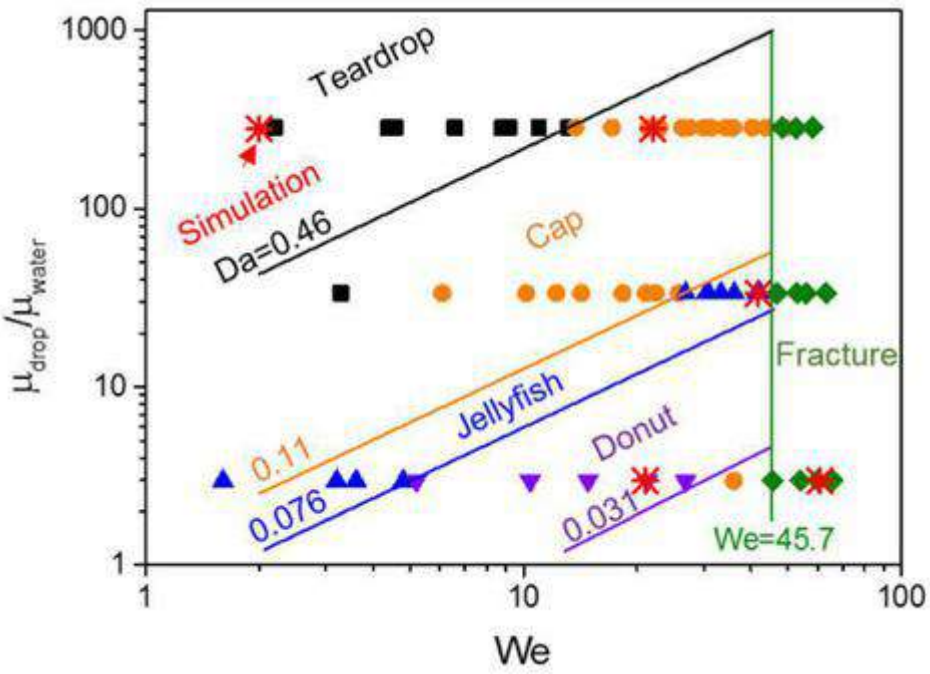

Figure 2. Diagram illustrating experimental results for particle shapes frozen during vortex ring evolution for different parameters. Results of simulations using a phase-field approach are shown as red stars.

Results of particle shapes obtained in the experiments are plotted as symbols on the μ_{drop}/μ_{water} versus *We* phase diagram, Figure 2. Regardless of viscosity ratio, an impacting droplet with inertia above *We* ~ 45.7 cannot be frozen. This empirical limit is marked by the vertical green line. Additional lines on the phase plot are contours of constant *Da* using the correlation, $Da = const\ Oh^{0.5}\left(\mu_{drop}/\mu_{water}\right)^{0.5} We^{-0.5}$, where $const$ is evaluated empirically. The lines of constant *Da* are seen to partition the shapes. Simulations were also performed, and the results matched well with the experiments and the correlation. Note that the progression with decreasing *Da* in Figure 2 – Teardrop-Cap-Jellyfish-Donut – follows the progression with increasing time in Figure 1 with one exception – the Cap and Jellyfish shapes are flipped between the two progressions. This is correct and the reason will be explained in the talk.

CONCLUSIONS

The gelation reaction of vortex formations into shaped particles is reported, along with a phase diagram giving shape control.

References

[1] Xie, J., Jiang, J., Davoodi, P., Srinivasan, M. P. & Wang, C. H. Electrohydrodynamic atomization: A two-decade effort to produce and process micro-nanoparticulate materials. *Chem. Eng. Sci.* **125,** 32-57 (2015).

[2] Hsiao MY, Lichter S, Quintero LG. The critical weber number for vortex and jet formation for drops impinging on a liquid pool. *Phys Fluids* **31**, 3560-3562 (1988).

[3] Peck B, Sigurdson L. The 3-dimensional vortex structure of an impacting water drop. *Phys Fluids* **6**, 564-576 (1994).

[4] Walker, T. W., Logia, A. N. & Fuller, G. G. Multiphase flow of miscible liquids: jets and drops. *Exp. Fluids* **56,** 1–14 (2015).

FROM THE ONSET OF ELECTROSPRAY AND DISINTIGRATION OF LEAKY-DIELECTRIC DROPS TO STEADY CONE-JET

A. M. Gañán-Calvo*[1], J. M. López-Herrera[1], N. Rebollo-Muñoz[2], and J. M. Montanero[2]
[1]*Depto. de Ingeniería Aeroespacial y Mecánica de Fluidos,Universidad de Sevilla, Sevilla, Spain*
[2]*Depto. de Ingeniería Mecánica, Energética y de los Materiales,Universidad de Extremadura, Badajoz, Spain*

Summary We describe the disintegration of a leaky-dielectric drop from the unsteady phenomenon giving rise to the first ejected droplet to the steady cone-jet mode of electrospray. We summarize the differentiated scaling laws of the two limiting regimes for the relevant quantities and show their validation from comparison with both numerical simulations and experimental data.

Under certain conditions, a leaky-dielectric drop subject to a strong electric field ejects a thin liquid ligament, which issues a stream of tiny drops (Fig. 1). The masses and charges of those droplets are essentially determined by the liquid properties, and reflect the electrohydrodynamic history leading to them. The first droplet produced by this unsteady process is particularly important due to its very small diameter d_1 and large electric charge q_1 (per unit volume). After this first phase of the ejection process, the system reaches spontaneously a quasi-steady regime characterized by a natural (intrinsic) flow rate Q^*, electric current I^*, and droplet diameter d^*, which essentially depend upon the liquid properties too. If a flow rate $Q \geq Q^*$ is prescribed by, for instance, injecting liquid across a feeding capillary, the above quasi-steady process gives rise to the steady cone-jet mode of electrospray, which emits droplets of diameter d that transport the electric current I. While the unsteady ejection of the first droplet is affected by charge relaxation effects, the bulk charge density is negligible in both the quasi-steady and steady regimes. The complete understanding of the transition from the first unsteady process to the steady cone-jet mode opens new avenues for the conception of global (e.g. atmospheric) predictive models and innovative technologies using the liquid ejecta.

The parameters which essentially characterize this electrohydrodynamic problem are the liquid density ρ, viscosity μ, surface tension σ, electrical conductivity K, and electrical permittivity ε_i, as well as the environment electrical permittivity ε_o. From these parameters, one defines the characteristic length $d_o = (\sigma\varepsilon_o^2/\rho K^2)^{1/3}$, velocity $v_o = (\sigma K/\rho\varepsilon_o)^{1/3}$, electric field magnitude $E_o = (\sigma/d_o\varepsilon_o)^{1/2}$, electric charge $q_o = \varepsilon_o E_o d_o^2$, and intensity $I_o = \sigma\rho^{-1/2}\varepsilon_o^{1/2}$, and the intrinsic dimensionless numbers $\delta_\mu = \rho d_o v_o/\mu$ and $\beta = \varepsilon_i/\varepsilon_o$. The unsteady ejection of the first droplet consists in a self-similar ultra-fast collapse of the droplet's tip where charge relaxation plays a relevant role [1]. In the final state of this process, inertia, axial viscous stresses, electrostatic suction, and surface tension balance, which leads to the universal scaling laws [1]

$$d_1 = d_o\delta_\mu^{-1/3}\beta^{5/12}\ , \quad q_1 = q_o\delta_\mu^{-2/3}\beta^{7/12}\ , \tag{1}$$

for the first droplet diameter d_1 and its electric charge q_1, which were derived and validated in Ref. [1] (Fig. 2).

The unsteady process described above is followed by a quasi-steady regime characterized by a natural (intrinsic) flow rate Q^* and droplet diameter d^*. The scaling laws for these two quantities are [2]

$$Q^* = Q_o\delta_\mu^{-1}\ , d^* = d_o\delta_\mu^{-1/2} \quad \text{and} \quad Q^* = Q_o\beta\ , d^* = d_o\beta^{1/2} \tag{2}$$

when the viscosity and polarization force becomes dominant, respectively. These two scenarios arise for $\beta\delta_\mu < 1$ and $\beta\delta_\mu > 1$, respectively. In both cases, the conservation of mass, momentum, energy, and electric charge leads to the scaling

$$d^* = d_o(Q^*/Q_o)^{1/2} \quad \text{and} \quad I^* = I_o(Q^*/Q_o)^{1/2}\ . \tag{3}$$

Figure 3 shows the experimental values for the ratio $Q^*/(Q_o\beta)$ as a function of $(\beta\delta_\mu)^{-1}$. For $(\beta\delta_\mu)^{-1} > 1$, the minimum flow rate is essentially independent of β over two orders of magnitude of the parameter $(\beta\delta_\mu)^{-1}$. The minimum value of $Q^*/(Q_o\delta_\mu^{-1})$ is approximately unity for all the liquids of this interval, and thus the validity of the scaling law (2)-left is shown even for large values of δ_μ.

Finally, if a flow rate $Q \geq Q^*$ is imposed by injecting liquid across a feeding capillary, the above quasi-steady process gives rise to the steady cone-jet mode of electrospray characterized by the droplet diameter d and electric current I. The scaling laws (3) also provide the values of these quantities, i.e., $d = d_o(Q/Q_o)^{1/2}$ and $I = I_o(Q/Q_o)^{1/2}$. These scaling laws have been widely validated from comparison with experiments [3].

This work is supported by the Spanish Ministry of Economy through Grant No. DPI2013-46485

References

[1] A. M. Gañán-Calvo, J. M. López-Herrera, N. Rebollo-Muñoz, and J. M. Montanero, PNAS **submitted** (2016).
[2] A. M. Gañán-Calvo, N. Rebollo-Muñoz, and J. M. Montanero, "Physical symmetries and scaling laws for the minimum or natural rate of flow and droplet size ejected by taylor cone-jets," New J. Phys. **15**, 033035 (2013).
[3] A. M. Gañán-Calvo and J. M. Montanero, "Revision of capillary cone-jet physics: Electrospray and flow focusing," Phys. Rev. E **79**, 066305 (2009).

*Corresponding author. Email: amgc@us.es

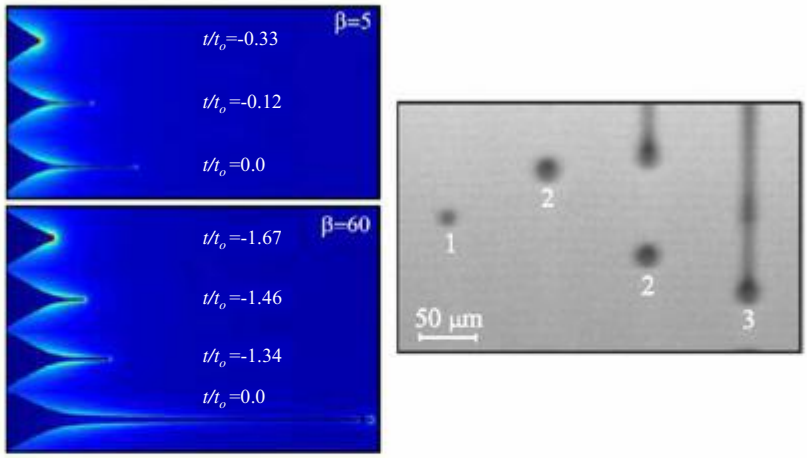

Figure 1: (Left) Numerical simulation of the droplet ejection for $\delta_\mu = 5$ and $\beta = 5$ and 60. The color indicates the magnitude of the electric field (red/blue corresponds to high/low values of that quantity). (Right) Experimental images of the first ejected droplets of 1-Octanol produced with 3000 kV. The labels indicate the droplet number.

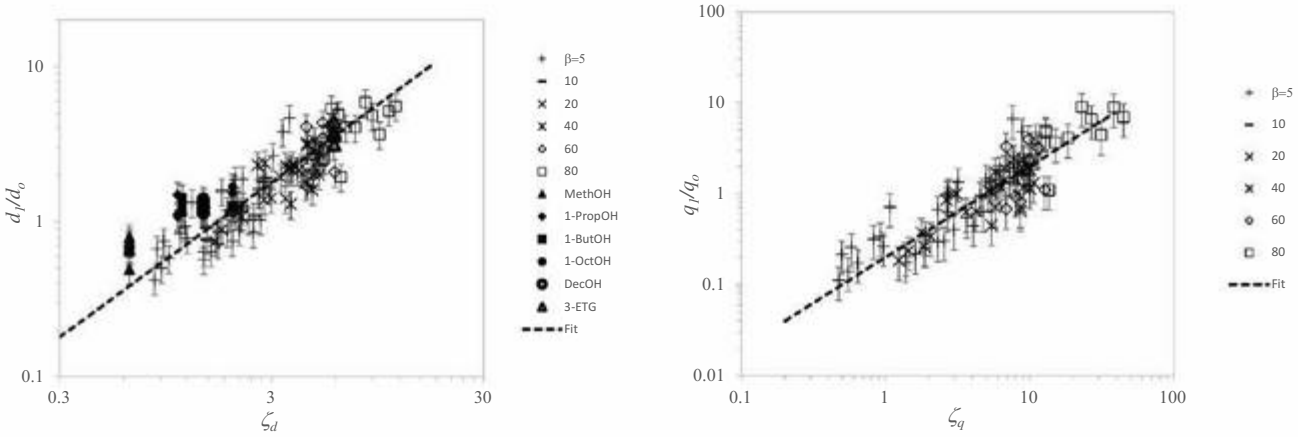

Figure 2: Diameter d_1/d_o versus $\zeta_d = \delta_\mu^{-1/3}\beta^{5/12}$ (left) and electric charge as a function of $\zeta_q = \delta_\mu^{-2/3}\beta^{7/12}$ (right) of the first ejected droplet obtained from numerical simulations (open symbols) and experiments (solid symbols) [1]. The dashed lines correspond to the fits $d_1/d_o = 0.6\ \zeta_d$ and $q_1/q_o = 0.2\ \zeta_q$.

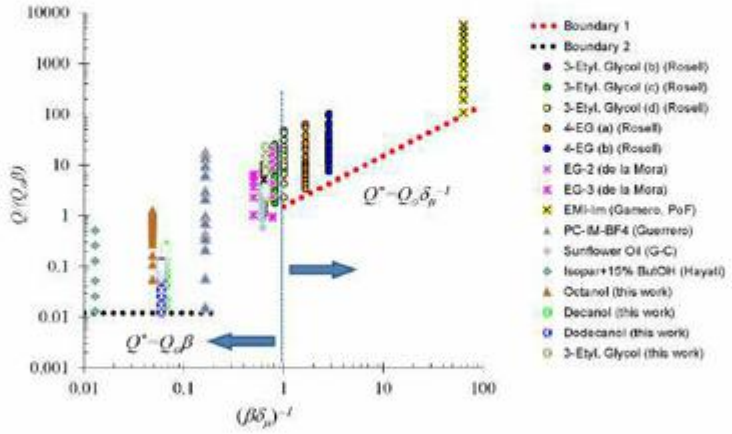

Figure 3: $Q^*/(Q_o\beta)$ as a function of $(\beta\delta_\mu)^{-1}$ [2].

MAGNETICALLY INDUCED CAVITATION AND NANOPARTICLE DISPERSION IN LIQUID METALS

Gunter Gerbeth[1a)], Martins Sarma[1], Ilmars Grants[1,2], Imants Kaldre[2], Andris Bojarevics[2]
[1]*Helmholtz-Zentrum Dresden – Rossendorf, Dresden, Germany*
[2]*Institute of Physics, University of Latvia, Salaspils, Latvia*

Summary Cavitation in liquid metals is supposed to provide conditions for the desired homogeneous dispersion of nanoparticles, leading for metal matrix nano-composites to improved mechanical properties. A contactless magnetic field approach to induce cavitation in liquid metals is demonstrated, and first results on the dispersion of nanoparticles in various metal samples are given.

INTRODUCTION

Acoustic cavitation by power ultrasound is widely used for the purpose of nanoparticle dispersion in room temperature liquids. There are also numerous experimental reports demonstrating that power ultrasound facilitates the dispersion of nanoparticles in a molten metal. So far, this technique has been applied for the production of metal matrix nano-composites (MMNC) of light metal alloys [1,2]. Being extremely violent on the micro-scale, the cavitation degrades also the vibrating surface transmitting the ultrasound into the liquid. A contactless technique for cavitation excitation is, therefore, desirable, in particular for high-melting liquid metals such as steel for which no ultrasonic transducers exist with a reasonable life-time in the molten metal. A contactless excitation of cavitation is possible by superposition of induction heating with a steady axial magnetic field. This combination creates an alternating radial magnetic body force in a cylinder [3]. The irrotational part of this force produces pressure oscillations. This contactless magnetic excitation of cavitation was first demonstrated recently [4]. Our experiment is designed to maximize the induction currents and, thus, allow to keep the static field moderate. We continue our studies [4] by considering the cavitation inception condition in molten stainless steel and in various Al alloys. Results on the dispersion of SiC and TiN nanoparticles in various liquid metals will be presented.

THEORETICAL BACKGROUND

Consider an infinite liquid metal cylinder of radius a in a uniform magnetic field with a steady and an alternating component

$$\mathbf{B} = \left(B_z + b(r)e^{i\omega t}\right)\mathbf{e}_z. \tag{1}$$

The alternating component of the magnetic field induces an azimuthal current, which in combination with the static axial field creates an oscillating radial force. This force is curl-free and, therefore, is balanced by an oscillating pressure field. Suppose the frequency ω is high enough to cause a strong skin-effect ($\sigma\omega\mu_0 a^2 >> 1$, where σ and μ_0 are the electric conductivity and magnetic permeability of the metal, respectively), yet low enough to form a long acoustic wave with a wave length much larger than a. Additionally suppose that the alternating field component is much smaller than the steady one ($b_A << B_z$) where $b_A = |b(a)|$. Under these conditions the alternating magnetic pressure is uniform in the bulk and has the amplitude [4]

$$p = \frac{B_z b_A}{\mu_0}. \tag{2}$$

Acoustic cavitation is recurring non-linear growth and subsequent collapse of small bubbles due to the oscillating pressure in the liquid. In an ideal liquid, where transient voids are only created by thermodynamic fluctuations, the critical tension is comparable to the yield strength of metals. Such tension is out of reach for power ultrasound. Thus, the observed beneficial effects of power ultrasound in metal casting [1,2] depend on size and density of cavitation nuclei, which is largely unknown and uncontrolled. As bubbles start to cavitate, they emit their own sound containing characteristic sub-harmonics f_0/n, where f_0 is the drive frequency and n = 2,3… [5,6]. We use this property for the identification of cavitation inception.

EXPERIMENTAL SET-UP

Experiments are either made in a cell with a free liquid metal surface or an evacuated cell ($p_0 < 400$ Pa) as shown in Fig. 1. The latter consists of a quartz tube 5 and water cooled copper caps 3. The cell is placed in a 82 mm wide vertical gap of an electromagnet. Water cooled copper screens 8 are used to protect the ferromagnetic pole shoes 9 from the induced currents. The refractory side support 6 accomodates vertical variations of the magnetic pressure. The electromagnet provides a magnetic flux density of up to 0.5 T in the experimental volume, and the maximum inductor current r.m.s value is I_{AC} = 1300 A that corresponds to b_A = 0.130 T. The AC frequency is f_0 = 14.7 kHz.

[a)] Corresponding author. Email: g.gerbeth@hzdr.de.

Four piezoelectric sensors 4 are glued at the surface of the bottom cap for the purpose of sound detection. The electric signal from these elements is acquired by a digital oscilloscope at 3.2 µs temporal resolution in packets of 5000 measurements. More details of the setup are given in Ref. [4]. The sample 1 is placed between two water cooled replaceable vertical supports 2 (diameter 20 mm). This configuration allows to increase the induction current without overheating the sample. Besides, it constrains the sample to the space in between.

A multitude of samples have been processed up to now. Cavitation onset has clearly been detected for tin, zinc and aluminum [4]. Meanwhile several aluminum alloys and the commercial non-magnetic stainless steel SAE 304 have been processed as well. In addition, many tests with the addition of various nano-particles such as SiC, Y_2O_3, TiN, etc. have been performed.

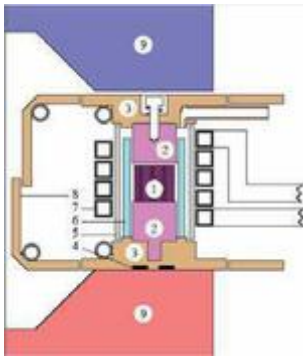

Fig. 1: Scheme of the experimental set-up.

RESULTS

The onset of cavitation has been clearly observed in all liquid metals mentioned above at pressure oscillations (2) in the range of 28…48 kPa. Figure 2 displays the transient sound spectrum in case of an Al+Pb sample. The static magnetic field induction was 0.5 T. The inductor current was varied stepwise: raised to 1200 A at t = 590 s and sustained for about 10 minutes. The first short burst of an $f_0/2$ sub-harmonic was observed at t = 610 s. A continuous cavitation signal with pronounced $f_0/2$ and $f_0/4$ modes set in after some delay at t = 850 s. Recently, additional experiments have been realized with an increased value of the steady magnetic field B_z using a superconducting magnet of up to 5 T. First results will be shown in the presentation.

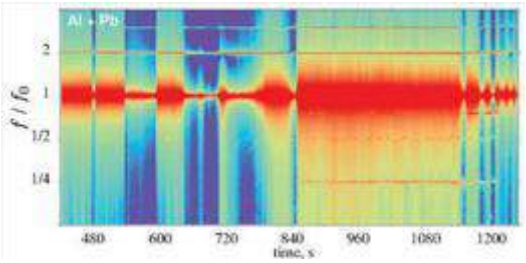

Fig. 2: Temporal dependency of the sound power spectrum in case of aluminium with lead. Depth of the logarithmic colour palette is 40 dB.

The results on the dispersion of the various types of nanoparticles in the liquid metals are more diverse due to influences of material compatibilities, possible chemical reactions and the interfacial tension between particles and melts, as well as various approaches of nanoparticle insertion into the melts. For the latter our main approach consists in using MMNC with an elevated particle concentration prepared by the powder metallurgical route, and melting it together with the pure metal. Promising results have been obtained recently for SiC as well as TiN nanoparticles in Al melts (see Fig. 3 with dispersed 100 nm SiC particles in Al-Mg, obtained in the experiments with a superconducting magnet), whereas for Y_2O_3 particles in steel melts there was evidence for chemical reactions and the occurrence of further compounds in the solidified sample. More detailed results will be given in the presentation.

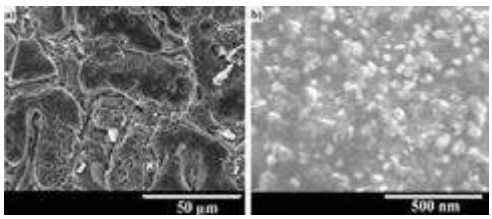

Fig. 3: SiC particle doped Al-6%wt.Mg. a) Particles are concentrated at the grain boundaries; b) fully dispersed nanoparticles within the metallic grains.

CONCLUSIONS

A contactless route based on magnetic field action has been demonstrated for the purpose of causing cavitation in liquid metals. This cavitation is the main clue to avoid agglomeration or to break-up agglomerated compounds of nanoparticles in metal melts. Systematic studies on the dispersion of various nanoparticles in various metal melts are going on.

References

[1] Cao G., Konishi H., Li X.: Recent developments on ultrasonic cavitation based solidification processing. *Int. J. Metalcast.* **2**: 57–68, 2008.

[2] Li X., Yang Y., Weiss D.: Theoretical and exp. study on ultrasonic dispersion of nanoparticles. *Metall. Sci. Technol.* **26**: 12–20, 2008.

[3] Wang Q., et al.: Direct generation of intense compression waves in molten metals. *J. Mater. Sci. Technol.* **19**: 5–9, 2003.

[4] Grants I., Gerbeth G., Bojarevics A.: Contactless magn. excitation of acoustic cavitation in liquid metals. *J. Appl. Phys.* **117**: 204901, 2015.

[5] Neppiras E.A.: Acoustic cavitation. *Phys. Rep.* **61**: 159–251, 1980.

[6] Cramer E., Lauterborn W.: Acoustic cavitation noise spectra. *Appl. Sci. Res.* **38**: 209–214, 1982.

THE CHARACTERISTICS OF DROPLETS IMPACTING ON CLOSED-CELL HYDROPHOBIC SURFACES

Rui Zhang[1], Feng He[1a)] & Pengfei Hao[1]
[1]*School of Aerospace Engineering, Tsinghua University, Beijing, China*

Summary Super-hydrophobic surfaces with different shapes of closed-cell micro-pits are designed in this paper to study the influences of factors such as solid fraction, cell size and depth to critical pressure and droplet rebounding property. Droplets impacting on open-cell textured surfaces undergo a transition from the Cassie state to the Wenzel state whereby the surface gets impregnated by the liquid and temporarily loses its super-hydrophobicity. Cassie-to-Wenzel transition would induce the loss of super-hydrophobicity and the so-called self-cleaning effect of the substrates since a Wenzel state would lead to a strong increase of adhesion and friction properties. Owing to the preservation of air cushion in the micro-pits, droplets impacting on closed-cell micro-structured surfaces can undergo a "mixed state" instead of transferring into Wenzel state. Proper design of closed-cell micro-structured surfaces can delay the so-called Cassie-to-Wenzel transition and maintain hydrophobicity and water-repellency even under high-speed droplets impact.

INTRODUCTION

Droplets impacting on solid surface, which consists of interesting physical phenomena and obsesses scientists all the time, is commonplace in nature and relevant for many industrial and technical applications, playing important roles in ink-jet printing, spray coating and cooling, forensic science, aircraft and power-line designing.

Designing of ice-repellent surface is of more application value than studying deicing strategies after ice accumulation. Much attention has been paid to sessile droplets or static liquid film resting on super-cooled surface[1,2]. Nevertheless every icing process undergoes the collision between the drop and surface before ice nucleation begins. Early experiments and study have demonstrated that drops impacting on super-hydrophobic substrates would experience a harmonic spring-like behaviour—impacting, spreading and bouncing[3,4]. However, when the impact velocity increases, splashing arises from the breakup of a fine liquid sheet that is ejected radially along the substrate before receding breakup appears. Most recent studies focus on the dynamic behaviors of droplets impacting on super-hydrophobic substrates with smooth surfaces, rough surfaces and surfaces structured with regular micro-posts. However, closed-cell textured surfaces with micro-pits performed much better repellency against drop impact due to their improved mechanical and pressure stability.

Since the collision of droplets and substrates can induce the CWT transition from non-wetting to wetting state[5], another essential indicator for designing anti-icing surfaces is to have high static pressure stability and dynamic pressure stability, that is the substrate should preserve super-hydrophobicity even after high speed droplets impacting. Lidiya et al.(2010) [6]emphasize the potential of hydrophobic polymeric coatings bearing closed-cell surface geometries(such as bricks or honeycombs) is significantly higher than that of open-cell structures(such as posts) due to the confinement of air underneath the droplet in closed cells. This paper designed closed-cell micro-structured silicon surfaces with varied cell pitch, cell depth and solid ratio. The OTS self-assembled membrane technology was used for long lasting hydrophobic treatment. The impact behaviors and pressure stability under different falling height of the droplets are studied here.

MATERIALS AND METHODS

Materials preparation

Different shapes of closed-cell micro-structured silicon surfaces in this work were fabricated using the etching technology which are honeycombs, squares and triangles, as shown is Fig. 1. Micro-posts structured surfaces with the same solid fraction were prepared as the control group. All the micro-structured surfaces were treated with Octadecyl trifluoro silane to improve the wetting property. The static and dynamic contact angle on the as-prepared substrates was measured from needle water drops of 5μL with a Standard Contact Angle Goniometer.

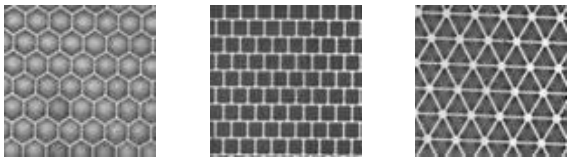

(a) (b) (c)

Fig.1. Microscopic structure of three different shapes of closed-cell microstructure surfaces:
(a) honeycombs; (b)squares; (c)triangles

Experimental setup

[a)] Corresponding author. Email: hefeng@tsinghua.edu.cn.

Droplet impacting studies were performed on closed-cell and open-cell micro-structured hydrophobic surfaces at different speeds. Water droplets of ~8μL at room temperature are generated from a fine capillary tube equipped with a syringe pump from varied heights and fall onto the sample substrate positioned in a desiccator chamber. The temperature and humidity in the chamber are controlled constant to reduce the condensation on the substrates. The dynamics of droplet impact was recorded by a high-speed camera (Fastcam Mini UX100, Photron) at the frame rate of 5,000 fps with a shutter speed 1/25,000s. After each experiment, the substrate were dried using the air blower to remove the residue of water drops.

RESULTS AND DISCUSSIONS

In Fig.2. we could see clear air bubbles in the wetted region of the micro-pits surface under high-speed impact, which weaken the adhesion resistance and result in easy rebound. Cassie-to-Wenzel transition is presented in the wetted region of micro-posts surface and impalement occurs as a result.

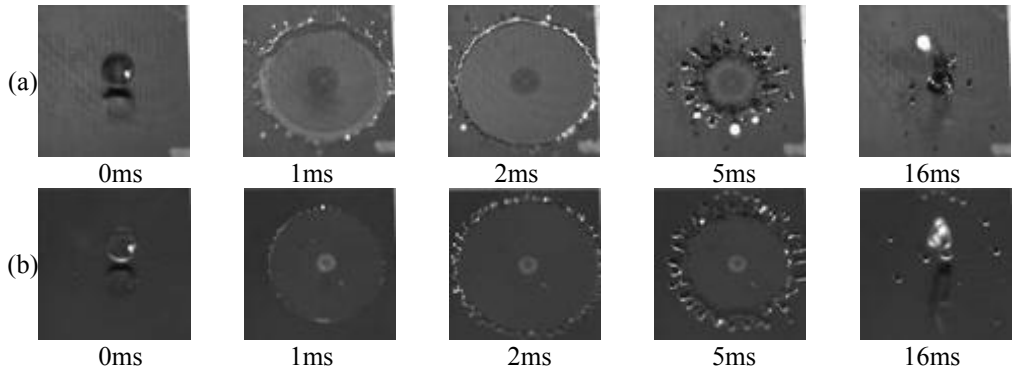

Fig.2.Dynamic behaviours of droplet with velocity of 5.2m/s impacting on (a) micro-post structured surface and (b) micro-pit structured surface

When droplets impact on textured surfaces, the main force that hinders the wetting of microstructure is the capillary forces [7]. According to mechanical equilibrium, we can obtain the equilibrium pressure $P_{eq} \sim cos\ \theta/a$. The contact angle θ has an upper limit, namely the advancing contact angle θ_a. If $\theta > \theta_a$, the three-phase contact line will spontaneously slide downward along the walls of the pits/posts. Therefore, the critical "sliding" impalement pressure is obtained as $P_{crt} \sim cos\ \theta_a /a \sim \eta\ cos\ \theta_a$. Here we define the ratio of perimeter and area $\eta = L/S$ ($\eta_h > \eta_s = \eta_t$). Therefore the critical pressure of the honeycombs is the maximum. We can also conclude that the critical pressure increases as the cell size decreases.

CONCLUSIONS

We have presented a systematic experimental and theoretical study of the dynamic process of water droplets impacting on micro-pits and micro-posts structured surfaces by analyzing a broad range of wetting and bouncing behaviours including critical pressure, wetting area, contact time and so on. Compared to open-cell surfaces, the closed-cell micro-structured surfaces present a better rebounding property under high-speed drop impacts.

Micro-post surfaces are easily wetted by impacting droplets and the wetted area is larger than their counterparts, where wetting and adhesion are synchronous. By comparison, the micro-pits can preserve the air cushion better, which acts as a spring upon droplets impact, effectively preventing the Cassie-to-Wenzel transition and resulting in a "mixed state". Adhesion does not occur simultaneously with wetting and the bouncing performance depends on the initial kinetic energy, wetting and resistance characteristic and the remaining kinetic energy. The smaller and deeper the cell is, the better bouncing behaviour the micro-pit structured surface performs.

References

[1] Eberle, P., Tiwari, M. K., Maitra, T., Poulikakos, D. Rational Nanostructuring of Surfaces for Extraordinary Icephobicity. Nanoscale 2014, 6, 4874−4881.

[2] Jung, S., Tiwari, M. K., Doan, N. V., Poulikakos, D. Mechanism of Supercooled Droplet Freezing on Surfaces. Nat. Commun. 2012, 3, 615.

[3] A. L. Yarin. Drop Impact Dynamics: Splashing, Spreading, Receding, Bouncing…. Annu. Rev. Fluid Mech., 2006.38:159-92.

[4] C. Josserand and S.T. Thoroddsen. Drop impact on a solid surface. Annu. Rev. Fluid Mech., 2016,48: 365-91.

[5] Choongyeop Lee et al. Two types of Cassie-to-Wenzel wetting transitions on superhydrophobic surfaces during drop impact. Soft Matter, 2015, 11, 4592-4599.

[6] Lidiya Mishchenko et al. Design of Ice-free Nanostructured Surfaces Based on Repulsion of Impacting Water Droplets. ACS NANO, 2010, 4:7699-7707.

[7] Denis Bartolo et al. Bouncing or sticky droplets: impalement transitions on micropatterned surfaces. Europhys Lett., 2007, 74(2):299.

ON MODELING DROP IMPACTS AT SHALLOW ANGLES ON FLOWING SOAP FILMS

Saikat Basu *[1], Ali Yawar[2], Andres Concha[3], and Mahesh Bandi[1]
[1]*Collective Interactions Unit, Okinawa Instiutute of Science and Technology, Onna, Japan*
[2]*Department of Mechanical Engineering and Material Science, Yale University, New Haven, U.S.A.*
[3]*School of Engineering and Sciences, Adolfo Ibañez University, Santiago, Chile*

Summary Small drops impinging on soap films flowing at an angle exhibit three fundamental post-impact dynamics regimes: (a) the drop pierces through the film, (b) it coalesces with the flow, and (c) it bounces off the surface. During impact, the drop deforms along with bulk elastic deformation of the film. The system thus presents the rare opportunity to explore in-tandem effects of bulk elasticity and hydrodynamics. For shallow angles of film inclination, bounce-off regime predominates. We outline the analytical framework to characterize the impact dynamics. The model assumes a deformable drop and a deformable three-dimensional film, and invokes phase space based parametric analysis. Results can offer a significant step towards optimizing interactions between a spray and a flowing liquid. Findings for the bounce-off case also indicate a momentum transfer leading to vortex dipole shedding, along with capillary wave generation. Such an impulsive regime can be relevant for biolocomotion of water-walking animals.

INTRODUCTION

In problems of mechanics, soap films are typically idealized as a two-dimensional system. However, if we track the dynamics of small drops impinging into a flowing film, the three-dimensionality of the film material becomes significant. During the impact, the drop shoots into the film and deforms it leading to bulk elastic forces being induced upon the drop. This works in tandem with the interfacial tension. Quite notably, the problem also includes hydrodynamic effects (like shed vortices) owing to the shear layers generated from the relative motion between the gravity-driven drop and the film flow. The impacts can be broadly classified into: (a) the falling energy of the drop is high enough to make it tunnel down through the film (*piercing* regime), (b) the drop hits the film surface and moves downstream with the background stream (*coalescence* regime), and (c) it hits the film surface, moves downstream for a finite time, and then bounces off the surface (designated as the *bounce-off* regime).

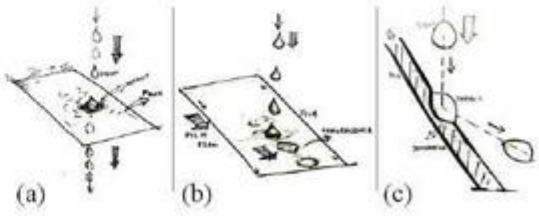

Figure 1: Simple artistic representations of the three major regimes when drops impinge on a soap film.

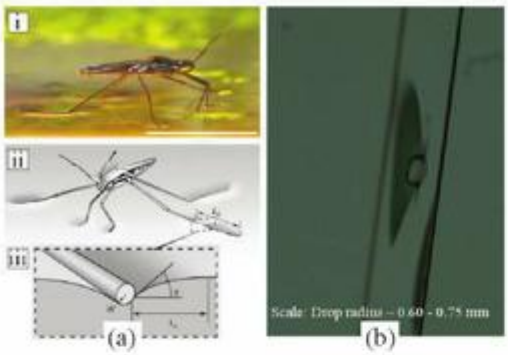

Figure 2: (a) The panels (i), (ii), and (iii) have been adapted from [1]. Panel (i) shows a natural water strider (*Gerris remigis*). Panels (ii) and (iii) represent the distortion of the interface when the strider is static at the air-water interface. Scale bar is 1 cm. (b) A representative impact as observed in our experiments.

We perform a series of experiments where the drop hits the film surface at shallow angles ($< 10^\circ$). Bounce-off regime is predominant when the angle subtended between the pre-impact drop trajectory and the film plane is that small. A quasi-2D projection of the resultant impact is remarkably similar (see Fig. 2) to certain aspects of the impulsive interaction observed in water strider locomotion at air-water interface, as studied by Hu et al. [1].

Our work can be schematized into: (1) experimental visualization of drops impacting the film at shallow angles, and (2) developing a mathematical model to identify the parameter space for the observed bounce-off regime. Comparison of the model predictions with experimental observations is crucial towards validating the model idealizations.

EXPERIMENTAL PARAMETERS AND OBSERVATIONS

We have done a detailed experimental study of droplet impacts on a soap film flow, for a number of inclination angles of the film and heights of fall of the drop. Fig. 3(a) depicts an artistic rendering of our experimental setup. The design involves gravity-driven soap film flow (under a constant potential head) channeled through a slightly inclined wired network. Drops are impinged into the film via a syringe injection system. Film thickness measures approximately in the order of 40–50 microns and the averaged drop diameter is approximately 1.2 mm. The film length is 194 cm and its width is 5 cm. The soap solution has a concentration of 2.5% by volume in deionized water. The drops are also made from deionized water. We have 48 bounce-off data-points obtained for 3 different heights of free descent for the drop, combined with 8 angles of film inclination for each, with 2 trials in each orientation. The imaging techniques used include observing thickness fluctuations (through interferometry) and flow fluctuations (through particle tracking velocimetry). Digital high speed cameras (Vision Research Phantom v641) have been used for front and side imaging of the impact, with typical imaging speed range of 4500–6000 frames s^{-1}. As stated above, we mostly observe the bounce-off regime for smaller angles of film inclination. However, for higher angles of impact, puncture of the film leading to the drop tunneling through becomes a more common occurrence [2]. It should be noted that a larger drop size significantly complicates the dynamics leading to a pinch-off regime where a part of the drop connects with the flow and is sheared away while the

*Corresponding author. Email: saikat25@vt.edu Note: Co-author Ali Yawar participated in the project as a research intern at OIST, Japan

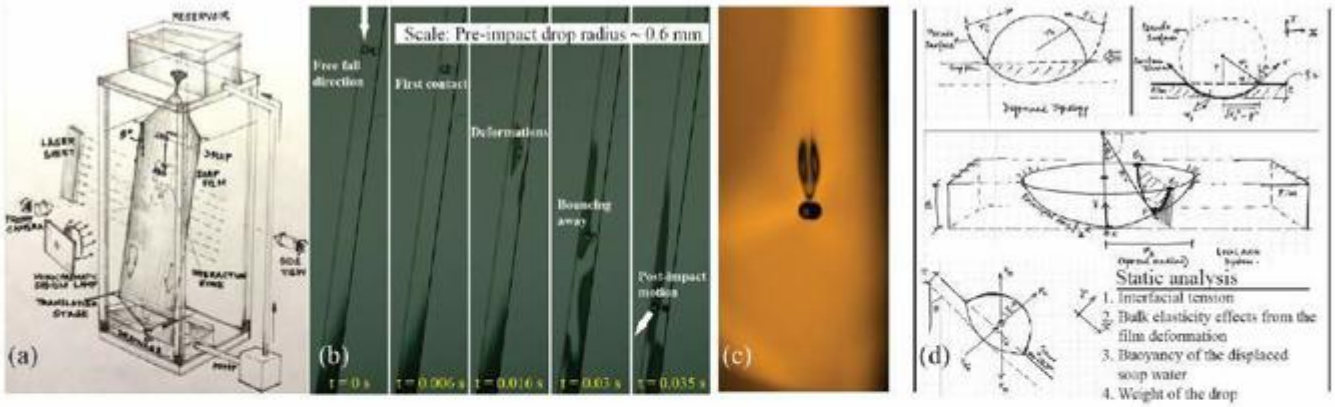

Figure 3: (a) An artistic rendering of the experimental setup. (b) Representative experiment depicting the bounce-off regime (the line of sight is almost in plane with the soap film, and has been imaged from the side). (c) Vortex dipole and waves shed by the impacting drop. (d) Outlines of the mathematical idealization. The details are discussed in the section for model analysis. Note that θ in these sketches is the inclination angle of the film to the vertical.

rest of the drop mass tries to track an inertial trajectory. Such an interaction is beyond this work's purview. Fig. 3(b) shows a representative bounce-off case, imaged from the side with the line of sight being almost in-plane with the film. The front image in Fig. 3(c) shows the vortex dipole shed by the drop when it is in contact with the background film flow.

MODEL ANALYSIS

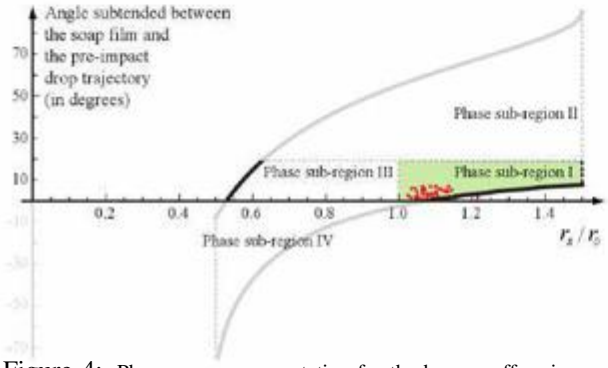

Figure 4: Phase space representation for the bounce-off regime. The solid red circles indicate the parametric location of the experimental data-points.

The mathematical model to track the drop impact on the film entails static analysis of the drop after it has impinged into the film, thereby deforming itself (it spreads out on the film surface) and also the film. It is assumed that the falling energy of the drop has been used up to deform the film material and it is at rest for an infinitesimal time. Our analysis captures this stationary point and considers the forces that are acting on the drop. Similar modeling techniques, albeit for different problems of drop impacts have been adopted before, for example by Chappelear [3] where he studied vertical drop impacts and entrance in a liquid bath. To capture the parameters necessary for the bounce-off regime, the resultant force component perpendicular to the film plane should exceed zero. This gives the force criterion: $F_\sigma(r_s) + \mathbb{F}_E(r_s) + [F_B(r_s) - F_W]\sin\theta = \mathbb{F}(r_s, \theta) > 0$. Here F_σ is the interfacial tensile force component perpendicular to the stream, $\mathbb{F}_E$ is the bulk elastic force component (assuming linearized elastic deformation transverse to the film flow), F_B is the buoyant force, F_W is the drop weight, and r_s is the spread radius of the intersectional periphery of the drop on film plane.

Phase space representation

Fig. 4 shows the phase space representation depicting the physical parametric bounds that lead to a bounce-off. The region enclosed by the curves is determined from the force criterion on $\mathbb{F}(r_s, \theta)$. Ratio r_s/r_0 quantifies the spreading of the drop as it impinges into the film surface, with r_0 being the pre-impact radius of curvature of the drop. For phase sub-region II, the higher angle of inclination would lead to a sagging of the film and that results in flow from peripheries on to the test section. The complication is beyond the scope of this work. In phase sub-region III, $r_s < r_0$ defies the experimental observation that the small drops mostly spread out on impact. Phase sub-region IV consists of negative angles of inclination and is just a "mathematical construct" owing to the dependence of $\mathbb{F}$ on θ. Thus, the predicted model region for the observed bounce-off regime is only phase sub-region I, colored green. Its vertical extent is tentatively marked by the dashed line at 20° inclination. However, it is an open question as to at what angle the film sagging becomes appreciable (resulting in contamination of the impact region from peripheral flows) and this demarcation is just a rough estimate. Comparison with experiments turns out satisfactory as all the experimental data-points, except one, could be located in the predicted phase domain.

Concluding remarks: *Momentum transfer and physical applications*

A final component of this work compares the momentum transfer from the drop to the film with the locomotion characteristics of water-walking animals. From the particle tracking velocimetry data, the shed vortex dipole is found to carry a mean momentum of order 10^{-7} N-s. It fits well with vortex momentum calculated from Bühler's theory [4] for water insect locomotion, which predicts the mean momentum transfer to the shed vortices as 1.48×10^{-7} N-s. This correlation suggests that this impulsive regime may indeed be relevant for investigating the locomotion of water striders.

References

[1] Hu D. L., Chan B., Bush J. W. M.: The hydrodynamics of water strider locomotion. Nature **424**:663-666, 2003.
[2] Kim I., Wu X. L.: Tunneling of micron-sized droplets through soap films. Physical Review E **82**, 2010.
[3] Chappelear D. C.: Models of a liquid drop approaching an interface. J. Colloid Science **16**, 1961.
[4] Bühler O.: Impulsive fluid forcing and water strider locomotion. J. Fluid Mech **573**, 2007.

Universal rescaling of drop impact on smooth and rough surfaces

Daniel Bonn[1,a], Nick Laan[1], Karla de Bruin[2], Noushine Shahidzadeh[1]
[1]*Van der Waals-Zeeman Institute, Institute of Physics, University of Amsterdam, Science Park 904, 1098 XH Amsterdam, Netherlands*
[2] *Netherlands Forensic Institute, Laan van Ypenburg 6, 2497 GB The Hague, Netherlands*

Summary The maximum diameter a droplet that impacts on a surface will attain is the subject of controversy, notably for high-velocity impacts of low-viscosity liquids such as water or blood. We study the impact of droplets of simple liquids of different viscosities for a wide range of surfaces, impact speeds, and impact angles. We show that the spreading behavior cannot simply be predicted by equating the inertial to either capillary or viscous forces, since, for most situations of practical interest, all three forces are important. We determine the correct scaling behaviors for the viscous and capillary regimes and, by interpolating between the two, allow for a universal rescaling.

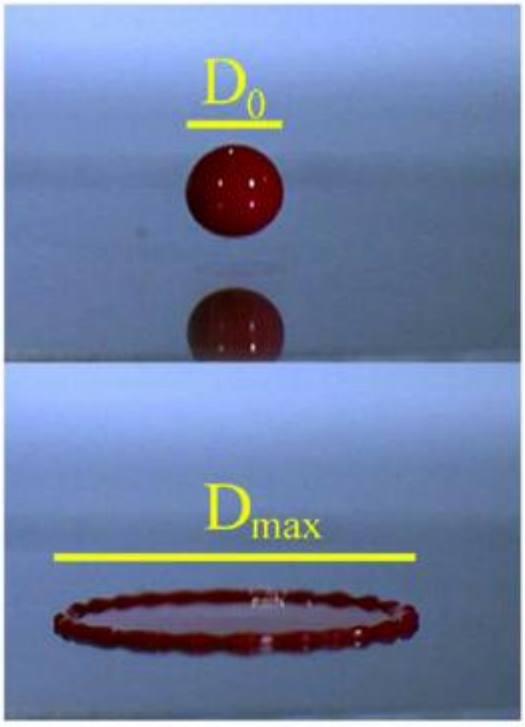

We show that all drop impact, can be rescaled on a universal curve given by intertial, capillary and viscous forces. This is in fact a crossover regime, and so simple scalings do not work. We also include impacts for different impact angles that can be rescaled on the same curve by doing a simple geometrical correction for the impact angle. Also, for a complex fluid like blood (see image), we show that the shear-thinning properties do not affect the maximum diameter and only the high-shear rate viscosity is relevant. With our study, we solve a long-standing problem within the fluid-dynamics community: We attest that the spreading behavior of droplets is governed by the conversion of kinetic energy into surface energy or dissipated heat. Energy transfer into internal flows marginally hinders droplet spreading upon impact. We also demonstrate that dynamic wetting plays an important role in

[a)] Corresponding author. Email: d.bonn@uva.nl

the spreading at low velocity, characterized by the dynamic contact angle at maximum spreading. In the energy balance, we account for the dynamic wettability by introducing the capillary energy at zero impact velocity, which relates to the spreading ratio at zero impact velocity. Correcting the measured spreading ratio by the spreading ratio at zero velocity, we find a correct scaling behaviour for low and high impact velocity. The influence of the liquid as well as the nature and roughness of the surface are taken into account properly by subtracting the spreading ratio at zero velocity

References

[1] Nick Laan, Karla G de Bruin, Denis Bartolo, Christophe Josserand, Daniel Bonn, Physical Review Applied 2 044018 (2014)
[2] JB Lee, N Laan, KG de Bruin, G Skantzaris, N Shahidzadeh, D Derome, J. Carmeliet, D. Bonn Journal of Fluid Mechanics 786, R4 (2015)

CONTROLLING CRACK DYNAMICS USING DROP IMPACT ON COLD SUBSTRATES

Christophe Josserand,* Elisabeth Ghabache, and Thomas Séon

Sorbonne Universités, UPMC Univ Paris 06, CNRS, UMR 7190, Institut Jean Le Rond d'Alembert, F-75005 Paris, France

Summary We perform water drop impact experiments on a solid cold substrate for temperature ranging from 20 to -60° C. Different behaviors are observed depending on the impact parameters and the substrate temperature. In particular, cracks are observed when the solid substrate is cold enough. We identify different crack propagation corresponding to dynamical fractures at intermediate low temperature and quasi-static fracture propagation at very low temperature. A phase diagram is obtained that is interpreted using classical fracture theory.

INTRODUCTION

Drop impact is now an iconic problem of fluid mechanics, concentrating many key-features of multiphase flows [1, 2]. Drop impact exhibits large surface deformation with high stresses, surface flows instabilities and liquid break-up, and it is present in many physical situations ranging from atomization process in combustion to raindrop erosion, from drop printing or coating to models for meteorite impacts. In the present work, we investigate experimentally the dynamics of drop impact on a very cold substrate such that the liquid (water here) would solidify for this substrate temperature. Such configuration is present in the context of ice formation for aircrafts [3] or liquid metal coating [4]. Since the solidified splat of ice created by the impact experiences high shrinking due to the thermal shock, we study here the different cracks patterns that can be formed.

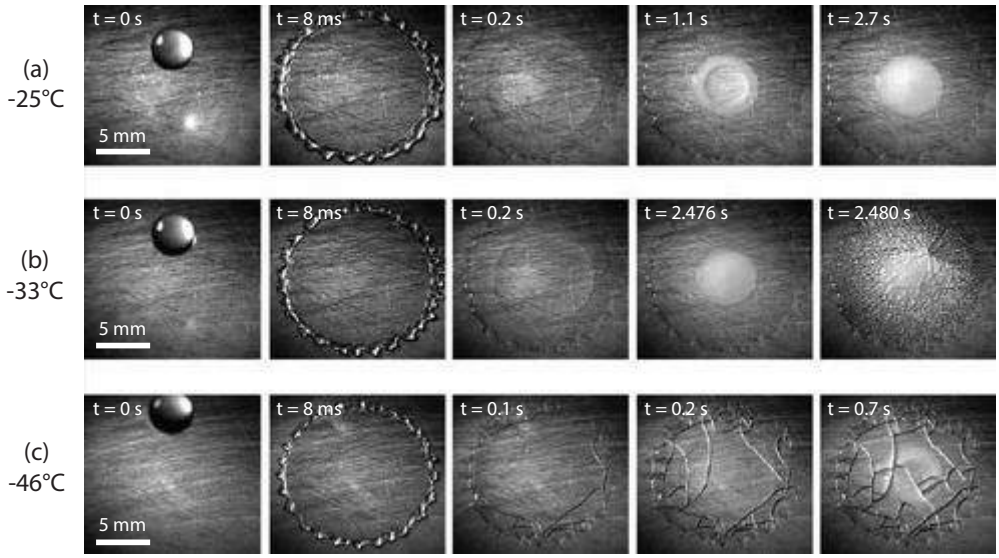

Figure 1: Snapshots of the drop impact dynamics on cold surface at different substrate temperature, with $D = 3.9$ mm and $U_0 = 2.4\,\mathrm{m}\cdot\mathrm{s}^{-1}$. In each case, a solidification front can be observed on the $t = 0.2$ s figure. For the case (a) $T = \circ\, 25^\circ$, no crack are present, while different cracks patterns are formed for the two other cases. While a complex cracks pattern appear suddenly for $T = \circ\, 33^\circ$, a netweork of orthogonal cracks appear step by step for $T = \circ\, 46^\circ$.

EXPERIMENT

We study the impact of a drop of water (diameter $D = 3.9$ mm) falling by gravity on a steel substrate so that the impact velocity is thus close to the free fall $U_0 \sim \sqrt{gH}$ where H is the falling height. The temperature of the substrate can vary typically from room temperature to $\circ\, 60^\circ$ C. It is reached by plunging a large cube of metal (radius 10 cm) into a liquid nitrogen bath until the desired temperature is reached. The whole experiment is made into a controlled atmosphere box in order to avoid frost formation on the substrate. Because of the small impact time (of the order of D/U_0), we can consider that the substrate is at constant temperature during the dynamics, but the small area beneath the spreading drop where thermal

*Corresponding author. Email: christophe.josserand@upmc.fr

exchanges are present. The drop dynamics is visualized using two high-speed cameras that allow simultaneous side and top views. A typical sequence of the impact dynamics is shown on figure 1 for three different temperature. For relatively low temperature ($T = \circ 25°$), right after the impact, the drop spreads rapidly on the substrate until it reaches its maximal extension. No retraction of the drop is further observed since it is pinned on the solid substrate because of ice formation on the substrate. Later a solidification front is observed on the surface until the whole liquid splat is solid. When the substrate temperature is decreased, this general dynamics for the drop impact survives but with important changes during and after the solidification. Firstly, for intermediate temperature, the solidification front appears earlier, and the maximum spreading radius decreases slightly. Then, a dramatic change is observed for low enough temperature (here for $T \sim \circ 33°$) some time after the solid splat is formed. Indeed, while the splat is solid, a very dense crack pattern appear suddenly between two successive images. When increasing the frame rate acquisition in order to estimate the speed of propagation of the cracks, we obtain that this value is varying between 800 and $1000\, m \cdot s^{-1}$, which is a fraction of the Rayleigh wave speed. Moreover, high frequency sequences show that the crack patterns propagates from a localized emission point. As the substrate temperature still decreases further on ($T \sim \circ 46°$), the crack patterns and dynamics exhibit a strong transition: the cracks appear more rapidly after the impact but in successive steps so that the cracks patterns are very different.

ANALYSIS

Varying the velocity impact and the substrate temperature, we have obtained a phase diagram identifying the three main domains of the impact output: no cracks, fast (sudden) craks and slow (by step) cracks, see figure 2. In the presentation, we will analyse this phase diagram using energetic argument [5, 6].

CONCLUSION

Using drop impact on solid substrate, we obtain different cracks patterns by varying the impact conditions and the substrate temperature. Since the drop spreading can be control by changing its dynamical parameters, it can be used to investigate and further on to control the cracks patterns of thin structures.

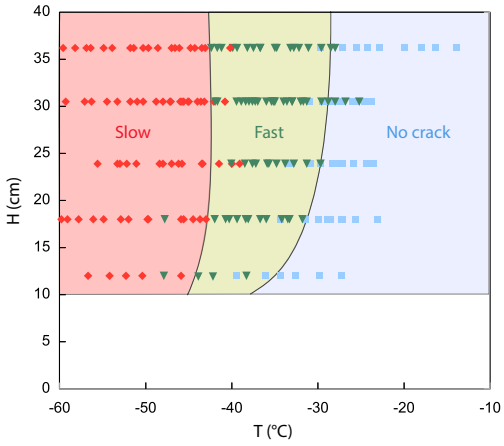

Figure 2: Phase diagram for the cracks pattern as the substrate temperature and the drop impact velocity (here noted by H the height of drop fall) vary.

References

[1] Yarin A.L.: Drop Impact Dynamics: Splashing, Spreading, Receding, Bouncing... Annu. Rev. Fluid Mech 38:159, 2006.

[2] Josserand C. and Thoroddsen S.: Drop Impact on a Solid Surface. Annu. Rev. Fluid Mech 48:365-391, 2016.

[3] Hauk T. Bonaccurso E., Roisman I.V. and Tropea C.: Ice crystal impact onto a dry solid wall. Particle fragmentation. Proc. Roy. Soc. A 471:20150399, 2015.

[4] Ghafouri-Azar R., Shakeri S., Chandra S. and Mostaghimi J.: Interaction between molten metal droplets impinging on a solid surface. Int. J. Heat Mass Transf. 46:1395-1407 2003.

[5] Adda-Bedia M., Ben Amar M. and Pomeau Y.: Morphological instabilities of dynamic fractures in brittle solids. Phys. Rev. E 54: 5774-5779, 1996.

[6] Bourdin B., Marigo J.-J., Maurini C. and Sicsic P.: Morphogenesis and Propagation of Complex Cracks Induced by Thermal Shocks. Phys. Rev. Lett. 112:014301, 2014.

SEQUENTIAL DROPLET DEPOSITION ON GEOMETRICALLY AND CHEMICALLY PATTERNED SUBSTRATES

Pallav Kant[1], Mark Dowling[2] Andrew Hazel[1] & Anne Juel[3]
[1] *School of Mathematics and Manchester Centre for Nonlinear Dynamics, University of Manchester, Oxford Road, Manchester M13 9PL*
[2] *Cambridge Display Technology Limited, Technology Development Centre, Unit 12, Cardinal Business Park, Godmanchester, Cambridgeshire PE29 2XG, UK*
[3] *School of Physics and Astronomy and Manchester Centre for Nonlinear Dynamics, University of Manchester, Oxford Road, Manchester M13 9PL*

Summary: We experimentally investigate the use of topographical features and spatially varying wettability (with moderate receding contact angle) to fill and confine a linearly deposited sequence of overlapping micro-droplets (30 μm in diameter) into a stadium-shaped well region (Figure 1). Our experiments determine the parameter regimes for which droplet lines are contained within shallow wells (~1 μm depth) and, moreover, reveal that the presence of topography results in the formation of contact line cusps during fluid redistribution .On surfaces with wettability variations, controlled wetting resulting in accurate fluid positioning is achieved without any extreme deformation of the contact line. We extend a previously developed quasi-static lubrication model that predicts the post-impact, drop by drop evolution of a liquid line on a flat substrate [1] to include topographical and wettability patterns. The model is shown to reproduce the overall experimental features accurately.

INTRODUCTION

Sequential droplet deposition using inkjet printing technology spans applications from tissue engineering to microelectronics. It relies on the high-precision deposition of material on a target substrate via droplets printed at predetermined locations. However, compared to photolithography, inkjet printing alone often results in insufficient accuracy of the fabricated product so that its practical applications remain limited. Hence, hybrid processes involving photolithographic treatment of the substrate coupled to inkjet deposition are commonly employed in industry to achieve high resolution products. In order to evaluate the full potential of the inkjet printing technique for microfabrication, the underlying physical processes need to be understood, and predictive models are required for the deposition, coalescence and spreading of multiple droplets on variety of substrates.

In the current study, we both experimentally and numerically investigate the deposition of equally spaced, overlapping droplets on substrates with geometrical and chemical patterns. Using high speed imaging technique, we visualize the drop by drop deposition process on the substrates and based on the observations we extend, a previously developed numerical model [1]. Its predictive capabilities are discussed through a quantitative comparison between experiments and theory for wells combining topography and wettability variations used in the microelectronic industry.

EXPERIMENTS

The experimental facility (Figure 1) has been designed to record bottom views using a Photron Fastcam SA5 digital high-speed camera fitted with long distance magnifying optics (Navitar) at 100-1000 fps. After droplet deposition, side view image is recorded to measure the thickness of the deposited morphology. A drop on demand printhead (SX3, FUJIFILM Inc.) is used to generate droplets with deposition frequency 60Hz-200Hz. The printhead is mounted on a linear motion stage (Aerotech – ANT95 L) for accurate positioning of droplets. The inter drop distance (δ) is varied by changing the droplet deposition frequency and printhead speed. Substrates with stadium shaped pixel wells are provided by CDT (*Cambridge Display Technology*).

NUMERICAL MODEL

We extend the Model-I derived by A. Thompson et. al [1] to include the effects of geometric and chemical patterning. We assume that there is no viscous resistance to the fluid movement within the deposited morphology and fluid arranges itself so that pressure is spatially uniform. Under the thin film approximation, the pressure is linked to the interface curvature by the Young-Laplace equation as:

$$\mathbf{P}(\boldsymbol{t}) = -\boldsymbol{\sigma}\boldsymbol{\nabla}^{\boldsymbol{2}}(\boldsymbol{h} - \boldsymbol{B}) \quad \textbf{(1)}$$

[1)] Corresponding author. Email: pallav.kant@postgrad.manchester.ac.uk
* This study is funded by EPSRC and CDT

Where *h(x,y)* is the height distribution of the deposited fluid interface and *B(x,y)* is topographical description of the substrate. For a known value of the deposited fluid volume, we determine both h*(x,y)* and P*(t)* through

$$\boldsymbol{V = \iint (h - B)\, dx\, dy} \quad \textbf{(2)}$$

The contact line motion is defined by the following spreading law:

$$-\cdot\frac{\vec{}}{dt} = \boldsymbol{U(\theta)} = \begin{cases} (\boldsymbol{\theta - \theta_A(x,y)})\boldsymbol{U_0} & \theta > \theta_A \\ (\boldsymbol{\theta_R(x,y) - \theta})\boldsymbol{U_1} & \theta < \theta_R \end{cases}$$

$\theta \approx -n.xh$. Here $\bar{n}$ is the 2D unit normal directed out of the footprint of fluid interface on the substrate, $\theta_A(x,y)$ and $\theta_R(x,y)$ define the spatial variation of the advancing and receding angles on the substrate (chemical patterning). U_0 and U_1 are calculated experimentally.

CONCLUSION

We separately evaluate the effects of geometrical and chemical patterning on the controlled wetting during sequential droplet deposition. The interaction between the contact line and the shallow geometrical features leads to the extreme deformation of the contact lines locally (Figure 2). Similar observations were also made in the experimental study by R. Seemann et.al [2]. The wettability patterning on substrates proves to be an effective method to achieve high resolution features by controlled wetting. The extended model is shown to reproduce the overall experimental features accurately and its predictive capabilities are discussed through a quantitative comparison between experiments and theory.

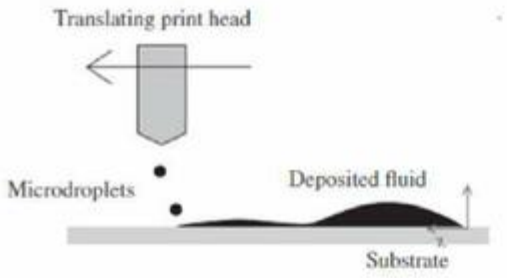

Figure 1: Schematic representation of experimental setup

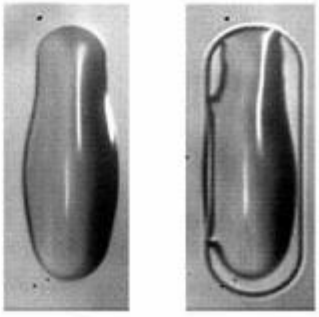

(a) (b)

Figure 2: (a) Morphology of the deposited droplets on a flat substrate **(b)** Formation of the cusps as a result of the interaction between the shallow topographical features with the contact line

References

[1] Thompson, A. B., et al. (2014) "Sequential deposition of overlapping droplets to form a liquid line" *J. Fluid Mech*. 761, 261-281.

[2] Seemann, Ralf, et al. (2005) "Wetting morphologies at microstructured surfaces" *PNAS* 102.6 : 1848-1852.

[3] Sirringhaus, H., et al. (2000) "High-resolution inkjet printing of all-polymer transistor circuits." *Science* 290.5499: 2123-2126.

LEIDENFROST DROPS ON A LIQUID SUBSTRATE: THEORY AND EXPERIMENTS

Benjamin Sobac[1], Alexey Rednikov[1], Laurent Maquet[2], Baptiste Darbois-Texier[2], Alexis Duchesne[2], Martin Brandenbourger[2], Stéphane Dorbolo[2] & Pierre Colinet[1a)]
[1]*Université libre de Bruxelles, TIPs – Fluid Physics, CP 165/67, B-1050 Brussels, Belgium*
[2]*Université de Liège, Physics Department, GRASP, B-4000 Liège, Belgium*

Summary The Leidenfrost effect is studied for drops on a superheated yet non-volatile liquid pool, and contrasted with the more classical situation implying a solid substrate. Experiments reveal the absence of a critical superheat for drops to "levitate" over the roughness-free liquid surface, even when the latter is significantly deformed (i.e. for large drops). Inspired from a previous work, a theoretical model is presented which compares fairly well to experiments without any fitting parameter. Contrary to the case of a solid substrate, the vapor film here does not appear to form chimneys, even for large drops. The evaporation dynamics is also studied, and scaling laws are discussed versus classical ones.

INTRODUCTION

It is common knowledge that a water drop released over a sufficiently hot surface does not contact the plate nor boils but rather "levitates" over a thin vapor film generated by its own evaporation. Although discovered in 1756 [1] and widely studied in connection with heat transfer (cooling) technologies, this so-called Leidenfrost effect is the subject of a renewed interest nowadays (for a recent review, see [2]), partly in view of new perspectives in the field of microfluidics. Indeed, as the small thermal conductivity of the vapor layer slows down the phase change process, while its low viscosity confers a large mobility to the drop, the control and manipulation of Leidenfrost drops (envisaged as contactless micro-reactors for chemical synthesis/analysis) turns out to be possible using ratchets or other surface structures, external fields, ...

Most of the attention has been focused on the case of Leidenfrost drops over a hot solid substrate however, and in that case the threshold temperature above which the drop does not contact the plate is significantly higher than the boiling temperature (e.g. for water on polished aluminum, the Leidenfrost temperature is about 150°C [3]). This critical superheat is notably affected by the roughness of the solid substrate, and also by its thermal properties. In order to separate these two effects, it is therefore of primary interest to study the Leidenfrost effect over a pool of liquid, the free surface of which being truly smooth down to molecular scales.

In addition to the question of the critical superheat, it is also interesting to study the shape of the underlying vapor film as a function of the two main control parameters of the problem: the superheat and the drop size (or its volume). Indeed, in the case of a solid substrate, it is known that this vapor "cushion" generally displays a pocket/neck structure [4], such as seen in Fig. 1. Importantly, when the radius of the drop (as viewed from the top) exceeds about four times the capillary length, the central vapor pocket pierces the liquid upwards and forms a "chimney", as also observed experimentally [3].

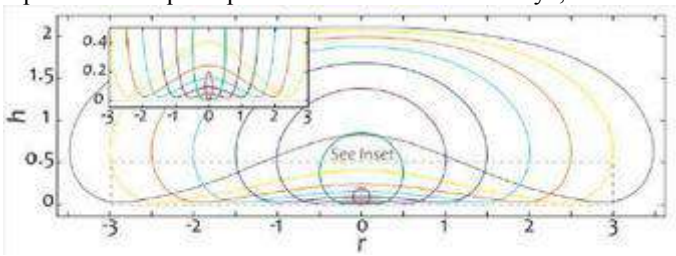

Figure 1: Calculated shapes of water drops of various sizes (dimensionless radius of 0.1, 0.5, 1, 1.5, 2, 2.5, 3, 3.5) in Leidenfrost state over a flat solid substrate superheated by ΔT=270K above the boiling point of water (100°C). All lengths are scaled by the capillary length (2.5 mm for water at 100°C). Reproduced from Sobac *et al.* [5].

METHODS

Experiments are conducted using drops of ethanol on a pool of silicone oil maintained at a constant temperature thanks to a heating plate, a PID controller and a thermocouple that is immersed in the pool close to its surface. Sufficiently viscous silicone oils can be heated up to roughly 200°C and are practically non-volatile as compared to other liquids at these temperatures. The boiling temperature of ethanol is 78°C, hence the superheat ranges from 0°C to more than 100°C. The depth, length and width of the liquid pool are more than ten times larger than the drop radius to avoid finite-size effects.

On the theoretical side, the axisymmetric model used here is based on the model described in [5] for solid substrates, which was successfully validated by direct fitting-parameter-free comparison with the earlier interferometric measurements of the vapor cushion shape by Burton *et al.* [4]. It is also similar to the model proposed by Snoeijer *et al.* [6] in that it assumes an equilibrium (Young-Laplace) shape for the upper part of the superhydrophobic-like drop, but includes a more realistic description of the (heat-conduction-limited) evaporation and vapor flow underneath the drop. The lubrication-type

a) Corresponding author. Email: pcolinet@ulb.ac.be.

formulation of this low-Reynolds number flow is similar though more general than that proposed by Pomeau *et al.* [7], enabling in particular to study drops of sizes comparable to the capillary length. An important difference with all previous models is clearly related to the deformation of the pool free surface, here assumed to be governed by a quasi-static balance between capillarity, gravity and pressure excess in the vapor film. The resulting system of ODE's is solved by a finite-difference method, using numerical matching between the upper and lower drop shapes (and similarly for the pool surface).

RESULTS AND DISCUSSION

Figure 2(left) shows a drop of ethanol over a pool of silicone oil maintained at 79°C, i.e. just above the boiling temperature of ethanol (78°C), hence demonstrating the absence of measurable critical superheat in this roughness-free situation. The surface deformation produced by a drop of the same size on a pool at 118°C is shown in Fig. 2(center), and the extracted profile is compared to the prediction of the theoretical model in Fig. 3(right), showing a rather satisfactory agreement.



Figure 2: Left: An ethanol drop (of radius 1.2 mm) on a pool of silicone oil V20 heated at 79°C, just above the boiling point of ethanol (78°C). Center: View from underneath the pool free surface, for a 1.2 mm ethanol drop on a pool of silicone oil V20 at 118°C. Right: Comparison of model predictions with the free surface shape extracted from the center experimental picture (sizes are rescaled by the capillary length of ethanol, namely 1.5 mm at 78°C).

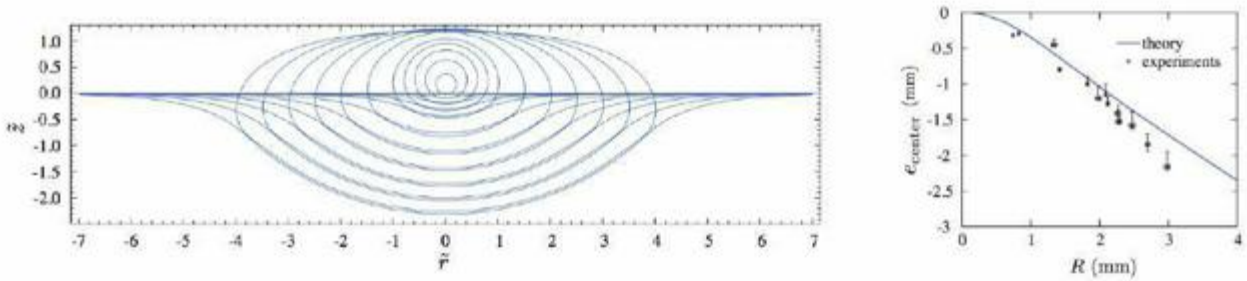

Figure 3: Left: Calculated shapes of ethanol drops of various sizes (dimensionless radius of 0.2, 0.4, 0.6, 0.8, 1, 1.5, 2, 2.5, 3, 3.5, 4) in Leidenfrost state over the free surface of a pool of silicone oil V20 heated at 118°C. All lengths are scaled by the capillary length (1.5 mm for ethanol at 78°C). Right: maximal pool surface deformation as a function of drop radius R (seen from above).

Figure 3(left) presents the calculated shapes of drops of sizes ranging from 0.2 to 4 times the capillary length for the same experimental conditions. While the upper part of the drop does not exceed a certain height, the deformation of the pool free surface increases with the drop size, and its maximal value at the center is satisfactorily compared to experimental measurements on Fig. 3 (right). A rather thin vapor film is visible between the drop and the pool, and even though a neck exists close to the edge, no pronounced vapor pocket is predicted as was the case for a solid substrate (see Fig. 1). No evidence of vapor pocket or chimney has been found in experiments either, although it has turned out to be difficult to generate droplets larger than three times the capillary length. Finally, results have also been obtained about the evaporation dynamics of drops on a bath, and about scaling laws for the typical dimensions of the vapor film under the drop. These results will be presented during the Conference.

The authors are grateful to Jacco Snoeijer for promising discussions on further modeling, and thankfully acknowledge the financial support of BELSPO (IAP 7/38 Micro-MAST project), ESA-BELSPO (PRODEX Heat Transfer Project), and of the Fonds de la Recherche Scientifique – FNRS. This research is also carried out under the umbrella of COST Action MP1106.

References

[1] Leidenfrost J.G.: De Aquae Communis Nonnullis Qualitatibus Tractatus, Part 2. Duisburg, 1756.

[2] Quéré D.:. Leidenfrost Dynamics. *Ann. Rev. Fluid Mech.* **45**:197-215, 2013.

[3] Biance A.-L., Clanet Ch., Quéré D.: Leidenfrost drops. *Phys. Fluids* **15**:1632–37, 2003.

[4] Burton J.C., Sharpe A.L., van der Veen R.C.A., Franco A., Nagel S.R. Geometry of the vapor layer under a Leidenfrost drop. *Phys. Rev. Lett.* **109**:074301, 2012.

[5] Sobac B., Rednikov A., Dorbolo S., Colinet P.: Leidenfrost effect: accurate drop shape modelling and refined scaling laws. *Phys. Rev. E* **90**:053011, 2014.

[6] Snoeijer J.H., Brunet Ph., Eggers J.: Maximum size of drops levitated by an air cushion. *Phys. Rev. E* **79**:036307, 2009.

[7] Pomeau Y., Le Berre M., Celestini F., Frisch Th.: The Leidenfrost effect: from quasi-spherical droplets to puddles. *C.R. Mécanique* **340**:867-881, 2012.

SHORT- AND LONG-TERM TAILING DYNAMICS DURING THE SETTLING OF A SPHERE THROUGH AN INTERFACE

Jean-Lou Pierson[1] and Jacques Magnaudet[2]

[1,2]*Institut Français du Pétrole, Solaize, France*
[2]*Institut de Mécanique des Fluides de Toulouse - Université de Toulouse, CNRS-INPT-UPS, Toulouse, France*

Summary We carry out a joint experimental and computational investigation of the settling of spheres made of various materials across the horizontal interface separating two viscous fluids. Over a wide range of conditions, the spheres tow a column of the upper fluid through the lower one for a while. Considering three situations characterized by markedly different inertia-to-viscosity and viscosity ratios, we show that this tail may exhibit strikingly different long-term evolutions. We identify the underlying mechanisms and discuss them in connection with several canonical phenomena, especially the instabilities of sheared viscous interfaces and those of stretched viscous threads.

INTRODUCTION

The situation in which a rigid body settles through a horizontal interface separating two layers of fluid with comparable densities and otherwise at rest is encountered in a wide variety of applications ranging from environmental sciences (ashes released in volcanic eruptions, sedimentation of marine snow,...) to engineering (coating processes, phase detection in oil industry). This flow configuration is known to give rise to two strikingly different behaviours [1]. The regime in which viscous and capillary effects dominate frequently yields a flotation configuration in which the body is stopped nearby the interface until the film located ahead of it is entirely drained. In contrast, when capillary effects are small enough and/or inertia effects are large enough, the interface deforms more easily, so that the body may fall across it, then towing a tail of the upper fluid while settling into the other. Although the first configuration has been extensively studied because of its relevance with respect to coalescence, much less is known about the tailing configuration, except in the Stokes limit [2]. We focused on that configuration in the regime in which inertia, viscosity and capillary effects all matter. To better understand the basic hydrodynamic processes that contribute to the development and later the retraction of the tail, we carried out an extensive investigation of this generic problem, based on a combination of experiments and direct numerical simulations.

METHODS AND PROBLEM DEFINITION

Experimentally, single rigid spheres made of various materials were released well above an interface separating a layer of water or of a mixture of glycerin and water, and an upper, slightly lighter, layer of silicon oil. A detailed evolution of the sphere motion and of the interface shape was obtained using a high-speed video camera and image processing techniques. Computations were carried out by solving the full Navier-Stokes equations with a Volume of Fluid approach combined with an Immersed Boundary Method to follow the sphere and enforce the no-slip condition at its surface.
The problem is governed by five dimensionless parameters, among which the Archimedes (Ar) and Bond (Bo) numbers which compare gravitational effects to viscous and capillary effects, respectively, and the viscosity ratio of the two fluids (λ) were varied by several orders of magnitude. The solid-to-fluid density contrast (ζ_p) and the fluid density contrast (ζ) were only varied by one order of magnitude. Depending on the value of these parameters, a variety of flow regimes, settling velocity evolutions and short- and long-time tail dynamics was observed. In this talk we shall focus on three specific configurations that we find illustrative of the richness of the dynamics that take place in these systems.

THE CONICAL-BLOB AND BULGE-COROLLA REGIMES

When the lower fluid is much less viscous than the upper one ($\lambda \ll 1$), only slightly heavier ($\zeta \ll 1$), and inertia effects are moderate ($Ar \lesssim 10$), the tail first takes a long, conical shape until pinch-off occurs slightly above the top of the sphere. The latter then continues to settle while carrying a drop of the upper fluid, the volume of which may be of the same order as or even larger than its own volume. The tail then retracts without breaking, in agreement with previous observations with very viscous pre-elongated drops [3]. The blob at the the bottom of the tail recedes with a velocity of the order of that predicted by the inviscid Taylor-Culick-Keller model but may exceed it by nearly 40%, owing to buoyancy effects resulting from the fluid density contrast ζ. A different scenario takes place when inertia effects are strong enough ($Ar \gtrsim 10$). Here a small bulge forms at the film surface in the rear region of the sphere and evolves in a series of skirts that develop along the tail and propagate upstream (left sequence in figure 1). Detailed examination of the evolution of the initial disturbance and comparison with the case of air bubbles crossing a similar fluid-fluid interface, in which this scenario has never been observed [4], suggest that the instability at work is similar to those observed at the interface between two shearing fluids. The thin oil film encapsulating the sphere being much more viscous than the outer fluid and the wavelength of the amplified disturbance being much larger than the film thickness, the phenomenon is reminiscent of the long-wave viscous instability described by Yih [5].

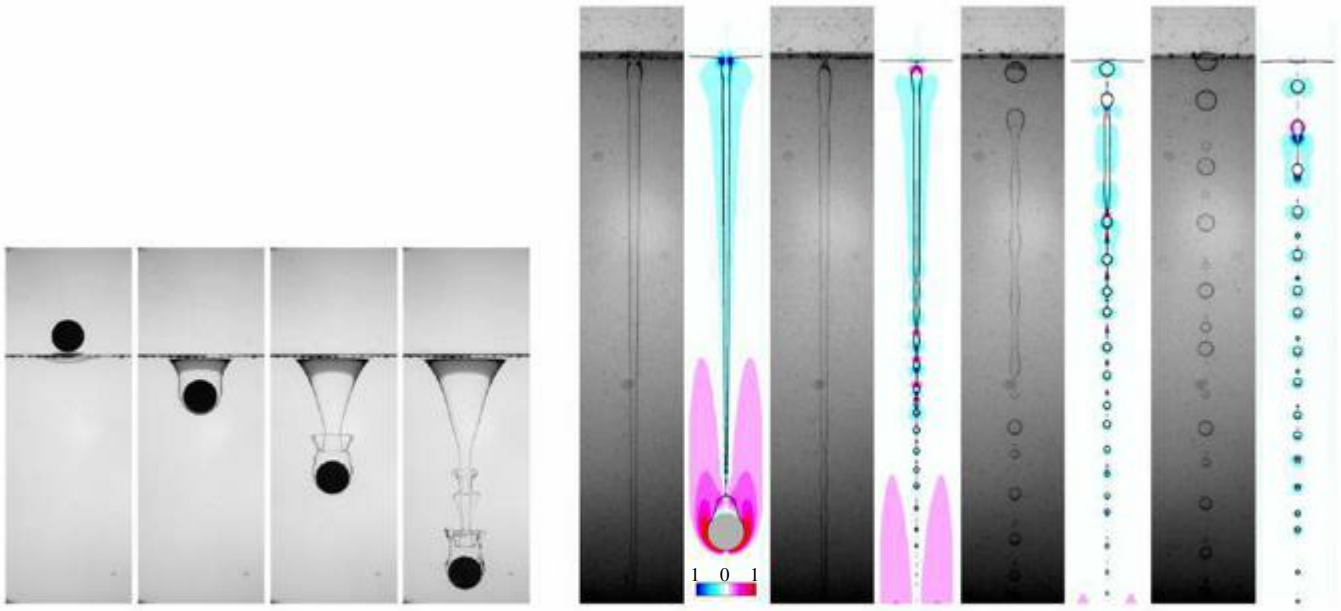

Figure 1: Left sequence: A steel sphere with $Ar = 9.2$ and $Bo = 0.46$ settling through a silicon oil/water interface with $\lambda \approx 2.10^{-3}, \zeta = 0.03$. Right sequence: a Teflon sphere with $Ar = 23.1$ and $Bo = 1.9$ settling through a silicon oil/water-glycerin interface with $\lambda \approx 0.84, \zeta = 0.26$; experimental images have been magnified by a factor of 1.4 with respect to computational snapshots; colors in the computational sequence refer to the magnitude and sign of the azimuthal vorticity.

THE CYLINDRICAL-BEADS REGIME

A strikingly different phenomenology takes place for $\mathcal{O}(1)$ viscosity ratios and Bond numbers, $\mathcal{O}(10^{-1})$ fluid density contrasts and $\mathcal{O}(10)$ Archimedes numbers. In that regime, the thick initial basis of the column gently thins down and a long cylindrical tail develops for a while. At some point it is about to break at its very top but, as the computations reveal, the neck reopens owing to the restoring effect of the standing wave system that develops since the early stages of the tail formation on the initial plane of the interface. After pinch-off eventually occurs at the back of the sphere, an end-pinching process takes place, in line with the findings of [3]. The tail bursts into an essentially bi-modal series of mother and satellite droplets along the scenario described in [6] (right sequence in figure 1). The size of the primary droplets that form during this process agrees well with Tomotika's predictions [7].

CONCLUSIONS

A joint experimental and computational investigation of the settling of a sphere across a horizontal fluid-fluid interface allowed us to identify a series of markedly different crossing scenarios. In particular, the long-term evolution of the light fluid column towed by the sphere follows strikingly different routes, depending on λ and Ar and, in a more subtle manner, on the other three dimensionless parameters. The driving mechanisms at work in these late evolutions turn out to be closely related to canonical situations examined so far in very different contexts, especially those of sheared viscous films or the retraction of viscous or inviscid threads.

References

[1] Maru H. C., Wasan D. T., Kintner R. C.: Behavior of a rigid sphere at a liquid-liquid interface. Chem. Eng. Sci. 26:1615-1628, 1971.

[2] Geller A. S., Lee S. H., Leal L. G.: The creeping motion of a spherical particle normal to a deformable interface. J. Fluid Mech 169:27-69, 1986.

[3] Stone H. A., Bentley B. J., Leal, L. G. An experimental study of transient effects in the breakup of viscous drops. J. Fluid Mech. 173:131-158, 1986.

[4] Bonhomme R., Magnaudet J., Duval F. and Piar B. Inertial dynamics of air bubbles crossing a horizontal fluid-fluid interface. J. Fluid Mech. 707: 405-443, 2012.

[5] Yih C. S. Instability due to viscosity stratification. J. Fluid Mech. 27, 337-352, 1967.

[6] Tjahjadi M. S. H. A., Stone H. A., Ottino J. M. Satellite and subsatellite formation in capillary breakup. J. Fluid Mech. 243: 297-317, 1992.

[7] Tomotika S. On the instability of a cylindrical thread of a viscous liquid surrounded by another viscous fluid. Proc. R. Soc. London Ser. A-Math. Phys. Sci. 150:322-337, 1935.

Explosive Fragmentation

E. Villermaux *[1,2], A. Vledouts[1], J. Quinard[1], and N. Vandenberghe[1]
[1]*Aix Marseille Université, CNRS, Centrale Marseille, IRPHE UMR 7342, 13384 Marseille, France*
[2]*Institut Universitaire de France, Paris*

Summary The forced radial expansion of a spherical liquid shell by an exothermic chemical reaction is a prototypical configuration for the explosion of cohesive materials in three dimensions. The shell is formed by the capillary pinch off of a thin liquid annular jet surrounding a jet of reactive gaseous mixture at ambient pressure. The encapsulated gas in the resulting liquid bubble is a mixture of hydrogen and oxygen in controlled relative proportions, which is ignited by a laser plasma aimed at the center of the bubble. The strongly exothermic combustion of the mixture induces the expansion of the hot burnt gas, pushing the shell radially outwards in a violently accelerated motion. That motion triggers the instability of the shell, developing thickness modulations ultimately piercing it in a number of holes. The capillary retraction of the holes concentrates the liquid constitutive of the shell into a web of ligaments, whose breakup leads to stable drops. We offer a comprehensive description of the overall process, from the kinematics of the shell initial expansion, to the final drops size distribution as a function of the composition of the gas mixture, the initial shell radius and thickness.

INTRODUCTION

Capillarity is the familiar manifestation of the cohesion of Liquids. Since Laplace (1805), we know that intense attractive forces between the molecules bridge the small with the large since they shape liquid/vapor interfaces (meniscii, liquid bridges, bubbles, drops etc...) at macroscopic scales through the concept of surface tension. In some situations however, liquids *disgregate*, following the neologism of R. Clausius (1862), meaning that they fragment by the action of deformations whose intensity competes with that of cohesion forces [1]. We consider here a liquid bubble encapsulating a hydrogen/oxygen gas mixture [2], fragmenting by the sudden deflagration of the mixture, and we offer a comprehensive description of the overall process, from the kinematics of the shell initial expansion, to the final drops size distribution as a function of the composition of the gas, and the initial shell radius and thickness of the bubble.

PRINCIPLE AND OBSERVATIONS

The shell is formed by the capillary pinch off of a thin liquid annular jet surrounding a jet of reactive gaseous mixture at ambient pressure. The encapsulated gas in the resulting liquid bubble is a mixture of hydrogen and oxygen in controlled relative proportions, which is ignited by a laser plasma aimed at the center of the bubble (Fig. 1a). The strongly exothermic combustion of the mixture induces the expansion of the hot burnt gas. The flame radius is

$$r_f = \dot{r}_f t \tag{1}$$

where $\dot{r}_f$ is the flame velocity (Fig. 1b). This expansion motion pushes the liquid shell radially outwards in a violently accelerated motion so that its radius is

$$\frac{R}{R_0} = 1 + \frac{1}{4}\left(\frac{r_f}{R_0}\right)^3 \tag{2}$$

This super-accelerated motion ($R \sim t^3$) triggers a Rayleigh-Taylor type instability of the shell, developing thickness modulations, which ultimately puncture the shell in a number of holes. This happens a time $t_\star$ after the mixture ignition, corresponding to an instability radius $R(t_\star)$ given by

$$\frac{r_f t_\star}{R_0} \sim We^{-1/4} \quad \text{and} \quad \frac{R(t_\star)}{R_0} - 1 \sim We^{-3/4}, \quad \text{where} \quad We = \frac{\rho \dot{r}_f^2 h}{\sigma} \tag{3}$$

The mean distance between the holes is given by the most amplified instability wavelength as (Fig. 1c)

$$\frac{\lambda}{R_0} \approx \frac{2\pi}{We^{3/4}}, \tag{4}$$

The capillary retraction of the holes concentrates the liquid constitutive of the shell into a web of ligaments, whose breakup leads to stable drops. These are distributed in size d as [3]

$$\Gamma_\nu(x = d/\langle d\rangle) = \frac{\nu^\nu}{\Gamma(\nu)}\, x^{\nu-1}\, e^{-\nu x}, \tag{5}$$

*Corresponding author. Email: emmanuel.villermaux@univ-amu.fr

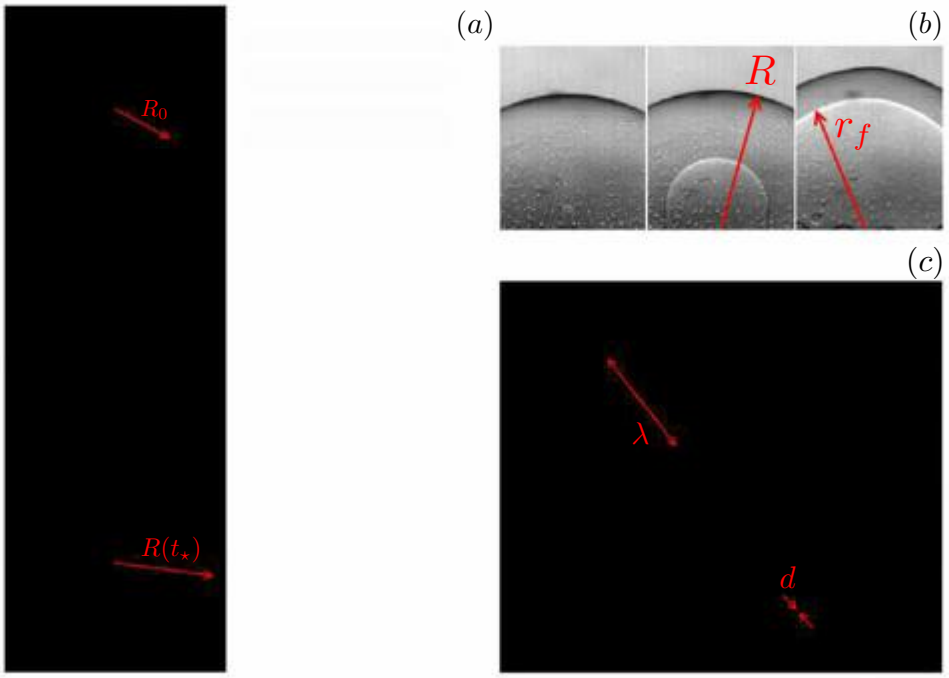

Figure 1: (a) Fragmentation of a liquid shell with initial radius $R_0 = 2.5$ cm by the combustion of a hydrogen/oxygen mixture, showing sequentially the shell expansion, the onset of the shell piercing at $t = t_\star$, the nucleation and coalescence of the holes, the formation of a web of ligaments, and finally the breakup of the ligaments in a dispersion of droplets. (b) Detail of the flame front propagation inside the liquid shell. (c) Holes rims collisions, ligaments destabilization, and drops formation.

with an index ν function of the ligaments initial corrugation, itself depending on the holes density while the mean droplet size $\langle d \rangle$ simply results from mass conservation

$$\langle d \rangle \sim \sqrt{\frac{2\lambda h}{\pi}}, \tag{6}$$

thus completing the description of this problem in which the fragments distribution is the result of a competition between deformation, breakup and cohesion [4].

CONCLUSION

A spherical liquid shell expanded by the deflagration of the gas mixture it encloses is a prototype of explosive fragmentation relevant to a collection of phenomena spanning over a broad range of length scales, among which are: Exploding blood cells in the human body, spore dispersal from plants, boiling droplets, underwater explosions, magma eruption in volcanoes. The objective of the present study is to illustrate a fragmentation scenario in a particular instance where each step can be documented and rationalized with certitude: We depict successively the dynamics of the flame in the gas, inducing that of the shell itself, the stability of the shell in its radially accelerated motion and its final disintegration into stable fragments. All steps, from the initial state to the final dispersion of droplets, are described quantitatively, and rationalized by simple but accurate arguments. The connexion with generally admitted lumped descriptions in fragmentation will be made.

References

[1] Rowlinson, J. S.: Cohesion. Cambridge University Press, 2002.
[2] Marangoni, C. and P. Stefanelli, P.: Monografia delle bolle liquide. Nuovo Cimento, 9, (1), 236-256, 1873.
[3] Eggers, J. and Villermaux, E.: Physics of liquid jets. Rep. Prog. Physics, 71, 036601, 2008.
[4] Vledouts, A., Quinard, J., Vandenberghe, N. and Villermaux, E.: Explosive Fragmentation of Liquid Shells. J. Fluid Mech., 788, 246-273, 2016.

FULLY RESOLVED SIMULATION OF FLUID FLOWS WITH SUSPENDED PARTICLES

Andrea Prosperetti [*1,2], Adam Sierakowski[1], Daniel Willen[1], and Yayun Wang[1]

[1]*Department of Mechanical Engineering, Johns Hopkins University, Baltimore USA*
[2]*Department of Applied Sciences, University of Twente, The Netherlands*

Summary PHYSALIS is a physics-based method for the numerical simulation of fluid flows with many suspended spherical particles. After a brief exposition of the method, we present results on the sedimentation of thousands of particles, illustrating in particular the presence of concentration waves, and on the random rotation of a fixed particle in an incident turbulent flow.

Progress in computational capabilities – and specifically in the realm of massively parallel architectures – render possible the simulation of fully resolved fluid-particle systems. This development holds the promise of major improvements in the physical understanding and modelling of these systems when the particle size is not small and their concentration appreciable. This work starts with a brief overview of the PHYSALIS method for the solution of the incompressible Navier-Stokes equations with finite-sized spheres, and then describes the results of several simulations.

PHYSALIS starts from the simple observation that, due to the no-slip condition, the flow near a solid particle differs very little from a rigid-body motion and it can, therefore, be linearized about such a motion. Thus, after a simple change of the dependent variables from the original velocity $\mathbf{u}$ and pressure p to modified velocity $\tilde{\mathbf{u}}$ and pressure $\tilde{p}$, the momentum equation can be reduced to a Stokes-like form in the immediate neighborhood of each particle. An exact analytic solution of this equation exists in the form

$$\tilde{\mathbf{u}}\left(r,\theta,\varphi\right)=\sum_{l=0}^{\infty}\sum_{m=-l}^{l}A_{lm}\tilde{\mathbf{u}}_{lm}\left(r\right)Y_{l}^{m}\left(\theta,\varphi\right),\qquad\tilde{p}\left(r,\theta,\varphi\right)=\sum_{l=0}^{\infty}\sum_{m=-l}^{l}B_{lm}\tilde{p}_{lm}\left(r\right)Y_{l}^{m}\left(\theta,\varphi\right),\tag{1}$$

Here (r,θ,φ) are local spherical coordinates with origin at the particle center and Y_l^m are spherical harmonics. The functions $\tilde{\mathbf{u}}_{lm}$ and $\tilde{p}_{lm}$ are simple algebraic functions of r known analytically. The no-slip condition at the particle surface is satisfied exactly due to the form of the functions $\tilde{\mathbf{u}}_{lm}$ whatever the order of truncation of the infinite summations. The time-dependent Lamb's coefficients A_{lm} and B_{lm} account for an arbitrary flow in the neighborhood of the particle and are simply related to the force, couple, and higher-order multipoles associated with the particle. The expressions (1) are used as a "bridge" from the particle surface to the closest grid nodes, away from which the full Navier-Stokes momentum equation is solved by a finite

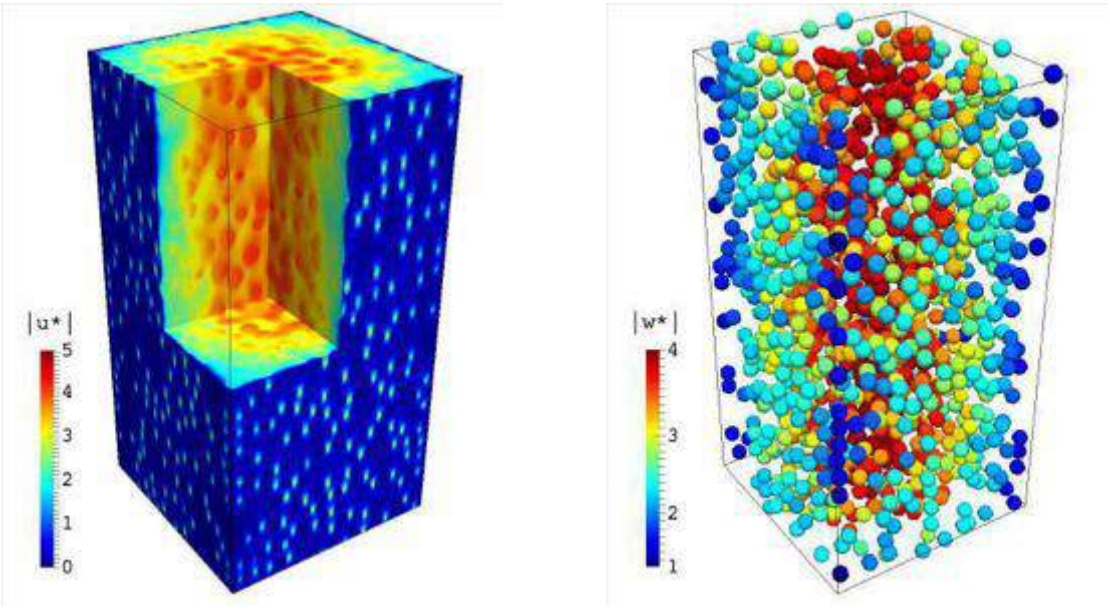

Figure 1: Snapshot of 2048 particles sedimenting under gravity; $|u^*|$ and $|w^*|$ are the fluid and particle velocities normalized by the single-particle terminal velocity. Color indicates the magnitude of the vertical velocity. The left panel is the fluid velocity and the right panel the particle velocity.

*Corresponding author. Email: prosperetti@jhu.edu

difference method. The Lamb coefficients are determined iteratively by matching the local solution (1) to the finite-difference solution. Advantages of the method are the spectral convergence of the expansions in (1), which permits the use of a relatively coarse discretization without loss of accuracy, the use of a regular Cartesian grid in spite of the curvature of the particle boundaries and the information on forces, couples and higher-order multipoles directly available from the Lamb coefficients with no need for further computations.

An example of the possibilities offered by PHYSALIS is shown in figure 1, taken from a recent paper [1]. Here 2048 spheres settle under gravity in a computational domain with no-slip lateral walls and periodicity in the vertical direction; the mean particle volume fraction is 20%. The figures show the fluid (left) and particle (right) vertical velocities after statistical steady state has been reached. The grid has 8 mesh lengths per particle radius and the summations in (1) contain 49 terms. The particle Galileo number $\mathrm{Ga} = \nu^{-1}\left(|\rho_p/\rho_f - 1|\, 8a^3 g\right)^{1/2}$, with ρ_p and ρ_f the particle and fluid densities, respectively, a the particle radius and g the acceleration of gravity, equals 49.

Results of this type contain a wealth of information and one of the challenges is to find useful way to extract them. We have found that the use of the Fourier series is a useful tool to extract information related to the particles. For example, let $\alpha(z,t)$ be the particle volume fraction averaged over horizontal planes. The Fourier expansion of this quantity is given by

$$\alpha(z,t) \;=\; v \sum_{\ell=-\infty}^{\infty} n_\ell(t) e^{-ik_\ell z}\,, \qquad \text{with} \qquad n_\ell(t) \;=\; \frac{1}{L_x L_y L_z}\left\langle \sum_{\alpha=1}^{N_p} e^{ik_\ell z_\alpha(t)} \right\rangle . \tag{2}$$

Here v is the particle volume, L_x, L_y and L_z are the dimensions of the computational domain and $k_\ell = 2\pi\ell/L_z$; the sum is over all the N_p particles, located at $z_\alpha(t)$, and the angle brackets indicate horizontal averages. A similar method can be used to extract the horizontally averaged vertical particle velocity $w(z,t)$. A space-time representation of $\alpha(z,t)$ and $w(z,t)$ obtained in this way is shown in figure 2 where the color is the magnitude of the function. These results were obtained from a simulation similar to that of figure 1 except that fully periodic boundary condition were imposed on all the boundaries of the domain; there were 500 particles with a mean volume fraction of 8.7%, Ga = 75 and ρ_p/ρ = 3.3. It is evident that there are upward-propagating concentration waves in the system, with the higher velocities coinciding with higher volume fractions. Several other features can be extracted from such simulations such as the dynamics of particle tetrads, clustering and multi-particle statistics.

Another interesting example of the application of PHYSALIS concerns the random rotation of a fixed particle in an incident turbulent flow. One finds, for example, that, while the flatness of the three components of the hydrodynamic couple is significantly larger than for a Gaussian (about 3.8 for Re_λ = 47.2, Re_p = 150, ρ_p/ρ = 2, a/η_k = 16, a/ℓ = 0.38 with a the particle radius, η_k the Kolmogorov length and ℓ the integral length scale), the flatness of the angular velocity is close to the Gaussian value of 3.

Acknowledgment: This study has been supported by NSF grant CBET 1335965.

References

[1] A. Sierakowski and A. Prosperetti, "Resolved-particle simulation by the Physalis method: Enhancements and new capabilities", *J. Comput. Phys.*, in press.

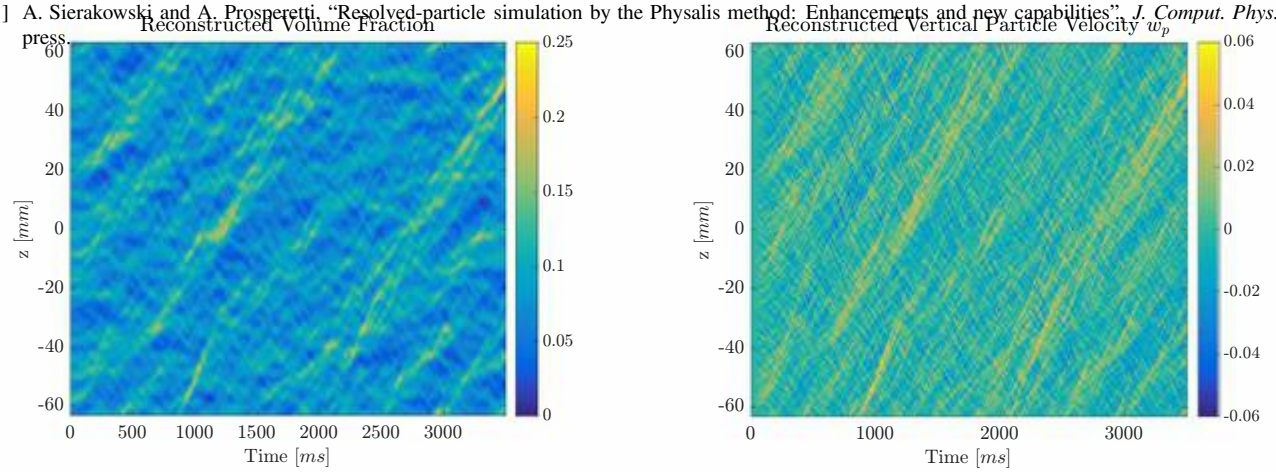

Figure 2: Space-time diagrams of the particle volume fraction (left) and vertical particle velocity (color indicates the magnitude of the function) for the sedimentation of 500 particles; note the upward-propagating concentration waves.

3D DNS OF SPRAY FORMATION IN GAS-ASSISTED ATOMIZATION

Yue Ling[1], Daniel Fuster[1], Gretar Tryggvason[2], Ruben Scardovelli[3], and Stéphane Zaleski [*1]

[1]*Institut Jean Le Rond d'Alembert, Sorbonne Univ. UPMC (Paris 6), CNRS (UMR 7190), F-75005 Paris, France*
[2]*Dept of Aerospace & Mechanical Engineering, University of Notre Dame, Notre Dame, IN 46556, United States*
[3]*DIN–Lab. di Montecuccolino, Universit di Bologna, Via dei Colli 16, 40136 Bologna, Italy*

Summary In this paper, 3D direct numerical simulations of gas-assisted atomization are performed to investigate the spray formation mechanisms. The shear between the gas and liquid jets introduces breakups of the liquid and turbulent flows in the gas. Particular attention is focused on the effect of grid resolution on the turbulence and spray characteristics.

INTRODUCTION

Gas-assisted atomization is commonly seen in many industrial applications and natural phenomena. In a typical configuration of gas-assisted atomization, the breakup of a slow liquid jet is assisted by a fast coflowing gas jet. Due to the large velocity difference between the liquid and gas jets, a Kelvin-Helmholtz instability develops at the gas-liquid interface. The resulting wavy structure on the interface grow temporally and spatially, which eventually leads to significant breakup and atomization of the liquid jet. Despite the substantial previous theoretical, numerical, and experimental research efforts on gas-assisted atomization [1], the underlying mechanisms (in particular in three-dimension) that leads to spray formation remain unclear. The interaction between the turbulence and the interfacial flows is still poorly understood [2]. In order to better understand the mechanisms of spray formation, in this work we simulate a model of the quasi-planar experiment of [3].

SIMULATION METHODS AND SETUP

The computational domain is a box of dimensions $L_x \times L_y \times L_z$, where we inject two streams, liquid and gas, separated by a solid plate of size $\ell_x \times e_y \times L_z$ through the boundary at $x = 0$, with velocities U_g and U_l. The thickness of the liquid and gas streams are H and $H \circ e_y$, respectively. The dimensions of the box are $L_x = 16H$ and $L_y = 8H$ and $L_z = 2H$. If the physical parameters, such as the large liquid-to-gas density ratio, exactly as in the experiments [3] is used, then it is impractical to fully resolve down the smallest physical scales with the current computational power. Therefore, here we choose a set of parameters that allow faster and easier simulations while still placing the flow in the high-speed atomization regime. The values of the corresponding dimensionless parameters are given in Table 1, using standard notations.

$M = \rho_g U_g^2/(\rho_l U_l^2)$	$r = \rho_l/\rho_g$	$m = \mu_l/\mu_g$	$\mathrm{Re}_{g,\delta} = \rho_g U_g \delta/\mu_g$	$\mathrm{We}_{g,\delta} = \rho_g U_g^2 \delta/\sigma$	$\mathrm{Re}_g \rho_g U_g H/\mu_g$
20	20	20	1000	10	8000

Table 1: Key dimensionless parameters. The thickness of the gas boundary layer above the separator plate is denoted by δ.

We solve the Navier-Stokes equations for incompressible flow with sharp interfaces and constant surface tension. The fields are discretized using a fixed regular cubic grid, and use a projection method for the time stepping to incorporate the incompressibility condition. The interface is tracked using a Volume-of-Fluid (VOF) method with a Mixed Youngs-Centered Scheme to determine the normal vector and a Lagrangian-Explicit scheme for the VOF advection. Curvature is computed using the height-function method. Surface tension is computed from curvature by a well-balanced Continuous-Surface-Force method. The whole method is implemented in the a free code *PARIS* [4] and described in [5, 6].

The simulations are performed on three grids called M0, M1 and M2, so that Mn has $H/\Delta x = 32 \times 2^n$ points in the liquid layer. An approximate steady state is reached at about $U_g t/H = 200$ and the simulations are then continued until $U_g t/H = 400$. For the M2 mesh, the simulation was perfomed using 2048 processors and the total simulation time is about 5×10^5 CPU hours. The results presented correspond to the M2 mesh, unless stated otherwise.

RESULTS

A global view of the atomizing liquid jet is shown in Fig. 1 (a), and a closeup of the vortical structures arising from the gas-gas and the gas-liquid mixing layers is shown in Fig. 1 (b). The interface is unstable due to the shear between the gas and the liquid and an interfacial wave develops. The interfacial wave grows and forms a thin liquid sheet which in turn breaks into ligaments and droplets. The unbroken part of the liquid sheet eventually reattaches to the domain bottom. Turbulence develops from the mixing layers and the downstream flow becomes fairly violent and chaotic.

*Corresponding author. Email: stephane.zaleski@upmc.fr

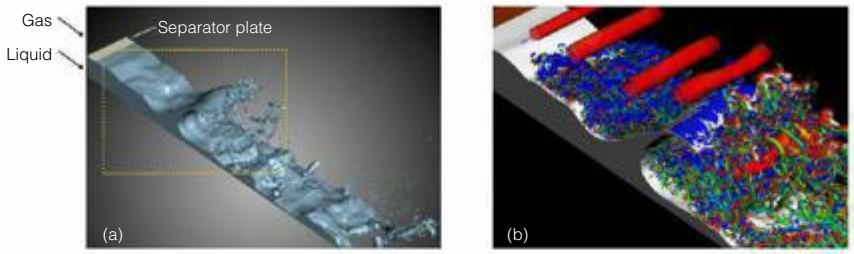

Figure 1: (a) The atomizing jet. (b) Turbulent vortical structures in the primary breakup region.

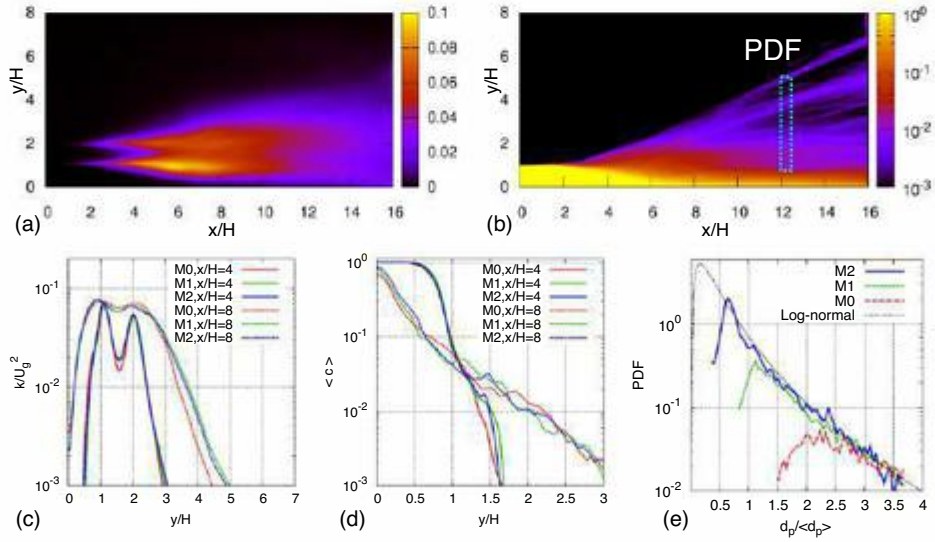

Figure 2: Turbulence and atomization characteristics: (a) TKE; (b) liquid volume fraction; results of (c) TKE and (d) liquid volume fraction obtained by different mesh resolution; (e) droplet-size distribution.

The statistical characteristics of the turbulent multiphase flows are investigated by averaging the data obtained from DNS. The average flow field is two dimensional, depending only on x and y. Therefore, averaging is conducted temporally and spatially (in the z direction) and the results of turbulent kinetic energy and average liquid volume fraction are shown in Fig. 2 (a) and (b). The TKE of the gas-liquid mixing layer is observed to be more intense than that of the gas-gas mixing layer. The average liquid jet core and the spreading liquids can be seen in the contour of liquid volume fraction. The open angle of the liquid spray is measured about 14.9 degrees.

Finally, we examine the effect of grid resolution on the TKE, the liquid volume fraction, and the droplet size PDF, see Fig. 2 (c), (d), and (e). It is seen that the results of TKE and liquid volume fraction obtained by M1 and M2 meshes agree well at different streamwise locations, indicating that the fine mesh M2 used is sufficient to capture the major characteristics of turbulent multiphase flows. It is also shown that the grid resolution requirement is more demanding for droplet size distribution. The size distributions of large droplets for different meshes are in good agreement. Nevertheless, to capture the small droplets formed a fine mesh has to be used. Even the finest mesh used here seems to be insufficient to capture all the small droplets formed. At last, the highly skewed log-normal distribution, is shown to well capture the size distribution profile. To better resolve the formation of these very small droplets, a finer mesh is required and this is relegated to future works.

References

[1] Lasheras J. C. and Hopfinger E. J.: Liquid jet instability and atomization in a coaxial gas stream. Annu. Rev. Fluid Mech. 32:275–308, 2000.

[2] Lakehal D. and Liovic P.: Turbulence structure and interaction with steep breaking waves. J. Fluid Mech. 674:522–577, 2011.

[3] Matas J.-P., Marty S. and Cartellier A.: Experimental and analytical study of the shear instability of a gas-liquid mixing layer. Phys. Fluids 23:094112, 2011.

[4] Arrufat T. J., Dabiri S., Fuster D., Ling Y., Malan L., Scardovelli R., Tryggvason G., Yecko P., and Zaleski S.. The PARIS-Simulator code, available from http://www.lmm.jussieu.fr/ zaleski/paris/index.html.

[5] Tryggvason G., Scardovelli R., and Zaleski S. Direct numerical simulations of gas-liquid multiphase flows. Cambridge University Press, 2011.

[6] Ling Y., Zaleski S., and Scardovelli R. Multiscale simulation of atomization with small droplets represented by a lagrangian point-particle model. Int. J. Multiphase Flow 76:122–143, 2015.

GEOMETRICALLY CONTROLLED DYNAMICS IN EVAPORATING SESSILE DROPS

P. J. Sáenz[1 a)], J. Kim[2], P. Valluri[3], K. Sefiane[3], A. Wray[4], Z. Che[4] & O. K. Matar[4]
[1]*Department of Mathematics, Massachusetts Institute of Technology, Cambridge, Massachusetts, USA*
[2]*Department of Mechanical Engineering, University of Maryland, College Park, Maryland, USA*
[3]*Institute for Materials and Processes, University of Edinburgh, Edinburgh, UK*
[4]*Department of Chemical Engineering, Imperial College London, London, UK*

Summary Geometry is found to play a critical role in the evaporation kinetics and flow dynamics of volatile sessile drops of pure liquids and binary mixtures. In non-spherical drops, the coffee ring effect leads to a spatially uneven pattern along the contact line with high-concentration of particles observed at the "corners". This contrasts to the homogeneous ring stain observed in spherical drops. The local and overall evaporation rates are found to change accordingly. The spontaneous onset and growth of thermocapillary instabilities in more volatile drops also becomes spatially dependent. In this case, "corners" become the areas where the instabilities are first detected, i.e. the most unstable regions. Finally, a segregation process is observed during the alcohol depletion in water-ethanol drops. This phenomenon, once again, is governed by geometry. All the observations are rationalized in terms of the contact-line curvature.

The evaporation of a liquid droplet on a solid substrate is a common physical phenomenon encountered in a vast variety of situations; it is therefore unsurprising that it has received significant attention in the literature. This is an intricate two-phase problem whose most significant ingredients include phase change, contact-line dynamics, non-uniform geometry and a complex Marangoni effect resulting from not only spatially but also temporally varying gradients of temperature (and of solutal concentration in binary mixtures). Due to the intricacy of these phenomena, the study of volatile sessile drops has thus been restricted to spherical configurations for the most part to take advantage of axisymmetry to simplify the problem to 2D. In most real-life situations, however, spherical sessile drops are the exception rather than the rule. We thus revisit milestone investigations dealing with the bulk flow [1], evaporation kinetics [2], stability [3], and binary-mixture dynamics [4] of spherical sessile drops and extend their scope to the poorly understood and largely unexplored case of non-spherical geometries. Experiments and numerical simulations are combined to illustrate the findings of our work [5,6].

Fig. 1 illustrates the different pattern left by a drying drop of coffee when the contact area is (a) spherical and (b) triangular. In accordance with the explanation offered by Deegan *et al.* [1], mass conservation leads to a radially outwards flow towards the contact-line which results into the typical uniform ring stain pattern (Fig. 1a). When the contact area is triangular (Fig. 1b), however, the pattern shows darker regions at the "corners" (larger contact-line curvature). This also indicates that corners are areas where the local evaporation rate is higher and where there emerge preferential evaporation-driven currents in the bulk flow. The overall evaporation rate also depends on the drop shape. These experimental finding show good agreement with the accompanying numerical simulations.

We then consider drops of a liquid with higher vapour pressure. Sefiane *et al.* [3] discovered the spontaneous emergence of thermocapillary instabilities in spherical drops of FC-72, ethanol and methanol while no thermal motion was observed for water drops. Fig. 2 shows the onset and growth of these instabilities in ethanol drops with different shapes.

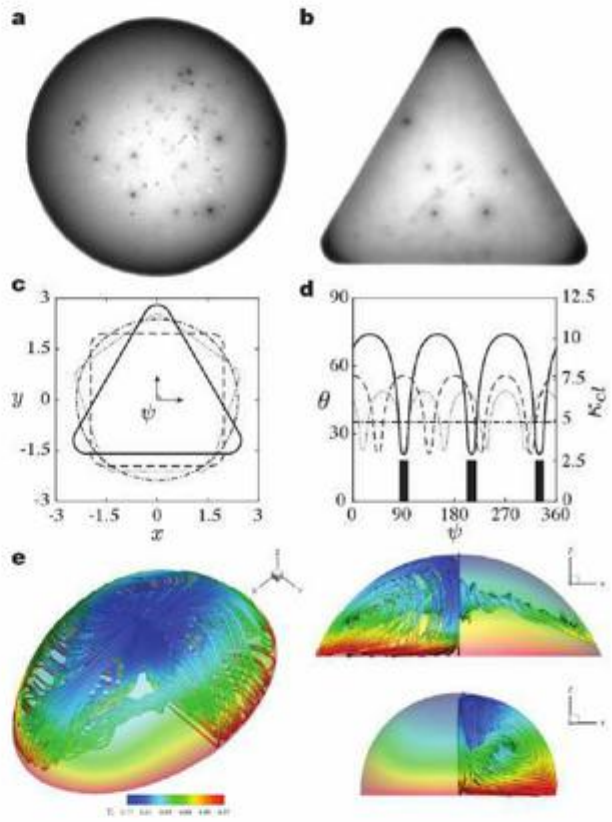

Fig. 1 - Different stains left by a (a) spherical and a (b) non-spherical sessile drop of coffee. As expected, the coffee particles form a uniform ring stain when the contact area circular. However, in a drop with triangular contact area the particles accumulate preferentially at the "corners" of the contact area. Similar observations are made with other non-spherical geometries. Figure c depicts the contact line of the fundamental drop shapes considered in this investigation. The corresponding contact angle θ and contact-line curvature κ_{cl} distributions are illustrated in g. (Reproduce from [6]). Figure e illustrates the thermal distribution and bulk flow of a non-spherical drop calculated by means of direct numerical simulations in 3D. (Reproduced from [5]).

[a)] Corresponding author. Email: psaenz@mit.edu.

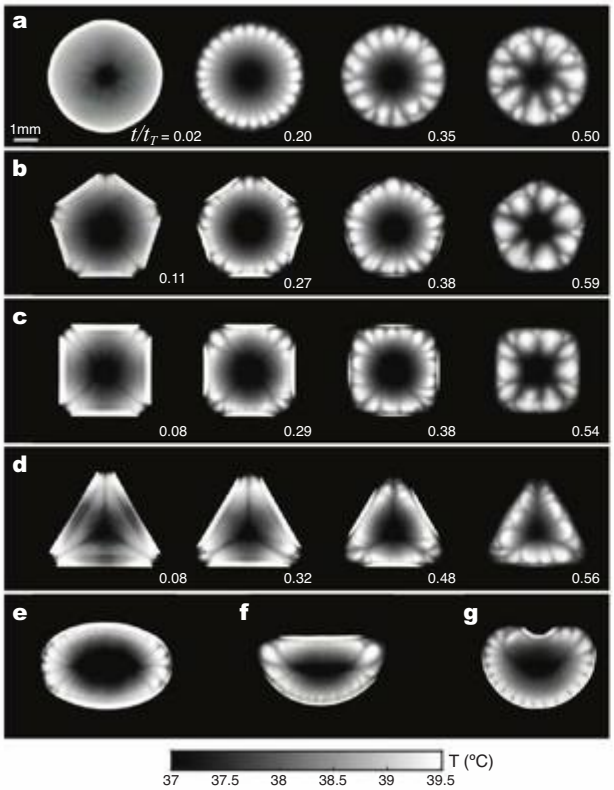

Fig. 2 – IR images showing the temperature distribution (top view) of evaporating sessile drops of ethanol. Non-spherical geometries lead to spatially non-uniform onset and growth of thermocapillary instabilities. The instabilities always grow first (last) where the contact-line curvature is maximum (minimum). The contact-line curvature is $\kappa_{cl} = 0.42\ \mathrm{mm}^{-1}$ in (a) and ranges between $0 \leq \kappa_{cl} \leq 2.5\ \mathrm{mm}^{-1}$ in (b-d). Figures (e-g) show drops with other principal curvature combinations supporting this observation. (Reproduced from [6])

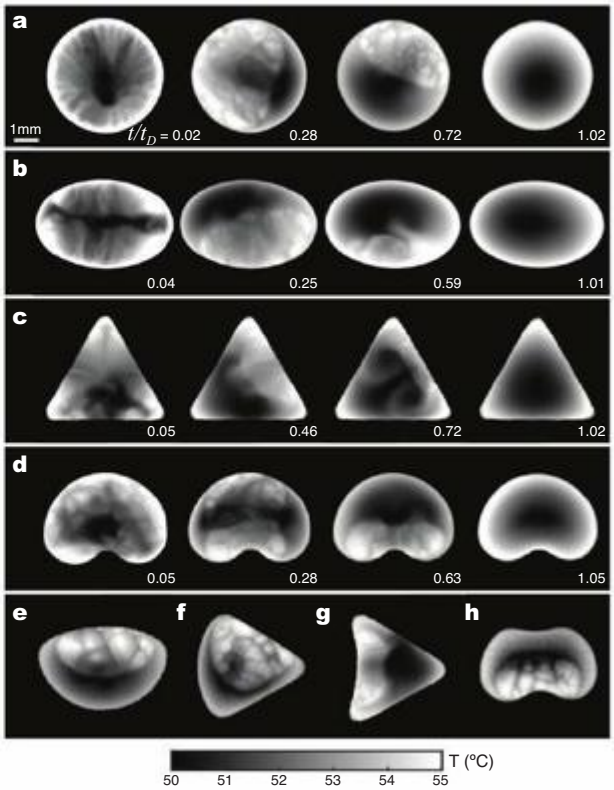

Fig. 3 - IR images illustrating the ethanol depletion occurring in evaporating sessile drops of binary mixtures (25% vol ethanol, 75% vol distilled water) with different shapes. The interfacial turbulences give a measure of the ethanol concentration. In non-spherical drops, the segregation area always corresponds to the region where the contact-line curvature κ_{cl} is minimum. Figures (e-h) show other shapes with different principal curvature combinations (namely, positive-positive, zero-positive, negative-zero, negative-negative). (Reproduced from [6])

In the spherical case (Fig. 2a), the initial temperature distribution is almost concentric until the thermal gradient along the interface becomes supercritical and the drop develops petal-like thermal fluctuations that travel in the azimuthal direction. The shape, size and direction of propagation of these instabilities change as the drop dries. This behaviour changes in non-spherical drops. For instance, in triangular drops (Fig. 2d) the initial flow shows a well defined three-fold structure and, as the drop evaporates, the thermal fluctuations are first observed at the corners while the rest of the drop flow is stable. Eventually thermocapillary instabilities plague the whole drop but these experiments show how some regions are more stable than others in irregular drops, i.e. there is a previously unknown spatial dependence in the instability threshold.

Finally, we consider drops of binary mixtures. Using PIV, Christy *et al.* [4] have recently discovered the existence of three stages in the evaporation process of spherical water-ethanol drops. We revisit their experiments using IR thermography and also considering non-spherical geometries (Fig. 3). Initially the flow is subject to very chaotic solutal-driven interfacial turbulences. As evaporation goes on, the IR images show that the turbulences, which give a measure of the ethanol concentration, become localized at some region near the contact line while the rest of the interfacial thermal field appears to be at rest (similarly to what is observed for pure water). In spherical drops, the segregation point moves around the contact line and its final location cannot be predicted. In non-spherical drops, on the other hand, we find that the segregation point is governed by geometry and always coincides with the point with minimum contact-line curvature.

References

[1] Deegan *et al.* (1997). Capillary flow as the cause of ring stains from dried liquid drops. *Nature*, **389**, 827–829.

[2] Hu & Larson (2002). Evaporation of a sessile droplet on a substrate. *J. Phys. Chem. B*, **106**(6), 1334–1344.

[3] Sefiane *et al*. (2008). Self-excited hydrothermal waves in evaporating sessile drops. *Appl. Phys. Lett.,* **93**(7), 74103.

[4] Christy *et al*. (2011). Flow transition within an evaporating binary mixture sessile drop. *Phys. Rev. Lett.*, **106**(20), 1–4.

[5] Sáenz *et al.* (2015). Evaporation of sessile drops: a three-dimensional approach. *J. Fluid Mech.*, ***772***, 705–739.

[6] Sáenz *et al.* (2016). Geometrically controlled dynamics in evaporating sessile drops. *(submitted)*.

PARTICLE RESUSPENSION BY A PERIODICALLY-FORCED IMPINGING JET

Wen Wu*[1], Giovanni Soligo[2], Cristian Marchioli[2], Ugo Piomelli[1], Francesco Zonta[2], and Alfredo Soldati[2]

[1]*Department of Mechanical and Materials Engineering, Queen's University, Kingston, Ontario, Canada*

[2]*Department of Electrical, Management and Mechanical Engineering, University of Udine, Udine, Italy*

Summary In this work, we investigate numerically the mechanisms of the dust cloud formation that occurs when a helicopter hovers near the ground. We use a numerical approach that combines Large-eddy simulation of the flow field with Lagrangian particle tracking. The wake generated by the helicopter is modeled as a round impinging jet perturbed by a sequence of periodically forced azimuthal vortices. Particles are initially placed on a thin layer just above the ground. Particle resuspension occurs as the large-scale vortices strike the ground. We characterize statistically the local interaction between the particles and turbulence, as well as the tendency of particles to segregate and concentrate preferentially in specific flow regions. We also clarify the role of the periodic and stochastic fluctuating velocity and vorticity on the inception of particle resuspension.

INTRODUCTION

When hovering near arid grounds, the rotor of helicopters generates a downward jet that interacts with the soil and induces resuspension of sand grains, dust or dirt. This phenomenon, called helicopter brownout (HB), can be dangerous because it drastically reduces the pilot's vision during landing. To mitigate the impact of HB, a detailed knowledge of the turbulent flow field generated by the recirculating rotor downwash, and of the particle resuspension mechanisms is needed. Due to the simplicity of the configuration and the similarity to the rotor-wake flow, the round impinging jet can be used as a model of the wake of a rotorcraft hovering near the ground. The Kelvin-Helmholz instability in the jet shear-layer generates an array of azimuthal vortices, which are advected by the jet and impinge on the ground. These embedded large-scale vortices, representing the rotor-tip vortices, are found to dominate this flow [1]. When the vortex ring approaches the ground it creates locally an adverse pressure gradient in the radial direction; a counter-rotating secondary vortex ring is formed, and the interaction between the large-scale vortices and the near-wall flow plays an important role in the heat and momentum transfer. The secondary instability of the vortices forms rib-like structures that rise up into the free-stream, and can be related to the dust cloud formation in HB [1]. In this work, we investigate precisely the resuspension of dust particles resulting from their interaction with the flow structures that develop along the jet. To this aim, we use a numerical approach that combines Large-eddy simulation (LES) of the flow field with Lagrangian particle tracking.

CONFIGURATION AND METHODOLOGY

We exploited a LES database of a forced round impinging jet [1] to compute the detailed statistics of inertial particles transported by the turbulent carrier flow. The air jet, whose Reynolds number based on the jet diameter $D = 0.1$ m and the mean jet velocity $U_0 = 10$ m/s is 66,000, has outlet-to-target wall distance $H/D = 1$, and is excited at a frequency of 75 Hz. This configuration matched the experiments in Ref. [2]. Assuming one-way coupling between fluid and particles, a swarm of $N_p = 50,000$ particles of size d_p =20 μm is tracked using Lagrangian approach, in which the dynamics of particles is computed as:

$$\frac{d\mathbf{x}_p}{dt} = \mathbf{u}_p, \quad \frac{d\mathbf{u}_p}{dt} = \mathbf{F} \tag{1}$$

with $\mathbf{x}_p$, $\mathbf{u}_p$, and $\mathbf{F}$ are the particle position, velocity, and the overall forces exerted by the fluid on the particles, respectively. The drag, buoyancy and Saffman lift forces are considered. Further details on the Lagrangian particle tracking can be found in Ref. [3]. The particles are initially randomly distributed in a thin layer just above the ground. They are allowed to evolve from the initial state for 30 forcing periods to reach statistically steady state. Statistics are then collected for further 24 forcing periods. This time interval is long enough to obtain reliable results on ejection rates and other Eulerian statistics.

RESULTS

The particles concentrate preferentially around the primary vortices after being ejected from the surface (Fig. 1 *(a)*). The regions corresponding to the vortex cores are almost completely depleted of particles, as was also observed in other multiphase flow studies [5]. In the present configuration, the particles reach up to $z/D = 0.9$, and may affect the pilot's visibility during HB. Particles cluster also in the azimuthal direction θ (Fig. 1 *(b)*). The separation between the particle clusters in θ corresponds to $\pi/12$ wavelength that was found to be a primary mechanism for the instability of the ring vortex [1].

*Corresponding author. Email: w.wu@queensu.ca

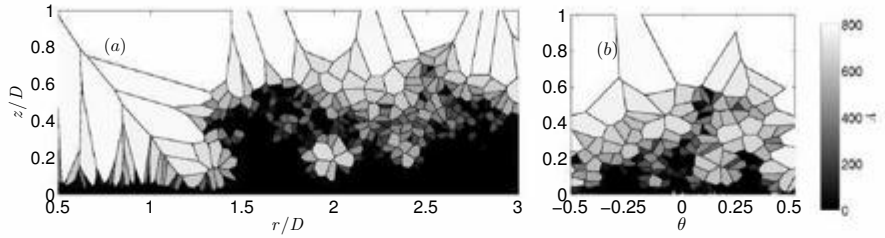

Figure 1: Visualization of instantaneous particle clusters (dark gray) and voids (light gray) in *(a)* $r - z$ plane, $z_p \in [-\pi/6, \pi/6]$, *(b)* $\theta - z$ plane, $r_p/D \in [1.65, 1.85]$, by Voronoï tessellation [4] at $t = 23.75T$. Colored by the Voronoï polygon area A/D^2.

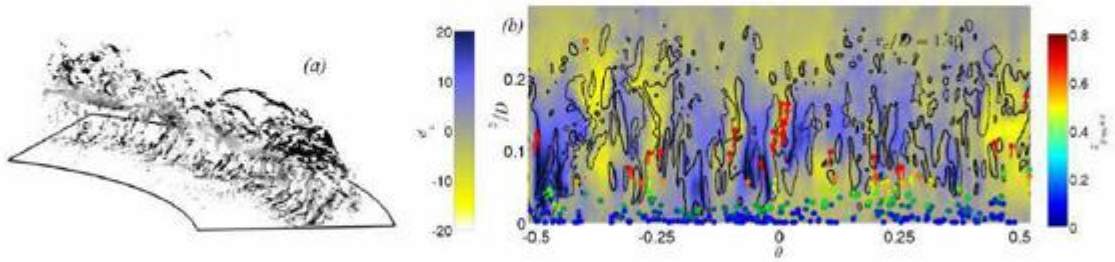

Figure 2: Contours of *(a)* Q-isosurfaces showing the rib-like vortices around the primary vortex; *(b)* fluid velocity u_r' (in yellow and blue, value refer to the colormap on the left), and ω_z' = -20 (dashed) and 20 (solid). Fields showed are instantaneous ones at $t = 23.75T$, averaged in a slice region $r = 1.40 \pm 0.01D$. Particles within this region are also plotted by dots, with solid tails represent their trajectories during the past $T/2$, colored by the maximum heights they reach later (value refer to the colormap on the right).

Figure 2 *(a)* shows the behavior of the rib-like vortices emerging around the primary vortices, whereas Fig. 2 *(b)* shows the contours of the wall-normal fluctuating vorticity (lines), ω_z', and the radial velocity fluctuations of the fluid (map) u_r' in a slice slightly downstream of the primary vortex. The instantaneous particles distribution, together with their trajectories during the preceding half period $T/2$, is also plotted. In this region, the rib-like vortices (shown in Fig. 2 *(a)*) around the primary vortex are almost vertical, like "fences" with different u_r' distributed in the slots between each pair. Particles ejected far away from the surface (red dots) are found in the $u_r' < 0$ region (in yellow) formed by the negative ω_z' on the left and by the positive ω_z' on the right. Particles entrained in the near-wall inclined part of the rib-like vortices (green dots) are less affected by these fences and their ejection is weaker. They fall back to the surface soon, though may be ejected by the downstream turbulent structures again. Particles that do not interact with the fences (blue dots) are barely ejected. Therefore, the fence-like vortices screen the particles, block the ones in the $u_r' < 0$ region, and eject them to the height comparable to H. To prove our conclusions on the role of the fluctuating velocities in the ejection of particles, we performed two more simulations considering only the periodic or the fluctuating velocity components (plus the mean wall jet). It is found (not shown here) that the fluctuating velocity itself leads to similar particle behaviour (with enhanced particle deposition) as the one using the total velocity, while the periodic velocity cannot eject particles from the surface. This indicates that the fluctuating turbulence related to the fence-like vortices plays the most important role in ejecting the particles from the surface. The periodic roller has only a minor effect on particle ejection, but it is important in preventing the particles from falling below the flow region occupied by the primary vortex.

CONCLUSIONS

An Eulerian-Lagrangian multiphase solver is used to simulate the motion of small heavy particles, mimicking sand grains during HB. Particles concentrate preferentially around the primary vortices upon being ejected from the ground. The rib-like vortices generated by the secondary instability play a crucial role in ejecting particles and determining their maximum heights. The primary vortex has only little effect on particle ejection, but it prevents the particles from falling back to the ground.

References

[1] Wu W., Piomelli U.: Large-eddy simulation of impinging jets with embedded azimuthal vortices. J. Turbul. 16: 44–66, 2015.

[2] Geiser J., Kiger K. T.: Vortex ring breakdown induced by topographic forcing. J. Phys. Conf. Series. 318(6): 062013, 1–10, 2011.

[3] Marchioli C., Giusti A., Salvetti M. V., Soldati A.: Direct numerical simulation of particle wall transfer and deposition in upward turbulent pipe flow. Int. J. Multiphas. Flow 29: 1017–1038, 2003.

[4] Monchaux R., Bourgoin M., Cartellier A.: Preferential concentration of heavy particles: a Voronoï analysis. Phys. Fluids 22, 103304–1–10, 2010.

[5] Squires .K. D., Eaton J. K.: Preferential concentration of particles by turbulence. Phys. Fluids 3(5): 1169–1178, 1991.

*Corresponding author. Email: w.wu@queensu.ca

HEALING CAPILLARY FILMS

Z. Zheng[1], M. A. Fontelos *[2], S. Shin[3], M. C. Dallaston[4], D. O. Tseluiko[5], S. Kalliadasis[6], and H. A. Stone[7]

[1,3,7]*Department of Mechanical and Aerospace Engineering, Princeton University, Princeton NJ, USA*
[2]*Instituto de Ciencias Matemáticas, CSIC, Madrid, Spain*
[4,6]*Department of Chemical Engineering, Imperial College London, LondoN, UK*
[5]*Department of Mathematical Sciences, Loughborough University, Loughborough, UK*

Summary We investigate, by means of theoretical arguments, numerical simulation and numerics, the closing of a circular cavity (healing) in a thin liquid film. We assume that the process is dominated by capillary forces. The final stages of the evolution can be described by means of self-similar solutions to the problem. A comparison with experimental data is also presented.

INTRODUCTION AND MAIN RESULTS

We study the healing process of a viscous thin film driven by surface tension. Such phenomena occur in lots of physical and industrial processes [1], [2]. The effect of surface tension suggests a fourth-order nonlinear partial differential equation that has completely different behaviours from the nonlinear diffusion equation for the buoyancy-driven processes. The novel part of this study is to seek a self-similar solution for the fourth-order equation that describes the dynamics of the film thickness.

We consider a converging thin film driven by surface tension in axisymmetric geometry. We assume that the air-fluid interface is long and thin, so the flow is mainly one-dimensional, and the lubrication approximation holds. We assume that initially viscous fluid of height $\tilde{h}_0$ fills the gap between $\tilde{r}_0$, the location of a lock gate, and $\tilde{r}_{out}$, the location of an outer boundary; or equivalently, the thin film spreads toward the origin ($\tilde{r} = 0$) from an initial condition that takes the form of a step function. After defining dimesionless variables, one can obtain the following partial differential equation:

$$\frac{\partial h}{\partial t} + \frac{1}{r}\frac{\partial}{\partial r}\left(rh^3\frac{\partial}{\partial r}\left(\frac{1}{r}\frac{\partial}{\partial r}\left(r\frac{\partial h}{\partial r}\right)\right)\right) = 0. \tag{1}$$

We now look for a self-similar solution for equation (1) of the form

$$h(r,t) = (t_0 \circ\ t)^{\alpha} f\left(\xi \equiv \frac{r}{(t_0 \circ\ t)^{\beta}}\right), \tag{2}$$

where t_0 denotes the dimensionless time for the (circular) front of the air-fluid interface to reach the origin ($r = 0$). Immediately, from dimensional analysis, the form of solution (2) suggests that $\alpha = \frac{(4\beta-1)}{3}$, and we can rewrite equation (1) as an ordinary differential equation (ODE):

$$\circ\ \frac{(4\beta \circ\ 1)}{3} f + \beta\xi\frac{\mathrm{d}f}{\mathrm{d}\xi} + \frac{1}{\xi}\frac{\mathrm{d}}{\mathrm{d}\xi}\left(\xi f^3\frac{\mathrm{d}}{\mathrm{d}\xi}\left(\frac{1}{\xi}\frac{\mathrm{d}}{\mathrm{d}\xi}\left(\xi\frac{\mathrm{d}f}{\mathrm{d}\xi}\right)\right)\right) = 0. \tag{3}$$

We look now at a distance R from the center of the hole. Since fluid has to enter through $r = R$ in order to fill the hole, a certain flow rate $J = 2\pi r h^3 \frac{\partial}{\partial r}\left(\frac{1}{r}\frac{\partial}{\partial r}\left(r\frac{\partial h}{\partial r}\right)\right)$ has to be established and it is natural to assume that it is constant near t_0. This leads to an exponent $\beta = \frac{2}{5}$. On the other hand, the contact line must move with a nonzero velocity $v = h^2\frac{\partial}{\partial r}\left(\frac{1}{r}\frac{\partial}{\partial r}\left(r\frac{\partial h}{\partial r}\right)\right)$. Numerical evidence suggests the presence of a region near the contact line where such condition implies $\beta \approx 0.48\ldots$.

Numerical evidence

We solved (1) with no flux boundary condition at $r = 10$ and an initial step at $r = 1$. The evolution is sketched in figure 1(*a*). In figure 1(*b*) we represent the same profiles rescaled according to the similarity exponent $\beta = \frac{2}{5}$ and comparison with the similarity solution obtained from equation (3).

EXPERIMENTS

Laboratory experiments have been designed and conducted to verify the self-similar solutions we obtained from the theoretical model. We first prepare a clean oil-wetting slide glass as the flat substrate. We then place a Teflon container above the slide glass which forms a non-wetting circular outer boundary. A plastic cylinder is then placed at the center of the circular area created by the Teflon container, and used as a cylindrical lock gate in our experiments.

*Corresponding author. Email: marco.fontelos@icmat.es

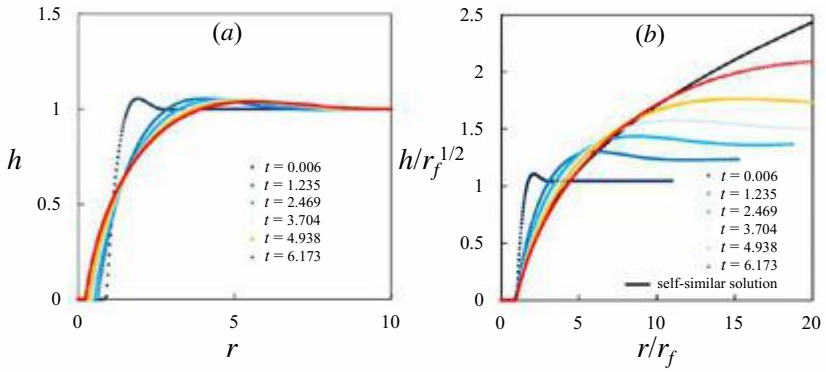

Figure 1: Time evolution of the profile shape from direct numerical simulation: (*a*) raw data; (*b*) rescaled data. The collapse of the profile shapes occurs near the location of the propagating front. The black curve represents the prediction from the self-similar solution with $\beta = 2/5$.

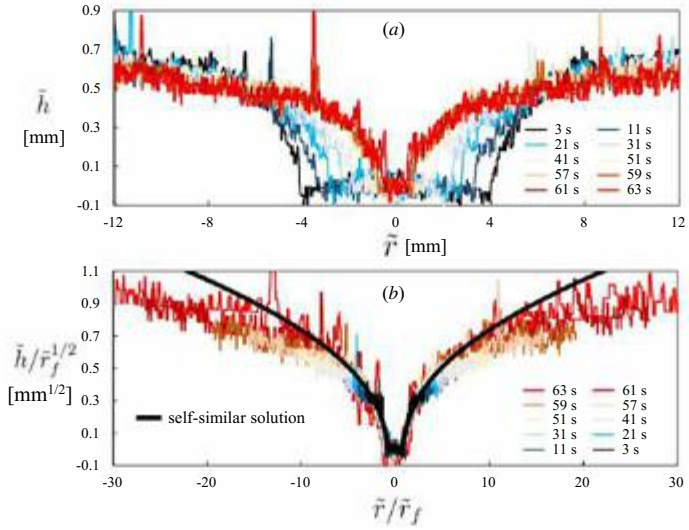

Figure 2: Time evolution of the shape of the fluid-fluid interface: (*a*) raw experimental data, and (*b*) rescaled experimental data.

In each experiment, we first fill the gap between the lock gate (plastic cylinder) and the outer boundary (Teflon container) with a viscous fluid (e.g., silicone oil). Upon the removal of the lock gate, the fluid film spreads toward the center, driven by surface tension. A digital camera (Nikon 7100) is placed right above the setup, and takes pictures of the healing thin films from the top. The propagating front appears to be circular, and we can measure the radius of the circular front $r_f(t)$ as a function of time t.

We use different silicone oils with varying viscosities (e.g., 100 cst, or 500 cst) as the working fluid. In our post-experimental data analysis, based on the calibration, we are able to conduct the interface shapes $h\ r, t)$ at different times t. The profile shapes from a representative experiment are shown in figure 2*a*. Silicone oil of viscosity $\mu \approx 100$ cst and surface tension $\gamma \approx 20$ mN/m was used in this experiment. The time for the front to reach the origin is $t \approx 40$ s. The rescaled profile shape based on our theoretical arguments is also shown in figure 2*b*. The theoretical prediction from the self-similar solution is also plotted as the black curve in figure 2*b*.

References

[1] J. A. Dijksman and S. Mukhopadhyay and C. Gaebler and T. P. Witelski and R. P. Behringer, Self-similar scaling in focusing flows, Phys. Rev. E 92 (2015), 043016.

[2] M. Backholm and M. Benzaquen and T. Salez and E. Raphael and K. Dalnoki-Veress, Capillary leveling of a cylindrical hole in a viscous film, Soft Matter 10 (2014), 2550–2558.

TAYLER INSTABILITY IN LIQUID METAL COLUMNS AND LIQUID METAL BATTERIES

Caroline Nore *[1], Wietze Herreman[1], Jean-Luc Guermond[2], and Loïc Cappanera[1]
[1]*Laboratoire d'Informatique pour la Mécanique et les Sciences de l'Ingénieur, CNRS, Univ. Paris-Sud, Université Paris-Saclay, Campus Universitaire, Orsay, France*
[2]*Department of Mathematics, Texas A&M University 3368 TAMU, College Station, U.S.A.*

Summary This paper investigates the Tayler instability in an incompressible, viscous and resistive liquid metal column and in a model of liquid metal battery. We perform detailed comparisons between numerical simulations and some simplified theoretical models, both in the linear and nonlinear regimes. We present the first direct numerical multiphase simulation of the Tayler instability in a model battery. (Key words: Liquid Metal Batteries, Energy storage, Multiphase flows, Magnetohydrodynamics).

INTRODUCTION

Energy storage is a key societal challenge that hampers the development of renewable energies. One bottleneck is the development of highly efficient large scale batteries. A breakthrough has recently been made by Sadoway et al. [1], based on the assembly of three liquid layers composed of a low density liquid metal electrode, a medium density electrolyte and a heavier liquid metal electrode. This setting yields high reaction rates in electrochemistry [2]. Moreover, these batteries do not use any solid active material and are thus immune to cracking and degradation over time, contrary to conventional batteries. The self-segregating nature of the assembly (using gravity) and the use of low-cost materials make liquid metal batteries (LMBs) promising candidates for almost unlimited scalability which is essential for economic competitiveness. Large scale LMBs are however prone to magnetohydrodynamic instabilities. For instance, the Tayler instability induces flows that could disrupt the stratified three layer state. We investigate this problem in an incompressible, viscous and resistive liquid metal column and in a model of liquid metal batteries.

ANALYTICAL AND NUMERICAL RESULTS

We perform detailed comparisons between numerical simulations and some simplified theoretical models, both in the linear and nonlinear regimes, in a cylindrical column of radius R and height H. The problem depends on three control

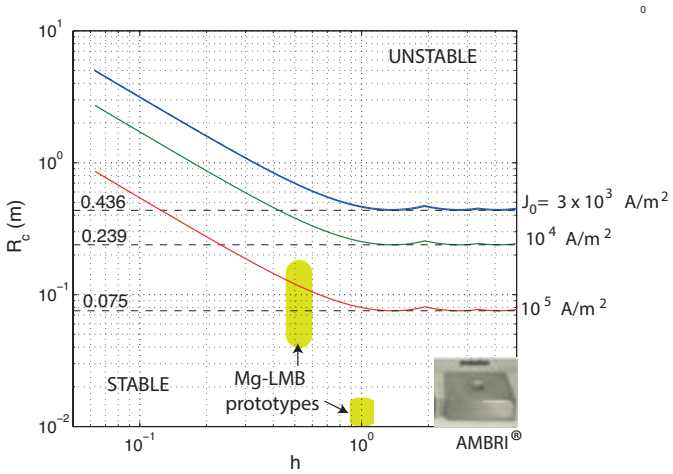

Figure 1: Critical radius R_c vs. aspect ratio h for Tayler instability (TI) in Mg-based LMBs for the three J_0-scenarios. **Risk** of TI only in batteries with $R \geq R_c$. Yellow zones are estimated dimensions of LMB prototypes shown in insert (AMBRI).

parameters: the Hartmann number $Ha = 0.5\mu_0 J_0 R^2\sqrt{\sigma/\rho\nu}$ measuring the charge/discharge current density and comparing the Lorentz and the viscous forces, the magnetic Prandtl number $Pm = \sigma\mu_0\nu$ and the aspect ratio $h = H/R$. We identify the timescale that is well adapted to the low-Pm regime and find the range of Hartmann numbers where this approximation applies. Above a threshold Ha_c independent of Pm, the Tayler instability gives rise to a non-axisymmetric flow with velocity U_T (associated to a Reynolds number $Re = U_T R/\nu$). The scaling law $Re \sim Ha^2$ for the amplitude of the Tayler destabilized

*Corresponding author. Email: caroline.nore@limsi.fr

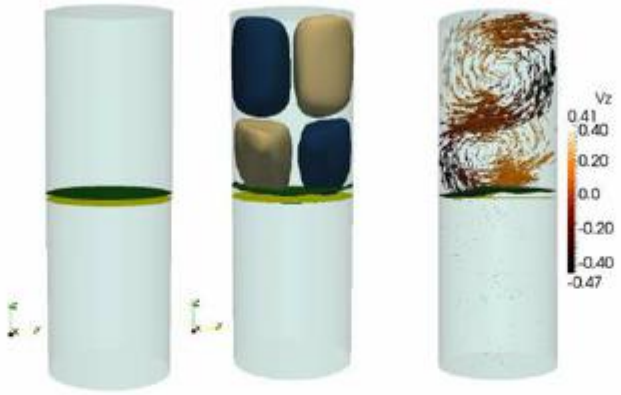

(a) Initial condition (b) $Ha = 47.3$, B_z blobs (c) $Ha = 47.3$, velocity field

Figure 2: Tayler instability in a LMB of aspect ratio $h = 5.74$: (a) initial condition, (b)-(c) just before the pinch of the electrolyte layer at Hartmann number $Ha = 47.3$. B_z contours visualize $\pm 10\%$ of the maximum and minimum value, velocity field vectors are colored by U_z. The top and bottom interfaces are visualized by isosurfaces of two level sets $\Phi_1 = 0.5$ (yellow) and $\Phi_2 = 0.5$ (green).

flow is explained using a weakly nonlinear argument. Depending on the possible current density J_0, instability arises in the top layer of a Mg-based battery for a radius $R \geq R_c$ reported in figure 1.

We also calculate a critical electrolyte height above which the Tayler instability is too weak to disrupt the electrolyte layer. Applied to present day Mg-based batteries, this criterion shows that short-circuits can occur only in very large batteries.

CONCLUSION

Preliminary results (see figure 2) based on a new multiphase algorithm implemented in our locally-developed MHD code called SFEMaNS [3] demonstrate the feasibility of direct numerical multiphase simulations of the Tayler instability in a model battery. We refer to [4] for more details. Finally LMBs seem to be immune to Tayler instability in practice but thermal convection which is inevitable in this system needs to be investigated in the future.

References

[1] Bradwell, David J and Kim, Hojong and Sirk, Aislinn HC and Sadoway, Donald R, *Magnesium–Antimony Liquid Metal Battery for Stationary Energy Storage*, Journal of the American Chemical Society **134**, 4, p.1895–1897 (2012).

[2] Kim, Hojong, Boysen, Dane A., Newhouse, Jocelyn M., Spatocco, Brian L., Chung, Brice, Burke, Paul J., Bradwell, David J., Jiang, Kai, Tomaszowska, Alina A., Wang, Kangli, Wei, Weifeng, Ortiz, Luis A., Barriga, Salvador A., Poizeau, Sophie M. and Sadoway, Donald R., *Liquid metal batteries: Past, present, and future*, Chemical Reviews **113** (3), p. 2075–2099 (2013).

[3] Guermond, J.-L., Léorat, J., Luddens, F., Nore, C. and Ribeiro, A., *Effects of discontinuous magnetic permeability on magnetodynamic problems*, J. Comput. Phys. **230**, 6299–6319 (2011).

[4] Herreman W., Nore C., Cappanera L. and Guermond J.-L., *Tayler instability in liquid metal columns and liquid metal batteries*, J. Fluid Mech. **771**, p. 79–114 (2015).

BUBBLE-BASED ACOUSTIC MICROPROPULSION: MIXING AND ADVANCED SWIMMERS

Nicolas Bertin *[1], Tamsin Spelman[2], Herve Hue[3], Olivier Stephan[4], Eric Lauga[5], and Philippe Marmottant[6]
[1,3,4, 6]*LIPhy, University Grenoble Alpes, Grenoble, France*
[2,5]*DAMTP, University of Cambridge, Cambridge, United Kingdom*

Summary Acoustic microswimmers present great potential for microfluidic applications and targeted drug delivery. Here we introduce armoured microbubbles (size range, 10-20 m) made by three-dimensional microfabrication which allows the bubbles to last for hours even under forced oscillations. The acoustic resonance of the armoured microbubbles is found to be dictated by capillary forces and not by gas volume, and its measurements agree with a theoretical calculation. This flow, a consequence of steady streaming in the fluid, can reach 100 mm/s. A collection of devices is fabricated and can be used inside microchannels for efficient mixing. Complex shapes are also achieved, with devices containing multiple bubbles. A direct application is to build multidirection microswimmers, each bubble having a different resonance frequency that can be excited by scanning frequencies with the broadband acoustic source.

INTRODUCTION

Microswimmers have been widely used over the past decade for payload carrying and mixing in microchannels. Bubble-based acoustic microswimmers can achieve high velocity thanks to the efficiency of bubble microstreaming. Microfabrication allows to build hollow objects that, when immersed in water, contain a bubble actuated with an acoustic source. The bubble vibration (see fig. 1(b)) generates a steady flow (acoustic streaming), due to the non-linear response of the fluid, that can be used for propulsion. This mechanism has been used at the 50-100 μm scale, in two-dimensional (2D) microchannels with contact piezo-transducers [1]. Here, the technique we use, two-photon polymerisation, allows us to build three-dimensional objects at the 10-20 μm scale (see fig. 1(a)). Contactless acoustic sources are prefered in order to scan frequencies and excite the bubble at its resonance, enhancing the efficiency of the streaming.

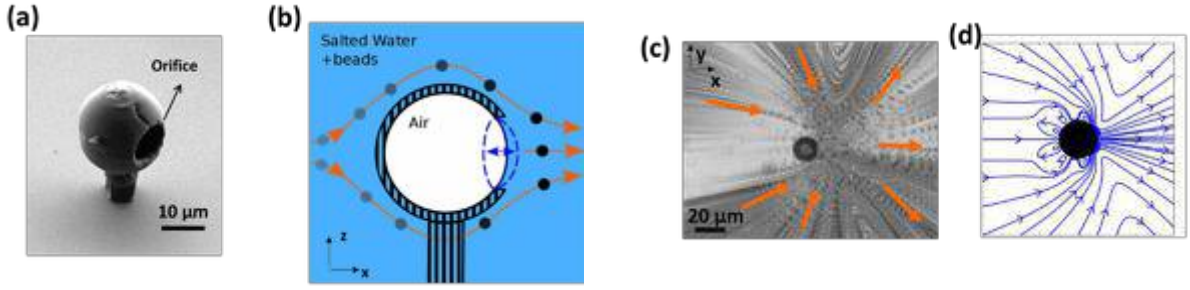

Figure 1: (a) SEM image of a capsule of radius $r = 9\,\mu$m and aperture radius $a = 5\,\mu$m on a pole of length $H = 10\,\mu$m; (b) schematic of the bubble first vibration mode; (c) streamlines generated by device (a) submersed in water (viewed from below) at transducer's frequency $f_{transd} = 320$ kHz and acoustic pressure $P_{ac} = 9.2$ kPa; (d) theoretical streamline prediction.

PROPULSION: CAPILLARY RESONANCE AND STREAMLINE PREDICTIONS

Free bubbles have well predicted resonance frequencies. In the case of an encapsulated bubble with an aperture like ours, the origin of the resonance is related to that of a Helmoltz resonator, with the additional ingredient of the capillary restoring force. Previous experiments showed that the capillary effects are dominant over the physics of the gas inside the bubble. At the 10-20 μm scale, the resonance frequency then depends on the aperture radius, and not on the volume of gas inside the bubble. Modeling the encapsulated bubble as a rigid sphere with an oscillating cap, and a purely capillary restoring force, we are able to predict the resonance as well as the generated 3D streamlines [2] (see fig. 1(c-d)). Near the resonance, the streaming is very efficient and can reach thousands of body lengths per second.

COLLECTION OF PROPULSORS: MICROFLUIDIC APPLICATIONS

A new automated fabrication process allows us to fabricate a great number of objects on the same sample. On fig. 2(a) we show 120 capsules arranged in a pyramid shape and the associated streamlines. It is also possible to complexify the shape

*Corresponding author. Email: nicolas.bertin@ujf-grenoble.fr

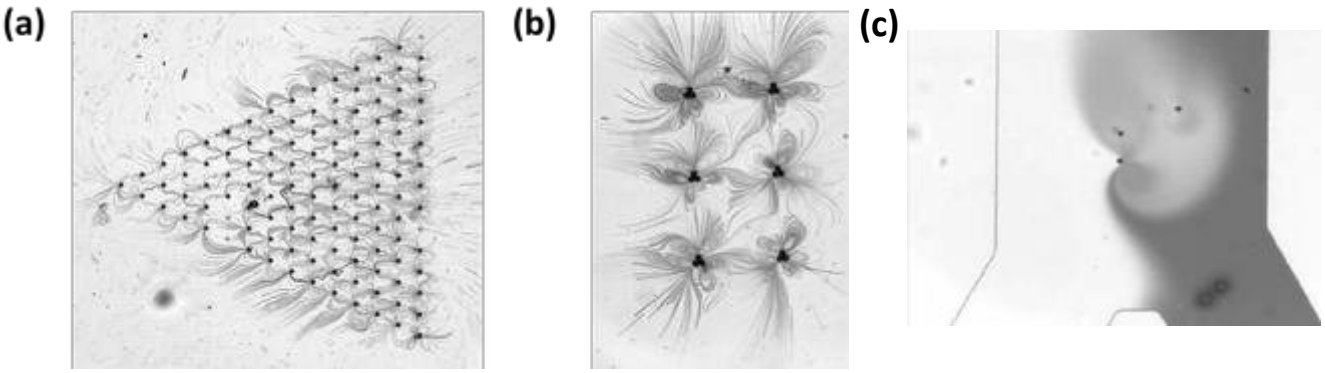

Figure 2: (a) Pyramid of capsules; (b) streamlines generated by triple capsules; (c) mixing with three active capsules inside a Y-shaped microchannel.

of the capsules, with several cavities, to make a triple capsule (see 2(b)). An interesting application is to fabricate capsules arranged so that the generated flows induce mixing in a Y-shaped microchannel with two liquids (see 2(c)).

ADVANCED SWIMMERS

A capsule mounted on a ballast is able to swim easily a 1 mm/s in a single direction [2], see fig. 3(a). We are able now to build an object with several cavities of different aperture radii in order to activate them independently by scanning frequencies. Such a device (see fig. 3(a)) consists of a cube acting as ballast with four cavities pointing in each horizontal direction. The goal is to guide the swimmer in a given direction by changing the excitation frequency towards the resonance of the cavity pointing in the opposite direction. Our theoretical model is able to predict the resonance frequency of all those cavities. On fig. 3(b) we see that when excited at the resonance frequency of the largest cavity, it is here that the streaming is the most efficient.

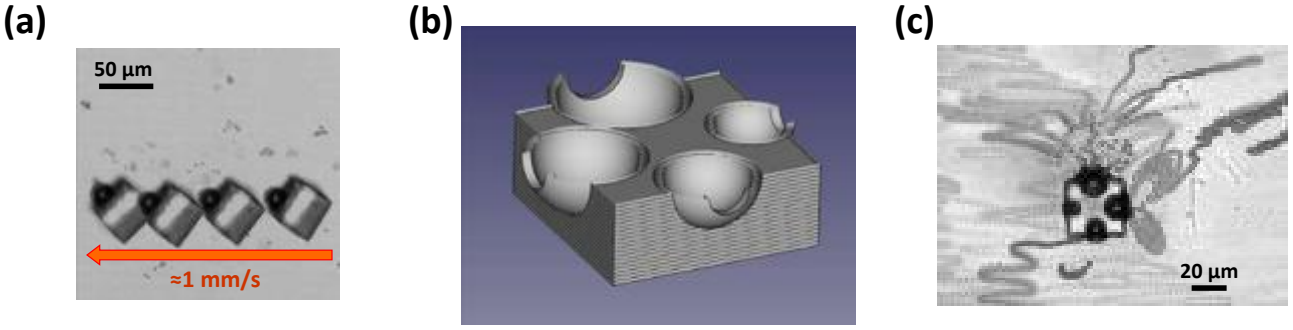

Figure 3: (a) Single direction swimmer actuated at 320 kHz, 5.6 kPa; (b) CAD software cut image of an advanced swimmer with 4 cavities; (c) streamlines generated by such a swimmer at 320 kHz, the resonance frequency of the largest cavity.

References

[1] Ahmed D., Lu M., Nourhani A., Lammert P. E., Stratton Z., Muddana H. S., Crespi V. H., and Huang T. J., Selectively manipulable acoustic-powered microswimmers, Sci. Rep., **5**, 9744, 2015.

[2] Bertin N., Spelman T.A., Stephan O., Gredy L., Bouriau M., Lauga E., and Marmottant P.: Propulsion of Bubble-Based Acoustic Microswimmers, Phys. Rev. Applied, **4**, 064012, 2015.

A NUMERICAL STUDY OF THE EFFECT OF ROUGHNESS TOPOLOGY ON SURFACE HYDROPHOBICITY

Reza Attarzadeh[1], Moussa Tembely[1], and Ali Dolatabadi *[1]
[1]*Department of Mechanical engineering, Concordia University, Montreal, Quebec, Canada*

Summary Understanding the various effects of micro and sub-micron roughness on dynamics of micro-droplet is of interest for many industrial applications such as aerospace industries, spray coating, etc. In this paper, numerical modeling of roughness topology through series of micro arrays is performed to explore the direct effect of surface roughness on super-hydrophobic enhancement, droplet penetration depth, and droplet restitution coefficient. The comparative study is performed on smooth hydrophobic surface and three rough surfaces following similar pattern with varying width to pitch ratio. The intrinsic contact angle of 111° is applied to all surfaces. Mimicking the impact of cloud particles, the droplet size of 20 μm with terminal velocity of 1.6 m.s^{-1} is opted in this study. The simulation successfully captured different stages of a bouncing drop and the air beneath droplet . It was observed that decreasing the width to pitch ratio of arrays, will results in higher droplet mobility, and higher apparent contact angle.

INTRODUCTION

Surfaces with designed microscopic roughness possess remarkable non-wetting properties, and extensive attention is drawn recently by the micro and nano-technology research communities [1, 2, 3] into development of the materials, aiming at finding new ways of controlling solid surface-fluid interface properties. Although according to the Young's correlation, a flat surface with a contact angle approaching 180° could theoretically be possible, no physical evidence have been reported that demonstrates this situation. Theoretical models describing the influence of surface roughening with respect to the wetting properties of the surface have been introduced earlier by (i)Wenzel [4] , and (ii) Cassie-Baxter [5]. A large number of numerical investigations on droplets-surface interaction has been reported, but they are based the outcome of impact on smooth surfaces with intrinsic contact angles [7, 8]. However, the outcome of micro-droplet impact on roughened surface is different from that on smooth surface. Due to the impact force, the liquid penetrates into the micro-cavities, and exhibits different wetting scenario on textured surface.It is known [9] that topology of roughness can control interplaying parameters associated with surface wettability, such as capillary pressure and viscous dissipation rate. Unfortunately due to some uncertainties, such as penetration depth, geometrical configuration of recoiling droplet and the complicated viscous dissipation rate, a direct theoretical and experimental investigation of the bounding behavior of the droplet on roughened surface is difficult.

METHODOLOGY

The Navier stokes equation expressing flow distribution of the liquid and the gas, coupled with the Volume of Fluid (VOF) method for tracking the interface between the liquid and the gas are solved numerically using finite volume methodology. In VOF model [6], tracking of the interface is modeled by solving continuity equation for one of the two phases in each computational cell at every time steps. The governing equations for continuity and momentum are,

$$\vec{\nabla}.\vec{V} = 0 \tag{1}$$

$$\frac{\partial \rho \vec{V}}{\partial t} + \vec{\nabla}.(\rho \vec{V}\vec{V}) = \circ \nabla. \underbrace{\left[\left(p + \frac{2}{3}\mu \nabla.\vec{V}\right) I + \mu\left[\nabla \vec{V} + \left(\nabla \vec{V}\right)^T\right]\right]}_{\text{Stress Tensor}} \circ \underbrace{\sigma \vec{\nabla}.\left(\frac{\vec{\nabla}\alpha}{|\vec{\nabla}\alpha|}\right)\vec{\nabla}\alpha}_{\text{Continuum Surface Force}} \tag{2}$$

Where second term represents the continuum surface force model which is of great importance in modeling of small sized droplet as one driving force during recoiling stage. As Bond number is too small it is evident that the effect of the gravitational force is negligible. In terms of finding the interface, a modified VOF method is used which has additional convective term :

$$\frac{\partial \alpha}{\partial t} + (\vec{V}\vec{\nabla})\alpha + \vec{\nabla}.(\vec{V_r}\alpha(1 \circ \ \alpha)) = 0 \tag{3}$$

where α is the VOF volume fraction scalar function which is used to calculate the viscosity(μ), and density(ρ), as weighted averages based on the distribution of the liquid fraction, The Kistler's correlation [10]is used to calculate the dynamic contact angle in each time step, $\theta_d = f_H[Ca + f_H^{-1}(\theta_e)]$ Surface roughness is modeled as a series of patterned micro arrays (Fig1) with constrained pitch size (l), but varying array width (W) in contact.

*Corresponding author. Email: ali.dolatabadi@concordia.ca

RESULTS & DISCUSSION

Figure1. representing the cross sectional view of a micro-droplet in maximum spreading stage on micro arrays with squared pattern. As shown in the Figure, droplet has partially penetrated into the micro grooves. The penetrated volume, geometrically preserves its spherical shape, due to the effect of surface tension. The entrapment of air helped droplet on sustaining the energy of rebounding. The presence of air pockets is captured, and is shown in red shaded area.

Figure2, the normalized kinetic energy of the droplet are calculated by integration over the entire computational domain during impact and recoiling process for different surface models. As shown in the graph (a), most of the kinetic energy of the droplet has been dissipated due to the maximum area in contact with the smooth surface. This caused droplet to remain on the surface after the least number of oscillation. The same scenario is repeated for the textured surface with 1μm arrays where the solid fraction decayed the kinetic energy of droplet gradually. In graphs(c-d), droplet is partially penetrated into the spaces between arrays before it detaches from the surface. It is observed that droplet onto smallest arrays, undergoing more number of oscillations. However reducing the size of arrays results in reducing the maximum spreading diameter, and reducing the contact time of the bouncing drop. The coefficient of restitution started increasing as the with to pitch ratio of arrays is reduced.

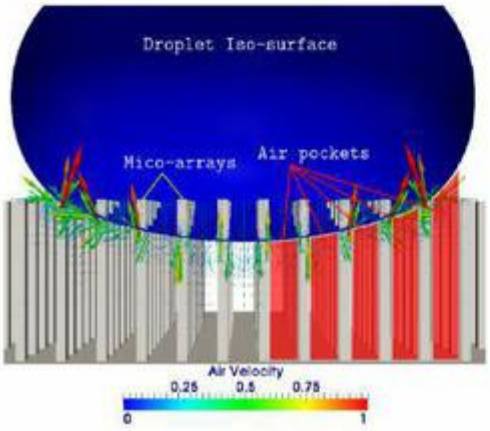

Figure 1: Presence of air pockets beneath micro-drop between the arrays, shaded red.

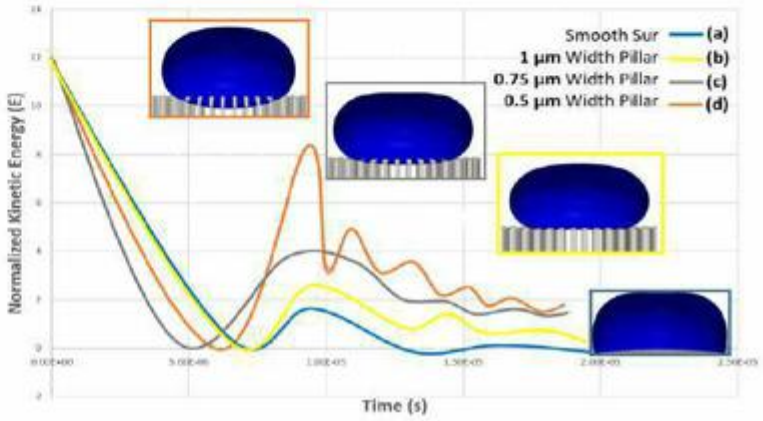

Figure 2: Normalized Kinetic energy of the impinging Micro-droplet on; a)smooth surface, and roughed surfaces b)W=1μm, c)W=0.75μm, d)W=0.5μm

CONCLUSIONS

The numerical simulation of the impact of a micro-droplet onto a smooth and roughened surfaces is performed using a volume of fluid method. Considering low wettability of the material, droplet start rebounding from the surface at some point by direct modeling of micro roughness. The simulation successfully captured the effect of the air beneath droplet inside micro grooves, which increased the apparent contact angle, and reduced surface energy level. The pillars width is found to control both the contact time and the maximum spreading diameter of the droplet, making it one interesting design parameter for textured surfaces.

References

[1] Shang, HM., Wang, Y.: ”Optically transparent superhydrophobic silica-based films”, Thin Solid Films 472:3743, 2005.

[2] Sun, T., Feng, L.:”Bioinspired surfaces with special wettability”, Acc Chem Res 38:644-652, 2005.

[3] Feng, L., Song Y.: ”Superhydrophobicity of Nanostructured Carbon Films in a Wide Range of pH Values”, Angewandte Chem Int Ed 115:4349-4352, 2003.

[4] Wenzel RN.: ”Resistance of solid surfaces to wetting by water”, Ind Eng Chemistry 28:988-994, 1963.

[5] Cassie, A., Baxter S.: ”Wettability of porous surfaces”, Trans Faraday Soc, 10:546551, 1944.

[6] Hirt, C. W., Nichols, B. D.: ”Volume of Fluid (VOF) Method for the Dynamics of Free Boundaries”, J. Comput. Phys 39:201225, 1981.

[7] Gunjal, P. R., Ranade, V. V., Chaudhari, R. V.: ”Dynamics of Drop Impact on Solid Surface”. AIChE J. 51:59-78, 2005.

[8] Mitra, S., Sathe, M., Doroodchi, E., Utikar, R., Shah, M., Pareek, V., Joshi, J. B., Evans, G.: ”Droplet Impact Dynamics on A Spherical Particle”, Chem Eng Sci 100:105-119, 2013.

[9] Deng, T., Varanasi, K.: ”Nonwetting of impinging droplet” 94:1333109, 2009.

[10] Kistler, S. F.: ”Hydrodynamics of wetting”, Wettability, Applied Physics Letter 6:311-430, 1993.

WAVE INDUCED FLUCTUATIONS IN THE GAS-PHASE OF A STRATIFIED AIR/WATER PIPE FLOW

Anis A. Ayati*[1] and Atle Jensen[2]

[1,2]*Department of Mathematics, University of Oslo, N-0316 Oslo, Norway*

Summary The combination of PIV, conductance probing and hot wire anemometry allows us to obtain deeper insight into the physical mechanisms that govern stratified gas-liquid pipe flows. In this paper, we turn our attention towards one of such mechanisms; wave-induced fluctuations in the air velocity field and we raise two questions that will hopefully be answered in future analysis of the present data set. Gas-phase PIV was achieved by using water droplets to seed the gas-phase and provides us with instantaneous and phase-averaged velocity profiles. Conductance probes measured interface elevation at two positions in the axial direction, while a hot-wire probe measured air fluctuations at a set of points between the interface and the pipe wall. This combination of techniques demonstrates clearly how a deformed interface obliges the gas flow to fluctuate at the same frequency as the dominating interfacial wave components.

INTRODUCTION

In the petroleum industry, the widespread use 1D models is due to the need of computation cost efficiency and also because this approach has provided acceptable predictions of global flow parameters such as the pressure drop and liquid hold-up, [1]. The non-uniform nature of the velocity profile, either in the gas or liquid phase is represented by a shape factor times the ensemble averaged velocity, $c_g u_g$ or $c_l u_l$, for gas and liquid, respectively. When it comes to predicting transitions from stratified to slug flow caused by unstable wave growth [5], 1D models have traditionally been combined with viscous or non-viscous Kelvin Helmholtz analysis [2]. This paper is meant as an introduction to the sort of analysis possible to achieve now that a phase-averaging routine as been developed since previously published results, see f.ex [3].

EXPERIMETNAL TECHNIQUE

The experimental work presented in this paper was conducted at the Hydrodynamics Laboratory, University of Oslo. The lab facilities dispose a 31 m long horizontal acrylic pipe with an internal diameter of 100 mm. The two-phase test fluids are air and water at atmospheric pressure with an average temperature of 22°C. At the pipe inlet, honeycomb flow straighteners are placed right before and after the contact point between the air and water in order to dampen secondary flows. More details about the flow loop and the mentioned measuring instruments can be found in [3]. The main test-section combines three different experimental techniques: i) Simultaneous two-phase PIV. Water micro droplets 5-10 μm in diameter were injected at the pipe inlet to seed the gas-phase. This approach minimalizes any impact on the surface tension of the water layer. In this paper, we only focus on gas-phase results, ii) interface elevation measurements using conductance probes (CP) and, iii) gas-phase Hot-Wire anemometry (HW).

RESULTS AND DISCUSSIONS

We study an air/water flow determined by the superficial velocity combination, $U_{sg} = 2.0$m/s and $U_{sl} = 0.1$m/s or in terms of bulk velocities; 3.4m/s and 0.24 m/s, respectively. This combination led to a mean liquid height of $\overline{H_l} = 42.3$mm and relatively regular two-dimensional waves at the interface with the following characteristics: wave amplitude $A_{rms} = 3.14$ mm, dominating wave length $\lambda_D = 0.21$m and dominating wave speed $c_D = 0.79$m/s.

Figure 1 shows the power spectral density (psd) of the interface elevation time series $\eta(t)$ plotted together with low-frequency part of the psd of the air velocity fluctuations measured by a hot-wire probe placed at three different positions from the interface. The figure shows the dominant wave component causes both the axial and wall normal air velocity components to fluctuate at exactly the same frequency. In fact, the vertical velocity component near the interface even perceives both the first and second dominating wave component.

With the help of PIV, we can actually see, in terms of instantaneous velocity fields, how the deformed interface causes the air flow to fluctuate, see fig. 2. Above a wave crest, the velocity is generally larger than above a trough. That is because the area above a crest is smaller than above a trough, and thus by means of mass conservation, the waves induce dynamic fluctuations on the air. By taking the average of velocity profiles above all crests and trough of 1000 PIV realizations, we obtain the phase-averaged velocity profiles shown in fig. 3. The semilogarithmic highlights the difference between crest/trough velocities and also unveils a logarithmic behavior in the interfacial boundary layer. This raises a question: How does this affect the momentum transfer to the waves, [4]? We then compute profile coefficients for crest and troughs separately, $c = \frac{1}{A_f U_{bf}^2} \int_{A_f} u^2 dA$, which in this specific case, are: $c_{cr} = 1.05$ and $c_{tr} = 1.12$, for crest and trough, respectively. This yields a relative difference of approx. 6.5%. Should this difference be incorporated in the stability analysis of [2]?

*Corresponding author. Email: awalaa@math.uio.no

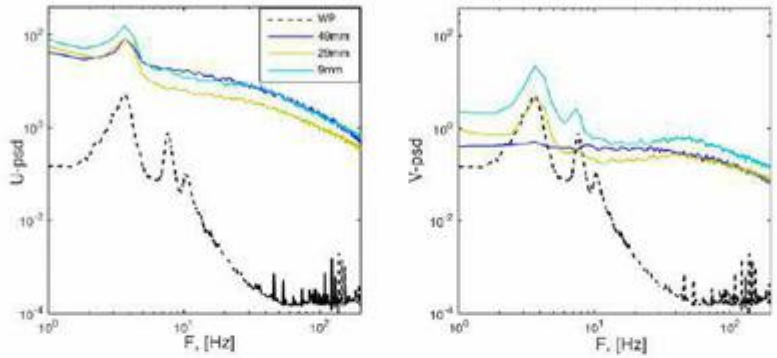

Figure 1: PSD of interfacial waves plotted against gas-phase velocity spectra measured at three different vertical positions (49, 29 and 9 mm) from the interface with hot wire. On the right side is the U-component hot wire spectrum, while on the left side is V-component. The wave and hot wire spectra are scaled with ρ_l and ρ_g, respectively.

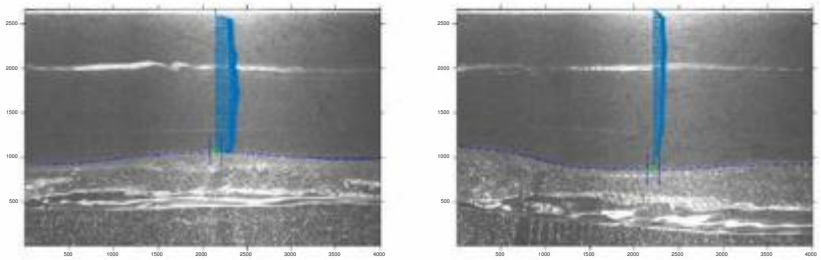

Figure 2: Velocity vectors (in pixels) averaged over 4 IW above a crest (right) and a trough (left) showing the fluctuations .

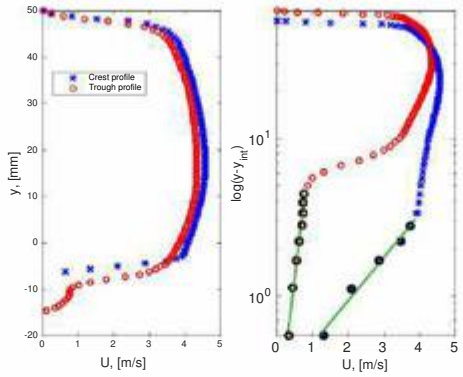

Figure 3: Phase-averaged velocity profiles above crests and troughs, linear plot (left) and semilog plot (right).

References

[1] Andritsos, N. and Hanratty, T.J. *Influence of interfacial waves in stratified gas-liquid flows.* AIChE Journal, 33:444-454, 1987.

[2] Barnea, D. and Taitel, Y. *Kelvin-Helmholtz stability criteria for stratified flow: viscous versus non-viscous (inviscid) approaches.* I. J. Multiphase Flow, 19:639-649, 1993.

[3] Ayati, A.A., Kolaas, J., Jensen, A. and Johnson, G.W. *The effect of interfacial waves on the turbulence structure of stratified air/water pipe flow.* I.J. of Multiphase Flow, 78: 104-116, 2016.

[4] Sajjadi, S.G., Hunt, J.C.R and Drullion, F. *Asymptotic multi-layer analysis of wind over unsteady monochromatic surface waves.* J. of Eng. Math., 2013.

[5] Sanchis, A., Johnson, G. and Jensen, A. *The formation of hydrodynamic slugs by the interaction of waves in gas-liquid two-phase pipe flow.* I.J. of Multiphase Flow, 37:358-368, 2011.

LASER HEATING AND EVAPORATION OF A LEVITATED WATER DROP

Timothy E. Tracey & Cody J. Brownell[a]
Mechanical Engineering Department, United States Naval Academy, Annapolis, Maryland, USA

Summary Single water drops with initial diameter of approximately 1-mm are acoustically levitated and subject to laser radiation from a 1070 nm cw laser with mean irradiance of 530 W/cm^2. Effects of the radiation on the drop are measured using high speed video, and a beam profiler measures the corresponding effects of the drop on the laser beam. Turbulent convection within the drop is visible from the video, unlike what has been seen in prior laser heating experiments using smaller drops. Phase change begins immediately upon initiation of the laser strike, with no obvious sensible heating period. The drop evaporation rate is measured, and shows good agreement with a simple 1-D laser heating model.

INTRODUCTION

The U.S. Navy is actively developing both offensive and defensive technologies related to the use of lasers in warfare. For the Navy, the complexity of a maritime environment poses particular challenges for laser propagation due to high probabilities of liquid water in the form of fog, rain, or sea spray along the beam path. Several previous studies have examined laser heating effects on water droplets with diameters less than 100 microns [1], but less is known about laser interactions with larger drops with diameters upwards of 1-mm. At this size, geometric optics may be used to describe the beam propagation through the drop, and convection within the drop is expected to play a much more important role. Current interest in this problem lies in both predicting the laser's effect on the drop, including the evaporation rate and the fate of the subsequent water vapor, and in understanding the drop's effect on the transmission of the laser beam.

EXPERIMENT

To quantify the effects of a high energy NIR laser on a water drop, a series of experiments were conducted using acoustic levitation to isolate single water drops from solid boundaries, preserving a near-spherical drop shape and allowing a free path for the laser. Levitation was achieved using a tec5™ acoustic levitator, which creates a standing wave between a fixed transducer and an adjustable reflector. Using the acoustic pressure at the nodes, the levitator is capable of stably supporting drops up to approximately 2.4-mm in diameter [2].

The water samples used in the present data are tap water, with an absorptivity of 14.1 m^{-1} at 1070-nm measured using a Jasco NIR spectrometer. The light source is an IPG continuous wave fiber laser with a wavelength of 1070-nm, power of 105 W, and a beam diameter of approximately 5-mm. Drop imaging is achieved using a Hamamatsu ORCA Flash2.8 CMOS scientific camera with a Navatar macro lens. The Hamamatsu is equipped with an IR filter to protect the instrument, and extra ambient lighting is supplied through either a pair of 500W halogen bulbs or a pair of 500W equivalent LED spotlights. After passing through the drop interrogation region, the laser beam passes through an optical wedge and a series of ND filters before the beam is profiled using a Spiricon beam profiler with 1600 x 1200 pixels at full resolution. A schematic of the experimental setup is shown in Fig. 1 below, and a sample drop image is shown in Fig. 2.

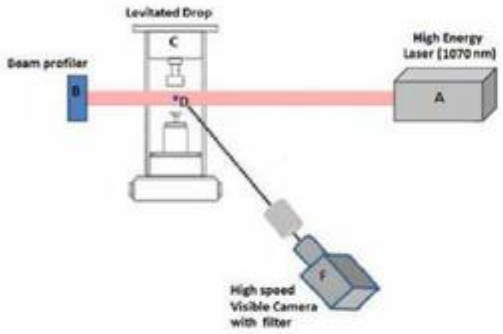

Fig. 1 – Experiment schematic

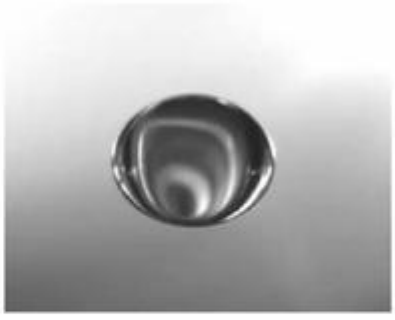

Fig. 2 – Nearly-spherical drop in levitator

The experiments shown here consist of drops with an initial size of approximately 1-mm, centered on the laser beam, which is operating at full power of 105-W. The levitator causes some distortion of the drop, making the horizontal diameter slightly larger than the vertical diameter. The range of major to minor drop diameter for these experiments is typically $H/D \approx 1.05$, and this value tends towards 1.00 as the drop evaporates and shrinks. Experimental runs typically last 40-sec or more, assuming the drop is not lost from the levitator. When placing the drop in the levitator, care is taken to reduce the probability of introducing trapped gases inside the drop, which result in instability of the drop during irradiation.

[a] Corresponding author. Email: brownell@usna.edu.

RESULTS

A few interesting qualitative results have been found from observing the drop evaporation. First, strong convective processes within the drop are visible during and after irradiation. Small vapor bubbles within the drop arrange along vortex lines, and can be seen circulating in an apparently turbulent manner. The speed of this circulation has not been quantified, but the dissipation of kinetic energy within the drop after the end of the laser strike is also observable. This is in contrast to laser heating of aerosols, which is characterized by either a slow diffusive heating regime dominated by thermal diffusion, or a fast, explosive regime controlled by the pressure wave from fluid that has exceeded the superheat limit. A second observation is that when the ellipticity of the sphere is particularly large (due to tuning or "over-tightening" of the levitator's reflector) vapor bubbles can be seen escaping from the top of the drop as would be expected with nucleate boiling. This has not been observed with more spherical drops.

Unexpectedly, vaporization appears to begin immediately after the beginning of the laser strike, with no clear sensible heating phase. Because the drops are initially at room temperature, some delay in the onset of phase change (determined from the rate of change of the drop size) was expected. The irradiance of the laser, with a mean value of approximately 530 W/cm^2, is unlikely to provide enough energy for any part of the drop to reach the superheat limit in the first few seconds of exposure, or for the drop as a whole to reach saturation within the same timeframe. Along with the observation of vigorous mixing within the drop, this is therefore a somewhat surprising finding.

From the video data of the irradiated drop, major and minor drop diameters were calculated throughout the process to produce a time history of drop volume. Figure 3 below shows the results from eight different runs, each lasting 40-s or more. The run-to-run repeatability is good, suggesting that changes in absorptivity from one liquid sample to the next are small. The outliers in the data are due to instability of the drop within the levitator. Occasionally during a laser strike, likely due to the formation and release of a vapor bubble, the drop will shake or oscillate around the acoustic node for a second or two before stability is re-established. Because these movements are very fast, the drop images can appear blurry and measurement accuracy of drop size is temporarily reduced. The decay in drop size vs time is not exponential, so it is characterized with a half-life value found to be 18.3-s for the laser at full power. This number agrees with a half-life of 20-s calculated from a simple 1-D numerical model that assumes uniform irradiance, an initially saturated drop, and approximates the drop as a thin film normal to the incoming laser (see Fig. 4).

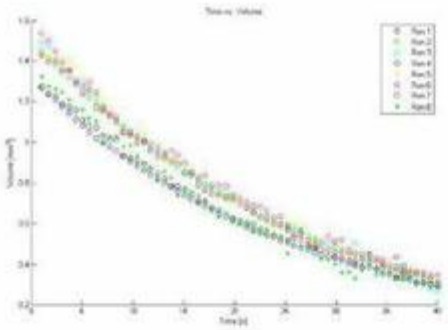

Fig. 3 – Drop volume vs time for eight water samples

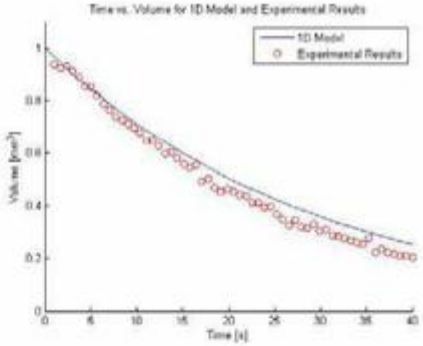

Fig. 4 – Comparison of data and 1-D model

CONCLUSIONS

Acoustic levitation is a promising method for the study of laser heating of spherical water drops. Results show good sample-to-sample repeatability, and agreement with a simple 1-D model. Effects of drop size and irradiance on convection within the drop require further study, as does the effect of the drop (and the escaped water vapor) on the beam profile.

ACKNOWLEDGEMENTS

The authors would like to thank the Office of Naval Research, the High Energy Laser – Joint Technology Office, and the USNA Trident Scholar Program for their support of this research.

References

[1] Armstrong, R.L., and Park, B.S.: Laser Induced Droplet Heating. *in Optical Effects Associated with Small Particles,* ed. PW Barber and RK Chang, World Scientific, 1988.

[2] "Basics About Ultrasonic Levitation." In *Ultrasonic Levitator Manual*, tec5 – Technology for Spectroscopy, 2014.

ELECTROSTATIC SUPPRESSION OF THE LEIDENFROST STATE

Soumik Das[1], Arjang Shahriari[2], Vaibhav Bahadur[2] & Roger T. Bonnecaze[1a)]
[1]*Department of Chemical Engineering, The University of Texas at Austin, Austin, Texas, USA*
[2]*Department of Mechanical Engineering, The University of Texas at Austin, Austin, Texas, USA*

Abstract The mechanisms of electrostatic suppression of the Leidenfrost state in an evaporating droplet with finite electrical conductivity is studied theoretically and experimentally. Using linear stability analyses for 2D and axisymmetric models of the electrohydrodynamic flow, the minimum voltage required for the suppression of the vapor gap (Leidenfrost effect) between the drop and hot surface is determined as a function of their voltage and temperature differences and the physical properties of the liquid and vapor. The dynamics of the liquid-vapor gap depends on the interplay of a destabilizing electrostatic force and stabilizing capillary and evaporation-driven hydrodynamic forces. The critical voltage required for Leidenfrost suppression is found to increase with both the droplet volume and the surface temperature. The critical wavelength of the applied perturbation is of the order of the droplet dimensions. There is very good agreement between theoretical predictions and experimental measurements.

INTRODUCTION

Boiling heat transfer is vital to several industrial processes like steam generation, desalination and distillation. In the film boiling regime, the heat transfer is significantly smaller than in the nucleate boiling regime due to the formation of a vapor layer at the solid-liquid interface (Leidenfrost effect). This vapor layer severely degrades heat transfer and causes surface dryout, which results in temperature excursions[1-3] that can cause equipment failure. Electrostatic elimination of the vapor layer increases heat transfer in film boiling by more than an order of magnitude. The suppression process happens upon application of voltage due to electrostatic attraction between the liquid drop and solid surface. The critical voltage for the attachment of the droplet to the surface appears to occur when fluctuations at the liquid-vapor interface amplify to bridge the gap[4] (Fig. 1).



FIG. 1. Illustration of Leidenfrost state suppression of a 100 μL 2-propanol droplet on a 360°C surface. a) Leidenfrost state with a visible vapor gap. b) At the threshold voltage, (65 Volts) liquid fingers protrude towards the surface. c) Enhanced suppression of the Leidenfrost state at a higher voltage (130 Volts).

The competition between electrostatic forces and capillary forces along with pressure buildup beneath the droplet due to evaporation will determine whether these fluctuations are damped or amplified and also the minimum voltage requirements which will lead to the growth of these instabilities. These instabilities bridge the vapor gap at a critical or threshold voltage leading to liquid-solid contact. There have been studies on instabilities of thin films used in electrohydrodynamic patterning[5-6], but no study has been done on electrostatic suppression of the Leidenfrost state. Here we predict the influence of concentrated interfacial electric fields on interface instabilities and develop an analytical model to predict the conditions to collapse the vapor gap and suppress the Leidenfrost state.

METHOD

The 2D model illustrated in Fig. 2 is used to analytically investigate the instabilities on the liquid-vapor interface upon application of voltage differences between drops and the solid surface. The purpose is to find the critical voltage that results in the growth of those instabilities (initiation of Leidenfrost suppression). Energy and momentum balances are applied to determine the initial vapor gap thickness in the system. An evolution equation for the liquid-vapor interface is then written under the conditions of approximately constant drop volume and electric field present only across the vapor gap. The interface evolution is assumed to be unaffected by flow inside the liquid drop and gravitational and van der Waals forces are negligible. Finally, we perform a linear stability analysis to analyze the behavior of the perturbed interface.

[a)] Corresponding author. Email: rtb@che.utexas.edu.

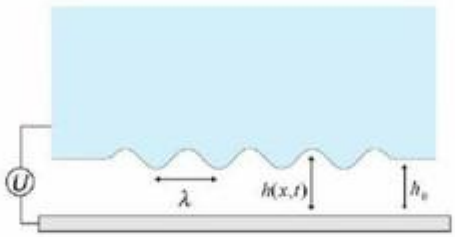

FIG. 2. Two-dimensional model to investigate evolution of liquid-vapor interface

PRELIMINARY RESULTS

Fig. 3a shows the neutral stability curve for non-dimensional electrowetting number $N_E = \varepsilon_0\varepsilon_{vap}V^2h_0^2/3\ _1\mu^2$ for varying capillary number $N_C = 3\mu A_1L^4/\gamma\ _0^5$ (Fig. 3a) for the 2D model; here $\varepsilon_0\varepsilon_{vap}$ is permittivity of the vapor, V is voltage, h_0 is nominal gap thickness, A_1 is evaporation rate, μ is viscosity of the vapor, γ is interfacial tension and L is length of the droplet. When the dimensionless wave number k is high, stabilizing capillary forces dominate. For low k evaporation effects dominate as the stabilizing mechanism. The critical voltage V_{Crit} is set by the minimum N_E. Fig. 3b depicts the variations of V_{Crit} for different surface temperatures and droplet volumes. V_{Crit} is found to increase with increasing surface temperatures and modestly so with droplet volumes. Very good agreement is found between theoretical predictions and experimental observations. Fig. 3c shows a comparison of the experimental and predicted values of V_{Crit} for a 5μL drop at different surface temperatures. The two plots show good agreement, qualitatively as well as quantitatively. Analysis using axisymmetric flow models will also be presented.

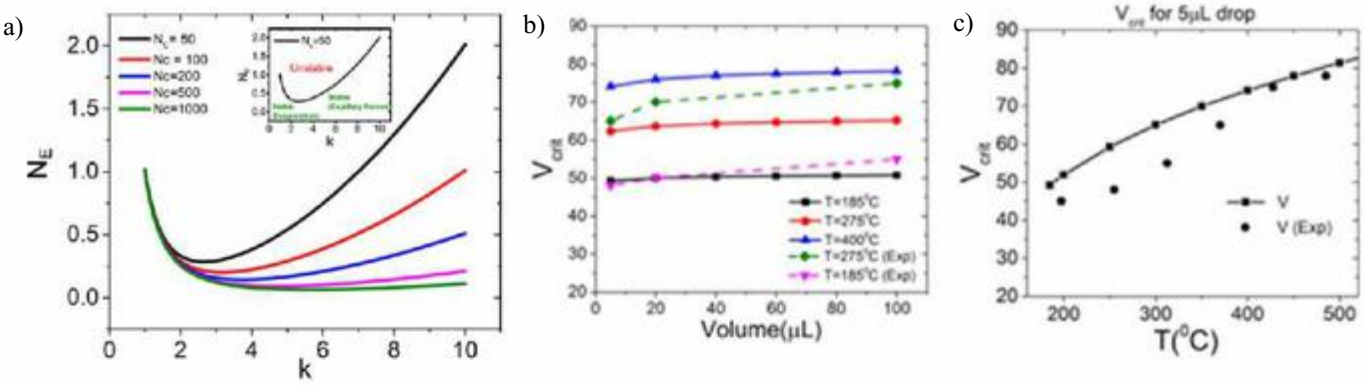

FIG. 3 a) Neutral stability curve (N_E vs k). b) V_{Crit} versus droplet volume for different surface temperatures. c) V_{Crit} versus surface temperature for a 5μL drop.

CONCLUSIONS

The present work lays the foundation for electrically tunable boiling heat transfer and offers a powerful tool to control boiling heat transfer in the film boiling regime. Using a simplified 2D and axisymmetric flow models we predicted the critical voltage required to suppress the leidenfrost state through an extensive linear stability analysis. The critical voltages obtained were in the range of 60 – 80 Volts which are in very good agreement with values obtained from experiments. The analysis accurately predicted the qualitative dependency of the critical voltage on surface temperature and droplet volume.

References

[1] Dhir, V. Boiling heat transfer. Annu. Rev. Fluid Mech. 1998, **30**, 365-401.
[2] Orzechowski, T.; Wcislik, S. Instantaneous heat transfer for large drops levitating over a hot surface. Int. J. Heat Mass Transfer 2014, 73, 110-117.
[3] Carey, V. Liquid Vapor Phase Change Phenomena, 2nd edition, Washington, D.C.: Taylor and Francis, 2007.
[4] Shahriari A., Wurz J., Bahadur V. Heat transfer enhancement accompanying leidenfrost state suppression at ultrahigh temperatures. Langmuir 2014, **30** (40), 12074-12081.
[5] Schaffer E., Thurn-Albrecht T., Russel T.P., Steiner U. Electrically induced structure formation and pattern transfer. Nature 2000, **403**, 874-877.
[6] Gambhire P., Thaokar R.M., Linear stability analysis of electrohydrodynamic instabilities at fluid interfaces in the "small feature" limit. Eur. Phys. J. E. 2011, 34:84.

MASS TRANSFER WITH SLENDER DROPS IN SHEAR AND EXTENSIONAL FLOWS

Moshe Favelukis*
Department of Chemical Engineering, Shenkar College, Ramat-Gan, Israel

Summary Mass transfer between a slender drop and a viscous liquid in shear and extensional creeping flows has been theoretically studied. The problem is governed by three dimensionless parameters: the capillary number (Ca), the viscosity ratio (λ) and the Peclet number (Pe). As the shear or extension rate increases, the drop becomes thinner, longer, the surface area increases, leading to larger mass transfer rates.

INTRODUCTION

High viscosity liquids such as polymer melts, are generally processed in rotary equipment which can generate shear or extensional flow. A drop present in these types of flows will deform and if the strength of the flows exceeds some critical value, the drop may even break. For incompressible Newtonian fluids under creeping flow conditions (Re = 0), the deformation problem is governed by two dimensionless parameters: the capillary number (Ca) and the viscosity ratio (λ): drop over external fluid. At $Ca \ll 1$, the drop is considered to be a slightly deformed sphere. This report is dedicated to slender drops only, these are obtained at $Ca \gg 1$ and $\lambda \ll 1$. A summary of this fundamental topic having many industrial applications can be found in excellent reviews by Rallison [1] and Stone [2].

The first one to suggest a theory for a slender drop flow was G.I. Taylor [3]. He considered a slender drop in axisymmetric extensional creeping flow, where the cross section of the drop is circular. The theory, that was refined by Acrivos and Lo [4] and others suggests that the slender drop has a parabolic radius profile with pointed ends. Hinch and Acrivos [5] developed a model for a slender drop in simple shear and creeping flow with the assumption that the drop has a circular cross section. The theory predicts an S-shaped drop with pointed ends. Both models for extensional and shear flows predict: (a) as the capillary number increases, the drop becomes thinner, longer and its surface area increases; (b) the critical capillary number needed for breakup increases as the viscosity ratio decreases.

Mass transfer between slender drops and viscous liquids can be found in several industrial applications such as: polymer melt devolatilization, the production of polymeric foam materials, the production of glasses, and more. Since mass transfer is proportional to the surface area of the drop, we can expect slender drops to be very efficient in mass transfer operations. It is the purpose of this report to review as well as present new results to the subject of mass transfer with slender drops. In axisymmetric extensional flow we present recent theoretical studies by Favelukis [6-7] for both large and small Peclet numbers. In simple shear flow, we have past theoretical and experimental results at large Peclet numbers (Favelukis et al., [8-9]) and we suggest here an expression for small Peclet numbers.

FLUID MECHANICS

Figure 1 shows slender drops ($R/L \ll 1$), having a local radius R and a half-length L. The undisturbed motion, is axisymmetric extensional flow ($v_r = -Er/2$, $v_\theta = 0$, $v_z = Ez$) and simple shear flow ($v_x = Ey$, $v_y = 0$, $v_z = 0$). The problem is governed by the capillary number: $Ca = \mu Ea/\sigma$ and viscosity ratio: $\lambda = \mu_{in}/\mu$. Here μ_{in} and μ are the viscosity of the drop and of the external fluid respectively, $E > 0$ is the extension or shear rate, a is the radius of sphere of equal volume, and σ is the surface tension. The dimensionless parameters can be reduce from two to one O(1): $G_{ext} = Ca\lambda^{1/6}$ and $G_{shear} = Ca\lambda^{2/3}$.



Figure 1: Left: A slender drop in an axisymmetric extensional flow; Right: A slender drop in a simple shear flow.

Figure 2 describes the deformation curve with $L^*_{ext} = L/(aCa^2)$ and $L^*_{shear} = L/(aCa^{1/2})$ both with O(1). In an extensional flow, the deformation curve contains a lower stable branch and an upper unstable branch. The two branches are separated by a bifurcation turning (breakup) point at G = 0.148, and no stationary drop can exists beyond this point. In shear flow, stationary drops can be found for every value of G, with the breakup point at G = 0.0519.

*Corresponding author. Email: favelukis@gmail.com

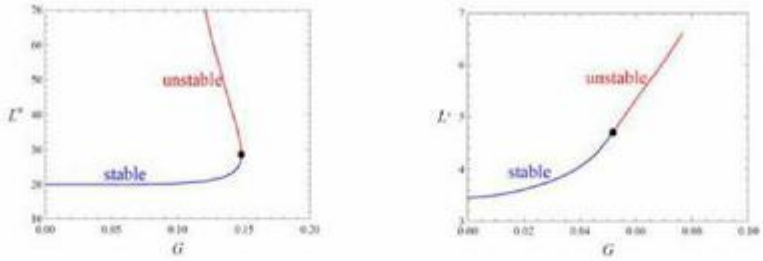

Figure 2: Deformation curves. Left: axisymmetric extensional flow; Right: simple shear flow.

MASS TRANSFER

The differential binary mass balance in the continuous phase, at constant density and diffusion coefficient (D) is governed by the Peclet number, the ratio of convection to diffusion: $Pe = Ea^2/D$. When $Pe \to \infty$, the thin concentration boundary layer approximation is valid, while $Pe \to 0$ suggests diffusion only with a thick concentration boundary layer.

Large Peclet numbers ($Pe \to \infty$)

In axisymmetric extensional flow, an exact analytical solution is presented in Favelukis [6]. The solution can be found by applying the theory of Lochiel and Calderbank [10] for axisymmetric bodies of revolution, with the only requirements being the shape and the tangential surface velocity of the drop. In simple shear flow, an order of magnitude model was suggested by Favelukis et al. [8], which was experimentally confirmed by bubble dissolution and growth experiments ([8-9]):

$$\overline{Sh}A^*_{\text{ext}} = 5\sqrt{\frac{2}{3\pi}}\left(\frac{\nu}{2}\right)CaPe^{1/2} \sim E^{3/2} \quad ; \quad \overline{Sh}A^*_{\text{shear,inv.}} \sim Ca^{-1/8}Pe^{1/2} \sim E^{3/8} \tag{1}$$

Where $\overline{Sh} = \overline{k}a/D$ is the average Sherwood number (average flux), $A^* = A/4\pi a^2$ is the dimensionless surface area, and their product is the mass transfer rate. In extensional flow, $\nu = 2$ ($G = 0$) denotes an inviscid drop (bubble), while $\nu > 2$ a viscous drop. For both types of flows, as the shear or extension rate increases, the rate of mass transfer also increases.

Small Peclet numbers ($Pe \to 0$)

In axisymmetric extensional flow, the shape of the drop is an approximated slender spindle suggesting the usage of bispherical coordinates. The electrostatic capacity of a spindle was obtained by Payne [11] and others. Making use of the analogy between electrostatics and diffusion, both governed by the Laplace equation, Favelukis [7] recently obtained the exact solution involving conal functions. It was found that the diffusion around a slender prolate spheroid (rounded ends), Szegö [12], gives an excellent approximation to the exact solution (pointed ends). As a result, for shear flow, we suggest:

$$\overline{Sh}A^*_{\text{ext}} \approx \frac{20(\nu/2)^2 \cdot Ca^2}{\ln\left[160(\nu/2)^3 \cdot Ca^3\right]} \quad ; \quad \overline{Sh}A^*_{\text{shear, inv.}} \approx \frac{3.45Ca^{1/2}}{\ln\left[11.9Ca^{3/4}\right]} \quad ; \quad \overline{Sh}A^*_{\text{shear, crit.}} \approx \frac{4.71Ca^{1/2}}{\ln\left[20.1Ca^{3/4}\right]} \tag{2}$$

The first eq. (2) is valid for inviscid ($\nu = 2$) and viscous ($\nu > 2$) drops. The second eq. (2) corresponds to an inviscid drop ($G = 0$, $L^* = 3.45$), while the last eq. (2) represents a viscous drop at the breakup point ($G = 0.0519$, $L^* = 4.71$). As expected, for both shear or extensional flows, as the capillary number increases, the rate of mass transfer also increases.

CONCLUSIONS

Mass transfer between a slender drop and a viscous liquid in shear and extensional creeping flows has been theoretically studied at small and large Peclet numbers. For both types of flows and regimes, as the shear or extension rate increases, the rate of mass transfer also increases. Slender drops, having large surface area, can offer very high mass transfer rates.

References

[1] Rallison J.M.: The Deformation of Small Viscous Drops and Bubbles in Shear Flows. Ann. Rev. Fluid Mech. 16: 45-66, 1984.
[2] Stone H.A.: Dynamics of Drop Deformation and Breakup in Viscous Fluids. Ann. Rev. Fluid Mech. 26: 65-102, 1994.
[3] Taylor G.I.: Conical Free Surfaces and Fluid Interfaces, in: Proc. 11th Int. Congr. on Appl. Mech., Munich, Springer, Berlin, pp. 790-796, 1964.
[4] Acrivos A., Lo T.S.: Deformation and Breakup of a Single Slender Drop in an Extensional Flow. J. Fluid Mech. 86: 641-672, 1978.
[5] Hinch E.J., Acrivos A.: Long Slender Drops in a Simple Shear Flow. J. Fluid Mech. 98: 305-328, 1980.
[6] Favelukis M.: Mass Transfer around Slender Drops in an Extensional Flow: Inertial Effects at Large Pe. Can. J. Chem. Eng. 93: 2274-2285, 2015.
[7] Favelukis M.: On the Diffusion from a Slender Drop in an Extensional Flow: Inertial effects at Zero Pe. Colloids Surf. A. in press, 2015.
[8] Favelukis M., Tadmor Z., Talmon Y.: Bubble Dissolution in Viscous Liquids in a Simple Shear Flow. AIChE J. 41: 2637-2641, (1995).
[9] Favelukis M., Tadmor Z., Semiat R.: Bubble Growth in a Viscous Liquid in a Simple Shear Flow. AIChE J. 45: 691-695, (1999).
[10] Lochiel A.C., Calderbank P.H.: Mass Transfer in the Cont. Phase around Axisymmetric Bodies of Rev. Chem. Eng. Sci. 19: 471-484, 1964.
[11] Payne L.E.: On the Axially Flow and the Method of Generalized Electrostatics. Q. Appl. Math. 10: 197-204, 1952.
[12] Szegö G.: On the Capacity of a Condenser. Bull. Am. Math. Soc. 51: 325-350, 1945.

EFFECTS OF ATMOSPHERIC PRESSURE ON WATER ENTRY OF HYDROPHOBIC SPHERES

Zhaoxin Gong[a)], Yongliu Fang, Hua Liu, Jie Li, Ying Chen, Chuanjing Lu
Department of Engineering Mechanics, MOE Key Laboratory of Hydrodynamics, Shanghai Jiao Tong University, Shanghai, China

Summary We report an experimental study of water entry of a hydrophobic sphere, which is initially released by an electromagnet and freely falls downward in a sealed equipment. The sphere firstly impacts the water surface and generate a splash, then a cavity is developed when the sphere moves inside the water, and finally a jet is formed after the cavity pinch-off. Here, the effects of atmospheric pressure on such water entry phenomena are presented. Our work especially demonstrates its influence on the splash shape, the surface seal and cavity moving velocity.

INTRODUCTION

When a sphere enters water with certain impacting velocity, the phenomena of interests are splash, cavity and jet, as shown in Figure 1. Splash refers to the water curtain above the free surface, cavity is the gas attached to the sphere and formed by the air entrainment, and jet here means the re-entrance jet after the pinch-off of the cavity. The first research on water entry can dates back to 1897, when Worthington & Cole investigated spheres impacting onto liquid surfaces using single-spark illumination photography. With the developments in experimental techniques and numerical simulation schemes, there are notable progresses on understanding the mechanism and characteristics of the water-entry cavity in the past decades. The behaviours of splash, cavity and jet are determined by various factors, such as sphere diameter, impacting velocity, water depth, surface coating, vacuum degree and so on. Here, we pay attention to the effects of atmospheric pressure on water entry of hydrophobic spheres.



Figure 1. phenomena of a sphere entering water: splash, cavity and jet.

EXPERIMENTAL SETUP

Experiments are conducted in a octagonal water tank with 800mm diameter and 1400mm height and filled with 764mm height of water. A 500mm long hollow cylinder is placed on the top of the water tank and a electromagnet is contained on its cover. The sphere is initially suspended from the electromagnet. The air pressure inside the water tank is adjusted by a vacuum pump. The sphere is made up of cast steel and coated with hydrophobic material. The pressures at the top of the water tank are measured by a pressure gauges. A high speed camera is used to record the sphere motion and the images are taken at 1000frames/sec. The sphere used in our experiments is with 29mm diameter and 100g mass. The contact angle of the hydrophobic sphere is 134°. The impacting velocity is 4.7m/s.

RESULTS

Several atmospheric pressure conditions are tested to observe its impacts on the splash, cavity and jet during the sphere entering water process. It can be concluded that the atmospheric pressure effects on the sphere trajectory can be neglected. In all cases, the sphere slightly accelerates at first, then almost keeps constant velocity, and shortly before cavity pinch-off, the sphere starts decelerating. The most obvious effects is on the splash, which height and width varies with the atmospheric pressures. Besides that, when the pressure above the water surface approaching vacuum, there is no surface seal, i.e. the top of the splash cannot merge and form a dome-shape space. The surface seal affects the jet performances. The cavity pinch-off happens at the same time for all cases , which agrees well with previous studies. After the pinch-off, the cavity are divided into two parts, one is moving upward and generates jets into the splash, and the other is moving downward and generates jets inside the cavity. The upward velocity decay significantly shortly after the pinch-off, whereas the downward velocity changes relatively slowly.

[a)]Corresponding author. Email: jackyff@sjtu.edu.cn.

CONCLUSIONS

A series of experiments results are presented to study the water entry problems of hydrophobic spheres. We describe the water entry process in detail and demonstrate the effect of atmospheric pressure on the hydrodynamics phenomena, including splash, cavity and jet .

References

[1] Worthington A. M. and Cole R. S.: Phil. Trans. R. Soc. Lond. Ser. A, 1897, 189: 137-148.
[2] Gilbarg D. and Anderson R. A.:J. App. Phys., 1948, 19(2):127-139.
[3] Aristoff J. M. and Bush J. W. M., Water entry of small hydrophobic spheres, J. Fluid Mech. 2009,619:45-78.
[4] Mansoor M. M., Marston J. O., Vakarelski I. U. and Thoroddsen S. T.:J. Fluid Mech., 2014, 743:295-326.
[5] Grumstrup T., Keller J. B. and Belmonte A.:Phys. Rev. Lett., 2007, 99:114502 .
[6] Truscott T. T., Epps B. P. and Techer A. H.:J. Fluid Mech., 2012, 704:173-210.
[7] Bodily K., Langley K., Huey J. and Truscott T. T.:Phys. Fluids., 2013, 25(9):091109.
[8] Bodily K., Carlson S. J. and Truscott T. T.:Phys. Fluids., 2014, 26(7):072108.

INFLUENSE OF OSCILLATIONS ON COAGULATION AND SEDIMENTATION OF AEROSOLS IN TUBES

Damir Gubaidullin[1a)], Rinat Zaripov[1] & Liudmila Tkachenko[1]
[1]*Institute of Mechanics and Engineering, Kazan Science Center, Russian Academy of Sciences, Kazan, Russia*

Summary Experimental investigations of oscillations of an aerosol were carried out for tubes with various geometry on end in shock-wave and shock-free modes near resonance frequencies. Numerical concentration of aerosol droplets monotonously decreases with time. With increase of intensity of oscillations, these times decrease. The dependence of the time scale of sedimentation of aerosol in closed tube and time scale of clearing of aerosol in an open tube on the excitation frequency likewise exhibits a nonmonotonic pattern. It is established, that presence of a flange slows down process of the sedimentation of aerosol. Reduction of internal diameter of a flange results in increase in the time scale of sedimentation of aerosol. The time scale of sedimentation of aerosol in the closed tube is 2-4 times, time scale of clearing of aerosol in an open tube is 6-12 times and a partially open tube is 5-10 times lower than at natural depositing.

INTRODCTION

Different multiphase media are the main working fluids in a number of power-generating equipments, apparatus of chemical technology. One of acute problems of thermophysics and mechanics of multiphase systems is investigation of wave processes. Basic models of wave dynamics of multiphase media and some related results are given in monograph [1]. The acoustic coagulation of aerosols, which is accompanied by agglomeration of small particles or droplets under the effect of acoustic waves, is a well-known phenomenon treated in detail in the monographs [2, 3] and in other publications. Widely employed is a system of the type of resonance tube, in which the excitation of the medium near resonance causes the emergence of highly nonlinear pressure waves up to periodic shock waves at resonance. The behaviour of the aerosol with its nonlinear oscillations in tubes near resonance frequencies was studied in experimental works [4-12]. The main nonlinear effect was accelerated coagulation and deposition of the droplets of machine oil and tobacco smoke [4], oleic acid droplets [5], smoke particles produced by the combustion of an incense stick [6], and droplets obtained from liquid Di-ethyl-hexyl-sebacate (DEHS) [7-12] on the tube walls. The geometric diameter of the aerosol droplets and particles was 1–10 μm [4, 5], 0.3 μm [6], and 0.863 μm [7-12]. This work is aimed at experimental study of the features of sedimentation of the oscillating aerosol (with a droplet diameter of less than 1 μm) near the resonance frequencies in tubes of different lengths with various geometry on the end in the shock-wave and the shock-free modes.

RESULTS

Experimental investigations of oscillations of aerosol were carried out for different length of tubes in a shock-wave and shock-free modes near to subharmonic and natural resonances. Di-ethyl-hexyl-sebacate $C_{26}H_{50}O_4$ was used as the working fluid to generate aerosol. The majority of droplets have the geometric diameter 0.863 μm. As experiments have shown, the concentration of droplets monotonically decreases with time. Moreover, under natural deposition a slower decrease in the aerosol concentration with time takes place. In the closed tube, this process includes the coagulation of aerosol droplets upon their coalescence and sedimentation on the tube walls. The time of variation of concentration is the time scale of sedimentation of aerosol. In the open and the partially open tubes, the monotonic process of the decrease in concentration with time includes mainly the coagulation of aerosol droplets, their sedimentation on the tube walls, and the unsteady discharge of aerosol from the open end of the tube in the form of a pulsating jet. Therefore, we will refer to the characteristic time of this process as the time scale of clearing of the aerosol.

The obtained dates were used to determine the time scale of sedimentation of aerosol and the time scale of clearing of aerosol as a function of frequency and amplitude of piston travel for different values of the tube length. The dependence of the time scale of sedimentation of aerosol and the time scale of clearing of aerosol on the excitation frequency exhibits a nonmonotonic pattern. This pattern of the dependence is attributed to the fact that the amplitude of forced oscillation of aerosol increases when resonance is approached and this leads to a decrease in the time scale of sedimentation of aerosol and the time scale of clearing of aerosol. At resonance, the amplitude reaches its maximal value; accordingly, the time scale of sedimentation of aerosol and the time scale of clearing of aerosol is minimal. Behind resonance, the amplitude decreases; as a result, the time scale of sedimentation of aerosol and the time scale of clearing of aerosol increases.

We will examine the data on the dependence of the time scale of coagulation and deposition of aerosol on the intensity of aerosol oscillation. It is known that, in a tube, the amplitude of pressure oscillation of the medium at resonance is proportional to $\varepsilon = l/L$ [13]. Therefore, a decrease in the tube length or raising the amplitude of the travel piston causes an increase in the amplitude of pressure oscillation and, accordingly, of intensity of oscillation. The increase in ε leads to reduction of the time scale of sedimentation of aerosol in the closed tube and time scale of clearing of the aerosol in the open tube.

[a)] Corresponding author. Email: damirgubaidullin@gmail.com.

It is possible to note that the time scale of the sedimentation of aerosol in closed tube is 2-4 times, and the time scale of clearing of aerosol in open tube is 6-12 times and in partially open tube is 5-12 times less than time scale of natural deposition in the absence of oscillations. Effective coagulation of aerosol droplets and their deposition in the tube due to the secondary flow in the manner of two toroid vortices is observed [13], formed as a result of the nonlinearity of the resonant oscillations.

In addition, the influence of the flanges at the passive end of the tube on the process of the clearing of aerosol is studied. It is shown that the decrease of the internal diameter of the flange results in an increase the time scale of clearing of aerosol that reaches a maximum value in the case of the closed tube. This is due, firstly, to the significant influence of the unsteady discharge of aerosol from the open end of the tube, and secondly, with the approach of the investigated excitation frequencies of aerosol in an open tube to its resonance frequency [14, 15]. Note that the time scale of clearing of aerosol in an open tube with the flange is longer than in an open tube without a flange. This is because an open tube with a flange, which is in connection with the tube forms a right angle, the consumption on the formation of vortices near the outlet section, is greater than in the tube with the rounded open end [16].

CONCLUSIONS

It is shown that the presence of oscillations leads to acceleration of sedimentation of aerosol. The increase in intensity of the oscillations, caused by increase of amplitude of piston travel or a decrease of the tube length, leads to reduction of process time. The time scale of the sedimentation of aerosol in closed tube is 2-4 times, and the time scale of clearing of aerosol in open tube is 6-12 times and in partially open tube is 5-12 times less than time scale of natural deposition. It is established, that presence of a flange slows down process of the clearing of aerosol. Reduction of internal diameter of a flange results in increase in the time scale of clearing of aerosol. The nonmonotonic pattern of the dependence of the time scale of sedimentation of aerosol in a closed tube and the time scale of clearing of aerosol in an open tube on the frequency of excitation with a minimal value at resonance frequencies has been found.

ACKNOWLEDGMENTS

The study was performed by a grant from the Russian Science Foundation (project No. 15-11-10016).

References

[1] Nigmatulin R. I.: Dynamics of Multiphase Media. *Hemisphere*. New York, 1990.

[2] Mednikov E.P.: Acoustic Coagulation and Precipitation of Aerosols. *Consultant Bureau*. New York, 1965.

[3] Temkin S.: Suspension Acoustics: an Introduction to the Physics of Suspensions. *Cambridge University Press*. New York, 2005.

[4] Gulyaev A.I. and Kuznetsov V.M.: Aerosol Coagulation under Periodic Shock Waves. *Sov. Phys. Acoustic* **8**(4):236–238, 1963.

[5] Temkin S.: Droplet Agglomeration Induced by Weak Shock Waves. *Phys. Fluids* **13**:1639–1641, 1970.

[6] Shuster K., Fichman M., Goldshtein A. and Gutfinger C., Agglomeration of Submicrometer Particles in Weak Periodic Shock Waves. *Phys. Fluids* **14**(5):1802–1805, 2002.

[7] Gubaidullin D.A., Zaripov R.G., Galiullin R.G., Galiullina E.R. and Tkachenko L.A.: An Experimental Investigation of the Coagulation of Aerosol in a Tube in the Vicinity of Subharmonic Resonance. *High Temperature* **42**(5):794–802, 2004.

[8] Gubaidullin D.A., Zaripov R.G. and Tkachenko L.A.: Experimental Study of Coagulation and Sedimentation of Aerosols in a Closed Tube in the Shock-Free Mode. *High Temperature* **50**(4):564–566, 2012.

[9] Gubaidullin D.A., Zaripov R.G. and Tkachenko L.A.: Experimental Study of Oscillations of Aerosols in an Open Tube in the Shock-Free Mode. *High Temperature* **51**(6):955–957, 2013.

[10] D. A. Gubaidullin, R. G. Zaripov, and L. A. Tkachenko, Experimental Study of Nonlinear Oscillations of Aerosols in Tubes in the Shock-Free Mode near Resonance. *Doklady Physics* **58**(9): 392–395, 2013.

[11] Gubaidullin D.A., Zaripov R.G. and Tkachenko L.A.: Nonlinear Oscillations of Finely Dispersed Aerosol in a Flanged Pipe. *J. of Engin. Physics and Thermophysics* **85**(2): 259–264, 2012.

[12] Gubaidullin D.A., Zaripov R.G. and Tkachenko L.A.: Resonance Oscillations of an Aerosol in a Tube with a Diaphragm in the Shock_Free Wave Mode. *High Temperature* **52**(6):895-899, 2014.

[13] Ilgamov M.A., Zaripov R.G., Galiullin R.G. and Repin V.B.: Nonlinear oscillations of a gas in a tube. *Appl. Mech. Rev.* **49**(3):137–154, 1996.

[14] Jimenez J.: Nonlinear gas oscillations in pines. Pt.1. Theory. *J. Fluid Mech* **59**:23-46, 1973.

[15] Sturtevant B.B.: Nonlinear gas oscillations in pines. Pt. 2. Experiment. *J. Fluid Mech* **63**:97-120, 1974.

[16] Sturtevant B.B. and Keller J.J.: Subharmonic non-linear acoustic resonances in open tubes. Pt. 2: Experimental investigation of the open-end boundary condition. *Z. Angew. Math. Physics* **29**(3):473-485, 1978.

TRANSIENT FLUID PHENOMENA DURING A RAPID TWO-PHASE DEPRESSURISATION

Ouajih Hamouda[1a)], David S. Weaver[1] & Jovica Riznic[2]
[1]*Mechanical Engineering, McMaster University, Hamilton, Ontario, Canada*
[2]*Operational Engineering Assessment, Canadian Nuclear Safety Commission, Ottawa, Ontario, Canada*

Abstract Experiments were carried out using a custom-built facility to determine the loading on a model nuclear steam generator tube array during a simulated Main Steam Line Break accident. The working fluid was refrigerant R-134a. Measurements were taken of temperature and pressure during the fluid transient and high-speed videos from synchronised cameras were used to help understand the related flow physics. Sudden depressurisation was created using a rupture disc that opened fully in a few milliseconds. Parametric studies were undertaken to investigate the effects of varying initial conditions and liquid levels. The results provide valuable insights into the two-phase flow physics during such an event and have significant potential for benchmarking numerical code development as well as predicting tube loading.

INTRODUCTION

This paper presents the results of an experimental study of two-phase flow transients following sudden depressurisation from a pressurised subcooled liquid state. While the overall purpose of the research was to determine the fluid loading on the U-bend tubes of a nuclear steam generator during a simulated Main Steam Line Break (MSLB), an understanding of the physics of the fluid transient phenomena must first be developed. Indeed, such an understanding is useful for a wide range of applications including the design of boilers, refrigeration systems, desalination equipment, cryogenic systems, the transfer and storage of liquefied gases, and pressurised water nuclear reactors. The authors are unaware of any similar thorough experimental investigations of the relevant phenomena published in the open literature.

EXPERIMENTS

The present experiments were carried out using R-134a which, for the present purposes, scales well with steam-water transients. The experimental rig consists of a vertical 15.2 cm diameter pipe reservoir that contains quiescent pressurised liquid, a test section that contains the model tube array, a rupture disc that produces the sudden depressurisation upon opening, and a downstream vacuum reservoir of sufficient volume that the downstream increase in pressure during the transient has no effect on the results. The rupture disc opens in a couple of milliseconds and presents no obstruction to the flow after rupture. The vertical rig is shown schematically at the right side of Fig. 1 without the large vacuum tank at the downstream pipe exit. Each experiment consisted of drawing the rig down to a vacuum upstream and downstream of the rupture disc, charging the liquid reservoir to the desired volume and pressure, initiating the transient, and monitoring the dynamic temperatures and pressures at the 3 axial locations on the pipe as numbered in Fig. 1. All instruments were carefully validated, calibrated and synchronised. High-speed videos from two synchronised cameras above and below the test section permitted visualisation of the flow to assist in understanding the flow physics. Parametric studies were carried out to study the effects of varying the initial liquid volume and its free surface level relative to the tube bundle.

Overview of experimental results

The research objective was to provide a unique and reliable dataset and to perform analysis that supports the major two-phase fluid phenomena observed. The accurate inclusion of two-phase fluid effects in numerical simulations is one of the main areas for improvement in present computational modelling tools. The rapid depressurisation process is initialised by the propagation of a rarefaction wave from the point of disc rupture. The fluid is subsequently depressurised and transitions into a superheated metastable state, which triggers an extremely rapid boiling process.

A sample set of pressures measured in a typical experiment is presented in Fig. 1. In the first 10 ms, a pressure wave propagates rapidly at the speed of sound. The arrival of the wave is recorded at different times because of

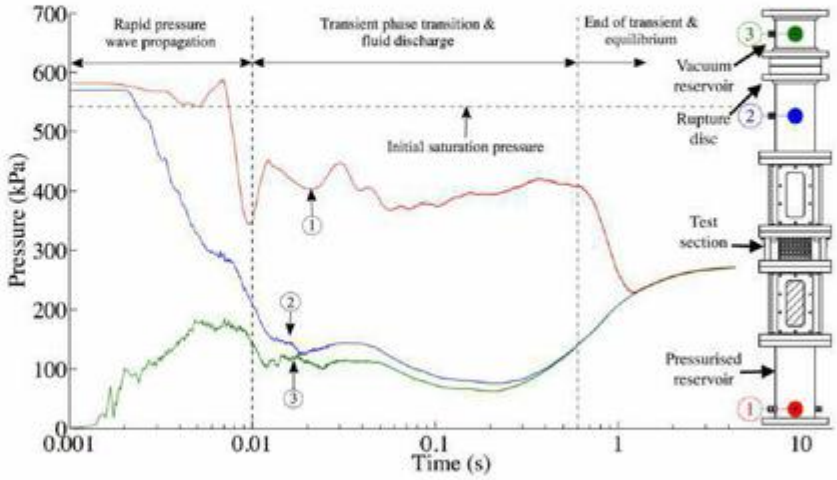

Figure 1. Sample fluid pressures measured during a transient experiment

a) Corresponding author. Email: hamoudo@mcmaster.ca

the locations of the pressure sensors relative to the rupture disc. This is followed by a period of vigorous phase transition in which the ratio of vapour-to-liquid in the pressure vessel increases rapidly. At the same time, the two-phase fluid mixture is discharged through the open rupture disc due to the pressure difference between the pipe and the downstream vacuum tank. A quasi-steady choked flow condition is established beginning at about 100 ms. At about 600 ms, the pressures everywhere in the system begin to equalise until equilibrium conditions are established, signalling the end of the transient. Around 1 second following the opening of the rupture disc, the 14 litre liquid inventory is essentially completely boiled off.

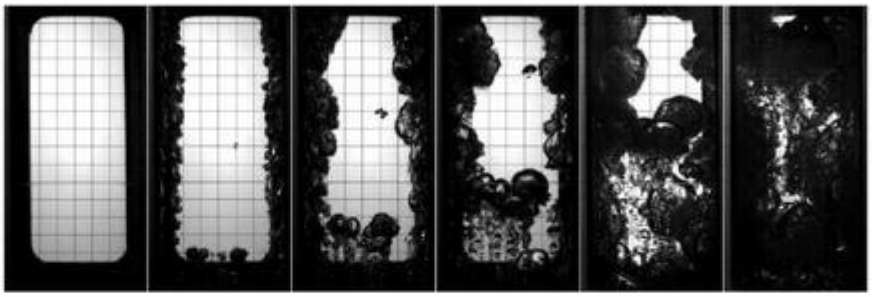

Figure 2. High-speed flow visualisation sequence of bubble growth – 50 ms time step, 10 mm grid

The specific details of the initial wave propagation behaviour depend on the initial liquid level in the pressure vessel. Wave velocity measurements indicated that the tube bundle had no discernible influence on wave propagation. The two-phase mixture accelerates rapidly towards the discharge plane. The velocity of the accelerating front was traced using high-speed images and pressure signals. Since the pressure ratio between the upstream pipe and the vacuum reservoir is very high, the flow becomes choked in the early stages of the transient. This critical flow condition establishes the maximum possible discharge mass flow rate. The velocity was found to approach the single-phase vapour speed of sound at higher void fractions.

The initial rapid depressurisation of the liquid proceeds to a minimum pressure that is lower than the initial saturation pressure, as shown at about 9 ms in Fig. 1. Following this point, the pressure recovers to a pressure amplitude that typically remains steady for the next several hundred milliseconds. The recovery in the pressure amplitude is caused by rapid expansion and growth of the vapour phase. An analysis of the transient thermal phenomena was made possible by measurements from fast response thermocouples. The expected equilibrium saturation temperatures computed from local pressure measurements were compared to the measured transient temperatures. The results indicated a significant amount of thermal non-equilibrium between the liquid and vapour phases. The liquid was observed to remain in a prolonged superheated state, whereas the vapour temperatures rapidly dropped towards saturated thermodynamic conditions.

Flow pattern visualisations provided interesting insights into the physical mechanisms of phase transition, vapour growth, and transient fluid regime development. A sample image sequence of the rapid vapour growth filmed is shown in Fig. 2. The images show that the generation of vapour occurs mainly at the solid-liquid pipe wall boundaries. The vapour that is generated grows radially into the liquid bulk and rises upwards towards the vacuum reservoir. The bubble velocities and growth rates were significantly under-predicted by theoretical pool boiling models.

The pressure amplitude during the transient is determined by the net effect of the rate of vapour generation, which produces an increase in pressure, and the rate of fluid discharge, which results in a decrease in pressure. The effects of the initial conditions were found to be as follows. The rate of phase transition and the amplitude of pressure recovery in these experiments were mainly influenced by the rate and mechanism of vapour generation. Larger initial interfacial surface area between the two phases resulted in greater heat and mass transfer, which promoted faster phase transitions and higher pressures. The volume of liquid in the pipe determines to a certain extent the transient pressure amplitudes and the duration of the discharge. When the initial liquid inventory is smaller, less vapour is generated, and the overall pressure amplitudes are lower. Smaller liquid inventories also produce shorter transients. The inclusion of the tube bundle restricted the rate of fluid discharge, resulting in smaller departures from non-equilibrium conditions compared to full-bore pipe transients.

CONCLUSIONS

The general two-phase flow phenomena can be summarised as follows. The initial rapid transient stages directly following the sudden pressure release are dominated by unsteady acoustic phenomena. Significant liquid flashing to vapour develops a few milliseconds later and the mass flow rate of the discharging fluid increases rapidly. This is a period of strong thermodynamic non-equilibrium. Subsequently, the upstream pressure stabilises and remains steady for a few hundred milliseconds, which indicates that the two-phase flow is choked during this time. The duration of this quasi-steady discharge stage depends strongly on the initial liquid level in the reservoir and the restriction to the flow imposed by the tube bundle in the test section. The upstream pressure tapers off when the liquid inventory is reduced sufficiently that the pressure level cannot be maintained by vapour generation. The results of this study provide a basic understanding of the transient flow physics during a rapid depressurisation such as caused by a MSLB, generate the data required for related numerical code development, as well as create the basis for predicting the steam generator tube loading during such an event.

ROTATIONAL SAPERATION IN BINARY DROPLET COLLISON

Kuan-Ling Huang, Chi-Ru Lu & Kuo-Long Pan[a)]
Department of Mechanical Engineering, National Taiwan University, Taipei 10617, Taiwan, R. O. C.

Summary We have studied experimentally the collision regimes between two identical droplets made of alkane or water. In contrast to five typical regimes generally known, i.e., (I) coalescence after minor deformation, (II) bouncing, (III) coalescence after substantial deformation, (IV) reflexive separation, and (V) stretching separation, we have found additional regime named as (VI) rotational separation. This regime is characterized by separation of a merged droplet with a scenario different from that reported in previous studies. In comparison with the existing models, interpretation is provided based on the resultant of the momenta in the reflexive and rotating masses of the merged droplet. Separation may happen if this resultant overcomes the restraining of the surface and viscous forces. The three types of separation can thus be unified into one model and the inconsistency among previous models could be eliminated.

INTRODUCTION

The collision dynamics between two droplets has been widely studied in near decades [1-5] due to its significance in various disciplines of nature and practical interests. The outcomes of droplet collision are illustrated in Fig. 1, showing characteristic transitions from (I) coalescence after minor droplet deformation to (II) bouncing, to (III) coalescence after substantial droplet deformation, and to (IV) temporary coalescence followed by separation of primary binary droplets and further formation of satellite droplets when a governing dimensionless parameter of Weber number is increased. It is defined as $We = \rho_l U^2 D/\sigma$, where U is the relative velocity, D the diameter of the droplet, and ρ_l and σ respectively the density and surface tension of the liquid.

Another key factor dominating the collision is the impact parameter, $B = \chi/D$, where χ is the projection of the separation distance between the droplet centers in the direction normal to the vector $\boldsymbol{U}$. Thus $B = 0$ indicates head-on collision and $B = 1$ means grazing condition. If We is sufficiently large, with increase of B, two distinct scenarios of separation after merging of droplets have been reported. That is, (IV) reflexive separation due to the reflection of colliding masses and (V) stretching separation at large B caused by stretching of temporarily coalesced masses that are however not aligned in a collinear path. The models proposed to predict the transition boundary from regime (III)-(V) were referred to the competition between the rotational [1] or stretching [2-4] energy to the surface energy. These predictions are somehow not consistent with each other and the accuracy may degenerate in different studies. In this work we investigate a new regime diagram according to the experimental finding as shown in Fig. 2(a) and 2(b) and this could eliminate the inconsistency raised in previous studies.

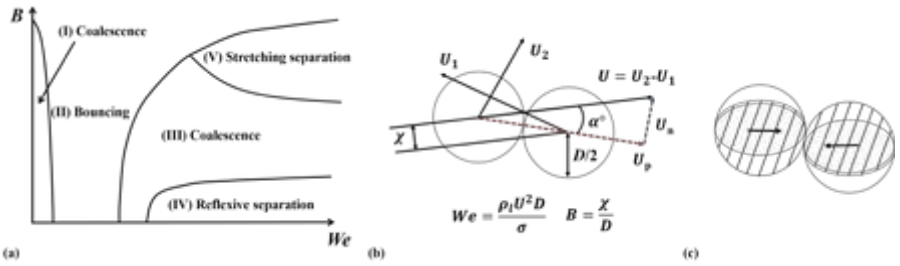

Fig. 1 (a) The typical regime diagram of hydrocarbon at 1 atm [4]. (b) Definition of parameters in binary droplet collision. (c) Schematic scheme of the reflexive portion (cross hatched) for the colliding droplets [1].

EXPERIMANTAL METHOD

The experimental setup was similar to that described in Refs. [5] and [6]. Two identical droplets were generated by nozzles that were triggered by the vibration of piezoelectric plates. They were made to impinge onto each other with adjusted angles of the colliding path. Time-resolved images were either taken through stroboscopy synchronized with the droplet generation circuit or recorded by a high-speed CMOS digital camera (X-StreamTM Vision, XS-4), which supported a maximum resolution of 512×512 pixels with 5100 frames per second (fps). The shutter of the high-speed camera was synchronized with a LED lamp that can support the shortest duration of 1 μs, so as to capture images with sufficiently small exposure and adequate light intensity while avoiding slurring due to background scattering. In contrast, for high spatial resolution, a standard CCD was used to take droplet pictures as the motion was synchronized with the stroboscopic light. However, this technique might not readily render desired points on the regime diagram; thus the high-speed camera system was implemented.

RESULTS AND DISCUSSION

Decane, dodecane, tetradecane, hexadecane and water droplets with two different diameters (0.3 and 0.6 mm) have been tested, for which the new regime diagram was recorded and shown in Fig. 2(a) and 2(b). Specifically in Fig. 2(a), as B is

[a)] Corresponding author. Email: panpeter@ntu.edu.tw.

increased, the collision outcome can be compared for the marked points and shown in Fig. 3. These results all demonstrate the existence of a new regime (VI) of separation, and a strip of coalescence regime between regime (V) and (VI). The sequential images in Fig. 3(c) show that the coalesced droplet is stretched out in the same manner as reflexive separation but eventually separated after a rotation of about 3π/4 in phase difference. This is distinct from the known scenarios of reflexive and stretching separation regimes. In Fig. 2(b), the minimum value of *We* on the transition boundary from regime (III) to (VI) is defined as We_r and is compared to We_c, as shown in Fig 2(c). It indicates that We_r linearly increases with Ohnesorge number, which is defined as $Oh = \mu_l/\sqrt{\rho_l D\sigma}$, where μ_l is the viscosity of the liquid. This tendency is similar to that of the model proposed in [4], whereas the values and the slope of the regression line of We_r are higher than We_c. This reveals that the mechanism leading to the variation of regime (V) from (VI), intercepted by (III), may relate to the dominance between the momentum in the rotating masses, which originally move toward the trajectories of the colliding droplets, and the momentum in the reflexive zone (Fig. 1c) of the merged droplet which can lead to oscillation. If the resultant of these momenta is large enough to overcome the surface and viscous forces, separation happens. This model would unify the mechanisms interpreted by the models based on rotational energy [1] and on stretching kinetic energy [2-3], respectively; thereby the discrepancy could be elucidated.

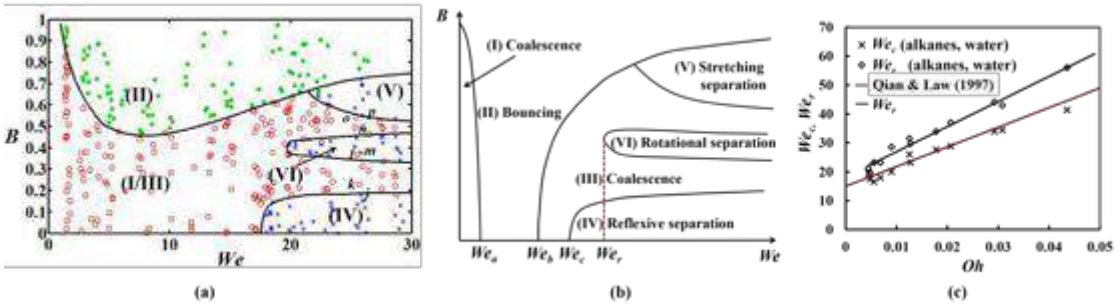

Fig .2 (a) Regime diagram for water droplets with 0.6 mm diameter. ○: coalescence, ×: separation, ✶: bouncing. (b) The new regime diagram of alkanes. (c) Comparison of We_c and We_r with the model based on energy conservation [4].

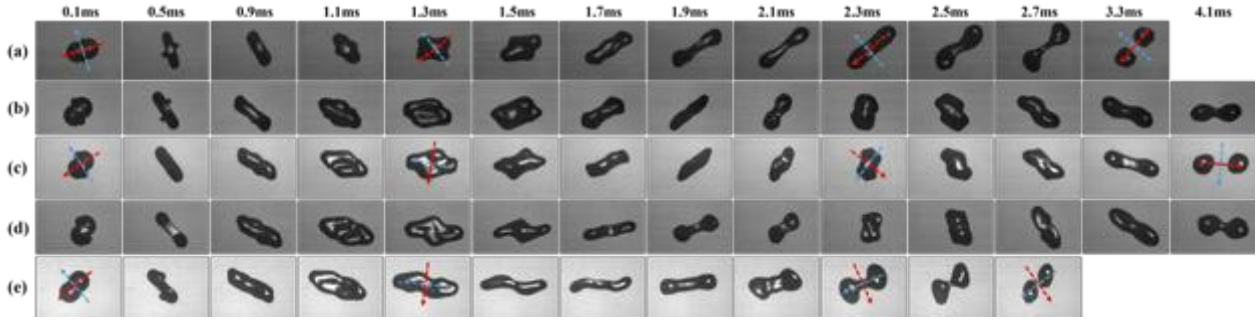

Fig. 3 Different sequences of water droplet collision with 0.6 mm diameter for points *j-p* (*We, B*) in Fig. 2(a). (a) *j* (25.8, 0.177), (b) *l* (25.7, 0.374), (c) *m* (25.9, 0.377), (d) n (26.5, 0.463), (e) *p* (26.0, 0.551).

CONCLUSIONS

In this work, a new regime of droplet separation following temporary coalescence is investigated. This phenomenon can be related to the competing dominance between the resultant of the momenta and the restraining of the surface and viscous forces. To eliminate the inconsistency raised in previous studies, we have been deriving a model which includes the reflexive, rotational, and stretching kinetic energies for comprehensive interpretation of three patterns of separations.

References

[1] Brazier-Smith P. R., Jennings S. G., Latham J.: The Interaction of Falling Water Drops: Coalescence. *Proc. R. Soc. Lond. A* **326**:393-408, 1972.

[2] Ashgriz N., Poo J. Y.: Coalescence and Separation in Binary Collisions of Liquid Drops. *J. Fluid Mech.* **221**:183-204, 1990.

[3] Jiang Y. J., Umemura A., Law C. K.: An Experimental Investigation on the Collision Behaviour of Hydrocarbon Droplets. *J. Fluid Mech.*, **234**:171-190, 1992.

[4] Qian J., Law C. K.: Regimes of Coalescence and Separation in Droplet Collision. *J. Fluid Mech.* **331**:59-80, 1997.

[5] Pan K. L., Law C. K., Zhou B.: Experimental and Mechanistic Description of Merging and Bouncing in Head-on Binary Droplet Collision. *J. Appl. Phys.* **103**:064901, 2008.

[6] Pan K. L., Chou P. C., and Tseng Y. J.: Binary Droplet Collision at High Weber Number. *Phys. Rev. E* **80**: 036301, 2009.

QUANTITATIVE MEASUREMENT OF ACOUSTIC SEPARATION OF SUBMICRON SOLID AEROSOLS

Ramin J. Imani*[1] and Etienne Robert[2]

[1]*Linné Flow Centre, KTH Royal Institute of Technology, 100 44 Stockholm, Sweden*
[2]*Polytechnique Montreal, Dep. of Mechanical Engineering, Montréal, Quebéc, Canada*

Summary An experimental study is carried out to measure the acoustic force on aerosol particles as a function of their size and quantify deviations, for very small particles, from the acoustophoresis theory established when the fluid is treated as a continuum. To do so, the size distribution is acquired as a function of position in a flow-through resonator. Considering the size range of the aerosols investigated and the mean free path of air molecules, the acoustophoretic phenomenon reported here falls in the transition and molecular regimes. An electrostatic transducer is used to generate a standing wave in the 50-80 kHz frequency range, concentrating the particles at the pressure nodes. A section of the flow is then sampled isokinetically and sent to the analysis system which provides quantitative data on size distribution. The results demonstrate the possibility of performing acoustic separation on aerosols with particle diameters as small as 100 nm.

INTRODUCTION

The use of ultrasonic standing wave to manipulate the position of particles suspended in a liquid in a microfluidic channel, i.e. acoustofluidics, is now a mature technique capable of performing advanced tasks such as sorting according to size, compressibility and density of particles [1]. For the last two decades, these developments in microfluidics have been driven mainly by life science applications as a tool for the treatment of cell or particle suspensions [2]. The adaptation of advanced acoustic manipulation techniques developed in the liquid phase to gaseous media can potentially bring desirable capabilities for a wide range of other scientific and industrial applications. However, there are limitations imposed by the nature of the gaseous media such as molecular effect at submicron length scales, high attenuation of acoustic energy in gases and the effect of turbulence which need to be taken into account. The acoustic separation of aerosols, especially at submicron scales, has received very limited attention from the research community relative to liquid suspensions and only a few works have addressed this situation experimentally. For instance, Anderson [3] and Budwig [4] studied the manipulation of micron size particles in an acoustic field using optical techniques and compared it with a theoretical model. Recently, Imani & Robert [5] investigated the separation of submicron solid particles in a flow-through resonator using a light scattering technique and quantified the efficiency of the process.

EXPERIMENTAL SETUP

With the work presented here, we aim to provide an experimental characterization of the acoustic separation of submicron aerosols in gases. The experimental setup consists of a rectangular acoustic separation channel, 30 mm wide and with a variable height (H) adjustable from 0 to 20 mm. A commercially available electrostatic broadband transducer is flush mounted in the bottom surface, generating ultrasound standing waves at frequencies in the 50 kHz to 80 kHz range with sound pressure levels up to approximately 155 dB (re 20 µpa). The side walls and a part of the reflector, exactly above the transducer, are made of Plexiglas and glass to provide optical access to the separation region along two perpendicular axes. A fluidized bed seeder is used to introduce a polydispersed suspension of TiO_2 particles in the acoustic channel and the size distribution measured using a Scanning Mobility Particle Sizer (SMPS, GRIMM 5410, with 11–1110 nm measurement range in 44 channels). To bring the particles flowing at a specific location in the resonator to the SMPS system, a section of the flow is sampled isokinetically between adjustable plates with spacing of 1 mm, as shown in Fig. 1 a). A laser sheet is inserted from the top to illuminate the channel mid-plane, parallel to the flow direction and just downstream of the transducer, thus revealing the nodal pattern in the resonator through light scattering. A tuning procedure [5] is used to find the resonance frequency that results in the best separation of particles, with a sample picture shown in Fig. 1 b) inverted for clarity with darker shades denoting regions with higher particle number density. The visualisation of the nodal pattern formed in the resonator ensures that the sampling slit captures the desired portion of the flow. In the example of Fig. 1 b), the channel height is approximately 6.86 mm and the excitation frequency is 75 kHz, resulting in a $\frac{3\lambda}{2}$ standing wave with three particle enriched-bands across the channel located $\frac{\lambda}{4}$, $\frac{3\lambda}{4}$ and $\frac{5\lambda}{4}$ from the transducer face.

*Corresponding author. Email: ramin@mech.kth.se

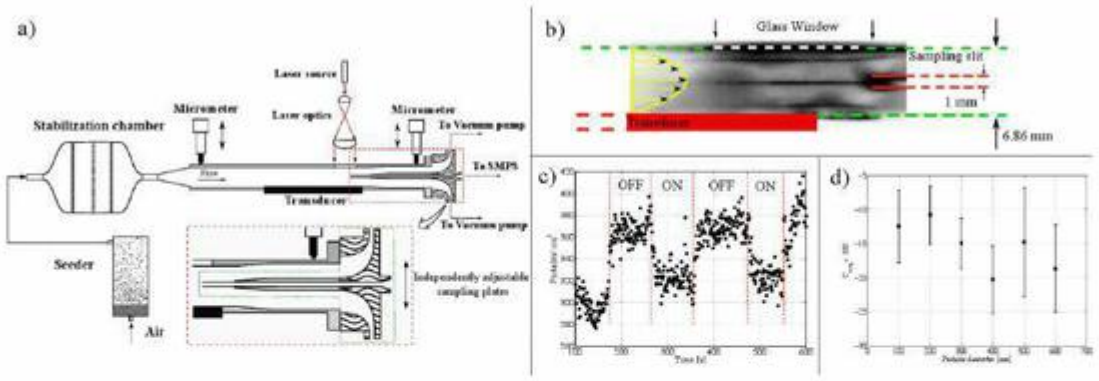

Figure 1: a) Schematic representation of the experimental setup. Inset shows a magnified view of the independently adjustable plates making the sampling slit. b) Visualisation of particle distribution within the channel using laser light scattering with 75 kHz excitation frequency, c) Time resolved signal of the particle number density for 300 nm diameter particles, acquired with the SMPS system. d) Relative change in the number density for different particle sizes.

RESULTS

Preliminarily experiments were performed to validate the sampling and analysis techniques with the sampling slit positioned $\frac{\lambda}{2}$ from the reflector when a $\frac{3\lambda}{2}$ standing wave is established in the channel, probing the flow at a pressure antinode, where the number density is expected to decrease when a standing wave is present in the channel. For these measurements, the sound excitation was turned on and off at time intervals of 2 minutes (50% duty cycle), for 40 minutes of total acquisition. Fig. 1 c) shows an example of the raw time-resolved signal for number density of 300 nm diameter particles. Jumps in particle concentration are clearly visible when the sound is turned on and off. To assess the effect of acoustic for particles of different sizes, a simple separation metric was defined as the difference between the particle number density with and without sound excitation divided by the particle number density without sound excitation. The procedure was repeated while monitoring different particle sizes. Results are presented in Fig. 1 d) for the 100 nm to 600 nm size range, with the error bar representing the standard deviation in the separation metric, showing a clear separation of TiO_2 aerosols, measured here for the first time for distinct particle sizes. The trend observed reveal that smaller particles appear to be more difficult to separate. This is expected from the equilibrium of forces on the suspended particles, dominated here by the primary axial radiation force and Stokes drag. The primary axial radiation force scales with the volume of the particles, while the Stokes drag scales with the particles radius. Therefore, the net force responsible for particle displacement to the pressure nodal planes is expected to decrease with the square of the particle radius. The trend observed in Fig. 1 d) confirms that the acoustic separation of smaller particles is indeed more difficult, but the dependence could not be quantitatively verified mainly because the 1mm thick sampling slit used results in significant spatial averaging. This will be addressed in future works.

CONCLUSION

The results demonstrate for the first time the size-resolved acoustic separation of submicron solid aerosols in the 100 nm to 600 nm size range. This hints that there might be critical size below which acoustic separation is impossible for a given acoustic pressure amplitude. It is reasonable to assume that the acoustic separation of particles with diameters on the order of 100 nm may not be properly modelled when the fluid is as a continuum as the flow around the particles falls well within the transition regime. The preliminary results presented here highlights desirable improvement to the facilities to be implemented in future works, such as increased temporal stability for the particle generation system and higher spatial resolution for the aerosol sampling that will result in a quantitative evaluation of the acoustic force as a function of particle size.

References

[1] F. Petersson, A. Nilsson, C. Holm, H. Jonsson, T. Laurell: Separation of lipids from blood utilizing ultrasonic standing waves in microfluidic channels, Analyst 129, 938-943, 2004.

[2] Laurell, T., Petersson, F., Nilsson, A.: Chip integrated strategies for acoustic separation and manipulation of cells and particles. Chem. Soc. Rev. 36,492-506, 2007.

[3] Anderson, M., Budwig, R. S., Line, K., Frankel, J.: Use of acoustic radiation pressure to concentrate small particles in an air flow. Ultrasonics Symposium,1, 481-484, 2002.

[4] Budwig, R. S., Anderson, M. J., Putnam, G., Manning, C.: Ultrasonic particle size fractionation in a moving air stream. Ultrasonics 50 (1), 26-31, 2010.

[5] Imani, Ramin J., Etienne Robert: Acoustic separation of submicron solid particles in air. Ultrasonics 63, 135-140, 2015.

THE EFFECT OF INHOMOGENEOUS MOBILITY ON IMMISCIBLE HELE-SHAW FLOW

S.J. Jackson, H. Power *, D. Giddings, and N. Johnson
Faculty of Engineering, Division of Energy and Sustainability, University of Nottingham, UK

Summary We investigate immiscible radial displacement in a Hele-Shaw cell with an inhomogeneous mobility using two coupled high resolution numerical methods. A Cartesian periodic perturbation in the Hele-Shaw plate separation gives rise to an inhomogeneous mobility, which we explore in a high capillary number regime. Under Cartesian periodic geometry, secondary tip splitting instabilities are significantly altered and different fingering structures are formed around an initially symmetric interface. Viscous fingers are sharpened when aligned with the periodic grid, as the fingers travel in regions of high permeability that accelerate the finger fronts. Fingers displacing at 45° to the axes show close resemblance to their uniform cell counterparts due to the homogeneity of the plate perturbation at the length scale of the interfacial displacement.

INTRODUCTION

During the immiscible displacement of a high viscosity fluid by the radial injection of a low viscosity fluid in a Hele-Shaw cell, interfacial instabilities can evolve forming complex viscous fingering patterns. Hele-Shaw cells are often used to provide insight into the more complex problem in porous media, whereby effects such as inhomogeneous permeability and wetting conditions play a significant role in the interface evolution. A spatially varying permeability can be considered in a Hele-Shaw cell context as a variation in the plate separation, giving rise to an inhomogeneous fluid mobility. Recently, several analytical and experimental works have shown that small changes in the plate separation in a Hele-Shaw cell can have significant effects on the interface evolution, allowing the control and suppression of fingering instabilities [1].

In rectilinear Hele-Shaw flows at low capillary numbers, the fingering instability can be completely suppressed in a converging cell if the capillary number is below a critical value [2]. This is due to the increase in transverse curvature in the flow direction that helps to stabilise the interface. When the capillary number is raised, the fingers are sharpened, as the finger fronts are more strongly accelerated than the finger sides [3]. In diverging cases, the front is decelerated leading to stubbier, less ramified fingers. These experimental findings have been confirmed by linear stability theory that analyses the growth rate and finger morphology at early time stages for small perturbations [1][4]. However, to fully understand the non-linear finger interactions and late stage interfacial evolution in radial Hele-Shaw flow subject to a variable plate separation requires extensive numerical simulation [4].

This short paper uses recently developed numerical methods to analyse late stage finger tip-splitting instabilities at high capillary number in periodic Hele-Shaw geometry, providing insight into the effects of inhomogeneous mobility on immiscible displacement.

THEORETICAL MODEL

For the flow in a Hele-Shaw cell, the depth averaged pressure P and 2D Darcy velocity u in each fluid region l can be expressed through Darcy's law: $u_i^l(x) = \circ\, M_l(x)\frac{\partial P_l}{\partial x_i}$. The mobility M_l is related to the fluid viscosity μ_l and plate spacing $b(x)$ by: $M_l(x) = b(x)^2/12\mu_l$. The flow field satisfies conservation of mass, which takes into account the varying plate separation: $\partial(b(x)u_i^l)/\partial x_i = 0$. At the interface between the fluids, the kinematic matching condition requires continuity of normal velocity, whilst the dynamic condition requires a jump in pressure equal to the capillary pressure. Substituting the Darcy velocity into the conservation of mass, and splitting the plate spacing, mobility and pressure into homogeneous ($^-$) and perturbed ($\tilde{}$) components we form the following equation:

$$m_l(x)\frac{\partial^2 \tilde{p}_l}{\partial x_i^2} + m_l(x)\frac{\partial^2 \bar{p}_l}{\partial x_i^2} + \frac{\partial \tilde{m}_l(x)}{\partial x_i}\frac{\partial \tilde{p}_l}{\partial x_i} = \circ\, \frac{\partial \tilde{m}_l(x)}{\partial x_i}\frac{\partial \bar{p}_l}{\partial x_i} \tag{1}$$

Where, $m_l(x) = b(x)M_l(x)$. Equation (1) represents a convection-diffusion transport equation, with a steady-state pressure field that must be solved in order to evaluate the 2D Darcy velocity at the interface. The inhomogeneous source term on the RHS of (1) can be found through the evaluation of the homogeneous pressure, which we constrain to satisfy Laplace's equation.

Equation (1) is solved to find the perturbed pressure using a strong form radial basis function finite collocation (RBF-FC) method with adaptive quadtree dataset that makes use of the symmetry of the problem and equivalent boundary conditions [5]. The homogeneous pressure is represented by the sum of a double layer potential density and a source injection term, which is solved using a boundary element method shown in [6]. Taking the normal derivatives of the pressure components at the interface, the normal interface velocity can be reconstructed and the interface advanced with a forward euler time stepping procedure.

*Corresponding author. Email: Henry.Power@nottingham.ac.uk

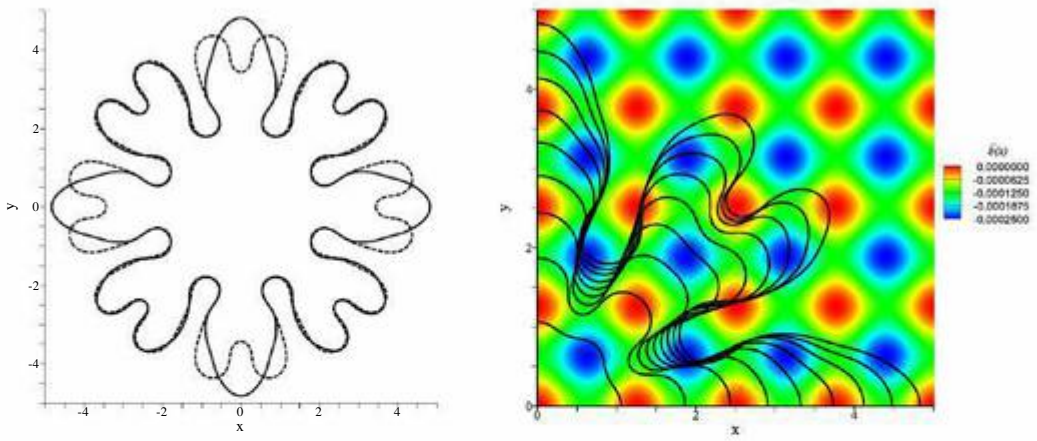

(a) (b)

Figure 1: (a) Interface plot at $t = 40$ for the periodic and uniform cell. **—** Cartesian periodic cell,**- - -** Uniform cell. (b) Interface plots at $\Delta t = 5$ increments from $t = 0$ to $t = 40$ for the periodic case overlaying the plate separation variation, $\tilde{}(x)$.

PERIODIC GEOMETRY RESULT

Here, we present interfacial displacement results for a 2D periodic Hele-Shaw cell geometry with a variation in plate spacing as: $\tilde{}(x) = \frac{A_s}{4}(\cos(f_s(x_1)) + \cos(f_s(x_2)) - 2)$ where, A_s is the wave amplitude and f_s is the wave frequency. For the case presented here we take $f_s = 5$, $A_s = 0.00025$ and $r_0 = 5\ cm$. We use a low mobility ratio between the fluids M_1/M_2 = 10, with the global capillary number $Ca_g = 2500$. $Ca_g = r_0 Q/\gamma M_2$, where Q is the injection flux,γ is the surface tension between the fluids and r_0 is the unperturbed bubble radius.

In Figure 1(a), the interface plots for the periodic cell and a corresponding uniform cell ($b(x) = 0$) can be seen. The finger evolving in the periodic cell at 45° to the horizontal (and corresponding symmetric fingers) has a completely different bifurcation mode to the fingers travelling parallel to the x- and y-axis. The fingers travelling parallel to the axes have been sharpened significantly due to continued acceleration of the finger tips, whereas the 45° finger has a very similar structure to the uniform case. The capillary number is large in the case presented here, meaning the transverse curvature has very little effect on the overall finger evolution.

The time evolution of the fingers with respect to the variation in plate separation are shown in Figure 1(b). The fingers parallel to the axes generally have their tips in regions of higher mobility compared to the sides of finger fronts as the interface displaces with time. This means that the homogeneous velocity is larger around the tip, creating a larger source term and perturbed velocity, sharpening the finger. This behaviour is similar in nature to the sharpening of the fingers in the rectilinear case presented by [3]. The sharpening of the fingers in the present case and the case in [3] are both caused by locally high sources of perturbed pressure that act to add a larger perturbed velocity to the finger tips compared to the sides.

For the finger that is displacing at 45° to the x-axis we see a morphology very similar to the uniform case. The bifurcation is only slightly different to the uniform case as the finger travels through both a peak and a trough in the cell separation before bifurcating. The 45° degree finger evolves in a cell whose plate spacing can be considered homogeneous at the scale of displacement, with a small perturbation term slightly altering the finger shape. However, the fingers parallel to the axes evolve in a highly inhomogeneous environment, where the tips travel through regions of high permeability (like a fracture) compared to the sides, resulting in highly sharpened fingers. The result in Figure 1 shows the significant differences in finger morphologies that can occur when the plate separation varies non-uniformly with respect to the flow direction.

References

[1] T.T. Al-Housseiny and H.A. Stone. Controlling viscous fingering in tapered Hele-Shaw cells. *Physics of Fluids*, 25(092102), 2013.

[2] T.T. Al-Housseiny, P.A. Tsai, and H.A. Stone. Control of interfacial instabilties using flow geometry. *Nature Physics*, 8:747 – 750, 2012.

[3] H. Zhao, J. Casedemunt, C. Yeung, and J.V. Maher. Perturbing Hele-Shaw flow with a small gap gradient. *Physical Review A*, 45:2455 – 2460, 1992.

[4] E.O. Dias and J.A. Miranda. Finger tip behaviour in small gap gradient flows. *Physical Review E*, 82(056319), 2010.

[5] S.J. Jackson, D. Stevens, D. Giddings, and H. Power. An adaptive RBF finite collocation approach to track transport processes across moving fronts. *Computers and Mathematics with Applications*, 71(1):278 – 300, 2016.

[6] S.J. Jackson, D. R. Stevens, H. Power, and D. Giddings. A boundary element method for the solution of finite mobility ratio immiscible displacement in a Hele-Shaw cell. *International Journal for Numerical Methods in Fluids*, 78(9):521 – 551, 2015.

STABILITY AND EQUILIBRIUM OF CHARGED ROTATING DROPS

M. A. Fontelos[1], V. J. García-Garrido[1], and U. Kindelán*[2]
[1]*Instituto de Ciencias Matemáticas (CSIC - UAM - UC3M - UCM). C/Nicolás Cabrera, 13-15, Campus de Cantoblanco, 28049 Madrid, Spain.*
[3]*Departamento de Ingeniería Geológica y Minera, Universidad Politécnica de Madrid, Alenza 4, 28003 Madrid, Spain.*

Summary In this contribution we use the Boundary Element Method to study the stability of a viscous conducting and charged drop, submmitted to rotation at constant angular momentum. This droplet is considered to be contained in another viscous and insulating fluid. Our numerical simulations show that the Rayleigh fissibility ratio at which charged drops become unstable decreases with angular momentum. We have also considered neutral drops subject to an electric field, in this case the critical value of the field which destabilizes the drop increases with rotation. Concerning equilibrium shapes, approximate spheroids and ellipsoids are obtained and the transition values between these two families of solutions is described.

DESCRIPTION OF THE MODEL

We are interested in the evolution, stability and equilibrium configurations of a viscous and conducting drop surrounded by another viscous and insulating fluid. Both fluids rotate about a common axis (e.g. the z axis) with constant angular momentum $\mathcal{L}$ and are assumed to be incompressible. We consider the following two situations: in the first, the droplet has an amount of charge Q distributed over its surface, and in the second, the drop is neutral and subject to a uniform external electric field of magnitude $\mathcal{E}_\infty$ along its axis of rotation. In this contribution we will study the case where viscous forces dominate inertial and Coriolis forces. This regime is known as Stokes flow and is characterized by Reynolds number $\ll 1$ and Ekman number$\gg 1$. Thus we have Stokes system:

$$\begin{cases} \circ\, \nabla \Pi^{(i)} + \lambda^{i-1} \Delta \mathbf{u}^{(i)} = \mathbf{0} & , \quad \text{in} \mathcal{D}_i\left(t\right) \\ \nabla \cdot \mathbf{u}^{(i)} = 0 & , \quad \text{in } \mathcal{D}_i\left(t\right) \end{cases} , \tag{1}$$

where $\mathcal{D}_1(t)$ is the region enclosed by the droplet and $\mathcal{D}_2(t)$ that of the surrounding fluid, $\lambda = \frac{\mu_2}{\mu_1}$, μ_i is the viscosity of fluid i, $\mathbf{u}^{(i)}$ is the velocity field of fluid i and, supposing that $\rho_2 \ll \rho_1$,

$$\Pi^{(1)} = p^{(1)} \circ\ \varrho_1 \frac{\mathcal{L}^2}{2\mathcal{I}^2} r_{axis}^2 \quad , \quad \Pi^{(2)} = p^{(2)}.$$

Where ρ_i is the density of fluid i and $\mathcal{I}$ is the moment of inertia of the drop.

We also impose that the normal component of the velocity is continuous across the boundary:

$$\mathbf{u}^{(1)} \cdot \mathbf{n} = \mathbf{u}^{(2)} \cdot \mathbf{n} \equiv \mathbf{u} \cdot \mathbf{n}\ , \tag{2}$$

and the kinematic condition:

$$v_n = \mathbf{u} \cdot \mathbf{n} \quad , \quad \text{on} \quad \partial\mathcal{D}\left(t\right)\ , \tag{3}$$

with v_n being the normal velocity of the free boundary.

Now, since the drop is considered an ideal conductor, the potential $\mathcal{V}$ must be constant inside and at the drop's surface, and all the charge is located at the boundary. The electric potential satisfies the Laplace equation:

$$\begin{cases} \Delta \mathcal{V} = 0 & , \quad \text{in } \mathcal{D}_2\left(t\right) \\ \mathcal{V} = \mathcal{V}_0 & , \quad \text{in } \partial\mathcal{D}\left(t\right) \\ \mathcal{V} \to \circ\, \mathcal{E}_\infty z + O(|\mathbf{r}|^{-1}) & , \quad \text{as } |\mathbf{r}| \to \infty \end{cases} , \tag{4}$$

and $\mathcal{V}_0$ has to be chosen so that the total charge is Q. At the boundary of the drop the surface charge density σ is given by the normal derivative of the potential, $\sigma = \circ\, \varepsilon_0 \frac{\partial \mathcal{V}}{\partial \mathbf{n}}$, with ε_0 the permittivity of the surrounding fluid and $\mathbf{n}$ is the outward unit normal to the surface of the droplet. At the surface of a conductor, the repulsive electrostatic force per unit area is:

$$\mathbf{F}_e = \frac{\varepsilon_0}{2} \left(\frac{\partial \mathcal{V}}{\partial \mathbf{n}} \right)^2 \mathbf{n} = \frac{\sigma^2}{2\varepsilon_0} \mathbf{n}\ ,$$

To solve (1) we set a balance between viscous stresses and capillary, electrostatic and centrifugal forces at the interface of both fluids:

$$\left(T^{(2)} \circ\ T^{(1)} \right) \mathbf{n} = \left(2\gamma\mathcal{H} \circ\ \varrho_1 \frac{\mathcal{L}^2}{2\mathcal{I}^2} r_{axis}^2 \circ\ \frac{\sigma^2}{2\varepsilon_0} \right) \mathbf{n} \quad , \quad \text{on } \partial\mathcal{D}_1\left(t\right)\ , \tag{5}$$

*Corresponding author. Email: ultano.kindelan@upm.es

NUMERICAL SOLUTION

We use the Boundary Element Method (BEM) to solve (1) and (4) with the boundary conditions (2), (3) and (5). More precisely, in each time step we use the BEM to solve a boundary integral equation (obtained from (1)) that describes the velocity of the drop's interface. In order to do this we need to calculate the mean curvature and the surface charge density (solving (4)) at each node of the surface mesh as well as the moment of inertia of the drop. Once the velocity field is known, we can move the boundary mesh in the normal direction (the tangential component of velocity is not considered because it only redistributes the nodes over the boundary) with an Euler explicit scheme. The algorithm is implemented to be adaptive, since a good resolution is needed in regions of the mesh where singularities develop.

DISCUSSION

In the presentation we will discuss the evolution and stability of axisymmetric rotating drops in electric fields and the effects of rotation on dynamic Taylor cones, regarding the latter it is worth noting that when the drop becomes unstable, a two-lobed structure forms where a pinch-off occurs in finite time or dynamic Taylor cones (in the sense of [1]) develop, whose semiangle, for small $\mathcal{L}$, remains the same as if there was no rotation in the system. Finally, a 3D stability analysis is conducted for charged rotating drops or rotating drops immersed in an electric field. In figure 1 we depict the diagram that summarize this analysis.

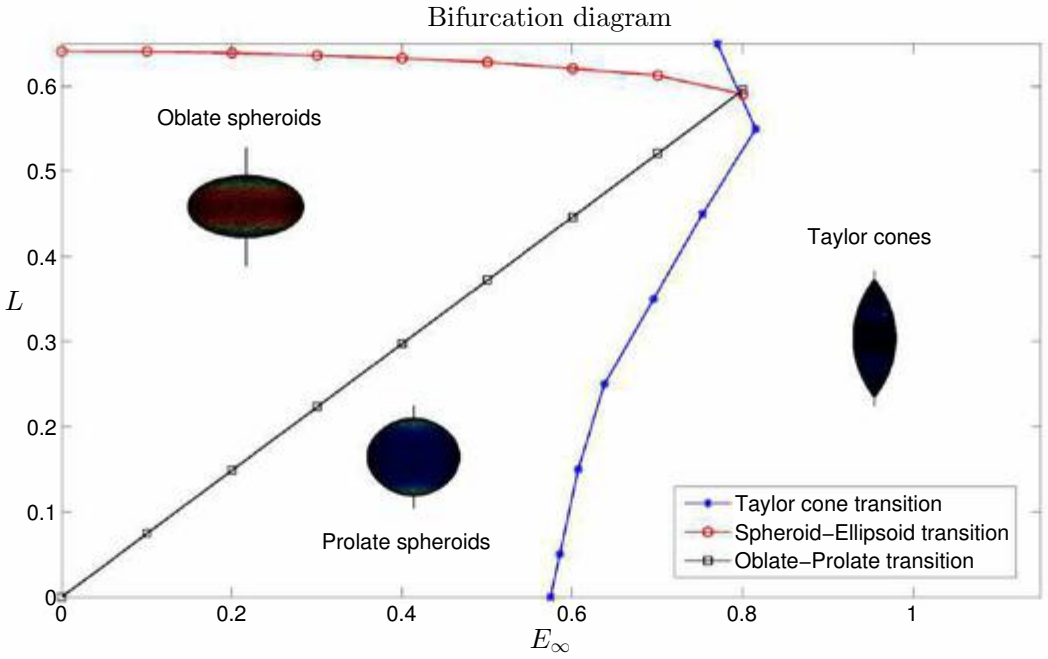

Figure 1: Sketch of the bifurcation diagram summarizing numerical results (symbols) for the transition points between different regimes obtained with the full 3D model.

Note: Most of this work has been published in [2] and [3].

References

[1] S. I. Betelú, M. A. Fontelos, U. Kindelán, O. Vantzos, Singularities on charged viscous droplets, Phys. Fluids **18** (2006) 051706.

[2] V. J. García-Garrido, M. A. Fontelos, U. Kindelán, Evolution, stability and equilibrium shapes of rotating drops which are charged or subject to electric fields Q. Jl Mech. Appl. Math November 2013. doi:10.1093/qjmam/hbt015.

[3] V. J. García-Garrido, *The Mathematical models of rotating droplets which charge or subject to electric fields*. PhD Thesis, Universidad Autónoma de Madrid 2014.

EFFECTS OF A WATER HAMMER AND CAVITATION ON THE MOTION OF A GAS-LIQUID INTERFACE

Akihito Kiyama[1], Chihiro Kurihara[1], Keisuke Hayasaka[1] & Yoshiyuki Tagawa [*1]
[1]*Department of Mechanical systems engineering, Tokyo University of Agriculture and Technology, Tokyo, Japan*

Summary The interaction among a water hammer and the motion of a gas-liquid interface is of great importance in various fluid systems. We recently reported a simplified model for clarifying the interaction. However, the most dominant event (i.e. the pressure wave propagation) of the model has not been experimentally verified. This study measures the pressure near the interface in order to experimentally reveal the mechanism of the interface motion. We impact a liquid-filled container and generate a pressure wave in a liquid. The pressure impulse *in the early stage of the wave propagation event* is compared with the maximum volume of cavitation bubbles. Remarkably, a linear relation between the pressure impulse and bubble volume is found. The trend is the same as the relation between the interface velocity and the bubble volume we beforehand reported. It indicates that the pressure impulse decides the motion of the interface.

INTRODUCTION

Impacting a container partially filled with a liquid leads to interesting motion of a gas-liquid interface [1]. Antkowiak et al. [2] reported that a focused liquid jet emerges from a curved interface. They assumed the incompressible fluid and then described velocity field and pressure field near the interface based on the "Pressure Impulse Approach". Recently, we investigated that the influences of the water hammer on the motion of the interface [3]. We reported two characteristic motions: (i) the periodical vibration of the interface caused by the reflection of pressure waves; (ii) the jet velocity increment due to the cavitation appearance. The jet velocity can be up to twice faster than that of the jet with no cavitation. Both phenomena are obviously related to the effect of water hammer and hence "Pressure Impulse Approach" was not applicable. We paid attention to the propagation of pressure waves before jet formation and proposed simplified model for describing phenomena. Especially we considered that the scaling law, which is based on the maximum volume of bubbles, is applicable to explaining the jet velocity. We showed that the jet velocity increases linearly as the bubble volume increases. The model [3] reasonably describes the motion of the interface.

However, pressure in the liquid, which is an essential part of the model, has not been measured directly. The measurement of pressure near the interface is meaningful for understanding the detailed mechanism of the interaction between the jet motion and cavitation. In this study, we construct a new experimental setup in order to measure pressure in the liquid. We calculate the pressure impulse near the interface and compare it with the bubble volume. Finally, we revisit the scaling law [3] and give an interpretation on the mechanism of the jet velocity increment.

MODEL

The model [3] is based on the water hammer theory assuming linear waves since the pressure perturbations are small enough [4]. In the model, we consider a stationary test tube filled with the liquid. One end of the test tube is closed and the other end has the interface. The tube is suddenly accelerated by the impact and then starts to move with the velocity V. At this moment, a pressure wave generates in the liquid. Pressure waves continue to propagate in the liquid (Figure 1a). The pressure of the pressure wave p can be estimated as $p=\rho cV$, where ρ and c are the density and the sound speed, respectively.

When cavitation nuclei exist in a liquid and pressure in the liquid becomes negative (state 3 in Figure 1b), cavitation may occur. During bubble expansion, pressure in a liquid relaxes from negative to atmospheric pressure. Expansion wave propagating through the liquid is attenuated during pressure relaxation. When the expansion wave in state 3 is completely attenuated, the interface holds faster speed than the tube bottom (Figure 1b, green line). Based on the model, the maximum jet velocity is twice larger than that of the test tube. The model indicates that the dominant factor for deciding the jet velocity increment is the extent of pressure relaxation at state 3.

EXPERIMENTAL SETUP

The aim of this experiment is to investigate the relation between the pressure impulse and the bubble volume. Thus, here we do not record the jet. Our experimental setup is shown in Figure 1c. We fill the glass test tube (inner diameter d=8.0 mm, length L=90 mm) with pure water (density ρ=1,000 kg/m^3, sound speed c=1483 m/s). The shape of the free surface is almost flat since we aim to easily capture the reflection of pressure waves. We strike the tube bottom and move the tube with the velocity V. The tube velocity V, which is only the controllable parameter, is varied from 0.076 m/s to 0.596 m/s. We insert a hydrophone probe (Mueller Instruments) near the interface (60 mm from the tube bottom) and measure the pressure.

Cavitation bubbles are illuminated by a LED light and filmed by a high-speed camera (Photron, Fastcam SA-X), whose frame rate and spatial resolution are 100,000 f.p.s. and 0.1 mm/pixel, respectively. Matlab image processing is applied to compute the bubble volume. The experiment is repeated 5 times for each condition.

* Corresponding author. Email: tagawayo@cc.tuat.ac.jp.

RESULTS AND DISCUSSION

Typical time histories of pressure are shown in Figure 2a. Blue and red lines show the case with no cavitation (V=0.154 m/s) and the case with cavitation (V=0.366 m/s), respectively. Vertical and horizontal axes show the pressure in gauge normalized by water hammer pressure ρcV and the time normalized by a time scale L/c, respectively. The pressure of the first peak is $p \sim \rho cV$ for both cases. When cavitation does not occur (blue line in Figure 2a), pressure waves continue to propagate in the liquid. When cavitation occurs (red line in Figure 2a), the pressure goes back to the atmospheric pressure. The timing for starting pressure relaxation fairly matches with that of bubble appearance. It implies that the pressure relaxation is caused by cavitation, which agrees with the model [3].

The relation between pressure impulse P and the bubble volume Ω is presented in Figure 2b. According to that the motion of the interface is dominantly characterized by the event until the end of state 3 in Figure 1a, we calculate P as the integration of pressure from t=0 to t=4L/c. Each marker presents the mean value for the same tube velocity V and error bar shows the standard deviation.

When cavitation does not occur, pressure impulse P is nearly equal to zero (blue marker in Figure 2b). On the other hand, when cavitation occurs (red marker in Figure 2b), pressure impulse P increases with bubble volume Ω. It indicates that the extent of pressure relaxation is described by bubble volume Ω. If the revisiting discussion in previous study [3] is allowable, we mention that the jet velocity may be decided by the pressure impulse P in the early stage ($t \sim 4L/c$) of the event.

CONCLUSIONS

In this paper, we experimentally revisit the effect of a water hammer on the motion of the interface. We construct a new experimental setup based on the model [3] in order to measure pressure near the interface. We find that the proportional relation between the pressure impulse P and the bubble volume Ω, which was not discussed in the previous study [3]. According to this relation, the jet velocity is supposed to be decided by the pressure impulse P in the early stage ($t \sim 4L/c$) of the event.

This work was supported by JSPS KAKENHI Grant Number 26709007.

References

[1] Milgram J. H.: The motion of a fluid in a cylindrical container with a free surface following vertical impact. *J. Fluid Mech* **37**:435-448, 1969.

[2] Antkowiak A., Bremond N., Le Dizes S. and Villermaux, E.: Short-term dynamics of a density interface following an impact. *J. Fluid Mech* **577**:241-250, 2007.

[3] Kiyama A., Tagawa Y., Ando K. and Kameda M.: Effects of a water hammer and cavitation on jet formation in a test tube. *J. Fluid Mech* **787**:224-236, 2016.

[4] Thompson P. A., Compressible-Fluid Dynamics. McGraw-Hill, 1972.

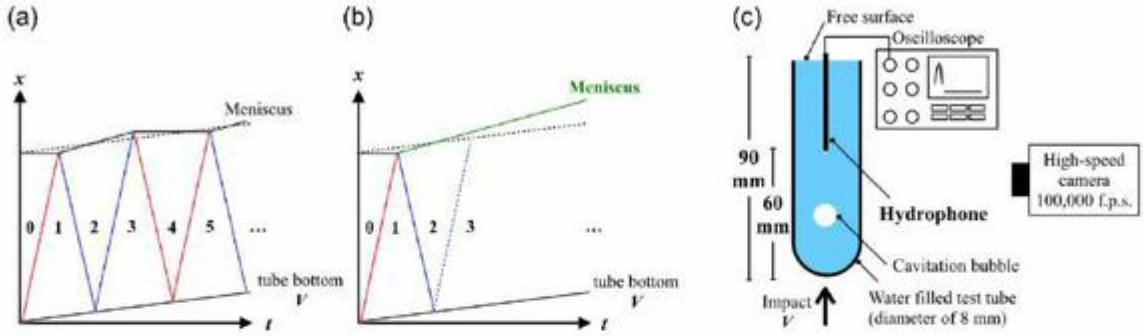

Figure 1: (a) x-t diagram of the wave propagation model for the case with no cavitation [3]. (b) x-t diagram for the case with cavitation. Red line shows a compression wave and blue line shows an expansion wave in the x-t diagram. (c) the schematic of our experimental setup.

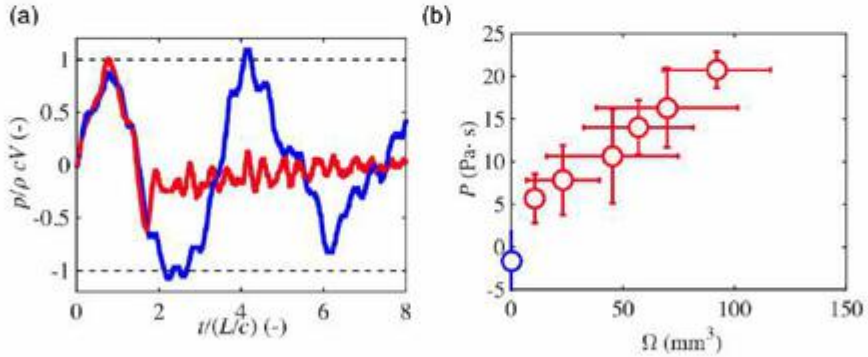

Figure 2: (a) typical time histories of pressure near the free surface (L=60 mm). Red marker shows the data with cavitation and blue marker shows the data with no cavitation. Dashed lines show the water hammer pressure $\pm\rho cV$. (b) the pressure impulse P vs. the bubble volume Ω.

OSCILLATION AND PINCHOFF OF AXISYMMETRIC DROPLETS

Kazuki Koga [*1] and Mitsuaki Funakoshi[1]

[1]*Department of Applied Analysis and Complex Dynamical Systems, Graduate School of Informatics, Kyoto University, Yoshida Honmachi, Sakyo-ku, Kyoto 606-8501, Japan*

Summary Oscillation and pinchoff of axisymmetric droplets are studied numerically using the model of axisymmetric vortex sheets with surface tension in inviscid fluids. Droplets are initially at rest and biconcave, and then evolve under the action of surface tension. Oscillation of a droplet is observed for a sufficiently small depth of the initial dent. For a large value of this depth that causes the high curvature of a vortex sheet, however, it pinches off at two points and breaks into two end-droplets and a satellite droplet. We observe that a significantly small satellite droplet is generated for the smallest depth of the initial dent within the region where pinchoff occurs.

FORMULATIONS

There have been many numerical studies on the motion of axisymmetric droplets with the boundary integral method. In the present paper, we examine the time evolution of axisymmetric droplets of high curvature by using the boundary integral method and numerical techniques of high accuracy developed in [1] and [2] recently. In our simulations, biconcave droplets with different depths of the dents are released from rest and evolve under the action of surface tension. We observe the oscillation of the droplets or their pinchoff in a finite time depending on their depth of the initial dent. Our main purpose is to find the relation between the initial shape (and initial distribution of mean curvature) of the droplets and their final state.

We consider the irrotational motion of two inviscid, incompressible fluids of the same density in $\mathbb{R}^3$ separated by a closed smooth surface S. For simplicity, let the densities be equal to 1. The governing equations for the fluid velocity $\boldsymbol{u}$ and pressure p in $\mathbb{R}^3\backslash S$ are the Euler equations, the equation of continuity and the condition of no vorticity written as

$$\partial_t \boldsymbol{u} + (\boldsymbol{u}\cdot\boldsymbol{\nabla})\boldsymbol{u} = -\boldsymbol{\nabla} p, \qquad \boldsymbol{\nabla}\cdot\boldsymbol{u} = 0, \qquad \boldsymbol{\nabla}\times\boldsymbol{u} = 0, \qquad \text{in } \mathbb{R}^3\backslash S, \tag{1}$$

where t is the time, and the external forces are neglected . In addition, there are three boundary conditions given by

$$[\boldsymbol{u}]_S\cdot\boldsymbol{n} = 0, \qquad [p]_S = \tau\kappa, \qquad \text{on } S, \qquad \boldsymbol{u}\to 0 \quad \text{as} \quad |(x,y,z)|\to\infty. \tag{2}$$

Here, $\boldsymbol{n}$ is the unit normal vector of S towards the outer fluid, κ is the mean curvature of S, and τ is the surface tension coefficient. Brackets $[\cdot]_S$ give the jump of physical quantities across S. The first condition in (2) is the kinematic boundary condition on S, which forces S to move with both fluids. The second condition, called the Laplace-Young boundary condition, represents the effect of surface tension on S. The last condition is the far-field condition for the fluid velocity.

We assume that the flow possesses axial symmetry. That is, in cylindrical coordinates (r,φ,z), all the physical quantities are independent of the azimuthal coordinate φ and depend only on r, z, and t (see Fig.1(a)). Therefore, the fluid velocity $\boldsymbol{u}$ can be written as

$$\boldsymbol{u} = u_r(r,z,t)\ \boldsymbol{e}_r + u_\varphi(r,z,t)\ \boldsymbol{e}_\varphi + u_z(r,z,t)\ \boldsymbol{e}_z, \tag{3}$$

where $\boldsymbol{e}_r$, $\boldsymbol{e}_\varphi$, and $\boldsymbol{e}_z$ are unit vectors in the r, φ, and z directions, respectively. The flow without swirl defined by $u_\varphi(r,z,t)\equiv 0$ is assumed. The time evolution of the shape of the axisymmetric free boundary S is specified by the motion of a curve on the plane of $\varphi = const.$ called a plane curve. To introduce a Lagrangian representation, we define the following mappings with the parameter $\alpha\in[0,\pi]$:

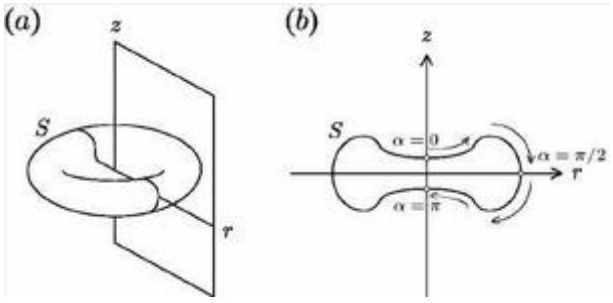

Figure 1: Axial symmetry and parametrization.

$$\boldsymbol{X}(\alpha,t) = (z(\alpha,t), r(\alpha,t)), \qquad \mu(\alpha,t) = -[\phi]_S(\boldsymbol{X}(\alpha,t),t), \tag{4}$$

where $\boldsymbol{X}(\alpha,t)$ is the location of a point on S specified by α and t, and ϕ is the velocity potential satisfying $\boldsymbol{u} = \boldsymbol{\nabla}\phi$. An example of the parametrization of initial plane curve of a droplet is shown in Fig.1(b). Upper and lower points of the curve on the z axis correspond to $\alpha = 0$ and $\alpha = \pi$ for all t, respectively. The curved arrows along the plane curve in the right half plane indicate the direction of increasing α.

*Corresponding author. Email: k.kazuki@acs.i.kyoto-u.ac.jp

If the definition $\partial_t \boldsymbol{X} = \dfrac{1}{2}\lim_{h\to+0}(\boldsymbol{u}(\boldsymbol{X}+\boldsymbol{n}h,t)+\boldsymbol{u}(\boldsymbol{X}-\boldsymbol{n}h,t))$ is adopted, the equations governing the time evolution of $\boldsymbol{X}(\alpha,t)$ and $\mu(\alpha,t)$ are expressed as

$$\begin{cases} \partial_t z(\alpha,t) = \dfrac{1}{2\pi}\ \text{p.v.}\displaystyle\int_0^\pi \mu'_\alpha \frac{1}{\rho_2}\left[F(\lambda) - \frac{(z'-z)^2+r^2-r'^2}{\rho_1^2}E(\lambda)\right]d\alpha', \\ \partial_t r(\alpha,t) = \dfrac{1}{2\pi r}\ \text{p.v.}\displaystyle\int_0^\pi \mu'_\alpha \frac{z'-z}{\rho_2}\left[F(\lambda) - \frac{(z'-z)^2+r^2+r'^2}{\rho_1^2}E(\lambda)\right]d\alpha', \\ \partial_t \mu(\alpha,t) = \tau\kappa \end{cases} \tag{5}$$

where, for example, z and z' are values at α and α' respectively, and the subscript α implies the differentiation with respect to α or α'. Here, $\rho_1^2 = (z'-z)^2+(r'-r)^2$, $\rho_2^2 = (z'-z)^2+(r'+r)^2$, $F(\lambda)$ and $E(\lambda)$ are the complete elliptic integrals of the first and second kind, and $\lambda^2 = 4r'r/\rho_2^2$. The symbols p.v. in front of integrals indicate that they are interpreted as the principal value integrals.

NUMERICAL RESULTS

We employ the Crank-Nicolson discretization used in [1] for the time integration and the modified dBM approximation proposed in [2] for the evaluation of the singular integrals in (5). Initial shapes of droplets at $t = 0$ can be determined by giving $\theta = \tan^{-1}(r_\alpha/z_\alpha)$, the tangent angle to a plane curve for all α, with a uniform grid spacing satisfying $|\boldsymbol{X}_\alpha|(\alpha,0) = const.$ The initial condition used in the present study is written as

$$\theta(\alpha,0) = \frac{\pi}{2} + \alpha - 0.5\sin 2\alpha - A\sin^k 2\alpha, \qquad \mu(\alpha,0) = 0, \qquad L(0) = L_0, \tag{6}$$

where $L(t)$ is the length of the plane curve at the time t. The constant A in (6) determines the depth of the initial dent. For positive A, the resulting shape of the droplet is biconcave. Larger k yields higher curvatures near the points where the sign of the curvature of a plane curve changes. The second condition of (6) means that the droplet is initially at rest. In the present paper, we show a few results for $\tau = 2$, $k = 1$, and $L_0 = 2\pi$.

For $A = 0$, the shape of the droplet oscillates, similarly to the motion of a droplet obtained in [1] for a different initial condition. Its initial shape has no dent, and it repeats the deformation between this initial shape and the shape of a capsule (see Fig.2(a)). For A =0−0.4125, the droplet still oscillates, but high curvatures corresponding to the pinching near $(z,r) = (0,0)$ are observed for A close to 0.4125. For A =0.421−0.5, the droplet pinches off at two points on the symmetric axis and breaks into two end-droplets and a satellite droplet. For smaller A within this region, the size of the generated satellite droplet is smaller, and the pinchoff time is larger. As an example illustrating this property, the shapes just before the pinchoff for $A = 0.421$ and $A = 0.5$ are shown in Figs.2 (b) and (c) respectively. For $A = 0.421$, the sizes of the satellite droplet in the z and r directions are 0.076 and 0.014 respectively and the pinchoff time is $t = 2.39$, while for $A = 0.5$ the sizes are 1.20 and 0.19 and the pinchoff time is $t = 1.81$.

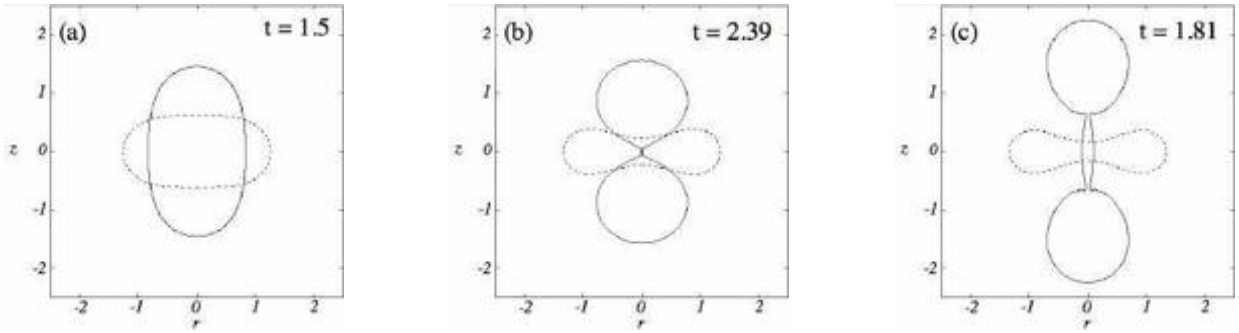

Figure 2: Initial shapes (dashed lines) and axially elongated shapes (solid lines) at t shown in the figures : (a) $A = 0$, (b) $A = 0.421$, and (c) $A = 0.5$.

We will also show results for k larger than 1 in the presentation.

References

[1] Nie Q.: The Nonlinear Evolution of Vortex Sheets with Surface Tension in Axisymmetric Flows. *J. Comp. Phys.* **174**: 438-459, 2001.

[2] Nitsche M.: Axisymmetric Vortex Sheet Motion: Accurate Evaluation of The Principal Value Integral. *SIAM J. Sci. Comput.* **21 (3)**: 1066-1084, 1999.

THE COILING AND WHIPPING INSTABILITY OF AN ELECTRICALLY CHARGED LIQUID JET

Tiantian Kong[1, 2, 3, a)], Liqiu Wang[2,3,a)], Howard A. Stone[4] & Ho Cheung Shum[2,5,a)]
[1]*Guangdong Key Laboratory for Biomedical Measurements and Ultrasound Imaging, Department of Biomedical Engineering, School of Medicine, Shenzhen University, Shenzhen, China*
[2] *Department of Mechanical Engineering, University of Hong Kong, Hong Kong*
[3] *HKU-Zhejiang Institute of Research and Innovation (HKU-ZIRI), Hangzhou, Zhejiang, China*
[4]*Department of Mechanical and Aerospace Engineering, Princeton University, Princeton, New Jersey, USA*
[5]*HKU-Shenzhen Institute of Research and Innovation (HKU-SIRI), Shenzhen, Guangdong*

Summary We show and characterize the relative importance of the coiling and whipping instabilities of an electrified liquid jet, which dictate the dynamic path of the jet among three regimes include "coiling jet", "whipping jet" and "straight jet".

.INTRODUCTION

The dynamics of an electrically charged jet is fascinating with enormously rich underlying physics and wide applications[1,2]. The applied electric stress deforms the liquid interface into a jet, which either breaks up into droplets or elongates, enabling the production of nano-sized particles or fibers[3]. The application of an electric field enables multiple unstable modes. For example, the repulsion between surface charges has been known to trigger the whipping instability[1,2]. The tangential stress to which the surface charges are subjected can induce the "liquid coiling instability"[4]. The whipping instability of electrified jets and the coiling of un-charged jet have been extensively investigated separately[1–3,5–7]. However, the transition from a charged coiling jet to a whipping one has not been systematically reported. Moreover, few comprehensive studies are available, to describe the relative importance of the coiling and whipping instabilities when a liquid jet is electrified. To address these, we have characterized the onset of the coiling and whipping instabilities for liquid jets as the charging voltage is tuned. We show that a critical capillary number and a representative electro-capillary number determine the dynamics of the charged jet, among regimes of "coiling jet", "whipping jet" and "straight jet" (Fig.1).

EXPERIMENTS

We formed a straight jet of glycerine in paraffin oil by a metallic nozzle (d_{nozzle}~0.92mm), and the aspect ratio of the jet was controlled by the volumetric flow rate and the distance between the nozzle and substrate (L~10mm). The straight jet was charged by connecting the nozzle and substrate to a high voltage power supply (Fig.1 (a)). The interfacial tension of the system was tuned by varying the concentration of the surfactants, Tween 20 and Span 80, in glycerine and paraffin oil, respectively. The dynamic behaviors of the jet is visualized and recorded by a using a high-speed camera (Phantom V 9.1) coupled with a zoom lens (Nikon).

RESULTS

When a straight jet is charged with an increasing voltage, it accelerates towards the substrate connecting the opposite electrode and thus thins. The subsequent impact of the jet with a solid substrate requires a dramatic deceleration that gives rise to a compressive stress, resulting in jet bending at a sufficiently large compression (Fig.1(b)). Thus, charging a liquid jet can trigger the coiling instability, where a jet starts to rotate steadily[7]. A coiled jet has more interfacial area than a straight one, which is resisted by the interface tension. The electric compression relative to the interfacial tension can be characterized by the capillary number of the jet, $Ca=\mu v/\gamma$, where μ,v and γ are the viscosity, velocity and interfacial tension of the liquid jet respectively. We show that with increasing applied charging voltage, which corresponds to an increasing Ca, coiling occurs as Ca reaches a magnitude of ~10^1 (Fig. 2(a)).

Meanwhile, when a charged jet is subjected to an electric field, charges migrate from the bulk to the interface and accumulate. The surface charge density rises sharply as the applied voltage increases. As a result, the repulsion between surface charges becomes significant. When the charge repulsion dominates surface tension which is stabilizing, the liquid jet develops a lateral instability and starts to whip violently and chaotically[8] (Fig. 2(b)). In this manner, the whipping instability is induced. The charge repulsion relative to surface tension can be characterized by an electro-capillary number, $\varepsilon\varepsilon_0E^2a_{average}/\gamma$, where ε, ε_0, E, a_{average} are the permeability of vacuum, the dielectric constant of the liquid, the applied electric field strength, and the initial average radius of the straight jet, respectively. Experimentally, the electro-capillary number increases with the increase of the applied electric field. When $\varepsilon\varepsilon_0E^2a_{average}/\gamma$ is on the order of 10^0, we observe a transition from a stable jet to a whipping jet (Fig. 2(b)). To summarize the effect of electric charging, we characterize the dynamics of the liquid jet using a phase diagram with axes of Ca and $\varepsilon\varepsilon_0E^2a_{average}/\gamma$ shown in Fig. 3(a). With increasing charging voltage, both Ca and $\varepsilon\varepsilon_0E^2a_{average}/\gamma$ increase. The relative importance of these two numbers dictates the dynamic path of the charged jet. For instance, if a critical Ca is reached, the jet first enters the "coiling" regime; as the charging voltage increases further, the jet starts to "whip" (Fig. 3((b)). However, if a critical $\varepsilon\varepsilon_0E^2a_{average}/\gamma$ is attained before Ca, a straight jet directly start to "whip" without any observable "coiling" (Fig. 3(c)).

[a)] Corresponding author. Email: ttkong@szu.edu.cn, lqwang@hku.hk, ashum@hku.hk.

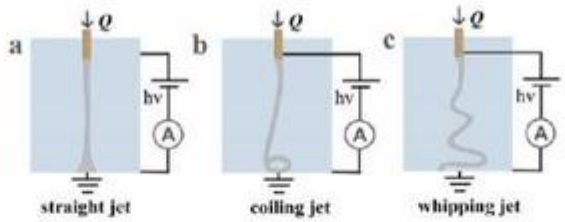

Figure 1. Schematic showing (a) a straight jet in insulating oil is charged by high-voltage (hv) power supply, and the possible dynamic behaviors of the jet, including (b) coiling jet, and (c) whipping jet.

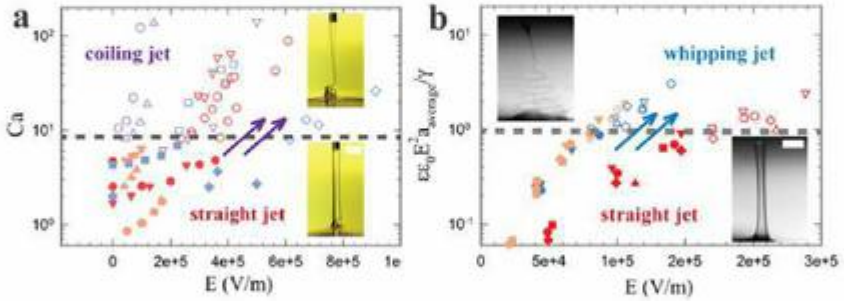

Figure 2. (a) The capillary number *Ca* as a function of the applied potential gradient E. Open symbols denote "coiling" (insert: top); filled symbols denote "straight jet" (insert: bottom). Red, pink, blue and purple colors denote liquid lecithin from soy bean, glycerine with 10wt% tween20, polyglycerolpolyricinoleate and tween20 respectively; shapes of symbols correspond to different volumetric flow rates. Purple arrows indicate the transition from "straight jet" to "coiling jet"; (b) The electro-capillary number $\varepsilon\varepsilon_0E^2a_{average}/\gamma$ as a function of the applied potential gradient E. Open symbols denote "whipping jet" (insert: top); filled symbols denote "straight jet" (insert: bottom). Red, pink and blue colors denote interfacial tensions of 3.5mN/m^2, 1.5 mN/m^2 and 0.8 mN/m^2 respectively; shapes of symbols correspond to different volumetric flow rates. The scale bar is 2mm. Blue arrows indicate the transition from "straight jet" to "whipping jet". Both diagrams are obtained with the nozzle diameter~0.92mm and a distance between the nozzle and the substrate, *L*~10mm.

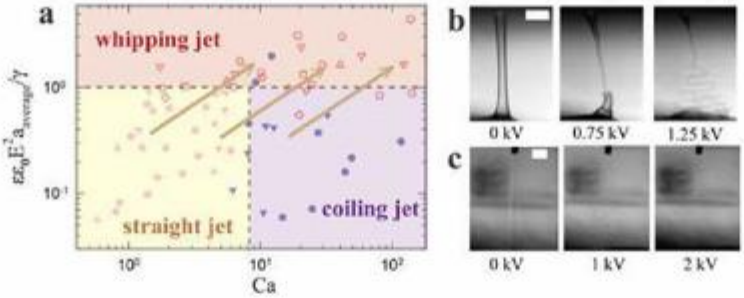

Figure 3. (a) A phase diagram of an electrically charged liquid jet: The top, bottom left and right are "whipping jet" (open red symbols), "straight jet" (filled pink symbols) and "coiling jet" (filed purple symbols) respectively. Arrows indicate the dynamic path of the liquid jet; A series of high speed images showing (b) a transition from "straight jet" to "coiling jet" and then to "whipping jet"; The scale bar is 2mm. (c) a transition from "straight jet" to "whipping jet" directly. The phase diagram is obtained with *L*~10mm.

CONCLUSIONS

We have studied the dynamic behaviors of an electrically charged jet in an axial electric field. We show that as the charging voltage increases, both coiling and whipping instability can be triggered. We emphasize the relative importance of two dimensionless numbers, *Ca* and $\varepsilon\varepsilon_0E^2a_{average}/\gamma$, which dictates the dynamic path of the jet as the charging voltage increases. Our results enrich the physical understanding of an electrically charged jet, and enable the control of jet behaviors for applications such as electrohydrodynamic 3D printing and patterning.

References

[1] M.M. Hohman, M. Shin, G. Rutledge, and M.P. Brenner, Phys. Fluids **13**, 2201 (2001).

[2] M.M. Hohman, M. Shin, G. Rutledge, and M.P. Brenner, Phys. Fluids **13**, 2221 (2001).

[3] Y.M. Shin, M.M. Hohman, M.P. Brenner, and G.C. Rutledge, Appl. Phys. Lett. **78**, 1149 (2001).

[4] T. Kong, J. Li, Z. Liu, Z. Zhou, P.H.Y. Ng, L. Wang, and H.C. Shum, Sci. Rep. In Print (2016).

[5] S. V. Fridrikh, J.H. Yu, M.P. Brenner, and G.C. Rutledge, Phys. Rev. Lett. **90**, 144502 (2003).

[6] M. Le Merrer, D. Quéré, and C. Clanet, Phys. Rev. Lett. **109**, 8 (2012).

[7] N.M. Ribe, M. Habibi, and D. Bonn, Annu. Rev. Fluid Mech. **44**, 249 (2012).

[8] J. Guerrero, J. Rivero, V.R. Gundabala, M. Perez-Saborid, and a. Fernandez-Nieves, Proc. Natl. Acad. Sci. **111**, 13763 (2014).

DYNAMIC DEFORMATION OF TOROIDAL DROPS IN COMPRESSIONAL STOKES FLOW

Olga M. Lavrenteva[1a)], Michael Zabarankin[2], Irina Smagin[1] & Avinoam Nir
[1] *Department of Chemical Engineering, Technion-Israel Institute of Technology, Haifa 32000, Israel*
[2] *Department of Mathematical Sciences, Stevens Institute of Technology, Castle Point on Hudson, Hoboken, NJ 07030, USA.*

Summary The deformation of toroidal drop in an axisymmetric compressional viscous flow (also known as bi-axial extension) is studied making use of boundary integral equations. It is demonstrated that the initially circular torus cross section first deforms to a shape close to elliptic. Then, depending on the governing parameters and initial shape, the torus collapses to the center, expands indefinitely or assumes a stationary shape.

INTRODUCTION

Non spherical droplets are of interest in various areas, and recently also as potential carriers of drugs (Champion et al., 2007) or building blocks for more complex assemblies (Velev et al., 2000). Toroidal drops are known since the experiments by Plateau (1854) in rotating fluids. Such geometry is obtained also when a drop, falling free in a viscous fluid, experiences a finite surface deformation which develops into a toroidal form (Kojima et al., 1984; Baumann et al., 1992; Sostarecz & Belmonte 2003).

Zabarankin et al (2013) studied on the deformation of viscous drops in an axisymmetric compressional viscous flow and showed that the drops deform to steady shapes until critical condition (intensity of the flow characterized by the capillary number, Ca) are obtained. At supercritical capillary number, a fast thinning occurs near the middle of the drop, forming a nearly flat layer enclosed by a large bulbous ring. This shape continues to stretch and thin until the width of the layer become so small that intermolecular forces will lead to its break up and formation of liquid torus. Zabarankin et al (2015) simulated the deformation of such tori, embedded in viscous compressional flow, for a special case of equal viscosity of the phases. In the present study, the case of arbitrary viscosity ratio is considered.

FORMULATION OF THE PROBLEM

Consider a drop of volume $4\pi l^3/3$ (equal to that of a sphere with radius l) and viscosity μ^{drop} that is embedded in an unbounded viscous flow with viscosity μ. In the absence of the drop, the ambient fluid is subject to an undisturbed flow: $\boldsymbol{u} = G\,(x_1\boldsymbol{e}_1 + x_2\boldsymbol{e}_2 - 2x_3\boldsymbol{e}_3)$, where $x_1; x_2; x_3$ is a Cartesian coordinate system with the basis $\boldsymbol{e}_1; \boldsymbol{e}_2; \boldsymbol{e}_3$ and G is a constant shear rate, characterizing the intensity of the flow. We assume a creeping flow, i.e. the velocity and pressure fields satisfying the Stokes equations. Under this assumption, the governing parameters are the viscosity ratio μ^{drop}/μ denoted by λ and the capillary number, $Ca = \mu G l/\gamma$, with γ being the interfacial tension. The initial shape of the drop is assumed to be a torus with circular cross-section and major radius R, as depicted in figure 1.

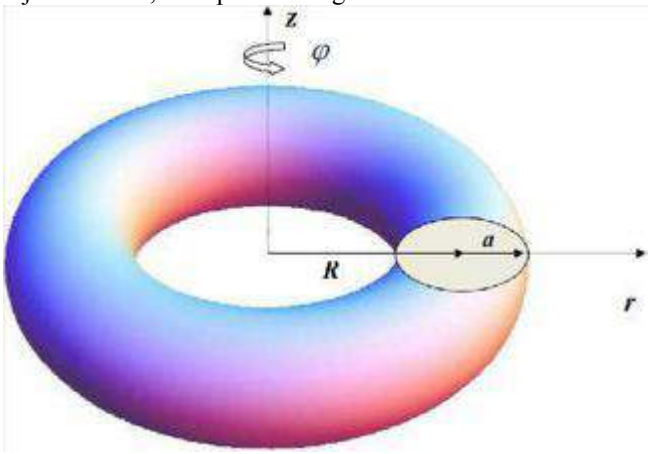

FIGURE 1. Toroidal drop: R and a are the major and minor radii respectively. The cross section of the torus is shown in the rz half-plane in the cylindrical coordinate system (r; φ, z), where the z-axis is the axis of revolution.

[a)] Corresponding author. Email: ceolga@tx.technion.ac.il

RESULTS

Dynamic deformations of toroidal drop in the compressional flow, with initially circular cross section, are studied making use of Boundary Integral Equations. It was shown that the initially circular torus cross first deforms to a shape close to elliptic. Then the torus either collapses to the center, or expands indefinitely. If the capillary number is below some critical value $Ca_{cr}(\lambda)$, a stationary state is possible as well. For moderate Ca, the cross section of stationary torus is close to ellipse. As $Ca \to 0$, the eccentricity of this stationary ellipse tends to zero. When the initial $R > R_{cr}(Ca, \lambda)$, the torus expands indefinitely and gradually assumes a circular cross section. It reflects the ever growing local curvature of the cross section perimeter which renders the tension forces there increasingly dominant. For $R < R_{cr}(Ca, \lambda)$, the torus collapses toward the axis of symmetry. When the radius of the inner interface shrinks, the local surface surrounding the gap at the axis of symmetry deforms into a cylindrical shape. With time, a circular depression develops about the symmetry plain — indication that some of the outer fluid remains trapped within this dimpled shape, and that the contact (and perhaps coalescence) of the torus may occur above and below this symmetry plain. These 3 scenarios are illustrated in figure 2. In this figure, the cylindrical radius r and initial major radius of the torus are scaled by the radius of the equivalent sphere l, while τ denotes time scaled by $1/G$.

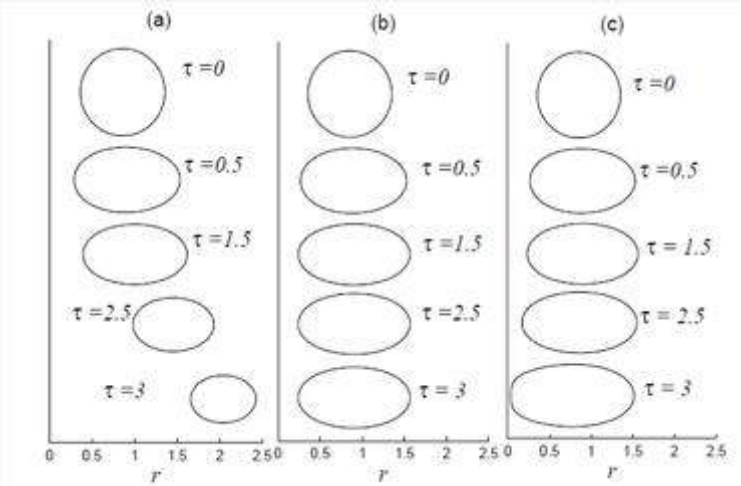

FIGURE 2. Dynamic deformations of initially circular cross section of toroidal drop at $Ca = 0.16$, $\lambda = 1$.
(a) R=0.86, (b) R=0.85236, (c) R=0.852

For super critical capillary number and sufficiently low initial major radius, the resulting dynamics has a different character. The initial circular cross section deforms to a highly asymmetric egg shape. Then, either the extended inner circular tip of the torus collapses to complete contact, or the torus expands until it is sufficiently far from the axis of symmetry, at which stage the cross section becomes gradually circular again. For higher supercritical values of Ca, after an initial short lived deformation of the cross section into elliptical shape, the drop keeps on flattening and attains very thin shapes that might be susceptible to collapse and disintegration. If this does not happen, with further toroidal expansion, the circular small cross section is regained. These examples reflect the dominance of the distorting viscous stresses upon the interfacial tension.

Acknowledgement A.N. and O.M.L. acknowledge partial support by the Israel Science Foundation (grant no. ISF/327.17) O.M.L. also acknowledges the support of the Israel Ministry of Immigrant Absorption.

References

[1] Baumann N., Joseph, D.D., Mohr P., Renardy, Y. Vortex rings of one fluid in another in free fall. *Phys. Fluids* A **4** (3) 567-580, 1992.
[2] Champion J.A., Katare Y.K., Mitragotri S. Particle shape: A new design parameter for micro- and nanoscale drug delivery carriers. *J. Contr. Release* **121** (1–2) 3-9, 2007.
[3] KojimaM., Hinch E.J., Acrivos A. The formation and expansion of a toroidal drop moving in a viscous fluid. *Phys. Fluids* **27** (1) 19-32, 1984.
[4] Plateau J. I. Experimental and theoretical researches on the figures of equilibrium of a liquid mass withdrawn from the action of gravity.–Third series. *Philosophical Magazine* Series 4 14 (90) 1-22, 1857.
[5] Sostarecz M.C., Belmonte A. Motion and shape of a viscoelastic drop falling through a viscous fluid. *J. Fluid Mech.* **497** 235-252, 2003.
[6] Velev O.D., Lenhoff A.M. & Kaler E.W. A class of microstructured particles through colloidal crystallization. *Science* **287** (5461) 2240–2243, 2000.
[7] Zabarankin M., Smagin I., Lavrenteva O.M. & Nir, A. Viscous drop in compressional Stokes flow. *J. Fluid Mech.* **720**, 169–191, 2013.
[8] Zabarankin M., Lavrenteva O.M. & Nir, A. Liquid toroidal drops in compressional Stokes flow. *J. Fluid Mech.* **785**, 372–400, 2015.

FRAGMENTATION AND EXCHANGES DURING PLANETARY CORE FORMATION

Jean-Baptiste Wacheul[1] and Michael Le Bars [*1]

[1]*CNRS, Aix-Marseille University, ECM, IRPHE UMR 7342, Marseille cedex 13, France*

Summary Telluric planet formation involved the settling of large amounts of liquid iron coming from impactors into an ambient viscous magma ocean. Planetary initial state was largely determined by diffusive exchanges of heat and elements during this iron rain. Current models often assume that the metal rapidly equilibrated as drops of single capillary size settling at the Stokes velocity. But the dynamics is more complex, and influenced by the large viscosity ratio between the metal and ambient fluid. We study this two-phase flow using a model experiment, where a balloon of heated liquid metal is popped at the top of a tank filled with viscous liquid. We explore the relevant planetary regimes, including the whole range of viscosity ratios. High-speed videos allow determining the statistics of drop sizes, shapes, and velocities. Measures of the temperature decrease during settling allow defining a global turbulent diffusion coefficient, confronted to current analytical models.

INTRODUCTION AND METHOD

As described in detail in the seminal study of [1], telluric planets formed progressively by accretion, initially of grains, then of planetesimals with growing sizes, made mostly of silicate and iron. At some stage of planet accretion, heat generated by large impacts resulted in melting in the proto-planet surface, allowing the denser metallic compound already present, as well as the metal brought by further impacting planetesimals, to separate and settle in the form of drops down to the bottom of the magma ocean (the so-called "iron rain"). The gravitational energy released in this process was enough to raise the core temperature by several thousand degrees; thus, also considering radiogenic and impact heating, the early core was entirely liquid. The initial thermochemical state of planets was mostly determined by exchanges of heat and chemical elements (i.e. siderophile vs. lithophile) taking place during this iron rain, where the surface of exchange between the main iron and silicate compounds was large. Up to now, most models of planet formation don't account for fluid mechanics: they assume that the whole metal rapidly equilibrated with the whole amount of melted mantle. Other models account for simplified fluid dynamics of the iron rain, supposing for instance that all drops had the same radius given by the capillary length and settled at the corresponding Stokes velocity with no further mixing. The fluid dynamics of iron sedimentation and fragmentation is much more complex, and influences the effective exchange coefficients as well as the amount of mantle effectively seen by the metal. It has been the subject of a renewed interest in the planetary sciences community, combining analytical models, simulations and experiments (e.g. [2, 3]). But the key ingredient of the large viscosity ratio between the metal and the viscous ambient fluid has been mostly ignored up to now, while it is known from studies of rising gas bubbles to play a significant role in the dynamics (e.g. [4]).

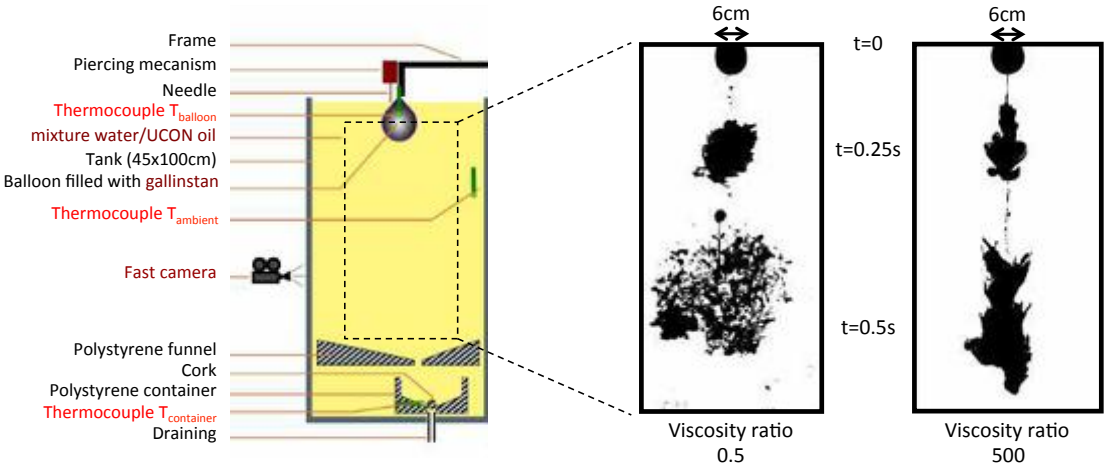

Figure 1: sketch of the experimental set-up (left) and two examples of the observed sedimentation and fragmentation processes for identical initial metal blobs (right). Only the viscosity of the ambient fluid is changed between the two experiments, with pure water on the left and a mixture of water and Ucon oil on the right, leading to a viscosity ratio of 0.5 and 500 respectively. Each picture shows the liquid metal blob at two times following the balloon piercing at $t = 0$.

*Corresponding author. Email: lebars@irphe.univ-mrs.fr

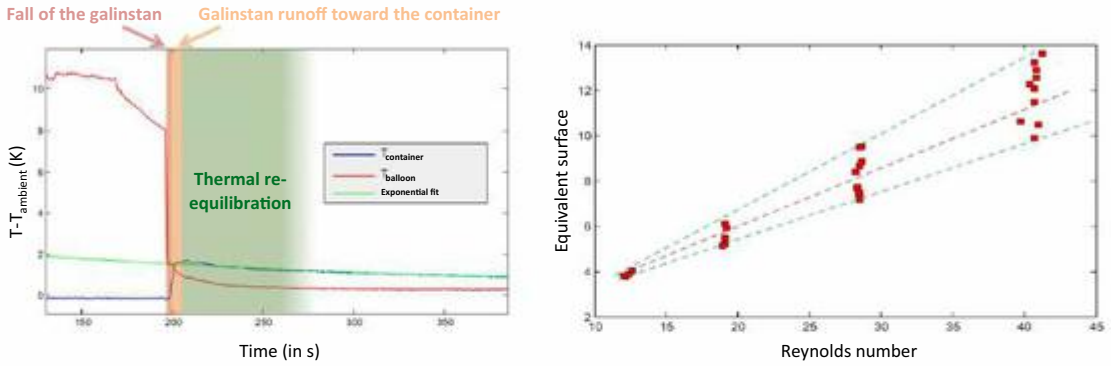

Figure 2: example of temperature measurements during one experiment (left), and systematic study of the equivalent blob surface (divided by the initial blob surface) as a function of the Reynolds number for a fixed viscosity ratio of 500 (right). Dotted lines highlight the linear interpolation of experimental results (red squares) and measured dispersion.

Our purpose is to develop a global understanding of the real dynamics of the iron rain, and provide on this basis a reliable set of parameterization, directly useable in planet formation models. As skeched in figure 1, our study relies on an experimental approach, consisting in popping a balloon filled with heated metal liquid (i.e. Galinstan) at the top of a large tank filled with a viscous liquid (i.e. mixtures of Ucon Oil and water). The set-up is capable of reaching the relevant planetary dynamical regimes, with a fully turbulent flow and a Weber number above the critical value for breakup. It also tackles for the first time almost the whole range of realistic viscosity ratios. High-speed video recording from the side of the tank determines the global dynamics of drops and drop clouds, as well as the statistics of drop sizes, shapes, and velocities. We also test the classical analytical model of thermal turbulent diffusion during settling, by measuring the global temperature decrease of the Galinstan blob during its descent using thermocouples (figure 2).

RESULTS AND CONCLUSIONS

Our first conclusion is directly visible in the pictures of figure 1: while the mean settling of a metal blob does not depend on the ambient viscosity (i.e. our study is indeed in the Newtonion regime), the fragmentation dynamics strongly depends on the ratio between the ambient and internal viscosities. A low viscosity ratio leads to the standard formation of an “iron rain”, with a Gamma distribution of drop sizes [5]. But a large viscosity ratio leads to the overall stabilisation of large blobs with a significantly distorded surface. It is then expected that these different behaviors lead to different equilibration scalings.

The classical approach of equilibration consists in quantifying temperature exchanges by considering diffusion across a turbulent boundary layer scaling as the square root of the Péclet number (e.g. [3]). To assess this model, we systematically measure the temperature decrease of the metal blob during settling in our tank, which we express in the form of an “equivalent blob surface”, i.e. the surface of exchange necessary to explain the measured temperature decrease while using the turbulent boundary layer diffusive scaling. The evolution of this equivalent surface, non-dimensionalized by the initial blob surface, is shown in figure 2 for a fixed viscosity ratio 500: it exhibits a linear scaling with the Reynolds number, with a factor 12 increase in the most extreme case reached by our set-up. The same results, now non-dimensionalized by the total surface of a model iron rain, provide a factor 1.6 increase, smaller but still significant.

In conclusion, our experimental model confirms the primordial role of the viscosity ratio on the fragmentation and exchanges dynamics of a settling metal blob, even in the Newtonian regime where the ambient viscosity is supposed to be unimportant. Using systematic experiments, we propose new scalings laws regarding the evolution of the turbulent diffusion coefficient as a function of the Reynolds number and viscosity ratio. Building upon a better understanding of the sedimentation and fragmentation processes provided by our fluid mechanics approach, more relevant models of planet formation based on a reliable dynamical ground will be developed.

References

[1] Stevenson D. J.: Fluid dynamics of core formation. Origin of the Earth 1:231-249, 1990.
[2] Deguen R. et al.: Experiments on turbulent metal-silicate mixing in a magma ocean. Earth Planet. Sci. Lett. 310:303-313, 2011.
[3] Samuel H.: A re-evaluation of metal diapir breakup and equilibration in terrestrial magma oceans. Earth Planet. Sci. Lett. 313:105-114, 2012.
[4] Bonometti T. & Magnaudet J.: Transition from spherical cap to toroidal bubbles. Phys. Fluids 18:052102, 2006.
[5] Wacheul J. B. et al.: Laboratory experiments on the breakup of liquid metal diapirs. Earth Planet. Sci. Lett. 403:236-245, 2014.

LUBRICATION AND ADHESION OF DROPLETS IN MICROCHANNELS

Haosheng Chen [1] & Jiang Li[2a)]
[1]*State Key Laboratory of Tribology, Tsinghua University, Beijing, China*
[2]*School of Mechanical Engineering, University of Science and Technology Beijing, Beijing, China*

Summary The thin lubrication film around bubbles moving in microchannels was measured using an optical interference method, and the three-dimensional profile of the lubrication film around the bubble was obtained experimentally. The minimum film thickness of the axial section in the downstream direction was found to agree well with the prediction of the Bretherton equation; while the minimum film thickness in the across-stream direction was found to be proportion to the capillary number as the film thickness was decreasing. When the lubrication film was broken, adhesion of the droplets occurred and it was demonstrated to have potential application on the breakup of the emulsion droplet.

THIN LUBRICATION FILM AROUND DROPLET IN MICROCHANNELS

The droplets/bubbles flowing in microchannels are either in wetting or in a lubrication configuration. In the former, the droplet/bubble contacts the inner surface of the microchannel, while in the latter, the droplet/bubble is encapsulated in the continuous phase and a thin lubrication film separates the droplet/bubble from the channel surface. The dynamics of this lubrication film was firstly studied by Bretherton [1], and the film thickness h is theoretically derived to have a relationship with the capillary number Ca as $h \sim Ca^{2/3}$ for a long bubble moving in a square capillary. In experiments, it is difficult to distinguish the wetting status when the lubrication film was very thin, for example, in the scale of 10^{-1}~10^{1} μm. Moreover, in a channel with noncircular cross section the lubrication film varies in both directions of downstream and cross-stream, so it is still a challenge to get the three-dimensional profile of the film through the microscope.

Method to measure the thin lubrication film

A polydimethylsiloxane (PDMS) microfluidic device is fabricated to generate bubbles in a microchannel using a flow focusing method [2]. The flow rates of the fluids are controlled by syringe pumps, and the size of the bubble is adjusted by the flow rate ratios of the continuous phase to the dispersed phase. An optical interference method is adopted to measure the thickness of the lubrication film between the moving bubble and the channel wall. A monochromatic green light with a wavelength of 550 nm is used as the incident light. When the incident light is shown through the glass it undergoes a division of amplitude, with one beam reflecting directly back from the semi-reflective layer while the other passes through the lubricant film before being reflected back from the bubble surface. This latter beam has thus travelled two times the lubricant film thicknesses further than the former reflected beam. Therefore, the two beams are out of phase and on recombination they interfere, constructively or destructively, to form light and dark interference fringes, respectively.

According to the image of the interference pattern, the thickness of the lubrication film can be calculated according to the relative optical interference intensity (ROII) method [3], after the zero film thickness is calibrated [4]. Therefore, the thickness of the lubrication film can be acquired according to the relative intensity of each fringe in the interference pattern. From the acquired interference fringe patterns, the three-dimensional profile of the lubrication film can be established from the interference fringe patterns.

Lubrication film thickness vs. capillary number

In our experiments, we change the capillary number Ca in two different ways. One is to change the flow velocity of the continuous water phase by the syringe pump, and the other is to increase the viscosity of the aqueous solution by changing the concentration of glycerol dissolved in water. The resultant Ca was in the range of 10^{-6}-10^{-4}. With the measured minimum thickness h_{min} of the lubrication film under different Ca, the relationship between h_{min} and Ca was acquired. In the downstream distance, the minimum lubrication film thickness $h_{min\text{-}x}$ increases as the Ca increases. The best fit line in the log-log plot has a slope of 0.63, which agrees well with the predicted relationship $h_{min} \sim Ca^{2/3}$ according to Bretherton equation. In the cross-stream direction, the best fit line of the film thickness has a slope of 0.92. This deviation is considered to be caused by the tangential-convection according to the analysis by Wong et al [5] that the relationship between $h_{min\text{-}y}$ and Ca is derived as $h_{min} \sim Ca^{1}$.

BREAKUP OF LUBRICATION FILM AND ADHESION OF DROPLET

When the lubrication film was broken under a low Ca, the adhesion of the droplet would occur. This adhesion would also be induced for the oil-in-water droplet when the surface of the microchannel was hydrophobically treated. The experiments of the droplet adhesion were performed in a microfluidics device where oil-in-water emulsion droplets were generated and transported through a section of hydrophilic-to-hydrophobic square capillary with controlled moving speed. The adhesion of the droplets on the hydrophobic surface was observed as the oil-in-water emulsion droplets were flowing

[a)] Corresponding author. lijiang@ustb.edu.cn

into the hydrophobic part of the capillary. The oil-in-water emulsion droplets dyed in red adhered on the hydrophobic surface and the emulsion droplets broke, the oil phase occupied the channel surface and the water phase was encapsulated by the oil phase to form the water-in-oil emulsion droplets.

Critical *Ca* for the breakup of lubrication film

The droplet adhesion was found to be affected by the flowing speed and the droplet size. In the experiment, we gradually reduced the flowing velocity, and the critical velocity to induce the adhesion was measured. Then, we changed the size of the droplets and found the critical velocity of adhesion increased as the droplet size increased. The critical *Ca* for the adhesion was then acquired as $Ca \sim (D/d)^{3/4}$, where D is the drop size and d is the channel size [6]. This experiment result was consistent with our theoretical analysis.

Adhesion of droplets to break emulsions

Here, we demonstrate how to use droplet adhesion to recycle the ingredient materials of emulsions in microfluidics. In some applications, the materials of the emulsions are valuable and so recycling is needed. However, typically the emulsions are very stable and not easily broken down to two separated phases. As a specific example, for a typical oil-in-water emulsion system, the collected emulsion droplets still remain an emulsion and the oil droplets are mixed with the water phase. However, when we use the technology of droplet adhesion illustrated above, then below a critical speed the oil emulsion droplets formed in the hydrophilic region will break up in the hydrophobic region. Thus, we can separate the oil phase from the water phase and collect the pure oil phase from the original emulsion fluids.

CONCLUSIONS

In this work, we used the optical interference method to reveal the profile of the thin lubrication film around the droplet/bubble moving in the microchannels. The measured film thickness validates the Bretherton equation experimentally. The breakup of the lubrication film was also investigated and it was found to obey the rules of $Ca \sim (D/d)^{3/4}$. The surface wetting induced adhesion of the emulsion droplets in the microchannel was demonstrated to be used in the breakup of the emulsions.

References

[1] Bretherton F.P.: The motion of long bubbles in tubes. *J. Fluid Mech.* **10**: 166-188, 1961.
[2] Anna S.L., Bontoux N., Stone H.A.: Formation of dispersions using "flow focusing" in microchannels. *Applied physics letters* **82**: 364-366, 2003.
[3] Luo J.B., Shen M.W., Wen S.Z.: Tribological properties of nanoliquid film under an external electric field. *J. Appl. Phys.* **96**: 6733-6738, 2004.
[4] Chen H., Meng Q., Li J.: Thin lubrication film around moving bubbles measured in square microchannels. *Appl. Phys. Lett.* **107**: 141608, 2015.
[5] Wong H., Radke C.J., Morris S.: The motion of long bubbles in polygonal capillaries. Part 1. Thin films. *J. Fluid Mech.* **292**: 71-94, 1995.
[6] Chen H., Dong E., Li J., Stone H.A.: Adhesion of moving droplets in microchannels. *Appl. Phys. Lett.* **103**: 131605, 2013.

TRANSLATION OF TWO ENCAPSULATED BUBBLES IN AN ULTRASOUND FIELD

Yunqiao Liu*[1], Kazuyasu Sugiyama[2], and Shu Takagi[3]

[1]Department of Engineering Mechanics, Shanghai Jiao Tong University, Shanghai, China
[2]Department of Mechanical Science and Bioengineering, Graduate School of Engineering Science, Osaka University, Osaka, Japan
[3]Department of Mechanical Engineering, School of Engineering, The University of Tokyo, Tokyo, Japan

Summary The expressions of the radial oscillation and translation of two encapsulated bubbles in an ultrasound field are derived analytically based on a potential flow with a viscous correction. The in-plane stress and bending moment of a viscoelastic membrane are balanced on the interface of the bubble with the hydrodynamic traction. The history force, in addition to the quasisteady viscous drag, is calculated by numerical solving the vorticity equation in toroidal direction. The translations of two bubbles agree with the prediction by Bjerknes' theory in the attractive or repulsive movements under specific driving frequency. The encapsulating membrane shows more damping than the shear-free gas bubble due to the no-slip condition on encasulating membrane.

INTRODUCTION

In the applications of contrast-enhanced agents and drug-carrier capsules, encapsulated bubbles do not exist independently. Surrounding bubbles affect the behavior of each bubble. The interaction of two gas bubbles without encapsulation has been well studied. The pioneer work traces back to that of Bjerknes in 1906 [1]. The famous secondary Bjerknes force is the reason of motion of a bubble due to fluid acceleration caused by the volume oscillations of another bubble. The coupled pulsation and translation were studied in recent decades [2,3]. The effects of the shape oscillation are included in the theoretical work of Takahira et al. [4] and in numerical work by Pelekasis et al. [5,6] and Chatzidai et al. [7]. Most of the previous work on encapsulated bubbles focused on the single encapsulated bubble [8-10]. Our work in this paper focuses on the translation motion of two encapsulated bubble.

BASIC EQUATIONS

The dynamics of two bubbles suspended in an unbounded fluid are studied. We establish an axisymmetric coordinate system with the symmety axis connecting the centres of the two bubbles. In the following equations, the subscript i denotes the one bubble, and $j = 3 - i$ denotes the other one. Only the equations for the bubble i are written, while the equations for the bubble j are equivalent with the i and j exchanged.

The bubbles are coated by a viscoelastic membrane, characterized by the surface modulus G_{si}, the bending modulus G_{bi}, the membrane viscosity μ_{si}, and the Poisson ratio υ_{si}.

We consider nonlinearity in radial motions R_i, which yields the Rayleigh-Plesset like equation:

$$R_iR_i + \frac{3}{2}R_i^2 + \frac{1}{\rho}\Big[p_\infty - p_{g0}\big(\frac{R_{0i}}{R_i}\big)^{3\Gamma} + \frac{2\gamma}{R_i} + 4\mu_l\frac{R_i}{R_i}\Big] - \frac{\mathrm{d}}{\mathrm{d}t}\Big(\frac{q_{0j}}{L}\Big) + \frac{R_j^3 q_{0i}}{L^4} - \frac{3v_{ri}^2}{4} + \frac{v_i^2}{2} \tag{1}$$
$$= -\frac{1}{\rho}\Big[\frac{2G_{si}(R_i^6 - R_{0i}^6)}{R_i^7} + 4\mu_{si}\frac{R_i}{R_i^2}\Big],$$

where ρ is the liquid density, μ_l the liquid viscosity, Γ the polytropic index. The surface tension term with coefficient γ is kept here to include the gas bubble case and will be zero for encapsulated bubble. The last four terms on the left hand side of the equation represent the effect of the other bubble and the translations. $q_{0i} = -R_iR_i^2$ is a coefficient from velocity potential. L is the distance between two bubbles. v_i is the velocity of the bubble center. $v_{ri} = v_i - q_{0j}/L^2$ is a reference velocity. The right hand side of the equation is the membrane force.

The equation of translational motion is:

$$\frac{\mathrm{d}}{\mathrm{d}t}\big(\frac{1}{2}\rho V_b v_{ri}\big) = \rho V_b\frac{\mathrm{d}}{\mathrm{d}t}\Big(\frac{q_{0j}}{L^2}\Big) - 4\pi\mu_l R_i T_i(R_i, t), \tag{2}$$

where $V_b = 4\pi R_i^3/3$. The left hand side of the above equation represents the inertia the added mass. The first term in the right hand side is the Bjerknes force. The second term is the drag force, in which $T_i(R_i, t)$ is the toroidal component of vorticity, obtained by numerical solving

$$\rho\frac{\partial T_i}{\partial t} + \rho\frac{\partial}{\partial r_i}[R_i(R_i/r_i)^2T_i] - \mu_l\frac{\partial^2 T_i}{\partial r_i^2} + \mu_l k(k+1)r_i^{-2}T_i = 0, \tag{3}$$

with the boundary condition $T_i \to 0$ as $r_i \to \infty$. T_i on the bubble surface is determined by satisfying the tangential force balance as

$$2\mu_l\Big(\frac{3v_{ri}}{2R_i} - \frac{T_i(R_i,t)}{2R_i} - R_i^{-1}\int_{R_i}^{\infty} s^{-1}T_i(s,t)ds\Big) = 6G_{si}\frac{R_{0i}^6}{R_i^8}b_{1i} + (1+\upsilon_i)\frac{G_{bi}}{R_i^4}b_{1i} + \frac{2\mu_{si}}{R_i^3}(R_ib_{1i} - R_ib_{1i}), \tag{4}$$

*Corresponding author. Email: yunqiaoliu@sjtu.edu.cn

where b_{1i} is the movement of material points along the bubble interface, satisfying the no-velocity-jump condition as:

$$-\frac{3}{2}v_{ri} + \int_{R_i}^{\infty} s^{-1}T_i(s,t)ds = b_{1i} - \frac{R_i b_{1i}}{R_i}. \tag{5}$$

The toroidal field $T_i(R_i, t)$ can be also solved under the Stokes flow. For shear-free gas bubble, the RHS of (4) is zero. Accordingly, we can obtain the Levich drag $12\pi\mu_l R_i v_{ri}$. For no-slip rigid sphere, the RHS of (5) is zero, from which we obtain the drag force $6\pi\mu_l R_i v_{ri} + 6\pi\mu_l R_i^2 v_{ri}/\chi_i$, where χ_i is the thickness of boundary layer. For the above equations, the readers are referred to [11] for a detailed derivation.

RESULTS

Both gas bubbles and encapsulated bubbles are investigated. For gas bubbles, the coefficient of surface tension is chosen as $\gamma = 0.0729$ N/m. For encapsulated bubbles, the elastic modulus is $G_s = 0.5$N/m, the bending modulus is $G_b = 2 \times 10^{-13}$ N·m, and the membrane viscosity is $\mu_m = 10^{-8}$ kg/s.

According to Bjerknes' theory, two bubbles will move away from each other when the driving frequency is between the two natural frequencies $\omega_{01} < \omega_d < \omega_{02}$; otherwise, the two bubble will attract to each other at $\omega_d < \omega_{01}$ or $\omega_d > \omega_{02}$. To validate this theory, we choose two bubbles with $R_{01} = 10$ μm and $R_{02} = 5$ μm. We plot the final distances between the two bubbles after 20 driving cycles versus the driving frequencies in Fig. 1. For gas bubbles, the zeroth-order natural frequencies are $\omega_{01} = 2\pi \times 0.34$ MHz and $\omega_{02} = 2\pi \times 0.72$ MHz, respectively. We can see that the two bubbles attract each other when the driving frequency is smaller than both of the natural frequencies. When the driving frequency approximates to the smaller natural frequency, i.e. $\omega_d = \omega_{01}$, the distance has a minimum. After this minimum, the relative translation becomes repulsive. When the driving frequency approaches the other natural frequency, i.e. $\omega_d = \omega_{02}$, the two bubbles repel to a maximal distance. After this maximum, the translational motion of the bubbles returns to a weak attraction. For encapsulated bubbles, the zeroth-order natural frequencies are $\omega_{01} = 2\pi \times 0.51$ MHz and $\omega_{02} = 2\pi \times 1.28$ MHz, respectively. Similar to the gas bubbles, the distance approaches to minimum/maximum near the two natural frequencies respectively. However, the magnitudes of the translation is smaller than those of gas bubbles. The reason is that the no-slip interface on the membrane enhances the viscous dissipation and the resultant history force is comparable to the quasisteady viscous drag or even overwhelm it.

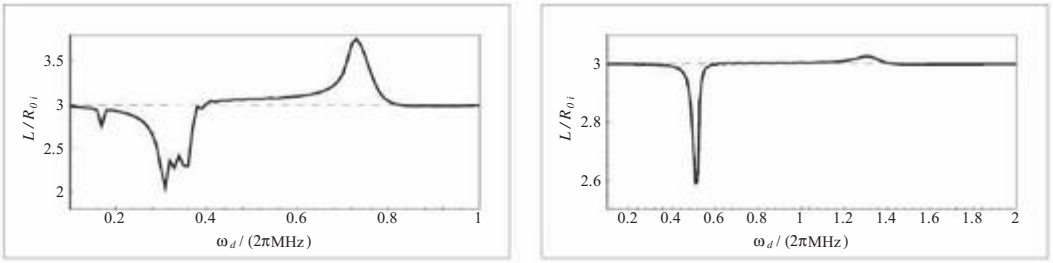

(a) Gas bubbles (b) Encapsulated bubbles

Figure 1: The final distance after 20 driving cycles at different driving frequencies with driving amplitude $\varepsilon = 0.1$. $R_{01} = 10$ μm, $R_{02} = 5$ μm.

ACKNOWLEDGMENTS

This work was supported by the National Natural Science Foundation of China (11302128).

References

[1] Bjerknes V F K 1906 *Fields of Force*, Columbia University Press.
[2] Barbat T, Ashgriz N and Liu C *J. Fluid Mech.*. **389** 137, 1999.
[3] Harkin A, Kaper T J and Nadim A *J. Fluid Mech.* **445** 377, 2001.
[4] Takahira H, Akamatsu T and Fujikawa S *Trans. JSME B* **57** 447, 1991.
[5] Pelekasis N A and Tsamopoulos *J. Fluid Mech.* **254** 467, 1993.
[6] Pelekasis N A and Tsamopoulos *J. Fluid Mech.* **254** 501, 1993.
[7] Chatzidai N, Dimakopoulos Y and Tsamopoulos *J. Fluid Mech.* **673** 513, 2011.
[8] Tsiglifis K and Pelekasis N A *Phys. Fluids* **23** 012102, 2011.
[9] Liu Y, Sugiyama K, Takagi S and Matsumoto Y *Phys. Fluids* **23** 041904, 2011.
[10] Liu Y, Sugiyama K, Takagi S and Matsumoto Y *J. Fluid Mech.* **691** 315, 2012.
[11] Liu Y, Sugiyama K and Takagi S *in preparation*.
[12] Lauterborn W and Bolle H *J. Fluid Mech.* **72** 391, 1975.

EXPERIMENTAL INVESTIGATION OF SLUG FLOW IN A PIPE SUBJECTED TO FLUID INJECTION AT THE WALL

Francisco J. S. Bandeira, Gabriel F. N. Gonçalves, Juliana B. R. Loureiro *, and Atila P. Silva Freire
Programa de Engenharia Mecanica (COPPE/UFRJ), Universidade Federal do Rio de Janeiro, C.P. 68503, 21941-972, Brazil

Summary The present work investigates experimentally the changes on the properties of horizontal gas-liquid slug flows subject to fluid injection at the wall. Measurements include data on global parameters including flow rates and pressure drop for ten different conditions. A Shadow Sizer system is used to determine the geometric and kinematic properties of the flow. Three flow transpiration rates are discussed, $v_w^{++} = v_w/U_m = 0.0$, 0.0005 and 0.001. The effects of flow transpiration induce bubble break-up and large changes in the passage frequency and characteristic lengths of unit cells. The work introduces modifications to single-phase wall injection models and unit cell models for gas-liquid slug flow to propose a unified theory capable of dealing with the effects of wall injection on slug flow. All theoretical predictions are compared with the experimental data.

INTRODUCTION

The uniform injection of fluid into flows bounded by porous walls is normally referred to in literature as transpiration. This is a problem of great industrial interest, whose typical examples include the thermal protection of walls, filtration or the production of oil in horizontal or vertical wells.

For laminar flow, analytical solutions to the Navier-Stokes equations can be obtained to find the dependence of the velocity components and pressure on position coordinates, pipe dimensions and fluid properties. For turbulent flow, the search for analytical solutions is much complicated by the natural requirement of closure. However, some authors have shown [1, 2] that some simple algebraic closure hypotheses and perturbation arguments can be used to find local analytical solutions.

The occurrence of a second flow phase – gas – is frequent in many cases of interest, in particular, in flow conditions typical of slug flow. Thus, a problem of great practical relevance is the description of slug flow subject to fluid transpiration at the wall.

The purpose of the present work is to perform reference experiments in horizontal pipes with flow injection at the wall for single- and two-phase (slug) flow patterns. Measurements of global flow rates and pressure drop are obtained for ten different experimental conditions. The properties of the two-phase flow are measured through a Shadow Sizer system and laser-based sensors.

To extend the theoretical single-phase results to slug flow, unit cell models are considered.

THEORETICAL BACKGROUND

A law of resistance for rough pipes with wall transpiration can be introduced as shown in [3]. Define $Re^{++} = R/k_s$, $v_w^{++} = v_w/U_m$ and $A_k = B \circ 512\, v_w^{++}$. It follows immediately that

$$1 = \frac{\sqrt{f}}{2\sqrt{2}}(2.5\ln(Re^{++}) + A_k \circ 3.75) + v_w^{++}(1.56\ln^2(Re^{++}) + (1.25A_k \circ 4.68)\ln(Re^{++}) + \frac{A_k^2}{4} + 1.86A_k + 5.47). \quad (1)$$

where f denotes the friction coefficient, U_m the bulk velocity and v_w the injection velocity.

In unit cell models, a typical structure is postulated to repeat itself moving down a pipe. Provided a reference frame exists where the liquid and gas phases are considered to travel in a fully developed state with about the same velocity, the flow randomness can be encapsulated in models with fixed or stochastic cell lengths. In the present work, we consider the unit cell models of [4] and [5].

Uniform mass injection through a pipe wall alters the pressure drop due to the acceleration of the slow moving fluid. The pressure drop resulting from wall shear is also affected through a dual effect: the fluid injection increases the mixture velocity of the flow but decreases the liquid friction coefficient.

Since the length of the unit cell is unknown and the mixture velocity depends on the amount of liquid that is transpired through the wall, an iterative scheme needs to be used to find the flow properties, which now obviously change from cell to cell. In the extension of the models of [4] and [5] to transpired walls, the addition of mass needs to be considered accordingly. The friction coefficient also needs to be modified due to its dependence on the injection rate and bulk velocity.

*Corresponding author. Email: jbrloureiro@mecanica.coppe.ufrj.br

EXPERIMENTS AND RESULTS

The experiments were conducted in a 15 meter long porous pipe (31.75 mm in diameter) with uniform fluid injection at the wall. The test section consisted of three concentric stainless-steel tubes, assembled as shown in Fig. 1.

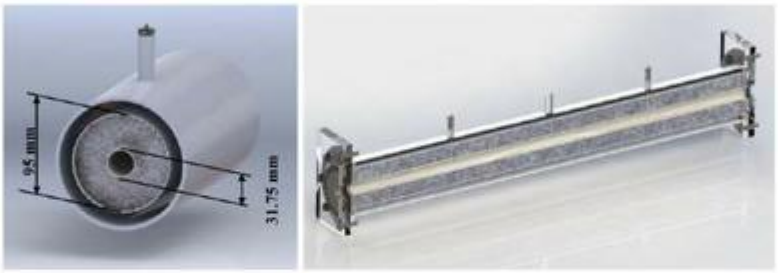

Figure 1: Test section: a) main pipe dimensions, b) geometric arrangement.

The total pressure losses are compared with predictions obtained through the models of [4] and [5] in Fig. 2. For the lower liquid and gas flow rates the agreement between theories and experiments is within 26% in error. For the highest flow rates, the maximum difference reaches 38%. It is clear that for the lower gas flow rates the theoretical results for both injection rates slightly under predict the experimental data (by a maximum of 10%). For the highest gas low rate, the extended models of [4] and [5] over predict the data by 12%.

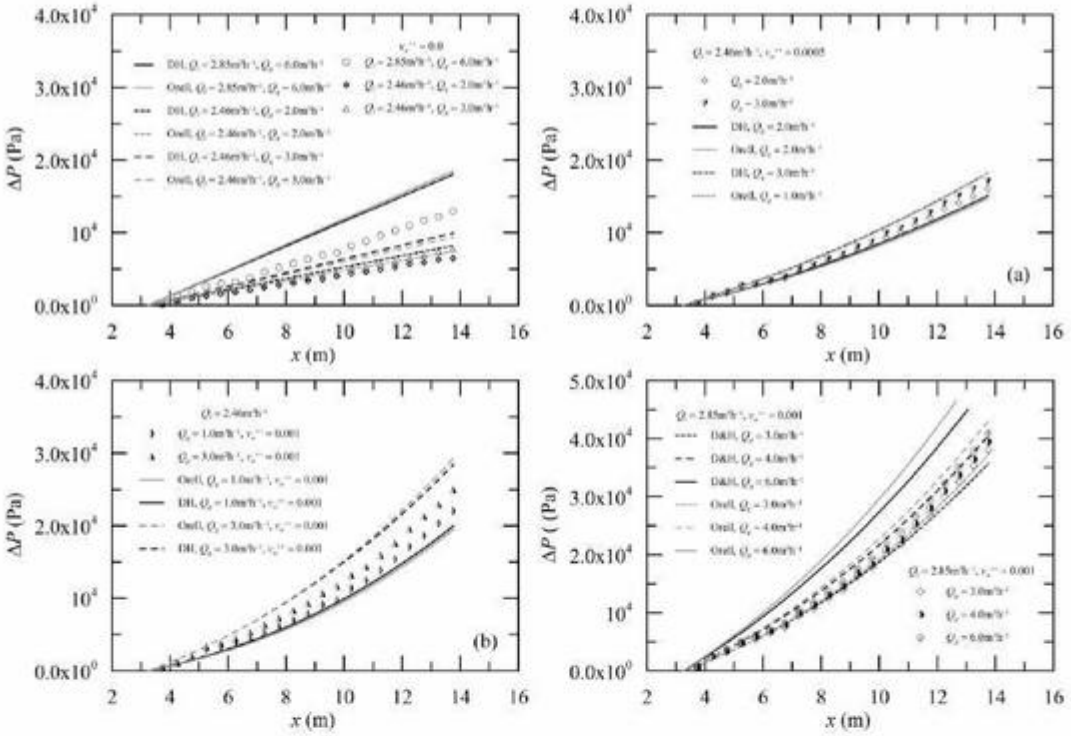

Figure 2: Pressure drop predictions for two-phase slug flow with and without wall transpiration.

References

[1] Stevenson, T. N.: A law of the wall for turbulent boundary layers with suction or injection. Cranfield Rep. Aero. **166**, The College of Aeronautics, Cranfield, England, U.K. (1963)

[2] Silva Freire, A.P.: An asymptotic solution for transpired incompressible turbulent boundary layers. Int. J. Heat Mass Transfer, **31**, 1011-1021 (1988)

[3] Loureiro, J.B.R., Silva Freire, A.P.: Slug flow in horizontal pipes with transpiration at the wall. Journal of Physics. Conference Series (Online), **318** (2011)

[4] Dukler, A. E., Hubbard, M. G.: A model for gas-liquid slug flow in horizontal and near horizontal tubes. Ind. Eng. Chem. Fund., **14**, 337–347 (1975)

[5] Orell, A.: Experimental validation of a simple model for gas-liquid slug flow in horizontal pipes. Chem. Eng. Sci., 60, 1371–1381 (2005)

RAPID GENERATION OF SMALL WATER-WATER DROPLETS AT THE INTERFACE OF A JET FLOWING AT HIGH SPEED

Sze Yi Mak[1,2] & Ho Cheung Shum [1,2a)]
[1]*Department of Mechanical Engineering, The University of Hong Kong, Hong Kong*
[2]*HKU-Shenzhen Institute of Research and Innovation (HKU-SIRI), Guangdong, China*

Summary All-aqueous droplets have promising potential in biomedical applications such as enzyme encapsulation. However, it remains difficult to generate water-water droplets with a narrow size distribution, a high degree of control over droplet size and a high generation frequency. We propose a robust method to generate all-aqueous droplets of a relatively small size (~ 10 microns), at an ultra-high rate (several kilohertz), and with a high size uniformity (c.v. less than 1%). Our technique is based on the shearing of the droplet phase off of the interface of a jet, which is flowing at a significantly higher speed than the continuous phase. We anticipate that by generating size controllable water-water droplets in a rapid and scalable manner, this technique will inspire new application of all-aqueous emulsion droplets.

INTRODUCTION

Through addition of incompatible additives, such as polymers and salts, a single-phase aqueous solution can separate into two immiscible aqueous phases, enabling the possibility to form water-in-water emulsions. Current technology has thus far only been able to form water-water droplets with a relatively large size of around 20 μm to 200 μm[1, 2] and typically at low production rate of a few tenths to a few droplets per second. Emulsification by homogenization results in a high production rate but does not yield size uniformity[3]. All-aqueous droplet makers typically require the introduction of external disturbances, such as piezoelectric actuation[4] and mechanical perturbation[2, 5, 6]. We develop a novel robust technique to produce water-water emulsions with the elimination of the current limitation on size, size uniformity and generation rate.

RESULTS

In all our experiments, we propel a fast aqueous jet from the nozzle into an aqueous continuous phase. The aqueous-aqueous interface is characterized by an ultralow interfacial tension[7]. As the flow rate of the jet is increased, three distinctive dynamic regimes are classified: namely Jetting, Jet-folding and Droplet-Shearing. When the inner flow rate is higher than the outer flow rate, a stable expanding jet is formed in the Jetting regime. When the inner flow rate is increased to Q_i = 13 ml/h, the jet surface starts to fold and becomes corrugated in the Jet-Folding regime. When the inner flow rate is further increased to Q_i = 25 ml/h, the corrugations of the interface eventually shear the outer phase into droplets within the jet phase in the Droplet-Shearing regime. The resultant droplets follow the flow of the jet and propagate downstream.

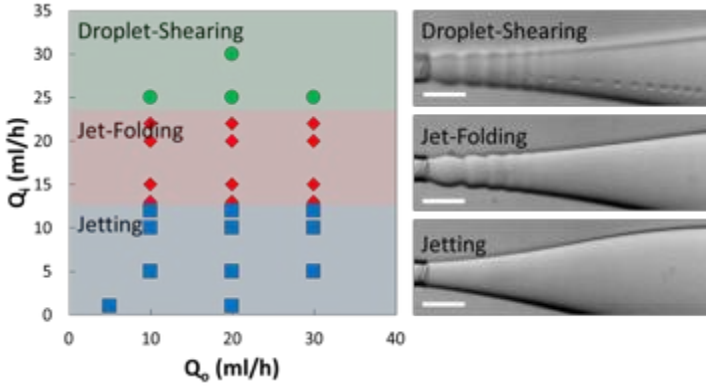

Figure 1: Phase map (Left) and microscopic images (Right) of the three regimes at a fixed outer flow rate Q_o = 30 ml/h. Droplet-Shearing, Jet-Folding and Jetting regime, Q_i = 30, 25, 12 ml/h (Top to bottom). Scale bars are 100 μm.

The transition from a stable jet to an unstable one, followed by the formation of small droplets of the outer phase fluid occurs at a fixed inner flow rate for a wide range of outer flow rate tested (Q_o = 5 ml/h to 30 ml/h), as shown in the phase map of the two-phase system in Figure 1. Here, we demonstrate using a fast propelling inner jet phase to produce small outer phase droplets. This method of droplet generation can result in droplets with size significantly smaller than the nozzle size which is 59 μm.

We further investigate the droplet size dependence on the flow rates. When the inner flow rate is increased from Q_i = 25 ml/h to 30 ml/h at a fixed outer flow rate of Q_o = 20 ml/h, the droplet size decreases from (15.2 ± 0.1) μm to (12.1 ± 0.1) μm. These droplets have a low size polydispersity of 0.8 %. Hence, the droplet size can be tuned simply by adjusting the relative velocity of the inner and outer phases.

[a)] Corresponding author. Email: ashum@hku.hk.



Figure 2: Trains of droplets generated from multiple zones, Q_i = 30 ml/h and Q_o = 20 ml/h. Scale bar is 100 µm.

Moreover, the droplet generation rate follows the frequency of the interfacial corrugation and is significantly higher than other existing microfluidic approaches for forming water-water droplets. For example, the droplet generation rate can be as high as over 5000 Hz per one shearing zone when the flow rates of the inner and outer phases are Q_i = 30 ml/h and Q_o = 20 ml/h respectively. At a sufficiently high inner flow rate, multiple shearing zones are developed and distributed at different radial positions on the jet interface (Fig. 2). All shearing zones have almost the same droplet generation rate with a slight deviation of 1.3%. Therefore, the total droplet generation rate can be numbered up.

DISCUSSIONS

The stable Jetting regime has been studied extensively. Hence, we focus on the Jet-Folding regime, which arises when the inner flow rate exceeds a certain threshold value. When a fast jet is ejected into a continuous phase in a microfluidic channel, a huge velocity difference is created at the interface of the inner and outer phases. The mean velocity difference between the jet phase and the continuous phase exceeds 1 m/s. The interface is destabilized and thereafter the outer fluid is sheared off at the interface and breaks up into droplets within the jet. We notice that the transition from a stable jet to a folding one is insensitive to the variation in the outer flow rate, since the jet diameter is significantly smaller than the channel diameter. Variation in inner flow rate will significantly alter the jet velocity while the variation in outer flow rate will not significantly change the velocity of the outer phase. Ultra-fast droplet generation is realized for two reasons. Firstly, the high frequency of corrugation at the interface, which is on the order of kilohertz, sets the high droplet generation frequency. Secondly, droplets are emitted simultaneously at different radial planes at the interface of the jet. The parallel generation allows multiplication of the droplet generation rate within a single jet.

EXPERIMENTS

Glass capillaries are used to construct the microfluidic device. A round capillary which is tapered to have a nozzle size of around 60 µm is inserted into a square capillary with an inner dimension of around 1.1 mm. The aqueous two-phase system (ATPS) is formed by phase separation of a mixture of 9.7 wt% sodium carbonate (Na_2CO_3) and 23.285 wt% Poly(Ethylene Glycol) with a molecular weight of 4000 Da (PEG 4000). The bottom and top phases are injected into the round and square capillaries to form the inner and outer phases respectively. The interfacial tension of this ATPS is 1.99 mN/m. The flow rates of the inner and outer phases range from 1 ml/h to 30 ml/h. In all the experiments, the co-flow system is in a jetting regime where the velocity of the inner phase is much higher than that of the outer phase. This provides a huge velocity contrast between the inner and outer fluids. Microscopic images are taken using a high speed camera (FASTCAM SA4, Photron) connected to a microscope (AE2000, Motic).

CONCLUSIONS

We show a robust method to shear off tiny droplets with a size of around ten microns with high generation rate, based on a sufficiently large velocity difference between the liquid phases and the possibility to have multiple shearing zones. We anticipate this technique to be highly adoptable in various applications that require mass production of all-aqueous emulsions.

ACKNOWLEDGEMENTS

This research was supported by the General Research Fund (Nos. HKU 719813E, 17304514 and 17306315) from the Research Grants Council of Hong Kong, and the General Program (No. 21476189/B060201)from the National Natural Science Foundation of China.

References

[1] Moon B. U. et al.: Microfluidic generation of aqueous two-phase system (ATPS) droplets by controlled pulsating inlet pressures. *Lab Chip* **15**: 2437-2444, 2015.

[2] Sauret A., Shum H. C.: Forced generation of simple and double emulsions in all-aqueous system. *Appl. Phys. Lett.* **100**:154106, 2012.

[3] Franssen O., Hennink W. E.: A novel preparation method for polymeric microparticles without the use of organic solvents. *Int. J. Pharm.* **168**: 1-7, 1998.

[4] Geschiere S. D. et al.: Slow growth of the Rayleigh-Plateau instability in aqueous two phase systems. *Biomicrofluidics* **6**:022007, 2012.

[5] Shum H. C. et al: Corrugated interfaces in multiphase core-annular flow. *Phys. Fluids* **22**:8:082002, 2010.

[6] Sauret A. et al: Fluctuation-induced dynamics of multiphase liquid jets with ultra-low interfacial tension. *Lab Chip* **12**:3380, 2012.

[7] Atefi E. et al.: Ultralow Interfacial Tensions of Aqueous Two-Phase Systems Measured Using Drop Shape. *Langmuir* **30**:32:9691-9699, 2014.

MULTISCALE SIMULATION OF SOAP BUBBLES RUPTURE

Shucheng Pan[a)], Xiangyu Hu & Nikolaus A. Adams
Institute of Aerodynamics and fluid mechanics, Technische Universität München, Garching, Germany

Abstract The development of numerical method for soap bubble dynamics is of academic significance to understanding the underlying physics of the foams. In this study, we propose an efficient, robust and accuracy numerical method for simulating the dynamics of dry foams, including macroscopic evolution of membranes and its rupture on microscopic scale. The main feature of the method is its simplicity in implementation, both for the macroscopic interface advection and microscopic drainage. Regarding the interface advection we use a recently developed multi-region level-set method with high order discretization schemes while for drainage equation we use smooth particle hydrodynamics (SPH) to solve it. And the remesh method is employed to maintain the conservation during interface evolution and suddenly topology change. The results show the success in capturing the dynamics and rupture of soap cluster.

INTRODUCTION

Although the Reynolds number of soap bubbles is relatively low and the flow usually keeps laminar, the interconnected interface of the soap foams is complex and encounters frequent topology change during membrane rupture which leads to challenges in developing numerical method for solving this type of flow mechanics. A typical soap bubble cluster is composed of thin liquid membrane (also known as lamella), Plateau borders (multi-lamella junction) and gas inside/outside the lamella. Under the surface tension effect, the macroscopic motion of the lamella network always try to approach the minimal surface energy state. Inside the lamella, the liquid is governed by the gravity and curvature which make the thickness of the lamella alter, leading to a sudden rupture once the lamella is too thin. Therefore this phenomena breaks the balanced state of the interface network, which need find a new equilibrium under surface tension effect. The total system is driven by the interplay of the two types of dynamics with disparate time and space scales which allow us use the scale separation when investigate the bubble cluster dynamics [1]. Recently Saye and Sethian [1] developed a multiscale framework for soap bubble dynamics. They use voronoi implicit interface method [2] and finite element method for interface advection and drainage equation, respectively. However the frequent mesh generation for the finite element method is time consuming. In this manuscript we present another multiscale framework with each part different with Saye's method to simulate the soap bubble dynamics more efficiently.

NUMERICAL METHODS

The method developed in this paper is based on the idea of scale separation proposed by Saye and Sethian [1] who suggest using different equations at different scales of foams. The whole simulation includes rearrangement, drainage, and rupture.

Rearrangement

In this stage, the surface tension and gas dynamics rearrange the global geometry of soap foam cluster in order to get an equilibrium with minimal surface energy. In this process, if we only care about the geometry of bubble cluster, it is not necessary to fully resolve the thin liquid film and its mass is neglected, which eliminates the difficulty in capturing the interface network. Here we can couple the multi-region level-set method with weakly compressible Navier-Stokes equations. Like voronoi implicit interface method [2], the multi-region level-set method uses only an unsigned level-set value ϕ and an additional phase indicator χ. The interface evolution is based on the idea that away from singularities this evolution is identical to the motion of region-boundary while in singularities additional operators are required to determine how the singularities move. So instead of the interface of the multi-region system, we prefer to capture the evolution of the boundary of each region (Fig.1a). Obviously singularities are never resolved, but they never affect the adjacent resolved interface segments, therefore numerically it is not necessary to consider the motion of these points in an explicit manner, instead the operator only need determine the changes of ϕ and χ. This method will automatically degenerate to traditional in two-phase region, while in the multiple junctions this method it need three simple operators to capture the advection:

$$\phi^{n+1} = \mathcal{I}^{\phi}\left(\mathcal{E}^{\phi}\left(\mathcal{R}(\phi,\chi)\right)\right), \quad \chi^{n+1} = \mathcal{I}^{\chi}\left(\mathcal{E}^{\phi}\left(\mathcal{R}(\phi,\chi)\right)\right)$$

Where the operators $\mathcal{E}$, $\mathcal{I}$, and $\mathcal{R}$ indicate the evolution, interaction, and reconstruction in multiple junctions. The function of $\mathcal{R}$ is to locally reconstruct the signed distance level-set field by judging the sign of all cells in the stencil or invoke re-initialization procedure. After local reconstruction, the evolution is determined by $\mathcal{E}$, depending on the spatial and temporal discretization scheme. Then we consider at every cell center, the point has an interaction with the region if it is located at the stencil of the current cell. Thus the boundary of region is evolved by the interaction. All the interaction of the neighbouring regions need be considered (see Fig.1c). To choose one region from all the candidates, we consider the dominating interaction belongs to the

[a)] Corresponding author. Email: shucheng.pan@tum.de.

region and its ghost (grey part in Fig.1c) which lead to minimal signed distance, that is to say under this interaction, the cell center is closest to the corresponding region-boundary.

Afterwards, the multi-region level-set method is coupled with Navier-Stokes equations:

$$\frac{\partial \mathbf{U}}{\partial t} + \nabla \cdot \mathbf{F}_c = \nabla \cdot \mathbf{F}_v + \sigma\kappa\delta\mathbf{n}$$

In order to obtain high accuracy, both level-set advection and NS equations are solved by WENO scheme and second-order TVD Runge-Kutta time integration. A multi-material multi-resolution solver is developed based on our previous two-phase multi-resolution solver [3].

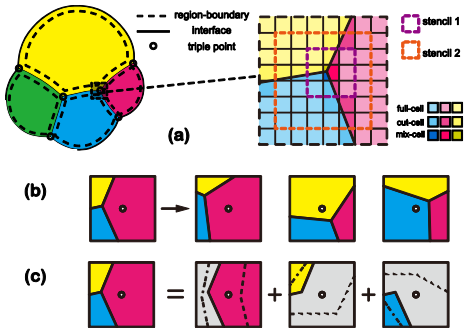

Fig.1. A schematic representation of multi-region method.

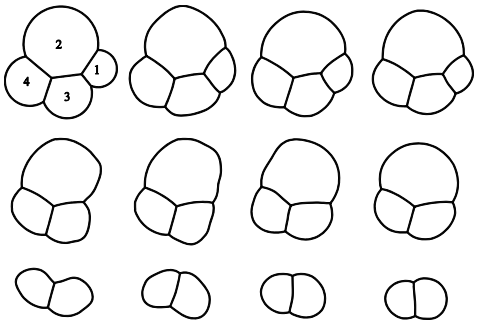

Fig.2. Four-bubble cluster dynamics

Drainage

Assuming the lamella network is in macroscopic equilibrium, the drainage process is studied by solving the thin-film equation derived in [1]:

$$\frac{\partial \eta}{\partial t} + \frac{1}{\mu}\nabla_s \cdot \left(\sigma\eta^3\nabla_s\left((k_1^2 + k_2^2)\eta + \Delta_s\eta\right) + \rho\mathbf{g}_s\right) = 0$$

$$\frac{\partial \lambda}{\partial t} + \frac{C_\Delta}{\mu}\frac{\partial}{\partial \ell}\left(-\frac{1}{2}\left(\sqrt{3} - \frac{\pi}{2}\right)^{1/2}\sigma\lambda^{1/2}\partial_\ell\lambda + \lambda^2\rho g_t\right) = S$$

However these equations are defined in curved surface, requiring high quality mesh generation every macroscopic tem step which reduce the computational efficiency dramatically. Here we use meshless SPH method to solve the issue. Another issue is that since the equations are high-order nonlinear PDE implicit scheme is usually more suitable. Here we employ an operator-spitting scheme [4] for solving SPH.

Once the thickness becomes too small, the rupture stage is triggered and this phenomenon is completed immediately. Thus we just delete the corresponding region in the multi-region method and use re-initialization to re-calculate the new level-set fields.

RESULTS AND CONCLUSIONS

For simplicity, the gas exchange across permeable membranes and Marangoni forces at the liquid-gas interface are neglected in our simulation. Symmetric boundary condition is applied. The CFL number is set as 0.6 and the resolution of the simulation is $h = 1/256$. Initially, four soap bubbles are evolved from an artificial configuration to an equilibrium state, as shown in the first row of Fig.2. Then region 1 breakups, after sometime, the second equilibrium is attained under the surface tension force, see the second row of Fig.2. Then region 2 breakups and the similar process is observed for the remaining two bubbles.

In summary we propose a multiscale framework that can capture the foam dynamics in an efficient and robust manner. The framework is composed of multi-region level-set method, weakly compressible NS solver and SPH method. The result shows its ability to capture the dynamics of bubble cluster and its rupture.

References

[1] Saye, Robert I., and James A. Sethian. "Multiscale modeling of membrane rearrangement, drainage, and rupture in evolving foams." Science 340.6133 (2013): 720-724.

[2] Saye, Robert I., and James A. Sethian. "The Voronoi implicit interface method for computing multiphase physics." Proceedings of the National Academy of Sciences 108.49 (2011): 19498-19503.

[3] Han, L. H., X. Y. Hu, and N. A. Adams. "Adaptive multi-resolution method for compressible multi-phase flows with sharp interface model and pyramid data structure." Journal of Computational Physics 262 (2014): 131-152.

[4] Litvinov, S., et al. "A splitting scheme for highly dissipative smoothed particle dynamics." Journal of Computational Physics 229.15 (2010): 5457-5464.

NON-SPHERICAL BUBBLE COLLAPSE DYNAMICS IN VISCOELASTIC MEDIA

Mauro Rodriguez[1] and Eric Johnsen*[2]

[1,2]*Department of Mechanical Engineering, University of Michigan, Ann Arbor, Michigan, USA*

Summary Understanding the dynamics of cavitation bubbles and the shock waves emitted by their collapse in and near viscoelastic media is important for various naval and medical applications, particularly in the context of cavitation damage. Although not fully understood, the damage mechanism combines the effect of the incoming pulses and cavitation produced by the high tension. Additionally, the influence of the shock on the material and the response of the material to the shock are not well known. A novel Eulerian numerical method for simulating shock and acoustic wave propagation in a Zener-like viscoelastic media is leveraged. The method is high-order accurate, solution-adaptive and based on a weighted essentially non-oscillatory scheme for shock capturing. Validation results and studies for two-dimensional simulations of the bubble collapse dynamics will be presented. Three-dimensional studies of the bubble collapse dynamics for various experimental studies of viscous and viscoelastic media will also be presented.

INTRODUCTION

Understanding the mechanics of shock waves in viscoelastic media is important for various naval and medical applications, particularly in the context of cavitation-induced damage. Two examples are erosion to drag-reducing elastomeric coatings along propellers and therapeutic ultrasound such as histotripsy. Histotripsy uses high-amplitude (100 MPa peak positive pressure, -25 MPa peak negative pressure) and high-frequency (MHz) ultrasound waves to destroy tissue. The local and transient pressure changes may lead to the formation of cavitation bubbles that grow and then violently collapse, thus producing shock waves that propagate in the surrounding medium. Although not fully understood, the damage mechanism combines the effect of the incoming pulses and cavitation (bubble oscillation and collapse) produced by the high tension. The constitutive models describing these materials are non-trivial and include effects such as (nonlinear) elasticity, history (relaxation effects) and viscosity. Thus, the influence of the shock on the material and the response of the material to the shock are poorly understood. For medical applications, understanding these mechanism will be invaluable to the further the development of histotripsy as a therapy tool for treating malignant tissues. For naval research, understanding the shock wave influence and the response of the coating on the shock wave can further technological developments on propeller and rudder design to mitigate cavitation damage.

A finite-difference numerical approach is proposed for simulating shock and acoustic wave propagation in multi-component flows including Zener-like viscoelastic media [9]. The governing equations are conservation of mass, momentum, energy in a Eulerian framework. For closure, an equation of state and a constitutive relations are used to determine the pressure, heat flux and stress tensor, respectively. All of the media is modeled using the stiffened equation of state. This equation is used to describe compressible flow phenomena in liquid and dense gases. An interface-capturing approach is used to represent compressible phenomena interacting with different materials. For the constitutive equation, the generalized version of the Zener model, which captures the viscous, elastic stresses and relaxation frequencies is used. Although strains can not be readily calculated in an Eulerian framework, strain rates, however, can be. Thus, we perform a temporal differentiation of the constitutive relation to readily calculate strain rates as spatial velocity gradients. As a result, additional evolution equations for the elastic component of the stresses are used in the numerical model.

NUMERICAL METHODS

For the time marching, we use the fourth-order Runge-Kutta scheme. For the spatial flux discretization, we implement the sensor presented by Henry de Frahan et al. [5] for finite elements and adapted to finite differences by Alahyari Beig et al. [1]. The sensor identifies smooth and discontinous regions that contain material interfaces, shockwaves, or both. For smooth regions, the convective fluxes for the equations are calculated using the fourth-order finite difference scheme [8]. For regions with discontinuities, the finite-volume approach presented in Johnsen and Colonius [7] is leveraged with the HLL Riemann solver for upwinding [4]. The fifth-order weighted essentially non-oscillatory (WENO) scheme [6] is used for the reconstruction of the primitive variables. The source terms in the system have first and second order derivatives. The first order derivatives are calculated using a finite-difference fourth-order discretization. Similarily, for the second order derivatives (e.g., diffusion and source terms), the finite-difference fourth-order discretization is used.

RESULTS

Two-dimensional results of single and multiple shock-induced bubble collapse problems will be presented at the meeting. Using the two-dimensional canonical bubble collapse problem [2], the re-entrant jet velocity during the collapse and total bubble collapse time numerical results are compared with the experimental results to validate the numerical

*Corresponding author. Email: ejohnsen@umich.edu

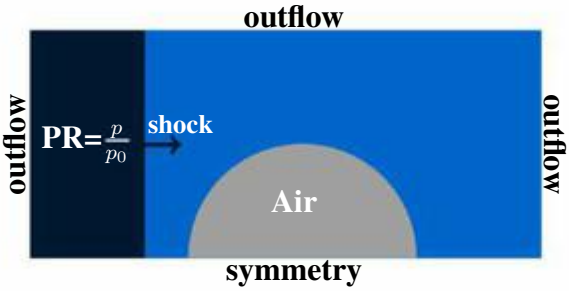

Figure 1: Bubble collapse setup initial condition analogous to the two-dimensional experiments by Bourne et al. [3]

method. The material properties of the gel of the study are comparable with the two-dimensional experiments by Bourne et al. [3] and Swantek et al. [10]. The initial condition of the problem is presented in Fig. 1, half of the domain is simulated given the symmetry of the problem. Moreover, the problem will also be used to study effect of elasticy and viscoelasticity on the single shock-induced bubble dynamics by increasing the shear modulus of the surrounding medium. The pressure contours for the two-dimensional simulations of the water and a Kelvin-Voigt-like material with μ = 50mPa s and G = 1.1MPa are presented in Fig. 2 showing the effect of viscoelasticity on the bubble dynamics. An initial bubble radius of 3mm and pressure ratio of 250 was be considered for these simulations.

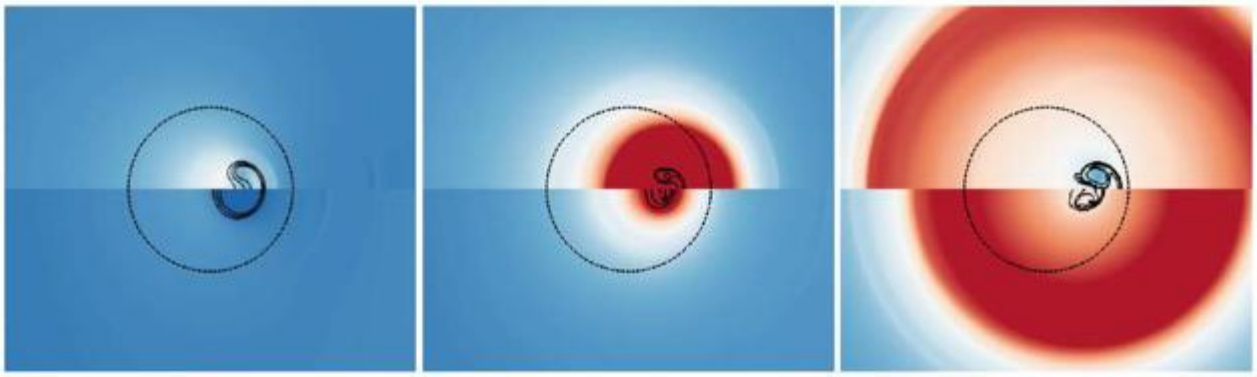

(a) time=30μs (b) time=32μs (c) time=36μs

Figure 2: Pressure contours for the 2D shock-induced bubble collapse problem. Top contours: water case. Bottom contours: Kelvin-Voigt-like material with μ = 50mPa s and G =1.1MPa. Black dashed lines: bubble initial condition. Black solid lines: approximate locations of the bubbles' interfaces.

The first frame show the viscoelasticity delaying the formation of the re-entrant jet (bottom contour) that is visibly formed in the water case (top contour). As a result, the re-entrant jet velocities and time of the bubble collapsing are reduced relative to the water case seen in the second frame. The third frame shows that, despite the shock wave generated from the bubble collapse is delayed, the pressure response between the two cases to be similar between water and a Kelvin-Voigt-like material at this shear modulus [9]. Different single and multiple bubble and compliant viscoelastic surfaces configurations where the acoustic impedance and bubble-bubble interactions effect the resulting pressure and temperatures from the bubble dynamics will also be presented at the meeting.

References

[1] S. Alahyari Beig, E. Johnsen: Maintaining interface equilibrium conditions in compressible multiphase flows using interface capturing, J. Comput. Phys. 302 (2015) 548-566.

[2] G.J. Ball, B.P. Howell, T.G. Leighton, M.J. Schofield, Shock Waves 10 (2000) 265.

[3] N. K. Bourne, J. E. Field: Shock-induced collapse of single cavities in liquids, J. Fluid Mech. 244 (1992) 255.

[4] A. Harten, P. D. Lax, B. Vanleer: On upstream differencing and Godunov-type schemes for hyperbolic conservation laws 25 (1) (1982) 35-61.

[5] M. T. Henry De Frahan, S. Varadan, E. Johnsen: A new limiting procedure for discontinuous Galerkin methods applied to compressible multiphase flows with shocks and interfaces, J. Comput. Phys. 280 (2015) 489-509.

[6] G.-S. Jiang, C.-W. Shu: Efficient implementation of weighted ENO schemes, J. Comput. Phys. 228 (126) (1995) 202-228.

[7] E. Johnsen, T. Colonius: Implementation of WENO schemes in compressible multicomponent flow, 284 problems, J. Comput. Phys. 219 (2006) 715-732.

[8] P. Movahed, E. Johnsen: A solution-adaptive method for efficient compressible multifluid simulations, with application to the Richtmyer-Meshkov instability, J. Comput. Phys. 239 (2013) 166-186.

[9] M. Rodriguez, E. Johnsen: A high-order finite-difference method for numerical simulations of shock waves in heterogenous, linear viscoelastic media. In preparation.

[10] A. B. Swantek, J. M. Austin: Collapse of void arrays under stress wave loading, J. Fluid Mech. 301 (2010) 399.

PRESSURE DISTRIBUTION ON A LEVITATING DROP OVER A MOVING SURFACE

Erina Sawaguchi[1], Kai Hama[1], Masafumi Saito[1] & Yoshiyuki Tagawa [*1]
[1]*Department of Mechanical systems engineering, Tokyo University of Agriculture and Technology, Tokyo, Japan*

Summary When a drop is deposited onto a moving wall, it can steadily levitate. The lubrication pressure generated inside an air film between the drop and the wall plays a crucial role for the levitation. In this paper, based on our experiments, we for the first time report the three-dimensional pressure distribution under the levitating drop. The pressure distribution is calculated by two different methods: One method computes the pressure distribution by applying lubrication theory. The other method estimates the pressure by a balance with surface tension and hydrostatic pressure. We find that the areas for positive or negative pressure agree well between the two methods. It experimentally confirms that the lubrication pressure steadily balances the surface tension of the deformed free surface of the levitating drop.

INTRODUCTION

When a drop is deposited onto a static wall, it touches the wall. However, when onto a moving wall, it can steadily levitate (see figure 1 and our movie: https://www.youtube.com/watch?v=VFpPb8WsaVE). It has been confirmed that the drops can levitate in a wide range of wall velocity, viscosity, and drop size. The non-coalescence phenomenon is expected to be used in liquid transportation without contacting the wall of transport pipe, or significantly affects the efficiency of ink-jet printer. Towards implementation, it is hoped to clarify the mechanism of the levitating drop.

There exists an air thin film between the levitating drop and the moving wall. Lhuissier[1] *et al*. computed the air film shape by a balance between surface tension, hydrostatic pressure, and pressure generated inside the air film. They conducted the two-dimensional numerical calculation, but did not experimentally verify the balance in three dimensions. As a result, the numerical shape of the air film qualitatively agreed with the experimental result, but only in two dimensions.

In our study, we consider the three-dimensional pressure distribution generated inside the air film. We measure the air film shape, and then calculate the pressure distribution by two different methods. One method computes the pressure distribution by applying lubrication theory. The other method estimates the pressure by a balance of the force acting on the bottom of the levitating drop. From comparison of the two pressures, we experimentally indicate the relation between the pressure generated inside the air film and the shape of the gas-liquid surface.

EXPERIMENT

The experimental setup in our study is schematized in figure 2(a). A hollow glass cylinder with diameter 200 mm rotates on its axis in the horizontal direction with constant circumferential velocity U = 1.57 m/s. A drop is deposited onto the inner wall of the cylinder, and then it is steadily levitated. The air film shape under the drop is measured by using interferometric method. Monochromatic incident light with wavelength 630 nm through coaxial zoom lens reflects off the drop's bottom and the wall respectively, which makes interference fringes. We obtain an image of the fringes with a high-speed camera (FASTCAM SA-X, Photoron). In this experiment, we use the drop of silicon oil (surface tension σ = 20.9 mN/m, density ρ = 960 kg/m^3, and viscosity ν = 100 cSt) with diameter 1.98 mm.

PRESSURE DISTRIBUTION

We calculate the pressure distribution p generated inside the air film based on three-dimensional measurement by two difference methods.

On the one hand, by applying lubrication theory, the gauge pressure p is given by motion equation of the air film[2] [3]

$$\frac{\partial}{\partial x}\left(\frac{h^3}{\mu}\frac{\partial p}{\partial x}\right)+\frac{\partial}{\partial y}\left(\frac{h^3}{\mu}\frac{\partial p}{\partial y}\right)=6U\frac{\partial h}{\partial x}$$

where h and μ respectively stand for the thickness and the dynamic viscosity of the air film and the coordinates $\{x, y, z\}$ are shown as figure 2(b). Boundary condition gives atmospheric pressure to the rim of the thin film area (diameter d_f). It was verified that the weight of the drop agreed with the lift force calculated by integrating the lubrication pressure p[3].

On the other hand, Lhuissier[1] *et al*. described Laplace's equation considering a balance between the force by surface tension, the hydrostatic pressure and the lubrication pressure at the drop's bottom. We combine the equation of the balance with the pressure by the drop's weight p_g into

$$2\sigma(\kappa_0-\kappa)+\Delta\rho g\{(z_0-z)\cos\theta+(x_0-x)\sin\theta\}=p-p_g$$

where κ, $\Delta\rho$ and θ stand for the mean curvature of the drop, the density difference between the air and the liquid, and the angular position to the gravity. $\{x_0, y_0, z_0\}$ and κ_0 respectively stand for the coordinates and the mean curvature at the rim of the thin film area, that is, $x_0 = d_f/2$, $y_0 = 0$, $z_0 = h(x_0, y_0)$ (see figure 2(b)).

* Corresponding author. Email: tagawayo@cc.tuat.ac.jp.

Now, we state the method deciding p_g. The shape of the levitating drop mostly agrees with that of the sessile drop with contact angle of 180° [3]. It is thought that the weight of the levitating drop acts on contact area where the sessile drop touches the wall. Within the contact area, we give p_c of the drop's weight divided into the contact area (diameter d_c). Atmospheric pressure is given at the rim of the thin film area, and line interpolation is performed between the rims of the thin film area and the contact area.

COMPARISON

Figure 3(a, b) shows the pressure distribution by different two methods, respectively. We verify that the lift force by integrating the lubrication pressure quantitatively agrees with the drop's weight. The both pressure distributions have positive pressure in a whole range of the thin film area and negative pressure near the downstream rim of the thin film area. In three dimensions, the two pressure distributions show quite qualitative agreement although the orders of the negative pressure are different due to the limit of the interferometric method. The surface tension of the gas-liquid surface dominantly affects the pressure distribution at the drop's bottom. Therefore, it is experimentally verified that the agreement between the two pressure distributions decides the steady shape of the free surface of the levitating drop.

CONCLUSION

We calculate with the three-dimensional pressure distribution generated inside the air film by two methods. One method computes the pressure distribution by applying lubrication theory. The other method estimates the pressure by the balance of the force acting on the drop's bottom. In three dimensions, the two pressure distributions show quite qualitative agreement that positive pressure widely ranges within the thin film area and negative pressure exists near the downstream rim of the thin film area. We experimentally indicate that lubrication pressure steadily balances the surface tension of the deformed free surface of the levitating drop.

This work was supported by JSPS KAKENHI Grant Number 26709007.

References

[1] Lhuissier, H., Tagawa, Y., Tran, T. and Sun, C., Levitation of a drop over a moving surface, *Journal of Fluid Mechanics*, Vol. 733 (2013), R4.
[2] Tipei, N., Theory of lubrication: with applications to liquid- and gas-film lubrication (1962), *Stanford University Press*, pp.144-151.
[3] Saito, M., Tagawa, Y., Lift force acting on a levitating drop over a moving wall, *Transactions of the JSME* (in Japanese), **81**, No. 825, p.15-00059 (2015).

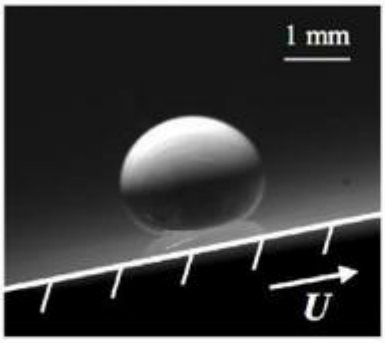

Fig.1 Side view of a steadily levitating drop.

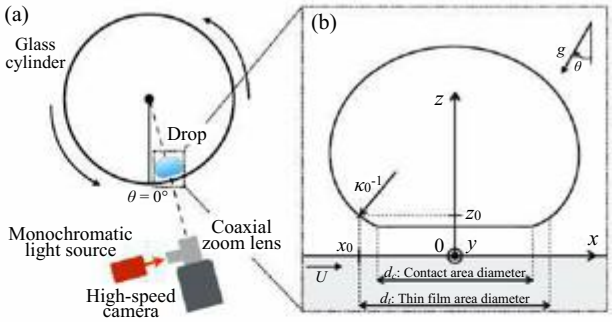

Fig.2 Schematic views of (a) the experimental setup and (b) the levitating drop.

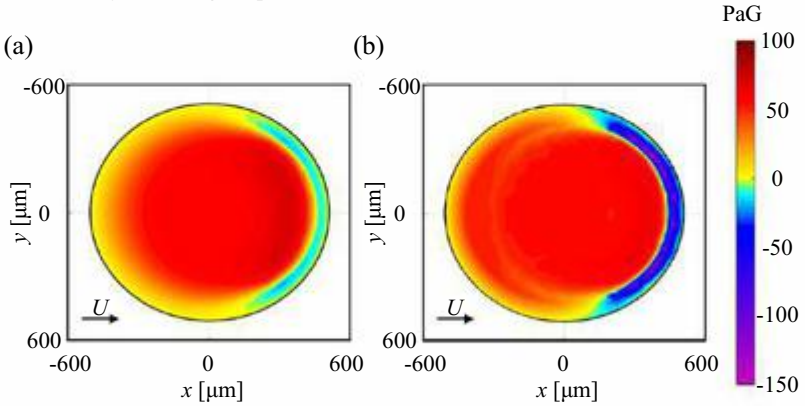

Fig.3 Pressure distributions (a) by applying lubrication theory and (b) by a balance of the force at the drop's bottom.

MESOSCALE MODELLING OF MULTIPHASE FLOW IN CONTACT WITH ELASTIC SURFACES

Ciro Semprebon*[1], Timm Krüger[1], and Halim Kusumaatmaja[2]

[1]*School of Engineering, University of Edinburgh, Edinburgh, UK*
[2]*Department of Physics, Durham University, Durham, UK*

Summary Coupling wetting and elasticity is of fundamental importance to the physics of wetting in general. It also plays an increasingly relevant role in many technological applications. One such potential application involves particles at interfaces, where the softness enhances their stabilising effects on emulsions. Here we present a novel simulation approach where the fluid phases are simulated adopting a free-energy lattice-Boltzmann method [1], while the deformable elastic structure is modelled with a finite element representation. The coupling between the solid and fluid dynamics is handled through an immersed boundary method [2]. The approach is validated by simulating the statics and dynamics of soft particles at liquid-liquid interfaces.

MOTIVATION

Flexible materials are ubiquitous in nature and cover a wide range of length scales. At microscopic scales, surface-tension forces are extremely important, and the interplay with elasticity has a pivotal role in determining the structural stability and the dynamic response of deformable materials. For example, softness of particles enhances their stabilising effects on emulsions [3]. The same applies to fibrous systems where, in addition, elasticity has a strong impact on the stability of the liquid morphologies [4]. While a wide range of simulation techniques is already present in the literature, there is a growing need for a numerical platform able to couple fluid dynamics, solid mechanics and capillary forces.

SIMULATION TECHNIQUE

In our approach we employ the lattice-Boltzmann method to incorporate fluid dynamics, combined with a recently developed ternary model based on a Landau free energy functional [1]. Deformable boundaries representing the surface of soft materials (either shells or bulk) are introduced with a finite element approach [2], while the coupling of the fluid momentum is provided by the immersed boundary method [5]. The key aspect of our approach is the coupling mechanism for the surface tensions that relies on the thermodynamic properties of the free energy approach, by confining one of the fluid phases to the interior of the deformable object.

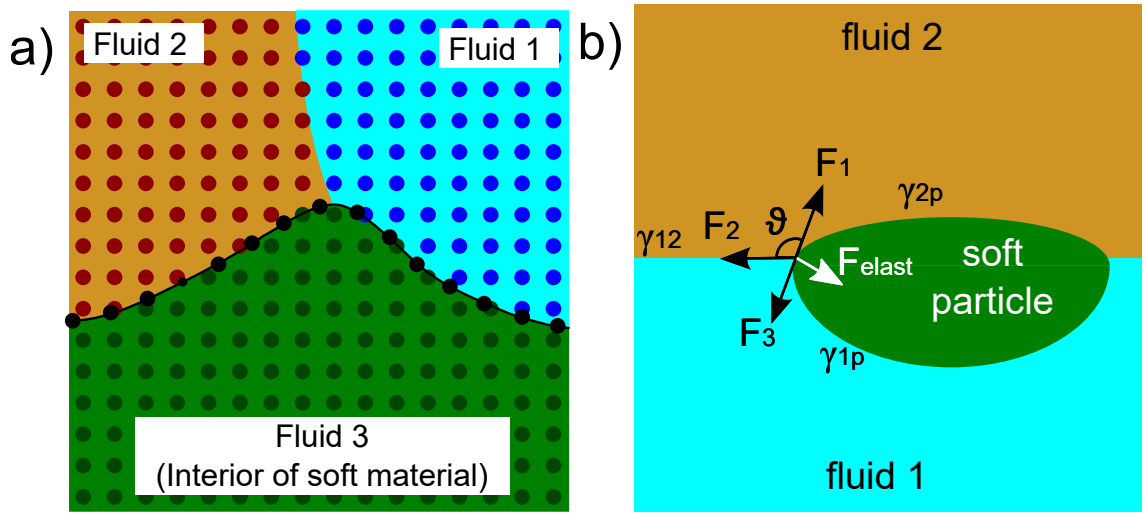

Figure 1: (a) Coupling between the three fluids and the deformable membrane: one of the fluids is assigned to the interior of the soft object. (b) Sketch of a deformed soft particle at an interface.

*Corresponding author. Email: ciro.semprebon@ed.ac.uk

WETTING OF SOFT PARTICLES

Soft particles are of primary importance for a variety of applications ranging from the production of food and cosmetics to the synthesis of pharmaceuticals. For example, particles at the interface between two fluids can be employed to replace surfactants [6]. To illustrate the potential of our numerical approach, we will show preliminary simulation results of soft particles at a fluid-fluid interface (cf. Fig. 1b), compared to recent experimental and numerical investigations [7, 8].

References

[1] C. Semprebon, T. Krüger, and Halim Kusumaatmaja. Ternary Free Energy Lattice Boltzmann Model with Tunable Surface Tensions and Contact Angles. *arXiv:1511.02155v1*, 2015.

[2] T. Krüger, F. Varnik, and D. Raabe. Efficient and accurate simulations of deformable particles immersed in a fluid using a combined immersed boundary lattice Boltzmann finite element method. *Comp. Math. App.*, 61(12):3485–3505, jun 2011.

[3] M. Destribats, V. Lapeyre, M. Wolfs, E. Sellier, F. Leal-Calderon, V. Ravaine, and V. Schmitt. Soft microgels as Pickering emulsion stabilisers: role of deformability. *Soft Matter*, 7(17):7689, aug 2011.

[4] C. Duprat, S. Protière, a. Y. Beebe, and H. a. Stone. Wetting of flexible fibre arrays. *Nature*, 482(7386):510–513, feb 2012.

[5] C. S. Peskin. The immersed boundary method. *Acta Numerica*, 11:479–517, 2002.

[6] S. Deshmukh, D. van den Ende, M. C. Stuart, F. Mugele, and M. H.G. Duits. Hard and soft colloids at fluid interfaces: Adsorption, interactions, assembly & rheology. *Adv. Coll. Int. Sci.*, 222:215–227, 2014.

[7] R. W. Style, L. Isa, and E. R. Dufresne. Adsorption of soft particles at fluid interfaces. *Soft Matter*, 2015.

[8] H. Mehrabian, J. Harting, and J. H. Snoeijer. Soft particles at a fluid interface. *Soft Matter*, 12:1–17, 2015.

INSTABILITY OF LIQUID JETS IN WEAK GASEOUS CROSSFLOW

Ghobad Amini[1a)], Ali Dolatabadi
Mechanical and Industrial Engineering, Concordia University, Montreal, Quebec, Canada

Summary Development in spray technology requires more basic understanding on primary breakup mechanism. Insight concerning this issue can be gained by studying the properties of waves that appear on the surface of the jet during the breakup process. In an effort to elucidate the primary breakup of liquid jets injected transversely into a gaseous flow, a three-dimensional temporal linear stability analysis is developed. A characteristic equation accounting for the growth of columnar waves is obtained and the instability dynamics is parametrically investigated in the presence of capillary, viscous, and aerodynamic forces.

INTRODUCTION

Due to the enhanced mass and momentum exchange between two perpendicular streams, a liquid jet injected into a gaseous crossflow (LJICF), liquid sprays in transverse flows have a wide application in a number of industrial systems including fuel injection and thermal spray [1, 4, 9]. Theoretically, the flow of a gas over streaming of a liquid causes instabilities at the interface and the growth of these instabilities leads to breakup of the liquid jet into smaller droplets and increasing the surface area, which enhances the mixing of the liquid and the gas.

The experimental results show that subjecting a liquid column to a gradually increasing crossflow velocity, four regimes are formed: column breakup, bag breakup, multimode breakup, and shear breakup [2, 3]. By increasing the gas velocity through these regimes, the wavelength of surface waves and the size of ligaments and droplets decreased. For small crossflow velocities, which is the focus of this work, the ratio of wavelength to jet diameter is greater than or approximately equal to unity. In the column breakup regime, the liquid jet column is somehow deformed to yield an ellipsoidal and kidney cross section [3] and deflected in the direction of the crossflow. The increased drag forces due to the flattened shape of the liquid jet enhances deflection in the crossflow direction and eventually causes to break. Numerical simulations [10] show that two types of disturbances exist on the jet windward surface: (I) the azimuthal disturbances which leads to the surface breakup and (II) the axial disturbances leading to the breakup of column. Experimental and numerical studies have shown that the surface breakup is the dominant breakup process in the high crossflow velocities [1, 2, 3] and the surface breakup of a jet can be a result of the shear instability on the jet lateral sides. For type (II) the evolution of the jet surface show that the column breakup occurs due to propagation of the long waves on the windward surface of the jet. With distance down the jet, these waves grow on the surface until sufficiently amplified to break up the liquid column.

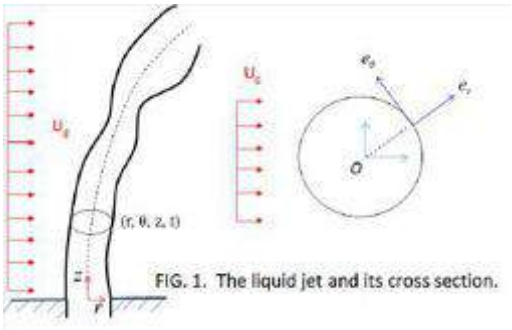

FIG. 1. The liquid jet and its cross section.

Due to the motion and interaction of the jet and the gas phase, the flow structures involved in the LJICF problem are very complex. Experimental techniques are not able to completely visualize and quantify the breakup mechanism and, on the other hand, numerical simulation of this problem requires a considerable amount of computational resources. However, theoretical models are able to capture the essential physics and can facilitate the experimental and numerical studies through parametric studies. The analysis of primary atomization of liquid jets using linear theory is generally well established [4, 5, 6, 7, 8], however, for to support columnar breakup mechanism of LJICF no theoretical investigation has been reported [10]. This work is aimed to provide this part.

PROBLEM DESCRIPTION AND GOVERNING EQUATIONS

Due to the complexity of the flow field inside and around the liquid jet, in order to tract the theoretical analysis, it is assumed the boundary layer thickness is very thin compared to the jet radius and there is no separation of the boundary layer. Additionally, it is assumed that the length scale of baseflow liquid jet velocity W_l in the axial direction is much larger than the one for axial wavelengths of interface disturbance. This assumption eliminates requirement of developing a complicated multiscale stability analysis. Furthermore, our analysis of the instabilities is applied to the region sufficiently close to the nozzle where the liquid jet deflects negligibly and assumed to preserves its nearly cylindrical shape.

For a nonturbulent viscous liquid jet, as illustrated in Fig. 1, the three-dimensional cylindrical coordinate system (r,θ,z) corresponds to the velocity vector (u,v,w), i.e. z-direction is aligned with the direction of liquid jet. The jet cross section is described by r and θ coordinates as shown in Fig.1. The liquid jet with density ρ_l, dynamic viscosity μ_l and surface tension σ is issuing with a uniform axial velocity W_l from a round nozzle with radius R through a viscous and incompressible gas with density ρ_g, dynamic viscosity μ_g, streaming with velocity U_g.

In order to carry out an instability analysis, a baseflow for the transverse jet needs to be defined. Since no steady exact solution to the Navier-Stokes equations exists for the baseflow of this three-dimensional flow field, we make use of the viscous

[a)] Corresponding author. Email: ghobad@encs.concordia.ca

potential flow model [8]. The complete set of equations includes conservation equations for mass and momentum, which by introducing the velocity potential ϕ, reduces to Laplace's equation. Based on above assumptions, the potential solution of flow around a solid cylinder can reasonably represent the external baseflow about the liquid jet as,

$$\phi_g = U_g(r + \frac{R^2}{r})\cos\theta. \quad (1)$$

For liquid baseflow it is assumed that there is only a uniform axial velocity and the other velocity components are zero.

The stability analysis is carried out by decomposing any instantaneous flow-field quantity ψ into a baseflow (mean) quantity, and a disturbance (fluctuating) quantity. Following the classic normal mode analysis, the disturbances, denoted as (.'), are expanded into normal modes through

$$\psi'(r,\theta,z,t) = \psi'(r)e^{i(kz+m\theta)+\alpha t},$$

where k and m are the real-valued axial and azimuthal wavenumber, and $\alpha=\alpha_r+i\alpha_i$ is the complex-valued frequency, with real and imaginary components corresponding to the frequency of the Fourier wave and the exponential growth rate, respectively. By substituting the normal modes into the governing equations, subtracting the baseflow, and linearizing the resulting perturbation equations, two generalized wave equations are formed. The solution for perturbed viscous potential flow for liquid and gas, considering that the solution must exist at r=0 and r→∞, is then sought in the form of

$$\phi_l' = C_1 I_m(kr)e^{i(kz+m\theta)+\alpha t}, \quad \phi_g' = C_2 K_m(kr)e^{i(kz+m\theta)+\alpha t}, \quad (2)$$

where I_m and K_m are the mth order modified Bessel functions of the first and second kind, respectively. The boundary conditions to be applied at the interface require that there is no net flux of mass across the interface and that the normal stress is continuous. These kinematic and dynamic boundary conditions are employed as.

$$U_l = \frac{\partial\eta}{\partial t} + W_l\frac{\partial\eta}{\partial z}, \quad U_g = \frac{\partial\eta}{\partial t} + V_g\frac{\partial\eta}{r\partial\theta}, \quad \tau_{rr(l)} - \tau_{rr(g)} = \frac{-\sigma}{R^2}(1-m^2-k^2R^2)\eta, \quad (3)$$

where η is interface displacement as $\eta = \eta_0 e^{i(kz+m\theta)+\alpha t}$ with initial value of η_0 and τ_{rr} is the normal stress tensor which its pressure term is obtained using Bernoulli's equation and equation (1). Linearized expansion of equation (2) using equation (3) yields two homogeneous equations which their nontrivial solution yields a local dispersion relation as D (k,α)=0. The coefficients of this equation are function of velocity and physical properties of fluids. In the next section, the instability dynamics is parametrically investigated by using the roots of this equation.

RESULTS AND DISCUSSION

In the following, the effect of surface tension, viscosity, and aerodynamic forces on the perturbation dynamics of a liquid jet in crossflow is investigated. The ratio of these forces identifies the dimensionless groups: liquid Weber number, gas Weber number, and Ohnesorge number as

$$We_l = \frac{\rho_l W_l^2 R}{\sigma}, \quad We_g = \frac{\rho_g U_g^2 R}{\sigma}, \quad Oh = \frac{\mu_l}{\sqrt{\rho_l \sigma R}}, \quad (4)$$

respectively. Additionally, we introduce momentum flux ratio $q=We_l/We_g$, density ratio $Q=\rho_g/\rho_l$, and viscosity ratio $\beta=\mu_g/\mu_l$.

For the case of zero crossflow velocity (stagnation surrounding fluid), the results obtained from the present formulation are compared with results by Avital [5] for viscous coflow case. The excellent agreement serves as verification of the developed stability formulation. By increasing the crossflow velocity, the instability growth rate is increased. The cut off wave number is a weak function of the crossflow velocity. Instability is maximum at windward direction and minimum at lateral direction. Linear hydrodynamic instability analysis is able to capture the main physics in the primary breakup step.

References

[1] Behzad M., Ashgriz N., Mashayek A.: Azimuthal Shear Instability of a Liquid Jet Injected into a Gaseous Cross-Flow. *J. Fluid Mech*. **767**:146-172, 2015.

[2] Sallam K.A., Aalburg C., Faeth G.M.: Breakup of Round Nonturbulent Liquid Jets in Gaseous Crossflow. *AIAA J*. **42,** 12:2529-2540, 2004.

[3] Wu P.K., Kirkendall K.A., Fuller R.P., A.S. Nejad A.S., Breakup processes of liquid jets in subsonic cross flows *J. Propuls. Power,* **13** , 64-73, 1997.

[4] Alves L.S., Kelly R.E., Karagozian A.R.: Local Stability Analysis of an Inviscid Transverse Jet. *J. Fluid Mech*. **581**:401-418, 2007.

[5] Avital E.: Asymmetric Instability of a Viscid Capillary Jet in an Inviscid Media. *Phys. Fluids*, **7**(**5**):1162-1164, 1995.

[6] Amini G., Ihme M, Dolatabadi A.: Effect of gravity on capillary instability of liquid jets. *Phys. Review E*., **87**, 053017, 2013.

[7] Amini G., Y Lv Y., A Dolatabadi A., M Ihme M:Instability of Elliptic Liquid Jets: Temporal Linear Stability Theory and Experimental Analysis. *Phys. Fluids*, **26**:114105, 2014.

[8] Funada T., Joseph D.D.: Viscous Potential Flow Analysis of Capillary Instability. *Int. J. Multiph. Flow* **28**:1459-1478, 2002.

[9] Farvardin E., Johnson M., Alaee H., Martinez A., Dolatabadi A.: Comparative Study of Biodiesel and Diesel Jets in Gaseous Crossflow. *AIAA J. of Prop*., **29,** 6, 1292-1302, 2013.

[10] Behzad M, Ashgriz N, Karney B.W.: Surface Breakup of a Non-turbulent Liquid Jet Injected into a High Pressure Gaseous Crossflow. *Int. J. Multiph. Flow* **80**:100-117, 2016.

STUDY OF PATH INSTABILITY OF A RISING OIL DROPLET USING PIV

Arun Kumar[1], Aman Jain[2] & P. Shukla[3]
[1, 2, 3]*Department of Mechanical Engineering, Indian Institute of Technology (Banaras Hindu University) Varanasi, India*

Abstract: This paper presents an experimental study of the dynamics of a rising oil droplet in water. The motion is associated with path, velocity and shape instabilities. In this work, the former two instabilities have been studied. A three-dimensional visualization of the trajectory of the rising droplet has been presented. A stereo-PIV analysis was conducted on the system for visualization of the velocity field generated by the motion of the droplet. Two distinct type of trajectories were observed and the liquid droplet were found to follow two types of paths - straight and zig-zag. Helical paths were not observed in our study. Vorticity plots calculated from the velocity field are used to explain the observed trajectories.

INTRODUCTION

The droplet motion of one immiscible fluid within a continuum phase of another fluid is of great importance in several industrial and technological applications such as extraction of liquid–liquid mixture, breakup of emulsions, pipeline transportation of liquid–liquid mixture, and in the oil industry where oil and water are often produced and transported together. Droplet rise in an immiscible liquid is a complex phenomenon because unlike the motion of solid particles in liquids, the no-slip velocity condition does not hold true in this case. What further compounds the problem are the associated path, velocity and shape instabilities [2].

Several computational and experimental studies have studied the phenomenon of rising droplets in water [2-4]. In a recent work, Albert *et al*. [2] conducted an extensive computational study of a high viscosity liquid droplet rising in water. Chaotic helical trajectories associated with the motion of bubbles [5] were not observed in their study. An experimental investigation related to the phenomenon of rising droplets in water, similar to the one studied computationally in [2] was conducted, using a highly viscous fluid (~320 cP). The aim of this study is to visualize the flow field induced due to a rising droplet in quiescent water using stereo-PIV and its relation with the droplet trajectory. The trajectory of the rising oil droplets was traced in three dimensions using two digital cameras positioned perpendicular to each other, in a separate experiment under the same conditions.

EXPERIMENTAL PROCEDURE

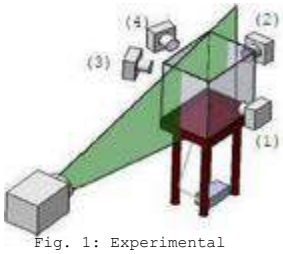

Fig. 1: Experimental Setup

Oil of viscosity 320 cP was injected into a water tank (24 cm x 30 cm x 31 cm) seeded with neutral buoyant glass particles. An infusion pump connected to a nozzle was used to control the flow rate and the following experiments were performed in succession for each droplet: Droplets in the size range 2.4 to 2.6 mm were generated using a needle of internal diameter 0.18 mm and a flow rate of 1 ml/hr while larger droplets (4.0 to 4.2 mm) were produced using a needle of diameter 0.65 mm and a flow rate of 5 ml/hr.

Experiment 1: Two digital cameras 1 and 2 (1280 x 720-pixels resolution, 60 fps) were placed at 90° to each other with sufficient illumination to track the trajectory of the coloured oil droplet in two mutually perpendicular planes.

Experiment 2: After Experiment 1 was performed, liquid was allowed to settle overnight and stereo-PIV measurements were taken to visualize flow field around the rising droplet under identical experimental conditions. The reason for not performing both the experiments simultaneously was the practical difficulty associated with taking pictures from digital cameras with the laser firing simultaneously.

OBSERVATIONS

The size of droplets generated depends on the nozzle diameter and the flow rate of the pump. Different trajectories were observed for droplets of different sizes. As shown in fig. 2(a), smaller droplets of size range 2.4 mm to 2.6 mm follow an approximately vertical path with slight oscillations while larger droplets of size range 4.0 mm to 4.2 mm. initially moved linearly and then follow a zig-zag trajectory (fig. 3(a)). The plane of zig-zag motion differed for each droplet and cannot be ascertained beforehand. However, the nature of the trajectory for a droplet of a particular size was found to be the same after multiple runs. The height at which the oscillations began and the shape of the path obtained were nearly the same for a droplet of a given size. The phenomena of smaller droplets rising linearly and larger droplets exhibiting a zig-zag trajectory has also been reported by Albert *et al*. [2]. The velocity field for the droplet moving in a linear fashion shows a small component of velocity (~ 1 mm/s) in the Z-direction as illustrated by the yellow patches in fig. 2(b) whereas for the case of the larger droplets (fig. 3(b)), the Z-direction velocities vary from approximately -10 mm/s (blue region) to 5 mm/s (red region). The zig zag motion of the larger droplet induces both positive and negative values of the Z-velocity. In this case, the droplet was found to move out of the X-Y plane at x = 40 mm which is depicted by a large velocity in the Z-direction.

[3)]Corresponding author. Email: pshukla.mec@iitbhu.ac.in

The vortices formed in 2(c) have strengths ranging from nearly -2.3 s^{-1} (blue) to 1.3 s^{-1} (orange) and are smaller in size while in (fig. 3(c), region b), because of the larger size of the droplet, the vortices spread over a larger area. Interestingly, the region where the larger droplet leaves the X-Y plane (x=40 mm), an unpaired vortex of strength (~1.2 s^{-1}, fig. 3(c), region c) was observed.

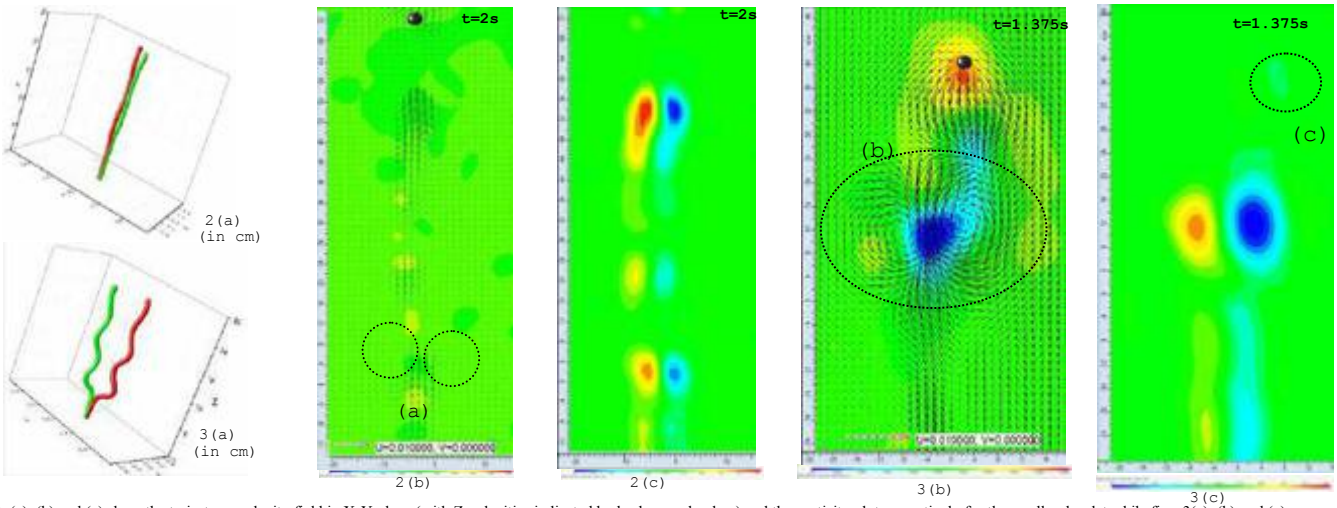

Figs. 2: (a), (b) and (c) show the trajectory, velocity field in X-Y plane (with Z-velocities indicated by background colors) and the vorticity plot respectively for the smaller droplet while figs. 3(a), (b) and (c) show the corresponding data for larger droplets. Reference vector: U=0.01 m/s.

DISCUSSIONS

The rectilinear rise of smaller droplets is consistent with the observation of low velocities in the Z-direction. The existence of oscillations (Fig. 3(b)) in the trajectory for larger droplets is justified by the presence of a large velocity component in the Z-direction associated with the flow field near the droplet. The rising droplet pushes the liquid ahead while the liquid behind it is sucked into droplet wake. A pair of counter-rotating vortices were observed for smaller droplets (see Fig. 2(b), region a). Similarly, for larger droplets, an unsymmetrical wake region was clearly visualized and two vortices tilted opposite to each other were observed (see Fig. 3(b), region b). The wake region was also visualized via vorticity plots (see Figs. 2(c) and 3(c)) which indicate that larger droplets leave behind a larger disturbed area. Also, a shorter extent of impact was observed ahead of the droplets. It is speculated that the unsymmetrical wake region behind the larger droplet is responsible for the movement of the droplet away from the plane of the laser sheet as shown in Fig. 3(b). Some authors [3] believe that the onset of zig-zag motion must be due to superposition of the droplet shape oscillation and its translational oscillation. It was argued that the existence of deformation will change the effective area of the drag force, causing unbalanced force couples on the drop and making the drop rotation and further deformation, and finally leading to oscillations [3].

.

CONCLUSIONS

Smaller droplets (2.4 to 2.6 mm) were found to rise in an approximately straight path whereas larger droplets (4.0 to 4.2 mm) followed a zig zag trajectory. Chaotic helical trajectories associated with bubble motion were not observed in this study. Due to their zig zag motion, larger droplets were found to move out of the laser plane. An unsymmetrical wake region with counter-rotating vortices oblique to each other was observed for larger droplets. Stereo-PIV results indicated a large Z-velocity component associated with the flow field near the droplet when it begins its oscillating. The zig zag motion of the larger droplet induces both positive and negative values of the Z-velocity.

References

[1] C. Albert, J. Kromer, A. M. Robertson, D. Bothe: Dynamic behaviour of buoyant high viscosity droplets rising in a quiescent liquid, J. Fluid Mech. (2015), Vol. 778, pp. 485-533, Cambridge University Press 2015

[2] Zhengming Gao, Li Rao, Yuyun Bao and Ziqi Cai: Hydrodynamics and Deformation of Single Drop Rising in Newtonian Fluids, Journal of Chemical Engineering of Japan, Vol. 48, No. 5, pp. 345–352, 2015.

[3] Mirco Wegener and Matthias Kraume, Terminal and Transient Drop Rise Velocity of Single Toluene Droplets in Water, Fluid Mechanics and Transport Phenomena (2009), DOI 10.1002/aic.11969

[4] A.W.G. de Vries: Path and wake of a rising bubble, PhD Thesis (2009), University of Twente, Netherlands

INERTIAL AND VISCOUS FORCES ON DRIPPING-TO-JETTING TRANSITION IN AQUEOUS TWO-PHASE SYSTEMS

Sze Yi Mak[1,2] , Youchuang Chao[1,2] & Ho Cheung Shum [1,2a)]
[1]*Department of Mechanical Engineering, The University of Hong Kong, Hong Kong*
[2]*HKU-Shenzhen Institute of Research and Innovation (HKU-SIRI), Guangdong, China*

Summary The dripping-to-jetting transition of a co-flow has been extensively studied. Jetting often occurs due to a sufficiently large inertial force for a non-viscous jet or a considerably large viscous force for a viscous jet. However, in an aqueous two-phase system (ATPS) with an ultra-low interfacial tension, the force required to overcome the tension to form a jet is significantly smaller. We show that the viscous force of a non-viscous jet can be sufficient to induce jetting. The dripping-to-jetting transition is governed by the sum of viscous and inertial force instead of by any of them alone.

INTRODUCTION

Weber number and Capillary number of the inner phase describe the balance of inertial and viscous forces, respectively, against interfacial force. It is known that a widening jet is achieved by a large inertial force that compensates for the interfacial force; hence this transition is often characterized by the Weber number of the inner phase We_i approaching unity[1-3]. In another extreme case where the viscosity of the inner phase is high, the dripping-to-jetting transition is instead indicated by the Capillary number of the inner phase Ca_i approaching a tenth[4]. While these parameters serve well in characterizing the transition for oil-water systems, which generally have a relatively higher interfacial tension than aqueous two-phase systems (ATPSs), they fail to characterize the transition for water-water system. We revisit the dripping-to-jetting transition in a core-annular flow in a microfluidic glass capillary channel by replacing oil-water systems with an aqueous two-phase system. We discover that the dripping-to-jetting transition of such ATPS is attributed to the combined effect of inertial and viscous force of the inner phase.

RESULTS AND DISCUSSIONS



Figure 1: Microscopic images of two-phase microfluidic flow. Dripping and Jetting regimes. Scale bars are 200 μm.

We consider the transition of a widening jet. Figure 1 shows the typical microscopic images of dripping and jetting. Dripping-to-jetting transition occurs when the inner flow rate is increased to a certain threshold value. Firstly, we notice that the threshold inner flow rate can be as low as 50 μl/h. At this flow rate, the inertial force alone is not sufficient to overcome the interfacial tension. Interestingly, we find, for ATPSs with low interfacial tension, the transition is not characterized by either $We_i \sim 1$ (Figure 2a) or $Ca_i \sim 0.1$ as expected for oil-water systems. Instead, it is represented by $(We_i + Ca_i) \sim 1$, as shown in the phase map in Figure 2b.

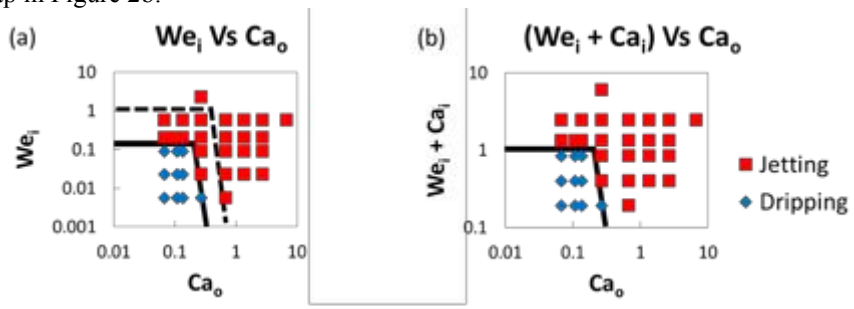

Figure 2: (a) Phase map of We_i against the Capillary number of the outer phase Ca_o. Dashed line is the literature dripping-to-jetting transition from Ref. 1. Solid line is the transition found for our ATPS. (b) Phase map of $(We_i + Ca_i)$ against Ca_o.

In case of low interfacial tension system like ATPS, the interfacial force is so weak that the dripping-to-jetting transition typically occurs at extremely low inner flow rate (Q_i = 50 μl/h in some cases). At such low flow rate, both the inertial and viscous forces of the inner phase are very minute; and the Reynolds number of the inner phase Re_i, which characterizes their relative importance, is in the range of O(-2) and O(0) (see Figure 3). To better describe the dripping-to-jetting transition for low

[a)] Corresponding author. Email: ashum@hku.hk.

interfacial tension systems which yields such a wide distribution of Re_i throughout the transition, we propose adopting the sum of inertial and viscous forces relative to the force of interfacial tension, i.e., $We_i + Ca_i$, with the rationale illustrated as follows.

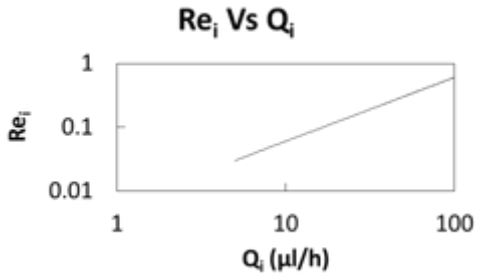

Figure 3: Re_i against Q_i. The Reynolds number of the inner phase spans two decades as the inner flow rate increases.

At a low viscosity of the inner fluid of 1.79 mPa.s, the viscous force observed at a low flow rate of Q_i = 50 µl/h is sufficient to overcome the interfacial tension and cause jetting. Hence, despite the low viscosity, viscous force of the inner phase may still become dominant. Meanwhile, as the inner flow rate is increased, the inertial force increases significantly. The Reynolds number of the inner phase Re_i indeed increases by ten-fold as the flow rate is increased. Since the transition takes place in this range of inner flow rate for which Re_i varies significantly, meaning the relative importance of viscous force and inertial force is changing, we believe the dripping-to-jetting transition is best characterized by the combined value of Weber and Capillary numbers of the inner phase.

EXPERIMENTS

The microfluidic devices are made of glass capillaries. A round glass capillary is tapered into desired nozzle size of ~ 40 µm and is placed into a square capillary with an inner size of around 1 mm. An additional untapered round capillary with an inner diameter of ~ 600 µm is put inside the square capillary enveloping the tapered nozzle to further reduce the channel dimension. All capillaries are co-axially aligned. The aqueous two-phase system (ATPS) is prepared by dissolving 10.27 wt% of sodium citrate with 10.91 wt% of Poly(Ethylene Glycol) with a molecular weight of 8000 Da (PEG 8000) in deionized water. After phase separation, a PEG-rich top phase and a salt-rich bottom phase are obtained. The interfacial tension of the ATPS is 0.013 mN/m, as measured by a spinning drop tensiometer (SITE 100, Krüss). The bottom and top phases are fed into the square and tapered round capillary as the inner and outer phase respectively. The viscosity of the inner phase is 1.79 mPa.s, measured with a viscometer (MicroVisc, RheoSense). The inner and outer flow rates are Q_i = 5 µl/h to 1 ml/h and Q_o = 50 µl/h to 5 ml/h. The two-phase co-flow is monitored by an inverted microscope (AE2000, Motic) and a high speed camera (V9, Phantom).

CONCLUSIONS

This study has revealed a unique situation of the breakup dynamics in aqueous two-phase co-flow where the interfacial tension is ultra-low. Even the jet phase is not highly viscous, the viscous force of the inner phase together with the inertial force cause jetting at a very low inner flow rate. This work demonstrates the need for a different treatment of the dripping-to-jetting transition for liquid-liquid systems with an ultra-low interfacial tension.

ACKNOWLEDGEMENTS

We thank Prof. Howard A. Stone and Dr. Yuan Liu for valuable discussions. This research was supported by the Early Career Scheme (No. HKU 707712P) and the General Research Fund (Nos. HKU 719813E, 17304514 and 17306315) from the Research Grants Council of Hong Kong, the General Program (No. 21476189/B060201), Young Scholar's Program (No. NSFC51206138/E0605) and the Major Research plan (No. 91434202) from the National Natural Science Foundation of China, as well as the Seed Funding Programme for Basic Research (Nos. 201211159090, 201311159105) from the University of Hong Kong.

References

[1] Utada A. S. et al.: Dripping to jetting transitions in coflowing liquid streams. *Phys. Rev. Lett.* **99**:094502, 2007.

[2] Nunes J. K et al.: Dripping and jetting in microfluidic multiphase flows applied to particle and fibre synthesis. *J. Phys. D: Appl. Phys.* **46**:114002, 2013.

[3] Ren Y. et al: Breakup dynamics and dripping-to-jetting transition in a Newtonian/shear-thinning multiphase microsystem. *Lab Chip* **15**:121, 2014.

[4] Cubaud T. et al.: Capillary threads and viscous droplets in square microchannels. *Phys. Fluids* **20**:053302, 2008.

NUMERICAL SIMULATION OF COLLOID EVAPORATION IN CONFINED CONVECTIVE COATING

Hochan Hwang[1] and Gihun Son *[1]
[1]*Department of Mechanical Engineering, Sogang University, Seoul, South Korea*

Summary Confined convective assembly coating based on the evaporation of a colloidal suspension including nanoparticles is investigated numerically solving the conservation equations of mass, momentum, and energy in the liquid-gas phases, the vapor mass fraction in the gas phase, and the particle concentration in the liquid phase. A sharp-interface level-set method for tracking the liquid-gas interface is extended to include the effects of phase change, contact angle and particle deposition. The computation demonstrates particle accumulation near the contact line. The present method is proved to be applicable to investigation of the effect of plate velocity on the particle deposition pattern in the confined convective coating.

INTRODUCTION

Convective assembly coating has been extensively investigated as a novel fabrication method for micro- and nano-structures in the last decade, as reviewed by Wang and Zhou [1]. The convective assembly has been further improved employing a confined geometry, such as between two parallel or non-parallel plates [2, 3], for rapid and well-controlled fabrication of micro film structures. However, a general predictive model for the confined convective coating has not yet been developed due to the complexity of the evaporating interface phenomena coupled to the heat and mass transfer in the liquid-gas phases and the particle deposition near the liquid-gas-solid contact line.

Recently, numerical simulations were performed for sessile droplet evaporation and particle deposition using body-fitted moving-grid methods [4], finite elements methods [5], a volume-of-fluid method [6] and a level-set (LS) method [7]. Very recently, Lee and Son [8] developed the LS method for analysis of liquid evaporation and particle deposition in dip coating.

In this work, the LS method is further extended for computation of the particle deposition in confined convective coating. Numerical techniques are developed for implementation of evaporation, contact line motion and particle deposition on a moving substrate.

NUMERICAL ANALYSIS

The present numerical approach is based on the sharp-interface LS method for liquid film evaporation and particle distribution in dip coating developed in our previous work [8] and extended for the confined convective coating. The liquid-gas interface is tracked by the LS function ϕ, which is defined as a signed distance from the interface. The positive sign is chosen for the liquid phase and the negative sign for the gas phase.

The conservation equations of mass, momentum and energy in the liquid and gas phases, vapor mass fraction (Y_v) in the gas phase, and particle volume fraction (Y_p) in the liquid phase can be expressed as

$$\nabla \cdot \mathbf{u} = \beta \dot{m} \mathbf{n} \cdot \nabla \alpha \tag{1}$$

$$\hat{\rho}\left(\frac{\partial \mathbf{u}}{\partial t} + \mathbf{u}_f \cdot \nabla \mathbf{u}_f\right) = -[\nabla p + (\sigma\kappa - \beta \dot{m}^2)\nabla\alpha] + \hat{\rho}\mathbf{g} + \nabla \cdot [\hat{\mu}\nabla \mathbf{u} + (\nabla \mathbf{u}_f - \beta \dot{m}\mathbf{n}\nabla\alpha)^T] \tag{2}$$

$$(\hat{\rho c})\left(\frac{\partial T}{\partial t} + \mathbf{u}_f \cdot \nabla T\right) = \nabla \cdot \hat{\lambda}\nabla T \quad \text{if } \phi \neq 0; \qquad T = T_I \quad \text{if } \phi = 0 \tag{3}$$

$$\frac{\partial Y_v}{\partial t} + \mathbf{u}_g \cdot \nabla Y_v = \nabla \cdot \hat{D}_v \nabla Y_v \quad \text{if } \phi < 0; \qquad Y_v = Y_{v,I} \quad \text{if } \phi = 0 \tag{4}$$

$$\frac{\partial Y_p}{\partial t} + \mathbf{u}_l \cdot \nabla Y_p = \nabla \cdot \hat{D}_p \nabla Y_p \quad \text{if } \phi > 0; \qquad -\dot{m} Y_p = \rho_l \hat{D}_p \nabla Y_p \cdot \mathbf{n} \quad \text{if } \phi = 0 \tag{5}$$

Here, the subscript f denotes the liquid phase (l) for $\phi > 0$ and the gas phase (g) for $\phi \leq 0$. The discontinuous step function α, the interface normal $\mathbf{n}$, and the interface curvature κ are evaluated from the LS function. The velocity $\mathbf{u}_f$ ($\mathbf{u}_l$ or $\mathbf{u}_g$) for each phase is extrapolated into the entire domain (or a narrow band near the interface) from the real velocity.

The temperature T_I and vapor fraction $Y_{v,I}$ at the interface ($\phi = 0$) and the evaporation mass flux $\dot{m}$ are simultaneously determined from the following coupled equations for the mass and energy balances at the interface and the thermodynamic relation

$$\dot{m} = \frac{\mathbf{n} \cdot \rho_g \hat{D}_v \nabla Y_v}{(1 - Y_{v,I})} = \frac{\mathbf{n} \cdot \left[(\hat{\lambda}\nabla T)_{\phi>0} - (\hat{\lambda}\nabla T)_{\phi<0}\right]}{h_{lg}} \qquad Y_{v,I} = \frac{M_v p_{v,sat}(T_I)}{M_v p_{v,sat}(T_I) + M_a\left[p_\infty - p_{v,sat}(T_I)\right]} \tag{6}$$

*Corresponding author. Email: gihun@sogang.ac.kr

The LS function ϕ is advanced and reinitialized as

$$\frac{\partial \phi}{\partial t} = -(\mathbf{u}_l + \frac{m}{\rho_l}\mathbf{n}) \cdot \nabla \phi; \qquad \frac{\partial \phi}{\partial \tau} = \frac{\phi}{\sqrt{\phi^2 + h^2}}(1 - |\nabla \phi|) \qquad \text{if} \quad |\phi| \geq h/2 \tag{7}$$

The boundary conditions at the bottom wall (y=0) are as follows:

$$u = u_w, \quad v = 0, \quad T = T_w, \quad \frac{\partial \phi}{\partial y} = -\cos\theta_w, \quad \frac{\partial Y_v}{\partial y} = 0, \quad \hat{D}_p \frac{\partial Y_p}{\partial y} = k_d Y_p \tag{8}$$

RESULTS AND DISCUSSION

Numerical simulation is performed for the evaporation of a colloidal suspension between a lower moving plate and an upper stationary plate. The results are plotted in Fig. 1. The computation demonstrates liquid circulation due to plate movement, vapor expansion caused by non-uniform evaporation and particle accumulation near the contact line.

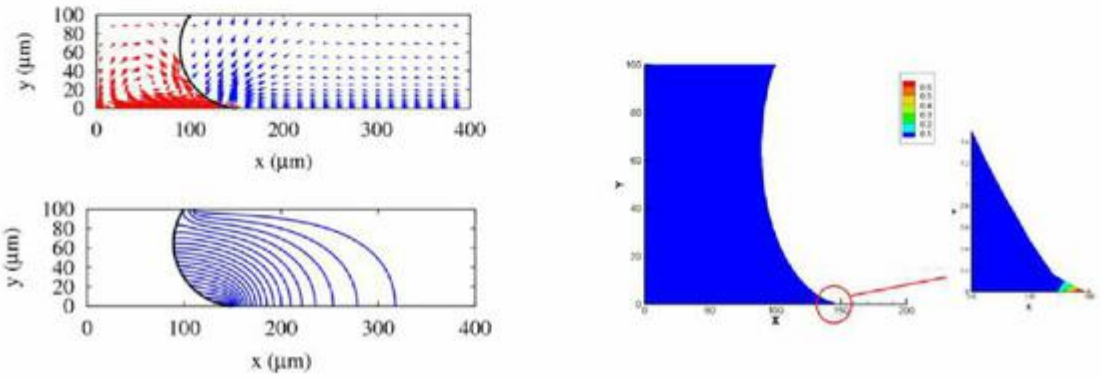

Figure 1: Colloid evaporation in convective coating: velocity, vapor fraction and particle concentration fields.

CONCLUSIONS

Numerical simulations were performed for the particle deposition in a confined convective coating condition using a sharp-interface level-set method modified to include the evaporation at the liquid-gas interface, the contact line movement and the particle deposition. The present computations demonstrated that the plate velocity significantly affects the liquid film formation and particle deposition thickness. The present LS method is proved to be applicable to investigation of the effect of plate velocity on the particle deposition pattern in the confined convective coating.

ACKNOWLEDGMENTS

This work was supported by the National Research Foundation of Korea (NRF) funded by the Korean government (MSIP) (Grant No. 2013R1A2A2A01068333).

References

[1] Wang Y., Zhou W.: A Review on Inorganic Nanostructure Self-assembly. J. Nanosci. Nanotechnol. 10:1563-1583, 2010.
[2] Prevo B.G., Velev O.D.: Controlled, Rapid Deposition of Structured Coatings from Micro- and Nanoparticle Suspensions. Langmuir 20:2099-2107, 2004.
[3] Kim M.H., Im S.H., Park O.O.: Rapid Fabrication of Two- and Three-Dimensional Colloidal Crystal Films via Confined Convective Assembly. Adv. Funct. Mater. 15:1329-1335, 2005.
[4] Maki K.L., Kumar S.: Fast Evaporation of Spreading Droplets of Colloidal Suspensions. Langmuir 27:11347-11363, 2011.
[5] Bhardwaj R., Fang X., Attinger D.: Pattern Formation during the Evaporation of a Colloidal Nanoliter Drop: a Numerical and Experimental Study. New J. Phys. 11:075020, 2009.
[6] Briones A.M., Ervin J.S., Putnam S.A., Byrd L.W., Jones, J.G.: A Novel Kinetically-Controlled De-Pinning Model for Evaporating Water Microdroplets. Int. Commun. Heat Mass Transf. 39:1311-1319, 2012.
[7] Son G.: Numerical Simulation of Microdroplet Impact and Evaporation on a Solid Surface. J. Heat Transf. 134:101502, 2012.
[8] Lee J., Son G.: Numerical Simulation of Liquid Film Formation and Evaporation in Dip Coating. Int. Commun. Heat Mass Transf. 68:220-227, 2015.

ON DROP INDUCED VORTEX RING AND ITS RELATED OSCILLATION PARAMETER

Pei-Hsun Tsai, Tetuko Kurniawan, Yu-Wen Hsieh & An-Bang Wang
Institute of Applied Mechanics, National Taiwan University, Taipei, 10617, Taiwan, R.O.C.

Summary Drop oscillation has long since been considered as the possible parameter to influence the penetration depth of vortex rings. However, for the simplicity, the conventional knowledge about drop oscillation on drop impact is restricted only on the 2nd mode without higher modes. Here, we demonstrated that this neglect has caused the contradictory ambiguity about the oscillation effect on transport phenomena over hundred years. In fact, instead of theoretically complex nonlinear expressions, a combination of both 2nd and 3rd oscillation modes are enough to describe the general characteristics of drop oscillation in practice and also are necessary to explain its induced outcomes. We therefore derive a theoretical prediction for ring penetration so as to highlight a quantitative design guideline for efficient transportation and mixing across free liquid surface.

AMBIGUOUS "DROP SHAPE" FOR DROP-INDUCED VORTEX RING PENETRATION

Vortex formation is omnipresent after a drop has impacted and merged into liquid surface [1]. Among different observations, some reported that the deepest penetration appeared when the drop shape at impact was vertically prolate [2,3], but some others indicated that it occurred for drops with spherical shape oscillating from (vertically) oblate to prolate [4,5]. This puzzle of contradictory arguments was attributed to the incomplete oscillation parameter used in the past [6]. Observation of the outer shape is always the most direct way to describe the oscillation of a drop. The theoretical time-varying outer shape of a drop can be written [7] as

$$R\ \theta\ \tau\ = R_0\left[1+\sum_{n=2}^{\infty} C_n\ \tau\ P_n(\cos\theta\ \right] \tag{1}$$

where R_0 is the undisturbed drop radius, θ is the polar angle and P_n is the associated Legendre polynomial. The coefficient $C_n(\tau)$ represents the amplitude coefficient of the n-th oscillation mode with respect to R_0. To get a better and quantitative understanding of the oscillating drop, Fig. 1(a) shows the experimental images of an oscillating drop after pinch-off, compared with truncated summations of different oscillation modes (mode 2 only is denoted as S_1, summation of mode 2 and mode 3 as S_2 and so forth). It shows clearly that mode 2 alone (S_1) could not correctly describe the outer shape of a real drop with strong non-symmetric oscillations (see photos at the bottom row). Importantly, there is no significant difference from the comparisons of S_2 and truncated results of more terms (cf. the rows with respect to S_2, S_3 and S_4); the results of S_2 (red dashed contours) overlap experimental images in a quite satisfactory manner, as shown in the last row. This reveals that the characteristic oscillation of a drop, to a first approximation, can be well represented by the two-term summation of the first two modes for general analysis. It brings about the advantages of drop shape description that the effects of gravity, aerodynamic resistance and nonlinear behaviors of drop could be negligible since all of them are excluded in the theory. On the other hand, the drop shape in consideration of superposition of at least oscillation mode 2 and mode 3 is deemed necessary for understanding the oscillatory outcomes. In the literature, drop shape parameter, axis ratio e (= b/a, see the inset of Fig. 1(b)), is the most frequently used; however, it can only reflect the characteristics of oscillation mode 2. Alternatively, the newly proposed oscillation index O_i (= b_1/R_0) can fully reflect the dynamics of drop with higher oscillation modes [6]. To demonstrate the incompleteness of using e to describe the outcomes of oscillating drops, values of the penetration depth L of the vortex ring by drops with different diameters (1.66 mm < D < 6.25 mm), impacting onto the same liquid pool, were carefully measured after significant improvement of measuring techniques [8]. These values were represented as circles with different sizes in Figs. 1(b) and 1(c), where $\Delta\tau$ denotes the time difference between e or O_i at drop impact and those at peaks (e_m or $O_{i,m}$), and T_2 denotes the oscillation period of mode 2. The less the $\Delta\tau$, the closer the drop shape at impact approaches to the peaks of shape parameters (e_m or $O_{i,m}$). It shows clearly that $O_{i,m}$ predicts the timing of the maximum penetration depth (L_{max}, red circles, in which one L_{max} regards to one drop size) much more precisely than e_m since L_{max} distributes much narrower with respect to O_i (-8% ~ 6%) than e (-27% ~ 6%).

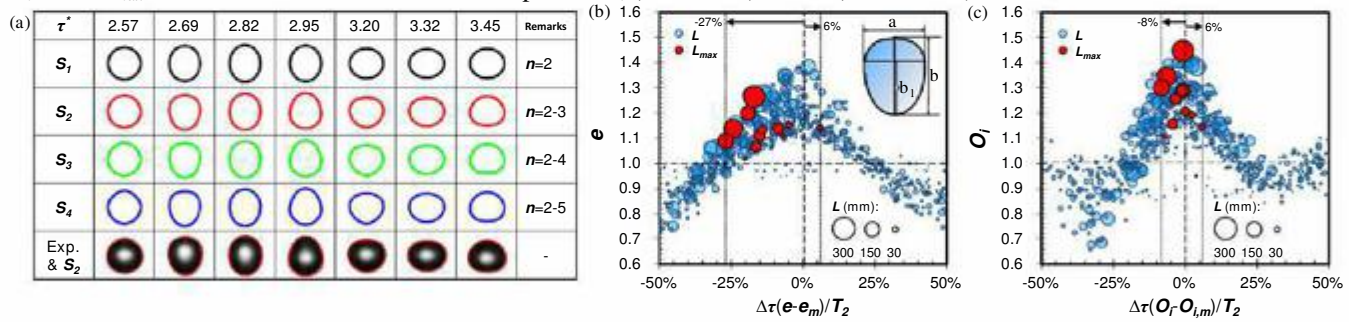

Fig 1. (a) Decomposition analysis of an oscillating drop. (b) Relation between the axis ratio e and the penetration depth L of vortex rings. (c) Relation between the oscillation index O_i and the penetration depth L of vortex rings.

[a] Corresponding author. Email: abwang@spring.iam.ntu.edu.tw.

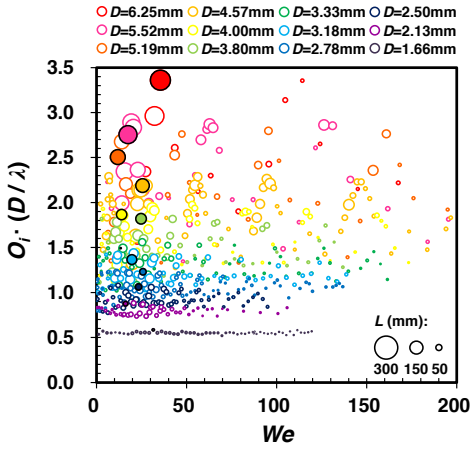

Fig. 2 Relation of O_i, *We* and penetration depth *L* of drop-induced vortex rings.

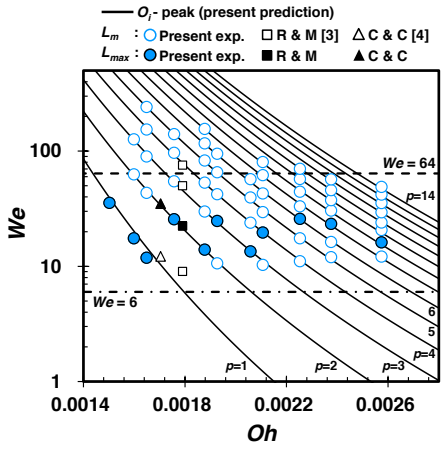

Fig. 3 Phase diagram of local (L_m) and absolute (L_{max}) max. penetration depth of vortex rings.

INFLUENCE OF DROP OSCILLATION AND PREDICTION OF RING PENETRATION

Fig. 2 shows a counter-intuitive fact that the penetration depth of drop-induced vortex rings decreases with Weber number *We* (= $\rho VD^2/\sigma$, where ρ, V, and σ are the density, impact velocity, and surface tension of drop, respectively). It implies that the drop with higher impact velocity (higher *We*) does not lead to deeper penetration depth. Instead, the L_{max} (solid circles) has a positive correlation regarding to O_iD/λ, where λ is the capillary length of liquid drops. Since O_iD/λ equals $b_1/(\lambda/2)$, this ratio reveals how significantly the drop oscillates, especially as b_1 larger than $\lambda/2$ (or $O_iD/\lambda > 1$). It can be concluded that the vortex ring penetrates more into the pool as drop size increases due to the magnification of oscillation.

Rather than only taking the Ohnesorge number *Oh* (= $\mu/(\rho\sigma D)^{1/2}$, where μ stands for the viscosity of drop), which determines whether a vortex ring forms [9], and *We* into account as shown in Fig. 3, we derived a theoretical prediction of the local peaks of O_i based on the Newton's law and drop oscillation theory to pin down the key influential parameters for the maximum penetration depth of vortex rings. As a result, the velocity V_p for each peak p of O_i can be obtained as follows:

$$V_{p(O_i)} = V_T \tanh\left\{\frac{g}{V_T}\left[\frac{90(4p+1)-\phi_{Oi}}{360}\right]T_{O_i} + \tanh^{-1}\left(\frac{V_0}{V_T}\right)\right\}, p = 1,2,3,... \quad (2)$$

where V_T and V_0 correspondingly denote the terminal and initial velocities of drops after pinch off, and T_{oi} (= $3T_2T_3/(T_2+T_3)$, where T_3 is the oscillation period of mode 3) and ϕ_{oi} are the period and phase angle of O_i, respectively. The experimental results, including data from literatures [3,4], as well as the predicted lines are compared in the phase diagram as shown in Fig. 3, and the local and absolute maximum penetration depths of vortex rings (L_m and L_{max}) can be well-predicted by Eqn. (2). It not only reveals the preference of drop shape with O_i-peak for upgrading the penetration depth but also highlights the quantum-like distribution of maximum penetration depth of vortex rings in the (*Oh*, *We*)-plane due to drop oscillation.

Acknowledgement

We thank the National Science Council of Taiwan for financial support under Grant No. 102-2221-E-002-081-MY3.

References

[1] Peck B., Sigurdson L.: The Three-dimensional Vortex Structure of an Impacting Water Drop. *Phys. Fluids* **6**, 564. 1994.

[2] Kutter V. V.: Die anwendung von Wirbelringen zur Bestimmung von Oberflachenspannungen. *Physikalische Zeithchrift XVII* **23** 573-579, 1916

[3] Rodriguez F., Mesler R.: The Penetration of Drop-Formed Vortex Rings into Pools of Liquid. *J. Colloid Interf. Sci*.**121** 121-129, 1988.

[4] Chapman D. S., Critchlow P. R.: Formation of Vortex Rings from Falling Drops. *J. Fluid Mech*. **29,** 177-185, 1967

[5] Durst F.: Penetration Length and Diameter Development of Vortex Rings Generated by Impacting Water Drops. *Exp. Fluids* **21,** 110-117, 1996.

[6] Wang A. B., Kurniawan T. and Tsai P. H.: About Oscillation Effect on the Penetration Depth of Water Drop Induced Vortex Ring, the 23rd International Congress of Theoretical and Applied Mechanics, Beijing, China. August 19-24, 2012.

[7] Becker E., Hiller W. J. and Kowalewski T. A.: Experimental and Theoretical Investigation of Large-amplitude Oscillations of Liquid Droplets. *J. Fluid Mech*. **231,** 189-210, 1991.

[8] Tsai P. H., Kurniawan T. and Wang A. B.: On a Quantitative Feature of Maximum Penetration Depth of Drop-Formed Vortex Rings, the 15th International Symposium on Flow Visualization, Minsk, Belarus. June 25-28, 2012.

[9] Lee J. S., Park S. J., Lee J. H., Weon B. M., Fezzaa K. and Je J. H.: Origin and Dynamics of Vortex Rings in Drop Splashing. *Nat. Communications*, **6**, 8187, 2015.

STEADY ELECTROROTATION OF A DROP IN A CONSTANT ELECTRIC FIELD

Alexander Tyatyushkin*[1]

[1]*Institute of Mechanics, Moscow State University, Moscow, Russia*

Summary The electrorotation of a drop of a viscous weakly electrically conducting polarizable liquid suspended in another viscous weakly electrically conducting polarizable liquid immiscible with the former as well as the electrohydrodynamic flow inside and outside the drop in a constant electric field is theoretically investigated. The influence of the surface electric conductivity is taken into account. The surface tension of the drop is regarded as sufficiently large in order to neglect the deformation of the drop when calculating the electric field and flow. The governing equations and boundary conditions are written down. The used methods and the obtained results are described. The expressions for the intensity of the electric field, velocity, and pressure inside and outside the drop are written down for the case when the viscosity of the drop is much greater than that of the surrounding liquid. The obtained results are summarized and discussed.

INTRODUCTION

Under certain conditions, weakly electrically conducting bodies rotate under action of an applied constant electric field. The study of this interesting phenomenon, called electrorotation, has a long history (see [1] and [2]). Melcher and Taylor [1] investigated theoretically the electrorotation of a solid cylinder, Jones [2] investigated the electrorotation of a solid spherical particle. He, Salipante, and Vlahovska [3] studied the electrorotation of a fluid drop. The present work is devoted to the theoretical investigation of the influence of the surface conductivity on the electrorotation of a drop and to the calculation of the corrections arising due to the finite viscosity of the drop.

PROBLEM ABOUT THE STEADY ELECTROROTATION OF A DROP

Setting: subject of the investigation, equations, and boundary conditions

Consider a spherical drop of radius a in a constant uniform electric field with intensity $\vec{E}_\mathrm{a}$. The viscosity, electric conductivity, and dielectric permittivity of the liquid inside the drop are η_i, λ_i, and ε_i. The drop is suspended in a liquid with viscosity η_e, electric conductivity λ_e, and dielectric permittivity ε_i. The surface tension and surface electric conductivity of the interface between the liquids are σ_s and λ_s. The Reynolds number is so small that the convective acceleration can be neglected, and σ_s is so high that the deformation of the drop can be neglected.

The system of equations for the velocity, pressure, and electric field intensity, $\vec{v} = \vec{v}(\vec{r})$, $p = p(\vec{r})$, and $\vec{E} = \vec{E}(\vec{r})$, consists of the continuity and Navier–Stokes equations for a steady flow of an incompressible fluid in the low Reynolds number approximation, the Maxwell's equations in the electrohydrodynamic approximation [1] for a constant electric field, and the constitutive relations

$$\nabla \cdot \vec{v} = 0, \quad \circ\, \nabla p + \eta \Delta \vec{v} = 0, \quad \nabla \cdot \vec{D} = 0, \quad \nabla \times \vec{E} = 0, \quad \vec{D} = \varepsilon \vec{E}, \quad \vec{j} = \lambda \vec{E}. \tag{1}$$

Here, $\eta = \eta_\mathrm{i}$, $\lambda = \lambda_\mathrm{i}$, and $\varepsilon = \varepsilon_\mathrm{i}$ inside the drop, $\eta = \eta_\mathrm{e}$, $\lambda = \lambda_\mathrm{e}$, and $\varepsilon = \varepsilon_\mathrm{e}$ outside it, ∇ is the nabla operator, Δ is the Laplacian, $\vec{r}$ is the radius vector with the origin at the center of the drop, $\cdot$ and $\times$ denote the scalar and vector products.

The boundary conditions on the interface between the liquids include the impenetrability and no-slip conditions, the conditions for the jumps of the normal and tangential components of the stress vector,

$$\vec{n} \times (\vec{v}|_\mathrm{i} \times \vec{n}) = \vec{n} \times (\vec{v}|_\mathrm{e} \times \vec{n}) = \vec{v}_\mathrm{s}, \quad [\vec{v}]_\mathrm{s} \times \vec{n} = 0, \quad [p]_\mathrm{s} = \circ\, \frac{2\sigma_\mathrm{s}}{a}, \quad \circ \left(\vec{n} \times \left\{ \left[2\eta \left(\nabla \vec{v} \right)^\mathrm{S} \right]_\mathrm{s} \cdot \vec{n} \right\} \right) \times \vec{n} = q_\mathrm{s} \vec{E}_\mathrm{s}, \tag{2}$$

the continuity condition for the tangential component of the intensity of the electric field, and the conditions for the jumps of the normal components of the electric induction and of the density of the electric current,

$$\vec{n} \times \left(\vec{E}\Big|_\mathrm{i} \times \vec{n} \right) = \vec{n} \times \left(\vec{E}\Big|_\mathrm{e} \times \vec{n} \right) = \vec{E}_\mathrm{s}, \quad \left[\varepsilon \vec{E} \right]_\mathrm{s} \cdot \vec{n} = 4\pi q_\mathrm{s}, \quad \left[\lambda \vec{E} \right]_\mathrm{s} \cdot \vec{n} = \circ\, \nabla_\mathrm{s} \cdot \left(\lambda_\mathrm{s} \vec{E}_\mathrm{s} \right) \circ\ \nabla_\mathrm{s} \cdot (q_\mathrm{s} \vec{v}_\mathrm{s}) \,. \tag{3}$$

Here, $A|_\mathrm{i}$ and $A|_\mathrm{e}$ denote the values of the quantity A on the interface between the liquids approached from inside and outside the drop, respectively, $[A]_\mathrm{s} = A|_\mathrm{e} \circ\ A|_\mathrm{i}$ denotes the jump of the quantity A at the interface when moving from the inside to the outside, ∇_s denotes the surface nabla operator, $\vec{n}$ is the external normal unit vector at a given point of the interface, $\nabla \vec{f}$ denotes the dyadic product of the nabla operator and the vector field $\vec{f} = \vec{f}(\vec{r})$, $\hat{T}^\mathrm{S}$ denotes symmetric part of the tensor $\hat{T}$.

The boundary conditions at infinity have the form

$$\vec{v} \to 0, \quad p \to p_\infty, \quad \vec{E} \to \vec{E}_\mathrm{a} \quad \text{as} \quad r \to \infty, \tag{4}$$

where p_∞ is the pressure at infinity.

Besides, $\vec{v}(\vec{r})$, $p(\vec{r})$, and $\vec{E}(\vec{r})$ should be bounded for all the bounded values of $\vec{r}$.

*Corresponding author. Email: tan@imec.msu.ru

Solution: used methods and obtained results

The electric filed intensity, velocity, and pressure are sought for in the form of series with vector and tensor coefficients for which some relations are obtained that allow one to determine these coefficients. With the use of these relations, the coefficients are sought for in the form of asymptotic expansions over the parameter $\eta^* = \eta_e/(\eta_e + \eta_i)$, the smallness of which corresponds to the sufficiently large viscosity of the drop with respect to that of the surrounding liquid. The terms of the dimensionless expansions up to the first order with respect to η^* are found in the explicit form.

For sufficiently small values of the parameter η^*, the intensity of the electric field, pressure, and velocity are as follows

$$\vec{E} = \begin{cases} \vec{E}_a \circ \dfrac{\vec{d}}{r^3} + 3\dfrac{\vec{d}\cdot\vec{r}\,\vec{r}}{r^5}, & r > a, \\ \vec{E}_a \circ \dfrac{\vec{d}}{a^3}, & r < a, \end{cases} \qquad p = \begin{cases} \dfrac{4\eta_e V a^2}{r^3}\left(3\vec{b}\cdot\dfrac{\vec{r}}{r}\,\vec{c}\cdot\dfrac{\vec{r}}{r} \circ \vec{b}\cdot\vec{c}\right) + p_\infty, & r > a, \\ \dfrac{14\eta_i V r^2}{a^3}\left(3\vec{b}\cdot\dfrac{\vec{r}}{r}\,\vec{c}\cdot\dfrac{\vec{r}}{r} \circ \vec{b}\cdot\vec{c}\right) + \dfrac{2\sigma_s}{a} + p_\infty, & r < a, \end{cases} \tag{5}$$

$$\vec{v} = \begin{cases} \dfrac{a^3}{r^3}\vec{\Omega}_0\times\vec{r} + 2V\dfrac{a^4}{r^4}\left(\vec{b}\,\vec{c}\cdot\dfrac{\vec{r}}{r} + \vec{c}\,\vec{b}\cdot\dfrac{\vec{r}}{r}\right) \circ 2V\left(\dfrac{a^2}{r^2} \circ \dfrac{a^4}{r^4}\right)\vec{b}\cdot\vec{c}\,\dfrac{\vec{r}}{r} + 2V\left(3\dfrac{a^2}{r^2} \circ 5\dfrac{a^4}{r^4}\right)\vec{b}\cdot\dfrac{\vec{r}}{r}\,\vec{c}\cdot\dfrac{\vec{r}}{r}\,\dfrac{\vec{r}}{r}, & r > a, \\ \vec{\Omega}_0\times\vec{r} + V\left(5\dfrac{r^3}{a^3} \circ 3\dfrac{r}{a}\right)\left(\vec{b}\,\vec{c}\cdot\dfrac{\vec{r}}{r} + \vec{c}\,\vec{b}\cdot\dfrac{\vec{r}}{r}\right) \circ 2V\left(\dfrac{r^3}{a^3} \circ \dfrac{r}{a}\right)\vec{b}\cdot\vec{c}\,\dfrac{\vec{r}}{r} \circ 4V\dfrac{r^3}{a^3}\vec{b}\cdot\dfrac{\vec{r}}{r}\,\vec{c}\cdot\dfrac{\vec{r}}{r}\,\dfrac{\vec{r}}{r}, & r \leqslant a, \end{cases} \tag{6}$$

where

$$\vec{d} = \varkappa a^3\vec{E}_a + \gamma a^3\vec{E}_a\times\frac{\vec{\Omega}_0}{\Omega_0}, \quad \varkappa = \chi \circ \frac{4\pi\lambda_e\gamma}{\varepsilon_e\Omega_0}\frac{\lambda^*}{\varepsilon^*}, \quad \gamma = \frac{8\pi\eta_e\Omega_0}{\varepsilon_e E_a^2}, \ \lambda^* = 2 + \frac{\lambda_i}{\lambda_e} + \frac{2\lambda_s}{a\lambda_e}, \ \varepsilon^* = 2 + \frac{\varepsilon_i}{\varepsilon_e}, \ \chi = \frac{3 \circ \varepsilon^*}{\varepsilon^*}, \tag{7}$$

$$V = \frac{1}{10}\frac{\varepsilon_e E_a^2 a}{8\pi(\eta_e + \eta_i)}, \quad \vec{b} = \chi\varepsilon^*\frac{\vec{E}_a}{E_a} + \varepsilon^*\frac{\vec{d}}{a^3 E_a}, \quad \vec{c} = \frac{\vec{E}_a}{E_a} \circ \frac{\vec{d}}{a^3 E_a}, \tag{8}$$

$$\Omega_0 = \frac{4\pi\lambda_e}{\varepsilon_e}\frac{\lambda^*}{\varepsilon^*}\sqrt{\frac{E_a^2}{E_c^2} \circ 1}, \quad \vec{\Omega}_0\cdot\vec{E}_a = 0, \quad E_c = \sqrt{\frac{32\pi^2\lambda_e\eta_e}{3\varepsilon_e^2}\frac{\lambda^{*2}}{\varepsilon^* \circ \lambda^*}}. \tag{9}$$

Calculating the surface normal force arising under action of the electric field and flow with the use of (5) and (6) and analyzing its dependence on the normal vector on the surface of the drop, one concludes that this normal force tends to deform the spherical drop into an ellipsoid the principal axes of which are determined by the following unit vectors

$$\vec{l}_{1,2} = \cos\phi_{1,2}\frac{\vec{E}_a}{E_a} + \sin\phi_{1,2}\frac{\vec{E}_a}{E_a}\times\frac{\vec{\Omega}_0}{\Omega_0}, \quad \vec{l}_3 = \frac{\vec{\Omega}_0}{\Omega_0}, \tag{10}$$

where

$$\phi_1 = \frac{1}{2}\arctan\frac{2(45 \circ 19\varepsilon^*)\gamma\varkappa + 19\varepsilon^*(1 \circ \chi)\gamma}{19\varepsilon^*(\chi + \varkappa \circ \chi\varkappa) + (45 \circ 19\varepsilon^*)(\varkappa^2 \circ \gamma^2)}, \quad \phi_2 = \phi_1 + \frac{\pi}{2}. \tag{11}$$

SUMMARY AND DISCUSSION

Note that, according to (9), the angular velocity of the electrorotation, $\vec{\Omega}_0$, is determined only if the intensity of the applied electric field is more than some critical value, E_c, and the latter is determined only if $\varepsilon^* \circ \lambda^* = \varepsilon_i/\varepsilon_e \circ \lambda_i/\lambda_e \circ 2\lambda_s/(a\lambda_e) > 0$. The expressions for $\vec{\Omega}_0$ in (9) and $\vec{E}$ and p at $r < a$ in (5) are written down with accuracy up to the terms of zeroth order and those for p at $r > a$ and $\vec{v}$ in (5) and (6), up to the terms of the first order with respect to η^*. These expressions together with (10) and (11) describe the phenomenon of the drop tilt [3].

With accuracy up to the first order with respect to η^*, $\vec{\Omega} = \vec{\Omega}_0 + \eta^*\vec{\Omega}_1$, where

$$\vec{\Omega}_1 = \circ\,\frac{1}{50}\left[\frac{16\tau_\eta^*}{\tau_\lambda^*}\frac{\lambda^*\left(\lambda^{*2} + \tau_\lambda^{*2}\varepsilon^{*2}\right)}{\varepsilon^{*2}} + \frac{15\lambda^{*2} + 9\tau_\lambda^{*2}\varepsilon^{*2}}{\varepsilon^{*2}}\right]\frac{\tau_\eta^*}{\tau_\lambda^{*3}}\vec{\Omega}_0, \quad \tau_\eta^* = \frac{4\pi\eta_e\Omega_0}{\varepsilon_e E_a^2}, \quad \tau_\lambda^* = \frac{\varepsilon_e\Omega_0}{4\pi\lambda_e}. \tag{12}$$

The found corrections of the first order with respect to η^* for $\vec{E}$, and p at $r < a$ are not written down because they are too cumbersome for the present article. With accuracy up to the first order with respect to η^*, the drop possesses not only the electric dipole moment, $\vec{d}$, but also some electric octupole moment, and the normal surface force tends to deform the drop not precisely into an ellipsoid but to give it a more complex shape.

References

[1] Melcher J.R. and Taylor G.I.: Electrohydrodynamics: a Review of the Role of Interfacial Shear Stresses. Annu Rev Fluid Mech 1:111-146,1969.

[2] Jones T.B.: Quincke Rotation of Spheres. IEEE T. Ind Appl IA-20:4:845-849, 1984.

[3] He H., Salipante P.F., and Vlahovska P.M.: Electrorotation of a Viscous Droplet in a Uniform Direct Current Electric Field. Phys Fluids 25:032106, 2013.

INVESTIGATION ON THE BREAKUP MECHANISM OF THE LIQUID JET UNDER LONGITUDINAL DISTURBANCE

Zhenyan Xia[a], Zhenni Li&Yan Tian
Department of Mechanics, Tianjin University, Tianjin, China

*Summary*The research on the breakup mechanism of the liquid jet is not only a traditional fluid mechanics problem, but also a topic with great theoretical research value and engineering application background. A liquid jet experimental system mainly consisting of liquid jet driving system, exciting system and photographing system has been designed and established. A longitudinal vibration produced by the vibration exciter applied on the nozzle, and the effects of vibration frequency and vibration amplitude on the breakup of the liquid jet were investigated.

EXPERIMENTAL SYSTEM

A schematic diagram of the experimental apparatus is presented in Fig.1. Fluid from a reservoir was pumped through a flowmeter into the nozzle, and the flow range is 8.5ml/min~500ml/min. The nozzle is fitted to the vibration exciter and is vibrated longitudinally. The vibration frequency and vibration amplitude of sine wave vibration are controlled by an signal generator and a power amplifier. Photron SA1.1 high-speed camera is used to obtained the shadowgraph images of the liquid jet. The frame rate is 5000fps and the frame resolution is 1024×1024 piexls. The Glycerol-water mixtures are used as test fluids with the mass fraction of 60% glycerol concentrations. The physical properties is shown in table1.

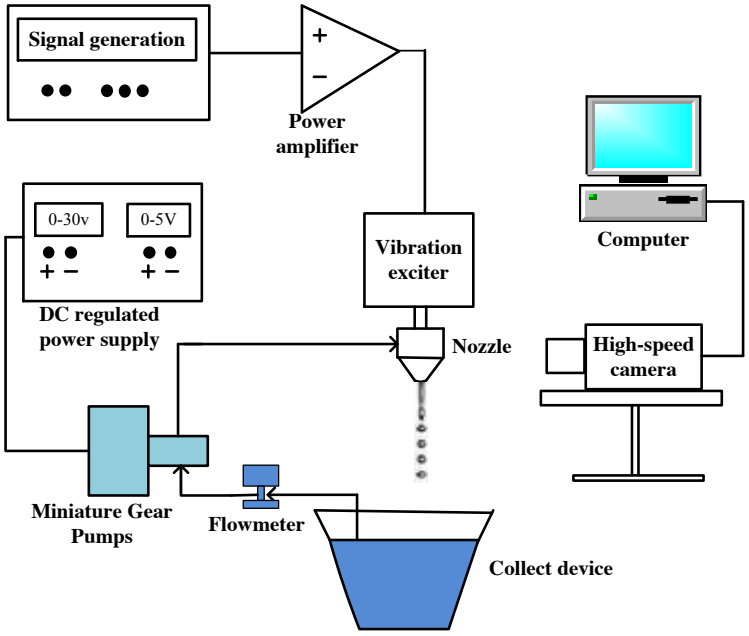

Figure.1 schematic diagram of the experimental apparatus

Tab.1 Physical properties

Liquid	Density(kg/m^3)	Viscosity(mPa.s)	Surface tension(mN/m)
60%glycerol	1.12×10^3	10.8	64

RESULTS

Fig.2 shows that the variation of the breakup length with vibration frequency under different jet velocities. It is apparently that as the increasing of the vibration frequency, the breakup length first decreases and then increases. In addition, the value of the vibration frequency under which the breakup length is the most shortest decreases as the increase of jet velocity.
The effect of vibration amplitude on the liquid jet is shown in Fig.3(a). It can be observed that as the increasing of the vibration amplitude, the satellite droplet is moving closer to the forward main droplet(vibration amplitude A=0.01~0.5cm/s), and eventually the satellite droplet merges with the forward main droplet and disappears(A=0.6cm/s~0.9cm/s). Moreover, the increase of the vibration amplitude can lead to the decrease of the breakup length. In order to quantitatively investigate the effect of the vibration amplitude on the breakup length, the breakup length under different vibration amplitudes is

[a]Corresponding author. Email: xia_zhy@hotmail.com.

extracted and the vibration tendency is shown in Fig.3(b). It can be seen that when the vibration amplitude is small, the breakup length decreases acutely as vibration amplitude increases.

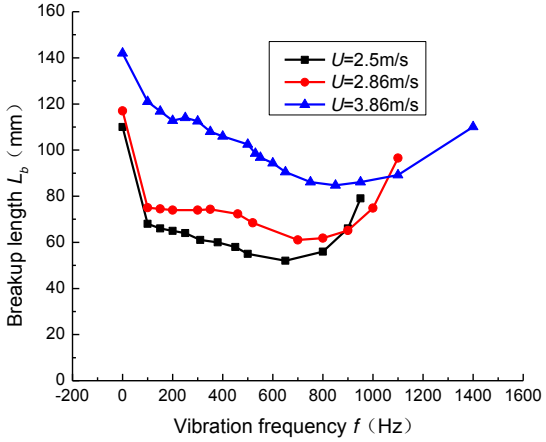

Figure 2 Variation of the breakup length with the vibration frequency under different jet velocities(d=0.9mm, vibration amplitude A=0.35cm/s)

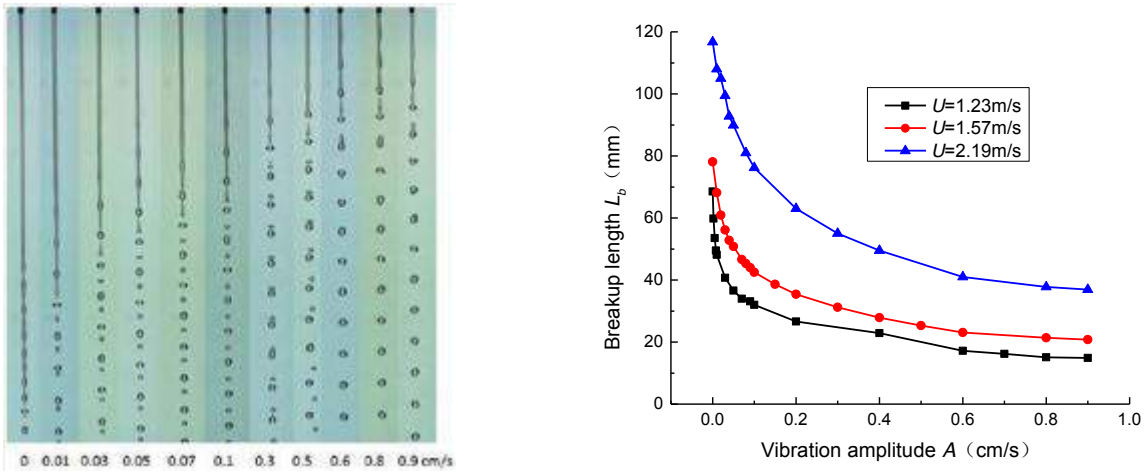

(a) (b)

Fig 3(a)The image of the liquid jet under different vibration amplitudes(d=0.9mm, f=300hz, U=1.57m/s);(b)The variation of the breakup length with the vibration amplitude(d=0.9mm, f=300hz)

CONCLUSIONS

With the increase of the vibration frequency, the breakup length of the liquid jet first decreases and then decreases. There exists a vibration frequency under which the breakup length is the shortest. Moreover, the increase of the vibration can lead to the decrease of the breakup length.

Acknowledgements

The support of National Natural Science Foundation of China (No.11172205 and No.11372219) is gratefully acknowledge.

FM07 - Flow Instability and Transition

TS.FM07-1.01	Tuckerman, Laurette - Can frequencies be predicted from mean flows? RZIF for thermosolutal convection (INVITED)	911
TS.FM07-1.02	Sipp, Denis - Mathematical foundations for mean flow stability analysis	913
TS.FM07-1.03	Kambe, Tsutomu - New Scenario of Turbulence Theory and Wall Turbulence	915
TS.FM07-1.04	Tao, Jianjun - Helical-wave instabilities of an annulus flow in a helical magnetic field	917
TS.FM07-1.05	Henningson, Dan S - Bypass transition in boundary layers	919
TS.FM07-1.06	Ait Moussa, Nabila - Stability of lobed Taylor-Couette flows by numerical simulations	921
TS.FM07-2.01	Bonne, Nicolas - Global stability analysis of a shock wave boundary layer interaction, including a transition model	923
TS.FM07-2.02	Healey, Jonathan - Using inflexion points to stabilize boundary layers	925
TS.FM07-2.03	Farano, Mirko - Nonlinear optimal coherent structures in turbulent channel flow	927
TS.FM07-2.04	Kunii, Kohei - Helical turbulence and puff in transitional sliding Couette flow	929
TS.FM07-2.05	Mittal, Sanjay - Experimental investigation of flow past a sphere in the regime of boundary layer transition	931
TS.FM07-2.06	Eckhardt, Bruno - Exact coherent structures for the turbulent cascade	933
TS.FM07-3.01	Kanazawa, Takahiro - Exponential increase of the lifetime with the number of coherent structures	935
TS.FM07-3.02	Wesfreid, José - Instabilities in the flow behind rotating bluff bodies	937
TS.FM07-3.03	Marquet, Olivier - A new formalism for identifying wavemaker regions of linear instabilities	939
TS.FM07-3.04	Asai, Masahito - Experimental investigation of instability of convecting local high-shear layer	941
TS.FM07-3.05	Fukudome, Koji - Relaminarization of stably stratified turbulent Poiseuille flows at low Reynolds number	943
TS.FM07-3.06	Chomaz, Jean-Marc - Optimal Perturbations of a Counter-rotating Vortex Pair in Stratified Flows	945
TS.FM07-4.01	Kida, Shigeo - Flow instability in a precessing sphere	947
TS.FM07-4.02	Majji, Madhu - Flow transition of neutrally buoyant suspension between concentric cylinders	949
TS.FM07-4.03	Mutabazi, Innocent - Thermoelectric convection in dielectric liquids in a cylindrical annulus	951
TS.FM07-4.04	Di Giovanni, Antonio - Boundary-layer stability of a generic reentry capsule with real-gas effects	953
TS.FM07-4.05	Shoji, Takeshi - Effects of external forcing on transverse jet structure and mixing	955
TS.FM07-4.06	Huerre, Patrick - Local and global instability of buoyant jets and plumes	957
TS.FM07-5.01	Egorov, Ivan - Direct numerical simulations of laminar-turbulent transition in hypersonic flows over flat plate	959
TS.FM07-5.02	Jallas, Damien - Wake deviation of a flapping foil: A symmetry-breaking bifurcation	961
TS.FM07-5.03	Kozlov, Victor - Longitudinal vortices and their secondary instability on swept wing	963

TS.FM07-5.04	Lusseyran, François - Nonlinear temporal dynamics of axisymmetric wavepackets in subsonic jets	965
TS.FM07-5.05	Poncet, Sebastien - DNS of turbulent flows inside a simplified stage of high-pressure compressor	967
TS.FM07-6.01	Kaiser, Robert - Large-scale flow modes in turbulent Rayleigh-Bénard convection	969
TS.FM07-6.02	Yakeno, Aiko - Transient dynamics and stability on spanwise-oscillatory turbulent channel	971
TS.FM07-6.03	Yokoyama, Naoto - Initial-condition dependence of large-scale structures in rotating turbulence	973
TS.FM07-6.04	Xie, Chenyue - Viscous Rayleigh-Taylor instability with and without the diffusion effect	975
TS.FM07-6.05	Leonov, Sergey - Boundary layer receptivity to transient plasma in m=4.5 airflow	977
TS.FM07-7.01	Luchini, Paolo - Higher-order WKBJ correction in spatially-developing open flows	979
TS.FM07-7.02	Ziade, Paul - Sensibility of Rayleigh and Orr-Sommerfeld equations to changes in base flow	981
TS.FM07-7.03	Bihi, Ilyesse - Microparticles effects on the stability of an air-water interface	983
TS.FM07-7.04	Gepner, Stanislaw - Stability of flow in a diverging-converging channel at moderate amplitudes of corrugation	985
TS.FM07-7.05	Ren, Jie - Secondary instabilities of Görtler vortices in high-speed boundary layer flows	987
PO.FM07-1.01.117	Abe, Yoshiaki - Flow instability on airfoil separation control at optimum actuation frequency	989
PO.FM07-1.02.118	Adachi, Shizuko - Lagrangian analysis of energy conversion in the taconis oscillations	991
PO.FM07-1.04.120	Amiroudine, Sakir - A Lagrange-euler Modelling of Thermovibrational Instabilities in Supercritical Fluids	993
PO.FM07-1.05.121	Bhowmick, Aklant - Effect of pressure fluctuations on Richtmyer Meshkov coherent structure	995
PO.FM07-1.06.122	Chopra, Gaurav - Intermittency of laminar seperaration bubble during drag crisis in flow past a circular cylinder	997
PO.FM07-1.07.123	Dong, Shuai - Secondary Optimal Perturbation Growth in Hartmann Channel Flow	999
PO.FM07-1.08.124	Kozlov, Nikolai - Flow structure in a rotating cylinder with fluid and a free light body at vibration	1001
PO.FM07-1.09.125	Marques, Larissa - Effects of curvature variations in a transitional boundary layer on heat transfer	1003
PO.FM07-1.11.127	Panina, Alexandra - Nonlinear disturbance evolution in supersonic boundary layers on the swept wing	1005
PO.FM07-1.12.128	Rouquier, Anthony - Numerical study of the transition to turbulence in particulate pipe flows	1007
PO.FM07-1.13.129	Seddighi, Amirreza - Use of natural instabilities for enhancement of flow mixing in annuli	1009
PO.FM07-1.14.130	Subbotin, Stanislav - Effect of librations on the dynamics of free inner core and liquid in rotating cavity	1011
PO.FM07-1.15.131	Takagi, Shohei - Detection of a logarithmic singular point behind an airfoil model at low Reynolds numbers	1013

PO.FM07-1.16.132	Tuliszka-Sznitko, Ewa - Numerical study of the Tsylor-Couette flow using DNS/SVV	1015
PO.FM07-1.17.133	Vafadar Moradi, Hadi - Sliding Couette flow in ribbed annuli	1017
PO.FM07-1.18.134	Verschaeve, Joris - Convective instability of the boundary layer under solitary waves	1019
PO.FM07-1.19.135	Yang, Changwei - Flow characteristics and structural stability in a ventilated cabin mock-up	1021
PO.FM07-1.20.136	Yatskikh, Aleksey - Evolution of Localized Artificial Disturbance in 2d Supersonic Boundary Layer	1023
PO.FM07-1.21.137	Yudin, Mikhail - Cylinder instability in circulation flow bounded by external cylindrical wall	1025

CAN FREQUENCIES BE PREDICTED FROM MEAN FLOWS? RZIF FOR THERMOSOLUTAL CONVECTION

Laurette S. Tuckerman *[1], Yacine Bengana[1], Nicolas Périnet[2], and Sam E. Turton[3]
[1]*PMMH (UMR 7636 CNRS - ESPCI - UPMC Paris 6 - UPD Paris 7 - ParisTech - PSL), Paris, France*
[2]*Departamento de Física, Universidad de Chile, Santiago, Chile*
[3]*Department of Mathematics, MIT, Cambridge MA, U.S.A.*

Summary Motivated by studies of the cylinder wake, in which the vortex-shedding frequency can be obtained from the mean flow, we study 2D thermosolutal convection driven by opposing thermal and solutal gradients, in which branches of traveling waves (TW) and standing waves (SW) are created simultaneously by a Hopf bifurcation. We find that the TW of thermosolutal convection have the RZIF property, meaning that linearization about the mean fields of the traveling waves yields an eigenvalue whose real part is almost zero and whose imaginary part corresponds very closely to the nonlinear frequency. In contrast, this is not the case for the SW. This difference can be attributed to the fact that the temporal power spectrum for the TW is peaked, while that of the SW is broad, and we show why this is so. We demonstrate that the frequency of any quasi-monochromatic oscillation can be predicted from its temporal mean.

The von Kármán vortex street generated in the wake of a circular cylinder is one of the archetypical hydrodynamic instabilities. Because it arises from a Hopf bifurcation, its frequency at onset is necessarily the imaginary part of the eigenvalue responsible for the bifurcation. However, away from the bifurcation, the frequencies differ substantially from those obtained from linear stability analysis, and so even quite close to onset, standard stability analysis of steady base flows dramatically fails to predict observed oscillation frequencies. However, it has been found that linear stability analysis, not of the base state, but of the temporal average of the nonlinear flow, yields an eigenvalue whose imaginary part corresponds very closely to the nonlinear frequency [1, 2, 3, 4] and whose real part is virtually zero, which can be interpreted [3] as the marginal stability of the mean flow. We call this the real-zero imaginary-frequency property, or RZIF [5]. The RZIF property has been further studied and extended by a number of researchers. It has been shown [6] that RZIF can be analyzed by means of a weakly nonlinear expansion and that RZIF is not verified by the oscillatory flow over a square cavity. The mean flow in the cylinder wake has been calculated without time integration merely by assuming the RZIF property [7]. Another recent investigation [8] proposes a generalization of this property for turbulent flows.

RZIF has been investigated primarily for open flows and almost exclusively the cylinder wake. Here and in [5] we report on an investigation of RZIF in thermosolutal convection [9, 10], motion driven by an unstable density gradient, which is caused in turn by independently imposed gradients in the temperature and concentration of a fluid. In a domain which is horizontally spatially periodic, branches of traveling waves (TW) and standing waves (SW) emerge simultaneously at a Hopf bifurcation [9]. We calculate these two temporally periodic states numerically via a 2D time-stepping code (imposing reflection symmetry to calculate the otherwise unstable SW). Instantaneous temperature fields are shown in figure 1 and phase portrait projections are shown in figure 2 (left). We then carried out linear stability analysis of the conductive state and of the temporal mean of the TW and the SW. The resulting eigenvalues are shown in figure 2 (middle). where it can be seen that the TW are an ideal case of RZIF, but the SW do not have this property. RZIF can easily be shown to result from a highly peaked spectrum of the nonlinear oscillations. Writing the governing equations in the abbreviated form $\partial_t \mathbf{U} = \mathcal{L}\mathbf{U} + \mathcal{N}(\mathbf{U},\mathbf{U})$ and decomposing $\mathbf{U} = \overline{\mathbf{U}} + \sum_{n\neq 0} \mathbf{u}_n e^{in\omega t}$, where $\mathbf{U}$ is the mean flow and ω is the nonlinear frequency, the component $\mathbf{u}_1$ satisfies

$$i\omega\mathbf{u}_1 = \left[\mathcal{L}\mathbf{u}_1 + \mathcal{N}(\overline{\mathbf{U}},\mathbf{u}_1) + \mathcal{N}(\mathbf{u}_1,\overline{\mathbf{U}})\right] + \sum_{m\neq 0,n} \mathcal{N}(\mathbf{u}_m,\mathbf{u}_{1-m}) \equiv \mathcal{L}_{\mathbf{U}}\mathbf{u}_1 + \mathcal{N}_1 \tag{1}$$

If $|\mathbf{u}_m| \ll |\mathbf{u}_1|$, then $\mathcal{N}_1$ is much smaller than the other terms of (1), and so $\mathbf{u}_1$ is an eigenvector of $\mathcal{L}_{\overline{\mathbf{U}}}$ with eigenvalue $0 \pm i\omega$, i.e. the RZIF property is satisfied. To explain why the temporal spectrum is highly peaked for TW and not for SW, as shown in figure 2 (right), we consider the nonlinear interaction $\nabla\psi \times \nabla\Theta$ between the streamfunction ψ and the temperature perturbation Θ, with a temporal phase difference Δ.

$$\mathbf{TW}: \quad \left.\begin{array}{l}\psi(x,z,t) = \psi_1 \sin(kx \circ\ \omega t)\sin\pi z \\ \Theta(x,z,t) = \Theta_1 \sin(kx \circ\ \omega t + \Delta)\sin\pi z\end{array}\right\} \implies \nabla\psi\times\nabla\Theta = \frac{\pi k}{2}\psi_1\Theta_1 \sin\Delta \sin 2\pi z$$

$$\mathbf{SW}: \quad \left.\begin{array}{l}\psi(x,z,t) = \psi_1 \sin kx \sin\omega t \sin\pi z \\ \Theta(x,z,t) = \Theta_1 \cos kx \cos(\omega t + \Delta)\sin\pi z\end{array}\right\} \implies \nabla\psi\times\nabla\Theta = \frac{\pi k}{4}\psi_1\Theta_1 \left[\sin\Delta + \sin(2\omega t + \Delta)\right]\sin 2\pi z$$

Thus, for TW the nonlinear interaction generates a mean flow but no second temporal harmonic $2\omega t$, while for SW, the nonlinear interaction generates both a mean flow and a second temporal harmonic.

*Corresponding author. Email: laurette@pmmh.espci.fr

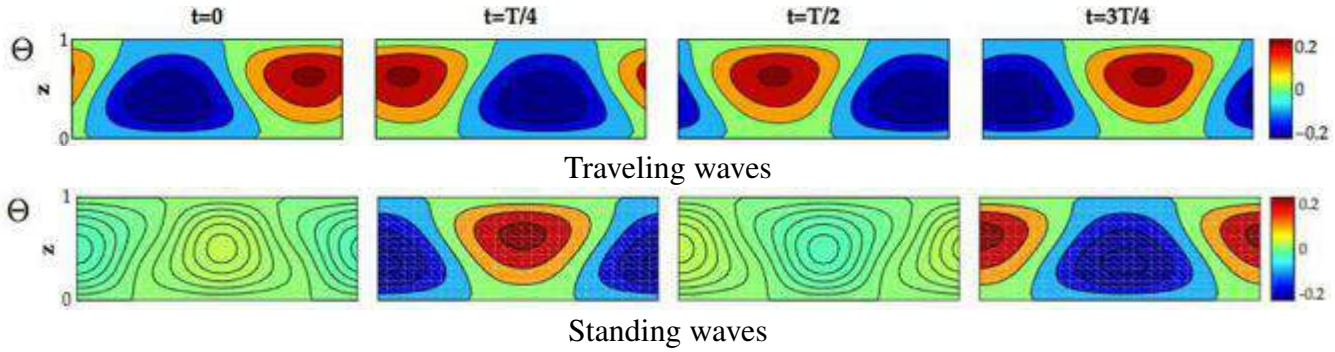

Figure 1: Temperature field at four successive instants for traveling waves (above) and standing waves (below) for thermosolutal convection at the same parameter values, $P = 10$, $L = 0.1$, $S = \circ\, 0.5$, and $r = 2.5$.

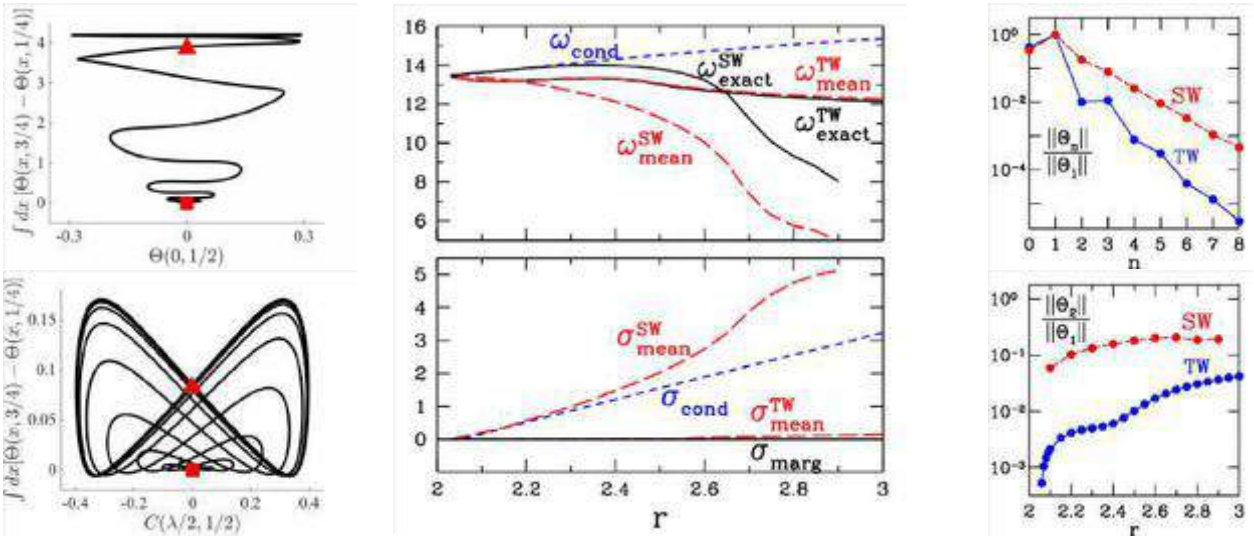

Figure 2: Left: phase portraits of traveling waves (above) and standing waves (below). The conductive state and the mean flow are represented by squares and triangles respectively. Traveling waves (TW) execute oscillation in a plane about the mean flow, while the motion of the standing waves (SW) can be seen to contain a second temporal harmonic. Middle: Frequencies (above) and growth rates (below) associated with TW and SW. Linearization about the conductive state (blue) and about the mean flow (red). Measured (exact) nonlinear frequencies and zero (marginal) growth rate (black). For TW, linearization about the mean flow yields the exact results as shown by resemblance of red and black curves; this is not the case for SW. Right: temporal spectrum is far more highly peaked for TW than for SW.

References

[1] D.A. Hammond and L.G. Redekopp, *Global dynamics of symmetric and asymmetric wakes*, J. Fluid Mech. **331**, 231 (1997).

[2] B. Pier, *On the frequency selection of finite-amplitude vortex shedding in the cylinder wake*, J. Fluid Mech. **458**, 407 (2002).

[3] D. Barkley, *Linear analysis of the cylinder wake mean flow*, Europhys. Lett. **75**, 750 (2006).

[4] S. Mittal, *Global linear stability analysis of time-averaged flows*, Int. J. Numer. Meth. Fluids **58**, 111 (2007).

[5] S.E. Turton, L.S. Tuckerman, D. Barkley, Prediction of frequencies in thermosolutal convection from mean flows, Phys. Rev. E **91**, 043009 (2015).

[6] D. Sipp and A. Lebedev, *Global stability of base and mean flows: a general approach and its applications to cylinder and open cavity flows*, J. Fluid Mech. **593**, 333 (2007).

[7] V. Mantič-Lugo, C. Arratia, F. Gallaire, *Self-consistent mean flow description of the nonlinear saturation of the vortex shedding in the cylinder wake*, Phys. Rev. Lett. **113**, 084501 (2014).

[8] S. Beneddine, D. Sipp, A. Arnault, J. Dandois, L. Lesshafft, *Mathematical foundations for mean flow stability analysis*, preprint.

[9] E. Knobloch, *Oscillatory convection in binary mixtures*, Phys. Rev. A **34**, 1538 (1986).

[10] L.S. Tuckerman, *Thermosolutal and binary fluid convection as a* 2×2 *matrix problem*, Physica D **156**, 325 (2001).

MATHEMATICAL FOUNDATIONS FOR MEAN-FLOW STABILITY ANALYSIS

Samir Beneddine[1], Denis Sipp [*1], Anthony Arnault[1], Julien Dandois[1], and Lutz Lesshafft[2]
[1]*ONERA, Meudon, France*
[2]*Ladhyx, CNRS-Ecole Polytechnique, Palaiseau, France*

Summary This presentation provides theoretical foundations for the use and meaning of a stability analysis around a mean flow. Considering a Reynolds decomposition of the flow field, the Fourier transform of the fluctuation field is found to be equal to the product of the resolvent operator by a turbulent forcing term. If the dominant singular value of the resolvent is much larger than all others, then the Fourier transform of the fluctuation field is directly related to the dominant optimal response mode of the resolvent. In the case of weakly non-parallel flows, the spatial structure of this mode may be approximated by a local spatial stability analysis based on parabolized stability equations (PSE). Results are illustrated for the case of a turbulent backward facing step.

INTRODUCTION

Turbulent flows are encountered in a wide variety of industrial applications, and they often present low frequency unsteadiness. One of the main goal is the prediction of the unsteady features of those flows, such as the characteristic frequencies or the spatial stucture of the unsteadiness. A substantial quantity of studies has been devoted to the use of stability theory to achieve this goal. The classical linear stability theory around a steady base flow fails to do so, by not accounting for the nonlinearities that have a strong influence on the unsteady behavior of the flow. However, there are many papers showing that those nonlinear effects may be factored in by using the time averaged field (the mean flow) instead of the base flow. For example, in the cylinder case, a linear stability analysis around the mean flow gives excellent prediction of the vortex shedding frequency, even far from criticality [1]. The same approach has been successfully used for amplifiers, *i.e.* flows that present a broadband spectrum originating from convective instabilities that amplify the external background perturbations. For instance, Gudmundsson *et al.* [2] focused on turbulent round jets: using an array of microphones, they experimentally measured the pressure fluctuations outside the jet shear layer and showed that the pressure amplitude and phase of the data accurately matched predictions from a local stability analysis around the mean flow. Those examples are just a part of the large number of studies that acknowledge the capability of a mean flow stability analysis to predict the unsteady features of a turbulent flow. On the other hand, a formal justification for the well-foundedness of such an approach is still wanting, and only few studies have been carried out to adress this question. Among these, Sipp *et al.* [6] focused on self-excited systems which present a strong dominating frequency (ocillator flows). They showed that, in the vicinity of the bifurcation threshold, if the mean flow harmonic dominates the second harmonic, a global linear stability analysis around the mean flow yields a marginally stable mode whose frequency matches the natural frequency of the flow. Recently, Turton *et al.* [7] more generally demonstrated that if the flow exhibits monochromatic harmonic oscillations, then the linearized operator around the mean flow indeed exhibits a purely imaginary eigenvalue equal to the frequency of the flow. This criterion has even been considered by Mantič *et al.* [4] to build a self-consistent model of cylinder flow that predicts the frequency of the vortex shedding for Reynolds numbers up to 110. But the conclusions of those studies cannot be extended to the more general case where a flow presents a broadband spectrum. The present study aims at providing, in the case of a flow field presenting a broadband spectrum and not just a peak, mathematical foundations to justify the efficiency of a mean flow stability approach to predict the spatio-temporal features of a flow field. It is an extension of the work of McKeon *et al.* [5], based on the optimal response modes computed from a singular value decomposition of the resolvent operator. Yet, they restricted their analysis to a turbulent pipe configuration, which is invariant (homogeneous) in the streamwise direction. Hence, the mean flow was constant in the streamwise direction and all fluctuating quantities were Fourier-transformed in this direction. In so far, only a local stability analysis was required. In the present study, we consider more general configurations, in particular open-flows which are not invariant in the streamwise direction, such as backward-facing step or jet configurations. Finally, we also aim at elucidating the link between the global stability results and those provided by local stability approaches, such as spatial stability or PSE (parabolized stability equations, see Herbert *et al.* [3]) analyses.

THEORY

We consider the equation governing the fluctuations of the flowfield around the mean-flow. This equation involves the linearized Navier-Stokes operator around the mean-flow and a non-linear driving term, which is usually unknown. Performing a Fourier transform of this equation, a singular value decomposition of the Resolvent operator provides a rank 1 approximation for the Fourier mode $\hat{\mathbf{u}}$ in the form:

$$\hat{\mathbf{u}}(\mathbf{x},\omega) \approx \tilde{\mathbf{u}}_1(\mathbf{x},\omega)\mu_1(\omega)\langle\tilde{\mathbf{f}}_1(\omega),\hat{\mathbf{f}}(\omega)\rangle \tag{1}$$

*Corresponding author. Email: denis.sipp@onera.fr

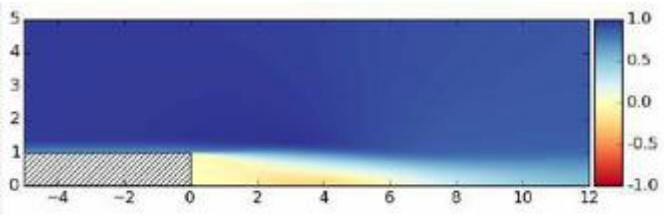

Figure 1: Streamwise velocity of the mean flow.

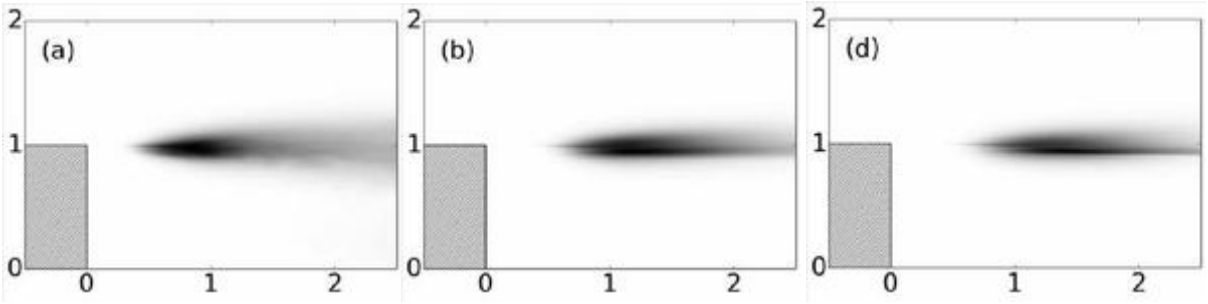

Figure 2: Comparison between $\hat{\mathbf{u}} \cdot \hat{\mathbf{u}}$ computed from the simulation (a), the optimal response $\tilde{\mathbf{u}}_1 \cdot \tilde{\mathbf{u}}_1$ (b), and the field reconstructed with PSE (c), for $\omega = 5.5$ and two-dimensional perturbations $\beta = 0$.

This approximation holds if the first singular value is much larger than the others. In this equation, (μ_1, $\tilde{\mathbf{u}}_1$, $\tilde{\mathbf{f}}_1$) are the dominant optimal gain, response and forcing of the singular value decomposition, while $\hat{\mathbf{f}}$ stands for the Fourier transform of the above mentioned unknown driving term. Hence, this shows that the Fourier mode is directly proportional to the dominant optimal response. We will further show that this mode may straightforwardly be approximated by a PSE analysis.

RESULTS

We consider the case of a two-dimensional backward facing step. We performed an unsteady 3D simulation at $Re = 57460$. A 2D mean flow was obtained by averaging the results in time and over the spanwise direction (see figure 1). The configuration being invariant in the spanwise direction, Fourier modes of the fluctuation field depend both on the frequency ω and on the spanwise wavenumber β. The resolvent operator therefore also depends on β and we expect that the Fourier mode $\hat{\mathbf{u}}(\omega, \beta)$ is proportional to $\tilde{\mathbf{u}}_1(\omega, \beta)$ if $\mu_1(\omega, \beta) \gg \mu_2(\omega, \beta)$. In the following, we will focus on two-dimensional perturbations ($\beta = 0$), for which the spanwise component u_3' is null. It was found that the first singular value μ_1 is several orders of magnitude larger than all others. Therefore, at a fixed frequency, the Fourier mode $\hat{\mathbf{u}}$ is supposed to be proportional to the dominant optimal response $\tilde{\mathbf{u}}_1$. We will now check this assertion by comparing the Fourier mode $\hat{\mathbf{u}}(\omega, \beta = 0)$ to the optimal response $\tilde{\mathbf{u}}_1(\omega, \beta = 0)$. We have checked that the norm of $\hat{\mathbf{u}}(\omega, \mathbf{x})$ compares well with the norm of the first optimal response $\tilde{\mathbf{u}}_1(\mathbf{x}, \omega)$ for several frequencies. Figures 2a and 2b illustrate, for example, the similarity between those two fields for $\omega = 5.5$. Finally, figure 2c shows the result obtained from a PSE analysis. We observe a strong similarity between this field and the two others.

References

[1] Barkley D. 2006 Linear analysis of the cylinder wake mean flow. EPL (Europhysics Letters) 75 (5), 750.

[2] Gudmundsson K. & Colonius T. Instability wave models for the near-field fluctuations of turbulent jets. Journal of Fluid Mechanics 689:97–128, 2011.

[3] Herbert T.: Parabolized stability equations. Annual Review of Fluid Mechanics, 29 (1):245–283, 1997.

[4] Mantič-Lugo V., Arratia, C. & Gallaire, F. Self-consistent mean flow description of the nonlinear saturation of the vortex shedding in the cylinder wake. Physical review letters 113 (8):084501, 2014.

[5] McKeon B.J. & Sharma A.S. A critical-layer framework for turbulent pipe flow. Journal of Fluid Mechanics 658, 336–382, 2010.

[6] Sipp D. & Lebedev A. Global stability of base and mean flows: a general approach and its applications to cylinder and open cavity flows. Journal of Fluid Mechanics 593:333–358, 2007.

[7] Turton S. E., Tuckerman L. S. & Barkley, D. Prediction of frequencies in thermosolutal convection from mean flows. Physical Review E 91 (4):043009, 2015.

NEW SCENARIO OF TURBULENCE THEORY AND WALL TURBULENCE

Tsutomu Kambe[1a)]
[1]*Former Professor, University of Tokyo, Tokyo Japan*

Summary: New general scenario of turbulence theory is proposed and applied to wall turbulence. The theory introduces a new wave field supported by a mathematical theorem, and predicts transverse traveling waves. The predictions are consistent with characteristic features of wall turbulence observed in experimental studies. There is a dynamical mechanism in streaky wall flows to excite a wave field, and there exists an energy channel from the flow field to the wave field. Traveling waves predicted by the theory are characterized by two scales of wave-length and damping-length, whose significance is discussed in relation to the two large scales of LSM and VLSM observed in experiments. The waves are accompanied with a new mechanism of energy dissipation, *i.e.* a new law of internal friction analogous to the Joule effect of electric current. Bulk energy dissipation is expressed in a form analogous to those of eddy-viscosity.

WALL TURBULENCE AND NEW FIELD

Large scale features is one of the main subjects in the study of wall turbulence such as boundary layer flows or pipe flows. Studies of pipe flows in the past decades have revealed that, at transition to turbulence, the flow supports transverse *traveling waves* with cross-stream modes. A new scenario of turbulence theory [1] is proposed by introducing a new field into the turbulence field. The theory supports transverse traveling waves. Significance of this formulation rests on a mathematical *theorem* and formulation by [2 *a ,b*], stating that a *conservation law* of current flux implies existence of fields governed by Maxwell-like equations, which supports transverse traveling waves. Along with the fields, a new dissipation mechanism of energy is introduced with the action of an internal friction (Joule-like effect).

From numerical studies of pipe-flow and wall-bounded flows [3 *a, b, c*], it is found that transverse *traveling* waves are generated by the help of body forces (*i.e*. introducing *external* agents), although final results are obtained without such forces. It is not clear why such a complex procedure is required in the study of natural phenomena. A stability analysis of channel turbulence [4] found existence of a disturbance wave-mode observed in the experiments. However, in order to obtain such a wave, a variable turbulent eddy viscosity had to be used instead of the constant molecular viscosity. Turning our attention to the drag coefficient, empirical laws must be used for fully developed pipe turbulence. These may imply that the current theory fails to predict the pipe turbulence adequately.

A wind-tunnel experiment of boundary layer flows [5] verified delay of transition to turbulence by a worked-out design on the wall enforcing streaky flow in the wall layer. In wall turbulence, there are ample experimental evidences of streaky large-scale structures: LSM (large-scale motions) and VLSM (very-large-scale motions) [6*a,* 6*b*, 7], which are characterized with streamwise streaks and long meandering structures. The LSMs are considered to be created by the vortex packets consisting of hairpin structures, while question of how the scale VLSM is mechanically generated remains open.

With a streamwise energy spectrum $E_x(k)$ with respect to a wave number k, the pre-multiplied streamwise spectra $k\,E_x(k)$ have two *peaks* at LSM of $\lambda_x/2 \approx 1 \sim 3$ and at VLSM of $\lambda_x/2 \approx 15 \sim 20$ (where 2 is the pipe radius and λ_x the streamwise scale), and decays beyond VLSM. The energy spectrum $E_x(k)$ takes a scaling form $E_x \propto k^{-1}$ in the wavenumber section between the two scales, while $E_x \propto k^{-5/3}$ at higher k's.

Here, the newly introduced field is called *Transverse-Wave* field, *TW*-field *in short*. Two dynamical mechanisms are newly found: a mechanism exciting the TW-waves and the other a channel supplying energy to the TW-field. This is studied by a model equation: $\nabla^2\boldsymbol{e} - {c_t}^2{\partial_t}^2\boldsymbol{e} = 2\rho\,\partial_t\boldsymbol{u} + 2\sigma\partial_t\boldsymbol{e}$, derived from the present theory described in the next section. The LHS is a wave equation describing a transverse traveling wave of $\boldsymbol{e}$ (a fluid-electric field defined below). The second term on RHS is a damping term, while the first is a term exciting the wave and supplying energy to the TW-field by extracting from the flow field $\boldsymbol{u}$.

Most importantly, the TW-field accompanies its own mechanism of energy dissipation due to a *fluid*-Joule effect. This effect is caused by a drift current $\boldsymbol{j}_d = \sigma\boldsymbol{e}$, newly introduced to the new field, where σ^{-1} is a fluid-resistivity. The fluid-Joule loss is given by $Q_\mathrm{J} = \boldsymbol{e}\cdot j_d = \sigma^{-1}|\boldsymbol{j}_d|^2$. The Joule loss Q_J can be written in a form analogous to the viscous rate of dissipation. In fact, using $|\boldsymbol{j}_d| = \rho v_d$ and $\sigma \sim \rho d/c_t$, we have

$$Q_\mathrm{J}/\rho \sim \nu_J\,(v_d/d)^2, \qquad \nu_J = c_t d$$

The Joule viscosity $\nu_J = c_t d$ is analogous to the eddy-viscosity. Here, the velocity is the speed c_t of transverse wave in turbulence and the length is the damping distance d.

NEW SCENARIO OF TURBULENCE THEORY

A new scenario of turbulence theory is formulated here without self-contradiction by introducing a new TW-field, which is governed by *fluid-Maxwell* equations, because conservation of the current $\boldsymbol{j}$ is a basic property of fluid turbulence.

[a)] Corresponding author. Email: kambe@ruby.dti.ne.jp

(*i*) Governing Equations: In order to represent the TW-field, we introduce a four-vector potential $(\phi, \boldsymbol{a})$ depending on time d and space coordinates $\boldsymbol{x} = (x_1, x_2, x_3)$. Then the TW-field is governed by the following fluid-Maxwell equations:

$$\partial_t d + \text{curl}\, \boldsymbol{e} = 0, \quad \text{div}\, d = 0, \quad -\partial_t \boldsymbol{d} + \text{curl}\, \boldsymbol{h} = \boldsymbol{j}, \quad \text{div}\, \boldsymbol{d} = \rho, \qquad (1{:}\, a, b, c, d)$$

where ρ is the density, $\boldsymbol{j}$ the current flux of fluid, $\boldsymbol{e} \equiv$-$\partial_t a - \nabla\phi$ the *fluid*-electric field, and $d \equiv \nabla \times \boldsymbol{a}$ the *fluid* magnetic field. First pair of equations (1*a, b*) are satisfied identically by the definitions of $\boldsymbol{e}$ and d. From the second pair of equations (1*c, d*), it is readily shown that the current conservation equation, $\partial_t \rho + \text{div}\, \boldsymbol{j} = 0$, is satisfied identically on the assumption that both of secondly-differentiable fields $\boldsymbol{d}$ and $\boldsymbol{h}$ exist. By analogy with the electromagnetism, we assume $\boldsymbol{d} = \epsilon \boldsymbol{e}$ and $\boldsymbol{h} = \mu^{-1} d$ with ϵ and μ being field parameters. Transverse waves are naturally supported by the system of $(1a \sim 1d)$. In turbulence too, transverse waves are accommodated by the following system. From $(1a \sim 1d)$, the following conservation equations of energy and momentum are immediately derived:

$$\partial_t w + \text{div}\, \boldsymbol{q}_{\text{TW}} = -\boldsymbol{j} \cdot \boldsymbol{e}\,, \quad \partial_t \boldsymbol{g} + \partial_{x_j} T_{ij} = -\boldsymbol{F}_{\text{L}}\,, \quad \text{where} \quad \boldsymbol{q}_{\text{TW}} = \boldsymbol{e} \times \boldsymbol{h}\,, \quad \boldsymbol{F}_{\text{L}} \equiv \rho\, \boldsymbol{e} + \boldsymbol{j} \times d\,, \qquad (2{:}\, a, b, c, d)$$

where $w = \frac{1}{2}(\boldsymbol{e} \cdot \boldsymbol{d} + \boldsymbol{h} \cdot d)$ is a field energy density, $\boldsymbol{q}_{\text{TW}}$ is *fluid*-Poynting-vector (TW-energy flux), and $\boldsymbol{g} = \boldsymbol{d} \times d = \boldsymbol{q}/\boldsymbol{c_t^2}$ is a field momentum, and T_{ij} is *fluid*-Maxwell-stress, where $c_t = 1/\sqrt{\epsilon\mu}$ is the velocity of transverse waves. The right hand sides of (2*a*) and (2*b*) are energy source (or loss) and *fluid*-Lorentz-force reaction, respectively.

Whole field consists of *Fluid Flow* (FF) and *TW*- field. Energy equation of the whole system is given by

$$\partial_t \left[\rho\, d\tfrac{1}{2} v^2 + \varepsilon\right) + w\,\Big] + \text{div}\,(\boldsymbol{q}_{\text{FF}} + q_{\text{TW}}) = 0, \qquad \boldsymbol{q}_{\text{FF}} = \rho\, \boldsymbol{v}\, d\tfrac{1}{2} v^2 + \varepsilon + P\Big) - \boldsymbol{v} \cdot \boldsymbol{\tau}^{(\text{vis})} - \boldsymbol{\kappa} \nabla \text{T}\,,$$

where ε is the internal energy of fluid, and $\boldsymbol{q}_{\text{FF}}$ is the FF-energy flux, with $\boldsymbol{\tau}^{(\text{vis})}$ the viscous stress tensor, T the temperature and κ the thermal diffusivity.

The FF-momentum equation is given by $\partial_t(\rho \boldsymbol{v}) + \partial_{x_j} \Pi_{ij} = \boldsymbol{F}_{\text{L}}$, where $\Pi_{ij} = \rho v_i v_j + p\, \delta_{ij} - \tau_{ij}^{(\text{vis})}$. There are interaction terms $\pm \boldsymbol{F}_{\text{L}}$ on the RHS of this and (2*b*), which cancel out by adding both equations side by side. Thus we obtain the momentum equation of whole field:

$$\partial_t(\rho \boldsymbol{v} + \boldsymbol{g}) + \partial_j(\Pi_{ij} + T_{ij}) = 0.$$

(*ii*) Dissipation: Our system is dissipative. The current flux is represented as $\boldsymbol{j} = \rho \boldsymbol{v} + \boldsymbol{j}_d$, where the term $\rho \boldsymbol{v}$ is a convection current, while $\boldsymbol{j}_d = \sigma \boldsymbol{e}$ is a *drift* (or conduction) current. This is a *fluid*-Ohm's law. Then, the *fluid*-Joule heat is given by $Q_{\text{J}} = \boldsymbol{e} \cdot j_d = \sigma |\boldsymbol{e}|^2$ $(d\ 0)$.

A fluid particle (*i.e.* a mass m of a macroscopic scale) is a *soft* cluster of an immense number of molecules and its macroscopic velocity $\boldsymbol{v}_c$ is the motion of the center of mass. Its macroscopic mass flux is $m\boldsymbol{v}_c$. If the fluid particle is exposed to strong acceleration (like in turbulence), it is very likely that its mass flux is forced to deviate from the value $m\boldsymbol{v}_c$, and may be modified by an additional term $\boldsymbol{j}_d$. The drift current $\boldsymbol{j}_d$ is regarded to be inherent in turbulent medium.

Owing to this dissipative heat, the equation for the entropy s is described by

$$\rho\, \text{T}\, \frac{\text{D}\, s}{\text{D}d} = Q_{\text{vis}} + Q_{\text{J}}$$

where $\text{D}/\text{D}d$ is the convective derivative and Q_{vis} the viscous heat. The second term is new due to the Joule heat.

Conclusion: The present scenario is successfully applied to pipe turbulence, by predicting traveling waves having two characteristic scales of a wave-length λ and a length d of wave damping. Significance of λ and d is discussed in relation to the two large scales, LSM and VLSM, of wall turbulence.

Perhaps, most remarkable outcome of the present scenario is the dissipation due to the fluid-Joule effect caused by the drift current. Its magnitude is comparable with models of eddy viscosity. Note that the fluid-Joule effect is derived *analytically* from the basic governing equations, while the eddy viscosities are not like that.

References

[1] Kambe, T.: A new scenario of turbulence theory and application to pipe turbulence. ETC15 (Delft), 2015.

[2] (*a*) Scofield D. F. & Pablo Huq,: Concordances among electromagnetic, fluid dynamical, and gravitational field theories. Phys. Lett. A, **374**, 3476-3482, 2010; (*b*) Scofield & Pablo Huq,: Fluid dynamical Lorentz force law and Poynting theorem --derivation and implications. Fluid Dyn. Res. **46**, 055514 (22pp), 2014.

[3] (*a*) Brosa, U.: Disturbances in pipe flow excited by magnetic fields. Z. Naturforsch. **46**a, 473--480, 1991; (*b*) Waleffe, F.: Three-dimensional coherent states in plane shear flows. Phys. Rev. Lett. **81**, 4140-4143, 1998; (*c*) Faisst, H. & Eckhardt, B.: Traveling waves in pipe flow. Phys. Rev. Lett. **91**, 224502, 2003.

[4] Del Alamo, J. C. & Jiménez, J.: Linear energy amplification in turbulent channels. J. F. M. **559**, 205-213, 2006.

[5] Fransson, J.H.M., Talamelli, A., Brandt, L. and Cossu, C.: Delaying transition to turbulence by a passive mechanism. Phys. Rev. Lett. **96**, 064501, 2006.

[6] (*a*) Hutchins, N. & Marusic, I.: Evidence of very long meandering features in the logarithmic region of turbulent boundary layers. J. Fluid Mech. **579,** 1-28, 2007; (*b*) Monty, J.P., Stewart, J.A., Williams, R.C. & Chong, M.S.: Large-scale features in turbulent pipe and channel flow. J. Fluid Mech. **589**,147--156, 2007.

[7] Kim, K.C. and Adrian, R.J.: Very large-scale motion in the outer layer. Phys. Fluids **11**, 417-422, 1999.

HELICAL-WAVE INSTABILITIES OF AN ANNULUS FLOW IN A HELICAL MAGNETIC FIELD

Xiangming Xiong, Jianjun Tao[a)], Yurong Zhao, Dong Luo
CAPT-HEDPS, SKLTCS, Department of Mechanics and Engineering Science, Peking University, Beijing, China

Summary The stabilities of an annulus flow with an external helical magnetic field is studied theoretically and numerically by using the quasi-static approximation. For the case with zero axial pressure gradient, it is shown numerically that when the Reynolds number is larger than a threshold value, the helical magnetic field will yield a right-handed traveling-wave instability. At higher Reynolds numbers, the first wave mode is superposed by a secondary anti-symmetric helical wave mode, which travels in the opposite direction of the first one. Linear stability analysis is carried out, and the critical parameters of the most unstable mode are consistent quantitatively with the numerical observations. Furthermore, when a finite axial pressure gradient is applied to guarantee a zero axial flow rate, the annulus flow is found to be more unstable than the case with zero axial pressure gradient.

INTRODUCTION

The magneto-rotational instability (MRI) was firstly studied in a Taylor-Couette flow by Velikhov[1], and now is of particular interest in astrophysics, where it is thought to be the main formation mechanism of stars in the accretion disks [2]. Recently, a helical magnetic field is proposed theoretically by Hollerbach & Rüdiger [3], and the critical Reynolds number of MRI can be reduced to $O(10^3)$. The corresponding experiment was conducted with "PROMISE" facility by Stefani et al.[4]. In experiments, the cylinders may not be completely electrically isolated from each other. Priede [5] assumed that the endcap was perfectly conducting and the radial voltage drop between the cylinders was constant as ignoring the resistance of the sliding liquid-metal contact between the inner cylinder and the endcap. Consequently, a base state composed of an upward flow along the inner cylinder and a return one along the outer cylinder was obtained.

Different from these previous studies, in this paper the effect of a helical magnetic field on an annulus flow between differentially co-rotating cylinders with the same electrical potential (i.e. both cylinders are electrically connected to the ground) is investigated.

NUMERICAL SIMULATIONS

The radius of the outer cylinder R_o is twice as much as that of the inner cylinder R_i, and they rotate with angular velocities Ω_o and Ω_i, respectively. In this paper $\Omega_o/\Omega_i = 0.27 > (R_i/R_o)^2 = 0.25$, the threshold value for centrifugally stable state according to the viscous extension of the Rayleigh criterion, hence the flow is hydrodynamically stable without external magnetic field. A constant axial magnetic field B_z and a purely azimuthal magnetic field $B_\theta(R_i/r)$ are imposed. The latter can be produced by a constant axial electric current flowing through the center rod of the cylinders and was studied numerically in our recent paper [6]. Another parameter is $\beta = B_\theta/B_z$, the ratio of the azimuthal magnetic field to the axial magnetic field. It is assumed that the magnetic Prandtl number and the magnetic Reynolds number are much smaller than 1. Consequently, the quasi-static approximation is applied. In addition, the inner and outer cylinders are perfectly conducting and connected electrically to the ground, hence their electric potentials always keep zero.

We used the radius of the inner cylinder R_i as the length scale, B_z as the scale of the magnetic field, and $\Omega_i R_i$ as the velocity scale. The scales of pressure, electric potential, and electric current density are $\rho R_i^2\Omega_i^2$, $R_i^2\Omega_i B_z$, and $\sigma R_i\Omega_i B_z$, respectively, where ρ and σ are the density and the electrical conductivity of the fluid, respectively. The Reynolds number and the Hartmann number are defined as $Re \equiv R_i^2\Omega_i/\nu$ and $Ha \equiv B_z R_i(\sigma/\nu\rho)^{1/2}$, respectively. Two kinds of basic flows are considered: one with a zero axial pressure gradient (BF1) and the other with a zero axial flow rate (BF2).

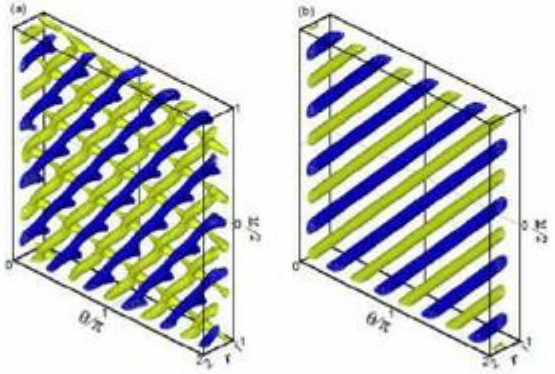

Fig1. (a)The instantaneous iso-surfaces of $u_r = \pm 0.02$ in a part of the computational domain at Re = 850 for BF1. The iso-surface of $u_r = \pm 0.01$ at Re = 600 is shown in (b) as a reference.

[a)]Corresponding author. Email: jjtao@pku.edu.cn

The governing equations are solved numerically using the highly conservative finite difference scheme studied by Krasnov *et al.*[7]. The radial point distribution is clustered toward the cylinder walls as $r = 1 + 0.5[1 + \tanh(H\zeta)/\tanh(H)]$, where $H = 1.5$ and $-1 < \zeta < 1$ is the transformed coordinate, in which the grid is uniform. Periodic conditions are used at the top and the bottom boundaries. In order to simulate the flow structures for infinitely long cylinders, different axial lengths (i.e. 2π, 3π, 4π, 6π and 12π) are tested. In addition, two sets of grid sizes in the azimuthal, radial and axial directions $[n_\theta, n_r, n_z]$=[192, 64, 512] and [256, 96, 768] are tested as well for the flow at Re=850 with the axial length of 12π. It was found numerically that the azimuthal and axial wave numbers of the first and the secondary unstable modes were the same for the two sets of grids and a relative difference of the mean total disturbance kinetic energy was less than 1.3%. Therefore, the mesh $[n_\theta, n_r, n_z] = [192, 64, 512]$ and the axial length 12π are used in the simulations. We choose $Ha = 7.8$ and $\beta = 5.37$, the parameters used in laboratory experiments by Stefani *et al.*[4].

For the case of zero axial pressure gradient (BF1), it is found that the flow becomes unstable first to a right-handed helical travelling wave as shown in Fig.1(b), and at higher Reynolds number a secondary left-handed wave appears (Fig.1a), travelling in the opposite direction of the first one. By extrapolating the volume-averaged kinetic energy as Re<600, we get the critical Reynolds number of the first instability is 500.2.

LINEAR INSTABILITY ANALYSIS

In order to understand the onset mechanism of these helical travelling waves, linear stability analysis is carried out. By introducing the normal mode $(\boldsymbol{v}', \phi', p') \sim \exp[i(k_z z + k_\theta \theta - \omega t)]$, we obtain an eigenvalue problem, which is discretized over 65 Chebyshev-Gauss-Lobatto collocation points, and solved with the QZ function in Matlab. $k_z k_\theta < 0$ and $k_z k_\theta > 0$ correspond to the right-handed and the left-handed helical modes, respectively.

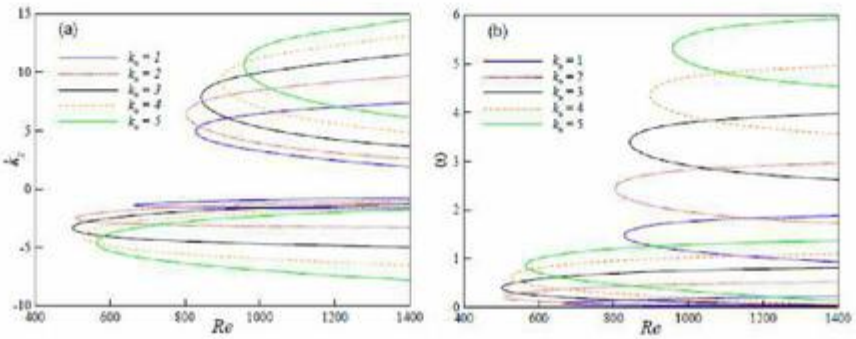

Fig.2 The neutral curves for the case with zero axial pressure gradient in (a) k_z-*Re* plane and (b) ω-*Re* plane.

As shown in Fig.2, the critical Reynolds number is 500.23, which agrees very well with the numerical value 500.2, and other critical parameters $(k_\theta, k_z, \omega) = (3, -3.35, 0.394)$ are consistent as well with $(3, -3.33, 0.402)$, the simulation data of the first helical travelling wave obtained at $Re = 510$.

The linear stability of the base flow with zero axial flow rate (BF2) is studied as well, and the most unstable mode is still the right-handed travelling wave mode with a critical Reynolds number of 202.47, which is much smaller than the BF1 value 500.23. In addition, the critical azimuthal wavenumber is changed from 3 of BF1 to 1 of BF2, and the axial phase velocity of the critical right-handed wave mode is positive for BF2 but negative for BF1.

CONCLUSIONS

Different from the previous studies of the helical MRI, in this paper both cylindrical walls are assumed to be electrically connected with the ground and two kinds of base flows are considered. The base flow without the axial pressure gradient (BF1) is vulnerable to a right-handed helical travelling wave, which is explained as the most unstable mode based on the linear stability theory. When an axial pressure gradient is exerted to guarantee a zero axial flow rate, the annulus flow becomes more unstable than the BF1 case. These results are expected to be helpful in understanding the helical MRI where the annulus is closed by insulating endcaps.

References

[1] Velikhov, E. P.: Stability of an Ideally Conducting Liquid Flowing Between Cylinders Rotating in a Magnetic Field. *J. Exptl. Theoret. Phys.* **36**, 1398–1404,1959

[2] Balbus, S. A. & Hawley, J. F.: A powerful local shear instability in weakly magnetized disks. I - Linear analysis. II - Nonlinear evolution. *Astrophys. J.* **376**, 214–233, 1991

[3] Hollerbach, R., Rüdiger: New Type of Magnetorotational Instability in Cylindrical Taylor-Couette Flow. *Phys. Rev. Lett.* **95**, 124501,2005

[4] Stefani, F., Gundrum, T., Gerbeth, G., Rüdiger, G., Schultz, M., Szklarski, J. & Hollerbach, R. 2006 Experimental Evidence for Magnetorotational Instability in a Taylor-Couette Flow under the Influence of a Helical Magnetic Field. *Phys. Rev. Lett.* **97**,184502, 2006

[5] Priede, J.: Pseudo-magnetorotational instability in a Taylor-Dean flow between electrically connected cylinders. *Phys. Rev. E* **79**, 066314, 2009

[6] Zhao, Y., Tao, J. & Zikanov, O.: Transition to two-dimensionality in magnetohydrodynamic turbulent Taylor-Couette flow. *Phys. Rev. E* **89**, 033002, 2014

[7] Krasnov, D., Zikanov, O. & Boeck, T.: Comparative study of finite difference approaches to simulation of magnetohydrodynamic turbulence at low magnetic Reynolds number. *Comp. Fluids* **50**, 46–59, 2011

BYPASS TRANSITION IN BOUNDARY LAYERS

Dan S. Henningson *[1], Tobias Kreilos[2], Taras Khapko[1], Philip Schlatter[1], Yohann Duguet[3], and Bruno Eckhardt[4,5]

[1]*Linné Flow Center, KTH Mechanics, Royal Institue of Technology, 10044 Stockholm, Sweden*
[2]*EPFL, School of Engineering, CH-1015 Lausanne, Switzerland*
[5]*LIMSI-CNRS, UPR 3251, Université Paris-Sud, 91403 Orsay, France*
[4]*Fachbereich Physik, Philipps-Universität Marburg, D-35032 Marburg, Germany*
[5]*JM Burgercentrum, Delft University of Technology, 2628CD Delft, The Netherland*

Summary The boundary layer above a flat plate exposed to free-stream turbulence becomes turbulent through the initiation of turbulent patches that spread as they are advected downstream. In order to model and describe the intermittency factor (a measures of the fraction of space that is filled with turbulence) we combine results on the receptivity of the boundary layer with nonlinear concepts developed in internal flows. The model gives a physically motivated expression for the spatial distribution of spot nucleation events that is then integrated into a probabilistic cellular automaton. The free parameters are fixed by fits to numerical simulations. The model reproduces the spatial variation of the intermittency factor for different turbulence levels. The results show how the recent theoretical progress on transitional wall-bounded flows can be extended to the much wider class of spatially developing boundary layers flow.

INTRODUCTION

The Blasius boundary layers shows a linear instability to the formation of Tollmien-Schlichting waves far down the plate and a transition that is not connected with a linear instability further upstream [1,2]. This second transition requires finite amplitude perturbations, and can be triggered, e.g., by free stream turbulence. A similar phenomenology is observed in plane Couette and pipe flow, where the transition could be explained with the appearance of exact three-dimensional coherent structures [3]. It has been possible to study how the phase space is organized, and how this determines the conditions under which the bypass process is the more dominant one, with the linear instability confined to a small set of initial conditions.

MODELLING THE TRANSITION

In the case of the boundary layer, we have already calculated one key structure, the state that is intermediate between laminar and turbulent, the edge state [4]. Its stable manifold separates perturbations that return to laminar from those that trigger a turbulent spot. In the present study we extend this concept to describe the probability that an incoming perturbation nucleates a turbulent spot and use it to derive the intermittency factor.

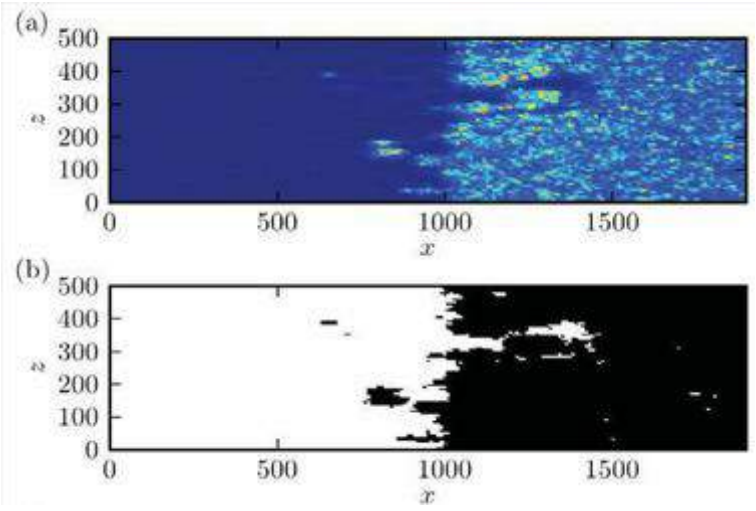

Figure 1: Visualization of turbulent spots in the LES data. (a) The untreated LES data. The colors indicate the level of turbulence by measuring the wall-normal velocity gradient at the wall. Dark blue indicates low intensities, the bright regions higher intensities. (b) Digitized LES data where only laminar (white) and turbulent (black) regions are distinguished. These data are then used to extract the parameters for the cellular automaton model.

*Corresponding author. Email: henning@mech.kth.se

For the implementation and test of this model for boundary layers, we appeal to the successful modeling of shear flows with probabilistic cellular automata and concepts from directed percolation. We fit a cellular automaton to the data from a large eddy simulation by discretizing space, time and the turbulent intensity to obtain a discrete map that has two states, laminar (white) and turbulent (black), see Figure 1. Within this automaton we can now model the breakdown of the laminar flow and the spreading of turbulent spots. Observables like the intermittency factor, the number of turbulent spots and their width calculated from the DNS and the automaton model are in very good agreement (Figure 2).

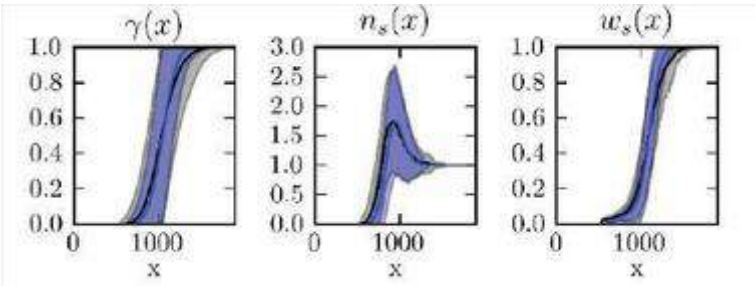

Figure 2: Comparison of statistics between the LES data (black) and the probabilistic cellular automaton (blue). (a) Intermittency factor. (b) Number of spots at every downstream position. (c) Width of independent spots in units of the domain width as a function of downstream position.

CONCLUSIONS

The results show how the receptivity of the boundary layer, which to a large extent is a linear or weakly nonlinear process, can be combined with the nonlinear concept of a threshold curve to explain the spot nucleation mechanism. When the nucleation model is introduced into the constructed simple cellular automaton the simulation data is fully reproduced. The results demonstrate how the understanding that has been obtained for parallel, internal flows can be extended to the much wider class of spatially developing boundary layers.

REFERENCES

[1] H. Schlichting, Boundary-layer theory (Springer, 2004).

[2] P. J. Schmid and D. S. Henningson, Stability and Transition in Shear Flows, Applied mathematical sciences No. Bd. 142 (Springer, 2001).

[3] B. Eckhardt, T. M. Schneider, B. Hof, and J. Westerweel, Annu. Rev. Fluid Mech. 39, 447 (2007).

[4] Y. Duguet, P. Schlatter, D. S. Henningson, and B. Eckhardt, Phys. Rev. Lett. 108, 044501 (2012).

STABILIT OF LOBED TA LOR-COUETTE FLOWS B NUMERICAL SIMULATIONS

Nabila Ait Moussa[1,3a)], Sébastien Poncet[2] & Abderrahmane Ghezal[3]
[1] *Ecole nationale sup rieure d informati ue, ued Smar, Alger, Alg rie*
[2] *partment de g nie m cani ue, facult de g nie, universit de Sherbroo e, u bec, Canada*
acult de physi ue, universit de ab E ouar UST , Alger, Alg rie

Abstract The stability analysis for the three-dimensional Taylor-Couette flow with triangular lobed inner cylinder is considered. The numerical simulations using a finite volume solver are carried out to characterize the transition to the two first bifurcations: the Taylor Vortex Flow (TVF) and Wavy Vortex Flow (WVF) regimes. The critical parameters such as the Reynolds number and wave number signaling the onset of Taylor vortices are determined. It is found that a destabilization of the Taylor vortices results from the application of a non-constant gap width along the radial direction and the vortical structures are more pronounced compared to the classical system.

INTRODUCTION

The flow between two concentric cylinders, which is termed as Taylor–Couette flow, has been the subject of considerable studies since the pioneering work of Taylor [1]. Although this flow is well known today theoretically and experimentally, applying some modifications on the shape of either the inner or outer cylinder opens the way to develop new generations of electrical rotating machineries or advanced reactors for dynamic membrane filtration. Soos et al. [2] investigated both experimentally and numerically the Taylor–Couette flow with a lobed inner cylinder. This new device, much less studied, was designed in order to improve the performance of classical Taylor-Couette (CTC) bioreactors in cell cultivation. Indeed, the authors indicated that the lobed configuration drastically reduces the shear rates and deforms the vortices, and therefore improves the mixing in the vortex core. More recently, Li et al [3] studied numerically the lobed Taylor Couette (LTC) system with eccentric inner cylinder for the synthesis of nanopowders. These investigations are limited to the specific flow conditions of a turbulent LTC flow. No attention has been paid up to now to the transition process in such system.
The present work is concerned with the CFD modelling of the LTC flow having the same cross-section geometry as in the experiments of Soos et al [2]. The motivation of this study, in addition to its connection with the classical Taylor-Couette system, is to gain basic understanding of the transition from circular Couette flow (CCF) to Taylor vortex flow (TVF), and then to the Wavy Vortex Flow (WVF) and to analyze the effect of inner cylinder cross-section on the transition process.

PROBLEM DESCRIPTION AND NUMERICAL METHOD

The classical device (CTC) is composed of two coaxial cylinders of height H=160mm, inner radius R_1=62mm and gap width d=8mm (Fig.1a). The aspect ratio of the system is then fixed to $\Gamma = 20$ and the radius ratio $\eta = 0.886$. The inner cylinder rotates with constant angular velocity Ω_1 while the outer one remains stationary. The flow is controlled by the Reynolds number $Re = \Omega_1 R_1 d/\nu$, where ν is the kinematic viscosity. The lobed configuration considered here is the triangular model with minimum and maximum gap widths of d_{min} and d_{max} respectively (Fig.1b). To characterize the effect of the inner cylinder radius variation, a new parameter χ is defined as: $\chi = d_{max}/d_{min}$. Here, d_{min}=8mm and χ is varied from 1 (CTC) to 3. Because of the non-constant gap between the cylinders in the LTC system, two local Reynolds numbers may be defined: e_{min} $R_1\Omega_1 d_{min}$ ν and e_{ma} $R_{1m}\Omega_1 d_{ma}$ ν respectively, where $R_{1m} = R_1-(d_{max}-d_{min})$.
The three-dimensional Navier-Stokes equations are solved using a finite volume approach. A third -order MUSCL scheme is used to discretize the convective terms in the momentum equations. For the pressure-velocity coupling, the PISO algorithm is employed. The mesh is uniformly distributed in the azimuthal and axial directions and refined near the cylinders in the radial direction for a total of 112 000 cells. No-slip boundary conditions are imposed at the walls.

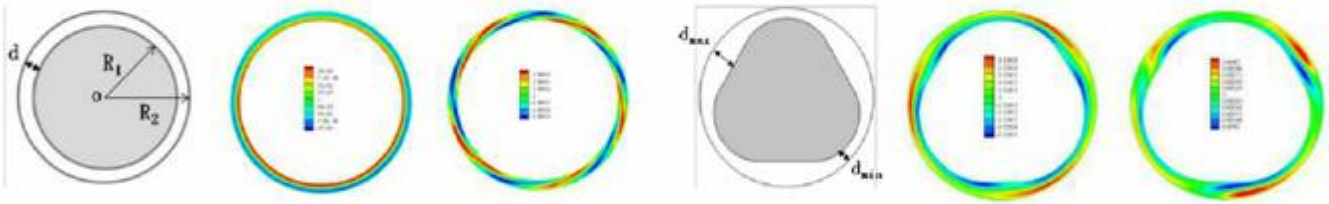

(a) CTC TVF (Re = 1.05 Re_{c1}) WVF (Re = 1.22 Re_{c1}) (b) LTC TVF (Re = 1.06 Re_{c1}) WVF (Re = 1.4 Re_{c1})

F re Contours of the axial velocity in a (r, θ) plane at z=H/2

[a)]Corresponding author. Email:n_ait_moussa@esi.dz

MAIN RESULTS

The critical parameters, the Reynolds number (Re_c) and the axial wave number (κ_c), corresponding to the first instability (TVF) for CTC (χ=1) are found to be 122.8 and 3.14 respectively. This flow regime is characterized by the axially piled of 20 vortices occurring over the cylinder height. It is in perfect agreement with the values found in previous experiments [4].

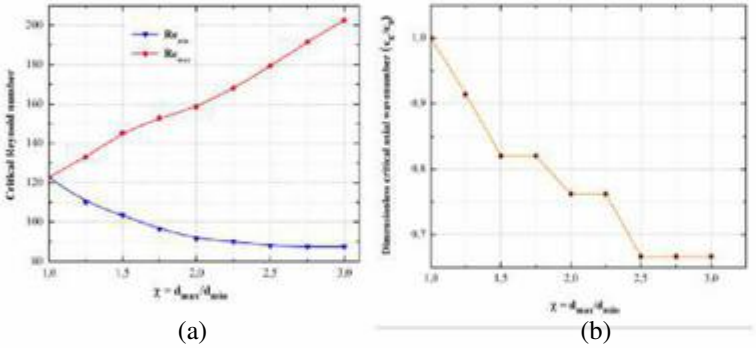

(a) (b)

F re 2 (a): Critical Reynolds number and (b) dimensionless critical axial wave number versus gap ratio χ.

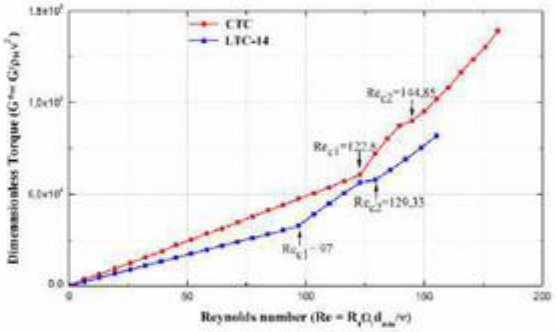

F re 3 Dimensionless torque G* against the inner Reynolds number.

For the LTC system, Figure 2a presents the variation of the first critical Reynolds numbers Re_{cmin} and Re_{cmax} with the gap ratio χ. It is shown that the minimal Reynolds number value (Re_{min}) decreases rapidly until Re_{cmin} = 87.42 for χ =3 with a rate of 28.81%. On the other hand, the maximal value Re_{cmax} substantially increases with the gap ratio χ. For χ=3, the critical Reynolds number reaches its maximum value of 202.66, corresponding to a growth rate of 65.03% significantly delaying the transition to the first instability compared to the classical case. In addition, one can note that the critical maximum Reynolds number evolves quasi linearly with χ in a pronounced positive slope of 39.12. From Figure 2b, it can be seen that the axial wave number decreases with the gap ratio. The axial waves number passes from 3.14 (20 vortices) for χ=1 to 2.1 (12 vortices) for χ=2.5-3. The axial wavelength exhibits sensitiveness to the variation of the gap shape.

The torque has been evaluated along the inner cylinder for a wide range of the inner Reynolds number and is shown in Figure 3. Two cases are considered, the CTC and LTC-14 corresponding to χ=1 and 1.75 respectively. The critical parameters for the primary (TVF) and secondary (WVF) transitions are indicated by a discontinuity in both the slope and magnitude of the torque curve. For the classical case, one can see that the position of the second mode (WVF) is reached at Re_{c2} = 144.85=1.18 Re_{c1}, in good accordance with the measurements of Andereck et al. [4] where the transition TVF-WVF was obtained for 1.17 Re_{c1}. In the lobed system, this regime occurs at Re_{c2} = 129.33=1.33 Re_{c1}. Thus, one can note that the TVF in the LTC can sustain longer than in the CTC by 12.71%. From Figure 3, one can also see that the gradient of the torque-speed relationship in the TVF regime is 3.2 times the laminar value. This result was observed by Cole [5]. In the LTC case, the TVF gradient is 2.71 times the laminar one. As the Reynolds number is further increase above the Re_{c1} value, the second change in slope corresponding to the onset of wavy vortices is less pronounced. The WVF gradient of the CTC case is 1.165 (0.9751 in the LTC case) times the TVF gradient.

CONCLUSION

The transition to the first (TVF) and second (WVF) instability regimes has been considered numerically in a novel geometry of Taylor-Couette system with a lobed inner cylinder. The results obtained show that the transition behaviors depend strongly on the gap shape. The threshold for the first transition from CCF to TVF is accelerated comparatively to the classical case. A similar behavior is also obtained for the transition to the WVF regime.

References

[1] Taylor G. I.: Stability of a viscous liquid contained between two rotating cylinders. *hil Trans Soc ondon Ser* A 223, 289-343, 1923

[2] Soos M., Wu H., Morbidelli M.: Taylor–Couette unit with a lobed inner cylinder cross section. *AIC E J* 53, 1109-1120, 2007.

[3] Li G., Yang X., Ye H.: CFD simulation of shear flow and mixing in a Taylor-Couette reactor with variable cross-section inner cylinders. *owder Technology* 280, 53-66, 2015.

[4] Andereck C.D., Liu S.S., Swinney H.L.: Flow regimes in a circular Couette system with independently rotating cylinders. *J luid ech.* 164, 155-183, 1986.

[5] Cole J.A.: Taylor-vortex instability and annulus-length effects. *J luid ech* 75 (1), 1-15, 1976.

GLOBAL STABILITY ANALYSIS OF A SHOCK WAVE/ BOUNDARY LAYER INTERACTION, INCLUDING A TRANSITION MODEL

Nicolas Bonne[1], Vincent Brion[1], Denis Sipp[1], and Laurent Jacquin[1]
[1]*Département d'aérodynamique fondamentale et expérimentale, ONERA, Meudon, France*

Summary The aim of this abstract is to present a global stability analysis of a shock wave boundary layer interaction which triggers the transition from a laminar to a turbulent state and leads to a separation bubble. The base flow is computed using the $k-\omega$ model with the SST correction and the transition model of Langtry. The global stability analysis and the sensitivity analysis take into account not only the laminar and turbulent variables but also the variables leading to the transition process.

INTRODUCTION

Shock wave/ boundary layer interactions play a predominant role in high-speed aerodynamics. Conditions for which they induce deterioration of the flow need to be understood in order to design efficient and robust vehicles. Typically a deficient SWBLI flow can be responsible for additional drag, wall heating and unsteadiness. Recent interest for laminar flow adds another item to this list, since in this case it is often seen that the boundary layer becomes turbulent at the shock location. The lower resilience of a laminar boundary layer compared to a turbulent one justifies fears that the transition triggered by SWBLI may lead to dramatic flow situations, the most dangerous one being a strong unsteadiness that would initiate a structural forcing. As a consequence this paper analyses the stability of a generic oblique shock wave interacting with a laminar boundary layer at M=1.6 with the aim of describing the fate of small perturbations to the flow and the triggering of flow unsteadiness. Interactions with a turbulent BL has been accomplished by Sartor [3], in a fully laminar setting (no transition) by Robinet [1] and in the transitional case by Spalart [4], Sansica [2] and Windle [5]. In particular Windle shows that a RANS computation can resolved Kelvin-Helmoltz instability in a case of a TSWBLI.

Stability analysis of SWBLI have been accomplished by Sartor [3]. For a normal shock wave on a transonic wing, Sartor showed, using a RANS baseflow, that a global unstable mode is associated with the buffet of the shock. Importantly the global mode comes out only if the turbulent viscosity is also perturbated. This shows that a linearization of the full RANS equations is required in order to model correctly the dynamics of such flows.

The present paper deals with including a transition model in the stability analysis methodology. To the author knowledge, the perturbation of a RANS system including the transition model has never been made. This work is carried out using the $k \circ \omega$ menter with the SST correction turbulence model and the Langtry transition model. This transition model has been chosen because it performs well in the configuration investigated here and because it is well suited to the perturbation method.

The paper is organized as follows . The first part presents the baseflow. Finally, we will perform the global stability analysis, including a sensitivity analysis.

FLOW CONFIGURATION AND COMPUTED BASEFLOW

The computation consists in a nozzle which imposes a Mach number of 1.62 in the test section (Figure 1). The lower part of the test section (BC) represents the flat plate and is modelled by an adiabatic wall. The upper part of the test section (DG) is deformed (EF) to create the shock wave, and is modelled by a wallslip condition. The line (GA) is a subsonic injection condition and (CD) is a supersonic outflow condition.

The steady solution of the RANS system has been found using the compressible solver elsA, developed at ONERA, with a second-order finite volume methods and a local time-stepping strategy. In figure 2 is shown the ρk field of base flow. The dashed line represents the incident shock wave. Continues lines are streamlines. One can see a separation bubble. The transition takes place after the impact of the shock. The turbulent kinetic energy reaches a maximum close to the reattachement point.This is in qualitative agreement with [5].

STABILITY ANALYSIS

For both stability and sensitivity analysis, we have first considered the conservatives variables (fixed μ_t), then we have added the variables of the turbulence model (fixed γ), and finally we have considered the all set of variables (complete). For the Global stability analysis, one can see on figure 1 that in the 3 different cases, the flow remains globally stable. The least stable modes are related to the accoustic of the nozzle and are of no interest for our purpose. Since the flow is globally stable, it is interesting to look at the noise amplifier behaviour of the flow. This is made by a sensitivity analysis.

In figure 4 are shown three different curves obtained maximizing the kinetic energie. One can see a pike at 30kHz for the three curves. The amplitude of this peak grows with the number of variables. One can see a gain much higher at lower

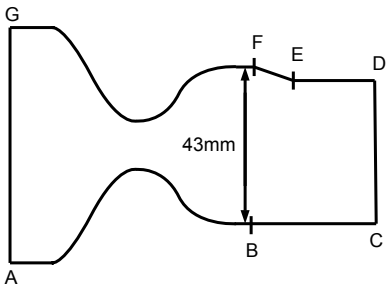

Figure 1: Scheme of the computational domain. The line GA represents the subsonic injection, the line CD the supersonic outflow, the line BC adiabatic wall. The other lines are wallslip conditions

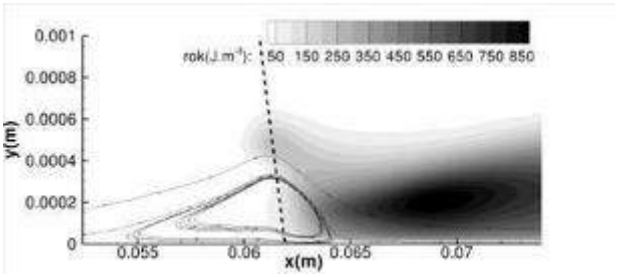

Figure 2: ρk field of the base flow. The dashed line represents the incident shock wave. Continues lines are streamlines

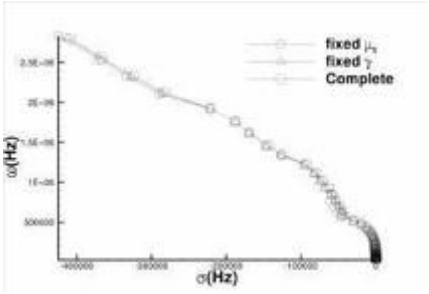

Figure 3: Spectrum in fixed μ_t (squares), fixed γ (triangles) and complete cases (circles). ω is the frequency of the mode, and σ it's growth rate

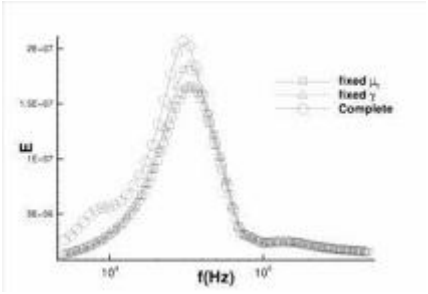

Figure 4: Sensitivity spectrum in fixed μ_t (squares), fixed γ (triangles) and complete cases (circles). f is the frequency of the mode and $E = f\lambda$, λ being it's gain

frequency (8.8kHz) in the complete case. This shows that the coupling between the transition model and the other equation of the system can emphasize a specific dynamics. Nevertheless, one can ask whether this dynamics is related to the physic or to the numerical modeling of the transition. To answer this question, the optimal forcing and response are also studied.

CONCLUSIONS

In the next few weeks, the mesh convergence of the sensitivity analysis will be tested. The influence of a free parameters which have been introduced to defined a derivative will be studied as well. Once the mesh convergence is reached, and this last analysis completed, a parameter analysis will be made on the angle of the shock.

References

[1] J-Ch Robinet. Bifurcations in shock-wave/laminar-boundary-layer interaction: global instability approach. *Journal of Fluid Mechanics*, 579:85–112, 2007.

[2] A Sansica, ND Sandham, and Z Hu. Forced response of a laminar shock-induced separation bubble. *Physics of Fluids (1994-present)*, 26(9):093601, 2014.

[3] F Sartor. *Instationnarités dans les interactions choc/couche-limite en régime transsonique: étude expérimentale et analyse de stabilité*. PhD thesis, Aix-Marseille Université, 2014.

[4] Philippe R Spalart and Michael Kh Strelets. Mechanisms of transition and heat transfer in a separation bubble. *Journal of Fluid Mechanics*, 403:329–349, 2000.

[5] Jan Windte, Ulrich Scholz, and Rolf Radespiel. Validation of the rans-simulation of laminar separation bubbles on airfoils. *Aerospace science and technology*, 10(6):484–494, 2006.

USING INFLEXION POINTS TO STABILIZE BOUNDARY LAYERS

Jonathan Healey *[1]

[1]*Department of Mathematics, Keele University, UK*

Summary We propose strategies for modifying a basic velocity profile so as to make it more stable. It is found that small modifications can produce very large increases in the critical Reynolds number for linear instability. What is especially surprising is that these stabilizing modifications create inflexion points in the profile. Our usual understanding of boundary layer stability suggests that introducing an inflexion point will be destabilizing, as it will create an inviscid instability. We use Orr-Sommerfeld calculations to show that while this destabilization does indeed take place at very large Reynolds numbers, there can be a simultaneous strong stabilization at lower Reynolds numbers. Recognising that some inflexional profiles can be very stable opens up possibilities for new stabilization strategies for transition delay.

THE PROBLEM

This paper is concerned with delaying the laminar-turbulent transition that occurs in boundary layers that form over aerofoils. Although there are many mechanisms, not all well understood, that can be involved in the transition process, we focus attention on perhaps the simplest of these, the linear amplification of waves, which forms the basis of the widely used 'e^n-method'. According to this linear theory, inflectional velocity profiles, like those produced by adverse pressure gradients and cross-flows, are most unstable and have low critical Reynolds number, Re_c, while favourable pressure gradients and the asymptotic suction profile, which produce flows with no inflexion points, and are much more stable. Indeed, strong favourable pressure gradients often create laminar flow near stagnation points, and suction is successful in stabilizing boundary layers.

These observations suggest that linear stability theory provides a useful rough guide to transition prediction, even though receptivity, nonlinearity and transient growth mechanisms would be needed for a more detailed transition analysis. The observations also suggest that modifications to a profile that significantly increase Re_c could delay transition. Large enough flow modifications, like suction, can achieve stabilization, but there may be an excessive cost in creating large modifications. Our goal is to identify relatively small flow modifications that nonetheless produce significant inreases in Re_c.

It seems likely that the easiest part of the flow to modify is the flow closest to the wall. But if we only modify the flow near the wall then we will typically introduce an inflexion point. For example, in a region close enough to the wall, the basic velocity profile is approximately linear. Any localized deviation from the linear profile produced by a modification must necessarily produce at least one inflexion point since the modified profile asymptotes back towards the unmodified linear profile as distance from the wall increases. Therefore, localized modifications to a profile near the wall would appear to make unpromising candidates for stabilization since they create inflexion points.

However, we show that near-wall modifications can produce large increases in Re_c even when producing inflexion points.

RESULTS

We illustrate the approach by stabilizing the Blasius boundary layer profile, $U_B(y)$, where the wall is at $y = 0$, the parallel flow approximation is made, and the flow has been nondimensionalized using the freestream velocity and displacement thickness. For Blasius flow $Re_c \approx 519$ according to Orr-Sommerfeld theory. This flow is a relatively challenging test case because it is the most unstable non-inflexional profile of the Falkner-Skan family, and, because it has zero curvature at the wall, it is highly susceptible to having inflexion points created by even small near-wall flow modifications.

The flow modification needs to be realizable in a physical flow. Consider the modification produced by a wall-jet

$$U_m(y) = u_j y^2 \exp(\circ\, y/d) \tag{1}$$

where $u_j > 0$ characterizes the strength of the wall jet, and d gives a measure of the thickness of the jet. When d is small the jet thickness is $O(d)$, and its velocity is $O(d^2)$ when $u_j = O(1)$, thus giving a small flow modification. However, $U_m'' = O(1)$, and since curvature is important to stability, this allows the small modification to have a significant effect on Re_c.

The modification (1) has inflexion points at $y/d = 2 \pm \sqrt{2}$, and for small d the combined profile $U = U_B + U_m$ has inflexion points at approximately the same places since U_B is approximately linear near the wall. Graphs of U_m and U_m'' are shown in figure 1 (a) and (b).

In figure 1 (c) and (d) we show examples of the Blasius profile modified by the wall jet, i.e. $U = U_B + U_m$ and the curvature of the modified profile U''. There is only one inflexion point produced in this case (the one near $y/d = 2 + \sqrt{2}$ in U_m has been eliminated by the stronger negative curvature of the Blasius profile). The appearance of the inflexion point in the modified profile, U, produced by adding this wall jet, creates an inviscid instability, which is obviously a destabilizing effect.

*Corresponding author. Email: j.j.healey@keele.ac.uk

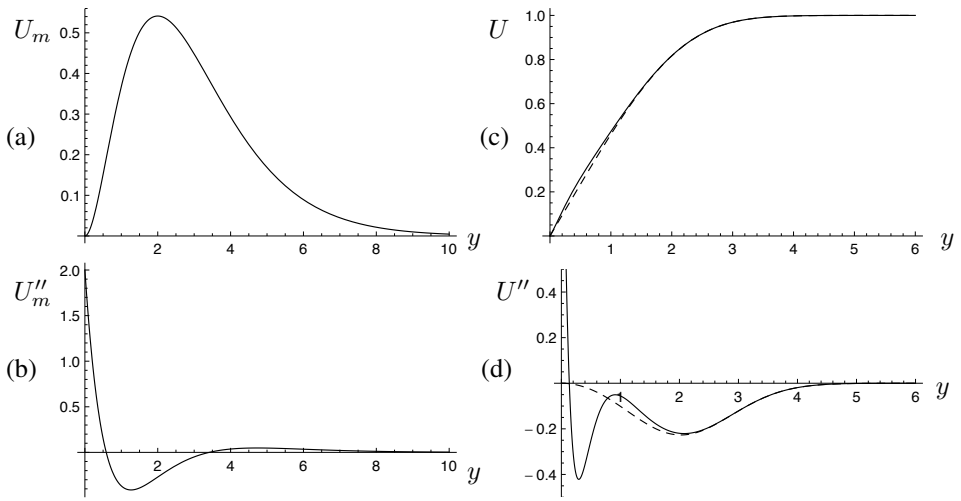

Figure 1: (a) The wall-jet flow modification (1) for $u_j = d = 1$ and (b) its second derivative also for $u_j = d = 1$. (c) The dashed line is the unmodified Blasius profile, U_B, ($u_j = 0$) and the solid line is the wall-modified profile $U = U_B + U_m$ for $u_j = 1$, $d = 0.23$; (d) shows the second derivatives of the curves in (c).

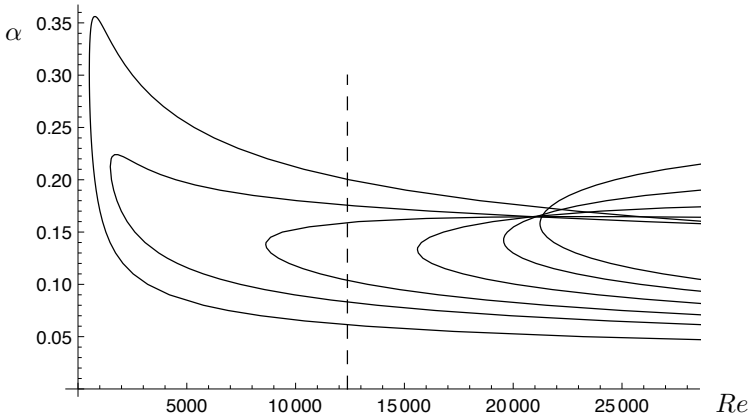

Figure 2: Neutral curves for wall-modified Blasius profiles for $d = 0.3$. The curve with lowest Re_c is for the Blasius profile, $u_j = 0$. The curves with increasing Re_c have $u_j = 0.333,\ 0.5,\ 0.667,\ 0.833,\ 1$, respectively. The dashed line marks the critical Reynolds number for stagnation point flow.

However, this is only an asymptotic prediction — it tells us that as $Re \to \infty$ there will be a finite band of unstable wavenumbers corresponding to the inviscid instability. Since no such instabilty exists for the Blasius profile, there is destabilization at large enough Re. But stabilization is still possible at lower Re.

Questions concerning finite parameter values are not easily addressed within an asymptotic framework alone, and require a complementary numerical study. We have therefore obtained numerical solutions of the Orr-Sommerfeld equation for the modified profile $U = U_B + U_m$. Figure 2 shows a family of neutral curves for a fixed value of d and a range of values of u_j.

CONCLUSIONS

In fact, very strong stabilization is obtained at lower Re, even though the modification introduces an inflexion point. The destabilization predicted in the inviscid limit due to the inflexion point only sets in for $Re > 22,000$. The critical Reynolds number for linear instability can be pushed above $20,000$, which is well above that for stagnation point flow.

Of course, some words of caution should be noted: we don't yet know if the modification increases transient growth mechanisms, nor how strong nonparallel effects are for the modified profile. The modification will decay with downstream distance and is likely to evolve on a shorter length scale than the Blasius profile, but on the other hand, at $Re \sim 20,000$ viscous diffusion of the modification will be weak. A more serious difficulty might be how a wall jet with the correct stabilizing characteristics can be introduced to a physical flow. Nonetheless, the stabilizing effect of a modification that produces an inflexion point is so strong, and yet counter-intuitive, that this seems to be a promising area for further investigation.

NONLINEAR OPTIMAL COHERENT STRUCTURES IN TURBULENT CHANNEL FLOW

Mirko Farano*[1,2], Stefania Cherubini[2], Jean-Christophe Robinet[2], and Pietro De Palma[1]
[1]*DMMM, Politecnico di Bari, Via Re David 200, 70125, Bari, Italy*
[2]*DynFluid Laboratory, Arts et Metiers ParisTech, 151 Boulevard de l' Hopital, 75013 Paris, France*

Summary Nonlinear optimal coherent structures have been computed in the turbulent channel flow at $Re_\tau = 180$. A scale separation has been obtained suitably choosing the optimization time scale characterising the inner and the outer region dynamics. The optimization provides wavy streaky structures in the inner region and hairpin vortices in the outer one at the target time. The time evolution of the hairpin optimal vortices has been analysed to understand its role in sustaining turbulence.

The main goal of this work is to show that the near wall coherent structures, observed in fully developed wall bounded turbulent flows, could be obtained as the result of an energy optimization process as it is observed in transitional flows [1]. In particular, here we focus on a non-linear global optimization, looking for finite-amplitude optimal coherent structures in the turbulent channel flow at $Re_\tau = 180$ [2].

The equations governing the motion of the coherent perturbations of a turbulent mean flow have been proposed in [3], and are reported here:

$$\frac{\partial \tilde{\mathbf{u}}}{\partial t} + \nabla\tilde{\mathbf{u}}\cdot\tilde{\mathbf{u}} + \nabla\mathbf{U}\cdot\tilde{\mathbf{u}} + \nabla\tilde{\mathbf{u}}\cdot\mathbf{U} = \circ\,\nabla\tilde{\mathrm{p}} + \frac{1}{Re}\nabla^2\tilde{\mathbf{u}} \circ\ \nabla\cdot(<\mathbf{u}'\mathbf{u}'>) + \nabla\cdot\left(\overline{(\tilde{\mathbf{u}}\tilde{\mathbf{u}})} + \overline{(\mathbf{u}'\mathbf{u}')}\right), \tag{1}$$

where $\tilde{\mathbf{u}}$ represent the coherent part of the perturbation, $\mathbf{U}$ is the turbulent mean flow, and $\mathbf{u}'$ is the background noise. The last two terms in equation (1) represent the phase average of the random fluctuation tensor and the Reynolds stress tensor (i.e., the time average of the perturbations of the mean flow obtained as the sum of the coherent and fluctuating parts), respectively. Since the main purpose of this work is to study the finite-amplitude coherent structures characterising turbulence, we assume that the term $<\mathbf{u}'\mathbf{u}'>$ is negligible, namely means that the variance of the probability distribution of the non-coherent part of the perturbation is rather small. On the contrary, concerning the Reynolds stress, both contributions to the tensor are taken into account, being evaluated by DNS computation.

Using this formulation, we compute the coherent structures which maximise the energy growth $\frac{E(T)}{E_0}$, for a fixed time horizon T, where:

$$E = \int_V \left(\widetilde{u}^2 + \widetilde{v}^2 + \widetilde{w}^2\right) dV. \tag{2}$$

This problem is solved by using the Lagrange multiplier technique coupled with a direct adjoint iterative procedure considering equation (1) as a constraint.

Concerning the choice of the optimization time, we focus on two distinct time scales existing in bounded turbulent flow, namely the inner and the outer one, associated with two spatial regions characterized by a different kind of flow dynamics: i) low and high speed streaks with typical dimension of $\lambda_z^+ \approx 80 \circ\ 100$ and $\lambda_x^+ \approx 1000$ surrounded by counter rotating vortices spaced of $\lambda_z^+ \approx 50$ with a length of $\lambda_x^+ \approx 100 \circ\ 200$; ii) hairpin vortices of different size and type, respectively [4]. The choice of the time scale associated with these two regions can be addressed in several ways as in [5, 6]. Here, we have chosen as target time the eddy turnover time at $y^+ \approx 20$ for the inner region, and the one at centreline for the outer region, obtaining respectively $T^+ \approx 80$ and $T \approx 31$.

The results of the nonlinear optimization at these two target times are shown in figure 1. Concerning the optimization for the inner scales, as one can note in the left panel of figure 1, the optimal coherent structure is characterised by streamwise-elongated streaks, which show a wavy modulation, inducing the formation of spots of counter-rotating vortices on their two sides. This structure is very similar to that obtained using a local linear optimization (see [5]) with similar parameters, except for the streamwise modulation and the presence of localised spots which are typically due to non-linear effects. This optimal structure well represents the streaky structures observed near the wall in turbulent bounded flow, having a spanwise spacing $\lambda_z^+ \approx 100$, supporting the idea that such structures can be considered as quasi optimal ones.

Concerning the optimal structures for the outer scale, they result in hairpin packets surrounding large scale streaks (see right panel of figure 1). Two different kinds of hairpin vortices can be distinguished: i) a smaller one linked to the presence of long low speed streaks starting to break down and allowing the side-by-side counter rotating vortices to join into a non symmetric arch; ii) a bigger one involving the varicose instability of two near streaks, leading to the merging of two counter rotating near-vortices in a bigger symmetric hairpin.

The dynamics of the outer optimal structure has been analysed looking at the evolution of the coherent perturbation from $t = 0$ up to $10\ T_{opt}$. The vortex dynamics involved into the hairpin formation is investigated, and its role into self sustaining

*Corresponding author. Email: m.farano@libero.it

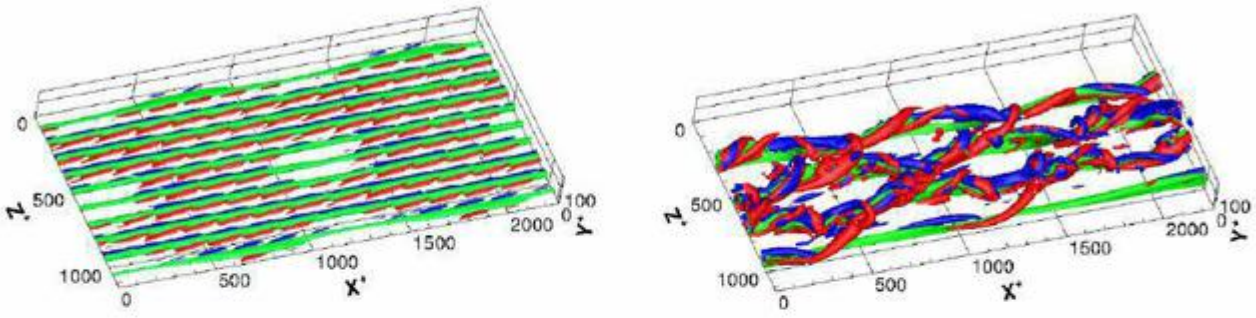

Figure 1: Optimal perturbation for $T^+ \approx 80$ (left) and $T \approx 31$ (right) with $E_0 = 10^{-2}$. Isosurface of negative streamwise velocity (green) and Q-criterion coloured with streamwise velocity (blue positive, red negative).

turbulence is enlightened. In particular, looking at the production and dissipation terms extracted from the energy equation obtained from equation (1) we have observed a strong initial energy growth until the formation of the largest hairpin vortices at a short time, which corresponds approximately to the target time (see figure 2, right frame). Then a breakdown of the large scale structures towards the smallest ones is observed, and a chaotic behaviour, typical of turbulent flows, starts to appear, inducing a balance between dissipation and production which is able to maintain the turbulence. The time evolution of the energy budget terms is shown in figure 2. The robustness of this structures has also be confirmed comparing the time scales and the spatial ones with those found in the literature for DNSs or experiments on turbulent channel flows.

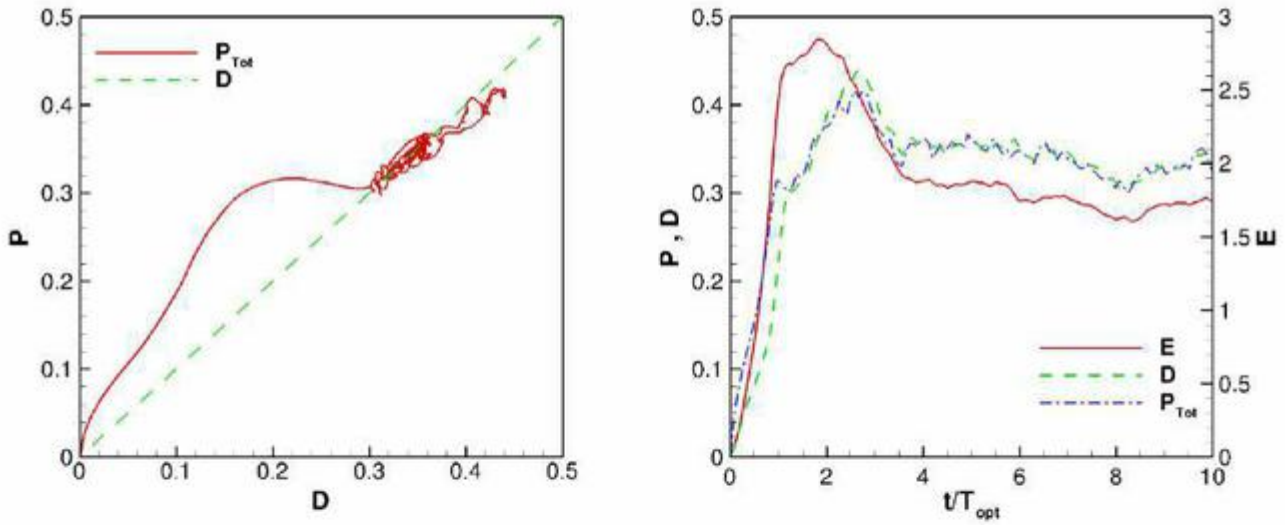

Figure 2: (Left) Time evolution of total production (P_{Tot}) versus dissipation (D). (Right) Time evolution of total production (P_{Tot}) dissipation (D) and energy (E).

Thus, the main result of this work is to characterize optimal finite-amplitude coherent perturbations in a fully turbulent shear flow, whose structure mimics the statistical properties of the flow near the wall.

References

[1] Farano M., Cherubini S., Robinet J.-C., De Palma P. : Hairpin-like optimal perturbations in plane Poiseuille flow J. Fluid Mech 775:R2, 2015.

[2] Kim J., Moin P., Moser R. : Turbulence statistics in fully developed channel flow at low reynolds number. J. Fluid Mech 177:133-166, 1987.

[3] Reynolds W.C., Hussain A.K.M.F. : The mechanics of an organized wave in turbulent shear flow. part 3. theoretical models and comparisons with experiments. J. Fluid Mech 54:263-288, 1972.

[4] Adrian J. R. : Hairpin vortex organization in wall turbulence. Phys. Fluid. 19:041301, 2007

[5] Buttler K. M. Farrel B. F.: Optimal perturbations and streak spacing in wall- bounded turbulent shear flow. Phys. Fluid. 5:774-777, 1993

[6] Pujals G., Garcia-Vilalba M., Cossu C., Depardon S. : A note on optimal transient growth in turbulent channel flows. Phys. Fluid. 21:015109, 2009

HELICAL TURBUELNCE AND PUFF IN TRANSITIONAL SLIDING COUETTE FLOW

Kohei Kunii, Takahiro Ishida & Takahiro Tsukahara[a)]
Department of Mechanical Engineering, Tokyo University of Science, Noda-shi, Chiba, Japan

Summary We performed direct numerical simulations of flows between two concentric cylinders, which flow is driven by a steady sliding motion of the inner cylinder in the axial direction. We parametrically investigated intermittent turbulence in the transitional regime for different radius ratio η. We found that the reducing Reynolds number (Re) from fully-developed turbulent state gave rise to organized large-scale structures, where localized turbulence and laminar coexisted with some spatial regularities. For η = 0.8, a helical pattern of laminar-turbulent structure occurred at Re = 375 and this structure sustained its shape until Re = 337.5. For η = 0.5 and 0.1, although the flow became laminar at Re = 375, the laminar patches were observed for η = 0.5 at higher Reynolds numbers. The localized turbulence observed for η = 0.1 was intermittent only in the axial direction, which was similar to a turbulent puff in pipe flow.

INTRODUCTION

Subcritical transition of wall-bounded flow exhibits characteristic structures of localized turbulence, such as the puff in pipe flows and the turbulent band/stripe in planar shear flows. Those structures are expected to play a key role in sustaining localized turbulence at very low Reynolds numbers close to the lower critical value for sustaining turbulence. Sliding Couette flow (SCF) is a flow between two concentric cylinders and driven by the inner cylinder, which slides in the axial direction. With a very low radius ratio $\eta = r_i/r_o$ (r_i, inner radius; r_o, outer radius), SCF can be regarded as a flow like the pipe flow, while SCF with $\eta \to 1$ becomes the plane Couette flow. According to a linear stability analysis [1], SCF is linearly stable against axisymmetric perturbations for $\eta > 0.1415$, while the flow encounters axisymmetric instability, i.e., upper stability boundary, at very large Reynolds numbers ($Re > 10^5$) for $\eta < 0.1415$. With respect to the lower critical boundary below which no fluctuation can survive, we require three-dimensional simulation and nonlinear analysis considering non-axisymmetric perturbation. Deguchi et al. [2] determined the lower critical Reynolds number (global Reynolds number Re_G) obtaining finite-amplitude non-axisymmetric solutions. They reported Re_G of 255.4, 256.7, and 288.7 for η = 1, 0.5, and 0.1, respectively. As for the plane Couette flow, many recent attentions have been paid to the turbulent band/stripe occurring near the lower critical Reynolds number [3-5]. The turbulent band is a large-scale transitional structure that spontaneously emerges for $Re_G \leq Re \leq 380$, where $Re_G = 324 \pm 1$ [4], and reveals their regularly-organized oblique pattern. Such a state accompanied by band/stripe is intrinsic for the subcritical transition of various planar shear flows [5]. Our present interests are in the subcritical transition process and the organized large-scale transitional structures in SCF, a non-planar shear flow. One may expect that the transitional structures occurring in SCF would be similar to either puffs or bands dependently on the radius ratio.

In this work, we perform direct numerical simulation (DNS) on SCF for η = 0.1, 0.5, and 0.8. By reducing the Reynolds number gradually, we research the transitional structure variation from featureless turbulence to laminar regime. The value of Re_G is also investigated for each radius ratio. The present parametric knowledge of the SCF in terms of the transitional structure may allow us to bridge together the limiting cases of the pipe flow and the plane Couette flow.

DIRECT NUMERICAL SIMULATION

The test field we considered here is an incompressible flow through an annular section between two concentric cylinders, which driven by a steady sliding motion of the inner cylinder. The tested radius ratios are 0.1, 0.5, and 0.8. The gap between the cylinders is denoted as h. The Navier-Stokes equation described in the cylindrical coordinate system is used and we employ the finite difference method for spatial discretization. The computational domain corresponds to the whole annular section and has a streamwise (x) length of $102.4h$ with a periodic boundary condition. The number of grids is $N_x \times N_r \times N_\theta$ = 1024 × 64 × 256 for η = 0.1 and 0.5 with the non-uniform radial mesh, but we use 512 grid points in the circumferential direction (θ) for η = 0.8 because of a wider domain. The control Reynolds number is $Re = U_w h/4\nu$, where U_w is the inner wall speed and ν the kinematic viscosity. For reference, the friction Reynolds number defined below will be also presented:

$$Re_\tau = \frac{u_{\tau,\mathrm{ave}} h}{2\nu}, \qquad u_{\tau,\mathrm{ave}} = \frac{\eta u_{\tau,\mathrm{inner}} + u_{\tau,\mathrm{outer}}}{\eta + 1}.$$

RESULTS AND DISCUSSION

Firstly, we have performed DNS of SCF at a moderate Reynolds number of Re = 750, at which the flow exhibits featureless turbulence. The friction Reynolds numbers are Re_τ = 34.2, 49.0, and 51.1 for η = 0.1, 0.5, and 0.8, respectively. By using those flows as initial fields, the flows at lower Reynolds numbers were obtained. Figure 1 shows a typical flow field in the transitional regime for η = 0.8, where we can see clearly the spatial patterning of localized turbulence. The highly-fluctuating

[a)] Corresponding author. Email: tsuka@rs.tus.ac.jp

region is unevenly distributed, taking a form of single band oblique to the streamwise direction. The angle of obliqueness is about 27° and the streamwise interval is about 50h, which are consistent with those in the plane Couette flow [3-5]. This turbulent band coiling around the inner cylinder is named here "helical turbulence". The helical turbulence has been also found in the annular Poiseuille flow [6]. By decreasing the Reynolds number, we found the helical turbulence sustains until Re = 337.5 (Re_τ = 24.1) and decays at 325. This scenario and the estimated Re_G are consistent with the case of plane Couette flow, even with a curved and closed geometry in the spanwise (azimuthal) direction.

If the radius ratio is reduced, the helical turbulence seems hard to exist because of the spanwise extent is too narrow. The spanwise domain length is only 9.4h at the gap center with η = 0.5, being shorter than the expected interval of the turbulent band. As a result, the intermittent flow of η = 0.5 exhibits laminar patches, as shown in Fig. 2(a). One may find out a fuzzy helical pattern that tilts in the opposite direction compared to the helical turbulence in Fig. 1. However, the turbulent region becomes intermittent only in the streamwise direction as the Reynolds number decreases further. The laminarization for η = 0.5 occurs at 375, which is much higher than the case of for η = 0.8. A much small radius ratio of η = 0.1 does not allow the helical turbulence to occur. In this case, the observed transitional structure is like a puff in the pipe flow, as seen in Fig. 2(b). The number of turbulent patches were found to increase and decrease via splitting and decaying, as similarly to the pipe flow. In our present simulations, any turbulent puff cannot survive for a long period at Re = 400. If normalized by the hydraulic equivalent diameter (4h), this lower critical Reynolds number is 1600 and much lower than the well-known threshold, e.g., 2040, for the pipe flow.

CONCLUSIONS

We found that the transitional structure of sliding Couette flow would take forms of helical bands and puffs for high and low radius ratios, respectively. The transitional flow accompanied by the helical turbulence undergoes laminarization at a low Reynolds number, resulting in a Re_G value similar to the plane Couette flow. Below η = 0.5, the puff-like structure emerges and the flow becomes laminar at Re = 375–400. This critical value is much lower than the corresponding threshold of pipe flow.

References

[1] Gittler, Ph.: Stability of axial Poiseuille-Couette flow between concentric cylinders. *Acta Mechanica* **101**: 1-13, 1993.
[2] Deguchi K., Nagata, M.: Bifurcations and instabilities in sliding Couette flow. *J. Fluid Mech.* **678**: 156-178, 2011.
[3] Prigent, A. et al.: Largescale finite-wavelength modulation within turbulent shear flows. *Phys. Rev. Lett.* **89**, 014501, 2002.
[4] Duguet, Y. et al.: Formation of turbulent patterns near the onset of transition in plane Couette flow. *J. Fluid Mech.* **650**: 119-129, 2010.
[5] Brethouwer, G.: Turbulent-laminar coexistence in wall flows with Coriolis, buoyancy or Lorentz forces. *J. Fluid Mech.* **704**: 137-172, 2012.
[6] Ishida, T. et al.: Transitional structures in annular Poiseuille flow depending on radius ratio. Under review, 2016.

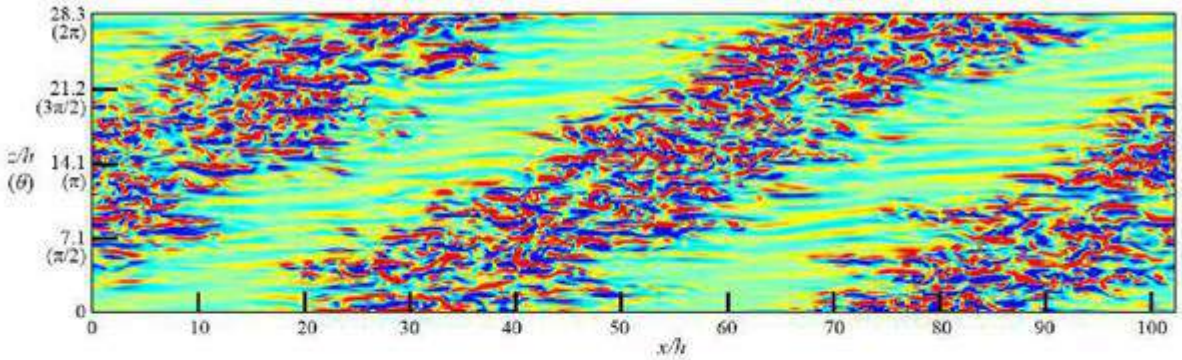

Fig. 1 Instantaneous flow field of a sliding Couette flow (SCF) for Re = 375 (Re_τ = 27.1) and η = 0.8. Contour shows the wall-normal velocity in the x-z (or x-θ) plane at the gap center of annular section: red, $u_r > 0.03U_w$; blue, $u_r < -0.03U_w$. The spanwise coordinate z is equivalent to $\theta(r_i + r_o)/2$. The mean flow is from left to right. The flow has reached a statistically steady state.

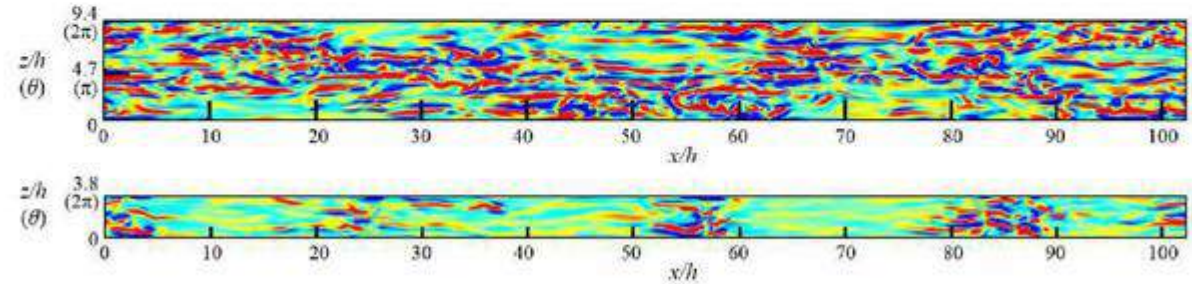

Fig. 2 Same as Fig. 1, but (a) for Re = 387.5 (Re_τ = 27.8) and η = 0.5, and (b) for Re = 400 (Re_τ = 19.3) and η = 0.1.

EXPERIMENTAL INVESTIGATION OF FLOW PAST A SPHERE IN THE REGIME OF BOUNDARY LAYER TRANSITION

Rahul Deshpande[1], Aditya Desai[1], Vivek Kanti[2], and Sanjay Mittal*[1,2]

[1]*Department of Aerospace Engineering, Indian Institute of Technology, Kanpur, Uttar Pradesh, India*
[2]*National Wind Tunnel Facility, Indian Institute of Technology, Kanpur, Uttar Pradesh, India*

Summary The flow over a smooth sphere is experimentally investigated for $1.5 \times 10^5 \leq Re \leq 5.5 \times 10^5$ via unsteady force and 2–D Particle Image Velocimetry(PIV) measurements. For $Re > 3.3 \times 10^5$, it is observed from the force measurements that the drag coefficient significantly reduces with increase in Re. This phenomenon, popularly known as the drag crisis, occurs in the critical flow regime due to the transition of the boundary layer over the sphere from laminar to turbulent state. The statistics from the force measurements reveal that the fluctuations in the force coefficients increase with Re in the subcritical regime. A steep fall in the fluctuations is observed in the critical regime. The normal Reynolds stresses in the separated shear layer, from the PIV measurements, are found to be one order lower in magnitude for the supercritical regime in comparison to the subcritical regime.

INTRODUCTION

The phenomenon of *drag crisis*, which is observed for the flow past a bluff body, has been of continued interest for the fluid mechanics community. Several experimental and numerical studies have been carried out till date for understanding its mechanism and analyzing its impact on flow properties. Drag crisis is characterized by a sudden decrease in the drag coefficient of the body due to the transition of the boundary layer from a laminar to turbulent state. This leads to a delayed flow separation from the surface which subsequently reduces the size of the wake and increases the base pressure. Achenbach [1] proposed four flow regimes based on the nature of the $\overline{C_D}$ vs Re curve for flow past a sphere: (i) *subcritical regime* - where the drag coefficient is almost independent of the Reynolds number and maintains a constant value of approximately 0.5, (ii) *critical regime* - where a rapid drop in the drag coefficient,i.e., the drag crisis is observed with the minimum $\overline{C_D}$ measured at the critical Reynolds number, (iii) *supercritical regime* - where the $\overline{C_D}$ is observed to increase slowly with Re and the point of transition of the laminar boundary layer to a turbulent state remains fixed at a particular azimuthal angle and (iv) *transcritical regime* - where the $\overline{C_D}$ is seen to increase due to the upstream shift of the point of boundary layer transition with an increase in Re.

Norman and McKeon [2] measured the statistics of the force coefficients in the range $5 \times 10^4 \leq Re \leq 5 \times 10^5$ and showed that the standard deviation of the lateral forces increased rapidly with increasing Re in the subcritical regime. On increasing Re further, the fluctuations are seen to jump to a lower value in the critical regime and remain approximately constant for supercritical Re. However, no explanation was provided for the abrupt change in the force fluctuations. In the present study, we attempt to investigate this abrupt fall in the force fluctuations, as the flow regime changes from subcritical to supercritical, by performing unsteady force and 2–D PIV measurements.

RESULTS AND DISCUSSIONS

Figure 1(a) depicts the variation of the mean force coefficients with the Reynolds number. Similar to what is reported in the literature, $\overline{C_D}$ tends to be almost constant in the subcritical regime after which it suddenly falls in the critical regime. In the early supercritical regime, the $\overline{C_D}$ is almost constant, following which it gradually starts increasing with Re. The present results show an excellent agreement with the results in the literature [1],[3](not shown here). $\overline{C_L}$ and $\overline{C_S}$, which represent the lateral force coefficients on the sphere, are negligible in the early subcritical regime and gradually increase in magnitude as the Re approaches the critical regime. Norman and McKeon [2] also reported non–zero magnitude of lateral forces in the critical flow regime and attributed it to the minute manufacturing imperfections existing on the sphere surface. A change in the direction of the lateral forces is observed at $Re = 3.5 \times 10^5$, which indicates the randomness in the orientation of the resultant lateral force in the critical flow regime. As the Re increases in the supercritical regime, the lateral force coefficients decrease in magnitude. Measurements were also carried out after rotating the sphere about the freestream axis at arbitrary angles to check for a bias in the lateral plane. On rotation, even though the magnitude of $\overline{C_L}$ and $\overline{C_S}$ changed, the resultant lateral force coefficient remained same, irrespective of the rotations at a particular Re.

The standard deviation of the three force coefficients, calculated for various Re, is shown in Figure 1(b). The lateral force fluctuations are almost four times larger than the drag fluctuations in the subcritical regime. In the critical flow regime, maximum drag and lateral force fluctuations occur at nearly the same Re, following which they jump to a lower value. However, the jump in the C_D fluctuations is very small compared to that of C_L and C_S. Such an observation suggests a

*Corresponding author. Email: smittal@iitk.ac.in

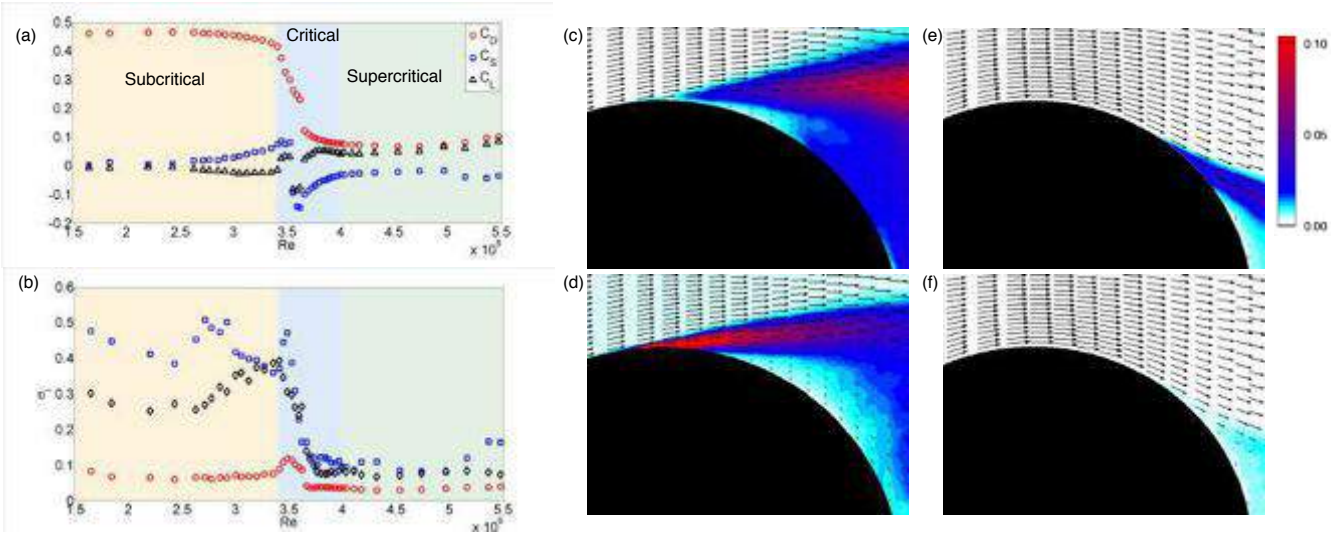

Figure 1: Flow past a sphere: (a)variation of the mean force coefficients with Re. (b)variation of standard deviation of the force coefficients with Re. (c) $\overline{u_r{'}u_r{'}}/U^2{}_\infty$ stresses and (d) $\overline{u_\theta{'}u_\theta{'}}/U^2{}_\infty$ stresses for subcritical $Re = 3.08 \times 10^5$. (e) $\overline{u_r{'}u_r{'}}/U^2{}_\infty$ stresses and (f) $\overline{u_\theta{'}u_\theta{'}}/U^2{}_\infty$ stresses for supercritical $Re = 4.28 \times 10^5$.

change in the flow physics near the shoulder of the sphere as the flow separation from the surface changes from laminar to turbulent. Once in the supercritical regime, the force fluctuations remain nearly constant with Re.

To investigate the physics behind decrease in lateral force fluctuations, we conducted 2–D Particle Image Velocimetry (PIV) measurements in a planar cut near the sphere surface for both subcritical and supercritical Re. Figures 1(c) and (d) show the non-dimensionalized radial ($\overline{u_r{'}u_r{'}}/U^2{}_\infty$) and tangential Reynolds stresses ($\overline{u_\theta{'}u_\theta{'}}/U^2{}_\infty$) at a subcritical $Re = 3.08 \times 10^5$. The contour plots depict the unsteadiness after the flow separates as a laminar boundary layer. The radial Reynolds stresses increase in magnitude along the separated shear layer, as a result of which we see the unsteadiness near the surface of the sphere. On the other hand, the tangential Reynolds stresses have a maximum value near the shoulder, where the flow separates from the sphere, and these stresses eventually decrease in magnitude along the shear layer downstream. The corresponding Reynolds stresses for supercritical regime are shown in Figure 1(e) and (f) at $Re = 4.28 \times 10^5$. In comparison to the laminar flow separation in the subcritical regime, the turbulent separation occurs at a greater azimuthal angle, the wake size is reduced and the unsteadiness close to the sphere surface decreases for the supercritical regime. Figure 1(e) shows that moderate values of radial Reynolds stresses are observed along the separated shear layer, while the stress levels are seen to be low near the sphere surface downstream. Similarly, the tangential Reynolds stress distribution for the supercritical flow regime depicts a decrease in the unsteadiness in the separated shear layer, when compared with the subcritical regime. This shows that the unsteadiness near the sphere surface decreases when the laminar separation changes to a turbulent separation after the drag crisis. This decrease in the unsteadiness near the sphere shoulder can be correlated with the abrupt decrease in the lateral force fluctuations, shown in Figure 1(b), as the Re increases from subcritical to supercritical regime.

CONCLUSIONS

The present study explores the variation in the flow physics in the vicinity of a sphere for the Re range $1.5 \times 10^5 \leq Re \leq 5.5 \times 10^5$ via force measurements and 2–D PIV. As the Re increases from subcritical to supercritical regime, it is found that the Reynolds stresses near the sphere surface decrease along with the reduction in the lateral force fluctuations in the critical regime.

References

[1] Achenbach E.: Experiments on the flow past spheres at very high Reynolds numbers. J. Fluid Mech 54(03):565575, 1972.

[2] Norman A. K., McKeon B. J.: Unsteady force measurements in sphere flow from subcritical to supercritical reynolds numbers. Exp Fluids 51.5:1439-1453, 2011.

[3] Norman A. K., Kerrigan E. C., McKeon B. J.: The effect of small amplitude time-dependent changes to the surface morphology of a sphere. J. Fluid Mech 675:268296, 2011.

EXACT COHERENT STRUCTURES FOR THE TURBULENT CASCADE

Stefan Zammert *[1,2] and Bruno Eckhardt [1,3]

[1]*Fachbereich Physik, Philipps-Universität Marburg, D-35032 Marburg, Germany*
[2]*Laboratory for Aero and Hydrodynamics, Delft University of Technology, 2628CD Delft, The Netherlands*
[3]*JM Burgercentrum, Delft University of Technology, 2628CD Delft, The Netherlands*

Summary The exact coherent structures that are connected with the transition to turbulence usually extend across the full height of the shear layer. Using scaling ideas for the Navier-Stokes equation that combine length and Reynolds number, we show how such large scale structures can be morphed into coherent structures at the Kolmogorov scale at high Reynolds numbers. We present the structure and dynamical properties of several families of exact coherent solution with different degrees of spatial localization.

INTRODUCTION

From a dynamical systems point of view, the transition to turbulence is connected with the appearance of persistent, non-trivial structures in the state space of the system. They are exact 3-d solutions to the Navier-Stokes equations with often simple temporal patterns, known as exact coherent structures (ECS). In some cases, like convection, they appear in sequences of bifurcations from the laminar state, in others, like pipe flow, they appear in saddle-node bifurcations that are not connected to the laminar profile. Since the identification of the first ECS in plane Couette flow [1], many further examples have been documented in a variety of flows. The study of these solutions, combined with the use of methods from dynamical systems theory, has improved our understanding of the emergence of turbulence in linearly stable flows [2]. In addition to the spatially extended ECS there are others that are localized in one or several directions [3, 4, 5, 6, 7] and that can contribute to an understanding of the spatio-temporal behavior of turbulence close to onset.

Many of the currently available ECS can be traced over a wide range in Reynolds numbers, but they all remain 'large' in the sense that they reach across the full width of the shear layer and often do not develop small scale structures. These states can therefore not capture the small scale dynamics of turbulent flows, other states must take over. Among the few studies that have addressed the scaling of ECS with increasing Reynolds number, the one by [8] stands out because it indicates how structures on small scales can be obtained asymptotically for large Reynolds numbers. Here, we present a general approach which allows to transfer ECS from large to small scales and demonstrate it for the case of plane Couette flow. For the numerical simulation we use the Channelflow-code [9].

RESCALING OF EXACT SOLUTIONS

The starting point for our solutions are ECS that are localized in the normal direction. Then a reduction in height, together with a reduction in the streamwise and spanwise scales, reduces the influence from the walls and opens up the path towards ECS on smaller scales. However, the change in length scales also mandates a change in Reynolds number. Specifically, we take a flow field $\vec{u}_0$ that is an ECS at Reynolds number Re_0 and form the flow field

$$\vec{u}_\lambda = \lambda \vec{u}_0(\vec{x}/\lambda), \tag{1}$$

which is rescaled by a factor λ in all spatial directions. The Navier-Stokes equation is invariant under this transformation if the Reynolds number is adjusted according to $Re = \lambda^{-2} Re_0$. The scaling invariance is broken by the presence of walls, but their influences becomes weaker if the solutions maintain their scaling properties. Therefore, the scaled solutions provide very good initial conditions for a Newton search for ECS of this scale, at the higher Reynolds number.

RESULTS

Using the described rescaling, we were able to identify several families of exact solutions in PCF. In figure 1a) a family of equilibrium solutions located in the center between the walls is shown. The visualized solutions differ by factors of 2, while the corresponding Reynolds number increase by factors of 4. Although the scaling is not perfect due to the weak wall-normal localization, the vortex structures which are visualized in the figure are almost identical but at different scales. The solutions are reminiscent of the states studied by Deguchi [8].

The stability of the states follows from the linearized equations, which have a similar scaling. We find that all states are unstable but they only have a small number of unstable directions. In particular, for the lower branch the number of

*Corresponding author. Email: Stefan.Zammert@gmail.com

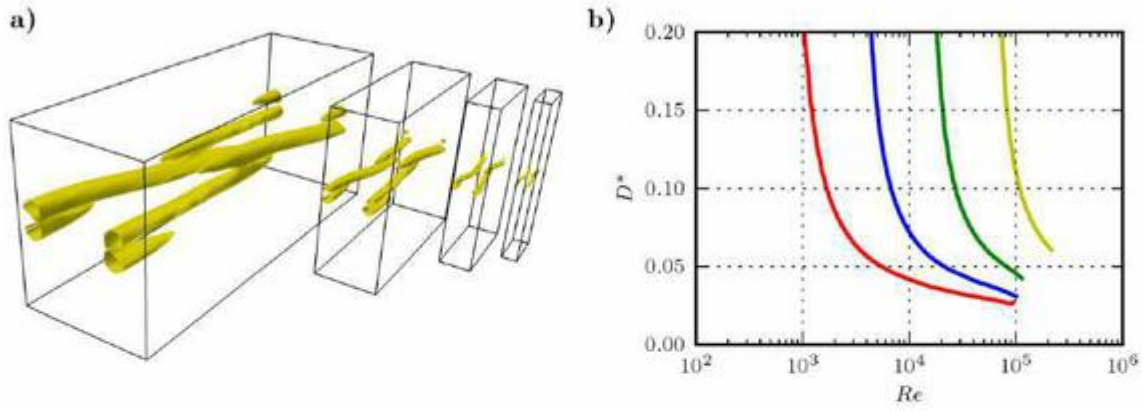

Figure 1: ECS on different scales and for different Reynolds numbers. (a) Visualization of the exact solutions using isosurfaces $Q = 0.0015$. The Reynolds numbers are, from left to right, $3,375$, $13,500$, $54,000$ and $216,000$. For each state the spanwise and streamwise wavelength decreases by a factor of 2, and the Reynolds number increases by factors of 4. (b) Bifurcation diagram of the four states shown in panel a). On the ordinate the total dissipation divided by the area (streamwise times spanwise wavelength) of the computational domain is shown.

superharmonic instabilities of the states and also their growth rate is retained by the rescaling. In a subspace with spanwise reflection symmetry $s_z : [u, v, w](x, y, z) = [u, v, -w](x, y, -z)$ and rotation symmetry $s_x s_y : [u, v, w](x, y, z) = [-u, -v, w](-x, -y, z)$ the lower branch of the states has one unstable direction and is an edge state [10].

In figure 1b) the bifurcation diagram of the solutions is shown, with the dissipation rate along the ordinate. The bifurcation diagram indicates an increasing number of states of different scales that populate the state space. The widest solutions appear at the lowest Reynolds numbers, and with increasing Reynolds number smaller solutions appear. By construction, it is possible to map the solution curves onto each other by an appropriate rescaling: this mapping becomes asymptotically exact for large Reynolds numbers, and the deviations at low Reynolds numbers are connected with the influence of the walls in the normal direction.

In addition to the ECS shown in figure 1, we have identified further families of ECS that are streamwise and spanwise localized, as well as travelling waves that are located close to the walls.

CONCLUSIONS

The families of ever more localized states presented here show how exact coherent structures at high Reynolds numbers can be constructed. The reduction in scales and the fact that their instabilities are retained by the rescaling suggests that many results obtained at low Reynolds numbers and on large scales can be transferred to high values of Re and small scales. These ECS will play a key role in extensions of the dynamical systems approach to turbulence from the transition region towards fully developed turbulence.

References

[1] M. Nagata, "Three-dimensional finite-amplitude solutions in plane Couette flow: bifurcation from infinity," *J. Fluid Mech*, vol. 217, pp. 519–527, 1990.

[2] T. Kreilos and B. Eckhardt, "Periodic orbits near onset of chaos in plane Couette flow.," *Chaos*, vol. 22, p. 047505, 2012.

[3] F. Mellibovsky, A. Meseguer, T. Schneider, and B. Eckhardt, "Transition in Localized Pipe Flow Turbulence," *Phys. Rev. Lett.*, vol. 103, p. 054502, 2009.

[4] M. Avila, F. Mellibovsky, N. Roland, and B. Hof, "Streamwise-Localized Solutions at the Onset of Turbulence in Pipe Flow," *Phys. Rev. Lett.*, vol. 110, p. 224502, 2013.

[5] E. Brand and J. Gibson, "A doubly-localized equilibrium solution of plane Couette flow," *J. Fluid Mech.*, vol. 750, p. R1, 2014.

[6] S. Zammert and B. Eckhardt, "Streamwise and doubly-localised periodic orbits in plane Poiseuille flow," *J. Fluid Mech.*, vol. 761, pp. 348–359, 2014.

[7] P. Ritter, F. Mellibovsky, and M. Avila, "Dynamical-systems approach to localised turbulence in pipe flow," *arxiv*, 1512.02382, 2015.

[8] K. Deguchi, "Self-sustained states at Kolmogorov microscale," *J. Fluid Mech.*, vol. 781, p. R6, 2015.

[9] J. F. Gibson, "Channelflow: A spectral Navier-Stokes simulator in C++," tech. rep., U. New Hampshire, 2012.

[10] J. Skufca, J. A. Yorke, and B. Eckhardt, "Edge of Chaos in a Parallel Shear Flow," *Phys. Rev. Lett.*, vol. 96, p. 174101, 2006.

XP NT A C AS T L ETI W TH T MB F CO R T ST CTU S

T h ro Ka w M s k S mizu , d Gent K
G aduat h l of Dr e r g S c a a U iv s ty O aka. Japa

Sum ary N r w r s z. s y s s y h r st r s s w-s st 's st w s r s. I h s st r s s r s y, r s s r . P r r r r s t s w s t m s z r h f w y h g h s w s h h r v s h r p h r h r st r s. s d h h r. f r R y s cr r s s s y s h b r h r st uc r s. Th s s h h h r st r o r s h y.

I I N

In p n u w th ugh t n un t t n t t n d nu , t n t n t tu u n n u uf nt g d tu n v n t w n d nu In th t th f t d f u tt d nt fy th ut t tu u n n mpa n t u n f fu t n n up t t n t n nd t h ng n n p n u t n

On f th t u kth ugh f th p l th d v f th f t f tu u n (f p S h g nd B kh dt) f w n tw n d t d f d tu n nd p t nt tu u n (t t f v t) d t n t n w nt w k h v ugg t d th t th f t n th d u p n nt fun t n f th n d nu (I f t 2 v t 2) G d nf d t (2) nt p t d th d u p n nt h v w th th n d nu u ng n t d t ut n th

In t n t n p n P u w nd t n t n p n u tt w n t tu u n z d n tw d t n th t w nd p nw d t n nd d tu u nt p t (ntw t 7) t h gh n d nu t p p tt n f tu u n d tu u nt nd n v d (uk h t 2 5). th ugh u h z d tu u n t n nt (Sh t 2 3, ng t 2) th n d t d u nt f f t n th ff t f th p nw ngth f tu u n u th p p th n n p p ll w In th p p w f u n th nu f h nt t u tu nt n d n t n nt tu u n h ng t p ng d t n t p nw ngth f th put t n d n nd d nt f th nt ut n t th f t wh h h n ugg t d G d nf d t (2)

S G

M C HOD

W n d n p w w th th n t nt u k v t U d v n p t n t nt d f tw n tw p p t p t d d t n $2h$ h x, y nd z f th t n d n t t t k n n th t w w n nd p nw d t n p t v In th d t n p t th p t x nd z d t n p d und nd t n p d w th p d L_x nd L_z p t v In th w n d t n n p nd p nd t n p d h t g v n d th n p N v St k u t n n n n d n n f u ng th h t t d t n h nd nt n v t f n w $U_c = 3U/2$ h n d nu d n d $Re = \frac{hU_c}{\nu} = \frac{3hU}{2\nu} = \frac{3}{2}Re_m$ wh ν th k n t v t f p t d t z t n w u p t G k n th d f u n th x nd z d t n nd h h v p n n th y d t n nd th ng v d f d t n h qu t n nt g t d u ng C nk- n th d f th v u t nd 2nd d d B hf th th d f th th h t w p d t t $L_x = 100$ nd th ngth n d d t uf nt f ng puff v th p nw p d L_z n th ng f $0.5 \leq L_z \leq 5$ nd th p t t A d n d $A = L_z/2$ h u w v nu n th x nd z d t n nd th u d f p n n th y d t n t t $(533, 47, [(64A - 1)/3])$ wh $\lfloor \cdot \rfloor$ n G u fi th t n nt t $\Delta t = 0.01$

L F EA U

nv t g t th d p nd n f th f t f tu u nt puff n Re_m nd A h f t d n d w nd ng du t n t h t nv nt t n ph p f n z t n wh h th un u t ut n f Re_m f u u v n t nd t n w p p t f tu u nt puff t d ff nt Re_m th th d n v t (2 0) ff f th t f th n t nd t n t pp d und w nd ng t t w n t t th h t t t t p f t th f t h 2 v t d t k n t v t nt v t p (d t) v u f th R n d nu u d t f n t nd t n

u th 1 f d th f h tu u nt puff nd nv t g t th t d p nd n f th u v v p t u u nt puff judg d t d d wh n t w k n f t n c th n t f n w $\langle |\mathrm{d}u_x/\mathrm{d}y|_{wall}\rangle/3 \leq 1.05$ wh $\langle\cdot\rangle$ n v g v th w

M u nt f th f t t n t d t $t_c = 500$ h di t ut n upp d t p n nt $P(t) = \exp(-t/\tau)$ h u k h d t t f n f t τ f n d d t p 2 n ng n w (982) g v n

$$\hat{\tau} = \frac{1}{r}\left\{\sum_{i=1}^{r}(t_i - t_0) + (n-r)(t_r - t_0)\right\}, \tag{1}$$

wh r $t_i (i = 1, 2, \ldots, r)$ th r t f t v d unt t_c $t_0 < t_1 < t_2 < \cdots < t_r < t_c$

R T

h f t not n n ng fun t n f th n d nu nd th p t t A n th d p nd n n th n d nu tt d w th d u xp n nt fun t n $\tau = \exp\{\exp(aRe_m + b)\}$ In th f w ng w nv t g t th d p nd n n th p t t A

L t u n d nd p nd nt nd d nt t wh h t nd d d n th p nw d t n nd g d d th n un t d t ng n w p d t k u u n u t n d h t p d f w p d t k nd n t d t w v t nd d pp wh n t d t th t If th f t f t u t τ_0 th f t f tu u nt puff wh h h N t n d t f b τ_0^N If w upp th t N p p t n t th p t t A

$$\ln(\tau) \propto A. \tag{2}$$

F gu h w th g th f th t t d f t $\ln(\tau)$ fun t n f th p t t A E u t n(2) t t u f t n nt tu u n h th h gh f t h t n h p tw n N t nd th fct ugg ts th t n n t d n tu u n t n nt v n f th n d nu u h h gh Tu u nt nd n n d d t p t nt n th h v n t

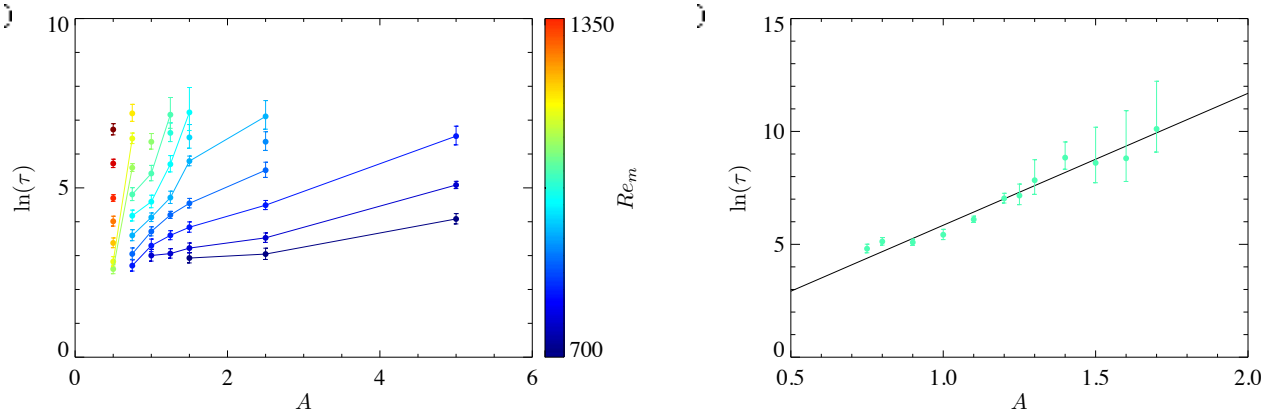

F gu h d p nd n f th f t n th p t t A ( ): t f th g th f th f t n(τ) t v u v u f A h n d nu t h p nt d t ngu h d n f ng ng f 700 t 1350 ( ) t t $Re_m = 1000$ F $A \geq 1.4$ u nt t n t d t $t_c = 1000$ S d n p nt th pp t fun t n $\ln(\tau) = cA$ wh $c \simeq 5.85$.

eferences

[ ] g E B c 79 3
[ ] H K k D ? M d T
P R 101 1 2
[ ] A : O x x f .. 646 1 7- .
[ ] G N, f *Phys. Rev. E.* **81** ( )
[ ] o S n e 87
[ ] T T Y T e I T 5 6
[ ] C r 110
[8] X Te J & L 0 T y *Phys. Fluids* **27**
[9] w F w

INSTABILITIES IN THE FLOW BEHIND ROTATING BLUFF BODIES

M. Krutnik[1], M. Skarysz[1], K. Gibiński[1], S. Goujon-Durand[2] and J.E. Wesfreid[2a]

[1] *Institute of Aeronautics and Applied Mechanics, MEiL, Warsaw University of Technology, Warsaw, Poland*

[2] *PMMH, Ecole Supérieure de Physique et de Chimie Industrielles de la Ville de Paris, UMR7636 CNRS-ESPCI-P6-P7, Paris, France*

Summary The wake and its instabilities behind rotating sphere and a simplified model of propeller were investigated for moderate Reynolds numbers, in a low- velocity water channel. We observed different vortex structures with LIF method and the velocity field was measured with PIV. The influence of rotation speed on vortex shape and size was analysed. The explored range of Reynolds number was from 0 to 400 and the swirl or rotation parameter Ω was not higher than 4 for the sphere and 2 for the rotor. For non-rotating bodies, is very well know the existence of various flow regimes with axisymmetric base flow, pairs of stationary counter-rotating vortices, and unsteady vortex shedding with hairpins. We described the occurrence of new regimes in presence of rotation with lower and higher helical modes. In this talk new results about the non-linear evolution of the instability modes are presented.

Introduction

Many experimental and numerical researches were carried out to describe the phenomenon of wakes and instabilities behind 3D bluff bodies. The structures created by fluid instabilities past spheres, cubes, disks and models of propeller have been investigated by our group [1-4]. This paper presents the first experimental results concerning wakes and its instabilities behind rotating sphere and a model of propeller. For static bodies, it is well known the existence of three main regimes, depending on Reynolds number. The initial regime is an axisymmetric base flow in the case of the sphere with a bifurcation with two counter-rotating streamwise vortices (CRV) with a planar symmetry between each other, at Re = 212. After a second transition, at Re = 270, two CRV evolve into hairpin, unsteady periodic vortex shedding. When rotation is introduced [5-6], in the case of two counter-rotating vortices, one of them becomes stronger and another one is weakened and is observed the phenomenon of "frozen" spiral and subsequent unsteady behavior.

Experimental details

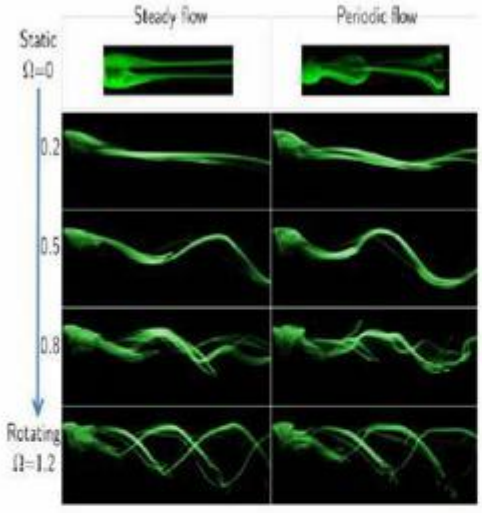

Figure 1: Visualization of the wake behind the sphere for Re = 250 (left) and Re =300 (right)as a function of Ω

The experimental set up consists of a low-velocity water channel of 86 cm length and with a cross-section of 10 cm x 10 cm. Both, the sphere and propeller were fixed by a rigid thin hollow tube (d=0,2cm) connected to a brushless electric motor and a dye input. The pipe axis was aligned with free stream direction. The motor was also located inside the channel, around one meter behind the support. The water stream achieved the velocity up to 4 cm/sec.

To perform flow visualization, fluorescein dye was injected through the slits in the objects, using Laser Induced Fluorescence (LIF) techniques. For velocity measurements, Particle Image Velocimetry (PIV) was adopted and the video camera was capable of recording images with the frequency of 15 Hz. Tracer particles, with the diameter around a few μm, were seeded in the water. For the velocity field calculation, the program used cross-correlation method and multi-pass iteration. Laser slices, perpendicular to the flow, were located at the distance of 2,5 diameter of the object (where we found maximum amplitude of the velocity perturbations), which is around 0,5 diameter behind the recirculation zone, in order to evaluate the streamwise vorticity behind the bodies. The Reynolds number range was up to 1000 with the possibility of steps increment of ΔRe equal to 2 and the swirl or rotation parameter Ω was not higher than 4 for the sphere and 2 for the rotor, with steps of ΔΩ

[a] Corresponding author,E-mail:wesfreid@espci.fr

equal to 0.1. This fine change in the flow parameters let us to perform very detailed description of the frequencies and the non-linear evolution of the instability fluctuations. The rotor was built from three identical propellers, which thickness was 0,06 cm. The blade width was 0,3 cm. In both cases of rotor and sphere, the diameter was 2 cm.

Results

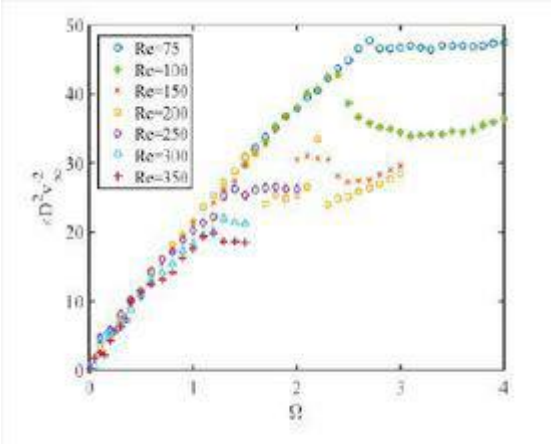

Figure 2: Dimensionless enstrophy of mode=0 as a function of Ω and Re

The investigation was focused on different regimes of wakes behind bodies, changing the swirl parameter Ω, which is the ratio of the maximum azimuthal velocity of the object to the free streamwise velocity, to explore the influence of rotation. In the case of the sphere (Figure 1), different structures are observed for Re = 250 and Re = 300. In particular, for Re=250, the steady flow (Ω=0) becomes a "frozen" flow up to Ω=0,2. With the increment of the swirl parameter, low helical frozen wake appears. The next images presents unsteady flow, which changes into high helical, when Ω=1,2.

Having the possibility to perform detailed measurements of the bifurcation branches of perturbation, we study the modification of the content of the azimuthal modes of enstrophy, obtained by polar Fourier decomposition. We present in our talk the first experimental evidence of the changes of the mean mode of homogeneous or global vorticity induced by the nonlinear interaction of the fluctuating perturbations. One example of this behavior is observed in the figure 2, showing in the axisymmetric mode of vorticity (azimuthal mode m = 0) this nonlinear anticyclonic contribution due to the presence of instabilities, at different Reynolds numbers.

In addition, we present on the figure 3, a flow visualization and the measurements of the streamwise vorticity and its spatio-temporal reconstruction, for the case of a rotating rotor with three blades at Ω = 1, with indication of the CRVs twist, where is observed as the negative vortex is pushed to the middle of the wake and surrounded by positive ones.

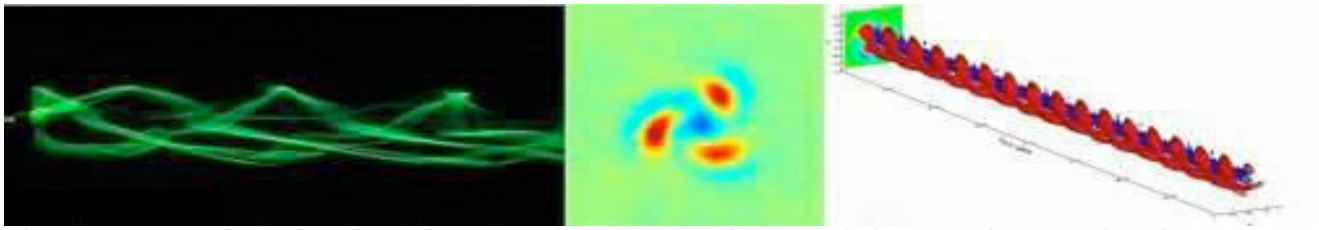

Figure 3: The visualization, instantaneous streamwise vorticity and its spatio-time reconstruction for the simple rotor, at Ω = 1

References

[1] K. Gumowski, J. Miedzik, S. Goujon-Durand, P. Jenffer, and J. E. Wesfreid, Transition to a time-dependent state of fluid flow in the wake of a sphere *Phys. Rev. E* **77**, 055308(R), 2008

[2] Szaltys, P., Chrust, M., Przadka, A., Goujon-Durand, S., Tuckerman, L. and Wesfreid, J. E., Nonlinear evolution of instabilities behind spheres and disks; *Journal of Fluids and Structures* **28**, 483-487, 2012

[3] Klotz, L.; Goujon-Durand, S.; Rokicki, J ; Wesfreid, J.E. ; Experimental investigation of flow behind a cube for moderate Reynolds numbers ; *Journal of Fluid Mechanics* **750**, 73-98, 2014

[4] Bobinski, T.; Goujon-Durand, S.; Wesfreid, J. E. ; Instabilities in the wake of a circular disk ; *Physical Review E* **89**, 053021, 2014

[5] Kim D. and Choi H., Laminar flow past a sphere rotating in the streamwise direction; *Journal of Fluid Mechanics* **461** 365386, 2002

[6] Pier B., Periodic and quasiperiodic vortex shedding in the wake of a rotating sphere; *Journal of Fluids and Structures* **41** 43-50, 2012

A NEW FORMALISM FOR IDENTIFYING WAVEMAKER REGIONS OF LINEAR INSTABILITIES

Olivier Marquet*[1] and Lutz Lesshafft[2]

[1]*ONERA, The French Aerospace Lab, DAFE, Meudon, France.*
[2]*LadHyX, Ecole polytechnique, Palaiseau, France.*

Summary A new formalism is introduced that allows to identify the wavemaker regions of linear instability eigenmodes of nonparallel open shear flows. The formalism is based on a decomposition of the governing linear operator into locally acting components that extract the localized dynamics. The unique contribution of the local dynamics to the global dynamics of an eigenmode is identified and computed by an orthogonal projection with the adjoint eigenmode. It is demonstrated, for the example of a spring-mounted cylinder in uniform flow, how this analysis can be used to motivate a physical discussion on the frequency selection of fluid/solid eigenmodes.

INTRODUCTION

We are interested in identifying wavemaker regions of linear instabilities, i.e. the regions in physical space which contribute most strongly to the temporal dynamics of an instability. In open shear flows, due to the non-normality of the Navier-Stokes operator [1], this region corresponds neither to the most energetic location of an eigenmode $\mathbf{q}$, nor to the most receptive region to external forcing, identified with the associated adjoint mode $\mathbf{q}^\dagger$. A commonly used characterization of the wavemaker region for instabilities in spatially developing flows is due to Giannetti & Luchini [2]. These authors investigated where local feedback mechanisms have the strongest impact on an hydrodynamic instability by considering a structural sensitivity analysis of the underlying eigenvalue problem (3). The analysis consists in modifying the structure of the linearized Navier-Stokes equations by introducing an artificial local feedback in the momentum equations. The resulting eigenvalue variation $\delta\sigma$ is linearly related to the structural modification via the adjoint eigenmode, and the following upper bound for the eigenvalue variation is obtained as

$$|\delta\sigma(\mathbf{x}_0)| < |\mathbf{q}^\dagger(\mathbf{x}_0)| \cdot |\mathbf{q}(\mathbf{x}_0)| \tag{1}$$

where $\mathbf{x}_0$ indicates the feedback location. Defining the wavemaker region as the region where local feedback mechanisms induce the largest eigenvalue variation, it is then identified by overlapping the direct and associated adjoint modes.

Wavemaker identification is now a widely used analysis tool in hydrodynamic instability studies, but the approach described above suffers from a major drawback. When perturbing the eigenvalue problem in order to identify a local feedback mechanism, artificial coupling mechanisms are introduced, which are absent in the original dynamics, but which might have a large effect on the eigenvalue variation. Without means to distinguish between intrinsic and artificial local feedback mechanisms, the inequality (1) only guarantees that local feedback mechanisms are unimportant for the global dynamics in regions where the overlap between adjoint and direct modes is weak. In regions of strong overlap, the large eigenvalue variations may arise from either intrinsic or artificial feedback.

A new wavemaker formalism is proposed in this study that is claimed to identify the local feedback action of the original linear operator. Rather than considering structural operator modifications, the approach relies on a decomposition of the governing operator $\mathcal{L}$ as the sum of *local* operators $\mathcal{L}_0$ that represent the dynamics at a given point $\mathbf{x}_0$. The product of this local operator with the eigenmode of interest is then decomposed onto the full basis of eigenmodes. The contribution from local feedback acting in $\mathbf{x}_0$ to the global temporal dynamics is determined by an orthogonal projection, by way of multiplication with the adjoint global mode. As a result of this analysis, we obtain the equality

$$\sigma = \int_{\mathcal{D}} \mathbf{q}^{\dagger *}(\mathbf{x}_0) \cdot (\mathcal{L}\mathbf{q})(\mathbf{x}_0)\, d\mathbf{x}_0, \tag{2}$$

where the integrand is proven to be the unique contribution of the local dynamics to the temporal dynamics of the global eigenmode. Interestingly, by separating the real and imaginary parts in the above equality, the analysis allows to discriminate between local contributions to the frequency selection on the one hand, and to the temporal growth rate on the other hand. The new formalism is detailed in this abstract. Results of this wavemaker analysis will be shown in the talk for the fluid-structure instability at the origin of the vortex-induced vibration of a spring-mounted cylinder.

*Corresponding author. Email: olivier.marquet@onera.fr

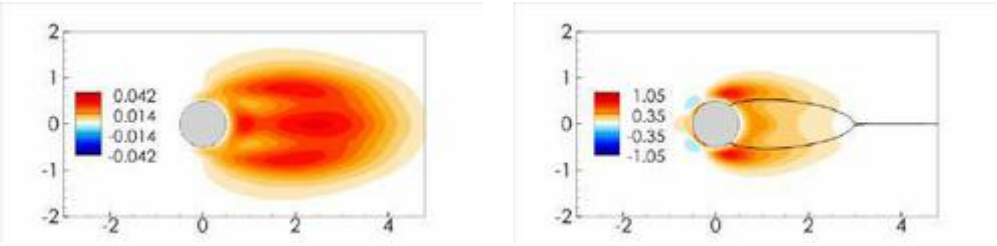

Figure 1: Frequency selection for a fluid/solid mode in the spring-mounted cylinder configuration at the Reynolds number $Re = 43$ in (a) the large mass limit $\rho = 1000$ and (b) the small mass limit $\rho = 0.01$. When varying the solid-to-fluid density ratio ρ, the frequency selection changes in nature and in space. The imaginary part of (7) for the fluid operator is displayed.

FORMALISM

Consider a linear hydrodynamic perturbation in normal mode form, $\mathbf{q}' = \mathbf{q}(\mathbf{x})\,\exp(\sigma t) + c.c.$, where $\sigma = \lambda + \mathrm{i}\omega$ is a complex quantity, of which the real and imaginary parts respectively represent the temporal growth rate and frequency of the mode with spatial structure $\mathbf{q}(\mathbf{x})$. These modes are obtained by solving the eigenvalue problem

$$\sigma\,\mathbf{q}(\mathbf{x}) = \mathcal{L}\,\mathbf{q}(\mathbf{x}), \tag{3}$$

where $\mathcal{L}$ is a linear operator, obtained from a linearization of the Navier-Stokes equations around a steady state in a spatial domain $\mathcal{D}$. In order to investigate which regions of this domain mostly contribute to the temporal dynamics of an eigenmode, we first decompose the linear operator into localized spatial components as

$$\mathcal{L} = \int_{\mathcal{D}} \mathcal{L}_0\; d\mathbf{x}_0, \tag{4}$$

where the operator $\mathcal{L}_0$ acts on an eigenmode and extracts its local dynamics at the location $\mathbf{x}_0$. It is mathematically defined by $(\mathcal{L}_0\mathbf{q})(\mathbf{x}_0) = (\mathcal{L}\mathbf{q})(\mathbf{x}_0)$ and $(\mathcal{L}_0\mathbf{q})(\mathbf{x}) = \mathbf{0}$ for $\mathbf{x} \neq \mathbf{x}_0$. In order to specifically determine the contribution of the local dynamics in $\mathbf{x}_0$ to the global dynamics of an eigenmode $\mathbf{q}$, the product of the local operator with the eigenmode is expanded in the basis of eigenmodes,

$$\mathcal{L}_0\,\mathbf{q} = \sigma_0\,\mathbf{q} + \sum_{j>1} \sigma_j\,\mathbf{q}_j, \tag{5}$$

where σ_0 and σ_j are complex coefficients that depend on the location $\mathbf{x}_0$. Since $\mathbf{q}$ is an eigenmode of $\mathcal{L}$ but not of $\mathcal{L}_0$, the coefficients σ_j are non-zero and the sum in the above relation does not vanish. The coefficient σ_0 expresses the unique contribution of the local dynamics, represented by $\mathcal{L}_0$, to the global dynamics of the eigenmode. In order to obtain the numerical value of σ_0, the adjoint eigenmode $\mathbf{q}^\dagger$ is first computed as the solution of the eigenvalue problem

$$\sigma^*\,\mathbf{q}^\dagger(\mathbf{x}) = \mathcal{L}^\dagger\,\mathbf{q}^\dagger(\mathbf{x}), \tag{6}$$

and the orthogonal projection of the decomposition (5) via the adjoint eigenmode then yields the complex coefficient

$$\sigma_0 = \int \mathbf{q}^{\dagger *}\,(\mathcal{L}_0\,\mathbf{q})\,d\mathbf{x} = \mathbf{q}^{\dagger *}(\mathbf{x}_0)\,(\mathcal{L}\mathbf{q})(\mathbf{x}_0). \tag{7}$$

Inserting the operator decomposition (4) into the eigenvalue problem (3) yields, after straightforward manipulation and use of (5), the identity

$$\sigma \;\; = \;\; \int_{\mathcal{D}} \sigma_0(\mathbf{x}_0)\; d\mathbf{x}_0. \tag{8}$$

This is the unique decomposition where the integrand represents unambiguously the contribution of the local dynamics to the temporal evolution of a global eigenmode. Such formalism extends straighforwardly to eigenvalue problems arising in fluid/structure interaction problem. It will be used to determine the respective contributions of the fluid and solid dynamics to the temporal dynamics of fluid/solid eigenmodes obtained for the example of a spring-mounted cylinder in uniform flow.

References

[1] Chomaz J.-M.: Global instabilities in spatially developing flows: nonnormality and nonlinearity, Annual Review of Fluid Mechanics, vol. 37, pp. 357–392, 2005.

[2] Giannetti F., Luchini P.: Structural sensitivity of the first instability of the cylinder wake, Journal of Fluid Mechanics, vol. 581, pp. 167–197, 2007.

EXPERIMENTAL INVESTIGATION OF INSTABILITY OF CONVECTING LOCAL HIGH-SHEAR LAYER

Masahito Asai[1a)], Yusuke Yoshida[1], Shohei Takagi[1]
[1]*Department of Aerospace Engineering, Tokyo Metropolitan University, Hino, Tokyo, Japan*

Summary To obtain a better understanding of the mechanism of wave breakdown into high-frequency hairpin eddies (which was identified as appearance of high-frequency spikes in the waveform of velocity fluctuation) in boundary-layer transition initially caused by the growth of Tollmien-Schlichting waves, development of pulse-like disturbances superposed on a convecting three-dimensional local high-shear layer artificially generated in laminar boundary layer was examined experimentally. In the flow immediately prior to the appearance of high-frequency spike, the group velocity of a wave-packet originating from the pulse disturbance was found to be almost equal to the convection velocity of the high-shear layer. This caused the disturbance to continue growing on the high-shear layer with strong frequency-selectivity, just like in an absolutely unstable flow.

INTRODUCTION

Boundary-layer transition starting with linear growth of Tollmien-Schlichting (T-S) waves has been studied by many authors and now our understanding of the transition process and the underlying mechanisms have been much advanced. However, a question regarding the mechanism of high-frequency breakdown of the primary T-S wave into small-scale hairpin vortices, which is identified as onset of spikes in the waveform of velocity fluctuation [1, 2], is still remained open. A few theoretical models have been proposed on the mechanism of very fast and frequency-selective growth of high-frequency spikes [3, 4], but they could not explain the actual phenomenon sufficiently. We revisited this fundamental problem here. In the present paper, a convecting local three-dimensional high-shear layer was generated artificially by means of periodic sucking/blowing with low frequency through a hole in a laminar boundary layer to realize a transition stage similar to the breakdown stage of high-shear layer in a well-controlled manner. Then, a pulse-like disturbance was introduced (superposed) on the convecting high-shear layer. and its development into high-frequency spikes was followed up. Particular focus was on the relationship of convection velocity of high-shear layer and the propagation (group) velocity of such localized disturbances. When the convection velocity of high-shear layer coincided to the group velocity of wave packet, we may expect a possibility of rapid and frequency-selective growth, like as in an absolutely unstable flow [5, 6].

EXPERIMENTAL SETUP

The whole experiment was conducted in a wind tunnel with a rectangular test section of 300 × 200 mm^2 in cross section. The turbulence in the free-stream, measured at the upstream end of the test section, is less than 0.15% of U_∞. A boundary-layer plate of 4 mm thick and 540 mm long was set in the test section. A small hole of 4 mm in diameter was drilled at the spanwise center, 280 mm downstream of the leading edge, and was connected to a loudspeaker by a vinyl hose. By periodically injecting and sucking air through the hole, the forcing system could produce a local three-dimensional high-shear layer away from the wall, which convected downstream. By adjusting a input current to the loudspeaker, we could realize various stages of breakdown of the high-shear layer into small-scale (high-frequency) hairpin vortices, i.e. a stage just prior to the onset of high-frequency spike, 1-spike stage, 2-spike stage, etc. As for the coordinate system, x is the streamwise distance, measured from the leading edge, y the normal-to-wall distance, and z the spanwise distance. The free-stream velocity was fixed at 4 m/s. The forcing frequency for producing the high-shear layer periodically was 20 Hz and the pulse-like disturbance was superposed on the primary wave (20 Hz). The streamwise velocity, th time-mean and fluctuation components of which are denoted by U and u respectively, is measured with a constant temperature hot-wire anemometer.

EXPERIMENTAL RESULTS

Fig. 1 illustrates waveforms of u-fluctuations at a location x-x_0 = 60 mm for two different excitation amplitudes (of 20 Hz) without any pulse-like disturbance. Here, x_0 = 280 mm, the x-position of the hole. We could see onset of high-frequency spikes in the waveform, just like the spike stage observed in the transition process of Klebanoff type when the initial disturbance (forcing) amplitude exceeded some critical value. We focused on the flow just before the appearance of high-frequency spike, and introduced a pulse-like disturbance mentioned above to follow up its development in detail. Fig. 2 illustrates the velocity profiles at the spanwise center (z = 0) in one forcing period T (= 1/20 s), measured at x-x_0 = 30 mm. We see that a local high-shear layer whose forward part was lifted up away from the wall is formed, which is very similar to that observed in the transition process [1, 2]. The local high-shear layer was intensified and moved gradually away from the wall as the primary wave grew downstream. When a pulse disturbance was given into this high shear layer by superposing it to the primary wave, the disturbance could develop with a form of wave packet on the high-shear layer, as shown in Fig. 3.

[a)] Corresponding author. Email: masai@tmu.ac.jp

The frequency of growing disturbance coincided with the frequency of spikes (see Fig. 1) appearing as the initial amplitude of the primary wave was increased. Besides, the wave packet propagated downstream at a group velocity C_g of about 0.57-0.59U_∞ over x-x_0 = 30 mm to 60 mm (which was estimated as the propagation velocity of the packet envelop). On the other hand, the convection velocity C_s of the high-shear layer increased downstream because the high-shear layer moved away from the wall. For instance, C_s was about 0.37U_∞ and 0.55U_∞ at x-x_0 = 30 mm and 60 mm, respectively. Thus the high-frequency wave packet tended to propagate at the same velocity as the convection velocity C_s so that it could continue to undergo strong amplification due to inflectional instability.

CONCLUSIONS

In the present experiment, a local three-dimensional high-shear layer was directly generated in a laminar boundary layer to model the late stage of secondary three-dimensional instability in transition initially caused by growth of Tollmien-Schlichting waves, and a localized disturbance (wave packet) was introduced there to examine the high-frequency instability of high-shear layer leading to breakdown into small-scale hairpin eddies. In the flow just prior to the appearance of hairpin eddies which was identified as high-frequency spikes in the waveform of velocity fluctuation, the group velocity C_g of the localized disturbance (wave packet) introduced was found to be very close to the convection velocity C_s of the high-shear layer. Thus, in the reference frame moving at the convection velocity C_s the wave packet could always stay on the high-shear layer and continue to grow by the inflectional instability, like as in absolutely unstable flows. The frequency of growing disturbance was found to be the same as that of high-frequency spikes.

References

[1] Klebanoff, P.S., Tidstrom, K.D. and Sargent, L.M.: The three-dimensional nature of boundary-layer instability, J. Fluid Mech. 12, 1-34, 1962.

[2] Nishioka, M. Asai, M. and Iida, S.: An experimental investigation of the secondary instability. In Laminar-Turbulent Transition (eds. R.Eppler and H. Fasel), Springer, 37-46, 1980.

[3] Itoh, N.: Secondary instability of laminar flows, Proc. Roy. Soc. London, A 375, 565-578, 1981.

[4] Kachanov, Y.S., Ryzhov, O.S. and Smith, F.T.: Formation of solitons in transitional boundary layers: theory and experiment, J. Fluid Mech. 251, 273-297, 1993..

[5] Huerre, P. and Monkewitz, P. A. Local and global instabilities in spatially developing flows. Annu. Rev. Fluid Mech. 22, 473–537, 1990.

[6] Chomaz, J. M. Global instabilities in spatially developing flows: Non-normality and nonlinearity. Annu. Rev. Fluid Mech. 37, 357‑392, 2005.

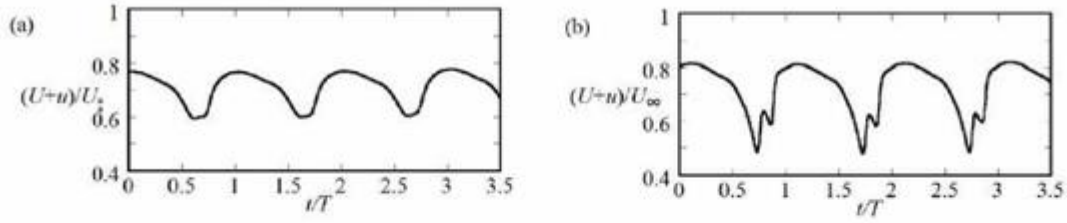

Fig. 1. Waveforms of velocity fluctuations at x-x_0 = 60 mm for different forcing amplitudes (20 Hz). (a) Just prior to onset of high-frequency spikes. (b) After onset of high-frequency spikes.

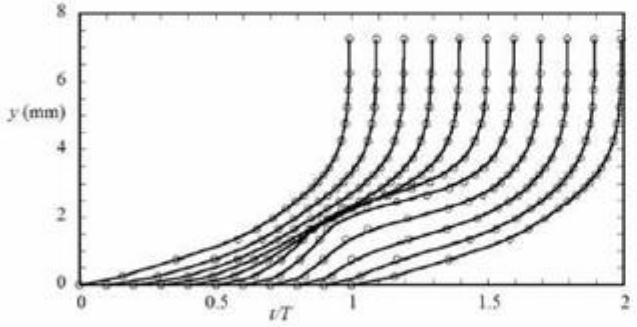

Fig. 2. Instantaneous velocity profile in one forcing period at x-x_0 = 30 mm without pulse disturbance.

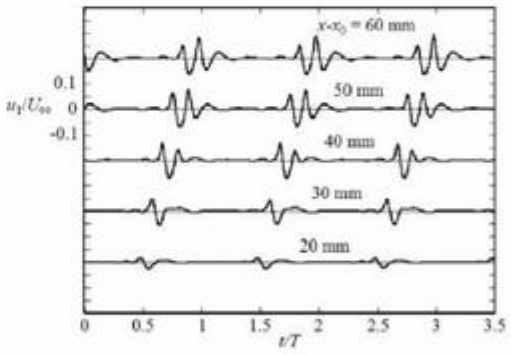

Fig. 3. Development of high-frequency wave packet in the convecting high-shear layer.

RELAMINARIZATION OF STABLY STRATIFIED TURBULENT POISEUILLE FLOWS AT LOW REYNOLDS NUMBER

Koji Fukudome[1a)] , Kento Higashitsutsumi [2] & Yoshifumi Ogami [1]
[1] *Department of Mechanical Engineering, Ritsumeikan University, Kusatsu, Shiga, Japan*
[2]*Graduate School of Mechanical Engineering, Ritsumeikan University, Kusatsu, Shiga, Japan*

Summary Direct numerical simulations of spectral method were performed to study relaminarizing turbulent structures in Poiseuille flow under stable density stratification. In the case of small computational domain, the turbulence attenuated with increasing effect of stable stratification, and relaminarization occurred on one wall side at $Ri > 0.30$ where the turbulence remain on the other wall. Here, Ri is the bulk Richardson number defined by bulk mean velocity. On the other hand, in the case of large computational domain, relaminarization on one wall side was not observed and large scale intermittent flow structure appeared at $Ri > 0.17$. Also, turbulent stripes were observed at $Ri = 0.56$. Therefore, the flow dynamics in SB and LB were different from each other. The flow structure of the turbulent stripe was similar to the ones in turbulent Poiseuille flow in transitional regions without any external forces.

INTRODUCTION

Turbulence under stable density stratification is observed in the atmosphere at night, in the oceans, and in the industrial systems. Hence, stably stratified turbulence is important for both physics and engineering. Hence, we focus on the relationship between stratification and the shear effects. Garg et al. [1] and Iida et al. [2] carried out direct numerical simulation (DNS) with relatively small computational domain and confirmed that the turbulence in horizontal Poiseuille flows is attenuated by stable density stratification. Iida et al. [2] also clarified that an internal gravity wave becomes dominant in the channel center, and strong stratification causes relaminarization on one wall side, whereas turbulence still remains on the other wall. On the other hand, García-Villalba et al. [3] carried out DNSs in a large computational domain, and found a very large scale intermittent flow structure consisting of turbulent and spotty quasi-laminar regions in stably stratified turbulent Poiseuille flow. However, the flow structures under stable stratification have not been studied systematically with the change of the stratification. Authors [4] performed DNSs of stably stratified Poiseuille flow and showed that the turbulent stripe consisting of turbulent and quasi-laminar bands appeared in large computational domain. This turbulent stripe was also found in turbulent channel flows consisting of open channel flows [5,6] and Couette flow [7] with moderate stratification. In this study, we performed DNSs to examine the turbulent structure in Poiseuille flows with stable density stratification, and clarified the flow structure more in detail to compare the flow structure in two computational domains.

NUMERICAL PROCEDURE

The objective flow is a Poiseuille flow, which is bounded by parallel walls consisting of an upper hot wall and a lower cold wall and is driven by a constant pressure gradient. The numerical method used in this study was the same as that used by Iida et al. [2] and previous research [4]. The governing equations were the incompressible Navier–Stokes equation with an added buoyancy term using a Boussinesq approximation, and continuity and energy equations. DNSs of the equations were carried out by the spectral method, using Fourier series in the streamwise x (= x_1) and spanwise z (= x_3) directions and a Chebyshev polynomial expansion in the wall-normal direction y (= x_2). The boundary conditions were periodic for the x and z directions and non-slip at the walls. For dealiasing, the 3/2 rule was adapted for both spatial discretizations. Time advancement was carried out by the Crank–Nicolson method for the viscous terms and the second-order Adams–Bashforth method for the nonlinear and buoyancy terms. All calculations were carried out at a Reynolds number of $Re_e = u_e\delta/\nu = 150$ and Prandtl number of $Pr = \nu/a = 0.71$. Here, u_e, δ, ν and α are the characteristic velocity at the mean pressure gradient, the channel half width, the kinetic viscosity, and thermal diffusivity, respectively. The computational domains in the x-, y-, and z-directions are $5\pi\delta\times2\delta\times2\pi\delta$ (SB) as in [1], of a $128\times129\times128$ grid system and $20\pi\delta\times2\delta\times10\pi\delta$ (LB) of a $512\times129\times512$ grid system. As an initial condition, fully developed flows at $Re_e = 150$ were calculated in advance. The Grashof number $Gr = g\beta\Delta\Theta(2\delta)^3/\nu^2$ was then systematically increased as shown in Table 1. Here, g, β, and $\Delta\Theta$ are the gravitational acceleration, the volumetric expansion coefficient, and the temperature difference between the hot and cold walls, respectively. Hereinafter, all parameters are normalized by u_e and ν ; normalization is indicated by the superscript $+$.

RESULT AND DISCUSSION

Table 1 show the flow statistics of our results, consisting of flow rate (bulk Reynolds number) $Re_m = 2U_m\delta/\nu$, friction coefficient $C_f = 2\tau_w/\rho U_m^2$, and bulk Richardson number $Ri = Gr/Re_m^2$ as a function of Gr in both cases of SB and LB. Here, U_m, τ_w, and ρ are the mean velocity in the entire channel, the wall shear stress, and the density, respectively.

[a)] Corresponding author. Email: fukudome@cfd.ritsumei.ac.jp

Table 1 Computational conditions and basic statistics in small computational domain.

Re_e	Gr	SB Re_m	SB C_f	SB Ri	LB Re_m	LB C_f	LB Ri
150	0.00	4579	× $^{-3}$	0.00	4522	× $^{-3}$	0.00
	× ^{5}	4771	× $^{-3}$	0.06	4715	× $^{-3}$	0.06
	× ^{5}	5129	× $^{-3}$	0.17	5100	× $^{-3}$	0.17
	× ^{5}	5466	× $^{-3}$	0.24	5408	× $^{-3}$	0.25
	× ^{5}	5766	× $^{-3}$	0.30	5605	× $^{-3}$	0.32
	× ^{5}	6532	× $^{-3}$	0.35	5849	× $^{-3}$	0.44
	× ^{5}	6599	× $^{-3}$	0.40	5927	× $^{-3}$	0.50
	× ^{5}	6751	× $^{-3}$	0.44	5976	5.06 10^{-3}	0.56
	× ^{5}	7497	× $^{-3}$	0.53	5924	× $^{-3}$	0.85

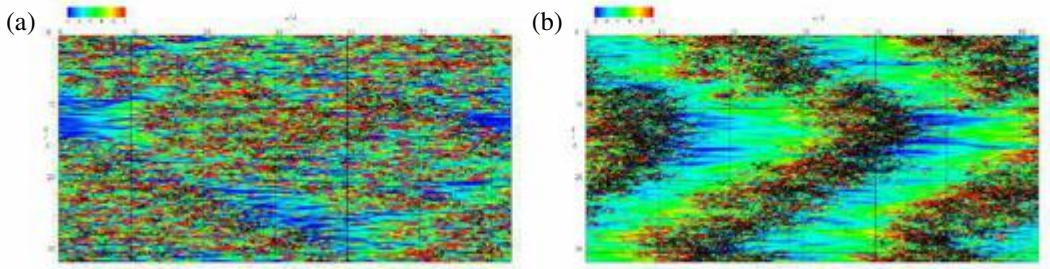

Figure 1 Instantaneous distributions of high- and low-speed fluids in the near-wall region and the vortical structure identified by the second invariant of the velocity gradient tensor $II = -0.5 u_{i\,j} u_{j,i}$ over the entire channel in LB. The black iso-surfaces correspond to $II^+ = 0.05$. The red to blue contours correspond to $u^+ = -3$ to 3. (a) $Ri = 0.17$. (b) $Ri = 0.56$.

Present results show good agreement with the results of Iida et al.[2] using a fine grid. The flows were relaminarized by the stratification, so that the increase of Re_m and decrease of C_f were raised. It is noted that the deviation of the flow rate Re_m between SB and LB becomes significant in the case of Ri > 0.3, where the one-wall-side turbulence which was observed in SB as reported by Iida et al. [2] was not shown here.

Figure 1 illustrates the instantaneous flow structure in the case of LB for Ri = 0.17 and Ri = 0.56. At Ri = 0.17, intermittent flow structure is clearly observed as reported by García-Villalba et al. [3]. The week turbulent regions tended to incline from streamwise direction. This intermittent flow structure was not observed at this Reynolds number flow without the stratification. At Ri = 0.56, one-wall-side turbulence were obtained in the case of SB. High- and low-speed fluids exist upstream and downstream of the turbulent region where many vortical structures were clustered. The turbulent regions formed stripe pattern, which is called turbulent stripe. Hence, the flow structure of the turbulent stripe was similar to the ones in turbulent Poiseuille flow in transitional regions without any external forces [7,8]. As a result, the turbulent stripe appears at higher Reynolds numbers to impose the stable density stratification in Poiseuille flows. Moreover, one-wall side turbulence was not observed when the turbulent stripe appeared in LB. Hence, the flow dynamics were not similar between SB and LB.

CONCLUSIONS

Direct numerical simulations were performed to study the turbulent structure in Poiseuille flow under stable stratification. In the case of SB, the turbulence attenuated with increasing effect of stable stratification, and relaminarization occurred on one wall side at Ri > 0.30. On the other hand, in the case of LB, relaminarization on one wall side was not observed consistently and large scale intermittent flow structure appeared at Ri > 0.17. Also, V-shape turbulent stripes were observed at Ri = 0.56. Therefore, the flow dynamics in SB and LB were different from each other. The flow structure of the turbulent stripe was similar to the ones in turbulent Poiseuille flow in transitional regions without any external forces.

References

[1] Garg, R. P., Ferziger, J. H., Monismith, S. G., & Koseff, J. R.: *Physics of Fluids* (1994-present), 12(10), pp. 2569-2594, 2000.

[2] Iida, O., Kasagi, N., & Nagano, Y.: *International Journal of Heat and Mass Transfer*, 45(8), pp. 1693–1703, 2002.

[3] García-Villalba, M., & Del Álamo, J. C.: *Physics of Fluids*, 23(4), 045104 , 2011.

[4] Fukudome, K., Yamasaki, S., & Ogami, Y.: *Proceedings of the First Pacific Rim Thermal Engineering Conference*, Hawaii's Big Island, USA, 2016.

[5] Brethouwer, G., Duguet, Y., & Schlatter, P.: *Journal of Fluid Mechanics*, 704, pp. 137–172, 2012.

[6] He, P., & Basu, S.: *Nonlinear Processes in Geophysics Discussions*, 2(1), pp. 179-241, 2015.

[7] Fukudome, K., & Iida, O.: *Journal of Fluid Science and Technology*, 7(1), pp. 181-195, 2012.

[8] Manneville, P.: *European Journal of Mechanics-B/Fluids*, 49, pp. 345-362, 2015.

OPTIMAL PERTURBATIONS OF A COUNTER-ROTATING VORTEX PAIR IN STRATIFIED FLOWS

Sabine Ortiz *[1], Jean-Marc Chomaz[2], and Claire Donnadieu[3]
[1]*UME/DFA, ENSTA, chemin de la Hunière, 91761 Palaiseau Cedex, France*
[2]*LadHyX,École Polytechnique, Palaiseau Cedex 91128, France*
[3]*LadHyX,École Polytechnique, Palaiseau Cedex 91128, France*

Summary This paper investigates the three dimensional perturbations developping on a pair of horizontal counter-rotating vortices in stably stratified flow. The 2D flow is unsteady and the stability is reformulated by searching transient energy growth of perturbations around a time varying flow. For weak and moderate stratifications (large Froude numbers), the stratification acts on a long timescale compared to the advection time of the dipole, when 3D instabilities are added, transient analysis at different instant retrieves the instability peaks corresponding to the Crow instability for the long wavelengths and to the elliptic instability. This shows the validity of the quasi-steady approximation and that stratification destabilizes the flow by bringing vortices closer. For strong stratifications (Froude numbers smaller than 2), the quasi-steady approximation is not valid. Optimal perturbations depart from their homogeneous counterpart with large perturbation in the wake of the dipole associated with density effects.

INTRODUCTION

Vortex dipole are characteristic of the wake of airplanes, their persistance depends on the instability mechanism leading or not to turbulence. In the homogeneous case Crow and elliptic instabilities are controlling this evolution but in the presence of a vertical stratification of density, the mechanisms involved are largely unknown. In the present study we consider an academic case with vortices not as slend as in aeronautical case to allow us to fully analyse with reasonable CPU time their stability.
The base flow is obtained by integration of the non-linear two-dimensional Navier-Stokes equations with a pseudo-spectral method in Cartesian coordinates (x, z) and periodic boundary conditions (Delbende *et al.* (1)). The initial state is the superposition of two circular Lamb-Oseen vortices of initial circulation Γ_0, initial radius a_0 and initial separation distance b_0 with $a_0/b_0 = 0.2$. The flow evolves in a stable linear vertically stratified flow characterized by the Brunt-Väisälä frequency N. The Reynolds number based on the initial circulation of the vortices is $Re_{_0} = 2400$, and the Froude number $Fr = \frac{W_0}{Nb_0}$, the ratio of the characteristic timescale of the stratification $1/N$ to the characteristic timescale of the flow (W_0 is the initial advection velocity of the dipole), is varied. As the counter-rotating vortices propagate downwards, they evolve under the influence of the stratification.

OPTIMAL PERTURBATIONS

In the case of strong stratification, i.e. for small Froude numbers, the unsteadiness of the flow validates the classical quasi-steady approximation. In order to study the dynamics of this unsteady flow, we explore here a different approach valid with no restriction when base flow and perturbations evolve on a similar time scale. We compute for each time horizon τ, the initial perturbation that will exhibit the largest gain $G(\tau)$ in total energy by time τ. A direct-adjoint technique (Corbett & Bottaro (2)) has been developed in order to compute the optimal perturbations while taking into account the evolution of the base flow.

The analysis shows that the growth of the perturbation at short wavelength is dominated by inertial mechanism associated with the development of elliptic modes for both symmetries. Up to time $Nt^* = Fr^{-1}t = 4$ and for Froude numbers down to unity, the effect of the stratification is mainly to enhance the development of the elliptic instability by bringing the vortices closer together and therefore increasing their ellipticity confirming the mechanism proposed by Nomura *et al.* (3). At larger times of optimisation and for stronger stratifications (Ortiz *et al.* (4)) the dynamics is driven by density effects and optimal response is concentrated in the wake of the dipole and not in the vortex cores.

At long wavelenth, the optimal response Fig. 1(a) is mainly located in the core of the vortices where its shape is characteristic of the Crow mode, the density perturbation in the wake being passively driven. For stronger stratifications, even though inertial effects in the vortices dominate the dynamics, optimal response is not limited to the core of the vortices and affects also the wake of the dipole Fig. 1(b).

*Corresponding author. Email: ortiz@ladhyx.polytechnique.fr

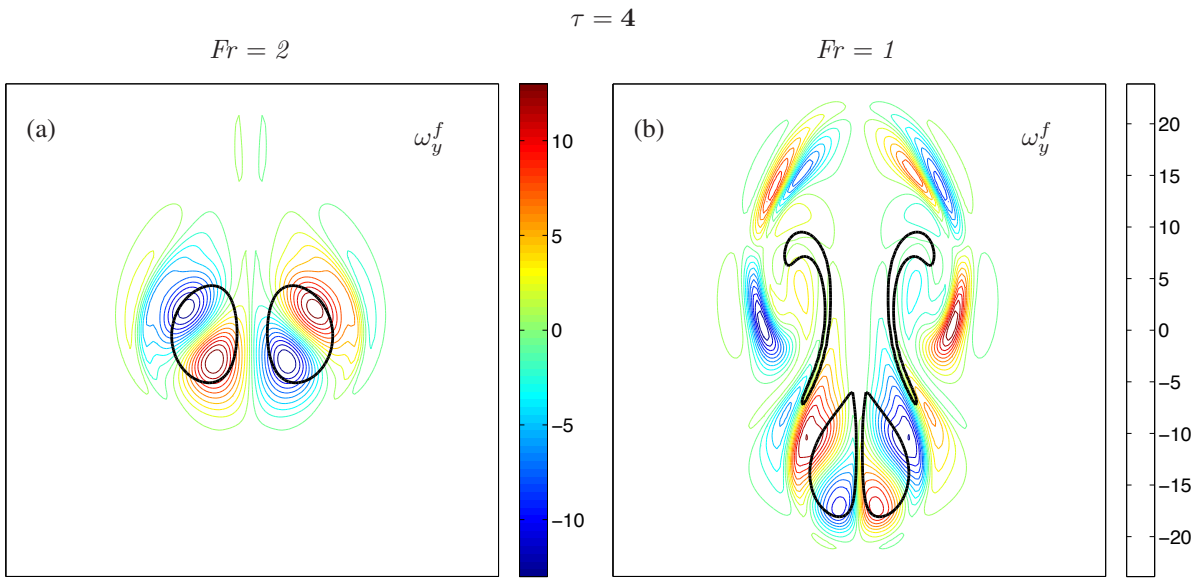

Figure 1: **Transient Crow type instability: Symmetric optimal perturbations for the long-wavelength peaks ($k_y^* a_0 = 0.2$ at $\tau = 4$)** - Isovalues of the axial vorticity of the (a)-(b) optimal responses ω_y^f at the time horizon $\tau = 4$ in the (x, z) plane normed by the total energy of the optimal initial perturbation. For (a) $Fr = 2$ and (b) $Fr = 1$. The thick black lines materialize the "core" of the vortices and correspond to the isocontours $\omega_{By}/\omega_{By}^{max} = \pm exp(-1)$. The size of the domain shown is $3.5b_0 \times 3.5b_0$ whereas the computation domain is $12b_0 \times 12b_0$ and the domain is shifted to follow the vortices in their descent.

CONCLUSIONS

In the present study, we analyze the transient growth of perturbation for an horizontal vortex dipole in a stratified fluid. One ratio of the core to the distance of the vortices $a_0/b_0 = 0.2$, have been considered. We show that down to Froude number unity the dynamics is mainly led by the elliptic instability, therefore by inertial effects rather than gravity effects. We may conjecture that the mechanism described in this study should be retreived for aircraft wakes even if the corresponding dipoles are far more concentrated with an aspect ratio a_0/b_0 several order of magnitude smaller. Investigation of such aircraft trailing vortices that requires very high resolution and higher Reynolds numbers are too CPU consuming to be exhaustive and one specific case has been computed and seems to confirm this conjecture.

References

[1] Delbende I., Chomaz J.-M.and Huerre P.: Absolute/convective instabilities in the batchelor vortex: a numerical study of the linear impulse response J. Fluid Mech 355:229-254, 1998.

[2] Corbett P., Bottaro A: Optimal perturbations for boundary layers subject to stream-wise pressure gradient Phys. Fluids 12:120-130, 2000.

[3] Nomura K.K., Tsutsui H., Mahoney D. and Rottman J. W.: Short-wavelength instability and decay of a vortex pair in stratified fluid J. Fluid Mech 553:283-322, 2006.

[4] Ortiz S., Donnadieu C. and Chomaz J.-M.: Three-dimensional instabilities and optimal perturbations of a counter-rotating vortex pair in stratified flows Phys. Fluids 27:106603, 2015.

FLOW IN BILITY IN A PRECE SING HERE

Sh geo Kida *
Dox i Univer i y T tar -Miy kod ni I 3 Kyo n be hi J p n

Summary In t b t rd t lo t ta r t t b t boa d o t d o r p rg p rv tg t d b t a o d t t.m r m t on o t t m. A g t rg o ont o p m t m y a d t rg r bot t t mpo vo t on (g t o t on p od rd p) rd t p t t t a g p t t t p tto t p e rt o t o T m r mo t t t st on s m r d w th t p o 3D o v a z t on r t

We co er e mo o o a com re b e co a rece ere e a rece o a ar e oc e Ω_s a Ω_p are co a me a e r ave are or o o a o eac o er y em e arac er e by o o me o a arame er e Rey o mber $Re = a^2\Omega_s/\nu$ a e Po caré mber $Po = \Omega_p/\Omega_s$ ere a e ere ra a ν e k ema e co y o

e ab y bo ary o e ea y o be e a e by e re e a or ere ro re are o re l w ere e o e r e e ab y bo ary e co r e e by a ar e y o ab e mo e pa er e oc o r a e o o e o e arac er e aro $(Re, Po) = (1540, 0.165)$ ch ca e by a o ro o a arro re l e e y o o e ar e e e ere e o ab e a e o e e e a ab e a e o e re e

e ab y o ea y o are evam e by er omm e rec mer ea m a o o e o y em ar arb rary a co o We ca e a e e em ora e o o o e o me e ra o e er y a a o e e oc y q are e ro y e or e y q are a e e y e er ro e o e oc y a or e y) ere e e oc y a or e y are e e e rece o ra e e o e e a y e o be e er ea y or er o e me e e y o e ab y bo ary

re e a e a ram o e e er y e ro y a e crea ea y a e a ear a a o crea a er o e o a a e o e r e e a ac e a abe corre o o o e ea a e o [re l T e o e o ea y a e or A B C D ll a mea a e ea y a e ab e or ea e e ob er e a e o e orb a ee e e o re e ma fie by 500 me e a e o r a -e oc e a o e orb er o $0.96T_s$ ere T_s e ro a o er o e o me e ra o e er y e ro y a e e y e a ea mo o a y me fi re om e A e a e o co ro arame er e er Re or Po rom o ll ea o a ra e e a e e a e d a ram ere o ee a o y 0 6 crea e i $Re \rightarrow$ or 0 l% $Po \rightarrow$ br abo a b e a e e e er y a e ro y a e or er o e era re me ea am e a abo (X) me o e a o er o ee be o

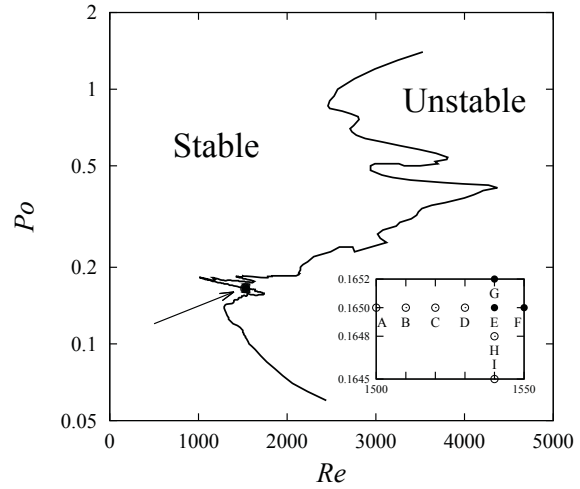

re l Sab y bo ary o e ea y llo e ea y o are s ab e or ab e o e e or e r o e o e r e e e y o e o ro of a arro e ar e e e

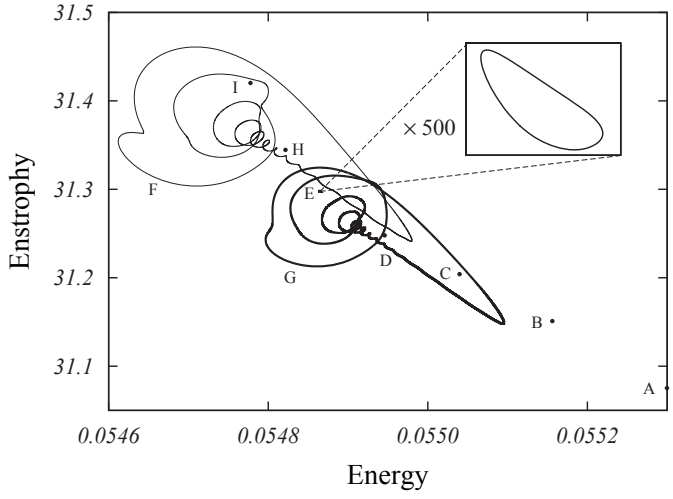

re a e a ram e e er y e ro y a e A a be A– corre o o o e ar o co ro arame er o e e o re l e a e o r a e oc e a o e orb or a

*C r es o g f , Dr Sh 6 ko J p

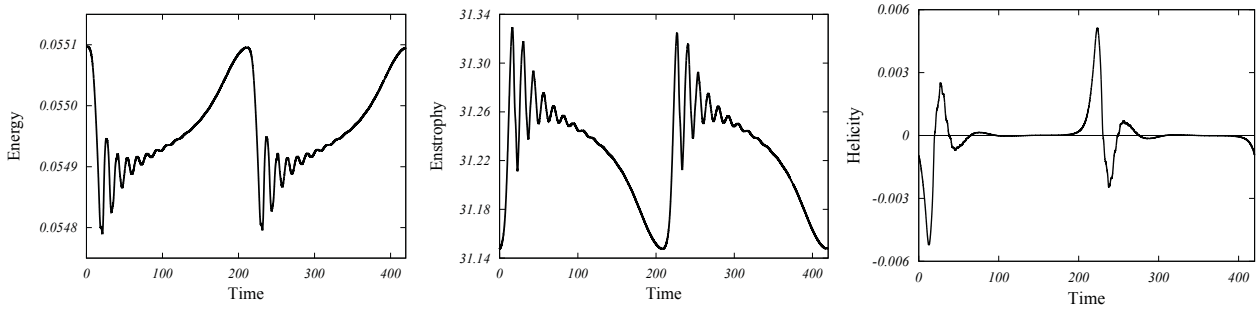

re 3 em ora e o 1 o o e er y e e ro y ee er a e e y (r o er o e er o $\approx 420T_s$ $(Po, Re) = (0.1652, 1540)$

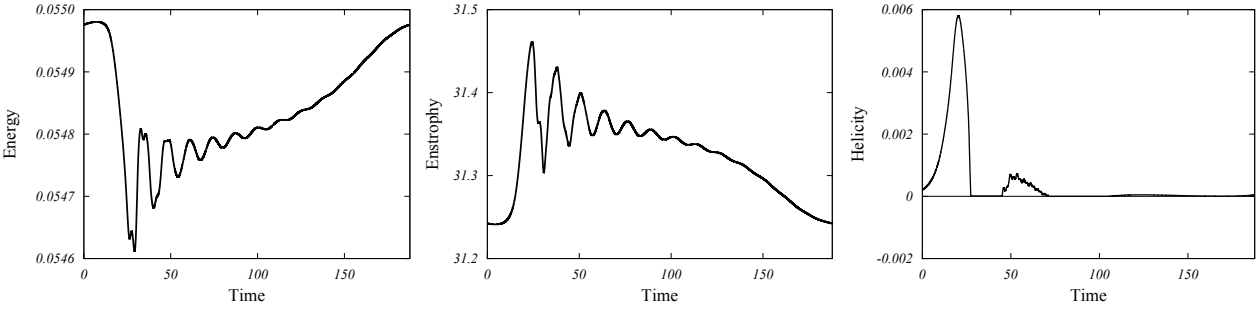

re : em ora e o o o e er y e e ro y ee er a e e y r g o er o e er o $\approx 188T_s$ $(Po, Re) = (0.1650, 1550)$

e em ora e o o o e er y e ro y a e e y or ca e a are ra re 3 a re ee e y ere o no e a a o e e er y a e ro y ary m ar y e o ca e e e e y oe o or ca e G a ee e r a e o re 3 e e e y a e bo o ve a e a e a e a re er e com e ely e ery a er o . or ca e o e o er a e e e y a e o y a e ee e r a e o re o a are e ame er o e e er y a e ro y e er o or ca e ear y a o a or ca e a u re o e rob em ere ere ee e be a or o e e y be ee e o ca e come rom e a o em ora r e re o e ab e mo e e e era o mee a m o ab y a e ere ee e e e y be a or are o er e a o e e o 3 o a za o a e re be re e e e co ere ee

Acknowledgements or a ar a y or e by ra A or e e fic Re earc 2 540 16 15K 5 19 rom e Ja a oce y or e Promo o o e e ee e mer ca ca e a o ere earr e o o R16000 a Y P yo o U er y

FLOW TRANSITION OF NEUTRALLY BUOYANT SUSPENSION BETWEEN CONCENTRIC CYLINDERS

Madhu V Majji[1,2], Jeffrey Morris [1] & Sanjoy Banerjee [2]
[1]*Levich Institute and Department of Chemical Engineering, City College of New York, New York, NY 10031, USA.*
[2]*Energy Institute and Department of Chemical Engineering, City College of New York, New York, NY 10031, USA.*

Abstract: Experiments were performed to observe the flow transitions when a neutrally buoyant non-Brownian suspension of rigid particles in Newtonian fluid rotated in the annulus between two concentric cylinders. For pure fluid and very dilute suspensions, the flow transitioned from Taylor Vortex Flow (TVF) into Circular Couette Flow (CCF) as the Reynolds number (*Re*) of the inner cylinder was reduced. By contrast, for suspension concentrations between 5% and 20% particles, the flow transitioned from TVF into Spiral Vortex flow (SVF) and eventually into CCF. This indicates appearance of SVF under inner cylinder rotation only, a behaviour not seen for single-phase fluids. The initial transition was moved to a significantly lower *Re,* when the effective viscosity was considered. The transition values of *Re* corresponding to both TVF-SVF and SVF-CCF ware observed to reduce with increase in particle concentration indicating earlier onset of instability.

Understanding of flow transition and instabilities of particle-laden fluids (suspensions) is useful in developing predictive models for multiphase flows in industries and nature. Most of the past work on suspension flows was focused in Stokes and low Reynolds number (*Re)* regimes. Efforts to understand flows of suspensions close to and beyond the transition Reynolds number, *Re,* for various flows has received only slight attention[1,2].

We have performed experiments with neutrally buoyant non-Brownian suspension in the Taylor-Couette geometry to understand the effect of particles on various flow transitions. This flow represents an extremely well-studied baseline case for the pure fluid, and we make use of existing theory to guide our efforts [3,4,5]. The particle phase was made up of PMMA particles (212 μm < d_p <250 μm) and the fluid phase was a glycerin-water mixture, with minute amount surfactant added to reduce bubble adhesion to particles. A very small volume of mica flakes (flat particles of large dimension 50 microns) was added for visualization of flow structures. The Taylor-Couette set up consists of concentric cylinders placed inside a cooling jacket to maintain temperature at 20°C. The annular gap was filled with the suspension. The outer acrylic cylinder (diameter d_o=114 mm) was held fixed at all times while the inner solid aluminum cylinder (diameter, d_i=100 mm) was rotated. The annulus gap (a) was 7 mm and the ratio of height of the inner cylinder to the annulus gap (L/a) was 20.5. The radius ratio (d_i/d_o) was 0.88 and the annulus gap to particle diameter ratio (a/d_p) was 30.3. For pure fluid, Taylor vortices appeared at the top and bottom walls with Circular Couette Flow (CCF) in the middle and eventually filled the whole annulus length at a transition *Re* of 120 in accordance with linear stability theory. For a suspension, as *Re* (based on annulus gap, velocity of inner cylinder and the bulk viscosity of the suspension, using Krieger and Dougherty correlation[6]) was increased slowly, significant migration of particles was observed from the central CCF region into the Eckman vortices near the top and bottom boundaries resulting in non-uniform concentration profile along the annulus length before the transition *Re* was reached. To avoid migration effects in determining transitions, for a given particle concentration of the suspension, ϕ, initially, the inner cylinder was rotated at a *Re* corresponding to Taylor Vortex flow (TVF) until the steady state was established. The inner cylinder *Re* was then decreased at a small acceleration of $dRe/dt \approx -0.01$ (t is the time non-dimensionalized with viscous time scale) until the flow transitioned to CCF. The experiment was repeated for $dRe/dt \approx -0.005$ to make sure the results are independent of the acceleration applied.

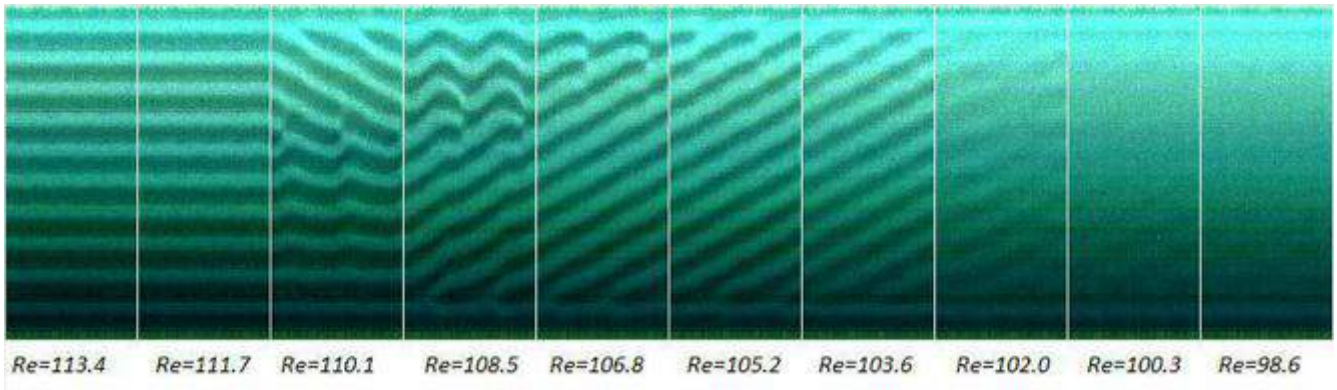

Figure 1: Space-time diagrams for 15% suspension. Vertical and horizontal axes are annulus length and time, respectively.

[a] Corresponding author. Email: madhuvr@gmail.com.

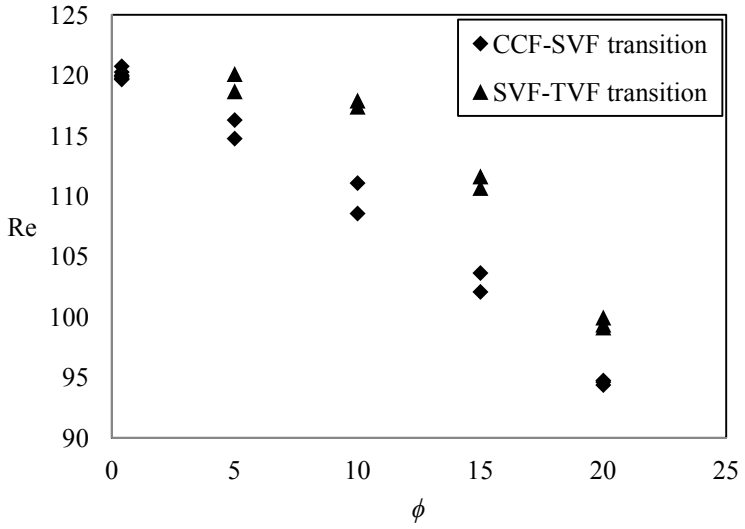

Figure 2: Reynolds number of CCF-SVF and SVF-TVF transitions for various suspension concentrations.

For a typical suspension concentration of ϕ=15%, steady TVF was established at Re=123. Figure 1 shows the space-time diagrams at different *Re* as the *Re* was reduced. It was observed that the TVF was stable for 123>*Re*>111, the flow transitioned from TVF into Spiral Vortex Flow (SVF) at *Re*≈111. For 111>*Re*>102, SVF was observed to be stable. A mixed state of spiral and wavy-TVF filling parts of the annulus length was observed in this range of *Re*. At *Re*≈102, SVF transitions into CCF. The flow was observed to be CCF for *Re*<102. The experiment was repeated for suspension concentrations 0%<ϕ<20% and the results are plotted in figure 2. For pure fluid and very dilute suspensions, the TVF transitioned into CCF with reducing *Re*. whereas, for suspension concentrations between 5% and 20 %, TVF transitioned into SVF which eventually transitioned into CCF at lower *Re*. Also, as the suspension concentration was increased from 0% to 20%, both TVF-SVF and SVF-CCF transition *Re* reduced considerably from TVF-CCF transition *Re* of pure fluid.

CONCLUSIONS

We observed an earlier onset of instability with increasing suspension concentration and the appearance of new stable SVF state between TVF and CCF compared to pure fluid. A remarkable feature is that the initial (lowest-*Re)* instability of the flow is to spiral vortex flow (SVF) under conditions of only inner cylinder motion. Note that for pure fluid case with rotating inner cylinder and stationary outer cylinder, the first instability transitions CCF into TVF and the SVF does not appear at all in the full range of Re[5]. For pure fluid case, the SVF appears only when the two cylinders are counter rotating [4,5]. Our results indicate that the viscosity alteration alone is not sufficient to account for the influence of the particles, and the normal stresses are quite weak at loadings of 20% solids or smaller. The particle-scale Reynolds number ($Re_p=d_p^2\,\gamma/4\,\nu$, where γ is the shear rate and ν is the kinematic viscosity of the fluid) had value of $Re_p \approx 0.03$. At particle level, though the flow is near the Stokes regime and roughly force and torque-free, the surface traction moment (stresslet) from particles may contribute to a change in the instability relative to the pure fluid. The weak inertia may play a role, as suggested in an examination of laminar to turbulent transition of suspension flow in pipes[2].

References

[1] M. E. Ali, Hydrodynamic stability of a suspension in cylindrical couette flow, *Physics of Fluids*, 14(3):1236–1243, 2002.

[2] J.P. Matas, J. F. Morris & E. Guazzelli, Transition to turbulence in particulate pipe flow, *Phys. Rev. Lett*., 90, 014501, 2003.

[3] Taylor G. I., "Stability of a viscous liquid contained between two rotating cylinders", Phil. Trans. R. Soc. Lond. A, (1923), 289-343.

[4] J. Sanchez, D. Crespo, F. Marques, Spiral Vortices Between Concentric Cylinders *Applied Scientific Research* 51: 55–59, 1993.

[5] Andereck C. D., Lui S. S., and Swinney H. L., Flow regimes in a circular Couette system with independently rotating cylinders, J. Fluid Mech. (1986), vol. 164, pp. 155-183.

[6] M. Krieger, T.J. Dougherty, A Mechanism for Non Newtonian Flow in Suspensions of Rigid Spheres, Trans. Soc. Rheol. 3, 137 (1959)

THERMOELECTRIC CONVECTION IN DIELECTRIC LIQUIDS IN A CYLINDRICAL ANNULUS

Innocent Mutabazi[1a], Antoine Meyer[1], Olivier Crumeyrolle[1] and Harunori Yoshikawa[2]
[1]Laboratoire Ondes et Milieux Complexes, UMR 6294, CNRS- Université du Havre, Le Havre, France
[2]Laboratoire de Mathématiques J-A. Dieudonné, UMR 7351, CNRS-Université de Nice Sofia Antipolis, Nice, France

Summary The stability of a dielectric liquid confined in a cylindrical annulus with a radial temperature gradient and an alternating electric tension shows the existence of different modes (thermal modes, hydrodynamic modes, electric modes and columnar modes) depending on the relative importance of the electric tension and the temperature difference. A comparison is made with the stability of the corotating Couette-Taylor flow with a radial temperature gradient where the centrifugal buoyancy replaces the dielectrophoretic force.

INRODUCTION

Flows in cylindrical annulus are encountered in many applications and represent hydrodynamic prototypes of closed flow systems. The cylindrical annulus has the advantage of the existence of a large group of symmetries that can be broken when a control parameter is varied and then lead to the occurrence of new states. For this reason, the Couette-Taylor flow between differentially rotating annulus has drawn much attention for the investigation of the transition to turbulence [1]. When a radial temperature gradient is added, the centrifugal force competes with the Archimedean buoyancy and new bifurcations states occur that are different of the isothermal case: helicoidal vortices become critical and their inclination angle depends on the temperature gradient [2, 3, 4]. When a dielectric liquid is confined in a cylindrical annulus with a radial temperature gradient and an alternating electric tension, it undergoes the combined action of the Archimedean buoyancy and the dielectrophoretic force due to the coupling between the electric field $\vec{E}$ and the variation of the electric permittivity with the temperature [5]. The present paper presents the results from the stability analysis of the flow of a dielectric liquid in the field of the Earth gravity and the dielectrophoretic force. This force dominates over the Coulomb force when the field frequency is much larger than the inverse of the fluid characteristic times [5].

FLOW EQUATIONS

We consider a dielectric liquid with density ρ, a kinematic viscosity ν and an electric permittivity ε in an infinite-length cylindrical annulus of inner radius a and outer radius b so that the gap width is d = b - a. The dielectrophoretic force $\vec{f}_{DEP} = -\frac{1}{2}\vec{E}^2\vec{\nabla}\varepsilon$ can be seen as a buoyancy force if one introduces the electric gravity defined as follows :

$$\vec{g}_e = \frac{1}{\rho\alpha}\vec{\nabla}\left(\frac{\varepsilon_0\varepsilon_r e\vec{E}^2}{2}\right)$$

where $\varepsilon_0 = 8.85\ 10^{-12} C^2/(N.m^2)$ is the vacuum permittivity. The density and the electric permittivity are assumed to be linear functions of the temperature:

$$\rho\,T = \rho_0\,1-\alpha\,T-T_{ref} \quad ; \quad \varepsilon\,T = \varepsilon_0\varepsilon_r\,1-e\,T-T_{ref} \quad .$$

For an incompressible fluid, viscous dissipation and Joule heating may be neglected under certain circumstances [4]. In the Boussinesq approximation, the governing flow equations read

$$\begin{cases} \vec{\nabla}\vec{u} = 0 \quad ; \quad \vec{\nabla}.\left(\varepsilon\vec{E}\right) = 0 \\ \left(\frac{\partial}{\partial t} + \vec{u}.\vec{\nabla}\right)\vec{u} = -\vec{\nabla}\Pi + \nu\Delta\vec{u} - \alpha\,\left(\vec{g} + \vec{g}_e\right) \qquad \left(\frac{\partial}{\partial t} + \vec{u}.\vec{\nabla}\right)T = \kappa\Delta T \end{cases}$$

where the electric field is supposed to vary in time so quickly so that its effective value can be considered as deriving from a potential ϕ and the reduced pressure Π is given by

$$\Pi = \frac{P}{\rho} - \frac{\varepsilon_0\varepsilon_r e T\vec{E}^2}{2\rho} - \frac{1}{2}\left(\frac{\partial\varepsilon}{\partial\rho}\right)_T\vec{E}^2$$

The boundary conditions at the cylindrical surfaces are

$$\begin{cases} \vec{u} = 0, T = T_1 \quad \phi = V_0 \quad \text{at} \quad r = a \\ \vec{u} = 0, T = T_2 \quad \phi = 0 \quad \text{at} \quad r = b \end{cases}$$

[a)] Corresponding author. Email: innocent.mutabazi@univ-lehavre.fr

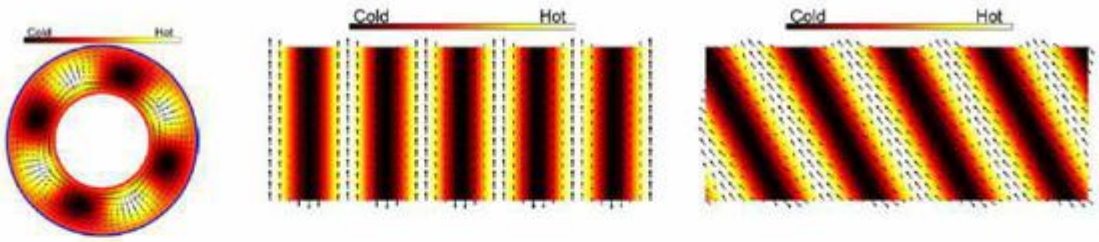

Figure : Cylindrical annulus with a radial temperature gradient and a high frequency electric tension : a) cross-section of the flow patterns, b) stationary columnar vortices, c) electric modes (stationary helicoidal vortices).

The base flow is characterized by the axisymmetry with a vertical velocity component $\vec{u} = W(r)\vec{e}_z$, a temperature profile $T\ r\ = \ln\left[(1-\eta)r\right]/\ln\eta$ and an electric tension given by $T\ r\ = \ln 1 - e\ T - T_{ref}\ /\ln(1-e$.

Scaling the lengths by the gap width d, the time by d^2/κ and the temperature by the temperature difference between the cylindrical surfaces $\delta T = T_1 - T_2$, one gets the flow control parameters :

$$Gr = \frac{\alpha \delta T\ g d^{\ 3}}{\nu^2},\ L = \frac{\alpha \delta T\ g_e d^{\ 3}}{\nu\kappa},\ \mathrm{Pr} = \frac{\nu}{\kappa}.$$

As the Grashof number Gr and the electric Rayleigh number L depend both on the temperature difference $\delta T = T_1 - T_2$, L can be replaced by the dimensionless electric tension: $V_E = V_0 / V_{ref}$ with $V_{ref} = \sqrt{\rho\nu\kappa / \varepsilon_0\varepsilon_r}$ being a characteristic tension that depends only on the fluid thermal and electric properties. Therefore Gr and V_E are independent parameters.

RESULTS

The linear stability analysis was performed in order to determine the critical parameters and the nature of the critical modes for different values of Pr, δ and η. Four critical regimes:

1) For weak values of the electric potential V_E, critical modes are oscillatory either axisymmetric for ($\eta > \eta^*$) or non-axisymmetric for ($\eta < \eta^*$) where η^* depends on values of Pr. The threshold Ra_c of these modes is almost constant with respect to V_E. These modes may have large wavenumber for small values of Pr (hydrodynamic modes) or small wavenumber for large values of Pr (thermal modes).

2) For large values of the electric potential V_E, critical modes are steady and non-axisymmetric. The threshold decreases with V_E and vanishes for $\mathrm{V_E} = \mathrm{V_E^c}\ \eta$. These modes are associated with the thermo-electric instability encountered in the microgravity conditions [2].

3) For intermediate values of V_E, the critical mode is a stationary critical mode with zero axial wavenumber and finite azimuthal wavenumber. This mode corresponds to columnar vortices, similar to those obtained in a differential heated cylindrical annulus in a solid body rotation and a heated outer cylinder [6].

4) Nonlinear stability analysis has shown that the electric modes are supercritical.

CONCLUSIONS

The stability of the flow of a dielectric liquid confined in a cylindrical annulus subject to a combined action of the Archimedean force and the dielectrophoretic force has been performed for a wide range of the control parameters. The results may be tested in experiments in zero-G flight during parabolic flight campaigns.

References

[1] S. Chandrasekhar, *Hydrodynamic and Hydromagnetic Stability*, Oxford University Press, 1961.
[2] H. Yoshikawa, M. Nagata and I. Mutabazi, *Phys. Fluids* **25**, 114104 (2013).
[3] C. Kang, K.S.Yang and I. Mutabazi, *J. Fluid Mech*. **771**, 57-78 (2015).
[4] H. Yoshikawa, O. Crumeyrolle and I. Mutabazi, *Phys. Fluids* **25**, 024106 (2013).
[5] V. Travnikov, O. Crumeyrolle and I. Mutabazi, *Phys. Fluids* **27**, 054103 (2015).
[6] M. Auer, F.H. Busse and R.M. Clever, *J. Fluid Mech.* **301**, 371-382 (1995).

Acknowledgments

The present work benefits from the support from the CNES and the program Investissements d'Avenir (ANR-10-LABX-09-01), LABEX EMC^3.

BOUNDARY-LAYER STABILITY OF A GENERIC REENTRY CAPSULE WITH REAL-GAS EFFECTS

Antonio Di Giovanni * and Christian Stemmer
Lehrstuhl für Aerodynamik und Strömungsmechanik, Technische Universität München, Munich, Germany.

Summary On the base of a generic Apollo capsule geometry, the present work focuses on the influence of high-temperature gas effects on the flow around the windward side of the blunt body. By means of Direct Numerical Simulations and Linear Stability Analysis, the influence of chemical dissociations and non-equilibrium on the stability of the boundary layer will be investigated.

INTRODUCTION

In order to ensure a safe atmosferic reentry, capsules are equipped with ablative Thermal Protection Systems (TPS) to protect and insulate the vehicle. In the realisation of a TPS, the prediction of the laminar-turbulent transition of the boundary layer on the capsule surface is a crucial issue. In the turbulent regime, the heat-transfer rate at the wall can be much higher than the one occurring in the laminar regime. However, in spite of the multi-decennial experience in hypersonic flows, there is still no effective and reliable method to predict transition. Although the flow is laminar in the first phase of typical return paths, with transition moving from back to front with decreasing altitude, the design of current TPSs is based on a fully turbulent boundary layer, followed by an increase of capsule weight and manufacturing costs [1]. A further challenge in the prediction of hypersonic transition arises because of the presence of high-temperature gas effects [2]. To this regard, Direct Numerical Simulations (DNS) represent a valuable investigation tool, as wind-tunnel experiments at reentry conditions matching all relevant dimensionless parameters including the Damköhler number are extremely difficult.

The presented work is part of a joint effort to investigate laminar-turbulent transition on the high-enthalpy boundary layer of a generic Apollo capsule geometry and it focuses on the influence of the high-temperature effects, such as molecular dissociation and thermal non-equilibrium. DNS are performed for both an axisymmetric case (angle of attack 0°) and a three-dimensional geometry (angle of attack 24°). By means of the linear stability analysis (LSA), it is shown how the stability properties of the flow considerably depends on the gas model adopted in the simulation. In fact, the inclusion of chemical reactions and non-equilibrium effects may lead to a premature destabilisation of the flow and, possibly, to an early transition.

RESULTS

Computation of the base flows

A simulation database of boundary-layer flows has been generated, including various freestream conditions and different gas models (ideal gas, chemical/thermal equilibrium as well as non-equilibrium). DNS, based on the finite-volume code NSMB, are performed with a second-order central difference scheme on a simulation grid consisting of $26.5 \cdot 10^6$ points. With regard to reentry missions, a realistic scenario at $Ma = 20$ at an altitude of $H = 57.7$ km has been chosen. The influence of chemical dissociation and thermal non-equilibrium on the flow is fully investigated and quantified and an analysis of the boundary-layer properties is performed in view of a first characterisation of the base-flow stability.

Due to the strong flow deceleration induced by the shock ahead of the capsule, the boundary layer remains subsonic to transonic (Fig. 2a). Therefore, no acoustic instabilities are expected. Moreover, the absence of a generalised inflection point in the boundary-layer profiles anticipates the stability of the boundary layer with respect to inviscid modes, independently of the gas model. However, in the case of reacting gas a significant decrease of the temperature and velocity values and of their respective gradients is observed. The inclusion of chemical non-equilibrium determines a further reduction of the temperature gradient (Fig. 2b). This behaviour will affect the stability of the boundary layer.

Comparison with experimental data

Direct numerical simulations at wind-tunnel conditions have been performed to validate the method used to generate the base flows (Fig. 1). Experimental data in the case of cold flow (i.e. ideal gas) are retrieved from the experimental campaign conducted at the Ludwieg-tube in Braunschweig, Germany, whereas data for a high-temperature reacting flow have been provided by the Japan Aerospace Exploration Agency (JAXA) [3].

Linear stability analysis

The LSA of the base flows is performed to provide a preliminary estimation of the frequency spectrum of those perturbations which are more likely to induce the laminar-turbulent transition. Although no unstable modes were found, the analysis revealed that in the case of reacting gas the damping rate of the stable modes is much less pronounced than for the ideal gas. The incorporation of chemical non-equilibrium further reduces the stability of the boundary layer (Fig. 2c).

*Corresponding author. Email: antonio.digiovanni@aer.mw.tum.de

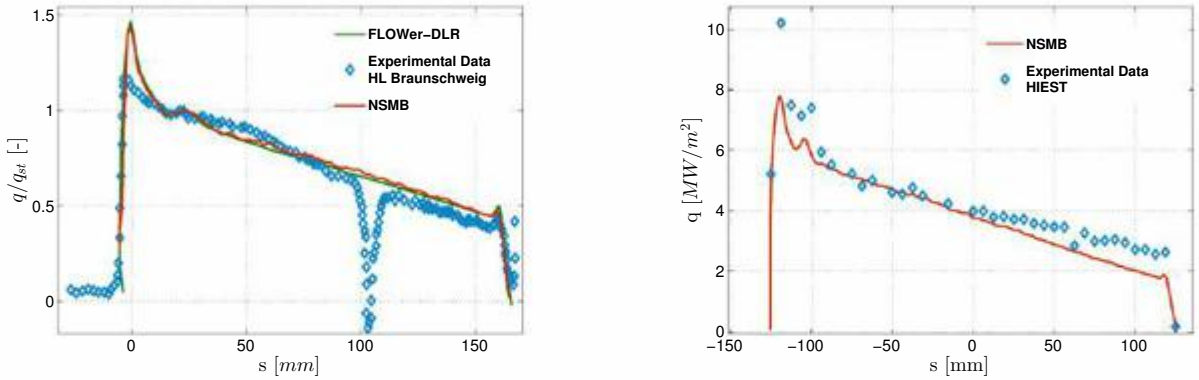

(a) *(b)*

Figure 1: Quantitative comparison between experimental and numerical heat flux (based on the code NSMB) at cold flow conditions (a) and at high-temperature reacting-flow conditions (b).

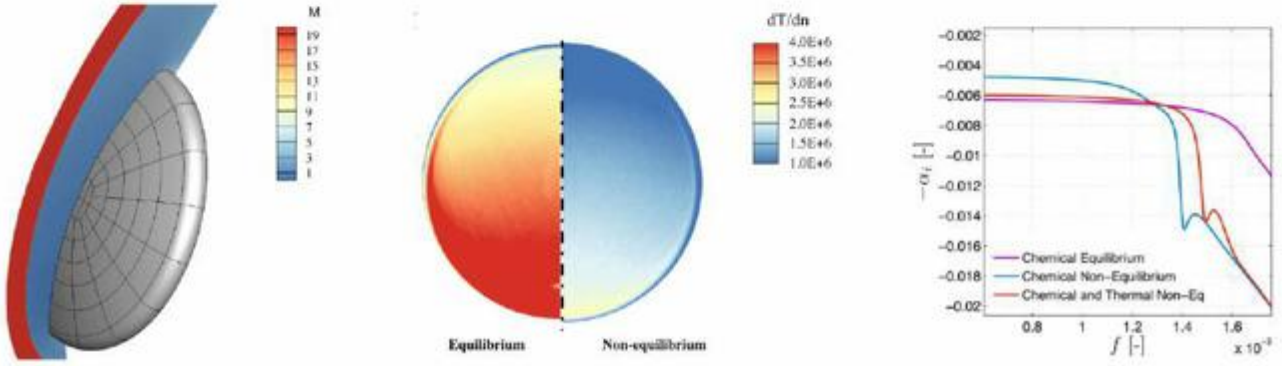

(a) *(b)* *(c)*

Figure 2: (a) Symmetry plane coloured by the value of the Mach number; (b) comparison of the wall-normal component of the temperature gradient in equilibrium and in non-equilibrium conditions and (c) growth rates of linear perturbations for different gas models. The values in the case of ideal gas are much lower than the ones of reacting gas and are not represented here.

CONCLUSIONS

For the angle of attack of 0 and 24 degrees, Direct Numerical Simulations have been undertaken to investigate the influence of the chemical and thermal modelling on the steady base flow of a generic Apollo capsule geometry. The linear stability analysis revealed that the inclusion of high-temperature gas effects considerably reduces the stability of the boundary layer in the wind-ward side of the capsule. These results highlight the importance of including chemical reactions and non-equilibrium in the investigation of the perturbation growth in the boundary layer of reentry capsules and it lays ground for future investigations on roughness-induced transition.

References

[1] Hollis B.R., Berger K.T., Horvath T.J., Coblish J.J., Norris J.D., Lillard R.P., Kirk B.S.: Aeroheating Testing and Predictions for Project Orion Crew Exploration Vehicle, Journal of Spacecraft and Rockets, Vol. 46, No.4, 2009.

[2] Malik M.R., Anderson E.C.: Real gas effects on hypersonic boundary-layer stability, Phys.Fluids A 3(5), 803-821, May 1991.

[3] Tanno H., Komuro T., Sato K., Itoh K., Lillard R.P., Olejniczak J., Grinstead J.H.: Aeroheating measurement of Apollo shaped capsule with boundary layer trip in the free-piston shock tunnel HIEST, AIAA SciTech, AIAA 2014-0434.

[4] Stemmer C., Adams N.A., Hein S., Schrder W., Meinke M., Olivier H., Radespiel R., Heitmann D.: Experimental and numerical investigation of hypersonic instabilities in a boundary layer on a capsule with and without high-temperature gas effects. RTO-AVT 200 Specialists Meeting on "Hypersonic Laminar-Turbulent Transition", 32.1-32.26, April 16-19, 2012, San Diego, USA.

[5] Stemmer C., Fehn J.: High-temperature gas effects at a capsule under re-entry and wind-tunnel conditions, AIAA-Paper 2014-2645.

EFFECTS OF EXTERNAL FORCING ON TRANSVERSE JET STRUCTURE AND MIXING

Takeshi Shoji[*], Andrea Besnard[*], Elijah W. Harris[*], Robert T. M'Closkey[*], and Ann R. Karagozian[*a)]
[*]*Department of Mechanical and Aerospace Engineering*
UCLA Henry Samueli School of Engineering and Applied Science
Los Angeles, CA 90095-1597, USA

Summary This experimental study explores the effect of temporal forcing on gaseous transverse jets, quantifying jet response via optical diagnostics. Low level sinusoidal jet excitation is observed to significantly affect structural and mixing characteristics for transverse jets with convectively unstable jet shear layers under unforced conditions. Such excitation, especially in a frequency range close to the fundamental, is found to attenuate the cross-sectional asymmetry naturally occurring in such unforced jets. There is also improved molecular mixing for excited jets with more symmetric cross sections. Yet when the transverse jet's upstream shear layer is absolutely unstable in the absence of forcing, sinusoidal jet excitation barely affects jet structure or mixing, even with a very high forcing amplitude and wider range of forcing frequencies. Different forcing methods, e.g., creating alternative temporal waveforms for jet excitation, are clearly required to control the structural and mixing characteristics of transverse jets based on these differing instabilities.

BACKGROUND AND CONTEXT OF PRESENT STUDIES

The transverse jet or jet in crossflow (JICF)[1,2] is a canonical flowfield that has been studied for several decades, principally for its extensive applications in engineering propulsion systems[3]. Extensive prior studies of such jets in the absence of external forcing[4,5,6] have documented a transition in the jet's upstream shear layer from convective to absolute instability as the jet-to-momentum flux ratio J and/or jet-to-crossflow density ratio S are brought below approximately 10 and 0.40, respectively. JICF structural characteristics have also been studied in relation to shear layer stability characteristics[7], in part because of the potential contribution of shear layer vortical structures to formation of the well-known counter-rotating vortex pair (CVP) associated with the jet cross-section and its possible role in improving transverse jet mixing as compared with that for a free jet[2]. It is observed[7] that as J decreases for the flush-injected transverse jet, initiation of upstream shear layer vortical structures occurs closer to the jet exit. As J is reduced below the transitional value of 10, a relatively symmetric CVP is observed under equidensity and low density conditions. On the other hand, at higher momentum flux ratios, e.g., J = 41, the flush-injected, equidensity JICF is observed to have delayed shear layer vorticity rollup, consistent with a weaker, convective instability, in many cases creating an asymmetric cross-section. Such asymmetries diminish as the jet density is reduced and absolute instability in the shear layer is achieved.

As noted above, the transverse jet is generally considered to be a better mixer than is a free jet[8], where typical mixing metrics include scalar concentration decay, jet spread and penetration, and the probability density function (pdf) associated with the scalar field. The implications of JICF structure and instability characteristics on molecular mixing have been studied in recent experiments[9], employing acetone PLIF to quantify traditional mixing metrics as well as jet centerplane- and cross-section-based Unmixedness under diffusion-limited flow conditions. In general, absolutely unstable jets are observed to create improved mixing with crossflow as compared with convectively unstable jets, yet with a few exceptions, notably those associated with jet-crossflow density differences.

Achieving improved mixing via active flow control can take advantage of the relationships among JICF shear layer instabilities, structure, and mixing parameters. Earlier studies[10] on strategic excitation of the JICF show that sinusoidal excitation of convectively unstable jets can significantly enhance jet penetration and spread, while such excitation of absolutely unstable jets has little impact on jet response. In contrast, square wave excitation[10,11,12] at prescribed temporal pulsewidths associated with optimal vortex ring formation[13] dramatically alters jet penetration and spread, even for absolutely unstable transverse jets. It is of interest in the present studies to utilize more extensive optical diagnostics to examine the effect of strategic JICF forcing on jet structural characteristics and, in particular, on molecular mixing.

EXPERIMENTAL APPROACH AND SAMPLE RESULTS

The present transverse jet experiments are performed in a low-velocity wind tunnel, utilizing non-intrusive PLIF of acetone vapor seeded in the jet fluid, which consists of mixtures of nitrogen and helium. The excitation source for PLIF is a dual cavity Q-switched Nd:YAG laser (Litron Nano L PIV); details on the optical diagnostics may be found in prior studies[7,9]. Several alternative jet injectors, including a contoured nozzle and straight pipe, are used to create jets issuing into a crossflow of air for a range of jet-to-crossflow momentum flux ratios J ($5 \le J \le 41$) and density ratios S ($0.35 \le S \le 1.0$) at a fixed jet Reynolds number, Re_j=1900. Axisymmetric excitation for the JICF is applied below the injection system via a loud speaker, which can create sinusoidal oscillations or, with control[11], temporal square wave oscillations in the jet velocity. Hot wire anemometry is used to match the root-mean-square (RMS) of the jet excitation, $U_{j,rms}$, at the jet exit among different excitation conditions for the range of jet and crossflow conditions explored here.

[a)] Corresponding author. Email: ark@seas.ucla.edu

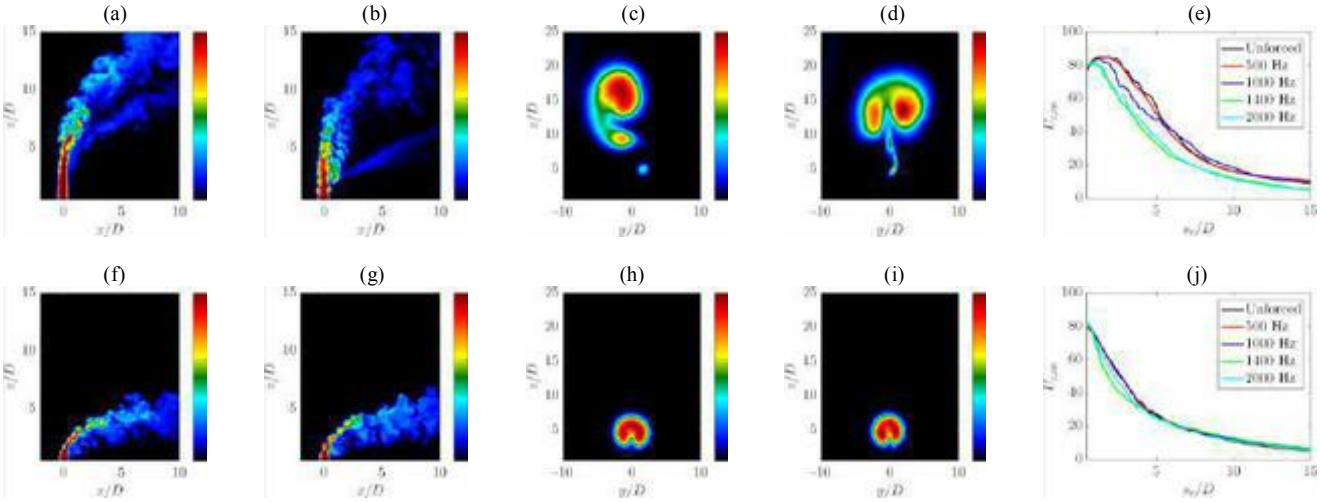

Figure 1. PLIF imaging and quantification of centerplane-based Unmixedness for equidensity transverse jets (S=1.00) for J=41 (top row) and J=5 (bottom row). Excitation conditions correspond to $U_{j,rms}$=0.07 m/s at f_f=1400 Hz, with a mean jet exit velocity of U_j ~ 6.5 m/s. Results correspond to PLIF imaging of: (a,f) the instantaneous unforced jet centerplane, (b,g) the instantaneous forced jet centerplane, (c,h) the averaged cross-section of the unforced jet at downstream location x/D=10.5, and (d,i) the averaged cross-section of the forced jet at x/D=10.5. Centerplane-based Unmixedness as a function of the unforced jet's centerline trajectory location s_c/D, for various forcing frequencies (500-2000 Hz) and in the absence of forcing, is shown in (e) and (j) for J = 41 and 5, respectively.

Representative results for the influence of sinusoidal jet excitation are shown in Figure 1. Data in the top row of the figure correspond to J=41, where the unforced jet's upstream shear layer is convectively unstable, and in the bottom row, to J=5, where the unforced jet is absolutely unstable. The RMS of the jet perturbation is matched at $U_{j,rms}$=0.07 m/s, approximately 1% of the mean jet velocity U_j, for all forcing conditions. Spectral characteristics of the upstream shear layer of the unforced equidensity jets with acetone seeding show that the fundamental frequency of the instability, f_o, is approximately 2000 Hz for J=5 and in the range 1600-1900 Hz for J=41. Sinusoidal excitation of the J=41 JICF at a forcing frequency f_f=1400Hz is seen to create a much more rapid initiation of rolled-up vortices closer to the jet exit (Fig. 1(b)) than those naturally occurring in the unforced jet (Fig. 1(a)); such forcing also attenuates the degree of natural asymmetry in the cross-sectional structure (c.f. Figs. 1(c,d), with averaging over 500 images). A relatively symmetric cross-sectional structure is observed for the forced JICF at J=41 for excitation frequencies in the range f_f=1400-2500 Hz, relatively close to the jet's fundamental frequency in the absence of forcing; outside of this range there is less influence of forcing on the jet's cross-sectional structure for a matched $U_{j,rms}$. Centerplane-based Unmixedness for this convectively unstable JICF in Fig. 1(e) shows a rather significant enhancement of the mixing (i.e., a lowered Unmixedness) for excitation in this symmetry-inducing frequency range. This result is particularly interesting given that Unmixedness is computed based on centerplane images such as those in Figs. 1(a,b), rather than cross-sectional images in Figs. 1(c,d). In contrast, sinusoidal excitation of the absolutely unstable JICF at J = 5 has less of an impact on both centerplane (Figs. 1(f,g)) and cross-sectional structural characteristics (Figs. 1(h,i)). In turn, the jet's mixing characteristics for J = 5 are relatively minimally influenced by forcing, especially in the farfield region (Fig. 1(j)), irrespective of forcing frequency. Clearly, alternative modes of excitation are required to control the degree of mixing for absolutely unstable jets in crossflow, as also documented in this study.

References

[1] Kelso R. M., Lim T. T., Perry A. E.: An Experimental Study of Round Jets in Cross-flow. **J. Fluid Mech** 306:111-144, 1996.
[2] Karagozian A. R.: Transverse Jets and Their Control. **Prog. Energy Comb. Science** 36(5):531-553, 2010.
[3] Margason R. J.: Fifty Years of Jet in Cross flow Research. AGARD-CP-534 1:1-141, 1993.
[4] Megerian S., Davitian J., Alves L. S. de B., Karagozian A. R.: Transverse Jet Shear Layer Instabilities. Part I: Experimental Studies. **J. Fluid Mech** 593:93–129, 2007.
[5] Davitian J., Getsinger D., Hendrickson C., Karagozian, A. R.: Transition to Global Instability in Transverse Jet Shear Layers. **J. Fluid Mech** 661:294-315, 2010.
[6] Getsinger D. R., Hendrickson C., Karagozian A. R.: Shear Layer Instabilities in Low-density Transverse Jets. **Expts in Fluids** 53:783–801, 2012.
[7] Getsinger D. R., Gevorkyan L., Smith O. I., Karagozian A. R.: Structural and Stability Characteristics of Jets in Crossflow. **J. Fluid Mech** 760:342-367, 2014.
[8] Smith S. H., Mungal M. G.: Mixing, Structure and Scaling of the Jet in Crossflow. **J. Fluid Mech** 357:83-122, 1998.
[9] Gevorkyan, L., Shoji, T., Getsinger, D. R., Smith, O. I., and Karagozian, A. R., Transverse Jet Mixing Characteristics, **J. Fluid Mech**, to appear.
[10] Davitian J., Hendrickson C., Getsinger D., M'Closkey R. T., Karagozian A. R.: Strategic Control of Transverse Jet Shear Layer Instabilities. **AIAA Journal** 48(9):2145-2156, 2010.
[11] M'Closkey R. T., King J., Cortelezzi L., Karagozian A. R.: The Actively Controlled Jet in Crossflow. **J. Fluid Mech** 452:325-335, 2002.
[12] Shapiro S., King J., M'Closkey R. T., Karagozian A. R.: Optimization of Controlled Jets in Crossflow. **AIAA Journal** 44:1292-1298, 2006.
[13] Gharib, M., Rambod, E., and Shariff, K., "A universal time scale for vortex ring formation", **J. Fluid Mech**. 360: 121-140, 1998.

LOCAL AND GLOBAL INSTABILITY OF BUOYANT JETS AND PLUMES

Patrick Huerre[1a)], R.V.K. Chakravarthy[1] & Lutz Lesshafft [1]
[1]*Laboratoire d'Hydrodynamique (LadHyX), Ecole Polytechnique, Paris, France*

Summary The local and global linear stability of buoyant jets and plumes has been studied as a function of the Richardson number *Ri* and density ratio *S* in the low Mach number approximation. Only the $m = 0$ axisymmetric mode is shown to become globally unstable, provided that the local absolute instability is strong enough. The helical mode of azimuthal wavenumber $m = 1$ is always globally stable. A sensitivity analysis indicates that in buoyant jets (low *Ri*), shear is the dominant contributor to the growth rate, while, for plumes (large *Ri*), it is the buoyancy. A theoretical prediction of the Strouhal number of the self-sustained oscillations in helium jets is obtained that is in good agreement with experimental observations over seven decades of Richardson numbers.

INTRODUCTION

Buoyant jets and plumes occur in a wide variety of environmental and industrial contexts, for instance fires, accidental gas releases, ventilation flows, geothermal vents, and volcanic eruptions. Understanding the onset of instabilities leading to turbulence is a research challenge of great practical and fundamental interest. Somewhat surprisingly, there have been relatively few studies of the linear stability properties of buoyant jets and plumes, in contrast to the related purely momentum driven classical jet. In the present study, local and global stability analyses are conducted to account for the self-sustained oscillations experimentally observed in buoyant jets of helium and helium-air mixtures [1].

FORMULATION AND METHODOLOGY

The flow is assumed to be governed by the compressible Navier-Stokes equations in the low Mach number approximation, a feature that allows for large density variations but filters out acoustic waves. In the limit of small density variations, this system reduces to the Boussinesq approximation. The steady axisymmetric base flow is obtained by resorting to the Newton-Raphson technique for given hyperbolic tangent axial velocity and density profiles at the inlet. Let R denote the inlet radius, ρ_j and U_j the inlet density and axial velocity and ρ_∞ the outer density. The most important parameters of the problem are then the Richardson number $Ri = gR(\rho_\infty - \rho_j)/(\rho_j U_j^2)$ and the density ratio $S = \rho_\infty / \rho_j$ with *Ri* and *S* in the range $10^{-4} < Ri < 10^3$ and $1 < S < 7$. At low Richardson numbers, buoyancy forces are much smaller than inertia forces, in which case the base flow is referred to as a *buoyant jet*, while at large Richardson numbers, buoyancy is dominant and the base flow is said to be a *plume*. The pure jet and pure plume are reached in the limit $Ri = 0$ and $Ri = \infty$ respectively.

The linearized system of partial differential equations associated with the non-parallel base flow then gives rise to a two-dimensional eigenvalue problem in the axial and radial directions, where the eigenvalue is the complex circular frequency $\omega = \omega_r + i\omega_i$ of frequency ω_r and temporal growth rate ω_i. A suitable finite-element discretization of the system followed by the implementation of a shift-invert scheme then leads to the determination of the eigenvalues and associated two-dimensional eigenfunctions. The same methodology is applied to the locally parallel base state at each axial station to compute the eigenvalues ω of the local instability problem as a function of axial wavenumber k and azimuthal wavenumber m. The convectively/absolutely unstable nature of the base flow is then readily determined as shown in [2] and [3].

LOCAL AND GLOBAL INSTABILITY CHARACTERISTICS

For buoyant jets (low *Ri*), the axisymmetric $m = 0$ global spectrum typically displays a single unstable discrete frequency, whereas for plumes (large *Ri*), it is composed of several unstable discrete modes with a maximum growth rate and corresponding frequency that are larger by two or three orders of magnitude. The local and global instability results may be summarized in the $Ri - S$ state diagram displayed in Figure 1. As the density ratio *S* and the Richardson number *Ri* increase along a diagonal line, the base flow changes from locally convectively unstable (white region) to locally absolutely unstable (blue and red regions) as the zero absolute growth rate neutral curve (thin line) is crossed. As the streamwise extent of the absolutely unstable domain reaches a critical size, the base flow becomes globally unstable (red region) as the neutral global stability curve (thick line) is crossed. Buoyant jets (low *Ri*) successively experience all three qualitative states as *S* increases while plumes are much more unstable and exhibit a rapid transition to global instability. The dip in the global neutral curve at intermediate *Ri*'s is due to a shift from an inertia driven instability mechanism for buoyant jets to a buoyancy dominated mechanism for plumes. No globally unstable discrete frequency is obtained for the $m = 1$ helical mode, but the downstream sponge region needs to be carefully tuned in order to stabilize the continuous spectrum, as in classical jets. A local stability analysis [2] in the Boussinesq approximation framework (*S* close to unity), recently reported that the $m = 1$ mode is the only

[a)] Corresponding author. Email: huerre@ladhyx.polytechnique.fr

one to become absolutely unstable. It may be concluded that the magnitude of the absolute growth rate is then too weak to drive an unstable global mode.

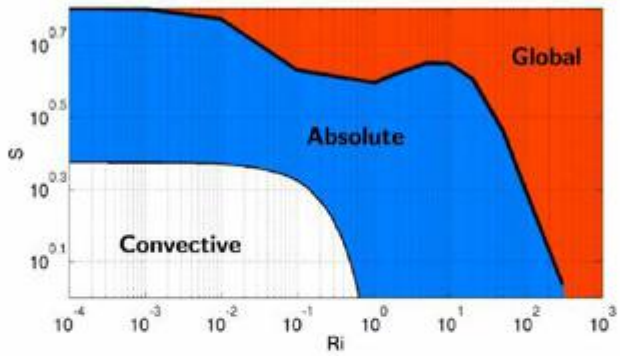

Figure 1: Instability regions and associated neutral curves in $Ri - S$ plane (log-log scale) for the axisymmetric mode $m = 0$ at Reynolds number 200. White region: locally convectively unstable; Blue region: locally absolutely unstable; Red region: globally unstable (and absolutely unstable).

A sensitivity analysis on the relative contributions to the global growth rate and frequency of shear, buoyancy and other terms in the linear dynamical operator, reveals that shear is the dominant factor for the global instability of buoyant jets while buoyancy becomes dominant for plumes.

GLOBAL FREQUENCY AND SELF-SUSTAINED OSCILLATIONS

Light jets have been known for some time to give rise to axisymmetric self-sustained oscillations. Prior theoretical investigations have relied on local stability approaches, thereby implicitly assuming that the base flow is weakly non-parallel. The predictions of the global analysis are compared in Figure 2 with the experimental observations of Cetegen & Kasper [1]. The blue line represents the empirical formula resulting from experiments and the red line the theoretical prediction of the present study.

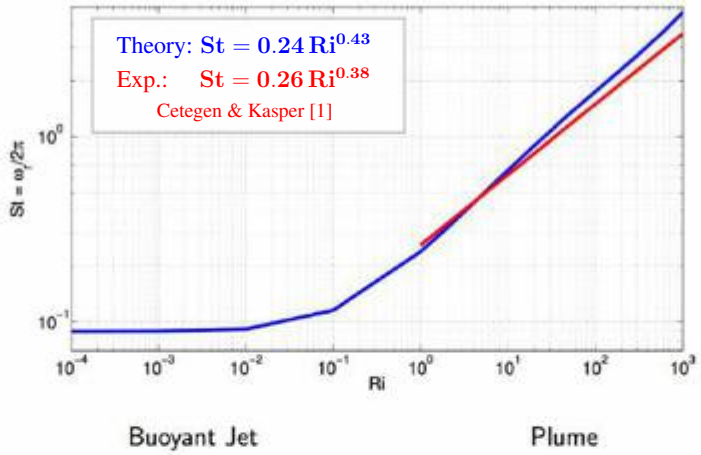

Figure 2: Strouhal number $St = \omega_r/2\pi$ versus Richardson number (log-log scale) in the range $10^{-4} < Ri < 10^{3}$: Comparison between prediction of global stability theory (blue line) and experimental observations of Cetegen & Kasper [1].

The linear global mode theory is seen to closely agree with the observations over 7 decades of Richardson numbers. For buoyant jets (low Ri), the Strouhal number is almost constant with Ri, while for plumes (large Ri), it continuously increases.

References

[1] Cetegen B.M. & Kasper K.D.: Experiments on the Oscillatory Behavior of Buoyant Plumes of Helium and Helium-Air Mixtures *Phys. Fluids* **8**(11):2074-2984, 1996.

[2] Chakravarthy R.V. K., Lesshafft, L. & Huerre, P.: Local Linear Stability of Laminar Axisymmetric Plumes. *J. Fluid Mech* **580**:344-369, 2015.

[3] Chakravarthy R.V. K.: Local and Global Instabilities in Buoyant Jets and Plumes. *PhD Thesis*, Ecole Polytechnique, LadHyX, Paris, France, 2015.

DIRECT NUMERICAL SIMULATIONS OF LAMINAR-TURBULENT TRANSITION IN HYPERSONIC FLOWS OVER FLAT PLATE

Ivan Egorov[1a] & Andrey Novikov[2]
[1]*Central Aerohydrodynamic Institute (TsAGI), Zhukovsky, Moscow region, Russia*
[2]*Moscow Institute of Physics and Technology, Zhukovsky, Moscow region, Russia*

Summary In this paper we simulate 3D wave trains generated by a periodic suction-blowing actuator working at a fixed frequency. These disturbances brake down within the computational domain that allows for simulations of the early stage of LTT. DNS are performed by solving the 3D Navier-Stokes equations for unsteady compressible flows of viscous perfect gas using the in-house solver "HSFlow" (High Speed Flow solver).

The problem of laminar-turbulent transition (LTT) in hypersonic flows over bodies is one of the main tasks of high-speed aerodynamics. LTT leads to a substantial increase of the surface heating and aerodynamic drag of hypersonic vehicles as well as affects the efficiency of propulsion system and control surfaces. To solve this problem it is needed to clarify physical mechanisms causing transition to turbulence. In the case of low free-stream disturbances typical for flight conditions, the LTT includes the three main stages [1]: receptivity to external disturbances; growth of unstable modes (such as first and second Mack modes, cross flow instability and Görtler vortices); nonlinear breakdown of disturbances leading to the fully turbulent flow regime.

A holistic computation of the all LTT stages is possible only using direct numerical simulations (DNS), where the full unsteady three-dimensional (3D) Navier–Stokes equations are solved without any restriction on the mean (unperturbed laminar) flow and disturbance amplitudes. In addition, as opposed to physical experiments, DNS gives full information about 3D disturbance field, which enables to identify and study in detail different LTT mechanisms. The modern methods of parallel computations and rapid developments of multi-processor supercomputers make it feasible to conduct such numerical experiments for hypersonic boundary layers for simple configurations such as a flat plate and a cone at zero angle of attack [2].

In this paper we consider a plat plate at the freestream Mach number 5.373 and unit Reynolds number $\mathrm{Re}_{\infty,1} = 17.9\times10^6$ m^{-1}. These flow parameters are relevant to the Hyper-X model tested in the NASA LaRC 20-Inch Mach 6 Air Tunnel [3]. The earlier stability and numerical studies in these conditions were performed for the 5.5 degree compression corner in 2D [4, 5] and 3D cases [6, 7]. In this paper we simulate 3D wave trains generated by a periodic suction-blowing actuator working at a fixed frequency. These disturbances brake down within the computational domain that allows for simulations of the early stage of LTT. DNS are performed by solving the 3D Navier-Stokes equations for unsteady compressible flows of viscous perfect gas using the in-house solver "HSFlow" (High Speed Flow solver).

Computations are performed on an orthogonal grid with $6001\times n_y \times 151$ nodes, where the number of nodes in vertical direction n_y varies from 126 to 376 through the computational domain depending on the bow shock location. It is clustered near the surface so that 55% of nodes are within the boundary layer with the smallest cell y-size of $\Delta y = 0.0001$. In the spanwise direction the grid is equidistant with the step size of $\Delta z = 0.0013$. Near the outflow boundary the size of 160 grid cells is gradually increased from $\Delta x = 0.0005$ to $\Delta x = 0.1$. This part of computational domain acts as "buffer" zone where the unsteady disturbances dissipates via numerical viscosity. The solution in this zone is inaccurate and is ignored during the analysis below. The grid contains 251×10^6 nodes in total.

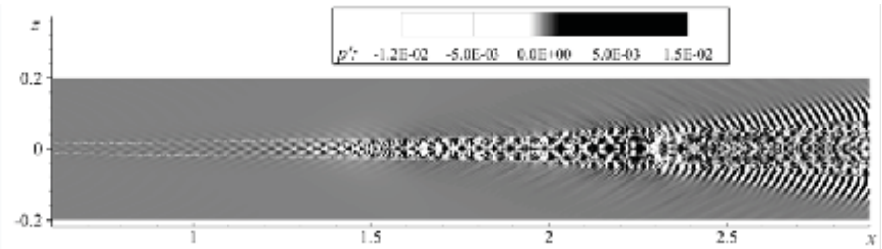

Figure 1. Instantaneous wall pressure disturbances field at t = 5.704. Dashed lines mark the core part of the wave train.

Figure 1 illustrates the instantaneous pressure disturbance field on the plate surface. Shown is the time moment t = 5.704 after switching-on the actuator, when the induced wave train reached the outflow boundary of the domain. Hereafter the disturbance fields are obtained by subtracting the basic flow field from the fields at different time instances. Note that the

[a] Ivan Egorov. Email: ivan.egorov@tsagi.ru.

calculations were done only in the half $z \geq 0$ of the shown domain with symmetric boundary condition at the central $z = 0$ plane. The full patterns shown in the all figures hereafter are obtained by mirroring the computed half to another.

Figure 1 shows that upstream from the x-section $x \approx 1.4$ the wave train consist of oblique waves with the front angle being around 66 degrees. They form a v-shape pattern typical for the first-mode dominated disturbance. Near the central line, the wave train exhibit a staggered pattern surrounded by oblique waves from both sides. With the *x*-coordinate the wave train disperses in the spanwise direction so that its core part lies within a wedge marked by the dashed lines in Fig. 1.

The amplitude of disturbance waves grows monotonically and, ultimately, the nonlinear breakdown is observed downstream of the point $x \simeq 1.4$ where the regular pattern of wave train starts to be distorted. Downstream of the section $x \approx 2.25$ the disturbances near the wave-train center exhibits a chaotic appearance. Here the process of laminar-turbulent transition begins and a "young" turbulent wedge is formed. Features of instability development in the linear and nonlinear stages are explored using disturbances spectra, disturbances profiles and visualizations of the 3D disturbances field. The disturbances in the turbulent wedge core at the symmetry plane $z = 0$ is shown in Fig. 2 using the shadowgraph pattern (density Laplacian $\nabla^2\rho$).

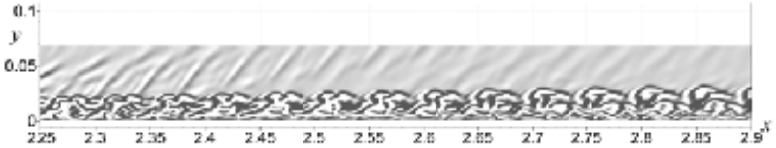

Figure 2. Shadowgraph of the boundary layer disturbance in the symmetry plane $z = 0$ at $t = 7.3125$.

Figure 3 shows 3D vortical structures visualized at the time instance $t = 7.3125$ using an isosurface of Q criterion. Small-scale hairpin vortices fill up the central portion of the wave train surrounded by oblique waves. On the whole there are vortices of many scales that is typical for turbulent boundary layers. However, regular-in-space structures indicate that the flow is not fully turbulent yet.

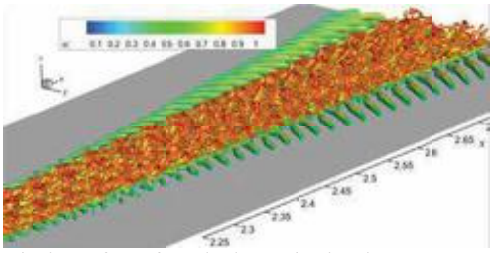

Figure 3. Visualization of flow structures by isosurface of Q criterion at the time instance $t = 7.3125$, Q = 100. Side, top and perspective views. The isosurface is coloured using the streamwise velocity magnitude.

Features of instability development in the linear and nonlinear stages are explored using disturbances spectra, disturbances profiles and visualizations of the 3D disturbances field. Distributions of the average skin friction coefficient help to detect the beginning of LTT.

ACKNOWLEDGMENTS

This work was supported by Russian Scientific Foundation (Project No.14-19-00821).

References

[1] Fedorov A., "Transition and Stability of High-Speed Boundary Layers," *Annu. Rev. Fluid Mech*., Vol. 43, 2011.

[2] Zhong X., and Wang X., "Direct Numerical Simulation on the Receptivity, Instability, and Transition of Hypersonic Boundary Layers," *Annu. Rev. Fluid Mech*., Vol. 44, 2012.

[3] Berry S. A., DiFulvio M., and Kowalkowski M. K., "Forced Boundary Layer Transition on X-43 (Hyper-X) in NASA LaRC 20-Inch Mach 6 Air Tunnel," *NASA TM-2000-210316*, Aug. 2000.

[4] Balakumar P., Zhao H., and Atkins H., "Stability of Hypersonic Boundary Layers over a Compression Corner," *AIAA J*., Vol. 43, No. 4, 2005.

[5] Egorov I.V., Novikov F.V., and Fedorov A.V., "Numerical Modeling of the Disturbances of the Separated Flow in a Rounded Compression Corner," *Fluid Dynamics*, Vol. 41, No. 4, 2006.

[6] Zhao H., and Balakumar P., "Nonlinear Disturbance Evolution Across a Hypersonic Compression Corner," *AIAA J*., Vol. 43, No. 5, 2005.

[7] Egorov I., Novikov A., and Fedorov A., "Numerical simulation of three-dimensional wave packet in supersonic flow over a compression corner," AIAA-2015-2624, 2015.

WAKE DEVIATION BEHIND A FLAPPING FOIL : A SYMMETRY-BREAKING BIFURCATION

Damien Jallas*[1], Olivier Marquet[1], and David Fabre[2]
[1]*ONERA, The French Aerospace Lab, Fundamental and Experimental Aerodynamics Department (DAFE)*
[2]*Université de Toulouse, INPT, UPS - Institut de Mecanique des Fluides de Toulouse (IMFT)*

Summary The mean deviation of the time-periodic wake observed behind flapping foils is investigated with a two-dimensional linear stability analysis. A method preserving the spatio-temporal flow symmetry imposed by the foil motion is specifically developed to determine the non-deviated flow. A Floquet stability analysis of this time-periodic flow then shows the existence of an unstable real Floquet mode for a pitching frequency corresponding to the onset of the mean wake deviation.

INTRODUCTION

At moderate Reynolds numbers, several flow regimes are observed in the wake of flapping foils depending on flapping frequency and amplitude [1]. When increasing one of the parameters, the pattern of the time-periodic wake evolves from the classical Bénard-von Karman vortex street, characteristic of drag regimes, to the reverse Bénard-von Karman vortex street, characteristic of propulsive regimes [2]. For even larger flapping frequencies, a deviation of the vortex street from the streamwise direction, shown in Figure 1(b), has been observed experimentally on pitching foils [3] and captured in two-dimensional simulations of heaving foils [4]. Recently, a linear stability analysis of the time-periodic wake have been performed to investigate the three-dimensional destabilisation of the wake [5]. The objective of the present study is to explain the wake deviation as a two-dimensional instability of the time-periodic wake. Flow configuration and results of unsteady direct simulations are first described. The numerical method, based on a damping of the flow component breaking a spatio-temporal symmetry, is presented and used to obtain the time-periodic non-deviated flow. Its stability is then investigated by performing a Floquet stability analysis.

FLOW CONFIGURATION AND UNSTEADY SIMULATIONS

We investigate the incompressible viscous flow around a foil immersed in a fluid of uniform upstream velocity. The geometry of the foil is a half-cylinder closed by a triangle, as in the experimental investigation [3]. All the variables are made non-dimensional using the diameter and the upstream velocity. The non-dimensional chord is equal to 4.6 and the Reynolds number is fixed to $Re = 255$. The pitching motion imposed at the center of the cylinder is a sinusoidal law characterised by the non-dimensional amplitude $A = 1.07$ and a varying non-dimensional frequency f.
A snapshot of the vorticity for $f = 0.45$ is displayed in Figure 1(b) and shows the deviation of the vortex street from the streamwise direction. At this fixed flapping amplitude, we observed deviation of the wake for flapping frequencies greater than $f_c \sim 0.4$. The critical frequency obtained numerically is larger than the critical frequency $f_c \sim 0.3$ reported in the experimental investigation [3]. We suspect that such a discrepancy is due to confinement effects.

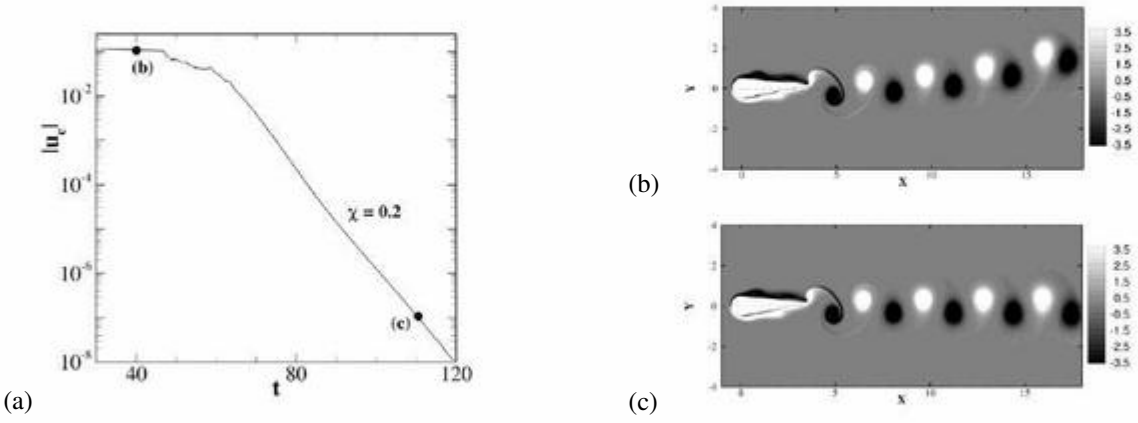

Figure 1: (a) Norm of the complementary part as a function of time at $f = 0.45$. Spatial distribution snapshot of the vorticity behind the pitching foil for different values of the damping coefficient at $f = 0.45$. (b) $\chi = 0$ and (c) $\chi = 0.2$.

*Corresponding author. Email: damien.jallas@onera.fr

FLOW SYMMETRY PRESERVING METHOD

For large flapping frequencies, the time-periodic wake is deviated and the flow breaks the following spatio-temporal symmetry $\omega_z(x, y, t) = \circ\, \omega_z(x, \circ\, y, t + T/2)$ satisfied for small flapping frequencies. The numerical technique developed here preserves the above symmetry by damping the symmetry-breaking component of the flow. The flow field $\boldsymbol{q}$ is decomposed as the sum of the symmetric component $\boldsymbol{q_s}$, which respects the above symmetry condition, and a symmetry-breaking component $\boldsymbol{q_c}$. Introducing such decomposition into the incompressible Navier-Stokes equations and extracting the symmetry and symmetry-breaking terms gives the system of coupled equations

$$\frac{\partial \boldsymbol{q_s}}{\partial t} + \mathcal{R}_s(\boldsymbol{q_s}, \boldsymbol{q_c}) = 0 \qquad\qquad \frac{\partial \boldsymbol{q_c}}{\partial t} + \mathcal{R}_c(\boldsymbol{q_s}, \boldsymbol{q_c}) = \circ\, \chi \mathcal{B} \boldsymbol{q_c}$$

where the original nonlinear operator $\mathcal{R} = \mathcal{R}_s + \mathcal{R}_c$ is decomposed into its symmetry and symmetry-breaking component. The second equation describes the linear dynamics of the symmetry-breaking component q_c around the unsteady symmetric component q_s. The source term $\circ\, \chi \mathcal{B} \boldsymbol{q_c}$ is introduced in this equation to suppress the symmetry-breaking component. An appropriate choice of the damping coefficient χ leads to the stabilisation of the second equation and ensures the suppression of the symmetry-breaking component. When q_c vanishes, the operator $\mathcal{R}_s$ is equal to the operator $\mathcal{R}$ and the solution q_s satisfies the original equation. Figure 1(a) displays the magnitude of the complementary component as a function of time, for the flapping frequency $f = 0.45$ and the damping coefficient $\chi = 0.2$. The method is activated for $t > 45$. The damping of the complementary component is clearly visible and transforms a deviated wake in Figure 1(b) at $t = 40$ into a stabilised wake in Figure 1(c) at $t = 110$.

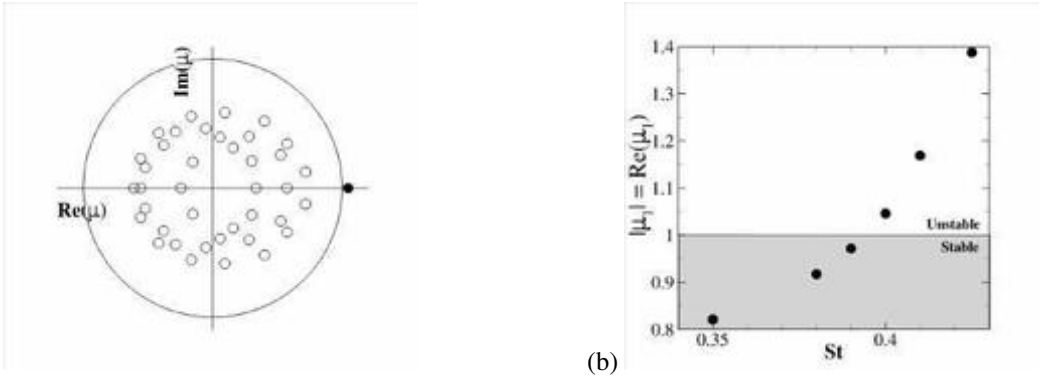

(a) (b)

Figure 2: (a) Spectrum of the Floquet multiplier μ at $f = 0.4$. The leading Floquet mode is $\mu_1 \simeq 1.046$. (b) Leading Floquet multiplier modulus as a function of f.

FLOQUET STABILITY ANALYSIS

The linear stability of the time-periodic flow computed in the previous section is adressed here with a Floquet analysis. Forty Floquet multipliers, corresponding to the growth of Floquet modes over one flapping period, are displayed in Figure 2(a) for the frequency $f = 0.4$. One real Floquet mode (black circle) is outside the unit circle, showing that the time-periodic base flow is unstable and its period is not modified by the instability. The Floquet multiplier of largest magnitude has been determined and is shown in Figure 2(b) for several flapping frequencies. The Floquet mode gets unstable for a critical frequency $0.39 < f_c < 0.4$. It is expected to break the spatio-temporal symmetry of the flow. The analysis of this mode and its time-averaged component is an on-going work necessary to further explain the onset of the wake deviation by a linear symmetry-breaking instability.

References

[1] Jones, K. D., Dohring, C. M., & Platzer, M. F. (1996). Wake structures behind plunging airfoils: a comparison of numerical and experimental results. AIAA paper, 78, 1996.

[2] Alben, S., & Shelley, M. (2005). Coherent locomotion as an attracting state for a free flapping body. Proceedings of the National Academy of Sciences of the United States of America, 102(32), 11163-11166.

[3] Godoy-Diana, R., Aider, J.-L., & Wesfreid, J. E. (2008). Transitions in the wake of a flapping foil. Physical Review E, 77(1), 016308.

[4] Zheng, Z. C., & Wei, Z. (2012). Study of mechanisms and factors that influence the formation of vortical wake of a heaving airfoil. Physics of Fluids (1994-present), 24(10), 103601.

[5] Deng, J., & Caulfield, C. P. (2015). Three-dimensional transition after wake deflection behind a flapping foil. Physical Review E, 91(4), 043017.

LONGITUDINAL VORTICES AND THEIR SECONDARY INSTABILITY ON SWEPT WING

Victor Kozlov[a)] & Stepan Tolkachev
Khristianovich Institute of Theoretical and Applied Mechanics SB RAS Novosibirsk, Russia

Summary In the study, the development of stationary and secondary disturbances excited by cylindrical and two-dimensional roughness elements were investigated using hot-wire anemometry and liquid crystal thermography. A pair of stationary vortices forms behind the cylindrical roughness element and modifies the boundary layer by destabilizing it. The used experimental techniques allowed us to find the area of maximal receptivity to the roughness location away from the attachment line. It was shown, that two-dimensional roughness element has a destabilizing effect on disturbances, induced by cylindrical roughness element. Also the two-dimensional roughness element is able to excite the stationary structures, and then the secondary disturbances, whose frequency range is lower than in the case of stationary vortices excitation by cylindrical roughness element.

It is well known that swept wing boundary layers are subject to the so-called cross-flow instability, which leads to formation of vortices prone to a secondary instability [1]. The aim of this work is to investigate further the role of localized roughness on the process of laminar-turbulent transition on the swept wing under favourable pressure gradient condition. For this purpose hot-wire anemometry was used in combination with liquid crystal thermography.

Experimental conditions

The experiment was carried out in the low-turbulent wind tunnel T–324 in the Institute of Theoretical and Applied Mechanics SB RAS. The cross section of the working area is 1000×1000 mm, its length is 4000 mm. Flow turbulence degree was laess than 0.03%. Free stream velocity varied within the range of a U_∞ = 4.2 – 14.6 m/s and was monitored with the Pitot-Prandtl tube connected to electronic manometer. The swept wing model (Fig.1.) had sweep angle 45°. To prevent separation on the upper side of model angle of attack was set up -16.1°. To exclude a laminar separation on the down side of the model, the flow there was tripped with an array of 15 mm height cones put on the position of airfoil maximal thickness. In the diffuser of wind tunnel, a loudspeaker was mounted for creating acoustic field. For excitation of longitudinal vortices cylindrical roughness elements with diameter 1.6 mm, height 0.4 mm, 0.7 mm and 1 mm were used. Also for this purpose two-dimensional roughness element was used with length 200 mm, width 15 mm and height varied from 0 mm to 1.6 mm.

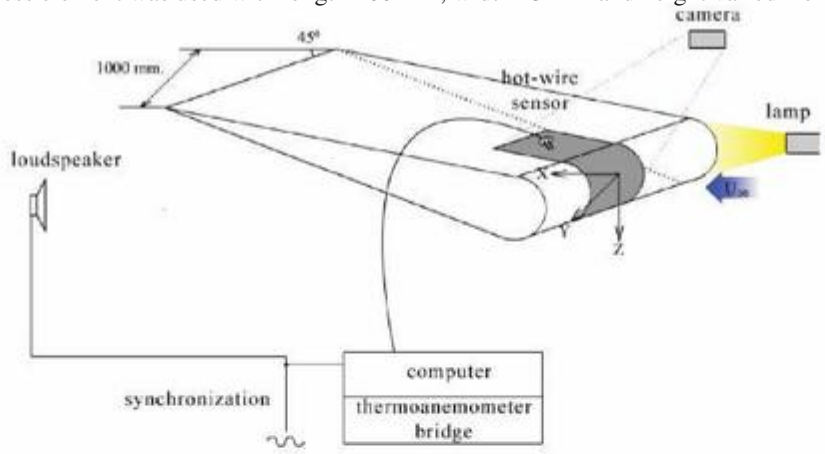

Fig.1. Experimental setup.

Combining of hot-wire anemometry and liquid crystal thermography techniques allowed us to choose the most effective regimes and investigate them quantitatively.

Results

Roughness element located at the leading edge excited a pair of counter rotating vortices, one of which decayed due to the presence of crossflow. The position of maximal cross-flow receptivity to the position of roughness element on the leading edge and it was on 55.1° from the line of airfoil symmetry. Increasing of roughness height or flow velocity are destabilizing factors for the cross-flow instability (Fig.2.). For investigation of secondary disturbances we have chosen the following configuration: roughness element with height 0.8 mm on the position 55.1° from the line of airfoil symmetry.

[a)] V.V. Kozlov. Email: kozlov@itam.nsc.ru.

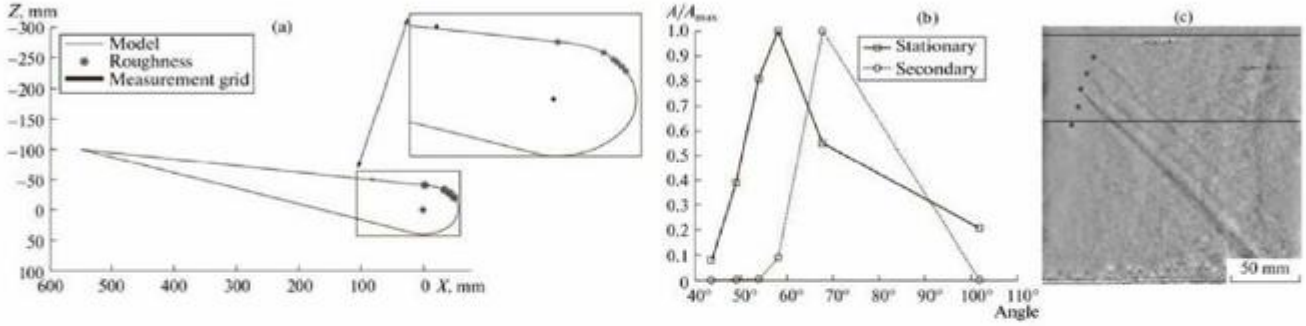

Fig.2. The region of maximum susceptibility to the roughness on the leading edge of an swept wing: the position of roughness elements (a); characteristics of susceptibility for stationary and secondary disturbances (b); and visualization of longitudinal structures behind roughness elements (c).

Two-dimensional roughness element was placed on the flat part of the wing model near the joint of cylindrical to flat part of the airfoil. Starting from 0.91 mm of roughness height it created longitudinal structures with wavelength 4 mm.

In the position of stationary vortex core, high-frequency wavepacket of the secondary disturbances appears. Depending on the flow velocity, different scenarios of secondary disturbance development occur. At small velocity (7.7 m/s) no wavepacket was observed. At moderate velocity (10.4 m/s) the wavepacket appeared and developed through linear stage (amplitude growth without change of spectra shape), nonlinear stage (growth of low frequency part of the spectra) to turbulence. At quite high velocity (13.2 m/s) appearance of super harmonics of wavepacket was observed followed by the grows of frequencies of the rest of the spectra.

Using low-amplitude acoustic field (70 dBA) to excite controlled disturbances, their phase velocity defined in linear regime was $0.55U_\infty$ and sharply increased in the nonlinear regime to $0.63U_\infty$. The position of change of the phase velocity is in a good agreement with a point of deviation of amplitude growing from exponential law.

Experiments with high-amplitude acoustic field (85 dBA) showed appearance of additional longitudinal structures in case of localized roughness element and in case of two-dimensional roughness element.

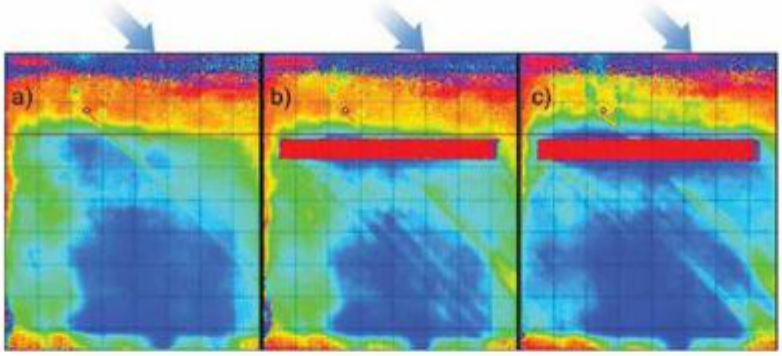

Fig.3. Influence of two-dimensional roughness height h_{2d} on the stationary structure development: а) h_{2d} = 0 mm; б) h_{2d} = 0.91 mm; в) h_{2d} = 1.3 mm.

CONCLUSIONS

This work is a further step to understand process of laminar-turbulent transition on the swept wing. Experimental techniques, used in this work could be used for defining the position of maximal receptivity in respect to the roughness element position.

This work was supported by the project of the President of the Russian Federation for Leading Scientific Schools (NSH-НШ-8788.2016.1), RFBR 15-08-01945 and 16-19-10330.

References

1. Saric, W. S., Reed, H. L. & White, E. B. 2003 Stability and Transition of Three - Dimensional Boundary Layers. // Annu. Rev. Fluid Mech. 35, 413–440.

NONLINEAR TEMPORAL DYNAMICS OF AXISYMMETRIC WAVEPACKETS IN SUBSONIC JETS

Onofrio Semeraro[1], François Lusseyran [*2], Peter Jordan[3], and Luc Pastur[4]

[1]*LadHyX, CNRS – Ecole polytechnique, Palaiseau, France*
[2]*LIMSI, CNRS, Université Paris-Saclay, Orsay, France*
[3]*Institute PPrime, Université de Poitiers, Poitiers, France*
[4]*LIMSI, CNRS, Univ. Paris-Sud, Université Paris-Saclay, Orsay, France*

Summary It is well established that turbulent jets are characterized by large-scale coherent structures. These structures exhibit a remarkable spatio-temporal coherence, despite turbulence. In this work, we analyse from the qualitative point of view the temporal dynamics of axisymmetric, coherent structures educed from experimental, subsonic iso-thermal jets. We use the data presented by Breaky et al. [2], where time-series describing the temporal behaviour of the wavepackets are extracted at different locations along the streamwise direction of the jet. The final goal of the contribution is assessing to what extent non-linear models can reproduce the temporal dynamics of the coherent structures and analysing the resulting dynamics from a qualitative point of view.

INTRODUCTION AND EXPERIMENTAL SETUP

As demonstrated in the experiments by Mollo-Christensen [7] and by Crow & Champagne [3], turbulent jets are characterized by large-coherent structures, exhibiting a remarkable spatio-temporal coherence. These observations have been further corroborated in recent years: indeed, it has been recognized that these structures can be modelled as linear or nonlinear instability wavepackets, obtained as solution of instability analysis based on appropriate steady solutions (for instance, the meanflow of the turbulent jet). The comparison between linear or nonlinear instability wavepackets and the large coherent structures of turbulent jets is typically verified *a-posteriori*, by directly comparing the experimental/numerical results with the stability analysis. A complete account of recent studies is contained in the review by Jordan & Colonius [5].

A last, important aspect is the associated acoustic far-field of these jets: it has been found that the dominating components of the acoustic field are correlated with these low-frequency structures (see, for instance [4]). In this sense, the analogy between the wavepackets in turbulent jets and the instability waves is particularly appealing as it might provide explanations for the basic mechanisms of the sound generation in turbulent jets and - possibly - strategies for the control of the acoustic radiation.

Our contribution enters into this framework as a follow-up of the investigations by Breaky et al. [2]; in [2], the analysis of the sound-field radiating at low-angles is performed by relating the radiation to the near-field pressure fluctuations. The setup of the experiment is shown in Fig. 1a, while a scheme of the ring of microphones used for the investigation is sketched in Fig. 1b. The experiment runs at Mach numbers $Ma = 0.4 - 0.6$. For our investigation, we consider the time-series associated with axisymmetric wavepackets, educed using the azimuthal ring of microphones and post-processed by mean of proper-orthogonal decomposition (POD) analysis. In particular, we study the runs at $Ma = 0.6$ and Reynolds number $Re = 5.7 \times 10^5$, at different locations along the streamwise direction ($0.5 < x/D < 8.9$).

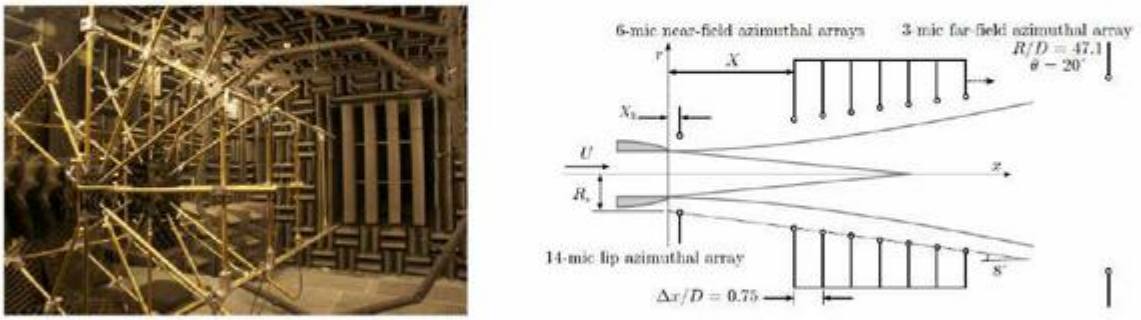

(a) Nozzle and installed ring.

(b) Sketch of the 7-ring near-field array.

Figure 1: Experimental setup for the analysis of turbulent, subsonic jets. Adapted from [2].

*Corresponding author. Email: francois.lusseyran@limsi.fr

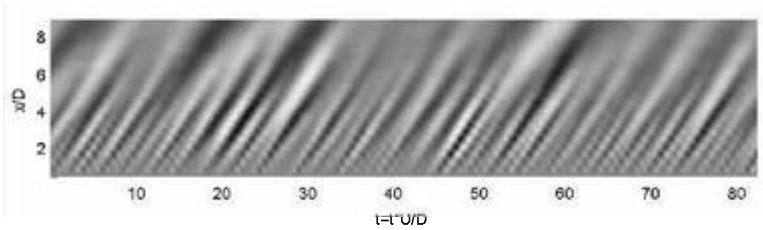

Figure 2: Time-series as a function of time and streamwise locations x/D.

TEMPORAL DYNAMICS: PRELIMINARY RESULTS AND PERSPECTIVES

In Fig. 2, the temporal behaviour associated with the wavepackets is shown as a function of time $t = t*U/D$, adimensionalised with the velocity U and the diameter of the nozzle D, and the streamwise direction. By means of nonlinear dynamical system tools by Kantz and Schreiber (see [6]), the temporal dynamics is characterized by computing the embedding dimension and the correlation dimension d at each position in x/D. A thorough parametric analysis is carried out over several parameters for assessing the convergence of our results; for instance, a minimal time-windows $t \approx 2500$ is identified by studying the convergence of d as a function of time (Fig. $3a$). It is shown that upstream positions are characterized by a more complex dynamics. Despite the dimension d is rather small, the analysis of the qualitative dynamics requires a modelling step for identifying the *essential* dynamics underlying the system. The identification is performed by producing nonlinear polynomial models of the time-series, by mean of the nonlinear auto-regressive-moving-average (N-ARMA) algorithm, see [1]. In Fig. $3b$, the resulting phase-space portrait is shown for a N-ARMA model of the time-series extracted at location $x/D = 5.75$, using delayed temporal-coordinates along y and z.

A qualitative analysis of the attractor will be completed and the control-oriented application of the linear and nonlinear models will be discussed. In particular, the possibility of using linear models for the description of the input-output behaviour of the system will be highlighted.

Acknowledgments The authors wish to acknowledge Luis A. Aguirre for sharing his system identification package and Christophe Letellier for fruitful discussions. This work is supported by the Agence Nationale de la Recherche (ANR) under the "Cool Jazz" project, grant number ANR-12-BS09-0024.

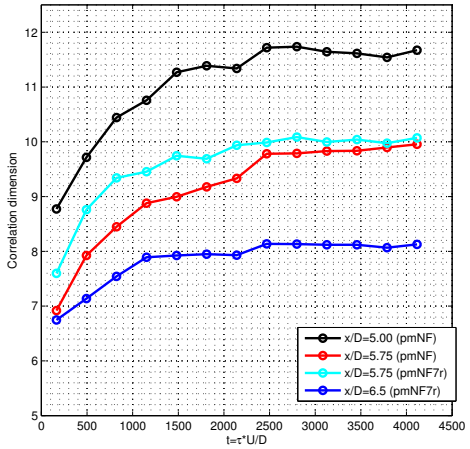

(a) Correlation dimension.

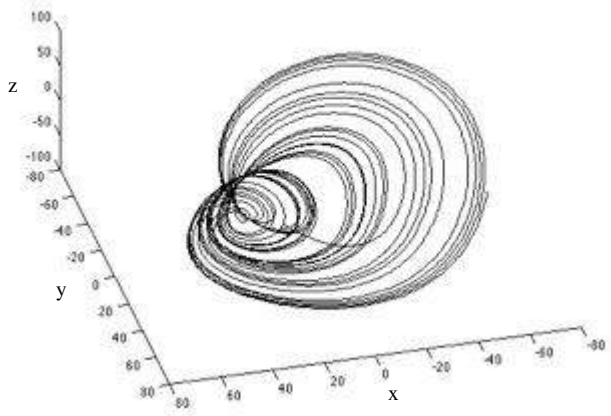

(b) Phase-space portrait in delayed coordinates.

Figure 3: Correlation dimension at 3 different locations, as a function of the time-window of analysis (a), and phase-space portrait of a N-ARMA model based on the measurements at $x/D = 5.75$, (b).

References

[1] Aguirre L. A., Letellier C.: Modeling nonlinear dynamics and chaos: a review, Mathematical Problems in Engineering, 2009.
[2] Breakey D. E. S, Jordan P., Cavalieri A. V. G., Léon O., Zhang M., Lehnasch G., Colonius T., Rodriguez D.: Near-field wavepackets and the far-field sound of a subsonic jet, 19th AIAA/CEAS Aeroacoustics Conference, AIAA Paper, 2013.
[3] Crow S. C., Champagne, F. H.: Orderly structure in jet turbulence, Journal of Fluid Mechanics, 1971.
[4] Freund J. B.: Noise sources in a low-Reynolds-number turbulent jet at Mach 0.9. Journal of Fluid Mechanics, 2001
[5] Jordan P., and Colonius T.: Wave packets and turbulent jet noise, Annual Review of Fluid Mechanics, 2013.
[6] Kantz H. and Schreiber T.: Nonlinear time series analysis, Cambridge university press, 2004.
[7] Mollo-Christensen E.: Measurements of near field pressure of subsonic jets, 1963.

DIRECT NUMERICAL SIMULATION OF THE TURBULENT FLOW INSIDE A SIMPLIFIED STAGE OF HIGH-PRESSURE COMPRESSOR

Romain Oguic[1], Stéphane Viazzo[1], and Sébastien Poncet *[1,2]

[1]*Laboratoire M2P2, Aix-Marseille Université, Marseille, France*
[2]*Mechanical Engineering Department, Université de Sherbrooke, Sherbrooke, Québec, Canada*

Summary The present work reports high-order direct numerical simulations (DNS) of the turbulent flow inside a simplified stage of high-pressure compressor. The geometry corresponds to the experimental set-up of Owen and Pincombe [4] and Farthing et $al.$ [1]. The axial Reynolds number is fixed to $Re = 5300$, while five values of the Rossby number are considered: $Ro = 1, 2, 4, 40$ and $+\infty$. For $Ro = +\infty$, the main flow along the axis is similar to a round jet with packets of helicoidal turbulent structures. A vortex stretching mechanism generates elongated structures in the axial direction. A secondary flow is produced inside the cavity with a main recirculation. For $Ro = 2$ and 1, modes 1b and 2b are obtained respectively, coexisting with type 1 and type 2 instabilities developed along the disks.

INTRODUCTION

The present objective is to investigate by high-order DNS the turbulent flow inside a simplified stage of high-pressure compressor (Fig.1a). Such flows, encountered in various types of gas turbine, are the site of important mechanical and thermal constraints. The compressor is composed of two disks of radius b separated by an interdisk spacing s. Two cylindrical pipes of radius a and length h_1 and h_2 respectively are located from either side of the cavity. The hydrodynamic fields depend on two parameters: the axial Reynolds number $Re = 2aU_b/\nu$, based on the axial velocity U_b imposed at the inlet, and the Rossby number $Ro = U_b/(\Omega a)$, where ν is the kinematic viscosity of the fluid and Ω the rotation rate. The geometrical and physical parameters correspond to those considered experimentally by Owen and Pincombe [4] and Farthing et $al.$ [1]. These authors were the first to characterize by velocity measurements the four flow regimes appearing in such a cavity: Mode 1a is characterized by a non-axisymmetric vortex breakdown (VB) and the appearance of an oscillating jet within the cavity for $20 < Ro < 100$; Mode 2a is characterized by an axisymmetric VB and occasionally, an oscillation of the main flow inside the cavity for $2.6 < Ro \leq 20$; Mode 1b is characterized by a non-axisymmetric VB and a flickering flame effect inside the cavity for $1.5 < Ro \leq 2.6$; Mode 2b is characterized by an axisymmetric VB and occasionally, a re-entry of fluid for $Ro \leq 1.5$. For a detailed state-of-art, the reader can refer to the review of Owen and Long [3].

NUMERICAL METHOD

The Navier-Stokes equations written in primitive variables are discretized in cylindrical coordinates using a second-order semi-implicit temporal scheme. The pressure-velocity coupling is overcame through a projection scheme reducing the equations into a set of Helmholtz and Poisson equations solved by a diagonalization technique. The spatial discretization is achieved by fourth-order compact schemes in the radial and axial directions and Fourier series in the tangential direction. The axis singularity is treated by the method proposed by Sandberg [5] extended to the fourth-order. A multidomain approach based on the continuity influence matrix technique has been coupled with an hybrid MPI/OpenMP parallelization [2].

A turbulent velocity profile calculated in preprocessing is imposed at the inlet, while convective conditions are imposed at the outlet. In the non-rotating (resp. rotating) case, the cavity is decomposed into 4 (resp. 7) subdomains with 7.5 (resp. 13.1) millions of nodes. The time step is fixed to 10^{-3}s ($Ro \geq 40$) and 5×10^{-4}s ($Ro \leq 4$).

RESULTS

The Reynolds number is fixed to $Re = 5300$, while five values of the Rossby number are considered: $Ro = 1, 2, 4, 40$ and $+\infty$. The geometrical parameters are fixed to $G = s/b = 0.533$, $a/b = 0.1$, $h_1/b = 0.5$ and $h_2/b = 0.97$.

In the non-rotating case ($Ro = +\infty$), the main axial flow is strongly influenced by the sudden enlargement due to the cavity. Fluid impinges the second disk, which creates a large recirculation bubble within the cavity, whose center is located at $(z \circ h_1)/s \simeq 0.54$ and $r/b \simeq 0.678$, in good agreement with the experimental value [4, 1]. Smaller recirculations appear also at each corner between the disks and the shroud. The flow generated at the pipe inlet is highly turbulent with some turbulent structures dissipated before the cavity inlet (Fig.1b). Helicoidal turbulent structures are formed around the axis and then advected by the main axial flow. Thinner structures under the form of elongated axial structures produced by

*Corresponding author. Email: sebastien.poncet@USherbrooke.ca

a vortex-stretching phenomenon roll up around them. For $Ro = 40$, the flow structure is very close to the one obtained without rotation. The main difference lies in the high tangential velocity values at $r/b \approx 0.13$ due to the formation of a free vortex. For $Ro \leq 4$, the flow within the cavity is very similar to the flow inside a rotating cavity with a superimposed radial outflow. Two boundary layers, known as Ekman layers, develop on the disks. They are separated by a central inviscid region in quasi solid body rotation. The tangential velocity varies in the radial direction there: the pressure gradient is balanced by the centrifugal force. Figure 1c shows that the mode 1b corresponding to a flickering flame effect is recovered for $Ro = 2$. The fluid enters the cavity because of the oscillating jet and leaves it through a large arm. The oscillating jet presents two characteristic frequencies $(2\pi f)/\Omega$: 2.71 and 7.26. For $Ro = 1$ and 2, two types of Ekman layer instabilities appear along the disks (Fig.1d). Type 2 instabilities, related to the effects of Coriolis and viscous forces, develop, for $0.2 < r/b < 0.5$, as negative counter-rotating spirals. Their angle α varies with r in the range $[-22, -5.5]^\circ$ (resp. $[-14, -5.4]^\circ$) for $Ro = 1$ (resp. 2). The normalized wavelengths λ/δ are equal to 19.04 and 20.02 for $Ro = 1$ and 2 respectively, where $\delta = 0.6\sqrt{\nu/\Omega}$ is the Ekman layer thickness. Type 1 instabilities are observed for $0.1 \leq r/b \leq 0.2$. This inviscid instability appears under the form of positive spirals characterized by a normalized frequency $(2\pi f)/\Omega$ equal to 2 and 6.2 for $Ro = 1$ and 2 respectively.

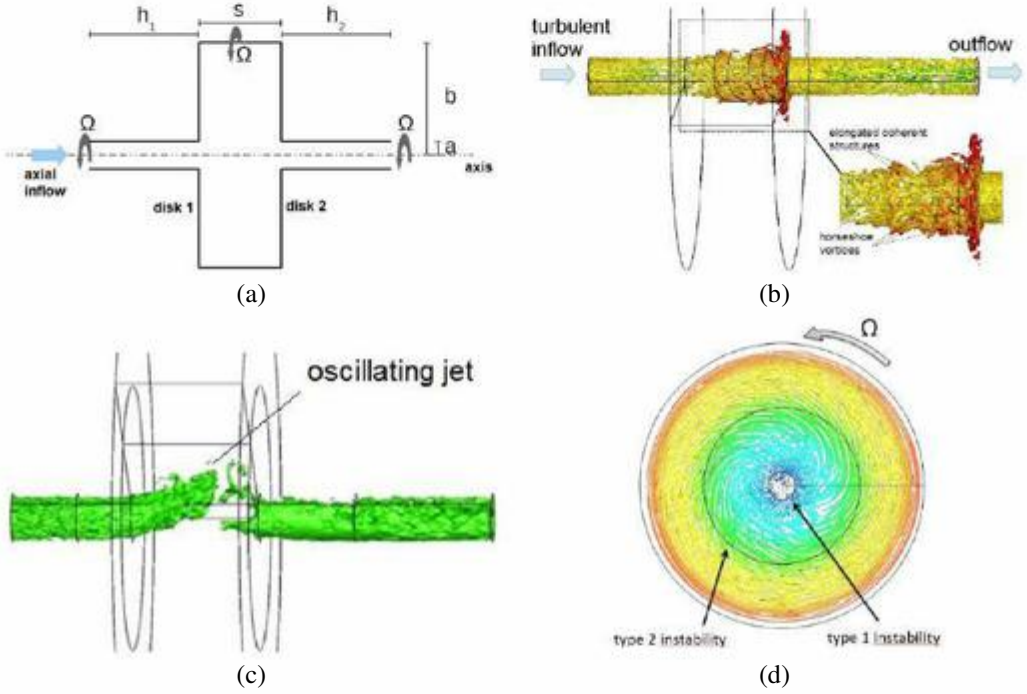

Figure 1: (a) Schematic representation of the system; (b) Isosurfaces $Q = 1$ of the Q-criterion colored by the radius r for $Ro = +\infty$; (c) Isovalues of $\overline{u_z}/U_b = 1$ for $Ro = 2$; (d) Isovalues $Q = 0.01$ of the Q-criterion colored by r for $Ro = 1$.

CONCLUSIONS

High-order DNS have been performed in a simplified stage of high-pressure compressor corresponding to the experiments of Owen and Pincombe [4] and Farthing et $al.$ [1]. The axial Reynolds number has been fixed to $Re = 5300$ and five values of the Rossby number have been considered: $Ro = 1, 2, 4, 40$ and $+\infty$. For $Ro = +\infty$, the main flow close to the axis is similar to a round jet with packets of helicoidal turbulent structures. This axial flow produces also a secondary flow inside the cavity with a main recirculation. For $Ro = 1$ and 2, modes 1b (oscillating jet) and 2b have been obtained respectively. Both coexist with spiral patterns developed in the disk boundary layers under the form of type 1 and type 2 instabilities.

References

[1] Farthing P.R., Long C.A., Owen J.M., Pincombe J.R.: Rotating cavity with axial throughflow of cooling air: Flow structure. J. Turbomach. 114:237-246, 1992.
[2] Oguic R., Viazzo S., Poncet S.: A parallelized multidomain compact solver for incompressible turbulent flows in cylindrical geometries. J. Comp. Phys. 300:710-731, 2015.
[3] Owen J.M., Long C.A.: Review of Buoyancy-Induced Flow in Rotating Cavities. J. Turbomach. 137(11): 111001, 2015.
[4] Owen J.M., Pincombe J.R.: Vortex breakdown in a rotating cylindrical cavity. J. Fluid Mech. 90:109-127, 1979.
[5] Sandberg R.D.: An axis treatment for flow equations in cylindrical coordinates based on parity conditions. Comput. Fluids 49:166-172, 2011.

Large-scale flow modes in turbulent Rayleigh-Bénard convection

Robert Kaiser* and Ronald du Puits
Institute of Thermodynamics and Fluid Mechanics, Technische Universitaet Ilmenau, Ilmenau, Germany

Summary The modes of the global flow structure in turbulent Rayleigh-Bénard convection in air ($Pr = 0.7$) at various aspect ratios between $1 \leq \Gamma \leq 4$ were studied experimentally. By the use of an infrared camera, high resolution distributions of the local wall heat flux at the surface of the heated bottom plate were measured. The data reveals a spot of enhanced heat flux, which is correlated to the down-welling motion of the fluid. Based on this, the position of the large-scale vortex can be identified. Varying the height of the fluid layer, a critical aspect ratios of $\Gamma_{crit} = 1.65$ was found for the transition from a single vortex to a double vortex structure, which agrees very well with previous experimental and numerical investigations if one takes into account a Rayleigh number dependency of that quantity.

INTRODUCTION

A model experiment to study thermally driven flows in nature and technology is the Rayleigh-Bénard set-up. In this canonical flow, a horizontally infinite fluid layer is heated from below at a constant temperature T_h and cooled from above at a constant temperature T_c under the gravitional acceleration of the Earth g. The entire set-up is fully described by three dimensionless input parameters. The Rayleigh number Ra characterizes the thermal driving force $Ra = \beta g H^3 (T_h \circ T_c)/(a\nu)$ with β as the thermal expansion coefficient. The Prandtl number Pr is defined as the ratio of the momentum diffusivity ν and the thermal diffusivity a. The third parameter, the aspecto ratio Γ, emerge from the vertical confinement in experiments and describes the geometry of the convection cell as the ratio of the horizontal dimension D compared to the vertical dimension H. The main interest is the convective heat flux $\dot{q}_c$ from the bottom to the top plate expressed as the Nusselt number $Nu = \dot{q}_c H/(\kappa(T_h \circ T_c))$, which is defined as the ratio of the convective heat flux compared to pure heat conduction through the fluid layer. Here, κ is the thermal conductivity of the fluid layer.
In the last three decades, a lot of experimental apparatuses were built up to scan systematically the $Ra \circ Pr$ parmeter space with respect to Nusselt scaling $Nu \approx Ra^{\gamma_1} Pr^{\gamma_2}$ [2]. At the same time, several theories were evolved to predict the convective heat flux by an estimation of γ_1 and γ_2 [5]. While the measurements were conducted in convection cells with aspect ratios equal or smaller than one, the theoretical predections are derived for $\Gamma \to \infty$. Therefore we performed measurements of the convective heat flux locally on the heating plate at various apect ratios between $1.1 \leq \Gamma \leq 4$ by keeping the Rayleigh number virtually constant $4 \cdot 10^{10} \leq Ra \leq 4 \cdot 10^{11}$. In order to understand the aspect ratio dependency, local measurements of the wall heat flux has been conducted with highly spatial resolution using infrared thermography.

EXPERIMENTAL FACILITY AND MEASUREMENT TECHNIQUE

The measurements were performed in the large-scale convection facility called the Barrel of Ilmenau. Inside this upright cylinder, air at ambient pressure ($Pr = 0.7$) is confined between two horizontal plates with a diameter of $D = 7.15$ m. The vertical distance of the plates can be continuously changed from $H = 0.15$ m to $H = 6.30$ m, while the temperature difference can be set up to 60 K. Based on this boundary conditions, a Rayleigh number variation from $Ra = 10^8$ to $Ra = 10^{12}$ is achievable. For detailed information of the convection cell, we refer to [6].
The processes of the heat transport is investigated in the vicinity of the heating plate using an infrared camera, see figure **??**. Therefore, a thin layer of well-known heat conductivity, commonly called slab, is coated on the surface of the temperature regulated bottom plate [3]. While the temperature of the lower surface of the slab is maintained at the heating plate temperature, the free surface is cooled by the near wall flow phenomena which is observed with a high resolution infrared camera (640x480 pxs^2). All measurement runs were performed for 5h with a sampling rate ig 1Hz. Based on this measurement technique, the two-dimensional wall heat flux is calculated with highly spatial and temporal resolution and the global heat flux can be investigated as the sum of all underlaying local transport processes near the heating plate [7].

RESULTS

First of all, the measurement results show that the local wall heat flux is distributed strongly inhomogeneous on the heating plate, whereas a variation of up to 30% of the spatial and temporal average is observable, see figure **??**. Based on previous investigations combining infrared thermography and planar PIV in a slender rectangular convection cell [7, 8], the near wall flow field along one large-scale vortex could be divided into three characteristics flows: the impinging jet (down-welling fluid), the plate parallel shear flow (central region) and the boundary layer deflection (up-welling fluid). Especially the impingement

*Corresponding author. Email: robert.kaiser@tu-ilmenau.de

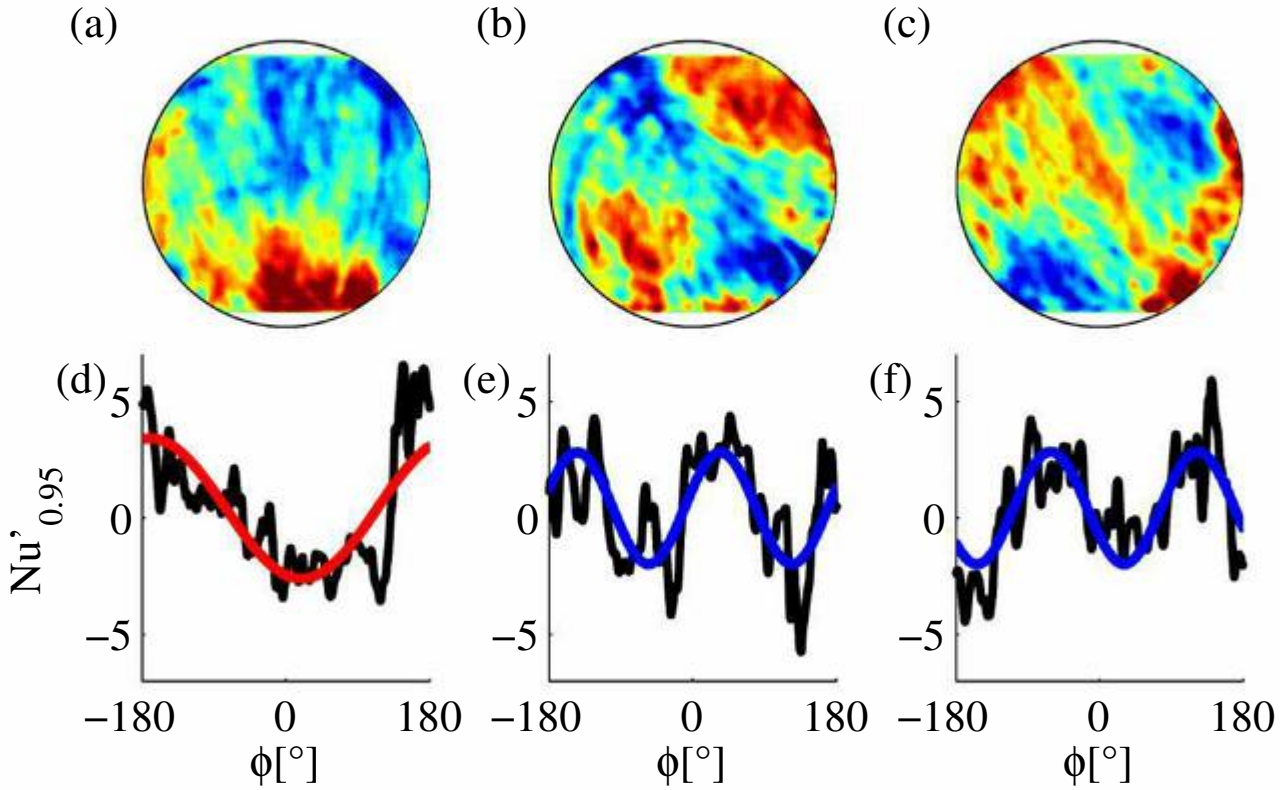

Figure 1: (a)-(c) instanteneous distribution of the fluctuation of the local wall heat flux $Nu' = Nu - \langle Nu \rangle_t$ on the heating plate at $Ra = 4 \cdot 10^{10}$ and .75. (d)-(f) corresponding azimutal profile of Nu' in a distance from the center of the heating plate of $r = 0.95R$, whereas $R = D/2$.

on the heating plate of the down-welling fluid causes a spot of enhanced heat flux and the position of the large-scale vortex can be identified. Based on the time resolved data set for $1 \leq \Gamma \leq 4$, the transitional behaviour of the modes of the global flow structure is investigated by the calculation of the averaged life-time of either one large-scale vortex or two smaller vortices. The critical aspect ratio is given by the equal probability of both structures and appears at $\Gamma_{crit} = 1.65$. This result is in good agreement with a previous estimation by du Puits et al. [1]. They measured the profiles of the horiztonal velocity components inside the boundary layer near the cooling plate and observed a velocity reduction of 20% between $1.47 < \Gamma < 1.89$. By linear interpolation of the averaged horiztonal velocity, a critical aspect ratio of $\Gamma_{crit} = 1.68$ was estimated. Furthmore, Bailon-Cuba et al. [4] performed serveral direct numerical simulations at moderate Rayleigh numbers and various aspect ratios. Using the global Nusselt number $Nu(\Gamma)$, critical aspect ratios of $\Gamma_{crit} = 2.5$ at $Ra = 10^7$ and $\Gamma_{crit} = 2.25$ at $Ra = 10^8$ were calculated. If a Rayleigh number dependency is considered, all experimental and numerical results are in very good agreement.

References

[1] du Puits, R., Resagk, C., Thess, A.: Breakdown of wind in turbulent thermal convection. Phy. Rev. E: 75, 016302, 2007.

[2] Ahlers, G., Grossmann S., Lohse, D.: Heat transfer and large scale dynamics in turbulent Rayleigh-Bénard convection. Rev. Mod. Phys.: 81:2, 2008.

[3] Carlomagno, G.M., Cardone, G.: Infrared thermography for convective heat transfer measurements Exp. Fluids: 49:11871218, 2010.

[4] Bailon-Cuba, J., Schumacher, J.: Aspect ratio dependence of heat transfer and large-scale flow in turbulent convection, J. Fluid Mech.: 655, 152173, 2010.

[5] Chillá, F., Schumacher, J.: New perspectives in turbulent Rayleigh-Bénard convection. Eruo. Phys. J. E: 35:58, 2012.

[6] du Puits, R., Resagk, C., Thess, A.: Thermal boundary layers in turbulent Rayleigh-Bnard convection at aspect ratios between 1 and 9, New J. Phys. 15: 013040, 2013.

[7] Kaiser, R., du Puits, R.: Local wall heat flux in cconfined thermal convection, Int. J. Heat Mas Trans.: 73, 2014.

[8] du Puits, R., Willert C.: The evolution of the boundary layer in turbulent Rayleigh-Bénard convection in air. Phys. Fluids.: Under revision, 2014.

TRANSIENT DYNAMICS AND STABILITY ON SPANWISE-OSCILLATORY TURBULENT CHANNEL

A. Yakeno*[1] and K. Fujii[1, 2]

[1]*Institute of Space and Astronautical Science, Japan Aerospace Exploration Agency, Kanagawa, Japan*
[2]*Department of Management Engineering, Tokyo University of Science, Tokyo, Japan*

Summary We suggested the new prediction parameter for drag reduction effect of the spanwise wall-oscillation control based on both the acceleration and shear rate in the wall-normal direction, which is available for the larger oscillation time-period ($T > 150$). Additionally, we conducted direct stability analysis on spanwise-oscillatory turbulent-channel. The present results suggest that the wall oscillation affects on the transient growth rate, while it does not quantitatively correlate with the control performance. The drag reduction effect of the spanwise wall-oscillation is not dominated only by the linear transient behavior of the streak.

PROBLEM SETTING

Spanwise wall-oscillation control for friction-drag reduction [1] have been discussed about its performance and mechanism for the past few decades. The control achieves a considerable drag reduction rate [2]. It still attracts attention about the drag-reduction mechanism in order to improve the methods. Prediction methods for the drag reduction rate had been suggested [3, 4, 2, 5]. The drag reduction is correlated with a parameter combination of height from the wall, acceleration scale or penetration length scale of the Stokes layer for the cases of high frequency oscillation, which the time period is $T < 150$. However, that is not true for the cases of low frequency oscillation. In the present report, we suggest the new dominant parameter for the drag reduction, basically to use the acceleration and shear rate in both time and wall-normal directions. We calculate the parameter by the theoretical laminar solution of the second Stokes problem [6] (as shown in Fig. 3 (b)) and compare with computation results obtained by previous papers [7, 8].

On the other hand, several trials to make a connection with streak modification to drag reduction have been conducted in these years [9, 10, 11, 12]. The secondary instability of streak is considered to be a significant part to maintain turbulence [13]. Duque-Daza *et al.* (2012) showed that there was a good qualitative correlation between the change in streak growth and drag reduction in streamwise-travelling spanwise oscillatoru channel by solving the initial value problem for linearized Navier-Stokes equations. Hack *et al.* (2015) referred that the flow was stabilized due to the weaker non-modal growth when bypass mechanisms were dominant, although transition could be promoted due to fast growth of the modal instability at large amplitude oscillation. In the present study, we conduct direct stability analysis on spanwise-oscillatory turbulent channel flow as shown in Fig. 1. We include the unsteady turbulence effect on the analysis to discuss the transient dynamics more precisely, which is dominated by the new prediction parameter.

CONTROL PERFORMANCE & NEW PREDICTION METHOD

The bulk mean velocity, U_b, is increased in the spanwise-oscillatory channel under constant pressure gradient, $\partial\bar{p}/\partial x$. The amplitude of the oscillation is W_0 and the time period is T. All variables are normalized by the viscous wall unit in the paper. The increase of U_b is described in Fig. 2 (a) obtained by [7, 8]. There are the optimal oscillation time period around $T = 75$ for each oscillation amplitude W_0. Relationship of the increase, ΔU_b, and the acceleration of the oscillating spanwise shear rate, $\left|\partial^2 \langle w \rangle / \partial y \partial t\right|$, at $y(= y_d) = 13$ as the transient effect is represented in Fig. 2(b), which is described in Eq. (1). This new prediction method is available for the cases of large time period ($T > 150$).

$$\left|\partial^2 \langle w \rangle / \partial y \partial t\right| = 2\sqrt{2}\pi/T \cdot \exp\left(-y_d/\delta\right), \quad \delta = \sqrt{T/\pi} \tag{1}$$

DIRECT STABILITY ANALYSIS ON OSCILLATORY TURBULENT CHANNEL

In the direct stability analysis on the spanwise-oscillatory turbulent channel flow, variables, f_i, are decomposed in the phase-averaged and the perturbation, $\langle f_i \rangle$ and f_i", respectively. The resultant linearlized Navier-Stokes equations and the continuity equation of the perturbation in the oscillatory turbulent-channel are given in Eqs. (2), which includes the total viscosity defined as $\nu_T (= \nu_T^*/\nu^*) = 1 + \nu_t$.

$$\partial u_i" / \partial t + \langle u_j \rangle \partial u"_i / \partial x_j + u"_j \partial \langle u_i \rangle / \partial x_j = -\partial p" / \partial x_i + \partial / \partial x_j (\nu_T \partial u"_i / \partial x_j) \tag{2}$$

*Corresponding author. Email: yakeno@flab.isas.jaxa.jp

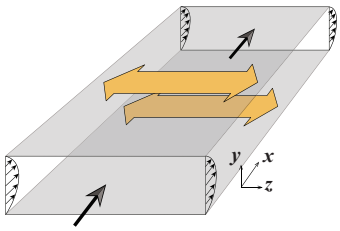

Figure 1: Schematic of the spanwise-oscillatory turbulent-channel.

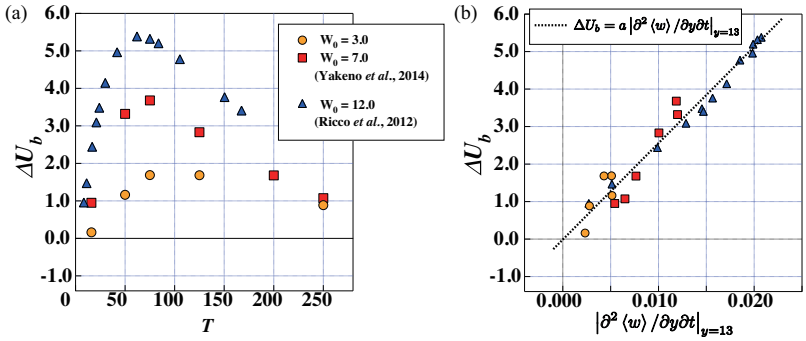

Figure 2: (a) The increase of bulk mean velocities under spanwise oscillation, ΔU_b, those are obtained by [7, 8]. (b) Relationship of ΔU_b and the acceleration effect of the spanwise shear rate, $\left|\partial^2\langle w\rangle/\partial y\partial t\right|$, at $y = 13$.

Since the oscillatory base-flow $\langle u_i\rangle$ is homogeneous in x and z direction, all perturbations are expressed in Fourier space as $f"_i(x, y, z, t) = \hat{f}_i(y, t)e^{i(\alpha x+\beta z)}$. Here, the hat superscript represents the Fourier coefficient, which is time dependent, while α and β denote the streamwise and spanwise wave numbers, respectively. We obtain the maximum transient growth rate G_{rate} of the kinetic energy for each combination of (α, β) and the target time, τ. The computation method is expanded for that of a certain wave number from that of other papers [14, 15]. The program code is validated based on comparison with other papers [16, 17].

We show the oscillatory base-flow in Fig. 3 and G_{rate} in Fig. 4 for the inner optimal mode of turbulent channel, $(\alpha, \beta) = (0, 31.4)$, which scale corresponds to that of streak ($\lambda_z(= 2\pi/\beta) = 100$) at $Re_\tau = 500$. We compare G_{rate} for controlled cases starting from four different phases of oscillation, those time periods are $T = 16, 75$ and 250. At a glance, the change in linear growth in spanwise-oscillatory turbulent-channel does not quantitatively correlate with the control performance. The growth rates with the oscillation of $T = 16$ are mostly affected for any target times than those of other cases (Fig. 4 (a)), although the increase of U_b of that case is not larger than others (Fig. 2). Further discussions will be described in the presentation.

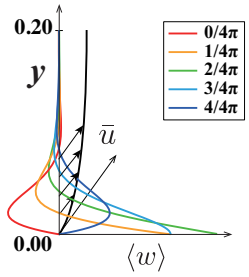

Figure 3: Oscillatory base-flow, $\langle w\rangle$, based on the theoretical solution and $\bar{u}$ ($\approx \langle u\rangle$).

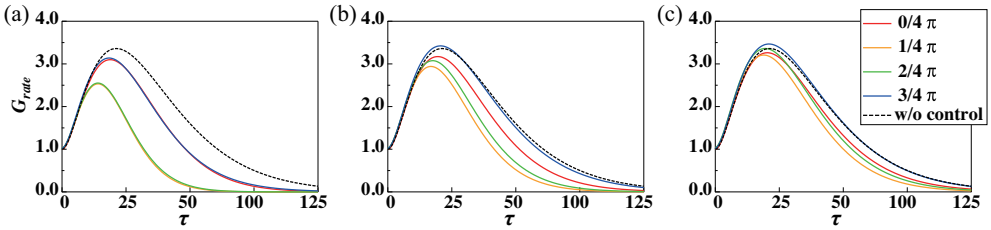

Figure 4: Transient maximum growth rate, G_{rate}, for controlled cases starting from four different phases; oscillation time-period of (a) $T = 16$, (b) 75 and (c) 250.

ACKNOWLEDGEMENT

We acknowledges the support of the Grant-in-Aid for Scientific Research (B) (No. 30634331) by the Ministry of Education, Culture, Sports, Science and Technology (MEXT). We would like to express our sincere gratitude to the late Prof. Nobuhide Kasagi for his supervising to conduct the research. We would also like to appreciate Prof. Tamer Zaki and Prof. Yosuke Hasegawa. Without their guidance and persistent help, the research would not have been possible. We thank them for permission to use the direct stability code developed with their support.

References

[1] W. J. Jung *et al.*. 1992. [2] M. Quadrio and P. Ricco. 2004. [3] M. R. Dhanak and C. Si. 1999. [4] J. I. Choi *et al.*. 2002. [5] A. Cimarelli *et al.*. 2013. [6] H. Schlichting *et al.*. 2000. [7] P. Ricco *et al.*. 2012. [8] A. Yakeno *et al.*. 2014. [9] E. Touber and M. A. Leschziner. 2012. [10] C. A. Duque-Daza *et al.*. 2012. [11] O. Blesbois *et al.*. 2013. [12] M. J. P. Hack and T. A. Zaki. 2015. [13] J. Jiménez and A. Pinelli. 1999. [14] D. Barkley *et al.*. 2008. [15] H. M. Blackburn *et al.*. 2008. [16] K. M. Butler and B. F. Farrell. 1992. [17] G. Pujals *et al.*. 2009.

INITIAL-CONDITION DEPENDENCE OF LARGE-SCALE STRUCTURES IN ROTATING TURBULENCE

Naoto Yokoyama *[1] and Masanori Takaoka[2]

[1]*Department of Aeronautics and Astronautics, Kyoto University, Kyoto, Kyoto, Japan*
[2]*Department of Mechanical Engineering, Doshisha University, Kyotanabe, Kyoto, Japan*

Summary Direct numerical simulations of rotating turbulence driven by an external force are performed. In strongly rotating systems, the flow in the statistically steady state has a coherent cyclonic vortex (a Taylor column), and is two-dimensional and anisotropic. In weakly rotating systems, the flow in the statistically steady state is in the three-dimensional isotropic Kolmogorov turbulence regime. The two-dimensional anisotropic flow and a three-dimensional isotropic Kolmogorov turbulence are bistable at the system's angular velocities in a range. The transitions between the two flow regimes are discontinuous, when the angular velocity is increased or decreased. This hysteretic behavior can be understood by stability of the cyclonic vortex.

INTRODUCTION

In the rotating turbulence, the crossover of two-dimensional (2D) turbulence in strongly rotating systems and three-dimensional (3D) turbulence in weakly rotating systems was numerically observed in Ref. [1]. In the 2D turbulence, the cyclonic vortices emerge more than the anticyclonic vortices, and such asymmetry strongly depends on the external force and the boundary condition (e.g., Ref. [2]). The cyclonic vortices are stable for small perturbation [3]. Initial-condition dependence of formation of the cyclonic vortices was also found in our preliminary simulations. In this work, the transition between the 2D flow and the 3D flow in the statistically steady states is numerically investigated through variation of the angular velocity of the system's rotation.

NUMERICAL RESULTS

The governing equations for the velocity $\boldsymbol{u}$ of the incompressible fluid are the Navier–Stokes equation with the Coriolis term and the divergence-free condition:

$$\frac{\partial}{\partial t}\boldsymbol{u} + (\boldsymbol{u}\cdot\nabla)\boldsymbol{u} + 2\Omega\boldsymbol{e}_z\times\boldsymbol{u} = \circ\,\nabla p + \nu\nabla^2\boldsymbol{u} + \boldsymbol{f}, \qquad \nabla\cdot\boldsymbol{u} = 0, \tag{1}$$

where the rotation axis is taken as the z axis, and the angular velocity of the system's rotation is denoted by Ω. The kinematic viscosity is expressed by ν. The external force $\boldsymbol{f}$ is given by the three-dimensional two-component force of a steady Taylor–Green type $\boldsymbol{f} = f_0(\cos k_\mathrm{f}x \sin k_\mathrm{f}y \sin k_\mathrm{f}z, \sin k_\mathrm{f}x \cos k_\mathrm{f}y \sin k_\mathrm{f}z, 0)$, where $k_\mathrm{f} = 2$. The periodic boundary condition with the period $(2\pi)^3$ is employed, and the standard pseudo-spectral method with the aliasing removal by the phase-shift method and the spherical truncation is used.

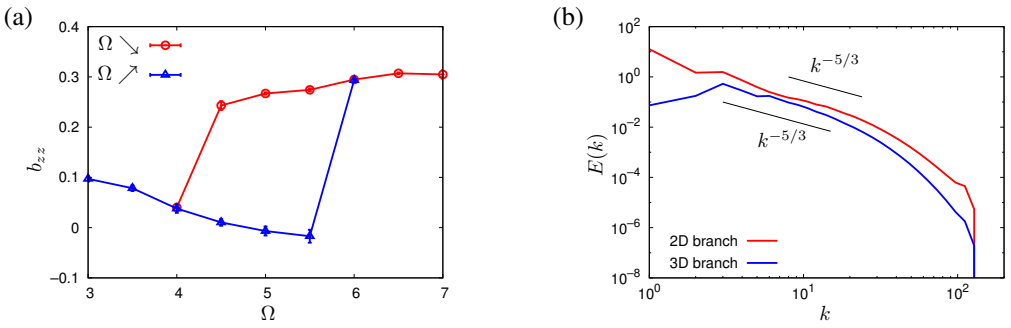

Figure 1: (a): zz component of anisotropy tensor vs. angular velocity. The red curve (Ω ↘) and the blue curve (Ω ↗) respectively show the zz components, when the angular velocity decreases from $\Omega = 7$ and increases from $\Omega = 3$. The error bars represent the standard deviation due to the time variation. (b): energy spectra of the bistable states at $\Omega = 5$.

The zz component of anisotropy tensor $b_{zz} = 1/3 \circ \langle u_z^2\rangle/\langle|\boldsymbol{u}|^2\rangle$ is used to evaluate the anisotropy of the system. (Fig. 1 a) At $\Omega = 3$, $b_{zz} \approx 0.1$, which comes from the anisotropic external force of the Taylor–Green type. When the angular velocity

*Corresponding author. Email: yokoyama@kuaero.kyoto-u.ac.jp

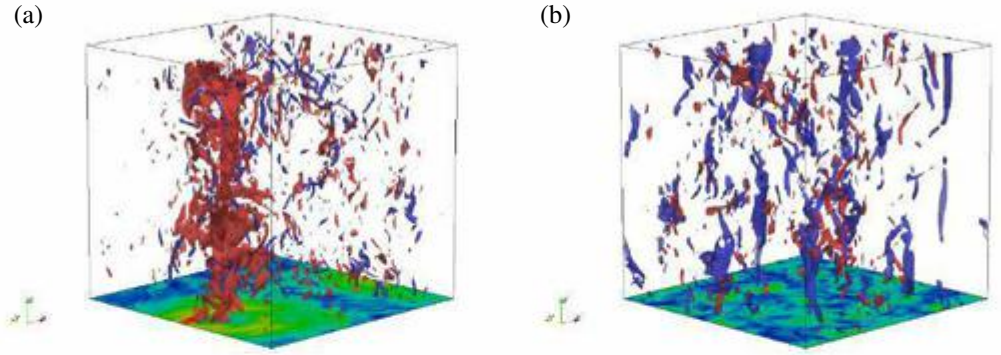

Figure 2: Isosurfaces of $\omega_z = 4\sqrt{\langle\omega_z^2\rangle}$ (red) and $\omega_z = -4\sqrt{\langle\omega_z^2\rangle}$ (blue) for $\Omega = 5$, where the 2D flow and the 3D flow are bistable. (a): 2D flow, and (b): 3D flow. The speed $|\boldsymbol{u}|$ on the $z = 0$ plane is represented by color map.

is increased from $\Omega = 3$, b_{zz} decreases to 0, where the flow is 3D and almost isotropic. It jumps in the range of $5.5 < \Omega < 6$ to 0.3, where the flow is almost 2D and strongly anisotropic. At $\Omega = 7$, $b_{zz} \approx 0.3$ owing to the strong rotation. When the angular velocity is decreased from $\Omega = 7$, b_{zz} slowly decreases. In the range of $4 < \Omega < 4.5$, b_{zz} drops sharply, representing the abrupt transition from the 2D anisotropic flow to the 3D isotropic flow. In the range of $4.5 \lessapprox \Omega \lessapprox 5.5$, the two regimes, the 2D anisotropic flow and the 3D isotropic flow, are bistable. The transitions between the 2D flow and the 3D flow show hysteretic phenomena.

The energy spectra at $\Omega = 5$, where the 2D flow and the 3D flow are bistable, are shown in Fig. 1(b). It is worth noting that in both spectra, the Kolmogorov spectrum, $E(k) \propto k^{-5/3}$, is observed at the large wavenumbers in the inertial subrange.

The difference is significant at the wavenumbers smaller than the forced wavenumber $\sqrt{3}k_{\mathrm{f}} \approx 3$. The accumulation at the small wavenumbers in the 2D flow is caused by the inverse cascade. Once the accumulation is built up, the accumulation acts like the energy source. In the 3D flow, the energy supplied by the external force is almost completely transferred to the large wavenumbers owing to the forward cascade, and the accumulation is weak. The 2D flow has more energy than the 3D flow has all over the wavenumbers. The fact indicates that the hystereses for other quantities all over the wavenumbers similar to the one shown in Fig. 1(a) can be observed.

The accumulation of the energy at $k = 1$ in the 2D flow indicates one large vortex in the periodic box. In fact, the isosurface of z component of vorticity ω_z in the real space shows the cyclonic vortex aligned along the rotation (z) axis, which is a Taylor column, as drawn in Fig. 2(a). The cyclonic vortices make strongly sheared regions between the vortex and its images due to the periodicity, where small-scale 3D structures are produced. The external force of the Taylor–Green type in the present study develops vortices every $2\pi/(2k_{\mathrm{f}})$ length in the horizontal directions in the periodic box. We can observe the 3D vortices due to the external force if the Taylor column is not formed as shown in Fig. 2(b).

At the transition from the 3D flow to the 2D flow, the strong cyclonic vortex is formed over the external force. On the other hand, at the transition from the 2D flow to the 3D flow, the coherent cyclonic vortex collapses into pieces. The creation and annihilation of the coherent cyclonic vortex cannot be continuous for the variation of the system's angular velocity. Therefore, the transitions exhibits the hysteresis. This hysteresis robustly exists, though the fluctuations due to turbulence are large. Similar hysteresis appears also for the variation of the amplitude of the external force.

CONCLUSIONS

Direct numerical simulations of forced rotating turbulence were performed, and the dependence of the statistically steady flow on the initial conditions is investigated. When the angular velocity of the system's rotation is small, the flow regime is in a 3D Kolmogorov turbulence. On the other hand, when the angular velocity is large, the flow in the statistically steady state has a coherent 2D cyclonic vortex. The transitions between the 2D flow and the 3D flow are discontinuous when the angular velocity is increased or decreased. In other words, it exhibits the hysteresis which can be understood by the stability of the coherent cyclonic vortex.

References

[1] Smith L. M., Chasnov J. R., Waleffe F.: Crossover from two- to three-dimensional turbulence. Phys. Rev. Lett., 77:2467–2470, 1996.

[2] Godeferd F. S., Moisy F.: Structure and dynamics of rotating turbulence: A review of recent experimental and numerical results. Appl. Mech. Rev., 67:030802, 2015.

[3] Carnevale G. F., Briscolin M., Kloosterziel R. C., Vallis G. K.: Three-dimensionally perturbed vortex tubes in a rotating flow. J. Fluid Mech., 341:127–163, 1997.

VISCOUS RAYLEIGH-TAYLOR INSTABILITY WITH AND WITHOUT THE DIFFUSION EFFECT

Chenyue Xie[1], Jianjun Tao[1a)] &Jie Li[2]
[1]*CAPT-HEDPS, SKLTCS, Department of Mechanics and Engineering Science, College of Engineering, Peking University, Beijing, 100871 P. R. China*
[2]*Department of Engineering, University of Cambridge, CB2 1PZ, UK*

Summary: The approximate but analytical solution of the viscous Rayleigh-Taylor instability (RTI) has been widely used recently in theoretical and numerical investigations due to its concept clarity. In this letter, a modified analytical solution of the growth rate for the viscous RTI of incompressible fluids is obtained based on an approximate method. It is confirmed numerically that its accuracy is significantly improved in comparison to the previous ones in the whole wave number range for different viscosity ratios and Atwood numbers. Furthermore, this solution is expanded for viscous RTI including the concentration-diffusion effect.

INTRODUCTION

The linear Rayleigh-Taylor instability (RTI) of viscous fluids was first studied by Harrison [1], and its implicit dispersion relation was simplified by Bellman and Pennington [2] to obtain an approximate but analytical solution of the linear growth rate, where the viscous effect is shown explicitly. Later on, this solution was expanded to include the concentration diffusion [3]. It should be noted that clear discrepancies between the molecular dynamics simulations and the linear theory for different viscosities were observed both at the low wave number region [4] and at high wave numbers [5], and hence the dispersion relation hasn't been verified completely. In addition, the approximate solutions were found to deviate from the exact values with a maximum error about 12% [6]. However, due to their clarity and ease of use, the approximate solutions have been used recently in numerical and theoretical studies of the late-time growth of a single mode, the accel-decel-accel profile, multiphase flow, and the Knudsen-number dependence [7-10]. The main motivation of this paper is to propose a new explicit solution of the implicit dispersion relation with better accuracy and verify it for fluids with different viscosities in the whole wave number range.

THEORETICAL AND NUMERICAL RESULTS

The implicit dispersion relation for two-dimensional incompressible and viscous RTI is as follows,

$$[g(\rho_2-\rho_1)k+(\rho_1+\rho_2)n^2]M+4nk=0, \tag{1}$$

$$M=\frac{1}{\mu_1 k+(\mu_2^2k^2+\rho_2 n\mu_2)^{1/2}}+\frac{1}{\mu_2 k+(\mu_1^2k^2+\rho_1 n\mu_1)^{1/2}}$$

where ρ, μ, g, k and n are the fluid density, the dynamic viscosity, the absolute value of gravity, the wave number and the linear growth rate of normal mode, respectively. The subscript 1 and 2 correspond to the light and the heavy fluids, respectively. $A=(\rho_2-\rho_1)/(\rho_2+\rho_1)$ is the Atwood number. By assuming $\rho_1 n<<\mu_1 k^2$, $\rho_2 n<<\mu_2 k^2$, Bellman and Pennington [2] simplified the above equation to an explicit manner and obtained its analytical solution N (an approximate value of n),

$$N=\sqrt{gkA+\nu^2k^4}-\nu k^2, \tag{2}$$

where $\nu=(\mu_1+\mu_2)/(\rho_1+\rho_2)$. However, this simplification leads to a maximum error of 12% [8].

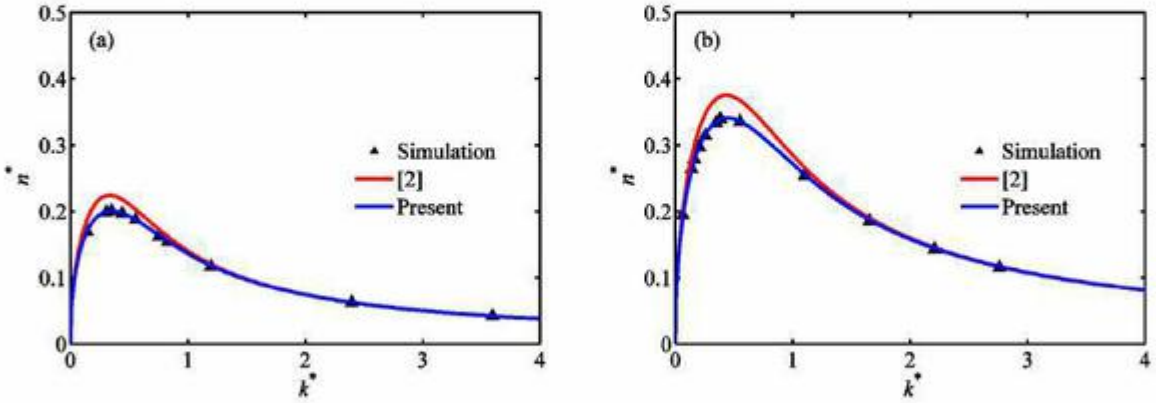

Fig.1 The dimensionless growth rate n^*as a function of the dimensionless wave number k^*: (a) $\nu_1/\nu_2=0.5, A=0.3$; (b) $\nu_1/\nu_2=10, A=0.65$.

[a)]Corresponding author. Email: jjtao@pku.edu.cn.

In order to improve the accuracy of this solution, the contribution of n to M is not ignored completely but estimated by replacing n with N. Consequently, we get

$$[g(\rho_2 - \rho_1)k + (\rho_1 + \rho_2)n^2]M_1 + 4nk = 0 \tag{3}$$

$$M_1 = \frac{1}{\mu_1 k + (\mu_2^2 k^2 + \rho_2 N \mu_2)^{1/2}} + \frac{1}{\mu_2 k + (\mu_1^2 k^2 + \rho_1 N \mu_1)^{1/2}}.$$

The analytical positive root of this explicit equation is:

$$n = \sqrt{gkA + Q^2} - Q, \quad Q = 2k/(\rho_1 + \rho_2)M_1 \tag{4}$$

The two-dimensional, incompressible N-S equations are solved by a projection method in Cartesian coordinates to examine this new solution. VOF method and the multi-grid method are used to track the interface and solve the pressure Poisson equation, respectively. Parameters are dimensionalized by the character length and time scales $(\nu^2/g)^{1/3}$and $(\nu/g^2)^{1/3}$, respectively. The aspect ratio of the computational domain is 1:4, and the uniform mesh 1024x4096 is found to be fine enough to calculate the initial growth stage of a one-wavelength cosine interface perturbation.

In Fig.1 the approximate solutions are compared with the numerical simulations (triangle). It is illustrated that at different viscosity ratios and Atwood numbers, Eq.(2) has a maximum error (about 12%) near the maximum growth rate, while the present analytical solutions (Eq.4) consistent with the numerical simulations very well in the whole wave number range with a relative error less than 1%. In addition, it is the first time to our knowledge that the dispersion relation of RTI for fluids with different viscosities is verified successfully.

When the concentration-diffusion effect is included, Duff *et al.* [3] developed an approximate theory based on Eq.(2) by assuming that $v\epsilon$ was so small to be neglected and then the viscous and the diffusive effects were independent, where $\epsilon = 2(Dt)^{1/2}$, a length scale at the diffusivity D and the elapsed time t. The diffusion effect includes two parts: the dynamic diffusion effect-broadening the density transition zone between the fluids, decreasing the effective Atwood number, and then reducing the linear growth rate; the static diffusion effect – reducing the amplitude of the mean density perturbation. Based on the above ideas, Duff *et al.* derived the following approximate growth rate:

$$n = \sqrt{gkA/\psi + \nu^2 k^4} - (\nu + D)k^2, a = 1/k\epsilon, \tag{5}$$

where ψ is a function of a and A. Obviously, this solution inherits the maximum error (about 12%) from Bellman's solution N (Eq.2). Therefore, it is convenient to improve its accuracy by replacing the contribution of the viscous part with the proposed solution as follows:

$$n = \sqrt{gkA/\psi(a, A) + Q^2} - (Q + Dk^2),\ a = 1/k\epsilon,\ \epsilon = 2(Dt)^{1/2}. \tag{6}$$

It can be seen from Eq.(5) and (6) that both the momentum diffusion (viscosity) and the concentration diffusion tend to stabilize RTI. The coupled N-S equation and the concentration equation are solved numerically as well at different Prandtl numbers, and it is confirmed that the growth rates predicted by Eq.(6) agree with the simulation results better than those of Eq.(5).

CONCLUSIONS

The implicit dispersion relation of viscous RTI is solved by an approximate method to obtain an analytical solution of the growth rate, which is at least one order of magnitude more accurate than the Bellman solution. According to the numerical simulations, the maximum relative error is reduced from 12% to less than 1%. In addition, this solution is extended successfully to include the concentration-diffusion effect. Because of its explicit manner and ease of use, these solutions are expected to be used to validate numerical schemes and to include more effects, e.g. the electromagnetic effect and the thermal diffusion.

References

[1] Harrison W.J.: The influence of viscosity on the oscillations of superposed fluids.*Proc. London. Math.Soc***6**:396-405, 1908.

[2] Bellman R., Pennington R. H.: Effects of surface tension and viscosity on Taylor instability. *Q. Appl. Math***12**:151-162, 1954.

[3] Duff R. E., Harlow F. H. & Hirt C.W.: Effects of Diffusion on Interface Instability between Gases.*Phys. Fluids***5**:417-425, 1962.

[4] Kadau K., Germann T. C., Hadjiconstantinou N. G., Lomdahl P.S., Dimonte G.,Holian B.L. & Alder B.J.: Nanohydrodynamics simulations: An atomistic viewof the Rayleigh–Taylor instability. *Proc. Nat. Acad. Sci***101**: 5851-5855,2004.

[5] Barber J. L., Kadau K., Germann T. C. & Alder B. J.:Initial growth of the Rayleigh-Taylor instability via moleculardynamics.*Eur. Phys.J. B***64**:271-276,2008.

[6] Mikaelian K.O.: Effect of viscosity on Rayleigh-Taylor and Richtmyer-Meshkov instabilities. *Phys. Rev. E* **47**: 375-383,1993.

[7] Wei T., Livescu D.: Late-time quadratic growth in single-mode Rayleigh-Taylor instability.*Phys. Rev. E***86**:046405, 2012.

[8] Ramaprabhu P., Karkhanis V.&LawrieA. G. W.: The Rayleigh-Taylor Instability driven by an accel-decel-accel profile. *Phys.Fluids***25**:115104, 2013.

[9] Liang H., Shi B. C., Guo Z. L. & Chai Z. H.:Phase-field-based multiple-relaxation-time lattice Boltzmannmodel for incompressible multiphase flows.*Phys. Rev. E***89**:053320, 2014.

[10] Sagert I., Howell J., Staber A., Strother T., Colbry D.&Bauer W.: Knudsen-number dependence of two-dimensional single-mode Rayleigh-Taylor fluid instabilities.*Phys. Rev. E***92**:013009, 2015.

BOUNDARY LAYER RECEPTIVITY TO TRANSIENT PLASMA IN M=4.5 AIRFLOW

Alec Houpt, Stanislav Gordeyev, Thomas Juliano & Sergey Leonov [a)]
FlowPAC Institute, AME Dept, University of Notre Dame, Notre Dame, IN, 46556, USA

Summary: This work is focused on experimental studies of promoting flow instability with a weakly ionized transient plasma in the corner separation zone of a compression surface within a hypersonic boundary layer. Optical measurements have been successfully performed using a high-speed Shack-Hartmann sensor to quantify a characteristic frequency of flow perturbations at different locations in the flowfield and the plasma impact on the spectrum of disturbances in the boundary layer and in the separation bubble. It was shown that the near-surface plasma, generated at a frequency of repetition higher than a dominant natural frequency of perturbations in the boundary layer (the first mode F_1), $f = 100\ kHz > F_1 \approx 65\ kHz$, lead to a significant intensification of the amplitude of the high-frequency disturbances in the range of $A / A_0 = 2 - 8$. The plasma effect was negligible or insignificant at excitation frequencies below F_1.

INTRODUCTION

The need for tripping of a hypersonic boundary layer is motivated by the control of flow instabilities and, consequently, a steering of processes of laminar-turbulent transition and separation [1-2]. Particularly, for airframe-integrated scramjet engines, the forebody ahead of the inlet is designed to process and pre-condition the flow that will be ingested by the air inlet. Turbulent flow is desirable at the entrance to the inlet to mitigate flow separations on compression ramps and prevent air inlet unstarts. This issue stimulates development of various boundary layer tripping methods to promote turbulent flow in order to properly scale the engine flight test results to future full-scale vehicles. It is suggested that the most effective tripping mechanism requires the formation of streamwise vorticity within the boundary layer [3-4]. Typically obstacles, moving elements, or non-steady gas jets are used to promote transition on the forebody. Recently, a thermal type of BL management was considered to be feasible [5].

The intense, localized, rapid heating produced by plasmas in pulsed electric discharges produce strong shock waves which can considerably modify supersonic flows over blunt bodies. The energy transfer from the electric field to the electrons is almost instantaneous while the transfer of energy from the electrons to the gas molecules goes through a series of processes: vibrational excitation, dissociation, and ionization followed by relaxation. Basically, rapid near-adiabatic heating results in an abrupt pressure jump in the current filament. This suggests that rapidly heated regions located near aerodynamic surfaces could be used to force various instabilities in shear layers and jets. The key benefit of localized plasma actuators, compared to mechanical and acoustic actuators, is that they uniquely combine a wide range of operation frequencies with large forcing amplitude [6-8]. Multiple plasma actuators can be independently controlled by varying the repetition rate, duty cycle, and the phase, making it possible to trigger and amplify specific flow instabilities. As a result, significant flow field changes can be produced at a relatively small energy cost to operate plasma actuators.

The objective of this work is to perform a feasibility study on the steering effect of a weakly ionized transient plasma on the corner separation zone of a compression surface with a hypersonic boundary layer. Specific tasks of current experiments included: (1) - experimental study of the dynamics of the gas pressure/density disturbances realized in the zone of flow separation with upstream generation of transient plasma; (2) - experimental demonstration of the BL receptivity to plasma-based gas perturbations in supersonic/hypersonic flow.

TEST DESCRIPTION

The diagram of the test arrangement is shown in Fig. 1a. The experiments were performed in the high-enthalpy ACT-1 facility at the University of Notre Dame under the following test parameters: Mach number $M = 4.5$ (at nozzle exit); Reynolds number $Re_L = 10^7 (\text{m}^{-1})$; stagnation pressure $P_0 = 0.8$ Bar; stagnation temperature $T_0 = 300\ K$ and $1800\ K$; flow enthalpy from $h \cdot \dot{m} \approx 10\ kW$ (cold flow) to $50\ kW$ (hot flow). The model has length $L = 229\ mm$, width $W = 102\ mm$, and thickness $H = 19\ mm$. It consists of a base plate with a sharp leading edge with $\alpha = 15°$. The compression ramp is formed with a second plate of equal thickness and a ramp angle $\alpha = 20°$. The test duration was $t < 1\ s$ including the arc operation (in the hot regime) for $0.3\ s$ and the plasma operation for $0.1\ s$ within the flow. A photograph of the experimental model is shown in Fig. 1b. The model was equipped with a ceramic insertion where multiple plasma generators, using the Shallow Cavity Discharge design [9] and working at frequencies $f = 50\ kHz$ and $100\ kHz$, Fig.1c, were arranged in the spanwise-direction upstream of the ramp. Instrumentation and data acquisition included: flow perturbation measurements made by a high-speed wavefront sensor; schlieren visualization; fast cam imaging; and electrical measurements of the discharge parameters. Aero-optical measurements were performed using a high-speed Shack-Hartmann Wavefront Sensor [10]. The laser beam was expanded to a $50\ mm$ diameter collimated beam and passed along the spanwise direction over the corner region of the model in the test section. After exiting the test section, the beam is reflected off the return mirror, which sends the beam along exactly the same path from which it came. The returning beam is split off using a cube beam splitter, sent though a contracting telescope which reduces the beam size to $12\ mm$ in diameter and goes into a high-speed Phantom v1610 digital camera. The camera had a 70×60 lenslet, $0.3\ mm$ pitch array attached to it. After passing through

[a)] Corresponding author. Email: leonov.1@nd.edu

the lenslet array, the beam was split into subaperture beams and focused on the camera sensor, creating a series of dots. To achieve the high sampling rate, only a small, 128×64-pixel portion of the image was sampled at $531{,}645\ Hz$ for 4 seconds. This image size corresponds to a $15 \times 7\ mm$ measurement region over the model, with $1.2\ mm$ spacing between dots.

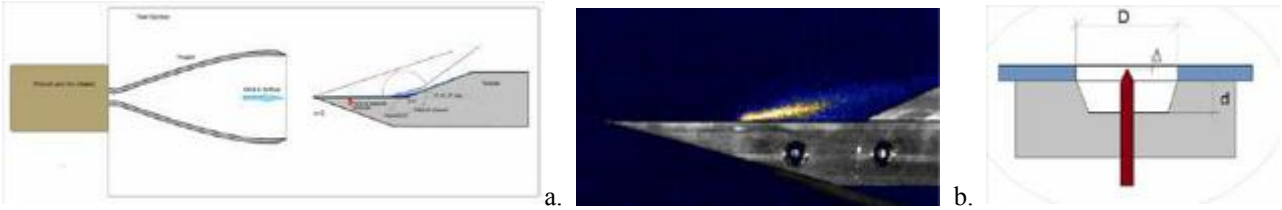

a. b. c.

Fig. 1. Experimental arrangement: a – test layout; b - photograph of the model with plasma generator in $M = 4.5$ flow; c - principal schematic of plasma BL actuator based on Shallow Cavity Discharge [9].

TEST RESULTS

After a series of measurements it was found that the plasma generation affects the spectrum of the flow perturbations only slightly if the repetition frequency is less than the dominant frequency of the first-mode instability, $F_1 = 60 - 80\ kHz$. For a plasma frequency greater than F_1, the plasma effect is significant. Figures 2a and 2b show data for plasma actuation frequencies of 50 and $100\ kHz$, respectively. Every test included $0.1\ s$ of spectrum analysis prior to plasma actuation, $0.1\ s$ with plasma operation, and $0.1\ s$ after the plasma has turned off (to ensure there was no shift of flow parameters during operation).

At $f = 50\ kHz$, the plasma effect is really small in most areas (Fig. 2a). Some effect is visible in the shear layer, point A3. Amplitudes of high-frequency disturbances ($> 80\ kHz$) appear to increase. At the plasma repetition frequency $f = 100\ kHz$ (Fig. 2b), the plasma effects were observed at all points except A4 located above the corner separation zone. Amongst the points observed in this test the maximal effect of the plasma was detected for the flowfield zone close to a root part of the ramp-related shock. It results in an amplification of the amplitude of gas perturbations, $A/A_0 = 2 - 8$, in a wide range of spectra including high-frequency oscillations $f > 100\ kHz$.

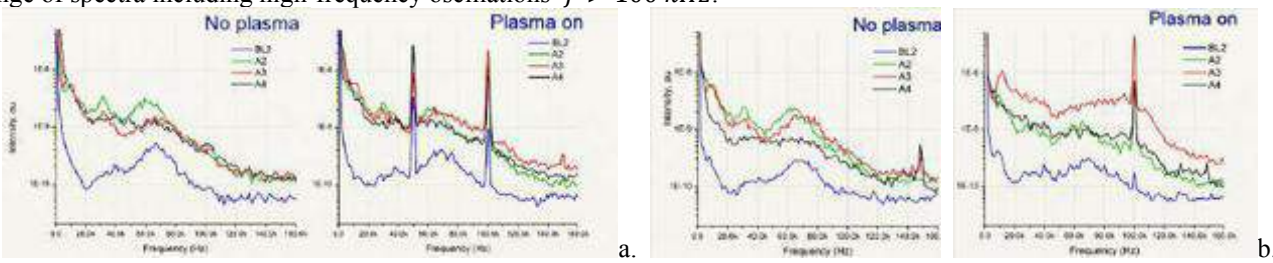

a. b.

Fig. 2. Spectra of flow disturbances with plasma on and off. a – plasma excitation $f = 50\ kHz$; b – plasma excitation $f = 100\ kHz$. Points for the analysis: BL2 – in boundary layer upstream the corner; A2-A4 – in separation bubble $y = 2, 3.2$ and $4.4\ mm$ from the model surface, respectively.

CONCLUSIONS

The current results of the study of using a transient electrical discharge for the control of boundary layer transition in a high-speed flow demonstrate the following:

- the hypersonic BL is highly receptive to repetitive plasma generated near the surface upstream of the separation zone;
- active tripping of a hypersonic BL using electric discharges with a frequency of repetition $f > F_1$ is certainly feasible;
- the high potential of aero-optical techniques to perform non-intrusive, high-frequency (up to 1 MHz), spatially-resolved measurements of flow structure and dynamics.

References

[1] Scott Berry, Roger Kimmel, and Eli Reshotko, AIAA Paper 2011-3415
[2] A. Valdivia, K. B. Yuceil, J. L. Wagner, N. T. Clemens, and D. S. Dolling, AIAA J, 2014, Vol. 52, No. 6 : pp. 1207-1218
[3] Schneider, S.P., J. of Spacecraft and Rockets, Vol. 45, No. 2, pp. 193–209, March-April 2008.
[4] Reshotko, E., and Tumin, A., AIAA J., Vol. 42, No. 4, pp. 766–770, April 2004.
[5] Yan, H., and Gaitonde, D., Physics of Fluids, Vol. 22, 2010, 064101(1-17).
[6] Samimy, M., Adamovich, I., Webb, B., Kastner, J., Hileman, J., Keshav, S., and Palm, P., Experiments in Fluids, Vol. 37, No. 4, 2004, pp. 577-588.
[7] Moreau, E., Journal of Physics D: Applied Physics, vol. 40, No.3, 2007, pp. 605-636
[8] F. Falempin, A. Firsov, D. Yarantsev, M. Goldfeld, K. Timofeev, S. Leonov, Experiments in Fluids, 2015, Vol 56, # 3,
[9] Sergey B. Leonov, Alec Houpt, Francois H. Falempin, AIAA 2015-3602
[10] Tyson RK. 1997. Principles of Adaptive Optics. New York: Academic. 345 pp. 2th ed.

HIGHER-ORDER WKBJ CORRECTION IN SPATIALLY-DEVELOPING OPEN FLOWS

Lorenzo Siconolfi[1], Paolo Luchini [*2], Vincenzo Citro[2], Flavio Giannetti[2], and Simone Camarri[1]
[1]*Dipartimento di Ingegneria Civile ed Industriale, Università di Pisa, Via Girolamo Caruso, 56122 Pisa, Italy*
[2]*DIIN, Università degli Studi di Salerno, Via Giovanni Paolo II, 84084 Fisciano (SA), Italy*

Summary We apply a WKBJ approximation to 2D and 3D bluff-body wakes. A correction term to the classical saddle-point estimation of the eigenfrequency is here calculated through a robust complex-plane extrapolation procedure based on rational Chebyshev approximation. Such correction is shown to decrease the error in the estimated eigenvalue by about an order of magnitude. Both the direct and adjoint global-mode structures are determined from local stability properties and compared with results obtained from a full 3D global stability analysis. Results show excellent agreement between the numerical global solution and its local approximation.

INTRODUCTION

Huerre & Monkewitz [1], Chomaz et al.[2] and Monkewitz et al.[3] discussed in detail the connection between local and global dynamics in spatially-developing open flows by means of a WKBJ asymptotic analysis. In particular, they explained the occurrence of an unstable global mode in terms of the local properties of the flow field, highlighting the role of a region of absolute instability and identifying a precise location in the streamwise direction which acts as a wavemaker for the entire field. Such an asymptotic approach is justified whenever the streamwise variations of the base flow are slow over a typical instability wavelength. Nevertheless, pushing the approximation to the limit of its validity, [4] and [5] applied the local analysis to the wake of a circular cylinder obtaining reasonable results compared to a global 2D stability computation. The aim of the present work is twofold: first, we will show that by including a higher order correction terms, the local approach is able to provide very accurate estimation of the global eigenfrequency, reducing the error by about one order of magnitude; second, we will show that the asymptotic analysis can be used to analyze 3D flow configurations, such as wakes behind bluff bodies, obtaining good results compared to a full 3D stability analysis at a highly reduced cost. Such approach could be useful for large parametric studies when many computations are needed. Moreover, following Juniper & Pier [6], we will also rebuild from the local 2D stability properties the 3D shape of the direct and adjoint global mode. The structural sensitivity obtained from the local and global approach will be compared and discussed.

PRELIMINARY RESULTS

For flows depending an all spatial directions the global stability approach consists in considering the entire domain and looking for eigensolutions of the form $\hat{\mathbf{u}}(\mathbf{x})exp\{\circ\, i\omega_{glob.}t\}$. On the other hand, if the base flow changes over a slow streamwise scale $X = \epsilon x$, then, the dynamics can be retrieved using a weakly non-parallel approximation [7]. In particular, the perturbation can be decomposed by using a WKBJ approximation as follows:

$$\mathbf{q} = \exp\{i(\omega t \circ\ \theta(X))/\epsilon\} \sum_{n=0}^{\infty} \mathbf{q_n}(X, y, z)\epsilon^n$$

where $\mathbf{q_n}$ is a vector coefficient and $\theta(X)$ is the complex phase. The homogeneous eigenvalue problem for $\mathbf{q_0}$ determines a dispersion relation of the form $\omega = D(k, X)$ where $k = d\theta/dX$.

Reference	ω	$(\lvert\omega_{\text{glob}} \circ\ \omega_{\text{loc}}\rvert)/\lvert\omega_{\text{glob}}\rvert$	Type
Giannetti and Luchini (2007)	0.750+0.013i	-	Global analysis
Pier (2002)	0.785+0.091i	11.40%	Local analysis
Juniper and Pier (2014)	0.791+0.083i	10.83%	Local analysis
Present (without correction)	0.750+0.084i	9.49%	Local analysis
Present (with correction)	0.729+0.012i	2.80%	Local analysis

Table 1: Leading eigenvalue for the flow past a circular cylinder at Re=50. Comparison between the global eigenvalue and the eigenvalue obtained by using the local theory.

*Corresponding author. Email: luchini@unisa.it

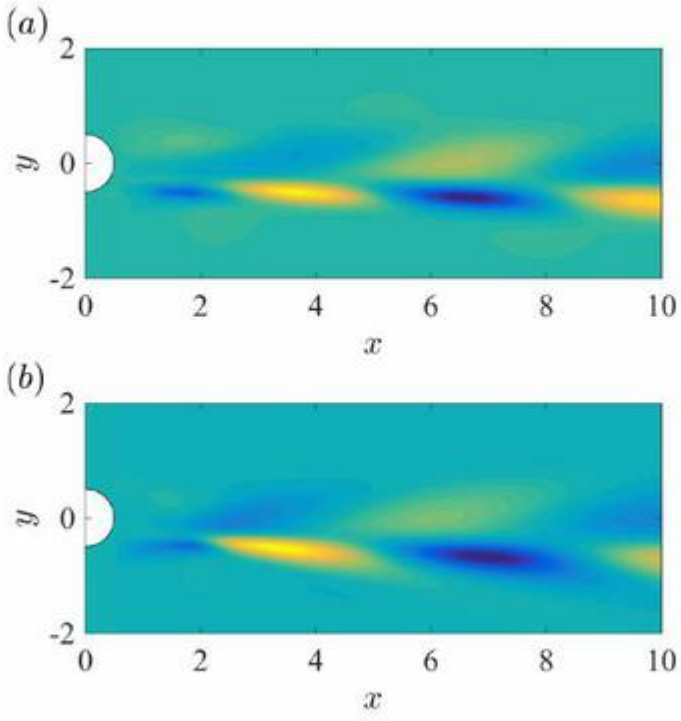

Figure 1: Contour plot of direct leading global mode calculated by using the (a) full 3D analysis and (b) the two-dimensional local analysis on the wake asymmetric wake of the sphere. Here, we show the real part of u, i.e. the streamwise component, at $Re = 275$.

Huerre & Monkewitz [1] showed that, in presence of a finite region of absolute instability, the dispersion relation provides an estimate for the global mode frequency via the saddle-point criterion

$$\omega_g = D(k_s, X_s) \quad \text{with} \quad \frac{\partial D}{\partial k}(k_s, X_s) = \frac{\partial D}{\partial X}(k_s, X_s) = 0.$$

Such formula is based on the analytic continuation of the dispersion relation in the complex-X plane. In the present work we will show that including higher order WKBJ correction terms greatly improves the accuracy of the estimated global eigenvalue.

Since the base flow is not known in the complex plane a delicate step of the procedure is the analytic prolongation of the dispersion relation. A robust extrapolation procedure based on rational Chebyshev approximation is here used to obtain a precise determination of the complex saddle point and the calculation of frequency corrections. Results will be shown first for a classical 2D example (the flow past a circular cylinder, table 1) and then for a genuine 3D flow (the flow past a sphere, figure 1).

References

[1] Huerre P., Monkewitz P. A.: Local and global instabilities in spatially developing flows. Annu. Rev. Fluid Mech. 22:473-537, 1990.
[2] Chomaz J.-M., Huerre, P., Redekopp, L.: A frequency selection criterion in spatially developing flows. Stud. Appl. Maths 84:119-144, 1991.
[3] Monkewitz, P. A., Huerre, P., Chomaz, J.-M.: Global linear stability analysis of weakly non-parallel shear flows. J. Fluid Mech. 251:1-20, 1993.
[4] Pier, B.: On the frequency selection of finite-amplitude vortex shedding in the cylinder wake. J. Fluid Mech. 458:407-417, 2002.
[5] Giannetti F., Luchini P.: Structural sensitivity of the first instability of the cylinder wake. J. Fluid Mech. 581:167-197, 2007.
[6] Juniper M. P., Pier B. The structural sensitivity of open shear flows calculated with a local stability analysis. Eur. J. Mech. B/Fluid 49:426-437, 2015.
[7] Chomaz J.-M.: Global instabilities in spatially developing flows: Non-normality and Nonlinearity. Annu. Rev. Fluid Mech. 37:357-392, 2005.

SENSITIVITY OF THE RAYLEIGH AND ORR-SOMMERFELD EQUATIONS TO CHANGES IN BASE FLOW

Paul Ziadé*[1] and Pierre E. Sullivan[1]

[1]*Department of Mechanical & Industrial Engineering, University of Toronto, Toronto, Ontario, Canada*

Summary Inviscid and viscous stability analysis is performed on mean velocity profiles obtained from large-eddy simulations. The effects of changes in reverse flow magnitude, inflexion point location, and maximum second derivative are analyzed with respect to their resulting effects on stability behaviour. It is found that the velocity profile second derivative is the dominant parameter, with changes thereof resulting in non-negligible shifts in peak growth rate and frequency, whereas the other two velocity parameters result in much less pronounced changes in stability behaviour.

INTRODUCTION

Low Reynolds number flows ($Re_c < 500,000$) over airfoils are prone to boundary layer separation. The flow over these configurations can exhibit complex behaviour, such as post-separation shear layer transition to turbulence and reattachment to the airfoil surface. The unstable shear layer undergoes transition due to amplification of instabilities. The understanding of these instabilities and their growth mechanism is therefore very important for airfoil performance prediction and the application of flow control strategies. Hydrodynamic stability is typically investigated using linear stability analysis. The perturbation amplitude, $\tilde{v}(y)$, is given by the Orr-Sommerfeld equation (OSE),

$$\left(U \circ \frac{\omega}{\alpha}\right)\left(\frac{d^2\tilde{v}}{dy^2} \circ \alpha^2\tilde{v}\right) \circ \frac{d^2U}{dy^2}\tilde{v} = \circ \frac{i}{\alpha Re}\left(\frac{d^4\tilde{v}}{dy^4} \circ 2\alpha^2\frac{d^2\tilde{v}}{dy^2} + \alpha^4\tilde{v}\right), \tag{1}$$

where U is the mean flow, ω is the real radial frequency, and $\alpha = \alpha_r + i\alpha_i$ is the complex wavenumber. By assuming an inviscid instability mechanism, this idealization reduces Eqn. (1) to the Rayleigh equation,

$$(\alpha U \circ \omega)\left[\frac{d^2\tilde{v}}{dy^2} \circ \alpha^2\tilde{v}\right] \circ \alpha\frac{d^2U}{dy^2} = 0. \tag{2}$$

During a recent study evaluating the flow behaviour over a low-Reynolds number airfoil at $Re_c = 100,000$ using large-eddy simulation (LES) and wind tunnel experiments[1], it was found that the computed stability characteristics exhibited large variations despite very good agreement in the base velocity profiles. LES, which provides a very fine boundary layer resolution, can be preferable to experiments as the much coarser resolution of the latter has been shown to affect the resulting stability profiles[2]. This present study is a preliminary attempt to isolate and quantify the individual contributions of the flow reversal magnitude, the maximum value of the second second derivative, and the location of the inflexion point, towards the growth rate spectrum as calculated by the Rayleigh and Orr-Sommerfeld equations.

COMPUTATIONAL METHODOLOGY

Chebyshev Collocation Method

A Chebyshev collocation approach is employed to solve Eqns.(1) and (2). An algebraic mapping function, $f(\eta)$, is used to transform the semi-infinite domain of the shear layer profile, $y \in [0, \infty)$, to the domain $\eta \in [\circ\, 1, 1]$ in which the Chebyshev polynomials are defined. The vertical velocity fluctuation in (1) and (2) is expressed as a Chebyshev polynomial series, $\tilde{v}(\eta) = \sum_{n=1}^{N} a_n T_n(\eta)$, where $T_n(\eta)$ is the nth Chebyshev polynomial of the first kind. The Chebyshev expansions are substituted in (1) and (2) with boundary conditions $\tilde{v}(\pm 1) = \tilde{v}'(\pm 1) = 0$. Both cases yield polynomial eigenvalue problems[3] with matrix coefficients, C_j. The eigenvalue problem is reformulated using a companion matrix method to yield a complex generalized eigenvalue problem, which is solved using the QZ algorithm. In the spatial instability formulation, the unstable eigenvalues are those which assume negative values, $\circ\, \alpha_i$.

Mean Velocity Profiles

A hyperbolic tangent velocity profile[4] was used to fit the LES data.

$$\frac{U(y)}{U_e} = \frac{\tanh[a_1(y \circ a_2)] + \tanh(a_1 a_2)}{1 + \tanh(a_1 a_2)} + a_3\frac{y}{a_2}\exp\left[\circ\, 1.5\left(\frac{y}{a_2}\right)^2 + 0.5\right], \tag{3}$$

where a_1, a_2 and a_3 are the fit parameters and U_e is the edge velocity. This curvefit follows the finely-spaced LES data very well with a least-squares residual of $R = 0.0001$ for the base profile. The base velocity data was altered to independently change the flow reversal magnitude, inflexion point, and maximum second derivative by a relative amount of $\pm 30\%$. Care has been taken to minimize as best as possible any secondary modifications in the velocity profile while altering the desired parameter.

*Corresponding author. Email: paul.ziade@mail.utoronto.ca

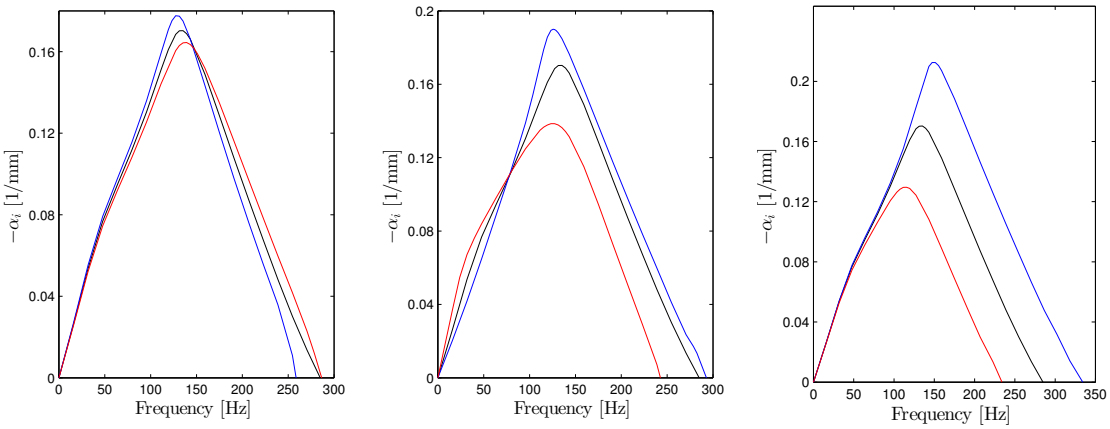

(a) $\min(U) \pm 30\%$ (b) $y(d^2U/dy^2 = 0) \pm 30\%$ (c) $\max(d^2U/dy^2) \pm 30\%$

Figure 1: Inviscid stability profiles with altered base velocity parameters. ——:$\circ$ 30%, ——:$\pm 0\%$ (base profile), ——:$+30\%$.

RESULTS

Linear stability analysis was performed on the base and modified velocity profiles (Figure 1 and Table 1). Of note is that change in reverse flow magnitude has a minimal effect on the resulting stability profile. Moderate changes in growth rate magnitude but not peak frequency are seen with a change of inflexion point location. The largest changes in growth rate and frequency are due to changes in the maximum second derivative of the velocity profile. Changes in d^2U/dy^2 shift the stability profiles in the $f \circ \alpha_i$ plane by non-negligible amounts and widen/shrink the spectrum of unstable frequencies. Solutions to viscous instability demonstrate lower absolute growth rate magnitudes but very similar relative changes due to changes in base velocity profile (Table 1).

	$\min(U)$		Inflexion Point		2nd Derivative	
	-30%	$+30\%$	-30%	$+30\%$	-30%	$+30\%$
$\Delta(\alpha_i)$	-3%/-3%	+4%/+3%	-18%/-20%	+11%/+11%	-24%/-24%	+25%/+25%
$\Delta(f)$	+3%/0%	+3%/0%	-3%/-3%	-4%/-3%	-15%/-15%	+15%/+15%

Table 1: Relative change in peak growth rate and associated frequency due to changes in base velocity profile parameters by $\pm 30\%$. Inviscid (blue font), viscous (red font).

CONCLUSIONS

The flow reversal magnitude, inflexion point location, and maximum second derivative were analyzed independently in order to quantify their respective contributions to instability. It was found that, for both viscous and inviscid analysis, the dominant factor affecting the stability curve (peak growth rate and associated frequency) is the maximum second derivative of the velocity profile, while the inflexion point location and reverse flow have much less pronounced effects. This preliminary analysis is to be extended and generalized by repeating this study with different curve fitting methods and velocity profiles.

ACKNOWLEDGMENTS

Computations were performed on the GPC supercomputer at the SciNet HPC Consortium. SciNet is funded by: the Canada Foundation for Innovation under the auspices of Compute Canada; the Government of Ontario; Ontario Research Fund - Research Excellence; and the University of Toronto. Computations were also performed on the SOSCIP Consortiums Blue Gene/Q computing platform(s). SOSCIP is funded by the Federal Economic Development Agency of Southern Ontario, IBM Canada Ltd., Ontario Centres of Excellence, Mitacs and 14 academic member institutions.

References

[1] P. Ziadé, M. Feero, P. Lavoie, P. Sullivan: Shear Layer Development, Separation, and Stability Over a Low-Reynolds Number Airfoil, AIAA Journal (Submitted).

[2] M.S.H Boutilier, S. Yarusevych: Sensitivity of linear stability analysis of measured separated shear layers. European J. Mechanics B/Fluids, 37, 129-142, 2013.

[3] T.J. Bridges, P.J. Morris: Differential eigenvalue problems in which the parameter appears nonlinearly. J. Comp. Phys., 55, 437-460, 1984.

[4] A.V. Dovgal, V.V. Kozlov, A. Michalke: Laminar boundary layer separation: Instability and associated phenomena. Prog. Aerospace Sci., 30, 61-94, 1994.

MICROPARTICLES EFFECTS ON THE STABILITY OF AN AIR-WATER INTERFACE.

Ilyesse Bihi *[1,2], Michael Baudoin[1], Jason E. Butler[2], Christine Faille[3], and Farzam Zoueshtiagh[1]

[1]*Univ. Lille, CNRS, ECLille, ISEN, Univ. Valenciennes, UMR 8520 - IEMN, F-59000 Lille, France*
[2]*Department of Chemical Engineering, University of Florida, Gainesville, Florida ,USA*
[3]*INRA, UR638, Villeneuve d'Ascq, France*

Summary When air is pushed inside a Hele-shaw cell containing a viscous liquid above a critical capillary number, Saffman Taylor instability leads to the formation of fingers, a phenomenon known as viscous fingering. Here Saffman-taylor experience is revisited when partially wettable hydrophilic particles are lying on the walls. It is shown that the presence of the particles leads to the reverse situation wherein liquid pushed inside a cell filled with air results in a fingering instability at low capillary number. This capillary-driven instability is due to the integration of particles to the interface resulting from interfacial energy minimization. Both axisymmetric and rectangular geometries are considered in order to quantify this phenomenon.

INTRODUCTION

Since the work of Saffman-Taylor [1] on the instability of an interface between two immiscible fluids, there has been an unprecedented growth of literature in this field. Developing viscous fingering as an instability occurs whenever a low viscosity fluid displaces a high viscosity fluid. Beside the beauty of the structures and the experiments, this great deal of attention is explained by the daily life applications, such as, flow in porous media[2], the flame propagation[3], and growth of bacterial colonies[4]. On the other hand, no instability occurs when we inject a highly viscous fluid in a low viscous one. Nevertheless, this case is of importance in cleaning processes when bacteria, spores, dust or particles are prensent on surfaces. We experimentally study this case in presence of micro-particles.

MATERIALS AND METHODS

Two geometries are used for this investigation: (i) a radial Hele-Shaw cell and (ii) a rectangular tube (see Fig.1). The first cell (i) is made of two circular glass of 50mm radius. They are centred and placed on top of each other, separated by a narrow gap, typically between 0.1 and 1mm. We lye a bed of roughly shaped Rilsan (Polyamide 11) particles of 15m radius, on the surfaces. DI Water is injected by a syringe pump to the cell through a hole drilled at the center of the bottom plate at constant flow rates (2,20,200 or 2000 ml/h). the evolution of the liquid-air interface was recorded with a CCD camera. The second set of experiments (ii) were performed in a rectangular Borosilicate capillary tube of height $H = 0.40$ mm and width $W = 10H$. After cleaning the inner walls, they were covered by Rilsan (Polyamide11) particles by gently blowing them into the channel with an air jet. Water was injected through the tube at a constant flow rate $Q = 0.1$ ml/h, corresponding to a capillary number $Ca = \mu_l Q/(\gamma_{GL} WH) = 2.38\times10^{-7}$, while recording the dynamics of the moving meniscus as described previously.

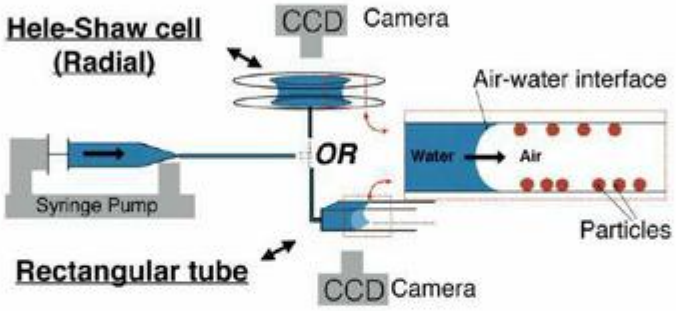

Figure 1: Schematic of the experimental setup: water is injected into air using a syringe pump either between two parallel plates (radial Hele-Shaw cell) or inside a rectangular tube. Micro-particles were deposited on the surfaces prior to water injection.

*Corresponding author. Email: bihi.ily@ufl.edu

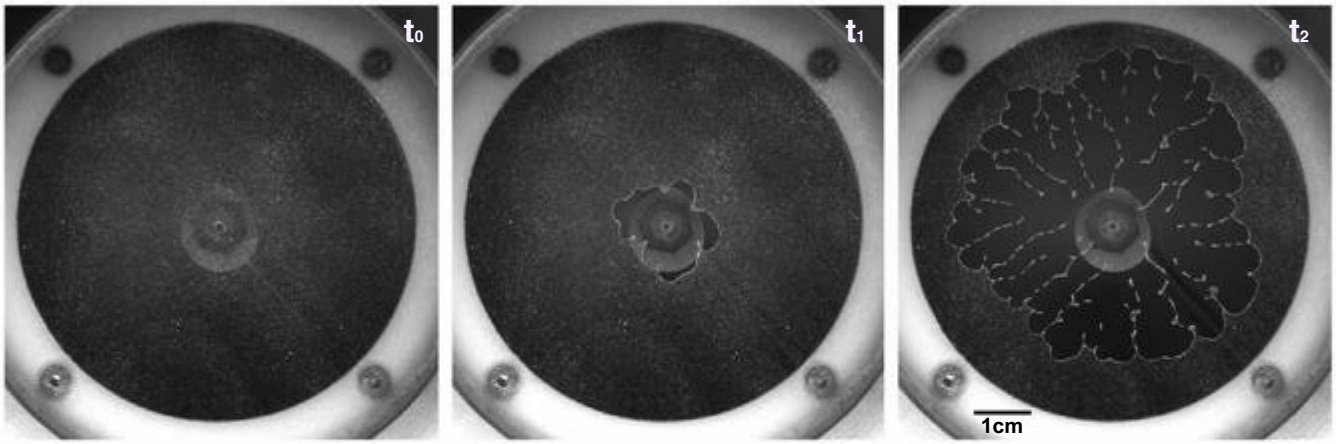

Figure 2: Images showing a time sequence of the interfacial instability in a radial Hele-Shaw cell with a plate spacing of 150 μm, $C = 0.45$, flow rate $Q = 2000\ ml/h$ and $[t_0, t_1, t_2 = 0, 5, 31s]$.



Figure 3: Image showing the interface instability "Semi-armoured bubbles" in a rectangular capillary tube with capillary number $Ca = 2.38 \times 10^{-7}$. The air appears dark gray and the water is light gray.

RESULTS

This study examines the influence of the micro-particles on the stability of the water-air interface. We show that the particles clings to the liquid interface, leading to a non-linear interfacial pattern formation. Diffrent structures of patterns (Fig.2,3) are reported depending on three key parameters: the concentration of particles, the gap between the plates and the flow rate. It was found that the emerging patterns develop fingers,labyrinths or a deposition of a liquid film ahead of the meniscus, similar to what was observed previously in cylindrical tubes [5]. We then focus on two aspects of the instability: (i) The critical radius where the instability appears. (ii) The characteristic lengths obtained from these patterns. This instability is driven by interfacial energy minimization. Once liquid/air meniscus is entirely covered by particles collected from the walls, it will expand in an asymmetric way to increase the surface to volume ratio and incorporate new particles encountred by the meniscus. Two models are developed to predict the two resulting parameters (i) and (ii) based on the balance between the space available on the meniscus with the area needed to accomodate additional particles encountered by the liquid-air interface during its motion. The models captures the qualitative trends and matches all the experimental data. Therefore we can predict the conditions of the stability of the interface.

CONCLUSIONS

This work demonstrate that the presence of partially wettable particles on the walls can dramatically affect the dynamics of a liquid interface that is injected into a Hele-Shaw cell filled with air. Different pattern structres emerge, eventough in absence of microparticles the air-water interface in stable. The destabilization of the interface occurs due to interfacial energy minimization, which requires that all particles intersected by the meniscus are collected.

References

[1] P. G. Saffman and G. Taylor, Roy. Soc. **245**, 312 (1958).
[2] B. Sandnes, H. A. Knudsen, K. J. Maloy, and E. G. Flekkoy, Phys. Rev. Lett. **99**, 038001 (2007).
[3] P. Pelcé, *Dynamics of curved Fronts* (Academic Press, Inc. 1988).
[4] E. Ben-Jacob, O. Schochet, A. Tenenbaum, I. Cohen, A. Czirok and T. Vicsek, Nature **368**, 46 (1994).
[5] F. Zoueshtiagh, M. Baudoin and D. Guerrin, Soft Matter **10**, 9403 (2014).

STABILITY OF FLOW IN A DIVERGING-CONVERGING CHANNEL AT MODERATE AMPLITUDES OF CORRUGATION

S. W. Gepner *[1] and J. M. Floryan[2]

[1]*Institute of Aeronautics and Applied Mechanics, Warsaw University of Technology, Warsaw, Poland*
[2]*Department of Mechanical and Materials Engineering, The University of Western Ontario, London, Ontario, Canada*

Summary Flow in a diverging-converging channel of moderate amplitudes has been studied. The analysis is carried out up to Reynolds numbers resulting in the formation of secondary states. The first part of the analysis is based on a two-dimensional model and demonstrates that reducing the corrugation wavelength results in the appearance of an unsteady separation whose onset correlates with the onset of the travelling wave instability. The second part of the analysis is based on a three-dimensional model and demonstrates that the flow dynamics are dominated by the centrifugal instability over a large range of geometric parameters, resulting in the formation of streamwise vortices. The critical Reynolds number for the vortex onset initially decreases as the groove amplitude increases but an excessive increase leads to reduction of the centrifugal forces. The flow dynamics under such conditions are dominated by the onset of the travelling wave instability.

INTRODUCTION

It is known that presence of grooves results in the appearance of two instability modes. The first one is the travelling wave mode [1, 2] which, in the smooth channel limit, connects to the classical Tollmien-Schlichting (TS) wave. This mode is driven by shear and is responsible for the transition from stationary to oscillatory states and, eventually, to aperiodic states [3]. The second mode has the form of streamwise vortices and its existence has been documented both experimentally [4] and numerically [1, 5]. It is attributed to the centrifugal forces associated with the groove-imposed changes of the stream direction. This mode connects in the smooth channel limit to a Squire mode and, thus, one may argue that the centrifugal effect amplifies (and modifies) a suitable Squire mode [5]. This instability becomes critical in channels with a certain class of grooves.

The onset of the two-dimensional, travelling wave instability is well discussed in the literature (see e.g., [2, 6]) and its dependence on the geometric parameters is known for small amplitude grooves [2] and for selected large-amplitude grooves [1, 6]. The centrifugal instability has been studied less frequently, primarily due to its three-dimensional character. Some limited investigation of both modes only for a single corrugation wavelength $\lambda = 3$ and with amplitudes large enough for the recirculation zone to form within troughs is given in [1]. Full range of corrugation wavelengths, but limited to small amplitudes is investigated in [5]. Critical conditions leading to both types of instabilities have been investigated in [2]. It was shown that the two-dimensional travelling wave is dominant for small amplitudes but is quickly overcome by the centrifugal instability as soon as the corrugation amplitude is increased. The conclusions are similar to those given in [1] indicating that while moderate corrugation amplitudes result in the centrifugal instability being dominant, their increase results in a larger separation zone which brings back the travelling wave instability.

PROBLEM SPECIFICATION

The main focus of this work is mapping of the dynamics of flow in a converging-diverging channel with the groove wave number varied from $\alpha = 10$ (short wavelength grooves) to $\alpha = 0.5$ (long wavelength grooves) which covers the full range of wavelengths of practical importance. The analysis is limited to moderate groove amplitudes, i.e. $S < 0.2$, and relies on DNS based on the spectral finite-element method in the $(x, y)-$plane combined with the Fourier decomposition in the spanwise direction, as implemented in NEKTAR++ [7].

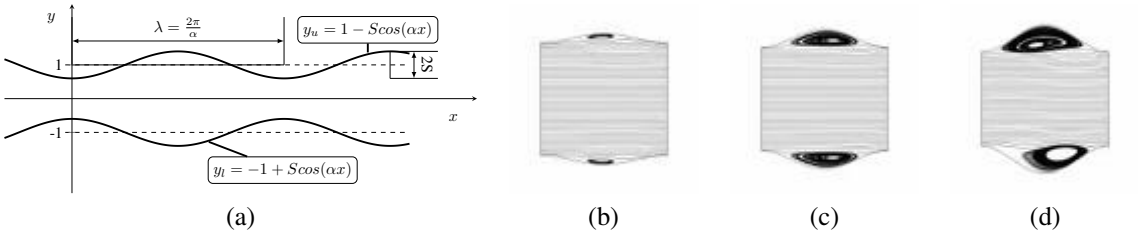

Figure 1: Geometry of the channel (a). Development of the recirculation zone for $\alpha = 3$, $Re = 2300$, at corrugation amplitudes $S = 0.075$ (b), $S = 0.150$ (c) and $S = 0.225$ (d)

*Corresponding author. Email: sgepner@meil.pw.edu.pl

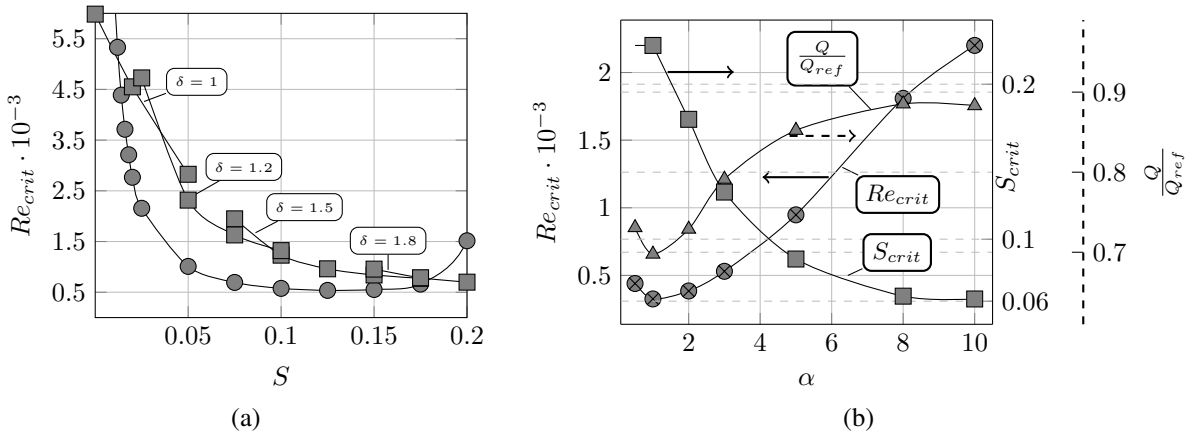

(a) (b)

Figure 2: Variation of critical the Reynolds number necessary for the onset of a 3D vortices and a competing 2D wave instability with various wavelengths δ as a function of the groove amplitude S for $\alpha = 3$ (a). Variations of the minimum critical Reynolds number, the corresponding critical corrugation amplitude S_{crit} and the corresponding reduction of the flow rate as function of the corrugation wave number α (b).

The analysis is divided into two steps, with the first one focused on the two-dimensional dynamics and presenting flow properties up to the formation of secondary states. Issues of particular interest are the onset and growth of the separation zone (see figure 1b, c), particularly the unsteady separation (figure 1d) and the drag penalty associated with the grooves.

The second step involves analysis of three-dimensional dynamics and identification of conditions when it precedes the two-dimensional dynamics (see figure 2a). Determination of conditions leading to the onset of streamwise vortices is of particular interest. Still, there has been little research committed to it. The process of vortex creation can be interfered with by the travelling waves. It is thus important to establish conditions where such vortices are likely to dominate the system dynamics. Figure 2a displays variations of the critical Reynolds number as a function of the groove amplitude required for the onset of the travelling waves (of various wavelengths δ) and for the onset of the vortices for $\alpha = 3$. At small amplitudes it is the travelling wave that dominates having a smaller Re_{crit}. For both instabilities an initial monotonic decrease in Re_{crit} is observed as S increases, with the centrifugal instability quickly becoming dominant. i.e. having smaller Re_{crit}. Further increase of S eventually reverses the character of variations of Re_{crit} for vortices with Re_{crit} increasing as growing recirculation prohibits the flow from producing enough of the centrifugal effect. As a result, the travelling wave becomes dominant again.

Here we view configuration which can amplify vortices at the smallest Re as being the most effective for designing an efficient mixing device. Figure 2b displays variations of the minimum critical Reynolds number and the corresponding critical corrugation amplitude S_{crit}, as functions of the corrugation wave number. Depending on α, the minimum Re_{crit} changes from 300 to 2200 and S_{crit} changes from 0.22 to 0.06. The cost of creating vortices can be expressed in terms of the flow rate reduction caused by the grooves. The flow rate reduction corresponding to the use of the optimal configuration varies as a function of α from 30% to 11% (see figure 2b).

CONCLUSIONS

Both two- and three-dimensional flow dynamics at previously uninvestigated flow conditions have been studied. Formation of various possible secondary states has been considered, respective critical conditions have been determined and compared. Obtained results provide basis for the identification of the most effective geometric configuration for the generation of the vortices and possible application in designing efficient mixing devices operating at low Reynolds number regimes.

References

[1] Cho, K. J., Kim, M. and Shin, H. D., Linear stability of two-dimensional steady flow in wavy-walled channels. Fluid Dynamics Research 23 (6), 349-370, 1998.

[2] Floryan, J. M. and Floryan, C., Travelling wave instability in a diverging-converging channel. Fluid Dynamics Research 42 (2), 2010.

[3] Guzman, A. M. and Amon, C. H., Transition to chaos in converging-diverging channel flows: Ruelle-takens-newhouse scenario. Physics of Fluids 6 (6), 1994.

[4] Nishimura, T., Yano, K., Yoshino, T. and Kawamura, Y., Occurrence and structure of Taylor-Goertler vortices induced in two-dimensional wavy channels for steady flow. Journal Of Chemical Engineering of Japan 23 (6), 697-703, 1990

[5] Floryan, J. M., Vortex instability in a diverging-converging channel. Journal of Fluid Mechanics 482, 17-50, 2003.

[6] Rivera-Alvarez, A. and Ordonez, J. C., Global stability of flow in symmetric wavy channels. Journal of Fluid Mechanics 733, 625-649, 2013.

[7] Cantwell, C.D., Moxey, D., Comerford, A., Bolis, A., Rocco, G., Mengaldo, G., Grazia, D. De, Yakovlev, S., Lombard, J.-E., Ekelschot, D., Jordi, B., Xu, H., Mohamied, Y., Eskilsson, C., Nelson, B., Vos, P., Biotto, C., Kirby, R.M. and Sherwin, S.J., 2015 Nektar++: An open-source spectral/ element framework. Computer Physics Communications 192, 205 - 219, 2015.

SECONDARY INSTABILITIES OF GORTLER VORTICES IN HIGH-SPEED BOUNDARY LAYER FLOWS

Jie Ren[1] and Song Fu*[1]

[1]*School of Aerospace Engineering, Tsinghua University, Beijing, China*

Summary Görtler vortices developed in laminar boundary layer experience remarkable changes when the flow is subjected to compressibility effect. In the present study, five *Ma* numbers, covering incompressible to hypersonic flows, at $Ma = 0.015,\ 1.5,\ 3.0,\ 4.5$ and 6.0 are specified to illustrate this compressibility effect. Görtler vortices in subsonic and moderate supersonic flows ($Ma = 0.015,\ 1.5,\ 3.0$) are governed by the conventional wall-layer mode (mode W). In hypersonic flows ($Ma = 4.5,\ 6.0$), the trapped-layer mode (mode T) becomes dominant. This difference maintains and intensifies downstream leading to different scenarios of secondary instabilities. The secondary instabilities of Görtler vortices set in when the resulting streaks are adequately developed. The secondary perturbations become unstable downstream following the sequence of sinuous mode type I, varicose mode and sinuous mode type II indicating an increasing threshold amplitude. Onset conditions are determined for these modes. The above three modes each can have the largest growth rate under the right conditions.

INTRODUCTION

Görtler instability [1], known as the centrifugal instability of boundary layer over a concave wall, arises due to the imbalance between the centrifugal force and the wall-normal pressure gradient. The streamwise-oriented, counter-rotating vortices (Görtler vortices) are consequently generated, maintained and can be significantly intensified downstream promoting flow transition. Most of early studies are conducted within the framework of incompressible flows (see reviews, e.g., by Floryan [2] and Saric [3]).

For hypersonic Görtler flows, the most significant flow feature is the existence of the temperature adjustment layer near the upper edge of the boundary layer which gives rise to the trapped-layer mode (mode T, disturbances rest in the layer near the upper edge of boundary layer). This mode becomes the most dangerous when the *Ma* number is larger than a critical value, e.g., $Ma \geq 4$. The present study, thus, attempts to investigate, comprehensively to clarify the effect of *Ma* number on the secondary instability with mode T being the governing mode.

METHODOLOGY

The local normal mode analysis (LST) and nonlinear parabolized stability equations (NPSE) are used for the generation of the base flows. The secondary instability is then performed in a Bi-Global framework of the normal mode analysis. Detailed formulation and numerical treatments can be found in the authors' previous papers [4, 5].

RESULTS AND DISCUSSIONS

Spatial development of Görtler vortices

Nonlinear development of Görtler vortices for the five groups of Mach numbers ($Ma = 0.015,\ 1.5,\ 3.0,\ 4.5$ and 6.0) and three wavenumbers ($B = \beta/Re = 0.5,\ 1.0$ and 2.0×10^{-3}) are performed.



Figure 1: Nonlinear development of Görtler vortices and the formation of low- and high-speed streaks. Contour plots of the streamwise velocity are within $Re \in [520, 720]$. Contour levels $= 0.1,\ 0.2,\ \cdots, 0.9$. Global spanwise wavenumber B=1.0×10^{-3}. (a)$Ma = 1.5$, (b)$Ma = 3.0$, (c)$Ma = 4.5$, (d)$Ma = 6.0$.

It can be found in Fig. 1 that the counter-rotating streamwise vortices carry the fluids with high momentum & low tem-

Secondary instabilities of Görtler vortices

A global view of the normalized disturbance u_s (under subharmonic conditions) of the varicose mode, sinuous mode type I and sinuous mode type II is provided in Fig. 2. Onset conditions for the five Mach numbers are obtained in Table. 1. Results are based on the spanwise wavenumber $B = 1 \times 10^{-3}$.

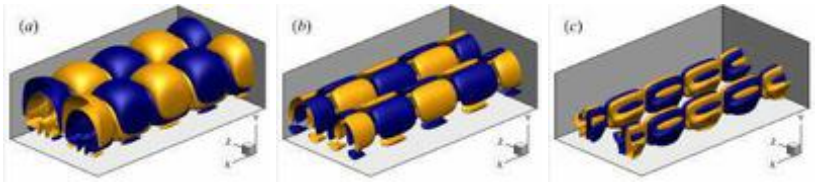

Figure 2: Contour surfaces of the normalized streamwise velocity perturbations u_s at $Ma = 1.5$, $B = 1.0 \times 10^{-3}$, $Re = 700$. The surfaces colored yellow and blue indicate $u_s = 0.1$ and -0.1, respectively. (a) Varicose mode; (b) Sinuous mode type I; (c) Sinuous mode type II.

Mach number	Sinuous-I	Sinuous-II	Varicose
$Ma = 0.015$	28%	59%	41%
$Ma = 1.5$	31%	63%	45%
$Ma = 3.0$	31%	63%	44%
$Ma = 4.5$	9%	/	/
$Ma = 6.0$	5%	/	/

Table 1: Onset conditions of the secondary instability modes measured by the streak amplitude $A(u)$. Spanwise wavenumber $B = 1 \times 10^{-3}$.

CONCLUSIONS

The development of Görtler vortices acts to strengthen the boundary layer streaks regardless of the Mach number. In the current study, the streak amplitude $A(u)$ keeps growing downstream (before the right-branch regime is reached). The sinuous mode type I becomes unstable first, followed by the varicose mode and then the sinuous mode type II.

Mach number affects Görtler vortices in two aspects. (1) The growth rate of primary Görtler mode decreases with Mach number. The streaks are thus weakened. (2) Increase in *Ma* gives rise to the trapped-layer mode (mode T) for the primary instability. This mode has its disturbances detached from the wall. As a result of the above changes, conventional *mushroom* structures are replaced by *bell*-shaped structures leaving the near-wall region an unperturbed area. The difference in the primary instability leads to a deserved and remarkable change on the secondary instability. In subsonic and moderate supersonic flows, varicose and sinuous (type I and type II) modes can both be responsible for the transition process. The sinuous mode type II, whose disturbances concentrate near the *stem* of the *mushroom*, is demonstrated to have the largest growth rate when the streak amplitude is large. However, it is missing in existing studies. The relationship between the dominance of sinuous or varicose modes and the primary wavelength in incompressible flow [6] is no longer valid in hypersonic flows. The sinuous mode becomes the most dangerous regardless of the spanwise wavelength when $Ma > 3$.

References

[1] H. Görtler, "Über eine dreidimensionale instabilität laminarer grenzschichten an konkaven wänden," *Ges. D. Wiss. Göttingen, Nachr*, vol. 1, no. 2, 1940. Translated as "On the three-dimensional instability of laminar boundary layers on concave walls. NACA TM 1375, 1954".

[2] J. Floryan, "On the görtler instability of boundary layers," *Progress in Aerospace Sciences*, vol. 28, no. 3, pp. 235–271, 1991.

[3] W. S. Saric, "Görtler vortices," *Annual Review of Fluid Mechanics*, vol. 26, no. 1, pp. 379–409, 1994.

[4] J. Ren and S. Fu, "Study of the discrete spectrum in a Mach 4.5 Görtler flow," *Flow, Turbulence and Combustion*, vol. 94, no. 2, pp. 339–357, 2015.

[5] J. Ren and S. Fu, "Secondary instabilities of görtler vortices in high-speed boundary layer flows," *Journal of Fluid Mechanics*, vol. 781, pp. 388–421, 2015.

[6] F. Li and M. R. Malik, "Fundamental and subharmonic secondary instabilities of Görtler vortices," *Journal of Fluid Mechanics*, vol. 297, pp. 77–100, 1995.

FLOW INSTABILITY ON AIRFOIL SEPARATION CONTROL AT OPTIMUM ACTUATION FREQUENCY

Yoshiaki Abe[1], Taku Nonomura *[2], and Kozo Fujii[2]
[1]*Department of Aeronautics and Astronautics, University of Tokyo, Sagamihara, Kanagawa, Japan*
[2]*Institute of Space and Astronautical Science, JAXA, Sagamihara, Kanagawa, Japan*

Summary The present study reveals a role of flow instabilities in the spatially developing disturbance induced by a synthetic jet device (SJ) with an optimum actuation frequency, which improves a separation-control capability around an airfoil. For this purpose, a high fidelity flow computation (large-eddy simulation) is conducted, where the chord Reynolds number and angle of attack are set to be 63,000 and 12 [deg], respectively. The linear stability analysis is conducted to detect an unstable mode of the wall-normal fluctuation in the separation controlled flows. In the well-controlled flows, the harmonics of the input fluctuation directly enhances the Kelvin-Helmholtz instability which linearly develops in the separated shear layer, followed by higher- and lower-frequency modes that are triggered by the most unstable modes (nonlinear growth regime). The process above effectively enhances a turbulent transition and generation of large-scale coherent vortices.

INTRODUCTION AND PROBLEM SETTINGS

Recently, microdevices for separated-flow control have been investigated because they attain low energy consumption, simple structures, and offer active control for unsteady flow fields compared with conventional devices such as "steady jet" and "vortex generator". This paper focuses on a "synthetic jet" device (SJ)[2], which is regarded as one of the most effective and promising microdevices. The SJ consists of a cavity with a connected orifice. The bottom of the cavity oscillates with a small amplitude, which generates periodic blowing and suction flow from the orifice. The induced flow fluctuates a separated shear layer near the SJ, and then the fluctuation is amplified as it convects downstream. Finally, the entire separated flow is modified to the attached one. However, the detail of the present separation-control mechanism has not been adequately clarified from the viewpoint of the relation between a chordwise-momentum injection and turbulent flow structures generated near the airfoil surface, which results in the gap of an optimum actuator condition of the SJ among several researchers. For example, the optimum actuation frequency F^+ (a nondimensional frequency normalized by the chord length and freestream velocity) has been separately shown to be $F^+ = 1$[5] and $F^+ = 10$[4] due to a lack of consistent explanation on the separation-control mechanism. The present study conducts a highly-accurate unsteady flow computation[3], i.e., a large-eddy simulation (LES), which can correctly resolve turbulent statistics inside the deforming cavity as well as the external flows around an airfoil. The sixth-order compact scheme is adopted for spatial discretization, and a deforming grid is used for the SJ cavity[1] (total number of the grid points is approximately 30 million). In this study, the relation between the optimum actuation frequency and the momentum injection methods in the separation-controlled flows is investigated from the viewpoint of a shear-layer instability and spatial growth of the disturbance introduced by the SJ.

CHORDWISE-MOMENTUM EXCHANGE IN THE CONTROLLED FLOWS

Figure 1(a) shows the effect of the actuation frequency F^+ on the control capability (the lift-to-drag ratio), where the optimum actuation frequency is localized in between $F^+ = 6.0$ and 20 for both of strong ($C_\mu = 2.0 \times 10^{-3}$) and weak ($C_\mu = 2.0 \times 10^{-5}$) input cases. In these well-controlled flows, the instantaneous flow field of Fig.1(b) shows strong turbulent vortex structures over an airfoil as well as inside the SJ cavity, where the isosurfaces of the second invariant of the velocity

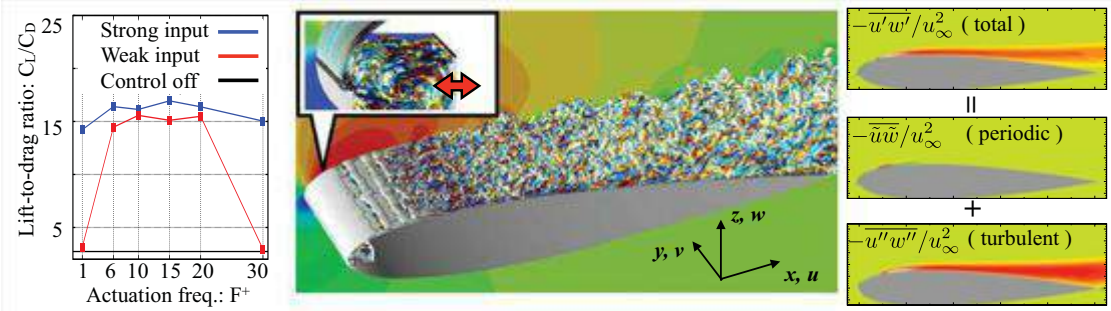

(a) Lift-to-drag ratio (b) Instantaneous flow field (controlled by F^+=6.0) (c) Reynolds stress

Figure 1: Characteristics of the separation-controlled flows: (a) effects of F^+ on the lift-to-drag ratio; (b)instantaneous flow field ($C_\mu = 2.0 \times 10^{-3}$, $F^+ = 6.0$); (c)phase decomposition of the Reynolds stress of the controlled flow.

*Corresponding author. Email: abe@flab.isas.jaxa.jp

gradient tensor is shown. The laminar-separation bubble (LSB) is generated near the leading edge, and the smaller LSB exhibits a strong suction peak at the leading edge, which results in the better capability (C_L/C_D). On the other hand, Fig.1(c) shows the phase decomposition of the Reynolds stress, which is decomposed into the periodic and turbulent component, i.e., $\overline{u'w'} = \widetilde{u}\widetilde{w} + \overline{u''w''}$. The present decomposition indicates that the chordwise momentum exchange is mainly achieved by the turbulent component of the Reynolds stress ($-\overline{u''w''}$), which is generated by the turbulent vortices. Therefore, one of the key mechanism for the separation control is the turbulent structure so that the promotion of the turbulent transition is important for the improvement of the control capabilities.

LINEAR STABILITY ANALYSIS ON THE SPATIAL DEVELOPMENT OF DISTURBANCE

The LST is conducted to extract the linear unstable mode in the spatially developing disturbance (wall-normal fluctuation) in the separated-shear layer near the leading edge, which is assumed to be $u'_n = \hat{u}_n \exp[i(\alpha x - \omega t)]$ ($\alpha = \alpha_r + i\alpha_i$). The spatial growth rate α_i can be also computed from unsteady data of the LES. Figure2(a) shows the comparison of LST and LES results of α_i, where both are corresponding to each other at $x/c_h = 3\%$. This indicates that the linear instability regime appears near the leading edge even in the separation-controlled flow. On the other hand, the higher- and lower-frequency modes are enhanced at $x/c_h = 5\%$, which indicates the region where the nonlinear growth regime begins. The higher- and lower-frequency modes promotes a turbulent transition and generation of coherent vortex structures (see top figures of Fig.2(a)), respectively. Note that the coherent vortex entrains the turbulent vortex structures over the airfoil, which is the another key for the chordwise-momentum exchange[3]. Figure2(b) apparently shows the comparison of α_i between the LST and LES results on the St-x plane. The power spectrum density (PSD) of the fluctuation is visualized in Fig.2(c). The higher- and lower-frequency modes are triggered by the well-developed linear instability mode (LST), which indicates that the LST mode should be excited in the upstream position. In the controlled flows with an optimum actuation frequency, the LST mode is introduced by the harmonics of the actuation frequency F^+ as well as the lower-frequency mode is given by disturbance of actuation frequency F^+.

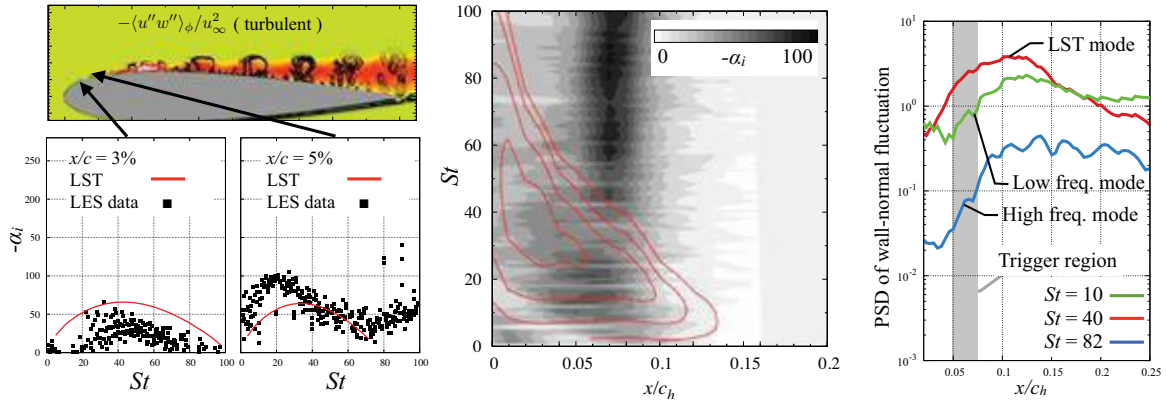

(a) Spatial growth rate (b) Spatial growth rate on *St*-*x* plane (c) Growth of disturbance

Figure 2: Comparison of LST and LES results in the spatial growth rate in the controlled flow ($C_\mu = 2.0 \times 10^{-3}$, $F^+ = 6.0$): (a)top figure shows the phase-averaged field, and bottom figures show the spatial growth rate $-\alpha_i$ at $x/c_h = 3$ and 5%; (b)spatial growth rate on the St-x plane; (c)spatial development of the PSD of wall-normal fluctuation obtained from the LES data.

CONCLUSIONS

The high-fidelity LES has been conducted on the separated flow control using the SJ around an NACA0015 airfoil. The followings have been newly represented: 1) the chordwise momentum injection is mainly achieved by turbulent vortex structures over the airfoil based on the phase-decomposition of the Reynolds shear stress, which are entrained by spanwise coherent vortex structures periodically generated and convecting downstream; 2) the linear growth regime of the spatially-developping disturbance from the SJ was verified by a linear stability theory (LST) in the separation-contolled flows; 3) based on the unsteady flow data of the LES, the spatial growth rate of disturbance from the SJ exhibits linear- and nonlinear-growth regime sequentially. 4) the optimum actuation frequency around $F^+ = 6.0$ to 20 directly excites a generation of large-scale coherent vortices (lower-nonlinear growth regime) as well as promoting a turbulent transition by introducing harmonic modes of F^+ (higher-nonlinear growth regime).

References

[1] Abe, Y. and Iizuka, N. and Nonomura, T. and Fujii, K., J. Comput. Phys. 260:163-203, 2014.
[2] Smith, B. L. and Glezer, A.: The formation and evolution of synthetic jets, Phys. Fluids, 10:2281, 1998.
[3] Abe, Y. and Okada, K. and Nonomura, T. and Fujii, K., Progress in Flight Physics (TORUS PRESS) 7:147-168, 2015.
[4] Glezer, A and Amitay, M: Synthetic Jets, Annual Review of Fluid Mechanics, 34:503-529, 2002.
[5] Seifert, A. and Darabi, A. and Wygnanski, I.: Delay of Airfoil Stall by Periodic Excitation, J. Aircraft, 33:691-698, 1996

LAGRANGIAN ANALYSIS OF ENERGY CONVERSION IN THE TACONIS OSCILLATIONS

Katsuya Ishii[1] & Shizuko Adachi[2a)]
[1]*Information Technology Center, Nagoya University, Nagoya, Japan*
[2]*School of Business and Commerce, Tokyo International University, Kawagoe, Japan*

Summary Energy conversion in the Taconis oscillations is numerically studied from the Lagrangian point of view. By solving the axisymmetric compressible Navier-Stokes equations, spontaneous thermoacoustic oscillations in a closed cylindrical tube are observed when a strong temperature gradient is imposed along the tube axis. The ratio of the high wall temperature near both ends of the tube to the low wall temperature of the central part is fixed at 15. Temporal evolution of dynamical and thermodynamical properties of fluid particles in the fundamental mode oscillation of a standing wave and the second mode oscillation is obtained from the field data. The state of the fluid particle is represented on a pressure-volume diagram. Fluid particles moving near the tube end perform a nearly cyclic transformation in both modes. When displacement of fluid particles is large, a regular pattern is not found on a pressure-volume diagram.

INTRODUCTION

Thermoacoustic oscillations in a long tube which spontaneously occurs when a strong temperature gradient is imposed along the tube axis are called the Taconis oscillations. Rott [1] succeeded in obtaining theoretical stability curves for the Taconis oscillations of a helium gas in an open-closed tube. The stability curves were confirmed later by the experiments of Yazaki *et al*. [2]. In their experiments they used tubes with both ends closed, and the central part of the tube is cooled and both ends are kept hot at room temperature. We [3-6] have numerically studied the Taconis oscillations in a 2D rectangular tube and a cylindrical tube with both closed ends.

In the previous paper [6], we showed that steady oscillations in a closed tube are observed in a certain range of ξ which is the ratio of the length of the hot part to that of the cold part. Three oscillation modes are observed: the second mode in which pressures at both ends oscillate in phase, a shock-wave mode and the fundamental mode in which pressures at both tube ends oscillate pi out of phase.

In the present paper, we study the energy conversion in the Taconis oscillations from the Lagrangian point of view.

FORMULATION AND NUMERICAL METHOD

We performed numerical simulations of the Taconis oscillations of a helium gas in a cylindrical tube with both closed ends. The tube wall temperature of the regions near the tube ends is kept at T_H=300K and that of the central part at T_C=20K. The temperature of the end walls is T_H=300K. The temperature ratio T_H/T_C is 15. The illustration of the temperature distribution on the tube wall along the tube axis is presented in Fig.1. The temperature distribution has a linear gradient between the hot part and the cold part. The tube length L is 280mm and tube radius r_0 is 0.756mm. The length of the interval with finite temperature gradient Δl is 7.5mm. The ratio of the length of the hot part to that of the cold part is defined as $\xi = 2l/(L-2l)$. In the present paper, we show the results for the length ratio ξ =0.4 and 1.0. Because the ratio of the radius to the length of the tube r_0/L is small enough (2.7×10^{-3}), we assume that the flow motion is axially symmetric around the tube axis.

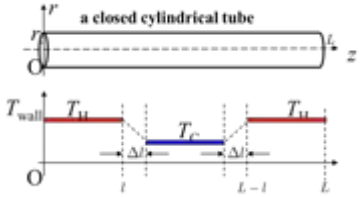

Figure 1. The temperature distribution on the tube wall.

The governing axisymmetric compressible Navier-Stokes equations of a perfect gas are solved with the block pentadiagonal matrix scheme. For the time integration, the second-order accurate three-point backward implicit scheme is employed. Fourth-order accurate central differencing is used for the convective terms, and second-order accurate three-point central differencing for the viscous terms.

We use a rectangular grid system consisting of 300 points along the tube length and 34 points in the radial direction. The grid points are clustered near the side wall and the end walls of the tube in order to resolve the motion in the boundary layer. The non-slip and isothermal boundary conditions are applied to the tube wall. A pressure gradient in the normal direction of the wall is assumed to be zero because the pressure gradient is negligible in the viscous boundary layer. Variables are normalized with respect to the appropriate combination of the tube length L, the density ρ_0= 0.167kg/m^3 and the sound speed a_0 = 1004m/s.

a) Corresponding author. Email: sadachi@tiu.ac.jp.

RUSULTS

For the fundamental mode oscillation (ξ = 1.0) and the second mode oscillation (ξ = 0.4), temporal evolution of dynamical and thermodynamical properties of fluid particles is obtained from the field data. Fluid particles start from various points in a tube. The state of the fluid particle is represented on a pressure-volume diagram. In Fig.2, position (a) and a pressure-volume diagram (b) are presented for fluid particles which start from (z=0.1, r=0.2) and (z=0.4, r=0.2) during three periods of the fundamental mode oscillation.

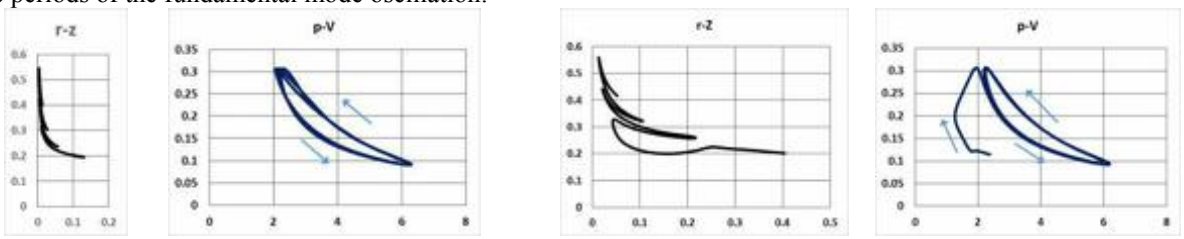

(1a) position (1b) p-V diagram (2a) position (2b) p-V diagram

Figure 2. Position and pressure-volume diagram of the fluid particles starting from (1) (z=0.1, r=0.2) and (2)(z=0.4, r=0.2)

Starting points of both fluid particles are near the tube axis. The fluid particle which starts in the cold region (2) moves toward the hot region, then it moves upward near the tube end as in the other fluid particle (1). The motion near the tube end corresponds to a cyclic transformation on a pressure-volume diagram. This cycle is performed in a counterclockwise direction, which means that the total work done is negative. The state of fluid particles moving near the end tube is similar also in the second mode oscillation.

Figure 3 presents position (a) and a pressure-volume diagram (b) for a fluid particle during two periods of the fundamental mode oscillation. This fluid particle begins to move at a point (z=0.4, r=0.5) which is between the wall and the axis in the cold region. It moves across the finite temperature gradient region (z=0.25) and goes upward.

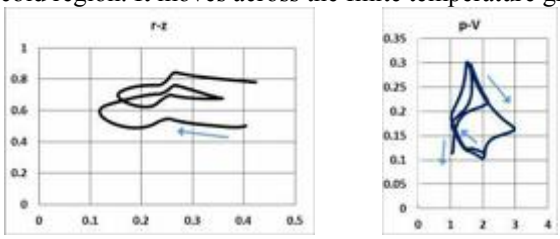

(a) position (b) p-V diagram

Figure 3. Position and pressure-volume diagram of the fluid particle starting from (z=0.4, r=0.5).

This is one example in which a fluid particle has large displacement and does not perform a cyclic transformation on a pressure-volume diagram. In the second mode oscillation which has smaller pressure amplitude than the fundamental mode oscillation, fluid particles starting from a point in the cold region do not have so large displacement as the fundamental mode oscillation.

CONCLUDING REMARKS

Fluid particles moving near the tube end perform a nearly cyclic transformation on a pressure-volume diagram. When displacement of fluid particles is large, a cyclic transformation is not found on a pressure-volume diagram.

References

[1] Rott N.: *Z. Angew. Math. Phys.***20**:230-243, 1969; *Z. Angew. Math. Phys.***24**:54-72, 1973.

[2] Yazaki T., Tominaga A. and Narahara Y.: *J. Low. Temp. Phys.***41**:45-60, 1980; *Phys. Lett.* **79A**: 407-409, 1980.

[3] Ishigaki M. Kuzuu M., Adachi S. and Ishii K.: *Theor. Appl. Mech. Japan* **56**:307-316, 2008.

[4] Ishigaki M., Adachi S. and Ishii K.: *Fluid Dyn. Res.* **43**: 041403 (12pp), 2011.

[5] Ishigaki M., Shirai K., Adachi S. and Ishii K.: "Numerical Analysis of Thermoacoustic Spontaneous Oscillations in a 2D Rectangular and an Axisymmetric Closed Tube," in NONLINEAR ACOUSTICS State-of-the-Art and Perspectives, AIP Conference Proceedings 1474, edited by T. Kamakura and N. Sugimoto(American Institute of Physics, Melville, NY, 2012), pp. 295–298.

[6] Ishii K., Kitagawa S., Ishigaki M. andAdachi S.: *Fluid Dyn. Res.* **46**: 061408 (14pp), 2014.

A LAGRANGE-EULER MODELLING OF THERMOVIBRATIONAL INSTABILITIES IN SUPERCRITICAL FLUIDS

D. Sharma[1], A. Erriguible[2], G.Gandikota[1], S. Amiroudine[1]

[1] Université of Bordeaux, I2M, UMR CNRS 5295, 16 Av. Pey-Berland, 33607 Pessac, France
[2] Bordeaux INP, I2M, UMR CNRS 5295, 16 Av. Pey-Berland, 33607 Pessac, France

Summary: A numerical modelling of thermo-vibrational instabilities in supercritical fluids is performed under zero-gravity conditions. The model is based on a new formulation where the density is calculated from the continuity equation (mass conservation is achieved at a machine precision). The numerical results are compared with experimental data in zero-gravity conditions based on magnetic compensation field (levitation). They show excellent agreement. Stability diagrams will be shown as a function of different given parameters (amplitude, frequency, heating rate, proximity to the critical point).

INTRODUCTION

The liquid-gas critical point on the phase diagram represents a singular equilibrium state, beyond which the boundary between the liquid and gas phases no longer exists and the fluid becomes supercritical. As one approaches the critical point, some peculiar thermo-physical properties emerge such as the heat of vaporization approaches zero, the constant-pressure specific heat increases substantially along-with diverging compressibility [1]. When these fluids are subject to thermal quench (or heating) along with longitudinal vibrations of frequencies of the order 10-50 Hz [2-5], the dynamic response of the fluid has been observed to originate in the boundary layers. A number of intriguing phenomena have been observed in literature when near-critical fluids are submitted to longitudinal vibrations such as the layering of the gas-liquid phases [2], or the acceleration of the gas-liquid phase transition dynamics [3].

The experiments pertaining to super-critical fluid subjected to vibrations under weightlessness have been performed using CO_2 on-board a sounding rocket (see [2] for details). These experiments have reported the appearance of fingers which shows destabilization of thermal boundary layer under the aforementioned conditions. Amiroudine and Beysens [4] were the first to perform numerical study for supercritical fluids subjected to vibrations and observed the fingering structure in the thermal boundary layers with different proximities to the critical point. It was found that fingering wavelength and the vibrational Rayleigh number $\left(Ra_v = \frac{(A\omega\beta_P\delta Te)^2}{2\nu D_T}\right)$ decrease as a power law with the distance in temperature to the critical point. Gandikota *et al.* [5] then performed numerical simulation with supercritical hydrogen subjected to longitudinal vibrations. They evaluated the effect of vibrations using three different combinations of boundary conditions thus providing insight into the mechanisms of corner, parametric and Rayleigh vibrational instability.

The work mentioned so far in the literature has assumed a linear equation of state being valid near the critical point. This poses limitations on the quench (or heating) conditions that may be considered in the numerical study (assumed to be 10% of initial temperature distance from critical point in [5]). The purpose of this study is to evaluate the effect of longitudinal vibrations not limited by temperature conditions. This has been achieved using a numerical model which does not require any equation of state and directly calculates properties from NIST data base. The numerical results are first validated with the experimental results followed by detailed analysis for different heating conditions, different proximities to the critical point and different vibrational parameters (frequency and amplitude).

PROBLEM DESCRIPTION AND MATHEMATICAL MODEL

The problem to be investigated consists of supercritical Hydrogen at its critical density filled in a 2-D square cavity of length $h = 7mm$ subjected to longitudinal vibrations $A\sin\omega t$ (shown in Fig. 1). The problem is mathematically modelled using Navier-Stokes equations comprising of conservation of mass, momentum and energy which can be described as following (see [6] for more details),

$$\rho\frac{D\boldsymbol{V}}{Dt} = -\nabla[P^0 - \delta t(\frac{1}{\chi_T} + \frac{\beta_P^2 T}{\rho C_v \chi_T^2})\nabla.\boldsymbol{V} - \delta t\frac{\beta_P}{\rho C_v \chi_T})\nabla.\boldsymbol{\phi}] + \rho A\omega^2 sin\ \omega t\ \boldsymbol{i} + \nabla.[\mu(\nabla\boldsymbol{V} + \nabla^t\boldsymbol{V} - \frac{2}{3}\nabla.V\bar{\bar{I}})]$$

$$\rho C_v\frac{DT}{Dt} = \nabla.(k\nabla T) - \frac{\beta_P T}{\chi_T}\nabla.\boldsymbol{V}$$

$$\rho = \rho^0 e^{-\delta t\nabla.\boldsymbol{V}}$$

$$Properties:\ \beta_p, \chi_T, C_v, \mu\ and\ k$$

[a] Corresponding author. Email: sakir.amiroudine@u-bordeaux.fr.

Here P^0 and T^0 are the equilibrium pressure and temperature at a defined time instant. The thermo-physical properties are calculated directly from NIST database while the density is evaluated directly from the continuity equation. These equations are solved numerically by a home-made code (Thetis [6]).

RESULTS AND DISCUSSION

The amplitude of vibrations varies from 0.2 to 5 mm while the frequency varies from 2 to 50 Hz. The initial temperature in the study is varied from 10 mK to 1K from critical point and walls are subjected to different heating rates.

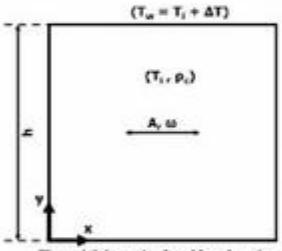

Figure 1 Schematic of problem domain.

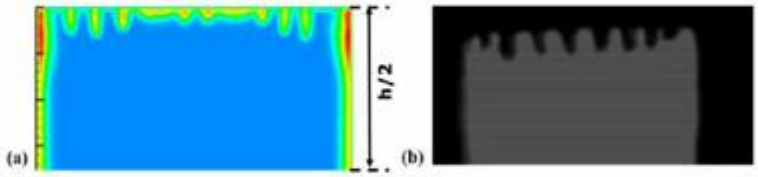

Figure 2. Evolution of temperature field when subjected to longitudinal vibrations (A=0.875 mm , ω = 20 Hz) (a) Numerical (b) Experimental at time 1.6 s

Fig. 2 shows an example of our numerical results in comparison with experimental data in zero-g (based on the magnetic field levitation, see details about experimental set-up in [7-8]) when the cell is subjected to vibrations with an amplitude of 0.875 mm and frequency of 20 Hz (T_i=33.739 K). The wall boundary condition used in the numerical simulation corresponds to a cubic polynomial fit to experimental values. Owing to the vertical symmetry only upper half of the cell has been shown. One can observe that the numerical results match closely with the experimental data. Further, if one tries to superimpose the two figures, the height of the fingers matches within a reasonable accuracy. The appearance of fingers is attributed to Rayleigh vibrational instability which appears due to Bernoulli like pressure difference ($\Delta p \approx \rho_c \Delta V^2 = \rho(\frac{\Delta\rho}{\rho_c})^2 A^2\omega^2$) in thermal boundary layers. The results show that the present model is thus able to predict instabilities without any constraint on the heating rate. With an increase in the distance from the critical point, the number of fingers decreases while their amplitude grows faster. The latter is attributed to that fact that diffusion time increases significantly as we move closer to the critical point thereby causing a delay in the growth of instability in the thermal boundary layer. A stability curve will be presented for different proximities to the critical point, different values of frequency and amplitude and different heating rates.

CONCLUSIONS

A numerical simulation with a mathematical model based on the determination of the density from the mass conservation equation and thermophysical properties from the NIST database has been performed. The results show a fingering structure in the thermal boundary layer and confirmed with the experimental results based on the magnetic field levitation. Stability diagrams will be shown as a function of the different parameters described above.

Acknowledgments: S.A and G.G would like to thank CEA (Atomic and Alternative Energy Research Center in Grenoble, France) through D.Chatain and D.Beysens for the experimental results in G.G's thesis

References

[1] B. Shen and P. Zhang, "An overview of heat transfer near the liquid–gas critical point under the influence of the piston effect: Phenomena and theory," *International Journal of Thermal Sciences,* vol. 71, pp. 1-19, 9, 2013.

[2] R. Wunenburger, P. Evesque, C. Chabot, Y. Garrabos, S. Fauve, and D. Beysens, "Frozen wave induced by high frequency horizontal vibrations on a CO_2 liquid-gas interface near the critical point," *Physical Review E,* vol. 59, pp. 5440-5445, 05/01/ 1999.

[3] D. Beysens, D. Chatain, P. Evesque, and Y. Garrabos, "High-Frequency Driven Capillary Flows Speed Up the Gas-Liquid Phase Transition in Zero-Gravity Conditions," *Physical Review Letters,* vol. 95, p. 034502, 07/14/ 2005.

[4] S. Amiroudine and D. Beysens, "Thermovibrational instability in supercritical fluids under weightlessness," *Phys Rev E,* vol. 78, p. 036325, 2008.

[5] G. Gandikota, S. Amiroudine, D. Chatain, T. Lyubimova, and D. Beysens, "Rayleigh and parametric thermo-vibrational instabilities in supercritical fluids under weightlessness," *Physics of Fluids,* vol. 25, p. 064103, 2013.

[6] S. Amiroudine, J. P. Caltagirone, and A. Erriguible, "A Lagrangian–Eulerian compressible model for the trans-critical path of near-critical fluids," *International Journal of Multiphase Flow,* vol. 59, pp. 15-23, 2, 2014.

[7] G. Gandikota, D. Chatain, S. Amiroudine, T. Lyubimova, and D. Beysens, Frozen-wave instability in near-critical hydrogen subjected to horizontal vibration under various gravity fields, *Phys. Rev. E* 89, 012309 (2014).

[8] G. Gandikota, Instabilités d'interfaces fluides en apesanteur spatiale lors d'un changement brutal ou périodique d'accélération, PhD Thesis, Université Joseph Fourier, Grenoble, France, Dec 2013.

EFFECT OF PRESSURE FLUCTUATIONS ON THE EVOLUTION OF RICHTMYER-MESHKOV COHERENT STRUCTURE

Aklant Kumar Bhowmick[1] & Snezhana Abarzhi[1]
[1]*Carnegie Mellon University, Pittsburgh, USA*

Summary We consider the effect of pressure fluctuations on the evolution of Richtmyer-Meshkov (RM) flows. The pressure fluctuations are induced by non-uniformities in the fluid bulk and are modeled as a time dependent acceleration with the power-law exponent (-2). We consider a large scale periodic coherent structure of bubbles and spikes in a two-dimensional RM flow, and obtain asymptotic solutions describing nonlinear dynamics of the structure using group theory analysis. We show that regular asymptotic solutions describing the bubble dynamics form a one-dimensional family. The family can be parametrized by the curvature of the bubble front. The stability of the family solutions is analyzed. The physically significant solution in the family is interpreted as the stable solution with the maximum velocity. The associated flow fields in the vicinity of the bubble tip indicate the formation of vortices and the presence of shear at the interface, which may lead to cascading of energy to smaller scales.

INTRODUCTION

Richtmyer Meshkov (RM) instability develops when a shock refracts at the interface between fluids with different acoustic impedances. In the incompressible limit, it may occur when a light fluid impulsively accelerates a heavy fluid. These instabilities hold one of the keys to understanding a variety of physical phenomena occurring in a wide range of length and time scales. Sharp density gradients occur in phenomena such as inertial and magnetic confinement fusion, supernova explosions, flames, formation of salt domains etc. Developing a reliable theoretical framework to describe the turbulent mixing in these processes is one of the fundamental objectives of doing such studies.

The interfacial dynamics is often decoupled into small and large scales. At large scales, the instabilities lead to a coherent structure of bubbles and spikes in the plane normal to the direction of the acceleration. At small scales, there are secondary instabilities and vorticities which may lead to the formation of singularities, thereby making the non-linear evolution fairly complicated and chaotic at these scales. Considerable progress has been made in the mathematical modelling of the large scale coherent structure.

SMALL SCALE DYNAMICS IN THE BULK: PRESSURE FLUCTUATIONS

It is traditionally believed that in RMI, the non-uniformities in the small scale dynamics is confined to the vicinity of the interface, and the bulk dynamics is uniform at small scales. However, recent simulations [2] have indicated that small-scale dynamics in the indeed exist in the bulk of RM flow. Figures 1a and 1b clearly show these non-uniformities in the form of hot spots and reverse cumulative jets. These non-uniformities induce pressure fluctuations, which may have significant impact on the morphology and the dynamics of RM bubbles. In this work, we study the effect of pressure fluctuations on nonlinear evolution of RMI. In the process, we study the impact of small scale non-uniformities on the large scale coherent structure, and show that pressure fluctuations have significant impact on morphology and dynamics of RM bubbles.

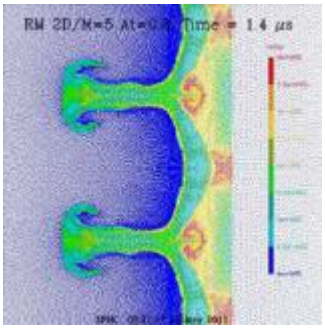

(a) Temperature from 4000 K(blue) to 8000 K(red)

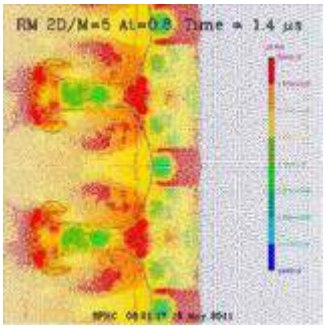

(b) Pressure from 10^{11}Pa (blue) to 2×10^{11} Pa (red)

Figure 1: RMI small scale structures obtained using SPH simulations (Stanic et. al., 2012)

[a] Corresponding author. Email: akbhowmi@andrew.cmu.edu, aklant.app@gmail.com

PROBLEM FORMULATION AND GOVERNING EQUATIONS

We consider 2D flow of heavy and light ideal incompressible fluids separated by an interface. We further assume that the flow is irrotational at scales comparable to the large scale coherent structure. The resulting system of equations in the potential approximation for the heavy and light fluid bulks are

$$\nabla^2 \Phi_{h/l} = 0, \tag{1}$$

$$\left(\rho \frac{\partial \Phi}{\partial t} + \frac{\rho}{2}\left|\vec{\nabla}\Phi\right|^2 + \rho\left(g(t) + \frac{\partial v}{\partial t}\right) z\right)_{h/l} = -P_{h/l}. \tag{2}$$

where Φ is the flow potential, ρ is the mass density. $g(t)$ is the effective acceleration term caused by pressure fluctuations. $\frac{\partial v}{\partial t}$ is a non-inertial term appearing as a consequence of being in the rest frame of the bubble tip, where v is the bubble tip velocity. The indices h and l represent heavy and light fluids respectively. The boundary conditions assume no fluid motion at large scales far away from the interface, and are given by

$$\vec{\nabla}\Phi = -\vec{v}\,, \quad z = \pm\infty. \tag{3}$$

The conditions of mass and momentum conservation at the interface are given by,

$$\left(\rho\left(\frac{\dot{\theta}}{|\vec{\nabla}\theta|} + \vec{\nabla}\Phi.\hat{n}\right)\right)_{h/l} = 0 \tag{4}$$

$$P_h = P_l \tag{5}$$

MODELLING OF PRESSURE FLUCTUATIONS: TIME DEPENDENT ACCELERATION

The effect of pressure fluctuations is contained in the acceleration term $g(t)$. These pressure fluctuations may not be due to dissipation and diffusion effects because they seem to occur at scales larger than the dissipative or diffusive scales. Thus the pressure fluctuations may be scale invariant, and could be modelled by a scale invariant function such as the power law, i.e. $g(t) \sim t^a$. In this work, we consider $g(t) = L_g/t^2$ because the resulting asymptotic solutions are of the form $v \sim \frac{1}{t}$, which is the same as the case of no fluctuations [1].

ASYMPTOTIC SOLUTIONS FOR RM EVOLUTION WITH PRESSURE FLUCTUATIONS

We solve for the tip velocity and the velocity fields and show that the solutions may be convergent and are asymptotically stable. The details of the approach shall be presented later. The solution for the tip velocity v as shown in figures 2a and 2b, bring out the essential features of the morphology of the RM bubble. The plots are at different Atwood numbers $A = \frac{\rho_h - \rho_l}{\rho_h + \rho_l}$
The solutions form a one parameter family, parametrized by the bubble curvature ζ_1. The physically significant solution corresponds to the maxima of these curves. Thus, RM bubbles are flat for small fluctuations and curved for large fluctuations.

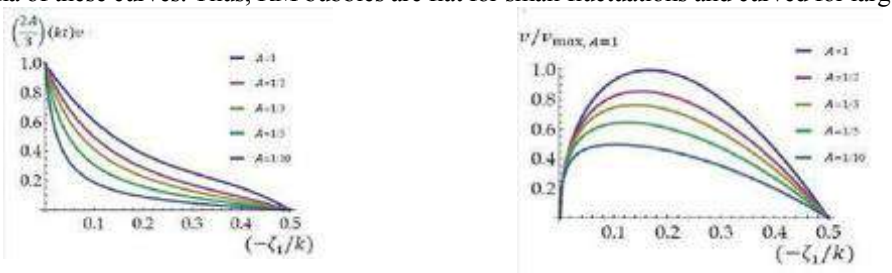

(a) Small pressure fluctuations (b) Large pressure fluctuations

Figure 2: Tip velocity as a function of curvature for large and small pressure fluctuations

CONCLUSIONS

Qualitative and quantitative distinctions in the solutions for small and large pressure fluctuations indicate that the solutions exhibit sensitivity to pressure fluctuations and this is one of the key results of our work. This clearly demonstrates that small scale structures in the bulk may have significant impact on the dynamics at large scales. The solutions also indicated the presence of shear and the formation of vortices at the interface, which provides a mechanism for energy cascade to smaller scales at the interface possible giving rise to small scale structures at the interface via mechanisms such as Kelvin Helmholtz instability.

References

[1] Nonlinear evolution of unstable fluid interface, S.I. Abarzhi, Physical Review E 66, 036301 (2002)

[2] Scale coupling in Richtmyer Meshkov flows induced by strong shocks, M. Stanic, R. F. Stellingwerf, J. T. Cassibry, and S. I. Abarzhi, Physics of Plasmas 19, 082706 (2012)

INTERMITTENCY OF LAMINAR SEPARATION BUBBLE DURING DRAG CRISIS IN FLOW PAST A CIRCULAR CYLINDER

Gaurav Chopra[1] and Sanjay Mittal*[1]

[1]*Department of Aerospace Engineering, Indian Institute of Technology, Kanpur, Uttar Pradesh, India*

Summary This work explores the phenomenon of drag crisis in flow past circular cylinder: a significant reduction in drag with increase in Re due to transition of boundary layer from laminar to turbulent state. The incompressible flow equations are solved using a stabilized finite element method for $1 \times 10^4 \leq Re \leq 4 \times 10^5$, in three dimensions. The computations successfully capture the phenomenon. It is shown that the drag crisis is accompanied with appearance of a Laminar Separation Bubble (LSB). The intermittent nature of the LSB during the transition is explored. In addition to the streamlines, the LSB may also be tracked via filtered Reynolds stress and fluctuations in surface pressure.

INTRODUCTION

Understanding the phenomenon of drag crisis in flow past a circular cylinder has relevance in several engineering applications. It has been a subject of research in the past via experimental and numerical studies. The boundary layer on the cylinder transitions from a laminar to turbulent state during drag crisis. The flow can be broadly classified in four regimes as a function of Re: sub-critical, critical, super-critical and trans-critical ([1], [3] and, [4]). In the sub-critical regime ($Re < 2 \times 10^5$) the boundary layer is laminar until separation and, the mean coefficient of drag ($\overline{C}_D$) is almost constant with Re. In the critical regime ($2 \times 10^5 \leq Re \leq 4 \times 10^5$) the laminar boundary layer separates near the shoulder of cylinder. The separated shear layer undergoes transition to a turbulent state and reattaches to the surface of the cylinder ([2]), leading to the formation of a Laminar Separation Bubble (LSB). The reattached turbulent boundary layer separates further downstream. As a result, the wake is narrower and base suction pressure higher, leading to a rapid reduction in $\overline{C}_D$ with increase in Re. In the supercritical regime ($Re \geq 4 \times 10^5$) $\overline{C}_D$ increases with increase in Re. The main objective of the present work is to understand the phenomenon of drag crisis. Does it occur abruptly, or is it a relatively gradual process that occurs over a range of Re? We attempt a statistical analysis of the computed flow to understand the intermittent nature of the LSB.

RESULTS AND DISCUSSIONS

Figure 1(a) shows the variation of $\overline{C_D}$ with Re from the present computations along with their comparison from earlier studies. We observe that both two- and three-dimensional simulations predict drag crisis. The range of Re for which the flow lies in the critical regime is very similar from the two sets of computations. This suggests that the phenomenon itself is largely two-dimensional. Of course, the three-dimensional effects are quite significant as indicated by the difference in $\overline{C}_D$ in the sub- and super-critical regime from the 2D and 3D computations. However, the mechanism of transition in a span-averaged sense appears to be two-dimensional. Compared to the measurements from experiments, the present results predict the drag-crisis at a slightly lower Re. Results are also shown in Figure 1(a) for the Large Large Eddy Simulation (LES) with a static Smagorinsky model to account for the subgrid scales. Compared to results from model-free computations, these results are in closer agreement with the experimental data. Since the model-free computations also capture the essential trend, therefore, all the analysis in this work is carried out for data from model-free computations. Both, the computational and experimental data in Figure 1(a) shows that the variation of $\overline{C}_D$ with Re during the transition is smooth, and not abrupt. We explore the changes in the flow during transition.

The instability of the separated shear layer and its subsequent rolling up into vortices plays a major role in the reattachment of the boundary layer and formation of LSB. To study this we need to filter out the activity due to the Karman shedding that has a much lower frequency compared to the activity of the shear layer. For the same, consider the time variation of the span-averaged surface coefficient of pressure $C_P(\theta, t)$ at different Re. We compute a moving average of $C_P(\theta, t)$: $\widetilde{C_P}(\theta, t)$ over a time window of size $T_k/10$, where T_k is the time period of the Karman shedding. This averaging filters out the shear layer activity while retaining the vortex shedding effects. By subtracting $\widetilde{C_P}(\theta, t)$ from the original signal, we compute the rms of the fluctuations that correspond to shear layer activity: $\widetilde{C'_P C'_P}(\theta, t)$. Figure 1(b) shows a space-time diagram of the variation of $\widetilde{C'_P C'_P}(\theta, t)$ for $Re = 1.5 \times 10^5$. The flow is in the transitional regime at this Re and undergoing drag-crisis. Figure 1(d) shows the streamlines for the moving time-averaged flow that are also span averaged at two time instants that are marked in figure 1(b). These figures reveal the co-relation between the presence/absence of LSB with the level of fluctuations due to shear layer activity as observed in $\widetilde{C'_P C'_P}(\theta, t)$. At $t = t_1$ the fluctuations in the figure 1(b) are high at $\theta \approx 105^o$

*Corresponding author. Email: smittal@iitk.ac.in

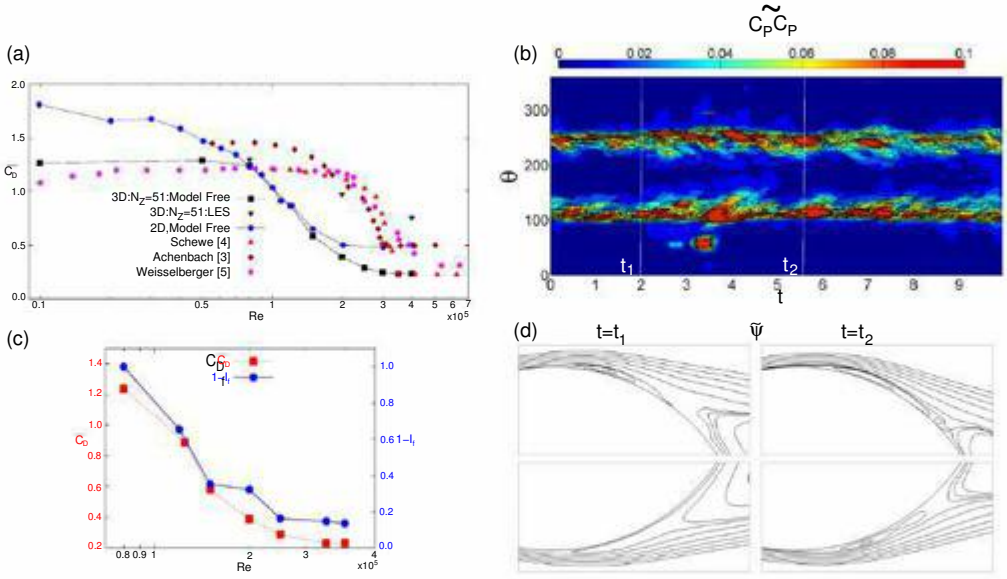

Figure 1: Flow past a cylinder: (a) variation of the mean drag coefficient with Re, (b) space-time diagram of the *rms* of the fluctuations $\widetilde{C'_P C'_P}(\theta, t)$ subjected to high pass filter at $Re = 1.5 \times 10^5$, (c) variation of the intermittency factor $(1 - I_f)$ with Re in solid line. Also shown in broken line is the span- and time-averaged drag coefficient. (d) Close-up views of the streamlines for the span- and moving time-averaged flow at two time instants marked in (b).

but relatively low at $\theta \approx 250^o$. Correspondingly a LSB can be seen in the time-averaged streamlines shown in figure 1(d) on the upper shoulder of the cylinder. At $t = t_2$, an LSB appears on both the upper and lower shoulder of the cylinder. Correspondingly, high fluctuations in $\widetilde{C'_P C'_P}(\theta, t)$ can be seen at $\theta \approx 105^o$ and $\theta \approx 250^o$. This demonstrates that high fluctuations in $\widetilde{C'_P C'_P}(\theta, t)$ correspond to increased shear layer activity and formation of LSB. As seen from figure 1(b), the high fluctuations in $\widetilde{C'_P C'_P}(\theta, t)$ appear in bursts. The space-time diagram is utilized to compute the Intermittency factor, I_f. An LSB exists on the shoulder if $\widetilde{C'_P C'_P}(\theta = 105^o \text{ or } 250^o, t)$ exceeds a certain threshold value. The concept of intermittency is very well established in transitional flows where it represents the fraction of time that the flow is in a turbulent state. In the present work, I_f represents the fraction of time during which LSB appears in the flow. Figure 1(c) shows the variation of $1 - I_f$ and C_D with Re. This figure clearly shows the correlation between $1 - I_f$ and C_D. In the subcritical regime $I_f \approx 0$, indicating LSB does not appear in the flow. In the early stages of critical regime, I_f starts increasing from a zero value and reaches unity towards the end of the critical regime. This shows that LSB appears intermittently during the regime of drag crisis and its frequency of appearance increases towards the end of drag crisis. Thus it can be said that in the transitional regime during the drag crisis, the flow fluctuates between laminar and turbulent states. The laminar state is associated with larger drag and is devoid of LSB. The turbulent state has a lower drag and is associated with an LSB. The average drag at any Re depends on the relative time spent in the two states.

CONCLUSIONS

The numerical simulations capture the drag-crisis. The Laminar separation bubble (LSB) is found to exhibit an intermittent behaviour. This nature of LSB is utilized to explain the gradual change in $\overline{C_D}$ in the transition regime during drag crisis as opposed to a sudden decrease in drag at a certain Re.

References

[1] Roshko A.: Experiments on the flow past a circular cylinder at very high Reynolds number. J. Fluid Mech 10:345-356, 1961.

[2] Singh S.P., Mittal S.: Flow past a cylinder: shear layer instability and drag crisis. Int. J. Numer. Meth. Fluids 47:75-98, 2005.

[3] Achenbach E.: Distribution of local pressure and skin friction around a circular cylinder in cross-flow up to Re= 5×10^6. J. Fluid Mech 34: 625-639, 1968.

[4] Schewe G.: On the force fluctuations acting on a circular cylinder in crossflow from subcritical up to transcritical Reynolds numbers. J. Fluid Mech 133:265-285, 1983.

[5] Schlichting H., Gersten K.,: Boundary layer theory. Springer Science and Business Media: 2000.

SECONDARY OPTIMAL PERTURBATION GROWTH IN HARTMANN CHANNEL FLOW

Shuai Dong*[1], Dmitry Krasnov[2], and Thomas Boeck[2]

[1]*School of Energy, Power and Mechanical Engineering, North China Electric Power University, Baoding, China*
[2]*Institute of Thermodynamics and Fluid Mechanics, Ilmenau University of Technology, Ilmenau, Germany*

Summary The algebraic growth of secondary optimal perturbations in a channel flow with a transverse magnetic field is investigated. Linear growth of perturbation on the streaky base flow is calculated by iteratively solving the direct and adjoint governing equations. For small amplitude streaks evolving on the channel flow, the secondary optimal perturbations resemble the primary ones. For large amplitude streaks cases, there is still residual interaction between the top and bottom Hartmann layer at relatively high Hartmann number. The optimal streamwise wavenumber is found to be finite and scaled with the thickness of the Hartmann layer.

INTRODUCTION

Hartmann channel flow is the prototype of many MHD flows in the casting and material processing industry. When the conducting liquid is passing through two unbounded plate in the presence of a constant transverse magnetic field, the core of the flow becomes flat and two electromagnetic boundary layers, i.e., Hartmann layers, develop at the walls perpendicular to the magnetic field. The thickness of the Hartmann layer δ is scaled as the inverse of the Hartmann number Ha. The stability of the Hartmann channel flow usually can be determined by the local Reynolds number R with δ as the length scale. A recent experiment identified transition in the Hartmann layers at critical local Reynolds number $R_c \sim 380$ [1]. Theoretical work with normal mode linear stability analysis overestimate this value. It is two orders of magnitude higher than that of experiment [2]. Recent developments in non-modal stability theory revealed that the transient growth, or algebraic growth of perturbations may play a significant role in the so-called sub-critical transition of shear flows [3]. We study this topic by means of a transient linear perturbation analysis using channel flow with unsteady streaks as the basic state.

FORMULATION OF THE PROBLEM

The Hartmann channel flow is considered in the present study, i.e., an incompressible electrically conducting fluid between two infinite parallel plates in the presence of an uniform transverse magnetic field. The flow is driven by the pressure gradient and the mass flux is maintained constant. A constant and uniform static magnetic field is oriented along the wall-normal z-axis. With the assumption of low magnetic Reynolds number, the nondimensional governing equations and boundary conditions are:

$$\frac{\partial \boldsymbol{u}}{\partial t} + (\boldsymbol{u}\cdot\nabla)\boldsymbol{u} = -\nabla p + \frac{1}{Re}\nabla^2\boldsymbol{u} + \frac{Ha^2}{Re}\left(-\nabla\phi\times\boldsymbol{e}_z + (\boldsymbol{u}\times\boldsymbol{e}_z)\times\boldsymbol{e}_z\right), \tag{1}$$

$$\nabla\cdot\boldsymbol{u} = 0, \tag{2}$$

$$\nabla^2\phi = \nabla\cdot(\boldsymbol{u}\times\boldsymbol{e}_z), \tag{3}$$

$$u = v = w = \frac{\partial\phi}{\partial z} = 0 \quad \text{at } z = \pm 1, \quad \text{periodicity in } x \text{ and } y \text{ directions.} \tag{4}$$

Here $\boldsymbol{e}_z \equiv (0,0,1)$ is the unit vector of the applied magnetic field and x, y, z denote the streamwise, spanwise and wall-normal directions, respectively. The nondimensional parameters in equation (1) are the Reynolds number $Re \equiv UL/\nu$ and the Hartmann number $Ha = L/\delta$, where δ denotes the Hartmann layer thickness, $\delta = \sqrt{\rho\nu/\sigma B^2}$. The local Reynolds number is then defined as $R = U\delta/\nu = Re/Ha$.

For the analysis of secondary perturbations, the governing equations (1–3) are linearized around the modulated Hartmann flow $\mathbf{U}(y,z,t)$. The secondary linear perturbations take the form $\mathbf{u}_p(x,y,z,t) = \frac{1}{2}\left[\hat{\mathbf{u}}(y,z,t)\exp(i\alpha x) + c.c.\right]$, where α denotes the streamwise wavenumber and $c.c.$ denotes the complex conjugate. An energy norm is then defined as $E(t) \equiv \int(\hat{u}\hat{u}^* + \hat{v}\hat{v}^* + \hat{w}\hat{w}^*)dydz$, thus the ratio of $E(t)$ and the initial value $E(0)$ is the perturbation energy amplification factor $G(t) = E(t)/E(0)$.

Using a Lagrangian formalism, the maximum value of G for given parameters $G_{\max}(Re, Ha, T, \alpha)$ is determined via optimization constraints, which are enforced by the adjoint fields [3]. The optimal perturbation and amplification at time T are obtained by an iterative scheme, in which forward integration of the linearized governing equation is followed by backward integration of the corresponding adjoint equations. For comparison of secondary growth at different values of Re and Ha, we require a comparable velocity amplitude of the developed streak. Thus, an energy amplitude A is defined as $A = E_0/E_{\mathrm{B}}$, where E_{B} is the mean kinetic energy of the Hartmann channel flow. The value of ARe^2/Ha is decisive and must remain constant between different cases for comparison.

*Corresponding author. Email: shuai.dong@ncepu.edu.cn

RESULTS

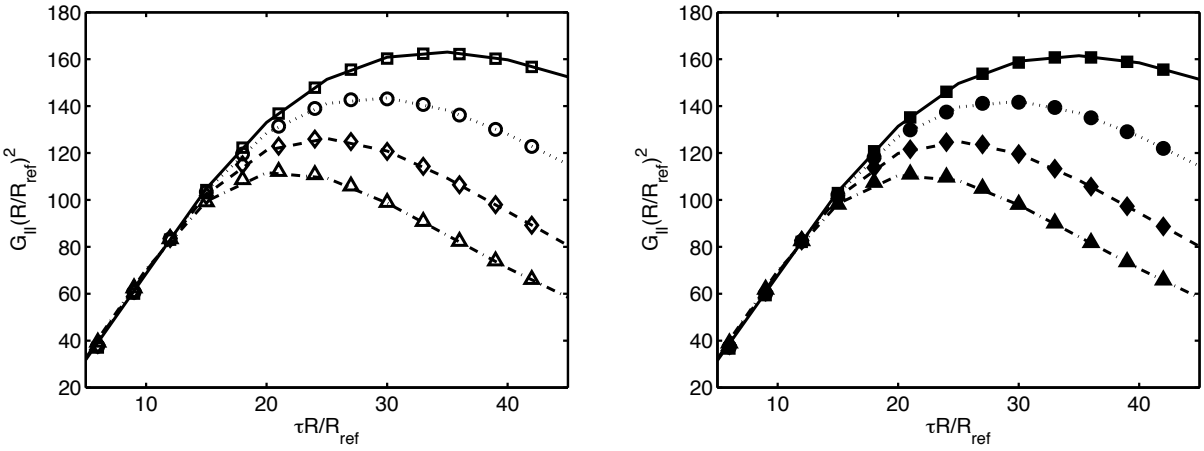

Figure 1: Amplification of perturbations with small α evolving on modulated channel flow with lower amplitude streaks, symmetric (left) and antisymmetric case(right). The parameters are $Ha = 10$ at $R = 500$(symbols) and $R = 300$(lines). Different line(symbol) corresponds to different value of rescaled α, which is increased from top to bottom.

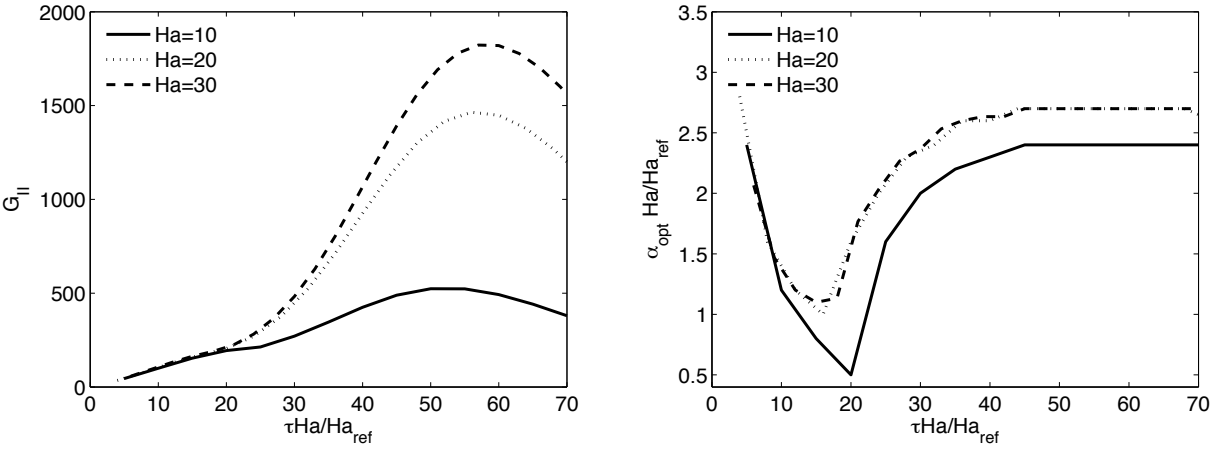

Figure 2: Maximum of secondary perturbation energy amplification (left) and the corresponding optimal wavenumber $\alpha_{\rm opt}$ (right) for higher amplitude streaks at $R = 300$ and $Ha = 10, 20, 30$.

Fig.1 shows the rescaled optimal secondary amplification $G_{\rm II}(R/R_{\rm ref})^2$ as function of the rescaled time $\tau R/R_{\rm ref}$ for corresponding rescaled wavenumbers $\alpha R/R_{\rm ref}$, and $R_{\rm ref} = 300$. The rescaled amplifications of perturbations coincide at the two Reynolds numbers $R = 300$ and $R = 500$. This scaling behaviour is in agreement with that of primary optimal perturbations [4]. There are no apparent differences between the modulation by antisymmetric and symmetric primary perturbations, that implies the secondary perturbations are localized in the top and bottom Hartmann layers. For higher amplitude streaks, the scaling is not valid due to the strong modulation of channel flow. The maximum value of secondary perturbation energy and the corresponding optimal wavenumber $\alpha_{\rm opt}$ are shown in Fig.2, as a function of time τ for $R = 300$ and different Ha. The maximum of energy amplification increases as the Hartmann number is increased from $Ha = 10$ to $Ha = 30$. The small differences in $G_{\rm II}$ between $Ha = 20$ and $Ha = 30$ indicate that the perturbations become localized at the walls for $Ha = 30$. The optimal wavenumber $\alpha_{\rm opt}$ is approximately proportional to Ha at larger values of τ.

Acknowledgment

DK and TB acknowledge financial support by the Helmholz alliance "Liquid Metal Technologies" (Limtech). SD's work is supported by the National Natural Science Foundation of China (No.11302076), the Natural Science Foundation of Hebei Province (No.A2014502047) and the Fundamental Research Funds for the Central Universities (No.2014MS111).

References

[1] Moresco P., Alboussière T.: Experimental study of the instability of the Hartmann layer. J. Fluid Mech. 504: 167-181, 2015.

[2] Lingwood R. J., Alboussière T.: On the stability of the Hartmann layer. Phys. Fluids 11: 2058-2068, 1999.

[3] Schmid P. J., Henningson D. S.: Stability and Transition in Shear Flows. Springer, 2001.

[4] Cossu C., Chevalier M., Henningson D. S.: Optimal secondary energy growth in a plane channel. Phys. Fluids 19: 058107, 2007.

FLOW STRUCTURE IN A ROTATING CYLINDER WITH FLUID AND A FREE LIGHT BODY AT VIBRATION

Nikolai V. Kozlov*[1]
[1]*Lab. of Vibrational Hydromechanics, Perm State Humanitarian-Pedagogical University, Perm, Russia*

Summary A system of two quasi-concentric cylinders at rotation is studied experimentally. The gap between the cylinders is filled with a fluid. The outer cylinder (cuvette) is installed horizontally and brought to rotation, the inner cylinder (core) is lighter than the fluid and occupies a steady position on the rotation axis due to the centrifugal force. The action of transversal vibration on the system leads to the excitation of core inertial oscillations, steady streaming generation in the Stokes layers and core differential rotation. Heavy particles are added into the fluid to study the flow in the annulus. The core oscillations make the sedimented particles redistribute on the cylinder wall surface forming a regular pattern, azimuthal rings periodic along the rotation axis. The spatial period of the pattern depends on the regime of the core motion.

INTRODUCTION

A flow in an annulus between two concentric independently rotating cylinders, known as Couette–Taylor flow, possesses a large number of regimes [1]. One of the most known is a pattern of vortices periodic along the axial coordinate – Taylor vortex flow. Oscillations of the outer cylinder, e.g. librations, lead to the excitation of inertial waves in the fluid [2]. Circular oscillations of a free cylindrical core in a rotating cylinder lead to steady flow generation and spinning of the core [3]. The study of Couette–Taylor flow is a key to understanding the physics of interior of planets and stars [4] and a promising approach for industrial application [5].

EXPERIMENTAL RESULTS

A system of two quasi-concentric cylinders at rotation is studied experimentally. The gap between the cylinders is filled with a fluid. The outer cylinder (cuvette) is installed horizontally on the platform of an electrodynamic vibrator and is brought to rotation about its axis with the rate Ω_r by a stepper motor. The inner cylinder (core) is lighter than the fluid and occupies a steady position on the rotation axis due to the centrifugal force. The core rotates with the rate Ω_s. Heavy particles are added into the fluid to study the flow structure in the annulus.

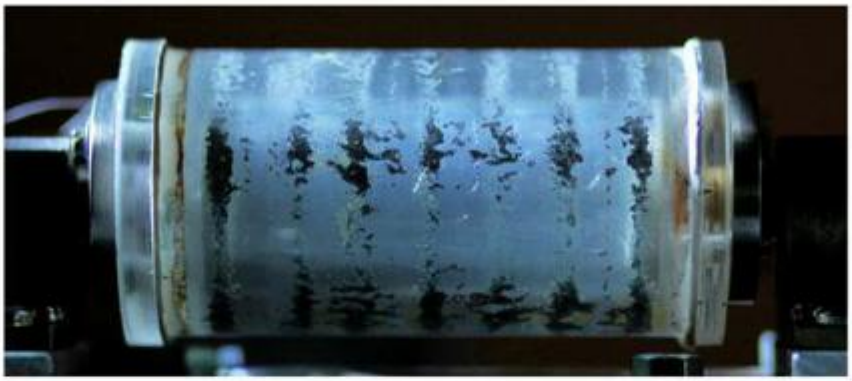

Figure 1: Regular pattern of heavy particles of different size – aluminium flakes, polymeric spheres, and carbon – deposited on the wall of the outer cylinder. Cuvette rotation rate $\Omega_r = 113.6$ rad/s, vibration angular frequency $\Omega_v = 251.3$ rad/s, vibration amplitude $b_v = 0.30$ mm, differential rate of core rotation $\Delta\Omega = 33.9$ rad/s

The action of transversal vibrations on the system leads to a resonant excitation of the core inertial oscillations of circular polarization. This leads to a steady streaming generation in the Stokes layers. Depending on the direction of oscillations, either they are prograde or retrograde with respect to the cavity rotation, the steady flow is directed positive or negative relative to the cavity. Accordingly, the free core is entrained by this flow in an average differential rotation, either leading or lagging. The mechanism of steady flow generation in this system is theoretically explained in [6]. In Figure 1, the pattern photograph

*Corresponding author. Email: kozlovn@pspu.ru

is presented for the case when the core oscillates in the prograde direction and its rotation is leading. In the annulus, a strong azimuthal flow is present, which moves faster than the cavity wall.

At simultaneous oscillations and differential rotation of the core, the sedimented particles redistribute on the cylinder wall surface, forming a regular pattern: azimuthal rings periodic along the rotation axis (Figure 1). This indicates the occurrence of a regular system of toroidal vortices. This phenomenon is observed for both leading and lagging differential rotation of the core. Depending on the dimensionless frequency of vibration ($n \equiv \Omega_v/\Omega_r$), the spatial period of the pattern changes and the rings of particles may become wavy. At high oscillation amplitude of the core, the large particles are washed to the end-walls, and the aluminium flakes visualize small-scale patterns (spatial period of the order of ten times the boundary layer thickness) periodic along the axis.

Analysis of the pattern wavelength and Reynolds numbers makes it possible to suggest two mechanisms of vortex generation. First, since the core is oscillating, the propagation of inertial waves should be considered, which may lead to the redistribution of the particles in the points of wave reflection. Second, at sufficiently high values of the Reynolds numbers, the Taylor instability should be taken into account. In a certain range of experimental parameters, a coexistence and an interaction of the two mechanisms is possible, which makes the problem quite complicated. Different types of the sub-scale structure of the particle rings are found, which supports the idea of a competition between two mechanisms of flow generation.

Acknowledgements

The work is supported by the Russian Scientific Foundation, project 14-11-00476.

References

[1] Andereck C. D., Liu S. S., Swinney H. L.: Flow regimes in a circular Couette system with independently rotating cylinders. J. Fluid Mech. 164: 155–183, 1986.

[2] Borcia I. D., Ghasemi A. V., Harlander U.: Inertial wave mode excitation in a rotating annulus with partially librating boundaries. Fluid Dyn. Res. 46(4): 041423, 2014.

[3] Kozlov V. G., Kozlov N. V.: Vibrational hydrodynamic gyroscope. Dokl. Phys. 52(8): 458–461, 2007.

[4] Le Bars M., Cébron D., Le Gal P.: Flows driven by libration, precession, and tides. Annu. Rev. Fluid Mech. 47: 163–193, 2014.

[5] Lee S., Lueptow R. M.: Rotating membrane filtration and rotating reverse osmosis. J. Chem. Eng. Jpn. 37(4): 471–482, 2004.

[6] Kozlov N.: Theory of the vibrational hydrodynamic top. Acta Astronaut. 114: 123–129, 2015.

EFFECTS OF CURVATURE VARIATIONS IN A TRANSITIONAL BOUNDARY LAYER ON HEAT TRANSFER

Larissa Ferreira Marques *[1], Josuel Kruppa Rogenski[1], Leandro Franco de Souza[1], and Jerzy M. Floryan[2]
[1]*Dept. of Applied Mathematics and Statistics, ICMC - University of Sao Paulo, Sao Carlos, Sao Paulo, Brazil*
[2]*Dept. of Mechanical and Materials Engineering, University of Western Ontario, London, Ontario, Canada*

Summary It is known that the boundary layer over concave surfaces can be unstable to centrifugal forces, giving rise to counter-rotating vortices, aligned in the streamwise direction. The effects caused by these vortices distort the hydrodynamic and thermal boundary layer profiles, and they may modify the heat transfer rates. Results of a numerical investigation of the effects of Goertler vortices on heat transfer enhancement from a boundary layer flow over walls of variable curvature are reported. Fully concave, concave-flat and concave-convex configurations are considered. The results provide evidence that one may effectively decrease heat transfer rates of a transitional flow by changing curvature.

INTRODUCTION

The laminar-turbulent transition phenomenon and its effect on heat transfer have been investigated for several decades. The literature relating to this subject is covered by different types of approaches, whether analytical, numerical or experimental. The first study regarding the effects of Goertler vortices on heat transfer was conducted by [3]. The experimental study [4] compares the enhancement in heat transfer in Goertler flow with turbulent values, proving that the enhancement in heat transfer in Goertler flow can be higher than the one in turbulent flows. In [5], experimental results of streamwise variation of the Stanton number on heated flat and concave walls with three different favorable streamwise pressure gradients at Mach number 0.015 show one increase up to 110% in the Stanton number due to the presence of the Goertler vortices. Studies related to nonlinear spatial stability computations for walls with variable concave curvature were published in [1], where is studied numerically the influence of variations in the curvature using the parabolized disturbance equations. Results presented in [2] show that steady Goertler flow can increase the heat transfer rates to values close to the values of turbulence, without the existence of a secondary instability. In the present paper we extend some analyses of [1] by discussing the effects of curvature variations on heat transfer rates.

PROBLEM FORMULATION AND RESULTS

The problem is modeled through a Navier-Stokes system equations written in vorticity-velocity formulation. The governing equations are complemented by the specification of boundary conditions. A simulation code was developed and implemented using a high-order, pseudo-spectral numerical simulation method. Further details can be seen in [2]. The schematic diagram of the computational domain is illustrated in Fig.1.

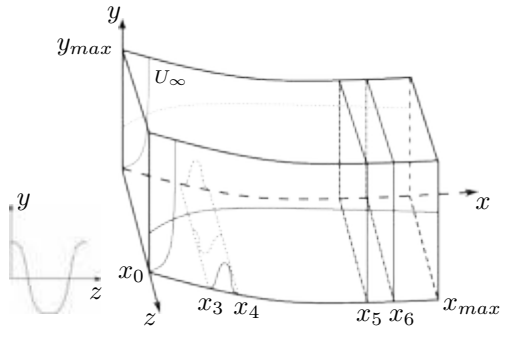

Figure 1: Computational domain

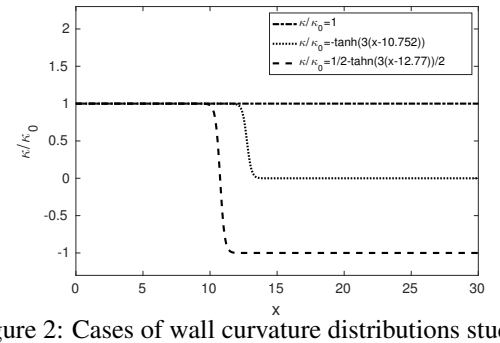

Figure 2: Cases of wall curvature distributions studied

The nonlinear simulations were made adopting the same physical parameters of the classical experiment [6]. We consider the radius of the concave surface $R^* = 3.2\ m$, the free stream velocity $U^*_\infty = 5\ ms^{-1}$, and the kinematic viscosity $\nu^* = 1,5 \times 10^{-5}\ m^2 s^{-1}$. For analysis of heat transfer we verify the evolution of the spanwise–average Stanton number in the streamwise direction, where this nondimensional parameter is defined as $St_x = \frac{Nu_x}{PrRe_x}$. Nu_x, Re_x and Pr denote the Nusselt, Reynolds and Prandtl numbers and they are defined by $Nu_x = \left.\frac{\partial T}{\partial y}\right|_{wall} \frac{L}{T_e - T_w}$, where T_e and T_w are the temperature

*Corresponding author. Email:laraposmac@gmail.com

values outside from the thermal boundary layer and at the wall, $Re_x = \frac{U^*_\infty x^*}{\nu^*}$ and $Pr = \frac{\nu^*}{\alpha^*}$, where x^* is a plate characteristic length and α^* is the thermal diffusivity of the fluid.

Figure 2 illustrates the cases of wall curvature distributions studied. These distributions are modeled by the function $\frac{\kappa}{\kappa_0}$, where κ_0 and κ represent the curvature at $x = 1$ and x position respectively and they are similar to the functions presented in [1]. The evolution of the spanwise–average Stanton number in the streamwise direction for each of the curvature distributions is shown in Fig. 3. The first distribution of curvature to be analysed is a classic case where the curvature is fully concave, i.e., $\frac{k}{k_0} = 1$. The second case studied displays a wall consisting of a concave section attached to a flat section by a section with continuous variable curvature. They are modeled by $\frac{k}{k_0} = \frac{1}{2} - \frac{1}{2}\tanh[3(x - 12.77)]$. For the last case analysed, we consider concave circular plate attached to a convex circular one of the same radius $\frac{1}{k_0}$ by a section with continuously variable curvature. The function representing the curvature distribution is given by $\frac{k}{k_0} = -\tanh[3(x - 10.752)]$. For each case of curvature variation three Prandtl numbers were considered, $Pr = 0.72$, $Pr = 1.0$ and $Pr = 7.07$. As can be seen in Fig

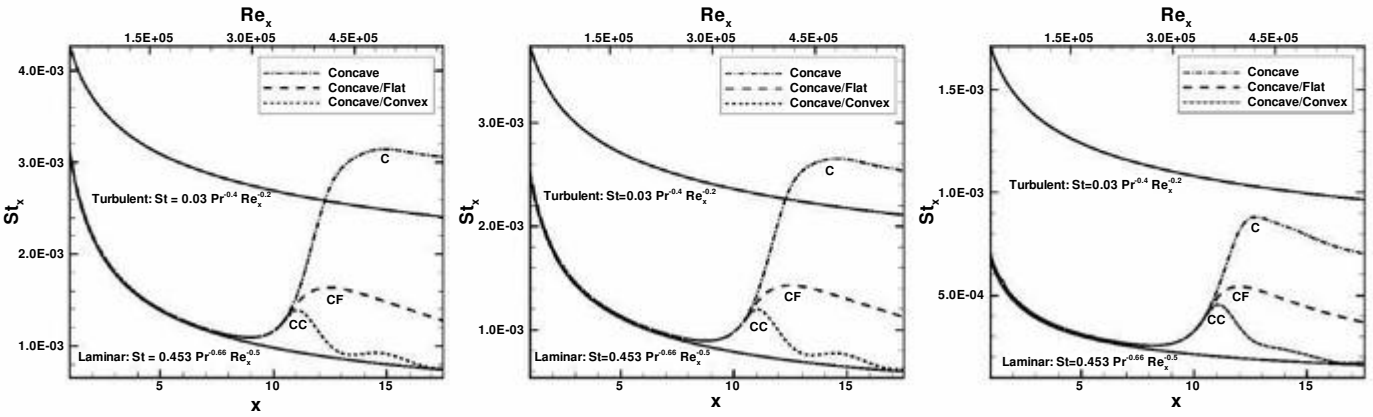

(a) $Pr = 0.72$ (b) $Pr = 1.0$ (c) $Pr = 7.07$

Figure 3: Streamwise evolution of the spanwise-averaged Stanton number for $\lambda_z = 0.18$. Transitional results are compared with laminar and turbulent boundary layer theoretical Stanton functions.

3 all cases of wall curvature distributions are showing the spanwise-averaged Stanton number for the Goertler flow similar to laminar flow at region until $Re_x \sim 2.25 \times 10^5$ $(x \sim 7)$. For the cases illustrated in the Fig.3, items (a) and (b), the intensification of rate of heat transfer caused by the Goertler vortice can be observed from $Re_x \sim 3.0 \times 10^5$ $(x \sim 10)$. In the first case, where the curvature distribution is fully concave, at the Re_x around 4.0×10^5 $(x \sim 12.5)$, the Stanton number reaches higher values than the turbulent ones. In the cases where the curvature is changed, we can observe that the centrifugal effect caused by the concave curvature is turned off, resulting in a decrease in heat transfer rates. For concave/flat wall this decrease can be seen from $Re_x = 4.0 \times 10^5$ $(x = 12.75)$, and from $Re_x = 3.75 \times 10^5$ $(x = 10.75)$ on the concave/convex curvature distribution. Fig 3 (c) displays results with $Pr = 7.07$. In this case the Stanton numbers for the transitional flow does not reach the Stanton values obtained in turbulent flow in any of the curvature distributions. This behavior is expected since the thermal boundary layer is thicker than the hydrodynamic boundary layer, therefore the influence of Goertler vortices is smaller.

CONCLUSIONS

Results show that the case of concave/convex curvature has effects of stability on Goertler vortices generated by the concave curvature. Thus there is evidence that the convex curvature can be most useful for the control of a laminar flow. This was also happen for concave/flat wall, but with a lower intensity. Considering the fully concave curvature distribution it was observed that the steady Goertler flow can increase the heat transfer rates to values higher than the turbulent ones.

References

[1] Benmalek, A. and Saric, W.S.: Effects of curvature variation on the nonlinear evolution of Goertler vortices. *Physics of Fluids.* **6,** 3353-3367, 1994.

[2] Malatesta, V., Souza, L. F. and Liu, J.T.C.: Influence of Goertler vortices spanwise wavelenght on heat transfer hates. *Computational Thermal Sciences: An International Journal.* **5,** 389-400, 2013.

[3] McCormack P. D., Welker H. and Kelleher M.: Taylor-Grtler vortices and their effect on heat transfer. *ASME J. Heat Transfer.* **92,** 101-112, 1970.

[4] Peerhossaini, H.: LInstabilite dune couche limite sur une paroi concave: les tourbilons de Goertler. Ph.D. thesis, Univ. Pierre et Marie Curie, 1987.

[5] Umur, H and Karagz I.: An investigation of external flows with various pressures and surfaces. *Int. Comm. Heat Mass Transfer.* **26,** 411-419, 1999.

[6] Swearingen, J.D. and Blackwelder, R.F.: The growth and breakdown of streamwise vortices in the presence of a wall. *J. Fluid Mech.*. **182,** 255-290, 1887.

NONLINEAR DISTURBANCE EVOLUTION IN SUPERSONIC BOUNDARY LAYERS ON THE SWEPT WING

Alexandra Panina[1,a)], Gleb Kolosov[1], Alexander Kosinov[1], Nikolay Semionov[1] & Yury Yermolaev[1]
[1]*Khristianovich Institute of Theoretical and Applied Mechanics, Novosibirsk, Russia*

Summary The paper presented the results on the generation and development of the wave train in uniform and spanwise modulated boundary layer at Mach 2. A swept-wing model was used in the experiments. In 3D boundary layer the oblique breakdown mechanism is detected, which previously observed only in a supersonic boundary layer on flat plate. It was obtained that in the spanwise modulated boundary layer the oblique breakdown mechanism occurs at lower values of the longitudinal coordinate *x*.

INTRODUCTION

For fluid mechanics, the laminar-turbulent transition in supersonic 3D boundary-layer flows is one of the most important issue. In ITAM SB RAS, which has low-turbulence wind tunnel T-325, controlled experiments on a 45° swept wing were carried out. First of all, detailed hot-wire measurements of unstable wave trains propagating at free-stream Mach number M = 2 were performed [1]. Most recently, the experimental validation of predicted nonlinear mechanism of subharmonic resonance on smooth swept wing was achieved [2]. From data available to us we can state that the subharmonic resonance plays a major role in transition in swept wing boundary layer with roughness. But not only subharmonic resonance mechanism will cause a transition to turbulence. Another nonlinear mechanism is oblique breakdown mechanism obtained earlier on flat plate [3, 4]. Using the distributed roughness near the leading edge it was able to intensify the mechanism of oblique breakdown in the boundary layer on the flat plate [5]. In this paper, similar experiments on the smooth swept wing and swept wing with roughness were presented.

EXPERIMENTAL SETUP

The experiments were conducted in the T-325 low noise supersonic wind tunnel of ITAM SB RAS at M = 2 and unit Reynolds number $Re_1=7\times10^6$ m^{-1} in experiments on the smooth model and $Re_1=5\times10^6$ m^{-1} in experiments on the model with roughness. A swept-wing model was used in the experiments. The model had a sweep angle of 45° and a slightly blunted leading edge of radius 0.2 mm [1]. A sketch of the experimental model and the coordinate systems are shown in Figure 1; dimensions are given in mm. The model was fixed in the central plane of the test section at approximately zero angle of attack. A source of localized artificial disturbances was built in the model [6]. Controlled pulsations have been generated using high-frequency glow discharge in a chamber and they were injected into the boundary layer through an aperture 0.4 mm in diameter in the upper surface of the model. A sine-wave generator and amplifier with transformer output were used to produce high voltage at a frequency of 10 kHz. The actuator work at frequency 20 kHz that enabled artificial perturbations to be excited at frequencies of 10 and 20 kHz in the boundary layer. The square stickers from a scotch tape were applied to induce the spanwise modulation of mean flow in the boundary layer. The sizes of labels were 3 mm × 3 mm, the height in both case was 60 microns. Some details concerning to the coordinate systems and location of the stickers are shown in Figure 1. The wind tunnel has an automated measuring system that allows determining the flow parameters in "real time". The flow disturbances were measured by a constant-temperature anemometer (CTA). A tungsten hotwire of 10 μm in diameter and 1.6 mm in length was used. The pulsation measurements were synchronized with a disturbance source and sine wave generator by a special device in a computer-automated measurement and control crate. The AC and DC signals from the CTA were written to the PC using a 12-bit analog-to-digital converter with sampling rate 750 kHz and by DC voltmeter, respectively. Four time traces of 65536 points in length were measured and written to file in each space position of the hotwire.

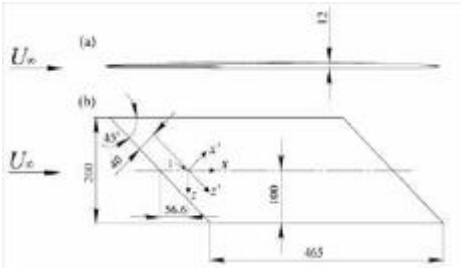

Fig. 1. A sketch of the swept wing and coordinate systems used; (a) – side view; (b) – plan view; (1) marks the disturbance source.

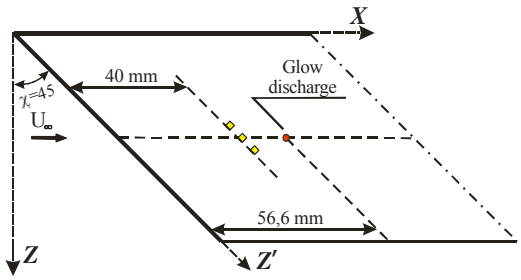

Fig. 2. Model of the swept wing with roughness.

[a)] Corresponding author. Email: avpanina@itam.nsc.ru

Mean and pulsation characteristics of the flow were obtained after data processing using a standard technique [1]. The mean flow distortion was determined by using the ratio between the relative change of the average mass flow and relative change of mean voltage output from CTA [5].

RESULTS

The source of controlled disturbances introduced pulsations at frequencies $f = 10$, 20, 40 kHz in the supersonic boundary layer. However, disturbances at 40 kHz attenuate downstream whereas those at 10 and 20 kHz have grown. Figure 3,*a* shows the amplitude β'-spectra of the controlled disturbances for the fundamental frequency $f = 20$ kHz on the smooth swept wing. The greatest amplitude growth is observed at $\beta' = 1.21$ rad/mm, which correspond to linear development of unstable waves. In sections $x = 70$, 80 mm the amplitude growth at $\beta' = -0.88$ rad/mm is occurred. The presence of additional peak in the amplitude spectra for the fundamental frequency cannot be explained in terms of subharmonic resonance. It is likely formed by nonlinear interaction between stationary and travelling waves.

For occurring oblique breakdown mechanism synchronism condition must be satisfied:

$$f_1+f_2=f_3$$
$$\alpha_1+\alpha_2=\alpha_3$$
$$\beta_1+\beta_2=\beta_3.$$

Dispersion relations $\alpha_r'(\beta')$ are estimated from phase β'-spectra and these results are shown in Figure 3,*b*. For $f = 10$, 20 kHz the dependence $\alpha_r'(\beta')$ are seen to be close to the linear ones. For $f = 0$ kHz the line $\alpha_r'(\beta')$ is drawn parallel to those at frequencies $f = 10$, 20 kHz. The arrows on the plot indicate the increasing waves. From these data we consider that nonlinear amplification of disturbances in 3D supersonic boundary-layer is described well by oblique breakdown mechanism.

In experiments on the swept wing with roughness the greatest amplitude growth is observed at $\beta' = 1.19$ rad/mm (Figure 3,*c*). In sections $x = 40$, 50, 60 mm the amplitude growth at $\beta' = -0.6$ rad/mm is occurred. This additional peak in the amplitude spectra for the fundamental frequency formed by nonlinear interaction between stationary and travelling waves - oblique breakdown mechanism.

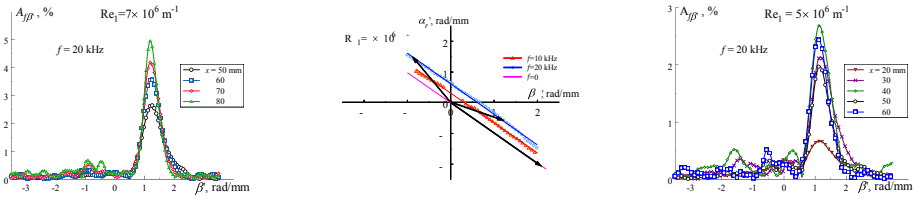

Fig. 3. (a) Amplitude β'-spectra of disturbances. $f = 20$ kHz, smooth model; (b) Dispersion relations $\alpha_r'(\beta')$. $f = 20$ kHz, smooth model; (c) Amplitude β'-spectra of disturbances. $f = 20$ kHz, model with roughness.

CONCLUSIONS

In uniform and non-uniform flows in 3D boundary layer the oblique breakdown mechanism is detected, which previously observed only in a supersonic boundary layer on flat plate. Thus, subharmonic and oblique breakdown are the mechanisms of weakly nonlinear interaction in 3D supersonic boundary layer, similar to the case on a flat plate. It was obtained that in the spanwise modulated boundary layer the oblique breakdown mechanism occurs at lower values of the longitudinal coordinate x. The results are suitable for the CFD code verification.

This work has been supported by the RFBR grant 16-31-00290, 16-01-00743.

References

[1] Ermolaev Yu.G., Kolosov G.L., Kosinov A.D., Semenov N.V. Linear evolution of controlled disturb-ances in the supersonic boundary layer on a swept wing. *J. Fluid Dynamics* **49(2)**:188-197, 2014.

[2] Kolosov G.L., Kosinov A.D., Yermolaev Yu.G., Semionov N.V. On nonlinear interaction of controlled disturbances in 3D supersonic boundary layer. *Intern. Conf. on Methods of Aerophys. Research: Proc. Pt I.*:113-114, 2014.

[3] Mayer C., Fasel H.F. Investigation of Asymmetric Subharmonic Resonance in a Supersonic Boundary Layer at Mach 2 Using DNS. *AIAA-paper №2008-0591*, 2008.

[4] Kosinov A.D., Yermolaev Y.G., Semionov N.V., and Tagaev S.N. Mean flow distortion effect on the nonlinear wave interaction at the transition in supersonic boundary layer. *Abstracts of XIII International Conference on the Methods of Aerophysical Research, Novosibirsk, Part I*:168-169, 2008.

[5] A.V. Panina, A.D. Kosinov, Yu.G. Yermolaev, V.N. Gorev, N.V. Semionov. Experimental study of mean and pulsation flow characteristics in the 2D/3D supersonic boundary layer behind flat roughness elements. *Thermo-physics and Aeromechanics* **21(1)**:3-13, 2014.

[6] A.D. Kosinov, A.A. Maslov, S.G. Shevelkov. Experiments on the stability of supersonic laminar boundary layers. *J. Fluid Mech.* **219**:621-633, 1990.

NUMERICAL STUDY OF THE TRANSITION TO TURBULENCE IN PARTICULATE PIPE FLOWS

Anthony Rouquier[1], Chris Pringle[2], and Alban Potherat[3]

[1,2,3]*Department of Applied Mathematics, University of Coventry, Coventry, United Kingdom*

Summary We present a stability analysis of a pipe flow with particle suspension. Particles are considered solid, spherical, heavy with an unique size and density. The particles are, in our physical model, modelled as a continuous phase and for the fluid-particles interactions only the Stokes drag is taken into account, the other forces being neglected. We first use a linear stability analysis to study the influence of the addition of particles to the global stability of the flow. Single phase pipe flows have been proven to be globally stable for any Reynolds number, we find that this is also the case for particulate pipe flows. The effect of particles varies with the concentration and the size of the particles, but it remains relatively weak. Then a nonlinear transient growth analysis allows us to look for the optimal perturbation triggering turbulence and the effects of particles.

Pipe flow is a classical problem in fluid dynamics. The simplicity of geometry and relevance to industry and engineering has made it one of the main research topic in fluid dynamics. Thus a lot of knowledge has been accumulated, yet research is mostly focused on single phase flows. The characteristics of laminar and turbulents flows and the conditions for the transitions from one to the other has been a major source of interest for decades because of the wide range of applications. Today the transition for single phase shear flows is relatively well understood and little is known for flows having differents phases, and the focus on this topic has risen recently in the scientific community.
One of the major difficulty in simulating a particulate laden flow is the modeling of particles. The representation of a high number of discrete entities and accompanying boundary layers is very expensive and limits the possibilities. In order to circumvent the problem, instead of modeling particles as discrete entities, we parametrize them with continuous variables, much like the fluid. A similar model is used in [Klinkenberg et al., 2011] for a study of channel flows. Because it requires a lot less computational power than a realistic description of particles, this model is not as constrained as the complete description of particle. The drawback is that this representation is not always physically realistic. For small particles and low volumic concentration the model should give a good approximation but it is supposed to break if those parameters increase too much. The system of equations for our model is :

$$\frac{\partial u}{\partial t} = \circ\ \frac{\nabla p}{\rho}\ \circ\ (u.\nabla)u + \nu\nabla^2 u + \frac{KN}{\rho}(u_p \circ\ u)$$

$$\frac{\partial u_p}{\partial t} = \circ\ m\,N(u_p.\nabla)u_p + KN(u \circ\ u_p)$$

$$\frac{\partial N}{\partial t} = \circ\ \nabla(N u_p)$$

$$\nabla.u = 0$$

With u and u_p the velocity fields for the fluid and particles, p the pressure, ρ the density of the fluid and ν its viscosity. N is the concentration of particles and m the mass of one particle, so mN represents the mass of the particles per unit volume. K is the Stokes drag defined such as $K = 6\,\pi\,r\,\rho\,\nu$ with r the radius of a particle.

We used in a first time a linear stability analysis to study the influence of the addition of particles to the global stability of the flow. The equations for the perturbation leads to a modified Orr-Sommerfeld problem. Linear stability analysis have been carried out extensively for single phase pipe flows. It is well known that the pipe flow is linearly stable to very high Reynolds numbers and it is theorised that pipe flows are always linearly stable. We find the same result for particle laden pipe flows, but the addition of particles does affect the temporal growthrate of the perturbation, effect which varies linearly with the particle concentration. While the increase of the effect with the particle concentration is consistent with our model, it is likely that the linearity is due to the physical model and the absence of nonlinear effects rather than to physical effects. The impact on the flow also depends on the particle size as seen in the figure below. Is represented the normalised growthrate (particles have a stabilising effect on the flow if is superior to 1, destsabilising otherwise). against SR, a nondimensional Stokes number proportional to the square of the particle radius for several Reynolds number and a mass concentration of 10% :

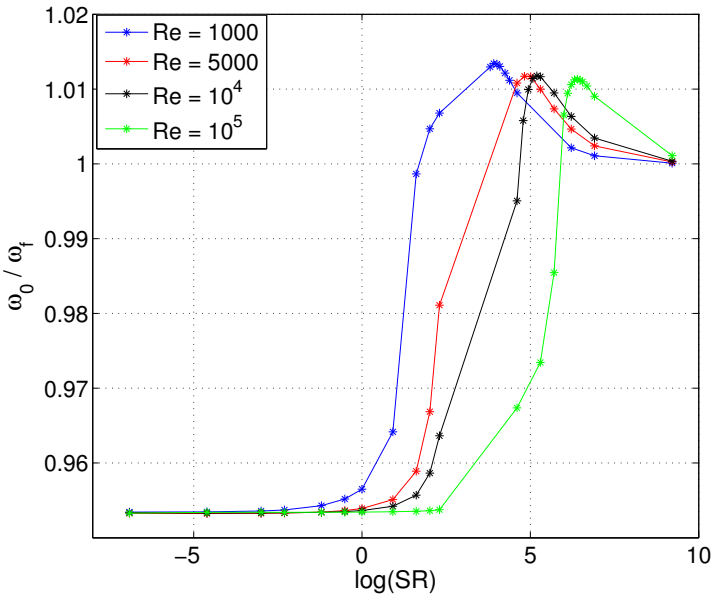

Figure 1: Evolution of the energy (f=0.1, $\alpha = 1$)

In the limit of very small particles, the particles behave as passive tracers only affect the linear stability by modifying the global density of the flow. In the limit of larges particles, the fluid and particles velocities are decoupled (the Stokes drag is converging towards 0) so the particles do not affect the growthrate of the perturbation. This last property is the opposite of what is physically expected and illustrates the limit of our model. Intermediate sized particles have a stabilising effect on the flow with a peak so we have a "optimal" particle size for a given set of Reynolds number Re and perturbation wavelength α. The amplitude of the effect is also inversely proportional to the Reynolds number. The optimal value follows a simple heuristic formula, expressed here in terms of a Stokes number SR :

$$SR_{peak}(Re, \alpha) \approx \frac{1.85}{\sqrt{Re\,\alpha}} \tag{1}$$

Then a nonlinear transient growth analysis is done to obtain further results. The method for nonlinear transient growth in our work has been defined in [Pringle and Kerswell, 2010]. Our code is a modified version of the DNS code for pipe flows created by Dr Willis ([Willis, 2015]). It can be used in two different ways, either a perturbation is given, and the program looks at how it evolves with time, or for a given time T it find the optimal perturbation, producing the maximal growth at that time. The analysis is still ongoing, but first results seems to indicate stronger effects than in the linear model. For initial perturbations with a small energy (less than 1% of the mean flow) and stable cases the addition of particles still do not make an important difference. Whereas for unstable cases, when transition happens, the general behaviour is similar but the difference in energy between single phase and particle laden flows are more important. Thus we expect particles to play a role in the transition in the boundary cases.

References

[Klinkenberg et al., 2011] Klinkenberg, J., de Lange, H., and Brandt, L. (2011). Modal and non-modal stability of particle-laden channel flow. *Physics of Fluids (1994-present)*, 23(6):064110.

[Pringle and Kerswell, 2010] Pringle, C. C. and Kerswell, R. R. (2010). Using nonlinear transient growth to construct the minimal seed for shear flow turbulence. *Physical review letters*, 105(15):154502.

[Willis, 2015] Willis, A. P. (2015). The openpipeflow.org Navier–Stokes solver. Technical report. openpipeflow.org/index.php?title=File:TheOpenpipeflowSolver.pdf.

USE OF NATURAL INSTABILITIES FOR ENHANCEMENT OF FLOW MIXING IN ANNULI

Amirreza Seddighi, Hadi Vafadar Moradi & Jerzy Maciej Floryan
Dept. of Mechanical and Materials Engineering, University of Western Ontario, London, Ontario, Canada

Summary A technique has been proposed to increase flow mixing in annuli through efficient vortex generation. Corrugations in the form of axisymmetric ribs have been placed at the walls to modulate the axial flow in a manner which leads to centrifugal instabilities which result in the formation of streamwise vortices. This technique results in only a small increase in the pressure drop, unlike other vortex generation methods. A spectral algorithm based on Fourier and Chebyshev expansions has been used to study the stationary state and its stability. Due to the irregularities of the boundaries, the immersed boundary conditions (IBC) method has been used to enforce the flow boundary conditions. The effects of geometric and flow parameters on the pressure losses and on the stability characteristics have been thoroughly investigated. Characteristics of both the vortex mode and the travelling mode of instability, as well as the region of dominance of each mode, have been determined.

INTRODUCTION

Axial flow between two concentric cylindrical shells (annulus) is widely encountered in applications, e.g. flow in tubular heat exchangers, movement of drilling mud in oil and gas wells, heavy oil extraction industry, fuel cells, etc. [1]. The main objective of this study is the identification of conditions which lead to the formation of vortex instabilities which can be used to increase mixing. It is known that radial mixing in flows with vortices can increase by an order of magnitude when compared with flows without vortices [2]. As the same system is subject to the travelling wave instability, one needs to know its characteristics in order to avoid interference with the formation of vortices. Thus, we are interested in the determination of conditions where the vortex instabilities dominate.

PROBLEM FORMULATION AND RESULTS

Steady, pressure-gradient-driven axial flow of viscous incompressible fluid in an annulus extending to $\pm\infty$ in the z-direction is investigated. The flow field is described using the cylindrical system of coordinates with z, r and θ corresponding to the axial, radial and circumferential directions, respectively. With the transverse, sinusoidal ribs placed on both cylinders, the annulus geometry is described by four geometric parameters: R_1- radius of the inner cylinder, S-rib amplitude, α-rib wave number (rib wavelength $\lambda = 2V/\alpha$) and φ- phase shift between ribs at the inner and outer cylinders (Fig. 1).

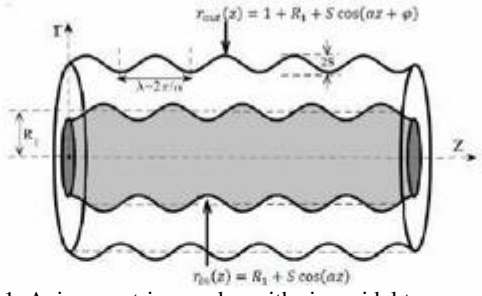

Figure 1. Axisymmetric annulus with sinusoidal transverse ribs.

The mass flow rate through the ribbed annuli is kept the same as through the smooth annuli (reference flow) and pressure losses are assessed by determining the added pressure gradient (denoted by A) required to maintain this flow rate. After solving the mean flow and determining the velocity and pressure fields ($\bar{V}$ and P), a disturbance field of the form

$$\bar{}_{disturbance}(z,r,\theta,t),\ P_{disturbance}(z,r,\theta,t)\big] = \big[\vec{G}_V(z,r), G_p(z,r)\big]e^{i(\delta z + M\theta - \sigma t)}$$

is introduced. In the above equation, $\vec{G}_V$ and G_p are the z-periodic amplitude functions, δ and M are the axial and circumferential disturbance wave numbers, respectively, and σ is the complex frequency. The solution of the relevant eigenvalue problem leads to the determination of σ. Figures 2 to 4 illustrate the effects of geometric parameters on the pressure losses. It can be seen that an increase of R_1, S, α and φ increases the losses (Fig.2 and Fig.4). Variations of the phase difference φ are relevant only for ribs with small α's (Fig. 3). It can also be seen that in the case of $R_1 \to \infty$ the pressure losses approach losses found in channels with the same ribs (Fig. 4).

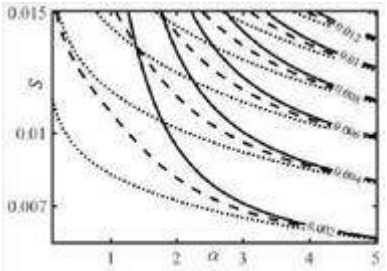

Figure 2. Variation of the ratio of the pressure gradient correction A to the reference flow pressure gradient as a function of α and S for R_1=1 and *Re*=1000. Solid, dashed, dot lines indicate φ=0, $\pi/2$, π, respectively.

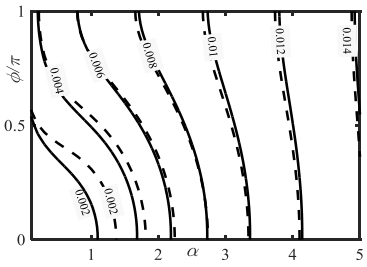

Figure 3. Variation of the ratio of the pressure gradient correction A to the reference flow pressure gradient as a function of α and φ for S=0.015, *Re*=1000. Solid, dashed lines indicate R_1=1, 10, respectively.

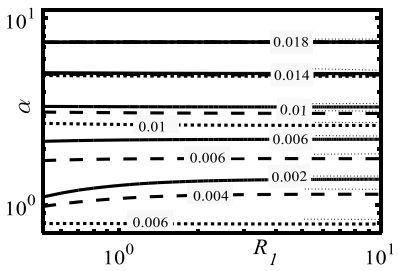

Figure 4. Variation of the ratio of the pressure gradient correction A to the reference flow pressure gradient as a function of α and R_1 for S=0.015 and *Re*=1000. Solid, dashed, dotted lines indicate φ=0,$\pi/2$, π, respectively.

Figure 5 illustrates the flow topology resulting from the introduction of vortices. The formation of these vortices can be affected if the onset of the travelling wave instabilities precedes the onset of the vortices. Therefore, the favorable conditions are defined as those for which the critical Reynolds number for the onset of the vortex mode is smaller than the critical Reynolds number for the onset of the travelling wave mode. Such conditions are identified using grey in Fig. 6, which displays variations of the Re_{cr} for both instability modes as functions of the rib amplitude and the rib wave number. These results show that an increase of α beyond 4 does not have a significant effect on the reduction of Re_{cr} required for the formation of the vortices. However, since an increase of α increases the pressure losses (Fig. 2), one can conclude that $\alpha = 4$ represents the optimal rib wave number for the formation of vortices. We use the term "optimal" to signify the rib wave number which gives the smallest critical Reynolds number for the formation of the vortices and which, at the same time, produces the smallest pressure drop.

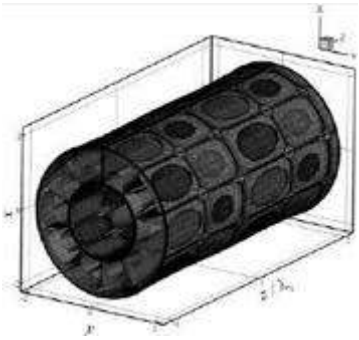

Figure 5. Topology of the disturbance velocity field associated with the formation of vortices in an annulus with $R_1 = 1$, $\alpha = 5$, $S = 0.015$, $\varphi = 0$, M = 5 at the onset ($Re = 3401.5$).

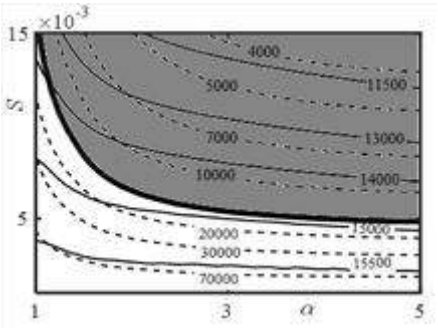

Figure 6. Variations of Re_{cr} as a function of α and S for the onset of the travelling wave (solid lines) and the vortex instabilities (dashed lines) in an annulus with $R_1 = 1$ and $\varphi = 0$. The thick line separates zones of dominance of the travelling wave and the vortex modes of instability.

CONCLUSIONS

Characteristics of flow in ribbed annuli have been studied to identify conditions leading to the formation of streamwise vortices without interference from the travelling waves. It was shown that the rib amplitude should be large enough for the vortices to dominate over the travelling waves. It was also observed that the rib wave number should not be larger than 4 in order to avoid excessive pressure losses. Finally, the annulus with the phase shift of φ=π (a converging-diverging annulus) was shown to offer the most favorable conditions for the generation of vortices.

References

[1] Moritis G.: Heavy oil expansions gather momentum worldwide. Oil & Gas Journal, 93, 31-38, 1995.

[2] Lograni P. M., Oliviera M. M., Blaskovich T.: Comparison of heat transfer augmentation techniques, AIAA J., 41, 337-362, 2003.

EFFECT OF LIBRATIONS ON THE DYNAMICS OF FREE INNER CORE AND LIQUID IN ROTATING CAVITY

Stanislav Subbotin[1]
[1]*Perm State Humanitarian Pedagogical University, Perm, Russia*

Summary. The motion of fluid and a free spherical core in a cavity rotating about a horizontal axis is experimentally investigated. The cavity rotation speed is modulated (librations). It is found that the action of librations leads to the generation of the azimuthal fluid motion, resulting in the averaged lagging differential rotation of the free core. It is shown that the contribution of librations in differential rotation is determined by the amplitude of librations, which depends on the Ekman number.

INTRODUCTION

Fluid motion excited by oscillations in rotating cavities is an actual geophysical problem. It is known that the oscillating motion in liquid cores of planets can be excited by a periodic change of the rotation speed (librations). In works [1, 2, 3] it was shown that the zonal flow in the fluid interior is generated as a result of oscillatory motion in the Ekman layers. On the other hand, the oscillation of fluid can be excited by oscillation of the inner solid core. An example is the free oscillations of the planet inner core of buoyant nature, which are named a "Slichter triplet" [4]. A theoretical and experimental study of the effect of circular oscillations of free inner core on its dynamics has been studied in works [5, 6, 7]. The investigations have shown that as a result of the oscillations the core which is located near the axis of rotation comes into a differential rotation relative to the cavity. The direction of rotation is determined by a dimensionless frequency (the ratio of oscillation frequency and rotation frequency) $n = \Omega_{osc} / \Omega_{rot}$. In this paper the motion of the fluid and free oscillating core excited by librations of the cavity is experimentally investigated.

EXPERIMENTAL TECHNIQUE

A light spherical body (core) is located in a fluid-filled spherical cavity. The fluid density is higher than the core density. The cavity rotates around a horizontal axis. The rotation speed is high enough to make that the light core to take place in the central part of the cavity under the action of centrifugal force. The cavity rotation speed in the inertial reference frame changes according to the law: $\Omega(t) = \Omega_{rot} + \Delta\varphi\, \Omega_L \sin(\Omega_L t)$. The azimuthal velocity profile in a spherical shell is investigated by PIV-method.

RESULTS

In the absence of librations the core performs a slow lagging differential rotation with the speed $\Delta\Omega < 0$ under the action of the gravity force. The average differential rotation of the core has a vibrational nature and is explained by the fact that the static in the laboratory frame gravitational field rotates in the non-inertial frame in the direction opposite to the cavity rotation with the frequency $\Omega_{osc} = -\Omega_{rot}$. The action of the rotating field on the nonhomogeneous in density system “solid core – liquid” leads to a circular oscillation of the core relative to the cavity. As a result of nonlinear effects in dynamical boundary layers, an average torque which spins the core relative to the cavity appears [6, 7]. Librations of the cavity leads to variations of the core rotation speed, which changes periodically with the frequency Ω_L. With an increase in the amplitude of the libration the core differential rotation increases monotonically. Simultaneously, the range of $\Delta\Omega$ variations expands, and at a critical value of the amplitude the maximum differential rotation exceeds the average cavity rotation speed ($\Delta\Omega_{\max} > 0$). At the same time, the average lagging differential rotation speed increases. Intensification of the differential rotation of the core is due to the emergence of steady flow associated with an oscillating motion in the Ekman layer caused by librations.

ACKNOWLEDGMENTS

The work was supported by RFBR (project No. 16-31-60099 mol_a_dk and 16-31-00169 mol_a).

References

[1] Busse F.H.: Mean zonal flows generated by librations of a rotating spherical cavity. *J. Fluid Mech.* **650**: 505–512, 2010

[2] Sauret A., Cebron D., Morize C., Le Bars M.: Experimental and numerical study of mean zonal flows generated by librations of a rotating spherical cavity. *J. Fluid Mech.* **662**: 260–268, 2010.

[a)] Corresponding author. Email: subbotin_sv@pspu.ru.

[3] Calkins M.A., Noir J., Eldredge J.D., Aurnou J.M.: Axisymmetric simulations of libration-driven fluid dynamics in a spherical shell geometry. *Phys. Fluids.* **22**: 086602, 2010.

[4] Slichter L.B.: The fundamental free mode of the Earth's inner core. *Proc. Natl. Acad. Sci. U.S.A.* **47**: 186–190, 1961.

[5] Kozlov V.G., Kozlov N.V.: Vibrational hydrodynamic gyroscope. *Dokl. Phys.* **52**: 458–461, 2007.

[6] Kozlov V.G., Kozlov N.V., Subbotin S.V.: Influence of an external force field on the dynamics of a free core and fluid in a rotating spherical cavity. *Phys. Fluids* **27**: 074106, 2015.

[7] Kozlov V.G., Kozlov N.V., Subbotin S.V.: The effect of oscillating force field on the dynamics of free inner core in a rotating fluid-filled spherical cavity. *Phys. Fluids* **27**: 124101, 2015.

DETECTION OF A LOGARITHMIC SINGULAR POINT BEHIND AN AIRFOIL MODEL AT LOW REYNOLDS NUMBERS

Shohei Takagi[1a)], Yasufumi Konishi[2], Nobutake Itoh[1], Masahito Asai[1] and Shigeru Obayashi[2]
[1]*Department of Aerospace Engineering, Tokyo Metropolitan University, Hino, Tokyo, Japan*
[2]*Institute of Fluid Science, Tohoku University, Sendai, Miyagi, Japan*

Summary Regular-vortex formation behind circular cylinders or 2-D blunt bodies is associated with the global instability of the wake, which selectively induces a monochromatic disturbance. The complex ray theory predicts that the monochromatic disturbance is selected at the logarithmic singular point in the wake of a flat plate, which corresponds to the turning point in the global theory. Experiments at low Reynolds numbers were performed to detect this singularity behind an airfoil-shaped model in a low–turbulence wind tunnel. The onset of the global mode with extreme frequency selectivity and much larger spatial growth rate than that of convective instability was observed in the recirculation region very near the trailing edge of the model.

INTRODUCTION

It is known that regular-vortex formation behind circular cylinders or 2-D blunt bodies is associated with the so-called global instability of the wake, which selectively induces a monochromatic disturbance [1, 2]. The complex ray theory [3] also shows that this instability and the frequency selection may be explained from the viewpoint of a logarithmic singularity, which corresponds to the turning point in the global theory and is associated with the recirculation region of the wake. However, the fact that the singular point is located in a complex extension of the streamwise coordinate with a small imaginary part leads to a question as to how the singularity manifests its effects in the real flow field experimentally observed. Main objectives of the present study are experimentally to detect a reflection of the singular point and to investigate the spatial structure of the monochromatic disturbances. An airfoil-shaped model was deployed in order to increase the critical Reynolds number up to the one order of magnitude higher than that of blunt models and to allow accurate measurements in the velocity range of 3-6m/s.

EXPERIMENTAL SETUP

All experiments were conducted in the low-turbulence wind tunnel at the Institute of Fluid Science, Tohoku University, Japan. The test section is a closed octagonal shape with a diagonal length of 290 mm. Residual turbulence level in free stream to the free stream velocity U_0 is approximately 0.03% at 5m/s, consisting of the frequency components lower than 100Hz. A constant-temperature anemometer was used to measure mean and fluctuating velocities. An NACA0010 airfoil model, made of stainless steel, was used, whose chord length c and maximum thickness t are 24mm and 2.4mm, respectively. The airfoil model at no incidence was vertically set in the middle of the test section. The freestream velocity U_0 was varied from 3 to 6m/s, corresponding to Reynolds numbers of approximately 460-920, based on U_0 and t. As for the coordinate system, X and Y are taken in the streamwise and transversal directions. The origin of X and Y are placed at the trailing edge of the airfoil.

EXPERIMENTAL RESULTS

Figures 1a and 1b illustrate power spectra at the peak positions of fluctuating velocity components across X=20mm at U_0 =3m/s and X=12.5mm at 5m/s, respectively. In Fig.1a, two peak components approximately at 60Hz and 250Hz are observed. The former may be due to mechanical vibration of the hot-wire support, and the selective peak at 250Hz accompanies slightly broad side-lobe components around the peak. Also, Figure 1b represents an extremely sharp line component at 480Hz and also its higher harmonics. There is no comparison in amplitude between Figs 1a and 1b at each peak frequency, showing that the wake-instability mechanism between two cases is obviously different. So, we measured profiles of mean and fluctuating velocities across the wake at various X locations varying free-stream velocities.

Figure 2 shows distributions of the maximum rms values of the most amplified component u_f normalized by U_0 against X. At U_0=3m/s and 4m/s, the most amplified components exponentially grow in the streamwise direction, indicating that the wake instability is convective. However, when U_0 exceeds 4.5-5m/s, the spatial growth rates are drastically increased by abrupt growth of a monochromatic disturbance as shown in Fig.1b. This implies that such abrupt growth may be attributed to existence of the logarithmic singularity near the trailing edge of the model.

Considering that the anemometer output is rectified for reverse flow, we made an attempt to estimate the magnitude of reverse flow by fitting a curve $U/U_0=1-U_D \exp(-0.69315(Y/h)^m)$ on the measured mean velocity profiles, where h is the half-value-half-width of each mean velocity profile. Figure 3 presents U_D versus X at various U_0. At lower than 4.5m/s, U_D

[1a)] Corresponding author. Email: pantaka@tmu.ac.jp

monotonically increases in the downstream direction, while U_D for the cases exceeding 5m/s is slightly negative or almost zero between X=2 and 3.5mm, indicating that a small-scale reverse flow exists. It is important to point out that the first appearance of a monochromatic disturbance is located in the recirculation region.

CONCLUSIONS

Experiments with the use of an airfoil-shaped model at low Reynolds numbers were found to be successful in switching the wake from subcritical to supercritical states by means of a slight Reynolds-number increase. In contrast to the subcritical wake dominated by growing disturbances of broad-band frequencies, the supercritical wake exhibits a sharp line spectrum of disturbances after its strong frequency selection. Another remarkable feature of the supercritical wake is that the selected component has a much larger spatial growth rate than the one experienced in convective instability. It could be concluded that a singular point exists near the middle portion of the recirculation region and manifests its effect in both formation and abrupt spatial growth of the global mode.

References

[1] Monkewitz, P. A., Huerre, P. and Chomaz, J.-M.: Global linear stability analysis of weakly non-linear shear flows, *J. Fluid Mech.*, 251(1993), pp. 1-20.

[2] Chomaz, J.-M.: Global instabilities in spatially developing flows: Non-normality and nonlinearity, *Ann. Rev. Fluid Mech.*, 37(2005), pp. 357-392.

[3] Itoh, N., Takagi, S. and Ikeda T.: "Instability and frequency selection of the wake behind a flat plate", *Trans. Jpn. Soc. Aeronaut. Space Sci.*, Vol. 55, No.6 (2012) pp.356-363.

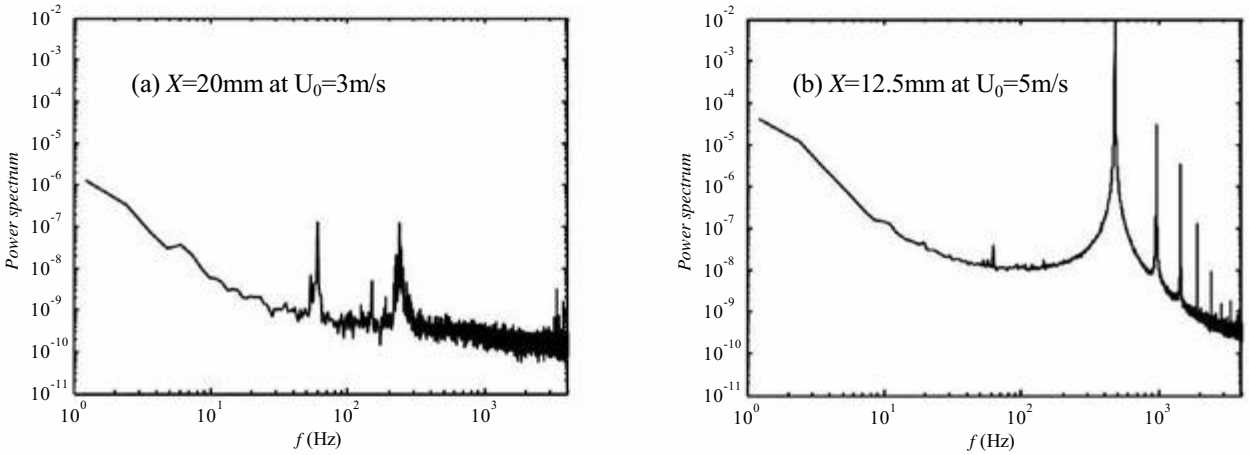

Fig.1 Power spectra of fluctuating velocity in the wake behind an NACA0010 airfoil model.

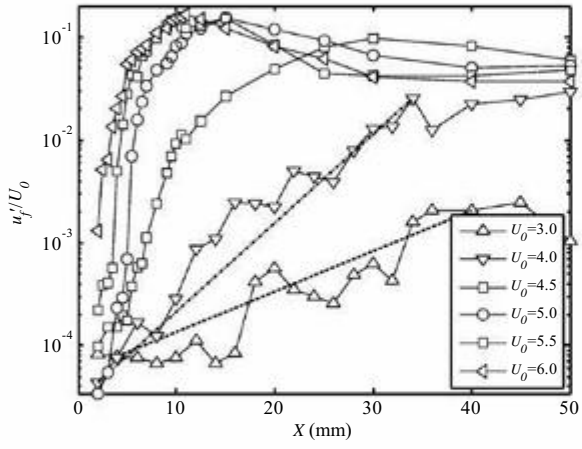

Fig.2 Distributions of maximum rms values of most-amplified component against X at various free-stream velocities U_0(m/s).

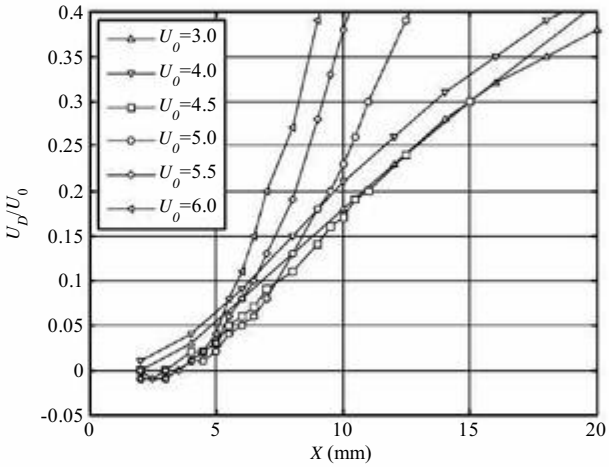

Fig.3 Distributions of maximum velocity defect U_D against X at various free-stream velocities U_0(m/s).

NUMERICAL STUDY OF THE TAYLOR-COUETTE FLOW USING DNS/SVV

Ewa Tuliszka-Sznitko, Kamil Kiełczewski
Institute of Thermal Engineering, Poznań University of Technology, Poland

Summary The authors present the results obtained during a numerical investigations of the Tylor-Couette flow in configurations of aspect ratios 11.75 and 3.76, different radii ratios and end-wall boundary conditions. The main purpose of the research is to investigate the influence of geometrical parameters and end-walls boundary conditions on the flow structure, the torque fluctuations and its total values. The results are discussed in the light of Brauckmann, Eckhardt [1] and Dong [2] data obtained with periodicity condition in axial direction. The results are compared also with Wendt [3] experimental results. For the cavity of aspect ratio 3.76 the authors study the laminar-turbulent transition for the radii ratio from the range: 0.375 - 0.821. The authors have found that the transition from the three-cell structure to the one-cell structure occurs only for the lower ratios. Computations are performed for Re up to 3100. All presented results have been obtained with the use of DNS/SVV method in which an artificial viscous operator is added to Laplace operator to stabilize the computational process for higher Reynolds numbers.

RESULTS AND NUMERICAL APPROACH

With the increase of Reynolds number in the Taylor-Couette flows we observe a series of successive bifurcations leading from the cylindrical Couette flow to the periodic Taylor vortex flow, then to a state with waves developed on the vortices, and finally, to a turbulent Taylor vortex flow. Literature on the Taylor-Couette flow is very extensive and different configurations are considered. The main purpose of the investigations of the phenomena which occur in the Taylor-Couette flow is to answer the fundamental question concerning transitional and turbulent structures, their origins and their role in creating stresses. This knowledge can help to control the boundary layer flow in more complex industrial configurations. The Taylor-Couette flows are governed by Reynolds number defined on the basis of the rotational speeds of the cylinders $Re_1 = (R_2-R_1)R_1\Omega_1/\nu$ and by the geometrical parameters: aspect ratio $\Gamma = H/(R_2-R_1)$ and radii ratio $\eta = R_1/R_2$. The dependence of the flow structure on the control parameters were analyzed in many papers (among others in Eckardt et al. [4]). In the present work we study the Taylor-Couette flow using DNS/SVV (direct numerical method/spectral vanishing viscosity method) in the cavity of rotating inner cylinder and stationary outer one with the symmetric and asymmetric end-wall boundary conditions. In the study we focus on influence of the end-walls boundary conditions, as well as, Γ and η on the flow structure, the torque distributions, the radial profiles of the mean angular velocity, the mean angular momentum, the Reynolds stress tensor components and the thickness of the boundary layers. The obtained results are analyzed in the light of data published in [1, 2] in which the authors, presented results obtained in similar cavities but with periodicity condition in axial direction. The results we also compare to the experimental results published in [3].

In the paper two groups of the flow cases are discussed. In the first one the computations have been performed for the cavity of aspect ratio 11.75, $\eta = 0.9$ (with the symmetric and asymmetric end-wall boundary conditions) and for Reynolds number up to 3100. These results are compared with numerical data published in [1] obtained by DNS for η=0.71 and with data obtained for cavity of $\eta = 0.93$ published in [3]. In connection with the theoretical analysis carried out in [4] we consider the local transverse angular momentum current $j^{\omega}(R,\varphi,Z,t) = R^3[v_r v_\varphi / R - \nu\partial(v_\varphi/R)/\partial R]$ and its averaged values $J^{\omega} = < j^{\omega}(R,\varphi,Z,t) >_{A(R),t} = R^3[< v_r v_\varphi / R >_{A(R),t} - \nu\partial(< v_\varphi / R >_{A(R),t})/\partial R]$ over concentric cylindrical surface, where v_r and v_ϕ denote the radial and azimuthal velocity components. The velocity decomposition to the turbulent velocity and the mean velocity allows to analyze contribution of the turbulent term $R^3 < v'_r v'_\varphi / R >_{A(R),t}$, the mean convection term $R^3 < \bar{v}_r \bar{v}_\varphi / R >_{A(R),t}$ and the viscous term $\nu\partial(< \bar{v}_\varphi / R >_{A(R),t})/\partial R]$ to the total J^{ω}. We analyze the spatial fluctuations of the local torque which show different characteristics near the cylinders and in the middle section of cavity as well as, the influence of aspect ratio on the $J^{\omega}/J^{\omega}_{lam}$. The influence of Γ we investigate by keeping constant Re and η, and by increasing and decreasing slowly Γ, with $\Delta\Gamma = 0.2$. This analysis is performed for the symmetric and asymmetric end-wall boundary conditions, and for two Reynolds numbers Re=150. Figure 1 presents the exemplary results obtained for configuration of aspect ratio 11.75 and $\eta = 0.9$ from which, among others, we can see that the maximum of the torque takes place at the bottom rotating disk (r = -1).

In the second part, we analyze the influence of the radii ratio η on the flow structure and statistics obtained in the cavity of aspect ratio $\Gamma = 3.76$. For the configuration of aspect ratio $\Gamma = 3.76$ and $\eta = 0.375$ with a rotating inner cylinder and bottom disk, and with a stationary outer cylinder and top disk the sequence of events occurring with the increasing Re is as follows: The three-cell structure is fully formulated at Reynolds number Re = 77 (the odd number of vortices is a characteristic feature of the Taylor-Couette flow with the asymmetric end-wall boundary conditions, Mullin, Blohm, [5]). At slightly larger Re (about 270) the middle vortex is squeezed by the growth of the top and bottom vortices, and finally at Re

[a] Corresponding author. Email: ewa.tuliszka-sznitko@put.poznan.pl.

= 281 the transition from a steady three-cell structure to a steady one cell-structure takes place. The transition to unsteadiness occurs at Re = 492 (six spiral vortices have been found of the dimensionless azimuthal wavelength $\lambda_a = 8.6$). After this transition with increasing Re we observe gradual development of the boundary layers on both cylinders and disks. The development of these boundaries is the main area of our interest: we analyze the axial and radial distributions of the Reynolds stress tensor components, the thickness of boundary layers and many structural parameters useful for modeling purposes. For small Reynolds numbers the results are compared to those published in [5]. The procedure of the transition from three-cell structure to one-cell structure takes place for $\eta = 0.375$ and 0.524. With further increase of η ($\eta = 0.615$, 0.756, 0.821) the classical Taylor-Couette scenario with consecutive bifurcations is observed. For higher Re (η =0.375) we observe vortices which appear very close to the inner cylinder as thin negative spiral patterns (they roll up in the opposite direction to the rotation of the inner cylinder). For $\eta = 0.821$ we also study the influence of temperature field on the flow structure and the distributions of the Nusselt number.

All presented numerical results have been obtained with the use of DNS/SVV method with meshes of 4-12 million collocation points. In the numerical approach the time scheme is second-order semi-implicit, which combines an implicit treatment of the diffusive term and an explicit Adams- Bashforth scheme for the non-linear convective terms. The spatial scheme is based on a pseudo-spectral Chebyshev-Fourier-Galerkin collocation approximation. All dependent variables have been obtained by solving Helmholtz equation. In the DNS/SVV method an artificial viscous operator is added to Laplace operator to stabilize the computational process for higher Reynolds numbers, Severac, Serre [6]. The precision of computations is checked by convergence analysis (we analyze $J^{\omega}/J^{\omega}_{lam}$ obtained for different resolutions) and by analyzing parameters $(z)^{+}_{2/1}, (r)^{+}_{2/1}, (\Delta\varphi, R_{2/1})^{+}$ along the inner and the outer cylinders. From the identification techniques based on the pointwise analysis of the velocity gradient tensor we chose the λ_2 criterion, which represents the topology of vortex cores very well.

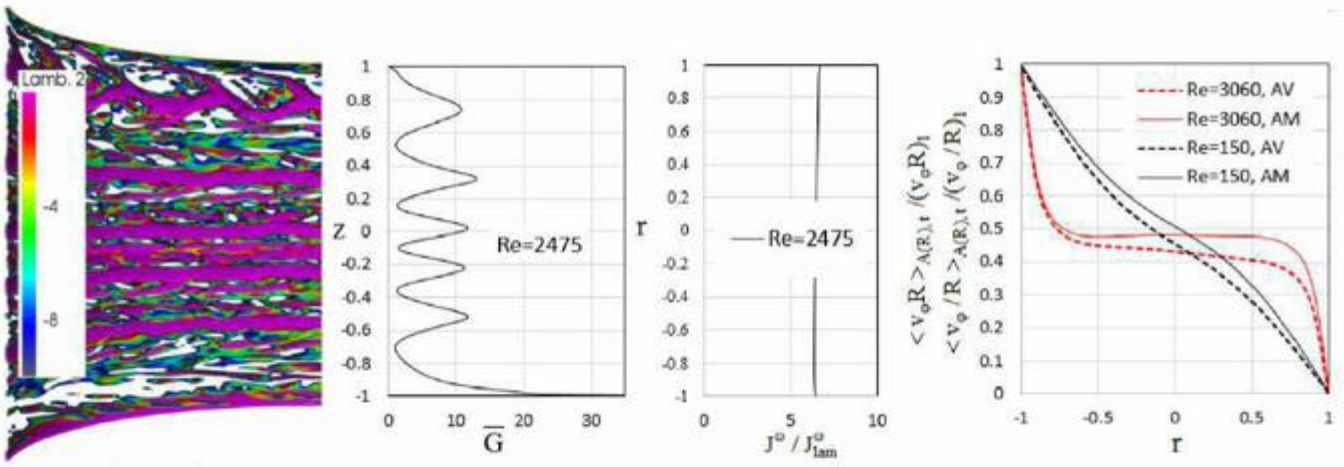

Figure 1. a) The iso-surfaces of the λ_2 near the outer cylinder (1/4 of cylinder), Re=2475, b) the axial distribution (along the outer cylinder) of the local transverse angular momentum current averaged in time and in azimuthal direction, and normalized by its laminar value for the circular Couette flow denotes here by $\overline{G}$, z denotes the dimensionless axial coordinate, c) the radial profiles of the total current J^{ω} normalized by its laminar value, r denotes the dimensionless radial coordinate, d) the radial profiles of the mean angular velocity and the mean angular momentum, $\Gamma = 11.75$, $\eta = 0.9$.

References

[1] Brauckmann, H., Eckhardt, B.: Direct numerical simulations of local and global torque in Taylor-Couette flow up to Re D 30000. *J. Fluid Mech*., 718, 398, 2013.

[2] Dong, S.: Direct numerical simulation of turbulent Taylor-Couette flow. *J. Fluid Mech*., 587, 373, 2007.

[3] Wendt, F.: Turbulente Strömungen zwischen zwei rotierenden koaxialen Zylindern. *Ing.-Arch*., 4, 577–595, 1933.

[4] Eckhardt, B., Grossmann, S., Lohse, D.: Torque scaling in turbulent Taylor–Couette flow between independently rotating cylinders. *J. Fluid Mech*., 581, 221–250, 2007.

[5] Mullin, T., Blohm, C.: Bifurcation phenomena in a Taylor-Couette flow with asymmetric boundary conditions. *Phys. Fluids*, 13, 136, 2001.

[6] Severac, E. and Serre, E.: A spectral viscosity LES for the simulation of turbulent flows within rotating cavities. *J. Comp. Phys*., 226, 2, 1234, 2007.

SLIDING COUETTE FLOW IN RIBBED ANNULI

Hadi Vafadar Moradi[*a)] & Jerzy M. Floryan[*]
[*]*Dept. of Mechanical and Materials Engineering, University of Western Ontario, London, Ontario, Canada*

Summary. The flow in an annulus driven by the axial movement of one of the cylinders has been studied. The stationary cylinder has been fitted with axisymmetric ribs. It has been shown that the flow is subject to a centrifugal-force-driven instability giving rise to the formation of axial vortices. The critical stability conditions have been determined for a wide range of geometries of practical interest. Reduction of the annulus' radius leads to qualitatively different flow responses depending on the position of the cylinder driving the flow. The critical Reynolds number is reduced and the range of the rib wave numbers that are capable of inducing the instability is increased when the outer cylinder drives the flow. The trend is reversed when the inner cylinder drives the flow.

INTRODUCTION

Flow between two concentric cylinders sliding with respect to each other in the axial direction is referred to as the sliding Couette flow (SCF) [1]. SCF occurs in a wide range of situations, e.g. piston-cylinder systems, a train moving through a tunnel, a catheter injected in a blood vessel, coating technology, etc. Since it is known that a vortex instability can be created in the planar Couette flow either through the use of transverse ribs [2] or through the use of wall transpiration [3], we wish to determine if a similar instability can be created in SCF. The main objective of this study is, therefore, the determination of conditions leading to the formation of such an instability, if at all possible.

PROBLEM FORMULATION AND RESULTS

Steady flow of an incompressible viscous Newtonian fluid confined between two concentric cylinders extending to $\mp\infty$ in the z-direction is considered. The flow, which is driven by the sliding motion of the outer cylinder with a constant velocity U in the positive z-direction, while the inner cylinder is kept at rest, is referred to as SCF. We modify the inner cylinder through addition of sinusoidal axisymmetric ribs (see Fig. 1). The stationary flow in the modified annulus is represented as a superposition of the SCF and modifications generated by the ribs. Introduction of the stream function defined in the usual manner leads to a single fourth-order partial differential equation which is discretized using the Fourier-Chebyshev spectral method [4]. The Immersed Boundary Conditions method (IBC) is employed to resolve the problem associated with the irregularities of the geometry [5].

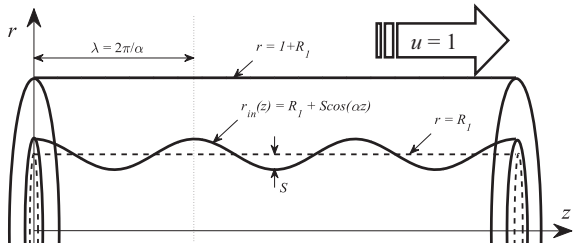

Figure 1: Sketch of the flow geometry - axisymmetric annulus with sinusoidal transverse ribs placed at the inner cylinder.

While the above flow modifications are caused directly by the ribs, additional changes may be caused indirectly through the formation of secondary flows. Conditions which lead to the onset of such flows and the determination of their form can be deduced using linear stability theory [2]. Unsteady, three-dimensional disturbances of the form $\mathbf{V}_D(x,y,z,t) = \sum_{n=-\infty}^{+\infty}\left[g_u^{(n)}(r), g_v^{(n)}(r), g_w^{(n)}(r)\right] e^{i[(\delta+n\alpha)x+M\theta-\sigma t]}$ are superposed on the mean flow where $V_D = (u_D, v_D, w_D)$ is the disturbance velocity vector, $g_{u,v,w}^{(n)}(r)$ are the unknown modal functions, δ stands for the real wave number in the axial direction, M denotes an integer wave number in the circumferential direction, and $\sigma = \sigma_r + i\sigma_i$ is a complex amplification rate whose real part stands for the frequency and whose imaginary part represents the amplification rate of the disturbances. Subtraction of the mean flow and linearization lead to the disturbance equations which form an eigenvalue problem. This problem has to be solved numerically [2].

The flow topology associated with the vortices for flow in an annulus with $R_1 = 1, \alpha = 5, S = 0.015$, $Re = 6568$ and $M = 4$ is well illustrated in Fig. 2A displaying iso-surfaces of the axial vorticity component. The formation of streaky structures aligned in the axial direction and being modulated by the ribs is clearly visible. The streaks are located close to the inner (ribbed) wall. The conditions which determine the appearance of the vortex instability can be expressed in terms of a critical Reynolds number Re_c, i.e. the minimum Reynolds number required for the onset of the instability for a given geometry of the annulus. Results displayed in Fig. 2B illustrate the role played by both R_1 and α. In general, when outer cylinder drives the flow, an increase of R_1 for a fixed α stabilizes the flow with annulus for $R_1 \to \infty$ being the most stable. The situation is reversed when the flow is driven by the inner cylinder. It can also be seen that the reduction of α stabilizes the flow. This is associated with the fact that the use of the long wavelength ribs reduces the streamwise flow modulations which, in turn, weaken the centrifugal force until it is unable to support the instability. Increase of α also stabilizes the flow but the mechanics of this process is different. In this case the troughs are filled in with the separation bubbles and the stream lifts up above the rib peaks. As a result, the fluid movement becomes nearly

[a)] Corresponding author. Email: hvafadar@uwo.ca

rectilinear, weakening the centrifugal force field. Figure 2C shows variations of Re_c as a function of the rib wave number and R_1 when flow is driven by the outer cylinder. It can be seen that an increase of Re increases the range of α capable of flow destabilization and expands the range of R_1 where the instability may occur. For $Re = 9000$, the instability may occur in the limit of $R_1 \to \infty$ (channel flow) but only for a narrow range of rib wave numbers, i.e. $\alpha \in (2.3,7.17)$; reduction of R_1 with Re fixed leads to a huge expansion of this range. These results also demonstrate that the reduction of R_1 has a strong destabilizing effects as the critical Reynolds number can be reduced from $Re = 8200$ for $R_1 \to \infty$ down to $Re < 4500$ for $R_1 \leq 0.1$ while, at the same time, the most effective rib wave number shifts from $\alpha \approx 3.5$ to $\alpha \approx 10$. Results presented in Fig. 2D illustrate the effect of the increase of the rib amplitude. The use of taller ribs amplifies the flow modulations, increases the centrifugal force field and, as a result, reduces the critical Reynolds number.

The ribbed wall can be viewed as hydraulically smooth as long as it is unable to create a system bifurcation. It is convenient to introduce the global critical Reynolds number, $Re_{c,g}$, which corresponds to the minimum of Re_c over all rib wave numbers for the specified rib amplitude and the annulus curvature. $Re_{c,g}$ has a very simple dependence on S if R_1 is fixed as illustrated in Fig. 2E. These curves define the upper limit of S which guarantees the flow stability. As the flow is stable for conditions below these curves for any rib distribution, the cylinders with such ribs can be viewed as hydraulically smooth. A general correlation of the form $Re_{c,g} = (-50.24R_1^{-0.04861} + 81.99)S^{(0.02703R_1^{-0.5274} - 1.293)}$, provides a very good approximation of $Re_{c,g}$ which guarantees the flow stability for all R_1 and S considered.

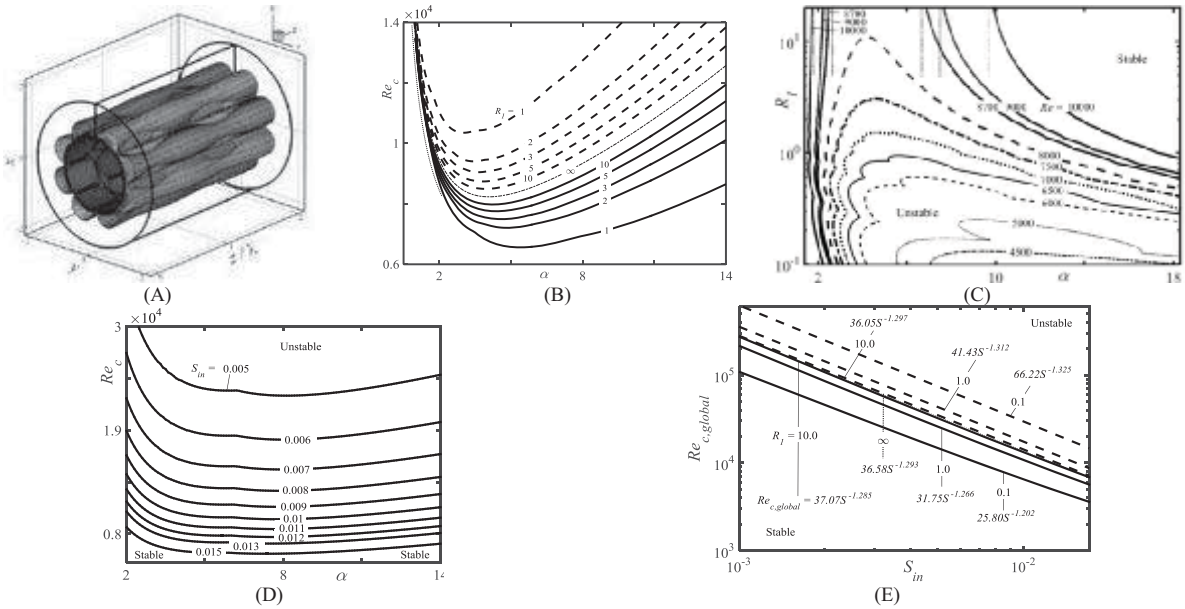

Fig. 2: Disturbance flow topology associated with the vortex instability (Fig. 2A), variations of Re_c as a function of different geometric parameters (Fig. 2B, C, and D), and variations of the global critical Reynolds as a function of ribs amplitude (E).

CONCLUSIONS

The Couette flow in an annulus formed by two co-axial cylinders, one of which is fitted with axisymmetric ribs, has been studied. Linear stability analysis shows that the flow undergoes transition to a secondary state, resulting in the formation of pairs of counter-rotating axial vortices. In the case of flow driven by the movement of the outer cylinder with the inner cylinder being ribbed, the flow is destabilized by reduction of R_1, with the lowest critical Reynolds number corresponding to the smallest R_1 considered, i.e. $R_1 = 0.1$. The range of the rib wave numbers capable of flow destabilization expands at the same time. In the case of the flow driven by the movement of the inner cylinder with the outer cylinder being ribbed, the flow is stabilized by a reduction of R_1 and the range of α capable of flow destabilization decreases at the same time. The most unstable configuration corresponds in this case to $R_1 \to \infty$. Conditions when the ribbed annulus can be viewed as being a hydraulically smooth annulus have been determined.

References

[1] Joseph, D. D. 1976 *Stability of Fluid Motions*, Vols I and II. Springer.

[2] Floryan, J. M. 2002 Centrifugal instability of Couette flow over a wavy wall, *Phys. Fluids* **14**, 312-322.

[3] Floryan, J. M. 2003 Wall-Transpiration-Induced Instabilities in Plane Couette Flow, *J. Fluid Mech.* **488**, 151-188.

[4] Moradi, H. V., Floryan, J. M.: Algorithm for analysis of flows in ribbed annuli. *Int. J. Numer. Meth. Fluids* **68** (2011), 805–838.

[5] Szumbarski, J., Floryan, J. M.: A direct spectral method for determination of flows over corrugated boundaries, Journal of Computational Physics **153** (1999), 378-402.

CONVECTIVE INSTABILITY OF THE BOUNDARY LAYER UNDER SOLITARY WAVES

Joris C. G. Verschaeve* and Geir K. Pedersen
Department of Mathematics, University of Oslo, Norway

Summary The stability of boundary layers under surface and internal solitary waves has been investigated. The parabolized stability equation method has been used in order to compute the neutral curves and amplification factors for this flow. A direct numerical simulation has been performed in order to validate the results by model equations. As a main result the instability is found to be of convective type opposed to what has been assumed in literature so far. A range of cases has been investigated for surface and internal solitary waves.

INTRODUCTION

The stability of the boundary layer under a solitary wave has been investigated experimentally or by direct numerical simulation in several works, see for instance [4, 2, 1]. These works suggest that the nature of the instability is of absolute type but report diverging critical Reynolds numbers. A study on the linear stability of boundary layers under solitary waves suggesting that the instability is of convective type has been performed in [3]. In the present paper, we shall also elaborate on some of the results in the latter work.

Given the fully nonlinear inviscid solution for this flow, the boundary layer equations are solved numerically. Using this boundary layer solution, the parabolized stability equation method has been used in order to compute the neutral curves and amplification factors for this flow. The amplications of the perturbation have been verified by comparison to a direct numerical simulation using a high order accurate solver.

RESULTS

The boundary layer under surface solitary waves is controlled by two parameters, the Reynolds number and the wave elevation. On the other hand, for the internal solitary wave of a two fluid system, the ratio of the density of the two layers and the respective height of the two layers are additional parameters. Qualitatively, the boundary layer profiles are similar for both cases. They display an acceleration region in front of the crest and a deceleration region in the rear of the crest, cf. figure 1 (LEFT). As a main result, we find that in the rear of the wave crest, the boundary layer displays amplification of perturbations for all Reynolds numbers considered, which ought to be expected due to the inflection point in the profile in this region, cf. figure 1 (RIGHT). However, for small surface elevations and small Reynolds numbers the total amplification is rather weak, implying that, depending on the background level of noise in experiments or direct numerical simulation, the perturbation might or might not grow to such levels to be observable. This contributes to an explanation of the different results in the literature concerning the critical Reynolds numbers obtained by experiments or direct numerical simulation. As the signal to noise ratio is less favorable for internal solitary wave experiments compared to surface solitary wave experiments, the perturbations in the boundary layer of internal solitary waves are expected to be observable for amplifications factors much lower than for the corresponding surface solitary waves.

CONCLUSIONS

By means of the parabolized stability equation, amplification factors and neutral curves are computed for the boundary layer under solitary waves. A range of cases is considered for surface and internal solitary waves. The results obtained in this study suggest that the appearance of instabilities for lower Reynolds numbers depends strongly on the level of the initial perturbations/noise in the experiments/direct numerical simulation. Control of the perturbations is thus a prerequisite in order to obtain repeatable results in experiments or simulations.

*Corresponding author. Email: joris@math.uio.no

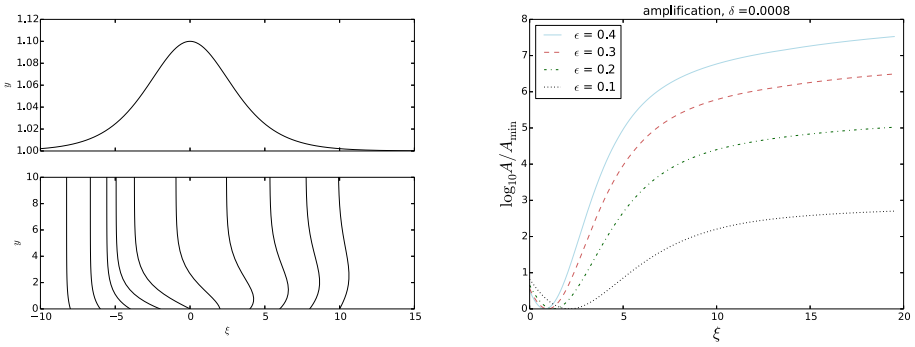

Figure 1: LEFT: Surface elevation η and profiles of the horizontal velocity component in the boundary layer under a surface solitary wave moving from right to left. The profiles have been multiplied by 40. The moving horizontal coordinate ξ has been scaled by the water depth, whereas the normal coordinate y has been scaled by the boundary layer thickness. The value at $y = 0$ of the profiles shown corresponds to the position ξ, where the profile has been taken. The horizontal velocity vanishes at $y = 0$ in order to satisfy the no-slip boundary condition. RIGHT: Amplification of the critical perturbation in the boundary layer under surface solitary waves of different amplitude ϵ, for a Reynolds number $\mathrm{Re} = 2/\delta = 2500$.

References

[1] C. E. Ozdemir, T.-J. Hsu, and S. Balachandar. Direct numerical simulations of instability and boundary layer turbulence under a solitay wave. *Journal of Fluid Mechanics*, 731:545–578, 2013.

[2] B. M. Sumer, P. M. Jensen, L. B. Sørensen, J. Fredsøe, P. L.-F. Liu, and S. Carstensen. Coherent structures in wave boundary layers. part 2. solitary motion. *Journal of Fluid Mechanics*, 646:207–231, 2010.

[3] J. C. G. Verschaeve and G. K. Pedersen. Linear stability of boundary layers under solitary waves. *Journal of Fluid Mechanics*, 761:62–104, 2014.

[4] G. Vittori and P. Blondeaux. Turbulent boundary layer under a solitary wave. *Journal of Fluid Mechanics*, 615:433–443, 2008.

INSTANTANEOUS FLOW CHARACTERISTICS AND STRUCTURAL STABILITY IN A BIDIRECTIONAL VENTILATED CABIN MOCK-UP

Changwei Yang[1], Feng He[1a)], Zhanyou Lin[1], Jiawei Liu[1], Xiwen Zhang[1], & Pengfei Hao[1]
[1]*School of Aerospace Engineering, Tsinghua University, Beijing, China*

Summary Airflow movement is one of the most important physical factors greatly influencing contaminants transmission in aircraft cabin. Since various perturbations are hard to control and experimental measurements are hard to handle in full-size aircraft cabin, the researches on instantaneous characteristics are seldom reported. In this work, PIV experimental investigations on the structural stability of velocity fields in a bidirectional ventilated cabin mock-up are conducted. It indicates that the velocity field is obviously unstable and there are coherent auto-oscillation of the large-scale flow structures in this cabin mock-up. The spatial and temporal behaviors of the large-scale flow structures and the evolution of topological characteristics of the velocity fields are presented. The structural stability theory is also used to further interpret the unstable phenomena of the velocity fields. Our present findings can serve as a base for forthcoming study of contaminants transmission and a simplified model for problem of cabin ventilation.

INTRODUCTION

As a result of the popularity of air transportation and the growing mobility of people, more and more people are travelling by commercial airplanes. The air quality, especially the air safety, in aircraft cabin has been the focus of many passengers and crews [1]. Airflow movement is one of most important physical factors greatly influencing the contaminants transmission in aircraft cabin environment [2]. Although many measured and computational results showed that the airflows in aircraft cabins were highly unsteady or even unstable in various aircraft cabins, most of the existing studies mainly focused on the time-averaged air distributions. Since various perturbations are hard to control and experimental measurements are hard to handle in full-size aircraft cabin, the researches on instantaneous characteristics of velocity fields are seldom reported [3, 4].

EXPERIMENTAL SETUP AND METHOD

Fig. 1(a) shows the aircraft cabin model of Boeing 737-200 in Ref. [4]. Fig.1 (b) and (c) show the schematic of simplified cabin mock-up and PIV measurement setup. There are two opposing inlets close to the ceiling and two outlets close to the bottom of the mock-up. One hundred diffusers are distributing uniformly in each inlet over the full depth (D=400mm). The size of the each diffuser is 20mm×2mm. In order to research the structural stability of velocity fields in this type of cabin, various perturbations are removed as much as possible. The geometries are created symmetrical with the symmetrical surface. As shown in Fig.1 (d), (e) and (f), the velocity distribution along the X and Y directions is determined by hot wire. The velocities is set at fixed and symmetrical with the middle plane. The PIV (Laser model: YAG double pulse laser. CCD model: REDLAKE MegaPlus II. Laser power: 200 mJ/pulse) is used to obtain the velocity field.

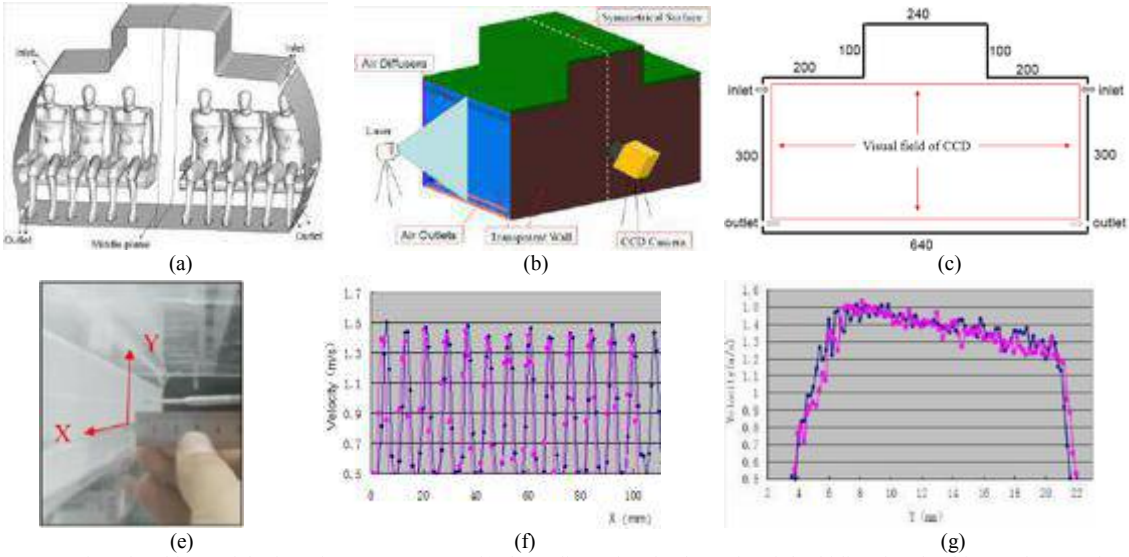

(a) (b) (c)

(e) (f) (g)

Fig. 1. (a)One row aircraft cabin model of Boeing 737-200 [4]. (b)Three dimensional schematic of the bidirectional cabin mock-up and PIV setup. (c) Cross-section of cabin mock-up at 0.5D and the corresponding sizes in millimeter. (d)The Cartesian coordinates used for determination of the velocity magnitude of inlets by hot wire. The velocity magnitudes along (e) the X direction and (f) the Y direction. The black lines and points stand for the velocity magnitudes on the left side. And the pink lines and points stand for the velocity magnitudes on the right side.

[a)] Corresponding author. Email: hefeng@tisnghua.edu.cn

RESULTS AND DISCUSSION

Fig. 2 depicts the large-scale flow structures in the cross section of visual field (CSVF) of CCD. There are obvious large-scale swing motions of the air flow in the cabin mock-up. The topological characteristic and structural stability analysis of the velocity fields [5] are shown in Fig.3. There are one saddle point (SP) and one half saddle points (HSP) in the CSVF. Moreover, one hetero-clinic orbit, connecting the SP and HSP exists in the CSVF. According to the third condition of Peixoto theorem [6], when there is a hetero-clinic orbit connecting saddle points in a two-dimensional vector field, it is not a structurally stable system. In this case, a sufficient perturbation, such as a small unequal velocity of two sides' diffusers, could destroy the hetero-clinic orbit and cause complicated bifurcation of the velocity field. The unstable velocity field is the intrinsic features in this bidirectional cabin. The instantaneous spatial and temporal behaviors of the large-scale flow structures and the dependence of the flow structures on the Reynolds number Re would be presented in our full paper.

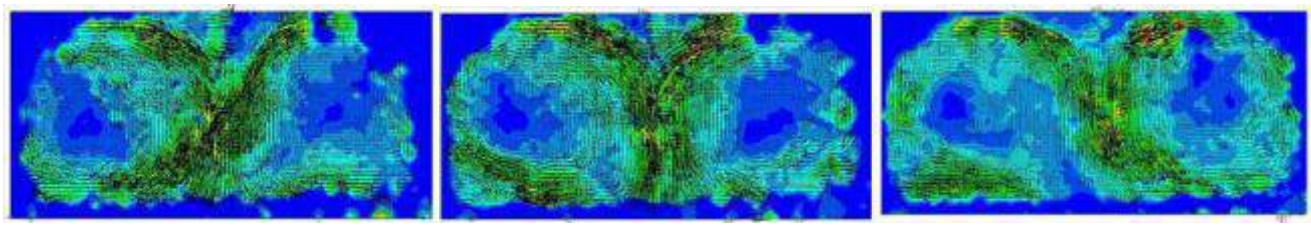

Fig. 2. The large-scale flow structures in the cross section of the ventilated aircraft cabin mock-up.

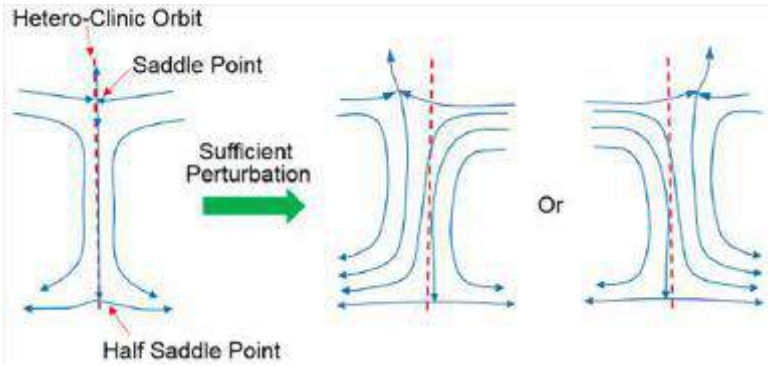

Fig. 3. The topological characteristic and structural stability analysis of the velocity field.

CONCLUSIONS

In this paper, the detailed instantaneous information and evolution of velocity field in a bidirectional ventilated cabin mock-up are investigated by PIV measurement. We can conclude that:

1) Although the boundary conditions are set at fixed and symmetrical with the middle plane as much as possible, the instantaneous velocity fields in aircraft cabin mock-up display intrinsic obvious continuing quasi-periodic large scale instabilities.

2) The instantaneous flow fields are very complicated due to the coexistence and interaction of the large-scale flow structures and turbulent fluctuations. Repeated reversal of the velocity components in the horizontal and longitudinal directions exist universally. The instantaneous spatial and temporal behaviors of the large-scale flow structures and the dependence of the flow structures on the Reynolds number are also studied.

4) The Peixoto theorem well interprets the mechanism of such unstable flow fields in this generic aircraft cabin mock-up.

5) The alteration of topological characteristics in the bidirectional ventilated muck-up allows the lateral airflow movements carrying infectious gaseous contaminants to move across the middle plane and influence the opposite region. This is a reasonable mechanism explanation of gaseous contaminants transmission in aircraft cabin.

References

[1] Mangili A, Gendreau MA, Transmission of infectious diseases during commercial air travel, *Lancet* 365 (9463): 989-996, 2005.

[2] Zhang Z, Chen X, Mazumdar S, Zhang T, Chen Q. Experimental and numerical investigation of airflow and contaminant transport in an airliner cabin mockup, *Build. Environ* 44 (1), 85-94, 2009.

[3] C.H. Lin, T.T. Wu, R.H. Horstman, P.A. Lebbin, M.H. Hosni, B.W. Jones, B.T. Beck, Comparison of large eddy simulation predictions with particle image velocimetry data for the airflow in a generic cabin model, *HVAC R Res*. 12 (S3), 935-951, 2006.

[4] Yang C, Zhang X, Yao, Cao X, Liu J, He F. Numerical study of the instantaneous flow fields by large eddy simulation and stability analysis in a single aisle cabin model. *Building and Environment* 96, 1-11, 2016.

[5] Anosov D V. Structurally stable systems, *Tr. Mat. Inst. VA Steklova* 169, 59-93, 1985.

[6] Peixoto M M. Structural stability on two-dimensional manifolds. *Topology*, 1(2): 101-120, 1962.

EVOLUTION OF LOCALIZED ARTIFICIAL DISTURBANCE IN 2D SUPERSONIC BOUNDARY LAYER

AlekseyYatskikh[1,2a)], Yury Yermolaev[1], Alexander Kosinov[1,2] & Nikolay Semionov[1]
[1]*Khristianovich Institute of Theoretical and Applied Mechanics SB RAS, Novosibirsk, Russia*
[2]*Novosibirsk State University, Novosibirsk, Russia*

Summary The evolution of the artificial pulsed wave packet in laminar flat-plate boundary layer was experimentally studied by hot-wire measurements at M=2. The localized disturbances were generated by pulsed glow discharge. The angle of the spreading and the velocity of propagation downstream of the wave packet were estimated. Also, wave analysis was provided. It was found, that for different frequencies the most unstable waves are oblique.

INTRODUCTION

For solving the problem of laminarization the detailed knowledge of the mechanisms of laminar-turbulent transition are required. At present it is generally recognized that the onset of turbulence is connected with the loss of stability of the initial laminar flow. There are many experimental and theoretical studies of the stability of subsonic boundary layer. However, the stability of supersonic boundary layer is much less studied.

The study of the evolution of artificial controlled perturbations allows find out the wave characteristics of the boundary layers. The commonly used method of the actuation of controlled perturbations in the supersonic experiment is the high-frequency electric glow discharge. This method has proved to be effective in the study of the stability of supersonic boundary layer. The linear and nonlinear theories of hydrodynamic stability were proved by this method [1, 2]. However, this method allows the study the evolution of narrowband disturbances while natural laminar-turbulent transition is associated with the evolution downstream of fluctuations consisted of a wide range of frequencies and wavenumbers excited by freestream turbulence. Therefore the study of the evolution of broadband disturbance (wave packets) is perspective.

The first experimental studies of wave packet propagation in boundary layer were provided at low speed of flow [3]. The evolution of wave packet generated by a short-duration pulse through a small hole in the surface of the flat plate was investigated by hot-wire measurements. These measurements compared very well with results obtained from the theoretical model which represented the wave packet as a superposition of individual disturbances for all frequencies and spanwise wave numbers of the most unstable linear waves [4]. At high speeds of flows the method of the excitation of artificial wave packets is actively developing. The evolution of wave packets in the hypersonic boundary layer of nozzle was experimentally studied in [5]. The measurements were taken along the axial line of the nozzle using surface pressure transducers. The linear and non-linear growth of wave packets and their transformation into turbulent spot were founded. The spectra of wave packets corresponded with the second mode of instability which, as known, is the most unstable at hypersonic flow. The evolution and transformation into turbulent spots of wave packets is shown as a continuous process. Also, the method of wave packets is widely used in numerical study of laminar-turbulent transition [6-8].

The goal of this work is to experimentally study the evolution of wave packet in laminar supersonic flat-plat boundary layer at Mach number of flow M=2.

EXPERIMENTAL SETUP

The evolution of wave packets in the supersonic boundary layer was studied on flat plate model. The experiments were carried out in the quiet supersonic tunnel T-325 of ITAM SB RAS at Mach number M=2 and unit Reynolds number $Re_1=6\times10^6$ m^{-1}. Artificial localized disturbances were actuated by pulsed electric glow discharge between isolated electrodes located 30 mm from leading edge on the surface of model. Pulsations in the boundary layer were measured with the help of constant temperature hot-wire anemometer. Hot-wire probe from tungsten with 10 micron in diameter and 1.5 mm in length was used. The measurements were carried out with overheat of the probe wire to 0.8. The hot-wire measurements were synchronized with glow discharge ignition. Ensemble-averaged fluctuation traces were computed for 320 disturbances to increase the signal-to-noise ratio. All data in this work were obtained in layer with maximum level of natural boundary layer pulsation.

RESULTS

Contour lines mass flow pulsations of the wave packet in the plane (z, t) measured at the different distance from the leading edge of the flat plate x = 60, 80, 100 mm are shown in figure 1. The wave packet has a three-dimension structure. It is obtained that the wave packet is expanded in the spanwise direction (z). The estimates of the angle of the spreading of the wave packet were done. It was found that the half-angle spanwise spreading of the wave packet is about 5°. It is close to the

[a)] Corresponding author. Email: 73.yatskikh@gmail.com.

experimental data of a linear development of controlled wave trains generated by high-frequency discharge. The leading edge of the wave packet propagates with a velocity about 0.9 U_∞, the speed of the trailing edge is about 0.3 U_∞.

In addition, the spectral analysis of the evolution of wave packet was made. Time and spatial Fourier transforms were done for five transverse sections: x=60, 70, 80, 90 and 100 mm. The distributions of the normalized amplitude from the inclination angle of the wave vector χ for frequencies f=8, 10, 12, 14 kHz are shown in figure 2. For each frequency amplitude was normalized on the maximum value at initial (x=60 mm) transverse section. As can be seen, for different frequencies the most unstable waves are oblique. This corresponds with the theory results for compressible shear layers. Also, the phase velocities were estimated too. For these frequencies it was obtained that $C_x \approx 0.6 \div 0.7$.

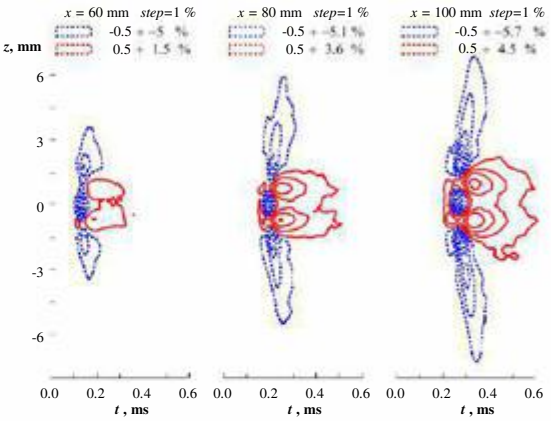

Fig. 1. Countor plots of wave packet.

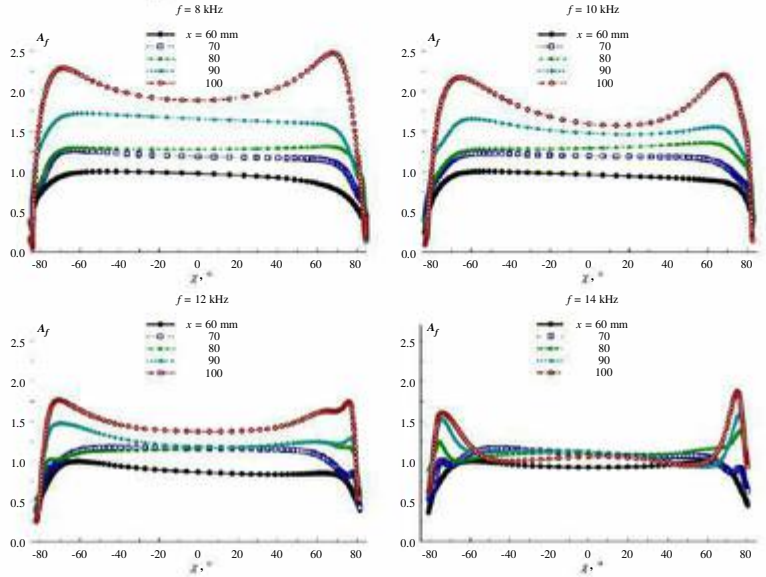

Fig. 2. The distributions of the normalized amplitude from the inclination angle of the wave vector for different frequencies.

CONCLUSION

The evolution of single wave packet generated by pulsed glow discharge in supersonic boundary layer was experimentally studied by hot-wire measurements. It was found that a pulsed glow discharge generates three dimensional wave packets. The wave packet spanwise spreading was observed. The spectral analysis of the evolution of wave packet showed that the most unstable waves have big inclination angle.

The obtained experimental data may be useful for verification of numerical models.

This work is supported by the Russian Foundation for Basic Research (grant number 16-31-00388).

References

[1] Kosinov A.D., Maslov A.A., Shevelkov S.G.: Experiments on the stability of supersonic laminar boundary layers. *J. Fluid Mech* **219:**621-633, 1990.

[2] Kosinov A.D., Tumin A.: Resonance interaction of wave trains in supersonic boundary layer. *Nonlinear Instability and Transition in Three-Dimensional Boundary Layers*: 397-388, 1996.

[3] Gaster, M., Grant I: An experimental investigation of the formation and development of a wave packet in a laminar boundary layer. *Proc. R Soc. Lond., A.* **347**:253-269, 1975.

[4] Gaster, M.: A theoretical model of a wavepacket in the boundary layer on a flat plate. *Proc. R Soc. Lond., A.* **347**:271-289, 1975.

[5] Casper, K.M., Beresh, S.J., Schneider, S.P.: Pressure fluctuations beneath instability wavepackets and turbulent spots in a hypersonic boundary layer. *J. Fluid Mech* **756**:1058-1091, 2014.

[6] Sivasubramanian J., Fasel H.F.: Numerical investigation of the development of three-dimensional wavepackets in a sharp cone boundary layer at Mach 6. *J. Fluid Mech* **756**:600-649, 2014.

[7] Mayer C.S. J., Laible A.C., Fasel H.F. Numerical Investigation of Wave Packets in a Mach 3.5 Cone Boundary Layer. *AIAA Journal* **49.1**: 67-86, 2011.

[8] Novikov A., Egorov I., Fedorov A.: Numerical simulation of three-dimensional wave packet in supersonic flow over a compression corner. *AIAA Paper:* 2015-2624, 2015.

CYLINDER INSTABILITY IN CIRCULATION FLOW BOUNDED BY EXTERNAL CYLINDRICAL WALL

Victor Kopiev[1a)], Sergey Chernyshev[1], Mikhail Yudin[1,2]
[1]*Acoustic Department, TsAGI, Moscow Branch, Moscow, Russia*
[2]*Moscow Institute of Physics and technology (State University), Dolgoprudny, Russia*

Summary Within the framework of two-dimensional incompressible Euler equations, we study stability of the system composed of an inner free circular cylinder, the fluid with circular streamlines around the cylinder, and an exterior cylindrical wall. A dispersion relation is obtained for different mean flows realized between the cylinder and the wall: potential flow, flow with constant vorticity and flow with weakly decreasing/increasing vorticity. Exact solutions of the dispersion relation are provided and analyzed. It is shown that unlike the unbounded problem, the heavy cylinder in this case becomes unstable even in the potential flow. The sheared instability which is characteristic feature for the unbounded problem for the flow with decreasing vorticity, is realized in the bounded case not only for decreasing, but also for increasing vorticity. Arnol'd theorem is used to perform the energy study of the stability loss in the system.

INTRODUCTION

Instabilities of three-dimensional vortices play a key role in the problem of turbulence onset. One of these instabilities, so called shear instability, is related to the energy transfer to the vortex core from the critical layer, which appears due to core oscillations in the circulation flow (Fig.1a). In particular, this kind of instability could be responsible for turbulization of the "atmosphere" of a solitary vortex ring for high Reynolds numbers [1].

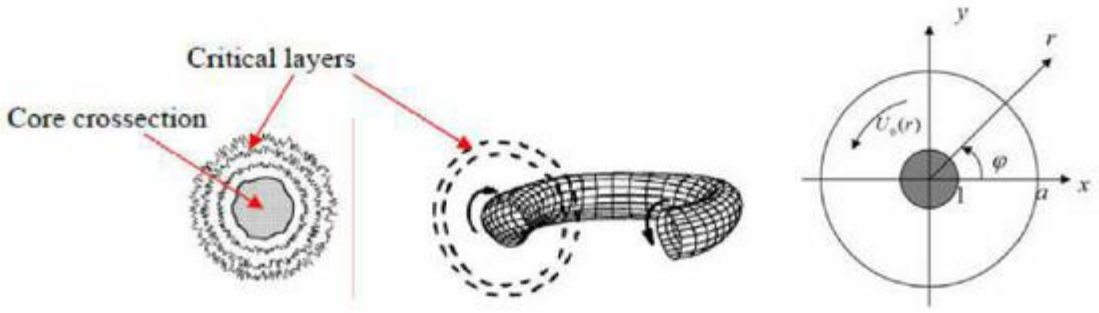

a) b)

Fig.1 a) A scheme of stability loss of vortex ring core oscillations due to energy transfer from the mean flow to the oscillations via a system of multiple critical layers; b) a free cylinder in a circulation flow of the fluid bounded by an external cylindrical wall, 2D.

Difficulties of studying the shear instability in vortex circulation flows are relating to the fact that it appears only for curved vortex filaments, while cylindrical vortex flow is stable for any monotonically decreasing (non-increasing) vorticity profile. It is known that two-dimensional oscillations of a Rankine vortex (a circular vortex with constant vorticity in an infinite potential circulation flow) are neutrally stable. Since any non-increasing vorticity distribution in infinite flow is stable [2], a circular vortex with constant vorticity keeps its stability after being placed in a circulation flow with decreasing vorticity. Shear instability could appear in 2D simple system if rigid cylinder being placed instead of the Rankine vortex in streamlining circular flow. Ref. [3] studied an oscillator composed of a circular cylinder with elastic fixation streamlined by a potential or vortical circulation flow with decreasing vorticity in the infinite fluid. It is shown that unlike Rankine vortex oscillations, oscillations of this system can be unstable. The flow seems to be simplest two-dimensional flow where the shear instability can be realized.

The mechanism of shear instability, which is related with the interactions of oscillation of discrete spectrum with critical layer perturbations, takes place also in a plane-parallel flow. It could realized due to interaction of surface waves of the sea and the shear flow over the surface of the sea with the wind [4,5]. However, in this case the flow has a different topology in comparison with the circulation flow around a vortex core. Therefore it is difficult to transfer the results of studying water wave appearance to the processes of perturbation evolution in a flow with vortical filaments. Besides, the flows with circular streamlines have an advantage in a mathematical description of such effects, because they allow for nontrivial potential flow with a weak shear, which in its turn allows obtaining exact solutions as approximations to the potential one. In a plane-parallel flow, the changing velocity necessarily assumes the strong shear or a trivial case of potential flow with zero velocity.

Thus, a theoretical study of the shear instability is enabled by a system composed of circular rigid cylinder with elastic or free fixation, streamlined by a circulation flow. Unlike the case of a cylindrical vortex, which oscillations have negative

[a)] Corresponding author. Email: vkopiev@mktsagi.ru.

energy; oscillations of an elastic heavy cylinder have positive energy, which allows the shear instability to be realized in this simple two-dimensional system due to the positive energy flux from the critical layer to the oscillations.

FORMULATION OF THE PROBLEM

Experimental investigation of the instability mechanism implies finiteness of the flow region. However, in [3] the shear instability of an elastic cylinder in a circulation flow has been obtained for the infinite flow. This brings about a stability problem of a flow in a "cup" of large but finite radius, when the flow is bounded on the one hand by the wall of an exterior fixed cylinder, and on the other hand by a movable circular cylinder inside (Fig.1b). It turns out that limitation of the system size by the cup wall results in appearance of one more kind of instability, which is realized already in a potential flow and can mask the shear instability.

The objective of this work consists in investigation of stability of a free (not fixed) cylinder related with the finiteness of the circulation flow, as well as analysis of system parameters which allow the shear instability to be discerned from the other instabilities for its further experimental investigation.

MAIN RESULTS

Two cases are considered: potential flow and weakly vertical flow. For these cases, the dispersion relation is obtained, its analytical roots are determined, and the instability regions are found. In case of a potential flow around a cylinder in a bounded fluid, a new instability related with the finiteness of the flow region is obtained. This instability is characteristic only for the flows with external boundaries and is absent for potential flows in infinite fluid. The instability region appears for sufficiently heavy cylinders. For an arbitrary large radius of the cup, always there is a region of parameters for which the flow will be unstable. An energy study is also performed accordingly Arnol'd approach [6,7], which shows that for the entire region of unstable parameters the energy of perturbations identically vanishes. For region of stable parameters, there are two branches of dispersion curve, one with positive energy, and the other with negative energy.

Addition of weakly decreasing vorticity in the potential flow gives rise to the shear instability, known from the problem of the infinite flow [1,3]. However, in the bounded case the situation is complicated by the onset of the instability in the case of potential flow, which persists for weakly vortical flow as well, albeit for heavy cylinders. Therefore this instability can be avoid by considering cylinders with moderate masses. Another problem might be related with the new instability on the lower branch of the dispersion curve (unlike the infinite case, this branch is not trivial). However, for decreasing vorticity this instability is not realized. The instability on the lower branch does exist, but only for increasing vorticity when there is an energy flux not from but to the critical layer.

CONCLUSIONS

Therefore, the analysis of the described two-dimensional case allows establishing new instabilities in a simple system composed of two cylinders and a circulation flow between them, and giving them a physical interpretation. Besides, the results demonstrate how the shear instability, which is important for three-dimensional vortices (vortex rings), can be realized in an experiment.

References

[1] Kopiev V.F., Chernyshev S.A. Physics-Uspekhi. **43**(7), 663-690, 2000

[2] Kop'ev V.F., Leont'ev E.A. Akust. Zh. **34** (3) 475-480 (1988) [Sov. Phys. Acoust. **34**, 276 (1988)]

[3] Kopiev V.F., Chernyshev S.A. Fluid Dynamics **35**(6), 858-871, 2000

[4] Miles J.W. J. of Fluid Mech. **3,** 185–204, 1957

[5] Miles J.W. J. of Fluid Mech. 6 (4), 568–582, 1959

[6] Arnol'd V.I. Dokl. Akad. Nauk SSSR, **162** (5) 975-978, 1965

[7] Arnol'd V.I. Prikl. Mat. Mekh. **29** (5) 846-850 (1965)

FM08 - Flow in Thin Films

TS.FM08-1.01	Eggers, Jens - Arrested bubble rise in a narrow tube (INVITED)	1029
TS.FM08-1.02	Jensen, Oliver - Drop spreading with random viscosity	1031
TS.FM08-1.03	Wilson, Stephen - A fluid dynamical model for anti-surfactant solutions	1033
TS.FM08-1.04	Dallaston, Michael - Axisymmetric self-similar rupture of thin films with general disjoining pressure	1034
TS.FM08-1.05	Goel, Sachin - Drainage of a thin film of Bingham fluid between two viscous Newtonian drops	1036
TS.FM08-1.06	Ait Abderrahmane, Hamid - Tear Film Dynamics on a Spherical Cornea	1038
TS.FM08-2.01	Bestehorn, Michael - Pattern forming instabilities in mechanically vibrating thin films (INVITED)	1040
TS.FM08-2.02	Nepomnyashchy, Alexander - Waves in a heated liquid layer covered by insoluble surfactant (INVITED)	1042
TS.FM08-2.03	Ruyer-Quil, Christian - Sheared falling film flows: An experimental and numerical study	1044
TS.FM08-2.04	Denner, Fabian - On solitary waves in periodically excited falling liquid films	1046
TS.FM08-2.05	Mendez, Miguel - Experimental Characterization of 2D Traveling Waves in Low Kapitza Liquid Film down a Vertical Wall	1048
TS.FM08-2.06	Afkhami, Shahriar - On the computation of viscous forces near the moving contact line	1050
TS.FM08-3.01	Vila, Jean-Paul - 2D versus 1D models for thin film flows (INVITED)	1052
TS.FM08-3.02	Noble, Pascal - Numerical simulations of capillary thin film flows under hyperbolic CFL conditions	1054
TS.FM08-3.03	Sellier, Mathieu - Towards optimal crêpe making	1056
TS.FM08-3.04	Scheichl, Bernhard - Capillary effects and short-scale interaction in a weakly viscous supercritical overfall	1058
TS.FM08-3.05	Christensen, Kenneth - Flow Interactions Between Water and CO2 in 2D Heterogeneous Porous Micromodels	1060
PO.FM08-1.01.36	Aktershev, Sergey - Nonlinear Waves in a Falling Film with Phase Transition	1062
PO.FM08-1.02.37	Codrignani, Andrea - Viscous dissipation impact on pressure loss in compressible lubricants	1064
PO.FM08-1.03.38	Dagois-Bohy, Simon - Stability of a Non-Newtonian Flow down an Incline	1066
PO.FM08-1.04.39	Guion, Alexandre - Mesh convergence of moving contact lines in VOF simulations	1068
PO.FM08-1.05.40	Guzanov, Vladimir - Rivulets formation during transition to 3D wave regime in isothermal liquid film	1070
PO.FM08-1.06.41	Kvon, Alexandr - Statistical characteristics of 3D waves & stationary 3D wave regimes for falling liquid films	1072
PO.FM08-1.07.42	Lavalle, Gianluca - Reduced order modelling for flooding onset prediction	1074
PO.FM08-1.08.43	Leivadarou, Evgenia - Fluid Shearing for Enhanced Collisions and Accelerated Reactions	1076
PO.FM08-1.09.44	Nazaripoor, Hadi - Interface morphology of thin films: electrohydrodynamic vs electrokinetic model	1078
PO.FM08-1.10.45	Villedieu, Philippe - Dealing with contact line forces in shallow water models	1080
PO.FM08-1.11.46	Yang, Hao - Numerical study of falling film on flexible wall in the presence of	1082

insoluble surfactant
PO.FM08-1.12.47 Zhou, Zhi-Qiang - Instabilities of liquid-lined flexible tubes with interfacial surfactant 1084

ARRESTED BUBBLE RISE IN A NARROW TUBE

Jens Eggers[1] and Catherine Lamstaes[1]

[1]*Department of Mathematics, University of Bristol*

Summary If a large air bubble is placed inside a vertical tube closed at the top it will rise, displacing the fluid above it. However, Bretherton found that if the tube radius, R, is smaller than a critical value $R_c = 0.918\ \ell_c$, where $\ell_c = \sqrt{\gamma/\rho g}$ is the capillary length, there is no solution corresponding to steady rise. Experimentally, the bubble rise appears to have stopped altogether. Here we explain this observation by studying the unsteady bubble motion for $R < R_c$. We find that the minimum spacing between the bubble and the tube goes to zero in limit of large t like $t^{-4/5}$, leading to a rapid slow-down of the bubble's speed $U \propto t^{-2}$. As a result, the total bubble rise in infinite time remains very small, giving the appearance of arrested motion.

A very common and useful observation, for example in the biological sciences, is that the flow of liquid out of a narrow capillary can be arrested by sealing off the top or bottom (for example using a finger). This is illustrated in the sequence on the right of Fig. 1: a capillary of inner radius $R = 1.9$ mm is closed off at the bottom. As a result, a column of water remains suspended above an air bubble (munch longer than the radius of the tube) at the bottom, without any apparent motion, even over long periods of time.

If however the tube is slightly wider, as seen on the left of Fig. 1, a bubble rises steadily, as liquid is allowed to pass through a thin film surrounding the bubble. Such constant-speed solutions are possible only if the radius of the tube is larger than a critical value $R_c = 0.918\ \ell_c$ [1]. The question we address in this paper is how it is possible that no more liquid is allowed to flow past the bubble if $R < R_c$. This is surprising, since a liquid is not able to support a constant shear stress, as would a solid.

To study this question, we solve the dynamical equation for the film thickness $h(x,t)$, which reads in dimensionless form:

$$\frac{\partial h}{\partial t} + [h^3(\kappa_x \circ\ 1)]_x = 0. \tag{1}$$

Here κ is the curvature of the interface, and the following term comes from gravity. If $R > R_c$, any solution of (1) converges toward a solution of traveling wave type. If $R < R_c$, the minimum film thickness goes to zero in infinite time, as shown in Fig. 2. We show that the local solution close to the point of touchdown x_0 has the similarity form:

$$h(x,t) = t^{-4/5} H(\xi), \quad \xi = (x \circ\ x_0) t^{2/5}. \tag{2}$$

The similarity exponents are determined by matching the local solution (2) to the static front of the bubble on one hand, and to a film solution on the other hand, the latter representing a balance of surface tension, gravity, and viscosity. As a result, the minimum film thickness is described by

$$h_{min} \approx 1.39 \ell_c^{1/5} \left(\eta/\gamma\right)^{4/5} (R_c \circ\ R)^{-1/2} t^{-4/5}. \tag{3}$$

Since the motion of the bubble is controlled by the amount of fluid which can pass by the minimum, the speed goes to zero rapidly, as described by

$$U(t) \approx 2.97 \nu/(gR(R_c \circ\ R)^{1/2}) t^{-2}. \tag{4}$$

Thus even in infinite time, the bubble travels only a short distance, given the appearance of the bubble motion having stopped altogether.

References

[1] F. P. Bretherton. The motion of long bubbles in tubes. *J. Fluid Mech.*, 10:166, 1961.

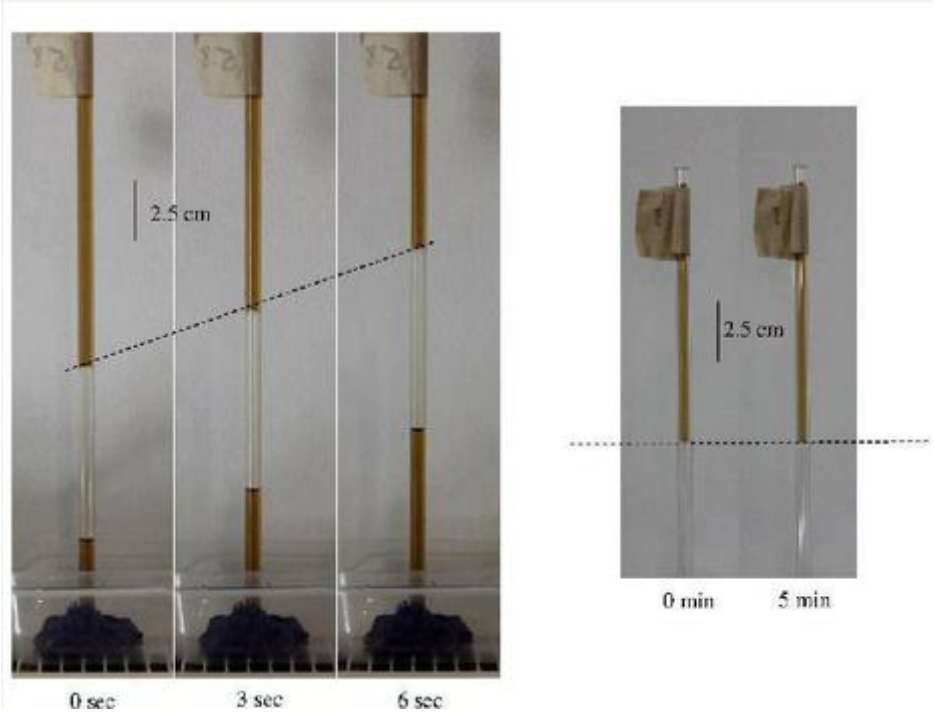

Figure 1: A home experiment illustrating the motion of long bubbles in tubes filled with water (using coffee as a colorant), closed off at the end. Based on the surface tension of water, $R_c \approx 2.5$mm. On the left, a bubble rises steadily in a tube with inner radius $R = 2.9$ mm. On the right, no motion is detectable even over a long period in a tube with $R = 1.9$ mm.

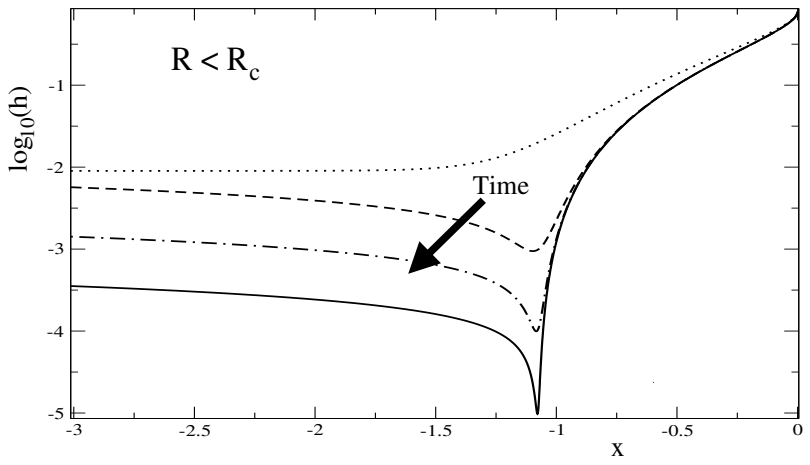

Figure 2: Plot of the film height $h(x,t)$ as found from (1) for R = 0.794 at time $t = 0$ (dotted curve), $log_{10}(t) = 3.02$ (dashed curve), $\log_{10} t = 4.50$ (dashed-dotted curve) and $\log_{10} t = 7.02$ (solid line).

DROP SPREADING WITH RANDOM VISCOSITY

Feng Xu and Oliver E. Jensen*
School of Mathematics, University of Manchester, UK

Summary This study addresses the influence of stochastic heterogeneity in thin-film flows of biological liquids. We consider the manner in which the spreading of an inhaled aerosol droplet over the liquid lining of a lung airway is regulated by intrinsic non-uniformities in the liquid film. One source of variability is associated with the distribution of biochemical constituents that influence the physical properties of the film, and which may themselves be transported by the spreading flow. We investigate this through a model problem in which a drop spreads over a Newtonian film having viscosity that depends on the concentration of a passive solute. Using PDE simulations and a surrogate ODE model that exploits physical insights into mass transport across the drop's contact lines, we quantify the variability in drop spreading rates in terms of the statistical properties of the initial solute distribution.

INTRODUCTION

Many biological systems have intrinsic spatial heterogeneity which, because of the difficulty of experimental measurement, may (at best) be estimated in terms of a few statistical variables. Ideally, transport processes in such environments must then be characterized in terms of distributions, requiring initial uncertainties to be propagated through a mechanistic model in order to quantify the likely variability of outcomes. In the present study we examine such a problem involving liquid transport in a lung airway, focusing on constitutive heterogeneity of the liquid film. Lung mucus has complex rheological properties that are regulated by mucin proteins released from goblet cells distributed within the airway epithelium. We investigate how the spatial heterogeneity of the mucus layer, associated with non-uniform mucin distributions, influences the spreading of an inhaled aerosol droplet over the airway liquid lining. This study provides a vehicle to explore techniques that complement expensive stochastic simulations, by exploiting physical understanding of the flow structure to derive low-order "surrogate" models that capture both the dominant physics and the variability of outcomes.

THE MODEL PROBLEM

We work in the framework of lubrication theory and assume that the drop and underlying mucus layer have Newtonian rheology. The mucus viscosity is assumed to depend on the concentration of a dissolved solute that is transported passively within the liquid. We derive coupled PDEs for the film thickness and cross-sectionally averaged solute concentration, assuming that diffusion is sufficient to suppress gradients across, but not along, the film. The drop spreads under the action of surface tension over a precursor mucus layer, regularising the singularity at the moving contact line. The initial solute distribution is a Gaussian random field with prescribed variance and correlation length, represented numerically using a Karhunen–Loève expansion.

Complementing Monte Carlo simulations of the PDE system, we derive a reduced ODE formulation of model when the precursor film is thin, extending previous asymptotic methods to account for solute transport. An analysis of characteristics shows that the solute distribution is stretched beneath the bulk of the drop, while being compressed in a region close to each advancing contact line, as illustrated in Figure 1.

RESULTS

Spreading rates are strongly influenced by the viscosity of the liquid in the neighbourhood of the contact line. When the solute variance is small, the initial solute distribution near each contact line turns out to have a long-lived influence. In this instance we derive explicit predictions of the variance of drop centre location and width, showing how the former decreases, and the latter increases, as the correlation length of the initial solute distribution increases, consistent with previous studies of drop-spreading on rough surfaces [1]. The solute field concertinas within the contact line region so that, when the solute variance is larger, fluctuations in viscosity encountered by the advancing contact line influence the local contact line speed.

CONCLUSIONS

While the model is subject to a number of strong assumptions, it reveals how spatial fluctuations in film properties influence the speed of an advancing contact line and quantifies the variability of spreading rates. The problem is characteristic of situations in which different physical processes, acting over distinct lengthscales, lead to only a subset of features of the underlying stochastic distribution being "sampled" by the flow, a feature that can be exploited in deriving low-order representations of the dynamics. The influence of additional heterogeneities in airway liquid lining flows, associated with non-uniform spatial domains, will also be discussed.

*Corresponding author. Email: Oliver.Jensen@manchester.ac.uk

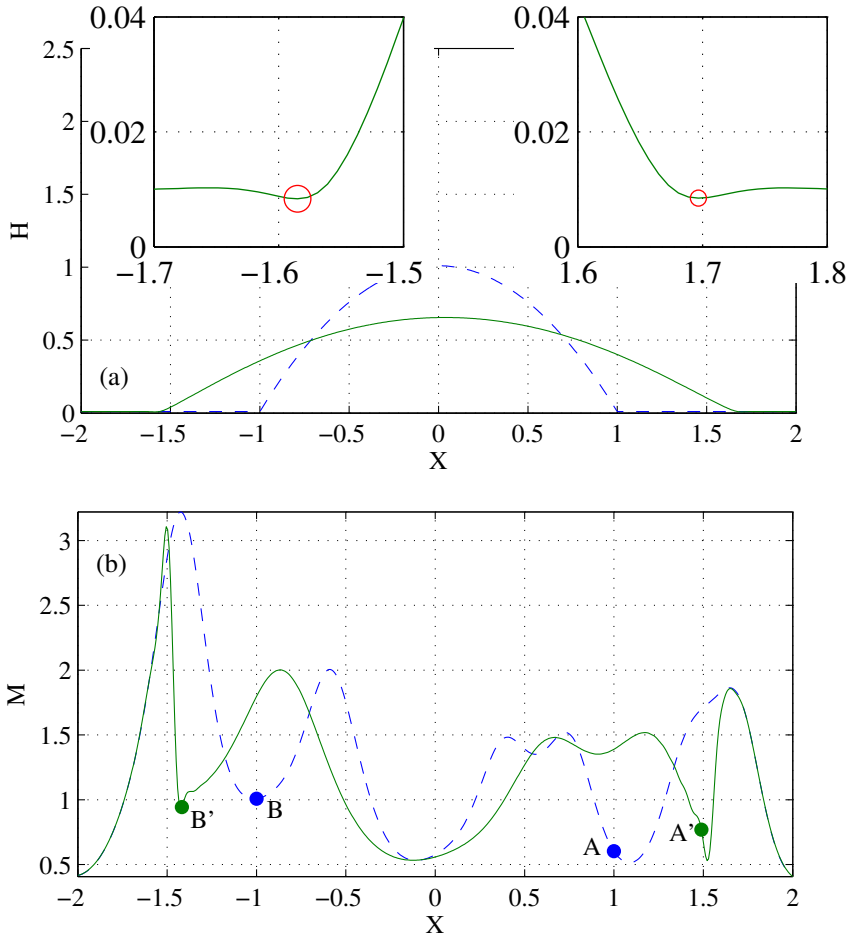

Figure 1: Simulations showing (a) film thickness H and (b) a realisation of the solute distribution M at initial (dashed) and later times (solid), as functions of position X. The film viscosity is regulated by M, which is stretched beneath the bulk of the drop but compressed near each contact line. Insets near each contact line in (a) show how the drop connects to a precursor film. The viscosity distribution within each contact-line region plays a dominant role in the spreading dynamics. The viscosities at the initial (A, B) and later (A', B') contact-line locations are indicated in (b).

ACKNOWLEDGEMENTS

Funding for this project is provided by EPSRC grant EP/K037145/1.

References

[1] Savva, N., Kalliadasis, S. & Pavliotis G.A. Phys. Rev. Lett. 104:084501, 2010.

A FLUID DYNAMICAL MODEL FOR ANTI-SURFACTANT SOLUTIONS

Stephen K. Wilson*[1], Justin Conn[1], David Pritchard[1], Brian R. Duffy[1], Peter J. Halling[2], and Khellil Sefiane[3]

[1]*Department of Mathematics and Statistics, University of Strathclyde, Livingstone Tower, 26 Richmond Street, Glasgow, G1 1XH, Scotland, United Kingdom*

[2]*Department of Pure and Applied Chemistry, University of Strathclyde, Thomas Graham Building, 295 Cathedral Street, Glasgow, G1 1XL, Scotland, United Kingdom*

[3]*School of Engineering, College of Science and Engineering, University of Edinburgh, The King's Buildings, Mayfield Road, Edinburgh, EH9 3JL, Scotland, United Kingdom*

Summary A fluid-dynamical model for surfactants and anti-surfactants based on the concept of surface excess (rather than simply surface concentration) is formulated and analysed. In particular, this model predicts a novel instability which occurs for anti-surfactants but not for surfactants.

In recent years there has been considerable progress on the mathematical modelling of solutions of surfactants. Surfactants are solutes which preferentially accumulate near the free surface and reduce the surface tension of the solution. Mathematical models for surfactants in which the surface tension is taken to be a decreasing function of the surface concentration of surfactant have been applied with considerable success to a wide variety of different physical systems (see, for example, Craster and Matar [1]).

However, there are other solutes, (such as, for example, salt dissolved in water) which preferentially *deplete* near the free surface and *increase* the surface tension of the solution. Such solutes are sometimes called "anti-surfactants" and cannot be modelled simply by considering the surface tension to be a function of the surface concentration. Instead a promising approach is to take the surface tension to be a function of the *surface excess*, an appropriate measure of the difference between bulk and surface concentrations. Thus, in the present work we construct a fluid-dynamical model for anti-surfactants based on the concept of surface excess which reduces to the classical model for surfactants when the surface concentration much larger than the bulk concentration, but has qualitatively different behaviour for anti-surfactants when the surface concentration is much smaller then the bulk concentration. In particular, this model is consistent with the Henry and Gibbs isotherms in surface-bulk equilibrium.

We use this model to analyse the stability of a quiescent layer of solution and demonstrate the occurrence of a novel instability which occurs for anti-surfactants but not for surfactants.

In addition, we formulate and analyse an asymptotically reduced version of the model applicable to thin layers of anti-surfactants and use it explore the complex non-linear dynamics which this system can display. In particular, the derive and analyse semi-analytical similarity solutions which capture and elucidate aspects of the long-time behaviour of such systems.

Finally, some of the many possible directions for future work will be indicated.

References

[1] Craster, R. V., Matar O. K.: Rev. Mod. Phys. 81:1131–1198, 2009

*Corresponding author. Email: s.k.wilson@strath.ac.uk

AXISYMMETRIC SELF-SIMILAR RUPTURE OF THIN FILMS WITH GENERAL DISJOINING PRESSURE

Michael Dallaston * [1], Dmitri Tseluiko[2], Serafim Kalliadasis[1], Zhong Zheng[3], Marco Fontelos[4], and Howard Stone[3]

[1]*Department of Chemical Engineering, Imperial College London, London, UK*
[2]*Department of Mathematical Sciences, Loughborough University, Loughborough, UK*
[3]*Mechanical and Aerospace Engineering, Princeton University, Princeton NJ, USA*
[4]*Departamento de Ciencia e Ingenieria, Universidad Rey Juan Carlos, Madrid, Spain*

Summary A thin film coating a dewetting substrate may be unstable to perturbations in the thickness, which leads to finite time rupture. The self-similar nature of the rupture has been studied by numerous authors for a particular form of the disjoining pressure, with exponent $n = 3$. In the present study we use a numerical continuation method to compute discrete solutions to self-similar rupture for a general disjoining pressure exponent n. Pairs of solution branches merge when n is close to unity, indicating that a more detailed examination of the dynamics of a thin film in this regime is warranted. We also numerically evaluate the power law behaviour of characteristic quantities of solutions in the limit of large branch number.

FORMULATION

A thin film on a dewetting substrate is dominated by the effects of surface tension and van der Waals forces. Invoking the *lubrication* or *thin film* approximation [3], the thickness of the film $h(\boldsymbol{x}, t)$ may be modelled by the (dimensionless) equation

$$\frac{\partial h}{\partial t} = \circ\, \nabla \cdot \left[h^3 \nabla \left(\nabla^2 h + \Pi(h)\right)\right], \qquad \Pi(h) = \circ\, \frac{1}{nh^n}. \tag{1}$$

As long as $n > 1$, the *disjoining pressure* $\Pi(h)$, which captures the effect of van der Waals forces, destabilises the film.This leads to finite time rupture, where h vanishes at a point or line at time t_0. Assuming axisymmetry and self-similarity near a rupture point ($r = 0$), the film thickness may be expressed as $h(r, t) = (t_0 \circ\ t)^\alpha f(\xi)$, $\xi = r/(t_0 \circ\ t)^\beta$, where f satisfies the following ordinary differential equation

$$\circ\, \alpha f + \beta \xi f' = \circ\, \frac{1}{\xi}\left[\xi f^3 \left(f'' + \tfrac{1}{\xi} f'\right)' + \xi f^{2-n} f'\right]', \quad f'(0) = f'''(0) = 0, \quad f \sim c\xi^{\alpha/\beta},\ \xi \to \infty. \tag{2}$$

The similarity exponents α and β are simple functions of the exponent n, while the far field condition is derived from the assumption of quasi-steadiness away from the rupture point. The conditions at $\xi = 0$ are required for symmetry and boundedness of the solution at the origin.

For $n = 3$, it has been shown that (2) has a discrete family of solutions, which may be characterised by the scaled film thickness at the origin $f_0 = f(0)$. Previously, these solutions have been computed numerically, using a shooting method [7], and Newton iteration on a discretised boundary value problem [5]. In each case, the numerical computation is highly sensitive to an initial guess (the right-hand initial condition for shooting, or the initial guess of the Newton scheme, respectively). The selection mechanism in the plane symmetry (line-rupture) version of (2) was explored in [1], where the exponential asymptotics of the large branch-number (equivalent to small f_0 was performed). The plane-symmetric version has also recently been resolved numerically [4] using the continuation algorithms implemented in the open source package AUTO07p [2].

The purpose of the present study is two-fold: firstly, we compute discrete solutions to (2) using numerical continuation, which has been shown to be highly effective on the plane-symmetric version of this problem [4]. Secondly, numerical continuation allows us to compute the discrete solution branches as the disjoining pressure exponent n is varied.

NUMERICAL CONTINUATION

The idea behind numerical continuation is to compute a solution to a boundary value problem that features a number of parameters, then gradually vary one or more of those parameters, using the previous solution as an initial guess (say, in a Newton iteration) to compute the new solution. The smooth dependence of the solution on parameters may thus be harnessed. The parameters in question may be model parameters, or *artificial parameters* introduced for numerical expediency, as we use here.

*Corresponding author. Email: m.dallaston@imperial.ac.uk

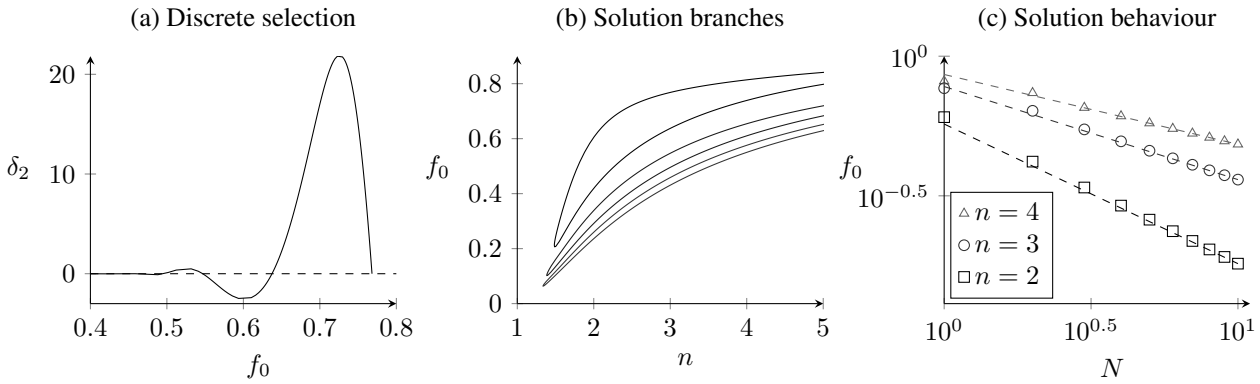

Figure 1: (a) The artificial parameter δ_2 as a function of the scaled film thickness at the origin f_0; The roots $\delta_2 = 0$ correspond to solutions of (2). (b) The first six solution branches vs the disjoining pressure exponent n. Pairs of solution branches merge near $n = 1$. (c) Discrete solutions f_0 vs solution index N; solutions appear to asymptote to $\propto N^{-1/n}$ for large N.

As a starting point, we note that when $n = 3$, (2) has the exact solution $f_{\rm e}(\xi) = c\sqrt{\xi}$ satisfying the far field conditions, but not the conditions at $r = 0$. We thus introduce the artificial parameters δ_1 and δ_2 into the boundary conditions, as well as an approximate left hand boundary location $\xi_0 \ll 1$, and enforce the conditions

$$f(\xi_0) = f_0, \qquad f'(\xi_0) = \delta_1, \qquad f'''(\xi_0) = \delta_2.$$

(the far field boundary conditions are also enforced at a large but finite value $\xi = L$). Given appropriate values of δ_1 and δ_2 , $f_{\rm e}(\xi)$ also satisfies these boundary conditions, so may be used as an initial guess in our computation. Using numerical continuation, we now take δ_2 and δ_1 to zero, allowing f_0 to be free in each case. Now as ξ_0 is taken to zero, we approach a solution to the original problem (2).

The introduction of the artificial parameters also provides a systematic way of computing the other members of the discrete family of solutions. For $\delta_1 = 0$ and $\xi_0 > 0$ we allow f_0 to vary, letting δ_2 be free. The curve of δ_2 against f_0 oscillates around $\delta_2 = 0$, each intersection corresponding to a solution of (2). This approach is similar to that used for the plane symmetric problem [4], although in our case the variation of the artificial parameters in the boundary conditions cannot take place on $\xi = 0$ due to the coordinate singularity.

Finally, after finding the discrete solutions for $n = 3$, we continue in n to trace out discrete solution branches.

RESULTS

In figure 1a we plot the curve of the artificial parameter δ against f_0 for $n = 3$, showing the selection of discrete solutions where $\delta_2 = 0$. In figure 1b we plot the discrete branches of solutions, characterised by f_0, over a range of values of n. The most interesting phenomenon we observe is the merging of pairs of branches at a value $n > 1$ as n decreases. Thus, for small values of n, the branch with largest f_0 (the only which is stable [5]) disappears. The dynamical behaviour of the time-dependent problem (1) in this regime is therefore of further interest, something which we intend to explore further by numerical computation of (1).

In addition we compute the relationship between f_0 on the discrete solution branches and the index N of the branch (starting with the largest value as $N = 1$), particularly in the limit that N is large. As shown in figure 1c, the discrete values of f_0 appear to behave as $\propto N^{-1/n}$ as $N \to \infty$ for $n = 3, 4$ and 5. When $n = 3$, the far field coefficient c behaves as $N^{-0.43}$, as previously computed [6, 4]. The relationship between these numerically observed power laws, as well as the connection with the asymptotic result of [1], is ongoing work.

References

[1] S. J. Chapman, P. H. Trinh, and T. P. Witelski. Exponential asymptotics for thin film rupture. *SIAM J. Appl. Math.*, 73(1):232–253, 2013.

[2] E. J. Doedel, A. R. Champneys, F. Dercole, T. F. Fairgrieve, Yu. A. Kuznetsov, B. Oldeman, R. C. Paffenroth, B. Sandstede, X. J. Wang, and C. H. Zhang. Auto-07p. *Continuation and bifurcation software for ordinary differential equations*, 2007.

[3] A. Oron, S. H. Davis, and S. G. Bankoff. Long-scale evolution of thin liquid films. *Rev. Mod. Phys.*, 69(3):931–980, 1997.

[4] D. Tseluiko, J. Baxter, and U. Thiele. A homotopy continuation approach for analysing finite-time singularities in thin liquid films. *IMA J. Appl. Math.*, 78(4):762–776, 2013.

[5] T. P. Witelski and A. J. Bernoff. Stability of self-similar solutions for van der Waals driven thin film rupture. *Phys. Fluids*, 11(9):2443–2445, 1999.

[6] T. P. Witelski and A. J. Bernoff. Dynamics of three-dimensional thin film rupture. *Physica D*, 147(1-2):155–176, 2000.

[7] W. W. Zhang and J. R. Lister. Similarity solutions for van der Waals rupture of a thin film on a solid substrate. *Phys. Fluids*, 11(9):2454–2462, 1999.

DRAINAGE OF A THIN FILM OF BINGHAM FLUID BETWEEN TWO VISCOUS NEWTONIAN DROPS UNDERGOING A HEAD-ON COLLISION

Sachin Goel[1] and Arun Ramachandran*[1]
[1]*Department of Chemical Engineering and Applied Chemistry, University of Toronto, Toronto, Ontario, Canada*

Summary The drainage of a film of Bingham fluid between two colliding Newtonian drops differs from that of a Newtonian film in three principal ways. First, drainage rates are slower for yield stress films as compared to Newtonian films of the same viscosity. Second, the spherical regime of drainage is characterized by higher curvatures in the film region, and it transitions to the dimpled regime at times later than the Newtonian case. Third, the Bingham film can freeze completely at a critical thickness, h_f, which counterintuitively, is independent of the force pushing the drops against each other. The results suggest that for a given shear rate, coalescence will occur at a slower rate, and will be completely hindered above a critical drop size.

Keywords: Bingham fluid, film drainage, coalescence, emulsion

INTRODUCTION

In this work, we consider the canonical problem of the drainage of the thin film of Bingham fluid between two spherical, Newtonian drops pushed against each other under the action of an external force. The only prior research to have studied this problem is the analytical work due to Jeelani and coworkers [1] [2]. Unfortunately, these results have been obtained from a simplistic lubrication analysis for nearly planar films, or for dimpled films with *ad-hoc* assumptions about the film shape. In this work, we have performed detailed numerical simulations of the evolution of the shape of a thin, Bingham film with an immobile interface based on the lubrication equations, and we compare our trends with existing work on the drainage of Newtonian films.

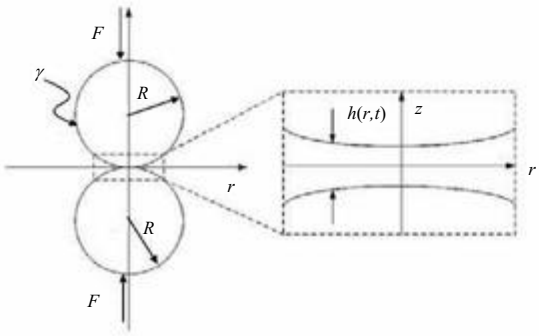

Figure 1: Schematic of the flow problem.

METHOD AND RESULTS

Consider two Newtonian drops each of radius R suspended in a Bingham fluid of yield stress τ_0 and viscosity μ [see Fig. 1]. The interfacial tension between the two fluids is γ, and the interface is assumed to be immobile. The drops are pushed into contact by a force F acting on each drop, which results in the formation of a film in the contact zone with a thickness profile h in the cylindrical co-ordinates r and z, as shown in Fig. 1. Ultimately, the film can be rendered unstable by an attractive van der Waal's force characterized by a Hamaker constant A. The governing equations for the drainage of the film are the same as has been derived in previous works [3,4], except that the depth-integrated flow rate of the fluid in the radial direction is given by

$$q_r^* = -\mathrm{Ca}\frac{h^{*3}}{12}\frac{\partial p^*}{\partial r^*}\left[1 - \frac{3}{2}\frac{\tau_0^*}{\tau^*} + \frac{1}{2}\left(\frac{\tau_0^*}{\tau^*}\right)^3\right] H\left(\tau^* - \tau_0^*\right), \tag{1}$$

where, $r = r^* R\mathrm{Ca}^{1/2}$, $p = p^*\gamma/R$, $\tau = \tau^*(\gamma/R)\mathrm{Ca}^{0.5}$, $h = h^* R\mathrm{Ca}$, and H is the Heaviside step function. The capillary number, Ca, is defined as $F/(\gamma R)$.

In Fig. 2, we compare the evolution of the shape of a Newtonian film [Fig. 2(a)] and a Bingham film with $\tau_0^* = 0.1$ [Fig. 2(b)] for Ca = 10^{-3} and a dimensionless Hamaker constant of $A^* = A/\left(4\pi\gamma R^2\right) = 10^{-10}$. The shapes are shown until the point of thin-film instability, which occurs at $t^* = 217.5$ and $t^* = 262.8$ for the Newtonian and Bingham cases, respectively, where $t = t^* R\mu/(\gamma\mathrm{Ca}^{0.5})$. As is obvious, at the same Ca and A^*, the drainage of the Bingham film is slower than that of the Newtonian film. However, what may be noticed is that just prior to the instability, while the Newtonian film has dimpled, the Bingham film is still spherical, implying that the time spent in the spherical regime is much greater in the latter case. In spite of this and the fact the spherical films are expected to drain faster than dimpled ones, unexpectedly, the Bingham film drains more slowly.

*Corresponding author. Email: Arun.Ramchandran@utoronto.ca

At sufficiently high Ca, the Bingham film does flatten and dimple, but when this happens, the shear stress in the film decreases with time. If the yield stress is large enough, film drainage can be arrested completely below a critical thickness, h_f. A scaling analysis reveals that this thickness varies as $\tau_0^2 R^3/\gamma^2$, and our simulations verified this. Interestingly, this trend is independent of the force F. These and other counterintuitive trends will be explained in detail in the presentation.

CONCLUSIONS AND IMPLICATIONS

The introduction of a yield stress not only slows down the rate of drainage, but also modifies the shape of the film during the drainage process, increasing the time spent by the film during the spherical regime. The retardation of drainage, coupled with the arresting of drainage beyond a critical yield stress and capillary number for a given drop size and interfacial tension, implies that the coalescence of two drops colliding with each other due to an imposed shear can be strongly mitigated for a Bingham suspending fluid relative to a Newtonian one of the same viscosity.

REFERENCES

[1] S. Hartland and S. A. Jeelani, "Drainage in Thin Planar Non-Newtonian Fluid Films," Can. J. Chem. Eng., vol. 65, pp. 384-390, 1987.

[2] S. Hartland and S. A. Jeelani, "Drainage of Thin Dimpled Non-Newtonian Fluid Films," J. Phys. Chem., vol. 90, pp. 6054-6059, 1986.

[3] A. Saboni, C. Gourdon and A. K. Chesters, "Drainage and Rupture of partially mobile films during coalescence in liquid-liquid systems under a constant interaction force," JCIS, vol. 175, pp. 27-35, 1995.

[4] P. Santoro and M. Lowenberg, "Coalescence of drops with tangentially mobile interfaces: effect of ambient flow," Ann. N.Y. Acad. Sci., vol. 1161, pp. 277-291, 2009.

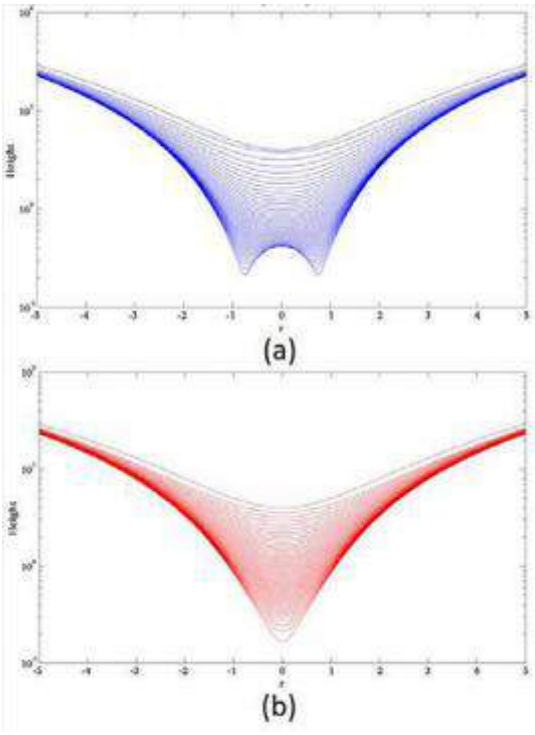

Figure 2: The shapes of the draining (a) Newtonian and (b) Bingham fluid, as functions of time.

TEAR FILM DYNAMICS ON A SPHERICAL CORNEA

Moussa Allouche[1], Faical Nait Bouda[2], and Hamid Ait Abderrahmane*[3]

[1]*Mechanical Engineering, Abderrahmane Mira University, Bejaia, Bejaia, Algeria*
[2]*Mechanical Engineering, Abderrahmane Mira University, Bejaia, Bejaia, Algeria*
[3]*Mechanical Engineering, Masdar Institute, Abu Dhabi, Abu Dhabi, United Arab Emirates*

Summary. We re-examine the effect of the human cornea curvature on the tear film thinning by investigating the tear film dynamics on a spherical geometry. The model, which consists of two nonlinear partial differential equations for the aqueous layer thickness and the lipid concentration, is solved in domain squeezed between a moving upper and fixed lower lids. We show that curvature influences the thinning rate of the tear film behind the upper eyelid. This contrasts with the accepted result that the corneal shape has a weak influence on the tear film dynamics.

INTRODUCTION

Tear film plays a key role in protecting the cornea surface against contaminations and providing high-quality optical surface during the period of a time, the eye remains open. During this interblink period the deposited tear film on the cornea surface thins and eventually breaks. The need to understand this tear film breakup, often associated with dry eye syndrome, from the fluid dynamics perspective, gave rise to a variety of studies, which are thoroughly reviewed by Braun [1]. Nearly all tear film models assume the cornea under the tear film to be flat and very few of those models include the curvature of the human cornea. For instance, Braun *et al.*[2] considered the evolution of a thin fluid layer deposited on a prolate spheroidal surface, driven only by the pressure gradient due to the variations of the surface curvatures. They conclude, based on the tear film thinning rate at the center of the cornea, that the curvature does not have a strong effect on the tear film dynamics. In this note, we re-examine this question by considering the interplay of the cornea curvature with the motion of the eyelids and the flows driven by Marangoni, capillarity and gravity effects.

FORMULATION OF THE POROBLEM



Figure 1: Sketch of the tear film cross section on a spherical cornea

We consider a two-dimensional tear film layer spreading between two eyelids on impermeable, stationary, spherical corneal surface of constant radius R. The upper eyelid is moving while the lower one is considered stationary; see Figure 1. We assume that the polar lipid layer acts like an insoluble surfactant at the surface of the tear layer and its convection-diffusion is described by the mass transport equation. We use a system of curvilinear coordinates (x, y) where x indicates the curvilinear abscissa along the corneal surface and y is the normal ordinate. We also assume that the tear layer is a Newtonian and incompressible liquid, bound by passive air layer. Exploiting the thinness of the tear layer, the flow governing equations are considerably simplified and reduce to the following lubrication model for the tear film thickness, h, and the lipid concentration, Γ:

$$h_t = \frac{2}{2}\frac{\mathcal{M}\left(\sin(\kappa x - \theta_0)\, h^2 \Gamma_x\right)_x}{\sin(\kappa x + \theta_0)} - \frac{\mathcal{C}\,\mathcal{B}}{3}\frac{\left[h^3 \sin^2(\kappa x - \theta_0)\right]_x}{\sin(\kappa x - \theta_0)} + \frac{\mathcal{C}}{3}\frac{\left[\sin(\kappa x - \theta_0)\, h^3 \left(\kappa^2 h_x - h_{xxx} - \kappa h_{xx}\cot(\kappa x + \theta_0) - \kappa^2 h_x \cot^2(\kappa x - \theta_0)\right)\right]_x}{\sin(\kappa x - \theta_0)} = 0 \qquad (1)$$

*Corresponding author: Email: hait-abdelah@mail.com

$$\partial_t - \mathcal{M}\,(\partial_t(\Gamma_s) \quad -\frac{1}{2}\mathcal{C}\,\mathcal{C}a^1\,(\mathcal{B}\,\sin\,(\alpha c - \theta_0)^2_{,} - \tag{2}$$

$$\frac{1}{2}\mathcal{C}\,\mathcal{C}a^1\,(\kappa^2 h_{,} + h_{,xx} + \kappa h_{,} \cos(\alpha_{,} + \theta_0) \quad \kappa^2 h_{,} \cos^2(\alpha_{,} + \theta_0)\big)^2_{,} = 0$$

Where $\mathcal{C} = \frac{d}{L_0}$, $\mathcal{B} = \frac{\rho_0}{\rho}$ and $\mathcal{M} = \epsilon Ma$ ($\epsilon \ll$ is the aspect ratio of the problem and $\kappa = \frac{L_0}{R_c}$ is the cornea surface curvature. $Ca = \frac{\mu U}{\gamma_0}$, $Si = \frac{\gamma_s m L_0}{\gamma_0}$ and $Ma = \frac{\rho_0 g L_0}{\gamma_0}$ are the capillary, Stokes and Marangoni numbers, respectively. g, $\rho_0, \rho_s, h^*, \Gamma^*, \mathcal{D}_s^* R$ and T are the gravity, density, tear fluid dynamic viscosity, surface tension in the absence of lipid at the free surface, meniscus initial height, initial lipid concentration, lipid diffusion coefficient, the universal gas constant and absolute temperature, respectively. L_0 is the maximal value of opening function of the upper eyelid, $L(t)$, defined in [4]. These equations are solved in the variable domain $0 \leq x \leq L(t)$ subject to the appropriate boundary and initial conditions.

RESULTS AND DISCUSSION

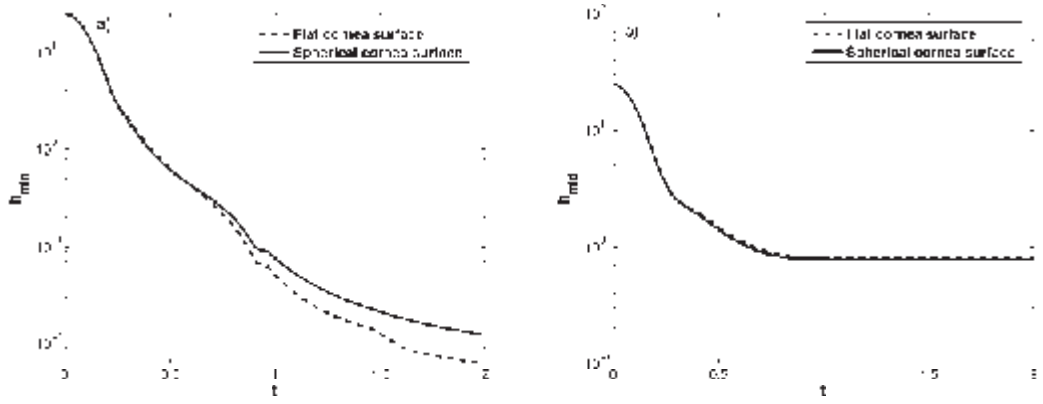

Figure 2: Comparison between the tear film flow dynamics for flat and spherical cornea surfaces. a) evolution of minimum film thickness $h_{min(t)}$, b) evolution of the film thickness at the middle of the cornea surface. The parameters of the simulations are $P_{e^*} = 0.01$ m, $g = 9.8$ m/s^2, $\rho_0 \approx 1.3$ Kg/m^3, $\mu \approx 1.0 \times 10^{-3}$ Ns/m^2, $\gamma_0 \approx 4.5 \times 10^{-2}$ N/m, $h^* = 10^{-6}$ m, $\Gamma^* \approx 4 \times 10^{-7}$ mol/m^2, $\mathcal{D}_s \approx 3.8 \times 10^{-9}$ m^2/s, $R = 8.31$ J/mol K, $T \approx 310$ K, $L_{z_0} = 0.01$ m, $\mathcal{C} = 6.79\,10^{-4}$, $\mathcal{M} = 1.5\,10^{-3}$, $\mathcal{B} = 2.18\,10^{1}$ and $\mathcal{U} = 25$. The letter ϵ is the dimensionless meniscus initial height.

The Figures 2 compare the evolutions of the profiles of the minimum tear film thickness and the film thickness at the middle of the cornea surface up to $t = 3$. This time is within the interblink period. The figure 2a shows that the tear film thinning occurs during interblink phase, which starts at approximately $t = 0.78$, and the curvature reduces the thinning rate of $h_{min(t)}$ the minimum film thickness. Figure 2b indicates that the curvature does not influence the thinning rate at the middle of the cornea. We could have drawn similar conclusion as Braun *et al.*[2], if we had only focused at the thinning rate of the tear film at the center of the cornea.

CONCLUSION

In this paper, we have shown that the interplays of the cornea curvature with the motion of the eyelid, gravity, capillarity and lipid concentration gradient on the surface of the tear layer influence the thinning rate of the minimum film thickness. This result, which is of interest for dry eye syndrome, break-up time and tear film stability, contrasts with the current belief that the curvature of the cornea surface has a weak influence on tear film dynamics.

References

[1] Braun R. J.: Dynamics of the Tear Film. Annu Rev. Fluid Mech 44: 267-297, 2012.

[2] Braun R. J., Usha R., McFadden G.B., Driscoll T.A., Cook L.P. and King-Smith P.E.: Thin film dynamics on a prolate spheroid with application to the cornea. J Eng Math 73: 121–138, 2012.

[3] Nelson Rojas, R., Bevilacqua, A. L. and Simpson, M. L.: A model of flowing foam over a porous substrate in space. J. Fluid Mech 484, 253-261,2003.

[4] Braun, M. and Berard, C.: Influence of non-polar fluids on tear film dynamics. J. of Fluid Mech. 768: 560-585, 2014.

PATTERN FORMING INSTABILITIES IN MECHANICALLY VIBRATING THIN FILMS

Michael Bestehorn* and Sebastian Richter

Department of Theoretical Physics, Brandenburg University of Technology, Cottbus, Germany

Summary Thin liquid films with a free surface on a planar horizontal substrate are examined. The substrate is subjected to oscillatory accelerations in normal direction. The description is based on the longwave approximation including inertia effects which are important due to the large velocities imparted by external vibrations. The linearized system is studied using Floquet analysis. Pattern formation in the nonlinear regime is computed numerically from an integrated model of two (three) coupled PDEs for the thickness and the flow rate of the fluid in two (three) spatial dimensions. The treatment can be systematically extended to multi-layer systems of stratified inmiscible liquids.

BASIC EQUATIONS

Lubrication approximation

Consider a thin liquid film with a free surface on a planar horizontal solid substrate in the gravity field g. The average thickness of the film is d. Its kinematic viscosity ν, its surface tension γ and its density ρ are assumed constant. The velocity field is denoted by $\vec{v}_h$ and v_z for the horizontal and vertical components, respectively. The fluid is subjected to vertical harmonic accelerations of the substrate located at $\tilde{z} = \tilde{A}\cos(\tilde{\omega}\tilde{t})$. We adopt the usual scaling in the lubrication approximation [1] (variables with a tilde are dimensional) $\vec{x} = \tilde{\vec{x}}/\ell,\ z = \tilde{z}/d,\ t = (\nu/d^2)\,\tilde{t}$ where $\vec{x} = (x, y)$ denotes the horizontal coordinates and ℓ is a typical horizontal scale (wavelength). Expanding the dependent variables of the Navier-Stokes eqs. with respect to powers of $\delta = d/\ell \ll 1$, one finds in the accelerated frame of reference at zero order

$$\partial_t \vec{v}_H + (\vec{v}_H \cdot \nabla)\vec{v}_H + v_z \partial_z \vec{v}_H = \partial_z^2 \vec{v}_H - \nabla\big(G\,(1 + a(t))h - \Gamma\nabla^2 h\big)\,, \tag{1}$$

where $h(\vec{x}, t)$ is the local film thickness, ∇ and ∇^2 are the horizontal gradient and Laplacian, respectively. The dimensionless numbers are the Galileo number $G = gd^5/(\ell^2\nu^2)$ and the inverse capillary number $\Gamma = \gamma d^5/(\ell^4\nu^2\rho)$. The normal acceleration results in a virtual force $a(t) = A\omega^2\nu^2/(gd^3)\cos(\omega t + \varphi)$ with the dimensionless amplitude $A = \tilde{A}/d$. We assume periodic boundary conditions (b.c.) in the horizontal directions. In the normal direction, we have at the substrate ($z = 0$) $\vec{v}_H = 0$ and $\partial_z \vec{v}_H = 0$ at the free surface $z = h(\vec{x}, t)$. The surface itself is determined by the kinematic boundary condition

$$\partial_t h + \nabla \cdot \vec{q} = 0 \tag{2}$$

where we already introduced the local horizontal flow rate $\quad \vec{q}(x, y, t) = \displaystyle\int_0^{h(x,y,t)} dz\ \vec{v}_H(x, y, z, t).$

Reduced model

The system consisting of Eq. (1) and the kinematic boundary condition Eq. (2) forms a set of 3D partial differential equations. Assuming $\vec{v}_H = 3\vec{q}(zh - \frac{1}{2}z^2)/h^3$ (closure), multiplying (1) by the weight function $W(z) = zh - \frac{1}{2}z^2$ and integrating over z across the film yields a set of 2D partial differential eqs. for $\vec{q}$ and h (for details see [2])

$$\frac{6}{5}\left(\partial_t \vec{q} + \nabla \cdot \underline{Q} - \frac{1}{7}\frac{\vec{q}(\nabla \cdot \vec{q})}{h}\right) = -\frac{3}{h^2}\,\vec{q} - h\nabla\big(G(1 + a(t))h - \Gamma\nabla^2 h\big) \tag{3}$$

with the matrix $Q_{ij} = (9/7)q_i q_j/h$. Note that weighting Eq. (1) with other polynomials yields different coefficients in Eq. (3), [3].

NUMERICAL RESULTS

Linearized system

Linearization of (2,3) around the quiescent state with a flat interface $h = 1 + \eta_k \exp(ikx),\ q = q_k \exp(ikx)$, yields a linear algebraic system for the deviations from which the flow rate q_k can be eliminated. A damped Mathieu equation

$$\frac{6}{5}\,\ddot{\eta}_k(t) + 3\,\dot{\eta}_k(t) + k^2\Big(G(1 + a(t)) + \Gamma k^2\Big)\eta_k(t) = 0 \tag{4}$$

is obtained for the surface deflection η_k. A solution of (4) is found by the Floquet analysis with $\eta_k(t) \sim \exp(\lambda_k t)w_k(t)$ and a periodic function w_k. A negative real part of all λ_k is crucial for the stability of the flat film. Fig.1 shows the marginal lines

*Corresponding author. Email: bestehorn@b-tu.de

Reλ_k=0 in the k-A plane for a certain silicone oil, together with direct numerical results of the linearization of (2,3). The agreement is excellent.

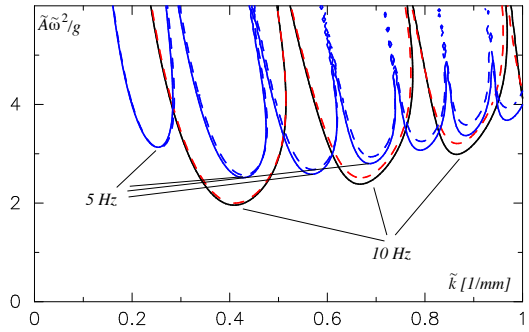

Fig.1: Marginal growth rate Re$\lambda_k = 0$. The parameters are for silicone oil with $\nu = 5 \cdot 10^{-6}\mathrm{m}^2/\mathrm{s}$, $\rho = 920\,\mathrm{kg/m}^3$, $\gamma_0 = 0.02\,\mathrm{N/m}$, $d = 0.7$ mm, and two different frequencies $\tilde{\omega}/2\pi = 10$ Hz (red), $\tilde{\omega}/2\pi = 5$ Hz (blue). The solid lines result from the Mathieu Eq. (4), The dashed curves are found by direct numerical solution of Eq. (1). the regions of instability are located inside the tongues.

Nonlinear pattern formation

Solving the full system Eqs. (2,3) numerically, we have always found square patterns in the subharmonic range and hexagonal patterns in the harmonic one, in agreement with [4]. For multi frequency excitation with certain frequency and amplitude ratios also quasi-periodic structures can be seen (fig.2, right frame) [5].

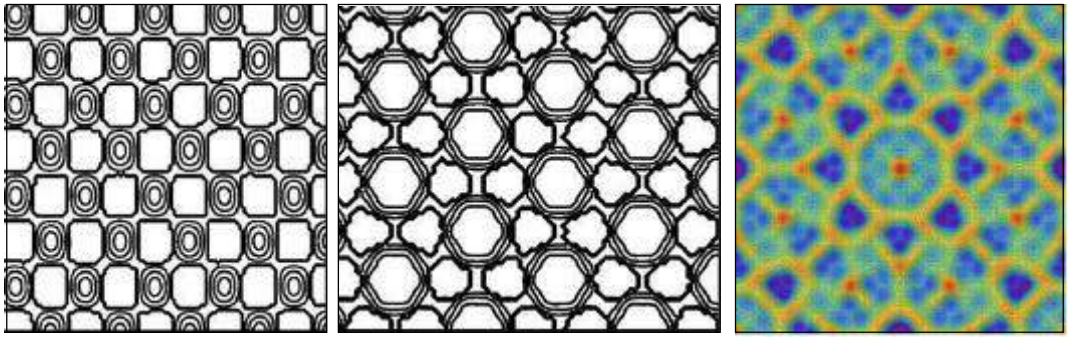

Fig.2: Various surface patterns, depending on frequency and kind of excitation.

MULTY-LAYERS

The model (2,3) can be systematically extented to a system of N stratified layers of inmiscible liquids separated by N deformable interfaces. Let h_i be the depth and $\vec{q}_i$ the local flow rate of layer i, then the system of $3N$ PDEs reads

$$\partial_t \vec{q}_i + \nabla \cdot \underline{Q}_i = \sum_j^N A_{ij}(h_1..h_N)\vec{q}_j - h_i \nabla P_i \tag{5}$$

$$\partial_t h_i + \nabla \cdot \vec{q}_i = 0 \tag{6}$$

with the generalized pressures $P_i(h_1,..h_N,t)$ and the matrices

$$\underline{Q}_i = \int_{h_i} dz\ \vec{v}_{iH} \otimes \vec{v}_{iH}\ .$$

To compute $\underline{Q}$ as a function of h_i and $\vec{q}_i$, a closure via the Karman-Pohlhausen approach can be used [6]. This work is currently under progress [7].

References

[1] Oron A., Davis S.H., Bankoff S.G.: Long-scale evolution of thin liquid films, Rev. Mod. Phys. 69:931-980, 1997
[2] Bestehorn M.: Laterally extended thin liquid films with inertia under external vibrations, Phys. Fluids 25:114106, 2013
[3] Trevelyan P.M.J., Scheid B., Ruyer-Quil C., Kalliadasis S.: Heated falling films, J. Fluid Mech. 592:295-334, 2007
[4] Perinet N., Juric D., Tuckerman L.S.: Numerical simulation of Faraday waves, J. Fluid Mech. 635:1-29, 2009
[5] S. Richter, Master thesis BTU Cottbus, 2015, to be published
[6] Craster R.V., Matar O.K.: Dynamics and stability of thin liquid films, Rev. Mod. Phys. 81:1131-1198, 2009
[7] Pototsky A., Bestehorn M., in preparation

WAVES IN A HEATED LIQUID LAYER COVERED BY INSOLUBLE SURFACTANT

Alexander Mikishev[1,2] and Alexander Nepomnyashchy [*3]

[1]*Department of Physics, Sam Houston State University, Huntsville, USA*
[2]*Embry-Riddle Aeronautical University - Worldwide, Daytona Beach, USA*
[3]*Department of Mathematics, Technion, Haifa, Israel*

Summary It is known that there are two types of wavy motions in a liquid layer covered by surfactant: (i) transverse capillary-gravity waves; (ii) longitudinal waves caused by the surfactant advection and tangential stresses generated by the inhomogeneity of the surfactant concentration. We derive and investigate, analytically and numerically, the general dispersion relation, which describes both wavy modes. We study the parametric excitation of both kinds of waves by heat flux modulation or vibration (i) in the case where there is no instability in the absence of parameter modulation; (ii) in the case of a pre-existing oscillatory instability. The nonlinear development of instability modes is analysed in the framework of the longwave asymptotic approach.

We consider a horizontal liquid layer with the free surface covered by insoluble surfactant. The liquid is subjected to a transverse temperature gradient directed downward (heating from below) or upward (heating from above). The surface tension of the liquid depends on both the temperature and surfactant concentration. Two types of wavy motions are possible in that case: (i) transverse capillary-gravity waves; (ii) longitudinal waves generated by interfacial tangential stresses caused by the dependence of the surface tension on the concentration of the surfactant adsorbed on the interface [1]. Without heating, both kinds of waves decay due to the viscous dissipation, but they may develop spontaneously if a temperature gradient is applied.

The existence of a longitudinal oscillatory mode and the possibility of its instability can be easily revealed in the case where the transverse waves are suppressed by a strong gravity (infinite value of the Galileo number), hence the surface can be considered as non-deformable. In the limit of a small wavenumber ($k \ll 1$) and vanishing Biot number, one obtains an analytical expression for the growth rate $\Lambda(k)$,

$$\Lambda/k^2 = \frac{1}{96}\{M \circ\ 48L \circ\ 12N \circ\ 48 \pm [192(ML \circ\ 48L \circ\ 12N) + (48L + 12N \circ\ M)^2]^{1/2}]\},$$

where M, L, and N are the Marangoni number, Lewis number, and elasticity parameter, correspondingly. An oscillatory instability takes place if $N > 4L^2/(1 \circ\ L)$ as

$$M > M_{osc} = 48 + 12(4L + N).$$

Analytical expressions for the dispersion relation in the implicit form $f(\Lambda, k) = 0$ can be found also for finite values of the Galileo number G, specifically, in the longwave limit and in the opposite limit, when the wavelength is small with respect to the layer thickness. In the latter case, one can clear distinguish between transverse waves with the dependence of the frequency $Im\Lambda$ on the wavenumber k similar to that for usual capillary-gravity waves, and longitudinal waves with a quite different frequency dependence. In a certain interval wavenumber a mixing and even a reconnection between two oscillatory modes is observed. An example of the competition between two instability modes in a layer heated from below is shown in Fig. 1. Both kinds of waves can be excited by a parameter modulation, e.g., by vibration [2] or temporal modulation of the heat flux on the surface [3]-[5]. In the former case, the Galileo number G in the gravity normal stress on the surface is replaced with $G[1 \circ\ F\sin(2\omega t)]$, where F is the dimensionless ratio between the forcing-induced acceleration and the gravity acceleration. In the latter case, the base temperature profile in the layer is changed as $T_b(z) = \bar{T}_b(z) + \tilde{T}_b(z)$, where $\bar{T}_b(z)$ is the stationary linear profile, while the non-stationary component of the temperature profile is given by the formula

$$\tilde{T}_b(z) = Re\left[\left(ae^{\sqrt{2i\omega}z} + be^{-\sqrt{2i\omega}z}\right)e^{2i\omega t}\right],$$

where a and b are some constants. Above-mentioned parameter modulations create subharmonic and harmonic "tongue-like" instability zones. Near the pre-existing stability curves, one observes the appearance of parametric instability "bubbles".

In the longwave limit we derive nonlinear equations governing the waves excited by the parametric instabilities.

*Corresponding author. Email: nepom@math.technion.ac.il

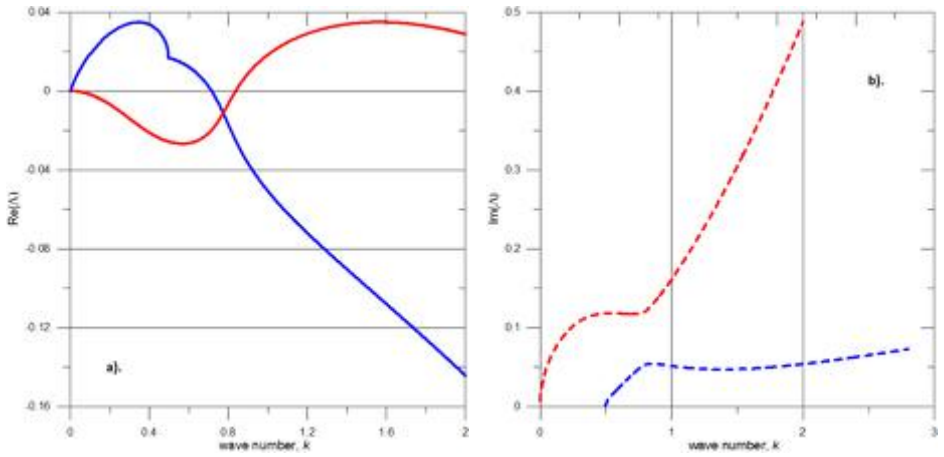

Figure 1: Dependence of the growth rate on the wavenumber k. (a) The instability growth rate $Re\Lambda(k)$ and (b) the frequency $Im\Lambda(k)$. Blue color lines correspond to Marangoni instability, red color lines corresponds to capillary-gravity waves. Parameters of the problem:the Marangoni number $M = 10$, the Galileo $G = 5$, the Prandtl number $P = 0.01$, the elasticity number $N = 0.1$, and the Lewis number $L = 0.01$.

References

[1] Nepomnyashchy A.A., Velarde M.G., Colinet P.: Interfacial Phenomena and Convection. Boca Raton, Chapman and Hall/CRC Press 2002.

[2] Mikishev A.B., Friedman B.A., Nepomnyashchy A.A.: Generation of transverse waves in a liquid layer with insoluble surfactant subjected to temperature gradient. Preprint, 2016.

[3] Mikishev A.B., Nepomnyashchy A.A.: Large-scale Marangoni convection in a liquid layer with insoluble surfactant under heat flux modulation. J. Adhesion Sci. and Techn. 25:1411-1423, 2011.

[4] Mikishev A.B., Nepomnyashchy A.A.: Marangoni instability of a liquid layer with insoluble surfactant under heat flux modulation. Eur. Phys. J. Special Topics 219:81-88, 2013.

[5] Mikishev A.B., Nepomnyashchy A.A.: On dynamic excitation of Marangoni instability of a liquid layer with insoluble surfactant on the deformable surface. Eur. Phys. J. Special Topics 224:229-239, 2015.

SHEARED FALLING FILM FLOWS: AN EXPERIMENTAL AND NUMERICAL STUDY

Nicolas Kofman[1], Christian Ruyer-Quil [*2], and Sophie Mergui[3]

[1]*École Polytechnique Fédérale de Lausanne, Lausanne, Switzerland*
[2]*Université de Savoie Mont-Blanc and Institut Universitaire de France, Chambéry, France*
[3]*Université Pierre et Marie Curie, Paris, France*

Summary We document experimentally and numerically the influence of a counter-current turbulent gas stream on a falling liquid film flow. Though only qualitative, the proposed one-sided modelling is able to retrieve qualitatively the experimental observations: enhancement of wave amplitude, lowering of phase velocity and reduction of the number of capillary ripples.

INTRODUCTION

Sheared and falling liquid films have been the subject of numerous experimental and theoretical studies in the recent past [1, 2, 3, 4]. This renewed interest stems from the wide range of applications of this type of flow in chemical engineering. Indeed, falling films still constitute the state-of-the art technical solution for multiphase chemical reactors, evaporators or distillation columns [5, 6] as their intrinsic dynamics is well known to intensify heat and mass transfer. The presence of nonlinear waves in interaction is probably the key element for the intensification mechanisms in such flows as the onset of rolls and backflows promote transfers and wave merging generates an efficient mixing. This work is devoted to the analysis of a counter-current gas-liquid film flow in an inclined channel. Our purpose is to consider how travelling waves generated at the free surface of the film by the classical Kapitza instability mechanism are affected by the gaseous turbulent flow.

EXPERIMENTS

A devoted experimental set-up has been constructed consisting of a glass plate above which a plexiglas channel is placed. The glass plate is inclined at an angle β with the horizontal plane ($3^\circ \leq \beta \leq 18^\circ$). A falling water film flow is controlled by means of a gear pump and a collection tank thus ensuring a constant inlet liquid flow rate, whereas a fan generates a counter-current air stream. Special care has been taken for the construction of the inlet and outlet sections in order to limit the interaction of the gas and liquid flows to the middle section of the plane at which saturated travelling waves are observed on the liquid film. The frequency of the travelling waves is controlled by means of a temporal forcing at the liquid inlet. The film height is measured via a one-point CCI (confocal chromatic imaging) technique. Figure 1 presents a series of wave profiles for different speeds of the gas stream. As the gas speed is raised, the amplitude of the wave humps increases whereas the number of capillary ripples preceding each hump is reduced. The speed, and consequently the wavelength of the wave, drop with the onset of the air stream.

CONSTRUCTION OF TRAVELLING WAVE SOLUTIONS

Travelling wave solutions, i.e. waves which remain stationary in their moving frame, have been found numerically. The approach is one-sided as a constant interfacial shear stress is assumed at the gas-liquid interface. A pseudo-spectral approach is followed where a projection of the unknowns onto Chebyshev polynomial functions is performed and the primitive equations are evaluated at the Gauss-Lobatto points, which results in the elimination of the normal coordinate. By invoking a penalization method to account for the continuity of the stresses at the free surface, an autonomous dynamical system of large dimension is obtained. Travelling wave solutions are then obtained as Hopf bifurcations of the Nusselt flat-film solution by means of a predictor-corrector continuation method (ATO07p software [7]). Figure 1 compares numerical travelling-wave profiles to experimental data. As the experimental pressure drop is unknown, the comparison remains qualitative. A good agreement is found at a relatively low superficial gas speed. However, the constant shear stress assumption is insufficient to retrieve the experimental results at larger values of U_G.

CONCLUSION

The influence of a shear exerted by a gas stream on a falling liquid film has been documented experimentally and numerically. Though only qualitative, the proposed one-sided modelling is able to retrieve qualitatively the experimental observations: enhancement of wave amplitude, lowering of phase velocity and reduction of the number of capillary ripples. A better agreement to the experimental observations may be achieved through the Benjamin-Miles approach [2, 3] and will be the subject of future work.

[*]Corresponding author. Email: christian.ruyer-quil@univ-smb.fr

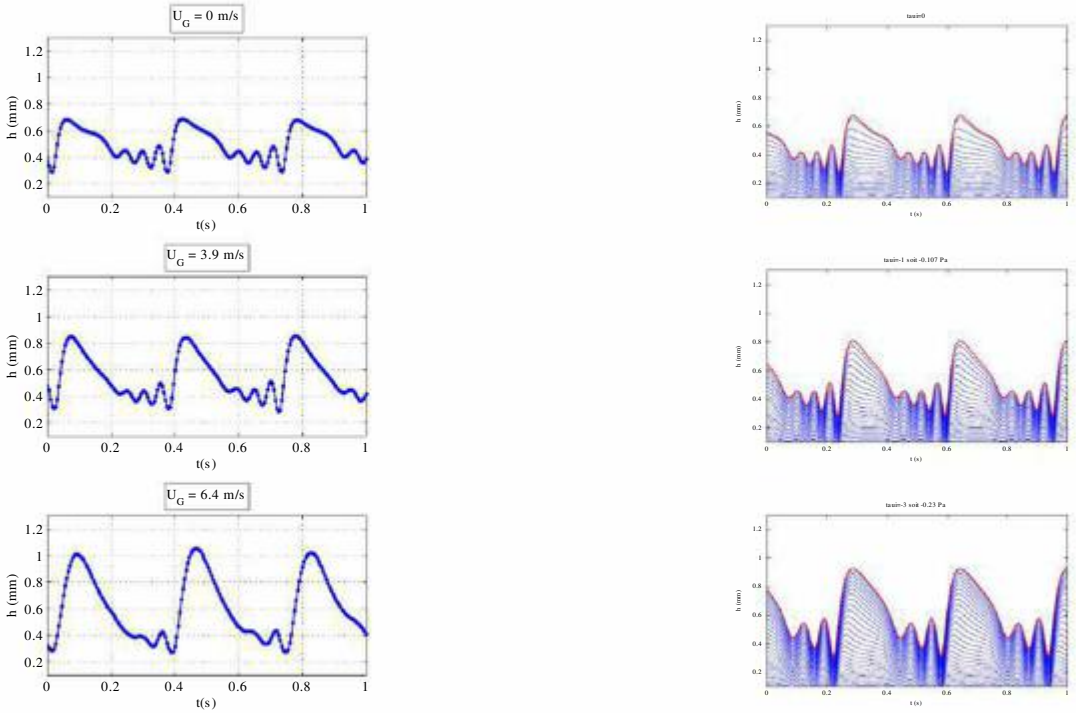

Figure 1: Left: CCI measurements of wave profiles at different superficial speeds U_G (liquid Reynolds number $R_L = 34$, canal height $e = 18$ mm, inclination angle $\beta = 5°$ and frequency $f = 2.8$ Hz). Right: Travelling-wave solutions to the primitive equations assuming a constant shear stress (top: $\tau_i = 0$; middle: $\tau_i = -0.1$ Pa ;bottom: $\tau_i = -0.3$ Pa).

References

[1] Vlachos, N. A., Paras, S. V., Mouza, A. A. and Karabelas, A. J. Visual observations of flooding in narrow rectangular channels. Intl J. Multiphase Flow 27: 1415-1430, 2001.

[2] Trifonov, Y. Y.: Counter-current gas-liquid wavy film flow between the vertical plates analyzed using the Navier-Stokes equations. AIChE J. 56 (8): 1975-1987, 2010.

[3] Tseluiko, D. and Kalliadasis, S. Nonlinear waves in counter-current gas-liquid film flow. J. Fluid Mech. 673: 19-59, 2011.

[4] Dietze, G. F. and Ruyer-Quil, C. Wavy liquid films in interaction with a confined laminar gas flow. J. Fluid Mech. 722: 348-393, 2013.

[5] Valluri, P., Matar, O. K., Hewitt, G. F. and Mendes, M. A.: Thin film flow over structured packings at moderate Reynolds numbers. Chem. Engng Sci. 60: 1965-1975, 2005.

[6] Haroun, Y., Legendre, D. and Raynal, L.Direct numerical simulation of reactive absorption in gas-liquid flow on structured packing using interface capturing method. Chem.Engng Sci. 65: 351-356, 2010.

[7] Doedel, E. J. AUTO07p: continuation and bifurcation software for ordinary differential equations. Montreal Concordia University, 2008.

ON SOLITARY WAVES IN PERIODICALLY EXCITED FALLING LIQUID FILMS

Fabian Denner*[1], Alexandros Charogiannis[2], Marc Pradas[3], Christos N. Markides[2], Berend G.M. van Wachem[1], and Serafim Kalliadasis[2]

[1]*Department of Mechanical Engineering, Imperial College London, London, United Kingdom*
[2]*Department of Chemical Engineering, Imperial College London, London, United Kingdom*
[3]*Department of Mathematics and Statistics, The Open University, Milton Keynes, United Kingdom*

Summary We present a detailed and systematic computational and experimental study of the hydrodynamics of solitary waves on periodically excited falling liquid films. We also offer a novel scaling for inertia-dominated falling liquid films that allows for a self-similar characterisation of the shape and dispersion of solitary waves in the films and unravels the main hydrodynamic mechanisms that dominate the dynamic behaviour of such waves. Furthermore, our results yield new insight pertaining to the onset of flow recirculation in the moving frame of reference of the waves, the flow reversal due to capillary effects as well as mechanisms related to capillary ripples preceding the main solitary humps that cause a significant reduction in film height and speed.

INTRODUCTION

A falling liquid film is an open-flow hydrodynamic system that is convectively unstable to long-wave disturbances and exhibits a rich variety of spatiotemporal structures, including a sequence of wave instabilities and transitions which are generic to a large class of hydrodynamic and other nonlinear systems. Due to their typically low flow rates resulting in low pressure drops but also small thermal resistance and large contact area, falling films are utilised in a wide spectrum of engineering applications, such as evaporators, heat exchangers and chemical reactor columns. When applying a periodic excitation with a sufficiently large amplitude, interfacial waves form as a result of the long-wave instability mechanism. A secondary modulation instability eventually transforms the primary wave field into fast solitary waves. These solitary waves have a dominant wave hump typically preceded by capillary ripples. If inertia is sufficiently high, solitary waves exhibit a separation of scales between the front of the main wave hump, where gravity, viscous drag and surface tension balance, and the tail of the wave, characterised by a balance between gravity, viscous drag and inertia [1]. This leads to a strongly non-parabolic velocity profile at the front of the solitary wave [2, 3], including a recirculation zone in the main wave hump in the moving frame of reference and flow reversal underneath the wave trough, which have a significant impact on the heat and mass transfer in the film.

Despite considerable research efforts in recent decades, many aspects of solitary wave dynamics still elude us. Using direct numerical simulation (DNS) [4, 5] and detailed experimental measurements [2] we have recently conducted an extensive synergistic computational-theoretical-experimental study to elucidate the hydrodynamics and characteristics of solitary waves in falling liquid films [3, 6]. Here we present some recent and largely unexpected findings with regards to the physical mechanism and hydrodynamics of solitary waves and their relation to the shape and the non-linear dispersion of the waves.

PARAMETRISATION AND SELF-SIMILARITY OF SOLITARY WAVES

Consider a liquid film flowing down a planar inclined substrate with angle β with respect to the horizontal. The equilibrium (flat) film height, referred to often as the Nusselt film height, is $h_\mathrm{N} = \sqrt[3]{3\,\mu\,q/(\rho\,g\,\sin\beta)}$ and the corresponding average film velocity, referred to often as the Nusselt velocity, is $u_\mathrm{N} = g\,\sin\beta\,\rho\,h_\mathrm{N}^2/(3\mu)$, where q is the flow rate per unit length and μ, ρ and g are the liquid viscosity, liquid density and gravity, respectively. Using the pressure scales corresponding to the three dominant physical effects, namely inertia, viscous stresses and surface tension, the flow can be parameterised by the Reynolds number $Re = \rho\,h_\mathrm{N}\,u_\mathrm{N}/\mu$ and the Weber number $We = \rho\,h_\mathrm{N}\,u_\mathrm{N}^2/\sigma$, where σ represents the surface tension coefficient. However, these dimensionless groups do not take the driving mechanisms of solitary waves into account.

An interfacial wave evolving from a long-wave perturbation is always unstable (for all Re) on a vertically falling liquid film ($\beta = 90°$) and stable on a horizontal liquid film ($\beta = 0°$) [1]. Consequently, since the horizontal component of velocity does not contribute to sustaining the solitary wave, a fully-developed solitary wave is only affected by the vertical component of the velocity, leading to the *driving Nusselt velocity* $u_\mathrm{N}^* = u_\mathrm{N}\,\sin\beta$. By substituting u_N^* for u_N, we can then define a driving Reynolds number Re^* and driving Weber number We^* [6].

Using Re^* and We^* to parameterise the shape and dispersion of solitary waves leads to a self-similar characterisation of the asymmetry $d/\lambda \sim 1/\sqrt{We^*}$ – where d is the distance between wave crest and wave trough, and λ is the wavelength – and the wave speed $c \sim \sqrt{Re^*}$ of the solitary wave. Figure 1a shows an example of the wave speed c as a function of driving Reynolds number Re^* for a water film with different surface tension coefficients σ and on substrates with different inclination angles β. The correlation of c and Re suggests that the dispersion of solitary waves in the inertia-dominated regime is mainly influenced by inertia, whereas frequency dispersion (i.e. due to surface tension and gravity) has no significant influence.

*Corresponding author. Email: f.denner09@imperial.ac.uk

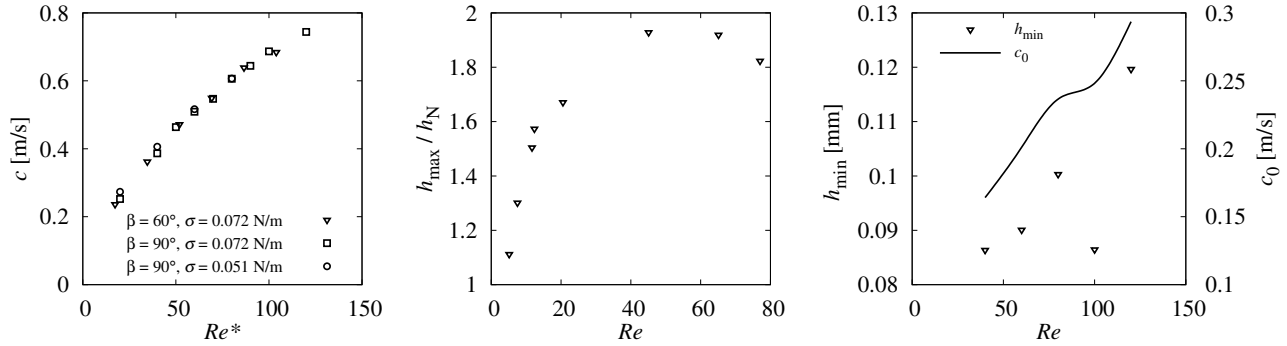

(a) Wave speed c as a function of driving Reynolds number Re^*

(b) Maximum film height $h_{\max}/h_{\mathrm{N}}$ as a function of Reynolds number Re

(c) Minimum film height $h_{\min}$ and net wave speed c_0 as a function of Reynolds number Re

Figure 1: Wave speed and film height as a function of Reynolds number for different periodically excited falling liquid films.

HYDRODYNAMICS OF SOLITARY WAVES

As mentioned earlier, the hydrodynamics of solitary waves are governed by a complex interplay of inertia, viscous stresses and surface tension. If inertia is sufficiently high, a recirculation in the main wave hump can be observed in the moving frame of reference and the flow separates from the substrate leading to flow reversal underneath the wave trough in the laboratory frame of reference. Our results suggest that the onset of flow recirculation inverts the long-wave instability mechanism and, thus, reduces the equilibrium wave height. For example, Fig. 1b shows experimental measurements of the height of the crest of solitary waves $h_{\max}$ with excitation frequency $f = 7\,\mathrm{s}^{-1}$ on a falling aqueous glycerol film on a substrate with $\beta = 20^\circ$ as a function of Reynolds number Re, where the maximum film height is observed just before the onset of flow recirculation at $Re \approx 46$. With regards to the flow separation and reversal underneath the wave trough, Chakraborty et al. [7] reported that the flow reversal is bounded by a lower and an upper limit with respect to the Reynolds number. At low Reynolds numbers the curvature at the wave trough and the ensuing pressure gradient are too small to induce flow reversal, whereas at high Reynolds numbers the low-pressure region in the vicinity of the wave trough is not able to reach the low-velocity region close to the substrate, which is necessary for the onset of flow reversal, as shown by our results.

The minimum film height $h_{\min}$ (i.e. at the trough immediately downstream of the main wave hump) adopts a minimum with respect to the Reynolds number Re, which coincides with a stagnation of the corresponding net wave speed $c_0 = c \circ u_{\mathrm{N}}$, i.e. the speed of the solitary wave relative to the film. For instance, Fig. 1c depicts $h_{\min}$ and c_0 as a function of Re for a vertically falling water film with excitation frequency $f = 50\,\mathrm{s}^{-1}$, where the minimum in $h_{\min}$ and the stagnation of c_0 for $Re \approx 100$ are clearly discernible. This phenomenon occurs at Reynolds numbers just below the threshold at which an additional capillary ripple develops. At higher Reynolds numbers ($Re \gtrsim 100$ in Fig. 1c) the number of capillary ripples preceding the main hump increases, along with an increase of the minimum film height $h_{\min}$ and the net wave speed c_0.

CONCLUSIONS

We have conducted an extensive computational and experimental study of the hydrodynamics of solitary waves in periodically excited falling liquid films, revealing new insights into the complex physical mechanisms that govern solitary waves, such as the long-wave instability mechanism and the complex interactions between solitary waves and capillary ripples. These observations should have important consequences with respect to maximising heat and mass transfer in the film, where the depth of the wave trough and the increased mixing associated with flow recirculation and flow separation play a crucial role (see e.g. [8]). Furthermore, by introducing a novel scaling derived from the Nusselt flat film solution based on the driving physical mechanisms, we have unraveled an unexpected self-similarity of the shape and dispersion of solitary waves.

References

[1] S. Kalliadasis, C. Ruyer-Quil, B. Scheid and M.G. Velarde, *Falling Liquid Films*, Springer (2012).

[2] A. Charogiannis, J.S. An and C.N. Markides, *Exp. Therm. Fluid Sci.* **68**, 516 (2015).

[3] F. Denner, A. Charogiannis, M. Pradas, C.N. Markides, B. van Wachem and S. Kalliadasis, *submitted to J. Fluid Mech.* (2015).

[4] F. Denner and B. van Wachem, *Numer. Heat Trans. B-Fund.* **65**, 218 (2014).

[5] F. Denner and B. van Wachem, *J. Comput. Phys.* **279**, 127 (2014).

[6] F. Denner, M. Pradas, A. Charogiannis, C.N. Markides, B. van Wachem and S. Kalliadasis, *submitted to Phys. Rev. E* (2015).

[7] S. Chakraborty, P.-K. Nguyen, C. Ruyer-Quil and V. Bontozoglou, *J. Fluid Mech.* **745**, 564 (2014).

[8] R. Mathie, H. Nakamura and C.N. Markides, *Intl J. Heat Mass Transfer* **56**, 819 (2013).

EXPERIMENTAL CHARACTERIZATION OF 2D TRAVELING WAVES IN LOW KAPITZA LIQUID FILM DOWN A VERTICAL WALL

Miguel Alfonso Mendez[1], Jean-Marie Buchlin [1]
[1]*Environmental and Applied Fluid Dynamics, von Karman Institute, Rhode-Saint-Genese*

Summary: Two-dimensional waves travelling on a vertical falling, low Kapizta (Ka=4.6) liquid film are characterized using Light Absorption (LAbs) and Laser Tomography (LT), in the low Reynolds number regime (Re=1-8). The waves are produced by introducing sinusoidal flow rate pulsations of controlled frequency (in the range 12-18 Hz) and amplitude (6-12% of the mean). The measurements, spatially and temporally resolved, include thickness profiles and wave celerity, non-dimensionalized using the Skhadov scaling.

INTRODUCTION

The evolution of a 2D travelling wave is a fundamental test case for validating theoretical and numerical models for liquid film flows. As the wave profile reaches a steady state in a reference frame moving at the wave velocity, analytical models can be formulated as a system of Ordinary Differential Equations (ODEs) and the wave evolution can be analyzed in the framework of dynamical system theory [1]. Saturated waves are typically produced experimentally by forcing the flow at frequencies much lower than the natural film cut-off frequency (e.g [2-3]). However, most of the experiments concern high Kapizta liquid such as water or alcohols (Ka~ $O(10^3)$), while little attention has been payed to low Kapitza liquids such as organic oils or paint (Ka~ O(1)). This paper presents the optical characterization of 2D traveling waves on a film of Dipropilene Glycol (Ka~4), using two optical techniques: the Light Absorption (LAbs) and the Laser Tomography (LT).

METHODOLOGY

The liquid film facility developed at the von Karman Institute (VKI) is shown in Fig.1a. It consists of a closed loop in which the liquid falls along a vertical test section and is recirculated, by a volumetric pump, into a pneumatic chamber. In this chamber a controlled pressure pulsation is introduced by a system of rotating butterfly valves, which open and close the inlet and the discharge lines of compressed air. This results in a pulsating Poiseuille flow in the distributing channel supplying the test section, and thus in a pulsating liquid film whose flow rate is linked to the measured pressure oscillation by a transfer function [4]. The experimental setups for the LAbs and the LT techniques are shown in Fig.1b and 1c.



1a) 1b) 1c)

Figure 1: a) Liquid Film Facility developed at the VKI, b) Set up for LAbs measurement, c) Set up for LT measurements.

The LAbs technique relates the film thickness to the amount of light it absorbs from a backlighting source. The set up include an array of LEDs, an Opal PLEXIGLAS screen and a CMOS camera synchronized with the LEDS. To maximize the absorption, a colorant is diluted in the liquid. The measurement consists in acquiring a set of transmittance images (Fig2a, top) and computing the corresponding thickness using the Beer-Lambert's law, being the total amount of light availailable and the liquid absorbance coefficient provided by a calibration. This method is 2D and time resolved, with sensitivity and uncertainty adjustable by a suitable choice of the colorant concentration [4]. A typical snapshot is proposed in Fig.2a, bottom.

The LT technique measures the film thickness from planar laser induced images, taken on a plane perpendicular to the test section and aligned with the stream-wise direction. The setup include a laser sheet and a CMOS camera, equipped with

[a] Corresponding author. Email: mendez@vki.ac.be.

zoom lens and optical high-pass filter, placed on one side. The image processing consists in recontrasting and edge enhancement (Fig. 2b, top), and gray-level gradient analysis, to locate the liquid interface in each image column. This method is 1D and time resolved, and needs no calibration. A typical measurement snapshot is proposed in Fig.2b, bottom.

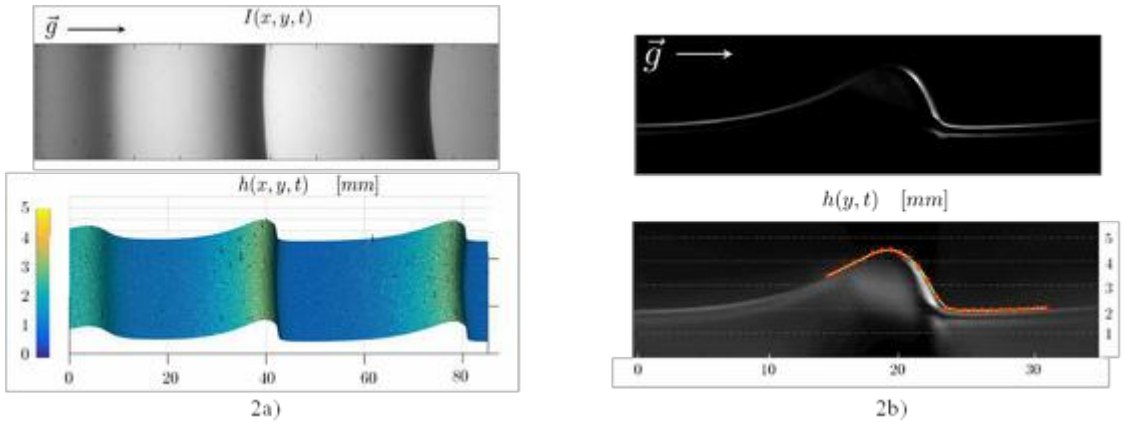

Figure 2: a) Example of gray scale transmittance image (top) and corresponding film thickness reconstruction (bottom) b) Example of edge processed LT image and corresponding interface tracking (bottom).

RESULTS

Measurements of the film thickness, h, are scaled with respect to the Nusselt thickness $h_N = (3\mu q/\rho g)^{1/3}$, while the wave celerity, obtained by cross-correlating wave profiles in time, is scaled with respect to kinematic wave speed $gh_N^2\rho/\mu$. The flow regime is defined in terms of reduced Reynolds number $\delta = (3Re)^{11/9}/Ka^{1/3}$. Fig.3a shows the evolution of the wave maxima/minima (h_M/h_m) as a function of δ, for several perturbation frequencies. Besides a slight overestimation for the LT, both measurements show an asymptotic behavior of h_m ($h_m \approx 3/2$) and a slight growth of h_M. Fig.3b plots the corresponding wave celerity, which is growing for lower perturbation frequency and is weakly affected by δ.

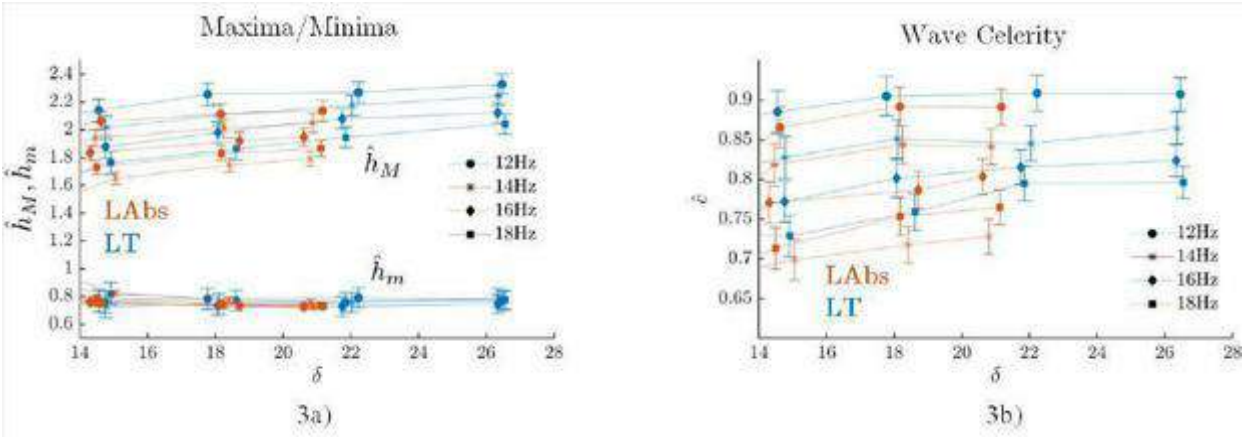

Figure 3: 3) Maxima/Minima thickness and (3b) wave celerity XX as functions of the reduced Reynolds Number.

Acknowledgement. M.A. Mendez is supported by a FNRS Fria Grant; VKI research is supported by ArcelorMittal.

References

[1] S.Kalliadasis,C.Ruyer-Quil,B.Scheid,M.G.Velarde. Falling Liquid Films, volume 176. Springer, Applied Mathematical Sciences, 2012.

[2] Liu J, Gollub J.P., Solitary wave dynamics of film flows, *Phys. Fluids 6(5):1702-1713*, 1994

[3] Charogiannis, A., Jae Sik A., Markides C.N. A simultaneous planar laser-induced fluorescence, particle image velocimetry and particle tracking velocimetry technique for the investigation of thin liquid-film flows, *Exp. Therm. Fluid Sci 68*:516-536, 2015.

[4] Mendez M.A., Nemeth L., Buchlin J.-M.. Measurement of Liquid Film Thickness using Light Absorption and Laser Tomography, EFM 2015, Prague, Czech Republic .

[5] Mendez M.A., Buchlin J.-M. Notes on 2D Pulsing Poiseuille Flows, VKI Technical Note 215, 2016

ON THE COMPUTATION OF VISCOUS FORCES NEAR THE MOVING CONTACT LINE

S. Afkhami *[1], S. Zaleski[2], S. Popinet[2], A. Guion[3], and J. Buongiorno[3]
[1]*New Jersey Institute of Technology, Newark, NJ, USA*
[2]*Institut Jean Le Rond d'Alembert, UPMC & CNRS-UMR 7190, Paris, FRANCE*
[3]*Massachusetts Institute of Technology, Cambridge, MA, USA*

Summary We present a numerical modeling of partially wetting plate withdrawn from a liquid reservoir at small capillary numbers in situations where a dynamic contact line at a certain height forms. We show that the main part of the dissipation on the plate arrises from the viscous friction near the contact line region. Previously, we showed in [J. Comp. Phys., 228:5370–5389, 2009] that the computed viscous dissipation on the plate depends on the mesh resolution. Here we investigate the effects of viscosity ratio on the calculation of viscous friction near the contact line region. We use an adaptive flow solver to focus the computations on contact line region. We discuss the computations of frictional drag close to the contact line region when varying the mesh resolution and the viscosity ratio.

NUMERICAL MODEL

We consider a computational domain $0 \leq x, y \leq 1$, with fluid 1 occupying $y < 0.35$ and fluid 2, $y > 0.35$ (see Fig. 1(a)). We use GERRIS [2-4] to numerically solve the Navier-Stokes and continuity equations, $\rho D\mathbf{u}/Dt = -\nabla p + \nabla \cdot \left[\mu \left(\nabla \mathbf{u} + \nabla \mathbf{u}^{\top}\right)\right] + \gamma\kappa\delta_s\mathbf{n} + \rho\mathbf{g}$, $\nabla \cdot \mathbf{u} = 0$, respectively, where $D/Dt = \partial_t + \mathbf{u} \cdot \nabla$, $\rho = \rho_1 C + \rho_2(1 - C)$, and $\delta_s\mathbf{n} = \nabla C$. Here, $\mathbf{u}$ is the velocity field, p the pressure, ρ the density, μ the viscosity, γ the surface tension, κ the interface curvature, $\mathbf{n}$ the normal to the interface (pointing from fluid 1 to fluid 2), δ_s the delta function centered at the interface, $\mathbf{g}$ the gravitational acceleration, and C(= 1 in fluid 1 and 0 in fluid 2) the color function. The location of the interface is determined from where the density jumps in value and is updated according to $D\rho/Dt = (\partial_t + \mathbf{u} \cdot \nabla)\,\rho = 0$. We solve this equation using a volume of fluid interface tracking method [1,2]. We use a volume wighted averaging and a harmonic mean averaging method for the computation of the viscosity in an interfacial cell, $\mu = \mu_2 C + \mu_2(1 - C)$, $1/\mu = 1(\mu_2 C) + 1/(\mu_2(1 - C))$, respectively.

RESULTS AND DISCUSSIONS

Consider a solid plate ($x = 0$) withdrawn from a fluid reservoir, as illustrated in Fig. 1(a), with a velocity $V_s = 1$. We fix the capillary number, $Ca = \mu_1 V_s/\sigma = 0.01$, the Reynolds number, $Re = \rho_1 V_s L/\mu_1 = 1$ (L is the size of the computational domain), the capillary length, $l_c = \sqrt{\sigma/(\rho_1 g)} \approx 0.3$, the density ratio, $\rho_1/\rho_2 = 100$, and vary the viscosity ratio, μ_1/μ_2, the mesh resolution, with the maximum mesh size Δ, and the equilibrium contact angle θ_{eq}. The results are computed to the stationary state, $t \to \infty$.

Here we report on the computation of the shear rate near the contact line region to shed light on the nature of the contact line friction force. We vary the viscosity ratio as well as the contact angle to understand the effect of the surrounding fluid and the surface wetting on the viscous dissipation. In Fig. 1(b), we plot the shear rates along the solid boundary. First, we show that the results depend on the mesh size. As shown, the maximum shear rate near the contact line is significantly increased by only doubling the mesh resolution. We note that further mesh refinement will lead to logarithmic divergence of the shear rate. When the viscosity ratio is increased, it appears that the maximum shear rate at the contact line only increases slightly. However, the location of this maximum shear rate is changed noticeably when changing the viscosity ratio. Interestingly, changing the equilibrium contact angle appears to have an insignificant effect on the maximum shear rate at the contact line. In Fig. 1(c), we show that using a volume weighted averaging versus a harmonic mean averaging can shift the location of the maximum shear rate, but it has no significant effect on the value of the maximum shear rate near the contact line. Figure 2 illustrates the flow fields near the contact line, at stationary state, when varying the viscosity ratio and the equilibrium contact angle. The streamline plots show a major shift in the stagnation point near the contact line when varying the viscosity ratio; i.e. for $\mu_1/\mu_2 = 1$, it is on the interface, while for $\mu_1/\mu_2 = 50$, it is inside liquid 2. The plot also shows the split streamlines in liquid 2. We observe that the angle of the split streamline varies when varying the viscosity ratio and the equilibrium contact angle.

CONCLUSIONS

We study the dynamics of moving contact lines for fluids with a large viscosity contrast. We report on the computation of the shear rate exerted by the solid wall on the liquid near the contact line region, and compare the results when varying the mesh size, viscosity ratio, and the equilibrium contact angle. We show that the shear rate diverges with mesh refinement. Interestingly, changing the equilibrium contact has no significant effect on the maximum shear rate at the contact line. The results of the flow topology suggest that for high viscosity ratios, a stagnation point near the contact line resides in the bulk, while for low viscosity ratios it is on the interface. This mechanism can be responsible for the difference in the bending of the interface and the topology of the flow close to the contact line.

*Corresponding author. Email: shahriar.afkhami@njit.edu

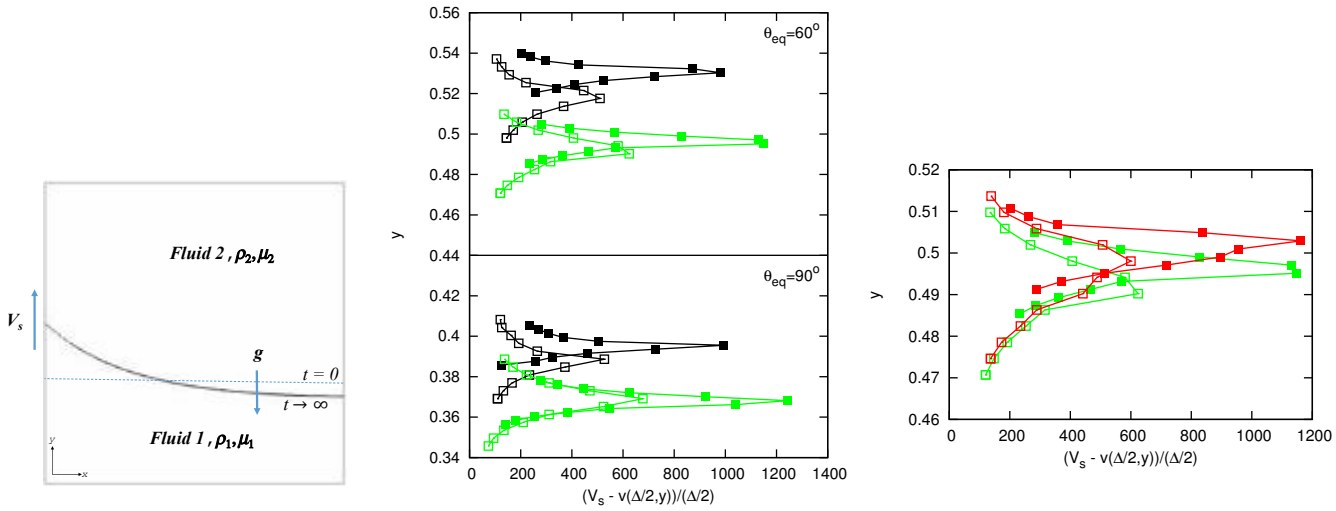

(a) (b) (c)

Figure 1: (a) Schematic of the withdrawing plate, initially at $t = 0$, and at the stationary state $t \to \infty$. (b) Stationary state shear rates at mesh resolutions $\Delta = 1/256$ (□) and $\Delta = 1/512$ (■), for $\mu_1/\mu_2 = 1$ (black) and $\mu_1/\mu_2 = 50$ (green). (c) Volume weighted averaging (red) versus harmonic mean averaging (green), $\mu_1/\mu_2 = 50$.

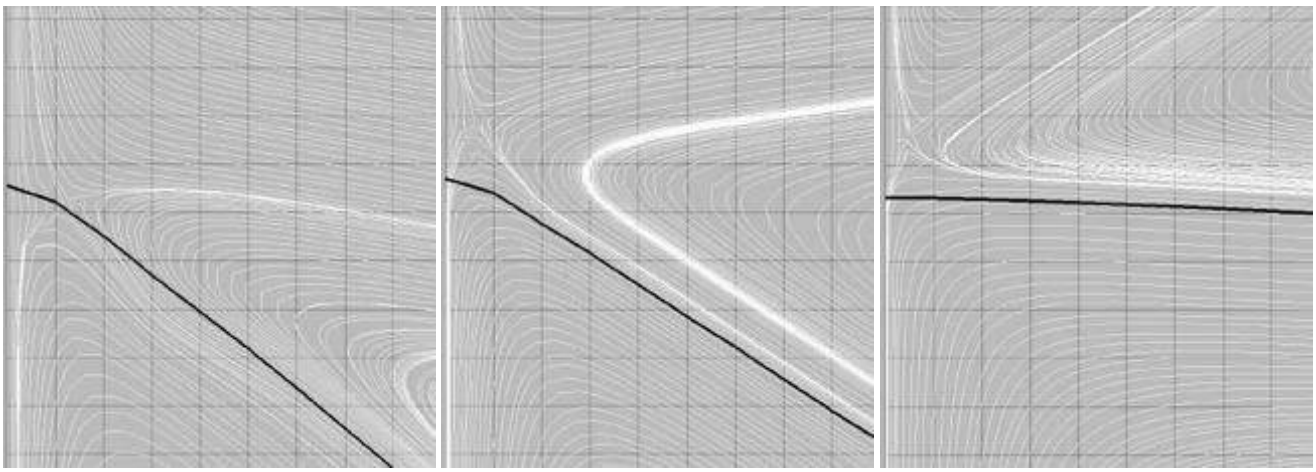

(a) (b) (c)

Figure 2: The flow fields near the contact line, at stationary state. The streamlines depict the slip of the contact line along the wall, as well as the parabolic flow field in fluid 1 and the split streamlines in liquid 2. (a) $\mu_1/\mu_2 = 1$, $\theta_{\text{eq}} = 60°$, (b) $\mu_1/\mu_2 = 50$, and $\theta_{\text{eq}} = 60°$, and (c) $\mu_1/\mu_2 = 50$, $\theta_{\text{eq}} = 90°$. $\Delta = 1/512$.

References

[1] Afkhami S., Zaleski S., Bussmann M.: A mesh-dependent model for applying dynamic contact angles to vof simulations. J. Comp. Phys., 228:5370–5389, 2009.

[2] Popinet S.: Gerris: a tree-based adaptive solver for the incompressible Euler equations in complex geometries. J. Comp. Phys., 190:572–600, 2003.

[3] Popinet S.: An accurate adaptive solver for surface-tension-driven interfacial flows. J. Comp. Phys., 228:5838–5866, 2009.

[4] Gerris Flow Solver, http://gfs.sourceforge.net.

2D VERSUS 1D MODELS FOR THIN FILM FLOWS

Jean Paul VILA *[1], Florent Chazel[1], and Florent Chazel[1]
[1]*Institut de Mathématique de Toulouse, Toulouse, France*

Summary The present paper first develop by using Prandtl shift system of coordinate an efficient tool for computing simple asymptotic expansion of 3D flow of thin films over a general non flat topography. 2D related two equations models are thus presented and generalize those classicaly obtained on plane surface. An asymptotic framework is also presented in order to elaborate simplified 1D two (or 3) equations models when the topography of the 2D models presents characteristics of 1 dimensionnal channel with general shape of cross sections. In the special case of Shallow water equations of hydraulic the new models are compared to the classical one used in standart hydraulic

ASYMPTOTIC EXPANSION OF THIN FILM FLOW OVER ARBITRARY TOPOGRAPHY

The motion of a thin liquid film of a viscous laminar fluid over a general topography is considered. For a flat substrate, general framework for deriving asymptotic expansion (with respect to the small parameter h/L where h is the characteristic hight of the flow and L a characteristic longitudinal length) is presented eg in [1]. Recently Charru and Luchini [2], Boutounet et al [3] have used Prandtl shift to build asymptotic expansion and one or two equations models for 1 dimensionnal flow over arbitrary one dimensionnal topography. By using technics such as those developped in [4] a new asymptotic expansion of all fields (velocity, pressure...) is build in the case of a general 2D topography. It generalizes the one given in [1] and reference therein.

1D FLOW OVER 2D TOPOGRAPHY

When the arbitrary topography presents some features involving one dimensionnal channel of arbitrary shape eg in the case where the bottom surface $b\,(x,y)$ is given by an equation of the form

$$Z = b(x,y) = B_0 b_0\left(\frac{x}{L}\right) + h_0\varphi\left(\frac{x}{L_X},\frac{y}{L_y}\right)$$

a theory is proposed to build asymptotic expansion of 1D flow along the $x$line.

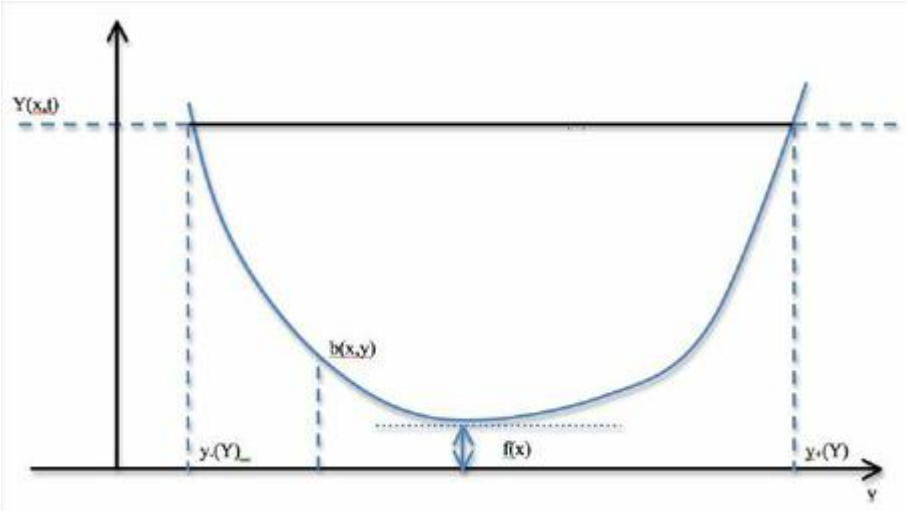

Figure 1: transverse section

One dimensionnal averaged two equations models are derived over such topography.

*Corresponding author. Email: vila@insa-toulouse.fr

CASE OF SAINT VENANT EQUATIONS

In the special case of Saint Venant hydraulic equations which writes in 2D

$$\left\{\begin{array}{l} h_t + (hu)_x + (hv)_y = 0 \\ u_t + uu_x + vu_y + gh_x = g\left(\circ\, Z_x \circ\, \dfrac{u}{C_v^2 h^m}\sqrt{u^2+v^2}\right) \\ v_t + uv_x + vv_y + gh_y = g\left(\circ\, Z_y \circ\, \dfrac{v}{C^2 h^m}\sqrt{u^2+v^2}\right) \end{array}\right. \tag{1}$$

one dimensional averaged models are build, they takes the form

$$\left\{\begin{array}{l} S_t + Q_x = 0 \\ Q_t + \left(\dfrac{Q^2}{S}\right)_x + gH_x S + R\left(H\right)H_x = gS\left(\mathcal{I}\circ\, \dfrac{Q\left|Q\right|}{C_h^2 R_h S^2}\right) \end{array}\right. \tag{2}$$

In the case of U shaped channel $R\left(H\right) = 0$, and these models are those classicaly used in hydraulics. It is proven that unless the channel is U schaped, additionnal terms in $R(H)$ arises and are needed to get consistency of 2D averaged models with 1D models. A special care is taken for the case of small Froude number. A new class of nonlinear models is presented, they requires an additionnal third equation to achieve first order consistency of 1D averaged models with 2D equations.

References

[1] S. Kalliadasis, C. Ruyer-Quil, B. Scheid, M.G. Velarde, Falling Liquid Films, Vol. 176, Springer-Verlag, 2012.

[2] P. Luchini, F. Charru, The phase lead of shear stress in shallow-water flow over a perturbed bottom, J. Fluid Mech. 665 (2010) 516–539.

[3] M. Boutounet, J. Monnier∗, J.-P. Vila, Multi-regime shallow free surface laminar flow models for quasi-Newtonian fluids, European Journal of Mechanics B/Fluids 55 (2016) 182–206

[4] C. Roget, J. Brazier, J. Cousteix, J. Mauss, A contribution to the physical analysis of separated flows past three-dimensional humps, Eur. J. Mech. B Fluids 17 (1998) 307–329.

[5] M. Boutounet, L. Chupin, P. Noble, J.-P. Vila, Shallow water flows for arbitrary topography, Commun. Math. Sci. 6 (2008) 531–536.

Numerical simulations of capillary thin film flows under hyperbolic CFL conditions

Didier Bresch[1], Pascal Noble [*2], and Jean-Paul Vila[3]
[1]*LAboratoire de MAthématiques; UMR 5127, Université Savoie Mont Blanc; CNRS, Chambéry, France*
[2]*Institut de Mathématiques de Toulouse; UMR 5219, Université de Toulouse; CNRS, INSA, Toulouse, France*
[3]*Institut de Mathématiques de Toulouse; UMR 5219, Université de Toulouse; CNRS, INSA, Toulouse, France*

Summary In this note, we introduce a *new* extended formulation of the so-called Euler-Korteweg equations. This formulation allows to design a numerical scheme with entropy stability property under a hyperbolic CFL condition in the multi-dimensional setting. We apply this strategy to perform fast and accurate numerical simulations of capillary thin films. We focus on the roll-wave phenomenon and wet-dry front both modeled by the shallow water equations with surface tension.

THE EULER-KORTEWEG EQUATIONS AND EXTENDED FORMULATION

The Euler-Korteweg equations are written as

$$\partial_t \varrho + \mathrm{div}(\varrho \mathbf{u}) = 0, \quad \partial_t(\varrho \mathbf{u}) + \mathrm{div}(\varrho \mathbf{u} \otimes \mathbf{u} + p(\varrho)\mathbf{I}_{R^n}) = \mathrm{div}(\mathbf{K}), \tag{1}$$

where ϱ denotes the fluid density, $\mathbf{u}$ the fluid velocity, $p(\varrho)$ the fluid pressure and $\mathbf{K}$ the Korteweg stress tensor defined as

$$\mathbf{K} = \left(\varrho \mathrm{div}(K(\varrho)\nabla\varrho) + \frac{1}{2}(K(\varrho) \circ \ \varrho K'(\varrho))|\nabla\varrho|^2 \right) \mathbf{I}_{R^n} \circ \ K(\varrho)\nabla\varrho \otimes \nabla\varrho.$$

with $K(\varrho)$ the capillary coefficient. These models comprise liquid-vapor mixture [3], superfluids [4] or regular fluids at sufficiently small scales (think of ripples on shallow waters) [5]. In classical fluid mechanics, the capillary coefficient $K(\varrho)$ is chosen constant. The system (1) admits additional conservations laws. In particular, the conservation of total (kinetic+potential) energy reads:

$$\partial_t \left(\frac{\varrho}{2}|\mathbf{u}|^2 + \mathcal{E} \right) + \mathrm{div} \left(\mathbf{u} \left(\frac{\varrho}{2}|\mathbf{u}|^2 + \mathcal{E} + p(\varrho) \right) \right) = \mathrm{div} \Big(F(\varrho)(\nabla \mathbf{w}\, \mathbf{u} \circ \ \nabla \mathbf{u}\, \mathbf{w}) \circ \ (F(\varrho) \circ \ \varrho F'(\varrho))(\mathrm{div}(\mathbf{w})\mathbf{u} \circ \ \mathrm{div}(\mathbf{u})\mathbf{w}) \Big),$$

with $\mathcal{E} = F_0(\varrho) + \frac{1}{2}K(\varrho)|\nabla\varrho|^2$ and F_0 the classical potential energy in Euler equations. The main issue in the numerical simulations of (1) is to preserve or, at least, dissipate this total energy. Following the strategy of [1], we introduce a "good" additional unknown, homogeneous to a velocity. We denote this additional velocity $\mathbf{w} = \nabla\varphi(\varrho)$ with $\sqrt{\varrho}\varphi'(\varrho) = \sqrt{K(\varrho)}$. We also define $F(\varrho)$ so that $F'(\varrho) = \sqrt{K(\varrho)\varrho}$. The Euler Korteweg system admits the extended formulation

$$\begin{cases} \partial_t \varrho + \mathrm{div}(\varrho\, \mathbf{u}) = 0, \\ \partial_t(\varrho\, \mathbf{u}) + \mathrm{div}(\varrho \mathbf{u} \otimes \mathbf{u}) + \nabla p(\varrho) = \mathrm{div}(F(\varrho)\nabla \mathbf{w}^T) \circ \ \nabla \left((F(\varrho) \circ \ \varrho F'(\varrho))\mathrm{div}(\mathbf{w}) \right), \\ \partial_t(\varrho\, \mathbf{w}) + \mathrm{div}(\varrho \mathbf{w} \otimes \mathbf{u}) = \circ\, \mathrm{div}(F(\varrho)\nabla \mathbf{u}^T) + \nabla \left((F(\varrho) \circ \ \varrho F'(\varrho))\mathrm{div}(\mathbf{u}) \right), \end{cases} \tag{2}$$

Note that we performed a reduction of order and the second order term is skew-symmetric: this latter property plays a central role in the design of numerical schemes which dissipate the generalized entropy $\mathcal{E} + \frac{\varrho}{2}|u|^2$.

NUMERICAL SIMULATIONS OF THIN FILM FLOWS

As an application, we carried out a numerical simulation of a thin film falling down an inclined plane. A consistent shallow water model [2] is given by

$$\partial_t h + \mathrm{div}\,(h\mathbf{u}) = 0, \tag{3}$$

$$\partial_t(h\mathbf{u}) + \mathrm{div}\,(h\, \mathbf{u} \otimes \ \mathbf{u}) + \nabla(p(h)) + \left(\frac{g\sin(\theta)}{\nu} \right)^2 \partial_x \left(\frac{2h^5}{225} \right) \mathbf{e}_1 = S(h, \mathbf{u}) + \frac{\sigma h}{\rho} \nabla(\Delta h). \tag{4}$$

with $p(h) = g\cos(\theta)h^2/2$ and $S(h, \mathbf{u}) = gh\sin(\theta)\mathbf{e}_1 \circ \ 3\nu\mathbf{u}/h$ and $\mathbf{e}_1$ the first vector of the canonical base directed downstream. Here g is the gravity constant, ρ, ν, σ are respectively the fluid density, kinematic viscosity and surface tension

*Corresponding author. Email: pascal.noble@math.univ-toulouse.fr

whereas θ is the inclination of the plane. We picked the values found in [5]. The convection terms are treated explicitly whereas the second order terms and the source term are treated implicitly: since both terms are only founds in the equations for $\mathbf{u}$ and are linear with respect to $\mathbf{u}$, the implicit step is *linear*. Moreover, we can prove that the scheme is entropy stable under a *hyperbolic CFL condition* (in contrast to classical approach where the stability condition reads $\delta t = O(\delta x^2)$). We first carried out a numerical simulation of the original experience in [5] but imposed periodic boundary conditions in both directions. The numerical scheme is second order accurate both in time and space: we implemented IMEX type strategy [6] to reach order two and implicit capillary and source terms.

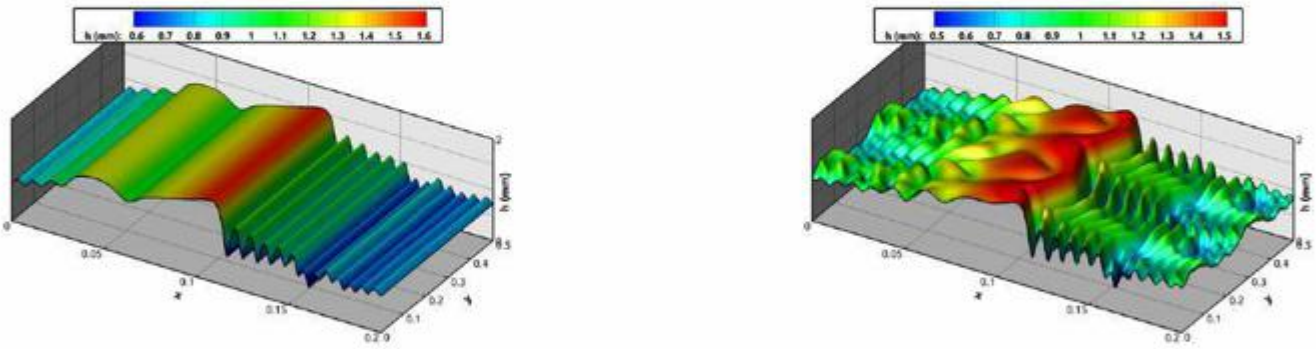

Figure 1: Numerical simulation of a roll-wave in presence of surface tension. On the left: one dimensional roll-wave without transverse perturbations. On the right: a two-dimensional roll-wave

In order to test the robustness of the scheme, we also carried various numerical experiments of a drop falling down a plane in order to deal with wet/dry fronts. For that purpose, we introduced a precursor film with a thickness of $1.0 \times 10^{-5}\, mm$.

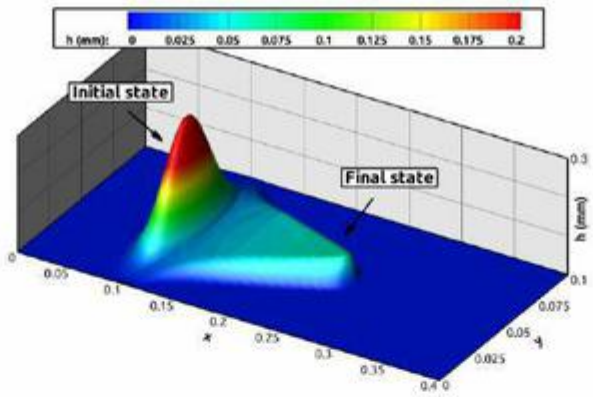

Figure 2: Drop falling down an incline plane ($\theta = 60^o$) at time $t = 0$ and $t = 1s$. The fluid density, kinematic viscosity and surface tension are respectively $\rho = 1.0 \times 10^3\, kg.m^{-3}$, $\nu = 1.0 \times 10^{-6}\, m^2.s^{-1}$ and $\sigma = 67 \times 10^{-3}\, kg.s^{-2}$.

References

[1] S. BENZONI-GAVAGE, R. DANCHIN, S. DESCOMBES. On the well-posedness for the Euler-Korteweg model in several space dimensions. *Indiana University Mathematics Journal,* 56, no 4, 1499–1579 (2007).

[2] M. BOUTOUNET, L. CHUPIN, P. NOBLE, J.–P. VILA. Shallow water flows for arbitrary topography. *Comm. Math. Sci.,*6 (2008) no 1, p. 73–90.

[3] D. JAMET, D. TORRES, J.U. BRACKBILL. On the theory and computation of surface Tension: The elimination of parasitic currents through energy conservation in the second-gradient Method. *Journal of Computational Physics* 182 (2002) 262–276.

[4] M.A. HOEFER, M.J. ABLOWITZ, I. CODDINGTON, E.A. CORNELL, P. ENGELS, V. SCHWEIKHARD. Dispersive and classical shock waves in Bose-Einstein condensates and gas dynamics. *Physical Review A* 74 (2006) no 2, 023623.

[5] J. LIU, J.B. SCHNEIDER, J.P. GOLLUB. Three-dimensional instabilities of film flows. *Physics of Fluids* 7 (1995) no 1, 55–67.

[6] L.PARESCHI, G.RUSSO, Implicit-Explicit Runge-Kutta methods and applications to hyperbolic systems with relaxation, *J. Sci. Comput.* 25 (2005), no. 1-2, 129–155.

TOWARDS OPTIMAL CRÊPE MAKING

Mathieu Sellier[1], & Younes Roqai Chaoui[2]
[1]*Department of Mechanical Engineering, University of Canterbury, Christchurch, New Zealand*
[2]*Ergonomie, Design et Ingénierie Mécanique, Université de Technologie de Belfort-Montbéliard, France*

Summary This contribution explores the familiar process of crêpe making whereby a fixed amount of batter is deposited on a pan and cooked. We treat the crêpe as a gravity current and solve the corresponding equation for a non-isothermal fluid on a rotating surface. We show that imparting a rotating motion of the pan can improve the coverage and uniformity of the resulting crêpe, as observed in practice. The modelling framework presented here can be applied in the wider context of surface coatings.

INTRODUCTION

Crêpes, unlike pancakes, are best appreciated when uniformly thin and most aesthetically pleasing when perfectly circular. Achieving these goals is, however, not necessarily easy to the inexperienced cook because as the batter spreads, it cooks at the same time and if the pan is left horizontal, the batter tends to solidify before reaching uniformly the rim of the pan. There are two strategies known to the authors to circumvent the issue. The first involves using a blade to force spread a uniform layer of batter on the pan in a process reminiscent of blade coating. The other strategy, preferred by the authors, consists in tilting the pan in a swirling motion and force the batter to spread preferably in the downslope direction of the span. As soon as this tilting is initiated, the axial-symmetry of the problem is broken and one cannot help but wondering what is the optimal swirling motion one should aim for to achieve an optimally thin and round crêpe. This contribution is a preliminary attempt at solving this very mundane yet interesting, practical problem using mathematical modelling and numerical simulations.

MODELLING FRAMEWORK

In order to tackle this problem, the batter layer is treated as a gravity current spreading over a surface whose inclination varies over time. The liquid viscosity is assumed to be a function of the temperature in order to model the solidification process. Gravity currents have received considerable attention in the past and an excellent account of the current knowledge can be found in [1]. To leading order in the liquid film aspect ratio, the momentum and energy conservation equations applied to an incompressible liquid film of reduce to:

x-momentum: $$\frac{\partial}{\partial z}\left(\mu\frac{\partial u}{\partial z}\right)=\frac{\partial p}{\partial x}-\rho g_x$$

y-momentum: $$\frac{\partial}{\partial z}\left(\mu\frac{\partial v}{\partial z}\right)=\frac{\partial p}{\partial y}-\rho g_y$$

z-momentum: $$-\frac{\partial p}{\partial z}-\rho g_z=0$$

Mass: $$\frac{\partial u}{\partial x}+\frac{\partial v}{\partial y}+\frac{\partial w}{\partial z}=0$$

Energy: $$\frac{d^2T}{dz^2}=0$$

where (u,v,w) is the velocity vector, p the pressure, T the temperature, $\mu(T)$ is the temperature-dependent batter viscosity, ρ the density, and (g_x,g_y,g_z) are the components of the acceleration of gravity vector projected on the x,y,z axis, respectively. The coordinate system (x,y,z) is attached to the pan but the rotation of the pan is assumed sufficiently slow that centrifugal or Coriolis forces may be neglected. The batter layer is bounded by the $x-y$ plane from below and the surface $h(x,y,t)$ from above. As the pan rotates, the orientation of the acceleration of gravity vector changes with respect to time. We represent the cyclic rotation of the pan by two angles $\theta(t)$ and $\beta(t)$ such that $g_x=g\sin\theta$, $g_y=g\sin\beta$, and $g_z=g\cos\theta\cos\beta$. The pan is assumed to be at a fixed temperature of T_s and the upper surface of the batter subject to convective heat transfer with the surrounding atmosphere at temperature T_∞ with a convective heat transfer coefficient h_c. Accordingly, $k\frac{\partial T}{\partial z}\Big|_{z=h}=h_c\big(T_\infty-T(h)\big)$ where k is the thermal conductivity. The governing equations above are subject to the no-slip boundary condition on the pan and a shear free boundary condition at the free surface which is subject to the passive atmosphere. Various models may be assumed for the variation of the viscosity with temperature, see [2,3] for example. We adopt here an exponential model such that:

$$\mu(T)=\mu_0 e^{-\alpha T}$$

Integration of the x- and y- momentum equations with respect to z yield the velocity field in terms of the pressure gradient which can be seen to be hydro-static from the z-momentum equation. Plugging this velocity field in the continuity equation integrated over the film thickness yields the following partial differential equation for the crêpe thickness $h(x,y,t)$:

[a] Corresponding author. Email: mathieu.sellier@canterbury.ac.nz.

$$\frac{\partial h}{\partial t} + \nabla \cdot \left(\frac{e^{\alpha T_s} \rho g h^3}{\mu_0 (A'\alpha)^3} \left(2e^{A'\alpha} - \left(\alpha^2 A'^2 + 2A'\alpha + 2 \right) \right) \left(\cos\theta \cos\beta \, \nabla h - (\sin\theta \, \vec{\imath} + \sin\beta \, \vec{\jmath}) \right) \right) = 0$$

where $A' = \frac{h_c(T_\infty - T_s)}{\frac{k}{h} + h_c}$. In the following and for the sake of illustration, we choose the following values for the parameters ρ=1000 kg/m^3, μ_0=2 Pa.s, α=10^{-4} K^{-1}, k=1.2 W.m^{-1}.K^{-1}, h_c=5 W.m^{-2}.K^{-1}, T_∞= 200 ^{o}C, T_s=20 ^{o}C. In this preliminary modelling attempt, the cooking of the batter is represented by an increase of the viscosity with a decreasing temperature, an unrealistic representation of the true process but at this early stage, the intent is merely to introduce a temperature-dependent solidification process.

The governing equation is solved in the Finite Element Multiphysics modelling software COMSOL. The computational domain, representing a circular pan, is a disk of radius 12.5 cm. Natural boundary conditions are applied at the boundary and the batter is initially a flat disk of thickness H_0=2.5 cm and radius 5 cm. In order circumvent the singularity which arises at the wetting front, the gravity current spread on a precursor film of thickness H_0/1000. Typical meshes have on the order of 6,500 quadratic elements which lead to good convergence and agreement with experimental measurement for the spreading on a flat, horizontal surface.

RESULTS

The cyclic rotation of the pan is imposed by letting $\theta(t) = A_1 \sin\omega_1 t$ and $\beta(t) = A_2 \sin\left(\omega_2 t - {}^{\pi}/_{2}\right)$ where ω_1, ω_2 are the angular frequencies and A_1, A_2 are the amplitudes of the tilting motion. These parameters are optimized in COMSOL to maximize an objective function I representative of the closeness of the solidified batter layer to the optimal thickness $h_{opt} = {}^{V}/_{A}$ where V is the initial volume of batter and A is the cross-section of the pan. Accordingly, the objective function is $I = \int_D \left(h - h_{opt}\right)^2 dxdy$. The Nelder-Mead algorithm is used for the optimization process.

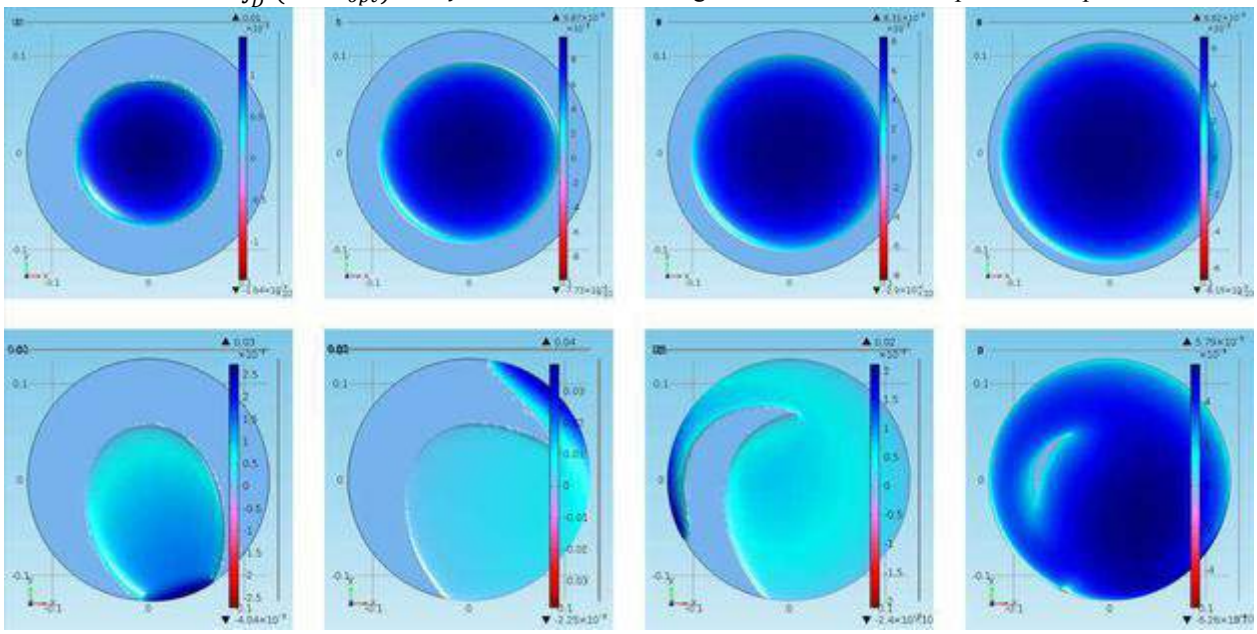

Figure 1: Top-view of the spreading batter on a circular pan. The top picture sequence shows the spreading on a flat, horizontal surface and the bottom sequence shows the spreading on a rotating surface. Times from left to right are: t=0.2 s, t=1 s, t=2 s, t=5 s

The top picture sequence shows that on a flat, horizontal surface, the gravity current spreads radially and solidifies before reaching the rim of the pan. The corresponding value of the objective function is 1.41e-5 m^3. The lower picture sequence shows the spreading when a swirling motion is imparted to the pan. The pan is periodically rotated about the x-axis and the y-axis. The batter is seen to reach the edge of the pan. The optimized application of rotation leads to an improved coverage of the pan and the corresponding value of the objective function is 1.06e-5 m^3. Over ~50 runs, the optimal parameters were found to be A_1=51.6^o, A_2=45.8^o, $\omega_1 = 2.77$ rad.s^{-1}, and $\omega_2 = 2.96$ rad.s^{-1}, a set of values specific to this case.

This preliminary study shows, as intuitively guessed, that imposing a rotating motion to the pan can improve the coverage and uniformity of the crêpe and the developed modelling framework should be relevant in the wider context of coatings.

References

[1] Leal L.G.: Advanced Transport Phenomena. Cambridge Series in Chemical Engineering, 2010.

[2] Sansom A., King J.R., Riley D.S.: Degenerate-diffusion models for the spreading of non-isothermal gravity currents. J. Eng. Math. **48**: 43-68, 2004.

[3] Bercovici D.: A theoretical model of cooling of viscous gravity currents with temperature-dependent viscosity. Geophys. Res. Let. **21**: 1177-1180, 1994.

CAPILLARY EFFECTS AND SHORT-SCALE INTERACTION IN A WEAKLY VISCOUS SUPERCRITICAL OVERFALL

Bernhard Scheichl [*1,2] and Robert I. Bowles[3]
[1] *Institute of Fluid Mechanics and Heat Transfer, Technische Universität Wien, Vienna, Austria*
[2] *AC2T research GmbH (Austrian Center of Competence for Tribology), Wiener Neustadt, Austria*
[3] *Department of Mathematics, University College London, United Kingdom*

Summary We consider a thin liquid film past a semi-infinite horizontal plate under the action of gravity acting vertically, surface tension, and relatively low viscosity. This scenario comprises a manifold of effects at play, given the two disparate length scales involved: distance from jet impingement generating the layer to the trailing edge of the plate, height of the film. The yet not fully understood behaviour of a developed viscous film near the edge and previous studies on bores and hydraulic jumps in weakly viscous horizontal layers stimulate the present investigation. In sharp contrast to these, here the flow remains supercritical, and isolated regimes of strong viscous–inviscid interaction are dictated by the short length scale rather than the common shallow-water approximation. Specifically, we show how viscosity produces standing waves upstream of localised interaction and how weak capillarity modifies drastically the potential-flow singularity close to the edge, which in turn affects crucially its viscous regularisation.

MOTIVATION AND SCOPE

Higuera [1] was the first who elucidated in detail the asymptotic structure of a steady developed viscous liquid film as this passes the plate edge in the configuration given in the summary under the assumption of shallow-water theory and supercritical initial conditions. He showed how the film undergoes a hydraulic jump, for a developed film meaning transition from super- to subcritical film at a streamwise scale that measures the distance from its initial stages to the edge, before it finally becomes critical in the sense of the Burns–Lighthill criterion for long waves. However (and as he conceded), the type of singularity the solution of the thin-film equations terminates in at the edge is not unambiguous. An alternative to the one proposed in [1] is provided by the expansive singularity in freely interacting hypersonic boundary layer (BL) flow as already pointed out in [2]. In addition, it is not fully understood how the flow becomes strongly interactive and how Higuera's singularity accommodates to the situation of a very supercritcal film and the associated shortening of the streamwise scale at play around the edge.

This contribution is devoted to the clarification of this issue, where we address the problem from the viewpoint of the high-Reynolds-number (Re) limit. Then a BL forms in an otherwise uniform flow, and the associated separation of scales gives rise to a myriad of intriguing phenomena not encountered in developed flow. Specifically, the short scale becoming essential and finally provoking localised strong viscous-inviscid interactive is given by the shallow-water parameter, ϵ, rather than the largeness of the Froude and/or Weber numbers, as in the investigation [3] of strong hydraulic jumps in a developed film. Also, the situation is unlike that in the preceding study [4] where those were considered in the high-Re and long-wave limit. Hence, our study is a paradigm for genuine short-scale interaction and the associated plate-normal momentum transfer in such flows as its generation is imprinted by the potential flow falling off the edge. The flow is then governed by the reciprocal forms G and T of the squared Froude and the Weber number, respectively, apart from the asymptotic parameters $\epsilon \ll 1$ and $Re \gg 1$, the latter formed with the speed $\tilde{U}$ and heigth $\tilde{H}$ of the unperturbed film and reduced by ϵ. The flow is critical/sub-/supercritical in the sense adopted in shallow-water theory for $G = / > / < 1$. Let us tacitily refer to figure 1 (*a*) subsequently: the flow velocity and Cartesian coordinates x, y are non-dimensional with $\tilde{U}$ and $\tilde{H}$; the long scale is thus represented by $1/\epsilon$.

We first justify strict supercriticality of the flow, then envisage the short-scale characteristics of the weakly/strongly interactive BL flow by advanced asymptotic techniques. As an exciting finding, a triple deck (TD) structure having an extent of $O(1)$ emerges at a distance $-x = O(\ln \epsilon)$. This new TD allows for the destabilising effect of viscosity and the generation of stationary waves upstream but their suppression downstream of it. Also, the solutions of the BL equations form a singularity at and thus a further interactive stage around the edge. We finally use this surprisingly rich flow picture to approach the situation of a developed flow addressed in [1] by letting ϵ (the plate) to become so small (so long) that strict supercriticality is questioned and local critical conditions do or do not point to the terminal structure of the BL close to the edge.

POTENTIAL-FLOW LIMIT: THERE IS NO STEADY SUBCRITICAL WATERFALL

We commence the investigation by analysing the potential flow falling off the edge, parametrised by G where first $T \ll 1$ is assumed as in [1]. Interestingly, though posing a fundamental member of closely related (more complex) ideal-fluid flow problems of great importance in hydraulics, cf. [5], converged numerical solutions to it are rare and not reliable at all for $G > 1$. This is not so surprising as one commonly associates subcritical flows with standing waves far upstream, which here

*Corresponding author. Email: bernhard.scheichl@tuwien.ac.at

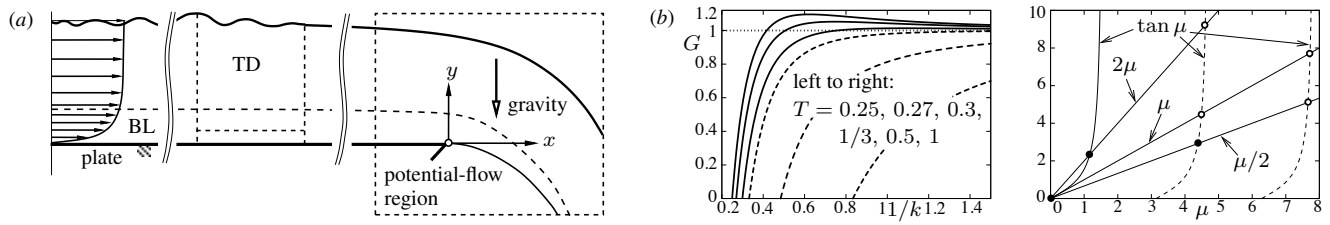

Figure 1: (*a*) flow configuration; (*b*) $\delta_0 = 0$: $G > 1$ can be double-valued for $T < 1/3$ ($\mu = 0$), μ jumps as G exceeds 1 ($T = k = 0$).

conflict with the required approach towards uniform flow. Moreover, in the aforementioned related situations solutions have been observed to exist if G does not exceed some critical value $G_c < 1$. Proving existence of such a threshold with sufficient rigour and determining its value analytically has not been successful so far. However, we demonstrate that $G_c = 1$ holds for the classical downfall problem; this value might even be lower if a sill or dent modifies locally the horizontal surface.

If q denotes the flow speed, the proof essentially exploits the extremal properties of $\ln q$ in consideration of the isotaches and their possible branching points. We first show that the detached streamline has negative curvature, i.e. bends towards the direction of gravity, throughout. Evaluating the global momentum balance in horizontal direction then yields the remarkable result $G < 4$. In particular, the flow past a flat plate is shown to be strictly accelerating, which in combination with its far-upstream variation finally yields $G \leq 1$. For $T \geq 0$, the latter is algebraic for $G = 1$ and purely exponential otherwise, and our restriction to the as appealing as geometrically simple overfall scenario includes the delicate near-critical case $G \to 1_-$.

The first part of that proof implies forced flow detachment at the edge for $T = 0$. With q equal to $q_0 := \sqrt{1 + 2G}$ there in this limit, we find the position $z := x + \mathrm{i}y$ very close to the edge as a function of the complex flow potential, w, in the form

$$q_0\bar{z} \sim w - \mathrm{i}c_1 w^{3/2} - \frac{9c_1^2 w^2}{16} - \left[\frac{2c_1 G}{5q_0^3}\Big(\frac{\mathrm{i}\ln w}{\pi} + 1\Big) + \mathrm{i}c_2\right] w^{5/2} - T\left[\frac{3c_1}{2q_0}\Big(\frac{\mathrm{i}\ln w}{\pi} + 1\Big) + \mathrm{i}d\right] w^{1/2} + O\big(w^3 \ln w, T^2 w^{-1/2}\big) \quad (1)$$

for $w \to 0$, $T \to 0$. Here we have $\bar{z} := z - x_d$, actual detachment at some $z = x_d(T) = O(T \ln T)$, and undetermined coefficients $c_1(G) > 0$, $c_2(G)$, $d(G)$. Resolving the non-uniformity of (1) proves a delicate matter; see [5] and the relevant references therein. At the critical stage $z = O(T)$, the procedure involves the (non-unique) solution of the celebrated *dock problem* by the Wiener–Hopf method. One finally finds the bottom streamline detaching at a stagnation point $z = x_d$ and an angle $\sim -\alpha c_1 T^{1/2} \ln T$ with the plate. This and the solution to the separation problem given in [5] differ by the number $\alpha > 0$ and the logarithmic term, which crucially affecting its viscous modification by the aforementioned second interaction process.

UPSTREAM BOUNDARY LAYER AND SHORT-SCALE INTERACTION

The exponentially varying short-scale disturbances imposed far upstream of the trailing-edge region $|z| = O(1)$ interact strongly with the BL if the rescaled reference wavelength $\Lambda := \epsilon Re^{3/2}$ is kept fixed. They satisfy the dispersion relation

$$\Lambda^{1/3}\,\delta_0 \sim \chi\,\delta_1, \quad [\delta_0, \delta_1] := [\lambda - (G - T\lambda^2)\tan\lambda,\ \lambda^{4/3}(G - T\lambda^2 + \lambda\tan\lambda)], \quad \chi := \Gamma(\tfrac{1}{3})(2/3)^{2/3}\beta^{-5/3} \doteq 7.2059. \quad (2)$$

for steady weakly viscous linear gravity–capillary waves with wavenumbers $k := \Im\lambda$ and damping rates $\mu := \Re\lambda > 0$; $\beta \doteq 0.4696$ is the wall shear rate of the unperturbed Blasius BL. The imposed, purely non-oscillatory perturbations are recovered for $\Lambda \gg 1$; for $G > 1$ they could also be strictly oscillatory: see figure 1 (*b*). Even slightly subcritical flows might be possible given the weak damping of these inviscid waves. The localised nonlinear lower-deck pocket associated with the new TD absorbs the waves upstream of it and described by (2) and achieve consistency with the overall flow structure by shedding the non-wavy potential-flow perturbations downstream. Accordingly, the generalised Fourier transforms $-\mathcal{A}$, $\mathcal{P}$ of the displacement function and the induced pressure perturbations, respectively, satisfy the interaction law $\mathrm{i}k\mathcal{A}(k) = \mathcal{P}(k)\,(\delta_0/\delta_1)(\mathrm{i}k)$.

The current efforts are directed towards resolving the trailing-edge singularity for $\Lambda \ll 1$ and the new TD. Specifically, we expect the limit $G \to 1$ to reveal how the long-wave TD structure in [6] governing transcritical flow resides in our setting.

References

[1] Higuera F. J.: The hydraulic jump in a viscous laminar flow. J. Fluid Mech. 274:69–92, 1994.

[2] Bowles R. I.: Applications of nonlinear viscous–inviscid interactions in liquid layer flows and transonic boundary layer transition. PhD thesis, Dept. Math., University of London, 1990.

[3] Bowles R. I., Smith F. T.: The standing hydraulic jump: theory, computations and comparisons with experiments. J. Fluid Mech. 242:145–168, 1992.

[4] Gajjar J. S. B., Smith F. T.: On hypersonic self-induced separation, hydraulic jumps and boundary layers with algebraic growth. Mathematika 30 (59):77–91, 1983.

[5] Vanden-Broeck J.-M.: Gravity–Capillary Free-Surface Flows (Cambridge Monographs on Mechanics). Cambridge University Press, 2010.

[6] Kluwick A., Cox E. A., Exner A., Grinschgl Ch.: On the internal structure of weakly nonlinear bores in laminar high Reynolds number flow. Acta Mech. 210 (1–2):135–157, 2010.

FLOW INTERACTIONS BETWEEN WATER AND CO_2 IN 2D HETEROGENEOUS POROUS MICROMODELS

Yaofa Li[1,3], Farzan Kazemifar[1,3], Gianluca Blois[1,3], Kenneth T. Christensen[1,2,3,a)]
[1]*Department of Aerospace and Mechanical Engineering, University of Notre Dame, Notre Dame, Indiana, USA*
[2]*Department of Civil and Environmental Engineering and Earth Sciences, University of Notre Dame, Notre Dame, Indiana, USA*
[3]*International Institute for Carbon-Neutral Energy Research (I²CNER), Kyushu University, Fukuoka, Japan*

Summary Multiphase flow of water and supercritical CO_2 in porous media is central to the geologic sequestration of CO_2 within saline aquifers. The coupled flow dynamics of CO_2 and brine in geologic media must be better understood, particularly at the pore scale, as pore-scale processes represent a critical component of accurately predicting large-scale migration of injected CO_2. In this work, the pore-scale flow interactions of water and liquid/supercritical CO_2 are being quantified in 2D heterogeneous porous micromodels at reservoir-relevant conditions (*i.e.*, 80 bar, 20°C), in an attempt to accurately mimic the process of CO_2 injection into saline aquifers. The initial results show that the dominant CO_2 flow paths have very complex spatial configuration, which highlights the importance of the local pressure (*e.g.*, capillary) gradient in CO_2 front migration.

INTRODUCTION

Carbon capture and sequestration (CCS) is a viable technique for reducing carbon emissions from large CO_2 sources, such as fossil fuel thermal power plants [1]. An important stage in the CCS process is the injection of supercritical CO_2 into saline aquifers, which are porous formations saturated with brine, and thus CO_2 must displace the resident brine during and post injection. At reservoir conditions, the CO_2 is in either a liquid or supercritical state, and thus less dense and less viscous than the resident brine. These conditions therefore lead to complex displacement patterns as the CO_2 infiltrates the pore space, particularly the onset of fingering phenomena driven by the balance between viscous and capillary effects [2]. Our fundamental understanding of the coupled flow dynamics of CO_2 and brine in geologic media is still limited. This is particularly true at the pore scale, despite pore-scale processes representing a critical component of accurately predicting large-scale migration of injected CO_2.

To this end, fluorescent microscopy and the micro-PIV method are simultaneously employed to capture the pore-scale flow dynamics of liquid/supercritical CO_2 infiltration into water-saturated 2D *heterogeneous* porous micro-models at reservoir conditions (80 bar, 20 °C). These results provide valuable insight into flow processes at the pore scale in natural rock.

EXPERIMENTAL METHODS

The micromodels used in these experiments were fabricated from silicon, with the porous matrix formed from the reprint of the pore structure of real sandstone as shown in Figure 1 [3].

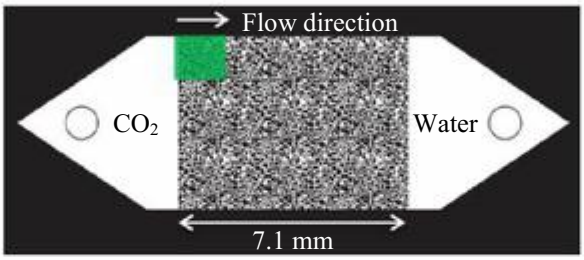

Figure 1: Schematic diagram (to scale) of the micromodel with the green region indicating the imaging field of view.

The coupled flow of water and CO_2 through the micromodel is accurately controlled by two high-pressure syringe pumps. One pump is connected to the inlet (*i.e.*, the left port) of the micromodel and is used to push the supercritical CO_2, while the other pump is connected to the exit (*i.e.*, the right port) to withdraw water as well as maintain the back pressure of the flow system. In order to keep the micromodel from breaking at reservoir-relevant pressures, *i.e.*, 80 bar, the micromodel is placed within an overburden pressure cell, whose pressure is controlled by a third high-pressure syringe pump. Fluorescent microscopy and the micro-PIV method are simultaneously employed by seeding the water phase with fluorescent particles and tagging the CO_2 phase with a fluorescent dye of a different spectral emission. Doing so allows for simultaneous measurement of the spatially-resolved instantaneous water velocity field and quantification of the instantaneous spatial configuration of both phases [4].

a) Corresponding author. Email: kchrist7@nd.edu.

INITIAL RESULTS

The initial results provide a unique view of the flow dynamics during the migration of the CO_2 front, the evolution of individual menisci and the growth of dendritic structures, so-called fingers [2, 4]. Before the CO_2 front arrives, the test section features a steady single-phase flow of pressurized water, which is predominantly from left to right owing to the driving pressure gradient (Fig. 2*a*). During the CO_2 infiltration process, CO_2 suddenly breaks through the resident water, forming fingers which grow in directions both along and normal to the bulk pressure gradient, and even against the bulk pressure gradient, indicative of capillary fingering (Fig. 2*b*). The complex spatial configuration of each fluid phase highlights the importance of local pressure gradients in CO_2 front migration. Although results are not shown here, experiments at a much higher flowrate (*i.e.*, 0.05 ml/min or 10 times higher), and thus a much higher capillary number, show that the CO_2 fingers grow predominantly in the bulk flow direction, which suggests that the flow is more likely dominated by viscous fingering (*vs.*, capillary fingering) as the capillary number increases [2].

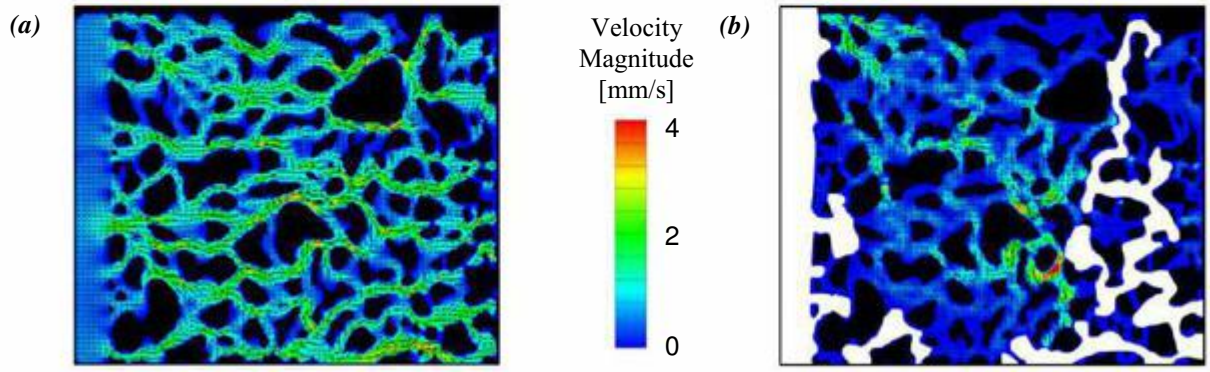

Figure 2: Sample flow fields (80 bar, 20 °C, 0.005 ml/min) before CO_2 front arrives (*a*) and after it passes (*b*), showing water velocities as color contours; CO_2 and silicon grains as white and dark, respectively.

CONCLUSIONS

Fluorescent microscopy and micro-PIV have proved to be powerful tools to quantify of the flow interactions of supercritical CO_2 and water under reservoir-relevant conditions. For single-phase flow, the flow is steady and predominantly in the direction of the bulk driving pressure gradient. For multi-phase flow, dominant flow paths have complex spatial configuration, highlighting the importance of local pressure gradients in front migration; capillary fingering in the CO_2 phase are noted at both low and high flow rates, with relatively stronger capillary effects at the lower flow rate, as expected.

CURRENT WORK

Experiments are ongoing for a broad range of reservoir-relevant conditions to study the sensitivity of these flow patterns on pressure. In addition, similar heterogeneous micromodels are being constructed with varying wettability to study the impact of grain wettability on the observed fingering physics upon injection of CO_2 and concomitant displacement of the resident water. Finally, complementary numerical simulations that replicate the conditions studied herein (pore geometry, thermodynamic conditions and wettability) are underway with collaborators to both validate these numerical tools as well as explore a broad span of the relevant parameter space.

References

[1] S. Pacala and R. Socolow, Science **305**, 968-972, (2004).
[2] R. Lenormand, E. Touboul, and C. Zarcone, J. Fluid Mech. **189**, 165-187, (1988).
[3] L. Zuo, C. Zhang, R.W. Falta, and S.M. Benson, Adv. Water Resour. **53**, 188-197, (2013).
[4] F. Kazemifar, G. Blois, D. C. Kyritsis, and K. T. Christensen, Adv. Water Resour. **000**, 1-17, (2015).

Acknowledgements

This work was primarily supported as part of the Center for Geologic Storage of CO_2, an Energy Frontier Research Center funded by the U.S. Department of Energy, Office of Science and partially supported by the International Institute for Carbon-Neutral Energy Research (WPI-I^{2}CNER) based at Kyushu University, Japan.

NONLINEAR WAVES IN A FALLING FILM WITH PHASE TRANSITION

Alekseenko S. V.,[1, 2] Aktershev S. P.[1, 2 a)]
[1] *Institute of Thermophysics, Siberian Branch, Russian Academy of Sciences, Novosibirsk, Russia*
[2] *Novosibirsk State University, Novosibirsk, Russia*

Summary Intensive investigation of thin liquid films is caused by their wide application in engineering. In the majority of practical situations the film flow is unstable and waves develop on the liquid surface. It is known that the waves in liquid film intensify processes of heat and mass transfer even for laminar flow. Wave generation and transport processes in falling liquid films without phase transition were investigated in many studies; the results of these studies are summarized in [1]. The wave dynamics and heat transfer in non-isothermal films are much less studied. The purpose of the presented research is to study the nonlinear evolution of waves in the film with a phase transition, and to determine the effect of waves on heat transfer. Nonlinear evolution of the two-dimensional both natural and forced waves in a liquid film is studied by numerical method. An integral-boundary-layer model [2] modified to consideration of phase transition is applied to describing nonlinear waves in a liquid film.

UNSTEADY FILM FLOW EQUATIONS

Let us consider a vertical laminar film flow on a uniformly heated or cooled plate. Let us introduce Cartesian coordinate system *Oxy* with *Ox* axis directed downward, and *Oy* axis normal to the plate. Let us assume the following basic simplifications, acceptable for a wide range of practically important flow conditions: 1) Plate temperature $T_w = const$, the liquid surface is in contact with stagnant saturated vapor with temperature $T_s = const$. 2) Film essentially contributes to the thermal resistance. 3) The perturbation of the film surface is considered to be long wave (the typical length of the perturbation is much greater than the film thickness). 4) Density ρ, dynamic viscosity μ, liquid conductivity λ, surface tension σ, and latent heat of evaporation r are assumed constant. We introduce the distance scale l along the *Ox* axis. We take film thickness h_m at $x = 0$ as the distance scale along the *Oy* axis. Let us introduce velocity scale $u_m = gh_m^2/3\nu$, time scale $t_m = l/u_m$, flow rate scale $q_m = u_m h_m$, temperature scale $\Delta T = |T_s - T_w|$, and move on to the dimensionless variables x/l, y/h_m, h/h_m, q/q_m, t/t_m, u/u_m, keeping for them the same notations. In dimensionless variables the film flow with phase transition is described by the set of equations [3, 4] with respect to film thickness $h(x,t)$, flow rate $q(x,t)$ and temperature $\theta(x,\eta,t) = \pm (T - T_w)/\Delta T$:

$$\frac{\partial q}{\partial t} + \frac{\partial}{\partial x}\left(\frac{6F_0 q^2}{5h}\right) = \frac{3}{\chi \mathrm{Re}_m}\left(h - \frac{F_1 q}{h^2}\right) + \chi^2 We h \frac{\partial^3 h}{\partial x^3},$$
$$\frac{\partial h}{\partial t} + \frac{\partial q}{\partial x} = \pm \frac{A}{\chi \mathrm{Re}_m h}, \qquad (1)$$
$$\frac{\partial \theta}{\partial t} + u\frac{\partial \theta}{\partial x} + \frac{W}{h}\frac{\partial \theta}{\partial \eta} = \frac{1}{\chi \mathrm{Re}_m \mathrm{Pr} h^2}\frac{\partial^2 \theta}{\partial \eta^2}.$$

Here and in other formulae sign "plus" corresponds to condensation and sign "minus" corresponds to evaporation; $A = \varepsilon \left.\frac{\partial \theta}{\partial \eta}\right|_{\eta=1}$; $\varepsilon = c_p \Delta T/(r\,\mathrm{Pr})$ is a parameter of phase transition; $\mathrm{Re}_m = gh_m^3/3\nu^2$ is the Reynolds number at the inlet; $\chi = h_m/l$ is the ratio of scales; $We = (3Fi/\mathrm{Re}_m^5)^{1/3}$; $Fi = \sigma^3/\rho^3 g \nu^4$ is the Kapitza number; coefficients $F_0 = 1 - A/(4+A)^2$ and $F_1 = 1 + A/(4+A)$ take into account the effect of condensation on the velocity profile in the film; $W = \left(\eta - \frac{3\eta^2}{2} + \frac{\eta^3}{2}\right)\frac{\partial q}{\partial x} - \frac{3\eta^2 - \eta^3}{2}\frac{\partial}{\partial x}\left(\frac{qA}{4+A}\right) - \frac{A\eta}{\chi \mathrm{Re}_m h}$. For smooth film (without waves) the effect of surface tension can be neglected. If we take a linear temperature profile $\theta = \eta$, the solution to the first two equations (1) will be as follows

$$h_{steady} = \left(1 \pm \frac{4\varepsilon(F_1 + 2F_0\varepsilon/3)x}{3\chi \mathrm{Re}_m}\right)^{1/4}, \qquad (2)$$
$$q_{steady} = \frac{h^3}{F_1 + 2F_0\varepsilon/3}$$

Wave flow regimes are obtained by numerical solution to equations (1) using the finite-difference method. Region of computation was large enough to be able to trace the development of the waves downstream. Duration of calculations was also chosen sufficiently large to assure that the wave regime is developed over the all computation region.

[a)]Corresponding author. Email: **sergey-aktershev**@mail.ru

Boundary and initial conditions. The waves were generated by a small perturbation of the flow rate at the inlet: $q(0,t) = q_0\left(1 + Q_a \sin 2\pi\right)$. Here q_0 is the undisturbed flow rate, Q_a is small amplitude, and f is flow rate oscillation frequency. The constant film thickness $h(0,t) = 1$ and the linear temperature profile $\theta(0,\eta,t) = \eta$ were set at the inlet. Linear temperature profile was set at time t = 0 for the all region of calculation; distributions of $h(x,0)$ and $q(x,0)$ were set by formulas (2). Boundary conditions for the energy equation are $\theta\big|_{\eta=1} = 1$, $\theta\big|_{\eta=0} = 0$.

SIMULATION RESULTS

All calculations were carried out for water at the temperature of 373 K (Pr = 1.75, $Fi^{1/3}$= 14700) for Q_a= 0.01, ε = 0.005. Reynolds number at the inlet Re_m = 1 in a case of condensation and Re_m = 40 in a case of evaporation. Simulation shows natural waves caused by instability of flow develop which intensify considerably heat transfer in a film. Natural waves occurred without inlet perturbation were also observed in [5] at numerical simulation of the R11 condensate film flow. For the first time the evolution of forced waves in a film with phase transition is studied in a wide range of frequencies. The wave film surface at forcing frequency of 18 Hz is shown in Fig. 1 (condensation) and Fig. 2 (evaporation). It can be seen from figures that forced waves have the regular character and develop at a certain distance from the inlet. The coordinate, at which the nonlinear wave starts to develop, depends on frequency, but in all cases the forced waves develop earlier than the natural ones. At sufficiently low forcing frequency, the intermediate peaks (generation of higher harmonics) are observed. This results in the wave interaction with the subsequent merge of the individual peaks.

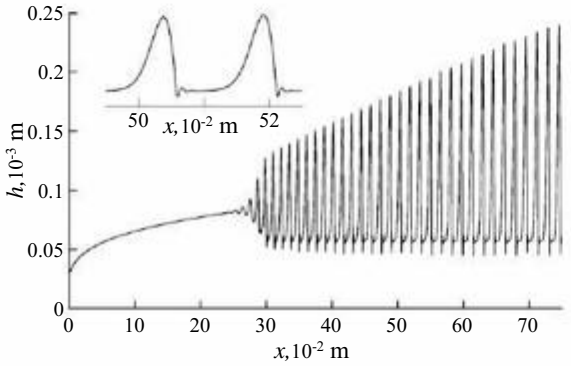

Fig.1. Forced waves in a condensate film; f=18 Hz; Detail structure of the wave is shown in the upper insertion.

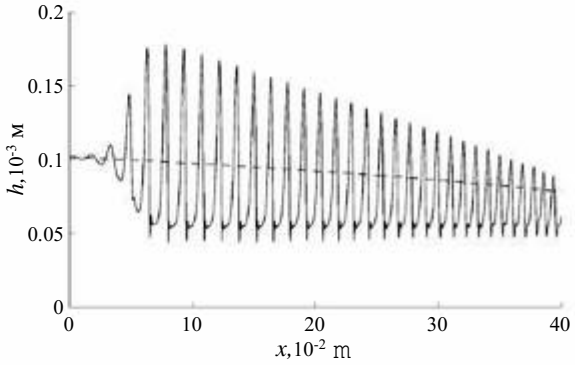

Fig. 2. Forced waves in an evaporating film; f=18 Hz;

CONCLUSIONS

In the presented study a numerical method is used to simulate nonlinear waves and heat transfer in the film of water flowing down a vertical wall in the presence of a phase transition. The evolution of both natural waves arising due to the instability of the flow, and forced waves generated by small periodic perturbation of flow rate at the inlet, was investigated. Natural waves appear at some distance from the inlet and very quickly transform into large-amplitude nonlinear waves with a thin residual layer between them. The application of small periodic forced perturbation within a certain frequency range results in appearance of regular waves with stable characteristics. The distance, at which the nonlinear wave starts to develop, depends on frequency, but in all cases the forced waves develop earlier than the natural ones. At sufficiently low forcing frequency, the intermediate peaks (generation of higher harmonics) are observed. It results in the wave interaction with the subsequent merge of the individual peaks. Sufficiently high forcing frequency results in appearance of subharmonic instability, which also leads to the interaction and merging of the waves. Heat transfer calculations show that at the appearance of waves (both natural and forced) heat transfer coefficient abruptly increases up to a certain level, depending on the frequency of the waves.

References

[1] S.V. Alekseenko, V.E. Nakoryakov, B.G. Pokusaev, Wave Flow of Liquid Films. Begell House, NY 1994.

[2] V.Ya. Shkadov, Wave-flow theory for a thin viscous liquid layer. *Fluid Dynamics* **3**, 12–15, 1968.

[3] S.P. Aktershev, S.V. Alekseenko, Influence of condensation on the stability of a liquid film moving under the effect of gravity and turbulent vapor flow. *Int. J. Heat Mass Transfer*, **48**, 1039-1052, 2005.

[4] S.P. Aktershev, S.V. Alekseenko, Nonlinear waves and heat transfer in a falling film of condensate. *Phys. Fluids*, **25**, 083602, 2013.

[5] A. Miyara, Flow dynamics and heat transfer of wavy condensate film. *ASME, J. Heat Transfer* **123**. 492-500, 2001.

VISCOUS DISSIPATION IMPACT ON PRESSURE LOSS IN COMPRESSIBLE LUBRICANTS

Andrea Codrignani*, Franco Magagnato, and Bettina Frohnapfel
Institute of Fluid Mechanics, Karlsruhe Institute of Technology, Karlsruhe, Germany

Summary In the present work we consider compressible viscous lubrication oils in a channel flow. With the aim to study the effects of viscous dissipation and thermodynamics in a very thin lubricant film. Direct numerical simulations of the compressible Navier-Stokes equations and the energy equation are performed for a lubricant oil whose equation of state is represented by a stiffened gas model. Particular attention is paid to the resulting pressure losses in the plane channel. It is shown that these viscous effects, that alter the classical Couette velocity profile towards a Couett-Poiseuille one, scale with the parameter $\alpha = \mu LU/h^2$, and that the losses are proportional to the square of α.

INTRODUCTION

In tribological applications the ability of the lubricant film to generate a net load capacity is the key performance factor. For many different reasons (*e.g.* viscous effects, roughness, compressibility, cavitation...), the lubricant flow generates undesired pressure losses which degrades the overall load carrying capacity. Several aspects of these losses are discussed in literature based on numerical (Gropper *et. al.* [2]) and experimental (Morini [1]) studies. In the present work we focus exclusively on effects related to the compressibility of the lubricant fluid by taking into account the related thermodynamics without any simplification.

In usual sliding contacts, the lubricant film is very thin but the contact area between the two surfaces may extend over a very large distance in comparison. For this reason, even in absence of pressure gradients due to inclined walls, severe pressure drops can be encountered due to viscous dissipation. This kind of effect can be described, from the numerical viewpoint, only by solving the compressible Navier–Stokes equations jointly with the energy equation. Such a numerical approach can also provide the thermal dependency which is not discussed in the presently available analytical solutions (*e.g.* Venerus [3], Housiadas [4]) where isothermal flows are considered.

PROCEDURE

In oder to study the generation of a pressure gradient due to compressibility effects, the laminar flow between two parallel surfaces is considered. The gap height is h, its length L and the upper wall moves with constant velocity U. At the inlet, a linear velocity profile (Couette flow) with a uniform temperature T is prescribed, while the static pressure P_0 is assigned at the outlet boundary. In order to describe the lubricant oil properties we apply the stiffened gas equation of state in the following form:

$$P = (\gamma \circ\ 1)\rho e \circ\ \gamma \bar{P} \tag{1}$$

where γ and $\bar{P}$ are liquid dependent constants, ρ is the density and e the internal energy of the fluid. In this case the selected oil is a Polyalphaolefin whose viscosity depends exponentially on temperature and not on pressure. The two liquid dependent constants are $\gamma = 2.8$ and $\bar{P} = 3.16e^8[Pa]$.

The compressible Navier–Stokes equations and the energy equation with the above oil properties are solved with a Finite Volume scheme [5]. All results are tested to be mesh independent by means of a multi-level method.

A parametric analysis is carried out by varying important aspects of the flow such as temperature, inlet velocity and the aspect ratio of the channel. All these aspects can be summarized in a unique parameter $\alpha = \frac{\mu LU}{h^2}$ which represents the influence of the viscous dissipation on energy and pressure. This parameter originates from the dimensional analysis of the energy equation which, for a compressible flow in a thin channel, can be reduced to:

$$u\frac{\partial H^t}{\partial x} = \mu\left(\frac{\partial u}{\partial y}\right)^2 \tag{2}$$

where H^t is the total enthalpy $H^t = \rho e + \frac{1}{2}\rho u^2 + P$. We can note that, by isolating the enthalpy on the left side of the equation, the right hand side becomes dimensionally proportional to the already mentioned parameter $\alpha = \frac{\mu LU}{h^2}$.

Three main sets of simulations are carried out in order to investigate the influence of α by varying the moving wall speed and the viscosity (temperature). For every set, six different channel aspect ratios L/h are considered.

*Corresponding author. Email: andrea.codrignani@kit.edu

RESULTS

Figure 1a shows the relative pressure difference between inlet and outlet $\frac{P-P_0}{P_0}$ as a function of α. The solid symbols represent one simulation result each and it can be seen that the pressure drop increases with increasing value of α. In fact, it appears to be directly proportional to α^2. For example, at $\alpha = 4.26$ the relative pressure drop is $\frac{\Delta P}{P_0} = 1.86$ times the reference pressure at the outlet. It is interesting to note that this case can easily correspond to a typical tribological application, since it is obtained for a channel of height $h = 1\mu m$, length $L = 1mm$, at a temperature of $T = 50°C$, and with a sliding velocity of $U = 0.5m/s$.

The above case is shown also in figure 1b, where the relative pressure drop and temperature distribution are plotted along the longitudinal axis x of the channel. Due to viscous dissipation, the thermodynamic state of the initial Couette flow changes through the channel and the temperature increases. The consequent temperature gradient yields a density decrease and thus generates a streamwise pressure gradient which must exist in order to maintain the mass flow rate. Due to this pressure gradient the velocity profile at the outlet assumes the typical shape of a Couette-Poiseuille flow. Moreover, the change in the velocity profile leads to an increasing wall shear stress in streamwise direction and thus to a higher overall friction coefficient.

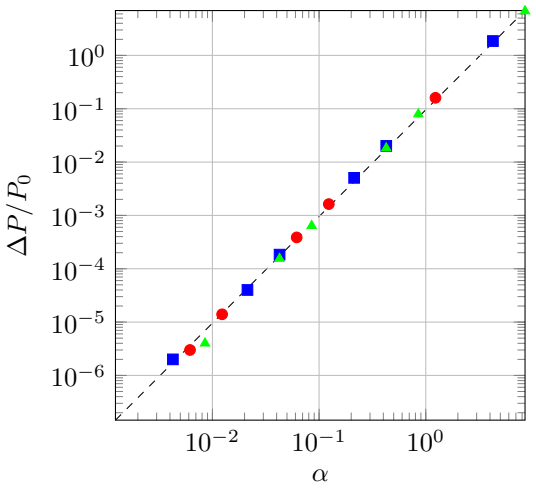

(a) Pressure losses as function of the parameter α. ■ $T = 50°C$, $U = 0.5m/s$. ● $T = 100°C$, $U = 0.5m/s$. ▲ $T = 50°C, U = 1m/s$.

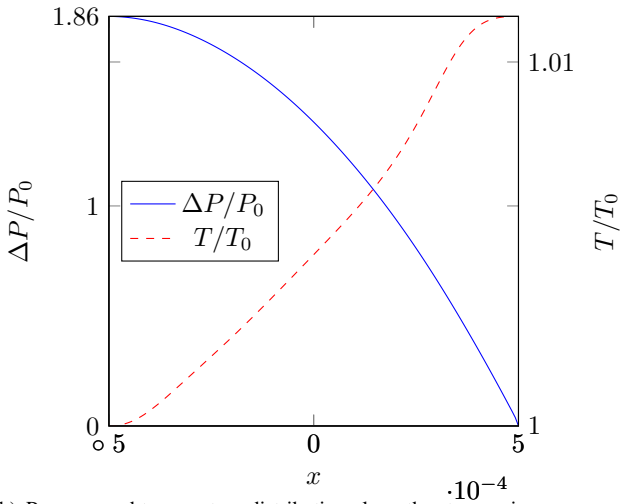

(b) Pressure and temperature distribution along the streamwise direction x. $T = 50°C, U = 0.5m/s, h = 1\mu m, L = 1mm$.

CONCLUSION

The pressure losses due to viscous dissipation are quantitatively studied for a generic compressible lubricant oil, pointing out the relevance of this phenomena for a typical lubrication case. As a result, a common scaling is found which directly captures the influence of viscous dissipation on the pressure losses. Further work that we intend to present at the conference includes the extension towards more realistic tribological cases, particularly for bearing applications with prescribed pressure and temperature gradients.

References

[1] Morini, G. L. "Single-phase convective heat transfer in microchannels: a review of experimental results." International Journal of Thermal Sciences 43.7 (2004): 631-651.

[2] Gropper, D, Ling W, and Terry J. H. "Hydrodynamic lubrication of textured surfaces: A review of modeling techniques and key findings." Tribology International 94 (2016): 509-529.

[3] Venerus, D. C. "Laminar capillary flow of compressible viscous fluids." Journal of Fluid Mechanics 555 (2006): 59-80.

[4] Housiadas, K. D. "Compressible Poiseuille flows with exponential type pressure-dependent mass density." Journal of Non-Newtonian Fluid Mechanics 201 (2013): 94-106.

[5] Magagnato F., Claas A. G. "Simulation of Compressible Cavitating Flows using a Novel Stochastic Method Field Formulation". Proceedings of the 8th International Symposium on Cavitation (2012). Singapore CAV2012

STABILITY OF A NON-NEWTONIAN FLOW DOWN AN INCLINE

Simon Dagois-Bohy*[1], M.H. Allouche[1], S. Millet[1], V. Botton[1], D. Henry[1], H. Ben Hadid[1], and F. Rousset[2]

[1]*Laboratoire de Mécanique des Fluides et d'Acoustique, CNRS/Université de Lyon, École Centrale de Lyon/Université Lyon 1/INSA de Lyon*

[2]*CETHIL, UMR CNRS 5008, Université de Lyon, INSA de Lyon/Université Lyon 1*

Summary We investigate experimentally the stability of a shear-thinning flow down an inclined plane. We focus on low-concentrated polymer solutions following a Carreau rheology. By measuring the wave numbers and amplification coefficients at different frequencies, we reach the marginal conditions and determine the stability threshold in the (Re, k) plane. We find this threshold to be in good agreement with numerical results obtained by a resolution of the generalized Orr-Sommerfeld equations, as well as with results found in the literature. This confirms the destabilizing effect of the shear-thinning properties, observed through a lower critical Reynolds number and a higher wave celerity.

The hydrodynamics of viscous film flows driven by gravity down an inclined plane cover a very large scope of natural phenomena and industrial applications. The stability of such flows has been studied extensively in the Newtonian case, most notably by Yih [1] and Benjamin [2], and Liu et al. [3] for the experimental part. The main features unravelled by these authors are that the instabilities occur at very long waves (compared to the thickness of the film) and that inertia plays a major role in the destabilization of the flow.

However, in many real cases, industrial (coating, transport, ...) or environmental (mud, glacier, lava flows), the fluid is not Newtonian and exhibits a complex rheological behavior. In particular, relatively few studies have investigated the stability of such flows when the fluid is shear-thinning. Ng and Mei [4] considered a power-law fluid and, using a long-wave approximation, they demonstrated a linear evolution of the critical Reynolds number for the onset of instability as a function of both the cotangent of the slope and the power-law exponent n. This study, however, is limited by the singularity introduced by the viscosity law in the model: a power-law describes an infinite viscosity at the free surface characterized by a zero shear-rate, which is not physically consistent. To remove this singularity, Ruyer-Quil *et al.* [5] introduced a Newtonian plateau at small strain rate. Their use of integrated Navier-Stokes equations allowed them to predict an analytical expression of the critical Reynolds number. Another approach consists in numerically solving the generalized Orr-Sommerfeld equations that arise from the linearization of the Navier-Stokes equations. This was carried by Rousset *et al.* [6] who studied a fluid following a Carreau law, *i.e.* whose viscosity varies (in a dimensionless form) as :

$$\bar{\eta} = I + (1 \circ\ I) \left[1 + \left(L \frac{du_b}{dy} \right)^2 \right]^{(n-1)/2}$$

where $I = \eta_0/\eta_\infty$, $L = \delta Q \left(\frac{\rho g \sin\gamma}{\eta_0 Q} \right)^{2/3}$, with Q the flow rate, γ the slope angle, η_0 (η_∞) the 0 (resp infinite) shear rate viscosity, δ a parameter of the Carreau law, and u_b is the dimensionless basic flow velocity.

They found that the critical Reynolds number is lowered by the shear-thinning properties, whereas the wave celerity is increased. They also showed in a subsequent paper that the Squire relations cannot be extended to this configuration, and even that 3D waves become less stable than 2D waves when the non-dimensional parameter L is high, another signature of the rich behavior of non-Newtonian flows [7].

In this paper we present experimental measurements of the linear stability threshold of two shear-thinning fluids flowing down an inclined plane, which was never done before, and we compare those measurements with the aforementioned numerical models. The two chosen fluids are composed of a mixture of Carboxymethylcellulose (CMC, E466) and Xanthan gum (Xg, E415), with two different concentrations. These mixtures were carefully elaborated so that the non-Newtonian effect *i)* can be observed, *ii)* is not too strong for the simulations, *iii)* keeps the L parameter within ranges where the instability is 2D. The viscosity of both these mixtures follows a Carreau law (Fig. 1b). Because the Newtonian plateau is sometimes difficult to observe on conventional rheometers, we also used an electro-capillarity technique to measure the rheology of those fluids over the full range of shear rates in the inclined plate experiment [8].

The experiment consists in an inclined channel with a free surface (47 cm X 200 cm) and two reservoirs (upstream and downstream) linked by a pump. The upstream reservoir is constantly alimented by the pump and overflows in the channel, ensuring a continuous thin flow with a rate imposed by the pump (Fig. 1a).

Upstream, a shaker actions a plate in the fluid and generates small surface perturbations at a controlled frequency. The slope of the surface is measured locally by the deflection of a laser beam shot through the channel (the bottom is transparent). The

*Corresponding author. Email: simon.dagois-bohy@univ-lyon1.fr

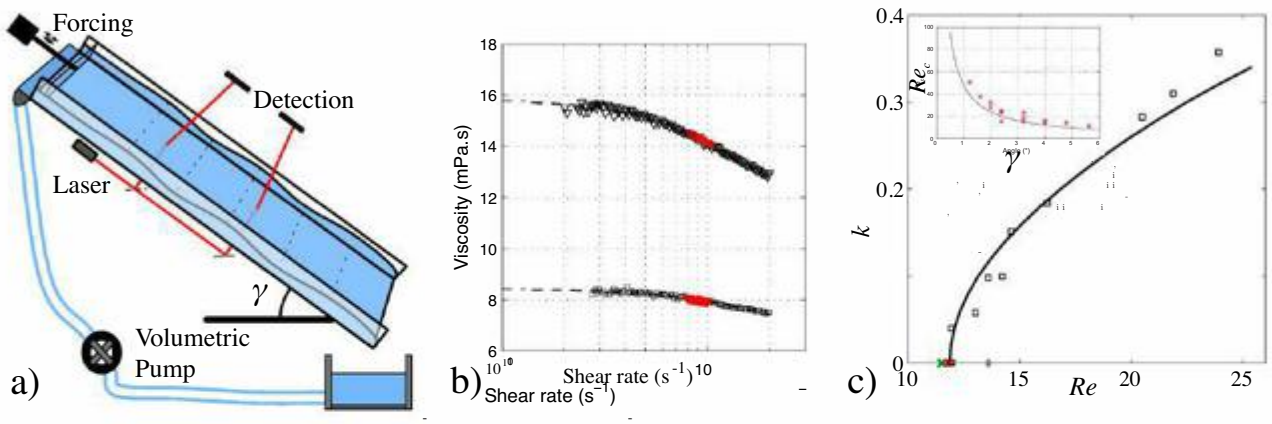

Figure 1: *a-*
Xanthan gum. Fluid 1 (top curve) corresponds to a higher proportion of CFC/Xg, whereas fluid 2 (lower curve) has a lower proportion and is less viscous. *c-* Marginally stable wave number k as a function of the Reynolds number Re, for fluid 1 (empty square dots). Black line : simulation results with Rousset *et al.* method [6]. The other points correspond to predictions by Ng & Mei (green cross), Ruyer-Quil (red square) [4, 5], and to the Newtonian case (grey diamond). Inset : Critical Reynolds number as a function of the inclination angle, in the Newtonian case.

measurement system is set on a translational stage in order to get longitudinal profiles of wave amplitude and phase-shift. By varying the frequency at a given slope and flow rate, we were able to determine the wave number k at the marginal stability threshold, *i.e.* when the growth rate changes sign.
To verify the validity of this setup, this threshold k was first measured with a Newtonian water-glycerol mixture for different Re, and the critical Reynolds number Re_c at zero k was extrapolated from the curve, for different inclination angles γ. The good agreement we found between our measurements and the theory (inset of Fig. 1c) shows the validity of the experimental setup.
We then measured this threshold wave number for the shear-thinning fluids at an angle $\gamma = 7°$. Fig. 1c shows this wave number as a function of the Reynolds number of the flow (empty square dots), as well as the numerical resolution of the generalized Orr-Sommerfeld equations (solid line) [6]. Again, a good agreement is found. The critical Reynolds number that we extrapolate from this instability threshold is also consistent with the predictions of Ruyer-Quil and Ng & Mei [4, 5]. The predicted $\cot\gamma$ dependency of Re_c [4, 5, 6] is confirmed, and as expected, Re_c is lower than in the Newtonian case, and the wave celerity is larger, thus confirming the destabilizing effect of the shear-thinning properties.

References

[1] C.S. Yih. Stability of liquid flow down an inclined plane. *Physics of Fluids*, 6:321–334, 1963.
[2] T.B. Benjamin. Wave formation in laminar flow down an inclined plane. *Journal of Fluid Mechanics*, 2:554–573, 1957.
[3] J. Liu, J.D. Paul, and J.P. Gollub. Measurements of the primary instabilities of film flows. *Journal of Fluid Mechanics*, 250:69–101, 1993.
[4] C.O. Ng and C.C. Mei. Roll waves on a shallow layer of mud modeled as a power-law fluid. *Journal of Fluid Mechanics*, 263:151–183, 1994.
[5] C. Ruyer-Quil, S. Chakraborty, and B.S. Dandapat. Wavy regime of a power-law film flow. *Journal of Fluid Mechanics*, 692:220–256, 2012.
[6] F. Rousset, S. Millet, V. Botton, and H. Ben Hadid. Temporal stability of Carreau fluid flow down an incline. *Journal of Fluids Engineering - transactions of the ASME*, 129:913–920, 2007.
[7] M.H. Allouche, S. Millet, V. Botton, D. Henry, H. Ben Hadid, F. Rousset. Stability of a flow down an incline with respect to two-dimensional and three-dimensional disturbances for Newtonian and non-Newtonian fluids. *Phys. Rev. E.*, 92 (2015) 063010.
[8] M.H. Allouche, V. Botton, D. Henry, S. Millet, R. Usha, and H. Ben Hadid. Experimental determination of the viscosity at very low shear rate for shear thinning fluids by electrocapillarity. *J. non-Newt. Fluid. Mech.*, 215 (2015) 60-69.

MESH CONVERGENCE OF MOVING CONTACT LINES IN VOF SIMULATIONS

A. Guion*[1], J. Buongiorno[1], S. Afkhami[2], and S. Zaleski[3]
[1]*Massachusetts Institute of Technology, Cambridge, MA, USA*
[2]*New Jersey Institute of Technology, Newark, NJ, USA*
[3]*Institut Jean Le Rond ∂'Alembert, UPMC & CNRS-UMR 7190, Paris, FRANCE*

Summary The numerical simulation of moving contact lines is complicated by the stress singularity at the contact point, which prevents results from converging in a standard way. The objective of this work is to achieve mesh convergence of moving contact line results in VOF simulations, and to assess the applicability for a wide range of capillary numbers of the numerical model proposed by Afkhami et al. [1]. Based on fundamental hydrodynamics, the numerical model serves as a new boundary condition that adapts the microscopic contact angle as the mesh is refined, eliminating the stress singularity at the contact line. Systematic computations are performed to obtain convergence of the macroscopic interface shape near the moving contact line at a solid plate withdrawing from a fluid pool.

INTRODUCTION

Contact line motion has been studied in the limit of small capillary numbers, when capillary forces dominate. Cox [2] and others have used matched asymptotic expansions to relate the microscopic contact angle (θ_m) with the macroscopic contact angle (θ_w) of the interface relative to the solid, respectively near the moving contact line (distance r_{in}) and away from the moving contact line (distance r_{out}, $r_{out} >> r_{in}$). An approximation of this asymptotic matching [3] has been used to obtain a contact angle boundary condition as a function of mesh size [1], in order to achieve mesh convergence in VOF simulations of moving contact lines. Same macroscopic contact line configurations were obtained for different microscopic mesh sizes, in the simulation of a partially wetting and withdrawing plate from a liquid reservoir at a small capillary number $\mathbf{Ca} = 0.03$.

NUMERICAL METHODS

We use the open-source code Gerris to solve the incompressible, variable-density, Navier-Stokes equations with surface tension [4]. The volume fraction c of the first fluid (ρ_1, μ_1) is used to define density $\rho \equiv c\rho_1 + (1-c)\rho_2$ and viscosity $\mu \equiv c\mu_1 + (1-c)\mu_2$, where ($\rho_2, \mu_2$) are properties of the second fluid. A time-splitting projection method is used, and requires an iterative solution procedure. Space is discretized using quad tree partitioning. A Volume Of Fluid (VOF) scheme is used to track (advect and reconstruct) the interface.

SIMULATION PROPERTIES

Consider a solid plate withdrawing at a velocity U from a square fluid pool of length $L/l_c = 20$, with l_c the capillary length: $l_c = \sqrt{\sigma/\rho g}$. The density ratio is set to 20, and viscosity ratio to 1. The interface between the two fluids is initially flat at height $h_0/l_c = 7$. No slip and a fixed microscopic contact angle θ_m are prescribed at the wall. The contact line motion along the wall evolves to a stationary state for $\tau >> 1$, with $\tau = (U \cdot t)/l_c$. Systematic computations are performed to span a wide range of contact angles θ, Capillary numbers, and cell sizes at the contact line dx/l_c, as detailed in Table 1.

Mesh refinement is increased at the interface, in the vicinity of the contact line, and where the error on velocity is the highest. In Figure 1, the inner region (in blue) in the vicinity of the contact line is sufficiently refined to resolve small scale effects, up to the inflexion point of the interface, where its curvature becomes positive (in red). The computational domain shown in Figure 1 is truncated: a static microscopic contact angle, and no-slip, are prescribed at the left boundary of the domain; symmetry on the right boundary of the domain (at $x/l_c = 20$); top and bottom boundaries allow flow in and out of the domain.

Table 1: Simulation parameters

Contact angle θ [°]	Capillary number Ca [−]	Minimum cell size dx/l_c [-]
50, 55, 60, 65, 70, 75, 80, 85, 90	0.01, 0.02, 0.04, 0.08, 0.16	1/16, 1/32, 1/64, 1/128, 1/256

*Corresponding author. Email: aguion@mit.edu

RESULTS

In the wide range of capillary numbers simulated, we both observe the development of a steady meniscus at the partially wetting wall (see blue, black and magenta profiles in Figure 2 (a)), and the Landau-Levich transition at higher values of Ca, where the liquid meniscus is entrained and leads to the formation of a thin film at the wall (red profiles, Figure 2 (a)). The position of the meniscus once it has reached its stationary state, e.g. when all forces are in equilibrium, is reported for all Ca, θ and dx/l_c (see Figure 2 (b)). This work systematically quantifies the effect of mesh refinement and contact angle on the final position of the contact line, for a range of capillary numbers below the Landau-Levich transition threshold. It is then possible to adjust the microscopic contact angle a priori with mesh refinement to obtain convergence of the results (see Figure 2 (c)).

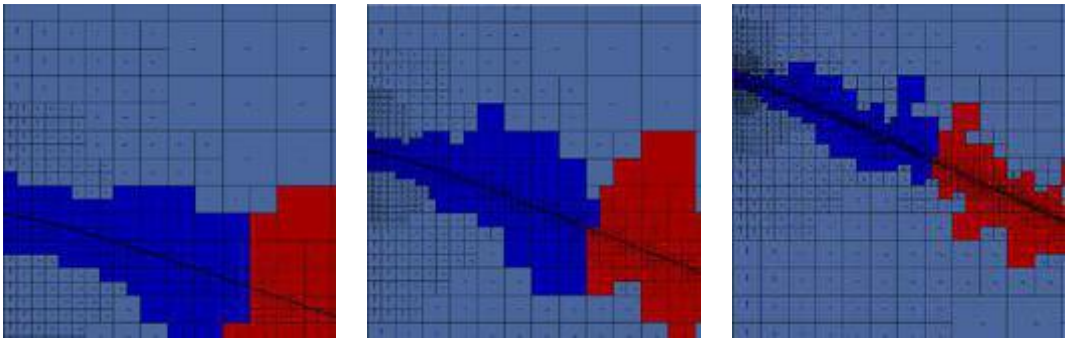

a b c

Figure 1: Stationary shape and position of the contact line (black line), for the same window of observation, but different minimum cell sizes $dx/l_c = 1/16$ (a), $1/32$ (b), $1/64$ (c). The curvature is negative (blue) then positive (red).

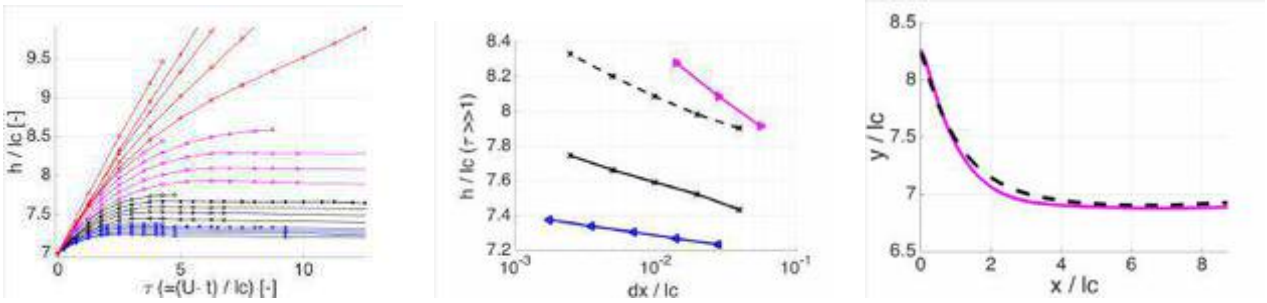

(a) (b) (c)

Figure 2: (a) Contact line height as function of time for $\theta_m = 90°$, Ca $\in \{10^{-2}$(blue), $2 \cdot 10^{-2}$(black), $4 \cdot 10^{-2}$(magenta), $8 \cdot 10^{-2}$(red)$\}$, and dx$/l_c \in \{1/16(\triangleleft), 1/32(\triangleright), 1/64(\square), 1/128(\star), 1/256(\circ)\}$. (b) Stationary heights of the contact line as function of cell size. Dashed line for $\theta_m = 70°$. (c) Stationary contact line shapes for $(dx/l_c, \theta) \in \{(1/64, 70°), (1/32, 90°)\}$

CONCLUSIONS

The numerical model proposed in [1] is applied to a wider range of capillary numbers. The systematic adjustment of microscopic contact angles with mesh refinements makes it possible to refine the grid arbitrarily, while still eliminating the stress singularity at the contact line and obtaining mesh convergence of the results.

References

[1] S. Afkhami, S. Zaleski, M. Bussmann: A mesh-dependent model for applying dynamic contact angles to vof simulations. J. Comp. Phys., 228:5370 5389, 2009.

[2] R.G. Cox, The dynamics of the spreading of liquids on a solid surface. Part 1. Viscous flow, J. Fluid Mech., 168:169194, 1986

[3] P. Sheng, M. Zhou, Immiscible-fluid displacement: contact-line dynamics and the velocity-dependent capillary pressure, Phys. Rev. A 45 (8):56945708, 1992

[4] S. Popinet: An accurate adaptive solver for surface-tension-driven interfacial flows J. Comp. Phys., 228:58385866, 2009

RIVULETS FORMATION DURING TRANSITION TO 3D WAVE REGIME IN ISOTHERMAL LIQUID FILM

Vladimir Guzanov[1,2a)], Aleksey Bobylev[1,2], Alexandr Kvon[1,2], Dmitry Markovich[1,2], Sergey Alekseenko[1,2] & Sergey Kharlamov[1,2]

[1] *Institute of Thermophysics, Siberian Branch of RAS, Novosibirsk, Russia*
[2] *Novosibirsk State University, Novosibirsk, Russia*

Summary. Results of experimental study of transition processes from two-dimensional to three-dimensional wave regimes for the case of isothermal falling liquid film are presented. Instantaneous and time-averaged film thickness fields are obtained and analyzed. It is shown that the process of transition to the three-dimensional wave motion is accompanied by formation of rivulets and that the downflow evolution of the rivulets usually has non-monotonic character.

INTRODUCTION

Three-dimensional wave regimes are considered to be the last stage of film flow evolution at moderate Reynolds numbers. In such regimes the film surface is covered by the numerous amounts of 3D waves chaotically interacting with each other. Usually 3D waves arise due to transverse instability of nonlinear 2D waves which in turn can be formed during the process of natural wave evolution or generated by artificial modulation of liquid flow rate. The case of transition to three-dimensional wave regimes for excited 2D waves is more investigated by now. Recent experimental ([1], [2], [3]) and theoretical ([4], [5], [6]) investigations show good agreement in some characteristic dimensions of 3D waves despite on some differences in their shape. Using modern experimental techniques, in the first place Laser Induced Fluorescence technique, allow us to reveal sufficient redistribution of liquid in transverse direction in the processes of 2D – 3D transition ([2], [3]) for the case of isothermal film flow, which leads to the formation of well pronounced rivulets on the time-averaged fields of film thickness. Such behaviour is unexpected for isothermal film flow and previously was not observed in experiments basically because of using local probes or shadowgraph technique adjusted for registration of the waves' parts which have high curvature of free boundary. Main aim of this work is to investigate experimentally general dependencies of process of transition from two-dimensional to three-dimensional wave motion and associated formation of rivulets on the vertically falling liquid film surface in the range of $5 < Re < 100$ for the downflow distances up to 140 cm.

EXPERIMENTAL TECHNIQUES AND OPERATING CONDITIONS

On the vertical transparent glass plate the liquid film with width of 50 cm and length of 140 cm was formed by adjustable slot distributor. The film freely flows down onto one side of the glass by the action of gravity. Water and water-glycerol solutions (WGS) with different concentrations were used as working liquids which allowed us to cover range of Kapitsa number from 1100 for more viscous WGS up to 3675 for water. The range of investigated Reynolds numbers $5 < Re=q/\nu < 100$, where q – volumetric flow rate per unit width and ν – kinematic viscosity of liquid. The 2D – 3D transition processes in the case of the natural wave evolution as well as for the case of initially regular excited 2D waves were investigated. For the last case the regular two-dimensional waves were forced by the periodic flow rate modulation with prescribed frequency F. With help of regular 2D waves the uniformity of local flow rate distribution over the plate's surface was controlled. In the case of uniform distribution of liquid the wave's front in the upper part of the flow is a straight line perpendicular to the flow direction. The procedure of control and adjustment of uniformity of liquid distribution was performed obligatory before each experiment.

The shadowgraph imaging was used for registration of the wave patterns over whole area of the plate. The white matt screen placed behind the glass plate on the variable distance was used for the technique realization. The halogen light source and registering camera were placed from the film side. Varying the distance between the screen and the plate allows obtaining shadow images for parts of liquid surface with different curvature. When the screen is placed close to the glass plate, shadow images represent the areas with high curvature and are similar to those obtained in other works (e.g. [1]). If the screen is placed at distances of a few centimeters from the plate, the film areas with much lower curvature form evident shadows on the screen. The distance between the screen and the glass plate was selected before each experiment in order to register capillary ripples having high curvature as well as the rivulets having lower curvature of film surface (fig. 1).

The Laser-Induced Fluorescence (LIF) technique was used for measurement of instant film thickness distribution with high time and spatial resolutions. High-speed camera registers LIF images with frequency of 1 kHz on film areas with sizes from 13x13 cm^2 up to 19x19 cm^2 dependently on flow conditions; this leads to spatial resolution from 0.13 mm/pix to 0.19mm/pix accordingly. Record length of each set of LIF images was 2 seconds. For each investigated regime the sets were obtained independently on the different distances from inlet. The time-average film thickness distributions were obtained for each set of LIF images using full length of the set.

[a)]Corresponding author. Email: guzanov@itp.nsc.ru.

RESULTS

For all investigated liquids three typical scenarios of wave evolution against Reynolds number can be noted in the range of $5 < Re < 100$. Major difference between liquids consist in different values of boundary Reynolds numbers which exact definition is the complex problem and lies beyond the scope of this work.

First scenario of wave evolution is observed for low $Re < Re_1$ when transition to three-dimensional wave regimes does not occur even in the bottom part of the test section. The waves have a shape close to two-dimensional up to the end of test section and time-average film thickness distributions over the plate are flat. Upper limit for Re_1 is 15 for all investigated liquids. Over this value ($Re > Re_1$) transition from two-dimensional to three-dimensional wave regimes occur which is characterized by fast degradation of transverse size of the waves. In the upper part of the flow initially 2D wave, no matter natural or excited, are breaking down into numerous 3D waves with characteristic dimension of 1 – 2 cm in transverse and longitudinal directions. In that region time-averaged film thickness distribution reveals formation of rivulets.

For $Re_1 < Re < Re_2$ (where $40 < Re_2 < 60$) the second scenario of wave evolution with well pronounced rivulets is observed. In this case evolution of natural and excited waves is different and rivulets are observed up to the end of test section (fig.1). Forming 3D waves move mainly upon the rivulets and form chains. At the same time wave motion between rivulets looks depressed. Despite some differences in regimes of natural and excited wave evolution the 3D waves in bottom part of test section have similar characteristics.

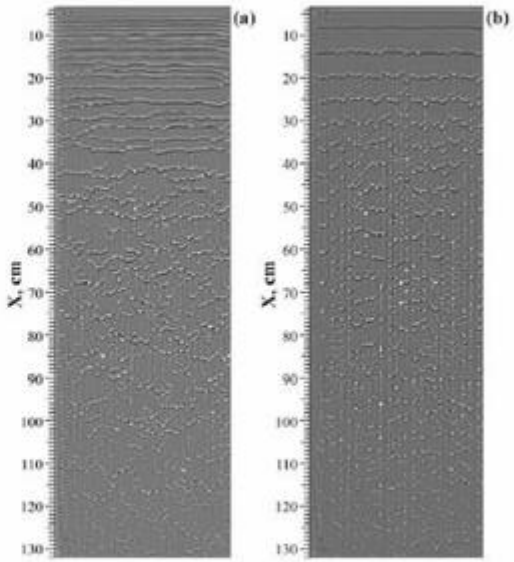

Figure 1. Shadowgraph images of water film at Re = 25. a) natural wave evolution, b) evolution of excited waves, F = 8Hz. X – downstream distance.

Because the formation of rivulets in the film flow usually connects with non-isothermal effects, direct measurements of film surface temperature were performed with help of Titanium ATR-570M infrared scanner. Measured with total error not exceeded 0.05K temperature fields show that the flow is isothermal on the whole flow area.

In third scenario of wave evolution which is observed for Reynolds number $Re > Re_2$ the 2D-3D transition appears in the upper part of the flow over a few wavelengths of 2D waves. Rivulets formation in such regimes is not monotonic. Till 40 – 50 cm rivulets can increase and further they begin to decay up to full disappearance at the end of the flow. Difference between cases of natural and excited wave evolution is revealed only in the upper part of the plate at the distances up to a few wavelengths from the film inlet, after that the wave patterns for both cases become similar and appeared to be steady state 3D wave flow regime.

CONCLUSIONS

Performed in a wide range of parameters experimental study of wave evolution of isothermal film flowing down a big plate reveals formation of rivulets during the process of transition from two-dimensional to three-dimensional wave motion. Evolution of forming rivulets depends on flow parameters but their transverse sizes weakly affects by Re. For regimes with well pronounced rivulets the decay of wave motion is observed for both natural and excited wave evolution. Characteristics of 3D waves in such regimes are similar in the bottom part of the flow despite on differences in the upper part. For $Re > Re_2$ fast evolution of the film flow toward steady state 3D wave regimes is observed and the rivulets exist only in the upper part of the flow. Direct measurements of temperature fields of film surface indicate that the flow in a range of measurements errors is isothermal on the whole test section. Therefore observed redistribution of liquid in transverse direction leading to rivulets formation should be described in the terms of hydrodynamics of isothermal film flow.

This work was supported by the Russian Foundation for Basic Research (project no. 15-01-06702)

References

[1] Park C.D., Nosoko T.: Three-dimensional wave dynamics on a falling film and associated mass transfer. *AIChE J* **49**(11): 2715-2727, 2003.

[2] Alekseenko S.V., Guzanov V.V., Markovich D.M., and Kharlamov S.M.: Specific features of a transition from the regular two-dimensional to three-dimensional waves on falling liquid films. *Tech. Phys. Lett.* **38**(8): 739-742, 2012.

[3] Kharlamov S.M., Guzanov V.V., Bobylev A.V., Alekseenko S.V. and Markovich D.M.: The transition from two-dimensional to three-dimensional waves in falling liquid films: Wave patterns and transverse redistribution of local flow rates. *PHYSICS OF FLUIDS* **27**: 114106, 2015.

[4] Kalliadasis S., Ruyer-Quil C., Scheid B. and Velarde M. G.: Falling liquid films. Springer Science & Business Media, 2012. T. 176.

[5] Scheid B., Ruyer-Quil C., Manneville P.: Wave patterns in film flows: modelling and three-dimensional waves. *J. Fluid Mech* **562**: 183-222, 2006.

[6] Dietze G., Kneer R.: Flow separation in falling liquid films. *Frontiers in Heat and Mass Transfer* **2**: 033001, 2011.

STATISTICAL CHARACTERISTICS OF 3D WAVES & STATIONARY 3D WAVE REGIMES FOR FALLING LIQUID FILMS.

Alexandr Kvon[1,2a)], Aleksey Bobylev[1,2], Vladimir Guzanov[1,2], Sergey Kharlamov[1,2]& Dmitry Markovich[1,2].
[1] *Institute of Thermophysics, Siberian Branch of RAS, Novosibirsk, Russia*
[2]*Novosibirsk State University, Novosibirsk, Russia*

Summary. In this paper we present results of experimental study of three-dimensional (3D) waves characteristics on the surface of the vertically falling liquid films. Experiments were carried out using liquids with various physical properties in the range of Reynolds numbers 5 < Re < 100. The statistical analysis of the 3D wave's characteristics allowed us to characterize in detail different scenarios of downflow evolution of 3D waves and to determine the regimes of fully developed steady-state 3D wave flow. Noticeable differences between natural and forced wave evolution have been observed for the relatively small Reynolds numbers whereas for the higher Reynolds numbers fast evolution of the all characteristics with achievement of the steady-state 3D wave flow is distinctive.

INTRODUCTION

Three-dimensional wave regimes are considered to be the last stage of the wave evolution at moderate Reynolds numbers of liquid film flow down vertical plate. In such regimes liquid film surface are covered with numerous interacting 3D waves. Statistical description of these regimes is often used due to large number of the waves [1]. Recent experimental investigations have shown that rivulets formation occurs during transition process from the two-dimensional (2D) to the 3D wave flow regimes [2]. The fact of the rivulets formation in the process of 2D to 3D wave transition has never been taken into account in the previous attempts to classify film flow regimes. In order to describe in detail the 2D to 3D waves transition process we carried out experimental investigation of film flow down the vertical plate of large dimensions using measuring system allowing reconstruction the form of 3D waves. The main consideration was given to the analysis of statistical characteristics of the waves and their connection with flow regimes including formation of the rivulets

METHODS AND EXPERIMENTAL SETUP

The experimental setup represents a close-looped hydrodynamic contour. Liquid film flow was formed by an adjustable slot distributor on a vertical glass plate with dimensions 50cm x 140cm. Three types of working fluids were used in experiments: water ($\nu = 0.99*10^{-6}$ m^2/s), water-glycerol solution WGS1 ($\nu = 1.5*10^{-6}$ m^2/s), and water-glycerol solution WGS2 ($\nu = 2.2*10^{-6}$ m^2/s). Experiments were carried out in the range of Reynolds numbers $5 < Re = q/\nu < 100$, where q is a volumetric flow rate per unit width and ν is kinematic viscosity of liquid. Detailed structures of the waves were studied by means of the high-speed laser induced fluorescence (LIF) method [3]. In this method, special fluorescent dye Rodamin 6G is dissolved in the working fluid, so that obtained solutions acquire fluorescent properties. Green solid state continuous laser is used for the fluorescence excitation. Intensity of the emitted from the liquid light is proportional to the film thickness **H**. The LIF method allowed us to obtain instantaneous film thickness fields whereas extensively used shadowgraph method [4] gives only qualitative information about waves shapes. The most demonstrative in the matter of evaluating the direction of the wave evolution downwards were such statistical characteristics as the film thickness probability density function (PDF), dispersion and spectral power density of film thickness temporal variation.

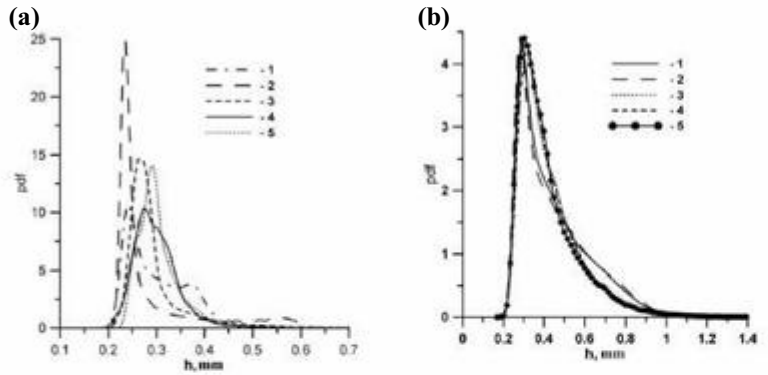

Figure 1. Film thickness PDFs, working liquid - WGS2. a) Re=19, distance X from the flow inlet: 1 – X=26cm, 2 – X=26cm, f=8Hz, 3 – X = 92cm, 4 – X = 133cm, 5 – X = 133cm, f = 8Hz. b) Re = 54, 1 – X = 26см, 2 – X=26cm, f=8Hz, 3 – X=92cm, 4 – X = 133cm, f = 8Hz, 5 – X = 133cm.

EXPERIMENTAL RESULTS

The analysis of the statistical characteristics allows us to classify in detail the studied flow regimes. It was found that for all working fluids there exists a threshold value of Reynolds number Re_1 beneath which ($Re < Re_1$) no transition from two- dimensional to three-dimensional wave motion occurs throughout the length of the working section both for

[a)] Corresponding author. Email: azkvon@gmail.com.

natural and forced two-dimensional waves. Re_1 is different for the different liquids and lies in the range from 5 to 15. Several statistical quantities were obtained and analyzed in order to determine direction of the wave motion evolution on the falling liquid film. Probability density functions of the liquid film thickness are shown in figure 1 for WGS2. Distributions have characteristic asymmetric right-tailed shape. For the high Reynolds numbers the film thickness PDFs almost don't change with downflow distance (fig.1(b)). However transform of the PDFs with shifting of the most probable film thickness can be observed for the case of lower Re (fig. 1(a)).

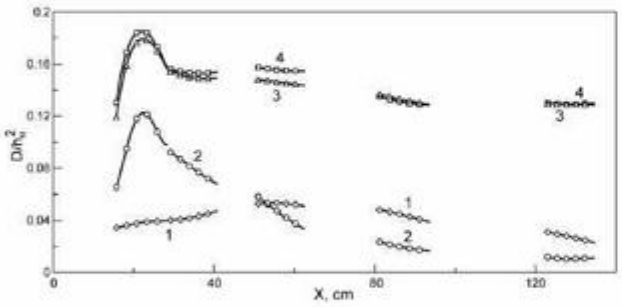

Figure 2. Film thickness dispersion D normalized to the squared undisturbed film thickness (h^2). Working liquid - WGS2. 1 – Re = 19, natural waves; 2 – Re = 19, forced waves F = 7 Hz; 3 – Re = 54, forced waves F = 7 Hz; 4 – Re = 54, natural waves.

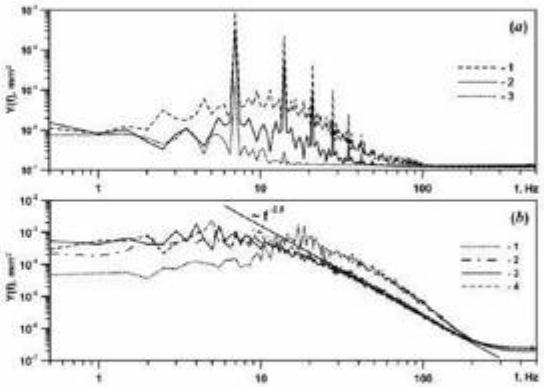

Figure 3. Spectral power density Y(f) at various distances from the distributor. Working liquid – WGS2 a) Re = 13.5,forced waves F = 7 Hz.. 1 – X = 21 cm, 2 – X = 56 cm, 3 – X = 128 cm. b) Re = 54, natural waves, 1 – X = 21 cm, 2 –X = 87 cm, 3 – X = 128 cm; 4 – forced F = 7 Hz, X = 128cm.

Values of the dispersion D were obtained by averaging of the calculated local D values over the each transverse section of the measuring area. Intensive growth of the D was observed up to 40cm from the inlet for the high Re. After fast evolution in the upper part of flow D reaches steady-state value in cases of both natural and forced 2D waves (fig.2). Behavior of the D value while moving downstream in the case of lower Re is different: the change of D is observed up to the end of the plate (fig.2). It should be noted that in such regimes transition from 2D to 3D waves is accompanied with formation of well pronounced rivulets on the time-averaged film thickness distributions. Fast forming of the three-dimensional wave motion for the case of large Re was also observed while analyzing spectral power (fig. 3(b)). Interestingly that for the steady-state flow regimes in the area of the high frequencies the spectral power decay by law of $Y \sim f^{\alpha}$, with index of power $\alpha = -2.8$. This index is close to that obtained in the work [5] and as it turned out it doesn't depend on the liquid properties.

CONCLUSIONS

The analysis of the statistical characteristics allows characterizing in detail regimes of the film flow at $5 < Re < 100$. Stabilizing of the dispersion value as well as of the PDFs and spectral power densities of film thickness fluctuations for the flow regimes with high Reynolds numbers apparently indicates that at these regimes stabilization of 3D wave motion occurs. However at lower Re continuous evolution of the waves throughout the whole plate takes place with different behavior of statistical characteristics for the cases of natural and forced waves

AKNOWLEDGEMENTS

This work was supported by Russian Science Foundation (project no.14-22-00174).

References

[1] Telles, A. S., and A. E. Dukler. "Statistical characteristics of thin, vertical, wavy, liquid films." Industrial & Engineering Chemistry Fundamentals 9.3, 1970.

[2] Alekseenko S.V., Bobylev A.V, Guzanov V.V., Markovich D.M. and Kharlamov S.M.. Formation of Rivulets in Isothermal Liquid Film Flow during Transition to a Three-Dimensional Wave Regime. Technical Physics Letters, 40(11), 2014.

[3] Alekseenko S.V., Cherdantsev A.V., Cherdantsev M.V., Isaenkov S.V., Kharlamov S.M. and Markovich D.M.. Application of a high-speed laser-induced fluorescence technique for studying the three-dimensional structure of annular gas–liquid flow. Experiments in fluids, 53(1): 77-89, 2012.

[4] Park C. D., Nosoko T. Three-dimensional wave dynamics on a falling film and associated mass transfer. AIChE Journal, V. 49. № 11. P. 2715, 2003.

[5] Chu K. J., Dukler A. E. Statistical characteristics of thin, wavy films III. Structure of the large waves and their resistance to gas flow. AIChE Journal.V. 21. №. 3, 1975.

REDUCED ORDER MODELLING FOR FLOODING ONSET PREDICTION

Gianluca Lavalle *[1], Jean-Paul Vila[2,3], Mathieu Lucquiaud[1], and Prashant Valluri[1]
[1]*School of Engineering, The University of Edinburgh, Edinburgh, EH9 3JL, United Kingdom*
[2]*Institut de Mathématiques de Toulouse, INSA, GMM, 31055 Toulouse, France*
[3]*ONERA, Aerodynamics and Energetics Modelling Department, 31055 Toulouse, France*

Summary We investigate numerically the flooding onset occurring in two-layer channel flows at low density contrast and low surface tension. An integral film model is used in the bottom layer, which is supposed much thinner than the interfacial wavelength. This low-dimensional model allows us to cut down the computational cost and data with respect to DNS (Direct Numerical Simulation). The validation of our methodology is achieved by comparing the growth rate of linear wave with the Orr-Sommerfeld theory, and the non-linear wave profiles with DNS.

INTRODUCTION

Counter-current two-layer flows are encountered in numerous chemical applications, such as in distillation and absorption. The performance of such processes in terms of transfer rate is governed by the flow pattern and the interface evolution. However, under certain conditions, two-layer flows manifest flow reversal, which drives to a dramatic loss of performances of the technological equipments. During the past, several studies have therefore aimed to understand and predict the flooding onset, focusing on experimental observations, linear stability analysis and numerical simulations. More recently, for those applications involving thin films, the flooding onset has been also investigated by means of reduced models, such as for turbulent gas over liquid films as in Tseluiko & Kalliadasis [1], and gas-liquid flows in narrow channels as in Dietze & Ruyer-Quil [2].

Here, we introduce a two-phase numerical model for counter-current channel flows with the aim to predict the flooding onset and provide a map relevant for industrial uptake for a quick evaluation of the regions where flooding occurs. This numerical model is based on the coupling between a low-dimensional model for the lower layer and compressible Navier-Stokes equations in the upper layer, as developed by Lavalle et al. [3] for co-flowing liquid-gas channel flows.

MODEL DEVELOPMENT

Consider a liquid film flowing at the bottom of a channel driven by gravity, while an opposite pressure gradient drives an upper layer counter-currently. Shear stress and pressure exerted by the upper phase at the interface feed the film, which in turn can become unstable. The integral formulation is based on the assumption that the film thickness h is thinner than the wavelength λ of interfacial waves. The Navier-Stokes equations can be therefore integrated over the film thickness, aiming to reduce the order of the system by enslaving the film dynamics to thickness and flow rate only. However, those depth-integrated equations need closure laws for the wall shear stress and the integral of squared velocity, and many choices are possible. We use a first-order gradient expansion of the velocity field in terms of the small parameter $\varepsilon = h/\lambda$. At this stage, computing the velocity profile allows us to close the system of depth-integrated equations.

However, the interfacial shear stress and pressure must be given by the upper layer. This long-wave integral model is therefore coupled to compressible Navier-Stokes equations in the upper phase, with the aim to couple the two phases. At the interface, we choose to transfer the stresses from the top phase to the bottom one, while the interfacial velocity and shape of the interface is given by the film to the upper phase. Numerically, a moving mesh technique has been implemented in order to guarantee the correct transfer of the interface shape.

NUMERICAL RESULTS

We apply our model to counter-current two-layer flows at low density contrast and low surface tension. Given a small sinusoidal perturbation, we compute periodic simulations with our coupled model. We firstly validate the linear regime by comparing the growth rate of linear waves with the Orr-Sommerfeld problem. Subsequently, we investigate the non-linear saturated waves developing at the interface. Our model provides good comparisons with our in-house DNS [4] in terms of wave profiles, as well as pressure and streamline distribution.

Furthermore,at the most unstable wavelength, we look at the speed of the developed waves in order to plot the map of Figure 1. This Figure shows the regions where the saturated waves travel downwards with the gravity, stand in a fixed position or travel upwards against the gravity. The latter is the condition for flooding, according to our definition. This map is highly important for industrial uptake because links the applied pressure gradient and the liquid flow rate (directly from the uniform film thickness h_0) and therefore has an immediate interpretation.

*Corresponding author. Email: g.lavalle@ed.ac.uk

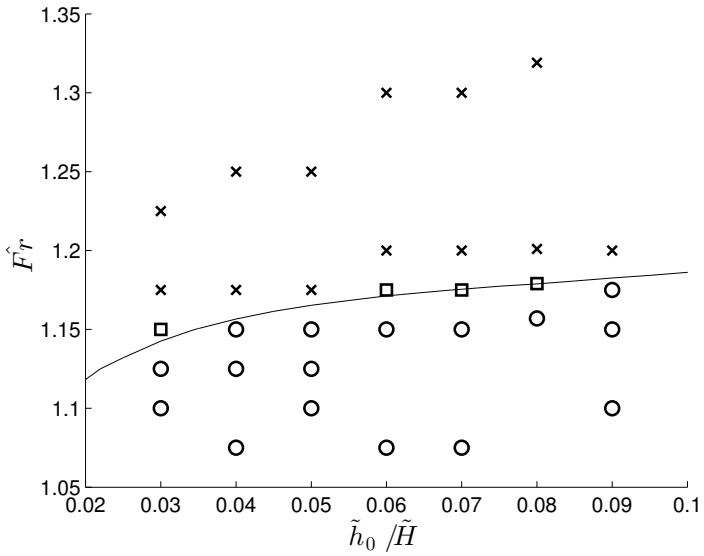

Figure 1: Map obtained from our model simulations, showing cases of downwards waves (circles), standing waves (squares) and upwards waves (crosses) at the most unstable wavelength. The solid line is the Orr-Sommerfeld loading curve. The applied pressure gradient plays with $\hat{Fr}^2 = \Delta\tilde{p}/\tilde{\lambda}/(\rho_2 g)$.

CONCLUSIONS

This work addresses the problem of the flooding onset in counter-current two-layer flows. We provide a two-phase numerical model based on a low-dimensional formulation for the film at the bottom, which is considered thinner than the wavelength of interfacial waves. Not only our model shows agreement with Orr-Sommerfeld theory and DNS within the linear and nonlinear regimes, but also is an efficient and fast methodology to predict the flooding onset. The implementation of turbulence to study gas-liquid flows is left to future works, as well as the inclusion of mass transfer.

ACKNOWLEDGEMENTS

The authors gratefully acknowledge EPSRC Grant No. EP/M001482/1.

References

[1] Tseluiko D., Kalliadasis S.: Nonlinear waves in counter-current gasliquid film flow. J. Fluid Mech. 673, 19-59, 2011.

[2] Dietze G.F., Ruyer-Quil, C.: Wavy liquid films in interaction with a confined laminar gas flow. J. Fluid Mech. 722, 348-393, 2013.

[3] Lavalle G., Vila J.P., Blanchard G., Laurent C., Charru F.: A numerical reduced model for thin liquid films sheared by a gas flow. J. Comput. Phys. 301, 119-140, 2015.

[4] Ó Náraigh L., Valluri P., Scott D.M., Bethune I., Spelt P.D.M.: Linear instability, nonlinear instability and ligament dynamics in three-dimensional laminar two-layer liquid-liquid flows. J. Fluid Mech. 750, 464-506, 2014.

FLUID SHEARING FOR ENHANCED COLLISIONS AND ACCELERATED REACTIONS

Evgenia Leivadarou [*1] and Dr. Stuart Dalziel [1]

[1] *Department of Applied Mathematics and Theoretical Physics, University of Cambridge, UK*

Summary The aim of this project is to explain the fluid motion and maximise the performance of the Vortex Fluidic Device, a rapidly rotating tube with pipettes feeding liquid reactants to the base of the tube. It is a novel 'greener' technology for industrial applications such as pharmaceutical production and protein folding. The problem is approached according to the stages of fluid spreading, with the most promising area being at the bottom of the hemispherical tube as the fluid reaches the solid surface and spreads along the walls. The parameters that affect the spreading are defined and their role is explored theoretically and experimentally with respect to the geometry of the tube. The spreading pattern is explained and the optimum fluid volume, release height and rotation rate are established for both a flat disk and a hemispherical bowl.

INTRODUCTION

The Vortex Fluidic Device (VFD) is a novel thin film reactor developed by the Raston Laboratory at Flinders University. This technology is focused on the synthesis of organic chemicals and in material processing. The thickness of the thin film produced depends primarily on the rotational speed, flow rate, the position of the feed nozzles and the tilt angle of the tube (Britton et al., [1]).

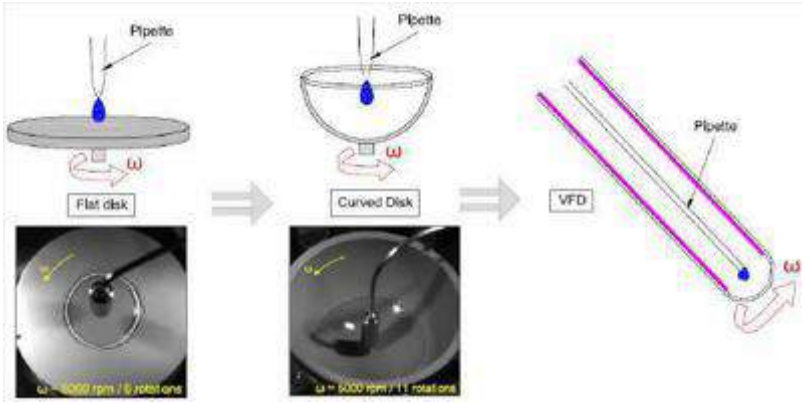

Figure 1: Methodology - geometrical approach.

To understand the efficiency of the VFD, we consider a model reaction $A + B \rightarrow C$. If Z is the collisional frequency between the reactants of respective concentration $[A]$ and $[B]$, the main hypothesis is based on the idea that the rate of reaction is enhanced when collision rate Z is increased. The fluid mechanics of the tube can control the collision rate Z by altering the conditions of intense shearing, e.g. by achieving high velocity gradients at the interface with the solid surface.

This project focuses on explaining the fluid mechanics responsible for enhancing the reactions in the VFD and will seek optimal conditions with respect to the geometry of the tube and the fluid mechanical parameters such as the rotation rate, flow rate, wettability and contact line dynamics, gravity, the orientation of the tube and environmental conditions, such as overheating.

As the film is thin, the base of the tube can be considered locally flat and can be modelled as a horizontal disc. This presentation describes the experiments conducted so far for a broad range of parameters from moving on a flat disc to moving in a curved bowl, as illustrated in Figure 1.

OVERVIEW OF FLUID MOTION IN THE VFD

There is very little literature describing the fluid mechanics in the VFD, i.e. landing, spreading, climbing, etc. First, despite the continuous flow, surface tension at the nozzle promotes the formation of droplets, which fall vertically onto the rotating disc with angular velocity ω. The spreading pattern is affected by the height of the release (Chou et al, [2]). At the stage of the landing, the top of the droplet and the base of the droplet move with different velocities forming a 'Rayleigh layer' at the bottom of the volume of increasing thickness $\delta \sim (\nu t)^{1/2}$, where ν is the kinematic viscosity of the fluid.

At the next stage, of centripetal acceleration, the bottom of the liquid droplet adheres on the surface and is simultaneously dragged by the moving substrate. The spreading is axisymmetric and the thickness of the 'Ekman layer' at the bottom, which rotates with the disc is $\delta \sim (\nu/\omega)^{1/2}$. At the third stage, the fluid is ejected by the Ekman layer, it spreads with viscous forces

*Corresponding author. Email: el393@cam.ac.uk

balancing the centrifugal force as a 'Nusselt film' (Espig and Hoyle, [3]) and eventually climbs the curved base, moving within the 'Stewartson layers'.

During fluid spreading, waves alter the curvature at the contact line. These waves cause azimuthal variations in pressure, triggering an instability mechanism at a critical radius r_c (Spaid et al., [4]). Since fingering instability decreases the overall shear stress it is therefore desirable to suppress or delay its onset.

According to our analysis, the concentration of the product with respect to fluid mechanics, before the formation of fingers, is predicted to follow

$$\Delta C \sim \int_o^T Z dt \sim \left(\frac{\omega^2 r_c^5}{Q\nu} \right)^{\frac{1}{3}}.$$

The above relation indicates that there is an enhanced shear stress when the shearing duration, the angular velocity and the axisymmetric spreading are maximised and the flow rate Q is low.

EXPERIMENTS

The aim of the first experiments was to understand the different patterns of spreading at different rotation rates, heights of release and landing points. For this purpose, experiments were conducted on a flat disc and on a curved bowl at rotation rates ranging from 1000 rpm to 12000 rpm and with heights of release from 5 mm to 15 mm. In one set of runs, the nozzle was positioned above the axis of the disc, while in a second set the nozzle was positioned off axis. The droplet volume was kept constant and the rotation rate was changed in steps of 1000 rpm.

RESULTS AND CONCLUSIONS

According to our theoretical approach and experimental observations, the height of the droplet release should be close to the disc to avoid high kinetic energy on impact which leads to faster spreading and fingering. A volume of 40μl, released 5 mm above the disc, is sufficient to cause axisymmetric spreading. Although maximum axisymmetric spreading occurs at 5000 rpm, the maximum collision rate, prior to the onset of instability, is likely to occur at 9000 rpm.

Since velocity gradients increase with increased rotation rates, the shearing after the fingers form requires further investigation. The duration of the acceleration of the fluid after landing is also important. An off-axis landing increases the spreading time at the boundary layer which can be beneficial for the desirable shearing. The spreading is slower on a curved bowl due to the reduced tangential component of centrifugal force and instability is delayed due to the normal component of gravity.

The research will continue according to the factors that affect instability and shear stress. Tilting is a component that affects the performance of the VFD. Current experiments investigate whether it is the landing point that changes the performance or the tilting that has multiple effects on the device. Once optimum conditions are established, reactions will be monitored in the VFD.

References

[1] Britton J., Dalziel S., and Raston C.: Continuous flow Fischer esteriications harnessing vibrational-coupled thin film fluidics. RSC Advances 5:1655-1660, 2015.

[2] Chou F.C., Zen T.S., and Lee K.A.: An experimental study of a water droplet impacting on a rotating wafer. Atomization and Sprays 19:905-915, 2009.

[3] Espig H. and Hoyle R.: Waves in a thin liquid layer on a rotating disk. J. Fluid Mech, 22:671-677, 1965.

[4] Spaid M. A., and Homsy G.M.: Stability of Newtonian and viscoelastic dynamic contact lines. Physics of Fluids, 8:460, 1996.

INTERFACE MORPHOLOGY OF THIN FILMS: ELECTROHYDRODYNAMIC VS ELECTROKINETIC MODEL

Hadi Nazaripoor[1], Behnam Khorshidi[1], Charles R. Koch[1], and Mohtada Sadrzadeh *[1]
[1]*Department of Mechanical Engineering, University of Alberta, Edmonton, Alberta, Canada*

Summary Dynamics and morphological evolution of thin liquid films (thickness<100 nm) are numerically investigated using electrohydrodynamic (EHD) and electrokinetic (EK) models. In the EHD patterning process, the thin film is typically considered as either perfect dielectric (PD) or leaky dielectric (LD) and the EHD model can be used to investigate the spatiotemporal evolution of the thin film. In the case of having a finite diffuse layer of charges accumulated at the interface (i.e. double layer), the EK model is applied. The effect of the ionic strength of an ionic liquid film which is determined by its molarity is included in the EK model. The 3-D nonlinear thin film equation is solved numerically resulting in spatiotemporal evolution of interface.

INTRODUCTION

Electrically assisted patterning of polymer films has received extensive attention over the past decades as a unique and interesting approach for creating micron and submicron sized features [1, 2]. In this process, a thin liquid film is sandwiched between two electrodes and an electric field is applied to the film in the transverse direction (see Fig.1(a)). Disparity of electrical properties of the film and the bounding fluid (the material which fills the gap between the film and the upper electrode) results in an net electrostatic force acting on the interface[3]. As the film thickness is less than 100 nm, the short range intermolecular forces are considered in addition to long range electrostatic, viscous and interfacial forces. The film motion can be described by nonlinear *thin film* equation employing long-wave approximation [4]:

$$3\mu h_t + [h^3(\gamma[h_{xx} + h_{yy}] \circ \phi)_x]_x + [h^3(\gamma[h_{xx} + h_{yy}] \circ \phi)_y]_y = 0 \tag{1}$$

In this equation, the subscripts x and y denote the spatial derivatives and subscript t denotes the time derivative. The term ϕ, often called conjoining/disjoining pressures, is the summation of van der Waals, Born repulsion and electrostatic pressures. Initial linear stages in growth of instabilities was investigated through linear stability (LS) analysis [1]. The LS analysis provides prediction of the maximum wavelength, λ_m, for growth of instabilities which characterize the center-to-center distance of pillars (raised columnar structure) in the hexagonal pillar pattern formation[1, 2]. In this analysis, it is shown that the lateral size of pillars decreases when increasing the applied voltage ψ_l, mean initial film thickness h_0, electric permittivity of film ε and its conductivity σ. A significant discrepancy between the theoretical predictions and experimental results was observed during formation of nano-sized features at the high electric field strength [5] which is primarily attributed to the electric breakdown of the polymer film and the bounding fluid. This phenomenon that typically occurs at higher electric field strength is reported as the main limitation of the EHD patterning for generation of submicron sized features. In the work of Lau and Russel, an ionic conductive liquid (IL) is used as a bounding fluid to prevent electric breakdown happening in the bounding layer [5]. In the EHD patterning process, the thin liquid film and/or bounding layers is considered as either perfect dielectric (PD) or leaky dielectric (LD). In the PD film there is no free charge and the film is polarized under applied electric field. In contrast, for the LD film the infinitesimal amount of charge present moves and accumulates at the interface. Both LS and non-linear analysis of the EHD patterning shows that the presence of free charges, albeit infinitesimal, reduces the characteristic wavelength λ_m.

In ILs, the free ions move easily and form a diffuse layer called double layer (DL) adjacent to the charged surfaces. In the PD and LD models, the thickness of the DL is assumed infinitesimally large and small, respectively. Between these two limiting cases, an electrokinetic (EK) model has been initially developed for drop deformation in an electric field[6]. More recently, LS analysis of thin films has also been considered using EK model based on the linearized Debye Huckel approximation [7]. The more general model based on the nonlinear Poisson Boltzmann equation to investigate the dynamics and stability of IL-PD bilayers [8].

In this study, morphologyical evolution and the process of pattern formation on the thin liquid films under applied electric field are numerically simulated using both the EHD and the EK models. A system of two planar fluids layer (thin PD or IL films below and a PD bounding media above) confined between two flat electrodes is considered.

The main contributions of this paper are: (1) developing an electrostatic model for dynamic modeling of the EHD patterning process using ultra-thin IL film; (2) investigating the dynamics and pattern formation on IL films that includes the initial linear stages and further nonlinear stages in growth of instabilities; and (3) evaluating the effects of ionic strength and the IL film initial thickness on the shape and size of structures forming on the film.

*Corresponding author. Email:sadrzade@ualberta.ca

RESULTS AND DISCUSSION

In the present work the ionic strength of an IL which is determined by IL molarity, M, is incorporated in our analysis. This is in addition to typical design parameters such as applied voltage, electric permittivity of layers and electrodes distance. Higher values of M (i.e. 100 and 1000 mMol L^{-1}) account for higher concentration of charges in the film, thinner DL, which results in perfect conducting (PC) behavior whereas lower values of M (i.e. 0.001 mMol L^{-1}), thicker DL, represent poor conductive medium similar to PDs . The Poisson-Nernst-Plank (PNP) model is used to develop the electrostatic model and find the dynamics of free ions in the ionic conducting layer. It should be noted that, in this study the process time is much longer than the charge relaxation time. This diminishes the effect of the free ions (charges) dynamics during pattern formation process. The effect of molarity on the electrostatic component of conjoining pressure, as the main force for pattern formation process, is examined. Higher electrostatic force is applied to the film interface in the EK model compared to the EHD model.

An overview of the interface morphology at the quasi-steady state in the pattern formation process is shown in Fig.1(b). The effects of ionic conductivity and film initial filling ratio (mean initial film thickness to electrodes distance ratio) on the shape and size of structures are presented. The addition of ionic conductivity to the film results in an increase in the number of pillars forming on the interface and consequently more compact structures (pillars with smaller size) are created. The number of pillars formed in the IL films also increase at higher filling ratios. The PD film shows similar trend below the critical filling ratio of $h_0/d = 0.5$.

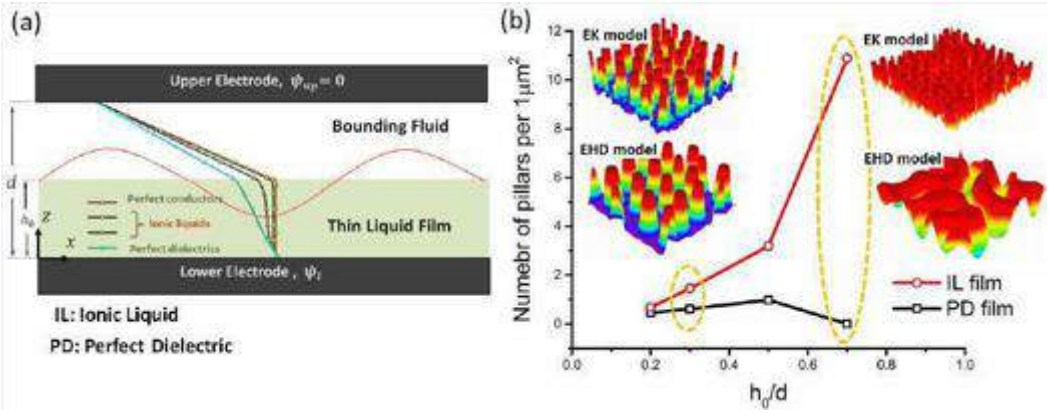

Figure 1: (a) Schematic of the thin film sandwiched between electrodes and electric potential distribution within each layer. (b) Interface morphology and total number of pillars versus initial filling ratio of film. 3-D snapshots of the patterns formed in PD and IL films with h_0 = 30 and 70 nm. d= 100 nm, ψ_l = 20 V.

CONCLUSIONS

In the EK model, ILs are defined to be materials having properties between two limiting cases of PC and PD materials based on their ionic strength. The IL films experience a much higher electrostatic pressure compared to similar PD films and this increase in ionic strength results in higher electrostatic pressure. More compact structures are created in the IL film (using the EK model) when compared to the similar PD films (using the EHD model) and the compaction is increased by increasing the initial film height.

References

[1] Schaffer E., Thurn-Albrecht T., Russell T. P., Steiner U.: Electrically Induced Structure Formation and Pattern Transfer. Nature, 403:874-877, 2000.

[2] Wu N., Russel W. B.: Micro- and Nanopatterns Created via Electrohydrodynamic Instabilities. Nano Today, 4(2):180-192, 2009.

[3] Landau L. D., Lifshitz E. M.: Electrodynamics of Continuous Media. Pergamon Press, 1960.

[4] Oron A., Davis S. H., Bankoff S. G.: Long Scale Evolution of Thin Liquid Films. Reviews of Modern Physics, 69:931-980, 1997.

[5] Lau C. Y., and Russel W. B.: Fundamental Limitations on Ordered Electrohydrodynamic Patterning. Macromolecules, 44(19):7746-7751, 2011.

[6] Zholkovskij E. k., Masliyah J. H., Czarnecki J.:An Electrokinetic Model of Drop Deformation in an Electric Field. Journal of Fluid Mechanics, 472(12):1-27, 2002.

[7] Gambhire P., Thaokar R.: Electrokinetic Model for Electric- Field-Induced Interfacial Instabilities. Physical Review E, 89:032409-9, 2014.

[8] Nazaripoor H., Koch C. R., Bhattacharjee S.: Electrical Perturbations of Ultrathin Bilayers: Role of Ionic Conductive Layer. Langmuir, 30(49):14734-14744, 2014.

DEALING WITH CONTACT LINE FORCES IN SHALLOW WATER MODELS

Philippe Villedieu[1,2,a)], Julien Lallement[2], Pierre Trontin[2], Claire Laurent[2] & Jean-Paul Vila[1]
[1]*Department of Mathematics, INSA, Toulouse, France*
[2]*Department of Models for Aerodynamics and Energetics, ONERA, Toulouse, France*

Summary The objective of this paper is to present a simple approach for taking into account the contact line forces in shallow water models for partially wetting liquid films onto a solid substrate. The method is inspired by the idea proposed by Brackbill et al in [1] to deal with capillary forces in two-phase flows. It consists in reformulating the shallow water equations by introducing a "colour function" α which is equal to 1 where the film is present and 0 elsewhere and which is advected at the film velocity. The introduction of this new variable allows reformulating the shallow water system in a new way which is much more suited to the numerical discretization than the original one. First numerical results, issued from the currently ongoing tests, will be presented during the conference.

INTRODUCTION

Liquid films moving onto a solid substrate are present in a lot of natural and industrial processes and have been the object of a lot of research studies for several decades. For thin films, capillary forces generally play an important role and could strongly influence both the motion of the contact line and the development of longitudinal (surface waves) and transversal instabilities (dewetting and rivulets formation) [2,3]. To predict such flows, shallow water models are generally preferred to the full Navier-Stokes equations. The derivation of such models is based on closure assumptions on the normal film velocity profile which can be justified either by asymptotic analysis or by empirical arguments. In the present paper, since the objective is not to justify the formulation of a particular model but to focus on the numerical treatment of capillary forces both inside the film and at the contact line, we will restrict our attention to the simplest model accounting for surface tension and gravity effects. For the sake of simplicity, viscous effect and other forces will not be considered but it is worth pointed out that the present approach could be easily extended to more complex and more realistic film models. In the following the model of interest will read:

$$(1)\qquad \begin{cases} (a) \quad \partial_t h + \partial_x(hu) = 0 \\ (b) \quad \rho\partial_t hu + \rho\partial_x\left(hu^2 + \frac{1}{2}gh^2\right) = h\partial_x\left(\frac{\gamma_{lg}\partial_{xx}h}{[1+(\partial_x h)^2]^{\frac{3}{2}}}\right) + \left(\gamma_{sg} - \gamma_{lg}\frac{1}{\sqrt{1+(\partial_x h)^2}} - \gamma_{sl}\right)n_{cl}\delta_{cl} \end{cases}$$

where h denotes the film thickness, u is the film velocity, g is the gravity acceleration, ρ is the liquid density, γ_{sl}, γ_{lg} and γ_{sg} denote the interfacial energy of the solid-liquid interface, liquid-gas interface and solid-gas interface respectively, $n_{cl} = \pm 1$ is the x-component of the outward unit normal to the contact line, and δ_{cl} is the Dirac measure concentrated at the contact line position. System (1) can be interpreted as a model for the motion of an inviscid incompressible fluid over a horizontal flat plate. The last term in the r.h.s. of the momentum equation accounts for the surface tension forces acting on the contact line. It allows to impose the Young-dupré boundary condition at the contact line (or by modifying its expression to prescribe a dynamic contact angle model). This term is generally not taken into account in the shallow water models used in the literature.

In this paper, we propose a regularizing method which allows dealing easily with this term at the discrete level. It consists in introducing in the shallow water model a "colour function" α which is equal to 1 where the film is present and 0 elsewhere and which is advected at the film velocity. Thanks to this additional variable, it is possible to reformulate the surface tension terms in the momentum equation in a more tractable way as regards numerical purposes.

REVISITED SHALLOW WATER MODEL

Model derivation

Let α denotes the indicator function of the film, defined as:

$$\begin{cases} \alpha(t,x) = 0, & if\ \exists\ \varepsilon > 0\ such\ that\ h(t,x') = 0\ for\ all\ x' \in]x-\varepsilon, x+\varepsilon[\\ \alpha(t,x) = 1, & elsewhere \end{cases}$$

Obviously α is solution of the following (non-conservative) equation:

$$(2)\qquad \partial_t\alpha + u\partial_x\alpha = 0$$

Noticing that, by definition, $\alpha\, h = h$ and $\partial_x\alpha = n_{cl}\delta_{cl}$, system (1) is equivalent to:

$$(3)\qquad \begin{cases} \partial_t(\alpha h) + \partial_x(\alpha hu) = 0 \\ \rho\partial_t(\alpha hu) + \rho\partial_x\left(\alpha hu^2 + \frac{1}{2}\alpha gh^2\right) = \partial_x\left(\frac{\gamma_{lg}\,\alpha\, h\,\partial_x p}{[1+p^2]^{\frac{3}{2}}}\right) + \partial_x\left(\frac{\gamma_{lg}\alpha}{\sqrt{1+p^2}}\right) + \left(\gamma_{sl} - \gamma_{sg}\right)\partial_x\alpha \end{cases}$$

a) Corresponding author: philippe.villedieu@onera.fr.

where we have set p = $\partial_x h$ and we have used that $\partial_x\left(\frac{\alpha}{\sqrt{1+p^2}}p\right) = -\frac{\alpha\, p\, \partial_x p}{[1+p^2]^{\frac{3}{2}}} + \frac{1}{\sqrt{1+p^2}}\,\partial_x\alpha$. Using equation (1)-(a), equation (2) and the property $\alpha\, h = h$, the following equation can be derived for p:

(4) $$\partial_t(\alpha p) + \partial_x(\alpha p u) = -\partial_x(\alpha h\, \partial_x u)$$

Combining (3) and (4), we finally get the following model:

(5) $$\begin{cases} \partial_t\alpha + u\partial_x\alpha = 0 \\ \partial_t(\alpha h) + \partial_x(\alpha h u) = 0 \\ \partial_t(\alpha p) + \partial_x(\alpha p u) = -\partial_x(\alpha h\, \partial_x u) \\ \partial_t(\alpha h u) + \partial_x\left(p\alpha h u^2 + \frac{1}{2}\alpha g h^2\right) - \partial_x\left(\frac{\gamma_{lg}\alpha}{\rho\sqrt{1+p^2}}p - \partial_x\, p\frac{(\gamma_{sl}-\gamma_{sg})}{\rho}\alpha\right) = \partial_x\left(\frac{\gamma_{lg}\,\alpha\, h\,\partial_x p}{\rho[1+p^2]^{\frac{3}{2}}}\right) \end{cases}$$

It is worth pointing out that (5) is exactly equivalent to (1) as soon as α is the exact indicator function of the film support. But, if α is only a regularization of the indicator function (as it will be the case at numerical level due to artificial diffusion), system (5) is no more equivalent to system (1). It must simply be considered as a regularization of (1) in which the singular capillary force acting at the contact line have been replaced by a continuous force as in the CSF method.

Energy equation associated with the model

Given the definition of α, it is natural to define the energy of the system as:

(6) $$E = \int \alpha\, e\, dx \qquad \text{where: } e = \frac{1}{2}\rho h u^2 + \frac{1}{2}\rho g h^2 + \gamma_{lg}\sqrt{1+p^2} + \left(\gamma_{sl} - \gamma_{sg}\right)$$

Noticing that $\frac{\partial_x p}{[1+p^2]^{\frac{3}{2}}} = \partial_x\left(\frac{p}{\sqrt{1+p^2}}p\right)$, it is possible to prove that the following additional equation is satisfied by the solution of (5) [4]:

(7) $$\partial_t(\alpha e) + \partial_x(\alpha e u) + \partial_x\left(\alpha\left(\gamma_{sg} - \gamma_{sl} - \frac{\gamma_{lg}}{\sqrt{1+p^2}}p\right)up = \partial_x\left(\gamma_{lg}\alpha h\, u\, \partial_x\left(\frac{p}{\sqrt{1+p^2}}p\right)\right) - \partial_x\left(\gamma_{lg}\,\alpha h\,\frac{p}{\sqrt{1+p^2}}\partial_x up\right.\right.$$

Equation (6) is the energy balance equation corresponding to model (5). It implies the conservation of E. Such a result was mandatory since viscous effects are not accounted for in model (1). The existence of this energy balance equation was used as a criterion to select system (5) among the multiple models which could be formally consistently derived from (1) and the definition of α. It is also worth mentioning that each term of equation (7) can be easily interpreted from a physical point of view [4].

NUMERICAL DISCRETIZATION

Model (5) is much more suited for numerical purposes than system (1). First of all, system (5) only involves second order derivatives instead of third order derivatives. Moreover the second order terms present in the r.h.s. of (5) satisfy a mathematical property (linked to the energy conservation) which allows building energy stable schemes by extending the ideas introduced by Noble and Vila in [5]. Last but not least, by construction, model (5) allows to easily take into account the singular force located at the moving contact line.

Equation (2) being a non-conservative equation, it cannot be discretized by using a finite volume scheme. However a second order upwind scheme may be used, with a special attention paid to the choice of the slope limiter in order to avoid excessive numerical diffusion. Regarding the three other equations of system (5), a finite volume method can be applied. A suitable scheme has to be chosen for the second order derivative terms in order to preserve their compatibility with equation (7) at the discrete level. Details on the chosen numerical method will be given during the conference.

CONCLUSIONS

An original way to deal with capillary forces in shallow water models has been proposed. This new formulation is well adapted for numerical purposes. Its numerical implementation (using a more general model which also takes into account viscous effects) is on-going and application results for partially wetting films will be presented during the conference. The extension of the method to 3D problems is also currently in progress.

References

[1] Brackbill J.U., Kothe D.B., Zemach C. : A continuum method for modelling surface tension, J. Comp. Phys., 100, 1992

[2] Kondic L.: Instabilities in gravity driven flow of thin fluid films, *SIAM Review*, 45(1), 2003.

[3] Young G.W, Davis S.H.: Rivulet instabilities, J. Fluid Mech. **176**, 1987

[4] Villedieu P. et al : paper in preparation

[5] Noble P., Vila J.P. : Stability theory for difference approximations of Euler–Korteweg equations and application to thin film flows, SIAM J. Numer. Anal.52 (6), 2014

NUMERICAL STUDY OF FALLING FILM ON FLEXIBLE WALL IN THE PRESENCE OF INSOLUBLE SURFACTANT

Hao YANG[1], Rong-Qi SHI[1], and Jie PENG *[1]
[1]*Department of Engineering Mechanics, Tsinghua University, Beijing, China*

Summary The dynamics of falling film down an inclined flexible wall have been studied by means of a numerical simulation, in which the algorithm is based on marker and cell (MAC) method. The free surface of liquid film is occupied by insoluble surfactant. The equations governing the fluid motion are discretized on a semi-staggered grid fixed on a physical space. The interfacial boundary conditions on the free surface are treated with the donor cell method. The displacement of flexible wall are treated according to the conservation of mass for liquid film. The surfactant evolution is simulated by separating the convection and diffusion into two steps. Simulation results indicate that the surfactant acts to suppress the dispersion of interfacial wave. Both the wall damping and tension acts to suppress the fluctuations of the flexible wall. However, they play different roles in the evolution of the liquid-air interface.

PROBLEM DESCRIPTION

We consider a two-dimensional incompressible liquid film flow down an infinitely long flexible wall under the effect of gravity force, as illustrated in figure 1. The liquid is postulated as Newtonian fluid. The film is bounded by a gas, which is assumed to be inviscid. Thus, the flow of the gas is ignored in this model. Phase change at the interface, condensation or evaporation, does not occur and the shear stress from the vapor phase may be neglected. The insoluble surfactant occupies the liquid-gas interface, which convects and diffuses along the interface to alter the local surface tension. In this study, we consider that the surfactant is present in dilute concentration. Thus, a linear relation between surface tension and surfactant concentration is adopted. Moreover, the flexible wall is assumed to be tethered and non-stretchable. The bending stresses are neglected and the wall inertia is negligible relative to wall damping.

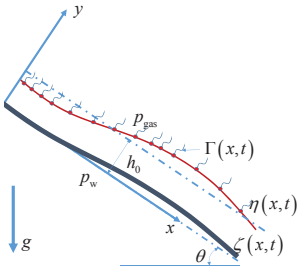

Figure 1: Schematic of the problem. The inclination angle is θ. The unperturbed thickness is h_0.

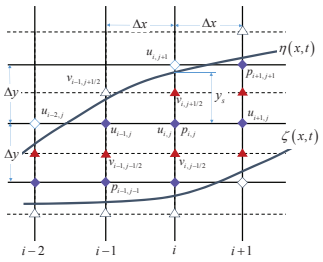

Figure 2: Semi-staggered grid fixed on the physical space near the interface. Here, ⧫ and ▲ denote the grid inside the film where the velocity u, pressure p, and velocity v are defined, respectively. Corresponding ◊ and △ indicate the grid outside the film.

COMPUTATIONAL METHOD

In this study, an algorithm technique based on the MAC method is adopted to directly simulate the moving interfacial problem. The computational framework is built on an Eulerian Cartesian grid to facilitate the field equation computation. A finite differential, semi-implicit method is used to discretize the governing equations on a semi-staggered grid, as illustrated in figure 2. Inside the liquid film, both the convection terms and the diffusion terms of basic equations are discretized by the second-order upwind scheme and the second-order central-difference scheme, respectively.

Evolution of free-surface and flexible wall

The values at the grid points outside the liquid-gas interface and the flexible wall, which are shown as open symbols in figure 2, are unknown, though they are necessary for the numerical procedure. Similar to those presented by [1], they are extrapolated according to the values inside the film and the boundary conditions on the liquid-gas interface or flexible wall. The x-direction velocity component at the liquid-air interface $u_{i,\eta}$ is then obtained by interpolate from $u_{i,j}$ and $u_{i,j+1}$, and the y-direction velocity component can be obtained according to the conservation of mass. The velocity of flexible wall is obtained by integrating the continuity equation from $y = \zeta$ to $y = \eta$ and combining with the flexible wall velocity conditions and kinematic boundary condition at the liquid-gas surface. Therefore, the film thickness on each time step satisfies the mass conservation strictly. The movement of the both the liquid-gas interface and flexible wall can be obtained.

*Corresponding author. Email: peng-jie@tsinghua.edu.cn

Strategy for surfactant evolution

In this work, unlike those presented in [2], the movement of free-surface are captured with the position of marker points. The surface area can be calculated accurately. Thus, we do not solve the surfactant convective and diffusion equation directly and instead relate the surfactant concentration to the ratio of the surfactant mass M and surface area A. In current approach, the evolution of surfactant is simulated by the following three separated steps: (i) the convection which is attributed to the movement of free-surface, (ii) the marker point update and (iii) the diffusion induced by the concentration gradient within the surface, as illustrated in figure 3.

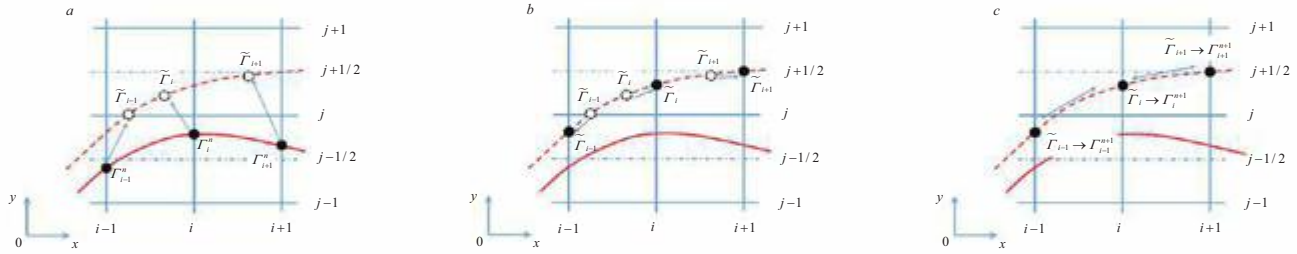

Figure 3: Computation for the concentration of surfactant. It includes (a) convection, (b) marker point update and (c) diffusion step. The initial position of free-surface at time step n is profiled with solid line, while the position of free-surface at time step $n+1$ is represented with dashed line.

RESULTS AND CONCLUSIONS

Many cases were performed to study the effect of surfactant, wall damping and wall tension on such problem. As illustrated in figure 4, the wave characteristics of the wave agree well with the simulation result presented in [1]. For the flow with clean liquid-gas interface ($M = 0.0$), it can be found in figure 5a that the wave celerity is much larger than that of the mean flow. However, for the contaminate interface $M = 0.01$, as illustrated in figure 5b, the development of the initial imposed wave packet is weakened due to the presence of surfactant. Moreover, the surfactant plays a role to weaken the dispersion of the initially imposed perturbation wave.

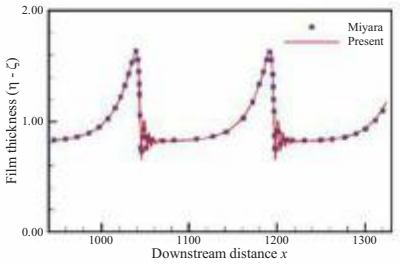

Figure 4: Comparison of a calculated solitary-like waveform to the previous simulation results on a rigid wall. $Re = 29$, $We = 0.414$, $\theta = 6.4^{\circ}$, $\omega = 0.0135$ and $\delta = 0.03$ with clean liquid-gas interface.

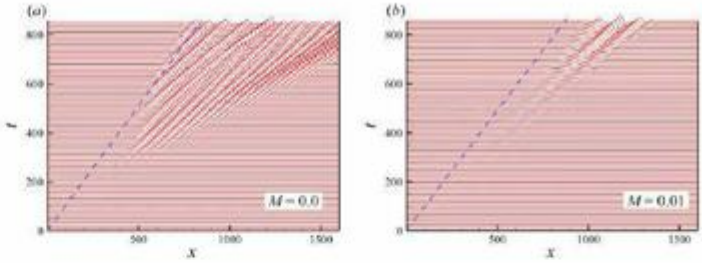

Figure 5: Effect of surfactant on the dispersion of initial imposed wave on the rigid wall, where (a) $M = 0.0$ and (b) $M = 0.01$. The rest parameters are $Re = 45.0$, $We = 0.05$, $\theta = 90^{\circ}$, $Pe_s = 10^3$. The dashed line indicates the convection velocity due to the mean flow.

The effect of wall damping and wall tension on the evolution of initial imposed wave packet have also been studied. Both the wall damping and wall tension act to suppress the fluctuations of the flexible wall. In the case of small wall damping, it suppresses the proceeding capillary ripples of the solitary-like wave. However, for the strong wall damping case, the capillary ripples are intensified with increasing of wall damping. The wall tension, which acts to reduce the displacement of the wall, acts to intensify the proceeding ripples, constantly. Moreover, the wall flexibility has little influence on the dispersion of the initially imposed perturbation wave packet.

References

[1] Miyara A.: Numerical simulation of wavy liquid film flowing down on a vertical wall and an inclined wall. INT J. THERM SCI 39: 1015-1027, 2000.

[2] James A. J., Lowengrub J.: A surfactant-conserving volume-of-fluid method for interfacial flows with insoluble surfactant. J. COMPUT PHYS 201: 685-722, 2004.

Instabilities of liquid-lined flexible tubes with interfacial surfactant

Zhi-Qiang Zhou[1] and Jie Peng *[1]

[1]*Department of Mechanics Engineering, Tsinghua University, Beijing, China*

Summary The linear instability and dynamic behaviours of a liquid-lined flexible tube are studied as a simplified model of pulmonary airway. The liquid-air interface is occupied with an insoluble surfactant. The primary flow can be driven by an external force (e.g. gravity), an interfacial shearing stress, or their combination. A modified lubrication approximation is proposed with the pressure being assumed to vary linearly with the radial position. The linear instability property of the system is examined using normal-mode analysis. For the extremely thin liquid film ($\varepsilon \to 0$), the approximate dispersion relations are derived. For liquid film with relative small thickness (e.g. $\varepsilon = 0.1$), though either the interfacial shearing stress or the external force destabilizes the interface, the combination can cause stabilization in the presence of surfactant. Island of stability, which is caused by the dual role of primary flow in affecting the instability, is detected in the $\sigma_s - Bo$ plane.

PROBLEM FORMULATION

In this work, we consider an incompressible annular liquid film coating the inner surface of a flexible tube, surrounding an infinitely long cylindrical air core. The pressure in the core (p^*_{in}) is constant while the dynamics of the core is neglected. Without loss of generality, the gravity $\boldsymbol{g}^*$ is considered as the external force. An additional constant shearing stress σ^*_s induced by airflow is applied to the liquid-air interface, and its direction can either assist or oppose the flow caused by the external force. The liquid-air interface is occupied by an insoluble surfactant, which can convect and diffuse across the interface to alter the local surface tension. The liquid film with density ρ^* and viscosity μ^* occupies the annular region $\eta^*(z^*,t^*) < r^* < \zeta^*(z^*,t^*)$, where $\eta^*(z^*,t^*)$ and $\zeta^*(z^*,t^*)$ denote the position of liquid-air interface and inner wall of the flexible tube, respectively. Throughout this work, we assume that the flows and geometry are axisymmetric.

The non-dimensionalized evolution equation for the liquid-air interface position ($r = \eta$) is given by

$$\frac{\partial \eta}{\partial t} + \frac{\overline{u}_z(\eta)}{\varepsilon^3}\frac{\partial \eta}{\partial z} = \frac{\zeta}{\eta}\left(\frac{\partial \zeta}{\partial t} + \frac{\overline{u}_z(\zeta)}{\varepsilon^3}\frac{\partial \zeta}{\partial z}\right) + \frac{1}{2\pi\eta}\frac{\partial Q}{\partial z}. \tag{1}$$

Here, Q means axial flow rate of the perturbation field. The surfactant convection-diffusion equation takes the form (at $r = \eta$)

$$\frac{\partial}{\partial t}\left[\eta(1+\Gamma)\Delta_\eta\right] + \frac{\partial}{\partial z}\left[\left(\frac{\overline{u}_z(\eta)}{\varepsilon^3} + u_z\right)\eta(1+\Gamma)\Delta_\eta\right] = \frac{1}{Pe}\frac{\partial}{\partial z}\left(\frac{\eta}{\Delta_\eta}\frac{\partial \Gamma}{\partial z}\right), \tag{2}$$

where $Pe = Ub^*/\kappa^*$ denotes the interfacial diffusivity of the surfactant. The evolution equation for the displacement of the tube wall (at $r = \zeta$) is given by

$$\frac{\phi}{\Delta_\zeta}\frac{\partial \zeta}{\partial t} + \beta\frac{\zeta - 1}{\zeta^2\Delta_\zeta} - \frac{T_z}{\Delta^3_\zeta}\frac{\partial^2 \zeta}{\partial z^2} = \varepsilon p + \frac{2\overline{\sigma}_{rz}(\zeta)}{\Delta^2_\zeta}\left(\frac{\partial \zeta}{\partial z}\right)^3 + T_0\left(1 - \frac{1}{\zeta\Delta_\zeta}\right). \tag{3}$$

Here, $\Delta_\zeta = \sqrt{1 + (\partial\zeta/\partial z)^2}$, $\phi = \varepsilon^3\rho^*_w H^*\lambda^* b^*/\mu^*$ is the damping parameter, which remains finite in the limit $\varepsilon \to 0$. $\beta = E^*H^*/\left(\gamma^*_0(1-\chi^2)\right)$ is the ratio of elastic forces to the surface tension. $T_z = T^*_z/\gamma^*_0$ is the ratio of longitudinal wall tension to the surface tension and $T_0 = T^*_0/\gamma^*_0$ is the ratio of initial circumferential tension to the surface tension. The evolution equations (1) – (3) constitute an initial value problem for η, γ and ζ, respectively.

RESULTS

The results of present work are compared with those of traditional lubrication approximation and an Orr-Sommerfeld computation that comes from a linearization of the full Navier-Stokes equations, which is named as full linear instability analysis. The value of β is marked on the curve. For $\beta = 1.5$, the growth rates predicted by the lubrication approximation (dashed lines) lie below those from the modification method in the present work (solid lines), which are consistent with the results from the full linear instability analysis (solid squares). This indicates that the modification method proposed in the present study is sufficient to capture the linear regime satisfactorily, while the lubrication approximation without modification is unsatisfactory for the compliant tube wall in the presence of primary axial shearing flow caused by either gravity force ($Bo = 2.0$, in figure 1a) or interfacial shearing stress ($\sigma_s = 0.5$, in figure 1b). However, for $\beta = 100.0$, the tube wall is

*Corresponding author. Email: peng-jie@tsinghua.edu.cn

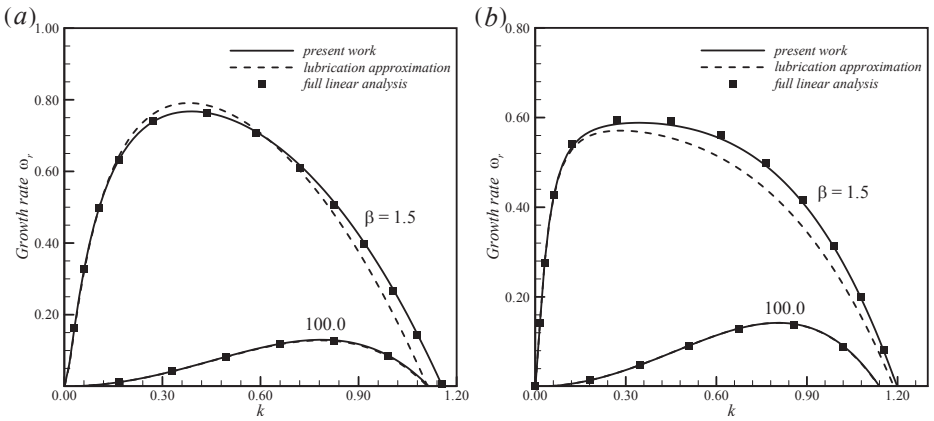

Figure 1: Comparison of the results in this work with those from the lubrication approximation and full linear instability analysis for $\varepsilon = 0.1$, $\phi = 0.1$, $T_0 = 0.0$, $T_z = 0.0$, $M = 0.0$ and (a) $Bo = 2.0$, $\sigma_s = 0.0$; (b) $Bo = 0.0$, $\sigma_s = 0.5$. Numbers marked on the curve denote the value of β, which indicates the ratio of elastic forces to the surface tension.

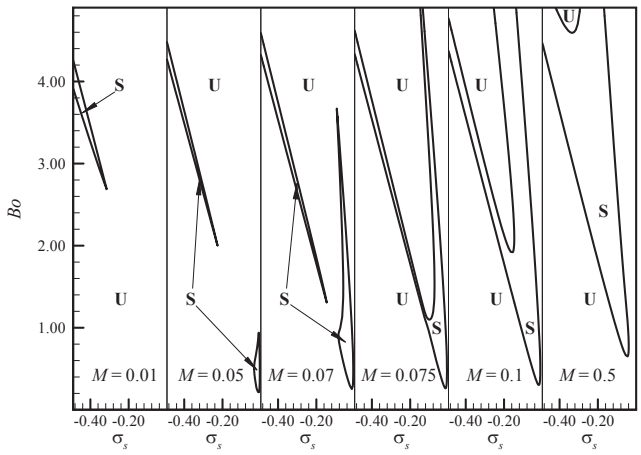

Figure 2: Formation and evolution of an island of stability on the $\sigma_s - Bo$ plane for $\phi = 0.1$, $T_0 = 0.0$, $T_z = 0.0$, $\beta = 1.5$ and $Pe = 10^3$ with Marangoni number M being a parameter. The stable and unstable regions are identified with the symbol $'\mathbf{S}'$ and $'\mathbf{U}'$, respectively.

assumed to be stiff, and the differences between the profiles become very small (see in figure 1). The lubrication approximation without modification is now acceptable.

For compliant tube wall ($\beta = 1.5$), as illustrated in figure 2 with $\phi = 0.1$, $T_0 = 0.0$, and $T_z = 0.0$, the neutral stability curves are distinctively different from those with stiff tube wall. For $M = 0.01$, a small stable region with sharp profile can be identified. The minimum value of Bo, below which the flow is linearly unstable with whatever value of σ_s, is $Bo_{min} = 2.688$. This is much larger than that with stiff tube wall. However, for $M = 0.02956$, an island of stability close to the origin point of coordinates is developed. The island becomes larger with increasing of Marangoni number M (e.g. $M = 0.05, 0.07$), and integrates together with the rest stable region while M is big enough (e.g. $M = 0.075$, etc.). A stable streak, which looks like character $'\mathbf{V}'$, is formed on the neutral plane, and the stable region expands with increasing of M (e.g. $M = 0.1, 0.5$). Physically, as being mentioned before, for the compliant tube wall, a remarkable axial perturbation flow rate can be induced and result in destabilization. Combining with the Marangoni traction forces due to the surfactant gradient, the primary flow, which acts to stabilize for stiff tube wall, tends to play a dual role in the flow instability.

References

[1] Halpern, D. & Grotberg, J. B.: Fluid-elastic instabilities of liquid-lined flexible tubes. J. Fluid Mech. 1992(244), 615632.

[2] Kas-Danouche, D. T., Papageorgiou, D. T. & Siegel, M.: Nonlinear dynamics of core-annular film flows in the presence of surfactant. J. Fluid Mech 2009(626), 415448.

[3] Matar, O. K., Craster, R. V. & Kumar, S.: Falling films on flexible inclines. Phys. Rev. E 2007(76), 056301.

FM09 - Geophysical and Environmental Fluid Dynamics

TS.FM09-1.01	Linden, Paul - Experiments on stratified turbulence and mixing in an inclined duct (INVITED)	1087
TS.FM09-1.02	Salehipour, Hesam - Turbulent mixing in strongly stratified shear flows	1089
TS.FM09-1.03	Delache, Alexandre - Isotropy restored at small scales in stratified turbulence : Thorpe's scale vs Ozmidov's scale	1091
TS.FM09-1.04	Arratia, Cristobal - Transient growth on time-dependent strongly-stratified flows	1093
TS.FM09-1.05	Kaminski, Alexis - Nonlinear evolution of optimal perturbations to strongly stratified shear layers	1095
TS.FM09-1.06	Yang, Bernard - High frequency observations of under-ice convection	1097
TS.FM09-2.01	Dauxois, Thierry - Energy Cascade in Internal Wave Attractors (INVITED)	1099
TS.FM09-2.02	Heijst, Gertjan - Tidal flushing of semi-enclosed basins (INVITED)	1101
TS.FM09-2.03	Scase, Matthew - Suppression of the Rayleigh-Taylor Instability by Rotation	1103
TS.FM09-2.04	Billant, Paul - Instabilities of baroclinic vortices in stratified-rotating fluids	1105
TS.FM09-2.05	Reinaud, Jean - Interaction of a surface Quasi-Geostrophic buoyancy strip and an internal vortex	1107
TS.FM09-3.01	Davarpanah Jazi, Shahrzad - Enhanced Sedimentation Beneath Sediment Laden Overflows and Interflows	1109
TS.FM09-3.02	Shimokawa, Shinya - Oceanic oscillation phenomena related synchronization and stochastic resonance	1111
TS.FM09-3.03	Khani, Sina - Evaluation of eddy- and non-eddy-viscosity subgrid scale models in stratified turbulence	1113
TS.FM09-3.04	Penney, Jared - Numerical simulation of free-slip double-diffusive gravity currents	1115
TS.FM09-3.05	Laizet, Sylvain - Reynolds number effects for non-channelized non-axisymmetric particle-driven gravity currents	1117
TS.FM09-4.01	Waite, Michael - Numerical simulations of the atmospheric kinetic energy spectrum (INVITED)	1119
TS.FM09-4.02	Kimura, Yoshifumi - Temperature front genesis in stably stratified turbulence	1121
TS.FM09-4.03	Hossain, Md Monir - Simulation of flow field inside a coral colony	1123
TS.FM09-4.04	Gurka, Roi - 3D POD examination of streamwise enstrophy in a stably stratified sphere wake	1125
TS.FM09-4.05	Mizerski, Krzysztof - New turbulent large-scale magnetic dynamo mechanism	1127
PO.FM09-1.01.49	Gu, Haihua - The influence of particles on turbulence intensity in a high Reynolds number ABL flow	1129
PO.FM09-1.02.50	Jin, Ting - The influence of large-scale turbulent structure on saltation sand transport	1131
PO.FM09-1.03.51	Kong, Linghai - A dynamical study on the north pacific low-latitude western boundary currents	1133
PO.FM09-1.05.53	Soomere, Tarmo - Water level extremes at the Baltic Sea coast	1135
PO.FM09-1.06.54	Wu, Zhouhu - Theoretical concentration contours equation of sewage mixing zone in rivers and its application	1137

EXPERIMENTS ON STRATIFIED TURBULENCE AND MIXING IN AN INCLINED DUCT

Adrien Lefauve*[1] and P. F. Linden[1]

[1]*Department of Applied Mathematics and Theoretical Physics, University of Cambridge, Cambridge, UK*

Summary Laboratory experiments on the stratified shear flows in an inclined duct are reported. Stratified turbulence is observed in this two-layered exchange flow, whose dissipation is controlled by the duct inclination and compares with that observed in geophysical contexts. Three-dimensional simultaneous particle image velocimetry (PIV) and laser-induced fluorescence (LIF) measurements are presented together with arguments as to how they can be employed to advance our understanding of the dynamics and mixing of stratified turbulence.

FROM THE OCEAN TO THE INCLINED DUCT

Between quasi-geostrophic and small-scale isotropic turbulence lies a range of scales strongly affected by buoyancy. The realm of *stratified turbulence*, characterized by high Reynolds number (Re), low horizontal Froude number (Fr_h) but high buoyancy Reynolds number ($Re_b \equiv Re\, Fr_h^2$, a measure of turbulence intensity), exhibits complex dynamics and mixing properties [1]. A better understanding of the laminar-turbulent transition, spatio-temporal intermittency, energy dissipation and mixing poses serious mathematical challenges and would enable progress in atmospheric and oceanic modelling. Although typical geophysical values are $Re_b = O(10^5 - 10^7)$, it was argued that $Re_b > O(10)$ was sufficient to investigate this regime [2]. However, sustaining high-Re and "high" Re_b turbulence proves challenging both experimentally and numerically.

The experiment sketched in Fig. 1 consists of a long duct connecting two reservoirs of brine and water, in which a two-layer exchange flow is established. As shown in Fig. 2, the flow can exhibit laminar, wavy behaviour, spatio-temporally intermittent 'weak' turbulence or developed turbulence in a well mixed layer. This experiment was first investigated in [3],

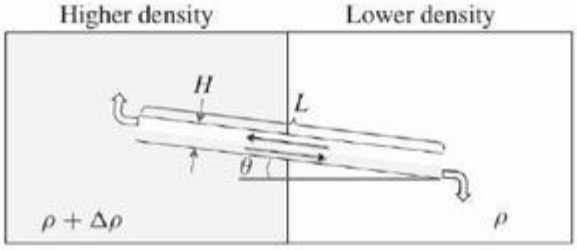

Figure 1: Schematic of the inclined duct experiment. The square duct is 135 cm long and 4.5cm high. Adapted from [4]).

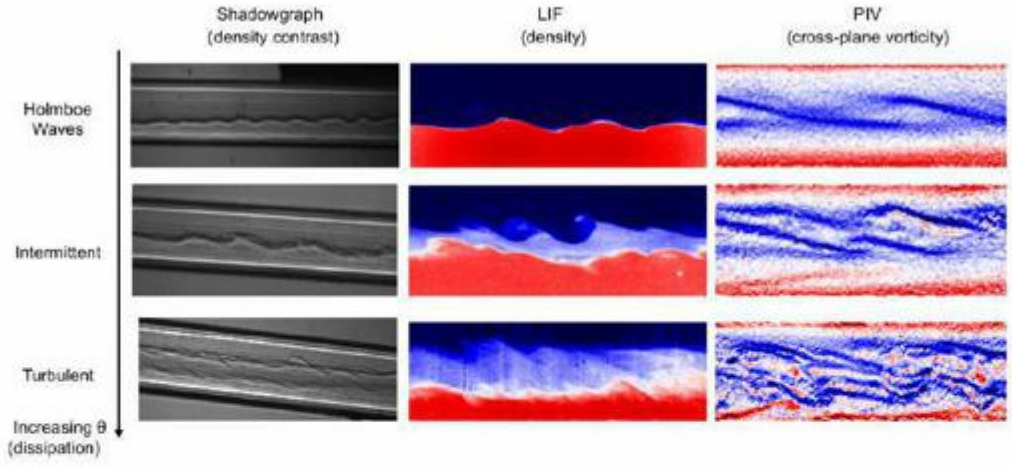

Figure 2: Shadowgraph, laser-induced fluorescence (LIF) and particle image velocimetry (PIV) visualisations of the flows.

and more recently in [4], who mapped the flow states in the $(Re = \sqrt{g'H}H/\nu, \theta)$ space and proposed that the transition to turbulence was triggered by increasing $\theta > 0$. Due to the flow velocity being hydraulically controlled by the duct ends, the inclination provides excess energy that needs to be dissipated. They argued that the ensuing stratified turbulence, generated by the internal flow dynamics and whose dissipation is controlled, could maintain values up to $Re_b = O(10^2)$ for extended periods of time.

*Corresponding author. Email: lefauve@damtp.cam.ac.uk

PIV AND LIF EXPERIMENTS

Using non-simultaneous LIF and PIV measurements, it was possible to estimate the vertical time- and space-average shear distribution in the mid-plane of the duct $S = \partial u/\partial z$, as well as the buoyancy frequency $N^2 = (\circ\ g/\rho)(\partial\rho/\partial z)$, and deduce the gradient Richardson number $Ri_g \equiv N^2/S^2$ (Fig. 3). Low values ($Ri_g < 0.5$) on both sides of the interface (Fig. 3a) are thought to be responsible for the Holmboe waves, while the turbulent, mixed layer (Fig. 3b-e) seems associated with even lower, near constant $Ri_g \approx 0.1 \circ\ 0.2$. This can be substantiated by arguing that this interior mixed layer, insulated by two peaks of high stability ($Ri_g \approx 1$), is not influenced by the duct upper and lower boundaries. Its thickness is thought to be internally set by the flow, which is consistent with a constant $Ri_g = Ri_e$, where Ri_e is an equilibrium Richardson number [5], which can be shown to provide the link between the turbulent transition and mixing efficiency.

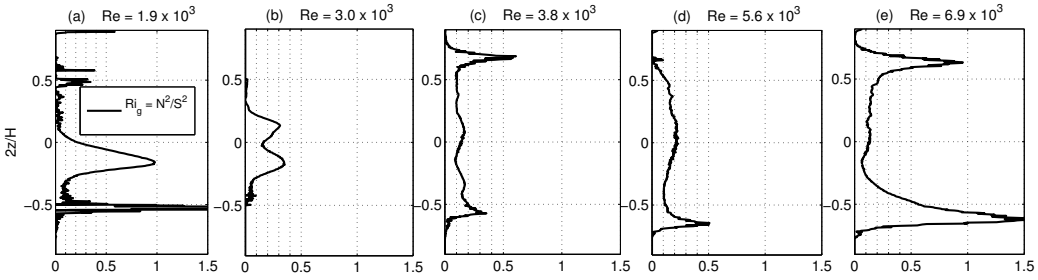

Figure 3: Time- and space-averaged $Ri_g(z)$ from non-simultaneous LIF and PIV at various Re and $\theta = 2°$.

State-of-the-art experimental capabilities (Fig 4) now allow us to probe the flow with simultaneous LIF and PIV and extract buoyancy fluxes as well as coherent structures. The latest results obtained with those techniques will be presented.

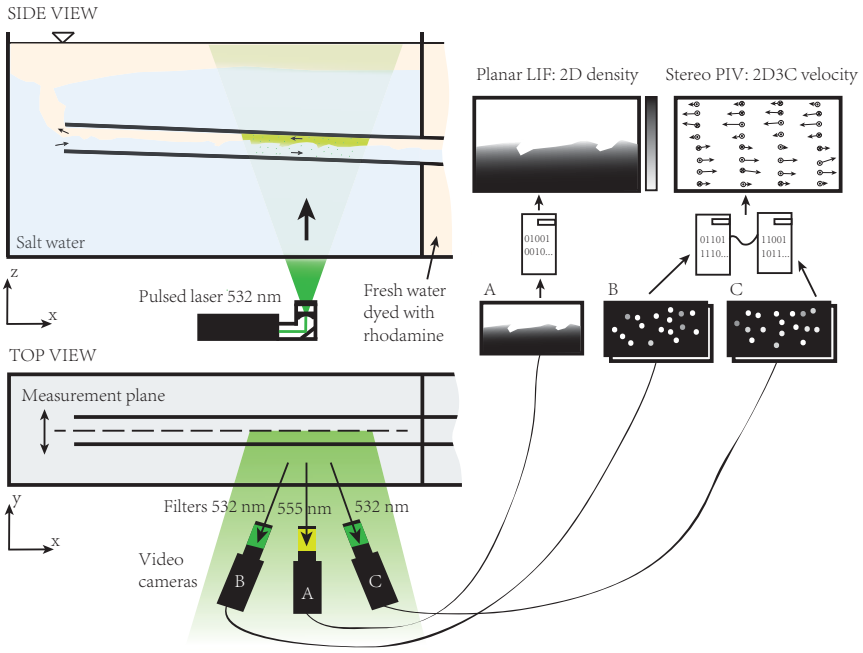

Figure 4: Schematic of the 3D simultaneous LIF-PIV system.

References

[1] Waite, M. L. Direct Numerical Simulations of Laboratory-Scale Stratified Turbulence. AGU, Washington DC. USA (2013)

[2] Bartello, P., & Tobias, S. M.. Sensitivity of Stratified Turbulence to the Buoyancy Reynolds Number. *J. Fluid Mech.* **725** (2013)

[3] Kiel, D. E. Buoyancy driven counterflow and interfacial mixing. PhD Thesis, Department of Engineering, University of Cambridge, Cambridge UK (1991)

[4] Meyer, C. R. & Linden, P. F.. Stratified Shear Flow: Experiments in an Inclined Duct. *J. Fluid Mech.* **753** (2014)

[5] Turner, J. S. Buoyancy Effects in Fluids. Cambridge University Press, Cambridge UK (1973)

TURBULENT MIXING IN STRONGLY STRATIFIED SHEAR FLOWS

Hesam Salehipour *[1], W. Richard Peltier[1], and Colm-cille Caulfield[2,3]

[1]*Dept. of Physics, University of Toronto, Toronto, ON M5S 1A7, Canada*
[2]*BP Institute, University of Cambridge, Madingley Road, Cambridge CB3 0EZ, UK*
[3]*Department of Applied Mathematics and Theoretical Physics, University of Cambridge, Centre for Mathematical Sciences, Wilberforce Road, Cambridge CB3 0WA, UK*

Summary Motivated by the importance of irreversible mixing in geophysical and environmental flows, we seek to understand the dependence of its efficiency under strongly stratified conditions through an investigation of two types of stratified shear instabilities: the Kelvin-Helmholtz and Holmboe wave instabilities. Our numerical findings suggests that mixing efficiency of energetically turbulent flows may never become suppressed despite arbitrarily strong stratification in the Holmboe wave case.

INTRODUCTION

Turbulent mixing of a stably stratified flow has a leading role in controlling the large scale meridional overturning circulation of the ocean [1]. Although the precise nature of physical processes that are involved in the downscale cascade of energy, from global to dissipation scales, is not well understood, it is generally believed that shear instabilities occur as the last step to mediate the transition to turbulence at the smallest scales. In fact, a layered or stepwise density structure (i.e. layers of well-mixed flow separated by sheets of sharp density interfaces), is commonly observed in nature. For a stably stratified density layer that is embedded by a shear layer of a similar finite depth, the classical Kelvin-Helmholtz instability (KHI) may grow. However if the density interface is sufficiently sharper than the shear layer, another class of shear instability, the Holmboe wave instability (HWI), emerges in spite of arbitrarily large values of stratification.

The turbulent mixing induced by these instabilities may be characterized by an efficiency, E, that quantifies the proportion of the total rate of dissipation into internal energy which is expended on useful irreversible mixing (M). Furthermore, a fundamental non-dimensional parameter in stratified shear flows is the bulk Richardson number, Ri, which characterizes the relative strength of density stratification to the velocity shear. Formally these parameters may be defined mathematically as:

$$E = \frac{M}{M+\epsilon}, \qquad Ri = \frac{g\Delta\rho/(\rho_0 L_\rho)}{(\Delta U/L_u)^2}, \tag{1}$$

in which L_ρ and L_u represent respectively the thickness of the density and shear layers across which these quantities vary by $\Delta\rho$ and ΔU. In addition, for a stratified flow to be recognized as *turbulent*, the rate of kinetic energy dissipation, ϵ, should exceed a limit of approximately $20\nu N^2$ [2], where $N^2 = \circ\,(g/\rho_0)d\overline{\rho}/dz$ is the squared buoyancy frequency associated with the background stratification and ν is the kinematic viscosity. In other words, the so-called buoyancy Reynolds number, $Re_b = \epsilon/(\nu N^2) > 20$ for a stratified flow to be considered *turbulent*.

An outstanding question in stratified turbulence concerns the behavior of E when the flow is subjected to *strongly* stratified conditions with arbitrarily large values of Ri. As illustrated in figure 1 (left), it is unclear whether mixing (I) stays at its maximum efficiency, (II) asymptotes to an efficiency less than its maximum or (III) becomes completely suppressed. While previous laboratory studies support (III) [3], recent studies seem to suggest that (II) is most likely [4, 5]. Both cases (I) and (II) would imply the absence of a critical bulk Richardson number as suggested by [6]. Nevertheless, none of these studies discuss the vigor of turbulence as e.g. characterized by Re_b. As a result, the true behavior of E with Ri for geophysically relevant energetic turbulence (i.e. $Re_b > 20$) has hitherto remained enigmatic.

In particular, in the context of the aforementioned shear instabilities, it is not known whether the growth of the two-dimensional Holmboe instability, which is guaranteed in spite of an arbitrarily large Ri, would lead to a fully three-dimensional turbulent flow. In fact, previous Direct Numerical Simulations (DNS) of this instability at exceedingly low Reynolds number [7] suggest that the saturated Holmboe waves may never become turbulent (i.e. $Re_b \ll 20$) which supports a complete suppression of irreversible mixing as suggested by case (III). Nonetheless, it has most recently been demonstrated in [8] that sufficient increase in the flow Reynolds number renders the induced flow truly turbulent by promoting the strength of the secondary instabilities which directly contribute to the three-dimensionalization process.

In the present work, we aim to investigate the behavior of E with respect to Ri under the stringent condition that the induced flow after the saturation of two-dimensional instability must be sufficiently turbulent (i.e. $Re_b \gg 20$). This condition is particularly important for studies of mixing in *strongly* stratified flows [9].

*Corresponding author. Email: h.salehipour@utoronto.ca

RESULTS

Figure 1 (right) illustrates E^* as a function of Ri where E^* is the maximum value of the mixing efficiency that is achieved after the saturation of three-dimensional kinetic energy. Note that $E = E^*$ approximately when Re_b also becomes maximum. Hence E^* characterizes the mixing efficiency when the flow is most vigorously turbulent. This figure contains a rich collection of DNS data associated with both Kelvin-Helmholtz and Holmboe wave instabilities (KHI and HWI) where the KHI dataset is that available from [10]. Note that every symbol indicates the result for a single DNS analysis.

Unlike KHI that is suppressed for the *bulk* Richardson numbers $Ri \gtrsim 1/4$, under such strongly stratified conditions HWI not only emerges but also produces highly turbulent flows. Although the emergence of two-dimensional HWI is expected based on linear theory alone, the transition to a fully three-dimensional turbulent flow has been achieved only by increasing the flow Reynolds number to sufficiently high values so as to lead to $Re_b > 20$ (this condition has demanded the application of massive computational resources). As a result, the mixing induced by HWI is apparently never fully suppressed. Moreover, the highest value of mixing efficiency, as high as $E^* \sim 0.4$ when $Ri \sim 1/4$, is only attainable through KHI. For $Ri \gtrsim 1/4$, mixing efficiency quickly decreases to approximately $E^* \sim 0.15$ and remains at this value up to $Ri \sim 2$.

CONCLUSIONS

Although further DNS analysis of HWI have not been conducted beyond $Ri \sim 2$, our findings in figure 1 (right) clearly support scenario (II) in figure 1 (left) which suggests that turbulent mixing may *never* become completely suppressed so long as the stratified flow is sufficiently energetic with $Re_b > 20$.

References

[1] Wunsch, C., & Ferrari, R. (2004): Annu. Rev. Fluid Mech., 36, 281-314.

[2] Smyth, W. D., Moum, J. N., & Caldwell, D. R.: J. Phys. Oceanogr., 31(8), 1969-1992, 2001.

[3] Linden, P. F. : Geophys. Astrophys. Fluid Dyn., 13,3–23, 1979.

[4] Strang, E. J. & Fernando, H. J. S.: J. Fluid Mech., 428, 349–386, 2001.

[5] Oglethorpe, R. L. F., Caulfield, C. P. & Woods, Andrew W: J. Fluid. Mech., 721, 2013.

[6] Galperin, B., Sukoriansky, S. & Anderson, P. S.: Atmospheric Science Letters, 8.3, 65–69, 2007

[7] Smyth, W.D., Carpenter, J. R. & Lawrence, G. A.: J. Phys. Oceanogr., 37, 1566–1583, 2007.

[8] Salehipour, H., Caulfield, C. P., & Peltier, W. R.: J. Fluid Mech., submitted.

[9] Brethouwer, G., Billant, P., Lindborg, E. & Chomaz, J.-M.: J. Fluid Mech., 585, 343–368, 2007.

[10] Salehipour, H., & Peltier, W. R.: J. Fluid Mech., 775, 464–500, 2015.

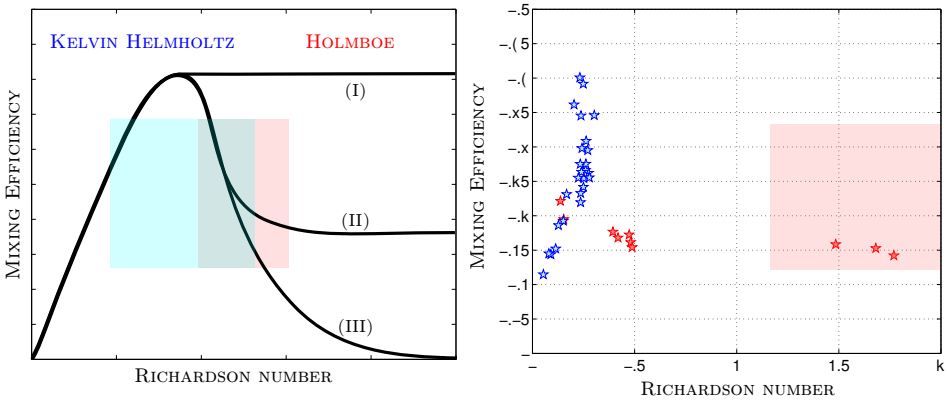

Figure 1: Left: Schematic illustration of three hypothetical behaviors for mixing efficiency as a function of the bulk Richardson number (Ri). The shaded areas represent schematically the region of the Ri space where Kelvin-Helmholtz instability (KHI) or Holmboe wave instability (HWI) may mediate the transition to turbulence. Right: DNS data of KHI [10] indicated by blue stars, along with a set of original DNS analysis of HWI indicated by red stars (a single symbol represents the result for a single DNS case). Note that all DNS analyses have been conducted at sufficiently high Reynolds numbers yielding $Re_b \gg 20$.

ISOTROPY RESTORED AT SMALL SCALES IN FREELY DECAYING STRATIFIED TURBULENCE : A CONFIRMATION OF THORPE'S SCALE AND OZMIDOV'S SCALE.

Alexandre Delache * [1], Louis Gostiaux[2], Fabien S. Godeferd[2], and Claude Cambon[2]
[1]*LMFA, site de Saint-Etienne, Université de Lyon, Université Jean Monnet de Saint-Etienne, France*
[2]*LMFA UMR 5509 CNRS, École centrale de Lyon, Université de Lyon, France*

Summary The unobvious relation between Ozmidov's scale L_o [2] and Thorpe's scale L_T [1] is extended to a large regime of stratification by investigating the corresponding dynamics using Direct Numerical Simulations (DNS) in freely decaying turbulence at different stratification rates. Moreover, we confirm the return to isotropy of the small scales by analyzing the orientation-dependent power spectrum and energy modes. To some extent, many characteristics of isotropic universality are restored at small scales but, surprisingly, the density spectrum (also potential energy spectrum) plays a particular role.

THORPE'S SCALE AND OZMIDOV'S SCALE

In oceanic, atmospheric or engineering flows, turbulence can be strongly affected by stratification. In stably stratified homogeneous turbulence, the flow contains quasi-horizontal structures organized in vertically sheared layers. These structures are a mix between internal waves and turbulence. Different lengthscales are used to characterise the overturning of buoyancy; the most used in oceanography are Thorpe's scale L_T which is a measure of large-scale vertical overturns [1] and Ozmidov's scale $L_o = \left(\varepsilon/N^3\right)^{\frac{1}{2}}$ (with N the Brunt-Väisälä frequency and ε the dissipation) which compares the relative effects of inertia and of the buoyancy force [2].

Structures larger than L_o are strongly influenced by stratification whereas structures smaller than L_o recover three-dimensional isotropy. These two scales L_o and L_T are related by Dillon's relation $L_o \simeq 0.8 L_T$ [3] which is obtained in the Ocean. This relation allows to find the value of dissipation ε in the ocean, directly by a measure of Thorpe's scale L_T. Nonetheless, the proportionality coefficient 0.8 depends on stratification and on the flow regime, so that Dillon's relation was recently extended using DNS [4]. Moreover the scales L_o and L_T are widely used for the analysis of numerical simulations [6, 7] or experiments [8, 9]. Such a refined description is thus important for an accurate characterization of turbulent mixing in stratified flows. We propose here a parametric study of scale-by-scale anisotropy of stratified turbulence using dedicated spectra.

In order to analyze further the extension of Dillon's relation and small-scale isotropisation, we present results from high resolution DNS (2048^3 points) of freely decaying turbulence at four different stratification rates. On figures 1(a) and (b), we illustrate a typical distribution of the fluctuations of density and of Thorpe's deplacement.

SCALE BY SCALE ANALYSIS

Classically, to measure the energy by scale — or for each wave number k in Fourier space —, one uses averages of energy over spheres of radius k, and thus averages out the anisotropic contents of the energy distribution. In the case of stratified turbulence with axisymetric statistics about the vertical axis of gravity, the distribution of energy is not equi-distributed over the spherical shell of radius k by contrast to isotropic turbulence. We characterise this non equi-distribution of kinetic energy and potential energy by introducing the angular dependence of the power spectrum [10]. In the case of discrete analysis in DNS, we decompose the sphere into several rings O_i (six rings in our simulation as shown on the sketch of figure 1 d)) and we define the kinetic E_c and potential E_{pot} energy spectra for each ring as:

$$E_c(k, O_i) = \frac{1}{m_k^i} \sum_{\mathbf{k} \in O_i} |\hat{\mathbf{u}}_\mathbf{k}|^2 \qquad \text{and} \qquad E_{pot}(k, O_i) = \frac{1}{m_k^i} \sum_{\mathbf{k} \in O_i} |\hat{\rho}_\mathbf{k}|^2 \tag{1}$$

where $\hat{\mathbf{u}}_\mathbf{k}$ is the Fourier velocity vector, $\hat{\rho}_\mathbf{k}$ is the Fourier component of density and $m_k^i = (\pi/4)(\theta_i \circ\ \theta_{i+1})^{-1}(\sin(\theta_i) \circ\ \sin(\theta_{i+1})^{-1}$ is a normalization term (so that E_c recovers isotropic scalings $k^{-5/3}$ of classical Kolmogorov spectrum in absence of stratification).

We have performed simulations at four stratification intensities, thus at different Froude numbers ranging from about 0.13 to 1.06, with 2048^3 grid points, so that the Reynolds numbers are rather high and of order $Re \simeq 3000$–4000. For instance, figures 1 (c) and (d) show power spectra for two stratification rates. On each plot the Ozmidov wavenumber $k_N \simeq 1/L_O$ is indicated to delimitate the large scale stratification-affected range from the smaller-scale range.

*Corresponding author. Email: alexandre.delache@univ-st-etienne.fr

We show that at Froude number of order one (the lowest stratification rate in our parametric study), on figure 1(c), large scales are clearly anisotropic (kinetic energy is concentrated towards the polar ring O_1), whereas at scales smaller than the Ozmidov one (wavenumbers larger than k_N), the spectra join again, as a sign that 3D isotropy is recovered. At very high stratification rate on figure 1(d) (very low Froude number), all scales are strongly anistropic with at least one decade difference in the energy between horizontal motion (vertical wavenumbers in ring O_1) and vertical one (horizontal wavenumbers in ring O_6). During the colloquium, we shall present all the results of our simulations, which confirm that the Ozmidov scale is a separating scale between anisotropic and isotropic ranges: for moderate stratification, the large scales are preferentially horizontally oriented but the smaller scales recover a classical isotropic behaviour whereas for increased stratification, small scales also become quasi horizontal. This work was granted access to the HPC resources of IDRIS under the allocation i20152a2206 and i20152a7411 made by GENCI.

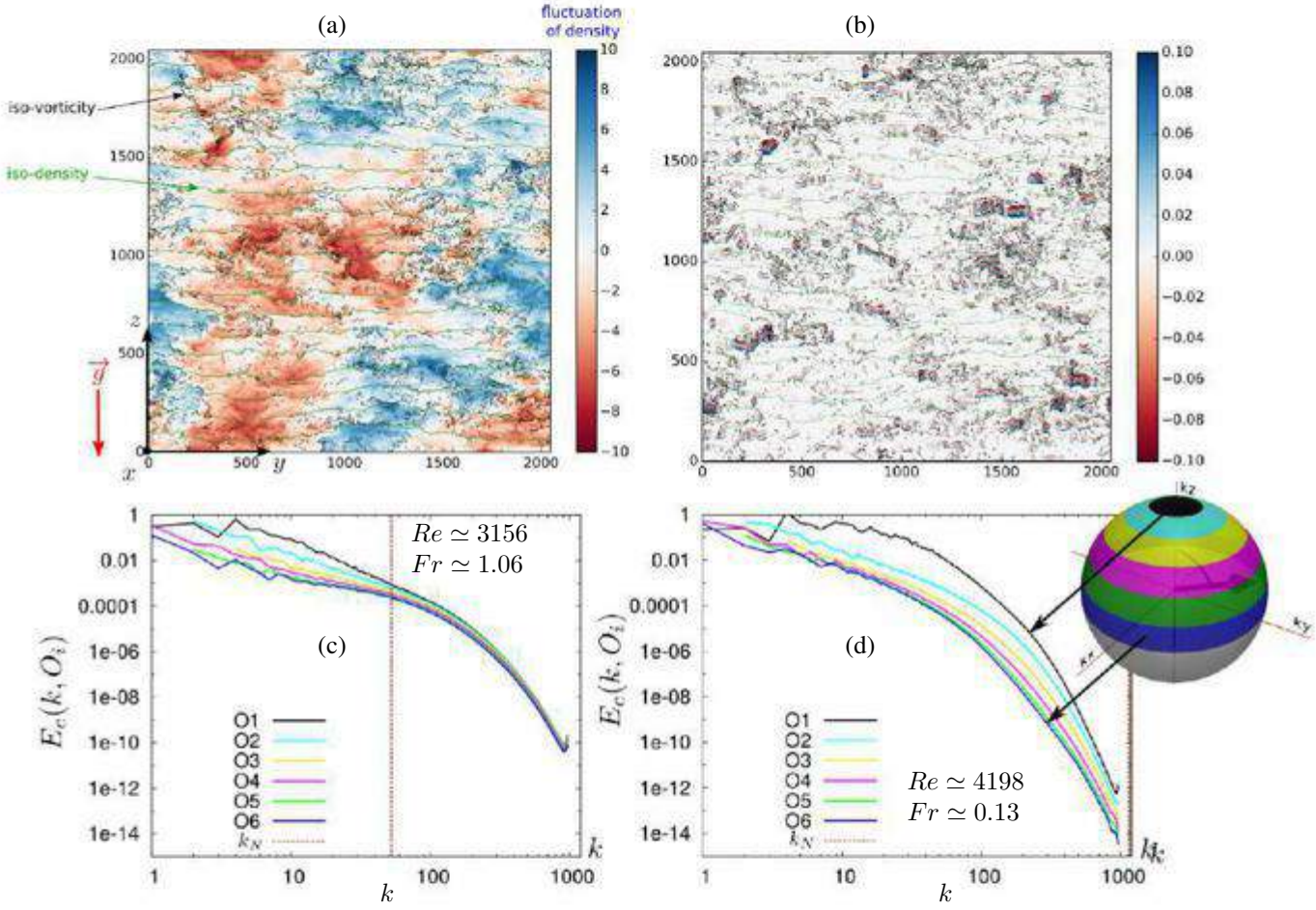

Figure 1: Illustration of the layering through distribution in a vertical section: (a) fluctuation of density with vorticity and iso-density, and (b)Thorpe's deplacement. Angle-dependent power spectrum at increasing Froude numbers as indicated from (c) to (d) -(different stratification rates), and sketch of the angular decomposition into six spectral rings.

References

[1] S. A. Thorpe, Philos. Trans. R. Soc. London, Ser. A 286, 125-181 (1977)
[2] Ozmidov R.V. Izvestia Acad. Sci. USSR, Atmosphere and Ocean Physics, 1965,$N^\circ 8$
[3] T. M. Dillon, J. Geophys. Res. 87, 9601-9613, (1982).
[4] B. D. Mater, S. M. Schaad, and S. K. Venayagamoorthy, Physics of Fluids 25, 076604 (2013);
[5] F.S. Godeferd, C. Cambon, Phys. Fluids 6, 2084-2100, (1994).
[6] Marino, R. and Mininni, P. D. and Rosenberg, D. L. and Pouquet, A., Phys. Rev. E, 90, 2, (2014).
[7] Augier, P., Chomaz J.M and Billant P., J. Fluid Mech., 713, pp 86-108, (2012).
[8] J. J. Riley and E. Lindborg. J. Atmos. Sci., 65, 2416-2424, (2008).
[9] van Haren, H., and L. Gostiaux. Oceanography 25(2):124-131, (2012).
[10] P. Sagaut and C. Cambon, *Homogeneous Turbulence Dynamics* , Cambridge University Press, Cambridge, England, 2008.

TRANSIENT GROWTH ON TIME-DEPENDENT STRONGLY-STRATIFIED FLOWS

Cristobal Arratia*[1] and Jean-Marc Chomaz[2]
[1]*Departamento de Física, FCFM, Universidad de Chile. Santiago, Chile*
[2]*LadHyX, CNRS-Ecole Polytechnique, F-91128 Palaiseau Cedex, France*

Summary We study the competition between the zigzag instability and Lilly's mechanism of vertical decorrelation through independently-evolving horizontal layers by computing the linear optimal perturbations to different types of vertically-invariant base flows with strong stratification. This allows us to find, as a function of vertical wavelength, the potential of linear perturbations to extract energy from each base flow. We observe that the zigzag instability is more relevant than Lilly's mechanism only when the base flow is composed of distinct vortices, while the zigzag scaling laws remain always valid except for viscous effects. Additionaly, the optimal perturbations reveal other, more efficient mechanisms of transient energy extraction. Performing toroidal-poloidal decomposition of the optimal perturbations we observe that, as the vertical wavenumber increases, the optimal perturbations are increasingly associated to energy extraction from the vertical vorticity into vertical velocity and density perturbations.

INTRODUCTION

Similar to the zigzag instability [1], the vertical scale of the anisotropic direct cascade of strongly stratified turbulence is given by the buoyancy length scale [2]. In both cases this length scale selection follows from the inviscid self-similarity of the strongly stratified Boussinesq equations [3], but it is not clear what role, if any, does the zigzag instability play in the development of stratified turbulence. In fact, Lilly's mechanism of vertical decorrelation between different horizontal layers [4] also predicts small vertical scales and is consistent with the strongly stratified scaling of Billant & Chomaz [3].

The dynamical differences between Lilly's mechanism and the zigzag instability are important. Lilly's mechanism involves two-dimensional (2D) dynamics on each of the essentially uncorrelated horizontal layers, and is similar to the toroidal cascade in that it does not involve vertical transport (except for 'secondary' instabilities that may arrive from the vertical shear between adjacent horizontal layers). For the zigzag instability, on the other hand, vertical transport is a key ingredient that leads to the destabilization of an otherwise neutral 2D mode associated with rotation and translation of the vortices.

Despite the differences, both mechanisms can lead to the formation of thin horizontal layers from an initial flow which is nearly invariant in the vertical direction. While a layering induced by the zigzag instability is expected when there are well separated interacting vortices, Lilly's mechanism will induce decorrelation of horizontal layers on any nearly vertically invariant base flow through the sensitivity to initial conditions of the 2D flow. The question arises of whether the zigzag instability, or a similar mechanism inducing the destabilization of the 2D dynamics for long vertical wavelengths, will generically be the most efficient in determining the vertical wavelength appearing naturally from a vertically invariant flow.

METHODOLOGY AND MAIN RESULTS

Here we evaluate the different mechanisms that may be involved in the layering process by computing transient energy growth on different types of vertically-invariant, time-dependent horizontal flows. These flows are computed by 2D direct numerical simulations of the Navier-Stokes equations, and the resulting evolution is stored and used as a vertically invariant base flow for computing three-dimensional (3D) optimal perturbations (maximizing perturbation energy growth in a prescribed evolution interval) with a direct-adjoint method [5]. We are thus able to identify and characterize, as a function of the vertical wavenumber and for each of the base flows considered, the mechanisms which are the most efficient in extracting energy from the vertically-invariant base flow to a 3D flow.

Figure 1 shows horizontal cuts of the vertical vorticity at different times of the evolution of optimal perturbations to a base flow composed of well separated vortices. The base flow was initialized at $t = 0$ with a superposition of four Gaussian vortices of the form $\pm 2\exp(-\boldsymbol{x}^2)$ initially located at random positions and indicated at later times by the dashed (negative vortices) and solid (positive vortices) black lines. The different columns in the figure correspond to different times during the evolution of the optimal perturbation. The different rows in the figure correspond to optimal perturbations with different Froude numbers $F_h = 1/N$ (where N is the Brunt-Väisälä frequency) and vertical wavenumbers k_z while keeping $F_h k_z$ in accordance to the inviscid scaling of strongly stratified flow [3]. The vorticity plots are very similar between the different rows, showing that the evolution of the optimal perturbations indeed satisfy the inviscid self-similarity.

At the final time of the evolution of the optimal perturbations shown in the example of figure 1 (right column for $t = 25$), it can be noted that the vertical vorticity corresponds to a simultaneous displacement of all the base flow vortices in a similar direction. This indicates that the zigzag instability is active in the example of the figure, as can be expected from the presence of well separated vortices. It will be seen that this 'zigzag-like' optimal perturbation is of no particular significance in

*Corresponding author. Email: cristobal.arratia@gmail.com

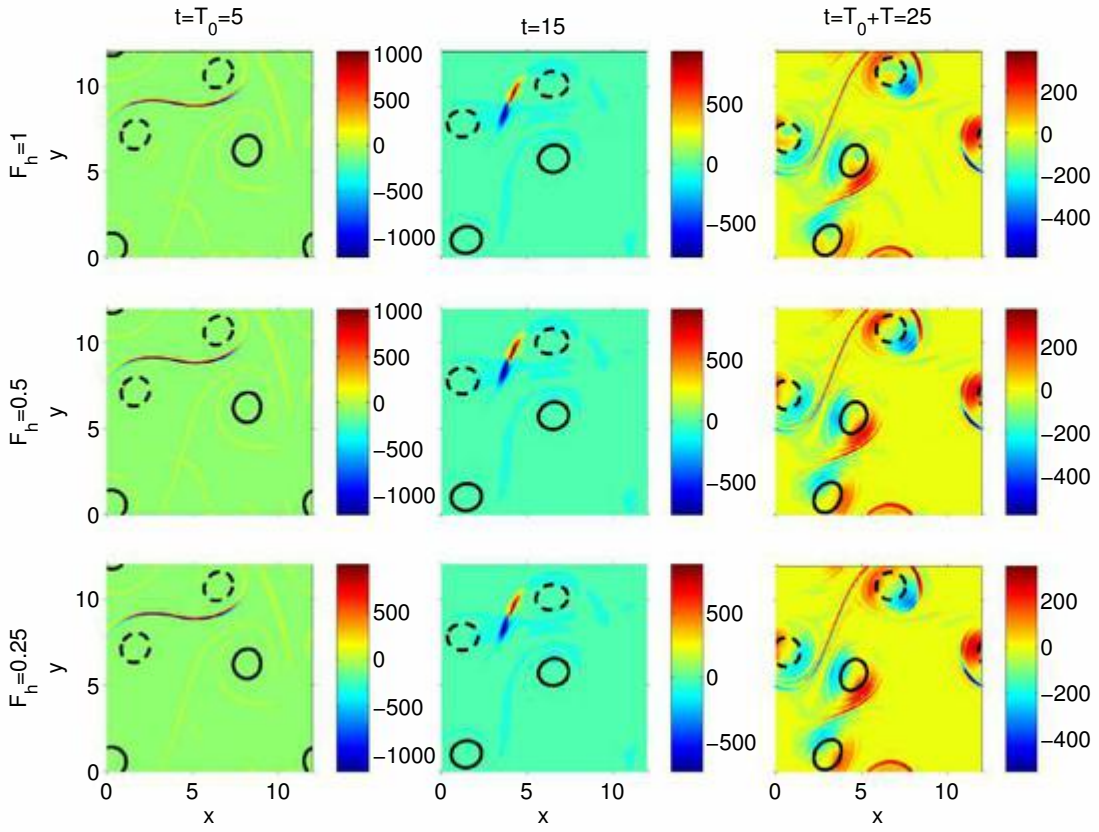

Figure 1: *Snapshots of the initial ($t = 5$, left column), intermediate ($t = 15$, middle column) and final ($t = 25$, right column) vertical vorticity of the optimal perturbation for $k_z F_h = 1.26$, and $F_h = 1$ (top), $F_h = 0.5$ (middle) and $F_h = 0.25$ (bottom). The solid (dashed) black lines correspond to iso-values where the vorticity of the instantaneous base flow is equal to 1 (-1).*

terms of energy growth, and that depending on the base flow and the vertical wavenumber, different and more efficient mechanisms are present in the optimal perturbations. These include but are not restricted to the 2D mode associated to the leading (finite time) Lyapunov exponent corresponding to the optimal perturbations associated to Lilly's mechanism. For the different types of base flow, strong energy extraction is remarkably found for short-wavelength perturbations, only limited by viscous effects. A poloidal-toroidal decomposition shows that this short-wavelength optimal perturbations are, initially, almost exclusively composed of toroidal energy, and at the final times their energy is predominantly poloidal. Thus, the corresponding mechanisms are associated to energy transfer from the predominant vortical flow to density perturbations and horizontally divergent flow.

References

[1] P. Billant and J.-M. Chomaz 2000 *Experimental evidence for a new instability of a vertical columnar vortex pair in a strongly stratified fluid*, J. Fluid Mech. **418**, 167 – 188.

[2] E. Lindborg 2006 *The energy cascade in a strongly stratified fluid*, J. Fluid Mech. **550**, 207 – 242.

[3] P. Billant and J.-M. Chomaz 2001 *Self-similarity of strongly stratified inviscid flows*, Phys. Fluids **13**, 1645 – 1651.

[4] D.K. Lilly 1983 *Stratified turbulence and the mesoscale variability of the atmosphere*, J. Atmos. Sci. **40**, 749 – 761.

[5] C. Arratia, C.P. Caulfield and J.-M. Chomaz 2013 *Transient perturbation growth in time-dependent mixing layers*, J. Fluid Mech. **717**, 90 – 133.

NONLINEAR EVOLUTION OF OPTIMAL PERTURBATIONS TO STRONGLY STRATIFIED SHEAR LAYERS

Alexis Kaminski*[1], Colm-cille Caulfield[1,2], and John Taylor[1]
[1]*Department of Applied Mathematics and Theoretical Physics, University of Cambridge, Cambridge, UK*
[2]*BP Institute, University of Cambridge, Cambridge, UK*

Summary Vertical mixing in the stably-stratified ocean interior is often assumed to arise due to shear instabilities. However, there is observational, experimental, and numerical evidence that suggests increased dissipation may also occur in more strongly stratified flows. The non-normality of the Navier-Stokes and buoyancy equations may allow for substantial perturbation energy growth at finite times, even in flows which are stable in the Miles-Howard sense. Here we show that this transient growth mechanism may be sufficient to trigger strongly nonlinear effects and breakdown into small-scale structures, thereby leading to enhanced dissipation and non-trivial modification of the background flow. The effects of nonlinearity are felt more strongly for higher Re and lower Ri_b. As such, this may point to transient non-normal growth as a possible linear mechanism to trigger turbulence and mixing in stably-stratified shear flows.

INTRODUCTION

Vertical mixing in the stably-stratified ocean interior is thought to be a key player in setting the vertical density structure and distributions of tracers which are important for climate and biogeochemical cycles. However, the turbulent eddies responsible for mixing are typically on the order of several meters in size, and are unresolved in ocean circulation models. Parameterizations of the physics leading to mixing are therefore required.

Mixing is often assumed to arise in the ocean interior as the result of shear instabilities. The Miles-Howard theorem states that, for parallel, steady, inviscid stratified shear flows, a necessary condition for instability is that the gradient Richardson number (the ratio of stratification, which stabilizes a flow, and shear, which destabilizes a flow) be less than 1/4 somewhere in the domain. This concept has been used as the basis of several mixing parameterizations which employ a critical Richardson number below which the effects of turbulence are felt. However, despite the correlation between enhanced dissipation and low Richardson numbers, there is observational [1, 2], experimental [3], and numerical evidence [4] suggesting that increased dissipation may also occur in more strongly-stratified flows.

LINEAR OPTIMAL PERTURBATIONS

The Miles-Howard theorem is based on the behaviour of normal-mode perturbations to a given steady inviscid parallel flow and their subsequent exponential growth rates. However, due to the non-normality of the Navier-Stokes operator, transient perturbation growth may be possible at finite times even when no normal-mode instabilities exist. By employing a direct-adjoint-looping technique, Kaminski et al. (2014) [5] computed the "linear optimal perturbations", i.e. the perturbations which maximize perturbation energy gain at a finite target time T, for a uniform stable stratification and hyperbolic-tangent shear layer. They considered a range of target times T and bulk Richardson numbers Ri_b (where, for the base state in question, Ri_b corresponded to the minimum gradient Richardson number of the flow) and showed that perturbation energy gains of $\mathcal{O}(10 \circ\ 100)$ could be achieved, even in flows which were were stable in the Miles-Howard sense.

Here, we consider the same base flow as in [5] and a target time of $T = 15$. Both the stratification Ri_b and the Reynolds number Re are varied. Higher gains are achieved for higher values of Re, as shown in figure 2(a), and for lower Ri_b. At this target time, the linear optimal perturbations found are two-dimensional and consist of a series of rolls tilted against the background shear (figure 1(a)). Perturbation energy grows via the Orr mechanism as the rolls are tilted upwards by the background shear (figure 2(b)).

NONLINEAR EVOLUTION

Given the substantial gains achieved via linear transient growth, it is natural to question what the nonlinear evolution of these perturbations might be. To examine this, the optimal perturbations computed for $T = 15$ are given small but finite initial amplitudes E_0 and used to initialize full direct numerical simulations. Random noise is also added to allow for the possibility of secondary instabilities arising. The full nonlinear Navier-Stokes and buoyancy conservation equations are solved using DIABLO, which employs a third-order mixed Runge-Kutta-Wray/Crank-Nicolson timestepper. The horizontal directions are periodic and treated pseudospectrally, while a second-order finite-difference discretization is used in the vertical [6].

We find that the perturbations initially grow linearly, as seen in figure 2(b). After this initial growth period, nonlinear effects become important and the perturbations saturate. In some cases, perturbations have grown enough to become susceptible to

*Corresponding author. Email: alexis.kaminski@gmail.com

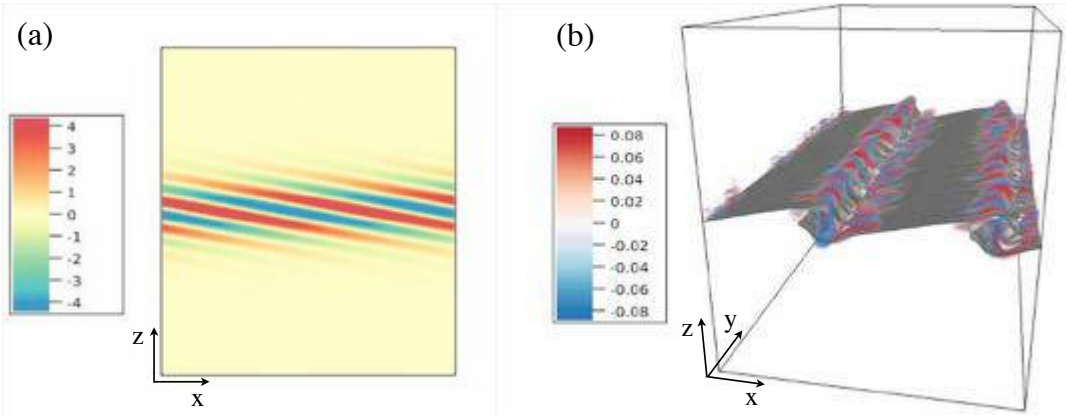

Figure 1: (a) Buoyancy perturbation of linear optimal perturbation for $Ri_b = 0.40$, $Re = 4000$, and $T = 15$. Note that the magnitudes are arbitrary. (b) Total buoyancy (isosurface) and vertical vorticity $\omega_z = \partial v/\partial x \circ \partial u/\partial y$ (colour) for $Ri_b = 0.40$, $Re = 4000$, and $E_0 = 2 \times 10^{-5}$ at $t = 24.4$. Note that only the region around the shear layer is shown and the aspect ratio is stretched in the vertical in order to better show the detailed structure in both (a) and (b).

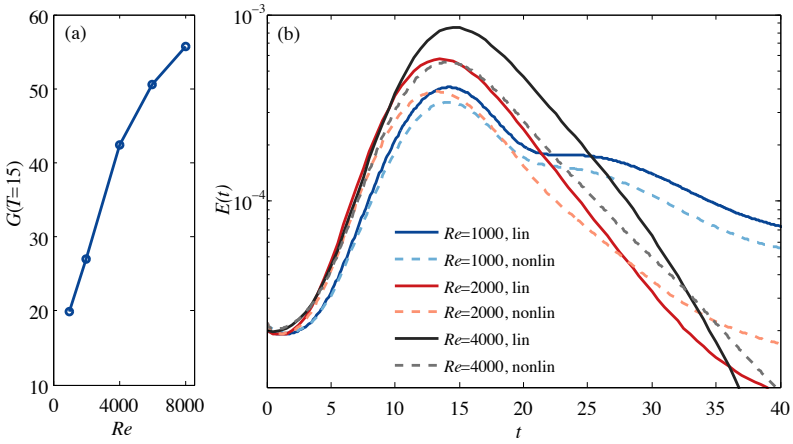

Figure 2: (a) Linear perturbation energy gains for $Ri_b = 0.40$ and $T = 15$. (b) Perturbation energy evolution for $Ri_b = 0.40$, $E_0 = 2 \times 10^{-5}$, and $Re = 1000$, 2000, and 4000. Linear perturbation evolutions are shown with solid lines, while dashed lines denote the perturbation energy from the full DNS.

secondary instabilities which then break down into small-scale turbulence. For example, in figure 1(b) (for which $Re = 4000$, $Ri_b = 0.40$, and $E_0 = 2 \times 10^{-5}$), we observe that after the rolls are tilted by the Orr mechanism, billows reminiscent of the classical Kelvin-Helmholtz instability form. These billows then become unstable to a three-dimensional secondary instability. We find that the effects of nonlinearity are more important for flows with higher Re, higher initial amplitude, and lower Ri_b.

As a result of the effects of nonlinearity, we find that the perturbations are able to modify the background flow non-trivially, leading to layer formation in the background buoyancy field. Enhanced kinetic energy dissipation is observed for higher-Re and lower-Ri_b flows, and the mixing efficiency, quantified here by the ratio of the potential energy dissipation to the total dissipation, $\varepsilon_p/(\varepsilon_p + \varepsilon_k)$, is found to be approximately 0.35 for the most strongly nonlinear cases.

References

[1] Polzin, K.: Statistics of the Richardson number: mixing models and finestructure. J. Phys. Oceanogr. 26:1409-1425, 1996.

[2] Mack, S.A. & Schoeberlein, H.C.: Richardson number and ocean mixing: towed chain observations. J. Phys. Oceanogr. 34:736-754, 2004.

[3] Augier, P., Billant, P., Negretti, M.E., & Chomaz, J.-M.: Experimental study of stratified turbulence forced with columnar dipoles. Phys. Fluids 26(4):046603, 2014.

[4] Riley, J.J. & deBruynKops, S.M.: Dynamics of turbulence strongly influenced by buoyancy. Phys. Fluids 15(7):2047-2059, 2003.

[5] Kaminski, A.K., Caulfield, C.P., & Taylor, J.R.: Transient growth in strongly stratified shear layers. J. Fluid Mech. 758:R4, 2014.

[6] Taylor, J.R.: Numerical simulations of the stratified oceanic bottom boundary layer. PhD thesis, University of California, San Diego, 2008.

HIGH FREQUENCY OBSERVATIONS OF TEMPERATURE AND DISSOLVED OXYGEN DURING UNDER-ICE CONVECTION IN LAKE SIMCOE

Bernard Yang[1], Joelle Young[2], Laura Brown[3]& Mathew Wells [1a)]
[1]*Department of Physical and Environmental Sciences, University of Toronto Scarborough, Scarborough, Ontario, Canada*
[2]*Environmental Monitoring and Reporting Branch, Ministry of the Environment, Toronto, Ontario, Canada*
[3]*Department of Geography, University of Toronto Mississauga, Mississauga, Ontario, Canada*

Summary High-frequency observations of thermal structure under the ice of a large lake reveal the presence of large (10-20 m) overturning convection cells, driven by solar heating. Two winters observations are used to quantify the under-ice mixing and dissolved oxygen dynamics. The most vigorous convection occurred near the end of winter, as the water surface layer started warming, with a gradually deepening of the mixed layer over time. This coincided with the prediction by the Canadian Lake Ice Model of when the ice cover began to melt and decrease in thickness. During the same period the dissolved oxygen had become super-saturated from the surface to 23 m below the surface, suggesting abundant algal growth. Thorpe scale analysis revealed that very large scale mixing occurred beneath the ice; the mixed layer depth increased during the melting period, and mixing was most active during the day.

INTRODUCTION

Vigorous circulation can occur under the surface of ice-covered lakes that is driven by the penetration of solar radiation. The extent of this circulation is strongly influenced by underlying inverse stratification that typically forms under ice: near the floating ice was is close to 0°C, while water at the base of lakes is near the density maximum of 4°C water near the bottom of the lake. Due to isolation of the water in an ice covered lake from the atmosphere it has often been assumed that circulation is very small. However heat fluxes through clear ice can drive very large overturn convection near the end of winter, as reviewed by [1]. The main goal of this study is to quantitatively investigate the effect of solar radiation penetrating through the ice on the magnitude of convection and how this influences the dissolved oxygen (DO) concentrations in ice-covered lakes. Specifically, we investigate how the surface mixing layer evolves near the end of the ice-cover period; and how mixing influence dissolved oxygen concentrations in lakes.

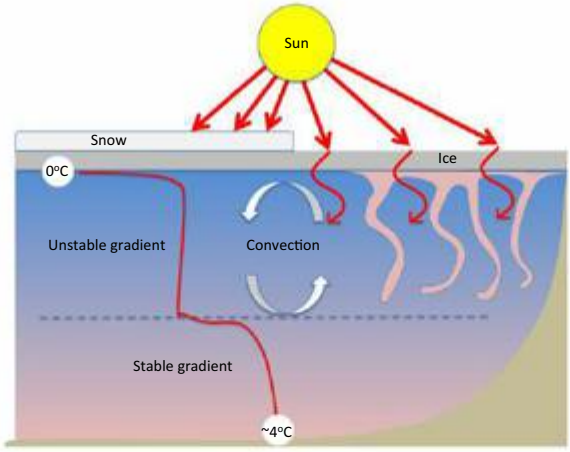

Figure 1: Schematic representation of under ice convection, showing how solar radiation penetrating through clear ice can drive heating of the water column. For water below 4°C such heating drives convective overturn of the water column (figure modified after [1]).

FIELD SITE AND METHODS

The field study was conducted in Lake Simcoe (44°25'N, 79°30'W), a large dimictic lake located in southern Ontario, Canada. A mooring with temperature and DO sensors was lowered between November 27, 2014 and April 27, 2015 into Lake Simcoe. Complete ice cover over the lake was observed between January 7 and April 25, 2015. The depth of the water column at the location of the mooring is about 42 m. The temperature loggers were configured to record at a spatial measurement interval of 2.5 m with the topmost one being at 5m deep on the rope. Each temperature logger samples at a frequency of 20 seconds. The DO loggers were configured at a spatial measurement interval of 7.5 m, with the topmost one being at 7.5 m deep. Each DO logger samples at a frequency of 30 minutes.

[a)] Corresponding author. Email: wells@utsc.utoronto.ca

We quantify the stability of the water column using two parameters, namely the buoyancy frequency and by estimations of Thorpe scales of density inversions. The buoyancy frequency N is defined by $N^2 = -(g/\rho_o)\, d\rho/dz$, where $g = 9.8\, m/s^2$ and $\rho_o = 1000\, kg/m^3$. Thorpe displacements were calculated by sorting the instantaneous density profile and tracking the distance moved by each water parcel. The minimum temperature difference we could resolve was twice the uncertainty of the accuracy of the temperature loggers. The corresponding instantaneous Thorpe scales were calculated by taking the root mean square of the Thorpe displacements. Buoyancy frequencies and Thorpe scales are calculated from the raw temperature data, and then smoothed with a 6-hour running average. The depth of the surface mixed layer beneath the ice was determined as the depth from the surface to where the buoyancy frequency first exceeds $N = 10^{-5}\, s^{-1}$

RESULTS

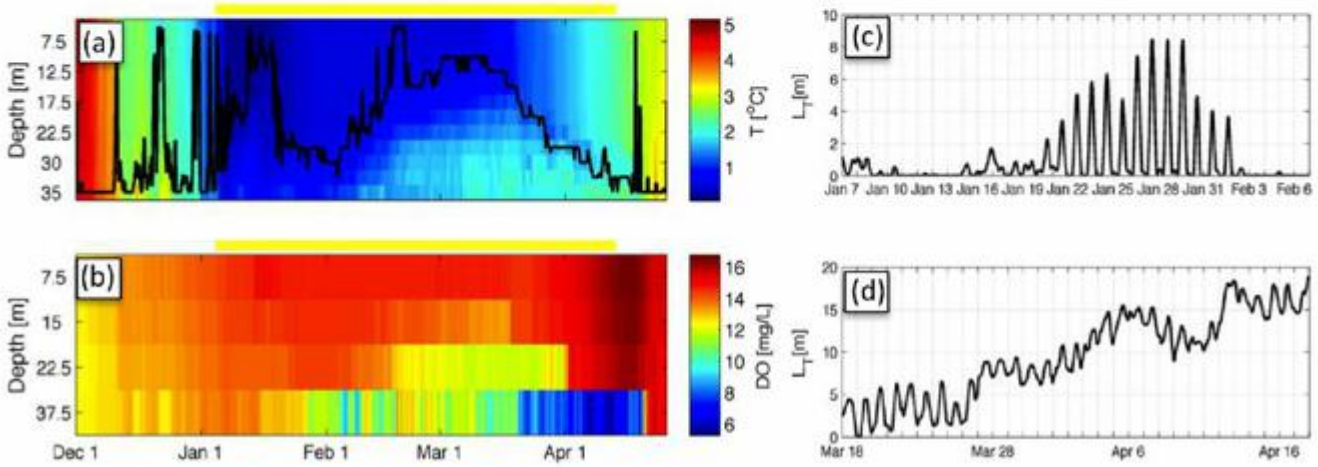

Figure 2: Water column temperature time series, black line indicates estimated mixed layer depth (a), DO concentration time series (b). Yellow bar on top of graph indicates ice cover. Calculated Thorpe scales between the periods January 7 to February 7 (c) and March 18 to April 18 (d).

Figure 2 shows that before the ice-cover period, the mixing layer spans the entire water column with overturns as large as 15-20 m occurring. Ice covered the lake on January 7, and there was a vigorous period of mixing from Jan 16 to 31st, after which the snow cover was sufficient to block any light. Calculations of Thorpe scales show that the water column is highly unstable in this period of time. From the time series of the Thorpe scales in this period of time, it is clear that there is a periodic behaviour of convection. In particular, the maximum Thorpe scales occur around noon, suggesting that the main driving mechanism of mixing is solar radiation. Between February 3 and March 18, the water column stratifies with warm water at the bottom and cold water at the top. The mixing layer shallows and DO concentrations decrease in the water column. The bottom levels of the water column gradually increase in temperature over this period, suggesting positive surface heat flux from the bottom. After March 18, steady increase in mixed layer depth and Thorpe scales are observed. The calculated Thorpe scales once again exhibit a periodic behaviour. DO concentrations in the water column homogenize as the mixed layer extends deeper. There is a clear increasing trend of DO in the mixing layer while the bottom stratified region still shows a decreasing trend of DO. This suggests algal growth in the water column. Algae then produce oxygen by photosynthesis. The maximum DO concentration observed in the water column is about 17 mg/L, which is supersaturated relative to the surface.

A new field deployment in the winter 2015/2016 includes a velocity meter, light sensor and faster response DO and T sensors. We use this new data to discuss the energetics of under-ice convective mixing in more detail in our presentation.

References

[1] Kirillin, G., Leppäranta, M., Terzhevik, A., Granin, N., Bernhardt, J., Engelhardt, C., Tatyana Efremova, T., Golosov, S., Palshin, N., Sherstyankin, P. , Zdorovennov, R. (2012). Physics of seasonally ice-covered lakes: a review. Aquatic sciences, 74(4), 659-682.

ENERGY CASCADE IN INTERNAL WAVE ATTRACTORS

Thierry Dauxois[1], C. Brouzet [*1], E. Ermanyuk[1,2], S. Joubaud[1], H. Scolan[3], and I. Sibgatullin[1,4,5]

[1]*Laboratoire de Physique, ENS de Lyon, Université de Lyon, CNRS, Lyon, France*
[2]*Lavrentyev Institute of Hydrodynamics, Novosibirsk, Russia*
[3]*Atmospheric, Oceanic and Planetary Physics, Department of Physics, University of Oxford, Oxford, UK*
[4]*Institute of Mechanics and Department of Mechanics and Mathematics, Moscow State University, Russia*
[5]*Shirshov Institute of Oceanology, Moscow, Russia*

Summary One of the pivotal questions in the dynamics of the oceans is related to the cascade of mechanical energy in the abyss and its contribution to mixing. Here, we propose a unique self-consistent experimental and numerical setup that models a cascade of triadic interactions transferring energy from large-scale monochromatic input to multi-scale internal wave motion. We also provide, for the first time, explicit evidence of a wave turbulence framework for internal waves. Finally, we show how beyond this regime, we have a clear transition to a cascade of small-scale overturning events which induce mixing.

The continuous energy input to the ocean interior comes from the interaction of global tides with the bottom topography yielding a global rate of energy conversion to internal tides on the order of 1TW. The subsequent mechanical energy cascade to small-scale internal-wave motion and mixing is a subject of active debate in view of the important role played by abyssal mixing in existing models of ocean dynamics. The oceanographic data support the important role of internal waves in mixing, at least locally: increased rates of diapycnal mixing are reported in the bulk of abyssal regions over rough topography in contrast to regions with smooth bottom topography. A question remains: how does energy injected through internal waves at large vertical scales induce the mixing of the fluid?

In a stratified fluid with an initially constant buoyancy frequency $N = [(-g/\bar{})(\mathrm{d}\rho/\mathrm{d}z)]^{1/2}$, where $\rho(z)$ is the density distribution over vertical coordinate z, and g the gravity acceleration, the dispersion relation is $\theta = \arcsin(\Omega)$. Here θ is the slope of the wave beam to the horizontal, and Ω (resp. $\omega = \Omega N$) is the non-dimensional (resp. dimensional) frequency of oscillations. The anisotropic dispersion relation requires preservation of the slope of the internal wave beam upon reflection at a rigid boundary. In the case of a sloping boundary, this property gives a purely geometric reason for a strong variation of the width of internal wave beams (focusing or defocusing) upon reflection. Internal wave focusing leads to shortening of wavelengths and amplification of wave amplitudes, which provides a necessary condition for large shear and overturning, as well as shear and bottom layer instabilities at slopes.

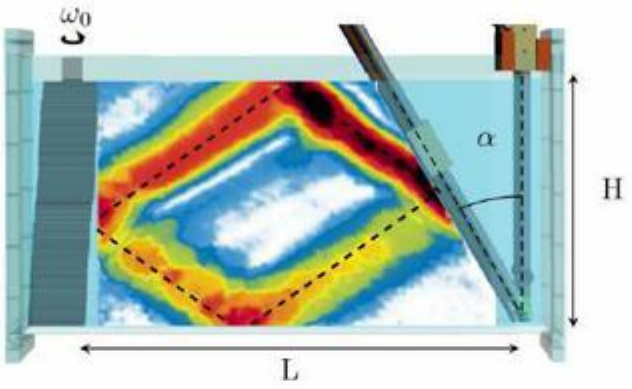

Figure 1: Experimental set-up showing the wave generator on the left and the inclined slope on the right. The color inset is a typical PIV snapshot showing the magnitude of the experimental two-dimensional velocity field obtained at $t = 15\ T_0$ with $T_0 = 2\pi/(N\Omega_0)$. Black dashed lines show the billiard geometric prediction of the attractor.

In a confined fluid domain, focusing usually prevails, leading to a concentration of wave energy on a closed loop, the internal wave attractor [1]. At the level of linear mechanisms, the widths of the attractor branches are set by the competition between geometric focusing and viscous broadening. High concentration of energy at attractors make them prone to parametric subharmonic instability (PSI) which sets in as the energy injected into the system increases [2]. The onset of instability in this case is similar to the classic concept of triadic resonance, which is best studied for the idealized case, with monochromatic in time and space carrier wave as a basic state which feeds two secondary waves via nonlinear resonant interactions. The

*Corresponding author. Email: Thierry.Dauxois@ens-lyon.fr

resonance occurs when temporal and spatial conditions are satisfied: $\Omega_1 + \Omega_2 = \Omega_0$ and $\overrightarrow{k_1} + \overrightarrow{k_2} = \overrightarrow{k_0}$, where $\overrightarrow{k}$ is the wave vector while subscripts 0, 1 and 2 refer to the primary, and two secondary waves, respectively. In a wave attractor, the wave beams serve as a primary wave, and the resonance conditions are satisfied with good accuracy [2], providing a consistent physical framework for the short-term behavior of the instability.

Using laboratory experiments and numerical simulations, we suggest the energy cascade in internal wave attractors as a novel laboratory model of a natural cascade. We show here that energy transfer from global to small scales in attractors operates via a hierarchy of triadic interactions producing a complex internal wave field with a rich multi-peak discrete frequency spectrum embedded in a continuous spectrum of weaker magnitude. Convincing evidence of a wave turbulence framework for internal waves is also provided for the first time. Spontaneous summation of the wave-field components produces moreover a statistically significant amount of extreme overturning events which eventually lead to an easily measurable mixing.

It is important to emphasize that the final stage of overturning and mixing is non-trivial since these phenomena are beyond the domain of pure wave-wave interactions, a regime usually called wave turbulence. A similar situation takes place for surface waves, where the flourishing literature gives a fully consistent description of energy cascades between components of wave spectra, only in the case of weakly nonlinear processes, while experimental reality deals with cascades significantly "contaminated" by effects of a finite size fluid domain, wave breaking, wave cusps, nonlinear dispersion, viscous damping of wave-field components, etc. The very specific dispersion relation for internal waves introduces additional complications. For instance, in rotating fluids, which have a dispersion relation analogous to stratified fluids, the usefulness of the formalism turbulence as a basis for the studies in rotating turbulence has been reported for experiments only recently [3]. For internal waves, the question is still fully open, from both experimental and numerical points of view. Its consequences on mixing were moreover widely open, until the present work.

Conclusion

We report and describe a novel experimental and numerical setup, an "internal wave mixing box", which presents a complete cascade of triadic interactions transferring energy from large-scale monochromatic input to multi-scale internal wave motion, and subsequent cascade to mixing. We report interesting signatures of discrete wave turbulence in a stratified idealized fluid problem. Moreover, we show how statistics of extreme vorticity events leads to mixing that occur in the bulk of the fluid.

References

[1] Maas, L.R.M., Benielli, D., Sommeria, J. & Lam, F.P.A. . Observations of an internal wave attractor in a confined stably stratified fluid. Nature 388:557-561, 1997.

[2] Scolan, H., Ermanyuk, E. & Dauxois, T.: Nonlinear fate of internal waves attractors. Physical Review Letters 110:234501 (2013).

[3] Yarom, E. & Sharon, E.: Experimental observation of steady inertial wave turbulence in deep rotating flows. Nature Phys. 10:510-514 (2014).

[4] Brouzet, C., Ermanyuk, E.V., Joubaud, S., Sibgatullin, I. & Dauxois, T.: Energy cascade in internal wave attractors. Submitted to Europhysics Letters (2016).

[5] Brouzet, C., Sibgatullin, I., Scolan, H., Ermanyuk, E.V. & Dauxois,T.: Internal wave attractors examined using laboratory experiments and 3D numerical simulations. Submitted to Journal of Fluid Mechanics (2016).

TIDAL FLUSHING OF SEMI-ENCLOSED BASINS

GertJan van Heijst[a], Leon Kamp, Matias Duran Matute & Stan Thorez
Department of Physics, Eindhoven University of Technology, The Netherlands

Summary The tidal flushing of coastal basins is studied both experimentally and numerically. Two key parameters are the shape of the basin and the position of the connection to the open sea. For the case of a rectangular basin, the opening position has been varied systematically, and three different flow regimes have been observed, with different flushing characteristics.

INTRODUCTION

Partly enclosed coastal basins, such as harbours and estuaries, usually have one or more connections to the open sea. Through these connections, coastal basins are subjected to marine influences like tides, which lead to the generation of residual circulation patterns. The tidally induced flow through the opening between the coastal basin and the open sea has an asymmetric structure, being essentially a potential sink flow towards the opening, while the outflow on the other side has the character of a jet, often with a dipolar vortex structure at its head. Such a dipolar vortex, when strong enough, may propagate into the basin, due to its self-propelling mechanism, and may thus greatly influence the exchange of matter between the coastal basin and the open sea. The propagation of such dipolar flow structures in an oscillating tidal flow has previously been studied in the laboratory by Kashiwai (1984), who argued that the tidal dipoles can propagate away from the opening region if the dimensionless parameter W/UT (with U the maximum velocity, W the width of the opening, and T the tidal period) is larger than some critical value. This analysis was later extended by Wells & van Heijst (2003), and the analytical predictions were verified by their laboratory observations. In later studies by Nicolau del Roure et al. (2009) the effect of the inlet geometry was investigated.

The asymmetry between the periodic jet-like inflow, together with the self-propelling dipolar vortex structures, and the sink-type outflow may result in the generation of a residual circulation in the coastal region. In a recently started study, we have studied this issue in detail by a combination of laboratory experiments and two-dimensional (2D) numerical simulations. It was found that the shape of the basin and the positioning of the inlet/outlet opening has a profound effect on the resulting circulation pattern, and hence on the flushing of the basin. Some results of this study will be presented here.

LABORATORY EXPERIMENTS AND NUMERICAL SIMULATIONS

Laboratory experiments have been performed in a rectangular container (length L_0 = 1 m, width W_0 = 0.5 m) filled with a layer of fresh water. In order to minimize the effects of bottom friction, an additional layer (thickness 1 mm) of salty fluid was added, so that the total fluid depth measured H = 11 mm. The experimental configuration is shown in Figure 1. The tidal motion is generated by moving a partially submerged cylindrical weight harmonically up and down. The frequency of this harmonic motion was low enough to prevent gravity waves being formed. A barrier with a narrow opening was placed in the tank, thus separating the 'coastal basin' from the 'open sea', in which the tidal motion is generated. The shape of the opening plays a crucial role in the generation of the exchange flow. The present study focusses on the case of a thin-walled separating barrier, with sharp edges at the sides of the opening. Flow visualization experiments were performed in order to obtain a clear qualitative picture of the overall flow (structure of inflow and outflow, vortex formation, structure of the residual circulation pattern). Detailed quantitative information about the flow was obtained by PIV measurements.

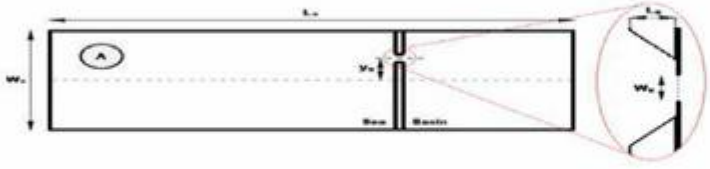

Figure 1 Experimental configuration.

Numerical simulations of the tidal exchange flow in this geometry were performed by using the COMSOL Multiphysics modelling software. The simulations were carried out for the 2D case, so neglecting any effects and velocities in the vertical direction. The tidal motion was introduced by prescribing a harmonically varying in/outflow at the far end of the 'open sea' region of the flow domain. This in/outflow results in a harmonically changing free-surface level of the fluid, and hence in a harmonically changing horizontal divergence. In all simulations, no-slip conditions were imposed at the boundaries of the coastal basin.

In the present study the position of the opening of the barrier was varied. This position is given by the coordinate y_g, measured from the long (symmetry) axis of the domain. The gap position was varied from y_g = 0 (corresponding to a symmetric configuration, with the gap on the symmetry axis of the domain) to y_g = 7.5 (corresponding to the opening touching the side wall).

[a] Corresponding author. Email: g.j.f.v.heijst@tue.nl

RESULTS

The simulations, carried out for y_g = 0, 1.35, 2.7, 4.05, 5.4 and 6.75, with the non-dimensional gap width fixed at the value W_g = 0.5, revealed the occurrence of three different flow regimes The first regime is observed for the symmetric opening position y_g = 0. During the first few tidal periods, the flow is symmetric with respect to the long domain axis. The starting dipole travels straightforward, towards the end wall of the coastal basin, and subsequent dipoles catch up with the previous ones, thus forming a larger dipolar structure that tends to fill the coastal basin. After approximately 15 periods, this pattern changes: the symmetry is broken and the flow changes into one large domain-filling circulation cell. Newly arriving dipoles are deflected by the circulating flow, thus further forcing this cellular motion.

The second regime is observed for the gap positions y_g = 1.35, 2.7, 4.05 and 5.4, so not on the centreline (y_g = 0) and not touching the sidewall (y_g = 6.75). The flow pattern observed for these y_g-values after 200 periods is shown in Figure 2. After a few tidal cycles, a single cell is formed, which appears to be very robust. The circulation Γ of this cell was found to be significantly larger than that of the cell observed in regime 1. A circulation pattern consisting of two oppositely rotating cells is established in the 'open sea' part of the domain. The occurrence of these cells is determined by the presence of the solid boundaries in this model system.

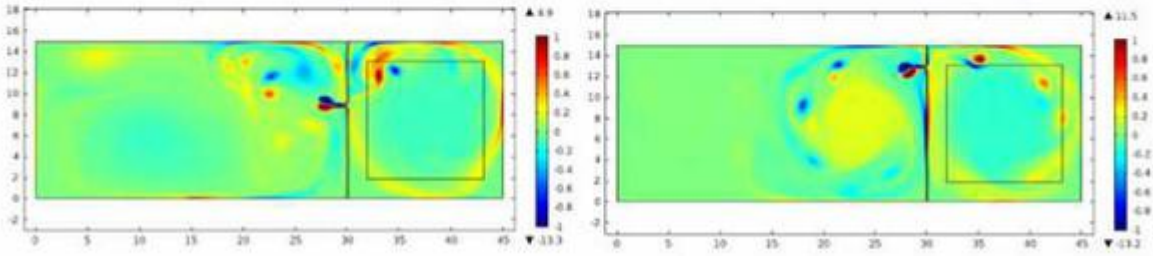

Figure 2 Vorticity distribution after 200 periods for y_g = 1.35 (left) and y_g = 5.4 (right), corresponding with regime 2.

The third flow regime is observed for the case y_g = 6.75, so with the gap touching the side wall. Very soon after the tidal forcing has started, the dipoles are deflected to the centre of the basin and then follow a curved trajectory back towards the gap. Boundary-layer vorticity generated at the no-slip sidewall is partially taken up into the dipole, thus giving it a negative net circulation and hence resulting in a curved trajectory. Although one observes also a larger cell filling the basin, this cell is much weaker than that found in regime 2.

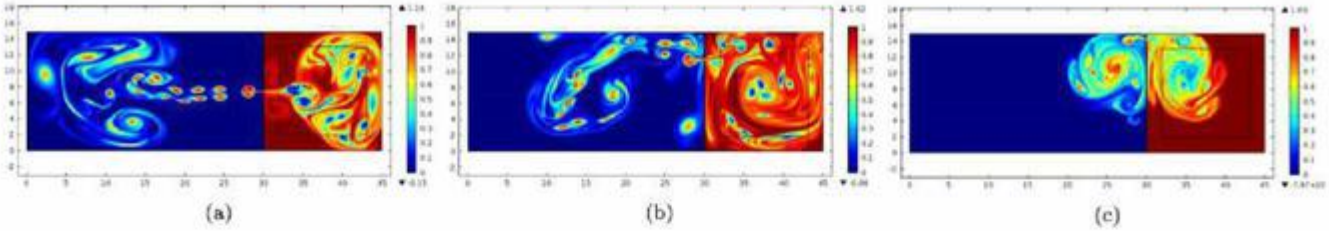

Figure 3 Tracer distributions after 25 periods for y_g = 0 (a), 4.05 (b), and 6.75 (c).

In order to examine the flushing characteristics, the transport of a tracer with concentration c was simulated by numerically solving the 2D advection-diffusion equation for c, with initial concentrations c = 0 in the 'open sea' and c = 1 in the 'coastal basin'. Figure 3 shows some typical results, with the concentration values varying between 0 (blue) and 1 (red), as indicated by the colour bars. It is obvious that the most efficient flushing of the coastal basin is obtained in regime 2. Putting the opening symmetrically (y_g = 0) or touching the side wall (y_g = 6.75) leads to locally good mixing, but with large portions of the domain still having their initial concentration values.

CONCLUSIONS

The tidal flushing characteristics of a coastal basin are highly determined by the geometry of the basin, and in particular the position of the inlet/outlet.

References

[1] Kashiwai M.: J. Oceanogr. Soc. Japan **40**, 437-444, 1984.

[2] Wells M.G., van Heijst G.J.F.: Dyn. Atmos. Oceans **37**, 223-245, 2003.

[3] Nicolau del Roure F., Socolofsky S.A., Chang K.-A.: J. Geophys. Res. **114**, C05024.

SUPPRESSION OF THE RAYLEIGH-TAYLOR INSTABILITY BY ROTATION

Matthew M. Scase*[1], Kyle A. Baldwin[2], and Richard J. A. Hill[2]
[1]*School of Mathematical Sciences, University of Nottingham, Nottingham, UK*
[2]*School of Physics and Astronomy, University of Nottingham, Nottingham, UK*

Summary The effect of rotation upon the classical Rayleigh-Taylor instability is considered both theoretically and using superconducting magnets in a novel experimental configuration. We show that in many cases, rotating the system above a critical rate associated with the mode's wavelength, the Atwood number and the flow's aspect ratio may stabilize unstable axisymmetric wave modes. The growth rate of the instability and its dominant lengthscale may be significantly reduced by rotation.

Experiments conducted in a magnetic field with 'heavy' diamagnetic and 'light' paramagnetic fluids are used to show the effects of rotation and to compare with our theoretical predictions. By rotating the system the growth rate of the instability is typically suppressed and the scale of the structures observed are significantly reduced. We investigate the effect of increasing fluid viscosity on the observed structures and conclude that both rotation rate and fluid viscosity control the form of the instability that develops.

INTRODUCTION

The Rayleigh-Taylor instability is a fundamental fluid dynamical phenomenon that occurs at the interface between a dense fluid supported by a lighter fluid under gravity, or, equivalently, in a system that is accelerating in the direction of the denser fluid. The instability is a common occurrence in many geo- and astrophysical phenomena including, for example, the finger-like structures of the Crab nebula, created by the acceleration of pulsar winds through a dense supernova remnant [**?**], and salt tectonics, where deep salt sediments protrude upwards through denser rock into finger-like 'diapirs' [**?**]. The instability appears in many industrial applications involving, for example, thin film flows, pool boiling and aerosol transport [see e.g., 3]. In some cases we may wish to influence the Rayleigh-Taylor instability through means beyond imposing the initial density difference. In particular there are many situations in which it is desirable to stabilize a system, as in inertial confinement fusion. Here we investigate the effect of rotation on the system.

MODELLING

We consider a fluid system that consists of a two-layer gravitationally unstable stratification that is subject to steady rotation about an axis parallel to the direction of gravity. A rotating fluid is known to organize itself into coherent vertical

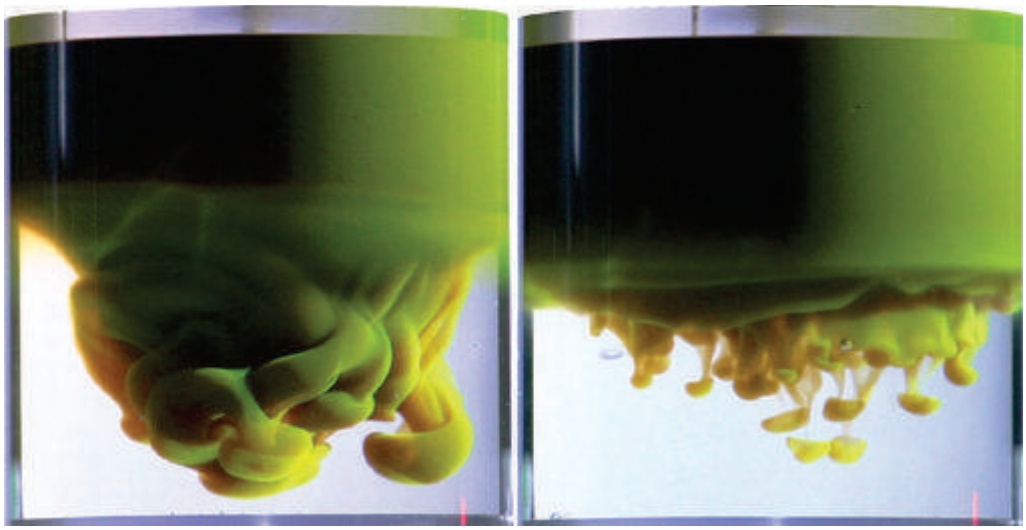

Figure 1: The image on the left hand side is of the Rayleigh-Taylor instability developing in a non-rotating system. The instability develops in time, forming large vortices that transport the 'denser' (green) fluid downwards. The image on the right hand side is of the same fluids, but here the system is rotating. The effect of the rotation can be seen to restrict the size of the vortices that form and inhibit the bulk vertical transport of fluid.

structures aligned with the axis of rotation, so-called 'Taylor columns' [**?**], whereas a perturbation to an unstable two-layer density stratification will lead to baroclinic generation of vorticity at the interface, tending to break-up any vertical structures.

*Corresponding author. Email: matthew.scase@nottingham.ac.uk



Figure 2: Images from a series of experiments investigating the role of viscosity in determining the scale of instability observed. The rotation rate was fixed at $\Omega = 7.8 \pm 0.1\,\mathrm{rad\,s^{-1}}$. The left image shows the instability in a system that has viscosity approximately equal to that of water. The middle image shows the instability in a system that has viscosity approximately 8.36 times that of water. In the right hand image the viscosity of the system is approximately 20.50 times that of water. It can be seen that the observed length scale increases with increasing fluid viscosity.

Hence the system under investigation undergoes competition between the destabilizing effect of the denser fluid overlying the lighter fluid that generates an overturning motion at the interface, and the stabilizing effect of the rotation that is organizing the flow into vertical structures and preventing the two layers passing each other. With increased rotation rate the ability of the fluid layers to move radially, with opposite sense to each other, in order to rearrange themselves into a more stable configuration, is increasingly prohibited by the Taylor-Proudman theorem [**?**, **?**]. The radial movement is therefore reduced and the observed structures that materialize as the instability develops are smaller in scale.

We model the system using an unpublished variational approach that represents the governing wave equation and the associated boundary conditions as stationary points of a multivariate functional. It can be shown that in the appropriate limits the well-known results for gravity waves in both non-rotating and rotating systems, and the classical non-rotating Rayleigh-Taylor instability can be recovered. We are also able to show that in a finite domain there exists a critical rotation rate above which axisymmetric modes may be stabilized. This demonstrates that although Chandrasekhar's statement [**?**] that '... rotation does not affect the instability or stability, as such, of a stratification' applies in the limiting case of an infinite aspect ratio, any confinement of the flow, i.e., a finite aspect ratio, permits the stabilization of modes of instability by rotation of the system.

EXPERIMENTAL VALIDATION

In order to compare our experiments with theory we show that the additional magnetic effects that modify the stress tensor in the fluid may be regarded as a modified gravitational field. In this way we are able to create a gravitationally stable stratification and spin it up into solid body rotation. We are then able to use the magnet to create a modified gravitational field that renders the interface unstable such that the fluid system behaves, to a good approximation, as a classical Rayleigh-Taylor instability. We show that there is good agreement between our theoretical prediction for the stabilization of the dominant axisymmetric mode of instability and our experimental observations. We are also able to demonstrate good agreement between the predicted growth rate of the instability and our observations. At high rotation rates large-scale structures in the instability are inhibited and the dominant lengthscale of the instability is controlled by the fluid viscosity (figure 2). We conclude that the observed nature of the instability is determined by both the rotation rate of the system and the fluid's viscosity.

References

[1] CHANDRASEKHAR, S. 1961 *Hydrodynamic and Hydromagnetic Stability*. New York: Dover.

[2] GELFAND, J. D., SLANE, P. O. & ZHANG, W. 2009 A dynamical model for the evolution of a pulsar wind nebula inside a nonradiative supernova remnant. *Astrophys. J.* **703**, 2051.

[3] LIMAT, L. *et al.* 1992 Gravitational instabilities of thin liquid layers: dynamics of pattern selection. *Physica D* **61**, 166–182.

[4] PROUDMAN, J. 1916 On the motion of solids in a fluid possessing vorticity. *Proc. Roy. Soc. Lond. A* **92** (642), 408–424.

[5] TAYLOR, G. I. 1917 Motion of solids in fluids when the flow is not irrotational. *Proc. Roy. Soc. Lond. A* **93** (648), 99–113.

[6] TAYLOR, G. I. 1923 Experiments on the motion of solid bodies in rotating fluids. *Proc. Roy. Soc. Lond. A* **104**, 213–218.

[7] ZALESKI, S. & JULIEN, P. 1992 Numerical simulation of Rayleigh-Taylor instability for single and multiple salt diapirs. *Tectonophysics* **206**, 55–69.

INSTABILITIES OF BAROCLINIC VORTICES IN STRATIFIED-ROTATING FLUIDS

Eunok Yim*[1], Paul Billant[1], and Claire Ménesguen[2]
[1]*LadHyX, CNRS, École polytechnique, Palaiseau, 91128, France*
[2]*LPO, IFREMER, CNRS, BP 70, 29280 Plouzané, France*

Summary We investigate the stability of an axisymmetric pancake vortex in a continuously stratified and rotating fluid. The characteristics and domains of existence of the different instabilities are determined as a function of the Froude number F_h, Rossby number Ro, aspect ratio α and Reynolds number Re. The centrifugal instability is almost independent of the aspect ratio of the vortex due to its short-wavelength nature and depends mostly on the Rossby number Ro and the buoyancy Reynolds number $\mathcal{R} = ReF_h^2$. The shear instability exists for the azimuthal wavenumber $m = 2$ only when F_h/α is below a threshold depending on Ro. This condition comes from confinement effects along the vertical. The shear instability transforms into a mixed baroclinic-shear instability when the Burger number $Bu = \alpha^2 Ro^2/(4F_h^2)$ is smaller than unity. The baroclinic instability develops when $F_h/\alpha|1 + 1/Ro| > 1.46$ in qualitative agreement with an analytical model.

INTRODUCTION

In stably stratified rotating fluids, vortices have a pancake shape with a small thickness compared to their radial extent. An example is the Mediterranean eddies (Meddies) which are formed by salty water flowing from the Mediterranean sea into the Atlantic ocean [1, 2]. The stability of such vortices has been studied with multi-layer models under the quasi-gesotrophic or shallow water approximations [3, 4, 5]. More recently, continuously stratified non-rotating fluids [8, 9, 10] or quasi-geostrophic fluids [6, 7] have been considered. In order to link these two limits, the linear stability of an isolated axisymmetric pancake vortex is studied here in a continuously stratified fluid with arbitrary background rotation.

METHODS

The base vortex is chosen to have a Gaussian angular velocity profile in radial (r) and vertical (z) directions

$$\Omega = \Omega_0 \exp\left(\circ \frac{r^2}{R^2} \circ \frac{z^2}{\Lambda^2} \right), \tag{1}$$

where Ω_0 is the maximum angular velocity, Λ the half thickness and R the radius. The base density inside the vortex is deduced from the thermal-wind relation. The stability problem is solved numerically by discretizing the linearized Boussinesq equations with finite element methods and by solving the eigenvalue problem with the Krylov-Schur method of SLEPc library [11]. The most unstable modes have been determined as a function of azimuthal wavenumber m, Froude number $F_h = \Omega_0/N$, Rossby number $Ro = \Omega_0/\Omega_b$, Reynolds number $Re = \Omega_0 R^2/\nu$ and aspect ratio $\alpha = \Lambda/R$, where N is the Brunt-Väisälä frequency, Ω_b the ambient rotation and ν the viscosity. The Schmidt number $Sc = \nu/\kappa$ (where κ is the mass diffusivity of the stratifying agent) is set to unity.

RESULTS

The pancake vortex is unstable to many kinds of instabilities depending on the azimuthal wavenumber, Froude and Rossby numbers. As an example, Figure 1a shows the domains of existence of each instability for the azimuthal wavenumber $m = 2$ in the parameter space $(F_h/\alpha, Ro)$. The corresponding eigenmodes are displayed in Figure 1b-e. The origin of each instability has been identified thanks to stability criteria or from their resemblance with the instabilities in the columnar limit ($\alpha \to \infty$). The centrifugal instability (Fig. 1b) exists for the azimuthal wavenumbers $m = 0, 1, 2$ when the Rossby number $|Ro|$ is larger than a critical value such that the generalized Rayleigh discriminant is negative. For a given Rossby number, its maximum growth rate is almost independent of the aspect ratio α and scales mostly as $\mathcal{R}^{-1/3}$ where $\mathcal{R} = ReF_h^2$ is the Buoyancy Reynolds number. For a given Reynolds number, the centrifugal instability is therefore stabilized for small Froude number (Fig. 1a). The shear instability (Fig. 1b) due to the radial shear exists for $m = 2$ when the vertical Froude number F_h/α is below a threshold depending on the Rossby number (Fig. 1a). This condition derives directly from the fact that the shear instability for a columnar vortex exists only in the vertical wavenumber band $0 \leq kRF_h \leq c(Ro)$, where $c(Ro)$ is a constant depending on Ro. The pancake vortex should be therefore tall enough so that the minimum vertical wavenumber fitting inside the pancake vortex, $kR \simeq \pi/\alpha$, is unstable, i.e. $F_h/\alpha \leq c(Ro)/\pi$. When the Burger number $Bu = \alpha^2 Ro^2/(4F_h^2)$ is smaller than unity, the shear instability transforms continuously into a mixed baroclinic-shear instability (Fig. 1a). The eigenmode of the latter instability (Fig. 1d) resembles the shear instability one (Fig. 1c) but its energy source is the potential energy of

*Corresponding author. Email: eunok@ladhyx.polytechnique.fr

the base flow instead of the kinetic energy. A similar mode has been found by [7] in the quasi-geostrophic limit. The pure baroclinic instability (Fig. 1e) exists for $F_h/\alpha|1+1/Ro| \geq 1.46$ (Fig. 1a), just below the threshold for the gravitational instability [9], i.e. when the isopycnals of the base vortex are almost about to overturn. It can destabilize a large band of azimuthal wavenumbers $m \geq 1$. An analytical model consisting in a bounded vortex with an angular velocity only varying slowly in the vertical direction shows that this threshold comes from confinement effects. This model further shows that the maximum growth rate and the most amplified azimuthal wavenumber of the baroclinic instability scale as $F_h/\alpha|1+1/Ro|$ in good agreement with the numerical results. For the azimuthal wavenumber $m = 1$ (not shown), there exists an additional instability: the Gent-McWilliams instability [12] which bends the vortex. It continuously changes into a mixed baroclinic-Gent-McWilliams instability for Burger number below unity, as reported by [7] in the quasi-geostrophic limit. Comparison to oceanic observations will be discussed.

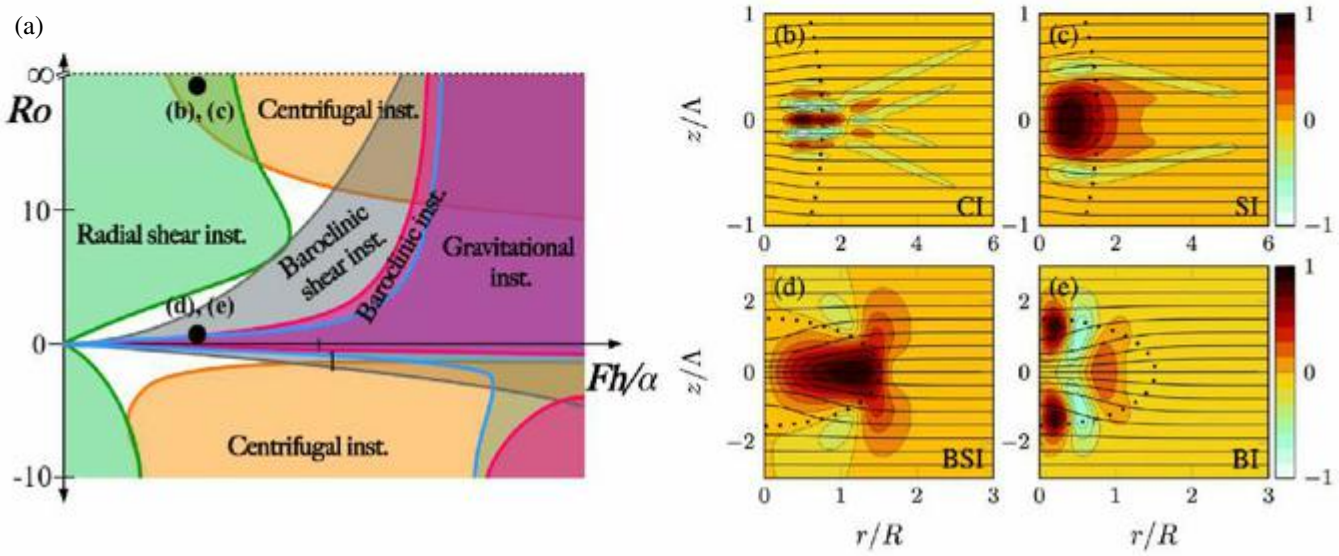

Figure 1: (a) Stability map as a function of the vertical Froude number F_h/α and the Rossby number Ro for $m = 2$ and $Re = 10000$: — gravitational instability, — centrifugal instability, — horizontal shear instability, — baroclinic shear instability and — baroclinic instability. Real part of the radial velocity perturbation $\mathrm{Re}(u_r)$ of the (b) centrifugal instability for $Ro = 20$, (c) shear instability for $Ro = 20$, (d) baroclinic-shear instability for $Ro = 0.25$ and (e) baroclinic instability for $Ro = 0.25$ for $m = 2$, $\alpha = 1.2, F_h = 0.5$ and $Re = 10000$. The dotted line indicates the extension of the base flow where $\Omega = 0.1\Omega_0$. Horizontal lines represent isopycnals.

References

[1] Armi L., Hebert D., Oakey N., Price J. F., Richardson P. L., Rossby H. T., Ruddick B.: Two years in the life of a mediterranean salt lens. J. Phys. Oceanogr. 19: 354-370, 1989.

[2] Hobbs R.: A new tool to understand the thermal structure and dynamics of oceans. European Union Newsletter, 2, 2007.

[3] Baey J.M., Carton X.: Vortex multipoles in two-layer rotating shallow-water flows. J. Fluid Mech. 460: 151-175, 2002.

[4] Benilov E.: Instability of quasi-geostrophic vortices in a two-layer ocean with a thin upper layer. J. Fluid Mech. 475: 303-331, 2003.

[5] Lahaye N., Zeitlin V.: Centrifugal, barotropic and baroclinic instabilities of isolated ageostrophic anticyclones in the two-layer rotating shallow water model and their nonlinear saturation. J. Fluid Mech. 762: 5-34, 2015.

[6] Hua B.L., Menesguen C., Le Gentil S., Schopp R., Marsset B., Aiki H.: Layering and turbulence surrounding an anticyclonic oceanic vortex: in situ observations and quasi-geostrophic numerical simulations J. Fluid Mech. 731:418-442, 2013.

[7] Nguyen H.Y., Hua B. L., Schopp R., Carton X.: Slow quasigeostrophic unstable modes of a lens vortex in a continuously stratified flow. Geophys. Astrophys. Fluid Dyn. 10:14-19, 2010.

[8] Beckers M., Verzicco R., Clercx H. J. H., van Heijst G. J. F.: Evolution and instability of monopolar vortices in a stratified fluid. Phys. Fluids 15:1033-1045, 2003.

[9] Negretti E.M., Billant P.: Stability of a gaussian pancake vortex in a stratified fluid. J. Fluid Mech. 718:457-480, 2013.

[10] Yim E., Billant P.: Analogies and differences between the stability of an isolated pancake vortex and a columnar vortex in stratified fluid. J. Fluid Mech. 796:732-766, 2016.

[11] Garnaud X.: Modes, transient dynamics and forced response of circular jets. PhD. thesis, Ecole Polytechnique Palaiseau, France, 2012.

[12] Gent P.R., McWilliams J.C.: The instability of barotropic circular vortices. Geophys. Astrophys. Fluid Dyn. 35:209-233, 1986.

INTERACTION OF A SURFACE QUASI-GEOSTROPHIC BUOYANCY STRIP AND AN INTERNAL VORTEX

Jean N. Reinaud *[1], David G. Dritschel[1], and Xavier Carton[2]
[1]*University of St Andrews, UK*
[2]*Université de Bretagne Occidentale, France*

Summary We consider the interaction between a surface buoyancy strip and an internal vortex. This research investigates the coupling between the observable ocean surface and the less well observed deeper ocean. We show that the strip?vortex interaction depends on the ratio of the time scales of the two features, and on their relative displacement (horizontally and vertically). Intense buoyancy strips break down rapidly once perturbed by the vortex, whereas weak strips tend to wrap due to the vortex rotation. When the vortex is close to the surface and below an intense strip, the vortex may destabilise and break into smaller vortices. Importantly, the interaction depends on the sign of the buoyancy strip relative to that of the internal vortex. Above a cyclone, a surface strip with positive buoyancy rolls up into a spiral filament, while a strip with negative buoyancy forms a row of billows on both sides of the vortex.

INTRODUCTION

The availability of data at the ocean's surface has increased both in quantity and quality with the increase of satellite measurements. These data provide detailed information about the ocean surface dynamics, from which one may infer information on the internal dynamics, invisible to direct satellite observations. Our ability to relate the surface dynamics to the interior dynamics greatly depends on our theoretical understanding of the coupling and interaction between the two. At meso-scales, the dynamics of the surface alone is well documented, in particular within the context of the Surface Quasi-Geostrophic (SQG) model, see [1,2] for buoyancy strips. It should be noted that SQG remains relevant at submeso-scales. Similarly, the dynamics of internal vortices under the quasi-geostrophic approximation is now well known, see [3] for isolated ellipsoidal vortices. Much less is known, however, for the coupled system. Perrot *at al* [4] studied the interaction between a internal vortex and an elliptical patch of buoyancy at the surface. Here we consider a different situation where the surface elliptical patch is replaced by a strip of buoyancy, modelling a filament. The main difference is that the (isolated) strip is always intrinsically unstable, while an elliptical surface vortex is stable for aspect ratios < 2.34 [5]. The internal vortex is taken to be spherical (after stretching by the ratio of buoyancy to Coriolis frequencies), implying it is stable if taken alone. We investigate the influence of the relative sign of the buoyancy anomaly with respect to the sign of the vortex as well as their displacement.

RESULTS

We consider a strip of buoyancy anomaly b of half-width $a = 0.5$ located at the top surface of a $(2\pi)^3$ computational domain. The transverse buoyancy profile is $b = b_m\sqrt{1 \circ (x/a)^2}$, leading to a linear profile of velocity within the strip, $v(x) = \frac{b_m}{a}x. |x| < a$. The linear stability of the strip has been examined, and we find that the strip is unstable to perturbations with wavenumber $k \in [0, k_{max}]$, $k_{max} \simeq 1.1/a$. The most amplified mode has $k \simeq 0.73/a$. The domain is periodic in both horizontal coordinates. A sphere of uniform potential vorticity $q = 1$, of radius $r = a$, is centred at a depth H from the surface and is displaced horizontally from the central axis of the strip by a distance ϱ. In this study we investigate the influence of b_m, H and ϱ on the dynamics of the interaction.

Simulations are performed using the Contour-Advective Semi-Lagrangian algorithm described in [4] and references therein. The coarse grid on which the interior velocity field is obtained has a resolution of 256^3 while is it 1024^2 at the surface where smaller scale features are expected.

Figure 1 illustrates the interaction in cases where there is no horizontal displacement between the surface strip and the internal vortex. By symmetry, the centroid of the vortex remains at the centre of the domain. For small values of b_m, the strip is nearly passive and is wound up by rotating vortex. The strip will eventually destabilise once it gets sufficiently thin. The vortex remains almost exactly spherical throughout the simulation. The shear flow induced by the strip is not strong enough to disrupt the vortex. On the other hand, we see a topological differences between the cases $b_m > 0$ and $b_m < 0$, even for small values of $|b_m|$. Buoyancy tends to accumulate directly above the vortex when $b_m < 0$, in a region of cooperative shear, and is depleted from this region when $b_m > 0$ (adverse shear). The reason for this behaviour becomes clearer with increasing $|b_m|$, and is related to the destabilisation of the strip. The vortex first deforms the strip. In the case $b_m > 0$, the deformation of the strip above the vortex initiates a saddle point between two consecutive billows along the strip while in the case $b_m < 0$ it seeds the formation a billow (again due to the cooperative shear). For an intense strip, the shear induced by the strip is able to deform, and even tear the vortex apart. This effect is more pronounced in adverse shear.

*Corresponding author. Email: jean.reinaud@st-andrews.ac.uk

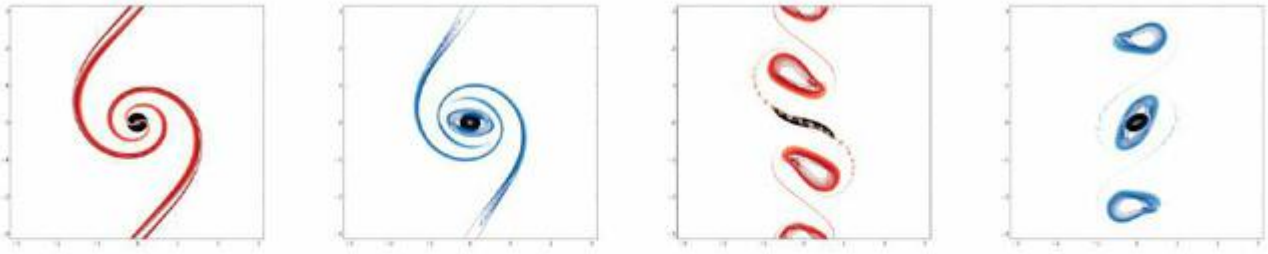

Figure 1: Surface buoyancy strip (blue for $b < 0$, red for > 0, and internal vortex (black) with $q = 1$. From left to right. First frame: $\varrho = 0$, $H = 0.5$, $b_m = 0.01$ at $t = 600$. Second frame: same as left but $b_m = -0.01$. Third frame: $\rho = 0$, $H = 0.5$ $b_m = 1$ and $t = 17.5$. Fourth frame: same as third one but $b_m = -1$.

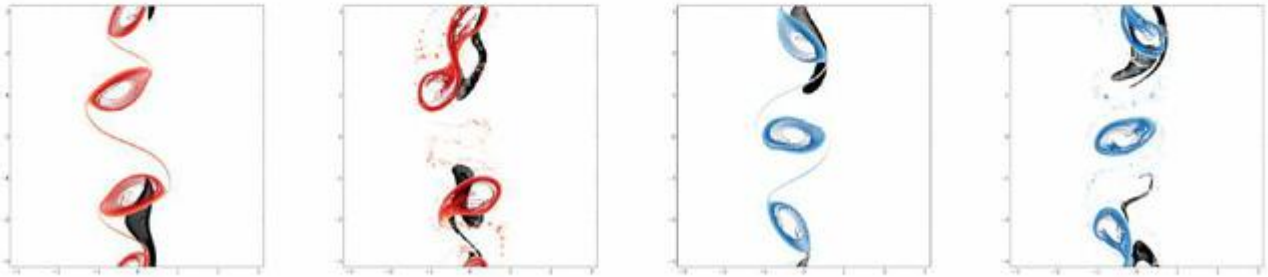

Figure 2: Surface buoyancy strip (blue for $b_m < 0$, red for > 0, and internal vortex (black) with $q = 1$. From left to right. First two frame: $\varrho = r$, $H = 0.25$, $b_m = 2$ at $t = 7.5$ (first) and $t = 12.5$ (second). Last two frames same as first two, but $b_m = -2$.

Figure 2 illustrates how a horizontal displacement between the strip and the vortex changes the flow evolution. For illustration purposes, the vortex is located closer to the surface ($H = 0.25$) and near an edge of the strip ($\varrho = a = r$) where the velocity induced by the strip is maximum (and equal to b_m). We can see that the vortex now travels along the edge of the strip and produces a more complex deformation field on the strip. Indeed, it becomes a moving source of perturbations feeding further instabilities along the strip. The strip breaks asymmetrically, and the vortex is caught in a complex shear flow which disrupts and eventually tears it apart. Both the strip and the vortex are now sources of smaller-scale structures in the flow, inducing a cascade of both enstrophy and energy to higher wavenumbers (smaller scales).

CONCLUSION

The examples discussed illustrate the richness of the interaction between a strip of surface buoyancy and a deep vortex. Both are potential sources of smaller-scale structures in the flow. The details of the interaction depends on the time scales associated with the features and whether they are in a cooperative or an adverse shear situation. As regards applications to ocean dynamics, we find that the link between an observable surface structure and the internal dynamics is tenuous at best. In particular, the existence of a buoyancy patch at the surface is not always associated with the presence of the internal vortex directly below it. The presentation will also analyse energy cascades at the surface and in the interior, as well as the exchange of energy between the surface and the interior.

References

[1] Harvey, B.J., Ambaum, M.H.P. *Quart. J. Roy. Meteorol. Soc. Part B.* 2010, **136**, 1506–1513, 2010.

[2] Juckes, M. *J. Atmos. Sci.*, **52**, 3247–3262, 1995.

[3] Dritschel, D.G., Scott, R.K., Reinaud, J.N. *J. Fluid Mech.*, **505**, 201–223, 2004.

[4] Perrot, X., Reinaud, J.N., Carton, X., Dritschel, D.G. *Regul. Chaotic Dyn.*, **15**, 66–83, 2010.

[5] Dritschel, D.G. *Geophys. Astrophys. Fluid Dyn.*, **105**, 368–376, 2011.

ENHANCED SEDIMENTATION BENEATH SEDIMENT LADEN OVERFLOWS AND INTERFLOWS

Shahrzad Davarpanah Jazi[1a)] & Mathew Wells[1]
[1]*Department of Physical & Environmental Sciences, University of Toronto, Toronto, Ontario, Canada*

Summary Double-diffusive and settling-driven convection processes can enhance the sedimentation rate of particles beneath a sediment-laden plume. The two mechanisms can be active simultaneously, and previous experimental studies had difficulty distinguishing them visually. In experiments with a sediment-laden fluid overlying a saline layer, visual measurements of mean velocities can only be made in the optically clear lower layer. We measured the velocity and turbulence components of the flow field above and below the initial sediment/salt interface, using an Acoustic Doppler Velocimeter. The velocity of the sediment fingers in the lower layer were always larger than the Stokes settling velocity of the particles, leading to an asymmetry in the flow field of the two convective layers. Sediment fingers only dominated when there were marginal density differences between the two layers. We conclude that double diffusive sediment fingers control sedimentation beneath interflows in most lakes, whereas settling-driven convection is dominant in most oceanic overflows.

When a sediment-laden river enters in to a stratified lake or the coastal ocean, it is of great interest to know how fast the sediment settles from the base of the resulting surface or subsurface flow (overflow or interflow). There is observational evidence of enhanced sedimentation near the mouth of the rivers, in the coastal ocean [6] and lakes [9], where the apparent particle settling rate is larger than that based on Stokes settling velocity of a single particle. However it is not clear whether such enhanced settling is due to flocculation [8], double-diffusive convection [4, 7] or settling-driven convection [5]. In the absence of flocculation, two related processes of enhanced particle sedimentation could occur beneath a sediment-laden intrusion; namely double-diffusive convection (illustrated in Figure 1a) and settling-driven convection (illustrated in Figure 1b). When a sediment-laden fluid overlies a denser saline layer, the accumulation of particles at the interface can develop a gravitationally unstable bulk density profile that produces Rayleigh-Taylor instability at the sediment front [5, 10, 11, 1, 2], shown in Figure 1b. In this case the settling-driven mechanism leads to convective sediment plumes below the interface, which drives vigorous convection. Double-diffusive "sediment-fingering" is another instability that arises due to the diffusion of salt being much faster than the Brownian diffusion of sediment. This process results in rapidly descending fingers of sediment beneath the intrusion as shown in Figure 1a.

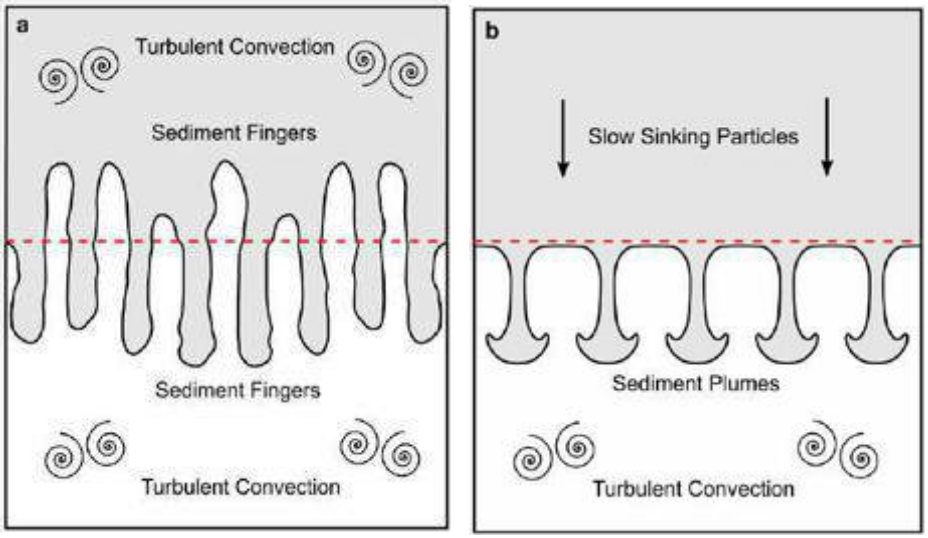

Figure1. Schematic figures indicating (a) the horizontally symmetric double-diffusive instability and (b) the vertically symmetric Rayleigh-Taylor instability (the red lines show the initial interface between the saline and sediment laden layers).

While there has been great progress in direct numerical simulations of double diffusion [10, 11, 1, 2], there is a paucity of solid experimental or theoretical descriptions of the process, which limits our understanding of sediment transport. A critical limitation of all previous experiments [3, 4, 5, 7] was that the sediment layer was optically opaque, which greatly hampered an understanding of the physical processes at work. In this experimental study we investigated the responsible mechanisms for the enhanced sedimentation of non-cohesive SiC particles with a median diameter of 7.8 μm. We conducted a series of geophysical relevant experiments to distinguish enhanced sedimentation due to double-diffusive fingering versus settling-driven convection. By measuring the turbulence characteristics using a NORTEK Vectrino+ Acoustic Doppler

[a)] Corresponding author. Email: sh.davarpanahjazi@mail.utoronto.ca.

Velocimeter (ADV) in the sediment-laden and saline layers of a two-layer configuration, we determined what conditions were consistent with double-diffusive or settling-driven convections. Our data covered a geophysical relevant range of salinity and sediment concentration differences (Figure 2a), which we used to provide a sedimentation process regime diagram (Figure 2b). We then applied the diagram to predict the occurrence of enhanced sedimentation beneath overflows and interflows in oceans and lakes.

Our main conclusion was that for 7.8 μm SiC particles, sediment fingers due to double-diffusive convection dominated only for $1 \leq R_\rho < 1.1$. However, settling-driven convection was significant for $R_\rho > 2$, and strength of turbulence in the bottom layer only depended on density difference due to the added sediment. We anticipate that for particles with slower settling velocities (i.e. smaller or lighter) there would be a greater range of R_ρ, where double-diffusive processes dominate. Sediment-laden underflows or interflows are rare in the coastal ocean, due to the large density difference between fresh water and seawater ($\Delta\rho \sim 20$ kg m^{-3}). This implies that sediment laden overflows and river plumes in ocean generally have $Rp >> 1$ and hence settling-driven convection is the dominant sedimentation mechanism (Figure 2b). An interflow by definition occurs at its depth of neutral buoyancy, where the density difference is minimal ($R_\rho \sim 1$). Therefore based on our regime diagram (Figure 2b) double-diffusive convection is the primary mechanism for sedimentation in these flows.

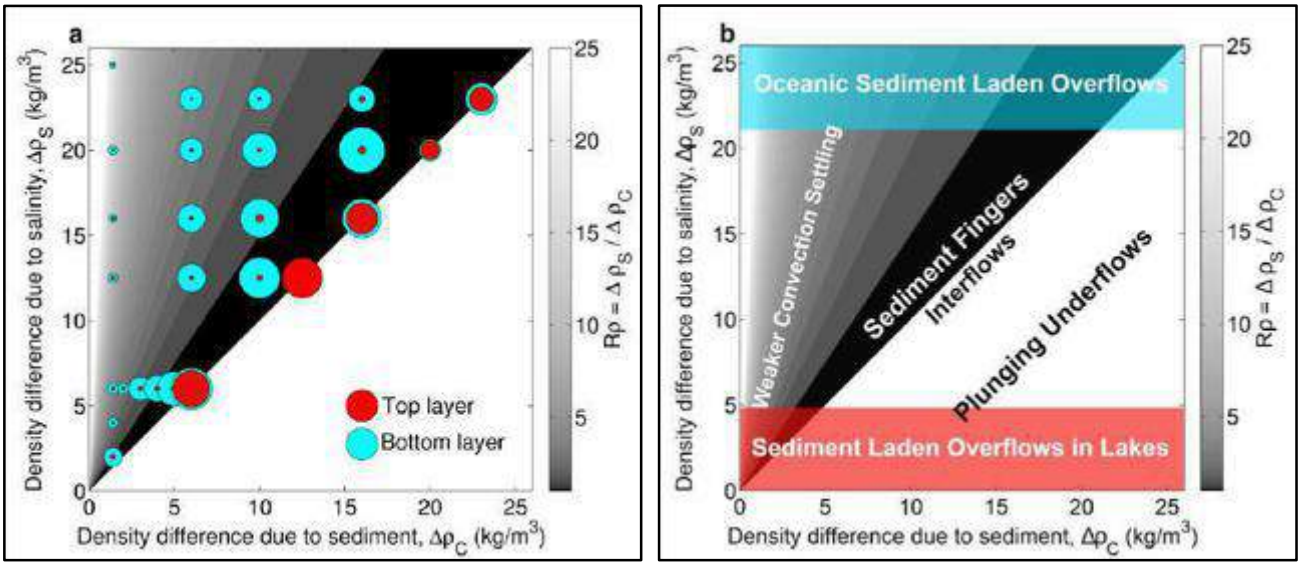

Figure 2. (a) The turbulence strength normalized by Stokes settling velocity in the first 500s for the top and bottom layers as a function of the density difference due to sediment and salinity or R_ρ (The size of the red and blue circles in lower right corner represents normalized turbulence strength of 27.5) and (b) A regime diagram showing the occurrence of overflows, underflows and interflows.

References

[1] Burns, P., and E. Meiburg: Sediment-laden fresh water above salt water: linear stability analysis, *J. F. M.*, 691: 279-314, 2012.

[2] Burns, P., and E. Meiburg: Sediment-laden fresh water above salt water: nonlinear stability analysis, *J. F. M.*, 762: 156-195, 2015.

[3] Chen, C. F.: Particle flux through sediment fingers, *Deep-Sea Res.*, 44(9-10): 1645-1654, 1997.

[4] Hoyal, D. C. J. D., Bursik M. I., and J. F. Atkinson: The influence of diffusive convection on sedimentation from buoyant plumes. *Mar. Geol.*, 159: 205-220, 1999a.

[5] Hoyal, D. C. J. D., M. I. Bursik and J. F. Atkinson: Settling-driven convection: A mechanism of sedimentation from stratified fluids. *J. Geophys. Res.*, 104, No. C4: 7953-7966, 1999b.

[6] Nowacki, D. J., Horner-Devine, A. R., Nash J. D. and D. A. Jay: Rapid sediment removal from the Columbia River plume near field. *Cont. Shelf Res.*, 35: 16 – 28, 2012.

[7] Parsons, J. D. J. W. M. Bush and J. P. M. Syvitsky: Hyperpycnal plume formation from riverine outflows with small sediment concentrations. *Sedimentology*, 48: 465-478, 2001.

[8] Rouhnia, M., and K. Strom: Sedimentation from flocculated suspensions in the presence of settling-driven gravitational interface instabilities. *J. Geophys. Res: Oceans*, 120(9): 6384-6404, 2015.

[9] Scheu, K. R., Fong, D. A., Monismith, S. G., and Fringer, O. B.: Sediment transport dynamics near a river inflow in a large alpine lake. *Limnol. Oceanogr.*, 2015.

[10] Yu, X., T.-J. Hsu, and S. Balachandar: Convective instability in sedimentation: Linear stability analysis, *J. Geophys. Res.: Oceans*, 118: 256–272, 2013.

[11] Yu, X., T. J. Hsu and S. Balachandar: Convective instability in sedimentation: 3-D numerical study. *J. Geophys. Res.: Oceans*, 119: 8141-8161, 2014.

OCEANIC OSCILLATION PHENOMENA RELATED SYNCHRONIZATION AND STOCHASTIC RESONANCE

Shinya Shimokawa [1] & Tomonori Matsuura [2]
[1] *National Research Institute for Earth Science and Disaster Prevention, Tsukuba, Ibaraki, Japan*
[2] *University of Toyama, Toyama, Toyama, Japan*

Summary Various oscillation phenomena, such as the transitions between stable and unstable states of western boundary currents (e.g., the Kuroshio), are present in the oceanic circulation of the North Pacific Ocean. These phenomena are considered to be related to non-linear rhythmic phenomena, such as the synchronization and the stochastic resonance, which are often observed in non-linear ocean systems. However, oceanic applications of these non-linear rhythmic phenomena have not been investigated in detail. Thus, we investigated the responses of oceanic double gyres to external wind forcing with and without noise using a 1.5 layer quasi-geostrophic model and considered the possibility of the occurrence of these non-linear rhythmic phenomena in general oceanic circulation.

INTRODUCTION

Synchronization is an adjustment (e.g., frequency and/or phase locking) of the rhythms of two or more self-sustained oscillating systems that have different periods because of their non-linear interaction [1, 2]. Stochastic resonance is a phenomenon in which parts of potential signals can exceed the threshold when adequate noise is added to non-linear systems; these can then be detected as actual signals [3, 4]. Both phenomena are general characteristics of highly non-linear open systems and have been observed in living systems and electrical circuits [2, 4]. They are considered to be related to formation of ordered structure, such as in the rhythm adjustment observed in non-linear systems.

The ocean system can be regarded as a highly non-linear open system driven by external forcing (i.e., the wind stress on the sea surface). The variability in the oceanic general circulation results in a non-linear interaction between the atmospheric wind stress oscillator and the oceanic circulation oscillator. In fact, previous studies [5-11] have noted the possibility that both the synchronization and the stochastic resonance should play an important role in causing the variability of strong oceanic currents and of the concurrent eddy shedding. The aim of this study is to understand the relevance of synchronization and stochastic resonance in the generation of oceanic turbulence.

NUMERICAL MODEL AND METHODS

The model used in this study was a 1.5 layer, reduced-gravity, quasi-geostrophic numerical model with Rayleigh-type interfacial friction and a nonslip boundary condition [12]. The model domain was a rectangular area of 3600 km × 2800 km representing the mid-latitude North Pacific. Further details of the numerical model are provided in [8].

The external wind forcing, $\tau(y, t)$, has the following form:

$$\tau(y, t) = [1 + \alpha \cos(\omega t) + \varepsilon\, n(t)/\sigma_n] \times \tau_0 \cos(2\pi y/L), \quad \text{Eq. (1)}$$

where α is the amplitude of seasonal variation (see below in this section), ω is the frequency of seasonal variation (= 1/1 year^{-1}), ε is the amplitude of red noise $n(t)$ [13], σ_n is the root mean square of $n(t)$, τ_0 is the amplitude of wind stress (= 0.1 N m^{-2}), and L is the length of the region in the N-S direction (= 2800 km). The basic external forcing field, $\tau_0 \cos(2\pi y/L)$, has only an E-W component, is constant in time and varies in the N-S direction, representing a simplified spatial distribution of wind stress in the mid-latitude North Pacific. Seasonal variation and red noise were added to the basic field after year 50 in the integration. Further details of the red noise calculation are provided in [10].

The experiments for constant external forcing (i.e., $\alpha = \varepsilon = 0.0$) [9] showed that the energy level changes discontinuously and represents a different quality state. As a result, the state of Re = 39 represents the state in which the modelled ocean regularly oscillates with a characteristic period. The state with Re = 157 represents the situation in which potential signals exist in the model ocean but are not apparent.

Based on the above results, we conduct the following experiments:

[Seasonally changing experiments] These experiments were conducted under seasonally varying external forcing with a 1 year period for Re = 39. In these experiments, the only variable parameter was α, the amplitude of the seasonal variation (i.e., $\varepsilon = 0.0$), which can vary from 0.0 to 1.0: $\alpha = 0.0$ corresponds to no seasonal variation, and $\alpha = 1.0$ indicates that the amplitude of the seasonal variation is equal to that of the average external force.

[Noise-added experiments] These experiments were conducted under red-noise-added external forcing for Re = 150. In these experiments, the only variable parameter was ε, the amplitude of the seasonal variation (i.e., $\alpha = 0.0$), which can vary from 0.0 to 0.1: $\varepsilon = 0.0$ corresponds to no added red noise, and $\varepsilon = 0.25$ indicates that the amplitude of the red noise is equal to that of the average of external force because the range of $x(t)/\sigma_x$ in Eq. (1) is roughly equal to ±4.0 [6].

[a] Corresponding author. Email: simokawa@bosai.go.jp

RESULTS AND DISCUSSION

The results obtained in this study can be summarized as follows.

(1) The response of the oceanic double-gyre to seasonally changing external forcing was investigated by changing only the seasonal variation amplitude α in the numerical model. We focused on the state Re = 39, in which the modelled ocean regularly oscillated with a characteristic period.

(2) With seasonally varying external forcing, the characteristic period of the modelled ocean (2.45 years) was synchronized to twice the period of the external forcing (2 years). In this case, the period of the whole system is believed to adjust due to the interactions between the ocean system and the external forcing.

(3) The response of the oceanic double-gyre to red-noise-added external forcing was investigated by varying only the red noise amplitude ε in the numerical model. We focused on the condition Re = 157, in which potential signals existed in the model ocean but did not appear in the results.

(4) With the noise-added external forcing, an adequate noise amplified the potential signals in the system (i.e., stochastic resonances occur), but strong noise buried the potential signals within the noise.

(5) An optimum noise strength in stochastic resonance is considered to exist at least in the parameter range corresponding to a noise that is not excessively strong.

The result (5) is interesting because it is formally identical to the "intermediate-disturbance hypothesis" [14, 15], that has been demonstrated in ecology and in which species diversity in a local area is maximized when the environmental disturbances are neither excessively weak nor excessively strong. The relation between them and the generality should be investigated.

Our previous studies [8-11] have noted also the possibility that both the synchronization and the stochastic resonance significantly influence the variability of strong oceanic currents and of the concurrent eddy shedding. These phenomena may affect the periods of oceanic oscillation phenomena, such as the transitions between stable and unstable states of western boundary currents (e.g., the Kuroshio). The roles of these phenomena in the real ocean should be investigated.

The coupling of synchronization and stochastic resonance has also been discovered and is known as stochastic synchronization [16]. However, only one study [17] related to stochastic synchronization in oceanic circulation has been conducted so far; thus, additional investigations on this topic are required.

References

[1] Kuramoto, Y., 1984, Chemical Oscillations, Waves, and Turbulence, Springer, Berlin.

[2] Pikovsky, A., M. Rosenblum and J. Kurths, 2001, Synchronization: A Universal Concept in Nonlinear Sciences, Cambridge Univ. Press., Cambridge.

[3] Benzi, R., A. Sutera and A. Vulpiani, 1981, The Mechanism of Stochastic Resonance, J. Phys., 14A, L453-L457.

[4] Moss, F. and K. Wisenfeld, 1995, The Benefits of Background Noise, Scientific American, August 1995, 66-69.

[5] Dijkstra, H. A., 2000, Nonlinear Physical Oceanography: A Dynamical Systems Approach to the Large Scale Ocean Circulation and El Nino, Springer, Dordrecht.

[6] Pierini, S., 2010, Coherence Resonance in a Double-Gyre Model of the Kuroshio Extension, J. Phys. Oceanogr., 40, 238–248.

[7] Pierini, S., 2011, Low-Frequency Variability, Coherence Resonance, and Phase Selection in a Low-Order Model of the Wind-Driven Ocean Circulation, J. Phys. Oceanogr., 41, 1585-1604.

[8] Shimokawa, S. and T. Matsuura, 2010, Chaotic Behaviors in the Response of Q-G Oceanic Double-Gyre to Seasonal External Forcing, J. Phys. Oceanogr., 40, 1458-1472.

[9] Shimokawa, S., T. Matsuura and H. Hashimoto, 2013, Instability and Long-Term Variability of Strong Current Extension in an Oceanic Double-Gyre, Theor. Appl. Mech. Jpn., 61, 23-30.

[10] Shimokawa, S., K. Shiratori, and T. Matsuura, 2014, Responses of Oceanic Double-Gyre to External Wind Forcing with Noise, Theor. Appl. Mech. Jpn., 62, 49-57.

[11] S. Shimokawa and T. Matsuura, 2015, Oscillation Phenomena in the Oceanic General Circulation and Rhythmic Phenomena in Nonlinear Systems, Japanese J. Multiphase Flow, 28, 583-590 (in Japanese).

[12] McCalpin, J. D., 1995, The Statistics and Sensitivity of a Double-Gyre Model: The Reduced-Gravity, Quasigeostrophic Case, J. Phys. Oceanogr., 25, 806–824.

[13] Ornstein, L. S., and Uhlenbeck, G. E., 1930, On the Theory of the Brownian Motion, Phys. Rev., 36, 823-841.

[14] Connell, J. H., 1978, Diversity in Tropical Rain Forests and Coral Reefs, Science, 199, 1302-1310.

[15] Shimokawa, S., T. Murakami, A. Ukai, H. Kohno, A. Mizutani, and K. Nakase, 2014, Relationship Between Coral Distributions and Physical Variables in Amitori Bay, Iriomote Island, Japan, J. Geophys. Res. Oceans, 119, 8336-8356, doi: 10.1002/2014JC010307.

[16] Fukuda, H., H. Nagano, and S. Kai, 2003, Stochastic Synchronization in Two-Dimensional Coupled Lattice Oscillators in the Belousov–Zhabotinsky Reaction, J. Phys. Soc. Jpn., 72, 487-490.

[17] Shimokawa, S. and T. Matsuura, 2015, Stochastic synchronization in an oceanic double gyre, Theor. Appl. Mech. Jpn., 63, 99-107.

EVALUATION OF EDDY- AND NON-EDDY-VISCOSITY SUBGRID SCALE MODELS IN STRATIFIED TURBULENCE

Sina Khani* and Fernando Porté-Agel
École Polytechnique Fédérale de Lausanne (EPFL)

Summary This paper presents a detailed study on the performance of eddy- and non-eddy-viscosity subgrid scale (SGS) models using direct numerical simulations (DNS) of decaying stratified turbulence, when two types of test filters – the Gaussian and sharp spectral filters – are applied. It is shown that non-eddy-viscosity models yield very good results when a Gaussian filter is applied. On the other hand, the eddy-viscosity models show less dissipative results when the spectral filter is applied. Overall, this study provides a strong support for the choice of minimum grid spacing in eddy- and non-eddy-viscosity SGS parameterizations using theoretical scale analysis and DNS data.

INTRODUCTION

Due to the high computational costs of direct numerical simulations (DNS), large eddy simulations (LES) has been considered in the computational studies of stratified turbulence in the last few years (e.g. Remmler & Hickel, 2012; Paoli et al., 2013; Khani & Waite, 2014 and 2015). In particular, Khani & Waite (2014 and 2015) have studied the performance of three common eddy-viscosity models in LES of forced stratified turbulence. They have shown that the robustness of LES in capturing the fundamental characteristics of stratified turbulence depends on the resolution of the buoyancy scale L_b and also the SGS models: the Kraichnan (1976) model requires $\Delta/L_b < 0.47$, the Smagorinsky (1963) model requires $\Delta/L_b < 0.17$ and the dynamic Smagorinsky model requires $\Delta/L_b < 0.24$, where Δ is the grid spacing (Khani & Waite, 2014 and 2015). The resolution of L_b might not be computationally practical when the buoyancy Reynolds number Re_b is very large, as in, for example, mesoscale motions in the atmosphere (e.g. Riley & Lindborg, 2008; Waite, 2014). As a result, improving the capability of current SGS models in LES of stratified turbulence, when L_b is not resolved, is motivated. The first step for this improvement is to evaluate different SGS models, including non-eddy-viscosity SGS parameterizations, using DNS data through an $a\ priori$ study. The results of this study will provide strong supports for the $a\ posteriori$ study of Khani & Waite (2014 and 2015). In addition, we will investigate the importance of resolving buoyancy scale L_b in LES of stratified turbulence through the theoretical scale analysis on the SGS stress tensor τ_{ij}, and using the fact that the vertical scale l_z in stratified turbulence is squeezed and scaled by the buoyancy scale L_b due to the buoyancy effects.

MATERIALS AND METHODS

An idealized case of study for decaying stratified turbulence in a cubic domain of size $L = 2\pi$ with triply periodic boundary conditions is considered. Taylor-Green vortices of size π, i.e.

$$\boldsymbol{u}(\boldsymbol{x}, 0) = \cos(z) \begin{pmatrix} \cos(x)\sin(y) \\ \circ\ \sin(x)\cos(y) \\ 0 \end{pmatrix}, \tag{1}$$

along with low-level noise, are considered for the initial conditions. Spatial derivatives are discretized using the spectral transform method with the cubic truncation. The two-thirds rule is considered for eliminating aliasing errors. The time advancement includes the explicit third order Adams-Bashforth scheme for all terms except the diffusion terms, for which the implicit trapezoidal method is employed. A sharp spectral filter with $k_c = \pi/\Delta_f$, a long with a Gaussian filter $G(k)$ with the isotropic form

$$G(k) = exp\left(\circ\ \frac{k^2\Delta_f^2}{24}\right), \tag{2}$$

are applied, where Δ_f is the test filter scale. The test filtering wavenumbers are $k_c = 10$, 20, 32 and 44, which are smaller or around the Ozmidov wavenumber $k_o = (N^3/\epsilon)^{1/2}$. Since the vertical kinetic energy is relatively small, the root-mean-square velocity u_{rms} is set to $\sqrt{E}$ at the time when the kinetic dissipation rate ϵ is large.

*Corresponding author. Email: sina.khani@epfl.ch

CONCLUDING RESULTS AND DISCUSSION

Layered structures are seen in the x-z field of the actual and SGS stress tensors τ_{13}, dissipation rate $\tau_{ij}\bar{s}_{ij}$ and the dynamic Smagorinsky coefficient c_s. During the $a\ priori$ study, different SGS models show both up- and downscale energy transfer, except the regular Smagorinsky model that is a purely dissipative scheme. With a Gaussian test filter, the Smagorinsky and dynamic Smagorinsky parameterizations are more dissipative in comparison with the nonlinear and modulated gradient parameterizations. The histograms of SGS dissipation $\tau_{ij}\bar{s}_{ij}$ are dramatically changed with changing the type of test filters. The correlation coefficient γ, which shows the correlation between actual and SGS stress tensors, depend on the SGS model and the type of filter scale. Moreover, the leading order of the SGS tensor τ_{ij} depends on the resolution of L_b: when L_b is not resolved, $\tau_{ij} \sim u_{rms}^2$, which shows that the SGS stress removes the turbulent kinetic energy at the smallest resolved scale (isotropic dissipation); when L_b is resolved, however, $\tau_{ij} \sim \Delta_f^2 N^2$, which shows that the SGS stress depends on the test filter scale Δ_f and the buoyancy frequency N, and that increased N requires smaller grid spacing to prevent excessive SGS dissipation (consistent with the picture of anisotropic dissipation, as seen in LES of Khani & Waite, 2014 and 2015). In conclusion, both the $a\ priori$ and $a\ posteriori$ studies suggest that the resolution of L_b is required in order to capture the fundamental characteristics of stratified turbulence if common isotropic SGS models are employed. In other words, we require to develop a new anisotropic SGS model for LES of stratified turbulence if the buoyancy scale L_b is not resolved.

References

[1] Khani, S. & Waite, M. L. *J. Fluid Mech.* **773**, 327-344, 2015.

[2] Khani, S. & Waite, M. L. *J. Fluid Mech.* **754**, 75-97, 2014.

[3] Kraichnan, R. H. *J. Atmos. Sci.* **33**, 1521-1536, 1976.

[4] Paoli, R., Thouron, O., Escobar, J., Picot, J. & Cariolle, D. *Atmos. Chem. Phys. Discuss.* **13**, 31891-31932, 2013.

[5] Remmler, S. & Hickel, S. *Int. J. Heat Fluid Flow* **35**, 13-24, 2012.

[6] Riley, J. J., & Lindborg, E. *J. Atmos. Sci.* **65**, 2416-2424, 2008.

[7] Smagorinsky, J. *Mon. Weather Rev.* **91(3)**, 99-164, 1963.

[8] Waite, M. L. *American Geophysical Union*, Washington, DC., 159-175, 2014.

NUMERICAL SIMULATION OF FREE-SLIP DOUBLE-DIFFUSIVE GRAVITY CURRENTS

Jared Penney*[1] and Marek Stastna[1]

[1]*Department of Applied Mathematics, University of Waterloo, Waterloo, Ontario, Canada*

Summary In situations where gravity currents develop due to thermohaline gradients, double-diffusive instabilities may also arise. When simulating these flows numerically, because of the low diffusivities of both heat and salt, highly refined grids are required for adequate resolution of the resulting small scale diffusive processes. This paper presents several high-resolution direct numerical simulations of gravity currents formed by thermohaline gradients that induce double-diffusive salt fingering.

INTRODUCTION

Gravity currents are a well-documented phenomenon that arises due to density differences between interacting fluid masses as a result of gradients in temperature or dissolved material (e.g., salinity). When both of these quantities contribute to the density gradient, the difference in diffusion coefficients may result in double-diffusive instabilities. The primary challenge in the numerical simulation of these instabilities is the adequate resolution of the different diffusive length scales of the tracers. Because diffusivity of salinity is so small (typically on the the order of $10^{-9}\,\mathrm{m^2 s^{-1}}$), sharp saline interfaces may arise in the flow that require a high number of grid points to resolve. This paper examines several high-resolution direct numerical simulations (DNS) of double-diffusive, near-surface gravity currents. Initially, the flows are horizontally stratified in heat and salt to simulate dam-break experiments so that a less dense current of hot, salty water flows over top of cooler, fresh water. Although this causes the flow to become stably-stratified in density, the top layer sees a loss of both heat and salt to the bottom layer due to diffusion. However, because the diffusivity of heat is larger than the diffusivity of salinity, the saline layer retains most of its salt along the thermohaline interface while experiencing a relatively rapid decrease in temperature. This causes the salty layer to increase in density near the interface, where denser fluid parcels begin to sink in the form of thin convective cells called salt fingers. In a typical two layer system, the motion of the fingers would be primarily vertical. In this configuration, the shear along the interface of the current causes them to slope down and away from the direction of flow. The shear also has the effect of aligning the fingers in rows parallel to the direction of the flow. Depending on the size of the current, the salt lost due to fingering may be enough to make the gravity current lose coherence and hinder its motion in the streamwise direction.

METHODOLOGY

The double-diffusive gravity currents presented in this paper are simulated using the Boussinesq approximation to the Navier-Stokes equations under the effects of incompressibility. Salinity, s, and temperature, T, are governed by typical conservation laws, and are coupled to the momentum equations using a nonlinear approximation to the UNESCO equation of state for seawater density, ρ,

$$\frac{\partial \boldsymbol{u}}{\partial t} + \boldsymbol{u}\cdot\boldsymbol{\nabla}\boldsymbol{u} = -\frac{1}{\rho_0}\boldsymbol{\nabla}p - g\frac{\rho}{\rho_0}\delta_{i3} + \nu\nabla^2\boldsymbol{u}, \quad \boldsymbol{\nabla}\cdot\boldsymbol{u} = 0, \quad \frac{\partial T}{\partial t} + \boldsymbol{u}\cdot\boldsymbol{\nabla}T = \kappa_T\nabla^2 T, \quad \frac{\partial s}{\partial t} + \boldsymbol{u}\cdot\boldsymbol{\nabla}s = \kappa_s\nabla^2 s,$$

$$\rho\left(T,s\right) = \rho_0 + c_1 + c_2 T + c_3 s + c_4 T^2 + c_5 sT + c_6 T^3 + c_7 sT^2.$$

In these equations, $\boldsymbol{u} = (u,v,w)$ is the velocity in the x-, y-, and z- (or streamwise, spanwise, and vertical) directions, respectively, p is the pressure, g is the gravitational constant, δ_{i3} is the Kronecker delta, and $\nu = 2\times10^{-6}\,\mathrm{m^2/s}$ is the kinematic viscosity. $\kappa_T = 3.4\times10^{-8}\,\mathrm{m^2/s}$ and $\kappa_s = 2\times10^{-8}\,\mathrm{m^2/s}$ are the thermal and saline diffusivity coefficients, while $\rho_0 = 1000\,\mathrm{kg/m^3}$ is the reference density, and c_i, $i = 1,\ldots,7$, are the coefficients of the nonlinear equation of state described by [2]. The initial thermohaline stratification is defined by

$$\frac{s\left(\boldsymbol{x},t=0\right)}{\Delta s} = \frac{T\left(\boldsymbol{x},t=0\right)-T_0}{\Delta T} = \frac{1}{2}\left(1+\tanh\left(\frac{x_0-x}{\Delta x}\right)\right), \tag{1}$$

where x_0 gives the midpoint of the stratification, and $\Delta x = 0.5\,\mathrm{cm}$ sets the width. $T_0 = 15\,^\circ\mathrm{C}$ is chosen as the temperature of the cool water, while the change in temperature and salinity between the layers are $\Delta T = 25\,^\circ\mathrm{C}$ and $\Delta s = 5\,\mathrm{psu}$, respectively. This arrangement gives lighter, hot, salty water to the left of $x = x_0$, and denser, cool, fresh water to the right. The fluid is initially stationary, with all motion arising from the stratification. In each direction, free-slip boundary conditions are chosen

*Corresponding author. Email: j2penney@uwaterloo.ca

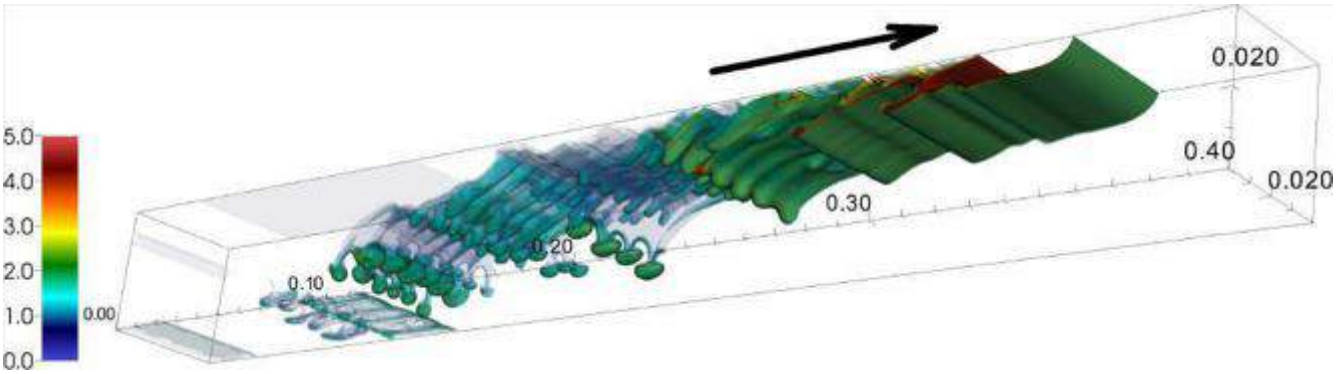

Figure 1: Salinity isosurfaces in psu for a gravity current in a $40\,\mathrm{cm} \times 4\,\mathrm{cm} \times 4\,\mathrm{cm}$ tank with free-slip boundary conditions in all directions after $25\,\mathrm{s}$. The arrow indicates the direction of travel of the current.

for the velocity fields, while no-flux conditions are chosen for the tracers. In the vertical direction, the free-slip condition has the effect of simulating a near-surface gravity current in a tank with an open top.

Direct numerical simulation was performed using the Spectral Parallel Incompressible Navier-Stokes Solver (SPINS) model [6]. Spatial derivatives are calculated using cosine transforms, while the time-stepping method is variable third-order Adams-Bashforth. In each experiment, the midpoint of the pycnocline is varied to examine the effect of different initial volumes of salty water, and thus, different current sizes. The grid spacing is $9.766 \times 10^{-3}\,\mathrm{cm}$ in the streamwise direction, $3.125 \times 10^{-2}\,\mathrm{cm}$ in the spanwise direction, and $2.083 \times 10^{-2}\,\mathrm{cm}$ in the vertical direction.

RESULTS

Each numerical experiment exhibits a similar flow pattern. To stabilize the density gradient, the less dense, warm, salty water moves along top the denser, cool, fresh water, forming a near-surface gravity current that travels toward the right side of the tank. The current head takes the shape described by inviscid theory [1] and observed in moving boundary experiments [5]. Towards the back of each current, horizontal salt fingers that are two-dimensional in the streamwise and vertical direction begin to form. The heads of these fingers eventually begin to sink, causing the fingers to slope down and away from the direction in which the current is traveling. The streamwise shear causes spanwise undulations in the two-dimensional fingers, which is the beginning of the salt sheet instability as described by [3] and [4]. The sheets give way to the full three-dimensionalization of the fingers, which arrange themselves parallel to the direction of the shear. Meanwhile, the head of the current remains mostly two-dimensional, even upon colliding with the far wall. These features are observable in Figure 1, which presents isosurfaces of the salinity field of the lowest salt water volume experiment, where the midpoint of the pycnocline is set $2\,\mathrm{cm}$ from the left-hand wall. This simulation shows an increase in three-dimensionalization moving from the head of the current towards the back.

In general, prior to collision with the wall, the current head in each experiment was observed to travel at a roughly constant velocity of $1.7\,\mathrm{cm/s}$, independent of current volume. However, the low volume current presented in Figure 1 loses enough of its salt content due to fingering that it slows down significantly. Additionally, upon colliding with the wall, the current loses enough coherence that it breaks down. In contrast, the larger current simulations retain enough of their volume and shape that they do not slow down, and upon colliding with the wall, rebound and travel leftward. In an experiment using the same initial conditions as presented in Figure 1, but with a domain that is half as long, the flow manages to stay two-dimensional until shortly after colliding with the wall.

References

[1] T. Brooke Benjamin. Gravity currents and related phenomena. *J. Fluid Mech.*, 31(2):209–248, 1968.

[2] D. Brydon, S. Sun, and R. Bleck. A new approximation of the equation of state for seawater, suitable for numerical ocean models. *J. Geophys. Res.*, 104(C1):2156–2202, 1999.

[3] S. Kimura and W. Smyth. Direct numerical simulation of salt sheets and turbulence in a double-diffusive shear layer. *Geophys. Res. Lett.*, 34(21):L21610, 2007.

[4] P. F. Linden. Salt fingers in a steady shear flow. *Geophys. Fluid Dynamics*, 6(1):1–27, 1974.

[5] J. E. Simpson. Effects of the lower boundary on the head of a gravity current. *J. Fluid Mech.*, 53(04):759–768, 1972.

[6] C. J. Subich, K. G. Lamb, and M. Stastna. Simulation of the Navier-Stokes equations in three dimensions with a spectral collocation method. *Int. J. Numer. Meth. Fluids*, pages 103–129, 2013.

REYNOLDS NUMBER EFFECTS FOR NON-CHANNELIZED NON-AXISYMMETRIC PARTICLE-DRIVEN GRAVITY CURRENTS

S. Laizet*[1], E.P. Francisco[2], L.F.R. Espath[2], C.A.S Moser[2], and J.H. Silvestrini[2]

[1]*Department of Aeronautics, Imperial College London, UK*
[2]*Faculdade de Engenharia, Pontificia Universidade Catlica do Rio Grande do Sul, Porto Alegre, Brasil*

Summary The purpose of this numerical work is to investigate the influence of the Reynolds number on the evolution of particle-laden gravity currents in a non-channelized non-axisymmetric lock-exchange configuration by means of high-fidelity simulations. Such configurations are largely understudied by comparison to more conventional channelized or axisymmetric lock-exchange configurations, despite the fact that most of gravity currents in nature originate from non-channelized non-axisymmetric configurations. It is found that the Reynolds number has a strong influence on the lobe-and-cleft structures at the head of the current and on the deposition patterns over the flat bed.

INTRODUCTION

Turbidity currents are particle-laden gravity-driven currents in which the gravitational driving force is supplied by a density excess associated with the suspension of particles. They exhibit a highly complex dynamic with the presence of the lobe-and-cleft patterns at the front of the head and a region of mixing with intense spanwise Kelvin-Helmholtz vortices. Understanding the physical mechanism associated with these currents as well as the correct prediction of their main features are of great importance for practical and theoretical purposes. They have been under scrutiny for a very long time with many experimental investigations and more recently with numerical investigations based on Direct Numerical Simulations. However, most of those investigations were performed in a channelized flow configuration for which the flow is constraint by the wall in the spanwise direction. Following our previous work on channelized turbidity currents [2], high-fidelity simulations are performed in a non-channelized non-axisymmetric configuration where the current can freely evolved in the streamwise direction as well as in the spanwise direction. In the present numerical investigations, the aim is to better understand the effect of the Reynolds number on the spatio-temporal evolution of a non-channelized non-axisymmetric gravity current. The focus will be on the lobe-and-cleft structures at the front of the current and on the deposition pattern at the bottom wall.

NUMERICAL METHODS AND FLOW CONFIGURATION

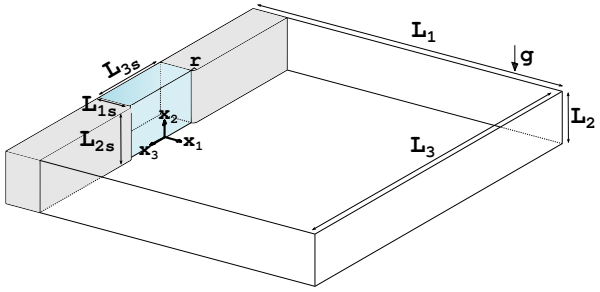

Figure 1: Schematic view of the flow configuration.

The fluid-particle mixture (in blue in Figure 1) is enclosed in a small portion of the domain $L_{1s} \times L_{2s} \times L_{3s}$ separated by a gate from the clear fluid. Then, the gate is removed and the particles flow due to gravity, without any constraint in the spanwise direction. We choose half of the box height as the characteristic length scale $h = L_2/2$. The velocity scale is defined by the buoyancy velocity as $u_b = \sqrt{g'h}$. The reduced gravitational acceleration g' is defined as $g' = g(\rho_p - \rho_0)c_i/\rho_0$ where ρ_p and ρ_0 are the particle and clear fluid density respectively, g is the gravitational acceleration and c_i is the initial volume fraction of the particles in the lock. With these two scales and the kinematic viscosity of the fluid ν, we can define the Reynolds number as $Re = u_b h/\nu$. All variables are made dimensionless using c_i, h or/and u_b.

Free-slip boundary conditions are imposed for the velocity field in the streamwise and spanwise directions x_1 and x_3 while no-slip boundary conditions are used in the vertical direction x_2. For the scalar field, no-flux conditions are used in the streamwise and spanwise directions x_1 and x_3, and in the vertical direction x_2 at the top of the domain. For the particles deposition in the vertical direction x_2 at the bottom of the domain, a simple 1D outflow boundary condition is imposed, meaning that the particles can virtually leave the computational domain (non conservative simulations). The modelling of the initial reservoir is performed with a customized immersed boundary method based on a direct forcing approach that ensures zero-velocity boundary conditions and a no-flux boundary condition for the fluid-particle mixture at the wall of the solid geometry. We solve the incompressible Navier-Stokes equations using the Boussinesq approximation along with a scalar transport equation on a Cartesian mesh with our high-order flow solver **Incompact3d** (www.incompact3d.com) which is based on sixth-order compact schemes for spatial discretization, a third order Adams-Bashforth scheme for time advancement and a fully spectral Poisson solver. Full details about the code can be found in [1].

*Corresponding author. Email: s.laizet@imperial.ac.uk

RESULTS

For this study, three simulations are performed with three different Reynolds numbers equal to 1000, 5000 and 10000. The computational domain $L_1 \times L_2 \times L_3 = 12 \times 2 \times 12$ is discretized with $1201 \times n_y \times 1201$ mesh points with n_y equal to 193, 289 and 385 for $Re = 1000,\ 5000$ and 10000 respectively. For the three simulations we use the same lock dimensions $L_{1s} \times L_{2s} \times L_{3s} = 1 \times 2 \times 2$ with a dimensionless settling velocity of $u_s = 0.02$ and a Schmidt number equal to 1. The formation, merging and meandering of the lobe-and-cleft structures at the front of the current can be seen in Figure 1. The observed slightly curved structures are different from the straight ones obtained with channelized or axisymmetric locks. For Re=1000, the structures are almost symmetric with respect to $x_3 = 0$ with very large lobe-and-left structures. When the Reynolds number is increased the structures become smaller and more curved. Note that the streamwise and spanwise extension of the current is the same for Re=5000 and Re=10000 suggesting a geometric similarity for the shape of the current for high Reynolds numbers.

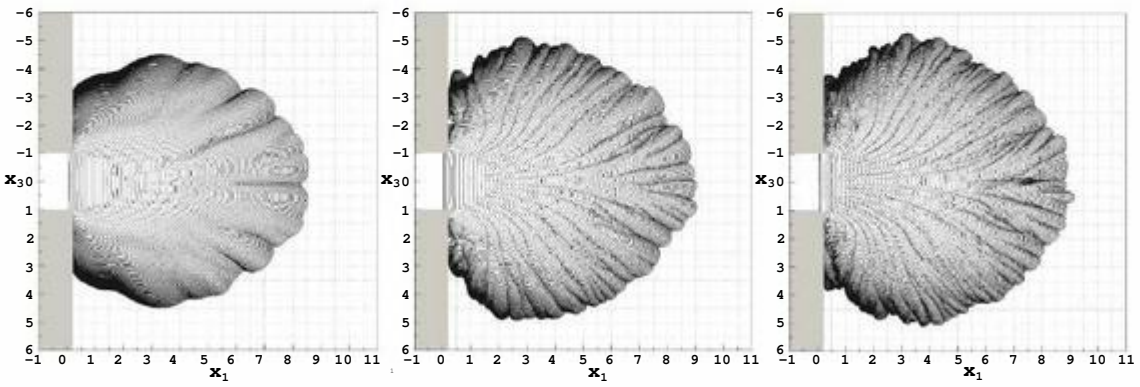

Figure 2: Time evolution of isolines of the bottom wall concentration for Re=1000 (left), 5000 (middle) and 10000 (right).

2D maps of the wall deposition $D_t(x_1, x_3, t) = \int_0^t c_w(x_1, x_3, \tau) u_s \, d\tau$ (where c_w is the concentration at the wall) are presented in Figure 3. As already explained for the channel configuration in a previous study [2], the lines starting from the initial volume and expanding with the current corresponds to the signature of the clefts. These maps can therefore be seen as a footprint of the front structures and can be used to better understand the lobe-and-cleft patterns. It can be seen that most of the deposition is location very close to the gate regardless of the Reynolds number. Once again, we can observe a very symmetric shape for the deposition at Re=1000 whereas at Re=10000 a large-scale bifurcation seems to split the deposit map in two large areas.

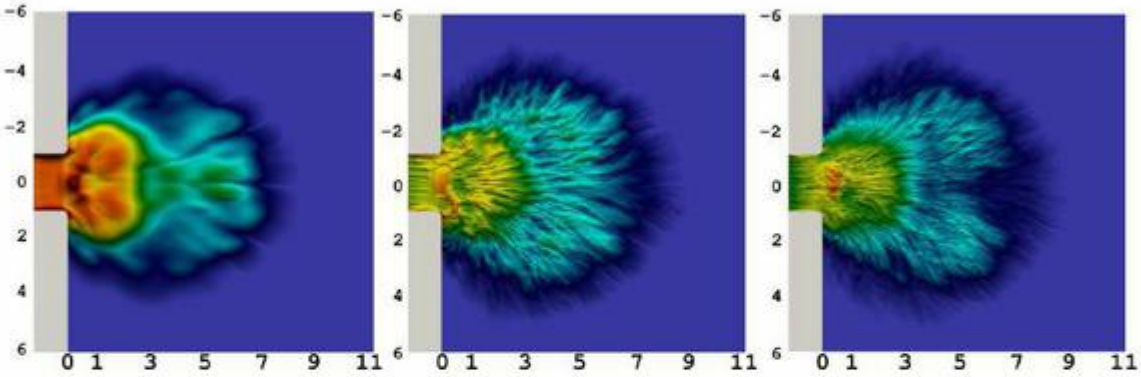

Figure 3: Deposit maps at $t = 20$ for Re=1000 (left), 5000 (middle) and 10000 (right). The data are normalized with the maximum values (red is 1, blue is 0).

References

[1] Laizet S. & Lamballais E.: High-order compact schemes for incompressible flows: a simple and efficient method with the quasi-spectral accuracy. J. Comp. Phys. 228: 5989-6015, 2009.

[2] Espath L.F., Pinto L.C., Laizet S. & Silvestrini J.H.: High-fidelity simulations of the lobe-and-cleft structures and the deposition map in particle-driven gravity currents. Physics of Fluids 27(5): 056604

NUMERICAL SIMULATIONS OF THE ATMOSPHERIC KINETIC ENERGY SPECTRUM

Michael L. Waite *[1]
[1]*Department of Applied Mathematics, University of Waterloo, Waterloo, Ontario, Canada*

Summary Idealized numerical simulations of the atmospheric kinetic energy spectrum are analyzed to better understand the wide range of results reported in the literature. In particular, the role of stratified turbulence, vertical mixing, and vertical grid resolution are investigated in simulations forced by baroclinic instability. Spectra are converged when the vertical grid spacing $\Delta z < 200$ m – which is quite high by comprehensive atmospheric model standards – but are very sensitive to resolution with coarser grids. When the vertical mixing scheme is weak, the under-resolved spectra are energized in the mesoscale. By contrast, when strong mixing is employed, the under-resolved mesoscale cascade is suppressed. Convergence requires that vertical scales associated with the full range of horizontal scales – including quasi-geostrophic scales of large-scale vortices and the buoyancy-scale of small-scale stratified turbulence – be resolved.

INTRODUCTION

Over the last two decades, there has been increasing interest in using atmospheric models to study the atmospheric kinetic energy spectrum and the energy cascade through the mesoscale (horizontal scales from $O(1)$-$O(100)$ km). A variety of models are able to reproduce the qualitative shape of the observed spectrum, which has a spectral slope of -3 at large scales, shallowing to approximately -5/3 in the mesoscale [1, 2, 4]. Different driving mechanisms have been identified for the mesoscale cascade, including stratified turbulence [3] and inertia–gravity waves [5]. There has naturally been a strong focus on increasing the horizontal resolution of such studies, in order to capture more of the mesoscale spectrum at small scales. By contrast, vertical resolution has received less attention, and coarse vertical grids with grid spacing $\Delta z \approx 1$ km outside the boundary layer are often employed [2] in global and regional atmospheric models. Sensitivity to Δz is rarely considered, but when it has been investigated, spectra have been found to be possibly very dependent on Δz [1]. In addition to practical implications, this grid dependence gives insight into the mechanics of the cascade because some mechanisms (e.g. stratified turbulence) require very fine vertical grids to be resolved. In this work, we present a careful investigation of the dependence of the energy spectrum on the vertical resolution and vertical mixing, and discuss implications for theories of the mesoscale cascade.

METHODOLOGY

Forced simulations of the Boussinesq equations on an f-plane are performed and analyzed. A sinusoidal zonal jet is initialized with Rossby and Froude numbers of 0.1. Simulations are seeded with low-level noise and forced by relaxation to the initial jet. The numerical model is fully spectral (transform-based with full dealiasing in the horizontal and vertical). Primary horizontal resolution is 512×512 grid points, with an effective grid spacing of 12 km, though some higher-resolution cases are also discussed. Baroclinic instability of the initial jet grows over the first few days. Simulations are run for 24 days. A wide range of vertical resolutions, from 16 levels ($\Delta z = 2$ km) to 256 levels ($\Delta z = 120$ m) are considered. In addition, three different vertical mixing schemes are employed: no explicit mixing, hyperviscosity with a grid-dependent but otherwise fixed coefficient, and stability-dependent Smagorinsky. Additional simulations testing the sensitivity to Coriolis parameter and buoyancy frequency are also performed. In each case, horizontal wavenumber spectra of kinetic energy are computed, averaged in the vertical, and averaged over the last few days of integration.

RESULTS

In simulations with no explicit vertical mixing, the energy spectra converge for $\Delta z < 200$ m. The converged spectra show the familiar double power law shape, with a large-scale spectral slope of -3 that shallows below scales of ≈ 100 km. By contrast, the under-resolved simulations have an exaggerated mesoscale spectrum, with a very shallow slope that extends to much larger scales. In the most extreme case ($\Delta z = 2$ km), the spectrum shallows below scales of 300 km, and the mesoscale slope is around $\circ$ 1. Convergence occurs when the vertical grid is fine enough to capture the thickness of quasi-geostrophic vortices at all scales with small Rossby number, as well as the buoyancy scale associated with smaller-scale motions. Indeed, the small-scale features in the well-resolved cases have some similarities with idealized simulations of stratified turbulence.

In addition to vertical resolution, the details of the vertical mixing scheme also affect the simulated energy spectra. When fixed vertical hyperviscosity is employed, the under-resolved simulations are strongly damped: vertical mixing removes kinetic energy from a wide range of horizontal scales, suppressing the shallowing of the mesoscale spectrum. Well-resolved simulations are very similar to cases without vertical mixing. Stability-dependent Smagorinsky mixing behaves differently:

*Corresponding author. Email: mwaite@uwaterloo.ca

under-resolved simulations are not affected by mixing because of their grid-scale stability, and these simulations resemble experiments without mixing. However, high-resolution simulations have small grid-scale Richardson numbers, and the mesoscale spectrum is correspondingly strongly damped. Stability-dependent Smagorinsky does not appear to be appropriate for simulations with high vertical resolution. Implications for sub-grid scale modelling are discussed.

CONCLUSIONS

These findings suggest that, in some cases, kinetic energy spectra from atmospheric model simulations may be contaminated by low vertical resolution. Vertical grid spacings larger than 200 m and stability-dependent vertical mixing schemes are commonly employed. Our work implies that the mesoscale spectra in such simulations may be exaggerated by under-resolution in the vertical. Sensitivity to vertical resolution should always be checked directly.

References

[1] Brune, S., and E. Becker: Indications of stratified turbulence in a mechanistic GCM. J. Atmos. Sci. 70:231–247, 2013.

[2] Hamilton, K., Y. O. Takahashi, and W. Ohfuchi: The mesoscale spectrum of atmospheric motions investigated in a very fine resolution global general circulation model. J. Geophys. Res. 113:D18110, 2008.

[3] Lindborg, E., 2006: The energy cascade in a strongly stratified fluid. J. Fluid Mech. 550, 207–242.

[4] Skamarock, W. C.: Evaluating mesoscale NWP models using kinetic energy spectra. Mon. Wea. Rev. 132:3019–3032, 2013.

[5] Waite, M. L., and C. Snyder, 2009: The mesoscale kinetic energy spectrum of a baroclinic life cycle. J. Atmos. Sci. 66, 883–901.

TEMPERATURE FRONTS IN STABLY STRATIFIED TURBULENCE

Yoshifumi Kimura*[1], Peter P. Sullivan[2], and Jackson R. Herring[2]
[1]*Graduate School of Mathematics, Nagoya University, Nagoya, Japan*
[2]*National Center for Atmospheric Research, Boulder, USA*

Summary Temperature fronts and associated cliff-ramp structures in stably stratified turbulence are investigated using DNS of the Navier-Stokes equations under the Bousinesq approximation. Vertical profiles of temperature fluctuations show sawtooth wave structures which result in a skewed PDF of the derivative of temperature fluctuation in the z-direction. The mechanisms for generating and maintaining these structures are considered.

In the atmosphere and oceans, flows are often stably stratified, and ongoing research seeks to understand the dynamics of stratification in geophysical turbulence. An important feature of stably stratified turbulence is the significant influence of internal gravity waves which makes stably stratified turbulence unique compared to homogeneous isotropic turbulence. In this paper, we investigate the genesis of temperature fronts–a crucial subject both practically and fundamentally–in stably stratified turbulence using Direct Numerical Simulations (DNS) with 1024^3 grid points.

The simulations are done by solving the following non-dimensionalized 3D momentum and temperature fluctuation equations under the Boussinesq approximation pseudo-spectrally,

$$(\partial_t - \nu\nabla^2)\mathbf{u} = -\mathbf{u}\cdot\nabla\mathbf{u} - \nabla p + \theta\mathbf{z} + \mathbf{f} \quad (1)$$

$$(\partial_t - \kappa\nabla^2)\theta = -N^2 w - \mathbf{u}\cdot\nabla\theta \quad (2)$$

$$\nabla\cdot\mathbf{u} = 0 \quad (3)$$

where $\mathbf{u} = (u, v, w)$ are velocity components, θ is the temperature fluctuation about the linear (stable) mean temperature profile $\mathrm{d}\overline{T}/\mathrm{d}z \equiv -N^2$, and N is the Brunt–Väisälä frequency, $\sqrt{g\alpha(\partial\overline{T}/\partial z)/T_0}$. $\mathbf{f}$ is a stochastic forcing applied to the large scales of the horizontal velocity. In wavenumber space, we set $\mathbf{f}(\mathbf{k}) = (f_x(k_x, k_y, 0), f_y(k_x, k_y, 0), 0)$ so that the forcing excites pure 2D velocity modes uniform in the z-direction and isotropic in (x,y). For the analysis of velocity field, we use the so-called Craya-Herring decomposition, which decomposes the velocity field into a vortex mode (ϕ_1) and a wave mode (ϕ_2). As an initial condition, we set all velocity components zero, and excite the velocity without coupling to the temperature field. After the 2D velocity field is developed, we switch on the velocity-temperature coupling [1]. Figure 1 shows the temporal growth of the energy in ϕ_1 and ϕ_2 for $N^2 = 10$ and forcing wavenumber $k_f = 4$. Stratification is switched on at $t = 10$, and because of the interaction with the vortex mode, the wave mode ϕ_2 grows nearly exponentially and becomes comparable with ϕ_1 around $t = 20$. It takes a rather long period for the ϕ_1 and ϕ_2 modes to become stationary around $t = 50$.

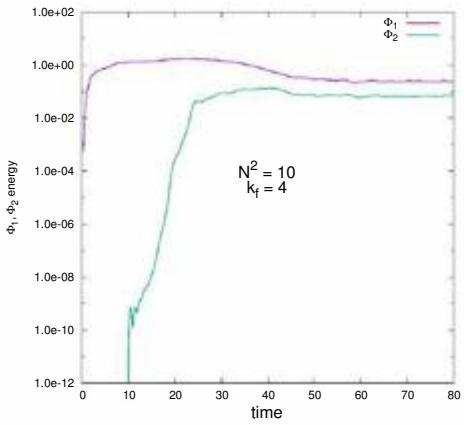

Figure 1: The growth of ϕ_1 and ϕ_2 energy.

Figure 2 shows a gray-scale contour plot of temperature fluctuations at slice $y = \pi$ (or $y = 512$ in grid number coordinates) at $t = 64.7$. We observe many (almost vertically periodic) wavy structures with black (negative) and white (positive) layers stacked together with clear boundaries implying a sharp temperature fronts. Similar temperature front structures are observed in simulations of homogeneous shear flows [2],[3] as well as in large-eddy simulations of the stably stratified atmospheric boundary layer [4]. Also, temperature fronts are ubiquitous features in passive scalar turbulence [5]. The fronts are tilted at angles that depend on the ratio of horizontal to vertical gradients of temperature; Chung and Matheou [3] show that for fixed shear the fronts become nearly horizontally when the mean temperature gradient is very large.

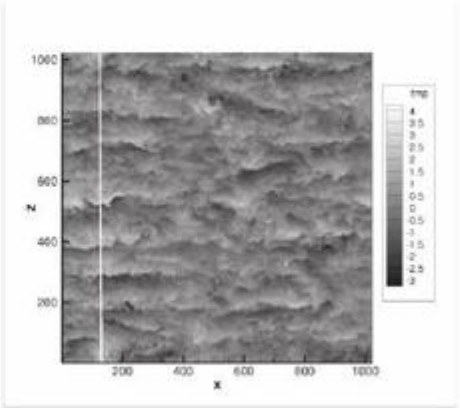

Figure 2: Contour plot of the temperature fluctuations on the slice at $y = \pi$ at $t = 64.7$.

*Corresponding author. Email: kimura@math.nagoya-u.ac.jp

Cliff-ramp structures are one of the signatures of temperature fronts, and to show this more clearly, a vertical cut is taken at $x = 132$ in the region where the most intense fronts are visible in Figure 2 (see the white line in Figure 2). Temperature fluctuations and the total temperature along this cut are plotted in Figure 3. Figure 3-a) shows numerous sharp jumps in the temperature fluctuations with increasing z. These large jumps result in a staircase pattern for the total temperature shown in Figure 3-b). The sawtooth waves consist of gradual decreasing θ with z with rapid recovery to a positive value as the frontal boundary is crossed. This asymmetry of gradients comes from the structure that warm temperature region lies on top of cool temperature region.

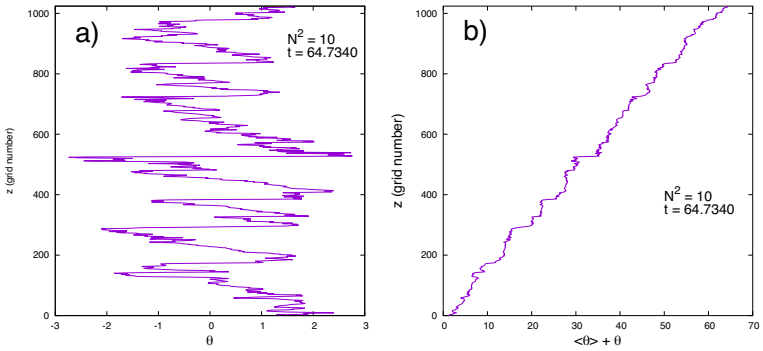

Figure 3: a): Temperature fluctuations along the line at $x = 132$, b): The total temperature

The asymmetry of the positive and negative gradients in the z direction is further shown in the probability density function (PDF) of temperature. Figure 4 shows the PDFs of θ and the three components of its derivatives. We see that the PDF of θ is near Gaussian for small values, while the tails exhibit strong non-Gaussianity for all components of the gradient of θ. Among the three components, $\partial\theta/\partial z$ shows skewness while the horizontal derivatives are not skewed.

Based on the above observations, the objectives of this work are to seek the answers to the following questions:

(1) How is the strong temperature front produced in relation of the effects of gravity waves? (How does it grow along the development of ϕ_1 and ϕ_2 in Figure 1 ?)

(2) What are the relevant flow structures to maintain the strong temperature front in stably stratified turbulence? (Are they (approximate) vortex rings [4], pancake vortices [6] or any kind of colliding waves?)

(3) How does the intermittency of the derivative of temperature fluctuations develop as stratification varies? (Departure from Gaussian increases/decreases with stratification?)

(4) What kind of interactions do flow instabilities in stably stratified turbulence have with temperature fronts? zig-zag or Kelvin-Helmholtz (Zigzag instability [7][8] causes the front genesis ? Kelvin-Helmholtz instability enhances/suppresses it ?)

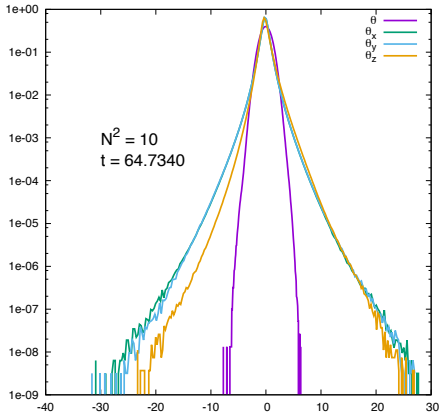

Figure 4: PDFs of the temperature fluctuations and the derivatives.

References

[1] Herring, J.R. & Métais O. : Numerical experiments in forced stably stratified turbulence. *J. Fluid Mech.* **202**, 97–115 (1989).

[2] Gerz, T., Howell, J. & Mahrt L. : Vortex structures and microfronts. *Phys. Fluids* **6**, 1242–1251 (1994).

[3] Chung, D. & Matheou, G.: Direct numerical simulation of stationary homogenous stratified sheared turbulence. *J. Fluid Mech.* **696**, 434–467 (2012).

[4] Sullivan, P.P., Weil, J.C., Patton, E.G., Jonker, H.J.J. & Mironov, D.V.: Turbulent winds and temperature fronts in large eddy simulations of the stable atmospheric boundary layer. accepted to *J. Atmos. Sci.*

[5] Warhaft, Z. : Passive scalars in turbulent flows. *Annual Review of Fluid Mechanics*, **32**, 203–240 (2000).

[6] Kimura, Y. & Herring, J.R. : Diffusion in stably stratified turbulence. *J. Fluid Mech.* **328**, 253–269 (1996).

[7] Billant, P. & Chomaz, J.-M. : Experimental evidence for a new instability of a vertical columnar vortex pair in a strongly stratified fluid. *J. Fluid Mech.* **418**, 167–188 (2000).

[8] Billant, P. & Chomaz, J.-M. : Theoretical analysis of the zigzag instability of a vertical columnar vortex pair in a strongly stratified fluid. *J. Fluid Mech.* **419**, 29–63 (2000).

SIMULATION OF FLOW FIELD INSIDE A CORAL COLONY

Md Monir Hossain[a] & Anne Staples
Department of Biomedical Engineering and Mechanics, Virginia Tech, Blacksburg, Virginia, USA

Summary Three-dimensional simulations of flow through a single *Pocillopora* coral colony were performed to examine the interaction between coral geometry and hydrodynamics. The complex shape of a coral colony poses a significant challenge for numerical simulation. To simplify grid generation and minimize computational cost, the immersed boundary method was implemented. Large eddy simulation was chosen as the framework to capture the turbulent flow field in the range of realistic Reynolds numbers of 5,000 to 30,000. These results presented here give insight into internal coral colony flow fields and the interaction between coral and surrounding ocean hydrodynamics. We found that, in contrast with the one previous numerical study of flow inside a coral colony, the maximum water velocity value in the colony interior was comparable to the value of the uniform flow velocity exterior to the coral.

INTRODUCTION

Coral reefs are the largest shallow-water marine ecosystem. They form the habitat of more than 25% of all marine life, though they cover less than 1% of the ocean floor. In addition, coral reefs provide natural protection against storms and coastal erosion. But most of the world's corals are currently under serious threat

Developing methods for measuring the flow field inside coral colonies is a key issue for understanding coral nutrient uptake, photosynthesis and wave dissipation capabilities [1-3]. Most of the physical and numerical experiments conducted previously have measured or modeled the flow over and external to the coral reef canopies, and theory and computations have treated the corals as an isotropic porous medium [4]. Experimental studies are also constrained due to the limitations of the measurement techniques and the limited environmental conditions in the laboratory. Numerical simulations can be an answer to overcome some of these shortcomings. Here, we compute the flow through and around a single *Pocillopora* coral colony whose geometry was obtained from the coral skeleton via computed tomography scanning.

METHODS AND PROCEDURES

The immersed boundary (IB) method was implemented in order to handle the complex boundary. The *Pocillopora* coral colony geometry we used was obtained from the coral skeleton via computed tomography scanning by our colleagues in the Environmental Fluid Mechanics Research Laboratory at the Technion – Israel Institute of Technology.

The IB methodology applied in this work solves the Navier-Stokes equation in all liquid and mixed cells. Large eddy simulation (LES) was chosen as the framework in which the IB technique was implemented, so that the turbulent flow field could be captured without requiring extensive modeling. The largest scales of motion are calculated explicitly in LES while the effects of the small scales on the large scales, or the sub grid dynamics, are modeled. In the present study, a top-hat filter in physical space is applied implicitly by the finite difference operators. The resulting filtered equations of motion are:

$$\frac{\partial \bar{u}_i}{\partial t} + \frac{\partial}{\partial x_j}\left(\bar{u}_i \bar{u}_j\right) = -\frac{1}{\rho}\frac{\partial \bar{P}}{\partial x_i} - \frac{\partial \tau_{ij}}{\partial x_j} + \upsilon \frac{\partial^2 \bar{u}_i}{\partial x_j x_j} + f_i$$

$$\frac{\partial \bar{u}_i}{\partial x_i} = 0$$

where $\bar{u}_i$ is the large-scale velocity vector, P is the pressure, ρ is the fluid density and υ is the kinematic viscosity; f represents an external body force field, which in the present case is designed to enforce the proper boundary conditions on an arbitrary immersed body that does not coincide with the grid. The effect of the small scales upon the resolved part of turbulence appears in the SGS stress term, $\tau_{ij} = \overline{u_i u_j} - \bar{u}_i \bar{u}_j$ which must be modeled. The dynamic eddy-viscosity model [5] used in this study is of the following form:

$$\tau_{ij} - \frac{\delta_{ij}}{3}\tau_{kk} = -2\upsilon_T \bar{S}_{ij} = -2\,C\Delta^2 |\bar{S}| \bar{S}_{ij}$$

where $|\bar{S}| = (2\bar{S}_{ij}\bar{S}_{ij})^{0.5}$ is the magnitude of large scale strain rate tensor,

$$\bar{S}_{ij} = \frac{1}{2}\left(\frac{\partial \bar{u}_i}{\partial x_j} + \frac{\partial \bar{u}_j}{\partial x_i}\right)$$

and the coefficient C is determined from a Lagrangian averaging procedure.

The flow domain was set up as rectangular box where X represented the streamwise direction and Y and Z the width and the height of the domain, respectively. These dimensions allowed adequate space around each coral to build natural flow inside and outside of this coral colony. To further resolve the region of interest close to the coral with enhanced mixing, the grid was locally refined.

[a] Corresponding author. Email: mdmoh81@vt.edu

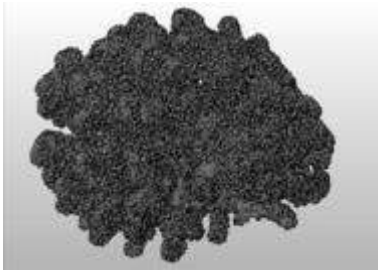

Figure 1. Rendering from STL file of *Pocillopora* coral colony.

RESULTS & DISCUSSION

To quantify the field flow variations in the computational domain, velocities were extracted as a function of location along the span of the coral. The slices of the velocity field at different locations inside the coral gave a complete picture of the flow formation inside the coral colony. The simulations were performed at Reynold numbers ranging from 4,000 to 50,000 to simulate natural low and high flow condition. The results of the simulations were compared and validated against the results of Chang *et al*. [6] for another *Pocillopora* colony geometry under similar flow condition. Surprisingly, high velocities were observed in some regions inside the coral colony. This indicates that some high velocities were still able to penetrate into the interior of coral, and were in fact accelerated.

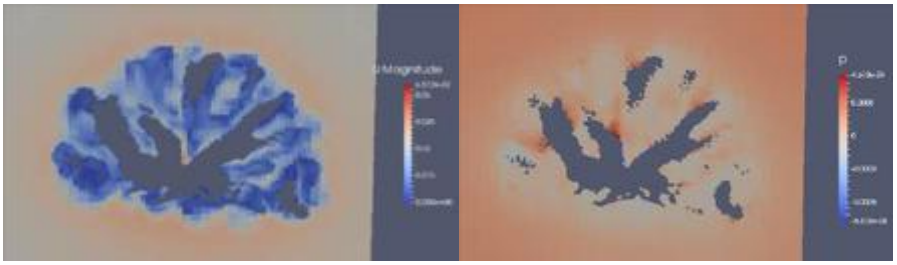

(a) (b)

Figure 2. Slices of (a) velocity and (b) pressure field inside the *Pocillopora* colony.

CONCLUSIONS

The velocity field inside a *Pocillopora* coral coral was simulated using the immersed boundary method over a range of realistic Reynolds numbers. LES was used as the framework to capture the turbulent flow. The simulations were validated against previous experimental and numerical investigations, and give clear insight into the flow formation inside a single coral colony. The findings contradicted previous numerical findings, in that internal colony velocities comparable to the external uniform velocity were found in our study. The present work will help us to understand the interaction between coral geometry and hydrodynamics and the impact of hydrodynamics on biological processes of coral.

Acknowledgments

The authors thank Elias Balaras of GWU whose immersed boundary code was used for some of the simulations, and Uri Shavit of the Technion for the STL file describing the *Pocillopora* colony geometry.

References

[1] Bilger R., Atkinson M.: Anomalous Mass Transfer of Phosphate on Coral Reef Flats. *Limnology and Oceanography* **37**(2):261-272, 1992.

[2] Mass T., Genin A.: Environmental Versus Intrinsic Determination of Colony Symmetry in the Coral Pocillopora Verrucosa. *Mar Ecol Prog Ser* **369**:131-137, 2008.

[3] Dennison W.C., Barnes D.J.: Effect of Water Motion on Coral Photosynthesis and Calcification. *Journal of Experimental Marine Biology and Ecology* **115**(1):67-77, 1988.

[4] Ong R.H.: Development and Validation of Computational Fluid Dynamics Models for Prediction of Heat Transfer and Thermal Microenvironments of Corals. *PloS one* **7**(6):e37842, 2012.

[5] Germano M.: A Dynamic Subgrid‐Scale Eddy Viscosity Model. *Physics of Fluids A: Fluid Dynamics (1989-1993)* **3**(7):1760-1765, 1991.

[6] Chang S.: Local Shear and Mass Transfer on Individual Coral Colonies: Computations in Unidirectional and Wave‐Driven Flows. *Journal of Geophysical Research: Oceans* **119**(4):2599-2619, 2014.

3D POD EXAMINATION OF STREAMWISE ENSTROPHY IN A STABLY STRATIFIED SPHERE WAKE

Zachary J. Taylor[1], Roi Gurka *[2], Alex Liberzon[1], and Peter J. Diamessis[3]
[1]*School of Mechanical Engineering, Tel Aviv University, Tel Aviv, Israel*
[2]*School of Coastal and Marine Systems Science, Coastal Carolina University, Conway, SC, US*
[3]*School of Civil and Environmental Engineering, Cornell University, Ithaca, NY, USA*

Summary A three-dimensional proper orthogonal decomposition (POD) is applied to the wake of a sphere in a stably stratified environment. The wake data are obtained through a spectral implicit LES numerical simulation highly resolved in both space and time. The Reynolds number based on the tow velocity and diameter of the sphere is $Re = 5 \times 10^3$ and the buoyancy Froude number is $Fr = 4$. Due to the nature of the stably stratified wake, the decomposition analysis suggests the possibility of decomposing the flow field into an "inner" portion and an "outer" portion, both representing different flow phenomena. This type of decomposition allows for further examination of the enstrophy variation in the two dominant features of these flows: the turbulent wake core and the internal gravity waves radiated from the wake core.

INTRODUCTION

Due to the prevalence of stably stratified environments in the atmosphere and oceans, the understanding of energy flux paths in these environments is of considerable interest. One of the most important - yet not fully understood - energy flux paths in a stably stratified medium is the formation and propagation of internal gravity waves due to turbulence [1]. It is well known that the propagation angle of internal gravity waves (IGWs) is directly related to the forcing frequency of the generating source [2]; however, the wide spectrum of frequencies typical of turbulent flows leaves many open questions about how IGWs are generated and propagated from turbulent spots in a stratified medium.

Proper orthogonal decomposition (POD) is used for a variety of purposes in the analysis and simulation of turbulent flows after first being suggested for use in the study of turbulence by Lumley [3]. The POD technique has been used to quantify the dominant flow features in many types of flows (e.g., [4]), and is often applied to the velocity field in which case the spatial modes represent those which maximize the turbulent kinetic energy. However, in other cases [5, 6] the vorticity is used as the set of basis functions. In the case where vorticity is used the spatial modes represent those which maximize the enstrophy. In each case spatial and temporal characteristics of the turbulent dynamics are revealed by examining and reconstructing the turbulent flow field based on the obtained eigenmodes.

The study of [5] has previously assessed a sphere wake in stable stratification using two-dimensional POD by focusing on key planes normal to the lateral and streamwise directions. The results of this analysis showed that each mode was responsible for different angles of IGW propagation. The boundary conditions imposed by the numerical simulations in that study meant that the data could be assessed until $Nt \approx 35$ before re-entrant IGWs contaminated the flow field. In the current study, the analysis is extended to three dimensions and the numerical simulations have incorporated sponge layers to allow for longer examination times up to approximately $Nt = 100$.

NUMERICAL SIMULATIONS

The numerical model and initialization used in the present study is detailed in [7, 8] and is best described as a spectral implicit LES solution. The definition of the geometry and the co-ordinate system are given in Fig. 1. The Reynolds number of the simulation based on the tow velocity, U, and the diameter, D, of the sphere is set to $Re = 5 \times 10^3$, and the size of the domain is approximately $X \times Y \times Z = 27D \times 27D \times 12D$ with a resolution of $256 \times 256 \times 175$. The effect of stratification is provided through the Froude number, $Fr = 2U/(DN)$, and in this case is set to $Fr = 4$, where N is the buoyancy frequency $N = \sqrt{(-g/\rho_0)/(\partial\rho/\partial z)}$, and ρ is the density.

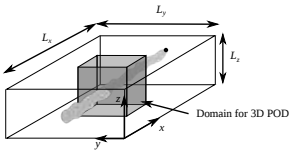

Figure 1: Schematic defining the problem geometry and the three-dimensional domain used for the POD.

*Corresponding author. Email: rgurka@coastal.edu

RESULTS & DISCUSSION

The functionality of proper orthogonal decomposition maximizes a set of functions in terms of the variance. In many implementations of POD the set of functions to be analyzed are snapshots of the velocity field at different times [9]; in these cases the modes represent those features contributing most significantly to the the turbulent kinetic energy (i.e., the variance of the velocity). In the current study, the set of functions to be analyzed are snapshots of the streamwise vorticity component, ω_x. Therefore, the modes found are those which contribute most significantly to the turbulent enstrophy. It is noted that the horizontal components of vorticity contain contributions from both wake turbulence and IGWs whereas the vertical component contains only contributions from turbulence [10].

We choose to classify the modes into two main categories: (i) those which contribute relatively more to the wake core, and (ii) those which have relatively more enstrophy outside of the wake core. The former are referred to as "inner" modes with the latter being "outer" modes. The selection of which modes are inner or outer modes is necessarily subjective. In the current study the distinction is defined by the following ratio where the wake core definitions follow from the late-time size of the wake [7], $\gamma_m = \langle \phi_m^2 \left(y \geq 4D, z \geq D\right) \rangle / \langle \phi_m^2 \left(y < 4D, z < D\right) \rangle$, where the angle brackets denote a three-dimensional spatial average. The ratio γ_m quantifies the relative streamwise enstrophy content in the outer wake versus the inner wake for an individual mode. Due to the shear in the mean velocity profile within the wake core, the enstrophy is highest in this location. Examples of so-called "inner" and "outer" modes are shown in Fig. 2.

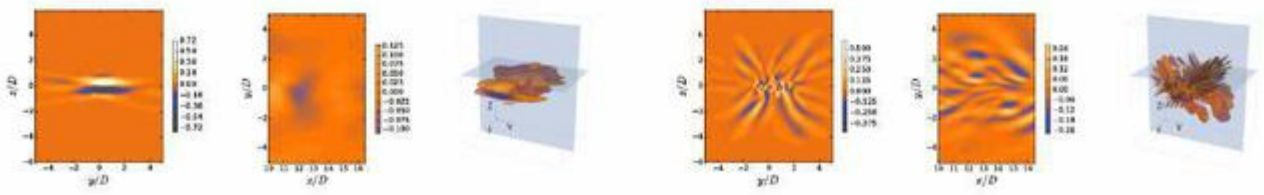

(a) (b) (c) (d) (e) (f)

Figure 2: Normalized values of the POD eigenmodes (an analogue to streamwise vorticity) showing an example of an "inner" mode (mode 1, (a)-(c)) and "outer" mode (mode 10, (d)-(f)). The y-z transect is taken at the midpoint on the x-axis, and the x-y transect is taken at $z/D = 1$ as shown by the cut planes in (c) and (f).

CONCLUSIONS

It is somewhat challenging to provide a generic description of the individual mode shapes to physical flow features since the decomposed data sets vary as a function of the flow phenomena - in this case wake turbulence and IGWs. Therefore, care must be taken to associate the mode distribution with the specific flow phenomena which is under investigation. Inherent in the POD is the ability to reconstruct flow fields using selected modes through linear superposition. By selectively reconstructing the flow fields using the "inner" modes and "outer" modes it will be shown that the relative contributions to the total enstrophy of the turbulent wake core and the IGW field can be examined and quantified using the 3D POD technique. This type of decomposition will enable the study of the coupling between turbulence and stratification and shed light on the dynamics of vorticity in this type of flow.

References

[1] S.A. Thorpe. *The Turbulent Ocean*. Cambridge University Press, 2005.

[2] B.R. Sutherland. *Internal Gravity Waves*. Cambridge University Press, 2010.

[3] J.L. Lumley. *Stochastic tools in turbulence*. Dover Publications, 1970.

[4] S.L. Tang, L. Djenidi, R.A. Antonia, and Y. Zhou. Comparison between velocity- and vorticity-based pod methods in a turbulent wake. *Exp. Fluids*, 2015.

[5] P.J. Diamessis, R. Gurka, and A. Liberzon. Spatial characterization of vortical structures and internal waves in a stratified turbulent wake using proper orthogonal decomposition. *Phys. Fluids*, 22:086601, 2010.

[6] Z.J. Taylor, G.A. Kopp, and R. Gurka. Distribution of spanwise enstrophy in the near wake of three symmetric elongated bluff bodies at high Reynolds number. *Phys. Fluids*, 25:055103, 2013.

[7] P.J. Diamessis, G.R. Spedding, and J.A. Domaradzki. Similarity scaling and vorticity structure in high-reynolds-number stably stratified turbulent wakes. *J. Fluid Mech.*, 671:52–95, 2011.

[8] A.M. Abdilghanie and P.J. Diamessis. The internal gravity wave field emitted by a stably stratified turbulent wake. *J. Fluid Mech.*, 720:104–139, 2013.

[9] T.R. Smith, J. Moehlis, and P. Holmes. Low-dimensional modeling of turbulence using the proper orthogonal decomposition: A tutorial. *Nonlinear Dyn.*, 41:275–307, 2005.

[10] J.J. Riley and M.-P. Lelong. Fluid motions in the presence of strong stable stratification. *Annu. Rev. Fluid Mech.*, 32:613–657, 2000.

NEW TURBULENT LARGE-SCALE MAGNETIC DYNAMO MECHANISM

Krzysztof A. Mizerski*[1]

[1]*Department of Magnetism, Institute of Geophysics, Polish Academy of Sciences - Centre for Polar Studies KNOW, Leading National Research Centre, Warsaw, Poland*

Summary Among the large scale magnetic dynamo mechanisms occurring in turbulent MHD flows in many astrophysical objects such as stars, planets, accretions disks, galaxies etc. the so-called α-effect based on nonlinear interactions between the velocity and the magnetic fields of the fluctuating turbulent components is without a doubt the most commonly invoked. The large scale electromotive force, whcih is responsible for generation of the mean magnetic field is calculated as the cross-product of the wave-like solutions of the linearised equations for the velocity $\mathbf{u}'$ and magnetic field $\mathbf{b}'$ of the same mode, i.e. with the same complex growth rate. Here it is demonstrated that there exists a mechanism for mean electromotive force generation based on interactions of turbulent small scale fields of different modes, which does not even require the fluid's resistivity to operate and which is potentially very effective.

INTRODUCTION

The mean field theory [1, 2] is most commonly used to describe large scale magnetic fields in natural systems. It is based on the following induction equation for magnetic field resulting from the Maxwell laws and the OhmâĂŹs law and averaged over a statistical ensemble

$$\frac{\partial \langle \mathbf{B} \rangle}{\partial t} = \nabla \times (\langle \mathbf{u} \rangle \times \langle \mathbf{B} \rangle) + \nabla \times \langle \mathbf{u}' \times \mathbf{B}' \rangle + \eta \nabla^2 \mathbf{B}. \tag{1}$$

The ensemble average removes the quickly varying in space and time turbulent fluctuations in magnetic and velocity fields, $\mathbf{B}'$ and $\mathbf{u}'$, leaving the fields $\langle \mathbf{B} \rangle$ and $\langle \mathbf{u} \rangle$ which possess only slowly varying components. The averaged interactions of small scale fluctuations generate a large scale electromotive force (EMF) $\langle \mathbf{u}' \times \mathbf{B}' \rangle$, which is a physical foundation of the mechanism of generation of the large scale magnetic fields.

THE NEW MECHANISM

The mean electromotive force is typically calculated as an average of the cross product of the perturbation velocity and magnetic fields corresponding to a single eigenmode obtained from linearised problem. In such case, it was shown by [1], that generation of the mean EMF is impossible without the magnetic diffusion, which creates a phase shift between the velocity and magnetic fields within one eigenmode, i.e. perturbation fields associated with the same complex eigenvalue. However, in [3] it was shown, that the interactions between different unstable tidal modes lead to generation of the electromotive force and consequently, the possibility of exciting the magnetic dynamo instability, i.e. large scale magnetic field generation through the well-known α-effect. It was also demonstrated for the first time, that the magnetic dissipation (i.e. the fluidâĂŹs resistivity) is not necessary for generation of the electromotive force. A new mechanism of the EMF generation was found, based on interactions between two eigenmodes with the same wave-vector and the EMFs were calculated, generated by both, the resonance modes excited through the parametric instability mechanism and horizontal modes excited by interactions of the Coriolis force and strain in the basic elliptic flow.

The theory of [3] is further developed in here on general grounds for the basic flow $\mathbf{U}_0$ in the form of axial jet and arbitrary geometry. It is demonstrated that in the two asymptotic cases of double limits $kU_0 \ll \Omega k/k_z$ and either $\left|\langle \mathbf{B} \rangle \cdot \mathbf{k}/\sqrt{\mu_0 \rho}\right| \ll |2\boldsymbol{\Omega} \cdot \mathbf{k}/k|$ or the opposite $|2\boldsymbol{\Omega} \cdot \mathbf{k}/k| \ll \left|\langle \mathbf{B} \rangle \cdot \mathbf{k}/\sqrt{\mu_0 \rho}\right|$, where $\mathbf{k}$ is the wave-vector and $\boldsymbol{\Omega} = \Omega \hat{\mathbf{e}_z}$ is the background rotation, the large scale electromotive force induced via interactions between fluctuations belonging to two different eigenmodes, i.e.

$$\mathbf{u}' = C_1 \mathbf{u}'^{(1)} + C_2 \mathbf{u}'^{(2)}, \qquad \mathbf{B}' = C_1 \mathbf{B}'^{(1)} + C_2 \mathbf{B}'^{(2)} \tag{2}$$

$$\begin{aligned} \boldsymbol{\mathcal{E}} &= \frac{1}{2} \Re\mathfrak{e} \left(\mathbf{u}' \times \mathbf{B}'^{*} \right) \\ &= \frac{1}{2} \sqrt{\mu_0 \rho} \Re\mathfrak{e} \left[\left(C_1 \hat{\mathbf{u}}^{(1)} \mathrm{e}^{\mathrm{i}\omega_1 t} + C_2 \hat{\mathbf{u}}^{(2)} \mathrm{e}^{\mathrm{i}\omega_2 t} \right) \mathrm{e}^{\mathrm{i}\mathbf{k}\cdot\mathbf{x}} \times \left(C_1^* \hat{\mathbf{B}}^{(1)*} \mathrm{e}^{-\mathrm{i}\omega_1 t} + C_2^* \hat{\mathbf{B}}^{(2)*} \mathrm{e}^{-\mathrm{i}\omega_2 t} \right) \mathrm{e}^{-\mathrm{i}\mathbf{k}\cdot\mathbf{x}} \right] \\ &= \frac{1}{2} \sqrt{\mu_0 \rho} \Re\mathfrak{e} \left[C_1 C_2^* \hat{\mathbf{u}}^{(1)} \times \hat{\mathbf{B}}^{(2)*} \mathrm{e}^{\mathrm{i}\Delta\omega t} + C_1^* C_2 \hat{\mathbf{u}}^{(2)} \times \hat{\mathbf{B}}^{(1)*} \mathrm{e}^{-\mathrm{i}\Delta\omega t} \right], \end{aligned} \tag{3}$$

*Corresponding author. Email: kamiz@igf.edu.pl

oscillates on a timescale $1/\Delta\omega$ much larger than that of the mean magnetic field growth and hence can lead to mean field dynamo, as long as $k_z/k \ll 1$. In the above $\Delta\omega = \omega_1 \circ \omega_2$ denotes the difference between the two eigenvalues associated with the two interacting eigenmodes.

The new mechanism of EMF generation based on the interactions between fluctuations of the velocity and magnetic fields with the same wavelength of a structure resulting from superposition of at least two different eigenmodes can be particularly effective in systems with degenerate (multiple) eigenvalues. In such case the superposition of eigenmodes associated with one eigenvalue and their nonlinear interactions result in the EMF growing in time as t to a power dependent on multiplicity (and structure) of the eigenvalue, which enhances the mean field dynamo action. In the case of negligible resistivity of the fluid, which extracts the new mechanism by eliminating the mean EMF generation through resistive phase shift between velocity and magnetic fields, the large scale elctromotive force induced in systems with multiple eigenvalues takes the forllowing form

$$\mathbf{u}' = C_1\mathbf{u}'^{(1)} + C_2 t\mathbf{u}'^{(2)}, \qquad \mathbf{B}' = C_1\mathbf{B}'^{(1)} + C_2 t\mathbf{B}'^{(2)} \tag{4}$$

$$\begin{aligned}
\boldsymbol{\mathcal{E}} &= \frac{1}{2}\Re\mathfrak{e}\left(\mathbf{u}' \times \mathbf{B}'^{*}\right) \\
&= \frac{1}{2}\sqrt{\mu_0\rho}\Re\mathfrak{e}\left[\left(C_1\tilde{\mathbf{u}}^{(1)} + C_2 t\tilde{\mathbf{u}}^{(2)}\right)\mathrm{e}^{\mathrm{i}(\mathbf{k}\cdot\mathbf{x}+\omega t)} \times \left(C_1^{*}\tilde{\mathbf{B}}^{(1)*} + C_2^{*}t\tilde{\mathbf{B}}^{(2)*}\right)\mathrm{e}^{-\mathrm{i}(\mathbf{k}\cdot\mathbf{x}+\omega t)}\right] \\
&= t\frac{1}{2}\sqrt{\mu_0\rho}\Re\mathfrak{e}\left[C_1C_2^{*}\tilde{\mathbf{u}}^{(1)} \times \tilde{\mathbf{B}}^{(2)*} + C_2C_1^{*}\tilde{\mathbf{u}}^{(2)} \times \tilde{\mathbf{B}}^{(1)*}\right],
\end{aligned} \tag{5}$$

where λ_1, λ_2, λ_3 and λ_4 are constants and the subscripts 1 and 2 at the fluctuating velocity and magnetic fields correspond to two different eigenmodes assiciated with the same eigenvalue. The EMF obtained in such a way grows linearly in time, however, in the case of higher multiplicites of eigenvalues in the problem the dominant contrbution to the mean electromotive force can grow as a higher power of t.

CONCLUSIONS

A new mechanism of generation of mean electromotive force is presented, which operates even for perfectly conducting fluids. The physical basis of the mechanism relies on nonlinear interactions between the magnetic and velocity fields of two different MHD waves, which can produce non-zero EMF that either oscillates in time very slowly or grows in time as a power of t. A thorugh analysis of this new mechanism may allow for determination of its role in generation of astrophysical large scale magnetic fields, however, the relation of this mechanism to small scale dynamo mechanisms operating at high magnetic Reynolds numbers $Rm = U_0L/\eta \gg 1$ needs to be established.

References

[1] Moffatt H. K.: Magnetic field generation in electrically conducting fluids. Cambridge University Press, 1978 (available at http://moffatt.tc).

[2] Tobias, S.M., Cattaneo, F., Boldyrev, S.: MHD Dynamos and Turbulence, in Ten Chapters in Turbulence. ed. by P.A. Davidson, Y. Kaneda and K.R. Sreenivasan, pp. 351-404, Cambridge University Press: Cambridge, 2013.

[3] Mizerski, K.A., Bajer, K., Moffatt, H.K., The mean electromotive force generated by elliptic instability, J. Fluid Mech. 707, 111-128, 2012.

THE INFLUENCE OF PARTICLES ON TURBULENCE INTENSITY IN A HIGH REYNOLDS NUMBER ABL FLOW

Hai-Hua Gu[1], Tian-Li Bo[1] & Xiao-Jing Zheng [1,2a)]
[1]*Key Laboratory of Mechanics on Western Disaster and Environment, Lanzhou University, Lanzhou, Gansu, China*
[2] *Electronical and Mechanical Engineering, Xidian University, Xi'an, Shaanxi, China*

Summary A dust storm is a particle-laden two-phase flow with a Reynolds number of up to $Re_\tau(10^6)$. The effect of particles on wind flow has gotten more and more attention; meanwhile it is important to understand the turbulence statistics in boundary-layer flow with particles. Therefore, field observations were conducted in the Desert of Qingtu Lake in western China, Results from these data revealed that a) the presence of sand particles appears to enhance both the streamwise and vertical turbulence intensities, with increases up to 20%; b) vertical turbulence intensity is likely to be more affected by particle than streamwise intensity; and c) with an increase in Reynolds number, the increases of streamwise and vertical intensities caused by particles are likely to be more significant. We also provide a physical interpretation of these phenomena. These results contribute to understanding the turbulence characteristics of a high Reynolds number ABL flow with particles.

INTRODUCTION

It is important to understand the turbulence statistics, such as how turbulent kinetic energy is a key factor in maintaining turbulent flow (Perry et al , 1986 ; Marusic et al , 1997). However, most measurements have been expended in turbulent wind field or DNS, meanwhile this previous measurements almost in clean air flows (Hultmark et al, 2012; Hutchins and Marusic, 2007). Therefore, the analysis of the effect of particles on wind flow will contribute to understanding the turbulence characteristics of a high Reynolds number ABL flow.

As we all know, a dust storm is a particle-laden two-phase flow with a Reynolds number of up to $Re_\tau(10^6)$. The effect of particles on wind flow has gotten more and more attention from scholars. Wei Zhang (2008) comparison of the turbulence statistics with and without sand reveals that the significant influence of sand movement on the wind field; Kenning and Crowe (1997) also discovery that the turbulence intensity variation was related to the turbulent wakes separated behind the particles; Bailiang Li(2012) used a commercial LDA system in wind tunnel, they find that turbulence intensities and Reynolds stress increase with the particles and that aeolian saltation increase the magnitude but not the frequency of burst-sweep events. But field experiments, the presence of sand are how to influence the development of turbulence? How to influence the turbulence intensity? At present, we do not know this clearly, Therefore, field observations were conducted in the Desert of Qingtu Lake in western China (E: 103° 40′ 03″, N: 39° 12′ 27″). Results from these data revealed the effect of particles on turbulence flow.

FIELD MEASUREMENTS AND PRE-TREATMENT

Field observations were conducted in the Desert of Qingtu Lake in western China (E: 103° 40′ 03″, N: 39° 12′ 27″). 3D sonic anemometers (50Hz) and a sand particle counter (1Hz) were used to measure the three components of wind velocity and sediment process (sand transport rate Q (g/m/s)) under the condition of time synchronization. The 3D sonic anemometers installed at 11 levels (0.9m,1.71m,2.5m,3.49m,5m,7.15m,8.5m,10.24m,14.65m,20.96m,30m, just as Fig 1) and the sand particle counter installed at 4 levels (0.2 m, 0.3 m, 0.5 m and 0.7 m). This paper distinguishes the flow with or without sand from the sediment process Q at 0.2m.Of course, before analyzing the data, we calibrate and correct the raw data of sediment process. The more details can be found from Masao Mikami et al (2005). The process of diversion and subtracting synoptic-scale fluctuations from the raw wind-velocity signals and more details can be found from Liu, H. Y. et al (2014).

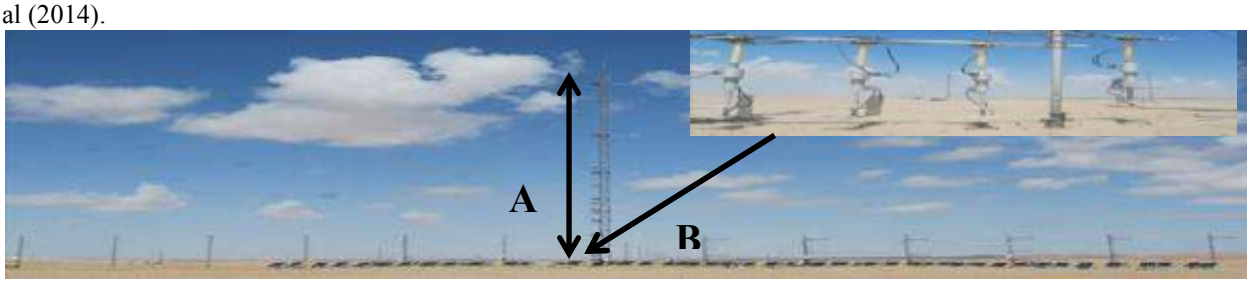

Figure 1 the 3D sonic anemometers installed and the sand particle counter installed at the test site. A shows the 3D sonic anemometers installed at 11levels and B shows the SPC installed at 4 levels.

[a)] Corresponding author. Email: guhh13@lzu.edu.cn.

Due to space limitations, The mean velocity profiles and the streamwise turbulence intensities (Picture doesn't show) show that the near-neutral ASL at the test site behaves like a canonical turbulent boundary layer during the selected hour of data. The more details is same as (Liu, H. Y. et al (2014); Hutchins. et al (2012)) .

RESULTS

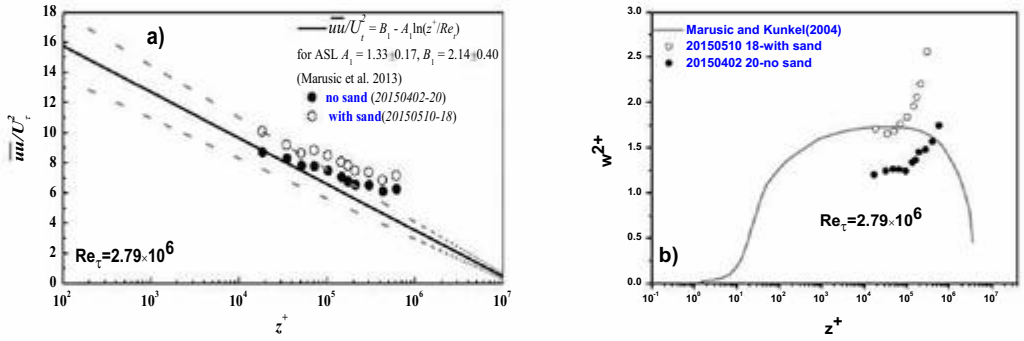

Figure 2 Figure a shows streamwise turbulent intensities normalized by U_τ at different heights The solid line indicates the normalized streamwise velocity fluctuation from Marusic et al .2013, dash line shows the variation of parameters A and B; Figure b shows vertical turbulent intensities. The dash line shows the formulation of Marusic and Kunkel (2004). Both of figures of Solid dot and circle are current ASL data with and without sand at Re_τ =2.79× 10^6.

Figure 2a is a comparison of the streamwise turbulent intensity with and without sand. Due to space limitations, we just show one group data at Re_τ =2.79× 10^6(The same of following analysis) . Marusic et al .2013 have given variation of parameters A and B about streamwise turbulent intensity, we can seem that our data agree well with their results without sand. Considering the formulation is presented based on a canonical zero-pressure-gradient turbulent boundary layer, it is reasonable that the ASL can also be considered as a model of the canonical bounder layer. But when full of sand of flow, we can seem the streamwise turbulent intensity increasing clearly, about 15%.

Figure 2b is a comparison of the vertical turbulent intensity with and without sand.From this figure, we see a different between our results and Marusic and Kunkel (2004), which is mainly in atmospheric surface layer flows, the top surface layer with a certain energy input, resulting in difference with low Reynolds number experiments. At the same time, we find the presence of sand will increase vertical turbulent kinetic energy (about 22%), which are consistent with the laboratory results (Bailiang Li, 2012 ; zhang et al, 2008). On the other hand, vertical turbulence intensity is likely to be more affected by particle than streamwise intensity.

CONCLUSIONS

The enhanced turbulence in the presence of sand particles can be explained by the wake structure behind individual sand particles, just the same as Wei Zhang (2008). In the particle-bed collision event, the vertical turbulence intensity is more influenced than the streamwise turbulence intensity, which could be a direct result of the particle-bed collision. During this progress, the gravity plays an important role, which will cause the increasing of vertical turbulence intensity. The analysis of this paper, we show this influence of particles on flow by field observations, which contribute to understanding the turbulence characteristics of a high Reynolds number ABL flow with particles.

References

[1] Perry, A. E., S. Henbest, and M. S. Chong. "A theoretical and experimental study of wall turbulence." Journal of Fluid Mechanics 165 (1986): 163-199.

[2] Marusic, I., A. K. M. Uddin, and A. E. Perry. "Similarity law for the streamwise turbulence intensity in zero-pressure-gradient turbulent boundary layers." Physics of Fluids (1994-present) 9.12 (1997): 3718-3726.

[3] Hutchins, Nicholas, and Ivan Marusic. "Large-scale influences in near-wall turbulence." Philosophical Transactions of the Royal Society of London A: Mathematical, Physical and Engineering Sciences 365.1852 (2007): 647-664.

[4] Zhang, Wei, Yuan Wang, and Sang Joon Lee. "Simultaneous PIV and PTV measurements of wind and sand particle velocities." Experiments in Fluids45.2 (2008): 241-256.

[5] Li, Bailiang, and Cheryl McKenna Neuman. "Boundary‐layer turbulence characteristics during aeolian saltation." Geophysical Research Letters39.11 (2012).

[6] Mikami M, Yamada Y, Ishizuka M, et al. Measurement of saltation process over gobi and sand dunes in the Taklimakan desert, China, with newly developed sand particle counter[J]. Journal of Geophysical Research: Atmospheres (1984–2012), 2005, 110(D18).

[7] Liu H Y, Bo T L, Wang G H, et al. The Analysis of Turbulence Intensity and Reynolds Shear Stress in Wall-Bounded Turbulent Flows at High Reynolds Numbers[J]. Boundary-layer meteorology, 2014, 150(1): 33-47.

[8] Kunkel, Gary J., and Ivan Marusic. "Study of the near-wall-turbulent region of the high-Reynolds-number boundary layer using an atmospheric flow."Journal of Fluid Mechanics 548 (2006): 375-402.

THE INFLUENCE OF LARGE-SCALE TURBULENT STRUCTURE ON SALTATION SAND TRANSPORT

Ting Jin[1, 2a)], Ping Wang[1,2], Xiaojing Zheng[3], Shengjun Feng[1,2]
[1]*Key Laboratory of Mechanics on Western Disaster and Environment, Lanzhou University, Lanzhou, China*
[2]*Department of Mechanics, Lanzhou University, Lanzhou, China*
[3]*School of Electronical and Mechanical Engineering, Xidian University, Xi'an, China*

Summary Saltation is an important process on aeolian sand transport, as it contributes to dust raising, bedform dynamics, and aeolian abrasion. However, the mass flux prediction remains notoriously unreliable, especially for close-to-onset saltation. Large eddy simulation and discrete particle method are employed to model the close-to-onset sand saltation in this paper. Two kinds of wall models for large eddy simulation are used as wall boundary condition, the standard model that can predict the mean wall shear stress and a new wall-model that is able to predict the fluctuating wall shear-stress from a large-scale velocity input. The results show that the latter can lead to more fluid-sheared particles and therefore higher mass flux, which demonstrate the significance of large-scale turbulent structure to unsteady environmental sediment transport.

INTRODUCTION

Aeolian sand saltation contributes the majority of mass flux during sand/dust storm events [1]. The onset of saltation transport is classically associated with a critical mean shear velocity. However, the recent measurements [2][3]suggested that discontinuity and intermittency dominate saltation transport when the wind velocity fluctuates around the threshold. Most importantly, the mass flux prediction remains notoriously unreliable, especially for close-to-onset saltation [4]. By analyzing the observed data, it is believed that the coherent structure in the turbulent wind in atmospheric surface layer is crucial [5].

There are four key sub-processes [4] in saltation. We focus on aerodynamic entrainment process first. Based on recent researches on high Reynolds number wall-bounded turbulent flows that the large and very-large scale motions in the outer region interact with the near-wall region, a model (IOSI) for the wall shear stress prediction was proposed[6] and applied in large eddy simulation[4]. Comparing to standard wall model [7], it is able to reconstruct the fluctuating wall shear-stress based on large-scale log-layer velocity input, which will directly influence the number of aerodynamic-entrainment sand particle. Therefore, large eddy simulation and discrete particle method are employed to model saltation.

The scale-dependent dynamic subgrid-scale model [8] is adopted in equation (1) to calculated filter stress. The governing equations (1) are discretized in time using the Crank-Nicholson scheme and resolved in space using the second-order central difference scheme with a staggered mesh. The computational domain in each direction (L_x , L_y , L_z) is (8 ,1,2 π)m, where x (i = 1), y (i = 2), and z (i = 3) denote the streamwise, vertical and spanwise coordinates, respectively. The upper boundary has a stress-free condition, i.e. ∂u/∂y=∂w/∂y=0, where u, v, and w are the streamwise, vertical and spanwise velocity, respectively. Periodic boundary conditions are used in the streamwise and spanwise direction. At the surface, the wall stresses are provided based on aforementioned wall models.

$$\frac{\partial \overline{u}_i}{\partial t}+\frac{\partial \overline{u}_i\,\overline{u}_j}{\partial x_j}=-\frac{1}{\rho}\frac{\partial \overline{p}}{\partial x_i}+\nu\frac{\partial^2 \overline{u}_i}{\partial x_j x_j}+\frac{\partial \overline{\tau}_{ij}}{\partial x_j}+F_i;\qquad \frac{\partial \overline{u}_i}{\partial x_i}=0$$

Sand particles are presumed to travel only under the act of drag force and the gravity force,

$$m_P\frac{d\mathbf{u}_P}{dt}=\frac{1}{2}\rho C_D A\left|\mathbf{v}-\mathbf{u}_P\right|(\mathbf{v}-\mathbf{u}_P)+m_P\mathbf{g};\qquad \frac{d\mathbf{x}_P}{dt}=\mathbf{u}_P$$

where m_p $\mathbf{u}_p$ $\mathbf{x}_p$ are the particle density, velocity and position vector, C_D, A denote the drag coefficient and cross-sectional area of sand particle, ρ and $\mathbf{v}$ are the atmospheric density and wind velocity vector at particle position obtained through linear interpolating. The particle number of aerodynamic liftoff is proportional to the excess shear stress $N=10^7\cdot(\ -\ _c)$. The splash process is modeled according to the stochastic methods [9].

The Reynolds number of the simulated turbulent wind is Re =22000. The density and particle diameter are 2650 kg/m^3 and 0.48 mm so that the mean wall shear-stress is slightly larger than the particle's threshold stress, □□=1.05□$_c$. The mean wind velocity profile with and without saltation sand are shown in figure 1. It can be seen that the wall model has a small effect on mean velocity profile in the outer-regions of the boundary layer without sand particle. However, the mean velocity apparently decrease in the saltation layer. The evolution of aerodynamic entrainment is show in fig.2， indicating that particle number lifted directly by aerodynamic shear is much larger than in fluctuating wall shear stress case. Apparent large structures existed for the IOSI-model simulation which deserves further discussion.

[a)] Corresponding author. Email: jint15@lzu.edu.cn..

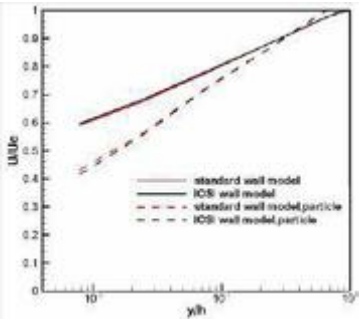

Fig. 1 Mean velocity profile with and without sand saltation.

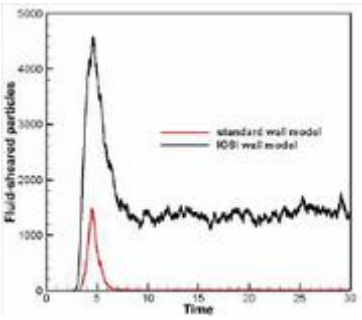

Fig. 2 Particle number entrained by aerodynamic shear.

CONCLUSIONS

The inner outer interaction wall model which can predict fluctuating wall shear stress is included in large eddy simulation to discuss the effect of large scale turbulent structure on sand saltation. The model results show that the aerodynamic liftoff particles are significantly increased.

ACKNOWLEDGEMENT

This research was supported by Grants from the National Natural Science Foundation of China (Nos.11490553, 11302090, 11232006) and Innovative Research Group of the National Natural Science Foundation of China (No. 11421062).

References

[1] Sidebottom W, Cabrit O, Marusic I, et al. Modelling of Wall Shear-Stress Fluctuations for Large-Eddy Simulation[J]. 2014.
[2] Stout J E, Zobeck T M. Intermittent saltation[J]. Sedimentology, 1997, 44(5): 959-970.
[3] Carneiro M V, Rasmussen K R, Herrmann H J. Bursts in discontinuous Aeolian saltation[J]. Scientific reports, 2015, 5.
[4] Wang P, Zheng X. Saltation transport rate in unsteady wind variations[J]. The European Physical Journal E, 2014, 37(5): 1-11.
[5] Baas A C W. Complex systems in Aeoliangeomorphology[J]. Geomorphology, 2007, 91(3): 311-331.
[6] Mathis R, Marusic I, Chernyshenko S I, et al. Estimating wall-shear-stress fluctuations given an outer region input[J]. Journal of Fluid Mechanics, 2013, 715: 163-180.
[7] Piomelli U. Wall-layer models for large-eddy simulations[J]. Progress in aerospace sciences, 2008, 44(6): 437-446.
[8] Porté-Agel F, Meneveau C, Parlange M B. A scale-dependent dynamic model for large-eddy simulation: application to a neutral atmospheric boundary layer[J]. Journal of Fluid Mechanics, 2000, 415: 261-284.
[9] [Dupont S, Bergametti G, Marticorena B, et al. Modeling saltation intermittency[J]. Journal of Geophysical Research: Atmospheres, 2013, 118(13): 7109-7128.

A DYNAMICAL STUDY ON THE NORTH PACIFIC LOW-LATITUDE WESTERN BOUNDARY CURRENTS

Linghai Kong[1], Lingbo Kong[2], & Fujun Wang[3]

[1]*Institute of Applied Physics and Computational Mathematics, Beijing China*
[2]*School of Software Engineering, Beijing Jiaotong University, Beijing China*
[3]*Institute of Oceanology, Chinese Academy of Science, Qingdao China*

Summary A weakly-coupled evolution model of stratified ocean is proposed to build upon our knowledge on the interacting mechanism of North Pacific Low-Latitude Western Boundary Currents (NP-LLWBCs), which takes the influence of the surface wind forcing, dissipation and understratum configuration into account. The solvability of its initial and/or boundary problem is established, moreover, some analytical and numerical results on the dynamical behaviour of the currents are advanced by its simplified versions, including our comment on the decadal variability in the bifurcation of the North Pacific Current.

INTRODUCTION

Western intensified wind-driven currents are ubiquitous in world oceans, among which NP-LLWBCs, including the Mindanao Current (MC), the New Guinea Coastal Current (NGCC), the New Guinea Coastal Undercurrent (NGCUC) and the Mindanao Undercurrent (MUC), play a prominent role in the understanding of the climate dynamics and the meridional conveying of mass, heat and salt of the world ocean [1-5]. The southward flowing MC is deemed to not only blocks the surface water and the subtropical water in NGCC and NGCUC and forces them turning into the Northern Equatorial Countercurrent (NECC) and the Equatorial Undercurrent (EUC), but also constitutes the two branches of the North Equatorial Current (NEC) together with the northward flowing Kuroshio (KC), as NEC encounters its western boundary along the Philippine coast, where the bifurcation latitude indicates the separation of the subtropical and the tropical gyres of North Pacific Ocean.

Considerable progress has been achieved in the last several decades towards the dynamics of the NEC bifurcation in the oceanographic observation and mathematical modelling, with seminal works [6-14] among many others, while discrepancy still remains and the models used are usually linear ones or oversimplified. On the subject of ocean circulation models, many important contributions have also been made, among which we recommend [15-24] for more inspiration. Concerning the NP-LLWBCs, our knowledge is still not comprehensive and we need more endeavours or speculations on their driving mechanism and interacting mode, especially with the view of nonlinear evolution. This talk is an attempt at the puzzle with the Sverdrup theory and the multi-layer potential vorticity theory.

GOVERNING EQUATIONS AND MATHEMATICAL SETTINGS

With proper assumptions, such as taking dissipation or friction, bottom topography, and thickness and density of currents into account while ignoring the relative vorticity and the Indonesian throughflow (ITF), our model ocean is characterized by the following two-layer evolutional system

$$\partial/\partial t\left(-(1+\theta)\psi_1+\theta\psi_2\right)+J\left(\psi_1,q_1\right)=H_1\mathrm{curl}_z\tau_T-\nabla\cdot\Phi_1,\quad \partial/\partial t\left(\theta\left(\psi_1-\psi_2\right)\right)+J\left(\psi_2,q_2\right)=-\nabla\cdot\Phi_2, \tag{1}$$

and

$$q_1=\left(H_1g\beta/f_0^2\right)f-(1+\theta)\psi_1+\theta\psi_2,\quad q_2=\left(H_2g\beta/f_0^2\right)f+\left(g/f_0\right)\eta+\theta\left(\psi_1-\psi_2\right), \tag{2}$$

$$\Phi_1=-R_1\nabla\left(-(1+\theta)\psi_1+\theta\psi_2\right)-\left(\kappa gf/f_0^2\right)\nabla\left(fH_1\right),\Phi_2=-R_2\nabla\left(\theta\left(\psi_1-\psi_2\right)\right)-\left(\kappa gf/f_0^2\right)\nabla\left(fH_2\right)-\left(g/f_0\right)\nabla\eta \tag{3}$$

in an extended ocean basin, where $\psi_i,\rho_i,i=1,2$ are the stream function (upper=1) and density ($\rho_1<\rho_2$) at the k-th layer, respectively, g is the gravitational constant, $\theta=\rho_1/\left(\rho_2-\rho_1\right)$, ψ_1 and $\psi_2-\psi_1$ are proportional to the interface displacement from the basic resting state, J is the general Jacobian operator with $J(a,b)=a_xb_y-a_yb_x$, $H_i,i=1,2$ denote the functions of layer height, $f=f\left(x,y\right),f_0$ are the Coriolis frequency equation and its reference value, respectively, $\mathrm{curl}_z\tau_T$ in this talk represents a zonally-averaged synthetic seasonal or interannual wind stress curl field with the form

$$\mathrm{curl}_z\tau_T=\mathrm{curl}_z\tau_T\left(y,t\right)=-\sum_{i=0,\mathrm{k}=0}^{1,N}M_{ik}(\mathrm{y})\sin\left(\tfrac{i\pi}{2}-k\omega t\right). \tag{4}$$

In application, $\eta=\eta\left(x,y\right)$ can be regarded as the understratum function, which can be a bottom topographic function or a shape function of an extra layer. The system can be regarded as a generalization of the Stommel model (e.g.[22]).

[1]Corresponding author. Email: kong_linghai@iapcm.ac.cn.

CONTRIBUTION

Using the weakly-coupled system ($R=(R_1,R_2)\neq 0$) and its reduced version ($R=0$), we investigate the interacting mechanism of the system. The monthly wind stress curl used in our talk is derived from the European Center for Medium-Range Weather Forecasts (ECMWF) Ocean Analysis System ORA-S3 (Figure 1) with horizontal resolution 11 and period from January 1959 to December 2009.

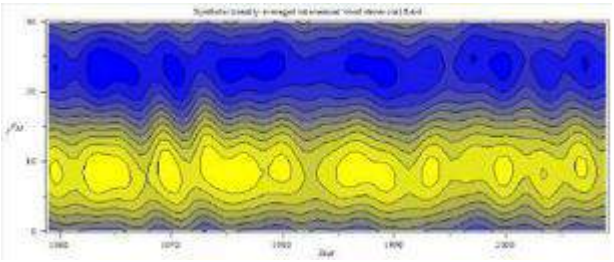

Figure 1. A synthetic zonally averaged interannual wind stress curl field from ORA-S3(1959-2009)

The solvability to the initial and/or boundary problem of the weakly coupled system 1)-3) is developed firstly, and the existence and uniqueness of its solutions are established to present an evolution pattern of the currents. With Sverdrup's balance, its formal solutions are presented for each layer. In the case of $0<R_i=1, i=1,2$, it can be seen as a viscosity regularization of its corresponding transport system, i.e. the case of $R_i=0, i=1,2.$ Our upper layer equation can be regarded as a generalization of the reduced gravity equation given by Qiu and Lukas (1996).

Secondly, with further simplifications, such as $\Delta\psi_1 \propto \varepsilon\psi_1$, the transport system of wind-induced and form-dragged type is used to interpret their interacting mode of the two layers. In this case, the system can be regarded as a generalization of Meyer's single layer transport equation. Analytical solutions of the system are established and applied to enlighten the cause of swerve for the western boundary currents and the decadal variability in the NEC bifurcation latitude.

Some numerical results on application of our proposed models are issued.

References

[1] Nitani H.: Beginning of the Kuroshio, in Kuroshio: Its Physical Aspects, edited by H. Stommel and K Yoshida 129-163,1972.

[2] Lindstrom E., Lukas R., Fine R. et al.: The western equatorial Pacific Ocean circulation study. *Nature* **330**:533-537,1987.

[3] Hu D., Cui M.: The western boundary current of the Pacific and its role in the climate. *Chin. J. Oceanol. Limnol.* **9**:1-14,1991.

[4] Lukas R., Firing E., et al.: Observations of the Mindanao Current during the Western Equatorial Pacific Ocean Circulation study. *J. Geophys. Res.*,**96:**7089-7104,1991.

[5] Kawabe M., Fujio S.: Pacific ocean circulation based on observation. *J. Oceanogr.* **66**:389-403,2010.

[6] Meyers G.: On the annual Rossby wave in the tropical North Pacific Ocean. *J. Phys. Oceanogr.* **9(4)**:663-674,1979.

[7] Toole J. M. Zou E.,Millard R. C.: On the circulation of the upper waters in the western equatorial Pacific Ocean, *Deep Sea Res., Part A*,**35**:1451-1482,1988.

[8] Fine R. A., Lukas R. B., Bingham F. M., et al.: The western equatorial Pacific: A water mass crossroads. *J. Geophys. Res.* **99**:25063-25080,1994.

[9] Qiu B., Lukas R.: Seasonal and interannual variability of the North Equatorial Current, the Mindanao Current, and the Kuroshio along the Pacific western boundary. *J. Phys. Oceanogr.* **33**:5-18,1996.

[10] Wang F., Hu D.: Dynamic and thermohaline properties of the mindanao undercurrent I. Dynamic structure. *Chin. J. Oceanol. Limnol.*, **16(2)**:122-127,1998.

[11] Qu T. Lukas R.: On the bifurcation of the North Equatorial Current in the Pacific. *J. Phy. Oceano.*,**33(5)**:5-18, 2003.

[12] Kim Y. Y., Qu T., Jensen T. et al.: Seasonal and interannual variations of the North Equatorial Current bifurcation in a high-resolution OGCM. *J. Geophys. Res.* **109**:C03040, 2004.

[13] Jensen T. G.: Bifurcation of Pacific North Equatorial Current in a wind-driven model: response to climatological winds. *Ocean Dynamics* **61:**1329-1344**,** 2011**.**

[14] Zhao J., Li Y., Wang F.: The role of Mindanao dome in the variability of the Pacific North equatorial current bifurcation. J. Oceanogr. 69:313-327,2013.

[15] Munk W. H.: On the wind-driven ocean circulation. *J. Meteorol.* **7**: 79-93, 1950.

[16] Carrier G. F., Robison A. R.: On the theory of the wind-driven ocean circulation. *J. Fluid Mech.* **12(1)**:49-80, 1962.

[17] Holland W.R.: The role of mesoscale eddies in the general circulation of the ocean-numerical experiments using a wind-driven quasi-geostrophic model. *J. Phys. Oceanogr.* **8**:363-392,1972.

[18] Rhines P. B., Young W. R.: A theory of wind-driven circulation. I. Mid-ocean gyres. *J. Marine Research* **40(suppl.)**:559-596, 1982.

[19] Young W. R ,Rhines P. B..: A theory of wind-driven circulation. II. Gyres with western boundary layers. *J. Marine Research* **40(3)**:849-872, 1982.

[20] Pedlosky J. : Geophysical fluid dynamics. Springer, Berlin, 1987.

[21] Medjo T. T.: Robust Control Problems associated with the multilayer quasi-geostrophic equations of the ocean. *Appl. Math. Optim.* **51**:333-360,2005.

[22] Valis G. K.: Atmospheric and Ocean Fluid Dynamics: Fundamentals and Large-Scale Circulation. Cambridge University Press, 2006.

[23] Mu L., Zhong L., et al.: Low-frequency variability of a semi-closed sea induced by the circulation in an adjacent ocean in a wind-driven, quasi-geostrophic, eddy-resolving simulation. *Ocean Dynamics*,**61**:1459-1473,2011.

[24] Crisciani F., Badin G.: A note on the symmetric and antisymmetric constituents of weakly nonlinear solutions of a classical wind-driven ocean circulation model. *Eur. Phys. J. Plus* **129**:142,2014.

WATER LEVEL EXTREMES AT THE BALTIC SEA COAST

Tarmo Soomere[1a)]
[1]*Institute of Cybernetics at Tallinn University of Technology, Tallinn, Estonia*

Summary The paper describes several new options to analyse and forecast possible changes in extreme water levels at the coasts of sea areas hosting substantial subtidal weekly-scale variations in the water level. The test area is the Baltic Sea. For a certain averaging interval (about 8 days) there exists a straightforward separation of the total water level into components driven by Gaussian and Poisson processes and representing the basin-scale and local phenomena, respectively. The contribution of the basin-scale phenomena into the increase in extreme water levels is almost constant for the entire study area whereas the contribution of local storm surges exhibit substantial spatial variations. The entire pattern of the changes in water level extremes signals a rotation of strong wind directions rather than an increase in the wind speed.

INTRODUCTION

The risks and damages associated with coastal flooding that are associated with an increase in the magnitude of extreme storm surges are one of the largest concerns of countries with extensive low-lying nearshore areas. It is often unclear which component of the water level (or its physical driver) is responsible for an increase in the extreme water levels. For example, changes in high sea levels matched mean sea level changes on the German North Sea coast prior to the mid-1950s and from about 1990 onwards, but obvious mismatch was observed in the 1960s to 1980s [1]. The largest challenges in the analysis of the water level data sets from the past and in modelling of the future (extreme) water levels offer semi-enclosed water bodies such as the Baltic Sea. The sea-level change in such basins may be faster than in the adjacent regions and the course of water level may depend on specific factors such as local salinity or spatial variations in the tectonic motions.

The core question is: Which mechanism has the largest contribution into the changes in sea level extremes and associated coastal floodings? Classic approaches address this question by means of a separation of the water level course into periodic and random components, or components driven by fundamentally different mechanisms such as the long-term mean and its slow variations, tides and storm surges. We demonstrate that a natural, straightforward and rich in content separation can be produced for sea areas of certain type by means of a surprisingly simple operation of the running average.

MODELLED AND OBSERVED TIME SERIES OF WATER LEVEL

The focus is on the possibilities of the analysis and modelling of large-amplitude subtidal (with time scales from a day up to a few weeks) variations in the water volume of semi-enclosed water bodies from the viewpoint of possible changes in water level extremes. The presence of such variations substantially complicates the analysis of the future projections of the course of local water level extremes. For example, in the Baltic Sea these fundamentally aperiodic variations are driven by the atmospheric impact, usually occur on time scales of a few weeks and contribute about 50% of the extreme storm surges [2].

We employ time series of sea levels numerically reconstructed using the three-dimensional RCO (Rossby Center, Swedish Meteorological and Hydrological Institute) ocean circulation model and kindly provided in the framework of BONUS BalticWay cooperation. The horizontal and vertical resolutions of the model are 2×2 nautical miles (about 3.7 km) and 3–12 m, respectively. The model run for May 1961–May 2005 includes information about sea ice and is driven by a meteorological data set with a horizontal resolution of 22 km produced from the ERA-40 re-analysis. The modelled data set (sampled once in 6 h) is complemented with observed water level time series at four coastal locations in the eastern Baltic Sea: Tallinn 1945–1995, Narva-Jõesuu 1950–2010, Ristna 1950–2012 and Pärnu 1950–2010.

SEPARATION OF WATER LEVEL TIME SERIES INTO WEEKLY AVERAGE AND STORM SURGES

Application of a running average with a variable averaging length (from one day up to a few months) and subsequently evaluating the residual naturally produces a separation of the total water level into slowly and rapidly changing constituents [3]. For averaging lengths of the order of one week the distribution of the slowly changing component mimics the water volume of the entire Baltic Sea (and has, as expected, an almost Gaussian shape). The residual characterises the heights of storm surges. It contains all outliers of the water level time series for averaging intervals longer than about 3 days. Surprisingly, its distribution (equivalently, the frequency of occurrence of local storm surges of different height) almost exactly matches an exponential distribution for the 8-day average. Therefore, for this averaging length we reach a separation of the total water level into a Gaussian process (that governs the large-scale water level of the entire sea) and a component driven by a Poisson process. The slopes of the positive and negative branches of the resulting exponential distribution provide a useful quantification of different coastal sections with respect to the probability of coastal flooding and extremely low water levels.

[a)] Corresponding author. Email: soomere@cs.ioc.ee.

CONTRIBUTION OF SUBTIDAL PROCESSES AND STORM SURGES INTO EXTREME WATER LEVELS

It is well known that the water level maxima increase rapidly at many ocean coasts. This increase has a spatially variable rate of 5–10 cm/decade in the eastern Baltic Sea [4] and is relatively rapid in the interiors of bays deeply cut into the mainland and slower on the coasts of the open sea. The introduced separation makes it possible to evaluate the contribution of different processes into this increase. The weekly-scale component reflects the cumulative impact of long sequences of storms. The relevant increase rate is almost constant along the entire eastern coast of the Baltic Sea. Therefore, either the wind speed in associated storms or the duration of storm sequences has increased.

Importantly, almost all spatial variability in the trends in the total water level maxima stems from the component that reflects the impact of single storms. This component reveals almost no changes in locations that are open to the predominant directions of strong storms. The changes in the maxima of the total water level in such locations are thus almost exclusively governed by the water volume of the entire Baltic Sea. Consequently, it is very likely that the wind speed in strong storms has not increased significantly in the Baltic Sea region but the length of sequences of storms that push water into the Baltic Sea has increased.

The maxima of storm surge heights exhibit a substantial increase in bayheads of large subbasins cut deeply into the mainland such as the eastern Gulf of Riga and the eastern Gulf of Finland. Therefore, most of the changes in the spatial variability in the local water level extremes are driven by changes in single storms. This remarkable spatial variation suggests that, most likely, wind directions in strong storms may have rotated since the 1960s.

ENSEMBLE APPROACH TO HIGHLIGHT THE MAGNITUDE OF LOFAL EFFECTS

The spatially varying contribution of various drivers to the water level in the eastern Baltic Sea and the frequent presence of outliers in the observed and modelled water levels lead to large uncertainties in the projections of future extreme water levels. A natural way to more reliably evaluate return periods of extreme water levels is the use of an ensemble of projections to. An appropriate example is constructed by means of fitting several sets of block maxima (annual maxima and stormy season maxima) with the classic generalised extreme value distributions. As the shape parameter of the Generalised Extreme Value distribution changes its sign along the coast of Estonia, projections based on the Gumbel and Weibull distributions are also included. The ensemble involves projections based on two data sets (resolution of 6 h and 1 h) hindcast by different circulation models and atmospheric drivers.

For coastal segments where the observations represent the offshore water level well, the overall appearance of the ensembles signals that the errors of single projections are randomly distributed and that the median of the ensemble provides a sensible result. For locations where the observed water level involves strong local effects (e.g. wave set-up) the block maxima are split into clearly separated populations. The resulting ensemble consists of two distinct clusters, the difference between which can be interpreted as a measure of the impact of local features on the water level observations [5].

CONCLUSIONS

By means of a simple and straightforward averaging procedure we have separated the local water level time series of semi-enclosed water bodies into two components with fundamentally different probability distribution functions. A weekly-scale average large follows a Gaussian distribution whereas the residual (the total water level minus the weekly average) exhibits features of a Poisson process. The latter is not particularly surprising as the formation of storm cyclones can be described by a Poisson process. A further analysis of the contribution of these components indicates an interesting feature of climate changes in the Baltic Sea basin and possibly in other areas. Namely an increase in wind speed in strong storms is unlikely in this area but storm duration may have increased and wind direction may have rotated. In general, one or even set of a few projections based on single general extreme value distribution are not appropriate for the estimates of future extreme water levels and their return periods at the eastern coast of the Baltic Sea.

References

[1] Mudersbach, C., Wahl, T., Haigh, I. D., Jensen, J.: Trends in high sea levels of German North Sea gauges compared to regional mean sea level changes. *Cont. Shelf Res.* **65**:111–120, 2013.

[2] Leppäranta, M., Myrberg, K.: 2009. Physical Oceanography of the Baltic Sea. Springer, Berlin, 2009.

[3] Soomere, T., Eelsalu, M., Kurkin, A., Rybin, A.: Separation of the Baltic Sea water level into daily and multi-weekly components. *Cont. Shelf Res.* **103**:23–32, 2015.

[4] Suursaar, Ü., Sooäär, J.: Decadal variations in mean and extreme sea level values along the Estonian coast of the Baltic Sea. Tellus A **59**:249–260, 2007.

[5] Eelsalu, M., Soomere, T., Pindsoo, K., Lagemaa, P.: Ensemble approach for projections of return periods of extreme water levels in Estonian waters. *Cont. Shelf. Res.* **91**:201–210, 2014.

THEORETICAL CONCENTRATION CONTOURS EQUATION OF SEWAGE MIXING ZONE IN RIVERS AND ITS APPLICATION *

Zhouhu Wu†[1], Wen Wu[2], and Ni Chen[1]

[1]*School of Environmental and Municipal Engineering, Qingdao University of Technology, Qingdao, China P. R.*

[2]*Department of Mechanical and Materials Engineering, Queen's University, Kingston, Ontario, Canada*

Summary In this study, we derived the theoretical formulas characterizing the geometry of the pollutant mixing zone (PMZ) formed by a constant discharge, point source in straight-bank, wide open rivers, using the analytical solution of the simplified two-dimensional advection-diffusion equation of the pollutant. In such flow configuration, only the convection in the longitudinal direction and diffusion in the lateral direction are significant in the pollutant transport. The obtained formulas for the maximum length, maximum width and its corresponding longitudinal location, and area of PMZ, and the concentration contours equation defining the PMZ boundary, show excellent agreement with the onsite observations. These theoretical formulas can also be used in the inverse problems to determine the lateral diffusion coefficient in the river, or to design the sewage discharge load based on the PMZ range limitations in the water environmental quality standard.

INTRODUCTION

Industrial wastewater or municipal sewage, after being treated to achieve the appropriate discharge standards, is discharged along the river bank through pipes or open channels in the coastal area of rivers. Because the depth of the natural rivers is usually much smaller than the width, the initial dilution stage of the pollutant mixing is rather short, and the vertical diffusion is soon finished within a short distance downstream of the sewage outfall. Therefore, the pollutant concentration and its characterization in the river are commonly considered as the two-dimensional (longitudinal and lateral) advection and diffusion during the mixing zone development stage [1, 2].

Pollutant mixing zone (PMZ) is the allocated impact zone where water quality criteria can be exceeded as long as acutely toxic conditions are prevented. One of the PMZ technical procedure manuals (drafts) was proposed by the Idaho Department of Environmental Quality in 2008. It includes the PMZ setup rules, approval process, monitoring, determination and water quality modelling *etc.* [3]. Wu Z.-H. *et al.* developed an analytical PMZ calculation method for constant lateral diffusion coefficient cases corresponding to the wide, rectangular and straight rivers [4, 5]. In this study, we derived a set of analytical formulas of the geometric scales and area of the PMZ, for constant, point source riverbank discharging. The goal is to provide analytical mathematical tools for both scientific studies and environmental flow applications.

GEOMETRIC CHARACTERISTICS OF CONCENTRATION CONTOURS

At the steady state of pollutant transport downstream of the sewage outfall, the diffusion in the longitudinal direction (x) is negligible compared to the advection. Then, the only remaining terms give the simplified two-dimensional advection-diffusion equation of the pollutant concentration, C, as [1]

$$U\frac{\partial C}{\partial x} = E_{\mathrm{y}}\frac{\partial^2 C}{\partial y^2} \tag{1}$$

in which positive x-axis points downstream of river, and y is the lateral direction (positive y-axis points towards the opposite bank). Both axises are oriented from the sewage outfall; U is the mean longitudinal velocity (dim. LT^{-1}), and E_{y} is the lateral diffusion coefficient (dim. $\mathrm{L}^2\mathrm{T}^{-1}$). For constant, point source riverbank discharging, the analytical solution of Eq. (1) is [1]

$$C(x,y) = \frac{m}{H\sqrt{\pi E_{\mathrm{y}} U x}}\exp\left(\circ\,\frac{Uy^2}{4E_{\mathrm{y}}x}\right) \tag{2}$$

in which m is the discharge rate (dim. MT^{-1}), and H is the mean depth of the river (dim. L).

Let $C(x,y) = C_{\mathrm{a}}$ to be the threshold defining the boundary of the PMZ, and $y = 0$, the theoretical formula of the maximum length of PMZ along the riverbank reads

$$L_{\mathrm{s}} = \frac{1}{\pi E_{\mathrm{y}} U}\left(\frac{m}{HC_{\mathrm{a}}}\right)^2 \tag{3}$$

Take derivative of each term in both sides of Eq. (2), and let $dy/dx = 0$, we obtained the theoretical formula of the maximum width of the PMZ, b_{s}, and its relation with L_{s} as

$$b_{\mathrm{s}} = \sqrt{\frac{2}{\pi \mathrm{e}}}\frac{m}{HUC_{\mathrm{a}}} = \sqrt{\frac{2E_{\mathrm{y}}L_{\mathrm{s}}}{\mathrm{e}U}} \tag{4}$$

†Corresponding author. Email: wu_zh2008@aliyun.com.

*This research is supported by the National Natural Science Foundation of China (51379097).

where e is the mathematical constant. This maximum width occurs at $L_c = L_s/e$ in the longitudinal direction.

Substitute Eq. (3) and (4) into (2), the concentration contours equation of the PMZ at $C = C_a$ is

$$y = b_s\sqrt{-e\frac{x}{L_s}\ln\left(\frac{x}{L_s}\right)} \tag{5}$$

Figure 1 shows an example of the nearly semi-elliptical shape of PMZ described by Eq. (5). Take definite integral of Eq. (5) in the x direction from 0 to L_s, the area enclosed by the boundary is

$$S \equiv \int_0^{L_s} y dx = \int_0^{L_s} b_s\sqrt{-e\frac{x}{L_s}\ln\left(\frac{x}{L_s}\right)}dx = \left(\frac{2}{3}\right)^{3/2}\frac{\sqrt{\pi e}}{2}L_s b_s \approx 0.795 L_s b_s \tag{6}$$

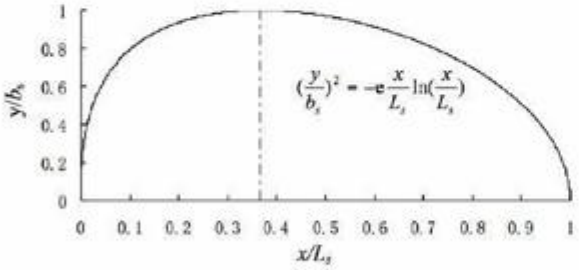

Figure 1: The standard curve of the boundary of pollutant mixing zone defined by Eq. (5) near the sewage outfall.

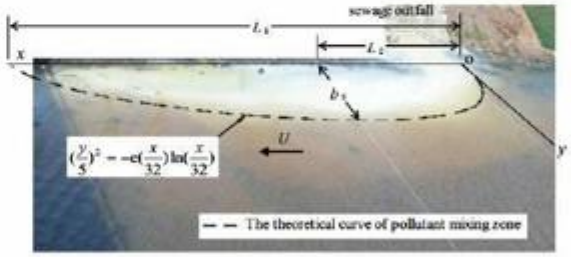

Figure 2: An onsite observation of the pollutant mixing zone near the outfall of a starch factory in the Guangfu River.

APPLICATION: DIFFUSION IN A RIVER

Figure 2 is the onsite observation of the PMZ near the outfall of a starch factory in the Guangfu River in Shandong, China [5]. The high pollutant concentration, white PMZ in this river is independent from the other side of boundary, thanks to the sufficient river width and strong longitudinal advection. The maximum length and width of the PMZ are measured to be L_s = 32 m and b_s = 5 m. The corresponding longitudinal location of b_s is at L_c = 12 m, which agrees very well with the value predicted by the formula derived in this study, *i.e.* $L_c = L_s/e \approx 11.8$ m. Substitute the measured value of L_s and b_s into Eq. (5), the concentration contours equation of the PMZ boundary is predicted to be $y = 5\sqrt{-e\xi\ln(\xi)}$, where $\xi = x/32$, and is showed in Fig. 2 as the dashed line. It is in excellent agreement with the visual boundary identified by the water color.

The theoretical formulas obtained above also have significant values in the inverse problem to determine E_y in the river. Rewrite Eq. (4), the formula to calculate E_y is

$$E_y = \frac{eU}{2L_s}b_s^2 \tag{7}$$

The parameters U, L_s and b_s in Eq. (7) are easy to measure onsite. E_y in the Guangfu River, for instance, is calculated to be 0.27 m^2/s using the measured L_s and b_s of the white PMZ (U = 0.25 m/s).

CONCLUSIONS

In this paper, the theoretical formulas describing the geometry of the pollutant mixing zone in rivers are derived from the simplified two-dimensional advection-diffusion pollutant transport equation. Application of these formulas shows excellent agreement with the onsite observation. These theoretical tools are powerful and easy-to-use in estimating the PMZ in water environmental impact prediction, and can be used as the basis for water quality model validation. They can also be applied to the inverse problems, such as determining the lateral diffusion coefficient of the river, or the maximum pollutant discharge load limited by the allowable range of the PMZ.

References

[1] Fischer H. B., List E. G., Koh R. C. Y., Imberger J., Brooks N. H.: Mixing in Inland and Coastal Waters, Academic Press, New York, NY, 1979.

[2] Wu Z.-H.: Correction of "Pollution Belt Extension Stage" in Environmental Hydraulics. J. Qingdao Tech. Univ. 36 (2): 1–6, 2015.

[3] Idaho Dept. Enviro. Quality: Mixing Zone Technical Procedures Manual (DRAFT). Boise: Idaho Dept. Enviro. Quality, USA, 2008.

[4] Wu Z.-H, Jia H.-Y.: Analytic Method for Pollutant Mixing Zone in River. Adv. Water Sci. 20(4): 544–548, 2009.

[5] Wu Z.-H., Wu W., Wu G.-Z.: Calculation Method of Lateral and Vertical Diffusion Coefficients in Wide Straight Rivers and Reservoirs. J. Comp. 6 (6): 1102–1109, 2011.

FM10 - Low Reynolds Number Flow

TS.FM10-1.01	Stone, Howard - Hydrodynamics of a hot particle in a viscous fluid	1140
TS.FM10-1.02	Slowicka, Agnieszka - Three modes of the dynamics of flexible fibers in shear flow	1142
TS.FM10-1.03	Duprat, Camille - Complex Trajectories of Confined Fibers in Viscous Flows	1144
TS.FM10-1.04	Mitchell, William - Generalized traction integral equations and viscous erosion	1146
TS.FM10-1.05	Shelley, Michael - Fluid-structure interactions in cellular biophysics (INVITED)	1148
TS.FM10-1.06	Singh, Pushpendra - Fluid dynamics of hydrophilous pollination in Ruppia (widgeon grass) (INVITED)	1150
TS.FM10-2.01	Lemaire, Elisabeth - Rheology of non-brownian suspensions: The role of inter-particle contact forces (INVITED)	1152
TS.FM10-2.02	Wilson, Helen - Simulations of a heavy ball falling through a sheared suspension	1154
TS.FM10-2.03	Guazzelli, Elisabeth - Rheology of dense Newtonian and viscoplastic suspensions	1156
TS.FM10-2.04	Wierschem, Andreas - Shear-induced granular motion on regular substrates at low particle Reynolds numbers	1158
TS.FM10-2.05	Inasawa, Ayumu - Experimental study on drag reduction due to periodically heated wall	1160
TS.FM10-3.01	Ardekani, Arezoo - Collective motion of microorganisms in complex fluids (INVITED)	1162
TS.FM10-3.02	Djellouli, Adel - Artificial swimmers through shell buckling	1164
TS.FM10-3.03	Barthes-Biesel, Dominique - Effect of membrane bending resistance on capsule wrinkling in simple shear flow	1166
TS.FM10-3.04	Amah, Edison - Electric Field Driven Hierarchical Self-assembly of Monolayers of Mixtures of Particles	1168
TS.FM10-3.05	Bonnecaze, Roger - Multi-scale model of magnetically-driven flows in dead-end channels	1170
TS.FM10-4.01	Ramchandran, Arun - Hele-Shaw flow of a concentrated, non-colloidal suspension (INVITED)	1172
TS.FM10-4.02	Kim, Jungchul - Particle-induced viscous fingering	1174
TS.FM10-4.03	Cater, John - Flow in a Human Nasal Cavity Obtained by Improved Shape Standardization	1176
TS.FM10-4.04	Cebers, Andrejs - Magnetic micro-convection	1178
TS.FM10-4.05	Yu, Jie - Ratcheting viscous fluids in a vibrating channel	1180
PO.FM10-1.01.56	Hormozi, Sarah - Dispersion of solids in fracturing flows of yield stress fluids	1182
PO.FM10-1.02.57	Lee, Donghwi - Effects of cross-sectional aspect ratio of flat plate on flow characteristics	1184
PO.FM10-1.03.58	Masoud, Hassan - A reciprocal theorem for convective scalar transfer from a particle in linear flows	1186
PO.FM10-1.04.59	Sumetc, Pavel - Flow through the channel coated with charged porous media	1188

HYDRODYNAMICS OF A HOT PARTICLE IN A VISCOUS FLUID

Howard A. Stone *[1], Shahin Navardi[2], and Naomi Oppenheimer[1]
[1]*Department of Mechanical and Aerospace Engineering, Princeton University, Princeton, NJ USA*
[2]*Department of Mechanical Engineering, Texas Tech University, Lubbock, TX USA*

Summary We study the motion of a hot particle in a viscous liquid at low Reynolds numbers. The calculation is inspired by experiments of laser heating of Brownian particles. The difference in temperature between the particle and the fluid causes a spatial variation of the viscosity. We derive formulae for the force and the torque on the particle by exploiting the reciprocal theorem. For small viscosity variations, a perturbation analysis provides the leading-order correction to the hydrodynamic force and torque. The results are applied to describe dynamics of a uniformly hot spherical particle and to spherical particles with non-uniform surface temperature distributions.

INTRODUCTION

There are many problems of physicochemical hydrodynamics where temperature gradients affect the motion of suspended particles, e.g. thermophoresis [1, 2]. The standard analyses of these problems assume the viscosity of the solution is constant. More recently, the Brownian motion of a small heated sphere – a hot particle – has been investigated [3] and the particle diffusion has distinct features from diffusion in isothermal systems since the temperature field produces spatial variations in viscosity. This problem motivates our study where we present an asymptotic calculation for the corrections to the hydrodynamic force and torque on a particle due to viscosity variations in the surrounding fluid.

Several recent studies report approximate formulae for the force on hot particles considering variation in the viscosity of the surrounding liquid (e.g. [4]). To the best of our knowledge there are no analytical expressions available for the force or torque on a particle that have been derived with a self-consistent asymptotic analysis. Obviously, numerical solutions can be developed on a case-by-case basis for a given viscosity distribution. We seek analytical results by combining the reciprocal theorem with a perturbation analysis in a parameter characterizing small viscosity changes. Thus, we obtain equations for the force-velocity and torque-rotational velocity relations that account for the influence of the viscosity variation.

PROBLEM FORMULATION AND SOLUTION

We present a theory for the force on a hot particle of arbitrary shape, which produces a variation of viscosity, in a low-Reynolds-number flow. We assume that advective transport of thermal energy is negligible compared to conduction, i.e. the Péclet number is small, and so (i) distortions induced by the flow on the temperature field can be neglected and (ii) particle-scale features of the temperature distribution are imprinted on the thermal field in the fluid. The viscosity in liquids is temperature dependent and hence the viscosity varies with position. Therefore, both the flow field and the hydrodynamic force on a translating particle will differ from their respective results in the well known case of a constant viscosity fluid.

We denote the position vector as $\boldsymbol{r}$. For an incompressible flow, the velocity $\boldsymbol{u}$ and stress $\boldsymbol{\sigma}$ fields are determined by

$$\nabla \cdot \boldsymbol{u} = 0 \qquad \text{and} \qquad \nabla \cdot \boldsymbol{\sigma} = \boldsymbol{0}. \tag{1}$$

For a Newtonian fluid and a temperature distribution $T(\boldsymbol{r})$, the stress $\boldsymbol{\sigma}$, pressure p, spatially varying viscosity $\eta\left(T(\boldsymbol{r})\right)$ or $\eta(\boldsymbol{r})$, and the rate of strain tensor $\boldsymbol{E} = \frac{1}{2}\left(\nabla\boldsymbol{u} + (\nabla\boldsymbol{u})^T\right)$ are related by $\boldsymbol{\sigma} = \circ\, p\boldsymbol{I} + 2\eta(\boldsymbol{r})\boldsymbol{E}$, where $\boldsymbol{I}$ is the identity tensor. The corresponding force and torque on a particle (surface S_p) are $\boldsymbol{F} = \int_{S_p} \boldsymbol{n}\cdot\boldsymbol{\sigma}\, \mathrm{d}S$ and $\boldsymbol{T} = \int_{S_p} \boldsymbol{r}\wedge(\boldsymbol{n}\cdot\boldsymbol{\sigma})\, \mathrm{d}S$.

Our main objective is to quantify the difference of the force calculated from equation (1) to the force obtained from the Stokes equations when the viscosity is constant, i.e. $\eta = \eta_0$ does not depend on position,

$$\nabla \cdot \boldsymbol{u}_0 = 0, \quad \text{and} \qquad \circ\ \nabla p_0 + \eta_0 \nabla^2 \boldsymbol{u}_0 = \nabla \cdot \boldsymbol{\sigma}_0 = \boldsymbol{0}, \tag{2}$$

where the subscript 0 refers to the constant viscosity problem. In this case, for particle translation $\boldsymbol{U}_0$ and rotation $\boldsymbol{\Omega}_0$, the force and torque are given by $\begin{pmatrix}\boldsymbol{F}_0\\ \boldsymbol{T}_0\end{pmatrix} = \boldsymbol{R}_0 \cdot \begin{pmatrix}\boldsymbol{U}_0\\ \boldsymbol{\Omega}_0\end{pmatrix}$, where $\boldsymbol{R}_0$ is the resistance tensor (each term proportional to η_0).

In order to avoid the complexities of solving the differential equation (1) or (2) arising from the variations of the viscosity with position, we exploit the reciprocal theorem [5]. To relate the solution of the Stokes equations (1) and (2), we note that $(\nabla\cdot\boldsymbol{\sigma})\cdot\boldsymbol{u}_0 = 0$, and so we have $\nabla\cdot(\boldsymbol{\sigma}\cdot\boldsymbol{u}_0) \circ \boldsymbol{\sigma} : \nabla\boldsymbol{u}_0 = 0$; as a result of incompressibility and the symmetry of the stress tensor we can write $\nabla\cdot(\boldsymbol{\sigma}\cdot\boldsymbol{u}_0) \circ 2\eta(\boldsymbol{r})\boldsymbol{E} : \boldsymbol{E}_0 = 0$. Following the usual steps we find

$$\circ \int_{S_p} \boldsymbol{n}\cdot\boldsymbol{\sigma}\cdot\boldsymbol{u}_0\, \mathrm{d}S + \int_{S_p} \boldsymbol{n}\cdot\boldsymbol{\sigma}_0\cdot\boldsymbol{u}\, \mathrm{d}S = 2\int_V \big(\eta(\boldsymbol{r}) \circ \eta_0\big)\boldsymbol{E} : \boldsymbol{E}_0\, \mathrm{d}V. \tag{3}$$

*Corresponding author. Email: hastone@princeton.edu

Now we apply (3) to translation and rotation of a particle, where the boundary condition on S_p for the main problem is $\boldsymbol{u} = \boldsymbol{U} + \boldsymbol{\Omega} \wedge \mathbf{r}$ and for the model constant viscosity problem is $\boldsymbol{u}_0 = \boldsymbol{U}_0 + \boldsymbol{\Omega}_0 \wedge \mathbf{r}$. Owing to the linearity of the Stokes equations and the boundary conditions, which involve both translation with velocity $\boldsymbol{U}$ (or $\boldsymbol{U}_0$) and rotation with angular velocity $\boldsymbol{\Omega}$ (or $\boldsymbol{\Omega}_0$) we can write the strain tensor as a sum of two tensors, $\boldsymbol{E}^U$, due to translation, and $\boldsymbol{E}^\Omega$, due to rotation. We also define corresponding third-order tensors, $\boldsymbol{\mathcal{E}}^\beta$, which we shall call the normalized strain tensor, such that:

$$\boldsymbol{E} = \boldsymbol{E}^U + \boldsymbol{E}^\Omega = \boldsymbol{\mathcal{E}}^U \cdot \boldsymbol{U} + \boldsymbol{\mathcal{E}}^\Omega \cdot \boldsymbol{\Omega} \quad \text{and} \quad \boldsymbol{E}_0 = \boldsymbol{E}_0^U + \boldsymbol{E}_0^\Omega = \boldsymbol{\mathcal{E}}_0 \cdot \boldsymbol{U}_0 + \boldsymbol{\mathcal{E}}_0 \cdot \boldsymbol{\Omega}_0. \tag{4}$$

Then, we eliminate the otherwise arbitrary vectors $\boldsymbol{U}_0$ and $\boldsymbol{\Omega}_0$ to arrive at

$$\begin{pmatrix} \boldsymbol{F} \\ \boldsymbol{T} \end{pmatrix} = \boldsymbol{R}_0 \cdot \begin{pmatrix} \boldsymbol{U} \\ \boldsymbol{\Omega} \end{pmatrix} + 2\eta_0 \int_V \left(1 \circ \frac{\eta(\boldsymbol{r})}{\eta_0} \right) \boldsymbol{\Lambda} \, \mathrm{d}V \cdot \begin{pmatrix} \boldsymbol{U} \\ \boldsymbol{\Omega} \end{pmatrix} \quad \text{with} \quad \boldsymbol{R}_0 \equiv \begin{pmatrix} \boldsymbol{R}_0^{FU} & \boldsymbol{R}_0^{F\Omega} \\ \boldsymbol{R}_0^{TU} & \boldsymbol{R}_0^{T\Omega} \end{pmatrix} \text{ and } \boldsymbol{\Lambda} \equiv \begin{pmatrix} \boldsymbol{\mathcal{E}}_0^U : \boldsymbol{\mathcal{E}}^U & \boldsymbol{\mathcal{E}}_0^U : \boldsymbol{\mathcal{E}}^\Omega \\ \boldsymbol{\mathcal{E}}_0^\Omega : \boldsymbol{\mathcal{E}}^U & \boldsymbol{\mathcal{E}}_0^\Omega : \boldsymbol{\mathcal{E}}^\Omega \end{pmatrix}, \tag{5}$$

where we have defined the double inner product : of third-order tensors according to $\boldsymbol{\mathcal{E}}_0 : \boldsymbol{\mathcal{E}} = \mathcal{E}_{0(kji)} \mathcal{E}_{jk\ell} \mathbf{e}_i \mathbf{e}_\ell$.

A PERTURBATION EXPANSION FOR MOTION OF A SPHERE

For a heated particle we describe the local temperature variations away from T_0 with the first terms of a multipole expansion, which can be written in terms of the characteristic change in temperature caused by the particle (ΔT_m, ΔT_d and ΔT_q, respectively, for monopole, dipole and quadruple), i.e. using $\tilde{}$ to denote the normalized dipole $\tilde{\boldsymbol{\Delta}}$ and quadrupole $\tilde{\boldsymbol{Q}}$, we write

$$T(\boldsymbol{r}) \circ \ T_0 = \Delta T_m \frac{a}{r} + \Delta T_d \frac{a^2 \tilde{\boldsymbol{\Delta}} \cdot \boldsymbol{r}}{r^3} + \Delta T_q \frac{a^3 \tilde{\boldsymbol{Q}} : \left(3\boldsymbol{rr} \circ \ r^2 \boldsymbol{I} \right)}{6r^5} + \cdots . \tag{6}$$

We can show for a sphere that moments higher than a quadrupole do not contribute to the leading-order correction given below.

For small temperature variations characterized by ΔT_m, the viscosity can be expanded as a Taylor series around T_0,

$$\eta \approx \eta_0 \left(1 + \frac{\Delta T_m}{\eta_0} \frac{\partial \eta}{\partial T} \bigg|_{T_0} \mathcal{T}(\boldsymbol{r}) + O(\mathcal{T})^2 \right) \quad \text{where} \quad \mathcal{T}(\boldsymbol{r}) = \frac{T(\boldsymbol{r}) \circ \ T_0}{\Delta T_m}. \tag{7}$$

Introducing a small parameter ϵ that captures the (small) temperature and viscosity variations produced by a heated particle, we define $\epsilon = \circ \ \frac{\Delta T_m}{\eta_0} \frac{\partial \eta}{\partial T} \Big|_{T_0}$ since typically $\frac{\partial \eta}{\partial T} < 0$. Clearly, ϵ represents the fractional change of viscosity, $\frac{\Delta \eta}{\eta_0}$,

Then, for the velocity and the pressure fields, we write regular perturbation expansions

$$\boldsymbol{u}(\boldsymbol{r}; \eta(\boldsymbol{r})) = \boldsymbol{u}_0(\boldsymbol{r}) + \epsilon \boldsymbol{u}_1(\boldsymbol{r}) + \epsilon^2 \boldsymbol{u}_2(\boldsymbol{r}) + \cdots \quad \text{and} \quad p(\boldsymbol{r}; \eta(\boldsymbol{r})) = p_0(\boldsymbol{r}) + \epsilon p_1(\boldsymbol{r}) + \epsilon^2 p_2(\boldsymbol{r}) + \cdots . \tag{8}$$

Here the zeroth-order solution is the well known solution for a constant viscosity. Thus, using equations (5) and (7) we have

$$\begin{pmatrix} \boldsymbol{F} \\ \boldsymbol{T} \end{pmatrix} = \left(\boldsymbol{R}_0 + \epsilon \boldsymbol{R}_1 + O\left(\epsilon^2\right) \right) \cdot \begin{pmatrix} \boldsymbol{U} \\ \boldsymbol{\Omega} \end{pmatrix} \quad \text{with} \quad \boldsymbol{R}_1 = 2\eta_0 \int \mathcal{T}(\boldsymbol{r}) \begin{pmatrix} \boldsymbol{\mathcal{E}}_0^U : \boldsymbol{\mathcal{E}}_0^U & \boldsymbol{\mathcal{E}}_0^U : \boldsymbol{\mathcal{E}}_0^\Omega \\ \boldsymbol{\mathcal{E}}_0^\Omega : \boldsymbol{\mathcal{E}}_0^U & \boldsymbol{\mathcal{E}}_0^\Omega : \boldsymbol{\mathcal{E}}_0^\Omega \end{pmatrix} \mathrm{d}V. \tag{9}$$

where $\boldsymbol{R}_1$ can be evaluated in terms of the thermal field and known quantities for the constant viscosity zeroth-order solution. This equation is our main result; it introduces the first effects of viscosity variations on the dynamics of a hot particle.

In our presentation we consider different thermal characterizations of small particles, as described by a thermal monopole, dipole and quadrupole. Then, we use (9) to obtain analytical corrections to the force and torque on a sphere. Among other results, we find for dipolar thermal fields that there is coupling of the translational and rotational motions when there are local viscosity variations; such coupling is absent in an isothermal fluid.

CONCLUSIONS

We describe a systematic asymptotic approach accounting for viscosity variations on the motion of small particles. The analysis is applicable to recent experiments where laser heating of Brownian particles produces local viscosity variations.

References

[1] Schermer, R. T. and Olson, C. C. and Coleman, J. P. and Bucholtz, F.: Laser-induced thermophoresis of individual particles in a viscous liquid. Optics Express 19, 10571–10586, 2011.

[2] Bickel, T. and Majee, A. and Würger, A.: Flow pattern in the vicinity of self-propelling hot Janus particles, Phys. Rev. E 88, 012301, 2013.

[3] Rings, D. and Schachoff, R. and Selmke, M. and Cichos, F. and Kroy, K.: Hot Brownian motion/ Phys. Rev. Lett. 105, 090604, 2010.

[4] Rings, D. and Selmke, M. and Cichos, F. and Kroy, K.: Theory of hot Brownian motion. Soft Matter 7:3441–3452, 2011.

[5] Happel, J. and Brenner, H.: Low Reynolds Number Hydrodynamics. p. 85. Prentice-Hall. 1965.

THREE MODES OF THE DYNAMICS OF FLEXIBLE FIBERS IN SHEAR FLOW

Agnieszka M. Słowicka [1], Howard A. Stone[2], Eligiusz Wajnryb[1], and Maria L. Ekiel-Jeżewska [*1]

[1]*Institute of Fundamental Technological Research, Polish Academy of Sciences, Pawińskiego 5b, 02-106 Warsaw, Poland*

[2]*Department of Mechanical and Aerospace Engineering, Princeton University, Princeton NJ 08544*

Summary Dynamics of a single non-Brownian flexible fiber in shear flow at low Reynolds number is investigated numerically. Initially, the fiber is straight and at the equilibrium. For different initial orientations and values of bending stiffness, three generic scenarios are observed: the fiber tends to: align along the vorticity direction, tumble within the plane perpendicular to vorticity, or perform a periodic motion superposed with translation along the flow.

SYSTEM

Dynamics of non-Brownian flexible microfibers in external flows have been recently intensively investigated experimentally and numerically, see e.g. [1, 2] and the references therein. One of the basic questions is how to classify the modes of their dynamics in shear flow, depending on the initial position [3, 4, 5] and flexibility [6]. In this work, we contribute towards solving this problem. We denote the fluid viscosity as η and the shear flow velocity as $\mathbf{v} = \dot{\gamma} z \mathbf{e}_x$, where $\mathbf{e}_x$ is the unit vector along x. A flexible fiber is modeled as a chain of N beads of equal diameters d, with the consecutive beads connected by springs, and resisting bending [7]. At equilibrium, the fiber is straight with a very small distance l_0 between the centers of the consecutive beads. As in [1, 6], the constraint forces are characterized by the dimensionless bending stiffness parameter A equal to the ratio of the Young modulus to $\pi\eta\dot{\gamma}$, and the dimensionless ratio k of the spring constant to the hydrodynamic force per unit length, $\pi\eta d\dot{\gamma}$. The value of k is assumed to be large, to provide almost constant fiber length.

The Reynolds number of the system is much smaller than unity, and the fluid motion satisfies the Stokes equations. Numerical simulations of the dynamics of each fiber bead are performed using the multipole expansion, corrected for lubrication [8], and implemented in the HYDROMULTIPOLE numerical code. We choose $N = 40$, $k = 1000$, $l_0 = 1.02$. We assume that initially the fiber is at equilibrium, and we perform a systematic study of how the evolution depends on the bending stiffness A and the initial orientation, which is determined by two angles: Θ_0 - the angle between the end-to-end vector of the fiber and the vorticity direction y, and Φ_0 - the angle between the projection of the end-to-end vector on the $x-z$ plane and the x axis.

RESULTS

Identification of modes

In our simulations of the fiber motion, we have found three generic types of evolution. Basic features of these three modes of the fiber dynamics are illustrated in three columns of Figure 1, where we plot the time-dependent angle Θ between the instantaneous end-to-end vector and the vorticity direction, and the time-dependent distance ΔL between the centers of the first and last beads, normalized by its equilibrium value L_0. The time unit is $1/\dot{\gamma}$.

In the first mode, shown in the left column of Figure 1, colored blue and called spin-rotation [4], the fiber tends to stay straight, $\Delta L/L_0 \to 1$, and along the vorticity direction y, $\Theta \to 0$, rolling around it. In the second (red) mode, called the tumbling one, the fiber tends to the $x-z$ plane, $\Theta \to 90^o$, and it regularly straightens out and becomes coiled while tumbling, with large-amplitude oscillations of $\Delta L/L_0$. In the third (green) mode, each bead of the fiber evolves towards a periodic orbit of a very complex three-dimensional shape, translating along the flow with a constant speed. This mode, called the periodic one, has not been observed before.

Diagrams of the modes

We have systematically investigated the dependence of the dynamical modes on the fiber initial orientation (Φ_0, Θ_0) with respect to the vorticity direction. The results for fibers of a different bending stiffness $A = 4, 10$ and 40 are shown in Figure 2. Very flexible fibers ($A = 4$, left) with all the initial orientations belong to the spin-rotation (blue) mode. For very stiff fibers ($A = 40$, right), the tumbling (red) mode dominates for most of the initial positions, excluding some of those which are close to the vorticity direction and lead to the spin-rotation (blue mode). For fibers of a moderate stiffness ($A = 10$, middle), there exists a range of the initial orientations which correspond to the periodic (green) mode. The boundaries of this range are not smooth, and a relatively small change of initial orientations can result in a different dynamical mode.

*Corresponding author. Email: mekiel@ippt.pan.pl

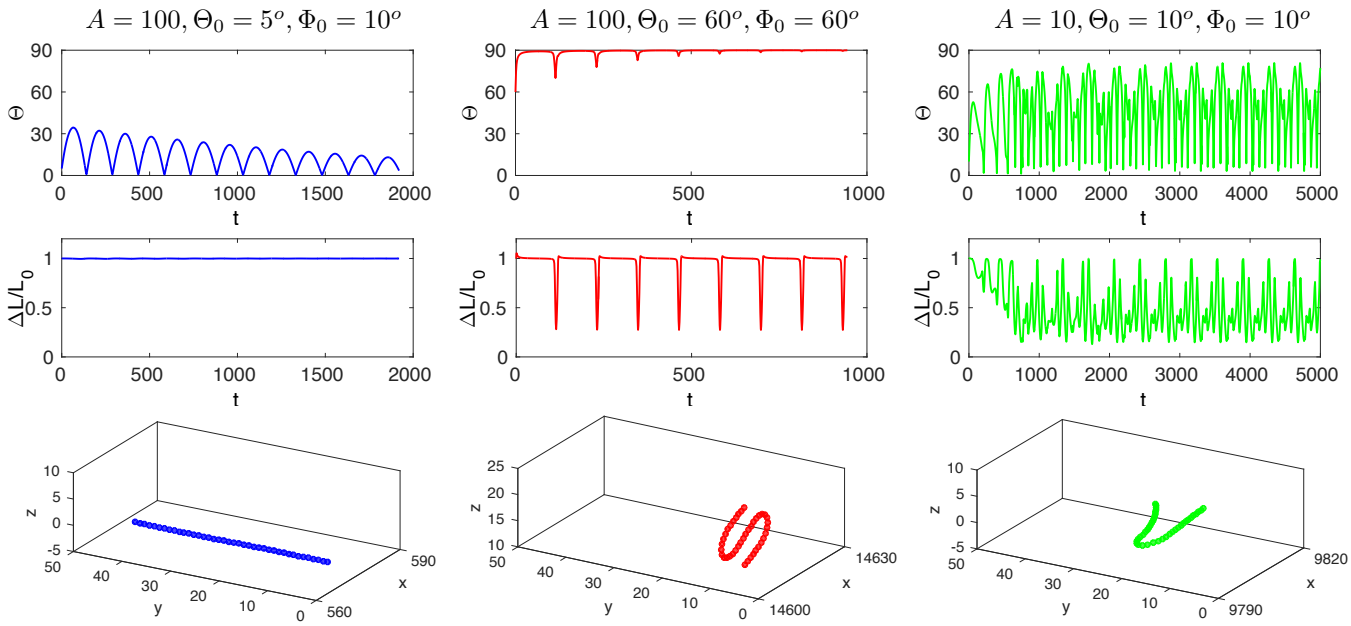

Figure 1: Typical examples of three modes of the fiber dynamics: blue, red and green. Top: the time dependent angle Θ. Middle: the instantaneous relative length $\Delta L/L_0$ of the fiber end-to-end vector. Bottom: examples of shapes when the end-to-end vector is perpendicular to the flow.

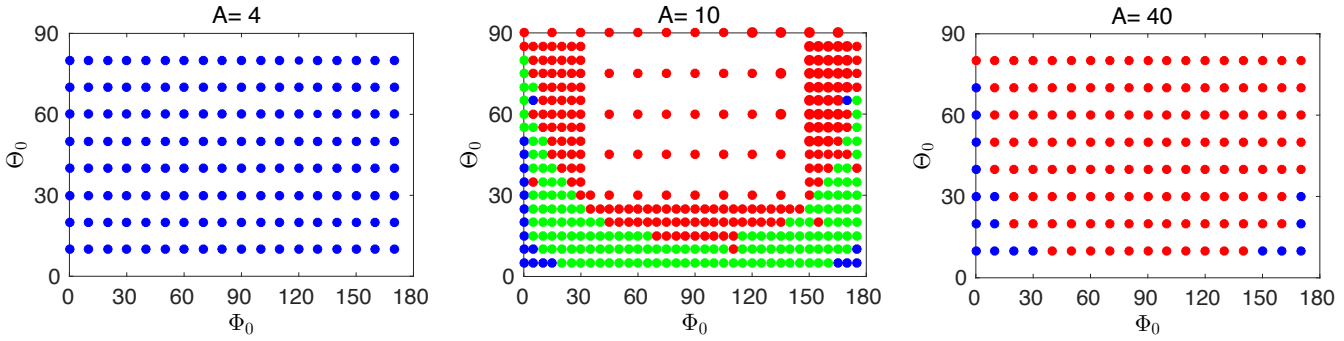

Figure 2: Dynamical modes of fibers at different initial orientations (Φ_0, Θ_0), depending on their bending stiffness A.

CONCLUSIONS

We have shown numerically that there exist three – rather than two as reported before [3, 4, 5] – essentially different modes of the flexible fiber dynamics in shear flow. The remarkable feature is that for moderate values of the bending stiffness, periodic solutions exist, with a very complex three-dimensional shape of the periodic trajectories. These orbits are essentially different than the classical Jeffery's orbits.

This work was supported in part by the National Science Centre under grant No. 2014/15/B/ST8/04359.

References

[1] Kuei S., Słowicka A.M., Ekiel-Jeżewska M.L. Wajnryb E., Stone H.A.:Dynamics and topology of a flexible chain: knots in steady shear flow. New J. Phys.: 17: 053009-1-15, 2015

[2] Słowicka A.M., Ekiel-Jeżewska M.L., Wajnryb E.:Lateral migration of flexible fibers in Poiseuille flow between two parallel planar solid walls.Eur. Phys. J. E 36:1-12, 2013

[3] Arlov A.P., Forgacs O.L., Mason S.G.: Particle motions in sheared suspensions IV. General behaviour of wood pulp fibres. Sven. Papperstidn. 61: 61-67, 1958.

[4] Skjetne P., Ross R. F. and Klingenberg D. J.: Simulation of single fiber dynamics. J. Chem. Phys. 107: 2108, 1997.

[5] Joung C.G., Phan-Thien N. and Fan X.J.: Direct simulation of flexible fibers. J. Non-Newtonian Fluid Mech. 99:1-36, 2001.

[6] Słowicka A.M., Wajnryb E., Ekiel-Jeżewska M.L.: Dynamics of flexible fibers in shear flow. J. Chem. Phys. 143:124904-1-6, 2015

[7] Gauger E. and Stark. H.: Numerical study of a microscopic artificial swimmer. Phys. Rev. E, 74:021907, 2006.

[8] Cichocki B., Ekiel-Jeżewska M.L., Wajnryb E.: Lubrication corrections for three-particle contribution to short-time self-diffusion coefficients in colloidal dispersions. J. Chem. Phys. 111: 3265, 1999.

COMPLEX TRAJECTORIES OF CONFINED FIBERS IN VISCOUS FLOWS

Camille Duprat *[1], Marine Daieff[2], and Anke Lindner[2]

[1]*Laboratoire d'hydrodynamique (LadHyX), Ecole polytechnique, Palaiseau, France*
[2]*Laboratoire PMMH, ESPCI, Paris, France*

Summary We study the trajectories of elongated objects transported in microfluidic Hele Shaw cells. The transverse confinement (and the resulting viscous friction on the particle), as well as lateral confinement (i.e. the presence of lateral walls), lead to complex trajectories that we characterize experimentally and numerically. We show that the fiber behaves as an oscillator and obtain a complete bifurcation diagram. We then study the effect of the particle asymmetry by considering L-shaped particles; in that case, there is a coupling between translation and rotation that leads to a reorientation of the particle. We show that this reorientation stabilizes the particle motion.

The motion of rigid or flexible particles in viscous flows has been extensively studied; a particular example are elongated objects, like fibers, whose transport is important in a variety of small-scale applications, from swimming micro-organisms and biofilm streamers in blood capillaries to fabrication of non-woven fibrous media. A canonical situation is the sedimentation of such an elongated object in a Stokes flow; due to its drag anisotropy, a randomly oriented fiber does not translate in the direction of gravity but at an angle depending on its orientation. The presence of a vertical wall leads to a rotation of the fiber, with either glancing or reversing motions. Other hydrodynamics effects, linked to the shape or deformability of the particle, the features of the flow or of the flow boundaries can lead to complex trajectories. For example, the flexibility of the fiber can induce changes in the trajectory and significantly affect its transport [1]. When a flexible filament sediments in a viscous fluid, it deforms due to the viscous drag; this deformation modifies its trajectory, i.e. the filament rotates and aligns perpendicular to the flow. In addition, highly flexible filaments are susceptible to a buckling instability [2]. These motions influence the stability of a suspension of flexible fibers sedimenting in a viscous fluid: the deformation of the fibres leads to an anisotropic base state that renders the suspension more unstable, while the subsequent self-rotation of the fibres prevents clustering and thus stabilizes the suspension [2]. Here, we consider the transport of elongated objects in pressure-driven flows in microfluidic Hele-Shaw cells, and study the effect of confinement, shape and flexibility on the trajectories.

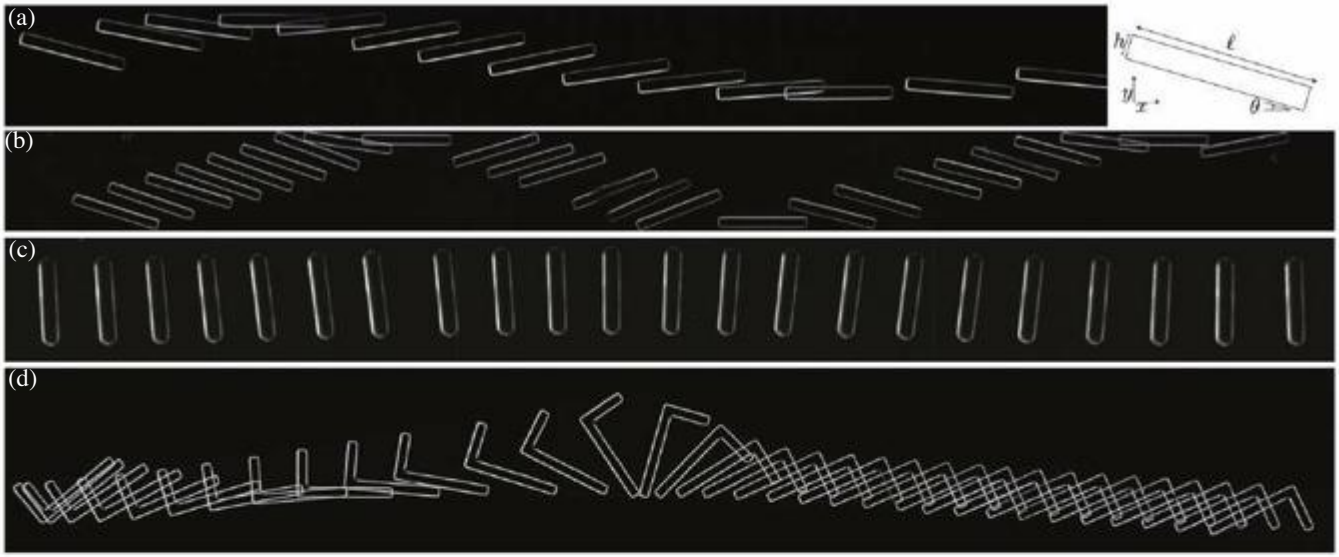

Figure 1: Inset: notations. (a-c) Experimental chronophotographies of a fiber flowing in a microchannel exhibiting (a,b) glancing (with two different initial angles) and (c) reversing oscillations. (d) Experimental chronophotographies of the flow of an L-shaped fiber. Flow is from left to right.

*Corresponding author. Email: camille.duprat@ladhyx.polytechnique.fr

FLOW OF CONFINED RIGID SYMMETRIC FIBERS

We fabricate polymeric particles directly in microchannels by using a stop-flow photolithography method [1, 4]. This allows for a good control over the shape and mechanical properties of the fiber. We first consider rigid symmetric particles, i.e. fibers with a square cross-section (inset in Fig. 1). When the particle dimensions are small compared to the channel dimensions, the particle is unconfined and is simply advected at the flow velocity. However, in shallow cells in which the fiber size is of the same order as the channel height (i.e. nearly blocks the channel), the particle is confined and its trajectory and velocity are modified due to the friction with the walls. In that case, the transport anisotropy is reversed compared to sedimentation: a fiber moves faster when perpendicular to the flow direction than when parallel to the flow [3]. When oriented at an arbitrary angle θ with the flow direction, the fiber thus drifts, albeit in the opposite direction than the one found in sedimenting fibers (see Fig. 1 (a-c) near the center of the channel). By varying the confinement, i.e. the ratio of the particle height to the channel height, we can tune the magnitude of the friction and thus the velocities. The drift angle, as well as the spanwise drift velocity, increase with increasing confinement and are maximal for an orientation close to $\theta = 45^\circ$. We then consider the effect of lateral confinement, i.e. interactions with the lateral walls. In that case, the trajectory of the fiber is a combination of drift and rotation due to the presence of the bounding walls. When the orientation of the fiber deviates from $\theta = 0^\circ$, the fiber exhibits oscillations around $\theta = 0^\circ$ (*glancing*) as shown in Fig. 1 (a-b). As the initial fiber angle increases, the drift velocity increases, while the rotation velocity remains nearly constant: as a consequence, the amplitude of the oscillations increases with increasing angle, i.e. the fiber glances closer to the wall and explores a larger part of the channel (Fig. 1 (a-b)). If we increase the angle above 45°, the fiber exhibits qualitatively different oscillations (Fig. 1 (c)): the rotation induced by the wall is reminiscent of the *reversing* regime, i.e. the fiber now oscillates around $\theta = 90^\circ$. When the fiber is not placed at the center of the channel but in the vicinity of the wall, it remains in the boundary layer close to the wall and we observe different trajectories (not shown): the fiber either rotates and completely reverses orientation with a repeated movement of *pole-vaulting*, or exhibits small oscillations (*wiggling*).

The fiber thus behaves like an oscillator. We build a bifurcation diagram as a function of the fiber orientation and spanwise position in the channel. The fiber either exhibits closed orbits (glancing and reversing oscillations) or open orbits near the walls (pole-vaulting and wiggling). We analyze the oscillatory regimes and show that the trajectories can be tuned by adjusting the confinement, i.e. changing the magnitude of the viscous drag. We also note that the fiber position is unstable to small perturbations, i.e. the fiber can jump from one orbit to the other. For example, fibers of orientation close to $\theta = 50^\circ$ oscillate between glancing and reversing motions. Finally, our experimental data compares well with numerical simulations using modified Brinkman equations developed by M. Nagel, P-T. Brun and F. Gallaire at EPFL (Lausanne). With these simulations, we can obtain a complete phase diagram exhibiting both glancing and reversing regimes, as well as pole-vaulting and wiggling, for various transverse and lateral confinements, and extract the rotation and drift velocities from which we rationalize our observations.

ASYMMETRIC AND FLEXIBLE FIBERS

We then turn to asymmetric particles, by first considering an L- shaped fiber. Here, the anisotropy of the viscous drag exerted between the fiber and the walls leads to a reorientation of the fiber due to its asymmetry: the fiber rotates until it reaches an equilibrium orientation, i.e. its angle remains constant (Fig. 1 (d)). As we vary the transverse confinement and the shape of the particle (i.e. the ratio of lengths between the short and long branches of the "L"), the equilibrium angle varies: it decreases (i.e. the long branch tends to align with the flow) as the confinement increases or as the length ratio increases. This model experiment shows that a small perturbation of the shape (here the presence of a small branch on one side) can lead to particle rotation, and the particles always reorient towards their equilibrium orientation. While this can lead to complex trajectories, it also stabilizes the fiber motion: slightly asymmetric particles return to a constant angle even if perturbed, and are thus more stable than straight fibers. These experiments are a first step towards understanding the motion of a flexible fiber in a confined geometry. Due to the transverse confinement, strong hydrodynamics forces can deform the fiber. As a first step, we have used this flow-induced deformation, on anchored fibers, to develop an in-situ method to measure the mechanical properties of photo-polymerized gels [4]. When freely transported by the flow, the fiber can deform due to a change in flow conditions or the presence of a wall, and we expect complex trajectories as suggested from our results with L-shaped particles.

References

[1] A. Lindner and M. Shelley, Elastic fibers in flows, in *Fluid-Structure Interactions in Low-Reynolds-Number Flows*, eds: C. Duprat and H. A. Stone, Royal Society of Chemistry (2016)

[2] Li. L, H. Manikantan, D. Saintillan, S. Spagnolie, The sedimentation of flexible filaments, *J. Fluid Mech.* 735 (2013); H. Manikantan, L. Li, S. Spagnolie, D. Saintillan, The instability of a sedimenting suspension of weakly flexible fibres, *J. Fluid Mech.* 756 (2014)

[3] H. Berthet, M. Fermigier, A. Lindner, Single fiber transport in a confined channel: Microfluidic experiments and numerical study, *Phys. Fluids* 25 (2013)

[4] C. Duprat, H. Berthet, J. S. Wexler, O. du Roure, A. Lindner, Microfluidic in situ mechanical testing of photopolymerized gels, *Lab on a Chip* 15 (2015)

GENERALIZED TRACTION INTEGRAL EQUATIONS AND VISCOUS EROSION

William H. Mitchell[1] and Saverio E. Spagnolie *[1]
[1]*Department of Mathematics, University of Wisconsin-Madison*

Summary Motivated by the problem of an eroding particle immersed in a viscous fluid, we present some new results on surface tractions in Stokes flows. In particular, we derive new integral equations for the surface tractions on a rigid particle immersed in a low Reynolds number fluid which may have a non-trivial background flow and/or a no-slip plane wall. The integral operator enjoys the conditioning advantages of second kind integral equations while avoiding the traditional obstacles of hypersingularity and rank deficiency. Moreover, the derivation is a simple argument using the Lorentz reciprocal theorem. This work builds on a 2011 paper of Keaveny and Shelley which considered the case of an infinite quiescent fluid. The formulation is used to explore viscous erosion of bodies in a selection of fundamental background flows, resulting in the emergence of distinct limiting body shapes involving sharp corners and ridges.

THE COMPLETED TRACTION BOUNDARY INTEGRAL EQUATION WITH IMPOSED BACKGROUND FLOW

Consider the following Stokes resistance problem. The boundary D and centroid Y of a suspended particle are given along with a background linear flow $u_i^\infty(\boldsymbol{x}) = A_{ij}x_j$, where A is trace-free. The equations of motion in the fluid are the Stokes equations,

$$\boldsymbol{0} = \circ\, \nabla p + \mu \nabla^2 \boldsymbol{u} \tag{1}$$

$$0 = \nabla \cdot \boldsymbol{u} \tag{2}$$

where $\boldsymbol{u}$ is the fluid velocity, μ is the viscosity, and p is the pressure. We wish to determine the surface tractions on the particle. The boundary conditions consist of an imposed rigid-body motion at the surface, $\boldsymbol{u} = \boldsymbol{U} + \boldsymbol{\Omega} \times (\boldsymbol{x} \circ\ \boldsymbol{Y})$, and decay of the disturbance flow at infinity, $|\boldsymbol{u} \circ\ \boldsymbol{u}^\infty| = \mathcal{O}\left(1/|\boldsymbol{x} \circ\ \boldsymbol{Y}|\right)$ as $|\boldsymbol{x} \circ\ \boldsymbol{Y}| \to \infty$. The desired tractions can be obtained by solving the second-kind integral equation

$$\begin{aligned} &\frac{\circ\, 1}{2\mu} f_j(\boldsymbol{y}) + n_k(\boldsymbol{y}) \int_D T_{ijk}(\boldsymbol{y}' \circ\ \boldsymbol{y}) f_i(\boldsymbol{y}') dS_{\boldsymbol{y}'} + \int_D C_{ij}(\boldsymbol{y}', \boldsymbol{y}) f_i(\boldsymbol{y}') dS_{\boldsymbol{y}'} \\ &= U_j + \epsilon_{jk\ell}\Omega_k(y_\ell \circ\ Y_\ell) \circ\ (A_{jk} + A_{kj}) n_k(\boldsymbol{y}) + \frac{1}{2}(A_{jk} \circ\ A_{kj}) y_k + \frac{1}{2}(A_{jk} + A_{kj}) z_k(\boldsymbol{y}). \end{aligned} \tag{3}$$

This equation holds for $j = 1, 2, 3$ and at each point $\boldsymbol{y}$ on the particle surface D. We have written T_{ijk} for the free-space stresslet and C_{ij} for the kernel of a *completion flow*:

$$T_{ijk}(\boldsymbol{x}, \boldsymbol{y}) = \frac{\circ\, 3}{4\pi\mu} \frac{(x_i \circ\ y_i)(x_j \circ\ y_j)(x_k \circ\ y_k)}{|\boldsymbol{x} \circ\ \boldsymbol{y}|^5} \tag{4}$$

$$C_{ij}(\boldsymbol{x}, \boldsymbol{y}) = \frac{\delta_{ij}}{8\pi\mu|\boldsymbol{x} \circ\ \boldsymbol{z}(\boldsymbol{y})|} + \frac{(x_i \circ\ z_i(\boldsymbol{y}))(x_j \circ\ z_j(\boldsymbol{y}))}{8\pi\mu|\boldsymbol{x} \circ\ \boldsymbol{z}(\boldsymbol{y})|^3} + \epsilon_{m\ell j} \frac{\epsilon_{imp}(x_p \circ\ z_p(\boldsymbol{y}))}{8\pi\mu|\boldsymbol{x} \circ\ \boldsymbol{z}(\boldsymbol{y})|^3} (y_\ell \circ\ z_\ell(\boldsymbol{y})) \tag{5}$$

where $\boldsymbol{z} : D \to \operatorname{Int} D$ is a map from the surface to the interior of the particle; in the case that $\boldsymbol{z} \equiv \boldsymbol{Y}$ this reduces to the Power and Miranda formulation [1]. The inclusion of completion flow makes the operator acting on $\boldsymbol{f}$ invertible. The integral equation (3) may be derived through a simple Lorentz reciprocal theorem argument. The formulation can also be extended to address problems with several particles, problems with more general background flows, problems involving a no-slip plane wall, and mobility formulations. This work generalizes the argument presented in [2], which considered the case of an infinite quiescent fluid and which in turn drew on [3]. Previous works in this area also include [4, 5, 6] and others; the current method is advantageous because it leads to invertible integral operators with singularity equivalent to a jump discontinuity.

DISCRETIZATION AND APPLICATION TO LOW-REYNOLDS NUMBER EROSION

We employ a simple collocation discretization of the integral equations, following a suitable subtraction of the singularity which reduces its order to that of a jump discontinuity. After presenting numerical tests indicating third-order convergence under mesh refinement, we use the method to examine the erosion of several bodies when they are held fixed in various background flows. A recent study of erosion of clay in a high Reynolds number fluid flow found support for a model of surface ablation as proportional to the tangential surface stress [7]. We use the same ablation model to explore the erosion of bodies in a variety of low Reynolds number settings. We also apply the method to obtain surface tractions on spheroidal bodies sedimenting under gravity near a plane wall as studied in [8], clarifying the role of particle eccentricity in determining three-dimensional glancing versus reversing type trajectories.

*Corresponding author. Email: spagnolie@math.wisc.edu

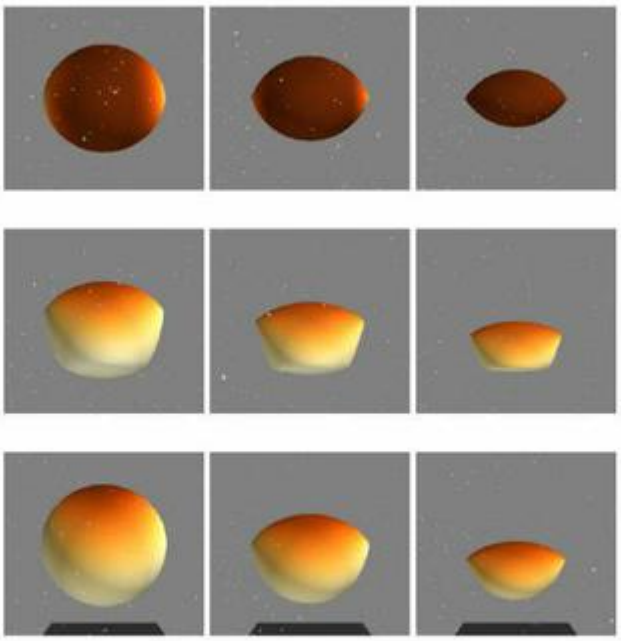

Figure 1: Erosion of three initially spherical particles at low Reynolds number while held immobile in non-trivial background flows. Top row: uniform horizontal flow. Second row: shear flow with plane of zero background flow below the sphere. Third row: shear flow above a no-slip plane wall. The surface color indicates shear stress. The white tracers illustrate the background flow in the animations from which these images are taken.

CONCLUSIONS

We have presented new integral equations for the surface tractions on a rigid body in a viscous fluid with background flow. These equations were applied to the study of several erosion processes including those depicted above; in each case we see the emergence of a distinct limiting body shape, which has sharp corners or ridges. In particular, the body shape that emerges in a uniform background flow is the drag-optimizing profile obtained by Pironneau [9]. Future applications of this integral equation will include problems in microscale chemical processes and biophysics where local stress information may be critically important in inducing/inhibiting growth, as well as other stress-influenced phenomena such as plaque rupture in arteries [10].

References

[1] H. Power and G. Miranda: Second Kind Integral Equation Formulation of Stokes' Flows Past a Particle of Arbitrary Shape. SIAM Journal on Applied Mathematics 47.4: 689-698 (1987).

[2] E. E. Keaveny and M. J. Shelley: Applying a Second-Kind Boundary Integral Equation for Surface Tractions in Stokes Flow. J. Comp. Phys. 230, 2141 (2011).

[3] S. Kim and S. J. Karrila, Microhydrodynamics: Principles and Selected Applications (Butterworth-Heinemann, Boston, 1991).

[4] N. Liron and E. Barta: Motion of a Rigid Particle in Stokes Flow: a New Second-Kind Boundary-Integral Equation Formulation. J. Fluid Mech 238, 579 (1992).

[5] S. Kim and H. Power: A Note on Two Boundary Integral Formulations for Particle Mobilities in Stokes Flow. J. Fluid Mech 257, 637 (1993).

[6] M. Ingber and L. Mondy: Direct Second Kind Boundary Integral Formulation for Stokes Flow Problems. Computational mechanics 11, 11 (1993).

[7] L. Ristroph, M. N. Moore, S. Childress, M. J. Shelley, and J. Zhang: Sculpting of an Erodible Body by Flowing Water. Proceedings of the National Academy of Sciences 109, 19606 (2012).

[8] W. H. Mitchell and S. E. Spagnolie: Sedimentation of Spheroidal Bodies Near Walls in Viscous Fluids: Glancing, Reversing, Tumbling and Sliding. J. Fluid Mech. 772: 600–629 (2015).

[9] R. Glowinski and O. Pironneau: On the Numerical Computation of the Minimum-Drag Profile in Laminar Flow. Journal of Fluid Mechanics 72, 385 (1975).

[10] Groen, Harald C., Frank JH Gijsen, Aad van der Lugt, Marina S. Ferguson, Thomas S. Hatsukami, Anton FW van der Steen, Chun Yuan, and Jolanda J. Wentzel: Plaque Rupture in the Carotid Artery Is Localized at the High Shear Stress Region. Stroke 38, no. 8: 2379-2381 (2007).

FLUID-STRUCTURE INTERACTIONS IN CELLULAR BIOPHYSICS

[a]Michael J. Shelley [a)]
Courant Institute of Mathematical Sciences, New York University, New York, New York
and
Center for Computational Biology, Simons Foundation, New York, New York

Summary The cellular cytoskeleton is an assembly of microscopic filaments and molecular motors, and is the machinery for performing many cellular processes vital to life such as mitosis and cell division. Despite its critical role, important aspects of cytoskeletal mechanics remain poorly understood, particularly how the interactions of microscopic cytoskeletal elements — filaments and motor-proteins — with each other and the cellular cytoplasm relate to observed larger-scale behavior. One reason for this lack of understanding is the complexity of the fluid-structure interactions involved – mitosis and chromosome segregation can involve hundreds to tens-of-thousands of microtubules – and, when modeling, the difficulty in determining the key actors driving the phenomena. I will discuss recent advances in our theoretical understanding of some important cytoskeletally-driven processes, achieved partly through the development of highly efficient and flexible numerical methods for resolving and evolving large assemblies of microtubules, and partly through careful combinations of experimental observation and biophysical modeling.

INTRODUCTION

Biology has long been the inspiration for studying how actively driven structures interact with fluids, with the flight of birds and swimming of fish being classical examples. However, the microcosm of the cell provides other, less easily observed, likewise fascinating instances. Figure 1 shows some of the events leading to the first cell division in a *Caenorhabditis elegans* embryo. Figure 1a–c shows the migration and positioning of the pronuclear complex (PNC), which carries the male and female genetic material to the center of the cell. However this process might be effectuated, the proper positioning and orientation of the complex, and thus that of the subsequent mitotic spindle (Figure 1c–e), are crucial for asymmetric cell division and the generation of cell diversity during development. Pronuclear positioning is a daunting problem in fluid-structure interactions as the PNC is itself geometrically complex given its association with two dense arrays of stiff biopolymers -- microtubules, or MTs -- which are themselves involved in driving the complex through the cytoplasm. Figure 1d,e captures another fluid-structure interaction as chromosome copies are divided and are then moved to opposite ends of a cell before cell division (Figure 1f). See [1] for a recent review. To study these problems in developmental biology, we have developed new numerical tools to resolve some of the complex fluid-structure interactions involved, and new theoretical models of the active cytoskeletal materials involved.

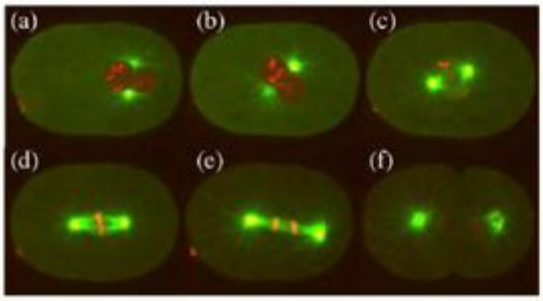

Figure 1: Snapshots of different stages of the first cell division in a single-cell *C. elegans* embryo: (a–c) pronuclear centering and rotation, (c,d) spindle formation, (e) asymmetric spindle elongation and chromosome segregation, and (f) cell division. Here tubulin is labeled with a green fluorescing molecule, and the chromosomes are labeled with a red fluorescing molecule. Figure modified with the permission of Asako Sugimoto.

Spindle Positioning as a Fluid-Structure Interaction Problem

To this end, we have created a highly efficient, large-scale numerical platform for dynamic simulation of cytoskeletal assemblages of MTs and motor-proteins [2]. It is, to our knowledge, the first method to incorporate many-body hydrodynamic interactions between MTs and other intracellular bodies with the cytoplasmic fluid, while also accounting for MT flexibility, their "dynamic instability", and interactions with motor proteins [3]. Our method is based upon a boundary integral formulation for efficiently solving the Stokes equations around immersed bodies in confinement [4], and uses nonlocal slender body theory for the accurate, but dimensionally reduced, representation of MT biopolymers [5]. Figure 2 shows the application of this platform to the study the mitotic spindle positioning in the first cell division in *C. elegans* embryo [3]. Achieving proper position is indispensible for faithful chromosome segregation. This simulation instantiates a model of pronuclear positioning proposed by Kimura & Onami [6] wherein motor proteins bound to the cell periphery pull upon MTs attached to the pronucleus; see also [7]. Specifically, we show that different proposed active mechanisms for spindle positioning produce qualitatively different

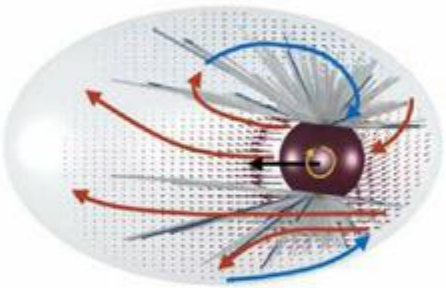

Figure 2: The computed cytoplasmic flow during nuclear positioning where ~1000 MTs are pulled upon by motor-proteins bound to the cell periphery. Adapted with permission from Nazockdast *et al* [3].

[a)] Corresponding author. Email: **shelley@cims.nyu.edu or mshelley@simonsfoundation.org**

signatures in their induced cytoplasmic flow, suggesting flow visualization as a tool for studying different active mechanisms in cellular processes. For the simulation in Figure 2, the cytoplasmic flow is predominantly that induced by a Stokeslet moving under confinement. In related work, we use a combination of structural data from electron tomography and computer simulations to study the interaction of MTs within the spindle with chromosomes during chromosomal division (Redemann *et al*, 2016, in preparation).

Mathematical Modeling of Contractile MT/Motor-Protein Networks

It remains unclear how cytoskeletal filaments and motor proteins organize into cellular scale structures such as the mitotic spindle, and how molecular properties of cytoskeletal components affect the large-scale behaviors of such systems. To help understand this in the context of the mitotic spindle, recent work from the Needleman Lab (Harvard) investigated the self-organization of microtubules in cellular extracts [8]. These experiments show that MTs can form macroscopic networks that spontaneously contract; See the two left panels of Figure 3. As part of this study, we proposed that these contractions are driven by the clustering of microtubule minus ends by the motor-protein dynein, and constructed an active fluid theory based on this idea. In this mathematical model, motion of MTs is driven by the active stresses arising from motor-protein driven bundling of their minus ends, and is ultimately resisted by steric repulsion. This theory predicts a dependence of the time-scale of contraction on initial network geometry, a development of density inhomogeneities, and a constant final network density, all in quantitative agreement with experiments. The right panel of Figure 3 shows a comparison of the MT density predicted by simulating the active fluid model with experimental measurements of the active material density. These results demonstrate that the motor-driven clustering of MT ends is a generic mechanism leading to contraction, and its consequences are being investigated in the context of active fluid models of the mitotic spindle (Furthauer et al, (2016), in preparation).

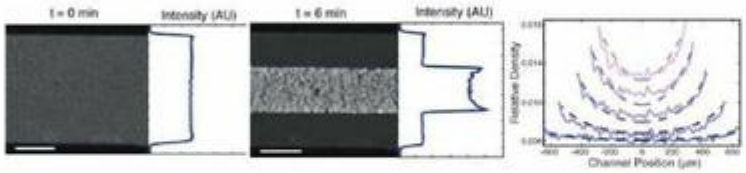

Figure 3: Left and Middle panels: Contraction of a cellular extract containing "stabilized" MTs in a microfluidic channel, and showing intensity averaged along the length of the channel (rightward graphs). The average intensity peaks at the network's edges due to increased local microtubule density. Right panel: Comparison of measured density (solid lines) with density from simulation of the active fluid model (dashed lines). Adapted with permission from Foster *et al* [8].

Conclusions

Cell biophysics provides complex new fluid-structure interaction problems that are central to our understanding of basic developmental biology, and which impinges on new areas of materials science and self-assembly. Understanding these requires the development of new computational tools that can resolve the geometric complexity of the phenomena, and the derivation and analysis of new "active-matter" models that explore the peculiarities of how motor-proteins interact with cytoskeletal filaments such as microtubules.

References

[1] Shelley, M.J.: The Dynamics of Microtubule/Motor-Protein Assemblies in Biology and Physics, in *Annual Reviews of Fluid Mechanics* **48**, 487-506 (2016).
[2] Nazockdast, E., Rahimian, A., Zorin, D., Shelley, M.J.: A Fast Platform for Simulating Flexible Fiber Suspensions applied to Cell Mechanics. Submitted (2016).
[3] Nazockdast, E., Rahimian, A., Needleman, D., Shelley, M.J.: Cytoplasmic Flows as Signatures for the Mechanics of Mitotic Spindle Positioning. Submitted (2016).
[4] Veerapaneni, S., Rahimian, A., Biros, G., Zorin, D.: A fast algorithm for simulating vesicle flows in three dimensions. In *Journal of Computational Physics* **230**, 5160-5634 (2011).
[5] Tornberg, A.-K., Shelley, M.J.: Simulating the Dynamics and Interactions of Flexible Fibers in Stokes Flows. In *Journal of Computational Physics* **196**, 8-40 (2004).
[6] Kimura A., Onami S.: 2005. Computer simulations and image processing reveal length-dependent pulling force as the primary mechanism for *C. elegans* male pronuclear migration. In *Developmental Cell* **8**, 765–75 (2005).
[7] Shinar T., Mano M., Piano F., Shelley M.J.: A model of cytoplasmically driven microtubule-based motion in the single-celled *Caenorhabditis elegans* embryo. In *PNAS* 108:10508–13 (2011).
[8] Foster, P., Furthauer, S., Shelley, M., Needleman, D.: Active contraction of microtubule networks. In *eLife*, 10837 (2015)

FLUID DYNAMICS OF HYDROPHILOUS POLLINATION IN *RUPPIA* (WIDGEON GRASS)

Naga Musunuri[1], Daniel E. Bunker[2], Susan Pell[3], Ian Fischer[1] and Pushpendra Singh[1a)]
[1]*Department of Mechanical Engineering, New Jersey Institute of Technology, Newark, New Jersey*
[2]*Department of Biological Sciences, New Jersey Institute of Technology, Newark, New Jersey*
[3]*Science Department, Brooklyn Botanic Garden, Brooklyn, New York*

Summary The aim is to understand the physics underlying the mechanisms of two-dimensional aquatic pollen dispersal, known as hydrophily. We observed two mechanisms by which the pollen released from male inflorescences of *Ruppia* is adsorbed on a water surface: 1) inflorescences rise above the surface and after they mature their pollen mass falls onto the surface as clumps and disperses on the surface; 2) inflorescences remain below the surface and produce air bubbles which carry pollen mass to the surface where it disperses. In both cases dispersed pollen masses combined under the action of capillary forces to form pollen rafts. This increases the probability of pollination since the capillary force on a pollen raft towards a stigma is much larger than on a single pollen grain. The presence of a trace amount of surfactant can disrupt the pollination process as the pollen is not captured or transported on the water surface.

INTRODUCTION

In *Ruppia maritima*, the transport of pollen from an anther to a stigma takes place primarily on a water surface [1,2]. To model the transport process, we need to understand the mechanisms by which the pollen grains released from an anther are adsorbed and disperse on the water surface and the hydrodynamic forces that govern their subsequent motion on the surface towards the sigma. Our objective is also to study the role of surface tension in the transport process and how it is affected by the presence of surfactants that may be present because of water contamination. It is well known that particles trapped in liquid surfaces interact with each other via lateral capillary forces, which arise because of their weight, to form clusters. This, as discussed below, is also the mechanism by which pollen particles cluster together to form pollen rafts.

Clusters of pollen adsorbed in a water surface are subjected to hydrodynamic drag and capillary forces. The vertical component of capillary force keeps them afloat, and its lateral component moves them tangentially on the water surface (Fig. 1). A depression in the water surface created by a stigma gives rise to a lateral capillary force that transports the pollen towards the stigma. The latter is the key mechanism that enhances the probability of pollination which is especially important because these plants produce pollen in limited quantities in comparison to the plants that rely on three-dimensional pollination. Flow on the surface of oceans or lakes changes with changing wind and water currents. Therefore, in addition to lateral capillary forces, floating pollen clusters are subjected to hydrodynamic forces. This makes a study of the role of capillary forces in the pollen transport process difficult to carry out under natural conditions.

For the last three years, we have collected *Ruppia maritima* from the north coast of Long Island and the Jersey Shore just as it was coming into bloom. This was the optimal condition in which to manipulate and observe pollen release and its interaction with the water surface. Field samples of male and female flowers were collected for experimentation and whole plants were transferred to saltwater aquariums at Brooklyn Botanic Garden and New Jersey Institute of Technology for observation. We made video recordings of the pollen release, transport to the surface, adsorption, dispersion, and transport on the water surface under the controlled laboratory conditions. We also conducted experiments to understand the effect of trace amounts of surfactant in the water, for which we added detergent to the water and observed its influence on each of these steps.

(i)  (ii) 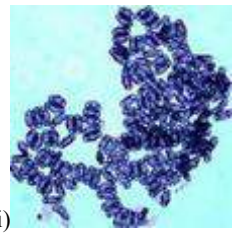 (iii) 

Figure 1. Anthers and pollen grains of *Ruppia*. (i) Male flower (anthers); (ii) Magnified view of kidney-shaped pollen grains (length ~40 μm) in 100x, and (iii) Magnified view of a stigma in contact with the water surface. Notice that the water surface around the stigma is depressed which can be inferred from the reflection pattern around the upper tip of the stigma. This attracted the attached pollen clusters.

RESULTS AND DISCUSSION

We observed two mechanisms by which the pollen released from male inflorescences of *Ruppia maritima* is adsorbed on a water surface: 1) inflorescences rise above the water surface and after they mature their pollen mass falls onto the surface as clumps and disperses as it comes in contact with the surface [3-5]; 2) inflorescences remain below the surface and produce air bubbles which carry kidney-shaped pollen mass to the surface where it disperses. In the second case, some pollen grains were

[a)] Corresponding author. Email: singhp@njit.edu

also released onto the bubble surfaces before they detached from the inflorescences. These pollen grains adsorbed on the bubble surfaces were also carried to the water surface.

The video recordings show that in the second mechanism often the pollen mass within a bubble remained undispersed for several seconds and then suddenly the bubble bursted causing the dispersion of the pollen onto the water surface (Fig. 2). The dispersion occurs in two-dimensions, i.e., on the water surface, in the sense that a significant fraction of the pollen grains are adsorbed at the surface. Pollen grains are slightly denser than water and so if they are not adsorbed at the surface, they slowly sediment to the bottom.

For both mechanisms, the pollen mass partially dispersed with a densely packed region of pollen grains in the middle which was surrounded by a monolayer of pollen grains. The latter appeared translucent compared to the densely packed region because it contained mostly a single layer of grains with some smaller clumps within. The process by which a pollen mass disperses is qualitatively similar to the process by which a clump of powder disperses on a water surface. The dispersed area of a pollen mass released above the water surface was smaller than that of a pollen mass released below the water surface. Pollen dispersion on the surface is a crucial first step in the formation of floating porous pollen structures called "pollen rafts." In both cases dispersed pollen masses floated and combined with others to form pollen rafts.

The presence of a trace amount of surfactant (~100 ppm) interfered with the pollen adsorption process. For anthers released below the water surface most pollen masses were not transported to the surface. The surface tension force, reduced because of the surfactant, was not large enough to keep them attached to the bubbles as they rose to the surface, and so pollen masses sedimented to the bottom. Although some pollen masses were transported to the water surface, they did not disperse and after remaining on the water surface for a few minutes they also sedimented. The reduced surface tension was not large enough to keep them afloat or to disperse them. For pollen masses released above the water surface, most of the pollen was not trapped at the surface, especially the larger sized clumps. The pollen that was adsorbed formed a monolayer which was not dense enough and pollen rafts were not formed, and so it was only weakly attracted towards a depression in the water surface created by a stigma.

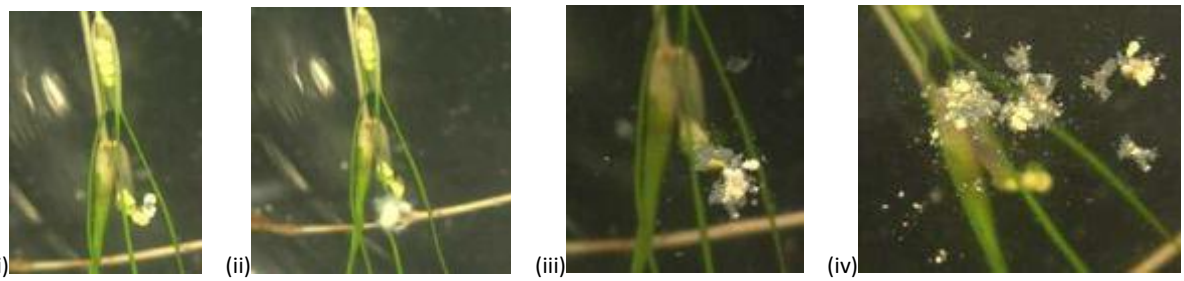

Figure 2. Pollen mass released from anthers below the air-water interface disperses upon reaching the water surface to form a partially dispersed clump and subsequently combined with other pollen masses to form a pollen raft (i-ii) A pollen mass is rising to the water surface, (iii) The pollen mass dispersed as soon as it came in contact with the water surface, and (iv) Several dispersed pollen masses cluster together to form a pollen raft.

CONCLUSIONS

Surface tension is essential for efficient pollination of *Ruppia maritima*. It causes pollen masses released above or below the water surface to disperse when they are adsorbed in the surface. This increases their surface area allowing pollen masses to float on the surface. Furthermore, lateral capillary forces cause dispersed pollen masses to come together to form pollen rafts. Pollen rafts deform the water surface substantially more than a single pollen grain because of their larger size and buoyant weight, and therefore, they are more strongly attracted to the depressions created by the stigmas. For this reason the pollen rafts are also referred to as the search vehicles. The presence of a trace amount of surfactant can disrupt the pollination process. When pollen is released above the water surface it sinks as it is not trapped at the surface because of the reduced surface tension, and when it is released below the surface either it does not reach the surface or if it does, it does not disperse on the surface and eventually sinks.

Acknowledgements: The work was supported by the National Science Foundation grant (Award # 1067004).

References

[1] Cox, P. A. Hydrophilous pollination, Annu. Rev. Ecol, Syst., 19, 261-280 (1988).
[2] Ackerman, J.D., *Plant Syst. Evol*. 222, 167–185 (2000).
[3] Singh, P., D.D. Joseph, S.K. Gurupatham, B. Dalal and S. Nudurupati, PNAS, 106, 19761-19764 (2009).
[4] Gurupatham, S.K., B. Dalal, Md. Hossain, I. Fischer, P. Singh and D.D. Joseph, *Particle Technology*, 217, 288–297 (2012).
[5] Musunuri, N., D. Codjoe, B. Dalal, I.S. Fischer and P. Singh, KONA, 31, 135-145 (2014).

RHEOLOGY OF NON-BROWNIAN SUSPENSIONS/ THE ROLE OF INTER-PARTICLE CONTACT FORCES

Elisabeth Lemaire[1a)], Frédéric Blanc[1], Stany Gallier[2], Laurent Lobry[1] & François Peters [1]
[1]*Laboratoire de Physique de la Matière Condensée - UMR 7336 - CNRS Université de Nice Sophia-Antipolis Parc Valrose - 06108 Nice cedex 2, France*
[2]*SAFRAN-Herakles, Le Bouchet Research Center, 91710 Vert le Petit, France*

Summary Suspensions of non-Brownian particles display a complex rheology that originates in a subtle balance between hydrodynamic interactions and direct forces between particles, together with the so-called shear-induced microstructure. In particular, the influence of the microstructure has been qualitatively evidenced years ago in shear-reversal experiments. At the particle scale, experimental studies pointed the role played by the surface roughness of the particles in promoting direct contact between particles, and recent numerical computations suggest that contact friction between particles could be part of the explanation for the large viscosity of non-Brownian suspensions. We shall present both experimental and numerical results that highlight the links between contact forces, microstructure and rheology.

INTRODUCTION

Creeping flows of non-Brownion suspensions are ubiquitous in industrial processes as in nature and have been the subject of numerous studies from about the 1970s. Significant efforts have been devoted to modelling the rheological behaviour of these suspensions and, in particular, the variation of the viscosity, η, with shear rate, $\dot{\gamma}$, or particle volume fraction, ϕ. The viscosity dependence on the shear rate is still ambiguous for highly concentrated suspensions. Suspensions appear to change from slight shear-thinning behaviour to shear-thickening one, as the ratio of viscous to Brownian forces increases [1], [2]. Recently the work of Mari et al. [3] showed that discontinuous shear-thickening could be explained by the involvement of friction forces between particles when the shear stress is high enough and Gallier et al. [4] have conducted a comprehensive study on the effect of friction between particles on the rheological behaviour of Non-Brownian suspensions showing that friction was responsible for a significant increase of both the viscosity and the magnitude of normal stress differences. The idea that particles interact not only through hydrodynamic forces, though often ignored, was proposed as early as 1980 by Gadala-Maria & Acrivos to explain the transient response of the viscosity under shear reversal [5]. Indeed, Gadala-Maria & Acrivos proposed to explain the step-like reduction followed by a slower decrease that undergoes the suspension viscosity after shear reversal by the destruction of an asymmetric shear-induced microstructure. Few years latter, this conjecture was confirmed by Parsi & Acrivos who measured the pair distribution function in a non-Brownian suspension [6]. Owing to the reversibility of Stokes equations that hold in low Reynolds number flows, an asymmetric microstructure can develop only if non hydrodynamic forces are involved in particle interactions. Later, Blanc et al. [7] showed that the fore-aft asymmetry observed in the pair distribution of a diluted suspension under shear is explained quantitatively by the direct contacts experienced by the particles through their roughness.
Here, we present some experiments that evidence the role of contact both on microstructure and on rheology and, in a second part we give some numerical results that characterize the role of friction on rheology.

LOCAL RHEOMETRY AND MICROSTRUCTURE

Using Particle Image Velocimetry (PIV) method, we measure the velocity field in a buoyant index-matched suspension sheared in a Couette rheometer [8]. We thus access to the viscosity everywhere in the gap between the concentric cylinders. This local method provides two main advantages compared to conventional macroscopic rheometry: it allows us to avoid or, at least, to control experimental artefacts such as wall slip or shear-induced particle migration and it enables us to observe the microstructure that develops under the flow. We used this technique to measure the response of suspensions of various particle volume fractions under shear reversal. Fig. 1 shows the viscosity response as well as the change in microstructure during shear reversal tests. These results corroborate those of Gadala-Maria & Acrivos and of Pari & Acrivos but since they are almost free from the experimental artefacts mentioned above, we can extract the viscosity values at the minimum and at the plateau. Furthermore, since the microstructure measured at the minimum is almost isotropic, the minimum viscosity should be that of a random suspension where the particles interact only through hydrodynamic interactions. On the opposite, at the plateau, the suspension has a microstructure with pairs of contacting particles in the compressional quadrant. Thus the difference between the viscosity at the plateau, η_{pl}, and the viscosity at the minimum, η_{min}, corresponds to the enhancement of the dissipation due the microstructure and should give an estimate of the so called contact viscosity that is the non hydrodynamic contribution to the viscosity.

[a)] Corresponding author. Email: elemail@unice.fr.

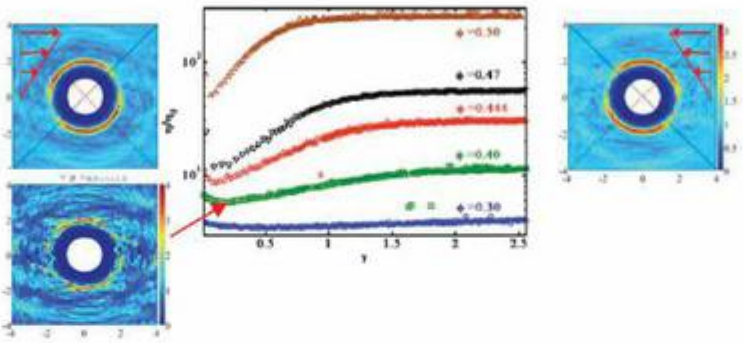

Figure1*. Viscosity response during shear reversal experiments and associated pair distribution functions, obtained for a suspension with ϕ=0.35. When the flow direction is changed, the microstructure pair distribution function is changed into its par distribution function. After shear reversal, the viscosity undergoes a step-like decrease, passes through a minimum and increases again to its steady value. At the minimum the microstructure is almost isotropic (in the shear plane) while, at the plateau contacting pairs are present in the compressional quadrant.*

A detailed numerical study conducted with the Force Coupling Method of Peters et al. proposes a correlation between the contact viscosity, η^c, and the difference η_{pl}-η_{min}:

$$\eta^c=0.85.(\eta_{pl}-\eta_{min})$$

Even though this correlation seems to hold whatever the roughness of the particles and the friction coefficient, friction plays a significant role on rheology and tunes both the viscosity and the normal stress differences, as shown in fig.2 [4]

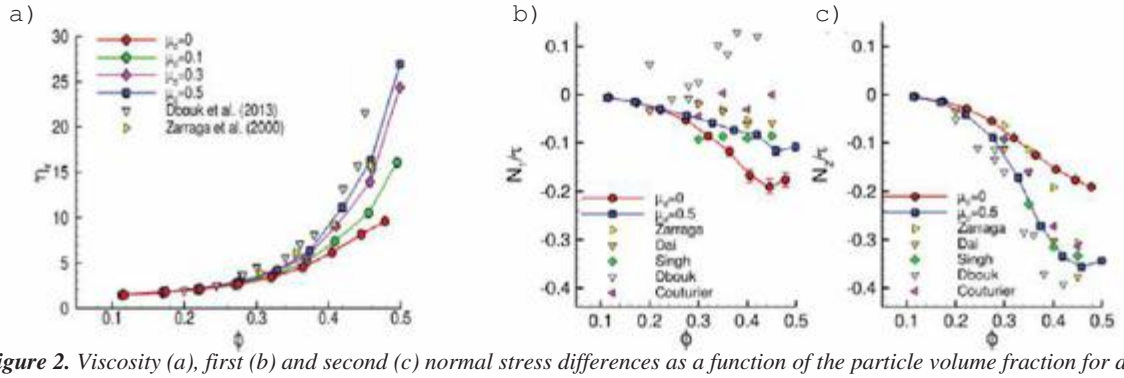

Figure 2. *Viscosity (a), first (b) and second (c) normal stress differences as a function of the particle volume fraction for different friction coefficients.*

CONCLUSIONS

From experiments (local rheometry and pair distribution function measurement), links between rheology, microstructure and solid contact interactions between particles have been evidenced and the role of friction between particles has been studied from numerical simulations.

References

[1] Stickel, J. J., & Powell, R. L.: Fluid mechanics and rheology of dense suspensions. Annu. Rev. Fluid Mech., 37, 129-149, 2005.

[2] Denn, M. M., & Morris, J. F.: Rheology of non-Brownian suspensions. Annual review of chemical and biomolecular engineering, 5, 203-228, 2014.

[3] Mari, R., Seto, R., Morris, J. F., & Denn, M. M.: Shear thickening, frictionless and frictional rheologies in non-Brownian suspensions. J. Rheol. 58(6), 1693-1724, 2014.

[4] Gallier, S., Lemaire, E., Peters, F., & Lobry, L.: Rheology of sheared suspensions of rough frictional particles. J. Fluid Mech. 757, 514-549, 2014.

[5] Gadala‐Maria, F., & Acrivos, A.: Shear‐Induced Structure in a Concentrated Suspension of Solid Spheres. J. Rheol., 24(6), 799-814, 1980.

[6] Parsi, F., & Gadala‐Maria, F.: Fore‐and‐Aft Asymmetry in a Concentrated Suspension of Solid Spheres. J. Rheol., 31(8), 725-732, 1987.

[7] Blanc, F., Peters, F., & Lemaire, E.: Experimental signature of the pair trajectories of rough spheres in the shear-induced microstructure in noncolloidal suspensions. Phys. Rev. Lett., 107(20), 208302, 2011.

[8] Blanc, F., Peters, F., & Lemaire, E. . Local transient rheological behavior of concentrated suspensions. J. Rheol. 55(4), 835-854, 2011.

[9] Peters, F., Ghigliotti, G., Gallier, S., Blanc, F., Lemaire, E., & Lobry, L.: Shear-reversal in non-Brownian suspensions: experiments and simulations. Submitted to J. Rheol. 2016.

SIMULATIONS OF A HEAVY BALL FALLING THROUGH A SHEARED SUSPENSION

Adam K. Townsend and Helen J. Wilson *

Department of Mathematics, UCL, London, UK

Summary In recent experiments, Blanc, Lemaire and Peters dropped a heavy sphere through a concentrated suspension of smaller, neutrally buoyant particles. They found that the application of a lateral oscillatory shear flow caused the heavy ball to fall faster on average; and that for highly concentrated suspensions, at certain moments of the cycle of shear oscillation, the heavy ball moves upwards.

We use Accelerated Stokesian Dynamics to model these experiments and other related scenarios. We show how the motion of the heavy particle depends on two key dimensionless parameters: the frequency of the oscillations (relative to a typical settling time) and the strength of repulsive interparticle forces, such as DLVO, relative to the buoyancy-adjusted weight of the heavy ball. At the conference, we will also present results on the dependence on oscillation amplitude, suspension concentration, and the orientation of the shear flow.

INTRODUCTION

Blanc and coworkers [1] recently discovered that a heavy ball falling through a dense suspension of smaller particles can be made to fall much faster by applying a transverse oscillatory shear to the system, as in geometry **[A]** of figure 1. The mechanism, they hypothesise, is all in the microstructure created in the small-particle suspension by each flow. A falling ball creates an asymmetric density disturbance, with more particles ahead of it than are found in its wake; this naturally hinders its falling. The cross-shear, on the other hand, may encourage the small particles to align in the vertical direction, making it easier for the large sphere to pass.

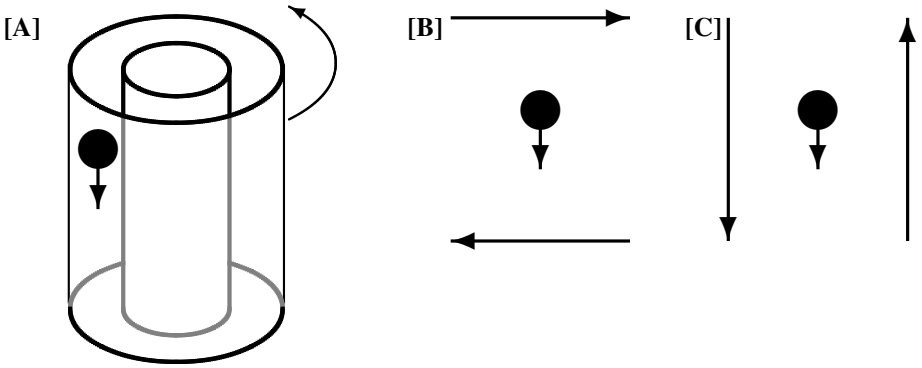

Figure 1: Three different possible orientations of the fall direction relative to the oscillatory shear flow. **[A]** Vorticity direction, as in the Couette device experiments of [1]; **[B]** Flow gradient direction, as reported below; **[C]** Flow direction.

They also found that for very concentrated suspensions (a volume concentration of $\phi = 0.47$), if they tracked the large ball's fall speed during a shear oscillation, its variation was so extreme that at some moments of the shear cycle it was actually travelling upwards. In this paper we aim to reproduce some of these observations numerically, and therefore elucidate the importance of various physical parameters on the two phenomena.

SIMULATION METHOD

We use Accelerated Stokesian Dynamics [2], modified to allow for spheres of different sizes, along with a DLVO-type repulsive force between each close pair of particles (to prevent overlap); for particles of radius a and b whose surface separation is h, the magnitude of this force is $[2ab/(a+b)]\overline{k}e^{-\tau h}$. Here $\overline{k}$ governs the force strength and τ its extent.

The physical system we are simulating can be completely specified in terms of the following physical parameters: the radius of the small particles, a_s, and of the large ball, a_f; the volume concentration ϕ, or area concentration, c of small particles; the shear oscillation amplitude, γ_0, and frequency, $\overline{f}$ (defined here as the inverse of the period); the solvent viscosity, μ; the buoyancy-adjusted weight of the heavy ball, W; and the two parameters of the DLVO repulsive force, $\overline{k}$ and τ. There are additional parameters introduced by the fact that we are simulating a small imitation of the real physical system: the length of our simulation region, L; the number of preshear oscillations we carry out before "turning on" gravity, N_p; the number of shear oscillations we simulate during settling, N_{osc}; and the timestep Δt.

We choose to use the large ball radius a_f as our fundamental lengthscale; its buoyancy-adjusted weight W as our fundamental scale of force; and as our fundamental timescale, the Stokes time $T_s = W/6\pi\mu a_f^2$ over which the large ball would fall through its own radius in pure solvent. The system is then governed by the dimensionless parameters given in table 1.

*Corresponding author. Email: helen.wilson@ucl.ac.uk

Physical parameters			Simulation parameters		Ideal	Used
$\lambda = a_s/a_f$	0.1	Particle size ratio	L/a_f	Box size	Large	5–10
γ_0	1/3	Shear amplitude	N_p	Pre-shear oscillations	Large	2
$(\tau a_f)^{-1}$	0.05	Repulsion decay length	N_{osc}	Main oscillations	Large	2
$k = \overline{k}/W$	Free	Strength of DLVO force	$\Delta t/T_s$	Step size	Small	Varies
$f = \overline{f}T_s$	Free	Dimensionless frequency	c	Area concentration (2D)	–	0.60

Table 1: Dimensionless parameters governing our simulations. On the left are physical parameters, along with typical values as used in the simulations presented below. On the right we give numerical parameters as we have used them; we also show the "ideal" value these parameters would take if we had unlimited computing resource.

Since simulations are such a flexible tool, we have also considered the two other possible orientations of the shearing flow relative to the fall direction (figure 1). The experiments correspond to geometry **[A]**; in cases **[B]** and **[C]** the direction out of the plane of shear is essentially neutral and we can make a reasonable approximation by considering a single layer of spheres (here we parametrise the suspension in terms of its area concentration, c, rather than volume fraction, ϕ). Preliminary results for a layer in case **[B]** are presented below; results for **[A]** and from fully 3D simulations will be presented at the conference.

PRELIMINARY RESULTS

In figure 2 we show the transient fall speed v (normalised by the Stokes velocity of the large sphere in pure solvent) during a single oscillation of the shear flow for four different parameter combinations with the ball falling in the flow gradient direction **[B]**. The system is first presheared for two oscillations before the ball begins to fall; we show here the trajectory of the second oscillation after the large ball begins its settling motion.

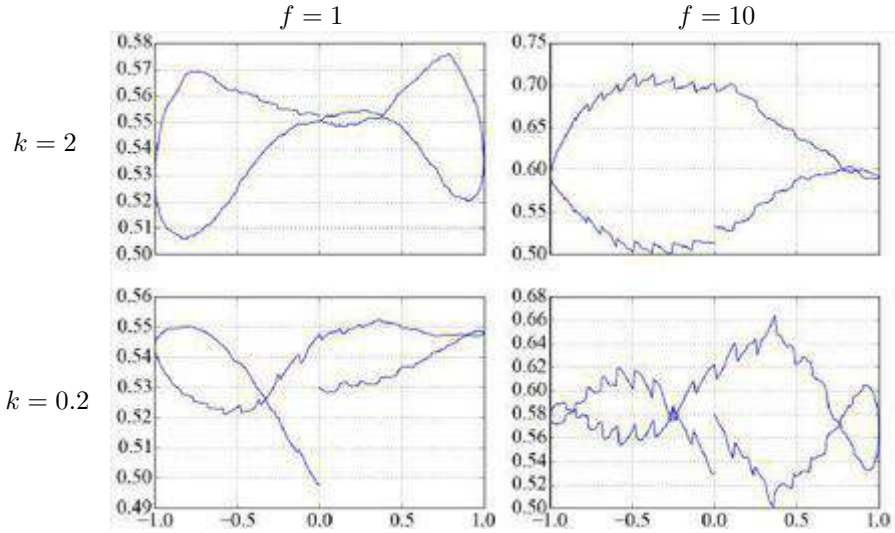

Figure 2: Two-dimensional simulations of a ball falling in the flow-gradient direction (geometry **[B]** of figure 1). We plot the instantaneous fall speed v against state of shear. In each plot, the oscillation begins with motion to the right. The timestep is $\Delta t/T_s = 1/(100f)$ in each case and the other parameters are as in table 1.

Looking first at the mean velocity, we see that, as expected, the ball falls more slowly if the magnitude of the repulsive force between particles is increased (lower plots), because the falling ball naturally comes close to more of its neighbours on the underside than on the top, so the repulsive force has a net upwards effect on the large ball. This is, however, a weak effect (as we would hope, since the purpose of the repulsive force is primarily to reduce numerical overlap problems).

When we investigate the dependence on frequency, however, the results are more dramatic. When the shear has a higher frequency (plots on the right) the mean fall velocity is enhanced by roughly 10%. If we think of low frequencies as the no-shear limit, this is a reproduction (in a different geometry) of the effect discovered by [1]. However, in our geometry we are yet to find any parameter values for which there is reproducible upwards motion.

References

[1] Blanc F., Lemaire E., Peters F.: Tunable fall velocity of a dense ball in oscillatory cross-sheared concentrated suspensions. J. Fluid Mech 746:R4, 2014.

[2] Sierou A., Brady J.F.: Accelerated Stokesian Dynamics simulations. J. Fluid Mech 448:115-146, 2001.

RHEOLOGY OF DENSE NEWTONIAN AND VISCOPLASTIC SUSPENSIONS

Élisabeth Guazzelli*[1], Simon Dagois-Bohy[2], Sarah Hormozi[3], and Olivier Pouliquen [1]

[1]*Aix-Marseille Université, CNRS, IUSTI UMR 7343, 13453 Marseille, France*
[2]*Université Claude Bernard Lyon 1, LMFA, UMR CNRS 5509, 69134 Écully, France*
[3]*Department of Mechanical Engineering, Ohio University, Athens, Ohio 45701-2979, USA*

Summary Despite its long research history and its practical relevance, the mechanics of dense suspensions remain poorly understood. A frictional approach, which stems from the rheology of dry granular materials, has been successfully applied to Newtonian suspensions using an original pressure-imposed shear cell. This alternative way of looking at suspensions provides a way to circumvent the divergence observed in volume-imposed rheometry and yields examination of the rheology close to the jamming transition. This has been also applied to suspensions of non-Brownian spheres in yield-stress fluids. Accurate measurements of the shear stress and particle normal stress are favorably compared with a model based on scaling arguments and homogenization method.

Dense or highly concentrated particulate flows belong to an intermediate regime between pure suspensions and granular flows. These dense mixture of non-Brownian particles and fluid are found very commonly in practical engineering applications (e.g. waste disposal, concrete, drilling muds, metalworking chips transport, and food processing) but also in natural phenomena (e.g. flows of slurries, debris, and lava). In order to understand their flowing behavior, it is desirable to know their response to imposed forces and motions at their boundary. The fundamental problem is then to determine the rheological properties of these media (considered as equivalent homogeneous materials) from a knowledge of the mechanics of the particles and the interstitial fluid. In other words, the key problem is to understand the relationship between the macroscopic or bulk properties of the medium and its microscopic structure at these large concentrations. The major difficulty of dense particulate flows is that the grains interact both by hydrodynamic interactions through the liquid and by mechanical contact. The complex nature of these particle interactions greatly contribute to the lack of understanding of these systems.

Over the last century, there has been extensive work on the rheology of Newtonian suspensions, i.e. suspensions composed of a Newtonian suspending fluid and of non-colloidal particles interacting mainly through hydrodynamics, see e.g. [1]. In the case of neutrally-buoyant solid spheres subjected to a steady shear flow, the linearity of the Stokes equation implies that the scaling of the shear stress τ is viscous, i.e. $\tau = \eta_s(\phi)\,\eta_f\dot{\gamma}$ where $\dot{\gamma}$ is the shear rate and η_f the viscosity of the suspending Newtonian fluid. The dimensionless effective shear viscosity η_s only depends on the particle volume fraction ϕ and increases with increasing ϕ, diverging at maximum packing fraction, ϕ_m. In addition to this quasi-Newtonian shear-stress law, there exists a particle normal stress P which also scales viscously. To be more precise, P is linear in the modulus of the shear rate, because it must be independent of the sign of the shear rate. It can be written as $P = \eta_n(\phi)\,\eta_f\dot{\gamma}$ where $\dot{\gamma}$ is conveniently defined in an invariant form as $\dot{\gamma} = \sqrt{2\,\mathbf{E}:\mathbf{E}}$ where $\mathbf{E}$ is the rate of strain. The dimensionless effective normal viscosity η_n is again a sole function of ϕ and presents the same divergence as $\eta_s(\phi)$ when approaching jamming at ϕ_m. The rheology of the suspension is solely determined by the knowledge of the two functions $\eta_s(\phi)$ and $\eta_n(\phi)$.

There is an equivalent approach to this classical view in terms of effective viscosities which is coming from the rheology of dry granular materials and hinges on a frictional view of the problem, see e.g. [2]. When an assembly of particles is subjected to steady shear under a confining particle pressure P, there is only one dimensionless control parameter, a dimensionless shear rate which can be interpreted as the ratio of the time scale for particles to rearrange due to the pressure P to the time scale of the flow $\dot{\gamma}^{-1}$, see figure 1 (a). The friction $\mu = \tau/P$ and the volume fraction ϕ are sole function of this dimensionless number. In the case of immersed granular media, when viscous forces are dominant, the dimensionless number is $J = \eta_f\dot{\gamma}/P$ and is viscous in contrast to dry granular flows where it is inertial. Using an original pressure-imposed shear cell, $\mu(J)$ and $\phi(J)$ has been found once again to collapse onto universal curves [3]. This alternative way of looking at suspensions enabled to circumvent the divergence observed in volume-imposed rheometry and provided examination of the rheology close to the jamming transition. In particular, this approach yields accurate measurements of the particle pressure, a quantity not often easily captured.

The new unconventional rheological tool that is the pressure-imposed shear cell offers a brand new perspective of analysis, see figure 1 (b). We have undertaken systematic investigations and examined how the macroscopic rheology close to the jamming transition is influenced by the nature of the suspending fluid. In particular, we have explored the rheology of non colloidal suspensions composed of a yield-stress fluid and of neutrally-buoyant solid spheres in the dense regime [4]. The particles used were polystyrene spheres having a diameter $d = 580 \pm 10\ \mu$m and thus are insensitive to Brownian motion and colloidal interactions. Four suspending fluids having different rheological behaviors were selected. A test case Newtonian

*Corresponding author. Email: elisabeth.guazzelli@univ-amu.fr

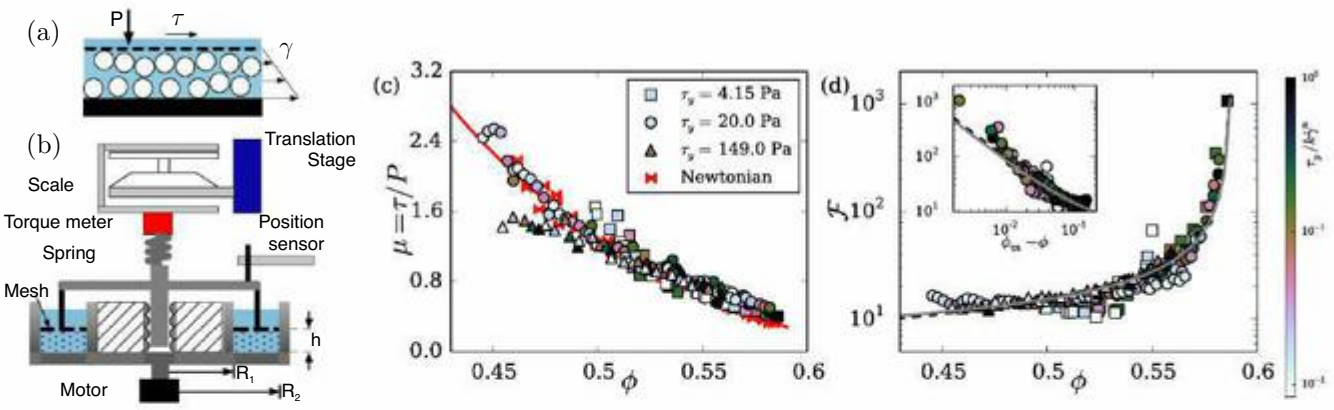

Figure 1: (a) Principle of the pressure-imposed rheometry: the porous plate exerts a pressure (P) on the grains while the suspension is sheared ($\dot{\gamma}$) and the shear stress (τ) is measured. (b) Sketch of the experimental apparatus. (c) Friction coefficient $\mu = \tau/P$ and (d) the function $\mathcal{F}$ relating the local shear rate seen by the particles to the macroscopic shear rate versus ϕ (grey line : $2.8\sqrt{\eta_s(\phi)}$ [6], black dashed line : $2\sqrt{\eta_s(\phi)/1-\phi}$ [5], inset : $\mathcal{F}$ versus $\phi_m - \phi$) for the viscoplastic suspensions as well as for the test Newtonian suspension. The symbols correspond to the suspending fluids (the viscoplastic fluid having different yield stresses τ_y and consistencies k and the Newtonian fluid) and the colormap to the range of $\tau_y/k\dot{\gamma}^n$.

fluid was chosen to be polyethylene glycol-ran-propylene glycol monobutylether of viscosity $\eta = 2.27$ Pa.s at a temperature of 24°C and of density closely matched to that of the particles. The three other non-Newtonian suspending fluids were emulsions of water droplets in dodecane at different water volume-percentage (68%, 72%, and 80%). Their rheological behaviors followed a Herschel-Bulkley law with the same exponent but with different yield stresses τ_y and consistencies k.

The rheological measurements are in agreement with a model based on scaling arguments and homogenisation methods [5, 6]. In particular, all the data including the Newtonian test case show a perfect collapse of the friction $\tau/P = \mu(\phi)$, see figure 1 (c). This shows that the constitutive laws close to jamming has a form similar to that for a Newtonian suspending fluid and thus demonstrates unambiguously that the dynamics of the particles close to jamming are mainly controlled by geometrical constraints and are independent of the suspending fluid. This scaling approach has been further tested by inferring the function $\mathcal{F}(\phi)$ relating the local shear rate seen by the particles to the macroscopic shear rate imposed by the rheological flow and by showing that an excellent collapse is obtained with a sole dependence in ϕ, see figure 1 (d). This experimental master curve agrees well with the prediction proposed by [5] and by [6].

As previously found by [5], the properties of the viscoplastic suspensions can be satisfactorily modelled as that of a Herschel-Bulkley fluid with an exponent equal to that of the suspending fluid. The dimensionless effective yield-stress and consistency are found to be sole functions of ϕ that can be deduced from the knowledge of $\mathcal{F}(\phi)$ and the dimensionless effective viscosity $\eta_s(\phi)$ of the test Newtonian suspending fluid.

The present study offers new perspective in the study of even more complex particulate systems as the knowledge of the rheological constitutive laws in the Newtonian case and the calculation of the function relating the local to the macroscopic shear rate seem to be the sole ingredients needed to infer the rheological properties of these suspensions.

References

[1] Guazzelli E., Morris J. F.: A Physical Introduction to Suspension Dynamics. Cambridge Texts In Applied Mathematics. Cambridge University Press 2012.

[2] Andreotti B., Forterre Y., Pouliquen O.: Granular Media: Between Fluid and Solid. Cambridge University Press 2013.

[3] Boyer F., Guazzelli E., Pouliquen O.: Unifying suspension and granular rheology. Phys. Rev. Lett. 107:188301, 2011.

[4] Dagois-Bohy S., Hormozi S., Guazzelli E., Pouliquen O.: Rheology of dense suspensions of non-colloidal spheres in yield-stress fluids. J. Fluid Mech. 776:R2, 2015.

[5] Chateau X., Ovarlez G., Trung, K.L: Homogenization approach to the behavior of suspensions of noncolloidal particles in yield stress fluids. J. Rheol. 52:489-506, 2008.

[6] Lerner E., Düring G., Wyart M.: A unified framework for non-Brownian suspension flows and soft amorphous solids. PNAS 109:4798-4803, 2012.

SHEAR-INDUCED GRANULAR MOTION ON REGULAR SUBSTRATES AT LOW PARTICLE REYNOLDS NUMBERS

José R. Agudo[2], Christian Illigmann[1], Giovanni Luzi[2], Antonio Delgado[1,2] & Andreas Wierschem[1a)]

[1]*Institute of Fluid Mechanics, Friedrich-Alexander-Universität Erlangen-Nürnberg (FAU), Erlangen, Germany*
[2]*Institute of Fluid Mechanics, FAU Busan Campus, University of Erlangen-Nuremberg, Busan, Republic of Korea*

Summary We study incipient motion of single spherical particles in shear flow over regular substrates at low particle Reynolds numbers. Experimental studies show a strong dependence on the substrate geometry. Numerical studies covering the entire range of particle spacings on quadratically arranged substrates show that rolling motion is always preferred to sliding motion. It also reveals how the effective zero level depends on the particle spacing. Taking into account the substrate geometry, we propose a model for the incipient motion at low particle Reynolds numbers that only relies on the effective zero level and compares well with experiments and numerics.

INTRODUCTION

Prediction of particle incipient motion is important in a wide variety of industrial and natural processes like cleaning of surfaces and conveying as well as sediment transport in rivers, granular beds erosion and dune formation. Given the wide range of applications, onset of particle motion has been studied intensively during the last century, yet mostly under turbulent conditions. During the last decade, several authors have focused on incipient particle motion under laminar conditions, which is encountered, for instance, in heavy oil transportation [1], deposition and cleaning in filtration processes or microfluidics [2], [3]. Even in high Reynolds number flows, the particle Reynolds numbers may be of order one or smaller [4].

In recent experimental studies at low particle Reynolds numbers with regularly arranged monolayers of spheres as substrates, we observed a strong impact of the substrate geometry on the incipient motion of a single bead [2]. Further experiments also revealed the role of the substrate geometry on the incipient particle motion for multi-particle systems [3]. The local grain arrangement on the incipient particle motion has been considered by taking into account the angle of repose [5], [6] and exposure to the flow [7] or grain protrusion [8]. The models for predicting the incipient motion usually rely on effective empirical values for the drag coefficient and assume an effective zero level independent from the bed geometry [9]. Depending on the assumed effective and empirical values, the models provide threshold values that scatter significantly [10]. Focusing on creeping-flow conditions, we propose here a model that takes into account the substrate geometry and only relies on the effective zero level. The dependence of the effective zero level on the particle spacing is determined numerically.

SYSTEM

We consider a single sphere of diameter D_P and density ρ_S deposited on a regular substrate and exposed to a steady shear flow (see Figure 1) with shear rate $\dot{\gamma}$ of a viscous incompressible Newtonian fluid of constant density ρ and kinematic viscosity ν. The substrate consists of a layer of fixed spheres of same size that are regularly arranged in quadratic configurations. In experiments, the spacing was achieved using sieves of different mesh size [2], [3]. For irregular substrates, it has been shown that the shear flow penetrates slightly into the substrate [1], [11], [12]. Extrapolating the linear shear flow results in an effective zero level z_0 below substrate protrusions.

We consider particle Reynolds numbers smaller than 1. The particle Reynolds number is given by $\mathrm{Re}_P = \dot{\gamma} D_P^2 / \nu$. The incipient motion is characterized by the critical Shields number θ_C, which compares the characteristic shear force acting on the particle to the resistant specific particle weight that retains the particle in its place. The Shields number is defined by $\theta = \nu\dot{\gamma} / \left[(\rho_S / \rho - 1) g D_P\right]$, where g is the acceleration of gravity.

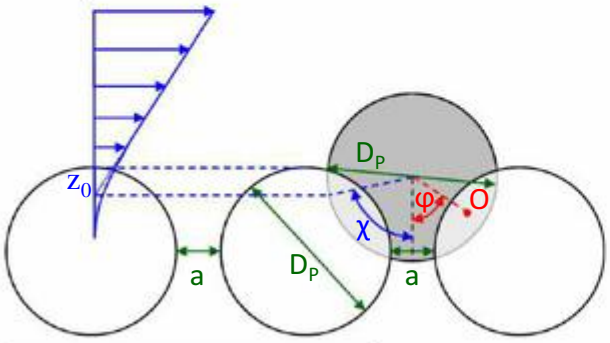

Figure 1: Sketch of the system: Single bead resting on a quadratic substrate exposed to a shear flow. D_P: particle diameter; a: substrate spacing; z_0: effective zero level below the top of the substrate; O: downstream contact point between mobile bead and substrate; φ: angle of repose.

a) Corresponding author. Email: andreas.wierschem@fau.de.

RESULTS

At particle Reynolds numbers below 1, the critical Shields number does not depend on inertia but increases with substrate spacing [2]. The substrate hinders the motion in two ways: The mobile particle is partially shielded to the shear flow and it has to overcome the angle of repose at the downstream side. The latter is a function of the substrate spacing. The former has been studied numerically. As shows Figure 2(a), the effective zero level below substrate protrusions increases linearly with substrate spacing from about 10% to 20%.

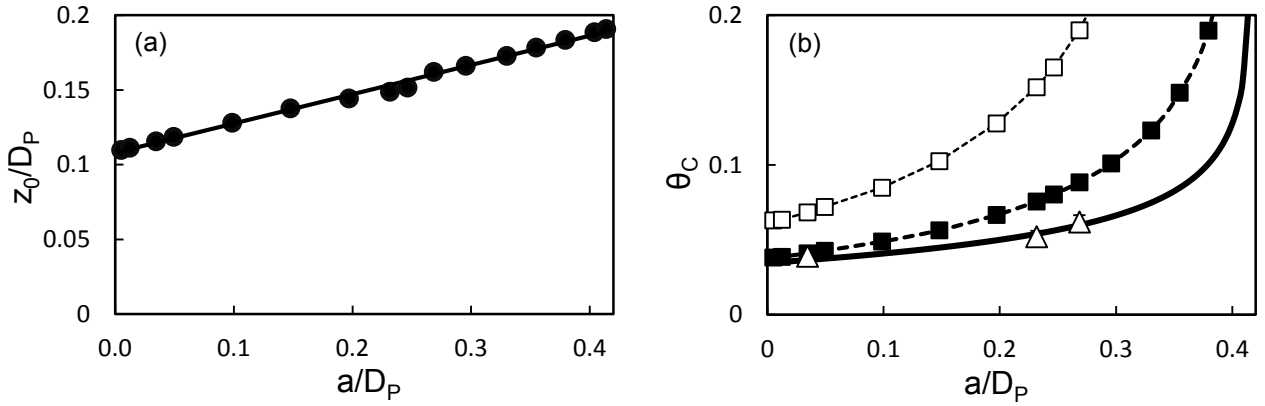

Figure 2: (a): Effective zero level below substrate protrusions. The symbols show the numerically determined values; the line is to guide the eye. (b): Critical Shields number as a function of the angle of repose. Triangles indicate the experimental data [2], [3]; open and solid squares indicate the numeric values for frictionless sliding and for rolling motion, respectively. The solid line represents the critical Shields number obtained from the analytical model.

Figure 2(b) shows the critical Shields number determined numerically for the entire range of particle spacings. For each geometry, it was determined using the particle density for which the torque balance or the force balance is zero, respectively. The former corresponds to the onset of rolling motion, the latter to that for sliding motion. It shows that rolling motion is always preferred to sliding motion. The numerical studies also show that lift forces are negligible.

Assuming a linear velocity profile for the effective zero level obtained numerically, we derive a model for the incipient motion as an extension of Goldman's model for a single particle near a plain surface [13]. The critical Shields number for rolling motion can be expressed as: $\theta_c = 0.13\left(1+\cos\chi\right)^{-1} L_G/L_D$, where L_G and L_D are the lever arms of the effective gravity force and of the drag force with respect to the center of rotation O, respectively. Like χ, they are related to the bead diameter and to the spacing. As shows Figure 2(b), it recovers quite well the experimental and numerical data.

CONCLUSIONS

Incipient motion depends strongly on the substrate geometry. At low particle Reynolds numbers, rolling motion is always preferred to sliding motion. The effective zero level depends on the particle spacing. Based on the effective zero level and taking into account the substrate geometry as the only parameters, we propose a model for the incipient motion at low particle Reynolds numbers that compares well with experiments and numerics.

References

[1] Mouilleron H., Charru F., Eiff O.: Inside the moving layer of a sheared granular bed. *J. Fluid Mech.* **628**:229-239, 2009.
[2] Agudo J. R., Wierschem A.: Incipient motion of a single particle on regular substrates in laminar shear flow. *Phys. Fluids* **24**:093302, 2012.
[3] Agudo J. R., Dasilva S., Wierschem A.: How do neighbors affect incipient particle motion in laminar shear flow? *Phys. Fluids* **26**:053303, 2014.
[4] Guazzelli E., Morris J. F.: A Physical Introduction to Suspension Dynamics. Cambridge University Press, 2012.
[5] Wiberg P. L., Smith J. D.: Calculations of the critical shear-stress for motion of uniform and heterogeneous sediments. *Water Resour. Res.* **23**:1471-1480, 1987.
[6] Dey S.: Sediment threshold. *Appl. Math. Model.* **23**:399-417, 1999.
[7] Armanini A., Gregoretti C.: Incipient sediment motion at high slopes in uniform flow condition. *Water Resour. Res.* **41**:W12431, 2005.
[8] Chin C. O., Chiew Y. M.: Effect of bed surface-structure on spherical particle stability. *J. Waterw. Port Coastal Ocean Eng.* **119**:231-242, 1993.
[9] Yergey B. A., Beninati M. L., Marshall J. S.: Sensitivity of incipient particle motion to fluid flow penetration depth within a packed bed. *Sedimentology* **57**:418-428, 2010.
[10] Marsh A. N., Western A. W., Grayson R. B.: Comparison of methods for predicting incipient motion for sand beds. *J. Hydraul. Eng.* **130**:616-621, 2004.
[11] Ouriemi M., Aussillous P., Guazzelli E.: Sediment dynamics. Part 1. Bed-load transport by laminar shearing flows. *J. Fluid Mech.* **636**:295-319, 2009.
[12] Derksen J. J., Larsen R. A.: Drag and lift forces on random assemblies of wall-attached spheres in low-Reynolds number shear flow. *J. Fluid Mech.* **673**, 548-573, 2011.
[13] Goldman A. J., Cox R. G., Brenner H.: Slow viscous motion of a sphere parallel to a plane wall-II. *Chem. Eng. Sci.* **22**:653-660, 1966.

EXPERIMENTAL STUDY ON DRAG REDUCTION DUE TO PERIODICALLY HEATED WALL

Ayumu Inasawa[1a], Keinosuke Taneda[1], and Jerzy M. Floryan[2]
[1]*Dept. of Aerospace Engineering, Tokyo Metropolitan University, Hino, Tokyo, JAPAN*
[2]*Dept. of Mechanical and Materials Engineering, University of Western Ontario, London, Ontario, CANADA*

Summary Flow in a channel with spatially periodic wall heating is examined experimentally at Reynolds numbers below Re=20 and at the Rayleigh number based on the amplitude of the periodic heating and the channel half width Ra_p=3500, to verify the super-thermohydrophobic effect leading to a friction-drag reduction. Periodic heating with a non-dimensional wavenumber of 1 is applied at the lower wall while the temperature of the upper wall is uniform and kept constant at the average temperature of lower wall. The results show that steady separation bubbles are created by periodic heating, which separate the main stream from the wall. About 12% drag reduction is found at Re=1, demonstrating that separation bubbles due to the super-thermohydrophobic effect surely contribute to the friction drag reduction.

INTRODUCTION

Drag reduction due to the super-hydrophobic effect is well known, in which gas bubbles trapped in surface micro pores prevent direct contact of the liquid with the solid surface and, thus, the shear between the liquid flow and the solid wall is replaced by a shear between the flow and the trapped gas bubbles [1]. This mechanism, however, is active only when the fluid of the main stream is liquid, and usually requires fine surface topography in order to trap the gas bubbles. In recent years, Floryan [2] proposed a novel methodology to reduce friction drag using spatially distributed wall heating, in which buoyancy-generated steady separation bubbles isolate the main stream from the solid wall. Accordingly, he referred to this effect as the super-thermohydrophobic effect. A significant advantage of this method is that it is applicable to single phase flows, including gas flows, and is independent of surface topography. A qualitative discussion of the drag reducing effect due to distributed wall heating was reported by Hossain et al.[3] who analyzed the dependency of the intensity and wave length of periodic wall heating on the flow topology and drag reducing effect in detail, and showed that up to 87% drag reduction could be achieved. In addition, a proper combination of spatially periodic and spatially uniform heating enhances the drag reducing effect [4]. Although the characteristics of flow exposed to a distributed wall heating have been revealed analytically, an experimental study has not yet been reported. In the present experimental study, flow in a channel with spatially periodic wall heating is examined to verify the friction drag reduction due to the super-thermohydrophobic effect.

RESULTS

The experiment is conducted in a rectangular channel whose width, height and length are 420mm, 20mm (=2h) and 2000mm, respectively, giving an aspect ratio (the ratio of width to height) of 21 (Fig. 1a). The channel is set horizontally in the laboratory. The main flow is driven by a piston connected to a stepper motor controlled ball screw. The spatially (streamwise) periodic wall heating is applied at the lower wall while the upper wall temperature is uniform and is kept constant. Hot and cold water is supplied in square pipes installed in the back of the lower wall made of thin water proof paper, creating a streamwise periodic temperature variation along the bottom surface (Fig. 1b). The wavelength of the heating is λ=62.8mm, giving a non-dimensional wavenumber of $\alpha=2\pi h/\lambda=1$. The Reynolds number is defined as $Re=U_c h/\nu$, where U_c denotes the center velocity of the plane Poiseuille flow upstream of the heated wall and ν stands for the kinematic viscosity. The Rayleigh number measuring the intensity of periodic heating is defined as $Ra_p=g\beta h^3\Delta T_p/(\nu\kappa)$, where ΔT_p denotes the peak-to-peak amplitude of the absolute temperature along the lower wall, g stands for the gravitational acceleration, β is the thermal expansion coefficient and κ denotes thermal diffusivity. Properties of the fluid (air) are defined at the upper wall temperature. A particle image velocimetry (PIV) system (Dantec) consisting of a double-pulsed Nd:Yag laser and a CCD camera of 2048 × 2048 pixels is used to obtain instantaneous velocity fields. The surface temperature is measured using thermography and thermocouples. In the present paper, the average temperature of the lower wall is set equal to the temperature of the upper wall.

Figures 2(a)-(c) display the time-averaged flow expressed in terms of a map of the transverse velocity V and streamlines. In the absence of net horizontal flow at Re=0, pairs of counter rotating rolls whose upward and downward motions occur above the hot (maximum temperature at $(x-x_0)/h$=94) and the cold (minimum temperature at $(x-x_0)/h$=97) spots, respectively, are observed (Fig. 2a). When a weak flow is imposed at Re=1, the main stream meanders remarkably, i.e. the net stream flows along the lower wall at $91\leq(x-x_0)/h\leq94$ and along the upper wall at $94\leq(x-x_0)/h\leq97$ (Fig. 2b). This stream divides a pair of rotating rolls into distinct separation bubbles which separate the main stream from the wall. With increasing Reynolds

[a] ainasawa@tmu.ac.jp

number, separation bubbles on the upper (non-heated) wall become smaller than those on the lower (heated) wall (Fig. 2c). Figure 3 illustrates the Reynolds number dependency of the drag reducing effect compared with the unheated (plane Poiseuille) flow. Local skin friction is measured by measuring the y-profile of the streamwise velocity U at each x location, and the net wall shear stress over one heating wavelength τ_1 is examined. About 6-12% drag reduction is found at $Re \leq 5$, demonstrating that the presence of the separation bubbles surely contributes to the friction drag reduction.

CONCLUSIONS AND OUTLOOK

Flows in a channel with spatially periodic wall heating are examined experimentally. The results have shown that periodic heating creates steady separation bubbles which reduce the net friction drag by about 12% at Re=1, verifying the existence of the super-thermohydrophobic effect. In the presentation, the influence of the heating wave number as well as the average temperature difference between the upper and lower walls on the drag reduction will be discussed in detail.

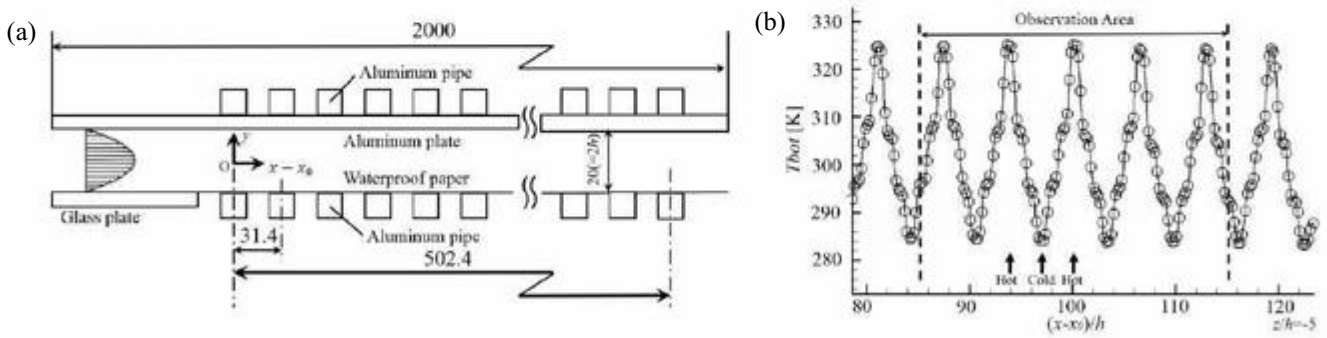

Fig. 1. (a) Experimental setup (dimensions in mm) and (b) streamwise variation of the bottom surface temperature (Ra_p=3500).

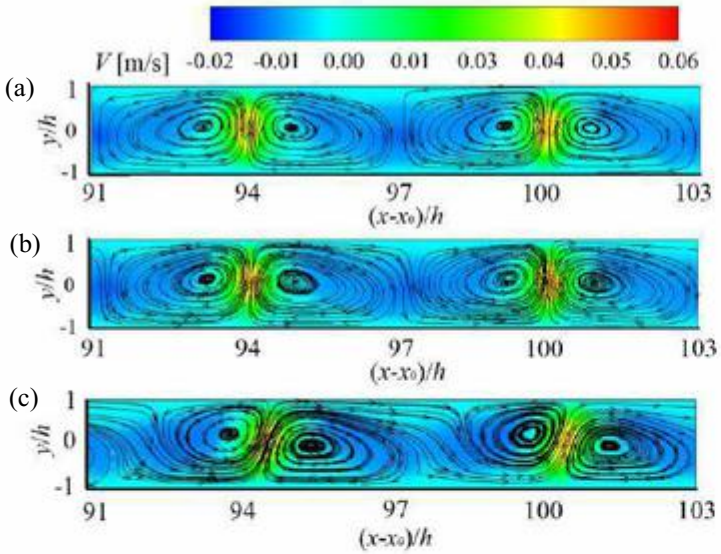

Fig. 2. Maps of V velocity component and the stream lines. (a)Re=0, (b) Re=1, (c) Re=5.

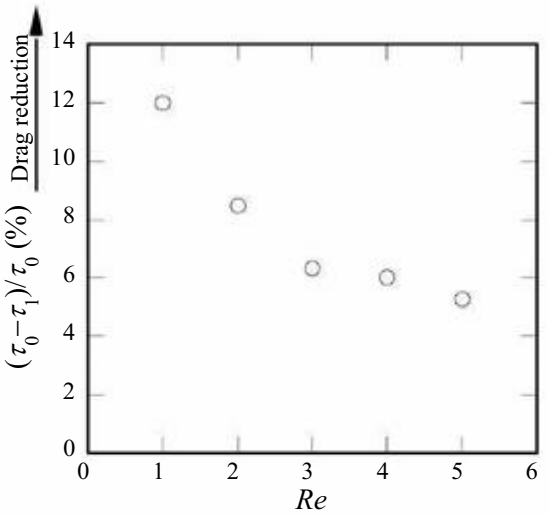

Fig. 3. Variations of the reduction of the friction drag as a function of Re. τ_0 denotes wall shear stress of the unheated (plane Poiseuille) flow.

References

[1] Rothstein, J.P. : Slip on superhydrophobic surfaces, *Annu. Rev. Fluid Mech.* **42**, 89-109, 2010.

[2] Floryan, J.M. : The thermo-superhydrophobic effect. *Bull. Am. Phys. Sci.* **57** (1), X50.00015, 2012.

[3] Hossain, M.Z., Floryan, D., and Floryan, J.M. : Drag reduction due to spatial thermal modulations, *J. Fluid Mech.* **713**, 398-419, 2012.

[4] Floryan, D, and Floryan, J.M.: Drag reduction in heated channels, *J. Fluid Mech.* **765**, 353-395, 2015.

COLLECTIVE MOTION OF MICROORGANISMS IN COMPLEX FLUIDS

Gaojin Li[1] & Arezoo M. Ardekani[1a)]
[1]*School of Mechanical Engineering, Purdue University, West Lafayette, USA*

Summary Suspensions of microorganisms are characterized by large scale correlated flow structures, enhanced diffusion of passive tracers, and enhanced fluid mixing. Most previous studies on the collective motion of microorganisms have been limited to Newtonian fluids. The non-Newtonian fluid properties, such as viscoelasticity and shear-dependent viscosity in biological flows, such as saliva, mucus and biofilm, significantly affect the swimming dynamics of a single swimmer. However, the role of fluid rheology on the collective motion of microorganisms is poorly understood. In this work, we use direct numerical simulations to investigate the effects of fluid properties on the collective motion of rod-like microswimmers in a low Reynolds number regime. For both pushers and pullers, we find that the viscoelasticity does not qualitatively alter the collective motion of microorganisms. The average speed and spatial correlations in a suspension of pushers decrease with Deborah number, but they are less affected for pullers.

INTRODUCTION

Collective motion of microorganisms, which is also referred to as "active turbulence", is characterized by complex dynamics including large-scale correlated motions, strong fluctuations and enhanced diffusion and fluid mixing [1]. The energy source of the active turbulence is intrinsically different from the classical turbulence at high Reynolds numbers. The high Reynolds number turbulent flow arises from energy input on large scales. For the microbial turbulent flow, the energy is provided by the microorganisms at microscale and flow is highly dissipative at such low Reynolds numbers (Re~10^{-5}). Although the active turbulence in a Newtonian fluid has been recently studied [2], the role of non-Newtonian fluid properties on the collective dynamics is poorly understood. Microorganisms and spermatozoa often swim in non-Newtonian fluids exhibiting both viscoelasticity and shear-thinning viscosity [3, 4]. For an isolated swimmer or a swimmer in a dilute suspension, fluid rheological properties are found to greatly affect the swimming speed [5, 6]. Using a modified mean-field theory, the viscoelasticity is found to affect the wavenumber corresponding to the largest growth rate [7]. Despite widespread applications of swimming in complex fluids, the role of fluid properties on the hydrodynamic interaction of microorganisms in a suspension is poorly understood.

GOVERNING EQUATIONS AND NUMERICAL METHODS

We conduct two-dimensional simulations of suspension of N identical slender rod-like swimmers of length l, propelling themselves by a slip velocity $2U$ over half of their body. Two types of swimmers are considered: pushers, for which a constant slip velocity is imposed on the tail half side of the rod, and pullers, for which slip velocity is imposed on the head half side. In a Newtonian fluid, a single pusher and puller swimmer have the same swimming speed U. In the following, the length is scaled by l, velocity by U, time by l/U, and pressure and stress by $\mu U/l$, where μ is the fluid viscosity. Simulations are performed in a periodic square box of size L=10. Volume fraction is defined as $c = N/L^2$.

The dimensionless equations for conservation of momentum and mass are

$$Re\frac{\partial \boldsymbol{u}}{\partial t} = -\nabla p + \nabla \cdot \boldsymbol{\tau} - \alpha \boldsymbol{u}$$
$$\nabla \cdot \boldsymbol{u} = 0,$$

where the Reynolds number is defined as $Re = {\rho U l}/{\mu} = 5 \times 10^{-3}$, ρ is the fluid density, **u** is the velocity vector, p is the pressure, and $\boldsymbol{\tau}$ is the deviatoric stress tensor. The extra dissipative term $-\alpha \boldsymbol{u}$ corresponds to the mechanical friction between the soap film and the surrounding air. This dissipation is important in the energy budget for high Reynolds two-dimensional turbulent flows, however, it is not necessary for an active turbulence at low Reynolds numbers. We set $\alpha = 0$ in the following, unless otherwise mentioned. In a Newtonian fluid, the stress tensor is simply determined by the shear rate tensor $\dot{\boldsymbol{\gamma}} = \nabla \boldsymbol{u} + \nabla \boldsymbol{u}^T$ and fluid viscosity, i.e., $\boldsymbol{\tau} = \dot{\boldsymbol{\gamma}}$ in dimensionless form. For the elastic fluid, we use the Oldroyd-B constitutive relation, in which $\boldsymbol{\tau}$ can be split into solvent and polymer contributions as $\boldsymbol{\tau} = \boldsymbol{\tau}^s + \boldsymbol{\tau}^p$, where $\boldsymbol{\tau}^s = \beta_s \dot{\boldsymbol{\gamma}}$,

$$\boldsymbol{\tau}^p + De\widehat{\boldsymbol{\tau}^p} = (1 - \beta_s)\dot{\boldsymbol{\gamma}},$$

where $\beta_s = 0.5$ is the ratio of the solvent viscosity to the zero-shear-rate viscosity of the polymeric solution. The Deborah number $De = \lambda U/l$ is the ratio of the polymer relaxation time λ and the characteristic flow time scale l/U. The notation $\wedge$ represents the upper-convected derivative. Simulations are conducted using a finite-volume method based on a staggered grid. A conventional operator-splitting method is applied to enforce the continuity equation. The swimmer is modelled by satisfying the above mentioned slip condition using a distributed Lagrange multiplier method. The viscoelastic stress is solved by implementing a commonly used formulation denoted as the elastic-viscous stress splitting method [8].

[a)] Corresponding author. Email: ardekani@purdue.edu

RESULTS AND DISCUSSIONS

As shown in figure 1, the flow field is characterized by large scale coherent structures much larger than the swimmer size. Pushers tend to align with their neighbours due to a side-by side attraction and show a local nematic ordering. The pullers aggregate at their head and form clusters. Similar results are also observed in confined 2D suspensions of microswimmers in a Newtonian fluid [9]. Although the viscoelasticity does not qualitatively change the collective motion for either pushers or pullers, it quantitatively affects the collective motion of pushers. Figure 2 shows the distribution of the swimming speeds and the spatial correlation for pushers and pullers. Pushers swim faster in a Newtonian fluid while pullers swim slower. Stronger spatial correlations are observed for pushers as Deborah number increases, while pullers are less affected.

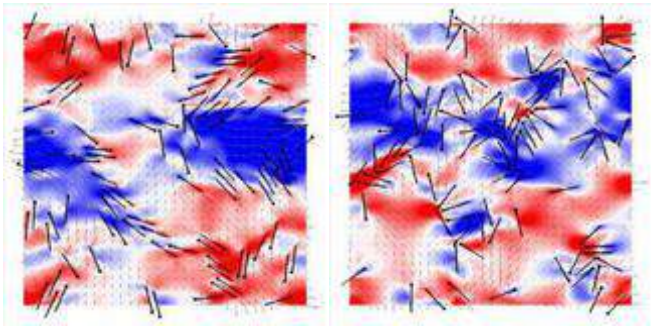

Suspension of pushers, $De = 1$ Suspension of pullers, $De = 1$

Figure 1. Distribution of swimmers and flow field. Colour contours show the u-velocity component.

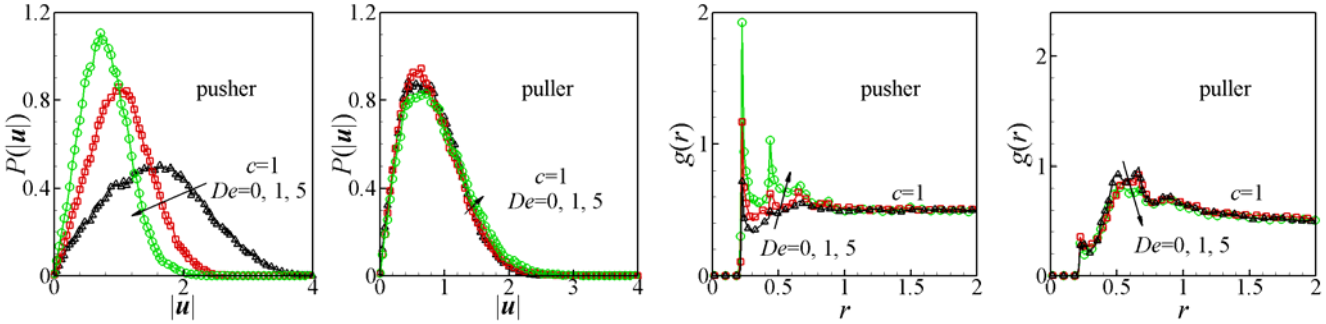

Figure 2. Swimming speed and spatial correlation in suspensions of pushers and pullers.

In summary, we have conducted fully resolved simulations of suspension of microswimmers and quantified the role of viscoelasticity of the surrounding fluid on suspensions of pushers and pullers.

References

[1] Saintillan, D., & Shelley, M. J.: Emergence of coherent structures and large-scale flows in motile suspensions. *J. R. Soc. Interface*, rsif20110355, 2011.

[2] Wensink. H. H., Dunkel, J., Heidenreich, S., Drescher, K., Goldstein, R. E., Löwen, H., Yeomans, J. M.: Meso-scale turbulence in living fluids. *Proc. Natl. Acad. Sci. U. S. A.,* **109**, 14308-14313, 2012.

[3] Hwang, S. H., Litt, M., & Forsman, W. C.: Rheological properties of mucus. *Rheol. Acta*, **8**: 438-448, 1969.

[4] Klapper, I., Rupp, C. J., Cargo, R., Purvedorj, B., & Stoodley, P.: Viscoelastic fluid description of bacterial biofilm material properties. *Biotechnol. Bioengng*, **80**: 289-296, 2002.

[5] Shen, X. N., & Arratia, P. E.: Undulatory swimming in viscoelastic fluids. *Phys. Rev. Lett.* **106**: 208101, 2011.

[6] Teran, J., Fauci, L., & Shelley, M.: Viscoelastic fluid response can increase the speed and efficiency of a free swimmer. *Phys. Rev. Lett.* **104**, 038101, 2010.

[7] Bozorgi, Y., & Underhill, P. T.: Effect of viscoelasticity on the collective behavior of swimming microorganisms. *Phys. Rev. E*, **84**, 061901, 2011.

[8] Guénette, R., & Fortin, M.: A new mixed finite element method for computing viscoelastic flows. *J. Non-Newtonian Fluid Mech.*, **60**, 27-52, 1995.

[9] Tsang, A. C. H., & Kanso, E.: Flagella-induced transitions in the collective behavior of confined microswimmers. *Phys. Rev. E*, **90**, 021001, 2014.

ARTIFICIAL SWIMMERS THROUGH SHELL BUCKLING

Adel Djellouli[1*], Gwennou Coupier[1], Catherine Quilliet[1] & Philippe Marmottant[1]
[1]*LIPHY, University Grenoble-Alpes and CNRS, Grenoble, France*

Summary In this study, we investigate the possibility to swim using a simple thin polymer encapsulated bubble, propelled through the buckling of its shell. This opens the way to obtaining microswimmers with high throughput.

INTRODUCTION

For a few years, microswimmers have mobilized increasing attention and research forces. This is due to fundamental motivations to understand mobility at small scale, together with an interest towards applications such as drug delivery or the challenging build-up of miniaturized labs-on-a-chip or nanorobots.
Since swimming at this scale is generally performed at a low Reynolds number, a necessary condition to fulfil is to achieve a non-reciprocal path in the deformation space [1]. The proposed candidate is a simple thin polymer spherical shell, propelled through the buckling of its shell and actuated by a scalar field: static pressure.

Previous works [C.Quilliet, G.Coupier, preprint] showed that a deformation happens through the sudden appearance of a depression (inverted bump), with a size determined by the thickness of the shell and its radius. This symmetry breaking generates a first-order transition with hysteresis. Indeed, re-inflation allows to observe situations non attainable during deflation. This hysteresis naturally fulfills the necessary condition previously mentioned.

EXPERIMENTAL STUDY

To study individual swimmer dynamics, we molded spherical shells in a rubber-like polymer, with various thickness over radius ratios (d/R), where $R \propto 1$ cm. Using an airtight tank and a pressure controller, we immerse the spherical shell in liquids which have different viscosities and submit it to external pressure cycles. The liquids used are water and glycerol, with a viscosity of 10^{-3} (Pa.s) and 1 (Pa.s) respectively. Knowing that the buckling occurs at the same spot, due to some imperfection in the shell, we use an attaching system to direct the ball in a targeted direction and keep the shell immersed.

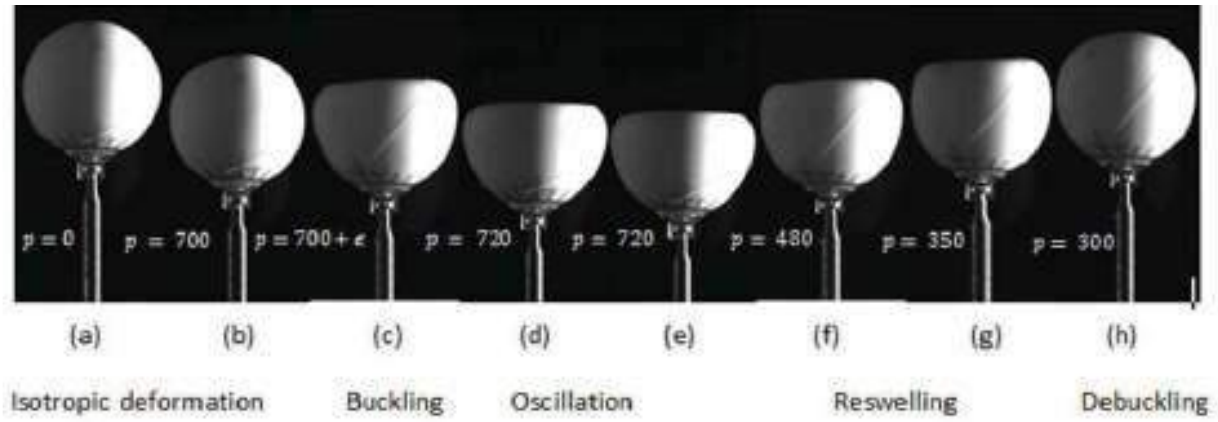

Fig. 1: snapshots from spring experiment
Pressure given in mbar, ball's radius70 mm, and liquid is water.

The experiment shown in (Fig. 1) consists in attaching a ball of a certain (d/R), to a well-calibrated spring, directing the buckling spot to obtain a 1-D displacement and immerse it in the liquid. By applying pressure cycles, and recording the ball's position, we obtain:
(i)The thrust $\vec{T}(\frac{d}{R}, \mu)$ delivered by the ball during the buckling/debuckling phases after fitting the recorded displacement during these phases using a quite simple model (Fig.2) and (ii) we get access to the different shapes undergone by the shell in respect to the applied pressure, which allows to quantify the deformation hysteresis as discussed in the introduction and shown in (Fig. 3).

The experimental results are coherent with the theory [2] and the simulations [3] for the quasi-static phase *i.e.* the isotropic compression and the expansion. These results allow us also to study the buckling dynamics which have not been studied yet and to get insights on the dissipation in the ball's material. In water, we could observe a buckling occurring in $\tau \sim 10$ ms, depending on the shell material, inducing a brief passage at a high Reynolds number, at the buckling spot.

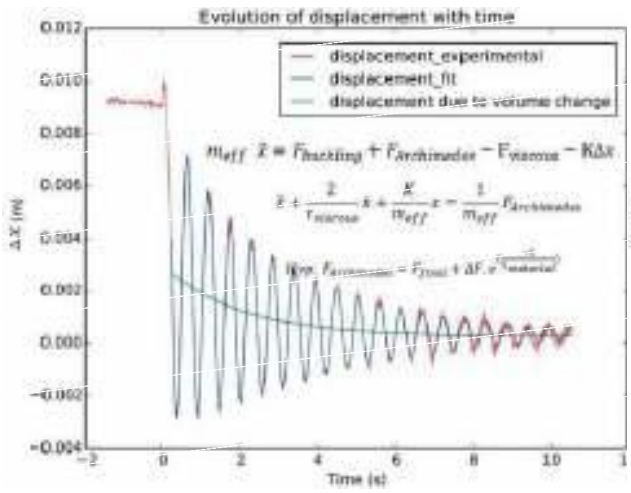

Fig.2: Shell's Displacement induced buckling for a ball of d/R = 0.2, in water.
ΔX representing the displacement of the center of mass.

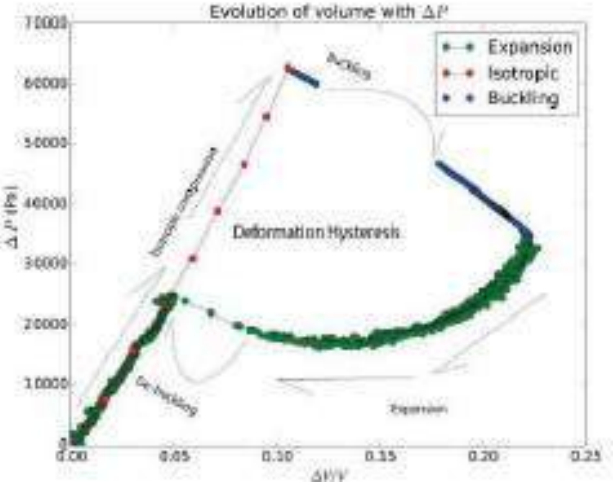

Fig. 3: Experimental evolution of shell's volume through a pressure cycle, for a ball of d/R = 0.2, in water.
Pressure given in Pa. ΔP is the pressure between the applied pressure and the shell internal pressure. $\Delta V/V$ is the difference between the initial volume and the volume during the process divided by the initial volume.

CONCLUSION AND PERSPECTIVES

From this experiment, we can study the swimming efficiency dependency in regards to the parameters $d\backslash R$ and μ. These experimental results would be completed by fluid simulation, taking as input the extracted shapes from the spring experiment and using it as time-dependent boundary layer for the fluid domain, hence reducing the problem complexity by getting rid of the coupled interaction between the solid and its surrounding fluid. It would allow us to get access to the velocity field and compare between the contribution of the swimming at low Reynolds due to undertaking a non-reciprocal path through the deformation space and the contribution due to the brief passage at an inertial regime which occurs at the buckling/debuckling phases.

The research leading to these results has received funding from the European Research Council under the European Union's Seventh Framework Programme (FP7/2007-2013) / ERC Grant agreement n° 614655 Bubbleboost.

References

[1] EM Purcell - Am. J. Phys, 1977.
[2] Knoche - Physical Review E, 2011.
[3] C Quilliet - The European Physical Journal E, 2012.

EFFECT OF MEMBRANE BENDING RESISTANCE ON CAPSULE WRINKLING IN SIMPLE SHEAR FLOW

Anne-Virginie Salsac*[1], Claire Dupont[1,2], Dominique Barthès-Biesel[1], Patrick Le Tallec[2], and Marina Vidrascu[3]

[1]*Biomechanics and Bioengineering Laboratory (UMR CNRS 7338), Université de technologie de Compiègne - CNRS, Sorbonne universités, Compiègne, France*

[2]*Solid Mechanics Laboratory (UMR CNRS 7649), Ecole Polytechnique, Palaiseau Cedex, France*

[3]*REO project–team, Inria de Paris & Sorbonne universités, UPMC Université de Paris VI, LJLL, Paris, France*

Summary We study the effect of wall bending resistance on the motion of an initially spherical capsule freely suspended in shear flow. The fluid–structure interactions are modeled by coupling a boundary integral method for the fluids with a shell finite element method for the capsule envelope. For a given wall material, the capsule deformability strongly decreases when the wall thickness (or bending resistance) increases. For low flow strength, membrane wrinkles can appear with a wavelength that depends on the wall bending resistance.

INTRODUCTION

Capsules, which consist of an internal liquid droplet enclosed by a membrane, are designed to protect fragile or volatile substances and control their liberation. Typical artificial capsules are quasi–spherical at rest and have a thin membrane whose thickness and mechanical properties depend on the fabrication process. When suspended in a simple shear flow, a spherical capsule is elongated in the straining direction by the hydrodynamic stresses, while the membrane rotates around the deformed shape because of the flow vorticity. However, for low flow strength, the capsule membrane is compressed in the equatorial region and may buckle [1]. Since membrane wrinkling may lead to fatigue breakup, it is important to predict this phenomenon in order to avoid/provoke membrane rupture. Numerical models of the fluid–structure interaction must then be developed to understand the complex behavior of a spherical capsule in an external flow. Most models that include bending effects have decomposed the wall strain energy into the sum of a membrane elastic energy and of a bending energy computed from the local curvature. Their relevance for artificial capsules can be questioned because unrealistically high values of the bending modulus have been used [4, 5].

The objective of this study is to analyze the deformation of an initially spherical capsule (radius ℓ) in a simple shear flow, assuming that the wall is made of a three–dimensional, incompressible, homogeneous, hyperelastic material (thickness $\alpha\ell$ ($\alpha < 1$), shear modulus G and Poisson ratio $\nu = 1/2$) that resists both membrane and bending deformations.

PROBLEM FORMULATION AND NUMERICAL MODEL

The wall is sufficiently thin to be modeled as a thin shell with mid–surface $\mathcal{S}_t$. The displacement field satisfies the Reissner–Mindlin kinematic assumption [2]. The wall's stress-strain relationship is the generalized Hooke's law. The capsule is freely suspended in a simple shear flow with shear rate $\dot{\gamma}$. The inner and outer fluids have the same viscosity μ and density ρ. As inertia effects are neglected, the internal and external flows are governed by the Stokes equations. For thin walls, the local velocity of the mid–surface points is then obtained from an integral over $\mathcal{S}_t$ of the viscous traction jump, weighted by a stokeslet. The problem parameters are the relative wall thickness α, the bulk capillary number $Ca_v = \mu\dot{\gamma}/G$, which compares the viscous to the elastic forces. When bending resistance is neglected ($\alpha \ll 1$), it is customary to introduce a surface shear modulus $G_s = G\alpha\ell$, to which corresponds a membrane capillary number $Ca_s = \mu\dot{\gamma}\ell/G_s = Ca_v/\alpha$. The bending number $K_b = \alpha^2/3$ measures the relative importance of bending and shearing effects.

To solve the fluid–structure interaction problem, we iteratively couple *(i)* a shell finite element method to solve the solid problem and find the viscous load acting on the capsule wall from the displacement field on $\mathcal{S}_t$, and (*ii*) a boundary integral method to compute the velocity field on $\mathcal{S}_t$ from the load transferred by the solid solver. We then update the position of the mid–surface by integrating the velocity using a first–order explicit Euler scheme. At time $t = 0$, the undeformed mid–surface of the capsule wall is discretized with linear triangular shell elements (MITC3 elements). A convergence analysis has shown that 5,120 elements are sufficient to obtain a precision of order 10^{-3} on the overall capsule deformation. s

EFFECT OF WALL THICKNESS ON CAPSULE DEFORMATION

We first study the influence of the wall thickness and consider capsules made of the same homogeneous 3D material but with different wall thicknesses, subjected to a linear shear flow corresponding to $Ca_v = 0.05$. As shown in Figure 1, the thinner the wall, the more elongated the capsule becomes under the influence of the external flow.

*Corresponding author. Email: anne-virginie.salsac@utc.fr

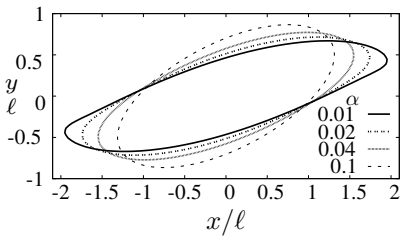

Figure 1: Influence of wall thickness on the mid–surface profile in the shear plane for $Ca_v = 0.05$. From Dupont et al. [3]

.

We now evaluate the effect of the bending resistance (as measured by α) on the behavior of a capsule for $Ca_s = 0.1$ and $\alpha \in [0.005, 0.02]$. The capsule is subjected to compressive tensions in the equator region as is observed with a membrane model with no bending resistance. As a consequence, buckling may occur at steady state for low bending resistance (small α) of the capsule wall (Figure 2). When the wall thickness is increased, the bending resistance increases and fewer wrinkles are formed. For $\alpha \geq 0.02$, the wall is too thick for wrinkles to form even if it is subjected to compressive tensions. It is thus possible to prevent buckling by increasing the wall thickness.

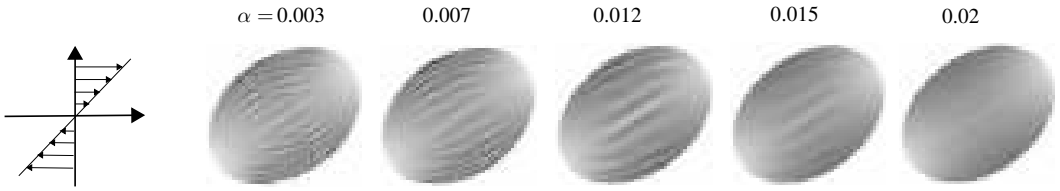

Figure 2: Steady profiles of an initially spherical capsule subjected to a simple shear flow at $Ca_s = 0.1$ for different wall thicknesses α. Thin membranes tend to buckle around the equator, which is under compression. Grey levels represent the load on the membrane. From Dupont et al. [3]

CONCLUSIONS

For a given wall material, the capsule deformability decreases when the wall thickness increases. However, the overall deformation of the capsule depends only on Ca_s with no influence of the bending resistance, because the stretching of the mid–surface is the prevailing phenomenon. Note that using Ca_s as the main parameter implies that the bulk elastic modulus G decreases when α is increased: thus, for a given flow strength and capsule size, the larger α, the softer the material. Other authors [4, 5] have observed that the bending resistance reduces the capsule deformability at a given Ca_s. But they have considered very large values of bending resistance corresponding to $\alpha \sim 0.3 - 0.9$, for which the thin shell hypothesis fails. Furthermore, it is difficult to imagine a thin material sheet that has both a very low shear elastic modulus and a very high bending modulus.

A shell model is needed to analyze the formation of the wrinkles, which appear at low Ca_s. We find that Ca_s has no influence on the wrinkle wavelength λ_e, which depends only on α (or K_b) and increases with it. The wrinkle wavelength can be correlated to the bending stiffness by a power function $\lambda_e/\ell \simeq 3.3\,(K_b)^{1/4}$, which is similar to the one obtained for a flat membrane stretched between two clamped ends [6]. The results from this study can be used to analyze experiments on wrinkled nylon capsules [7] and deduce the membrane thickness from the wavelength of the experimental folds.

References

[1] Barthès-Biesel D.: Motion and deformation of elastic capsules and vesicles in flow *Annu. Rev. Fluid Mech* **48**:25–52, 2016.

[2] Chapelle D., Bathe KJ.: *The finite element analysis of shells – fundamentals.* Computation Fluid and Solid Mechanics, 2003.

[3] Dupont C., Salsac A.-V., Barthès-Biesel D., Vidrascu M., Le Tallec P.: Influence of bending resistance on the dynamics of a spherical capsule in shear flow. *Phys. Fluids* **27**:051920, 2015.

[4] Pozrikidis C.: Effect of membrane bending stiffness on the deformation of capsules in simple shear flow. *J. Fluid Mech.* **440**:269–291, 2001.

[5] Le D.V., Tan Z.: Large deformation of liquid capsules enclosed by thin shells immersed in the fluid. *J. Comput. Phys.* **229**:4097–4116, 2010.

[6] Cerda E., Mahadevan L.: Geometry and physics of wrinkling. *Phys. Rev. Lett.* **90**:074302, 2003.

[7] Koleva I., Rehage H.: Deformation and orientation dynamics of polysiloxane microcapsules in linear shear flow. *Soft Matter* **8**:3681–3693, 2012.

ELECTRIC FIELD DRIVEN HIERARCHICAL SELF-ASSEMBLY OF MONOLAYERS OF MIXTURES OF PARTICLES

Edison Amah[1a)], Md. Hossain[2], Naga Musunuri[1], Ian Fischer[1] and Pushpendra Singh[1)]
[1]*Department of Mechanical Engineering, New Jersey Institute of Technology, Newark, New Jersey*
[2]*Department of Engineering Technology, QCC, CUNY, Bayside, New York*

Summary We numerically study the self-assembly process of particle mixtures on fluid-liquid interfaces when an electric field is applied in the direction normal to the interface. The resulting electric and capillary forces cause particles to self-assemble into molecular-like hierarchical arrangements, consisting of composite particles (analogous to molecules) arranged in a pattern. As in experiments, the structure of a composite particle depends on factors such as the relative sizes of the particles and their polarizibilities. If the particles sizes differ by a factor of two or more, the composite particle has a larger particle at its core and several smaller particles forming a ring around it. Approximately same sized particles, on the other hand, form chains (analogous to polymeric molecules) in which positively and negatively polarized particles alternate.

INTRODUCTION

In recent years, many studies have been conducted to understand the behavior of particles trapped at fluid-liquid interfaces because of their importance in a range of physical applications and biological processes, e.g., formation of pollen and insect egg rafts, stabilization of emulsions, and the formation of photonic crystals and biosensor arrays [1-2]. Particles trapped in fluid-liquid interfaces interact with each other via lateral capillary forces, and when present also by other forces such as electrostatic forces, to form monolayer arrangements. However, capillarity-driven self-assembly produces monolayers which lack long-range order, and for monolayers containing two or more types of particles the technique does not allow for any control of the particle-scale structure as capillary forces simply cause particles to cluster [3].

We have recently shown that monolayers containing two or more types of particles with different dielectric properties can be self-assembled by applying an electric field in the direction normal to the interface. The technique exploits the fact that the dipole-dipole force between two particles adsorbed in an interface can be repulsive or attractive depending on their polarizabilities and that the intensity of the force can be varied by selecting suitable upper and lower fluids. The force is repulsive when both particles are positively or negatively polarized, but attractive when one particle is positively polarized and the other is negatively polarized. The force also depends on the sizes of the particles and the electric field intensity.

The differences in the polarizibilities and sizes of the particles derive a hierarchical self-assembly process analogous to that which occurs at atomic scales. First, groups of particles combine to form composite particles (analogous to molecules) and then these composite particles self-assemble in a pattern (like molecules arrange in a material). The force between similar particles is repulsive (because they have the same polarizibilities), and so they move apart which allows particles that attract to come together unhindered to form composite particles. Furthermore, since particles trapped in a fluid-liquid interface are free to move laterally, they self-assemble even when the lateral forces driving the assembly are small. The only resistance to their lateral motion is hydrodynamic drag which can slow the motion but cannot stop it. A sufficiently strong electric field is applied to ensure that the electrically induced lateral forces remain stronger than Brownian forces.

In our experimental studies, the availability of liquids and particles with the specific dielectric properties limited the parameter range that could be investigated. This is not the case for the numerical study presented in this paper which has allowed us to discover new self-assembled arrangements.

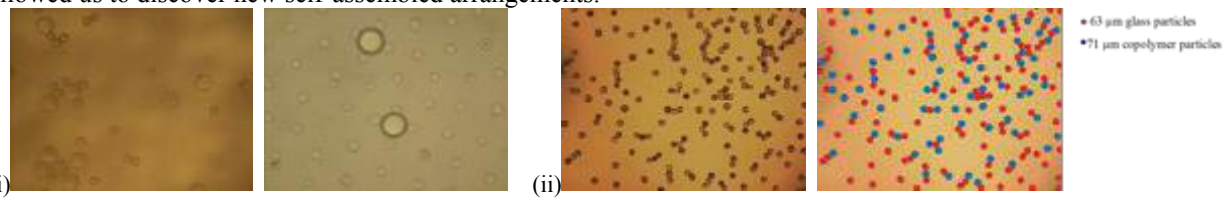

Figure 1. (i) Monolayers of mixtures of 20 μm glass and 71 μm copolymer particles formed on the surface of a 30% castor oil and 70% corn oil mixture: (left) Initial distribution and (right) final distribution. (ii) Monolayer of a mixture of 63 μm glass and 71 μm copolymer particles on silicone oil. The graphical representation (right) shows glass and copolymer particles in different colors.

RESULTS AND DISCUSSION

The self-assembly process of particles was simulated by placing *n* particles on a regular grid, and then integrating the governing momentum equations in time

$$m_i \frac{d\mathbf{u}_i}{dt} = \sum_{j=1,\, j\neq i}^{n} \left(-\frac{w_i\, w_j}{2\pi\gamma} \frac{\mathbf{e}_{ij}}{r_{ij}} + \frac{3 p_i p_j}{4\pi\varepsilon_o \varepsilon_L} \frac{\mathbf{e}_{ij}}{r_{ij}^4} \right) - 6\pi\mu\xi a_i \mathbf{u}_i, \; i = 1,n, \qquad (1)$$

a) Corresponding author. Email: eca8@njit.edu

where $\mathbf{u}_i$ is the velocity, m_i is the effective mass of the ith particle which includes the added mass contribution, $\mathbf{e}_{ij}$ is the unit vector from the center of particle i to the center of particle j, and r_{ij} is the distance between the centers of particle i and particle j. Here w_j is the vertical force and p_j is the induced dipole moment acting on the jth particle, ε_0 is the permittivity of free space, ε_L is the permittivity of the lower liquid, γ is the interfacial tension, and r is the distance between the particles. The last term on the right side is the Stokes drag, where μ is the viscosity of the lower fluid and ξ is a correction parameter which accounts for the fact that the particle is immersed in both upper and lower fluids. The system of equations was discretized using an implicit second order scheme in time.

The three distinct size dependent regimes identified in our experiments for the mixtures of glass and copolymer particles on corn oil were also found and validated in our numerical simulations. Fig. 2a shows numerical results for the mixture 71 μm copolymer and 150 μm glass particles. The larger sized particles were positively polarized and the smaller particles were negatively polarized. The larger sized particles attracted the smaller ones to form composite particles, similar to those seen in the experiments (see Fig. 1). In Fig. 2b, the smaller sized particles were more intensely polarized, which is the case for the mixture of 71 μm copolymer and 20 μm glass particles. As in the experiments, the smaller particles formed a triangular lattice in which the larger particles were imbedded. The larger particles attracted nearby smaller particles in the lattice and together they formed composite particles. Fig. 4c shows a third regime for which the sizes of positively and negatively polarized particles were comparable, which corresponds to the case of a mixture of 71 μm copolymer (red) and 63 μm glass (yellow) particles. In this case, instead of forming ring-like arrangements, the particles arranged in chains in which the positively and negatively polarized particles alternated.

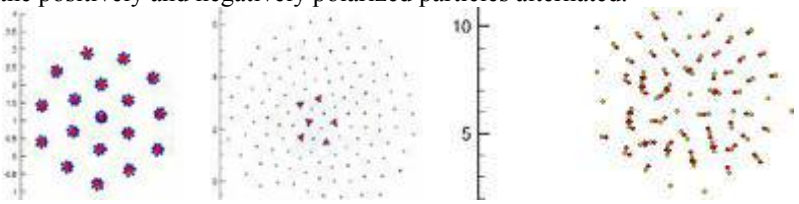

Figure 2. Numerical simulation of self-assembly on corn oil. The parameters were selected to match: (a) 71 μm copolymer and 150 μm glass particles; (b) 71 μm copolymer and 20 μm glass particles; and (c) 71 μm copolymer (red) and 63 μm glass (yellow) particles.

Fig. 3 shows how the monolayers for four different values of $\frac{p_1}{p_2}$, while keeping all other parameters fixed. When the smaller particles are more polarizable than the larger particles, the former arranged in a triangular lattice, and the larger particles clustered at the center as the capillary force was the dominant force for them (see Fig 3a). As the polarizability of the larger particles was increased, they moved apart and the smaller particles formed rings around them (see Fig 3b-d).

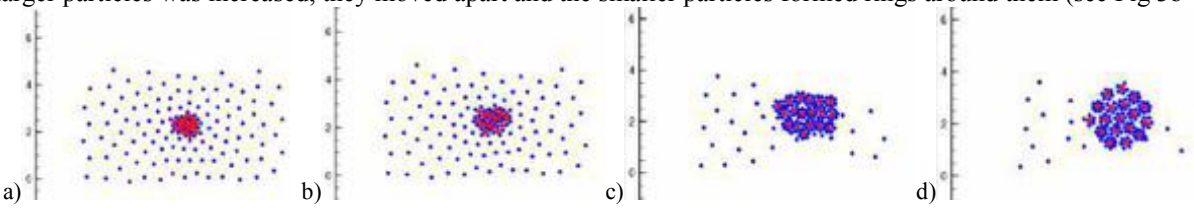

Figure 3: Monolayers of particle mixtures with $\frac{a_1}{a_2} = 1.2$. The ratio $\frac{p_1}{p_2}$ was varied: (a) 0.5, (b) 1.0, (c) 5.0, and (d) 7.5.

CONCLUSIONS

Our simulations show that the theoretical model given by Eq. 1 correctly captures the underlying physics of the self-assembly process. In agreement with our experiments, particles self-assemble into hierarchical arrangements, consisting of composite particles arranged in a pattern. If the particles sizes differ by a factor of two or more, the composite particle has a larger particle at its core with several smaller particles forming a ring around it. Approximately same sized particles form chains in which positively and negatively polarized particles alternate.

Acknowledgements: The work was supported by the National Science Foundation grants (CBET-1067004 and CBET-1236035).

References

[1] Binks, B.P., *Current opinion in Colloid and Interface Science*, 7, 21-41 (2002).
[2] Blanco, A., et al., *Nature*, 405, 437-440 (2000).
[3] Singh, P. & Joseph, D.D., *J. Fluid Mech*., 530, 31-80 (2005).
[4] Singh, P., et al., *Scientific Reports*, 4, 7427 (2014).

MULTI-SCALE MODEL OF MAGNETICALLY-DRIVEN FLOWS IN DEAD-END CHANNELS

Roger T. Bonnecaze[1a)] and Michael Clements[1]
[1]*Department of Chemical Engineering, The University of Texas at Austin, Austin, Texas, USA*

Abstract Observations show that dilute suspensions of iron particles in a rotating magnetic field form rotating rods along the wall of a blocked channel, creating a convective flow. We propose a multi-scale mechanism for this magnetically-driven flow. At the particle-scale, particles chain up to a length balancing magnetic and hydrodynamic forces on the resulting chains. The weak gradient of the magnetic field causes the chains to accumulate on one side of the channel. They rotate due to the rotating magnetic field, provided the field strength is high enough, which creates a localized body couple in the flow that drives a macroscopic convective flow in the channel. Coupled transport equations for the particles, chains and the suspension as a whole are presented and are successfully compared to experimental observations.

INTRODUCTION

Creating convective transport in dead-end channels is important for improving many processes, including enhanced oil recovery and delivery of thrombolytics (clot-dissolving drugs) to thrombi (clots) blocking an artery during stroke. For ischemic stroke patients, delivering the thrombolytics to the blood clot is time sensitive. Since the artery is blocked, there is no convective transport, and so the thrombolytic must be delivered by a usually too slow diffusion-limited process[1]. Inducing convection within the blocked artery can dramatically speed delivery of the thrombolytic to the clot and improve patient outcomes.

Pulse Therapeutics has developed a method for rapidly delivering thrombolytics that does not require imaging of the thrombus and can be easily performed by a nurse[2,3,4,5]. The apparatus for this delivery method is a permanent magnet that uses a two-motor system so that it can rotate in any plane. It generates a rotating magnetic field with a gradient and applies it to the affected area of the stroke victim's brain. Simultaneously, very low concentrations of 100 nm diameter ferroparticles are co-delivered with a thrombolytic during IV administration. These particles interact with the magnetic field, inducing a flow within the occluded vessel. The hypothesis for this process is the following. In the presence of a magnetic field, induced dipoles in the ferroparticles are attracted to one another so they form into chains. The chains accumulate on one side of the channel due to the gradient in the magnetic field. The chains also experience a magnetic torque and rotate as the field rotates. This creates a non-uniform body-couple in the fluid which generates a flow. Because the channel is blocked at one end, a pressure gradient is created so there is no net flow at any cross-section. A schematic of the chains (not to scale) and the flow field is shown in Fig. 1. A conveyor belt of flow up one side and down the other is created that can convectively transport the thrombolytic or other material to the dead-end.

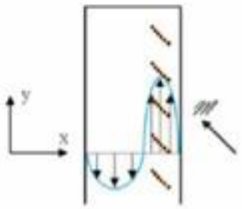

FIG 1. Schematic of model system showing particle aggregates, potential flow field, and rotating magnetic field source.

Here we develop and present a model and analysis of the proposed mechanism and compare with experimental observations.

METHOD

In order to predict the fluid velocity profile of a dilute suspension of ferroparticles in a 2D blocked channel (Fig. 1) when subjected to a rotating magnetic field and to better understand the physics leading to convective flow, a model was developed to describe both the particle dynamics and the flow field. The 2D model equation describing the suspension dynamics is given by,

$$0 = -\frac{dP}{dy} + \eta \frac{\partial\, u}{\partial x^2} + \frac{\partial}{\partial x}\left(nG_M\right)$$

where u is the velocity vector, P is pressure, and η is fluid viscosity and n is the number density of chains. G_M is the torque on the chains due to the applied magnetic field which is essentially the body-couple per particle in the fluid. Note that the torque is essentially constant across the channel and that the variation of the number density across the channel due to the gradient of the magnetic field is essential to drive the flow.

The dynamics of the chains are described by balancing the hydrodynamic and magnetic torques. The length and width of the chains is determined by a balance of the magnetic forces attracting the individual particles with the hydrodynamic forces due to rotation of the chain or the shear generated by the flow. The dimensions of the chain are determined using a model by Gomez-Ramirez *et al*.[6.] A general set of multiscale equations describing the fluid flow and particle dynamics will be shown in the presentation.

[a)] Corresponding author. Email: rtb@che.utexas.edu.

RESULTS

Fig. 2 shows the torque on the chain as function of the magnetic field. Here the chains are assumed constant in length. Both figures show that there is a threshold or critical field strength $H_{crit} \sim \sqrt{\eta L^3 \Omega / \mu_0 \ \alpha_L}$, where L is the length of the chain, Ω is the rotation rate of the field, μ_0 is magnetic permeability and α_L is a chain shape factor. Above the critical field strength the chains rotate at the same rate as the rotation of the applied field. Below this critical field strength, the viscous forces are too large for the chains to rotate, the average torque vanishes and there is no flow.

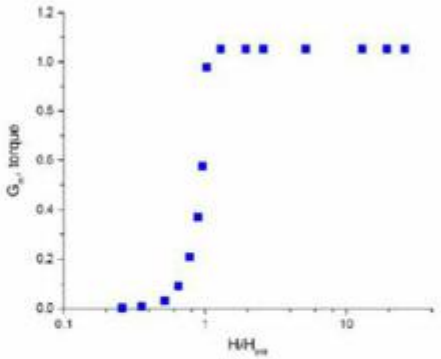

FIG 2. Dimensionless torque on rod-like aggregates of iron particles when subjected to magnetic fields of various amplitudes. The torque is constant above a threshold or critical field strength H_{crit}.

Fig 3a shows a typical velocity profile in the 2D channel. The length and width of the chains are computed self-consistently with the flow field. There is an upward flow on one side of the channel due to the magnetic forces and downward flow on the other side due to the pressure gradient created by the dead-end to ensure no net flow. Note it is unsteady due to the offset in the location of the source of the magnetic field. The flow speed on the order of mm/s is consistent with experimental observations[2]. The average magnetic component of the velocity is shown in Figs. 3b,c as a function of applied field and rotation rate. Note there are optimal values because of the flow strength depends on the length of the chains and the rotation rate, but increasing the flow strength can tear the chains apart. The optimum of rotation rate of about four Hz is consistent with experimental observations.

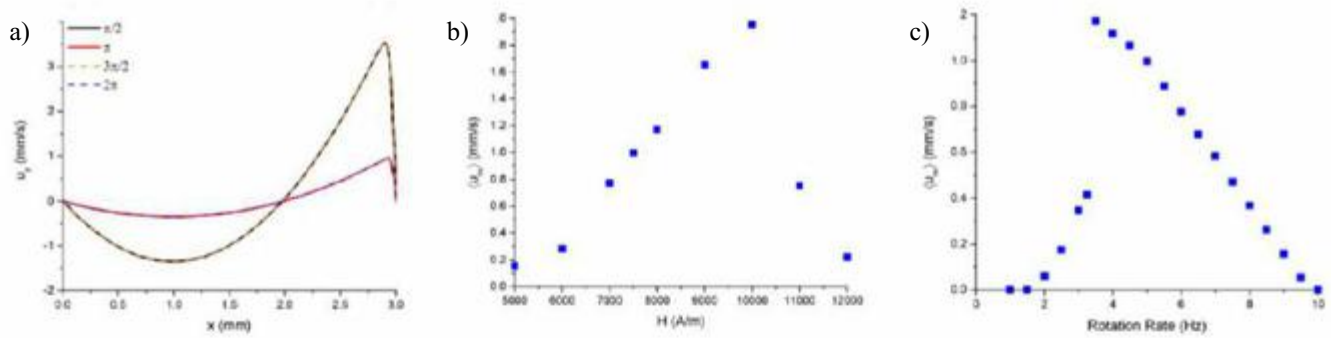

FIG 3. a) Velocity profiles across a blocked channel with an average ferroparticle volume fraction of 0.1% in the presence of a 7500A/m magnetic field rotating at 5Hz. Profiles shown at different times in a rotation cycle. b) Average magnetically-induced velocity in a channel with an average particle volume fraction of 0.1% under the influence of a 5Hz magnetic field at various field strengths c) Average magnetically-induced velocity in a channel with an average particle volume fraction of 0.1% under the influence of a 7500A/m magnetic field rotating at various frequencies

CONCLUSIONS

We develop a multi-scale model of magnetically-driven flows in dead-end channels that includes a coupling between chain formation and dynamics and the fluid flow. The flow requires a field strength above a critical value, and it must rotate and have gradient to interact with the ferroparticles. Preliminary results agree with experimental observations.

References

[1] Clements, M. & R.T. Bonnecaze, 2013 *Cardiovasc. Eng. Technol.* **4**(4) 364-373.
[2] Devices for controlling magnetic nanoparticles to treat fluid obstructions, F.M Creighton, US Patent 8,715,150 B2
[3] Methods of controlling magnetic nanoparticles to improve vascular flow, F.M. Creighton, US Patent 8,529,428 B2
[4] Magnetic-based methods for treating vessel obstructions, F.M. Creighton, US Patent 8,313,422 B2
[5] Magnetic-based systems for treating occluded vessels, F.M. Creighton, US Patent 8,308,628 B2
[6] Gomez-Ramirez A., P. Kuzhir, M. T. Lopez-Lopez, G. Bossis, A. Meunier and J. D. G. Duran, 2011 *J. Rheology* **55** (1), 43-67.

HELE-SHAW FLOW OF A CONCENTRATED, NON-COLLOIDAL SUSPENSION

Arun Ramachandran*[1]
[1]*Department of Chemical Engineering and Applied Chemistry, University of Toronto, Toronto, Ontario, Canada*

Summary This paper provides a set of macrotransport equations for determining the volume fraction and velocity distributions in the flow of a concentrated suspension of rigid, spherical particles through a Hele-Shaw cell. In this problem, Taylor dispersion relaxes volume fraction gradients in the flow direction, with a dispersivity that is proportional to $\overline{\mathbf{u}}B^3/a^2$, where $\overline{\mathbf{u}}$ is the local depth-averaged velocity, B is the half depth of the channel and a is the particle radius. Perpendicular to the flow, volume fraction gradients are relaxed by shear-induced migration at a rate proportional to $|\mathbf{u}|\,a^2/B$. The model predicts that negative volume fraction gradients should relax in the flow direction, while positive ones should self-sharpen to an asymptotic distribution in an appropriate frame of reference. However, the latter distribution is unstable to perturbations normal to flow, leading to viscous miscible fingering with a preferred wavelength that scales as $B^{5/3}/a^{2/3}$.

Keywords: Non-Brownian suspension, Taylor dispersion, shear-induced migration, viscous miscible fingering

INTRODUCTION

The development of the suspension balance model by Nott and Brady [1] represented a significant advancement in the area of modeling concentrated, non-Brownian suspension flows. It has explained experimentally-observed velocity and volume fraction distributions for several different flow geometries [2, 3, 4]. However, the numerical implementation of this model to calculate time and space dependent volume fraction distributions can be a highly challenging task [5, 6, 4], particularly in geometries with a region of vanishing shear stress in the cross-section. Fortunately, some geometries allow the simplification of the model in certain asymptotic limits. Previously, we have developed a macrotransport model for suspension flow through a circular tube that describes the spatial and temporal distribution of the cross-section-averaged volume fraction distribution. In this work, we present the corresponding macrotransport equation for Hele-Shaw of suspensions, and compare the results with tube flow.

METHOD AND RESULTS

In this work, we implement a two time scale perturbation [7] of the suspension balance model [1] coupled with the constitutive equations of Zarraga et al.[8], and formally derive the following depth-averaged convection-dispersion equation for the flow of a concentrated suspension of neutrally-buoyant, non-colloidal particles between two parallel plates.

$$\frac{\partial \overline{\phi}}{\partial t} + \underbrace{\nabla \cdot \left[g\left(\overline{\phi}\right)\mathbf{u}\right]}_{\text{Convection}} = \underbrace{\frac{B^3}{a^2}\nabla \cdot \left[h\left(\overline{\phi}\right)\frac{\mathbf{u}\cdot\nabla\overline{\phi}}{|\mathbf{u}|}\mathbf{u}\right]}_{\text{Taylor dispersion}} + \underbrace{\frac{a^2}{B}\nabla \cdot \left[q_A\left(\overline{\phi}\right)|\mathbf{u}|\,\mathbf{H}\cdot\nabla\overline{\phi}\right] + \frac{a^2}{B}\nabla \cdot \left[q_B\left(\overline{\phi}\right)\nabla\cdot\left(|\mathbf{u}|\,\mathbf{H}\right)\right]}_{\text{Shear-induced migration}} \tag{1}$$

The various variables here are the depth averaged velocity field $\overline{u}$, the local depth-averaged particle volume fraction $\overline{\phi}$, the half depth of the channel B, the particle radius a, a geometry tensor, $\mathbf{H}$, that attributes different weights to the flow and vorticity directions according to normal stress differences [4], and h, g, q_A and q_B, which are functions only of $\overline{\phi}$. At every time step, the pressure field, P, needs to be determined by solving the depth-averaged continuity equation,

$$\nabla \cdot \left[M\left(\overline{\phi}\right)\nabla P\right] = 0, \tag{2}$$

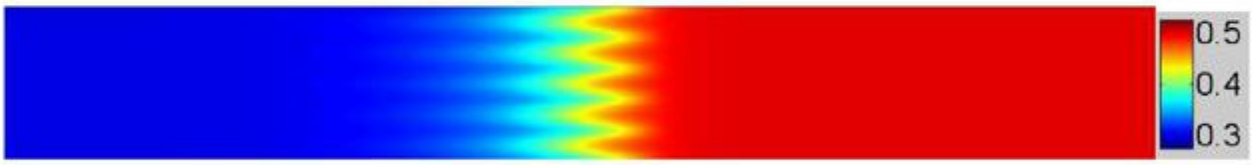

Figure 1: A positive step change in volume fraction from 30% to 50% in the flow direction is unstable to perturbations imposed normal to the flow.

*Corresponding author. Email: Arun.Ramchandran@utoronto.ca

from which $\overline{u}$ may be deduced as $-\left(B^2/\mu_0\right) M\left(\overline{\phi}\right) \nabla P$, μ_0 being the viscosity of the suspending fluid. The Taylor-dispersion coefficient in this macrotransport equation scales as B^3/a^2, and it is proportional to the local velocity. However, it acts only on gradients in the local flow direction. Normal to the flow, shear-induced migration terms can produce particle redistribution, and these are proportional to a^2/B .

Analogous to the macrotransport equation for tube suspension flow [9], the evolution of concentration distribution is dependent only on the total strain experienced by the suspension, and is independent of the suspension velocity. However, unlike tube suspension flow, a positive concentration gradient along the flow direction does not reach an asymptotic distribution; rather, it is susceptible to viscous miscible fingering, as shown in Fig. 1. A linear stability analysis performed for a step change in the volume fraction revealed that the wavenumber corresponding to fastest growing mode scales as $a^{2/3}/B^{5/3}$.

These phenomena will be explained in detail in the presentation. An inner solution in the vicinity of an obstacle surface with the details of the particle distribution and the velocity field in the inner region will also be elucidated.

CONCLUSIONS

The macrotransport equations presented here greatly reduce the complexity of determination of velocity and particle distributions in suspension flows. One only needs to solve two coupled PDEs in P and $\overline{\phi}$, which can be implemented on standard numerical software such as COMSOL or ANSYS. The equations will be useful in determining time-dependent volume fraction and velocity fields in processes such as powder injection molding or extrusion of films containing filler particles.

References

[1] P. R. Nott and J. F. Brady. Pressure-driven flow of suspensions: Simulations and theory. *J. Fluid Mech.*, 275:157–199, 1994.

[2] J. F. Morris and F. Boulay. Curvilinear flows of non-colloidal suspensions: The role of normal stresses. *J. Rheol.*, 43(5):1213–1237, 1999.

[3] Z. Fang, A. A. Mammoli, J. F. Brady, M. S. Ingber, L. A. Mondy, and A. L. Graham. Flow-aligned tensor models for suspension flows. *Int. J. Multiphase Flow*, 28(1):137–166, 2002.

[4] A. Ramachandran and D. T. Leighton. The influence of secondary flows induced by normal stress differences on the shear-induced migration of particles in concentrated suspensions. *J. Fluid Mech.*, 603:207–243, 2008.

[5] R. M. Miller and J. F. Morris. Normal stress-driven migration and axial development in pressure-driven flow of concentrated suspensions. *J. Non Newtonian Fluid Mech.*, 135(2-3):149–165, 2006.

[6] A. Ramachandran and D. T. Leighton. Viscous resuspension in a tube : The impact of secondary flows resulting from second normal stress differences. *Phys. Fluids*, 19(5):055301, 2007.

[7] M. Pagitsas, A. Nadim, and H. Brenner. Multiple time scale analysis of macrotransport processes. *Physica A*, 135:533–550, 1986.

[8] I. E. Zarraga, D. A. Hill, and D. T. Leighton. The characterization of the total stress of concentrated suspensions of noncolloidal spheres in Newtonian fluids. *J. Rheol.*, 52(2):185–220, 2000.

[9] A. Ramachandran. Secondary convection due to second normal stress differences: A new mechanism for the mass transport of solutes in pressure-driven flows of concentrated, non-colloidal suspensions. *Soft Matter*, 9:6824–6840, 2013.

PARTICLE-INDUCED VISCOUS FINGERING

Jungchul Kim[1], Feng Xu[1], and Sungyon Lee *[1]

[1]*Department of Mechanical Engineering, Texas A&M University, College Station, Texas, USA*

Summary Viscous fingering instability arises when a less viscous fluid displaces a more viscous one inside porous media. We introduce a novel fingering instability in the absence of the destabilizing viscosity ratio, when particles are added to the viscous invading fluid in a radial source flow inside a Hele-Shaw cell. The fingering regimes are characterized experimentally (from a stable regime to weak and band fingering) for varying particle volume fractions and ratios of the gap thickness to particle diameter. The mechanism of particle-induced fingering is rationalized based on the particle migration towards the channel centerline, and the transition between weak and band fingering regimes is theoretically resolved based on the rate of particle aggregation near the interface.

INTRODUCTION

Viscous fingering is ubiquitous in multiphase flows in porous media, and controlling them is important in numerous industrial applications that include enhanced oil recovery. While the invasion of a more viscous fluid into a less viscous fluid is inherently stable to fingering [1, 2], Tang et al. [3], followed by Ramachandran and Leighton [4], discovered the surprising destabilizing effect of particles which leads to particle-induced viscous fingering; however, much of the rich physics of this fingering phenomenon remains unexplored. In this paper, we experimentally quantify the particle-induced viscous fingering and derive a functional dependency of the fingering onset for varying key experimental parameters: particle volume fraction, ϕ_0, and gap thickness relative to particle diameter, h/D.

EXPERIMENTAL RESULTS

A mixture of silicone oil (density, $\rho = 0.98$ g/cm^3 and viscosity, $\mu = 0.1$ Pa$\cdot s$) and neutrally buoyant polyethylene particles ($D \approx 0.330$ mm) is injected into a Hele-Shaw cell at a constant flow rate, Q (schematic in Fig. 2(a)). The Hele-Shaw cell consists of two glass plates with gap thickness, h, that ranges from $0.635 - 1.39$ mm. We experimentally observe three distinct regimes of fingering, as the particle volume fraction, ϕ_0, is increased for given Q and h/D. As shown in Fig. 1, for $\phi_0 < 10\%$, the interface appears to be stable, which corresponds to a stable "no fingering" regime. As ϕ_0 increases, regularized particle clusters and slight interfacial deformations are observed, referred to as the "weak fingering" regime. For large values of ϕ_0, more pronounced fingers appear on the interface in the "band fingering" regime. Specifically, band fingering involves the formation of a torus band of particles on the interface, which subsequently breaks to form fingers (Fig. 2(b)). Fig. 2(c) shows that the radius at which the particle band breaks coincides with the peak in the dimensionless deviation of the interface from a circle, $\Lambda = \int_S (1 - (R_\mathrm{b}(s)/R_\mathrm{c}))^2 ds$, where R_b is the center-to-edge distance and R_c is the radius of the best fitted circle [4]. The value of Λ is calculated using MATLAB$^{\bigcirc}$ image processing tools for all values of ϕ_0 and h/D to differentiate band fingering from weak or/and no fingering, as summarized in a phase diagram of Fig. 2(f).

MECHANISM OF FINGERING

Fingering is caused by the particle aggregation on the interface, which results in the destabilizing local increase in effective viscosity [5, 6, 7], as illustrated in Fig. 2(d). The particle aggregation on the interface itself arises from the particle focusing on the channel centerline ($z = 0$) due to shear-induced migration [8], which leads to the faster motion of particles towards the interface relative to that of the mixture. Here, we define the ratio of the mean particle speed to that of the suspension as

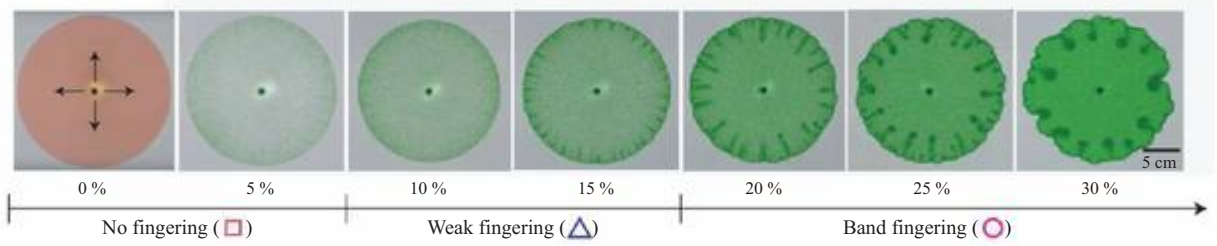

Figure 1: Gradual appearance of fingering with an increasing particle concentration, ϕ_0, for the gap thickness, $h = 1.15$ mm, particle diameter, $D = 330$ μm, and flow rate, $Q = 150$ mL/min. Arrows indicate the flow direction.

*Corresponding author. Email: sungyon.lee@tamu.edu

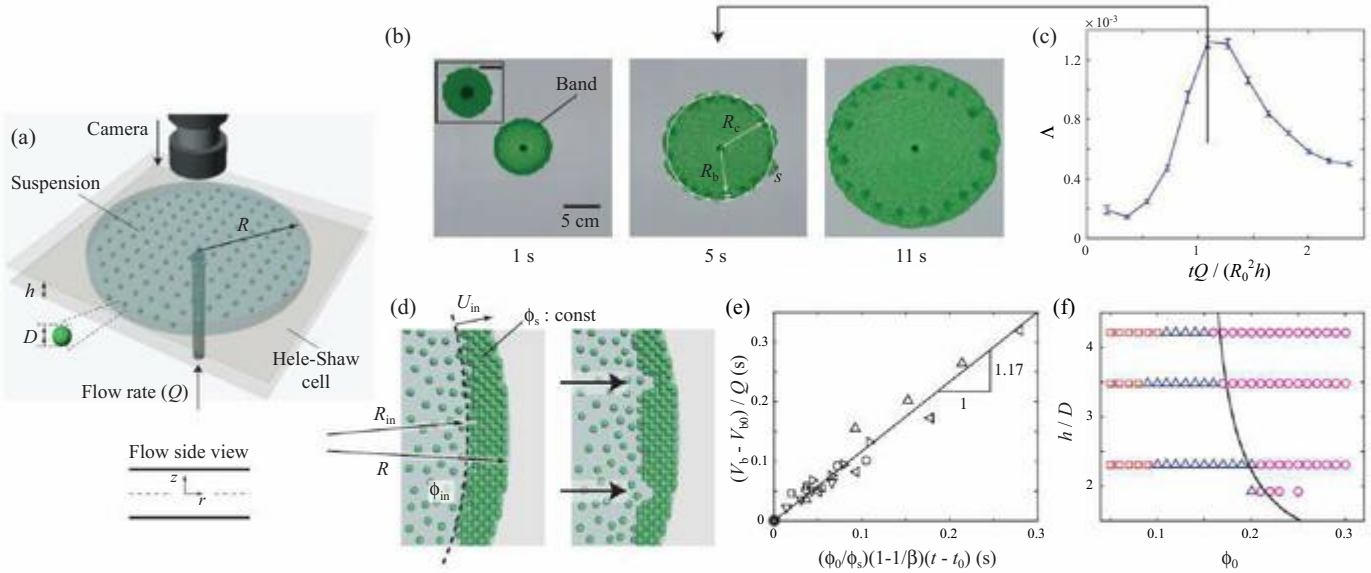

Figure 2: (a) Schematic of the experimental set-up. (b) Time evolution images of band fingering ($\phi_0 = 30\%$, $h = 0.762$ mm, and $D = 330$ μm.); inset: initial formation of the band with the scale bar of 2 cm. (c) Plot of $\Lambda = \int_0^S (1 - (R_\mathrm{b}(s)/R_\mathrm{c}))^2 ds$ over dimensionless time, which characterizes the interfacial deviation from a circle. (d) Schematic illustrating the sequence of events that lead to fingering due to the particle aggregation on the interface. (e) The rate of the particle volume increase in the band is predicted based on $q_p \approx Q\phi_0(1 - 1/\beta)$, in good agreement with the experimental data. (f) A ϕ_0-(h/D) phase diagram summarizes the fingering regimes with a solid line showing the theoretical transition between weak and band fingering.

$\beta = \int_{-h/2}^{h/2} u_p \phi \mathrm{d}z / (\bar{}(r) \int_{-h/2}^{h/2} u \mathrm{d}z)$, where $\bar{}(r) = \int_{-h/2}^{h/2} \phi(r,z)\mathrm{d}z/h$, and u and u_p denote local suspension and particle radial velocities, respectively. In order for the particle aggregation to occur, $\beta > 1$ must be satisfied. Furthermore, if we assume a uniform particle concentration, ϕ_in, away from the interface, $\phi_\mathrm{in} = \phi_0/\beta$ by mass conservation. In the limit of $h/D \to 1$, one can derive the expression for β to scale as $3/[2(1 + D/(3h))]$ assuming a monolayer of particles centered at $z = 0$. In the limit of $h/D \gg 1$, the suspension balance model [9, 10] is employed to compute β in a separate manuscript.

To identify the transition from weak to band fingering, the necessary condition to form and maintain a particle band of maximum monolayer volume fraction, $\phi_s \approx 0.46$, is considered. By balancing the increase in the band volume, V_b, with the particle flux at the inner edge, R_in (schematic in Fig. 2(d)), we obtain $\phi_s(V_b - V_{b0}) = Q\phi_0(1 - 1/\beta)(t - t_0)$ with $V_b(t_0) = V_{b0}$, which has been experimentally validated in Fig. 2(e). In order for the band fingering to occur, V_b must evolve in such a way that the band width is at least greater than or equal to the particle diameter, D: $\dot{V}_b = Q(\phi_0/\phi_s)(1 - 1/\beta) \gtrsim 2\pi h D R_\mathrm{in}$, where $R_\mathrm{in} = Q/(2\pi R_\mathrm{in} h)$. By plugging in $R_\mathrm{in} = r_0$ and rearranging the terms, we define the ratio of particle influx to the required band growth rate as $\Pi = \frac{r_0\phi_0}{D\phi_s}(1 - \frac{1}{\beta})$. When $\Pi \gtrsim 1$, band fingering is more likely to occur as the requirement for sustaining an initial particle band has been met. In contrast, for $\Pi \lesssim 1$, the rate of particles entering the band is not sufficiently fast to maintain it, resulting in weak or no fingering. As shown in the phase diagram of Fig. 2(f), the curve of $\Pi = 1.47$ successfully captures the boundary between the band fingering and weak fingering and shows that this simple model exhibits the correct functional dependence of the band fingering onset on ϕ_0 and h/D.

References

[1] Saffman P. G., Taylor G.: The penetration of a fluid into porous medium or Hele-Shaw cell containing a more viscous liquid. *Proc. Roy. Soc. A* **245**:312-329, 1958.

[2] Paterson L.: Radial fingering in a hele shaw cell. *J. Fluid Mech.* **113**:513-529, 1981.

[3] Tang H., Grivas W., Homentcovschi D., Geer J., Singler T.: Stability considerations associated with the meniscoid particle band at advancing interfaces in Hele-Shaw suspension flow. *Phys. Rev. Lett.* **85**:2112, 2000.

[4] Ramachandran A., Leighton D. T.: Particle migration in concentrated suspensions undergoing squeze flow. *J. Rheol.* **54**:563-589, 2010.

[5] Zarraga I. E., Hill D. A., Leighton D. T.: The characterization of the total stress of concentrated suspensions of non-colloidal spheres in Newtonian fluids. *J. Rheol.* **44**:185-220, 2000.

[6] Pramanik S., Wit A. D., Mishra M.: Viscous fingering and deformation of a miscible circular blob in a rectilinear displacement in porous media. *J. Fluid Mech.* **782**:R2, 2015.

[7] Homsy G. M.: Viscous fingering in porous media. *Ann. Rev. Fluid Mech.* **19**:271-311, 1987.

[8] A. Ramachandran and D. T. Leighton, The effect of gravity on the meniscus accumulation phenomenon in a tube, *J. Rheol.*, **51**:1073-1098, 2007.

[9] Morris J. F., Boulay F.: Curvilinear flows of noncolloidal suspensions: the role of normal stresses. *J. Rheol.* **43**:1213-1237, 1999.

[10] Nott P. R., Brady J. F.: Pressure-driven flow of suspensions - simulation and theory. *J. Fluid Mech.* **275**:157-199, 1994.

FLOW IN A HUMAN NASAL CAVITY OBTAINED BY IMPROVED SHAPE STANDARDIZATION

Alireza Nejati[1] and John Cater *[1]

[1]*Department of Engineering Science, University of Auckland, New Zealand*

Summary Numerical simulations of flow through healthy and diseased human airways suffer from significant inter-individual variation. We develop a method for standardizing the human nasal cavity to eliminate some of these differences. In this work we present preliminary CFD results for air flow through this standardized air way and demonstrate flow features that are reflective of average flow features in the population.

INTRODUCTION

It is important to understand the airflow through the human upper airways, for purposes of such as optimizing the delivery of drugs through aerosol deposition [8] and improvements of artificial respiratory devices [6]. To do this, first an airway geometry has to be obtained. Airway geometries are typically obtained from cadavers or CT scans of individual subjects [8, 7], however these are subject to excessive inter-individual variation [1]. Here, we analyze flow through a more representative geometry. A naive method of obtaining representative geometry would be taking the average of scans [3, 4] or the median of segmented scans [5]. However, these methods have difficulties with the very thin, convoluted structures present in the nasal cavity. In this work we use a deformable registration procedure to obtain a more accurate standardized geometry and we simulate the air flow through this geometry and compare with previous results obtained from individual scans.

METHODS

Standardization

The deformable registration procedure consists of three separate alignment procedures that are carried out in sequence: 1. Rigid alignment to common landmarks, 2. 'Straightening' of the nasal septum, 3. Fine-tuning via per-cross-section deformable registration. In the first step, all scans are aligned such that their anterior maxillary spine (AMS) and choana are coincident. In the second step, coronal cross-sections of the scans are obtained and the nasal septum is identified in each cross-section, and the septa are deformed to be straight while still preserving the position of their bottom-most point and total arc length. In the final step, a a multiple registration procedure is used based on the following functional [2]:

$$J\left(\{\mathbf{u}_k\}_{k=1}^m\right) = \sum_{k=1}^{m} \int_\Omega \left(f_k(\mathbf{x} \circ \ \mathbf{u}_k) \circ \ g(\mathbf{x})\right)^2 d\mathbf{x} + \lambda \int_\Omega |\nabla g|^2 \, d\mathbf{x} + \mu \sum_{k=1}^{m} \int_\Omega |\nabla \mathbf{u}_k|^2 \, d\mathbf{x} + \sigma \int_\Omega \left(\sum_{k=1}^{m} \mathbf{u}_k\right)^2 d\mathbf{x} \qquad (1)$$

where Ω is the image domain (e.g. $\mathbb{R}^2$), $\mathbf{u}_k$ are the deformations, and f_k represent the input images. The variables λ, μ, and σ are parameters of the model that may be set to different values to produce different alignment behavior. m is the number of images. After this alignment step, the 'average' image g is extracted and the slices are combined together to produce a solid 3-dimensional surface mesh.

Air flow simulation

The expiratory air flow through the mean geometry was modeled in ANSYS 16.0. The surface mesh was 'cleaned' by removal of overlapping faces and a CFD mesh was generated using 0.4 mm as the base element size and using 3 prism layers on the interior of the airway to resolve the boundary layer. We carry out a numerical solution of steady state air flow, with a shear stress transport (SST) turbulence model. The inlet was modeled as a source of 37 °C air at 5.5 $\times 10^{-4}$ g/s (28.8 litres/minute). This represents a typical expiratory air flow rate [6].

RESULTS

A pressure drop of 12.9 Pa was observed from the tracheal inlet to the nostril; the highest relative pressure (19.2 Pa) existed in the posterior section of the middle turbinate, superior turbinate, and olfactory section. This is similar to results obtained from individual airways (e.g. a relative pressure of 9.8 Pa was observed in [7]). Two recirculation regions (one in the superior nasopharynx area and one in the small cavity behind the tip of the nose) were observed. The flow appears transitional

*Corresponding author. Email: j.cater@auckland.ac.nz

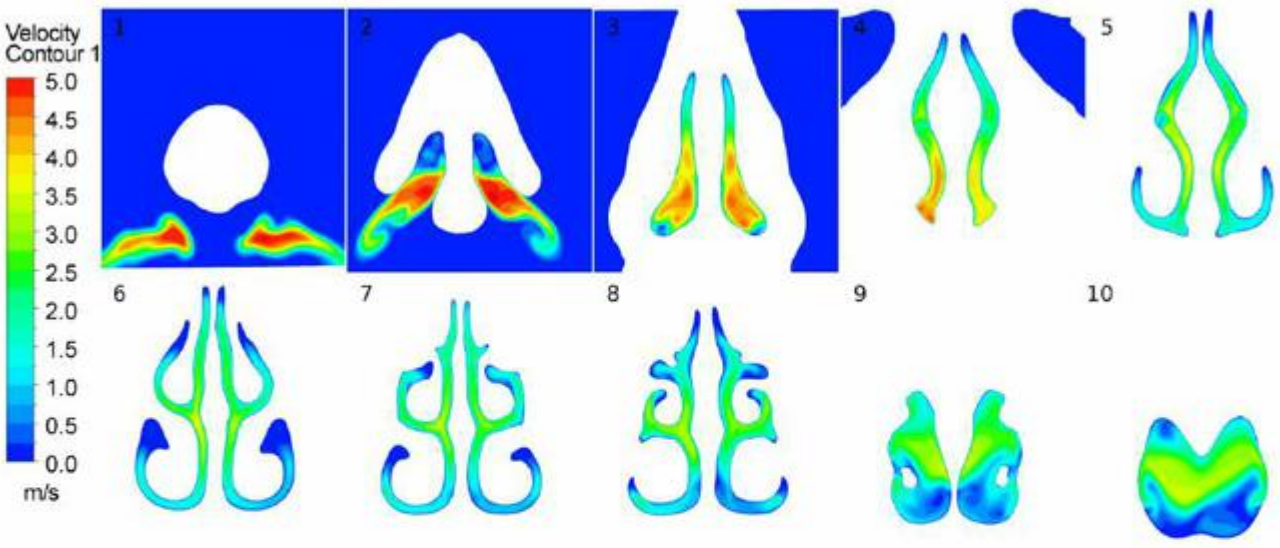

Figure 1: Flow velocity in coronal cross-sections of nasal cavity. Cross-sections 1-9 positioned 1-9 cm behind the tip of the nose, respectively; slice 10 positioned 9.5 cm behind the tip of the nose.

with some areas of relative laminar flow and other areas of turbulent flow. With the 2 million node mesh, the boundary layer appears well resolved and relatively thin (˜0.1 mm) in some areas. In the cross-sections, most of the flow appears to occur in the thin middle sections (velocities ranging from 3 to 5 m/s), with a relatively small portion of the flow occuring in the extremes of the inferior turbinates or the olfactory section. This is despite the inferior turbinates having large cross-sectional area.

CONCLUSIONS

The transitional flow and relative small thickness of boundary layer are consistent with the presumed role of the nasal cavity as heat and moisture exchange system. The airway shape is such that flow is forced through thin sections; this is consistent with the shape of the airway being optimal for heat and moisture exchange. Note that various developmental disorders of the nasal cavity (such as *concha bullosa*) interfere with this natural air flow pattern and cause air to flow through regions of relatively low resistance and high cross-sectional area, exchanging less heat and moisture. Compared with individual subjects, the standardized geometry is more symmetric (left and right passageways of similar shape and size; deviation of nasal septum not apparent) and this leads to a symmetric flow pattern, however due to the turbulence present, this symmetry is not exact, as can be seen.

References

[1] Steven E. Churchill, Laura L. Shackelford, J. Nicole Georgi, and Michael T. Black. Morphological variation and airflow dynamics in the human nose. *American Journal of Human Biology*, 16(6):625–638, 2004.

[2] Shun Inagaki, Hayato Itoh, and Atsushi Imiya. Multiple Alignment of Spatiotemporal Deformable Objects for the Average-Organ Computation. In *Computer Vision - ECCV 2014 Workshops*, volume 8928, pages 353–366, 2014.

[3] Chih Fang Lee, Mohd Zulkifly Abdullah, Kamarul Arifin Ahmad, and Ibrahim Lutfi Shuaib. Standardization of Malaysian adult female nasal cavity. *Computational and Mathematical Methods in Medicine*, 2013, 2013.

[4] Chih Fang Lee, Mohd. Zulkifly Abdullah, Kamarul Arifin Ahmad, and Ibrahim Lutfi Shuaib. Analytical Comparisons of Standardized Nasal Cavity. *Journal of Medical Imaging and Health Informatics*, 4(1):14–20, 2014.

[5] Y Liu, M R Johnson, E a Matida, S Kherani, and J Marsan. Creation of a standardized geometry of the human nasal cavity. *Journal of Applied Physiology*, 106:784–795, 2009.

[6] Callum J. T. Spence, Nicholas A. Buchmann, and Mark C. Jermy. Flow Field in the Human Nasal Cavity with Nasal High Flow Therapy from Stereoscopic PIV Measurements. In *8th International Symposium on Particle Image Velocimetry - PIV09*, Melbourne, Victoria, Australia, 2009.

[7] Nicholas M Stringer, John E Cater, J Eaton-Evans, and C White. Numerical Comparison of Air Flow Patterns in the Upper Airways of Adults and Neonates. In *17th Australasian Fluid Mechanics Conference, Auckland, New Zealand*, 2010.

[8] Jinxiang Xi, Xiuhua Si, Jong Won Kim, and Ariel Berlinski. Simulation of airflow and aerosol deposition in the nasal cavity of a 5-year-old child. *Journal of Aerosol Science*, 42(3):156–173, 2011.

MAGNETIC MICRO-CONVECTION

Andrejs Cebers *[1], Kaspars Erglis[1], Guntars Kitenbergs[1], Oksana Petrichenko[1], and Andrejs Tatulcenkovs[1]
[1]*Department of Physics, University of Latvia, Riga, Latvia*

Summary Magnetic micro-convection of a magnetic liquid in Hele-Shaw cells is caused by the action of non-potential ponderomotive forces of its self-magnetic field. The main experimental findings of a study of the magnetic micro-convection, which are in a good agreement with analytical and numerical results obtained in the frame of the Brinkman model, are presented. It is also found that the gravitational forces play important role in the horizontal Hele-Shaw cells due to the small density difference of miscible magnetic and non-magnetic fluids.

EXPERIMENTAL AND THEORETICAL STUDY

Magnetic liquids with a free boundary in Hele-Shaw cells under the action of perpendicular magnetic field form complex patterns due to the action of ponderomotive forces of their self-magnetic field [1].

Magnetic micro-convection occurs in the limit of zero surface tension on the interface between miscible magnetic and non-magnetic fluids [2, 3]. The flow in the Hele-Shaw cell with a thickness h caused by the non-potential ponderomotive force of the self-magnetic field is described in the frame of the Brinkman equation coupled with the diffusion equation for the normalized particle concentration c:

$$-\nabla p - \frac{12\eta}{h^2} v + \eta \Delta_2 v + \frac{2M_0 c \nabla \psi}{h} = 0\,, \tag{1}$$

$$\frac{\partial c}{\partial t} + v \cdot \nabla c = D \Delta_2 c\,. \tag{2}$$

Here M_0 is the magnetization of the liquid at $c = 1$, ψ is the potential of magnetostatic field on the boundary of Hele-Shaw cell.

Scaling the length and time by h and h^2/D respectively it follows that the flow arising on the planar interface between miscible magnetic and non-magnetic fluids is determined by the magnetic Rayleigh number $Ra_m = M_0^2 h^2/12\eta D$, which characterizes the ratio of the hydrodynamic M_0^2/η and diffusion h^2/D time scales. The calculation in the frame of linear perturbation theory in quasi-static approximation taking into the account the non-homogeneous self-magnetic field at the step-like initial concentration distribution ($c = 1;\ x < 0$ and $c = 0;\ x > 0$) gives the critical value of the magnetic Rayleigh number $Ra_m^c = 6.6$ and the characteristic wavenumber of the instability $kh = 1.8$. The flow in the non-linear stage of the instability described by Eqs.(1,2) is calculated by the pseudospectral technique.

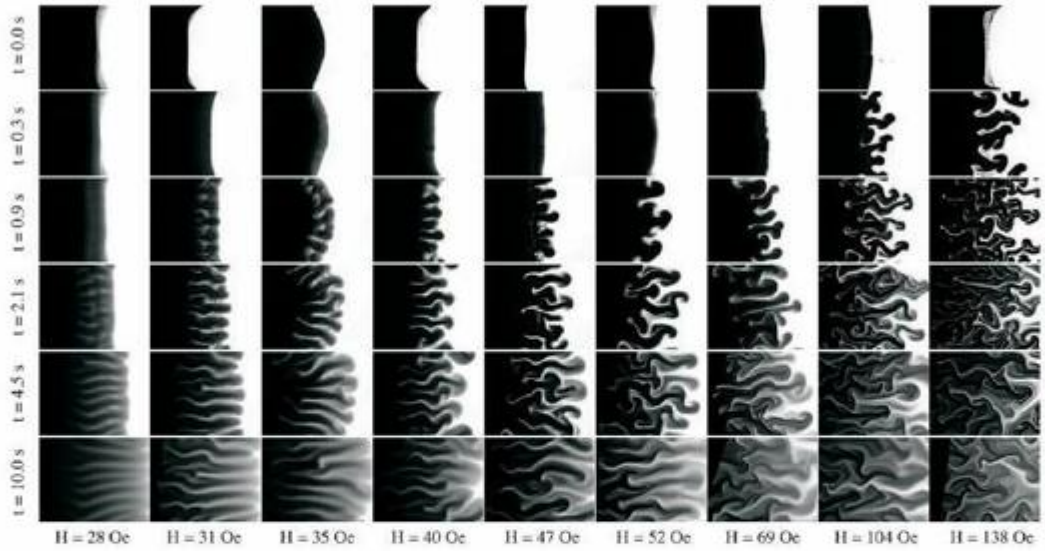

Figure 1: Magnetic micro-convection development [3].

Experimental study of the magnetic micro-convection is carried out in the horizontal Hele-Shaw cell with thickness $h = 120\ \mu$m, where two miscible fluids are put into a contact by a syringe pump. Water-based magnetic fluid with average particle diameter 7 nm, saturation magnetization $M = 8.4$ G and magnetic susceptibility $\chi = 0.016$ is used. The development of the patterns on the interface in dependence on the applied magnetic field is shown in Fig. 1.

*Corresponding author. Email: aceb@tesla.sal.lv

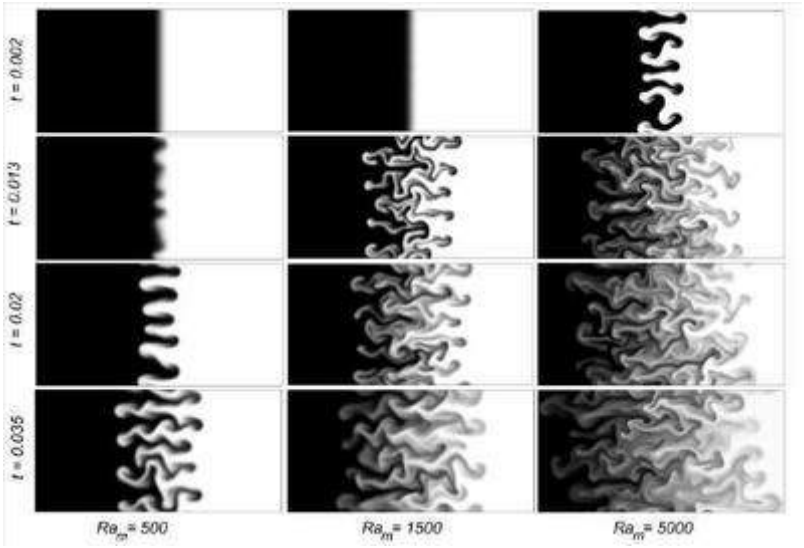

Figure 2: Numerical simulation of magnetic micro-convection development [3].

These data and the theoretical value of the critical magnetic Rayleigh number give us the effective diffusion coefficient of the particles which turned out to be much larger than determined by Dynamic Light Scattering measurements. Additional experimental and theoretical study has shown that it is due to the counter flows arising in the horizontal Hele-Shaw cell due to the small density difference of the magnetic liquid and its carrier liquid which causes effective smearing of the interface presumably accounted for by introduction of the effective diffusion coefficient.

As a result good quantitative and qualitative agreement of the experimental and numerical simulation results is obtained as may be seen by comparing experimental results in Fig. 1 and Fig. 2, where numerical simulation results for different magnetic Rayleigh numbers are shown. It should be remarked that the Brinkman model [3] contrary to the Darcy model [2] shows the formation of mushroomson the fingers of the developing micro-convection pattern (see Fig. 1), which is in agreement with the experimental observations.

Rather convincing results are obtained by the measurement of the velocities of the finger motion in dependence on the magnetic Rayleigh number shown in Fig. 3. The slope of the linear dependence of the finger velocity on the magnetic Rayleigh number 0.29 is close to the slope of numerical results in the frame of the Brinkman model 0.36 and is rather far from the one given by the Darcy model [2] .

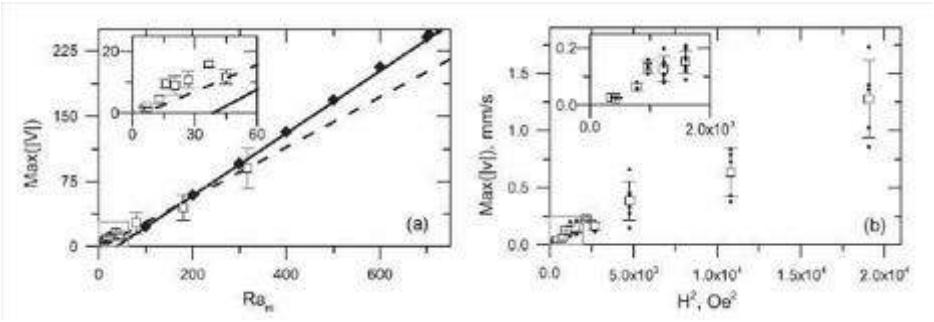

Figure 3: Maximal finger velocities in dimensionless (left) and dimensional (right) units. Empty squares mark average experimental data, black diamonds on the left – numerical data [3].

To conclude we may note that magnetic micro-convection could be interesting in microfluidics to enhance the mixing of magnetic and non-magnetic fluids.

References

[1] Cebers A., Maiorov M.M.: Magnetostatic instabilities in plane layers of magnetizable liquids. Magnetohydrodynamics 16:21-27,1980

[2] Erglis K., Tatulcenkovs A., Kitenbergs G., Petrichenko O., Ergin F.G., Watz B.B., Cebers A.: Magnetic field driven micro-convection in the Hele-Shaw cell. J.Fluid Mech 714:612-635,2013

[3] Kitenbergs G., Tatulcenkovs A., Erglis K., Petrichenko O., Perzynski R., Cebers A.: Magnetic field driven micro-convection in the Hele-Shaw cell: the Brinkman model and its comparison with experiment. J.Fluid Mech. 774:170-191,2015

RATCHETING VISCOUS FLUIDS IN A VIBRATING CHANNEL

Jie Yu *[1]

[1]*Department of Civil Engineering and, School of Marine and Atmospheric Sciences, Stony Brook University, Stony Brook, New York, USA*

Summary A laboratory experiment shows that fluid can be pumped from one end to another in a narrow channel with vibrating sawtooth walls. The phenomenon is referred to as ratcheting fluid. We here present a theory describing the mechanism of rectifying oscillatory momentum into steady motions and symmetry-breaking that lead to the directional pumping of fluids as observed. A 'terrain-following' theoretical framework is formulated using a conformal transformation to accurately resolve the Stokes boundary layer of oscillatory flows and boundary-driven effects. The theory correctly predicts the unidirectional pumping, clearly elucidating the working principle of this fluid rectifier: The nonlinear inertia rectifies the periodic fluctuations of the flow into a steady momentum flux, driving steady circulations against viscous resistance. The asymmetric wall geometry renders the steady circulations to be spatially biased, leading to the pumping. Various influences on the pumping rate are analyzed. Applications to viscoelastic flows will be discussed.

MOTIVATION, METHOD AND RESULTS

Motions rectified by symmetry-breaking mechanisms in oscillating flows have been of great interest in biological locomotion and engineering applications. The ratchet-based concepts have been extensively explored in applications of selective control and optimization of directed transport, separation (or mixing) of nanoparticles, micro and complex fluids, magnetic vortices, etc; see extensive reviews in [1, 3]. The importance of boundary conditions has led to techniques that exploit boundary-driven effects by microfluidic manipulation, e.g. electrokinetic effects, acoustic streaming (i.e. steady streaming) in oscillatory boundary layers and fluid-structure interactions [3].

As Yu [5] pointed out, the ratcheting effect of viscous fluids observed in [4] shares the same origin as the acoustic (steady) streaming in Stokes boundary layers of oscillatory flows. It is in fact akin to the steady streaming over sand ripples under water waves [2]. To deal with the large-amplitude sawteeth, Yu [5] adapted the method of constructing a conformal map for generally periodic boundary geometries that has been recently developed in the studies of water waves interacting with seabeds [6]. Under the transformation, the undisturbed flow domain between the sawtooth walls is mapped onto a uniform strip, while the symmetry with respect to the channel centerline is preserved; see figure 1. The large sawtooth height (relative to the mean channel width) limits wall vibrations to be of small amplitude, avoiding collisions of sawteeth. Thus, we can approximate the instantaneous wall position using the Taylor expansion at the mean position up to the accuracy that is necessary (for determining the steady streaming), avoiding the use of a time-dependent map, hence greatly simplifying the formulation.

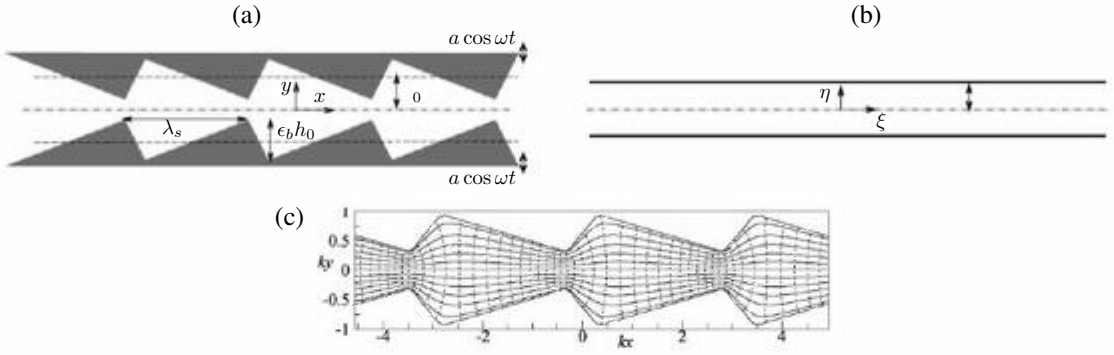

Figure 1: (a) A 2D sketch of a channel with oscillating sawtooth walls, showing the relevant scales. (b) The uniform strip of the undisturbed flow domain upon conformal transformation. (c) The curvilinear grids in the (x, y) plane that correspond to the regular grids $\xi = const$ and $\eta = const$, showing the 'terrain-following' contours near the walls. The actual sawtooth profile used is smoothed, considering the perturbation analysis.

The complete vorticity equation, the boundary conditions at the vibrating channel walls and centerline, are transformed to the mapped plane. A boundary layer approach is then invoked, considering long-wavelength sawtooth profiles, rendering analytical solutions to be attainable. The perturbation solution is sought for the stream function $\psi(\xi, \eta, t) = \widehat{\ }_0 \mathrm{e}^{-\mathrm{i}\omega t} + \alpha(\psi_{10} + \widehat{\psi}_{11}\mathrm{e}^{-\mathrm{i}\omega t} + \widehat{\psi}_{12}\mathrm{e}^{-2\mathrm{i}\omega t}) + \text{c.c.}$, where α is the amplitude of wall vibrations normalized by the mean half-channel width and, ψ_{10} is the rectified steady streaming flow field whose spatial average gives the net pumping; see figure 2. Good comparison

*Corresponding author. Email: jie.yu.1@stonybrook.edu

with the experiment is obtained; see figure 3. The theoretical method can be adapted to study viscoelastic flows in similar channels. This is ongoing.

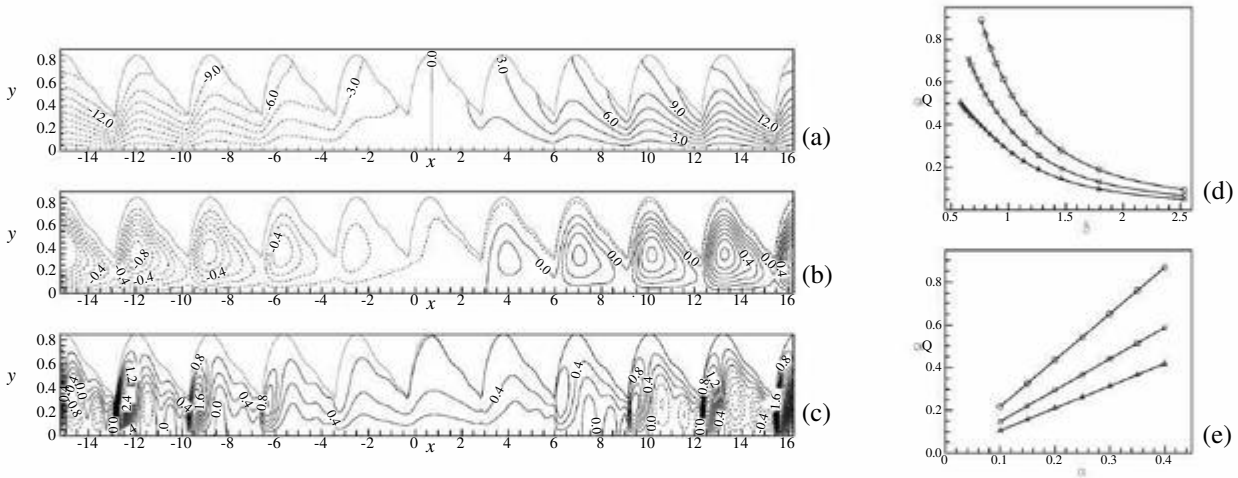

Figure 2: Contours of stream functions in the half plane $y > 0$. (a) ψ_0 at $t = \pi/2$. (b) ψ_0 at $t = \pi$, i.e. at the end of a closing half cycle when the flow is about to reverse. (c) The steady streaming flow field ψ_{10}, showing the net pumping from left to tight. Dashed lines indicate the negative contour values. The Reynolds number, based on the speed of vibration and channel width, is $Re = 2.47$ taking water as the working fluid. (d) The pumping rate αQ (for half channel width) as a function of frequency (via the dimensionless Stokes layer thickness $\delta = \sqrt{2\nu/\omega}/h_0$) for oscillation amplitude $\alpha = 0.3$; (e) αQ vs. α for $\delta = 0.9247$. Channel lengths: $\bigcirc$, $N = 15$; $\square$, $N = 10$; $\triangle$, $N = 5$ (multiple of λ_s). $\epsilon_b = 1.0$, $\beta = 0.3130$.

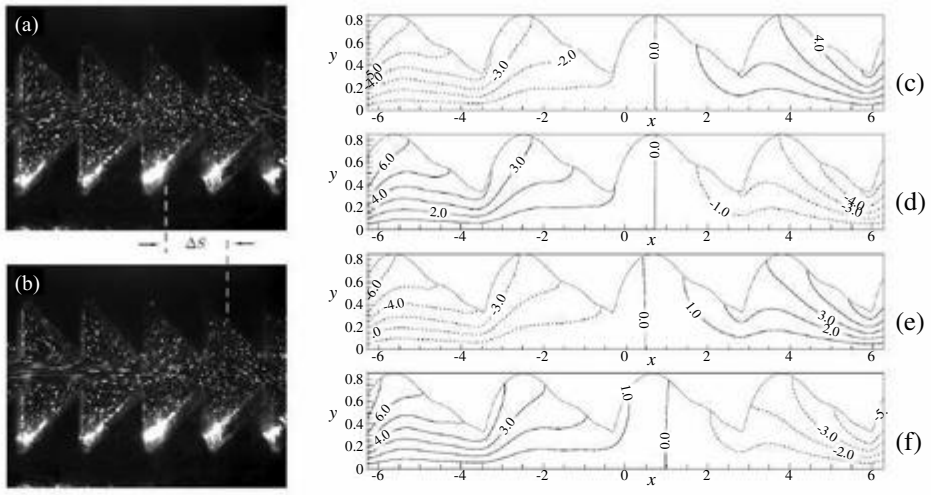

Figure 3: Experimental flow visualization (fig. 5 in [4]) at the central region of the oscillating channel (a) during the closing phase and (b) during the opening phase, showing the shift of stagnation point. Theoretical results: The leading order (linear dynamics) stream function ψ_0 (c) during the closing half cycle and (d) during the opening half cycle, showing the complete reversal of the flow pattern. The streaming function $\psi_0 + \psi_{10}$ including the steady streaming (e) during the closing phase and (f) during the opening phase, showing the shift of stagnation point that is consistent with the observation.

References

[1] HANGGI, P. AND MARCHESONI, F. 2009 Artificial Brownian motors: Controlling transport on the nanoscale. *Rev. Mod. Phys.*, **81**, 387–442.

[2] MEI, C. C. AND YU, J. 1997 The instability of sand ripples under partially standing surface waves. *Phys. Fluids*, **9(6)**, 1606–1620.

[3] SQUIRES, T. M. AND QUAKE, S. R. 2005 Microfluidics: Fluid physics at the nanoliter scale. *Rev. Mod. Phys.* **77**, 977–1026.

[4] THIRIA, B. AND ZHANG, J. 2015 Ratcheting fluid with geometric anisotropy. *Appl. Phys. Lett.*, **106**, 054106.

[5] YU, J. 2014 Fluid ratcheting by oscillating channel walls with sawteeth. *J. Fluid Mech.* **761**, 305–328. doi:10.1017/jfm.2014.636

[6] YU, J. AND HOWARD, L. N. 2012 Exact Floquet theory for waves over arbitrary periodic topographies. *J. Fluid Mech.*, **712**, 451–470. doi:10.1017/jfm.2012.432

DISPERSION OF SOLIDS IN FRACTURING FLOWS OF YIELD STRESS FLUIDS

Sarah Hormozi*[1] and Ian Frigaard[2]
[1]*Department of Mechanical Engineering, Ohio University, Athens, Ohio, USA.*
[2]*Departments of Mathematics and Mechanical Engineering, University of British Columbia, Vancouver, BC, Canada.*

Summary Recent trends in the hydraulic fracturing have included the use of cyclic pumping of solid particles (proppant) interspersed with yield stress fracturing fluid, which is found to increase the subsequent productivity. We propose a model framework for this scenario and analyse one of the simplifications. A key effect of including a yield stress is to focus high shear rates near the fracture walls. In typical fracturing flows this results in a large variation in shear rates across the fracture. With shear-thinning viscous frac fluids, suspensions may vary on the particle scale from Stokesian behaviour to inertial behaviour across the width of the fracture. Equally, according to the bulk flow rates, Hele-Shaw style models give way at higher Reynolds number to those in which inertia must be considered. We develop the Suspension Balance Model of Nott and Brady [1] to include this range of flows, while still representing a significant simplification over fully three-dimensional computations. In relatively straight fractures and for fluids of moderate rheology, this simplifies into a one-dimensional model that predicts the solids concentration along a streamline within the fracture. We use this model to make estimates of the streamwise dispersion in various relevant scenarios.

Fracture geometries can be very complex and the aim here is to develop a simplified description in which the transport equations can be applied locally to channel-like geometries, with length $\hat{L}$, width $\hat{D}$ and height $\hat{H}$. Fracture orientation and width are assumed to vary along the fracture on a length-scale $\hat{L}_t \lesssim \min\{\hat{L}, \hat{H}\}$. The essential parameters for describing the fracturing flows are the fracturing fluid with density, $\hat{\rho}_f$ and effective viscosity, $\hat{\mu}_f$ and proppant with density, $\hat{\rho}_s$, diameter size, $\hat{d}_p$ and volume fraction, ϕ_{in} are pumped in a cyclic fashion at the fracture inlet. Here, the fracturing fluid is described by a Herschel-Bulkley fluid with yield stress $\hat{\tau}_Y$, consistency $\hat{\kappa}$ and power law index n. With this simplistic description above, we expect that 8 dimensionless groups govern these flows. Four of these groups are geometric. On adopting $\hat{D}$ and $\hat{L}_t$ as natural length-scales for transverse and streamwise directions, we have 2 groups $L = \hat{L}/\hat{D}$ and $H = \hat{H}/\hat{D}$, that simply indicate the extent of the fracture. More relevant to the transport processes are: $\delta_p = \hat{d}_p/\hat{D}$ and $\delta_t = \hat{D}/\hat{L}_t$ i.e. a scaled particle diameter (particle diameter to fracture width ratio) and the local fracture aspect ratio. The remaining dimensionless groups are ϕ, the density ratio $s = \hat{\rho}_s/\hat{\rho}_f$ and two others that we take as the densimetric Froude number, $Fr = \hat{U}_0/\sqrt{\hat{g}(s \circ 1)\hat{D}}$, and Reynolds number, $Re = \hat{\rho}_f \hat{U}_0 \hat{D}/\hat{\mu}_f$. Further dimensionless groups may arise in characterizing the rheology.

The presence of shear thinning and yield stress lead to a huge variation in the viscosity of the fracturing fluid across the fracture. This will be amplified by the presence of particles. In a bulk rheological sense there is an effect of increase in viscosity due to the particles ($\eta_s(\phi)$), e.g. of classical Krieger-Dougherty type [2], but also local shear rates are amplified by the presence of particles (which do not deform) focusing the effective shear rate in the inter-particle liquid and increasing the shear-thinning. The form of local effective viscosity, $\hat{\eta}_f$ depends on the local shear rate, $\hat{\dot{\gamma}}_{loc}$, which itself depends on the solid volume fraction [3]. Therefore, the bulk suspension viscosity $\hat{\eta}$ can be decomposed as: $\hat{\eta} = \eta_s(\phi)\hat{\eta}_f(\hat{\dot{\gamma}}_{loc}(\phi))$. In considering the local micro-rheology it is of great interest to estimate the local particle Reynolds number, $Re_p = \hat{\rho}_f \hat{U}_0 \hat{d}_p/\hat{\eta}_f(\phi, \hat{\dot{\gamma}}_{loc})$ to understand the range of behaviors locally. It can be shown that there is a significant variation in this local particle Reynolds number across the fracture due to the change in local viscosity of yield stress fracturing fluid. In the high viscous central region the Stokesian particle regimes is applicable; however, in the wall layers with significant shear rates, particle regimes may vary from Stokesian to inertial.

Diffusive and dispersive effects combine with the averaged forces acting on the solids phase to distribute the particles. The solid phase mass conservation equation is typically manipulated to give a transport equation for evolution of ϕ. At least two general approaches have been taken to model particle phase diffusion: (i) the diffusive flux approach of Leighton & Acrivos [6]; (ii) the Suspension Balance Model (SBM) of Nott & Brady [1]. The diffusive flux approach is essentially phenomenological in bringing in a diffusive term to the right-hand side of the solid phase mass conservation equation. The physical origin of this term is stochastic and can be justified by ensemble averaging. The phenomena modelled by the diffusive flux approach of Leighton & Acrivos [6] are observable experimentally, but the derivation of the model has been criticised on two grounds. First, the form of diffusive closure predicts no diffusive fluxes where $\hat{\dot{\gamma}} = 0$, leading to unrealistic profiles for ϕ in pressure driven flows. Secondly, the point has been made that similar diffusive fluxes arise naturally from gradients in the suspension stress, which enter the solid phase mass conservation equation directly in considering the relative velocity. This is the idea underlying the SBM approach of Brady and co-workers, [1]. The relative velocity ($\hat{\mathbf{u}}_r = \hat{\mathbf{u}}_p \circ \hat{\mathbf{u}}_f$) is substituted into the solid phase mass conservation equation to give:

$$\frac{\partial \phi}{\partial \hat{t}} + \hat{\nabla} \cdot [\phi \hat{\mathbf{u}}] \quad = \quad \circ\, \hat{\nabla} \cdot [\phi(\hat{\mathbf{u}}_p \circ \hat{\mathbf{u}})] = \circ\, \hat{\nabla} \cdot [\phi(1 \circ \phi)\hat{\mathbf{u}}_r] = \hat{\nabla} \cdot [\phi(1 \circ \phi)\hat{M}(\hat{\eta}_f, \hat{d}_p, \phi)\hat{\mathbf{f}}_D], \tag{1}$$

*Corresponding author. Email: hormozi@ohio.edu

where $\hat{\mathbf{u}}$, $\hat{\mathbf{u}}_f$ and $\hat{\mathbf{u}}_p$ denote the suspension velocity, the fluid velocity and the particle velocity respectively. Here, $\hat{M}$ is the particle mobility and $\hat{\mathbf{f}}_D$ is the phase-averaged particle drag force. The usual approach now is to consider the solid momentum equation in the limit of small inertia. In this case, we may write $\hat{\mathbf{f}}_D \approx \circ\,[\hat{\mathbf{f}}_B + \hat{\mathbf{f}}_{D'} + \hat{\nabla}\cdot\hat{\Sigma}_p]$, where $\hat{\mathbf{f}}_B$ is the solid phase body force, $\hat{\mathbf{f}}_{D'}$ contains hydrodynamic forces excluding the drag (e.g., lift and Archimedes forces) and $\hat{\Sigma}_p$ is the solid phase stress. Then, $\hat{\mathbf{f}}_D$ may be substituted into (1) to derive a transport equation for the solid volume fraction. The objective is to include the non-Newtonian and inertial effects into SBM model to extend it for fracturing flows with yield stress frac fluids. This includes the suspension momentum equations and a transport equation for the solid volume fraction. The recent work of [3] implies that the non-Newtonian effects can be introduced to the SBM through adopting a local effective viscosity. With shear-thinning viscous suspending fluids, suspensions may vary on the particle scale from Stokesian behavior to inertial behavior depending on the shear rate. Here, we include inertial effects by following the approach of Koch and co-workers [4, 5], targeted primarily at dense inertial gas suspensions, but also applicable to liquid suspensions with sufficiently large density ratio. The idea is to include the growth of the fluctuating component of the particle velocity $\sqrt{\Theta}$ into the suspension stress.

We adopt the Hele-Shaw/lubrication approach to model fracture flows. In deriving this type of model equation the assumption is made that the velocity field and gradients can be scaled differentially, according to the fracture aspect ratio. We define dimensionless coordinates and velocity components as follows: $(x,y,z) = (\hat{x}/\hat{L}_t, \hat{y}/\hat{D}, \hat{z}/\hat{L}_t), (u,v,w) = (\hat{u}/\hat{U}_0, \delta_t\hat{v}/\hat{U}_0, \hat{w}/\hat{U}_0)$. Evidently, if we consider all $O(\delta_t)$ terms we invite suffocating geometric complexity, quite apart from the additional normal stresses and shear stress contributions. Neglecting terms strictly of $O(\delta_t)$, we see that the Hele-Shaw type of model is recovered as $\delta_t \to 0$ at fixed Re. If Re is $O(1)$ then anyway the Hele-Shaw type of averaging is valid, but in practice many fracturing flows have large Re. Insofar as the bulk suspension flow is concerned, the terms of $O(\delta_t Re)$ are probably the most important to include at high flow rates. These terms change the form of the momentum balance. Equally, at higher flow rates we would expect larger gradients in shear rates and thus inertial effects to appear at the particle scale in sheared layers nearer the walls. In summary, it appears that two types of model are feasible within this framework, according partly to the fracture geometry, fluid rheology and flow rates. Here we effectively assume $\delta_t \sim 1/L$, that Re is moderate and that the fracture width $\hat{D}$ is small enough for $\delta_p^2 \gg \delta_t$. We can show that the following model equations result:

$$0 = \nabla\cdot\mathbf{u} \tag{2}$$

$$0 = \circ\,\frac{\partial p_f}{\partial x} + \frac{\partial}{\partial y}\left[\eta_f\eta_s\frac{\partial u}{\partial y}\right], \tag{3}$$

$$0 = \circ\,\frac{\partial p_f}{\partial y} \tag{4}$$

$$0 = \frac{Re}{Fr^2}\phi\circ\,\frac{\partial p_f}{\partial z} + \frac{\partial}{\partial y}\left[\eta_f\eta_s\right]\frac{\partial w}{\partial y}\Big], \tag{5}$$

$$\begin{aligned}\frac{\partial\phi}{\partial t} &= \circ\,\nabla\cdot[\phi\mathbf{u}] + \frac{\delta_p^2}{\delta_t}\frac{\partial}{\partial y}\left[\phi(1\circ\,\phi)M\left(\left|\frac{\delta_p^2\phi Re}{Fr^2}\right|\right)\left(\lambda_y\frac{\partial\Pi}{\partial y}\circ\,\frac{\mathbf{f}_{D'},y}{\delta_p^2}\right)\right]\\ &\quad + \frac{\delta_p^2 Re}{Fr^2}\frac{\partial}{\partial z}\left[\phi^2(1\circ\,\phi)M\left(\left|\frac{\delta_p^2\phi Re}{Fr^2}\right|\right)\right]\end{aligned} \tag{6}$$

$$0 = \eta_f[\eta_s\circ\,1][u_y^2 + w_y^2]\circ\,12\eta_f\alpha(\phi,\Theta)\Theta + \delta_p^2\frac{\partial}{\partial y}\left[3\eta_f\kappa(\phi,\Theta)\frac{\partial\Theta}{\partial y}\right]. \tag{7}$$

This model appears to allow potential for analysis. We use this model and apply mathematical techniques to make estimates of the streamwise solid dispersion in various relevant scenarios of fracturing flows with yield stress suspending fluids.

References

[1] Nott, P.R. & Brady, J.F, Pressure-driven flow of suspensions: simulation and theory. J Fluid Mech **275**, 157–199 (1994).

[2] Krieger, I.M. Rheology of monodisperse lattices. Adv. Coll. Int. Sci. **3**, 111–136, (1972).

[3] Dagois-Bohy, S., Hormozi, S., Guazzelli, E. & Pouliquen, O. Rheology of dense suspensions of non-colloidal spheres in yield-stress fluids. J. Fluid Mech. **776**, R2 1–11 (2015).

[4] Sangani, A.S., Mo, G.B., Tsao, H.K. & Koch, D.L., Simple shear flows of dense gas solid suspensions at finite Stokes numbers, J. Fluid Mech. **313**, 309–341 (1996).

[5] Wylie, J.J. , Koch, D.L. & Ladd, A.J.C. Rheology of suspensions with high particle inertia and moderate fluid inertia, J. FluidMech. **480**, 95–118, (2003).

[6] Leighton, D. &Acrivos, A. The shear-induced migration of particles in concentrated suspensions. J. Fluid Mech. **181**, 415–439, (1987).

EFFECTS OF CROSS-SECTIONAL ASPECT RATIO OF FLAT PLATE ON FLOW CHARACTERISTICS

Donghwi Lee *[1], Taku Nonomura[2], Akira Oyama[2], and Kozo Fujii[2]

[1]*Department of Aeronautics and Astronautics, The university of Tokyo, Sagamihara, Kanagawa, Japan*
[2]*Institute of Space and Astronautical Science, JAXA, Sagamihara, Kanagawa, Japan*

Summary This study conducts two-dimensional unsteady laminar simulation and investigates effects of flat plates aspect ratio on the flow field characteristics under the constant Reynolds number based on the plate thickness. The flat plate aspect ratios (t/c, t: plate thickness, c: plate chord length) are set to be 0.01, 0.025, 0.05, and 0.1. The Reynolds numbers based on the plate thickness (Re_t) are set to be 250 (laminar reattachment), and $1,000$ (turbulent reattachment). The results suggest that the effects of t/c can relatively be negligible at $Re_t = 250$. After formation of three-dimensional turbulent structures at $Re_t = 1,000$, however, the reattachment points move to downstream as t/c decreases. In this Re_t, the flow fields characteristics such as instantaneous flow, turbulent kinetic energy, and boundary layer near the leading edge are different depending on t/c.

INTRODUCTION

Characteristics of low Reynolds number (Re) flow are drastically changed with a little variation of the Re, so it is important to understand the flow field characteristics in a wide range of low Re. Especially, one of the important features of the low Re flow is a formation of laminar seperation bubble (LSB) because it affects not only the flow field characteristics but also the mechanical efficiency (e.g., airfoil aerodynamic performance). Thus, it is important to understand the characteristics of LSB such as flow fields around the LSB or the length of LSB. Figure 1 shows the comparison of reattachment points of several previous experiment and numerical results[1]. The reattachment points are normalized by the plate thickness with respect to the thickness based Reynolds numbers (Re_t)[1]. It is commonly observed that the flow remains two-dimensional structures in a relatively low Re_t ($Re_t < 320 \sim 400$). The separated shear layer reattaches as laminar state in this Re_t. As increase in Re_t, the three-dimensionality appears at $Re_t > 320 \sim 400$ and the shear layer reattaches as turbulent state[2, 3]. In this Re_t region, all the results show the movement of reattachment points to the leading edge, but their values are not quantitatively consistent. One more point that many experimental studies have set the Reynolds numbers based on the plate thickness, because the plate length based Reynolds number cannot be specified by assuming as an infinite length. It has not been discussed, however, that comparisons of the reattachment point based on the plate thickness are reasonable or not. The discussion is also insufficient that these quantitative discrepancies with respect to the reattachment points is resulted by the physical phenomena depending on the plate thickness or error of each measurement method. Therefore, numerical experiments are conducted to investigate the effects of aspect ratio of flat plate on flow field characteristics under the constant Re which is based on the plate thickness.

COMPUTIATIONAL SETUP

The 3rd order MUSCL[4] with SHUS[5] are employed for evaluating the convective terms. The viscous terms are computed by the 2nd order central differencing without any turbulence model. The 2nd order backward differencing converged by the ADI-SGS method[6] is adopted for time integration. The methods used in this study have been verified by comparison with the Large-eddy simulation results[1] in terms of the reattachment point predictability, reattachment state, etc. The freestream Mach number is set to be 0.2 with zero turbulence intensity. Two cases of Re_t are conducted: $Re_t = 250$ for laminar reattachment and $Re_t = 1,000$ for turbulent reattachment. The flat plate aspect ratios (t/c, t : plate thickness, c : plate chord length) are set to be 0.01, 0.025, 0.05, and 0.1.

RESULTS

VERIFICATION OF NUMERICAL EXPERIMENTS

In performing numerical experiments, it should be firstly considered some factors which may produce numerical errors (e.g., the number of grid points N, time step Δt, and minimum grid spacing) to reduce numerical errors and prevent misleading of the discussion. Thus, the verification of simulations is conducted using $t/c = 0.05$ case. The results indicate that grid points used in this study (streamwise $\times$ wall-normal direction $= 471 \times 359$) are sufficient in terms of discussing the reattachment points. It is shown that the maximum CFL number should be lower than 1.2, and minimum grid spacing in the wall-normal direction Δy is sufficient in $\Delta y < 0.1/\sqrt{Re_c}$. One more important factor which should be considered is the minimum grid spacing in the streamwise direction near the leading edge Δx, because the resolution of shear layer thickness which flows

*Corresponding author. Email: lee@flab.isas.jaxa.jp

around the corner of the leading edge has significant effects on the accuracy of reattachment point predictability and the formation of shear layer is affected by the boundary layer resolution at the leading edge. The results show that $\Delta x = 3.5\Delta y$ is sufficient. Using the criteria above, four types of grids are prepared in each t/c. It is ensured that the quality of the grids near the leading edge (N, Δx, and Δy) is exactly same in each case when shown by the thickness base viewpoint. Detailed grids and verification results will be demonstrated at the presentation.

EFFECTS OF THE ASPECT RATIO OF FLAT PLATE TO THE REATTACHMENT POINTS

The present simulation results are also superimposed in Fig. 1. The results indicate that the effects of t/c of the plate can be ignored at $Re_t = 250$ where the laminar reattachment appears. At the turbulent reattachment Re_t ($Re_t = 1,000$), however, the reattachment points move downstream as t/c decreases. Figure 2 shows the instantaneous spanwise vorticity flow fields near the leading edge at $Re_t = 1,000$. From the figure, location of the spanwise vortex shedding from the shear layer moves downstream as decreasing in t/c. It can be considered that some flow fields characteristics in the downstream are different depending on t/c at this Re_t, and downstream flow affects the characteristics near the leading edge flows. Detailed results such as averaged and instantaneous flow fields, turbulent kinetic energy distributions, and boundary layer characteristics (displacement and momentum thickness) will be shown at the presentation.

CONCLUSIONS

The effects of flat plates aspect ratio (t/c, t : plate thickness, c : plate chord length) on the flow field characteristics under the constant Reynolds number based on the plate thickness (Re_t) are investigated by two-dimensional unsteady simulation. Four cases of t/c are conducted at the two different Reynolds numbers ($Re_t = 250$ and $Re_t = 1,000$). The results show that the effects of t/c can be negligible at $Re_t = 250$. At $Re_t = 1,000$, however, the reattachment points move to downstream as t/c decreases. In this Re_t, some flow fields characteristics (instantaneous flow, turbulent kinetic energy, and boundary layer) change near the leading edge. Therefore, it can be considered that the variation of the reattachment points at the turbulent reattachment Re_t which are shown in Fig. 1. might be largely affected by different physical phenomena depending on the t/c.

References

[1] Lee D. et al.: International Conference of Jets, Wakes and Seperated Flows. Stockholm, Sweden 2015.
[2] Sasaki K., Kiya M.: J. Fluid Eng. 113:405-410, 1991.
[3] Lee D. et al.: Phys. Fluids 27:023602, 2015.
[4] van Leer B.: J. Comput. Phys. 23:101-136, 1979.
[5] Shima E., Jounouchi T.: Proceedings of the 14th NAL Symposium on Aircraft Computational Aerodynamics, 1997.
[6] Fujii K.: Proceedings of the International CFD Workshop on Supersonic Transport Design. Tokyo, Japan 1998.

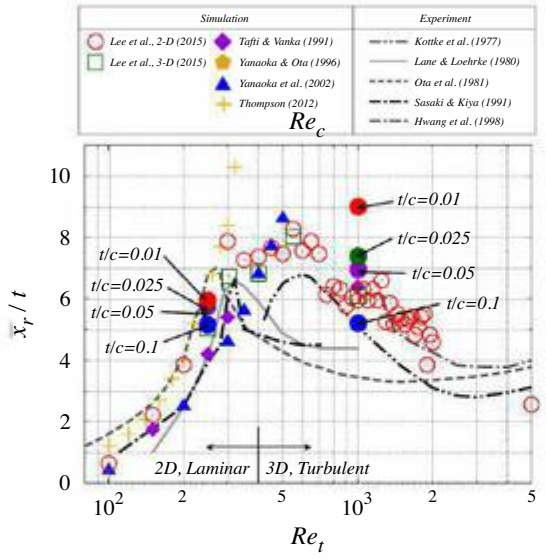

Figure 1: Comparison of the reattachment points normalized by the plate thickness[1].

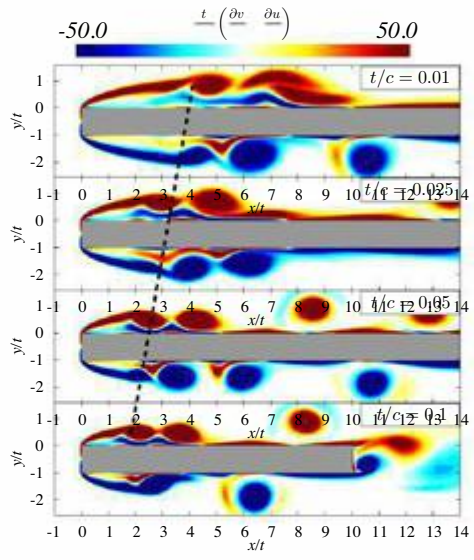

Figure 2: Instantaneous spanwise vorticity flow fields at $Re_t = 1,000$.

A RECIPROCAL THEOREM FOR CONVECTIVE SCALAR TRANSFER FROM A PARTICLE IN LINEAR FLOWS

Vahid Vandadi, Saeed Jafari Kang, and Hassan Masoud*
Department of Mechanical Engineering, University of Nevada, Reno, Reno, Nevada, USA

Summary We develop a reciprocal theorem for convective scalar transfer from an arbitrary-shaped particle in linear flows. In particular, we obtain a closed-form expression for the total transfer rate from a particle with a non-uniform surface distribution given the known solution of the scalar field for a constant surface distribution. Hence, eliminating the need for calculating a detailed scalar field corresponding to the non-uniform boundary condition. Employing this formula, we analytically calculate the convective heat transfer from a sphere with an arbitrary surface temperature in Stokes flow in the limits of small and large Péclet numbers.

INTRODUCTION

Since the seminal works of Acrivos [1], Acrivos and Taylor [2], and Brenner [3] more than half a century ago, there has been a significant theoretical progress in the area of transport phenomena in creeping and potential flows (see e.g. [4]). However, a vast majority of analytical results for the rate of convective heat and mass transfer from an object have been derived under the assumption of uniform boundary condition on the surface of the particle. This limits the applicability range of such results as in many practical applications convective transfer takes place from particles with non-uniform surface conditions.

Here, we introduce a reciprocal theorem for convective heat and mass transfer from an arbitrary-shaped particle in steady linear (e.g. Stokes and potential) flows. Specifically, we derive a formula relating the total transfer rate from a particle with a non-uniform surface distribution to the solution of the temperature/concentration field for a constant surface distribution. The formula enables us to readily extend the existing analytical results to accommodate non-uniformities in surface boundary condition without solving for new scalar fields. We note that the Lorentz reciprocal theorem has been used in a similar fashion for calculating drag, torque, and propulsion speed in Stokes flow without developing detailed flow fields (see e.g. [5, 6, 7, 8]). In the following, we explain how Green's second identity (a reciprocal relation between two scalar fields [9, 10]) is used to derive a closed-form expression for convective scalar transfer from a particle in a linear flow.

DERIVATION OF THE RECIPROCAL THEOREM

Consider a steady linear (e.g. Stokes or potential) flow with velocity $\boldsymbol{u}$ past a stationary rigid particle of arbitrary geometry. Let ϕ and ψ be two diffusing scalar fields that vanish at infinity and are transported, respectively, by the velocity fields $\boldsymbol{u}$ and $\circ\ \boldsymbol{u}$. Then, their Laplace transforms $\tilde{\phi}$ and $\tilde{\psi}$ satisfy

$$s\tilde{\phi} \circ\ \phi_0 + \boldsymbol{u}\cdot\nabla\tilde{\phi} = D\nabla^2\tilde{\phi}, \tag{1}$$

$$s\tilde{\psi} \circ\ \psi_0 \circ\ \boldsymbol{u}\cdot\nabla\tilde{\psi} = D\nabla^2\tilde{\psi}, \tag{2}$$

where D is the diffusion constant and ϕ_0 and ψ_0 are initial conditions at $t = 0$. Note that $\circ\ \boldsymbol{u}$ satisfies the reversed flow far from the particle as the velocity field is linear. Multiplying (1) by $\tilde{\psi}$ and (2) by $\tilde{\phi}$ and subtracting the resulting equations yield

$$\tilde{\phi}\psi_0 \circ\ \tilde{\psi}\phi_0 + \nabla\cdot\left(\tilde{\psi}\tilde{\phi}\boldsymbol{u}\right) = D\left(\tilde{\psi}\nabla^2\tilde{\phi} \circ\ \tilde{\phi}\nabla^2\tilde{\psi}\right). \tag{3}$$

According to Green's second identity

$$\int_V \left(\tilde{\psi}\nabla^2\tilde{\phi} \circ\ \tilde{\phi}\nabla^2\tilde{\psi}\right)\mathrm{d}V = \int_{S_p+S_\infty}\left[\tilde{\psi}(\nabla\tilde{\phi}\cdot\boldsymbol{n}) \circ\ \tilde{\phi}(\nabla\tilde{\psi}\cdot\boldsymbol{n})\right]\mathrm{d}S, \tag{4}$$

where V, S_p, and S_∞ denote the domain volume, surface of the particle, and bounding surfaces at infinity, respectively. Substituting from (3) into (4) and applying divergence theorem, we obtain

$$\int_V \left(\tilde{\phi}\psi_0 \circ\ \tilde{\psi}\phi_0\right)\mathrm{d}V + \int_{S_p}\tilde{\psi}\tilde{\phi}\,(\boldsymbol{u}\cdot\boldsymbol{n})\,\mathrm{d}S = D\int_{S_p}\left[\tilde{\psi}(\nabla\tilde{\phi}\cdot\boldsymbol{n}) \circ\ \tilde{\phi}(\nabla\tilde{\psi}.\boldsymbol{n})\right]\mathrm{d}S. \tag{5}$$

Integrals over S_∞ are zero since $\tilde{\psi}\tilde{\phi}$, $\tilde{\psi}(\nabla\tilde{\phi}\cdot\boldsymbol{n})$, and $\tilde{\phi}(\nabla\tilde{\psi}.\boldsymbol{n})$ decay faster than the inverse distance squared in the far field [11].

*Corresponding author. Email: Hassan.Masoud@masoud-lab.academy

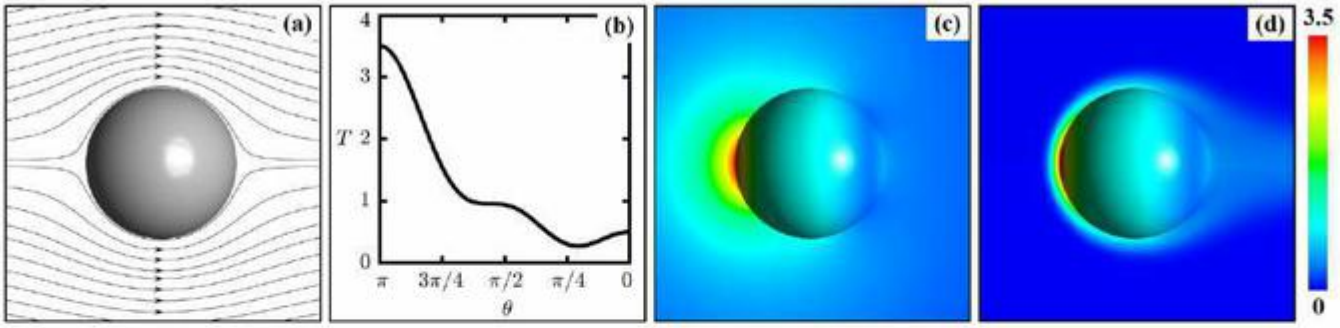

Figure 1: (a) The cross-sectional streamline for a uniform Stokes flow past a sphere with non-uniform surface temperature. (b) Distribution of temperature on the surface of the sphere. (c) and (d) The cross-sectional steady-state distribution of temperature corresponding to Péclet numbers $\mathrm{Pe} = 0.5$ and $\mathrm{Pe} = 100$, respectively. The temperature vanishes at infinity and its average value on the surface of the sphere is set to $T_{\mathrm{ave}} = 1$.

Given $\phi_0 = \psi_0 = 0$ everywhere in V except on S_p, the first integral on the left-hand side of (5) is zero. The second integral also vanishes since $\boldsymbol{u}$ is zero on S_p. Hence,

$$\int_{S_p} \psi \left(\nabla\phi \cdot \boldsymbol{n} \right) \mathrm{d}S = \int_{S_p} \phi \left(\nabla\psi \cdot \boldsymbol{n} \right) \mathrm{d}S. \tag{6}$$

Assuming ψ is uniform on S_p, we have

$$q_\phi = \int_{S_p} \phi \left(\frac{q''_\psi}{\psi} \right) \mathrm{d}S, \tag{7}$$

where $q_\phi = -D \int_{S_p} \left(\nabla\phi \cdot \boldsymbol{n} \right) \mathrm{d}S$ and $q''_\psi = -D \left(\nabla\psi \cdot \boldsymbol{n} \right)$. The left-hand side of (7) represents the instantaneous total convective flux q_ϕ from the particle corresponding to an arbitrarily non-uniform surface distribution ϕ_s. The right-hand side of (7) is a surface integral that only involves ϕ_s, ψ_s, and the local convective flux q''_ψ. The latter denotes the transfer due to the reversed flow (i.e. $-\boldsymbol{u}$) and a constant surface distribution ψ_s. Simply put, equation (7) relates the average quantity of interest q_ϕ to the boundary information (ϕ_s) and the solution of a much simpler problem ψ, which is often already known. Remember that conventionally $\tilde{}_\phi$ is directly calculated from $\int_{S_p} \left(\nabla\phi \cdot \boldsymbol{n} \right) \mathrm{d}S$. However, evaluating this integral requires the detailed knowledge of ϕ, which is analytically much more challenging to obtain than ψ. As an application of (7), we will extend the analytical results of Acrivos and Taylor [2] for temperature distribution around a sphere of constant temperature in a uniform Stokes flow to calculate convective heat transfer from a sphere with a non-uniform surface temperature (see figure 1).

References

[1] Acrivos A.: Solution of the Laminar Boundary Layer Energy Equation at High Prandtl Numbers. Phys. Fluids 3:657, 1960.

[2] Acrivos A., Taylor T. D.: Heat and Mass Transfer from Single spheres in Stokes Flow. Phys. Fluids 5:387, 1962.

[3] Brenner H.: Forced Convection Heat and Mass Transfer at Small Peclet Numbers from a Particle of Arbitrary Shape. Chem. Eng. Sci. 18:109-122, 1963.

[4] Leal L. G.: Advanced Transport Phenomena: Fluid Mechanics and Convective Transport Processes. Cambridge University Press, 2007.

[5] Leal L. G.: Particle Motions in a Viscous Fluid. Ann. Rev. Fluid Mech. 12:435476, 1980.

[6] Stone H. A., Samuel A. D. T.: Propulsion of Microorganisms by Surface Distortions. Phys. Rev. Lett. 77: 41024104, 1996.

[7] Masoud H., Stone H. A.: A Reciprocal Theorem for Marangoni Propulsion. J. Fluid. Mech. 741:R4, 2014.

[8] Stone H. A., Masoud H.: Mobility of Membrane-Trapped Particles. J. Fluid. Mech. 781:494505, 2015.

[9] Brenner H., Haber S.: Symbolic Operator Solutions of Laplace's and Stokes' Equations Part I Laplace's Equation. Chem. Eng. Commun., 27:283-295, 1984.

[10] Brenner H., Haber S.: Heat Transfer from a Rigid Sphere in a Nonuniform Flow and Temperature Field. Int. J. Heat Mass Transfer, 37:2069-2076, 1994.

[11] Brenner H.: On the Invariance of the Heat-Transfer Coefficient to Flow Reversal in Stokes and Potential Streaming Flows Past Particles of Arbitrary Shape. J. Math. Phys. Sci. 1:173, 1967.

FLOW TROUGH THE CHANNEL COATED WITH CHARGED POROUS MEDIA

Pavel Sumets[1], John Cater[2], David Long[3], and Richard Clarke [*4]
[1,2,4]*Department of Engineering Science, University of Auckland, Auckland, New Zealand*
[3]*Auckland Bioengineering Institute, University of Auckland, Auckland, New Zealand*

Summary We consider steady state flow of a viscous Newtonian fluid containing solution of water and ions through a wavy wall channel coated with electrically charged poroelastic layer. This is relevant to applied problems such as blood flow through a post-capillary vessel lined with the endothelial glycocalyx layer. A triphasic mixture theory is used for the mathematical description of the mechano-electrochemical behavior of the charged porous layer. The governing equations are solved numerically by means of combined Boundary Element and Finite Element Methods as well as analysed analytically using an asymptotic analysis. We examine the impact of geometry and electrical charge effect on hydrodynamics, as well as the role of the EGL in transmitting fluid shear stress exerted on the vessel wall.

INTRODUCTION

Past studies have shown that endothelial cells that line inner capillary wall surfaces are coated with a layer of macromolecules (the Endothelial Glycocalyx Layer)[1]. This layer has a gel-like structure and is comprised of polysaccharides. It is established that this layer acts as a mechanotransducer of fluid shear stress (FSS) to the endothelial cytoskeleton, including the resulting biochemical responses. In addition, the presence of the EGL can provide vessels with an anti-adhesive inner lining when a white blood cell pass through the vessel. Indirect measurements of the mechanical properties of the EGL show the layer is deformable and can restore its shape after being deformed by an applied force. However, there is some debate around the dominant mechanism by which this layer restores. There are two types of models accounting for the restoring mechanism, namely, elastohydrodynamic and mechano-electrochemical models. According to the elastohydrodynamic approach, the dominant source of restoration is due to the inherent elasticity of the EGL. The layer is modeled as a poroelastic media and the biphasic mixture theory is applied to mathematically describe the phenomenon.

The mechano-electrochemical model takes into account electrical properties of the EGL which contain electrostatically charged macromolecules hydrated in an electrolytic fluid. Electrostatic forces and associated osmotic pressure represent an additional restoring force for an EGL deformed by the fluid flow or passing blood cell. A triphasic mixture theory (TMT) is used for the mathematical description of the mechano-electrochemical behavior of the EGL. The TMT combines the physico-chemical theory for ionic and polyionic solutions with the biphasic theory for porous media [2]. This theory is successfully applied to model swelling and deformation of hydrated porous biological materials [3, 4]. In the absence of any flow, a pseudo-equilibrium approximation is often made for the mechano-electrochemical dynamics [3, 4, 5]. This means that the electroneutrality condition along with the Boltzmann distribution for ions is assumed. However, background flows introduce a streaming potential which modifies the transport of ions (the distributions of which can no longer be assumed to be Boltzmann), and hence generates an electric field. In this study we, for the first time, tackle the full problem incorporating flow, electrochemical effects, and EGL elasticity. Considering this coupled problem allows us to gauge the effect that electrochemical effects have on the shear stresses exerted on a vessel's walls, and hopefully ultimately inform the debate around the relative importance of different effects in EGL restoration.

MODEL FORMULATION

In the problem considered the blood is modeled as a solution containing water and salt ions (Na, Cl). The vessel is coated with the EGL which is considered as a negatively charged porous layer reflecting the electrical property of proteoglycans (PG). We consider two sets of non-dimensional equation: for the luminal region (index l) where blood flows unhindered

$$\nabla^2 \boldsymbol{v}_l = \nabla p_l \circ \ \alpha_l \nabla^2 \varphi_l \nabla \varphi_l, \tag{1}$$

$$\nabla \cdot [\gamma_{\pm} c_{l\pm} \boldsymbol{v}_l \circ \ \nabla c_{l\pm} \mp c_{l\pm} \nabla \varphi_l] = 0, \tag{2}$$

$$\circ \ \delta \nabla^2 \varphi_l = c_{l+} \circ \ c_{l-}, \tag{3}$$

and for the layer region having fluid (ϕ_f) and solid (ϕ_s) volume fractions

$$\nabla^2 \boldsymbol{v} = \nabla p \circ \ \alpha \nabla^2 \varphi \nabla \varphi + \hat{\chi} c_s \nabla \varphi + \chi \boldsymbol{v}, \tag{4}$$

$$\frac{1}{1 \circ \ 2\nu} \nabla \cdot (\nabla \boldsymbol{u}) + \nabla^2 \boldsymbol{u} = \phi \nabla p \circ \ \hat{\chi} c_s \nabla \varphi \circ \ \chi \boldsymbol{v}, \tag{5}$$

$$\nabla \cdot [\gamma_{\pm} c_{\pm} \boldsymbol{v} \circ \ \nabla c_{\pm} \mp c_{\pm} \nabla \varphi] = 0, \tag{6}$$

$$\circ \ \delta \nabla^2 \varphi = c_+ \circ \ c_- \circ \ c_s. \tag{7}$$

*Corresponding author. Email: rj.clarke@auckland.ac.nz

Here $\phi = \phi_s/\phi_f$, $\chi = KH^2/(\phi_f \mu_f)$, $\hat{\chi}_l = c_0 kTH/(\mu_f V)$, $\hat{\chi} = \hat{\chi}_l/\phi_f$, $\alpha_l = \epsilon k^2 T^2/(\mu e^2 VH)$, $\alpha = \alpha_l/\phi_f$ and $\delta = \epsilon kT/(c_0 e^2 H^2)$ are the non-dimensional parameters. Constant c_s models negative charge distribution fixed on the solid phase (i.e. EGL). The other notations are the following: $\boldsymbol{v}$ is the fluid velocity vector; μ_f is the fluid viscosity; p is the pressure; φ is the electric potential; $c_\pm$ positive (negative) mobile ions concentration; K is the hydraulic resistivity; $\boldsymbol{u}$ is the elastic displacement (assumes small strain); ν is Poisson's ratio; c_0 is the reference concentration; H is the characteristic length; constants $\varepsilon, e, k, T, D_\pm$ are the dielectric permittivity, elementary charge, Boltzmann constant, absolute temperature and ions diffusions coefficients respectively. The governing equations for the lumen region are given by the modified Stokes equation incorporating electric forcing term, extended Nernst-Plank equation for the ion diffusion and the Gaussian law for the electric potential. As to the EGL region, we obtain the Brinkman type equation for the fluid phase and Navier type equation for the solid phase both having the additional electrical forcing term. The small parameter δ captures the non-dimensional dielectric permittivity .

SOLUTION METHOD

The resulting nonlinear problem is solved using a Boundary Element Method (BEM) scheme for the momentum equations combined with Finite Element Method (FEM). The use of a hybrid scheme allows us to reduce computational cost. The nonlinear system is built in parallel across 48 CPUs, and solved iteratively.

RESULTS

Parameters values for the numerical simulation were chosen to be representative of a blood capillary having wavy wall shape. Simulation results have shown some features which are characteristics of the dynamics. Under the fluid flow state the electroneutrality condition is maintained in both lumen and EGL regions except in the neighborhood of the interface boundary. Within this zone we observe large electric potential and concentration gradients resulting in a nonlinear osmotic pressure distribution across the vessel. The smaller value of δ the narrower transitional zone and greater the gradients therein. The simulation was carried out with $\delta = 10^{-3}$ but physiologically it can reach the value of 10^{-6}. For such an extreme parameter value an asymptotic analysis was undertaken. The charge effect in the EGL along with wavy geometry leads to nonuniform fluid shear stress distribution exerted on the vessel wall (see Figure 1) different to that exerted in the absence of charge effects. It is believed that the EGL play an important role in transmitting mechanical signals to the underlying endothelial cells, and we shall report on how this mechanotransduction is predicted by our simulations to be affected by the EGL's charge.

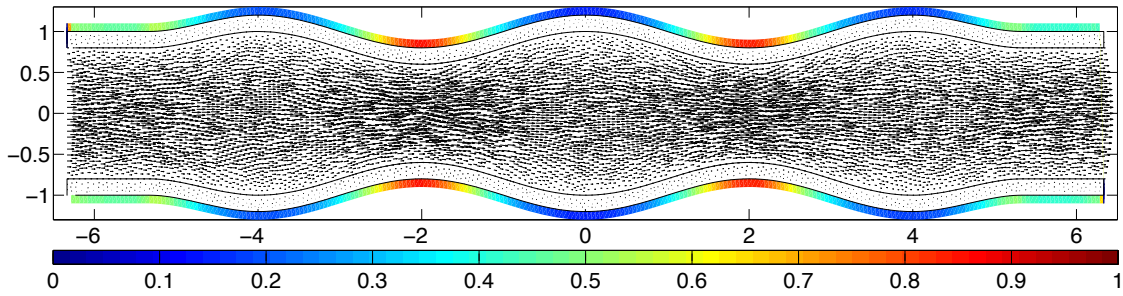

Figure 1: Varicose - type vessel showing flow field and fluid shear stress exerted on the solid wall. The scale beneath corresponds to the non-dimensional stress magnitude.

References

[1] Weinbaum S., Tarbell J. M., Damiano E.R.: The structure and function of the endothelial glycocalyx layer. Annu. Rev. Biomed. Eng., 9:121-167, 2007.

[2] Lai W. M., Hou J. S., Mow V. C.: A triphasic theory for the swelling and deformation behaviors of articular cartilage. Journal of Biomechanical Engineering, 113:245-258, 1991.

[3] Buschmann M. D., Grodzinsky A. J.: A molecular model of proteoglycan-associated electrostatic forces in cartilage mechanics. Journal of Biomechanical Engineering, 117:179-192, 1995.

[4] Damiano E. R., Stace T. M.: A mechano-electrochemical model of radial deformation of the capillary glycocalyx. Biophys. J., 82(3):1153-1175, 2002.

[5] Ehlers W., Karajan N., Markert B.: An extended biphasic model for charged hydrated tissues with application to the intervertebral disc. Biomech. Model. Mechanobiol., 8:233-251, 2009.

FM11 - Micro- and Nano-fluidics

TS.FM11-1.01	Sbragaglia, Mauro - Mesoscopic dynamics of droplets and emulsions in a microchannel (INVITED)	1192
TS.FM11-1.02	Juel, Anne - Sensitivity of Saffman-Taylor fingers to channel depth perturbations	1194
TS.FM11-1.03	Pawłowska, Sylwia - Mobility of highly deformable hydrogel nanofilaments	1196
TS.FM11-1.04	Silber-Li, Zhanhua - Swimming Mechanicsms of Janus Micromotors: From Self-diffusiophoresis to Bubble Propulsion	1198
TS.FM11-1.05	Chung, Aram - Inertial microfluidics for manufacturing and quantitative single-cell studies (INVITED)	1200
TS.FM11-1.06	Neild, Adrian - Ultrasonic Force Potential Wells for Trapping Arrays of Single Cells - One Cell Per Well (OCPW)	1202
TS.FM11-2.01	Pierini, Filippo - Particles double layer evaluation by atomic force microscopy-optical tweezers	1204
TS.FM11-2.02	Kiani, Mohammad - A biomimetic microfluid assay for rapid screening of anti-inflammatory drugs (INVITED)	1206
TS.FM11-2.03	Hao, Pengfei - Growth and Departure of Condensation Microdroplets on Superhydrophobic Surfaces	1208
TS.FM11-2.04	Sun, Xiaoze - Experimentally observed flows in inkjet-printed liquid rivulets	1210
TS.FM11-2.05	Kahouadji, Lyes - Massively parallel direct numerical simulation of 3D jet flows	1212
TS.FM11-3.01	Rosello, Maxime - Influence of nozzle shape on the break-up of non-newtonian ink jets	1214
TS.FM11-3.02	Duan, Huiling - Underwater superhydrophobiciy: Fundamentals and applications (INVITED)	1216
TS.FM11-3.03	Nold, Andreas - From the nano- to the macroscale - Bridging scales for the moving contact line problem	1218
TS.FM11-3.04	Park, Joonsik - Measurement of apparent slip near a high speed receding contact line on a hydrophobic surface	1220
TS.FM11-3.05	Fullana, Jose Maria - Effect of the lubrication film on the droplet dynamics in a Hele-Shaw microchannel	1222
PO.FM11-1.01.61	Chatterjee, Krishnashis - Slip flow in collapsing microchannels	1224
PO.FM11-1.02.62	Chen, Han - ACEO mixing of fluids in microchannels with asymmetric electrodes	1226
PO.FM11-1.03.63	Hou, Likai - Osmolarity-controlled swelling behaviors of dumbbell double emulsions	1228
PO.FM11-1.04.64	Hsieh, Ming-Che - A new flow control method based on multi-resonance valveless micropump	1230
PO.FM11-1.05.65	Hu, Guoqing - Inertial lift on a sphercial particle in microchannels	1232
PO.FM11-1.06.66	Juric, Damir - 3D plug formation in T-junctions & complex cross shaped microchannels	1234
PO.FM11-1.07.67	Lai, Kuan-Ruei - Optimal electro-osmotic pumping of a micro-duct with fin structures	1236
PO.FM11-1.08.68	McLaughlin, Richard - Geometric Control of Asymmetries in Passive Scalars Advected in Rectangular and Elliptical Pipes	1238
PO.FM11-1.09.69	Mitra, Surjyasish - Wetting Dynamics on under-liquid substrates	1240
PO.FM11-1.10.70	Naveira-Cotta, Carolina - Direct-inverse analysis of the biodiesel reaction in microreactors	1242

PO.FM11-1.11.71	Shi, Xinghua - Rotation-facilitated rapid transport of nanorods in mucosal tissues	1244
PO.FM11-1.12.72	Zheng, Xu - Probing the Non-Gaussianity in Confined Diffusion of Nanoparticles	1246
PO.FM11-1.13.73	Żuk, Paweł - From rheology to molecular detail - viscosity of suspension of complex molecules	1248

MESOSCOPIC DYNAMICS OF DROPLETS AND EMULSIONS IN A MICROCHANNEL

M. Sbragaglia*[1], A. Scagliarini[2], M. Lulli[3], and M. Bernaschi[4]
[1]*Department of Physics & INFN, University of Rome "Tor Vergata", Italy*
[2]*Helmholtz-Institute Erlangen-Nunberg, Germany*
[3]*Department of Physics, University of Rome "Tor Vergata", Italy*
[4]*Istituto per le Applicazioni del Calcolo CNR, Rome, Italy*

Summary By using fluid-kinetic simulations of confined and concentrated emulsion droplets in a rough microchannel, we explore the role of geometrical roughness in providing activation of plastic events close to the boundaries. Our results show the existence of a finite stress correlation scale, which can be mapped directly onto the cooperativity scale, recently introduced in the literature to capture non-local effects in the soft-glassy dynamics. Numerical simulations also allow to study the fluidity field, a continuous quantity which can be related to the rate of plastic events, thereby allowing us to establish a link between the mesoscopic plastic dynamics of the jammed material and the macroscopic flow behaviour.

INTRODUCTION

Soft-glassy materials (SGM) encompass a wide variety of systems such as emulsions, foams and granular media. The dynamics of these complex fluids is usually characterized by relatively large packing fractions, and the microscopic constituents (i.e., droplets for emulsions, bubbles for foams, etc) are *jammed* together so as to exhibit a yield stress, below which the material deforms elastically and above which it flows like a non-Newtonian fluid according to a Herschel-Bulkley rheology. The yielding behavior makes such systems as interesting for applications as challenging from the fundamental point of view of out-of-equilibrium statistical mechanics [1]. One challenging question concerns the formation of spatially non-homogeneous features, where the *global* rheology is not able to properly capture the complex space-time behavior of the system. It is now widely acknowledged that SGM flow as the result of a succession of plastic rearrangements, occurring when a local configuration of constituting micro-elements cannot sustain the accumulated stress and relaxes it in the form of long-ranged elastic waves which induce non-local behaviour in the rheological properties of the system. A number of theoretical frameworks have been developed recently accounting for these non-local effects (see [2, 3, 4] and references therein). One of them, the Kinetic Elasto-Plastic (KEP) model [4], captures the essential phenomenology in a mean-field spirit through a diffusion-relaxation equation for the *fluidity* field $f = \dot{\gamma}/\sigma$ (the ratio of the *local* shear rate and shear stress):

$$\xi^2 \Delta f = f \circ \ f_b, \tag{1}$$

where ξ is the so called *cooperativity length*, quantifying the spatial extension of the non-local correlations, and $f_b = f_b(\sigma)$ is the *bulk fluidity*, which is function of the shear stress σ only and equals the fluidity in absence of spatial heterogeneities. Together with (1), the other fundamental result of KEP, is the expected proportionality between f and the rate of occurrence of plastic events (whose prototypical instance, in 2d, is the so called $T1$, i.e. the neighbour-swapping of four adjacent droplets/bubbles), R_{T1}:

$$R_{T1} = \mathcal{A} f, \tag{2}$$

with $\mathcal{A}$ a constant, proportional to the elastic modulus G_0 in the KEP formulation. Equation (1) can be solved analytically in some simple cases, provided that a proper boundary condition is supplied for the fluidity at the wall. In a Couette flow, for instance, in which the stress is constant, a straightforward calculation for a Dirichlet-type boundary condition $f(\pm H/2) = f_w$ yields

$$f(z) = f_b + (f_w \circ \ f_b) \frac{\cosh(z/\xi)}{\cosh(H/(2\xi))} \tag{3}$$

whose corresponding velocity profile $v(z) = \sigma \int f(\zeta) d\zeta$ has been found consistent with numerical and experimental data [2]. Notice that a Von Neumann boundary condition of the type, e.g., $\frac{df}{dz}(\pm H/2) = 0$ (i.e. the wall does not act as a "source" of fluidity) would give $f = f_b$ everywhere, in clear contrast with all evidences. It must be noticed that, though it plays a crucial role, the fluidity at the wall f_w has no first principles ground and, as a matter of fact, enters the picture as a completely phenomenological free parameter of the model. Therefore, a challenging question, which certainly deserves thourough investigations, concerns the possibility of engineering a surface in such a way to control the fluidity, and hence the plastic activity, in its proximity. Nevertheless, only very few studies addressed the problem. Mansard *et al* [2] have performed experiments with dense emulsions flowing in microchannels with rough walls patterned with equally spaced posts of variable height, finding that slippage and surface fluidization depend non-monotonously on it. By means of numerical simulations,

*Corresponding author. Email: sbragaglia@roma2.infn.it

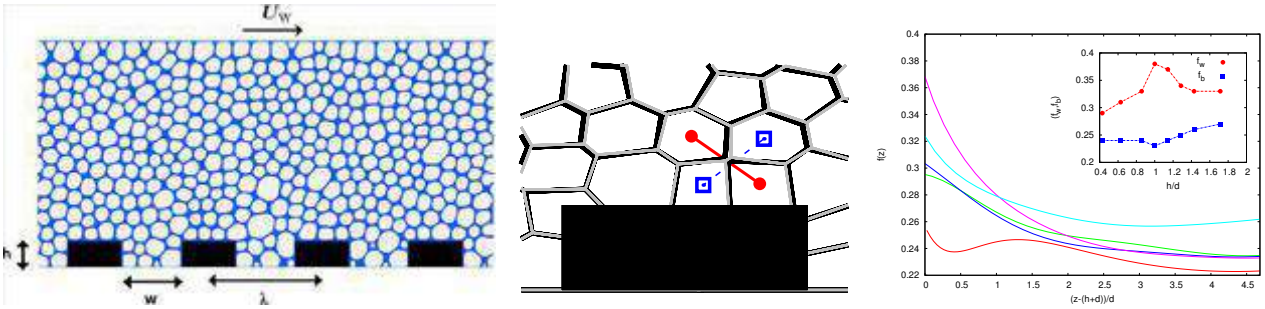

Figure 1: Left Panel: a Snapshot from lattice Boltzmann simulations in confined microchannels with structured roughness on the bottom wall. We report the main roughness parameters: λ, w and h refer to the roughness wavelength and inter-post width and height, respectively. Middle Panel: Sketch of a T1 plastic event. To systematically analyze plastic events, we perform a Voronoi tessellation from the centres of mass of the droplets. Following the Voronoi tessellation in time, we are able to identify T1 events and associated disappearing (red solid line) and appearing (blue dashed line) links. In grey (black) we indicate the Voronoi cells soon before (after) a T1 event. Right Panel: fluidity profiles for $\lambda/d = 7.3$ and $w/d = 3.5$ and various post heights. Inset: wall and bulk fluidity as a function of the post height.

based on the lattice Boltzmann method of Poiseuille flows of model soft-glassy materials [3], we have recently shown that there is a non-trivial dependence also on other geometrical parameters of the roughness (namely, the inter-post distance), and that the presence of the roughness may cause a breakdown of the proportionality relation predicted by KEP between fluidity and rate of occurrence of plastic events. To address in particular the latter problem in a more systematic way, in this paper we study two-dimensional Couette flows of dense emulsions. Our numerical setup is sketched in figure 1, where we show a snapshot from a simulation. The dense emulsion is confined between a top wall moving with the velocity U_w and a fixed bottom wall patterned with equally spaced posts of variable width w, height h and centre-to-centre inter-post distance λ. To gain insight into the statistics of plastic events, we perform a Voronoi tessellation (by using the *voro++* libraries [5]) of the centres of mass of the droplets so that we identify plastic rearrangements in the form of topological events, in which one "edge" of a given droplet collapses to zero length and neighbour droplets switching occurs. In connection with roughness-induced fluidisation of the material, deviations from the linear ($f(z) = f_b$) profile arise close to the wall, as highlighted in the right panel of figure 1, which is a signature of non-locality associated to a cooperative flow [4]. The enhanced friction effect induced by the roughness is accompanied by a triggered plastic activity which makes the dependence of the wall fluidity on the geometry of the wall roughness highly non-trivial.

CONCLUSIONS

Mesoscopic numerical simulations have been used to study the emergence of non-locality and the effects induced by roughness for the flow of concentrated emulsions in rough microchannels. Roughness effects are materialized through *enhanced friction* and *surface fluidization* induced by enhanced plastic activity. Numerical results are rationalized in the framework of KEP theory [4] for elastoplastic materials.

The authors kindly acknowledge funding from the European Research Council under the European Community's Seventh Framework Programme (FP7/2007-2013)/ERC Grant Agreement No. 279004. The authors kindly acknowledge useful discussions with R. Benzi.

References

[1] R. G. Larson, The Structure and Rheology of Complex Fluids, Oxford University Press (1999)

[2] V. Mansard, L. Bocquet & A. Colin, Boundary conditions for soft glassy flows: slippage and surface fluidization. Soft Matter **10**, 69846989 (2014)

[3] A. Scagliarini, M. Sbragaglia & M. Bernaschi, Mesoscopic simulation study of wall roughness effects in micro-channel flows of dense emulsions, *J. Stat. Phys.* **161**, 1482-1495 (2015)

[4] L. Bocquet, A. Colin & A. Ajdari, Kinetic theory of plastic flow in soft glassy materials, *Phys. Rev. Lett.* **103**, 036001 (2009)

[5] C.H. Rycroft, Voro++: A three-dimensional Voronoi cell library in C++, *Chaos* **19**, 041111 (2009)

SENSITIVITY OF SAFFMAN-TAYLOR FINGERS TO CHANNEL DEPTH PERTURBATIONS

Andres Franco-Gómez[1], Alice B. Thompson[2], Andrew L. Hazel[1] & Anne Juel[1 a)]
[1]*Manchester Centre for Nonlinear Dynamics, University of Manchester, Manchester, M13 9PL, United Kingdom*
[2]*Department of Mathematics, Imperial College London, London, SW7 2AZ, UK*

Summary We examine the sensitivity of Saffman-Taylor fingers to controlled variations in channel depth by investigating the effects of centred, rectangular occlusions in Hele-Shaw channels of increasing aspect ratio using a combination of experiments and numerical simulations of a depth-averaged lubrication model. The system is characterised by multiple modes of propagation which are first provoked for decreasing relative depth changes as the aspect ratio increases. We estimate that the required depth-changes become of the same order as the typical roughnesses of the experimental system (1 μm) for aspect ratios beyond 155, which we conjecture underlies the extreme sensitivity of experiments conducted in such (unoccluded) Hele-Shaw channels [1].

INTRODUCTION

Two-phase displacement flow in a confined geometry is a fundamental problem in fluid mechanics with applications in biomechanics, geophysics and industry. Following the classic work of Saffman and Taylor [2], the tube geometry that has attracted the most attention is the Hele-Shaw channel: an axially-uniform tube with rectangular cross-section of large width to height aspect ratio α. Only a single family of solutions is ever observed , although a depth-averaged model without surface tension possesses symmetric and asymmetric families of solutions. The introduction of finite surface tension selects a single family of stable, steadily propagating fingers, which depend uniquely on the modified capillary number $1/B=12\alpha^2 Ca$, where Ca corresponds to the ratio between viscous and surface tension forces [3]. However, the model also contains alternative families of multiple-tipped symmetric solutions, the Romero-Vanden-Broeck solutions [5], which are unstable. The Saffman-Taylor fingers have been observed up to a threshold in 1/B, which depends on the roughness of the experimental channel [4]. Motivated by the finger-selection problem, many groups have investigated the effects of geometric perturbations on two-phase flow in a Hele-Shaw channel, in the form of wires, threads or grooves, stabilising narrower fingers or generating dendrite growth. Unsteady finger propagation has also been observed in very large aspect ratio channels ($158 < \alpha < 490$) , where the fingertip exhibited significant lateral movement [1]. Fluctuations increased as the liquid films on the top and bottom channel walls thinned, and details of the wall roughness began to influence the system.

Here, we consider a Hele-Shaw channel with a small step change in depth provided by an axially-uniform rectangular block, which is known to support multiple stable modes of propagation, including asymmetric and oscillatory modes as well as the expected symmetric Saffman-Taylor mode [7]. We exploit this simple but robust system to probe the sensitivity of viscous fingering, because it enables transitions between multiple states to be clearly identified when the geometric variations are on a larger scale than the wall roughness.

EXPERIMENT

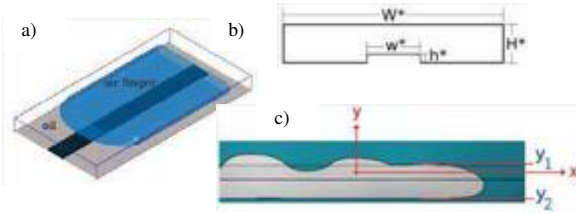

Fig. 1: (a) Experimental configuration. (b) Channel cross-section: $\alpha=W^*/H^*$, $\alpha_h=h^*/H^*$. (c) Example of an oscillating finger: finger width $\lambda=(y_1-y_2)/W^*$, finger offset $\delta=(y_1+y_2)/(2W^*)$.

The experimental channel is shown schematically in Fig.1(a-b). Air is drawn into the channel at one end by withdrawing silicone oil at constant flow rate from the other end, resulting in the steady propagation of an air finger that displaces the oil. The capillary number is $Ca=\mu U_f^*/\sigma$, where U_f^* is the dimensional speed of the finger, μ is the dynamic viscosity of the oil and σ the surface tension. Measurements are made of the finger width $\lambda=(y_1-y_2)/W^*$ and the finger offset $\delta=(y_1+y_2)/(2W^*)$ (see Fig. 1(c)).

DEPTH-AVERAGED MODEL

The variable-depth profile *b* is a smoothed step-like occlusion of fractional height α_h. The free-surface flow is modelled by the Reynolds lubrication equations with suitable boundary conditions [7]. The pressure jump at the interface becomes $\Delta p = \frac{1}{3Q}\left(\frac{1}{\alpha b}+\frac{\kappa}{\alpha}\right)$, where Q is the non-dimensional flow rate, κ the in-plane curvature and $Ca=QU_f$, with U_f the non-dimensional finger speed. For occluded channels, the cross-sectional curvature term 1/b is dynamically significant, and appears on the order of $\alpha_h\alpha^{-1}Q^{-1}$, whereas the effect of the in-plane curvature is on the order of $\alpha^{-2}Q^{-1}$.The model is integrated numerically using the finite-element library `oomph-lib`.

a) Corresponding author. Email: anne.juel@manchester.ac.uk

RESULTS

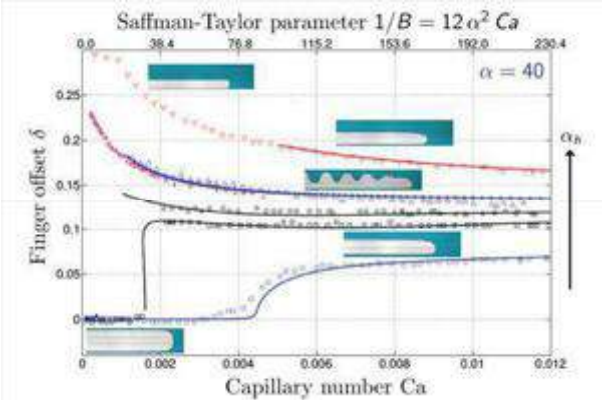

Fig. 2: Finger offset as a function of capillary number (1/B) for α =40. The symbols (lines) indicate experiments and numerical simulations, respectively. As the fractional depth α_h increases, the viscous finger undergoes supercritical then subcritical symmetry-breaking. Oscillatory fingers occur for a bounded range of α_h and Ca, respectively. The highest values of α_h yield a finger that localizes in one of the deeper side-channels.

We demonstrate that the depth-averaged model presented above is in quantitative agreement with the experimental results for $\alpha > 40$, provided that $Ca < 0.012$ – see Fig.2. The model is based on the lubrication approximation, which is expected to be valid for sufficiently high aspect ratio channels and small occlusion heights, in the limit of small Ca where the effect of liquid films on the top and bottom boundaries of the channel is negligible. Hence, this quantitative agreement means that we are able to use the model to follow the evolution of the solution structure in a large aspect ratio Hele-Shaw channel to that presented by [7] for a partially occluded channel with a high level of confidence that this represents the situation in the experiment. We believe that this evolution is the same for all aspect ratios which have been investigated, although we cannot confirm this without resorting to three-dimensional Stokes calculations. Thus we can demonstrate that the asymmetric and the double-tipped solutions observed in smaller aspect ratio channels by de Lozar et al. [8] and others are the unstable asymmetric Saffman-Taylor solutions and the first symmetric Romero-Vanden-Broeck solution having been stabilised by the presence of the occlusion – see Fig. 3. The occlusion height required to stabilise the asymmetric Saffman-Taylor solutions decreases with increasing aspect ratio, with the critical height for provoking pitchfork bifurcations being proportional to α^{-2} and that for Hopf bifurcations being proportional to α^{-1}.These scalings are consistent with the mechanisms underlying bifurcations described by Thompson et al. [7]. The pitchfork is principally associated with changes in viscous resistance, whereas the Hopf bifurcation is associated with coincidence of finger and occlusion edges.

a) b)

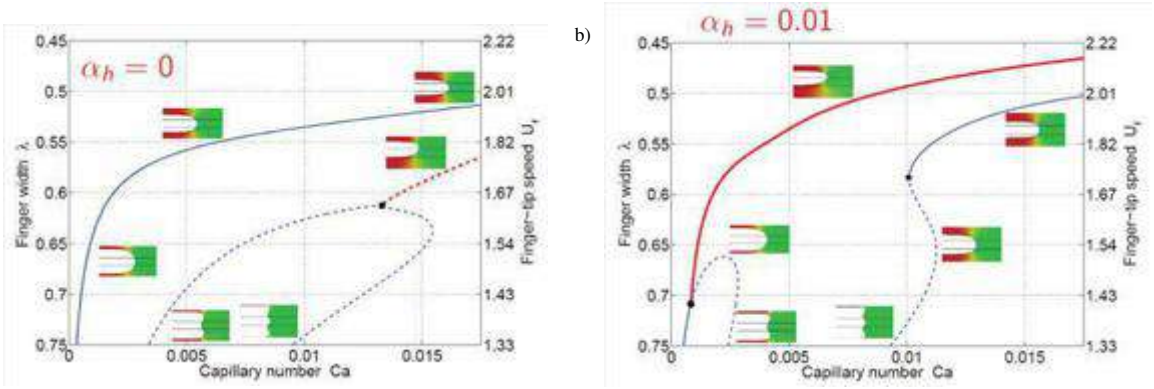

Fig. 3: Bifurcation diagrams for α=80 and (a) α_h=0, (b) α_h=0.01. The solid (dashed) lines represent stable (unstable) states, and blue (red) lines represent symmetric (asymmetric) fingers. Finite occlusion heights are required for stable asymmetric states to arise. In (a), the Saffman-Taylor mode is stable and the Romero-Vanden-Broeck solutions are unstable. In (b), the RVB solutions have interacted with the Saffman-Taylor mode, resulting in a bifurcation scenario with a supercritical symmetry-breaking bifurcation as Ca increases from small values.

References

[1] Moore, M. G., Juel, A., Burgess, J. M., McCormick, W. D. & Swinney, H. L. 2002 Fluctuations in viscous fingering. Phys. Rev. E. 65, 030601(R).

[2] Saffman, P. G. & Taylor, G. I. 1958 The penetration of a fluid into a porous medium or Hele-Shaw cell containing a more viscous liquid. Proc. R. Soc. Lond A 245, 312-329.

[3] McLean, J.W. & Saffman, P.G. 1981 The effect of surface tension on the shape of fingers in a Hele-Shaw cell. J. Fluid Mech. 102, 455-469.

[4] Tabeling, P., Zocchi, G. & Libchaber, A. 1987 An experimental study of the Saffman-Taylor instability. J. Fluid Mech. 177, 67-82.

[5] Romero, L. A. 1982 The fingering problem in a Hele-Shaw cell. PhD thesis, California Institute of Technology; Vanden-Broeck, J. M. 1983 Fingers in a Hele-Shaw cell with surface tension. Phys. Fluids 26, 2033-2034.

[6] Thompson, A. B., Juel, A. & Hazel A. L. 2014 Multiple finger propagation modes in Hele-Shaw channels of variable depth. J. Fluid Mech. 746, 123.

[7] de Lózar, A., Heap, A., Box, F., Hazel, A. L. & Juel, A. 2009 Tube geometry can force switchlike transitions in the behavior of propagating bubbles. Phys. Fluids 21, 101702.

MOBILITY OF HIGHLY DEFORMABLE NANOFILAMENTS

Sylwia Pawłowska[a)], Paweł Nakielski, Filippo Pierini, Krzysztof Zembrzycki & Tomasz Kowalewski
Institute of Fundamental Technological Research, Polish Academy of Sciences, Poland

Summary Mobility of hydrogel nanofilaments suspended in liquid is investigated to gain basic knowledge on hydrodynamic interactions biased by Brownian fluctuations. Typical for long macromolecules effects like spontaneous conformational changes and cross-flow migration are observed and evaluated. The collected experimental data can be used to validate assumptions present in numerical models describing intercellular transport of long biomolecules.

INTRODUCTION

Cross-flow migration of long micro objects is one of the fundamental mechanisms of lab-on-chip bio-processors. Moreover, behavior of long macromolecules is important in a variety of biological processes responsible for transport, aggregation and structure formation at the cellular level. Mobility of long deformable objects suspended in liquid depends on large number of parameters. Some of them like local flexibility, 3-D orientation, coiling - uncoiling are essential for resulting dynamics, however difficult to be accurately incorporated in practical models. Most common hydrodynamic models are based on several variants of classical *worm-like chain* (WLC) approach, describing flexible object as systems of interconnected identical spheres [1]. Its flexibility is usually defined by two parameters of stretching and bending. Experimental validation of such models using polymer solutions or DNA [2] is difficult and mainly limited to very general observations. In the following we propose more robust experimental study, based on optical observations of hydrogel filaments. Their characteristic size (dia. ~100 nm) allows for accurate evaluation of shape and orientation, but still remains small enough to reproduce characteristics of the flow regime influenced by Brownian fluctuations.

EXPERIMENT

We have developed new method allowing for fabrication of highly deformable microscopic filaments with typical diameter of 100 nm and contour length ranging from single micrometers to millimeters [3]. The nanofilaments are obtain by extracting hydrogel core of electrospun polymeric nanofibres. The composition of materials used allows for *in flight* modification of the hydrogel polymerization, tuning its mechanical properties to desired values. The surface topography of filaments is obtained by AFM equipped with a closed liquid cell and a rectangular silicon cantilever. Despite relatively large diameters, high deformability of our hydrogel filaments permits to obtain objects with mechanical properties resembling that of long biomolecules (comp. Table 1).

Table 1. Typical experimental parameters: mean flow velocity (Vm), contour length (L), radius (R), persistence length (Lp), and Young modulus (E) of the analyzed filament. Flow Reynolds number (Re) is based on the channel width (200 μm).

No	Vm [μm/s]	L [μm]	R [nm]	Re	Lp [μm]	E [kPa]
1	59.02	71.91	81	1.51E-02	17.62	2.17
2	77.78	72.87	81	1.98E-02	12.38	1.53
3	39.65	34.49	45	1.01E-02	3.44	4.45
4	68.87	54.31	45	1.76E-02	7.51	9.72

The dilute suspension of hydrogel nanofilaments is pumped through the 500 μm long PDMS microchannel and imaged by a fluorescent microscope coupled with high-gain EM-CCD camera. The experiment is based on observation of position and instantaneous shape of nanofilament conveyed by steady or pulsating flow. Some hundreds of long sequences of filament images are processed to extract their shape with specially designed Matlab software. The velocity profile in the channel is obtained from small amount of fluorescent tracers. For each analyzed filament its flexibility is determined by calculating Young modulus. For this purpose we analyze their Brownian shape fluctuations, and then used cosine correlation method to determine the persistence length [3]. Evaluation of geometry for three dimensional objects using 2-D projections obtained from the microscope is overwhelmed by unavoidable inaccuracy, it additionally complicates if parts of the filament tend to overlap. Hence, only clearly distinguishable objects with in plane shape deformations are taken into account. For this purpose constancy of apparent contour length of visualized filament is used as a control parameter. Channel depth is 60 μm. Hence, additional efforts (e.g. flow focusing) are undertaken to keep filaments far from the upper and bottom wall of the channel.

[a)] Corresponding author. Email: spaw@ippt.pan.pl

RESULTS

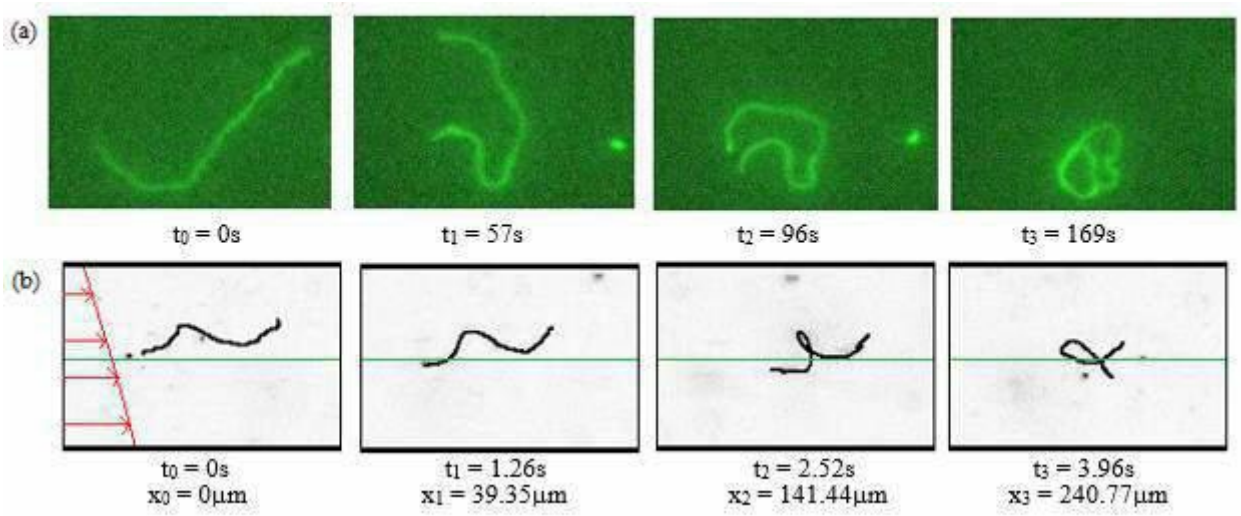

Figure 1. Sequence of images for a single flexible nanofilament suspended in liquid. (a) – Brownian motion observed for very long filament (R= 90 nm, L= 60 μm), image height 35 μm; (b) - filament conveyed by Poiseuille flow (no. 4 in Table 1), image centerline located 38 μm from the wall, t – time stamp, x – distance traveled from the channel entry (picture frame moves with the object), image height 66 μm.

Mobility of our filaments strongly depends on their length. For short pieces (10 – 20 μm) translational and rotational diffusion coefficients could be evaluated from Brownian motion. They are typically of the same order of magnitude as those obtained for rigid rods. For longer filaments their bending flexibility is well exhibited, especially pronounced for millimeters long objects (Fig. 1a). Interesting to note that despite negligible ionic interactions bending following characteristic coiling and knots formation is observed. This effect remains to dominate for objects conveyed by Poiseuille flow (Fig. 1b). The approximate center of mass for the conveyed filaments slightly lags behind the local flow field (Fig. 2), whereas cross-flow migration into the center of channel can be detected. Applying periodic flow we may notice evidence of broken reversibility of the Stokesian approximation. This is obvious for motion of deformable objects like droplets, bubbles and flexible fibers. In the present study it helps us to perform long time study for the same filament remaining in the field of observation.

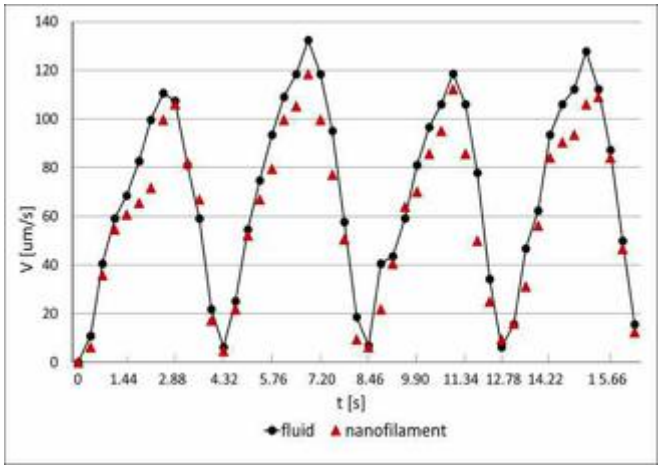

Figure 2. Velocity of fluid and for center of mass of the filament conveyed by pulsatile flow.

CONCLUSIONS

We have demonstrated possibility to create useful microscale experimental model to study hydrodynamic interactions for highly flexible long objects formed as hydrogel nanofilaments. Such objects can be used as possible carriers or indicators in biomedical applications. Our study gives evidence of difficulties to describe mobility of long flexible nanofilaments in terms of coarse parametric description, like hydrodynamic diameter and constant friction tensor. At each time step variable conformation of the observed objects strongly modifies hydrodynamic interactions, effects of wall and shear field forces, leading to more or less predictable evolution of their transport properties. Probably statistical analysis performed for large number of experiments is the only way to obtain plausible average mobility values convenient to predict longitudinal and cross-flow transport properties of such objects.

The support of NCN grant no. 2011/03/B/ST8/05481 and NCN Preludium grant no. 2015/17/N/ST8/02012 (S. P.) are acknowledged.

References

[1] Doyle P.S., Ladoux B., Viovy J.-L.: Dynamics of a tethered polymer in shear flow, *PRL* **84**(20), 4769-4772, 2000.
[2] Sadlej K, Wajnryb E, Ekiel-Jezewska ML, Lamparska D, Kowalewski T.A.: Dynamics of nanofibres conveyed by low Reynolds number flow in a microchannel, *Int. J. Heat & Fluid Flow* **31**, 996-1004, 2010
[3] Nakielski P., Pawlowska S., Pierini F., Liwinska V., Hejduk P., Zembrzycki K., Zabost E., Kowalewski T.A.: Hydrogel nanofilaments via core-shell electrospinning, *PLOS ONE* **10**(6), e0129816-1-16, 2015.

SWIMMING MECHANISMS OF JANUS MICROMOTORS: FROM SELF-DIFFUSIOPHORESIS TO BUBBLE PROPULSION

Xu Zheng [1], Jing Zhang [2], Leilei Wang [2], Haihang Cui [2] & Zhanhua Silber-Li [1a)]

[1] *State Key laboratory of Nonlinear Mechanics, Institute of Mechanics, Chinese Academy of Sciences, Beijing 100190, China*

[2] *Xi'an University of Architecture and Technology, Xi'an 710055, China*

Summary The self-propelled Janus micromotors moving in low Reynolds number environments have attracted extensive attention. In this paper, we measure the translational motion of Pt-SiO_2 Janus microparticles (size d=20-50μm) in H_2O_2 solutions, and report a three-stage typical behavior including self-diffusiophoresis, bubble growth, and bubble collapse. This behavior is found to coincide with a transition from self-diffusiophoresis to micro-bubble propulsion. The speed of the Janus microparticle due to bubble propulsion is observed to be about 1-2 order of magnitudes larger than that due to self-diffusiophoresis. Furthermore, we show that a strong jet flow towards the Janus microparticle emerges during bubble collapse, which reveals a new mechanism of bubble collapse.

INTRODUCTION

Self-propelled Janus microparticles are special types of active particles whose surfaces have two distinct physical or chemical properties [1]. Considering this special structure and the fact that no extra power is required, self-propulsion of Janus microparticles has attracted widespread interest in fields such as MEMS, drug delivery, enhancement of micromixing, environmental applications. As a simple and typical example, the Pt-SiO_2 Janus microparticles in H_2O_2 solutions are commonly used [2]. The catalytic reaction on the Pt surface, $2\ H_2O_2 \rightarrow 2H_2O_2 + O_2$, will generate more molecules and thus results in self-diffusiophoretic motion of Janus micropartilces driven by concentration gradient. In our previous study, we have demonstrated the typical behaviors of the self-diffusiophoresis [3]. Recently, a new type of self-propulsion due to micro-bubble propulsion (oxygen bubble on the Pt surface) was reported [4], which could significantly enhance the mobility of the Janus microparticles. Considering the possible wide applications of these Janus micromotors, we therefore perform systematic studies in this paper to investigate their swimming mechanisms.

EXPERIMENTS AND RESULTS

Experiments

The Pt-SiO_2 Janus microspheres were synthesized through the E-beam evaporation technology. We first deposited a monolayer of SiO_2 microspheres (30-65 μm in diameter) on a silicon wafer by spin-coating at 800 rpm for 10 s. Then, these silicon wafers were dried and baked at 80°C for 2 mins. Evaporation of 20 nm platinum on the upper half surfaces of these microspheres was performed using an e-beam evaporator, to them double faced. After that, the Janus microparticles were collected from the silicon wafer and re-suspended in di-water.

The Janus microparticles were set into motion in H_2O_2 aqueous solutions containing various concentrations (2-5 wt%). A 50μL droplet of Janus particles and H_2O_2 solutions were put on a glass slide. The motional behaviors of the Janus microparticles were then observed under a microscope (Nikon v7.3) with 20x or 40x objectives. A fast CCD camera Phantom Camera was used to record videos with a frame-to-frame interval of 100 μs. Video sequences were processed with Image J. The particle positions and the bubble growth can be tracked by the software video spot tracker (V07.02). And also, 2μm polystyrene tracers were added into the solution to show the flow field during bubble collapse.

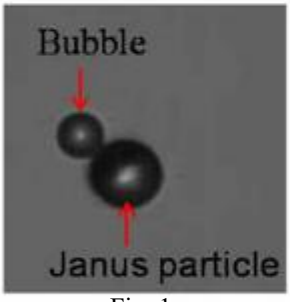

Fig. 1

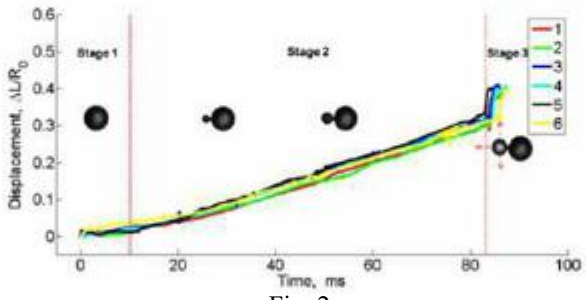

Fig. 2

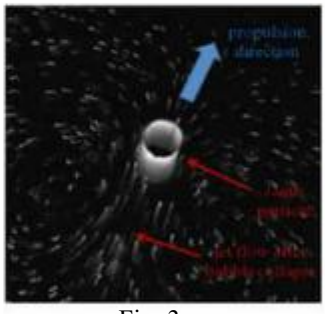

Fig. 3

Fig. 1 An image shows that a microbubble generates on the Pt surface of Janus micromotor to propel its motion.
Fig. 2 The three-stage behavior of the propulsion: (1) self-diffusiophoresis, (2) bubble growth and (3) bubble collapse.
Fig. 3 An overlapped image shows that a jet flow emerges after the bubble collapse in stage (3).

[a)] Corresponding author. Email: lili@ imech.ac.cn.

Results

Fig. 1 shows a typical image of a moving Janus microparticle with a growing bubble attached to its Pt surface (dark half) on the rear part. By analyzing the trajectories and displacements, we observe that the propulsion of the Janus microparitiicle can be divided into three stages: (1) self-diffusiophoresis; (2) bubble growth, and (3) bubble collapse, as shown in Fig. 2 (3% H_2O_2, results of six different Janus particles are assemble together). In stage 1, the bubble is still not visible, and the propulsion speed is about 5 μm/s, which is consistent with the typical speed of self-diffusiophoresis [2-3]. In stage 2, the Janus microparticle moves with an approximately constant speed (~ 100 μm/s), which means the propulsion force due to bubble growth is balanced by the Stokes drag force. This stage could last as long as 50-100 ms. In stage 3, the micro-bubble collapses when the pressure difference between its interface cannot be sustained. During bubble collapse, there will be instantaneous strong propulsion pushing the Janus microparticle forward, which results in a speed up to about 10 mm/s.

The fast propulsion in the third stage is of great interest. This process was considered as bubble burst that makes the Janus microparticle moving back and forth, and finally a local pressure depression will pull the Janus microparticle backward [5]. This explanation can only predict a negative pullback motion in stage 3. However, our measurements clearly show that the Janus micromotor emerges the strongest propulsion after bubble collapse. By overlapping 20 images (100 μs of each frame) recorded just after bubble collapse (Fig. 3), we observe that there is actually a jet flow from the bubble center pushing the Janus micromotor forward. This result shows a new mechanism of the bubble propulsion of Janus micromotors.

CONCLUSIONS

In this paper, we measure the characteristic motion of Janus microparticles in different H_2O_2 solutions (2-5 wt%). The catalytic reaction on the Pt surface of Janus microparitiicle will result in its self-propulsion. The swimming mechanisms are identified as both self-diffusiophoresis and bubble propulsion. Correspondingly, a three-stage behavior is reported, which includes (1) self-diffusiophoresis; (2) bubble growth, and (3) bubble collapse. A strong jet flow after bubble collapse is observed and considered as the reason of the strong propulsion in stage 3, which gives a new physical insight of this transient collapse process.

References

[1] Golestanian R, Leverpool T B, Ajdari A. Designing phoretic micro- and nano-swimmers. New J Phys, **9**:126, 2007.

[2] Howse J, Jones R, Ryan A et al. Self-motile colloidal particles: from directed propulsion to random walk. Phys. Rev. Letters, **99**: 048102, 2007.

[3] Zheng X, ten Hagen B, Wu M-L et al. Non-Gaussian statistics for the motion of self-propelled Janus particles: experiment versus theory, Phys. Rev. E, **88**: 032304, 2013.

[4] Wang S and Wu N, Selecting the swimming mechanisms of colloidal particles: bubble propulsion versus self-diffusiophoresis. Langmuir, **30**: 3477-3486, 2014

[5] Manjare M, Yang B and Zhao Y-P, Bubble driven quasioscillatory translational motion of catalytic micromotors. Phys. Rev. Letters, **109**: 128305, 2012.

INERTIAL MICROFLUIDICS FOR MANUFACTURING AND QUANTITATIVE SINGLE-CELL STUDIES

Aram J. Chung[1]

[1]*Department of Mechanical, Aerospace and Nuclear Engineering, Rensselaer Polytechnic Institute (RPI), Troy, NY, USA*

Summary Inertial microfluidics is a field of study involving interactions between fluids with particles and/or fluids with structures where both inertia and viscosity become important. In traditional microfluidics, inertia has generally been ignored since the associated Reynolds number is close to zero due to the small channel scale and low flow velocity. However, cases with fluid flows that involve non-zero Reynolds numbers (*i.e.*, non-zero inertia) are frequently encountered where fluid inertia should be accounted for. Inertial effects—inertial particle migration and secondary flow—have gained much attention in biology and medicine research because it inherently offers simple, sheathless, and high-throughput particle and cell manipulation that cannot be found in conventional active particle manipulation approaches. Through a deep understanding of fluid-particle-structure interactions, inertial microfluidics can be expanded to different fields, here in manufacturing and quantitative single-cell biology, in the sense of enabling technology.

3D PARTICLE MANUFACTURING: *OPTOFLUIDIC FABRICATION*

Many colloidal particles are spherical entities in order to minimize their interfacial energy. However, anisotropic particles can provide unique properties and additional functionalities not available in spherical particles. For instance, ellipsoids can randomly pack more densely in a given volume,[1] and non-spherical particles behave differently under electrical, chemical or mechanical stimuli. As such, shaped particles are now being used in various fields for self-assembly, photonics, biotechnology, structural materials and pharmaceutics.[2, 3] These intrinsic opportunities have driven the development of non-spherical polymer hydrogel particles,[4] and recent applications from various fields demand further functionalized, miniaturized and tailored hydrogel architectures at the micron scale. In order to meet these requirements, substantial efforts[5-11] have been made toward generating three dimensional (3D) tailored hydrogel particles. However, through these approaches, imposing high three-dimensionality into hydrogel architectures still remains challenging.[2, 3]

To address these limitations, recently we reported a novel inertial microfluidics based 3D particle generation method termed optofluidic fabrication.[12] The process is comprised of two sequential coupled procedures: (1) Fluid and (2) Light shaping. As a first step, we shape the fluid cross section using fluid inertia in microchannels with "obstacles". Although fluid inertia is ignored in conventional microfluidics,[13] non-negligible inertia can be of great use to change the flow cross sectional profile. With moderate inertia, the interaction between fluid and obstacles creates net lateral secondary flows, altering the cross sectional shape of multiple fluid streams. The flow is then quickly stopped (<1 sec), and patterned UV light is exposed to initiate a polymerization process (<1 sec) where UV light only polymerizes a photosensitive stream(s). The process can be considered as a polymerization of an intersection of two extruded bodies: horizontally shaped fluids by inertia and vertically patterned UV light. In this talk, I will present detailed numerical and experimental understandings of the interactions between fluid inertia and local obstacles in fluidic channels, and 3D shaped particle generation.

QUANTITIATVE SINGLE-CELL BIOLOGY: *NEXT GENERATION DEFORMABILITY CYTOMETRY*

Mechanical biomarkers associated with cytoskeletal structures have been reported as powerful label-free cell state identifiers.[14] Stiffness changes in red blood cells and stem cells are well known examples indicating cytoskeleton disorders[15, 16] and pluripotency,[17] respectively. This stiffness based cell state correlation also can be found in cancers,[18, 19] and cells possess different mechanical property upon their progression. Various recent studies[20-22] reported that a change in cell stiffness is shown between invasive and healthy cells where they can be distinguished. All of these facts suggest that the ability to measure cell stiffness is an extremely useful task for numerous applications, but the challenge is how to quantify a large number of cells precisely and rapidly. Due to the cellular heterogeneity, cells exhibit a distribution of responses in a probabilistic manner;[23] thus it is important to measure many individual cell behaviors rather than relying on the stochastic average masked by bulk measurements.[24] General approaches for measuring single-cell stiffness[25] are limited because of low throughput, non-bio-friendly measuring environments, and/or costly and time consuming labeling processes.

In this talk, I will present a development of a high-throughput and label-free inertial microsystem examining single-cell mechanical properties. Fluid inertia aligns cells into a single-cell train[26, 27] and guides them to collide with the channel wall at a T-junction where they can be stretched where we aim to establish a novel, simple, robust and high-throughput microfluidic cell stretcher for quantitative single-cell biology. I will discuss the details of cell positioning, ordering and manipulation strategies via localized microstructure induced secondary flows and a new image analysis algorithm for real-time data processing which may aid in next-generation deformability cytometry.

[a] Corresponding author. Email: chunga6@rpi.edu

References

[1] A. Donev, I. Cisse, D. Sachs, E. Variano, F. H. Stillinger, R. Connelly, S. Torquato and P. M. Chaikin, *Science*, **303:**990-993, 2004.

[2] H. C. Shum, A. R. Abate, D. Lee, A. R. Studart, B. G. Wang, C. H. Chen, J. Thiele, R. K. Shah, A. Krummel and D. A. Weitz, *Macromol. Rapid Commun.*, **31:**108-118, 2010.

[3] S. C. Glotzer and M. J. Solomon, *Nat. Mater.*, **6:**557-562, 2007.

[4] N. A. Peppas, J. Z. Hilt, A. Khademhosseini and R. Langer, *Adv. Mater.*, **18:**1345-1360, 2006.

[5] J. L. Perry, K. P. Herlihy, M. E. Napier and J. M. DeSimone, *Acc. Chem. Res.*, **44:**990-998, 2011.

[6] S.-K. Lee, H. S. Park, G.-R. Yi, J. H. Moon and S.-M. Yang, *Angew. Chem. Int. Ed.*, **48:**7000-7005, 2009.

[7] S. Q. Xu, Z. H. Nie, M. Seo, P. Lewis, E. Kumacheva, H. A. Stone, P. Garstecki, D. B. Weibel, I. Gitlin and G. M. Whitesides, *Angew. Chem. Int. Ed.*, **44:**724-728, 2005.

[8] M. Seo, Z. H. Nie, S. Q. Xu, M. Mok, P. C. Lewis, R. Graham and E. Kumacheva, *Langmuir*, **21:**11614-11622, 2005.

[9] J. R. Millman, K. H. Bhatt, B. G. Prevo and O. D. Velev, *Nat. Mater.*, **4:**98-102, 2005.

[10] K. W. Bong, D. C. Pregibon and P. S. Doyle, *Lab Chip*, **9:**863-866, 2009.

[11] Z. Nie, S. Xu, M. Seo, P. C. Lewis and E. Kumacheva, *J. Am. Chem. Soc.*, **127:**8058-8063, 2005.

[12] K. S. Paulsen, D. Di Carlo and A. J. Chung, *Nat Commun*, **6:**6976, 2015.

[13] D. Di Carlo, *Lab Chip*, **9:**3038-3046, 2009.

[14] D. Di Carlo, *Jala*, **17:**32-42, 2012.

[15] Y. Park, C. A. Best, K. Badizadegan, R. R. Dasari, M. S. Feld, T. Kuriabova, M. L. Henle, A. J. Levine and G. Popescu, *Proc. Natl. Acad. Sci. U.S.A*, **107:**6731-6736, 2010.

[16] A. Dondorp, B. Angus, K. Chotivanich, K. Silamut, R. Ruangveerayuth, M. Hardeman, P. Kager, J. Vreeken and N. White, *Am J Trop Med Hyg*, **60:**733-737, 1999.

[17] A. J. Engler, S. Sen, H. L. Sweeney and D. E. Discher, *Cell*, **126:**677-689, 2006.

[18] S. E. Cross, Y.-S. Jin, J. Rao and J. K. Gimzewski, *Nat nanotechnol*, **2:**780-783, 2007.

[19] S. Suresh, J. Spatz, J. Mills, A. Micoulet, M. Dao, C. Lim, M. Beil and T. Seufferlein, *Acta Biomater.*, **1:**15-30, 2005.

[20] S. Suresh, *Acta Mater.*, **55:**3989-4014, 2007.

[21] V. Swaminathan, K. Mythreye, E. T. O'Brien, A. Berchuck, G. C. Blobe and R. Superfine, *Cancer Res.*, **71:**5075-5080, 2011.

[22] J. Guck, S. Schinkinger, B. Lincoln, F. Wottawah, S. Ebert, M. Romeyke, D. Lenz, H. M. Erickson, R. Ananthakrishnan and D. Mitchell, *Biophys. J.*, **88:**3689-3698, 2005.

[23] D. Di Carlo and L. P. Lee, *Anal. Chem.*, **78:**7918-7925, 2006.

[24] D. Wang and S. Bodovitz, *Trends Biotechnol.*, **28:**281-290, 2010.

[25] A. J. Chung and S. C. Hur, *Micro-and Nanomanipulation Tools*, 2015.

[26] A. J. Chung, D. R. Gossett and D. Di Carlo, *Small*, **9:**685-690, 2013.

[27] A. J. Chung, D. Pulido, J. C. Oka, H. Amini, M. Masaeli and D. Di Carlo, *Lab Chip*, **13:**2942-2949, 2013.

ULTRASONIC FORCE POTENTIAL WELLS FOR TRAPPING ARRAYS OF SINGLE CELLS – ONE CELL PER WELL (OCPW)

Adrian Neild[1a], David J. Collins[1], Belinda Morahan[2], Jose Garcia-Bustos[2],
Christian Doerig[2] & Magdalena Plebanski[3, 4]
[1]*Department of Mechanical & Aerospace Engineering, Monash University, Clayton, Victoria, Australia*
[2]*Department of Microbiology, Infection and Immunity Program, Monash Biomedicine Discovery Institute, Monash University, Clayton, Victoria, Australia*
[3]*Department of Immunology, Alfred Hospital Precinct, Monash University, Clayton, Victoria, Australia*
[4]*MIME Immunotherapeutic Division, Monash University New Horizons, Clayton, Victoria, Australia*

Summary Single cell analysis enables the study of cellular activity and parameters at an individual, rather than population-average basis. This is made possible by retaining cells so that temporal data can be accessed. In contrast to previous capture approaches utilising mechanical traps, we present an ultrasonic method to capture and release spatially separated cells on demand, with potential for population screening and analysis. The transition from manipulation of particles in groups, which is routinely performed using ultrasound, to individuals requires the reduction of ultrasonic wavelength, but it also introduces a unique physical situation. This arises from the two key forces present: the acoustic radiation force and Bjerknes forces. The former collects particles at defined locations within the sound field, whereas the latter acts to coagulate particles. For collection of individual particles the former is beneficial, the later a hindrance; we show that over a defined range of parameters single particle and cell capture is possible.

INTRODUCTION

Single-cell analysis permits the interrogation of individual cells and their response to their local environment [1]. Due to heterogeneous cellular parameters, the examination of individual cells has the potential to offer a far more detailed picture of cellular response than the standard practice of analyzing the population as a whole. Further, the large-scale trapping of a cell population (100s-1000s of cells) permits this activity on an en-masse basis [2]. This study examines the use of acoustic force fields as a method of trapping grids of individual cells [3]. With the ability to rapidly activate the force field, this approach enables a method to flash the force potential so that a population can be rapidly screened, and cells of interest (for example, cells infected by a parasite) then held for more detailed examination. Whilst acoustic waves have been widely used for handling and trapping suspended cells [4, 5], this is the first study of trapping cells individually.

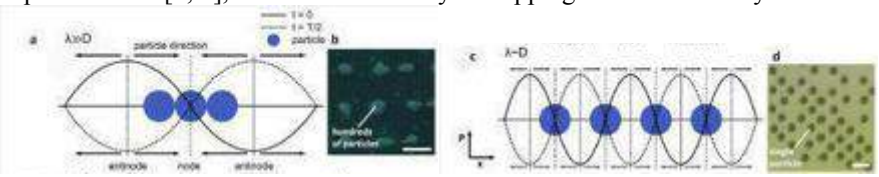

Figure 1. The two dimensional acoustic field is characterized by the ratio of wavelength to particle size. Looking at a 1D depiction, at large ratios multiple particles can cohabit a single potential minimum – the nodes of the standing pressure wave (left). Once the ratio falls below approximately 4 there is only enough physical space for a single particle (right) [3].

Previous work has shown the collection of cells in clumps by a 2D force field [6]. In order to transition from trapping clumps of cells at each acoustic radiation force potential minima to trapping of individual cells, the minima dimensions must be reduced (Figure 1). However, the underlying physics is more complex than simply a reduction in scaling. The sound field generates acoustic radiation forces on the particles which act to collect them in patterns dictated by the shape of the sound field. In addition Bjerknes forces are excited; these forces arise due particle-particle interactions and are attractive in nature. In contrast to previous acoustic cell manipulation studies in which patterns of cell clusters are formed, to pattern individual cells, the clustering effect of the Bjerknes force works against the patterning effect of the acoustic radiation forces.

METHODOLOGY

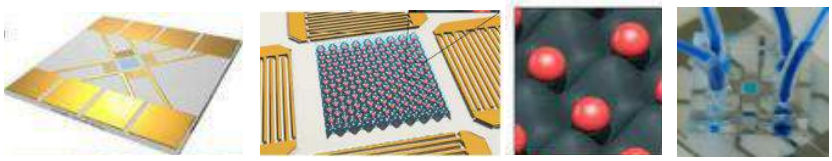

Figure 2. The one-cell-per-well device comprises a PDMS defined microfluidic chamber bonded onto a lithium niobate wafer on which two pairs of orthogonal IDTs are patterned (left). The result of actuating the four IDTs is a 2D pressure field in the fluid chamber, which leads to an acoustic radiation force potential field (right) capable of patterning cells [3].

[a)] Corresponding author. Email: adrian.neild@monash.edu

To achieve individual cell handling, we have designed a system which excites two orthogonal standing surface acoustic waves by excitation of four interdigital transducers (IDTs) patterned on a lithium niobate substrate (Figure 2). These waves couple into the fluid body defined by a PDMS chamber bonded onto the substrate, it is these coupled waves which define the sound field which patterns the particles.

RESULTS AND DISCUSSION

We have examined this unique physical situation, and found that a very specific range of frequency over diameter ratios is required in order to trap the cells individually. At a frequency which is too low, multiple particles fit in one well, and at a frequency which is too high, the cells do not conform to the pattern dictated by the acoustic radiation force field (Figure 3).

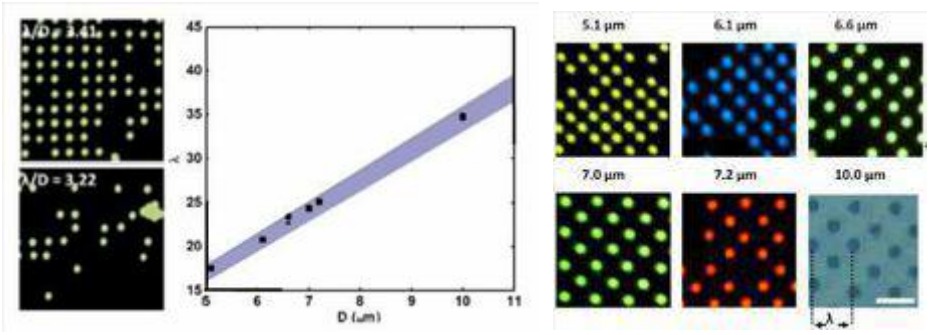

Figure 3. There is a limited range of λ/D in which single particles can be collected. Above approximately 4 there is space for more than one particle in each minimum. Within a specific range particles can be collected into a grid as shown for 6.1 μm particles (left, upper). At further reduced values of λ/D the particles form clumps across the force potential minima (left, lower). The optimum collection wavelength has been found experimentally for a range of particle sizes (right). It is observed that there is a linear relationship between wavelength and particle diameter [3].

Finally trapping of red blood cells in a flashing potential, has allowed cells to be screened by holding them statically against a fluid flow for visual inspection (Figure 4).



Figure 4. Red blood cells flowing (from the opening at the bottom right to that at bottom left) through the square chamber (left) can be captured by momentary excitation of the acoustic field (right) such that screening can take place [3].

CONCLUSIONS

This first study into acoustic single cell analysis shows the potential for using surface acoustic wave fields to trap and investigate multiple individually trapped cells, and highlights the intriguing underlying physics comprising the interplay between two acoustically generated forces.

References

[1] H. N. Joensson, H. A. Svahn: Droplet microfluidics: a tool for single-cell analysis, *Angewangte Chemie Int. Ed.* **51:**12176, 2012.

[2] N. Devervaud, J. Becker, R. Delgado-Gonzalo, P. Damay, A. S. Rajkumar, M. Unser, D. Shore, F. Naef, S. J. Maerkl: A chemostat array enables spatio-temporal analysis of the yeast proteome, *Proc. Nat. Acad. Sci.* **110**:15842, 2013.

[3] D. J. Collins, B. Morahan, J. Garcia-Bustos, C. Doerig, M. Plebanski, A. Neild: Two-dimensional single-cell patterning with one cell per well driven by surface acoustic waves, *Nature Communications* **6**:8686, 2015.

[4] R. Walker, I. Gralinski, K. K. Lay, T. Alan, A. Neild: Particle manipulation using an ultrasonic micro-gripper, *Applied Physics Letters* **101**:163504, 2012.

[5] T. Laurell, F. Petersson, A.Nilsson: Chip integrated strategies for acoustic separation and manipulation of cells and particles, *Chem Soc Rev* **36**:492, 2007.

[6] S. Oberti, A. Neild, J. Dual: Manipulation of micrometer sized particles within a micromachined fluidic device to form two-dimensional patterns using ultrasound, *J. Acoust. Soc. Am.* **121**:778, 2007.

PARTICLES DOUBLE LAYER EVALUATION BY ATOMIC FORCE MICROSCOPY-OPTICAL TWEEZERS

Filippo Pierini [a)], Paweł Nakielski, Sylwia Pawłowska, Krzysztof Zembrzycki & Tomasz Aleksander Kowalewski
Institute of Fundamental Technological Research, Polish Academy of Sciences, Poland

Summary Atomic force microscopy (AFM) is the most commonly used method of direct force evaluation, but due to its technical limitations this single probe technique is unable to detect forces with femtonewton resolution. We present the development of a combined atomic force microscopy and optical tweezers (AFM/OT) instrument. The optical tweezers system provides us the ability to manipulate small dielectric objects and to use it as a high spatial and temporal resolution displacement and force sensor in the same AFM scanning zone. We demonstrate the possibility to develop a combined instrument with high potential in nanomechanics, molecules manipulation and biological studies.
The presented study is aimed to quantify the interaction forces between two single polystyrene particles in the femtonewton scale by using the developed AFM/OT equipment.

INTRODUCTION

Materials containing suspended microparticles or nanoparticles are used extensively in fields of research and in the industry. In order to understand their behaviour in the liquid, the knowledge of stability and mobility of particles in the liquid is fundamental. In all applications it is vital to maintain single particles well dispersed and to avoid the formation of aggregates. For this reason, it is necessary to know the nanoscale fluid-solid interaction and the hydrodynamic properties of the particles. The equilibrium state and the hydrodynamic properties of many colloid's system in aqueous medium is affected by several environmental parameters. The addition of salt influences the stability of colloids. An explanation for this fact was given by the Derjaguin-Landau-Verwey-Overbeek (DLVO) theory, studying the surface charges at interfaces and the factors that affect the electrostatic double-layer forces [1]. This theory assumed that the interaction between two particles is due to the sum of the electrostatic double-layer repulsion and the van der Waals attraction. At low salt concentration, the double-layer repulsion is strong enough and the single particles are stable, but with increasing ionic strength the electrostatic repulsion is masked. If the saline concentration is high enough the colloid system will be unstable because the van der Waals attraction will be higher than the repulsive electrostatic barrier.
Atomic force microscopy (AFM) was developed for nanoscale imaging purposes, where a topographical reconstruction is obtained by scanning the sample surface using a tip fixed on a flexible cantilever [2]. AFM is not only a useful tool to visualize micro and nanomaterials with high resolution but it can also be used to quantify force in the nanonewtonscale (10^{-9} N). Optical tweezers were first realized by Arthur Ashkin in 1970. He was the first to observe and study light scattering on microparticles and the resulting gradient force. This is a technique with which it is possible to trap and manipulate nanometer and micrometer-sized material using a highly focused laser beam. Optical tweezers is a very sensitive technique used to manipulate objects with nanometer displacements and to measure forces with femtonewton (10^{-15} N) accuracy [3].

EXPERIMENT

The combination of atomic force microscopy and optical tweezers (AFM/OT) in one single piece of equipment (Figure 1) give us the ability to obtain images, to manipulate and quantify the motion and the forces directly in the same sample [4].
This research used an atomic force microscopy combined with optical tweezers system (AFM/OT) to measure the effect of ionic strength on the femtonewton scale interaction force between single polystyrene particles at different separation distances. Here, we describe forces involved in single polystyrene colloid stability according with the DLVO theory. At the beginning, AFM/OT system was used to isolate a 1.0 μm polystyrene particle into a microfluidic well using the dragging force of the trapping laser. Subsequently, a custom-made AFM colloidal probe cantilever in which a single fluorescent 5.5 μm particle was glued to the end of a tip-less AFM. It was used to quantify the interaction force between two polystyrene single particles The experiments were

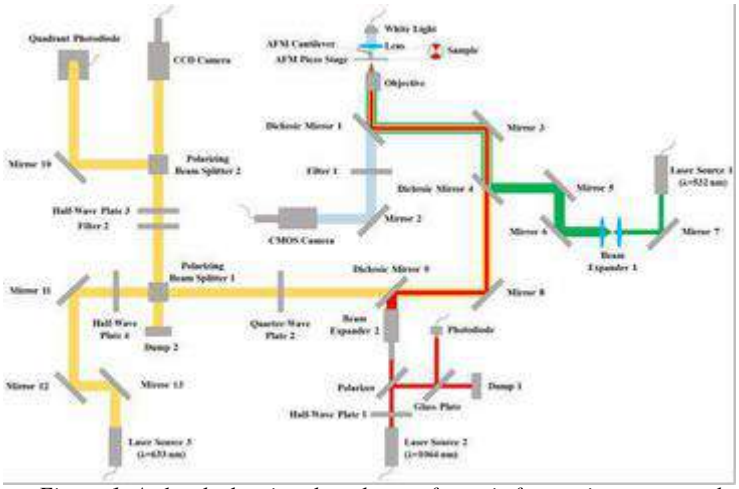

Figure 1. A sketch showing the scheme of atomic force microscopy and optical tweezers (AFM/OT) setup.

[a)] Corresponding author. Email: fpierini@ippt.pan.pl

carried out by approaching the trapped particle with the AFM particle probe at a constant velocity (200 nm/s) in pure water and recording the optical tweezers output signals with a resolution of ±100 fN. The same experiment was repeated in 10^{-5} M and 10^{-3} M KCl solutions in that order.

RESULTS

The obtained data (Figure 2) confirm that the behaviour of colloidal systems observed experimentally agrees with the theoretical predictions. In pure water, long range attraction is clearly measured, instead small short range repulsions that are still not strong enough to overcome the attractive component in the analysed range. A completely different behaviour is observed in presence of KCl, where no final attractive forces act in the analysed range, while repulsive forces that grow exponentially with decreasing particle-particle distance are visible. In all the studied systems, no interaction forces between the polystyrene particles could be observed at distances exceeding 450 nm.

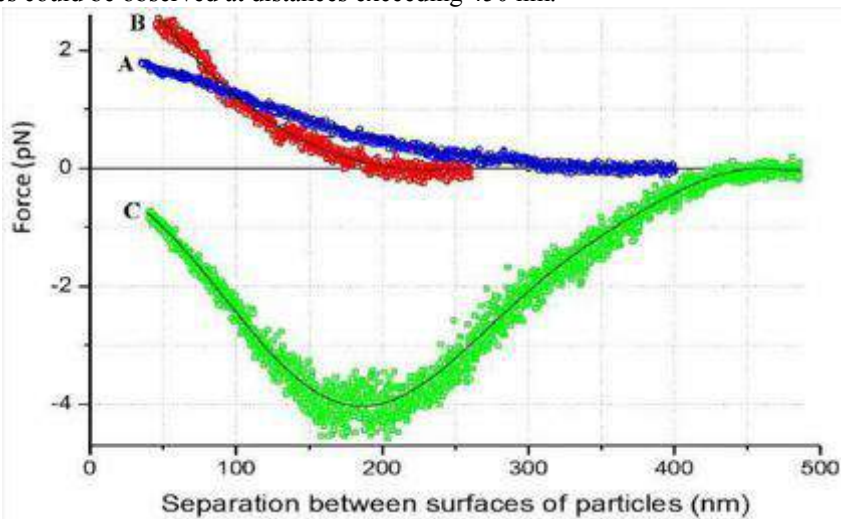

Figure 2. Force as a function of the relative distance between a single pair of polystyrene particles. The interaction force curves measured on approach between the polystyrene sphere attached to the AFM probe and the trapped sphere were collected varying KCl concentration: 10^{-3} M (blue circles; A), 10^{-5} M (red squares; B) and pure water (green triangles; C) at pH 7. The continuous lines correspond to the best fit in the particle-particle interaction range.

CONCLUSIONS

The hybrid AFM/OT allows quantifying the forces involved in the colloid stability with femtonewton resolution tacking in account only forces relative to the two analysed particles. The experiment performed using the developed instrument allows miming the natural colloidal system condition in which the studied single particle is completely bordered by the liquid through the use of the optical trap, giving us a more reliable result than similar experiment performed with AFM only. The used configuration can quantify the forces of interaction between single particles with good reproducibility.

The obtained experimental results confirm the applicability of our combined system to study single particle interaction forces. It is shown that the polystyrene particle colloid systems are more stable in a 10^{-3} M KCl solution, than a 10^{-5} M KCl solution and that is, in turn, more stable than the same system in water. The change of attractive and repulsive forces at various ionic strengths due to the modification of double layer structure affect the stability and the hydrodynamic properties of colloid systems.

ACKNOWLEDGEMENT

The support of NCN grant no. 2011/03/B/ST8/05481 is acknowledged.

References

[1] Maroto J.A., de las Nieves F.J.: Theoretical and experimental comparison of the colloid stability of two polystyrene latexes with different sign and value of the surface charge. *Colloid. Polym. Sci.*, **276**:453-458, 1998.

[2] Giessibl F.J.: Advances in atomic force microscopy. *Rev. Mod. Phys.* **75**:949, 2003.

[3] Moffitt J.R., Chemla Y.R., Smith S.B., Bustamante C.: Recent Advances in Optical Tweezers. *Annu. Rev. Biochem.*, **77**:205-228, 2008.

[4] Pierini F., Zembrzycki K., Nakielski P., Pawłowska S., Kowalewski T.A.: Atomic force microscopy combined with optical tweezers (AFM/OT). *Meas. Sci.Technol*, **27**:025904, 2016.

A BIOMIMETIC MICROFLUID ASSAY FOR RAPID SCREENING OF ANTI-INFLAMMATORY DRUGS

Mohammad F. Kiani[1a)], Fariborz Soroush[1], Balabashkar Prabhakarpandian[2] & Laurie Kilpatrick[3]
[1]*Department of Mechanical Engineering, Temple University, Philadelphia, PA, USA*
[2]*Biomedical Technology, CFD Research Corporation, Huntsville, AL, USA*
[3]*Department of Physiology, Lewis Katz School of Medicine, Temple University, Philadelphia, PA, USA*

Summary Almost all drugs recently developed in animal models to treat inflammatory disease have failed in clinical trials. There is therefore a significant need for rapid screening of anti-inflammatory drugs before they are tested for safety, efficacy and toxicity in expensive and time consuming large animal models and eventually human trials. We have developed and validated a novel biomimetic microfluidic assay (bMFA) that reproduces the entire leukocyte adhesion cascade in a physiologically realistic three-dimensional environment using human cells and allows for rapid screening of potential therapeutics. Protein Kinase C-delta (PKCδ TAT) inhibitor represents a new class of anti-inflammatory drug and we have used bMFA to show the potentially therapeutic effects of this novel drug on human neutrophil-endothelial interactions.

INTRODUCTION

Inflammation is a physiological response of the body to protect tissues from infection, injury, or disease. The inflammatory response starts a signaling cascade at the affected areas, followed by the production and release of chemical agents such as chemokines, cytokines and other inflammatory mediators. The evolving signals then recruit leukocytes to the inflammation site activating an acute inflammation process during three major stages at or near the affected site which include dilation of capillaries to increase blood flow, microvascular structural changes and increased endothelial permeability, and leukocyte transmigration through the endothelium and accumulation. Leukocyte transmigration and accumulation, depends on a multi-step process called the Leukocyte Adhesion Cascade, which includes 5 discrete steps: capture/attachment, rolling, firm arrest, spreading, and extravasation and migration. Recruitment of neutrophils to the site of injury or inflammation is an early key step in this process and neutrophil migration across the endothelium plays a key role in pathogenesis of lung injury in diseases such as sepsis [1].

Regulating leukocyte recruitment has been shown to reduce symptoms of inflammation in clinical studies [2] and identification of key molecules involved in the leukocyte adhesion cascade will allow for the development of novel therapeutics. However, while *in vivo* studies of mechanisms of inflammatory disease have mostly relied on murine models, *in vitro* studies of the inflammatory pathway have mostly relied on simplistic two-dimensional human cell culture models. A meta-analysis of a large number of studies found little overlap in gene activity between mouse models of inflammation and its clinical manifestations [3] which led The New York Times then to suggest that much time and money has been wasted studying mouse models of inflammation [4]. Of particular concern is that the reductions in mortality from sepsis has been primarily due to supportive care rather than effective medicines where, for example, all of the ~150 drugs recently developed in animal models to treat sepsis have failed in clinical trials [5]. Currently there are no specific pharmacologic therapies available that protect from neutrophil-mediated tissue damage and there is an increased preclinical effort to identify novel targets and develop new therapeutic paradigms.

To address some of these challenges, we have developed and validated a novel biomimetic microfluidic assay (bMFA) that reproduces the entire leukocyte adhesion cascade in a physiologically realistic three-dimensional environment, encompassing circulation, rolling, adhesion and migration of leukocytes [6-8]. In developing this technology we are specifically responding to the call by the scientific community for "translational medical research to focus on the more complex human conditions rather than relying on mouse models to study human inflammatory diseases" by developing a realistic fluidic model for "*in vitro* reconstitution of disease-related cell types or tissues" [3].

We have introduced a novel therapeutic paradigm which targets PKCδ and neutrophil-endothelial interactions and in an animal model have shown it to protect vascular endothelial integrity and attenuate sepsis-induced tissue damage [1, 9]. In this study, we investigated the mechanism of PKCδ inhibition on the interaction of human umbilical vein endothelial cells (HUVECs) and human neutrophils during the inflammatory response.

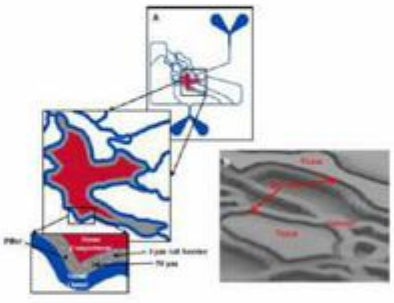

Figure 1: Schematic of the bMFA (A) and its scanning electron microscopic image showing the different compartments (B).

Novel Biomimetic Microfluidic Assay (bMFA)

Our modified Geographic Information System (GIS) approach was used to digitize the microvascular networks and generate the synthetic microvascular networks on Polydimethylsiloxane (PDMS) by soft lithographically (Figure 1). The device

a) Corresponding author. Email: mkiani@temple.edu

consists of a vascular compartment and connected to a tissue compartment connected by 3 μm gaps, the most common and optimum size for studying leukocyte migration. Similar to the *in vivo* vascular networks, the device has channels ranging from 15-100 μm. Confluent culture of human umbilical vein endothelial cells (HUVEC) in bMFA shows an elongated morphology in the direction of the flow and form a 3D culture as shown in confocal microscopic images (Figure 2). We have shown that the pattern of neutrophil adhesion to primary endothelial cells in bMFA is similar to that of leukocyte adhesion to the vessels in networks of the mouse cremaster muscle *in vivo* (Figure 3).

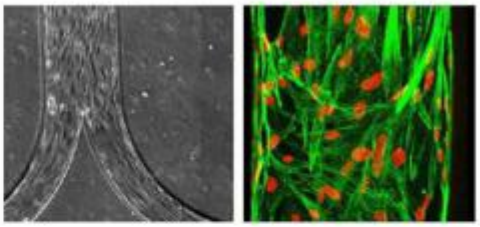

Figure 2: Endothelial cells in bMFA elongate in the direction of shear flow (A) and form a 3D culture (B).

Using bMFA to Screen a Potentially Novel Therapeutic

We have introduced a novel therapeutic paradigm which targets PKCδ and neutrophil-endothelial interactions to protect vascular endothelial integrity and attenuate sepsis-induced tissue damage [1, 9]. We have now used bMFA to characterize the effect of a PKCδ TAT peptide inhibitor on human neutrophil-endothelial interaction. As shown in Figure 4, PKCδ inhibition significantly decreases adhesion of human neutrophils to the TNF-α activated human endothelium in the presence of chemoattractant fMLP but only in channels with low shear rate flow (γ <30 1/sec) and at bifurcations. Please note that these latter observations regarding the spatial distribution of adhesion patterns within the vascular network cannot be easily made in other microfluidic devices. Migration of human neutrophils across TNF-α activated endothelial cells in response to fMLP also decreases significantly after inhibition of PKCδ (Figure 5).

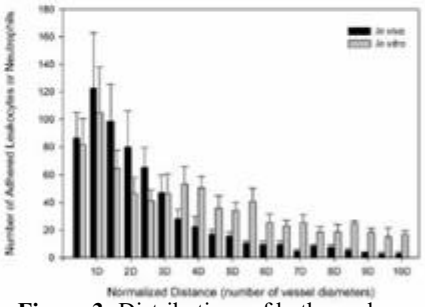

Figure 3: Distributions of both number of adhered leukocytes (*in vivo*, black bars) and neutrophils (*in vitro*, grey bars) as a function of distance from the nearest bifurcation indicate that leukocytes/neutrophils preferentially adhere near bifurcations.

CONCLUSIONS

Our novel biomimetic microfluidic assay (bMFA) provides an effective tool for rapid screening of promising anti-inflammatory therapeutics in a physiologically and functionally realistic *in vitro* environment and provides early indications of their potential success in clinical applications. We have used clinically relevant human cells to show that PKCδ TAT peptide is an effective therapy for reducing neutrophil-endothelial interaction during inflammation.

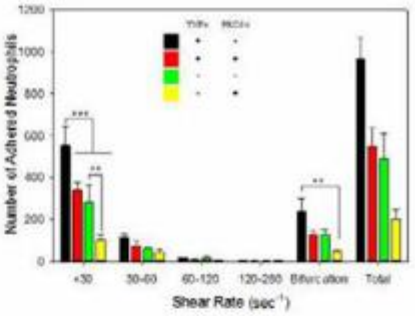

Figure 4: PKCδ inhibition significantly reduces adhesion of neutrophils to the endothelium in low shear regions and near bifurcations in bMFA in the presence of fMLP.

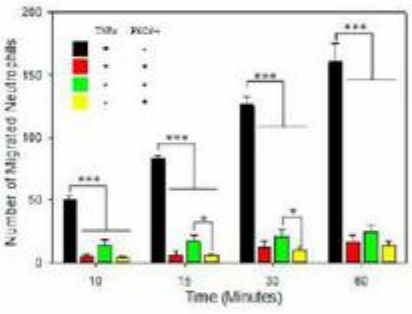

Figure 5: PKCδ inhibition significantly reduces migration of neutrophils from the vascular channels, across the activated endothelium, into the tissue compartment.

References

1. Mondrinos MJ, Zhang T, Sun S, Kennedy PA, King DJ, Wolfson MR, et al. Pulmonary endothelial protein kinase C-delta (PKCdelta) regulates neutrophil migration in acute lung inflammation. AmJPathol. 2014;184(1):200-13.
2. Kolaczkowska E, Kubes P. Neutrophil recruitment and function in health and inflammation. Nat Rev Immunol. 2013;13(3):159-75.
3. Seok J, Warren HS, Cuenca AG, Mindrinos MN, Baker HV, Xu W, et al. Genomic responses in mouse models poorly mimic human inflammatory diseases. ProcNatlAcadSciUSA. 2013;110(9):3507-12.
4. Kolata G. Mice Fall Short as Test Subjects for Some of Humans' Deadly Ills. The New York Times. 2013.
5. Drake AC. Of mice and men: what rodent models don't tell us. Cell MolImmunol. 2013;10(4):284-5.
6. Deosarkar SP, Prabhakarpandian B, Wang B, Sheffield JB, Krynska B, Kiani MF. A Novel Dynamic Neonatal Blood-Brain Barrier on a Chip. PLoS One. 2015;10(11):e0142725. doi: 10.1371/journal.pone.
7. Lamberti G, Prabhakarpandian B, Garson C, Smith A, Pant K, Wang B, et al. Bioinspired Microfluidic Assay for In Vitro Modeling of Leukocyte-Endothelium Interactions. AnalChem. 2014;86(16):8344-51.
8. Rosano JM, Tousi N, Scott RC, Krynska B, Rizzo V, Prabhakarpandian B, et al. A physiologically realistic in vitro model of microvascular networks. Biomed Microdevices. 2009;11(5):1051-7.
9. Mondrinos MJ, Kennedy PA, Lyons M, Deutschman CS, Kilpatrick LE. Protein kinase C and acute respiratory distress syndrome. Shock (Augusta, Ga). 2013;39(6):467-79.

GROWTH AND DEPARTURE OF CONDENSATION MICRODROPLETS ON SUPERHYDROPHOBIC SURFACES

Pengfei Hao*, Cunjing Lv, Zhaohui Yao, Xiwen Zhang and Feng He
Department of Engineering Mechanics, Tsinghua University, Beijing, China

Summary This article focuses on the growth, transition, coalescence and jumping of the condensation microdroplets (< 10 μm) on the superhydrophobic substrates with two-tier roughness. We report a spontaneous dewetting transition of condensed droplets occurring on pillared surfaces with micro/nanoscale roughness, from the valleys to the tops of the pillars, owing to the nanotexture enhanced superhydrophobicity. Three novel wetting transition modes are observed. It is found that a further decreased Laplace pressure on the top side of the individual droplets accounts for such a surprising transition and self-removal of condensed water. Our results also show that decrease the size and the space of the micro pillars is a good strategy to realize spontaneous dewetting and droplet jumping.

Condensation of water vapor is an everyday phenomenon which plays an important role in power generation, thermal management, chemical processing and water harvesting. The dropwise condensation has been shown to achieve heat and mass transfer coefficients over an order of magnitude higher than its filmwise counterpart.[1] Recently, there has been significant interest in developing superhydrophobic surfaces for promoting dropwise condensation.[2] Such surfaces benefit greatly from the combination of nano-/microstructures and the inherent hydrophobicity of their chemistry, which allows attaining extreme non-wetting properties with vapor trapped underneath (Cassie state) and coalescence-induced self-propelled dropwise condensation.[3] Most of the previous studies[4] have applied ESEM technique to visualize growth and merging of condensed droplets, however, low time resolution of ESEM has limited the investigation on the dynamics of growth and coalescence-induced jumping on such surfaces. The details and mechanisms of the growth and coalescence of microdroplets on micro/nano structured surfaces under natural condensation situation are still limited to date. This article focuses on growth, transition, coalescence and jumping of microdroplets (< 10 μm) on superhydrophobic substrates with two-tier (micro and nano) roughness. A moist ambient environment are employed, which allowing a systematical study of growth processes, wetting transitions, as well as jumping behaviors of microdroplets under optical microscopy.

Silicon wafer substrate with square-shaped micropillars (Fig.1) with side length L and spacing S of the neighbors, are employed. The height H of the micropillars in this work is fixed at 5 μm. The key feature is that the surface of the micropillars and the bottom of the substrate are treated with the coating agent, in which hydrophobic nanoparticles are contained to guarantee excellent superhydrophobicity, i.e., even on flat one-tier nanotextured surfaces , the apparent contact angle and hysteresis are found to be $\theta = 159.2°\pm1.5°$ and $\Delta\theta = 10.2°\pm2.1°$, respectively. There are four types of samples investigated with L = 2 μm, 3 μm, 4 μm, and 8.4 μm, respectively, and S = 3 μm, 4.5 μm, 6.5 μm, and 13 μm, respectively. For a 5 μL droplet dropped under an ambient environment, all of them demonstrate high apparent contact angles (> 160°) and low hysteresis (< 10°).

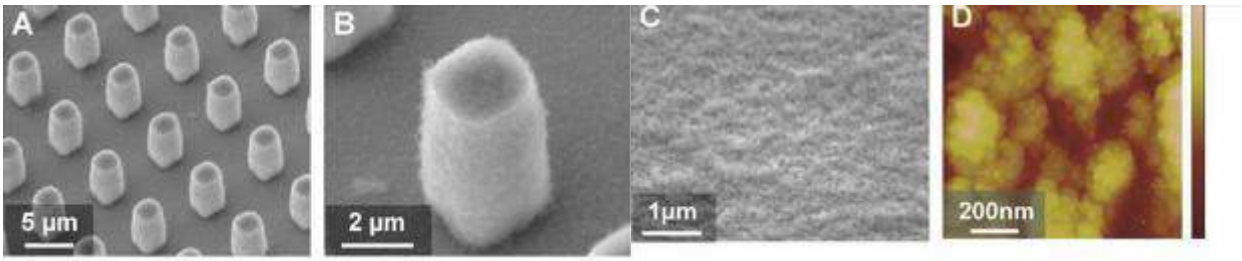

Fig.1 Topology of the two-tier nano-/microstructured surface (L = 3 μm, S = 4.5 μm, H = 5 μm) and its roughness characterized by SEM in micro (A) and nanoscale (B), (C), respectively. (C) and (D) are measured on flat surfaces. (D) is characterized by AFM, the roughness at the nanoscale is Ra = 24.5 nm, which corresponds to a 1 μm × 1 μm area.

All the experiments are performed using an optical microscopy technique under a moist ambient environment allowing for focusing on the *in situ* dynamic characteristics of the condensed droplets, thereby overcomes the limitations of the previous commonly used environmental scanning electron microscopy (ESEM) technique, such as slow imaging times, narrow ranges of operation pressures and temperatures, as well as beam heating effects. All of the samples are placed horizontally on a peltier cooling stage, which is fixed on the slider of an optical microscope with a high resolution of 0.2 μm. The laboratory temperature is measured at 29°C with a relative humidity of 40%. During the running of the cooling system, the temperature of the sample is well maintained at 10° ± 1°C. Top-down imaging of the processes is captured using a CCD camera installed on the microscope.

[a)]Corresponding author. Email: haopf@tsinghua.edu.cn.

We report a spontaneous dewetting of condensed microdroplets on superhydrophobic substrates owing to excellent superhydrophobicity at the nanoscale and the geometrical topologies at the microscle. Moreover, three dewetting modes are observed(Fig.2). Mode I: Wetting transition of an individual droplet**.** Mode II: Wetting transition triggered by a coalescence of two neighbor droplets**.** Mode III: Wetting transition triggered by coalescence of a flying droplet. We not only develop a theoretical expression which can be utilized to predict the Laplace pressure of the droplet with no fitting parameters, but also construct an explicit model which links the critical size of the droplet, and the spacing and height of the micropillars. Our experimental and theoretical results indicate that further decreased value of Laplace pressure on the top side of the individual droplet leads to instability, and subsequently a surprising spontaneous dewetting without any external force. We further reveal that the spacing of the micropillars is essential for determining the critical size of the droplet for dewetting. We have to emphasize that the contact angle hysteresis of the material/structure systems plays an essential role accounting for the motion of the droplets, only if it is further suppressed and overcome, the spontaneous dewetting can be realized effectively. We also display the statistical results between the number of dewetting transitions and transition modes, as well as the influence of the spacing of the micropillars. From Fig.3 it is clear that the wetting transition is dominant for the microstructures with the smallest value of space (S = 3 μm). On the contrary, the transition phenomenon is weakest for the microstructures with the largest value of space (S = 13 μm in *Mode I* and *Mode II*). For *Mode I*, the number of transitions decreases monotonously with S, and our findings suggest that decreasing the space of the micropillars constitutes a favorable strategy to decrease the critical size of the droplet for transitions.

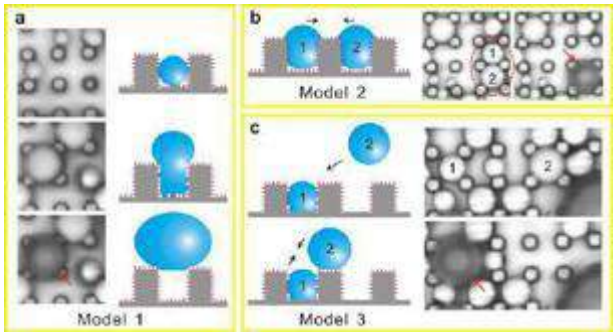

Fig. 2 Three wetting transition models of the microdroplets on the superhydrophobic substrates with two-tier roughness

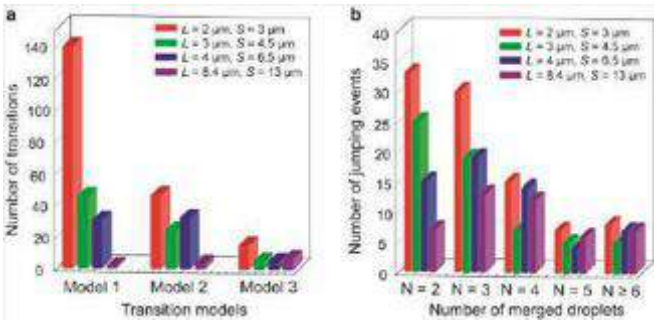

Fig. 3 (a) Number of transitions *vs* transition models; (b) Number of jumping events *vs* number of merging droplets.

References

[1] Miljkovic N. Wang E.N. *MRS Bull*. 38, 397–406,2013

[2] Wang, Q.; Yao, X.; Liu, H.; Quéré, D.; Jiang, L. *Proc*. *Natl*. *Acad*. *Sci*. *U.S.A*. *112*, 9247-9252. 2015

[3] Boreyko, J. B.; Chen, C. H. *Phys*. *Rev*. *Lett*. *103*, 184501. 2009

[4] Rykaczewski K., *Langmuir*, 28, 7720−7729. 2012

EXPERIMENTALLY OBSERVED FLOWS IN INKJET-PRINTED LIQUID RIVULETS

Xiaoze Sun, Liang Liu, Xiao Xiong & Timothy J. Singler[a)]
Department of Mechanical Engineering, SUNY Binghamton, Binghamton, New York, United States

Summary Inkjet printing technology has shown significant potential for the versatile and low-cost fabrication of micro-scale functional patterns that span applications from microelectronics to bio-engineering. Although theoretical and experimental investigations addressing the stability criteria and morphological evolution of rivulets have been discussed in literature, the transport phenomena within rivulets of dispersions or solutions have received little attention. Comprehensive study of transport in drops has firmly established the first-order role of transport process in determining the final deposition structure and functionality. This study focuses on the significantly more complex hierarchical structure in printing, the rivulet, and the corresponding role of transport on its final deposition structure and functionality. We elucidate the roles of capillary pressure and evaporation on the transport process in rivulets, the influence of liquid ink-substrate interaction and the relationship between transport and final deposition morphology.

LIQUID RIVULET FORMATION AND CAPILLARY PRESSURE DRIVEN FLOW

The inkjet printing of liquid rivulets was performed by a customized single nozzle inkjet printer coupled with three orthogonal μ-cameras enabling the visualization of the rivulet formation process and micro-scale flows inside rivulet. A typical size of the impinging droplet is about 50μm in diameter, and the width of the formed rivulet is about 100μm, depending on the advancing contact angle (θ_A) of the liquid ink on the surface of substrate. The receding contact angle is controlled at 0°, which is the prerequisite for the formation of hydrodynamically stable rivulet[1] and leads to the pinning of the contact line when the liquid starts to retract due to evaporation.

The printed liquid rivulet is characterized by the formation of a primary bulge at the initial drop landing position and linear ridge region as the leading edge of the rivulet moves forward due to continuous droplet overlapping (Fig. 1(a)). The formation of the primary bulge is due to the strong capillary pressure driven wetting process and contact angle hysteresis, according to Thompson.[2] Furthermore, the spatial gradient in the rivulet geometry (low curvature at the primary bulge and high curvature at the leading edge of the rivulet) leads to a capillary pressure gradient driven "axial flow" which pumps the liquid from the leading edge to the primary bulge continuously, as shown in Fig. 1(b) (the grey arrow represents the direction of the axial flow). The capillary pressure driven flow can be qualitatively represented by Eq. 1 as follows:

$$\Delta p = p_{front} - p_{back} \sim \gamma \left(\frac{\theta_d}{r_d} - \frac{\theta_A}{r_e} \right) > 0 \qquad (1)$$

Presumably, this capillary pressure driven transport process would be critical for the final deposition morphology and functionality if we are dealing with the patterning of functional materials via inkjet, and an elucidation of the transport in this microfluidic system would undoubtedly facilitate a fine control over this dynamic process and help with the structural optimization of the deposited materials in real-world manufacturing. Our microfluidic imaging measurement technique via tracking and decoding the motion of fluorescent particles seeded in the liquid rivulet serves as a powerful tool for the elaboration of the flow profile in the micro-scale liquid rivulet structure (Fig. 2(a)). Coupled with the new high-speed imaging technique, we are able to capture the μ-second time scale post-impact dynamics and strong surface tension driven liquid wetting and distribution, as well as the morphological evolution of the rivulet structure (Fig. 2(b)). More importantly, seeking a connection between the micro-flow profile and the morphological evolution of the rivulet provides information facilitating a fundamental understanding of the capillary pressure driven transport associated with the rivulet. Through these advanced characterization techniques, we clearly verified the existence of a pulsatile flow profile which is associated with the periodic impacts of the incoming droplets (inserted figure of Fig. 2(a) and Fig. 2(b)) for the first time. The frequency of pulsatile motion was characterized and matched with inkjet frequency.

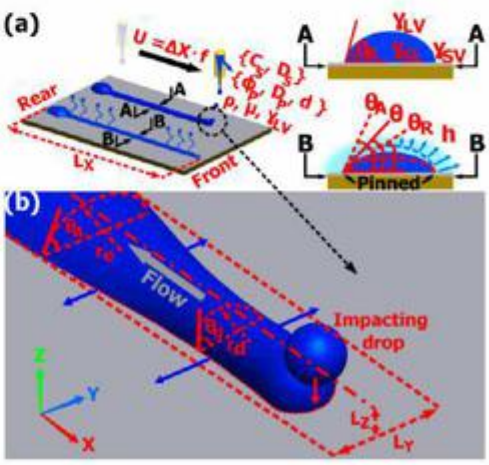

Figure 1. (a) Schematic representation of the liquid rivulet formation process via inkjet; (b) Leading edge of the rivulet depicting the surface tension driven wetting and liquid structure evolution.

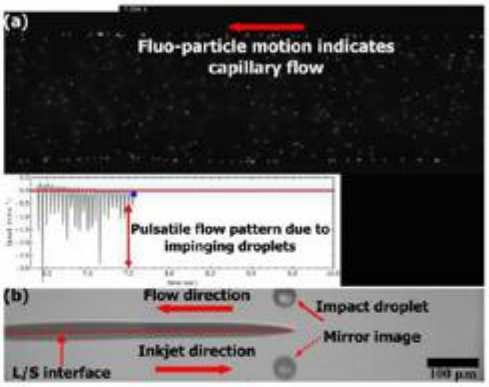

Figure 2. (a) The bottom-view fluorescent micrograph of the capillary pressure driven flow with particle motion; (b) The side-view optical micrograph of the droplet impact and rivulet formation process captured by high-speed imaging system.

[a)] Corresponding author. Email: singler@binghamton.edu.

Furthermore, the pulsation amplitude was also evaluated, and its relationship with the viscous dissipation of momentum (flow relaxation) has been drawn. The capillary pressure gradient existed in the liquid rivulet due to the geometric variation along the line axis, together with the momentum transfer due to droplet impact, leads to a strong capillary flow and axial distribution of the deposited materials. Further experiments will be performed for a quantitative characterization of the flow profiles along the line axis of the rivulet, which would provide information for a complete disclosure of the role of this capillary pressure driven transport process in material deposition and final functionality.

CONVECTIVE FLOW AND CONTROLLABLE PARTICLE SELF-ASSEMBLY AT THE CONTACT LINE

Besides the capillary pressure gradient driven flow in the line axial direction, we are also able to characterize the transverse convective flow existing in the printed rivulet, which is due to the enhanced evaporation at the contact line and usually leads to the so-called "coffee-stain" deposition profile. A fundamental investigation of the evaporatively driven convective flow would help to explain, and more importantly, mitigate the non-uniform material deposition and lead to an optimized functionality of the final product. Interestingly, one of our research projects focuses on rather mitigating, but taking advantage of such a seemly "harmful" transport process, and utilizes this convective flow for the generation of material deposition patterns which are 10 to 100 times smaller than the designed resolution of inkjet printing. The formation of the highly resolved "twin-line" patterns is due to the convectively driven particle self-assembly at the contact line (Fig. 3(a), left). Through a systematic control over the substrate surface energy, we produced high resolution patterns in a controllable manner (Fig. 3(a), middle and right). Water contact angle and pattern geometric characterization revealed reasonably good controllability over surface wetting property, quantitative matching between produced pattern width with theoretical prediction, and more interestingly, dependence of particle array width on liquid rivulet morphology (Fig. 3(b)), which haven't been explored previously. A numerical model for predicting the "twin-line" growth process was constructed, and a connection with the convective flow profile was sought, which captures the evaporation induced convective flow in inkjet printed rivulet and its relationship with the material transport and final deposition structure for the first time. This strategy also enables a fundamental understanding of the dynamic wetting process of sequentially overlapped droplets for rivulet formation and the transport in systems with varied morphologies (depending on the wetting behaviour).

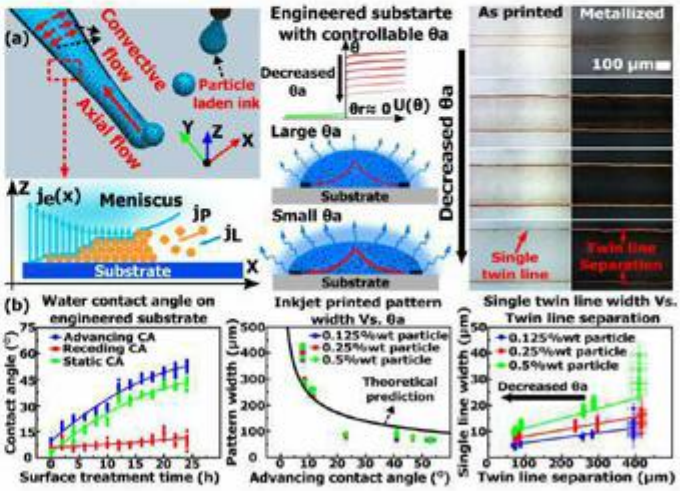

Figure 3. (a) Schematic of the particle suspension ink printing process and particle self-assembly at the contact line due to transverse convective flow (left), Engineered substrate surface with controllable wetting property (θ_A) and varied particle array formation processes (middle), high resolution "twin-line" formed on surfaces with varied wetting properties (right); (b) Measurement results of the "twin-line" width and separation distance with varied wetting property as indicated.

CONCLUSIONS

The capillary pressure gradient and evaporation induced flows in inkjet printed linear liquid rivulet have been investigated. Through tracking the fluorescent particles seeded in the liquid ink, the axial flow profiles with pulsatile feature were captured for the first time. The pulsatile characteristic of the flow inside the rivulet is due to the periodic impact of the droplets landing at the rivulet leading edge, which is coupled with the geometric variation of the rivulet and results in a strong capillary driven flow along the line axis towards the primary bulge. Furthermore, the evaporatively driven convective flow towards the contact line region was also visualized and characterized, and its relationship with the deposition morphology of the materials (nanoparticles) was drawn via a systematic control over the liquid ink wetting behaviour on the substrate surface. These two types of flows, both existing in the inkjet printed rivulet, have been proven to exert a significant influence on the final structure of deposited materials.

References

[1] Davis, S. H. *J. Fluid Mech.* **2006,** 98 (02), 225.

[2] Thompson, A. B.; Tipton, C. R.; Juel, A.; Hazel, A. L.; Dowling, M. *J. Fluid Mech.* **2014**, *761*, 261–281.

MASSIVELY PARALLEL DIRECT NUMERICAL SIMULATION OF 3D JET FLOWS

Lyes Kahouadji *[1], Jalel Chergui[2], Damir Juric[1,2], Omar Matar[1], and Seungwon Shin[3]
[1]*Department of Chemical Engineering, Imperial College London, London SW7 2AZ, United Kingdom*
[2]*LIMSI, CNRS, Universite Paris-Saclay, F-91405 Orsay, France*
[3]*Department of Mechanical and System Design Engineering, Hongik University, Seoul 121-791, Republic of Korea*

Summary We present three-dimensional simulations of two types of very challenging jet flow configurations. The first consists of a liquid jet surrounded by a faster coaxial air flow and the second consists of a global rotational motion. Such liquid jet flow configurations require a high spatial resolution and are performed with a newly developed high performance parallel code, called BLUE, for the simulation of two-phase, multi-physics and multi-scale incompressible flows, tested on up to 131072 threads on the IBM BlueGene/Q machine with excellent scalability performance. The method for the treatment of the fluid interfaces uses a hybrid Front Tracking/Level Set technique that defines the interface both by a discontinuous density field as well as by a local triangular Lagrangian mesh. Coriolis forces are taken into account and solved via an exact time-integration method that ensures numerical accuracy and stability.

INTRODUTION

Two-phase jet flows occur in a large variety of industrial configurations and also for artistic designs such as public fountains. Some jet flow configurations encompass complex hydrodynamic behaviour in many spatial scales such as the formation of primary and secondary interfacial instabilities, thin sheets, liquid rims, stretching ligaments and droplet atomization. Marmottant and Villermaux[1] highlight the process of spray formation of a liquid jet flow surrounded by a faster coaxial air flow (see fig.1-(a)). Kubitschek and Weidman [2, 3] studied a viscous liquid jet subjected to a global rotational motion for which the liquid jet shows, in the beginning, a clear preference for helical instabilities (see fig.1-(c)). The simulation of such jet flow configurations is very challenging since it requires particular numerical techniques able to handle large interface deformations and breakup phenomena and also the necessity of high spatial resolution for hydrodynamic motion occurring across many spatial scales.



Figure 1: (a) Jet flow snapshots from Marmottant and Villermaux[1] corresponding, from top to bottom, to 0.5m/s liquid jet surrounded by 15m/s air flow and 0.6m/s liquid jet surrounded by 35m/s air flow respectively. (b) Snapshot of three-dimensional simulation of 0.5m/s liquid jet surrounded by 15m/s air flow. (c) Snapshots of rotating jet flow from Kubitschek and Weidman [2, 3] at different angular velocity. (d) Snapshots of three-dimensional simulation of 4m/s liquid jet subjected to a global rotation of 400rad/s.

In figure1-(a) we show two examples of jet flows studied by Marmottant and Villermaux[1] for which we use the same physical and flow parameters in order to simulate numerically the complex process of spray formation (see Figure1-(b)). The jet flow configuration consists of a liquid jet exiting a nozzle, with inner diameter $D = 7.8$mm, and surrounded by a faster coaxial gas flow with an annulus gap width of $h = 1.7$mm. This simulation requires a very high resolution thus we decompose the entire domain into $8 \times 8 \times 32 = 2048$ subdomains and use 2048 cores with $32 \times 32 \times 32$ as the resolution per subdomain. The global resolution is $256 \times 256 \times 1024$. In figure1-(c) we show several jet flow shapes studied by Kubitschek and Weidman [2, 3] for different angular velocities of the nozzle. We also use similar physical properties with higher resolution than the previous example. We decompose the entire domain into $16 \times 16 \times 32 = 8192$ subdomains and use 8192 cores with $64 \times 64 \times 32$ as the resolution per subdomain. The global resolution is thus $512 \times 512 \times 2048$. Centrifugal and Coriolis forces are taken

*Corresponding author. Email: l.kahouadji@imperial.ac.uk

into account and treated via an exact time-integration method that ensures numerical accuracy and stability. The governing equations for transport of an incompressible two-phase flow are expressed by a single field formulation:

$$\nabla \cdot \mathbf{u} = 0, \tag{1}$$

$$\rho \left(\frac{\partial \mathbf{u}}{\partial t} + \mathbf{u} \cdot \nabla \mathbf{u} \right) = \circ \nabla P + \rho \mathbf{g} + \nabla \cdot \mu \left(\nabla \mathbf{u} + \nabla \mathbf{u}^T \right) + \rho \Omega \times (\Omega \times \mathbf{x}) \circ \ 2\rho \Omega \times \mathbf{u} + \mathbf{F} \tag{2}$$

The material properties such as density or viscosity are defined in the entire domain with the aid of the indicator function $I(\mathbf{x}, t)$, for the density for example :

$$\rho(\mathbf{x}, t) = \rho_1 + (\rho_2 \circ \ \rho_1) I(\mathbf{x}, t) \tag{3}$$

where the subscripts $_1$ and $_2$ stand for the respective phases. The fluid variables $\mathbf{u}$ and P are calculated by means of a projection method. A second order Gear scheme is used for time integration. Either explicit or implicit time integration of the viscous terms may be chosen depending on the problem. For the spatial discretization we use the well-known staggered mesh, MAC method with second order ENO advection. The pressure and distance function are located at cell centers while the x, y and z components of velocity are located at the faces. All spatial derivatives are approximated by standard second-order centred differences. The code BLUE [4] is written in Fortran 2003 which allows the definition of a set of dynamically allocated derived [data] types and generic procedures associated with the matrix of procedures, grids, scalar and vector fields, operators as well as the various solvers used in the Navier-Stokes and Lagrangian Tracking modules. The parallelization of the code is based on an algebraic domain decomposition technique where the velocity field is solved by a parallel GMRES method for the viscous terms and the pressure by a parallel multigrid method. Communication is handled by MPI message passing procedures able to be run on a simple laptop up to high performance supercomputers. The method for the treatment of the fluid interfaces uses a hybrid Front Tracking/Level Set technique which defines the interface both by a discontinuous density field as well as by a local triangular Lagrangian mesh. This structure allows the interface to undergo large deformations including the rupture and/or coalescence of fluid interfaces. The geometry of the nozzle is handled in the code by a module for the definition of immersed solid objects and their interaction with the flow for both single and two-phase flows.

CONCLUSION

We demonstrate through the simulation of two examples of jet flows the capabilities of BLUE, a new high performance parallel numerical code for the simulation of two-phase incompressible flows. The code combines high-fidelity algorithms for Lagrangian tracking of deformable phase interfaces for a precise treatment of surface tension forces, interface advection and mass conservation. The parallel structure allows calculation on highly refined grids of highly deforming fluid interfaces including rupture and coalescence. BLUE is, to our knowledge the first implementation of Lagrangian tracking on massively parallel architectures and is limited only by availability of computing resources as it has been run on up to 131072 cores on the IBM BlueGene/Q machine at the CNRS IDRIS computing center in Orsay, France.

ACKNOWLEDGEMENTS

This work is supported by (1) the Engineering & Physical Sciences Research Council, United Kingdom, through the MEMPHIS program grant, (2) the Basic Science Research Program through the National Research Foundation of Korea (NRF) funded by the Ministry of Science, ICT and future planning (NRF-2014R1A2A1A11051346) and (3) by computing time at the Institut du Developpement et des Ressources en Informatique Scientifique (IDRIS) of the Centre National de la Recherche Scientifique (CNRS), coordinated by GENCI (Grand Equipement National de Calcul Intensif). The authors wish to thank L. Tuckerman for helpful discussions.

References

[1] Marmottant P. and Villermaux E.: On spray formation. J. Fluid Mech 498:73-111, 2004.

[2] Kubitschek J. P. and Weidman P. D.: Helical instability of a rotating viscous liquid jet. Phys. Fluids 19:114108, 2007.

[3] Kubitschek J. P. and Weidman P. D.: Helical instability of a rotating viscous liquid jet. Phys. Fluids 20:091104, 2008.

[4] Shin S., Chergui J. and Juric D.: A solver for massively parallel direct numerical simulation of three-dimensional multiphase flows, arXiv 1410.8568, 2014.

INFLUENCE OF NOZZLE SHAPE ON THE BREAK-UP OF NON-NEWTONIAN INK JETS

Maxime Rosello *[1], Guillaume Maîtrejean[1], Denis Roux[1], and Pascal Jay[1]
[1]*Laboratoire Rhéologie et Procédés, Univ. Grenoble Alpes, Grenoble, France*

Summary The present work consists in an experimental study of the influence of nozzle shape onto the break-up of ink jets. Experimental data are obtained using a Continuous Ink Jet printing device and three low-viscosity inks. Several nozzle dimensions and shapes are investigated for different stimulation amplitudes. Droplet and satellites dynamics as well as jet break-up lengths for each fluid are compared and discussed with the numerical nozzle velocity profiles.

INTRODUCTION

Continuous Ink Jet printing technology relies on the efficient break-up of a micrometric ink jet issuing from a nozzle at very high speed. A periodic radius stimulation has to be applied to the fluid in order to trigger the capillary instability known as Rayleigh-Plateau instability. In order to widden the printability range of CIJ devices, one can take advantage of non-newtonian fluid properties like shear-thinning or viscoelasticity. The present work focuses on the influence of the nonlinear coupling between nozzle shape and rheological properties of inks and its influence onto the break-up dynamic. The shape of the jetting nozzle has a major influence on the velocity profile in the jet, which, in turn, influences the instability growth. Non-newtonian fluids behavior also involves modifications on the velocity profile and its relaxation when the jet leaves the nozzle. These statements motivated the present work and the understanding of interactions between nozzle shape and complex rheological properties.

EXPERIMENTAL SETUP

The experimental setup used for this study is shown on figure (1). The jet is stimulated by a piezoelectric actuator at a constant frequency of several kiloHertz. The stimulation frequency and pressure gradient are chosen in order to guarantee a wave number close to the optimal wave number calculated by Rayleigh [1]. A JetXpert® camera and a strobe light synchronized with the jet stimulation are used to observe jet and droplets. This setup is similar to the Rayleigh-Ohnesorgue Jetting Extensionnal Rheometer (ROJER) presented in [2] for the characterisation of elongationnal properties of weakly viscoelastic solutions.

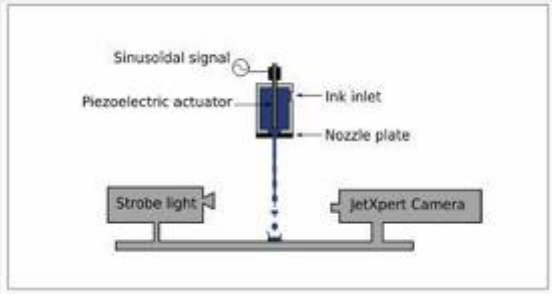

Figure 1: Experimental setup for ink jet break-up observation

Five micrometric home-designed nozzles with various shapes but a constant outlet diameter are compared. Tested fluids are low viscosity inks made of polymeric chains of various length and flexibility. The apporpriate choice of polymer made it possible to obtain three inks of comparable density, zero shear viscosity, and surface tension which display three distinct behavior : a newtonian behavior, a shear thinning behavior, and a viscoelastic behavior. Hence, a complete characterisation of rheological properties of inks has been performed beforehand. First of all, shear thinning characterisation has been made using a capillary rheometer (m-VROC from RheoSense) to obtain the dynamic viscosity at high shear rates ($\sim 5 \times 10^5\, s^{-1}$) and a rotationnal rheometer (ARG2 from TA-Instruments) to obtain the dynamic viscosity at low shear rate ($\sim 100\, s^{-1}$). Furthermore, elongationnal properties of our polymer solutions were obtained using the ROJER method.

*Corresponding author. Email: maxime.rosello@ujf-grenoble.fr

RESULTS

For each nozzle and ink, a wide stimulation amplitude sweep is performed. Figure (2) shows an example of two sweeps for the same ink but different nozzles. Although keeping the same jetting conditions, significant differences between data sets are observed, which emphasises the strong influence of nozzle shape onto droplets and satellites dynamics.

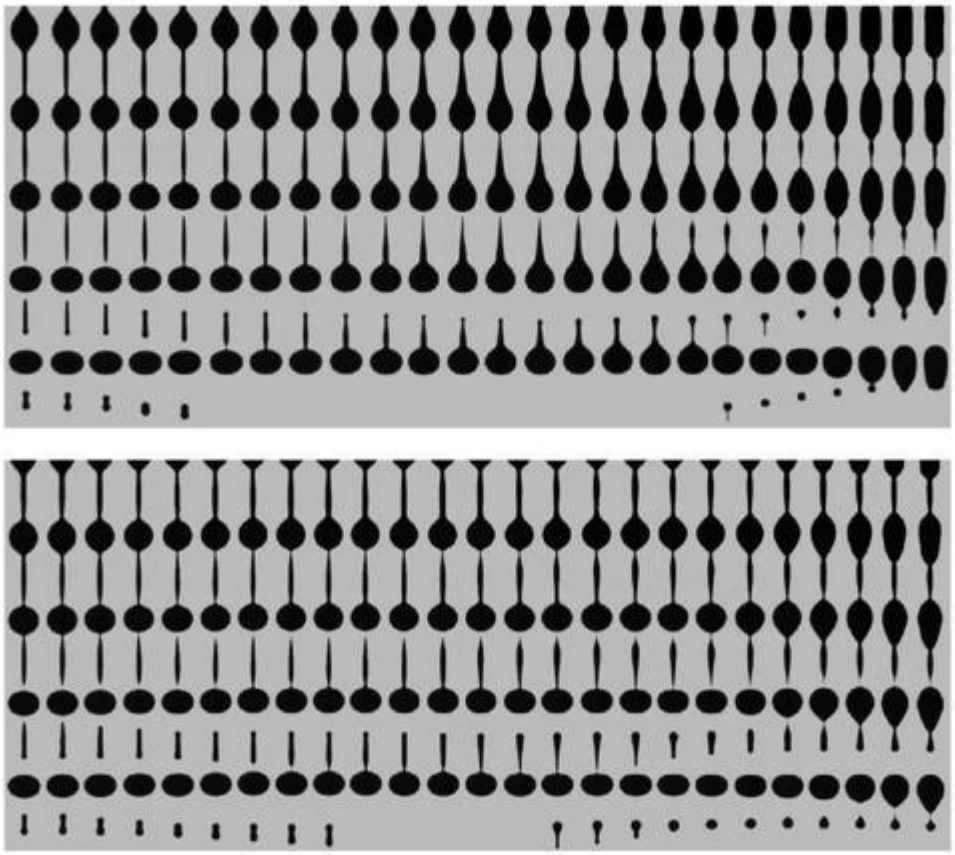

Figure 2: Amplitude sweeps for the same ink passing through two different nozzles. Constant dimensionless wave number $k = 0.6$.

Moreover, it is pointed out in the present work that the break-up length evolution as a function of stimulation amplitude reveals a strong dependency on the nozzle shape and ink rheological properties. Finally, a numerical calculation of the velocity profile in the nozzle for each case is performed for a better understanding of these links.

CONCLUSIONS

This study has been driven on a wide range of stimulation amplitude and experimental results have highlighted strong links between the nozzle shape and rheological properties of inks. These relations rely on the shape of the velocity profile and its relaxation into a plug flow.

AKNOWLEDGEMENT

The present work could not have been accomplished without the funding and assistance of Markem-Imaje, leading company in the field of printing technology and devices.

References

[1] Rayleigh L. : Proc. Lond. Math. Soc. 10(1)(1878) 4-13

[2] Keshavarz B.; Sharma, V.; Houze, E. C.; Koerner, M. R.; Moore, J. R.; Coots, P. M.; Threlfall-Holmes, P.; McKinley, G. H. : J. Non-Newtonian Fluid Mech. 2015, 222, 171.

UNDERWATER SUPERHYDROPHOBICIY: FUNDAMENTALS AND APPLICATIONS

Huiling Duan[a)]
State Key Laboratory for Turbulence and Complex Systems, Department of Mechanics and Engineering science, College of Engineering, Peking University, Beijing, China

Summary Bioinspired superhydrophobic surfaces have attracted great interest from fundamental research to engineering applications. The functioning of superhydrophobicity, especially under a submerged environment, depends on a large area fraction of entrapped liquid-air interfaces, which, however, are subject to instabilities as induced by physical phenomena such as pressurization, air diffusion, fluid flow, and condensation. The wetting states strongly impact various pertinent properties and phenomena such as liquid slippage and cavitation. This work is dedicated to elucidating the underlying mechanisms of stability and wetting transition of underwater superhydrophobicity, introducing novel strategies for durable and robust design, and probing the applications in drag reduction and cavitation control.

INTRODUCTION

Bioinspired superhydrophobic surfaces are enabled by an optimized combination of surface roughness and material chemistry [1], and have great potential for applications in self-cleaning, drag reduction, and energy conversion [2-4]. The key mechanism to realize superhydrophobicity is to maintain a large area fraction of liquid-air interfaces in a pinned Cassie-Baxter (CB) state. The collapse of the meniscus leads to wetting transition to a fully wetted Wenzel state and the failure of superhydrophobicity, as induced by pressurization. When these surfaces are fully submerged underwater, air diffusion from entrapped air cavities into bulk water may also gradually result in wetting transition, which is further deteriorated under fluid flow conditions. Moreover, microdroplet condensation within air cavities after long-time contact with water could also lead to wetting transition. Understanding the wetting transition dynamics is essential for the design and regulation of CB-based superhydrophobicity for its functionality. On the other hand, preexisting air cavities on structured hydrophobic surfaces may act as cavitation nuclei, which greatly reduce the cavitation threshold and preferentially initiate cavitation.

In this work, we elucidate the stability and wetting transition of superhydrophobic surfaces submerged underwater as influenced by pressure, air diffusion, fluid flow, and condensation, propose strategies for robust design, and investigate the application of these surfaces in liquid slippage and cavitation control.

STABILITY OF UNDERWATER SUPERHYDROPHOBICITY

Under a submerged environment, the entrapped air cavities on structured hydrophobic surfaces are isolated from the ambient, or in a closed state. The equilibrium of closed air cavities is established only if both mechanical and chemical ones are achieved. The mechanical equilibrium is governed by the balance of the liquid, the entrapped air and the capillary pressures, while the chemical one is controlled by air exchange between the entrapped air cavities and the bulk water, which is accelerated by fluid flow in a convection-diffusion regime. Moreover, microdroplet condensation within microcavities is another physical mechanism affecting the stability of underwater superhydrophobicity. In what follows, we will examine in details to see how physical factors lead to the wetting transition of submerged superhydrophobic surfaces.

Pressurization

Pressurization causes liquid penetration into entrapped air cavities, and the subsequent sliding of the three-phase contact line along the sidewalls gradually results in the failure of superhydrophobicity when the meniscus touches the pore bottom. However, the closed air cavities resist the liquid penetration under elevated liquid pressure due to air compressibility, leading to a new equilibrium state in-between the CB and Wenzel states, i.e., the depinned metastable state, which enhances the critical wetting transition pressure [5]. Laser scanning confocal microscopy (LSCM) was employed to investigate and quantify the CB-Wenzel transition and metastable states on regularly patterned surfaces submerged underwater [6]. LSCM is capable of dynamically resolving the liquid-air interfaces. The experiment results confirm the direct observation of the pinning CB and depinned metastable states, as shown in Fig. 1.

Air diffusion and fluid flow

The plastron supported on underwater superhydrophobic surfaces is susceptible to gas exchange with surrounding bulk water, especially under high liquid pressure, affecting the longevity of these surfaces. Under fluid flow conditions, a convection-diffusion regime accelerates the air exchange, and thus reduces the durability of underwater superhydrophobicity. The exchange of gas in entrapped air cavities with bulk water is controlled by a gradient of the gas partial pressure across a poorly-mixed region in water adjacent to the composite solid surface. This process was extensively quantified by LSCM under different ambient pressure conditions, and the experiment data are in good agreement with a diffusion-based model prediction. A similarity law along with a characteristic time scale is derived which governs the lifetime of the air pockets and which can be used to predict the longevity of underwater superhydrophobicity.

[a)] Corresponding author. Email: hlduan@pku.edu.cn.

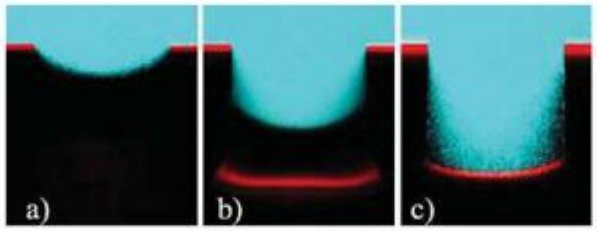

Figure 1. LSCM images of pined CB (a), depinned metastable (b), and Wenzel (c) states [6].

Condensation

Although microdroplet condensation on superhydrophobic surfaces has been extensively investigated, few researchers have noticed that when superhydrophobic surfaces are submerged underwater, microdroplet condensation occurring within entrapped air cavities after long-term contact with water can also result in wetting transition [7]. The process of microdroplet growth within hydrophobic textures submerged underwater was directly captured by LSCM, which eventually resulted in the collapse of the meniscus. The droplet growth is found to be induced by water condensation at hydrophilic defects. When the pore bottom was fabricated with sub-level structures, the condensed microdroplets were absent since the hierarchical structure enabled a sufficient self-cleaning of the pore bottom.

LIQUID SLIPPAGE REGULATION

We investigate experimentally how adhesion of superhydrophobic surfaces affects liquid slip [8-9]. Surface adhesion was regulated by sparsely grafting responsive hydrophilic polymer chains on superhydrophobic surfaces but without obviously changing the contact angle. It is found that the slip length of water on such surfaces decays quickly as the adhesive force increases. This intrinsic dependence is theoretically explained based on scaling descriptions for specific geometries. A slip length range of 87 μm can be achieved reversibly by changing the temperature below and above the low critical solution temperature (LCST) of the grafted temperature-sensitive polymer. The results shed light on the intrinsic mechanism of liquid slip on textured surfaces.

CAVITATION INCEPTION UNDER REDUCED PRESSURE

Gas cavities entrapped on structured hydrophobic surfaces play important roles in realizing their functionalities. We present a complete theoretical analysis to predict cavity morphological change under reduced liquid pressure, on a submerged hydrophobic surface patterned with cylindrical pores [10]. Equilibrium solutions are derived for five different phases, namely, (I) pinned recession, (II) depinned recession, (III) Cassie-Baxter, (IV) expansion, and (V) coalescence; their stabilities are also analyzed. A phase map is developed outlining the different regimes with respect to the gas amount and liquid pressure. Importantly, phase (IV) exhibits a complex stability behaviour that leads to two possible routes to coalescence, which lends two different mechanisms of cavitation. Accordingly, the threshold pressure for cavitation can be calculated. The theoretical model is supported by direct experimental measurements via confocal microscopy and demonstrates good quantitative accuracy. This work provides a predictive tool for the design of functional structured hydrophobic surfaces

References

[1] Onda, T., Shibuichi, S., Satoh, N., Tsujii, K.: Super-water-repellent fractal surfaces. *Langmuir* **12**: 2125-2127, 1996.

[2] Bixler, G., Theiss, A., Bhushan, B., Lee, S.: Anti-fouling properties of microstructured surfaces bio-inspired by rice leaves and butterfly wings. *J. Colloid Interface Sci.* **419**: 114–133, 2014.

[3] Rothstein, J.P.: Slip on Superhydrophobic Surfaces. *Annu. Rev. Fluid Mech.* **42**: 89-109, 2010.

[4] Miljkovic, N., Wang, E.: Condensation heat transfer on superhydrophobic surfaces. *MRS Bull.* **38**: 397–406, 2013.

[5] Xue, Y., Chu, S., Lv, P., Duan, H.: Importance of hierarchical structures in wetting stability on submersed superhydrophobic surfaces. *Langmuir* **28**: 9440-9450, 2012.

[6] Lv, P., Xue, Y., Shi, Y., Lin, H., Duan, H.: Metastable States and Wetting Transition of Submerged Superhydrophobic Structures. *Phys. Rev. Lett.* **112**: 196101, 2014.

[7] Lv, P., Xue, Y., Liu, H., Shi, Y., Xi, P. Lin, H., Duan, H.: Symmetric and Asymmetric Meniscus Collapse in Wetting Transition on Submerged Structured Surfaces. *Langmuir* 31: 1248-1254, 2015.

[8] Wu, Y., Xue, Y., Pei, X., Cai, M., Duan, H., Huck, W., Zhou, F., Xue, Q.: Adhesion-Regulated Switchable Fluid Slippage on Superhydrophobic Surfaces. *J. Phys. Chem. C* **118**: 2564-2569, 2014.

[9] Xue, Y., Wu, Y., Pei, X., Duan, H., Xue, Q., Zhou, F.: How Solid-Liquid Adhesive Property Regulates Liquid Slippage on Solid Surfaces?. *Langmuir* **31**: 226-232, 2014.

[10] Xue, Y., Lv, P., Liu, Y., Shi, Y., Lin, H., Duan, H.:, Morphology of gas cavities on patterned hydrophobic surfaces under reduced pressure. *Phys. Fluids* **27**: 092003, 2015.

FROM THE NANO- TO THE MACROSCALE — BRIDGING SCALES FOR THE MOVING CONTACT LINE PROBLEM

Andreas Nold * [1], Benjamin D. Goddard[2], David N. Sibley[3], and Serafim Kalliadasis[1]
[1]*Department of Chemical Engineering, Imperial College London, London, UK*
[2]*The School of Mathematics and Maxwell Institute for Mathematical Sciences, The University of Edinburgh, Edinburgh, UK*
[3]*Department of Mathematical Sciences, Loughborough University, Loughborough, UK*

Summary The moving contact line problem is one of the remaining unsolved fundamental problems in fluid mechanics. At the heart of the problem is its multiscale nature: a nanoscale region close to the solid boundary where the continuum assumption breaks down, must be bridged with a macroscopic region where the usual laws of hydrodynamics apply.

At the macroscale, we review our recent effort to show that direct matching between the inner (nanoscale) region and the outer (macroscale) region is possible through an overlap domain, thus simplifying the analysis presented to date in the literature. Our analysis is also in agreement with results from diffuse interface approaches.

At the nanoscale, the density profile at the contact line region is obtained using classical density-functional theory. This is used in combination with extended Navier-Stokes equations to compute advancing and receding contact lines. Our results are compared with predictions from molecular kinetic theory.

INTRODUCTION

It is well known that applying classical hydrodynamic equations to the moving contact line problem leads to a non-integrable stress singularity. Typically, it is concluded that the continuum assumption breaks down in the vicinity of the contact line and that nanoscale effects relieve the singularity. The main challenge in modelling the moving contact line is therefore twofold: First, the outer region (macroscopic) contact angle visible to the naked eye needs to be linked to the inner region contact angle at the nanoscale by bridging several lengthscales. Second, physical effects at the nanoscale need to be included in a self-consistent manner to predict the dynamic contact angle in the vicinity of the contact line.

In Ref. [8], we showed that the classical asymptotic analysis presented in Refs. [1, 3, 9], linking the inner region to the outer region via a viscocapillary balance can indeed be done in a systematic asymptotic manner and without the need for an intermediate region. Here, it is shown that our asymptotic results for the macroscopic equations are in agreement with diffuse interface computations, which also allow us to extract an effective slip. We then compute the nanoscale behaviour in the vicinity of the contact line by employing density-functional theory (DFT) in a dynamic setting. Our results compare well with predictions from molecular kinetic theory (MKT).

THE VISCOCAPILLARY BALANCE

In our recent work in Ref. [8], we demonstrated that direct matching between the inner and the outer region is possible without the need for an intermediate region as done in the literature. Therefore, any self-consistent model for the inner region should include the full overlap region, where viscous and surface tension forces balance (the viscocapillary region). We test this statement by modelling a binary fluid of two immiscible species using diffuse interface Navier-Stokes/Cahn-Hiliard (NS/CH) equations. In this case, the contact line singularity is relieved via diffusion along the substrate and along the fluid interface. The inner region length scale is defined by the diffusion length, which is independent from the interface thickness. For the computations presented here, the inner region is singled out following ideas outlined in Ref. [6].
In Fig. 1, it is shown that the model captures the full viscocapillary region. In particular, it is evident that away from the substrate, the slope of the fluid interface increases logarithmically with the distance to the substrate, in agreement with asymptotic results. The slip length, which here is employed as a fitting parameter, is shown to converge to approx. 0.45 ± 0.02 times the diffusion length. Away from the substrate, it can be shown that classical boundary conditions are retrieved at the fluid interface, as predicted analytically in Ref. [7].

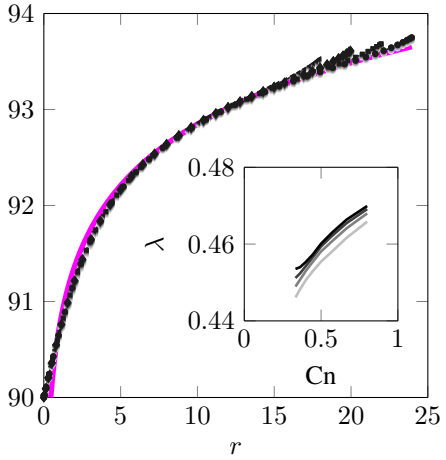

Figure 1: Angle of inclination of the fluid interface in $[^\circ]$ as a function to the distance to the contact line r (black symbols) and fit to the viscocapillary balance (magenta line). Inset: Slip length λ as a function of the Cahn number Cn.

*Corresponding author. Email: andreas.nold09@imperial.ac.uk

THE NANOSCALE

A more accurate description of the nanoscale effects in the vicinity of the contact line for a single fluid of spheres with diameter σ can be obtained by using DFT. This self-consistent statistical mechanics framework for equilibrium systems allows to model density oscillations close to the wall due to hard-sphere packing effects, as well as long-range dispersion forces. The density structure at the equilibrium contact line has been analysed in detail in Refs. [4, 5]. Here, we combine this equilibrium theory with the extended NS-like equations derived in Ref. [2], and compute advancing and receding contact lines (see Fig. 2). Computational results are compared with predictions from linear MKT theory, giving a good agreement.

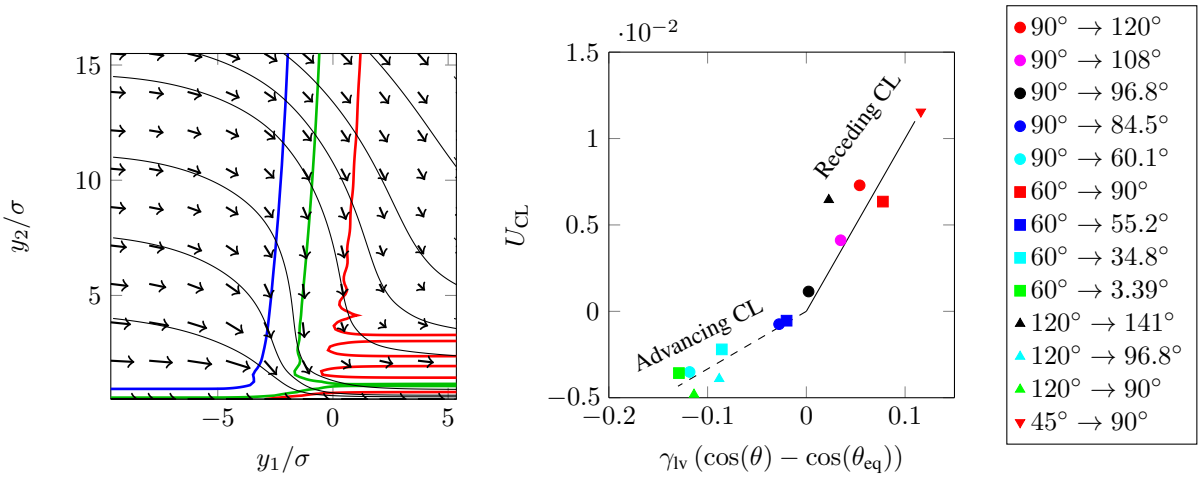

Figure 2: Dynamic DFT (DDFT) computations at the moving contact line. Left subplot: Density isolines (blue, green and red solid lines), and velocity field in the moving frame of reference (black solid streamlines and arrows). y_1 and y_2 are coordinates in direction parallel and perpendicular to the substrate, respectively. Right subplot: Contact line velocity U_{CL} vs. force acting at the contact line, where γ_{lv} is the liquid-vapour surface tension and θ_{eq} is the equilibrium contact angle. Coloured symbols are results from DDFT, with initial and equilibrium contact angles given in the legend. Black solid and dashed lines are fits to the prediction from linear MKT for receding and advancing contact lines, respectively.

CONCLUSIONS

Modelling a binary fluid contact line by NS/CH equations reveals the overlap between the inner and the viscocapillary region at the contact line, as shown in our previous effort for macroscopic/sharp-interface modes. The NS/CH computations also allow us to extract an effective slip length. For simple fluids, ideas from DFT are used in a dynamic framework to predict the inner region contact angle at the nanoscale. Results show a good agreement with linear MKT theory.

ACKNOWLEDGEMENTS

We acknowledge financial support from Imperial College through a DTG International Studentship and ERC Advanced Grant No. 247031.

References

[1] R. G. Cox. The dynamics of the spreading of liquids on a solid surface, Part 1. Viscous flow. *J. Fluid Mech.*, 168:169, 1986.
[2] B. D. Goddard, A. Nold, N. Savva, P. Yatsyshin, and S. Kalliadasis. Unification of dynamic density functional theory for colloidal fluids to include inertia and hydrodynamic interactions: derivation and numerical experiments. *J. Phys.: Condens. Matter*, 25:035101, 2013.
[3] L. M. Hocking and A. D. Rivers. The spreading of a drop by capillary action. *J. Fluid Mech.*, 121:425, 1982.
[4] A. Nold, D. N. Sibley, B. D. Goddard, and S. Kalliadasis. Fluid structure in the immediate vicinity of an equilibrium three-phase contact line and assessment of disjoining pressure models using density functional theory. *Phys. Fluids*, 26:072001, 2014.
[5] A. Nold, D. N. Sibley, B. D. Goddard, and S. Kalliadasis. Nanoscale fluid structure of liquid-solid-vapour contact lines for a wide range of contact angles. *Math. Model. Nat. Phenom.*, 10:111, 2015.
[6] P. Seppecher. Moving contact lines in the Cahn-Hilliard theory. *Int. J. Eng. Sci.*, 34:977, 1996.
[7] D. N. Sibley, A. Nold, and S. Kalliadasis. Unifying binary fluid diffuse-interface models in the sharp-interface limit. *J. Fluid Mech.*, 736:5, 2013.
[8] D. N. Sibley, A. Nold, and S. Kalliadasis. The asymptotics of the moving contact line: cracking an old nut. *J. Fluid Mech.*, 764:445, 2015.
[9] O. V. Voinov. Hydrodynamics of wetting. *Fluid Dynamics*, 11:714, 1976.

MEASUREMENT OF APPARENT SLIP NEAR A HIGH SPEED RECEDING CONTACT LINE ON A HYDROPHOBIC SURFACE

Joonsik Park[a], Kenneth S. Breuer
School of Engineering, Brown University, Providence, Rhode Island, USA

Summary The flow near a receding contact line on a hydrophobic surface was measured using a particle tracking velocimetry from two different experimental techniques: multi-layer flood illumination and Total Internal Reflection Fluorescent Microscopy. The high speed receding contact line motion was generated using a liquid bridge instability by stretching a liquid bridge formed between a syringe and a hydrophobic substrate. Significant apparent slip is observed and the derived slip velocity appears to be inversely proportional to the distance from the contact line, while the slip length changes from O(10 nm) to O(1u\μm) toward the contact line singularity.

INTRODUCTION

The boundary condition at a moving contact line remains as a challenge to the continuum description of fluid mechanics since it was first identified by Huh and Scriven [1]. When the no slip boundary condition applied to a creeping flow solution, the velocity at the contact line becomes multi-valued and the corresponding shear stress diverges infinitely. The resolution of this apparent paradox has become a lively topic of debate with suggestions ranging from the use of a slip model, a diffuse interface model, a variational method, molecular kinetic theory and the interface formation/disappearance model, to name a few [2]. Unlike the multifaceted theoretical debates, however, a few detailed, high resolution measurements of the boundary condition near a moving contact line have been made. In this work, we present particle tracking velocimetry (PTV) measurements of apparent slip near a receding contact line on a hydrophobic surface from two independent experimental techniques, multi-layer flood illumination and Total Internal Reflection Fluorescence Microscopy (TIRFM).

EXPERIMENTAL METHODS

The experimental setup for flood illumination and objective-based TIRFM on an inverted microscope is shown in figure 1. A syringe needle with a radius of 70 μm was lowered using a micro-stage until the pendant water droplet forms a liquid bridge in contact with a hydrophobic coverslip glass (contact angle of 110.8°). By retracting the syringe, a pinch-off instability was generated which generates a moving contact line that initially retreats slowly, in a quasi steady manner, but then accelerates to become a rapidly moving contact line as the liquid bridge pinches off to form a small droplet on the surface. Contact line velocities ranging from 150 to 3000 μm/s were repeatedly generated in this manner. The water filling the syringe was purified and mixed with 0.01% vol. fraction of fluorescent polystyrene particles (300 nm diameter). The fluorescent signals from either flood illumination or TIRFM were captured with a 100X objective and a 1.5X internal lens and recorded at 2000 fps with a CMOS camera coupled to a two-stage photon intensifier via 1:1 relay lens. The room temperature and humidity were regulated between 20 to 22°C and 10 to 20%, respectively. For multi-layer flood measurements, the objective was initially focused on the particles stuck on the glass and vertically translated twice in steps of 1 μm, for a total of three measurements. The mean vertical distances for each layer were computed accordingly from the depth of focus 800 nm of the objective and the size of particles. For TIRFM measurements, the penetration depth of the exponentially decaying evanescent field was measured as 214 nm. From the recorded images, contact line and particle positions were detected using a Canny edge detection algorithm and Gaussian fitting, respectively. The SPTV using Kalman filtering was implemented to reduce noise in particle velocities from Brownian motion and measurement error. Using more than 100,000 filtered particle trajectories, the velocity field was estimated using 2-D log-normal kernel density estimation.

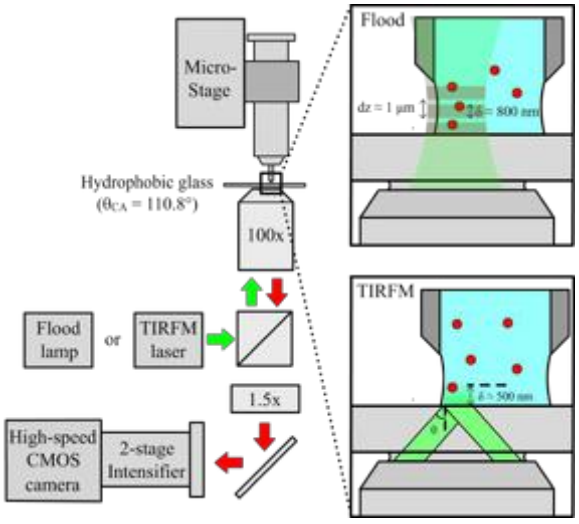

Figure 1. Experimental setup of flood illumination and total internal fluorescent microscopy. (δ: observation region, dz: interval between each depth of focus, θ: laser beam incident angle)

[a] Corresponding author. Email: Joon_Sik_Park@brown.edu

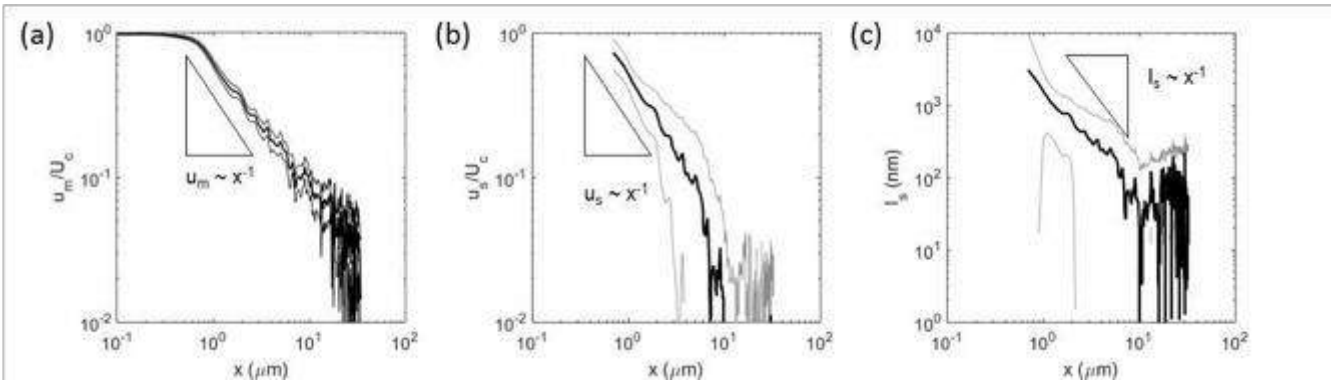

Figure 2. Flood illumination measurement of (a) normalized mean velocity near a substrate, (b) normalized slip velocity at the substrate, and (c) slip length near a moving contact line.

RESULTS

A result from multi-layer flood illumination is presented in Figure 2 with grey lines indicating standard errors. The particle velocities from the measurements are normalized by the corresponding contact line speed, U_c and are used to construct the velocity profile, $U(z)$, as a function of the distance from the contact line, x. In Figure 2(a), u_m is the mean velocity obtained from the bottom layer, with a mean distance of 300 nm from the glass surface. When $x < 1$ μm, the mean velocity u_m/U_c exhibits a power law dependence of x^{-1}. In figure 2(b), the slip velocity u_s was obtained by linear interpolation of the multi-layer measurements. Again, a power law dependence, $u_s \sim x^{-1}$ is observed until $x \sim 10$ μm where u_s become indistinguishable from the minimum resolvable velocity. Interestingly, in figure 2(c), the slip length, l_s, which is computed from the slip velocity and the shear rate, both derived from the linear interpolation, *also* exhibits a power law close to $l_s \sim x^{-1}$. At $x > 10$ μm, the slip length is in the order of 10 nm, which is consistent with the previous studies of slip length measurements between liquid-solid interface from a microfluidics channel [2].

CONCLUSIONS

The result presented here is quite startling as the apparent slip length becomes as high as in the order of 1μm close to the moving contact line. On the other hand, the universal power law dependence of $u_s \sim x^{-1}$ at various contact line speeds agrees with the theoretical analysis by Dussan [3]. The experimental artifacts such as particle size effect, near-surface particle-wall interaction, heating from the illumination, and measurement bias from a certain experimental technique have been ruled out as possible sources of error. The measurements from TIRFM with different size of particles will be presented in a future publication. The x^{-1} power law also is consistent with our previous measurement with a receding contact line at a low speed [4]. To the authors' best knowledge, our result is the first quantitative nanoscale observation of apparent slip near a moving contact line over a range of speeds, which can be utilized to test existing theoretical models.

References

[1] Huh C., Scriven L., Hydrodynamic model of steady movement of a solid/liquid/fluid contact line. *J. Colloid Interface Sci*. **35**, 85-10, 1971

[2] Lauga E., Brenner M., Stone H., Microfluidics: The no-slip boundary condition. *Handbook of Experimental Fluid Dynamics*, 1219-1240, 2007

[3] E. B. Dussan V, The moving contact line: The slip boundary condition. *J. Fluid Mech*. **77**, 665-684, 1976

[4] Qian B., Park J., Breuer K., Large apparent slip at a moving contact line, *Physics of Fluids* **27**, 091703, 2015

EFFECT OF THE LUBRICATION FILM ON THE DROPLET DYNAMICS IN A HELE-SHAW MICROCHANNEL

Jose-Maria Fullana*[1,2], Yue Ling[1,2], Stéphane Popinet[1,2], and Christophe Josserand[1,2]
[1] *CNRS, UMR 7190, Institut Jean le Rond d'Alembert, F-75005, Paris, France*
[2] *Sorbonne Universités, UPMC Univ Paris 06, UMR 7190, Institut Jean le Rond d'Alembert, Paris, France*

Summary We focus on the regime at low capillary number, where the droplet keeps a circular shape in the horizontal plane. Parametric studies are performed on the droplet horizontal radius and the capillary number, and particular attention is paid to the effect of the lubrication film on the droplet velocity. For droplets with an horizontal radius larger than half of the channel height, the droplet overfills the channel and a lubrication film is formed between the droplet and the wall. The lubrication film is shown to have a strong impact on the droplet migration velocity and the three-dimensional flow structure.

INTRODUCTION

A comprehensive understanding of droplet migration in confined microchannels is essential to many microfluidics applications i.e. for performing biochemical or chemical assays or to observe liquid-liquid extraction. Droplets are unit systems of controlled volume and content characterized by a radius R, within which mixing, reacting and/or transferring can be achieved. Rectangular confined channels with a width significantly larger than the height H are commonly used in microfluidics devices. The 3D simulations of droplet migration in a microchannel are challenging as well, in particular for droplets with large ratio R/H and small capillary number C_a which measures the relative importance of viscous stresses compared to surface tension. Numerical simulation can give supplementary information about droplet shape, streamlines, velocity patterns, stresses, which is difficult to extract from experimental data. We investigate the droplet migration in a Hele-Shaw microchannel through 3D direct numerical simulations. The capillary number ($2.3\ 10^{-2}$) of the droplet is considered to be small enough so that the horizontal shape of the droplet is near-circular. Particular attention will be paid to the effects of the lubrication film on the droplet dynamics to study the flow patterns around the droplet.

EQUATIONS

We use the incompressible ($\nabla U = 0$), three-dimensional variable-density NavierStokes equations with surface tension:

$$\rho\left(\frac{\partial U}{\partial t} + U\nabla U\right) = \circ\ \nabla p + \nabla(2\mu D) + \sigma\kappa\delta\bar{n}$$

with D the deformation tensor, $U = (u, v, w)$ the fluid velocity, $\rho = \rho(x, y, z, t)$ the fluid density, $\mu = \mu(x, y, z, t)$ the dynamic viscosity. The Dirac distribution function δ expresses the fact that the surface tension term is concentrated on the interface; σ is the surface tension coefficient, κ and $\bar{n}$ the curvature and normal to the interface. For two-phase flows we introduce the volume fraction $c(x, y, z, t)$ of the first fluid and define the density and viscosity as a function of c. The Navier-Stokes equations are solved using a finite volume approach based in a projection method. The spatial discretization is done using a octree cubic cells allowing dynamical grid refinement in the lubrication film and the accurate computation of the surface tension at such small scales. The numerical problem is solved using the open-source package Gerris [1]. The

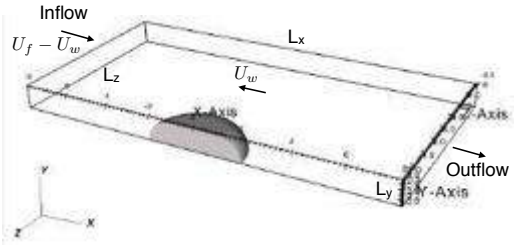

Figure 1: Microfluidic configuration: channel width is H, velocities are U_f the mean flow velocity and U_d the droplet velocity.

computational domain for 3D droplet migration in a Hele-Shaw microchannel is shown in Figure 1 where it is assumed that the droplet motion and the corresponding flow are symmetrical in the y and z directions, with respect to the planes $y = 0$ and $z = 0$. Taking the half-height of the channel H as the typical length scale, the length, height, and width of the computational domain are taken as L_x= $16H$, $L_y = H$, and$L_z = 8H$. An inflow boundary condition is imposed on the left of the domain with a parabolic velocity profile.

*Corresponding author. Email: jose.fullana@upmc.fr

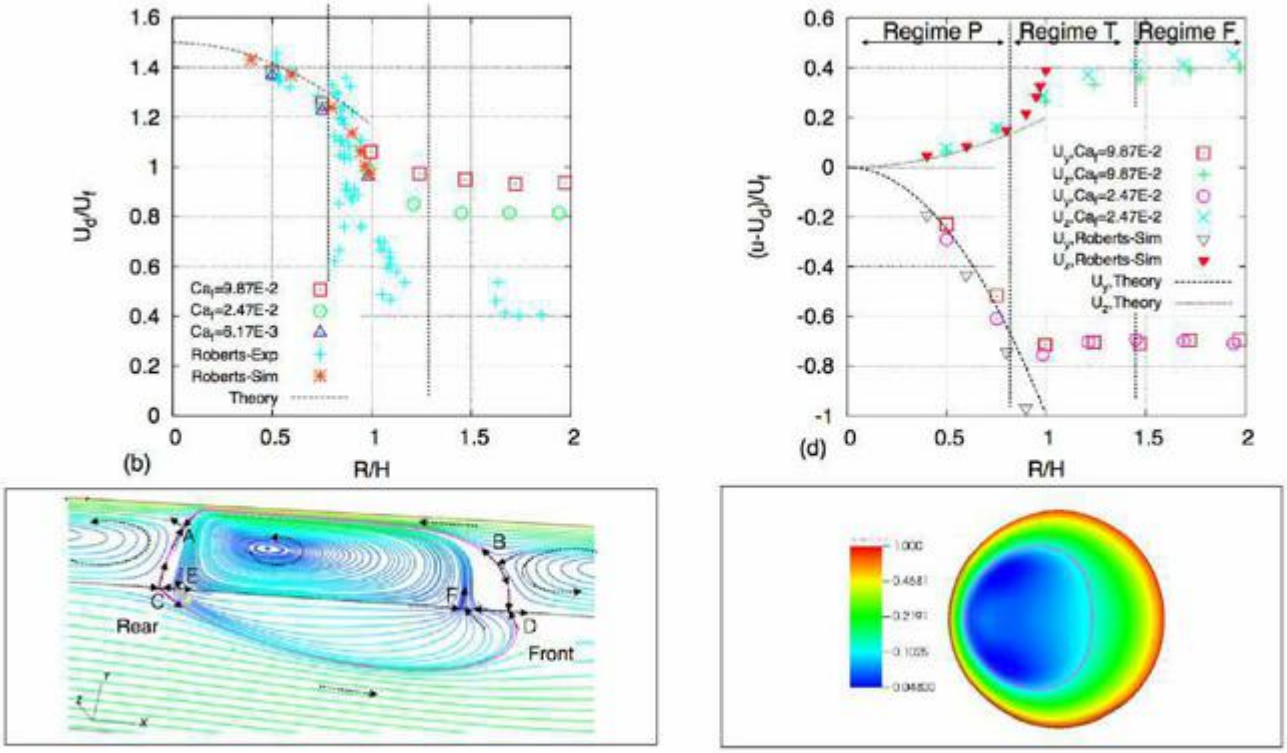

Figure 2: Top panel: Mean droplet velocity (left) and relative u-velocities (right) at the top and the side of the droplet as functions of droplet radius and capillary number. Bottom panel: streamlines in the droplet reference frame (left) and film thickness (right)

RESULTS

According to the numerical and experimental results [3, 5], the variation of U_d with R/H can be divided into three different regimes: the Poiseuille-dominated regime, the transient regime and the film-dominated regime, which are schematically shown in Figure 2 (top panel). In a Poiseuille-dominated regime (Regime P), the droplet velocity is close to the maximum fluid velocity, when R/H increases, U_d decreases (solid lines theory are from ref [4]). In a Transition regime (Regime T), the droplet just overfills the channel and the lubrication film just starts to form. Finally in the film-dominated regime (Regime F), $R/H >> 1$, the droplet velocity is controlled by the lubrication film. The film thickness becomes completely independent from the horizontal radius and becomes dependent on the Capillary number. For the film-dominated regime Figure 2 (bottom panel) shows the 3D streamlines (left) and the film thickness (right) using a color graduation between 1 and 0 in units of H (from red to dark blue). The stream lines concentration at the rear top of the droplet indicates a high shear stress region. This region is correlated with the bump in the shape observed in Figure 2 (bottom panel right). We note that the minimum dark blue is 5/100 of H. A complete description of film dynamics is presented in [5].

CONCLUSIONS

We have presented numerical simulations of a droplet in a channel. The good behavior of the numerical implementation of the Navier-Stokes equations with a surface tension model was demonstrated by comparisons with theory and experimental data. The quality of the numerical results are, in particular, a consequence of the grid refinement approach which allows the accurate computation of the very thin films of liquid between the droplet and the wall.

References

[1] Popinet, S. *An accurate adaptive solver for surface-tension-driven interfacial flows*, J. Comp. Physics, 228.16 (2009): 5838-5866.

[2] Bretherton, F. P. *The motion of long bubbles in tubes*, J. Fluid Mech., 10.02 (1961): 166-188.

[3] Roberts C. C., Roberts S. A., Nemer M. B., and Rao, R. R. *Circulation within confined droplets in HeleShaw channels*, Phys. Fluids, 26, 032105 (2014).

[4] Nadim A. and Stone H. A., *The motion of small particles and droplets in quadratic flows*, Stud. Appl. Math., 85, 5373 (1991).

[5] Ling Y., Fullana J-M, Popinet P. and Josserand Ch., Submitted to Phys. Fluids, 2016.

SLIP FLOW IN COLLASPING MICROCHANNELS

Krishnashis Chatterjee[1] and Anne Staples*[2]

[1,2]*Department of Biomedical Engineering And Mechanics, Virginia Tech, Blacksburg, Virginia, U.S.A*

Summary In this study we investigate the effects of rarefaction on the flow through a two-dimensional microchannel driven by periodically collapsing walls. The Navier Stokes equations are linearized using lubrication theory assumptions, and slip boundary conditions are imposed. Two up-down symmetric collapse sites in the channel are periodically actuated. The axial and vertical velocities, axial pressure gradient, and time averaged flow rates are found as a function of the phase lag between the two contraction sites, with and without slip. The optimal phase lag that maximizes the flow rate increases with the value of the slip parameter, from approximately 60° for no slip to approximately 70° for the largest value of the slip parameter considered, $\beta = 0.1$. As is the case for pressure driven flow through a microchannel, adding slip is found to reduce the rate of contraction-driven flow through the microchannel.

INTRODUCTION

Here, we extend the results of earlier studies [1],[3],[4],[7]. In that series of papers, inspired by features found in insect respiration, periodic collapses were established as a means for driving flow through a microchannel. In the earlier studies, only the upper wall of the channel contracted, and no-slip boundary conditions were imposed at the walls. The current study extends the earlier results by adding first-order slip boundary conditions and imposing contractions on both the upper and lower walls. These symmetric collapses are necessary in order to obey the assumptions of the slip flow model used. Slip effects can be assumed to occur in regions of insect tracheal networks, since the working fluid is air near atmospheric pressure and the diameter of the tracheal tubes for typical insects ranges from 1 to several hundred micrometers. Thus, the current study investigates the bio-inspired regime of low-Reynolds number flow in a microchannel with rarefaction effects.

PROBLEM FORMULATION

The incompressible flow in a two-dimensional rectangular microchannel is considered. The channel length L is assumed to be much greater than the width W so that $\delta = W/L << 1$. The upper and the lower wall contraction profiles are functions of time and distance from the beginning, and are given by $H_2(x,t)$ and $H_1(x,t)$ respectively.

For the microscale flow we can assume the Reynolds number to be of the same order of magnitude as the reciprocal of the channel aspect ratio, according to the lubrication theory assumptions. Neglecting the convective terms, the simplified form of Navier Stokes becomes

$$\frac{\partial u}{\partial x} + \frac{\partial v}{\partial y} = 0 \tag{1}$$

$$\circ\ \frac{\partial p}{\partial x} + \frac{\partial^2 u}{\partial y^2} = 0 \tag{2}$$

$$\frac{\partial p}{\partial y} = 0. \tag{3}$$

Using the following boundary conditions

(i) at $y = H_1(x,t)$, $u = \beta\frac{\partial u}{\partial y}$, $v = \frac{\partial H_1}{\partial t}$
(ii) at $y = H_2(x,t)$, $u = \beta\frac{\partial u}{\partial y}$, $v = \frac{\partial H_2}{\partial t}$
(iii) at $x = 0$, $p = p_o(t)$
(iv) at $x = 1$, $p = p_L(t)$.

we derive the expressions for the axial velocity, pressure gradient, total pressure and time averaged flow rate.

*Corresponding author. Email: staplesa@vt.edu

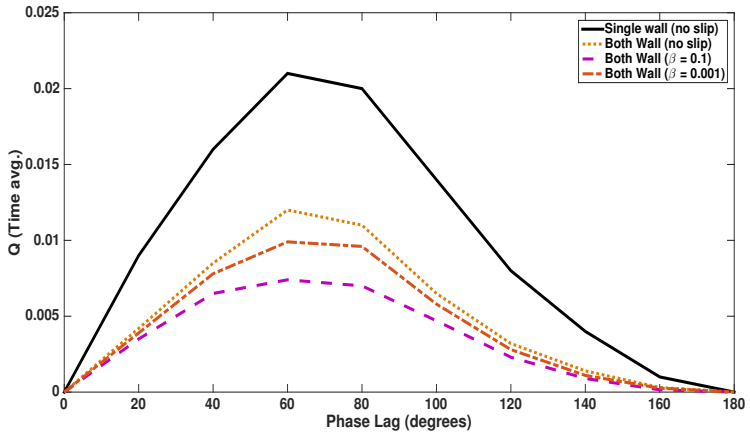

Figure 1: Time averaged net flow rate plotted for different phase lag values over an entire cycle at x = 0., the midpoint of the channel.

RESULTS

Three different values of the slip parameter β were considered, 0 (representing no-slip conditions), 0.001 (low-slip conditions), and 0.1 (high-slip conditions). Two collapse sites, one located at $0.25L$ and the other at $0.75L$, were actuated periodically. Details of the actuation and collpase functions can be found in [5] and [7]. We found that both the axial velocity and pressure gradient have higher values in the contraction regions of the channel, regardless of the value of the slip parameter. The velocity and the pressure gradient values for first half of the cycle (collapse) are identitical to that of the second half (re-expansion) in case of zero degree phase lag (i.e., collapse at the same time), regardless of the value of β, but for other phase lag values they differ. It is this temporal symmetry breaking between the first and the second half of the cycle that causes the unidirectional flow in the channel. Also, as seen in Figure 1, the time averaged flow over an entire cycle is significantly lower in case of double wall contractions than in the case of single (upper) wall contractions, even though the change in cross sectional area is preserved. This is because the momentum injected into the flow toward the center of the channel from the upper and lower walls tends to cancel. In Figure 1 it can also be seen that the introduction of slip reduces the net flow rate, with the reduction being proportional to the value of the slip parameter, β.

CONCLUSIONS

From the present study we conclude that in the absence of slip the time averaged flow rate is lower when both walls contract compared to when just a single wall contracts, even though the total reduction in cross-sectional area is the same in both cases. Adding slip decreases the flow rate further, with the reduction in flow rate found to be proportional to the value of the slip parameter β. The motivation of this study was to investigate the effect of slip boundary conditions on the fluid flow in microchannels driven by symmetric wall contractions. It can be concluded that adding slip to these flows decreases the net flow rate substantially. It has been established both theoretically and experimentally that adding slip to pressure-driven flow through a microchannel reduces the flow rate [6]. The results of this study indicate that the same is true for contraction-driven flow through a microchannel.

References

[1] Y. Aboelkassem and A.E. Staples, Selective pumping in a network: insect style microscale flow transport, Bioinspiration and biomimetics. Vol. 8, No. 2,026004

[2] S. Uchida and H. Aoki, Unsteady flows in a semi-infinite contracting or expanding pipe, J. Fluid Mech. 82 (1977), 371-387.

[3] Y.Aboelkassem and A.E.Staples, A three-dimensional model for flow pumping in a micro channel inspired by insect respiration, Acta Mech 225, 493-507(2013)

[4] Y. Aboelkassem and A.E.Staples, Stokeslets-meshfree computations and theory for flow in a collapsible micro channel, Theoretical and Computational Fluid Dynamics. Vol. 27, Issue 5, 681-700,(2013)

[5] Y. Aboelkassem, A.E. Staples, and J.J. Socha, Microscale flow pumping inspired by rhythmic tracheal compressions in insects, Proceedings of the ASME Pressure Vessels and Piping Conference, PVP2011 (2011), 57061.

[6] A. Agrawal, A comprehensive review on gas flow in microchannels, Volume 2, Number 1, (2011).

[7] Y. Aboelkassem, A.E. Staples, Flow transport in a micro channel induced by moving wall contractions: a novel micro pumping mechanism, Acta Mech 223, 463-480 (2012).

ACEO MIXING OF FLUIDS IN MICROCHANNELS WITH ASYMMETRIC ELECTRODES

Han Chen[1a)], Hua Liu[1], Feng Zhang[1] & Yuantai Hu[1]

[1]*Department of Mechanics, Huazhong University of Science and Technology, Wuhan, Hubei, China*

Summary In this paper, mixing of fluids in microchannels using AC electroosmotic(ACEO) flows with asymmetric electrodes are studied. Effects of geometric parametric of the asymmetric electrodes on the mixing efficiency are investigated using numerical simulation methods. Experimental results in PDMS-based microfluidic chips are compared with numerical results to confirm enhanced mixing in the micromixer, and optimal design of the asymmetric ACEO electrodes is proposed.

INTRODUCTION

Mixing is essential in many microfluidic devices, especially for those performing biochemical assays or chemical reactions. Due to the small characteristic dimensions of microfluidic channels, fluid flow is characterized by low Reynolds numbers and mixing of fluid streams is limited to molecular diffusion. Micromixers are generally divided into two groups, passive micromixers that utilize geometrical mixing by their physical structures and active micromixers that use movable parts or external forces like pressure, electric or magnetic field etc. [1]. AC electrokinetics has been employed extensively for mixing of fluids in microchannels. ACEO flow with a pair of asymmetric electrodes has been demonstrated to be effective in mixing of two fluid streams [2]. The goal of this work is to investigate the effects of electrode geometric parameters on the mixing efficiency in the micro-channel, and provide guidelines for the optimal design of ACEO micromixers with asymmetric electrodes.

DESCRIPTION OF THE MICROMIXER

In the micromixer, anti-symmetric AC voltages are applied on the two co-planar rectangular electrodes fabricated on the bottom of the microchannel, as shown in Fig.1. Geometric asymmetry of the electrodes results in ACEO flows with two asymmetric counter-rotating rolls of fluid motion above the two electrodes (Fig. 2). Stretching and folding of the material interface between the two fluid streams is significantly enhanced and mixing is hence improved.

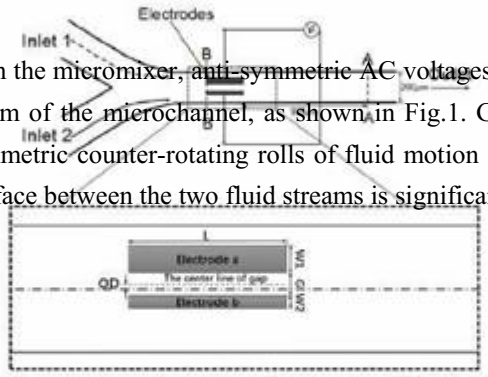

Fig. 1

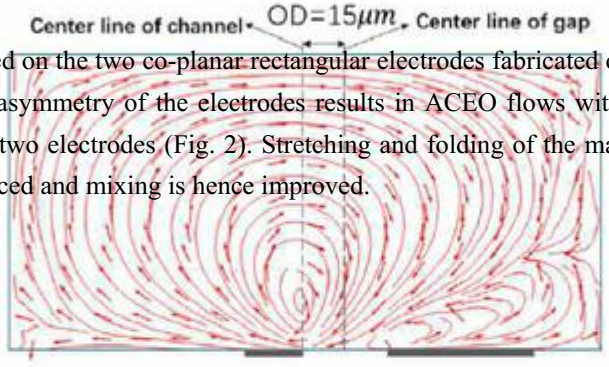

Fig. 2

RESULTS AND CONCLUSIONS

Steady 3D incompressible Navier-Stokes equations are solved numerically to obtain the ACEO flow in the microchannel, with ACEO slip velocity boundary conditions [3] on the electrode surfaces. Concentration distribution is governed by a steady convection diffusion equation. The coupled fluid flow and mass transfer problem is solved in Comsol Multiphysics 5.0. The mixing efficiency is calculated to be standard deviation of concentration in the region of interest.

The chips (Fig. 3) for generating ACEO are fabricated on a glass substrate, with a gold layer evaporated and patterned to be electrodes by a wet etching process. The Y shaped microfluidic channel, 2cm long, 200μm wide and 100 μm deep, is made of PDMS using standard soft-lithography techniques and precisely bonded onto the substrate after oxygen plasma treatment. An AC signal with peak-to-peak voltage V_{P-P} =14V at 10kHz is applied on the electrodes. Mixing efficiency in the square region in Fig. 3(b) is calculated acoording by fluorescence imaging to be 58%, which is in good agreement with a numerically computed value of 55%.

Effects of electrode geometric parameters are then studied numerically. Mixing efficiencies at a fixed cross section downstream the electrodes are plot in Fig. 4 for different offset distance (distance between the channel center line and electrode-gap center line) and different width w2 of the thin electrode. It is concluded that mixing efficiency increases with increasing size ratio of the two electrodes; when the sizes of the two electrodes are fixed, optimal mixing can be achieved if the inner edge of the thin electrode coincides with the channel center line (initial interface of the two fluids), as is the case in Fig. 2. For the configuration in our study, when w1=50μm, w2=10μm, electrode gap G=10μm, the optimal mixing efficiency can be as large as 93%, compared to the value of 25% without ACEO flows. Mixing efficiency of the micromixer also increases with decreasing gap between the electrodes, and increasing length of the electrodes.

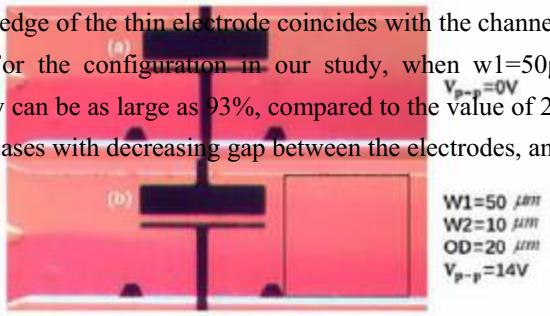

Fig. 3

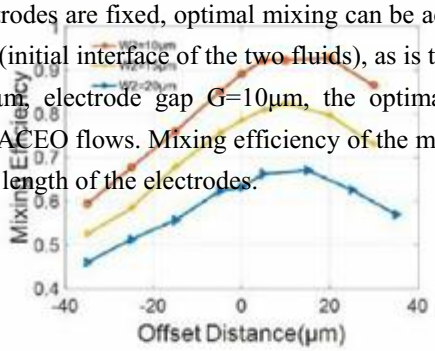

Fig. 4

References

[1] Yang Ng.W., Goh S., Lam Y.C.: DC-biased AC-Eelectroosmotic and AC-Eelectrothermal Flow Mixing in Microchannels. *Lab Chip* **9**:802-809, 2009.

[2] Wang Y.,Kang S.,Suh Y.: Enhancement of Mixing in a Microchannel by Using AC-Electroosmotic Effect. Proceedings of MNHT2008 Micro/Nanoscale Heat Transfer International Conference,Tainan, Taiwan, 2008.

[3] Brown A.B.D., Smith C.G., Rennie A.R.:Pumping of Water with AC-Electric Fields Applied to Asymmetric Pairs of Microelectrodes. *Phys. Rev. E* **63**:016305 1-8, 2000.

OSMOLARITY-CONTROLLED SWELLING BEHAVIORS OF DUMBBELL DOUBLE EMULSIONS

Likai Hou, Yukun Ren[a)], Xuewei Guan, Yankai Jia, Qingming Hu & Hongyuan Jiang[a)]
School of Mechatronics Engineering, Harbin Institute of Technology, Harbin, China

Summary We report a microfluidic approach to fabricate osmolarity-responsive dumbbell Water-in-Oil-in-Water(W/O/W) double emulsion with precisely osmolarity-controlled swelling behaviors. By using different concentration of KCL in the inner droplets and that in collection solutions, we independently control the swelling speed and size of each droplet in the dumbbell double emulsion. Interestingly, this osmolarity-controlled swelling behaviors of inner droplets facilitate two different kind of transformation in the dumbbell emulsion. One is core-coalescence between two inner droplets, when the two inner droplets have similar size and concentration of KCL. Another one is swelling-breakdown of one inner droplet, when the two inner droplets have different concentration of KCL. The swelling-caused core-coalescence behavior in a dumbbell double emulsion establishes a new reactor for protecting reaction materials and products from being contaminated or released. In addition, swelling-breakdown behavior has the potential for controlling release of important active ingredients.

INTRODUCTION

The advance in the microfluidic technologies provide new means for microencapsulating active ingredients such as drugs, microbes, living cells, and functional materials in isolated spaces, and separating them from the outer environment[1]. For instance, the core-shell double emulsions and the resulting microcapsules are thus attractive candidates in a wide range of applications, from materials science such as the synthesis of functional particles and fibers, to drugs for therapeutic applications, to components for cosmetics and food additives. To achieve these applications, the double emulsions or capsules have to be exposed to a range of specific stimulus to trigger the inner cores break or coalesce, such as mechanical stress, changing in PH or temperature, changing in the external chemical environment, or UV exposure[2-4]. In addition, the shape and size of an emulsion and capsule plays an important role in these trigger process. Thus, more active stimuli and shaped emulsions and capsules should be designed to enable the trigger process easier and more accurate, and extend the range of applications in variety areas.

RESULT AND DISCUSSION

In this work, we report fabrication of osmolarity-responsive dumbbell double emulsions with two different inner cores, which have precisely osmolarity-controlled swelling behaviors. As shown in Figure 1 a), we use a capillary microfluidic device to develop dumbbell Water-in-Oil-in-Water(W/O/W) double emulsions. The middle oil phase is Polydimethylsiloxane(PDMS), which allows the diffusion of only low-molecular weight molecules such as water, antibiotics, and signalling molecules. Moreover, its excellent bioinertness and biocompatibility are suitable for encapsulating important actives[5]. The inner droplet cores are KCL solutions. The outer phase is a 5 wt % Poly(vinyl alcohol) (PVA) aqueous solution.

By using different concentration of KCL in the inner droplets and that in collection solutions, we independently control the swelling speed and size of each droplet in the dumbbell double emulsion[6]. As shown in Figure 1 b) and c), the objectives of this osmolarity-controlled swelling behaviors are twofold. When the two inner droplets have similar size and concentration of KCL, the inner droplets swell with similar swelling speed and coalesce together at a certain size, as shown in Figure 1 b). When the two inner droplets have different concentration of KCL, the inner droplets swell with different swelling speed and reach different size. This un-equilibrium between the two inner droplets makes the dumbbell unstable, and facilitate the breakdown of the small inner droplet, as shown in Figure 1 c). Furthermore, by controlling the concentration of KCL in the inner droplets and that in the collection solution, the swelling caused core-coalescence behavior and the swelling-breakdown behavior in dumbbell emulsion can be controlled precisely.

CONCLUSIONS

In this work, a dumbbell Water-in-Oil-in-Water(W/O/W) double emulsion is developed using Polydimethylsiloxane(PDMS) as oily shell, which contains two inner droplets with different concentration of KCL. The swelling behaviors of this double emulsion is performed by precisely controlling the concentration of KCL in the inner droplets and that in outer phases of the double emulsions. Two different kind of swelling behaviors, core-coalescence between two inner droplets, and swelling-breakdown of one inner droplet, have been achieved by this osmolarity-controlled swelling. This approach is general and can be used as a kind of trigger for coalescing and releasing of dumbbell double emulsions. Thus, the development of swelling-caused core-coalescence behavior and swelling-breakdown behavior in a dumbbell double emulsion establishes a new tool for controlling release of important active ingredients and protecting them from being contaminated.

[a)] Corresponding authors. Email: rykhit@hit.edu.cn and jhy_hit@hit.edu.cn.

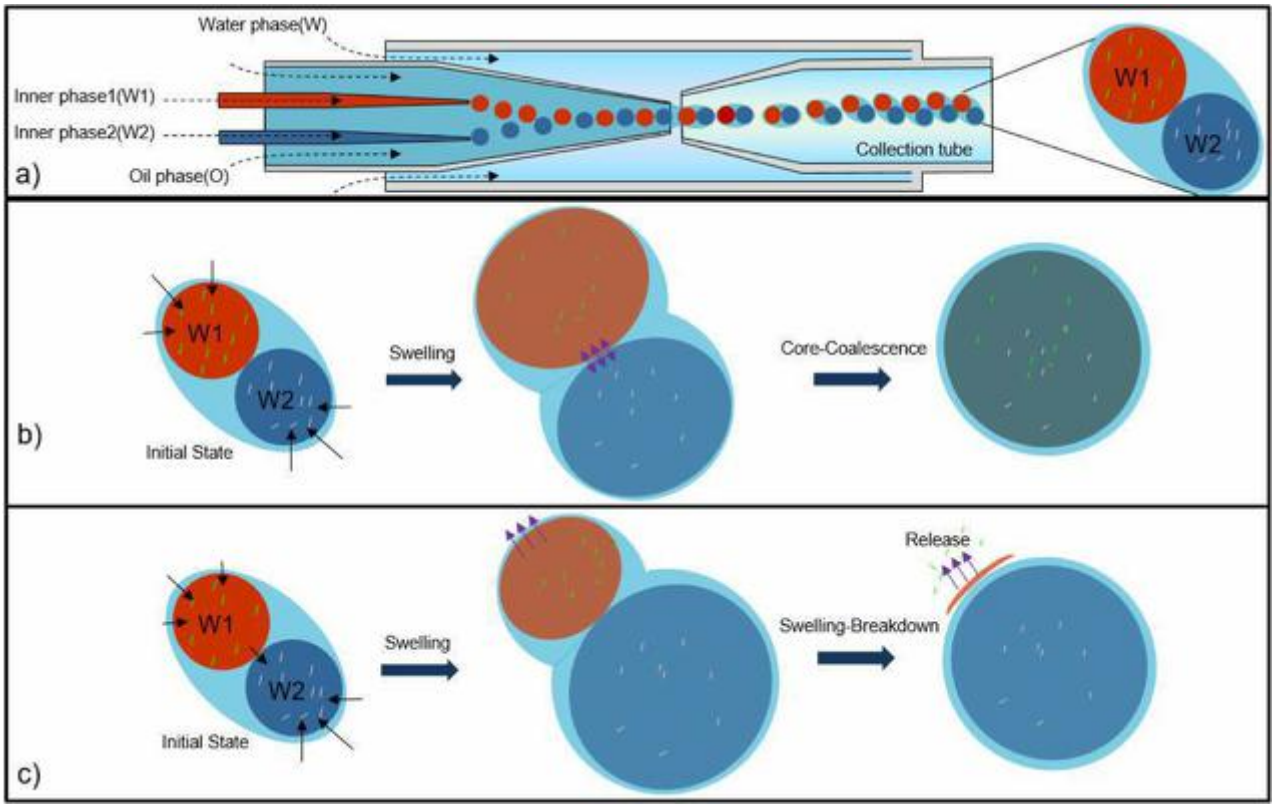

Figure 1. a) Schematic of the capillary microfluidic device for generating dumbbell W/O/W double emulsions. Two smaller separate capillaries are injected into the bigger round capillary as internal tubes, which enable two different fluids to enter the devices separately. b). Schematic diagram of the core-coalescence by swelling, when the inner droplets have similar size and concentration of KCL. c). Schematic diagram of the release mechanism by swelling-breakdown, when the inner droplets have different concentration of KCL.

References

[1] Datta S.S., Abbaspourrad A., Amstad E., Fan J., Kim S.H., Romanowsky M., Shum H.C., Sun B., Utada A.S., Windbergs M., Zhou S., Weitz D.A.: 25th anniversary article: double emulsion templated solid microcapsules: mechanics and controlled release. *Advanced materials* **26**:2205-2218, 2014.

[2] Amstad E., Kim S.H., Weitz D.A.: Photo- and thermoresponsive polymersomes for triggered release. *Angewandte Chemie* **51**:12499-12503, 2012.

[3] Abbaspourrad A., Datta S.S., Weitz D.A.: Controlling release from pH-responsive microcapsules. *Langmuir : the ACS journal of surfaces and colloids* **29**:12697-12702. 2013.

[4] Zhou S., Fan J., Datta S.S., Guo M., Guo X., Weitz D.A.: Thermally Switched Release from Nanoparticle Colloidosomes. *Advanced Functional Materials* **23**:5925-5929. 2013.

[5] Myeong-Jin O., Tae-Kyoung R., Choi S.W.: Hollow polydimethylsiloxane beads with a porous structure for cell encapsulation. *Macromolecular rapid communications* **34**:1728-1733. 2013.

[6] Tu F., Lee D.: Controlling the stability and size of double-emulsion-templated poly(lactic-co-glycolic) acid microcapsules. Langmuir : the ACS journal of surfaces and colloids **28**:9944-9952. 2012.

A NEW FLOW CONTROL METHOD BASED ON MULTI-RESONANCE VALVELESS MICROPUMP

Ming-Che Hsieh & An-Bang Wang [a)]
Institute of Applied Mechanics, National Taiwan University, Taipei, 10617, Taiwan, R.O.C.

Summary In comparison to traditional valveless micropumps, the pumping efficiency of the micropump proposed in this work has enhanced to about one order of magnitude with the aid of new elastomer design. A revised lumped model can effectively predict the frequency response of the system that could be well quantified by the geometry and material of elastomer design in the micropump. Furthermore, excellent consistency of various elastomer designs between experiment and theory has demonstrated another waveguide character of the present design. A micropump with three elastic outlet buffers was designed for having three distinct resonant frequencies, and a novel frequency-selective pumping method based upon Frequency-Division-Multiplexing (FDM) was used to execute the sequential and parallel flow manipulations without additional valves and the need of multi-pumps for general microfluidic applications.

MULTI-RESONANCE VALVELESS MICROPUMP

As the heart of mammals delivers and circulates blood flow inside vessels to sustain all functions of organs, tissues and cells, efficient fluid transportation and flow control are always the key issues in various microfluidic applications. To meet the need of delicate and precise flow manipulation in biochemical or biomedical reaction analysis, many valves and pumps were commonly designed and used to guarantee the reliable operations of the system [1]. However, the complexity of system could dramatically increase the cost and volume of system for involving more individual controllability and system reliability in the operation procedure. Hence, the alternative approaches with simple structures, such as droplet-based electrowetting [2], acoustophoresis [3], as well as frequency-specific pumping [4,5], have been proposed to reveal their control simplicity in comparison with those in complicated microfluidic systems.

In this study, a valveless micropump [6] equipped with two symmetric elastomers, e. g., elastic buffers, was first designed to create the multi-resonance behaviour as shown in the inset of Figure 1(a). It is mainly composed of "an active oscillator (actuation chamber)", inlet/outlet "rectifiers (nozzle/diffuser type)", "buffers with deformable boundaries", and "connecting tubes". To design the potential resonance frequency f_r below 10 kHz range in experiments, the PZT actuator was chosen as an oscillatory pressure-driven source and the thermoplastic polymer PMMA was adopted as the base material of microchannel due to its moderate elasticity. Here, γ is defined as r_b/r_a (the radius ratio of buffer and actuation chamber), and r_a is fixed as 12.5mm in all cases. Physically, γ can demonstrate the variation of structure compliance of buffer. Figure 1(a) shows that the dual resonance pump can be successfully activated in experiments and the net flow rate Q_{net} of the 2nd peak is significantly larger than the 1st peak for $\gamma > 0.64$. By increasing γ, the 2nd resonant peak f_{R2} would move leftward toward the 1st resonance due to the change of structure compliance and internal flow dynamics.

The lumped-element model (LEM) has been widely used to deal with such a Fluid-Structure-Interaction (FSI) problem according to Electric-Hydraulic Analogy (EHA) [7]. In our revised model, the structure compliance C_{struct} of all elastic components has been considered, and the hydraulic resistance R_{hyd} (viscous dissipation) of each element is modified as in series with a hydraulic inductance L_{hyd} (inertia) and in parallel with C_{struct}, denoted as $(R_{hyd}+L_{hyd})//C_{struct}$. The working fluid is water, which is regarded as incompressible with negligible hydraulic compliance. The corresponding ODEs for the designed system can then be numerically solved. In Figure 1(b), the model shows its excellent prediction of both f_{R1} and f_{R2}. Both of them decrease with increasing γ. As $\gamma > 1.4$, f_{R2} is insensitive to γ due to the dominant fluid inertia and f_{R1} disappears eventually. The amplification ratio of net flowrate Q_{net}* (the peak flowrate of designed pump divided by that of the original single peak of pump with $\gamma = 0.12$) has shown the significant efficiency enhancement (up to a factor of 15!) of the present design.

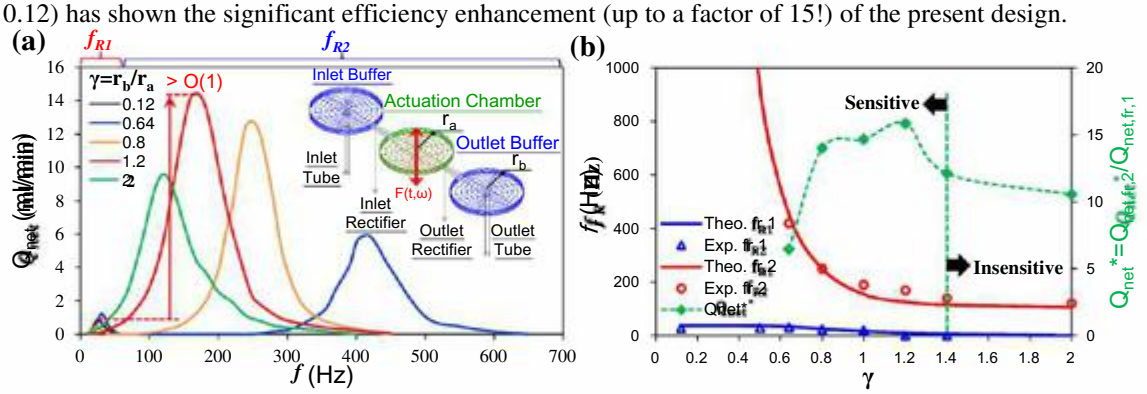

Figure 1. (a) Experimental net flowrate of the single- and dual-resonance pumps for various γ (= r_b/r_a), where γ =0.12 case has single Q_{net} peak while the rest cases have dual Q_{net} peaks; **(b)** Amplification ratio Q_{net}* and theoretical/experimental resonance frequency f_R versus γ relationship, respectively.

[a)] Corresponding author. Email: abwang@spring.iam.ntu.edu.tw.

FREQUENCY-DIVISION-MULTIPLEXING FLOW CONTROL METHOD

Similar to the wave-selection in the signal transmission technology, the elastic buffer could be also considered as a fluidic waveguide to transport (peak) flowrate under a specific (resonance) frequency. A micropump with three distinct radii of outlet buffers (γ = 0.71, 0.8 and 0.9), i.e., Single-Inlet and Multiple-Outlet (SIMO), was designed to create three distinct f_R, as shown in the inset of Figure 2. By the sweeping frequency technique, three resonant peaks locating in 977, 707, and 530 Hz (denoted as f_{RA}, f_{RB} and f_{RC} thereafter) were identified in the spectrum of the whole system. This means that the multi-bandpass-filters characterized by elastic outlet buffers can be further applied for the frequency-selective control of pump(s). However, the reverse net flow was found, shown as the blue and green dashed lines in Figure 2, by driving the PZT actuator with single frequency. To avoid the "crosstalk" phenomenon, taking the concept of Frequency-Division-Multiplexing (FDM) in telecommunication, the synthesized driving signal of PZT actuator was modulated by three sinusoidal waves with different f_R and driving amplitudes A_O. The multi-frequency driving signal can be represented as

$$A(t) = A_{o,A}\sin(2\pi f_{RA}t) + A_{o,B}\sin(2\pi f_{RB}t) + A_{o,C}\sin(2\pi f_{RC}t). \quad (1)$$

By properly choosing f_R and A_O for each sinusoidal wave, the reverse net flow from outlets (outlet A & C) can be easily eliminated , which is shown as solid lines in Figure 2. The designed route from the inlet to the outlet B was then successfully achieved without any additional valve or pump. Hence, the flow path control can be completed by simply adjusting the composition of driving signal, which shows the great simplicity and controllability of the newly proposed flow control method.

Furthermore, to illustrate the ability of sequential and parallel flow controls with only one actuator but without additional valves, three independent microchannels were individually connected to the three outlets of the above-mentioned micropump. The coloured droplet was placed in each microchannel as the tracer. The time-sequenced driving signal was pre-programmed as shown in Figure 3(a), and the sequential control (C→B→A→A&B) for driving the flow in three individual microchannels was successfully achieved as shown in Figure 3(b).

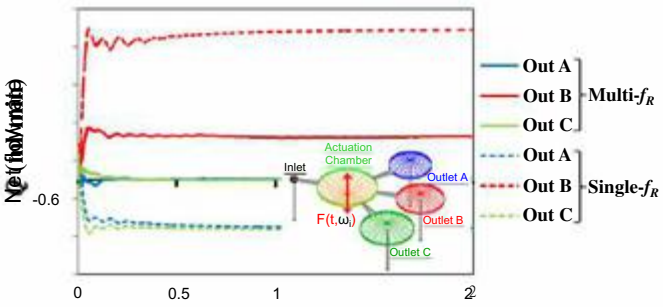

Figure 2. Transient net flow rate under different PZT driving signals of single and multiple resonant frequencies. Net flow through outlet B without reverse flow from the other outlets was achieved by driving the actuator with multi-frequency signal.

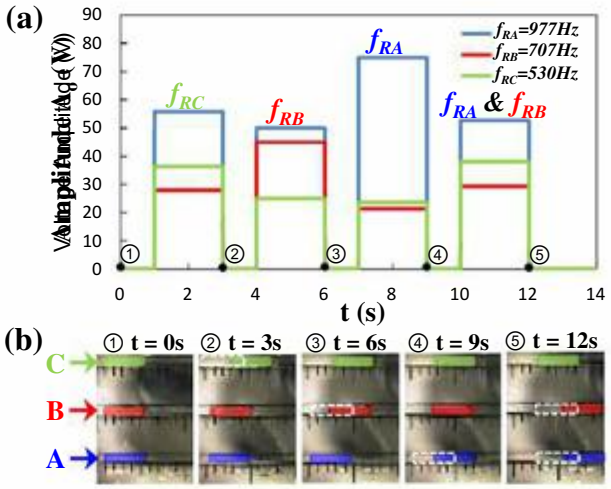

Figure 3. The sequential and parallel flow controls of the multi-resonance micropump in experiments: (a) The time-sequenced driving signal; (b) The control of droplet motion by FDM (white dashed lines show the position of droplet at the previous time step).

Acknowledgement

We thank for the financial support of Ministry of Science and Technology, Taiwan (MOST 101-2221-E-002-065-MY3).

References

[1] W. Grover, M. Muhlen and S. Manalis, Lab Chip, 2008, 8, 913.
[2] M. Prakash and N. Gershenfeld, Science, 2007, 315, 832.
[3] G. Destgeer and H. J. Sung, Lab Chip, 2015, 15, 2722.
[4] S. M. Langelier, D. S. Chang, R. I. Zeitoun, and M. A. Burns, Proc. Natl. Acad. Sci. U S A., 2009, 106(31), 12617.
[5] D. Leslie, C. Easley, E. Seker, J. Karlinsey, M. Utz, M. Begley and J. Landers, Nat. Phys., 2009, 5, 231.
[6] A. B. Wang and M. C. Hsieh, Lab Chip, 2012, 12, 3024.
[7] K. W. Oh, K. Lee, B. Ahna and E. P. Furlani, Lab Chip, 2012, 12, 515.

INERTIAL LIFT ON A SPHERICAL PARTICLE IN MICORCHANNELS

Chao Liu & Guoqing Hu[a)]
State Key Laboratory of Nonlinear Mechanics, Institute of Mechanics, CAS, Beijing 100190, China

Summary Inertial microfluidics has been extensively implemented for high-throughput manipulation of particles and cells, depending on hydrodynamic forces. The performance of inertial manipulation largely relies on the precise prediction of particle trajectories that are determined by the inertial lift acting on the particles. Here we propose a fitting formula for the inertial lift on a spherical particle drawn from the direct numerical simulation data obtained in straight channels. It consists of four terms that represent the shear-gradient-induced lift, the wall-induced lift, the slip-shear lift, and the correction of the shear-gradient-induced lift, respectively. Notably, as a function of the parameters of the local flow field, this generalized formula possesses good adaptability to complex channel geometry.

INTRODUCTION

The inertial lift on a particle stems from the asymmetry of pressure and viscous stresses on the particle surface in a Poiseuille flow with a finite Reynolds number. Analytical studies have been conducted to calculate the lift forces on a small sphere by solving the Navier-Stokes equations using perturbation methods. Investigating the motion of a sphere in a two-dimensional Poiseuille flow, Ho & Leal successfully explained the focusing pattern in tube flows[1] and obtained an explicit formula for the lift force[2]

$$F_L = \ _L\rho \ ^2_{\max} a^4 \ L^2 \tag{1}$$

where a is the particle diameter, C_L the lift coefficient, ρ the fluid density, $U_{\max}$ the maximum channel velocity, and L the characteristic length. The restriction of $Re << 1$ limits its application to practical applications where the Re is finite. Schonberg *et al*.[3] and Asmolov[4] extended the applicable Re up to 3000 by the matched asymptotic perturbation method. However, these theoretical studies fail to predict the lift forces when applied to the case of finite-sized particle in rectangular channel with high aspect ratio AR ($AR = W \ H$, where W is the channel width and H the height), which is a common situation in inertial microfluidic applications.

Several groups have conducted direct numerical simulation (DNS) to investigate the particle motion and lift distributions without the restrictions faced by the aforementioned perturbation methods. However, DNS could become dramatically burdensome for long microchannels encountered in practical devices, for example, serpentine or spiral ones. Here, we develop a generalized lift formula from DNS data obtained in straight rectangular microchannels.

RESULTS AND DISCUSSION

Figure 1a displays the schematics of simulation: a spherical particle with a diameter a suspended in a pressure-driven flow in a straight rectangular channel. Our previous dimensional analysis shows that the lift forces on a particle are determined by a dimensionless parameter group $F=F(\kappa, AR, Re, y^*, z^*)$.[5] Here κ is the particle blockage ratio ($\kappa = a \ H$). To re-examine the lift forces and develop the lift formula, we conduct systematic DNS in terms of these dimensionless parameters. The governing equations for the flow field are

$$\mathbf{u} \quad 0, \ \frac{\partial \mathbf{u}}{\partial t} + (\mathbf{u}\cdot\nabla)\mathbf{u} = -\frac{1}{\rho}\nabla \ + \ \nabla^2\mathbf{u} \tag{2}$$

where $\mathbf{u}$ is the fluid velocity, p the pressure, and ν the kinematic viscosity. The particle trajectory is predicted by Newton's second law

$$m_p \ \frac{d\mathbf{U}_p}{dt} = \int_\Sigma (-p\mathbf{1}+\boldsymbol{\tau})\cdot\mathbf{n}\,d\sigma + \ _p\mathbf{g}, \ \frac{d \ \mathbf{I}\cdot\boldsymbol{\Omega}_p)}{dt} = \int_\Sigma \mathbf{x} \quad \mathbf{x}_{cm}) \ \lfloor \quad p\mathbf{1}+\boldsymbol{\tau}) \ \mathbf{n} \rfloor d\sigma \tag{3}$$

where m_p is the mass of the particle, $\mathbf{U}_p$ the translational velocity, $\boldsymbol{\Omega}_p$ the angular velocity, $\mathbf{1}$ the unit tensor, $\mathbf{I} = diag\left(8\pi\rho_p a^5 \ 15\right)$ the moment of inertia tensor of the particle, and $\mathbf{x}_{cm}$ the position of the center of mass. Equations (2) and (3) are numerically solved on structured overlapping grids using the Overture C++ framework.[6] Figure 1b shows the computational grids and Figure 1c plots the lift force vectors in a quarter of the channel cross-section. The particles equilibrate at the positions where the lift forces vanish along both axes.

The proposed formula consists of four terms that represent the wall-induced lift F_w , the shear-gradient-induced lift F_s , the slip-shear lift F_{ss} , and the correction of the shear-gradient-induced lift F_c , respectively

$$F_L = C_1F_w + C_2F_s + C_3F_{ss} + C_4F_c \tag{4}$$

where C_1 , C_2 , C_3 , and C_4 are constants that will be determined by the fitting-analyses of the DNS data. After mathematical

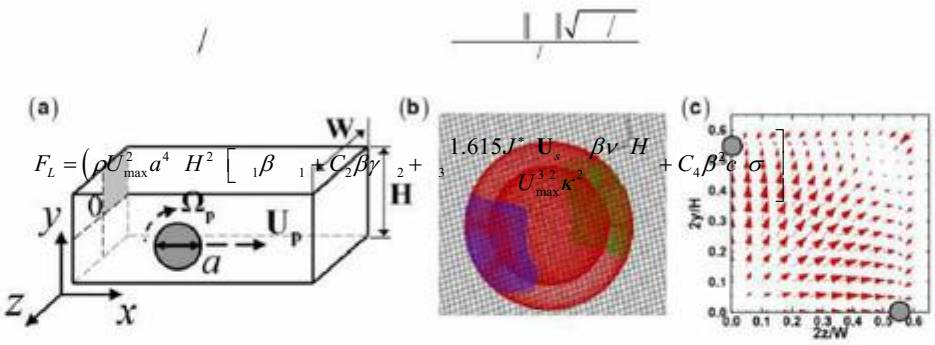

$$F_L = \left(\rho U_{\max}^2 a^4 / H^2\right)\left[{}_1\beta {}_1 + C_2\beta\gamma {}_2 + {}_3 1.615 J^* \mathbf{U}_s \beta v H / U_{\max}^3 \kappa^2 + C_4 \beta^2 c \sigma \right] \quad (5)$$

Figure 1. (a) The schematics of the computational system and the set of the coordinate system. (b) The overlapping grid used for calculating the inertial lift forces on a spherical particle in a rectangular microchannel. (c) Inertial lift forces are calculated for a quarter of a square channel cross-section and shown in vector plot for $\kappa = 0.3$ and $Re = 300$. The equilibrium positions are marked with the solid circles.

Equation (5) involves the parameters of the local flow field β and γ, the slip velocity $\mathbf{U}_s$, and the functions G_1 and G_2, *, and c that have been obtained by Ho & Leal,[2] Mei *et al*.,[7] and Asmolov,[4] respectively. As the lift forces directly depend on the local flow field, this formula has better adaptability for complex channel geometry, compared with those in terms of position's coordinates. Figure 2 shows that the C_L obtained by DNS for various AR ranging from 1 to 6 can be fitted by the proposed formula well. The proposed formula is then implemented in Lagrangian particle tracking method to realize fast prediction of particle trajectories in two types of widely used microchannels: a serpentine and a double spiral microchannels, demonstrating its ability to efficiently design and optimize inertial microfluidic devices by comparing against experimental observations.

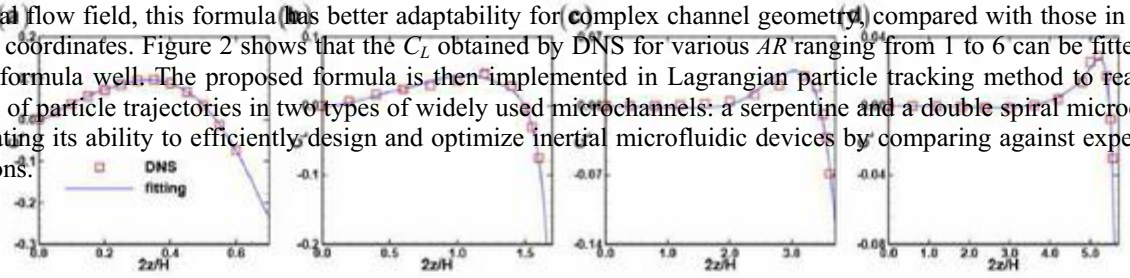

Figure 2. Comparison between C_L calculated by DNS (red marks) and the fitting results by the proposed formula (blue lines). $\kappa = 0.3$, $Re = 100$, and $R = 1$, 2, 4, and 6.

CONCLUSIONS

The proposed formula for the inertial lift consists of four terms that represent the wall-induced lift F_w, the shear-gradient-induced lift F_s, the slip-shear lift F_{ss}, and the correction of the shear-gradient-induced lift F_c, respectively. It could become an effective tool for predicting particle trajectories in real-world microfluidic devices when implemented in Lagrangian tracking method, as the effects of complex geometry on the acting forces can be automatically taken into account by prior solving the flow field.

References

[1] Segré G., Silberberg A.: Radial Particle Displacements in Poiseuille Flow of Suspensions. *Nature* **189**, 209-210, 1961.

[2] Ho B.P., Leal L.G.: Inertial Migration of Rigid Spheres in Two-dimensional Unidirectional Flows. *J Fluid Mech* **65**, 365-400, 1974.

[3] Schonberg J.A., Hinch E.J.: Inertial Migration of a Sphere in Poiseuille Flow. *J Fluid Mech* **203**, 517-524, 1989.

[4] Asmolov E.S.: The Inertial Lift on a Spherical Particle in a Plane Poiseuille Flow at Large Channel Reynolds Number. *J Fluid Mech* **381**, 63-87, 1999.

[5] Liu C., Hu G., Jiang X., Sun J.: Inertial Focusing of Spherical Particles in Rectangular Microchannels over a Wide Range of Reynolds Numbers. *Lab Chip* **15**, 1168-1177, 2015.

[6] Brown D.L., Henshaw W.D., Quinlan D.J.: Overture: An Object-oriented Framework for Solving Partial Differential Equations. Springer 1997.

[7] Mei R.: An Approximate Expression for the Shear Lift Force on a Spherical Particle at Finite Reynolds Number. *Int J Multiph Flow* **18**, 145-147, 1992.

3D PLUG FORMATION IN T-JUNCTIONS & COMPLEX CROSS SHAPED MICROCHANNELS

Damir Juric *[1,2], Jalel Chergui[2], Lyes Kahouadji[1], Omar Matar[1], and Seungwon Shin[3]

[1]*Department of Chemical Engineering, Imperial College London, London SW7 2AZ, United Kingdom*

[2]*LIMSI, CNRS, Universite Paris-Saclay, F-91405 Orsay, France*

[3]*Department of Mechanical and System Design Engineering, Hongik University, Seoul 121-791, Republic of Korea*

Summary We present three-dimensional direct numerical simulations of liquid-liquid plug formation in two kinds of microchannel configurations: circular T-junction and complex cross-junction microchannels. The simulations are carried out with a massively parallel two phase flow code, called BLUE. The method for the treatment of the fluid interfaces uses a hybrid Front Tracking/Level Set technique that defines the interface both by a discontinuous density field as well as by a triangular Lagrangian mesh. A static distance function represents the microchannel structures.

INTRODUCTION

Flows in small channels, with dimensions less than a millimiter, have found widespread applications in food processing, drug delivery and also in chemical reactions. At these scales, flows are generally laminar and governed mainly by viscous and interfacial forces, while gravity forces are neglected. In this work, we will focus on two kinds of microfluidic channel configurations. A circular T-junction where all branches have internal diameters equal to 200μm (see figure1(a)). The dispersed phase is chosen with the physical properties of a water/glycerol solution, injected from the vertical branch of the junction, while the continuous phase is silicon oil and was injected along the horizontal main channel axis. A similar configuration has been used and studied experimentally by Chinaud et al. [1] for which intriguing vortex formation is observed after the plug breakup process. The configuration shown in figure1(b) is a complex cross shaped microchannel for which the dispersed phase is injected from the horizontal main channel with a quasi-circular section and the continuous phase is injected from two vertical branches.

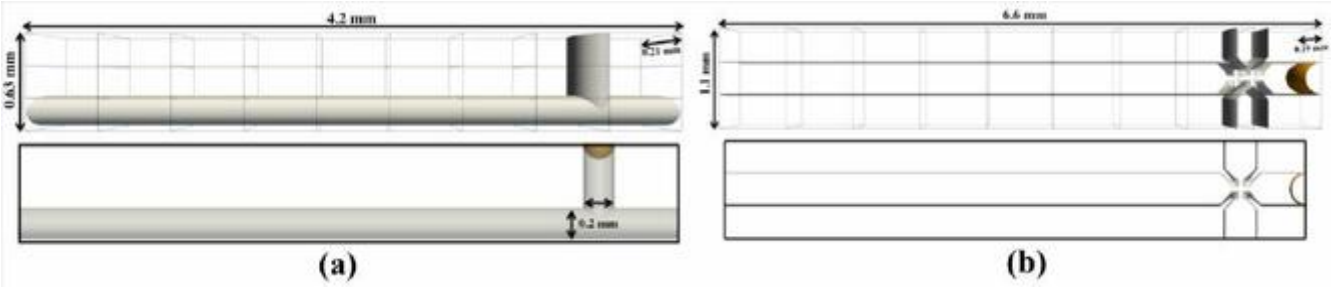

Figure 1: Microchannel configurations, (a) circular T-junction and (b) a complex cross-junction.

The geometry of both T-junction and the complex cross-junction is handled in our numerical study by implementation of a module for the definition of immersed solid objects and their interaction with the flow for both single and two-phase flows. Such simulations require an important spatial discretisation and figure1(top) represents the subdomain decomposition used in the parallel calculations. An example of one of our simulations is shown in figure 2 representing a snapshot of plug formation for the case of a T-junction. In the simulations it appears that the first plug is always longer than the following plugs.

GOVERNING EQUATIONS AND NUMERICAL METHODS

The governing equations for transport of an incompressible two-phase flow are expressed by a single field formulation:

$$\nabla \cdot \mathbf{u} = 0 \quad \text{and} \quad \rho \left(\frac{\partial \mathbf{u}}{\partial t} + \mathbf{u} \cdot \nabla \mathbf{u} \right) = \circ \nabla P + \nabla \cdot \mu \left(\nabla \mathbf{u} + \nabla \mathbf{u}^T \right) + \mathbf{F}. \tag{1}$$

Here $\mathbf{F}$ is the local surface tension force at the interface and described by the hybrid formulation $\mathbf{F} = \sigma \kappa \nabla I$ where σ is the surface tension coefficient assumed to be constant, I is the indicator function which is zero in one phase and one in the other

*Corresponding author. Email: damir.juric@alum.wpi.edu

phase and κ is twice the mean interface curvature field. The material properties such as density or viscosity are defined in the entire domain with the aid of the indicator function $I(\mathbf{x}, t)$, for the density for example :

$$\rho(\mathbf{x}, t) = \rho_1 + (\rho_2 - \rho_1)I(\mathbf{x}, t) \tag{2}$$

where the subscripts $_1$ and $_2$ stand for the respective phases. The gravity is neglected. The fluid variables $\mathbf{u}$ and P are

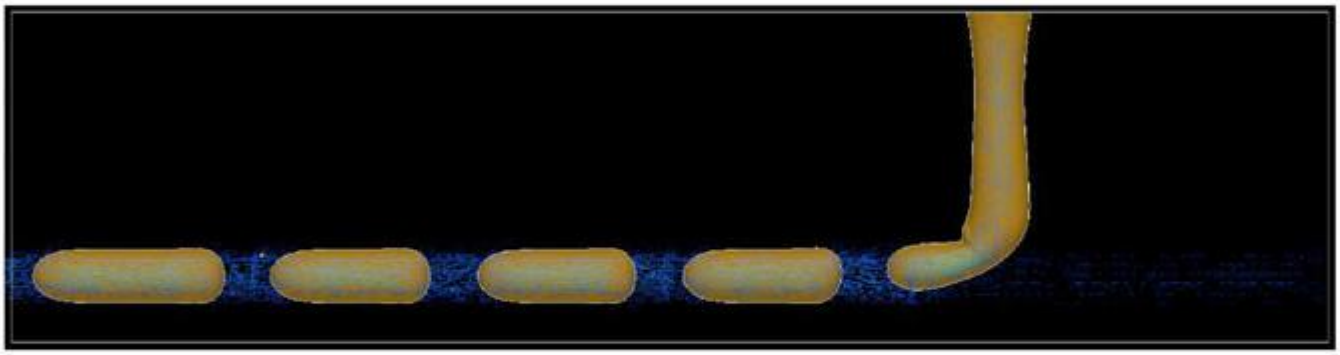

Figure 2: Snapshot of plug formation in a T-junction microchannel

calculated by means of a projection method. A second order Gear scheme is used for time integration. Either explicit or implicit time integration of the viscous terms may be chosen depending on the problem. For the spatial discretization we use the well-known staggered mesh, MAC method with second order ENO advection. The pressure and distance function are located at cell centers while the x, y and z components of velocity are located at the faces. All spatial derivatives are approximated by standard second-order centred differences. The code BLUE [2] is written in Fortran 2003 which allows for the definition of a set of dynamically allocated derived [data] types and generic procedures associated with the matrix of procedures, grids, scalar and vector fields, operators as well as the various solvers used in the Navier-Stokes and Lagrangian Tracking modules. The parallelization of the code is based on an algebraic domain decomposition technique where the velocity field is solved by a parallel GMRES method for the viscous terms and the pressure by a parallel multigrid method. Communication is handled by MPI message passing procedures able to be run on a simple laptop up to high performance supercomputers. The method for the treatment of the fluid interfaces uses a hybrid Front Tracking/Level Set technique which defines the interface both by a discontinuous density field as well as by a triangular Lagrangian mesh. This structure allows the interface to undergo large deformations including the rupture and/or coalescence of fluid interfaces.

CONCLUSION

We demonstrate, through simulations of two microchannel configurations, the capabilities of BLUE, a new high performance parallel numerical code for the simulation of two-phase incompressible flows. The code BLUE is, to our knowledge the first implementation of Lagrangian tracking on massively parallel architectures applied to two-phase microfluidic flows.

ACKNOWLEDGEMENTS

This work is supported by (1) the Engineering & Physical Sciences Research Council, United Kingdom, through the MEMPHIS program grant, (2) the Basic Science Research Program through the National Research Foundation of Korea (NRF) funded by the Ministry of Science, ICT and future planning (NRF-2014R1A2A1A11051346) and (3) by computing time at the Institut du Developpement et des Ressources en Informatique Scientifique (IDRIS) of the Centre National de la Recherche Scientifique (CNRS), coordinated by GENCI (Grand Equipement National de Calcul Intensif). The authors wish to thank L. Tuckerman for helpful discussions.

References

[1] Chinaud M., Roumpea E. P., Angeli P. : Studies of plug formation in microchannel liquid-liquid flows using advanced particle image velocimetry techniques. Exp. Therm. Fluid Sci. 69: 99-110 (2015).

[2] Shin S., Chergui J. and Juric D.: A solver for massively parallel direct numerical simulation of three-dimensional multiphase flows, arXiv 1410.8568, 2014.

OPTIMAL ELECTRO-OSMOTIC PUMPING OF A MICRO-DUCT WITH FIN STRUCTURES

Chun-Fei Kung[1], Kuan-Ruei Lai[1], Jen-Jen Lin[2], Chien-Cheng Chang[1,a)] & Chang-Yi Wang[3]
[1]*Institute of Applied Mechanics and Centre for Advanced Study in Theoretical Sciences, National Taiwan University, Taipei, Taiwan*
[2]*Department of Applied Statistics and Information Science, Ming Chuan University, Taipei, Taiwan*
[3]*Departments of Mathematics and Mechanical Engineering, Michigan State University, Easing Lansing, MI, USA*

Summary This study is aimed to present an analysis of electro-osmotic (EO) pumping of a micro-duct with fin vanes. Fin structures are known to be an efficient and very important tool in conducting heat generated in fluid transport system, such as Joule's heating in micro-fluidic devices. The present semi-analytical analysis, under the Debye-Hückel approximation (DHA), enables us to explicitly investigate the combined effects of various parameters for the purpose of optimizing the EO pumping while retaining substantial fin vanes for heat removal. A mathematical model based on the solutions of two fundamental EO flows is introduced to explain how the choice of the fin vane may optimize the EO pumping rate. Moreover, we identify and analyse several salient features of the optimized EO flow rates with the help of diagrams plotted on the plane of zeta potentials, which may serve as an easily used reference for engineering deign and applications.

INTRODUCTION

Microfluidic devices, as laboratory on a chip, have continued to find important applications in microbiological sensors and micro-electro-mechanical systems (MEMS). The electro-osmotic flow (EO flow) is inevitably subject to Joule's heating, and thus heat removal is also an essential issue in this type of fluid transport. In is well known from the heat transfer realm that fin plates or structures are excellent candidates for conducting heat generated in thermal-fluid system. A fundamental structure of using fin plates in EO flow inside a microtube or nanotube could consist of several plates radially inserted from the channel centre, as sketched in Fig. 1. It is of essential importance to seek understanding of the fluid transport mechanisms by solving appropriate equations based on the physical laws describing the EO flow. As there are several physical parameters involved, we aim to investigate the problem by the approach of mathematical analysis as much as possible so that the role of each parameter is easily identified. In the literature, analytical solutions to electroosmotic flow (EO flow) even under the Debye-Hückel approximation exist only for a few tube cross sections, and for a review we refer to some of our previous studies [1-4]. The several physical parameters involved include the width of the fin plates b, the radius of the cylindrical duct R, the numbers of sector P=2π/θ, the Debye length λ_D of the EDL as well as the zeta potential ζ_1 on the fin plate and the zeta potential ζ on the cylindrical surface and the externally applied electric field E (in the axial direction).

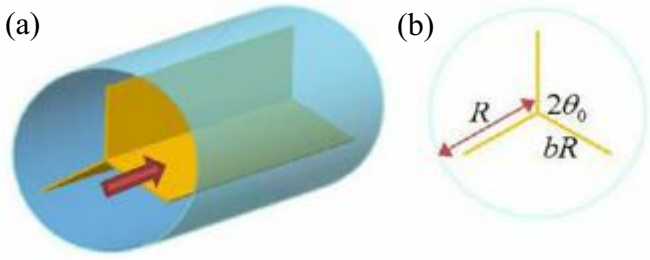

Figure 1. (a) Schematic of the fin vanes in the three dimensional setting. (b) The cross section of a cylindrical duct with inserted fin vanes with zeta potentials ζ_1 and ζ_2 developed on the fin vanes and duct surface, respectively, with *R* the radius of the duct, *bR* the width of the fin vanes, and *P* (=3 in this plot) the number of the vanes.

RESULT & DISCUSSION

For the geometry depicted in Fig. 1, we may only consider one sector of it with assuming symmetry, and formulate the EO problem for two fundamental problems. The idea is as follows. In the range of zeta potentials of possible interest, let the maximum of them (ζ_M) be normalized to be 1, then the solution (EO flow rate) to the problem for any pair of zeta potentials (α,β) with on the fin vanes and the duct surface can be obtained by linearly combining the two fundamental solutions, namely, $Q(\alpha,\beta)=\alpha Q(1,0)+\beta Q(0,1)$. The primary interest of this study is twofold. One is to obtain the solution to the two fundamental problems with detailed understanding of the EDL and flow velocity profiles as well as the general behaviours of the EO flow rate. And, more importantly, we would like to obtain the optimized EO flow rate in terms of the width of the fin plates for any given pair of zeta potentials on the fin plates and on duct surface.

a) Corresponding author. Email: **mechang@iam.ntu.edu.tw**

The fins complicate the analysis with involving a set of 4 normalized parameters: the vane width b, the electro-kinetic width $K = R/\lambda_D$, and the pair of zeta potentials (α, β) in addition to the number P of vanes. The findings are summarized below. In essence, there are two competing mechanisms that determine the optimal EO pumping when an external voltage is applied to drive the pumping: the no-slip condition hinders the EO flow yet the zeta potential helps the EO flow. The most significant finding is: it is more feasible for us to find a width b to optimize (maximize) the EO pumping rate if the ratio α/β is greater than 1. It can be shown that that Q(1,0) and Q(0,1) can be well approximated by simple algebraic functions. This simple model enables us to predict that the optimal width b=bmax for the occurrence of the maximum EO flow rate QM(α,β) for given (α, β) is proportional to the ratio α/β with other conditions specified. This behaviour is well confirmed by the accurate calculations with plots for the optimized EO flow rates. Figure 2 shows plots of typical EDL potentials and velocity profiles. The plots of Fig. 3 enable us to see how much the EO flow rate can be improved by optimization with respect to the width of the fin vanes. For example, given the point M in the (α, β), we may compare the level of QM(α,β) to the corresponding values at b=1 (full fin width) and 0 (zero fin width). The various diagrams plotted on the plane of zeta potentials contain all the useful information about the EO pumping and may serve as an easily used reference for engineering deign and applications.

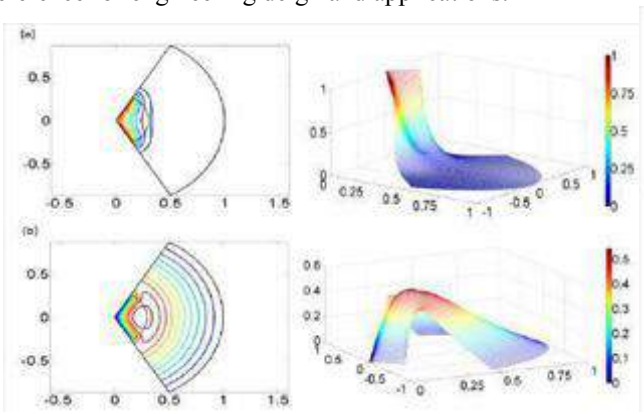

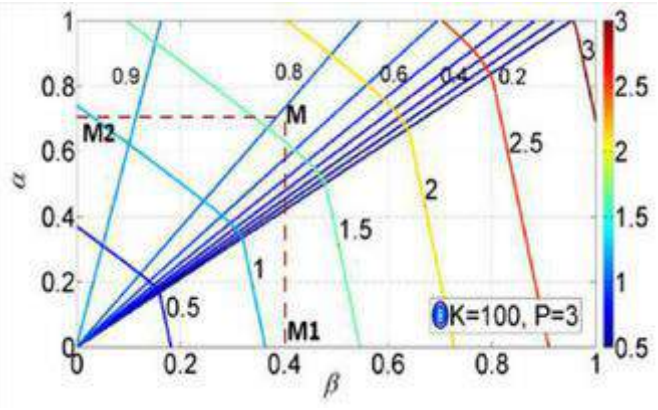

Figure 2. (left) Plots for the case $Q(1,0)$ with b=0.3, K=10, P=3: (a) EDL potential; (b) EO velocity profile. The left panel of each plot presents level lines of the field, and the right panel presents a three-dimensional view.

Figure 3. (right) Plots of several level lines of optimal EO pumping rate $Q_M(\alpha,\beta)$ for P=3 (with K=100). Also shown are several lines of constant b_{max} from 0.2 to 0.9 (counter-clockwise)

CONCLUSIONS

As a final remark, microfluidic devices in practice are often operated in a short time interval of impulse voltages. The steady-state EO pumping is reached after a transient time, which is on the order of ρR2/μ (see, e.g., [25]) (which is about 10-8 sec=10 ns for R=100nm). This is very efficient for the duct on the size of nanoscales. It must be emphasized that the present results were obtained under the Debye-Hückel approximation. In a wider range of applications with the ratio $\lambda = ze\zeta / k_b T$ being not small but close to 1, the DHA is no longer valid and one may resort to the analysis of the nonlinear Poisson-Boltzmann equation. In the line of our previous approach [26], the present DHA solution provides the base for extension of analysis to the Poisson-Boltzmann equation, or the more general Poisson-Nernst-Planck equations. In other realistic applications, one may need more accurate model to account for the physics and chemistry. (supported by MOST 103-2221-E-002-099-MY3)

References

[1] Liu YH, Kuo CY, Chang CC & Wang CY (2011) Electro-osmotic flow through a two-dimensional screen pump filter. Physical Review E 84, 036301
[2] Chang CC & Wang CY (2011) Rotating electroosmostic flow over a plate or between two plates. Physical Review E 84, 056320.
[3] Kung CF, Wang CY & Chang CC (2013) A periodic array of nano-scale slats for high-efficiency electro-osmotic pumping. Electrophoresis 34, 3133-3140.
[4] Kung CF, Wang CY & Chang CC (2014) Transition of the electrostatic potential from the inside of an open channel to the reservoir. RSC Advances 4, 45585-45591.

GEOMETRIC CONTROL OF ASYMMETRIES IN PASSIVE SCALARS ADVECTED IN RECTANGULAR AND ELLIPTICAL PIPES

Manuchehr Aminan[1,2], Francesca Bernardi[1,2], Roberto Camassa[1,2], and Richard M. McLaughlin*[1,2]

[1]*Department of Mathematics, University of North Carolina, Chapel Hill, NC, USA*
[2]*University of North Carolina Joint Fluids Laboratory, UNC, Chapel Hill, NC, USA*

Summary We explore the role different geometries (amongst rectangular and elliptical domains of arbitrary aspect ratios) play in controlling emerging up-stream/downstream asymmetries in the cross-sectionally averaged distribution of diffusing passive scalars advected by laminar, pressure driven shear flows. We show using a combination of rigorous analysis, asymptotic expansions, and Monte-Carlo simulations, that on short time scales relative to the shortest diffusion times, elliptical domains preserve initial uptream/downstream symmetric distributions, while rectangular ducts break this symmetry. Skinny ducts produce distributions with negative skewness, while fat ducts produce positive skewness for symmetric initial data which is uniformly distributed in the cross-section. There is a special aspect ratio of approximately 2-1 ratio for which symmetry is preserved. In turn, long-time (relative to the longest diffusion timescale) exact analysis shows that all geometries generically break symmetry before ultimately symmetrizing in infinite time.

INTRODUCTION

The evolution of diffusing passive scalars in laminar flows is of central importance to the discipline of micro and nano fluidics. Assessing precisely how geometry affects scalar spreading can provide a valuable design tool for producing mixers which deliver chemicals effectively. For example, if it is desirable to *deliver a chemical* from a source with a particular **heavy front-loaded** (as opposed to back-loaded) distribution, it is necessary to understand how the shear dispersion induced by pressure driven fluid flows manifests. To that end, we present a complete, comprehensive study which shows explicitly how a channel's cross sectional shape can be used to control such loading through a complete characterization of the dependence of the scalar's skewness (the centered, normalized third moment) upon the aspect ratio across elliptical and rectangular shaped pipes. We establish using a combination of exact and asymptotic analysis along with Monte-Carlo simulations several interesting new phenomena associated with the cross-sectional geometry.

First, we study the skewness of the distribution. The skewness is the centered, third moment of the distribution, taken as the integral of the product of the cube of the horizontal position, x, with the evolving distribution of the passive scalar, from minus infinity to plus infinity, then averaged over the cross-sectional area. This evolving quantity is the lowest order statistic which gauges asymmetries in a distribution. Closed evolution equations for arbitrary moments of a distribution were derived by Aris [1] in arbitrary cross-sectional domains. We succeed in deriving closed form exact expressions as single series formulas for the first three moments, along arbitrary slices for the special case of the flow between two infinite parallel plates. These formulas are used to carefully benchmark our Monte-Carlo simulations for arbitrary geometries.

Interestingly, we demonstrate that the case of the infinite channel has the property that for initial data which is symmetric in the upstream/downstream direction, but possesses no variation transverse to the flow, the skewness is strictly negative for all time. This is in contrast to the result of Barton [2], who showed that for the circular pipe, the analogous case is strictly negative. As such, alternative geometries with differing aspect ratios are expect to show an intriguing connection with interesting dynamics connecting the negative case for two infinite parallel plates, with the positive case involving the circular pipe.

We find that in fact, on short timescales compared to the shortest diffusion timescales, that elliptical domains preserve initial symmetries. On the other hand, rectangular ducts break this initial symmetry. Skinny ducts are seen to develop negative skewness, while fat ducts evolve passive scalar distributions to have positive skewness. Remarkably, a special aspect ratio of approximately 2-1 ratio separates negative skewness cases from positive ones.

We also document both analytically and numerically, that on long times relative to the longest diffusion timescale in the system, all geometries studied break symmetry. Of course, in infinite time, everything re-symmetrizes in accordance with the long time theory of homogenization theory and G.I. Taylor's pioneering work [3]. We establish similar "golden" ratios for ellipses and rectangles separating negative skewness from positive skewness at long time.

CONCLUSIONS

These results are expected to be of particular interest in the field of micro and nano=scale fluidics where geometry could potentially be used with these findings in mind to shape the distributions to be either front-loaded or back loaded, properties of natural interest in different mixing configurations. Some of our findings were just reported at **Physical Review Letters** [4].

*Corresponding author. Email: rmm@email.unc.edu

References

[1] R. Aris, *Proc. R. Soc. Lond. A*, 235, **67**, 1956.

[2] N. G. Barton, On the method of moments for solute dispersion, *J. Fluid Mech.*, **126** 205-218, 1983.

[3] G. I. Taylor, *Proc. R. Soc. Lond. A*, 219, **186**, 1953.

[4] M. Aminian, F. Bernardi, R. Camassa, and R. M. McLaughlin, *Phys. Rev. Lett.*, **115**, 154503, 2015.

WETTING DYNAMICS ON UNDER-LIQUID SUBSTRATES

Surjyasish Mitra and Sushanta K. Mitra *
Micro & Nano-scale Transport Laboratory, Department of Mechanical Engineering, Lassonde School of Engineering, York University, Toronto, Ontario, Canada, M3J 1P3

Summary An experimental study to characterize the spreading of a liquid drop on an under-liquid substrate has been presented. It was found that the spreading occurs over an initial distinct fast regime before transiting to a much slower regime close to its equilibrium. A comment has been made to delineate the distinction of spreading on under-liquid substrate with the well known framework of spreading-coalescence analogy commonly found in literature.

INTRODUCTION

Wetting of liquid drops on a substrate in air medium has been studied extensively over the past few decades due to its manifold applications in technology and industry [1]. This is a fairly well understood phenomenon where a liquid drop upon contact with a surface spreads by the virtue of minimization of surface energy. Recent studies have shown spreading occurs in two distinct regimes: an initial fast regime just at the instance after the liquid drop touches the substrate and a later slower regime close to equilibrium [2, 3, 4]. Though the latter regime is well understood from classical hydrodynamics [5, 6] as well as molecular kinetic theory [7], the initial faster regime is yet to be explained from a theoretical perspective. But what happens if we consider the same liquid drop spreading on a substrate in the presence of a surrounding liquid medium? This fundamental problem of liquid-liquid displacement poses some complexities due to lack of understanding of contact line dynamics in liquid-liquid systems. Though relatively less studied, it has significant applications in oil recovery [8], droplet microfluidics [9], interaction of marine systems with oil spills, etc. The present work aims at decoding the spreading of a liquid drop on a flat substrate submerged in another liquid medium.

EXPERIMENT AND RESULTS

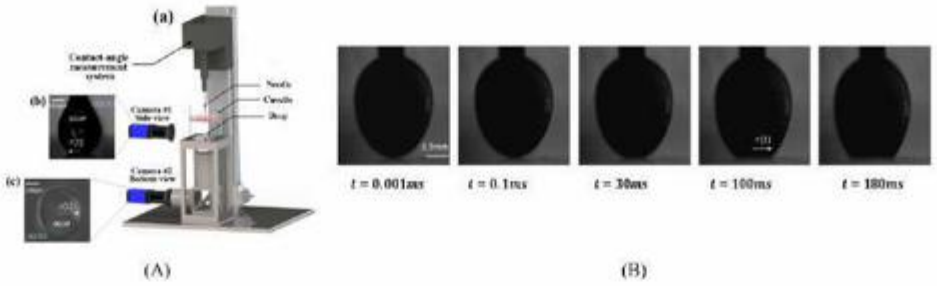

Figure 1: (Color online) (A) Schematic of the experimental set-up. Inset (b) and (c) shows an ideal representation of side-view and bottom-view images captured by the respective cameras. (B) Time snaps showing the growth of spreading radius r with time for oil-water-glass system used in the study.

The experimental set-up consist of a custom made contact angle measurement system (as shown in Fig. 1(A)). The working liquids used were deionized water ($\rho_W = 1000\text{kg/m}^3$, $\gamma_{WA} = 72.1\text{mN/m}$, $\mu_W = 0.001\text{Pa-s}$) and laser oil (Cargille Laboratories Inc., Cedar Grove, NJ, USA; $\rho_O = 1100\text{kg/m}^3$, $\gamma_{OA} = 24.5\text{mN/m}$, $\mu_O = 0.2\text{Pa-s}$). An oil drop of radius 0.7mm was generated at the tip of a stainless steel needle and was gently made to touch the glass substrate (microscope slides, Fisher Scientific) kept at the bottom of a water filled glass cuvette. Since the initial spreading dynamics is very fast, two high speed cameras (Photron UX-100) were used in tandem to simultaneously capture the spreading dynamics from side view as well as top view (see Fig. 1(A)). The entire process was captured at a frame rate of 10,000 fps. The drop contact radius was extracted from the captured images using an in-built image analysis tool in MATLAB.
Figure 1(B) shows the time snaps representing the growth of the drop contact radius, r with time. It can be seen that the spreading process was successfully captured with a temporal resolution of a few microseconds. Such high temporal resolution enabled us to track the growth of the spreading radius from as early as 4μm. Similar to spreading in air, here also spreading begins in an intial faster regime. Since, wetting on under-liquid substrate is in the domain of partial wetting with a final equilibrium contact angle greater than 90° (for the present oil-water-glass system, $\theta_{eq} = 134^\circ$), the spreading process slows down quickly and enters a period of much slower growth in spreading radius.

*Corresponding author. Email: mitras@yorku.ca

DISCUSSION

There has been a recent surge in applications of droplet microfluidics where the key idea is to generate and manipulate micro droplets. In such systems involving narrow confinement, spreading is often followed by coalescence of such drops and an eventual jet formation. Many recent studies have tried to understand spreading in analogy with coalescence due to their common self-similar flow characteristics [4]. When two free drops merge, the coalescence process essentially takes place by the formation of a liquid bridge between the drops which grows with time [10]. It has been argued that for spreading in air medium, growth of the spreading radius, r follows a similar scaling as growth of the liquid bridge when two free drops merge [4]. But, for spreading on an under-liquid substrate such analogy should not hold due to complexity in the nature of the contact line motion for a liquid-liquid system as well as different length scales over which the flow evolves in both the drop and the surrounding medium. Our recent study on under-liquid sessile drop coalescence has thrown some light into the growth of bridge height as two drops merge (see Fig. 2), where it has been found that the bridge height grows in a self-similar manner following a scaling of $h^* \sim t^{*0.89}$ (see Fig. 2(d))[11]. However, it is yet to be seen where for under-liquid substrates, spreading and coalescence can be merged into an single common theoretical framework.

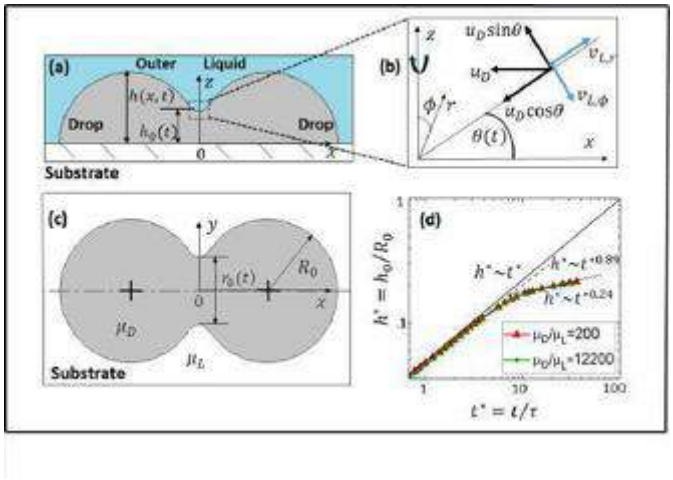

Figure 2: (Color online) Schematic of drop coalescence on an under-liquid substrate. (a) and (c) represents the side view and top view of the process, respectively. (b) represents an extended view of the bridge region connecting the two drops where the profiles has been conceived as a liquid wedge. The flow vectors are shown for the drop ad liquid medium. (d) shows the growth of the bridge height with time in non-dimensional terms where the curves for two different viscosity ratio of the drop liquid and surrounding liquid merge into a single curve. For more details, see Ref. [11].

References

[1] Ashgriz, N. ed.: Handbook of atomization and sprays: theory and applications. Springer Science & Business Media, 2011.

[2] Bird, J.C., Mandre, S., Stone, H. A.: Short-time dynamics of partial wetting. Phys. Rev. Lett **100**:234501, 2008.

[3] Biance, A.L., Clanet, C., Quere, D.: First steps in the spreading of a liquid droplet. Phys. Rev. E **69**:016301, 2004.

[4] Eddi, A., Winkels, K.G., Snoeijer, J.H.: Short time dynamics of viscous drop spreading. Phys. Fluids **25**:013102, 2013.

[5] Voinov, O.V.: Hydrodynamics of wetting. Fluid Dynamics **11**: 714-721, 1976.

[6] Cox, R.G.: The dynamics of the spreading of liquids on a solid surface. Part 1. Viscous flow. J. Fluid Mech **168**:169-194, 1986.

[7] Blake, T.D., Haynes, J.M.: Kinetics of liquid liquid displacement. J. Colloid Interface Sci **30**:421-423, 1969.

[8] Basu, S., Nandakumar, K., Lawrence, S., Masliyah, J.: Effect of calcium ion and montmorillonite clay on bitumen displacement by water on a glass surface. Fuel **83**:17-22, 2004.

[9] Kobayashi, I., Nakajima, M., Mukataka, S: Preparation characteristics of oil-in-water emulsions using differently charged surfactants in straight-through microchannel emulsification. Colloids Surf., A **229**:3341, 2003.

[10] Eggers, J., Lister, J.R., Stone, H.A.: Coalescence of liquid drops. J. Fluid Mech **401**:293-310, 1999.

[11] Mitra, S., Mitra, S.K.: Symmetric drop coalescence on an under-liquid substrate. Phys. Rev. E **92**:033013, 2015.

DIRECT-INVERSE ANALYSIS OF THE BIODIESEL REACTION IN MICROREACTORS

Péricles Crisiron Pontes & Carolina Palma Naveira Cotta
Dept. of Mechanical Engineering & Dept. of Nanoengineering
COPPE/UFRJ –Federal University of Rio de Janeiro
Cx. Postal 68503, Cidade Universitária, Rio de Janeiro, RJ, Brazil, 21945-970
E-mail: carolina@mecanica.coppe.ufrj.br

Summary A diffusive-convective-reactive coupled nonlinear mathematical model that governs the mass transfer process during the transesterification reaction in parallel plates microreactors in isothermal conditions is presented and a hybrid solution via Generalized Integral Transform Technique (GITT) is developed. The heuristic method Particle of Swarm Optimization (PSO) is applied in the inverse analysis to estimate the reaction kinetics constants. The results present a good agreement with experimental data from the literature and indicate that the GITT combined with PSO presents themselves as a efficient and robust combination for direct-inverse analysis in mass transfer problems.

INTRODUCTION

The theoretical analysis of the microreactors design for the biodiesel production via transesterification reaction is a complicated task due to the complex liquid-liquid reactant flow that takes place within these microsystems. So, the computational simulation is an important tool that helps to understand the physical-chemical phenomenon and, consequently, to determinate the suitable conditions that maximize the conversion of triglycerides during the biodiesel synthesis. Some works in the literature presents a theoretical and/or experimental study about the transesterification process within microreactors [1-2].

DIRECT AND INVERSE PROBLEM

The mathematical model was obtained from the literature [2] and it governs the concentration of the species involved in transesterification considering fully developed laminar stratified flow of two Newtonian reactants fluids, soybean oil and methanol, within parallel plates microreactors. It is considered that the second order consecutive elementary reaction occurs only in the oil phase in isothermal conditions.

$$U_{TG}\ Y\ \frac{\partial F_s\ X\ Y)}{\partial X} = \xi_s \frac{\partial^2 F_s\ X\ Y)}{\partial Y^2} + \varsigma G_s \tag{1a}$$

$$F_{TG}\left(0,Y\ =1;\ F_s\left(0,Y\right)=0 \text{ where} s = DG\ MG\ B\ A\ GL;\quad \left.\frac{\partial F_s}{\partial Y}\right|_{Y=0} = 0, \text{ where } s = TG\ DG\ MG\ B\ A\ GL \right. \tag{1b-d}$$

$$F_A\ \ X,1\ = F_{Ao}, \left.\frac{\partial F_s}{\partial Y}\right|_{Y=1} = 0, \text{ where } s = TG\ DG\ MG\ B\ GL$$

$$\text{where}\quad F_s = \frac{C_s}{C_{TGo}}, F_{Ao} = \frac{C_A^*}{C_{TGo}}\quad X = \frac{x}{L},\ Y = \frac{y}{H_{TG}}, U_{TG} = \frac{u_{TG}}{u_{TG\ Av}},\ \varsigma = \frac{LC_{TGo}}{u_{TG\ Av}},\ \xi_s = \frac{LD_s}{u_{TG\ Av}H_{TG}^2} \tag{1e-f}$$

where F is the dimensionless concentration of all six species involved: triglyceride (*TG*), diglyceride (*DG*), monoglyceride (*MG*), biodiesel (*B*), alcohol (*A*) and glycerol (*GL*), respectively. *L* and H_{TG} are the length of microreactor and the height of the oil phase in the stratified flow. C_{TGo} and C^*_A are, respectively, the concentration of the triglycerides specie at the entrance of microreactor and the equilibrium concentration of the alcohol species at the interface between the two phases. *D* is the mass diffusion coefficient of the species. $U_{TG}(Y)$ is the dimensionless velocity profile of the triglycerides species in the microreatcor. The G_s represents the kinetic equation for each specie, in accordance with Table 1.

TABLE 1. Chemical reaction equation.

Specie	G_s	Specie	G_s
B	$\left(k_1F_{TG}+k_3F_{DG}+k_5F_{MG}\right)F_A+\left(-k_2F_{DG}-k_4F_{MG}-k_6F_{GL}\right)F_B$	*MG*	$\left(k_3F_{DG}-k_5F_{MG}\right)F_A+\left(-k_4F_{MG}+k_6F_{GL}\right)F_B$
A	$\left(-k_1F_{TG}-k_3F_{DG}-k_5F_{MG}\right)F_A+\left(k_2F_{DG}+k_4F_{MG}+k_6F_{GL}\right)F_B$	*GL*	$k_5F\ \ F_A-k_6F\ \ F_B$
DG	$\left(k_1F_{TG}-k_3F_{DG}\right)F_A+\left(-k_2F_{DG}+k_4F_{MG}\right)F_B$	*TG*	$-k_1F\ \ F_A+k_2F\ \ F_B$

where k_1 to k_6 are the reaction kinetic constants.

The solution for the problem above was obtained by the hybrid method so called GITT [2, 3]. Some quantities of interest are the residence time and the triglycerides conversion, which are defined, respectively, by equations (2a-b):

[a] Corresponding author. Email: carolina@mecanica.coppe.ufrj.br

$$\tau = \frac{Triglyceride\ layer\ volume}{Triglyceride\ volumetric\ flow},\quad Conversion\,TG(\%) = \left(\frac{F_{TG,AV}(0) - F_{TG,AV}(1)}{F_{TG,AV}(0)} \right) \times 100 \tag{2a-b}$$

where $F_{TG,Av}$ is the average concentration of the triglyceride species.

To estimate the reaction kinetic constants, the least squares objective function is considered, and to minimize the objective function F_{obj}, the heuristic method Particle of Swarm Optimization (PSO) [4] was used.

$$F_{obj} = \sum_i \left[Conversion\,TG(\%)^{Exp} - Conversion\,TG(\%)^{Cal} \right]^2 \tag{3}$$

RESULTS

Table 2 presents the parameters used in the simulation of the concentration of the species, and Table 3 presents a comparison between the results obtained with the kinetic constants estimated in this work and the literature data [2].

TABLE 2. Parameters used in the simulation.

Parameter	Value	Parameter	Value	Parameter	Value
μ_{TG}	$5{,}825.10^{-2}$ [Pa.s]	Q_{TG}/Q_A	3,402	D_{DG}, D_{MG}, D_{GL} and D_B	$1{,}38.10^{-9}$ [m²/s]
μ_A	$5{,}47.10^{-4}$ [Pa.s]	C_{TGo}	1014 [mol/m³]	ρ_{TG}	885 [kg/m^3]
D_{TG}	$1{,}58.10^{-9}$ [m²/s]	F_{Ao}	4,4	W	0,0105 [m]
D_A	$1{,}182.10^{-10}$ [m²/s]	L	0,0233 [m]	H	100.10^{-6} [m]

TABLE 3. Reaction kinetics constants [mol/(m³.s)] estimated and conversion of triglyceride.

Parameter	Literature [2]	GITT+PSO	τ	Exp. [2]	Num. [2]	Num.(GITT+PSO)
k_1	$4.368x10^{-6}$	$3.170x10^{-6}$	0.41	12.33	20.36	15.90
k_2	$9.623x10^{-6}$	$2.461x10^{-6}$	0.79	36.98	40.68	35.70
k_3	$1.880x10^{-5}$	$5.378x10^{-5}$	1.69	66.56	66.78	66.31
k_4	$1.074\ x10^{-4}$	$2.874x10^{-4}$	3	84.48	80.57	83.98
k_5	$2.117x10^{-5}$	$1.000x10^{-1}$	5.3	89.5	88.29	90.13
k_6	$9.000\ x10^{-7}$	$3.221x10^{-2}$	10	91.1	90.95	90.88
F_{obj}	**0.00949**	**0.00152**	-	-	-	-

Figure 1 presents the conversion of triglycerides with the reaction kinetics constants from the literature and with the constants estimated by this work using the GITT and the PSO methods in the direct-inverse solutions, respectively.

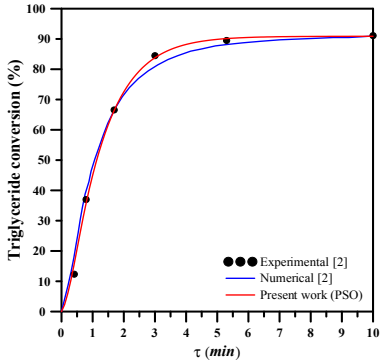

FIGURE 1. Conversion of triglycerides.

CONCLUSIONS

The GITT was successfully applied in the analysis of direct solution of the mass transfer process during the transesterification reaction in microreactors, and the heuristic method PSO was used to estimate the kinetic constants, providing a better agreement between the simulation and the experimental results than those previous available in the literature.

References

[1] A.A. Al-Dhubabian, *Production of biodiesel from Soybean Oil in a Micro Scale Reactor*, Thesis (M.Sc.), Oregon State University, USA, 2005.

[2] Pontes, P.C., Naveira-Cotta, C.P., Macedo , E.N. & Quaresma , J.N.N., Integral transforms analysis of three-dimensional mass transfer in the transesterification process in micro-reactors. *In: Proc. of the 7th Int. Symposium on Advances in Computational Heat Transfer, CHT-15*, *ICHMT*, 24–29 May 2015, Piscataway, USA

[3] Cotta, R.M., *Integral Transforms in Computational Heat and Fluid Flow*, CRC Press, Boca Raton, FL, 1993.

[4] Vu, T. V., 2012, "A comparison of Particle Swarm Optimization and Differential Evolution", *International Journal on Soft Computing* (*IJSC*), v. 3, n. 3, pp. 13-30.

ROTATION-FACILITATED RAPID TRANSPORT OF NANORODS IN MUCOSAL TISSUE

Xinghua Shi[1a)]
[1]*LNM, Institute of Mechanics, Chinese Academy of Sciences, Beijing, China*

Summary Mucus is a viscoelastic gel layer that typically protects exposed surfaces of the gastrointestinal (GI) tract, lung airways, and other mucosal tissues. Particles targeted to these tissues can be efficiently trapped and removed by mucus, thereby limiting the effectiveness of such drug delivery systems. In this study, we experimentally and theoretically demonstrated that cylindrical nanoparticles (NPs), such as mesoporous silica nanorods, have superior transport and trafficking capability in mucus compared with spheres of the same chemistry. The higher diffusivity of nanorods leads to deeper mucus penetration and a longer retention time in the GI tract than that of their spherical counterparts. Molecular simulations and stimulated emission of depletion (STED) microscopy revealed that this anomalous phenomenon can be attributed to the rotational dynamics of the NPs facilitated by the mucin fibers and the shear flow. These findings shed new light on the shape design of NP-based drug delivery systems targeted to mucosal and tumor sites that possess a fibrous structure/porous medium.

INTRODUCTION

Improving the mucus-penetrating ability of nanoparticles (NPs) is of great importance to avoid rapid drug clearance and achieve efficient drug delivery [1-3]. Mucus is a tenacious mesh structure with a thickness ranging from tens to hundreds of microns and an average pore size in the range of hundreds of nanometers. Small hydrophilic molecules can freely diffuse through this barrier while particles, especially foreign particles, are excluded in cases where the particle size is larger than the average pore size [4-7]. The trapped particles are then quickly washed away by the microflows of the mucus layer. Such a capture and clearance mechanism protects mucosal tissues against infectious agents; however, this mechanism limits opportunities for the controlled drug delivery of NPs. From the Nature, we know that most of the bacteria possessing a high mobility in mucus have a rod-like shape [8,9]. Pathogens such as Helicobacter pylori [10] and Vibrio cholera [11] are able to swim through the intestinal mucus and remain in the mucus layer for extended periods, instead of being easily washed away. This finding informs us that shape may contribute to the high mucus-penetrating ability of particles. The correlation between the shape of NPs and their diffusivity in mucus, however, is still missing, even though this aspect is potentially crucial in the design of NPs-based drug delivery systems.

RESULTS

Transport and tracking of NPs in rat intestinal mucus in vitro, ex vivo and in vivo

In this study, we fabricated mesoporous silica nanospheres (MSNSs) and mesoporous silica nanorods (MSNRs) with different aspect ratios (ARs) but identical surface chemistries and zeta potentials. We present evidence that, compared with spheres, cylindrical NPs display superior diffusion and penetration patterns in intestinal mucus, which can further lead to a longer intestinal retention time and higher villus absorption. This work provides insights into the effect of NP shape on the mucus-penetrating property and demonstrates the usability of nanorods for drug delivery to mucosal tissues.

Mechanism for the rapid diffusion of MSNRs

Through molecular simulations, we found that the better mucus-penetrating property of the nanorods is due to the rotational motions of the nanorods facilitated by the shear flow and the mesh structure of mucus. The rotational dynamics of nanorods were also confirmed using STED microscopy. A single MSNR is rotating in the mucus, which is consistent with the results of the molecular simulation.

CONCLUSIONS AND OUTLOOK

We note that in addition to transport in mucosal tissues, nanorods can have superiority in interstitial transport within the dense interstitial structure surrounding tumor cells. Because the microenvironment of the interstitial structure is similar to that of mucus, which is formed by fibrous tissues, we postulate that the mechanism for the rapid penetration of nanorods into tumor sites may be the same as that for mucus. Therefore, although conventional spherical NPs currently remain the dominant shape, non-spherical NPs may become common next-generation drug carriers. The barrier to using non-spherical particles lies partly with the difficulty in synthesis and characterization, but even more with the lack of understanding of the physics that govern the relationship between shape and various characteristics of non-spherical NPs. Our findings may inspire the novel and rational design of drug delivery systems for use in various diseases.

[a)]Corresponding author. Email: shixh@imech.ac.cn .

References

[1] Lai SK, Wang YY, Hanes J. *Advanced drug delivery reviews* **61**(2)**:** 158-171, 2009.

[2] Ensign LM, Cone R, Hanes J. *Advanced drug delivery reviews* **64**(6)**:** 557-570, 2012.

[3] Cu Y, Saltzman WM. *Nat Mater* **8**(1)**:** 11-13, 2009.

[4] Olmsted SS, Padgett JL, Yudin AI, Whaley KJ, Moench TR, Cone RA. *Biophys J* **81**(4)**:** 1930-1937, 2001.

[5] Horcajada P, Chalati T, Serre C, Gillet B, Sebrie C, Baati T, *et al*. *Nat Mater* **9**(2)**:** 172-178, 2010.

[6] Lieleg O, Ribbeck K. *Trends Cell Biol* **21**(9)**:** 543-551, 2011.

[7] Kirch J, Schneider A, Abou B, Hopf A, Schaefer UF, Schneider M, *et al*. *Proceedings of the National Academy of Sciences of the United States of America* **109**(45)**:** 18355-18360, 2012.

[8] Backhed F, Ley RE, Sonnenburg JL, Peterson DA, Gordon JI. *Science* **307**(5717)**:** 1915-1920, 2005.

[9] Johansson ME, Sjovall H, Hansson GC. *Nature reviews Gastroenterology & hepatology* **10**(6)**:** 352-361, 2013.

[10] Sycuro LK, Pincus Z, Gutierrez KD, Biboy J, Stern CA, Vollmer W, *et al*. *Cell* **141**(5)**:** 822-833, 2010.

[11] Schrank GD, Verwey WF. *Infection and immunity* **13**(1)**:** 195-203, 1976.

PROBING THE NON-GAUSSIANITY IN CONFINED DIFFUSION OF NANOPARTICLES

Xu Zheng [1a)], Chundong Xue [1] & Guoqing Hu [1]
[1]State Key Laboratory of Nonlinear Mechanics, Institute of Mechanics, Chinese Academy of Sciences, Beijing 100190, China

Summary Confined diffusion is ubiquitous in nature. Ever since the "anomalous yet Brownian" motion was observed, the non-Gaussianity in confined diffusion has been unveiled as an important issue. In this study, we experimentally investigate the characteristics and source of non-Gaussian behavior in confined diffusion of nanoparticles suspended in polymer solutions. A time-varied and size-dependent non-Gaussianity is reported based on non-Gaussian parameter and displacement probability distribution, especially when the nanoparticle's size is smaller than the typical polymer mesh size. The main source of the non-Gaussianity can therefore be attributed to hopping diffusion that results in an exponential probability distribution with the large displacements

INTRODUCTION

The diffusive motion of particulate matter (e.g., nanoparticle (NP), protein and DNA) in complex medium is of fundamental interest in many interdisciplinary fields, such as biophysics, soft matter and polymer physics. Different from free Brownian diffusion in simple liquids, the mean squared displacement (MSD) $\langle L^2(t)\rangle$ of the so called "anomalous diffusion" exhibits a nonlinear relation with elapsed time t, i.e., $\langle L^2(t)\rangle \sim t^{\beta}$ where $\beta \neq 1$. $\beta > 1$ corresponds to the super-diffusive motion, as observed in the self-motile motion of cells or Janus particles, whereas $\beta < 1$ corresponds to the confined and sub-diffusive motion, which is suggested to be more ubiquitous in nature.

Recently, as first observed by Granick's group, even Brownian diffusion with linear MSD could be non-Gaussian [1-2]. This "Brownian but not Gaussian" behavior has attracted much attention because it raises questions on the validity of the frequently invoked Gaussian approximation for describing the diffusive phenomenon in complex medium. To fully understand this phenomenon, one needs to know the origin and implication of the non-Gaussianity. However, the physical source of the non-Gaussianity and the influence from the complex environment on the non-Gaussianity remain an open question. Thus, the purpose of this study is to identify the physical source of non-Gaussianity in confined diffusion and clarify its characteristics.

EXPERIMENTS AND RESULTS

Experiment

We study the non-Gaussianity in a model system that contains diffusive polystyrene NPs in polyethylene oxide (PEO) solutions. The motions of NPs were measured using particle tracking method. The particle tracking method provides detailed displacements and facilitates statistical analysis to quantify non-Gaussianity based on high moment of displacement, displacement probability distribution (DPD) and displacement auto-correlation, which other techniques including dynamic light scattering or fluorescence correlation spectroscopy can hardly provide. The experiments were performed by controlling the NPs' size (diameter a = 40 nm, 100 nm and 200 nm, respectively), the PEO molecular weight (MW= 0.6 M, 2 M, 4 M and 8 M, respectively), and the PEO concentration (c = 0.05 to 1.5 wt %).

Results

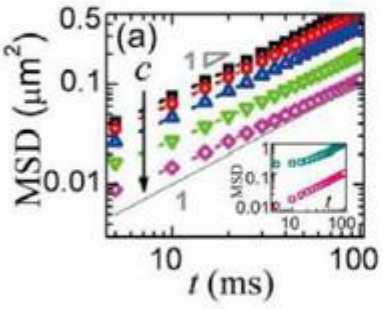

Fig. 1

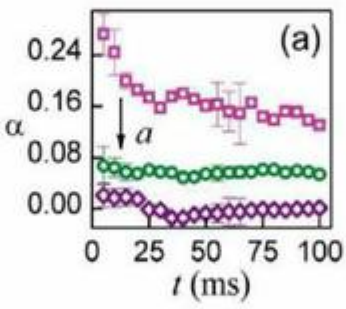

Fig. 2

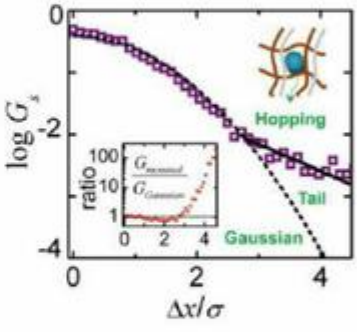

Fig. 3

Fig.1 The measured MSD of different NPs. The slope of 1 indicates the linear relation between MSD and t.
Fig.2 The measured non-Gaussian parameter α of 40nm (square), 100nm (circle) and 200nm (diamond) NPs in 0.5% PEO solution.
Fig.3 The fat tail distribution of DPD of 40nm NP, which is due to the long-distance hop through polymer networks.

[a)] Corresponding author. Email: zhengxu@lnm.imech.ac.cn.

Typical results of measured MSD are shown in Fig. 1. One sees that the MSD behavior varies from a sub-linear short-time stage ($t \sim 10$ ms, slope $\beta < 1$) to a linear Brownian stage ($t > 30$ ms, slope $\beta = 1$) in a long-time stage, and the slope on sub-linear stage decreases slightly with increasing PEO concentration. The transition between these two stages is in accordance with previous works [3].

However, there are several important questions that MSD results are unable to answer. First, as explained by Piskorz and Ochab-Marcinek [4], all those commonly-used models (*i.e.*, elastic force, walking confined diffusion with depletion layer or hopping diffusion) predict the same MSD feature as shown in Fig. 1. It is necessary to develop alternative approach to identify the source of non-Gaussian behavior. Second, it is still unclear why non-Gaussianity emerges not only in the sub-diffusive stage but also in the long-time Brownian stage. The non-Gaussianity needs to be quantified for a better understanding of the anomalous diffusion of NPs in complex medium.

Therefore, the non-Gaussian parameter, a fourth moment, α(= $< \Delta x^4 >$ $< \Delta x^2 >$ – , is introduced to quantitatively describe the variation of non-Gaussianity. Generally, α = 0 indicates a pure Gaussian process such as simple Brownian motion. In the current experiments, however, we obtain positive α which is observed to vary with particle size, elapsed time, PEO concentration and molecular weight. Fig. 2 shows a size-dependent non-Gaussianity, that is, smaller NPs result in a stronger non-Gaussianity regardless of PEO solutions. Explicitly, α is between 0.1-0.3 for 40 nm NP, while α is very close to zero for 200 nm NP indicating that the motion is still Brownian. Considering the PEO mesh size is in the order of 50 nm, it is not surprised that a more significant non-Gaussianity will be observed for those NPs smaller than the typical size of surrounding structure. Moreover, different time-varied tendencies of α are observed. For 40 nm NP, α decreases rapidly at short time and then reaches a nearly constant value at about $t \sim 30$ ms (Figure 2a-b). This time scale agrees with the transition time of the measured MSD shown in Figure 1. For 100 nm NP, α remains positive and varies slightly with time; while for 200 nm NP, α is always close to zero indicating that the non-Gaussianity becomes trivial. More interestingly, the non-Gaussianity of 40 nm and 100 nm NPs will not disappear even in the long-time Brownian stage.

The source of the non-Gaussianity will be analyzed with the aid of the measured DPD (Fig. 3, 40 nm NP in 4M PEO). The standard Gaussian distribution with probability density function $G_s = \frac{1}{\sqrt{2\pi}}$ $- \Delta x$ σ is introduced based on the normalized displacement $\Delta x/\sigma$, where σ is the standard deviation of displacements, which permits a direct comparison between different results. The most obvious deviation compared to standard Gaussian distribution is observed at the tails ($|\Delta / \sigma| > 3$), showing an approximately one hundred times higher probability of large displacements. The tail distribution is found to decay linearly on the logarithmic plot, implying that the probability function changes to $G_s \sim \exp[-(\Delta x/\sigma)]$ (solid lines in Figure 3). In the middle part of DPD, a sharper peak at $\Delta x/\sigma = 0$ and a narrower shoulder ($|\Delta / \sigma| = 1.5 - 2.5$) are visible, representing smaller displacements caused by confinements compared to simple Brownian motion. Based on the definition of non-Gaussian parameter α, *i.e.*, a fourth moment of displacement, the contribution from the tails with large displacements is much more significant than that from the center. Thus the non-Gaussianity depicted by α comes from the enhanced probability of large displacement through the surrounding structures. According to these features, we propose that the source of non-Gaussianity is mainly attributed to the hopping diffusion, which means that NPs could hop through the polymer mesh structures nearby intermittently. Multiple PEO molecular chains tend to overlap or entangle with each other to form heterogeneous structures like global networks and local compartments in which fast motion of NPs across networks or adjacent compartments would happen.

CONCLUSIONS

In summary, this letter investigates the diffusing behavior of NP interacting with surrounding polymer chains by means of non-Gaussian parameter α, DPD and displacement auto-correlation. A size-dependent and time-varied non-Gaussianity is observed, especially when the NP's size is smaller than the typical network mesh size. This non-Gaussianity does not vanish even at long-time Brownian stage with linear MSD, and thus results in the "anomalous yet Brownian" phenomenon. We thus propose that the main source of non-Gaussianity is connected to the exponential tail distribution with enhanced displacements, which is a clear signal of hopping diffusion. The present results provide physical insights into the particle-polymer interaction and shed light on the debate of the physical origin of NP dynamics in soft-matter systems.

References

[1] Wang, B., Anthony, S. M., Bae, S. C., Granick, S. *Proc. Natl. Acad. Sci. U. S. A.*, **106**, 15160-15164, 2009.

[2] Wang, B., Kuo, J.; Bae, S. C., Granick, S. *Nat. Mater.* **11**, 481-485, 2012.

[3] Ziębacz, N., Wieczorek, S. A., Kalwarczyk, T., Fiałkowski, M., Hołyst, R. *Soft Matter* **7**, 7181-7186, 2011.

[4] Piskorz, T. K.; Ochab-Marcinek, A. *J. Phys. Chem. B*, **118**, 4906-4912, 2014.

FROM RHEOLOGY TO MOLECULAR DETAIL - VISCOSITY OF SUSPENSION OF COMPLEX MOLECULES

Pawel Jan Zuk [*1,2] and Eligiusz Wajnryb[1]
[1]*Institute of Fundamental Technological Research, Polish Academy of Sciences, Warszawa, Polska*
[1]*Faculty of Physics, University of Warsaw, Warszawa, Polska*

Summary The viscosity of solution is intrinsically connected with its composition and the properties of individual particles. For complex macromolecules there often exist coupling between the flow and the state of the molecule. The distribution of particle shapes and movements reacts to the external flow and the flow reacts to this distribution change. This coupling determines the amount of stress induced by the molecules immersed in the fluid that results in change of the viscosity. Using the Rotne-Prager-Yamakawa approximation we show, that given molecular model, one can infer the details of the molecules based on rheology of the solution.

INTRODUCTION

Relation between effective solution viscosity and its composition, in principle, can be calculated from the Stokes equation. All the details of the system in a given time instant come into the solution. They include particles conformation and position but also characteristics of the external flow. Also the coupling of those play an important role due to the hydrodynamic interactions, since the flow affects particles and particles affect flow. Even the change in the strength of the flow change suspension state and the effective viscosity. These dependencies give an insight into the details of the molecules.

KEY IDEA

The effective viscosity η_{eff} is the proportionality coefficient between the stress tensor and the effective strain tensor. These three quantities are coupled and depend on the suspension and flow. The effective viscosity calculated for shear flow is different than for e.g. straining flow. In this report we will restrict to the shear flow even though the presented method is suitable for any kind of linear flow. For the shear flow stress tensor is given by

$$\boldsymbol{\sigma} = 2\eta_{\text{eff}}\mathbf{E}_\infty \quad : \quad \mathbf{E}_\infty = \frac{1}{2}\left(\nabla\mathbf{v}_0 + (\nabla\mathbf{v}_0)^T\right), \tag{1}$$

where $v_0 = (z\dot{\gamma}, 0, 0)$ is the ambient flow and $\mathbf{E}_\infty$ is the symmetric part of the ambient straining field. The stress tensor can be decomposed into the part originating from unperturbed fluid and the particle contribution

$$\boldsymbol{\sigma} = 2\eta_0\mathbf{E}_\infty + \left\langle \sum_i \boldsymbol{\mathcal{S}}_i \right\rangle_{\dot{\gamma}}, \tag{2}$$

where $\boldsymbol{\mathcal{S}}_i$ is the stresslet induced by particle i and $\langle\cdot\rangle_{\dot{\gamma}}$ denotes an average over all possible particle positions and states for a given flow strength $\dot{\gamma}$. The complete set of the components of the particle induced stresslet consists of: stresslet induced sole by the particle presence, stresslet induced by inter and intra particle forces, stresslet induced by torques acting on particles and stresslet induced by the translational and rotational Brownian motion. Some contributions can be neglected in the specific situations e.g. if all particles in the system are torque-free spheres, then the torque components of the stresslet can be neglected. In the shear flow the effective viscosity η_{eff} can be measured with force acting on the vessel walls required to sustain given shear rate. For the system between two parallel plates in xy plane only the $\boldsymbol{\sigma}_{xz}$ component will contribute to the measurements. In the dilute system - with volume fraction $\phi \ll 1$, the effective viscosity can be expressed in terms of intrinsic viscosity $[\eta]$ by the series expansion[1]

$$\eta_{\text{eff}} = \eta_0\left(1 + [\eta]\,\phi + O\left(\phi^2\right)\right). \tag{3}$$

For the arbitrary shear strength the intrinsic viscosity can be calculated as

$$[\eta] = \circ\,\frac{1}{\dot{\gamma}}\left\langle \sum_i \boldsymbol{\mathcal{S}}_i \right\rangle_{\dot{\gamma}}. \tag{4}$$

*Corresponding author. Email: pjzuk@fuw.edu.pl

METHOD

The total stresslet induced by every particle is calculated from the mobility matrix $\boldsymbol{\mu}$. Mobility matrix can be calculated for many different systems using bead models in different approximations. Here we use the Rotne-Prager-Yamakawa (RPY) approximation for the mobility matrix. This matrix is positive definite also for overlapping spheres of different radii[2]. Rigid, non-rigid and partially rigid molecules can be constructed in order to model real particle shapes that can interact with forces and torques. Depending on the partcle size, the Brownian or deterministic trajectory can be calculated. Finally the stresslet is averaged over the simulated trajectory. The method performance is demonstrated by the comparison of the different dumbbell intrinsic viscosities calculation in figure 1. The flow strength is expressed with dimensionless Péclet number $\mathrm{Pe} = 6\pi\eta a^3\gamma$.

RESULTS

On the example of Hookean dumbbell we show, that the equilibrium length of the spring can be determined based on the viscosity spectrum. We will consider a dilute suspension $\phi \ll 1$, that in practice is calculated as a single dumbbell in an unbounded fluid. Let the Hookean dumbbell be composed of spheres of radius a and a spring with an equilibrium length l_0 and stiffness k. The typical intrinsic viscosity dependence on the shear rate, for three different equilibrium lengths with fixed k is presented in figure 2. Significant shear thinning in rarefied solution is observed.

The simulation results for different l_0 and k show, that for spring constants bigger than certain threshold, the equilibrium length of the spring can be uniquely determined from the viscosity spectrum. There are two distinct regimes

- overlapping regime $l_0 \leq 2a : [\eta] = (a_1 + b_1 l_0\ \gamma^{c_1 l_0}$,
- non-overlapping regime $l_0 > 2a : [\eta] = (a_2 + b_2 l_0\ \gamma^{c_2 l_0}$,

where (a_i, b_i, c_i) are two sets constants independent of spring stiffness, that are calculated numerically.

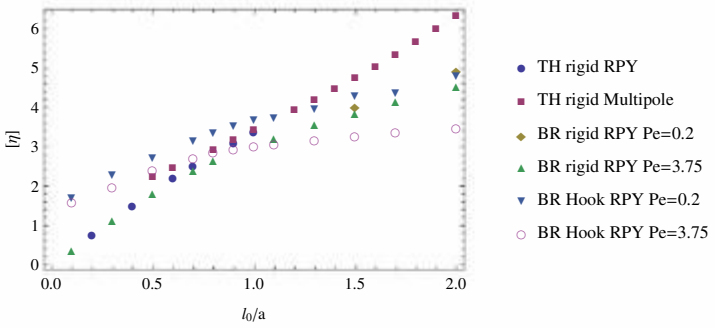

Figure 1: Comparison of intrinsic viscosities: theoretical (TH) results[3] including Brownian contribution for rigid dumbbell (RD) using multipole method and RPY approximation from linear response theory, RD in RPY approximation using Brownian dynamics (BD) and Hookean dumbbell (HD) with $k = 20k_BT$ using BD.

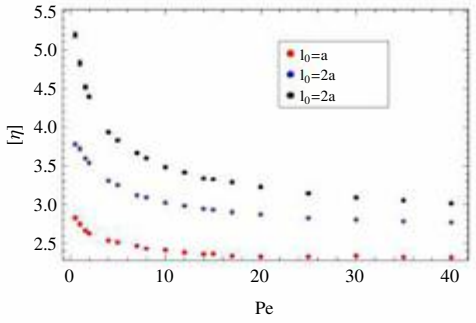

Figure 2: Dependence of intrinsic $[\eta]$ viscosity on the shear rate for $k = 20k_BT$ and different l_0.

CONCLUSIONS

The viscosity of suspension is a result of the coupled interactions between suspension structure and the flow. They both influence each other. Interesting molecular details can be deduced about the shape of the molecules and molecular intractions from the viscosity spectrum by exploiting the knowledge of the hydrodynamic interactions and a proper molecule model. This kind of measurements give insight into molecular details, that are not measurable by other techniques.

References

[1] Kim, Sangtae, and Seppo J. Karrila. Microhydrodynamics: principles and selected applications. Courier Corporation, 2013.

[2] Wajnryb, Eligiusz, et al. "Generalization of the RotnePragerYamakawa mobility and shear disturbance tensors." Journal of Fluid Mechanics 731 (2013): R3.

[3] Cichocki, Bogdan, Maria L. Ekiel-Jeewska, and Eligiusz Wajnryb. "Communication: Translational Brownian motion for particles of arbitrary shape." The Journal of chemical physics 136.7 (2012): 071102.

FM12 - Non-Newtonian and Complex Fluids

TS.FM12-1.01	Dimakopoulos, Yannis - What is the role of blood elasticity in the formation of CFL in microvessels? (INVITED)	1252
TS.FM12-1.02	Shinbrot, Troy - Paradoxical flows in complex fluids	1254
TS.FM12-1.03	Bryngelson, Spencer - Buckling and the rheology of an elastic capsule suspension	1256
TS.FM12-1.04	Harlen, Oliver - Capillary thinning and break-up of particulate suspensions	1258
TS.FM12-1.05	Muradoglu, Metin - Impact and spreading of a viscoelastic droplet on a solid surface	1260
TS.FM12-1.06	Leal, Gary - Flow induced inhomogeneity for a polymer solution in oscillatory shear flow	1262
TS.FM12-2.01	Pinho, Fernando - Purely-elastic instabilities in cross-channel flows with periodic forcing (INVITED)	1264
TS.FM12-2.02	Khomami, Bamin - Large-scale Brownian dynamics simulations of polymeric solutions	1266
TS.FM12-2.03	Yang, Mengfei - Rheology of Suspended Particles in Viscoelastic Fluids Under Shear	1268
TS.FM12-2.04	Gilbert, Peter - Molecular origins of higher harmonics in LAOS: Shear stress	1270
TS.FM12-2.05	Mikami, Fumihiko - Mach cones in a viscoelastic fluid	1272
TS.FM12-2.06	Giacomin, Alan - Elastomers in oscillatory extension	1274
TS.FM12-3.01	Frigaard, Ian - Creeping flow around particles in large yield stress Bingham fluids	1276
TS.FM12-3.02	Amiri, Amin - Displacement flows of viscoplastic fluids in an oscillating pipe	1278
TS.FM12-3.03	Jeon, Jaewoo - Displacing yield stress fluid by Newtonian fluid in a vertical circular channel	1280
TS.FM12-3.04	Roustaei, Ali - Darcy's law and critical pressure drops for yield stress fracture flows	1282
TS.FM12-3.05	Jalaal, Maziyar - Slip and no-slip of carbopol droplets: A direct experimental observation	1284
TS.FM12-3.06	Karimfazli, Ida - Pulsing thermal plumes in yield stress fluids	1286
TS.FM12-4.01	Anderson, Patrick - Start-up of shear flow of 2D particle suspensions in viscoelastic fluids (INVITED)	1288
TS.FM12-4.02	Sedes, Omer - Inertial Suspension Flows in Bifurcating Channels: Experiments and Modelling	1290
TS.FM12-4.03	Kunhappan, Deepak - Numerical modelling of cellulose micro/nanofibril suspensions	1292
TS.FM12-4.04	Evans, Arthur - Membrane dynamics in anisotropic media	1294
TS.FM12-4.05	Swan, James - Elasto-hydrodynamic Network Analysis of Colloidal Gels	1296
TS.FM12-4.06	Ness, Christopher - Rheological modelling and simulation of shear thickening in a bidisperse suspension	1298
TS.FM12-5.01	Hidema, Ruri - Vortex Deformation on Two-dimensional Turbulence Affected by Polymers (INVITED)	1300
TS.FM12-5.02	Choueiri, George - On the nature of elasto-inertial turbulence	1302
TS.FM12-5.03	Nguyen, Minh Quan - Effect of viscoelasticity on the small scale statistics of homogeneous isotropic turbulence	1304
TS.FM12-5.04	Horiuti, Kiyosi - Contravariant and Covariant Polymers in Elasto-inertial	1306

	Viscoelastic Turbulence	
TS.FM12-5.05	Schuh, Jonathon - Asymmetric surface textures and non-Newtonian fluids for decreased friction	1308
TS.FM12-5.06	Page, Jacob - Non-local vorticity generation by surface roughness in viscoelastic shear flows	1310
PO.FM12-1.01.139	Alexandrou, Andreas - Startup Poiseuille flow of a Bingham fluid with or without thixotropic benavior	1312
PO.FM12-1.03.141	Descher, Stefan - Viscoelastic and empirical models compared in context of flows in extruders	1314
PO.FM12-1.04.142	Jay, Pascal - Recirculating flow past a cylinder of a yield stress fluid	1316
PO.FM12-1.05.143	Maleki, Amir - Axial dispersion in weakly turbulent flows of viscoplastic fluids	1318
PO.FM12-1.06.144	Pierre, Saramito - A damped Newton algorithm for computing viscoplastic fluid flows	1320
PO.FM12-1.07.145	Ponakala, Nagarani - Effect of wall movement on dispersion of a solute in casson fluid flow in an annulus	1322
PO.FM12-1.08.146	Taghavi, Seyed Mohammad - Simulating particle sedimentation in yield stress fluids	1324
PO.FM12-1.09.147	Takaoka, Masanori - Dependence of energy spectra on forcing scales in elastic wave turbulence	1326

WHAT IS THE ROLE OF BLOOD ELASTICITY IN THE FORMATION OF CFL IN MICROVESSELS?

Yannis Dimakopoulos[1,a] & John Tsamopoulos[1]
[1]*Laboratory of Fluid Mechanics and Rheology, Department of Chemical Engineering, University of Patras, Patras, Greece*

Summary The current work investigates the effect of blood viscoelasticity on the stress, velocity and haematocrit fields as well as the formation of the cell-depletion-layer for haemodynamics in microvessels lined with glycocalyx layer. To this end, we advance the inhomogeneous constitutive model proposed by Moyers Gonzalez-Owens-Fang (2015), treating properly the shear induced rbc migration mechanism and incorporating the effect of plasma viscoelasticity. The enhanced model (e-model) can accurately reproduce the experimental data by Damiano-Long-Smith (2004) and provide reasonable predictions for the rbc distribution, the shear-stress along the luminal surface. It is shown that blood viscoelasticity expressed in terms of Deborah number is quite small (O(0.3)), but plays a crucial role in the formation of the cell-depletion-layer. In particular, there is a critical value of Deborah number above which the formation of the cell-depletion-layer occurs.

INTRODUCTION

The luminal surface of the endothelial cells that line our vasculature is coated with glycocalyx. Glycocalyx is a thin layer of membrane-bound macromolecules, which also plays a substantial role in the most striking non-homogenous effects[1,2] in blood flow in microvessels. Our work aims at the microrheological modelling of human blood, when it flows in confined vessels. A two-phase system is assumed, with one phase being a peripheral layer of filtered plasma flowing inside the glycocalyx layer, which is modelled as a porous medium that follows the Brinkman Law, and the other one a core region of suspension of all the erythrocytes, which is modelled as a non-Newtonian viscoelastic fluid. To this end, a new constitutive model for whole human blood is proposed for the description of the non-homogeneous behavior of blood in the core region. While the new model is based on the Moyers et al. model[3,4], it deviates from it in the conservation balance of red blood cells and aggregates where a new term replaces the stress gradient mechanism, and in the constitutive equations of stresses where the second order derivatives are omitted, since they are thermodynamically inconsistent. Also, the viscoelastic properties of plasma[5,6,7] could not be ignored, thus the behavior of plasma was approached by an Oldroyd-B model. Furthermore, the homogeneous apparent blood viscosity is obtained by a new equation, which optimally fits the data of Brooks et al.[8] and corrected from the experimentally measured apparent viscosity by Pries et al.[9,10,11]. The developed model was applied for the study of blood flow in small vessels lined with glycocalyx layer and reproduced with great accuracy all the experimental data of Damiano et al.[12] and concurrently captured properly the formation of the cell depleted layer near the glycocalyx layer. Our findings have showed that the elastic response and concentration of the erythrocytes along with the flow rate are the most crucial factors that affect the human blood behavior in microvessels.

RESULTS

In contrast to previous works[13,14] the e-model does not need any explicit or implicit assumption about the existence or location of the cell depletion layer. Its calculation is based only on the rheological properties and the geometric parameters of the flowing system. Figure 1 depicts the predictions of our model for (a) the velocity profile, (b) the number density of RBCs, and (c) the shear stress across a microvessel of diameter 21.8 μm, and glycocalyx thickness 0.15 μm. Apparently, we have accurately reproduced the experimental data by Damiano et al.[12] (Fig. 1(a)). Regarding the distribution of the red-blood-cells (number density in μm^{-3}), it is almost uniform across the core region of the vessel, but within its annular region there is a sharp reduction and zeroing of the local hematocrit indicating that there is no rbcs there. The thickness of the cell depletion layer id equal to 1.51 μm in agreement with the calculations of Secomb et al.[15]. The formation of the cell-depletion-layer affects the shear-stress field (Fig. 1(c)). Our predictions shows that in the core region its spatial variation is linear, having a slope smaller than the empirical model of Damiano et al.[12]. On the other hand, in the annular region the shear stress is also linear, with a smaller slope, due to the smaller value of the plasma shear-viscosity.

[a] Corresponding author. Email: dimako@chemeng.upatras.gr

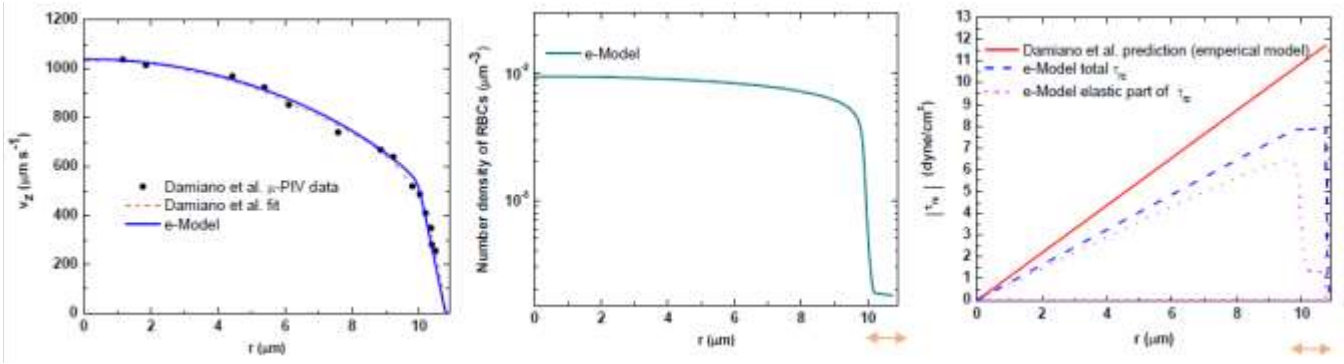

(a) (b) (c)

Figure 1*:* Predictions of the e-model for (a) the velocity profile, (b) the number density of RBCs, and (c) the shear stress across a microvessel of diameter 21.8 μm, and glycocalyx thickness 0.15 μm. The rest dimensionless numbers are equal to $De = 0.33 \quad Br = 50{,}140 \quad \beta = 0.14 \quad H_t = 0.56 \quad H_d = 0.67 \quad \dot{\gamma} = 16.4 s^{-1}$.

References

[1] Fåhraeus R, *Physiol*. *Rev*. **9**: 241–274, 1929.
[2] Fåhraeus R, Lindqvist T, *Am*. *J*. *Physiol*. **96**: 562–568, 1931.
[3] Moyers-Gonzalez MA, Owens RG, Fang J., *J*. *Fluid Mech*. **617**: 327–354, 2008.
[4] Dimakopoulos Y, Kelesidis G, Tsouka S, Georgiou GC, Tsamopoulos J, *Biorheol*. **52**(3): 183-210, 2015.
[5] Brust M, Schaefer C, Doerr R, Pan L, Garcia M, Arratia PE, Wagner C, *Phys*. *Review Lett*. **110**: 078305, 2013
[6] Pranay P, Henriquez Rivera RG, Graham MD, *Phys*. *Fluids* **24**(6): 061902, 2012.
[7] Jaishankar A, Sharma V, McKinley GH, *Soft Matter* **7**: 7623, 2011.
[8] Brooks DE, Goodwin JW, Seaman GVF, *J*. *Appl*. *Physiol*. **28**(2): 172–177, 1970.
[9] Pries AR, Secomb TW, Gaehtgens P, Gross JF, *Circ*. *Res*. **67**: 826–834, 1990.
[10] Pries AR, Neuhaus D, Gaehtgens P, *Am*. *J*. *Physiol*. **263**: H1770–H1778, 1992.
[11] Pries AR, Secomb TW, Geßner T, Sperandio MB, Gross JF, Gaehtgens P, *Circ*. *Res*. **75**: 904–915, 1994.
[12] Damiano ER, Long DS, Smith ML, *J*. *Fluid Mech*. **512**: 1–19, 2004.
[13] Sriram K, Intaglietta M, Tartakovsky DM, *Microcriculation* **21**: 628-639, 2014.
[14] Moyers-Gonzalez MA, Owens RG, *Biorheology* **47**(1): 39-71, 2010.
[15] Secomb TW, Hsu R, Pries AR, *Am J Physiol* **274**: H1016-H1022, 1998.

PARADOXICAL FLOWS IN COMPLEX FLUIDS

Troy Shinbrot[1]
[1]*Department of Biomedical Engineering, Rutgers University, Piscataway, NJ*

Summary It is well known that suspended particles strongly affect fluid flows. In this talk, we briefly describe two systems in which particles produce paradoxical motions in fluids. In a first example, we show that floating particles cause a flow reversal, leading to contamination of an upstream reservoir of clean water by particles in a dirty downstream reservoir, and in a second example, we demonstrate that vertically vibrating a plate in a cornstarch suspension causes the suspension to vigorously ratchet up the plate. Both examples produce motion against the direction imposed by gravity, and both can be analyzed in terms of well understood phenomena – the first due to interfacial forces, and the second due to non-Newtonian forces.

INTRODUCTION

When fluids are pipetted onto a culture plate, it is taken for granted that cells from the plate will not travel upstream to contaminate the fluid source. Yet we recognize that suspended particulates can interfere with the material properties of a fluid – for example reducing its surface tension or increasing its viscosity. In this conference proceeding, we demonstrate that these changes in material properties can produce paradoxical results that violate our expectations. In a first example, we show that the reduction in surface tension causes floating particles to contaminate upstream reservoirs. This occurs both on the micro-scale – in pipetting experiments over distances of millimetres to centimeters – and on the macro-scale – causing upstream flows over several meters in extent. In a second example, we show that vibrating a plate vertically in a shear thickening suspension causes the suspension to travel up the plate against the influence of gravity.

RESULTS

Over a century ago, Carlo Marangoni reported that floating particulates decrease the surface tension of water – an effect that we now recognize as being due to interference with hydrogen bonds. This observation has implications for modern applications ranging from microfluidics and cellular morphogenesis to colloidal dynamics and self-assembly. An underappreciated consequence of this effect is that when clean water is discharged into a dirty container, a gradient in surface tension is produced, with lower tension at the dirty downstream end of the flow, and higher tension upstream at the clean end.

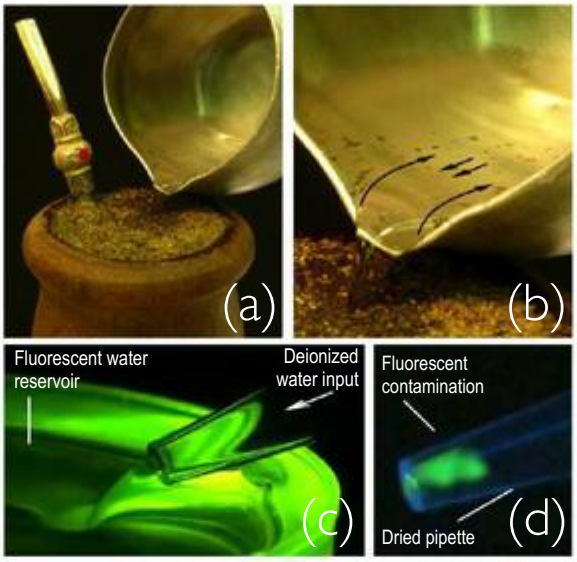

Figure 1 – Upstream contamination. (a) Clean water poured onto tea leaves; (b) expanded view shows that tea leaves travel upstream from cup into water source. *Figure credit: Sebastian Bianchini , Alejandro Lage & Ernesto Altshuler.* (c) Deionized water pipetted into petri dish containing fluorescein; (d) dried pipette afterward, showing contamination accumulated *inside* of tube.

Logically enough, the higher upstream tension causes fluid – and entrained contaminants – to be drawn upstream. This is shown qualitatively in Fig. 1 (details appear in Ref. [1]). In Fig's 1(a), we show mate tea being prepared by pouring clean water onto tea leaves: here the tea leaves downstream act as a contaminant, and as shown in the detail, Fig. 1(b), the leaves flow upstream – faster than the downstream flow imposed by gravity. The same thing can occur during pipetting, as shown in Fig's

[a] Troy Shinbrot, email: shinbrot@aps.org.

1(c)-(d). Although this effect is general insofar as it applies to many different problems, we hasten to point out that it requires a free and angled surface – meaning that upstream flow of contaminants is not observed in a vertical waterfall or in a closed pipe.

Paradoxical flows can be produced by other changes in fluid properties than surface tension. An example of this is shown in Fig. 2, where snapshots are displayed of a vertically vibrated plate partially submerged in a 50-50 w/w suspension of cornstarch in water. In this situation, the cornstarch is more strongly sheared when the shaft moves up than when it moves down – because in the first case the shaft and gravity act in opposing directions, while in the second they act in the same direction. It therefore follows that the suspension viscosity will be higher in the first case than in the second, and so we can expect the fluid to ratchet upward with every cycle of vibration of the shaft. This is in fact what we see, as shown in Fig. 2.

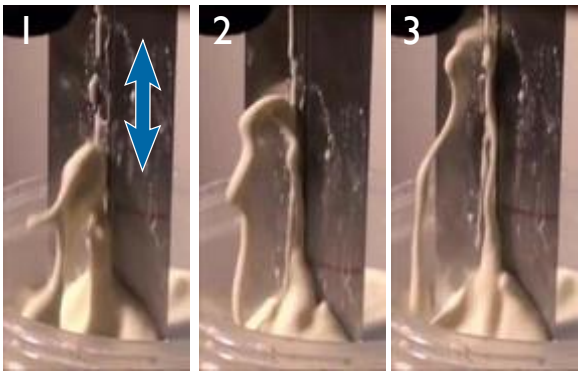

Figure 2 – Uphill ratcheting. Sequence of photos of plate partially submerged in cornstarch suspension and vibrated vertically as indicated by arrows. Suspension energetically ratchets upward as shown.

CONCLUSIONS

In this proceeding, we have presented two examples in which well-known effects of suspended particulates cause predictable paradoxical behaviors in fluids. In the first example, the particulates change the surface tension, and in the second they change the viscosity. Although predictable in retrospect, both of these paradoxical behaviors were encountered serendipitously, and we propose that other examples may be awaiting discovery.

References

[1] S. Bianchini, A. Lage, T. Siu, T. Shinbrot & E. Altshuler, "Upstream contamination by floating particles," Proceedings of the Royal Society A 469 (2013) 20130067.

[2] T. Shinbrot, M. Rutala, A. Montessori, P. Prestininzi & S. Succi, "Paradoxical ratcheting in cornstarch," Phys. Fluids 27 (2015) 103101.

BUCKLING AND THE RHEOLOGY OF AN ELASTIC CAPSULE SUSPENSION

Spencer H. Bryngelson*[1] and Jonathan B. Freund[2]

[1]*Mechanical Science & Engineering, University of Illinois at Urbana-Champaign, Urbana, Illinois, USA*
[2]*Mechanical Science & Engineering and Aerospace Engineering, University of Illinois at Urbana-Champaign, Urbana, Illinois, USA*

Summary The rheological behavior of an elastic capsule suspension is studied in a model two-dimensional channel using detailed numerical simulations. As the rest capsule membrane aspect ratio increases, the capsules become increasingly vulnerable to a buckling instability. This buckling behavior is concomitant with a sudden increase in the effective viscosity and a near disappearance of any near-wall capsule-free layer. The microstructure dynamics suggest elongated capsules make significant rotational contributions that disrupt organized flow, as computed by their rotlet capsule-capsule interactions.

INTRODUCTION

Flowing elastic capsule suspensions are well-known to have complex properties and rheology. We considered fluid-filled elastic membranes, which can be considered a model for both natural capsules like red blood cells, and artificial ones such as those used for drug delivery. The adjustment of the relative surface area of the capsule membrane leads to expected transitions in rest shape, from round, to biconcave, to elongated, and dog-bone-like. We examine how these shape changes contribute to the complex flow of the confined suspension, whose properties are then quantified by an effective viscosity. In blood or similar complex suspensions, when flowing in narrow confines on the cell scale, the effective viscosity is known to involve the formation of cell-free regions near the vessel wall, thus special attention is afforded to the behavior of this layer for different capsule shapes and its relation to the effective vicosity. This is carried out through the simulation of a two-dimensional simulation model.

METHODS

The flow geometry is a narrow streamwise-periodic two-dimensional channel, for which we vary width W and mean flow rate U. The capsule membranes are finite-deformation linear-elastic shells with finite-deformation bending (M) and tension (T) moduli; each of which contains an incompressible Newtonian fluid with viscosity μ matching that of the suspending fluid. The membrane rest shape is parameterized via $\xi_o = l_o/2\pi r_o$, where l_o is the length of the membrane and πr_o^2 the interior capsule area. We consider several different ξ_o, varying from circular geometries with $\xi_o = 1.0$ to very elongated shapes with $\xi_o = 3.0$. Figure 1 shows the flow of different capsule geometries at capillary number $u^* = \mu U/T = 1.0$.

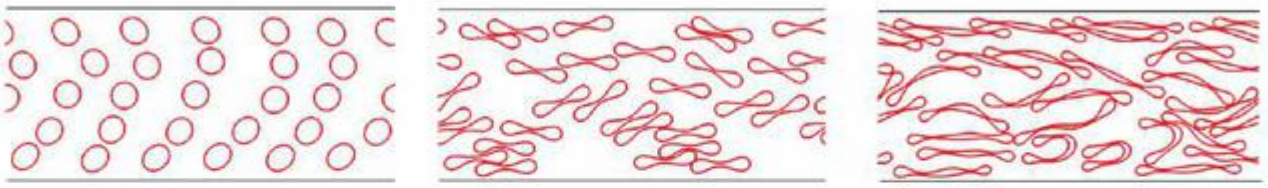

(a) $\xi_o = 1$ (b) $\xi_o = 1.7$ (c) $\xi_o = 3.0$

Figure 1: Flow visualizations of different ξ_o capsules as indicated flowing in the model channel.

Since the Reynolds number of cell-scale flow is small, inertia is neglected and the governing equations can be solved using a boundary integral formulation.[1] The computation of velocities is accelerated using a particle-mesh-Ewald scheme based on periodic Greens' functions, while channel walls impose a no-slip condition enforced by a penalty method.[2] The membrane positions $\mathbf{x}$ are then advected according to

$$\frac{\mathrm{d}\mathbf{x}}{\mathrm{d}t} = \mathbf{u}(\mathbf{x}), \tag{1}$$

where $\mathbf{u}(\mathbf{x})$ are the velocities of the capsule collocation points $\mathbf{x}$ as computed by the boundary integral equation. To evaluate elastic tractions on the fluid, derivatives are calculated using Fourier interpolants of the discrete collocation points representing the capsule membranes. A second-order Runge–Kutta scheme numerically integrates (1).

*Corresponding author. Email: bryngel2@illinois.edu

RESULTS

We see for the flowing capsules in figure 1, that the (a) circular $\xi_o = 1.0$ and (b) biconcave $\xi_o = 1.7$ cases only slightly deform from their equilibrium configuration, while the (c) $\xi_o = 3.0$ case shows significant folding of some capsules. This seemingly disrupts the otherwise orderly flow, and is considered subsequently as a buckling mechanism.

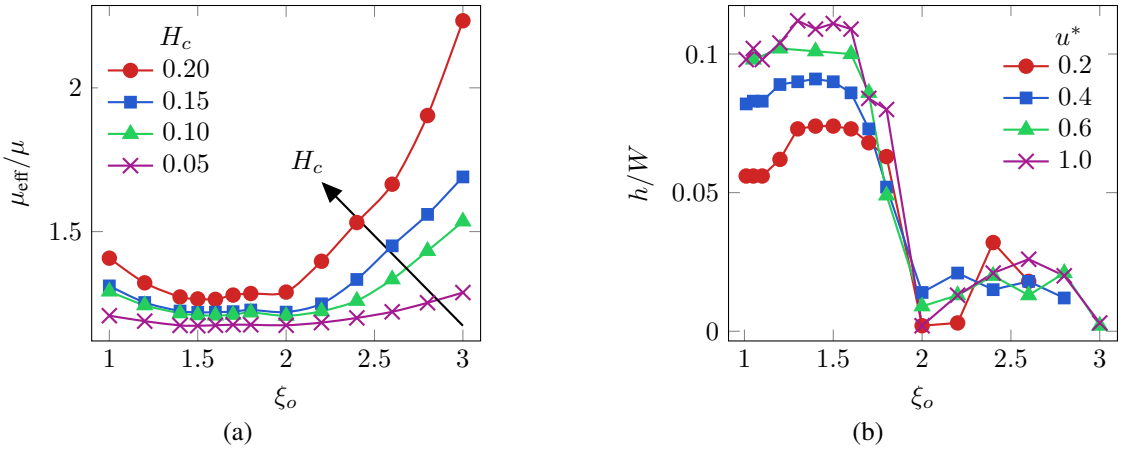

Figure 2: (a) Effective viscosity μ_{eff} for varying equilibrium shapes ξ_o, and (b) corresponding capsule-free layer thickness h.

The effective Newtonian-equivalent viscosities of the suspensions for different area fractions H_c and ξ_o are shown in figure 2 (a). Elongated capsules with $\xi_o \gtrsim 2.0$ have an increasingly large effective viscosity. In blood, the effective viscosity μ_{eff} is reduced through the formation of a cell-free layer. This is measured here as h in figure 2 (b), which decreases to near zero, also for $\xi_o \gtrsim 2.0$, presumably leading to the increase in μ_{eff}.

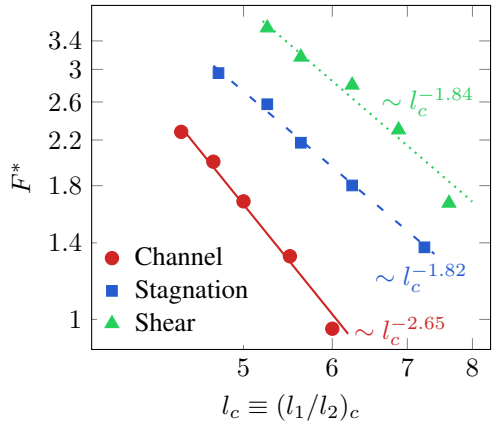

Figure 3: Non-dimensional force F^* versus resting capsule aspect ratio l_c. The straight lines are power-law fits.

We hypothesize that the capsules undergo a buckling transition. Figure 3 shows force $F^* \equiv F/\mu U l_o$ plotted against the aspect ratio $l_c = l_1/l_2$ of the corresponding at-rest capsules. This is compared for single capsules suspended in a Taylor–Green stagnation point flow, in a simple homogeneous shear flow, and in the channel flow. All three show a scaling reminiscent of Euler bucking though altered presumably due to the strong perturbation environment in the channel and the shell-like structure of the capsules.

This work was supported in part by the National Science Foundation under Grant No. CBET 13-36972.

References

[1] C. Pozrikidis, *Boundary integral and singularity methods for linearized viscous flow* (Cambridge University Press, Cambridge) (1992).
[2] J. B. Freund, "Leukocyte margination in a model microvessel," Phys. Fluids **19**, 023301 (2007).

CAPILLARY THINNING AND BREAK-UP OF PARTICULATE SUSPENSIONS

Oliver Harlen *[1], Claire McIlroy[1,2], Wouter Mathues[3], and Christian Clasen[3]
[1]*School of Mathematics, University of Leeds, Leeds, LS2 9JT, UK*
[2]*Department of Physics, Georgetown University, Washington D.C., USA*
[3]*Department of Chemical Engineering, K.U. Leuven, Leuven, Belgium*

Summary The capillary driven thinning and break-up of non-Brownian suspensions are considered. Experiments show that in the final stages of break-up (when the filament diameter is approximately five times that of the suspended particles) the thinning no longer follows the behaviour predicted by the bulk viscosity; instead thinning is accelerated due to the effects of finite particle size. A simple one-dimensional model is described in which the viscosity is determined from the local particle density, found by tracking individual particles within the suspension. Despite its simplicity this model is able to reproduce quantitively the thinning behaviour observed in experiments.

CAPILLARY THINNING OF NON-BROWNIAN SUSPENSIONS

The surface tension driven thinning and break-up of liquid bridges is a fundamental mechanism controlling jet break-up and droplet formation, and its prediction is vital to processes such as inkjet drop and spray formation. For Newtonian fluids considerable research has been done to understand the final stages of break-up, which have been shown to follow a progression of similarity thinning laws [1] depending upon the value of the Ohnesorge number ($Oh = \eta/\sqrt{\rho\gamma R}$, where η, ρ and γ are respectively the viscosity, density and surface tension and R is filament radius). However, many applications involve complex fluids such as polymer solutions or suspensions, which do not follow these scaling laws. In particular, the approach to break-up of non-Brownian suspensions depends upon the particle size, as well as particle concentration and so cannot be predicted from the bulk properties of the suspension alone.

Various experimental studies [2, 3] have demonstrated that the thinning behaviour of non-Brownian suspensions proceeds through a number of different regimes, illustrated in Fig 1 (left). While the radius of filament is relatively large compared the particle size, the thinning follows the appropriate Newtonian thinning law corresponding to the bulk viscosity. However, there is then transition to an "accelerated" regime in which the rate of decrease of the filament radius becomes faster even than that of the continuous fluid alone. This is followed by a further transition to a regime in which the filament appears to return to the Newtonian thinning law, but with a slope corresponding to the viscosity of the continuous phase.

MATHEMATICAL MODEL

In order to elucidate the mechanism responsible for this accelerated thinning, we have constructed a simple model [4] to examine the effects of axial variations in particle concentration on the thinning dynamics. In this model, the filament is assumed to be sufficiently long and thin that it can be modelled using the slender jet approximation, but with a viscosity given by the local particle concentration. The governing equations for the dimensionless filament radius $h(z,t)$ and velocity $v(z,t)$ are given by

$$\frac{\partial h^2}{\partial t} + \frac{\partial}{\partial z}(h^2 v) = 0,$$
$$\frac{\partial}{\partial t}(h^2 v) + \frac{\partial}{\partial z}(h^2 v^2) = \frac{\partial}{\partial z}\left(h^2\left(K + 3Oh\frac{\partial v}{\partial z}\right)\right).$$

where

$$K = \frac{1}{h(1+\left(\frac{\partial h}{\partial z}\right)^2)^{1/2}} + \frac{\frac{\partial^2 h}{\partial z^2}}{(1+\left(\frac{\partial h}{\partial z}\right)^2)^{3/2}},$$

is the surface tension contribution and

$$Oh = Oh_s\left(1 \circ \frac{\phi(z,t)}{\phi_{max}}\right)^{-2}$$

is the dimensionless local viscosity obtained from the local particle concentration $\phi(z,t)$ via the Maron-Pierce relation. To obtain $\phi(z,t)$ we track the positions of individual particles from an initial uniform distribution moving with the fluid velocity and determine the number density in a local section of filament. The particles only contribute to the dynamics through the local viscosity, so the direct effects of hydrodynamic interactions between particles and the effect of the individual particles on the free surface are not included. However, the model does capture the coupling between the local concentration fluctuations and the filament dynamics.

*Corresponding author. Email: o.g.harlen@leeds.ac.uk

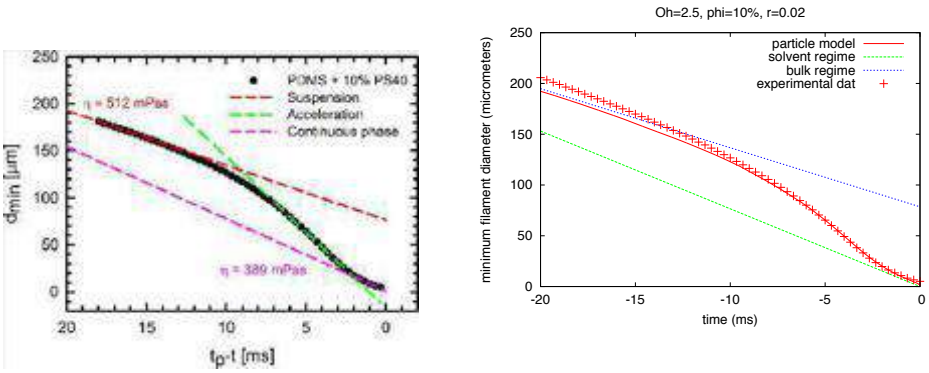

Figure 1: (left) Thinning dynamics of a 10% suspension of 40 μ m diameter polystyrene particles in a polydimethylsiloxane(PDMS)oil for Ohnesorge number $Oh = 2.5$. The thinning initially follows the thinning law for a Newtonian fluid of the bulk viscosity but then transitions to an accelerated regime where the rate of thinning is faster even than that of the continuous phase. (Right) Comparison with the predictions of the thinning dynamics, shown as solid line with the crosses showing the experimental data.

CAPILLARY THINNING EXPERIMENTS

The Capillary breakup experiments are performed using a CaBER-1 extensional rheometer (Thermo Scientific). This generates an unstable liquid bridge by stretching a sample of fluid between two end-plates. Unlike the pendant drop experiment, this setup has the advantage that the position of the minimum radius remains approximately fixed, so that the diameter can be followed more easily using a static high-speed camera. The experiments were performed using suspensions of three different particle sizes dispersed in Newtonian silicone oils with volume fractions, ϕ of between 0.02 and 0.40. The minimum filament diameters were obtained through analysis of the images from the high speed camera.

Since both the experiments and numerical simulations depend on the initial distribution of particles within the filament, each case was run with at least ten different realisations to obtain an ensemble average.

RESULTS AND CONCLUSIONS

The right-hand figure in Fig 1. compares the simulation results with the experimental data presented in the left-hand figure. It can be seen that despite the simplicity of the model it is not only able to reproduce the sequence of thinning regimes seen in experiments, but also provides a quantitatively accurate reproduction of the accelerated regime and its transitions. This demonstrates that accelerated thinning of these particulate suspensions results from local fluctuations in the particle density, amplified as the filament radius reduces, leading to the development of low-viscosity regions that allow the filament to thin more easily.

Whilst the model appears to capture the mechanism responsible for the acceleration phase in these moderate concentrations. Recent experiments [5] show that an acceleration of filament thinning is also observed in very dilute suspensions where the particles do not significantly change the fluid viscosity. This phenomenon occurs at a later stage when the minimum filament diameter is smaller than that of the particles and is beyond the scope of the current model. To address this requires a model that explicitly represents individual suspended particles, from which we hope to show preliminary results.

References

[1] Eggers J., Villermaux E.: Physics of liquid jets. Rep. Prog. Phys. 71:036601, 2008.
[2] Bonnoit, C., Clement E., Lindner, A.: Phys. Fluids 24:043304, 2012.
[3] Mathues, W., McIlroy C., Harlen O.G., Clasen C.: Phys. Fluids 27:093301, 2015.
[4] McIlroy C., Harlen O.G.: Phys. Fluids 26:033101, 2014.
[5] Lindner A., Fiscina J.E., Wagner C.: Euro. Phys. Lett, 110:64002, 2015.

IMPACT AND SPREADING OF A VISCOELASTIC DROPLET ON A SOLID SURFACE

Daulet Izbassarov and Metin Muradoglu *
Department of Mechanical Engineering, Koç University, Rumelifeneri Yolu, 34450 Sariyer, Istanbul, Turkey.

Summary The effects of viscoelasticity on impact and spreading of a drop on a solid surface are computationally studied. It is found that viscoelasticity favors advancement of contact line during the spreading phase leading to a slight increase in the maximum spreading in agreement with the experimental observations [5]. However, in contrast with the well-known anti-rebound effects of polymeric additives, the viscoelasticity is found to enhance the tendency of the drop rebound in the receding phase. These results suggest that the anti-rebound effects are mainly due to the polymer-induced modification of wetting properties of the substrate rather than the change in the material properties of the drop fluid. A model is developed to test this hypothesis. It is found that the model gives good qualitative agreement with the experimental observations and the anti-rebound behavior can be captured by modification of the surface wetting properties in the receding phase.

INTRODUCTION

Controlled deposition of a viscoelastic drop is an important problem in many applications including coating, ink jet printing, additive manufacturing, tissue engineering and single cell epitaxy [2]. It is particularly important to know whether a droplet will deposite or rebound after the impact. Unlike Newtonian systems, understanding of viscoelastic drop impact is severely limited, and yet of great importance for wide range of applications. It has been reported that a tiny amount of polymer, polyethylene oxide (POE), added to water can dramatically alter the drop dynamics, suppressing the rebounding of a drop on a hydrophobic substrate [1].

In this paper, we computationally study the effects of viscoelasticity on drop impact, spreading and rebound on a solid surface. We fully account for the effects of surface tension and treat the partially wetting cases with a dynamic contact angle. The Navier-Stokes and the viscoelastic model equations (FENE-CR) are solved in the entire computational domain using a front tracking method [7, 5]. Motivated by the recent experimental results of Bertola and Wang [3], a simple model is developed to mimic the hysteresis of the contact angle due to the deposition of polymer molecules on the substrate. Simulations are performed to investigate effects of viscoelasticity characterized by the Weissenberg number (Wi), polymeric viscosity ratio (β), the concentration parameter defined as the ratio of polymeric viscosity to solvent viscosity (c) and the extensibility parameter (L^2). Although the emphasis is placed on the effects of the viscoelasticity in the present study, simulations are also carried out to examine the effects of the Weber number (We), Reynolds number (Re) and equilibrium contact angle (θ_e).

RESULTS AND DISCUSSIONS

We first investigate the effects of viscoelasticity on drop impact, spreading and rebound without taking the polymer-induced modification of surface wetting properties into account. For this purpose, extensive simulations are performed to examine the effects of various flow parameters on the drop dynamics. Sample results are shown in Fig. 1(a) where the spread factor is plotted as a function of non-dimensional time for various Weissenberg numbers. The spread factor is defined as the radius of the wetted spot normalized by the equivalent drop radius. The results obtained for a Newtonian droplet are also plotted in this figure to directly show the effects of viscoelasticity. The viscosity in the Newtonian case is set to the total viscosity, i.e., $\mu_{Newtonian} = \mu_s + \mu_p$. The figure shows that the Weissenberg number does not have a significant influence on the spread factor in the initial stage of the impact where the inertial effects are dominant. However, its influence is more pronounced in the later stages especially in the receding phase. The maximum spread factor increases with Wi (Fig. 1(a)) mainly due to the additional viscoelastic stresses that act to favor the advancement of the contact line. The tendency for a drop rebound also increases with Wi and the drop rebounds when $Wi \geq 4$ in this case. These results are in contrast with the well-known polymeric anti-rebound phenomenon [1].

The recent experimental studies have revealed that there is a substantial hysteresis in the contact angle especially during the receding phase [2]. This hysteresis is believed to be related to the polymer molecules deposited on the substrate during the advancing phase [3]. Smith and Sharp [6] observed that the deposited polymers outside the drop are stretched during the receding phase, which in turn slows down the movement of the contact line. This mechanism can be interpreted as a dissipative force or an effective friction force acting in opposite direction of the contact line leading to a reduction in dynamic contact angle during the receding phase. Bertola and Wang [3] have recently shown that the contact angle decays nearly exponentially

*Corresponding author. Email: mmuradoglu@ku.edu.tr

during the first receding phase. Depending on the flow conditions, the contact angle may exhibit an under-damped or over-damped behavior until it reaches a steady value as the substrate gets fully saturated by the polymers. To mimic this behavior, we propose a simple model for the polymer-induced hysteresis and modify the equilibrium contact angle θ_e as

$$\theta_e = \begin{cases} \theta_c & \text{if } \mathrm{V_{col}} \geq 0 \text{ (advancing)} \\ \theta_s + (\theta_c \circ\ \theta_s) e^{-t/T_d} & \text{if } \mathrm{V_{col}} < 0 \text{ (receding),} \end{cases} \tag{1}$$

where t, T_d, V_{col}, θ_c and θ_s are the time, the time scale for the polymer deposition on the substrate, the impact velocity of the drop, the clean and saturated equilibrium contact angles, respectively. The deposition time scale characterizes how fast the polymers deposit on the substrate. The hysteresis effects are reduced as T_d increases and no-hysteresis conditions are recovered in the limit as $T_d \to \infty$. Simulations are carried out to examine the performance of this model and the sample results are shown in Fig. 1(b) where the evolution of the spread factor and the dynamic contact angle is plotted for various values of the non-dimensional deposition time scale $\tau = T_d V_{col}/d$ where d is the equivalent drop diameter. As seen, the drop rebound is suppressed as τ is reduced showing qualitatively good agreement with the anti-rebound effects of polymer additives observed in the experimental studies [2, 3]. These results support that the anti-rebound effect is mainly due to the modification of surface wetting properties by the deposited polymer molecules rather than alteration of the bulk fluid properties.

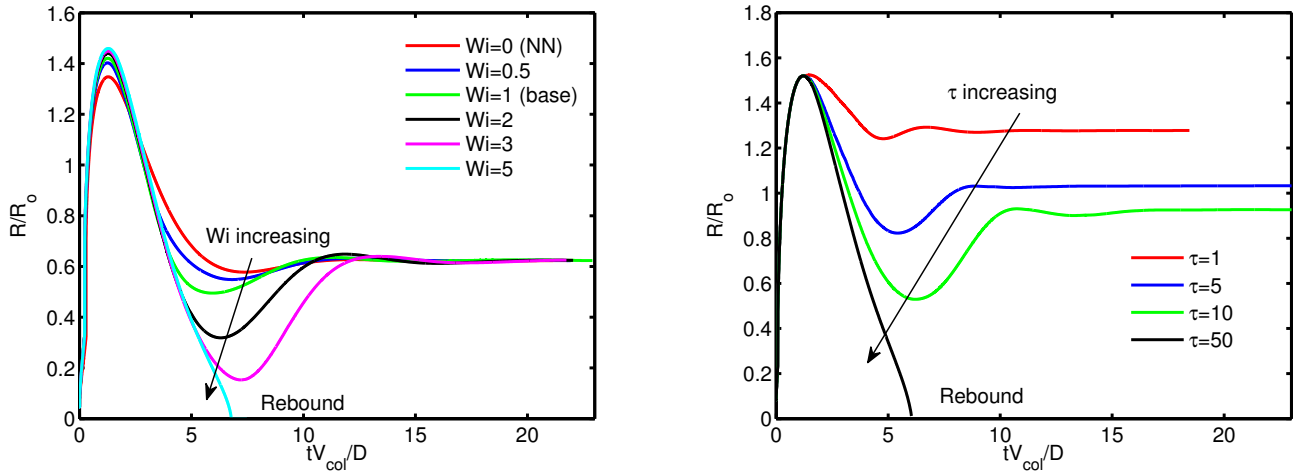

Figure 1: (a) The simulations without the polymer-induced hysteresis. Effects of the Weissenberg number on droplet impact and spreading. Time evolution of the spread factor with Wi ($Re = 35, We = 30, L^2 = 225, \beta = 0.56$ and $\theta_e = 145°$). (b) The simulations with the polymer-induced hysteresis. Effects of the non-dimensional deposition time (τ) on droplet impact and spreading. τ ranges between 1 and 50 ($Re = 75, We = 30, Wi = 1, L^2 = 225, \beta = 0.07, \theta_c = 145°$ and $\theta_s = 90°$).

References

[1] Bergeron V., Bonn D., Martin J.Y., Vovelle L.: Controlling droplet deposition with polymer additives. Nature 405:772-75, 2000.

[2] Bertola V.: Dynamic wetting of dilute polymer solutions: the case of impacting droplets. Adv. Colloids Interfaces 193-194:1-11, 2013.

[3] Bertola V., Wang M.: Dynamic contact angle of dilute polymer solution drops impacting on a hydrophobic surface. Colloids and Surfaces A: Physicochem. Eng. Aspects 481:600-608, 2015.

[4] Huh H.K., Jung S., Seo K.W., Lee S.J.: Role of polymer concentration and molecular weight on the rebounding behaviors of polymer solution droplet impacting on hydrophobic surfaces. Microfluid. Nanofluid. 18:1221-1232, 2015.

[5] Izbassarov D., Muradoglu M.: A front-tracking method for computational modeling of viscoelastic two-phase systems. J. Non-Newt. Fluid Mech. 223:122-140, 2015.

[6] Smith M.I., Sharp J.S.: Origin of contact line forces during the retraction of dilute polymer solution drops. Langmuir 30:5455-5459, 2014.

[7] Unverdi S.O., Tryggvason G.: A front-tracking method for viscous, incompressible, multi-fluid flows. J. Comput. Phys. 100(1):25-37, 1992.

Flow induced inhomogeneity for a polymer solution in oscillatory shear flow

Joseph D. Peterson and L. Gary Leal[a]
Department of Chemical Engineering, University of Santa Barbara, California

Summary Flow-induced concentration inhomogeneities are often neglected in fluid mechanics studies of polymer solutions, but recent work has shown that they can often occur and may lead to major changes in the flow kinematics. In this work, we consider this phenomena for the simple model problem of large amplitude oscillatory shear flow (LAOS).

Flow Induced Demixing and Two-Fluid Models

Entangled polymer solutions are known to exhibit enhanced light scattering and demixing for a broad range of flow geometries in both steady and unsteady flows[1, 4]. The resulting inhomogeneity in polymer concentration can, in turn, lead to major changes in the flow compared to what would be predicted for the same fluid rheology but uniform concentration. Early investigations[2] showed these phenomena arise due to a coupling between stress and concentration; in particular, the diffusive velocity of a polymer network is modified to account for the migration of polymer chains towards regions of higher stress. Such a coupling between stress and concentration is reasonably captured by two-fluid models that treat the polymer and solvent as superimposable continuum fluids coupled by friction and incompressibility. An example of such a two-fluid model is described in our previous research of flow induced demixing in steady shear flows[3]

Our recent 1D studies of a two-fluid model, based upon the Rolie-Poly constitutive theory, have shown that shear induced demixing leads to shear banded steady state velocity profiles[3]. The physics that drives this transition is relatively well understood at this point in time: a local depletion of polymer results in an immediate increase in the local shear rate to ensure stress continuity. This increased rate of deformation causes the polymer to experience an increase in compressive stresses along the flow gradient axis. For certain conditions, these elastic compressive stresses overpower the osmotic stresses and the low concentration domain squeezes solvent out of nearby concentrated regions, further enhancing the difference in concentration between the two regions of flow. This process will continue until the difference in concentration between the two domains is large enough to prevent further growth of concentration inhomogeneity.

Experimentally, shear induced demixing in polymer solutions has also been observed in large amplitude oscillatory shear flow[4] (LAOS), but the nonlinear, unsteady nature of the flow would initially seem to preclude the development of a comparatively concise explanation of the instability and its nonlinear evolution.

Multiple Scale Asymptotic Analysis

Numerical simulations of LAOS induced demixing, using the full two-fluid Rolie-Poly model, reveal that changes in concentration tended to evolve over a diffusive time-scale τ_{diff} that is much longer than the period of oscillation $1/\omega$ at the system boundary. For timescales on the order of $1/\omega$, the concentration profile is nearly unchanging, whereas oscillations in the velocity and polymer configuration are quasi-periodic. For much longer time-scales, any initial perturbation to the polymer concentration profile appears to evolve smoothly with negligible correlation to the oscillatory dynamics of the velocity profile and configuration tensor. Because the separation of time-scales is large ($\tau_{diff} \gg 1/\omega$), this suggests that an approximate analytic description of the dynamics can be achieved via the asymptotic method of multiple scales.

After formally applying the method of multiple scales, we found strong parallels between the physics of demixing in steady flows and demixing in oscillatory flows. In steady flows, changes in the configuration tensor may be approximated as quasi-steady with respect to changes in the polymer concentration. In oscillatory flows, the configuration tensor is always oscillating about a limit cycle, but the entire limit cycle can be approximated as quasi-steady with respect to changes in the polymer concentration. Thus, the relationships that provide an asymptotic description for the linear and non-linear behavior of flow induced demixing are identical for steady and unsteady flows, except that in unsteady flows the relationships are averaged through a limit cycle instead of computed for a stationary point.

Comparing: Simulations and the Asymptotic Theory

To evaluate the utility of the asymptotic model, we have tested its predictions of stability boundaries and shear band selection against a numerical simulation of demixing in the full two-fluid model. The choice of oscillatory flow is somewhat arbitrary, but for simplicity we impose a sinusoidal oscillation in the shear stress such that $\Sigma(\bar{\ }) = \Sigma_o \sin(2\pi\bar{t})$, where the

[a] Corresponding author. Email: lgl20@engr.ucsb.edu

shear stresses have been normalized by the elastic modulus of the solution. We evaluate the resulting velocity and concentration profiles for a well entangled semi-dilute polymer solution with 40 entanglements per chain and a solvent of viscosity 10^{-5} relative to the viscosity of the whole solution. The elastic modulus of the solution is 0.15 relative to the osmotic modulus, and the gap dimension is 35 times larger than the solution correlation length. To describe the coupling friction, we choose a 'magic length' at which diffusion and stress relaxation occur on similar time-scales. For present purposes, this magic length is defined as 1/10 of the gap dimension. Finally, the period of oscillation is chosen to be equal to the reptation time of the polymer chains.

For the material and flow protocol described above, demixing is predicted by the asymptotic theory to occur for $\Sigma_o = [0.6515,\ 0.6935]$. Here, we show simulations results for an initial small amplitude sinusoidal perturbation in the polymer concentration for values of Σ_o just below and just above the asymptotically predicted lower critical value for demixing. Note that the perturbation magnitude (as measured by the L2 norm of the departure from homogeneity) does oscillate slightly with the rest of the system, but the overall trend is consistent growth or decay.

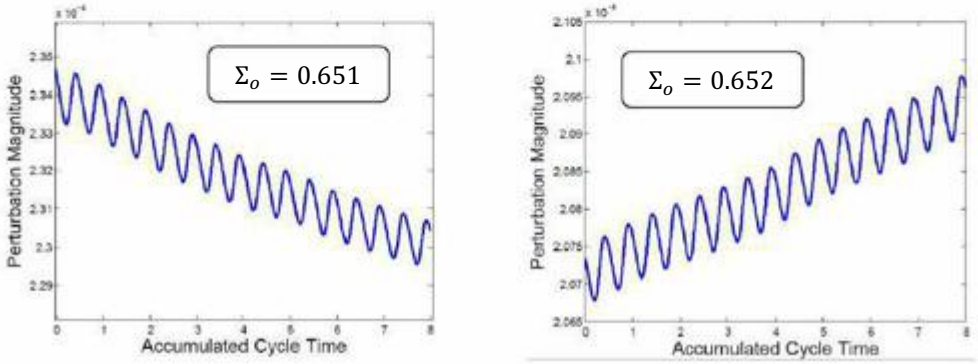

Figure 1: Perturbations decay for Σ_o below the stability boundary but grow in the expected unstable range of Σ_o.

The asymptotic theory seems well-equipped to describe the transition from homogeneous to demixing flows. As the perturbation amplitude grows larger still, the asymptotic theory predicts an eventual shear banded steady state. Simulations of the full model confirm the existence of shear banding, and the asymptotic model shows excellent agreement with the numerically predicted mean composition and velocity profiles. In the figures below, we show agreement in the steady state concentration profile (left) and time dependent local shear rates in the high shear band (middle) and low shear band (right). The concentration is scaled by its mean value and the shear rates are scaled by the oscillation frequency.

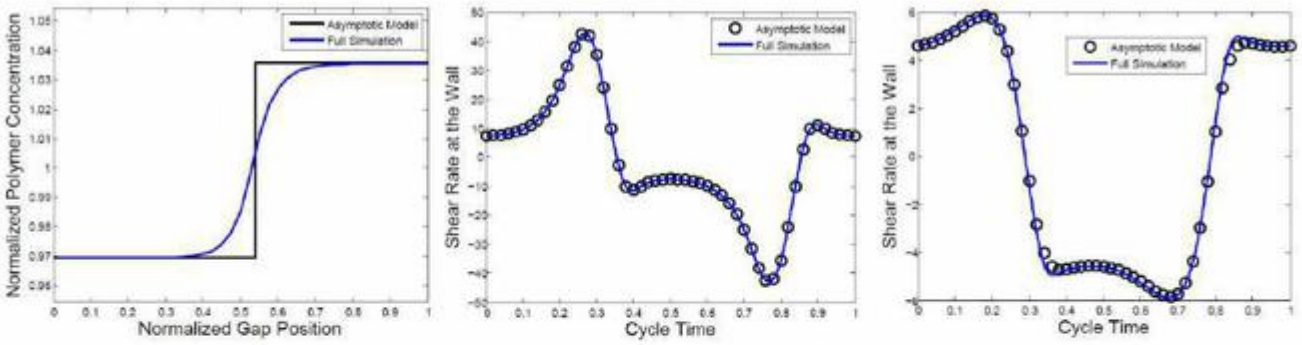

Figure 2: The asymptotic model can be used to obtain predictions for the concentration in the shear bands and the rheological behavior of the two bands. The figure on the left shows that the sigmoidal concentration profile obtained via numerical simulation approaches the limiting concentrations anticipated by the asympotic model. The center and right figures show that the rheological response of the two shear bands is also well described by the asymptotic model.

References

[1] Rangel-Nafaile C., Metzner A., Wissbrun K.: Analysis of Stress Induced Phase Separations in Polymer Solutions. Macromolecules, 17, 1187-1195 (1984)

[2] Helfand E. and Fredrickson G. H.: Large Fluctuations in Polymer Solutions under Shear. Physical Review Letters, 62, 21 (1989)

[3] Cromer M., Fredrickson G. H., and Leal L. G.: A Study of Shear Banding in Polymer Solutions. Physics of Fluids, 26 063101 (2014)

[4] Saito S., Matsuzaka K., Hashimoto T.: Structures of a Semidilute Polymer Solution under Oscillatory Shear Flow. Macromolecules, 32, 4879-4888 (1999)

PURELY-ELASTIC INSTABILITIES IN CROSS-CHANNEL FLOWS WITH PERIODIC FORCING

Alexandre M. Afonso[1], Manuel A. Alves[1] & Fernando T. Pinho [2a)]
[1]*CEFT, Department of Chemical Engineering, University of Porto, Porto, Portugal*
[2]*CEFT, Department of Mechanical Engineering, University of Porto, Porto, Portugal*

Summary We present results of a numerical investigation of the low Reynolds number flow of viscoelastic fluids, described by the Oldroyd-B model, in a 2D cross-slot channel with a main inlet flow and two periodic in-phase and out-of-phase forcings imposed on the opposing lateral inlets. Several types of flow transition are reported that depend on the amplitude and frequency of the forcing. We observed that for high Weissenberg numbers the flow becomes chaotic, with the path to the chaotic state depending on both the ratio of steady inlet velocity to oscillating velocity amplitude and Deborah number.

INTRODUCTION

Purely-elastic instabilities, i.e. induced by elastic normal stresses in the absence of significant inertial effects, have been observed in a range of flows, including ideal viscometric and complex flows. It is now well known that such instabilities can arise as a consequence of the combination of elastic stresses and streamline curvature, such as in the cross-slot microchannel flow investigated experimentally by Arratia et al. [1]. Poole et al. [2] numerically simulated such two-dimensional cross-slot flow for an Upper-Convected Maxwell (UCM) model under creeping-flow conditions, and were able to capture qualitatively the onset of a bi-stable steady asymmetric flow above a first critical Weissenberg number (*Wi*), followed by a second transition to a time-dependent flow at higher *Wi*. More recently, Cruz et al. [3] proposed the cross-slot flow as a benchmark problem due to its conceptually simple geometry and well defined steady asymmetric flow instability. The benchmark results were presented for a wide range of differential constitutive equations, namely the UCM, Oldroyd-B and Phan-Thien–Tanner (PTT) models, showing that, in the limit of negligible inertia, i.e. when the Reynolds number (*Re*) approaches zero, the flow exhibits two types of purely-elastic instabilities for fluids with high extensional viscosity. Above a first critical value of the Weissenberg number, Wi_{crit}, the steady flow becomes spatially asymmetric, even though the geometry is perfectly symmetric; at higher *Wi* a second instability occurs and the flow becomes time-dependent.

A flow-focusing configuration can also be realized in the same cross-shaped geometry in which a central inlet flow is shaped by two opposed side inlet streams, as in Jensen [4]. The steady low *Re* flow behavior for Newtonian fluids has been extensively investigated numerically by Oliveira et al. [5], whereas the corresponding viscoelastic flow was also characterized by the onset of elastic instabilities for UCM and linear simplified PTT models [6]. As for the cross-slot configuration above, the flow-focusing configuration showed a first pitchfork bifurcation from steady symmetric to steady asymmetric flow at a first critical Weissenberg number followed by a second transition to time-dependent flow above a second critical Weissenberg number provided the velocity ratio (*VR*) between side and main inlets was high, whereas for low *VR* there is a single transition from steady symmetric to time-dependent flow. However, what happens when the inlet lateral streams are not steady and how the elasticity and lateral inlet periodicity interact with the main steady inlet is still unknown and is the subject of the current investigation.

METHODS, RESULTS AND DISCUSSION

In this work we further extend the previous investigations of Oliveira et al. [6] by considering time periodic oscillating lateral streams of amplitude U_{max} and frequency *f*, defining the lateral inlet velocity as $u=U_{max}\cos(2\pi ft)$, stretching the main steady inlet stream of constant velocity U_{steady}, as sketched in Fig. 1a. The mesh used in the numerical simulations has 51 cells in the central square region of the cross slot along *x* and *y* directions (see partial view of the mesh in Fig. 1b), leading to minimum cell sizes of $\Delta x_{min} = \Delta x_{max} \approx 0.02$. We have used a finite-volume technique based on the kernel-conformation formulation, together with the high resolution 'CUBISTA' scheme for the convective terms in the constitutive equation, to study the low *Re* viscoelastic flow ($Re < 0.01$) inside the cross geometry, using an Oldroyd-B fluid with solvent viscosity ratio, β=0.575.

In order to explore the evolution of the flow dynamics due to the periodic oscillation we defined a parametric variable space based on the variation of the Weissenberg number ($Wi=\lambda U_{steady}/h$= 0 to 10), of the velocity ratio ($VR=U_{steady}/U_{max}$= 0.2, 1 and 5) and of the oscillation frequency, *f*, here quantified via the dimensionless Deborah number ($De=\lambda f$= 0.2, 1 and 5). Using two different periodic inlet flow configurations (in-phase and out-of-phase, as sketched in Fig. 1a) we were able to assess the importance of different types of flow near the stagnation point while assessing how the flow evolves along the outlet channel. We observed several types of flow transition, that depend on the amplitude and frequency of the forcing, and analyzed the corresponding velocity and stress fields in the exit channel, at the positions marked in Fig. 1a). As illustrated in Fig. 2, for the in-phase flow configuration the results at low *Wi* show the dampening of the oscillations on moving

a) Corresponding author. Email: fpinho@fe.up.pt

downstream along the outlet channel, whereas for high *Wi* the flow becomes chaotic. In contrast, for the out-of-phase forcing the outlet flow remains periodic up to *Wi*=10.

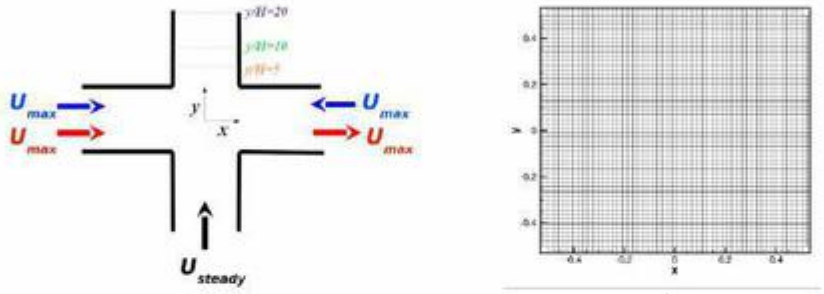

(a) (b)

Fig. 1. a) Schematic of the 2D cross-slot geometry and time periodic inlet configurations: in-phase (red) and out-of-phase (blue) configurations; b) partial view of the mesh at the central square.

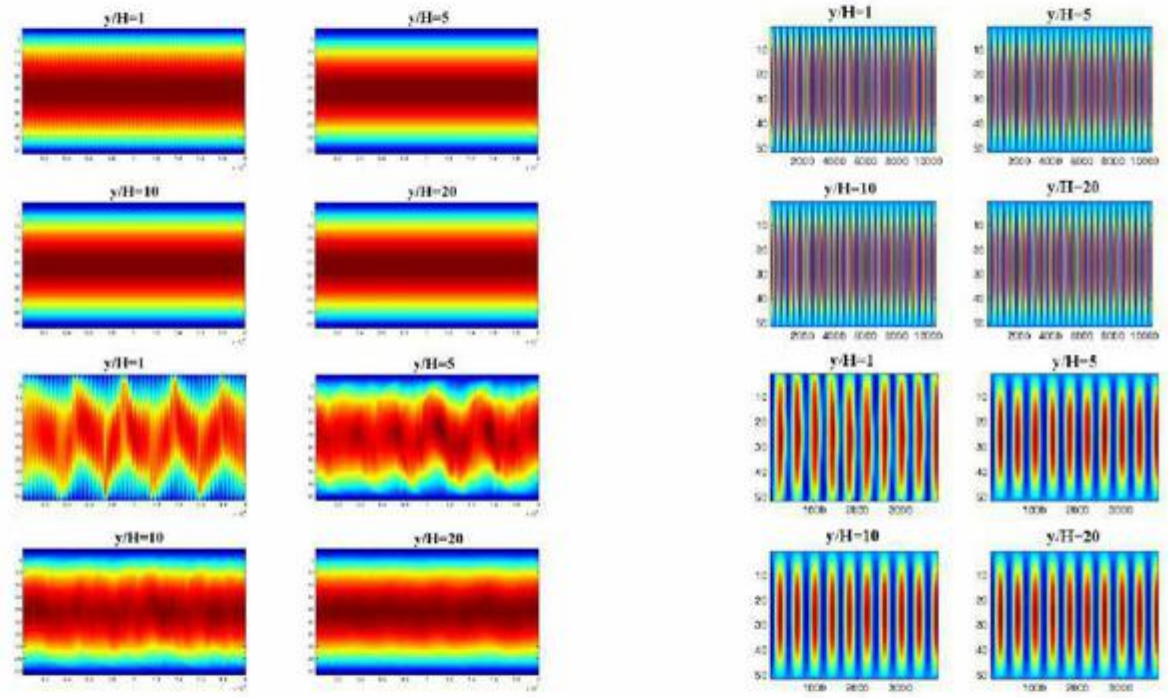

(a) (b)

Fig. 2. Time-space velocity maps at different cross-sections in the outlet channel at *Wi*= 0.1 (top two rows) and *Wi*= 10 (bottom two rows): a) in-phase configuration for *De*=0.2 and *VR*= 0.2; b) out-of-phase configuration for *De*= 5 and *VR*= 5.

References

[1] Arratia P. E, Thomas C. C., Diorio J. D., Gollub J. P. Elastic instabilities of polymer solutions in cross-channel flow. *Phys. Rev. Letters* **96**: 144502, 2006.

[2] Poole R. J, Alves M. A., Oliveira P. J. Purely elastic flow asymmetries. *Phys. Rev. Letters* **99**:164503, 2007.

[3] Cruz F. A, Poole R. J., Afonso A. M., Pinho, F. T., Oliveira P. J., Alves M. A. A new viscoelastic benchmark flow: Stationary bifurcation in a cross-slot. *J. Non-Newt. Fluid Mech.* **214**:57-68, 2014.

[4] Jensen K. Chemical kinetics: smaller, faster chemistry. *Nature* **393**:735-737, 1998.

[5] Oliveira M.S.N., Pinho F. T., Alves M. A. Divergent streamlines and free vortices in Newtonian fluid flows in microfluidic flow-focusing devices. *J. Fluid Mech.***711**: 171-191, 2012.

[6] Oliveira M.S.N., Pinho F. T., Poole R. J., Oliveira P. J., Alves M. A. Purely elastic flow asymmetries in flow-focusing devices. *J. Non-Newt. Fluid Mech.***160**: 31-39, 2009.

LARGE-SCALE BROWNIAN DYNAMICS SIMULATIONS OF POLYMERIC SOLUTIONS

Amir Saadat and Bamin Khomami *
Department of Chemical and Biomolecular Engineering, University of Tennessee, Knoxville, TN 37996, USA

Summary Excluded volume (EV) and hydrodynamic interactions (HI) play a central role in macromolecular dynamics under equilibrium and nonequilibrium settings, specifically in determining the concentration dependence of the properties of polymeric solutions. The computational cost of incorporating the influence of HI in Brownian dynamics simulations (BDS) of semidilute polymeric solutions has motivated much research on development of high-fidelity and efficient techniques. Here, a matrix-free approach for calculation of HI is implemented which leads to $O(N \log N)$ scaling of computational expense, where N is the number of beads in the simulation box. The fidelity of the algorithm is demonstrated by evaluating the properties of polymeric solutions and comparing the results with that of the blob theory. The scaling of relaxation time versus concentration is evaluated and compared with experiment. Furthermore, the matrix-free approach is implemented for nonequilibrium settings to simulate extension and relaxation of macromolecules of different architectures.

INTRODUCTION

The effect of concentration on equilibrium and dynamic properties of polymer solutions has been observed experimentally even at very low concentrations [1]. Accurate determination of the aforementioned properties of the polymer solutions near or above c^* (the concentration at which chains begin to partially overlap at equilibrium), i.e., the semidilute regime, is of great importance to the polymer physics as well as polymer processing communities. To this end, development of high-fidelity and computationally efficient simulation techniques for this class of fluids is important both from a scientific perspective and in industrial applications.

Calculating long-range HI

The perturbation of the velocity field around a polymer segment (or hydrodynamic coupling) is due to the movement of the segments of the same chain (intra-chain interaction) and the segments of other chains (inter-chain interaction). Simulations of such multichain systems are performed for homogeneous system in an unbounded domain using a periodic box. N_c chains with N_b identical beads are considered inside the primary box, so the number of interacting beads is $N = N_c N_b$. Due to the long-range nature of HI, each bead interacts not only with the beads inside the primary simulation box, but also with particles in all periodic replicas (images) of the primary box. The additive sum corresponding to this hydrodynamic coupling is known to be slowly and/or conditionally convergent [2]. Beenakker [2] used Ewald summation technique for Rotne-Prager-Yamakawa (RPY) HI tensor to split the original sum into two exponentially decaying sums in real and reciprocal spaces. In a straight forward implementation of the Ewald sum, the construction of the diffusion matrix requires $O\left(N^2\right)$ operations. This procedure followed by the calculation of Brownian displacements which also scales as $O\left(N^2\right)$ (if the Lanczos algorithm is used [3]) are the most cost prohibitive procedures in simulating polymer solutions with concentrations well above c^*.

Matrix-free Brownian Dynamics approach

In this study, the high computational cost of simulating long-range HI is reduced by using smooth particle mesh Ewald (SPME) technique where fast Fourier transform (FFT) is employed to accelerate the computations in reciprocal space. A small subset of interacting particles is treated in the real space while the main load is transferred to the reciprocal space sum. Efficient implementation of this method leads to the scaling of $O(N \log N)$ [6].

GOVERNING EQUATIONS

The dynamics of a macromolecule can be described using a coarse grained bead-spring model [4]. In this micromechanical model, a flexible polymer with N_K statistical Kuhn steps is discretized using N_b identical beads, which resemble the centers of hydrodynamic resistance, connected by $N_b \circ 1$ springs, which account for the entropic force between the neighboring beads. The simulation box is assumed to have sides with dimensions (L_x, L_y, L_z); i.e., $V = L_x L_y L_z$. Therefore, the concentration of beads in the box is given by $c = \frac{N}{V}$. The Itô stochastic differential equation of motion (SDE) is integrated in BDS to obtain the time evolution of the position of the beads, i.e., $\boldsymbol{r}$. The nondimensionalized form of SDE is written as

$$\mathrm{d}\boldsymbol{r} = \left[Pe\boldsymbol{K} \cdot \boldsymbol{r} + \frac{1}{4}\boldsymbol{D} \cdot \boldsymbol{F}^{\phi} \right] \mathrm{d}t + \frac{1}{\sqrt{2}}\boldsymbol{C} \cdot \mathrm{d}\boldsymbol{W} \tag{1}$$

where $\boldsymbol{K}$ is a block diagonal matrix which contains $N_b \times N_b$ blocks of 3×3 matrices which are equal to the transpose of the velocity gradient tensor. The diffusion matrix $\boldsymbol{D}$ is also a block matrix which contains $N_b \times N_b$ blocks and each block is the

*Corresponding author. Email: bkhomami@utk.edu

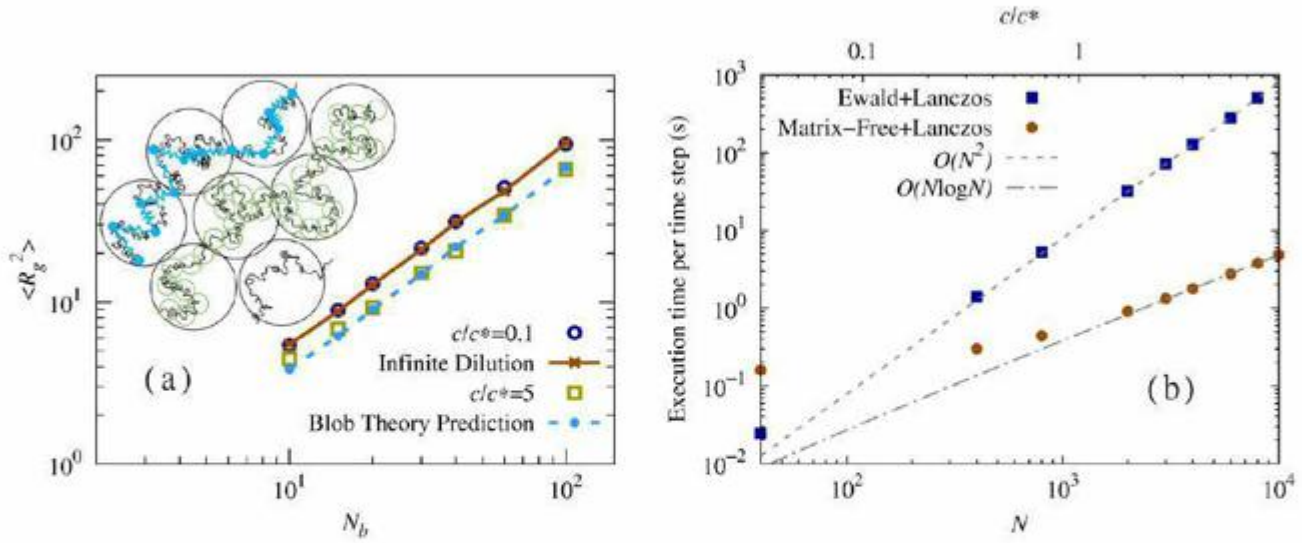

Figure 1: (a) The mean-square radius of gyration as a function of the number of beads in a bead-spring chain. The inset schematically depicts the blobs in the blob theory. (b) The execution time per time step as a function of the number of beads inside the periodic simulation box and the corresponding concentration.

3×3 pairwise RPY HI tensor. $\boldsymbol{F}^{\phi} = \boldsymbol{F}^{S} + \boldsymbol{F}^{EV}$ is the total conservative force on the beads, where $\boldsymbol{F}^{S}$ is the net spring force and the $\boldsymbol{F}^{EV}$ is the excluded volume force due to having a better than θ-solvent. $\boldsymbol{C}$ is the coefficient matrix which satisfies the following equation, $\boldsymbol{D} = \boldsymbol{C} \cdot \boldsymbol{C}^{T}$. In this work, $\boldsymbol{C}$ is calculated using the polynomial approximation to $\boldsymbol{D}^{1/2}$ based on the Lanczos technique [3]. $\boldsymbol{W}$ is a $3N$ dimensional Wiener process [4] defined for all beads in the simulation box.

RESULTS AND DISCUSSION

The static and dynamic behavior of multichain systems in θ and good solvents was evaluated both in dilute as well as semidilute regimes. The mean-square radius of gyration of the chains with different length in a good solvent is shown in Fig. 1(a). At low concentrations, i.e., ($c/c^* < 0.1$), $\langle R_g^2 \rangle$ is similar to the dimensions of the single chains at infinite dilution. At higher concentrations, an individual macromolecule experiences the repulsion due to the other chains in its vicinity which results in the reduction of its dimensions. The blob theory [5] (schematically shown in Fig. 1(a)) estimates this relative reduction of the chain size, i.e., $R_g/R_{g,0} = (c/c^*)^{-(2\nu-1)/(6\nu-2)}$, where $R_{g,0}$ is the radius of gyration in the limit of infinite dilution. To this end, the radius of gyration of the multi-chain systems with the relative concentration $c/c^* = 5$ is determined. It can be clearly seen that the simulated $\langle R_g^2 \rangle$ is consistent with the predictions of blob theory.

The execution time per time step as a function of N using both Ewald and matrix-free algorithms is depicted in Fig. 1(b). Clearly the matrix-free implementation with proper choice of the Ewald parameters [6] results in the total execution time which scales as $O(N \log N)$. As expected, the scaling of the execution time for the original Ewald algorithm is as $O(N^2)$.

The universal scaling of relaxation time for dilute and semidilute solutions is evaluated based on the correlation function of bead to center of mass relative distance to shed light into the dynamics of interacting macromolecules. The simulations are compared against the experimental data by Pan *et al.* [1]. Furthermore, the matrix-free approach is implemented for systems under homogeneous planar flow to simulate the transient and steady-state extension and relaxation of macromolecules of different molecular architectures.

References

[1] Pan S., Nguyen D. A., Sridhar T., Sunthar P., Prakash J. R.: Universal Solvent Quality Crossover of the Zero Shear Rate Viscosity of Semidilute DNA Solutions. J. Rheol. 58:339-368, 2014.

[2] Beenakker C. W. J.: Ewald Sum of the Rotne-Prager Tensor. J. Chem. Phys. 85:1581-1582, 1986.

[3] Saadat A., Khomami B.: Computationally Efficient Algorithms for Incorporation of Hydrodynamic and Excluded Volume Interactions in Brownian Dynamics Simulations: A Comparative Study of the Krylov Subspace and Chebyshev Based Techniques. J. Chem. Phys. 140:184903, 2014.

[4] Ottinger H. C.: Stochastic Processes in Polymeric Fluids. Springer-Verlag, Berlin 1996.

[5] Rubinstein M., Colby R. H.: Polymer Physics. Oxford, New York 2003.

[6] Saadat A., Khomami B.: Matrix-Free Brownian Dynamics Simulation Technique for Semidilute Polymeric Solutions. Phys. Rev. E 92:033307, 2015.

RHEOLOGY OF SUSPENDED PARTICLES IN VISCOELASTIC FLUIDS UNDER SHEAR

Mengfei Yang*[1], Sreenath Krishnan[2], Eric S. G. Shaqfeh[1, 2, 3], and Gianluca Iaccarino[3]

[1]*Department of Chemical Engineering, Stanford University, Stanford, California, United States*
[2]*Department of Mechanical Engineering, Stanford University, Stanford, California, United States*
[3]*Institute for Computational & Mathematical Eng, Stanford University, Stanford, California, United States*

Summary The study of viscoelastic fluids with particulate fillers is of considerable interest due to the prevalence of such materials in manufacturing, including injection molding and 3D printing, where the robustness of the process depends on controlling the suspension rheology. However, a fundamental understanding of the bulk stress of viscoelastic suspensions is complicated by the nonlinearities of the suspending fluid properties, which present a challenge for deriving analytical results. We present 3D simulations of neutrally buoyant spheres freely suspended in a viscoelastic fluid described by the Giesekus model under shear flow. Single particle results are used to validate the dilute limit and explore the effect of high shear rates, showing that the bulk rheology becomes dominated by polymer stresses induced in the fluid by particle disturbances. We also present multi-particle simulations at low volume fractions with fully resolved hydrodynamics to show how particle-particle interactions affect the pair-probabilities and resulting bulk stresses.

PROBLEM STATEMENT

Introduction

Because of the importance of viscoelastic suspensions in applied industrial applications, they have been studied mostly through experimental research devoted to concentrated suspensions. A deeper fundamental understanding of such systems is lacking in part because of the diverse nature of viscoelastic fluids and the nonlinearity of their stress-strain relationship. Few theoretical results exist and these predictions are often only valid in a flow regime (i.e. very weak flow and infinite dilution) where experimental measurements are difficult [1]. Numerical tools for computing the rheology of viscoelastic suspensions are few and most have focused on 2D, which produce results that often differ qualitatively and quantitatively from experiments [2]. As such there is a need for 3D simulations to not only validate the theoretical calculations but also provide a fundamental understanding of the mechanisms present in experimental results. We focus on the viscometric functions for non-colloidal suspensions of spheres in "Boger" fluids – i.e. nearly constant shear viscosity elastic fluid – since our primary goal is to gain insight into the effect of fluid *elasticity* on the rheological behavior of suspensions. There are several interesting observations from the experimental data which we explain through our numerical simulations. First, though the suspending Boger fluid is of constant shear viscosity, suspensions exhibit shear thickening even at low volume fractions [3, 4]. Second, experimental measurements of viscometric functions at low volume fractions exhibit larger viscosities and first normal stress difference coefficients than that predicted by dilute theory. Moreover, the measured second normal stress difference coefficients may differ in sign compared to that predicted by the dilute theory [4].

Numerical Methods

We use a 3D, parallel code based on an unstructured finite volume formulation for incompressible flow. The viscoelastic suspending fluid is described using the Giesekus constitutive model, which is fit to a number of existing experimentally measured Boger fluid rheologies, and added as a momentum source to the fluid solver. The code can accommodate boundary-fitted meshes, which allow high resolution of particle boundaries and can resolve all hydrodynamics (cf. Fig 1 a), as well as an immersed-boundary (IB) formulation that can efficiently handle multi-body dynamic simulations as well as all hydrodynamics if the particles remain separated by at least one grid spacing (cf. Fig 1 b). The IB code allows us to capture structure formation from flow inception to steady state (cf. Fig 1 c). The simulations are completed by solving the continuity and momentum equations for the flow around the particles and from this we can calculate any quantities of interest – e.g. the particle-induced fluid stress and the stresslet, which, when combined, determine the particle contribution to the bulk stress.

RESULTS

We first present a study of dilute suspensions as a function of the flow Weissenberg number, Wi, defined as the product of the shear rate and the polymer relaxation time, in Boger fuids. We found that the particle contribution to all viscometric functions exhibit shear thickening (cf. Fig 2 a). The shear-thickening was found to be created by the stretching of the polymers in the surrounding fluid induced by particle disturbances. These particle-induced fluid contributions increase with Wi, though, depending on the particular stress contribution, the trends may not be monotonic with Wi. We have also determined the

*Corresponding author. Email: mengfeiy@stanford.edu

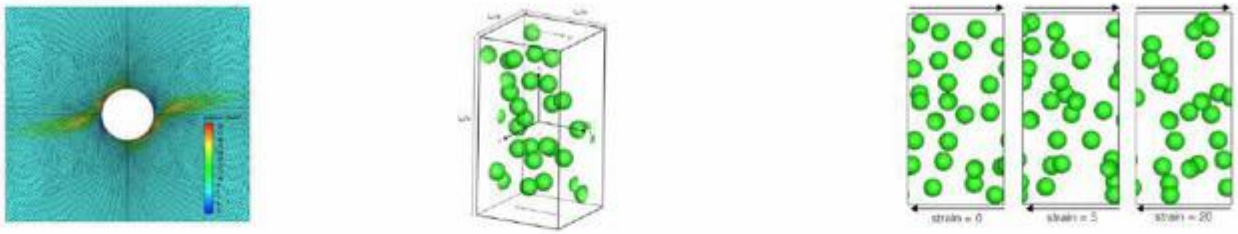

(a) (b) (c)

Figure 1: (a) body-fitted mesh for single particle simulations (b) initial configuration for immersed-boundary multi-particle simulations (c) 5 % suspension at various strains, $\gamma t = 0, 5, 10$

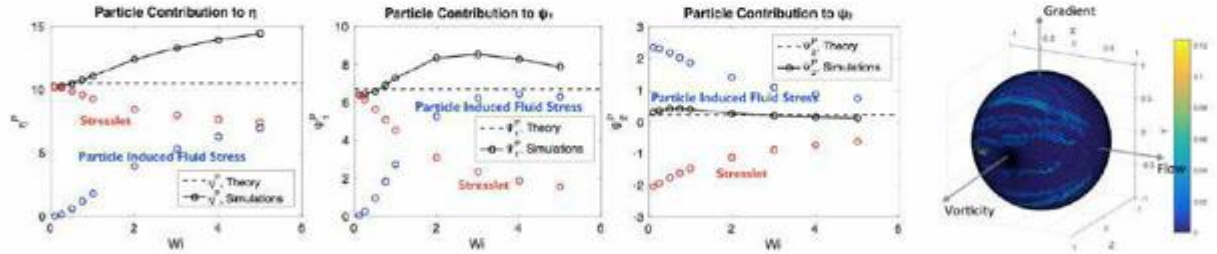

(a) (b)

Figure 2: (a) particle contribution to the viscosity, first normal stress coefficient, and second normal stress coefficient; stresslet in red, particle-induced fluid stress in blue, and total in black (b) cumulative pair probability of a 5 % suspension at $Wi = 1$

leading order Wi corrections (for $Wi << 1$) to the viscosity, first normal stress difference coefficient, and second normal stress difference coefficient for dilute suspensions.

We also performed multi-body simulations of suspensions at volume fractions of 0.05 in suspending Boger fluids. We can quantitatively evaluate the structure formation in the suspension by computing the cumulative pair probability and we find that there is a reduction of particle-particle interaction pairs in the flow direction while most interactions occur at an angle between the gradient direction and the vorticity direction (cf. Fig 2 b). We do not observe chaining in our simulations, which is in qualitative agreement with previous experimental observations of suspensions in Boger fluids [5]. On the other hand, 2D simulations do show chaining via flow-alignment, which suggests that our 3D multi-body simulations more accurately capture the physics of particle interactions than corresponding 2D simulations.

CONCLUSIONS

We have used a set of numerical tools to study the rheology of suspensions at low volume fractions for $Wi = 0 - 5$. In the dilute regime, we have validated our results by comparison to existing theory and, thereafter, extended the stress predictions to high Wi. In the non-dilute, low volume fraction regime, we are able to predict suspension structures similar to that observed in experiments. These tools allow us to study hydrodynamic interactions between particles and determine the solvent and polymer contributions to the bulk stress over a broad range of parameters. We anticipate that the present study will inform further fundamental investigations of suspensions in viscoelastic fluids as well as provide a starting point for the development of constitutive models for full particle loaded, viscoelastic suspensions.

References

[1] D. L. Koch, G. Subramanian, The stress in a dilute suspension of spheres suspended in a second-order fluid subject to a linear velocity field, J. Non-Newtonian Fluid Mech. 138 (2006) 87-97.

[2] N. O. Jaensson, M. A. Hulsen, P. D. Anderson, Simulations of the start-up of shear flow of 2D particle suspensions in viscoelastic fluids: structure formation and rheology, J. Non-Newtonian Fluid Mech. (2015) doi:10.1016/j.jnnfm.2015.09.006.

[3] R. Scirocco, J. Vermant, J. Mewis, Shear thickening in filled Boger fluids. J. Rheol. 49 (2005) 551-567.

[4] S. Dai, F. Qi, R. I. Tanner, Viscometric functions of concentrated non-colloidal suspensions of spheres in a viscoelastic matrix, J. Rheol. 58 (2014) 183-198.

[5] R. Scirocco, J. Vermant, J. Mewis, Effect of the viscoelasticity of the suspending fluid on structure formation in suspensions, J. Non-Newtonian Fluid Mech. 117 (2004) 183192.

MOLECULAR ORIGINS OF HIGHER HARMONICS IN LAOS: SHEAR STRESS

Peter H. Gilbert and A. Jeffrey Giacomin[a)]
Chemical Engineering Department, Queen's University, Kingston, Ontario, Canada

Summary Recent work focuses on understanding the molecular origins of higher harmonics arising in the shear stress response of polymeric liquids undergoing large-amplitude oscillatory shear (LAOS). These higher harmonics have been explained using orientation distribution of a dilute suspension of rigid dumbbells in a Newtonian fluid, neglecting polymer interaction. We explore these interactions by examining the Curtiss-Bird model, a kinetic molecular theory that accounts for restricted polymer motions arising when chains are concentrated.

INTRODUCTION

We examine the molecular origins of higher harmonics that arise in the shear stress response of a fluid undergoing LAOS [1] by exploring the predictions for several special cases of the Kramers freely-jointed chain [2]. We compare these predictions with those of rigid dumbbell [3] and reptation [4] theories. To explore the predicted behaviors, we plot loops of shear stress versus shear rate, since these best display distortions from ellipticity.

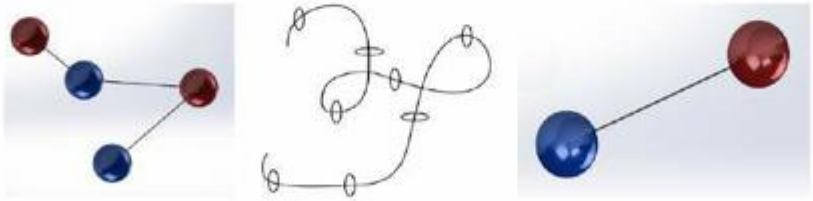

Figure 1: (Left to Right) Kramers freely-jointed chain (a), chain through slip-links (b), rigid dumbbell (c).

The Curtiss-Bird theory [2] models the polymer as an intertwined, interacting collection of freely jointed bead-rod chains (**Figure 1a**). A chain moves easily along its backbone ("reptation"), but neighboring chains restricts its lateral movement. The link tension coefficient, ϵ, quantifies this anisotropy, for which special cases arise: reptation ($\epsilon = 0$), rod-climbing ($\epsilon > 1/8$), reasonable shear-thinning ($1/5 \geq \epsilon \geq 3/4$), and dilute solution without hydrodynamic interaction ($\epsilon = 1$).

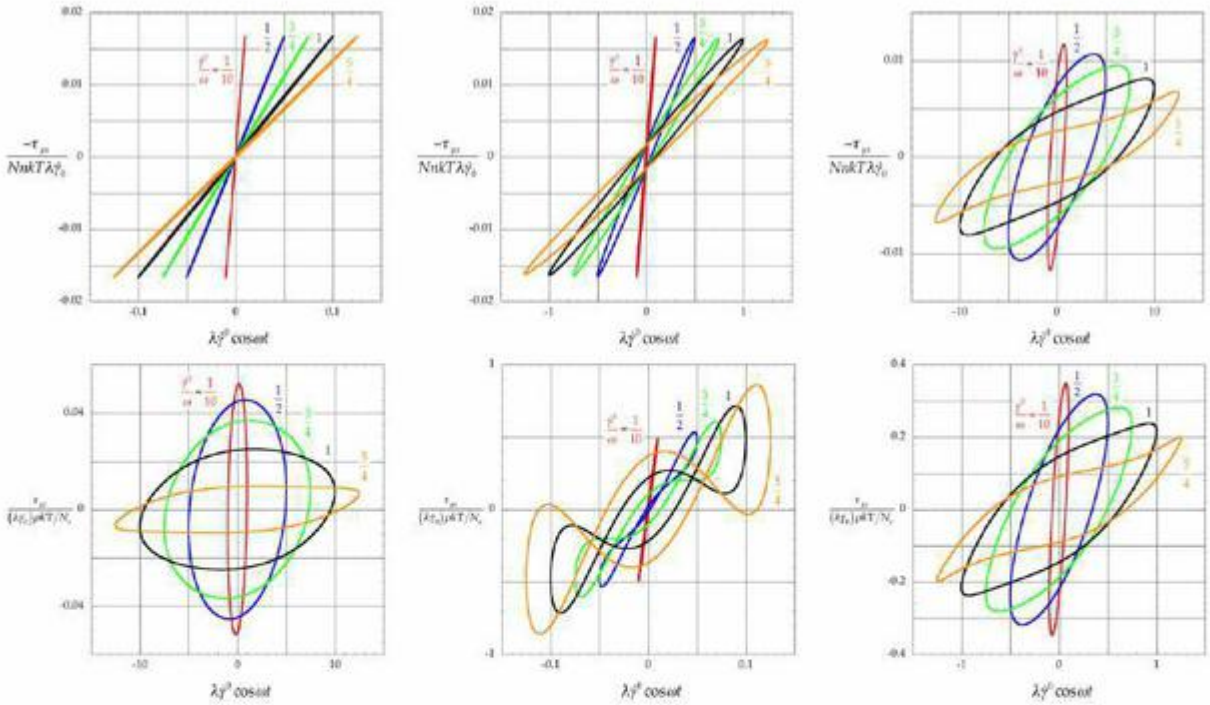

Figure 2: Curtiss-Bird model loops for $\epsilon = 0$ (*top row*) and slip-link reptation loops (*bottom row*) of dimensionless shear stress *versus* shear rate calculated for different values of Wi with (*left to right*) $\mathrm{De} = 0.1, 1, 10$.

In the dilute rigid dumbbell theory [3], a pair of beads, rigidly-separated, reorient in oscillatory shear flow, without interacting with any other dumbbells (**Figure 1c**). Doi-Edwards reptation theory includes hydrodynamic interaction by

[a)] Corresponding author. Email: giacomin@queensu.ca

confining the polymer chain to a tube [5] representing hydrodynamic interaction. For LAOS, reptation has been modeled using chains slipping through links (**Figure 1b**) [4]. We compare slip-link reptation with Curtiss-Bird theory [2] at $\epsilon = 0$.

COMPARISON: REPTATION THEORY

The Kramers freely-jointed chain (special case of $\epsilon = 0$) predicts an orientation distribution of the chains that matches the orientation distribution of Doi and Edwards. In other words, for the special case of $\epsilon = 0$, we can compare the Curtiss-Bird model, at least approximately, with predictions from slip-link reptation [4]. If we compare shear stress versus shear rate loops of Curtiss-Bird at $\epsilon = 0$ with those predicted by slip-link reptation (**Figure 2**), we immediately see that the reasonable loop shapes of Curtiss-Bird at $\mathrm{De} \le 1$ are not replicated by slip-link reptation. Instead, we obtain unphysical self-intersecting loops and loops with loop-end distortions resulting from the higher harmonics, which we call having *wrong convexity*. By *wrong convexity*, we mean that the loop tips are concave up rather than matching experimentally observed concave down shapes. Both models have *wrong convexity* at $\mathrm{De} > 1$, but they agree more closely.

COMPARISON: DILUTE SOLUTION OF RIGID DUMBELLS

When $\epsilon = 1$, the Curtiss-Bird model describes orientation distributions for dilute solutions. We can compare the Curtiss-Bird loops with those of a dilute solution of rigid dumbells (**Figure 3**). The increase of ϵ eliminates the *wrong convexity* we observed in the Curtiss-Bird loops when $\epsilon = 0$. However, the rigid dumbbell model still predicts *wrong convexity* when $\mathrm{De} > 1$. Furthermore, these two dilute solution models do not agree at any value of De.

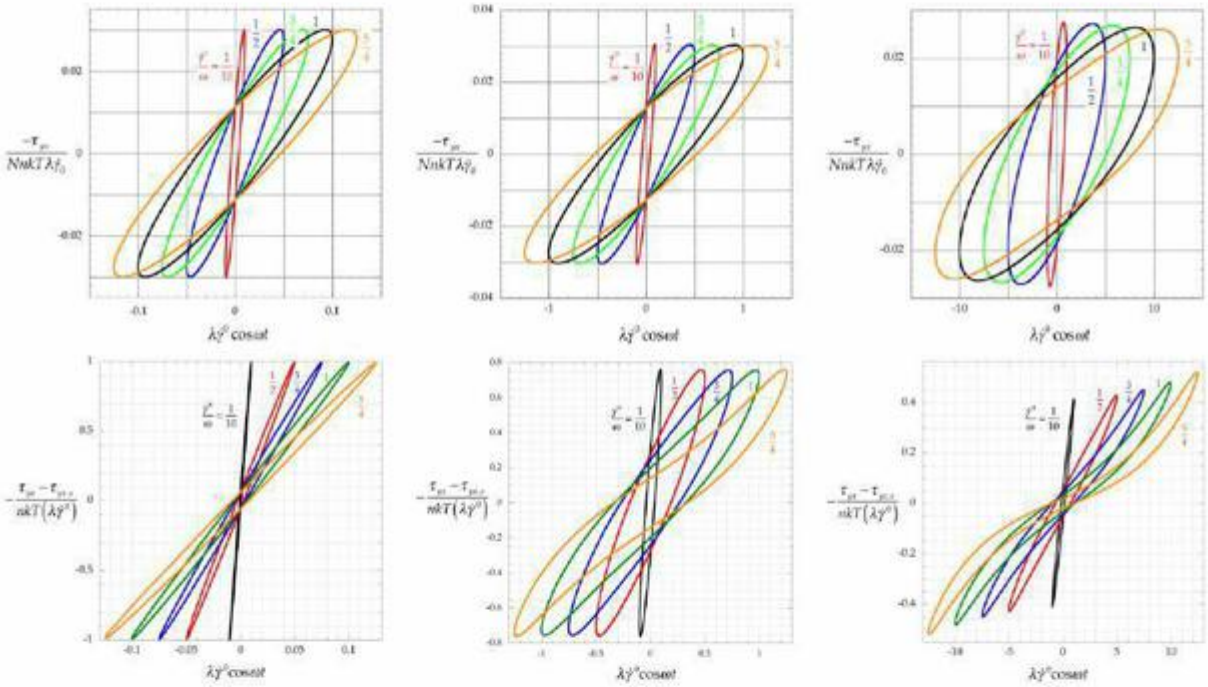

Figure 3: Curtiss-Bird model loops for $\epsilon = 1$ (*top row*) and rigid dumbell model loops (*bottom row*) of dimensionless shear stress *versus* shear rate calculated for different values of Wi with (*left to right*) $\mathrm{De} = 0.1, 1, 10$.

CONCLUSION

The higher harmonics in the fluid shear stress response are not correctly captured by molecular models, which predict *wrong convexity* for several values of De and Wi. Additionally, the *wrong convexity* manifested by each model disagrees with slip-link reptation and dilute solution predictions at similar conditions. Because the models do not capture convexity correctly and disagree with each other, one must further dissect these models to discover the source of these errant predictions.

References

[1] Oakley, J.G., J.A. Yosick and A.J. Giacomin, *Mikrochimica Acta*, **130**, 1 (1998).
[2] Fan X.-J. and R.B. Bird, *J. Non-Newt. Fluid Mech.*, **15**, 341 (1984).
[3] Bird, R.B., A.J. Giacomin, A.M. Schmalzer and C. Aumnate, *J. Chem. Phys.*, **140**, 074904 (2014).
[4] Pearson, D.S. and W.E. Rochefort, *J. Polym. Sci.: Pol. Phys. Ed.*, **20**, 83 (1982).
[5] Doi, M. and S.F. Edwards, *J. Chem. Soc., Faraday Trans.*, **2**, 1802 (1978).

MACH CONES IN A VISCOELASTIC FLUID

Fumihiko Mikami*[1] and Yoshiaki Yagi[1]
[1]*Department of Mechanical Engineering, Chiba University, Chiba-shi, Chiba, Japan*

Summary Mach cones created by a falling sphere are observed experimentally in a viscoelastic fluid. The fluid used is a dilute wormlike micelle solution of cetyletrimethylammonium bromide (CTAB) and sodium salicylate (NaSal) dissolved in water. A sphere falls through the fluid faster than the speed of shear waves. Mach cones are clearly observed in vorticity fields. They have a multiple-cone structure. The first cone is involved with forward shearing motion in the direction induced by the falling sphere, and it is followed by weaker cones with backward shearing motion accompanied by a relaxation of the initial shearing motion. The results suggest the importance of considering shear-wave-based Mach numbers that facilitates the understanding of a complex phenomenon associated with viscoelastic fluid flows.

INTRODUCTION

Shear waves, or equivoluminal waves can be propagated in viscoelastic fluids, and they can be interpreted as vorticity waves in the fluids. The speed of shear waves is given by $\sqrt{G/\rho}$, where G is the rigidity and ρ is the density of the fluid. The speed of shear waves propagating in a viscoelastic fluid is usually much smaller than that of compressional sound waves in the fluid. Therefore, it is easily possible that a shear-wave-based Mach number $M = V/c$ exceeds one, where V is the speed of an object through a fluid and $c = \sqrt{G/\rho}$ is the speed of shear waves in the fluid. The phase velocity of plane harmonic waves in wormlike micellar fluids decreases with the concentration and tends to zero [1], which is indicating that dilute conditions may give rise to supercritical flow of the fluids. Joseph [2] considered the problem of uniform flow of viscoelastic fluid past a body using linearized theory and showed that a Mach cone will develop if $M > 1$, where the governing vorticity equation is hyperbolic when $M > 1$ and elliptic when $M < 1$. In this study, we demonstrate experimentally that Mach cones are created by a falling sphere in a dilute wormlike micelle solution in the condition of $M > 1$.

METHODS

An aqueous solution of wormlike micelles was prepared by mixing 3 mM cetyltrimethylammonium bromide (CTAB) and 3 mM sodium salicylate (NaSal) in deionized water. The wormlike micelle solution was seeded with water-soluble acrylic paint containing luminous red pigment suspension for flow visualization purpose. It has been shown that the linear rheology of the wormlike micelle solution can be well described by a fit to a Maxwell model having single relaxation time [3]. Because the shear wave speed is the most important characterizing property of the fluid responsible for the formation of Mach cones, the speeds of plane shear waves generated by impulsive excitation in the fluid were directly measured instead of measuring the steady and dynamic shear rheology.

The fluid was contained in a transparent Plexiglas vessel having square cross section of 100 mm in side and a hight of 350 mm. The experiments were performed at a constant temperature of 25 °C. Shear waves were generated by a vertical thin plate moving in its own plane driven by an electric linear actuator. The plate undergoes a step increase of velocity from rest to 10 mm / s followed by a sudden stop. A generated shear wave pulse travels in the direction normal to the plate. The flow fields were visualized with laser sheet illumination of a central vertical slice normal to the plate. The sheet thickness of the laser was 0.8 mm. The emitted fluorescence from the tracer particles was imaged with a CCD camera (2336 ×1728 pixel, 8 bit) by using a sharp cut filter and captured on a PC. The flow fields associated with the shear waves were obtained by using a particle image velocimetry (PIV) and the vorticity was computed from the flow fields. The shear wave speed c was determined by tracking the position of a vorticity peak over several frames.

A polystyrene sphere of a density ρ_s = 1.04 × 10^3 kg / m^3 with a diameter of 6.36 mm was released from a guide pipe carefully. The lower end of the guide pipe was positioned a depth 12 mm below the center of the free surface. The flow fields around the sphere were obtained in a vertical plane coinciding with the center of the sphere, in the same way as described above for the wave speed measurement. The position of the sphere in each video frame was obtained by image analysis. The settling velocity V was determined from the trajectories of the sphere. The Mach number is defined as $M = V/c$.

RESULTS

In wave speed measurements, the generated shear waves have been damped before they reach walls and reflected waves were not observed. A vorticity peak was successively tracked over several video frames without any disturbance arising from the circulating flow in a cavity driven by a moving plate. The measured shear wave speed for the 3 mM CTAB/NaSal solution was 8.4 mm/s.

*Corresponding author. Email: fmikami@faculty.chiba-u.jp

Figure 1 shows the flow fields and the vorticity fields around a sphere falling at a constant speed of M = 1.5. The Mach cone is clearly visible and more easily identified on vorticity maps. The half-angle α of the Mach cone is nearly 40°, which obeys the relation $\sin\alpha = 1/M$. The undisturbed region in front of the Mach cone is visible in the vorticity fields. As can be seen in the vorticity maps, the initial Mach cone is followed by weaker cones with opposite sign of vorticity. The velocity and the vorticity fields show that in the first cone the fluid elements undergo forward shearing motion in the direction of shear flow induced by the falling sphere and in the following cones they undergo backward shearing motion. It is considered that the weaker Mach cones with opposite sign of vorticity are caused by a relaxation of the initial shearing motion in the first cone. A conical region of the negative wake is also visible in the flow fields behind relaxation waves.

Arigo and McKinley [4] examined negative wakes behind a sphere sedimenting in a viscoelastic solution of polyacrylamide in a water glycerol mixture. The Mach cones did not appear in their PIV results. By using the values given by them for the fluid, the shear wave speed is computed to be 58 mm/s and the Mach number is ranging from 0.07 to 0.09, which is subcritical. On the other hand, the formation of a conical upward flow zone that may be a Mach cone around a rising bubble in a polyacrylamide solution is reported in the experiment of Funfschilling and Li [5]. The flow patterns in their results are quite simillar to ours. Unfortunately, the shear wave speed can not be determined from their data, though the Mach number probably exceeded one in their experiments. They also observed a zone of a negative wake behind the conical upward flow. The distinct flow zones in their results could be attributed to the nature of the supercritical flows.

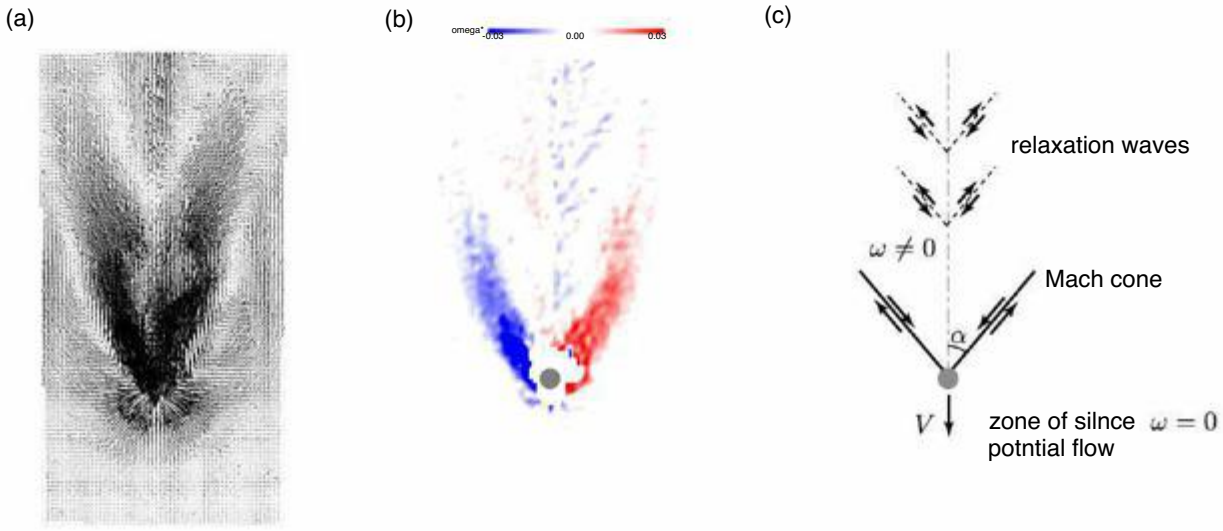

Figure 1: Flow around a sphere falling at a Mach number of 1.5 in a 3 mM CTAB/NaSal solution. (a) Velocity field. (b) Vorticity ω^* non-dimensionalized by the sphere velocity and the sphere diameter. (c) Wave system around a sphere.

CONCLUSIONS

Mach cones in a viscoelastic fluid were investigated experimentally by using a PIV. Mach cones were generated by a falling sphere in a viscoelastic wormlike micelle solution when the sphere velocity is faster than the shear wave speed in the fluid. The Mach cones were visible in the vorticity fields, and were found to have a multiple-cone structure. In the first cone the fluid elements undergo forward shearing motion in the direction induced by a sphere and in the following weaker cones they undergo relaxation by backward shearing motion. The results suggest the importance of considering shear-wave-based Mach numbers that facilitates the understanding of a complex phenomenon associated with viscoelastic fluid flow.

References

[1] Gladden, J. R., Gamble, A. M., Skelton, C. E., Mobley, J.: Shear Waves in Viscoelastic Wormlike Micellar Fluids over a Broad Concentration Range. J. Acoust. Soc. Am. 131:2063-2067, 2012.

[2] Joseph D. D.: Fluid Dynamics of Viscoelastic Liquids. New York, Springer-Verlag, 1990.

[3] Shikata, T., Hirata, H., Kotaka, T.: Micelle Formation of Detergent Molecules in Aqueous Media: Viscoelastic Properties of Aqueous Cetyltrimethylammonium Bromide Solutions. Langmuir 3:1081-1086, 1987.

[4] Arigo M. T., McKinley G. H.: An Experimental Investigation of Negative Wakes behind Spheres Settling in a Shear-Thinning Viscoelastic Fluid, Rheol. Acta 37:307-327, 1998.

[5] Funfschilling, D., Li, H. Z.: Flow of Non-Newtonian Fluids around Bubbles: PIV Measurements and Birefringence Visualisation. Chem. Eng. Sci. 56:1137-1141, 2001.

ELASTOMERS IN OSCILLATORY EXTENSION

C. Saengow[1], C. Dessi[2], D. Vlassopoulos[2], A.J. Giacomin[1,a)]
[1]*Chemical Engineering Department, Queen's University, Kingston, ON Canada*
[2]*F.O.R.T.H., Institute of Electronic Structure and Laser, Heraklion, Crete, Greece*

Summary We subject elastomers to a fixed pre-stretch in uniaxial extension upon which a large-amplitude oscillatory uniaxial extensional (LAOE) deformation is superposed. Our new continuum model, the *Voigt element with strain-hardening spring*, for this behavior combines a new nonlinear spring in parallel with a Newtonian dashpot. We consider this three-parameter model to be the simplest relevant one for the observed convex banana-shaped stress-strain ($\tau_{xx}-\varepsilon$) loops. We fit the three parameters (Young's modulus, viscosity and strain-hardening coefficient) to our LAOE measurements. We develop analytical expressions for the Fourier components to the parts of the stress response, both in-phase and out-of-phase with the strain, for the zeroth, first, second and third harmonics. We find that the part of the second harmonic that is out-of-phase with the strain must be negative, for proper banana convexity.

INTRODUCTION

We subject elastomers to a fixed pre-stretch in uniaxial extension upon which a large-amplitude oscillatory uniaxial extensional (LAOE) deformation is superposed (Figure 1a). Our continuum uniaxial spring, the strain-hardening spring follows:

$$\tau_{xx} = E\left([\ ] + \left\{ -\varepsilon^2 \left(+\tfrac{2}{3}\varepsilon \right)(1+\varepsilon)^{-2} \right\} + \left[\!\left[h\varepsilon^4 \right]\!\right] \right) \tag{1}$$

which, when combined in parallel with a Newtonian dashpot givess:

$$\tau_{xx} = E\left([\ ] + \left\{ -\varepsilon^2 \left(+\tfrac{2}{3}\varepsilon \right)(1+\varepsilon)^{-2} \right\} + \left[\!\left[h\varepsilon^4 \right]\!\right] \right) + \eta\dot{\varepsilon} \tag{2}$$

where for our LAOE protocol (Figure 1a):

$$\varepsilon = \varepsilon_p + \varepsilon_0 \sin\omega t \tag{3}$$

where the bracketed **[blue]** term is the linear elastic contribution, the braced **{green}**, the nonlinear, and the slot-bracketed ⟦red⟧ term accounts for strain-hardening. We call this the Voigt element with strain-hardening spring [Figure 1b and following Eq. (2)].

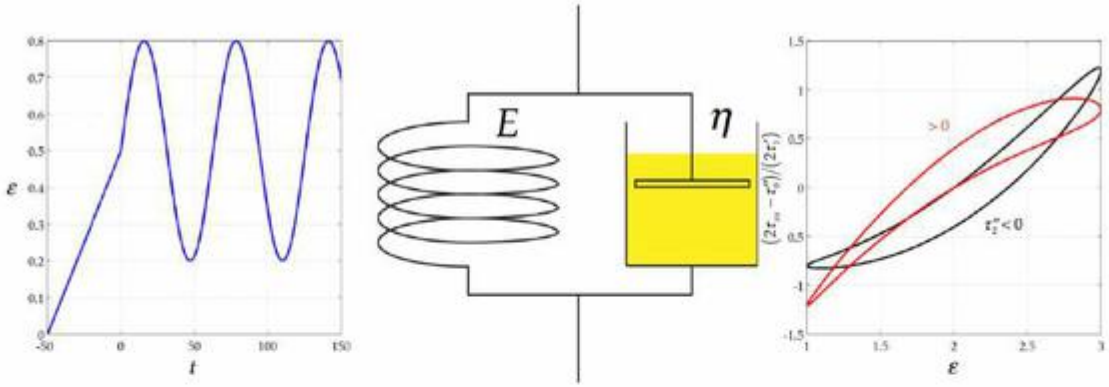

Figure 1: (Left to Right) (a) LAOE protocol, (b) Voigt element, (c) necessary condition for convex banana.

Figure 2a illustrates the static uniaxial extensional behavior for the new spring [Eq. (1)] and compares it with the classic natural rubber data of Treloar (FIG. 5.4 of [1]) for $E = 1.17\,\text{M Pa}$ and $h = 0.0210$. We see that the **green** term in Eq. (1) imparts concavity to the $\tau_{xx}-\varepsilon$ curve for low strain regime, and the red term imparts convexity for the large strain regime. From Figure 2a, we learn that our model agrees well the static observations. Figure 2b illustrates the steady uniaxial extensional behaviour of Eq. (2), for $E = 3.12\,\text{MPa}$, $\eta = 0.680\,\text{MPa s}$ and $h = 1.67$ with $\varepsilon_s = 0, \frac{1}{100}, \frac{1}{10}, 1\,\text{rad/s}$, and compare with our own measurements (*Figure 5.5* of [2]). Figure 2c illustrates the LAOE behavior of Eq. (2), for $E = 25.1\,\text{MPa}$, $\eta = 6.68\,\text{MPa s}$ and $h = 3.33$, and compares it with our own measurements (red loops in *Figure 5.10* of [2]). We see that the black term in Eq. (2) imparts area to the $\tau_{xx}-\varepsilon$ loop. We then rewrite Eq. (2) as a Fourier series:

a) Corresponding author. Email: giacomin@queensu.ca

$$\breve{\tau} \equiv \frac{E_0''}{2E} + \sum_{n=1,2}^{\infty} \mathbb{E}_n' \sin n\,\mathrm{De}\,\tau + \mathbb{E}_1'' + \sum_{n=2,2}^{\infty} \mathbb{E}_n'' \cos n\,\mathrm{De}\,\tau \tag{4}$$

$$\breve{\tau} \approx \frac{E_0''}{2E} + \frac{E_1'}{E}\sin \mathrm{De}\,\tau + \frac{E_3'}{E}\sin 3\,\mathrm{De}\,\tau + \frac{E_1''}{E} + \frac{E_2''}{E}\cos 2\,\mathrm{De}\,\tau \tag{5}$$

Further, our new model [Eq. (2)] satisfies the necessary condition:

$$\breve{\tau}_2'' \equiv \varepsilon_0 E_2'' < 0 \tag{6}$$

for banana convexity (Figure 1c).

CONCLUSION

We have studied the Voigt element with strain-hardening spring [Eq. (2)]. We find that this new model imparts convexity, and is adequate for static extension of natural rubber including at large extension. Our new model can also be fit to both steady uniaxial extensional and LAOE measurements on filled elastomer. However, we find that the best fit constants (E, η and h) for steady uniaxial extension differ significantly from those for LAOE [see above Eq. (4)]. We speculate that that multiple Voigt elements with strain-hardening springs in parallel would correct this.

In Eq. (6), we state the sufficient condition for $\tau_{xx} - \varepsilon$ banana convexity, and our new constitutive model predicts this banana convexity correctly. From this Fourier series, we conclude that harmonics higher than the third can be neglected for

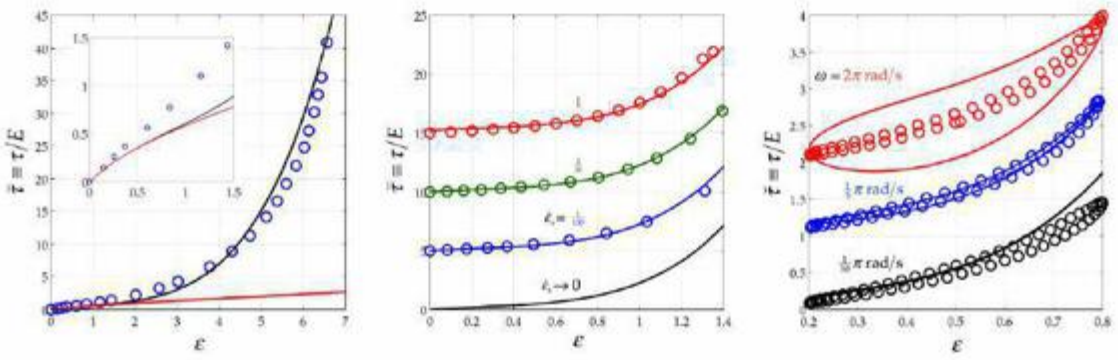

Figure 2: (Left to right) (a) Uniaxial static behavior of Treloar [1] spring (**red**) and (**black**) strain-hardening spring, (b) Steady uniaxial extension behavior of Voigt model with strain-hardening spring for $\dot{\varepsilon}_s = 0, \frac{1}{100}, \frac{1}{10}, 1\,\mathrm{s}^{-1}$ (from bottom to top). **Blue**, **green** and **red** curves and circles are shifted upward by 5,10 and 15. (c) LAOE behavior of Voigt model with strain-hardening spring for $\omega = \frac{1}{50}\pi, \frac{2}{10}\pi, 2\pi\,\mathrm{rad/s}$ (from bottom to top). **Blue** and **red** curves and circles are shifted upward by 1 and 2. Voigt element.

elastomers in LAOE. Our new model overpredicts the stress-strain loop area, and thus overpredicts the viscous dissipation at high frequency (top loop, Figure 2c). We speculate that that multiple Voigt elements with strain-hardening springs in parallel would correct this.

References

[1] Treloar, L.R.G, *The physics of rubber elasticity*, 3rd ed., Clarendon Press, Oxford (1975).

[2] Dessi, C., "Linear and Non-linear Rheology of Heterogeneous Polymeric Systems: from Entangled Polymeric Networks and Elastomers to Nanocomposites," PhD thesis, University of Crete, Greece (2016).

CREEPING FLOW AROUND PARTICLES IN LARGE YIELD STRESS BINGHAM FLUIDS

Emad Chaparian[1], Neil J. Balmforth[2], and Ian A. Frigaard [*1,2]

[1]*Department of Mechanical Engineering, University of British Columbia, Vancouver, British Columbia, Canada*
[2]*Department of Mathematics, University of British Columbia, Vancouver, British Columbia, Canada*

Summary Yield stress fluids can hold buoyant rigid particles static if their yield stress is large enough. This critical yield number, beyond which there is no flow, is an important parameter to estimate in addressing sedimentation of rigid particles in visco-plastic fluids. As we get close to this limit, viscous dissipation becomes negligible in comparison to the plastic contribution. Employing slipline theory for 2D plastic flows, we are able to approximate the yield number (lower bound) and the shape of the plugs attached to the falling particle in this limit. Numerical experiments of symmetric particles motion in visco-plastic fluid validate the predictions of slipline theory for a wide range of geometries and reveal some astonishing effects.

BACKGROUND

Particulate flow in viscoplastic fluid has been extensively investigated numerically and experimentally. One aspect however, that has not been addressed completely is the static stability problem: one expects that for large enough yield stress of the fluid, the particle will not move under the action of the body force (i.e. there is no particle settling). The yield number (Od_c) or critical plastic drag coefficient ($C^p_{D,c}$) is an important flow parameter. For a few specific geometries these critical numbers can be found in the literature [1–4]. However, a general method to find the yield number does not exist and also no study focuses on the features of the flow in the yield limit.

Putz and Frigaard [1] have shown that as we get close to the yield limit the viscous dissipation will be at least one order of magnitude less than the plastic dissipation. Ignoring the viscous contribution, here we consider a rigid-plastic rheological model. Slipline theory (which has been extensively used in solid mechanics and geotechnics) is a powerful tool for limit analysis in rigid-plastic problems. One of the best examples is the paper by Randolph and Houlsby [5] in which the authors constructed the slipline network around a circular pile to calculate the lateral resistance of it in the soil mass. This flow is equivalent to a 2D settling circular disc. In the present study, we attempt to shape a general framework for using slipline theory in calculating the critical plastic drag coefficient (or equivalently yield number) of particle motion in visco-plastic fluid and highlight the flow characteristics in the yield limit.

PROBLEM STATEMENT

The yield limit studied is identical for a range of yield stress models, e.g. Bingham, Casson, Herschel-Bulkley. Using the simplest (Bingham) model as the constitutive equation, we solve the following dimensionless equations:

$$\frac{\partial \tau_{ij}}{\partial x_j} - \frac{\partial p}{\partial x_i} = 0 \quad \text{and} \quad \partial u_i/\partial x_i = 0 \tag{1}$$

$$\begin{cases} \tau_{ij} = \left(1 + \dfrac{B}{\dot\gamma}\right)\dot\gamma_{ij} & \text{iff } \tau > B \\ \dot\gamma = 0 & \text{iff } \tau \leqslant B \end{cases} \tag{2}$$

where $B = \hat\tau_Y \hat L/\hat\mu \hat U$ is the Bingham number, $\dot\gamma = \sqrt{1/2\sum \dot\gamma_{ij}^2}$, and $\tau = \sqrt{1/2\sum \tau_{ij}^2}$. Here $\hat\tau_Y$ is the yield stress of the fluid, $\hat\mu$ the plastic viscosity, $\hat L$ the length scale, and $\hat U$ is the velocity of the particle. The stresses and pressure are scaled with viscous scale. For boundary condition we impose no-slip on the particle surface and $u_i = 0$ at infinity. Using variational principles we find the solution of (1)-(2) using the augmented Lagrangian formulation and Uzawa algorithm, e.g. [6].

SLIPLINE THEORY

Viscous dissipation is much smaller than the plastic dissipation in the yield limit. Hence, we ignore the role of viscosity in this limit for finding the critical plastic drag coefficient. In this case, the von Mises yield criterion and the Stokes equations form a closed set of hyperbolic equations along characteristic curves for which the magnitude of shear stress is maximal and is equal to the yield stress. These orthogonal characteristics (α and β lines) are found from the Hencky equations [7]):

$$\hat p + 2\hat\tau_Y \phi = \text{const. along } \alpha \text{ lines} \qquad \text{and} \qquad \hat p - 2\hat\tau_Y \phi = \text{const. along } \beta \text{ lines}, \tag{3}$$

*Corresponding author. Email: frigaard@math.ubc.ca

where ϕ by definition is the angle that the α-line makes with the x-axis. Solving these equations along the slipline network, we can find an admissible stress field and hence calculate a lower bound of $C^p_{D,c}$. In Fig. 1, the slipline network around example shapes is presented. In all the results presented the particle is moving vertically upward. Satisfactory agreement is found between the lower bound of $C^p_{D,c}$ predicted by slipline theory and that computed from iteratively solving (1)-(2) numerically.

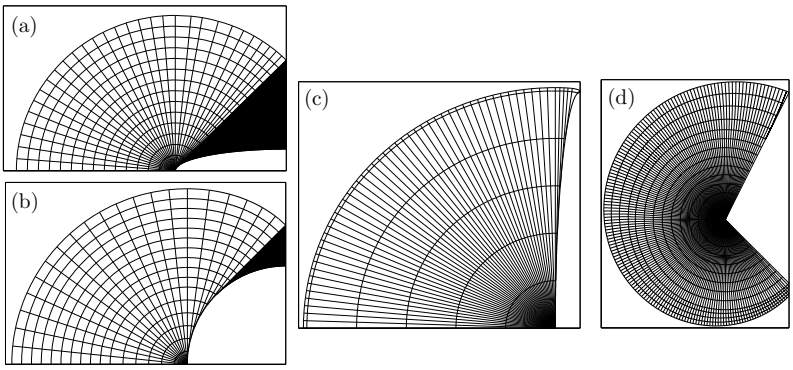

Figure 1: Slipline network for different geometries: (a) oblate ellipse (10.34,10.35), (b) circle (11.94,11.94), (c) prolate ellipse (27.43,27.9), (d) kite (11.78,11.85). The bracketed numbers in each case give the values of $C^p_{D,c}$ from slipline theory and numerical solution of (1)-(2), respectively.

CLOAKING EFFECTS

Close to the yield limit (large B), we observed that for different particle shapes, the flow can look very similar; see Fig. 2. Thus, the shape of the particle is 'cloaked'. Based on these observations, we developed a general methodology that can summarize all these flow features. Using this method, we can find the slipline network around arbitrary symmetric particles and calculate lower bounds estimates of the yield number that prove to be close to those from (1)-(2).

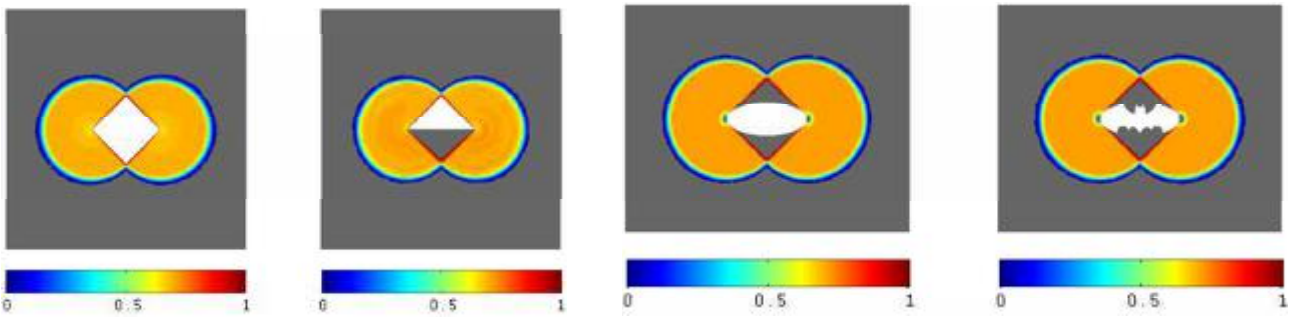

Figure 2: Different particles at large B. Colourmap shows speed contours and gray shaded regions are unyielded. The tilted square is like a triangle (a plug fills the rear side of the triangle). The 'Batman' and ellipse are very similar.

References

[1] Putz A., Frigaard I.A.: Creeping flow around particles in a Bingham fluid. J. Non-Newtonian Fluid Mech 165:263-280, 2010.

[2] Beris A.N., Tsamopoulos J.A., Armstrong R.C., Brown R.A.: Creeping motion of a sphere through a Bingham plastic. J. Fluid Mech 158:219-244, 1985.

[3] Tokpavi D.L., Magnin A., Jay P.: Very slow flow of Bingham viscoplastic fluid around a circular cylinder. J. Non-Newtonian Fluid Mech 154:65-76, 2008.

[4] Nirmalkar N., Chhabra R.P., Poole R.J.: On creeping flow of a Bingham plastic fluid past a square cylinder. J. Non-Newtonian Fluid Mech 171:17-30, 2012.

[5] Randolph M.F., Houlsby G.T.: The limiting pressure on a circular pile loaded laterally in cohesive soil. Géotechnique 34:613-623, 1984.

[6] Glowinski R., & le Tallec P.: Augmented Lagrangian and Operator-Splitting Methods in Nonlinear Mechanics, SIAM, (1989)

[7] Hill R.: The Mathematical Theory of Plasticity. Oxford, UK 1950.

DISPLACEMENT FLOWS OF VISCOPLASTIC FLUIDS IN AN OSCILLATING PIPE

A. Amiri, F. Larachi, and S.M. Taghavi*
Chemical Engineering Department, Laval University, Quebec, QC, Canada, G1V 0A6.

Summary We study experimentally the displacement flow of a viscoplastic fluid by a Newtonian fluid in a vertical pipe. The two fluids have a small density difference (i.e., 2%). The denser displacing fluid is placed above the displaced fluid. Although buoyancy is a driving force, there is also an imposed flow (from the top of the pipe) with a mean velocity V_0. We have considered two different situations: first, the pipe is stationary; second, the pipe slowly oscillates around its vertical position like an inverted pendulum. Considering displacement flows at different imposed flow rates in stationary and moving pipes, we find that at low imposed flows the displacement flow in a moving pipe is less efficient. This may have a negative impact in floating production storage and offloading (FPSO) applications, where displacement flows in moving geometry occurs.

INTRODUCTION

There are many industrial processes where it is necessary to remove viscoplastic materials from pipes and channels. Examples include bio-medical applications, cleaning of equipment and food processing, oil well cementing and waxy crude oil pipeline restarts. There are relatively few experimental studies of displacement of yield stress fluids by other fluids. Gabard & Hulin [1] studied iso-density miscible displacements in a vertical tube where a more viscous non-Newtonian fluid is displaced by a Newtonian fluid. They observed the effects of rheological features of the displaced fluid on the transient residual layer thickness during the displacement process. They reported that for yield stress fluid displacements the static residual wall layers have uniform thicknesses. Examples of other experimental studies on viscoplastic displacement flows in the pipe geometry are presented in [2, 3].

There are numerous situations where displacement flows occur in a geometry that is moving. Examples include various processes occurring in floating production storage and offloading (FPSO) applications and casing's reciprocative and rotative motions in primary cementing processes. However, displacement flows in moving geometry have not been studies in the literature. Our study considers displacement flows of a viscoplastic fluid and a Newtonian fluid in pipe moving with a specially interesting motion.

EXPERIMENT

Our experimental study was performed in a 2m long, 9.6mm diameter, transparent vertical pipe with a gate valve located 40cm from the top end. The displacement flow setup was mounted on an Hexapod parallel robot, which is a motion simulator that has six degrees of freedom (see Fig. 1). Based on the principle of the Stewart platform, the Hexapod includes a fixed platform and a mobile platform, which are linked together by six actuators (hydraulic jacks). The actuators are mounted in pairs on the fixed platform and cross over to three mounting points on the mobile platform. A software was used to move the mobile platform with the six degrees of freedom with a centre of rotation. The displacement setup placed on the top plate could be moved to experience the six degrees of freedom movement, including the three linear movements X (lateral), Y (longitudinal), and Z (vertical), and the three rotations pitch, roll, and yaw. Initially, the lower part of the pipe was filled with a less dense fluid (fluid 2) coloured with a small amount of ink. The upper part of the pipe, above the gate valve, was filled by the denser fluid (fluid 1). To avoid pump disturbances, the displacing upper fluid was fed by gravity from a large elevated tank. The flow rate was controlled by a valve and measured by a rotameter, located downstream of the pipe. At the start of the experiment the gate valve is opened. Images of the displacing fluid are recorded using a high-speed camera (covering 80cm below the gate valve), and subsequently analyzed to characterize different aspects of the flow. The camera was mounted on the setup to move with it; therefore, the (quite clear) images obtained were in a moving frame of reference. Regarding the pair fluids, we performed experiments with a Newtonian fluid (i.e., salt-water solution) as the displacing fluid and a viscoplastic fluid (i.e., Carbopol solution) as the displaced fluid. The characterization of our fluids was carried out using a rheometer.



Figure 1: Schematic of the Hexapod parallel robot.

*Corresponding author. Email: Seyed-Mohammad.Taghavi@gch.ulaval.ca

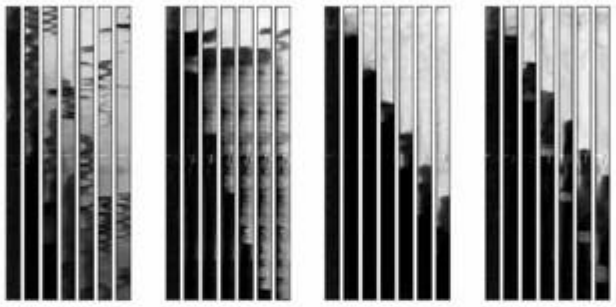

(a) (b) (c) (d)

Figure 2: Sequence of images showing the difference between the displacement flow in a stationary pipe and in a pipe in motion (with a frequency of 0.2 Hz over 15 degrees with respect to vertical). The field of view is 9.6×800 mm^2 right below the gate valve. In each subfigure, time grows from the left towards the right snapshot. (a) Stationary pipe flow: $V_0 = 8$ mm/s and $t = 0.25,\ 10,\ 20,\ 30\ ,40\ ,\ 50,\ 60$ s; (b) Flow in a pipe in motion at $V_0 = 8$ mm/s for $t = 0.25,\ 10,\ 20,\ 30\ ,40\ ,\ 50,\ 60$ s; (c) Stationary pipe flow: $V_0 = 41$ mm/s for $t = 0.25,\ 2,\ 4,\ 6\ ,8\ ,\ 10,\ 12$ s; (d) Flow in a pipe in motion at $V_0 = 41$ mm/s for $t = 0.25,\ 2,\ 4,\ 6\ ,8\ ,\ 10,\ 12$ s.

RESULTS & DISCUSSIONS

The experiments were performed at various density differences but for this paper we only present the results at a fixed density difference of 2%. The heavy fluid displaced the light fluid in a vertical pipe. The displaced fluid was a Carbopol solution as a viscoplastic fluid with $\tau_Y = 1.05$ Pa. Many experiments were performed at various imposed flow rates. To study the effect of the pipe motion on the displacement flow, the Hexapod simulator was used to impose an inverted pendulum like motion of 15 degrees (max amplitude with respect to the vertical position of pipe) at a small frequency of 0.2 Hz.

Fig. 2 shows examples of our results. Fig. 2(a) shows a sequence of images at a low imposed flow rate, i.e., $V_0 = 8$ mm/s ($Re \approx 76$), in a stationary pipe. As time grows, it can be seen that the heavy fluid displaces the light fluid downwards and there is not much mixing between the two fluids (although there are pieces of Carbopol moving upward). In fact the displacement process is efficient. As the displacement front moves further, the amount the displaced fluid left behind (called static residual wall layer) is not so significant. Fig. 2(b) shows that when the pipe is moving, there exists static residual wall layers and the displacement process is not as efficient as the case without motion. This observed behaviour might be due to the slumping effect (due to the density difference) that occurs in a moving pipe. At certain times when the pipe is inclined, the heavy displacing fluid slumps underneath the displaced fluid (for a moment) and it leaves behind a static residual layer of the displaced fluid. Fig. 2(c) and Fig. 2(d) show at a higher imposed flow rate, $V_0 = 41$ mm/s ($Re \approx 389.5$), the two displacements may have similar high efficiencies. In addition, visually, there is not a significant amount of static residual wall layers left behind in either case. For moving and stationary pipes, Fig. 3 shows the normalized average concentration (over the axial and the longitudinal directions) of the displacing fluid in the field of view shown in Fig. 2. As can be seen, the average concentration of the displacing fluid is similar at higher imposed velocities while at lower imposed velocities, the average concentration of the flow in a moving pipe is lower than that in a stationary pipe. We conclude that the displacement flow efficiency is a function of both the imposed flow rate and the motion of the geometry. At low imposed flows, the displacement flow in a moving pipe (in an inverted pendulum motion) may be be less efficient than that in a stationary pipe.

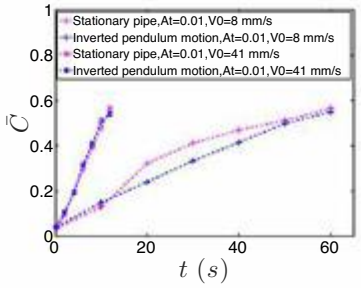

Figure 3: Average concentration against time for stationary and moving pipes.

References

[1] C. Gabard and J.-P. Hulin. Miscible displacements of non-Newtonian fluids in a vertical tube. *Eur. Phys. J. E*, 11:231–241, 2003.

[2] S.M. Taghavi, K. Alba, M. Moyers-Gonzalez, and I.A. Frigaard. Incomplete fluid-fluid displacement of yield stress fluids in near-horizontal pipes: experiments and theory. *J. non-Newt. Fluid Mech.*, 167-168:59–74, 2012.

[3] K. Alba, S.M. Taghavi, J.R. de Bruyn, and I.A. Frigaard. Incomplete fluid–fluid displacement of yield-stress fluids. part 2: Highly inclined pipes. *J. Non-Newt. Fluid Mech.*, 201:80–93, 2013.

DISPLACING YIELD STRESS FLUID BY NEWTONIAN FLUID IN A VERTICAL CIRCULAR CHANNEL

Jaewoo Jeon*[1], Ali Etrati†[1], Alondra Renteria[2], Reily Blackner[1], and Ian A. Frigaard[1,3]

[1]Department of Mechanical Engineering, University of British Columbia, Vancouver, British Columbia, Canada
[2]Departamento de Ingenieria Quimica, Universidad Nacional Autonoma de Mexico, Mexico
[3]Department of Mathematics, University of British Columbia, Vancouver, British Columbia, Canada

Summary We investigate the characteristics of displacement flow of a yield stress fluid by a Newtonian fluid. A neutralized solution of Carbopol, is placed at the bottom of a vertical pipe, displaced by pumping Newtonian fluid downwards from the top. During the displacement, 3 flow regimes are identified: central-type, slump-type and turbulent. Central-type displacements left non-uniform residual layer at the wall. Slump-type displacement normally have two fronts moving at different speeds, sometimes with Carbopol moving backwards against the imposed flow (when the Atwood number (At) is positive and the imposed velocity low). Turbulent mixing results in no discernible boundary between the displacing and displaced fluids, typically for $Re > 8000$. In some experiments with low velocity and negative At, the initial developing phase forms at the beginning of the experiment and a portion of initial phase stays until the end of the experiment without being displaced.

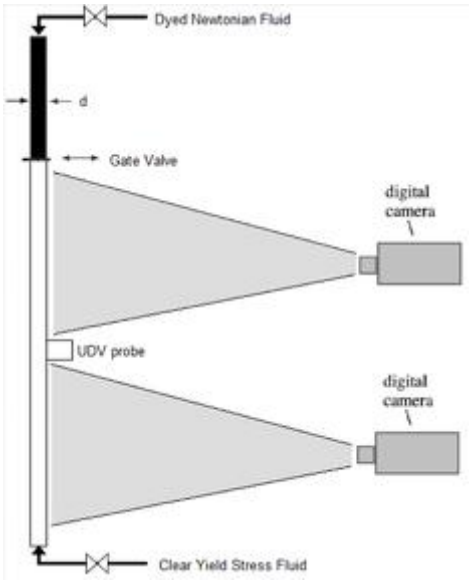

Figure 1: A schematic view of flow loop

INTRODUCTION AND SCOPE

In many industrial applications such as bio-medical, food processing, oilwell cementing and pipeline, it is required to remove a gel-like material from a duct. An oil industry application is chosen for this study where we consider the fluid to be removed is either a drilling mud or a pipe full of waxy crude oil, both with a yield stress. The yield stress is made at intermediate pH on neutralizing the Carbopol solution. Concentrations of Carbopol are chosen to give yield stresses of approximately 1, 5, 10 and 20Pa. Following [1,2], the experiment is performed in a 4m long, 19.05mm diameter acrylic pipe that stands vertically. Initially, the yield stress fluid (fluid 2) is filled in the bottom of the pipe up to a gate valve whereas Newtonian fluid (fluid 1) occupies the top section of the pipe. The gate valve is located at 80cm below the top end. The flow rate is controlled by imposed pressure and a flow control valve at the exit. It is measured by a magnetic flow meter, located at the inlet of the pipe, measures Newtonian fluid flowing into the pipe. An ultrasonic Doppler velocimeter (UDV) is mounted at the middle to measure the velocity through the central plane of the pipe; see Fig. 1.

The main experimental parameters are the fluid densities ($\hat{\rho}_k$), the mean imposed velocity ($\hat{V}_0$), the yield stress ($\hat{\tau}_y$) and other rheological parameters. The density difference is represented dimensionlessly by the Atwood number (At):

$$At = \frac{\hat{\rho}_1 \circ \hat{\rho}_2}{\hat{\rho}_1 + \hat{\rho}_2} \tag{1}$$

The flow is characterized by the Reynolds number (Re) and densimetric Froude number (Fr):

$$Re = \frac{\hat{\rho}_1 \hat{V}_0 \hat{D}}{\hat{\mu}_1}; \quad Fr = \frac{\hat{V}_0}{\sqrt{At\hat{g}\hat{D}}}, \tag{2}$$

with $\hat{\mu}_1$ the viscosity of the displacing fluid. The dimensionless number representing ratio of yield stress to viscous stress in the Bingham number. Here the viscous stress is imposed via the Newtonian fluid and hence we define:

$$B_N = \frac{\hat{\tau}_y \hat{D}}{\hat{\mu}_1 \hat{V}_0} \tag{3}$$

The range of the experiments is constrained to: $At = 0, \ \pm 0.0035, \ \pm 0.016$, $Re \in [200, 10000]$, $Fr \in [0, 20]$ and $B_N \in [90, 60000]$.

*Corresponding author. Email:jaewoo.jeon@alumni.ubc.ca
†Corresponding author. Email:etrati@alumni.ubc.ca

DISPLACEMENT

This work is to present results of an experimental study of buoyant miscible displacement flow of a yield stress fluid by Newtonian fluid in the geometry above. The main focus on this study is where the yield stress is significantly greater than a typical viscous stress in Newtonian fluid, $B_N \gg 1$. In some experiments where $\tau_y = 1$Pa and $At = -0.016$, the effect of buoyancy stress is significantly greater than τ_y. Flow regimes are identified into three different regimes: central-type, slump-type (including ripped, [2]) and turbulent displacements. In central displacements, static residual layers left behind after displacement are found to be non-uniform, showing long-wave variation along the pipe in the stream wise direction; see. Fig. 2. In slump-type displacement, we generally detect two propagating displacement fronts. A fast front propagates in a thin layer near to one wall. A slower second front follows and displaces a much thicker layer of the pipe but sometime stops altogether. The fast thin propagating flow is usually unsteady and flows through the yield stress fluid in an irregular fashion; see also [1,2].

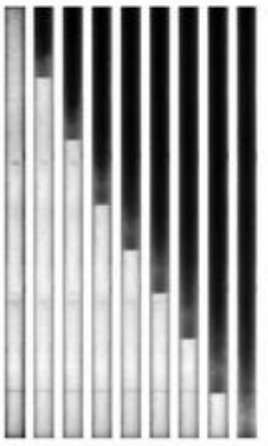

Figure 2: Central type
At=0.016, τ_y=6.91Pa, $\hat{}_0$=76.3mm/s



Figure 3: Backflow
At=0.016, τ_y=6.91Pa, V_0=2.3mm/s



Figure 4: Initial phase
At=-0.016, τ_y = 2.87 Pa, V_0=17.6 mm/s

Novel flow phenomena, compared to [1,2], are identified in slump-type displacements. Buoyancy-driven back-flow of Carbopol chunks rise upwards during displacement, in cases with high positive At and low $\hat{}_0$; see Fig. 3. Prominent Carbopol back flow occurs in the top half of the pipe rather than the bottom half. During the back-flow, Carbopol chunks generally becomes bullet-shaped and can flow upstream in a helical motion. Turbulent mixing occurs in some experiments with $Re > 8000$. In this regime, instead of a distinctive displacement front, there is no clear boundary between the displacing and displaced fluids and the length of the mixing area increases as the displacement progresses.

We also witnessed interesting flow development when negative At and low velocities coincide; see Fig. 4. The initial phase does not belong to any of the 3 flow regimes and occurs at the beginning of the displacement. The initial phase eventually grows to either the central or slump-type flow regime. In the initial phase, Carbopol displacement by Newtonian fluid is poor and it leaves a thicker non-uniform residual layer until it develops into central or slump type regimes. The portion of the initial phase in the pipe remains the same until the end of the displacement.

References

[1] Taghavi S.M., Alba K., Moyers-Gonzales M., Frigaard I.A.: Incomplete fluid-fluid displacement of yield stress fluids in near horizontal pipes: Experiment and theory. J. Non- Newtonian Fluid Mech 167-168(2012) 59-74.

[2] Alba K., Taghavi S.M., de Bruyn J., Frigaard I.A.: Incomplete fluid-fluid displacement of yield stress fluids. Part2: highly inclined pipes. J. Non-Newtonian Fluid Mech 201(2013) 80-93.

DARCY'S LAW & CRITICAL PRESSURE DROPS FOR YIELD STRESS FRACTURE FLOWS

Ali Roustaei*[1], Thibaud Chevalier[2], Laurent Talon[2], and Ian Frigaard[1,3]
[1]*Department of Mechanical Engineering, University of British Columbia, Vancouver, Canada*
[2]*Laboratoire FAST, Univ. Paris-Sud, CNRS, Universite Paris-Saclay, Orsay, France*
[3]*Department of Mathematics, University of British Columbia, Vancouver, Canada*

Summary Using numerical computation, we explore the validity of lubrication/Hele-Shaw approaches for 2D channel flows of a Bingham fluid: effectively Darcy's law. Wavy and linear profiles approximate a simple fracture and a shift between top/bottom walls adds tortuosity. The Darcy law estimate is valid as far as the geometry is *long* and *thin*, as expected. In other geometric ranges a major diversion occurs due to appearance of fouling layers, i.e. static fluid attached to the walls. Fouling gives an $O(1)$ modification to the aperture, resulting in $O(1)$ errors in Darcy law estimates. We show this can be improved. Second, we consider the critical pressure drop for the onset of flow, which is important in a variety of invasion/plugging and flow-back/cleaning applications. We study asymptotic behaviours and derive a simple toy model that gives good predictions for simple geometries. Illustrations are presented with more complex fractures.

INTRODUCTION

Cement injection for CO_2 storage reservoirs, flow of cement/drilling mud in thin annuli in primary cementing, repair of oil/gas wells in squeeze cementing, viscous frac fluids in hydraulic fracturing are some examples of industrial applications of yield stress fluid in fractures and irregular channels. Lubrication/Hele-Shaw approximations (Darcy's law) are widely used for Newtonian flows, so it is natural to develop the same yield stress fluids. Aside from standard "nonlinear filtration" modifications, the nature of yield stress fluids raises 3 additional issues. (i) It is known that naïve application of these approximations may result in significant errors in the stress fields. (ii) Fouling (static) layers can appear in uneven channels [2] which cause $O(1)$ changes in the aperture. (iii) Below a critical pressure drop these fluids are not expected to flow.

PROBLEM FORMULATION

We consider 2D Stokes flow of a Bingham fluid in 3 types of fractures: wavy, linear and affine fracture geometries. The Stokes equations are scaled with length scale $\hat{D}$, velocity scale $\hat{U}_0 = \hat{Q}/2\hat{D}$ ($\hat{Q}$ is the areal flow rate). A single dimensionless Bingham number B appears, which is the ratio of yield stress $\hat{\tau}_y$ to viscous stress $\hat{\mu}\hat{U}_0/\hat{D}$. Other dimensionless geometric parameters are $H,\ L,\ \psi$; see Fig. 1. Boundary conditions are no slip for top/bottom walls and periodicity on the left/right of the fracture. We have used the augmented Lagrangian method [1], implemented in the FreeFEM++ finite element environment. To improve solution accuracy, especially close to zero flow limit, we use five cycles of anisotropic mesh adaptation.

RESULTS

Lubrication approximation applicability

We have computed > 2000 flows over a wide range of (H, L, B, ψ). Assuming Poiseuille flow at each section of the fracture we find the corresponding pressure drop ΔP_L from lubrication approximation. This is compared with the 2D computed pressure drop along the fracture (ΔP_N), in Fig. 2a which shows the ratio $\Delta P_N/\Delta P_L$. Note that the 2D flow is expected to dissipate more energy than the pseudo-1D lubrication approximation, hence $\Delta P_N/\Delta P_L \geq 1$, but the 2 measures should coincide as the flow becomes progressively 1D. The main parameter affecting the prediction accuracy is H/L, as expected. For larger amplitudes H, fouling layers appear; see Fig. 3. These grow in size with B. The boundaries of the stagnant regions effectively define a new channel geometry (see red points in Fig. 3 at $B = 100$), which is *self-selected* by the flow. Self-selection also occurs in 1D duct flows [3]. Geometry and rheology are coupled by this novel non-Darcy effect. The pressure drop prediction may be improved by using the (unknown) fouled surface as the new geometry of the fracture (Fig. 2).

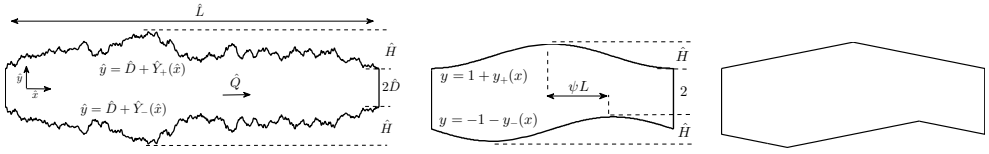

Figure 1: The fracture geometries used

*Corresponding author. Email: ali.rostai@gmail.com

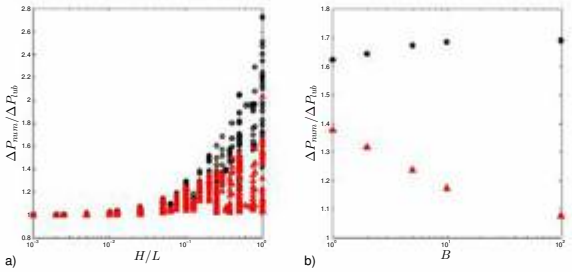

Figure 2: Plots of $\Delta P_N/\Delta P_L$: a) full range of geometries; b) $(H, L, \psi) = (2, 4, 0)$. Red marked points are from recomputing ΔP_L using the fouled yield surface as the wall.

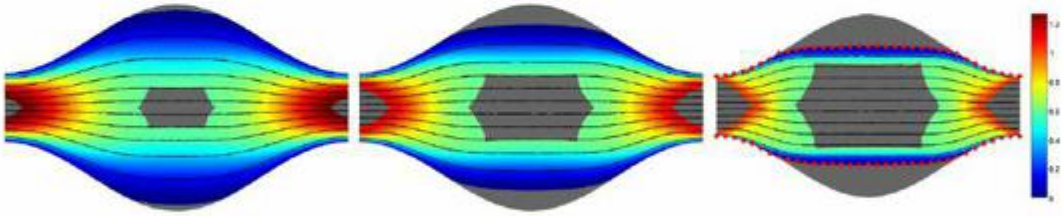

Figure 3: Speed & streamlines: $(H, L, \psi) = (2, 10, 0)$ and $B = 1, 5, 100$ (left to right); unyielded regions in gray. Self-selected channel marked by red points ($B = 100$).

Limit of zero flow

Due to the yield stress the pressure drop should exceed a minimum threshold ΔP_c to initiate flow. This limit (realised as $B \to \infty$) is studied by rescaling with the pressure drop $\Delta\hat{P}$, to give a problem dependent on the *Oldroyd* number: $Od = \hat{L}\hat{}_Y/(\hat{D}\Delta\hat{P})$. Using the mechanical energy balance of the flow, it can be shown that the critical Od_c for zero flow is:

$$Od_c = \sup_{\mathbf{v}*\in\mathcal{V},\mathbf{v}\ =0} \frac{Q(\mathbf{v}^*)}{j(\mathbf{v}^*)},\ Q(\mathbf{u}^*) \equiv \int_{-L/2}^{L/2}\int_{-1-y_-(x)}^{1+y_+(x)} u_1^*(x,y)\,dy\,dx,\ j(\mathbf{v}^*) \equiv \int_{-L/2}^{L/2}\int_{-1-y_-(x)}^{1+y_+(x)} \gamma(\mathbf{v}^*)\,dy\,dx \qquad (1)$$

Where $\mathcal{V}$ is the space of all velocity solutions. For $Od \geq Od_c$ ($\Delta P \leq \Delta P_c$) the fluid is stationary. By investigating velocity and stress fields of numerical solutions close to the zero flow limit, we can estimate the above supremum with simple algebraic expressions and hence predictions of Od_c over a wide range of parameters; see Fig. 4.

References

[1] R. Glowinski & P. le Tallec: Augmented Lagrangian and Operator-Splitting Methods in Nonlinear Mechanics, SIAM, (1989)

[2] A. Roustaei & I. Frigaard: The occurrence of fouling layers in the flow of a yield stress fluid along a wavy-walled channel, J. Non-Newt. Fluid Mech. 128 (2013), 109–124.

[3] P. Mosolov & V. Miasnikov: Variational methods in the theory of the fluidity of a viscous-plastic medium. J. Appl. Math. Mech. 29 (1965) 545–577.

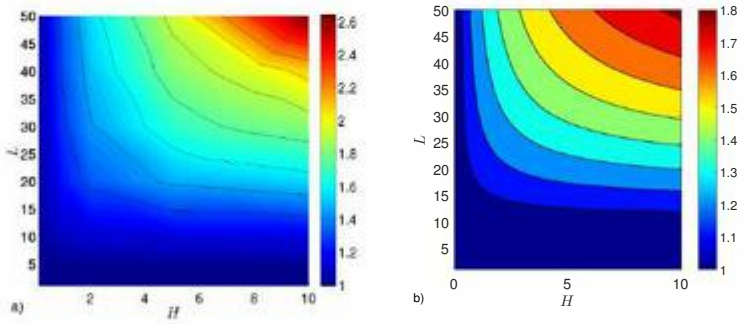

Figure 4: a) The Od_c values from numerical computation b) The Od_c estimated by the toy model

SLIP AND NO-SLIP OF CARBOPOL DROPLETS: A DIRECT EXPERIMENTAL OBSERVATION

Maziyar Jalaal*[1,2], Neil Balmforth[2,3], and Boris Stoeber[1,4]

[1]*Department of Mechanical Engineering, University of British Columbia, Vancouver, Canada.*
[2]*Institute of Applied Mathematics, University of British Columbia, Vancouver, Canada.*
[3]*Department of Mathematics, University of British Columbia, Vancouver, Canada.*
[4]*Department of Electrical and Computer Engineering, University of British Columbia, Vancouver, Canada.*

Summary The spreading of yield stress droplets extruded on glass surfaces is studied experimentally. We used a combination of shadowgraphy and swept-field confocal microscopy. The vertical profiles of the radial velocity were obtained, using Particle Image Velocimetry (PIV). On untreated glass surfaces, Carbopol droplets experience a significant amount of effective slip. However, on treated (through salinization) glass, where positive charges are permanently generated on the surface, PIV demonstrated a substantial reduction in slip.

INTRODUCTION

Spreading of yield stress materials occurs in several industrial applications such as painting, printing, and coating. Similar to many polymeric fluids, a large number of yield stress liquids undergo apparent slip in the vicinity of a smooth surface [1]. This often occurs due to the migration of the polymer particles away from a boundary, leaving a relatively dilute layer between the viscoplastic material and the wall. Direct observation of this lubrication layer (typically smaller than 1 μm) is challenging, however the macroscopic consequence of apparent slip can be perceived more easily (see e.g. [2] for the effect of slip on the rheology of Carbopol). In the current study, we explore experimentally the effect and control of wall slip for spreading droplets of Carbopol solutions as a prototypical yield stress fluid.

EXPERIMENTAL METHOD

Carbopol samples were made by preparing aqueous solutions of Carbopol Ultrez 21 (by Lubrizol) neutralized with triethanolamine. Carboxylated green (468-508nm) polystyrene fluorescent (PSF) particles of diameter of $3\pm0.1\mu$m were added to the samples and mixed gently to act as the flow tracers in our experiments. The pH of the final solutions was 6.25 ± 0.1. Material properties of the samples were measured using an Anton Paar (Physica MCR-30Z) rheometer and the yield stress values were obtained through the Herschel-Bulkley fits. The strongest and weakest solutions have yield stress of 0.14 Pa and 10.5 Pa, respectively.

The experimental setup for the droplet experiments is sketched in figure 1-a. Droplets of volume 0.1 mL were deposited onto glass slides at a rate of 2 mL/min, using a syringe pump connected to a stainless steel nozzle of inner and outer diameters of 0.15 and 0.31 mm, respectively, held 1.5 mm above the surface. Two different glass substrates were used: the first was a normal microscope glass slide. The second was a (3-aminopropyl) trimethoxysilane (APES) treated glass that had a positive surface charge.

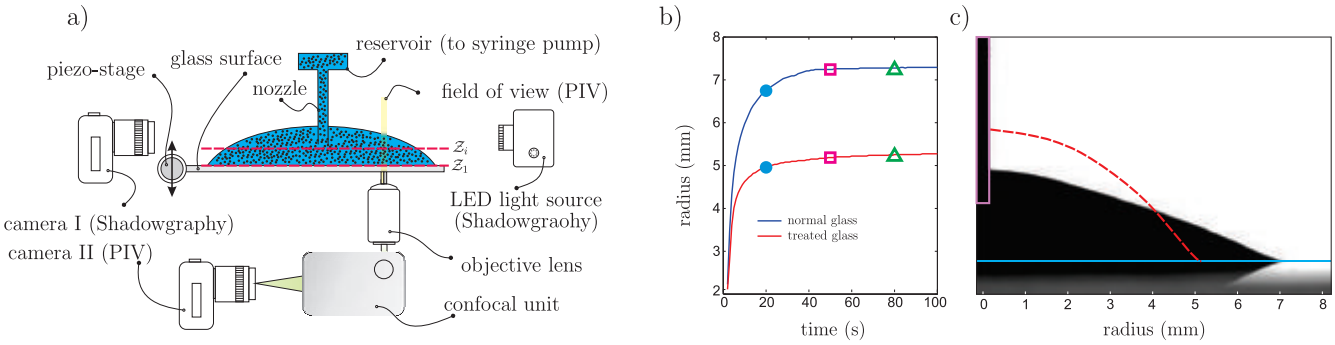

Figure 1: a) Sketch of the experimental setup. b) Droplet radius versus time for two different glass substrates. c) Shadowgraphy pictures of the final shapes, where the photograph shows the droplet on the untreated glass substrate and the red line shows the final shape on the treated glass substrate.

*Corresponding author. Email: mazi@alumni.ubc.ca

The side-view imaging was used for the shadowgraphy. The bottom view was used for swept-field confocal microscopy. A motorized piezo stage (Prior H101A ProScan) moved the glass slide vertically, enabling us to observe multiple horizontal planes. We focussed on the flow field very close to the substrate, scanning eleven planes with a vertical distance of 25 μm, starting at the surface of the glass slide and extending up to a total height of 250 μm. The images from microscopy were intensity-filtered to remove out-of-focus particles and then analysed using a cross-correlation PIV algorithm to obtain horizontal velocity fields. For the vertical profiles of the radial velocity, the magnitude of the instantaneous velocity field was averaged over the entire field of view for each of the horizontal planes.

RESULTS

Figure 1 (panels b and c) displays the side view results for the highest concentration Carbopol droplets spreading on the two glass surfaces. As can be seen from both the position of the contact radius (panel b) and the final shape of the droplets (panel c), the droplet spreads further over the untreated glass surface than the treated substrate. Figure 2 (panels a and b) displays vertical profiles of the radial velocity of the droplets at the three times indicated in Figure 1-b. Above the untreated glass surface (panel a), the wall slip is significant. By contrast, above the treated surface (panel b), no effective slip whatsoever could be detected to within the experimental precision.

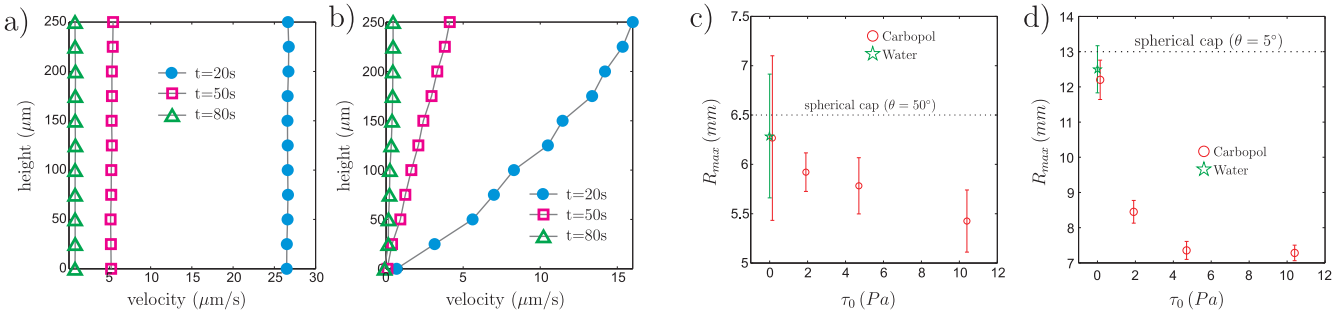

Figure 2: Vertical profiles of the radial velocity for the highest concentration Carbopol where droplet spreading over a) the untreated glass surface, and b) the treated glass surface. Maximum radius of the droplets over c) treated and d) untreated surfaces. The horizontal dashed lines show the predictions for a spherical cap with the contact angles of water.

A summary of final drop radii for the all concentrations is shown in Figure 2 (panels c and d). Over the treated surface, the droplets spread further when the Carbopol concentration is reduced, as would be expected for a reduction in the bulk yield stress without any significant change in surface tension and contact angle (see [3] for details). A similar trend is observed for the droplets over the untreated surfaces, where the slip rheology is expected to govern the spreading. For the lowest Carbopol concentration, the final droplet radii are similar to those measured for water. This agreement is not so surprising in view of the similarity of the observed contact angles. Indeed, the final radius is close to that predicted by assuming that the final shape is a spherical cap terminated at the contact angles of water.

CONCLUSIONS

We have provided evidence for apparent slip during the spreading of Carbopol drops, using a combination of shadowgraphy and confocal microscopy. It is known that glass surfaces obtain a negative surface charge in contact with aqueous solutions, mainly due to the dissociation of the terminal silanol groups. Therefore, a *repulsive* interaction between the Carbopol particles and the surface is expected, which results in an *apparent slip*. Wall slip however can be prevented if the glass is treated to feature positive surface charges. This substantiates the proposition that the lubrication layer can be breached with an *attractive* electrostatic interaction.

References

[1] Bonn D. et al.: Yield Stress Materials in Soft Condensed Matter arXiv:1502.05281, 2015.

[2] Roberts G.P., Barnes H.A.: New measurements of the flow-curves for Carbopol dispersions without slip artefacts Rheologica Acta, 40 2001.

[3] Jalaal M. et al.: Slip of Spreading Viscoplastic Droplets Langmuir, 31 2015.

PULSING THERMAL PLUMES IN YIELD STRESS FLUIDS

Ida Karimfazli *[1,2], Ian A. Frigaard[1,2], and Anthony Wachs[2,3]
[1]*Department of Mechanical Engineering, University of British Columbia, Vancouver, BC, Canada*
[2]*Department of Mathematics, University of British Columbia, Vancouver, BC, Canada*
[3] *IFP Energies nouvelles, Fluid Mechanics Department, Etablissement de Lyon, Solaize, France*

Summary We study flow development from a static background state in yield stress fluids, due to localized heating. The particular geometry of interest here is inspired by the experimental work of Davaille et al. [1]. Numerical and analytical techniques are used to explain the signature phenomena observed experimentally, namely delayed flow onset, cellular–like and plume–like flow development, and episodic development of multiple plumes.

BACKGROUND

When subject to shear stress, yield stress fluids (YSF) exhibit a finite resistance against motion. Once the *yield stress* is surpassed, the fluid starts to flow. Natural convection of YSF has been studied in a limited number of settings. Zhang et al. [2] showed that a layer of motionless YSF heated uniformly from below is linearly stable at all heating rates and that kinetic energy of small disturbances decays to zero in a finite time.

Recent experimental studies of Davaille et al. [1] revealed some peculiar features of naturally convecting flows of YSF at high Prandtl, Pr. They investigated the development of natural convection in a rectangular tank filled with otherwise static YSF. Localized heating was imposed on the bottom wall of the tank. Intuitively, when the yield limit is sufficiently high, fluid motion never starts. However, for smaller yield limits, there exists a measurable delay between the onset of heating and when motion starts. At lower heating rates, the motion is localized around the heater and develops smoothly. At higher heating rates however, multiple thermal plume heads may form close to the heater which then advect towards the top wall, episodically. We have studied a model problem to investigate the effect of the yield stress on the hydrodynamic features of the flow. A 2D square cavity filled with YSF is considered, as illustrated in Fig. 1. The fluid is initially at the reference (cold) temperature.

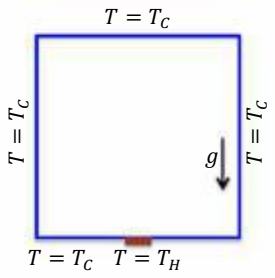

Figure 1: Model problem

MOTION ONSET

Initially, when the fluid is cold everywhere, there is no buoyancy stress in the domain. As the temperature field develops conductively, buoyancy stresses dominate the yield stress and promote fluid motion. The flow onset time, t_s, thus increases with Bingham number, B, which characterizes the ratio of buoyancy and yield stresses. This also indicates that t_s is independent of Rayleigh, Ra, and Pr numbers. Numerical and analytical estimates of t_s are illustrated in Fig. 2a. Analytical estimates of t_s are developed using asymptotic methods and assuming that at t_s yielded regions consist of a network of thin layers of slow–moving fluid (shown schematically in Fig. 2b). As B approaches the motionless limit, B_{cr}, the motion onset time approaches infinity. Our numerical and analytical estimates of the critical limit agree well and yield $B_{cr} \approx 0.003$.

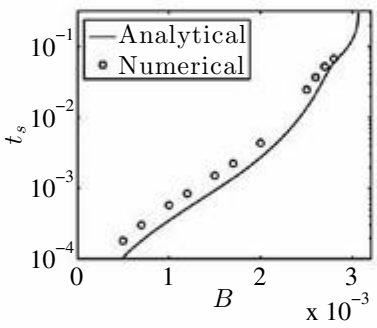

(a)

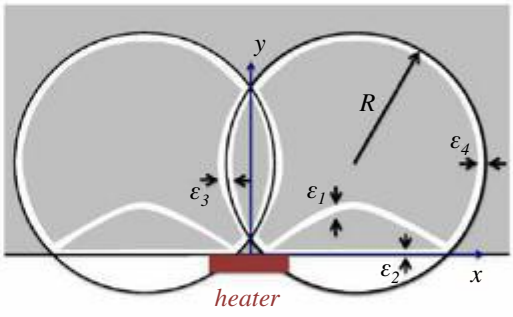

(b)

Figure 2: a) Variation of motion onset time, t_s, with Bingham number, B. b) Illustration of yieldded and unyielded zones just after t_s. The gray area represents the unyielded regions. The thin white layers are the yielded regions.

*Corresponding author. Email: idak@math.ubc.ca

PLUME DEVELOPMENT

Once motion starts, flow accelerates and advective heat transfer improves until a balance between thermal and effective viscous stresses is reached. When advection is sufficiently strong, the fluid around the heater becomes very buoyant and floats upwards. This *plume head* then advects towards the top wall, initially accelerating as it penetrates colder layers of fluid away from the heater. Ultimately it decelerates as it loses thermal energy and approaches the top wall. Figure 3 illustrates the development of the temperature field during the first two pulses at $Ra = 10^7, B = 0.0025, Pr = 10^4$.

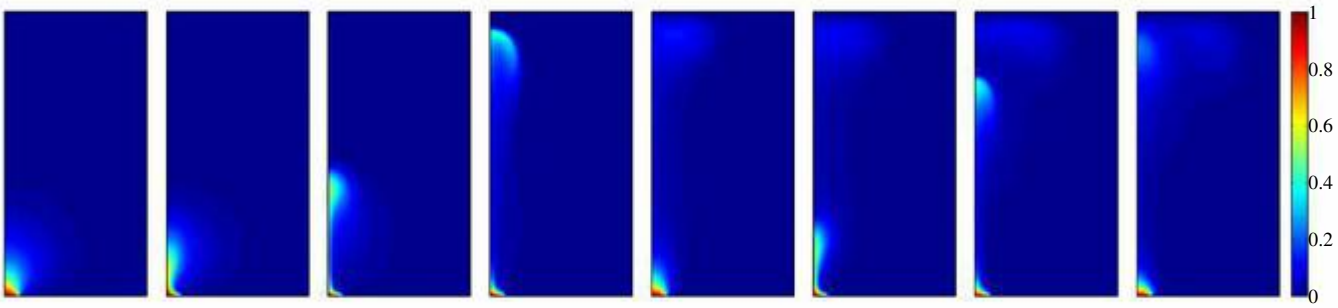

(a) $t = 0.0257$ (b) $t = 0.0259$ (c) $t = 0.0260$ (d) $t = 0.0262$ (e) $t = 0.0280$ (f) $t = 0.0287$ (g) $t = 0.0290$ (h) $t = 0.0297$

Figure 3: Development of temperature field at $Ra = 10^7, B = 0.0025, Pr = 10^4$ (half of the domain is omitted due to the symmetry with respect to the center–line).

This process is manifest in the temporal development of the kinetic energy of the domain; each plume head corresponds to a pulse–like feature. Multiple pulses can be observed depending on Ra and B. As Ra increases pulses become more pronounced and more numerous. B however plays a multifaceted role in the development of plume heads. The interplay of competing effects means that initially increasing B from zero results in formation and enhancement of plumes. However, ultimately as B gets close to the critical limit, advection becomes very weak and plume heads disappear.

CONCLUSIONS

The key qualitative observations made by Davaille et al. [1] are explained and the role of the yield stress is clarified. In particular, we have used numerical and analytical techniques to illustrate the possibility of development of motion in YSF from an initially static state regardless of the nature of disturbances in the domain. We have also illustrated that the static state is nevertheless linearly stable and may only be destabilized at sufficiently high Ra by imposing disturbances of a finite size.

Parallels to the two main flow development trends observed experimentally are identified and the role of dimensionless groups is explored. When $B < B_{cr}$, the temperature develops conductively until buoyancy stresses are sufficiently large to dominate the yield stress. The motion onset time, t_s, is therefore independent of Ra and Pr. After t_s flow development trends depend strongly on Ra. At low Ra, flow develops smoothly around the heater. At high Ra thermal plumes form and develop episodically.

References

[1] A. Davaille, B. Gueslin, A. Massmeyer, and E. Di Giuseppe. Thermal instabilities in a yield stress fluid: Existence and morphology. *J. Non-Newton Fluid*, 193:144–153, 2013.

[2] J. Zhang, D. Vola, and I. A. Frigaard. Yield stress effects on Rayleigh-Bénard convection. *J. Fluid Mech.*, 566:389–419, 2006.

START-UP OF SHEAR FLOW OF 2D PARTICLE SUSPENSIONS IN VISCOELASTIC FLUIDS

Patrick Anderson *[1], Martien Hulsen[1], and Nick Jaensson[1]
[1]*Department of Mechanical Engineering, Polymer Technology,, Eindhoven University of Technology,The Netherlands*

Summary We present simulations of the start-up of shear flow of 2D suspensions of rigid particles in viscoelastic fluids by applying a novel numerical method is applied that makes use of biperiodic domains. At Weissenberg numbers of 1 and higher, particle chaining is observed that leads to a decrease in bulk viscosity, an effect that was observed experimentally. Increasing the solid area fraction leads to the particle alignment occuring faster and the particles forming longer chains, causing a stronger decrease in bulk viscosity. In addition, at solid area fractions of 0.3 and higher, an increase of the bulk first normal stress difference is observed, which may be attributed to an increase in local shear rate in between the particle chains.

BIPERIODIC DOMAINS NUNDER SHEAR

Particle suspensions play an important role in science, nature and technology with many everyday examples such as food, pharmaceuticals, biological fluids, paint, etc. Consequently, the rheological behavior of suspensions has been subject to an increasing amount of research during recent decades. The use of boundary-fitted meshes allows for a high resolution in places where particle boundaries are in close proximity, while keeping the resolution lower in areas where gradients are low. We will use the model to study the influence of the elasticity of the suspending fluid and the particle concentration on the rheology of the suspension.

In this work we consider a suspension of rigid, non-Brownian, circular particles with a solid area fraction denoted by ϕ. The suspension is subject to a macroscopic shear field $\dot{\gamma}$, as is shown in Fig. 1. If the macroscopic length scale of the flow is large compared to the microscopic length scale (i.e. the inter particle distance), the suspension can be regarded as a homogeneous fluid with a linear velocity profile. However, the presence of the particles will cause a local disturbance of the linear velocity profile, which will be simulated by considering a biperiodic domain with length L and height H, as is shown in Fig. 1. The velocity in the biperiodic domain is given by $\boldsymbol{u}(x, y, t) = (u_x(x, y, t), u_y(x, y, t))$, which can be decomposed in a biperiodic part and a part from the macroscopic shear field: $\boldsymbol{u}(x, y, t) = \hat{\boldsymbol{u}}(x, y, t) + (\dot{\gamma}y, 0)$, where the vertical coordinate y is defined in Fig. 1. Since $\hat{u}_x(x, H, t) = \hat{u}_x(x, 0, t)$, there is a difference in u_x of $\dot{\gamma}H$ between the top and bottom of the biperiodic box.

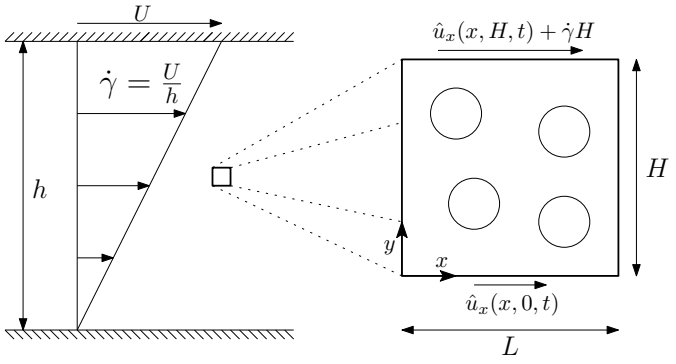

Fig. 1: A macroscopic shear field (left) and the biperiodic domain (right).

If there is a variable convected with the flow, the boundary conditions as shown in Fig. 1. By applying a novel numerical tool using the finite element method on moving, boundary fitted, biperiodic domains, we study the bulk behavior of particle suspensions in viscoelastic fluids.

*Corresponding author. Email:p.d.anderson@tue.nl

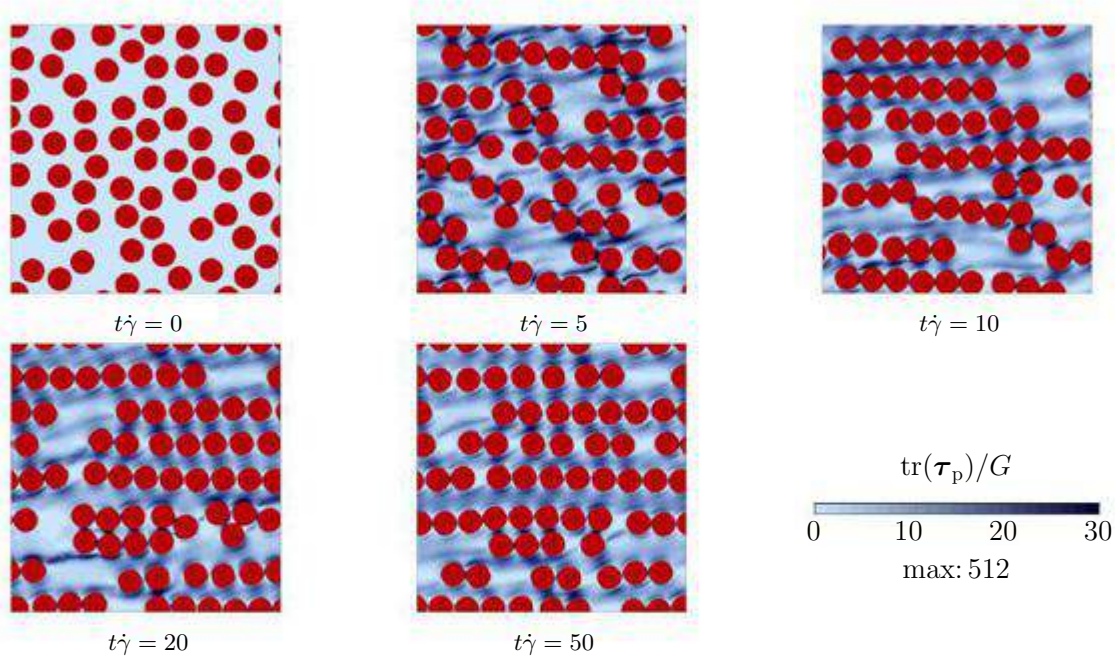

Fig. 2: Evolution of the polymer stress for $\mathrm{Wi} = 1$ *and* $\phi = 0.4$.

The evolution of the trace of the polymer stress is shown in Fig. 2 for a single realization with $\mathrm{Wi} = 1$ and $\phi = 0.4$. It results that the higher solid area fraction causes particle to align faster, with some string formation already visible at $t\gamma = 5$. Particle chains are observed of approximately the same length as the domain, possibly indicating that the finite box size is limiting the length of the chains. See Fig 3 for the relative viscosity and relative first normal stress coefficient.

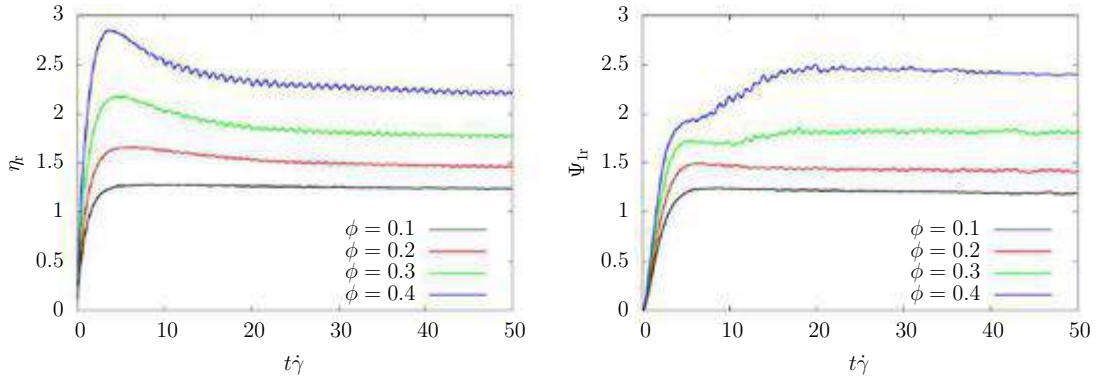

Fig. 3: The relative viscosity is shown left and relative first normal stress coefficient on the right.

CONCLUSIONS

For Weissenberg numbers ≥ 1 and solid area fractions ≥ 0.2, particle alignment plays a large role in the stress response of the suspension. A bulk viscosity that decreases with time is observed which may be related to the formation of particle strings in the fluid, an effect that was observed experimentally. The speed at which alignment takes place and the length of the particle strings depend for a large degree on ϕ: there is less fluid for the particles to move freely and hydrodynamic interactions push particles into string like formations. More details are available in Jaensson et al., Journal of Non-Newtonian Fluid Mechanics, 225, 70-85 (2015).

INERTIAL SUSPENSION FLOWS IN BIFURCATING CHANNELS: EXPERIMENTS AND MODELLING

Omer Sedes[1], Sojwal Manoorkar[1], and Jeffrey F. Morris[1]
[1]*Benjamin Levich Institute and Department of Chemical Engineering, The City College of New York, New York, NY 10031, USA.*

Summary Experiments of non-colloidal suspensions with finite inertia at both the particle and the bulk scale were performed in bifurcating channels focusing on the T-geometry to provide a benchmark for general suspension flows. Single-phase effective viscosity analyses fail to capture even the macroscopic characteristics of the flow. The non-Newtonian and multi-phase nature of this flow were examined using discrete particle Lattice-Boltzmann simulations and the continuum suspension-balance model and these provide a more accurate description and understanding of the experiments.

In recent years, there were significant developments in the understanding of the rheology of non-colloidal suspensions at finite inertia [1, 2, 3]. However extending this knowledge to non-viscometric flows and to suspension flows in general geometries remains a challenge [4]. In this work, we focus on the pressure-driven flow of inertial suspensions in straight channels and bifurcating asymmetric T-channels. These are geometries found in nature and industrial applications, and thus provide an important benchmark to examine the non-Newtonian and multi-phase behavior of inertial suspensions.

EXPERIMENTS

In the T-channels, we conducted experiments at bulk Reynolds numbers of $50 < Re < 900$ and covering particle volume fractions of $0.05 < \phi < 0.40$ at the inlet. The channel geometries consisted of an inlet branch of square cross section 2.4 mm wide and 128 mm long bifurcating into two daughter branches, one parallel and the other perpendicular to the inlet branch. In the two types of channel geometries considered, the parallel daughter branch dimensions were the same as the inlet, while the width of the perpendicular branch was either the same or one third of the inlet branch. Both channel outlets were open to the ambient air ($P_{out} = 1$ atm). We used neutrally buoyant suspensions of polystyrene particles ($d \approx 250$ μm) in 17% by volume of glycerol in water. The average flow rates and particle concentrations at each outlet were measured, and high speed camera images were captured to characterize the details of the flow at the bifurcation region during the experiments.

The results of these experiments demonstrate major macroscopic differences when compared with Newtonian fluid behavior, and provide a basis for comparison with modeling. Specifically, we observed highly non-trivial dependences of the suspension distribution among the daughter branches and of the particle concentrations at the branch outlets on Re and ϕ. The variation of the ratio of the straight branch flow rates to the inlet branch flow rates for the bulk suspension and the particle phase ($\beta_{\text{suspension}}$ and β_{particle}) at different inlet conditions show drastic differences compared to a simple Newtonian fluid. The detailed flow structure near the junction such as the size of the flow separation regions and particle concentrations inside these zones also demonstrated features that cannot be predicted by a single-phase flow description with an effective viscosity.

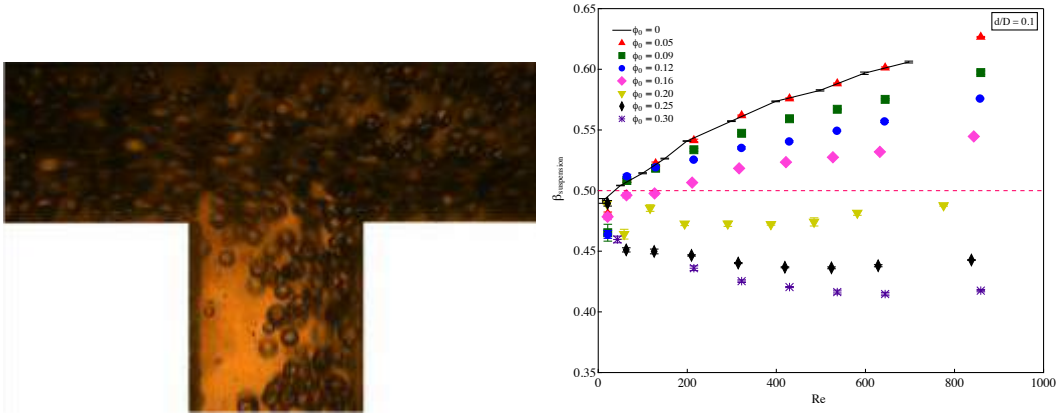

Figure 1: Image of the bifurcation region at $Re = 400$ and $\phi = 0.16$ (left). Experimental results for suspension splits at various Re and ϕ (right).

MODELLING

For particle loadings up to $\phi = 0.12$, Lattice-Boltzmann simulations of a pressure driven suspension flow in a square channel at the experimental Re range were performed to compute particle positions at the channel cross section near the T-junction. The dimensions of the periodic simulation box and the particle size in lattice units were chosen to match the experimental particle channel width to particle diameter ratio ($\alpha = d/W$). The simulations were conducted long enough for the suspension to travel a distance equivalent to the experimental inlet branch length. The results of these calculations demonstrate the transformation of cross-sectional particle positions from a ring structure to an almost uniform distribution of particles to a structure with more particles migrating to the core of the tube at high enough Re, as described in [5].

In addition, finite element method calculations of the Newtonian fluids were performed using Comsol Multiphysics in the experimental geometry. These calculations reveal the details of the highly three dimensional base flow and are used for calculating the complex evolution of the stream-surface partitioning the inlet flow into each branch with increasing Re.

The cross-sectional particle positions from LB calculations were superimposed with the streamlines entering into each branch obtained from FEM calculations for a Newtonian fluid. By assuming that the particles whose centers lie on the streamtube entering to a particular branch enters the corresponding branch we obtain a reasonably accurate estimate of the particle split among the branches ($\beta_{\mathrm{particle}}$). The interaction of the particle migration profiles with the streamlines provide the explanation of the experimentally observed cross-over from the particles preference of the side branch at low Re to the preference of straight branch at high Re.

For higher inlet particle concentrations, we present the predictions of the continuum suspension-balance model [6] extended to include inertial effects in a T-channel. We consider the influence of bulk level inertia, modeled through the inclusion of inertial terms to suspension momentum equations, along with the influence of the particle-scale inertia, modeled through rheological stress terms.

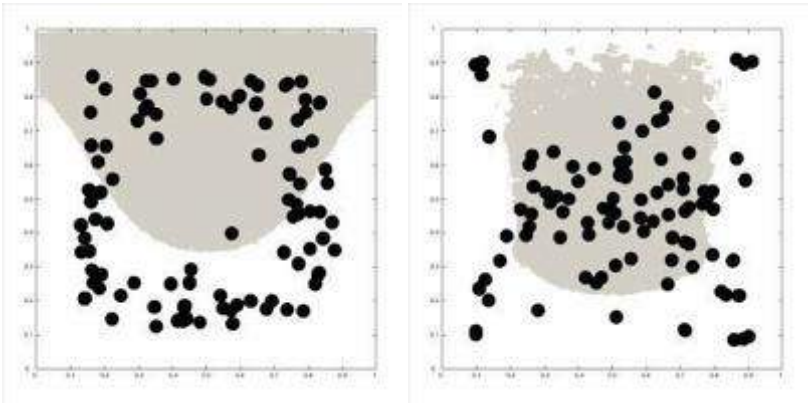

Figure 2: Combination of particle positions and streamline regions at the junction for $\phi = 0.05$ at $Re = 46$ (left) $Re = 525$ (right). Shaded regions indicate the regions corresponding to the straight branch; the side branch goes down the page.

CONCLUSIONS

The experiments of non-colloidal suspensions in T-channels reveal macroscopic and detailed flow behavior not explicable by a simple effective viscosity approach. Consideration of the particulate nature of the flow in simulations reveal the dominant influence of the upstream particle migration on the particle concentration in the daughter branches.

References

[1] Haddadi H, and Morris J.F.: Microstructure and rheology of finite inertia neutrally buoyant suspensions. J. Fluid Mech 749:431-459, (2014).

[2] Yeo K, and Maxey M.R.: Dynamics and rheology of concentrated, finite-Reynolds-number suspensions in a homogeneous shear flow. Physics of Fluids 25(5):053303, (2013).

[3] Kulkarni P.M., and Morris J.F.: Suspension properties at finite Reynolds number from simulated shear flow. Physics of Fluids 20(4):040602, (2008).

[4] Haddadi H., Shojaei-Zadeh S., Connington K., and Morris J.F.. Suspension flow past a cylinder: particle interactions with recirculating wakes. J. Fluid Mech 760:R2 (2014).

[5] Miura, K, Itano T., and Sugihara-Seki, M. Inertial migration of neutrally buoyant spheres in a pressure-driven flow through square channels. J. Fluid Mech 749: 320-330 (2014).

[6] Mirbod, P. Two-dimensional computational fluid dynamical investigation of particle migration in rotating eccentric cylinders using suspension balance model. Int J Multiphase Flow 80:79-88 (2015).

NUMERICAL MODELLING OF CELLULOSE MICRO/NANOFIBRIL SUSPENSIONS

Deepak Kunhappan[1,2,3,4], Pierre Dumont *[45], Barthélémy Harthong[1,2], Guillame Balarac[3,4], and Bruno Chareyre[1,2]

[1]*Univ. Grenoble Alpes, 3SR-Lab, F-38000 Grenoble, France*
[2]*CNRS, 3SR-Lab, F-3800 Grenoble, France*
[3]*Univ. Grenoble Alpes, LEGI-F38000 Grenoble, France*
[4]*CNRS, LEGI, F-38000 Grenoble, France*
[45]*Université de Lyon, INSA-Lyon, LaMCoS CNRS UMR5259,F-69621 Villeurbanne cedex, France*

Summary A numerical tool for the simulation of Nano/Micro Cellulose fibre suspensions is developed by means of coupling of a Computational Fluid Dynamics code and a Discrete Element code. The 3D Navier-Stokes equations are solved by a finite volume scheme, and the fibres are discretised into a chain of beam elements. Momentum exchange between the two phases are enforced by a two-way coupling. Compared to the conventional "prolate-spheroid" approximation [11] [12], we implement a hydrodynamic force model based on the drag of an infinite cylinder, as such a description of the hydrodynamic force tends to be free from the discretisation of the fibre. In the future work, it is planned to use the developed model for the simulation of dilute and dense NFC suspensions.

INTRODUCTION

Cellulose microfibrils exhibit strong mechanical properties ($E \sim 80Gpa$) and ultimate tensile stress around 1 GPa, making them attractive for applications in nano-fibrous based composites such as nano-films or packaging materials [1]. However the manipulation of these fibrous structures encounter obstacles in particular, at the process scale where their behaviour as suspensions are insufficiently understood, as they exhibit complex flow features such as shear banding, wall slippage and plug flow behaviour as described by Martoïa et al [1]. The objective of the present study is to develop a numerical model for the study of the complex rheology of N/MFC suspensions. Furthermore we review the applicability of the force models arising from the slender body theory and prolate-spheroid models for high aspect ratio fibres ($r_p \sim 100$) and propose an alternative model for the hydrodynamic force on the fibre segments based on the drag of an infinite cylinder derived by Tomotika et al [2] and Taylor [3].

METHODOLOGY

The methodology involved in the project is to couple a Finite Volume Method fluid flow solver (FVM) YALES2 [4] with a Discrete Element Method code (DEM) YADE [5]. In a nutshell YALES-2 accounts for the fluid flow physics and YADE accounts for the mechanical behaviour of the fibres. The codes are coupled with with in the Multiple Instruction Multiple Data (MIMD) framework of Message Passing Interface (MPI- 2), currently one-way coupling and two-way coupling methodologies are implemented. The one-way coupling deals with fluid $\Rightarrow$ fibre interactions and the two-way coupling adds fibre$\Leftrightarrow$fluid interactions.

A fibre is discretised into several beam segments with each segment having a local frame of reference fixed to its symmetric axis. Force and torque are applied to each of these segments. The cylindrical elements are modelled as discrete beams that respond elastically to normal, shear bending and twisting loads, the details are well explained in [6], [7]. For solving the three dimensional incompressible Navier-Stokes equations, a finite volume scheme with 4th order accuracy in space and time have been used as described in [4].

RESULTS

Comparison with Tritton's experiment

Tritton [8] performed experiments on the flow past a cylinder at various Reynolds numbers based on the fibre diameter ranging from 0.387 to 100. The experimental setup consisted of a high aspect ratio quartz fibres cemented at one end and the other free to move. A uniform flow was then imposed on the fibre. Based on the linear-beam theory, a beam in such a configuration (cantilever beam with uniform loading) would undergo a small deflection at the ends, ($l/h > 30$, l is the length of the beam, h the deflection).

In order to verify the drag force and the coupling of the methods, we repeat the experiments of Tritton [8] numerically with the prolate-spheroid model[10], Kaplun's expression [9] and Tomotika et al's expression, for the drag force on an infinite

*Corresponding author. Email: pierre.dumont@insa-lyon.fr

cylinder at low Reynolds number [2] and obtain the deflection of the fibre as shown in figure 1. From the figure it is observed that the prolate-spheroid model [10] tends to under-predict the deflection and the drag force, moreover on further examination of the prolate-spheroid model it was seen that the model is not independent of the fibre discretisation i.e, the net drag force on the fibre depends on the number of segments and this effect is more pronounced for higher aspect ratios.

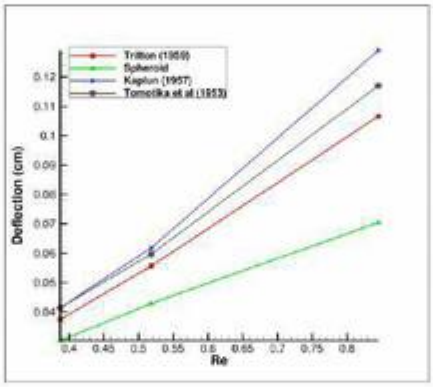

Figure 1: Comparison of Deflection with Tritton's experiments fibre-1 [8]

CONCLUSIONS

A numerical model for the simulation of flexible fibre suspensions has been developed and is currently under validation. The numerical tool dveloped would offer new insights on understanding the complex flow behaviour of N/MFC suspensions. An example of such a simulation of dense NFC suspension is shown in figure 2.

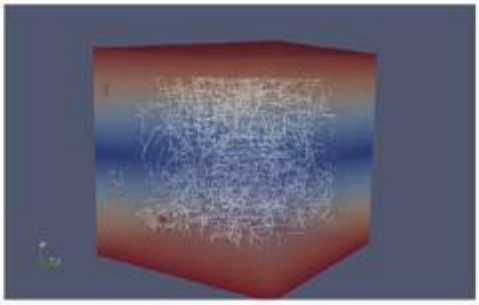

Figure 2: Suspension of N/MFc fibres

References

[1] Martoïa.F, et al.: Heterogeneous flow kinematics of cellulose nanofibril suspensions under shear. Soft matter 2015.

[2] Tomotika. S, et al.: On the forces acting on a circular cylinder set obliquely in a uniform stream at low values of Reynolds number. Proceedings of the Royal Society of London A: Mathematical, Physical and Engineering Sciences. Vol. 219. No. 1137. The Royal Society, 1953.

[3] Taylor, G.: Analysis of the swimming of long and narrow animals. Proceedings of the Royal Society of London A: Mathematical, Physical and Engineering Sciences Vol. 214, No. 1117. The Royal Society, 1952

[4] Moureau. V, et.al.: Design of a massively parallel CFD code for complex geometries. Comptes Rendus Mecanique 339.2, 2011

[5] Smilauer V. et al.: Yade Documentation 2nd ed. The Yade Project. http://yade-dem.org/doc/ 2015

[6] Bourrier, F. et al.: Discrete modeling of granular soils reinforcement by plant roots. Ecological Engineering 61, 2013

[7] Effeindzourou, A. et al.: Modelling of deformable structures in the general framework of the discrete element method. Geotextiles and Geomembranes 44.2, 2016

[8] Tritton, D.J.: Experiments on the flow past a circular cylinder at low Reynolds numbers. Journal of Fluid Mechanics 6.04 ,1959

[9] Kaplun S., Lagerström P.A.: Asymptotic expansions of Navier-Stokes solution for small Reynolds numbers. Journal of Mathematics and Mechanics, 6, 1957

[10] Sangtae K. and Karrila. S.J.: Microhydrodynamics: principles and selected applications. Courier Corporation, 2013.

[11] Lindström S.B, and Uesaka.T.: Simulation of the motion of flexible fibers in viscous fluid flow. Physics of Fluids. 19.11, 2007

[12] Schmid. C.F, et al.: Simulations of fiber flocculation: Effects of fiber properties and interfiber friction. Journal of Rheology. 44.4, 2000

MEMBRANE DYNAMICS IN ANISOTROPIC MEDIA

Arthur A. Evans *[1], Michael D. Graham[2], and Saverio E. Spagnolie[1]
[1]*Department of Mathematics, University of Wisconsin, Madison*
[2]*Department of Chemical and Biological Engineering, University of Wisconsin, Madison*

Summary Morphology and dynamics of soft structures depends on interactions with their environment. In the presence of anisotropic media, such as orthotropic gels or nematic liquid crystals, fluid anisotropy induces topological defects and long-range interactions between immersed particles. Understanding how anisotropic fluids deform particles and induce interactions over long distances is a theoretically and numerically challenging problem with applications to biological materials and soft device fabrication. In this paper we develop an immersed boundary method that efficiently simulates highly deformable particles in flowing liquid crystals.

INTRODUCTION

Microorganisms and biological materials inhabit highly viscous environments, and the overall behavior of soft cells and their molecular constituents depends sensitively on their interactions with the fluid in which they are immersed [1]. While many of these environments are purely viscous Newtonian fluids, a variety of biologically and technologically relevant phenomena occur between objects immersed in anisotropic fluids. Mucus and biofilms exhibit stress anisotropy (deformation direction dependence), which may have important implications for biological function. For instance, bacterial cells have been observed to swim along the preferred directions of fluid deformation in anisotropic environments [2, 3], which may be linked to urinary tract infections [4]. Moreover, the complicated cytoskeletal network of eukaryotes and even the transmembrane protein structure in lipid-based membranes exhibit orientational order that allows for these complex heterogeneous materials to be modeled as anisotropic fluids.

In this paper we consider the theoretical description of deformable bodies in a canonical class of anisotropic fluid, a nematic liquid crystal, a state of matter which exhibits orientational order but no positional order. Despite the myriad theoretical and experimental advances in studying nematic liquids crystals (NLCs), relatively little has been done to study dynamically evolving fluid-structure interactions in the presence of soft immersed boundaries. We develop an immersed boundary method that efficiently handles both the simpler Ericksen-Leslie model of NLCs and a more sophisticated Stark-Lubensky "**Q**-tensor" model [5]. Using semi-implicit time-stepping we construct a general framework that can be used to numerically study biologically relevant membrane dynamics, as well as various industrial applications associated with liquid crystal flow and device fabrication.

IMMERSED BOUNDARIES IN NEMATIC LIQUID CRYSTALS

For both the Ericksen-Leslie and Stark-Lubensky models of flowing liquids crystals, we examine the zero Reynolds number limit and solve a system of coupled equations for the fluid velocity and either the nematic director $\mathbf{n}$ (Fig. 1a) or the tensor order parameter $\mathbf{Q}$, respectively. Similar to the Landau-de Gennes model of liquid crystals, in the Stark-Lubensky model the orientational order of the fluid is represented by a second-rank order tensor $\mathbf{Q}$, which in a uniaxial system reduces to $\mathbf{Q} = S(\mathbf{nn} - \mathbf{I}/d)$, where S is a scalar order parameter, d is the dimension of the space, and $\mathbf{I}$ is the identity operator. The general Landau-de Gennes energy functional takes the form

$$\mathcal{F}(\mathbf{Q}, \nabla\mathbf{Q}) = \int_\Omega \left\{ -\frac{a}{2}\mathrm{Tr}(\mathbf{Q}^2) - \frac{b}{3}\mathrm{Tr}(\mathbf{Q}^3) + \frac{c}{4}\mathrm{Tr}(\mathbf{Q}^4) \right\} + \frac{1}{2}\left\{ L_1|\nabla\mathbf{Q}|^2 + L_2 Q_{ij,j}Q_{ik,k} + L_3 Q_{ij,k}Q_{ik,j} + L_4 Q_{ij}Q_{k\ell,i}Q_{k\ell,j} \right\} dV, \quad (1)$$

where the first bracketed term is the bulk energy, the second is the elastic energy, and the constants are material- and temperature-dependent. As in the Ericksen-Leslie model, variations of $\mathbf{Q}$ generate an added elastic stress and introduce anisotropy into the viscous stress, while itself satisfying a separate evolution equation [6]. The Stark-Lubensky formulation provides a coupled system of equations for the fluid velocity $\mathbf{v}$ and the order parameter tensor $\mathbf{Q}$ via this associated stress.

To efficiently compute the dynamics of deformable membranes in nematic liquid crystals we implement a spectral immersed boundary method with semi-implicit time stepping. In the immersed boundary formulation, the fluid equations are solved on a fixed rectangular (Eulerian) grid. The immersed boundary, however, is discretized according to Lagrangian points that do not conform to the background Eulerian mesh (Fig. 1b). In the present context, the immersed structure communicates forces onto the fluid as in Peskin's original method [7], but also communicates torques on the nematic director field through molecular anchoring boundary conditions. The immersed structure is modeled as a series of Lagrangian grid points that evolve

*Corresponding author. Email: aevans@math.wisc.edu

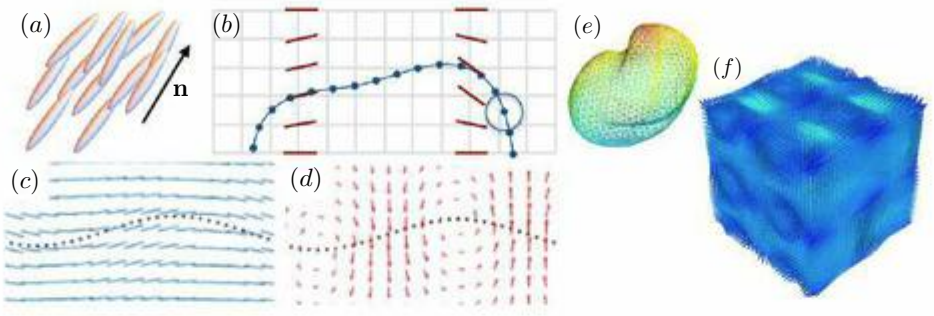

Figure 1: (a) The nematic director of a liquid crystal is written as a vector **n**. (b) Schematic of the immersed boundary formulation: the fluid equations are solved on a fixed rectangular (Eulerian) grid. The immersed boundary, however, is discretized according to Lagrangian points that do not conform to the background Eulerian mesh. [7] (c) Nematic director field for a "swimming sheet" with planar anchoring conditions immersed in a NLC, and (d) the corresponding velocity field. (e) Under imposed flow and weak anchoring conditions in a nematic LC, the membrane undergoes large amplitude deformations. (f) The director field (with scalar order parameter overlaid with color-code) for the simulation involving a deforming spherical membrane. High flow regions cause local areas of the nematic field to "melt", leading to locally isotropic regions and topological defects which further contribute to the complex deformations and dynamics of the immersed structure.

in time using semi-implicit time-stepping. The system is discretized in time such that at every time step n a nonlinear update for the position of the immersed structure $\mathbf{X}^n$ is required:

$$\mathbf{X}^{n+1} = \mathbf{X}^n + \Delta t S^* \mathcal{L}^{-1} S \mathbf{F}(\mathbf{X}^{n+1}), \tag{2}$$

where the time step is Δt, the force on the Lagrangian body points is $\mathbf{F}$, and S and S^* are "spreading operators". While S spreads vector- and tensor-valued fields from the Lagrangian to Eulerian grid, S^* accurately interpolates from the Eulerian to the Lagrangian grid. The inverse of the linear operator $\mathcal{L}$ is the matrix that solves the velocity system, which is nonlinear only in the order parameter, and thus amenable to standard splitting procedures for solving the Stokes equations. This method allows stable time stepping unburdened by classical Courant-Friedrichs-Lewy (CFL) constraints on Δt, and is related to efforts used to study the flow of other isotropic viscoelastic flows including those of the Oldroyd-B model fluid [8, 9].

RESULTS AND CONCLUSIONS

By developing a general numerical scheme for studying the dynamics of elastic membranes in anisotropic fluids we open the door to studying bio-locomotion in complex fluids (Fig. 1c-d), as well as explore key aspects associated with self-assembly in anisotropic fluids. For example, we explore the dynamics of an initially spherical elastic membrane in a Stark-Lubensky NLC in the presence of a 3D Taylor-Green vortex background field, as shown in Fig. 1e-f. Our simulations are valid over a wide range of material parameters, and we may explore a variety of dynamical phenomena, such as long-range interactions between particles [10], swimming bacteria in liquid crystals [2, 11], and defect dynamics in active matter [12].

References

[1] S.E. Spagnolie (ed.), *Complex Fluids in Biological Systems*, Springer, 2015.

[2] P.C. Mushenheim, R.R. Trivedi, H.H. Tuson, D.B. Weibel, and N.L. Abbott, Dynamic self-assembly of motile bacteria in liquid crystals, Soft Matter, 10:88–95, 2014.

[3] S. Zhou, A. Sokolov, O.D. Lavrentovich, and I.S. Aranson, Living liquid crystals, Proc. Natl. Acad. Sci. USA, 111:1265–1270, 2014.

[4] R.R. Trivedi, R. Maeda, N.L. Abbott, S.E. Spagnolie, and D.B. Weibel, Bacterial transport of colloids in liquid crystalline environments, Soft Matter, 11:8404–8408, 2015.

[5] H.Stark and T.C. Lubensky. Poisson-bracket approach to the dynamics of nematic liquid crystals. Phys.Rev.E, 67:061709,2003.

[6] P.-G. de Gennes, and J. Prost, *The Physics of Liquid Crystals*, Oxford University Press, 1993.

[7] C.S. Peskin, The immersed boundary method, Acta numerica, 11:479–517, 2002.

[8] J. Teran, L. Fauci, and M. Shelley, Peristaltic pumping and irreversibility of a Stokesian viscoelastic fluid, Phys. Fluids, 20:073101, 2008.

[9] R.D. Guy and B. Thomases. Computational challenges for simulating strongly elastic flows in biology. In *Complex Fluids in Biological Systems*, pages 359–397, Springer, 2015.

[10] C.P. Lapointe, T.G. Mason, and I.I. Smalyukh. Shape-controlled colloidal interactions in nematic liquid crystals. Science, 326:1083–1086, 2009.

[11] M.S. Krieger, S.E. Spagnolie, and T.R. Powers, Microscale locomotion in a nematic liquid crystal, Soft Matter, 11, 9115–9125, 2015.

[12] M.C. Marchetti, J.F. Joanny, S. Ramaswamy, T.B.Liverpool, J.Prost, M.Rao, and R.A. Simha. Hydrodynamics of soft active matter. Rev. Mod. Phys., 85:1143, 2013.

ELASTO-HYDRODYNAMIC NETWORK ANALYSIS OF COLLOIDAL GELS

James W. Swan*[1] and Zsigmond S. Varga [1]
[1]*Department of Chemical Engineering, Massachusetts Institute of Technology*

Summary We investigate the spectrum of relaxation times and relaxation normal modes in percolated colloidal networks. The relaxation spectrum is intimately tied to the linear viscoelasticity of such networks, and the spatial heterogeneity of the normal modes describes how susceptible structures of different length scales are to deformation. We show that these quantities are highly sensitive to hydrodynamic forces exerted on the network. Models for the hydrodynamic forces that neglect hydrodynamic interactions show significant departures from those that include them in dilute networks. In dense networks, hydrodynamic screening reduces the strength of the interactions, and the predicted relaxation spectra coincide regardless of hydrodynamic model. We show that modes of energy dissipation in the network are fundamentally altered by the presence of long-ranged hydrodynamic interactions. Analogous to the Zimm model in polymer dynamics, models describing network viscoelasticity must incorporate these effects of hydrodynamic coupling across the network to accurately predict the experimental response.

INTRODUCTION

Harmonic normal-mode analysis has been applied to study and predict liquid-state dynamics as well as the eigenmodes and eigenvalues and vibrational properties of numerous systems ranging from biomolecular structures such as membrane proteins, through jamming transitions of granular material to colloidal crystals and glasses. Normal modes provide a framework for understanding the dynamical excitations of a system in diverse fields. The normal modes are those degrees of freedom which, at least for small perturbations away from equilibrium, do not interact with each other. Each mode oscillates independently of the others with its own characteristic frequency. The distribution of these frequencies, known as the vibrational density of states (vDOS), is central in the investigation of solids,since, apart from the structure, it is probably the most relevant and direct quantity to characterize a system. For example, within the harmonic approximation, the vDOS allows one to calculate the temperature dependence of the specific heat, thermal conductivity, as well as the free energy. While much effort has been devoted to the investigation of dense glasses, much less is known for the case of weak colloidal gels. One of the reasons for this is that physically realistic modeling of such gels has become possible only recently [1].

In soft materials, normal mode analysis of the equations of motion of the load bearing constituents can be directly related to its macroscopic linear viscoelasticity. Conceptually, near any point of mechanical equilibrium, the load on each constituent can be modeled as a Hookean spring with a characteristic relaxation time related to the ratio of the spring constant to the viscosity of the suspending medium. There is a fundamental rheological relationship between the microscopic modes of particle relaxation within a colloidal gel and the macroscopic viscoelasticity of that material. The spectrum of these relaxation times, a density of states, of Maxwell-like normal modes, can be transformed into the linear viscoelasticity by summing the viscoelastic contributions of each mode.

Work by Rovigatti et al. [2] focused on the structural and relaxation properties of colloidal networks, the mechanisms responsible for the slowing down of the dynamics with decreasing temperature. However, such an analysis as all others before it neglected the role of hydrodynamic coupling. Contrary to atomic systems, where the phonon dispersion curve is entirely determined by inter-particle forces, in colloidal systems hydrodynamic interactions have to be considered. These interactions arise when moving colloids exchange momentum through the solvent. Because of their long-range nature these interactions are difficult to treat theoretically. We present computational methodologies for resolving this dilemma and results demonstrating that long-ranged hydrodynamic interactions are essential to relaxation spectrum of colloidal networks.

RESULTS

In a colloidal network the evolution of particle positions $\mathbf{x}$ is satisfies the equation:

$$\dot{\mathbf{x}} = \circ\, \mathbf{M} \cdot (\nabla U \circ\ \mathbf{F}_B)\,, \tag{1}$$

where $\mathbf{M}$ is the hydrodynamic mobility matrix, U is the inter-particle potential and $\mathbf{F}_B$ is the random fluctuating Brownian force. Using Cholesky decomposition the mobility matrix can also be expressed as $\mathbf{M} = \mathbf{B}^T \cdot \mathbf{B}$.

Close to mechanical equilibrium ($\nabla U = 0$), particles fluctuate about an equilibrium position $\mathbf{x}^{eq}$ such that $\mathbf{d} = \mathbf{x} \circ\ \mathbf{x}^{eq}$. The time evolution of the fluctuations to first order is

$$\dot{\mathbf{d}} = \circ\, \mathbf{M} \cdot \mathbf{H} \cdot \mathbf{d}, \tag{2}$$

*Corresponding author. Email:jswan@mit.edu

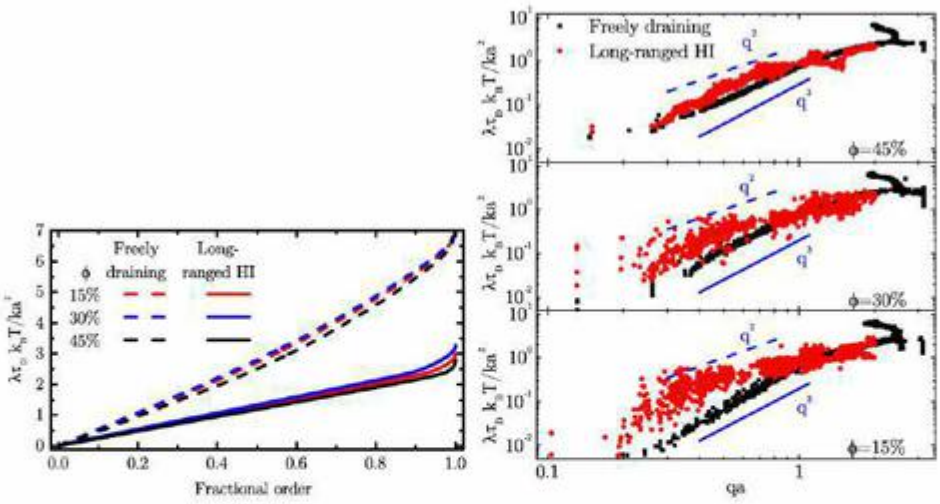

Figure 1: (Left) Relaxation rate λ as a function of the characteristic wavelength of energy dissipation q for the given mode, as calculated for each volume fraction and both hdyrodynamic models. (Right) Dispersion relation between relaxation rate and characteristic wave vector of different normal modes in gels with different volume fraction.

where $\mathbf{H}$ is the Hessian of the inter-particle potential, U. The solutions of this first order equation are exponentially decaying modes with rates satisfying the eigenvalue equation:

$$\lambda_i \mathbf{v}_i = \mathbf{M} \cdot \mathbf{H} \cdot \mathbf{v}_i. \tag{3}$$

Various computation methods can be applied to approximate the hydrodynamic mobility $\mathbf{M}$. The most common example is the so-called freely draining approximation in which $\mathbf{M}$ is replaced by an isotropic tensor describing the mobility of a single particle in the network neglecting all hydrodynamic interactions. A further approximation is the so-called Rotne-Prager tensor which couples the particle motions via long-ranged hydrodynamic interactions scaling with the inverse of inter-particle distance. We have recently shown that this approximation is the minimum acceptable for model gelation kinetics. It is the lowest order approximation capable of replicating the experimentally observed dependence of aggregation rate on the size of clusters during gelation.

Here we compare the relaxation specturm $\{\lambda_i\}$ and the normal modes of relaxation $\{\mathbf{B}^{-1} \cdot \mathbf{v}_i\}$, produced by the two models. Results from more sophisticated models which incorporate the effects of hydrodynamic lubrication can be shown to reduce to the Rotne-Prager mobility model as well. Figure 1 depicts the eigenspectrum as a function of the fractional order (position within the spectrum in accending order) for the freely draining and Rotne-Prager models applied to colloidal networks with 15, 30, 45% particles by volume. Differences in the relaxation rates across the entire spectrum can be attributed to the additional hydrodynamic drag imparted by the Rotne-Prager model. In the figure, the relaxation rate is normalized by $ka^3/k_BT/\tau_D$, where k is the mean stiffness of inter-particle bonds, a is the particle size, k_BT is the thermal energy, and τ_D is the characteristic relaxation time of a single particle.

The structure of each of the normal modes is interrogated by computing its spatial power spectrum. The power spectrum exhibits a peak at a particular wave vector q, which suggests the normal modes are correlated over a length scale $2\pi/q$. This describes the size of the relaxing unit associated with each normal mode. Figure 1 plots the relaxation rate versus the characteristic wave vector for networks with 15, 30, 45% particles. This dispersion relation is key for understanding relaxation and ultimately rheological properties of colloidal networks. At low volume fractions, the dispersion relations for the free draining approximation and the Rotne-Prager approximation differ in their power law scaling. Large structures relax more quickly in the Rotne-Prager approximation because of collective hydrodynamic enhancement to particle motion. At high volume fractions, hydrodynamic screening ensures that the approximations are indistinguishable. These differences in relaxation processes have profound consequences for how stress relaxes in colloidal networks and their viscoelastic properties.

References

[1] Varga, Z., Wang, G. and Swan, J., 2015. The hydrodynamics of colloidal gelation. Soft Matter, 11(46), pp.9009-9019.

[2] Rovigatti, L., Kob, W. and Sciortino, F., 2011. The vibrational density of states of a disordered gel model. The Journal of chemical physics, 135(10), p.104502.

RHEOLOGICAL MODELLING AND DISCRETE SIMULATION OF SHEAR THICKENING IN A BIDISPERSE SUSPENSION

Christopher Ness *[1] and Jin Sun[1]

[1]*School of Engineering, University of Edinburgh, Edinburgh EH9 3JL, United Kingdom*

Summary Concentrated suspensions of solid particles in liquid, such as pastes, exhibit many forms of nonlinear flow behaviour. Shear thickening, in which the suspension viscosity increases with applied stress, is of particular interest to engineers across disciplines as it can arise under minor variations in composition but leads to, for example, pump failure and extrusion blockages. We recently demonstrated that the increase in viscosity can be attributed to direct particle-particle contacts, which are frictional in nature. Furthermore, experiments have shown that the critical stress above which thickening occurs is intimately related to the particle size, with larger particles more likely to thicken than smaller ones. In the present work, we explore the implications of these findings for 'real' suspensions, which might be composed of particles spanning orders of magnitude in size, and propose how particle size distributions of future suspensions might be tuned to achieve or avoid certain shear thickening behaviour.

INTRODUCTION

Shear thickening, the increase of viscosity (e.g. of a densely packed suspension) with increasing shear rate, is a complex rheological phenomenon that has earned much attention from academia and industry. It can be desirable, for example during solidification upon impact of an otherwise highly flexible bullet proof vest, or detrimental, causing blockage and fracture during ceramic paste extrusion [1]. Until recently, the link between suspension composition and shear thickening has been somewhat misunderstood. A full understanding of this relationship could be used to establish design principles, allowing rational, as opposed to empirical, formulation of future suspensions, allowing predictable promotion or mitigation of thickening.

The classical explanation for shear thickening assumes that under large stresses or deformations, suspended particles approach each other extremely closely, leading to the diverging hydrodynamic lubrication forces becoming enormous in the interstices. This theory has recently been uprooted by experiments [2, 3] and simulations [4] demonstrating that above an onset stress σ^* particle surfaces come into contact, and the frictional nature of this interaction leads to enhanced dissipation and is responsible for shear thickening. Note that such a shear thickening mechanism is distinct from *inertial* shear thickening, which happens above a critical shear rate when the material adopts Bagnoldian stress scaling, analogous to dry grains [5]. The question remains of how to devise practical design principles that utilise this improved understanding.

In the present work, we propose how existing theory [6] might be extended to account for significant polydispersity of the suspended particles, using bidisperse suspensions of various diameter ratios at test cases.

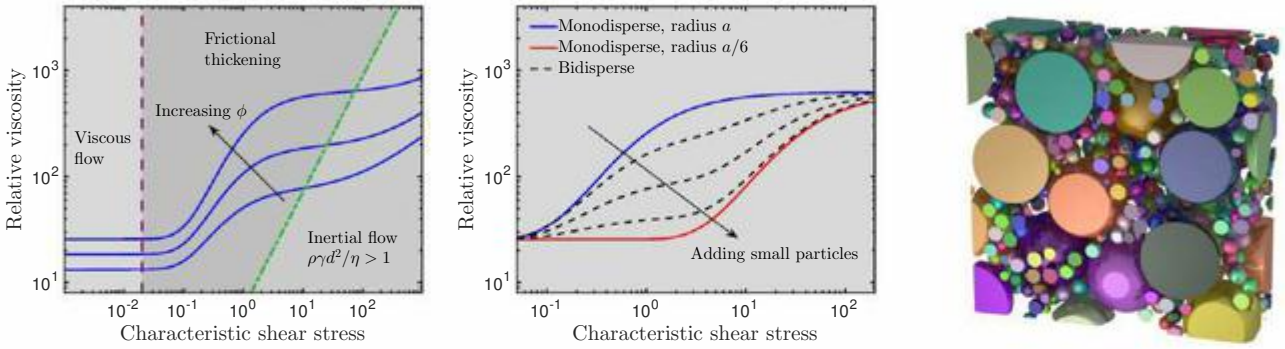

Figure 1: (a) Frictional and inertial flow regimes for a monodisperse suspension. Frictional shear thickening is governed by a critical shear stress (purple dashed line); inertial shear thickening is governed by a critical shear *rate* or Stokes number (dashed green line). (b) Highlighting frictional shear thickening behaviour for small and large particles, and a proposed interpolation for bidisperse mixtures. (c) Image of a sample simulation for diameter ratio 1:6;

*Corresponding author. Email: christopher.ness@cantab.net

THEORETICAL DEVELOPMENT

Recent theoretical work [6] proposes that above a critical applied stress σ^*, suspended particle surfaces may come into frictional contact. The fraction of particle-particle interactions that become frictional in this way as the stress σ is increased is given a simple exponential form

$$f \propto \exp(\circ\, \sigma^*/\sigma) \tag{1}$$

where f is a parameter varying from $0 \rightarrow 1$, quantifying the degree of frictional character of the suspension. This parameter may be built into a constitutive framework [7] by considering its influence on the critical solid fraction for flow arrest ϕ_{c}, as the contacts evolve from being frictionless (like a colloid, with flow arresting at $\phi_{\mathrm{rcp}} \approx 0.64$) to frictional (like a granular suspension, with flow arresting at $\phi_{\mathrm{m}} \approx 0.58$)

$$\phi_{\mathrm{c}} = \phi_{\mathrm{m}} f + \phi_{\mathrm{rcp}}(1 \circ\ f). \tag{2}$$

In Figure 1(a), we plot resultant viscosity-stress curves for varying solids fraction ϕ, further incorporating *inertial* shear thickening above a critical shear rate [5, 8]. Experiments [3] suggest that σ^* varies with $1/a_i^2$ for approximately monodisperse suspensions of particles of radius a_i, implying that large particles become 'frictional' at lower stresses than small ones. We therefore propose that in polydisperse suspensions, the large-large contacts become frictional at lower stresses than large-small or small-small, and therefore the frictional character of the suspension might be better characterised using a multi-modal f^{poly}, such as

$$f^{\mathrm{poly}} \propto \sum_i \kappa_i \exp(\circ\, \sigma_i^*/\sigma) \tag{3}$$

for a suspension with i distinct particle sizes, and where $\sum \kappa_i = 1$ and σ_i^*, the critical stress for shear thickening for particles of radius a_i, varies with $1/a_i^2$. Replacing f with f^{poly} in Eq 2 and assuming bidispersity, we obtain the family of shear thickening flow curves in Figure 1(b) (at fixed $\phi \circ\ \phi_{\mathrm{c}}$), where the weighting parameter κ_i is adjusted to represent varying the number ratio of small-to-large particles in the bidisperse suspension. The bidisperse flow curves demonstrate interesting shear thickening behaviour. Particularly, we observe significant non-monotonic behaviour in the viscosity, coupled with a large increase in the range of stresses over which thickening is observed. We note that having a wide window of frictional shear thickening stresses gives rise to the possibility of inertia of the large particles contributing to enhanced thickening. To elucidate these phenomena, and to validate our simplistic extension of Eq 1 for polydispersity, we carry out simulations of suspension shear flow.

SIMULATION DETAILS

Discrete element method simulations [9] enhanced for dense suspensions [10], implemented as described in [5] are carried out for bidisperse suspensions of particles of varying size and number ratios, with a sample cross-sectional slice being shown in Figure 1(c). We simulate the Newtonian dynamics of assemblies of ≈ 2000 particles in periodic, cubic domains subjected to Lees-Edwards boundary conditions and calculate the resulting shear viscosity as a function of shear stress, at fixed shearing rate.

We will discuss our simulation results in the context of the interpolating shear thickening regimes of Figure 1(b), discussing how that picture might be correctly extended to allow the emerging understanding of frictional shear thickening to be exploited as a design tool for general polydisperse suspensions.

We thank EPSRC and Johnson Matthey for funding, and Ben Guy, Michiel Hermes and Wilson Poon for fruitful discussions.

References

[1] N. Wagner and J. Brady. Shear thickening in colloidal dispersions. *Physics Today*, 62(10) 27, 2009.
[2] N. Lin, B. Guy, M. Hermes, C. Ness, J. Sun, W. Poon and I. Cohen. Hydrodynamic and contact contributions to shear thickening in colloidal suspensions. *Phys. Rev. Lett.*, 115:228304, 2015.
[3] B.Guy, M. Hermes and W. Poon. Towards a unified description of the rheology of hard-particle suspensions. *Phys. Rev. Lett.*, 115:088304, 2015.
[4] R. Seto, R. Mari, J. Morris and M. Denn. Discontinuous shear thickening of frictional hard-sphere suspensions. *Phys. Rev. Lett.*, 111:218301, 2013.
[5] C. Ness and J. Sun. Shear thickening regimes of dense non-Brownian suspensions. *Soft Matter*, 12:914-924, 2016.
[6] M. Wyart and M. Cates. Discontinuous shear thickening without inertial in dense non-Brownian suspensions. *Phys. Rev. Lett.*, 112:098302, 2014.
[7] F. Boyer, E. Guazzelli and O. Pouliquen. Unifying suspension and granular rheology. *Phys. Rev. Lett.*, 107:188301, 2011.
[8] C. Ness and J. Sun. Flow regime transitions in dense non-Brownian suspensions. *Phys. Rev. E*, 91(1) 12201, 2015.
[9] P. Cundall and O. Strack. A discrete numerical model for granular assemblies. *Geotechnique*, 29(1):47-65, 1979.
[10] R. Ball and J. Melrose. A simulation technique for many spheres in quasi-static motion under frame-invariant pair drag and Brownian forces. *Physica A*, 247:444-472, 1997.

VORTEX DEFORMATION ON TWO-DIMENSIONAL TURBULENCE AFFECTED BY POLYMERS

Ruri Hidema[1a)], Hiroshi Suzuki[2)]
[1]*Organization of Advanced Sicence and Technology, Kobe University, Kobe, Hyogo, Japan*
[2]*Department of Chemical Science and Engineering, Kobe University, Kobe, Hyogo, Japan*

Summary A drag reduction effect has been a long-standing issue. In order to consider the background mechanism of the drag reduction effect, we focus on vortex deformation in turbulence and extensional rheological properties of the fluids in this study. A flowing soap film as a two-dimensional flow was adopted to avoid shear stress effects. Vortex generation in a 2D flow was visualized and how the vortices deformed by polymer additives were analysed. Power spectra of the visualized 2D turbulence through interference patterns and velocity fluctuation obtained by a PIV analysis revealed the variation of energy transfer in 2D flow. A wavelet analysis was used to detect the variation of vortices in time. We considered how these variations were affected by a relaxation time of sample solution, and by several extensional rates added on the flow.

INTRODUCTION

Addition of little amounts of polymer in Newtonian-flow prohibits turbulence. This phenomenon is called a drag reduction effect. When polymers affect turbulence, vortices generated on the wall are deformed[1]. That is why frictional drag at the wall surfaces is reduced. Since the drag reduction effect is a useful technique to improve energy efficiency, this technique has been applied in many industries. In order to investigate the background mechanism of this phenomenon, the relationship between effects of polymers on the flow and rheological properties of the fluids has been studied in many previous studies. We have focused on how the relaxation time of solution related to extensional viscosity of solution affects turbulences[2,3,4]. Since the extensional viscosity is increased under the extensional rate, a flow that is free from shear stresses is needed. In order to realize such a flow system, a flowing soap film as a two-dimensional (2D) flow is installed[5]. 2D turbulence is generated on the flowing soap films, and vortices of the turbulence are visualized by interference patterns of the film in this study. Vortices deformation due to polymers is analysed by power spectra and a wavelet analysis of the images. Velocity fields of the two-dimensional flow are also measured by a PIV analysis to discuss turbulent statistics.

EXPERIMENTS

Material

Soap solutions contained sodium dodecylbenzenesulfonate (SDBS) as a surfactant at the concentration of 2wt%. As polymers, a flexible polymer and a rigid polymer were selected to vary rheological properties of the fluids. As a flexible polymer, polyethyleneoxide (PEO, molecular weight: 3.5×10^6) was used at the concentrations from 0.25 to 2.0×10^{-3}wt%. As a rigid polymer, hydroxypropyl cellulose (HPC, molecular weight: $>1.0\times10^6$) was used at the concentrations from 0.01 to 0.05wt%.

Method

Experiments were conducted on a flowing soap film shown in Figure 1(a). If we see the cross section of a soap film, water layer is sandwiched by surfactants. The surfactants are vanishingly small compared to the thickness of the water layer. Therefore, the flowing soap film is considered as a water layer itself, that is 2D flow. In this study, two nylon wires tightened by a weight were used to make a soap film channel. Sample solutions flowed between the two nylon wires from top to bottom by gravity-driven. The flow reached uniform velocities at about 30cm behind from the injection nozzle. The flow rate was measured by a flow meter. The mean velocity, $V(t)$ [m/s], was 130cm/s. The mean thickness of the water layer, $h(t)$ [m], was approximately 3.85μm, which is calculated by $h(t) = Q(t)/(V(t)W)$ with a flow flux, $Q(t)$ [m^3/s], of 0.5ml/s and the channel width W [m]. A grid of equally spaced cylinders was inserted to the flow perpendicular to the flow to generate 2D turbulence. The flow was illuminated and visualized through interference patterns (Figure 1(b)).

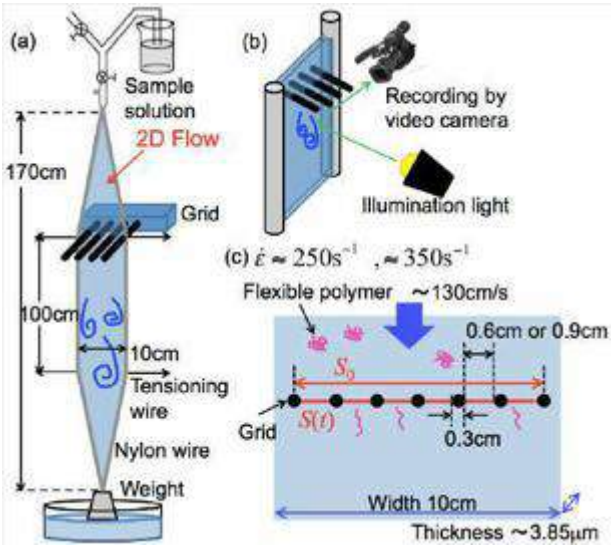

Figure 1. Experimental apparatus

a) Corresponding author. Email: hidema@port.kobe-u.ac.jp

Data acquisition area was 15cm behind the grid. Since the flow was self-standing, and was surrounded by air, shear stresses on the flow were negligible small. When polymers were added to the sample solution, polymers were mainly affected by extensional stresses at the grid due to an abrupt decrease of the cross section area of the water layer. Here, extensional rate, ε [1/s], added on flows were roughly calculated by $S(\ ) = S_0 \exp(-\dot{\varepsilon} t)$, where S_0 [m^2] is the cross section area before the grid, $S(t)$ [m^2] is the cross section area middle of the grid, and t [s] is the time needed to through the half distance of the grid. In order to change the extensional rate, the distance of the cylinder was changed. In this study, the extensional rates were 250 and 350 1/s. PIV was used to obtain local velocity fields around the cylinders. Polystyrene particles with 2.11μm of diameter were added to the solutions as tracers.

RESULTS AND DISCUSSION

Figures 2(a) and (b) show vortices of 2D turbulence visualized by interference patterns. The sample solution of Fig.2(a) was polymer free, and the sample solution of Fig.2(b) contains PEO at the concentration of 2.0×10^{-3}wt%. When PEO was added to the flow, vortices were clearly deformed. The deformation is due to variation of energy transfer in 2D flow. In order to investigate how the energy transfer was affected by polymers, power spectra of the interference patterns in the streamwise and the normal directions were calculated. The interference pattern is related to the thickness of water layer of 2D flow, and the thickness of 2D flow is a passive scalar. Therefore, we can adopt a dimension analysis of passive scalar scaling to the power spectra of interference patterns[4,5]. As shown in Fig.2(c) and (d), the scaling index of the power spectrum was changed to -5/3 to -1. In 2D flow, when the energy is well transferred to different scale, the index of passive scalar scaling shows -5/3, and when the energy transfer is prohibited the index becomes close to -1. The variation was detected by the power spectrum analysis. In addition, velocity field obtained by PIV and turbulent statistic analysis also confirmed that the variation of energy transfer was affected by polymers. When polymers were added to the flow, the third moment of velocity fluctuation of 2D flow, which indicates energy transfer, was depressed. Since vortices were generated at the grid and advected to downstream, rheological properties of the sample solution around the grid should affect the vortex generation. The relaxation times of polymer free solution and PEO 2.0×10^{-3}wt% added solution were 0.5ms ad 10ms. Relaxation time is related to extensional viscosity of the solution. In addition, when the extensional rate added at the grid was increased from 250 to 350 1/s, the variation of the scaling index occurred at a lower concentration. A wavelet analysis was also used to detect how polymers varied 2D turbulence(Fig.3). The wavelet intensity shows original vortices disappeared and new fluctuations appeared by addition of polymers. From all these results, we consider that the relationship between polymer effects on 2D flow and extensional viscosity of polymer solution were confirmed through vortex deformation in this system.

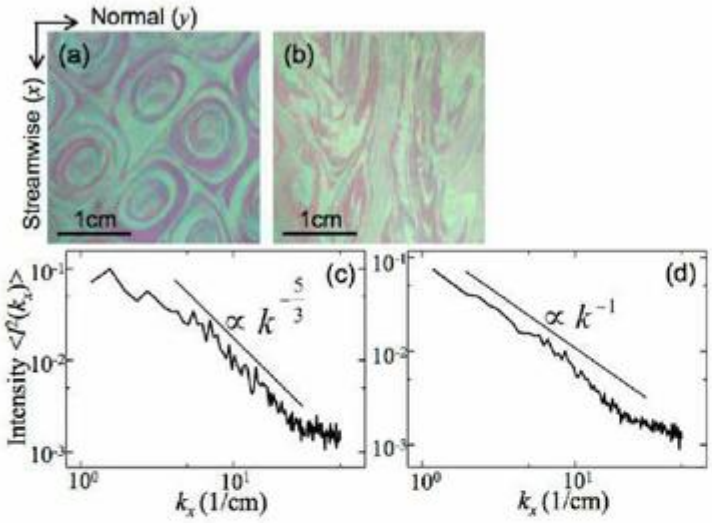

Figure 2. Interference patterns of 2D turbulence and power spectra

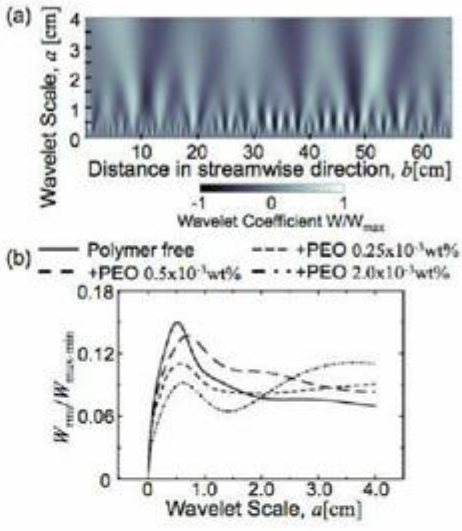

Figure 3. Wavelet coefficient map and intensity

ACKNOWLEDGEMENT

This work was funded by JSPS Grant-in-Aid for Young Scientists A, No. 15H05552.

References

[1] Motozawa M., Sawada T., Ishituka S., Iwamoto K., Ando H., Senda T., Kawaguchi Y.: *Int. J. Heat Fluid Flow* **50**:51–62, 2014 **[2]** Hidema R., Suzuki H., Hisamatsu, S., Komoda Y., Furukawa H.: *Rheol. Acta* **52**:949-961, 2013 **[3]** Hidema R., Suzuki H., Hisamatsu S., Komoda Y.: *AIChE J* **60**:1854-1862, 2014 **[4]** Hidema R., Suzuki H., Murao I., Hisamatsu S., Komoda Y.: *Flow Turbulence Combust.* **96**:227-244, 2016 **[5]** Boffetta G., Ecke R.E.: *Annu. Rev. Fluid Mech.* **44**:427–51, 2012

ON THE NATURE OF ELASTO-INERTIAL TURBULENCE

George H. Choueiri & Bjorn Hof[a)]
Institute of Science and Technology Austria, Klosterneuburg, Austria

Summary The instability arising in dilute polymer solutions has been studied experimentally. The effect of polymer concentration on the flow behaviour, with a focus on the friction factor and fluctuation intensity, was studied with the aim of better distinguishing between turbulence arising in Newtonian fluids and that in dilute polymer solutions. We concluded that long-chain polymers have the ability to completely supress Newtonian turbulence and give rise to an independent form of turbulence which has been termed elasto-inertial turbulence.

BACKGROUND

Dissolving minute amounts of long-chain polymers, such as polyacrylamide, in liquids has been shown to dramatically decrease the friction losses in wall bounded flows; the reduction can be as high as 80% in some cases with the addition of only a few parts per million of polymers by weight (ppmw). Applications which take advantage of this phenomenon range from reducing transport costs in oil pipelines [1] to reducing turbulence induced noise in military submarines [2]. While this phenomenon has been known about since the late 40's [3], several mysteries surrounding it have yet to be resolved. Of note, is an empirically derived asymptotic limit of drag reduction [4]; with increasing polymer concentration C, the drag of a turbulent flow progressively decreases from that of Newtonian turbulence (where the friction factor follows the Blasius scaling) to an asymptotic state which has been termed the maximum drag-reduction (MDR) asymptote [4,5] (see Figure 1). This limit does not depend on the type of long-chain polymer used, and in most cases cannot be exceeded irrespective of the quantity of polymers added. Another point of interest, and the focus of this paper, is the nature of the flow when it reaches this asymptotic state. It has recently been proposed that this state is not a modified version of ordinary turbulence but instead that ordinary turbulence gets completely supressed and replaced by a different state of motion which has been termed elasto-inertial turbulence (EIT) [6]. To illustrate this point Samanta et al. [6] plotted the transition to turbulence thresholds as a function of polymer concentrations; similar to what we have done in Figure 2. From this figure it is clear that adding more polymers delays the transition of ordinary turbulence to higher values of the Reynolds number while simultaneously promoting the emergence of a new type of turbulence; EIT.

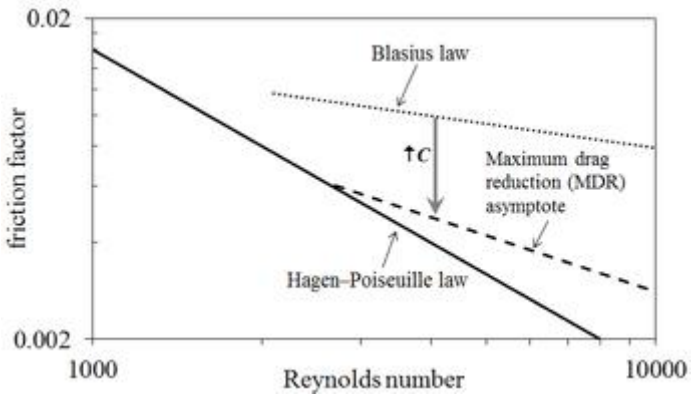

Figure 1 – Friction factor plot showing effect of increasing polymer concentration at a fixed Reynolds number.

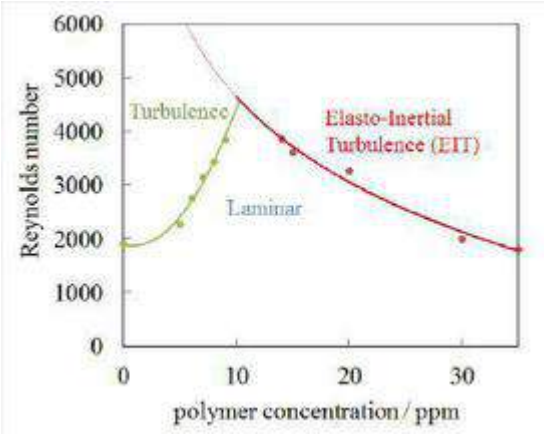

Figure 2 – Transition to turbulence thresholds as a function of polymer concentration.

EXPERIMENTAL FACILITY AND INSTRUMENTATION

The majority of experiments were conducted in a glass pipe of diameter D = 10mm consisting of several sections connected by precisely machined fittings into which pressure tap holes where added. Two differential pressure sensors were used; the first to measure pressure drop over a distance of 134.1D starting 200D away from the pipe inlet; and the second to measure pressure fluctuations across a distance of 5D starting from a distance of 323.3D from the inlet. The flow was driven by gravity and controlled by a precision control valve proceeded by a conditioning tank containing pressurized air which removed any flow fluctuations resulting from flow in the control valve. The flow rate was assessed by continuously measuring the mass of fluid collected at the outlet of the pipe. A solution of polyacrylamide (Batch#685910 with molecular weight up to 7 million as estimated by the distributor – Polysciences Europe GmbH, Eppelheim, Germany) was mixed in

[a)] Corresponding author. Email: bhof@ist.ac.at.

specially designed slow rotating drums to allow for a full dissolving of polymers while exerting the minimum amount of shear. In order to increase the repeatability of measurements, the fluid was mixed in a consistent manner, over a fixed amount of time (usually 24 hours) and once mixed, the fluid was only allowed to pass once through the pipe before being discarded. The viscosity of the solution was estimated from the pressure drop in the pipe by solving for the Reynolds numbers $\mathrm{Re}=UD/\nu < 500$, where U is the bulk flow velocity and ν the kinematic viscosity, with the assumption that at such low values of Re, the friction factor was consistent with that of Hagen-Poiseuille.

RESULTS AND DISCUSSION

Building on the work of Samanta et al. [6] we designed an experiment with the aim of showing definitively a clear distinction between Newtonian turbulence and EIT. The aforementioned authors showed that the critical shear rate ($\dot{\gamma} = 8U/D$) for the onset of EIT decreases with increased polymer concentration but this critical shear rate was independent of pipe diameter. Taking advantage of this and the fact that increased polymer concentrations tend to delay transition to Newtonian turbulence, we selected a pipe diameter which insured a laminar region would exist well beyond the natural transition point of ordinary turbulence.

For a turbulent flow at Re=5000, we increased the polymer concentration from 0 to 35ppmw and observed a steady decrease in the friction factor as well as the amplitude of pressure fluctuations as had been expected based on previous studies [5] and by examining Figure 2. At a fixed $\mathrm{Re}\simeq 3500$, we increased the polymer concentration starting from zero and initially observed similarities with the aforementioned trend. Interestingly this time, as the drag coefficient approached the MDR asymptote, the flow state changed from one of random fluctuations to one containing bursts of turbulence interlaced by regions of supressed turbulent activity resembling that of laminar flow; this observation could be related to the state referred to as “hibernating” turbulence [7] or may simply be a form of intermittency as known to exist in ordinary turbulence. Continuing to increase polymer concentration however lead to a surprising observation; the complete suppression of Newtonian turbulence; this is indicated by a suppression of observable pressure fluctuations and a friction factor which follows the Hagen–Poiseuille scaling. Even more surprisingly, increasing the polymer concentration further resulted in an increase in fluctuations accompanied by an increase in the friction factor which finally came to rest on the MDR asymptote. This time the fluctuations grew steadily in magnitude and no intermittency was observed. The complete suppression of ordinary turbulence and the introduction of a new type of turbulence (EIT) occurred by a continuous variation of a single quantity C; this leads us to the conclusion that the mechanisms driving the two types of turbulence are unique and the two resulting states are distinct.

A second point of distinction between the two types of turbulence raised by Samanta et al. [6] was the fact that unlike ordinary turbulence, the onset of EIT was not governed by Re, but rather by the critical shear rate (which can be expressed in dimensionless form as the Weissenberg number Wi). To test the limits of this assertion, we increased the viscosity of our polymer solution by adding various amounts of glycerine; this had the effect of lowering Re for a constant shear rate. By means of laser Doppler velocimetry (LDV) we measured the centreline axial velocity of the flow and by analysing the spectrum of velocity fluctuations we were able to determine that turbulent signatures could be resolved at Reynolds numbers as low as 7 (which was the smallest Reynolds number we tested). This further solidifies the argument of distinction between ordinary turbulence (which would be supressed in cases of high viscous forces in comparison to inertial forces) and EIT which persists under the same conditions.

CONCLUSIONS

From our experiments we conclude that long-chain polymers delay and completely suppress Newtonian turbulence under the right conditions. For large enough Weissenberg numbers on the other hand, polymers give rise to a distinct type of turbulence which we clearly demonstrated as being independent of Newtonian turbulence. Based on these observations, we conclude that MDR is in fact the asymptotic state of a unique type of turbulence which has been termed EIT.

References

[1] Burger, E. D., Munk, W. R., & Wahl, H. A.: Flow increase in the Trans Alaska Pipeline through use of a polymeric drag-reducing additive. *Journal of petroleum Technology* 34.02:377-386, 1982.

[2] Truong, V. T.: Drag reduction technologies. *Defence and Science Technology organisation Victoria (Australia) Aeronautical and Maritime Research Lab,* No. DSTO-GD-0290, 2001.

[3] Toms, Be A.: Some observations on the flow of linear polymer solutions through straight tubes at large Reynolds numbers. *Proceedings of the 1st International Congress on Rheology* 2, 1948.

[4] Virk, P. S., Mickley, H. S., & Smith, K. A.: The ultimate asymptote and mean flow structure in Toms’ phenomenon. *Journal of Applied Mechanics* 37.2:488-493, (1970).

[5] White, C. M., & Mungal, M. G.: Mechanics and prediction of turbulent drag reduction with polymer additives. *Annu. Rev. Fluid Mech*. 40:235-256, 2008.

[6] Samanta, D., Dubief, Y., Holzner, M., Schäfer, C., Morozov, A. N., Wagner, C., & Hof, B.: Elasto-inertial turbulence. *Proceedings of the National Academy of Sciences,* 110(26): 10557-10562, 2013.

[7] Graham, M. D.: Drag reduction and the dynamics of turbulence in simple and complex fluids. *Physics of Fluids* (1994-present) 26.10:101301, 2014.

EFFECT OF VISCOELASTICITY ON THE SMALL SCALE STATISTICS OF HOMOGENEOUS ISOTROPIC TURBULENCE

NGUYEN Minh Quan *[1], Alexandre DELACHE[2], Serge SIMONS[1], Wouter J.T BOS[1], and Mahmoud EL HAJEM[1]

[1]*LMFA UMR 5509 CNRS, Ecole Centrale de Lyon, Université de Lyon, France*

[2]*LMFA, site de Saint-Etienne, Université de Lyon, Université Jean Monnet de Saint-Etienne, France*

Summary The comparison of the results of direct numerical simulations (DNS) of homogeneous and isotropic turbulence (HIT) of viscoelastic fluid are done based on the FENE-P model. It provides evidence, comparing with DNS of Newtonian fluid HIT, that viscoelasticity modifies qualitatively the behaviour of the smallest scales.

INTRODUCTION

We have already reported [1] the influence of polymer on turbulence at the smallest scales by considering the dynamics of the FENE-P model and representing some key features of flow with a weak concentration of polymer molecules. The transfer of energy from large scale toward the smallest scales via interaction with polymer fields was observed. In this communication we will focus on the influence of these mechanisms on the classical statistical quantities issued from velocity or conformation fields of the viscoelastic fluid flows.

MODEL AND NUMERICAL SET-UP

We have implemented the FENE-P model in a standard pseudo-spectral solver. The model is given by

$$\partial_t \boldsymbol{u} + \boldsymbol{u} \times (\nabla \times \boldsymbol{u}) = -\nabla p + \nu \Delta \boldsymbol{u} + \nu_p \operatorname{div}(P.\boldsymbol{C} - \boldsymbol{I}) + \boldsymbol{f} \quad (1)$$

$$\partial_t \boldsymbol{C} + \boldsymbol{u}.\nabla \boldsymbol{C} = \boldsymbol{C}.\nabla \boldsymbol{u} + \nabla \boldsymbol{u}^t.\boldsymbol{C} + \frac{1}{\tau_p}(P.\boldsymbol{C} - \boldsymbol{I}) \quad (2)$$

where $p = p' + \frac{u^2}{2}$ is the total pressure, $\boldsymbol{C}$ is the conformation tensor of the polymer chains, $\boldsymbol{I}$ is the identity tensor, $P = \frac{L_m^2 - 1}{L_m^2 - Tr(\boldsymbol{C})}$ is the Peterlin's function with L_m the maximum extension of the spring, τ_p is the polymer relaxation time, ν_p is the polymer zero-shear-stress viscosity and $\boldsymbol{f}$ is a forcing term. The incompressibility condition is $\operatorname{div} \boldsymbol{u} = 0$. We use a symmetric factorization of the conformation tensor: $C_{ij} = B_{im}B_{mj}$ [2], which ensures $\boldsymbol{C}$ to remain positive definite. In order to accurately resolve the dissipation range, we simulate low Reynolds number flow (with a Taylor-scale Reynolds number of order $Re_\lambda \approx 30$) using 256^3 grid-points. The maximum stretching-length $L = 255$ and the ratio of solvent to total viscosity (β) is around 0.909. The parameter β is in a direct relation with the concentration of polymer. The Newtonian case can be considered as β equal to 1.

Case	Forcing type	ν $\times 10^{-2}$	τ_p	β
a1	S	1.25	0.5	1
a2	S	1.25	0.5	0.909
a3	S	2.5	0.5	0.909
a4	S	1.25	0.5	0.833
a5	S	1.25	0.75	0.909
b1	ABC	1.25	-	1
b2	ABC	1.25	0.5	0.909
c1	None	1.25		1
c2	None	1.25	0.5	0.909
d1	None	1.25	-	1
d2	None	1.25	0.5	0.909

Table 1: Parameter compilation for the different cases.

In order to investigate the issues in the following (dissipation range behaviour and drag-reduction), we consider five different flows at comparable Reynolds and Weissenberg ($Wi = \frac{\tau_p}{\lambda}$ numbers. Cases from a to b are forced to obtain a statistically steady state, the remaining cases c and d are decaying, starting from different initial conditions. We summarize them in the table 1. The label S denotes a stochastic forcing [3], ABC indicates a deterministic helical forcing [4]. The difference in the freely decaying simulations (non forcing type) is that in cases c the initial condition is a fully developed velocity field, in cases d it is a synthetic Gaussian flow field with prescribed energy distribution. The comparison of these different cases allows us to consider the issues discussed below.

*Corresponding author. Email: minh-quan.nguyen@ec-lyon.fr

RESULTS

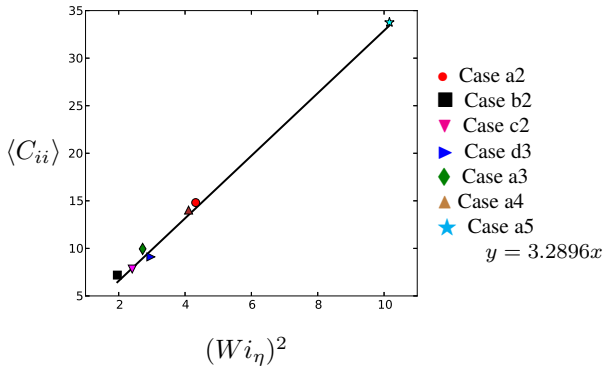

Figure 1: Dependence of the trace of the conformation tensor on the Weissenberg number

The polymer diluted in solvent will be stretched under the action of shear. In the linear regime of polymer stretching (small deformations), the polymer should be stretched more at the Kolmogorov's scale which corresponds to a peak of the shear rate. The extension of polymer is the competition between the relaxation rate $f_p = 1/\tau_p$ and the shear rate $s = \sqrt{\frac{\epsilon_f}{\nu}}$, where ϵ_f is the dissipation rate of kinetic energy. Hence, we expect that the polymer extension will scale with the ratio between the relaxation frequency of the polymer f_p and the characteristic shear rate (s) at the Kolmogorov scale.This ratio is the Weissenberg (Wi_η) number. The trace of conformation tensor scales with the square of the polymer extension, which yields:

$$\langle C_{ij} \rangle \sim \left(\tau_p \sqrt{\frac{\epsilon_f}{\nu}} \right)^2 = (Wi_\eta)^2 \tag{3}$$

Our data fit well the scaling law described in equation (3), as presented in figure 1. The linear regression coefficient is noted as $A = 3.29$. Thanks to this scaling law, we managed to collapse the kinetic energy spectrum (E_K) and the polymer elastic energy spectrum (E_p). The spectra of small scales in the dissipation range lead to a k^{-6} law and k^{-2} law respectively plotted on figure 2. The argument leading to this normalization will be detailed during the Colloquium. Finally, we will propose a phenomenological law on polymer extension, which is supported by a global and scale by scale analysis spectra. More statistical classical results, corresponding to Newtonian and viscoelastic cases will be presented and compared.

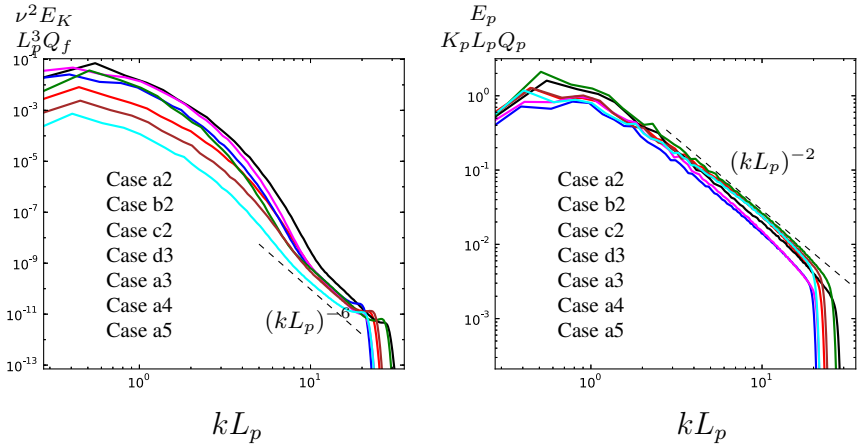

With:

$$Q_f = (\tfrac{\nu_p}{\tau_p})^2 \Big(3 \left(A(Wi_\eta)^2 - \langle B_{ij} \rangle^2 \right)^2 + 6 \langle B_{ij} \rangle^2 \left(A(Wi_\eta)^2 - \langle B_{ij} \rangle^2 \right) + \langle B_{ij} \rangle^4 \Big)$$

$$Q_p = A\,(Wi_n)^2 - \langle C_{ij} \rangle$$

$$K_p = \tfrac{\nu_p}{2\tau_p}$$

Figure 2: Normalized Kinetic and polymer energy spectra. L_p is the correlation length based on the elastic energy of polymer.

ACKNOWLEDGEMENT

This work was granted access to the HPC resources of IDRIS under the allocation i20152a2206 made by GENCI and the equip@meso center.

References

[1] M. Q. Nguyen, A. Delache, S. Simons, W. Bos, M. El Hajem, and R. Poole, Effect of viscoelasticity on the far-dissipation range of homogeneous isotropic turbulence, ETC 15, 2015.

[2] N. Balci, B. Thomases, M. Renardy, and C. Doering, Symmetric factorization of the conformation tensor in viscoelastic fluid models, J. Non-Newtonian Fluid Mech. **166**(11), 546 – 553 (2011).

[3] X. Chen, H. Marschall, M. Schfer, and D. Bothe, A Comparison of Stabilisation Approaches for Finite-volume Simulation of Viscoelastic Fluid Flow, Int. J. Comput. Fluid Dyn. **27**(6-7), 229–250 (2013).

[4] P. D. Mininni, D. Rosenberg, and A. Pouquet, Isotropization at small scales of rotating helically driven turbulence, JFM **699**, 263–279 (2012).

CONTRAVARIANT AND COVARIANT POLYMERS IN ELASTO-INERTIAL VISCOELASTIC TURBULENCE

Kiyosi Horiuti [*1] and Shu Suzuki[1]

[1]*Department of Mechano-Aerospace Engineering, Tokyo Institute of Technology, Tokyo, Japan*

Summary We conduct multi-scale study on energy transfer due to polymers dispersed in homogeneous isotropic turbulence in elasto-inertial regime (EIT). Effect of introduction of non-affinity with macroscopically-imposed deformation in the motion of polymers is examined by connecting mesoscopic Brownian dynamics of elastic dumbbells to macroscopic DNS for solvent. The dumbbells are allowed to be advected either affinely (contravariant) or completely non-affinely (covariant). The relaxation time of polymer is in the order of eddy turnover time. Contravariant polymers drain more energy from the large scales than they can dissipate and transfer the excess energy back into the solvent when they are highly-stretched. It is shown that the skewness of strain-rate tensor in the production term for elastic energy and dissipation rate transfer elastic energy back into the smallest scale of the solvent and increase the dissipation. In the covariant polymers, this backward transfer is eliminated and elastic energy is retained when highly stretched.

PROFILES OF BDS-DNS RESULTS AND CONVERSION OF SOLVENT ENERGY

It is well known that addition of small amount of long-chain polymers into the turbulent flow in the Newtonian fluid causes significant drag reduction (DR). A theoretical concept of DR due to Lumley [2] is that randomly coiled polymer molecules stretch in regions of strong deformation, increasing the elongation viscosity of the solution and results in damping of small turbulent eddies and DR. de Gennes [3] considered that Lumley scheme may hold for (rigid) rods, and in the coil-stretch transition, stretched chains behave elastically and it leads to modifications of turbulent cascade. It is generally assumed that the fluid surrounding the bead-spring configuration of the polymers moves affinely with an equivalent continuum. In the fluid diluted with stretched polymer or rod, molecular motions may not precisely correspond to the macroscopic deformation. In [4], the Johnson-Segalman (JS) constitutive model for the polymer stress τ_{ij} [5] was adopted to introduce non-affinity, where the strength of non-affinity is described by the slip parameter $\alpha(0 \leq \alpha \leq 1)$. Remarkable enhancement in DR was achieved when non-affinity is maximum ($\alpha = 1.0$) in homogeneous isotropic turbulence and pipe flow.

To extract exact distribution and orientation of the dumbbells, we adopt multi-scale BDS-DNS approach [6]. The position vectors of each bead of the $n-$th dumbbell are denoted by $\boldsymbol{x}_1{}^{(n)}$ and $\boldsymbol{x}_2{}^{(n)}$ ($n = 1, 2, \cdots N_t$, N_t is the number of dumbbells). When $\alpha = 0.0$, the governing equation for motion of the end-to-end connector vector $\boldsymbol{R}^{(n)}$ is given by

$$\frac{dR_i{}^{(n)}}{dt} = \{u_i(x_1{}^{(n)}) - u_i(x_2{}^{(n)})\} - \frac{1}{2\tau_s}\frac{R_i{}^{(n)}}{1 - (R_k{}^{(n)}R_k{}^{(n)}/{L_{max}}^2)} + \frac{r_{eq}}{\sqrt{2\tau_s}}\left((W_1{}^{(n)})_i - (W_2{}^{(n)})_i\right), \tag{1}$$

where $u_i(x)$ denotes the velocity field of the solvent fluid, and the finitely extensible nonlinear elastic (FENE) model is applied to the elastic force. $(W_{1,2}{}^{(n)})_i$ is a random force representing the Brownian motion of particles. τ_s denotes the relaxation time. We introduce the non-affinity by allowing a slippage in the motion of polymer strand [4]. The velocity imposed at bead i, is given as $\boldsymbol{u}_i = \boldsymbol{u}_g + (\nabla \boldsymbol{u}_g) \cdot (\boldsymbol{R}_i - \boldsymbol{R}_g) - 2\alpha\{\boldsymbol{S}_t \cdot (\boldsymbol{R}_i - \boldsymbol{R}_g)\}$, where $\boldsymbol{u}_g$ denotes the velocity at the center and $\nabla \boldsymbol{u}_g$ is the velocity gradient tensor and $\boldsymbol{S}_t$ is the strain rate. When $\alpha = 0.0$, Eq. (1) becomes analogous to the upper-convective derivative for evolution of a contravariant vector, $\frac{dR^i}{dt} = R^j \frac{\partial u^i}{\partial x^j}$. The dumbbells concentrate along the vortex lines. When $\alpha = 1.0$, Eq. (1) becomes analogous to the lower-convective derivative for material surface element with its covariant vector area, $\frac{dR_i}{dt} = -R_j \frac{\partial u^j}{\partial x^i}$. Elasticity arises in the sheet-like region and $\boldsymbol{R}$ aligns transversely with the vorticity vector $\boldsymbol{\omega}$. When $\alpha = 0.0$ $\boldsymbol{R}$ tends to become parallel to $\boldsymbol{\omega}$ [4]. By taking ensemble average over a small volume containing a large number of dumbbells, the JS model is obtained. We carried out DNS using 128^3 grid points, $\tau_s = 2.8$, $N_t = 10^9$. Weissenberg number $Wi = 10.0$ in which EIT arises. Pseudospectral technique with a $3/2$-rule de-aliasing is used. τ_{ij} due to the force acting on the fluid from the dispersed dumbbells are added to the Navier-Stokes equation, where replica method was used [6].

Figure 1 (a) shows the temporal variations in ε. Smaller ε implies larger DR. When $\alpha = 0.0$ DR occurs, but DR in $\alpha = 1.0$ is more remarkable. Figure 1 (b) shows the PDF for the length of the dumbbells. Covariant dumbbells exhibit larger extension close to the maximum length (≈ 0.1) and larger viscoelastic effect is caused in the covariant dumbbells. Note that the PDF for covariant dumbbells is segregated into two groups of large and smaller lengths.

The approximate solution of the the JS model expanded in τ_s becomes [4] $\tau_{ij} \approx \nu(1-\beta)\big[2S_{ij} + 2\tau_s\{(1-2\alpha)2S_{ik}S_{kj} - (S_{ik}\Omega_{kj} + S_{jk}\Omega_{ki})\}$ up to the first order in τ_s, where Ω_{ij} is the vorticity tensor. The production term for polymer elastic energy, P_e becomes $P_e \equiv \tau_{ij}S_{ji} \approx 4\nu(1-\beta)\tau_s(1-2\alpha)2S_{ik}S_{kj}S_{ji}$. The $-S_{ik}S_{kj}S_{ji}$ term is also responsible for production of dissipation ε, P_ε. Therefore, the solvent energy is converted to either elastic energy or dissipation. When the former case

*Corresponding author. Email: khoriuti@mes.titech.ac.jp

occurs, elasticity and tension force arises and it leads to DR, while in the latter, drag is enhanced. The shear stress comes from the $S_{ik}S_{kj}(i\ /\ j)$ term. It turned out that when the dumbbells are highly stretched, shear stress becomes large although the normal stress is dominant when the length is intermediate. Noting that $-S_{ik}S_{kj}S_{ji}$ is predominantly positive, when $\alpha = 0.0$, $P_e \propto S_{ik}S_{kj}S_{ji} < 0$ and $P_\varepsilon \propto -S_{ik}S_{kj}S_{ji} > 0$. When $\alpha = 1.0$, $P_e \propto -S_{ik}S_{kj}S_{ji} > 0$ and $P_\varepsilon \propto -S_{ik}S_{kj}S_{ji} > 0$. Thus, in the highly stretched dumbbells, the contravariant polymers transfer the elastic energy back into the solvent and it is converted to dissipation. In the covariant polymers, the transfer can proceed to both elastic energy and dissipation.

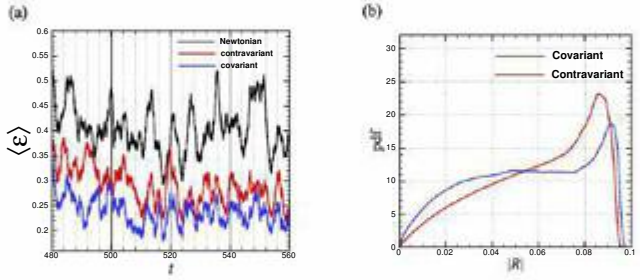

Figure 1: (a) Temporal variations in the dissipation rate ε.; (b) PDF for the length of the dumbbells.

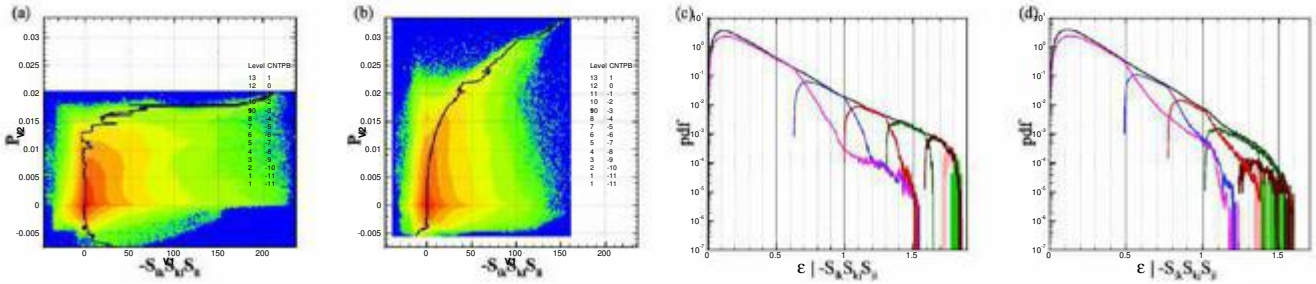

Figure 2: (a): joint PDF between $-S_{ik}S_{kj}S_{ji}$ (x-axis) and P_e (y-axis) from the case of $\alpha = 0.0$; (b): $\alpha = 1.0$; (c): PDF for ε taken conditionally on the magnitude of $-S_{ik}S_{kj}S_{ji}$ from the case of $\alpha = 0.0$; (d): $\alpha = 1.0$.

Figure 2 (a) and (b) show the joint PDF between $-S_{ik}S_{kj}S_{ji}$ and P_e in the cases of $\alpha = 0.0$ and 1.0, respectively. When $\alpha = 0.0$, large $-S_{ik}S_{kj}S_{ji}$ does not contribute to generation of large P_e, whereas large P_e occurs in association with large values of $-S_{ik}S_{kj}S_{ji}$ when $\alpha = 1.0$. Figure 2 (c) and (d) show the PDF for ε in $\alpha = 0.0$ and 1.0, respectively. The value of $-S_{ik}S_{kj}S_{ji}$is divided into 7 zones. PDF is taken in each zone. When $\alpha = 0.0$, ε monotonically increases as the value of $-S_{ik}S_{kj}S_{ji}$ increases. Transfer to dissipation overwhelms transfer to elastic energy in $\alpha = 0.0$. When $\alpha = 1.0$, the PDF of ε saturates in the intermediate zones of $-S_{ik}S_{kj}S_{ji}$. Transfer to elastic energy overwhelms transfer to dissipation, and the drawback of the contravariant polymer is eliminated in the covariant polymers.

CONCLUSIONS

Effect of introduction of non-affinity in the motion of polymers on elasto-inertial turbulence is studied using BDS-DNS. It is shown that contravariant polymers release the elastic energy back into the solvent when highly stretched and dissipation increases. Covariant polymers retain the elastic energy when highly elongated, which leads to larger DR. We consider that this difference is attributable to flexibility and rigidity in the contravariant and covariant polymers, respectively. Present results provide support for the hypothesis due to de Genne [3].

References

[1] P. C. Valente, C. B. da Silva and F. T. Pinho: J. Fluid Mech 760, 39-62, 2014.
[2] J.L. Lumley: Annual Rev. Fluid Mech 1, :367-384, 1969.
[3] P.G. de Gennes: Physica, 140A,:9-25, 1986.
[4] K. Horiuti, K. Matsumoto and K. Fujiwara: Phys. Fluids 25: 015106, 2013.
[5] M.W. Johnson Jr. and D. Segalman: J. Non-Newtonian Fluid Mech 2, 255-270, 1977.
[6] T. Watanabe, and T. Gotoh: J. Fluid Mech. 717, 535- 575, 2013.

ASYMMETRIC SURFACE TEXTURES AND NON-NEWTONIAN FLUIDS FOR DECREASED FRICTION

Jonathon K. Schuh and Randy H. Ewoldt *

Department of Mechanical Science and Engineering, University of Illinois at Urbana-Champaign, Urbana, Illinois, United States of America

Summary Using surface textures has been shown to decrease friction in lubricated sliding contact with Newtonian fluids (oils). Adding polymers to the oils increases their lubricating effectiveness, and also causes the solution to be Non-Newtonian. We present an experimental investigation varying both the surface texture depth profile and the viscoelastic lubricant in order to determine their effects on friction reduction. Gap-controlled experiments were performed on a custom tribo-rheometer in order to systematically examine the friction reduction by varying the Reynolds number, Weissenberg number, and Deborah number in bi-directional motion. Cavitation effects are not present so that the normal force is produced solely by the surface textures and the lubricants. We show that the symmetry of the surface textures must be broken in order to produce normal forces above the viscoelastic response, and that an optimal angle of asymmetry β exists for decreasing friction with asymmetric surface textures and viscoelastic lubricants.

INTRODUCTION

Surface texturing has been used in recent years in order to reduce the friction in lubricated sliding contact[1]. Surface textures can decrease the apparent area of contact in boundary lubrication, act as reservoirs that retain lubricant during startup [2], increase the film thickness and increase hydrodynamic pressure to further separate the plates [3], and decrease the local shear stress [4], all of which contribute to friction reduction.

We experimentally examine the effects of different surface texture depth profiles on decreasing friction through the reduction of apparent viscosity and the production of normal forces. Gap-controlled experiments were performed on a custom tribo-rheometer in order to systematically determine the normal force production and apparent viscosity reduction with varying Reynolds number up to a maximum Reynolds number with respect to gap height $Re_h = 59.54$. Previous experimental work [4, 5] only tested with the top plate moving in one direction. In our work here the top plate was allowed to rotate in both directions to verify symmetry in the experimental set up and to determine direction of motion dependence on the normal force and apparent viscosity reduction.

A recent trend in the lubrication industry is to use polymer additives with Newtonian oils in order to obtain better viscosity-temperature and viscosity-pressure dependence [6] and to increase the load carrying capacity [7]. We present an experimental examination of the effects of surface texture depth profiles with a viscoelastic lubricant. Gap controlled experiments were performed on a custom tribo-rheometer in order to systematically examine the friction reduction with varying Reynolds number, Weissenberg number $Wi = \lambda\dot{\gamma}$ where λ is the fluid relaxation time scale and $\dot{\gamma} = \Omega R_0/h$ is the nominal shear rate, and Deborah number $De = \lambda/t_{char}$ where $t_{char} = \Omega/\phi$ and ϕ is the periodic spacing of the surface texutres. Cavitation effects are not apparent in our measurements; therefore the normal force produced is solely from viscous effects caused by the surface textures and by the viscoelastic response of the fluid.

RESULTS AND DISCUSSION

The apparent viscosity reduction of the surface textures with the viscoelastic lubricant is given in Figure 1A. The flat plate matches the Carreau-Yasuda model obtained for the lubricant for all the gap heights tested, independent of the direction of motion. The surface textures decrease the apparent viscosity beyond the shear thinning effects, independent of the direction of motion.

The normal forces produced with the surface textures and the viscoelastic lubricant is given in Figure 1B. The forces produced by the flat plate are solely due to the viscoelastic response, independent of the direction of motion. The forces produced with the symmetric texture are barely above the viscoelastic response. The asymmetric textures produce normal forces above the viscoelastic response, and the magnitude of the normal force depends on the direction of motion and the value of β, suggesting there is an optimal surface texture for decreasing friction with viscoelastic lubricants.

The apparent viscosity reduction and normal force production can be combined as the effective friction coefficient, given as

$$\mu^* = \frac{M/R_0}{F_N}. \tag{1}$$

The effective friction coefficient for all the surface textures at each of the gap heights tested is given in Figure 2. A minimum is observed in the effective friction coefficient, suggesting that there is an optimal β for decreasing friction with a Non-Newtonian fluid.

*Corresponding author. Email: ewoldt@illinois.edu

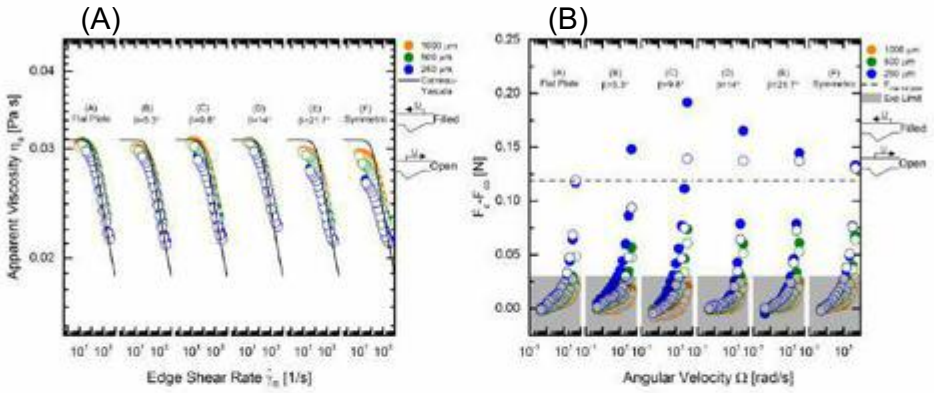

Figure 1: Results of the surface textures tested with a Non-Newtonian viscoelastic lubricant. (A) is the apparent viscosity reduction. (B) is the normal force production.

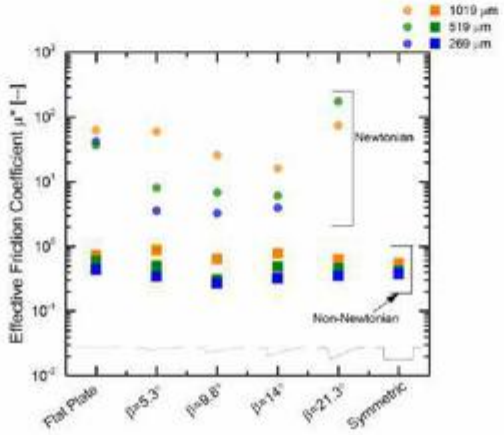

Figure 2: Effective friction coefficient $\mu^* = \frac{M/R_0}{F_N}$ for all the surface textures at each of the gaps tested experimentally with both Newtonian and Non-Newtonian fluids. The results with the Non-Newtonian fluid are always lower than those with the Newtonian fluid, meaning that the combined performance of the surface textures and Non-Newtonian fluids is better than the surface textures alone.

CONCLUSIONS

We show that the surface textures decrease the apparent viscosity of a viscoelastic lubricant beyond the shear thinning effects of the lubricant. We also show that symmetry must be broken in order to produce normal forces above the viscoelastic response, and the magnitude of the forces produced depend on the value of β of the asymmetric textures. Finally, we show that there appears to be a minimum in the effective friction coefficient as a function of the surface texture. This suggests that there is an optimal surface texture for decreasing friction in lubricated sliding systems with a viscoelastic lubricant.

References

[1] A. Erdemir, "Review of engineered tribological interfaces for improved boundary lubrication",Tribology International, vol. 38, pp.249-256, 2005.

[2] I. Etsion, "Improving tribological performance of mechanical components by laser surface texturing," Tribology Letters, vol. 17, no. 4, pp. 733-737, 2004.

[3] A. Ramesh et al., "Friction characteristics of microtextured surfaces under mixed and hydrodynamic lubrication," Tribology International, vol. 57, pp. 170-176, 2013.

[4] M.T. Johnston, W.P. King, and R.H. Ewoldt, "Shear stress characteristics on microtextured surfaces in gap-controlled hydrodynamic lubrication," Tribology International, vol. 82, pp. 123-132, 2015.

[5] C. Shen and M.M. Khonsari, "Effect of dimple's internal structure on hydrodynamic lubrication," Tribology Letters, vol. 52, pp. 415-430, 2013.

[6] G.W. Stachowiak and A.W. Bachelor, Engineering Tribolology, 4th ed.: Elsivier, 2014.

[7] D.R. Oliver, "Load enhancing effects due to polymer thickening in a short model journal bearing," Journal of Non-Newtonian Fluid Mechancis, vol. 30, pp. 185-196, 1988.

Non-local vorticity generation by surface roughness in viscoelastic shear flows

Jacob Page[1], Jin Lee[2], and Tamer A. Zaki *[2]

[1]*Department of Mechanical Engineering, Imperial College, London, SW7 2AZ, UK*
[2]*Department of Mechanical Engineering, Johns Hopkins University, MD 21218, USA*

Summary The vorticity response to small-amplitude surface undulations in a viscoelastic Couette flow is examined. An integral measure is defined to quantify the depth of vorticity penetration into the bulk flow. Three regimes of penetration are identified, and each occupies a sector of a phase diagram parameterized by the ratios of the channel depth and of the critical-layer (CL) height to the lengthscale of the surface roughness. The CL emerges due to the propagation of vorticity waves along the tensioned mean-flow streamlines. The most intriguing behavior, the *trans-critical* regime, occurs when the CL lies within one wavelength from the wall. In trans-critical flows a kinematic mechanism associated with the relative realignment of the polymer by the mean shear amplifies the vorticity in 'sheets' around the CL. The effect is dominant at this location since the vorticity waves appear steady to an observer advecting with the mean flow.

PROBLEM FORMULATION

Hoop stresses established in viscoelastic flows with curved streamlines can initiate linear instability even in the inertialess limit [1], a phenomenon which vanishes in parallel flows [2]. However, in planar configurations finite amplitude perturbations can generate streamline curvature which is susceptible to secondary instability [3]. In this work we consider an important related problem: how do small distortions in the surface topography of a parallel, viscoelastic shear flow affect streamline curvature in the bulk?

We consider viscoelastic Couette flow, $U^* = \dot{\gamma}^* y^*$, in a channel of depth d^* driven by motion of the top wall. The planar Couette flow has an associated viscoelastic streamwise stress $\mu_p T^*_{11} = \mu_p 2\dot{\gamma}^{*2}\varsigma$ and shear stress $\mu_p T^*_{12} = \mu_p \dot{\gamma}^*$, where μ_p is a polymeric viscosity and ς the relaxation time. The wavy surface of the lower wall is $y^* = h^*\cos(k^* x^*)$. In the linear regime, and assuming small wave slopes, $k^* h^* \ll 1$, the roughness leads to the slip boundary condition, $u^*(x^*, y^* = 0) = \circ\, \dot{\gamma}^* h^* \cos(k^* x^*)$. In these expressions the asterisk identifies a dimensional quantity. The problem is non-dimensionalized using the roughness wavenumber, k^*, and the shear rate, $\dot{\gamma}^*$. We seek steady solutions of the form $\phi'(\mathbf{x}) = \phi(y)\exp(\mathrm{i}kx)$, where the unit dimensional wavenumber $k = 1$ is retained for clarity.

The perturbation field is examined in terms of the vorticity, $\boldsymbol{\omega} = \nabla \wedge \mathbf{u}$, and the polymer torque, $\boldsymbol{\chi} = \nabla \wedge (\nabla \cdot \boldsymbol{\tau})$, where $\boldsymbol{\tau}$ is the perturbation polymer stress tensor. In the present problem the only relevant components of the vorticity and torque are in the spanwise direction, and in an Oldroyd-B fluid they satisfy [4, 5],

$$\overbrace{\mathrm{i}k\dot{\gamma}y\omega}^{\text{advection}} = \frac{\alpha^2}{R}\Big[\overbrace{\beta\left(\mathrm{d}_y^2 \circ\ k^2\right)\omega}^{\text{solvent diffusion}} + \overbrace{(1\circ\ \beta)\chi}^{\text{polymer torque}}\ \Big], \tag{1a}$$

$$\underbrace{\mathrm{i}k\dot{\gamma}y\chi}_{\text{advection}} + \underbrace{\frac{1}{W}\chi}_{\text{relaxation}} = \underbrace{2\mathrm{i}k\dot{\gamma}\mathrm{d}_y\varphi}_{\text{kinematics}} + \Big[\underbrace{\circ\, k^2 T_{11} + 2\mathrm{i}kT_{12}\mathrm{d}_y}_{\text{streamline tension}} + \underbrace{\frac{1}{W}\left(\mathrm{d}_y^2 \circ\ k^2\right)}_{\text{linear viscoelasticity}}\Big]\omega, \tag{1b}$$

where $\alpha \equiv k^* d^*$ is the normalized channel depth, $R = \dot{\gamma}^* d^{*2}/(\nu_s + \nu_p)$ is the bulk Reynolds number, $W = \dot{\gamma}^*\varsigma$ the Weissenberg number and $\beta = \nu_s/(\nu_s + \nu_p)$ the ratio of solvent to total viscosity. The variable φ is a polymer potential, $\nabla^2\varphi = \circ\, \chi$. Lines of constant φ are tangent to polymer force vectors. The most important terms in the torque equation (1b) are those labelled 'kinematics' and the T_{11} component of the 'streamline tension' term. The former generates torque as the mean shear re-aligns layers of varying polymer force. The latter provides a mechanism for the propagation of vorticity waves.

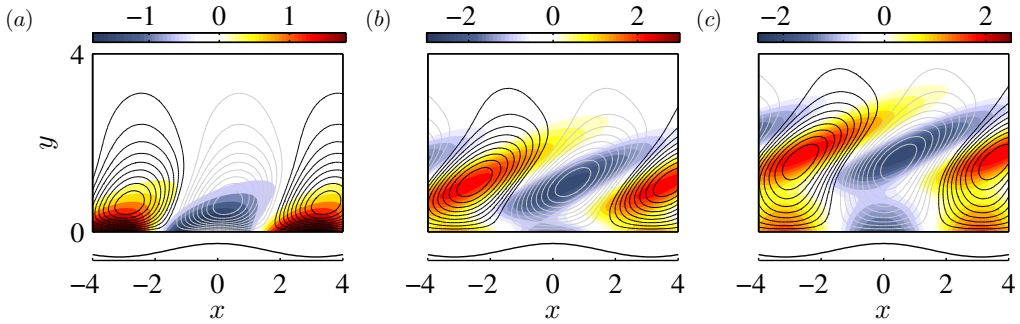

Figure 1: Perturbation spanwise vorticity (colors) and streamfunction (lines) due to surface waviness. Here $\alpha = 10$, $R = 800$. (a) Newtonian flow. (b) Viscoelastic flow, $\beta = 0.7$, $W = 30$. (c) Viscoelastic flow, $\beta = 0.7$, $W = 60$.

*Corresponding author. Email: t.zaki@jhu.edu

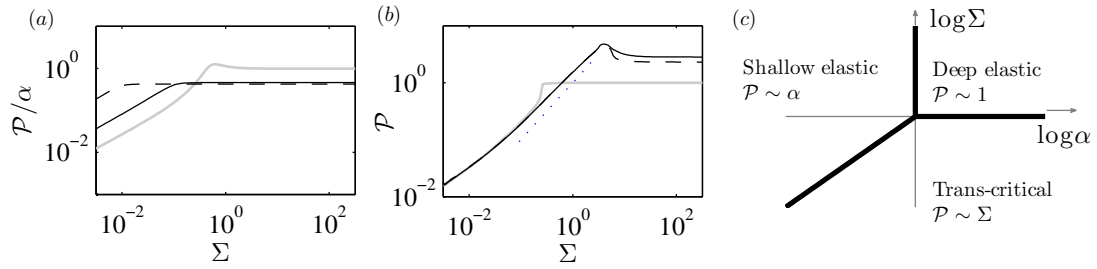

Figure 2: Penetration depth $\mathcal{P}$ in shallow ((a), '- - -' $\alpha = 0.01$, '——' $\alpha = 0.1$, '——' $\alpha = 0.5$) and deep ((b), '——' $\alpha = 1$, '——' $\alpha = 5$, '- - -' $\alpha = 10$) channels with with $W = 60$, $\beta = 0.7$. (c) Phase diagram of vorticity penetration.

TRANS-CRITICAL FLOWS

In inertia-dominated Newtonian flows where the viscous diffusion length is smaller than the channel height, $(\alpha^2/R)^{1/3} < \alpha$, the vorticity perturbations are swept downstream as they diffuse into the bulk flow [6], as shown in figure $1(a)$. Corresponding viscoelastic flows are considered in figures $1(b)$ and (c), and the influence of the polymer is increased by raising the Weissenberg number W. As W increases, the vorticity maximum detaches from the wall and moves upwards in the flow, where amplification occurs in 'stripes' which are aligned favorably with the shear.

The mechanics of this behavior are explained by examining the vorticity-torque system (1) in the limit $W \gg 1$. The leading approximation retains the effects of advection and the polymer torque in the spanwise vorticity equation (1a). In the polymer torque equation (1b) only the advection, kinematics and T_{11} component of the streamline tension term are kept. The reduced equations can be combined into a single 'elastic-Rayleigh' equation,

$$\underbrace{\mathrm{i}k\dot{\gamma}\left(y^2 \circ \Sigma^2\right)\omega_0}_{\text{advection \& wave propagation}} = \underbrace{\Sigma^2 \mathrm{d}_y\left(\varphi_0/W\right)}_{\text{kinematics}}, \tag{2}$$

where $\Sigma \equiv \alpha\sqrt{(1 \circ \beta)T_{11}/R}$. On the left hand side of (2) is the combination of base-flow advection and *steamwise wave propagation* along the tensioned mean-flow streamlines. The kinematic term from the torque equation (1b) is a source term.

The streamwise vorticity waves arise from an interplay between flow inertia and fluid elasticity, and affect the efficacy of the kinematic source term to generate vorticity. The source is most effective at $y = \Sigma$, or the *critical-layer* (CL) where the advection and vorticity wave speeds are equal. This is because the source term generates torque through the realignment of layers of varying polymer force by the mean shear, an effect which can operate most efficiently at the CL where an observer travelling with the mean flow would see a stationary vorticity wave. Equation (2) is singular at $y = \Sigma$, and we have constructed a uniformly valid solution using matched asymptotic expansions. This solution demonstrates that the CL thickness is set by the solvent diffusion lengthscale, $\delta_c \sim (\alpha^2\beta/R)^{1/3}$, and provides an explicit expression for the level of vorticity amplification there, $\omega_0(y = \Sigma) \sim \Sigma^{3/2}\mathrm{exp}(\circ\,\Sigma)/\delta_c^2$.

PHASE DIAGRAM

In order to quantify the induced vorticity perturbation, we introduce the integral penetration measure $\mathcal{P} \equiv y(\Lambda^r = 0.99)$ where $\Lambda^r(y) = \int_0^y |\omega(y')|^2\mathrm{d}y' / \int_0^\alpha |\omega(y')|^2\mathrm{d}y'$. This quantity depends on two parameters: the ratios of the channel depth and of the CL height to the roughness wavenumber, α and Σ respectively. Figures $2(a, b)$ report values of $\mathcal{P}$ in both shallow and deep channels. For shallow channels, $\alpha < 1$, the CL does not influence $\mathcal{P} \sim \alpha$ since it is outside of the domain, $\Sigma \gtrsim \alpha$. We term these cases 'shallow elastic' flows. In deep channels (figure $2b$) the penetration depth grows linearly with the CL height, $\mathcal{P} \sim \Sigma$ for $\Sigma \lesssim 1$. These are the 'trans-critical' flows described above. However, once the critical layer is sufficiently far from the wall, $\Sigma \gtrsim 1$, it no longer influences the perturbation field and the penetration depth reaches a maximum, $\mathcal{P} \sim 1$. These are termed 'deep elastic' flows'. These results are summarized in a phase diagram in figure $2(c)$.

The present analysis focused on trans-critical flows whose parameters are relevant to drag-reduced turbulence [7, 8], Furthermore, the shallow elastic regime has interesting features which were not discussed. In particular, there is an inertialess mechanism by which the vorticity amplifies at the top wall. Finally, while the analysis is performed with the Oldroyd-B model, the same behaviors are retained qualitatively in the more realistic FENE-P model.

References

[1] Shaqfeh, E. S. G.: Purely elastic instabilities in viscometric flows. Ann. Rev. Fluid Mech. 28:129-185, 1996.

[2] Pakdel, P. & McKinley, G. H.: Elastic instability and curved streamlines. Phys. Rev. Let. 77:2459-2462, 1996.

[3] Morozov, A. & Saarloos, W. V.: Subcritical finite-amplitude solutions for plane Couette flow of viscoelastic fluids. Phys. Rev. Let. 95:1-4, 2005.

[4] Page, J. & Zaki, T. A.: Streak evolution in viscoelastic Couette flow. J. Fluid Mech. 742:520-551, 2014.

[5] Page, J. & Zaki, T. A.: The dynamics of spanwise vorticity perturbations in homogeneous viscoelastic shear flow. J. Fluid Mech. 777:327-363, 2015.

[6] Charru, F. & Hinch, E. J.: 'Phase diagram' of interfacial instabilities in a two-layer Couette flow and mechanism of the long-wave instability. J. Fluid Mech. 414:195-223, 2000.

[7] White, C. M. & Mungal, M. G.: Mechanics and prediction of turbulent drag reduction with polymer additives. Ann. Rev. Fluid Mech. 40:235-256, 2008.

[8] Graham, M. D.: Drag reduction and the dynamics of turbulence in simple and complex fluids. Phys. Fluids 26:101301, 2014.

STARTUP POISEUILLE FLOW OF A BINGHAM FLUID WITH OR WITHOUT THIXOTROPIC BENAVIOR

Andreas Alexandrou[1], Georgios Georgiou[2], Raja Huilgol[3], Ian Frigaard[4]
[1]Department of Mechanical and Manufacturing University of Cyprus Nicosia, Cyprus
[2]Department of Mathematics University of Cyprus Nicosia, Cyprus
[3]Flinders Mathematical Sciences Laboratory School of Computer Science, Engineering and Mathematics, Flinders University of South Australia, Adelaide, Australia
[4]Department of Mechanical Engineering and Mathematics, University of British Columbia, Vancouver, BC, Canada

Summary In this work we focus attention on the startup flow version of the classical Poiseuille flow in a two dimensional channel for the case of a Bingham fluid by allowing the possibility for thixotropic behavior. We show results for the flow and unyielded core evolution and discuss the effects of the parameters on the final time needed to reach steady state.

INTRODUCTION

The unsteady startup Poiseuille flow is of great theoretical and practical importance. For a Bingham fluid the problem has been tackled mathematically by a variety of methods [1]. The ultimate objective of this work is to solve the flow numerically by using two competing numerical methods (for the case of viscoplastic fluids and to compare the results with those given by analytic solutions [1]. Eventually we seek to establish a widely accepted solution for this problem. Below however due to lack of space, after a brief description of the theoretical background we present and discuss high fidelity numerical results from finite element simulations of the regularized version of the theory.

Theoretical background

We consider the start-up flow of a Bingham plastic in a channel of height $2H$ initiated by a known constant pressure gradient G, such that $G > \tau_0/H$, where τ_0 is the yield stress. The flow field is divided into a yielded region (y_0, H) and an unyielded one $(0, y_0)$. The unyielded region is moving with a constant unknown velocity U_c. In the unsteady case both U_c and y_0 are functions of time. Conservation of linear momentum yields

$$\rho \frac{\partial u}{\partial t} = G + \frac{\partial \tau}{\partial y} \qquad (1)$$

where ρ is the density, $u=u(y,t)$ is the velocity in the x direction and τ is the shear stress. The shear stress τ is expressed using the Bingham flow model as

$$\tau = \tau_0 + \mu \frac{\partial u}{\partial y} \qquad (2)$$

where μ is the plastic viscosity. In case of thixotropy we use the following evolution equation for the structural parameter λ

$$\frac{D\lambda}{Dt} = \alpha(1-\lambda) - \beta\lambda\dot{\gamma} \qquad (3)$$

where α and β are the buildup and breakdown parameters and $\dot{\gamma}$ the rate of strain given by $\dot{\gamma} = du/dy$. For closure we assume that the yield stress is a linear function λ, i.e. $\tau_0 = \lambda\tau_1$ where τ_1 is the yield stress corresponding to the fully structured fluid.

Numerical solution and proposed extrapolation method

The numerical solution for the complete work is obtained by solving Eqs. (1)-(3) along with the constitutive relation for the yield stress with: (a) the augmented Lagrangian method [2] and (b) by regularization employing the Papanastasiou model [3]. The augmented Lagrangian method is implemented using Matlab and, the regularized approach is formulated using the classical Galerkin Finite Element method and solved by Newton-Raphson iteration procedure.

PRELIMINARY RESULTS AND DISCUSSION

Due to space limitation we are presenting here only for the regularized problem for *G=-5*, by using *1000* bi-quadratic elements and time increament *dt=5000*. The results are shown as a function of the Bingham number $Bn = {\tau_1 H}/{\mu U}$ and non-dimensional time $= {\mu t}/{\varrho H^2}$ where t is time and $U = \sqrt{{\tau_1}/{\varrho}}$. The velocity and thickness are scaled using U, and H respectively. Figures 1 and 2 show the non-dimensional thickness (green line) and non-dimensional velocity of the unyielded core region. As it is expected the thickness decreases with time while its velocity (red line) increases. Eventaully

the flow reaches steady state. The steady state results agree with the analytic solution to an accuracy of up to the sixth digit. A comparison between the two figures where the only difference is the magnitude of *Bn* shows that while the core thickens with increasing *Bn* and its velocity decreases. For the chosen parameters the time to reach steady state appears to be less sensitive to *Bn*. This issue however is investigated fully in the completed work.

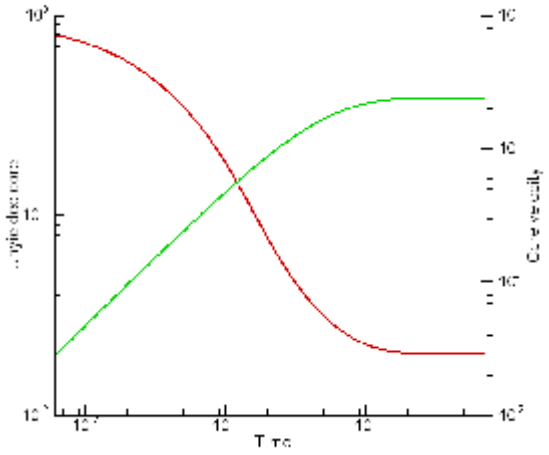

Fig. 1.: Velocity and size of core region (Bn=0.1)

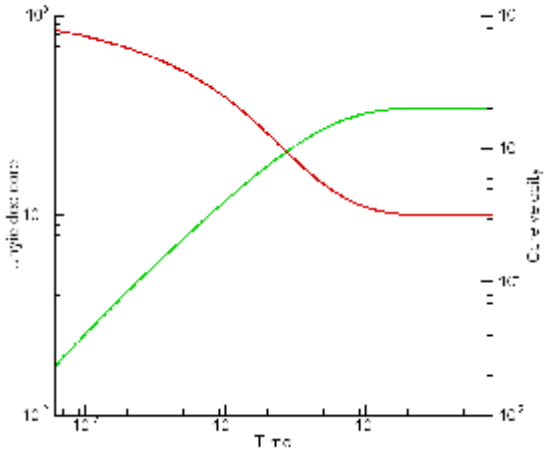

Fig. 2: Velocity and size of core region (Bn=0.5)

Figures 3 and 4 show the effects of thixotropy for Bn=0.5 and β=0.5. Depending on the relative ratio of the coeficients of breakdown and buildup the results are very different from the non-thixotropic cases. Figure 3 corresponds to a lower effective *Bn* because for lower buildup coefficient α less of the original yield stress survives during breakdown. Fig. 4 then corresponds to a case of higher effective Bn. Consistent then with these observations the final thickness for Fig.4 was 0.088039 and that for Fig. 3 *0.069147* (not a steady state value). The corresponding velocities are *2.138820* (Fig. 4) and 2.42848 (Fig.3). Please note that the time to reach steady state changes significantly as the flow represented by Fig. 3 has not reached steady state. This is another issue that is discussed in the completed work.

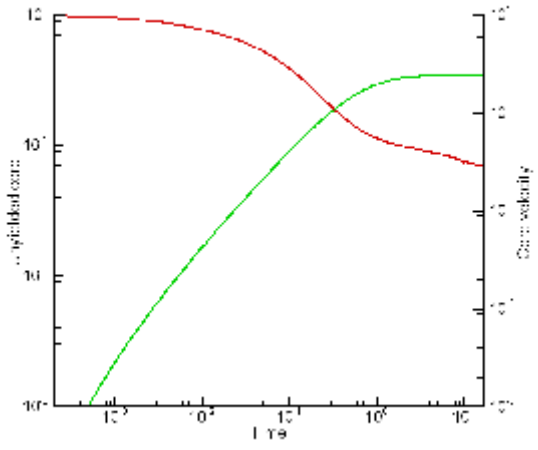

Fig. 3.: Velocity and size of core region *(α=0.1)*

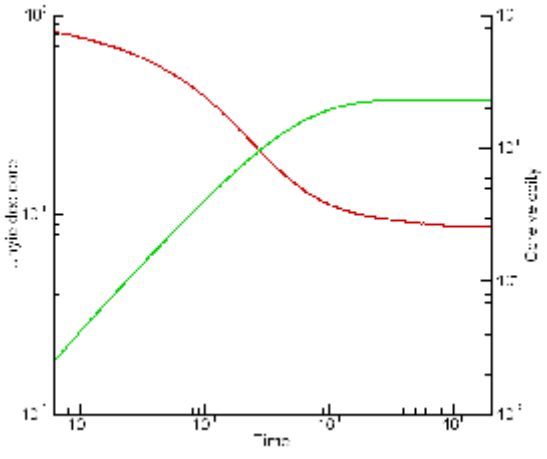

Fig. 4: Velocity and size of core region *(α=0.5)*

References

[1] Raja R. Huilgol, Fluid Mechanics of Viscoplasticity, Springer-Verlag, 2015.

[2] Frigaard, C. Nouar, On the usage of viscosity regularisation methods for visco-plastic fluid computation, Journal of Non-Newtonian Fluid Mechanics 127 (2005) 1-26.

[3] T. C. Papanastasiou, Flows of materials with yield, Journal of Rheology 31 (1987) 385-404.

VISCOELASTIC AND EMPIRICAL MODELS COMPARED IN CONTEXT OF FLOWS IN EXTRUDERS

Stefan Descher*[1] and Olaf Wünsch[1]
[1]*Chair of Fluid Mechanics, University of Kassel, Kassel, Germany*

Summary This contribution deals with the comparison of viscoelastic and empirical rheological models in context of flows in extruders. A simplified model based on the unwound helix channel is used to calculate the characteristic of the machine and the dissipation power curve. Results of computations with the exponential Phan-Thien-Tanner model and a model using only its shear thinning behavior are compared.

MOTIVATION

In modern CFD-analysis of process engineering applications the use of empirical rheological models like Cross or Carreau-Yasuda is common because they allow implementing a shear rate dependent viscosity at a low computational cost. In this approach the shear viscosity curve is modelled and all kinds of other effects that can occur in a fluid relevant to these processes are neglected. For example in polymer melts besides shear-thinning behavior also strain hardening, normal stress differences and transient effects like stress relaxation are relevant. But to consider these effects more complex models like e.g. the exponential form of the Phan-Thien-Tannner Model (EPTT) can be used. It includes all relevant effects, but is expensive with respect to the computation time. A question that may come up in everybody doing computational rheology is, if it is appropriate to just use empirical models or if the effort by using Maxwell-type models might be too high. Because the answer to that question is strongly dependent on the flow type, for every case an investigation should be performed.

In polymer processing extruders play a key role in melt conditioning and feeding casting processes. For these applications machine characteristics are relevant for process control which depends on the fluids properties. In this case it is useful to have numerical data that is reliable.

SHORT OUTLINE

To perform calculations an unwound extruder model for a single flighted machine introduced in [1] is used. Here the helically wound flow channel that is located between barrel and screw as shown in fig. 1 on the left is unwound which leads to the geometry on the right. In this model the screw surface is static and the barrel surface is moving with $v_b = \pi D_b n$, decomposed in the down-channel component v_{bz} and cross-channel component v_{bx} using the helix angle θ. Cyclic boundary conditions are used at the gap between barrel and screw for the cross direction flow and at the channel surface for the down direction flow. To calculate the characteristics of the machine a pressure gradient is implemented by using a body force in the momentum equation. The direction of this force is perpendicular to the velocity of the moving wall.

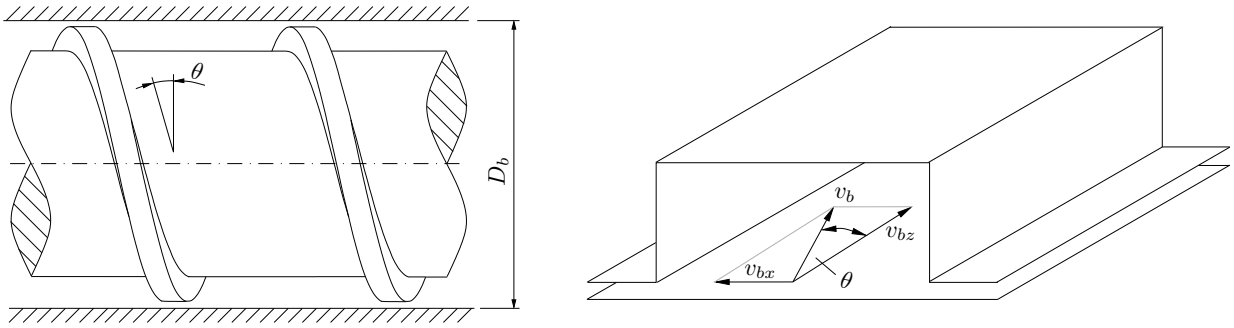

Figure 1: (Left) Single flighted screw in a barrel. (Right) Unwound helix channel model.

The study that is carried out deals with the case the pressure increases in direction of transport. This is given in extruders if e.g. a nozzle is mounted at the outlet. In this configuration one point of interest is when the volume flux is canceled out over the cross section of the channel. It is found by increasing the pressure gradient stepwise starting from zero. For each value one calculation is performed until the steady state is reached. In this work this is done also for a varying relaxation time λ of the EPTT model in a range of the Deborah-number $De = \lambda n$ from $10^{-3} - 10^{3}$. Besides the curve of power consumption is evaluated because it correlates with the dissipative heating. Although the calculations are performed isothermally this is

*Corresponding author. Email: descher@uni-kassel.de

important to know because the material behavior is highly temperature dependent. Investigations with this unwound model were done in [2] for the linear-PTT model analytically focused on the main and secondary flows.

The comparison with the empirical model is done by using the shear viscosity curve of the EPTT model in a list during calculations. For this purpose a solver that calculates the shear rate and uses this list to interpolate values for the viscosity was composed. The list is generated before the calculation using a semi analytical approach based on a Newton-Raphson method. Thereby in the computaion is guaranteed, that the empirical model has the same shear-thinning behavior as the viscoelastic model. The object of this approach is that if deviations occur in the calculations they will be caused by other material phenomena. The results will show the error that has to be taken into account if a fluid that behaves exactly like a EPTT model is described by a model that only concerns the shear properties.

The calculations are performed using foam-extend-3.1 [3] a version of OpenFOAM containing extensions contributed by the user community. For considering the EPTT model a solver based on the log-conformation reformulation [4] was composed. The solver interpolating the viscosity from a list uses a generalized shear rate based on the second invariant of the deformation rate tensor. In both solvers pressure and velocity are coupled with a block matrix method and they are based on outer corrections for stress respectively viscosity. For numerical stability the newtoinian solvent contribution had to be set to $\beta = 1\%$ which is also included in the empirical solver.

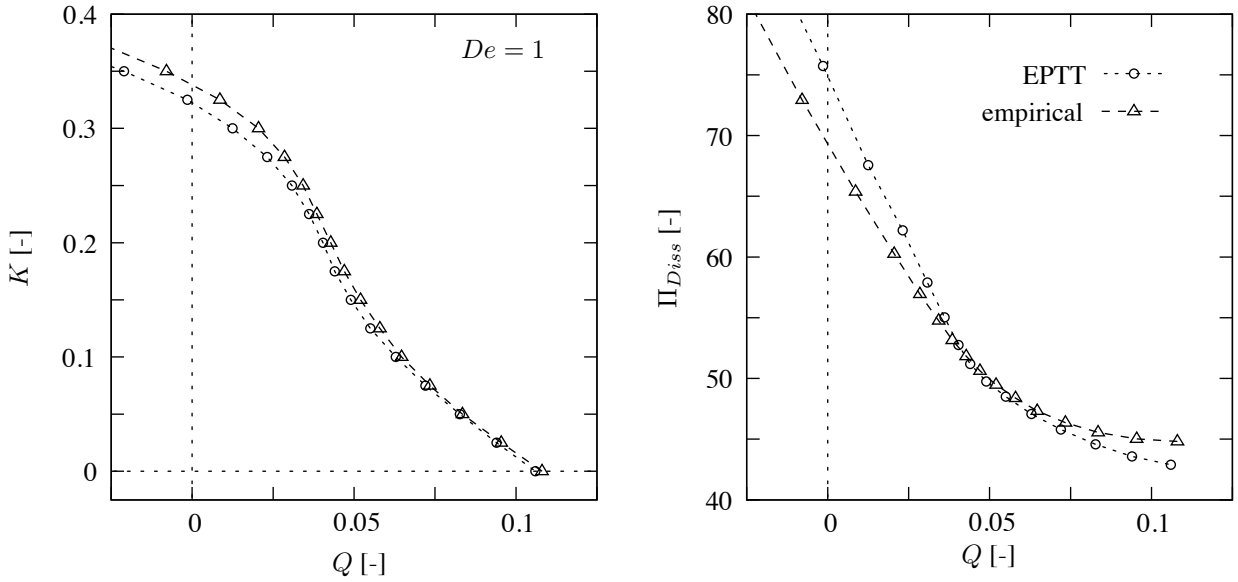

Figure 2: Comparison of the extruder characteristic and dissipation power curve for $De = 1$. (Left) Dimensionless pressure K over dimensionless volume flux Q. (Right) Dimensionless dissipation power Π_{Diss} over Q.

An example of one investigation with $De = 1$ is shown in fig. 2. In the left diagram the dimensionless pressure gradient K is plotted over the dimensionless volume flow rate Q. The right diagram shows the curve of the dimensionless dissipative power Π_{Diss}. The diagram for K shows that both models start with nearly the same value of Q in the pressure gradient free state and have the same shape. They have an increasing spacing that reaches a deviation of 4.9% at $K(Q = 0)$. The empirical model shows a weaker structure, because its curve is always above the one of the EPTT. This means smaller changes in the pressure gradient are needed for the same change in the volume flux. The curves of the dissipative power have a different slope and cross each other. Close to the pressure gradient free point the empirical model overestimates Π_{Diss} by 4.5% and at the characteristic point where $Q = 0$ underestimates it by -6.8%. In the investigated range of De the deviations of the models were in this magnitude. For the boundary values of De range both models behave newtonian and their deviation nearly vanishes. This is obvious for $De = 10^{-3}$ and must be for $De = 10^{3}$ because the viscosity of the EPTT model drops below the solvent viscosity.

References

[1] Tadmor Z., Gogos C.G.: Principles of Polymer Processing. Wiley Interscience, 2006.

[2] Cruz D.O.A., Adams J.A.: Analysis of isothermal flow of a Phan-Thien-Tanner fluid in a simplified model of a single-screw extruder. J. Non-Newtonian Fluid Mech. 167-168:95-105, 2011.

[3] The OpenFOAM® Extend Project: www.extend-project.de

[4] Fattal R., Kupferman R.: Constitutive laws for the matrix-logarithm of the conformation tensor. J. Non-Newtonian Fluid Mech. 123:281-285, 2004.

RECIRCULATING FLOW PAST A CYLINDER OF A YIELD STRESS FLUID

Hamdullah Ozogul[1], Pascal Jay[1a)] & Albert Magnin[1]
[1] *Laboratoire Rhéologie et Procédés, UMR 5520 Univ. Grenoble Alpes, LRP, F-38000 Grenoble, CNRS, LRP, F-38000 Grenoble, France*

Summary The recirculating flow around a circular cylinder is investigated experimentally and numerically in a Poiseuille configuration. A Newtonian fluid and two elasto-viscoplastic fluids without thixotropy prepared with Carbopol polymer are used. A regularised Herschel-Bulkley viscoplastic numerical model has been used to make comparison with experimental results. The morphologies and especially the geometrics characteristics of the twin vortices are described according to the Oldroyd and Reynolds numbers. The unyielded zones are defined. The parameters of the flow at the transition to the recirculating flow regime are provided.

INTRODUCTION

This paper is on the fundamental problem of the flow past a confined circular cylinder in the case of a Newtonian fluid and yield stress fluids. We focus on the recirculating regime of flow which has two vortices attached to the cylinder in a confined medium. The yield stress fluids concern a broad range of fluids used in the industry and in everyday life. An important property of this fluid category is that it takes a solid behaviour below a yield stress τ_0 and flows as a viscous fluid above.

The main features to describe the vortices at the rear of the cylinder are its length, the position of its centre and its separation angle in function of Reynolds number and Oldroyd number which represents the ratio of yield stress effects to viscous effects (Figure 1). In our confinement of 0.2, only two studies which focused on the description of the vortices have been found in the literature for newtonian fluid, Grove et al. [1] with a Poiseuille flow configuration and Coutanceau and Bouard [2] with a uniform velocity profile flow configuration. For yield stress fluids, Mossaz et al. [5] have given some results with a uniform velocity profile flow configuration. These results have been used to compare our results and to discuss about the effect of the flow configuration.

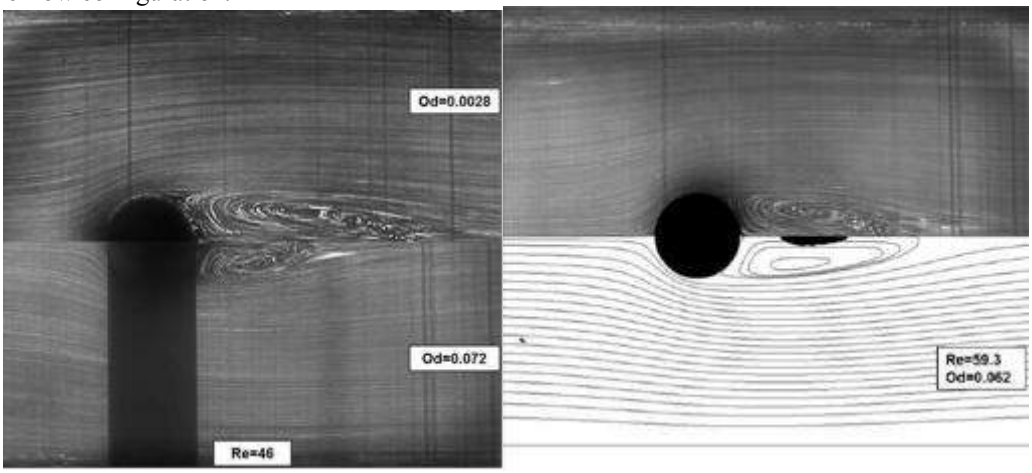

Figure 1: Example of vortices at the rear of the cylinder at Re=46 for the gel A (top part) and the gel B (bottom part) and comparison of numerical and experimental results at Re=59.3.

MATERIALS AND METHODS

Three different fluids have been used in this study: a Newtonian aqueous glucose solution and two yield stress fluids based on Carbopol polymer: gel A $(\tau_0 = 1.88\ Pa, K = 1.85\ Pa.s^n, n = 0.43)$ and gel B $(\tau_0 = 0.02\ Pa, K = 0.38\ Pa.s^n, n = 0.52)$. This polymer is used as a reference model for yield stress fluid experiences. Each fluid has been systematically characterised with rheometer by using specific methods [3]. For the yield stress fluids, the shear stress versus shear rate follows the Herschel-Bulkley constitutive law $\bar{\bar{\tau}} = \left(K\dot{\gamma}^{n-1} + \frac{\tau_0}{\dot{\gamma}}\right)\bar{\bar{\dot{\gamma}}}\ if\ \tau > \tau_0$ and $\bar{\bar{\dot{\gamma}}} = \bar{\bar{0}}$ else, where $\bar{\bar{\tau}}$ denotes the deviatoric part of the stress tensor, K the consistency, n the power index, τ_0 the yield stress. $\bar{\bar{\dot{\gamma}}}$ and $\dot{\gamma}$ are the strain rate tensor and the shear rate, respectively.

An experimental device has been built which consists in a loop working in closed circuit. The test duct has a rectangular cross section with a fixed confinement of $D/H = 0.2$ where D is the diameter of the cylinder and H the height of the channel. The visualisation system includes a high speed camera which allows us to make PIV. The Poiseuille flow is fully

a) Corresponding author. Email: pascal.jay@ujf-grenoble.fr.

developed upstream of the cylinder. A numerical method has been also developed with the ANSYS-Fluent software. The Herschel-Bulkley constitutive law has been implemented with the Papanastasiou's regularisation method

RESULTS

After a qualification of the experimental set-up by comparison to the literature results, the main characteristics of the vortices at the rear of the cylinders have been described for each fluid. The Figure 1 shows the typical influence of Oldroyd number ($Od = \tau_0/(K(V_{max}/D)^n)$ on the vortices at same Reynolds number ($Re = \rho {V_{max}}^{(2-n)} D^n/K$). The critical values of the parameters at the transition no recirculating to the recirculating flow regimes have been established. All the experimental results have been always compared to the numerical ones (Figure 1).
Globally, the yield stress effects are, on one hand, to delay the transition to the recirculating flow regime toward more inertial flow and on the other hand, to keep the vortices near to the cylinder (Figure 1). For this type of configuration, it is possible to distinguish different unyielded zones (Figure 2): first the confinement causes the appearance of a plug flow at the upstream and the downstream far from the cylinder. Then, around or on the cylinder, different unyielded zones rigid or moving can be observed. The size of these zones depends on both inertial and yield stress effects [4].

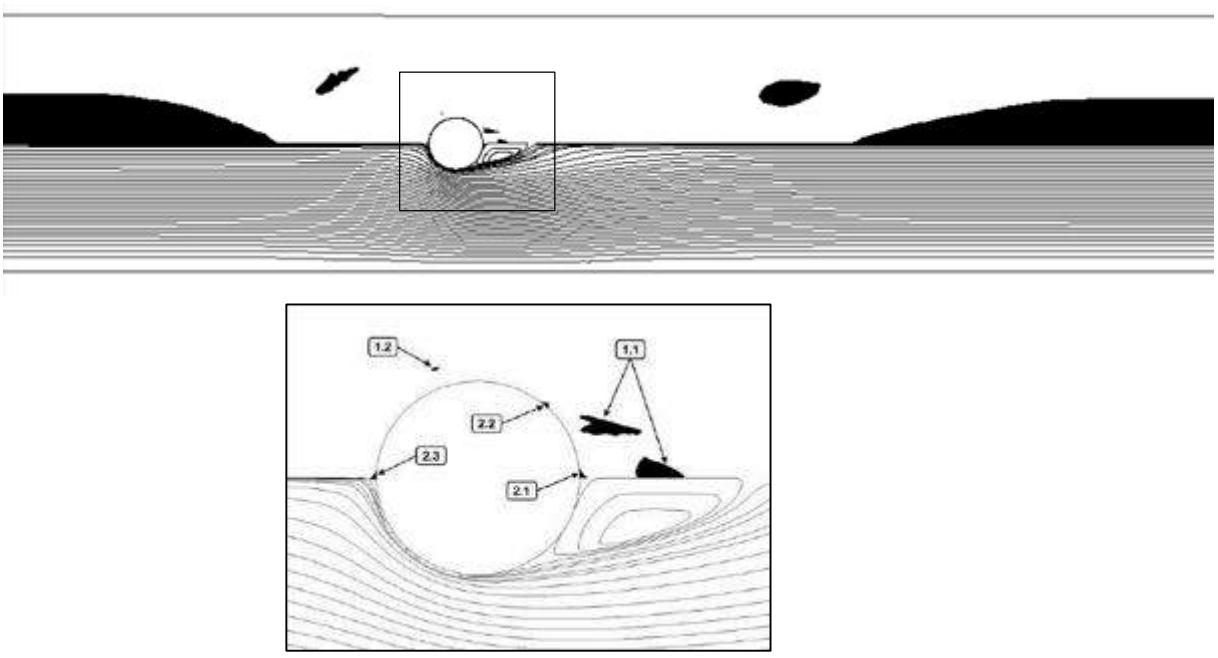

Figure 2: Streamlines and unyielded zones in the global flow (top part) and around the cylinder (bottom part, zoom on the cylinder). The unyielded zones are colored in black. $(Re, Od, n) = (52, 0.92, 0.5)$.

CONCLUSIONS

New results on flow morphologies and particularly on the structure of the vortex rear the cylinder have been determined experimentally and numerically for yield stress fluids. The influences of inertia, viscous and yields stress have been determined. The viscoplastic numerical simulation gives satisfactory results.

References

[1] Grove, A. S., Shair, F. H., and Petersen, E. E.: An experimental investigation of the steady separated flow past a circular cylinder. *J. Fluid Mech*. **19**(01):60-80, 1964.

[2] Coutanceau, M., and Bouard, R.: Experimental determination of the main features of the viscous flow in the wake of a circular cylinder in uniform translation. Part 1. Steady flow. *J. Fluid Mech*., **79**(02):231–256, 1977.

[3] Magnin, A., and Piau, J. M.: Cone-and-plate rheometry of yield stress fluids. Study of an aqueous gel. *J. Non-Newton. Fluid Mech*. **36**:85–108, 1990.

[4] Ozogul, H.: Ecoulement d'un fluide à seuil en milieu confiné : études expérimentale et numérique. *PhD Thesis*, Université Grenoble-Alpes, Grenoble, 2016.

[5] Mossaz, S., Jay, P., Magnin, A.: Non-recirculating and recirculating inertial flows of a viscoplastic fluid around a cylinder. *Journal of Non-Newton. Fluid Mech*. **177-178:**64-75, 2012.

AXIAL DISPERSION IN WEAKLY TURBULENT FLOWS OF VISCOPLASTIC FLUIDS

Amir Maleki*[1] and Ian Frigaard[1,2]
[1]*Department of Mechanical Engineering, University of British Columbia, Vancouver, British Columbia, Canada*
[2]*Department of Mathematics, University of British Columbia, Vancouver, British Columbia, Canada*

Summary In this study we present a framework to characterise the axial dispersion in the turbulent flow of viscoplastic fluids. Assuming Herschel-Bulkley model, we perform the hydraulic calculation for a viscoplastic fluid. Then, we propose a method to correct the well-known logarithmic turbulent velocity profile. Finally, we give an estimate for turbulent diffusivity and axial dispersion. This improves the earlier results of [1] as we demonstrate that the corrections suggested for velocity profile can contribute to significant change in the case of *weakly* turbulent flows. We also report on the effect of viscoplasticity on dispersion.

INTRODUCTION

The sequential flows of fluids along pipes or channels are ubiquitous in the industry. One particular example that we are interested in is the primary cementing of oil and gas wells. During primary cementing one fluid is pumped after another. These fluids have different densities and viscosities and may exhibit viscoplastic behaviour. They may also mix together. The objective of this study is to give an estimate of magnitude of mixing due to axial dispersion. That is, mixing due to difference of fluid parcel velocity with respect to the average velocity.

VISCOPLASTIC PIPE HYDRAULICS

The hydraulic calculations in general amount to defining the relationship between the wall shear stress $\hat{\tau}_w$ and the mean velocity $\hat{W}_0$ for the different flow regimes. A widely used approach is that of [2] in defining (Fanning) friction factor (f_f) as a function of the generalised (Metzner-Reed) Reynolds number $Re_{MR} = 8\hat{\rho}\hat{W}_0^2/\hat{\kappa}'(\hat{\dot{\gamma}}_N)^{n'}$ where $\hat{\kappa}' = \hat{\tau}_w/(\hat{\dot{\gamma}}_L)^{n'}$, $n' = \mathrm{d}\ln\hat{\tau}_w/\mathrm{d}\ln\hat{\dot{\gamma}}_L$, $\hat{\dot{\gamma}}_N$ is the Newtonian strain rate at the wall and $\hat{\dot{\gamma}}_L$ is the strain rate at the wall if the fluid would have been in a laminar flow. The definition of Re_{MR} is designed such that the classical relation $f_f = 16/Re_{MR}$ for laminar flows is recovered for power law fluid. However, the simplicity of this formulation is lost when we deal with more complicated generalized Newtonian fluids or different flow regimes, because Re_{MR} depends on both $\hat{W}_0$ and $\hat{\tau}_w$. This in fact makes it less useful in mapping $\hat{\tau}_w \leftrightarrow \hat{W}_0$. Therefore, we define a Reynolds number which depends only on $\hat{W}_0$:

$$Re_p = \frac{8\hat{\rho}\hat{W}_0^2}{\hat{\kappa}_p(\hat{\dot{\gamma}}_N)^n}, \qquad \hat{\kappa}_p = \hat{\kappa}\left[\frac{3n+1}{4n}\right]^n. \tag{1}$$

To represent the yield stress effect, we introduce a Hedström number that depends linearly on $\hat{\tau}_Y$ and is independent of both $\hat{W}_0$ and $\hat{\tau}_w$. Finally, we construct a similar dimensionless group representing $\hat{\tau}_w$.

$$He = \hat{\tau}_Y\left(\frac{\hat{\rho}^n\hat{D}^{2n}}{\hat{\kappa}_p^2}\right)^{1/(2-n)} \qquad H_w = \hat{\tau}_w\left(\frac{\hat{\rho}^n\hat{D}^{2n}}{\hat{\kappa}_p^2}\right)^{1/(2-n)}, \quad r_Y = \frac{\hat{\tau}_Y}{\hat{\tau}_w} = \frac{He}{H_w} \tag{2}$$

Given He, we show that there is a 1-1 relation between H_w and Re_p.

TURBULENT VELOCITY PROFILE

Following [2] we find that turbulent velocity profile is like:

$$W_0(r) = \sqrt{\frac{f_f}{2}}[A_0\ln(1-r) + B_0] \tag{3}$$

where $A_0 = A_0(n')$ and $B_0 = B_0(n', Re_{MR})$. Two common deficiencies of such log-law profiles are the centreline and near wall behaviours. The velocity profile is symmetric which demand a zero velocity gradient at centreline. Following [3] we add an exponential correction term to fix the centreline behaviour. In addition, as argued by [4] Reynolds stresses decay like $\sim (1-r)^3$ near the wall and therefore, a wall layer correction is needed. We eventually show that the velocity profile can be approximated by:

$$W = \begin{cases} \sqrt{\frac{f_f}{2}}[A_0\ln(1-r) + B_0 + B_{0,c} + B_w] & 0 < r < r_c \\ W^+(y^+) & r_c < r < 1 \end{cases} \tag{4}$$

*Corresponding author. Email: amaleki@mech.ubc.ca

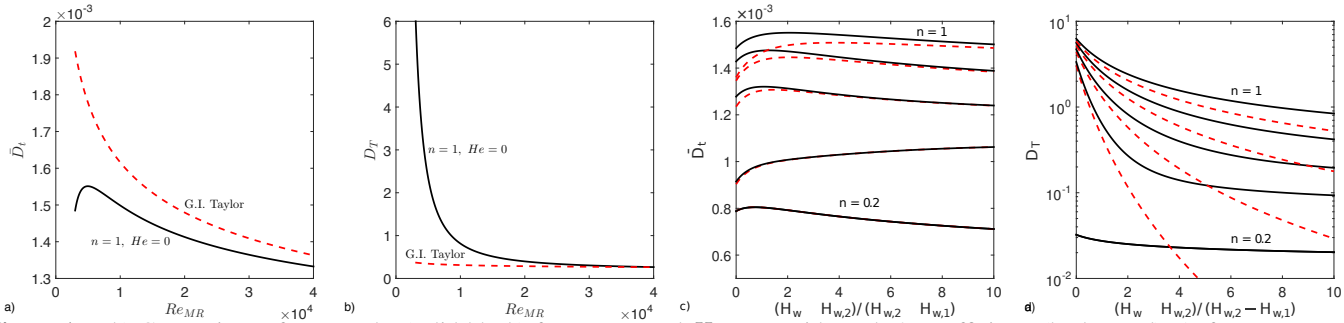

Figure 1: a,b) Comparison of our results (solid black) for $n = 1$ and $He = 0$ with Taylor's coefficients (broken red) [1] for average turbulent diffusivity ($\bar{D}_t$) and dispersion coefficient D_T. c,d)average turbulent diffusivity ($\bar{D}_t$) and dispersion coefficient D_T as a function of H_w and n for $He = 5$

where $B_{0,c}$ and B_w are centreline and wall corrections to the core velocity and W^+ is the wall layer velocity. $y^+ = \frac{1-r}{\psi}$ is the wall coordinate where ψ is a scaling factor. r_c is the wall layer width which is obtained by stitching the two velocity profiles together.

STREAMWISE DIFFUSIVITY AND DISPERSIVITY

We now follow a classical path towards estimating streamwise spreading of a passive tracer by the turbulent flow via diffusive and dispersive mechanisms. To do so, we first need an estimate of turbulent diffusivity D_t. We use the Reynolds analogy for the turbulent transport of mass and momentum, and the axial momentum balance to evaluate the shear stress. We eventually show that:

$$D_t = \begin{cases} \frac{1}{2Sc_t}\left(\frac{f_f}{2}\right)^{1/2} \frac{r}{r_c}\frac{1}{G(r)}\left[r_c - r_Y - \frac{8}{Re_p}\left[\frac{n}{3n+1}\right]^n [G(r_c)]^n \left(\frac{f_f}{2}\right)^{n/2-1}\right] & 0 < r < r_c \\ \frac{\psi}{2Sc_t}\left(\frac{f_f}{2}\right)^{1/2} \frac{\left[1-\psi y^+ - r_Y - (1-r_Y)\left|\frac{\mathrm{d}W^+}{\mathrm{d}y^+}\right|^n\right]}{\left|\frac{\mathrm{d}W^+}{\mathrm{d}y^+}\right|} & r_c < r < 1 \end{cases} \tag{5}$$

where Sc_t is turbulent Schmidt number, and $G(r) = \left|-\frac{A_0}{1-r} + \frac{\mathrm{d}}{\mathrm{d}r}B_{0,c}(r)\right|$. Finally we calculate the dispersion coefficient(D_T) which is defined as below:

$$D_T = \frac{1}{2}\int_0^1 \frac{\left(\int_0^r [W(\tilde{r}) - 1]\tilde{r}\,\mathrm{d}\tilde{r}\right)^2}{rD_D(r)}\,\mathrm{d}r \tag{6}$$

RESULTS

We compare our turbulent diffusivity and dispersion coefficient for the case of Newtonian fluid ($He = 0$, $n = 1$) with those of [1]. Figure 1(a,b) demonstrates the effect of velocity profile correction. Figure 1(c,d) shows averaged turbulent diffusivity ($\overline{D}_t$) and dispersion coefficient (D_T) as a function of dimensionless wall-shear stress (H_w) and power law index (n) for $He = 5$. The dashed red lines indicate the contributions from the turbulent core. We see that in the limit of weak turbulence, the contribution of wall layer is significant.

References

[1] TAYLOR, G. 1954 The Dispersion of Matter in Turbulent Flow through a Pipe *Proc. Roy. Soc. Lon. A, Math. Phys.* **223**(1155), 446–468.

[2] DODGE, D.W. AND METZNER, A.B. 1959 Turbulent flow of non-Newtonian systems *A.I.Ch.E. Journal* **5**(2), 189-204.

[3] BOGUE, D.C. AND METZNER, A.B. 1963 Velocity profiles in turbulent pipe flow; Newtonain and non-Newtonian fluids *Ind. Eng. Chem. Fundam.* **2**(2), 143-149.

[4] KRANTZ, W.B., WASAN, D.T. 1971 A correlation for velocity and eddy diffusivity for the flow of power-law fluids close to a pipe wall. *Ind. Eng. Chem. Fundam.* **10**(3), 424-427.

A DAMPED NEWTON ALGORITHM FOR COMPUTING VISCOPLASTIC FLUID FLOWS

Pierre Saramito *[1]
[1]*Lab. J. Kuntzmann, CNRS and Grenoble university, Grenoble, France*

Summary A new damped Newton algorithm for viscoelastic fluid flows is presented in this paper. This algorithm bases on a projection formulation of the viscoplastic problem and an efficient preconditioned iterative solver for the singular Jacobian. A demonstration is provided by computing a viscoplastic flow in a pipe with a square cross section and performance are compared with the augmented Lagrangian algorithm.

INTRODUCTION

The numerical resolution of viscoplastic fluid flows is still a challenging task. Two main main approaches are considered: the augmented Lagrangian algorithm, which is accurate and slow, and the regularization approach, which is faster but could be less accurate, as it solves a modified problem. This paper is a contribution to an ongoing effort for the development of faster algorithms than the augmented Lagrangian for the resolution of the unregularized viscoplastic model. One of the most efficient algorithm to solve nonlinear problems is the Newton method, due to its superlinear convergence properties. Applying the Newton method to the unregularized viscoplastic problem leads to a singular Jacobian matrix. In this paper, we address directly the singularity of the Jacobian matrix in the Newton method in order to preserve the superlinear convergence.

PROBLEM STATEMENT

The Bingham and Herschel-Bulkley models are characterized by the following property: the material starts to flow only if the applied forces exceed a certain limit σ_0, called the yield limit. We consider the fully developed flow in a prismatic tube (see [1, 2] for details and notations). The problem can be summarized as:

Find $\boldsymbol{\sigma}$ and u defined in Ω such that:

$$\nabla u = P_0(\boldsymbol{\sigma}) \quad (1)$$
$$\operatorname{div} \boldsymbol{\sigma} = \circ\, f \text{ in } \Omega \quad (2)$$
$$u = 0 \text{ on } \partial\Omega \quad (3)$$

where Ω is the pipe section, u is the velocity component along the pipe axis, $\boldsymbol{\sigma}$ is the shear stress vector and $f > 0$ is the given constant pressure force in the pipe. Here, P_0 denotes the following projection operator, defined for all $\boldsymbol{\tau} \in \mathbb{R}^2$ by

$$P_0(\boldsymbol{\tau}) = \begin{cases} \dfrac{1}{K^{1/n}} \left(|\boldsymbol{\tau}| \circ \sigma_0\right)^{1/n} \dfrac{\boldsymbol{\tau}}{|\boldsymbol{\tau}|} & \text{when } |\boldsymbol{\tau}| > \sigma_0 \\ 0 & \text{otherwise} \end{cases}$$

where $K > 0$ is the consistency. Here, (1) expresses the constitutive equation, (2) the conservation of momentum and (3) the no-slip boundary condition. The Bingham dimensionless number is defined by the ratio of the yield stress σ_0 by a representative viscous stress: $Bi = 2\sigma_0/(L\, f)$ where L is the half-length of an edge of a square section Ω of the pipe. The Bingham number Bi and the power law index n are the only two dimensionless numbers of the problem.

NUMERICAL RESULTS AND PERFORMANCES

Fig. 1 plots a comparison of the present inexact preconditioned damped Newton algorithm with the classical Uzawa/augmented Lagrangian method, as proposed in [1]. The augmentation parameter r for the augmented Lagrangian algorithm (AL) has been optimized for the present mesh (a pipe section with $h = 1/80$ and 5781 elements) in order to present the best possible convergence rate. Both algorithms are implemented in the `Rheolef` free software FEM library [3]. The Poisson matrix with no-slip boundary condition used by the AL is factored in sparse format one time for all, thanks to the SUITESPARSE library. At each iteration of the AL, a linear system is solved, based on this factorization. For the present inexact Newton algorithm, the Jacobian of the unregularized problem is solved by using a GMRES algorithm. The Jacobian matrix of the corresponding regularized problem is used as preconditioner and is also factored. This factorization has to be

*Corresponding author. Email: pierre.saramito@imag.fr

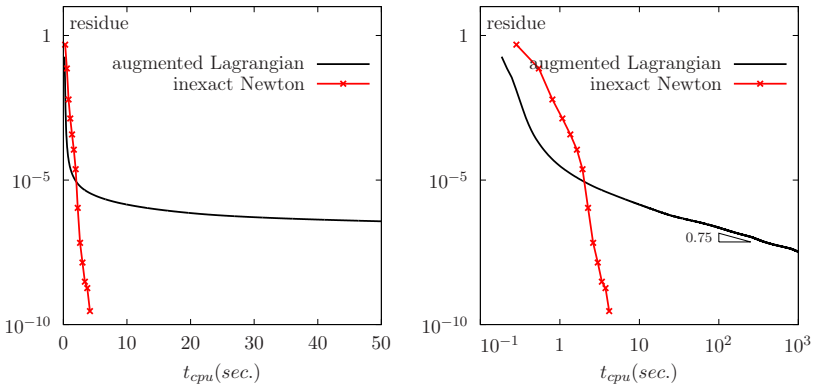

Figure 1: Comparison between the inexact damped Newton method and the augmented Lagrangian algorithm (AL) for the Herschel-Bulkley problem: residu vs CPU time, in seconds when $Bi = 0.1$, $n = 0.5$, $h = 1/80$ (a) in semi-log scale ; (b) in log-log scale.

performed at each iteration of the Newton method, so each iteration of the Newton method is expected to be slower than its AL counterpart. For this reason, Fig. 1 compares these two methods in term of the CPU time instead of iteration number. Observe the dramatic efficiency of the Newton algorithm, which converges in less than 5 seconds to a residue less than 10^{-10} while the AL becomes slower and slower in semi-log scale and adopts an asymptotic behaviour, as shown in semi-log scale, where the residue behaves as $1/t^{\alpha}$, with $\alpha \approx 0.75$. After about 15 minutes, the residue is of about 10^{-7} and, by extrapolation, reaching 10^{-10} would requires one day of computation.

CONCLUSION

For the first time, a Newton method is proposed for the unregularized viscoplastic fluid flow problem. It leads to a superlinear convergence for Herschel-Bulkley fluids when $0 < n < 1$. At each iteration, the singular Jacobian system is solved by an iterative method and an efficient preconditioner based on the regularized problem. An inexact approach permits to increase the performances of the algorithm. A demonstration is provided by the computing a viscoplastic flow in a pipe with a square cross section and performances are compared with the augmented Lagrangian algorithm. Future work will extend this approach to larger flow problems such as flows around obstacles and tridimensional geometries.

References

[1] P. Saramito and N. Roquet. An adaptive finite element method for viscoplastic fluid flows in pipes. *Comput. Meth. Appl. Mech. Eng.*, 190(40-41):5391–5412, 2001.

[2] P. Saramito. A damped newton algorithm for computing viscoplastic fluid flows. *submitted*, 2016. https://hal.archives-ouvertes.fr/hal-01228347/document.

[3] P. Saramito. *Efficient C++ finite element computing with Rheolef*. CNRS and LJK, 2013. http://cel.archives-ouvertes.fr/cel-00573970.

EFFECT OF WALL MOVEMENT ON DISPERSION OF A SOLUTE IN CASSON FLUID FLOW IN AN ANNULUS

Nagarani Ponakala[1a)]&Binil Thomas-Sebastian[2]
[1]*Department of Mathematics, The University of the West Indies, Mona Campus, Kingston, Jamaica, West Indies*
[2] *School of Mathematics and Statistics, University of Technology, Kingston, Jamaica, West Indies*

Summary The present model analyses the dispersion of a solute in Casson fluid in unsteady pressure driven flow through an annulus in which the outer wall is moving in its own plane. By using the generalized dispersion model, the expressions for dispersion coefficient and mean concentration are obtained. In the case of wall movement, the dispersion coefficient is observed to take both positive and negative values, which differ from the case of stationary boundary where the dispersion coefficient takes only positive values.

INTRODUCTION

The study of flow/dispersion in annular tube with wall movement has many applications in medical and industrial fields. Secomb (1978) studied two dimensional flow field of an incompressible viscous fluid in a long parallel side channel with pulsating walls. Hydon and Pedley (1993), studied axial dispersion in a channel and discussed the applications of their results in understanding low-volume high frequency ventilation of the human lung. Waters (2001) studied the uptake of passive solute through walls of pulsating, fluid filled channel into an adjacent medium in which the solute diffuses and is consumed at a constant rate. In this study, we aimed to study the combined effects of pressure pulsation and wall oscillation on the dispersion process in Casson fluid flow in an annulus. By using generalized dispersion model proposed by Gill and Sankarasubramanian (1970), the expressions for dispersion coefficient and mean concentration are obtained. The results are analysed for the variation of dispersion coefficient and mean concentration with different parameters in the model.

MATHEMATICAL FORMULATION

We considered the flow in an annulus between two coaxial cylinders with inner cylinder radius ka $(0 < k < 1)$ and outer radius a. The dispersion of a bolus of a solute, which is initially of $\bar{z}_s$ units in length and of uniform concentration C_0, is studied. For fully developed, axi-symmetric and incompressible flow, the unsteady convection-diffusion equation which describes the local concentration $\bar{C}(\bar{t}, \bar{z}, \bar{r})$ of a solute can be written in the non-dimensional form as,

$$\frac{\partial C}{\partial t} + w(r,t)\frac{\partial C}{\partial z} = \left(\frac{1}{r}\frac{\partial}{\partial r}\left(r\frac{\partial}{\partial r}\right) + \frac{1}{Pe^2}\frac{\partial^2}{\partial z^2}\right)C, \quad k \le r \le 1 \tag{1}$$

with the non-dimensional quantities

$$C = \frac{\bar{C}}{C_0},\ w = \frac{\bar{w}}{w_0},\ r = \frac{\bar{r}}{a},\ z = \frac{D_m \bar{z}}{a^2 w_0},\ t = \frac{D_m \bar{t}}{a^2}. \tag{2}$$

Here D_m is the coefficient of molecular diffusion, $w(r,t)$ is the axial velocity, $Pe = \frac{aw_0}{D_m}$, the Peclet number and w_0 is the reference velocity. The corresponding initial and boundary conditions are

$$C(0,z,r) = \begin{cases} 1, & |z| \le \frac{z_s}{2} \\ 0, & |z| > \frac{z_s}{2}, \end{cases} \tag{3a}$$

$$\frac{\partial C}{\partial r}(t,z,r) = 0, \text{ at } r = k \text{ and } 1, \quad C(t,\infty,r) = 0. \tag{3b-d}$$

The velocity expression for the case of pulsatile flow in Casson fluid flow in annulus with wall movement is obtained in different regions as:

[a)]Corresponding author. Email:nagaraniponakala@gmail.com.

$$w(t,r) = w^{+}(r,t) = \frac{\partial p}{\partial z}(t)\left[\lambda^2 \ln(r/k) - \left(\frac{r^2-k^2}{2}\right) + \Omega(r-k) - 2\Omega^{1/2}\int_k^r \left(\frac{\lambda^2 - r^2}{r}\right)^{1/2} dr\right] \quad \text{for} \quad k \le r \le \lambda_1$$

$$= w^{-} = w_p = w^{+}(t,\lambda_1) = w^{++}(t,\lambda_2) \quad \text{for } \lambda_1 \le r \le \lambda_2,$$

$$= w^{++}(r,t) = \frac{\partial p}{\partial z}(t)\left[\lambda^2 \ln(r) + \left(\frac{1-r^2}{2}\right) + \Omega(1-r) - 2\Omega^{1/2}\int_r^1 \left(\frac{r^2-\lambda^2}{r}\right)^{1/2} dr\right] + U_0(t) \quad \text{for } \lambda_2 \le r \le 1, \qquad \text{(4a-c)}$$

where $\lambda^2 = \lambda_1 \lambda_2$, the width of the yield plane region $\Omega = \lambda_2 - \lambda_1 = \tau_y / \frac{\partial p}{\partial z}(t)$, $\frac{\partial p}{\partial z}(t) = 1 + e\cos\alpha^2 Sct$,

$U_0(t) = W_0(1 + \xi\cos\alpha_w^2 Sct)$, $\alpha = a\sqrt{\frac{\omega}{\nu}}$, $\alpha_w = a\sqrt{\frac{\omega_1}{\nu}}$ and $Sc = \frac{\upsilon}{D_m}$. The superscripts "+" and "+ +" represent the shear flow regions $k \le r \le \lambda_1$ and $\lambda_2 \le r \le 1$, respectively, and the superscript "–" represents the plug flow region $\lambda_1 \le r \le \lambda_2$. The yield plane locations λ_1 and λ_2 are evaluated from the continuity condition of velocity.

METHOD OF SOLUTION

The solution of the convection-diffusion equation (1), with conditions (3 a-d) is solved, using the generalized dispersion method and hence the dispersion model reduces to

$$\frac{\partial C_m}{\partial t} = \sum_{i=1}^{\infty} K_i(t) \frac{\partial^i C_m}{\partial z^i}, \text{ where } C_m \text{ is defined as } C_m = \frac{2}{1-k^2}\int_k^1 C\, r\, dr, \qquad \text{(5a-b)}$$

with the transport coefficients K_i's as a function of time t and are given by

$$K_i(t) = \frac{\delta_{i2}}{Pe^2} - \frac{2}{1-k^2}\int_k^1 f_{i-1}(t,r)\, w(t,r)\, r\, dr \qquad i = 1, 2, \ldots$$

Here $K_1(t)$ is called convection coefficient and $K_2(t)$ is called dispersion coefficient.

Solving equation (5), by neglecting terms involved in K_3, K_4, etc., the solution of mean concentration C_m is obtained.

RESULTS AND DISCUSSION

We have discussed the effects of yield stress τ_y, inner cylinder radius k, steady component of the wall velocity W_0, fluctuating pressure gradient e, Womersely parameters α, α_w and amplitude of wall velocity ξ on dispersion coefficient and mean concentration by fixing both Pe and Sc as 1000. As ξ increases it is seen that fluctuations of K_2 are more and magnitude of K_2 is also increased. Here we made some of the important observations which are different from the stationary boundary problem. It is seen that as k increases the magnitude of K_2 increases and decreases with time when $\tau_y = 0$ .05 and the magnitude of K_2 increases for $\tau_y = 0.1$, but whereas in stationary boundary situation the magnitude of K_2 decreases for all times. As wall velocity increases the mean concentration increases, and also the curve shifts towards the right . The variation of mean concentration with annular gap is shown in Figure 6.18. As the annular gap decreases the mean concentration decreases and the curve shifts towards left as k increases.

CONCLUSIONS

Dispersion of a solute in an annulus in oscillatory flow in a Casson fluid with wall movement is studied using generalized dispersion model. It is found that dispersion coefficient in Casson fluid flow in an annulus in the presence of wall movement is a function of frequency parameter, Schmidt number, fluctuating pressure component, wall movement beside its dependency on time, annular gap, and yield stress of the fluid.

References

[1] Gill, W. N. and Sankarasubramanian, R.: Exact Analysis of Unsteady Convective Diffusion. *Pro.Royal Soc.London A 316*: 341-350, 1970.

[2] Hydon, P.E. and Pedley, T.J.: Axial Dispersion in a Channel with Oscillating Walls. *J Fluid Mech.* 249: 535-555, 1993.

[3] Secomb T.W.: Flow in a Channel with Pulsating Walls. *J Fluid Mech* 88:273-288, 1978.

[4] Waters S.L.: Solute Uptake through the Walls of a Pulsating Channel. *J Fluid Mech. 433*:193-208, 2001.

SIMULATING PARTICLE SEDIMENTATION IN YIELD STRESS FLUIDS

N.P. Khabazi[2], K. Sadeghy[2], S.M. Taghavi[1*]

[1]Chemical Engineering Department, Université Laval, Quebec, QC, G1V 0A6, Canada
[2]Center of Excellence in Design and Optimization of Energy Systems (CEDOES),
School of Mechanical Engineering, College of Engineering, University of Tehran, Tehran, Iran
Seyed-Mohammad.Taghavi@gch.ulaval.ca

Abstract

Sedimentation of rigid particles is numerically studied in Newtonian and Bingham fluids in this work. In Newtonian fluids it is found that an increase in the number of particles leads to a decrease in the average settling velocity of the particles whereas for yield stress fluids this is not necessarily true. For the latter fluids, it is found that for sufficiently large Bingham numbers the number of particles can have an increasing effect on the average settling velocity of the same particles. In general, it is concluded that the initial arrangement of the particles plays a more important role as compared with the number of particles in dictating their settling velocity in yield-stress fluids.

Introduction

Sedimentation of solid particles is encountered in a variety of industrial processes including fluidization, slurry flows, etc. While in the majority of cases the continuous phase is Newtonian, in food and oil industries the case in which the suspending medium is viscoplastic is quite common. Thanks to its technological impact, many researchers have studied single-particle sedimentation in yield stress fluids, either analytically or numerically [1-3]. To best of our knowledge, however, there is no published work addressing the case of multiple-particles settling in a yield stress fluid.

Problem Description and Results

We have studied sedimentation of particles under the influence of the gravitational force in yield stress fluids obeying the Bingham model. To figure out the interaction between particles during their fall, we have considered different initial configuration comprising one, two, four, and nine particles arranged in a symmetric fashion. The channel is assumed to have a width of 2 cm and a height of 8 cm. Initial positioning of the particles is chosen in such a way that, in all cases under investigation, their center of mass is located at a height of 7 cm from the center of the channel (see Fig. 1). The distance between two adjacent particles is set at 0.3 cm. The density of the fluid is set at $\rho_f = 1\ g/cm^3$ while the density of the solid particle is set at $\rho_s = 1.01\ g/cm^3$. The diameter of the planar particles is set at $D = 0.2\ cm$. The fluid and the particles are initially at rest. The viscoplastic fluid of interest is assumed to follow the Bingham model. Detailed descriptions of our numerical method (i.e., the LBM/SPM methods) and its verifications are presented in our recent publications [4,5]. The dimensionless parameters involved in this study are the Archimedes number and the dimensionless yield stress (say, the Bingham number); that is:

$$Ar = \frac{g D^3 (\rho_s - \rho_f)^2}{\mu^2},\ Y_g = \frac{\tau_y}{g D (\rho_s - \rho_f)}$$

where g is the gravitational acceleration, τ_y the yield stress, and μ is the dynamic viscosity of the fluid.

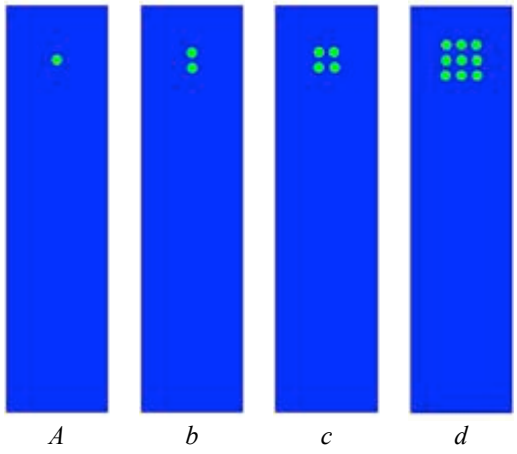

Fig. 1: Initial positioning of the particles in the two-dimensional channel.

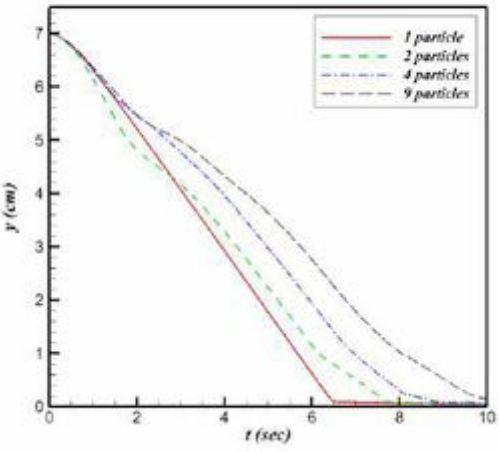

Fig. 2: Y-location of the center of gravity of the particles for the Newtonian case.

Figure 2 shows how the center of gravity of the particles varies with time during their sedimentation in a Newtonian fluid. In Figs. 3 and 4. we have shown the behavior when falling in a yield-stress fluid having $Y_g = 0.02$ and 0.05, respectively. As can be seen in Fig. 2, when the particles sediment in a Newtonian fluid, an increase in the number of particles results in a decrease in the average velocity of the particles settling velocity. In contrast, from Fig. 3 it can be

concluded that when the particles are falling in a slightly viscoplastic fluid, the two-particle scenario falls faster than the one-particle scenario. Similarly, the nine-particle case falls faster than the four-particle case. An increase in the yield stress of the fluids gives rise to an unexpected behavior, as can be seen in Fig. 4. The nine-particle combination settles faster than all other combinations. An interesting phenomenon that is seen in this figure is the change in the slope of the falling two and four particles. Two and four combinations of the particles start to fall with large velocity (with a high slope), but after a while the speed of their sedimentation decreases dramatically.

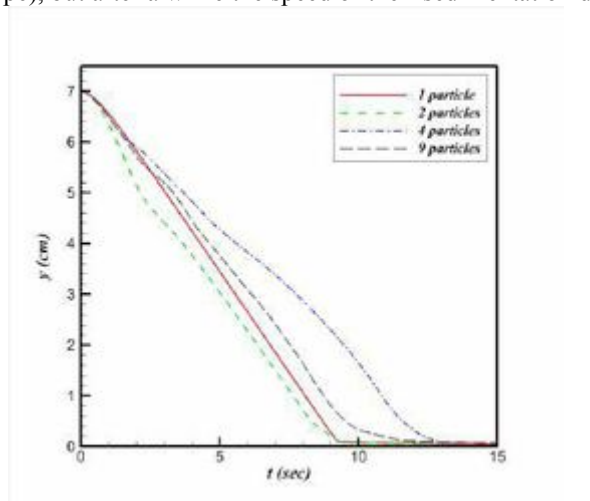

Fig. 3: Y-location of the center of gravity of the particles for the yield stress fluid (Y_g=0.02).

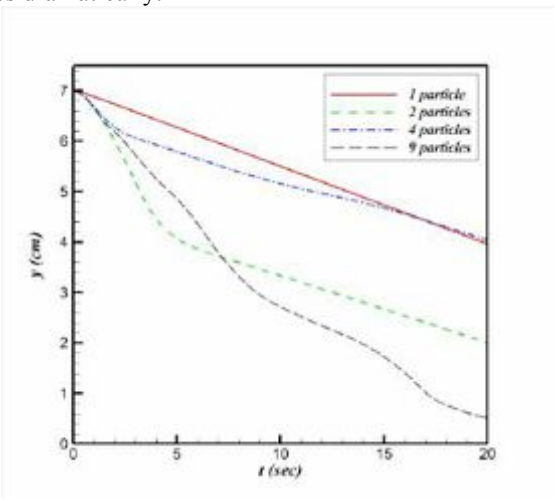

Fig. 4: Y-location of the center of gravity of the particles for the yield stress fluid (Y_g=0.05).

To have a better understanding of the mechanisms involved in the particles' settling, we have shown the vertical position of the particles in Figs. 5 and 6 for the cases of Y_g = 0.02, and Y_g = 0.05, respectively. A comparison between Fig. 5 and Fig. 3 reveals that the average settling velocity of the settling is directly related to their initial arrangment and not the number of the particles. Interestingly, as soon as the particles reach the same vertical position the speed of falling decreases. In fact, the best scenario for having a higher falling velocity is when the particles are arranged in a vertical line (cf. Fig. 6 with Fig. 4).

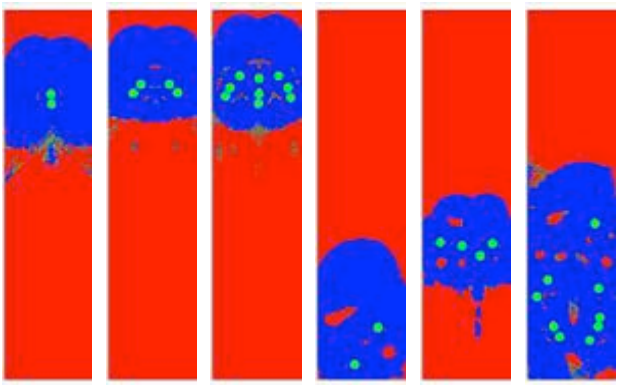

Fig. 5: Position of the particles during falling at times: t = 1.25 s (a,b,c), t = 8 s (d,e,f) (Y_g = 0.02, green: particles, red: unyielded regions, blue: yielded regions).

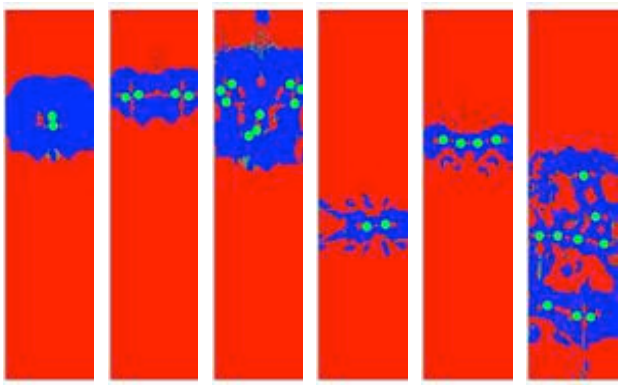

Fig. 6: Position of the particles during falling at times: t = 1.25 s (a,b,c), t = 8 s (d,e,f) (Y_g = 0.05, green: particles, red: unyielded regions, blue: yielded regions).

Conclusions

Based on the results obtained in this work, it can be concluded that the initial arrangement of particles before fall plays a key role in dictating the fall velocity when settling in a yield-stress fluid with the number of particles playing a secondary role.

References:

[1] R.W. Ansley, T.N. Smith, Motion of spherical particles in a Bingham plastic, AICHE Journal, 13 (1967) 1193.
[2] A.N. Beris, J.A. Tsamopoulos, R.C. Armstrong, R.A. Brown, Creeping motion of a sphere through a Bingham plastic, Journal of Fluid Mechanics, 158 (1985) 219-244.
[3] Prashant, J. Derksen, Direct simulations of spherical particle motion in Bingham liquids, Computers and Chemical Engineering, 35 (2011) 1200-1214.
[4] N.P. Khabazi, S.M. Taghavi, K. Sadeghy, Peristaltic flow of Bingham fluids at large Reynolds numbers: A numerical study, Journal of Non-Newtonian Fluid Mechanics, 227 (2016) 30-44.
[5] N.P. Khabazi, K. Sadeghy, Simulating peristaltic transport of solid particles immersed in a viscoplastic fluid using the LBM/SPM numerical method, submitted to Journal of Non-Newtonian Fluid Mechanics, 2016.

DEPENDENCE OF ENERGY SPECTRA ON FORCING SCALES IN ELASTIC WAVE TURBULENCE

Masanori Takaoka * [1] and Naoto Yokoyama[2]
[1]*Department of Mechanical Engineering, Doshisha University, Kyotanabe, Kyoto, Japan*
[2]*Department of Aeronautics and Astronautics, Kyoto University, Kyoto, Kyoto, Japan*

Summary Energy spectra of elastic wave turbulence are examined by simulating the Föppl-von Kármán equation for several forcing scales. There are two key scales: one is the system's scale and the other is the critical scale where the nonlinear frequencies are comparable with the linear ones. Although the energy spectra with the power law corresponding to the inverse wave-action cascade is observed in the middle stage, it eventually relaxes to that for the energy equipartition. Various power-law spectra are observed depending on the forcing scales.

INTRODUCTION

The wave turbulence propagating in a thin elastic plate is described by the Föppl-von Kármán (FvK) equation, which has Hamiltonian structure described easily in the Fourier representation. In the weak turbulence theory (WTT), complex amplitude $a_{\boldsymbol{k}} = \frac{\rho\omega_{\boldsymbol{k}}\zeta_{\boldsymbol{k}}+ip_{\boldsymbol{k}}}{\sqrt{2}\rho\omega_{\boldsymbol{k}}}$ is introduced as a canonical variable: $i\frac{da_{\boldsymbol{k}}}{dt} = \frac{\delta\mathcal{H}}{\delta a^*_{\boldsymbol{k}}}$, where $\zeta_{\boldsymbol{k}}$, $p_{\boldsymbol{k}}$, $\omega_{\boldsymbol{k}}$, and ρ are respectively the Fourier coefficients of the displacement and of the momentum, the frequency defined by the linear dispersion relation, and the density of the plate. The Hamiltonian is given as

$$\mathcal{H} = \sum_{\boldsymbol{k}} \omega_{\boldsymbol{k}}|a_{\boldsymbol{k}}|^2 + \sum_{\boldsymbol{k}+\boldsymbol{k}_1-\boldsymbol{k}_2-\boldsymbol{k}_3=\boldsymbol{0}} W^{\boldsymbol{k}\boldsymbol{k}_1}_{\boldsymbol{k}_2\boldsymbol{k}_3} a_{\boldsymbol{k}}a_{\boldsymbol{k}_1}a^*_{\boldsymbol{k}_2}a^*_{\boldsymbol{k}_3} + \sum_{\boldsymbol{k}-\boldsymbol{k}_1-\boldsymbol{k}_2-\boldsymbol{k}_3=\boldsymbol{0}} \left(G^{\boldsymbol{k}}_{\boldsymbol{k}_1\boldsymbol{k}_2\boldsymbol{k}_3} a_{\boldsymbol{k}}a^*_{\boldsymbol{k}_1}a^*_{\boldsymbol{k}_2}a^*_{\boldsymbol{k}_3} + \text{c.c.}\right). \tag{1}$$

The second and the third terms on the right-hand side respectively show the $2 \leftrightarrow 2$ and the $1 \leftrightarrow 3$ interactions of the four-wave interactions, and $W^{\boldsymbol{k}\boldsymbol{k}_1}_{\boldsymbol{k}_2\boldsymbol{k}_3} (= W^{\boldsymbol{k}_2\boldsymbol{k}_3*}_{\boldsymbol{k}\boldsymbol{k}_1})$ and $G^{\boldsymbol{k}}_{\boldsymbol{k}_1\boldsymbol{k}_2\boldsymbol{k}_3}$ are the corresponding matrix elements of the interactions. Although there exists the $0 \leftrightarrow 4$ interaction other than the above interactions, such interaction is omitted in Eq. (1), since it can be reduced by an appropriate canonical transformation. We have examined forward cascading turbulence in statistically steady states by adding external force at small wavenumbers and dissipation at large wavenumbers, and shown the coexistence of the weak and strong wave turbulence spectra as well as the variability of energy spectra depending on the energy level [1, 2].

Recently, Düring et al. [3] reported an inverse cascade of wave action in this system by adding external force at large wavenumbers, which seems like a contradiction to our understanding that steady inverse cascade of wave action does not exist in the framework of WTT. Although only the resonant interactions of the four-wave interactions are retained in WTT, the quadratic energy as well as the total energy is conserved, but the wave action is not conserved since the $1 \leftrightarrow 3$ resonant interactions exist in addition to the $2 \leftrightarrow 2$ resonant interactions. Furthermore, when a power-law solution of energy spectra $E(k) = Ak^p$ is assumed, the explicit expressions of the energy flux and the wave-action flux as well as the resonant interactions can be obtained formally [3, 4]. There exist four typical spectra: $\langle 1\rangle$ energy equipartition for $p = 1$, $\langle 2\rangle$ direct energy cascade for $p = 1$ with logarithmic correction, $\langle 3\rangle$ wave-action equipartition for $p = 3$, and $\langle 4\rangle$ inverse wave-action cascade for $p = 5/3$. Note here that for $p = 3$ and $p = 5/3$, the expression of the wave-action flux superficially diverges, and $E(k) = Ak^p$ cannot be a steady solution of the kinetic equation in WTT since the $1 \leftrightarrow 3$ resonant interactions do not vanish.

Alternatively, other two typical spectra are derived by using dimensional argument, where the physical parameter difined by the dispersion relation of the system is employed [5]. The one is $p = -1$ corresponding to the direct energy cascade and the other $p = -1/3$ to the inverse wave-action cascade. The dimensional argument is applicable to non-weak turbulent states.

Lastly, we have to be careful about the difference between FvK and the kinetic equation in WTT in terms of interaction and conserved quantities. The random phase approximation also makes the difference in nonlinearity, e.g. $n_{\boldsymbol{k}} = \langle|a_{\boldsymbol{k}}|^2\rangle \sim \omega_k\langle|\zeta_{\boldsymbol{k}}|^2\rangle$ as in Ref. [3]. The words "cascade" and "flux" have been often used for non-conservative quantities.

NUMERICAL RESULTS

Direct numerical simulations (DNS) were performed by using the standard pseudo-spectral method according to the canonical equation for the complex amplitude, added the external force and dissipation to achieve non-equilibrium statistically steady states. We used $N \times N = 2048 \times 2048$ modes in the calculation of the convolutions with the $4/2$ dealiasing rule. The forcing scale was changed, while the dissipation was always added at large wavenumbers. We also changed the system's scale $L \times L$ instead of changing N to investigate the dependence of energy spectra on the forcing scale, because too much computation time is consumed with much larger number of modes. Two types of forcing scales are chosen as a representative for the present analysis: one is the forcing at large wavenumbers, and the other at middle wavenumbers. The wavenumber range for the former is $\frac{512\pi}{L} \le k \le \frac{566\pi}{L}$ and that for the latter $\frac{32\pi}{L} \le k \le \frac{40\pi}{L}$.

*Corresponding author. Email: mtakaoka@mail.doshisha.ac.jp

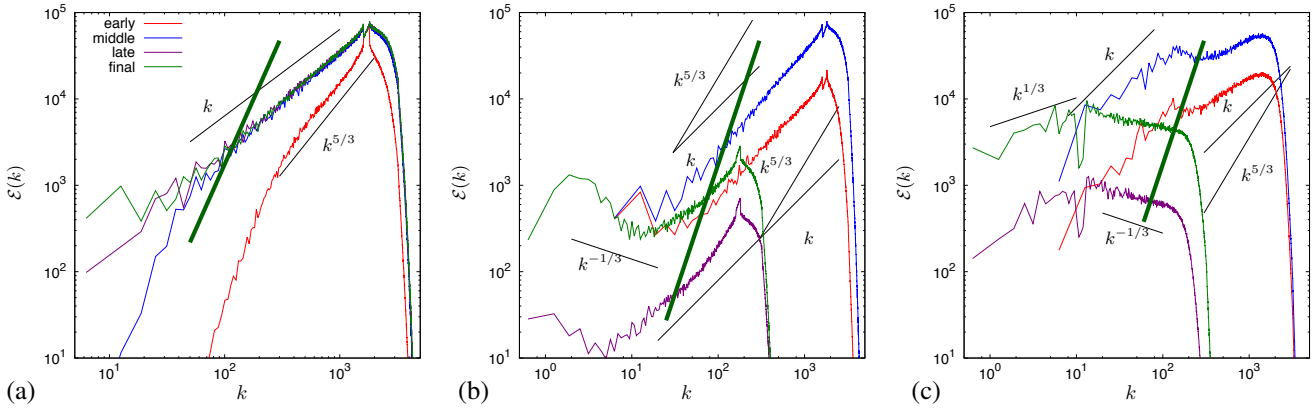

Figure 1: (a): representative energy spectra for external force at large wavenumbers with $L = 1$. (b) and (c): energy spectra in statistically steady states for external force at large wavenumbers and at middle wavenumbers. The system scales are $L = 1$ (red and blue curves) and 10 (purple and green curves). The thick straight lines represent the critical scale at each energy level.

In Fig. 1 (a) shown are the energy spectra at four representative times, when the external force is added at large wavenumbers. The spectrum (red curve) shows $k^{5/3}$ as reported in Ref. [3] at early stage, and the spectrum (blue curve) at middle stage becomes to have two power-law ranges which might correspond to the spectra in Fig. 8(b) of Ref. [3]. The spectra were described as a final spectra in a stationary regime with $\omega_k \langle |\zeta_k|^2 \rangle \sim k^{-4/3}$ for $k < 0.2$ and $\omega_k \langle |\zeta_k|^2 \rangle \sim k^{-2\times 0.873}$ for $0.5 < k < 5$. When the energy at the largest scales becomes significant, the energy spectrum (purple curve) grows to have the power law k which corresponds to the energy equipartition. In almost statistically steady state (green curve), the energy equipartion spectrum ends up being concave upward below the critical wavenumber where the nonlinear frequencies are comparable with the linear frequencies. Negative slope of energy spectrum appear in smaller wavenumber range where WTT cannot be applied but the dimensional analysis can be.

To investigate the importance of critical scales, we have performed DNS with the external force at large wavenumbers with changing L and the forcing amplitude. The energy spectra in almost statistically steady states are plotted in Fig. 1 (b). It is confirmed that the spectra in the larger wavenumber range than the critical wavenumber have the energy equipartition spectra k and that in smaller wavenumber range the negative slope spectra, though the fluctuation is large there, consistent with the dimensional analysis. There is no singular behavior at the smallest wavenumbers, though no drag was added at the smallest wavenumbers similarly to Ref. [3] .

We also performed DNS with the external force at middle wavenumbers in order to find the relation of the forcing scale with the system's scale. The results are shown in Fig. 1 (c). The energy spectra in the larger wavenumber range than the forcing wavenumbers show the similar behavior with those in Refs. [1, 2] where the external force was added at small wavenumbers to investigate the forward cascade. It is interesting to point out that the positive slope spectra appear in the smaller wavenumber range than the forcing wavenumbers even though such wavenumbers are smaller than the critical wavenumbers.

CONCLUSIONS

Direct numerical simulation of the Föppl-von Kármán equation are performed for various forcing scales and system's scales. Although the power-law spectrum $k^{-1/3}$ corresponding to the inverse wave-action cascade transiently appear, the energy spectrum in the larger wavenumber range than the critical wavenumbers relaxes to the energy equipartition spectrum k eventually. The spectra in larger wavenumber range than the forcing wavenumbers have weak and strong wave turbulence spectra as reported in Refs. [1, 2]. New power-law spectra are observed in the smaller wavenumber range than both the forcing wavenumbers and the critical wavenumbers.

References

[1] Yokoyama N., Takaoka M.: Weak and strong wave turbulence spectra for elastic thin plate. Phys. Rev. Lett. 110: 105501, 2013.

[2] *Id.*: Identification of a separation wave number between weak and strong turbulence spectra for a vibrating plate. Phys. Rev. E 89: 012909, 2014.

[3] Düring G., Josserand C., Rica S.: Self-similar formation of an inverse cascade in vibrating elastic plates. Phys. Rev. E 91: 052916, 2015.

[4] *Id.*: Weak turbulence for a vibrating plate: Can one hear a Kolmogorov spectrum? Phys. Rev. Lett. 97: 025503, 2006.

[5] Nazarenko, S.: Wave Turbulence. Springer, Berlin, 2011.

FM13 - Computational Fluid Dynamics

TS.FM13-1.01	Moser, Robert - Treating anisotropy in LES subgrid models (INVITED)	1330
TS.FM13-1.02	Lamballais, Eric - Explicit vs. implicit subgrid-scale modelling for les	1332
TS.FM13-1.03	Schlatter, Philipp - Pressure gradient turbulent boundary layers developing around a wing section	1334
TS.FM13-1.04	Vidal, Alvaro - Influence of duct corner geometry on secondary flow: Convergence from square duct to pipe	1336
TS.FM13-1.05	Kim, Pilbum - Non-equilibrium effects on hypersonic turbulent boundary layers	1338
TS.FM13-1.06	Köthe, Thomas - Adjoint shape optimization based on DNS of turbulent channel flow	1340
TS.FM13-2.01	Takagi, Shu - A full Eulerian method for fluid-structure interaction problems (INVITED)	1342
TS.FM13-2.02	Ekiel-Jezewska, Maria - Migration of vesicles and flexible fibers in Poiseuille flow	1344
TS.FM13-2.03	Van Hove, Sibylle - Apneaic airway gas concentrations during nasal high flow therapy	1346
TS.FM13-2.04	Zhao, Meng - An efficient adaptive rescaling scheme for computing Hele-Shaw problems	1348
TS.FM13-2.05	Maîtrejean, Guillaume - Kinetic theory of colloidal suspensions migration	1350
TS.FM13-2.06	Tan, Jennifer - Smart Morphing Blade for Vertical Axis Wind Turbines	1352
TS.FM13-3.01	Shen, Yiqing - High Order Global Smoothness Indicator for Improving the Fifth-order Weno-z Scheme	1354
TS.FM13-3.02	Ringue, Nicolas - Optimization-based anisotropic mesh-polynomial adaptation for high-order methods	1356
TS.FM13-3.03	Modesti, Davide - Efficient Algorithm for DNS of Compressible Turbulent Wall-Bounded Flows	1358
TS.FM13-3.04	Sakib, Md Nazmus - Spectrally-accurate immersed boundary conditions method for 3-D Navier-Stokes equations	1360
TS.FM13-3.05	Lv, Jun-Ming - Numerical study on radiative heat for hyper-velocity re-entry probes	1362
TS.FM13-3.06	Gelfgat, Alexander - On acceleration of Krylov-subspace Newton and Arnoldi iterations for incompressible CFD	1364
PO.FM13-1.01.149	Astafev, Vladimir - Numerical Calculation of Piton-like Oil Displacement for Different Schemes of Flooding	1366
PO.FM13-1.02.150	Baratchi, Farhad - A comparison between blade element actuator disk and actuator line methods for a tidal turbine	1368
PO.FM13-1.03.151	Bordet, Aurélien - Numerical simulation of solid suspension flows in a horizontal pipe	1370
PO.FM13-1.04.152	Doyle, Rob - Simulation of an unappended axisymmetric submarine hull during unsteady pitching	1372
PO.FM13-1.05.153	Falsafioon, Mehdi - Moving grid for large amplitude body motion	1374
PO.FM13-1.06.154	Florides, Georgios - Effect of groundwater flow on a ground heat exchanger	1376
PO.FM13-1.07.155	Ghazihesami, Rouzbeh - Assessment of numerical modelling for steady jet impingement cooling in different geometries	1378
PO.FM13-1.08.156	Huang, Wei-Xi - An immersed boundary projection method for flow over moving boundaries	1380

PO.FM13-1.10.158	Lizarraga-Garcia, Enrique - CFD-informed unified closure relation for the velocity of Taylor bubbles.	1382
PO.FM13-1.11.159	Maye, Ryan - AVT-251: a parametric study of modified saccon geometry	1384
PO.FM13-1.12.160	Palchekovskaya, Natalia - Numerical simulation of hypersonic flow over re-entry space vehicle	1386
PO.FM13-1.14.162	Untaroiu, Alexandrina - Flow field reconstruction for hole-pattern seals using reduced order modeling.	1388

TREATING ANISOTROPY IN LES SUBGRID MODELS

Sigfried W. Haering[1] and Robert D. Moser *[1,2]
[1]*The Center for Predictive Engineering and Computational Science, Institute for Engineering and Sciences, The University of Texas at Austin, Texas 78712, U.S.A.*
[2]*Department of Mechanical Engineering, The University of Texas at Austin, Texas 78712, U.S.A.*

Summary In many applications of large eddy simulation (LES), the grid or filter that defines the scales of turbulence to be simulated is anisotropic. Further, it is common for the turbulence to be so highly anisotropic and the filter scale so large that the unresolved turbulence cannot be assumed to be locally isotropic. However, LES subgrid models do not generally account for this turbulence and resolution anisotropy. In this talk we propose and evaluate an anisotropic subgrid modeling approach designed to address these shortcomings.

In large eddy simulations of complex turbulent flows, the geometry and important flow characteristics often demand that the grids employed be anisotropic (also inhomogeneous). The filter scale is therefore a function of the direction. To use classical large eddy simulation subgrid models such as Smagorinsky and its variants, which are formulated in terms of only a single filter scale, some sort of aggregated length scale must therefore be defined. But, this means that in some directions one must be simulating less turbulence than the grid could support and/or in some directions the model is formulated to simulate smaller scale turbulence than the grid can resolve. This results in poor LES performance in complex flows [Haering, 2015].

Further, in these complex flows, computational cost considerations demand that the resolved scales not extend deep into the inertial range, so isotropy of the unresolved scales is not generally a good assumption. Again, commonly used subgrid models like Smagorinsky are formulated based on a scalar and therefore isotropic description of the subgrid turbulence. The goal of the model development described here is to obtain an anisotropic subgrid model that accounts for the anisotropy of both the resolution and the turbulence. An anisotropic eddy diffusivity based on a tensor description of the resolution and a tensor measure of the subgrid turbulence intensity is sought.

To formulate an anisotropic filter metric, consider a transformed coordinate system in which the filter resolution is isotropic with unit filter width. Let $\mathcal{J}$ be the Jacobian of the transformation from this coordinate system to the physical coordinates, then the symmetric tensor $\mathcal{M} = (\mathcal{J}^T\mathcal{J})^{1/2}$ has the property that the quantity $\mathbf{e}^T\mathcal{M}\mathbf{e}$, where $\mathbf{e}$ is a unit vector, is the effective filter width in the direction of $\mathbf{e}$. $\mathcal{M}$ will be used as the tensor representation of the filter scale in the model formulated here.

To represent the scale anisotropy of the unresolved turbulence, a natural quantity to consider is the second order structure function evaluated with separation at the filter scale. Consider the second order structure function contracted on the velocity components:

$$S_2(\delta\mathbf{x}) = |\mathbf{u}'(\mathbf{x}+\delta\mathbf{x}) \circ \mathbf{u}'(\mathbf{x})|^2 \tag{1}$$

As is well known, $S_2/2$ is a measure of the kinetic energy of the turbulence at scales smaller than $|\delta\mathbf{x}|$. If we consider $\delta\mathbf{x}$ to be at the filter scale, then S_2 can be approximated as

$$S_2(\delta\mathbf{x}) \approx \left|\frac{\partial\overline{\mathbf{u}}'}{\partial x_m}\delta x_m\right|^2 \tag{2}$$

where $\overline{\mathbf{u}}$ is the resolved velocity. Using the resolution tensor defined above, a tensor $\mathcal{Q}$ representing the dependence of S_2 on the direction of the filter-scale separation can be defined as

$$\mathcal{Q}_{ij} = \frac{\partial\overline{u}'_k}{\partial x_m}\mathcal{M}_{mi}\frac{\partial\overline{u}'_k}{\partial x_n}\mathcal{M}_{nj}, \tag{3}$$

then the quantity $\mathbf{e}^T\mathcal{Q}\mathbf{e}$ is an approximation of S_2 with filter-scale separation in the direction $\mathbf{e}$.

A natural formulation for a second-order tensor eddy diffusivity can be found by generalizing the structure function model of Metais and Lesieur [1992]. The resulting tensor eddy diffusivity is given by

$$\nu = C_\nu(\mathcal{M}\mathcal{Q}\mathcal{M})^{1/2} \tag{4}$$

where consistency with the structure function model yields $C_\nu = 0.105C_k^{3/2}/3$ with C_k the Kolmogorov constant. The sub-filter stress tensor τ can then be written [Haering, 2015]

$$\tau_{ij} = \nu_{ik}\frac{\partial\overline{u}_j}{\partial x_k} + \nu_{jk}\frac{\partial\overline{u}_i}{\partial x_k}. \tag{5}$$

*Corresponding author. Email: rmoser@ices.utexas.edu

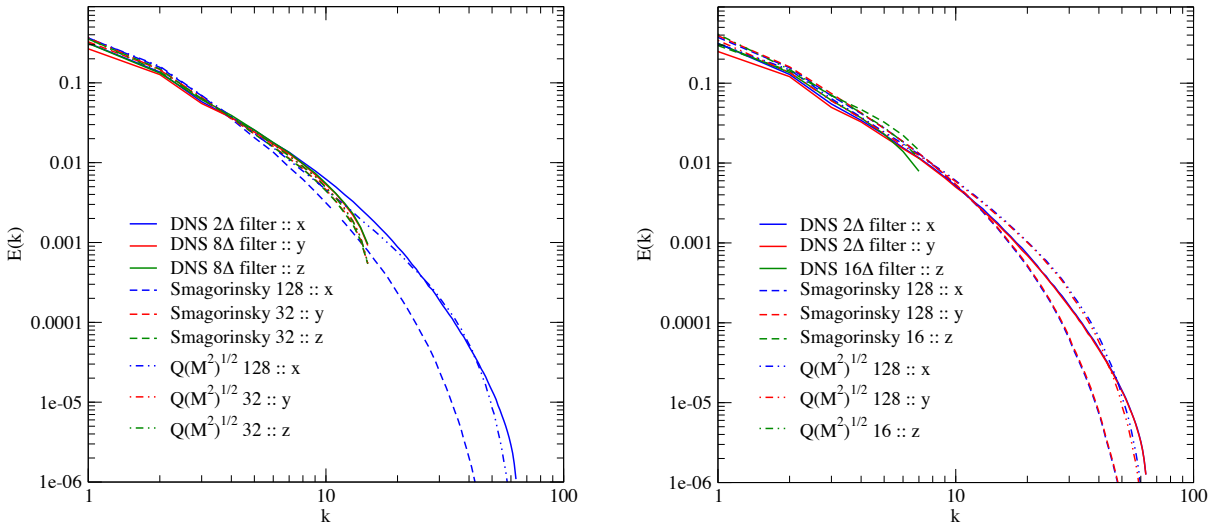

Figure 1: One dimensional energy spectrum of filtered DNS, LES with the proposed anisotropic model and standard Smagorinsky model. Compared to a DNS resolution of 256^3, the LES have effective grid sizes of 128×32^2 (left) and $128^2 \times 16$ (right).

This formulation of an anisotropic eddy diffusivity has been tested against filtered DNS. For example, to test the treatment of anisotropic filter widths, an anisotropically filtered forced isotropic turbulent DNS was compared to a forced isotropic turbulence LES performed with an anisotropic filter resolution. The resulting one-dimensional energy spectra are shown in figure 1 for two cases, one in which the filter resolution is coarse in two directions, and fine in the third, and one in which the filter resolution is coarse in one direction and fine in the other two. Also shown for reference are the spectra from the filtered DNS and from the standard Smagorinsky model. In both cases, the anisotropic model and the Smagorinsky model agree well with the filtered DNS in the coarsely resolved directions, but in the refined directions, the Smagorinsky model appears over dissipative, resulting in an under prediction of the spectrum at higher wavenumbers.

In this talk, we will discuss the model formulation and its testing, and examples of complex turbulent flows in which the anisotropy was found to be important.

References

Sigfried W. Haering. *Anisotropic hybrid turbulence modeling with specific application to the simulation of pulse-actuated dynamic stall control*. PhD thesis, University of Texas at Austin, 2015.

O. Metais and M. Lesieur. Spectral large-eddy simulation of isotropic and stably stratified turbulence. *Journal of Fluid Mechanics*, 239, 1992.

EXPLICIT vs. IMPLICIT SUBGRID-SCALE MODELLING FOR LES

Eric Lamballais *[1], Thibault Dairay[1], Sylvain Laizet[2], and John Christos Vassilicos[2]
[1]*Université de Poitiers, CNRS, ISAE-ENSMA, Institut Pprime, F-86962 Futuroscope Chasseneuil, France*†
[2]*Department of Aeronautics, Imperial College London, London SW7 2AZ, United Kingdom*

Summary This study compares explicit and implicit subgrid-scale modelling for large eddy simulation. The implicit modelling is based on a targeted numerical dissipation introduced by the discretization of the viscous term. The flexibility of the method ensures high-order accuracy while controlling the level and spectral features of the resulting numerical viscosity. A spectral closure can be used to scale it *a priori*. This relaxation strategy is found more efficient and accurate than the extremely popular Smagorinsky model in standard as well as in dynamic version. Its main advantage is the ability to regularise the solution at the mesh scale, a property that cannot be reached with any of the two versions of the Smagorinsky model that show a strong sensitivity to numerical errors. Despite its purely numerical nature, the present approach can also be viewed as explicit subgrid-scale modelling because of the equivalence with spectral viscosity prescribed on a physical basis.

INTRODUCTION

An alternative to conventional large-eddy simulation (LES) based on explicit subgrid-scale (SGS) modelling is to adopt a pragmatic approach mainly guided by basic physical and numerical considerations but free of clear formalism. This strategy is in continuous development since the MILES approach [1] and its various subsequent variants falling under the banner of implicit LES. In this work, we address the concept of implicit LES while suggesting a new balance between numerics and physics. How to combine numerics and physical modelling is a key issue for implicit LES. This study contributes to this challenging point in an alternative way where the built-in numerical dissipation does not come from the discretization of the convective term but of the viscous term in the Navier-Stokes equations. This switch from the convective term to the viscous term allows more flexibility in the prescription of the level of numerical dissipation, offering the opportunity to scale it as a conventional SGS model.

METHODOLOGY

To compare the implicit and explicit SGS modelling strategies, the academic Taylor-Green vortex problem is computed using the sixth-order flow solver Incompact3d which is kinetic energy conserving in the discrete and inviscid sense. To make this demanding benchmark more challenging and representative of realistic turbulence, high values of Reynolds are considered ($5000 \leq Re \leq 20000$) while using highly-resolved Direct Numerical Simulation (DNS) results as reference for the assessment of their LES counterparts.

The implementation of the standard and dynamic Smagorinsky model is based on conventional sixth-order compact centred finite difference schemes free from artificial dissipation. Alternatively, the implicit SGS modelling is ensured by the introduction of a targeted numerical dissipation via the discretization of the viscous term [3]. This approach can be seen as spectral vanishing viscosity $\nu_s(k)$ that can be easily shaped in order to control its value at the cutoff wavenumber k_c ($\nu_s(k_c) = \nu_0$) as well as its spectral shape (wavenumber k dependency of the kernel $\nu_s(k)/\nu_0$). Using this favourable feature, a simple method to scale the level of spectral viscosity has been proposed [2]. This method is based on a very simple closure of the Lin equation taking the numerical dissipation into account. The resulting Pao-like spectrum solutions are used to appropriately scale the spectral viscosity on a physical basis. For instance, to reduce the number of degrees of freedom (DOF) of the LES by a factor 8^3 by comparison to the DNS while using a highly concentrated numerical dissipation near the cutoff wavenumber, this simple closure model suggests the use of $\nu_0/\nu = 63$.

RESULTS

To the question "What is the most efficient and accurate SGS modelling between the present explicit and implicit strategies in the framework of the Taylor-Green benchmark?", the answer of this study is firmly in favour to the second strategy. To illustrate this conclusion, the time evolution of the total dissipation of the kinetic energy is presented in figure 1-left for three types of LES and for the reference DNS. The implicit SGS approach based on high-order numerical dissipation is clearly found in better agreement with DNS by comparison with the conventional standard and dynamic Smagorinsky models. The examination of turbulence spectra (see figure 1-middle) exhibits the fundamental difference between these two types of explicit/implicit SGS modelling. The Smagorinsky models are found unable to control the development of small-scale

*Corresponding author. Email: eric.lamballais@univ-poitiers.fr
†This work was granted access to the HPC resources of TGCC under the allocation 2015-2a0912 made by GENCI.

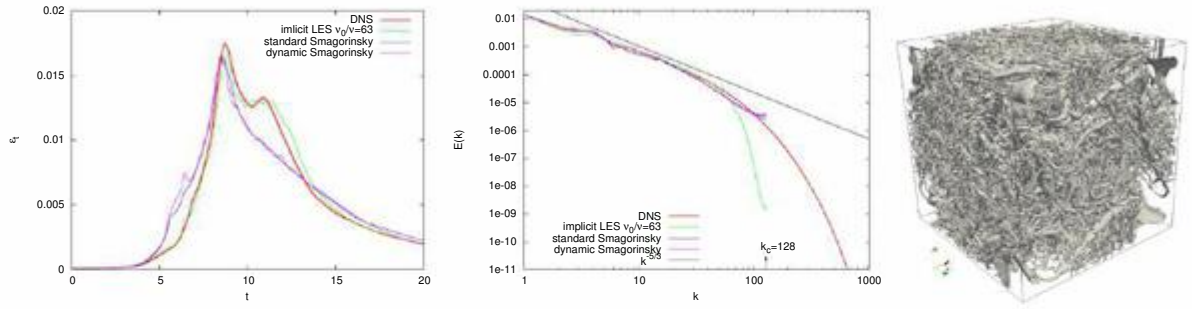

Figure 1: Left: time evolution of the total kinetic energy dissipation $\varepsilon_t = -dE_k/dt$. Middle: kinetic energy spectra $E(k,t)$ at $t = 14$. Right: isosurface of Q-criterion at $t = 14$ for the DNS. Results at $Re = 10000$ with 2048^3 and 256^3 mesh nodes on the computational domain $(2\pi)^3$ for the DNS and LES respectively.

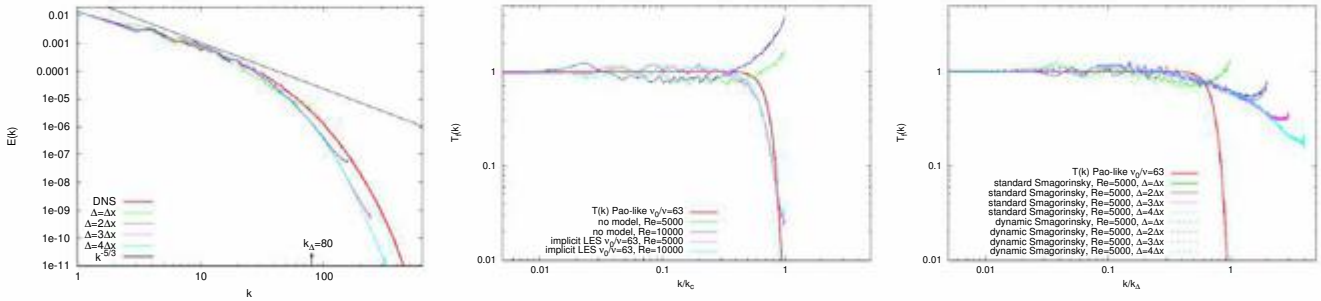

Figure 2: Left: Kinetic energy spectra $E(k,t)$ at $t = 14$ for different mesh refinements using a constant filter length Δ (DNS and LES with dynamic Smagorinsky at $Re = 5000$). Middle and right: Transfer functions T_f estimated *a posteriori* as $T_f(k,t) = \sqrt{E_{LES}(k,t)/E_{DNS}(k,t)}$ for various LES including the "no-model" case.

oscillations that can be seen as a partial thermalization of the turbulent flow that distorts strongly its kinetic energy spectrum not only at high wavenumbers (where a pile-up of energy is observed) but also in the mid-range wavenumbers. This contamination of low wavenumbers is assumed to be the consequence of triadic interactions between the unrealistic thermalized zone at high wavenumbers and the rest of the spectrum. This spurious behaviour (pile-up of energy at small scales and contamination of large scales) is not recovered for the present implicit SGS strategy.

To better understand the basic difference between the present explicit/implicit SGS modelling, a convergence study has been carried out through the use of a mesh size Δx significantly smaller than the filter length Δ. The conclusion is that the pile-up of energy observed near the cutoff wavenumber k_c when the Smagorinsky model is used (see figure 1-middle) is not a feature of the model but the consequence of numerical errors. On the contrary, the mesh refinement has no significant effect when the present high-order numerical dissipation is used, suggesting that the results can be seen as numerically converged even at the marginal resolution $\Delta x = \Delta$ (not shown for conciseness).

The use of very refined mesh $\Delta x \ll \Delta$, as required by the Smagorinsky model for the numerical errors to be negligible, is obviously very penalising computationally and a major drawback of this explicit SGS approach. This drawback is in fact more serious because even in this more favourable converged situation, the Smagorinsky model is found to ensure a very soft filtering effect. As a consequence, it is unable to provide a significant reduction in the number of DOF, missing the ultimate goal of any LES model. This conclusion is illustrated in figure 2 where the *a posteriori* transfer functions T_f of various LES are plotted. A "defiltering" effect associated with the pile-up of energy at small scales can be clearly observed at marginal resolution ($\Delta x = \Delta$) for the Smagorinsky model. This spurious defiltering can be removed using a finer mesh but the resulting T_f correspond to a very poor filtering effect. On the contrary, the present implicit SGS enables a strong damping of the kinetic energy at small scales as expected in order to allow a substantial reduction in the number of DOF.

References

[1] J.P. Boris, F.F. Grinstein, E.S. Oran, and R.L. Kolbe. *Fluid Dynamics Research*, 10:199–228, 1992.

[2] T. Dairay, E. Lamballais, S. Laizet, and J.C. Vassilicos. In *Proceedings of Direct and Large-Eddy Simulation X*, pages 1–6. ERCOFTAC series, 2015.

[3] E. Lamballais, V. Fortuné, and S. Laizet. *J. Comp. Phys.*, 230:3270–3275, 2011.

PRESSURE GRADIENT TURBULENT BOUNDARY LAYERS DEVELOPING AROUND A WING SECTION

Ricardo Vinuesa[1], Seyed M. Hosseini[1], Ardeshir Hanifi[1,2], Dan S. Henningson[1], and Philipp Schlatter [*1]
[1]*Linné FLOW Centre, KTH Mechanics, Swedish e-Science Research Centre (SeRC), Stockholm, Sweden*
[2]*Swedish Defence Research Agency, FOI, Stockholm, Sweden*

Summary The results of a DNS of the flow around a NACA4412 wing section at $Re_c = 400,000$ and 5° angle of attack are presented in this study. The high-order spectral element code Nek5000 was used for the simulations. The effect of a strong adverse pressure gradient ($\beta \simeq 4.1$) on the turbulent boundary layer at $x_{ss}/c \simeq 0.8$ is assessed, including a more prominent wake region, and steeper logarithmic and buffer layers. Increased production and dissipation are observed across the boundary layer, as well as enhanced viscous diffusion and velocity-pressure-gradient tensor close to the wall.

INTRODUCTION

Despite their great technological importance, the turbulent boundary layers developing around wing sections have not been characterized in detail in the available literature. One of the most remarkable studies in this regard is the work by Coles [1] 60 years ago, where among others he analyzed several sets of measurements on airfoils approaching separation, and he introduced the concept "law of the wake". Progressive increase in computer power has allowed in the recent years to perform numerical simulations on relatively complex geometries, which have shed some light on the physics taking place on wing sections. In the present study we report the results of a DNS of the flow around a NACA4412 wing section, at an unprecedented $Re_c = 400,000$, with 5° angle of attack. The emphasis of this work is on the streamwise development of the turbulent boundary layers around the wing, and the effect of the pressure gradient on the most relevant turbulent features.

NUMERICAL METHOD

In order to properly simulate the complex multi-scale character of turbulence, it is essential to use high-order numerical methods. The DNS described in this work was carried out with the code Nek5000 (Fischer *et al.* [2]), which is based on the spectral element method, and Lagrange interpolants of polynomial order $N = 11$ were considered for the spatial discretization. The computational domain has chord-wise and vertical lengths $L_x = 6.2c$ and $L_y = 2c$ respectively, and the periodic spanwise direction has a length of $L_z = 0.1c$. As can be observed in Figure 1 (left), we considered a C-mesh; a Dirichlet boundary condition extracted from a previous RANS simulation was imposed in all the boundaries except at the outflow, where the natural stress-free condition was imposed. A total of 1.85 million spectral elements was used to discretize the domain, which amounts to around 3.2 billion grid points. A comprehensive description of the setup can be found in the work by Hosseini *et al.* [3].

RESULTS AND DISCUSSION

In order to compute complete turbulence statistics, the simulation was run for a total of 10 flow-over times, which correspond to at least 12 eddy-turnover times throughout the whole wing except for $x_{ss}/c > 0.9$. Note that this region is subjected to a very strong adverse pressure gradient (APG), and therefore the turbulent scales are significantly larger than in the rest of the wing. According to the recent DNS of zero pressure gradient (ZPG) boundary layers by Sillero *et al.* [5], this averaging time is sufficient to obtain converged turbulence statistics.

The boundary layers developing around the wing were characterized at a total of 80 profiles on both sides, projected on the directions tangential (t) and normal (n) to the wing surface, and the magnitude of the pressure gradient was quantified in terms of the Clauser pressure gradient parameter $\beta = \delta^*/\tau_w \mathrm{d}P_e/\mathrm{d}x_t$. Figure 1 shows the inner-scaled mean flow and the turbulent kinetic energy (TKE) budget at $x_{ss}/c \simeq 0.8$. At this location the boundary layer is subjected to a strong APG, where the value of β is 4.1, and as can be observed in Figure 1 (center) the APG leads to a more prominent wake region, a steeper incipient log region, and reduced velocities in the buffer layer compared with the DNS of ZPG boundary layer by Schlatter and Örlü [4]. Table 1 shows several mean flow parameters of the boundary layer at $x_{ss}/c \simeq 0.8$ compared with the ZPG at approximately matching friction Reynolds number $Re_\tau = \delta_{99} u_\tau/\nu$. The APG effectively lifts up the boundary layer and increases its thickness, which leads to a larger shape factor $H = \delta^*/\theta$ (where θ is the momentum thickness), and also to a reduced skin friction coefficient. The lower value of the von Kármán coefficient κ is connected with a steeper log law, and the larger wake parameter Π shows the strong impact on the wake region. As shown by Monty *et al.* [6], the

*Corresponding author. Email: pschlatt@mech.kth.se

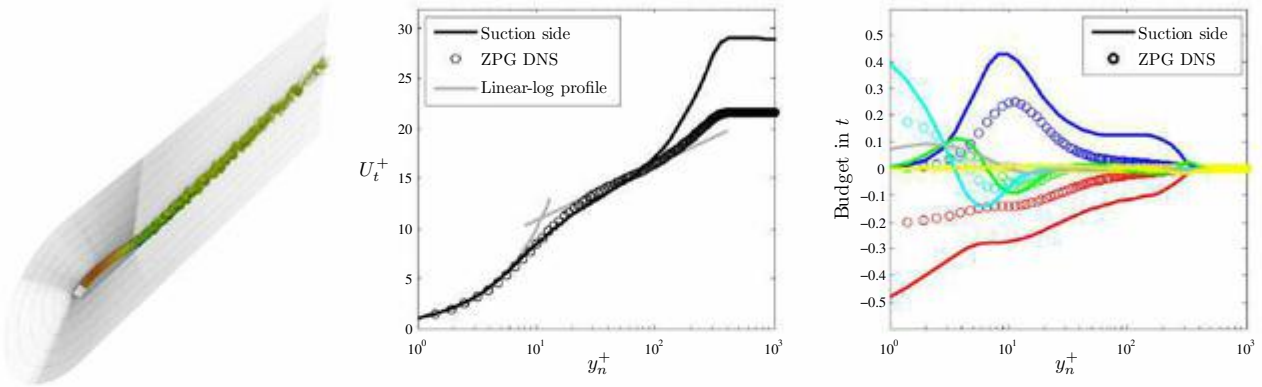

Figure 1: (Left) Instantaneous visualization of the DNS results showing coherent vortices identified by means of the λ_2 criterion. The spectral element mesh is also shown, but not the individual grid points within elements. (Center) inner-scaled mean flow (with reference low-Re values $\kappa = 0.41$ and $B = 5.2$) and (right) TKE budget scaled by u_τ^4/ν. Budget terms are represented as follows: (—) Production, (—) Dissipation, (—) Turbulent transport, (—) Viscous diffusion, (—) Velocity-pressure-gradient tensor and (—) Convection. Data extracted at $x_{ss}/c \simeq 0.8$, and compared with the ZPG data by Schlatter and Orlü [4].

Parameter	$x_{ss}/c \simeq 0.8$	ZPG DNS
Re_τ	373	359
β	4.1	$\simeq 0$
Re_θ	1,722	1,007
H	1.74	1.45
C_f	2.4×10^{-3}	4.3×10^{-3}
κ	0.33	0.41
B	2.08	4.87
Π	1.35	0.37

Table 1: Boundary layer parameters at $x_{ss}/c \simeq 0.8$ compared with ZPG results by Schlatter and Orlü (2010).

APG energizes the large-scale structures in the flow, which have a strong interaction with the outer flow (thus the impact on the wake region). These large-scale motions are usually wall-attached eddies, which leave their footprint at the wall and therefore significantly affect the overlap and buffer layers. The more energetic large-scale motions lead to the development of a prominent outer peak in the components of the Reynolds stress tensor [3]. The TKE budget presented in Figure 1 (right) shows increased production and dissipation throughout the boundary layer in comparison with the ZPG case, as well as the incipient emergence of an outer peak in the outer region of the production profile. Increased viscous diffusion is observed in the near-wall region ($y_n^+ < 10$), partly produced by the increased dissipation. Moreover, the other component balancing the increased dissipation is the velocity-pressure-gradient tensor, which exhibits moderate values in the near-wall region, and once again highlights the impact of the pressure gradient on the most relevant energy transfer mechanisms across the whole boundary layer.

References

[1] Coles, D.: The law of the wake in the turbulent boundary layer. J. Fluid Mech. 1:191–226, 1956.

[2] Fischer, P. F., Lottes, J. W. and Kerkemeier, S. G.: NEK5000: Open source spectral element CFD solver. Available at: `http://nek5000.mcs.anl.gov`, 2008.

[3] Hosseini, S. M., Vinuesa, R., Schlatter, P., Hanifi, A. and Henningson, D. S.: Direct numerical simulation of the flow around a wing section at moderate Reynolds number. Int. J. Heat Fluid Flow, To Appear, 2016.

[4] Schlatter, P. and Orlü, R.: Assessment of direct numerical simulation data of turbulent boundary layers. J. Fluid Mech. 659:116–126, 2010.

[5] Sillero, J. A., Jiménez, J. and Moser, R. D.: Two-point statistics for turbulent boundary layers and channels at Reynolds numbers up to $\delta^+ \simeq 2000$. Phys. Fluids 26:105109, 2014.

[6] Monty, J., Harun, Z. and Marusic, I.: A parametric study of adverse pressure gradient turbulent boundary layers. Int. J. Heat Fluid Flow 32:575–585, 2011.

INFLUENCE OF DUCT CORNER GEOMETRY ON SECONDARY FLOW: CONVERGENCE FROM SQUARE DUCT TO PIPE FLOW

Alvaro Vidal[1], Ricardo Vinuesa[2], Philipp Schlatter[2] & Hassan M. Nagib[1]
[1] *MMAE Department, Illinois Institute of Technology, Chicago, Illinois, USA*
[2] *Linné FLOW Centre, KTH Mechanics, Swedish e-Science Research Centre SeRC, Stockholm, Sweden*

Summary In the present study we present the results of a fully resolved direct numerical simulation (DNS) aimed at evaluating the influence of corner geometry in fully-developed turbulent duct flows by computing cases with increasing corner rounding radius r. Doing so, we evaluate the convergence from square duct $r = 0$ to pipe flow $r = 1$. We focus on the decay of the secondary flows present in turbulent duct flows and on further characterizing the mechanisms that produce them. The simulations are performed at friction Reynolds numbers $Re_{\tau,c} \cong 180$ and 360 using the spectral element code Nek5000.

SECONDARY FLOW OF PRANDTL'S SECOND KIND

According to Prandtl [1], there are two kind of secondary flows: skew-induced (Prandtl's first kind) and Reynolds-stress-induced (Prandtl's second kind). The first type, which involves vortex stretching and tilting terms, is found in curved geometries and thus it is not present in fully-developed straight ducts. The second type is associated with the deviatoric Reynolds shear stress $\overline{vw}$ and the anisotropy of the cross-stream Reynolds stress $\overline{v^2} - \overline{w^2}$ [2]. It is important to note that secondary flows of the second kind are entirely due to turbulence and are absent in laminar flows. As can be observed in Figure 1a), the secondary motions in a square duct consist of eight streamwise vortices, two counter-rotating in each corner, with the flow directed toward the corners along the bisectors. Although this kind of secondary flow is relatively weak (about 2-3% of the bulk velocity [3], as opposed to up to 10% or more for skew-induced secondary flow), its effect on the mean velocity distribution is important. The interaction between secondary flow and streamwise mean velocity is sketched in Figure 1b), which shows how the secondary flow modifies the primary mean flow by comparing the laminar and turbulent cases. As postulated by Prandtl [4], the secondary motions convect mean velocity from regions of large shear (along the walls) towards regions of low shear (along the corner bisectors). Secondary motions of Prandtl's second kind have been studied in detail through DNS simulations in ducts with varying aspect ratios AR (defined as the duct full width W divided by its full height H) and corners forming straight angles by Vinuesa *et al*. [5,6] (see figure 2). In the present study we study the effect of rounded corners on the secondary flow. The cases under consideration are with $AR = 1$, centerplane friction Reynolds numbers $Re_{\tau,c} \cong 180$ and 360, and radii of curvature of the corners $r = 0.25, 0.5$ and 0.75.

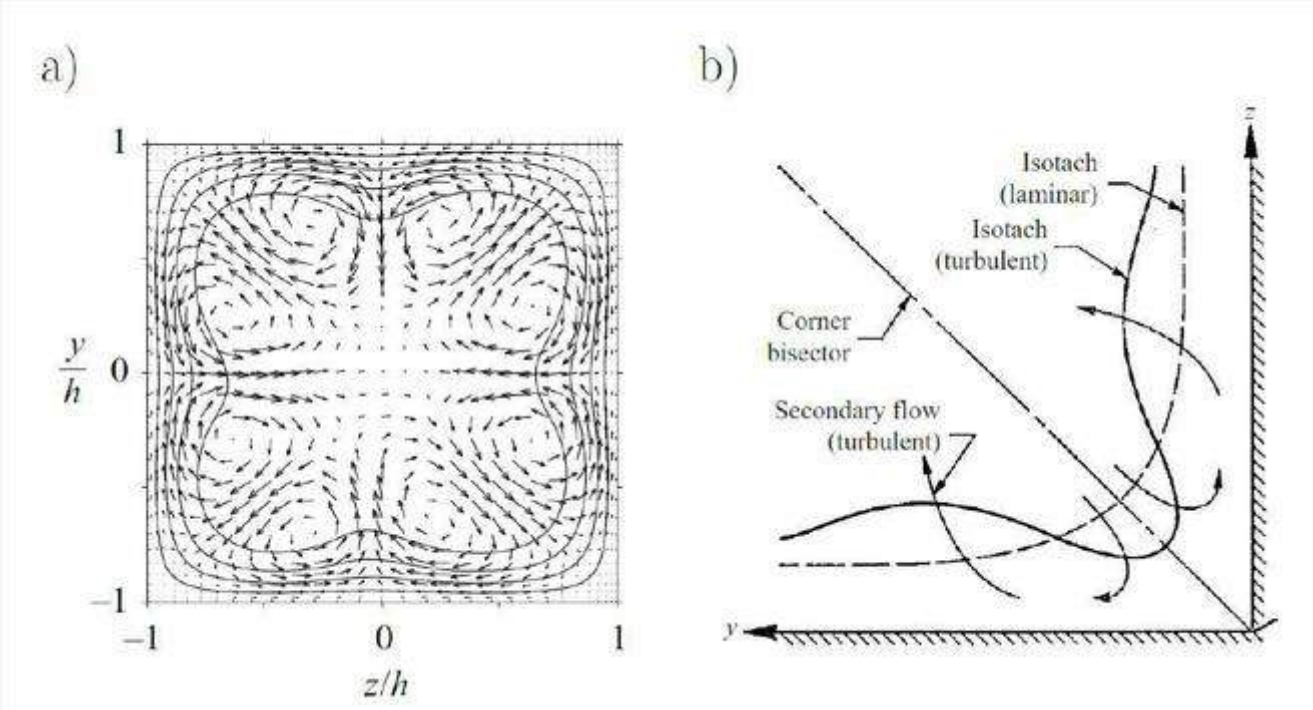

Figure 1: a) Contour lines of the primary mean flow U, and vectors of the secondary mean flow V ,W for a DNS at Reynolds number based on bulk velocity $Re_b = 1{,}205$ (this figure corresponds to Figure 3 in Uhlmann et al. [8]). b) Sketch of the mean flow U in the corner region of a straight duct (this figure corresponds to Figure 1 in Gessner [7]).

[a] Corresponding author. Email: avidalto@hawk.iit.edu

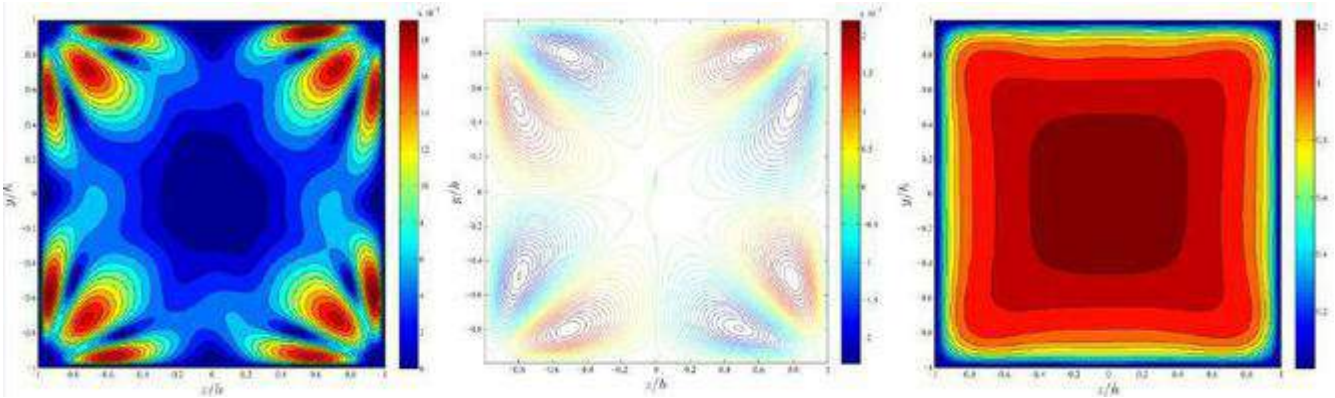

Figure 2: Cross-flow velocity magnitude $\sqrt{V^2+W^2}$ (left), contours of the streamfunction (center) and streamwise velocity (right) for the $AR=1$ duct case computed at $Re_{\tau,c} \cong 180$. Data extracted from Vinuesa *et al*. [5].

CONVERGENCE FROM DUCT TO PIPE FLOW

The above mentioned secondary motions are not present in straight pipes, where flow statistics are two-dimensional due to azimuthal symmetry. For this reason, by gradually increasing the rounding radius of the corners in the duct it is possible to characterize the decay of the secondary flow kinetic energy, and gain deeper fundamental knowledge of the mechanisms that produce the cross-flow. The idea is to determine the range of r values where these motions basically disappear. The rounding radius r here is defined as the ratio between the corner radius and the half height of the duct. Note that the 0 and 1 rounding radii cases correspond to the regular 90 degree corner duct and the canonical pipe flow respectively. Therefore, this study will serve as a link between two extensively studied cases helping the turbulence community to understand their differences. Figure 3 shows a visualization of instantaneous streamwise velocity in the $r=0.25$ case, as well as the computational mesh considered for the $r=0.5$ configuration.

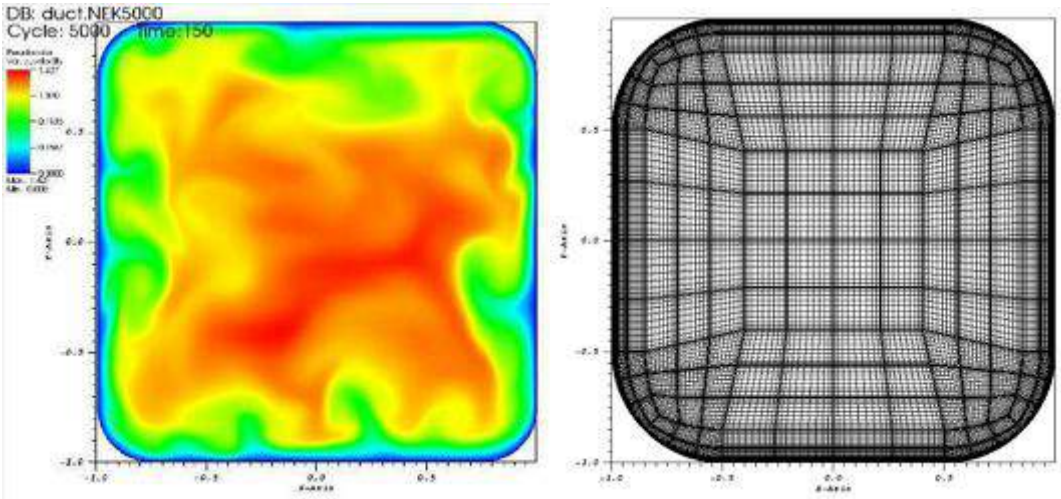

Figure 3: (Left) Cross-section view of the instantaneous turbulent streamwise velocity field in a duct with rounding radius $r=0.25$ and (right) detailed view of the computational mesh considered for the $r=0.5$ case.

References

[1] L. Prandtl, Über die ausgebildete Turbulenz [Turbulent Flow], Verh. 2nd Intl Kong. NACA Tech. Memo 62, 2nd Intl Kong. für Tech. Mech., Zürich. 1926, p. 435.

[2] Moinuddin, K. A. M., Joubert, P. N. & Ching, M. S.: Experimental investigation of turbulence-driven secondary motion over streamwise external corner, J. Fluid Mech., 511, 1-23, 2004.

[3] Huser, A. & Biringen, S.: Direct numerical simulation of turbulent flow is a square Duct, J. Fluid Mech., 257, 65-95, 1993.

[4] Prandtl, L. : Essentials of fluid dynamics, p. 145, Glasgow: Blackie, 1952.

[5] Vinuesa, R., Noorani, A., Lozano-Durán, A., El Khoury, G. K., Schlatter, P., Fischer, P. F.& Nagib H. M.: Aspect ratio effects in turbulent duct flows studied through direct numerical simulation, J. Turbul., 15:677-706, 2014.

[6] Vinuesa, R., Schlatter, P. and Nagib, H. M.: On minimum aspect ratio for duct flow facilities and the role of side walls in generating secondary flows, J. Turbul., 16:588--606, 2015.

[7] Gessner, F. B.: The origin of secondary flow in turbulent flow along a corner. J. Fluid Mech.,58, 1, 1973.

[8] Uhlmann, M., Pinelli, A., Kawahara, G. & Sekimoto, A.: Marginally turbulent flow in a square duct. J. Fluid Mech., 588, 153-162, 2007.

NON-EQUILIBRIUM EFFECTS ON HYPERSONIC TURBULENT BOUNDARY LAYERS

Pilbum Kim[1,2], John Kim *[1], Xiaolin Zhong[1], and Jeff Eldredge[1]
[1]*Department of Mechanical and Aerospace Engineering, University of California, Los Angeles, Los Angeles, California, USA*
[2]*Center for Exascale Simulation of Plasma-Coupled Combustion, University of Illinois Urbana-Champaign, Urbana, Illinois, USA*

Summary In the present study, direct numerical simulations (DNS) are performed to investigate the effects of thermal and chemical non-equilibrium on hypersonic turbulent boundary layers. In order to isolate the non-equilibrium effects, spatial developments of mean quantities, turbulence statistics and near-wall structures in non-equilibrium flows are compared with those in perfect gas flows. It is observed that the turbulent motions are intensified due to the non-equilibrium processes. Meanwhile, no direct energy exchanges between internal and turbulent kinetic energies are observed. The mechanisms of non-equilibrium effects on the flow fields are discussed in detail.

INTRODUCTION

In the present work, spatially developing hypersonic turbulent boundary layers over a cold wall are considered. Non-equilibrium states are described by Park's two temperature model with endothermic chemical reactions without ionizations [1]. The transport properties of the gas mixture are obtained by Gupta's mixing rule [2]. In order to reduce the computational costs, air is approximated as either pure oxygen or pure nitrogen, which are the main air species experiencing non-equilibrium processes in moderate and high enthalpy conditions, respectively.

The governing equations are approximated using a fifth-order hybrid weighted essentially non-oscillatory scheme with low dissipation finite difference scheme and a sixth-order central finite difference scheme for non-linear convective and viscous dissipative terms, respectively [3, 4]. The approximated difference equations are then advanced in time using the third-order total variation diminishing Runge-Kutta scheme [3].

HYPERSONIC TURBULENT BOUNDARY LAYERS

Results from DNS are presented in the current section. The same boundary conditions are applied to both the perfect gas and non-equilibrium flows of each species. The inlet flows are obtained from a separate simulation and assumed to be in thermal equilibrium with a constant mass fraction. Turbulent statistics, near-wall structures as well as mean properties are compared with those from perfect gas simulations with the same boundary conditions. The flow parameters are given in Table 1. All dimensional parameters are given in SI units.

	M_∞	Re_δ	Re_τ	δ_{in}	U_e	ρ_e	T_e	T_w	h_0
Oxygen	5.6	$13,073$	350	0.01013	$5,092$	0.0224	$2,275$	$3,042$	1.525×10^7
Nitrogen	5.2	$15,270$	380	0.00196	$7,129$	0.1205	$4,458$	$5,962$	3.104×10^7

Table 1: Flow parameters of hypersonic turbulent boundary layers in SI units.

Non-equilibrium effects

In order to rule out the different spatial development effects, all the quantities are normalized by either inlet wall units or boundary-edge values. The most noticeable non-equilibrium effects are observed in the van Driest effective velocity profiles, shown in Figure 1a. In non-equilibrium states, the additive constant in the low-law region becomes larger while the von Kármán constant remains the same. The difference in the additive constant between perfect gas and non-equilibrium flows depends on the degree of non-equilibrium, i.e. the stronger non-equilibrium, the larger difference. The non-equilibrium processes in the flow fields also reduce the growth rates of the momentum and boundary layer thicknesses, while the displacement thickness is hardly affected. Moreover, Figure 1b shows higher RMS of velocity fluctuations in non-equilibrium flows and, hence, the higher turbulence kinetic energy. The higher turbulent kinetic energy with endothermic reactions implies that there are no direct energy exchanges between internal and turbulent kinetic energies.

*Corresponding author. Email: jkim@seas.ucla.edu

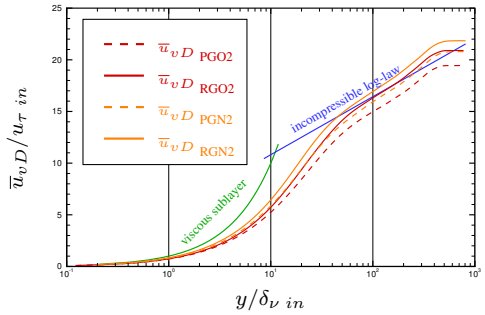

(a) van Driest effective velocity profiles.

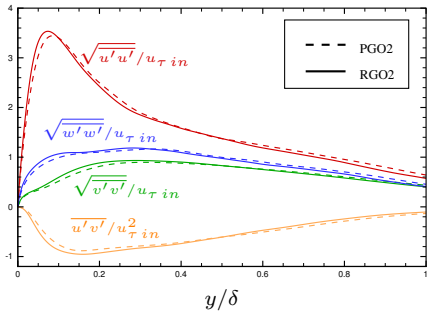

(b) RMS of velocity fluctuations in oxygen flows.

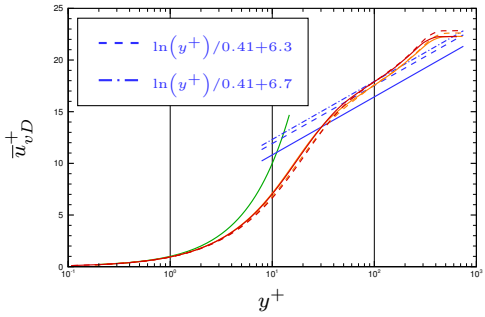

(c) Scaled van Driest effective velocity profiles.

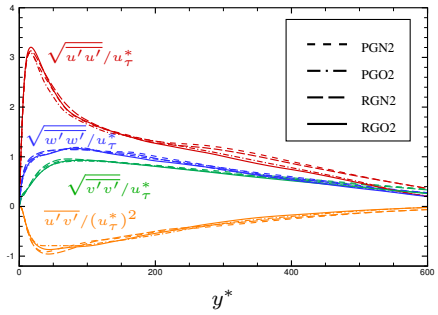

(d) RMS of velocity fluctuations in semilocal units.

Figure 1: Comparisons between prefect gas (PG) and non-equilibrium (RG) flows.

Mechanisms of non-equilibrium effects

The effects of non-equilibrium on turbulent boundary layers can be explained by changes in the mean temperature. Due to non-equilibrium processes, temperature fields are changed. In the non-equilibrium state of consideration in the current study, the flow fields experience cooling due to both the vibrational energy relaxation and endothermic reactions. The temperature drops result in an increase in density and a decrease in viscosity. The increased density causes slow streamwise velocities while the velocity gradient becomes stiff due to weak viscous diffusion. These two opposite phenomena are balanced by the conservation of mass and momentum. The perturbation fields are then adjusted according to the changes in the mean fields.

The differences between perfect gas and non-equilibrium flows can be compensated by taking the variations of density and viscosity into account, which implies Morkovin's hypothesis is still valid with thermal and chemical non-equilibrium. The van Driest effective velocities between perfect gas and non-equilibrium flows, normalized by local wall units, show excellent agreements in Figure 1c. The difference between species are mainly due to different degrees of non-equilibrium. In addition, by using semilocal scales, which are defined with the wall shear stress and local mean density and viscosity, and denoted by a superscript $*$ in Figure 1d, turbulent statistics curves collapse with each other. The RMS of velocity fluctuations are shown in Figure 1d as an example.

CONCLUSIONS

Based on the data from DNS, we have shown that changes in the mean temperatures are responsible for the modifications of the flows due to non-equilibrium processes. We have also shown that the proper scale for compressible turbulent boundary layers with isothermal wall conditions is the semilocal scale. From this, it can also be concluded that Morkovin's hypothesis is still valid even with thermal and chemical non-equilibrium.

References

[1] Park C.: Nonequilibrium Hypersonic Aerothermodynamics. John Wiley & Sons, USA 1990.

[2] Gupta R. N., Yos, J. M., Thompson R. A., Lee K.: A Review of Reaction Rates and Thermodynamics and Transport Properties for an 11-species Air Model for Chemical and Thermal Nonequilibrium Calculations to 30000 K. Technical report, NASA RP-1232, 1990.

[3] Jiang G.-S., Shu C.-W.: Efficient Implementation of Weighted ENO Schemes. J. Comput Phys 126:202-228, 1996.

[4] Zhong X.: High-Order Finite-Difference Schemes for Numerical Simulation of Hypersonic Boundary-Layer Transition. J. Comput Phys 144:662-709, 1998.

ADJOINT SHAPE OPTIMIZATION BASED ON DNS OF TURBULENT CHANNEL FLOW

Thomas Köthe *[1] and Claus Wagner[1,2]
[1]*Institute of Aerodynamics and Flow Technology, German Aerospace Center (DLR), Göttingen, Germany*
[2]*Institute of Thermodynamics and Fluid Mechanics, Technische Universität Ilmenau, Ilmenau, Germany*

Summary Direct Numerical Simulations (DNS) of turbulent channel flow are performed with the aim to reduce the skin friction by controlling the near-wall transport processes based on surface modifications. The latter are determined based on the solution of the adjoint Navier-Stokes equations which provides surface sensitivities indicating an optimal wall shape. With the modified geometry the DNS is continued until a new fully developed state is reached. Time-averaging of the instantaneous wall shapes produced with this approach will finally lead to a steady wall shape which controls the flow according to a prescribed objective function.
Considering that the objective function turbulence kinetic energy (TKE) is minimized, the approach produced a reduction of $\approx 9.3\%$ and a mean pressure gradient, required to drive the flow, which is reduced by $\approx 7.5\%$. Currently, different objective functions are tested to identify flow parameters which are suitable to effectively reduce the skin friction in turbulent channel flow.

ADJOINT SHAPE OPTIMIZATION

Passive flow control often relies on structural changes of the wall contours or on flow control devices which are installed on the wall. Although it is widely known that certain flow control devices like riblets or dimples can be used to control aerodynamic quantities like lift or drag, it is not fully understood, how they interact with near-wall flow structures and how the type and the size of these devices scale with the Reynolds number. On the other hand, it is well known that the wall-normal momentum transport is organized in sweep and ejection events in the boundary layer which control skin friction [1]. The final aim of this work is to identify surface modifications on the walls of a channel which influence the development of turbulent coherent flow structures and reduce the drag.
To achieve this, a finite volume method based on central differences and suitable to deal with unstructured grids solves the unsteady, incompressible Navier-Stokes equations

$$\begin{aligned} \frac{\partial v_i}{\partial t} + \frac{\partial}{\partial x_j}(v_i v_j) &= \circ\ \frac{\partial p}{\partial x_i} + \frac{\partial}{\partial x_j}\left[\nu\left(\frac{\partial v_i}{\partial x_j} + \frac{\partial v_j}{\partial x_i}\right)\right] \\ \circ\ \frac{\partial v_j}{\partial x_j} &= 0, \end{aligned} \tag{1}$$

with the velocity vector v_i, the specific pressure p and the kinematic viscosity ν. The investigated domain is a channel with periodic boundary conditions in streamwise and spanwise directions. Considering a bulk velocity $v_{bulk} = 1m/s$ leads to a Reynolds number, based on the channel half height and the friction velocity, of $Re_\tau = 180$. After reaching a statistically steady state in the DNS of fully developed turbulent channel flow, instantaneous velocity fields are averaged over one turn-around time based on the bulk velocity to obtain the turbulence kinetic energy (TKE). In [2] it was shown that due to the time-averaging, the minimization of the exact quantity of interest (skin friction) is not necessarily the most effective way. Therefore, the objective of the present study is to minimize the TKE of the turbulent channel flow by modifying the shape of the channel walls. The constraint R is to fulfill the unsteady, incompressible Navier-Stokes equations (1). The optimization problem

$$\begin{aligned} &\min\ J = \frac{1}{2}\left((v_x')^2 + (v_y')^2 + (v_z')^2\right) \\ &\text{wrt. } R = 0. \end{aligned} \tag{2}$$

is solved by the method of Lagrange multipliers. The latter is based on the Lagrange equation $L = J(v_i, p) + (u_i, q) \cdot R(v_i, p)$, with the Lagrange multipliers u_i and q. Minimization of the Lagrange equation is formally achieved by considering the total variation $\delta L = \delta_\beta L + \delta_{v_i} L + \delta_p L$, where β denotes the design variables. Since any change of β changes the state variables as well, a new solution of (1) would be required. To obviate the latter, an adjoint method [3], [4] is used, where the Lagrange multipliers are chosen in a way, that the relation $\delta_v L + \delta_p L = 0$ holds. This leads to the adjoint Navier-Stokes equations

$$\begin{aligned} v_j\left(\frac{\partial u_i}{\partial x_j} + \frac{\partial u_j}{\partial x_i}\right) &= \circ\ \nu\frac{\partial}{\partial x_j}\left(\frac{\partial u_i}{\partial x_j} + \frac{\partial u_j}{\partial x_i}\right) + \frac{\partial q}{\partial x_i} + \frac{\partial J}{\partial v_i} \\ \frac{\partial u_i}{\partial x_i} &= \frac{\partial J}{\partial p}. \end{aligned} \tag{3}$$

*Corresponding author. Email: thomas.koethe@dlr.de

With the solution of (3), the total variation of L reduces to $\delta L = \delta_\beta L$. To perform the shape optimization, all points of the surface mesh must serve as design variables β. Therefore, a superposition of local surface normal displacements β is introduced to describe the shape deformation [5]. Finally, one can compute the sensitivities in a post-processing step [6] with the solutions of (1) and (3) via

$$S = \delta L = \delta_\beta L = -A\nu \left(n_i \frac{\partial u_{t,j}}{\partial x_i} \cdot n_i \frac{\partial v_{t,j}}{\partial x_i} \right) \tag{4}$$

With these two solutions it is possible to compute sensitivities S for every cell of the boundary $\Gamma = \partial\Omega$, independent of the number of design variables. This reduces the computational costs extremely in comparison to other gradient based optimization methods and maximizes the degrees of freedom in the optimization process.
Since, the computed sensitivities represent local surface normal displacements, they can be used to deform the mesh by interpolating the sensitivities to the mesh points with radial basis functions (RBF). In [7] we developed a mesh deformation tool, which conserves the mesh quality. Thus, remeshing is not necessary.

RESULTS AND CONCLUSION

For the present study, the adjoint equation (3) has been solved based on the mean flow field obtained from the velocity fields of the DNS after time-averaging over one turn-around time. The resulting surface sensitivity distributions on both channel walls are shown in figure 1 (left). Based on them, the channels walls are deformed, as presented in figure 1 (right). Then, the DNS has been continued with the deformed channel domain until a new statistically steady state has been reached.

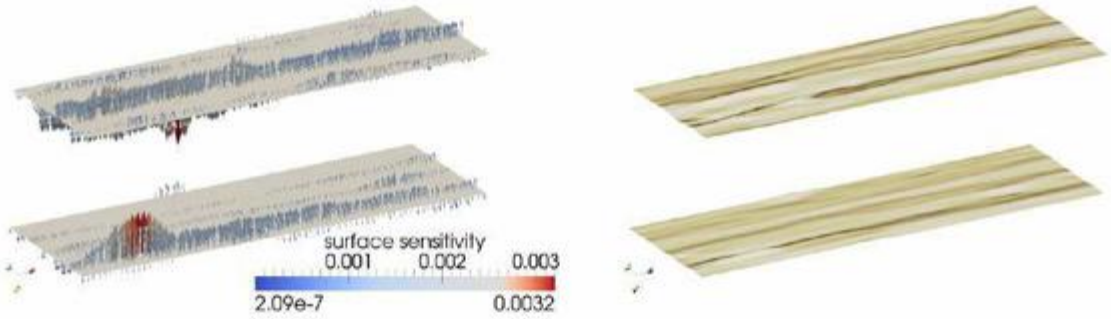

Figure 1: Computed surface sensitivities (left). TKE-optimized shape of the channel walls (right).

Time and volume averaging of the TKE fields obtained in the DNS of the turbulent flow in the channel with smooth walls resulted in a value of $2128.141\ m^2/s^2$. After the deformation of the channel walls (see figure 1), the corresponding TKE value evaluated based on the new flow fields drops to $1930.065\ m^2/s^2$. This is a reduction by 9.3%. Further, the pressure gradient, needed to drive the flow, drops from 0.00418 to 0.00387, which is a reduction by 7.4%.
The results show that the presented method has a high potential to identify passive flow control measures. Currently, other objective function are implemented which are suitable to reduce the pressure drop in turbulent channel flows. A comparison of the results which is performed to identify the most effective objective function for skin friction reduction in turbulent channel flows will be presented at the conference.

References

[1] Kim, J., Moin, P., and Moser, R., "Turbulence statistics in fully developed channel flow at low Reynolds number," *Journal of Fluid Mechanics*, Vol. 177, 1987, pp. 133–166.

[2] Bewley, T. R., Moin, P., and Temam, R., "DNS-based predictive control of turbulence: an optimal benchmark for feedback algorithms," *Journal of Fluid Mechanics*, Vol. 447, 2001, pp. 179–225.

[3] Giles, M. B. and Pierce, N. A., "An introduction to the adjoint approach to design," *Flow, Turbulence and Combustion*, Vol. 65, No. 3-4, 2000, pp. 393–415.

[4] Jameson, A., "Aerodynamic shape optimization using the adjoint method," *VKI Lecture Series 2003-02, Brussels.*, 2003.

[5] Pironneau, O., "Optimal shape design for elliptic systems," *System Modeling and Optimization*, edited by R. Drenick and F. Kozin, Vol. 38 of *Lecture Notes in Control and Information Sciences*, Springer Berlin Heidelberg, 1982, pp. 42–66.

[6] Soto, O. and Löhner, R., "On the computation of flow sensitivities from boundary integrals," *Proceedings of the 42nd AIAA Aerospace Sciences Meeting and Exhibit, Reno NV*, Vol. 112, 2004.

[7] Köthe, T., Herzog, S., and Wagner, C., "Shape optimization of aircraft cabin ventilation components using adjoint CFD," *Engineering Optimization 2014*, CRC Press, 2014, pp. 675–680.

A FULL EULERIAN METHOD FOR FLUID-STRUCTURE INTERACTION PROBLEMS

Shu Takagi[1], Kazuya Shimizu[1], Satoshi Ii[2], & Kazuyasu Sugiyama[2]
[1]*Department of Mechanical Engineering, The University of Tokyo, Tokyo, Japan*
[2]*Graduate School of Engineering Science, Osaka University, Osaka, Japan*

Summary A full Eulerian fluid-structure coupling method was proposed within the framework of the volume-of-fluid approach. All the basic equations are numerically solved on a fixed Cartesian grid in a finite difference manner. An incompressible fluid flow solver is extended to the incompressible fluid-structure system. The present method has been further developed for fluid-membrane interaction problems and applied to the blood flows containing Red Blood Cells (RBCs) and platelets. The method is further extended to multiscale thrombosis simulation, which couples Monte-Carlo simulations for the molecular scale protein-protein interactions with continuum scale simulations. These simulators are developed for the massively parallel computation and the method of having the good scalability of the computation will be also presented.

INTRODUCTION

Fluid-Structure Interaction (FSI) phenomena appear in many places, e.g., biological systems, and industrial processes. Conventionally, the computational Fluid dynamics is more commonly described in an Eulerian way, while the computational structure dynamics is more straightforward to be described in a Lagrangian way. The coupling of the Fluid and structure dynamics is a formidable task due to such a difference in the numerical framework. There are currently several major approaches classified, with respect to the computational treatment of FSI problems, on how the kinematic and dynamic interactions are coupled on the moving interface. In general, the methods with the body-fitted mesh can more accurately track the shape of the deformable body. These approaches are referred to as an interface-tracking approach, in which the surface mesh is shared between the fluid and solid phases, and thus automatically satisfies the kinematic condition. However, the computational domain has to be remeshed as the object is greatly distorted, and it is not always an easy task to keep the load of each computational core balanced. An alternative to the interface-tracking approach is an Eulerian-Lagrangian approach, in which the fluid and solid phases are separately formulated on the fixed Eulerian and Lagrangian grids, respectively. A noticeable contribution is the development of the immersed boundary (IB) method by Peskin[1], who introduces a smoothed approximation of Dirac δ function for communication between the Eulerian and Lagrangian quantities, and demonstrated the landmark simulation of the blood flow around heart valves. Here, we introduce another approach where both the fluid and solid phases are treating in Eulerian way.

Considering the utilization of voxel data converted from the medical image data of MRI or CT, it is straightforward to develop the full Eulerian finite difference methods, which directly access the voxel data to describe the boundary on the fixed Cartesian mesh and avoid difficulty in mesh generation and reconstruction. Sugiyama et al.[2] developed a novel full-Eulerian FSI solver, and it has been extended to a fluid and stiff material interaction and fluid and membrane interaction([3],[4]). Considering that the voxel data contain the volume fractions of fluid and solid, we apply the volume-of-fluid/volume-fraction (VOF) formulation to describing the multicomponent geometry. Because the Eulerian formulation lacks of the material points to link between the reference and current configurations, a method to quantify the level of deformation is required. To this end, we introduce the left Cauchy-Green deformation tensor defined on each grid point, and temporally update it. The full-Eulerian method has been reviewed by Takagi et al. [3]. In the present talk, this novel method is explained with its application to blood flows.

E AMPLES OF NUMERICAL RESULTS

The numerical results of large scale parallel computation with $O(10^6)$ flowing RBC-like particles are shown in Fig.1. The developed method is highly suitable for the massively parallel computing and the actual computational speed of 4.5 peta flops was achieved, which corresponds to 43% of the theoretical performance of the supercomputer, named “K”, used for the simulation. The method was also extended to simulate platelet adhesion process which occurs at the initial stage of thrombosis. The platelet adhesion to the vessel wall is given by the large numbers of protein-protein bindings. This binding process of protein molecules are treated stochastically using the Monte Carlo method. The snapshot of the numerical result of platelet adhesion is shown in Fig.2. More detail discussion will be given in the talk.

CONCLUSIONS

A novel simulation method for solving fluid-structure coupling problems suitable for the massively parallel computing was introduced. All the basic equations in continuum scales are numerically solved on a fixed Cartesian grid with finite difference discretization. An incompressible fluid flow solver is extended to the incompressible fluid-structure system. A

[a)] Corresponding author. Email: takagi@mech.t.u-tokyo.ac.jp

volume-of-fluid approach, which has been developed for computing multiphase flows, was applied to describing the multi-component geometry. So, the present method treats non-linear deformation of hyperelastic materials in fully Eulerian way on a fixed grid without generating the boundary-fitted meshes. The simulator was designed for the massively parallel computation and showed the excellent scalability of the computation which achieved the actual speed of 4.5 Peta Flops.

The method has been further developed for fluid-membrane interaction problems and applied to the blood flows containing Red Blood Cells and platelets. Then the method has been extended to multiscale thrombosis simulation. For this simulation, the molecular scale protein-protein interactions are solved using Monte-Carlo method [3] coupling with continuum scale simulations. The results show that the continuum scale flows affects the platelet adhesion on the vessel walls where the adhesion force itself is given by the molecular scale binding between GP1bα proteins on the platelet and vWF proteins on the damaged vessel wall.

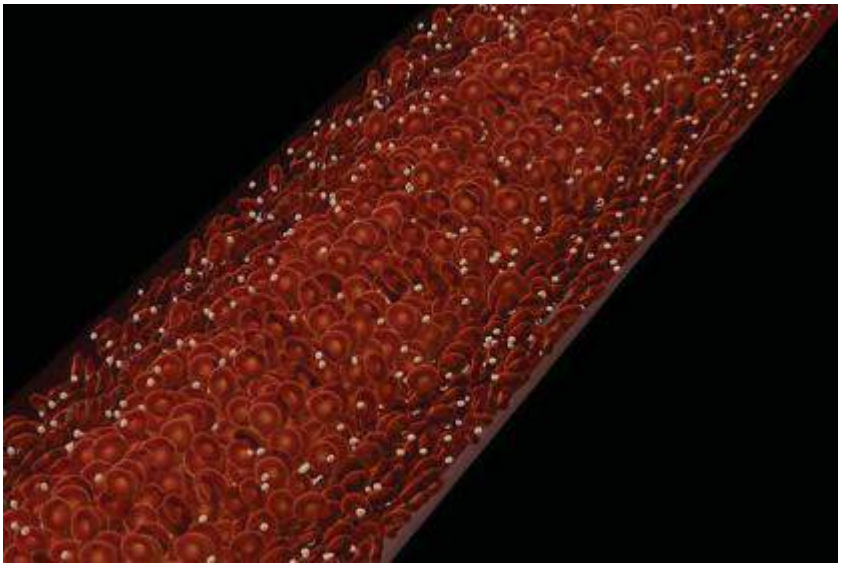

Fig.1 Large scale parallel computation with $O(10^6)$ particles
(Computational speed of 4.5 Peta Flops was achieved)

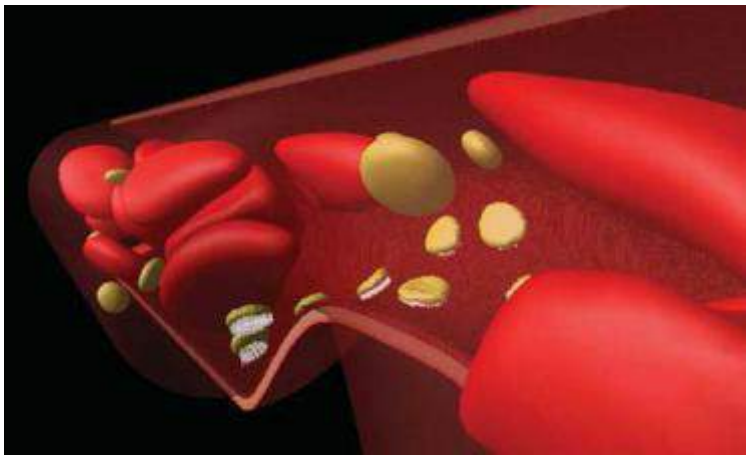

Fig.2 Simulation results of platelets adhesion on arteriosclerosis area in the presence of RBCs.

References

[1] C. Peskin, Flow patterns around heart valves: A numerical method, *J. Comput. Physics*, Vol.10, pp.252-271 (1972).

[2] K. Sugiyama et al. A full Eulerian finite difference approach for solving fluid–structure coupling problems. *J. Comput. Physics*. 230 , pp. 596–627 (2011)

[3] S, Takagi, et al., A Review of Full Eulerian Methods for Fluid-Structure Interaction Problems" *Journal of Applied Mechanics*, Vol.79, 010911(2011)

[4] S. Ii, et al., A Full Eulerian Fluid-Membrane Coupling Method. *Commun. Comput. Phys*, 12, pp. 544–576 (2012)

MIGRATION OF VESICLES AND FLEXIBLE FIBERS IN POISEUILLE FLOW

Alexander Farutin*[1,2], Tomasz Piasecki†[3], Agnieszka M. Słowicka[3], Chaouqi Misbah[1,2], Eligiusz Wajnryb[3], and Maria L. Ekiel-Jeżewska ‡[3]

[1]*Univ. Grenoble Alpes, LIPHY, F-38000 Grenoble, France*

[2]*CNRS, LIPHY, F-38000 Grenoble, France*

[3]*Institute of Fundamental Technological Research, Polish Academy of Sciences, Pawińskiego 5B, 02-106 Warsaw, Poland*

Summary Dynamics of flexible fibers and vesicles in unbounded planar Poiseuille flow at the low-Reynolds-number are shown to exhibit similar basic features, when their equilibrium (moderate) aspect ratio is the same and vesicle viscosity contrast is relatively high. The lateral migration and accumulation of these two types of flexible objects are analyzed numerically.

In this paper, we investigate whether different flexible objects – vesicles and flexible fibers made of beads – may share similar features, or even some universal behaviors, regarding their migration properties. Revealing similarities between apparently different systems would advance our understanding of the migration mechanism and allow for using simpler models, which are numerically more efficient.

A single flexible object is entrained by an unbounded Poiseuille flow with velocity $\boldsymbol{v}_\infty = \left(\alpha y^2 - v_m\right) \boldsymbol{e}_x$, where α is the flow curvature. The value $-v_m$ of the flow velocity at the central plane $y=0$ is irrelevant for the migration or shape evolution. The dynamics of the flexible object is derived from the Stokes equations, using the boundary integral method for vesicles [1, 2, 3] and the multipole expansion (implemented in the HYDROMULTIPOLE numerical codes) for the fiber beads [4, 5].

A vesicle has a constant area S and a constant volume V, and its geometry is described by the radius of the sphere having the same volume, $R_0 = (3V/4\pi)^{1/3}$, and the reduced volume $\nu = 6\sqrt{\pi} V S^{-3/2}$. The other parameters which determine the vesicle deformation and motion under flow are the ratio λ of the fluid viscosities inside and outside, and the dimensionless capillary number $C_a = \alpha R_0^4 \eta/\kappa$, defined as the dimensionless ratio of the hydrodynamic to bending forces (the first one proportional to the flow curvature α and fluid viscosity η, and the second one – to the vesicle bending modulus κ).

Flexible fiber is modeled as a chain of N identical spherical solid beads of diameter d. Following Refs. [4, 5, 6, 7, 8], we impose the constraint elastic and bending forces which act on each bead, in such a way that the total external force and torque on the fiber vanish. The bead centers are connected by springs with the equilibrium length $l_0 d$ only slightly larger than the bead diameter d, with $l_0 = 1.01$, and the Hooke's spring constant $\tilde{k}$. As in Ref. [5], the ratio of the elastic to viscous forces is given in terms of the dimensionless parameter $k = \tilde{k}/(\pi\eta v_m)$. We set $k = 80 >> 1$. With this choice, the fiber practically does not change its length during the motion, and the specific value of k is irrelevant. The relevant quantity is the ratio of bending and viscous forces, $A = \tilde{A}(625\pi\eta d^5\alpha)^{-1}$, where $\tilde{A}$ denotes the fiber bending stiffness. [5]

To match flexible fibers with vesicles, we focus on vesicles with relatively large viscosity contrast, $\lambda = 12$. Moreover, we choose relatively low aspect ratio – our fiber is made of $N = 5$ beads. We circumscribe the fiber at the equilibrium position by the spherocylinder, and match its volume and surface with the corresponding volume and surface of the vesicle at the equilibrium, what results in the choice of $\nu = 0.6$. The goal is to analyze how the dynamics of flexible objects depends on their dimensionless bending stiffness, i.e. A for fibers and C_a^{-1} for vesicles.

Each of our flexible objects is initially aligned with the flow. While translating with the flow, it tumbles and changes shape. The basic task, however, is to determine the motion of the center of the flexible object across the flow. For vesicles, the center is determined as the center of mass of the membrane. For fibers, we take their center of mass, with the position calculated as the arithmetic mean of the positions of all the bead centers. The center keeps the same z-coordinate, but its y-coordinate (denoted here as y_0) changes slowly with time. Examples of the time evolution of the dimensionless position y_0/R_0 of the center are shown in Fig. 1, with the use of $(\alpha R_0)^{-1}$ as the time unit. It is clear that both vesicles and flexible fibers migrate across the flow and their centers tend to a certain accumulation plane, $y_0 \to y_c$. The position y_c depends on the bending stiffness. In Fig. 1, we have matched the values of $C_a = 0.08$ and $A = 0.024$ in such a way that both vesicles and fibers accumulate at the same distance $y_0/R_0 \approx 8.2$ from the central plane.

The dynamics of a flexible object, which is relatively far from the central plane of the flow, satisfy a universal scaling [5, 9] – the fiber essential dynamics, including its deformation and migration, is determined only by the local shear rate $2\alpha y_0$. As the result, the accumulation position y_c is a linear function of the bending stiffness, as shown in Fig. 2. The same accumulation positions correspond to the bending stiffness of vesicles and fibers related to each other by the expression $1/C_a \approx 520A$.

*A. Farutin, T. Piasecki and A. M. Słowicka contributed equally to this work.

†Present address: Institute of Mathematics of the Polish Academy of Sciences, Śniadeckich 8, 00-656 Warsaw, Poland

‡Corresponding author. Email: mekiel@ippt.pan.pl

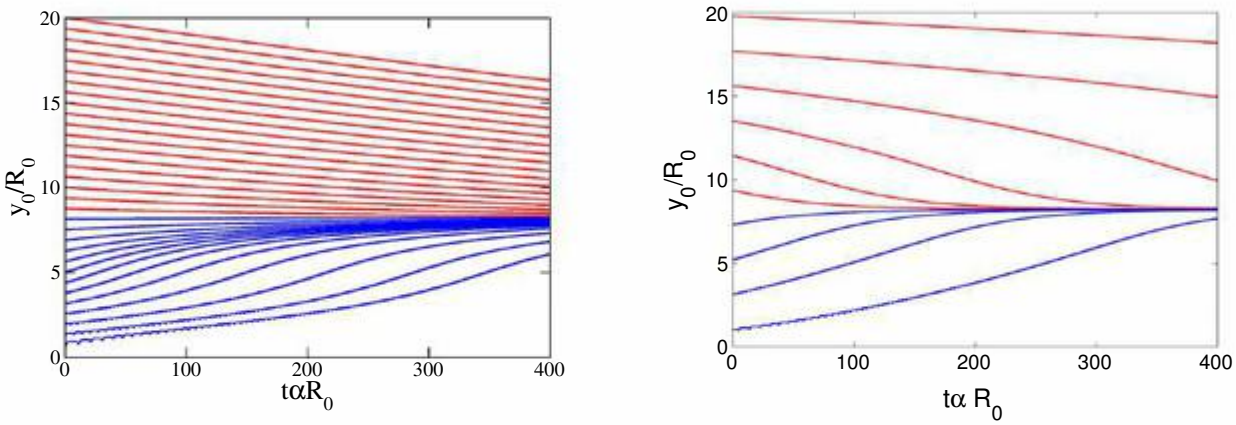

Figure 1: The time-dependent distance y_0/R_0 from the center of flexible object to the central plane of the flow. Vesicles with $C_a = 0.08$ (left) and fibers with A=0.024 (right) accumulate at the same distance $y_c/R_0 \approx 8.2$. The blue and red lines indicate migration outward and inward, respectively.

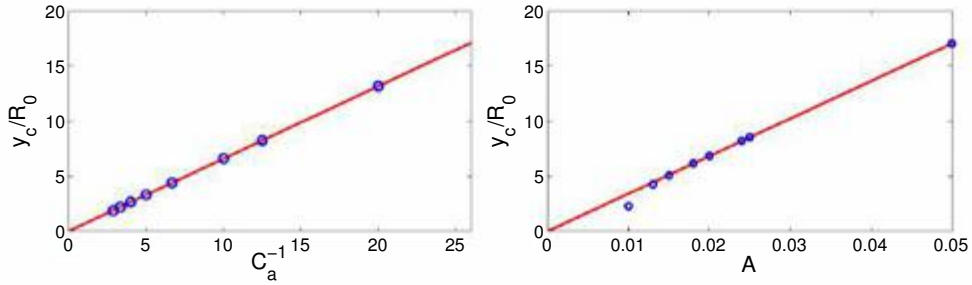

Figure 2: The accumulation position y_c/R_0 of vesicle (left) and fiber (right) vs. its bending stiffness.

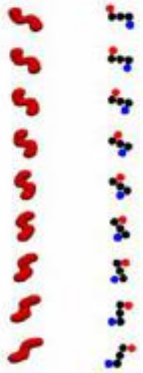

Figure 3: Evolution of shapes. $C_a = 0.15$, $y_0/R_0 = 9.3$.

In the following part of the paper, we analyze how other features of the dynamics of single vesicles and fibers depend on their bending stiffness. We evaluate the tumbling frequency and the migration velocity across the flow, study evolution of shape, compare the universal scaling based on the local shear with the dynamics in the pure shear flow. We also present examples of the motion and deformation of more elongated flexible objects, and demonstrate that the second (coiled) mode of the dynamics exists not only for fibers [8] but also for vesicles. We observe that fibers can migrate slower or faster than vesicles of the matched flexibility, depending on the range of the parameters. However, the overall similarity of the corresponding shapes (see Fig. 3) is evident, what allows to suppose that the accumulation mechanism of vesicles and fibers is essentially the same.

This work was supported in part by CNES, ESA and the National Science Centre under grant No. 2014/15/B/ST8/04359.

References

[1] A. Farutin T. Biben and C. Misbah. Three-dimensional vesicles under shear flow: Numerical study of dynamics and phase diagram. *Phys. Rev. E*, 83:031921, 2011.

[2] A. Farutin and C. Misbah. Squaring, parity breaking, and S tumbling of vesicles under shear flow. *Phys. Rev. Lett.*, 109:248106, 2012.

[3] C. Misbah A. Farutin. Symmetry breaking and cross-streamline migration of three-dimensional vesicles in an axial Poiseuille flow. *Phys. Rev. E*, 89:042709, 2014.

[4] A. M. Słowicka, M. L. Ekiel-Jeżewska, K. Sadlej, and E. Wajnryb. Dynamics of fibers in a wide microchannel. *J. Chem. Phys.*, 136:044904, 2012.

[5] A. M. Słowicka, E. Wajnryb, and M. L. Ekiel-Jeżewska. Lateral migration of flexible fibers in Poiseuille flow between two parallel planar solid walls. *Eur. Phys. J. E*, 36:1–12, 2013.

[6] E. Gauger and H. Stark. Numerical study of a microscopic artificial swimmer. *Phys. Rev. E*, 74(2):021907, 2006.

[7] S. Kuei, A. M. Słowicka, M. L. Ekiel-Jeżewska, E. Wajnryb, and H. A. Stone. Dynamics and topology of a flexible chain: knots in steady shear flow. *New J. Phys.*, 17(5):053009, 2015.

[8] A. M. Słowicka, E. Wajnryb, and M. L. Ekiel-Jeżewska. Dynamics of flexible fibers in shear flow. *J. Chem. Phys.*, 143:124904, 2015.

[9] A. Farutin and C. Misbah. Analytical and numerical study of three main migration laws for vesicles under flow. *Phys. Rev. Lett.*, 110:108104, 2013.

APNEAIC AIRWAY GAS CONCENTRATIONS DURING NASAL HIGH FLOW THERAPY

Sibylle Van Hove[1], Vinod Suresh[1,2], and John Cater *[1]

[1]*Department of Engineering Science, University of Auckland, Auckland, New Zealand*
[2]*Auckland Bioengineering Institute, University of Auckland, Auckland, New Zealand*

Summary Nasal high flow therapy has been used clinically to increase the intubation period in patients requiring mechanical ventilation, however the mechanisms through which the therapy achieves this have not been investigated. Computational fluid dynamics has been used in this study to demonstrate the effect of the therapy on the gas concentrations within the apneaic human airway. The complexity of the human airway gives rise to an intricate flow field in which the turbulence and mixing of gas species is augmented by the application of nasal high flow therapy. The therapy was found to flush the airway with oxygen thereby removing the stagnant, CO_2 rich gas via the nostrils and mouth and hence preventing CO_2 build-up during apnea. These results explain the previously reported clinical observations and give confidence in the application of the therapy during anaesthetic procedures.

INTRODUCTION

The intubation of patients requiring mechanical ventilation is a delicate procedure which can result in airway trauma - a situation in which intubation cannot occur and thus ventilation of the patient becomes impossible. Airway trauma happens most commonly in patients with difficult airway anatomies and prevents surgery from proceeding. Nasal high flow (NHF) oxygen therapy has been used on twenty five subjects to increase the apneaic period during which intubation occurs, thereby improving the chances of a successful intubation [1]. The apneaic window is the time period during which the surgeon provides the patient with an artificial windpipe that will be used throughout surgery for mechanical ventilation. During this period the patient is anaesthetised and paralysed, hence they are not breathing spontaneously and the procedure must be carried out rapidly. It is suggested that NHF aids in maintaining normal gas exchange in the alveoli during the apneaic window. However there are no studies to date that analyse the effect NHF has on the oxygen and carbon dioxide concentrations within the airway of apneaic subjects.

NHF therapy has traditionally been used to treat a variety of respiratory diseases, including chronic obstructive pulmonary disease and hypoxemic respiratory failure, through its five mechanisms of action [2]. One of the mechanisms of action of NHF therapy is the washout of the anatomical dead-space which is thought to improve patient oxygenation. Clinical studies have alluded to the existence of such a phenomenon [3] but the fluid dynamics causing this washout effect has not been investigated. Previous computational fluid dynamics (CFD) and experimental studies have focused on modeling the airflow patterns, temperature distribution, particle deposition and humidity variations within the airway during natural breathing. The size of flow re-circulations within the airway have been found to depend on flow rate [4] while anatomical features of the bronchi, such as large branching angles and quasi-monopodial branching, is thought to increase flow mixing by enhancing secondary flow [5]. Such flow features hint at the hypothesis that the nasopharyngeal washout produced by NHF therapy could maintain normal gas concentrations within the human airway during apnea. The focus of this study is to model, using CFD techniques, the gas concentrations within the apneaic airway of an adult human with applied NHF therapy in an attempt to explain the increased apneaic window observed in clinical studies.

MATERIALS & METHODS

The Reynolds Averaged Navier Stokes equations were solved numerically with the finite volume solver Fluent (ANSYS 16.0). A $k \circ \omega$ shear stress transport model was employed to model the turbulent features of the flow. The flow was assumed to be incompressible and isothermal as the effects of buoyancy are considered insignificant [6]. An anatomically accurate airway down to the 5th bronchiole generation was constructed from CT scans and is displayed in Figure 1(a). Fine anatomical details such as cilia and mucous were neglected and the airway was modeled as rigid, smooth, no-slip wall [6]. An Optiflow^{TM} nasal cannula was inserted into the model and a pipe extension was added to allow natural flow development. A box surrounding the terminals of the bronchi was generated to represent the remainder of the airway from the 5th generation through to the alveoli. A section of the atmosphere surrounding the nose was also included to allow air to pass through the nostrils at any angle. The box surrounding the lower airway was modeled as a wall with a constant CO_2 volume fraction representative of the alveolar CO_2 concentration.

The complexity of the nasal cavity geometry and the large variations in element size required to accurately capture the different sections of the model (i.e. the very fine bronchioles compared to the box) make generating a high quality mesh for this model arduous. An unstructured tetrahedral mesh, containing 4 million cells, was generated and used to solve the velocity,

*Corresponding author. Email: j.cater@auckland.ac.nz

pressure, carbon dioxide and oxygen volume fractions within the airway during the first 2 seconds after therapy was initiated. The airway was initialised with a gas composition that was representative of the alveolar gas composition to represent the end of an expiration prior to the patient becoming apneaic. Transient simulations were performed with therapy flow rates ranging between 0 - 70 Liters per minute. The model involves much faster flows around the nasal cannula compared to those in the lower airway. Hence the gas species transport within the upper airway is convection dominated while transport in the lower airway is primarily a result of diffusion and this is numerically challenging as it limits the solver time-step.

RESULTS

NHF therapy injects high flow oxygen into the upper airway which causes re-circulations within the nasal cavity. This in turn causes the high CO_2 concentrated gas that was initially in the airway to vent out of the mouth and nostrils. Over time, the concentration of carbon dioxide within the whole airway diminishes as oxygen coming from the therapy washes out the higher CO_2 concentrated gas. This washout along with the secondary flows produced by the airway branching helps the airway reach a steady state where the diffusion of CO_2 coming from the alveoli model is balanced by convective transport out of the airway. At higher therapy flow rates the flushing occurs faster, thus the airway reaches a steady state more quickly than at low flow rates. This is seen in Figure 1 (b) & (c), as the low CO_2 gas penetrates further down the airway at the higher therapy flow rate.

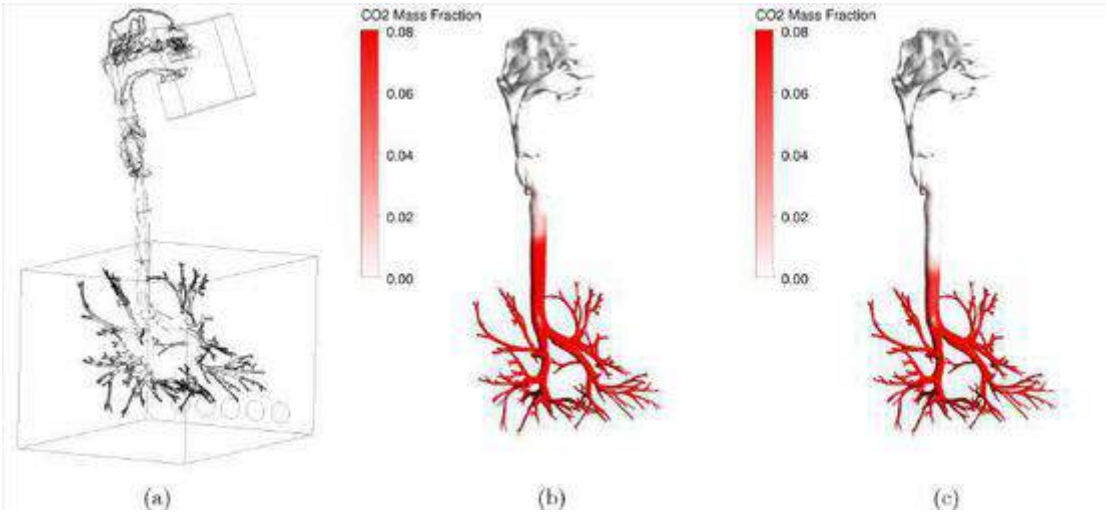

Figure 1: Outline of airway geometry and surrounding boxes (a). CO_2 distribution in airway after 2 s NHF therapy at flow rates of 30 L min^{-1} (b) & 70 L min^{-1} (c).

CONCLUSIONS

The results indicate that NHF can extend the apneaic window by enhancing CO_2 removal by a washout of the stagnant airway space during the process of intubation. The effect of airway geometry on the therapy remain to be studied.

Acknowledgements

The authors wish to acknowledge the contribution of NeSI high-performance computing facilities as well as Fisher & Paykel Healthcare Limited to the results of this research.

References

[1] Patel A., Nouraei S.A.R.: Transnasal Humidified Rapid-Insufflation Ventilatory Exchange (THRIVE): a physiological method of increasing apnoea time in patients with difficult airways. Anaesthesia 70:323-329, 2015.

[2] Dysart K., Miller T.L., Wolfson M.R, Shaffer T.H.: Research in high flow therapy: Mechanisms of action. Respiratory Medicine 103:1400-1405, 2009.

[3] Chatila W., Nugent T., Vance G., Gaughan J., Criner G.J.: The Effects of High-Flow vs Low-Flow Oxygen on Exercise in Advanced Obstructive Airways Disease. CHEST Journal 126:1108-1115, 2004.

[4] Martonen T.B., Quan L., Zhang Z., Musante C.J.: Flow Simulation in the Human Upper Respiratory Tract. Cell Biochemistry and Biophysics 37:27-36, 2002.

[5] Banko A.J., Coletti F., Schiavazzi D., Elkins C.J., Eaton J.K.: Three-dimensional inspiratory flow in the upper and central human airways. Experiments in Fluids 56:1-12, 2015.

[6] Keyhani K., Scherer P.W., Mozell M.M.: Numerical Simulation of Airflow in the Human Nasal Cavity. Journal of Biomedical Engineering 117: 429-441, 1995.

AN EFFICIENT ADAPTIVE RESCALING SCHEME FOR COMPUTING HELE-SHAW PROBLEMS

Meng Zhao*[1], Shuwang Li[1], and John Lowengrub[2]

[1]*Department of Applied Mathematics, Illinois Institute of Technology, Chicago, IL 60616, US.*
[2]*Department of Mathematics, University of California at Irvine, Irvine, CA 92697, US.*

Summary In this paper, we present an efficient rescaling scheme for computing moving interface problems. The idea is to design an adaptive time-space mapping such that in the new time scale, the interfaces can evolve logarithmic fast for small-sized interface at early stage of growth and exponentially fast for large-sized interface at later times. During the evolution, the new spatial scale guarantees the conservation of the area/volume enclosed by the interface. Comparing with the original rescaling idea in [3], this adaptive scheme dramatically improves the slow growth at early times when the interface size is small. Our results show that the original three-week computation in [3] can be done in just four days using the adaptive scheme.

THE HELE-SHAW PROBLEM

The Hele-Shaw problem is a classical example for studying interface dynamics or systems driven out of equilibrium. When a less viscous fluid is injected into a more viscous fluid contained in a Hele-Shaw cell, the interface separating the two fluids develops fingering patterns due to the Saffman-Taylor instabilities [4].

Let $\Gamma(t)$ be the moving interface separating the two fluid domains E_i, where $i = 1, 2$ indicates the injected fluid and the exterior viscous fluid, respectively. We assume the two fluids obey Darcy's Law, $\mathbf{u}_i = -M_i \nabla P_i$ for $\mathbf{x} \in E_i$, where $\mathbf{u}_i$ is the velocity of fluid i, P_i is the corresponding pressure, and $M_i = \dfrac{h^2}{12\mu_i}$ is the mobility of fluid i. The parameter h is the width of the gap between the two parallel plates and μ_i is the viscosity of fluid i. For incompressible fluids, i.e. $\nabla \cdot \mathbf{u}_i = 0$, we have

$$\nabla^2 P_i = 0, \qquad \mathbf{x} \in E_i. \tag{1}$$

Across the interface $\Gamma(t)$, the fluid normal velocity is continuous and the pressure has a jump given by the Laplace-Young condition

$$[P]_t = P_1 - P_2 = \sigma\kappa(\mathbf{x}), \qquad \mathbf{x} \in \Gamma(t), \tag{2}$$

where σ is the surface tension and κ is the curvature of the interface. Finally fluid is injected at flow rate $J(t) = \displaystyle\int_{\Sigma_0} \frac{\partial P_1}{\partial \mathbf{n}} ds$, where s is the arclength, Σ_0 is a small circle centered at origin and $\mathbf{n}$ is the outward normal. We reformulate Eq. (1) as a boundary integral equation and seek a solution in the form, $P(\mathbf{x}) = \dfrac{1}{2\pi}\displaystyle\int_{\Gamma(t)} \mu(\mathbf{x}')\Big[\frac{\partial ln|\mathbf{x}-\mathbf{x}'|}{\partial \mathbf{n}(\mathbf{x}')} + 1\Big] ds(\mathbf{x}') + Jln|\mathbf{x}|$, where $\mu(\mathbf{x})$ is the dipole density on $\Gamma(t)$. Using the boundary condition given by Eq. (2), μ can be calculated by solving a 2nd kind Fredholm integral equation, $\mu(\mathbf{x}) - \dfrac{1}{\pi}\displaystyle\int_{\Gamma(t)} \mu(\mathbf{x}')\Big[\frac{\partial ln|\mathbf{x}-\mathbf{x}'|}{\partial \mathbf{n}(\mathbf{x}')} + 1\Big] ds(\mathbf{x}') - 2Jln|\mathbf{x}| = 2\sigma\kappa(\mathbf{x}) \quad$ for $\mathbf{x} \in \Gamma(t)$, with $\int_{\Gamma(t)} \mu(\mathbf{x}') ds(\mathbf{x}') = 0$. The normal velocity of the interface can be calculated by the Dirichlet-Neumann map [2, 1].

THE RESCALING SCHEME

In [2, 3], the authors studied an air-oil interface in a radial Hele-Shaw cell with injection air flux $J = 1$. As predicted by the linear stability analysis, the interface develops ramified patterns by repeated tip-splitting of fingers. For a constant flux, the equivalent bubble radius evolves as $dR/dt \sim R^{-1}$, where R is the radius of a circle with the same area as the air bubble. Consequently the velocity of the interface, dR/dt, decreases as R increases (the bubble grows). From the perspective of numerical computation, this makes the large air bubble computation extremely expensive. In [3], the authors proposed a rescaling idea such that in the new rescaled time-space, the interface always evolves exponentially fast. The scheme works beautifully for large-sized interface at later times. However, at early times when the air bubble is small, the evolution is quite slow, and a significant portion of CPU time was used to compute the slow development of viscous fingers.

We introduce a new rescaled space and time frame $\mathbf{x}, \bar{}$) such that $\mathbf{x} = \bar{}(\bar{} \mathbf{x}(\bar{t}, \theta), \bar{} = \displaystyle\int_0^t \frac{1}{\rho(t')} dt'$, where $R(t)$ is the space scaling factor depending on a new time variable t, $\mathbf{x}$ is the position vector of the scaled interface, and $\rho(t) = \bar{\rho}(t)$

*Corresponding author. Email: mzhao8@hawk.iit.edu

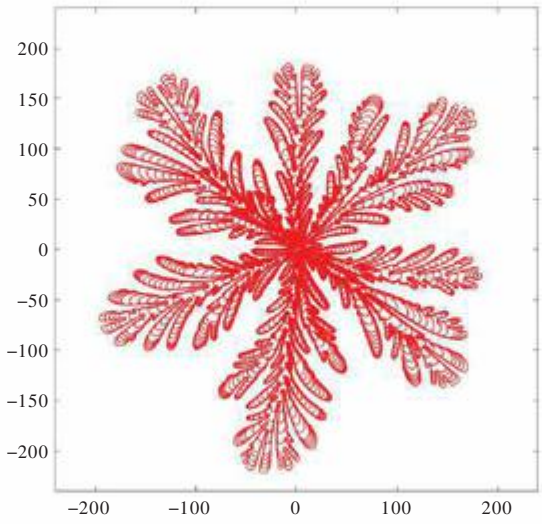

Figure 1: The largest and most complicated Hele-Shaw bubble simulation up to date.

is the time scaling factor. The rescaled normal velocity V satisfies $V(t) = \frac{\rho}{R}V(t(t)) - \frac{\mathbf{x}\cdot\mathbf{n}}{R}\frac{dR}{dt}$, where V is the original normal velocity. In the rescaled frame, we require the area enclosed by the interface remains constant. As a consequence, $\frac{dR}{dt} = \frac{\pi\rho J}{AR}$, where $J(t) = J(t(t))$ is the flux. Here we simply set the scaling time factor ρ_s as

$$\rho_s = \frac{b}{\log(a)}\frac{A(0)}{\pi J}R^2\Big(\underbrace{\frac{1}{a^R}}_{\text{logarithmic growth}} + \underbrace{\frac{1}{a^{R_0}R_0}}_{\text{exponential growth}}\Big). \tag{3}$$

At early growth stage, the evolution is dominated by the logarithm term in Eq. (3); at later stage, the evolution is dominated by the exponential term, where parameter R_0 is the switch point which can be chosen arbitrarily.

RESULTS AND CONCLUSION

We take an interface with initial shape, $x(\alpha,0), y(\alpha,0)) = \bar{r}(\alpha,0)(\cos\alpha,\sin\alpha))$ where $r(\alpha,0) = 1.0 + 0.1(\sin 2\alpha + \cos 3\alpha)$ following [2, 3]. The number of mesh points $N = 131,072$ along the interface and the time step $\Delta t = 2.5\times10^{-5}$. We set the injection flux to be a constant in time $J(t) = J(t(t)) = 1.0$, and the rescaling function $\rho_s = 20R^2(\frac{1}{1.05^R R} + \frac{1}{1.05^{11}\times 11})$. On a computer with CPU 1.6GHz running Linux, it takes about 5.8 days to get the results shown in Fig. 1. Note that it only takes four days to reproduce the simulation results in [3], which originally took three weeks [3]. In summary, the adaptive rescaling scheme significantly reduces the computation time, and enables one to efficiently simulate the long-time dynamics of moving interfaces.

References

[1] A. Greenbaum, L. Greengard, and G. B. McFadden. Laplace's equation and the Dirichlet-Nuemann map in multiply connected domains. *J. Comput. Phys.*, 105(2):267–278, 1993.

[2] Thomas Y. Hou, John S. Lowengrub, and Michael J. Shelley. Boundary integral methods for multicomponent fluids and multiphase materials. *J. Comput. Phys.*, 169(2):302–362, 2001.

[3] Shuwang Li, John S. Lowengrub, and Perry H. Leo. A rescaling scheme with application to the long-time simulation of viscous fingering in a Hele-Shaw cell. *J. Comput. Phys.*, 225(1):554–567, 2007.

[4] P. G. Saffman and Geoffrey Taylor. The penetration of a fluid into a porous medium or a Hele-Shaw cell containing a more viscous fluid. *Proc. R. Soc. London Ser. A*, 245(1242):312–329, 1958.

Kinetic theory of colloidal suspensions migration

Guillaume Maîtrejean*[1], Miroslav Grmela[2], Amine Ammar[3], and Francisco Chinesta[4]

[1]*Laboratoire Rhéologie et Procédés, Université Grenoble Alpes, Grenoble, France*
[2]*Department of Chemical Engineering, École Polytechnique de Montreal, Montreal, Quebec, Canada*
[3]*Arts et Métiers ParisTech, France – UMSSDT, ENSIT, Tunis, Tunisia*
[4]*EADS Corporate Fundation International Chair, École Centrale de Nantes, Nantes, France*

Summary Smoluchowski kinetic equation, which governs the time evolution of the pair correlation function of rigid spherical particles suspended in a Newtonian fluid, is extended to include particle migration. The extended kinetic equation takes into account three types of forces acting on the suspended particles: a direct force generated by an interparticle potential, hydrodynamic force mediated by the host fluid, and the Faxén-type forces bringing about the across-the-streamline particle migration. The enhanced Soluchowski model is solved numerically using the PGD method.

INTRODUCTION

Usual models of colloidal suspensions proceed within non-continuous approaches in which the suspensions are explicitly represented, the so-called Brownian dynamics (BD) or Stokesian dynamics (SD) framework. Thus, suspended particles are subjected to different kind of forces coming from the fluid drag, inter-particles potentials, particles-solvent interaction, Brownian forces describing the bombardment that colloidal particles suffer from other solvent and colloidal particles, etc. When the solvent is considered as continuum and the Reynolds number of particles is small, Stokesian dynamics account for interactions between colloidal suspension mediated by the solvent the so called hydrodynamics interactions (HI). However both BD and SD approaches fail in adressing flows on industrial interest for which the caracteristic length of the flow is several order of mignitude larger than suspensions one.

An alternative to the BD and SD simulations lies then in deriving a continuum and deterministic kinetic theory description. This formulation leads to the so called Smoluchowski equation that characterizes the microstructure through through the pair correlation function $g\left(\mathbf{r},\mathbf{R},t\right)$, where $\mathbf{r}$ is the position vector, $\mathbf{R}$ the vector connecting two particles

This approach has been successfully applied by Zmievski et al. [2] and more recently in [3] where the pair correlation function is taken as a micro-macro theory and is solved using high-dimensional strategy widely described in [5]. In this work we briefly present the extended Smoluchowski model that accounts for the particles migration. The new physics that is put into the governing equations is the physics behind the Faxén forces causing migration of suspended particles. Without the Faén forces, the kinetic equation arising in this paper is exactly the same as the classical Smoluchowski equation investigated in [2] and [3]. In order to see clearly how the new physics expressed in Faén forces modifies the kinetic equation, we invite the reader to refer to [4].

The dimensionless kinetic equations, based on the Smoluchowski equation and accounting for the migration takes the form:

$$\begin{aligned}\frac{\partial g}{\partial t} = \circ\, Pe\frac{\partial (gu_j)}{\partial r_j} + Pe\frac{\partial}{\partial r_j}\left[g(\kappa^{(I)}\mathcal{Y}_j^{(I)} + \kappa^{(II)}\mathcal{Y}_j^{(II)} + \kappa^{(III)}\mathcal{Y}_j^{(III)})\right] \circ\, Pe\frac{\partial}{\partial R_j}\left(R_k\frac{\partial u_j}{\partial r_k}\triangle g\right) \\ + Pe\frac{\partial}{\partial R_j}\left(g\lambda_{jk}\mathcal{X}_k\right) + \frac{\partial}{\partial r_i}\left(\kappa\frac{\partial g}{\partial r_i}\right) + \frac{\partial}{\partial R_j}\left(g_{eq}\Lambda_{jk}\frac{\partial}{\partial R_k}\left(\frac{g}{g_{eq}}\right)\right)\end{aligned} \tag{1}$$

The symbols appearing in previous equation have the following meaning: $\mathcal{Y}_i^{(I)} = R^2\mathcal{D}_{jji}$, $\mathcal{Y}_i^{(II)} = R_jR_k\mathcal{D}_{ijk}$, $\mathcal{Y}_i^{(III)} = R_iR_k\mathcal{D}_{jjk}$; the symbol $\mathcal{D}_{ijk}$ stands for $\mathcal{D}_{ijk} = \frac{1}{3}\left(\frac{\partial D_{jk}}{\partial r_i} + \frac{\partial D_{ik}}{\partial r_j} + \frac{\partial D_{ij}}{\partial r_k}\right)$ and λ_{ij}, Λ_{ij}, κ, $\kappa^{(I)}$, $\kappa^{(II)}$, $\kappa^{(III)}$ are material parameters. For more details about both the derivation of the equation (1) and the definition of the parameters, the reader is invited to refer to [4].

RESULTS

Due to the high dimensionality (7 in 3D and 5 in 2D) of function $g\left(\mathbf{r},\mathbf{R},t\right)$ the task is practically unfeasible if approached with traditional numerical methods. It has been demonstrated in [3] that with the PGD method, recently developed in [5], the problem of solving numerically the Smoluchowski kinetic equation becomes feasible without restoring to moments and closures.

*Corresponding author. Email: guillaume.maitrejean@ujf-grenoble.fr

We compare the results implied by the modified Smoluchowski model to the experimental results reported in [6]. The experimental setting is a micro channel of $2H \times 200H$ cross section and $1040H$ long with $H = 25\mu m$. The suspensions are slightly charged hard spheres of diameter in a flow characterized by a Péclet number $Pe = 69$. For more details concerning the experimental setting, please refer to [6].

Figure 1 presents $n_p(\mathbf{r}) = \int d\mathbf{R} g(\mathbf{r}, \mathbf{R})$ normalized by its value at rest for whole geometry. We can indeed observe the migration of the suspended particles toward the center of the channel.

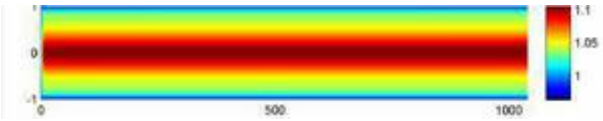

Figure 1: Normalized $n_p(\mathbf{r})$ for the whole channel. Note that for sake of clarity different scales are adopted for x and y axis.

Figure 2 shows the normalized local volume fraction of the suspended particles as they appear in the theoretical prediction and the experimental observations. Both types of results appear to be in relatively good agreement.

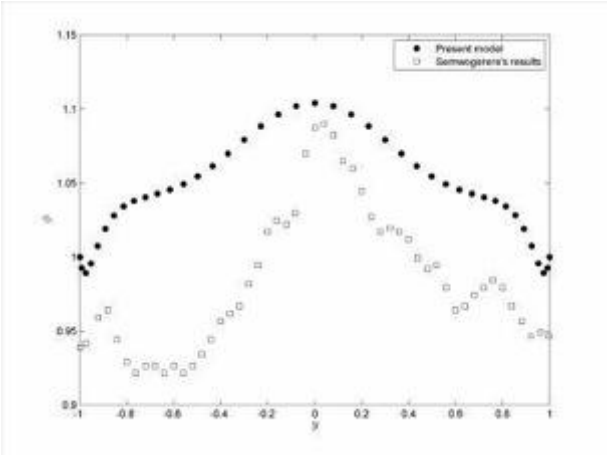

Figure 2: Normalized local volume fraction of particles for both experimental results (square, from [6]) and modified Smoluchowski's model (circle) accounting for migration effects.

CONCLUSIONS

In this paper we present an enhanced Smoluchowski model that accounts for the across-the-streamline migration of rigid particles in a Newtonian solvent. The use of the PGD makes the problem of finding numerical solutions to the Smoluchowski kinetic equation solvable. Finally, the enhanced model presented here is, as far as the authors know, the only continuous model thoroughly derived (from a thermodynamics point of view) describing the across-the-streamline migration of colloidal particles.

References

[1] Brady J., Morris J.: Microstructure of strongly sheared suspensions and its impact rheology and diffusion. J. Fluid Mech, 348 103, 1997

[2] Zmievski V., Grmela M., Bousmina M., Dagréau S.: Nonlinear microstructure and rheology of semidilute colloidal suspensions of stucturless particles. Phys. Rev. E 71, 051503, 2005

[3] Matrejean G., Ammar A., Chinesta F., Grmela M.: Deterministic solution of the kinetic theory model of colloidal suspensions of structureless particles. Rheologica acta, 51(6), 527-543, 2012.

[4] Grmela M., Matrejean G., Chinesta F., Ammar A.: Kinetic theory of colloidal suspensions: morphology, rheology, and migration. Rheologica Acta, 52(6), 557-577, 2013.

[5] Ammar A. , Mokdad B., Chinesta F., Keunings R.: A new family of solvers for some classes of multidimensional partial differential equations encountered in kinetic theory modeling of complex fluids, J. of Non-Newtonian Fluid Mech, 139(3), 153-176, 2006

[6] Frank M., Anderson D., Weeks E.R., Morris F.J.: Particle migration in pressure-driven flow of Brownian suspension, J. Fluid Mech,. 493 363, 2003

2D FLOW SIMULATION OF MORPHING BLADE FOR VERTICAL AXIS WIND TURBINES

Jennifer Tan[1], Matin Komeili[1], Marius Paraschivoiu[1a)], Alexander Pankonien[2], & Daniel Inman[2]
[1]*Department of Mechanical and Industrial Engineering, Concordia University, Montreal, Quebec, Canada*
[2]*Department of Aerospace Engineering, University of Michigan, Ann Arbor, Michigan, 41809, USA*

Summary The coefficient of power C_P generated by a Darrius vertical axis wind turbine is a function of the blade azimuthal position θ. For a given blade profile and tip speed ratio, there is always a given range of azimuthal position that gives the peak C_P. By using a blade with a morphing trailing edge, the blade camber is modified and the effective incidence angle can be controlled at different azimuthal position. The goal is to study the flow around the blade with morphing trailing edge to see which profile at which azimuthal position will result in the highest increase of C_P. Three blade profiles are used for the study, blade profiles with deflection angles of δ = -13.37°, δ = 6.98°, and δ = 0.48°, which include the highest negative and positive deflection angles of the actuation range as well as a nearly symmetric profile, respectively.

INTRODUCTION

The simulation of flow around a vertical axis wind turbine (VAWT) is complicated by the fact that the blade effective angle of attack changes as a function of its azimuthal position. Studies have been conducted in the last two decades in order to investigate the aerodynamic efficiency of VAWT with a constant pitching angle blade [1]. However, a constant pitching angle limits most of power generation to the upwind half of a cycle, and it also encounters self-starting difficulties. Studies have been done on the aerodynamic advantages of morphing the airfoil for wind turbine applications [2][3]. Pankonien, et al [4] developed a morphing flexure box mechanism in order to morph the trailing edge of a chord. They showed that this compliant mechanism performs better than a hinged box mechanism for a smooth trailing edge change. In the current research, the aerodynamic efficiency of three airfoil profiles that are formed by the flexure box mechanism are investigated. Therefore, in order to study the aerodynamic performance of the morphing trailing edge as it is implemented on the vertical axis wind turbine, the power coefficient is compared for the case of blade profiles at the available extreme ends of the morphing trailing edge deflection range and the blade profile that is closest to being a symmetric profile.

BLADE PROFILES AND NUMERICAL METHODOLOGY

Three blade profiles are demonstrated in Figure 1. ANSYS ICEM CFD is used to generate the 2D unstructured grid for positive camber profile δ = -13.37°. A grid convergence study is performed and the mesh with 3200 nodes on the blade surface is used which has an average y^+ of less than 10. The blade profile is deformed through FLUENT user-defined function (UDF) wherein each node points on the upper and lower surfaces are given new coordinates that are obtained through MATLAB's polynomial curve fitting of the experimental data points from the desired blade profile. The leading edge of the blade is the same as NACA0012, but the blade starts to morph at the location of 0.5 x/chord.

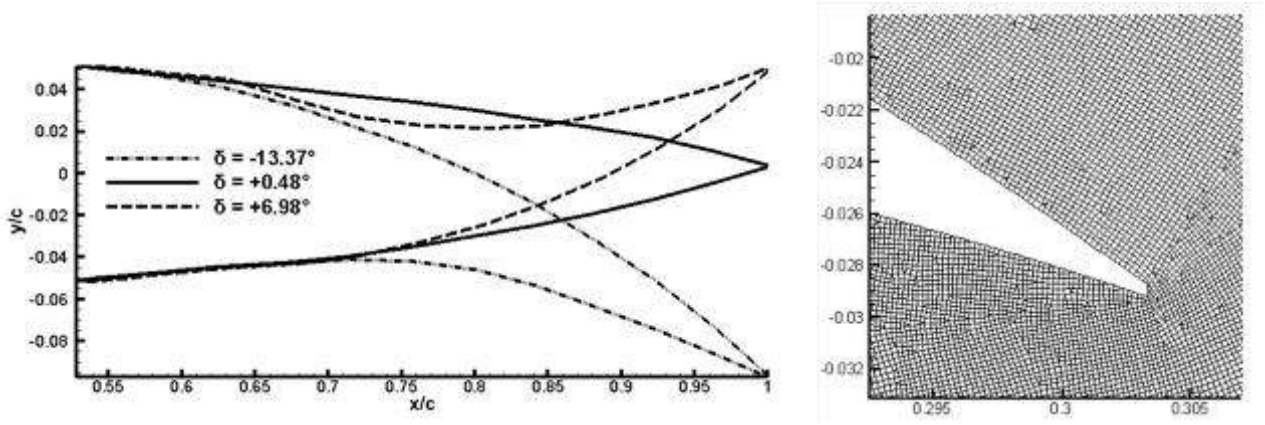

Figure 1: Morphing blade profile (left) and the mesh after diffusion-based smoothing (right)

After the blade profile is deformed, the resulting mesh motion is then smoothed by using FLUENT's boundary distance diffusion-based smoothing as it is shown in Figure 1 (right). The diffusion-based smoothing is governed by the equation $\nabla \cdot (\gamma \nabla \vec{u}) = 0$ where $\vec{u}$ is the displacement velocity of the mesh, and γ is the diffusion coefficient. The diffusion coefficient controls how the boundary motion affects the interior mesh movement. The region of nodes with higher diffusivity tend to move together. For this case, the diffusion coefficient is a function of the normalized boundary distance d and is represented by the equation $\gamma = 1/d^{\alpha}$

[a)] Corresponding author. Email: marius.paraschivoiu@concordia.ca.

where the diffusion parameter α is set to 1.5 in order to preserve larger regions of mesh near the deforming blade boundary and allow the regions further away from the blade to absorb most of the motion.

ANSYS FLUENT solver is used in order to simulate the flow past the turbine. The Unsteady Reynolds Averaged Navier-Stokes (URANS) model is used with the Spalart-Allmaras turbulence model having the far-field boundary condition turbulence viscosity ratio set to 0.1. The SIMPLE scheme pressure-velocity coupling is used with second order least-squares cell-based spatial discretization. The transient formulation used is the first order implicit with a time step size of $\Delta t = 0.0003$s or $\Delta\theta = 0.16°$. The rotor angular velocity ω is kept constant at 90rpm while the freestream velocity, V_∞, is set to 8 m/s for a tip speed ratio TSR = 3.18 where TSR is the ratio of the blade tip speed to the freestream velocity. C_P is calculated as $C_P = P/(0.5\rho AV^3)$, where P is the power generated and A = rotor diameter*span. The rotor diameter is 5.395m while a span length of 1m is used for the calculation.

RESULTS

The individual blade profiles δ = -13.37°, δ = 0.48°, δ = 6.98° are simulated individually at TSR = 3.18 until a periodic pattern has been achieved. The C_P curves for the last cycle is shown in Figure 2 along with the turbine diagram. The result shows that blade profile δ = 6.98° increases the maximum peak by as much as 22% compared to δ = 0.48° on the upwind half of a cycle; while on the downwind half, the blade profile δ = -13.37° gives the highest peak C_P.

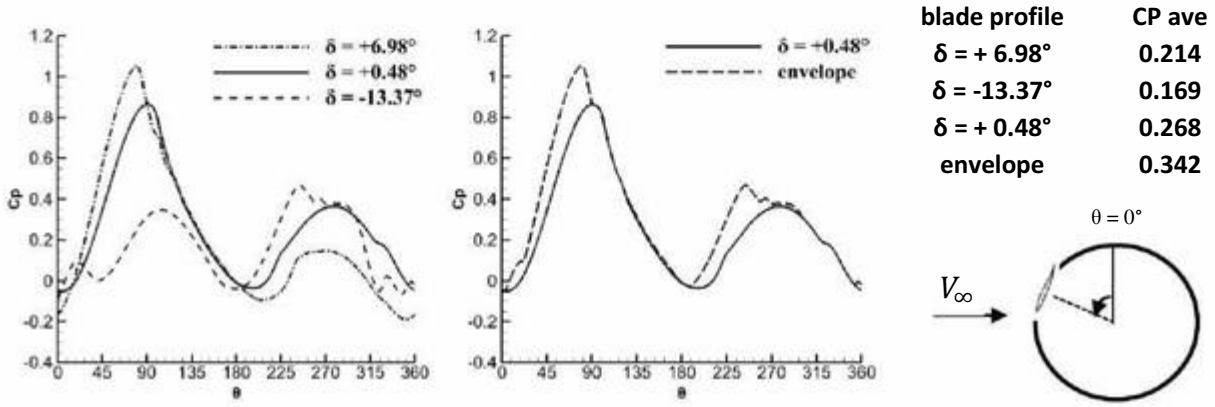

blade profile	CP ave
δ = + 6.98°	0.214
δ = -13.37°	0.169
δ = + 0.48°	0.268
envelope	0.342

Figure 2: C_P curve comparison for each blade profiles, average C_P values, and VAWT diagram

The C_P curves from the individual blade profiles in Figure 2 could be used to identify which profile should be used at which azimuthal position. It can be observed that the δ = 0.48° blade profile could be used for azimuthal positions $300° < \theta \leq 15°$, δ = 6.98° blade profile for $15° < \theta \leq 180°$, while δ = -13.37° blade profile performs better for $180° < \theta \leq 300°$. By doing so, this gives the envelope C_P curve, and it can be seen that although the average C_P is highest for the almost symmetric profile among the individual blade profiles, if the envelope is considered, there is a possibility of 28% increase in average C_P compared to the baseline profile of δ = 0.48°.

CONCLUSION AND FUTURE WORK

The current study demonstrates the advantages of utilizing the flexure box mechanism of morphing trailing edge by Pankonien & Inman [4] for a Vertical Axis Wind Turbine. The results show that using a smart blade increases the average CP of VAWT's by raising the CP peak in the upwind side and generating more power across the downwind side in a given cycle. The results also show that just by changing the camber line of the blade profile at different azimuthal positions, the average CP can be increased by as much as 28% compared to the baseline case of symmetric blade profile.

References

[1] S. N. Zadeh, M. Komeili, and M. Paraschivoiu, "Mesh Convergence Study for 2D Straight Blade Vertical Axis Wind Turbine Simulations and Estimation for 3D Simulations," *Trans. Can. Soc. Mech. Eng.*, vol. 38, no. No.4, pp. 487–504, 2014.

[2] G. Pechlivanoglou, J. Wagner, C. N. Nayeri, and C. O. Paschereit, "Active Aerodynamic Control of Wind Turbine Blades with High Deflection Flexible Flaps," *48th AIAA Aerosp. Sci. Meet. Incl. New Horizons Forum Aerosp. Expo.*, 2010.

[3] T. Wolff, B. Ernst, and J. R. Seume, "Aerodynamic Behavior of an Airfoil with Morphing Trailing Edge for Wind Turbine Applications," *Journal of Physics:* Conference Series 524 vol. 012018, 2014.

[4] A. M. Pankonien, K. Duraisamy, C. T. Faria, D. J. Inman, I. Introduction, and P. Scholar, "Synergistic Smart Morphing Aileron : Aero-structural Performance Analysis," no. January, pp. 1–14, 2014.

HIGH ORDER GLOBAL SMOOTHNESS INDICATOR FOR IMPROVING THE FIFTH-ORDER WENO-Z SCHEME

Yiqing Shen[1 a)], Shengping Liu[1], Bei Chen[1]&Jun Peng[1]
[1]*LHD, Institute of Mechanics, Chinese Academy of Sciences, Beijing, China*

Summary Two new high-order (sixth- and seventh-order) global smoothness indicators of the 5-point stencil used in the fifth-order WENO scheme are proposed. Using the new smoothness indicators to construct the WENO-Z type scheme, the sufficient condition of the fifth order convergence for a fifth-order WENO is satisfied even at critical points where the first-order derivatives are zero. Compared with existing global smoothness indicators, two new indicators contain all terms in the smoothness indicators of three sub-stencils, and the maximal ratio of the coefficients of different first-order undivided differences ($\triangle f_{i+1/2}=f_{i+1}-f_i$) is not greater than 3. Hence they can keep the property of essentially non-oscillation as well as low dissipation. Numerical results demonstrate the improved accuracy and robustness of the new WENO schemes.

INTRODUCTION

Weighted essentially non-oscillatory (WENO) schemes, which were first proposed by Liu et al. [1] and then improved by Jiang and Shu [2], have been widely applied in computational fluid dynamics. WENO schemes use a convex combination of all candidate reconstruction polynomials as the final numerical flux, in which each of polynomials is assigned a weight to determine the contribution of corresponding stencil based on a set of smoothness indicators of all candidate stencils. The smoothness indicator plays a very important role in the performance of a WENO scheme. Jiang and Shu[2] analyzed the fifth-order WENO scheme proposed by Liu et al. [1] and suggested a classic way of measuring the smoothness of a numerical solution. Thus, a WENO scheme with the optimal (2r−1)th order accuracy rather than (r+1)th order is obtained. Henrick et al. [3] pointed out that the original smoothness indicators of Jiang and Shu fail to improving the accuracy order of WENO scheme at critical points where the first derivatives are zero. By using a mapping function to Jiang and Shu's weights, a new WENO-M scheme is proposed. WENO-M scheme can achieve the fifth-order convergence order at critical points. Borges et al. [4] introduced a smoothness parameter for a global 5-point stencil and used it to devise a new set of WENO weights. The resulting WENO-Z scheme generates solutions that are sharp as the ones of the WENO-M scheme with a 25% reduction in CPU costs and presents less dissipation than WENO-JS, but it is difficult to guarantee both of sharp discontinuity profile and the sufficient condition for fifth-order convergence at the first order critical points. Recently, Ha et al [5] suggested a new method of measuring the smoothness of the numerical solution in a stencil, and a sixth-order smoothness indicator for a global 5-point stencil is also constructed to calculate the weights. The associated WENO scheme can get the fifth convergence order in smooth regions. Fan et al [6] devised several global smoothness indicator with truncation errors of up to 8th-order. With the new global smoothness indicators, the corresponding WENO schemes can achieve the fifth order convergence in smooth regions, even at critical points where the first and second derivatives vanish. The low diffusion of these new methods have been demonstrated by numerical examples in[5,6], however, by calculating more examples in this paper, we find that there still are shortcomings in these schemes, for example, poor symmetry, spurious numerical oscillation even incurs computation broken down. To overcome these shortcomings, this paper proposes new sixth-order and seventh-order global smoothness indicators to construct WENO-Z type scheme. The new scheme can achieve the fifth-order convergence in smooth regions with improved performance.

ALGORITHM

Consider a hyperbolic conservation law in the form

$$\frac{\partial u}{\partial t}+\frac{\partial f}{\partial x}=0 \tag{1}$$

and its semi-discretization form

$$\frac{du_i(t)}{dt}=-\frac{1}{\Delta x}(h_{i+1/2}-h_{i-1/2}) \tag{2}$$

The numerical flux $h_{i+1/2}$ of the fifth-order WENO-Z scheme[4] can be written as

$$h_{i+1/2}=\sum_{k=0}^{2}\omega_k q_k\ ,\quad \omega_k=\frac{\alpha_k}{\alpha_0+\cdots+\alpha_2}\ ,\quad \alpha_k=c_k\left[1+\frac{\tau_5}{IS_k+\varepsilon}\right] \tag{3}$$

where IS_k is called smoothness indicator at sub-stencil $S_k^3=(x_{i+k-2},\cdots,x_{i+k})$, its classic form is proposed by Jiang and Shu[2], and a more straightforward form is suggested by Shen and Zha[7]. To avoid confusion, parameter τ_5 can be called as global smoothness indicator of a 5-point stencil $S^5=(x_{i-2},x_{i-1},\cdots,x_{i+2})$. The τ_5 suggested by Borges et al [4] is

$$\tau_5=|IS_0-IS_2| \tag{4}$$

In smooth regions, there is $\tau_5=O(\Delta x^5)$. With the numerical flux (3), it is easy to analyze the accuracy of a scheme. To improve the accuracy of weights ω_k, two global smoothness indicators τ_6 and τ_8 are suggested by Fan et al.[5],

$$\tau_6=\left|[F^{'}(i-2,\cdots,i+2)]^2+[F^{''}(i-2,\cdots,i+2)]^2-(\eta_0+4\eta_1+\eta_2)/6\right| \tag{5}$$

$$\tau_8=(|F_0^{'}|-|F_2^{'}|)^2+(F_0^{''}-2F_1^{''}+F_2^{''})^2 \tag{6}$$

[a)]Corresponding author. Email:yqshen@imech.ac.cn

where, η_k is the smoothness indicator at sub-stencil S_k^3, and it is the form of Shen and Zha[7] with the coefficients $\gamma_1=\gamma_2=1$. Ha et al. [6] suggested using the approximation of the derivative $F_k^{(l)}$ ($l=1,2$, $k=0,1,2$) at $x_{i+1/2}$ on stencil S_k^3 to construct a local smoothness indicator IS_k, and a global smoothness indicator ζ is also suggested, i.e.,

$$IS_k=\beta_k^2,\quad \zeta=\frac{1}{2}\left[(\beta_0-\beta_2)^2+g(F'_{1,i+1/2})^2\right] \text{ with } \beta_k=\xi|F'_{k,i+1/2}|+|F''_{k,i+1/2}| \text{ and } g(x)=\frac{x^3}{1+x^3} \tag{7}$$

In this paper, two new indicators η_6 and η_7 is proposed as

$$\eta_6=[F'''(i-2,\cdots,i+2)]^2+[F^{(4)}(i-2,\cdots,i+2)]^2 \tag{8}$$

$$\eta_7=\left|[F'''(i-2,\cdots,i+1)]^2-[F'''(i-1,\cdots,i+2)]^2\right|+[F^{(4)}(i-2,\cdots,i+2)]^2 \tag{9}$$

Applying the Taylor expansion in smooth regions, we can be found that

$$\tau_5=O(\Delta x^5),\quad \tau_6=O(\Delta x^6),\quad \tau_8=O(\Delta x^8),\quad \zeta=O(\Delta x^6) \text{ and } \eta_6=O(\Delta x^6),\quad \eta_7=O(\Delta x^7).$$

Hence, compared with τ_5, it is clear that all these global indicators (τ_6, τ_8, ζ, η_6 and η_7) can improve the accuracy order of ω_k approximating to ideal weight c_k.

NUMERICAL EXAMPLES

In this section, several numerical examples are given to demonstrate the improved performance of the WENO-Z type scheme with the new global smoothness indicators. Table 1 gives the accuracy comparison of $f=x^2\exp(x)$. It can be seen that, at the critical point $x=0$, except τ_5 gives the fourth-order accuracy, others are fifth-order convergence. With decreasing Δx, the error of η_7 is closer to that of the 5th-order ideal scheme than those of τ_6, ζ, and η_6.

Table 1 Accuracy comparison of $f=x^2\exp(x)$

τ_5			τ_6			Ha			η_6			η_7			5th-order ideal scheme		
Δx	error	order	Δx	error	order	Δx	error	order	Δx	error	order	Δx	error	order	Δx	error	order
0.2500E+00	0.16237E-01	-----	0.2500E+00	0.61221E-02	-----	0.2500E+00	0.11954E-02	-----	0.2500E+00	0.86920E-02	-----	0.2500E+00	0.87159E-02	-----	0.2500E+00	0.42791E-03	-----
0.1250E+00	0.98866E-03	4.038	0.1250E+00	0.14197E-03	5.430	0.1250E+00	0.13893E-03	3.105	0.1250E+00	0.19860E-03	5.452	0.1250E+00	0.11800E-03	6.207	0.1250E+00	0.14220E-04	4.911
0.6250E-01	0.55315E-04	4.160	0.6250E-01	0.32037E-05	5.470	0.6250E-01	0.43230E-05	5.006	0.6250E-01	0.43326E-05	5.519	0.6250E-01	0.15022E-05	6.296	0.6250E-01	0.45980E-06	4.951
0.3125E-01	0.31259E-05	4.145	0.3125E-01	0.79429E-07	5.334	0.3125E-01	0.12074E-06	5.162	0.3125E-01	0.10518E-06	5.364	0.3125E-01	0.26397E-07	5.831	0.3125E-01	0.14628E-07	4.974
0.1563E-01	0.18086E-06	4.111	0.1563E-01	0.21550E-08	5.204	0.1563E-01	0.34525E-08	5.128	0.1563E-01	0.28171E-08	5.222	0.1563E-01	0.61156E-09	5.432	0.1563E-01	0.46135E-09	4.987
0.7813E-02	0.10737E-07	4.074	0.7813E-02	0.62234E-10	5.114	0.7813E-02	0.10224E-09	5.078	0.7813E-02	0.80740E-10	5.125	0.7813E-02	0.16576E-10	5.205	0.7813E-02	0.14484E-10	4.993
0.3906E-02	0.65090E-09	4.044	0.3906E-02	0.18659E-11	5.060	0.3906E-02	0.31021E-11	5.043	0.3906E-02	0.24096E-11	5.066	0.3906E-02	0.48440E-12	5.097	0.3906E-02	0.45368E-12	4.997

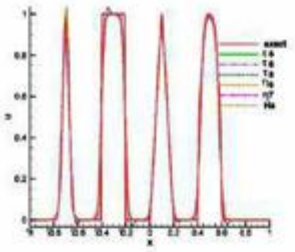

Fig.1 Four waves

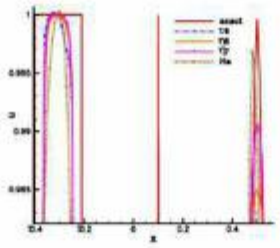

Fig.2 Zoomed of Fig.1

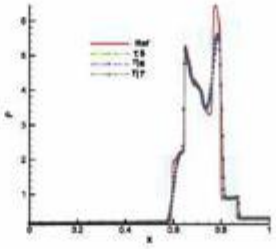

Fig.3 Shock tube

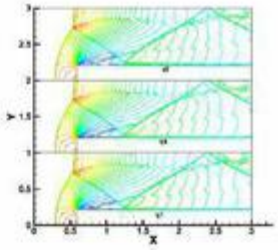

Fig.4 Forward step

Figs.1-2 give the solution contained a combination of Gaussians, a square wave, a sharp triangle wave, and a half ellipse. Ha scheme is overshoot for the Gaussians wave, τ_8 generates evident oscillation. In addition, Ha and τ_6 obtain evident asymmetric solution for square wave and half ellipse wave. While both η_6 and η_7 avoid above shortcomings greatly. For the 1D shock tube problem of interacting blast waves, the computations with τ_6, τ_8 and Ha schemes are broken down, while η_6 and η_7 work well as τ_5, see Fig.3. Fig.4 is the 2D supersonic flow over a forward step, similar as the 1D shock tube problem, η_6 and η_7 can capture the strong shock structures well, but the computations of τ_6 and Ha are broken down.

CONCLUSIONS

New higher-order global smoothness indicators are proposed to construct WENO-Z type scheme. With the news indicators, the new WENO-Z type scheme enhances the symmetry of solution, keeps the property of essentially non-oscillation well and improves the robustness.

ACKNOWLEDGEMENTS

This work was supported by the National Natural Science Foundation of China under Grants 11272325, 11272324.

References

[1] Liu X.D., Osher S., Chan T.: Weighted essentially non-oscillatory schemes. J. Comput. Phys. 115: 200-212, 1994.

[2] Jiang G.-S., Shu C.-W.: Efficient implementation of weighted ENO schemes. J.Comput.Phys. 126:202-228, 1996.

[3] Henrick A.K., Aslam T.D., Powers J.M.: Mapped weighted essentially non-oscillatory schemes: achieving optimal order near critical points. J. Comput. Phys. 208, 206-227, 2005.

[4] Borges R., Carmona M., Costa B., Don W.S.: An improved weighted essentially non-oscillatory scheme for hyperbolic conservation laws. J. Comput. Phys. 227:3191-3211, 2008.

[5] Ha Y.S, Kim C.H, Lee Y.J, Yoon J.H.: An improved weighted essentially non-oscillatory scheme with a new smoothness indicator, J. Comput. Phys., 232:68-86, 2013

[6] Fan P., Shen Y. Q., Tian B. L., Yang C.: A new smoothness indicator for improving the weighted essentially non-oscillatory scheme. J. Comput. Phys., 269:329-354, 2014.

[7] Shen Y.Q., Zha G.C.: A robust seventh-order WENO scheme and its applications. AIAA-2008-0757,2008.

OPTIMIZATION-BASED ANISOTROPIC MESH-POLYNOMIAL ADAPTATION FOR HIGH-ORDER METHODS

Nicolas Ringue * and Siva Nadarajah
Department of Mechanical Engineering, McGill University, Montreal, Quebec, Canada

Summary We present a general framework for anisotropic hp-adaptation of high-order discontinuous Galerkin finite element discretizations for compressible flow simulation. Using the sensitivities of an adjoint-based error estimate our method seeks optimal element mesh size h and polynomial degree p distributions. This approach results in an optimal hp-mesh tailored to yield the most accurate prediction of a quantity of interest, such as aerodynamic coefficients, at a given computational cost (number of degrees of freedom). The proposed approach features a reduced dependence on the initial mesh compared to established adjoint-based adaptive methods. It provides a unifying framework where adaptation choices such as isotropic/anisotropic, h-/p-refinement/coarsening do not only rely on local arbitrary measures of the solution's anisotropy and smoothness, but rather where a globally optimal distribution of degrees of freedom is sought to minimize the error in the chosen quantity of interest.

INTRODUCTION

Adaptive unstructured high-order methods form a promising framework to improve the computational efficiency, robustness and reliability of Computational Fluid Dynamics (CFD) algorithms, as well as to gain insight in aerodynamic flow physics [1]. The most widely used high-order discretization scheme for solving the compressible Navier-Stokes equations is arguably the discontinuous Galerkin (DG) method. The reason for the DG method's success is its arbitrary high-order accuracy, geometric flexibility (unstructured grids) and compact stencil. A number of variants to the DG method have been proposed including the promising Flux Reconstruction (FR) schemes [2].

Industrial CFD applications often result in complex flow solutions. Error estimation and control are hence essential to assess the validity of these numerical solutions. In addition since they rely on arbitrary discretizations of space and time, the efficiency and accuracy of the numerical methods can potentially be optimized for a given flow simulation. The development of reliable error estimates and robust procedures to adapt the mesh to the solution are subject to ongoing research efforts. Three types of error indicators are commonly used to drive mesh adaptation in CFD: feature-based, residual-based and adjoint-based indicators. Adjoint-based indicators provide information on the sensitivity of the error in a global quantity of interest with respect to the local solution error [3]. This type of indicator is arguably the best suited for CFD since it is the only one to account for error propagation. The approach is referred to as *goal-oriented* because it results in error estimates for outputs (such as aerodynamic coefficients), as well as local error indicators which can be used to adapt the mesh in order to obtain enhanced accuracy on chosen quantities of interest.

ADAPTIVE HIGH-ORDER METHODS

The discontinuous high-order methods provide a highly flexible framework for space discretization adaptation. Once an error indicator is available, several techniques enable to modify the discretization in order to seek an overall more accurate solution. To this end, the high efficiency of anisotropic mesh and polynomial (h- and p-adaptation) is well known. In addition to the error indicator, some solution anisotropy and smoothness information is commonly used to guide anisotropy and h/p adaptation choices [4]. A recently developed and unifying alternative to heuristic indicators is based on direct mesh optimization [5, 6, 4, 7]. Instead of assessing directivity or smoothness of the solution, trial element patches are used to compare all available local refinement choices. A merit function is then used to pick the optimal choice, i.e. locally minimizing the ratio of error reduction over number of added degrees of freedom. This approach is much better suited to be coupled with an adjoint-based adaptation technique since it allows a relevant use of the output sensitivity information provided by the dual solution.

In this context, it is reasonable to assume the existence of optimal meshes minimizing the error for a given number of degrees of freedom. Therefore, the use of optimization concepts have been recently increasingly considered to guide adaptation, from the use of local merit functions [4, 5] to the global mesh size optimization via a surrogate error model [7]. Following these recent developments, we propose a unifying optimization-based framework for anisotropic hp-adaptation.

A UNIFYING OPTIMIZATION-BASED FRAMEWORK FOR ADAPTATION

The proposed approach relies on the concept of mesh-metric duality [8] to optimize the computational hp-mesh $\{\Omega_k\}$ used to solve a system of governing equations $\mathcal{R}(u) = \nabla.\mathcal{F}(u) = 0$. A Riemannian metric is used to represent the discrete set of nodes forming the computational grid in a continuous mesh model. Every element of the mesh can be uniquely associated

with a positive definite symmetric matrix which contains information related to its geometric properties: size h, orientation φ and aspect ratio ρ. For a given two-dimensional element Ω_k, the metric is given by $\mathcal{M}_k = R(\varphi)^T \begin{bmatrix} h & 0 \\ 0 & h/\rho \end{bmatrix} R(\varphi)$, where R is a rotation matrix. By interpolation from the elements of the entire grid these matrices define a Riemannian metric field $\mathcal{M}(x)$. The knowledge of a metric enables to generate the corresponding mesh. To obtain an anisotropically adapted grid, the metric of a given initial mesh is modified in order to better approximate the solution. Based on this concept, the initial coarse hp-mesh is first represented in a continuous framework using its corresponding metric field $\mathcal{M}(x)$ and polynomial degree distribution $p(x)$. The adjoint solution ψ obtained from the linear system $\left[\frac{\partial \mathcal{R}}{\partial u}\right]^T \psi = \left[\frac{\partial \mathcal{J}}{\partial u}\right]^T$ provides a sensitivity of the global error on an output quantity of interest $J(u)$ with respect to the local error measured by the residual of the governing equations $\mathcal{R}(u)$. Adjoint-based error indicators η are computed on every element as $\eta = \psi^T \mathcal{R}(u)$ to provide an estimate of the contribution of the local error to the error on the functional $J(u)$, such as for example lift or drag coefficients for aerodynamic simulations. Given this information, it is possible to seek an hp-mesh minimizing the global error on the output of interest. To do so, we propose a method to evaluate the sensitivities of the error indicator η with respect to both the metric $\mathcal{M}(x)$ and the polynomial degree $p(x)$: $\frac{\partial \eta}{\partial \mathcal{M}}$ and $\frac{\partial \eta}{\partial p}$. These sensitivities are then used to guide a numerical optimization towards optimal $\mathcal{M}_{opt}(x)$ and $p_{opt}(x)$ minimizing the global error. Based on this optimized mesh representation, an adapted hp-mesh can be generated, either by adaptation of the initial mesh or by regeneration based on the metric field. Since the accuracy of the error indicator depends on the initial mesh, a constraint on the number of degrees of freedom of the adapted mesh has to be imposed. Several of the above described adaptation cycle have to be combined in an iterative procedure in order to drive the error under a specified tolerance. Since every adaptive cycle minimizes the error for a given number of degrees of freedom, few iterations are needed to converge to the coarsest mesh that meets a user-defined accuracy requirement.

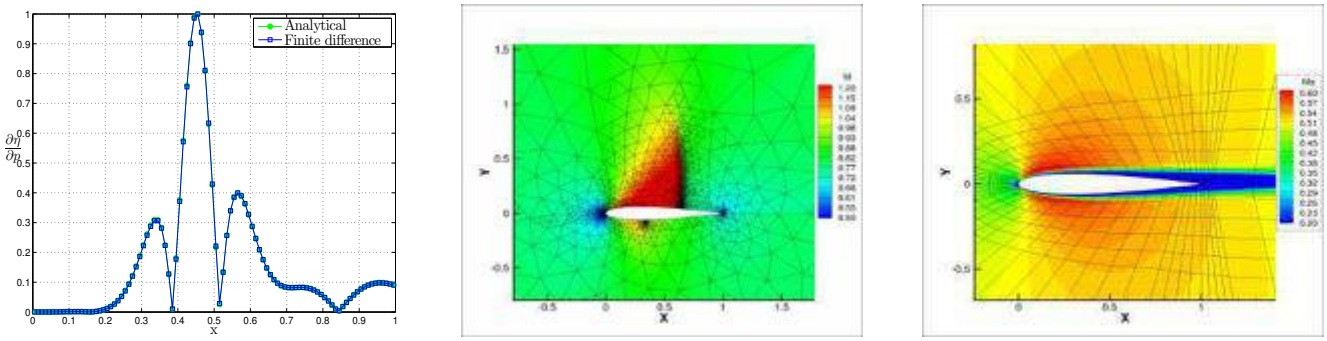

(a) (b) (c)

Figure: (a) Sensitivity $\frac{\partial \eta}{\partial p}$ for the manufactured solution of a linear steady advection equation using a 5th order FR scheme.

(b) Transonic inviscid flow over a NACA 0012 airfoil currently considered for optimization-based adaptation; Mach number solution obtained using a 3rd order adjoint-based adaptive DG scheme [9].

(c) Laminar viscous flow over a NACA 0012 airfoil also considered for optimization-based adaptation; Mach number solution obtained using a 6th order FR scheme.

References

[1] Z. J. Wang, K. Fidkowski, R. Abgrall, F. Bassi, D. Caraeni, A. Cary, H. Deconinck, R. Hartmann, K. Hillewaert, H. T. Huynh, et al. High-order CFD methods: current status and perspective. *International Journal for Numerical Methods in Fluids*, 72(8):pp. 811–845, 2013.

[2] H. T. Huynh. A flux reconstruction approach to high-order schemes including discontinuous Galerkin methods. In *18th AIAA Computational Fluid Dynamics Conference*, Miami, FL, June 2007. American Institute of Aeronautics and Astronautics, AIAA Paper 2007-4079.

[3] M. B. Giles and E. Süli. Adjoint methods for PDEs: a posteriori error analysis and postprocessing by duality. *Acta Numerica*, 11:pp. 145–236, 2002.

[4] S. Giani and P. Houston. Anisotropic *hp*-adaptive discontinuous Galerkin finite element methods for compressible fluid flows. *International Journal of Numerical Analysis & Modeling*, 9(4), 2012.

[5] M. Ceze and K. J. Fidkowski. Anisotropic *hp*-adaptation framework for functional prediction. *AIAA Journal*, 51(2):pp. 492–509, 2013.

[6] K. J. Fidkowski and D. L. Darmofal. Review of output-based error estimation and mesh adaptation in computational fluid dynamics. *AIAA Journal*, 49(4):pp. 673–694, 2011.

[7] M. Yano and D. L. Darmofal. An optimization-based framework for anisotropic simplex mesh adaptation. *Journal of Computational Physics*, 231:pp. 7626–7649, 2012.

[8] A. Loseille and F. Alauzet. Continuous mesh framework part I: well-posed continuous interpolation error. *SIAM Journal on Numerical Analysis*, 49(1):pp. 38–60, 2011.

[9] J.-S. Cagnone. *Mesh and Polynomial Adaptation for High-Order Discretizations of Compressible Flows*. PhD thesis, McGill University, 2012.

EFFICIENT ALGORITHM FOR DNS OF COMPRESSIBLE TURBULENT WALL-BOUNDED FLOWS

Davide Modesti [*1], Matteo Bernardini[2], and Sergio Pirozzoli[3]
[1-2-3]*Dipartimento di Ingegneria Meccanica e Aerospaziale, Università di Roma 'La Sapienza, via Eudossiana 18, 00184 Roma, Italia*

Summary We present a novel implicit algorithm which allows to remove the acoustic time step limitation in compressible shock-free flows. The key point of the algorithm is the use of the entropy equation in place of total energy. This allows to remove the acoustic time step restriction in the wall-normal direction by solving a single scalar tridiagonal system, which is considerably more efficient with respect to previous implicit algorithms [1, 2]. Direct Numerical Simulations(DNS) of compressible channel flows are presented to show accuracy and efficiency of the new approach.

INTRODUCTION

Compressible wall-bounded flows play an important role in many aerospace applications of industrial and academic interest [4, 3]. Despite that, compressible simulations of wall bounded flows remain often more time-consuming with respect to their incompressible counterparts, mostly due to the acoustic time step restriction. In the near-wall region in fact the gap between the hydrodynamic and acoustic time scale dictate the use of much smaller time steps than physically needed. In this respect the use of implicit time integration algorithms is attractive since it allows to relax, if not remove, the acoustic time step restriction. A crucial contribution in this sense was given by Beam and Warming [1], who proposed an implicit scheme for the solution of the Euler equations in conservative form, which relies on the inversion of block matrices, thus avoiding costly iterative algorithms. Many variations to Beam and Warming approach are available in literature, and special efforts have been devoted to the reduction of the operations count, such as the algorithm of Pulliam and Chausse[2], which involve the inversion of a series of scalar systems rather than block ones. The approach in this work is $20\% - 30\%$ faster than the Beam and Warming algorithm, but it is inaccurate for time dependent flows. We develop a novel implicit algorithm which is more efficient than previous ones as it barely requires the inversion of a single scalar tridiagonal system. A key role in the algorithm is played by the entropy equation which is used in place of the total energy. The novel implicit scheme can be used to efficiently predict Direct Numerical Simulation (DNS) of compressible wall-bounded flows. We perform DNS of compressible channel flows and compare the results in terms of accuracy and efficiency with the fully explicit case.

NUMERICAL APPROACH

The maximum eigenvalue of the Euler equations in the i-th direction is $u_i + c$, so that the inviscid time step limitation in the same direction is $\Delta t_I = (\mathrm{CFL}\Delta x_i/u_i + c)$, where u_i and Δx_i are the local velocity and mesh spacing in the i-th direction, c the local speed of sound and CFL is the Courant number. In the case of wall-bounded flows, the most restrictive limitation is in the wall-normal direction, since the mesh is clustered toward the wall, where the velocity goes to zero, but c is finite. The novel idea to remove the acoustic restriction is to treat implicitly only the terms in the Navier-Stokes equations which are responsible for the acoustic time step limitation in the wall-normal direction, namely the mass flux and the pressure gradient in the momentum equation. This alone would allow to invert a 2×2 block matrix rather than a 5×5 one as in the standard Beam and Warming approach. Further manipulations of the system of equations, which for the sake of brevity are omitted here, show that only a scalar system of equations needs to be solved. Depending on the Reynolds and Mach number and on the distance of the first mesh point from the wall, the viscous time step limitation in the wall-normal direction may also be restrictive, and the viscous terms also must be treated implicitly. This can be efficiently done by solving a series of scalar systems in sequence. The case in which both the acoustic limitation and the viscous one in the wall normal direction are removed is denoted as Acoustic and Viscous Terms Implicit (AVTI), whereas the case in which only the acoustic limitation is removed is denoted Acoustic Terms Implicit (ATI). The AVTI and ATI approaches are compared with the classical Beam and Warming algorithm (BM), and the explicit case (EXPL). In all cases a fourth order Runge-Kutta scheme is used as a wrapper for time stepping.

RESULTS

Six test cases have been performed, using the novel method (CH-AVTI and CH-ATI), Beam and Warming algorithm (CH-BW1 and CH-BW2) and two cases with fully explicit discretization (CH-EXPL1 CH-EXPL2). The cases denoted by 1 and 2

*Corresponding author. Email: davide.modesti@uniroma1.it

differ for the distance of the first mesh point from the wall, which is $\Delta y_w^+ = 0.15$ for the former and $\Delta y_w^+ = 0.7$ for the latter and are compared to CH-AVTI and CH-ATI respectively. In CH-BW1 both the viscous and inviscid limitation are removed, while in CH-BW2 only the Eulerian fluxes are implicit. The comparison of the time steps and computational times in table 1a shows that ATVI is $20\% - 30\%$ more efficient than BW. This is approximately the same speed up of Pulliam and Chausse variant [2], with the difference that ATVI can be applied to time-dependent flows. On the other hand the cases in table 1b show that the use of BW algorithm does not give any substantial advantage, while ATI allows a speed up of a factor 2.

Case	$\Delta t_I/\Delta t_E$	CPU_I/CPU_E
CH-EXPL1	1	1
CH-BW1	10	1.80
CH-AVTI	10	1.13

(a)

Case	$\Delta t_I/\Delta t_E$	CPU_I/CPU_E
CH-EXPL2	1	1
CH-BW2	2.3	1.80
CH-ATI	2.3	1.08

(b)

Table 1: Test cases. Turbulent channel flow at $M_b = 1.5$ $Re_\tau = 220$. The distance in inner units of the first mesh point from the wall is $\Delta y_w^+ = 0.15$ in table (a) and $\Delta y_w^+ = 0.7$ in table (b). $\Delta t_I/\Delta t_E$ is the ratio between the maximum allowable implicit end the explicit time step. CPU_E/CPU_I is the relative CPU effort with respect to the fully explicit case.

Figure 1 shows the mean velocity profile and the r.m.s. pressure fluctuations in wall units. Excellent agreement with the explicit case is found. The good agreement of the pressure fluctuations with the explicit case confirms that the method can also be used for time dependent flows.

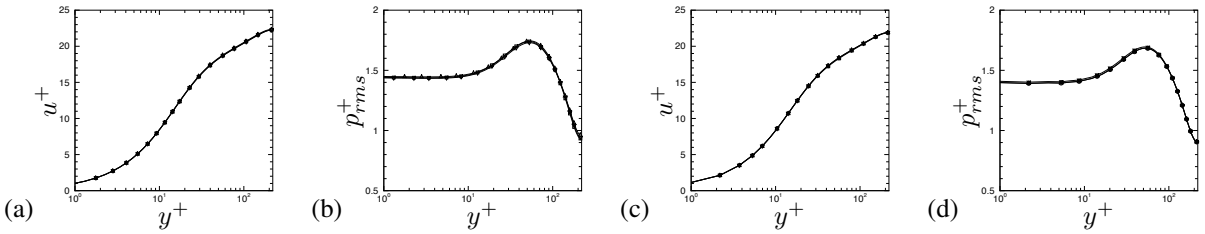

Figure 1: Turbulent channel flow at $M_b = 1.5$ $Re_\tau = 220$. $\Delta y_w^+ = 0.15$. (a-c)Mean velocity profile in wall units (b-d)r.m.s. pressure fluctuations in wall units. Figures (a-b) refer to the test cases of table 1a in which $\Delta y_w^+ = 0.15$, while figure (c-d) refer to table 1b, with $\Delta y_w^+ = 0.7$. The symbols denote CH-EXPL1,2(squares), CH-BW1,2(triangles),CH-ATI,AVTI(gradients).

CONCLUSIONS

A new algorithm for efficient removal of the acoustic time step limitation has been presented. The method is attractive as it barely requires the inversion of scalar systems rather than block ones[1], with subsequent efficiency gain. We performed DNS of a supersonic channel flow, which is a good prototype of wall bounded flows. The results of the test cases here presented shows an improvement which depends on the distance of the first mesh point from the wall. The speed up of AVTI is about $20\% - 30\%$ with respect to the BM approach, whereas a factor 2 is obtained when only the acoustic terms are treated implicitly (ATI). Future work will involve the application of the algorithm to other wall-bounded turbulent flows such as pipes and boundary layers, with special attention to pipe flow, for which the time step restriction is also severe in the azimuthal direction.

References

[1] R.M. Beam, R.F. Warming: An implicit finite-difference algorithm for hyperbolic systems in conservation-law form. J. Comput. Phys. 22(1) 87-100, 1976.

[2] T.H. Pulliam, D.S Chaussee: A diagonal form of an implicit approximate-factorization algorithm. J. Comput. Phys. 39(2) 347-363, 1981.

[3] D. Modesti, S. Pirozzoli: Reynolds and Mach number effects in compressible turbulent channel flow. Int. J. Heat Fluid Flow, 2016. Accepted.

[4] S.Pirozzoli, M. Bernardini: Turbulence in supersonic boundary layers at moderate Reynolds number. J. Fluid Mech. (68) 120-168, 2011.

SPECTRALLY-ACCURATE IMMERSED BOUNDARY CONDITIONS METHOD FOR 3-D NAVIER-STOKES EQUATIONS

Md Nazmus Sakib[1a)], J. M. Floryan[1]
[1]*Department of Mechanical and Materials Engineering, University of Western Ontario, London, Ontario, Canada*

Summary A three-dimensional, spectrally accurate algorithm based on the immersed boundary conditions (IBC) concept has been developed for the analysis of flows in channels bounded by rough boundaries. The algorithm is based on the velocity-vorticity formulation and uses a fixed computational domain with the flow domain immersed in its interior. The spatial discretization uses Fourier expansions in the stream-wise and span-wise directions and Chebyshev expansions in the wall-normal direction. Various tests confirm the spectral accuracy of the algorithm.

INTRODUCTION

The Immersed Boundary (IB) concept, first proposed by Peskin [1] in the context of cardiac dynamics, provides a general computational basis to develop efficient tools for the analysis of flows involving complex geometries. IB methods are mainly based on low-order finite-difference, finite-volume or finite-element techniques, limiting their spatial accuracy. Some recent implementations employ either a spectral discretization [2] or higher-order finite-difference techniques for the field equations [3], however, the complete solution is not spectrally accurate. A fully spectrally-accurate version of the IB algorithm, referred to as the Immersed Boundary Conditions (IBC) method, was proposed in [4] for two-dimensional flow problems. The IBC algorithm has been implemented for time-dependent problems, problems involving moving boundaries, and its accuracy has been improved through the use of the over-determined formulation. This algorithm has also been applied to three-dimensional problems governed by the Laplace operator. The current work describes the implementation of the IBC method for problems governed by the three-dimensional Navier-Stokes equations.

MATHEMATICAL FORMULATION AND SOLUTION METHOD

The problem of interest consists of a three-dimensional viscous steady flow in a channel bounded by rough walls. The geometry of the walls is described by the following relations:

$$y_U(x,z) = 1 + \sum_{n=-\infty}^{\infty}\sum_{m=-\infty}^{\infty} H_U^{(n,m)} e^{i(n\alpha x + m\beta z)},\quad y_L(x,z) = -1 + \sum_{n=-\infty}^{\infty}\sum_{m=-\infty}^{\infty} H_L^{(n,m)} e^{i(n\alpha x + m\beta z)} \qquad (1a, b)$$

where $H_U^{(n,m)} = H_U^{(-n,-m)^*}$, $H_U^{(-n,m)} = H_U^{(n,-m)^*}$, $H_L^{(n,m)} = H_L^{(-n,-m)^*}$, $H_L^{(-n,m)} = H_L^{(n,-m)^*}$ with stars denoting the complex conjugates. The walls are periodic and extend to $\pm\infty$ in the *x*- and *z*-directions, with $\lambda_x = 2\pi/\alpha$ and $\lambda_z = 2\pi/\beta$ denoting the wavelengths (Fig. 1).

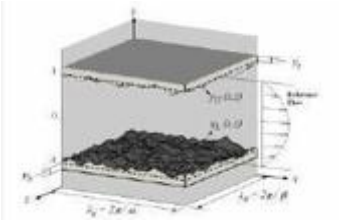

Figure 1: Sketch of the flow and computational domains.

The field equations in the vorticity-velocity form are used. Two types of closing conditions have been implemented, i.e. the fixed flow rate constraint and the fixed pressure gradient constraint. Fourier expansions are used for the discretization in the *x*- and *z*-directions and Chebyshev polynomials are used for the discretization in the *y*-direction. The solution takes the following form:

$$A(x,y,z) = \sum_{n=-N_M}^{N_M}\sum_{m=-M_M}^{M_M}\sum_{k=0}^{N_T-1} A_k^{(n,m)} T_k(y) e^{i(n\alpha x + m\beta z)}, \qquad (2)$$

where *A* stands for any of the unknowns, N_M and M_M are the number of Fourier modes used in the *x*- and *z*-directions, T_k represents the kth-order Chebyshev polynomial of the first kind and N_T is the number of Chebyshev polynomials retained in the solution. By applying the Galerkin procedure, a coupled nonlinear system of algebraic equations is obtained. All nonlinear terms are considered to be known during the iterative solution process with their values taken from the previous iteration.

PERFORMANCE OF THE ALGORITHM

To examine the performance of the algorithm a model problem is introduced where the upper wall is kept smooth and the shape of the lower wall is described by a combination of two Fourier modes of the form

[a)] Corresponding author. Email: msakib.uwo@gmail.com.

$$y_L = -1 + y_b sin(\alpha x) cos(\beta z). \quad (3)$$

Two error definitions have been used to measure the performance of the algorithm. The error of the whole solution domain ($||u_{er}||_\infty$) is defined as the maximum difference between the computed solution for the entire physical domain and a reference solution. The reference solution is computed using $N_M = M_M = 10$ Fourier modes and $N_T = 40$ Chebyshev polynomials. The other error measure is the boundary error ($||\mathrm{u_{er,BC}}||_\infty$) which is the maximum difference between the computed solution at the boundary and the known boundary condition.

Figure 2A demonstrates that the error decreases exponentially with an increase of the number of Chebyshev polynomials and, thus, the algorithm provides spectral accuracy in the *y*-direction. Figure 2B demonstrates that the algorithm delivers spectral accuracy when increasing the number of Fourier modes in the periodic directions. A spectral decomposition of the error at the rough wall (Fig. 2C) demonstrates the absence of the first eight Fourier modes in the *x*-direction and the first seven modes in the *z*-direction, in agreement with the construction of the boundary relations.

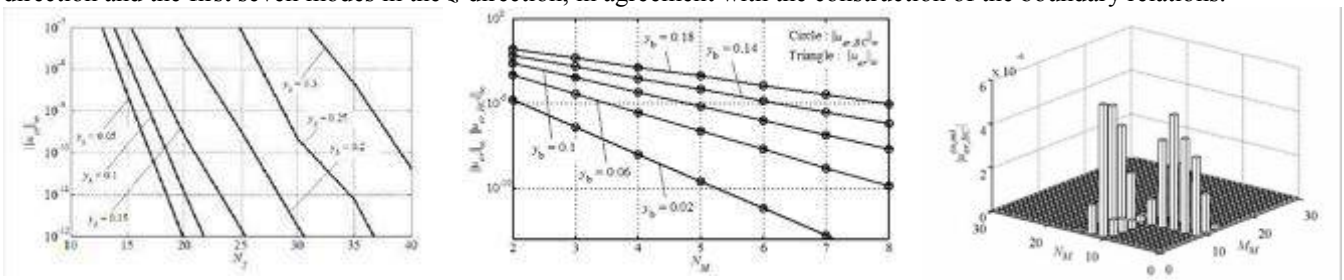

(A) (B) (C)

Figure 2: (A)- Variation of $||u_{er}||_\infty$ as a function of the number of Chebyshev polynomials N_T used. (B)-Variation of $||u_{er}||_\infty$ and $||\mathrm{u_{er,BC}}||_\infty$ as functions of the number of Fourier modes for $\alpha = \beta = 1$ and $Re = 5$, determined using $M_M = 10$ Fourier modes. (C)-Spectral decomposition of the boundary error for the roughness geometry described by (3) with $y_b = 0.1$ for $Re = 5$, $\alpha = \beta = 3$, determined using $N_M = 8$ and $M_M = 7$ Fourier modes.

Figure 3 illustrates variations of the pressure gradient correction dp_1/dx induced by the roughness of the form given by Eq.(3). Positive values of this correction indicate drag reduction.

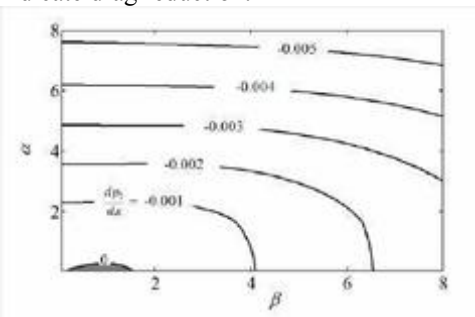

Figure 3: Variation of the pressure gradient correction dp_1/dx as a function of the roughness wave numbers α and β for the roughness geometry described by Eq.(3) with $y_b = 0.05$ for $Re = 5$ determined using $N_M = M_M = 12$ Fourier modes and $N_T = 50$ Chebyshev polynomials. Grey zone identifies the drag reducing corrugations.

CONCLUSION

A gridless, spectrally-accurate algorithm has been developed for the analysis of viscous flows in domains bounded by rough walls. It is demonstrated that the algorithm delivers spectral accuracy in spite of a complex shape of the solution domain. The solver represents a very efficient tool to explore flows over different surface topographies and to search for possible drag reduction.

References

[1] C.S. Peskin, The fluid dynamics of heart valves: experimental, theoretical and computational methods, Annu. Rev. Fluid Mech. 14 (1981) 235–259.

[2] Y. Mori, Convergence proof of the velocity field for a Stokes flow immersed boundary method, Commun. Pur. Appl. Math. 61 (2008) 1213–1263.

[3] Y. Jiang, X. Wang, X. Jing, X. Sun, A Study of Three-Dimensional Acoustic Scattering by Arbitrary Distribution Multibodies Using Extended Immersed Boundary Method, Journal of Vibration and Acoustics 136 (2014) 034505-1:7.

[4] J. Szumbarski, J.M. Floryan, A direct spectral method for determination of flows over corrugated boundaries, J. Comp. Phys. 153 (1999) 378–402.

NUMERICAL STUDY ON RADIATIVE HEAT FOR HYPER-VELOCITY RE-ENTRY PROBES

Jun-Ming Lv[a)], Jin-Ke Hao, Da-Chuan Li, Xiao-Li Cheng & Ji-Jun Yu
China Academy of Aerospace Aerodynamics, Beijing, China

Summary Radiative heat grows extremely fast as velocity increase to above 9 km/s. It is critical to precisely estimate radiation heating on surface of re-entry probes flying at hyper velocity for supporting thermal protection system design. Numerical simulations on FIRE II which is an Apollo like re-entry test vehicle have been carried out to analyse flow-field and radiation. Navier-Stokes equations with thermo-chemical non-equilibrium models, radiative narrow-band model accounting for both electronic and vibrational-rotational transition, and radiation transfer equation have been respectively solved to get the temperature, species number density, species emission intensity, average absorption coefficients, radiative intensity and radiation heating flux. It is shown that the emission intensity is highly related to the temperature distribution in shock layer. At typical status, the total computed heat rate at stagnation point is very close to the flight measurement.

INTRODUCTION

When vehicles re-enter to Earth's atmosphere at hyper velocity, high temperature gas in shock layer undergoes strong physical and chemical change, along with substantive radiation. Radiative heating will increase extremely fast along with the velocity goes up, may even be greater than convective heat when flying at the velocity above 10 km/s. It is essential to predict gas radiation accurately to guarantee thermal protection system. FIRE II project which is the first success flight experiment for radiation measurement is chosen to be studied.

MODEL AND NUMERICAL METHODS

Model and grid

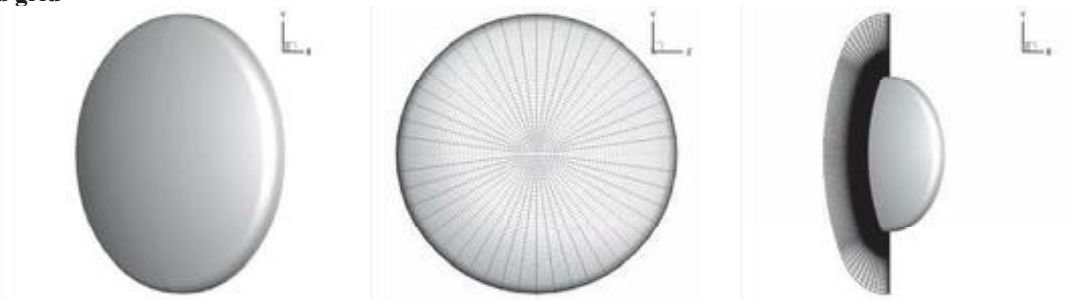

Fig.1 Geometry model and meshes on surface and symmetric plane of FIRE

Fire II is an Apollo like re-entry probe. At t=1643 s, the effective radius equals to 0.747 m. The C-H type mesh refined in shock layer has been used where the minimum grid length to wall is set to 1×10^{-7} m.

Equations and methods

Navier-Stokes equations with thermo-chemical non-equilibrium models have been solved to simulate high temperature flow in front of re-entry vehicles, to obtain the temperature and number density of all species. AUSM$^+$-up scheme was used to convection term, where the interface value was obtained by MUSCL method with minmod limiter; second-order central scheme was employed to viscous term; LU-SGS method was adopted in time marching; 11 species and 20 reactions model of Park was taken to compute chemical reaction sources. Narrowband model accounting for both electronic and vibrational-rotational transition mechanisms has been employed to calculate gas radiative characteristics, and then average absorption coefficients distribution in space was acquired. Radiation transfer equation has been computed by finite volume method on the same grid for flow solver to get radiative intensity distribution in azimuth angles and space positions. Radiation heating is obtained by integrating intensity in directions towards the wall over azimuth angles.

RESULTS AND ANALYSIS

Figure 1 show that in shock layer, O_2 and N_2 are completely dissociated in respect that the temperature is almost completely higher than 10,000 K. Atom N takes up the most mass concentration. It is noticed that there are quite a number of O^+ and N^+ produced behind the shock wave which will contribute a lot to gas radiation.

Based on the temperature and species number density, emission intensities between 0.2~10 μm of all species in chemical model have been calculated. In figure 3, $B\kappa$, the portion of emission energy in black body denotes the spectra

[a)] Corresponding author. Email: junminglyu@foxmail.com.

ranges selected cover the whole energy. Distributions of the absorption coefficients obtained by integrating over wavelengths and species are very similar to shock structure.

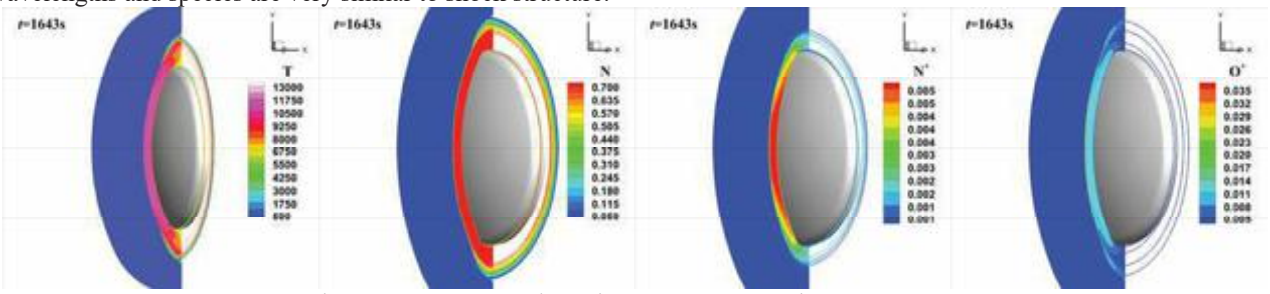

Fig.2 Temperature and species mass concentrations at t=1643 s

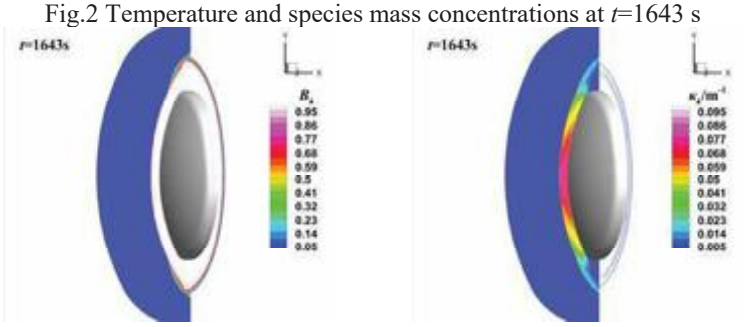

Fig.3 Average absorption coefficients at t=1643 s

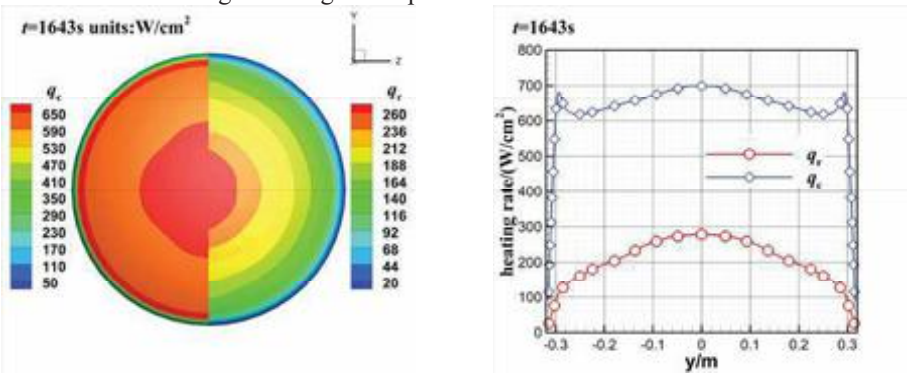

Fig.4 Convective and radiative heat on surface and along radial direction on symmetric plane

The radiation intensity is obtained by solving radiation transfer equation discretized by finite volume method in azimuth angles and space directions. The radiative heat is acquired by integrating radiation intensity on wall, which decrease slowly and monotonously along radial direction, while convective heat rises up again on the shoulder. The total heat rate at stagnation point is about 1007 W/cm^2 which is very close to the flight measurement of 1025 W/cm^2.

CONCLUSIONS

Three dimensional fluid dynamics equations, gas species radiation models and radiation transfer equation have been computed on FIRE II probes. It is found that a great number of atoms and ions produced by strong chemical reactions in high temperature shock layer emit much radiative intensities. Radiative and convective heating rates from the simulation at typical status agree well with the flight measurement.

ACKNOWLEDGEMENT

The authors gratefully acknowledge the support by the National Natural Science Foundation of China (Grant No.: 11402251).

References

[1] Palmer G. E., White T. and Pace A.: Direct Coupling of the NEQAIR Radiation and DPLR Computational Fluid Dynamics Codes. Journal of Spacecraft and Rockets, 48(5): 836-845, 2011.

[2] Johnston C. O., Kleb B.: Uncertainty Analysis of Air Radiation for Lunar-Return Shock Layers. Journal of Spacecraft and Rockets, 49(3):425-434, 2012.

ON ACCELERATION OF KRYLOV-SUBSPACE NEWTON AND ARNOLDI ITERATIONS FOR INCOMPRESSIBLE CFD

Alexander Gelfgat[a]
School of Mechanical Engineering, Faculty of Engineering, Tel-Aviv University, Tel-Aviv, Israel

Summary Looking for an improvement of convergence rate of steady state and eigenvalue solvers preconditioned by the inverse Stokes operator and realized via a time-stepping, we propose two independent additions. First, we suggest a generalization of the Stokes operator so that the resulting preconditioner operator depends on several parameters and whose action preserves zero divergence and boundary conditions. The parameters can be tuned for each problem to speed up the convergence of a Krylov-subspace-based linear algebra solver. Second, we propose to generate an initial guess of steady flow or eigenvalue and eigenvector using orthogonal projection on divergence free basis satisfying all boundary conditions. Both additions are illustrated on the solution of the linear stability problem for laterally heated square and cubic cavities.

INTRODUCTION

Stability of fluid flows, being one of the classical and oldest topics of theoretical fluid dynamics, attracted a lot of attention during the last decades. With the growth of computational power and fast development of numerical methods of linear algebra, it became possible to study stability of numerically calculated flows that require development of non-linear steady state solvers and the solution of eigenproblems for matrices of extremely large size [1-2]. Existing computational methods and computer power available allow one to study modal linear stability of two-dimensional flows relatively easy nowadays. Disturbances of these flows are usually assumed to be either two-dimensional or three-dimensional with prescribed spatial periodicity in one dimension, e.g., spanwise or circumferential one. The family of such problems is called BiGlobal in [1]. TriGlobal problems, where stability of fully three-dimensional flows should be studied without any preliminary assumptions about disturbances, remain challenging for computational simulations. Difficulties are usually caused either by available and not powerful enough computer resources, or by an enormous slowdown of convergence of numerical methods effectively applied to the BiGlobal problems. Thus, development of robust numerical methods for TriGlobal stability problems is one of the challenging problems of computational fluid dynamics.

One of the efficient and most popular approaches for application of Krylov-subspace linear algebra solvers to computation of incompressible flows and study of their stability was proposed in [3]. Within this approach, assuming availability of an efficient time-dependent CFD code, Krylov vectors are generated via the time stepping. This approach was successfully applied to a variety of BiGlobal problems, however applying this technique to TriGlobal problems usually leads to a very slow convergence, so that the final result cannot be obtained in a reasonable time.

As it is argued in [3], the time-stepping method for calculation of Krylov vectors can be interpreted as preconditioning by an inverse Stokes operator. The latter serves as a starting point for this study, in which we show how the Stokes preconditioning can be generalized. This allows for a faster convergence of the most inner iterative process, which produces Krylov vectors via iterative inverse of the preconditioner operator. Then, to reduce the number of outer iterations of either the Newton or Arnoldi solver, we propose to generate a close to solution initial guess using projections on divergence free bases. We argue also that having a good initial guess of the leading eigenvalue and eigenvector, the Arnoldi process can be replaced by a simpler and faster converging inverse iteration.

Application of the proposed approach is illustrated on the well-known problem of convection in square and cubic laterally heated cavities. Considering square cavities (BiGlobal) we reproduce previously published results for the critical Grashof number corresponding to the steady – oscillatory transition. We succeed also to compute the critical Grashof numbers also for laterally heated three-dimensional cubic boxes (TriGlobal) with different thermal boundary conditions on horizontal and spanwise boundaries. These results are obtained by means of linear stability analysis for the first time.

GENERALIZATION OF STOKES PRECONDITIONER

The Stokes operator acts of the three velocity components $u, v, w,$ and the pressure p and is defined as

$$\boldsymbol{S}\begin{bmatrix} u \\ v \\ w \\ p \end{bmatrix} = \begin{bmatrix} H_u & 0 & 0 & -\nabla_p^x \\ 0 & H_v & 0 & -\nabla_p^y \\ 0 & 0 & H_w & -\nabla_p^z \\ \nabla_u^x & \nabla_v^y & \nabla_w^z & 0 \end{bmatrix}\begin{bmatrix} u \\ v \\ w \\ p \end{bmatrix} = \begin{bmatrix} R_u \\ R_v \\ R_w \\ 0 \end{bmatrix} \tag{1}$$

where ∇^x, ∇^y and ∇^z are the first derivatives in the x, y and z directions, $H = \Delta - I/\delta t$ are Helmholtz operators, Δ is the Laplacian operator, and I is the identity operator. The lower indices show on which variable an operator acts. By assigning the lower indices, we emphasize that boundary conditions can be different for different velocity components, that different scalar variables can be assigned to different staggered grid nodes, and that numerical discretization of the same

[a] Corresponding author. Email: gelfgat@tau.ac.il

differential operators can be different for different scalar variables. As a result of the inverse Stokes operator $\boldsymbol{S}^{-1}$ action one obtains a divergence-free velocity field that satisfies all the boundary conditions. The product by $\boldsymbol{S}^{-1}$ can be interpreted as a semi-implicit time step of length δt, so that the result can be calculated by a time-dependent code [3], and $1/\delta t$ plays a role of an iteration parameter. The pressure gradient is needed here to remove the potential part of a vector resulting after the action of the three Helmholtz operators.

For the following we assume that velocity boundary conditions are linear and homogeneous. Note, that an inhomogeneity of a linear boundary condition can be removed by a change of variables. Then, for successful implementation of the Krylov-subspace iterations methods, vectors of the Krylov basis must be divergence free and satisfy all the boundary conditions. In other words the Krylov vectors and the solution must belong to the same linear space. Since the linearized Navier-Stokes operator alters the divergence and the boundary conditions, product by $\boldsymbol{S}^{-1}$ allows one to restore them. Observing that the boundary conditions are parts of the Helmholtz operators H, we can generalize the operators as

$$H_{(u,v,w)} = \alpha^{x}_{(u,v,w)} \frac{\partial^2}{\partial x^2} + \alpha^{y}_{(u,v,w)} \frac{\partial^2}{\partial y^2} + \alpha^{z}_{(u,v,w)} \frac{\partial^2}{\partial z^2} - \beta_{(u,v,w)} \tag{2}$$

The boundary conditions are incorporated into operators $H_{(u,v,w)}$, so that a product by newly formed $\boldsymbol{S}^{-1}$ yields a divergent free field satisfying the boundary conditions. The nine values of α-s and three values of β-s must be optimized for the fastest convergence. Clearly, there are too many parameters to optimize just by a numerical experiment. However, some partial optimization is possible, and allowed us to reduce by half the total computational time.

GENERATION OF INITIAL GUESS

Denoting the linearized part of the Navier-Stokes operator as $(\boldsymbol{N_U} + \boldsymbol{L})$[2,4,5], and the current Krylov basis vector as $\boldsymbol{w}^{(n)}$, the calculation of the next Krylov vector can be formally written as $\boldsymbol{w}^{(n+1)} = \boldsymbol{\Pi}(\boldsymbol{N_U} + \boldsymbol{L})\boldsymbol{w}^{(n)}$, where $\boldsymbol{\Pi}$ is an operator that projects a vector on the space of divergence free vectors satisfying all the boundary conditions. This operator can be built, for example, as an orthogonal projection on basis vectors of the above space. One possible way of construction of such basis as linear superpositions of the Chebyshev polynomials is proposed in [4], where all the definitions are given and technical details are described. Applying the Galerkin projections, $\boldsymbol{w}^{(n+1)}$ is calculated as a truncated Galerkin series. This yields approximation of the projection operator $\boldsymbol{\Pi}$ and allows one to obtain a rough approximation of a true numerical solution within a relatively short computational time. Then this rough approximation can be used as an initial guess either for computations with a larger truncation number, or for the complete computation using the above preconditioner operator.

PRELIMINARY RESULTS AND CONCLUSIONS

Applying two above approaches we succeeded to compute primary bifurcation points corresponding to a steady – oscillatory transition of convection in a laterally heated cube. The whole computations comprises several tens of hours on a PC with parallelization on six 2.6 GHz Intel CPUs. Further details can be found in [5]. Table 1 compares these results with those obtained by straight-forward integration in time (DNS) [6].

Table1. Critical Grashof number and critical oscillation frequency for primary instability of convection in a laterally heated cube. Comparison of results obtained by the stability analysis and DNS.

Horizontal boundaries	Spanwise boundaries	Stability analysis: Gr_{cr}/ω_{cr}	DNS: Gr_{cr}/ω_{cr}
conducting	conducting	$3.4136 \cdot 10^6$ /1.7651	$3.32{\cdot}10^6$ / 1.766
conducting	insulating	$3.3831 \cdot 10^6$ / 1.6489	$3.29{\cdot}10^6$ / 1.652
insulating	conducting	$1.226 \cdot 10^7$ / 0.9579	$1.28{\cdot}10^8$ / 0.987
insulating	insulating	$4.252 \cdot 10^7$ / 0.05385	$4.45{\cdot}10^7$ / 0.109

References

[1] Theofilis V.: Global linear stability, *Ann. Rev. Fluid Mech.* 43:319-3520, 2011.

[2] Dijkstra H.A., Wubs F.W., Cliffe A.K., Doedel E., Dragomirescu I.F., Eckhardt B., Gelfgat A.Yu., Hazel A.L., Lucarini V., Salinger A.G., Phipps E.T., Sanchez-Umbria J., Schuttelaars H., Tuckerman L.S., Thiele U.: Numerical bifurcation methods and their application to fluid dynamics: Analysis beyond simulation, *Comm. Comput. Phys.*, 15: 1-45, 2013.

[3] Tuckerman L. S., Bertagnolio F., Daube O., Le Quéré P., Barkley D.: Stokes preconditioning for the inverse Arnoldi method, in "Continuation Methods for Fluid Dynamics" (*Notes on Numerical Fluid Dynamics*, vol. 74), eds. D. Henry and A. Bergeon, Vieweg, Göttingen, 241-255, 2000.

[4] Gelfgat A. Yu.: Visualization of three-dimensional incompressible flows by quasi-two-dimensional divergence-free projections. *Computers & Fluids*, 97:143-155, 2014.

[5] Gelfgat A. Yu.: On calculation of quasi-two-dimensional divergence-free projections for visualization of three-dimensional incompressible flows, arXiv:1508.05603, submitted for publication.

[6] Gelfgat A. Yu.: Oscillatory instability of three-dimensional natural convection of air in a laterally heated cubic box, arXiv:1508.00652, submitted for publication.

NUMERICAL CALCULATION OF PISTON-LIKE OIL DISPLACEMENT FOR DIFFERENT SCHEMES OF FLOODING

Vladimir Astafev[1a)] & Andrey Kasatkint[2]
[1]*Department of Oil and Gas Field Development, Samara State Technical University, Samara, Russia*
[2]*Department of Continuum Mechanics, Samara State University, Samara, Russia*

Summary Prediction of the motion of oil-water contact has great importance in the problems of oilfield development by flooding. We consider a piston-like model of oil-water displacement, which takes into account differences in viscosity of two fluids. Filtration of liquids is described by Darcy's law. Both fluids are weakly compressible and the pressure in the reservoir satisfies the quasi-stationary diffusion equation. Piston-like model leads to discontinuity of the tangential velocity at the boundary L of oil-water contact. Using the generalized Cauchy integral we reduce the problem of finding the current boundary of oil-water contact to the system of singular integral equations for the velocity components and to the Cauchy problem for the boundary motion of oil-water contact. An algorithm for numerical solution of this problem is developed. The monitoring of oil-water boundary motion for different schemes of flooding (four-point, five-point, seven-point, nine-point, etc.) is carried out.

MATHEMATICAL MODEL AND NUMERICAL SOLUTION

Among the methods of oil fields development the flooding method [1] became widespread. The main objective of flooding is to maintain by flooding the reservoir pressure, inevitably falling in the primary field development. In this paper, the model of the piston-like oil displacement by water, which takes into account the difference in physical properties (density and viscosity) of oil and water. Consider the plane filtration flow of a viscous compressible fluid with viscosity μ and compressibility β in an infinite horizontal reservoir with permeability k, porosity m and thickness h. For the quasi-stationary state of filtration flow the pressure in the reservoir $p(x,y,t)$ satisfies the diffusivity equation and the velocity components $V_x(x,y,t)$ and $V_y(x,y,t)$ are calculated by the Darcy law [1]

$$\frac{\partial p}{\partial t} = \chi\left(\frac{\partial^2 p}{\partial x^2} + \frac{\partial^2 p}{\partial y^2}\right),\ V_x = -\frac{k}{\mu}\frac{\partial p}{\partial x},\ V_y = -\frac{k}{\mu}\frac{\partial p}{\partial y}, \tag{1}$$

where $\chi = k/m\mu\beta$ - the coefficient of diffusivity.

Solution of the equation (1) in the case of doubly periodic system of production and injection wells has been obtained in [2]. Discontinuous on the line L function $V_x(x,y,t) - iV_y(x,y,t)$ on the complex plane $z=x+iy$ will be sought in the form:

$$\overline{V}(z,t) = V_x(x,y,t) - iV_y(x,y,t) = F(z,t) + \frac{1}{2\pi i}\oint_L \zeta(\tau - z)\gamma(\tau,t)d\tau, \tag{2}$$

where $\zeta(z)$ - Weierstrass zeta function, $F(z,t)$ is given in paper [2].

Denoting the viscosity ratio as $\kappa = \mu_{(w)}/\mu_{(o)}$, the normal and tangential velocity components of the water as $N(s) = V_n^{(w)}$ and $T(s) = V_t^{(w)}$, equation (2) allows us to obtain singular integral equation for the unknown functions $T(s)$ and $N(s)$ on the line L:

$$\frac{1+\kappa}{2}T(s,t) + iN(s,t) = (F(s,t) + \frac{1-\kappa}{2\pi i}\int_0^S \zeta(z(\sigma) - z(s))T(\sigma,t)d\sigma)\frac{dz}{ds}, \tag{3}$$

The integral equation (3) must be supplemented by the differential equation that determines the time evolution of the line L. This equation has the following form [1]:

$$\begin{aligned} &m\frac{\partial\overline{z(s,t)}}{\partial t}\frac{\partial z}{\partial s} = \frac{(1+\kappa)}{2}T(s,t) + iN(s,t), \\ &z(s,0) = z_0 + r_w e^{i\theta}. \end{aligned} \tag{4}$$

where z_0 - the center of the injection well with radius r_w, through which water is pumped into the reservoir. The initial condition in the equation (4) indicates the starting position of the point in the beginning of flooding, the corresponding angle θ is determined on the contour of the injection well.

Consider the algorithm for the numerical solution of integro-differential equations (3) and (4). For the numerical solution of singular integral equation (3) we divide the contour L by discrete set of points on the elements $[z_i, z_{i+1}]$, $(i = 0, 1, \ldots N-1)$. Due to the closure of line L, the first and the last points of the partition are the same, i.e., $z_N = z_0$. Each of the points z_k corresponds to the length of the arc s_k. Let us choose and fix the point $z_k = z(s_k)$ on the contour L.

Omitting the rather cumbersome intermediate calculations, we write the approximation of the integral term in equation (3) as follows:

$$\int_0^S \zeta(z(\sigma) - z_k)T(\sigma,t)d\sigma = \frac{1}{2z_k'}\left[2T_k \ln\left(\frac{\Delta s_k}{\Delta s_{k-1}}\right) + T_{k-1} - T_{k-1} + \sum_{i=k+1}^{N+k-1}\zeta(z_i - z_k)T_i(\Delta s_i + \Delta s_{i-1})z_k'\right] \tag{5}$$

[a)] Corresponding author. Email: vladimir.astafev@mail.ru.

Equation (3) shows us that the real part of the singular integral equation (3) matches the finding of values of the unknown function $T_k=T(s_k)$ at a given time t_n on a discrete set of points $z_{k=}z(s_k)$. The imaginary part of this equation is, in fact, the formula for calculating the values of the function $N_k=N(s_k)$ at a given time t_n at the same discrete set of points.

The obtained values of T_k and N_k are then used to calculate the displacements of points $z_{k=}z(s_k)$ in the time interval $[t_n, t_{n+1}]$. These displacements are determined by the numerical solution of the Cauchy problem (4) with the Runge-Kutta method, modified in view of the complex nature of the differential equation (4). In the calculations it was chosen the dimensionless time τ, associated with the original time t as $\tau=10^{-4}Qt/2\pi mh\omega_1^2$, where Q is the flow rate of the injection well, ω_1 is the biggest complex period of doubly periodic system of production and injection wells.

RESULTS OF CALCULATIONS

To solve this problem there was developed a software system to track the evolution of the flooding front in time, as well as to quantify the effectiveness of a particular scheme of flooding (dimensionless water breakthrough time into the production wells $\tau_{breckthrough}$ and waterflooding coverages $K_{coverage}$). In numerical calculations there was considered frontal row, four-point, five-point, seven-point and nine-point scheme of flooding. To determine the current position of the flooding front it was involved 180 tracers - points coming out at the initial time of the injection well.

It is known [3] that the viscosity ratio κ has a negative impact on the ultimate recovery: the decrease in the parameter κ leads to the decrease in the volume of recoverable oil due to the growing instability of oil displacement by water. In addition, when viscosity ratio $\kappa<1$, the Saffman-Taylor instability [4] occurs, which is often called as "viscous fingering". The viscous fingering effect has been observed in the course of our numerical calculations. The fig. 1 shows the formation of viscous fingers for five-point scheme of flooding at $\kappa=1/5$ value. For comparison, the fig.1 is supplemented by the figure from [5] (fig. 6a in the cited paper) obtained experimentally for similar geometry placement of wells.

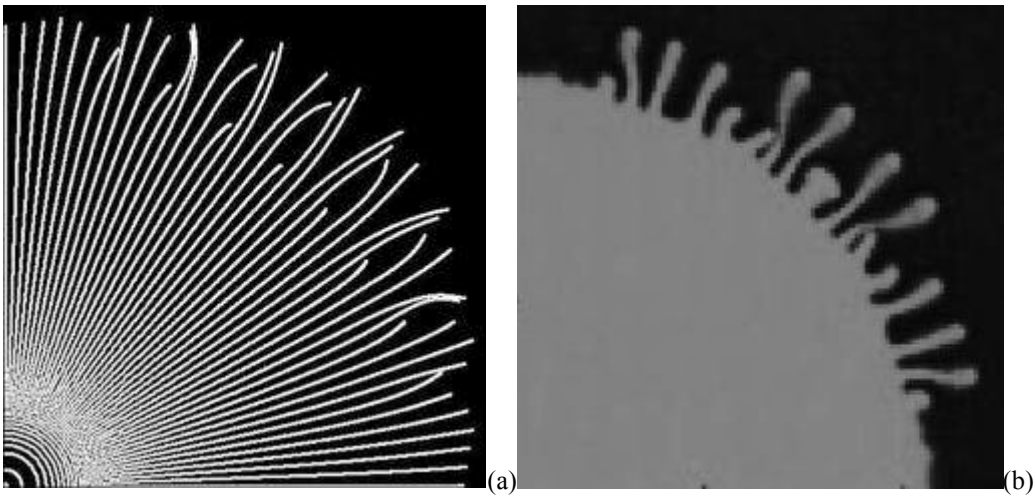
(a) (b)

Fig. 1. Saffman-Taylor instability of the front of flooding for the five-point scheme.

ACKNOWLEDGEMENTS

Authors are thankful the Russian Science Foundation for financial support under grant 15-17-00019.

References:

[1] Willhite G.P.: Waterflooding. SPE Textbook. Vol. 3. Society of Petroleum Engineers, Richardson, Texas, 1986.

[2] Astafev V.I., Roters P.V. Simulation of Oil Recovery using the Weierstrass Elliptic Functions. *Int. J. Mech.* **8**: 353-364, 2014.

[3] Craig F.F. The Reservoir Engineering Aspects of Waterflooding. Society of Petroleum Engineers, Dallas, 1971.

[4] Saffman P.G. Viscous Fingering in Hele-Shaw Cells. *J.Fluid Mech.* **173**: 73-84, 1986.

[5] Dapira P., Glimm J., Lindquist B. and McBryan O. Polymer Floods: A Case Study of Nonlinear Wave Analysis and of Instability Control in Tertiary Oil Recovery. *SIAM J.Appl. Math.* **48**: 353-373, 1988.

A COMPARISON BETWEEN BLADE ELEMENT ACTUATOR DISK AND ACTUATOR LINE METHODS FOR A TIDAL TURBINE

Farhad Baratchi[1 a)], Tiger Jeans[1] & Andrew Gerber[1]
[1] *Department of Mechanical Engineering, University of New Brunswick, Fredericton, NB, Canada*

Summary In this paper the operation of a tidal turbine has been simulated using the blade element actuator disk (BEAD) and actuator line (AL) methods for different values of tip speed ratio (TSR). Results show that the BEAD and AL give close results for power (C_P) and thrust (C_T) coefficients which agree well with the experiment [1]. On the other hand it is observed that for corresponding cases solved by the BEAD and AL, moving downstream, the wake experiences smaller velocity change behind the rotor centre in the AL method. This can be attributed to the presence of coherent root vortex structures which are captured in the AL method. In addition it is noted that the BEAD method, because of its averaged actuator disk methodology is not able to expose the flow unsteadiness as well as the AL method.

INTRODUCTION

Tidal energy and tidal turbines have drawn much attention in recent years. Among different methods that have been used to investigate tidal turbines, the blade element actuator disk (BEAD) and the actuator line techniques are feasible for turbine arrays and also have proven to have good performance. In the BEAD method, the turbine rotor is replaced with an actuator disk and the momentum source terms, calculated from the blade element theory, are distributed on the disk. The result is a permeable actuator disk which the flow can pass through and be influenced by the source terms which vary radially but are averaged in the rotational direction. In the AL method on the other hand, the blades body forces are placed as momentum source terms along the lines which represent the blades and rotate with time. The distribution of the source terms in these two methods have been shown in figure (1). As can be seen the source term distribution in the AL method is much closer to the real geometry of the rotor. In this study using the EXN/Aero CFD code, large eddy simulations are performed using the BEAD and AL methods and their performance is compared on the basis of their prediction of turbine performance and the wake pattern.

RESULTS

Figure (2) and (3) respectively show C_P and C_T coefficients versus TSR for the BEAD and AL methods. While from figure (2), the power coefficient increases with TSR until a maximum is reached (TSR ≈ 6) and falls off, in figure (3) the thrust coefficient increases continuously with TSR. Results from the present study have been compared with Bahaj et al. [1], Bai et al. [2] and Malki et al. [3] and a good correlation between them is observed. The velocity fields obtained from the BEAD and AL methods are shown in figure (4) and (5). A comparison between these two figures illustrates that the AL method shows a better performance in picking up the unsteadiness that is caused due to the spinning blades. In addition, when moving towards the wake core a smaller velocity gradient is obtained from the BEAD. This difference is due to the fast root vortex structures which maintain themselves in the AL method and are not captured by the BEAD method. Figure (6) and (7) show axial induction factor calculated from the two methods. While from figure (6) in the BEAD method the axial induction factor changes only with radius and is averaged in tangential direction, the plotted distribution from the AL method shows the capability of this method in giving a realistic picture of the turbine operation and its resulting velocity field. In figure (8) the change of normalized axial velocity in the cross stream direction have been shown at Z/D = 2 and Z/D = 5 downstream for both methods. This figure shows again that while in the AL method coherent structures due to the root vortex shedding maintain their higher velocity at the wake core, in the BEAD method because of their absence and overestimation of mixing process, axial velocity changes notably from Z/D = 2 to Z/D = 5. Figure (9) shows the changes in the normalized axial velocity behind the rotor at Z/D = 2. Since from figure (8) both methods predict the same value at this spot only results from the AL method have been shown here. From this figure it can be seen that the velocity deficit increases continuously with TSR. The vorticity field obtained from the AL method has been shown in figure (10). Tip and root vortices that can be seen in this picture are not detected by the BEAD method.

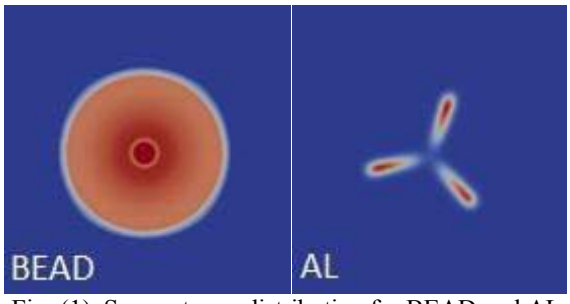

Fig. (1). Source terms distribution for BEAD and AL

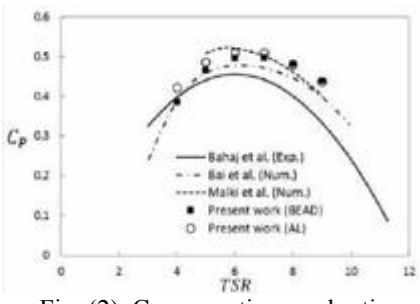

Fig. (2). C_p versus tip speed ratio

[a)] Corresponding author. Email: f.baratchi@unb.ca

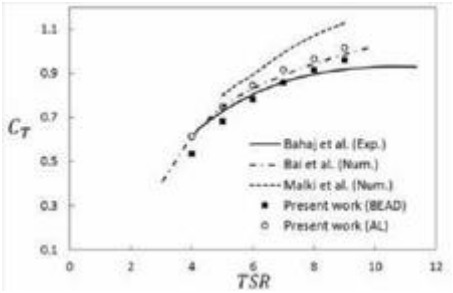

Fig. (3). C_T versus tip speed ratio

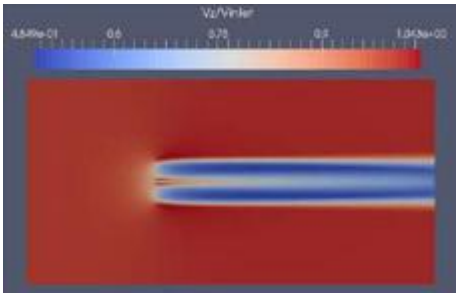

Fig. (4). Velocity field from BEAD method

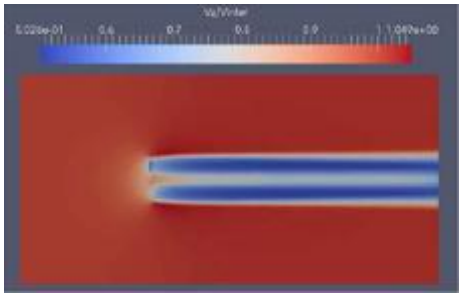

Fig. (5). Velocity field from AL method

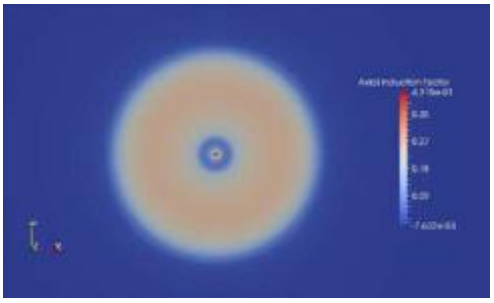

Fig. (6). Axial induction factor (BEAD)

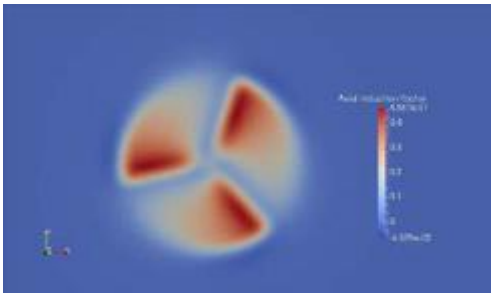

Fig. (7). Axial induction factor (AL)

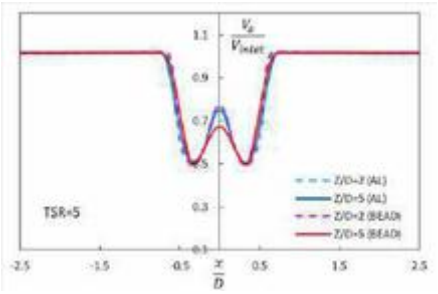

Fig. (8). Axial velocity behind the turbine

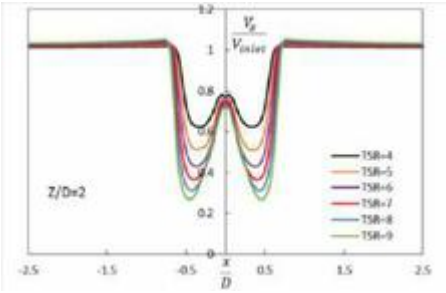

Fig. (9). Axial velocity for different TSRs

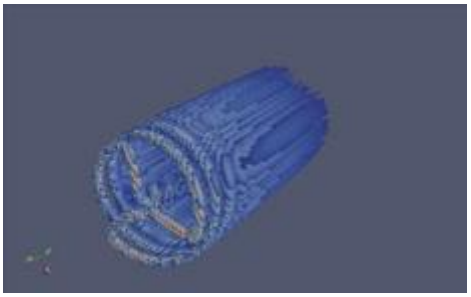

Fig. (10). Vorticity field from AL method

CONCLUSIONS

This study showed that while the BEAD method gives reasonable answers for turbine power and thrust coefficients, it does not capture the tip and root vortices and the unsteadiness that can be predicted by the AL method.

References

[1] Bahaj, A., Molland, A., Chaplin, J., and Batten, W., 2007. "Power and thrust measurements of marine current turbines under various hydrodynamic flow conditions in a cavitation tunnel and a towing tank". Renewable Energy, 32, pp. 407–426.
[2] Bai, G., Li, J., Fan, P., and Li, G., 2013. "Numerical investigation of the effects of different arrays on power extractions of horizontal axis tidal current turbines". Renewable Energy, 53, pp. 180–186.
[3] Malki, R., Williams, A., Croft, T., Togneri, M., and Masters, I., 2013. "A coupled blade element momentum-computational fluid dynamics model for evaluating tidal stream turbine performance". Applied Mathematical Modelling, 37, pp. 3006–3020.

NUMERICAL SIMULATION OF SOLID SUSPENSION FLOWS IN A HORIZONTAL PIPE

Aurélien Bordet *[1], Sébastien Poncet[1], Michel Poirier[2], and Nicolas Galanis[1]
[1]*Department of Mechanical Engineering, Université de Sherbrooke, Sherbrooke, Québec, Canada*
[2]*CanmetÉNERGIE, Varennes, Québec, Canada*

Summary The present work validates a numerical model used to describe the flow behavior of particle suspensions through horizontal pipes. The mixture of liquid water and polypropylene spheres is considered as single-phase and Newtonian fluid. The transport equation proposed by Phillips et al. [1] for the particle fraction is employed, including a term which accounts for buoyancy. Different flow conditions depending on the flow rate and initial particle concentration have been considered. The present simulations compare well to the experiments of Reghem [2] and improved the simulations of Darbouret [3].

INTRODUCTION

The primary objective of this project is the numerical simulation of ice slurry flows in different types of ducts and complex geometries for the transport of cold in refrigeration systems. The lack of reliable local measurements (velocity and ice concentration) has considerably slowed down the development of dedicated numerical models. Behaviour of flows involving solid particles scattered in liquid water tends to be very similar to the one of ice slurry flows. The velocity measurements and observations of Reghem [2] then constitute a very interesting database for the validation of the present model. Moreover, Darbouret [3] also proposed some numerical simulations based on the finite difference method and assuming a 2D steady-state laminar flow. This flow configuration is very challenging for numerical methods as the particle concentration may reach very high values at some locations inducing high shear stress flow regions.

MODEL DEVELOPMENT AND NUMERICAL PARAMETERS

The model presently used considers the fluid mixture as being single-phase and Newtonian. Phillips and al.'s equation [1] is employed to model the transport of the particle volume fraction. Originally, this transport equation gathered three components being a flux term accounting for the Brownian motion of the particles $\circ$ that can straightly be neglected in the present case $\circ$ and two other flux terms giving diffusion, due to the spatial variation of effective viscosity for the first and due to the spatial variation of particle interaction frequency for the second. The latter may also be neglected, according to [1], since the two resulting effects of this term auto-annihilate. A last flux term is added to obtain the particle buoyancy and the stratification phenomenon. The terminal particle settling velocity is calculated from [4] and a dumping function derived from Gurel's formula [5] is used to fit the mixture viscosity modelled with the Thomas'equation. The flow is isothermal and steady. The model has been implemented in a finite volume solver with second-order upwind schemes for the pressure, momentum and particle volume fraction transport equations. The pressure-velocity coupling is overcome through the SIMPLE algorithm. The particle suspension, a mixture of liquid water and polypropylene spheres of diameter $d = 0.0036$ m, flows through a cylindrical and horizontal pipe of length $L = 3$ m and diameter $D = 0.05$ m. The mesh comprises nearly 8×10^5 cells with about 1400 cells per cross-section. Mesh refinement is done in the near wall regions. At the inlet, uniform profiles for the velocity and the particle concentration are ruled. The flux of the particle volume fraction is turned to zero at the wall.

RESULTS AND DISCUSSION

Different values for the uniform axial velocity U_m and particle volume fraction Φ have been imposed at the inlet. The results are shown on Figures 1 and 2. They correspond to the radial profiles of the axial velocity and cross-section particle volume fraction at the pipe outlet $z/L = 1$, for each flow condition. The blue color corresponds to areas of high particle concentration ($\Phi > 0.35$) whereas the yellow region contains almost no particle. As the mixture flows along the pipe, the solid particles being lighter than liquid water rise to the top wall. Consequently, a heap of these particles is likely to form in the top region, slowing down the flow there considerably and reshaping the velocity profiles as shown on Figure 1. Thus, it appears essential to model accurately the dynamics of the particles within the mixture and especially the buoyancy term.

Case I corresponds to $U_m = 0.18\ m.s^{-1}$ and $\Phi = 0.15$, values typically encountered in ice slurry transport systems. The suspension is clearly heterogeneous, with a highly concentrated flow region at the top of the pipe and a part being poorly concentrated in the lower region (Fig.2-I). The mixture is accelerated in the lower-half of the pipe with a maximum velocity around $r/R \simeq \circ 0.18$ (Fig.1-I). A rather good agreement is obtained compared to the experiments [2], even if the model predicts a linear profile in the top region highlighting higher shear stresses there.

*Corresponding author. Email: aurelien.bordet@usherbrooke.ca

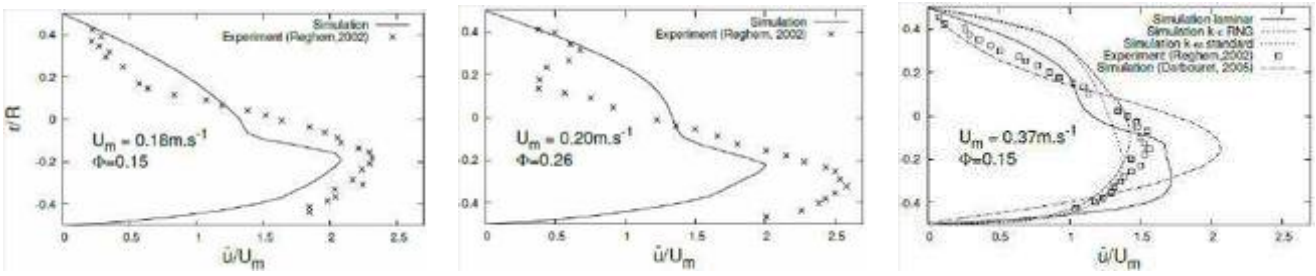

Figure 1: Radial profiles of the normalized axial velocity at the pipe outlet $z/L = 1$ for three sets of initial conditions (cases I to III). Comparisons with the experiments of Reghem [2] and the simulation of Darbouret [3].

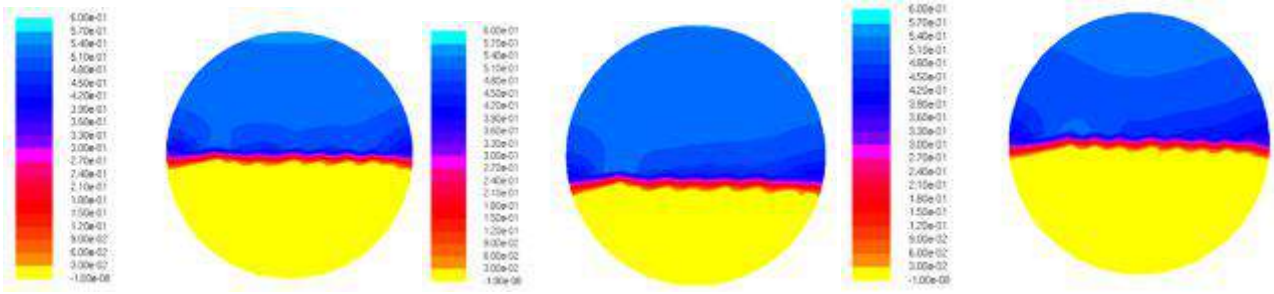

Figure 2: Corresponding simulated particle volume fraction over the same pipe section, i.e. at outlet.

The main difference between cases I and II is the increased initial concentration in solid particles to $\Phi = 0.26$. The radial distribution of the axial velocity is not significantly modified regarding the numerics. In the experiments, Reghem [2] observed the formation of a bed moving slowly in the top part of the pipe $0.1 < r/R < 0.5$, where the velocity remains almost constant ($\overline{u}/U_m \simeq 0.5$). The model fails to predict the right profile but Fig.2-II confirms a flow region with high and constant concentration in solid particles. A Bingham rheological law for such a flow regime would improve the capabilities of the model to reproduce packed-bed flows.

By comparing cases I and III, increasing the inlet velocity from $U_m = 0.18\ m.s^{-1}$ to $0.37\ m.s^{-1}$ clearly modifies the radial distributions of the axial velocity. The peak value at $r/R \simeq \circ\ 0.1$ is reduced. The flow regime is here turbulent, which slightly homogenizes the particle distributions (Fig.2-III). It explains why the turbulence models improve the predictions over the present laminar simulation and one of Darbouret [3]. The remaining discrepancies may be explained by the rheological law used there, valid for $\Phi \leq 0.6$, value locally exceeded at the top of the pipe. It will be shown also in the presentation that the model performs much better for ice slurry flows, with smaller particle diameter.

This work is part of the NSERC chair on industrial energy efficiency established at Université de Sherbrooke in 2014 with the support of Hydro-Qubec, CanmetÉNERGIE and Rio Tinto Alcan, which are gratefully acknowledged.

References

[1] Phillips R. J., Armstrong R. C., Brown R. A., Graham A. L., Abbott J. R.: A constitutive equation for concentrated suspensions that accounts for shear-induced particle migration. Physics of Fluids, 4(1):30-40, 1992.

[2] Reghem P.: Étude hydrodynamique de fluides diphasiques solide-liquide en conduite circulaire : application au coulis de glace. PhD Thesis, Université de Pau et des pays de l'Adour, Pau, France, 2002.

[3] Darbouret M.: Étude rhéologique d'une suspension d'hydrates en tant que fluide frigo-porteur diphasique. PhD Thesis, École Nationale Supérieure des Mines de Saint-Étienne, Saint-Étienne, France, 2005.

[4] Zhiyao S., Tingting W., Fumin X., Ruijie L.: A simple formula for predicting settling velocity of sediment particles. Water Science and Engineering, 1(1):37-43, 2008.

[5] Oliver D. R.: Sedimentation and effective viscosity. Nature, 185:912-913, 1960.

SIMULATION OF AN UNAPPENDED AXISYMMETRIC SUBMARINE HULL DURING UNSTEADY PITCHING

Robert Doyle*[1], Tiger Jeans[2], A. Gordon L. Holloway[2], J.T. Zhang[2], and George D. Watt[3]

[1]*PhD Student, Department of Mechanical Engineering, University of New Brunswick, Fredericton, New Brunswick, Canada*

[2]*Department of Mechanical Engineering, University of New Brunswick, Fredericton, New Brunswick, Canada*

[3]*Defence Research and Development Canada - Atlantic, Dartmouth, Nova Scotia, Canada*

Summary Unsteady CFD simulations of the unappended DARPA SUBOFF 5470 undergoing a pitch maneuver were conducted using Ansys CFX to support the development of hydrodynamic force models for simulating the transient dynamics of underwater vehicles. The simulations used a sliding mesh formulation and the BSL Reynolds stress turbulence model. Four simulations were conducted with varying pitch rates; the results from two of these were compared to experimental wind tunnel tests. The simulated flow was qualitatively correct, however comparisons show that the simulations under-predict the normal force and over-predict the pitching moment. This error grows in proportion to the angle of incidence. The body-normal vorticity moment distribution along the body and wake was calculated, and is seen to transition between from a steady translation distribution to a steady rotation distribution over the maneuver. This transition appears to be proportional to the local drift angle along the hull and the pitch rate.

INTRODUCTION

The design and safe operation of underwater vehicles depends critically on knowledge of the vehicles safe operating limits. This operating envelope is developed primarily by numerical dynamics simulations, which must be computationally fast and generally make use of simplified models for the vehicles hydrodynamics. Past work at the University of New Brunswick has investigated the hydrodynamic characteristics of submarines undergoing steady translations and rotations using computational fluid dynamics. The results of these investigations were accurate lower order models for the vehicle hydrodynamics, suitable for use in simulations of the vehicle dynamics.

In certain extreme conditions, such as emergency rising or collision avoidance, the fluid flow will experience significant unsteady effects and a model which resolves the transient hydrodynamics will be required. This work presents the results of CFD simulations of unsteady pitching maneuvers for the unappended DARPA SUBOFF submarine geometry at $Re = 6.1e6$, and an analysis of the hydrodynamic forces and moments. These results are compared to the unsteady experimental model tests of Granlund and Simposon [1], as well as previous simulations of the steady hydrodynamics, in an attempt to analyze both the accuracy of the CFD model and the effect of unsteadiness on the hydrodynamic forces.

METHODOLOGY

The geometry of interest is the unappended DARPA SUBOFF 5470 generic submarine hull in a steady cross flow of air at 44.56 m/s. The hull geometry is axisymmetric, measuring 2.24 m in length and 0.267 m in diameter. The maneuver and hull form are symmetric across the centreline, and so a half symmetry domain was used in the computational mesh. The hull surface was discretized with approximately 100 cells circumferentially and 216 cells longitudinally. A cell inflation layer with an initial cell height of between 5.52e-6 m at the bow and 8.62e-5 m at the stern was used; yielding $y^+ \approx 1$ along the hull. This mesh was simulated in Ansys CFX using a sliding mesh formulation. A cylindrical structured domain was used for the rotating mesh attached to the hull; this mesh was then embedded in a rectangular static hybrid domain. The total mesh, including both the rotating and static domains, contained approximately 12.2 million cells.

The maneuver consisted of the hull in a steady oncoming flow at an incidence of one degree, up to a non-dimensionalized time of 3 units, where $t' = tu/l$. At 3 units, the hull would begin pitching, sweeping up to 27 degrees incidence at approximately 9 units, at which point the motion ceased and the simulation was held for an additional 3 units. This corresponds to a constant linear pitch rate of $\omega = 1.36 rad/s$. Three additional unsteady cases were investigated. The first attempted to match the exact experimental kinematics of Granlund, which deviated slightly from a constant linear pitch rate, and were here fit to an 8th order polynomial. This was followed by two additional simulations at pitch rates of 4ω and 8ω and with the same range, in order further to investigate the effects of unsteadiness on the flow. Timestep sizes for these four simulations were $2.0e \circ 4$ seconds for the first two, $5.0e \circ 5$ seconds for the third, and $2.5e \circ 5$ seconds for the fourth. In addition, steady flow simulations were conducted for translation at incidence angles of 5, 10, 15, 20, and 27.6 degrees. All of the simulations utilized the BSL Reynolds stress turbulence model, as implemented in CFX v14.

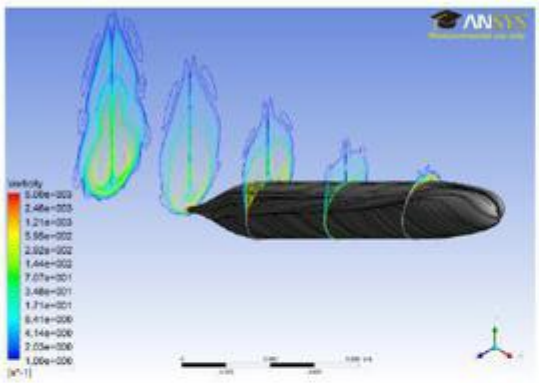

Figure 1: Vorticity Contours and Hull Streamlines

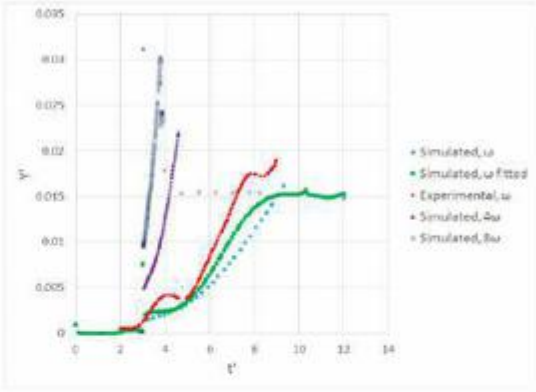

Figure 2: Comparison of Simulated and Experimental Normal Force

RESULTS

Qualitatively, as the hull is pitched, an open separation of the flow is seen to develop at the stern and gradually spread up the body towards the bow. Figure 1 displays the hull stream lines and select vorticity contours for the simulated flow with experimentally matched pitch rate at $t' = 12$. This corresponds to the end of the simulation, with a fixed incidence angle of 27 degrees. The separation line is clearly visible in the hull streamlines, while the formation and growth of the wake vortex is seen in the vorticity contours. This separation and wake vortex dominate the hydrodynamics of the hull, especially the hull normal force and pitching moment.

A plot of the body-frame normal force coefficient comparing the four unsteady simulations and experimental data is shown in Figure 2. It can be seen that both the linear and fitted kinematics simulations under-predict the normal force found in experiment, with the error magnitude increasing with time and thus with angle of incidence. The experimental result also shows two distinct plateaus, which Granlund attributes to separation events at the stern and bow of the hull respectively [1]. While the plateaus in the force data are not seen in the simulated results, the separation events discussed by Granlund are observed at the correct times and locations. As expected, the results at higher pitch rates show increased normal force, due to the greater added mass effects at the higher pitch rates. Similar results were found for the pitching moment, with the simulated results tending to over-predict the experimentally observed moment. Comparison with the steady state data at the corresponding angles of incidence throughout the maneuver shows that at this pitch rate, simulation predicts little effect due to unsteadiness. An analysis of the body normal vorticity moment distribution was also conducted. The results of this analysis showed that during the course of the maneuver, the vorticity moment transitions from a distribution which is characteristic of a steady translation to one which is characteristic of a steady rotation. The progress of this transition was seen to be proportional to the pitch rate and the instantaneous local drift angle along the body.

CONCLUSIONS

Simulations of the unsteady pitching of the DARPA SUBOFF hull geometry were conducted and compared to the experimental results of Granlund and Simpson. This comparison showed that despite the flow appearing qualitatively correct, the predictions for the normal force and pitching moment were under-predicted. Comparisons with steady simulations at varying angle of incidence showed that the unsteady result deviated little from the steady case, indicating little effect from simulation unsteadiness. Future work will investigate the effect of applying large eddy simulation to this maneuver, as well as the effect of the imposed symmetry on the domain. The vorticity moment analysis suggests that the body normal voriticy moment distribution transitions between that of a steady translation and a steady rotation during the maneuver, and that this transition depends on the local drift angle and the pitch rate. This suggests an avenue for exploring lower order models based on predicting the vorticity moment distribution, which merits further investigation for use with vehicle dynamics models.

References

[1] Grandlund K., Simpson R.L.: Experimentally Obtained Forces and Moments on Slender Bodies durng Steady and Unsteady Maneuvers. 47th AIAA Aerospace Sciences Meeting, Orlando Florida, 2009.

*Corresponding author. Email: rdoyle@unb.ca

MOVING GRID FOR LARGE AMPLITUDE BODY MOTION

Mehdi Falsafioon*[1], Ricardo Camarero[2], and François Guibault[3]
[1,2]*Department of Mechanical Engineering, Polytechnique Montréal, P.O. Box 6079, Montréal, QC, Canada, H4T 1J4,*
[3]*Department of Computer Engineering, Polytechnique Montréal, P.O. Box 6079, Montréal, QC, Canada, H4T 1J4,*

Summary A new approach is introduced and developed to generate moving grids for large amplitude rigid body motion. The approach can be interpreted as a solid body moving through, and displacing an existing mesh whose connectivity remains fixed. In this method, the elements ahead of the body are separated and reattached along a trajectory so as to preserve a fixed connectivity and maintain mesh validity. The procedure for the rotation is exactly the same where the grid nodes slide on the solid body during the rotation in order to maintain a fixed connectivity during the rotation.

INTRODUCTION

To achieve unsteady flow simulations with moving boundaries that incorporate the complete details of geometry as well as flow features, numerical algorithms with great fidelity are needed. This has led to the development of algorithms for simulating fluid physics using dynamic mesh generation for both viscous and inviscid flows. Generally, moving mesh generation is a conflicting situation between geometric complexity and algorithm robustness from several aspects points of view like boundaries with concave geometries, boundaries in contact, etc. The early attempts in dynamic grid generation are essentially remeshing techniques based on the new position of the boundaries in each time step (e.g. [1]). This approach can produce meshes of very high quality. However, it is very expensive computationally, as in addition to the actual remeshing, the technique requires the interpolation of the solution at each time step. Mesh motion algorithms with fixed topology have been presented in the literature, with various approaches according to the amplitude of the body motion: spring analogy, radial basis functions, grid deformation using PDE operators etc. However, all these methods finally fail to handle grid motion for large amplitude of motion since the cells remain attached to the boundary. The current work introduces a new method in order to allow the grid nodes to slide on the moving boundaries as particles flowing past the domain boundaries. This was first introduced by [2] where a generic configuration mimics the motion of the real object in the computational space followed by a mapping to physical space using an appropriate operator (e.g. Laplace's equation). In spite of numerous interesting features compared to other mesh motion strategies, this method suffers from a few short-comings. One of the most important weaknesses of the method is mapping the solution from the computational space to the physical space which is obviously costly. In addition, the distribution of the nodes in physical space depends on the choice of the mapping in computational space which is not necessarily compatible with geometry in physical space. Consequently, the current work is an extension of this method to manage the sliding procedure directly in physical space, to remove the previous shortcomings of the method, and to make the approach ready and compatible with any flow solver. Figure (1) shows generated grid for a moving circle passing several bumps. The whole motion can be watched on footage uploaded on [3].

Sliding Method for Translation

In the current work the sliding approach is directly handled in physical space. The procedure can be interpreted as the opening and stitching of a mesh around the moving body and along a defined path. Unlike the previous procedure for sliding method introduced by [2], where it was necessary to rearrange the grid in the leading node in order to generate a valid splitting, in the new approach, the initial grid is generated around the trajectory of the motion. As the topology of the grid is fixed during the entire motion, the edges are adapted to the specified motion and the arbitrary displacement of the body along the trajectory is satisfied with this strategy. The trajectory on the zipping path has two sides which are "inflated" as the body slips through the grid. This requires that the body be represented by its upper and lower sides which connect at the leading node and the trailing node. Therefore these two parts need to be determined together with the trajectory at the beginning of the procedure. Briefly, the procedure consists in the following steps: 1. Prescribing the path of the motion (trajectory) and generating the initial grid; 2. Defining the leading node and the trailing node on the body. This is equivalent to the determination of upper and lower parts of the body; 3. Setting the moving body on the trajectory; 4. Determining the number of time steps (of course this is dependent to the flow solver). 5. Displacing the body based on the time steps. 6. Smoothing the new grid using an appropriate operator. 7. Repeating the procedure from number 5 till to the end point of the motion.

*Corresponding author. Email: mehdi.falsafioon@gmail.com

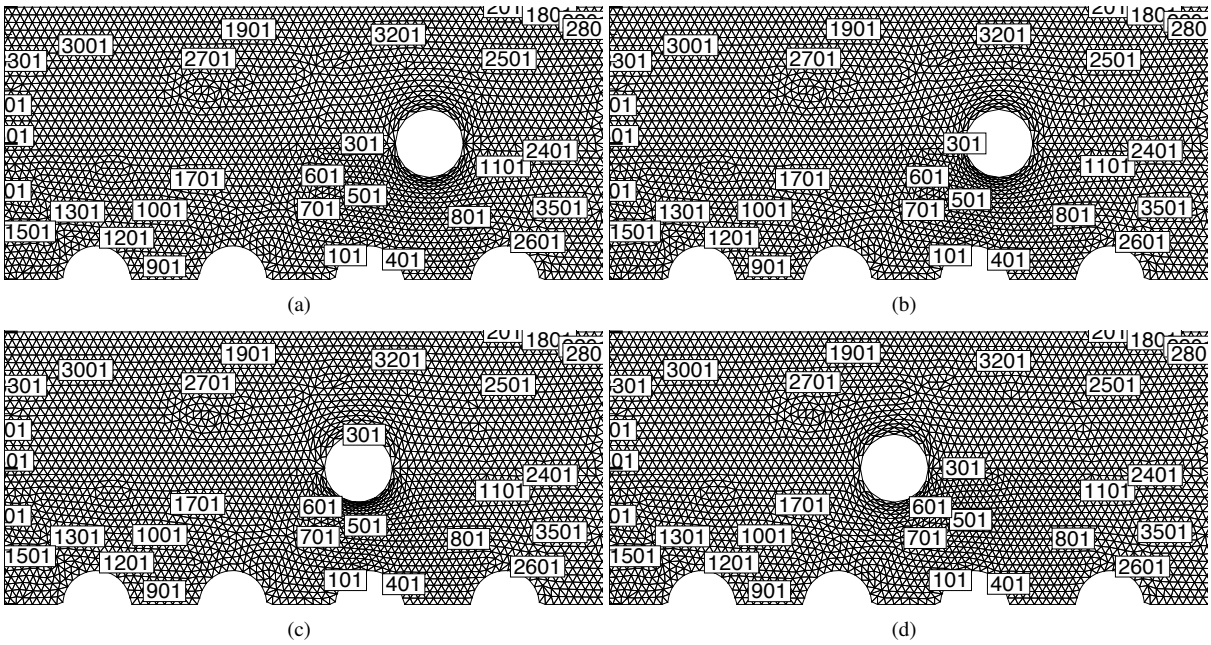

Figure 1: A moving circle passing several bumps

Sliding Method for Rotation

Similar to the translation motion, in the current work rotational motion is managed in physical space. This is to avoid the connectivity changes at each time step which obviously causes additional interpolation procedure for a flow solver. This is one of the major drawbacks of working in computational space which led to a modification for rotation in the present approach. Where, the mesh is constructed based on the geometry in computational space, it may not be well-adapted with the real geometry in physical space. In addition, managing the motion in computational space and then mapping the grid to the physical space with the use of an operator (e.g. Winslow equation) always requires a high number of iterations since at each time step, the grid in physical space does not have any information from previous time step to be used as an initial guess for the next time step. In the present study, working directly in physical space requires fewer iterations for the smoothing procedure since the initial guess comes from the previous time step and is a good approximation for the next time step. This is one of the main reasons of switching back to physical space. Another reason for working in physical space is the fact that smoothing operator does not smooth the grid in physical space but maps the grid from computational space to physical space. Accordingly sliding approach is directly applied in physical space. A step by step algorithm for this approach can be defined as follow 1. Generating the initial grid in physical space including the rotating object with its initial position; 2. Identifying the axis of the rotation; 3. Setting the angle of rotation; 4. Calculating the time step. This is obtained by dividing the entire rotation by the number of steps. The calculation of the time steps is not independent of the flow solver; 5. Rotating the object around the rotation axis based on the calculated time step; 6. Projecting the nodes on the rotating object(s) (boundary nodes) to their new positions based on the new position of the object; 7. Smoothing the mesh with the use of an appropriate smoothing operator. In the current work, Winslow's equation is employed for the configuration with sharp curvature(s) and a barycentric method is used for simpler cases; 8. Iterating the process from number 4 to complete the entire rotation. A footage of a generated grid for a rotating object with the use of presented approach can be found on [4].

References

[1] Zheng, Xiaoming, et al.: Adaptive unstructured volume remeshingII: Application to two-and three-dimensional level-set simulations of multiphase flow. Journal of Computational Physics 208.2 (2005): 626-650.

[2] Arabi, Sina, Ricardo Camarero, and François Guibault. "Unstructured meshes for large body motion using mapping operators." Mathematics and computers in simulation 106 (2014): 26-43.

[3] https://youtu.be/cK_mJzho9KI

[4] https://youtu.be/RB-im_Q6zzM

EFFECT OF GROUNDWATER FLOW ON A GROUND HEAT EXCHANGER

Lazaros Aresti[1], Georgios A. Florides[2a)], Paul Christodoulides[2] & Vassilios Messaritis[2]
[1]*Department of Electrical Engineering, Computer Engineering and Informatics, Cyprus University of Technology, Limassol, Cyprus*
[2]*Faculty of Engineering and Technology, Cyprus University of Technology, Limassol, Cyprus*

Summary Multiple layer underground and the flow of ground water in some layers have an important effect on the heating of vertical heat columns and heat exchangers (HE). This paper investigates the important implication on the design of the Ground HE with regard to their heating effect. For this reason a thermal model is constructed in Comsol Multiphysics software and the effect of various parameters such as thermal conductivity of the ground and the groundwater flow velocity is considered. The model parameters are set to present actual (known) parameters of an installed column and validated against experimental values. Although the key for an overall capital cost reduction is the borehole length, the results indicate that by using the groundwater available, construction of shallow Ground Source Heat Pump systems can be achieved with an increase of the coefficient of performance (COP).

INTRODUCTION

Ground Source Heat Pump (GSHP) systems constitute an evolving technology that has been given significant attention in recent years. GSHP systems have higher energy efficiency and lower environmental impact than regular ones [1]. Geothermal energy, although developed for many years, has not reached a stable and popular state to be widely used. This is due to the high manufacturing and installation cost of Ground Heat Exchangers (GHE) compared to similar, albeit not so effective systems. The capital cost of an air-to-air heat exchanger Heat Pump system is lower than that of a GSHP one, but the operation cost is higher compared to the GSHP system. Only recently the GSHP systems have gained more recognition due to energy shortage uses. It is noted that GSHP installations have increased dramatically in recent years (after 2010) with a rate of 10–30% annually [2].

The closed loop system, either vertical or horizontal, is the most common of the configurations. Pipes can be buried by drilling either vertical boreholes or horizontal trenches. Alternatively, if the building has access to an aquifer, pipes can run all the way down to utilize this natural underground water source. The effect of an aquifer with groundwater flow is examined in this paper through the use of the computational modeling. The model was constructed using the COMSOL v.5.1, which is a computational modeling software package allowing the use of general equations, but also adding and editing equations manually.

MATHEMATICAL MODEL

The three dimensional conservation of the transient heat equation for an incompressible fluid used is given as

$$\rho c_p \frac{\partial T}{\partial \mathrm{t}} + \rho_w c_{pw} u \nabla T + \nabla \cdot \mathbf{q} = Q, \tag{1}$$

where T is the temperature, t is time, ρ is the density of the borehole/soil material, c_p is the specific heat capacity of the borehole/soil material at constant pressure, ρ_w is the density of the ground water, c_{pw} is the specific heat capacity of the ground water at constant pressure, u is the velocity of the groundwater (seepage velocity is being used), Q is the heat source and q is given by the Fourier's law of heat conduction that describes the relationship between the heat flux vector field and the temperature gradient.

COMPUTATIONAL MODELING

The geometry includes five layers of ground with different thickness and thermal properties. Two cylinders represent the boreholes with a total depth of 100 m and a distance between them of 10 m. The geometry and the properties of the ground can be found in Florides et al. [3]. The multilayer ground was constructed with different material properties in order to achieve realistic results and the general model was scaled down on the z-axis. The groundwater velocity was set using the seepage velocity, where the hydraulic conductivity minimum and maximum values were taken from typical data presented in Domenico and Schwartz [4]. The boreholes were set as a heat source with an overall $Q = -40$ W m^{-1}. For presenting a nearly realistic model a pulse function was also applied, by equating the heat source term to 1 (on) for 12 hours and to zero (off) for the next 12 hours, for 7 consecutive days.

RESULTS AND DISCUSSION

By analyzing the borehole results at different regions (Figure 1), it is observed that the temperature decreases with time except in the region of the groundwater flow. This is due to the fact that heat is carried away from the borehole section

[a)] Corresponding author. Email: georgios.florides@cut.ac.cy.

where groundwater is present, while in the other sections heat is accumulated and maintained in the region. In addition, 7 lower peak points are noticeable due to the pulse function applied. The temperature reaches its lower peak point each day in the middle of the day after the 12 hours of continuous heat injection.

By plotting only the minimum temperature points in each borehole (Figure 2), it can be observed that by increasing the groundwater velocity the average surface temperature on the groundwater region increases. The results show that where the minimum hydraulic conductivity is applied (lower seepage velocity) there is not enough groundwater velocity to cool down the boreholes, whereas in the maximum hydraulic conductivity regime the boreholes response with lower average temperature and, in addition, they are reaching steady state in a shorter time. It is also noticeable that in the case of the first borehole, the average temperature reaches a steady state from the first day peak point, whereas on the second borehole (on the downstream) there is an increase in temperature before it reaches steady state again. Further on the heat carried away from the first borehole interferes with the second borehole (on the downstream) when the groundwater velocity is high enough, like in the case of the maximum seepage velocity (vS = 10^{-5} m s^{-1}).

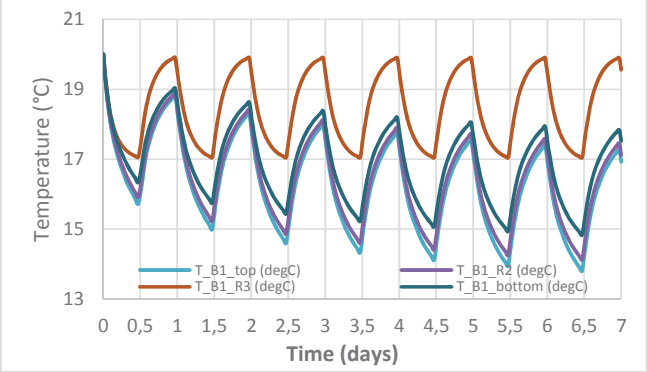

Figure 1. Temperature profiles versus time on the first borehole (B1) for a seepage velocity of vS = 10^{-5} m s^{-1}.

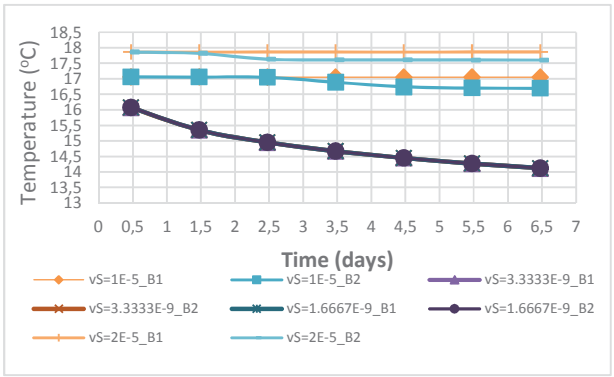

Figure 2. Average Temperature peak points versus time in the region of water flow for various values of seepage velocity (vS).

CONCLUSIONS

In this paper the effect of the groundwater flow on a GHE in heating mode is examined using the Comsol computational modeling. The average borehole surface temperature on every ground layer was calculated with lower and higher seepage velocities. The results indicate that groundwater flow has an effect on the temperature of the ground water flow region. It is also noticeable that in this region steady state is reached much sooner than in the other regions. Additionally, the two boreholes interfere with each other when the groundwater flow velocity is high influencing the downstream borehole temperature.

References

[1] Xiaohui Y., Yufeng Z., Na D., Jianshuan W., Dongwen Z., Jilin W.: Thermal response test and numerical analysis based on two models for ground-source heat pump system, *Energy and Buildings* **66**:657-666, 2003.

[2] Yang H., Cui P., Fang Z.: Vertical-borehole ground-coupled heat pumps: A review of models and systems, *Applied Energy* **87(1)**:16-27, 2010.

[3] Florides G., Theofanous E., Iosif-Stylianou I., Tassou S., Christodoulides P., Zomeni Z., Tsiolakis E., Kalogirou S., Messaritis V., Pouloupatis P., Panayiotou G.: Modeling and assessment of the efficiency of horizontal and vertical ground heat exchangers, *Energy* **58**:655-663, 2013.

[4] Domenico P., Schwartz F.: Physical and chemical hydrogeology, New York: John Wiley & Sons, 1990.

ASSESSMENT OF NUMERICAL MODELLING FOR STEADY STATE JET IMPINGEMENT COOLING IN DIFFERENT GEOMETRIES

Rouzbeh Ghazihesami, and Hoi Dick Ng
Department of Mechanical and Industrial Engineering, Concordia University, Montreal, Quebec, Canada

Summary In this paper, the suitability of Computational Fluid Dynamics (CFD) to evaluate and predict physical phenomena in lieu of experimental work in a jet impingement application is assessed. Previous experimental work looked at the effectiveness of different geometries in improving jet impingement cooling. This work was used to construct a numerical model of two of the geometries each running at three different Reynolds numbers. First a turbulence model is selected based on a simple two-dimensional axi-symmetric jet impingement case. The *k-ω* SST model produced the most accurate results and was thus selected. The model was then used to simulate jet impingement in both a basic flatplate and a corrugated geometry. The corrugated geometry was expected to improve cooling performance. The trend was seen in the numerical results, particularly at higher velocities and at the most downstream jets. The trend replicates that of the experimental results, with negligible impact of the corrugations before the 3-4th jet.

Gas turbines are one of the most effective power generation devices available today. They supply power to many applications, most commonly in aviation and utility power [1]. There is naturally a constant demand for higher fuel efficiency by gas turbine operators. Gas turbine efficiency can be improved by an increase in the turbine inlet temperature. Since these temperatures may exceed materials' allowable temperature, advanced cooling methods are involved [2]. Jet impingement cooling is one such technology and will be looked at more closely in this paper. Since experimental work can be both costly and time consuming, ideally a numerical model would be able to replace or reduce an experimental setup. A comparison is therefore made between experimental results based on available data in the literature [3, 4] to evaluate whether the same trends could be observed in the current numerical model. Two geometries are tested, a flatplate and a corrugated geometry. The geometry is given in Figure 1a. Each geometry consists of 10 inlet holes and a full streamwise length of over 40*D*.

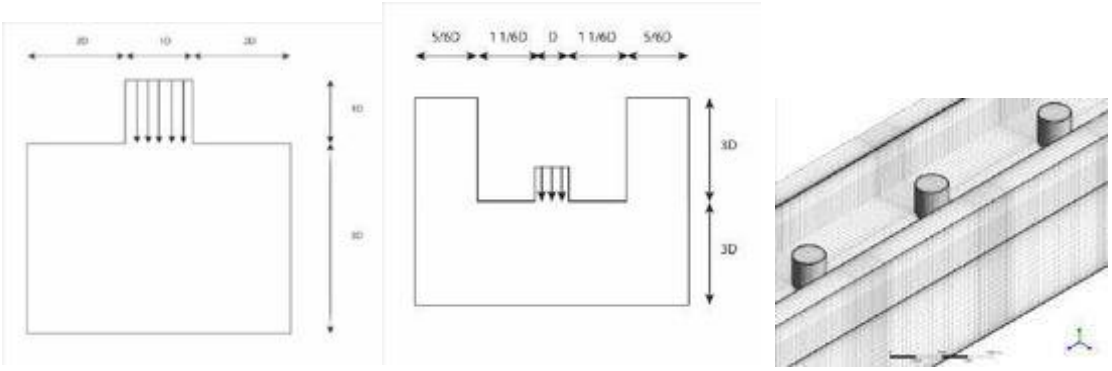

(a) (b)

Figure 1. a) Three-dimensional impingement geometries and dimensions; and b) sample mesh of the corrugated case

To select a numerical model for this study, a two-dimensional (2-D) axi-symmetric case was first simulated for validation. The results were compared to works of previous researchers who had done both numerical and experimental work [5]. The 2-D geometry was drawn in commercial software ANSYS Designmodeler, meshed in ICEM 14.5 and exported to FLUENT 14.5 to be solved [6], see Figure 1b. Three separate meshes were tested to determine the discretization error using the Grid Convergence Index (GCI) method [7], with the intermediate mesh size of 40,000 cells chosen as a sufficient compromise between accuracy and computational resources. The impingement target was set at a constant temperature of 315K with the air inlet at 300K, with the variation in heat flux providing the Nusselt number for comparison to the experimental results. There was a preference for a 2-equation model for the sake of computational efficiency. Of all 2 equation models, the *k-ω* SST model produced the most accurate results and was selected for use in the 3-D models. An example showing the comparison and mesh sensitivity is given in Figure 2. A linear regression analysis done on the two cases with respect to the experimental results over the full surface shows that the *k-ω* SST model fits the data with a R^2 value of 97.01% and standard error of 5.850 while the *k-ε* realizable model has a fit of 94.78% and standard error of 7.644. The *k-ω* SST model is the only 2-equation model that shows the second peak referred to by previous researchers and in the experimental results of Baughn [5], see Fig. 2b.

[a)] Corresponding author. Email: sorena.hessami@gmail.com

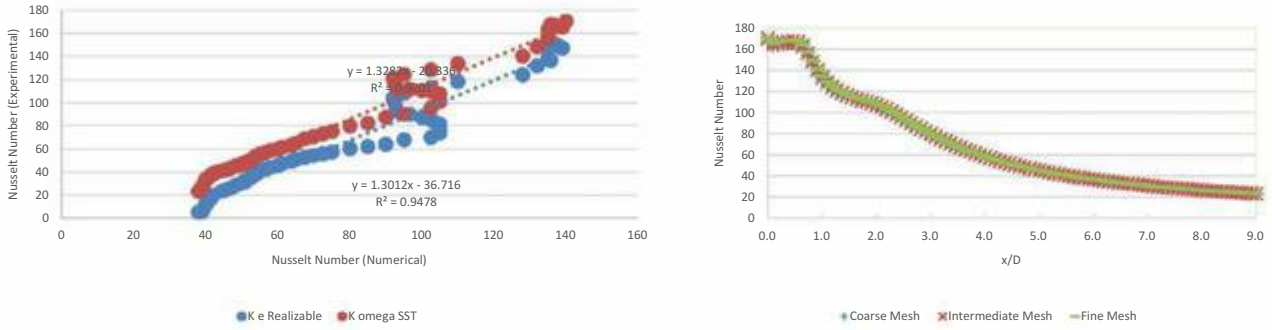

(a) (b)

Figure 2. a) Linear regression analysis for two different turbulence models; and b) the Mesh sensitivity using *k-ω* SST model for the 2-D axi-symmetric case

The same methodology as in the 2-D case was used in the 3-D case, with three separate meshes of roughly 2 million, 4 million and 9 million cells tested for each geometry. All meshes were found to be in the asymptotic range based on the analysis of the order, GCI and discretization errors. As a better compromise between accuracy and available computational requirements in all runs, the 4 million cell mesh was selected for all simulations cases.

Simulations were then run at steady state using the *k-ω* SST model and solutions of the governing equations were approximated using a second-order upwind scheme with the FLUENT solver [6]. Convergence was monitored at the impingement surface, which was 15K higher than the air inlet. Simulations using three Reynolds numbers of 20,000, 40,000, and 60,000 were conducted for each geometry case. As an example, the Nusselt contours of the 20,000 case for both the basic flat impingement case and the corrugated case are given in Figure 3a. The span-wise averaged Nusselt values were obtained to compare to experimental values. 400 lines were scripted to be drawn across the target plate with each line producing an average Nusselt value. Results for the 20,000 Reynolds case can be seen in Figure 3b.

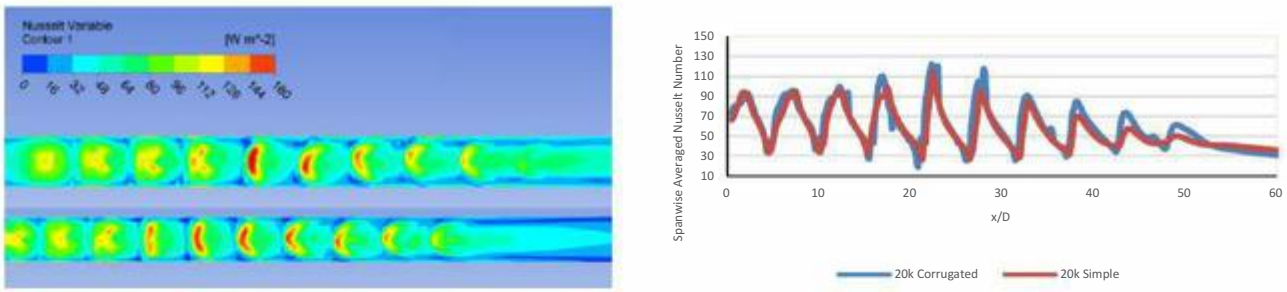

(a) (b)

Figure 3. a) Nusselt contours for flatplate (top) and corrugated (bottom) and b) Spanwise averaged Nusselt values for the two geometries, at Re=20,000

The corrugated geometry had improved cooling performance downstream, as suggested by the experimental results. The numerical model was therefore shown to successfully predict the trend though not the absolute Nusselt values. The cause of the error may be due to lack of turbulence intensity measurement in the experimental setup, which can greatly affect heat transfer. In the above cases, a turbulence intensity value of 5% was imposed at the inlets. Another cause of error may be the imposition of a uniform velocity profile at the inlets and lack of a plenum. The model was nonetheless accurate in replicating the trend seen in the experimental setup.

References

[1] Bathie W.: Fundamentals of Gas Turbines, New York, Wiley & Sons 1984.

[2] Han J.C., Dutta S., Ekkad S.: Gas Turbine Heat Transfer and Cooling Technology, Boca Raton: CRC Press, 2013.

[3] Esposito E.I., Ekkad S.V., Kim Y., Dutta P.: Novel Jet Impingement Cooling Geometry for Combustor Liner Backside Cooling. *J. Thermal Sci. Eng, Appl.* **1** (2), 021001, 2009.

[4] Xing Y., Spring S., Weigand B.: Experimental and Numerical Investigation of Heat Transfer Characteristics of Inline and Staggered Arrays of Impinging Jets. *J. Heat Transfer* **132**, 092201, 2010.

[5] Baughn J.W., Shimizu S.: Heat Transfer Measurements from a Surface with Uniform Heat Flux and an Impinging Jet. *Trans. ASME* **111**, 1096-1098, 1989.

[6] ANSYS Inc, ANSYS FLUENT 14.5 Theory Guide, USA, 2012.

[7] Roache P.J.: Perspective: A Method for Uniform Reporting of Grid Refinement Studies. *J. Fluids Eng.* **116**, 405-413, 1994.

AN IMMERSED BOUNDARY PROJECTION METHOD FOR FLOW OVER MOVING BOUNDARIES

Wei-Xi Huang[a)], Ru-Yang Li, Chun-Mei Xie & Chun-Xiao Xu
AML, Department of Engineering Mechanics, Tsinghua University, Beijing, P.R. China

Summary A revised immersed boundary projection method with the primitive variables is proposed by utilizing a two-step approximate factorization. Two computation sequences derived from the different factorization processes are introduced and compared. Benchmark problems are examined for validation of the proposed method for flow over moving boundaries.

INTRODUCTION

Flow over complex/moving boundaries is frequently seen in nature and engineering, but poses challenges for numerical simulation. As a representative of non-body conformal grid methods, the immersed boundary (IB) method has experienced a fast development during the past two decades [1-3]. Recently, a new IB formulation was proposed by Taira and Colonius [4]. In this method, the additional momentum forcing was interpreted as a Lagrangian multiplier to enforcing the no-slip condition along the IB, similar to the role of the pressure for satisfying the continuity equation of the impressible flow. Thus, the method was referred as the immersed boundary projection (IBP) method, which can be solved by using the approximate factorization [5]. However, it was found that the computational cost of the original IBP method with the primitive variables is high, where a modified Poisson equation needs to be solved by an iteration approach. In the present study, we propose a revised version of the IBP method, aiming at improving the computation efficiency.

NUMERICAL METHOD

The governing equations are the non-dimensional Navier-Stokes (N-S) equations for incompressible flow, which can be written into the matrix form after discretization [4], i.e.

$$\begin{bmatrix} A & H & G \\ E & 0 & 0 \\ D & 0 & 0 \end{bmatrix} \begin{bmatrix} \boldsymbol{u}^{n+1} \\ \delta \boldsymbol{F} \\ \delta p \end{bmatrix} = \begin{bmatrix} \boldsymbol{r}^{n} \\ \boldsymbol{U}_{B} \\ cbc \end{bmatrix} \tag{1}$$

where $\boldsymbol{u}$ is the velocity vector, p is the pressure, $\boldsymbol{F}$ is the momentum forcing applied to enforce the no-slip condition along the IB, $\delta \boldsymbol{F} \quad \boldsymbol{F} \quad \tilde{\boldsymbol{F}}$, and $\delta p = \quad - \tilde{}$, with $\tilde{\boldsymbol{F}}$ and $\tilde{}$ denoting the predictions of $\boldsymbol{F}$ and p respectively. In Eq. (1), the discrete interpolation operator E and the discrete regularization operator H are introduced for velocity interpolation and forcing spreading. Eq. (1) can be regarded as the Karush-Kuhn-Tucher (KKT) system and solved by the traditional fractional step method or equivalently the projection method [5], which can be implemented by utilizing a block-LU decomposition. In the original IBP method [4], the pressure and the momentum forcing are solved simultaneously from a modified Poisson equation by an iteration approach, which is not only computationally expensive but also prone to the convergence error. In order to retain the features of the original N-S solver after incorporating the IB method, especially the efficient Poisson solver for pressure which usually adopts the FFT algorithm, in the present study we propose a two-step LU decomposition of the above KKT system (Eq. (1)) to decouple the pressure and the momentum forcing sequentially from the velocity. Moreover, the three components of the intermediate velocity can be further decoupled by the approximate block LU decomposition [6], which significantly saves the computational cost and memory.

Two computation sequences derived from the different factorization processes are compared: In Algorithm 1, we first decouple δp from the system at the first fractional step and then decouple $\delta \boldsymbol{F}$ decoupled from the velocity field at the second fractional step; In Algorithm 2, the decoupling sequence of δp and $\delta \boldsymbol{F}$ is reversed. Moreover, we tried different schemes in the predicted momentum forcing $\tilde{\boldsymbol{F}}$ at each time step: (1) The simplest form is that $\tilde{\boldsymbol{F}} = 0$; (2) $\tilde{\boldsymbol{F}}$ is obtained by using the velocity of the previous step (3) $\tilde{\boldsymbol{F}}$ is calculated by using the predicted velocity obtained by an explicit advancement of the momentum equation without the forcing term.

RESULTS AND DISCUSSION

A series of cases of flow around the inline oscillating cylinder have been simulated with different computational algorithms and prediction schemes of the momentum forcing. The parameters are set consistent with Dütsch *et al.* [7]. By examining the time evolution of the drag coefficient, it is observed that the computation process has significant impact on the solution while the forcing prediction scheme has only slight influence. The solution obtained by Algorithm 1 is satisfactory except that unphysical oscillations appear at the very beginning stage. On the other hand, unphysical oscillations at the beginning stage can be eliminated by Algorithm 2, but the solution reliability can only be assured by

[a)] Corresponding author. Email: hwx@tsinghua.edu.cn.

using a relatively small computational time step. Moreover, the temporal and spatial accuracy are both between the first order and the second order.

Performance of the present method in the initial transient stage is further tested by simulating a circular cylinder impulsively started in a quiescent fluid, where Algorithm 2 together with the forcing prediction scheme 2 is chosen. The computational configuration is following Taira and Colonius [4] with Re=40. Fig. 1 displays the instantaneous vorticity contours behind the cylinder at t=1.0 and 3.5. We can see that a symmetric vortex pair grows as the cylinder moves. Time histories of the drag coefficient of the impulsively started cylinder is plotted in Fig. 2 for four different computational time steps. For comparison, the result of Taira and Colonius [4] and the analytical solution [8] are also included. As seen in Fig. 2, some differences exist among the results of the four time steps, especially at the beginning time (t < 0.5), while convergence of the results is observed as the time step decreases. The result of Δt=0.0005 agrees very well with that of Taira and Colonius [4] along the whole time and the analytical solution [8] at the very beginning stage, where it is valid.

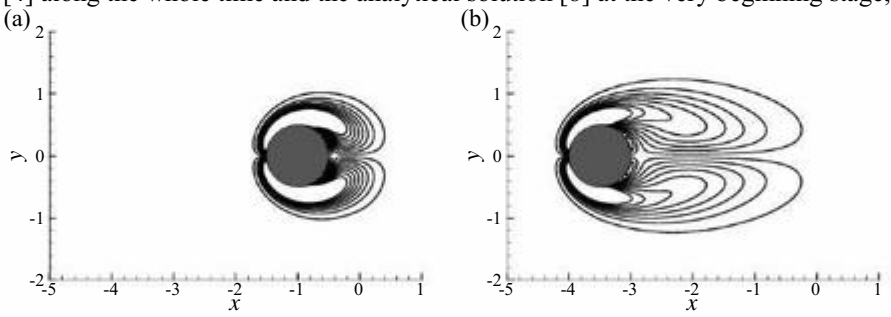

Fig. 1. Vorticity contours around an impulsively started circular cylinder at (a) t=1.0 and (b) t=3.5.

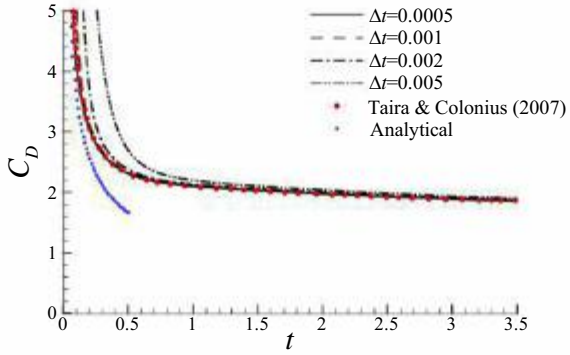

Fig. 2. Time history of the drag coefficient of the impulsively started cylinder.

CONCLUSIONS

In the current study, we presented a revised IBP method with the primitive variables, by utilizing a two-step approximate factorization. Both the pressure and the momentum forcing are decoupled from the system and solved sequentially, while an equation for the momentum forcing is derived. As a result, the computational cost is significantly saved as compared with original IBP method. Two computation algorithms, together with three prediction schemes of the momentum forcing at the beginning of each time step, were proposed and compared. More numerical examples will be presented in the conference, including both 2D and 3D benchmark problems. Furthermore, application of the proposed method to the insect flight problem will also be reported.

References

[1] C.S. Peskin,The immersed boundary method, Acta Numerica 11 (2002) 479-517.

[2] R. Mittal, G. Iaccarino, Immersed boundary methods, Annual Review of Fluid Mechanics 37 (2005) 239-261.

[3] S. Fotis, X.-L. Yang, Immersed boundary methods for simulating fluid-structure interaction, Progress in Aerospace Sciences 65 (2014) 1-21.

[4] K. Taira & T. Colonius, The immersed boundary method: A projection approach, Journal of Computational Physics 225 (2007) 2118-2137.

[5] J.B. Perot. An analysis of the fractional step method, Journal of Computational Physics 108 (1993) 51-58.

[6] K. Kim, S.-J. Baek and H. J. Sung, An implicit velocity decoupling procedure for the incompressible Navier-Stokes equations. International Journal for Numerical Methods in Fluids 38 (2002) 125-138.

[7] H. Dütsch, F. Durst, S. Becker, H. Lienhart, Low-Reynolds-number flow around an oscillating circular cylinder at low Keulegan-Carpenter numbers, Journal of Fluid Mechanics 360 (1998) 249–271.

[8] M. Bar-Lev, H.T. Yang, Initial flow field over an impulsively started circular cylinder, Journal of Fluid Mechanics 72 (4) (1997) 625–647.

CFD-INFORMED UNIFIED CLOSURE RELATION FOR THE VELOCITY OF TAYLOR BUBBLES.

Enrique Lizarraga-Garcia[1], Jacopo Buongiorno *[2], Eissa Al-Safran[3], and Djamel Lakehal[4]

[1]*Department of Mechanical Engineering, MIT, Cambridge, USA*
[2]*Department of Nuclear Science and Engineering, MIT, Cambridge, USA*
[3]*Department of Petroleum Engineering, Kuwait University, Kuwait City, Kuwait*
[4]*ASCOMP, Zurich, Switzerland*

Summary In the mechanistic modeling of slug flow, the Taylor bubble velocity has been determined to strongly affect the predictions of liquid holdup (or void fraction) and pressure gradient. The objective of this work is to improve these predictions through a better Taylor bubble velocity closure relation. Computational Fluid Dynamics (CFD) with Level-Set as the Interface Tracking Method (ITM) are employed to generate a large numerical database of Taylor bubbles in stagnant, upward and downward flow for an ample range of fluid properties and pipe geometries ($Mo \in [1 \cdot 10^{-6}, 5 \cdot 10^{3}], Eo \in [10, 700], \theta \in [-90°, 90°], Re \in [0, 1000]$). The new correlation, obtained using this database, has been applied to those mechanistic models observing higher improvements as the inclination with respect to the horizontal decreases.

INTRODUCTION

Two-phase slug flow occurs often in wells, riser pipes and pipelines of crude oil and natural gas systems. Current predictive methods are based on the mechanistic models, which require the use of closure relations to complement the conservation equations and predict integral flow parameters such as liquid holdup (or void fraction) and pressure gradient. These closure relations carry the highest uncertainties in the model, since they are obtained empirically or through the use of overly simplified assumptions. In particular, significant discrepancies have been found between experimental data and closure relations for the Taylor bubble velocity in slug flow, which has been determined to strongly affect the liquid holdup and pressure gradient calculations.

TAYLOR BUBBLE VELOCITY

Taylor bubble velocity, v_{TB}, in two-phase flow is generally modeled based on the drift flux approach of [5],

$$v_{TB} = C_0 \cdot v_m + v_d, \tag{1}$$

where v_d is the drift velocity of the bubble in stagnant liquid, and $C_0 \cdot v_m$ is the contribution of the mixture velocity, v_m, which is the sum of the liquid and gas superficial velocities, $v_m = v_{SL} + v_{Sg}$, respectively. The distribution parameter, C_0, is a dimensionless coefficient that depends on the velocity profile above the bubble, and is approximately the ratio of the maximum to the mean velocity profile for vertical pipes.

Taylor bubble's dynamics are influenced by the viscous, inertial, gravitational, and interfacial forces acting on it. Assuming that the liquid transport properties are dominant ($\rho_g/\rho_L \ll 1$, $\mu_g/\mu_L \ll 1$, where the subscripts g and L indicate the gas and liquid phases, respectively, ρ is density, and μ is the dynamics viscosity), dimensional analysis indicates the following five Π dimensionless groups are sufficient to determine the bubble dynamics: the Froude number, $Fr = v_{TB}^2/\sqrt{gd}$, where g is the gravitational acceleration and d is the pipe diameter; the Eötvös number, $Eo = \rho_L g d^2/\sigma$, where σ is the surface tension; the Morton number, $Mo = g\mu_L^4/(\rho_L \sigma^4)$; the liquid flow Reynolds number, $Re = \rho_L v_{SL} d/\mu_L$; and the inclination angle, θ.

Most multiphase models and correlations were developed based on and for low viscosity fluids. However, the oil and gas industry is currently moving towards the production of heavier oils. High density and high viscosity oils currently constitute nearly 70% of the available reserves in the world, increasing the need to gain and improve the knowledge of the flow behavior of these fluids. Furthermore, the combine effect of θ and Eo on the distribution parameter, C_0, needs further investigation.

The primary objective of this work is obtain Fr as a function of the other dimensionless numbers, $Fr = f(Eo, Mo, Re, \theta)$, for an ample range of fluid properties and pipe geometries.

CFD MATHEMATICAL MODEL

3-D CFD simulations have been performed with the CMFD code TransAT [6], a finite-volume software developed at ASCOMP. The code uses structured meshes and MPI parallel-based algorithm to solve multi-fluid Navier-Stokes equations. Computer resources for this work include the supercomputers of the Oak Ridge Leadership Computing Facility at the Oak Ridge National Laboratory. The code has been validated with experiments and correlations [3] (see blue circle cases ( ) in figure 1a). Simulations are initialized with the bubble in still water. Furthermore, for inclined pipes it is assumed that the thin film formed between the bubble and the pipe in its upper part exists, based on our proposed breakup criterion (figure 1b, [4]).

*Corresponding author. Email: jacopo@mit.edu

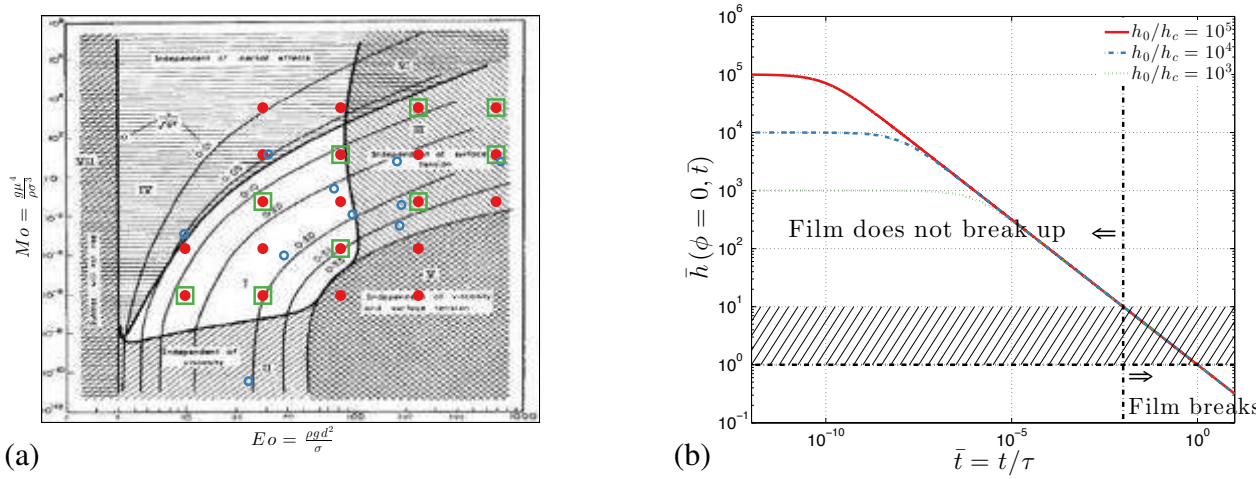

Figure 1: (a) Database for Taylor bubbles in stagnant liquid ( ), database for upward and downward flow (□), and cases used to validate the CFD code ( ), located in the map of [8]; (b) thin film drainage model and breakup criterion used in the inclined pipe simulations [4] .

NUMERICAL DATABASE

Our correlation covers from low to high viscosity oils ($Mo \in [1 \cdot 10^{-6}, 5 \cdot 10^{3}]$). Furthermore, Eo covers the whole range under which Taylor bubbles exist: $Eo \in [10, 700]$. The database text matrix is shown in figure 1a. The cases for stagnant liquid are depicted in red circle ( ), for which seven inclination angles ($5°, 15°, 30°, 45°, 60°, 75°, 90°$) are simulated. The cases for liquid flow are depicted in green square (□), for which six inclination angles ($\circ\, 90°, \circ\, 45°, \circ\, 5°, 5°, 45°, 90°$) and several liquid velocities ($Re \in [0, 1000]$) are simulated.

PROPOSED CORRELATION AND RESULTS

The proposed correlation for the terminal velocity in stagnant liquid, based on the procedure followed by [2], is

$$Fr/Fr_v = (1 + \cos\theta)^{Eo^{0.019} Mo^{0.0028}} \sqrt{\sin\theta}, \tag{2}$$

where F_v is obtain with the model of [7]. Equation 2 improves the velocity prediction of current correlations, and widens the dimensionless numbers range of applicability. Furthermore, it improves the prediction of the pressure drop by 2.1% for $\theta = 90°$, 5.9% for $\theta = 60°$, 11.3% for $\theta = 30°$, and up to 23.5% for $\theta = 15°$, using the modified mechanistic model of [1]. The correlation for upward and downward liquid flow is still under development.

CONCLUSIONS

A new approach to improve the prediction of mechanistic models through the use of CFD has been taken. A wide database of Taylor bubbles in round pipes has been generated, from which a unified correlation of their terminal velocity in stagnant liquid is obtained. The correlation improves the pressure drop prediction greater with lower inclination angles.

References

[1] A. M. Ansari, N. D. Sylvester, C. Sarica, O. Shoham, and J. P. Brill. A Comprehensive Mechanistic Model for Upward Two-Phase Flow in Wellbores. *SPE Production and Facilities*, 9(2):143 – 151, 1994.

[2] A. Hasan and C. Kabir. Predicting Multiphase Flow Behavior in a Deviated Well. *SPEPE*, 3(4):474–482, 1988.

[3] E. Lizarraga-Garcia, J. Buongiorno, E. Al-Safran, and D. Lakehal. Development of a new CFD-based unified closure relation for Taylor bubble velocity in two-phase slug flow in pipes. In *17th International Conference on Multiphase Production Technology, Cannes, France*. BHR Group, June 2015.

[4] E. Lizarraga-Garcia, J. Buongiorno, and M. Bucci. An analytical film drainage model and breakup criterion for Taylor bubbles in slug flow in inclined round pipes. *International Journal of Multiphase Flow*, Under review.

[5] DJ Nicklin, JO Wilkes, and JF Davidson. Two-phase flow in vertical tubes. *Trans. Inst. Chem. Eng*, 40(1):61–68, 1962.

[6] TransAT®. *version 5.1.1*. ASCOMP GmbH, Zurich, Switzerland, 2014.

[7] Flavia Viana, Raimundo Pardo, Rodolfo Yanez, Jose L Trallero, and Daniel D Joseph. Universal correlation for the rise velocity of long gas bubbles in round pipes. *Journal of Fluid Mechanics*, 494:379–398, 2003.

[8] E. T. White and R. H. Beardmore. The velocity of rise of single cylindrical air bubbles through liquids contained in vertical tubes. *Chemical Engineering Science*, 17(5):351–361, 1962.

AVT-251: A PARAMETRIC STUDY OF MODIFIED SACCON GEOMETRY

Ryan Maye[1a)], Brodie Torunski[1], Dr. Tiger Jeans[1] & Dr. Andrew G. Gerber [1]
[1]*Department of Mechanical Engineering, University of New Brunswick, Fredericton, NB, Canada*

Summary The North Atlantic Treaty Organization (NATO) has been tasked with completing a "Multi-Disciplinary design and performance assessment of effective, agile NATO Air Vehicles" which has been denoted the AVT-251 task group [1]. One of the goals of this subgroup, denoted the *"Aerodynamic Shaping group"*, is to determine how the overall leading edge shape effects the aerodynamic characteristics. This paper presents an initial parametric study focused on mesh development. The tasks were: 1) validate the CFD predictions for the latest unmanned combat aerial vehicle (UCAV) shape against previous experimental results, and 2) design and test a meshing topology to be used for future parametric studies. Preliminary simulations were run at M=0.2 and $\alpha = 10^0$ and 14^0 . Both the lift and drag coefficients correlated very well with previous results and pressure coefficient values were almost identical. The initial success of the simulations allows for continued validation and development of the mesh topology.

SIMULATION PARAMETERS

Geometry

The geometry of the SACCON has a great effect on the mesh creation process. The initial SACCON geometry used for previous AVT task groups can be found in the top of Figure 1.Three different air foil shapes were used at various sections along the UCAV, having varying shapes and chord lengths. The planform is a 1/10 scale model of the full SACCON geometry. The bottom portion of Figure 1 is a representation of the new planform shape used for simulations in the AVT-251 task group. This geometry has a different trailing edge sweep, 30^0, where the original designed used a consistent 53^0 sweep around the entire aircraft. The new planform geometry is for the full scale UCAV [2].

A structured mesh was used on this UCAV geometry, as it would allow for more control around the aircraft body. Due to the drastic variations in leading edge shape, it was impossible to create a mesh with both good minimum included angle values and proper aspect ratios. A delicate balance was met, ensuring that both the aspect ratios and minimum included angles were acceptable, in order to properly run in EXN/Aero. This resulted in a mesh with approximately 24 million cells. An initial grid spacing of 8mm around the aircraft body was set in order to reduce the overall skewness. Very few previous studies of the SACCON geometry used a structured mesh, due to the shear complexity of the aircrafts geometry. In order to reduce overall simulation time it was deemed more advantageous to run the CFD tests on half the UCAV, with a symmetry plane set at the root chord.

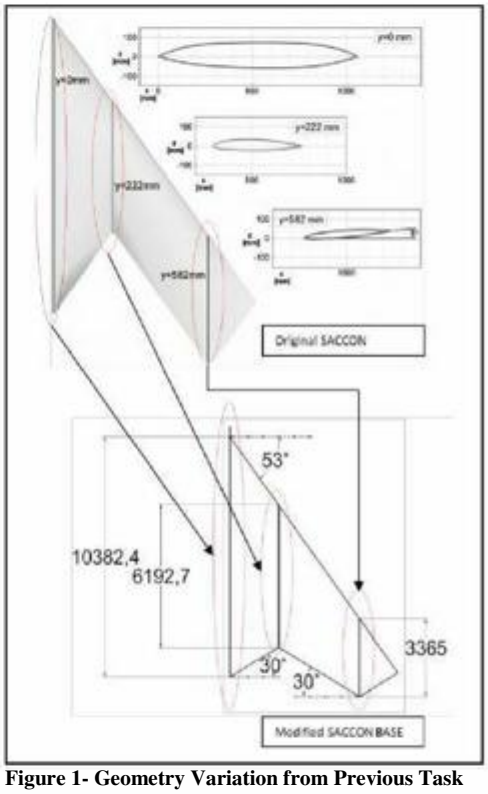

Figure 1- Geometry Variation from Previous Task group (AVT-161)

Flow Conditions and Simulation Parameters

Although it is anticipated that this UCAV will operate at both subsonic and supersonic speeds, this preliminary EXN/Aero test was subsonic flow at Ma=0.2. The focus is in the region where the pitching moment coefficient becomes inconsistent and sporadic (see Figure 4), occurring at an angle of incidence range of 10^0 to 20^0. The results shown are for $\alpha = 10^o$ and 14^0. The simulations were run at sea level conditions with a given $Re_\infty=50x10^6$ and an air density of 1.225 kg/m^3. Further simulations will be completed from $\alpha = 12^{\circ}$-20°, in order to fully understand the flow physics of this new planform shape.

The time step was set to $\Delta t = 0.001$sec with a total run time of 4.3 seconds for both simulations, using double precision blocks in the near field of the aircraft geometry, but single precision in the far-field, a capability found in EXN/Aero to optimize the use of GPU memory. Obtaining results employed the use of 6 CPUs and 4GPUs on a server system comprised of Intel Xeon E5-2600 processors and NVIDA Tesla K80 GPUs. EXN/Aero is a recently developed CFD solver designed specifically for use on many core hardware [3].

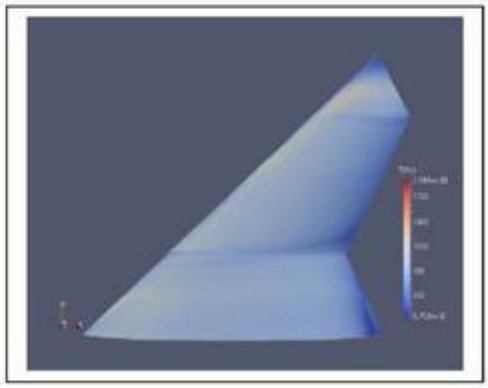

Figure 2- Y+ results around Surface

a) ryan.maye11@unb.ca,

SIMULATION RESULTS

Mesh Quality

The y+ results around the surface of the UCAV body can be found in Figure 2. As suspected the values are exceedingly high, ranging from 60 to an excess of 2000 in some very limited regions. This is due to the fact the initial distribution height off the body was set to be roughly 7mm, when the boundary layer height estimate was determined to be $\delta = 0.0119$mm, roughly 600 times smaller than the chosen value. Fortunately, this poor y+ estimate did not have a significant effect on the overall results, as the poor values were in such a localized region. Future work will require the proper y+ value of at most 1, for proper boundary layer resolution. Other important mesh quality parameters are: aspect ratio and skewness with the maximum values being 3665 and 0.84, respectively.

Pressure Results and Comparison

Prediction and Validation of Aerodynamic Characteristics for a Generic UCAV Configuration with Trailing-Edge Flaps is a report completed by Young et al. [4] that simulated flow over a 53^0 trailing edge sweep UCAV for the NATO AVT-201 task group. These simulations were conducted at 50 m/s[3]. Simulations were run on a 1/10 scale model of the original UCAV planform shape shown in Figure 1.

Figure 3 compares the results obtained in the EXN/Aero simulations (A) against the results obtained by Young et al. at an angle of attack of 10º(B). The important flow features include: a low pressure region on the leading edge of the aircraft, and a high pressure region at the tip and tail region of the aircraft.

As can be seen in Figure 3, a coefficient of pressure of approximately 0.3 is obtained at the nose and tail, and approximately -2 along the leading edge. Overall, it can be seen that the resultant pressure distribution has a strong correlation with work done by Young et al. Furthermore, it should be noted that work done by Young et al. was conducted with a tailing edge sweep of 53˚, while the new results were conducted on a 30˚ trailing edge sweep UCAV geometry.

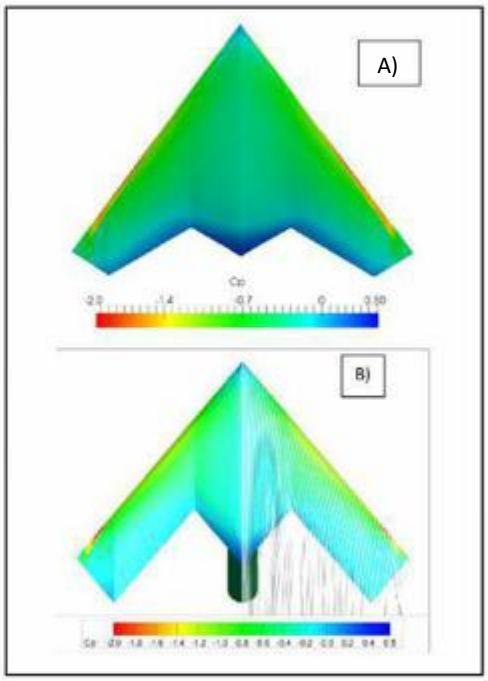

Figure 3- Pressure Coefficients. A) Xn/Aero B) Previous AVT-201 Simulations ($\alpha = 10^0$)[3]

Lift and Drag Results

The lift coefficient was found to be $C_L = 0.47$ and the drag coefficient was found to be $C_D = 0.039$ at $\alpha = 10^\circ$ and at $\alpha = 14^\circ$ $C_L = 0.56$ and $C_D = 0.076$. All the coefficients determined with EXN/Aero were integrated into a plot created by Loeser et al. (Figure 4). Loeser et al. conducted actual experiments on a model SACCON over a wide range of angles of attack with a Ma=0.15, close to the completed simulation values, making a qualitative comparison possible. As can be seen, the experimental data found by EXN/Aero shows a strong correlation with the data obtained by Young et al [4].

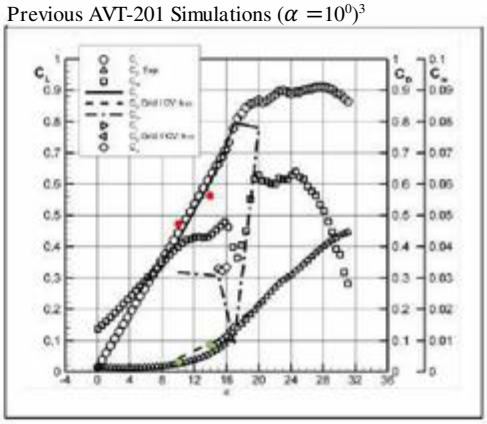

Figure 4- Lift and Drag Coefficients plotted against Experimental Results [1]. Red-Lift, Green-Drag.

CONCLUSIONS

Based on the close correlation between both experimental and previous CFD results, it can be conclude that these initial simulations were successful. In the future further refinement will be made to the mesh in order to improve the y+ values. More simulations will be completed at higher angles of attack, a requirement in order to better understand the new UCAV baseline flow characteristics.

References

[1] Schutte A., Cummings .R, "Multi-Disciplinary design and performance assessment of effective, agile NATO Air Vehicles," AVT 251 NATO presentation, published 2015

[2] Schutte A., Hummel. D and Hitzel. S, "Flow Physics Analyses of a Generic Unmanned Combat Aerial Vehicle Configuration," Journal of Aircraft, published November 2012; Vol. 49, DOI: 10.2514/1.C031386

[3] Gerber A., Wilcox K., Zhang J., "Benchmarking of a Massively Parallel Hybrid CFD Solver For Ocean Applications," ASME 32nd International Conference on Ocean, Offshore and Arctic Engineering, June 9-14, 2013.

[4] Young M., Cummings R., Jirasek A., et Al., "Prediction and Validation of Aerodynamic Characteristics for a Generic UCAV Configuration with Trailing-Edge Flaps," AIAA Aviation 32nd Applied Aerodynamics Conference, June 2014.

NUMERI AL SIM LATION F HYPE SONIC F OW OVE RE-ENTRY SPAC VEHICL

I an Egorov [1] Natalia Palchekovskay [1,2a)]
[1]*H personic de artment, Ce tral Aerohy rodynamic nstitute, Zhukovsky, Mos ow region, Russia*
[2]*Moscow Institute of hysics and echnology, olgoprudny, Moscow re ion, Russia*

Summary In t is work numerical simulation of flow over Martian space probe at wind tunnel conditions, corresponding to Mach numb rs M = 7.5, 10.5 and 14 for vari us angles of a tack (AoA) is arried out. Parallel computin is fulfilled on supercomputer using multiblock grids. Computational grids o various dimensions are used for verificatio of results. Comparison of b sic flow chara teristics, such as pressure coefficient and Mac number, for various flow regimes is implemented. Validation of numerical results using xperimental d ta is carried out.

I TRODUCT ON

There are urrently a lot of projects on developme t of re-entry vehicles for planet explor tion. Many of these proje ts involve experimental and theoretical studies for development of sp ce vehicles f r Mars inves igation. Main purpose of t is research is the develop ent of spa e probes f r various a plications. sually they represent strongly blunted axisymmetri al bodies, c ntour of which in meridional section is construct d from seg ents of ele entary curv s. Aerodynami characteristi s and aerodynamic heatin of a space robe during its motion in he planet at osphere can be determined by equations f viscous gas dynamics, hich can be solved numerically with high accuracy using softw re packages.

MERICAL IMULATION AND RES LTS

In this work numerical imulation of flow over M rtian space probe at wind tunnel conditions, corresp nding to Mach numbers M 7.5, 10.5 and 14 for various angles of attack, is carried out on basis of Navie -Stokes equa ions, which re solved using in-house sof ware packag HSFlow with possibility of distribute computing on multiproc ssor comput rs [1, 2]. It is assumed that temperature of the model surface is constant - T_w = 300 K. These flo regimes correspond to fl w parameters nd the model scale in h personic wi d tunnel T-117 of TsA I. Comparis n of numerical results and experimental data allows obtaining accuracy evaluation for results of mathematical simulation.

Calculations are fulfille on structured orthogonal computation l grids, consisting of 4 illion and 32 million nod s. Grids are clustered near the surface in order to resolve boundary l yer. In addition, for parall l calculation grid is splitted on smaller blocks, total amount of blocks – 96 and 38 correspondi gly.

Analysis of results is carried out using all test regimes in wind tunnel. In Figure 1 Mach numbe patterns with streamlines or angles of att ck 0°, 10°, 2 ° are given. hese patterns illustrate ho flow changes depending n angle of attack. E.g., it can be seen that rear separation zone shifts t ward leewar side of the v hicle with angle of attack increase.

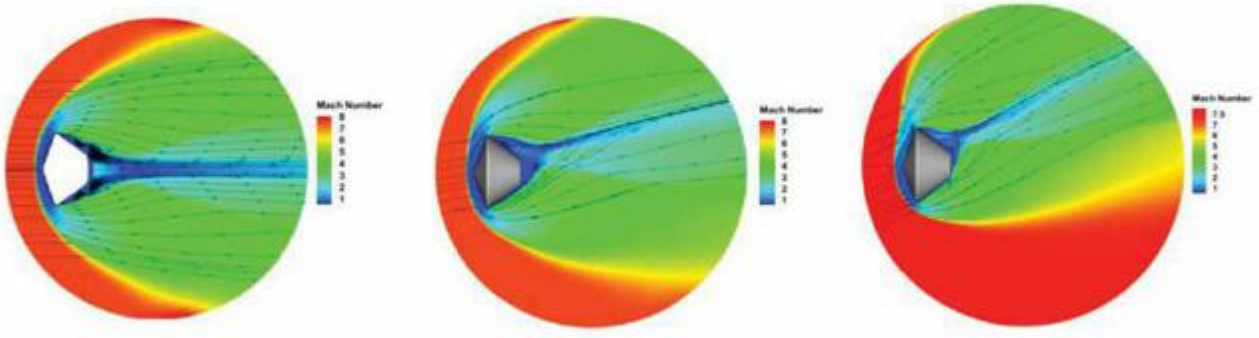

a b c

Figure 1. Mach num er fields at M = 7.5: a – A A = 0°, b - A A = 10°, c - oA = 25°

[a)] Corresponding author. Email: **nathalie.palchekovskaya gmail.com.**

In Figure 2 distribution of pressure coef icient along y coordinate fo three angles of attack at fixed Mach num er is shown. s seen from t ese dependencies, angle of attack ap reciably affects pressure coefficient behavior on l eward surfa e. Nonmonotonic behavior of pressure coefficient is specified the ve icle surface shape, which as curvature discontinuity at point of spherical and coni al parts conj nction.

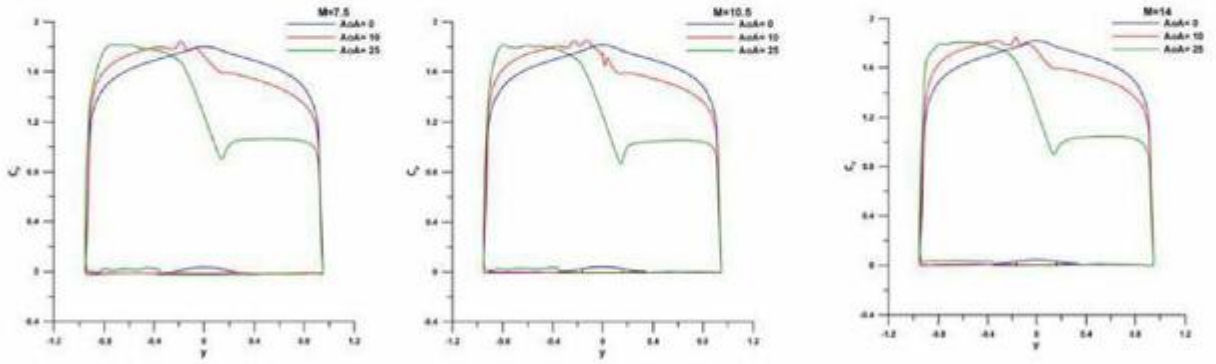

a b c

Figu e 2. Pressure oefficient dis ribution: a – $_\infty$ = 7.5, b - $_\infty$ = 10.5, c - $_\infty$ = 14

ONCLUSIONS

Numerical imulation of ypersonic flo over space ehicle is carri d out. Accor ing to calcul tions, in hyp rsonic flow the blunted edge is streamline without sep ration, and b undary layer separation occurs downstr am on the conical surface; in the global separation zone velocities achieve supersonic values, a d inside sho k wave is generated in th vicinity of the backward stagnation point. Back separation zone shif s closer to le ward surface with increase of the angle of attack. An le of attack has strong effect n values of pressure coefficient on the leeward surfac .

The reporte study was funded by RFBR according to the research project No. 16-38-00274 ол_а.

References

[1] Bashkin, V.A., and Egorov, I.V.: Numerical imulation of prefect viscous gas flow, Moscow: Fi matlit, 372 p., 2 12 (in Russian).

[2] Novikov A., Fedorov A., Egorov I.: Numerical simulation of three-dimensional wave packet in supersonic flo over a compre sion corner. AI A Paper 2015-2624, 2015.

FLOW FIELD RECONSTRUCTION FOR HOLE-PATTERN SEALS USING REDUCED ORDER MODELING

Alexandrina Untaroiu[1a)], Hanxiang Jin [1]& Wei Wei [2]
[1] *Dept. of Biomedical Engineering and Mechanics, Virginia Tech, Blacksburg, Virginia, United States*
[2] *School of Mechanical Engineering, Beijing Institute of Technology, Beijing, China*

Summary In annular pressure seals used in turbomachinery, the leakage of working fluid is reduced by the acceleration-deceleration effect of the fluid through a convoluted path. In order to better understand the mechanism that governs the leakage rate, this study proposes the utilization of Reduced Order Model and snapshot techniques. The goal is to study the energy distribution of the flow field by replacing a huge number of governing PDEs with only a few ODEs, to describe a complex system. As the results indicate, the first few modes contain the majority of the energy, therefore only these first few modes are needed to recreate the flow field. It is shown that energy distribution is concentrated on the clearance region. Considering that seal design studied is not efficiently using the space inside the grooves, a potential improvement from the energy flow point of view can be carried out to increase seal performance.

INTRODUCTION

Non-contact annular seals are widely used in turbomachinery to provide minimum leakage of the working fluid. A small clearance region exists between rotor and stator surfaces to avoid contact and keep the system stable, and thus a small amount of fluid leakage is inevitable. The leakage of working fluid is reduced through the acceleration and deceleration effect of the fluid through a convoluted path. For better performance of the non-contact annular seals, the study of the leakage path geometry is important since the leakage rate is significantly affected by the geometry.

Seal performance is typically calculated using bulk-flow method, CFD analysis, or a combination of the two [1]. The previous works on hole-pattern seals mostly connect the leakage rate and rotor dynamic coefficients to the geometry of the grooves directly. However the analysis of energy distribution can be used to improve the seal performance by providing insight into the underlying physical mechanisms. This paper focuses on the use of the method of Reduced Order Model (ROM) and snapshot techniques to understand the energy distribution of different elementary modes in control volume of working fluid of hole-pattern seals.

METHODOLOGY

In fluid dynamics, Reduced Order Modelling (ROMs) techniques have been widely used to describe a complex system with a few ODEs instead of a huge number of governing PDEs [2]. For a scalar function $u(\boldsymbol{x},t_i)$, i=1,2,…M, the time-average of the sequence can be defined by summation of time-dependent orthogonal amplitude coefficients $a_k(t)$ multiplied with time-independent orthogonal basis functions $\phi_k(x)$, which is $\bar{u}(\boldsymbol{x}) = \sum_{i=1}^{M} a_k(t)\phi_k(x)$. $\phi_k(x)$ and $a_k(t)$ are extracted using Proper Orthogonal Decomposition (POD) method to reconstruct the function. The optimum condition can be reduced to eigenvalue problem, and the snapshots method is used to find the eigenvector of ROM (ϕ_k), from which the eigenvectors can be written as a linear combination of the data vectors. Once the eigenvectors of matrix are calculated, the POD modes are derived, and the Galerkin procedure can be used to reduce a set of PDEs to a smaller set of ODEs. For flow field captured by POD of numerical simulation or experimental measurement, the relative energy of kth mode is defined by $E_k = \lambda_k/E = \sum_{j=1}^{M} \lambda_k$, where E is the total energy.

Computational Model The hole-pattern seal in this study is selected from the literature [3,4]. As shown in Fig.1, the grooves on the stator are evenly distributed in axial and circumferential direction. The repeated pattern allows to model only a sector of the seal using cyclic periodic boundary condition to reduce simulation time. A CFD model consisting of approx. 1 million grid elements is generated using ANSYS-Mesh (Fig. 2).

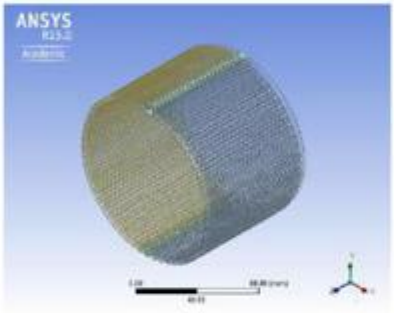

Figure 1. Hole-Pattern Seal Model- Fluid Domain

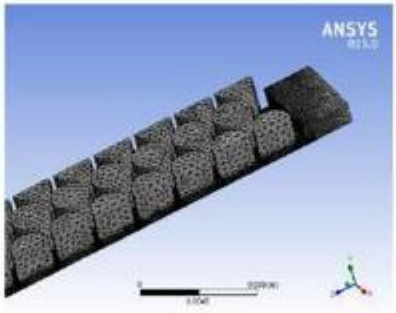

Figure 2. Computational Model

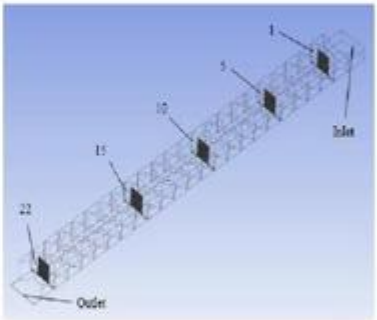

Figure 3. Five Representative Axial Locations

Numerical Modelling A transient flow simulation is then performed in ANSYS-CFX to calculate the leakage rate and flow field velocity distribution. The rotational speed of the rotor is set to high angular velocity with perturbation of 1/400 of the velocity ($n = (\quad + \quad \cdot \quad \pi ft)$ rpm). The perturbation frequency f is 60 Hz. In each cycle, 100 time steps are used for accurate POD snapshot. The sampling frequency is therefore 6000 Hz. The pressure at the inlet is set as 70 bar, and the

[a)] Corresponding author. Email: alexu@vt.edu

pressure ratio between outlet and inlet is 0.45. The isothermal heat transfer option and the $k-\varepsilon$ turbulence model in conjunction with a scalable wall function are selected. The air inlet temperature is set to $17.4\ ^{\circ}C$ as measured in the tests [3]. By using the ROM method described above, the flow field is deconstructed in elementary modes and their corresponding energy levels.To understand the flow pattern in the annular seal, five representative grooves (groove 1, 5, 10, 15, 22, shown in Fig. 3, are analysed with individual POD basis functions of velocities and their combination.

RESULTS

Velocity profile data is extracted for each of the 22 grooves along the axial direction of the seal in CFX-Post. These grooves are numbered by their distance from the inlet, from 1st to 22nd. The CFD results of velocity field are then used for the POD analysis. Fig. 4 shows the reconstructed flow pattern for section 1 using all modes Φ1~100 and only the first three Φ1~3, while Fig.5 shows the velocity vectors reconstructed at various axial locations along the seal. It can be seen that velocity magnitude and energy concentration are much higher in the jet flow region, which is the area near the rotor surface. The energy of all 100 modes are illustrated in Fig. 6. The first mode energy is much higher compared to other modes for both cases (groove and jet region together case and groove region only case). As the mode number increases, the energy of corresponding mode drops exponentially. As a result, only a few modes are required to reconstruct the entire flow pattern. Furthermore, if the same mode energy is compared for two different cases, it has been shown that the energy near the rotor surface is about one order of magnitude higher than the energy inside the groove. The results from the energy plots for all modes are consistent with the flow pattern reconstruction.

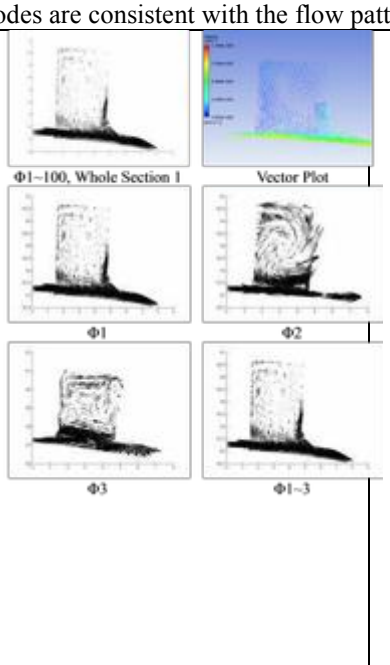

Figure 4. Flow pattern-Reconstructed vs. CFD for section 1

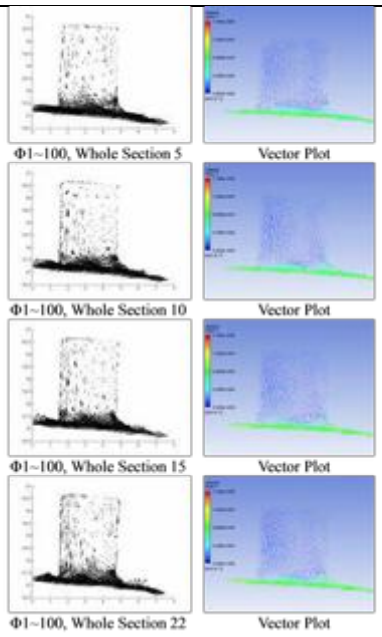

Figure. 5 Flow pattern-Reconstructed vs. CFD for section 15,10,15,22

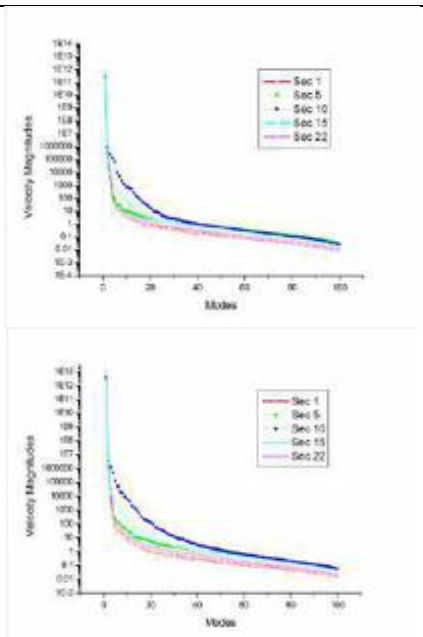

Figure. 6. Velocity magnitude (energy) plot for all modes a) groove and jet region, b) groove region only

CONCLUSIONS

The flow field in hole-pattern seals can be precisely reconstructed from energy decomposition by POD snapshots technique. The details of the velocity profile inside the grooves are accurately reassembled from the relative energy of elementary modes. The first few modes contain the majority of the energy, so only these first few modes are needed to illustrate the flow field. The energy concentration is much higher in the clearance region, therefore the groove depth is not efficiently used. Considering that the current hole-pattern seal design is not efficiently using the space deep inside the cavities, a potential performance improvement from the energy flow point of view can be carried out. The geometry could be adjusted to let energy flow more easily into the inner space of grooves and this might be achieved by tilting the groove orientation away from the normal of rotor surface.

References

[1] Migliorini P.J., Untaroiu A., Witt W.C., Morgan N.R., Wood H.G.: Hybrid Analysis of Gas Annular Seals with Energy Equation. *ASME. J. Tribol.* 136(3):031704-9, 2014.

[2] Cizmas, P. G. A., Palacios, A., O'Brien, T., Syamlal, M.: Proper-Orthogonal Decomposition of Spatio-Temporal Patterns in Fluidized Beds. *Chemical Engineering Science* 58(2003), 4417 – 4427, 2003.

[3] Childs, D. W., Wade, J.: Rotordynamic-Coefficient and Leakage Characteristics for Hole-Pattern-Stator Annular Gas Seals-Measurements versus Predictions. *ASME J. Tribol.* 126(2), 326-333, 2004.

[4] Untaroiu, A., Liu, C., Migliorini, P. J., Wood, H. G., Untaroiu, C. D.: Hole-Pattern Seals Performance Evaluation Using Computational Fluid Dynamics and Design of Experiment Techniques. *ASME J. Eng. Gas Turbines Power* 136(10), 102501, 2014.

FM14 - Turbulence

TS.FM14-1.01	Oberlack, Martin - Circumnavigating the closure problem of turbulence- A lie symmetry approach (INVITED)	1393
TS.FM14-1.02	Tatsumi, Tomomasa - Statistical normality of homogeneous isotropic turbulence	1395
TS.FM14-1.03	Okamura, Makoto - A Lagrangian closure approximation for homogeneous isotropic turbulence	1397
TS.FM14-1.04	Pollard, Andrew - Hot-wire spatial resolution effects in measurements of turbulent round jets	1399
TS.FM14-1.05	Nedić, Jovan - Energy dissipation scaling in uniformly sheared and in multi-structure turbulence	1401
TS.FM14-1.06	Kobayashi, Hiromichi - Energy transfer across scales around elliptic Burgers vortices	1403
TS.FM14-2.01	Lalescu, Cristian - Characterizing multi-scale interaction in turbulence	1405
TS.FM14-2.02	He, Guosheng - Multi-resolution Analysis of the Turbulent Boundary Layer with Orthogonal Wavelet and Pod	1407
TS.FM14-2.03	Buxton, Oliver - Concurrent scale interactions in a turbulent shear flow	1409
TS.FM14-2.04	Matsumoto, Takeshi - Mean-flow reversals in a two-dimensional randomly forced flow in a square domain	1411
TS.FM14-2.05	Toschi, Federico - Turbulence on a fractally decimated Fourier set	1413
TS.FM14-2.06	Alves Portela, Felipe - Scale by scale energy budget in the near wake of a square cylinder	1415
TS.FM14-3.01	Irvine, William - Conservation and flow of helicity across scales in reconnecting vortex knots and links (INVITED)	1417
TS.FM14-3.02	Sahoo, Ganapati - Effects of helicity on the energy transfer in three-dimensional turbulence	1419
TS.FM14-3.03	Obligado, Martin - Interaction of two high Reynolds number axisymmetric turbulent wakes	1421
TS.FM14-3.04	Yeung, Pui-Kuen (P.K) - Extreme Events and Acceleration Statistics at High Reynolds Number (INVITED)	1423
TS.FM14-3.05	Le Gal, Patrice - Rotating turbulence in a rotor/stator cavity at high Reynolds number	1425
TS.FM14-3.06	Osawa, Kosuke - Flow structure and torque transition process of turbulent Taylor-Couette flow	1427
TS.FM14-4.01	Biferale, Luca - Turbulence under rotation at high numerical resolution: Eulerian and Lagrangian statistics	1429
TS.FM14-4.02	Donzis, Diego - Asymptotic states in turbulence: The emergence of universality and intermittency	1431
TS.FM14-4.03	Gotoh, Toshiyuki - Inertial and inertial convective ranges and crossover lengths	1433
TS.FM14-4.04	Meneveau, Charles - High-order statistics and random additive model for turbulent boundary layers	1435
TS.FM14-4.05	Miura, Hideaki - Scale-hierarchy in homogeneous Hall MHD turbulence	1437
TS.FM14-4.06	Okamoto, Naoya - Turbulent/non-turbulent interface in magnetohydrodynamic channel flow	1439
TS.FM14-5.01	Pandit, R. - Turbulence in Cahn-Hilliard binary-fluid mixtures (INVITED)	1441

TS.FM14-5.02	Miyazaki, Takeshi - Clustering and Entropy Growth of Quasi-geostrophic Point Vortices	1443
TS.FM14-5.03	Favier, Benjamin - Generating Jovian-like zonal jets in a rapidly rotating fluid experiment	1445
TS.FM14-5.04	Caulfield, Colm-Cille - Turbulent layer dynamics in stratified Taylor-Couette flow	1447
TS.FM14-5.05	Lee, Myoungkyu - Extreme-Scale Motions in Turbulent Couette Flows	1449
TS.FM14-5.06	Kaneda, Yukio - Two-point statistics in the log-law region in DNS of turbulent channel flow	1451
TS.FM14-6.01	Okino, Shinya - Spectral analyses of high Prandtl number stratified turbulence	1453
TS.FM14-6.02	Gaskin, Susan - Effect of Background Turbulence on Passive Scalar Mixing Within a Turbulent Jet	1455
TS.FM14-6.03	Dodd, Michael S. - Effects of viscosity ratio on droplet-laden isotropic turbulence	1457
TS.FM14-6.04	Kametani, Yukinori - Optimal control input for skin friction drag reduction in turbulent channel flow	1459
TS.FM14-6.05	Rouhi, Amirreza - Application of the integral length-scale approximation to Wall Modelled LES	1461
TS.FM14-6.06	Stevens, Richard - Simulation and modeling of extended wind-farms	1463
PO.FM14-1.01.164	Anbarlooei, Hamidreza - Blasius-type Friction Equation for Yielding Fluids Based on Extended Kolmogorov Microscales	1465
PO.FM14-1.02.165	Araki, Keisuke - Energy transfer between ion cyclotron and whistler modes in Hall magnetohydrodynamic turbulence	1467
PO.FM14-1.03.166	Baj, Pawel - Mixing in a turbulent multiscale flow	1469
PO.FM14-1.04.167	Barge, Alexis - DNS assessment of fragmentation model of turbulent cascade	1471
PO.FM14-1.05.168	Benaissa, Azemi - Scalar dissipation in a turbulent round jet	1473
PO.FM14-1.06.169	Brahimi, Malek - Normal inverse gaussian PDF of velocity increments in a turbulent heated jet	1475
PO.FM14-1.07.170	Camp, Elizabeth - Influence of freestream turbulence intensity on wakes of side-by-side cylinders in crossflow	1477
PO.FM14-1.08.171	Chen, Yu - Discharge increment induced by groove in channel flow	1479
PO.FM14-1.09.172	Fraternale, Federico - Outer Helioshpere: a first attempt of magnetic field spectrum determination from Voyagers data	1481
PO.FM14-1.10.173	Griffin, Kevin - Correlated forcing with an active grid to control turbulence	1483
PO.FM14-1.11.174	Herault, Johann - A new model of turbulent mixing by a jet impacting a stratified interface	1485
PO.FM14-1.12.175	Iwayama, Takahiro - Spectral dynamics in enstrophy inertial range in α-turbulence	1487
PO.FM14-1.13.176	Izawa, Seiichiro - Geometric Relation of Vortices of Different Scales in Turbulent Flow	1489
PO.FM14-1.14.177	Lee, Inwon - Development of low frictional marine af paint based on a novel drag reducing polymer of FDR-SPC	1490
PO.FM14-1.15.178	Panidis, Thrassos (Thrasyvoulos) - Cross plane vorticity distributions in a rectangular wall jet	1492
PO.FM14-1.16.179	Patte-Rouland, Beatrice - Annular jet aerodynamic and passive control study by Proper Orthogonal Decomposition	1494

PO.FM14-1.17.180	Prabhu, Akhilesh - Torque scaling and mean velocity profiles in a wide-gap Taylor-Couette flow	1496
PO.FM14-1.18.181	Suryanarayanan, Saikishan - Some insights on turbulent plane mixing layers from extensive vortex-gas computations	1498
PO.FM14-1.19.182	Van Blitterswyk, Jared - Wall-pressure coherence beneath a low Reynolds number turbulent boundary layer	1500

CIRCUMNAVIGATING THE CLOSURE PROBLEM OF TURBULENCE - A LIE SYMMETRY APPROACH

Martin Oberlack *[1] and Andreas Rosteck[1]

[1]*Chair of Fluid Dynamics, Department of Mechanical Engineering, TU Darmstadt, Germany*

Summary Present text-book knowledge proclaims that Lie symmetries such as the Galilean transformation group lie at the heart of fluid dynamics. These important properties also carry over to the statistical description of turbulence, i.e. to the Reynolds stress transport equations and its generalization, the multi-point correlation equations (MPCE). Interesting enough, the MPCE admit a much larger set of symmetries, in fact, infinite dimensional, subsequently named statistical symmetries. The new statistical symmetries mirror key properties of turbulence such as intermittency and non-gaussianity. They have important consequences for our understanding and construction of turbulent scaling laws, as the symmetries form the essential foundation to derive exact solutions. Examples on classical and new shear flow scaling laws including higher order moments are presented.

SYMMETRIES OF NAVIER-STOKES EQUATIONS

The concept of symmetries may most easily be introduced by considering the Navier-Stokes equation

$$\frac{\partial U_i}{\partial t} + U_k \frac{\partial U_i}{\partial x_k} + \frac{\partial P}{\partial x_i} - \nu \frac{\partial^2 U_i}{\partial x_k \partial x_k} = 0 \ , \ \ i = 1,2,3 \ , \quad \frac{\partial U_k}{\partial x_k} = 0. \tag{1}$$

A symmetry or symmetry group is called a transformation, $\boldsymbol{x}^* = \boldsymbol{\phi}(\boldsymbol{x}, \boldsymbol{y})$ and $\boldsymbol{y}^* = \boldsymbol{\psi}(\boldsymbol{x}, \boldsymbol{y})$, where $\boldsymbol{x}$ and $\boldsymbol{y}$ are generic independent and dependent variables, such that the form of the original differential equations is unchanged in the new variables $\boldsymbol{x}^*$ and $\boldsymbol{y}^*$. For the Navier-Stokes equations (1) it is know that they admit a nine-parameter symmetry group, such as scaling, rotation, translation, and the prominent Galilean symmetry group

$$T_{Gal}: \ \ t^* = t, \ \ \boldsymbol{x}^* = \boldsymbol{x} + \boldsymbol{k}t, \ \ \boldsymbol{U}^* = \boldsymbol{U} + \boldsymbol{k}, \ \ P^* = P, \tag{2}$$

where $\boldsymbol{k}$ is the vector of group-parameters. In other words, inserting transformation (2) into equation (1) does not change the equations' shape, when written in terms of *-variables.

STATISTICAL SYMMETRIES OF THE CORRELATION EQUATIONS

From (1) we may define the correlation equation

$$\begin{aligned} &\frac{\partial R_{i_{\{n+1\}}}}{\partial t} + \sum_{l=0}^{n} \left[\bar{U}_{k_{(l)}}(\boldsymbol{x}_{(l)}) \frac{\partial R_{i_{\{n+1\}}}}{\partial x_{k_{(l)}}} + R_{i_{\{n+1\}}[i_{(l)} \mapsto k_{(l)}]} \frac{\partial \bar{U}_{i_{(l)}}(\boldsymbol{x}_{(l)})}{\partial x_{k_{(l)}}} + \frac{\partial P_{i_{\{n\}}[l]}}{\partial x_{i_{(l)}}} - \nu \frac{\partial^2 R_{i_{\{n+1\}}}}{\partial x_{k_{(l)}} \partial x_{k_{(l)}}} \right. \\ &\left. - R_{i_{\{n\}}[i_{(l)} \mapsto \emptyset]} \frac{\partial u_{i_{(l)}} u_{k_{(l)}}(\boldsymbol{x}_{(l)})}{\partial x_{k_{(l)}}} + \frac{\partial R_{i_{\{n+2\}}[i_{(n+1)} \mapsto k_{(l)}][\boldsymbol{x}_{(n+1)} \mapsto \boldsymbol{x}_{(l)}]}}{\partial x_{k_{(l)}}} \right] = 0, \ \text{ for } \ n = 1, \ldots, \infty \ , \end{aligned} \tag{3}$$

where the multi-point correlation is defined as

$$R_{i_{\{n+1\}}} = R_{i_{(0)} i_{(1)} \ldots i_{(n)}} = u_{i_{(0)}}(\boldsymbol{x}_{(0)}) \cdot \ldots \cdot u_{i_{(n)}}(\boldsymbol{x}_{(n)}) \ . \tag{4}$$

and the mean velocity is denoted by $\bar{\boldsymbol{U}}$ and $\boldsymbol{u}$ is the fluctuation velocity. Quite obvious, (3) admits all classical symmetries of (1) such as the Galilean group (2). Most important, however, the correlation equations (3) admit additional statistical symmetries such as

$$\begin{aligned} T^{*\prime}{}_{1_{\{1\}}}: \ & t^* = t, \ \ \boldsymbol{x}^* = \boldsymbol{x}, \ \ \boldsymbol{r}^*_{(l)} = \boldsymbol{r}_{(l)}, \ \ \bar{U}^*_{i_{(0)}} = \bar{U}_{i_{(0)}} + C_{i_{(0)}}, \\ & R^*_{i_{(0)} i_{(1)}} = R_{i_{(0)} i_{(1)}} + \bar{U}_{i_{(0)}} \bar{U}_{i_{(1)}} - \left(\bar{U}_{i_{(0)}} + C_{i_{(0)}}\right) \left(\bar{U}_{i_{(1)}} + C_{i_{(1)}}\right), \ \cdots \end{aligned} \tag{5}$$

$$T^{*\prime}{}_s: \ t^* = t, \ \ \boldsymbol{x}^* = \boldsymbol{x}, \ \ \boldsymbol{r}^*_{(l)} = \boldsymbol{r}_{(l)}, \ \ \bar{U}^*_{i_{(0)}} = \mathrm{e}^{k_s} \bar{U}_{i_{(0)}}, \ \ R^*_{i_{(0)} i_{(1)}} = \mathrm{e}^{k_s} \left[R_{i_{(0)} i_{(1)}} + \left(1 - \mathrm{e}^{k_s}\right) \bar{U}_{i_{(0)}} \bar{U}_{i_{(1)}} \right], \ \cdots, \tag{6}$$

see e.g. [1, 2]. It is to note that symmetries can be rigorously computed using the Lie algorithm from its underlying equations, and this algorithm has been implemented into various computer algebra systems.

*Corresponding author. Email: oberlack@fdy.tu-darmstadt.de

SYMMETRY INVARIANT SOLUTIONS - TURBULENT SCALING LAWS

For the understanding of the following results it is to note that symmetries are the key foundation of essentially all analytic solutions to ordinary and partial differential equations. For partial differential so-called symmetry invariant solutions may be computed, which comprise classical solutions such as similarity solutions, wave-type solutions, etc. to name only a few.

Presently we will only exemplary show a few solutions to equation (3) for the mean velocity and the second moment for plane shear flows. The condition for symmetry invariant solutions reads

$$\frac{\mathrm{d}x_2}{k_{NS}x_2 + k_{G,2}} = \frac{\mathrm{d}\bar{U}_i}{(-k_{NS}+k_s)\bar{U}_i + k_{tr,1} + k_{z1}} = \frac{\mathrm{d}\bar{P}}{(-2k_{NS}+k_s)\bar{P} + k_{\bar{P}}} = ... \tag{7}$$

where all k_α are group parameter and are usually considered constants. The complex conditions for the higher moments have been omitted. The first example is the well known case of the logarithmic law of the wall, which may easily obtained from the first two terms employing $k_{NS} = k_s$. Less well known is that also the stresses may be computed. The final results read

$$\begin{aligned} \bar{U}_1^+ &= \frac{1}{\kappa}\ln(x_2^+) + B \ , \\ \tilde{R}_{ij}^+ &= \frac{C_{I,ij}}{x_2^+} + \alpha_{ij} + \beta_{ij}^+ x_2 \ \text{ for } \ ij = 12, 22, 33 \ , \quad \tilde{R}_{11}^+ = \frac{C_{I,11}}{x_2^+} + \alpha_{11} + \beta_{11}x_2^+ - \frac{1}{\kappa^2}\ln^2(x_2^+) - \gamma\ln(x_2^+) \end{aligned} \tag{8}$$

while all constants in (8) are related to the group parameters in (7) by algebraic expressions and the constant $C_{I,12}$ is also conneted to von Kármán's constant due to the relation $C_{I,12} = \frac{1}{\kappa}$. Comparison to data has been waived due to lack of space.

The second example is the deficit law in the center of a Poiseuille flow

$$\bar{U}_1^{def\,+} = U_{cl}^+ - \bar{U}_1^+\left(\frac{x_2}{h}\right) = -C_{I,1}\left|\frac{x_2}{h}\right|^\gamma + B \ , \tag{9}$$

where U_{cl}^+ represents the normalized velocity of the centerline. The components of Reynolds stress tensor read

$$\tilde{R}_{ij}^+ = C_{I,ij}\left(\frac{x_2}{h}\right)^{\gamma-1} + \alpha_{ij} + \beta_{ij}\frac{x_2}{h} \ , \ \tilde{R}_{11}^+ = -C_{I,1}^2\left|\frac{x_2}{h}\right|^{2\gamma} + C_{I,11}\left|\frac{x_2}{h}\right|^{\gamma-1} + \sigma\left|\frac{x_2}{h}\right|^\gamma + \alpha_{11} + \beta_{11}\frac{x_2}{h} \ . \tag{10}$$

where $ij = 12, 22, 33$ and, further, there is a connection between coefficients according to $C_{I,12} = \frac{C_{I,1}\gamma}{Re}$. A comparison of the DNS data in [3] to the symmetry based scaling laws are presented in figure 1

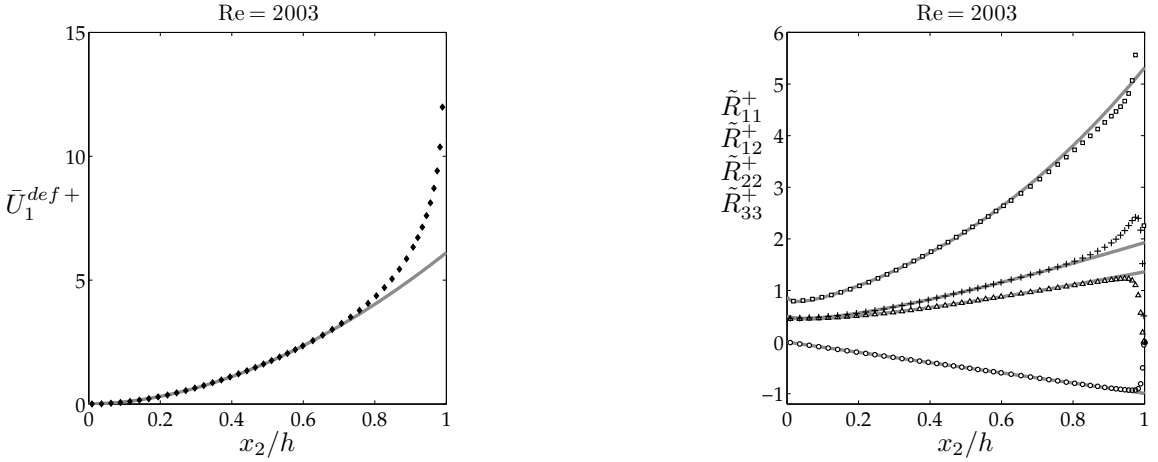

Figure 1: The mean velocity ♦ and the Reynolds stress components $\tilde{R}_{11}^+(\square)$, $\tilde{R}_{12}^+(\circ)$, $\tilde{R}_{22}^+(\triangle)$ and $\tilde{R}_{33}^+(+)$ from the DNS data in [3] are compared with symmetry based scaling law in (9) and (10) (solid lines).

CONCLUSION

Classical and new statistical symmetries allow to derive exact solutions to the MPCE for a very large number of canonical shear flows (only two were shown here), which turn out to be turbulent scaling laws.

References

[1] Oberlack M. Rosteck A. M.: New statistical symmetries of the multi-point equations and its importance for turbulent scaling laws. Discrete Contin. Dyn. Sys., Ser. S, vol. 3, pp. 451–471, 2010.

[2] Rosteck A. M.: Scaling Laws in Turbulence - A Theoretical Approach Using Lie-Point Symmetries. PhD thesis, TU Darmstadt, 2013.

[3] Hoyas S., Jimenez J.: Scaling of velocity fluctuations in turbulent channels up to $Re_\tau = 2000$. Phys. of Fluids, vol. 18, p. 011702, 2006.

STATISTICAL NORMALITY OF HOMOGENEOUS ISOTROPIC TURBULENCE

Tomomasa Tatsumi[1]
[1]*Kyoto University (Prof. Emer. Phys. / Sci.); Kyoto Institute of Technology (Prof. Emer.)*

Summary The one-point velocity distribution, the two-point velocity-sum distribution and the velocity-difference distributions of homogeneous isotropic turbulence are obtained exactly in the form of the *normal velocity distributions*. The consistency of this result with Kolmogorov's local similarity is discussed, and the above result is finally justified.

Closure problem of turbulence

One of the fundamental problems in statistical theory of turbulence lies in the 'unclosedness' of its equations governing the *mean products* of the multi-point turbulent velocities, since its n-th order equation, n being a positive integer, always includes the $(n+1)$-th order terms. Then, in order to make the equations solvable, we have to introduce a certain 'closure hypotheses' due to some physical consideration. Although a large number of the 'closure hypothesis' have been proposed so far, including those by the present author, no decisive answer seems to have been obtained yet.

An important progress in this problem has been made by Lundgren (1967) and Monin (1967) independently, using the statistical formulation in terms of the set of equations governing the *joint-probability distributions* of the turbulent velocities, instead of those for the *mean velocity products*.

This formalism had a definite merit in being indifferent from the above-mentioned statistical unclosedness, but it had its own unclosedness concerning the velocity distributions of different orders. This latter unclosedness is, however, much easier to deal with than the former, and actually the latter has been solved by the *cross-independence closure* proposed by Tatsumi (2011).

It has also been shown in this paper that the infinite set of the equations for the turbulent velocities can be minimized to the self-deterministic set of equations for the *one-point velocity distribution f, the two-point velocity-sum distribution g+* , and the *velocity-difference distribution g-* , and the closed set of equations for these distributions has been given explicitly in Tatsumi (2011).

Homogeneous isotropic turbulence

In the present work, this approach is applied **t**o *homogeneous isotropic turbulence* decaying in time, which has been first investigated by Taylor (1935, 1936) both experimentally and theoretically. In this turbulence, the *decay-law* of the *kinetic energy* per unit mass of fluid, $K(t)=\langle u^2\rangle/2$, u being the magnitude of the one-point *turbulent velocity* $\mathbf{u}(\mathbf{x},t)$, is determined as $K(t) = K_0 (t/t_0)^{-1}$, with K_0 being an initial value of $K(t)$. Then, the energy-dissipation rate, $D(t) = -d K(t)/dt$, is expressed as $D(t) = D_0 (t/t_0)^{-2}$ with an initial value D_0 .

Then, the velocity distributions f, g_+, g_- are expressed in the time-similar forms as

$$f(v,t) = (t/t_0)^{3/2} F(w) , \quad w= v (t/t_0)^{1/2} ;$$

$$g_+(v_+,r,t) = (t/t_0)^{3/2} G_+(w_+,s), g_-(v_-,r,t) = (t/t_0)^{3/2} G_-(w_-, s) , \quad s = r (t/t_0)^{-1/2} .$$

The equations governing the distributions f, g_+, g_- for homogeneous isotropic turbulence are derived from the corresponding general equations given in Tatsumi (2011), and the equations for the distributions F, G_+, G_- are obtained from these equations through the above time-similarity transformation. Then, the equations for the time-similar distributions F, G_+, G_- are solved analytically, and the following *normal* solutions are obtained:

One-point *normal* velocity distribution (N1):

$$F(w) = F_N (w) = (1/4(\mathrm{pi})A_0 t_0)^{3/2} \exp[- w^2/4A_0 t_0],$$

$$f(v,t) = f_N (v,t) = (t /4(\mathrm{pi})A_0 t_0^2)^{3/2} \exp[- v^2 t/ 4A_0 t_0^2],$$

where $A(t) = D(t)/3 = A_0(t/t_0)^{-2}$.

Two-point *normal* velocity-sum distribution (N2) for the energy-containing range:

$$G_+ (w_+, s) = G_{+N} (w_+, s) = (1/2(\mathrm{pi})A_0 t_0)^{3/2} \exp[- w_+^2/2A_0 t_0],$$

$$g_+ (v_+, t) = f_N (v_+ ,t) = (t /2(\mathrm{pi})A_0 t_0^2)^{3/2} \exp[- v_+^2 t/ 2A_0 t_0^2],$$

Two-point *normal* velocity-difference distribution (N2) for the energy-containing range:

$$G_- (w_+) = G_{+N} (w_+) = (1/2(\mathrm{pi})A_0 t_0)^{3/2} \exp[- w_+^2/2A_0 t_0],$$

$$g_- (v_-,t) = f_N (v_- ,t) = (t /2(\mathrm{pi})A_0 t_0^2)^{3/2} \exp[- v_-^2 t/ 2A_0 t_0^2],$$

It is to be noted that the above N2 is identical with the N1 except for that the parameter A_0 in the former is replaced by $A_0/2$. in the latter.

Two-point normal velocity-sum distribution (N3) for the energy-dissipation range:

[a] Corresponding author. Email tatsumi@skyblue.ocn.ne.jp

The velocity distributions in the *energy-dissipation range* are all normalized with respect to the Kolmogorov length and expressed in the local variables with *.

$G_+^*(w_+^*, s^*) = G_{+N}^*(w_+^*, s^*) = (1/4(\mathrm{pi})\, A_+^*(s^*)\, t_0^{*2}) \exp[-w_+^{*2}/4\, A_+^*(s^*)\, t_0^*]$,

$g_+^*(v_+^*, r^*, t^*) = f_N(v_+^*, r^*, t^*) = (t^*/4(\mathrm{pi})\, A_+^*(s^*)) \exp[-v_+^{*2} t/4\, A_+^*(s^*)\, t_0^{*2}]$,

Two-point normal velocity-difference distribution (N4) for the energy-dissipation range

$G_-^*(w_-^*, s^*) = G_{-N}^*(w_-^*, s^*) = (1/4(\mathrm{pi})\, A_-^*(s^*)\, t_0^{*2}) \exp[-w_-^{*2}/4\, A_-^*(s^*)\, t_0^*]$,

$g_-^*(v_-^*, r^*, t^*) = f_N(v^* - r^*, t^{*)}) = (t^*/4(\mathrm{pi})\, A_-^*(s^*)) \exp[-v_-^{*2} t/4\, A_-^*(s^*)]$,

where $A_+^*(s^*)$ ($= D_+^*(s^*)$) and $A_-^*(s^*)$ mean the local energy-dissipation rates related with the local velocity-sum $\mathbf{u}_+^*$ and the velocity-difference $\mathbf{u}_-^*$ respectively.

The local energy-dissipation rates $A_+^*(s^*)$ ($= D_+^*(s^*)/3$) and $A_-^*(s^*)$ ($= D_-^*(s^*)/3$) are expressed in terms of the error functions or the integral-normal forms. This result seems to be natural in view of the normality of the velocity distributions themselves.

Normal character of homogeneous isotropic turbulence

The *overall normality* of the statistics of homogeneous isotropic turbulence mentioned above is thought to be a natural consequence of the assumed *independence* of the velocity-*sum* and -*difference* assumed at small and large distances between the two points. This normality, however, seems to contradict with the notion of the *local similarity* due to Kolmogorov's theory (1941) of *local isotropic turbulence*, which predicted much non-normal characters of this turbulence. At the moment the author attribute this discrepancy to the time-stationality of his turbulence, while in homogeneous isotropic turbulence even the smallest components of turbulence are supposed to decay in time. Concerning this issue, reference may be made to the discussion by George (2013).

References

[1] George, W. (2013) In Farge, M. *et al* eds. *Fundamental Problems of Turbulence*, TCM 2011, EPS. pp.456-477

[2] Kolmogorov, A.N. (1941) Dokl Akad. Nauk SSSR **30**, 299-303.

[3] Lundgren, T. S. (1967) Phys. Fluids,**10**, 969-975.

[4] Monin, A. S. (1967) PMM **31**,1059-168.

[5] Tatsumi,T. (2011) J. Fluid Mech. **670,** 364-403**.**

[6] Taylor, G.I. (1935, 1936) Proc. Roy. Soc. A, **151**, 421 (1935), **156**, 307 (1936).

A LAGRANGIAN CLOSURE APPROXIMATION FOR HOMOGENEOUS ISOTROPIC TURBULENCE

Makoto OKAMURA*[1]

[1]*Research Institute for Applied Mechanics, Kyushu University, Kasuga, Japan*

Summary The closure problem of turbulence has been one of the most important subjects in fluid dynamics through many years. Now a large number of closure models, ranging from empirical to theoretical, are available. In this paper, we are interested in closure models which are compatible with Kolmogorov's five-thirds law without any adjustable free parameter. From this point of view, there are few closure models [1, 2], which are originated in the Lagrangian direct-interaction approximation (DIA) proposed by Kraichnan [3]. Their closure equations yield the Kolmogorov constant, $C_K = 1.72$. In this paper, a new closure approximation, which is completely different from the DIA, is proposed for homogeneous isotropic stationary turbulence in the Lagrangian description. A two-closed-equation set is derived without any adjustable free parameter. The Kolmogorov constant C_K is evaluated to be 1.66. This value is close to 1.62, which is the mean value of numerous experimental data collected by Sreenivasan [4].

GENERALIZED VELOCITY, LAGRANGIAN POSITION FUNCTION AND THEIR GOVERNING EQUATIONS

We introduce a generalized velocity $u_i(t|\boldsymbol{x}',t') = u_i\big(\boldsymbol{y}(t|\boldsymbol{x}',t'),t\big)$ defined by Kraichnan [3], where $\boldsymbol{y}(t|\boldsymbol{x}',t')$ is the position at time t of a fluid element which is at the position $\boldsymbol{x}'$ at time t', and the Lagrangian position function $\psi(\boldsymbol{x},t|\boldsymbol{x}',t') = \delta\big(\boldsymbol{x}-\boldsymbol{y}(t|\boldsymbol{x}',t')\big)$, where $\psi(\boldsymbol{x},t|\boldsymbol{x}',t) = \delta(\boldsymbol{x}-\boldsymbol{x}')$. Here these relations hold for all t and t'. We now move from real space to Fourier space. The Eulerian velocity $u_i(\boldsymbol{k},t)$ and the Lagrangian velocity $v_i(\boldsymbol{k},t)$ are the special cases of the generalized velocity $u_i(t|\boldsymbol{k},t')$ as follows:

$$u_i(\boldsymbol{k},t) = u_i(t|\boldsymbol{k},t) \quad \text{and} \quad v_i(\boldsymbol{k},t) = u_i(t|\boldsymbol{k},t_0), \tag{1}$$

where $t_0 = \pm\infty$. Because the Lagrangian velocity is most 'distant' from the Eulerian velocity regarding the labelling time t', the choice of $t' = t_0$ $(= \pm\infty)$ is more reasonable than that of $t' = 0$ for the Lagrangian velocity. The relation between the generalized velocities is expressed by

$$u_i(t|\boldsymbol{k}',t') = (2\pi)^3 \int d\boldsymbol{k}'' u_i(t|\boldsymbol{k}'',t'')\psi(-\boldsymbol{k}'',t''|\boldsymbol{k}',t'), \tag{2}$$

which shows that $\psi(-\boldsymbol{k},t|\boldsymbol{k}',t')$ is a time evolution operator of $u_i(t|\boldsymbol{k}',t')$ with respect to the labelling time t'. Setting $t' = t$ in (2), we obtain the Eulerian velocity expressed by the generalized velocity. The governing equation of the Lagrangian position function $\psi(\boldsymbol{k},t|\boldsymbol{k}',t')$ and its initial condition are

$$\frac{\partial}{\partial t}\psi(\boldsymbol{k},t|\boldsymbol{k}',t') = -\mathrm{i}k_j \iint d\boldsymbol{p}\, d\boldsymbol{q}\, \delta(\boldsymbol{k}-\boldsymbol{p}-\boldsymbol{q})u_j(\boldsymbol{p},t)\psi(\boldsymbol{q},t|\boldsymbol{k}',t') \quad (t \neq t'), \qquad \psi(\boldsymbol{k},t'|\boldsymbol{k}',t') = \frac{1}{(2\pi)^3}\delta(\boldsymbol{k}+\boldsymbol{k}'),$$

the formal solution to which is expressed by

$$\psi(\boldsymbol{k},t|\boldsymbol{k}',t') = \frac{1}{(2\pi)^3}\delta(\boldsymbol{k}+\boldsymbol{k}') - \mathrm{i}k_j \int_{t'}^{t} dt'' \iint d\boldsymbol{p}\, d\boldsymbol{q}\, \delta(\boldsymbol{k}-\boldsymbol{p}-\boldsymbol{q})u_j(\boldsymbol{p},t'')\psi(\boldsymbol{q},t''|\boldsymbol{k}',t'). \tag{3}$$

Under the isotropy, (3) yields $\big\langle\psi(\boldsymbol{k},t|\boldsymbol{k}',t')\big\rangle = \delta(\boldsymbol{k}+\boldsymbol{k}')/(2\pi)^3$ exactly, which makes it easy to derive the closure equations in the next section. The relations obtained from (3), such as $uuu\psi = uuu + uuuu\psi$ and $u = v + vv\psi$ with a symbolic representation, play an important role. Thus (3) is a key point in the present closure approximation.

We introduce the two-point, two-time velocity correlation function

$$Q_{ij}(\boldsymbol{k},t-t') = \int d\boldsymbol{k}'\big\langle v_i(\boldsymbol{k},t)v_j(\boldsymbol{k}',t')\big\rangle = \int d\boldsymbol{k}'\big\langle u_i(t|\boldsymbol{k},t')u_j(t'|\boldsymbol{k}',t_1)\big\rangle = \frac{1}{2}D_{ij}(\boldsymbol{k})Q(k,t-t') \tag{4}$$

for homogeneous isotropic stationary turbulence in an incompressible fluid. Here $D_{ij}(\boldsymbol{k}) = \delta_{ij} - (k_ik_j/k^2)$ and t_1 is an arbitrary constant. Setting $t_1 = t'$ in (4) and using the symmetry of the second-order isotropic tensor, we find that the third equation holds in spite of $k_iu_i(t|\boldsymbol{k},t') \neq 0$.

The governing equations of the Eulerian velocity $u_i(\boldsymbol{k},t)$ and the generalized velocity $u_i(t|\boldsymbol{k},t')$ are

$$\frac{\partial}{\partial t}u_i(\boldsymbol{k},t) = -\nu k^2 u_i(\boldsymbol{k},t) + M_{ijm}(\boldsymbol{k}) \iint d\boldsymbol{p}\, d\boldsymbol{q}\, \delta(\boldsymbol{k}-\boldsymbol{p}-\boldsymbol{q})u_j(\boldsymbol{p},t)u_m(\boldsymbol{q},t) + f_i(\boldsymbol{k},t) \quad \text{and} \tag{5}$$

*Corresponding author. Email: okamura@riam.kyushu-u.ac.jp

$$\frac{d}{dt}u_i(t|\boldsymbol{k},t') = -(2\pi)^3\nu\int d\boldsymbol{p}\,p^2u_i(\boldsymbol{p},t)\psi(-\boldsymbol{p},t|\boldsymbol{k},t') + (2\pi)^3\int d\boldsymbol{p}\,f_i(\boldsymbol{p},t)\psi(-\boldsymbol{p},t|\boldsymbol{k},t')$$
$$+ (2\pi)^3\mathrm{i}\iiint d\boldsymbol{p}\,d\boldsymbol{q}\,d\boldsymbol{r}\,\delta(\boldsymbol{r}-\boldsymbol{p}-\boldsymbol{q})\frac{r_ir_jr_m}{r^2}u_j(\boldsymbol{p},t)u_m(\boldsymbol{q},t)\psi(-\boldsymbol{r},t|\boldsymbol{k},t'), \tag{6}$$

where $M_{ijm}(\boldsymbol{k}) = [k_jD_{im}(\boldsymbol{k})+k_mD_{ij}(\boldsymbol{k})]/(2\mathrm{i})$, ν is the kinematic viscosity of the fluid and ϵ is the mean energy dissipation rate per unit mass. Here the external force $f_i(\boldsymbol{k},t)$ is given to satisfy the condition

$$\int d\boldsymbol{k}'\langle f_i(\boldsymbol{k},t)u_j(t'|\boldsymbol{k}',t_1)\rangle = \begin{cases}\dfrac{1}{2}\epsilon D_{ij}(\boldsymbol{k})\delta(\boldsymbol{k})\delta(\boldsymbol{k}+\boldsymbol{k}') & (t=t'),\\ 0 & (t\neq t').\end{cases} \tag{7}$$

CLOSURE APPROXIMATION

In order to obtain closure equations, we make the assumptions: (i) The Lagrangian position function $\psi(\boldsymbol{k},t|\boldsymbol{k}',t')$ is statistically independent of the Lagrangian velocity $v_i(\boldsymbol{k},t)$; (ii) The Lagrangian velocity $v_i(\boldsymbol{k},t)$ obeys a Gaussian distribution.

First, setting $i=j$ in (4), differentiating with respect to t, and then substituting (6), we obtain

$$\frac{\partial}{\partial t}Q(k,t-t') = \int d\boldsymbol{k}'\left\langle\frac{du_j(t|\boldsymbol{k},t')}{dt}u_j(t'|\boldsymbol{k}',t_1)\right\rangle = -(2\pi)^3\nu\iint d\boldsymbol{k}'d\boldsymbol{p}\,p^2\big\langle u_j(\boldsymbol{p},t)\psi(-\boldsymbol{p},t|\boldsymbol{k},t')u_j(t'|\boldsymbol{k}',t_1)\big\rangle$$
$$+ (2\pi)^3\mathrm{i}\iiint d\boldsymbol{k}'d\boldsymbol{p}\,d\boldsymbol{q}\,d\boldsymbol{r}\,\delta(\boldsymbol{r}-\boldsymbol{p}-\boldsymbol{q})\frac{r_jr_lr_m}{r^2}\big\langle u_l(\boldsymbol{p},t)u_m(\boldsymbol{q},t)\psi(-\boldsymbol{r},t|\boldsymbol{k},t')u_j(t'|\boldsymbol{k}',t_1)\big\rangle$$
$$+ (2\pi)^3\iint d\boldsymbol{k}'d\boldsymbol{p}\,\big\langle f_j(\boldsymbol{p},t)\psi(-\boldsymbol{p},t|\boldsymbol{k},t')u_j(t'|\boldsymbol{k}',t_1)\big\rangle. \tag{8}$$

The force term becomes zero under (7) and assumption (i). Substituting (3) into (8) and using (1), (2) [to eliminate $u_i(\boldsymbol{k},t)$], (4), assumptions (i), (ii), the incompressibility and the statistical steadiness, we obtain one of the two-closed-equation set

$$\left[\frac{\partial}{\partial t}+\nu k^2\right]Q(k,t-t') = -\frac{4}{3}\pi k^5\,\mathrm{sgn}(t-t')Q(k,t-t')\int_0^\infty dp\,p^{10/3}J(p^{2/3})\int_{t'}^t dt''Q(kp,t-t''), \tag{9}$$

which is the same as the former result [1, 2]. Here $\mathrm{sgn}(t) = t/|t|$, and $J(p)$ is defined in [2]. We have added $\mathrm{sgn}(t-t')$ to the right-hand side of (9) because (9) should be independent of the sign of $t-t'$ in stationary turbulence.

Second, setting $i=j$ in (4) and $t'=t$, and then differentiating with respect to t, we obtain

$$0 = \int d\boldsymbol{k}'\left\langle\frac{\partial u_j(\boldsymbol{k},t)}{\partial t}u_j(t|\boldsymbol{k}',t_1)\right\rangle + \int d\boldsymbol{k}'\left\langle u_j(\boldsymbol{k},t)\frac{\partial u_j(t|\boldsymbol{k}',t_1)}{\partial t}\right\rangle. \tag{10}$$

Substituting (5) and (6) into (10) and using (1), (2) [to eliminate $u_i(\boldsymbol{k},t)$], (3), (4), assumptions (i), (ii), the incompressibility and the statistical steadiness, we obtain another of the two-closed-equation set

$$0 = 2\Big[-\nu k^2Q(k,0)+\epsilon\delta(\boldsymbol{k})\Big] + \frac{1}{12}\,\mathrm{sgn}(t_0)\int_t^{t_0}dt'\iint d\boldsymbol{p}\,d\boldsymbol{q}\,\delta(\boldsymbol{k}-\boldsymbol{p}-\boldsymbol{q})$$
$$\Big\{kp\big[y(x+yz)Q(q,0)Q(k,t-t') + (z+xy)Q(k,0)Q(q,t-t')\big] - k^2a_1(k,p,q)Q(p,0)Q(q,t-t') + (p\leftrightarrow q)\Big\}, \tag{11}$$

which is different from the former result [1, 2]. Here the definitions of x, y, z and $a_1(k,p,q)$ are given in [3]. We have added $\mathrm{sgn}(t_0)$ to the right-hand side of (11) because (11) should be independent of the sign of t_0 in stationary turbulence. Note that (11) is independent of t because of $t_0 = \pm\infty$, which is reasonable in stationary turbulence.

Finally, we obtain a closed set of equations (9) and (11) using a new closure approximation. Substituting $Q(k,t) = (C_K/2\pi)\epsilon^{2/3}k^{-11/3}G\big(C_K^{1/2}\epsilon^{1/3}k^{2/3}t\big)$ and $G(0)=1$ into (9) and (11), we evaluate the Kolmogorov constant C_K to be 1.66. This values is close to 1.62, which is the mean value of numerous experimental and observational data [4]. We end this paper by adding a comment about an advantage of the present closure model over the Lagrangian DIA [1, 2]; The derivation of the closure equations in this model is much easier than that in the Lagrangian DIA because the former does not include the response function and the decomposition of physical quantities such as $u_i = u_i^{(0)} + u_i^{(1)}$.

References

[1] Y. Kaneda. Renormalized expansions in the theory of turbulence with the use of the Lagrangian position function. *J. Fluid Mech.*, **107**, 131 (1981).
[2] S. Kida and S. Goto. A Lagrangian direct-interaction approximation for homogeneous isotropic turbulence. *J. Fluid Mech.*, **345**, 307 (1997).
[3] R. H. Kraichnan. Lagrangian-history closure approximation for turbulence. *Phys. Fluids*, **8**, 575 (1965).
[4] K. R. Sreenivasan. On the universality of the Kolmogorov constant. *Phys. Fluids*, **7**, 2778 (1995).

HOT-WIRE SPATIAL RESOLUTION EFFECTS IN MEASUREMENTS OF THE TURBULENT ROUND JET

Hamed Sadeghi[1], Philippe Lavoie *[2], and Andrew Pollard[3]
[1,2]*Institute for Aerospace Studies, University of Toronto, Toronto, ON, Canada*
[1,3]*Department of Mechanical and Materials Engineering, Queen's University, Kingston, ON, Canada*

Summary The effect of hot-wire spatial resolution on turbulence statistics and velocity spectra in a round turbulent jet is investigated. To quantify spatial resolution effects, measurements were taken using conventional hot-wires with different sensing lengths of $l = 0.5$ mm and 1 mm and compared to results from a nano-scale thermal anemometry probe (NSTAP). Significant impact of spatial resolution on the velocity fluctuations, $\langle u^2 \rangle$, and dissipation, $\langle \epsilon \rangle$, is found along the jet centreline. Correction functions for the fluctuating velocity and dissipation data acquired with the conventional hot-wires are proposed. Along the jet centreline, the corrections are functions of l/η, where η is the Kolmogorov length scale defined as $\eta \equiv \nu^{3/4}/\langle \epsilon \rangle^{1/4}$.

INTRODUCTION

A significant source of error in hot-wire measurements of turbulence is its finite spatial resolution relative to the smallest (Kolmogorov) scale of the flow (i.e., the sensing length of the hot-wire probe is larger than the smallest turbulence length scale and therefore, the probe is not able to resolve the full range of scales). In some experiments, hot-wire measurements have been restricted to the jet far-field or low-Reynolds numbers, in which the Kolmogorov length-scale is typically large. In other cases, researchers have used the spectral correction approach, based on the method of Wyngaard [1] to minimise errors due to probe resolution. In a variety of other studies, however, it has been generally accepted that the magnitude of uncertainty due to the probe resolution is unknown. Therefore, the significance of spatial resolution effects remains an open question in jet flows. In this work, to quantify spatial resolution effects on the measurements of turbulence in jet flows, different hot-wire sensor lengths are used. The results obtained from two conventional probes (with 0.5 mm and 1 mm sensing lengths) are compared to those from a Nano-Scale Thermal Anemometry Probe (NSTAP) (see [2], [3]). The NSTAP is an order of magnitude smaller than conventional hot-wire probes and it displays also a considerably higher frequency response. In the current experiments, the NSTAP sensing length is smaller than the Kolmogorov scale for all test cases considered.

EXPERIMENTAL SET-UP

The experimental setup is the same as used in [4]. The experiments were carried out at Reynolds numbers of $Re_D = 30,000$ and 50,000, where Re_D is calculated based on the jet exit mean velocity and the nozzle exit diameter. The measurements were performed for $10 \leq x/D \leq 20$, where x represents streamwise distance. All data were obtained using single hot-wire anemometry probes. In this study, two types of thermal anemometry probes were employed: a new designed Nano-Scale Thermal Anemometry Probe (NSTAP) and two conventional hot-wire probes. The NSTAP probe used in this study was obtained from a series of standard semiconductor manufacturing techniques, as outlined in [3]. This probe had a 60-μm-long sensing element, measuring 100 nm by 2 μm in cross section, with a frequency response that exceeds 150 kHz [3]. The use of the NSTAP probe has previously been validated in pipe flows and grid turbulence in [2], [3] and [5]. The conventional hot-wires were made of 2.5 and 5 μm diameter tungsten wires with 0.5 mm and 1 mm sensing lengths, respectively.

RESULTS AND DISCUSSION

To determine the magnitude of spatial filtering on the turbulence statistics in the jet, the fluctuating velocity and dissipation measured by the conventional hot-wires along the jet centreline ($\langle u^2 \rangle_{\text{M}}$ $\langle \epsilon \rangle_{\text{M}}$), are compared to their fully resolved values obtained by the NSTAP ($\langle u^2 \rangle_{\text{N}}$ and $\langle \epsilon \rangle_{\text{N}}$) in Figure 1. Figure 1a shows the ratio of $\langle u^2 \rangle_{\text{M}}/\langle u^2 \rangle_{\text{N}}$, whereas Figure 1b provides the ratio of $\langle \epsilon \rangle_{\text{M}}/\langle \epsilon \rangle_{\text{N}}$. It can be observed that these ratios decrease with increasing l/η. This trend is more significant for the dissipation. Over the present range of l/η, the data are found to exhibit monotonic changes with l/η and can be described by:

$$\langle u^2 \rangle_{\text{M}}/\langle u^2 \rangle_{\text{N}} = \exp(\circ\ 0.005 l/\eta), \tag{1}$$

and

$$\langle \epsilon \rangle_{\text{M}}/\langle \epsilon \rangle_{\text{N}} = \exp(\circ\ 0.035 l/\eta). \tag{2}$$

*Corresponding author. Email: lavoie@utias.utoronto.ca

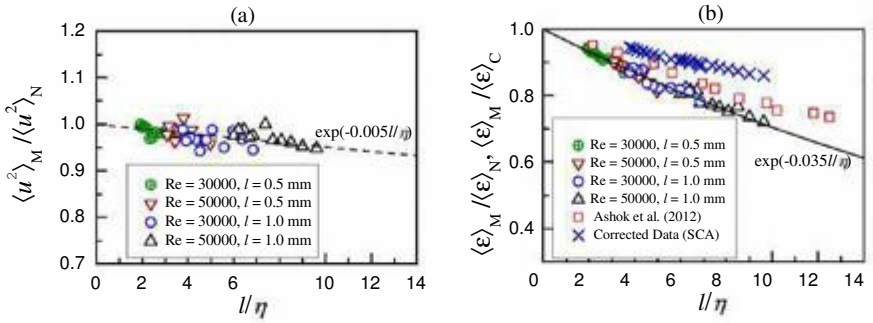

Figure 1: (a) The ratio of turbulent velocity measured by conventional HWA and NSTAP. The dashed line represents Eq (1). (b) The ratio of dissipation obtained by conventional HWA and NSTAP. The solid line represents Eq (2). The squares are the experimental data reported in [5] for grid generated turbulence. The crosses are the ratio of the measured dissipation to those corrected by spectral correction approach [1] .

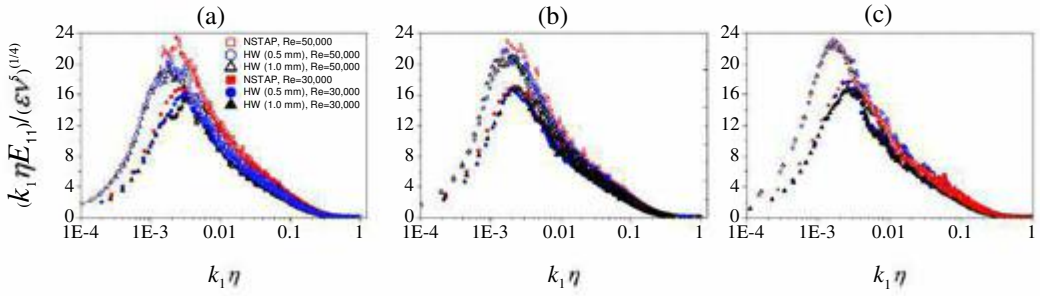

Figure 2: Measured streamwise wavenumber spectra normalized by the Kolmogorov scales in the pre-multiplied form at (a) $x/D = 10$, (b) $x/D = 15$ and (c) $x/D = 20$ for $Re_D = 30,000$ and 50,000 along the jet centreline .

The ratio of the dissipation obtained by the conventional hot-wires measurements to the corrected dissipation obtained by the spectral correction approach (SCA) [1], $\langle\epsilon\rangle_C$, is also included in Figure 1b. As can be observed, there is a significant deviation between $\langle\epsilon\rangle_C$ and $\langle\epsilon\rangle_N$, possibly because the SCA was developed for infinite Reynolds number. Also shown in Figure 1b is the dissipation measured by the conventional probes, normalized by the NSTAP, in grid-generated turbulence obtained in [5]. These data are within 5% of the present jet results.

In order to study the effect of spatial filtering on the energy spectra, the pre-multiplied form of the spectra, $k_1\eta E_{11}(k_1)$, at three selected axial locations ($x/D = 10$, 15 and 20) for $Re_D = 30,000$ and 50,000 along the centreline are provided in Figure 2. The reduced spectral response of the larger probes becomes more apparent when the spectra are viewed in the pre-multiplied forms, especially at $x/D = 10$, at which the energy measured by the conventional probes is lower than the NSTAP. It is noted that the conventional probes filter energy at wavelengths that are much larger than the wire length. This can be attributed to the one-dimensional filtering of a three-dimensional input, as previously noted in [2] and [3]. When x/D increases or Re decreases, η becomes larger and therefore the effect of spatial filtering on the spectra reduces.

CONCLUSIONS

In this work, spatial filtering effects on turbulence in a round turbulent jet were studied by conducting measurements with a new nanoscale probe and two conventional hot-wire probes. The turbulence fluctuation, dissipation distributions and energy spectra suggested that the conventional hot-wire results suffer from spatial filtering effects in the jet.

References

[1] J. C. Wyngaard, "Measurements of small-scale turbulence structure with hot wires," *J. Sci. Instr.*, vol. 1, no. 2, pp. 1105–1108, 1968.

[2] S. C. C. Bailey, G. J. Kunkel, M. Hultmark, M. Vallikivi, J. P. Hill, K. A. Meyer, C.Tsay, C. B. Arnold, and A. J. Smits, "Turbulence measurements using a nanoscale thermal anemometry probe," *J. Fluid Mech.*, vol. 663, pp. 160–179, 2010.

[3] M. Vallikivi, M. Hultmark, S. C. C. Bailey, and A. J. Smits, "Turbulence measurements in pipe flow using a nano-scale thermal anemometry probe," *Exp. Fluids*, vol. 51, pp. 1521–1527, 2011.

[4] H. Sadeghi, P. Lavoie, and A. Pollard, "Equilibrium similarity solution of the turbulent transport equation along the centreline of a round jet," *J. Fluid Mech.*, vol. 772, pp. 740–755, 2015.

[5] A. Ashok, S. C. C. Bailey, M. Hultmark, and A. J. Smits, "Hot-wire spatial resolution effects in measurements of grid-generated turbulence," *Exp. Fluids*, vol. 53, pp. 1713–1722, 2012.

ENERGY DISSIPATION SCALING IN UNIFORMLY SHEARED AND IN MULTI–STRUCTURE TURBULENCE

Jovan Nedić[1] and Stavros Tavoularis *[1]

[1]*Department of Mechanical Engineering, University of Ottawa, Ottawa, Ontario, Canada*

Summary First, we investigated the streamwise evolution of the dissipation parameter C_ε in uniformly sheared flow (USF). We observed three distinct regions in which $C_\varepsilon \propto Re_\lambda^\alpha$, with respective values of the exponent α equal to $-0.6, 0.5$ and 0, the latter one termed as "fully developed USF", where C_ε is constant. Second, we introduced a uniform grid within a developed USF and created a "multi–structure" turbulent flow, which had a region with $\alpha = -1$ and then eventually relaxed to fully developed USF again.

INTRODUCTION

Although dissipation of turbulent kinetic energy to heat is enacted by small–scale motions, the average rate of dissipation ε is known to depend on the large, energy–containing motions. Dimensional analysis leads to a dimensionless dissipation parameter $C_\varepsilon = \varepsilon L/(2k/3)^{3/2}$, where k is the turbulent kinetic energy and L is an integral length scale. Numerous experiments have shown that C_ε is approximately constant along the paths of canonical turbulent flows far downstream of their origin and has an asymptotic value that depends upon the geometry of flow and its boundary and/or initial conditions. The assumption of a constant C_ε has been employed in a wide variety of contexts, sometimes implicitly and often for the sake of convenience [1]. This assumption has been used in the derivation of far–field scalings laws for canonical turbulent flows, in the formulation of turbulence models for the solution of the Reynolds–averaged Navier–Stokes (RANS) equations and large–eddy simulations (LES), in the prediction of turbulent scalar dispersion and in the estimation of computer resources for direct numerical simulations (DNS) [2, 3, 4]. Recently, however, a growing body of research has shown that decaying grid turbulence [3] and turbulent axisymmetric wakes [4], both of which are canonical turbulent flows, contain a region in which $C_\varepsilon \neq$ const. In these "non–equilibrium" regions, C_ε could be fitted by a power law of turbulent Reynolds number $Re_\lambda = (2k/3)^{1/2}\lambda/\nu$, where λ is the Taylor microscale, related to the other parameters as $\lambda = \sqrt{10\nu k/\varepsilon}$. In both decaying grid turbulence and in turbulent axisymmetric wakes, $C_\varepsilon \propto Re_\lambda^\alpha$, where $\alpha = -1$ [3, 4].

As described in the following, we investigated the energy dissipation scaling in a uniformly sheared turbulent flow (USF). Most of the available literature on USF, which is also a canonical flow, has been concerned with its far–downstream, self–similar region, in which the turbulent kinetic energy grows exponentially [5]. Apart from a compilation of data from previous studies [6], there does not appear to be any clear analysis on the behaviour of C_ε in USF. The available data indicate that C_ε is constant in fully developed USF, a postulate that seems to be of general acceptance in the literature. We shall therefore focus our attention on the energy dissipation scaling in developing stages of USF, as it evolved towards its fully self–similar state. Uniform mean shear was generated in a wind tunnel, as depicted in Fig. 1, with the use of a shear generator, followed by a flow straightener, both of which had 12 channels with a spacing of $M = 25.4$ mm. Furthermore, we investigated the energy dissipation scaling in multi–structure turbulence, namely a flow which was generated by the insertion of a planar turbulence grid with a solidity of 0.25 and a mesh size M_g =18 mm across the USF. The streamwise and transverse velocity components were measured simultaneously with a cross-wire probe powered by constant temperature anemometers.

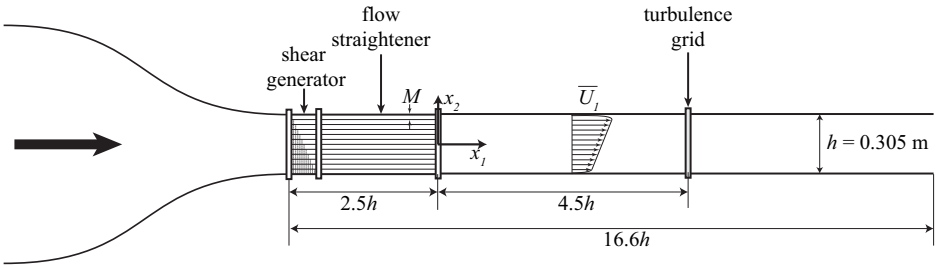

Figure 1: Schematic diagram of the wind tunnel, showing the shear–generating apparatus, the co–ordinate system and the location where the turbulence grid was inserted.

*Corresponding author. stavros.tavoularis@uottawa.ca

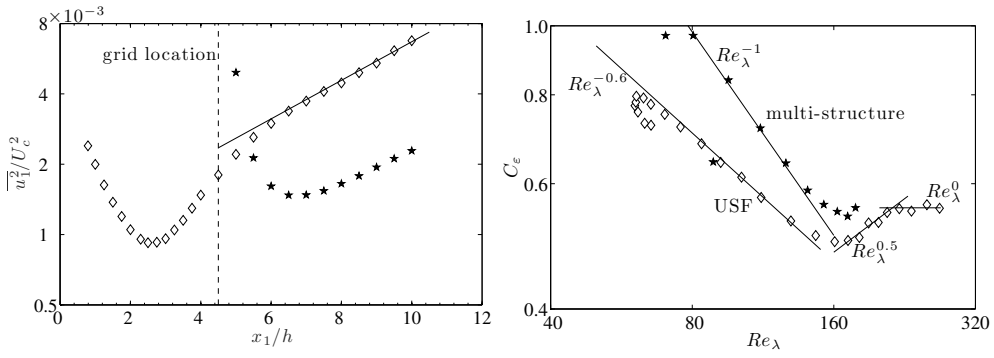

Figure 2: a) Streamwise evolution of the normalised streamwise velocity variance. b) Fitted relationships between the dissipation parameter C_ε and the turbulent Reynolds number Re_λ. In both plots, values are represented by diamonds for the unobstructed USF and by filled stars for the multi–structure case.

RESULTS

In Fig. 2a, we show the streamwise evolution of the normalised streamwise velocity variance $\overline{u_1^2}/U_c^2$, where $U_c = 10.8$ m/s was the centreline velocity. Near the shear generating apparatus, this property decayed with streamwise distance and reached a minimum, beyond which it increased monotonically as a result of production by the mean shear. In the unobstructed USF, $\overline{u_1^2}/U_c^2$ eventually grew at an exponential rate, denoted as the solid line in Fig. 2a. To generate the multi–structure flow, the turbulence grid was inserted at $x_1 = 4.5h$, which was just before the start of exponential growth. A region of decaying turbulence can be observed downstream of the grid, followed by a region of growth, which eventually reassumed an exponential growth rate.

In Fig. 2b, we show the relationship between the dissipation parameter C_ε and the turbulent Reynolds number Re_λ for the two cases. For regions with increasing turbulence (*i.e.* for $2.5h \leq x_1$ in Fig. 2a) in the USF case, three distinct regions can be identified. In the first region ($3h \leq x_1 \leq 4.5h$ in Fig. 2a), where the structure of device–generated turbulence gets transformed towards the USF structure, we found that $C_\varepsilon \propto Re_\lambda^{-0.6}$. This was followed by a second region ($6h \leq x_1 \leq 8h$ in Fig. 2a), in which $C_\varepsilon \propto Re_\lambda^{0.5}$; in this region, both k and ε were growing at their far–field, self–similar rates, however, L was not. Finally, in the far–field, self–similarity was established for all parameters and C_ε settled at a constant value. In the multi–structure case, we observed that $C_\varepsilon \propto Re_\lambda^{-1}$, which is the same scaling found in the "non–equilibrium" region of decaying grid turbulence [3]. Fig. 2b also suggests that, towards the end of the domain, C_ε began to increase again and one may speculate that, if measurements were taken further downstream, there would be a region in which C_ε would be constant.

CONCLUSIONS

We demonstrated that the studied USF had two distinct regions in which the dissipation parameter C_ε was not constant. The scalings in these regions were found to be $C_\varepsilon \propto Re_\lambda^{-0.6}$ and $C_\varepsilon \propto Re_\lambda^{0.5}$, both of which differ from the scaling $C_\varepsilon \propto Re_\lambda^{-1}$ found in "non–equilibrium" decaying grid turbulence. Towards the end of the measurement domain, C_ε became constant. For the multi–structure turbulence case, we again found that C_ε was not constant but instead scaled as $C_\varepsilon \propto Re_\lambda^{-1}$. These findings demonstrate that the common assumption that C_ε is a constant is not of universal applicability and that more work is required to understand the reasons behind the scaling of dissipation, if we are to improve, amongst other things, RANS and LES models.

This work was funded by the Natural Sciences and Engineering Research Council of Canada (NSERC).

References

[1] Tennekes H,. Lumley J. L.: A First Course in Turbulence. MIT, Cambridge, MA, USA,1972.

[2] Castro I.P.: Dissipative distinctions. J. Fluid. Mech. 788, pp.1-4, 2016.

[3] Vassilicos J.C.: Dissipation in Turbulent Flows. Annu. Rev. Fluid Mech. 47, 95, 2015.

[4] Nedić J., Vassilicos J.C., Ganapathisubramani B.: Axisymmetric turbulent wakes with new nonequilibrium similarity scalings. Phys. Rev. Lett. 111, 2013.

[5] Tavoularis S.: Asymptotic laws for transversely homogeneous turbulent shear flows. Phys. Fluids 28, 999, 1985.

[6] Sreenivasan K.R.: The energy dissipation in turbulent shear flows, in Symposium on Development in Fluid Dynamics and Aerospace Engineering, edited by S. M. Deshpande, A. Prabhu, K. R. Sreenivasan, and P. R. Viswanath. pp. 159-190. Interline Publishers, Bangalore, India, 1995.

ENERGY TRANSFER ACROSS SCALES AROUND ELLIPTIC BURGERS VORTICES

Hiromichi Kobayashi[1a)]
[1]*Department of Physics, Hiyoshi Campus, Keio University, Yokohama, Kanagawa, Japan*

Summary In turbulence, vortices emerge and the energy transfer across scales mainly occurs around the vortices. It is known that the vortices are approximated as elliptic Burgers vortices. We analytically and numerically examined the energy transfer across scales around the elliptic Burgers vortices. We found that the regions of the forward scatter (energy transfer from large-scale to small-scale) have a double-peak structure around the vortex and those appear in the direction of the minimum eigenvalue of the velocity strain tensor whereas the regions of the backward scatter (energy transfer from small-scale to large-scale) with a double-peak structure emerge in the direction of the maximum eigenvalue. Those double-peak structures distribute as a quadrupole around the vortex. By integrating the energy transfer distribution around the vortex in the azimuthal direction, we revealed that the net energy transfer becomes the forward scatter and takes place at the centre of the vortex.

MOTIVATION

Vortex tubes, in other words, coherent eddies or energy containing eddies, emerge in turbulence. The coherent eddies in direct numerical simulation (DNS) are well approximated by the elliptic Burgers vortex [1-3]. In large eddy simulation (LES), the energy transfer between large-scale and small-scale is of great importance. The energy transfer from large-scale to small-scale, the so-called forward scatter, around the vortex occurs at the different location of the high energy dissipation as shown in DNS [4]. The strong forward scatter region has also a double-peak structure around the vortex in the log layer of wall turbulence experiments whereas the strong backward scatter region where the energy transfers from small-scale to large-scale appears around the vortex with a double-peak structure [5]. In order to consider the energy transfer, using the DNS and experimental results is rigorous method. However, those results obtained from the DNS and experiment are complicated and are difficult to analyse. Thus, the analytical approach is useful to understand the feature of the energy transfer across the scales. In this study, the energy transfer around the elliptic Burgers vortex is analytically and numerically examined.

ANALYTICAL METHOD

We use the asymptotic solution of the elliptic Burgers vortices [3]. The background strain flow given to the elliptic vortex with the rotation axis in z direction is defined below.

$$U = (\alpha x, \beta y, \gamma z), \alpha + \beta + \gamma = 0, \alpha < 0 < \gamma, \beta > \alpha.$$

The normalized steady vorticity equation is described as

$$\frac{\partial(\psi,\omega)}{\partial(x,y)} = \varepsilon\left[\left(\alpha x\frac{\partial}{\partial x} + \beta y\frac{\partial}{\partial y}\right)\omega - \omega - \nabla^2\omega\right],$$

where the stream function expanded with Reynolds number defined by circulation and viscosity is

$$\psi = \psi_0(r) + \varepsilon_1 f(r)\sin 2\theta + \varepsilon^2\psi_2(r,\theta), \quad \varepsilon = 1/R_\Gamma = \nu/\Gamma, \quad \varepsilon_1 = \lambda\varepsilon, \quad \lambda = (\alpha-\beta)/(\alpha+\beta).$$

We used a typical condition of Re = 200 and $\lambda_0 = 9$ where λ_0 is the total stretching parameter and the value of 9 is commonly seen in homogeneous isotropic turbulence, turbulent mixing layer and turbulent channel flows [1]. In the DNS, λ_0 is computed using the velocity strain tensor at the centre of the vortex. However, the value consists in the background strain and the strain of the vortex. The stretching parameter λ by the background strain flow is analytically solved as 3.63.

Getting the velocity field of the elliptic Burgers vortex, we carried out the filtering operation using differential filter

$$\overline{u}_i = u_i + \frac{\overline{\Delta}^2}{24}\Delta u_i + O(\overline{\Delta}^4).$$

By using this filtering operation, we can calculate the energy transfer term $-\tau_{ij}\overline{S}_{ij}$ that is expressed by the multiplication of the subgrid-scale (SGS) stress tensor $\tau_{ij} = \overline{u_i u_j} - \overline{u}_i\overline{u}_j$ and the filtered velocity strain tensor. The positive and negative energy transfer terms indicate the forward scatter and backward scatter, respectively.

MAIN RESULTS

Figure 1 shows the distributions of vorticity and velocity vectors of the elliptic Burgers vortex at Re = 200 and $\lambda_0 = 9$. This is a typical vortex as seen in the turbulence [1]. By using the filtering operations, as shown in the left figure of Fig. 2, we obtain the energy transfer distribution where red and blue colours show the regions of the forward scatter and backward scatter, respectively. The forward scatter and backward scatter appear around the vortex as a quadrupole and those are located in the x and y directions that corresponds to the directions of the minimum and maximum eigenvalues. This

a) Corresponding author. Email: hkobayas@phys-h.keio.ac.jp.

distribution is analytically solved and decomposed with sine and cosine functions. By integrating that distribution in the azimuthal direction, we obtain the net energy transfer distribution as shown in the right figure of Fig. 2. We found that the net energy transfer occurs at the centre of the vortex. The amount of the net energy transfer is analytically derived as follows.

$$-\int_0^{\infty}\int_0^{2\pi}\tau_{ij}\overline{S}_{ij}rdrd\theta=\frac{\overline{\Delta}^2\varepsilon}{96\pi}\left[1-\frac{\overline{\Delta}^2}{64}\right]$$

We will elucidate the effects of the Reynolds number and the filter size on the energy transfer across scales in the presentation in detail.

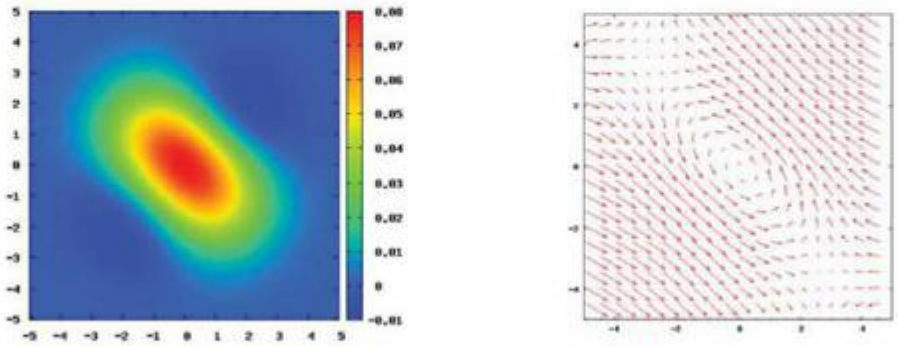

Figure 1 Distributions of vorticity (left) and velocity vectors (right).

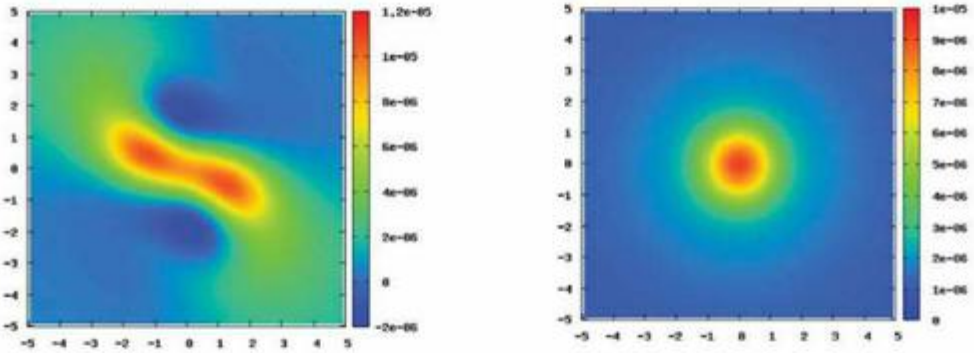

Figure 2 Distributions of energy transfer (left) and net energy transfer integrated in the azimuthal direction (right).

CONCLUSIONS

The energy transfer across scales around the elliptic Burgers vortices is examined analytically and numerically. The forward scatter with a double-peak structure appears in the direction of the minimum eigenvalue of the velocity strain tensor whereas the backward scatter with a double-peak structure emerges in the direction of the maximum eigenvalue. Although those double-peak structures distribute as a quadrupole around the vortex, the net energy transfer integrated in the azimuthal direction occurs at the centre of the vortex as the forward scatter. This analysis enable us to show the energy transfer decomposed into the Leonard, cross and Reynolds terms and to compare the energy transfer predicted through the Smagorinsky and Bardina models in LES.

References

[1] Wang, Y., Tanahashi, M., Miyauchi, T.: Coherent fine scale eddies in turbulence transition of spatially-developing mixing layer. *Int. J. Heat and Fluid Flow*, **28**:6, 1280-1290, 2007.

[2] Das, S. K., Tanahashi, M., Shoji, K., Miyauchi, T.: Statistical properties of coherent fine eddies in wall-bounded turbulent flows by direct numerical simulation. *Theor. Comp. Fluid Dyn.* **20**:2, 55-71, 2006.

[3] Moffatt, H. K., Kida, S. and Ohkitani, K.: Stretched vortices -- the sinews of turbulence; large-Reynolds-number asymptotics. *J. Fluid Mech.* **259**:241-264, 1994.

[4] Aoyama, T., Ishihara, T., Kaneda, Y., Yokokawa, M., Itakura, K., and Uno, A.: Statistics of Energy Transfer in High-Resolution Direct Numerical Simulation of Turbulence in a Periodic Box. *Journal of the Physical Society of Japan*, **74**:12, 3202–3212, 2005.

[5] Natrajan, V. K. and K. T. Christensen, K.T.: The role of coherent structures in subgrid-scale energy transfer within the log layer of wall turbulence. *Phys. Fluids*, **18**:065104, 2006.

CHARACTERIZING MULTI-SCALE INTERACTION IN TURBULENCE

Cristian C Lalescu *[1] and Michael Wilczek[1]
[1]*Max Planck Institute for Dynamics and Self-Organization, 37077 Goettingen, Germany*

Summary In fully developed turbulence, interactions take place between structures spanning a broad range of length and time scales. In this work, we aim to characterize these multi-scale interactions quantitatively. To this end, we identify the time scales relevant for structures of a given size, both from an Eulerian and a Lagrangian perspective. By employing filtering techniques in space and time, we compare turbulent velocity fields containing length scales above a given cutoff-scale with time-filtered fields. Varying the filter widths and times yields a precise picture of the various interactions. In a second step, we generalize the analysis to the Lagrangian frame to study the impact of large- and small-scale fluctuations on turbulent particle transport.

In fully developed three-dimensional turbulence, eddies of a wide range of sizes are dynamically active and energy is transferred from large to small scales. With respect to time scales, a naive application of the 1941 Kolmogorov theory predicts that eddies of scale ℓ, in the inertial range, should have a characteristic time scale $\tau \sim (\ell^2/\varepsilon)^{1/3}$, where ε is the mean energy dissipation rate. It is well known, however, that Eulerian statistical quantities are affected by random sweeping [1, 2], since structures of some characteristic size in the inertial and dissipative ranges are advected by the more energetic larger scales independently of any "scale-local dynamics" taking place at the same time. Random sweeping is known to have a significant impact on the decorrelation of Eulerian quantities in time [3, 4]. By analyzing both Lagrangian and Eulerian statistics for direct numerical simulations (DNS) of homogeneous isotropic turbulence, we aim to better distinguish between "scale-local dynamics" and random sweeping effects. While kinematic considerations have already led to the conclusion that only eddies of similar sizes interact effectively [5], here we progress towards quantifying how different time scales are associated to different length scales.

As a first step, we filter the DNS over time and space. If eddies of size ℓ evolve roughly on time scales τ, the naive expectation is that $\mathbf{u}_\ell \approx \mathbf{u}_\tau$, where $\mathbf{u}_\ell$ contains only eddies of size at least ℓ and $\mathbf{u}_\tau$ contains only components of $\mathbf{u}$ that evolve over time scales of at least τ. The removal of eddies smaller than ℓ is achieved by a spatial filtering, whereas fluctuating components that are faster than some τ are removed by temporal filtering.

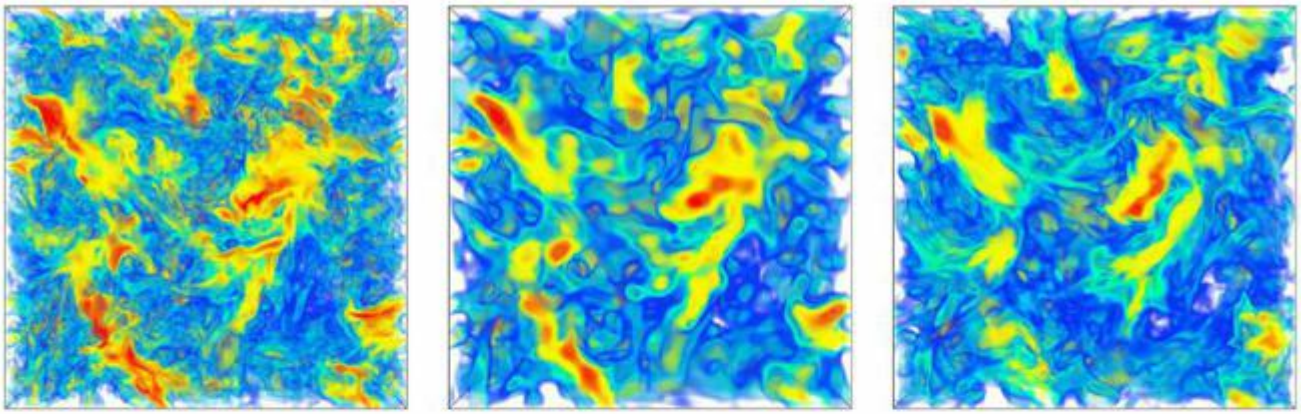

Figure 1: Snapshot of a turbulent velocity field. Velocity field containing all scales in space and time (left), result of spatial filtering (center) and result of temporal filtering (right). While the space- and time-filtered field show a similar large-scale structure comparable to the unfiltered field, small scales differ significantly. This points at the absence of a simple relationship between time and length scales.

In Fig. 1 we show, for illustration, an unfiltered velocity field $\mathbf{u}$ and the corresponding filtered fields, to emphasize the visually distinct details; differences are made more clear by the energy spectra shown in the left-hand plot of Fig. 2. It is evident that temporal filtering decreases the amplitudes of small-scale fluctuations. However, small scales are still present after temporal filtering, even though amplitudes are lowered progressively more for decreasing scales. This averaging effect, of course, is induced by both the scale-local dynamics as well as the random sweeping.

To quantify the difference between time-filtered and space-filtered fields we introduce the normalized difference:

$$\mathcal{M}(\tau, \ell) = \left\langle \frac{\|\mathbf{u}_\ell - \mathbf{u}_\tau\|_2}{\|\mathbf{u}\|_2} \right\rangle \tag{1}$$

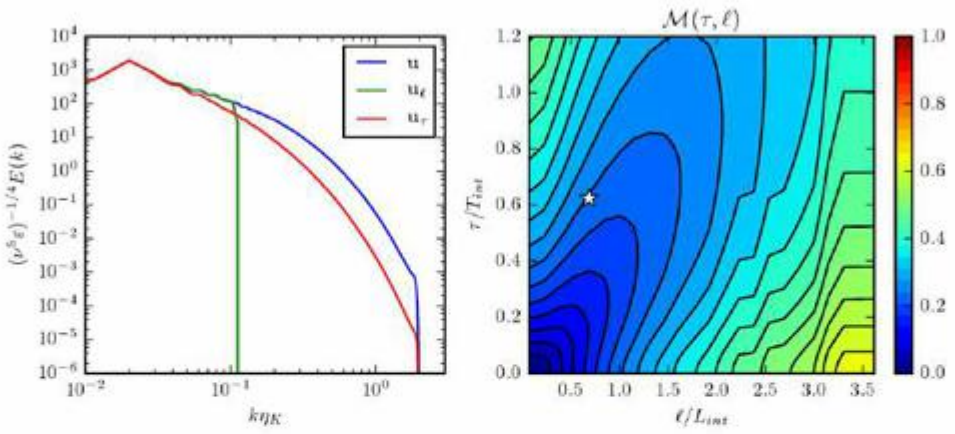

Figure 2: Spectra for original, spatially filtered and temporally filtered field (left) and difference between the two filtered fields, for different filter sizes (right). The white star corresponds to the ℓ and τ used for Fig. 1 and the spectra.

where the L^2 norms are taken over the spatial domain of the flow and the angular brackets denote ensemble averaging.

DNS data at $R_\lambda \approx 130$ is shown in Fig. 2. We observe that the different isocontours of $\mathcal{M}$ are not simply linear rescalings of each other; there is a nontrivial transformation as $\mathcal{M}$ increases and τ and ℓ reach integral scale values. Additional DNS at higher R_λ indicate that the normalized difference tends to scale with the large-eddy turn-over time and the integral length — which, as expected, points at random sweeping as the dominant effect. The results will be further quantified using a simple random sweeping model [6].

As a next step, complementary Lagrangian results will be presented. We will consider different "species" of Lagrangian tracers that follow Eulerian velocity fields filtered at various length scales. By this the dynamical influence of a range of scales is systematically eliminated. The elimination of small scales is expected to have only limited impact on single-particle statistics such as the mean square displacement because of the dominant influence of large-scale sweeping. Two-particle dispersion, on the other hand, largely eliminates sweeping effects and is expected to be more sensitive to smaller-scale fluctuations. This analysis will draw a detailed picture of the influence of Eulerian scales on Lagrangian statistics, yielding new insights into the problem of random sweeping by building on previous modeling attempts [7, 8, 6]. Besides characterizing fundamental aspects of turbulence, the results will also shed light on Lagrangian transport in large eddy simulations of turbulence relevant in many engineering applications, which has been a motivation for a number of recent studies [8, 9, 10].

References

[1] R. H. Kraichnan, "Relation between Lagrangian and Eulerian correlation times of a turbulent velocity field," *Phys. Fluids*, vol. 7, p. 142, 1964.

[2] H. Tennekes, "Eulerian and lagrangian time microscales in isotropic turbulence," *J. Fluid Mech.*, vol. 67, pp. 561–567, 1975.

[3] S. Chen and R. H. Kraichnan, "Sweeping decorrelation in isotropic turbulence," *Phys. Fluids A*, vol. 1, no. 12, pp. 2019–2024, 1989.

[4] M. Nelkin and M. Tabor, "Time correlations and random sweeping in isotropic turbulence," *Phys. Fluids A*, vol. 2, p. 81, 1990.

[5] G. L. Eyink, "Locality of turbulent cascades," *Physica D*, vol. 207, pp. 91–116, 2005.

[6] M. Wilczek and Y. Narita, "Wave-number-frequency spectrum for turbulence from a random sweeping hypothesis with mean flow," *Phys. Rev. E*, vol. 86, no. 6, 2012.

[7] G.-W. He and J.-B. Zhang, "Elliptic model for space-time correlations in turbulent shear flows," *Phys. Rev. E*, vol. 73, p. 055303, 2006.

[8] G.-W. He, G. Jin, and X. Zhao, "Scale-similarity model for Lagrangian velocity correlations in isotropic and stationary turbulence," *Phys. Rev. E*, vol. 80, p. 066313, 2009.

[9] J. Pozorski and S. V. Apte, "Filtered particle tracking in isotropic turbulence and stochastic modeling of subgrid-scale dispersion," *Int. J. Multiphas. Flow*, vol. 35, pp. 118–128, 2009.

[10] I. M. Mazzitelli, F. Toschi, and A. S. Lanotte, "An accurate and efficient Lagrangian sub-grid model," *Phys. Fluids*, vol. 26, p. 095101, 2014.

*Corresponding author. Email: Cristian.Lalescu@ds.mpg.de

MULTI-RESOLUTION ANALYSIS OF THE TURBULENT BOUNDARY LAYER WITH ORTHOGONAL WAVELET AND POD

Guo-Sheng He[1a)], Jin-Jun Wang[1]
[1]*Ministry-of-Education key laboratory of Fluid Mechanics, Beijing University of Aeronautics and Astronautics, Beijing, China*

Summary The flat plate turbulent boundary layer triggered by a tripwire is measured with two-dimensional particle image velocimetry (PIV) in the plane perpendicular to the plate. An orthogonal wavelet multi-resolution technique has been applied to decompose the flow into a number of wavelet components. The coherent structures in each wavelet component are examined by the proper orthogonal decomposition (POD) method. The POD modes of different wavelet components clearly reveal the cascade of scales in the turbulent boundary layer, while the POD modes of the measured data are only suitable to reveal the large coherent structures.

INTRODUCTION

Flow structures in turbulence consist of a wide range of scales. Previous studies on turbulent structures mostly focused on large-scale organized motions (large coherent structures), and the attention paid to other scales has been relatively scarce. The wavelet technique proposed by Mallat [1] provides a hierarchical frame work to represent a signal, which allows a muti-resolution analysis of the signal. Since then a lot of efforts have been made on applying this technique to investigate various scales in turbulence (see Meneveau [2], Farge[3] and Mouri[4] for a few examples). However, most of the previous studies in the literature are based on measurements of a single hot-wire, which cannot directly reveal the structures.

Recently, Rinoshika[5] used the wavelet technique to analyse the velocity data obtained by two rakes of hot-wires in the turbulent near wake of a circular cylinder. Using Taylor's frozen hypothesis, they were able to construct the sectional streamlines for the measured velocities and also each wavelet component. These streamlines, as well as a two-point velocity correlation in their study, showed the correspondence between the central frequencies (wavelet level) and spatial scales of the wavelet components.

In the present study, the wavelet technique is applied to velocity data of the turbulent boundary layer obtained by two-dimensional PIV measurements. Therefore the spatial structure can be revealed without relying on the Taylor's hypothesis. Moreover, POD method is used to examine the most important coherent structures in each wavelet component. POD method is widely used in the analysis of complex flow, but usually only the first a few modes (the large structures) are examined. In the present paper, a combination of the wavelet technique and POD method is expected to yield more details of the turbulent boundary layer.

EXPERIMENTAL SET-UP AND METHODOLOGY

The present experiment was conducted in a low-speed water tunnel. A flat plate with an elliptical leading edge was horizontally positioned at the center of the entire depth of the water tunnel. A rod with the diameter D=10mm placed on the flat plate, 300mm (15D) downstream of the leading edge, to trigger the boundary layer. The location of the rod on the flat plate is defined as the origin. x is in the streamwise direction and y is perpendicular to the flat plate. At x/D=100 (100D downstream of the rod, 115D from the leading edge), the boundary layer has become fully turbulent, which was verified by the mean streamwise velocity profile. The boundary layer thickness δ was about 76mm, corresponding to a friction Reynolds number Re_τ= 246 ($Re_\tau=\delta/y^*$, $y^*$is the inner length scale). Two-dimensional time-resolved particle image velocimetry was used to measure the flow-field in the rectangular region of about $100<x/D<122$ and $0<y/D<9$. There were a total of 256×100 vectors in each instantaneous velocity field and the spacing between adjacent vectors was 0.87mm (0.087D) in both x and y direction.

The velocity data obtained by the PIV technique was then decomposed by the one dimensional discrete orthogonal Daubechies wavelet basis with an order of 20 along the temporal direction (A detailed description of this kind of decomposition can be found in Mallat[1] and Rinoshika[5]). The decomposition depth was 10 levels. The flow field was then reconstructed with wavelet coefficient at each level, yielding 10 wavelet components of the flow field. The higher the level, the lower the central frequency. Wavelet component at the nth wavelet level (WL) was denoted as WL-n. For example, the wavelet component at the 10th level, WL-10, had the lowest temporal frequency and therefore should contain structures with the largest spatial wavelength (as shown in Figure 1(a) below).

The coherent structures in each wavelet component were then examined by the POD method. POD is a common tool in the analysis of fluid flow as it is very useful in extracting the dominant flow structures from the complex flow field. The theory and the application of POD method can be found in Berkooz[6] .

RESULTS AND DISCUSSIONS

a) Corresponding author. Email: heguosheng@buaa.edu.cn

Representative POD modes of WL5-10 are shown in Figure 1. The left column shows the modes for streamwise velocity *u* and the right column for vertical velocity *v*. Only the first or second mode of each wavelet component is shown, except that Figure1 (f) and (m) are the 6th mode of WL-6 for *u* and *v*, respectively. The cascade of scales in the turbulent boundary layer are evident. In figure 1(a) the coherent structure is featured as a long strip along the wall that extends out of the field of view. This may correspond to the long streamwise streaky structures in the sub-layer of the turbulent boundary layer. In figure 1(b), the streamwise extent of the strip decreases. Note that the coherent structure in figure 1(b) extends much further away from the wall than that in figure 1(a), suggesting this structure may have a wall-normal scale comparable to the boundary layer thickness. In Figure 1(c), (d), (e) and (g), with the decrease of the wavelet level, the streamwise wavelength of the modes also decreases. Although it is too early to speculate the flow structures of various scales based on the current POD modes, the hierarchical paradigm proposed by Kim[7], which is comprised of hairpin vortex, hairpin packet, large-scale-motions and very-large-scale-motions, may be a good candidate. However, we will not elaborate it here.

What we want to emphasize in the present paper is that the combination of wavelet technique and POD method yields more details about the turbulent boundary layer. If the POD is applied to the measured (undecomposed) data directly, only the modes in Figure 1 (a)-(d) (and (h)-(k)) can find their counterparts (not shown here due to length limitation). While for high wavenumber wavelet components (such as Figure 1 (g)), finding their counterparts may be very difficult or even impossible. This is because the POD modes are only orthogonal in space, so one mode may reflect contributions from high and low frequency components. As low frequency components are usually much more energetic, the POD modes for high frequency (wavenumber) components may easily be contaminated by the low frequency components. Therefore the present wavelet decomposition provides a good way to isolate the small scale structures from the influences of the large scale ones, and the POD method can then extract these small scale coherent structures.

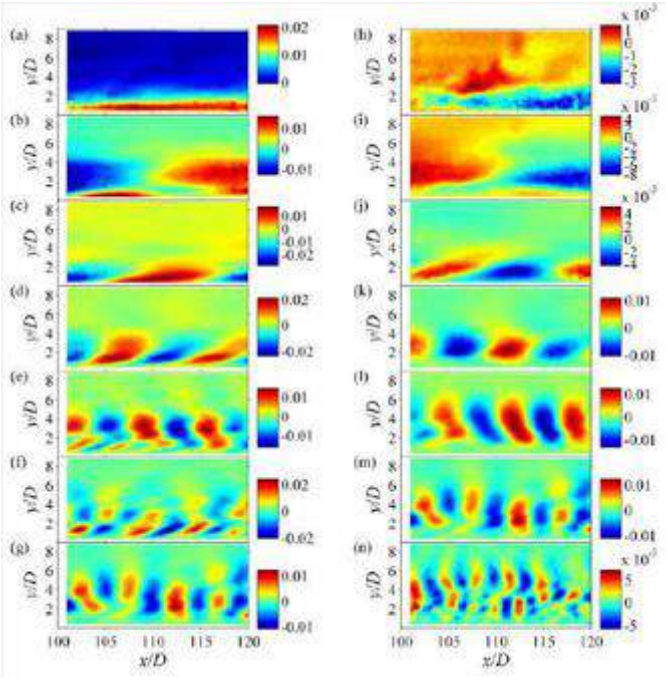

Figure 1 POD modes of the wavelet components. (a) and (h) WL-10, the first mode; (b) and (i) WL-9, the second mode; (c) and (j) WL-8, the first mode; (d) and (k) WL-7, the second mode; (e) and (l) WL-6, the first mode; (f) and (m) WL-6, the sixth mode; (g) and (n) WL-5, the first mode; Left column, the mode for streamwise velocity *u*; Right column, the mode for vertical velocity *v*.

This work has been supported by the National Natural Science Foundation of China (Grant No. 11502011) and Postdoctoral Science Foundation of China (Grant No. 2015M570023).

References

[1] Mallat S.: A Theory for Multi-Resolution Signal Decomposition: The Wavelet Representation. *IEEE Trans. PAMI* **11**: 674–693, 1989.

[2] Meneveau C.: Analysis of Turbulence in the Orthonormal Wavelet Representation. *Journal of Fluid Mechanics* **232**: 469–520, 1991.

[3] Farge M.: Wavelet Transforms and Their Applications to Turbulence. *Annual Review of Fluid Mechanics* **24**: 395–457, 1992.

[4] Mouri H., et al.: Wavelet Analysis of Velocities in Laboratory Isotropic Turbulence. *Journal of Fluid Mechanics* **389**: 229–254, 1999.

[5] Rinoshika A. and Zhou Y.: Orthogonal Wavelet Multi-Resolution Analysis of a Turbulent Cylinder Wake. *Journal of Fluid Mechanics* **524**: 229–248, 2005.

[6] Berkooz G., Holmes P. and Lumley J. L.: The Proper Orthogonal Decomposition in the Analysis of Turbulent Flows. *Annual Review of Fluid Mechanics* **25**: 539-575, 1993.

[7] Kim K. C. and Adrian R. J.: Very Large-Scale Motion in the Outer Layer. *Physics of Fluids* **11**(2): 417-422, 1999.

CONCURRENT SCALE INTERACTIONS IN A TURBULENT SHEAR FLOW

Oliver Buxton*[1]

[1]*Department of Aeronautics, Imperial College London, London, United Kingdom*

Summary The interaction between concurrent large-scale velocity fluctuations and small-scale velocity and velocity-gradient fluctuations is examined with both experimental and complementary DNS data. It is shown that both the sign and the magnitude of the large-scale velocity fluctuation affect this scale interaction, as does the definition of the "modulating" large scales, with a distinct peak interaction length-scale identified. The results are explained via a "convective" mechanism whereby high activity small-scale fluctuations are transported from the centre-line of the shear flow by the large-scale velocity fluctuations.

INTRODUCTION

Whilst turbulence is known to be a multi-scale phenomenon it has long been assumed that the smallest scales of motion, those responsible for the dissipation of turbulent kinetic energy to internal energy, possess a universal phenomenology. However, at practically realisable Reynolds numbers, there is a distinct interaction between the large and small scales. Recently there has been significant interest in these scale interaction effects in wall-bounded flows in which the large, outer scales are observed to leave a "footprint" on the inner small scales [e.g. 1]. However, little information is available concerning these interactions in free shear flows. The first study to examine the interaction between the large and small scales in a variety of shear flows (both wall bounded and free shear flows) was that of Bandyopadhyay and Hussain [2]. The authors examined the time correlations between the low and high frequency content of hot-wire time series data and observed a coupling between the large scales (low frequencies) and small scales (high frequencies) that was maximised when the two signals were concurrent. This manuscript combines the findings of Buxton and Ganapathisubramani [3] and Buxton [4], which examine these concurrent scale interactions in the far field of a turbulent mixing layer, thereby offering an explanation for these interactions.

DATA AND SCALE SEPARATION

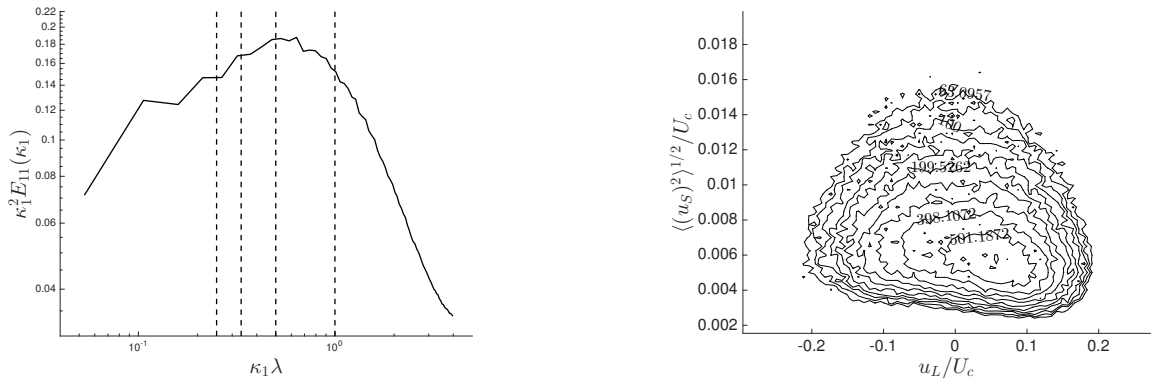

(a) (b)

Figure 1: (a) Dissipation spectrum along the centre-line of the mixing layer. (b) Joint PDF between the variance of the small-scale velocity fluctuations and the concurrent large-scale velocity fluctuation.

The data consists of experimental [3] and DNS [4] data from the far field of a planar mixing layer in which the turbulence is "fully developed". In both cases the centre-line turbulent Reynolds number (based on the Taylor microscale, λ) is $Re_\lambda \approx 260$. The dissipation spectrum for this flow is presented in figure 1(a). The experimental data consists of four simultaneously acquired particle image velocimetry (PIV) fields of view. Three of the fields of view are highly spatially resolved (1.2η, where η is the Kolmogorov length scale) and are embedded within the fourth, more coarsely resolved (12η) field of view. The highly resolved data, which comes from the high speed side of the mixing layer, is filtered to remove all length scales $> \lambda$, where λ is the Taylor microscale, and contrastingly the coarsely resolved field of view is filtered to remove all length scales $< \lambda$. The DNS data consists of the final 15% (in the streamwise direction) of the simulation domain of a planar mixing layer produced

*Email: o.buxton@imperial.ac.uk

by inlet flows U_1 and U_2 in the ratio $U_1/U_2 = 2$ either side of a splitter plate. The data was subsequently filtered with a sharp spectral filter at a variety of cutoff length scales marked on figure 1(a). Both the high wavenumber content and the low wavenumber content from the low speed side of the mixing layer were retained. Throughout this abstract the suffix "S" denotes the small-scale quantities (high wavenumbers) and "L" denotes the large-scale content.

DISCUSSION

Figure 1(b) shows a joint probability density function (PDF) between the variance of the small-scale velocity fluctuations and the concurrent large-scale velocity fluctuation from the experimental data set. The contours of the joint PDF are clearly sloped. This is illustrative of a scale interaction effect in which a concurrent low momentum large-scale fluctuation amplifies the concurrent small-scale fluctuations, with both the sign and magnitude of the large-scale fluctuation being important.

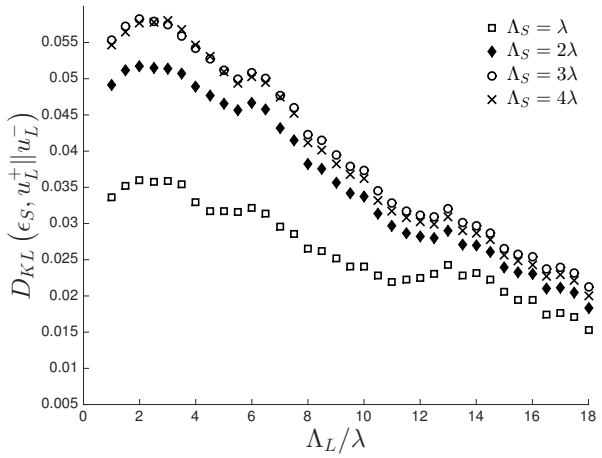

Figure 2: KLD between the PDFs of small-scale dissipation conditioned on positive and negative large-scale velocity fluctuations. The small-scale field consists of all length scales $\Lambda \leq \Lambda_S$ and the large-scale field consists of all length scales $\Lambda \geq \Lambda_L$.

Figure 2 shows that this scale interaction effect not only amplifies the energy content of the small-scale fluctuations but also the small-scale velocity-gradients. The figure shows the integrated difference between the PDF of the small-scale dissipation conditioned on the concurrent large-scale fluctuation being positive and the PDF of dissipation conditioned on the concurrent large-scale fluctuation being negative. This is quantified by means of the Kullback-Leibler divergence (KLD) [5], defined as

$$D_{KL}(A\|B) = \int_{-\infty}^{\infty} \ln\left[\frac{a(X)}{b(X)}\right] a(X)\mathrm{d}X$$

in which $a(X)$ and $b(X)$ are PDFs of fluctuating variable X. This is computed for various thresholds, $\{\Lambda_S, \Lambda_L\}$, defining the large and small scales. There is a peak in this interaction at $\Lambda_L \approx 2.5\lambda$, regardless of the definition of the small scales. This value of 2.5λ roughly corresponds to $L/4$, where L is the integral length scale, which is associated with the large, streamwise roller structures in a mixing layer.

The experimental data (figure 1(b)) is from the high speed side of the mixing layer whereas the DNS data (figure 2) is from the low speed side. The opposite scale interaction effect is observed in the low speed side to figure 1(b), in which the small-scale activity is amplified by a concurrent positive large-scale velocity fluctuation.

Neglecting smaller constituent term we may write the turbulent kinetic energy production term $\mathcal{P} \approx \circ\, \overline{u_L v_L}\partial U/\partial y$, which is positive. For a mixing layer the mean velocity gradient remains positive, hence for $\mathcal{P} > 0$ we require u_L and v_L to be inversely correlated. In the far field of a mixing layer the peak Reynolds stresses are located at the centre-line. Briefly, we may consider the proposed convective mechanism to work as follows: a positive v_L fluctuation in the high speed side of the mixing layer will originate from a region of higher turbulence intensity (Reynolds stresses). This is correlated to a negative u_L fluctuation, explaining the findings of figure 1(b). The opposite effect will of course be observed in the low speed side of the mixing layer, explaining the findings from the DNS data. The final manuscript will expand upon this proposed mechanism and will provide a fuller account of the scale interactions in a free shear flow, both of small-scale velocity fluctuations/Reynolds stresses and velocity-gradient phenomena, such as dissipation and enstrophy amplification via vortex stretching.

References

[1] N. Hutchins and I. Marusic. Large-scale influences in near-wall turbulence. *Phil. Trans. R. Soc. Lond.*, 365:647–664, 2007.

[2] P.R. Bandyopadhyay and A.K.M.F. Hussain. The coupling between scales in shear flows. *Phys. Fluids*, 27(9):2221–2228, 1984.

[3] O. R. H. Buxton and B. Ganapathisubramani. Concurrent scale interactions in the far-field of a turbulent mixing layer. *Phys. Fluids*, 26(12):125106:1–19, 2014.

[4] O.R.H. Buxton. Modulation of the velocity gradient tensor by concurrent large-scale velocity fluctuations in a turbulent mixing layer. *J. Fluid Mech.*, 777:R1:1–12, 2015.

[5] S. Kullback and R. A. Leibler. On information and sufficiency. *Ann. Math. Stat.*, 22(1):79–86, 1951.

TIME INTERVAL BETWEEN MEAN-FLOW REVERSALS IN A TWO-DIMENSIONAL RANDOMLY FORCED FLOW IN A SQUARE DOMAIN

Takeshi Matsumoto [*1]
[1]*Department of Physics, Kyoto University, Japan*

Summary We study time interval between random mean-flow reversals of a two-dimensional forced Navier-Stokes turbulence in a square domain. Via a heuristic modeling, we show that the interval scale is determined by the viscosity and the length scale given by the energy and the enstrophy.

INTRODUCTION

When a turbulent flow is somehow maintained inside a closed container, it is known that a large-scale mean flow can appear. More interestingly, it is also known that in certain cases the direction of the mean flow changes rather abruptly. A famous example is the high-Rayleigh number thermal convection, see, e.g., [1, 2]. How an organized mean flow of a confined turbulent flow suddenly switches its direction — mechanism of the reversal — is an important but unresolved question.

Another, perhaps simpler, example of such reversal is a two-dimensional (barotropic) forced flow in a square domain, which was first experimentally found by Sommeria [3] and was later modeled and numerically studied by Molenaar *et al*. [4] (see also [5]). According to Molenaar *et al*.'s numerical study [4], the reversal occurs irregularly but there is a typical time scale of the interval between reversals, which is order of 100 $\times$ (large-scale characteristic time). The large-scale characteristic time is here defined as the side length divided by the typical velocity given by the kinetic energy.

In the present study, we study the reversal in this two-dimensional flow formulated in [4]. In particular we consider determinant of the typical time interval via a heuristic, stochastic modeling of the integral quantities of the flow such as the energy, the enstrophy and the angular momentum.

NUMERICAL RESULTS AND MODELING

First, we numerically solve the two-dimensional randomly forced Navier-Stokes equation in the square domain as in [4]. The boundary condition is no-slip and the Reynolds number is about 3000. However, we use a slightly different Chebyshev tau method which is the streamfunction-vorticity formulation developed in [6] (the velocity-vorticity formulation was used in [4]). We reproduce the mean-flow reversals as obtained in [4]. The resultant normalized angular momentum of the flow, $L'(t)$, shown in Fig.1 indicates that the typical interval between reversals is indeed $O(100)$. The instantaneous kinetic energy, $E(t)$, the enstrophy, $Q(t)$, the angular momentum, $L(t)$, and the normalized angular momentum, $L'(t)$, of the flow are defined respectively as

$$E(t)=\frac{1}{2}\int_{\mathcal{D}}|\boldsymbol{u}(\boldsymbol{x},t)|^2d^2x,\quad Q(t)=\frac{1}{2}\int_{\mathcal{D}}\omega(\boldsymbol{x},t)^2d^2x,\quad L(t)=-\frac{1}{2}\int_{\mathcal{D}}|\boldsymbol{x}|^2\omega(\boldsymbol{x},t)d^2x,\quad L'(t)=\frac{\sqrt{3}L(t)}{D^2\sqrt{E(t)}}. \tag{1}$$

Here $\boldsymbol{u}$ and ω are the velocity and the vorticity; $\mathcal{D}$ denotes the square domain; D is the side length of the square.

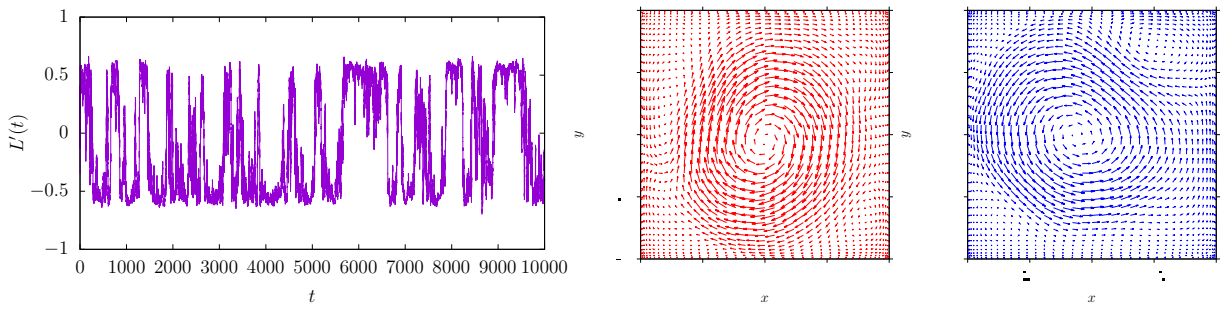

Figure 1: *Left:* time variation of the normalized angular momentum, $L'(t)$, obtained from one realization of the random forcing. *Middle:* typical velocity field of $L'(t)<0$ state. *Right:* typical velocity field of $L'(t)>0$ state.

*Corresponding author. Email: takeshi@kyoryu.scphys.kyoto-u.ac.jp

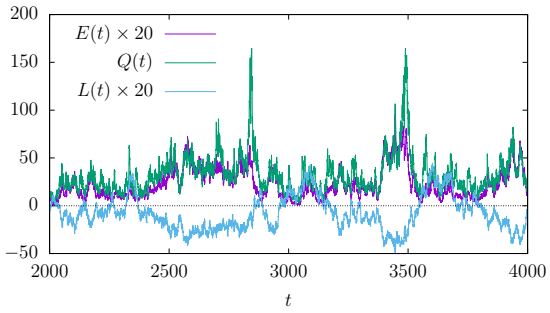

Figure 2: Time variation of the scaled energy, the enstrophy and the scaled angular momentum.

As already noticed in [4], $E(t)$, $Q(t)$ and $|L(t)|$ are almost perfectly correlated, which is shown in Fig.2. This implies that the integrals are characterized with a single length scale λ and a velocity scale U [4].

Now we start to model the time variation of the integrals with the two scales. First, we assume for simplicity that λ is a constant and only U depends on time. Second, by dimensional analysis, we assume that the integrals are expressed as $E(t) \sim D^2U(t)^2$, $Q(t) \sim (U(t)/\lambda)^2D^2$ and $L(t) \sim \lambda U(t)D^2$ (hence $L'(t) \sim \lambda \times \mathrm{sign}(U(t))$). Third, we consider the energy budget, which can be modeled roughly as $dE/dt = -\nu Q(t) + \xi(t)$. Here ν is the kinematic viscosity and $\xi(t)$ represents the energy input from the random forcing. This modeled budget is a stochastic process. On dimensional grounds, the random input term in the budget is $\xi(t) \sim U(t)\eta(t)D^2$, where $\eta(t)$ represents the random forcing added to the Navier-Stokes equation. Putting the scales λ and U into the modeled budget, we obtain

$$\frac{dU(t)}{dt} = -\frac{\nu}{2\lambda^2}U(t) + \frac{1}{2}\eta(t). \tag{2}$$

Lastly, we assume that $\eta(t)$ is a Brownian noise. Then Eq.(2) becomes an Ornstein-Uhlenbeck process. The correlation time of the random velocity scale, $U(t)$, is hence $T_c = 2\lambda^2/\nu$.

Does this time scale T_c agree with the interval time scale (~ 100) of the mean flow reversal? For the length scale λ, we take the time average of $\sqrt{E(t)/Q(t)}$, which is 0.19. The kinematic viscosity of our simulation is $\nu = 5.0 \times 10^{-4}$. This gives $T_c = 144$, which is in agreement with the interval time scale (here we cheat a bit: the factor 2 in T_c is crucial for getting the correct order). We speculate that the length scale 0.19 corresponds to the radius of the corner vortex such as the one seen in the top-right corner of the right panel of Fig.1.

SUMMARY AND DISCUSSION

It is known that the interval between the random mean-flow reversal of the two-dimensional randomly forced Navier-Stokes equation in the square domain is typically order of 100 [4], which is longer than the standard norm of the large scales of the flow. We inferred that the interval time is determined by the kinematic viscosity and the length scale defined by the energy and the enstrophy, $\sqrt{E/Q}$ by combining the scale representation of the integral quantities and the heuristic stochastic modeling of the energy budget.

However the model (2) has a drawback. If the model is correct, the resultant probability density function (PDF) of $U(t)$ or $L(t) \sim \lambda U(t)D^2$ is Gaussian. However, the PDF of $L(t)$ obtained in the direct numerical simulation differs qualitatively from Gaussian distribution: it has two peaks. A possible way to model the double peaks will be discussed in the conference.

References

[1] Niemela, Skerbek, Sreenivasan & Donnely: J. Fluid Mech. 449:169–178, 2001.
[2] Ahlers, Grossmann & Lohse: Rev. Mod. Phys., 81:503–537, 2009.
[3] Sommeria: J. Fluid Mech. 170:139–168, 1986.
[4] Molenaar, Clercx & van Heijst: Physica D, 196:324–340, 2004.
[5] Clercx & van Heijst: App. Mech. Rev. 62:020802, 2009.
[6] Peyret: Spectral Methods For Incompressible Viscous Flow. Springer, 2002.

Turbulence on a fractally decimated Fourier set

Federico Toschi*[1], Alessandra S. Lanotte[2], Roberto Benzi[3], Shiva K. Malapaka[4], and Luca Biferale[5]
[1]*Department of Applied Physics, Eindhoven University of Technology, 5600 MB Eindhoven, Netherlands and IAC CNR, Via dei Taurini 19, 00185 Roma, Italy*
[2]*ISAC-CNR and INFN Sez. Lecce, 73100 Lecce, Italy*
[3]*Department of Physics and INFN, University of Rome Tor Vergata, Via della Ricerca Scientifica 1, 00133 Roma, Italy*
[4]*IIT- Bangalore, Electronics City, Hosur Road, Bangalore 560100, India*
[5]*Department of Physics and INFN, University of Rome Tor Vergata, Via della Ricerca Scientifica 1, 00133 Roma, Italy*

Summary One of the most distinct features of the physics of fluid dynamics turbulence is the intermittency of the flux of energy. Here we present a recently proposed approach (Lanotte et al., Phys. Rev. Lett. 115 2015) to investigate the nature of the energy transfer in incompressible, homogenous and isotropic turbulence. The Navier-Stokes equations are projected on a fractally decimated skeleton in Fourier space. The robustness of the energy transfer and of the vortex stretching are tested by changing the fractal dimension D in Fourier space, from $D = 3$ to $D = 2.5$ (where about 3% of the modes are retained). This approach allows to study the statistical properties of the energy cascade preserving the symmetries of the Navier-Stokes equations. We find that a direct energy flux is maintained while clear deviations from the Kolmogorov scaling are observed in the energy spectra. A simple phenomenological model to rationalize to explain our findings is suggested.

INTRODUCTION

Understanding the nature of the energy transfer in fluid dynamics turbulence is a fascinating outstanding open problem of classical physics. Furthermore, being able to understand the statistics and to control the energy flux in turbulence would have an impact on a broad number of fields and applications, from astrophysics [2], atmospheric/ocean sciences [3], to mathematics and engineering [4]. One of the main difficulties hampering theoretical advancement is the presence of intermittency, i.e. strongly non Gaussian fluctuations over a broad range of scales. The energy flux in turbulence, transporting energy from the large to the small scales, is chaotic, intermittent, non-linear and it is influenced by the vortex stretching mechanism acting at the smaller scales (the amplification of vorticity in thin long filaments). The role of small-scale vorticity has been at the center of long debates, questioning whether or not the presence of such coherent structures correlates with the non-Gaussian intermittent statistics observed at the small scales. In our recent work [1] we employ a novel approach based on the modification of the Navier-Stokes equations by means of a fractally decimated mode reduction in Fourier space. An appropriate decimation operator (projector), $\mathcal{P}^D$, acts on the velocity field as proposed in [6]. By introducing the following notation for the real-space, $\mathbf{v}(\mathbf{x}, t)$, and Fourier-space, $\mathbf{u}(\mathbf{k}, t)$, representations of the velocity field in in $D = 3$ the decimated field, denoted as $\mathbf{v}^D(\mathbf{x}, t)$, can be in the following way:

$$\mathbf{v}^D(\mathbf{x}, t) = \mathcal{P}^D\mathbf{v}(\mathbf{x}, t) = \sum_{\mathbf{k}\in\mathcal{Z}^3} e^{i\mathbf{k}\cdot\mathbf{x}}\,\gamma_{\mathbf{k}}\mathbf{u}(\mathbf{k}, t)\,. \tag{1}$$

In this expression the random numbers $\gamma_{\mathbf{k}}$, that do not vary with time, express the projection operator and are defined to be: $\gamma_{\mathbf{k}} = 1$ with probability h_k and 0 with probability $1 - h_k$ where $k \equiv |\mathbf{k}$. Choosing the probability $h_k \propto (k/k_0)^{D-3}$ (where $0 < D \leq 3$) ensures that the dynamics is isotropically decimated on a D-dimensional Fourier-set. The factors h_k are independent for each k but are choosen such to respect Hermitian symmetry, i.e. $\gamma_k = \gamma_{-k}$, so that $\mathcal{P}^D$ is self-adjoint. The modified Navier-Stokes equations in the decimated Fourier space are:

$$\partial_t\mathbf{v}^D = \mathcal{P}^D N(\mathbf{v}^D, \mathbf{v}^D) + \nu\,\nabla^2\mathbf{v}^D + \mathbf{f}^D\,. \tag{2}$$

It is important to underline that the non linear term, $N(\mathbf{v}, \mathbf{v}) = -\mathbf{v}\cdot\nabla\mathbf{v} + \nabla p$, is projected at each time-step on the quenched fractal set. This in order to constrain the dynamics to evolve only on the decimated Fourier skeleton. It worths underlying that since $\mathcal{P}^D\mathbf{v}^D = \mathbf{v}^D$, both energy and helicity are conserved quantities in the inviscid and unforced limit, thus retaining the same invariants of the original Navier-Stokes equations.
The eqs. (2) are numerically integrated by means of a simple modification of a standard pseudo-spectral solver with fully dealiasing with the $2/3$-rule, time stepping was performed by means of a second-order Adams-Bashforth scheme. The numerical integration provides a stationary flow that is statistically isotropic and homogeneous. A large-scale forcing [7] was

*Corresponding author. Email: f.toschi@tue.nl

employed to keep the total kinetic energy constant in the range of shells $0.7 \leq |\mathbf{k}| < 1.7$. With this setting we performed several numerical simulations with different fractal dimension in the interval $2.5 \leq D \leq 3$, different space resolution and different realizations of the fractal mask for the projector operator.

To start disentangling the relation between large and small scales one can study the shell-to-shell energy transfer in Fourier space. Following the notation adopted in Ref. [5], we write the energy spectrum for a generic flow in dimension D as:

$$E^D(k) = \int_{|\mathbf{k}_1|=k} d^3k_1 \gamma_{\mathbf{k}_1} \int d^3k_2 \gamma_{\mathbf{k}_2} \langle \mathbf{u}(\mathbf{k}_1)\, \mathbf{u}(\mathbf{k}_2) \rangle \,, \tag{3}$$

and the energy flux across a Fourier mode k, $\Pi^D(k) = \int_{|\mathbf{k}_1|<k} d^3k_1 \partial_t E(k_1)$:

$$\Pi^D(k) = \int_{|\mathbf{k}_1|<k} d^3k_1 \gamma_{\mathbf{k}_1} \int d^3k_2 d^3k_3 \gamma_{\mathbf{k}_2} \gamma_{\mathbf{k}_3} S(\mathbf{k}_1|\mathbf{k}_2, \mathbf{k}_3), \tag{4}$$

where [8] $S(\mathbf{k}_1|\mathbf{k}_2, \mathbf{k}_3) = -Im[\langle (\mathbf{k}_1 \cdot \mathbf{u}(\mathbf{k}_3))(\mathbf{u}(\mathbf{k}_1) \cdot \mathbf{u}(\mathbf{k}_2)) \rangle + \langle (\mathbf{k}_1 \cdot \mathbf{u}(\mathbf{k}_2))(\mathbf{u}(\mathbf{k}_1) \cdot \mathbf{u}(\mathbf{k}_3)) \rangle]$.

CONCLUSIONS

Our first finding is that the energy flux is relatively robust under mode reduction meaning that an inertial range of scales with a constant-flux is observed even when D decreased from 3 and few modes survive. This finding can be explained by the fact that the Fourier Galerkin truncations that we apply do not alter the inviscid conservation of quadratic quantities. The energy spectrum in Fourier space gets a power law correction that we were able to predicted by means of dimensional arguments. Our second finding is that small-scale intermittency is quickly reduced for $D < 3$ and it almost vanishes already at $D \sim 2.98$. The Fourier decimation procedure here discussed could be seen as a possible way to introduce a control parameter in the original Navier-Stokes turbulence problem capable of modifying the scaling properties of the system and possibly making it amenable of semi-analytic or perturbative approach.

ACKNOWLEDGMENTS

We acknowledge useful discussions with S. Musacchio and P. Perlekar, who collaborated with us in the first part of the work. Numerical simulations were done at CINECA (Italy), within the EU-PRACE Project Pra04, No. 806. This work is part of the activity of the ERC AdG NewTURB, No. 339032. We thank F. Bonaccorso and G. Amati for technical support. We acknowledge support from the COST-Action MP1305 for support.

References

[1] A.S. Lanotte, R. Benzi, S.K. Malapaka, F. Toschi, L. Biferale, "Turbulence on a Fractal Fourier Set", Phys. Rev. Lett. 115, 264502 (2015).
[2] D. Biskamp, *Magnetohydrodynamic Turbulence* (Cambridge University Press, Cambridge, 2008).
[3] J. Pedlosky, *Geophysical Fluid Dynamics*, (Springer-Verlag 1987).
[4] S. B. Pope, *Turbulent Flows*, (Cambridge University Press, Cambridge, 2000).
[5] R. H. Kraichnan, J. Fluid Mech. **47**, 525–535 (1971).
[6] U. Frisch, A. Pomyalov, I. Procaccia, and S. S. Ray, Phys. Rev. Lett. **108**, 074501 (2012).
[7] A. G. Lamorgese, D. A. Caughey, and S. B. Pope, Phys. Fluids **17**, 015106 (2005).
[8] H. A. Rose and P. L. Sulem, J. Phys. France **39**, 441–484 (1978).

SCALE BY SCALE ENERGY BUDGET IN THE NEAR WAKE OF A SQUARE CYLINDER

Felipe Alves Portela *[1], George Papadakis[1], and John Christos Vassilicos[1]

[1]*Department of Aeronautics, Imperial College London, London, United Kingdom*

Summary We study the energy cascade downstream of, but close to, a square cylinder $Re = 3900$ using two-point statistics, by means of DNS. Shortly after the mean recirculation region the turbulent energy spectrum exhibits a near $-5/3$ slope in the frequency domain. Our DNS analysis of the general Kármán-Howarth-Monin equation show that the production, transport, advection and fluctuating pressure terms cannot be neglected as they are in the Richardson-Kolmogorov equilibrium theory. Even so, the term which is interpreted as an interscale energy flux divergence in the case of homogeneous turbulence is close to $-\epsilon$ over a significant range of small scales, where ϵ is the turbulence dissipation rate.

INTRODUCTION

In Kolmogorov's seminal work [1], the assumptions of equilibrium and local homogeneity lead to the well known $\circ\, 5/3$ law (1a) for the turbulent energy spectrum $E(k)$ or equivalently the $2/3$ law (1b) for the second order structure function $\langle \delta q^2 \rangle = \langle \delta u_i \delta u_i \rangle$.

$$E(k) \propto k^{-\frac{5}{3}}, \qquad \langle \delta q^2 \rangle \propto r^{\frac{2}{3}} \tag{1a,1b}$$

We use our DNS to study all the terms in the most general equation governing the evolution of $\langle \delta q^2 \rangle$, i.e. the generalised Kármán-Howarth-Monin equation (2) derived directly from the Navier-Stokes equations without assumptions [2] and is therefore valid in any turbulent flow with any inhomogeneity and anisotropy structure.

$$\overbrace{\frac{\partial \langle \delta q^2 \rangle}{\partial t}}^{\mathcal{A}_t} + \overbrace{\frac{\partial \frac{U_i^+ + U_i^-}{2} \langle \delta q^2 \rangle}{\partial x_i}}^{\mathcal{A}} + \overbrace{\frac{\partial \langle \delta u_i \delta q^2 \rangle}{\partial r_i}}^{\Pi} + \overbrace{\frac{\partial \delta U_i \langle \delta q^2 \rangle}{\partial r_i}}^{\Pi_U} = \overbrace{\circ\, 2 \langle \delta u_i \delta u_j \rangle \frac{\partial \delta U_j}{\partial r_i} \circ \langle \left(u_i^+ + u_i^- \right) \delta u_j \rangle \frac{\partial \delta U_j}{\partial x_i}}^{\mathcal{P}}$$
$$\underbrace{\circ\, \frac{\partial \langle \frac{u_i^+ + u_i^-}{2} \delta q^2 \rangle}{\partial x_i}}_{\mathcal{T}_u} \underbrace{\circ\, 2 \frac{\partial \langle \delta u_j \delta p \rangle}{\partial x_j}}_{\mathcal{T}_p} + \underbrace{\nu \frac{1}{2} \frac{\partial}{\partial x_i} \frac{\partial}{\partial x_i} \langle \delta q^2 \rangle}_{\mathcal{D}_x} + \underbrace{2\nu \frac{\partial}{\partial r_i} \frac{\partial}{\partial r_i} \langle \delta q^2 \rangle}_{\mathcal{D}_r} \underbrace{\circ\, 2\nu \left(\langle \frac{\partial \delta u_j}{\partial x_i^+} \frac{\partial \delta u_j}{\partial x_i^+} \rangle + \langle \frac{\partial \delta u_j}{\partial x_i^-} \frac{\partial \delta u_j}{\partial x_i^-} \rangle \right)}_{\epsilon} \tag{2}$$

Eq. (2) was used to investigate experimentally the flow immediately downstream of a fractal grid by [3] but they were not able to access all the terms of this equation. None of the terms of (2) which they were able to access was negligible but they nevertheless found that Π remains fairly constant at increasing separations $r = ||r_i||$ while all other terms increase (in absolute value) with r. They also observed a $\circ\, 5/3$ in the turbulent energy frequency spectrum even though the flow does not comply with the assumptions of [1].

RESULTS AND DISCUSSION

We used an in-house finite volume code with second order central discretisation in space and second order semi-implicit discretisation in time while the PISO algorithm is used for the pressure-velocity coupling. The spatial resolution in the wake was at worse about 4 times the Kolmogorov length scale and the statistics were collected over 30 shedding cycles and averaged along the span-wise direction.

Similarly to the observations of [3], our results show that at all positions where a near $\circ\, 5/3$ is observed (Fig. 1) many of the terms of eq. (2) which are neglected in [1] actually play a role in that equation. This can be seen in Fig. 2, where the ratio $\circ\, \frac{\Pi}{\epsilon}$ is shown for $x/d = 3$ on the centreline (d is the square cylinder width). In the framework of the Richardson-Kolmogorov cascade this ratio should be 1 over a range of scales. Instead, a ratio different from 1 is observed which equals the sum of the other terms in eq. (2) (normalised by ϵ). The individual contributions of each term are shown at two locations in Figs. 3 and 4 for stream-wise separations and Figs. 5 and 6 for separations averaged over all orientations.

The process of averaging extends the constant plateau in $\circ\, \frac{\Pi}{\epsilon}$ to larger r (Figs. 5 and 6). The non-linear interscale interactions represented by Π appear to act as a source in eq. (2) at separations normal to the mean flow direction (not shown for brevity) compensating their action as a sink at separations aligned with the mean flow. When averaged, the combined result is then a rate of transfer close to $\circ\, \epsilon$, similar to Kolmogorov's prediction of $\circ\, \frac{\Pi}{\epsilon} = 1$ but without satisfying the assumptions of equilibrium ($\mathcal{A} = 0$), local homogeneity and local isotropy.

*Corresponding author. Email: f.alves-portela13@imperial.ac.uk

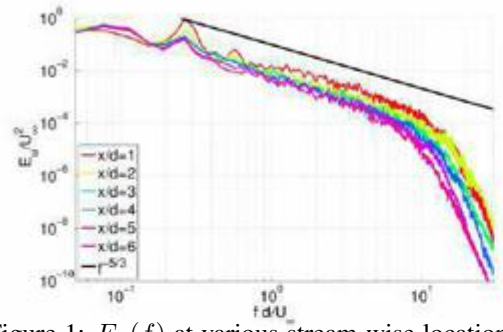

Figure 1: $E_u(f)$ at various stream-wise locations on the centreline.

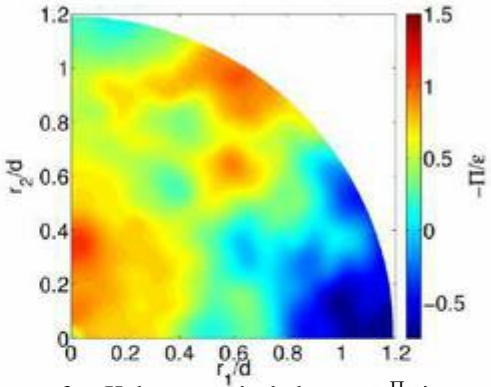

Figure 2: Kolmogorov's balance $-\frac{\Pi}{\epsilon}$ in scale space r_i ($r_3 = 0$), at $x/d = 3$.

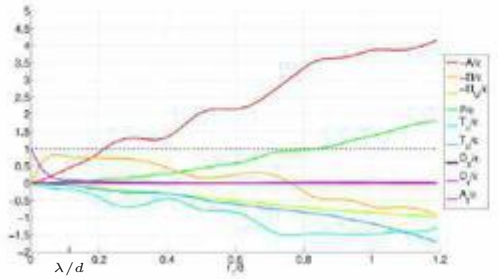

Figure 3: Terms in (2) at $x/d = 3$ along stream-wise separations r_1. λ is the Taylor micro-scale.

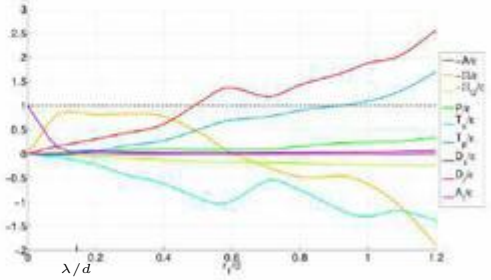

Figure 4: Terms in (2) at $x/d = 6$ along stream-wise separations r_1. λ is the Taylor micro-scale.

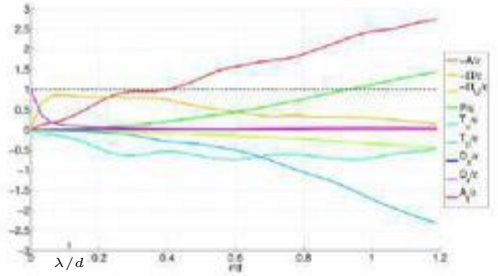

Figure 5: Terms in (2) at $x/d = 3$ averaged over the orientations r_i. λ is the Taylor micro-scale.

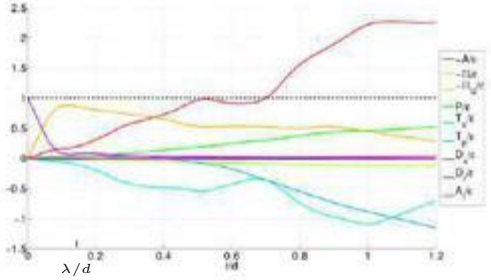

Figure 6: Terms in (2) at $x/d = 6$ averaged over the orientations r_i. λ is the Taylor micro-scale.

CONCLUSIONS

In the near-field of the planar turbulent wake the generalised Kármán-Howarth-Monin equation (2) does not only involve the non-linear transfer term Π and turbulent dissipation. The production, turbulent and mean flow transport and the pressure term are non-negligible. However we observe a clear $-5/3$ slope in the frequency energy spectrum at locations close to the cylinder. We find that Π is comparable (but not equal) to ϵ over a range of scales; this is particularly noticeable for larger separations r when averaged over the orientation, as the value of Π is smaller than ϵ for separations aligned with the centreline, but larger than ϵ at separations normal to the centreline.

ACKNOWLEDGEMENTS

The authors acknowledge the EU support through the FP7 Marie Curie MULTISOLVE project grant no. 317269 as well as the computational resources allocated in ARCHER HPC through the UKTC funded by the EPSRC grant no. EP/L000261/1.

References

[1] Kolmogorov A.: Dissipation of Energy in the Locally Isotropic Turbulence. Dokl. Akad. Nauk SSSR 32(1), 1941.
[2] Hill R.: Applicability of Kolmogorov's and Monin's equations of turbulence. Journal of Fluid Mechanics 353, 1997
[3] Gomes-Fernandes R., Ganapathisubramani B., Vassilicos J.C.: The energy cascade in near-field non-homogeneous non-isotropic turbulence. Journal of Fluid Mechanics 771, 2015.

HELICITY CONSERVATION AND THE FLOW OF KNOTTINESS ACROSS SCALES

Martin Scheeler[1], Dustin Kleckner[1], Hridesh Kedia[1], Stephane Perrard[1], and William T.M. Irvine [*1]
[1]*James Franck Institute and Department of Physics University of Chicago*

Summary The helicity of a fluid is a conserved quantity in idealized fluids, such as Euler fluids and thus offers the potential for fundamental insights into fluid flow. In real fluids, progress has been hindered by lack of accessible experimental and model systems. I will describe how to make vortex knots and links in water (in experiment), in the wave function of a superfluid (on a computer) and what happens thereafter. In particular, I will talk about how in helicity conservation, linking, coiling and twisting interplay across scales. Finally, I will describe experimental and numerical progress towards exploring the effects of helicity on turbulent flows.

HYDRODYNAMIC HELICITY

In addition to energy, momentum, and angular momentum, idealized (Euler) fluids have an additional conserved quantity, the hydrodynamic helicity $\mathcal{H}$:

$$\mathcal{H} = \int \mathbf{u} \cdot \omega \, \mathrm{d}V \tag{1}$$

where $\mathbf{u}$ and ω are respectively the velocity and vorticity of the flow. A natural interpretation of the hydrodynamic helicity is as a measure of the the linking and knotting of the vortex lines composing a flow:

$$\mathcal{H} = \sum_{i,j} \Gamma_i \Gamma_j L_{ij} \tag{2}$$

Where L_{ij} is the Gauss linking number between infinitesimal vortex tubes i and j having circulation Γ_i and Γ_j and the sum extends over all pairs of vortex tubes in a space-filling flow. For an Euler fluid, the conservation of helicity follows from the Helmholtz laws of vortex motion, which forbid vortex lines from crossing and preserve the flux of vorticity, making it impossible for linked or knotted vortices to untie.

Conservation laws are of fundamental importance in understanding flows so the question of whether this topological conservation law extends to real, dissipative systems is of clear and considerable interest. In particular determining whether and how helicity is conserved in the presence of dissipation could provide fundamental insights into the dynamics of complex and turbulent flows. Furthermore, since the dynamics of helicity are intrinsically geometric and topological in nature, lessons learned in fluids may well extend to the physics of tangling in other types of flow (e.g. plasmas) as well as other physical systems such as liquid crystals.

The robustness of helicity conservation in real fluids is unclear because dissipation allows the topology of field lines to change. For example, in viscous flows, vorticity will diffuse, allowing nearby vortex tubes to "reconnect", apparently creating or destroying the topological linking of vortices. This behavior is not unique to classical fluids: analogous reconnection events have also been experimentally observed in superfluids and coronal loops of plasma on the surface of the sun. In general, these observed reconnection events exhibit divergent, nonlinear dynamics that makes it difficult to resolve helicity dynamics theoretically. On the other hand, experimental tests of helicity conservation have been hindered by the lack of techniques to create vortices with topological structure.

GENERATION OF VORTEX KNOTS

Thanks to a recent advance in experimental vortex production [1] it is now possible to generate vortices with controlled shape and topology, such as the one shown in Figure 1 (Left). The technique is based on the acceleration of 3D printed hydrofoils in an otherwise stationary fluid. Upon acceleration, a "starting vortex" whose shape traces the trailing edge of the hydrofoil is shed and subsequently evolves under its own influence. In our experiments, we use this technique to produce vortex knots and links in water having a total length of approximately $1m$, a typical width of 150 mm and circulation $\Gamma = 20,000 mm^2/s$; the Reynolds number is of order $Re \sim 2 \times 10^4$.

By adding sparse micro-bubbles to the flow, we can clearly see the location of the vortex cores (see Figure 1 Left). Using a laser-sheet scanning apparatus, we can then reconstruct the three-dimensional shape of the vortices and track their evolution in time. This enables us to *measure* the evolution of helicity in a viscous fluid and probe how well it is conserved as well as what mechanisms exist for its conservation, for example through reconnections.

*Corresponding author. Email: wtmirvine@uchicago.edu

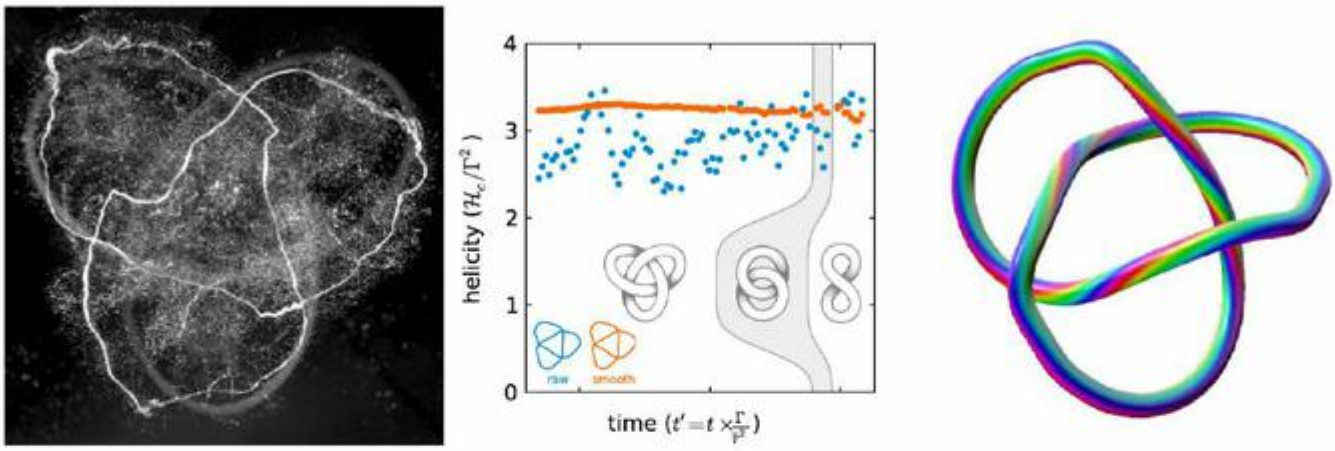

Figure 1: (Left: A vortex knot in water. Middle: The evolution of link and writhe in a reconnecting vortex trefoil knot. Right: a vortex knot in the Gross Pitaevskii model of a superfluid.

EVOLUTION OF HELICITY

We find that in both cases, the vortices distort towards a series of localized reconnections that appear to change their coarse topology. To quantitatively measure the evolution of the helicity we consider the three geometrically distinct contributions to helicity for thin vortex tubes: Linking, coiling and twist. These three geometrically distinct but topologically equivalent contributions arise in the case of finite thickness vortex tubes, by subdividing the tube into N infinitesimal filaments each with strength $\Gamma = \Gamma_0/N$, and computing their linking in the limit $N \to \infty$:

$$\mathcal{H} = \sum_{i \neq j} \Gamma_i \Gamma_j \, \mathcal{L}_{ij} + \sum_i \Gamma_i^2 \, \left(Wr_i + Tw_i \right), \tag{3}$$

where L_{ij} is the linking number between tubes i and j, Wr_i is the writhe of the tube center-line, and Tw_i is the total twist of each tube. Note that L_{ij} and Wr_i can be inferred from the shape of the tube centerline alone.

Remarkably, we find that immediately following the reconnections, the loss of linking between vortex tubes is completely balanced by the presence of writhe in the reconnected tube centerlines (Figure 1, center). This occurs through a geometric mechanism that converts link to writhe. By further decomposing the writhe on different scales using a 'helistogram' we track the flow of helicity across scales [2].

The mechanism we find for helicity conservation through reconnections is entirely geometric, suggesting it may be present in other fluid-like systems as well. To test this possibility, we simulate the evolution of vortex knots in a superfluid with the Gross-Pitaevskii equation (GPE). Although superfluids are inviscid, they are not ideal Euler fluids: vortex reconnections are possible and vortex cores do not have unconstrained structure. By simulating vortices with hundreds of distinct topologies we find that both aspect of topological vortex evolution outlined so far are general: all vortex knots untie efficiently and as they reconnect conserve the helicity of their centerline [3].

Measuring the total helicity however, requires additional information about how the vortex lines are locally twisted inside the vortex core. To bridge this gap, we have developed a novel technique for experimentally measuring twist helicity. Using this method, we are able to measure the production and eventual decay of twist for a variety of vortex evolutions. Remarkably, we observe twist dynamics capable of conserving total helicity even in the presence of rapidly changing writhe.

Injecting helicity in a turbulent flow (in experiment) enables us to explore the role helicity has to play in complex flows.

References

[1] Kleckner D., Irvine W.T.M.: Creation and dynamics of knotted vortices in fluids. Nature Physics **9** 253-258, 2013.

[2] Scheeler M., Kleckner D., Proment D., Kindlmann G., Irvine W.T.M: Helicity conservation by flow across scales in reconnecting vortex links and knots. Proceedings of the National Academy of Sciences **111** 15356-15361, 2014.

[3] Kleckner D., Kauffman H., Irvine W.T.M.: How superfluid vortex knots untie. Nature Physics, in press.

EFFECTS OF HELICITY ON THE ENERGY TRANSFER IN THREE-DIMENSIONAL TURBULENCE

Ganapati Sahoo*[1] and Luca Biferale[2]

[1]*Department of Physics and INFN, University of Rome Tor Vergata, Italy*
[2]*Department of Physics and INFN, University of Rome Tor Vergata, Italy*

Summary We investigated the effects of the helicity in the dynamics of the energy transfer in turbulent flows using a modified version of the Navier-Stokes equations with explicit breaking of the mirror symmetry. With an external parameter that controls the imbalance between the number of positive and negative helical Fourier modes we aim to disentangle the role of helicity in the direction of the turbulent energy transfer. In an earlier study with helical projection, an inverse cascade of energy was observed in the three-dimensional Navier-Stokes equations when helicity was maintained sign-definite [1, 2]. In this study we measure the degree to which the parity symmetry controls the direction of the cascade. We introduce a mechanism in which the parity is broken stochastically but in a time frozen manner with helical constraints. We keep triadic interactions in Fourier space involving modes with definite sign of helicity and decimate the triads of other modes with opposite sign of helicity with a fixed probability. We observed a singular behaviour of the direction of the energy cascade measuring a positive forward flux as soon as only a few modes with different helical polarities take part in the dynamics.

INTRODUCTION

Direct numerical simulations of three-dimensional Navier-Stokes equations for incompressible flows and experiments in the three-dimensional homogeneous and isotropic turbulence show cascade of energy from the forced scales to the dissipative scales. The direction of the energy transfer is however believed to be determined by the invariants of the system. In two-dimensions the two positive-definite invariants, energy and enstrophy, effect in transfer of energy to the large scales. For the three-dimensional Navier-Stokes equations two inviscid invariants are the energy $E = \int d^3r\ \vec{u} \cdot \vec{u}$ and the helicity $H = \int d^3r\ \vec{u} \cdot \vec{\omega}$, where $\vec{u}$ is the velocity and $\vec{\omega} = \nabla \times \vec{u}$ is the vorticity. The energy is positive and definite whereas the helicity could be either positive or negative. Helicity is known to play a key role in hydrodynamical and magnetohydrodynamical systems [3, 4]. In hydrodynamics both energy and helicity cascade forward from large scales to small scales [5]. However, There are evidences of inverse energy transfer to the large scales under special conditions. A turbulent flow confined in thick fluid layers due to formation of large scale vortex suppresses vertical motions and supports large scale energy transfer [6]. In a rotational turbulent flow with helical force a direct cascade of helicity and direct and inverse cascade of energy is observed [7]. Dynamics of the inverse energy transfer is studied in a subset of all interactions in the Navier-Stokes equations as in Ref. [1, 8]. Positive definiteness of helicity leads to inverse energy transfer. In this work we show that when relative weight between the positive and negative helical modes present in the system is changed a critical behaviour of the energy transfer is observed [9]. We, using a method to separate positive and negative helical modes to understand the dynamics of the energy cascade, show a transition of forward to inverse energy transfer.

NUMERICAL METHOD

Each Fourier mode of velocity $\boldsymbol{u}(\boldsymbol{k}, t)$ has two degrees of freedom as it satisfies the incompressibility condition, i.e., $\boldsymbol{k} \cdot \boldsymbol{u}(\boldsymbol{k}, t) = 0$. If we chose these degrees of freedom to be the projections on orthonormal helical waves with definite sign of helicity [10] we could write

$$\boldsymbol{u}(\boldsymbol{k}, t) = \boldsymbol{u}^{+}(\boldsymbol{k}, t) + \boldsymbol{u}^{-}(\boldsymbol{k}, t).$$

Using the complex eigenvectors of the curl operator $i\boldsymbol{k} \times \boldsymbol{h}^{\pm}(\boldsymbol{k}) = \pm k \boldsymbol{h}^{\pm}(\boldsymbol{k})$ we could define a projection operator

$$\mathcal{P}^{\pm}(\boldsymbol{k}) \equiv \frac{\boldsymbol{h}^{\pm}(\boldsymbol{k}) \otimes \boldsymbol{h}^{\pm}(\boldsymbol{k})^{*}}{\boldsymbol{h}^{\pm}(\boldsymbol{k})^{*} \cdot \boldsymbol{h}^{\pm}(\boldsymbol{k})}$$

such that $\boldsymbol{u}^{\pm}(\boldsymbol{k}, t) = \mathcal{P}^{\pm}(\boldsymbol{k}) \boldsymbol{u}(\boldsymbol{k}, t)$. The Navier-Stokes equations could be then independently written for each modes as

$$\partial_t \boldsymbol{u}^{\pm}(\boldsymbol{k}, t) = \mathcal{P}^{\pm}(\boldsymbol{k}) \boldsymbol{N}_{u^{\pm}}(\boldsymbol{k}, t) + \nu k^2 \boldsymbol{u}^{\pm}(\boldsymbol{k}, t) + \boldsymbol{f}^{\pm}(\boldsymbol{k}, t) \tag{1}$$

where ν is the kinematic viscosity and $\boldsymbol{f}$ is the external forcing and the nonlinear term containing all triadic interactions is

$$\boldsymbol{N}_{u^{\pm}}(\boldsymbol{k}, t) = \mathcal{F}T(\boldsymbol{u}^{\pm} \cdot \boldsymbol{\nabla} \boldsymbol{u}^{\pm} \circ \boldsymbol{\nabla} p).$$

*Corresponding author. Email: ganapati.sahoo@gmail.com

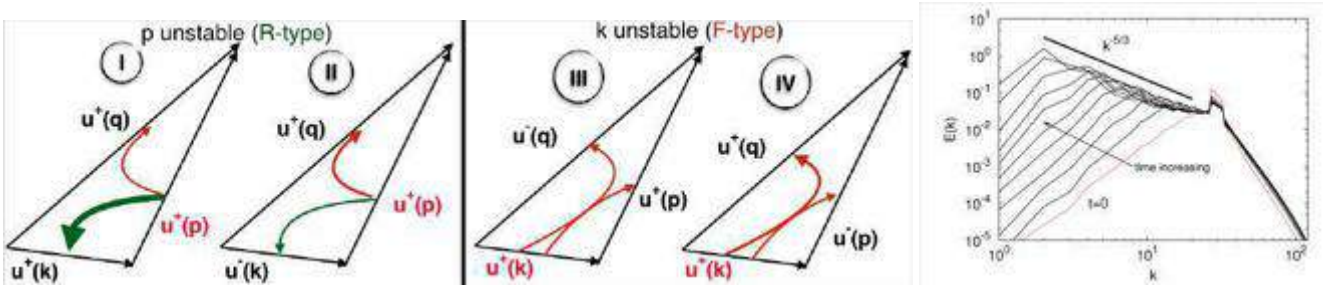

Figure 1: (a) All possible triadic interactions in Navier-Stokes equations based on the helicity content of the involving Fourier modes. The triads with only $\boldsymbol{u}^+$ (Class-I) lead to reversal of energy cascade (left). (b) Energy spectra $E(k) = \sum_{\boldsymbol{k} \ni |\boldsymbol{k}|=k} |\mathbf{u}(\boldsymbol{k})|^2$ in the inverse cascade regime shows $k^{-5/3}$ slope [1, 2] (right).

DISCUSSION AND RESULTS

There are four classes of nonlinear triadic interactions with definite helicity signs under helical decomposition of Navier-Stokes equations shown in Fig.1a. Energy and helicity are conserved for each triads. Restricting dynamics to subsets of these triads affects the direction of the energy transfer [10, 11]. Full decimation of triads involving either $\boldsymbol{u}^+$ or $\boldsymbol{u}^-$ shows inverse cascade of energy [1, 2] as shown in Fig.1b. To understand the transition of the forward energy transfer to the inverse energy transfer we decimated a fraction α of modes with helicity of one sign instead of all of them. We numerically found a *critical value* of α at which forward cascade of energy stops when force is applied at the large scales and alternatively, inverse cascade of energy stops if forced at small scales. We define the projection operator using the parameter α,

$$\mathcal{P}_\alpha^+(\boldsymbol{k})\boldsymbol{u}(\boldsymbol{k},t) = \boldsymbol{u}^+(\boldsymbol{k},t) + \theta_\alpha(\boldsymbol{k})\boldsymbol{u}^-(\boldsymbol{k},t) \tag{2}$$

where $\theta_\alpha(\boldsymbol{k})$ is 0 or 1 with probability α and $1 \circ \alpha$, respectively. When $\alpha = 0$ we obtain the results for standard Navier-Stokes equations and when $\alpha = 1$ we recover results for fully helical-decimated Navier-Stokes equations. We performed direct numerical simulations of Eq.(1) using a pseudo-spectral method on a periodic cubic domain of size $L = 2\pi$ with resolutions up to 1024^3 collocation points.

We observe that as we increase α, the contribution of triads leading to inverse energy cascade grows. Only when α is very close to 1 inverse energy cascade takes over the forward cascade; critical value of α is found to be $\simeq 1$ our simulations. We also measure the relative changes in the intermittency in the forward cascade regime at changing α.

ACKNOWLEDGEMENT

We acknowledge support from European Research Council under the ERC AdG No. 339032.

References

[1] L. Biferale, S. Musacchio, and F. Toschi, *Phys. Rev. Lett.* **108**, 164501 (2012).
[2] L. Biferale, S. Musacchio, and F. Toschi, *J. Fluid Mech.* **730**, 309 (2013).
[3] H. K. Moffatt, *J. Fluid Mech.* **35**, 117 (1969).
[4] H. K. Moffatt and A. Tsinober, *Annu. Rev. Fluid Mech.* **24**, 281 (1992).
[5] Q. Chen, S. Chen, and G. Eyink, *Phys. Fluids* **15**, 361-374 (2003).
[6] H. Xia, D. Byrne, G. Falkovich, and M. G. Shats, *Nat Phys* **7**, 321-324 (2011).
[7] P. D. Mininni, A. Alexakis, and A. Pouquet, *Phys. Fluids* **21**, 015108 (2009).
[8] L. Biferale and E.S. Titi, *J. Stat. Phys.* **151**, 1089 (2013).
[9] G. Sahoo, F. Bonaccorso, and L. Biferale, *Phys. Rev. E* **92**, 051002(R) (2015).
[10] F. Waleffe, *Phys. Fluids A* **4**, 350-363 (1992).
[11] G. Sahoo and L. Biferale *Euro. Phys. J. E* **38** (10), 114 (2015).

INTERACTION OF TWO HIGH REYNOLDS NUMBER AXISYMMETRIC TURBULENT WAKES

Martín Obligado*[1], Simon Klein[2], and J. C. Vassilicos[1]

[1]*Department of Aeronautics, Imperial College London, London, United Kingdom*
[2]*Institute of Fluid Mechanics, TU Braunschweig, Braunschweig, Germany*

Summary In the context of the recently discovered non-equilibrium high Reynolds number scalings in the wake of axisymmetric plates, we propose an application to the study of the interaction of two axisymmetric turbulent wakes generated by two bluff bodies. Our results show that non-equilibrium scalings properly describe the interaction of the turbulent wakes of the two bluff bodies, predicting both at which distance the wakes meet on average and the velocity fluctuation intensity at that point. Moreover, the streamwise evolution of the turbulence dissipation rate, estimated between both plates seems to follow the non-equilibrium law.

Recently, flow regions with non-equilibrium high Reynolds number turbulence at odds with usual Richardson-Kolmogorov phenomenology have been discovered in a number of turbulent flows [8], in particular axisymmetric and self-preserving turbulent wakes of plates with and without irregular edges. These regions are characterised by streamwise evolutions of the mean flow profiles which have only recently been documented and partially understood for the first time ever [5, 6]. Furthermore, these regions can extend as far as about 100 plate characteristic lengths (defined as $\sqrt{\mathcal{A}}$, with $\mathcal{A}$ the frontal area of the plate) in the streamwise direction. A further study [1], critically revised the classical theory of high Reynolds axisymmetric turbulent wakes [7, 2] to encompass these new scalings. Both direct numerical simulations and experiments were found to agree with the theory. A key point of this theory is an assumption of constant anisotropy which concerns the behaviour of the fluctuating velocity components at the edges of the wake.

In this work we focus on the interaction of turbulent axisymmetric wakes generated by two bluff bodies. This is an important configuration, present for instance in arrays of wind or marine tidal turbines, and the interaction of the two wakes can be expected to involve non-equilibrium turbulence. We present experimental evidence that the non-equilibrium theory in [1] properly models the interaction of these two wakes, for plates with both regular and irregular edges. We show that, by having knowledge of the values of δ and the centreline velocity deficit u_0 for a single wake, it is possible to predict the wake interaction length x_{12} which quantifies the position where the wakes meet. Furthermore, it is also possible to predict the intensity of the fluctuations at that particular point.

For this purpose, we propose an experimental set-up where streamwise profiles of streamwise fluctuating velocities are acquired via hot-wire anemometry (HWA) in a wind tunnel (figure 1a). We have studied two different sets of plates, one with square regular and another with irregular edges, the latter shown in figure 1b. All plates have a characteristic length $\sqrt{\mathcal{A}} = 64$ mm, and the freestream velocity U_∞ was kept constant at 10 m/s. Ten different plate separations S were tested: 240, 250, 260, 270, 280, 285, 290, 295, 300 and 305 mm. By acquiring streamwise profiles of the streamwise fluctuating velocity r.m.s $u\prime$ for different plate separations and identifying the streamwise distance x where the wakes meet for each separation it is possible to estimate the streamwise evolution of the single wake width δ. From the HWA measurements it is also possible to deduce the turbulence dissipation scalings.

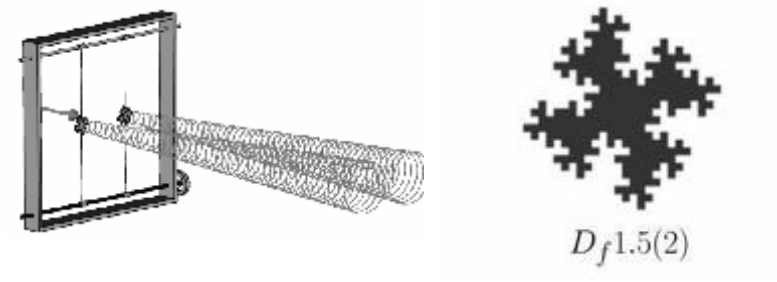

(a) **(b)**

Figure 1: (a) Sketch of the experimental wind tunnel set-up; (b) Irregular plates used herein. They are the second iteration of a fractal plate with dimension $D_f = 1.5$ and a square initial pattern, as described in [4].

As explained above, the interaction of the wakes can be characterized by the wake interaction length x_{12}. This parameter, previously proposed for planar wakes in fractal grids (see for instance [3]), can be easily generalized to include axisymmetric

*Corresponding author. Email: m.obligado@imperial.ac.uk

wakes, as it will depend linearly with the streamwise scaling of δ. Furthermore, the streamwise variation of this parameter will be different if the turbulence follows Richardson-Kolmogorov (where $\delta(x) \sim x^{1/3}$ and therefore $x_{12} \sim x^{1/3}$ as well) or non-equilibrium (where $\delta(x)$ and x_{12} vary according to $x^{1/2}$) phenomenology.

To scale the magnitude of velocity fluctuations, we use the assumption of constant anisotropy by Dairay *et al.*[1]. It implies that the turbulent kinetic energy is proportional to the Reynolds shear stress on the properly defined edges of the wake. This assumption also implies that the streamwise and radial velocity fluctuations are proportional at the edges of the wake. Therefore, an expression can be deduced for $u\prime$: $u\prime \sim \sqrt{2/3\, U_\infty u_0 (d/dx\, \delta(x))}$ at $r = n\delta(x)$, with n a constant (for this particular experiment $n \approx 2.2$). Scaling $u\prime$ with this expression and its streamwise development with the present interaction length scale $x_{12}(S)$ gives a very good collapse of the profiles of $u\prime(x)$ for almost all distances and both sets of plates (figure 2a). It is also important to note that the streamwise evolutions of the skewness and the flatness of the streamwise fluctuating velocities can also be collapsed with x_{12}.

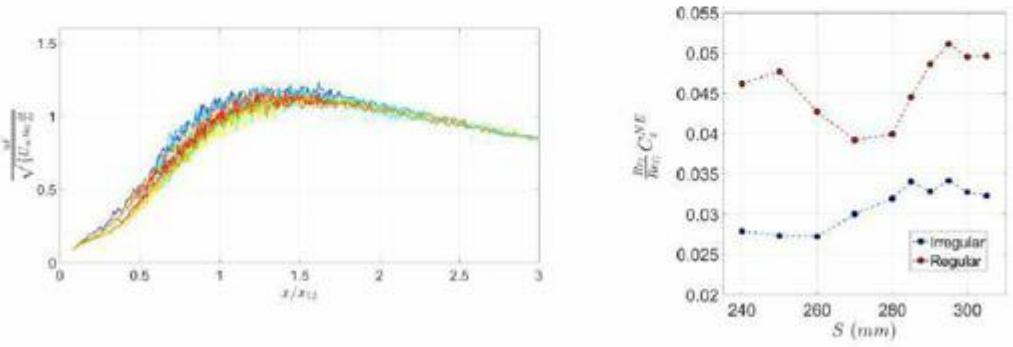

(a) **(b)**

Figure 2: (a) Streamwise evolution of velocity fluctuations for all distances and both sets of plates, collapsed horizontally with the values of x_{12} and vertically with $u\prime \sim \sqrt{2/3\, U_\infty u_0 (d/dx\, \delta(x))}$. The values of $S = 240$ and 250 mm for the square plates are not represented as the collapse is less good. (b) Values of $Re_l/Re_G C_\varepsilon^{NE}$ for different plates separations S for plates with regular and irregular edges.

Finally, to unequivocally demonstrate de presence of non-equilibrum scalings on the flow, we study the dissipation coefficient C_ε. It is well known that in the Richardson-Kolmogorov phenomenology, $C_\varepsilon \sim \varepsilon\delta/u\prime^3$ with C_ε a constant independent of Reynolds number. On the other hand, at high Reynolds numbers, the non-equilibrium dissipation coefficient is not constant, and obeys $C_\varepsilon^{NE} \sim Re_G/Re_l$, where $Re_l = K\delta/\nu$ is a local Reynolds number and $Re_G = U_\infty\sqrt{\mathcal{A}}/\nu$ is a Reynolds number based on global (inlet) properties. K and ν are the turbulent kinetic energy and the kinematic viscosity of the flow, respectively. Figure 2b shows the value of $(Re_l/Re_G)C_\varepsilon^{NE}$ at x_{12} for different values of S and both sets of plates. For both sets of plates, Re_l at $x = x_{12}(S)$ varies significantly with S. It can be seen that, as expected in the presence of non-equilibrium turbulence, $(Re_l/Re_G)C_\varepsilon^{NE}$ remains relatively constant.

In conclusion, this work shows that non-equilibrium turbulence properly models the interaction between two turbulent wakes. Furthermore, it adds to recent reported measurements suggesting that this non-equilibrium behaviour has some universality and is not limited to very specific turbulent flows.

References

[1] T Dairay, M Obligado, and JC Vassilicos. Non-equilibrium scaling laws in axisymmetric turbulent wakes. *Journal of Fluid Mechanics*, 781:166–195, 2015.

[2] W.K. George. The self-preservation of turbulent flows and its relation to initial conditions and coherent structures. *Advances in Turbulence*, pages 39–73, 1989.

[3] R Gomes-Fernandes, B Ganapathisubramani, and JC Vassilicos. Particle image velocimetry study of fractal-generated turbulence. *Journal of Fluid Mechanics*, 711:306–336, 2012.

[4] J. Nedić, B. Ganapathisubramani, and J.C. Vassilicos. Drag and near wake characteristics of flat plates normal to the flow with fractal edge geometries. *Fluid Dynamics Research*, 45(6):061406, 2013.

[5] J. Nedić, J.C. Vassilicos, and B. Ganapathisubramani. Axisymmetric turbulent wakes with new nonequilibrium similarity scalings. *Physical review letters*, 111(14):144503, 2013.

[6] M Obligado, T Dairay, and JC Vassilicos. Non-equilibrium scalings of turbulent wakes. *Submitted to PRL*, 2016.

[7] A.A. Townsend. *The structure of turbulent shear flow*. Cambridge university press, 1976.

[8] J.C. Vassilicos. Dissipation in turbulent flows. *Ann. Rev. Fluid Mech.*, 47(1), 2015.

EXTREME EVENTS AND ACCELERATION STATISTICS AT HIGH REYNOLDS NUMBER

P.K. Yeung*[1]

[1]*Schools of Aerospace Engineering and Mechanical Engineering, Georgia Institute of Technology, Atlanta, Georgia, USA*

Summary Statistics of dissipation, enstrophy and acceleration from a well-resolved high Reynolds number simulation of forced isotropic turbulence are reported. Observations of extreme events at intensity levels much higher than commonly reported and of a topologically distinct nature are related to conditional statistics that are useful for future efforts in improving stochastic modeling of turbulent dispersion, through incorporating the effects of fine-scale intermittency on the fluid particle acceleration.

BACKGROUND AND TECHNICAL APPROACH

Turbulent flows consist of disorderly fluctuations in time and space over a wide range of scales. At the small scales there is particular interest in the fluctuations of the dissipation rate ($\epsilon = 2\nu s_{ij}s_{ij}$, where s_{ij} is the strain-rate tensor) and the enstrophy ($\Omega = \omega_i\omega_i$, where ω_i is the vorticity). As the Reynolds number increases, the range of scales becomes wider, and intense fluctuations of ϵ and Ω localized in both time and space become more intense. Recent work [1] based on direct numerical simulations of forced isotropic turbulence at Taylor-scale Reynolds number (R_λ) about 1300 on an 8192^3 grid has shown that instantaneous values of both ϵ and Ω can take on extreme values that are as large as $O(10^4)$ or even $O(10^5)$ of their mean values, or higher. These "extreme events" are also observed to possess a spatial structure that is characteristically different from the classical notion of vortex filaments surrounded or wrapped around by sheets of high dissipation rate. Numerical tests indicate that actual occurrence or observation of events of these magnitudes is dependent on high Reynolds number as well as resolution of the small scales (which together require tremendous computing power to achieve).

In this short paper we first provide a basic description of extreme events in dissipation and enstrophy, and then focus on their connection to the acceleration experienced by a infinitesimal material fluid element in the flow. Both strong local straining and strong local rotation are expected to cause a fluid element to undergo rapid changes in the magnitude and orientation of its velocity, i.e. a large acceleration. A detailed understanding of the acceleration is, in turn, a key requirement [2] in long-standing efforts to improve the modeling of fluid particle dispersion and turbulent transport processes in a Lagrangian reference frame. However, in this paper it is convenient to compute the acceleration as the material derivative of the velocity, according to the Navier-Stokes equations, through a post-processing code that analyzes instantaneous velocity fields saved in the simulations. Both the simulation and post-processing are performed using massively parallel pseudo-spectral codes scaled up to 262,144 cores to date.

EXTREME EVENTS IN DISSIPATION, ENSTROPHY AND ACCELERATION

Figure 1 below shows visualizations of several representative snapshots of dissipation and enstrophy in regions closest to peak intensity in the simulations. Only the last image, at a lower Reynolds number, is dominated by structures resembling the conventional notion of worm-like vortex filaments surrounded by sheets of high dissipation. All others, from our 8192^3 DNS, show wider and less elongated structures with dissipation and enstrophy almost coincident at the highest magnitudes, although some vortex filaments at moderately high intensity are also visible. Our interest here is to investigate how this qualitative change in behavior at high Reynolds number affects other turbulence statistics of importance for various reasons.

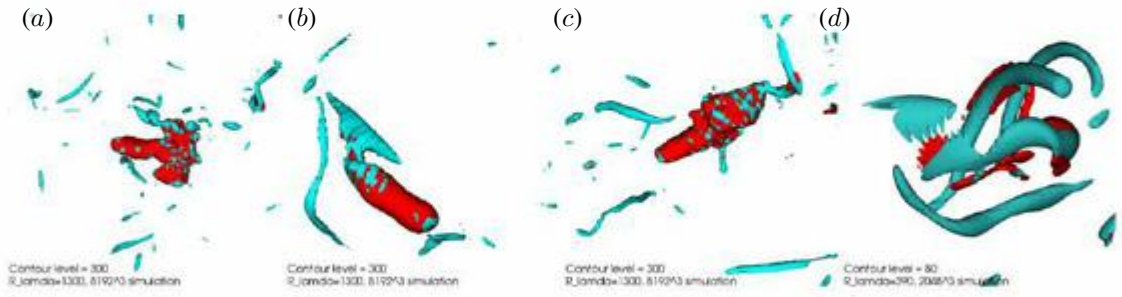

Figure 1: 3D contour surfaces for high ϵ (red) and high Ω (cyan) from DNS at R_λ 1000 (a-c) and 390 (d).

*Email: pk.yeung@ae.gatech.edu

PROBABILITY DISTRIBUTION AND CONDITIONAL STATISTICS OF THE ACCELERATION

In both simulations and experiments [3] acceleration in high Reynolds number turbulence is well known to be extremely intermittent. One consequence of this intermittency is that the acceleration variance does not follow classical Kolmogrov universality. In Eulerian terms, the acceleration may be computed as (neglecting any forcing at the large scales)

$$\mathbf{a} = \partial\mathbf{u}/\partial t + (\mathbf{u}\cdot\nabla)\mathbf{u} \;\; ; \quad \text{or} \quad \mathbf{a} = -\nabla(p/\rho) + \nu\nabla^2\mathbf{u}\,. \tag{1}$$

where unsteady and convective contributions are in strong mutual cancellation, and the pressure gradient dominates over the viscous term. The pressure fluctuation itself is governed by the Poisson $\nabla^2(p/\rho) = \frac{1}{2}(\Omega - \epsilon/\nu)$. In addition, a complete quadratic measure of the velocity gradients, including contributions from both straining and rotation, is given by the pseudo-dissipation $\varphi = \nu(\partial u_i/\partial x_j)^2$, which is useful for purposes of stochastic modeling.

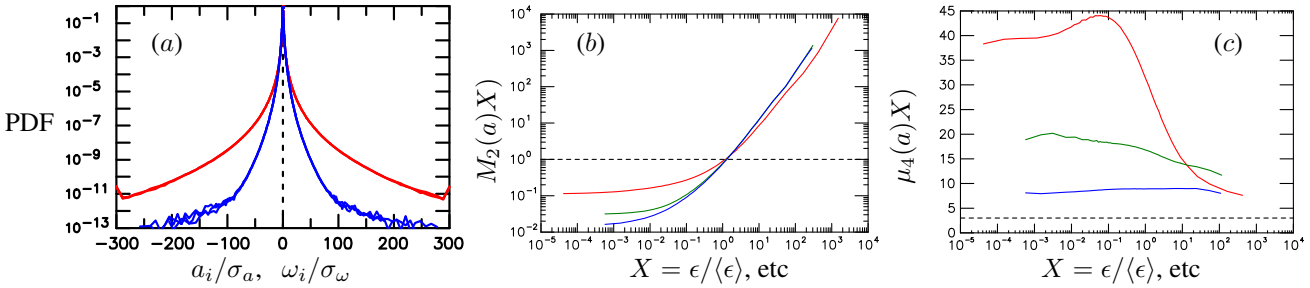

Figure 2: (a) PDF of normalized acceleration (red) and vorticity (blue) components; (b) acceleration variance conditioned upon $\epsilon/\langle\epsilon\rangle$ (red), $\Omega/\langle\Omega\rangle$ (green), $\varphi/\langle\varphi\rangle$ (blue); and (c) conditional flatness factors.

In Fig. 2(a) the probability density function (PDF) of the acceleration (normalized by its standard deviation) is seen to possess very wide tails, indicative of the systematic occurrence of extreme events at 300 standard deviations and beyond (which correspond to the square of the acceleration exceeding 10^5 of its mean value). The tails are in fact wider than that found in the PDF of the vorticity components that constitute the enstrophy. To relate, or partially explain, the intermittency of the acceleration to those of dissipation and enstrophy, we use conditional averaging [4], such as the conditional moments $M_n(a|X) = (1/3)\langle(\mathbf{a}\cdot\mathbf{a})^n|X\rangle$ where X can be either ϵ or Ω (and, by extension, also φ). Figure 2(b) shows that the conditional dependence is weak in regions of small velocity gradients, but that the conditional variance rises strongly at higher values of ϵ, Ω and φ, which means extreme events in these variables do tend to lead to extreme events in the acceleration. It is also interesting that (in Fig. 2(c)) the conditional flatness factor $\mu_4(a|X) = M_4(a|X)/M_2(a|X)^2$ decreases at large values of ϵ, Ω or φ. This decrease shows, in fact, that given a large ϵ (say), the likelihood of the acceleration-squared deviating far from its conditional mean (i.e. M_2) is somewhat low — or, conversely, that extreme events in all of these variables are indeed likely to correspond well to one another.

CONCLUSIONS

Direct numerical simulation results at Taylor-scale Reynolds number 1300 on a well-resolved 8192^3 domain have shown that dissipation, enstrophy and acceleration (squared) attain extreme values as high as $O(10^5)$ of their mean values. Conditional averaging shows that these extreme events are closely related to each other. Further results on the acceleration and other flow variables (such as the pressure gradient, and the inertial terms in the Navier-Stokes equation) in these conditions of extreme intermittency will be presented at the Congress.

Support from the NSF Petascale Computing Program through a large allocation of resources on the Blue Waters supercomputer at the University of Illinois at Urbana-Champaign is gratefully acknowledged.

References

[1] Yeung, P.K., Zhai, X.M., Sreenivasan, K.R.: Proc. Nat Acad Sci. USA 112(41):12633-12638, 2015.
[2] Sawford, B.L.: Phys Fluids A 3:1577-1586, 1991.
[3] La Porta, A., Voth, G.A, Crawford, A.M., Alexander, J., Bodenschatz, E.: Nature, 409:1017-1019, 2001.
[4] Yeung, P.K., Pope, S.B., Lamorgese, A.G., Donzis, D.A.: Phys Fluids 18:065103, 2006.

ROTATING TURBULENCE IN A ROTOR/STATOR CAVITY AT HIGH REYNOLDS NUMBER

C. Lachize, G. Verhille *, and P. Le Gal

Aix Marseille University - CNRS, Institut de Recherche sur les Phénomènes Hors Equilibre, Marseille, France

Summary This communication reports an experimental investigation of a turbulent flow confined within a rotor/stator cavity at high Reynolds numbers. The experiments have been driven by changing both the rotation rates of the disk and the density of the working fluid (sulfur hexafluoride near its critical point) by imposing the operating temperature and pressure inside a thermalized and pressurized vessel. This original set-up allows to get Reynolds numbers as high as $2\ 10^7$ with potential compressibility effects as the Mach number can reach 0.5. Pressure measurements reveal that the resulting fully turbulent flow shows both a direct and an inverse cascade in accordance with Kraichnan's conjecture. For the highest Reynolds numbers, the spectra are however dominated by low-frequency oscillations involving large scale modes with azimuthal wavenumbers $m = 1, 2, 3$ and 4. We interpret these modes as acoustico-inertial modes for which we have calculated their dispersion relation as function of the Mach number.

INTRODUCTION

The aim of this experimental work is to study rotating turbulence and its coherent large scale structures at high Reynolds numbers when turbulence is generated in a rotor-stator cylindrical cavity immersed in a pressurized vessel containing sulfur hexafluoride (SF_6). The use of this fluid permits to reach Reynolds numbers as high as $2\ 10^7$ and Mach numbers around 0.5. It is well known that flows driven by a rotating disk in cylindrical enclosures can generate azimuthal spiral coherent structures whose appearance is associated to Ekman (rotor) or Bödewadt (stator) layers instabilities. In general, the number of these spiral structures is around 20 and the increase of the Reynolds number makes them to disappear to give rise to an apparent homogeneous turbulence in the azimuthal direction [1]. The report of the experimental observation of a small number of azimuthal structures in rotor/stator cavity is scarce. To our knowledge, it was first described in the experimental visualizations of Czarny *et al.* [2] who reported the occurrence of unsteady large scale vortices. Jacques *et al.* [3] performed 2D-axisymmetric numerical simulations in a rotor/stator configuration that underlined the presence of inertial waves for fast enough rotation rates. Recently, three dimensional simulations of the flow inside a rapidly rotating cylinder split at mid-height show that the basic state loses stability through sidewall boundary layer breathing causing inertial waves to propagate in the core of the flow [4]. In this last work, when the cavity is axially extended, large amplitude subharmonics are discernible, leading to the complex superimposition of many inertial waves propagating at different angles. Independently of these rotating disk flow studies, rotating turbulence has been the subject of numerous experimental and numerical works as it is still today one of the main challenges of research on turbulence. To give a synthetic and simplistic view, it is admitted that if energy is injected in the turbulent rotating flow at a frequency f_0, it gives rise to both a direct and an inverse cascade which are similar for some aspects to the 2D turbulent cascades. Indeed, because of the bi-dimensionalisation of turbulence caused by the strong global rotation, a direct cascade of enstrophy should take place together with an inverse energy cascade towards frequencies lower than f_0 in agreement with Kraichnan's conjecture [5]. This inverse turbulence cascade has been revealed in recent experiments [6], [7]. Finally, as observed in the numerical simulations mentioned previously [4] and in experiments [7],[8], inertial waves can arise and superimpose on (and interact with?) turbulence through a process which is still debated.

EXPERIMENTAL SET-UP

The flow is generated within a cylindrical enclosure consisting of a stationary shroud, two smooth rotor and stator with diameters of respectively $2R_r = 68$ mm and $2R_s = 70$ mm. The outer wall is fixed to the stator and the rotor is driven by a brushless electric motor which could reach a rotation frequency $f_0 = 185$ Hz. The spacing between the disks is $H = 40$ mm. The rotor/ stator cavity with the motor is integrated into a pressurized 140 mm inner diameter cylindrical pressure vessel. The temperature control of the cavity is ensured by a thermostatically-controlled bath that regulates the entire vessel temperature through an internal circulation in the cylindrical wall of the pressure vessel. By changing the quantity of SF_6 in the vessel, different thermodynamics conditions (and so different viscosity, sound speed,...) can be reached. Measurements are performed at a rotation frequency f_0 from 17 Hz to 170 Hz, a density ρ from 6,17 (vapor) to 830 $\mathrm{kg/m^3}$ (supercritical phase). Variations of SF_6 dynamic viscosity and sound speed c_0 allow to explore a wide range of Reynolds numbers $5\ 10^4 < Re < 2\ 10^7$ and Mach numbers $0,03 < Ma = 2\pi R_r f_0/c_0 < 0.5$. Two dynamics pressure sensors are fixed flush on the stator at a radius of 15 mm and separated with an angle of $\pi/2$ in the azimuthal direction. These sensors have a frequency range that extends between 0.5 Hz and 10^5 Hz. Finally, a temperature probe is placed onto the cylindrical shroud, which allows us, a posteriori and associated with the absolute pressure measurements, to determine the working isochores and the corresponding thermodynamics conditions. Experimentally, these thermodynamics conditions are reached by varying the fluid density by evacuating SF_6 under pressure out of the vessel.

*Corresponding author. Email: verhille@irphe.univ-mrs.fr

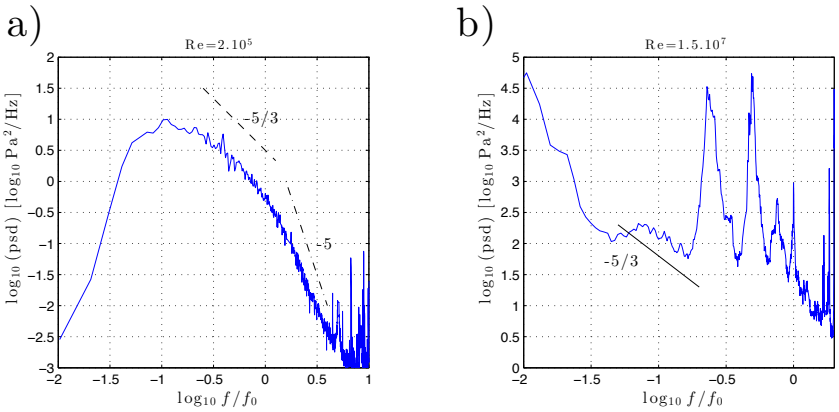

Figure 1: Pressure power spectral densities for $\rho = 830\ \mathrm{kg\,m^{-3}}$ and $Re = 10^5$ in a) and for $Re = 2\ 10^6$ in b).

RESULTS AND DISCUSSION

The power spectral densities of temporal pressure fluctuations are calculated and presented for two different Reynolds numbers in figure 1, for one of the two pressure sensors. Frequencies have been normalized by the rotor rotating frequency f_0 where energy is injected from the rotating disk to the fluid through the turbulent Ekman boundary layer. As can be observed, the spectra are divided in several frequency zones that we will describe starting from the highest frequencies. For all Reynolds numbers that we have explored and for frequencies higher than f_0, an inertial cascade is observed. This part of the spectra starts at the rotor frequency f_0 and is observable up to $3f_0$ with a slope very close to $\circ\ 5$ for the highest frequencies. This $\circ\ 5$ slope for the pressure fluctuation spectrum corresponds to the $\circ\ 3$ exponent of the velocity fluctuation power spectrum as predicted by Kraichnan [5] for the 2D turbulence direct enstrophy cascade. Starting at a Reynolds number around $\approx 10^6$ and in addition to this direct cascade, a series of peaks appears at frequencies in the range $1/4 < f/f_0 < 3/2$. They imply that non axisymmetric oscillating coherent structures come into play and lead to a complex flow topology. Whereas these peaks are numerous for Reynolds numbers in the range $10^5 < Re < 10^6$, when increasing the Reynolds number above $2\ 10^6$, only four of them are selected at frequencies $f/f_0 \approx 0.25, 0.5, 0.75$ and 1. The study of the phase difference between the two pressure probes shows that these modes possess azimuthal wavenumbers $m = 1, 2, 3$ and 4 respectively. We interpret them as acoustico-inertial modes for which we have calculated their dispersion relations as a function of the Mach number. Finally, for frequencies slightly lower than these series of peaks, one can detect a $\circ\ 5/3$ slope region which is, in fact, also present at lower Reynolds number before the appearance of the peaks (see figure1-a)). Although we have no direct proof of it, this range of frequencies - around one tenth of the injection frequency - should correspond to an inverse cascade of energy. Indeed, if we transform the $\circ\ 5/3$ exponent visible on our pressure fluctuation power spectra into the corresponding exponent for the velocity fluctuation power spectra, it becomes a $\circ\ 4/3$ in complete agreement with the temporal spectra exhibited in a recent rotating turbulence experiment [7]. As claim by these last authors, this exponent might appear by the interaction between inertial waves and may correspond to the inverse cascade. In our case, it seems however that the inverse cascade is independent of the presence or not of the low frequency azimuthal modes. Finally, as can be observed on figure 1-b), at very small frequencies we observe the appearance for the highest Reynolds numbers of a puzzling slow dynamics with periods as long as 100 times the disk rotation period.

References

[1] Cros A., Floriani E., Le Gal P., Lima R.:Transition to turbulence of the Batchelor flow in a rotor/stator device. Eur. J. Mech B/Fluids 24: 409-424, 2005.

[2] Czarny 0., Iacovides H., Launder B.E.: Precessing vortex structures in turbulent flow within rotor-stator disc cavities. Flow, Turb. & Comb. 69: 51-61, 2002.

[3] Jacques R., Daube O., Le Quéré P.: Axisymetric numerical simulations of turbulent flow in rotor-stator enclosures. Int. J. Heat & Fluid Flow 23: 381-397, 2002.

[4] Gutierrez-Castillo P., Lopez J.M.: Instabilities of the sidewall boundary layer in a rapidly rotating split cylinder. Eur. J. Mech B/Fluids 52: 76-84, 2015.

[5] Kraichnan R.: Inertial Ranges in Two Dimensional Turbulence. Phys. Fluids 10: 1417-1423, 1967.

[6] Campagne A., Gallet B., Moisy F., Cortet P. P.: Direct and inverse energy cascades in a forced rotating turbulence experiment. Phys. Fluids 26(12): 125112. 2014

[7] Yarom E., Sharon E.: Experimental observation of steady inertial wave turbulence in deep rotating flows. Nature Physics 10(7): 510-514. 2014

[8] Lamriben C., Cortet P. P., Moisy F., Maas L. R.: Excitation of inertial modes in a closed grid turbulence experiment under rotation. Phys. Fluids 23(1): 015102. 2011

FLOW STRUCTURE AND TORQUE TRANSITION PROCESS OF TURBULENT TAYLOR-COUETTE FLOW

Kosuke Osawa[1a)], Yoshitsugu Naka[1], Masayasu Shimura[1], Mamoru Tanahashi[1]
[1]*Department of Mechanical and Aerospace Engineering, Tokyo Institute of Technology, Tokyo, Japan*

Summary Direct numerical simulations of Taylor-Couette flow form Re = 8000 to 25000 are carried out to investigate the process of the transition in the Reynolds number dependency of the mean torque. The velocity fluctuations are decomposed into the contributions of the Taylor vortices and remaining turbulent fluctuations. Distinct Reynolds number dependencies of these components are observed in the Reynolds shear stress and the torque transmission. The net contributions of these components to the mean torque are evaluated. Relative contributions of The Taylor vortex component is overtaken by the turbulent counterpart around Re = 15000. This Reynolds number is close to the torque transition Reynolds number in the literature. These results suggest that the torque transition can be explained by the competition between the contributions of azimuthally averaged Taylor vortex and the remaining turbulent components.

INTRODUCTION

Taylor-Couette flow has been investigated because of its importance in engineering. Wendt et al. [1] found that the flow exhibits a transition in the Reynolds number dependency of the mean torque at Reynolds number Re = 10000. In the torque transition state, Lewis et al. [2] found the changes of azimuthally traveling wave of the velocity fluctuation in the center region as well as in the near wall region. The numerical study by He et al. [3] clarified that the universal fine scale eddy structures of turbulence develop in the domain around Re = 10 000. These results indicate the connection between the Reynolds number dependency of flow structures and the torque transition. In this study, the direct numerical simulations (DNS) of the Taylor-Couette flow have been conducted to clarify the Reynolds number dependency of the turbulence statistics in the torque transition state.

NUMERICAL METHODS

DNS of Taylor-Couette flow is conducted using Fourier-Chebyshev spectral methods. The governing equations are the incompressible Navier-Stokes equations and the continuity equation in the cylindrical coordinate system. These equations are non-dimentionalized by the rotation speed of the inner wall U_{in} and the gap width d. Boundary conditions are no-slip boundary condition for radial direction with only inner cylinder rotating, and the periodic boundary condition for axial direction. The time integration is implemented with 2nd order Adams-Bashforth method for non-linear terms and backward-Euler method for the other terms to satisfy the continuity equation with the influence matrix method. For the calculation conditions, the radius ratio η and the height of the domain h are fixed to 0.8 and 5d respectively. The DNS has been carried out at different Reynolds numbers Re (= $U_{in}\, d/\nu$) = 8000, 12 000, 20 000 and 25 000.

REYNOLDS NUMBER DEPENDENCY OF TURBULENCE STATISTICS

Figure 1 shows iso-surfaces of the second invariant of the velocity gradient tensor Q and mean velocity fields in r-z plane at Re = 8000 and 25 000. In the mean velocity field, two pairs of Taylor vortices are observed in both Re cases. The iso-surfaces of Q show that the fine scale eddy structures show preferential angle at Re = 8000 [3]. They distribute in the inflow and outflow regions existing between the Taylor vortices. In higher Reynolds number cases, the fine scale eddies gradually develop in the whole domain and they take more versatile angles.

As visually presented in Fig.1, both the large scale coherent motions of Taylor vortices and the fine scale structures exist around the transitional Reynolds number. To investigate the contributions of these flow structures to turbulence statistics, the velocity fluctuations are decomposed into the azimuthally-averaged velocity field and remaining turbulent components. $\langle f \rangle$ and $\tilde{f}$ denote the average of a variable in z and θ directions, respectively. f' and f'' are the fluctuations of from $\langle \tilde{f} \rangle$ and $\tilde{f}$. The Reynolds stress $R_{r\theta}$ is decomposed as

$$R_{r\theta} = \langle \widetilde{u_r' u_\theta'} \rangle = \langle \tilde{u}_r \tilde{u}_\theta \rangle + \langle \widetilde{u_r'' u_\theta''} \rangle = TV + T \,. \tag{1}$$

The first term TV is “Taylor vortex component” representing the contribution of the mean Taylor vortex motion. The second term T is “turbulent component”, which is the contribution of remaining turbulent fluctuations.

Transmission of the torque between cylinders is written as the function of the Reynolds stress and the viscosity terms [2].

$$G(r) = 2\pi Re^2 \left\{ R_{r\theta} r^2 - \frac{1}{Re} r^3 \frac{d}{dr} \frac{\langle \tilde{u}_\theta \rangle}{r} \right\} = \text{const.} \tag{2}$$

[a)] Corresponding author. Email: kosaw@navier.mes.titech.ac.jp.

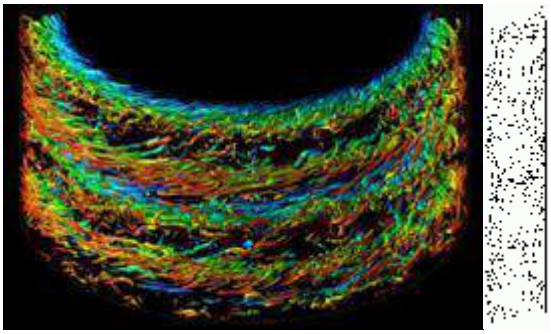

(a) Re = 8000

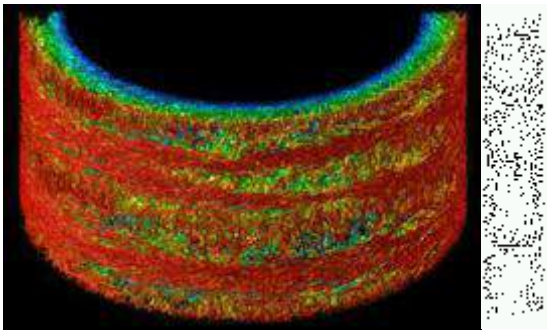

(b) Re = 25 000

Figure 1: Iso-surfaces of the second invariant of the velocity gradient tensor (Q = 1.0, colored by the radial position) and azimuthally averaged mean velocity in r-z plane.

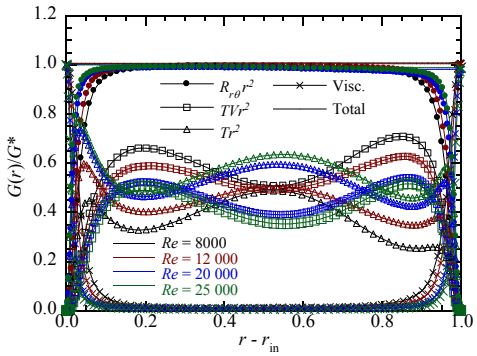

Figure 2: Radial profiles of the components of the torque transfer function.

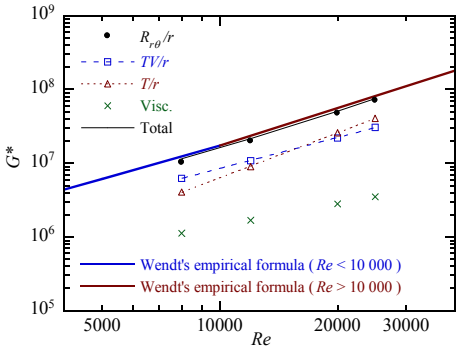

Figure 3: Reynolds number dependency of the components of the mean torque.

Fig. 2 shows the radial profiles of the each component of Eq. 2. The Reynolds stress term exhibits a major contribution in the torque transmission. The contributions of TV and T are comparable in the present Re range, and T apparently exceeds TV with Re increase. The viscosity term takes main role only in the near wall region.

The net contributions of each component in Eq. 2 to the mean torque can be written as

$$G = \int_{r_{in}}^{r_{out}} \frac{1}{r^3} G(r) dr \Big/ \int_{r_{in}}^{r_{out}} \frac{1}{r^3} dr \,. \tag{3}$$

Fig. 3 shows the contributions of the torque components at four Re cases. Wendt's empirical formula of the mean torque [1] are also plotted. Comparing the components of the Reynolds stress, TV is greater than T in lower Re cases, but due to the difference in their slope with respect to Re, the magnitude of T eventually excesses to TV. Assuming that TV and T follow the power law scaling, their trend lines are evaluated by the least squares method. The trend lines of TV and T cross near Re = 15 000, which is close to the transition Reynolds number proposed by Lewis et al. [2] Re = 13 000. Therefore it is considered that the torque transition can be explained by the competition between the large coherent motions of Taylor vortices and the fine scale turbulent structures.

CONCLUSIONS

A series of DNS of Taylor-Couette flow from Re = 8000 to 25 000 has been carried out to investigate the Reynolds number dependency of the turbulence statistics in torque transition state. The Reynolds stress and torque transmission show significant Reynolds number dependency when they are decomposed into the contribution of the mean Taylor vortex motion and remaining turbulent fluctuation. The contributions of these components to the net mean torque are evaluated from the torque transfer function. The turbulent fluctuation component excesses the Taylor vortex component around Re = 15 000, which is near the transition Reynolds number of the mean torque. These results show that the torque transition can be interpreted as the change of the major component from the Taylor vortices to turbulence.

References

[1] Wendt. F.: Turbulente stromungen zwischen zwei rotierenden konaxialen zylindern. *Arch. Appl. Mech.* **4**: 577–595, 1933.

[2] Lewis G. S., Swinney H. L.: Velocity structure functions, scaling, and transitions in high-Reynolds-number Couette-Taylor flow. *Phys. Rev. E* **59**(5): 5457, 1999.

[3] He. W., Tanahashi. M., Miyauchi. T.: Direct numerical simulation of turbulent Taylor-Couette flow with high Reynolds number. *ETC 11*: 215–217, 2007.

TURBULENCE UNDER ROTATION AT HIGH NUMERICAL RESOLUTION: EULERIAN AND LAGRANGIAN STATISTICS

Luca Biferale*[1], Fabio Bonaccorso[1], and Irene Mazzitelli[1]
[1]*Department of Physics and INFN, University of Rome Tor Vergata, Italy*

Summary Direct numerical simulations at unprecedented resolution of rotating turbulence at changing Reynolds and Rossby numbers are presented. Flow is also seeded with millions of particles, with and without inertia, light and heavy. We study two regimes, at high and low rotation. We mainly focus on extreme events for Eulerian and Lagrangian statistics, including the preferential sampling of inertial particles in presence of Coriolis and Centripetal forces.

EULERIAN ROTATING TURBULENCE

Turbulence under rotation is a paradigmatic problem involving complex physics and complex flow behavior. In presence of high rotation, i.e. low Rossby numbers, the flow tends to become more and more two-dimensional, being dominated by the presence of strong large-scale coherent structures aligned along the direction of rotation [1, 2, 5]. The transition is triggered by the presence of a non-vanishing inverse energy flux, as for genuine two dimensional flow (see Fig 1). Here, we present state-of-the-art direct numerical simulations of 3d turbulent flows under rotation at changing Reynolds number, up to record resolution (for the rotating case) of 4096^3 collocation points. Both the case of weak anisotropy (only forward energy cascade) and strong anisotropy (both forward and inverse cascades) are investigated, with assessment of isotropic and anisotropic scaling properties [4] of both the 2d mean field averaged along the rotation axis and the 3d underlying turbulent fluctuations.

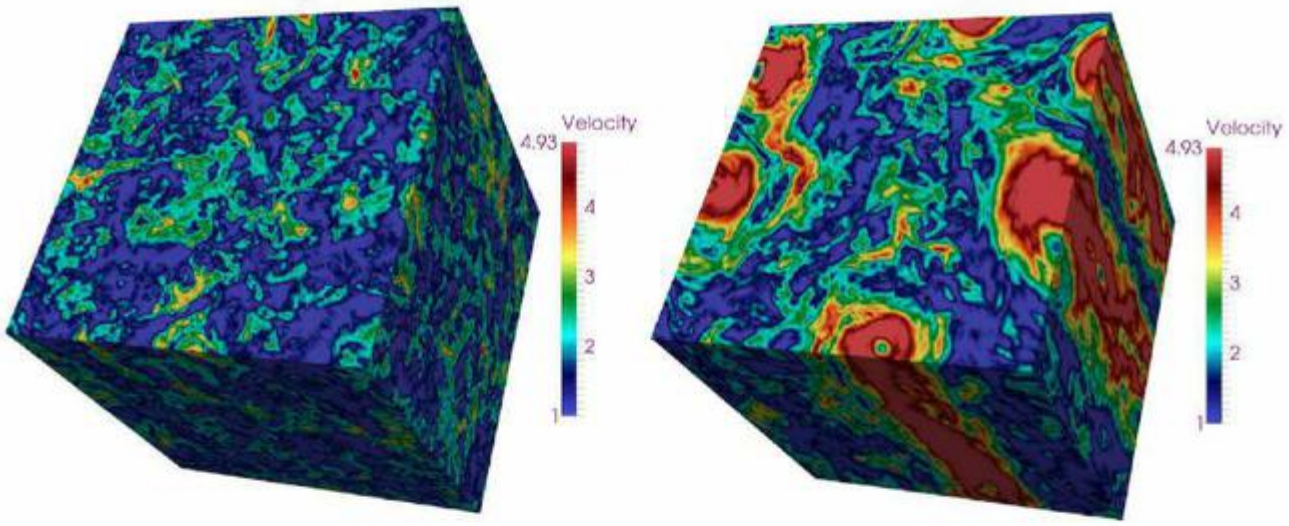

Figure 1: A 3D rendering of two turbulent flows at two Rossby numbers, one small enough to lead to an inverse energy cascade (right) and one with forward energy cascade only (left). At small Rossby, for the inverse energy cascade case, we observe the formation of three cyclonic coherent columnar vortices in a sea of 3D turbulent fluctuations.

LAGRANGIAN ROTATING TURBULENCE

The main novelty of our simulation is the advection of millions of light and heavy point-particles by the rotating flow. Following Maxey and Riley [6] the equations for the trajectory $\boldsymbol{x}$ and the velocity $\boldsymbol{v}$ of a small sphere of radius a and density ρ_p suspended in the fluid field $\boldsymbol{u}$ are:

$$\frac{d\boldsymbol{x}}{dt} = \boldsymbol{v} \tag{1}$$

$$\frac{d\boldsymbol{v}}{dt} = \beta\left[\frac{2}{3}\frac{D\boldsymbol{u}}{Dt}+\frac{1}{3}\frac{d\boldsymbol{u}}{dt}\right]-\frac{1}{\tau_p}(\boldsymbol{v}-\boldsymbol{u})-2\boldsymbol{\Omega}\times(\boldsymbol{v}-\beta\boldsymbol{u}) -(1-\beta)\boldsymbol{\Omega}\times(\boldsymbol{\Omega}\times\boldsymbol{r}) \tag{2}$$

*Corresponding author. Email: biferale@roma2.infn.it

The dynamics is controlled by two non-dimensional parameters, the density ratio $\beta = 3\rho_f/(\rho_f + 2\rho_p)$ and the Stokes number $St = \tau_p/\tau_\eta$ defined as the ratio between the particle relaxation time $\tau_p = a^2/3\beta\nu$ and the Kolmogorov time τ_η. The term $D\boldsymbol{u}/Dt = \partial\boldsymbol{u}/\partial t + \boldsymbol{u}\cdot\nabla\boldsymbol{u}$ is the fluid acceleration, while $d\boldsymbol{u}/dt$ is the derivative of the fluid velocity along the particle trajectory. Here we have neglected the Basset history force, the Faxen corrections and gravity force. At variance with the rotating Navier-Stokes equations for the fluid velocity field, the centrifugal force $(\beta \circ 1)\boldsymbol{\Omega}\times(\boldsymbol{\Omega}\times\boldsymbol{r})$ is explicitly present in the equation for the particles. Its sign depends on the factor $\beta \circ 1$: For heavy particles ($0 \leq \beta < 1$) the force is centrifugal, while for light particles ($1 < \beta \leq 3$) is centripetal. The presence of cyclonic structures (see Fig. 1) is key also for the dispersion and advection of inertial particles [4]. We present the first systematic investigation of dispersion of tracers, light and heavy particles in rotating turbulence, at high resolution and with a high number of particles trajectories. Both single particles quantities (acceleration, Lagrangian velocity structure functions) and two-particles quantities (Richardson dispersion) are studied, together with conditional statistics with respect to the underlying flow structures (preferential concentration).

CONCLUSIONS

We presented the first combined study of Eulerian and Lagrangian statistics for turbulence under strong rotation at high Reynolds and with a huge set of tracked particles' trajectories. Both single and multi-point statistics are investigated and the importance of the presence of stable coherent vortical structures for particles' distribution and particles' dispersion is analyzed.

ACKNOWLEDGEMENT

We acknowledge support from the European Research Council under the ERC AdG NewTURB, No. 339032.

References

[1] L. Smith, and F. Waleffe, *Phys. Fluids* **11**, 1608 (1999).
[2] A. Pouquet and P.D. Mininni, Phil. Trans. R. Soc. A **368**, 1635, (2010)
[3] L. Biferale and I. Procaccia Phys. Rep. **414** 43, (2005).
[4] T. Elperin, N. Kleeorin and I. Rogachevskii, Phys. Rev. Lett. **81**, 2898 (1998)
[5] C. Cambon N.M. Mansour and F.S. Godeferd, J. Fluid Mech. **337**, 303, (1997)
[6] M. R. Maxey and J. J. Riley, *Phys. Fluids* **26**, 883 (1983).

ASYMPTOTIC STATES IN TURBULENCE: THE EMERGENCE OF UNIVERSALITY AND INTERMITTENCY

Diego Donzis *[1]

[1]*Department of Aerospace Engineering, Texas A&M University, Texas, United States of America*

Summary Using a large database of well resolved direct numerical simulations, we show that small-scale universality, dissipative anomaly, and anomalous velocity gradients exponents attain an asymptotic character at very low Reynolds numbers—in fact, lower that those needed for the emergence of an inertial range. An implication of this observation is that inertial-range dynamics, for example, may not be responsible for small-scale intermittency. We also show that inertial range information can be accurately obtained from dissipative range statistics.

INTRODUCTION AND MOTIVATION

Most approaches to understand turbulence have sought universal behavior believed to manifest at high Reynolds numbers, R_λ. An underlying issue thus is the quantitative determination of the meaning of high Reynolds number. Neglecting this question could lead to varying conclusions when comparing flows in different configurations and different R_λ. Moreover, it has become clear now that different statistics approach their asymptotic state—if one actually exists—at different Reynolds numbers. For example, we recently suggested that anomalous scaling exponents of velocity gradients attain their high-R_λ asymptotic values at rather low R_λ [5]—in fact, lower than that required to observe an inertial range. This observation, which may seem counterintuitive, leads to important implications.

The thrust in this work is thus two fold. First, we identify asymptotic states for some of the most commonly studied statistics, namely, the mean dissipation rate, the energy spectrum, and moments of velocity gradients. We show that anomalous high-order exponents of velocity gradients emerge at lower Reynolds numbers than other lower-order statistics. This leads to the second objective, which is to assess whether quantities that emerge first already contain information about other aspects of fully developed turbulent flows. As we argue in this work this is indeed the case. A consequence of this is that, for example, information about the inertial range can be obtained from the dissipative range at very low Reynolds numbers.

THE EMERGENCE OF SMALL-SCALE UNIVERSALITY AND INTERMITTENCY

A basic assumption in phenomenological treatments of turbulence is that of dissipative anomaly—the idea that the mean energy dissipation rate, $\langle\epsilon\rangle$, is independent of viscosity as long as the latter is sufficiently small. This result, which was put forth by Taylor [8], has been verified experimentally and numerically [6, 2, 3]. Collectively data support an asymptotic $R_\lambda \sim O(10^2)$, above which the normalized dissipation rate is indeed independent of viscosity.

Dissipative anomaly is also an implicit assumption behind Kolmogorov 1941 theory (K41) which predicts certain universal behavior at small scales at high enough Reynolds numbers. This has been extensively assessed by examining the so-called compensated spectrum $\psi(k) = E(k)/\langle\epsilon\rangle^{2/3}k^{-5/3}$ where $E(k)$ is the three-dimensional energy spectrum at wavenumber k. Small-scale universality is then seen as a collapse of $\psi(k)$ at high wavenumbers for different Reynolds numbers and/or different flows. This is indeed observed in Fig. 1(a) where we show our data for a wide range of R_λ and different large scale forcing [1]. A question of interest is at what Reynolds number this universality emerges. In Fig. 1(b) we show data from new well-resolved DNS at much lower R_λ which shows that small-scale universality is maintained at R_λ as low as $O(1)$.

K41 also proposed the existance of the so-called inertial range of scales at high enough R_λ. Simulations and experiments show that it emerges also at $R_\lambda \sim O(10^2)$ (e.g. [3, 1] for recent data). We note, however, that the well-known spectral bump at $k\eta \sim 0.1$ [1] is established at a lower $R_\lambda \approx 50$. A significant inertial range—one in which the so-called 4/5th law can be meaningfully assessed—appears to be only obtained at R_λ exceeding 10^3 for forced flows or 10^6 for decaying flows [4]. The situation can be seen in Fig. 1(a). An inertial range would be seen as a plateau at intermediate scales. Careful investigation of the data, however, exposes two main difficulties which make an assessment of inertial-range quantities (such as the Kolmogorov constant) less than unambiguous as documented in [1]. These are intermittency corrections to the inertial-range slope, and the spectral bump. Difficulties in extracting information or even identifying the inertial range are even more severe for high-order statistics such as high-order structure functions. Finding an alternative way of doing so is, thus, highly desirable and possible as shown here.

While K41 has been shown to be approximately valid for low-order moments, it has become increasingly clear over the decades that high-order moments of velocity gradients, dissipation, enstrophy and velocity increments depart from K41 predictions [7]. This so-called anomalous scaling has been related to the phenomenon of intermittency—the tendency for extremely large but localized fluctuations in space and time. This fluctuations are resposible for strong departures from

*Corresponding author. Email: donzis@tamu.com

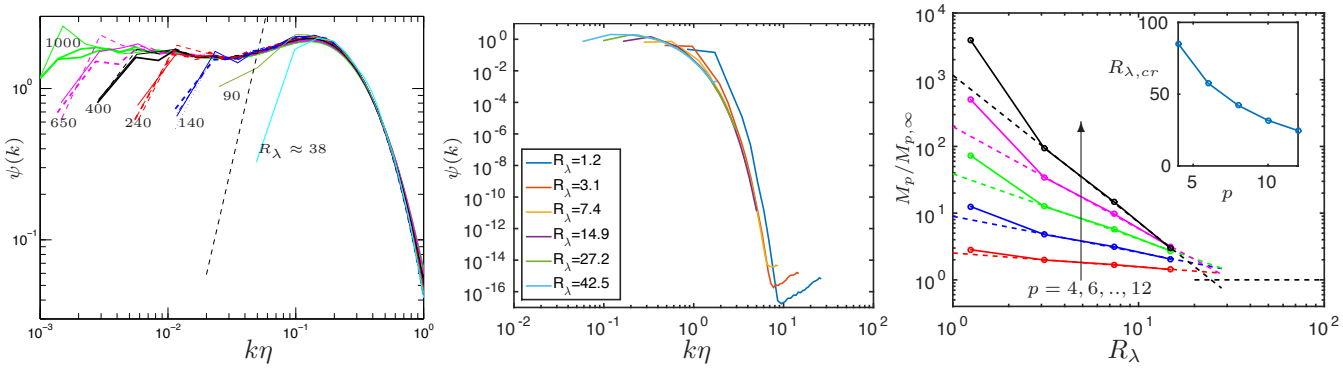

Figure 1: (a) Compensated energy spectrum at different Reynolds numbers. Different lines styles for different forcing and resolution. (b) Same as (a) at lower R_λ. (c) Normalized velocity gradient moments. Horizontal dashed line denotes asymptotic high-R_λ limit. Inset: critical R_λ at which each order approaches the high-R_λ limit.

Gaussian behavior as R_λ increases. Thus, intermittency has also been historically believed to be a high-R_λ feature. However, we recently showed [5] that anomalous scaling emerges at very low Reynolds numbers. Data suggest that the first few moments of velocity gradients transition from Gaussian to fully anomalous high-R_λ behavior at $R_\lambda \sim O(10)$. This implies the somewhat unexpected conclusion that the structure of very intense small-scale intermittent events emerges at lower R_λ that the inertial range or dissipative anomaly. Furthermore, in this work we show that normalized moments of different orders, $M_p = \langle(\partial u/\partial x)^p\rangle/\langle(\partial u/\partial x)^2\rangle^{p/2}$, approach their asymptotic behavior (the high-R_λ limit, $M_{p,\infty}$) at different Reynolds numbers (Fig. 1(c)). High-order moments do so at lower R_λ than low-order moments (inset of figure).

A number of studies have established relations between inertial range scaling exponents of structure functions and the scaling of velocity gradients which have been tested against DNS data. As we show here, this provides a key ingredient in a novel way we propose to study inertial-range dynamics from dissipative-range statistics.

THE OVERALL PICTURE

Taken together, all observations above suggest that as the Reynolds number is increased beyond $O(1)$ the energy spectrum display small-scale universality at high wavenumbers consistent with K41. At higher Reynolds numbers of $O(10)$ the most intense events appear as measured by high-order moments of velocity gradients. Further increase of R_λ to about 50 results in the formation of the spectral bump. Finally, it is only at $R_\lambda \sim O(10^2)$ that dissipative anomaly and an incipient inertial range appear. A number of interesting counterintuitive consequences follow from this result. First, since the spectral bump emerges before there is any inertial range, its origin cannot be attributed to inertial-range dynamics as commonly done. The same can be concluded for intermittency and anomalous scaling which appears at a Reynolds number and order of magnitude smaller than that required for the inertial range. Very strong fluctuations at the smallest scales, thus, are not produced by, e.g., fluctuations in the energy cascade as proposed in a number of intermittency models in the literature.

Additionally, since anomalous scaling of velocity gradients appears at very low R_λ, it is then possible to obtain very accurate velocity gradient moments from well resolved simulations at low Reynolds numbers and compute inertial-range scaling exponents for structure functions with well-known formulas relating the two. In this work we show this is indeed possible and compare against data in the literature. This approach provides a tremendous advantage, since as mentioned above, obtaining a sufficiently wide inertial range would require R_λ well beyond what is possible in the foreseeable future.

References

[1] D. A. Donzis and K. R. Sreenivasan. The bottleneck effect and the Kolmogorov constant in isotropic turbulence. *J. Fluid Mech.*, 657:171, 2010.

[2] D. A. Donzis, K. R. Sreenivasan, and P. K. Yeung. Scalar dissipation rate and dissipative anomaly in isotropic turbulence. *J. Fluid Mech.*, 532:199, 2005.

[3] T. Ishihara, T. Gotoh, and Y. Kaneda. Study of high-Reynolds number isotropic turbulence by direct numerical simulation. *Annu. Rev. Fluid Mech.*, 41:165, 2009.

[4] Antonia R. A. and Burattini P. Approach to the 4/5 law in homogeneous isotropic turbulence. *J. Fluid Mech.*, 550(1):175, 2006.

[5] J. Schumacher, J. D. Scheel, D. Krasnov, D. A. Donzis, V. Yakhot, and K. R. Sreenivasan. Small-scale universality in fluid turbulence. *Proceedings of the National Academy of Sciences*, 2014.

[6] K. R. Sreenivasan. On the scaling of the turbulence energy-dissipation rate. *Phys. Fluids*, 27:1048, 1984.

[7] K. R. Sreenivasan and R. A. Antonia. The phenomenology of small-scale turbulence. *Annu. Rev. Fluid Mech.*, 29:435, 1997.

[8] G. I. Taylor. Statistical theory of turbulence. *Proc. R. Soc. Lond. A*, 151:421, 1935.

INERTIAL AND INERTIAL CONVECT RANGES AND CROSSOVER LENGTH

Toshiyuki Gotoh*[1] and Takeshi Watanabe[1]

[1]*Department of Scientific and Engineering Simulation, Nagoya Institute of Technology, Nagoya, Japan*

Summary Local scaling exponents of the structure functions of the velocity and two passive scalar increments in steady isotropic turbulence at very high Reynolds numbers $R_\lambda = 805$ with the grid points $N = 4096^3$ are examined. The two passive scalars are convected by the identical turbulence but excited by the different scalar injections. It is found that all the exponents have plateaus at separation distance in between twice the Taylor microscale and a quarter of the integral scale, for which the inertial range is defined and does not coincide with the $-5/3$ kinetic energy spectrum range. The crossover lengths of the inertial (convective) and the dissipation (diffusive) ranges are found to be independent of the order of the structure functions.

INTRODUCTION

The scaling exponents have been one of the central issues in the fundamental physics of turbulence [1]. The theories of Kolmogorov for the velocity and Obukhov-Corrsin for the passive scalar predict the normal scaling with the exponent $n/3$ of the nth order structure functions, but the intermittency modifies the exponents to be non decreasing functions of n and smaller than $n/3$. The error bars of the exponents of the longitudinal velocity structure functions so far found are small, but the exponents of the passive scalar scatter considerably [1]. It is important and indispensable to quantitatively examine where the inertial range exists and at which scale the dissipation range begins. We try to find a quantitative measure of the position of the inertial (convective) range and the crossover scale to the dissipation (diffusive) range by using DNS at very high Reynolds number.

DIRECT NUMERICAL SIMULATION

We have numerically integrated the Navier-Stokes equations for the incompressible fluid with unit density and the transport equations of two passive scalars θ and q which are convected by the identical steady turbulent flow [2]. The scalar θ is excited by the Gaussian random source which is white in time and excited at low wavenumbers $1 \le k \le 3$, while q is excited by the uniform scalar gradient $\Gamma = 1$ applied in the x_3 direction. The pseudo spectral method and the 4th order Runge Kutta Gill method are used. The number of grid points are 4096^3 and the time average is taken over about 8.2 large eddy turnover time. The average Taylor microscale Reynolds number is $R_\lambda = 805$ and the Schmidt number is $Sc = 0.72$. The structure functions as functions of the separation vector $\boldsymbol{r}$ are defined by $Q_n^u(\boldsymbol{r}) = \langle(\boldsymbol{u}(\boldsymbol{x}+\boldsymbol{r}) - \boldsymbol{u}(\boldsymbol{x}))\cdot\boldsymbol{r}/r)^n\rangle, Q_n^\theta(\boldsymbol{r}) = \langle(\theta(\boldsymbol{x}+\boldsymbol{r}) - \theta(\boldsymbol{x}))^n\rangle, Q_n^q(\boldsymbol{r}) = \langle(q(\boldsymbol{x}+\boldsymbol{r}) - q(\boldsymbol{x}))^n\rangle$ and expanded in terms of the Legendre polynomial as $Q_n^\alpha(r,\phi) = \sum_{l=0} S_{n,l}^\alpha(r) P_l(\cos\phi), \quad \alpha = u, \theta, q$, where ϕ is the angle between the vector $\boldsymbol{r}$ and the x_3 direction [2]. This yields better statistical convergence at large separation distance.

RESULTS

Figure 1 shows the average spectra of the kinetic energy and the scalar variances which are compensated by multiplying $\bar{\epsilon}^{-2/3}k^{5/3}$ or $\chi_\alpha\bar{\epsilon}^{-1/3}k^{5/3}$, respectively, where $\alpha = \theta, q$. The plateaus of the curves with finite width are clearly seen. We assume that the separation distance $2r$ in the physical space corresponds to the wavelength and thus $k = \pi/r$.

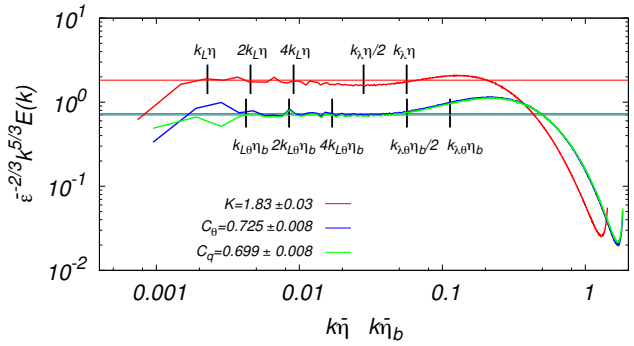

Figure 1: Average spectra of $\bar{\epsilon}^{-2/3}k^{5/3}E(k)$ (red), $\chi_\theta^{-1}\bar{\epsilon}^{1/3}k^{5/3}E_\theta(k)$ (blue), and $\chi_q^{-1}\bar{\epsilon}^{1/3}k^{5/3}E_q(k)$ (green).

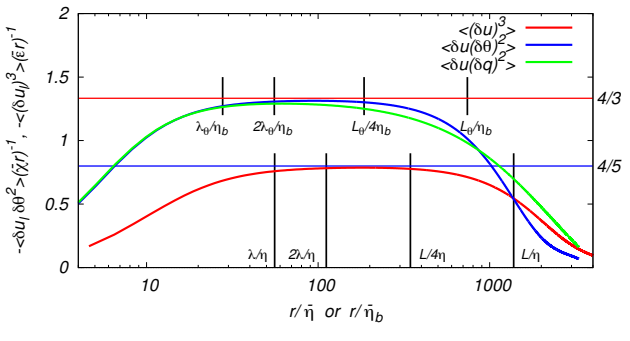

Figure 2: The 4/5 law $-\langle(\delta u_r)^3\rangle/(\bar{\epsilon}r)$ and the 4/3 laws $-\langle\delta u_r(\delta\theta_r)^2\rangle/(\chi_\theta r)$, $-\langle\delta u_r(\delta q_r)^2\rangle/(\chi_q r)$.

*Corresponding author. Email: gotoh.toshiyuki@nitech.ac.jp

The $k^{-5/3}$ plateau for the velocity is observed for $k_L < k < 4k_L$ and that for the scalar is for $k_{L_\theta} < k < k_{\lambda_\theta}/2$. Note that the tilted part exists in the kinetic energy spectrum for $4k_L < k < k_\lambda/2$ which corresponds to the scaling range of the velocity structure functions as we will see below. Figure 2 indicates the 4/5 law for the velocity and the 4/3 law for the passive scalars. It is seen that the approximate plateaus close to the 4/5 and 4/3 level occur for the range $2\lambda < r < L/4$ and $2\lambda_\alpha < r < L_\alpha/4 (\alpha = \theta, q)$, respectively. It should be noted that the range of $2\lambda < r < L/4$ corresponds to the tilted part in the compensated kinetic energy spectrum in Fig.1, not to the range where the fair $-5/3$ spectrum of the kinetic energy is observed.

Now we examine the local scaling exponents of the isotropic sector ($l = 0$) of the expansion coefficients that are defined by

$$\zeta^{\alpha}_{n,0}(r) = d \log S^{\alpha}_{n,0}(r) \; / \; d \log r, \qquad (\alpha = u, \theta, q)$$

and plotted in Fig.3. It is found that $\zeta^{u}_{n,0}(r)$ has the fair horizontal portion for $2\lambda < r < L/4$. When the crossover length of the inertial and dissipation ranges is defined as the length at which the curve leaves the plateau, it occurs at *the same length* of about 2λ and is independent of the order n within the present DNS. There is no trend that the lower end of the inertial range penetrates into the dissipation range with increase of the order [3]. Figure 3(b) is most remarkable result. There are no plateaus in the curves of the structure functions for the order higher than 2. The curves of $\zeta^{\theta}_{n,0}(r)$ are straight and approximated as $\zeta^{\theta}_{n,0}(r) = \xi^{\theta}_{n} + \beta_n (r - r_*)$, and thus the structure function for θ is given by the non-power law

$$S^{\theta}_{n,0} \quad = \quad A_{n,0} \, (r/r_*)^{\xi^{\theta}_n + \frac{1}{2}\beta_n \log(r/r_*)}, \quad r_* \approx 2\lambda_\theta,$$

for $2\lambda_\theta < r < L_\theta/2$. The slope of the curve is found to linearly increase with n [2]. On the other hand the local scaling exponents of the scalar q has fair plateaus for $2\lambda_q < r < L_q$. Again we observe that the crossover lengths are $2\lambda_\alpha (\alpha = \theta, q)$ and independent of the order.

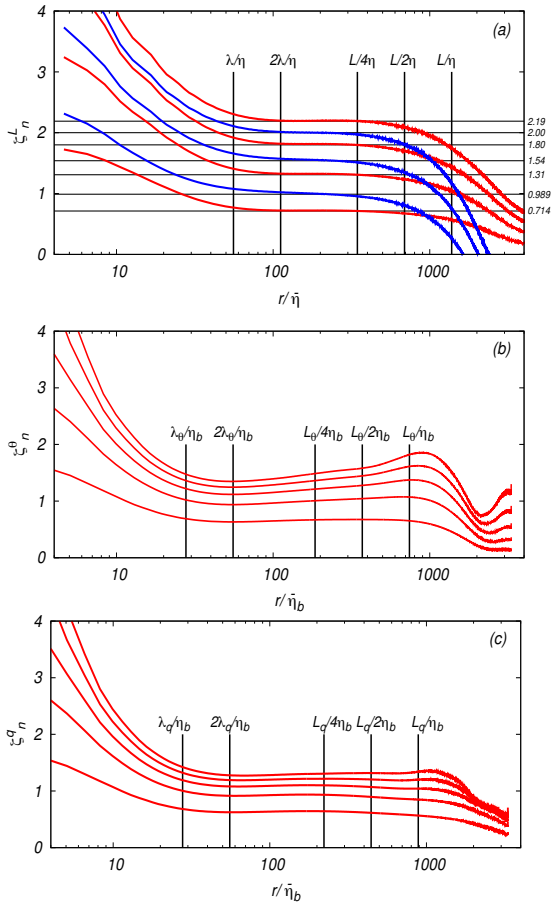

Figure 3: Local scaling exponents of (a) $S^{u,0}_n(r)$ for $n = 2, 3, \cdots, 8$, (b) $S^{\theta,0}_n(r)$ for $n = 2, 4, \cdots, 10$, and (c) $S^{q,0}_n(r)$ for $n = 2, 4, \cdots, 10$, respectively.

CONCLUSIONS

The range that the plateaus of the local scaling exponents of the longitudinal velocity is observed corresponds to the tilted part of the compensated kinetic energy spectrum, not to the range of $-5/3$ spectrum. The inertial range, when it is defined as the range of scales that the 4/5 and 4/3 laws hold, is approximately in between twice the microscale and one quarter of the integral scale within the present DNS study. The crossover length is at about $2\lambda_\alpha, (\alpha = u, \theta, q)$ and independent of the order. The physical reason for the non-power law will be discussed at the Congress.

This research used computational resources of Plasma Simulator provided by the National Institute for Fusion Science (NIFS) (NIFS14KNSS050), the K computer provided by the RIKEN Advanced Institute for Computational Science through the HPCI System Research project (hp150088). The work of T. G and T. W. was supported by Grants-in-Aid for Scientific Research Nos. 15H02218 and 26420106, respectively, from the Ministry of Education, Culture, Sports, Science, and Technology of Japan.

References

[1] P. Davidson, Y. Kaneda, and K. R. Sreenivasan Eds.: Ten Chapters in Turbulence, Cambridge Univ. Press, UK, 2013.

[2] Gotoh, T. and Watanabe, T.: Power and non-power laws of passive scalar moments convected by isotropic turbulence, Phys. Rev. Lett., **115**, 114502, 2015.

[3] Yakhot, V.: Probability densities in strong turbulence Physica D **215** 166-174, 2006.

HIGH-ORDER STATISTICS AND RANDOM ADDITIVE MODEL FOR TURBULENT BOUNDARY LAYERS

Charles Meneveau[a)1], Xiang I. A. Yang[1], and Ivan Marusic[2]
[1]*Department of Mechanical Engineering, Johns Hopkins University, Baltimore, Maryland, USA*
[2]*Department of Mechanical Engineering, University of Melbourne, Melbourne, Australia*

Summary A random additive process is introduced as a simplified version of the Townsend attached eddy hypothesis to describe fluctuations in the momentum cascade in wall turbulence at high Reynolds number. This formalism can provide economical predictions about scaling behaviors in single- and multiple-point turbulence statistics in the logarithmic region. New log laws for two-point quantities are identified and confirmed using experimental data. Secondly, properties of single- and two-point moment-generating- functions ($\langle \exp(qu) \rangle$ and $\langle \exp[qu(x,z) + q'u(x+r,z)] \rangle$) are investigated, where q, q' are real-valued parameters. Empirical evidence of power law behaviors with respect to the wall normal distance in the logarithmic region in single-point moment-generating-function (MGF) is observed. Moreover, a power-law scaling transition in two-point MGF $\langle \exp(qu(x,z)qu(x+r,z)) \rangle$ is predicted in the framework of the random additive process and Townsend's attached eddy hypothesis, and confirmed in experimental measurements.

INTRODUCTION

Townsend [1] hypothesized that at high Reynolds numbers boundary layer flow consists of self-similar, hierarchical eddies. The size of each eddy scales as its distance from the wall. This hypothesis leads to the prediction of logarithmic scaling of the variance of streamwise velocity fluctuations with wall normal distance z, $<u^+{}^2>= A_1 \log(\delta/z) + B_1$, where u is the streamwise velocity fluctuation, $+$ indicates normalization by friction velocity (for compactness, this notation is dropped hereafter), $\langle \cdot \rangle$ indicates ensemble average and $A_1 = 1.25$ is the Townsend-Perry constant, B_1 is yet another constant and δ is an outer-layer length scale such as the boundary layer thickness. In Refs. [2], [3], logarithmic scalings in $\left\langle u^{2p} \right\rangle^{1/p}$ as well as structure functions have been derived within the framework of Ref. [1].

Here we model the streamwise velocity fluctuation at a generic point P within the logarithmic region at height z above the wall to be an outcome of a random additive process:

$$u_z = \sum_{i=1}^{N_z} a_i, \quad N_z \sim \log(\delta/z). \tag{1}$$

For shorthand, the subscript z indicates height z above the wall in the logarithmic layer. The random additives a_i's are independently and identically distributed random variables, and each of them is associated with velocity induced at point P by an attached eddy of size $\delta/2^i$. The number of random additives is proportional to the number of eddies above and, in line with Ref. [1], $N_z \sim \int 1/z \, dz = \log(\delta/z)$. Using the assumed independency among a_i's, Eq.1 directly leads to generalized log laws in $\left\langle u^{2p} \right\rangle^{1/p}$. Also, Eq.1 leads to $u_z \circ u_r = \sum_{i=N_r}^{N_z} a_i$, also leading to logarithmic scalings in $\left\langle (u_z \circ u_r)^{2p} \right\rangle^{1/p}$. This random additive model is used to propose new log laws in the present contribution.

Taking exponential of both sides of Eq. 1 gives moment-generating-functions (MGFs) defined as the average of $\exp(qu) = \prod_{i=1}^{N_z} \exp(qa_i)$. As can be seen, power law scaling in the single-point MGFs $\langle \exp(qu) \rangle = z^{C \log\langle \exp(qa) \rangle}$ must hold for a random additive process. Besides this behavior for single-point MGFs, two-point MGFs are also examined.

We use Eq. 1 to derive new logarithmic laws. Eddies of height $< r \tan\theta$ cannot simultaneously affect a point at (x, z) and a point at $(x + r, z)$ and eddies of height $> r \tan\theta$ affect both points equally. θ is the inclination angle of a typical attached eddy. Decomposing the velocity fluctuation at a point into $u_z \circ u_{r\tan\theta}$ and $u_{r\tan\theta}$ the following new logarithmic scalings can be found (for more details see Refs.[4, 5]):

$$S_2 = \left\langle \frac{3}{2} u_z^2(x) u_z^2(x+r) - \frac{1}{2} u_z^4(x) \right\rangle^{1/2} = A_2 \log(\delta/r); \quad S_3 = \left\langle \frac{5}{2} u_z^3(x) u_z^3(x+r) - \frac{3}{2} u_z(x) u_z^5(x+r) \right\rangle^{1/3} = A_3 \log(\delta/r). \tag{2}$$

A_2, A_3 are the slopes in the logarithmic scalings in $\left\langle u^4 \right\rangle^{1/2}$ and $\left\langle u^6 \right\rangle^{1/3}$. The new log laws in Eq. 2 are confirmed using experimental measurements of a $Re_\tau = 19000$ boundary layer (figure 1, see Ref. [6] for details of the dataset).

The MGFs are computed for various q-values in a range between ± 2. The measured MGFs as function of wall distance in inner units are shown in figure 2 for representative values of q. The experimental measurements are taken at a boundary layer at $Re_\tau \approx 13000$ (see [7] for details of the dataset). In the range $600 < z^+$, $z < 0.2\delta$, power law behavior is observed. Moreover, there is significant difference in the scaling exponents of $\langle \exp(qu) \rangle$ for positive and negative q values of the same magnitude. A scaling transition in the two-point MGFs $\langle \exp(qu(x,z) \circ qu(x+r,z)) \rangle$ is observed in figure 2, (b)–the power-law scaling exponents increase as q increases for q being small, while beyond certain critical value q_{cr}, the scaling exponent becomes constant. Detailed derivation of this scaling transition can be done using the random additive formalism.

a) Corresponding author. Email: meneveau@jhu.edu.

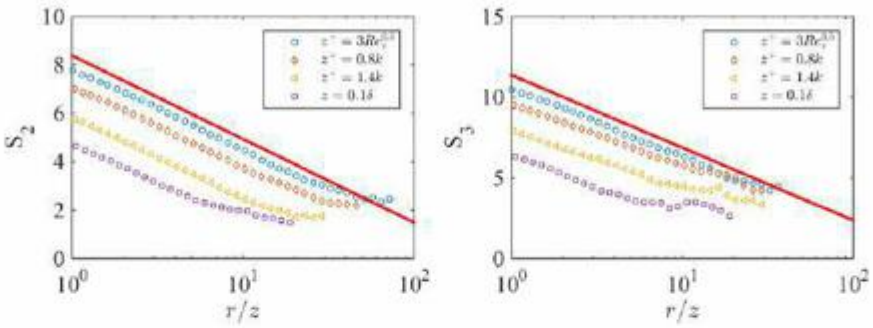

Figure 1: S_2, S_3 against r/z at $z^+ \approx 3Re_\tau^{0.5}, 800, 1400$ and $z = 0.10\delta$. The measured A_2, A_3 values [2] are used for the slope indicated in the figure (the solid red line).

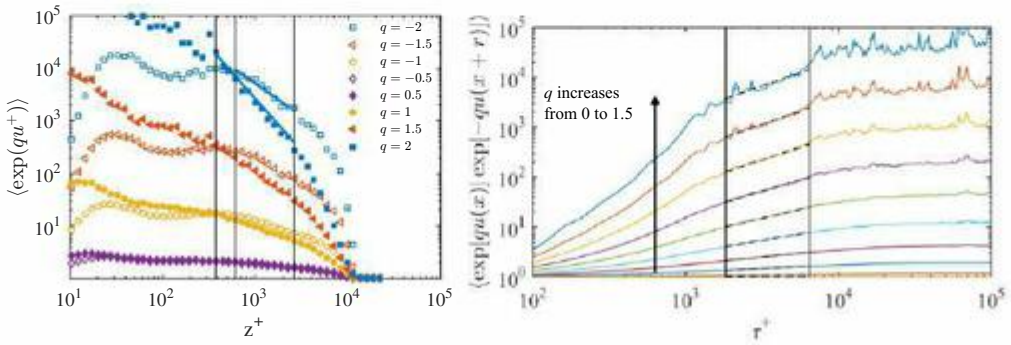

Figure 2: **a)** Log-log plot of $\langle \exp(qu^+) \rangle$ against z^+ for $q = \pm 0.5, \pm 1, \pm 1.5 \pm 2$. Solid symbols are used for positive q's and hollow symbols for negative q values. The extent of the scaling regions, $400 < z^+$, $z < 0.2\delta$ for $q>0$ and $600<z^+$, $z<0.2\delta$ for $q<0$ are indicated by vertical lines. **b)** Log-log plot of $W(q, -q; z, r)$ against r at $z^+ = 600$, for 9 values of q ranging from 0 to 1.5 (shown values are q =0,0.19,0.38,0.56,0.75,0.94,1.13,1.31 and 1.50). The range of r chosen to determine the power law scaling exponent (relevant for the log region) is $z/\tan\theta$, to $0.15\delta/\tan\theta$. At $z^+ = 600$, this range corresponds to (approximately) $2k<r^+<6.5k$, which is indicated by the vertical lines. The fits are indicated by dashed lines.

The random additive formalism is shown to be a convenient tool in providing economical yet accurate predictions of scaling behavior of turbulence statistics in the logarithmic region. New logarithmic laws are identified using this formalism. Properties of the single- and two-point moment generating functions in the logarithmic region are investigated. Power law behaviors are found in single-point MGFs and a scaling transition is found in two-point MGFs. We conclude that MGFs can provide new and statistically robust insights into turbulence structures and confirming essential ingredients of the attached eddy model.

Acknowledgements: The authors gratefully acknowledge the financial support of the Office of Naval Research, the National Science Foundation, and the Australian Research Council.

References

[1] Townsend A. A.: The structure of turbulent flow, Cambridge University Press, New York, 1976.

[2] Meneveau, C., Marusic, I.: Generalized logarithmic law for high-order moments in turbulent boundary layers. Journal of Fluid Mechanics, 719, R1, 2013. Chicago

[3] de Silva, C. M., Marusic, I., Woodcock, J. D., Meneveau, C.: Scaling of second-and higher-order structure functions in turbulent boundary layers. Journal of Fluid Mechanics, 769, 654-686, 2015.

[4] Yang, X.I.A., Marusic, I., Meneveau, C.: Logarithmic scaling of high order two-point correlations in turbulent boundary layer flow-data analysis and modeling. Preprint, 2016a

[5] Yang, X.I.A., Marusic, I., Meneveau, C.: Moment generating functions and scaling laws in the inertial layer of turbulent wall bounded flows. Preprint, 2016b

[6] Hutchins, N., Nickels, T. B., Marusic, I., Chong, M. S.: Hot-wire spatial resolution issues in wall-bounded turbulence. Journal of Fluid Mechanics, 635, 103-136, 2009.

[7] Marusic, I., Chauhan, K. A., Kulandaivelu, V., Hutchins, N.: Evolution of zero-pressure-gradient boundary layers from different tripping conditions. Journal of Fluid Mechanics, 783, 379-411. Chicago, 2015

Scale-hierarchy in homogeneous Hall MHD turbulence

Hideaki Miura [*1] and Keisuke Araki[2]
[1]*National Institute for Fusion Science, Oroshi 322-6, Toki, Gifu 509-5292, Japan*
[2]*Okayama University of Science, 1-1 Ridaicho, Okayama 700-0005, JAPAN*

Summary Direct numerical simulations are carried out to study scale-hierarchy in homogeneous Hall magnetohydrodynamic turbulence. It is shown that Hall term can cause from sheet to tubular structure transition in the vorticity field, changing the local structures without a clear change in the energy spectrum. Longitudinal structure functions of the velocity field tends to be refracted at the scale comparable to the ion skin depth. A relation between the refraction of the structure functions and the vorticity field is discussed.

INTRODUCTION

Magnetohydrodynamic (MHD) turbulence has been studied as a model of solar wind, nuclear fusion, and some other kinds of plasma turbulence in which ion skin depth scale can be important. While MHD equations provides a good plat form for studying plasma turbulence, the derivation of the equations can be invalid for very small scales comparable to or smaller than the ion skin depth and ion Larmor radius. An extension of the MHD equations to the small scales is the Hall MHD equations in which the ion skin depth scale, or two-fluid effects in other words, are taken into account.

The introduction of the two-fluid effects is considered to bring about modification of statistical structures as well as dynamical structures in turbulence. It has been reported in some numerical and theoretical works that the magnetic energy spectrum is likely to be proportional to $k^{-7/3}$ for a high k where k is the wave number[1, 2, 3]. The two-fluid effects can modify dynamical aspects and/or local structures of MHD turbulence. Dmitruk and Matthaeus have reported about the two-fluid effects on the electric field[5]. Recently we have shown that a transition from a sheet to a tubular vortex structures in freely decaying homogeneous and isotropic turbulence[4]. In this paper we study scale-hierarchy in statistics and its relation to spatial structures of Hall MHD turbulence.

DIRECT NUMERICAL SIMULATIONS

Direct Numerical Simulations (DNSes) of homogeneous turbulence under an uniform magnetic field $B_0 = 5$ are carried out by solving the Hall MHD equations by the use of the pseudo-spectral method and the Runge-Kutta-Gill scheme. Random forces are added to the equation of motions to keep turbulence to achieve statistically steady state. Because of the random forcing, the kinetic energy is much larger than the magnetic energy. The Hall parameter is set $\epsilon_H = 0.05$, and thus the wave number $k_\epsilon = 1/\epsilon_H = 20$ is the scale of the ion skin depth. DNSes of homogeneous MHD turbulence ($\epsilon_H = 0$) are also carried out so that we can compare the two kinds of turbulence closely as the initial value problem. The number of grid points in DNSes is typically 1024^3.

In Fig.1(a), isotropic energy spectra of the magnetic field in Hall MHD and MHD turbulence are shown. Since the resistivity and the viscosity in DNSes are set relatively low. In order to resolve the scale $k > k_\epsilon$, Kolmogorov's $k^{-5/3}$-law is not observed clearly. On the other hand, however, the spectrum in Hall MHD appears being proportional to $k^{-7/3}$, being consistent with earlier numerical works[1, 2, 3]. In Fig.1(b) energy spectra of the magnetic field perpendicular (square) and parallel (black circle) to the background magnetic field in in Hall MHD turbulence are shown. A clear power-law is observed both for the perpendicular and parallel components. In particularly, the perpendicular component exhibits a clear $k^{-7/3}$ scaling, showing a clear coincidence with earlier numerical simulations as well as solar wind observations by the Cluster satellites[6, 7].

Next we study scale-hierarchy in Hall MHD turbulence. Though the structure functions should be defined by the use of both the magnetic field and the velocity field as Galtier has derived the Kármán-Howarth equation[8] for homogeneous and isotropic turbulence, we can approximately define a structure function by the use of the velocity field only since the kinetic energy is quite larger than the magnetic energy. In Fig.2(a), structure functions of the velocity field in Hall MHD turbulence on the longitudinal displacement $S_n(r) \propto \langle (u_\alpha(x_\alpha + re_\alpha) - u_\alpha(x_\alpha)) \rangle$ for where e_α represents the α-th component of the unit vector $\mathbf{e}$ in the direction parallel to the uniform magnetic field of the strength B_0. Fig.2(b) is for the structure functions of MHD turbulence. Though both Fig.2(a) and (b) show a power-law in the even-number structure functions, it is clear that the structure functions in Fig.2(a) are refracted at $r/\eta \simeq 2$ and $r/\eta \simeq 4$ where η is the Kolmogorov's length scale. A possible understanding is that the generation of tubular vortices can influence the structure functions because radius of tubular vortices in hydrodynamic turbulence is typically $4\eta \sim 5\eta$ [9]. It may suggest that the refraction of structure functions originate from the tubular structure in the velocity field. However, since the velocity structure functions in hydrodynamic turbulence does not show a refraction at the scale of the vortex radius, the understanding may not be right. Another possible understanding is that the strong influences of whistler waves along the magnetic field lines may influences the scale smaller than $r/\eta < 4$, related with the magnetic field which is neglected here. The conjecture is to be examined.

*Corresponding author. Email: miura.hideaki@nifs.ac.jp

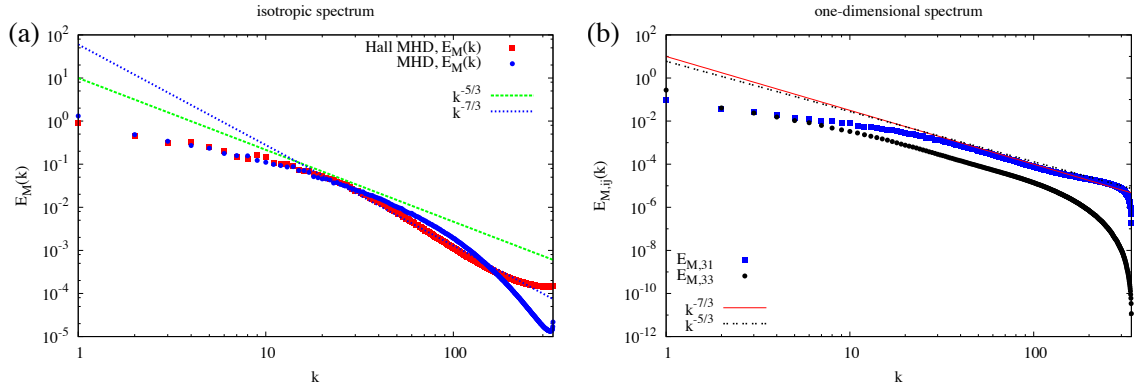

Figure 1: (a) Isotropic energy spectra of the magnetic field in Hall MHD and MHD turbulence. (b) Energy spectra of the magnetic field perpendicular (square) and parallel (black circle) to the background magnetic field in in Hall MHD turbulence.

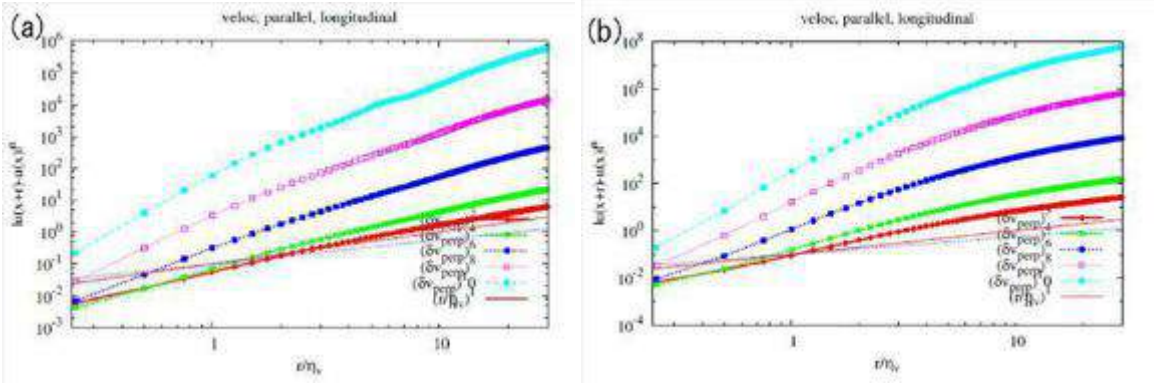

Figure 2: Structure functions of velocity fields in (a) Hall MHD and (b) MHD turbulence.

SUMMARY

DNSes of homogeneous Hall MHD turbulence shows that the introduction of the Hall term to MHD equations can cause from sheet to tubular structure transition in the vorticity field and change vortex structures. A clear $k^{-7/3}$-law is verified in the longitudinal structure (one-dimensional) spectrum of the magnetic field fluctuation, agreeing well with the satellite observations of the solar winds. It seems plausible that the refraction corresponds to the structure transition though the conjecture is left to be examined by more detailed analysis.

References

[1] Mininni, P., Alexakis, A., and Pouquet, A.: J. Plasma Phys. 73:377-401, 2007.

[2] Galtier, S., and Buchlin, E.: Astrophys. J. 656: 560-566, 2007.

[3] Hori, D., Miura, H.: Spectral Properties of Hall MHD Turbulence, Plasma Fusion Res. 3: S1053, 2008.

[4] Miura, H. and Araki, K.: Structure transitions induced by the Hall term in homogeneous and isotropic magnetohydrodynamic turbulence, Phys. Plasmas 21:072313, 2014.

[5] Dmitruk, P., and Matthaeus, W. H: Phys. Plasmas 13:042307, 2006.

[6] Alexandrova,, J. Saur, C. O, Lacombe, Mangeney, A., Mitchell, J., Schwartz, S. J., Robert, P.:Phys. Rev. Lett. 103: 165003, 2009. Universality of Solar-Wind Turbulent Spectrum from MHD to Electron Scales

[7] Kiyani, K. H., Chapman, S. C., Khotyaintsev, Yu. V., Dunlop, M. W., Sahraoui, F.: Phys. Rev. Lett. 103: 075006, 2009.

[8] Galtier, S.: Phy. Rev. E 77: 015302, 2008.

[9] Kida, S, and Miura, H.: J. Phy. Soc. Japan 67: 2166-2169, 1998.

TURBULENT/NON-TURBULENT INTERFACE IN MAGNETOHYDRODYNAMIC CHANNEL FLOW

Naoya Okamoto *[1], Yusuke Otake[1], and Takashi Ishihara[1]

[1]*Department of Computational Science and Engineering, Nagoya University*

Summary Direct numerical simulations (DNSs) are performed to show the presence of turbulent/non-turbulent interfaces in a magnetohydrodynamic (MHD) turbulent channel flow under the influence of a wall-normal magnetic field. Visualization of the vorticity field reveals flow structures consisting of two internal turbulent boundary layers (ITBLs) growing from each wall and a non-turbulent channel core. The flow structures suggest the presence of an interface between the ITBL and the core. The conditional statistics of the DNS data shows that vorticity components have sharp gradients at the interface as observed in external hydrodynamic shear flows. The Joule dissipation rate, a characteristic quantity in MHD flow, is shown to have sharp gradients at the interface. A phenomenological theory gives an estimate of the average thickness of the ITBL as a function of R, and the estimate is in close agreement with the DNS result. Here, R is the ratio of Reynolds and Hartmann numbers.

INTRODUCTION

Turbulence of electrically conducting fluids subjected to external magnetic field at low magnetic Reynolds number is encountered in many industrial applications e.g., electromagnetic casting of liquid metals and cooling blankets of nuclear reactors [1]. A typical role of the imposed magnetic field is the suppression of turbulence via Joule dissipation. Experiments with liquid-metal flows present difficulties for measuring and visualizing the relevant fields, owing to the opacity of the liquid metals and their corrosion. Therefore, direct numerical simulation (DNS) is an essential tool for obtaining statistics on the turbulent flows and flow structures encountered in those experiments. Boeck et al. [2] performed DNS studies of the effect of the wall-normal magnetic field on an MHD turbulent flow in a channel. For strong magnetic fields, the visualizations of the streamwise velocities of the DNS data showed flow structures consisting of two internal turbulent boundary layers (ITBLs) near each wall and a non-turbulent channel core. The flow structures suggest the presence of a turbulent/non-turbulent (T/NT) interface between the ITBL and the non-turbulent channel core. T/NT interfaces have been observed and studied for hydrodynamic (HD) turbulent shear flows, e.g., turbulent wakes [3], jets [4, 5], and boundary layers [6]. Across the T/NT interfaces, physical quantities such as vorticity have sharp gradients, and important exchanges of mass, energy and momentum take place [7]. In the present study, we perform DNSs to show the presence of T/NT interfaces in an MHD turbulent channel flow at low magnetic Reynolds number under the influence of a wall-normal magnetic field. Then, we characterize physical quantities near the interface using the conditional statistics of the DNS data.

DNS OF MHD CHANNEL FLOW

We consider the flow of an incompressible MHD fluid in a channel between electrically insulated walls. Figure 1 (a) shows a schematic of the channel and coordinate system used. A constant wall-normal magnetic field B_0 is imposed to the flow. The magnetic Reynolds number is assumed to be sufficiently small such that the so-called quasi-static (QS) approximation can be applied (see, e.g., Ref. [8]). Periodic boundary conditions are employed in the streamwise (x) and the spanwise (z) directions. On the walls, both the velocity and the wall-normal current vanish. Governing equations under the QS approximation are solved using a pseudo-spectral numerical method based on Fourier series in x- and z-directions and a Chebyshev polynomial expansion in the wall-normal direction (y). For time differencing, we use the implicit backward Euler scheme for the viscous and the magnetic terms, but for nonlinear terms, we use a third-order Runge-Kutta method. The average streamwise pressure gradient is controlled by maintaining the mass flow constant in time. Physical parameters and the numbers of grid points are listed in Fig. 1 (b), where Re and Ha are Reynolds and Hartmann numbers, respectively. The latter is a nondimensional measure for the strength of the Lorentz force to the viscous force. $R = Re/Ha$.

RESULTS

In Fig. 1 (c), we plot the mean streamwise velocity $U^+(y^+)$, obtained from the DNS data of the MHD channel flow at $R = 600$ and $Ha = 35$, where the superscript $+$ denotes a non-dimensional quantity scaled by the wall friction velocity and the kinematic viscosity. We see a three-layered structure consisting of a viscous region ($y^+ < 40$), logarithmic region ($40 < y^+ < 400$), and plateau region, as already observed in Boeck et al. [2].

*Corresponding author. Email: n.okamoto@nagoya-u.jp

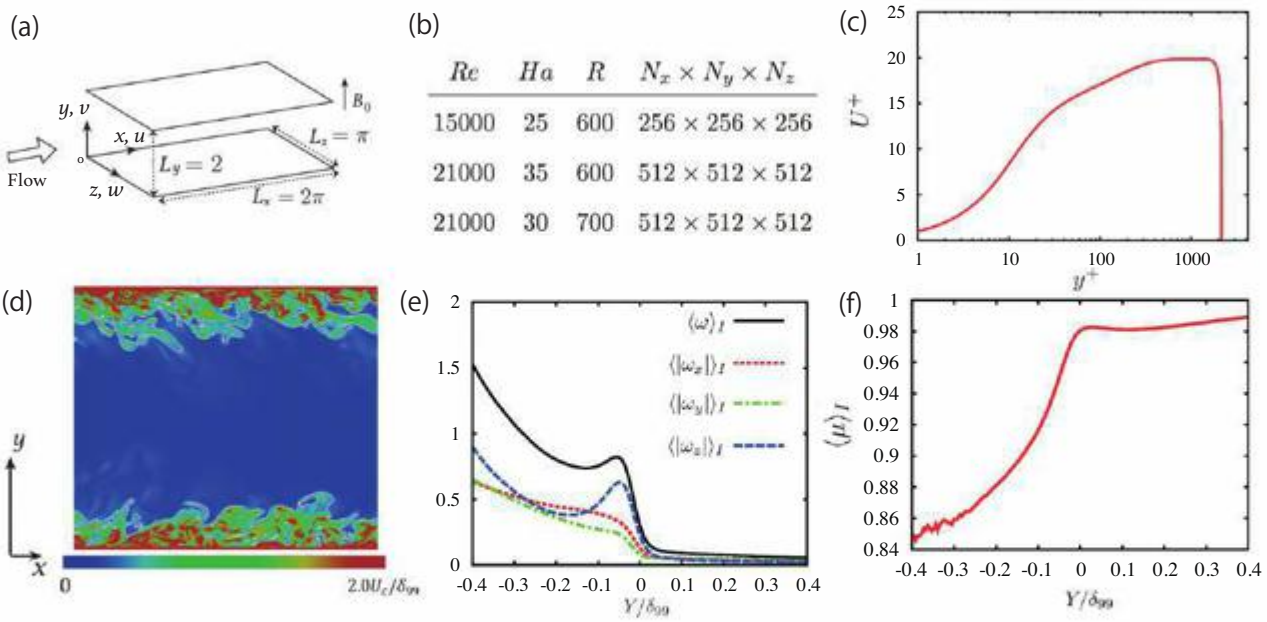

Re	Ha	R	$N_x \times N_y \times N_z$
15000	25	600	$256 \times 256 \times 256$
21000	35	600	$512 \times 512 \times 512$
21000	30	700	$512 \times 512 \times 512$

Figure 1: (a) Geometry and coordinate system. (b) Parameters of the DNS. (c) Mean profile of the streamwise velocity in wall units. (d) Contour plot of the amplitudes of vorticity on an xy-plane. Only the two-dimensional subregion $(0.37L_x) \times L_y$ is shown to enlarge the flow structure. White lines indicate the contour lines of $\omega = 0.3U_c/\delta_{99}$. (e) Conditional average of $\langle\omega\rangle_I$, $\langle|\omega_x|\rangle_I$, $\langle|\omega_y|\rangle_I$ and $\langle|\omega_z|\rangle_I$ (normalized by U_c/δ_{99}). (f) Conditional average of normalized Joule dissipation rate.

Figure 1 (d) is a contour plot of the amplitudes of vorticity $\omega = |\boldsymbol{\omega}|$ on a plane parallel to the streamwise and wall-normal directions. We observe that the vorticity magnitudes at the channel core are significantly reduced as compared to high vorticity regions near the walls. Following the analysis by Westerweel et al. [4], we first define the turbulent region as a set of regions where ω is greater than a given threshold. White lines indicate the isolines corresponding to the threshold value. The interface height $y_I(x, z)$ is then defined as a set of the outermost points of the turbulent region. The average interface height $\langle y_I^+ \rangle$ in the DNS data is found to be 340. This value approximately corresponds to the end of the logarithmic layer, as shown in Fig. 1 (c). Once the interface is defined, conditional statistics, $\langle\rangle_I$, are determined by averaging the data at fixed distances relative to the interface. In this study, a conditional average of any quantity is taken when the detected interface is locally more or less parallel to the channel walls [3]. Figure 1 (e) shows the conditional mean profiles of $\langle\omega\rangle_I$, $\langle|\omega_x|\rangle_I$, $\langle|\omega_y|\rangle_I$ and $\langle|\omega_z|\rangle_I$ (normalized by U_c/δ_{99}) as a function of the distance from the interface, Y/δ_{99}, where δ_{99} and U_c are the turbulent boundary layer thickness and channel centerline velocity, respectively. The turbulent region is on the side of negative Y, while the channel core is on the side of positive Y. The vorticity modulus $\langle\omega\rangle_I$ shows a sharp gradient from the core region to the turbulent region. This sharp gradient in the MHD channel is qualitatively similar to those across the T/NT interfaces observed in HD turbulent shear flows, e.g. turbulent boundary layers[6], wakes[3], and jets [5]. We observe that most of the values of $\langle\omega\rangle_I$ near the interface, say $-0.1 < Y/\delta_{99} < 0$, are retained by the spanwise component $\langle|\omega_z|\rangle_I$, followed by the streamwise component $\langle|\omega_x|\rangle_I$, and then the wall-normal component $\langle|\omega_y|\rangle_I$. Figure 1 (f) shows the mean conditional profile of normalized Joule dissipation rate $\langle\mu\rangle_I$, a characteristic quantity in MHD flow. We observe that $\langle\mu\rangle_I$ hardly changes in the core, and there is a rapid gradient near the interface. In the presentation, the average position of the interface is phenomenologically estimated as a function of $R = Re/Ha$, and the estimate is shown to be in good agreement with DNS results.

References

[1] Davidson P.A.: An Introduction to Magnetohydrodynamics. Cambridge University Press, Cambridge, England, 2001.

[2] Boeck T., Krasnov D., Zienicke E.: Numerical study of turbulent magnetohydrodynamic channel flow. J. Fluid Mech 572:179-188, 2007.

[3] Bisset B.K., Hunt J.C.R., Rogers M.M.: The turbulent/non-turbulent interface bounding a far wake. J. Fluid Mech 451:383-410, 2002.

[4] Westerweel J., Fukushima C., Pedersen J.M., Hunt J.C.R.: Momentum and scalar transport at the turbulent/non-turbulent interface of a jet. J. Fluid Mech 631:199-230, 2009.

[5] da Silva C.B., Pereira J.C.F.: Invariants of the velocity-gradient, rate-of-strain, and rate-of-rotation tensors across the turbulent/nonturbulent interface in jets. Phys. Fluids 20:055101, 2008.

[6] Ishihara T., Ogasawara H., Hunt J.C.R.: Analysis of conditional statistics obtained near the turbulent/non-turbulent interface of turbulent boundary layers. J. Fluids and Structures 53:50-57, 2014.

[7] da Silva C.B., Hunt J.C.R., Eames I., Westerweel J.: Interfacial layers between regions of different turbulence intensity. Annu. Rev. Fluid Mech 46:567-590, 2014.

[8] Knaepen B., Kassinos S., Carati D.: Magnetohydrodynamic turbulence at moderate magnetic Reynolds number, J. Fluid Mech 513:199-220, 2004.

TURBULENCE IN CAHN-HILLIARD BINARY-FLUID MIXTURES

Rahul Pandit *[1], Nairita Pal[2], Prasad Perlekar[3], and Anupam Gupta[4]
[1,2]*Centre for Condensed Matter Theory, Department of Physics, Indian Institute of Science, Bangalore 560012, India*
[3]*TIFR Centre for Interdisciplinary Sciences, 21 Brundavan Colony, Narsingi, Hyderabad 500075, India*
[4]*Department of Physics and INFN, University of "Tor Vergata", Via della Ricerca Scientifica 1, 00133 Rome, Italy*

Summary We give an overview of the coupled Cahn-Hilliard and Navier-Stokes (CHNS) equations and show that they provide a natural theoretical framework for studying turbulence in binary-fluid mixtures. In particular, we demonstrate, by using two recent studies that we have carried out, how the CHNS system can be used to study (a) the turbulence-induced suppression of phase separation in a symmetric binary-fluid mixture, (b) turbulence-induced multifractal dynamics in a droplet of the minority phase in a background of the majority phase, and (c) the reaction of the fluctuations of such a droplet on the turbulent fluid, which lead, eventually, to dissipation reduction.

RESULTS

The coupled Cahn-Hilliard and the incompressible Navier-Stokes (CHNS) equations provide us with a natural model for the dynamics of binary-fluid mixtures. They have been used to study the Rayleigh-Taylor instability [1] and, recently, turbulent-induced suppression of phase separation [2]. The CHNS equations are, in two dimensions (2D),

$$(\partial_t + \boldsymbol{u}\cdot\nabla)\,\omega = \nu\nabla^2\omega - \alpha\omega - \nabla\times(\phi\nabla\mu) + F_\omega, \quad (1)$$

$$(\partial_t + \boldsymbol{u}\cdot\nabla)\,\phi = \gamma\nabla^2\mu \text{ and } \nabla\cdot\boldsymbol{u} = 0, \quad (2)$$

where $\phi(\boldsymbol{x},t)$ is the order parameter field at the point $\boldsymbol{x}$ and time t [with $\phi(\boldsymbol{x},t) > 0$ in the majority phase and $\phi(\boldsymbol{x},t) < 0$ in the minority phase], $\mu(\boldsymbol{x},t) = \delta\mathcal{F}[\phi]/\delta\phi(\boldsymbol{x},t)$ is the chemical potential, $\mathcal{F}[\phi] = \Lambda\int[(\phi^2-1)^2/(4\xi^2) + |\nabla\phi|^2/2]d\boldsymbol{x}$ is the free energy, Λ is the energy density with which the two phases mix in the interfacial regime [1], ξ sets the scale of the interface width, ν is the kinematic viscosity, $\sigma = \frac{2\sqrt{2}\Lambda}{3\xi}$ is the surface tension, and the mobility of the binary-fluid mixture is γ, $\boldsymbol{u} \equiv (u_x, u_y)$ is the fluid velocity, the vorticity $\omega = (\nabla\times\boldsymbol{u})\hat{e}_z$. The forcing $F_\omega = F_0\cos(k_f y)$ is of the Kolmogorov-type with amplitude F_0 and forcing wave number k_f, and α is the air-drag induced friction. We concentrate on mixtures in which γ is independent of ϕ and both components have the same density and viscosity. The Grashof number $Gr = \frac{L^4F_0}{\nu^2}$ is a convenient dimensionless measure of the forcing . We keep the diffusivity $D = \frac{\gamma\beta}{\xi^2}$ of the system constant. The forcing-scale Weber number $We \equiv \rho L_f^3 F_0/\sigma$, where $L_f = 2\pi/k_f$, is a dimensionless measure of σ.

We use Eqs. (1) and (2) and extensive direct numerical simulations (DNSs) to study turbulence-induced (a) multifractal droplet dynamics of a minority-phase droplet in a turbulent background of the majority phase [3] and (b) suppression of phase separation in a symmetric, two-dimensional (2D) binary-fluid mixture [4].

For problem (a) we find [3] that the turbulence-induced fluctuations in the dimensionless deformation $\Gamma(t)$ of the droplet perimeter are intermittent. We obtain the probability distribution function (PDF) $P_\Gamma(\Gamma)$ at the mean steady-state droplet diameter $\langle d_p\rangle_t/L = 0.22$ and three different We (Fig. 1(a)) and the multifractal spectrum $f_\Gamma(\alpha)$ (Fig. 1(c)) of the time series $\Gamma(t)$ (Fig. 1(b)). We show, in Fig. 1(d), that the PDF of the y component a_y of the acceleration of the center of mass, $P(a_y)$, are similar to those for finite-size particles in turbulent flows; and the power-law dependence of $\langle a_{rms}\rangle_t$ on $\langle d_p\rangle_t/L$ in the inset of Fig. 1(d) is consistent with exponents that can be related to the inertial-range scaling of the pressure spectrum. We also find that the large-k tail of $E(k)$ is enhanced by the droplet fluctuations (Fig. 1(e)). The spectrum $E(k)$ also displays oscillations whose period is related inversely to the mean diameter of the droplet, and which appear prominently in the order parameter spectrum $S(k)$ (the Fourier transform of the spatial correlation function of ϕ) in Fig. 1(f).

For problem (b) we find that in the absence of any coupling, we get spinodal decomposition and domain growth, which we examine by the spatiotemporal evolution of ϕ. We then show that the Cahn-Hilliard-Navier-Stokes coupling leads to an arrest of phase separation at a length scale L_c, which we evaluate from $S(k)$, the spectrum of ϕ. In Fig. 1(g) we show pseudo-gray-scale plots of ϕ, at late times, when coarsening arrest has occurred, for four different values of We at $Re = 124$; we find that the larger the value of We the smaller is the linear size that can be associated with domains; this size is determined by the competition between turbulence-shear and interfacial-tension forces and can be related to the Hinze length scale [4].

Acknowledgements We thank S.S.Ray for discussions. NP and RP thank SERC (IISc) for computational resources, the Department of Science and Technology and the University Grants Commission (India) for support; PP thanks the Department of Atomic Energy (India); AG thanks a grant from the European Research Council (ERC) under the European Community's Seventh Framework Programme (FP7/2007-2013)/ERC Grant Agreement No.297004.

*rahul@physics.iisc.ernet.in

References

[1] A. Celani, A. Mazzino, P. Muratore–Ginanneschi and L. Vozella, J.Fluid Mech., **622**, 115-134 (2009).

[2] P. Perlekar, R. Benzi, J.H. Herman Clercx, D. R. Nelson and F. Toschi, Phys. Rev. Lett, **112**, 014502 (2014).

[3] N. Pal, P. Perlekar, A. Gupta and R. Pandit, arXiv:1512.09331, 2015.

[4] P. Perlekar, N. Pal and R. Pandit, arXiv:1506.08524v1, 2015.

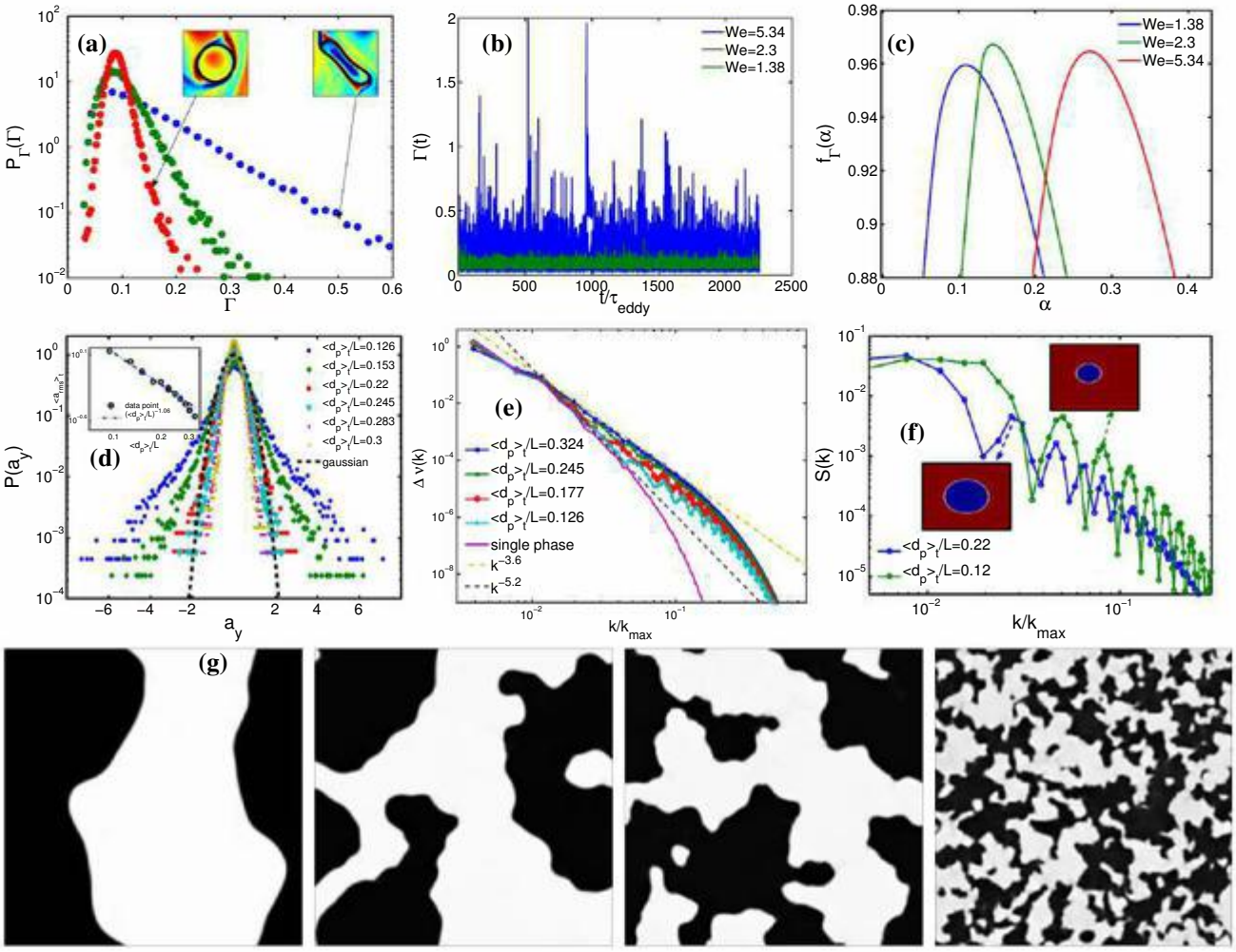

Figure 1: (Color online) Plots for the runs with $We = 5.34$, $We = 2.3$, and $We = 1.38$, shown respectively, by blue, green and red circles, (a) the PDFs $P(\Gamma)$, (b) $\Gamma(t)$ versus t/τ_{eddy} (where τ_{eddy} is the box-size eddy turnover time), and (c) the multifractal spectra $f_\Gamma(\alpha)$ for the times eries of Γ. The insets in (a) show pseudocolor plots of the vorticity field with ϕ-field contours superimposed on it; (d) semilog (base 10) plots of $P(a_y)$ for $\langle d_p \rangle_t / L = 0.126$ (deep-blue circles), $\langle d_p \rangle_t / L = 0.153$ (green diamonds), $\langle d_p \rangle_t / L = 0.22$ (red squares), $\langle d_p \rangle_t / L = 0.245$ (light-blue inverted triangles), $\langle d_p \rangle_t / L = 0.283$ (magenta plus signs) and $\langle d_p \rangle_t / L = 0.324$ (yellow asterisk) at $We = 1.38$. Inset: Plot of $\langle a_{rms} \rangle_t$ versus $\langle d_p \rangle_t / L$. In (d) the black dashed line shows a Gaussian fit. Log-log plots (base 10) versus the scaled wavenumber k/k_{max} of (e) $E(k)$ for runs with $\langle d_p \rangle_t / L = 0.324$ (deep-blue line with asterisks), $\langle d_p \rangle_t / L = 0.245$ (green line with crosses), $\langle d_p \rangle_t / L = 0.177$ (red line with circles), $\langle d_p \rangle_t / L = 0.126$ (light-blue line with plus signs), and single-phase fluid (magenta line); the power-laws $k^{-3.6}$ and $k^{-5.2}$ are depicted by yellow-dash-dot and black-dashed lines, respectively; (f) the order-parameter spectrum $S(k) = |\hat{}(k)|^2$ for the cases with $\langle d_p \rangle_t / L = 0.22$ (deep-blue line with circles) and $\langle d_p \rangle_t / L = 0.126$ (green line with circles); for details and run parameters see Ref. [3]; (g) pseudo-gray-scale plots of the order parameter field ϕ, at late times when coarsening arrest has occured, in 2D symmetric-binary-fluid turbulence with $Re = 124$. Note that the domain size decreases as we increase the Weber number We from the leftmost to the rightmost panel: $We = 1.2 \cdot 10^{-2}$; $We = 5.9 \cdot 10^{-2}$; $We = 1.2 \cdot 10^{-1}$; and $We = 5.9 \cdot 10^{-1}$; for details and run parameters see Ref. [4].

CLUSTERING AND ENTROPY GROWTH OF QUASI-GEOSTROPHIC POINT VORTICES UNDER PERIODIC BOUNDARY CONDITIONS

Takeshi Miyazaki *[1], Masaya Ishihara[1], Yuya Konno[1], and Naoya Takahashi[2]
[1]*Dept. Mechanical Engineering and Intelligent Systems, University of Electro-Communications, Tokyo, Japan*
[2]*Dept. Mechanical Engineering, Tokyo Denki University, Tokyo, Japan*

Summary The statistical mechanics of quasi-geostrophic point vortices of mixed sign is investigated numerically and theoretically. Direct numerical simulations of a point vortex system under periodic boundary conditions are performed using a fast special-purpose computer for molecular dynamics (GRAPE9). Clustering of point vortices of like sign is observed and two tall columnar vortices appear in the course of time. These numerical results are analyzed quantitatively using a density-based algorithm. The number of clusters decreases as about t^{-1}, which is significantly slower than $t^{-1.25}$ found in the previous spectral simulations of geostrophic turbulence (e.g. McWilliams *et al*., 1999). The equilibrium states are identified as the sn-sn dipole solutions of the two-dimensional mean field equation (the sinh-Poisson equation). A three-dimensional mean field equation is derived based on the maximum entropy theory, and several branches of two- and three-dimensional solutions are obtained. It is shown that the two-dimensional sn-sn dipole branch has the largest entropy.

INTRODUCTION

Geophysical flows are considered to be two-dimensional at the lowest order of approximation, because vertical fluid motion is suppressed by stable density stratification and the Coriolis force. In two-dimensional turbulence, many coherent vortices appear spontaneously and their interactions dominate the turbulence dynamics. The statistical mechanics of two-dimensional vortex system has been studied extensively, starting from Onsager (1949), who was the first to illustrate the existence of negative temperature states. Montgomery and Joyce (1974) derived the mean field equation (so called the sinh-Poisson equation) for a system of point vortices of mixed sign, based on the maximum entropy theory. In actual geophysical flows, the fluid motion is almost confined within a horizontal plane, but different flow patterns are realized on different horizontal planes. This three-dimensionality is incorporated in the 'quasi-geostrophic approximation'. The numerical simulations by McWilliams (1994) of decaying quasi-geostrophic turbulence indicated that the vorticity field developed coherent vortex structures. There was a period of self-similar dissipative temporal evolution, which terminated as the number of vortices decreased due to merger and alignment of like-sign vortices. The end state was consisted of a dipole pair of tall columnar vortices. It will be of interest to investigate the statistical mechanics of a simpler system, i.e., inviscid quasi-geostrophic point vortex system, to understand the turbulence dynamics deeply, which was undertaken by Funakoshi *et al*. (2012). The aim of the present paper is to extend their work. We perform larger numerical simulations with more point vortices, and determine the two- and three-dimensional maximum entropy states at higher energy level. In order to investigate the clustering process quantitatively, we also carry out clustering analysis using Density-Based Algorithm for discovering clusters.

NUMERICAL SIMULATIONS

As a simplest model of coherent vortices, we consider point vortices with infinitesimal size. The potential vorticity of point vortices is concentrated δ-function like $q(r) = \sum_{i=1}^{N_+ + N_-} \hat{\Gamma}_i \delta(r - R_i)$ at the location of vortices $R_i = (X_i, Y_i, Z_i)$. Here, N_+ and N_- denote the numbers of vortices with positive and negative sings, respectively. $\hat{\Gamma}_i$ is the strength of the i-th vortex. We consider a symmetric bi-disperse case, taking $N_+ = N_- = N$ and $|\hat{\Gamma}_i| = \hat{\Gamma}_0$. The point vortices move by mutual advection, and the motion of the i-th vortex is governed by the canonical equations : $\frac{dX_i}{dt} = \frac{1}{\hat{\Gamma}_i}\frac{\partial H}{\partial Y_i}$, $\frac{dY_i}{dt} = -\frac{1}{\hat{\Gamma}_i}\frac{\partial H}{\partial X_i}$. These equations look similar to those describing the motion of two-dimensional point vortices, in which the interaction energy is proportional to the logarithm of the distance between two vortices. It should, however, be noted that the interaction energy between two quasi-geostrophic point vortices is proportional to the inverse of the distance between them. The vertical coordinate Z_i remains constant, i.e., the vortices move on the horizontal plane on which they are initially located.

We illustrate the results of numerical simulation for a point vortex system in a cubic box of size $L_x = L_y = L_z = 2\pi$. We integrate the equations of motion for $N = N_\pm = 4000$ and 8000 point vortices of strength $\hat{\Gamma}_0 = 0.062$ and 0.031, respectively. The time is normalized by the mean potential vorticity $N\hat{\Gamma}_0/(2\pi)^3 = 1.00$, which is taken to be unity. The vertical distribution $P_\pm(z) = L_z^{-1} = 1/2\pi$ is assumed to be uniform, as in the dissipative numerical simulations by McWilliams *et al*. (1994). The energy is set to be $E = 4.428 \times 10^{-3}, 2.462 \times 10^{-3}$ for the computations with $N = 4000$ and 4.536×10^{-3} with $N = 8000$. In order to investigate the clustering process quantitatively, we carry out so called clustering analysis using Density-Based Algorithm for Discovering Clusters (DBADC). We search for a group of vortices, and identify it as a cluster, if its size exceeds a specified minimum radius and the number of vortices inside the group exceeds a specified minimum number.

*Takeshi Miyazaki. Email: miyazaki@mce.uec.ac.jp

We show in Fig. 1 (left) the time evolution for the case of $E = 4.428 \times 10^{-3}$, at the times $t = 0.0$, 14.0, 50.0 and 155.0, respectively. The initial unstable distribution is broken by about $t = 8.0$ and many ‘ almost spherical clusters are formed whose aspect ratio is about 2. We can see the growth in vertical height of the cluster, called alignment. In Figure 1, the number of clusters is shown as functions of time for three energy levels. The number of clusters decays like t^{-1} in all computations, which is significantly slower than $t^{-1.25}$ observed in the spectral numerical simulations of geostrophic turbulence by McWilliams *et al.* (1999). The cluster height grows while its radius remains unchanged, indicating that clusters of like sign align vertically but not being merged horizontally. This observation makes a sharp contrast with the fact that the size of coherent vortex structure grows both in radius and height, keeping its aspect ratio almost constant (about 1.6) in the spectral simulations of gestrophic turbulence. Our simulations of point vortices seem to capture the dynamics in later stages, in which the energy dissipation becomes very weak.

MAXIMUM ENTROPY THEORY

Funakoshi *et al.* (2012) derived the mean field equation based on the maximum entropy theory, i.e., maximizing the Shannon entropy under the constraints of the fixed energy E and the fixed vertical vorticity distributions $P_{\pm}(z)$: $\Delta\psi(r) + \lambda^2(z)\sinh\psi(r) = 0$. Here, $\psi(r) = -\beta\psi(r)$ denotes the rescaled stream function and $\lambda^2(z) = -2\beta e^{-\alpha(z)-1}$ is a combination of the Lagrangian multipliers. Coherent vortex structures appear only in the negative temperature region with $\beta < 0$. This equation is a natural extension of the sinh-Poisson equation derived for the two-dimensional point vortices. The mean field equation is solved utilizing an efficient iteration procedure proposed by Turkington and Whitaker (1996). Figure 1 (right) shows several branches of two- and three-dimensional solutions in the E–S (energy-entropy) plane, where the horizontal and vertical axes denote the energy and entropy, respectively. The inserted figures illustrate the potential vorticity distributions of two- and three-dimensional solutions. All branches emanate from the point $E = 0, S = 6\log(2\pi) \approx 11.027$, i.e., the uniformly random distributions $F_{\pm} = 1/(2\pi)^3$. As can be seen in Fig. 1, the sn-sn dipole branch has the largest entropy, among other two- and three-dimensional solution branches.

CONCLUSIONS

We have investigated the statistical mechanics of quasi-geostrophic point vortices of mixed sign under periodic boundary conditions numerically and theoretically. In the direct numerical simulations, clustering of point vortices of like sign is observed and a two-dimensional dipole structure forms gradually. The clusters align vertically and their number decreases as about t^{-1}, which is slower than $t^{-1.25}$ of the previous spectral simulations of geostrophic turbulence. This difference is due to the absence of horizontal merging process in our simulations. The mean field equation, which was derived as an extension of the sinh-Poisson equation, is solved to obtain the most probable states for the case with the uniform vertical distributions $P_{\pm}(z) = 1/2\pi$. Two- and three-dimensional solutions are obtained in a wide energy range. The two-dimensional sn-sn dipole solution has the largest entropy among them, explaining why it appears as the end state of the direct numerical simulations.

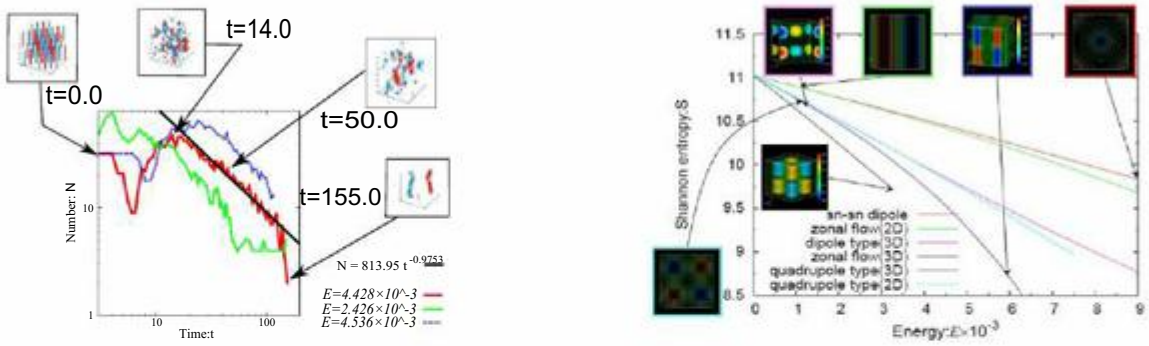

Figure 1: Left: Time-evolutions of the number of clusters, Right: Solution-branches of the mean field equation.

References

[1] Funakoshi S., Sato T., Miyazaki T.: Maximum entropy state of the quasi-geostrophic bi-disperse point vortex system: bifurcation phenomena under periodic boundary conditions. Fluid Dyn. Res. 44 031407 (13pp), 2012.

[2] McWilliams J. C. Anisotropy and coherent vortex structures in planetary turbulence. Science 264 410-413, 1994.

[3] McWilliams J. C., Weiss J. B., Yavneh I.: The vortices of homogeneous geostrophic turbulence. J. Fluid Mech. 401 1-26, 1999.

[4] Montgomery D., Joyce G.: Statistical mechanics of “negative temperature” states. Phys. Fluids 17 1139-1145, 1974

[5] Onsager L.: Statistical hydrodynamics. Nuovo Cimento Suppl. 6 279-287, 1949.

[6] Turkington B., Whitaker N.: Statistical equilibrium computations of coherent structures in turbulent shear layers. SIAM J. Sci. Comput. 17 1414-1433, 1996.

GENERATING jOVIAN-LIKE ZONAL JETS IN A RAPIDLY ROTATING FLUID EXPERIMENT

Simon Cabanes*[1], Jonathan Aurnou[2], Benjamin Favier[1], and Michael Le Bars[1]

[1]*CNRS, Aix-Marseille Université, Ecole Centrale Marseille, IRPHE UMR 7342, Marseille, France.*
[2]*Department of Earth, Planetary, and Space Sciences, University of California - Los Angeles, USA.*

Summary Using a combination of large-scale rotating fluid experiments and massively parallel Direct Numerical Simulations, we report the formation of strong zonal jets due to topographical effects in rotating turbulence. For the first time, we reach the so-called "zonostrophic" regime, thought to be relevant to Jupiter atmosphere for example. The jets dominate the small-scale turbulent fluctuations in amplitude and appear very stable and long-lived. Although their size is consistent with the so-called Rhines scale, we observe interesting dynamics over very long time-scales such as merging events where the number of jets decreases and their amplitude increases. These first results open new perspectives in the study of large-scale zonal flows in the laboratory.

EXPERIMENTAL AND NUMERICAL METHODS

For our experimental set up (see figure 1(b)), we use a cylindrical container 1.4 meter high with an internal radius of 0.5 meter filled with up to 400 liters of water. A turbulent small-scale flow is driven via a basal injection/suction system made of a square tiled set of 64 inlet/outlet ports, generating velocities in the range $U \approx 1-5$ cm/s (corresponding to a Reynolds number $2.5\times10^3 < Re < 1.3\times10^4$ and a Rossby number $3.3\times10^{-3} < Ro < 1.6\times10^{-2}$). As opposed to thermally-driven experiments (see [1] and references within for example), this set up allows a better control on the energy injection in terms of

1.

capacity and able to perform up to 100 revolutions per minute. Lagrangian surface velocities are measured using a Particle

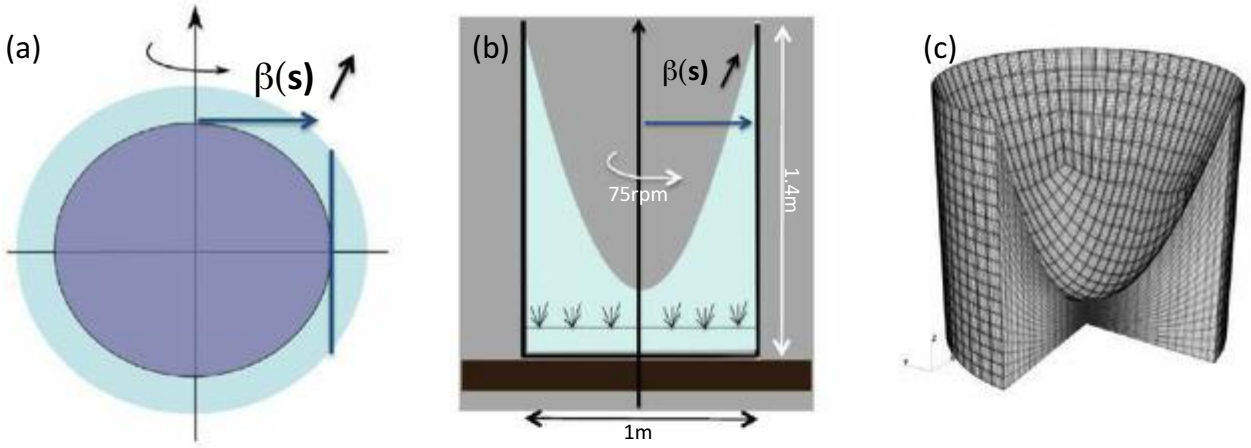

Figure 1: experimental and numerical methods. (a) Planetary configuration of interest, with the topographic "β"-effect due to the change of the fluid column depth with the distance from the rotation axis. (b) Sketch of our corresponding experimental model reproducing the same physical ingredients in a cylindrical geometry, i.e. fast rotation, topographic β-effect and small scale turbulent energy injection. (c) Cut through the numerical mesh used for the Direct Numerical Simulations.

Numerically, we consider the flow of an incompressible fluid of constant kinematic viscosity ν inside a cylindrical tank of radius R rotating at rate Ω around the vertical axis $\boldsymbol{z}$. The upper surface is stress-free and its paraboloid shape is fixed and given by the balance between centrifugal, gravitational and pressure forces (see figure 1(c)). Both the bottom and side walls are no-slip. The flow is forced by the steady volumic force $\boldsymbol{F}$ made of small Taylor-Green type vortices with a typical horizontal wave number of $k_f = 16$. It is purely horizontal initially but rapidly collapses into a three-dimensional small-scale turbulent flow at the base of the domain. The simulations are performed with the massively parallel spectral-element code Nek5000 (http://nek5000.mcs.anl.gov, see [2] and references within). Nek5000 solves the incompressible Navier-Stokes equations via a Legendre polynomial based Spectral Element Method which combines the geometrical flexibility of finite element methods with the accuracy of spectral methods. It is therefore particularly well adapted to our problem involving turbulent flows in complex geometries.

*Corresponding author. Email: ictam2016papers@legendconferences.com

RESULTS

Here, we report the experimental results with the following parameters. The depth of the fluid layer at rest is $h_0 = 50$cm and the rotation rate of the table is 75 RPM. This leads to a very large deformation of the fluid layer, with a minimum depth after the spin-up phase of $h = 20$cm at the center of the container and a maximum depth of on the side boundary of $h = 88cm$. The associated Ekman number based on the mean water depth is $E = 3 \cdot 10^{-7}$. The corresponding simulations are run with the same upper surface deformation but a slightly larger Ekman number of $E = 10^{-6}$, using 2048 processors, 53360 elements, and a Legendre polynomial order of $N = 10$.

After the spin-up is complete, we start the pumping system forcing quasi-homogeneous small-scale turbulence at the base of the domain. Due to the very low Rossby numbers, the basal forcing very quickly drives a nearly depth-invariant turbulent flow. The dominantly geostrophic flow is confirmed by the numerical simulations and shows that Lagrangian surface measurements are sufficient to characterize the system in a first approach. After several tens of rotation times, alternating zonal jets start to grow and eventually dominate the small-scale fluctuations. As shown in figure 2, this is observed in both the experiments and the numerics, although the time scales involved are different due to the different Ekman numbers used. The initial number of jets is consistent with the so-called Rhines scale, derived from a balance between the turbulent turn-over time scale and the typical frequency of Rossby waves [3]. Contrary to previous experiments, where the zonal jets are mainly observed after time averaging, our jets reach the so-called "zonostrophic" regime, where the instantaneous amplitude of the jets is greater than that of the small-scale fluctuations.

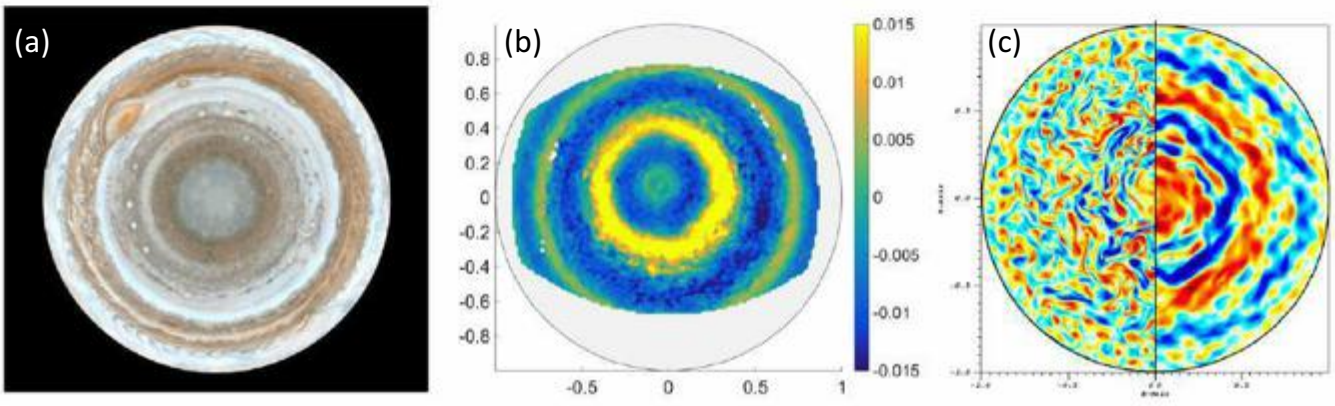

Figure 2: zonal jets visualization. (a) Polar view of Jupiter atmosphere (Credit: NASA/JPL/Space Science Institute). (b) Time averaged zonal velocity map obtained by particles tracking in our experiment: blue/yellow values are retrograde/prograde jets (velocity non-dimensionalized by the rotation rate times the tank radius). (c) Horizontal slice through the numerical domain showing the instantaneous vertical vorticity (left) and zonal velocity (right).

CONCLUSIONS

Using a combination of experimental and numerical approaches, we have obtained for the first time strong zonal jets in the so-called zonostrophic regime. These jets are extremely stable and live over many rotation timescales, but we nevertheless observe interesting merging events. Our systematic study allows to understand this dynamics, as well as what fixes the size and the amplitude of the jets. In the near future, implementations of our system will allow tacking many interesting questions in the laboratory, like the formation of large-scales vortices in the presence of a top stratified layer [4] and the existence of inertial wave turbulence [5] .

References

[1] P. L. Read, et al.: An experimental study of multiple zonal jet formation in rotating, thermally driven convective flows on a topographic beta-plane. Phys. Fluids 27, 085111, 2015.

[2] P. F. Fischer, et al.: Simulation of high-Reynolds number vascular flows. Comp. Meth. App. Mech. and Eng. 196 (31), 3049–3060, 2007.

[3] G. K. Vallis & M. E. Maltrud: Generation of mean flows and jets on a beta plane and over topography. Journal of Physical Oceanography 23, no. 7, 1346–1362, 1993.

[4] M. Heimpel, T. Gastine & J. Wicht: Simulation of deep-seated zonal jets and shallow vortices in gas giant atmospheres. Nature Geoscience 9, 19–23, 2016.

[5] E. Yarom & E. Sharon: Experimental observation of steady inertial wave turbulence in deep rotating flows. Nature Physics 10, 510–514, 2014.

TURBULENT LAYER DYNAMICS IN STRATIFIED TAYLOR-COUETTE FLOW

C. P. Caulfield *[1], P. Augier[2], Anne-Claire Le Bihan[3], C. Leclercq[4], and J. Partridge[5]
[1]*BP Institute and Department of Applied Mathematics & Theoretical Physics, University of Cambridge, Cambridge, U. K.*
[2]*Laboratoire des Écoulement Geophysiques et Industriels, LEGI-CNRS, Grenoble, France*
[4]*École polytechnique, Palaiseau, France*
[4]*School of Mathematics, University of Bristol, Bristol, U. K.*
[5]*Department of Applied Mathematics & Theoretical Physics, University of Cambridge, Cambridge, U. K.*

Summary We describe a series of laboratory experiments to study the turbulent mixing dynamics of an initially linear stratification in Taylor-Couette flow, i.e. the flow in the annular region between two concentric cylinders. As described in [1], relatively well-mixed layers separated by substantially thinner 'interfaces' of enhanced density gradient spontaneously form. Consistently with [1], these layers are extremely long-lived, and exhibit an average turbulent buoyancy flux that falls on a 'universal' curve independent of the number of the layers. However, by high-frequency measurements of density and image analysis, we show that the 'interfaces' are highly spatially and temporally intermittent, and for sufficiently small separation between interfaces, there is a dynamically robust, and profoundly nonlinear coupling between neighbouring interfaces. Such robust spatio-temporal intermittency has significant implications for the quantification and parameterisation of mixing driven by horizontal shear, as commonly arises in the environment.

INTRODUCTION

The spontaneous formation of relatively deep horizontal layers of weakly stratified fluid, separated by relatively thin interfaces of substantially stronger density gradient, is a common feature of strongly stably stratified flows and plays a major role in the dynamics of geophysical flows, particularly when the flow is both strongly stratified and turbulent. Dating from the seminal work of Phillips[2], such layer/interface formation is to be expected whenever the irreversible vertical buoyancy flux is a non-monotonic function of the overall stratification. However, little is known about the physical mechanisms which drive such robust layer formation, or indeed what sets their characteristic depth and subsequent evolution. When the mixing is driven by instabilities due to vertical velocity shear, the situation is further complicated by the instabilities themselves having a characteristic vertical length scale, which may or may not set the initial depth of the layers.

This uncertainty can be avoided by considering layer formation in 'stratified Taylor-Couette flow' (STC flow) in the annulus between a rotating inner cylinder and a fixed outer cylinder, initially filled with stably, axially or vertically and linearly stratified fluid. Here the dominant velocity shear is in the radial direction, and so the mixing due to turbulence can be considered in isolation from the large scale stirring associated with (vertical) velocity shear. However, such flows are still prone to various primary instabilities, including the inherently stratified strato-rotational instability[3], and unpicking the relative importance of such linear instabilities, nonlinear dynamics and disordered turbulent mixing events for the formation and subsequent evolution of layers and interfaces is still challenging. Relatively recently[4, 1], it has been demonstrated that the turbulent mixing in such flows is 'universal' in the sense that the vertical flux of buoyancy appears to depend only on an appropriately defined Richardson number: $Ri = [g\Delta\rho/\rho_0][R_O/(R_I\Omega)^2]$, where R_I is the radius of the inner cylinder with rotation rate Ω relative to the fixed outer cylinder R_O, and $\Delta\rho$ is the density jump across the interface. We investigate what actually causes this observed mixing, and also the robustness of the flow structures, since the layers and associated interfaces have previously been assumed to be extremely robust lasting several thousand rotation periods[1, 5].

EXPERIMENTAL PROCEDURE

The outer cylinder has an internal radius of 24 cm, and we use three different inner cylinders, with radii of 5, 10 and 15 cm. The outer cylinder, base and upper surface are stationary, while the flow is driven by the rotation of the inner cylinder, which has a range of angular velocities from 5 to 24 r.p.m. i.e. $0.5 < \Omega < 2.5\mathrm{rad/s}$. To analyse the time-dependent dynamics of the various interfaces, we record a shadowgraph image of the tank, which identifies the presence of regions of relatively strong density gradient, and hence the presence (or absence) of sharp interfaces. We then extract a particular vertical line from the image, and plot those vertical lines at several times. To investigate the robustness of the observed structures, and in particular to determine whether the initial spin-up from rest is significant, we run the experiment for 200 rotation periods, stop the rotation of the inner cylinder until the flow completely stops, and then restart the inner cylinder for 200 rotation periods. We then repeat the on-off cycle of 200 rotation periods several times. Images taken from a typical initial spin-up cycle for an experiment with $R_I = 10$cm are shown in the upper panel of figure 1.

*Corresponding author. Email: c.p.caulfield@bpi.cam.ac.uk

RESULTS

As is apparent to the left of the left panel of figure 1, the initial spin-up of the flow is quite complex, with clear evidence of spiral structures. These structures are reminiscent of the strato-rotational instability[3], but the characteristic length scale of the layers which clearly develop are different from the most unstable wavelength of linear theory, pointing to the central role played by nonlinear processes. More striking is the fact that the layers themselves continually appear and disappear, with a characteristic period of existence which is robust over the entire flow life cycle.

Even more surprising, as shown clearly by the black line marked on the left panel of figure 1, is that there is strong coupling between neighbouring interfaces, with a close to constant time lag between the reappearance onset of neighbouring interfaces as shown in the right panel of figure 1, across different 'runs' of (typically) 100 rotation periods. The disappearance of the interfaces appears to be associated with a coherent mode-1, inherently nonlinear structure, previously observed in such high Reynolds number (but two-layer by design) STC flow, localised on the single density interface[5]. For sufficiently small layers, apparently similar structures, localised on neighbouring interfaces, can couple strongly, and this coupling plays a central role in the ensuing vertical turbulent transport of salinity and hence buoyancy flux. The robustness of these structures across a wide range of flow parameters demonstrates that the layered state is strongly attracting, and that the predominant mixing mechanism, at least in flows of this type, effectively 'scours' rather than 'overturns' the interface[4]. Generic, robust scouring has significant implications for the appropriate parameterisation of diapycnal mixing in 'strongly' stratified flows.

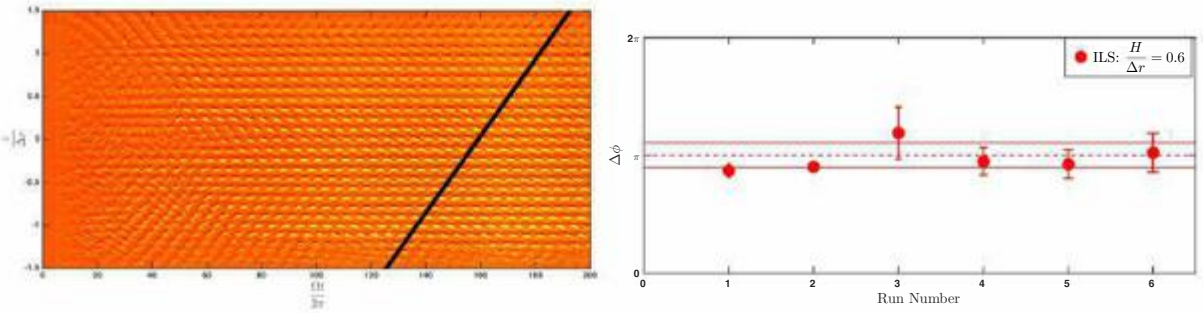

Figure 1: **Left panel:** Variation with time over initial 200-period run of shadowgraph images for an initially linearly stratified experiment with $R_I = 10\text{cm}$, $N_0 = 1.62\text{s}^{-1}$, and $Re = \Omega R_I(R_O - R_I)/\nu = 7000$, where ν is the kinematic viscosity of water. The formation of layers is visible with a well-defined wavelength, and a time-periodic structure is observed on each interface. Moreover, these structures appear to be coupled between each interface, with some constant phase difference between adjacent layers as indicated by the black solid line.
Right panel: Phase difference between adjacent layers for each run of an experiment with $Re = 14000$, and initial buoyancy frequency $N = 1.62\ \text{s}^{-1}$. The phase difference is calculated from the cross spectrum of the time varying signals on adjacent interfaces from the second 100 rotation period of each 200-period run (to minimise start-up influence), when the signal appears to be quasi-steady. Each point represents the mean over a number of layer pairs with the error bars indicating one standard deviation. The dashed line indicates the mean over all runs with the solid lines denoting one standard deviation.

References

[1] Oglethorpe R. L. F., Caulfield C. P. & Woods A. W.: Spontaneous layering in stratified turbulent Taylor-Couette flow. J. Fluid Mech. 721:R3 (12 pages), 2013.

[2] Phillips O.M.: Turbulence in a strongly stratified fluid - is it unstable? Deep-Sea Res. 19: 79-81, 1972.

[3] Le Bars M. & Le Gal P.: Experimental analysis of the stratorotational instability in a cylindrical Couette flow. Phys. Rev. Lett. 99:064502, 2007.

[4] Woods A. W., Caulfield C. P., Landel J. R. & Kuesters A.: Non-invasive turbulent mixing across a density interface in a turbulent Taylor-Couette flow. J. Fluid Mech. 663:347-357, 2010.

[5] Oglethorpe R. L. F.: Mixing in stably stratified turbulent Taylor-Couette flow. Ph.D. Thesis, University of Cambridge, 257 pages, 2014.

EXTREME-SCALE MOTIONS IN TURBULENT COUETTE FLOWS

Myoungkyu Lee[1] and Robert D. Moser *[1,2]

[1]*The Center for Predictive Engineering and Computational Science, Institute for Engineering and Sciences, The University of Texas at Austin, Texas 78712, U.S.A.*

[2]*Department of Mechanical Engineering, The University of Texas at Austin, Texas 78712, U.S.A.*

Summary The direct numerical simulation of turbulent plane Couette flows are performed at up to $Re_\tau \approx 500$ to investigate the existence of distinct large scale motion in streamwise direction. $100\pi\delta$ long simulation domain is used in streamwise direction. It is shown that there is extremely large scale motions exists in moderately high Re Couette flows and the scale of motions is strongly Re dependent.

Direct numerical simulation (DNS) has been a valuable vehicle for the study of wall-bounded turbulence. In the channel geometry, the DNS of Poiseuille flow at Re_τ up to approximately 5200 is available displaying many characteristics of high Re wall-bounded flows. [Lee and Moser, 2015] On the other hand, the Re of simulation of Couette flow is still limited. One of the reasons is that the largest scale motions in Couette flows are much larger than in Poiseuille flows. In particular, a low-wavenumber peak in the spanwise one-dimensional premultiplied energy spectra, which is indicative of the large-scale motions, has been observed. It has been speculated that there should be a similar peak in the streamwise spectrum, but this has not yet been observed, due to limited simulation domain sizes in previous studies. [Avsarkisov et al., 2014] In this work, we investigate the existence of strong distinct large scale motion in streamwise direction and its effect on statistics.

The simulation reported here are DNS of incompressible turbulent flow between two parallel planes without pressure gradient. Periodic boundary conditioned are applied in streamwise (x) directions and spanwise (z) directions. The no-slip and penetration conditions are applied at the walls. Both walls are moving at the same constant speed but in opposite directions. We simulated cases at three different Reynolds numbers, $Re_\tau = 93/220/505$. The computational domain sizes are $L_y = 2\delta$ and $L_z = 5\pi\delta$ where δ is channel half width. Two different domain sizes are used in streamwise direction, $L_x = 20\pi\delta$, labeled "small" and $L_x = 100\pi\delta$ labeled "large". A Fourier-Galerkin method was used in the streamwise and spanwise directions and a seventh-order B-Splines collocation method is used in the wall-normal direction. Effective grid spacings, normalized by wall-shear stress and viscosity (denotes "+", here after), are set to be smaller than 11.3, 0.006, 6.4 and 10.4 in x, y (at wall), y (at the center of channel) and z directions, respectively. For more details about the numerical method and code implementation, see Lee et al. [2013, 2014]. The convergence of statistics are monitored by examining total stress, which is known analytically, $\langle \partial_y U \rangle^+ - \langle u'v' \rangle^+ = 1$. The discrepancy between 1 and computed total stress of each case is less than 0.001.

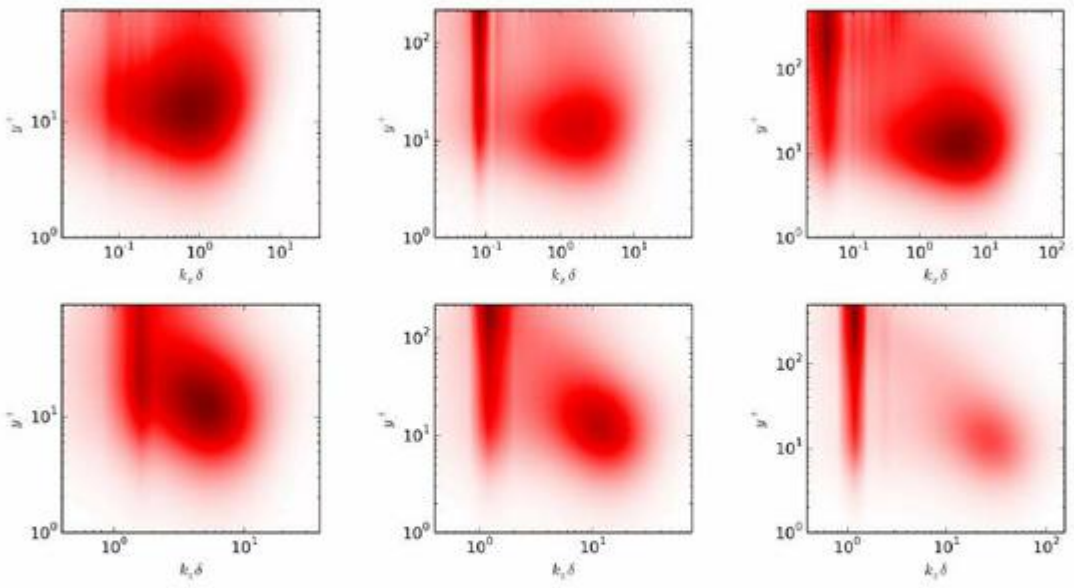

Figure 1: 1D premultiplied energy spectra of u'^2; left ($Re_\tau = 93$), middle ($Re_\tau = 220$), right ($Re_\tau = 505$); top ($k_x E_{uu}(k_x\delta, y^+)$), bottom ($k_z E_{uu}(k_z\delta, y^+)$), $L_x = 100\pi\delta$, $L_y = 2\delta$, $L_z = 5\pi\delta$

*Corresponding author. Email: rmoser@ices.utexas.edu

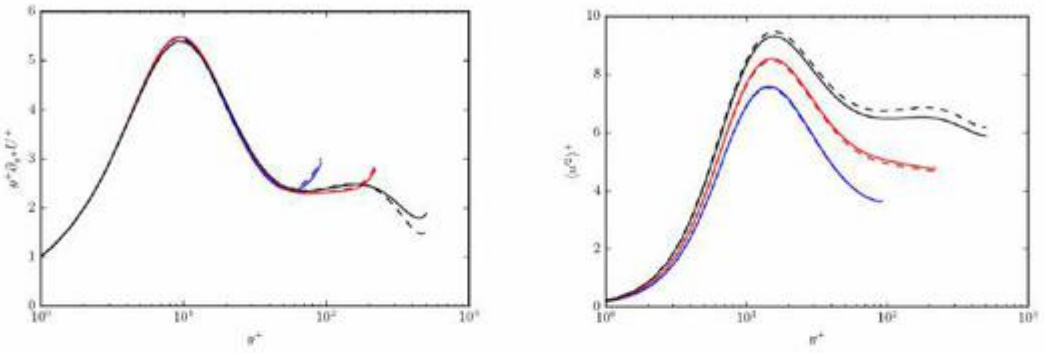

(a) Log-law test function: β

(b) Variance of u

Figure 2: Mean profiles and variances of u; — (blue, $Re_\tau = 93$ large domain), — (red, $Re_\tau = 220$ large domain), — (black, $Re_\tau = 505$ large domain), - - - (blue, $Re_\tau = 93$ small domain), - - - (red, $Re_\tau = 220$ small domain), - - - (black, $Re_\tau = 505$ small domain)

The one-dimensional premultiplied energy spectra of the streamwise velocity in the streamwise and spanwise directions for the large cases are shown in figure 1. Strong large scale motions of u are observed in spanwise direction with peak at $k_z\delta \approx 12$ in all cases. Also, the contribution of large scale motion at $k_z\delta \approx 12$ is getting stronger as Re increases. In all cases the simulation domain size in the spanwise direction ($L_z = 5\pi\delta$) is large enough to contain all motions of significant energy. Similarly, a strong large-scale contribution to the u'^2 is observed in streamwise direction. In the lowest Re case (Re_τ=93) there is no clear scale separation between the general turbulence and the large-scale motion. However, in the Re_τ=220 case, there is scale separation with a large-scale energy peak at $k_x \approx 0.1$, and in the Re_τ=505 the large scale energy peak is at separation at $k_x \approx 0.04$. Note that, the natural wavenumber of the large-scale peak is uncertain due to the discrete wavenumber resolution imposed by the limited domain size ($\Delta k_x = 0.02$). Nonetheless, it is clear that the large scale motions get larger as Re increases. Unfortunately it is difficult to determine the precise Re dependency of large streamwise scale from the current data set.

In the small domain ($L_x \leq 20\pi\delta$), the lowest non-zero wavenumber is $\Delta k_x = 0.1$ which is too large to include the large streamwise-scale energy peak observed in the large domain, especially in the Re_τ=505 case, and indeed it is not present in the spectra (not shown). A comparison of statistics from the large and small domain cases (figure 2) therefore provides an indication of the impact of the large streamwise scales on the statistics. The mean velocity profiles at the lower Reynolds numbers (Re_τ=93 and Re_τ=220) show only small differences in outer region between large and small domains. But, the difference is more substantial in the Re_τ=505 case. Similarly, there are not a big deviations in the profiles of u'^2 in the Re_τ=93 and Re_τ=220 cases. However there is a more significant difference in the Re_τ=505 case from $y^+ = 10$ to the center of the channel.

In this work, it is shown that there are extremely large streawise scales ($> 300\delta$) in fluctuations of u in turbulent Couette flow, and this size of these large scale motions increases with Re. In contrast, the size of the largest scales in spanwise direction does not appear to have a significant Re dependence. Another set of simulations with larger streamwise domain size would be required to accurately determine how the largest streamwise scale varies with Re. In the presentation we will demonstrate the nature of extreme scale motions and their contribution to various statistics in details.

References

V. Avsarkisov, S. Hoyas, M. Oberlack, and J. P. García-Galache. Turbulent plane Couette flow at moderately high Reynolds number. *Journal of Fluid Mechanics*, 751:R1, June 2014.

Myoungkyu Lee and Robert D. Moser. Direct numerical simulation of turbulent channel flow up to $Re_\tau \approx 5200$. *Journal of Fluid Mechanics*, 774:395–415, June 2015.

Myoungkyu Lee, Nicholas Malaya, and Robert D. Moser. Petascale direct numerical simulation of turbulent channel flow on up to 786K cores. In *the International Conference for High Performance Computing, Networking, Storage and Analysis*, pages 1–11, New York, New York, USA, 2013. ACM Press.

Myoungkyu Lee, Rhys Ulerich, Nicholas Malaya, and Robert D. Moser. Experiences from Leadership Computing in Simulations of Turbulent Fluid Flows. *Computing in Science Engineering*, 16(5):24–31, September 2014.

TWO-POINT STATISTICS IN THE LOG-LAW REGION IN DNS OF TURBULENT CHANNEL FLOW

Yukio Kaneda *[1], Koji Morishita[2], and Takashi Ishihara[3]
[1]*Department of Natural Science, Aichi Institute of Technology, Toyota, Japan*
[2]*Education Center on Computational Science and Engineering, Kobe University, Kobe, Japan*
[3]*Center for Computational Science, Nagoya University, Nagoya, Japan*

Summary Two-point statistics in the log-law region of turbulent channel flow are studied on the basis of high resolution direct numerical simulation (DNS) with the wall Reynolds number and the grid points up to 5120 and $2048 \times 1536 \times 2048$, respectively. The DNS data are consistent with the linear response theory of turbulence. According to the DNS, the Taylor microscale is anisotropic, but has a simple y-dependence ($\propto y^{1/2}$), and two-point fluctuating-velocity correlations at $|\mathbf{r}| \sim y$ depend on $\mathbf{r}$ approximately through $\mathbf{r}/y^{\alpha}$, where y is the distance from the wall, $\mathbf{r}$ is the displacement vector between the two points, and α is close to but a little different form 1.

INTRODUCTION

According to the idea of Kolmogorov (K41), there are a certain class of universal laws in the statistics of turbulence at high Reynolds number, where the influence of fluid boundaries is assumed to be negligible. On the other hand, in real flows in nature and technology, the flows are often bounded by walls, which may significantly affect the turbulence statistics.

Among canonical wall-bounded turbulent flows are those bounded by two parallel planes (channel flows). We consider the statistics of turbulent channel flow on the basis of high resolution direct numerical simulation (DNS) with the wall Reynolds number Re_τ up to 5120. A particular attention is paid on two-point statistics in the log-law region. The DNS uses a Fourier spectral method in the streamwise ($x_1 = x$) and the spanwise ($x_3 = z$) directions and Tchebycheff expansion method in the wall normal ($x_2 = y$) direction. Readers may refer to Morishita et al. [1] for some details of the numerical method. Characteristic parameter values of the DNS are listed in Table 1 (from [2]). Figure 1 is an example of visualization of the field and shows intense vorticity regions in the DNS at $Re_\tau = 5120$.

STATISTICS IN THE LOG-LAW REGION

In our DNS, it is confirmed that in a certain range of y the mean streamwise velocity U and the mean rate of energy dissipation ϵ per unit mass fit well to the log-law

$$U^+(y^+) = \frac{1}{\kappa}\log y^+ + C, \quad \text{and} \quad \epsilon^+ = 1/(\kappa y^+), \tag{1}$$

respectively, in accordance with studies so far made, where y is the distance from the wall and the superscript + denotes the normalization by the wall units. The constants are approximately $\kappa \approx 0.4$ and $C \approx 5$. The y-range depends on Re_τ. For example, it is approximately $50 < y^+ < 1000$ at $Re_\tau = 5120$ [2] .

Taylor microscale

As seen in Fig.1, the field consists of eddies of a wide scale range. Two-point velocity correlation $Q_{ij}(\mathbf{x}, \mathbf{r}) \equiv \langle u_i(\mathbf{x}) u_j(\mathbf{x}+\mathbf{r})\rangle$ is one of the most fundamental measures characterizing such a field, where $\mathbf{u}$ is the fluctuating part of the velocity field. In our DNS, because of the homogeneity in the x_1 and x_3 directions, $Q_{ij}(\mathbf{x}, \mathbf{r})$ is independent of x_1 and x_3, and depends on $\mathbf{x}$ only through $x_2 = y$. For small $r = |\mathbf{r}|$, Q_{ii} is well characterized by the so-called Taylor microscale λ_{ij} defined by $Q_{ii}(\mathbf{x}, 0)/\{\lambda_{ij}(\mathbf{x})\}^2 \equiv -[\partial^2 Q_{ii}(\mathbf{x}, \mathbf{r})/\partial r_j \partial r_j]_{\mathbf{r}=0}$ [1] (no summation over i nor j). In the log-law region in our DNS, the flow field is not isotropic. But they agree well with the scaling $\propto y^{1/2}$, which is in agreement with the scaling obtained by (1) and the scaling of λ_{ij} for isotropic turbulence.

Table 1: DNS parameters. h, the channel half width; L_x, L_z, fundamental periodic lengths; N_x, N_y, N_z, the number of grid points, $\Delta x^+, \Delta y_c^+, \Delta z^+$, grid width in the wall unit. The subscript denotes the direction. Δy_c is at the center of the channel.

	Re_τ	L_x/h	L_z/h	$N_x \times N_y \times N_z$	Δx^+	Δy_c^+	Δz^+
Case 1	320	π	$\pi/2$	$128 \times 192 \times 128$	7.9	7.9	3.9
Case 2	640	π	$\pi/2$	$256 \times 384 \times 256$	7.9	7.9	3.9
Case 3	1280	π	$\pi/2$	$512 \times 768 \times 512$	7.9	7.9	3.9
Case 4	2560	π	$\pi/2$	$1024 \times 1536 \times 1024$	7.9	7.9	3.9
Case 5	5120	π	$\pi/2$	$2048 \times 1536 \times 2048$	7.9	15.9	3.9

*Corresponding author. Email: ykaneda@aitech.ac.jp

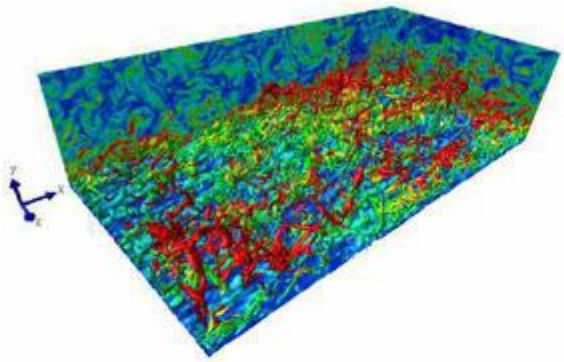

Figure 1: Intense vorticity region in the DNS at $Re_\tau = 5120$ in the domain $\{(x, y, z)|0 \leq x \leq L_x/4, 0 \leq y^+ \leq 1000, 0 \leq z \leq L_z/4)\}$. The color shows the distance y from the lower wall. The distribution of the vorticity amplitude is shown on the $x = L_x/4$ and $z = 0$ planes.

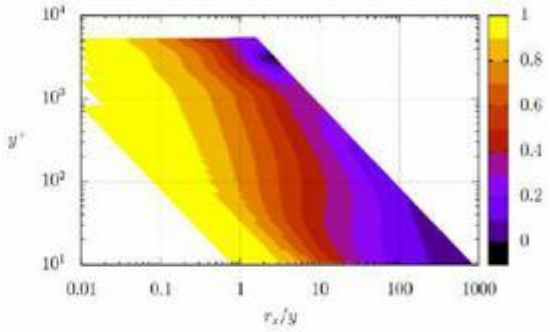

Figure 2: Contours of velocity correlation $C_{11} \equiv \langle u_1(x, y, z)u_1(x + r_x, y, z)\rangle / \left\langle \{u_1(x, y, z)\}^2 \right\rangle$ as a function of y^+ and r_x/y in the DNS at $Re_\tau = 5120$. The color correspond to the value of C_{11}.

Statistics at $y \gg r \gg \eta$ – Linear response theory

In general, the dominant dynamics in a scale range depends on the scale. Let L_S be the length scale defined by $L_S = \epsilon^{1/2}/S^{3/2}$, and η be the Kolmogorov microscale defined by $\eta \equiv (\nu^3/\epsilon)^{1/4}$, where $S \equiv \partial U/\partial y$ and ν is the kinematic viscosity of the fluid. According to (1), we have $L_S^+ = \kappa y^+$, $\eta^+ = (\kappa y^+)^{1/4}$. A simple dimensional analysis based on the idea of K41 suggests that in the scale range r such that $L_S \gg r \gg \eta$, the non-linear interaction with eddies of similar size r plays the dominant role, and the influence of the mean flow and the existence of the wall may be treated as perturbation added to the system dominated by the dynamics. This consideration leads us to apply the idea of the Linear Response Theory (LRT) [2,3]. The LRT gives a prediction on Q_{ij}, or its Fourier transform in the wavenumber range $1/L_S \gg k \gg 1/\eta$, The wavenumber dependence for fixed y has been shown to be consistent with DNS [2,3]. It is also confirmed that the y dependence is also consistent with the DNS.

Two-point statistics at $r \sim y$

If the log-law in fact exits, it is a challenging question whether we can derive the estimate of the Karman constant κ in (1) from the first principle, i.e., the Navier-Stokes equation. In such a derivation, it is expected that two points statistics, in particular the y-dependence at $r \sim y$ may play an important role.

According to our DNS, Q_{ij} in the log-law region fits fairly well to the form $Q_{ij}(\mathbf{x}, \mathbf{x} + \mathbf{r}) = Q_{ij}(y, \mathbf{r}/Y)$ where $Y \propto y^\alpha$ and α is close to 1 in agreement with the conjecture by Lesile[4]. But a close inspection shows that α is a little different from 1. Figure 2 shows the contours of the velocity correlation $Q_{ii}(\mathbf{x}, \mathbf{r})/Q_{ii}(\mathbf{x}, \mathbf{0})$ with $i = 1$, $\mathbf{r} = (r_x, 0, 0)$ as a function of y and r_x/y. If $\alpha = 1$, then the contours at $r_x/y \sim 1$ must be vertical, but they are seen a little tilted. The similar is true for the other i and direction of $\mathbf{r}$.

CONCLUSIONS

The analysis of the DNS data of turbulent channel flow with Re_τ up to 5120 shows the following. (i) The Taylor microscale is strongly anisotropic, but fits well to the simple scaling $\propto y^{1/2}$, (ii) the linear response theory is consistent with the velocity correlation spectra by the DNS, and (iii) the two-point correlation $Q_{ij}(\mathbf{x}, \mathbf{r})$ at $r \sim y$ depends on $\mathbf{r}$ approximately through $\mathbf{r}/Y$, where $Y = y^\alpha$ and α is not far from 1.

This work has been supported partly by JSPS KAKENHI Grant Number (C)26400410.

References

[1] Morishita K., Ishihara T., Kaneda Y.: Small-scale statistics in direct numerical simulation of turbulent channel flow at high-Reynolds number. *J. Phys.: Conference Series*, **318**, 022016-1–6, 2011.

[2] Kaneda Y., Morishita K., Ishihara T.: Small-scale universality and spectral characteristics in turbulent flows. Proceedings of TSFP8, 2013. http://www.tsfp-conference.org/proceedings/2013/v1/inv2.pdf.

[3] Kaneda Y., Morishita K.: Small-scale statistics and structure of turbulence – in the light of high resolution direct numerical simulation. *Ten Chapters in Turbulence*, edited by P. A. Davidson, Y. Kaneda and K. R. Sreenivasan, pp. 1-42. Cambridge University Press, 2012.

[4] Leslie, D. C.: Developments in the theory of turbulence, Clarendon Press, 1973.

SPECTRAL ANALYSES OF HIGH PRANDTL NUMBER STRATIFIED TURBULENCE

Shinya Okino[1] and Hideshi Hanazaki *[1]

[1]*Department of Mechanical Engineering and Science, Kyoto University, Kyoto, Japan*

Summary Spectra of decaying turbulence in a stratified fluid containing either an active (density stratifying) or a passive high Prandtl number scalar are investigated by direct numerical simulations. When the fluid is stratified by a low-Prandtl-number active scalar ($Pr_T = 1$) and simultaneouly contains a high-Prandtl-number passive scalar ($Pr_S = 25$), spectrum of the high-Prandtl-number passive scalar variance obeys the usual Batchelor scaling. On the other hand, when the fluid is stratified by a high-Prandtl-number active scalar ($Pr_T = 25$), horizontal spectrum of that active scalar (or potential energy) decreases rapidly at high wavenumbers to approach the kinetic energy spectrum, indicating the deviation from the Batchelor scaling. Examination of the spectral budget shows that the deviation is due to the persistent conversion from the potential energy to the kinetic energy at small scales.

METHODOLOGY

We consider a density stratified fluid due to a buoyant (or active) scalar T_*, which has a Prandtl number $Pr_T = \kappa_{T*}/\nu_*$ (dimensional quantities are denoted by asterisks.). Here, κ_{T*} and ν_* are the diffusion coefficient and the kinematic viscosity, respectively. The scalar has a constant mean vertical gradient $d\bar{T}_*/dz_* = \text{const} < 0$, where z_* is the vertical coordinate and the undisturbed mean density is given by $\bar{\rho}_*(z_*) = \rho_{0*}\{1 + \alpha_*(d\bar{T}_*/dz_*)z_*\}$ (ρ_{0*}: representative density of the fluid, α_*: contraction coefficient of the scalar).

The decaying turbulence in the stratified fluid are investigated by direct numerical simulations. We initially give isotropic velocity fluctuations, whose rms velocity and integral length scale are given by U_{0*} and L_{0*}, and zero scalar fluctuations. The Navier-Stokes equations under the Boussinesq approximation and the transport equation for the scalar perturbation are given by

$$\frac{\partial u_i}{\partial t} + u_j\frac{\partial u_i}{\partial x_j} = -\frac{\partial p}{\partial x_i} + \frac{1}{Re}\frac{\partial^2 u_i}{\partial x_j^2} - \frac{1}{Fr^2}T\delta_{i3} \quad \text{and} \quad \frac{\partial T}{\partial t} + u_j\frac{\partial T}{\partial x_j} = \frac{1}{RePr_T}\frac{\partial^2 T}{\partial x_j^2} + u_3 \tag{1}$$

in which physical quantities are non-dimensionalized by the length scale L_{0*}, the velocity scale U_{0*} and the scalar scale $L_{0*}d\bar{T}_*/dz_*$, and $i = 3$ denotes the vertical component. T represents the scalar deviation from the background. The initial Reynolds number and the Froude number are set to $Re = U_{0*}L_{0*}/\nu_* = 100$ and $Fr = U_{0*}/(N_*L_{0*}) = 1$, respectively, where N_* is the Brunt-Väisälä frequency. Additionally, we prescribe a linear stratification of a passive scalar S_*, which has a Prandtl number $Pr_S = \kappa_{S*}/\nu_*$. The passive scalar obeys a similar transport equation to the second equation of (1).

The governing equations are solved by the Fourier spectral method with the resolution of 1024^3 for the periodic cubic region with the domain size of 4π. We present the results of two simulations, in which the Prandtl numbers are set to $(Pr_T, Pr_S) = (1, 25), (25, 1)$. The simulation is terminated at $t = 40$, which approximately corresponds to seven buoyancy periods ($\sim 7 \times 2\pi/N_*$ in dimensional form).

RESULTS AND DISCUSSION

We first show the temporal evolution of the horizontal spectra in figure 1. In the left frame of figure 1, the passive scalar has a higher Prandtl number than the active scalar ($Pr_T = 1, Pr_S = 25$), and only the kinetic energy spectrum and the passive scalar variance spectrum are depicted. The passive scalar spectrum has much larger fluctuations at high wavenumbers than the kinetic energy spectrum as it is theoretically shown in [1]. In the right frame is shown the kinetic and potential energy spectrum when the active scalar has a high Prandtl number ($Pr_T = 25$). At an early stage ($t \sim 6$), the potential energy spectrum with $Pr_T = 25$ has large fluctuations at small scales as well as the passive scalar spectrum with $Pr_S = 25$. The influence of the buoyancy to small scales is not significant at this time since the Ozmidov wavenumber is at $k_H \sim 6$. The Ozmidov wavenumber monotonically increases and exceeds the Kolmogorov wavenumber at $t \sim 9$, at which even the smallest fluctuations of the flow are dominated by the buoyancy. Subsequently the potential energy spectrum rapidly decreases to approach the kinetic energy spectrum at high wavenumbers.

In the left frame of figure 2, the horizontal spectra of the passive scalar variance with $Pr_T = 1, Pr_S = 25$ normalized by the Kolmogorov wavenumber k_K, the passive scalar dissipation rate χ_S, the Prandtl number Pr_S and the Reynolds number Re are plotted as a function of k_H/k_B, where $k_B = k_K Pr_S^{1/2}$ is the Batchelor wavenumber. The normalized spectra almost converge with a single curve, showing the passive scalar spectrum follows the Batchelor scaling even though the turbulence is affected by buoyancy. For an isotropic turbulence, a similar result is presented in [2]. On the other hand, the normalized

*Corresponding author. Email: hanazaki@mech.kyoto-u.ac.jp

horizontal spectra of the potential energy with $Pr_T = 25$ disperse, reflecting the rapid decrease of the potential energy at small scales and the deviation from the Batchelor scaling for a high-Prandtl number active scalar. Though the potential energy spectrum of the stratified turbulent flow with $Pr_T > 1$ is presented in [3], such a phenomenon is not reported. Note that the Batchelor scaling holds for the vertical spectrum of both the passive scalar variance with $Pr_T = 1, Pr_S = 25$ and the potential energy with $Pr_T = 25$ (figures are omitted.).

To explain the difference between the active scalar spectrum and the passive scalar spectrum described above, we examine the budget of the scalar spectrum, which consists of the molecular diffusion, the vertical scalar flux and the scalar transfer from large to small scales. Compared to the passive scalar, the large vertical scalar flux for the active scalar (i.e., conversion from the potential energy to the vertical kinetic energy) significantly contributes to the rapid decrease of the spectrum at small scales.

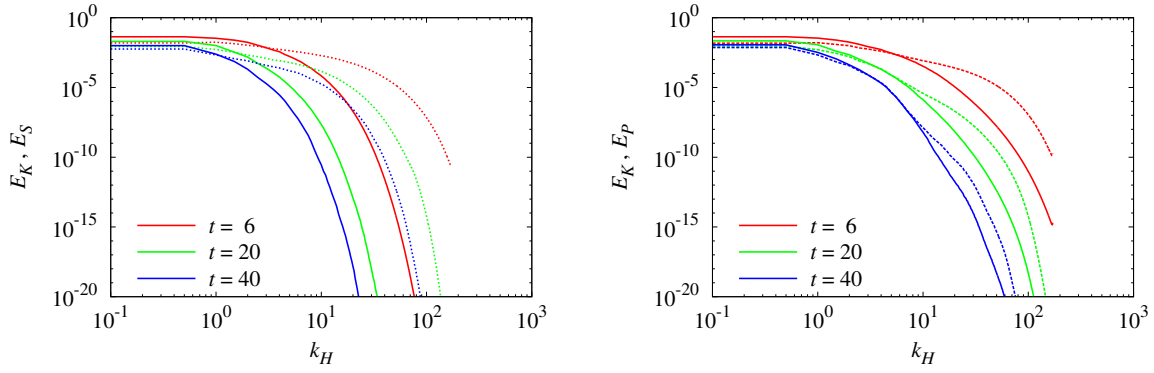

Figure 1: Temporal evolution of the horizontal spectra of (solid) the kinetic energy, (dashed) the potential energy and (dotted) the passive scalar variance. The spectra satisfy $\overline{u_i^2}/2 = \int E_K(k_H)dk_H, \overline{T^2}/(2Fr^2) = \int E_P(k_H)dk_H$, and $\overline{S^2}/(2Fr^2) = \int E_S(k_H)dk_H$, where the overbar denotes the space average, and k_H is the horizontal wavenumber. (Left) $Pr_T = 1, Pr_S = 25$. (Right) $Pr_T = 25, Pr_S = 1$.

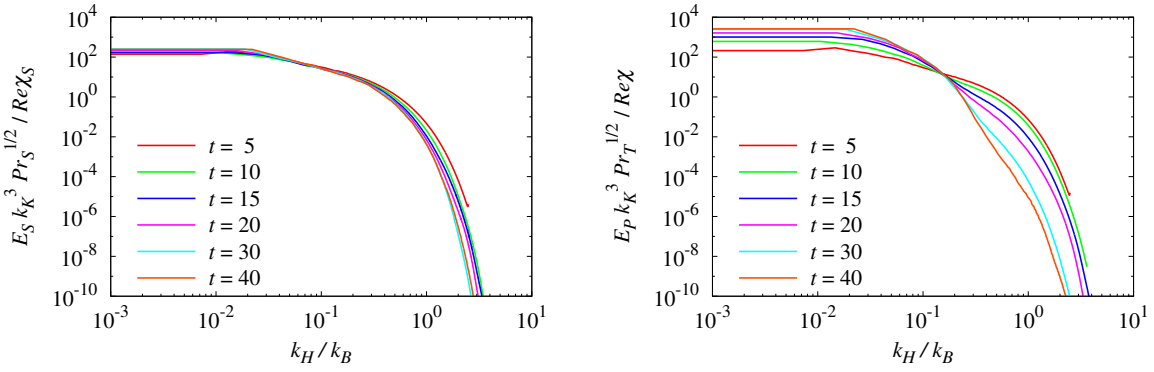

Figure 2: Normalized horizontal spectra of (left) the passive scalar variance with $Pr_S = 25$ and (right) the potential energy with $Pr_T = 25$.

References

[1] G. K. Batchelor. Small-scale variation of convected quantities like temperature in turbulent fluid. Part 1. General discussion and the case of small conductivity. *J. Fluid Mech.* **5**: 113–133, 1959.

[2] D. Bogucki, J. A. Domaradzki and P. K. Yeung. Direct numerical simulations of passive scalars with $Pr > 1$ advected by turbulent flow. *J. Fluid Mech.* **343**: 111–130, 1997.

[3] W. D. Smyth. Dissipation-range geometry and scalar spectra in sheared stratified turbulence. *J. Fluid Mech.* **401**: 209–242, 1999.

EFFECT OF BACKGROUND TURBULENCE ON PASSIVE SCALAR MIXING WITHIN A TURBULENT JET

Alejandro Pérez-Alvarado[1], Susan Gaskin*[2], and Laurent Mydlarski[1]
[1]*Department of Mechanical Engineering, McGill University, Montreal, Quebec, Canada*
[2]*Department of Civil Engineering and Applied Mechanics, McGill University, Montreal, Quebec, Canada*

Summary Despite the fact that most jets (natural or man-made) discharge into turbulent environments, the vast majority of previous studies of turbulent jets have considered the emission of jets into quiescent or laminar surroundings. The present investigation builds on the work of Khorsandi *et al.* [1], who studied the velocity field of a turbulent jet emitted into a turbulent background. We examine herein the effect of an approximately homogeneous, isotropic, zero-mean-flow turbulent background on the scalar field of a turbulent jet. To this end, we measured the concentrations of a high-Schmidt-number passive scalar within the jet by means of planar laser-induced fluorescence. We present the statistics of the jet's scalar field and compare them with the results of a jet emitted into a quiescent ambient.

INTRODUCTION

The velocity and scalar fields of an axisymmetric jet discharging into a quiescent background have been thoroughly investigated. However, most natural and industrial jet-like flows occur in the presence of external turbulence, and relatively few studies of jets issuing into a turbulent background have been carried out [1,2,3,4,5]. This prevents the complete understanding and prediction of the behavior of turbulent jets in more realistic situations, such as the discharge of pollutants into the atmosphere or hydrosphere, or the injection of fuels into combustion chambers. Consequently, the effect of background turbulence on both the scalar and velocity fields of turbulent jets is not well described. Furthermore, of the few previous works studying jets emitted into turbulent backgrounds, most have focused on the velocity field, with some studies predicting higher levels of mixing [3,4,5], while others predicted lower mixing [1,2]. Scalar mixing was studied quantitatively in one of these studies, which observed lower mixing [2], while most works obtained only qualitative data using flow visualization. To aid in resolving these contradictions, the present investigation undertakes a systematic study of the scalar field within the simple classic flow of a turbulent jet emitted into a quasi-homogeneous, isotropic, zero-mean-flow turbulent background.

Khorsandi *et al.* [1] studied the effect of background turbulence on the velocity field of a turbulent jet and showed that, in addition to increased decay rates of the mean axial velocities, jet widths, and rms axial velocities in the presence of background turbulence, the mass flow rate of the jet decreased compared to the quiescent case. The latter is an especially interesting finding since it is associated with lower entrainment into the jet. The reduced mass flow rates of a jet emitted into a turbulent background may imply lower levels of scalar mixing. Herein, we present the results pertaining to the scalar field of a jet emitted into a turbulent background necessary to confirm or refute the hypothesis of a reduction of the scalar mixing.

EXPERIMENTAL METHOD

The experiments were performed in a $1.5 \times 2.4 \times 0.9$ m^3 section of a large glass tank ($1.5 \times 6.0 \times 0.9$ m^3) filled with water in the Environmental Hydraulics Laboratory in the Department of Civil Engineering and Applied Mechanics at McGill University. The flow conditions of the jet and background turbulence were identical to those of Khorsandi *et al.* [1] in the same experimental facility. The turbulent jet had an exit velocity (U_j) of 1.3 m s^{-1} and a nozzle diameter (D) of 8 mm, resulting in a jet Reynolds number ($= U_j D/\nu$) of 10600. Planar laser-induced fluorescence was used to obtain concentration measurements of dye (disodium fluorescein, Schmidt number $= 2000$) within the turbulent jet. The approximately homogeneous, isotropic, zero-mean-flow background turbulence was generated by a random jet array [6]. The generated background turbulence had a turbulent kinetic energy ($1/2\langle u_i u_i \rangle$) of 4.4 cm^{2}s^{-2} (i.e. $u_{rms} = 1.7$ cm s^{-1}) and an integral length scale (ℓ) of 11.6 cm, resulting in a Reynolds number ($= u_{rms}\ell/\nu$) of 2000.

RESULTS

Figure 1 depicts the radial profiles of the normalized mean concentration ($\langle C \rangle / C_o$) at different downstream distances ($x/D = 20$, 40 and 50). The mean concentrations near the centerline ($r/x = 0$) are lower in the presence of background turbulence. However, slightly higher mean concentrations are measured at the edges of the jet ($r/x > 0.15$), which can be attributed to the moderately increased width of the jet emitted into turbulent surroundings. Examination of the downstream evolution of the centerline mean concentration ($\langle C_{(r=0)} \rangle / C_o$ vs x/D – not shown) revealed a higher decay rate for the jet emitted into turbulent surroundings. However, examination of the instantaneous concentrations showed a higher degree of intermittency in the presence of the turbulent background resulting in higher rms concentrations (Figure 2) due in part to meandering of the jet. Although the mean concentrations may contradict the hypothesis of Khorsandi *et al.* [1] of possible lower mixing based on the decreased mass flow rate of the jet (associated with lower entrainment), the combination of mean and

*Corresponding author email: susan.gaskin@mcgill.ca

rms concentrations may imply a more complex entrainment and mixing process of jet flow in the presence of the background turbulence.

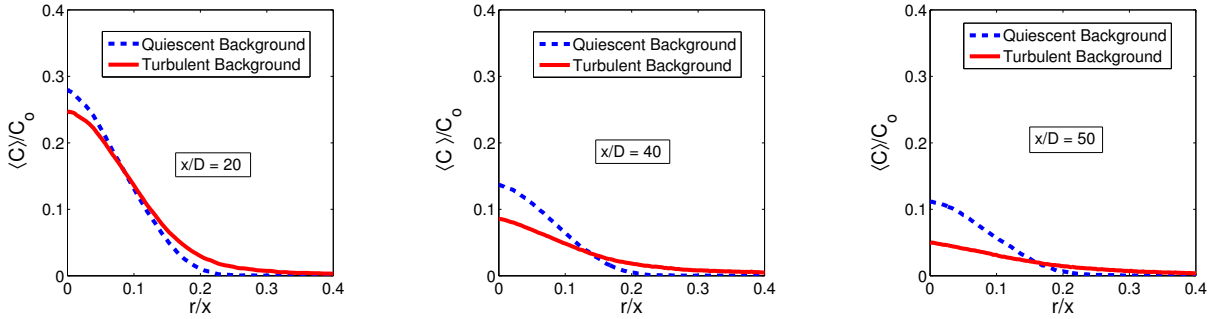

Figure 1: Radial profiles of mean concentration ($\langle C \rangle$) normalized by the initial concentration (C_o) at different x/D.

Figure 3 depicts the probability density function of concentration at the jet axis for quiescent and turbulent backgrounds at $x/D = 40$. (Similar results were obtained at different x/D.) In the presence of background turbulence, the concentrations at the jet axis spanned values of similar magnitude to those for the jet emitted into a quiescent background, even though the two jets exhibited significant differences in the mean concentrations (Figure 1). The shape of the probability density function is significantly modified (from a unimodal distribution to a bimodal one) as a result of the highly intermittent scalar field. These results indicate a large degree of meandering of the path of the jet due to the larger length scale of background turbulence, and indicate that the mean concentration is not as representative of the instantaneous concentration.

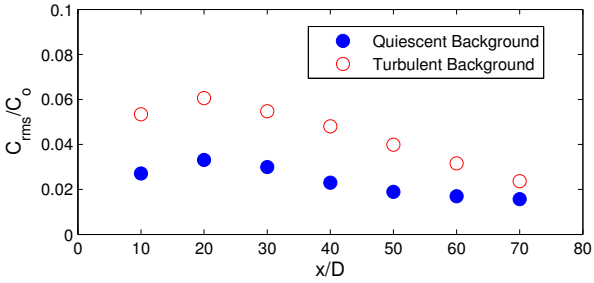

Figure 2: Downstream evolution of the normalized rms concentration (C_{rms}/C_o) at the jet axis ($r = 0$).

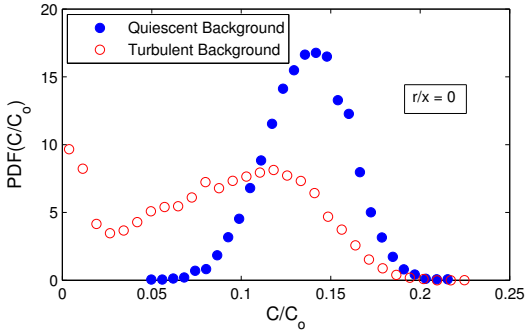

Figure 3: Probability density function of the concentration at the jet axis ($r = 0$) at $x/D = 40$.

In the presence of background turbulence, the entrainment and mixing in the jet may potentially be dominated by i) turbulent diffusion that is significantly enhanced by the turbulent background, and ii) apparent dilution due to meandering of the jet caused by large scales in the background turbulence. However, simultaneous velocity-concentration measurements would be beneficial in confirming these hypotheses. In the presentation, additional statistics of the scalar field will be presented, as well as the results for a jet at Re $= 5800$.

CONCLUSIONS

In the presence of background turbulence, the scalar field becomes highly intermittent (with concentrations on the order of those of a jet emitted into a quiescent background) and its statistics are significantly changed. An interesting finding is the observation of a more complex mechanism of entrainment and mixing in the jet emitted into a turbulent background due to the meandering of the jet, which explains the absence of significantly higher concentrations as hypothesized by Khorsandi *et al.* [1], who had assumed that the effect of the jet's meandering would not be as prominent.

References

[1] Khorsandi B., Gaskin S. & Mydlarski L.: Effect of background turbulence on an axisymmetric turbulent jet. J. Fluid Mech., 736:250-286, 2013.

[2] Gaskin S., McKeman M. & Xue F.: The effect of background turbulence on jet entrainment: an experimental study of a plane jet in a shallow coflow. J. Hydraul. Res., 42(5):531-540, 2004.

[3] Law A. W. K., Cheng N. S. & Davidson M.J.: Jet spreading in oscillating-grid turbulence. Proc. 3rd Int. Symp. on Env. Hydraul., 1-6, 2001.

[4] Guo Y., Malcangio D., Davies P. A. & Fernando H. J. S.: A laboratory investigation into the influence of a localized region of turbulence on the evolution of a round turbulent jet. Fluid Dyn. Res., 36:78-89, 2005.

[5] Cuthbertson A. J., Malcangio D., Davies P. A. & Mossa M.: The influence of a localized region of turbulence on the structural development of a turbulent, round, buoyant jet. Fluid Dyn. Res., 38:683-698, 2006.

[6] Variano E. A. & Cowen E. A.: A random-jet-stirred turbulence tank. J. Fluid Mech., 604:1-32, 2008.

EFFECTS OF VISCOSITY RATIO ON DROPLET-LADEN ISOTROPIC TURBULENCE

Michael S. Dodd[1] and Antonino Ferrante *[1]
[1]*William E. Boeing Dept. of Aeronautics & Astronautics, University of Washington, Seattle, WA, USA*

Summary We performed direct numerical simulation (DNS) of droplet-laden isotropic turbulence. We released 3130 non-evaporating droplets of diameter approximately equal to the Taylor lengthscale (corresponding to 5% droplet volume fraction) in decaying isotropic turbulence at initial Taylor-scale Reynolds number $\mathrm{Re}_\lambda = 83$. We studied four cases: one single-phase case and three droplet-laden cases in which we varied the droplet- to carrier-fluid viscosity ratio ($1 \leq \mu_d/\mu_c \leq 100$). We first derived the turbulence kinetic energy (TKE) equations for the two-fluid, carrier-fluid and droplet-fluid flow. This allows us to explain the pathways for TKE exchange between the turbulent flow of the carrier fluid and the flow inside the droplet. Then, we analyze the effects of varying μ_d/μ_c on the turbulent kinetic energy budget of the carrier fluid, the droplet fluid and the two fluids, and, finally, we explain the underlying physical mechanisms for their modulation.

The interaction of dispersed droplets and turbulence is important in many natural and industrial processes, e.g. rain formation [1], liquid-liquid emulsion [2], spray cooling [3] and spray atomization in combustors [4, 5]. Often, e.g., during secondary atomization or the latter stages of rain formation, the droplets are larger than the Kolmogorov lengthscale, i.e., finite-size. The interaction of finite-size droplets and turbulence, in comparison to the interaction of finite-size particles and turbulence (e.g., in [6]), is expected to incorporate new physical mechanisms. These new mechanisms are a result of the droplet's ability to deform, develop internal circulation, break up and coalesce with other droplets. The first two processes are characterized by two additional non-dimensional parameters: the Weber number, We, and the viscosity ratio between the droplet fluid and carrier fluid $\gamma = \mu_d/\mu_c$. In [7], we have reported on the effects of varying We on droplet/turbulence interaction, and we now focus on the effects of varying γ on such interaction.

We have performed direct numerical simulation (DNS) of decaying isotropic turbulence laden with deformable droplets, whose diameter is approximately equal to the Taylor lengthscale at the time of droplet release in the flow field. We released 3130 non-evaporating droplets from rest in the isotropic turbulent flow at time $t = 1$. Figure 1 shows a snapshot of the computational domain after the droplets are released ($t = 1.5$). The non-dimensional parameters characterizing the two-fluid flow are the initial Taylor-scale Reynolds number at droplet release time, $\mathrm{Re}_\lambda = 83$, droplet Weber number based on the r.m.s. velocity at release time, $\mathrm{We}_{\mathrm{rms}} = 1$, the droplet- to carrier-fluid density ratio, $\rho_d/\rho_c = 10$, the droplet volume fraction, $\phi_v = 0.05$, and the droplet- to carrier-fluid viscosity ratio which is varied from 1 to 100 in the three droplet-laden cases studied. The initial droplet diameter is 1.1 Taylor lengthscales and 20 Kolmogorov lengthscales. The computational domain is a periodic cube, which is discretized using 1024^3 grid points, giving a droplet resolution of 32 grid points per diameter. The governing equations were solved numerically using a fast pressure-correction method [8] that has been verified and validated. To capture the droplet interface and to track the motion of the finite-size deforming droplets, we used a mass-conserving Volume-of-Fluid (VoF) method [9].

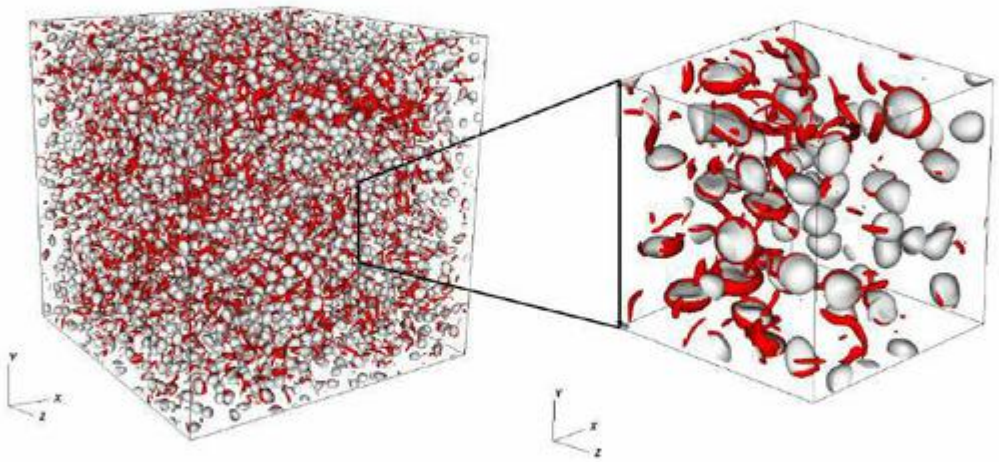

Figure 1: Instantaneous droplet interfaces in shaded white ($C = 0.5$ isosurface) and vortical structures in red ($\lambda_2 = -50$ isosurfaces) at $t = 1.5$. (Left) full domain ($1 \times 1 \times 1$); (right) sub-domain ($0.25 \times 0.25 \times 0.25$).

*Corresponding author. Email: ferrante@aa.washington.edu

We simulate four cases: a single-phase case and three cases in which the viscosity ratio (γ) is increased from 1 to 10 to 100. Figure 2(a) shows the time evolution of the carrier-fluid turbulence kinetic energy (TKE) normalized by its initial value, $k_c(t)/k_0$, in the four cases. The presence of the droplets increases the decay rate of carrier-fluid TKE compared to the single-phase case. As the viscosity ratio (γ) increases from 1 to 100, the decay rate of $k_c(t)$ increases. By analyzing the evolution of the terms in the carrier-fluid TKE budget, the results show that as γ increases, the enhanced decay of $k_c(t)$ is due primarily to an increase in the dissipation rate of carrier-fluid TKE, $\varepsilon_c(t)$ (figure 2(b)). $\varepsilon_c(t)$ increases because as γ increases, the velocity gradient near the droplet interface increases in the carrier fluid and decreases in the droplet fluid (figure 3). Therefore, the carrier-fluid dissipation rate ($\varepsilon_c(t)$) increases, while the droplet fluid dissipation rate decreases.

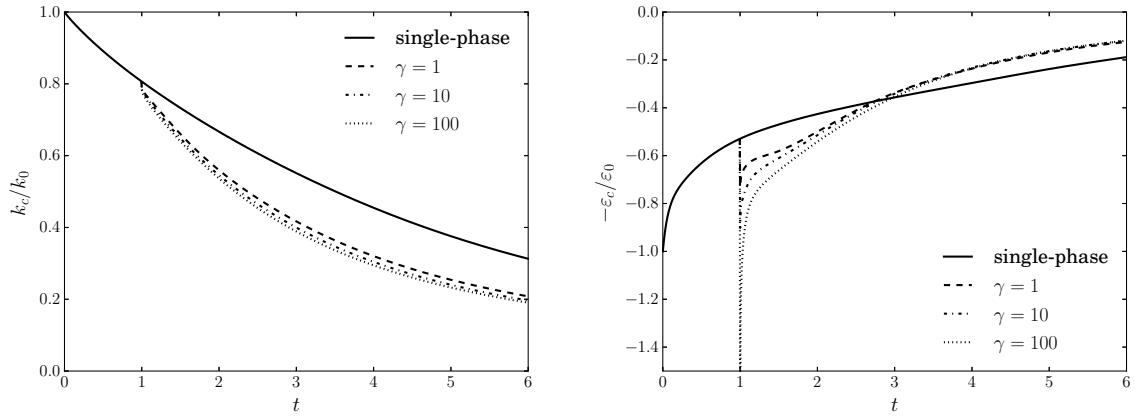

Figure 2: Temporal evolution of (a) the carrier-fluid turbulence kinetic energy, k_c, normalized by its initial value, k_0 and (b) the carrier-fluid dissipation rate of turbulence kinetic energy, ε_c, normalized by its initial value, k_0.

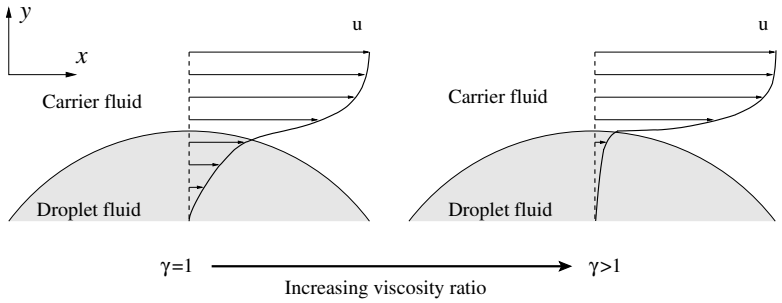

Figure 3: Illustration of the velocity profile, $u(y)$, at the interface of a droplet released from rest in uniform flow. The illustration depicts the effects of varying the viscosity ratio, γ. Unity viscosity ratio ($\gamma = 1$): at the interface, the velocity is continuous and the velocity gradient is continuous (left); viscosity ratio greater than unity ($\gamma > 1$): at the interface, the velocity is continuous and the velocity gradient is discontinuous (right).

References

[1] R. A. Shaw. Particle-turbulence interactions in atmospheric clouds. 35(1):183–227, 2003.

[2] P. D. Berkman and R. V. Calabrese. Dispersion of viscous liquids by turbulent flow in a static mixer. *AIChE J.*, 34(4):602–609, 1988.

[3] C. Qin, E. Loth, P. Li, T. Simon, and J. Van de Ven. Spray-cooling concept for wind-based compressed air energy storage. *J. Renew. Sustain. Energy*, 6(4):043125, 2014.

[4] W. A. Sirignano. Fuel droplet vaporization and spray combustion theory. *Prog. Energy and Combust. Sci.*, 9(4):291–322, 1983.

[5] G. M. Faeth, L. P. Hsiang, and P. K. Wu. Structure and breakup properties of sprays. *Int. J. Multiphase Flow*, 21:99–127, 1995.

[6] F. Lucci, A. Ferrante, and S. Elghobashi. Modulation of isotropic turbulence by particles of Taylor length-scale size. *J. Fluid Mech.*, 650:1–51, 2010.

[7] M. Dodd and A. Ferrante. Modulation of isotropic turbulence by deformable droplets of Taylor lengthscale size. *Bulletin of the American Physical Society*, 59, 2014.

[8] M. S. Dodd and A. Ferrante. A fast pressure-correction method for incompressible two-fluid flows. *J. Comput. Phys.*, 273:416–434, 2014.

[9] A. Baraldi, M. S. Dodd, and A. Ferrante. A mass-conserving volume-of-fluid method: Volume tracking and droplet surface-tension in incompressible isotropic turbulence. *Comput. Fluids*, 96:322–337, 2014.

OPTIMAL CONTROL INPUT FOR SKIN FRICTION DRAG REDUCTION IN TURBULENT CHANNEL FLOW

Yukinori Kametani and Yosuke Hasegawa *
Institute of Industrial Science, The University of Tokyo, Tokyo, Japan

Summary The optimal control theory is applied to determine wall blowing and suction for skin friction drag reduction in direct numerical simulations of a fully developed turbulent channel flow. A particular focus is on the effects of the time horizon used in the optimal control on the resultant control input and the control performance. Compared with the well-known opposition control[2], higher drag reduction is commonly achieved with the optimal control. Through the detailed comparison between the control inputs obtained by the opposition and optimal controls, the drag reduction mechanisms in the optimal control are discussed.

BACKGROUND

In the modern society, the reduction of turbulent skin friction drag is in huge demand in order to mitigate the environmental burden. The skin friction is mainly governed by microscopic coherent structures near the wall, so that the effective control within the thin near-wall layer is essential. So far, a wide variety of control schemes has been proposed. Passive schemes are advantageous in the sense that they don't require additional power consumption for control. On the other hand, active control schemes are in general more flexible, and results in higher control performance, since they can adapt their control inputs to instantaneous flow states. Among active control schemes, the optimal control theory provides a unique opportunity to mathematically optimize the control input to minimize a prescribed cost functional, and generally achieves highest control performance[1, 3, 4]. Despite its remarkable control performance, the optimized input and its control mechanisms are still not well understood. In the present study, we revisit the optimal control for skin friction drag in a fully developed channel flow. The resultant optimized control input are compared with that in one of the most well-known control schemes, i.e., the opposition control [2] in order to clarify the drag reduction mechanisms in the optimal control.

NUMERICAL PROCEDURES

In the present study, we conduct direct numerical simulations of a fully developed turbulent channel flow. The streamwise, wall-normal and spanwise directions are denoted by x, y, z. The governing equations of incompressible fluid are the Navier-Stokes and continuity equations. The streamwise and spanwise widths of the computational domain are $L_x = 2.5\pi\delta$ and $L_z = \pi\delta$, respectively, where δ is the channel half depth. The Reynolds number based on the friction velocity u_τ in the uncontrolled flow and δ is set to be $Re_\tau = u_\tau\delta/\nu = 150$ throughout of this work. Regardless of the presence of control, the flow rate is kept constant, so that the wall friction decreases when an applied control is successful. Periodic boundary conditions are applied in x and z directions, whereas the no-slip condition, i.e., $u = w = 0$, are used for the tangential velocity components at top and bottom walls. As for the wall-normal velocity on the wall, it is also set to be zero for the uncontrolled case, whereas the zero-net-mass-flux wall blowing/suction ϕ is applied as a control input. The fluid governing equations are solved by a pseudo-spectral method. The present code has been validated in simultaneous suboptimal control of wall friction drag and heat transfer [3], and then extended to apply the optimal control theory [4].

As a reference case, the opposition control[2] is considered. In this case, the control input, i.e., wall blowing/suction, is determined so that it opposes to the wall-normal velocity fluctuation at a prescribed distance from the wall. The wall distance of the sensing location is set to be $y^+ = 15$, which is optimal at the present Reynolds number, where the cross represents a value in wall unit. In the case of the optimal control, we first define a cost functional J as follows:

$$J = \int_0^T \int_{d\Omega} \left(-\frac{1}{Re_\tau} \frac{\partial \overline{u}}{\partial y} n_2 + \alpha \phi^2 \right) dS dt, \tag{1}$$

where $d\Omega$ is the wall boundary of the computational domain, and n_j is the unit outer-normal vector on $d\Omega$. Obviously, the first term is the wall friction integrated over an entire wall and within a time horizon T. The second term corresponds to the cost of control, where the weight coefficient α is set to be unity in this study. The optimization procedure is essentially the same as those reported in [1] and [4]. In all controlled cases, we start applying control at $t = 0$. In the case of the optimal control, the time horizon, in which the control input is optimized, is systematically changed as $T^+ = 50, 100, 150$ and 200, which are referred as T50, T100, T150 and T200, respectively.

*Corresponding author. Email: yukkam@iis.u-tokyo.ac.jp. ysk@iis.u-tokyo.ac.jp

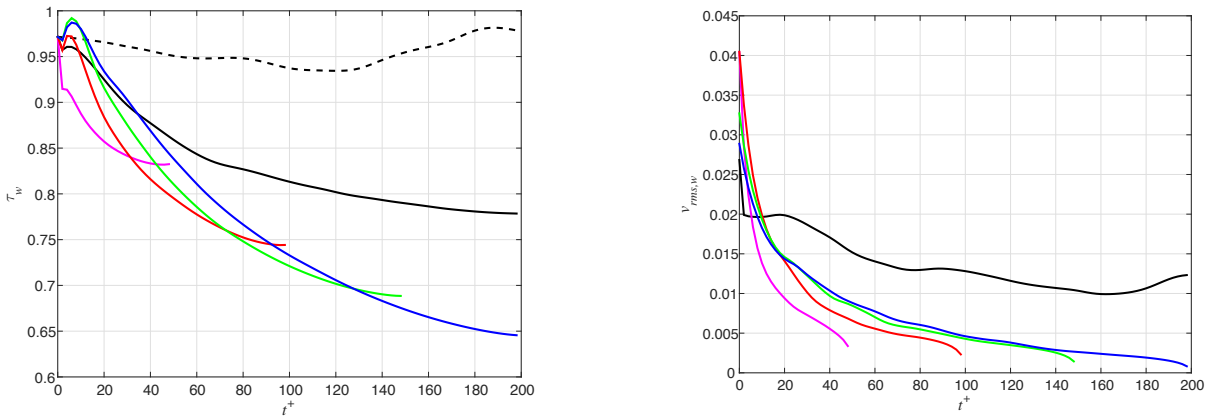

Figure 1: Time traces of Left) the wall shear stress; right) root-mean-square of blowing velocity after applying control at $t^+ = 0$. Magenta, T50; red, T100; green, T150; blue, T200. Solid black, the opposition control; broken, the uncontrolled.

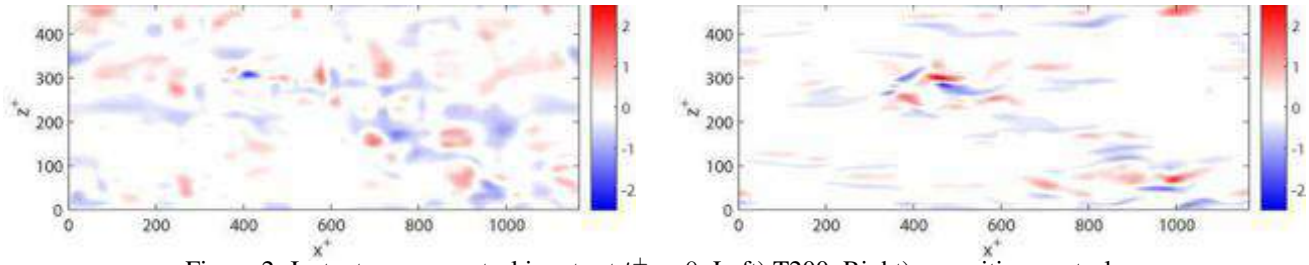

Figure 2: Instantaneous control inputs at $t^+ = 0$. Left) T200; Right) opposition control.

RESULTS

The time histories of the wall shear stress in the uncontrolled and controlled cases are plotted in Fig. 1. It should be noted that all controls are applied to the exactly same initial flow field at $t^+ = 0$. As the initial flow condition, a fully developed turbulent state is used. The optimal control commonly achieves higher drag reduction than the opposition control for all time horizons considered. It is also found that a longer time horizon results in higher drag reduction. A closer look around $t^+ \approx 10$ reveals that the wall friction of T50 achieves larger drag reduction compared to the opposition control, while the other cases enhance the drag. Specifically, the wall friction in T150 and T200 are even larger than the uncontrolled value at the begging of the control, and then rapidly reduced after $t^+ > 20$ The time traces of the root-mean-square of the input wall-normal velocity are shown in Fig. 1. It is found that the optimal control generates strong blowing/suction at the very beginning of the control, i.e., $t^+ < 10$ and then the control inputs are attenuated drastically with time. On the other hand, the intensity of the control input in the opposition control does not change significantly in time, since it is always applied to oppose the wall normal velocity fluctuation at a detection plane. These results indicate that the there is a clear difference between the drag reducing mechanisms of the optimal and opposition controls. Finally, the instantaneous control inputs at the bottom wall in the optimal control T200 and the opposition control at $t_0^+ = 0$ are compared in Fig. 2. The control input in the opposition control has a streamwise-elongated structure, which corresponds to the presence of the quasi-streamwise vortices close to the wall. In contrast, the optimal control input has wider structures in the spanwise direction. These two control inputs are not entirely different, since the correlation coefficient between them is around 0.3. Nonetheless, the clear difference suggests different control mechanisms. In the final presentation, we will investigate the drag reduction mechanisms of the optimal control through detailed comparison between the control inputs in the opposition and optimal controls.

References

[1] Bewley, T.R., Moin, P., Temam, R.: DNS-based predictive control of turbulence: an optimal benchmark for feedback algorithms. J. Fluid Mech. 447: 179-225, 2001.

[2] Choi, H., Moin, P., Kim, J.: Active turbulence control for drag reduction in wall bounded flows. J. Fluid Mech. 262: 75-110, 1994.

[3] Hasegawa, Y., Kasagi, N.: Dissimilar Control of Momentum and Heat Transfer in a Fully Developed Turbulent Channel Flow. J. Fluid Mech. 683: 57-93, 2011.

[4] Yamamoto, A., Hasegawa, Y., Kasagi, N.: Optimal Control of Dissimilar Heat and Momentum Transfer in a Fully Developed Turbulent Channel Flow. J. Fluid Mech. 733: 189-220, 2013.

APPLICATION OF THE INTEGRAL LENGTH-SCALE APPROXIMATION TO WALL MODELLED LES

Amirreza Rouhi *[1], Ugo Piomelli[1], and Alexandre Silva-Lopes[2]
[1]*Department of Mechanical and Materials Engineering, Queen's University, Kingston, Ontario, Canada*
[2]*Faculty of Engineering, University of Porto, Porto, Portugal*

Summary We apply the Integral Length-Scale Approximation (ILSA) model [Piomelli et al., J. Fluid Mech., 766, 2015] in Wall-Modelled Large-Eddy Simulations. In the ILSA model the length scale used for the eddy viscosity is defined in terms of the integral scale, rather than the grid-size, as is common practice. The only model coefficient is determined by prescribing a target value of the contribution of subfilter-scales (SFS) to the turbulent stresses, called "SFS activity". By increasing the SFS activity near the wall, the model correctly represents the gradual transition from an LES, away from the wall, to a RANS-like model near the wall, where the grid is of the same order as the integral length scale, and all eddies become subfilter scale. The modified model was applied to channel flow at $Re_\tau = 5 \times 10^3$, 5×10^4, 5×10^5 using various resolutions and predicted the DNS data and log-law very well.

In large eddy simulation the governing equations are filtered with an assigned filter width, Δ, to separate the fields between resolved and unresolved (subfilter) scales as a function of the filter-width. The nonlinear nature of momentum equations results in additional stress terms, here called subfilter-scale (SFS) stresses. The SFS stresses are usually modelled using an eddy-viscosity hypothesis which depends on the filter width, Δ. In most LES simulations it is related to the local grid size, h, *i.e.* $\Delta \propto h$. This choice causes various shortcomings, extensively explained in Ref. [1].

Piomelli *et al.* [1] proposed an alternative definition of Δ, decoupled from the grid, and is proportional to the integral length-scale, $L_{\rm est}$ (Integral Length-Scale Approximation, ILSA). $L_{\rm est}$ is estimated based on the resolved turbulent kinetic energy (TKE) and total dissipation. The single model parameter, C_k, is determined based on the contribution of SFS to the turbulent stresses, called SFS activity. Two formulations were derived based on the volume averaged or local SFS activity [2].Here, we extend the application of the localized ILSA model to wall-modelled LES (WMLES). WMLES is an approach in which the inner layer scales (which demand most of computational power) are by-passed and only the outer flow eddies, that scale like the boundary layer thickness (or channel half-width), are resolved. Then the effect of the by-passed wall layer, reflected as a momentum flux at the wall, is modelled.

In this work we solve the filtered Navier-Stokes equations in an open channel with periodic conditions in streamwise and spanwise direction, and a symmetry condition at the top boundary. Since the grid is too coarse to resolve the near-wall eddies, we use approximate boundary conditions [3]. In particular, we employ the logarithmic law approach, requiring that the average velocity at the first grid point satisfies the logarithmic law. Then the averaged wall shear-stress, $\langle \tau_w \rangle$, is calculated from the log-law and is used to update the instantaneous streamwise and spanwise wall shear-stress which then are imposed as slip boundary conditions at the wall. The impermeability condition is imposed on the normal velocity.

In ILSA the eddy viscosity used to parametrize the SFS stresses is defined as:

$$\nu_{\rm sfs} = C_k^2 \frac{\langle \mathcal{K}_{\rm res} \rangle^3}{\langle \varepsilon_{\rm tot} \rangle^2} \left| \overline{S} \right| \tag{1}$$

where $\mathcal{K}_{\rm res} = \overline{u}_i' \overline{u}_i'/2$ and $\varepsilon_{\rm tot} = 2\left(\nu + \nu_{\rm sfs}\right) \overline{s}_{ij}' \overline{s}_{ij}'$ are the resolved TKE and dissipation, respectively. $\left|\overline{S}\right| = \left(\overline{S}_{ij}\overline{S}_{ij}\right)^{1/2}$ is the strain-rate magnitude of the resolved field. The model parameter, C_k, is determined based on the following formulation for SFS activity which quantifies the contribution of SFS to turbulent stresses, denoted as s_τ:

$$s_\tau = \left[\frac{\left\langle \tau_{ij}^a \tau_{ij}^a \right\rangle}{\left\langle \left(\tau_{mn}^a + R_{mn}^a\right)\left(\tau_{mn}^a + R_{mn}^a\right) \right\rangle} \right]^{1/2}, \tag{2}$$

where

$$R_{mn}^a = \overline{u}_m' \overline{u}_n' \circ \frac{\delta_{mn}}{3} \overline{u}_k' \overline{u}_k', \quad \tau_{ij}^a = \tau_{ij} \circ \frac{\delta_{ij}}{3} \tau_{kk} = \circ\, 2\nu_{\rm sfs} \overline{S}_{ij}. \tag{3}$$

The user assigns a desired value of s_τ, and the model coefficient C_k is calculated dynamically by solving (2) (which can be recast as a quadratic equation for C_k^2). The averaging operation, $\langle ... \rangle$, in (2) is local (Eulerian/Lagrangian time frame, homogeneous directions); here, for open channel flow, plane averaging is used [2]. In WMLES the grid, near the wall, is insufficient to resolve even the largest eddies. Therefore, the simulation effectively becomes a solution of the Reynolds-Averaged Navier-Stokes (RANS) equations. In this region the SFS activity must be increased (to reach 1 at the wall) to

*Corresponding author. Email: amirreza.rouhi@queensu.ca

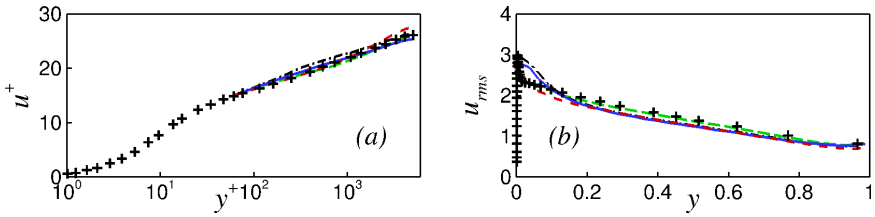

Figure 1: Application of wall-modelled ILSA on channel flow at $Re_\tau = 5 \times 10^3$ with $s_\tau^{\text{in}} = 0.02$. *(a)* mean velocity; *(b)* u_{rms} normalized by u_τ. ——— $64 \times 20 \times 32$; -·-· $64 \times 40 \times 32$; ——— $64 \times 40 \times 64$; - - - $128 \times 40 \times 64$; + DNS [4]

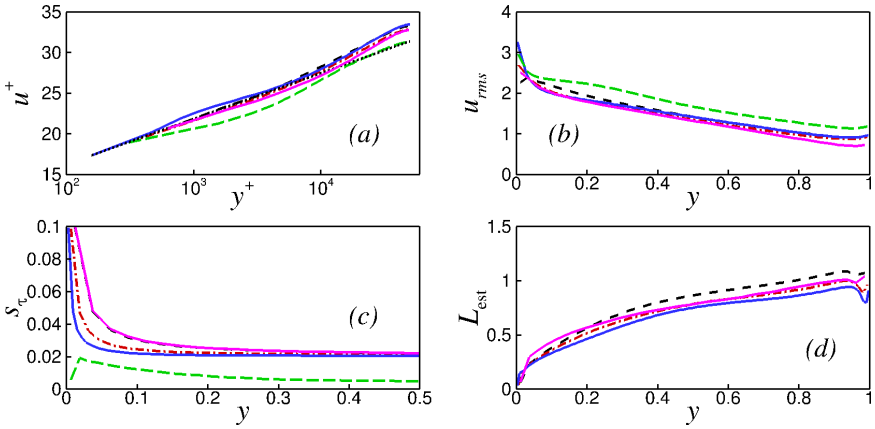

Figure 2: Application of wall-modelled ILSA on channel flow at $Re_\tau = 5 \times 10^4$ with $s_\tau^{\text{in}} = 0.02$. *(a)* mean velocity; *(b)* u_{rms}; *(c)* s_τ; *(d)* L_{est}. Wall-modelled ILSA: ——— $128 \times 40 \times 64$; - - - $256 \times 40 \times 128$; -·-· $256 \times 80 \times 128$; ——— $256 \times 160 \times 128$. Dynamic model: ——— $256 \times 80 \times 128$. Log-law: ····· .

account for the increased contribution of the unresolved eddies to the transport of momentum. The following distribution of s_τ for wall-modelled ILSA is used:

$$s_\tau(y) = s_\tau^{\text{in}} + \frac{1 \circ s_\tau^{\text{in}}}{y/D + 1} \tag{4}$$

where y is the normal distance to the wall, s_τ^{in} is the value of s_τ far away from the wall ($y > 20D$). The fitting hyperbola (4) bridges between a RANS like simulation at $y = 0$ to a well-resolved LES at $y \simeq 20D$. Numerical experiments suggested the use of $D = 0.1y_1$, where y_1 is the centre of first grid cell, which implies that the simulation is in RANS mode only for the first two or three grid cells.

The proposed model was applied on open-channel flow at $Re_\tau = 5 \times 10^3, 5 \times 10^4, 5 \times 10^5$; the domain size for all simulations was $(6\delta, \delta, 3\delta)$ with a uniformly distributed grid. Results at $Re_\tau = 5 \times 10^3$ are compared against DNS data [4] in Figure 1 for several grid resolutions. All the simulations predict the mean velocity accurately. For u_{rms}, agreement with DNS appears for $y > 0.2$ corresponding to $s_\tau < 0.025$ which falls within the resolved LES zone.

Figure 2 shows the application of wall-modelled ILSA and dynamic eddy-viscosity model [5] at $Re_\tau = 5 \times 10^4$. All cases with ILSA model performed accurately while the dynamic model results in incorrect prediction of log-law. This is due to the poorly resolved flow field near the wall and thus under-prediction of the dynamic model parameter. Using ILSA, as the number of grid points is increased in the normal direction, near-wall resolution is improved and the fitting hyperbola decays faster from the wall (due to decreasing D), to reduce the size of the RANS region close to the wall. Calculations at $Re_\tau = 5 \times 10^5$ (not shown here) revealed that the model is accurate for $0.01 \leq s_\tau^{\text{in}} \leq 0.03$, which is the same range observed in wall-resolved LES. Application of wall-modelled ILSA on high Reynolds number separating boundary layer is ongoing.

References

[1] Piomelli U., Rouhi A., and Geurts B. J.: A Grid-Independent Length Scale for Large-Eddy Simulations. J. Fluid Mech. 766, 499-527, 2015.

[2] Rouhi A., Piomelli U., and Geurts B. J.: A Dynamic Subfilter-Scale Stress Model for Large Eddy Simulations based on Physical Flow Scales. 15th European Turbulence Conference, Delft, Netherlands, 2015.

[3] Piomelli U., and Balaras E.: Wall Layer Models for Large-Eddy Simulations. Annu. Rev. Fluid Mech. 34:34974, 2002.

[4] Lee M., and Moser R. D.: Direct Numerical Simulation of Turbulent Channel Flow up to $Re_\tau \approx 5000$. J. Fluid Mech. 774, 395-415, 2015.

[5] Germano M., Piomelli U., Moin P., and Cabot W. H.,:A Dynamic Subgrid-Scale Eddy Viscosity Model, Physics of Fluids. 3, 7, 1760-1765, 1991.

SIMULATION AND MODELING OF EXTENDED WIND-FARMS

Richard J.A.M. Stevens [*1], Luis A. Martínez Tossas[2], Dennice Gayme[2], and Charles Meneveau[2]
[1]*Department of Science and Technology and J.M. Burgers Center for Fluid Dynamics, University of Twente, The Netherlands*
[2]*Department of Mechanical Engineering, The Johns Hopkins University, USA*

Summary We present a comparison between large eddy simulations (LES) using an actuator disk or an actuator line method with wind tunnel measurements performed at EPFL to analyze the accuracy of different wind turbine modeling approaches. We observe a very good agreement between the simulation results and wind tunnel measurements. We find that even on relatively coarse grids including the turbine nacelle improves the accuracy, compared to the wind tunnel data, of the flow profiles just behind the turbine in the LES. Subsequently, we use these LES to simulate the turbulent flow in extended wind-farms with very large inter turbine spacings. These LES results are compared to analytical predictions for the performance of different wind-farm configurations obtained from the Coupled Wake Boundary Layer (CWBL). We show that the CWBL model reproduces the LES results for many conditions and discuss the observed discrepancies.

INTRODUCTION

Wind turbines interact with the environment over a wide range of length scales ranging from millimeters (viscous scales) and meters (wakes and tip vortices) up to "geophysical scales" of hundreds of meters (inter-turbine spacing) to kilometers (windfarms). The large scale separation makes analysis and design of windfarms challenging from both a theoretical and a numerical perspective. However, a detailed understanding of the relevant physics is critical for efficient windfarm designs. In this work we first present a validation of a detailed large eddy simulation (LES) wind-farm modeling approach against wind tunnel measurements. Subsequently, this LES model is used to obtain data for different wind-farm configurations to validate the analytical Coupled Wake Boundary Layer (CWBL) model that can be used to get a very fast estimate of the wind-farm performance for many conditions.

COMPARISON LES WITH WIND TUNNEL MEASUREMENTS

To simulate wind-farms we use a LES code which solves the filtered Navier-Stokes Equations using a pseudo-spectral scheme in the two horizontal directions and second-order finite differencing in the vertical direction. The subgrid-scale model that is used is the scale-dependent Lagrangian dynamic model [2]. The turbines are modeled using an actuator disk or an actuator line method. Figure 1 [3] compares LES results obtained using an actuator line model to represent the turbines with wind

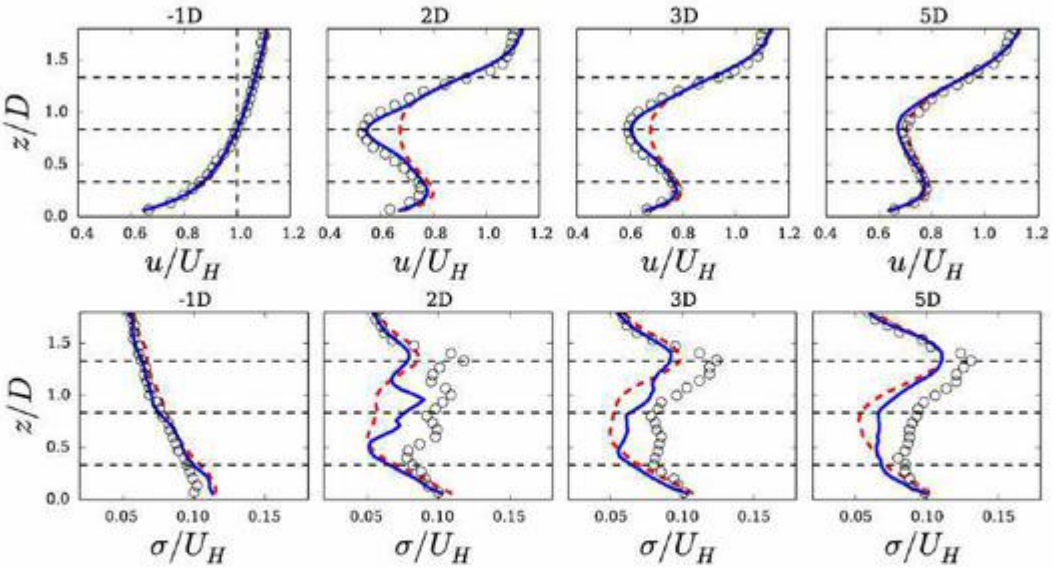

Figure 1: Comparison of the mean streamwise velocity (top panels) and turbulence intensity (lower panels) profiles as a function of height for different streamwise locations behind the turbine. The circles are data from a wind tunnel experiment by Chamorro and Porté-Agel [1]. The blue and red lines indicate actuator line model LES results with and without the modeling of a nacelle.

*Corresponding author. Email: r.j.a.m.stevens@utwente.nl

tunnel measurements performed at EPFL [1]. A comparison with the measurement data reveals that even on a relatively coarse grid including the nacelle, which is not a standard procedure, significantly improves the agreement between the LES and the wind tunnel data.

COUPLED WAKE BOUNDARY LAYER MODEL

With an experimentally validated LES mode available, it is possible to use it in development and testing of simpler, engineering wind-farm models. Two common wind-farm modeling approaches are wake models and the top-down model. Wake models [4] approximate the growth of velocity deficits behind each turbine as linear and account for wake-wake interactions through superposition of squared velocity deficits. This approach captures the entrance effects well, but is less accurate in modeling the deep-array effects. Top-down models [5] are able to capture the coupling between the wind-farm and the atmospheric boundary layer, but do not capture the effects of relative turbine positioning. The CWBL model [6] introduces a two-way coupling between these approaches and provides improved predictions over its constitutive models.

To test the CWBL model under conditions where it has not yet been evaluated, we model turbulent flow in wind-farms that consist of a regular array of wind turbines. We consider wind-farms with ten (or more) rows in the streamwise direction in order to study the fully developed regime. This number of turbine rows ensures that the power output of the later rows is approximately constant in both aligned and staggered wind-farm configurations. The distances between wind turbines are s_xD and s_yD, where D is the turbine diameter, in the streamwise and spanwise directions, respectively. We vary the streamwise spacing in the range $\sim [3.5, 36]$ and the spanwise spacing in the range $\sim [3.5, 12]$ and consider different combinations of these spacings in these parameter ranges. The inflow in our simulations is obtained using a concurrent-precursor method [7] and the turbines are represented by an area averaged actuator disk model using a constant thrust coefficient C_T, which is representative of turbines operating in region II. Figure 1 shows a sample comparison of LES and CWBL model predictions. The various comparisons to be presented show that the CWBL model reproduces the LES results under many conditions. Conditions under which discrepancies exist are also identified and discussed.

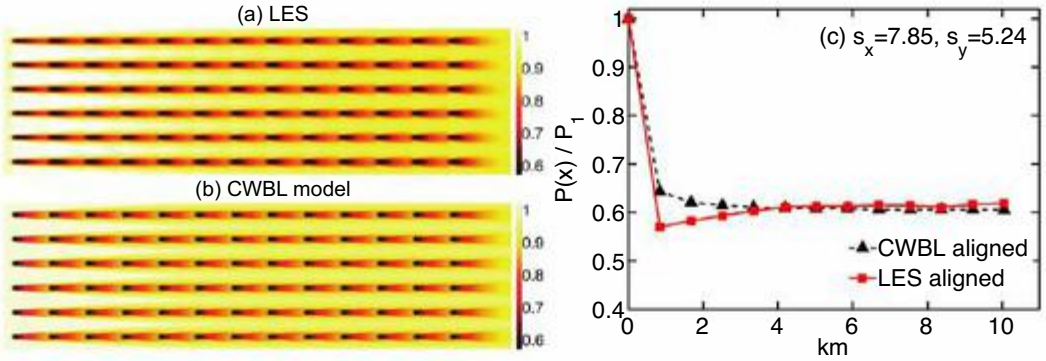

Figure 2: Normalized velocities at hub-height obtained in (a) LES and from (b) the CWBL model for an aligned wind-farm with $s_x = 7.85$ and $s_y = 5.24$. (c) Corresponding normalized power output $P(x)/P(1)$ development. Figure from Ref. [6].

ACKNOWLEDGMENTS

RJAMS's work is supported by the program 'Fellowships for Young Energy Scientists' (YES!) of the Foundation for Fundamental Research on Matter (FOM), which is financially supported by the Netherlands Organization for Scientific Research (NWO). CM, DG and LAMT are supported by the US National Science Foundation from grant IIA 1243482 (the WINDINSPIRE project).

References

[1] L. P. Chamorro and F. Porté-Agel, Bound-Lay. Meteorol. **136**, 515 (2010).
[2] E. Bou-Zeid, C. Meneveau, and M. B. Parlange, Phys. Fluids **17**, 025105 (2005).
[3] L. A. Martínez-Tossas, R. J. Stevens, and C. Meneveau, submitted to AIAA (2016).
[4] N. O. Jensen, Risø-M-2411, Risø National Laboratory, Roskilde (1983).
[5] S. Frandsen *et al.*, Wind Energy **9**, 39 (2006).
[6] R. J. A. M. Stevens, D. F. Gayme, and C. Meneveau, J. Renewable and Sustainable Energy **7**, 023115 (2015).
[7] R. J. A. M. Stevens, J. Graham, and C. Meneveau, Renewable Energy **68**, 46 (2014).

BLASIUS-TYPE FRICTION EQUATION FOR YIELDING FLUIDS BASED ON EXTENDED KOLMOGOROV MICROSCALES

Hamidreza Anbarlooei[1], Cecilia M.M. Santos[2], Daniel O.A. Cruz *[3], and Atila P. Silva Freire[4]
[1,2,3,4]*Mechanical Engineering Program (PEM/COPPE), Universidade Federal do Rio de Janeiro,C.P. 68503, 21941-972, Rio de Janeiro, Brazil*

Summary In previous works [1-2], the extension of the Kolmogorov K41 theory for purely viscous power-law fluids was developed. In the present work, the same procedure is used to find Kolmogorov microscales for yielding fluids. This idea is applied for Bingham plastic rheology and the related scales are derived. As a direct application a friction equation is developed for Bingham fluids by relating the purposed velocity scale and friction factor using a phenomenological model for turbulence. Comparing the new Blasius-type friction equation with experimental results shows a good agreement.

INTRODUCTION

Turbulent flow of purely viscous non-Newtonian (PVNN) fluids is present in many industrial applications. Typical examples are the transport of some polymeric substances, sewage sludges, coal, china clay and many other mineral suspensions. Despite its great engineering importance, only few works have been dedicated in literature to this topic.

Recently, authors have developed an extended version of the Kolmogorov K41 theory for purely viscous non-Newtonian fluids [1-2]. The purpose of the current paper is to extend further this idea into yielding fluids. Also, using the phenomenological turbulence model of Gioia and Chakaborty [3], it is possible to related Kolmogorov microscales to friction. Using this model, a Blasius-type friction equation was developed for Newtonian [3] and non-Newtonian (Power-Law) fluids [1]. The second part of this paper is dedicated to develope such an equation for Bingham fluids. To our knowledge there is no such a theoretical equation in the literature.

KOLMOGOROV SCALES

For the sake of simplicity, in the reminder of this paper only Bingham rheology is considered. This model is expressed as $\tau = \tau_y + \mu_\infty \dot{\gamma}$ where τ_y stands for the yield stress, μ_∞ is plastic viscosity and $\dot{\gamma}$ is shear rate. It should be emphasized here that in the turbulent flow yielding fluid, it is believed the stress is higher than yielding limit in any point or at least, thixotropy of the fluid do not let the plug micro-regions to form [4]. Thus the unyielded situation is removed from the rheological model considered here.

The starting point of Kolmogorov's theory is Richardson's notion of energy cascade [1]. Based on experimental and numerical evidences it can be assumed that this picture of energy transfer through eddies remains same for PVNN fluids.

K41 theory is based on three important hypotheses combined with dimensional arguments and experimental observations. It is clear that the first hypotheses (local isotropy of turbulence) is still valid in turbulent flow of PVNN fluids. However, first similarity hypotheses should be changed as *in every turbulent flow at sufficiently high Reynolds number, the statistics of the small scale motions (micro-scales) have a universal form that is uniquely determined by ε (dissipation rate), and rheological properties of the fluid (τ_y and μ_∞)*. Finally Kolmogorovs second similarity hypothesis states that in every turbulent flow at sufficiently high Reynolds number, the statistics of the motions of scale l in the range $l_0 \gg l \gg \eta$ have a universal form that is uniquely determined by ε independent of viscosity. Because of independency on viscosity, this hypotheses remains unchanged for PVNN fluids.

To complete our extension of Kolmogorov Hypothesis, we just need to provide the relation between ϵ, τ_y and μ_∞ (Kolmogorov micro-scales). To do this, we start from dissipation. Generally, dissipation can be expressed as $\epsilon = \tau S$, where ϵ and $S(\sim \dot{\gamma})$ stand for dissipation and strain rate, respectively. Using Bingham model, we will have $\epsilon = (\tau_y + \mu_\infty \dot{\gamma})\dot{\gamma}$ where at dissipation range this can be approximated by $\epsilon = (\tau_y + \mu_\infty \frac{u}{l})(\frac{u}{l})$ where u and l are dissipation velocity and length. Combining this with dissipation calculated from integral scale (U^3/L), we will have:

$$\frac{U^3}{L} = \left(\tau_y + \mu_\infty \frac{u}{l}\right)\left(\frac{u}{l}\right) \tag{1}$$

It is logical to assume (same as Newtonian fluids) that in the limit of Kolmogorov scales, the local Reynolds number is equal to one. For the Bingham fluid , the local viscosity can be expressed as $\mu = \tau/\dot{\gamma} = \mu_\infty + \tau_0 \frac{l}{u}$. Using equations (1) and $Re_{local} = 1$, one can obtain velocity scale as following

$$\frac{u_\eta}{U} = \sqrt{\frac{\sqrt{\frac{He^2}{Re^4} + \frac{4}{Re}} + \frac{He}{Re^2}}{2}} \tag{2}$$

*Corresponding author. Email: doac@mecanica.coppe.ufrj.br

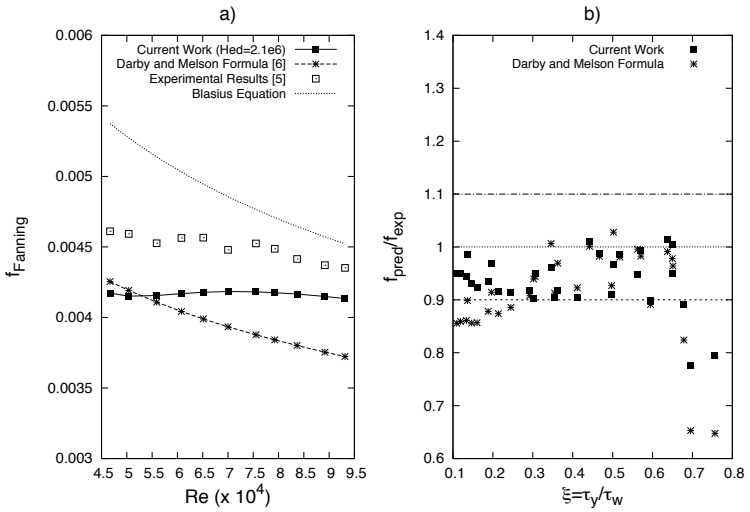

Figure 1: Comparison of Relative error of predictions of purposed formula with Darby-Melson and Blasius equations.

where $Re = \frac{\rho U L}{\mu_\infty}$ is the bulck flow Reylonds number and He is the Hedstrom number defined as $\frac{\rho \tau_y L^2}{\mu_\infty^2}$.

Friction Equation

Thanks to phenomenological theory developed by Gioia and Chakaborty [3], the Kolmogorov micro-scales can be related to friction factor [1-3]. Here we extend this idea to yielding fluids.

To derive an expression for τ_w, the shear stress at the wall, we follow the procedure set forward in [3]. We consider that the momentum transfer through the near the wall viscous layer balances wall shear stress and also yield stress of the fluid. On top of this layer, fluid has a high velocity which scales with U. However, in the viscous layer, the axial momentum transfer is negligible so that the net rate of momentum transfer is due to the normal velocity, which is induced by the small eddies. Thus, the stress scales as $\tau_w = \tau_w^{fluid} + \tau_y \sim \rho U u_n$, where u_n is the velocity of the dissipating eddies, which will be assumed equal to u_η. Combinign this idea with the velocity scale of the previous section, it easy to show

$$f_{fluid} = \frac{8\tau_w^{fluid}}{\rho U^2} = C(\xi)\sqrt{\frac{\sqrt{\frac{He^2}{Re^4} + \frac{4}{Re}} + \frac{He}{Re^2}}{2}} - 8\frac{He}{Re^2} \tag{3}$$

where f_{fluid} is Darcy friction factor and $C(\xi)$ is assumed to be equal to 0.316 for Newtonian case ($\xi = 0$) to comply with Blasius equation. Simple comparison with experimental data shows that C is not strong function of ξ at least for low values of ξ. So, it is assumed to be constant equal to 0.316 here. The accuracy of the predictions of equation (3) is compared with experimental results of [5], in Figure 1. For the sake of comparison, results obtained with the empirical equation of Darby and Melson [6] are also shown in this figure. This limited test seems to indicate that our analytic formula preforms even better than purely empirical equation Darby and Melson [6] (The maximum error of new equaiton is less than 10%, where the empirical equation shows up to 15% deviation from experimental results). However, further experimental evidence remains necessary for a final judgement. It is also interesting to note that developed equation approaches Blasius equation in the limit as expected, while Darby and Melson [6] equation does not.

References

[1] Anbarlooei H.R., Cruz D.O.A., Ramos F., Silva Freire A.P.: Phenomenological Blasius-Type Friction Equation for Turbulent Power-Law Fluid Flows. Phys. Rev. E 92:063006,2015.

[2] Anbarlooei H.R., Cruz D.O.A., Silva Freire A.P.: A Blasius Type Friction Equation for Purely Viscous non-Newtonian Fluid. 15th European Turbulence Conference, Netherlands 2015.

[3] Gioia G., Pinaki Chakraborty: Turbulent Friction in Rough Pipes and the Energy Spectrum of the Phenomenological Theory. Phys. Rev. Lett., 96:044502, 2006.

[4] Frigaard I.A., Howison S.D., Sobey I.J.: On the Stability of Poiseuille Flow of a Bingham Fluid. J. Fluid Mech. 263:133150, 1994.

[5] Bartosik A.: Simulation of the Friction Factor in a Yield-stress Slurry Flow which Exhibits Turbulence Damping Near the Pipe Wall. J. Theor. App. Mech. 49:283-300, 2011.

[6] Darby R., Melson J.: How to Predict the Friction Factor for Flow of Bingham Plastics. Ch.E. 28:5961, 1981.

ENERGY TRANSFER BETWEEN ION CYCLOTRON AND WHISTLER MODES IN HALL MAGNETOHYDRODYNAMIC TURBULENCE

Keisuke Araki*[1] and Hideaki Miura[2]

[1]*Okayama University of Science, 1-1 Ridai-cho, Kita-ku, Okayama 700-0005, Japan*
[2]*National Institute for Fusion Science, Toki, Gifu 509-5292, Japan*

Summary Using the generalized Elsasser variables expansion, we investigated the energy transfer by the interaction between ion cyclotron and whistler modes in fully developed turbulence of an incompressible Hall magnetohydrodynamic plasma. Asymmetry of energy budget between the ion cyclotron and whistler modes, i.e., energy transfer which tend to break chiral symmetry is observed.

INTRODUCTION

In the present study, we attempt to apply the analytical mechanical viewpoint to the results of direct numerical simulation (DNS) of fully developed turbulence of an incompressible Hall magnetohydrodynamic (HMHD) plasma. During Lagrangian mechanical analysis of the invariant action for the ideal, incompressible HMHD system, we found helicity-based particle-relabeling operator[1]. The eigenfunctions of this operator are double Beltrami flows (DBF), i.e., force-free stationary solutions to the equation of motion[2]. It was also shown that they provide a family of orthogonal function bases that yields the spectral representation of the equation of motion with a remarkably simple form. Among the DBFs, considering the influence of a uniform background magnetic field and the Hall term effect vanishing limit, the generalized Elsasser variables (GEV), which was introduced by Galtier to formulate the closure problem [3], are found to be the most suitable for avoiding problems with singularities in the standard magnetohydrodynamic limit. We developed the GEV application procedure to DNS datasets and calculated the energy spectra and transfer functions of the ion cyclotron and whistler modes[4]. However, the detailed analysis of transfer functions were left unresolved, because the analysis method that guaranteed the detailed energy balance was not established.

BASIC EQUATIONS AND CONSIDERATION ON THE QUADRATIC TERMS

The time development of an incompressible HMHD plasma motion is determined by the following equation: $\partial_t \vec{\boldsymbol{Z}} + (\vec{\boldsymbol{Z}} \circ \tilde{\nabla})\vec{\boldsymbol{Z}} = D\vec{\boldsymbol{Z}}$, where $\vec{\boldsymbol{Z}} := (\boldsymbol{V}, \boldsymbol{B})$ is a pair of velocity and magnetic fields; hereafter, called $\vec{\boldsymbol{Z}}$-variables. The quadratic and dissipation terms are respectively defined by:

$$(\vec{\boldsymbol{Z}}_1 \circ \tilde{\nabla})\vec{\boldsymbol{Z}}_2 \;=\; \frac{1}{2}\begin{pmatrix} \boldsymbol{\Omega}_1 \times \boldsymbol{V}_2 - \boldsymbol{V}_1 \times \boldsymbol{\Omega}_2 - \nabla \times (\boldsymbol{V}_1 \times \boldsymbol{V}_2) + \boldsymbol{B}_1 \times \boldsymbol{J}_2 - \boldsymbol{J}_1 \times \boldsymbol{B}_2 - \nabla P_V \\ \nabla \times (\boldsymbol{B}_1 \times (\boldsymbol{V}_2 - \alpha \boldsymbol{J}_2) - (\boldsymbol{V}_1 - \alpha \boldsymbol{J}_1) \times \boldsymbol{B}_2) - \boldsymbol{J}_1 \times \boldsymbol{V}_2 - \boldsymbol{V}_1 \times \boldsymbol{J}_2 + \alpha \boldsymbol{J}_1 \times \boldsymbol{J}_2 - \nabla P_B \end{pmatrix} \quad (1)$$

$D\vec{\boldsymbol{Z}} = (\nu\triangle\boldsymbol{V}, \kappa\triangle\boldsymbol{B})$, where $\boldsymbol{\Omega}$, $\boldsymbol{J}$, P_V, P_B, α, ν, and η are vorticity ($\boldsymbol{\Omega} = \nabla \times \boldsymbol{V}$), current field ($\boldsymbol{J} = \nabla \times \boldsymbol{B}$), generalized pressures to satisfy the divergence-free conditions, the Hall term strength parameter, kinematic viscosity, and resistivity, respectively. The expressions of quadratic terms in Eq. (1) are determined by postulating that the bilinear operator $(* \circ \tilde{\nabla})*$ is given by a linear combination of the Riemannian metric and the Lie bracket: $\big\langle \vec{\boldsymbol{Z}}_3 \big| (\vec{\boldsymbol{Z}}_1 \circ \tilde{\nabla})\vec{\boldsymbol{Z}}_2 \big\rangle_Z = C_1 \big\langle \vec{\boldsymbol{Z}}_1 \big| \big\{ \vec{\boldsymbol{Z}}_2, \vec{\boldsymbol{Z}}_3 \big\} \big\rangle_Z + C_2 \big\langle \vec{\boldsymbol{Z}}_2 \big| \big\{ \vec{\boldsymbol{Z}}_3, \vec{\boldsymbol{Z}}_1 \big\} \big\rangle_Z + C_3 \big\langle \vec{\boldsymbol{Z}}_3 \big| \big\{ \vec{\boldsymbol{Z}}_1, \vec{\boldsymbol{Z}}_2 \big\} \big\rangle_Z$, (the definitions of the symbols $\big\langle * \,\big|\, * \big\rangle_Z$ and $\big\{*, *\big\}$ are given in Sect. 3 of Ref. [5]). The coefficients are determined by the following three physical conditions: (1) when the dissipation terms are absent, the evolution equation, $\partial_t \vec{\boldsymbol{Z}} + (\vec{\boldsymbol{Z}} \circ \tilde{\nabla})\vec{\boldsymbol{Z}} = \vec{\boldsymbol{0}}$, agree with the Euler-Lagrange equation of the ideal HMHD system; (2) the detailed energy balance holds; i.e., the Riemannian metric is right-invariant in mathematical terminology: $\big\langle \vec{\boldsymbol{Z}}_3 \big| (\vec{\boldsymbol{Z}}_1 \circ \tilde{\nabla})\vec{\boldsymbol{Z}}_2 \big\rangle_Z + \big\langle (\vec{\boldsymbol{Z}}_1 \circ \tilde{\nabla})\vec{\boldsymbol{Z}}_3 \big| \vec{\boldsymbol{Z}}_2 \big\rangle_Z = 0$; (3) the substantial derivative operator $\partial_t + (\vec{\boldsymbol{Z}} \circ \tilde{\nabla})$ is Galilean invariant.

GENERALIZED ELSASSER VARIABLES

In the numerical analysis procedures, velocity and magnetic fields are firstly expanded by the complex helical waves [6], say $\boldsymbol{\phi}_{\sigma_k}(\vec{k})$: $\boldsymbol{V} = \sum \widehat{V}_{\sigma_k}(\vec{k})\boldsymbol{\phi}_{\sigma_k}(\vec{k})$, $\boldsymbol{B} = \sum \widehat{B}_{\sigma_k}(\vec{k})\boldsymbol{\phi}_{\sigma_k}(\vec{k})$, where $\sigma_k = \pm 1$, $\vec{k}$ are the helicity parameter and the wavenumber, respectively. Using these coefficients, we decompose $\vec{\boldsymbol{Z}}$-variables into the generalized Elsasser variables, say $\vec{\boldsymbol{Z}}^{s_k}_{\sigma_k}(\vec{k})$, as follows:

$$\vec{\boldsymbol{Z}}(\vec{x}, t) = \sum \widehat{Z}^{s_k}_{\sigma_k}(\vec{k}; t)\vec{\boldsymbol{Z}}^{s_k}_{\sigma_k}(\vec{k}; \vec{x}), \text{ where } \widehat{Z}^{s_k}_{\sigma_k}(\vec{k}) := \frac{\widehat{V}_{\sigma_k}(\vec{k}) + \lambda^{s_k}_{\sigma_k}(\vec{k})\,\widehat{B}_{\sigma_k}(\vec{k})}{1 + \lambda^{s_k}_{\sigma_k}(\vec{k})^2}, \;\; \vec{\boldsymbol{Z}}^{s_k}_{\sigma_k}(\vec{k}) := \begin{pmatrix} \boldsymbol{\phi}_{\sigma_k}(\vec{k}) \\ \lambda^{s_k}_{\sigma_k}(\vec{k})\boldsymbol{\phi}_{\sigma_k}(\vec{k}) \end{pmatrix},$$

*Corresponding author. Email: araki@are.ous.ac.jp

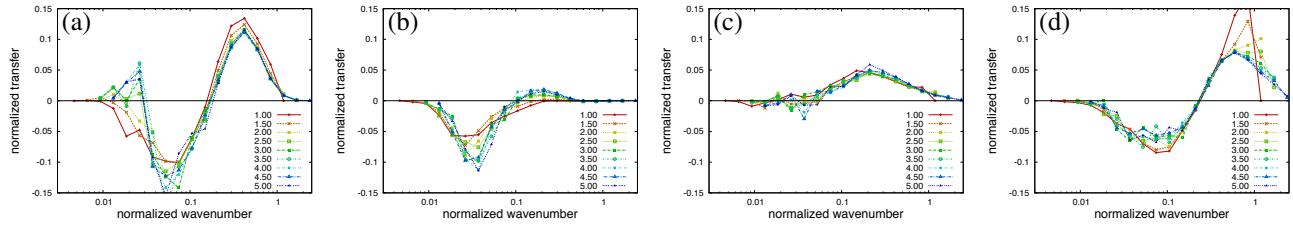

Figure 1: Time development of the energy transfer spectra (a) $-\langle \vec{\boldsymbol{Z}}_j^+ | (\vec{\boldsymbol{Z}} \circ \tilde{\nabla}) \vec{\boldsymbol{Z}}^+ \rangle_Z$, (b) $-\langle \vec{\boldsymbol{Z}}_j^+ | (\vec{\boldsymbol{Z}} \circ \tilde{\nabla}) \vec{\boldsymbol{Z}}^- \rangle_Z$, (c) $-\langle \vec{\boldsymbol{Z}}_j^- | (\vec{\boldsymbol{Z}} \circ \tilde{\nabla}) \vec{\boldsymbol{Z}}^+ \rangle_Z$, and (d) $-\langle \vec{\boldsymbol{Z}}_j^- | (\vec{\boldsymbol{Z}} \circ \tilde{\nabla}) \vec{\boldsymbol{Z}}^- \rangle_Z$.

and $s_k = \pm 1$ is the wave modes defining parameter. The eigenvalues, $\lambda_{\sigma_k}^{s_k}(\vec{k}) = \sigma_k s_k \lambda^{-s_k}$ (where $\lambda = \pi\alpha|\vec{k}| + [(\pi\alpha|\vec{k}|)^2 + 1]^{\frac{1}{2}}$), and the corresponding eigenfunctions, i.e., the GEVs, $\vec{\boldsymbol{Z}}_{\sigma_k}^{s_k}(\vec{k})$, are derived from the linearized dissipationless HMHD equations: $\partial_t \boldsymbol{V} = (\boldsymbol{B}_0 \cdot \nabla)\boldsymbol{B}$, $\partial_t \boldsymbol{B} = (\boldsymbol{B}_0 \cdot \nabla)\big[\boldsymbol{V} - \alpha(\nabla \times \boldsymbol{B})\big]$, where $\boldsymbol{B}_0$ is a uniform background magnetic field. The modes with $\sigma = +1$ (resp. -1) are the *ion cyclotron* waves (resp. the *whistler* waves). The set of these eigenfunctions work as an orthogonal basis of $\vec{\boldsymbol{Z}}$-variable space, even if the background magnetic field is absent ($\boldsymbol{B}_0 = \boldsymbol{0}$). The details of derivation and numerical procedures were described in [4].

NUMERICAL RESULTS

Energy budget is analyzed using the same DNS dataset as Refs. [4], [7], and [8], wherein the details of numerical methods and the principal features of the obtained turbulent snapshots were discussed. The quantities are normalized using the dissipation rate of the magnetic field, say $\epsilon_B(t)$, and the resistivity (η), and shell averaged in the wavenumber space on the intervals, $S_j := \{\vec{k}; 2^{-(j+1)/2} k_\eta(t) < |\vec{k}| < 2^{-j/2} k_\eta(t)\}$ for integers (j) and the characteristic wavenumber of the dissipation range ($k_\eta(t) := (\epsilon_B(t)/\eta^3)^{1/4}$). In the present study, we decompose $\vec{\boldsymbol{Z}}$-variable into the shell band-pass filtered components and the ion cyclotron and whistler modes: $\vec{\boldsymbol{Z}} = \sum_j (\vec{\boldsymbol{Z}}_j^+ + \vec{\boldsymbol{Z}}_j^-)$, where $\vec{\boldsymbol{Z}}_j^{s_k} := \sum_{\vec{k} \in S_j}^{\sigma = \pm 1} \widehat{Z}_{\sigma_k}^{s_k}(\vec{k}; t) \vec{\boldsymbol{Z}}_{\sigma_k}^{s_k}(\vec{k}; \vec{x})$ for $s_k = \pm 1$. We analyzed in the present study the budget equations given by $\partial_t \langle \vec{\boldsymbol{Z}}_j^s | \vec{\boldsymbol{Z}}_j^s \rangle_Z = -\sum_{s'} \langle \vec{\boldsymbol{Z}}_j^s | (\vec{\boldsymbol{Z}} \circ \tilde{\nabla}) \vec{\boldsymbol{Z}}^{s'} \rangle_Z + \langle \vec{\boldsymbol{Z}}_j^s | D \vec{\boldsymbol{Z}}_j^s \rangle_Z$.

As was shown in Ref. [4], the analysis of $\langle \vec{\boldsymbol{Z}}_j^+ | (\vec{\boldsymbol{Z}} \circ \tilde{\nabla}) \vec{\boldsymbol{Z}} \rangle_Z$ and $\langle \vec{\boldsymbol{Z}}_j^- | (\vec{\boldsymbol{Z}} \circ \tilde{\nabla}) \vec{\boldsymbol{Z}} \rangle_Z$ revealed that the energy is transferred from larger scales to smaller scales as a whole irrespective of the wave modes. Using Eq. (1), we decompose the nonlinear transfer as follows: $\langle \vec{\boldsymbol{Z}}_j^+ | (\vec{\boldsymbol{Z}} \circ \tilde{\nabla}) \vec{\boldsymbol{Z}} \rangle_Z = \langle \vec{\boldsymbol{Z}}_j^+ | (\vec{\boldsymbol{Z}} \circ \tilde{\nabla}) \vec{\boldsymbol{Z}}^+ \rangle_Z + \langle \vec{\boldsymbol{Z}}_j^+ | (\vec{\boldsymbol{Z}} \circ \tilde{\nabla}) \vec{\boldsymbol{Z}}^- \rangle_Z$, $\langle \vec{\boldsymbol{Z}}_j^- | (\vec{\boldsymbol{Z}} \circ \tilde{\nabla}) \vec{\boldsymbol{Z}} \rangle_Z = \langle \vec{\boldsymbol{Z}}_j^- | (\vec{\boldsymbol{Z}} \circ \tilde{\nabla}) \vec{\boldsymbol{Z}}^+ \rangle_Z + \langle \vec{\boldsymbol{Z}}_j^- | (\vec{\boldsymbol{Z}} \circ \tilde{\nabla}) \vec{\boldsymbol{Z}}^- \rangle_Z$. The transfers $\langle \vec{\boldsymbol{Z}}_j^+ | (\vec{\boldsymbol{Z}} \circ \tilde{\nabla}) \vec{\boldsymbol{Z}}^- \rangle_Z$ and $\langle \vec{\boldsymbol{Z}}_j^- | (\vec{\boldsymbol{Z}} \circ \tilde{\nabla}) \vec{\boldsymbol{Z}}^+ \rangle_Z$ evaluate the energy budget between the ion cyclotron modes ($\vec{\boldsymbol{Z}}^+$) and the whistler modes ($\vec{\boldsymbol{Z}}^-$), while the other two indicates the redistribution of energy among each of these modes.

In Fig. 1, the time development of these four energy transfer spectra is shown. It is most remarkable that the spectra of $\langle \vec{\boldsymbol{Z}}_j^- | (\vec{\boldsymbol{Z}} \circ \tilde{\nabla}) \vec{\boldsymbol{Z}}^+ \rangle_Z$, which evaluates the energy transfer from the ion cyclotron mode to the whistler mode, have almost stationary and positive functional profile for all the snapshots (see Fig. 1(c)). This implies that the energy is one-sidedly transferred from the ion cyclotron modes to the whistler modes. This suggests that the breaking of chiral symmetry[9] is spontaneous and intrinsic to the HMHD dynamics.

The counterparts of this excitation is given by $\langle \vec{\boldsymbol{Z}}_j^+ | (\vec{\boldsymbol{Z}} \circ \tilde{\nabla}) \vec{\boldsymbol{Z}}^- \rangle_Z$ (see Fig. 1(b)). The functional profile reads that the ion cyclotron mode energy is most actively extracted around $k \sim 0.03 k_\eta$, which corresponds to the peak of energy spectra (see Fig. 1 of Ref. [4]). Besides, the functional profile also tells us that the energy transfer to (or the mode excitation at) smaller scales around $k \sim k_\eta$ is remarkably small compared with the other three transfer functions (see Fig. 1(a), (c), (d)). In other words, the whistler modes practically has no feedback to the ion cyclotron modes in the dissipation range.

As a whole, we observed remarkable asymmetry of the energy transfer, i.e., almost one-way excitation of the whistler modes by the ion cyclotron modes, which leads to chiral symmetry breaking.

References

[1] K. Araki, Physical Review E **92**, 063106 (2015).
[2] S. M. Mahajan and Z. Yoshida, Phys. Rev. Lett. **81**, 4863 (1998).
[3] S. Galtier, Journal of Plasma Physics **72**, 721 (2006).
[4] K. Araki and H. Miura, Plasma Fusion Res. **10**, 3401030 (2015).
[5] K. Araki, Journal of Physics A: Mathematical and Theoretical **48**, 175501 (2015).
[6] F. Waleffe, Physics of Fluids A: Fluid Dynamics (1989-1993) **4**, 350 (1992).
[7] K. Araki and H. Miura, Plasma Fusion Res. **8**, 2401137 (2013).
[8] K. Araki and H. Miura, Plasma Fusion Res. **9**, 3401073 (2014).
[9] R. Meyrand and S. Galtier, Physical review letters **109**, 194501 (2012).

MIXING IN A TURBULENT MULTISCALE FLOW

Pawel Baj *[1], Yasumasa Ito[2], Koji Nagata[3], Yasuhiko Sakai[2], Paul J.K. Bruce[1], and Oliver R.H. Buxton[1]

[1]*Department of Aeronautics, Imperial College London, London, United Kingdom*
[2]*Department of Mechanical Science and Engineering, Nagoya University, Nagoya, Japan*
[3]*Department of Aerospace Engineering, Nagoya University, Nagoya, Japan*

Summary Results of a study examining the mixing of a passive scalar downstream of different single and multiscale turbulence generators (arrays of bars of various thicknesses) are reported in this work. Three different experiments were performed, each consisting of simultaneous velocity and concentration measurements, involving different dye release conditions: a mixing layer (solely in terms of the concentration field, the velocity field was uniform), a single point continuous release and a single point discrete release. The data was used to quantify the different mixing performance of the considered turbulence generators. Some concentration results are further linked to secondary coherent structures revealed during the velocity field analysis.

MULTISCALE FLOWS

Fractal generated turbulence has been widely discussed in the scientific community in recent years. In particular, its potential for mixing enhancement was reported by [1] as a significant increase in the turbulent cross-stream scalar transfer was observed. The authors postulated the concept of a scale-space unfolding (SSU) mechanism which is a plausible physical scenario linking such behaviour to the multiscale nature of the flow. The motivation behind the present work is to verify the SSU idea by providing experimental proof of its existence and quantifying its impact on mixing performance. This is approached via measuring velocity and concentration fields, using particle image velocimetry (PIV) and planar laser induced fluorescence (PLIF) techniques respectively, in the near-wake of a single and multiscale arrays of bars (the setup is shown in figure 1), as the latter can be seen as a canonical example of a multiscale flow.

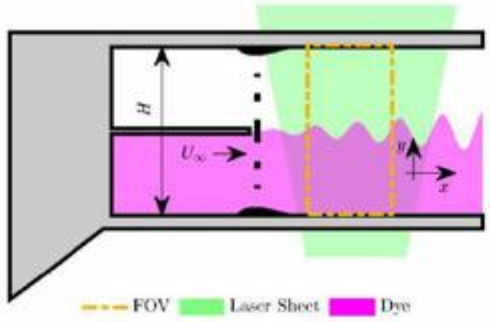

Figure 1: Experimental setups utilized in the study (the mixing layer case)

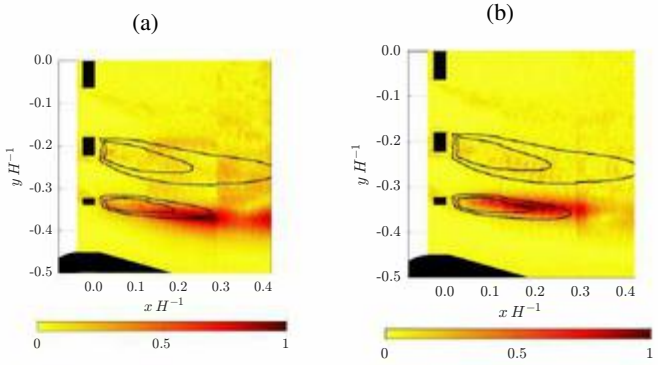

Figure 2: Normalized magnitudes of the secondary coherent structures associated with a) $f_1 - f_2$ and b) $f_1 + f_2$ frequencies (black contours indicate mean wake positions).

VELOCITY FIELD

As a near-wake contains energetic coherent structures, a triple decomposition (see [2]) was utilized for the velocity field analysis. The fluctuations were split into the stochastic part and coherent parts corresponding to shedding modes of various bars (a separate phase signal was associated with each of the resolved modes). The phase signals were further used in a conditional analysis which revealed some novel secondary coherent structures (see [3]). They appear to be the result of nonlinear triadic interactions between the shedding modes of adjacent bars, with the affiliated frequencies $f_1 \pm f_2$ (where f_1 and f_2 stand for the shedding frequencies). Spatially, they are located at the edges of the smaller wake,, as depicted in figure 2. The importance of these structures is to be studied by consideration of the spectra of the scalar flux terms (i.e. the transport of coherent concentration fluctuations by coherent velocity fluctuations, the transport of stochastic concentration fluctuations by coherent velocity fluctuations, etc.). The results will be delivered in the final paper.

*Corresponding author. Email: p.baj@imperial.ac.uk

CONCENTRATION FIELD

The improvement in mixing due to multiscale turbulence generation (compared to a single scale array) is going to be shown from both the global homogenization and the transverse scalar transport perspectives. The first comparison is achieved by studying the mean growth of a mixing layer downstream of different arrays. The mixing layer is generated by putting a splitter plate, which divides the flume's cross section into halves, upstream of an array and supplying one of the created sub-channels with a uniform dye solution instead of clean water (the velocity field stays uniform throughout). It is observed that the multiscale design homogenizes the concentration field more rapidly, as shown in figure 3.

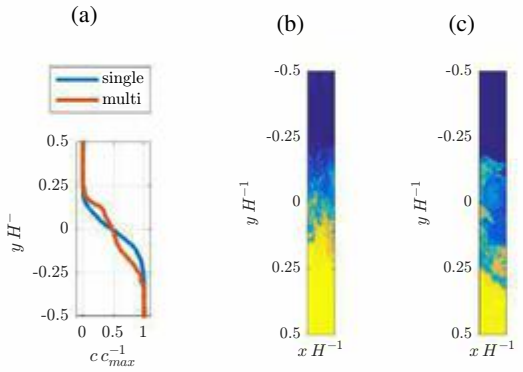

Figure 3: The bulk mixing comparison for single and multiscale arrays at an arbitrary downstream position: a) the mean profiles and instantaneous fields for b) single and c) multiscale arrays.

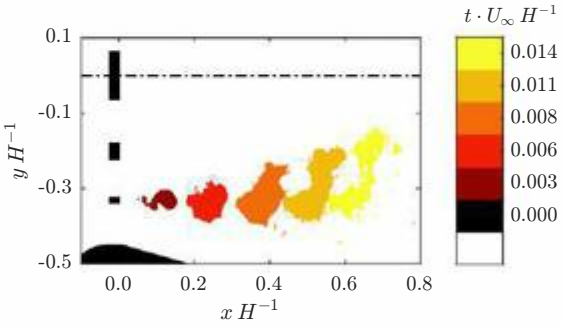

Figure 4: An example of the temporal evolution of a distinctive dye blob introduced into the multiscale flow.

The other comparison is completed by tracing dye released into the flow from a single point located at the rear face of the smallest bar within a given array. This approach, originally intended to mimic the SSU scenario, enables a visualisation of some quasi-periodic dye transfers between the adjacent wakes that occur in the multiscale flow. These are only observed at certain downstream positions, close to where the additional coherent structures are located. Examples of such bursts (an elongated transverse dye structure) are depicted in figure 5. It is believed that these engulfments are manifestations of the SSU mechanism.

Additionally, a similar experiment is performed in which the dye is released in short discrete "bursts" as opposed to continuously. Distinctive blobs of dye, originally of order of 1mm in diameter, are followed one by one so that the resulting point separation growth (when treating the single blob like a grouping of adjacent points) can be established. This experiment provides data for some Lagrangian mixing properties' estimation, e.g. $\overline{(y_t - y_0)^2}$, where y_t stays for a transverse coordinate of the fluid portion at time t thats originates form y_0 at the time 0. The example of the temporal growth of a single dye blob is given in figure 4. The full results will be presented in the final paper along with the comparison to the previous numerical simulations by [4].

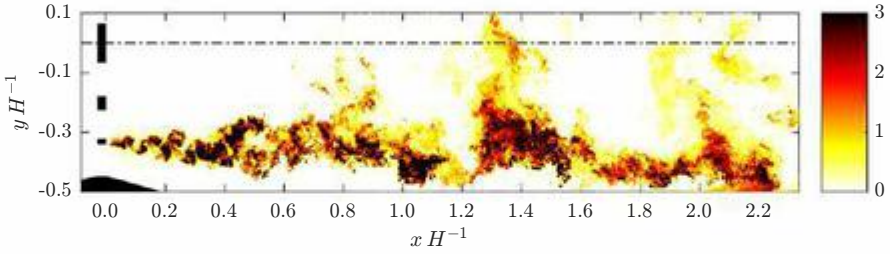

Figure 5: An example of the instantaneous concentration field behind the multiscale array (normalized with the local profile's rms). The dye is continuously released from the point source.

References

[1] Laizet S., and Vassilicos J.V.: Fractal space-scale unfolding mechanism for energy-efficient turbulent mixing. Phys. Rev. E 86.4, 2012.

[2] Baj P., Bruce P.J.K., Buxton O.R.H.: The triple decomposition of a fluctuating velocity field in a multiscale flow. Phys. Fluids 27(7), 2015.

[3] Baj P., Bruce P.J.K., Buxton O.R.H.: Space-scale unfolding mechanism in canonical multi-scale flows. Bull. Am. Phys. Soc. 60, 2015.

[4] Laizet S., and Vassilicos J.C.: Stirring and scalar transfer by grid-generated turbulence in the presence of a mean scalar gradient. J. Fluid Mech 764, 52-75, 2015.

DNS ASSESSMENT OF FRAGMENTATION MODEL OF TURBULENT CASCADE

Alexis Barge & Mikhael Gorokhovski
Laboratoire de Mécanique des Fluides et d'Acoustique, École Centrale de Lyon,
CNRS-Université Claude Bernard Lyon 1-INSA Lyon, Écully, France

Summary Recently in Saveliev & Gorokhovski (2012) Phys. Rev. E. 061112 the turbulent cascade model was proposed in the framework of renormalization of eddy-fragmentation equation under scaling symmetry. The analytical solutions to this equation for energy density and energy flux across length-scales have been obtained. Our present work consists in assessment of those solutions by DNS.

Fragmentation Model of Turbulent Cascade and Main Motivation

In applications to critical phenomena and field theory, the idea of scaling symmetry, i.e. an assumption of invariant to details statistical evolution of a non-equilibrium system with respect to change of the length-scale of observation, was successfully developed in celebrated works of Kadanoff and Wilson [1] and was successfully put into practice. However this idea is not exploited to its fullest extent in turbulence. Instead, the Kolmogorov 41 theory of turbulent cascade assumes the local statistical equilibrium in high-frequency motions, such that the overall turbulence decay is regarded as very slow, and the energy flux in spectrum of length-scales remains constant. In [2], the model of turbulent cascade was developed in the framework of fragmentation under scaling symmetry. To this end, the fragmentation equation was derived for the turbulent energy density in the space of length-scale, and this equation was renormalized, i.e. it was rewritten in the form of the continuity equation, in which the evolution in time is resulted from interaction of all length-scales. Thereby the divergence form of renormalized equation contained explicitly the energy flux towards zero-size. This equation conserves the total energy and is controlled by the "bare" flux of the specific energy, as a parameter. The auto-similar solutions to this equation for time-distributions of the energy and of its flux in the space of length-scale were found in the class of confluent hypergeometric functions, and they were expressed by elementary functions. Interestingly, with time translation to infinity, those solutions agreed with the Kolmogorov 41 law for the energy density $f(r) = C_0 \varepsilon_0^{2/3} r^{-1/3}$, including the value of constant $C_0 = 2$, which is usually presented in turbulence as an empirical one. The main motivation of our present work is to assess those solutions numerically.

Performed Simulations and Assessment.

The first case concerns the decaying statistically homogeneous turbulence. The DNS on the mesh containing 256^3 nods was performed in 3D-box of 2π-size for $Re_\lambda = 67$, $\varepsilon_0 = 2.077 m^2/s^3$, $\langle u'^2 \rangle = 2.58\, m/s$. An outcome from our simulations were time-distributions in the space of length-scale of the energy density and of the energy flux. The latter was computed first from the spectral energy balance in the space of wave numbers, and then it was recalculated for the length-scale r. From other side, in the fragmentation model of the turbulent cascade [2], the "bare" flux of the energy flux was attributed to the rate of the energy decay ε_0 at largest spatial scales. The results are shown in two following figures. The first one compares the energy density $f(r,t)$ at four times issued from DNS (discontinuous line), from fragmentation model [2] (continuous line) and from the Kolmogorov 41 (red symbols). It is seen that in the inertial zone, where the solution from the fragmentation model tends with time to the power function, there is a good agreement between theoretical and computed distributions, mimicking the both the behaviour of classical Kolmogorov 41 law.

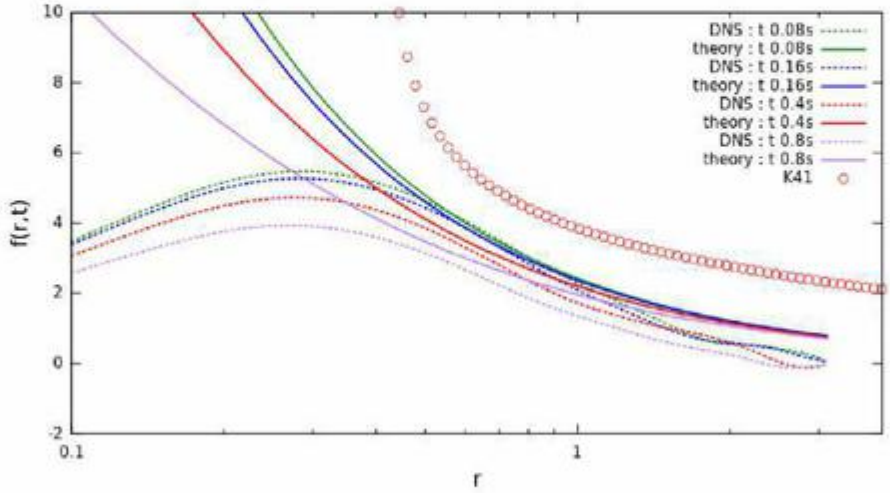

[a] Corresponding author. Email: mikhael.gorokhovski@ec-lyon.fr

The second figure below compares the energy flux distribution $j(r,t)$ towards smaller sizes for four times, indicating analytical solutions (continuous line) and DNS (discontinuous line). It is also seen that in the inertial range of scales the theory and computation display the similar behaviour. At small scales, the fragmentation model shows the continuous growth of the flux (manifested by accumulation of zero-size particles due to scaling symmetry), while DNS exhibits the viscous dissipation effect : distributions go to zero.

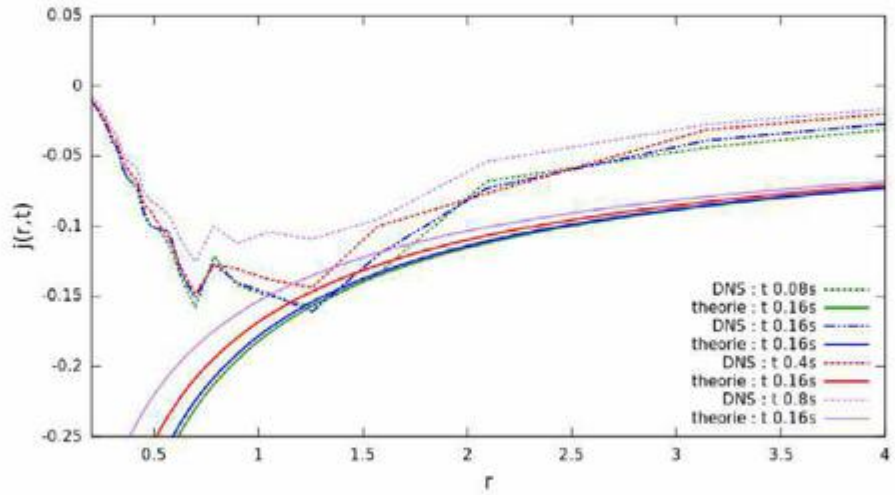

The next step of assessments concerned the model of the acceleration of fluids particles in the framework of the fragmentation model. Here we coupled the energy flux expression with the acceleration of fluid particles, and we compared DNS Lagrangian statistics with the model, as well as with the log-normal stochastic model given in [3, 4]. In the final paper these results will be presented.

At the moment, we develop the model of Lagrangian acceleration of fluid particles in the homogeneously stretched turbulence, and we are going to compare the fragmentation based model of the Lagrangian acceleration with DNS.

References

[1] Kadanoff Leo P., Statistical Physics: Statics, Dynamics, and Renormalization, World Scientific, River Edge, N.J., 2000

[2] Saveliev V.L. and Gorokhovski M.A. (2012) Phys. Rev. E. 061112

[3] Sabel'nikov V., Chtab A. and Gorokhovski M. (2011), Eur. Phys. J. B., 80, 177–187

[4] Zamansky R., Vinkovic I. and Gorokhovski M. (2013), JFM, V 721, pp 627-668

SCALAR DISSIPATION IN A TURBULENT ROUND JET

Azemi Benaissa[*a)], Jean Lemay[**], Alexis Darisse[**]
[*]Department of Mechanical and Aerospace Engineering, Royal Military College, Kingston Canada
[**]Department of Mechanical Engineering, Université Laval Quebec City Canada

Summary: Scalar dissipation is obtained in the self-preserving region of a free round turbulent air jet at high Reynolds number. Air is slightly heated and temperature is considered passive. Simultaneous laser Doppler velocimetry–cold-wire thermometry measurements were used to balance the temperature variance equation budget. Special care was paid to the statistical convergence of third-order moments. Temperature dissipation was deduced from the budget and directly measured with parallel cold wire probes. The validity and limitation of two point scalar measurements are presented.

INTRODUCTION

The control of the dispersion of pollutants in the atmosphere and fuels in a combustion chamber requires a good understanding of the mixing process of scalars in turbulent flows. This understanding is necessary in modeling the transport of scalars in industrial applications. Several works dealt with mixing in reacting flows. For non-reacting flows, different approaches were employed to characterise scalar mixing in turbulent jets (Antonia and Mi, 1993 (A.M); Pietri, *et al*. 2000). These later authors used LDV and cold wire thermometry to document the flow before the self-similar region (x/D = 15) of a slightly heated turbulent jet at Re_D =2.1x10^4. Their focus was on the statistics of individual fluctuations of velocity and temperature. In our case, Re_D was equal to 1.5x10^5, which corresponded to Re_λ = 548. High order moments and turbulent fluxes were measured in the self-similar region (x/D=30) and validated against the predictions of momentum and enthalpy equations (Darisse *et al,* 2013). In the present work the velocity measurements were performed with LDV technique. Extra care was devoted to the control of the boundary conditions, flow stability and statistical convergence. Most studies devoted to the direct measurement of the temperature dissipation rate have done so using an open loop approach. Since the target dissipation rate was obtained from the budget, it was possible to compare it to the direct measurements and analyse the validity of the temperature derivative measurements. This constitutes, to the authors' knowledge, the first time direct measurements of temperature dissipation were tested against a reliable estimate of this rate obtained in the same flow.

EXPERIMENTAL SYSTEM AND MEASUREMENT TECHNIQUES

The experimental system is composed of a slightly heated free jet produced with a convergent nozzle with a contraction factor of 25:1 and an exit diameter of 63.17 mm. The nozzle profile was a fifth degree polynomial that guaranteed a top hate velocity profile. The jet exits in a large room larger than 42D on each side to avoid confinement effect. Measurements were produced at x/D =30 with a jet exit velocity of U_{jet} = 36.4 m/s. Air was heated so that the nozzle exit temperature was 20 °C above ambient. The density ratio ρ_{jet} /ρ_{amb} was equal to 0.99 at x/D = 30 on the jet centerline. Velocity was measured with an LDV system from Dantec using a two color argon laser (blue 488 nm and green 514 nm) and a BSA-F60 analysing system. The focal distance of the optic system was equal to 1000 mm which allowed producing 22 interference fringes in the measurement point (0.14x0.14x3.70 mm^3 and 0.15x0.15x3.90 mm^3) for the blue and the green beam respectively. Temperature fluctuations were measured with current constant thermometry operating at an extremely low overheat (cold wire) and a low current of 0.1 mA. The sensors were made from Wollaston wire with a diameter of 0.58 mm. At x/D =30, on the jet axis, the ratio of the cut-off frequency over Kolmogorov frequency was estimated to be 2.20. The estimated error of the temperature dissipation was of the order of 5 %.

METHODOLOGY

The direct temperature dissipation was obtained using three different techniques: 1- from the use of Taylor's hypothesis assuming local isotropy; 2- from the temperature correlation at two point measurement; 3- from a finite difference method. As explained in Darisse *et al*. (2013), in the case of a round jet, the correlation coefficient and finite difference methods are essentially identical. The only difference lies in the potential calibration and gain errors introduced in the finite difference methods. Antonia *et al*. (1984) found the temporal and spatial correlation coefficient to yield similar results

DISCUSSION

In the $<\theta^2>/2$ budget, third-order correlations such as $<v\theta^2>$ require long samples in order to achieve statistical convergence, (Pietri *et al*. (2000)). This convergence is even more important considering that it is the gradient of this correlation that is required to estimate the turbulent diffusion term of the budget. In Figure 1, the radial distribution of $<v\theta^2>$ is presented and because no results could be found in the literature for comparison, we compared our results with data from Panchapakesan and Lumley, (1993) obtained in a Helium jet. The agreement around the centerline is due to

[a)] Corresponding author. Email: benaissa-a@rmc.ca

negligible buoyancy effect for the Helium jet. This agreement also confirms the soundness of the results for this difficult to measure correlation. The confidence in the data for all the production, convection and diffusion terms lead to balance the budget of the temperature fluctuation and deduce the remaining term (dissipation). In Figure 2, the normalized budget is represented with the results of Antonia and Mi, (1993) (grey lines). These authors measured directly the dissipation. The comparison shows a disagreement in the central region of the jet, where it seems, the direct measurements cannot resolve the presence of a hump at $\xi \approx 0.7$. Figure 3 presents the relative magnitude of ε_x, ε_r and ε_φ, the streamwise, radial and azimuthal components of temperature dissipation. The three curves are plotted against $\varepsilon_\theta/3$. Although, it is not expected that this reference will hold up away from jet centerline, it provides a useful basis for comparison. As found by Antonia and Mi, (1993), the three components of dissipation have roughly equal values on the jet centerline. This observation was already reported in Darisse *et al*. (2013). This near-equality prevails roughly up to $\xi = 0.5$. The value of ε_r and ε_φ remain approximately equal throughout the jet notwithstanding the spreading. Contrary to the results of A.M., ε_x becomes dominant around $\xi = 1$ and a large proportion of the peak reported in Figure 2 is attributed to the behavior of this component.

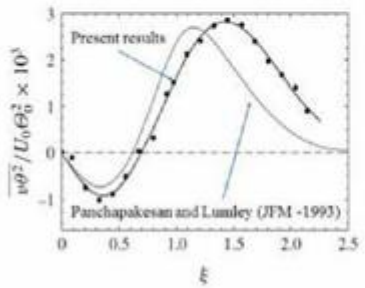

Figure 1: $<v\theta^2>$ radial distribution

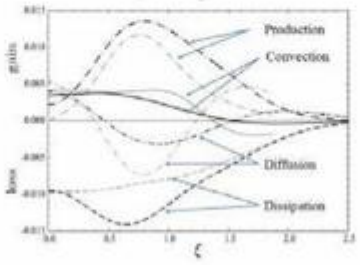

Figure 2: Budget of $<\theta^2>/2$.

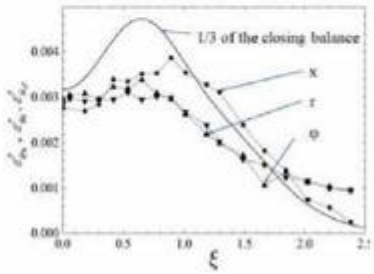

Figure 3: Three components of temperature dissipation

The spectral analysis of the streamwise temperature gradient obtained using a pair of probes presented in Darisse *et al*. (2013) revealed that for the most part, the attenuation present for high wavenumbers caused by wire separation was reasonably corrected using Wyngaard's analysis. However, departure from the spectra obtained using Taylor's hypothesis for low wave numbers was clearly reveled. The spectra obtained from the finite difference approximation would inevitably exhibit a very high level of low wave number content while the Taylor spectra would, as expected, monotonously decrease to zero when k_1 the wavenumber tends to zero.

The simulation of finite streamwise wire spacing using a convection velocity also provides an illustration of the effects of this distortion. When the simulated separation is wide enough, ripples start to appear in the derivative spectra as a consequence of the filtering effect (Darisse *et al*. (2013)). No such ripples are found in the streamwise derivative spectra, even for large wire separation. Ripples are thus not observed because under the presence of transverse instant velocities and the highly fluctuating streamwise velocity, the turbulent structures are distorted, so that they are not fully convected from the upstream probe to the one located just downstream. Antonia *et al*. (1984) simulated this effect by considering a fluctuating convection velocity in the calculation of their Taylor spectrum and observed that the ripples would then vanish. The mathematical operation performed would no longer be akin to a finite impulse response filter.

CONCLUSIONS

The direct measurement of the scalar dissipation is analysed and compared to one obtained from the budget of the transport equation of $<\theta^2>/2$. The limitation of temperature derivative measurements using two probes is shown and the reason of their failure identified. It is pointed out that a true derivative spectrum for the scalar is not attainable given the available approaches. Perhaps the knowledge of the passive scalar field obtained through direct numerical simulations could shed a new light on this behavior of the streamwise derivative spectrum and the mechanism through which the low wavenumber contents appear.

REFERENCES

1. Antonia, R. A. & Mi, J. 1993. Temperature dissipation in a turbulent round jet. Journal Fluid Mechanics 250, 531–551.
2. Antonia, R. A., Browne, L. W. B., Britz, D. & Chambers A. J. 1984. A comparison of properties of temporal and spatial temperature increments in a turbulent plane jet. Physics of Fluids 27 (1), 87–93.
3. Darisse, A., Lemay, J. & Benaïssa, A. 2013. Extensive study of temperature dissipation measurements on the centerline of a turbulent round jet based on the $\theta^2/2$ budget. Experiments in Fluids 55 (1), 1–15
4. Panchapakesan, N. R. & Lumley, J. L. 1993. Turbulence measurements in axisymmetric jets of air and helium. Part 2. Helium jet. J. Fluid Mech. 246, 225–247..
5. Pietri, L., Amielh, M. & Anselmet, F. 2000. Simultaneous measurements of temperature and velocity fluctuations in a slightly heated jet combining a cold wire and Laser Doppler Anemometry. International Journal of Heat and Fluid Flow 21 (1), 22 – 36.

NORMAL INVERSE GAUSSIAN PDF OF VELOCITY INCREMENTS IN A TURBULENT HEATED JET

Malek Brahimi[1a], Farida Benabbas[1] & Azemi Benaissa[2]
[1]*Department of Processes Engineering, University A. Mira of Bejaia, Bejaia, Algeria*
[2]*Department of Mechanical and Aerospace Engineering, Royal Military College of Canada, Kingston, Ontario, Canada*

Summary : Normal Inverse Gaussian law with four parameters α, β, δ and μ is shown to fit very well the experimental pronounced PDF shape with heavy tails at small scales and the Gaussian-like shape for the large scales. The probability density functions of velocity increments are obtained from recorded time series in the self-similarity region of a heated jet. The Reynolds number ($Re_j = 10^5$) is sufficiently high to consider the flow as fully turbulent.

INTRODUCTION

Because of intermittency, turbulent processes have the property to show a pronounced PDF shape with heavy tails for the increments at small scales of the velocity field. For the large scales, the PDF of increments tends to a Gaussian like type. A stochastic process approach to model this trait of turbulent process has recently been proposed [1]. The mathematical formulation is built in order to predict the correct shape of PDF at any scale of the velocity increments. Simulations of the process clearly show PDFs similar to those experimentally obtained. A maximum likelihood procedure is used by the authors to fit the PDFs by Normal Inverse Gaussian (NIG) law from small scales to large scales. The mathematical properties of the 4-parameter NIG $(\alpha, \beta, \delta, \mu)$ distribution are presented in [2] with its extensive use for three different data sets including data from a Jet flow. The analysis revealed a striking similarity scaling of α/δ of all three flow configurations. We consider that extended experimental support in different configurations of high Reynolds number turbulent flows is needed to comfort the proposed stochastic modeling. The present work is a contribution towards this goal by presenting some results on the PDF of velocity increments in a turbulent heated jet of Taylor Reynolds number $R_\lambda = 316$. We determine the 4-parameter NIG distributions for different lag time s and compare the results with those obtained by the previous authors in the case of a lower Taylor Reynolds number and frequency sampling.

EXPERIMENTS

The jet flow produced with a nozzle of $d = 63.5mm$ in diameter is slightly heated to consider the temperature as a passive scalar. Investigated Reynolds number 10^5 is sufficiently high for the flow to be fully turbulent as shown by the well separated ranges of large scales, inertial and dissipative scales in the spectra (fig.1). The longitudinal velocity u is recorded at $R/d = 30$ in the centerline of the jet with a sampling frequency of $f_s = 40\ kHz$ and each time series realization contains 2.10^6 samples. For more details about the experimental apparatus and techniques the reader can advantageously consult the references [3,4]. The data used in the present analysis have been kindly provided by Professor A. Benaissa. A huge number of data points is necessary to accurately estimate the PDF tails and consequently the effect of intermittency. A unique functional form of the 4-parameter class of NIG distributions is used to match all the experimental PDF of velocity increments for different scales.
The NIG distribution has PDF function given by the following analytical expression [1,2]:

$$p(R,\alpha,\beta,\delta,\mu) = \frac{\delta\alpha}{R.\sqrt{(\delta^2+(R-\mu)^2)}} K_1\left(\alpha.\sqrt{(\delta^2+(R-\mu)^2)}\right)\exp\left(\delta\sqrt{(\alpha^2-\beta^2)}\right)\exp(\beta(R-\mu))$$

K_1 is the Bessel function of the second kind with index one. In the present work, the parameters are determined by Maximum Likelihood estimation.

RESULTS AND DISCUSSION

The spectrum depicted in figure 1 reveals the inertial range where the classical $-5/3$ power law of Kolmogorov is verified followed by the dissipation range. Well separated ranges are observed owing to the high value of Reynolds number. Figure 2 reports the dynamic behavior of the velocity increment squared $(\Delta u)^2 = [u(t+s)-u(t)]^2$ with time lag $s = 10$ (1/f_s units). We can clearly visualize the intermittency phenomenon

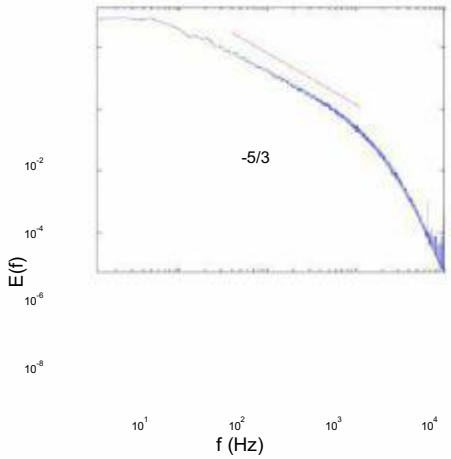

Figure 1- Spectrum of the velocity

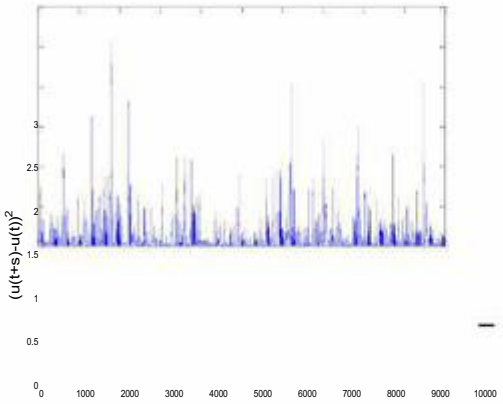

Figure 2- Dynamics of $(\Delta u)^2$ versus units of $\frac{1}{f_s}$

The PDF of velocity increments for different time lag s are reported on figure 3. As the time lag increases we go through the dissipation range, inertial range and the large scales range. We observe the heavy tails of the PDF at small scales and the Gaussian-like shape at large scales (for s = 2000, the red curve is the Gaussian pdf).

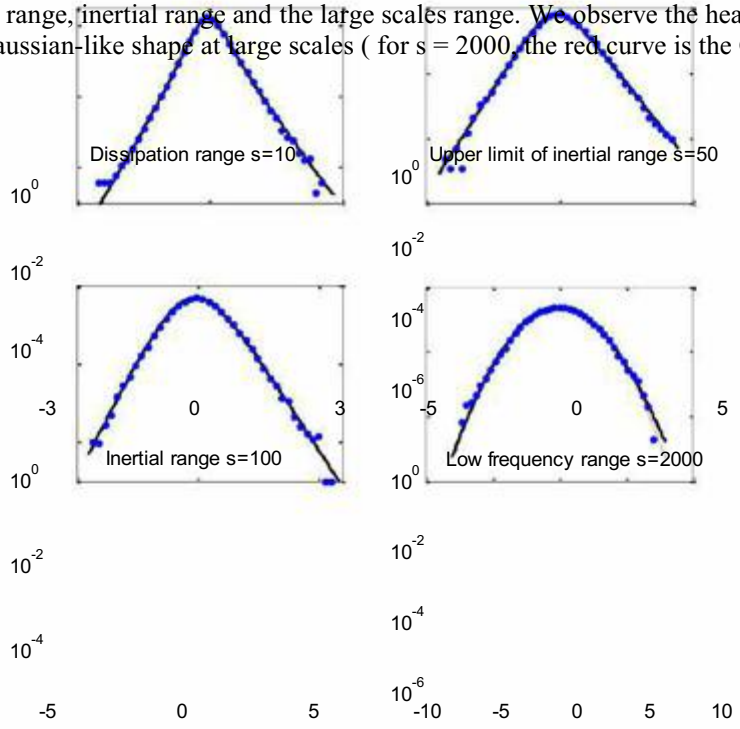

Figure 3- PDF (Δu) for different time lags s- (experimental data: blue points- NIG distributions: black curves)

It is clear that the Normal Inverse Gaussian fits accurately experimental pdf at all scales.

CONCLUSIONS

A unique functional form of 4-parameters Normal Inverse Gaussian law is shown to represent accurately the PDF of velocity increments from dissipative scales to the large scales where it collapses with the Gaussian distribution. Further analysis is being conducted to figure out scaling properties of the parameters.

References

[1] Barndorff-Nielsen O.E., Schmiegel J.: A stochastic differential equation framework for the timewise dynamics of turbulent velocities. *Theory. Probab. Appl.52,3,372-388,2008.*

[2] Barndorff-Nielsen O.E., Blæsild P., Schmiegel J.: A parsimonious and universal description of turbulent velocity increments. *Eur. Phy.J.,44,345-363,2004.*

[3] Benaissa A., Gisselbrecht Th.: Self-similar evolution of velocity and temperature small scales in a turbulent round jet. *Eur.J.Mech.B/fluids,42,169-175,2013.*

[4] Duffet J.C., Benaissa A.:Influence of initial conditions on the evolution towards similarity of passive scalar in turbulent round jets. *Experim. Therm. Fluid Sc.,44,834-843,2013.*

INFLUENCE OF FREESTREAM TURBULENCE INTENSITY ON WAKES OF SIDE-BY-SIDE CYLINDERS IN CROSSFLOW

Elizabeth Camp *[1] and Raúl Bayoán Cal[1]

[1]*Department of Mechanical and Materials Engineering, Portland State University, Portland, Oregon, USA*

Summary Stereo particle image velocimetry is used to examine the influence of varying levels of freestream turbulence on the wakes of a pair of side-by-side cylinders crossflow. Four different inflow conditions are employed. Each inflow condition is applied to three different cylinder-to-cylinder spacing values. The mean velocity components and Reynolds stresses are heavily affected by the inflow condition as well as the center-to-center spacing. Low dimensional representations found using Proper Orthogonal Decomposition recover energy at rates that are also dependent on the level of incoming turbulence intensity.

INTRODUCTION

In addition to being of fundamental interest, groups of cylinders are a commonly found in engineering applications such as heat exchangers, structural supports, and cables. In many applications, the incoming flow is highly turbulent. Much work has been done to examine the wake behind single cylinders and to a lesser extent pairs or groups of cylinders. Even fewer studies have been done to examine the changes in the wakes due to freestream turbulence. The present study examines the changes in the wakes of pairs of side-by-side cylinders as a function of varying freestream turbulence intensity and cylinder-to-cylinder spacing.

EXPERIMENTAL METHODS

Wind tunnel experiments are conducted at the facility at Portland State University. This closed circuit tunnel has a 9:1 contraction ratio. The test section is 5 m in length with a cross-section which is 0.8 m in height and 1.2 m in width. Four different inflow conditions are used in this experiment which vary in the inflow turbulence intensity. The inflow is dependent on a variable removable section at the tunnel inlet. In three of the inflow cases, the removable section houses an grid which is operated passively or actively using two different winglet rotation protocols. In the fourth inflow case, the removable section is a simple duct with a cross-section identical to that of the tunnel test section. Figure 1 illustrates the arrangement of the pair of cylinders employed herein. For each inflow condition, three different transverse spacing to diameter ratios (T/D) are employed: 1) T/D=1.5, 2) T/D=2.1, and 3) T/D=2.7. The four inflow conditions and T/D spacings compose a set of twelve unique cases. End plates with a design described by Szepessy [1] are attached to the cylinders 0.06 m from the tunnel floor and ceiling, respectively. Each cylinder has a diameter of 19.1 mm and has a ground surface. Based on the endplate-to-endplate distance, the cylinders have an aspect ratio of 35. The combined blockage of the cylinders and structural attachments at the floor and ceiling is 6.5%.

Stereo particle image velocimetry (SPIV) measurements are made at 0.4 m from the tunnel floor which is half of the test section height. The SPIV system is composed of two LaVision 4 megapixel Pro LX cameras fitted with Schiempflug adapters, a Litron Nano L 200-15 double pulsed Nd:YAG laser, and the software DaVis 8.1.5 by LaVision. The flow is seeded with Diethyl-Hexyl Sebacate that was aerosolized via a seeding generator which uses a Laskin nozzle. Images are processed using a multi-grid strategy for the stereo cross-correlation with two passes with interrogation area size of 64×64 pixels with 50% overlap followed by three passes of interrogation area size of 32×32 pixels. Erroneous vectors are removed using a median filter. Spurious vectors are replaced with vectors computed via a Gaussian interpolation of valid neighboring vectors.

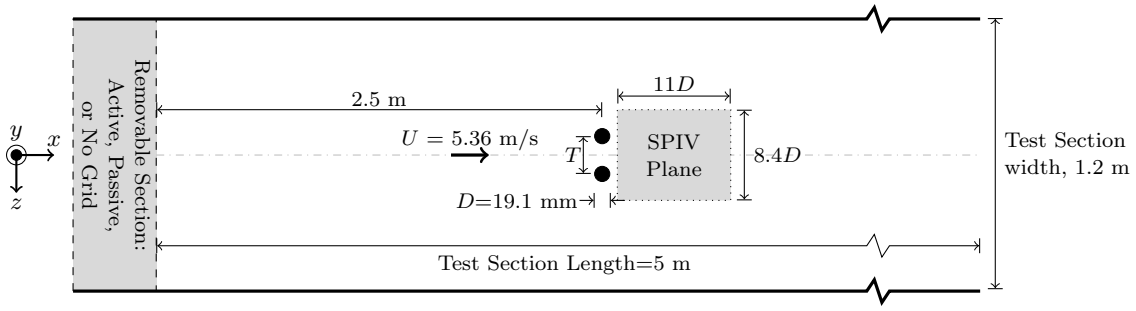

Figure 1: Top view of wind tunnel test section with experimental setup

*Corresponding author. Email: betsy.h.camp@gmail.com

RESULTS

Figure 2 shows the mean streamwise velocity component, U, for T/D=1.5 for four different freestream turbulence intensities. The lowest turbulence intensity employed was $Tu\%$=0.32 which is displayed in Figure 2(a). This set of inflow conditions the wake is consistent with bistability reported in previous studies for laminar inflow and low T/D ratios [2]. Figure 2(b) shows the same cylinder-to-cylinder spacing but with $Tu\%$=3%. At this higher turbulence intensity, asymmetry in the velocity is still present to a much smaller degree than in the laminar inflow case. The higher turbulence intensity cases with $Tu\%$=19.4% and $Tu\%$=16.4% are shown in Figure 2(c) and Figure 2(d), respectively. The velocity deficits are symmetrically distributed in both of these sets of conditions. For conciseness, the additional cases in which T/D=2.1 and 2.7 are not shown.

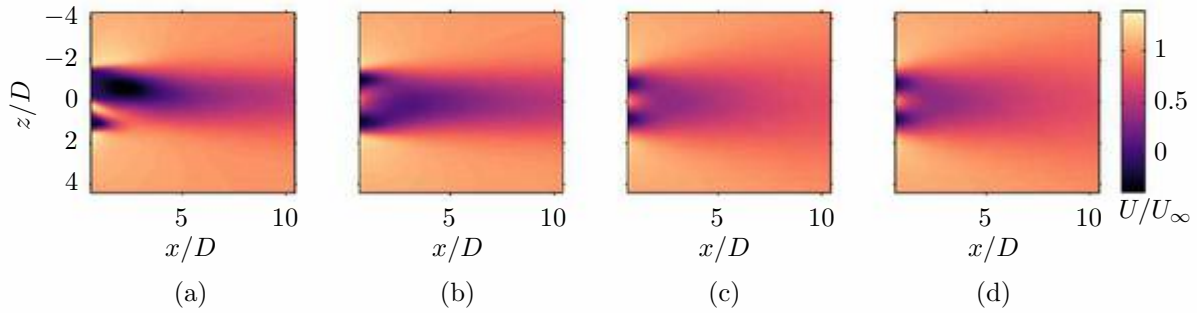

Figure 2: Mean normalized streamwise velocity for turbulence intensities (a) $Tu\%$=0.32%, (b) $Tu\%$=3%, (c) $Tu\%$=19.4%, and (d) $Tu\%$=16.4%. Origin of coordinate system set so that $x/D = 0$ coincides with the center of both cylinders.

Proper orthogonal decomposition (POD) using the method of snapshots [3] was done for each set of cases in order obtain a low dimensional representation of each case. Focusing on the only cases corresponding to those shown in Figure 2, a greater number of modes is needed to recover 50% of the turbulence kinetic energy as turbulence intensity is increased. As seen in Figure 3(a), the highest energy containing mode shows evidence of vortex streets in for the $Tu\%$=3% case. In contrast, as seen Figure 3(b) the highest energy containing mode for the $Tu\%$=19.4% case do not indicate the presence of vortex streets.

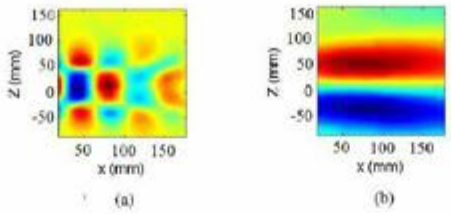

Figure 3: Highest energy containing POD modes for the cases with (a) $Tu\%$=3% and (b) $Tu\%$=19.4%.

CONCLUSIONS

The characteristics of the mean velocity components and Reynolds stresses are heavily impacted by turbulence intensity of the freestream turbulence impinging on a pair of side-by-side cylinders in crossflow. This influence is present for all three T/D spacing values employed in this study. From the POD, the rate of convergence the turbulence kinetic energy also varies as a function of the freestream turbulence intensity incident on the cylinders with lower turbulence intensity generally having more energy present in the first several modes. The characteristics of these the highest energy containing mode for each case also differs with the inflow conditions. Specifically, vortex streets are only evident in the highest energy containing modes for the inflow condition having $Tu\%$=0.32 and $Tu\%$=3%

References

[1] S. Szepessy and P. W. Bearman. Aspect ratio and end plate effects on vortex shedding from a circular cylinder. *Journal of Fluid Mechanics*, 234:191–217, 1992.

[2] D. Sumner. Two circular cylinders in cross-flow: a review. *Journal of Fluids and Structures*, 26(6):849–899, 2010.

[3] L. Sirovich. Turbulence and the dynamics of coherent structures. Part I: Coherent structures. *Quarterly of Applied Mathematics*, 45(3):561–571, 1987.

DISCHARGE INCREMENT INDUCED BY GROOVE IN CHANNEL FLOW

Yu Chen*[1,2], Jerzy Maciej Floryan †[3], Yong Tian Chew[2], and Boo Cheong Khoo[2]
[1]*Institute of High Performance Computing, 1 Fusionopolis Way, #16-16 Connexis North, Singapore*
[2]*Department of Mechanical Engineering, National University of Singapore, Singapore*
[3]*Department of Mechanical and Materials Engineering, The University of Western Ontario, London, Ontario, Canada*

Summary Flow in channels with longitudinal grooves has been theoretically and numerically studied in the current work. The changes in discharge are monitored for the pressure driven flow to investigate the efficiency of fluid flowing through the channels in laminar and turbulent flow regimes. It has been shown that the long wavelength grooves induce discharge increase up to 3–9%, while the short wavelength grooves reduce the discharge. Analysis of the flow patterns demonstrates that the increase in discharge results from the re-arrangement of the bulk fluid movement.

INTRODUCTION

Drag reduction in wall-bounded flows is an essential method to reduce the power consumption and energy costs. Thus, techniques to reduce friction drag attract lots of attention from the researchers since the reduction of pressure drag has been well studied. These techniques include both passive methods (such as riblets and super-hydrophobic surface [1, 2]) and active methods (such as wall-oscillations and jet injection [3, 4]). Recently, Mohammadi & Floryan [5] investigated the drag of a macro-scale device, the two dimensional grooves in channel flow. It was reported that the longitudinal grooves with long wavelengths potentially reduce drag in spite of the increase in the wetted surface area, while the short wavelength grooves increase the drag. Such drag reduction was found to be attributed to the redistribution of the bulk flow, with the largest mass flow taking place in the widest channel opening. Various shapes of groove have been investigated in laminar regime [6].

Considering the advantages of macro-scale devices over micro-scale devices and active methods (easy to manufacture and maintain, no additional energy input), turbulent flows in channels with longitudinal grooves with various wavelength and shapes are investigated to determine their capability to reduce drag in turbulent flow regime. The drag reducing potential is measured by comparing the discharge through the grooved channel with the discharge through a smooth channel when both channels are exposed to the same pressure gradient.

RESULTS

Consider fluid flow driven by a given pressure gradient through a channel extending to $\pm\infty$ in the x-direction bounded by sinusoidal grooves parallel to the flow direction (see Figure 1(a)). The sinusoidal grooves can be defined as plate with smooth longitudinal wavy grooves in such a way: $y_L = -1 - \frac{S}{2}\sin(\alpha z)$, $y_U = 1 + \frac{S}{2}\sin(\alpha z)$, where the subscripts L and U refer to the lower and upper walls, respectively. S and α are, respectively, the amplitude and wave number of grooves, thus the wavelength of grooves in the spanwise direction is $\lambda = 2\pi/\alpha$. Simulations of turbulent flow in grooved channel were conducted in a computational domain of length $L = 2\pi$, width $W = \min(2\pi, \lambda)$ and mean height $2H = 2$ at $Re_\tau = 180$ ($Re_{2H} \approx 6,000$) by DNS and DES methods [7, 8].

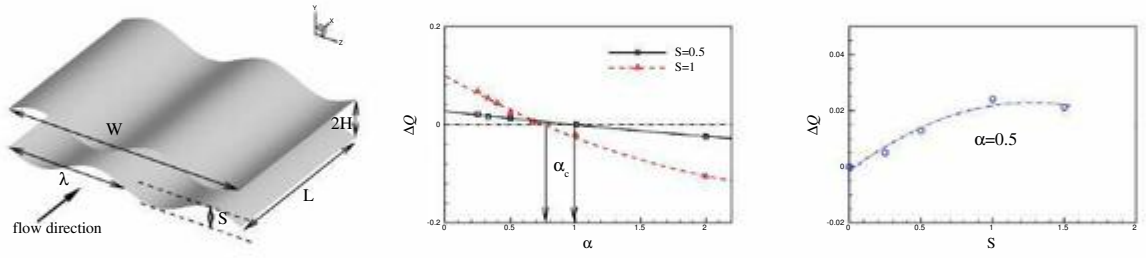

Figure 1: Channel with two corrugated walls (a); variations of the discharge correction ΔQ as a function of the groove wave number α (b), and as a function of the groove amplitude S (b) for channel with grooves at $Re_\tau = 180$.

*Corresponding author. Email: yuchen1986sg@gmail.com
†Corresponding author. Email: mfloryan@eng.uwo.ca

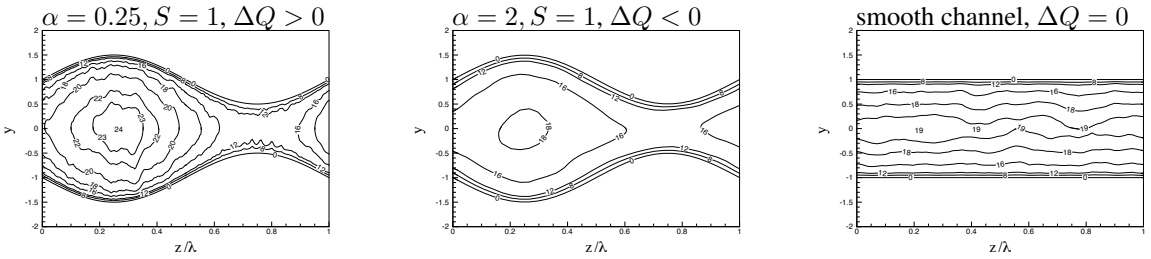

Figure 2: Distributions of the mean velocity component U in the y-z plane of channel with grooves $\alpha = 0.25, S = 1$ (a), $\alpha = 2, S = 1$ (b) and smooth channel (c) respectively, for $Re_\tau = 180$.

The normalized discharge difference between corrugated and smooth channels $\Delta Q\,(\alpha, S) = \frac{Q - Q_0}{Q_0}$ can be employed to evaluate the system effectiveness, and positive ΔQ indicates an increase in the effectiveness of the flow system, or effective drag reduction. Figures 1(b) and (c) display variations of the discharge difference between the corrugated and smooth channels generated by the same pressure gradient. A critical groove wave number α_c is observed, below which the grooves increase discharge and above which the discharge is reduced. The critical wave number is estimated to be $\alpha_c \approx 1$ for $S = 0.5$ and $\alpha_c \approx 0.8$ for $S = 1$. An increase in the groove amplitude S decreases the discharge when $\alpha > \alpha_c$ and, conversely, increases the discharge when $\alpha < \alpha_c$. A decrease of α increases the discharge but this increase rapidly approaches an asymptotic limit where any further decrease of α brings in negligible contributions. The highest increase of the discharge at $S = 0.5$ is about 2%–3%, and it is about 9% at $S = 1$.

Figure 2 displays distributions of U in the spanwise cross-sections of channel with grooves. In the presence of grooves, the fluid either accelerates or retains its velocity in the wide segment of the channel and slows down in the narrow segment, leading to the re-arrangement of the bulk motion and stream tubes. When $\alpha < \alpha_c$ (Figure 2(a)), the difference between the maximum velocity in the widest and narrowest sections of the channel is larger than the similar difference for channels with $\alpha > \alpha_c$ (Figure 2(b)). The maximum velocity at the widest section of the channel for $\alpha < \alpha_c$ is higher than the maximum velocity in the smooth channel ($U \approx 19$; Figure 2(c)) with a minor velocity decrease in the narrow section, resulting in an increase in the total discharge. When $\alpha > \alpha_c$ (Figure 2(b)), the maximum velocity in the widest portion of the channel is $U \approx$ 18–19, which is similar to that found in the smooth channel and, since velocity decreases in the narrow section, there is an overall reduction in the discharge.

CONCLUSIONS

The passive and macro-scale devices, grooved channels with small wave number ($\alpha < \alpha_c \approx 0.8$–1) and large amplitude, induce discharge increase up to 10% for turbulent flow under the same pressure gradient. The maximization of the discharge requires the use of the minimum possible groove wave number α as well as the largest possible groove amplitude S. Such discharge increase is associated with the rearrangement of the bulk velocity in the cross-section (y-z) plane with the largest fluid flux flowing through the widest channel opening.

References

[1] Walsh M. J.: Riblets as a viscous drag reduction technique. *AIAA J.*, 21:485–486, 1983.

[2] Rothstein J. P.: Slip on superhydrophobic surfaces. *Annual Review of Fluid Mechanics*, 42:89–109, 2010.

[3] Quadrio M.: Drag reduction in turbulent boundary layers by in-plane wall motion. *Philosophical Transactions of the Royal Society of London A: Mathematical, Physical and Engineering Sciences*, 369(1940):1428–1442, 2011.

[4] Iuso G., Onorato M., Spazzini P. G., and Di Cicca G. M. : Wall turbulence manipulation by large-scale streamwise vortices. *J. Fluid Mech.*, 473:23–58, 2002.

[5] Mohammadi M. and Floryan J. M.: Pressure losses in grooved channels. *J. Fluid Mech.*, 725:23–54, 2013.

[6] Mohammadi A. and Floryan J. M.: Numerical analysis of laminar-drag-reducing grooves. *J. Fluids Eng.*, 137(4):041201, 2015.

[7] Wang Z., Yeo K. S., and Khoo B. C.: DNS of low Reynolds number turbulent flows in dimpled channels. *J. Turbulence*, 7:37, 2006.

[8] Chen Yu, Chew Yong Tian, and Khoo Boo Cheong: Enhancement of heat transfer in turbulent channel flow over dimpled surface. *International Journal of Heat and Mass Transfer*, 55:8100–8121, 2012.

OUTER HELIOSPHERE: A FIRST ATTEMPT OF MAGNETIC FIELD SPECTRA DETERMINATION FROM VOYAGERS DATA

Federico Fraternale[1], Luca Gallana [1], Michele Iovieno[1], Merav Opher[2], John D. Richardson[3], and Daniela Tordella*[1]

[1]*Department of Aerospace and Mechanical Engineering, Politecnico di Torino, Torino, Italy*
[2]*Astronomy Department, Boston University, Boston (MA), USA*
[3]*Kavli Institute for Astrophysics and Space Research, Massachusetts Institute of Technology, Boston (MA), USA*

Summary The Voyager spacecrafts (V1-V2) are providing unique measurements of plasma and magnetic field at the helioshpere edge. We compare the magnetic field measured from the Voyagers inside the heliosheath (HS) (V1 years 2004-2012, V2 year 2007-). Observations of high variations of energetic particle fluxes at V2, recently suggested the existence of two regions with distinct magnetic field features: the SHS (sectored heliosheath), where the magnetic field alternates the polarity due to the current sheet flapping and piling up as the heliopause is approached, and the UHS (unipolar heliosheath) which extends outside the SHS, where the magnetic field polarity is constant. We present here the first magnetic field power spectra computation inside the heliosheath. The spectra differ in both anisotropy and inertial decay rate. The difference cannot be explained in terms of the different physics supposedly present in the sectored and unipolar regions.

Both the Voyagers have crossed the termination shock entering the heliosheath (V1 in December 2004 [13], V2 in August 2007 [10] . In this region, many observations are not completely understood [12, 8]. One of these is the difference observed by V1 and V2 in the flux of both energetic ions and electrons (ions: kinetic energy from about 40 KeV to >1 GeV (Galactic Cosmic Rays) and electrons: from about 50 KeV to >100 MeV) [6]. In particular, while particle fluxes time histories seen by V1 were almost constant in the period 2007-2012, those recorded by V2 showed variations with an amplitude 50 times larger. According to Hill et al. [6], possible physical interpretations to explain the enhancement or depression of energetic particle intensity are related to the Helioshperic Current Sheet (HCS) maximum latitudinal extensions. These northern and southern boundaries enclose the socalled sectored heliosheath region (SHS), where the magnetic field changes polarity as the HCS is crossed, according to the Parker spiral structure. At higher North and South latitudes, outside the sector region, the heliosheath is unipolar (UHS), see fig. 1. Traveling at a latitude of about 30° S, V2 is thought to have crossed different times the boundary of the SHS, and a correlation was found between the energetic particle flux at V2 and the alternation of unipolar and sectored zones crossed by V2. Different particle transport properties are expected in these regions. Opher et al. [9] suggested that in the SHS region the magnetic field was not laminar but disordered and turbulent, with the sector structure being replaced by a sea of nested magnetic islands. These bubbles would take origin from magnetic reconnection processes occurring near the heliopause, triggered by the compression of sectors and by the narrowing of the HCS (see Drake et al. [2]). Different scenarios may coexist, for instance the presence of magnetic reconnection or turbulence in the SHS can as well increase the ions and electrons transport.

We are here interested in analyzing the magnetic field fluctuations in the two different SHS and UHS heliosheath regions, see fig.1. We consider the highest resolution of recorded data (48-s averages) from this NASA mission [7] and we compute power spectra by exploiting a proper data gap treatment developed inside this group [5, 4]. The data gap problem arises from the fact that data can be lost due to telecommunication issues, noise, instrumental interferences and other reasons.

We consider four magnetic field ($\mathbf{B}$) datasets in the interval 2009-2012. In particular, for V1 we analyze the sequences 2009 DOY 1 - 2009 DOY 180 (A1) and 2010 DOY 180 - 2011 DOY 180 (B1). V1 is supposed to be in the SHS in this two periods, even if the constancy of polarity of $\mathbf{B}$ suggests that V1 remained within just one sector, see the azimuthal angle variations in fig 2a, and [1]. For V2, we choose the interval 2009 DOY 219 - 2010 DOY 180 (A2), when V2 was inside the unipolar region and measured a low flux of energetic particles, and the period 2010 DOY 255 - 2011 DOY 256 (B2), when V2 was in the SHS measuring an enhanced particles intensity. The power spectra of the magnetic energy and of the field components of $\mathbf{B}$ in the heliographic reference system for A1, A2, B1, B2, are shown in panels (c,d,e,f), respectively.

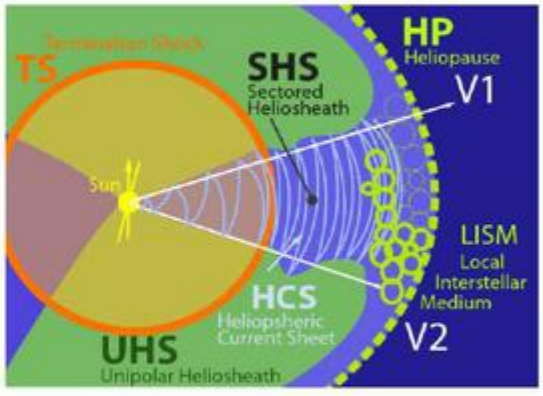

Figure 1: Qualitative scheme of the heliosphere

A few aspects are common to all spectra. They show a mild algebraic decay in the low-frequency range ($f < 10^{-5}$ Hz) a steeper algebraic decay in the intermediate range (about $10^{-5} < f < 3 \cdot 10^{-4}$ Hz) and a hi-frequency range ($3 \cdot 10^{-4} < f < 10^{-2}$ Hz) where the decay is likely affected by the accuracy of the magnetometers, which is around 0.03 nT. Concerning the magnetic energy fluctuation, in the low frequency range, spectral slopes are within

*Corresponding author. Email: daniela.tordella@polito.it

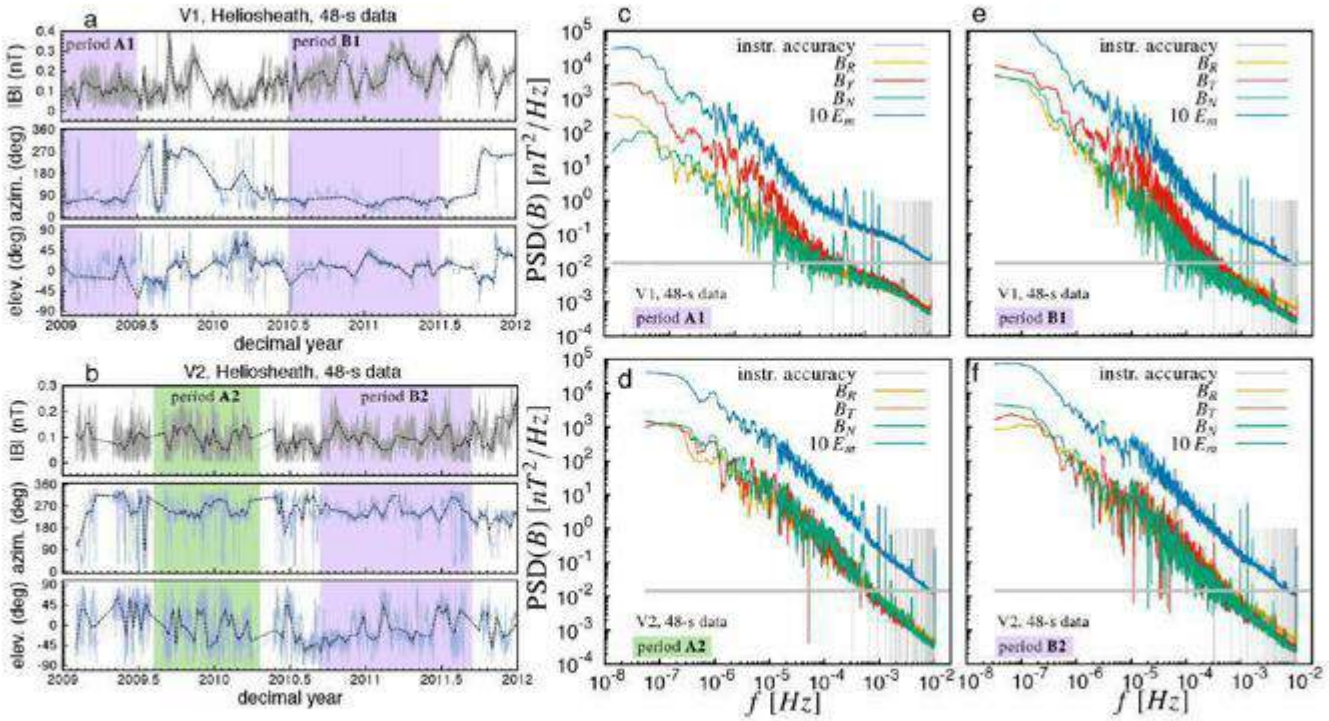

Figure 2: (**a**,**b**) Magnetic field module, azimuthal angle and elevation angle for V1 (top) and V2 (bottom). SHS periods are highlighted in purple (A1, B1, B2) and UHS periods in green (A2). (**c**,**d**) Magnetic field components and energy spectra during A1 and A2. All the spectra have been computed with the *compressed sensing* methodology, already tested in [4]. Vertical grey lines indicate probably instrumental-related peaks, harmonics of $2.3 \cdot 10^{-4}$ Hz. (**e**,**f**) Magnetic field spectra during the periods B1 and B2.

-1.24 ± 0.2 for both crafts and all the periods observed. However, in the portion of inertial range $10^{-5} < f < 3 \cdot 10^{-4}$ Hz, V1 and V2 show important differences which at this stage of knowledge seem associated to the different structures of the fluctuation of the field orientation. In particular, for the Voyager 1, either when located at the boundary between UHS and SHS or inside one single sector, the fluctuations level of the azimuthal and elevation angles is very low and their 48-s averages are constant. For V2 instead, both inside the unipolar period A2 and in sectored period B2 the orientation fluctuation is much more intense. These signal differences are reflected in a different structure of the spectra: the slope for V1 is 2.0 ± 0.19 while V2 shows a spectral decay of 1.68 ± 0.2, closer to the Kolmogorov value. By looking at the components, high anisotropy is observed by V1, where the tangential component is dominant and decays much faster than the radial and normal components a fact which is not observed by V2. In particular, the anisotropy can be observed in fig. 2a (B signal) and in fig. 2 c,e (power spectra). The anisotropy level in 2009 was $\sigma^2_{B_T}/\sigma^2_{B_R} = 10.5$, $\sigma^2_{B_T}/\sigma^2_{B_N} = 11.6$ while in 2011-2012 it reduced to 4.6 and 4, respectively. Spectrally this anisotropy is highlighted by the different decays showed by the normal and radial components (~ -1.5) and the tangential component (~ -2), see fig.2 c,e. By contrast, confer in fig. 2d,f, the nearly isotropic behavior as sensed by V2. It should be noted, in conclusion, that the highly different magnetic field structure we obtain by observing the solar wind along the Voyager different paths cannot be simply explained from being in or out the sectored heliosheath. For example, the V2 path seems to enter the unipolar region (A2) first and then the sectored region (B2), however, the signal and related spectra remain alike.

References

[1] L. F. Burlaga, L. F. Ness, and J. D. Richardson. *J. Geophys. Res.*, 119(8):6062–6073, 2014.
[2] J. F. Drake, M. Opher, M. Swisdak, and J. N. Chamoun. *Astrophys. J.*, 709(2):963–974, 2010.
[3] V Florinski. *Adv. Space Res.*, 48(2):308–313, 2011.
[4] L. Gallana, F. Fraternale, M. Iovieno, S. M. Fosson, E. Magli, M. Opher, J. D. Richardson, and D. Tordella. *Under revision for J. Geophys. Res.*, 2016.
[5] F. Fraternale, L. Gallana, M. Iovieno, M. Opher, J. D. Richardson, and D. Tordella. *Physica Scripta*, 91(2): 02301155, 2016.
[6] M. E. Hill, R. B. Decker, L. E. Brown, J. F. Drake, D. C. Hamilton, SM Krimigis, and M. Opher. *Astroph. J.*, 781(2):94, 2014.
[7] http://voyager.jpl.nasa.gov/mission/interstellar.html
[8] M. Opher. *Space Sci. Rev.*, pages 1–20, 2015.
[9] M. Opher, J. F. Drake, M. Swisdak, K. M. Schoeffler, J. D. Richardson, RB Decker, and G Toth. *Astrophys. J.*, 734(1):71, 2011.
[10] J. D. Richardson, J. C. Kasper, C. Wang, J. W. Belcher, and A. J. Lazarus. *Nature*, 454(7200):63–66, 2008.
[11] J. D. Richardson and L. F. Burlaga. *Space Sci. Rev.*, 176(1-4):217–235, 2013.
[12] J. D. Richardson and R. B. Decker. *Astrophys. J.*, 792(2):126, 2014.
[13] E. C. Stone, A. C. Cummings, F. B. McDonald, B. C. Heikkila, N. Lal, and W. R. Webber. *Science*, 309(5743):2017–2020, 2005.

CORRELATED FORCING WITH AN ACTIVE GRID TO CONTROL TURBULENCE

Kevin Griffin[1], Nathan Wei[1], Marcus Hultmark[1], Eberhard Bodenschatz[2], and Gregory Bewley*[2]
[1]*Department of Mechanical and Aerospace Engineering , Princeton University, Princeton, NJ, USA*
[2]*Max Planck Institute for Dynamics and Self-Organization, Göttingen, Germany*

Summary Research on classical turbulence theory has benefited from the use of active grids that allow a wider range of flow conditions to be generated than their passive counterparts [1]. We used a new type of active grid with 129 independently rotating paddles to imprint different correlations into wind tunnel turbulence. The grid's control over the RMS fluctuation velocity and integral length scale allowed the turbulence Reynolds number Re_λ to be held constant and isotropy to be controlled. We then imposed correlations into the otherwise random motions of the paddles through convolution with kernels of different shape. At constant Re_λ, the velocity correlation functions collapsed into different families based on kernel shape when scaled by the integral length scale, regardless of flow anisotropy. This suggested that the active grid could change the structures in the flow. The exceptional degree of control over flow properties offered by these methods could allow hypotheses about the influence of large-scale structure on the various properties of turbulence to be tested more precisely and extensively.

EXPERIMENTAL SETUP

The experimental apparatus consisted of a wind tunnel with the active grid mounted on the upstream end of the test section and a traverse to hold a hot wire constant temperature anemometer (single- or cross-wire). The probes were calibrated [2] using ten known velocities produced by a calibration unit. Measurements were taken in the center of the tunnel at a location 5.59 meters downstream of the grid. For all tests, the free stream velocity in the wind tunnel was approximately 1.5 m/s. The raw voltage data were corrected using these readings to control against temperature changes across tests.

The active grid, part of the Göttingen Turbulence Facility, was composed of 129 independently-moving paddles forming an 11×13 octagonal array. Each paddle was 11.5 cm wide and rotated on its diagonal, moving 90 degrees in either direction from the open orientation. The positions of the paddles were updated every 0.1 seconds by a computer program.

The positions of each paddle were stored in memory along with their past and future positions. Raw positions began as uniform random noise, which was then convolved with a 3-dimensional kernel function, composed of a spatial kernel function multiplied by a temporal kernel function, to produce correlated positions. The width of the spatial kernel, σ_s, corresponded to the size of the correlations in the cross-sectional dimensions of the flow. Taylor's Hypothesis allowed the temporal kernel length σ_t to be mapped to an effective correlation length in the streamwise dimension of the flow. Thus, altering the size of a kernel by changing σ_s and σ_t would change the relative physical dimensions of flow structures produced by the grid. Top hat and long tail functions, shown in blue and red in Figure 1(b), were used to create these correlations.

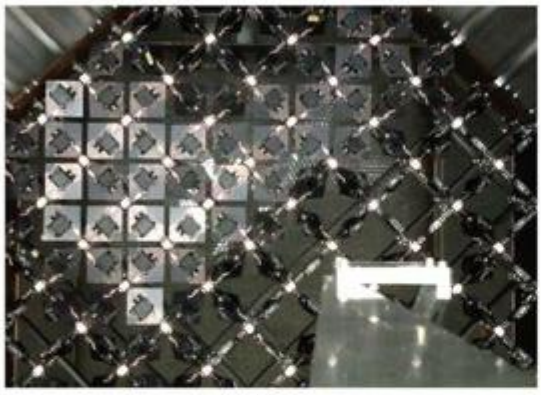

(a)

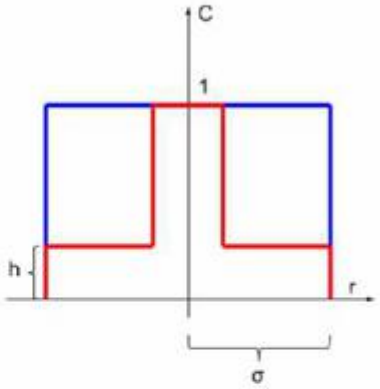

(b)

Figure 1: (a) Photograph of the active grids paddle configuration during operation, viewed from the probe mount.
(b) Correlation kernels used in the experiments, with top hat kernel shown in blue and long tail kernel shown in red. The correlation length σ represents either σ_s or σ_t. The height h of the long tail kernel was fixed to be 0.1.

*Corresponding author. Email: gregory.bewley@ds.mpg.de

RESULTS

Controlling Flow Parameters

θ' was defined as the root mean square of all paddle angles θ, where $\theta = 0$ for paddles parallel to the flow. Increasing θ' increased linearly u', the root mean square of the fluctuation velocities of the turbulence. Integral length scale was defined as the correlation distance ($r = U_{\text{avg}} \cdot t$) at which the normalized velocity correlation function dropped below $\frac{1}{e}$ [3]. Increasing σ_s and σ_t increased proportionally the integral length scale, with saturation occurring as the integral length scale approached the size of the tunnel. The Taylor length scale λ varied with the correlation kernel applied, so the turbulence Reynolds number Re_λ was controlled by adjusting θ' to change u'. Constructing kernels so that $\frac{\sigma_s}{\sigma_t} = 1$ produced near-isotropic turbulence. This ratio thus indicated the relative isotropy of a flow produced by a kernel with given correlation lengths.

Controlling Correlation Functions

Applying top hat and long tail correlation kernels with isotropic and anisotropic $\frac{\sigma_s}{\sigma_t}$ ratios created independent groups of velocity correlation functions in a series of tests all run at $Re_\lambda = 200 \pm 10$. In Figure 1(a), the much slower decay of the anisotropic correlation functions implied that greater anisotropy increased the spatial persistence of large-scale structures in the flow. In Figure 1(b), the type of correlation kernel affected the small-scale behavior of the flows independent of anisotropy.

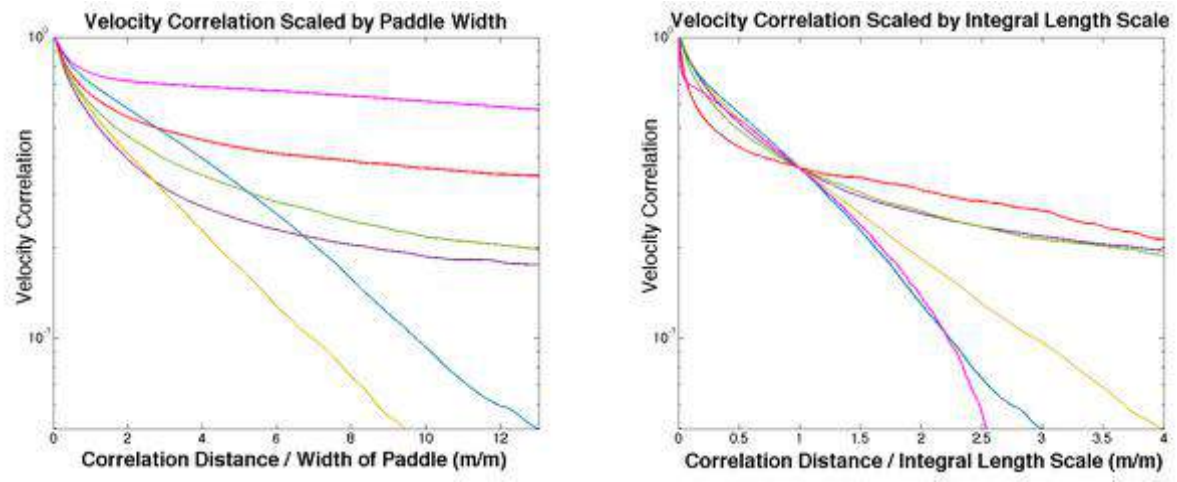

(a) (b)

Figure 2: Velocity correlation functions for several different correlation kernels of varying type and degree of anisotropy, normalized by (a) paddle width and (b) the integral length scale. The pink and blue curves represent anisotropic and isotropic top hat kernels, while the yellow, purple, green, and red curves are long tails of increasing anisotropy. The separation of the curves in (a) at large scales shows that persistence of large-scale structures increases with anisotropy. Normalizing the curves by the integral length scale in (b) isolates small-scale behavior, revealing that the type of correlation kernel affects flow behavior at small scales independent of anisotropy. Thus, by controlling the kernel shape and the relative dimensions of the temporal and spatial kernels, the small and large scales of the flow can be independently controlled.

CONCLUSIONS

Spatial and temporal correlations of the paddles on an active grid enabled control over a large number of flow parameters, including u', integral length scale, Re_λ, and isotropy. The ability to change the shape of velocity correlation functions using different correlation kernels demonstrated the grid's control over the shape and behavior of large- and small-scale structures in the flow, as well as the fact that grid and flow correlations were directly related. Such unprecedented control of the structures and properties of turbulence will have sizable implications for studies of the fundamentals of turbulence and for technological flows where mixing is important.

References

[1] Makita H.: Realization of a large-scale turbulence field in a small wind tunnel. Fluid Dyn. Res. 8, 53, 1991.
[2] Cekli H.E., Joosten R., van de Water W.: Stirring turbulence with turbulence. Phys. Fluids 27, 125107, 2015.
[3] Bewley G.P., Chang K., Bodenschatz E.: On Integral Length Scales in Anisotropic Turbulence. Phys. Fluids 24, 061702, 2012.

A NEW MODEL OF TURBULENT MIXING BY A JET IMPACTING A STRATIFIED INTERFACE

Johann Herault *[1,2], Giulio Facchini[2], and Michael LeBars[2]
[1]*Institut de Radioprotection et de Sûreté Nucléaire, BP 3, 13115 St Paul lez Durance, France*
[2]*CNRS, Aix-Marseille Université, Ecole Centrale Marseille, IRPHE UMR 7342, 49 rue F. Joliot-Curie, 13013 Marseille, France*

Summary We investigate experimentally the mechanism of erosion by a turbulent jet impinging a density interface with moderate Reynolds numbers and low Froude numbers. From our measurements, we present a new scenario of turbulent mixing. The turbulent eddies contribute indirectly to the mixing by generating surface gravity waves. The waves are then amplified by a mechanism similar to the Miles instability characterized by the presence of a critical layer, where the phase velocity of the waves matches the velocity of the mean flow. This amplification leads to the breaking of the wave, which mixes efficiently both fluids.

INTRODUCTION

Mixing between fluids with different density occurs in geophysical, in astrophysical and in industrial context [1]. It relies on a complex process where the kinetic energy is irreversibly converted into potential energy. Our work is motivated by the industrial applications in the nuclear safety context, where a lighter fluid (hydrogen) must be mixed with the ambient fluid (air) to avoid the ignition of explosive reactions [2]. We consider the case of a sharp density interface impinged by a turbulent round jet. The turbulent jet of light fluid (water) of density ρ_1 impinges a volume of heavier fluid (salty water) of density $\rho_2 > \rho_1$, such that the outflow of the jet is orientated in the gravity direction and orthogonal to the density interface. The jet is driven by an upstream pump and the buoyant effect are initially localized in the region of the impact (figure 1). The salty water is progressively mixed with the fresh water until the gradients of concentration disappear. We investigate the mechanism of erosion of the density interface by a turbulent jet for moderate Reynolds number $Re = u_i b_i/\nu$ ($Re \in [2 \circ\ 3] \times 10^3$) and low Froude number $Fr_i = u_i/\sqrt{b_i g'}$ ($Fr_i < 2$) with u_i and b_i the typical velocity and width of the jet at the interface and $g' = g(\rho_2 \circ\ \rho_1)/\rho_1$ the reduced gravity acceleration. The velocity field is measured by particle image velocimetry (PIV) process in the vertical plane of the laser sheet, which crosses the nozzle of the jet. The density is measured by planar laser-induced fluorescence (PLIF).

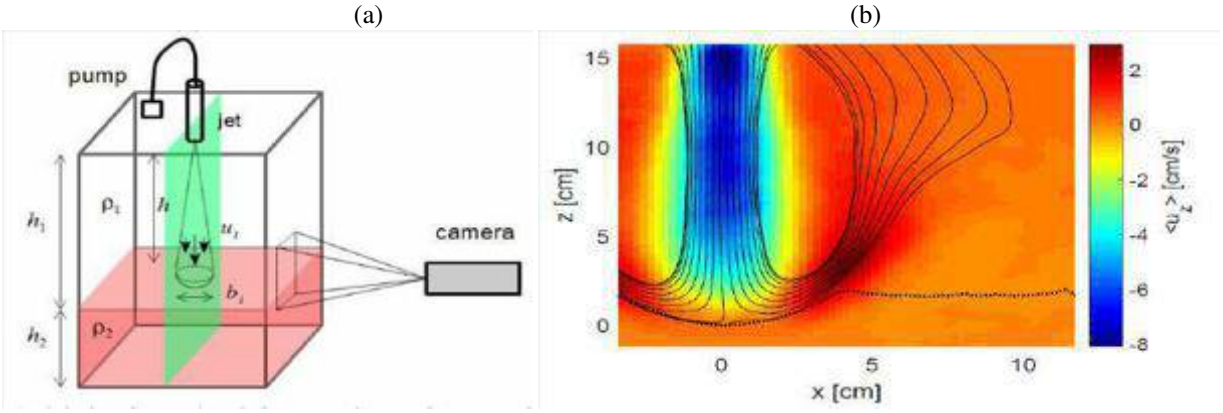

Figure 1: (a) A schematic of the experimental set-up showing a rectangular tank (30x30x50cm) filled with water (h_1) and a saline solution (h_2). The nozzle is located at a height h from the interface. (b) Streamlines (black curves) of the mean flow, superimposed on the vertical component of the mean velocity field $\langle u_z \rangle$ (cm/s). The black dotted curve corresponds to the time-averaged location of the interface separating both fluids.

AN NEW SCENARIO OF TURBULENT MIXING

The classical models of erosion (see e.g. [3, 4]) are commonly based on the mixing capacity of vortices, which engulf the heavy fluid at the interface before being advected by the mean flow outside the impinged region. However no experimental study has demonstrated quantitatively such mechanism in a non-buoyant jet. Our experimental results show that the mixing is

*Corresponding author. Email: herault@irphe.univ-mrs.fr

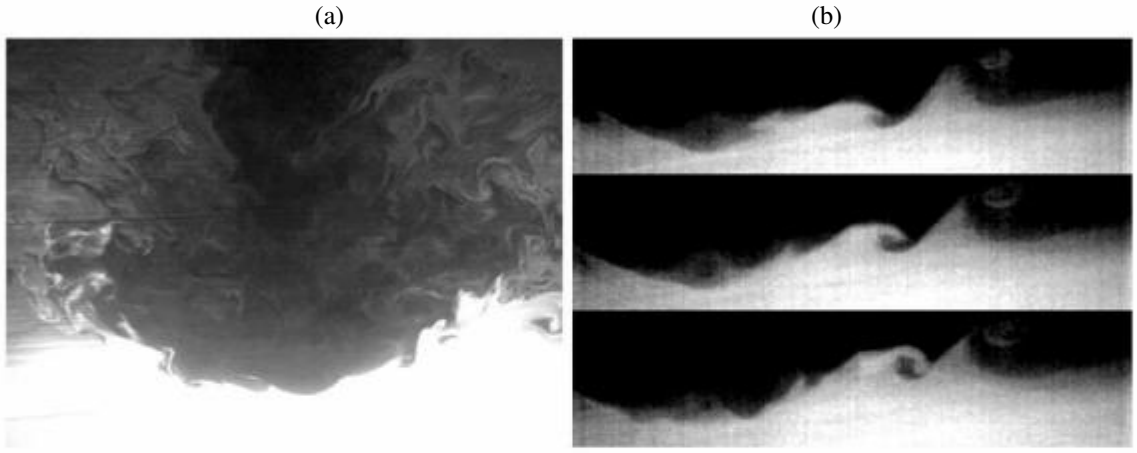

Figure 2: (a) Mixing process induced by surface-gravity waves in the vicinity of the interface ($15 \times 20cm^2$) and (b) of the dome head ($15 \times 8cm^2$). The heavy fluid has been dyed by rhodamine and corresponds to the bright region.

induced by the breaking of surface-gravity waves (figure 2.(a)) and the eddies play only the role of waves generator. We have investigated in details the different steps of this process: the generation, the amplification and the breaking of the waves.

We draw a global picture of the mechanism of erosion. The jet impinges the interface between both fluids and the time averaged impact describes a parabolic dome (figure 1.(b)). Inside the dome, the surface is convoluted by the turbulent fluctuations of the jet. Our measurements shows that the Kelvin-Helmholtz instability is inefficient to trigger perturbations, because the local shear is very weak in the vicinity of the dome head. The waves are rather generated by the turbulent eddies coming from the jet. The vortices excite surface-gravity waves, which propagate outward the impinged region, but the eddies do not contribute directly to a significant mixing as expected from the scenario of eddy engulfment. Theses waves are identifiable on figures 2.(a) and 2.(b). During the propagation, the height of the waves increases until they breakdown close to the border of the dome. This process is illustrated on the three successive pictures of the interface of the figure 2.(b), with waves propagating from left to right. As the Kelvin-Helmholtz instability is not able to amplify the waves, an other mechanism must transfer the energy to the waves.

For the first time, we show that the amplification of the waves is caused by an energy transfer from the mean flow via a mechanism similar to the one described by Miles [5] in shear flows. Indeed, we observe a critical region where the phase velocity of the waves matches the time-averaged tangential velocity following the interface. As described by Miles [5] , the waves are amplified below the critical layer. Finally, the breaking of the waves induces a strong mixing due to the wrapping of filaments. The heavy fluid is then transported in the bulk flow where the turbulence of the jet mixes both fluids (figure 2.(a)).

CONCLUSION

Our work shows the key role played by the waves in the erosion process at low Froude. The waves are amplified by a mechanism involving a critical layer [5] and this amplification leads to the breaking of the waves, which is here the main source of erosion. Waves being the primordial mechanism for mixing, we define a new scaling law for the entrainment rate as a function of local Froude number, based on waves properties. This law is in good agreement with present and past experimental measurements, hence solving a long standing problem [4]. This work is detailed in [1].

References

[1] Herault, J. and Facchini, G. and LeBars, M. :Erosion of a sharp density interface by a turbulent jet at low Froude number. Submitted to J. Fluid Mech.

[2] Studer, E. and Brinster, J. and Tkatschenko, I. and Mignot, G.and Paladino, D. and Andreani, M.: Interaction of a light gas stratified layer with an air jet coming from below : Large scale experiments and scaling issues. Nuclear Engineering and Design, vol. 253, pp. 406-412, 2012.

[3] Cotel, A. J. and Gjestvang, J. A. and Ramkhelawan, N. N. and Breidenthal, R. E.: Laboratory experiments of a jet impinging on a stratified interface. Exp. Fluids, 23(2),155-160, 1997.

[4] Shrinivas, A. B. and Hunt, G. R.: Unconfined turbulent entrainment across density interfaces. Journal of Fluid Mechanics 757, 573-598.

[5] Miles, J. W.: On the generation of surface waves by turbulent shear flows. J. Fluid Mech 7(03):469-478, 1960.

SPECTRAL DYNAMICS IN ENSTROPHY INERTIAL RANGE IN α-TURBULENCE

Takahiro Iwayama [*1] and Takeshi Watanabe[2]

[1]*Department of Planetology, Kobe University, Kobe, Japan*
[2]*Department of Scientific and Engineering Simulation, Nagoya Institute of Technology, Nagoya, Japan*

Summary We investigate spectral dynamics in the enstrophy inertial range in forced-dissipative turbulence for a generalized two-dimensional fluid system, the so-called α-turbulence, by the eddy damped quasi-normalized Markovianized (EDQNM) closure approximation equation for this system. As the non-local parameter α increases, the downward enstrophy flux dominates the net enstrophy flux and the triads responsible for the net enstrophy flux become more non-local. According to this analysis, we derive the transition of the exponent of the enstrophy spectrum at $\alpha = 2$, which has been observed by previous direct numerical simulations, from an asymptotic analysis of EDQNM approximation equation. The energy transfer in the enstrophy inertial range is also investigated similarly.

INTRODUCTION

The generalized two-dimensional (2D) fluid system was introduced by Pierrehumbert *et al*.[3] as a tool for studying effects of non-locality of triad interactions on 2D Navier-Stokes (NS) turbulence. The governing equation of the system is given by

$$\frac{\partial q}{\partial t} + \frac{\partial \psi}{\partial x}\frac{\partial q}{\partial y} - \frac{\partial \psi}{\partial y}\frac{\partial q}{\partial x} = \mathcal{D} + \mathcal{F}, \quad q = -(-\boldsymbol{\nabla}^2)^{\alpha/2}\psi, \tag{1}$$

where $\psi(\boldsymbol{x}, t)$ is the stream function and $q(\boldsymbol{x}, t)$ is a scalar advected by an incompressible velocity $\boldsymbol{v} = \boldsymbol{e}_z \times \boldsymbol{\nabla}\psi$. Here, $\boldsymbol{e}_z$ is a unit vector normal to the plane of motion, α is a real number, $\boldsymbol{\nabla}^2$ is the Laplacian in 2D space, and $\mathcal{D}$ and $\mathcal{F}$ are dissipation and forcing terms, respectively. When $\alpha = 2$, this system reduces to the 2D NS system. This system has two inviscid invariants, the generalized energy $\mathcal{E} \equiv -\langle \psi q \rangle /2$ and the generalized enstrophy $\mathcal{Q} \equiv \langle q^2 \rangle /2$. Here, those are frequently referred to as energy and enstrophy for simplicity, respectively, and the angle brackets denote a spatial average.

In the present paper, we consider statistically steady state of turbulent flows governed by (1) forced at a narrow wavenumber range around a forcing wavenumber k_{f} on an infinite plane with appropriate decay conditions at infinity. Turbulent flows governed by (1) is frequently referred to as α-turbulence.

Since there are two inviscid invariants, the cascade phenomenon of both invariants are realized in α-turbulence. Previous direct numerical simulations (DNSs)[3, 4] indicated that the enstrophy spectrum $Q(k)$ in the enstrophy inertial range, which is formed in larger wavenumber side than k_{f}, takes the form,

$$Q(k) \propto \begin{cases} k^{-(7-2\alpha)/3}, & (\text{for } 0 < \alpha < 2). \\ k^{-1}\{\ln k\}^{-1/3}, & (\text{for } \alpha = 2). \\ k^{-1}, & (\text{for } \alpha > 2). \end{cases} \tag{2}$$

The transition of the spectrum (2) was explained by a phenomenology proposed by Watanabe & Iwayama[5]. However, underlying physics of their phenomenology has not yet fully understood. Moreover, the spectrum (2) has not been analytically derived. Thus, to provide a dynamical basis to their phenomenology, we analyse the enstrophy transfer in the enstrophy inertial range and the triad interactions responsible for the enstrophy transfer using an eddy damped quasi-normal Markovianized (EDQNM) closure approximation equation of the present system[1, 2]. Furthermore, we derive (2) from the EDQNM closure approximation equation.

RESULTS

First, using the detailed conservations of energy and enstrophy, we decompose the enstrophy flux into two parts:

$$\Pi(k) = \Pi^{(+)}(k) - \Pi^{(-)}(k), \tag{3a}$$

$$\Pi^{(+)}(k) = \int_k^\infty \mathrm{d}k' \int_0^k \mathrm{d}l \int_0^l \mathrm{d}m\, T_\alpha^{\mathcal{Q}}(k', l, m), \;\; \Pi^{(-)}(k) = \int_0^k \mathrm{d}k' \int_k^\infty \mathrm{d}l \int_l^\infty \mathrm{d}m\, T_\alpha^{\mathcal{Q}}(k', l, m). \tag{3b}$$

Here, $T_\alpha^{\mathcal{Q}}(k', l, m)$ is the triad enstrophy transfer function in the EDQNM approximation[2]. Furthermore, normalizing the triads comprising $\Pi^{(+)}$ and $\Pi^{(-)}$, and assuming the enstrophy spectrum of the form $Q(k) = C_\alpha k^{-n}$, we obtain the exponent n in the enstrophy inertial range as $n = (7 - 2\alpha)/3$ for $0 < \alpha < 2$ and $n = 3 - \alpha$ for $\alpha > 2$, and two parts of the enstrophy flux in the enstrophy inertial range as a function of α. Two parts of enstrophy flux normalized by the net enstrophy flux are

*Corresponding author. Email: iwayama@kobe-u.ac.jp

shown in Figure 1. Figure 1 indicates that when α is small, $\Pi^{(+)}$ and $\Pi^{(-)}$ far exceed the net enstrophy flux and a small

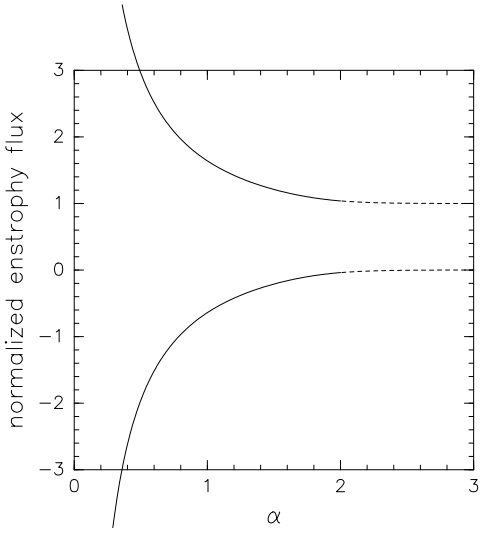

Figure 1: α-dependence of $\Pi^{(+)}(k)$ and $\Pi^{(-)}(k)$ normalized by the net enstrophy flux $\Pi(k)$ in the enstrophy inertial range. The bold and thin lines indicate $\Pi^{(+)}(k)/\Pi(k)$ and $-\Pi^{(-)}(k)/\Pi(k)$, respectively. Dotted lines indicate the normalized enstrophy fluxes for $\alpha > 2$, where our analysis fails to derive spectrum for $\alpha > 2$.

difference between them derives the net enstrophy flux downward. The upward enstrophy flux $\Pi^{(-)}$ exceeds the net enstrophy flux when $\alpha \lesssim 0.79$. As α increases, both upward and downward enstrophy fluxes decrease, and $\Pi^{(+)}$ dominate the net enstrophy flux up to and beyond $\alpha \simeq 2$. Note that the enstrophy fluxes calculated by the EDQNM closure approximation equation reasonably agree with the DNS results[6].

Next, we examine the characteristics of the triads responsible for enstrophy transfer in the enstrophy inertial range. (Figures are not shown.) Approximately 80% of the downward and upward enstrophy fluxes are carried by triads with minimum wavenumber below half of the medium wavenumber. The triads responsible for the downward enstrophy flux become more non-local as α increases, while those responsible for the upward enstrophy flux are insensitive to α.

According to the nature of the triad interactions responsible for the enstrophy transfer, we perform an asymptotic analysis of the EDQNM approximation equation and theoretically derive the transition of the exponent of the enstrophy spectrum (2). The phenomenology proposed by Watanabe and Iwayama[5] modifies the characteristic time scale of enstrophy transfer in Kraichnan-Leith-Batchelor phenomenology. This modification can be interpreted as the combined effects of the non-locality of the decaying time of the third-order moments associated with the triads and the dominance of non-local triad interactions.

The energy transfer in the enstrophy inertial range is investigated similarly. In the enstrophy inertial range, the downward and upward energy fluxes are equivalent; therefore, the net energy flux vanishes. The triads responsible for the energy transfers and those for the downward enstrophy transfer show identical characteristics.

ACKNOWLEDGMENTS

This study was supported by a Grant-in-aid for Scientific Research (C) No.15K05288 from the Japanese Society for the Promotion of Science. The GFD-DENNOU Library was used for drawing the figure.

References

[1] B. H. Burgess and T. G. Shepherd: Spectral nonlocality, absolute equilibria, and Kraichnan-Leith-Batchelor phenomenology in two-dimensional turbulent energy cascades. J. Fluid Mech. 725: 332, 2013.

[2] T. Iwayama and T. Watanabe: Universal spectrum in the infrared range of two-dimensional turbulent flows. Phys. Fluids 26: 025105, 2014.

[3] R. T. Pierrehumbert and I. M. Held and K. L. Swanson: Spectra of local and nonlocal two dimensional turbulence. Chaos, Solitons & Fractals 4: 1111, 1994.

[4] N. Schorghofer: Energy spectra of steady two-dimensional turbulent flows. Phys. Rev. E 61: 6572, 2000.

[5] T. Watanabe and T. Iwayama: Unified scaling theory for local and non-local transfers in generalized two-dimensional turbulence. J. Phys. Soc. Japan 73:3319, 2004.

[6] T. Watanabe and T. Iwayama: Interacting scales and triad enstrophy transfers in generalized two-dimensional turbulence. Phys. Rev. E 76:046303, 2007.

GEOMET IC RELA ION OF ORTICES OF DIFFE ENT SCALES IN TURBULENT FLOW

eiichiro Iza a[1a)], Masato irota[1], Yu Nishio[1] & Yu ukunishi[1]
[1]Departm nt of Mecha ical Systems nd Design, ohoku University, Sendai, Japan

Summary In h mogeneous iso ropic turbulenc , geometric relations between vortices of two groups, whose scales are twice different, are investigated by focusing on the vortex stretching. Hierarchical vor ices are extracted by Fourier band-pass filter and each vortex is r constructed by a group of vo tex segments aligned along the vortex axis. It is found that vortic s of larger scale contributing to t e stretching of ortices of a smaller scale are likely to be orthogonal to the smaller vortices an that the larger vortices tend to be aligned antiparallel to each other.

ACKGROUND AND OB ECTIVE

Turbulenc is characteri ed by vortex motions of va ious scales. Their mutual i teractions produce the flow of kinetic energy from t e energy-containing large- cale vortices to the high-dissipative small-scale vortices, which is a couple of times larger t an the Kolmogorov scale. Such turbulent behaviours are well described in a statistical sense;[1] however, the relation between the v rtex motions and the ener y transfer mechanism still remains unclear. Recent remarkable progress of computer environments permits us to directl access the detailed structu es of comple ly entangled ortices in turbulent flows. Goto and Kawahara [2] reported that anti-parallel pairs of vortex tu es creates further smaller vortices via vortex stretching process in a turbulent flo . Hirota et al. [3] found that fast stretching vortices ten to be orthog nal to the direction of larger vortices, while vortices not stretching are aligned parallel or anti parallel to the larger ones. his study investigates h w vortices are stretched in homogeneous isotropic tur ulence by analyzing the g ometric relation among vortices of dif erent scales, hich are extracted by a Fourier band-pass ilter.

ETHOD

Target tur ulent filed is obtained by a direct numeri al simulation using a pseudo-spectral method together ith phase shift method to eliminate aliasing errors. otal number f gird points is 512^3. Solenoidal force is randomly applied to the low wavenumber region ($1 \le k \le 2$) to eep the flow filed in statistical equilibri m.[4] Besi es, the JHU urbulence database of 1024^3 grids (htt ://turbulence. ha.jhu.edu) is also used to nalyze a higher Reynolds number flow. he Taylor Reynolds numbers Re_λ are 267 for the for er and 427 f r the latter. Filtering rages re $k_1 = 12\sqrt{2}$ ($12 \le k < 24$ for small scale and k_2 $8\sqrt{2}$ ($8 \le$ < 16) for large scale, where k_1 and k_2 re the center wavenumber of each band ass filter. Extracted vortices are replaced with a gr up of cylindrical vortex se ments in a f llowing man er:[3] (1) Find vortices using a certain threshold of the second inv riant of velocity gradient te sor Q, (2) Ide tify the vorte axes by con ecting the points at which Q become the local maxi a, (3) Estim te the vortex radii using a wavelet-based method. After that, the geometric relations between vortices of tw different scales are discuss d.

ESULTS

Figure 1 hows the joint probability density functio of relative p sitions of twi e larger vortices, k_2, to target vortices, k_1. Only the top 10% vortic s that show high stretching speed are picked up. The xes (ξ, η) in the figure represent the direction of target vortex a d its vertical direction, where R is the radius of larger segment. In t e vicinity of stretching vortices, twic larger vortices tend to ap ear in the ±45° directions. Beside, picking up the pri ary and the secondary vortices contributing the stretching, it is fo nd that they tend to be orth gonal each other and the correlatio of their cosi e angles beco es higher at round -1, regardless of the Reynolds number. This fact impli s that a vortex in a turbulent field tend to be stretched by a pai of larger anti-parallel vorti es.

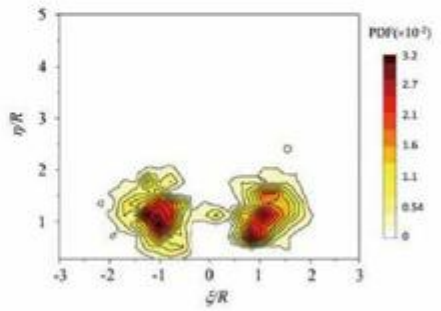

Fig. 1 Joint PDF o positions of t ice larger vortices relative to the target stretching vortices (512^3 case)

References

[1] Ishihara T., otoh T., Kaneda Y.: Study of Hig -Reynolds Numb r Isotropic Turbu ence by Direct Nume ical Simulation, Annu. Rev. Fluid Mech. 41:165-180, 2 09.

[2] Goto S., Ka ahara G.: Generation Mechanism of ierarchy of Coherent Vortices in Turbulence Sustained by Steady Force, Pro . ETC14, 2013.

[3] Masato H., oshihisa K., Nishio Y., Izawa S., F kunishi Y.: Stretc ing process of m lti-scale vortices in tu bulent flow, Proc. 12th ICFD, 796-7 7, 2015.

[4] Alvelius A.: Random forcing of three-dimensional homogeneous turbulence, Phys. Fluids, 11:1880-188 , 1999.

[a)] Correspondin author. Email: izawa@fluid.mech.tohoku.ac.jp

DEVELOPMENT OF LOW FRICTIONAL MARINE AF PAINT BASED ON A NOVEL DRAG REDUCING POLYMER OF FDR-SPC

Inwon Lee[1a)] & Hyun Park[2]
[1]*GCRC-SOP, Pusan National University, Busan, South Korea*
[2]*GCRC-SOP, Pusan National University, Busan, South Korea*

Summary In this study, a novel skin-friction reducing polymer named FDR-SPC (Frictional Drag Reduction Self-Polishing Copolymer) has been synthesized. The drag reducing functional radical such as PEGMA (Poly(ethylene) glycol methacrylate) has been utilized to participate in the synthesis process of the SPC. The types of the baseline SPC monomers, the molecular weight and the mole fraction of PEGMA were varied in the synthesis process. In the high-Reynolds number flow measurement with a flush-mounted balance and a LDV (Laser Doppler Velocimeter), the skin friction of the present FDR-SPC is found to be smaller than that of smooth plate in the entire Reynolds number range, with the average drag reduction efficiency being 13.5% over the smooth plate.

INTRODUCTION

The reduction of frictional drag of turbulent boundary layer is of great importance for the fuel economy of ship. Along with the development of hull form optimization technique, the wavemaking resistance has become less than 20% of the total drag of most modern ships. Therefore, the advantage from the reduction of the remaining frictional drag would be enormous. The skin frictional drag is closely associated with the coherent structures, e.g. hairpin vortices in the turbulent boundary layer flow. Various control strategies toward the attenuation of the drag-inducing flow structure have been proposed during several decades. One of the most effective drag reduction strategies is the polymer injection, which was first introduced by Toms [1]. Toms [1] found that addition of few ppm of a high molecular weight polymer to a turbulent water flow can result in large (up to 80%) reduction of skin friction drag. Added long chain polymer molecule extracts the turbulent energy out of the adjacent flow by coiling its chain structures and then releases the energy by becoming stretched back in the shear flow. The turbulent energy transfer between the freestream and the near-wall flow is thus interfered, leading to a significant skin friction reduction. This is named Toms effect after who discovered it. The polymer injection has been put into practice for the pipeline transportation of petroleum, demonstrating one of the most effective examples of drag reduction. It has been suggested that the polymer injection be applied to the frictional drag reduction for ships. There have been various researches to exemplifying the drag reduction efficiency of polymer injection in turbulent boundary layer [2]. From the aspect of implementation, however, the polymer injection is impractical for ship application. This is because it necessarily requires the injection holes to be installed onto the hull surface, which would cause significant structural strength issues. As a feasible alternative to the polymer injection method, Yang et al. [3] proposed a PEO-containing AF paint. They reported the release of PEO, the well-documented drag reducing agent leading to Toms effect, from the surface of coating. It was found that the PEO-mixed paint exhibited significant drag reduction efficiency in excess of 10% from various lab tests. In their paint, however, the PEO powders were physically mixed with the paint matrix, thereby giving rise to an increase in surface roughness and rapid release associated with the solubility of PEO in water. These factors may be detrimental to the longevity of drag reduction performance.

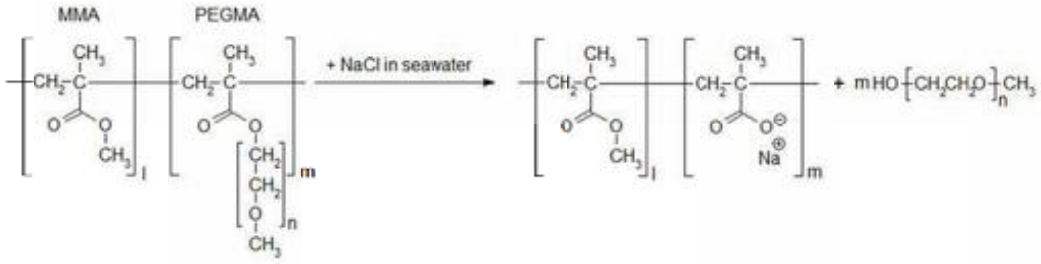

Fig. 1 Hydrolysis reaction of FDR-SPC

SYNTHESIS OF FDR-SPC

With a view to overcoming the drawbacks of the PEO-mixed paint in the previous research, a novel FDR-SPC is first synthesized in this study. The drag reducing functional radical such as PEGMA (Poly(ethylene) glycol methacrylate) has been utilized to participate in the synthesis process of the SPC. Figure 1 illustrates the release mechanism of PEO from the

[a)] Corresponding author. Email: inwon@pusan.ac.kr

hydrolysis reaction between the FDR-SPC and seawater. The types of the baseline SPC monomers, the molecular weight and the mole fraction of PEGMA were varied in the synthesis process.

The resulting SPCs were coated to the substrate plates for the subsequent hydrodynamic test for skin friction measurement. In a low-Reynolds number flow measurement using PIV (Particle Image Velocimeter), a significant reduction in Reynolds stress was observed in a range of specimen, with the maximum drag reduction being 15.9% relative to the smooth surface for PRD3-1, as shown in Table 1. Figure 2 shows the profiles of the streamwise turbulent intensity and the Reynolds stress. It is obvious that those turbulent quantities significanty decreased in the case of PRD3-1, corroborating the presence of Toms effect from the present FDR-SPC.

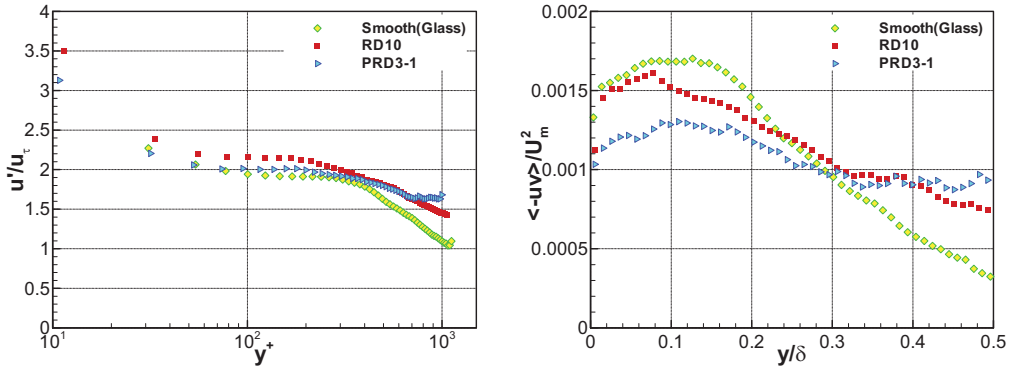

(a) Streamwise turbulence intensity (b) Reynolds stress

Fig. 2 Comparison of turbulent quantities in low-Reynolds number flow for FDR-SPC

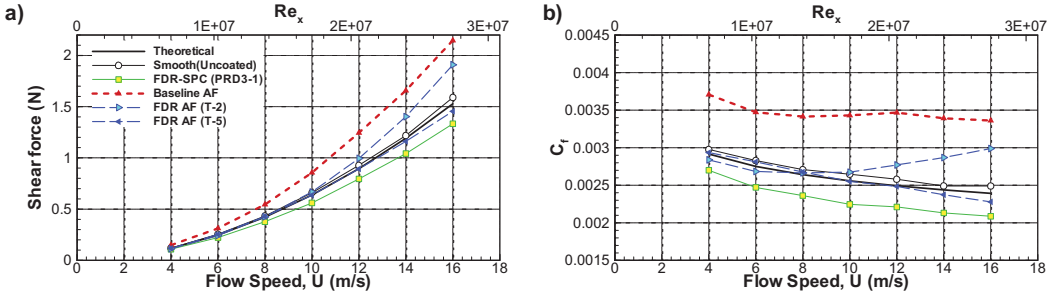

Fig. 3 Comparison of frictional drag in high Reynolds number flow for FDR-SPC and FDR AF coatings

PERFORMANCE OF FDR-SPC IN A HIGH REYNOLDS NUMBER FLOW

The present FDR-SPC was subsequently used as a binder for the FDR AF (AntiFouling) coating for marine application. The FDR AF coating consisted of FDR-SPC, antifouling pigment such as cuprous oxide (Cu_2O) and various additives. Measurement of the skin friction of the present FDR-SPC and the FDR AF coated surfaces was carried out in a high-Reynolds number flow measurement with a flush-mounted balance and a LDV (Laser Doppler Velocimeter). It is found that the FDR-SPC showed smaller skin friction than the smooth plate in the entire Reynolds number range, with the average drag reduction efficiency being 13.5% over the smooth plate. The FDR-AF (Anti-Fouling) coating manufactured from the present FDR-SPC exhibits drag reduction efficiency of about 20% over the conventional AF coatings, as shown in Fig. 3.

This work was supported by National Research Foundation of Korea (NRF) grant of the Korea government (MSIP) through GCRC-SOP (No. 2011-0030013)

References

[1] Toms B.: Observation on the flow of linear polymer solutions through straight tubes at large Reynolds numbers. *Proc. Intl Rheol. Congr.* **2**:135–141, 1948.

[2] Somandepalli V. S. R., Hou Y. X., Mungal, M. G.: Concentration flux measurements in a polymer drag-reduced turbulent boundary layer. *Journal of Fluid Mechanics*, **644**: 281-319, 2010.

[3] Yang J. W., Park H., Chun H. H., Ceccio S. L., Perlin M., Lee, I.: Development and performance at high Reynolds number of a skin-friction reducing marine paint using polymer additives. *Ocean Engineering*, **84**: 183-193, 2014.

CROSS PLANE VORTICITY DISTRIBUTIONS IN A RECTANGULAR WALL JET

Thrassos Panidis[1a)], Andrew Pollard[2] & Rainer Schwab[2]
[1]*Mechanical Engineering and Aeronautics Department, University of Patras, Patras, Greece*
[2]*Department of Mechanical and Materials Engineering, Queen's University, Kingston, Canada*

Summary Experimental results on the near field development of a turbulent rectangular wall jet with aspect ratio 10, issuing from a sharp-edged orifice at $Re_h \sim 23{,}000$ are presented and discussed. Hot wire X-probe measurements on cross plane grids provide information on the 3D characteristics of the flow field. Mean vorticity components were estimated by interpolation and derivation from the mean velocity measurements. Contour plots of flow characteristics are presented and discussed to uncover some complex flow physics.

INTRODUCTION

Wall jets have been studied extensively in the past, see Agelin-Chaab [1] for recent review. The initial 2D studies were rendered inadequate to provide proper physical understanding of these rather complicated flow fields. Several 3D studies have delivered significant information on wall jet development, see Schwab and Pollard [2]. Despite the consensus that vorticity plays an important role, the corresponding experimental information is rather scarce, see Craft and Launder [3]. In this work modern computer interpolation techniques are used in order to further exploit available 3D experimental measurements, providing first stage information on the vorticity distributions in a rectangular turbulent wall jet.

MATERIALS AND METHODS

The air jet was produced by a sharp-edged rectangular orifice (70x7 mm^2, equivalent hydraulic diameter $D_h = 12.73$ *mm*) mounted on the downstream end of a 1.05 m long, square cross sectioned settling chamber 0.350 *m* to the side. The exit Reynolds number, based on the slot height (h=7mm) and jet exit velocity, U_{exit}, was $Re_h = 23{,}000$. The velocity components in the streamwise (x-axis) and the spanwise (y-axis, parallel to the long side of the orifice) directions were measured with a miniature X-wire HWA probe and upon probe rotation the vertical velocity components were obtained (z-axis). Data were collected at equally spaced positions on cross plane grids at x/h= 1, 2, 3, 5, 7, 10, 15 and 20 distance from jet exit (see Schwab [4] for further details). The origin of the Cartesian coordinate system used in this work is located on the intersection of the wall plane and the short central axis of the orifice on the jet exit plane. Derivative variables and contour plots have been produced by applying the 'inverse distance interpolation' scheme on the raw measurements using Tecplot^{TM}. Contour plots of the measured and derived variables are presented in Figure 1. In all the plots, the black contour lines indicate the locations where the mean streamwise velocity takes values U/U_{cl}=0.5 and 0.95, where U_{cl} is the local centreline velocity.

EXPERIMENTAL RESULTS - DISCUSSION

Mean streamwise velocity distributions (Fig. 1a) present three main characteristics. The first is the appearance of two off centre peaks (saddle back profile) which reach a maximum of 23% over the central value at x/h=10. These peaks diminish downstream but persist to the last of the measurement stations at x/h=20. The second characteristic is the tendency of the wall jet towards axis switching indicated by the contraction of the jet in the spanwise direction and the spreading in the vertical direction away from the wall. The third characteristic is that although at the first cross plane the jet seems to diverge from the wall with peak values appearing over z/h=1, downstream a Coanda effect attracts the jet towards the wall and peak values appear at locations z/h<1. The **streamwise normal turbulent stress** distributions (Fig. 1b, very similar to those of the other normal stresses, not presented here) indicate that turbulence production is associated with the shear layers that develop between the jet and the ambient fluid, as well as between the mean velocity peaks and the centre of the jet. On the contrary, the wall impedes turbulence and the turbulent stresses gradually diminish downstream in the wall region. Shear layers also affect the vorticity distributions (normalized by h and U_{exit}). The **mean vorticity magnitude** ($|\boldsymbol{\Omega}|$, Fig. 1c) is higher around the jet core in the first downstream stations although far from the jet exit the shear layer developing close to the wall is responsible for the high vorticity values that dominate in this region. The **streamwise vorticity component** (Fig. 1d) presents in the first stations negative values more or less within the U/U_{cl}>0.5 zone and positive outside, whereas at farther downstream locations a system of four vortices seems to develop in the central area of the wall jet as indicated in Fig. 1d at x/h=20, which is a possible link to Ewing and Pollard [5] interpretation. The **transverse vorticity components** (Fig. 1e,f) are affected by the derivatives of the streamwise velocity across corresponding shear layers. Ω_y is in the first stations dominated by the shear layers along the large side edges of the jet, whereas the wall shear layer has a smaller effect which gradually becomes dominant downstream, not only for Ω_y but for $|\boldsymbol{\Omega}|$ as well. Similarly, at all measuring stations, Ω_z changes sign at the locations of U_x off-center peak ridges and the corresponding centerline trench developing in z-direction due to the saddle back profile. Extensive interpretation of the vorticity field evolution through examination of the axial mean vorticity equation will be presented with link to what is known in the case of the free jet (see Vouros et al. [6]).

[a)] Corresponding author. Email: panidis@upatras.gr

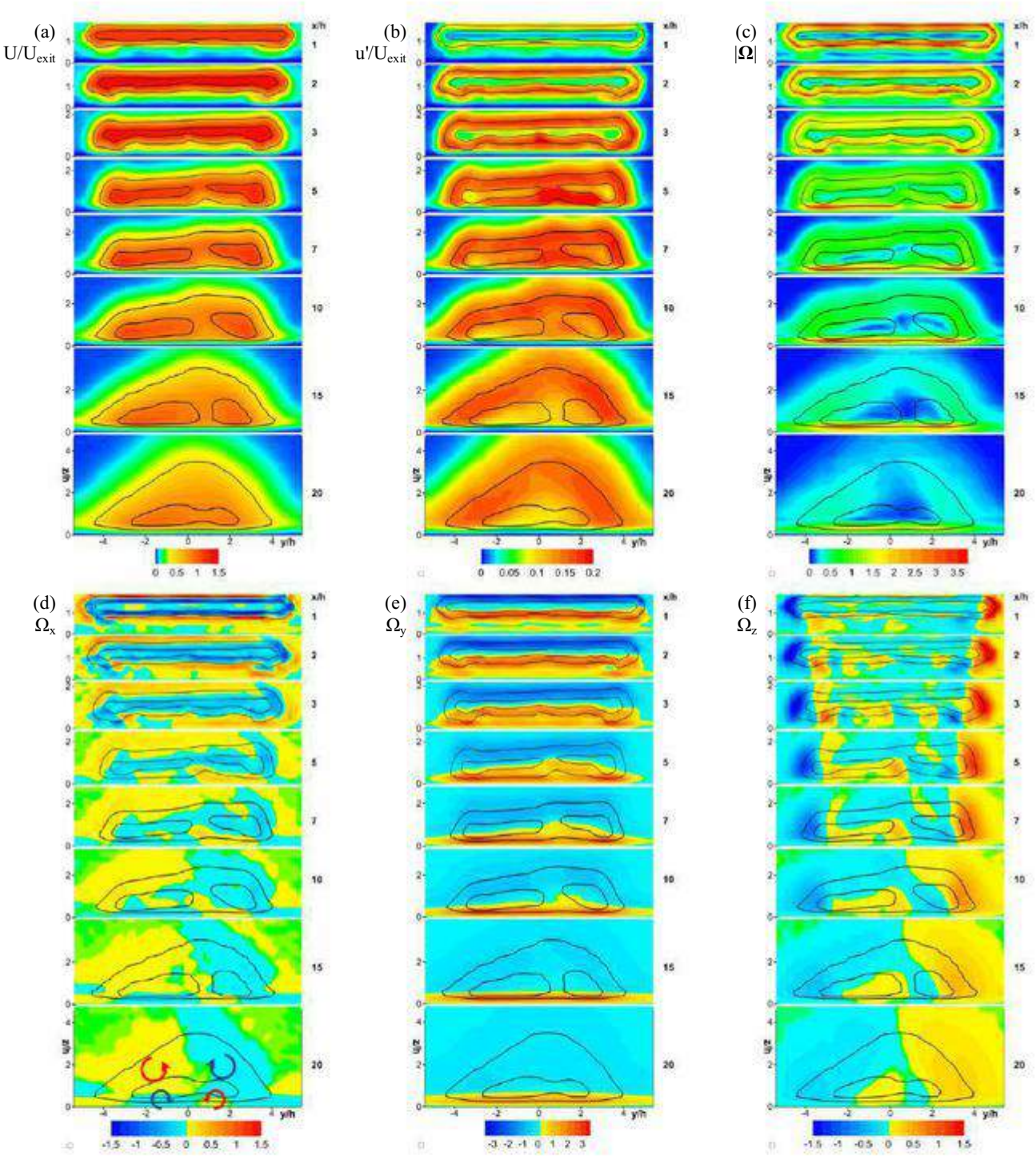

Figure 1. Contour plots of the axial mean (a) and rms (b) velocity and vorticity vector magnitude (c) and components (d, e, f) on cross planes at several distances (x/h) from jet exit

References

[1] Agelin-Chaab M.: Experimental Study of 3D Offset Jets and Wall Jets. *PhD Thesis*, Dept. Mech. & Manuf. Eng., Univ. Manitoba, Winnipeg, 2010.

[2] Schwab R.R., Pollard A.: An Experimental Investigation of Wall Jets Issuing from Rectangular Sharp-Edged Orifices. *Proc. 7th Symp. Turbulent Shear Flows*, Stanford University, Stanford, California, 1989.

[3] Craft T. J., Launder B. E.: On the spreading mechanism of the three-dimensional turbulent wall jet.. *J. Fluid Mech.* **435**: 305-326, 2001.

[4] Schwab R.: An Experimental and Numerical Investigation of 3D Jet Flows from Sharp-Edged Orifices. *Ph.D. Thesis*, Dept. Mech. & Mat. Eng., Queen's University, Kingston, 1986.

[5] Ewing D., Pollard A.: Evolution of the large-scale motions in a three-dimensional wall jet. *AIAA Paper* No. 97-1964, 1997.

[6] Vouros A. et al: Near field vorticity distributions from a sharp-edged rectangular jet. *Intl. J. Heat & Fluid Flow* **51**:383-394, 2015.

ANNULAR JET AERODYNAMIC AND PASSIVE CONTROL STUDY BY PROPER ORTHOGONAL DECOMPOSITION

B.Patte-Rouland [1], A.Danlos [2], E.Rouland [3]
[1] CORIA UMR 6614, Rouen University Avenue de l'université BP 12 76801 Saint -Etienne du Rouvray cedex
[2] Laboratoire de Dynamique des Fluides (DynFluid), EA 92, Arts et Métiers ParisTech, Paris,
[3] AREELIS Technologies 675 Rue Isaac Newton, 76800 Saint-Étienne-du-Rouvray FRANCE

Summary The annular jet is an example of complex shear flow situations. Two axisymmetric shear layers, originating at the jet exit, one at the nozzle lip and the other at the centre body, eventually meet downstream or interact with each other. The main aim of this study is to observe and analyze the effects of passive control on an annular jet with a great diameter ratio (r= 0.91), in order to find a new way to reduce jet instabilities. This contribution discusses the application of Proper Orthogonal Decomposition to the Particle Images Velocimetry (PIV) velocity fields of the initial zone of an annular jet. Passive control has already been used with round jets and has given promising results. This work will permit us essentially to have a better knowledge of annular jets and used the potential of Proper Orthogonal Decomposition for aerodynamic study.
Key-Words: - Annular jet, Particle Image Velocimetry, Proper Orthogonal Decomposition, Passive Control

INTRODUCTION

Annular jet is used in the industrial domain, in combustion (burners, bluff bodies…) or in industrial treatment processes. The geometry of the annular jet is determined by the ratio Di/Do, where Di represents the internal diameter and Do the external diameter. The interests of the flow here are the interaction between the jet and the recirculation zone near the nozzle of the annular jet. Many authors, like Ko [1], work on small diameter ratio annular jets, with a ratio Di/Do smaller than 0.7. Lumley [2] has proposed Proper Orthogonal Decomposition (P.O.D.) for identifying coherent and instantaneous structures in turbulent flow. This method provides a base for the modal decomposition of a set of functions, such as data obtained in the course of the experiments. The most striking property of this decomposition is optimality: it provides the most efficient way of capturing the dominant components of an infinite-dimensional process with only a few functions [3]. That is why the P.O.D. process has been applied in different turbulent flows to analyze experimental P.I.V. data with a view to extracting dominant features and trends: coherent structures [4]. The present study relies on an experimental investigation of the initial zone of a large diameter ratio annular air jet by the use of Particle Image Velocimetry (P.I.V.).

EXPERMENTAL SET-UP

The annular jet is characterized by the outer diameter Do, equal to 53.88 mm, and the inner diameter Di, equal to 48.75 mm. The thickness of the jet e is thus equal to 2.565 mm. In our set-up, Di/Do is equal to 0.91. The exit velocity Uo is equal to 30m/s which correspond to the value of the Reynolds number Re, based on the thickness e, of 7680. Nozzles used for experiments are presented on figure Fig.1.



Fig.1: annular jet nozzles with central obstacle made of (a) a cylindrical shape (b) a conical shape and (c) an ellipsoidal shape and experimental PIV set-up.

A double pulsed Nd-Yag laser is used to set up the light sheet. The output energy is nearly 30 mJ for each laser pulse. The wavelength is 532 nm. The observation field is 2.8*2.5 cm². In this study, the video images are recorded by a LAVISION Flow Master 3S camera. The acquisition frequency is 4 Hz. For all velocity fields, the sampling window has a size of 16 by 16 pixels (0.377 by 0.377 mm) and there is a 50 % overlap with the next window. 400 P.I.V. images have been recorded.

PROPER ORTHOGONAL DECOMPOSITION

Coherent structures are present in turbulent flow and P.I.V. is able to highlight those on the largest scale at any given moment. The scientific interest in the study of turbulence has led to the development of P.I.V. post-processing, which is able to bring out the inner driving mechanism of the flow [5]. P.O.D. provides an optimal set of basis functions for a set of data, Patte-Rouland [5] Danlos [6]. It is optimal in the sense that it is the most efficient way of extracting the most energetic components of an infinite dimensional process with only a few modes. The Proper Orthogonal Decomposition is a linear procedure, which decomposes a set of signals in modal base. Karhunen–Loève decomposition can be used to decompose flow in space and/or time and separate the key flow features from the transient flow.

EFFECTS OF PASSIVE CONTROL

For the annular jet, it appears that the stagnation point is put through important radial fluctuations and, axially, the maximal fluctuations are localized on the external-mixing layer. This was also observed by Ko and Chan [1], but they used a hot wire and this cannot measure null velocity. Figure 2 shows an example of the mean velocity field with the corresponding Reynolds decomposition fluctuation fields. The initial merging zone extends from the jet exit to the tip of the potential core.

[a] Corresponding author. beatrice.patte@coria.fr

This zone contains a recirculation zone. The stagnation point which marks the end of the recirculating region is located at x/Do=0.5.

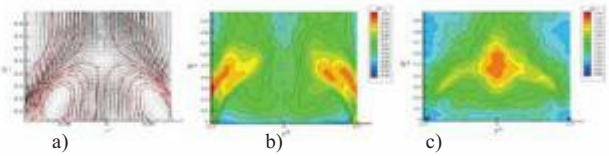

a) b) c)

Fig 2: Aerodynamic characteristics of the annular jet: a) Average velocity b) radial velocities c) axial velocities.

ELLIPSOIDAL ANNULAR JET

The ellipsoidal jet seems to narrow a little more towards the central axis than in the case of a basic annular jet. When we observe the field of average velocities, we notice that the recirculation zone completely disappears in the initial zone. We can see that the transversal fluctuations are no more situated in the stagnant point but rather in the separation point. The standard deviation of longitudinal velocities shows that there is only one zone of shear in the case of ellipsoidal obstacle. The flow of the ellipsoidal annular jet is then totally different from the basic annular jet.

The figure shows the results of the P.O.D. computation on an ellipsoidal annular jet. Mode 0 represents the mean velocity field of the flow. The transversal fluctuations of velocities situated in the separation zone (downstream the ellipsoid) seem to be reflected on mode 1 while the transversal fluctuations part dedicated to the shear flow on the rims of the jet seem to be represented by the mode 2. And then the mode 3 looks like the longitudinal fluctuations manager.

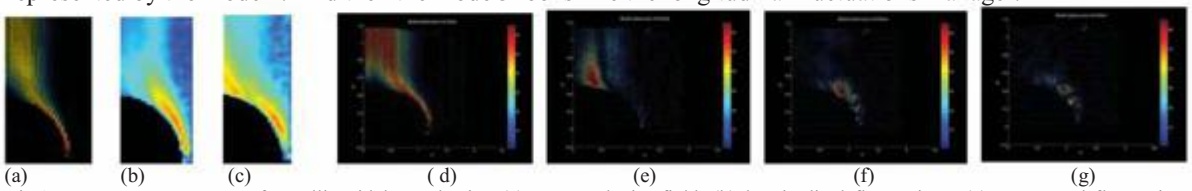

(a) (b) (c) (d) (e) (f) (g)

Fig.3: P.I.V. measurements of an ellipsoidal annular jet. (a) mean velocity field, (b) longitudinal fluctuations, (c) transversal fluctuations. and P.O.D. analysis of an ellipsoidal annular jet. (d) Mode 0, (e) Mode 1, (f) Mode 2, (g) Mode 3.

CONICAL ANNULAR JET

The flow of a conical jet seems to be more spread than in the case of an ellipsoidal annular jet. The jet seems to not narrow so much towards the central axis. The mode 0 shows the appearance of the mean velocity field. There is no real special characteristic drawn on the mode 2. Modes 1 and 3 seem to represent structures responsible for instabilities on the rims of the jet that we can see on the longitudinal (modes 1 and 3) as much as the transversal (mode 1) fluctuations of velocities.

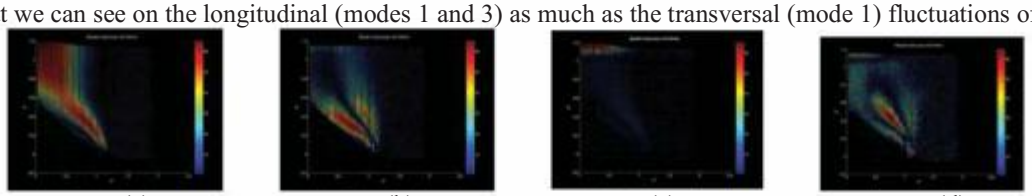

(a) (b) (c) (d)

Fig. 4: P.O.D. analysis of an ellipsoidal annular jet. (a) Mode 0, (b) Mode 1, (c) Mode 2, (d) Mode 3.

CONCLUSIONS

The study describes the recirculation zone of an annular jet by Particle Image Velocimetry. The Proper Orthogonal Decomposition has been applied to find the relationship of these radial fluctuations to the inner structures of the instantaneous P.I.V. fields. The mode 0 represents the carrier flow, which is the most energetic. The space fluctuation of the stagnation point is principally due to the mode 1. Each obstacle modifies different characteristics of the flow. Instabilities disappear in the stagnant point in the case of a conical annular jet but a new area of transversal fluctuations appears on the rims of the jet. The ellipsoidal annular jet suppresses the recirculation zone but there are always a lot of fluctuations in the flow, at the separation point or on the rims of the jet. This particular annular jet contains much more coherent structures than in the other configurations and then it has more energy represented in the first ten modes. This study shows that a partial control of the stagnant point fluctuations can result from a modification of the central obstacle but this obstacle has other effects on the rest of the flow. All effects have to be taken into account in order to determine the efficiency of the passive control.

References

[1]Ko N.W.M. & Chan W.T., Similarity in the initial region of annular jets: three configurations. J.Fluid Mech., 84, part 4, pp 641-656, 1978.

[2] Lumley J.L., Holmes P. & Berkooz G., The proper orthogonal decomposition in the analysis of turbulent flows, Annu. Rev. Fluid Mech, 25,pp 539-575, 1993.

[3] Adrian R.J., Christensen K.T. & Liu Z.C., Analysis and interpretation of instantaneous turbulent velocity fields, Experiment in Fluids, 29,pp 275-290, 2000.

[4]Moreau J., Patte-Rouland B., & Rouland E., Particle Image Velocimetry and Proper Orthogonal Decomposition., Euromech 411, s5, 2000.

[5]Patte-Rouland B., Lalizel G., Moreau J. and Rouland E. Flow analysis of an annular jet by Particle Image Velocimetry and Proper Orthogonal Decomposition. Measurement Science and Technology, 2001.

[6] Danlos A, Lalizel G, Patte-Rouland B Experimental characterization of the initial zone of an annular jet with a very large diameter ratio. Experiment in Fluids 54, 2013

TORQUE SCALING AND MEAN VELOCITY PROFILES IN A WIDE-GAP TAYLOR-COUETTE FLOW

Akhilesh M Prabhu[1], Shrutakeerti M V[2], R K Shukla[3], and J H Arakeri [*4]
[1,2,3,4]*Mechanical Engineering, Indian Institute of Science, Bangalore, India*

Summary A wide-gap Taylor-Couette (T-C) configuration with a radius ratio of 0.1 is investigated through direct numerical simulation. Both axis-symmetric and fully three dimensional cases are simulated for a range of Reynolds numbers (Re_a) from 100 to 1000. Rotating inner cylinder and a stationary outer cylinder result in distributions of angular momentum near the walls which are susceptible to Gortler instability. Unlike plane Couette flow which exhibits symmetry about the mid plane, wide-gap Taylor-Couette flow owing to circular geometry, has distinct and sharply contrasted behaviour of flow at the two walls. Our investigations into the low Re_a regime, shows the presence of circumferentially elongated eddies resembling Gortler vortices near the inner wall. These observations lend support to earlier studies which report experimental observations of near wall flow [3, 5, 6]. Mean angular momentum profiles show regions in the annulus with a negligible gradient. Further, scaling of the non-dimensional torque (G) with Re_a is reported.

NUMERICAL METHODOLOGY

High resolution direct numerical simulation of wide-gap T-C flow pose significant challenges in terms of efficient utilization of resources. Motivated by this, a high-order accurate incompressible flow solver has been developed with MPI slab decomposition. A high resolution compact scheme [12, 13] and Fourier spectral approximation [14] are used to discretize the aperiodic and periodic directions respectively. A second-order accurate semi-implicit projection method [9] is used for non-stiff temporal integration and to enforce incompressibility. The computational code has been extensively validated for both two and three-dimensional bluff body flows. Both axis-symmetric and fully three dimensional cases have been simulated for Re_a (based on inner cylinder radius and wall velocity) ranging from 100 to 1000. The simulations are run till a statistically steady flow field is obtained. At low Re_a the flow is nearly axis-symmetric and the spatio-temporally averaged velocities and fluctuations agree within a reasonable accuracy with the fully three dimensional cases. As Re_a is further increased, circumferential symmetry is lost resulting in a significant difference of mean statistics between the two cases. Global transport quantity such as the torque however, seems to be unaffected by the loss in circumferential symmetry.

RESULTS AND DISCUSSIONS

The data presented here on are from the fully three dimensional cases. Global transport quantity such as the torque in T-C flows has been subject to many previous investigations [3, 5, 7, 10, 15], albeit for higher radius ratios. Our DNS results show that the non-dimensional torque per unit length (G) scales as $Re^{1.41}$ as can be seen in Fig. 1(a). The exponent obtained here is smaller compared to the previous studies which however were concerned with flows at much higher Re_a .

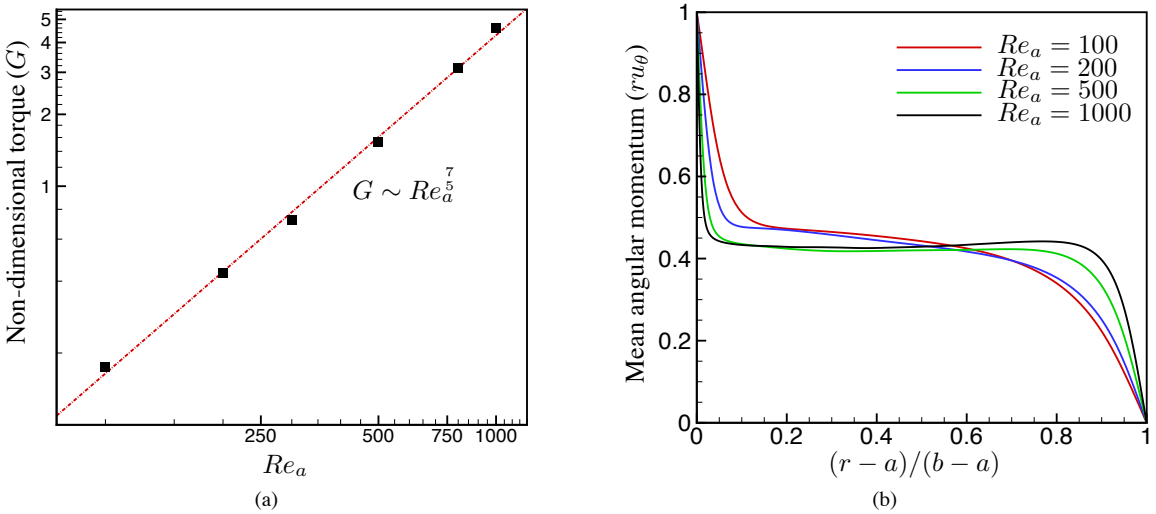

Figure 1: (a) Scaling of mean torque with Re_a (b) Mean angular momentum profiles for various Re_a

*Corresponding author. Email: jaywant@mechengg.iisc.ernet.in

Fig. 1(b) shows the radial variation of spatio-temporally averaged angular momentum. The profiles show two distinct regions, the two boundary layers near the walls with a steep gradient and a core of nearly constant angular momentum, as was also observed previously by [1, 4, 10, 7, 16]. Further, it is interesting to see that the mean axial vorticity in the core is nearly zero for all Re_a (see Fig. 2(a)). The inlet of Fig. 2(a) shows the full extent of the radial variation of mean axial vorticity for $Re_a = 100$. As can be seen, the flow is nearly irrotational in the mean, bounded on either side by sharp boundary layers with non-zero axial vorticity.

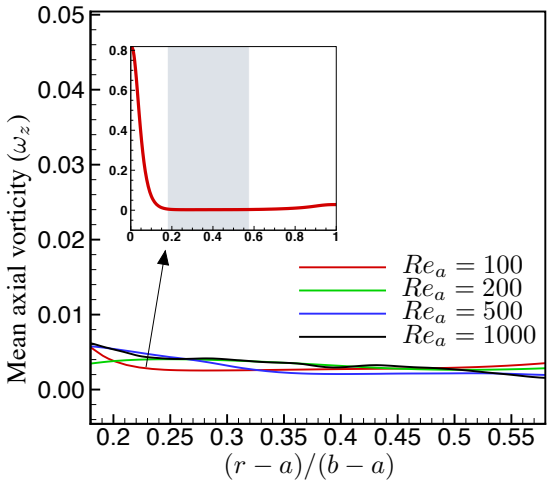

(a)

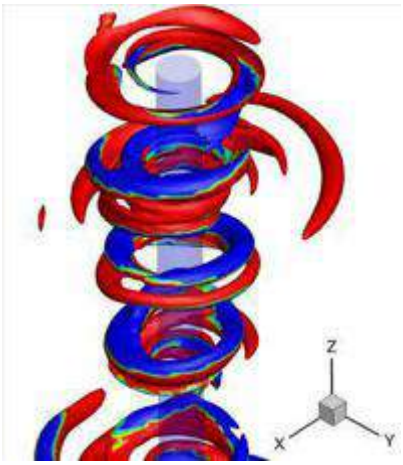

(b)

Figure 2: (a) Spatio-temporally averaged axial vorticity for various Re_a (b) Iso-contours of $\lambda_2 = -0.01$ for $Re_a = 200$ with the colours representing the sign of radial velocity, red being positive and blue negative.

Fig. 2(b) shows the presence of vortical structures (as illuminated by the λ_2 criterion [8]) in the flow near the inner wall, while no such coherent structures are observed at the outer wall. The iso-contours of λ_2 are coloured using the sign of radial velocity and indicate the presence of Gortler type vortices. These structures play a key role in the transport of torque and angular momentum to the outer reaches of the flow.

References

[1] TAYLOR, G. I. 1935 Distribution of velocity and temperature between concentric rotating cylinders. *Proc. R. Soc. Lond.* A. **151**, 494-512

[2] DONNELY R. J. & SIMON N. J. 1960 An empirical torque relation for supercritical flow between rotating cylinders. *J. Fluid Mech.* **7**, 401-418

[3] BARICLON A., BRINDLEY J., LESSEN M., & MOBBS F. R. 1979 Marginal instability in Taylor-Couette flows at a very high Taylor number. *J. Fluid Mech.* **94**, 453-463

[4] SMITH G. P. & TOWNSEND A. A. 1982 Turbulent Couette flow between concentric cylinders at large Taylor numbers. *J. Fluid Mech.* **123**, 187-217

[5] BARICLON A. & BRINDLEY J. 1984 Organized structures in turbulent Taylor-Couette flow. *J. Fluid Mech.* **143**, 429-449

[6] WEI T., KLINE E. M., LEE SHK & WOODRUFF S. 1992 Grtler vortex formation at the inner cylinder in TaylorCouette flow. *J. Fluid Mech.* **245**, 47-68

[7] LATHROP D. P., FINEBERG J., & SWINNEY H. L. 1992 Turbulent flow between concentric rotating cylinders at large Reynolds number. *Phys. Rev. Lett.* **68(10)**, 1515.

[8] JEONG J. & HUSSAIN F. 1995 On the identification of a vortex. *J. Fluid Mech.* **285**, 69-94

[9] SANDRINE HUGUES & RANDRIAMAMPIANINA A. 1998 An improved projection scheme applied to pseudospectral methods for the incompressible NavierStokes equations. *Int. j. numer. methods fluids* **28(3)**, 501-521.

[10] DONG S. 2007 Direct numerical simulation of turbulent TaylorCouette flow. *J. Fluid Mech.* **587**, 373-393

[11] DONG S. 2008 Herringbone streaks in Taylor-Couette turbulence. *Phys. Rev. E* **77(3)**, 035301.

[12] SHUKLA R. K. & ZHONG X. 2005 Derivation of high-order compact finite difference schemes for non-uniform grid using polynomial interpolation. *J. Comput. Phys* **204(2)**, 404-429.

[13] SHUKLA R. K., TATINENI M. & ZHONG X. 2007 Very high-order compact finite difference schemes on non-uniform grids for incompressible NavierStokes equations. *J. Comput. Phys* **224(2)**, 1064-1094.

[14] BOYD J. P. 2001 *Chebyshev and Fourier spectral methods*. Courier Corporation.

[15] ECKHARDT B., GROSSMANN S. & LOHSE D. 2007 Torque scaling in turbulent Taylor-Couette flow between independently rotating cylinders. *J. Fluid Mech.* **581**, 221-250

[16] GROSSMANN S., LOHSE D. & SUN C. 2016 High Reynolds Number Taylor-Couette Turbulence. *Annu. Rev. Fluid Mech.* (to be published)

SOME INSIGHTS ON TURBULENT PLANE MIXING LAYERS FROM EXTENSIVE VORTEX-GAS COMPUTATIONS

Saikishan Suryanarayanan[1a)], Roddam Narasimha[1] , Hari Dass N.D.[2] & Sunil D. Sherlekar[3]
[1]*Engineering Mechanics Unit, JNCASR, Jakkur, Bangalore – 560064, India.*
[2]*TIFR Centre for Interdisciplinary Sciences, Narsingi, Hyderabad - 500075, India.*
[3]*Sankhya Sutra Labs Pvt. Ltd., JNCASR campus, Jakkur, Bangalore – 560064, India.*

Summary We examine the extent of relevance of extensive point-vortex-gas simulations (of Suryanarayanan et al, 2014) to real world turbulent mixing layers. The vortex gas is a singular, 2D, inviscid method used in the 70s and 80s to understand some aspects of turbulent flows, but has since been relegated to the status of a toy model. We challenge this view, by revisiting the vortex gas using modern high performance computing enabling simulations involving much larger number of vortices (upto 32000) than earlier studies and more crucially, large (upto 10^3) member ensemble averages. The present vortex-gas results are shown to be highly relevant to the large scale dynamics of free shear layers, particularly on the central and controversial issue of universality of self-similar states. The present analysis provides new insights on understanding data from other simulations that seemingly point to non-universal self-preservation behaviour.

INTRODUCTION AND PROBLEM SETUP

We examine the evolution of a singly periodic array of N-point vortices of same sign and strength, initially distributed in the close neighbourhood of the x-axis with y-displacements drawn from a specified random or periodic distribution. Due to the 2D inviscid approximation, all the dynamics are condensed into the kinematics of the Biot-Savart relationship as a consequence of Kelvin's theorem and hence the system is governed by $2N$ ODEs which are solved using double precision RK4. The chosen scheme and time-step ensures conservation of the Hamiltonian to within 10^{-5} of its initial value. Different measures of layer thickness and other statistics are computed from the ensemble and x-averaged velocity field induced by the vortices on a grid. Further details are presented in Suryanarayanan et al (2014), where it was also demonstrated that the present simulations are far more extensive and accurate than existing simulations of this kind and that such an improvement was crucial for the conclusions that were drawn. The evolution of the layer was found to have three distinct regimes – an initial condition influenced RI, a periodic domain limited RIII and a linear intermediate asymptotic overlap RII with a universal spread rate. While connections were made between RIII and equilibrium statistical mechanics, the present paper would focus on the relevance of RI and RII on the dynamics of free shear layers as observed in experiments and 3D LES/DNS studies.

RESULTS ON SELF PRESERVATION SPREAD RATE

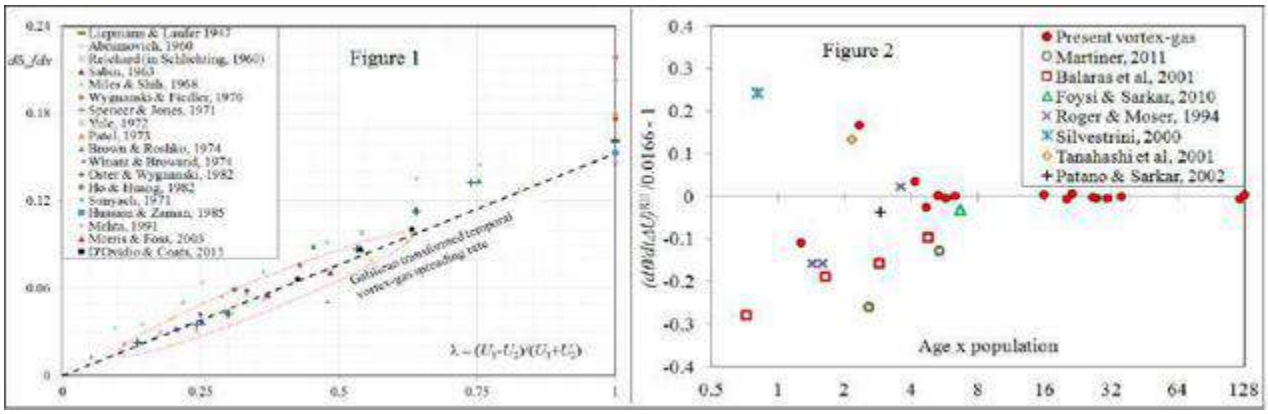

Figure 1. Galilean transformed Universal RII spread rate from temporal vortex-gas simulations compared with experimental results on plane mixing layers.
Figure 2. Departures of the reported growth rates in DNS/LES of 3D Navier-Stokes Temporal mixing layers and present vortex-gas simulations from the universal Regime II growth rate with the product of "age" and "population" parameters

It can be observed from Figure 1, that the transformed temporal vortex-gas results are within the range of the experimental scatter, and many high Reynolds number experiments with velocity ratio parameter $0.1 \lesssim \lambda \lesssim 0.6$ (at large values of λ the effects of spatial feedback may become dominant and Galilean transformation is no longer valid; further details in Suryanarayanan & Narasimha, 2015), including the recent post-mixing-transition experiments of D'Ovidio and Coats (2013) are in close agreement. This suggests that 2D inviscid mechanisms can explain the spread rate even in post-mixing-transition free shear layers. Implications and possible reasons for the experimental scatter shall be discussed.

[a)] Corresponding author. Email: saikishan.suryanarayanan@gmail.com

ANALYSIS OF PREVIOUS LES/DNS SIMULATIONS

We next examine results from 3D DNS / LES simulations of temporal mixing layers. The scatter in the reported self-preservation states is often used as an argument in support of existence of non-universal self-preservation states (e.g. Balaras et al, 2001). However, the present analysis shown in Fig.3, suggests a systematic departure from the universal spread rate when the product of two parameters – number of mergers ("age") and final number of structures ("population") becomes small. This suggests that non-universal self-preservation states are possible artefacts of fits over insufficient number of mergers or lack of appreciation of onset of the domain dependent RIII. The implications will be discussed.

LONG RANGE CORRELATIONS AND MULTIPLE SELF-PRESERVATION STATES

Another controversy concerns the proposal that there are multiple self-preservation solutions in the growth of a mixing layer. Such segmented growth curves are encountered in single realizations of vortex-gas simulations as well. Figure 3 shows a single realization in Regime II of a temporal vortex-gas shear layer that consists of four linear segments, each with a different slope varying by a factor of 2.35. However an ensemble average yields an excellent linear growth throughout, very close to the universal value in each of the indicated segments, suggesting that these "transient metastable states" (Narasimha, 1990) are eliminated by adequate averaging. The explanation for the segmented growth that appear under inadequate averaging is contained the vortex location snapshots that reveal long-range correlation via the presence of several co-oriented vortex 'trains'. The train of structures rotating nearly in unison creates a very strong fluctuation in the local growth rate, and thus averaging over sufficient number of such trains is required. It is thus possible that reports of multiple or serial self-preservation states (Carton de Wiart et al, 2010) are the result of inadequate averages.

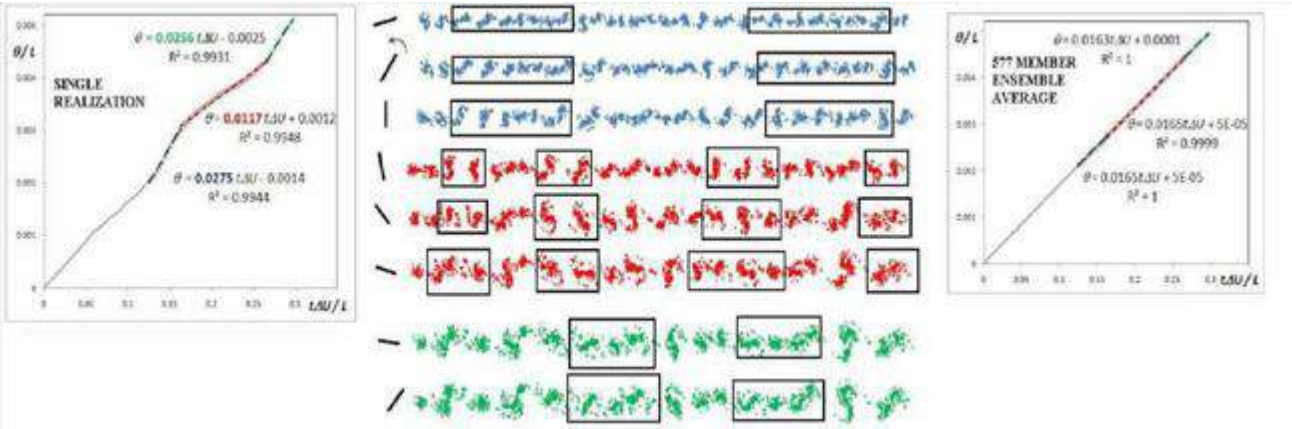

Figure 3. Insufficient averaging leads to multiple local self preservation states with different spread rates. The orientation of train of structures (marked in boxes) may be locally coherent (orientation indicated by the black lines) and may lead to a linear growth for a substantial duration but with a very different slope compared to the average.

CONCLUSIONS

Thus temporal vortex-gas shear layer satisfactorily describes the large scale evolution of 3D NS mixing layers despite of what may appear as severe approximations, suggesting the dominance of the 2D Kelvin-Biot-Savart in determining the vorticity dispersal in real mixing layers. Therefore the universality of spread rate in Regime II suggests that the self-preservation spread rate in real mixing layers is also likely to be universal and reports of non-universal or multiple self-preservation states may be due to inadequate appreciation of the long memory of initial conditions, insufficient averaging, unreliability of fits made over short temporal and / or spatial domains, and the lack of appreciation of the beginning of Regime III during which the size of the flow domain becomes an additional parameter in the problem.

References

[1] Suryanarayanan S., Narasimha R. and Hari Dass N.D. : Free turbulent shear layer in a point vortex gas as a problem in nonequilibrium statistical mechanics. *Phys.Rev.E* **89**, 013009, 2014.

[2] Suryanarayanan S. and Narasimha R. : Spatially evolving vortex-gas turbulent free shear layers. *ArXiV* 1509.00603 & 1511.05717, 2015.

[3] Balaras E., Piomelli U. and Wallace, J.M : Self-similar states in turbulent mixing layers, *J. Fluid Mech*. **446**, 1, 2001.

[4] D'Ovidio A. and Coats C.M. : Organized large structure in the post-transition mixing layer. Part 1. Experimental evidence., *J. Fluid Mech*. **737**, 466, 2013.

[5] Narasimha, R. : The utility and drawbacks of traditional approaches. In Whither Turbulence? Turbulence at the Crossroads (pp. 13-48). Springer Berlin Heidelberg. 1990.

[6] Carton de Wiart, C., et al. :Similarity in 2-D spatially developing and long shear layers." *APS Division of Fluid Dynamics Meeting Abstracts*, 1, 2010.

WALL-PRESSURE COHERENCE BENEATH A LOW REYNOLDS NUMBER TURBULENT BOUNDARY LAYER

Jared Van Blitterswyk *[1] and Joana Rocha [1]

[1]*Department of Mechanical and Aerospace Engineering, Carleton University, Ottawa, Ontario, Canada*

Summary Measurements of the unsteady wall-pressure field are acquired on the floor of a wind tunnel beneath a fully developed, zero pressure gradient turbulent boundary layer with a Reynolds number based on momentum thickness, Re_θ of 2593. The single point wall pressure spectrum and the streamwise coherence lengths are reported. The coherence lengths of streamwise pressure fluctuations are larger than predicted using existing models, and shows that large irrotational outer layer motions retain their coherent power for streamwise separations exceeding 3.6 boundary layer thicknesses, while smaller, high-frequency fluctuations decay within 0.75 boundary layer thicknesses. Further investigations with finer spatial resolution are required to understand the coherent nature of high-frequency pressure events.

INTRODUCTION

A thorough understanding of wall-pressure fluctuations produced beneath a turbulent boundary layer (TBL) is of principal importance to properly modelling flow-induced vibrations and sound radiation. Models of flow-induced noise depend on a deterministic model of the spatial characteristics of unsteady wall-pressure beneath a TBL. This includes the frequency spectrum of pressure fluctuations at a single point, and the spatial coherence of wall-pressure signatures. The streamwise cross-spectrum ($\gamma(\xi, f)$) between two microphones separated by a distance ξ, is calculated by taking the Fourier transform of the cross-correlation ($\chi = \langle p(x_0, t_0)p(x_0 + \xi, t_0 + \tau)\rangle$) and normalizing by the respective single-point autospectra (Eq. (1)).

$$\gamma(\xi, f) = \frac{|\phi(x_0, x_0 + \xi, f)|}{|\phi(x_0, x_0, f)|^{0.5}|\phi(x_0 + \xi, x_0 + \xi, f)|^{0.5}} \tag{1}$$

Corcos [1] proposed the most well-known model for predicting spatial coherence between two points, described by the product of coherent decay in the streamwise and spanwise directions (ξ and η, respectively) (Eq. 2).

$$\gamma(\xi, \eta, f) \propto e^{-2\pi f \alpha_x |\xi|/U_c} e^{-2\pi f \alpha_y |\eta|/U_c} \tag{2}$$

The spatial separation is normalized by an empirical constant, α_i and the convection velocity, U_c, and together represents the frequency-dependent 'coherence length', $L_i = U_c/2\pi f \alpha_i$. The inverse dependence on frequency results in overprediction at low frequencies, which was addressed by Efimtsov [2] who offered a corrected model of the form,

$$L_x = \delta \left[\left(\frac{2\pi f \delta a_1}{U_c} \right)^2 + \frac{a_2^2}{(2\pi f \delta/u_\tau)^2 + (a_2/a_3)^2} \right]^{-1/2} \tag{3}$$

where; the empirical constants a_i control the mid to high frequency coherence and the low frequency roll off from the Corcos model. Comparisons in the recent literature with both exponential models are not very satisfying as some researchers have measured sinusoidal variations in the coherence lengths or sustained coherence at large separations [3,4]. This lack of agreement encourages further research in this area, and will be studied here in the case of a low Reynolds number TBL.

EXPERIMENTAL METHODS

Streamwise measurements of wall-pressure fluctuations were made on an instrumented test panel along the test section floor in a closed-circuit wind tunnel facility. The microphone array consisted of five, 1/4 in.-diameter, Brüel and Kjaer 4944A type microphones, spaning x = 1.17 m to x = 1.3 m downstream of forced transition, with a minimum spacing of 25.4 mm. More information on the facility, test panel, and microphone array can be found in reference [5]. The test section has since been outfitted with an adjustable ceiling to control the streamwise pressure gradient. The boundary layer was characterized using a Dantec 55P11 miniature hot-wire probe, which was sampled at 8 kHz for 65 seconds. Over the center of the microphone array, at a freestream velocity of 10.4 m/s and zero pressure gradient conditions, the boudnary layer thickness, δ = 34.8 mm, the Reynolds number based on momentum thickness, $Re_\theta = U_\infty \theta/\nu$ = 2593, and the shape factor, $H = \delta^*/\theta$ = 1.43. The friction velocity, u_τ = 0.40 m/s, was found by fitting the mean velocity profile to a logarithmic law.

*Corresponding author. Email: jared.vanblitterswyk@carleton.ca

RESULTS AND DISCUSSION

The single point frequency spectrum of wall pressure fluctuations, shown in Fig.1a, posseses key features of a well developed turbulent boundary layer; including an increase in amplitude proportional to $f^{0.2} \circ f^{0.3}$ up to the spectrum peak ($f \approx 120$ Hz), followed by a decay in amplitude proportional to $f^{-0.7} \circ f^{-0.8}$, and a rapid decay at high frequencies. The normalized cross-spectrum for four different spatial separations, ranging from 0.73δ to 3.63δ, are shown in Fig.1b along with predictions using the Corcos and Efimtsov models for the case of $\xi = 2.54\delta$. The coherence length is calculated for a given frequency by fitting an exponential curve to the cross-spectrum amplitude at each of the measurement locations, with the frequency-dependent nature of the coherence length shown in Fig.1c.

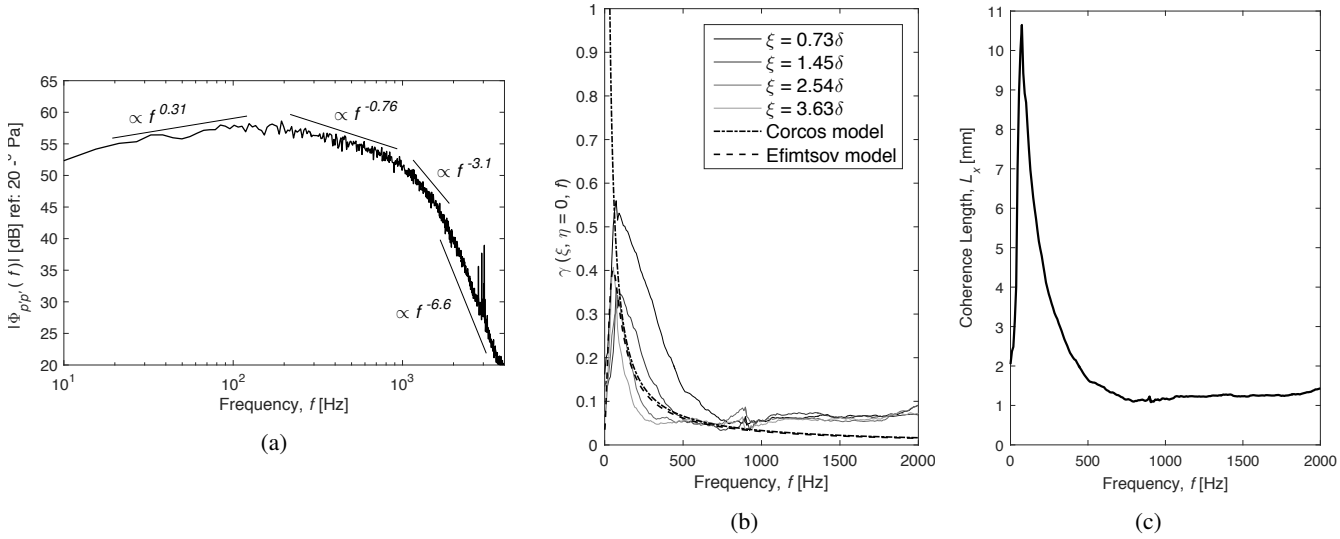

Figure 1: Single-sided frequency spectrum of wall-pressure fluctuations (a), normalized cross-spectral density measured between transducers with various spatial separations (b), and coherence length for all frequencies up to 2,000 Hz (c).

As shown in Fig.1b, the coherent power of the low-frequency pressure fluctuations exceeds the streamwise extent of the microphone array, suggesting that these events can retain their signature for atleast 3.6δ downstream. This prolonged coherence, reaching a maximum of 10.7 mm at $f = 73$ Hz (Fig.1c), is the signature of irrotational motions in the outer regions of the boundary layer. The cross-spectrum is not well predicted by either model for any of the measured cross-spectra. Assuming appropriate model constants are selected to match the low frequency behaviour, high-frequency coherent power is always under-predicted. The rapid decrease in coherence length, shown in Fig.1c, suggests that the spatial signatures of high-frequency fluctuations decay within travelling approximately 0.75δ downstream. The exponential form used to define the coherence length likely contributes to the asymptotic behaviour at high-frequencies (Fig.1c), but the non-zero cross-spectrum amplitudes (Fig.1b) suggests it may be a physical feature of the wall-pressure signature and requires further investigation.

CONCLUSIONS

Low-frequency wall-pressure signatures from irrotational outer layer motions are retained in the streamwise direction for at least 3.6 boundary layer thicknesses, with a maximum coherence length of 10.7 mm measured at a frequency of 73 Hz. The decrease in spatial coherence was not well predicted with exponential models from the literature. Further studies with refined spatial resolution would be useful for investigating the coherence of smaller, high-frequency, pressure events.

References

[1] Corcos G.M., "Resolution of Pressure in Turbulence", J. Acoust. Soc. Am., 35(2);192-199, 1963.

[2] B.M. Efimtsov, "Characteristics of the field of turbulent wall pressure fluctuations at large Reynolds numbers", Soviet Physics Acoustical, 28(4);289-292, 1982.

[3] Leclercq D.J.J., Bohineust X., "Investigation and modelling of the wall pressure field beneath a turbulent boundary layer at low and medium frequencies", J. Sound. Vib., 257(3);477-501, 2002.

[4] Arguillat B., et al., "Measured wavenumber: Frequency spectrum associated with acoustic and aerodynamic wall pressure fluctuations", J. Acoust. Soc. Am., 128(4);1647-1655, 2010.

[5] Van Blitterswyk J., Rocha J., "Prediction and Measurement of Flow-Induced Wall-Pressure Fluctuations at Low Mach Numbers", Canadian Acoustics, 42(4);3-14, 2014.

FM15 - Vortex Dynamics

TS.FM15-1.01	Quaranta, Umberto - Long-wave instabilities of two interlaced helical vortices	1504
TS.FM15-1.02	Stroh, Alexander - Secondary vortices over spanwise heterogeneous roughness	1506
TS.FM15-1.03	Goudar, Manu - Auto-generation by interaction of weak eddies	1508
TS.FM15-1.04	Krasny, Robert - Computation of the starting vortex past a flat plate (INVITED)	1510
TS.FM15-1.05	Hourigan, Kerry - The curious case of the vanishing vorticity (INVITED)	1512
TS.FM15-1.06	Yang, Wenchao - Two-dimensional wakes of an oscillating cylinder at low Reynolds number	1514
TS.FM15-2.01	Stremler, Mark - Point vortex models of exotic laminar vortex streets	1516
TS.FM15-2.02	Blackmore, Denis - Magnetic point vortex dynamics in the plane	1518
TS.FM15-2.03	Brøns, Morten - Topology of vortex creation and merging: Wakes and multi-Gaussian models	1520
TS.FM15-2.04	Rosi, Giuseppe - Entrainment in non-stationary flows	1522
TS.FM15-2.05	Franck, Jennifer - Vortex and wake interactions of multiple oscillating foils for energy harvesting	1524
TS.FM15-3.01	Ko, Lok Sun - Experimental investigation of a slender delta wing with apex and tail flap control	1526
TS.FM15-3.02	Rockwood, Matthew - Determining the shedding time of vortices in real-time	1528
TS.FM15-3.03	Fukumoto, Yasuhide - Motion of a vortex pair at high and low Reynolds numbers	1530
TS.FM15-3.04	Llewellyn Smith, Stefan - Motion of a compressible vortex pair	1532
TS.FM15-3.05	Kerr, Robert - What trefoil reconnection says about Navier-Stokes regularity	1534
TS.FM15-4.01	Kudela, Henryk - Collapse Vortices and Filaments of Vorticity	1536
TS.FM15-4.02	Le Dizes, Stéphane - Curvature and elliptic instabilities in helical vortices (INVITED)	1538
TS.FM15-4.03	Delbende, Ivan - Simulations of Helical Vortex Instability	1540
TS.FM15-4.04	Wood, David - The Use of Helical Vortex Solutions in Wind Turbine Performance Analysis	1542
TS.FM15-4.05	Heil, Matthias - Topological fluid mechanics of the formation of the Karman-vortex street	1544
PO.FM15-1.01.75	Chang, Chien-Cheng - An analysis of vorticity force versus pressure-friction for incompressible flow	1546
PO.FM15-1.02.76	Cuevas, Sergio - Free surface vortex instability in magnetically driven liquid metal swirling flow	1548
PO.FM15-1.03.77	Daneshvar, Sina - On the influence of end effects for stationary and vibrating circular cylinders	1550
PO.FM15-1.04.78	Elsas, José Hugo - Vortex Statistics from Vorticity Local Properties	1552
PO.FM15-1.05.79	Feys, Jan - Elliptical instability of the Moore-Saffman model for a trailing wingtip vortex	1554
PO.FM15-1.06.80	Hasegawa, Hideki - Characteristics of eigen-vortical-axis lines	1556
PO.FM15-1.07.81	Hu, Ruifeng - Far-field wake behind a rotating ellipse at a low Reynolds number	1558
PO.FM15-1.08.82	Itano, Toshihisa - Singular-value analyses of symmetric and asymmetric perturbations on a cylindrical vortex sheet	1560
PO.FM15-1.09.83	Krishnamurthy, Vikas - Analytical solutions for weakly compressible von Karman vortex streets	1562

PO.FM15-1.10.84	Limacher, Eric - Representation of real flows with dynamically equivalent concentrated point vortices	1564
PO.FM15-1.11.85	Liu, Xin - Cascade of vortex knots detected by HOMFLYPT polynomial	1566
PO.FM15-1.12.86	Mohseni, Kamran - Unsteady Kutta condition and vortex-sheet generation	1568
PO.FM15-1.13.87	Nakayama, Katsuyuki - Invariant local flow topology in transition into a vortex and property of its prediction	1570
PO.FM15-1.14.88	Nitsche, Monika - Deflection of a vortex dipole by a flat plate	1572
PO.FM15-1.15.89	O'Neil, Kevin - A vortex sheet / point vortex dipole	1574
PO.FM15-1.16.90	Paoli, Roberto - Hybrid rans-les simulation of wingtip vortices of an airliner	1576
PO.FM15-1.17.91	Velasco Fuentes, Oscar - Motion and flow topology of multiple helical vortices	1578

LONG-WAVE INSTABILITIES OF TWO INTERLACED HELICAL VORTICES

Hugo Umberto Quaranta[1,2], Mattias Brynjell-Rahkola[3], Thomas Leweke*[1], and Dan S. Henningson[3]

[1]*IRPHE UMR 7342, Aix-Marseille Université, CNRS, Centrale Marseille, Marseille, France*
[2]*Aerodynamics Department, AIRBUS HELICOPTERS, Marignane, France*
[3]*Linné FLOW Centre, KTH Mechanics, Royal Institute of Technology, Stockholm, Sweden*

Summary We present a comparison between theoretical predictions and experimental observations of the instabilities in the wake of a two-bladed rotor. The linear stability of the vortex system consisting of two helical vortices is described using the Biot–Savart induced velocity approach. Experiments are performed to investigate the breakdown scenario caused by both local and global pairing of successive vortex loops, and the observations are found to be in accordance with the theory.

The near wake behind multi-bladed rotors consists of several interlaced helical vortices, generated at the tips of the rotor blades. Various instabilities can exist in this system, involving perturbations at different wavelengths: long-wave displacement modes or short-wave vortex core deformations [1]. The linear stability of a single helical vortex was first analyzed by Widnall [2], followed by the work of Gupta & Loewy [3]. These authors determined the stability of long-wave displacement modes by perturbing the helices and deriving an eigenvalue problem considering the induced velocity obtained using the Biot–Savart law and the vorticity transport theorem (see [3] for details). A study aimed at verifying these theoretical results was recently performed by Quaranta & Leweke [4], who carried out detailed experiments with a single-bladed rotor in a water channel. By imposing perturbations with various wave numbers (i.e. number of perturbation wavelengths in one helix turn), they were able to obtain growth rates that closely matched those predicted by Widnall [2] and Gupta & Loewy [3]. It was also shown that the long-wave instability can be linked to the local pairing of successive loops of the helical vortex, and quantitative comparisons were made with the well-known pairing mechanisms of an infinite array of straight vortices [5, 6].

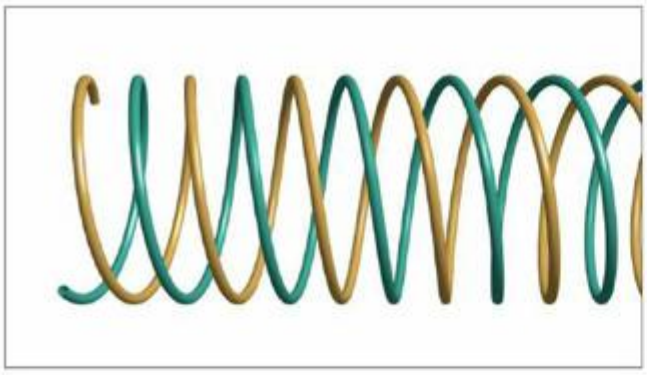

(a) Schematic of a double-helix, as seen from a distance of $8R$.

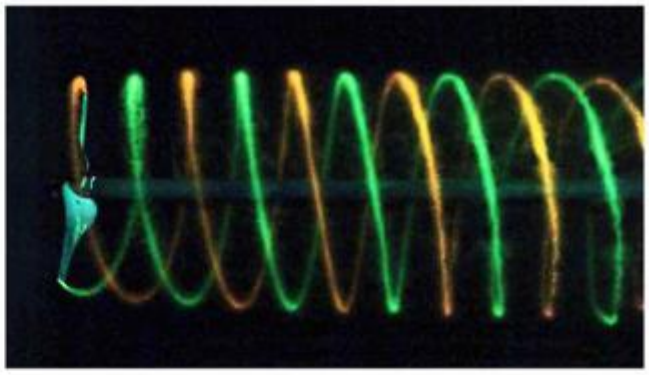

(b) Water channel dye visualization of the base flow.

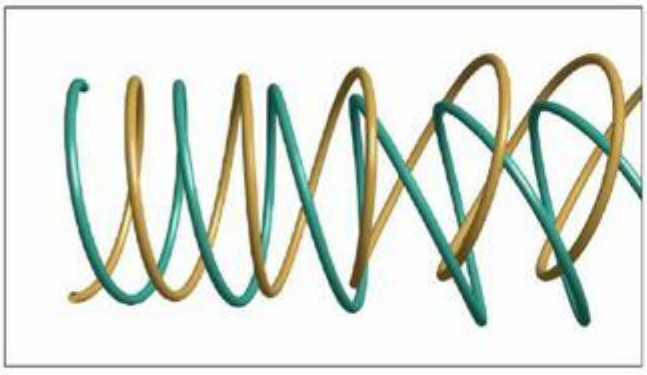

(c) Predicted shape for a spatially growing mode with $k = 1$.

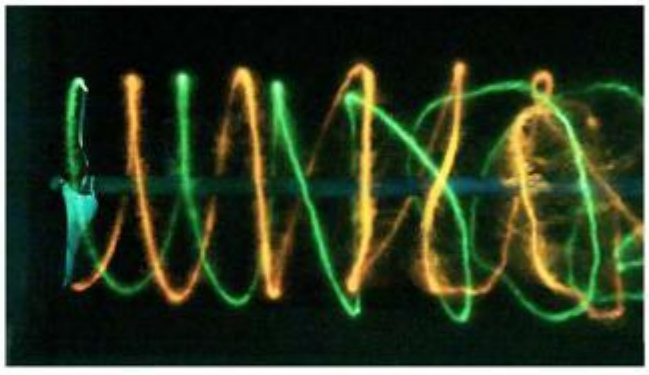

(d) Visualisation of the rotor wake perturbed with $k = 1$.

Figure 1: Vortices in the wake of a two-bladed rotor of radius $R = 8$ cm. (a,b) Unperturbed base flow. (c,d) Wake perturbed with a mode of wave number $k = 1$.

*Corresponding author. Email: Thomas.Leweke@irphe.univ-mrs.fr

(a)

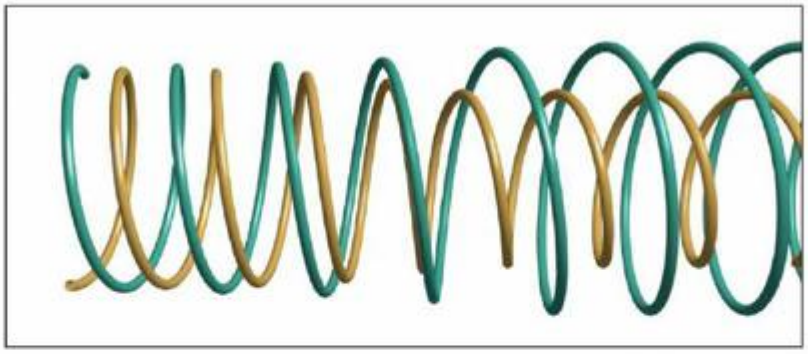

(b)

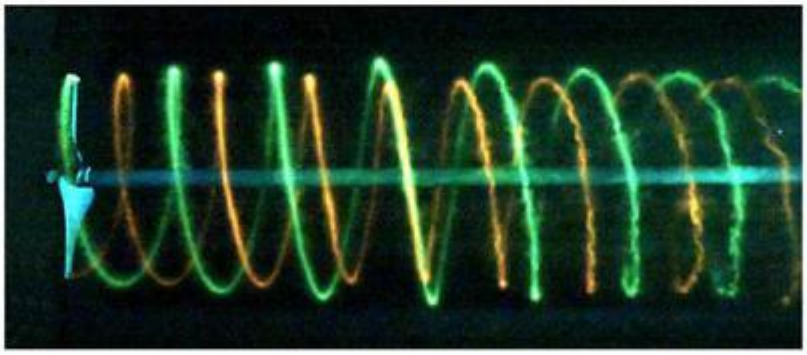

Figure 2: Uniform pairing mode ($k = 0$) of two helical vortices. (a) Prediction of the spatial growth, based on the linear instability mode. (b) Experimental dye visualization of the wake of a slightly asymmetric rotor.

In the present study, the work by Quaranta & Leweke [4] is extended to the configuration of two helical vortices. Similar cases have previously been considered theoretically by Gupta & Loewy [3], and by Okulov & Sørensen [7]. Both analyses predict instability of the system, involving again local pairing at various locations along the filaments, depending on the perturbation wave number k, as well as a new mode of global pairing, with an azimuthally uniform ($k = 0$) relative displacement of one helical vortex with respect to the other. When the perturbations are triggered by a rigid rotor, they are in phase on all vortices, and pairing can be expected for wave numbers $k = N(i + 1/2)$, where N is the number of blades and i an integer. This has recently been investigated numerically by Sarmast *et al.* [8], who noted that pairing can also occur for other wave numbers, including $k = 0$, when the perturbation imposed on the different vortices have different phases.

The experimental setup used is similar to the one described in [4], except that the rotor, of radius $R = 8$ cm, now has two blades instead of one. By modulating the velocity of the stepper motor driving the rotor, the local pairing mechanism is triggered with a prescribed wave number and an identical phase for both vortices (figure 1), whereas a very small eccentricity of the rotor with respect to the axis of rotation leads to global pairing (figure 2). Both cases, as well as their combination with various amplitude ratios, are investigated, including detailed measurements from dye visualizations and Particle Image Velocimetry.

The presentation includes a review of previous theoretical results concerning the long-wave instability of helical vortex systems and the pairing of vortex arrays, and a discussion of their limits of validity. Comparisons between theoretical predictions and experimental measurements of the instability mode structures and corresponding growth rates are presented, and the relevance of these results for the evolution of rotor wakes is considered.

References

[1] Leweke T., Quaranta H. U., Bolnot H., Blanco-Rodríguez F. J. & Le Dizès S.: Long- and short-wave instabilities in helical vortices. *J. Phys.: Conf. Ser.* **542**:012154, 2014.

[2] Widnall S. E.: The stability of a helical vortex filament. *J. Fluid Mech.* **54**:641-663, 1972.

[3] Gupta B. P. & Loewy R.: Theoretical analysis of the aerodynamic stability of multiple interdigitated helical vortices. *AIAA J.* **12**:1381-1387, 1974.

[4] Quaranta H. U. & Leweke T.: Long-wave instability of a helical vortex. *J. Fluid Mech.* **780**:687-716, 2015.

[5] Lamb H.: Hydrodynamics, §136. Cambridge, UK, 1932.

[6] Robinson A. C. & Saffman P. G.: Three-dimensional stability of vortex arrays. *J. Fluid Mech.* **125**:411-427, 1982.

[7] Okulov V. L. & Sørensen J. N.: Stability of helical tip vortices in a rotor far wake. *J. Fluid Mech.* **576**:1-25, 2007.

[8] Sarmast S., Dadfar R., Mikkelsen R. F., Schlatter P., Ivanell S., Sørensen J. N. & Henningson D. S.: Mutual inductance instability of the tip vortices behind a wind turbine. *J. Fluid Mech.* **755**:705-731, 2014.

Secondary vortices over spanwise heterogeneous roughness

Alexander Stroh *, Pourya Forooghi, Jochen Kriegseis, and Bettina Frohnapfel
Institute of Fluid Mechanics (ISTM), Karlsruhe Institute of Technology (KIT), Karlsruhe, Germany

Summary A spanwise heterogeneity of roughness is known to lead to the formation of large-scale secondary motions. The secondary motions are investigated based on the data sets extracted from direct numerical simulations (DNS) of fully developed turbulent channel flow where streamwise stripes of modeled rough surface with varying spanwise extension and roughness layer thickness are introduced. In order to study the character of the secondary flow structures, the calculated flow fields are further post-processed by means of streamline-based topology analysis. The extracted topology maps indicate that stronger secondary motions occur for wider roughness stripes and thicker roughness layer, while the height of the roughness layer appears to not alter the secondary motion topology.

INTRODUCTION

Secondary motions of Prandtl's second kind have recently been investigated numerically and experimentally for rough-wall turbulent boundary layer flows with spanwise roughness heterogeneity [1, 2]. Similar observations were made in direct numerical simulations of turbulent channel flows with superhydrophobic surfaces (SHS) where streamwise stripes of a slip surface are introduced [3]. In the case of SHS the presence of secondary motions results in a reduction of the flow rate when a turbulent channel flow driven by a constant pressure gradient (CPG) is considered. For rough-wall turbulent boundary layers there are some contradictory results with respect to the location of low- and high momentum pathways (LMP & HMP) above the rough surface [1, 2], while a reversal of the secondary motion and hence a switch in LMP & HMP location are reported for SHS when the spanwise extend of the structure is increased [3].

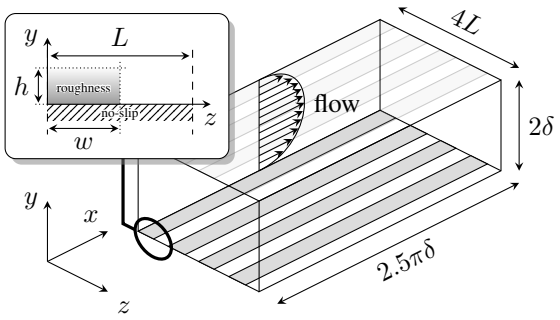

Figure 1: Schematic of the numerical domain with roughness strips at the walls.

The present contribution considers a detailed analysis of the secondary motions above a surface on which stripes of roughness are inserted as indicated in Figure 1. Topological evolution of the secondary flow and its properties are examined for variation of the wave-length, L, and roughness layer thickness, h, and compared to available literature results.

PROCEDURE

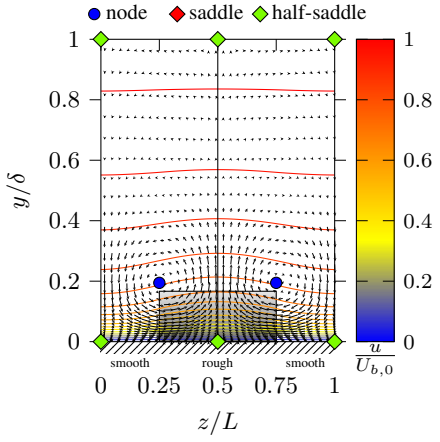

Figure 2: Vector plot of secondary motions, contours of streamwise mean velocity and singular points at $L/\delta = 0.78$.

A series of DNS has been carried out in a fully developed turbulent channel flow driven by CPG. The numerical code is identical to the implementation used by [3]. The schematic of the numerical domain is depicted in Figure 1. The friction Reynolds number is $\mathrm{Re}_\tau = u_\tau \delta/\nu = 180$. The wave-length, L, represents the size of the alternating structure with a constant roughness fraction $\Phi = w/L = 0.5$. For the variation of L we adjust the number of grid nodes in spanwise direction and, therefore, the spanwise extension of computational domain, while the wall area is always covered by four wave-lengths. Based on literature results the wave-length range $0.4 < L/\delta < 1.6$ is considered.

The roughness effect is modeled by the introduction of an additional drag force to the momentum equations in the corresponding areas of flow domain:

$$f_{d,i}(y) = \circ\, \frac{1}{2}\rho\alpha \cdot \sqrt{u_j u_j} \cdot u_i \cdot d(y)\,, \qquad (1)$$

where α represents the weighted drag coefficient depending on the roughness element density and the frontal element width defined as $d(y) = (1 \circ y/h)$ within the roughness element height h [4]. The particular wall-normal distribution, $d(y)$, and the value of α are chosen to represent the drag force exerted by an array of equidistantly distributed conical roughness elements with height h and cone base diameter $2h$ to the fluid. For the present analysis the roughness element height $h^+ = 10, 30$ and 50 are chosen.

The resulting secondary motions are characterized by means of singularity analysis, where nodes and saddles are extracted from the velocity maps in so as to develop a topology map of the flow structures; see Foss [5] for details on topology analysis. An example of a secondary motion vector plot with singular points is given in Figure 2.

*Corresponding authors Email: alexander.stroh / bettina.frohnapfel@kit.edu

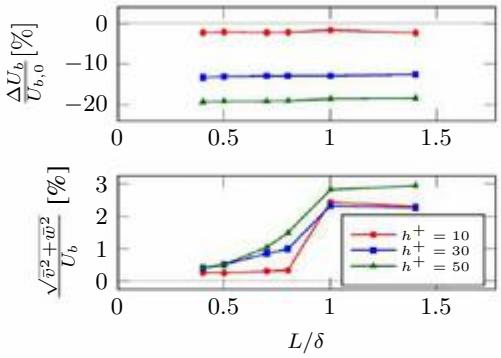

Figure 3: Change in the bulk mean velocity (upper plot) and the strength of secondary motions (lower plot).

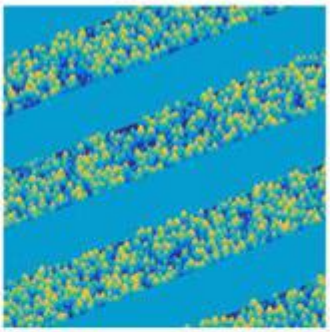

Figure 4: Heterogeneous roughness distribution with discrete elements.

RESULTS

The upper plot in Figure 3 shows the change of the bulk mean velocity with increasing L for three considered roughness heights. It is evident that the change of U_b is mainly governed by the roughness layer height and does not significantly change for different L, which is in contrast to the results obtained with stripes of free-slip surface [3]. In comparison to a plain channel flow the reduction in U_b is 2.5%, 13% and 19% for $h^+ = 10, 30$ and 50, resepectively. The lower plot in Figure 3 shows the maximum magnitude of the occuring secondary motion with variation of L and h. The secondary motion strength does not exceed 1% of U_b for $L/\delta < 0.75$ and rapidly increases for larger L. At $L/\delta = 1$ the secondary motion strength reaches $2 - 3\%$ of U_b and shows only slight variations for higher values.

For all investigated cases HMPs are found over the plain wall areas, while LMPs are located over the areas with roughness as exemplarily shown in Figure 2, which is in agreement with results presented in [2]. The HMPs & LMPs are generated due to the formation of a vortex pair with nodes located above the smooth / rough wall edges. The nodes slightly shift towards the middle of the channel with increasing L. Interestingly, the wall-normal position of the vortex nodes is almost independent of the considered roughnes layer height. This observation and analysis of the vorticity source term suggest that the secondary motions mainly occur due the presence of a spanwise heterogeneity of the stress close to the wall surface, where the height of surface roughness appears to only affect strength but not the topology of the secondary motion.

OUTLOOK

For the upcoming months, it is planned to extend the current analysis with a detailed evaluation of the vorticity transport equation in order to elucidate the mechanism of the vortex formation and the influence of the roughness properties on it. We also intend to carry out a similar investigation at higher Reynolds numbers ($\mathrm{Re}_\tau = 500$) with discrete roughness elements as shown in Figure 4 resolved in a DNS through immersed body method. The influence on the flow properties and characteristics of the secondary motions as well as the comparison to the current roughness modeling approach will be reported in the presentation.

ACKNOWLEDGMENTS

This work was performed on the computational resources bwUniCluster and ForHLR Phase I, funded by the Ministry of Science, Research and the Arts Baden-Wurttemberg, and the German Research Foundation (Deutsche Forschungsgemeinschaft, DFG) within the framework program bwHPC. The authors greatly acknowledge additional support by DFG through SFB/Transregio 150 project B02.

[1] Willingham, D., Anderson, W., Christensen, K. T., & Barros, J. M.: Turbulent boundary layer flow over transverse aerodynamic roughness transitions: Induced mixing and flow characterization. Phys. Fluids, 26(2), 025111, 2014.

[2] Vanderwel, C., & Ganapathisubramani, B.: Effects of spanwise spacing on large-scale secondary flows in rough-wall turbulent boundary layers. J. Fluid Mech., 774, R2, 2015.

[3] Türk, S., Daschiel, G., Stroh, A., Hasegawa, Y., & Frohnapfel, B.: Turbulent flow over superhydrophobic surfaces with streamwise grooves. J. Fluid Mech., 747, 186-217, 2014.

[4] Bons, J. P., McClain, S. T., Wang, Z. J., Chi, X., & Shih, T. I.: A Comparison of Approximate Versus Exact Geometrical Representations of Roughness for CFD Calculations of c_f and St. J. Turbomach., 130(2), 021024, 2008.

[5] Foss, J. F.: Surface selections and topological constraint evaluations for flow field analyses. Experiments in fluids, 37(6), 883-898, 2004.

AUTO-GENERATION BY INTERACTION OF WEAK EDDIES

Manu V Goudar*[1], Wim-Paul Breugem[2], Yoshifumi Jodai[3], and Gerrit E Elsinga[4]
[1,2,4]*Laboratory of Aero and Hydrodynamics, Delft University of Technology, Delft, The Netherlands*
[3]*National College of Technology, Kagawa College, Takamatsu, Kagawa, Japan*

Summary For channel flow, we explore how the interaction of weak eddies produces additional eddies by means of auto-generation. This is done by DNS of two eddies with different initial strengths, initial sizes and initial stream-wise spacing between them. The numerical procedure followed is similar to Zhou et al[1]. The two eddies merge into a single stronger eddy when a larger upstream and a smaller downstream eddy are placed within a certain initial stream-wise separation distance. Subsequently, the resulting stronger eddy is observed to auto-generate new eddies. The non-merging cases with small initial stream-wise separation also auto-generate. The auto-generation is characterized by a rapid lift-up of an initial eddy, which blocks the incoming flow and leads to shear-layer roll-up and formation of a new eddy. The same sequence of events is observed in a fully developed turbulent boundary layer[2].

INTRODUCTION

To create energy-efficient designs by reducing drag, it is essential to understand the internal structure and dynamics of wall-bounded turbulent flows. One of the ways to describe the dynamics of boundary-layer flows is the hairpin eddy model[3], based on coherent structures. The hairpin-like vortices are observed to populate the outer layer over a range of Reynolds numbers [4]. They are organized in the direction of the mean flow and occur in packets[5, 6, 7]. This packet organization not only enhances the Reynolds shear stress[5], but also, while occupying only 4% of total area of the flow, it contributes to more than 25% of the Reynolds shear stress[8]. Hence, vortex organization in packets is considered important. The packet formation has been explained by the auto-generation mechanism or parent-offspring concept[3]. Zhou et al[1] reported that the hairpins above a threshold strength can auto-generate. However, such strong vortices do not frequently appear in actual turbulent flows. Hence, we consider scenarios involving weak eddies, which are frequent in actual wall-bounded turbulence. The effect of low-speed streak on auto-generation, which is located under the eddy, is also studied. Finally, we examine the critical aspects leading to the onset of auto-generation and present a modified interpretation of the auto-generation mechanism.

The interactions between two ideal non auto-generating eddies is studied numerically by Direct Numerical Simulation (DNS). We follow a similar procedure to [1] in extracting the eddy from fully developed turbulent channel flow and simulate them dynamically. A variety of scenarios are created based on different initial strengths, event location and initial stream-wise spacing between the aligned eddies. The two eddies merge (Fig. 1a-b), when an eddy conditioned at higher wall-normal location is placed upstream of the one conditioned at the lower wall-normal location. The eddy with higher wall-normal location moves faster due to higher local flow velocity and merges with the downstream eddy creating an above threshold strength eddy, which auto-generates (Fig. 1c). However, only the merging cases with lower stream-wise separation auto-generate. Because, as the initial distance between the eddies increases, merging takes longer time, during which the eddies weaken individually and hence the merged eddy is not strong enough to create new vortices. Also, a few non-merging cases generate new structures, when the initial stream-wise separation between initial eddies is lower. From these observations, it is inferred that merging can create stronger eddies, but is not the sole mechanism. The auto-generation may depend upon a sufficiently small initial stream-wise separation of the two eddies as it is common between all the auto-generation cases.

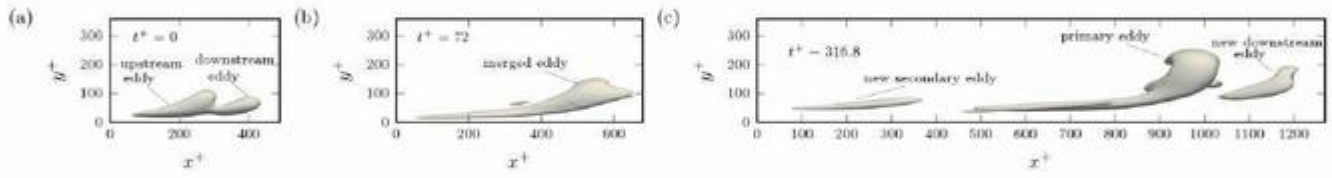

Figure 1: Iso-contours of swirling strength squared (10% of maximum) at time $t^+ = 0, 72$ and 316.8 for the two-eddy case with stream-wise separation $\Delta x^+ = 118$ (side view). Two eddies in (a) merge to form a single stronger eddy in (b). Merged eddy further auto-generates as shown in (c). x^+ and y^+ represent stream-wise and wall-normal directions, respectively, normalized by wall units.

The smaller stream-wise separation between eddies emulates the increasing threshold strength, as the velocity field of the two individually eddies gets superimposed and amplified. Hence, the role of the velocity field and specifically of the overlapping low-speed streak in the onset of auto-generation is explored. When the stream-wise separation is small, low-speed

*Corresponding author. Email: m.goudarvishwanathappa@tudelft.nl

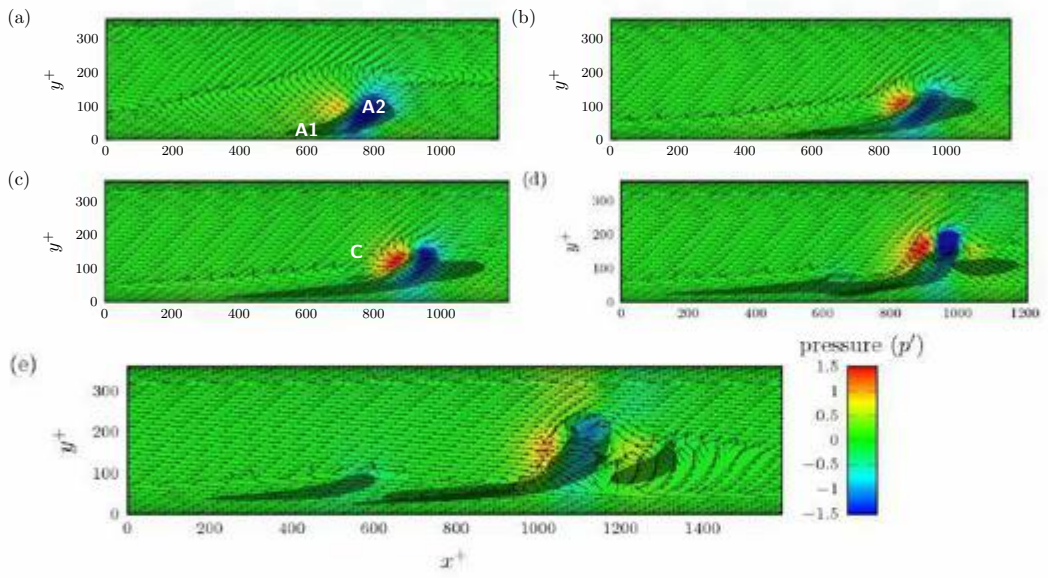

Figure 2: Auto-generation mechanism : Vector plots of velocity fluctuations (u'^+, v'^+) along with fluctuation pressure (p') contours in the symmetry plane which is between the two legs of an eddy. u'^+ and v'^+ are velocity fluctuations in stream-wise and wall-normal directions, respectively. All vectors are scaled by unit length, hence only indicate the flow direction. The iso-surfaces in the figures correspond the 10% of the initial maximum swirling strength. This is for two eddy case $(76, 51)$ at strength $\alpha = (1, 1)$ with $\Delta x^+ = 59$. Figures a-e represent the evolution of two eddies and vector plots in time at $t^+ = 28.8,\ 57.6,\ 86.4,\ 158.4$ and 244.8 respectively.

streaks from the two eddies overlap and get superimposed, which amplifies the strength of the resulting streak. A separate set of simulations has been performed by adding a divergence-free low-speed streak to a conditional eddy to understand the influence of vortex-streak interactions on auto-generation. However, these simulations do not show any auto-generation.

Finally, based on the above observations, the current picture of the auto-generation mechanism is modified. Analysis of the data suggests that the strong lift up of the initial hairpin head is due to the ejection event located at the hairpin head (Fig. 2a). Due to the lift up of the head, the in-rushing flow is blocked (Fig. 2b). This inrush of flow and the already existing ejection events cause the shear layer to deform and roll-up in the span-wise direction (z) just upstream of the vortex (Fig. 2c-d). As this span-wise roll-up becomes stronger, it connects to the leg/legs of the downstream vortex and becomes a new vortex by separating from the main vortex (Fig. 2d-e). When the ejection events are stronger in any of these two vortices, a third eddy will be formed in a similar way, else, the eddies are dissipated over time. The generation mechanism of new hairpin vortices is also observed in experiments by [2] within a fully turbulent boundary layer in a similar way.

This modified mechanism differs from the existing mechanism by [1] where induced vortex motions result in the formation of a kink in the legs of the initial eddy before a new hairpin head is created. In other words, kink formation in [1] is due to mutual and self induction of stream-wise legs, whereas in the present mechanism, it is the consequence of shear layer roll-up and ejection events. Also, the presence of two stream-wise vortex legs is not necessary to describe the onset of auto-generation as a single leg can lift up and block the incoming flow leading to the shear-layer roll up and further generation of a new eddy. The main implication of the present study is that commonly found weak eddies can also auto-generate, strengthening the existing hairpin eddy model[3].

References

[1] Zhou J., Adrian R.J., Balachandar S., Kendall T.M.: Mechanisms for generating coherent packets of hairpin vortices in channel flow, J. Fluid Mech 387:341-383, 1999.

[2] Jodai Y., Elsinga G.E.: Experimental observation of hairpin auto-generation events in a turbulent boundary layer. J. Fluid Mech submitted, 2015.

[3] Adrian R.J.:Hairpin vortex organization in wall turbulence, Phys. Fluids 19:041301, 2007.

[4] Bandyopadhyay P.: Large structure with a characteristic upstream interface in turbulent boundary layers, Phys. Fluids 23:2326, 1980.

[5] Adrian R.J., Meinhart C.D., Tomkins C.D.: Vortex organization in the outer region of the turbulent boundary layer, J. Fluid Mech 422:1-54, 2000.

[6] Head M.R., Bandyopadhyay P.: New aspects of turbulent boundary-layer structure, J. Fluid Mech 107:297-338, 1981.

[7] Smith C.R., Patterson G.K., Zakin J.L.: A synthesized model of the near-wall behavior in turbulent boundary layers, NASA STI/Recon Technical report N 84:19764, 1984.

[8] Ganapathisubramani B., Longmire E.K., Marusic I.: Characteristics of vortex packets in turbulent boundary layers, J. Fluid Mech 478:35-46, 2003.

COMPUTATION OF THE STARTING VORTEX PAST A FLAT PLATE

Monika Nitsche[1], Ling Xu[2], and Robert Krasny*[2]

[1]*Department of Mathematics and Statistics, University of New Mexico, Albuquerque, New Mexico, USA*
[2]*Department of Mathematics, University of Michigan, Ann Arbor, Michigan, USA*

Summary A comparison is presented of numerical methods applied to compute the starting vortex past a flat plate. The methods include (1) direct numerical simulation (DNS) by a finite-difference scheme, and (2) a vortex sheet model. Preliminary results will also be presented for (3) DNS by a viscous vortex method. The advantages and disadvantages of the methods will be discussed.

INTRODUCTION

When a viscous flow passes a solid body, the flow sticks to the body and a boundary layer forms along the body surface. The boundary layer thickens due to viscous diffusion and it is convected downstream until eventually it separates and rolls up into a starting vortex. The starting vortex affects the lift and drag forces on the body, and this has implications in many fields such as aerodynamics and biolocomotion.

Several groups have compared different models and numerical methods for computing this type of flow separation. For example a recent study compared a direct numerical simulation (DNS) with a discrete vortex model (DVM) for flow past an airfoil [9]. The results showed that the DVM captures some large scale features of the flow and was much less costly than the DNS, but the DVM was lacking in its treatment of the viscous boundary layer.

Here we consider the starting vortex past a flat plate and compare results obtained using several numerical methods, (1) DNS by a finite-difference scheme, and (2) a vortex sheet model. Preliminary results will also be presented for (3) DNS by a viscous vortex method. The advantages and disadvantages of the methods will be discussed.

PROBLEM DESCRIPTION

A flate plate is immersed in a viscous fluid. The plate is held fixed on the interval $\circ\, 0.5 \le x \le 0.5$ in the xy-plane. The incoming flow has speed $U = t^p$ and angle of incidence α. Here we consider the case of impulsively started flow $p = 0$ and normal incidence $\alpha = 90^\circ$, and we will report on other cases at the ICTAM. We consider the Navier-Stokes equations in vorticity form,

$$\partial_t \omega + \mathbf{u} \cdot \nabla \omega = Re^{-1} \nabla^2 \omega, \tag{1}$$

where ω is the vorticity, $\mathbf{u}$ is the velocity, and Re is the Reynolds number. The velocity is obtained from the stream function, $\mathbf{u} = (\psi_y, \circ\, \psi_x)$, where the vorticity and stream function are related by the Poisson equation $\nabla^2 \psi = \circ\, \omega$ with boundary conditions $\psi = 0$ on the plate surface, and $\psi \to \psi_\infty$ for $|\mathbf{x}| \to \infty$. The no-slip condition $\mathbf{u} = \mathbf{0}$ on holds on the plate surface.

NUMERICAL METHODS

DNS by a finite-difference scheme

The Navier-Stokes equations are solved by operator splitting, where the inviscid and viscous parts are computed in two successive stages per time step. The inviscid part, $\partial_t \omega + \mathbf{u} \cdot \nabla \omega = 0$, is computed by a semi-Lagrangian method, and the viscous part, $\partial_t \omega = Re^{-1} \nabla^2 \omega$, is computed by the Crank-Nicolson method. Details are in [8, 12, 13].

Vortex sheet model

The vorticity distribution has two components, a free vortex sheet that is shed at the edge of the plate, and a bound vortex sheet on the plate. The free sheet is represented by regularized point vortices (vortex blobs) with smoothing parameter δ, and the bound sheet is represented by singular point vortices. The vortex blobs are advected using the Biot-Savart integral. The bound vortex sheet strength is computed by solving an integral equation on the plate. The unsteady Kutta condition is imposed at the edge of the plate to account for circulation shedding. Details are in [7].

DNS by a viscous vortex method

Lighthill [5] advocated that the vorticity should be used in DNS of viscous flow past a solid body, where the no-slip condition can be satisfied by creating vorticity on the body surface, and then allowing it to diffuse and convect. This approach has been implemented in various ways by many investigators (see for example [2, 11, 3]). In the present work we implement this approach using recently developed adaptive refinement and remeshing techniques for accuracy [4, 1] and a treecode algorithm for efficiency [6]. This is current work and we will report on our preliminary results at the ICTAM.

*Corresponding author. Email: krasny@umich.edu

NUMERICAL RESULTS

Figure 1 compares results obtained using (1) DNS by a finite-difference scheme with several values of Reynolds number Re, and (2) a vortex sheet model with several values of the smoothing parameter δ. The DNS results show a streakline of passive particles introduced at the edge of the plate, and the vortex sheet results also show a streakline, but in this case these are the computed vortex blob locations. The streaklines roll up into spirals that become tighter as $Re \to \infty$ and $\delta \to 0$. There is good agreement between the DNS and vortex sheet model in terms of the size, shape, and location of the spiral. Similar results were previously obtained for the case in which a free shear layer rolls up in unbounded flow [10], and the present work

Γ as a function of time, again showing good agreement between the two models.

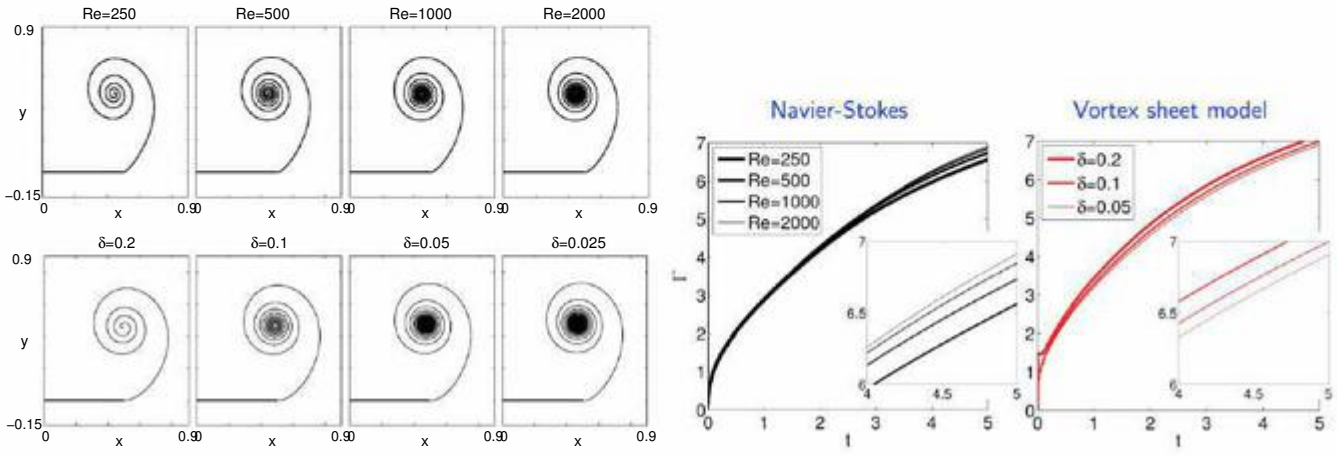

Figure 1: Starting vortex past a flat plate, comparison of numerical results, (left) streaklines of separating shear layer, (top left) DNS by a finite-difference scheme with Reynolds number Re, (bottom left) vortex sheet model with smoothing parameter δ, (right) shed circulation Γ as a function of time.

CONCLUSIONS

We computed the starting vortex in viscous flow past a flat plate using several numerical methods, direct numerical simulation (DNS) and a vortex sheet model. There is good agreement between the DNS and vortex sheet results in terms of the large scale features of the flow, namely the size, shape, and location of the spiral core, and the shed circulation as a function of time. The vortex sheet model is much less costly than the DNS, but it has limited applicability due to the omission of the boundary layers present in the true viscous flow. We are currently developing a viscous vortex method which should address the limitations of the vortex sheet model.

References

[1] Bosler P., Wang L., Jablonowski C., Krasny R.: A Lagrangian Particle/Panel Method for the Barotropic Vorticity Equations on a Rotating Sphere. Fluid Dyn Res 46:031406, 2014.

[2] Chorin A.J.: Numerical Study of Slightly Viscous Flow. J. Fluid Mech 57:785–796, 1973.

[3] Cottet G.-H., Koumoutsakos P., Vortex Methods: Theory and Practice. Cambridge University Press, 2000.

[4] Feng H., Kaganovskiy L., Krasny R.: Azimuthal Instability of a Vortex Ring Computed by a Vortex Sheet Panel Method. Fluid Dyn Res 41:051405, 2009.

[5] Lighthill M.J.: Introduction, Boundary Layer Theory, in: L. Rosenhead (Ed.), Laminar Boundary Layers. Oxford University Press, pp. 54–61, 1963.

[6] Lindsay K., Krasny R.: A Particle Method and Adaptive Treecode for Vortex Sheet Motion in Three-Dimensional Flow. J. Comput Phys 172:879–907, 2001.

[7] Nitsche M., Krasny, R.: A Numerical Study of Vortex Ring Formation at the Edge of a Circular Tube. J. Fluid Mech 276:139–161, 1994.

[8] Nitsche M., Xu L.: Circulation Shedding in Viscous Starting Flow Past a Flat Plate. Fluid Dyn Res 46:061420, 2014.

[9] Ramesh K., Gopalarathnam A., Granlund K., Ol M.V., Edwards J.R.: Discrete-Vortex Method with Novel Shedding Criterion for Unsteady Aerofoil Flows with Intermittent Leading-Edge Vortex Shedding. J. Fluid Mech 751:500–538, 2014.

[10] Tryggvason G., Dahm W.J.A., Sbieh K.: Fine Structure of Vortex Sheet Rollup by Viscous and Inviscid Simulation, J. Fluids Engin 113:31–36, 1991.

[11] Wu J.Z., Wu J.M.: Boundary Vorticity Dynamics Since Lighthill's 1963 Article: Review and Development. Theor Comput Fluid Dyn 10:459–474, 1998.

[12] Xu L., Nitsche M.: Scaling Behaviour in Impulsively Started Viscous Flow Past a Finite Flat Plate. J. Fluid Mech 756:689–715, 2014.

[13] Xu L., Nitsche M.: Start-Up Vortex Flow Past an Accelerated Flat Plate. Phys Fluids 27:033602, 2015.

THE CURIOUS CASE OF THE VANISHING VORTICITY

Mark Thompson[1], Morten Brøns[2], Thomas Leweke[3], and Kerry Hourigan*[1]

[1]*FLAIR, Department of Mechanical & Aerospace Engineering, Monash University 3880, Melbourne, Australia*
[2]*Department of Applied Mathematics and Computer Science, Technical University of Denmark, Lyngby, DK-2800, Denmark*
[3]*IRPHE UMR 7342, CNRS, Aix-Marseille Université, Centrale Marseille, 13384 Marseille, France*

Summary The flow over a submerged horizontally translating cylinder results in vorticity of opposite sign being shed from the top and bottom. However, when the cylinder is close to a stress-free surface, the vorticity shed from the top of the cylinder seems to disappear downstream, for zero and non-zero Froude number cases. For the zero Froude number flow case, vorticity shed from the top surface of the cylinder can diffuse from the body of the fluid into the interface. For high Froude numbers, the stress-free surface curves and vorticity can stream into the body of the fluid, cross-annihilating vorticity shed from the top surface of the cylinder. For each case, it is shown that circulation is conserved in the flow, by taking account of the circulation at the stress-free interface. Such an interface is therefore a potent source of vorticity, even in the absence of external forcing, and can dramatically modify vortex formation and evolution.

THE PROBLEM

The specific problem of interest involves the flow around a submerged circular cylinder translating at constant velocity horizontally to a stress-free surface [1, 2]. For an isolated circular cylinder, a Bénard-von Kármán array of alternating vortices (vortex street) forms in the wake. As the gap G between the cylinder and the free surface decreases, the vorticity shed strongly from the top surface of the cylinder remarkably disappears in the wake, leaving vorticity of only one sign in the flow downstream. At a Reynolds number Re of 180, and for the zero Froude number (Fr) case (figure 1a), the role of the stress-free surface is not obvious. For Fr = 0.2, the stress-free surface can distort, and patches of vorticity now appear (figure 1b). As the Froude number is increased further to 0.6, the free surface curves more and strong downward jetting of positive vorticity from the surface is seen to occur, leading to the rapid cross annihilation of the negative vorticity shed from the cylinder top surface (figure 1c).

Here, we consider this apparent violation of the conservation of circulation and why vorticity appears to vanish from the flow by first reflecting on how vorticity is generated and diffused at interfaces, and then analysing the particular case of the flow over a submerged circular cylinder.

THE THEORY

For simplicity, we consider the case where the normal motion of the stress-free surface is negligible. The source density σ, of vorticity ω, at a stress-free interface can be written as (the complete formulation for the generation of vorticity for 2D incompressible fluids is found in [3], building on the earlier work of [4, 5]):

$$\sigma = \frac{\mathrm{d}}{\mathrm{d}t}(\boldsymbol{u}\cdot\boldsymbol{t}) + \frac{1}{\rho}\frac{\partial p}{\partial s}, \tag{1}$$

where $\boldsymbol{u}$, p and ρ are the fluid velocity, pressure, and density, respectively, t is time, s is the curvilinear distance along the surface, and $\boldsymbol{t}$ is the unit vector tangential to the surface.

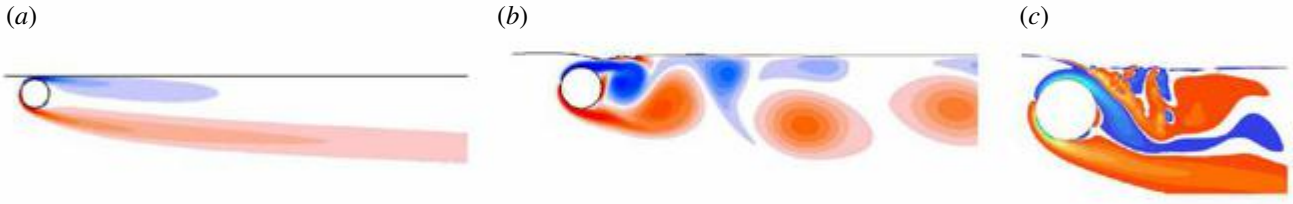

Figure 1: Vorticity field for a cylinder of diameter D translating to the left, horizontally at distance G under a free surface, for Re = 180: (*a*) Fr = 0, G/D = 0.125, (*b*) Fr = 0.2, G/D = 0.3 and (*c*) Fr = 0.6, G/D = 0.25 [3]. Red/blue denotes positive/negative vorticity, respectively.

*Corresponding author. Email: Kerry.Hourigan@monash.edu

The rate of change of the total circulation at the interface in an area A, perimeter C, and between the points a and b on the surface of the stress-free interface is given by:

$$\frac{\mathrm{d}}{\mathrm{d}t}\left(\int_A \omega \mathrm{d}A + \int_{\boldsymbol{a}}^{\boldsymbol{b}} \boldsymbol{u}\cdot\hat{\boldsymbol{t}}\,\mathrm{d}s\right) = \int_C \nu\nabla\omega\cdot\boldsymbol{n}\,\mathrm{d}s + \left(\left.\frac{p}{\rho_1}\right|_{\boldsymbol{b}} \circ \left.\frac{p}{\rho}\right|_{\boldsymbol{a}}\right). \tag{2}$$

This means that circulation is generated by a net pressure gradient in the fluid along the surface; viscosity serves to diffuse existing vorticity. If the tangential velocity at the surface changes with time (i.e., the fluid accelerates at the interface), then the circulation stored there evolves (second term in brackets on the left).

There is no constraint on the velocity of the fluid in the limit approaching the interface. However, from the dynamical boundary condition (zero tangential stress at the interface), the following relation can be derived [5, equation 11]:

$$\omega = 2\frac{\boldsymbol{u}\cdot\hat{\boldsymbol{t}}}{R} = 2\Omega. \tag{3}$$

This equation reflects the familiar statement that "surface vorticity is twice the curvature times tangential velocity", and it follows that the surface is point-wise in solid-body rotation with angular velocity $\Omega = \boldsymbol{u}\cdot\hat{\boldsymbol{t}}/R$, where $R = 1/\kappa$ is the radius of curvature.

THE SOLUTION

In general, for a curved surface with a stress-free boundary condition, the exchange of vorticity between the body of the fluid and the vortex sheet (velocity jump) representing this surface is such that the fluid at the surface is in solid-body rotation (see equation (3)). In the case of a flat surface, the radius of curvature is infinite and the vorticity at the surface is identically zero; therefore, the flow of vorticity can only be directed into the interface. A curved stress-free surface can also lead to active and substantial vorticity introduction into the body of the fluid from the interface. Both the flow of vorticity into the interface and the flow of vorticity away from a curved surface leading to cross-annihilation results in the diminution of opposite sign vorticity shed from the top of the circular cylinder.

A close examination of our flow predictions shows that the deficit in vorticity present in the body of the fluid is indeed balanced precisely by the increase in the circulation of the vortex sheet or velocity jump at the free surface. More generally, according to equation (2), a flux of vorticity to the free-surface interface, in the absence of normal motion, is associated with an acceleration of the fluid surface and/or a pressure gradient along this layer. For an initially uniform flow relative to the cylinder, the net pressure difference and the velocity difference at the fluid interface between far upstream and far downstream is zero; therefore, although local vorticity variations can occur and vorticity of one sign seems to vanish into the free surface, overall the circulation is conserved.

CONCLUSIONS

The generalised formulation of the stress-free interface facilitates the physical understanding of the generation and re-distribution of vorticity at the interface. The vorticity in the body of a fluid can be exchanged with that at a stress-free interface/boundary and be stored as a vortex sheet (velocity jump). This storage is not possible at a no-slip boundary as the fluid is forced to co-move with the boundary. Furthermore, tangential fluid motion induced at a curved stress-free boundary results in the appearance of (solid-body rotation) vorticity at the fluid surface, and a balance of opposite-sign circulation in the interface/boundary vortex sheet. In all cases, net vorticity (or circulation) is conserved in the system. The generation, transport and conservation of vorticity has been demonstrated in the case of the flow past a cylinder beneath a stress-free surface; the apparent loss in the fluid body of vorticity of in the body of the fluid is precisely balanced by the change in circulation stored at the stress-free surface. Where there is surface curvature, solid body rotation ensues at the stress-free surface, and significant amounts of vorticity can form (balanced by a change in the circulation at the interface); in certain cases, this vorticity can separate into the flow, leading to rapid cross-annihilation of vorticity shed from the cylinder.

Acknowledgments

This research was supported by Australian Research Council (ARC) Discovery Grants DP130100822 and DP150102879.

References

[1] Sheridan, J., Lin J.-C., Rockwell, D.: Flow past a cylinder close to a free-surface. J. Fluid Mech. 330:130, 1997.
[2] Reichl, P., Hourigan, K., Thompson, M.: Flow past a cylinder close to a free surface. J. Fluid Mech. 533:269–296, 2005.
[3] Brøns M., Thompson, M. C, Leweke, T., Hourigan, K.: Vorticity generation and conservation for two-dimensional interfaces and boundaries. J. Fluid Mech 758:63–93, 2014.
[4] Morton, B. R.: The generation and decay of vorticity. Geophys. Astrophys. Fluid Dyn. 28:277–308,1984.
[5] Lundgren, T., Koumoutsakos, P.: On the generation of vorticity at a free surface. J. Fluid Mech. 382:35–366, 1999.

TWO-DIMENSIONAL WAKES OF AN OSCILLATING CYLINDER AT LOW REYNOLDS NUMBER

Wenchao Yang and Mark A. Stremler*
Department of Biomedical Engineering and Mechanics, Virginia Tech, Blacksburg, Virginia, USA

Summary We will discuss the results of a systematic parametric study of the wake structure produced by a circular cylinder undergoing forced oscillations transverse to the background flow in an inclined soap film system. Comparisons with existing results for a three-dimensional experimental system and a two-dimensional computational model provide important insight into the role of system dimensionality in the formation and dynamics of complex vortex wakes.

Vortex-induced vibration is a classic problem in fluid mechanics with many applications. To better understand this phenomenon, numerous researchers have investigated the structure and dynamics of wakes that are generated by a circular cylinder undergoing controlled oscillations transverse to a uniform background flow. In their seminal paper, Williamson & Roshko [6] documented several distinct wake structures that appeared in water channel experiments over a broad range of oscillation parameters, as shown in Fig. 1(I). The normalized oscillation amplitude, $A^* = A/D$, and the normalized oscillation wavelength, $\lambda^* = U/fD$ (or normalized oscillation frequency, $f^* = (\lambda^* St)^{-1}$), play key roles in determining the wake structure, which is related to the forces felt by the wake-producing body [5]. Here, D is the cylinder diameter, A is the oscillation amplitude, f is the oscillation frequency, U is the (uniform) background flow speed, and $St = f_N D/U$ is the Strouhal number, where f_N is the frequency of vortex shedding from a fixed cylinder. The vortex wake structures documented in Ref. [6] include a '2S' mode corresponding to the standard von Kármán street having two single vortices formed per shedding cycle, a '2P' mode in which two pairs of vortices are formed per cycle, and an asymmetric 'P+S' mode comprised of a pair of vortices and a single vortex; examples of each are illustrated in Fig.1(I).

Leontini and collaborators [2] replicated the investigation from [6] using a two-dimensional computational model. The resulting bifurcation diagram for wake structure in (f^*, A^*)-space is shown in Fig. 1(II). Some general characteristics are shared between the results shown in panels I and II of Fig. 1, but the relationship between parameter values and wake structure as computed in the two-dimensional simulations is substantially different from that observed in the three-dimensional experimental system. Some of this difference can be explained by Reynolds number dependence, as considered by Leontini et al. [2]. Of particular note is the absence of any '2P' wake patterns in Ref. [2] for the wide range of parameter values considered in those numerical simulations, although Williamson & Roshko [6] do note that "for Re< 300 the P+S mode occurred instead of the 2P mode throughout that region as well." Leontini et al. [2] conclude that the primary explanation for the differences between the computational and experimental results (at similar Re values) lies in the difference in dimensionality between these two systems.

We are investigating the role of system dimensionality in the wake structure generated behind an oscillating cylinder by conducting experiments in a flowing soap film. Soap film systems have been established as a useful tool for investigating (quasi-) two-dimensional flows [7] and have been used by several different research groups for investigating wake structure (see, e.g., Refs. [1, 4]). Couder & Basdevant [1] demonstrated three decades ago that in-line oscillation of a circular cylinder can generate a '2P' wake in a soap film. Schnipper et al. [4] conducted an extensive parametric analysis of flow past a flapping foil and observed a rich collection of wake structures. However, a replication of Williamson & Roshko's [6] investigation of transverse cylinder oscillations has not been conducted previously in a soap film.

Our experimental system, illustrated in Fig. 1(III), consists of a gravity-driven, inclined flowing soap film that generates a quasi-two-dimensional flow with a controlled flow speed. The nylon wires forming the sides of the test system are stretched by four horizontal pull lines that are tensioned by springs to form a $1\,\mathrm{m} \times 0.1\,\mathrm{m}$ rectangular test section. Soap solution is pumped into a top reservoir with an overflow mechanism to maintain a constant pressure head at the valve, enabling a consistent average flow speed. The cylinder penetrates perpendicularly through the flowing soap film and is forced to oscillate in harmonic motion transverse to the film flow. A high-speed camera records the optical interference between the front and back surfaces of the film. Dark and bright fringes become visible on the film under monochromatic light from the sodium lamp, enabling direct visualization of the wake pattern.

Five example cases of the wake structure observed in our experimental system are shown in Fig. 1(IV). Case A shows evidence of a P+S wake structure, which consists of one pair of (two) vortices and one single vortex that are shed from the cylinder during each oscillation cycle. The generation of a P+S wake structure at these parameter values is consistent with the two-dimensional results in Ref. [2], as can be seen in Fig. 1(II), but differs from the 2P wake structure expected for these parameter values in the three-dimensional experimental system [6], as shown in Fig. 1(I). Case B does not show an established wake pattern, which is consistent with the findings of both Refs. [2] and [6]. Case C shows evidence of a 2S wake (with two

*Corresponding author. Email: stremler@vt.edu

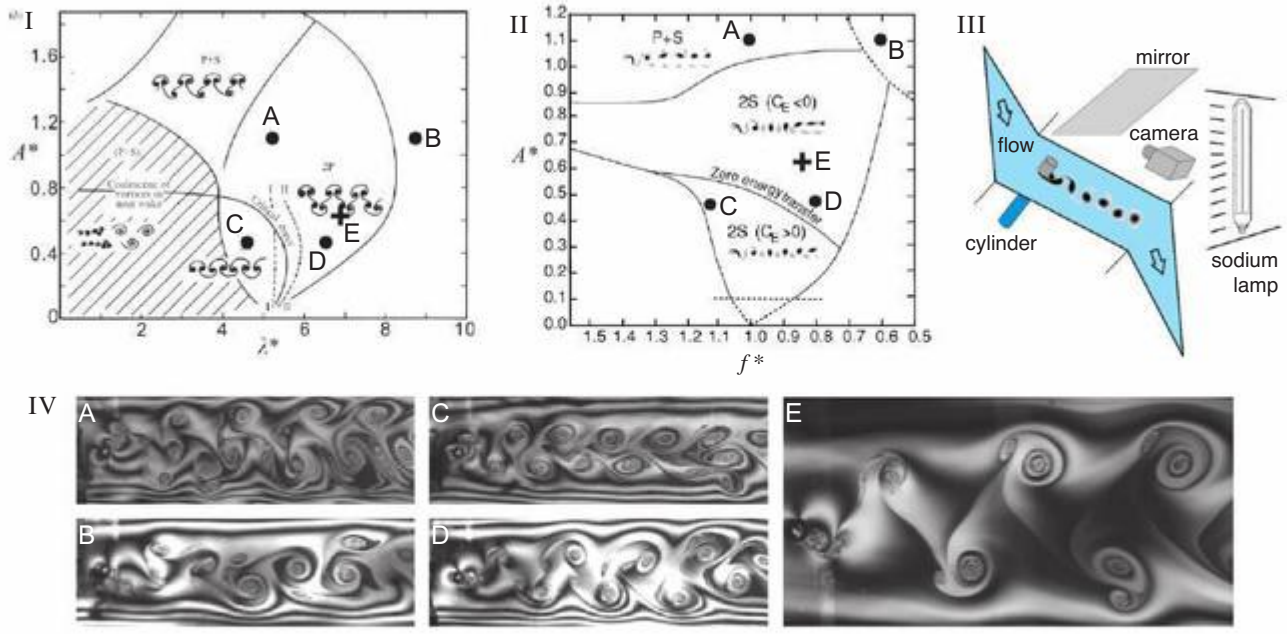

Figure 1: (I) Characterization of wake structure behind an oscillating cylinder (I) in a three-dimensional water channel by Williamson & Roshko [6] for $300 < \mathrm{Re} < 1000$ and (II) in a two-dimensional computational model by Leontini et al. [2] for $\mathrm{Re} \approx 100$. Points labeled A–E mark the parameters corresponding to images A–E in panel IV. (III) Schematic of the inclined flowing soap film system used in the present experimental study. (IV) Representative examples of wake patterns generated by a cylinder oscillating transverse to the flow in the inclined soap film system for $\mathrm{Re} \approx 170$ (cases A–D) and $\mathrm{Re} \approx 110$ (case E). Flow is from left to right.

single vortices formed per cycle) but lacks repeatability, which would seem most consistent with being near the bifurcation boundary for the two-dimensional system in Fig. 1(II), but does not fully agree with the results for either of the previous investigations. Case D shows evidence of being a $2P_O$ wake, which is similar to the $2P$ wake with four vortices (or two pairs of vortices) shed per cycle but exhibiting much weaker secondary vortices [3]. This wake structure is most consistent with that found in the three-dimensional system [3, 6] despite the difference in Re values, although the structure we observed is not invariably repetitive. Our final example, case E, shows a clear 2P wake structure; the occurrence of this structure matches well with the three-dimensional experimental results in Ref. [6] for $\mathrm{Re} > 300$ and contrasts sharply with the two-dimensional computational results in Ref. [2] and the statement in Ref. [6] that the 2P mode is not observed for $\mathrm{Re} < 300$, when the wake is expected to remain two-dimensional.

We will discuss the results of a systematic parametric study of the wake structure produced in the (λ^*, A^*)-space accessible to our experimental system. The examples presented here suggest that differences between the results from Williamson & Roshko [6] and Leontini et al. [2] and occurrence (or absence) of a 2P mode wake cannot be attributed solely to system dimensionality. Further insight into the formation and dynamics of complex vortex wakes produced behind oscillating bluff bodies can be obtained by consideration of this quasi-two-dimensional experimental model.

References

[1] Couder, Y. and Basdevant, C.: Experimental and numerical study of vortex couples in two-dimensional flows. J. Fluid Mech. 173:225–251, 1986.

[2] Leontini, J. S. et al.: Wake state and energy transitions of an oscillating cylinder at low Reynolds number. Phys. Fluids 067101, 2006.

[3] Morse, T. L. and Williamson, C. H. K.: Prediction of vortex-induced vibration response by employing controlled motion. J. Fluid Mech. 634:5–39, 2009.

[4] Schnipper, T., Andersen, A. and Bohr, T.: Vortex wakes of a flapping foil. J. Fluid Mech. 633:411–423, 2009.

[5] Williamson, C. H. K. and Govardhan, R.: Vortex-induced vibrations. Ann. Rev. Fluid Mech. 36:413–455, 2004.

[6] Williamson, C. H. K. and Roshko, A.: Vortex formation in the wake of an oscillating cylinder. J. Fluids Structures 2:355–381, 1988.

[7] Zhang, J., Childress, S., Libchaber, A. and Shelley, M.: Flexible filaments in a flowing soap film as a model for one-dimensional flags in a two-dimensional wind. Nature 408:835–839, 2000.

POINT VORTEX MODELS OF EXOTIC LAMINAR VORTEX STREETS

Mark A. Stremler*[1] and Saikat Basu[2]
[1]*Department of Biomedical Engineering and Mechanics, Virginia Tech, Blacksburg, Virginia, USA*
[2]*Collective Interactions Unit, Okinawa Institute of Science and Technology Graduate University, Okinawa, Japan*

Summary We will discuss the structure and dynamics of complicated, or exotic, laminar vortex streets using point vortex models in two-dimensional potential flow. The focus will be on singly-periodic systems containing four vortices per period having an assumed spatial symmetry that is preserved by the dynamics. This symmetry is inspired by the patterns observed in 2P-mode bluff body wakes, in which four neighboring vortices appear as two pairs with a glide-reflective symmetry: the position of each pair is related to the other by a reflection about and a half-period translation along the wake centerline. This problem can be reduced to an integrable Hamiltonian system. Vortex motions are classified using a bifurcation analysis of the phase space topology as determined by level curves of the Hamiltonian. The four-point-vortex system exhibits a rich variety of relative motions for almost all possible initial conditions.

Consider the laminar flow of a viscous fluid moving with a steady free-stream velocity U around a submerged bluff body. If the Reynolds number is sufficiently large, the vorticity generated by the body is periodically shed into the downstream wake. The most commonly occurring pattern for the shed vortices is the standard von Kármán (vK) street, such as that shown in Fig. 1(a), in which the vortices move in rows nearly parallel to the streamwise axis and with essentially constant inter-vortex spacing. This flow can be modeled as two oppositely-signed point vortices in a periodic "strip", i.e. in a singly-periodic domain. When the body oscillates, flaps, or is in close proximity to another body, the vortices in the wake can exhibit a variety of other patterns, most of which display relative vortex motion. Patterns such as those shown in Fig. 1(b,c) have been referred to as 'exotic wakes' [2].

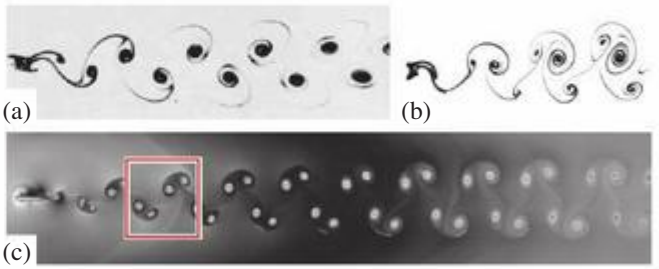

Figure 1: Various experimental wakes, with flow moving from left to right. (a) A 2S von Kármán street behind a stationary cylinder in water, adapted from [7]. (b) A P+S wake behind an oscillating cylinder in water, from C.H.K. Williamson [private communication]. (c) A 2P wake behind a flapping foil in a flowing soap film, adapted from [5].

The point vortex modeling approach introduced by von Kármán has been extended to wakes that can be represented by $N = 3$ [1] or $N = 4$ [3] vortices per period. The model represents one set of 'base' vortices in an exotic wake, say the four vortices highlighted by the box in Fig. 1(c). Each base vortex is considered to be at position $z_\alpha = x_\alpha + \mathrm{i}\, y_\alpha$ in the complex plan and have strength Γ_α. For simplicity, it is assumed that the influence of the remaining vortices can be approximated using spatially periodic images of these base vortices. These complicated, or exotic, wakes are thus modeled as periodic arrangements of N point vortices in a periodic strip of width L (i.e. as vortex streets); the focus of this presentation will be on the case $N = 4$. The downstream development of a wake is then examined in the vortex street model by considering the temporal evolution of the base vortices. The equations are formulated so that the vortex street is viewed in a frame of reference moving with the background flow.

Point vortex models of exotic vortex streets display a range of interesting, and sometimes quite complicated, behaviors. When $N = 4$, the model system can be made integrable by assuming a glide-reflective symmetry that is motivated by experimental observations of 2P wakes [6]. Each set of four base vortices are considered as two pairs, with the position of each pair related to the other by a reflection about the wake centerline and a half-period translation along the wake centerline. The strength of each vortex is taken to be the negative of its glide-reflective image, so that the sum of the vortex strengths is zero. Under these assumed constraints, the $N = 4$ problem can be reduced to an integrable Hamiltonian system that depends only on the relative separation between like-signed vortices, $Z = X + \mathrm{i}\, Y = \pi(z_1 - z_2)/L$, with the relative vortex strengths, $\gamma = \Gamma_1/(\Gamma_1 + \Gamma_2)$ and the imaginary component of the linear impulse, $\mathcal{P} = (\pi/L) \sum_\alpha \Gamma_\alpha/(\Gamma_1 + \Gamma_2)\, y_\alpha$, as parameters.

The Hamiltonian formulation allows for a full characterization of this integrable system using phase space representations and a bifurcation diagram in $(\gamma, \mathcal{P})$-space. Specifying values of γ and $\mathcal{P}$ establishes the topological structure of the phase space representation, as determined by the existence of and connectivity between fixed points in the (X, Y) plane. For a given initial vortex configuration, the relative vortex positions evolve along level curves of the Hamiltonian. Absolute motion of the vortex system is then determined by an additional integration of the relative motion. An example phase-space structure and several corresponding real-space trajectories are shown in Fig. 2 for $(\gamma, \mathcal{P}) = (2/5, -1)$.

Varying the values of γ and $\mathcal{P}$ can change the phase space structure, leading to bifurcations in which the connectivity of the saddle points changes. The topology of the phase space structure is the same within a given region of the bifurcation diagram,

*Corresponding author. Email: stremler@vt.edu

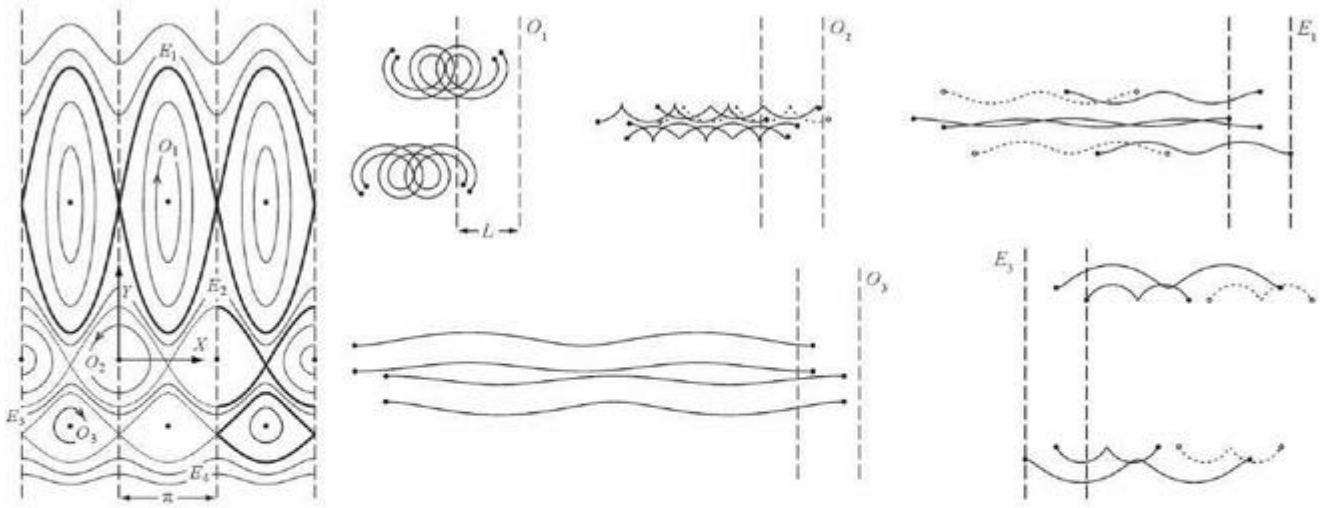

Figure 2: *(left)* Representative level curves of the Hamiltonian in the (X, Y) plane for the case $\gamma = 2/5$, $\mathcal{P} = -1$. Three spatial periods are shown. Level curves are marked with solid lines; separatrices joining the saddle points are shown with heavy lines, and these curves delineate seven distinct regimes of motion. Regimes with orbiting motion are labeled O_i, and those with exchanging motion are labeled E_i. *(right)* Representative real-space vortex trajectories, labeled according to the corresponding regime in the phase space diagram at left. Solid circles mark initial and final locations of the base vortices; open circles mark initial and final locations of selected image vortices. The trajectories taken by the base vortices are shown with solid lines; trajectories of the image vortices are shown with dotted lines.

shown in Fig. 3. Then, for a particular phase space structure, separatrices delineate regimes of vortex motion, and within any particular regime of motion the relative motion of vortices in the (x, y) plane is qualitatively the same. Thus, describing the possible vortex motions from a representative phase space example in each of the regions of bifurcation space gives a full characterization of the vortex motion in this system.

In the experimental literature, wakes with four vortices per period are generally classified as being 2P or 2C wakes [6], a distinction acknowledging that very different wake dynamics can arise from having strong interactions between the oppositely-signed vortices (generally 2P) or the like-signed vortices (generally 2C). Relatively recent experiments have expanded this classification to include a '$2P_{\mathrm{overlap}}$' mode, a 2P-like mode in which one of the vortices in a pair is much weaker than the other [4]. The present model results suggest that a wide variety of vortex dynamics may exist in experimental wakes, and classification of a wake based primarily on the number of vortices shed per cycle is likely insufficient.

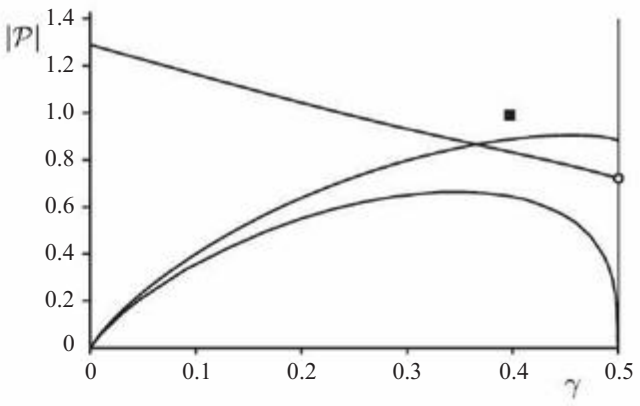

Figure 3: Bifurcation diagram for the phase space topology. Solid lines mark the $(\gamma, \mathcal{P})$ coordinates at which different phase space fixed points are connected by separatrices. The open circle marks a singularity in the bifurcation diagram. The example from Fig. 2 is marked with a square symbol.

[1] Aref, H. and Stremler, M. A.: On the motion of three point vortices in a periodic strip. J. Fluid Mech. 314:1–25, 1996.

[2] Aref, H. Stremler, M. A., and Ponta, F. L.: Exotic vortex wakes — point vortex solutions. J. Fluids Struct. 22:929–940, 2006.

[3] Basu, S. and Stremler, M. A.: On the motion of two point vortex pairs with glide-reflective symmetry in a periodic strip. Phys. Fluids 27:103603, 2015.

[4] Morse, T. L. and Williamson, C. H. K.: Prediction of vortex-induced vibration response by employing controlled motion. J. Fluid Mech. 634:5–39, 2009.

[5] Schnipper, T., Andersen, A., and Bohr, T.: Vortex wakes of an oscillating foil. J. Fluid Mech. 633:411–423, 2009.

[6] Stremler, M. A., Salmanzadeh, A., Basu, S., and Williamson, C. H. K.: A mathematical model of 2P and 2C vortex wakes. J. Fluids Struct. 27:774–783, 2011.

[7] Van Dyke, M.: An Album of Fluid Motion. Parabolic Press, 1982.

MAGNETIC POINT VORTEX DYNAMICS IN THE PLANE

Denis Blackmore[1], Anthony Rosato[2a)] & Surajit Sen[3]
[1]*Department. of Mathematical Sciences, New Jersey Institute of Technology, Newark, NJ, USA*
[2]*Department of Mechanical & Industrial Engineering, New Jersey Institute of Technology, Newark, NJ, USA*
[3]*Department of Physics, SUNY Buffalo, Buffalo, NY, USA*

Summary It is shown that an interpretation of the Hamiltonian dynamics of a one-dimensional chain of point magnets bears a striking resemblance to that of point vortices in a planar ideal fluid. This leads naturally to a consideration of planar generalizations of point magnet fields that exhibit vortex-like dynamical characteristics. A class of such generalizations – (quasi-) 2-dimensional approximations of Bose—Einstein condensate vortex dynamics – is analyzed using a combination of theory and simulations. Special attention is paid to integrability, bifurcations and perturbations of the Hamiltonian dynamics. Possible variations of the fields and extensions to approximate models of (topological) vortex dynamics in Maxwell—Chern—Simon—Higgs fields are also briefly considered.

INTRODUCTION

The dynamics of a 1-dimensional chain of small (point) magnets has several useful applications as shown in [5] and experiments and simulations by the authors indicate considerable energy harvesting potential. Naturally, this leads to an interest in higher dimensional generalizations, which catalyzed the work described in this paper on 2-dimensional extensions related to physical phenomena of current interest, especially those involving vortex-like dynamics. This emphasis is a result both of the resemblance of the equations of motion of to that of point vortices in fluid dynamics (see *e.g.* [1]) and certain similarities between these equations and those associated to vortex-like behavior in various electro-magnetic gauge fields, especially Bose—Einstein condensates (BEC) as illustrated in papers such as [2-4, 6].

This paper begins with a brief description of the Hamiltonian dynamics of a 1-dimensional chain of magnets; especially its similarity to the dynamics of point vortices in an ideal fluid. We also describe the Hamiltonian equations for point magnetic fields in general Euclidean spaces. Next, the vortex dynamics of quasi-two-dimensional BECs is recognized as a natural 2-dimensional generalization of the 1-dimensional point magnet chain. The remainder of the exposition is mainly devoted to an investigation of the BEC vortex dynamics, wherein we summarize one of the main results of our research so far. In the final section, we describe some of our conclusions and identify several possible generalizations and interesting problems related to vortex dynamics in other gauge fields.

POINT MAGNET AND RELATED DYNAMICS

We assume that the magnetic monopoles are continuously distributed along a line, but concentrated in finitely many minute intervals identified as *point magnets* at the interval midpoints. Integration of the $1/r^2$ forces over the intervals produces $1/r$ interaction forces among the point magnets. Let N point magnets of masses $m_1, \ldots, m_N$ and strengths per unit mass $\gamma_1, \ldots, \gamma_N$ lie along $\mathbb{R}$ at the points $x_1, \ldots, x_N$. The Hamiltonian equations of motion with $1/r$ interaction forces are

$$\dot{x}_k = \{H_0, x_k\}, \quad \dot{y}_k = \{H_0, y_k\} \quad (1 \le k \le N), \tag{1}$$

where the momenta y_k, Hamiltonian function H_0 and (nonstandard) Poisson bracket $\{\bullet,\bullet\}$ are defined, respectively, as

$$y_k := \dot{x}_k,\ H_0 := (1/2)\sum_{k=1}^{N} \gamma_k y_k^2 - \sum_{1 \le j < k \le N} \gamma_j \gamma_k \log\left|x_j - x_k\right| \text{ and } \{f, g\} := \sum_{k=1}^{N} \gamma_k^{-1} \{f_{y_k} g_{x_k} - f_{x_k} g_{y_k}\}. \tag{2}$$

For point magnets in Euclidean n-space $\mathbb{R}^n$, the equations of motion are the same *mutatis mutandis* the notation.

If one omits the kinetic energy in H_0 in (2) for massless point vortices [3], it is essentially identical to that of point vortices in an ideal fluid and has three independent invariants in involution [1], whereas the original has just two.

BOSE—EINSTEIN CONDENSATE VORTEX DYNAMICS IN THE PLANE

Vortices occur in BEC dynamics in the plane as shown in the experimental observation in Fig. 1, which can be inferred from a well-known approximate point vortex model of the form

$$\gamma_k \dot{z}_k = -2i\gamma_k \partial_{\overline{z}_k} \Phi(z) - i \sum_{1 \le j \ne k \le N} \gamma_j \gamma_k \left(\overline{z}_j - \overline{z}_k\right)^{-1} \quad (1 \le k \le N), \tag{3}$$

where $z_k = x_k + iy_k \in \mathbb{C}$, the complex plane, and the leading term on the right-hand side is the component of the *precession velocity*. We note that the system (3) is symplectic, with Poisson bracket as in (2) and Hamiltonian function

a) Corresponding author. Email: denis.l.blackmore@njit.edu

(4) $$H = \Phi(z) - \sum_{1 \le j < k \le N} \gamma_j \gamma_k \log \left| z_j - z_k \right|.$$

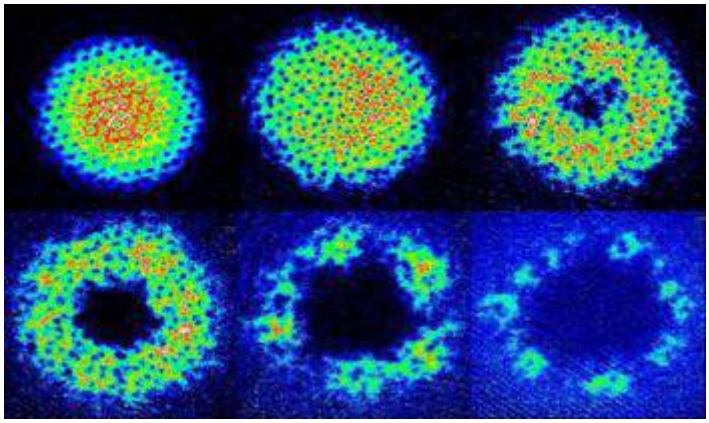

Fig. 1. Evolution of vortices in a BEC.

The Hamiltonian dynamical system corresponding to (3) is

(5) $$\dot{x}_k = \gamma_k^{-1} \partial_{y_k} H = \{H, x_k\}, \quad \dot{y}_k = -\gamma_k^{-1} \partial_{x_k} H = \{H, y_k\} \quad (1 \le k \le N).$$

As for the choice for the precession velocity, the function

(6) $$\Phi(z) := a \log \left[\prod_{k=1}^{N} \left(b - \left| z_k \right|^2 \right)^{\gamma_k} \right],$$

where a and b are positive constants, is realistic and often chosen [4].

As an example of the type of results we have been able to prove, we offer the following:

Theorem. *The Hamiltonian system* (5) *has, depending on* Φ, *either one, two or three independent constants of motion (including H) in involution, in which case it is completely Liouville—Arnold (L-A) integrable for* $N = 1$, $N = 2$ *or* $N = 3$ *point magnets, respectively. Additional point vortices in each of these cases can cause chaotic dynamics (proving that there are no additional independent invariants in involution).*

Indeed, if $\Phi = 0$, the Hamiltonian function is the same as for point vortices in a fluid, for which a system of at most three vortices is completely L-A integrable [1], when Φ is as in (6) it is not difficult to show that the system (5) is L-A integrable for $N = 2$, but not $N = 3$, and it is easy chose Φ so that H is the only independent integral of (5).

CONCLUDING REMARKS

We have shown how certain 2-dimensional generalizations of the dynamics of a 1-dimensional chain of point magnets includes well-known approximate 2-dimensional dynamical models of the evolution of BECs, and have begun to analyze these models. Additional investigation of these models is planned as part of our ongoing research. Moreover, inasmuch as the BEC models are derived from the 3-dimensional Gross—Pitaevskii partial differential equation, it is reasonable to assume that approximate planar point magnet models can be derived from gauge-field equations of more general types falling within the sphere of Maxwell—Chern—Simons—Higgs theory. We are also planning to delve into these possibilities.

References

[1] Blackmore, D., Ting, L., Knio, O.: Studies of Perturbed Three Vortex Dynamics. *J. Math. Phys.* **48**: 065402, 2007.

[2] Chen, R.-M., Guo, Y., Spirn, D., Yang, Y.: Electrically and Magnetically Charged Vortices in the Chern—Simons—Higgs Theory. *Proc. R. Soc. A* **465**: 3489-3516, 2009.

[3] Hirata, K.: The Electrodynamics with Magnetic Monopoles. I. *Progr. Theor. Phys*. **69**: 300-313, 1983.

[4] Kolokolnikov, T., Kevrekidis, P., Carretero-Gonźalez, R.: A Tale of Two Distributions: From Few to Many Vortices in Quasi-Two-Dimensional Bose—Einstein Condensates. *Proc. R. Soc. A* **470**: 21040048, 2014.

[5] Manciu, F., Manciu, M., Sen, S.: Possibility of Controlled Ejection of Ferrofluid Grains from a Magnetically Ordered Ferrofluid Using High Frequency Non-linear Acoustic Pulses – A Particle Dynamical Study. *J. Magnetism & Magnetic Materials* **220**: 285-292, 2000.

[6] Prykarpatsky, A., Blackmore, D.: New Vortex Invariants in Magneto-Hydrodynamics and a Related Helicity Theorem. *Chaotic Modeling and Simulation* **2:** 239-245, 2009.

[7] Rosato, A., Blackmore, D., Urban, K., Zuo, L., Tricoche, X.: Dynamical Systems Modelling and Discrete Element Simulation of a Tapped Granular Column. *Proc. Powders and Grains 2013* (AIP Conf. Pro. **1541**): 317-320, 2013.

TOPOLOGY OF VORTEX CREATION AND MERGING: WAKES AND MULTI-GAUSSIAN MODELS

Rasmus Ellebæk Christiansen[1], Allan Peter Engsig-Karup[1], and Morten Brøns*[1]
[1]*Department of Applied Mathematics and Computer Science, Technical University of Denmark, Lyngby, Denmark*

Summary With the purpose of clarifying the topology of vortex creation and vortex merging in 2D flows, we consider the dynamics of the critical points of vorticity. These include local extrema, which we identify as feature points of vortices, as well as saddle points. We present a precise criterion for the merging or creation of a vorticity extremum and a saddle, and describe the motion of the critical points close to the bifurcation. We show how creation of vortices in this sense occurs in the wake of a circular cylinder, and how vortex merging occur in a multi-Gaussian model of two vortices.

A vortex is a fundamental object in fluid mechanics, and understanding how vortices are created, interact, and merge is important for clarifying the features of the flow. Many definitions of a vortex exist, see e.g. [5, 4, 3], but no general or commonly accepted concept has emerged as yet. Furthermore, these definitions focus on a vortex as a coherent object in a way where the processes of creation and merging of vortices is not easily addressed.

One way to overcome this is to consider a *feature point* [7] of the vortex, rather than the spatially extended vortex as a whole. In 2D flows, the extrema of vorticity $\omega(x, y, t)$ naturally present themselves as generalizations of inviscid point vortices. They are defined by

$$\omega_x(x(t), y(t), t) = 0, \quad \omega_y(x(t), y(t), t) = 0, \tag{1}$$

where the subscripts denote differentiation. In [1] equations of motion of these points are derived,

$$\dot{x} = u - \nu \frac{\omega_{yy}\Delta\omega_x - \omega_{xy}\Delta\omega_y}{|H|}, \quad \dot{y} = v - \nu \frac{\omega_{xx}\Delta\omega_y - \omega_{xy}\Delta\omega_x}{|H|}. \tag{2}$$

Here Δ is the Laplace operator, ν is viscosity, and $|H|$ is the determinant of the Hessian matrix $H = \begin{pmatrix} \omega_{xx} & \omega_{xy} \\ \omega_{xy} & \omega_{yy} \end{pmatrix}$. Hence, a vorticity extremum is a material point in an inviscid flow, which is advected by the velocity field (u, v). Viscosity induces a deviation from this. Saddle points of vorticity also fulfill (1), and while they may have no immediate physical interpretation, they must be present for topological reasons. Vortex merging cannot occur directly between two vorticity extrema, but must include the interaction with a vorticity saddle. This occurs when $|H| = 0$ and the velocity of a critical point is not well-defined. It is the purpose of the present paper to explore these bifurcations. Examples of vortex creation through such bifurcations in a cylinder wake are shown in Fig. 1(a).

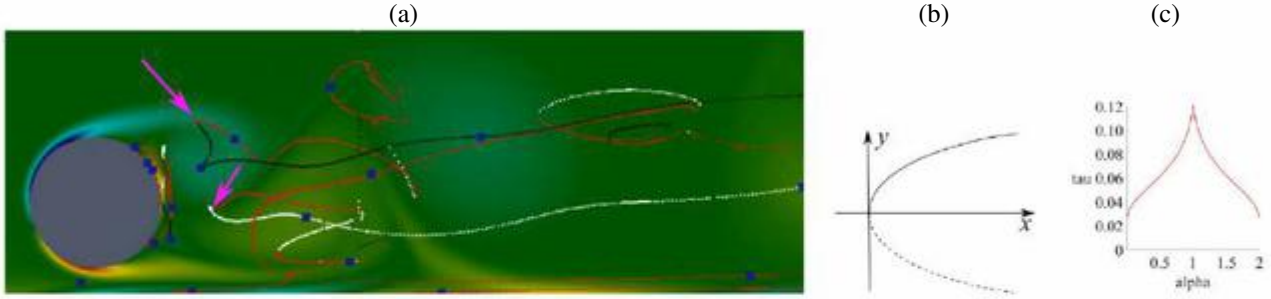

Figure 1: (a) Snapshot of the unsteady flow around a circular cylinder close to a wall at $Re = 300$. Gap width is 0.2 cylinder diameters. The colors indicate vorticity. The blue markers are instantaneous critical points. The black and blue curves are paths of critical points with negative and positive vorticity, respectively. The red curves are paths of saddle points. The arrows show the creation of the two main vortices (and corresponding saddles) which persist in the wake. Other vortices are created, but they disappear again in vortex destruction bifurcations. Generated with numerical methods from [2]. (b) Paths of a saddle and an extremum close to the creation, as given by (3). (c) Bifurcation diagram for the merging of vortices in the multi-Gaussian model. Merging of an extremum and a saddle occur at the red curve.

The main theoretical result is the following: We consider the simplest case where H has 0 as a simple eigenvalue at a critical point of vorticity at $t = 0$. We choose the coordinate system such that the critical point is at the origin and the Hessian

*Corresponding author. Email: mobr@dtu.dk

is in normal form, $H = \begin{pmatrix} A & 0 \\ 0 & 0 \end{pmatrix}$ with $A = \omega_{xx} \neq 0$ and $\omega_{xy} = \omega_{yy} = 0$. If further $B = \omega_{yt} \neq 0$, $C = \omega_{yyy} \neq 0$, we show that two critical points of vorticity, one an extremum, one a saddle, emanate from the origin, following a trajectory given by

$$x(t) = \left(\circ \frac{\omega_{xyy}}{A} + \frac{\omega_{xt}\omega_{xyy}}{AB} \right) t + O(t^{3/2}), \quad y(t) = \pm \sqrt{\circ \frac{C}{B}} t + O(t). \tag{3}$$

If $C/B < 0$ the critical points exist for $t > 0$, and the bifurcation describes a vortex creation. If $C/B > 0$, it is the destruction of a vortex at $t = 0$.

For small values of t, the curve (3) is approximately a parabola, with an extremum following one branch, and a saddle following the other. See Fig. 1(b). Furthermore, the local shape of the vortex close to the extremum is elliptic, and the half-axes are given from the eigenvalues of H. We will show that the ratio of the half-axes grows as $|t|^{1/4}$.

We use the theorem outlined above to study vortex merging as well. We revisit and extend the analysis of [6] of the multi-Gaussian model of the merging of two vortices. The vorticity field is given by

$$\omega = \frac{1}{4\pi\tau} \left[\Gamma_1 \exp\left(\frac{\circ\, |z \circ\, z_L|^2}{4\tau} \right) + \Gamma_2 \exp\left(\frac{\circ\, |z \circ\, z_R|^2}{4\tau} \right) \right]. \tag{4}$$

Here $z = x + iy$ is the complex representation of a point, z_L, z_R are the centers of the two vortices, each moving in the velocity field generated by the other as if they were point vortices with a strength decaying from the initial values Γ_1, Γ_2. Time is given on the viscous scale, $\tau = \nu t$. Initially, there are vorticity extrema located at the vortex centers z_L, z_R, but the extrema deviate from the centers as time progresses. The ultimate distribution is that of a single Gaussian vortex based at the center of vorticity. We explore the development of ω when $\Gamma_1 = \alpha$, $\Gamma_2 = 2 \circ\, \alpha$ to compare with the study of $\alpha = 1$ (symmetric case) and $\alpha = 4/3$ of [6].

If Γ_1 and Γ_2 have the same sign, $0 < \alpha < 2$, this state is reached through a vortex destruction as described above, where a vorticity extremum merges with a saddle. The time τ of merging as a function of α is shown in Fig. 1(c). The symmetric case $\alpha = 1$ is special, since the non-degeneracy condition $B \neq 0$ does not hold. The bifurcation is now a pitchfork bifurcation, where both vorticity extrema and the saddle merge at the same time into a single extremum.

If Γ_1 and Γ_2 have opposite signs, there is no saddle point, and no bifurcation occurs. Instead, the strongest vortex advects to the center of vorticity, while the other goes to infinity at a linear rate, while its strength goes to zero. Thus, in this case, there is no vortex merging.

In conclusion, we have presented a simple a rigorous method to study vortex merging and creation, and showed how it can be applied in a few specific flow situations. We believe this approach will be useful for classification of vortex interactions in general. If time permits, we will discuss the application to a system of three multi-Gaussian vortices.

References

[1] M. Brøns and A. V. Bisgaard. Topology of vortex creation in the cylinder wake. *Theoretical and Computational Fluid Dynamics*, 24(1-4):299–303, 2010.

[2] R. E. Christiansen. *Advanced techniques for investigating structures in computational fluid dynamics*. Master's thesis, Technical University of Denmark, Department of Applied Mathematics and Computer Science, 2013.

[3] L. Graftieaux, M. Michard, and N. Grosjean. Combining PIV, POD and vortex identification algorithms for the study of unsteady turbulent swirling flows. *Measurement Science and Technology*, 12(9):1422, 2001.

[4] G. Haller. An objective definition of a vortex. *Journal of Fluid Mechanics*, 525:1–26, 2005.

[5] J. Jeong and F. Hussain. On the identification of a vortex. *Journal of Fluid Mechanics*, 285:69–94, 1995.

[6] F. Jing, E. Kanso, and P. K. Newton. Insights into symmetric and asymmetric vortex mergers using the core growth model. *Physics of Fluids*, 24(7):073101, 2012.

[7] J. Kasten, J. Reininghaus, I. Hotz, H.-C. Hege, B. R. Noack, G. Daviller, and M. Morzynski. Acceleration feature points of unsteady shear flows. *arXiv:1401.2462 [physics]*, 2014.

ENTRAINMENT IN NON-STATIONARY FLOWS

Giuseppe A. Rosi* and David E. Rival

Department of Mechanical and Materials Engineering, Queen's University, Kingston, Ontario, Canada

Summary The current study reports on a generalized mechanism for entrainment in non-stationary flows. Towards this end, the starting vortex that forms behind a constantly-accelerating, normally-towed, circular plate is considered. Velocimetry measurements of the starting vortex suggest that the ratio between entrainment velocity and instantaneous plate velocity is independent of dimensionless acceleration. A statistically significant data set has been obtained, from which a final model is currently being developed.

Entrainment, which is the assimilation process of low-vorticity fluid by neighbouring high-vorticity fluid, is as ubiquitous as the shear layers that induce this disparity of vorticity in a flow. Studies on entrainment in non-stationary flows have typically investigated the parameter ε, which represents the entrainment rate normalized by the growth rate of the rotational region. By investigating vortex rings formed by piston-cylinder arrangements, recent studies have focused on the methods for measuring ε, and on the dependency of ε with Reynolds number or with the piston's velocity program [1, 2]. Although these studies represent significant contributions, the entrainment mechanism they propose is not valid for the early-stage growth of the rotational region. Thus, towards providing a mechanism for early-stage entrainment, the current study considers a basic, non-stationary problem: A constantly-accelerating, circular plate of diameter D being towed normal to its path from rest.

Consider two accelerating plates as shown in Fig. 1(a). One accelerates at a higher non-dimensional rate of a^*_H, resulting in an instantaneous plate velocity of U_H, while the other accelerates at a^*_L, resulting in an instantaneous plate velocity of U_L. Acceleration is non-dimensionalized here as $a^* = aD^3/\nu^2$, where ν is viscosity. The following question is posed: As each plate traverses a common dimensionless distance of $s/D = s^*$, how will the different acceleration rates modify the entrainment? The answer to this is uncertain. Since the plate accelerating at a^*_H results in a shear layer that produces vorticity at a greater rate, presumably the resulting entraining structures would be correspondingly more energetic, which may result in the greater ε. Nevertheless, the effect of acceleration remains unclear.

Towards answering the aforementioned question, planar, Particle Image Velocimetry (PIV) measurements of a circular plate accelerating from rest were performed in a glass towing-tank facility at Queen's University. The experimental setup is presented in Fig. 1(b). Accelerations $a^*_L = 2.1 \times 10^8$ and $a^*_H = 1.1 \times 10^{10}$, which are hereafter respectively referred to as the low- and high-acceleration cases, were tested. The imaging apparatus is shown in Fig. 1(c). $10^-\,\mathrm{m}$ hollow glass spheres were illuminated by a $2\mathrm{mm}$-thick laser sheet positioned at the plate's midspan. A high-speed camera acquired images of the bottom half of the starting vortex within the domain of $0.2 \leq s^* \leq 1.0$. The field-of-view size was $0.8c \times 0.8c$, and the camera's frame rate was set at $125\mathrm{Hz}$ and $1000\mathrm{Hz}$ for the low- and high-acceleration cases, respectively. Enstrophy ($|\omega^2|$) fields were derived from the images, and entrainment velocity $\vec{u}_e$ along starting vortex's periphery was calculated using the following equation, which is presented in [3]:

$$\vec{u}_e = \circ \, \frac{\mathrm{D}|\omega^2|}{\mathrm{D}t} / \left| \, \nabla |\omega^2| \, \right| . \tag{1}$$

Preliminary (instantaneous) results of the starting vortex at a dimensionless distance of $s^* = 1.0$ are shown in Fig. 2. Figs. 2(a) and (b) present the $|\omega^2|$ fields of the starting vortex for the low- and high-acceleration cases. $|\omega^2|$ has been normalized by U^2/D^2, where U is the instantaneous plate velocity. Correspondingly, Figs. 2(c) and (d) present $\vec{u}_e$ across rotational regions identified via the enstrophy-threshold technique described in [3]. The magnitude of $|\omega^2|$ scales well with U^2/c^2. Furthermore, the topology of the $|\omega^2|$ fields appears to scale with s^*, since the starting vortices in both cases are of equal size, and the number and positioning of Kelvin-Helmoltz instabilities are nearly identical. Finally, the length of $\vec{u}_e$ presented in (c) and (d) are both on the order of U, suggesting that $|\vec{u}_e|/U$ along the periphery of the starting vortex is independent of a^*.

The results presented here are derived from a single run of each acceleration case, and are by no means statistically significant. Thus, forty additional runs of each acceleration have been acquired. In all collected runs, $\vec{u}_e$ is evaluated directly from the spreading of $|\omega^2|$ iso-contours, which can be calculated more reliably from PIV data. From this data, the authors wish to make definitive conclusions regarding the global and regional effects that non-stationarity has on entrainment.

References

[1] S. C. Shadden, K. Katija, M. Rosenfeld, J. E. Marsden, and J. O. Dabiri. Transport and stirring induced by vortex formation. *Journal of Fluid Mechanics*, 593:315–331, 2007.

[2] A. B. Olcay and P. S. Krueger. Measurement of ambient fluid entrainment during laminar vortex ring formation. *Experiments in Fluids*, 44(2):235–247, 2008.

[3] M. Wolf, M. Holzner, D. Krug, B. Lüthi, W. Kinzelbach, and A. Tsinober. Effects of mean shear on the local turbulent entrainment process. *Journal of Fluid Mechanics*, 731:95–116, 2013.

*Corresponding author. Email: g.rosi@queensu.ca

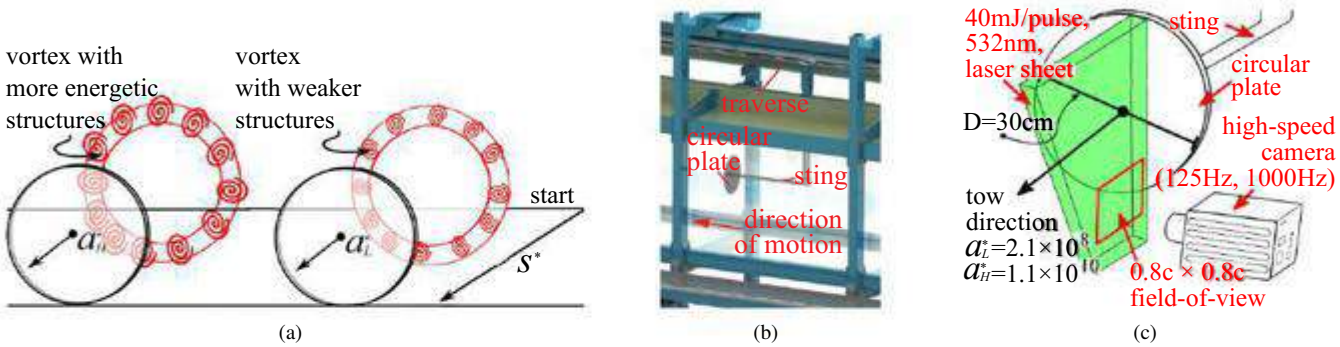

Figure 1: (a) A Schematic of two geometrically equivalent plates towed normally from rest to s^* at two different constant accelerations, a_H^* and a_L^*, where $a_H^* > a_L^*$. The current study investigates how entrainment responds to different a^*. (b) A schematic of the water-filled towing tank. A circular plate is towed from rest at two constant accelerations through a $1\text{m} \times 1\text{m}$ cross section. The sting attaches to the suction side, which then attaches to the traverse located above the tank. (c) A schematic of the imaging apparatus. The plate has a diameter of $D = 30\text{cm}$ and traverses through a $0.8c \times 0.8c$ interrogation field. Two accelerations were tested: $a_L^* = 2.1 \times 10^8$ and $a_H^* = 1.1 \times 10^{10}$. Images were acquired at 125Hz and 1000Hz, respectively.

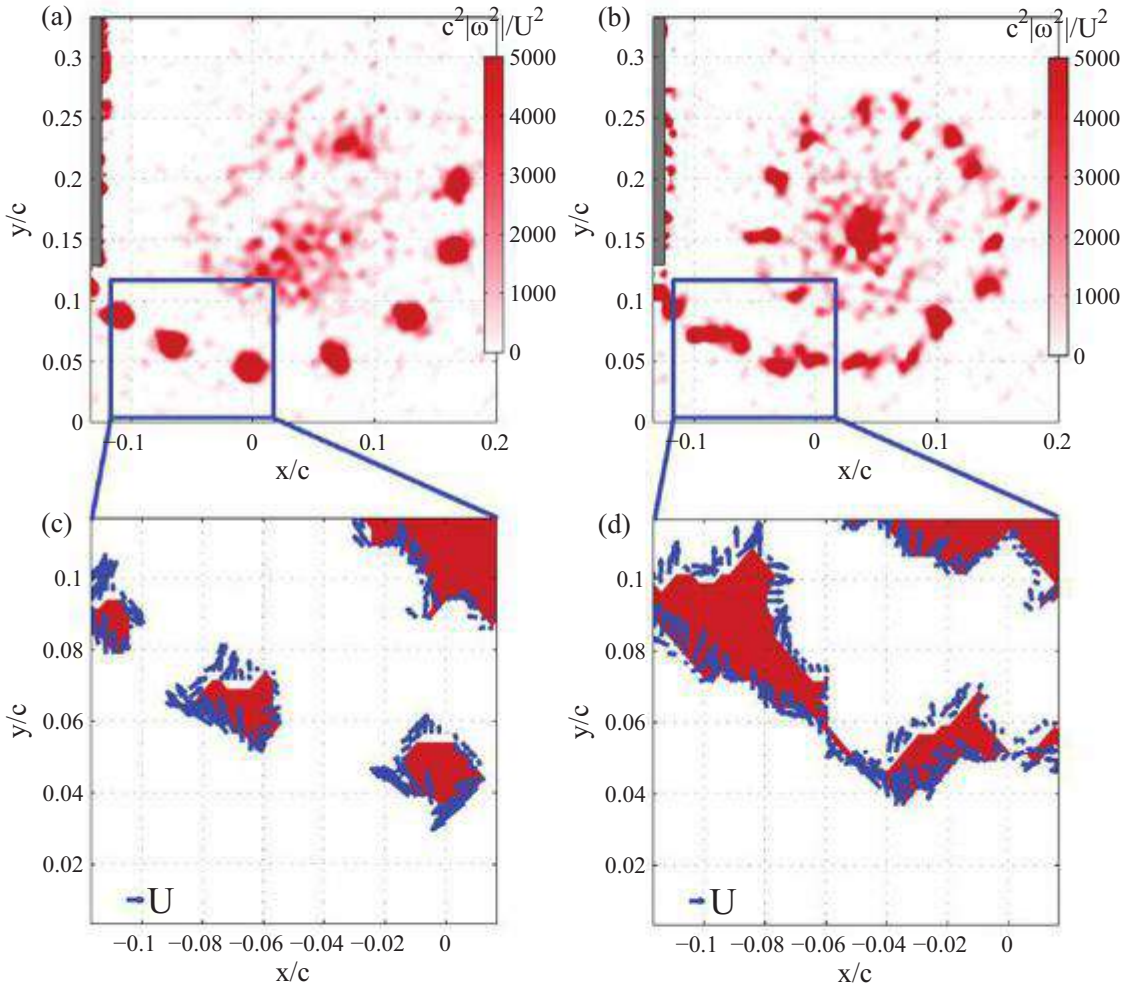

Figure 2: (a) presents the enstrophy field of the plate accelerating at a_L^*, while (c) presents entrainment-velocity vectors calculated within the blue-rectangle region in (a). (b) and (d) present similar results as (a) and (c) but for the plate accelerating at a_H^*. In all figures, the plate, which moves from right to left, has traversed a dimensionless distance of $s^* = 1.0$ and is indicated by a gray rectangle. The topology and and magnitude of the enstrophy fields for the low- and high-acceleration cases collapse well when enstrophy is normalized by U^2/c^2. Furthermore, the length of the vectors presented in (b) and (d) are both on the order of U. The result suggests that $|u_e|/U$ along the periphery of the starting vortex is independent of a^*.

VORTEX AND WAKE INTERACTIONS OF MULTIPLE OSCILLATING FOILS FOR ENERGY HARVESTING

Jennifer A Franck*[1], Filip Simeski[1], Jennifer Cardona[1], Yunxing Su[1], Kenny Breuer[1], and Shreyas Mandre[1]
[1]*School of Engineering, Brown University, Providence, RI*

Summary The vortex and wake interactions of multiple oscillating foils are investigated with computational fluid dynamics (CFD) and compared with experimental measurements for energy harvesting applications. Oscillating with high pitch and heave amplitudes to maximize power production, the elliptical-shaped foils generate large coherent vortices at the leading and trailing edge, which are shed downstream to create a large highly structured wake of vortices with alternating sign. Downstream foils oscillate within the large organized wake at a relative phase angle to the lead foil such that power efficiency is optimized. When placed directly downstream of one another, the optimal phase of a second foil is to avoid interactions with the first foil's wake, generating less than half of the total power of the first foil. However, when placed in a staggered configuration the downstream foil has a 20% increase in efficiency through constructive vortex-foil interactions.

INTRODUCTION AND METHODS

An oscillating foil at high heave and/or pitch amplitudes will generate a sequence of shed vortices into an organized wake. The structure and repeatability of the wake allows for interesting vortex interactions with subsequent strokes or with other bodies in the flow. These vortex interactions have been well noted in animal propulsion, for example with vortex recapture in insect wings [1] or by exploiting vortices while swimming [2]. Instead of propulsion, this paper focuses on energy harvesting, in which the pitch and heave amplitude of the foil can be optimized to extract power from the freestream flow. We show that with the proper configuration and kinematics, that a downstream foil can recapture the energy from the structured wake of the lead foil. For the application of an hydrokinetic energy device, these constructive vortex-foil interactions will boost the overall power, and increase the overall power density by placing devices in closer proximity of one another.

Energy Harvesting from Oscillating Foils

An oscillating foil generates power from a heaving motion defined by $h(t)$ coupled with a pitching motion, defined by an angular position $\theta(t)$. The instantaneous power generated is the combination of the two, $P(t) = L(t)h'(t) + M(t)\theta'(t)$ where L(t) is the lift force and M(t) is the moment about the pitching axis. Energy harvesting occurs when the pitch is 90 degrees out of phase with the heave cycle, thus generating large vertical force at maximum vertical velocity. A key component to maximizing the power is the generation of a leading edge vortex (LEV) at the high relative angles of attack, which enhances the lift force. For a single foil, maximum efficiency values are $30-34\%$ (reduced frequency $fc/U = 0.1-0.15$, normalized by chord c and freestream velocity U, heave amplitudes $h/c = 0.8-1.5$, pitch amplitudes $\alpha = 75-85$ deg) and most of the power is generated through the heave term $L(t)h'(t)$, with the pitch generating the high angle of attack necessary for the LEV formation. Many researchers have investigated the potential of energy harvesting from oscillating foils (see review [3]), and a few groups have looked at interactions of multiple foils. Tandem and parallel foil configurations have been investigated [4], but only for a handful of configurations, limited to either 90 or 180 degrees out of phase with one another. More recently a parallel, or stacked configuration of foils has been performed [5].

This paper explores the vortex dynamics between two foils in tandem configuration with (a) the foils aligned one behind the other, and (b) the foils staggered, with the trailing foil offset in the streamwise and vertical directions. Once a given configuration is fixed, a range of optimal kinematics is prescribed, varying the phase angle, ψ, between the foils. The efficiency and power production is computed for the upstream and downstream foils.

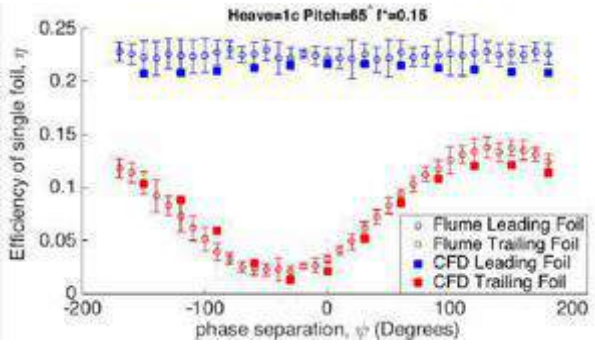

Figure 1: Linear arrangement: Efficiency of upstream (blue) and downstream (red) foils; 6 chords separation.

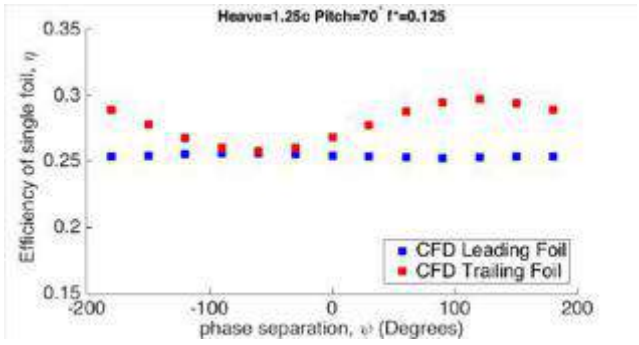

Figure 2: Staggered arrangement: 8 chords downstream and 4 chords vertical separation.

*Corresponding author. Email: jennifer franck@brown.edu

Numerical Methods

Direct numerical simulations are used to perform all simulations, and the efficiency values and instantaneous forces are compared with experimental flume data. The simulations are performed utilizing the *OpenFOAM* dynamic mesh libraries, where the kinematics of the foils are prescribed. An incompressible Navier-Stokes solver is used to solve the fluid flow and the solid body rotation stress equations for the mesh motion. An unstructured mesh of two elliptical foils is generated with *Gmsh*, with an outer boundary of 25 chord lengths in all directions. The simulations are performed at a Reynolds number of 1000, however the efficiency and forces are well validated against measurements performed in a water flume at Reynolds number $50,000$ (Fig 1).

RESULTS

To validate the simulations, a sequence of experiments are performed in the flume with a linear arrangement of foils. Figure 1 shows the efficiency of the lead and trailing foils for a separation distance of 6 chords apart for the flume and CFD, and the kinematics of $fc/U = 0.15$, $h/c = 1$, $\alpha = 65$ deg. Both the CFD and flume agree remarkably well with the ideal phase separation between foils. For these kinematics, the efficiency of a single foil is approximately 22%, which is the same as the results from the lead foil. Thus, the lead foil's performance is not influenced by the presence of a downstream foil. The efficiency of the downstream foil is influenced by the wake of the first foil, and depending on the phase difference the efficiency ranges from approximately 1% to 14%. Since the downstream foil is directly behind the first its relative freestream velocity is significantly slower, and a lower efficiency is expected. However, when the second foil is 150 degrees out of sync, its stroke avoids the shed vortices from the first foil, and corresponds to the optimal phase for this configuration. At -30 degrees, the downstream foil directly intersects the counterclockwise vortex on the downstroke and clockwise vortex on the upstroke, decreasing the lifting force and resulting in close to zero power production.

However, an arrangement of staggered foils (8c downstream and 4c vertical separation) in Figure 2, is able to benefit from the intersection of vortices. By placing the downstream foil above the wake from the first, it sees mostly undisturbed flow, and thus no drop in efficiency. Furthermore at optimal phase separation of 120 degrees, the second foil can favorably interact with the clockwise vortex during the downstroke increasing the efficiency from 25% to 30%. The clockwise rotation of the vortex is essential since the relative velocity in the proximity of the foil is increased, thus strengthening the LEV and enhancing the downward force on the foil.

Future work will include adding more foils in various staggered configurations to investigate how constructive interference can be achieved with multiple foil interactions.

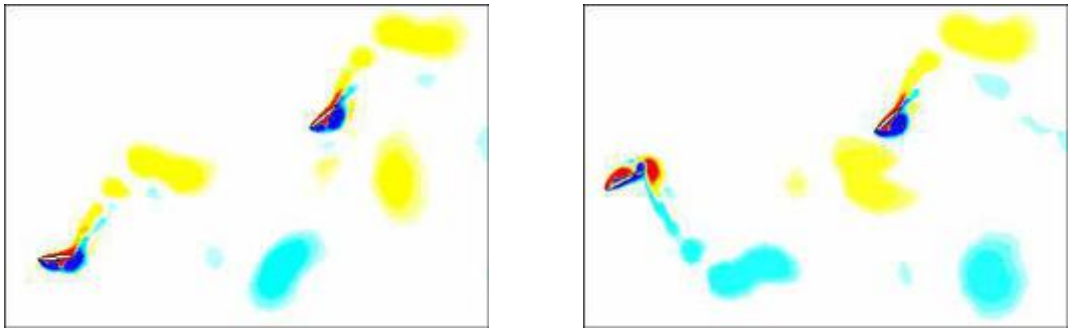

(a) $\psi = -30$ degrees (b) $\psi = 120$ degrees

Figure 3: Vorticity flow fields in the staggered configuration of Figure 2.

References

[1] Dickinson, M, Lehmann, F, Sane, SP, "Wing Rotation and the Aerodynamic Basis of Insect Flight", Science, 18 Jun 1999.

[2] Liao, JC, Beal, DN, Lauder, GV, Triantafyllou, MS. "Fish Exploiting Vortices Decrease Muscle Activity", Science, 28 Nov 2003.

[3] Xiao, Q, Zhu, Q. "A review on flow energy harvesters based on flapping foils", Journal of Fluids and Structures. 04/2014; 46.

[4] Kinsey T, Dumas G. "Optimal Tandem Configuration for Oscillating-Foils Hydrokinetic Turbine". ASME. J. Fluids Eng. 2012;134(3).

[5] Wu, J, Zhan, JP, Wang, X., Zhao, N. "Power extraction efficiency improvement of a fully-activated flapping foil: With the help of an auxiliary rotating foil", Journal of Fluids and Structures 08/2015; 57:219.

EXPERIMENTAL INVESTIGATION OF A SLENDER DELTA WING WITH APEX AND TAIL FLAP CONTROL

Lok Sun Ko[1a)] & Tim Lee[1]
[1]*Department of Mechanical Engineering, McGill University, Montreal, Quebec, Canada*

Summary An experimental investigation of a slender delta wing with a sweeping angle Λ=65° was conducted with apex and tail flap control at a Reynolds number Re = 12,900. Dye flow visualization revealed the flow pattern and vortex breakdown (VBD) location over the different wing configurations. The flow visualization showed that a tail flap with anhedral deflection angle of -15° (T-15) or -30° (T-30) promoted VBD while a tail flap with dihedral deflection angle of +15° (T+15) or +30° (T+30) delayed VBD. A combination of apex flap -15° and tail +30° (A-15/T+30) delayed VBD the most of all the cases. A particle image velocimetry (PIV) study was conducted to characterize the flow.

INTRODUCTION

For a slender delta wing, a pair of leading-edge vortices (LEVs) is formed on the suction side of the wing at moderate to high angle of attack. The LEVs provide additional suction vortex lift not found in a conventional rectangular wing. Furthermore, with increasing angle of attack, the LEVs undergo vortex breakdown (VBD), which is characterized by an increase in core size, decrease in vorticity, suction pressure and axial velocity. The core axial velocity, which can reach up to 3 U_c/U_∞, becomes wake-like downstream of the VBD location. The breakdown occurs initially in the trailing-edge region and moves upstream with increasing angle of attack until it reaches near the apex, stalling the wing. Furthermore, due to its unsteady nature VBD may cause large structural vibrations and dangerous fatigue damage of fins [1].

Rao and Campbell [2] summarized many different control methods for delta wing vortical flow control. One such device is the apex flap, where the apex region of the wing is hinged transversely (seen in red, Figure 2b). Lowson and Riley [3] believed that the key in controlling the vortex breakdown is at the apex region because the strength of the vorticity shed by the apex will vary with apex geometry. In addition, the vorticity shed from the apex will form the center of the LEV core, hence affecting the vorticity distribution inside the core. The effective angle of attack of the wing is also altered. Therefore, the apex flap should have a great impact on LEV control. A tail flap is formed by hinging one of the base angles in the streamwise direction (seen in blue, Figure 2b). The goal is to affect the pressure gradient in the rear region of the wing. The flap also introduces spanwise camber to the delta wing.

The objective of this study is to explore the use of both apex flap and tail flaps, deflected passively individually or as a combination, for VBD control. Based on flow visualization and particle image velocimetry (PIV), it is shown that certain flap deflections delay vortex breakdown.

EXPERIMENTAL SETUP

The experiments were conducted in a Rolling Hill Research Corporation (RHRC) model 0710 water tunnel. The chord Reynolds number was fixed at Re = 12,900. The 0.18 m × 0.25 m × 0.45 m test section was equipped with three optical windows. Furthermore, a dye flow visualization system was integrated into the test section. Ten test models, with a sweeping angle $\Lambda = 65°$ and chord c = 0.108 m, were made from 1 mm thick aluminium sheet metal. The apex flap was sized at 30% c while the tail flaps had a width of 50% trailing edge semispan. The flaps were bent to the deflection angles of $\delta = \pm 15°$ or $\pm 30°$.

The PIV experimental technique was used in order to study the flow field characteristics at different chordwise stations along the wing from 0.3 to 1.5 x/c, with $\Delta x/c = 0.10$ along the wing and 0.01 near VBD. A dual-head Continuum Nd:YAG laser was used to generate two overlapping light sheets. The test models' x/c location was changed using guided rails. A 4MP PowerView Plus CCD camera was set up downstream and outside of the test section to look upstream at the region of interest. The PIV calibration was 45.15μm/pixel. The water tunnel was seeded with Dantec PSP-20 polyamid particles with a mean diameter of 20μm and a density of 1.03g/cm^3. The pictures were processed with the TSI Insight 3G version 9.1.0.0 software. The TSI LaserPulse synchronizer model 610035 controlled all the components for picture taking.

RESULTS

Figure 1 shows the VBD location curves obtained by flow visualization. The worst case in terms of breakdown is the apex with upward deflection +15° (A+15), where VBD has been promoted due to the increase in effective angle of attack. Otherwise, A-15 delayed VBD beyond $\alpha > 22.5°$ due to the lowering of effective angle of attack. The cases of tail flap anhedral deflection -15° (T-15) and T-30 promoted VBD to a lesser throughout the range of angle of attack tested. The cases of T+15, T+30 and cropped all delayed VBD. The combination A-15/T-15 promoted VBD when $\alpha < 30°$ and delayed VBD at higher angles of attack. The combination A-15/T+30 delayed VBD significantly beyond $\alpha > 22.5°$.

[a)] Corresponding author. Email: lok.ko@mail.mcgill.ca.

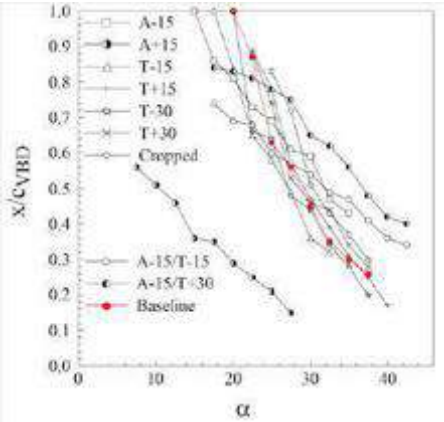

Figure 1. Vortex breakdown location curves obtained by flow visualization (vortex breakdown location vs. angle of attack).

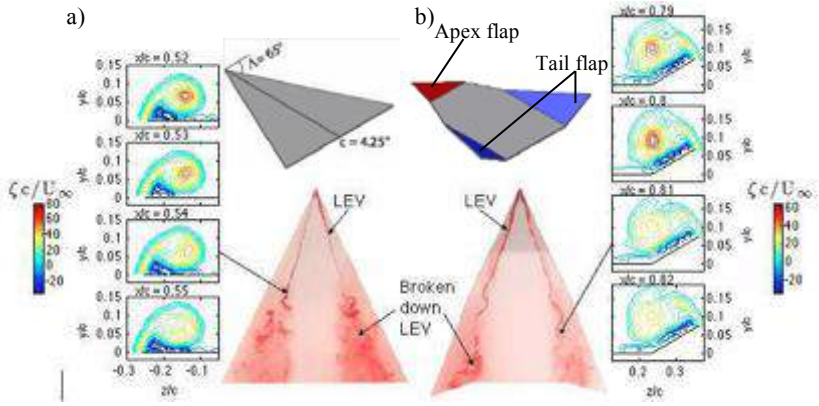

Figure 2. Flow visualization and PIV composite iso-vorticity results for a) baseline and b) combination of apex -15° deflection and tail +30° (A-15/T+30) deflection for α = 25°.

Figure 2 shows a set of typical flow visualization and PIV results for a) baseline and b) A-15/T+30 at α = 24°. Figure 2a shows four PIV x/c locations, two before and two after VBD. For x/c = 0.52 and 0.53, a strong concentric red core can clearly be observed. After VBD, for x/c = 0.54 and 0.55, a region of vorticity persisted but is more diffused with a significantly lower peak vorticity. In the flow visualization picture, two concentrated red lines, representing the trajectory of the vortex core center, can be seen originating from the apex and ending at the VBD location (x/c = 0.54). Downstream of VBD, the dye became a chaotic flow pattern with a larger diameter. Figure 2b shows the PIV result for A-15/T+30, which is the PIV case with the most delayed VBD (x/c = 0.81) at the same angle of attack. A red circular core of weaker vorticity intensity than the baseline can be observed for x/c = 0.79 and 0.80. Furthermore, the LEVs are mostly located on the tail flaps. From the apex to approximately x/c = 0.50, the LEV filaments are straight and concentrated. Around the tail flap hinge line, the LEV filaments begin to spiral before reaching VBD at x/c = 0.81. Post-VBD, the concentrated red core was no longer identifiable; instead a diffused region of low vorticity is observed. From flow visualization, the A-15/T-15 and A-15 cases also experienced spiralling before reaching VBD. This spiralling phenomenon could be caused by the downward deflection of the apex flap.

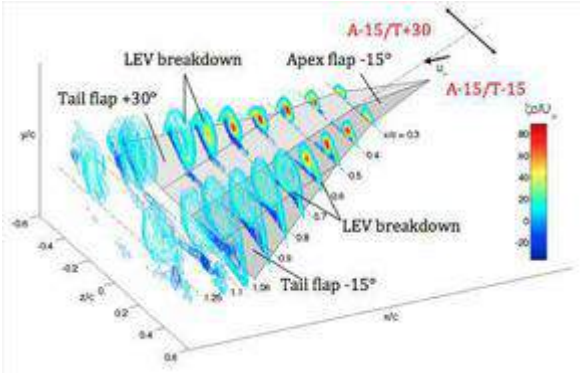

Figure 3. 3D composite iso-vorticity plot for combination of apex -15° and tail +30° (A-15/T+30) deflections, and combination of apex -15° and tail -15° (A-15/T-15) deflections at α = 24°.

Figure 3 shows the 3D composite iso-vorticity contours with Δx/c = 0.10 along the wing for the A-15/T+30 and A-15/T-15 cases. The difference in VBD locations (0.81 vs 0.62, respectively) can be seen clearly. Furthermore, the LEVs for the A-15/T+30 are located on the tail flap while the A-15/T-15 LEVs are situated mostly on the main body of the wing. The tail dihedral caused the LEV to be closer to the shear layer while an anhedral deflection had the effect of elongating the shear layer.

The vortex flow parameters calculated from the PIV results show that for all the cases the flap deflection rendered a weaker and more diffused LEV, with a lower outer circulation and tangential velocity, and a higher core radius. For all the control cases, peak tangential velocity and peak vorticity were also lower than baseline.

CONCLUSIONS

An experimental investigation of a slender delta wing was conducted with apex and tail flap control. The apex and tail flaps significantly modified VBD location and vortex parameters. The apex flap seemed to increase, for A+15, or decrease, for A-15, the effective angle of attack of the wing. Decreasing the effective angle attack causes the LEVs to become weaker, rendering a delayed VBD. Vortex spiralling before VBD was observed for some cases with apex flap control. Tail flap dihedral deflection is best for delaying VBD compared to tail anhedral deflection. The tail flaps were also able to change the shape of the shear layer. The best control case for VBD delay was the case of A-15/T+30.

References

[1] Gursul I.: Review of unsteady vortex flows over slender delta wings, *Journal of Aircraft*, 42:2 299-319, 2005.

[2] Rao D. M. and Campbell J. F.: Vortical flow management techniques. *Progress in Aerospace Sciences* 24, 173-224, 1987.

[3] Lowson M. V. and Riley A. J.: Vortex breakdown control by delta wing geometry. *Journal of Aircraft* 32:4, 832-838, 1995.

DETERMINING THE SHEDDING TIME OF VORTICES IN REAL-TIME

Matthew Rockwood[1] and Melissa Green *[1]
[1]*Mechanical and Aerospace Engineering Department, Syracuse University, Syracuse, New York, USA*

Summary Coherent vortex structures are tracked in the simulated wake of a circular cylinder. Topological Lagrangian saddle points are identified as intersections of positive and negative finite-time Lyapunov exponent (FTLE) ridges, and these points are then followed as the flow evolves in order to track individual coherent structures. Previous studies of a circular cylinder in cross-flow have shown that the acceleration of Lagrangian saddle points away from the cylinder surface provides an objective method to detect vortex shedding. This saddle point acceleration is combined with the static pressure distribution on the circular cylinder to provide a clear, more easily measured indication of the shedding time of a vortex than comparable techniques such as force measurements.

INTRODUCTION

Coherent structures, or vortices, are a key component of unsteady flows that include propulsive wakes, flow separation, or instabilities in shear layers. They are often found in the wake of bluff bodies, aerodynamic surfaces at high angles of attack, or in turbulent flows. The visualization and tracking of coherent structures helps to explain the basic physics of turbulent motions, and can be used to improve turbulent flow modeling, prediction, and the design and implementation of control systems.

Although studies on vortex dynamics have been carried out for decades, a widely-accepted, objective definition of a vortex and its boundaries remains an open question. Techniques used to define vortices can be classified as Eulerian, in which the instantaneous velocity field and its gradients are used to identify regions that contain vortices, and Lagrangian, where metrics are calculated using particle trajectories to determine which regions of the flow are dynamically distinct.

Lagrangian techniques have been shown to help identify and describe mass transport and vortex dynamics in a variety of unsteady flow fields, but they're computationally intensive and require future data when calculating forward-time quantities. In the current work, we consider how to detect Lagrangian phenomena from quantities such as surface pressure measurements in vortex shedding off a circular cylinder, as the static pressure is easily measurable in real-time using current sensors.

METHODS

The Q criterion, an Eulerian scalar, identifies regions of the flow as vortices when there is local rotational motion. Vortices are found where the norm of the local rate of rotation tensor is dominant over the norm of the local rate of strain tensor, which corresponds to Q values greater than zero [1]. The Q criterion is useful for visualizing vortex cores.

The Lagrangian finite-time Lyapunov exponent (FTLE) measures the maximum rate of separation around a certain location in space ($\boldsymbol{x}_0$) by first calculating the flow map of neighboring particles $\boldsymbol{\phi}(\boldsymbol{x}_0, t_0, \tau)$ over an integration time τ, and constructing the Cauchy-Green strain tensor from the spatial gradient of the flow map. Maximizing ridges in this field indicate high levels of Lagrangian stretching among nearby particle trajectories, and have been shown to represent structure boundaries in vortex dominated flows [2].

While repelling ridges of FTLE (pFTLE) can be calculated using forward-time integration, attracting ridges (nFTLE) at time t_0 can be found by calculating FTLE using particle trajectories initialized at t_0 and integrated in negative-time. The pFTLE and nFTLE ridges at time t_0 intersect at the outer boundaries of vortices but don't overlap. Vortex structures are tracked using points where the pFTLE ridges intersect with the nFTLE ridges. These intersections of the attracting and repelling ridges in the flow are Lagrangian saddle points, and have been shown to be dynamically important features of the vortex boundaries [3, 4].

RESULTS

In this section we compare the vortex shedding time found by the acceleration of a Lagrangian saddle point away from the cylinder surface to the static pressure signal at an angular location 100° from the upstream stagnation point, as well as to the cylinder lift history. Data was generated by a simulation run by Robert Reger advised by Drs. Taira and Cattafesta at Florida State University using the CHARLES™ solver run at $Re = 150$. FTLE was calculated using an integration time of two shedding periods ($\tau = 2T$).

*Corresponding author. Email: greenma@syr.edu

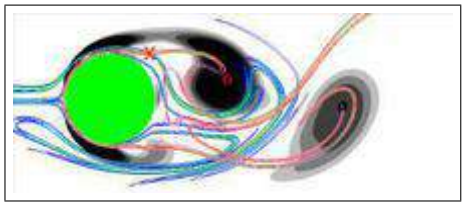

Figure 1: FTLE ridges (blue and red) and Q criterion (grey contours) at $t/T = 0.55$.

Figure 1 displays a zoomed-in view of the cylinder wake. The attracting nFTLE ridges (red) wrap around the outside boundaries of the vortices as they form, separate, and convect downstream. The repelling pFTLE ridges (blue) form the boundaries between vortices as well as between forming vortices and the cylinder surface. The vortex center, found as the location of maximum Q within the vortex of interest, is highlighted by a red "O", and the Lagrangian saddle point associated with that vortex is highlighted by a red "X".

The location of the vortex center and Lagrangian saddle point were tracked, and the results are displayed in figure 2(a). The track of the vortex center yields little information besides the vortex convection speed (dashed line), but the large change in slope of the saddle track as it sheds (departure from solid black line) gives a clear indication that $t/T = 0.44$ is the time of vortex shedding (vertical dash-dot line). See [5] for more details. Figure 2(b) shows that $C_p'(t)$ at the 100° location on the cylinder surface reaches its minimum just as the Lagrangian saddle point is beginning to accelerate away from the cylinder surface at $t/T = 0.44$. The pressure upstream and downstream of 100° reache a minimum at later and earlier times than the vortex shedding time, respectively. The vortex shedding time found by the Lagrangian saddle point departure also coincides with the maximum in lift, calculated by integrating the static pressure distribution, experienced by the cylinder as shown in figure 2(c). As the vortex sheds from the upper surface of the cylinder, the pressure values in this region begin to increase, resulting in an increase in negative lift. Preliminary experimental results for a circular cylinder at $Re = 9000$ are compared with the current results in figure 2(d). While the locations of the Lagrangian saddle point are not identical between the two cases, the overall trend is very similar. Experiments are ongoing to determine if a similar relationship exists between the saddle departure and the static pressure upstream of the separation point.

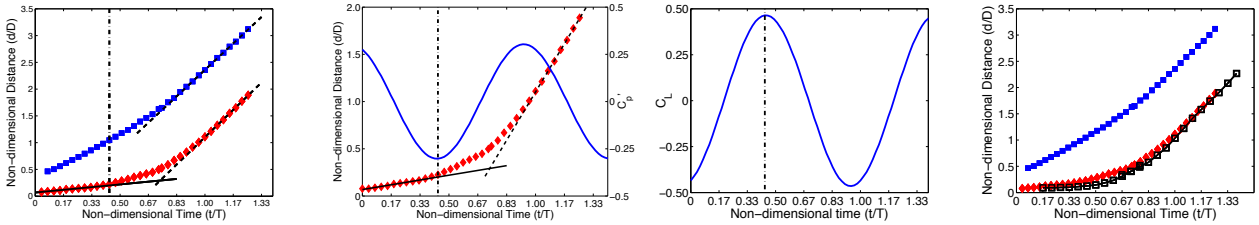

(a) Distance from cylinder to vortex center (blue squares) and Lagrangian saddle point (red diamonds).

(b) $C_p'(t)$ at 100° with saddle trace

(c) Coefficient of lift

(d) Experimental Lagrangian saddle point locations (black hollow squares) compared with numerical results

Figure 2: Three techniques for identifying vortex shedding time: (a) Lagrangian saddle departure, (b) pressure minimum, and (c) lift maximum. Includes preliminary experimental results (d). The shedding time of $t/T = 0.44$ is marked by a vertical dash-dot line in (a-c).

Discussion

The vortex shedding time found by the location of Lagrangian saddle points was compared with the shedding time determined by the force history, and the spatial track of the vortex center. The force history agreed well with the Lagrangian saddle point shedding time, but the location of the vortex center did not yield information that corresponded to minima in pressure or force on the cylinder. The surface static pressure 15° upstream of the mean separation point was found to reach its minimum just as the vortex was shed from the cylinder. This relationship makes the detection of vortex shedding, described objectively by the Lagrangian saddle point location, possible in a simple fashion using common sensors at an angular location near the mean separation point. The information found from a few specifically placed pressure sensors could then be used to inform closed-loop flow control around bluff bodies, deploy high-lift devices to prevent stall, or to inform fuel injection levels in a mixing application.

References

[1] J. C. Hunt, A. Wray, and P. Moin, Eddies, streams, and convergence zones in turbulent flows, in Studying Turbulence Using Numerical Simulation Databases, 2, Vol 1, 1988.

[2] G. Haller, Distinguished material surfaces and coherent structures in 3D fluid flows, Physica D 149, 2001.

[3] M. A. Green, C. W. Rowley, and A. J. Smits, The unsteady three-dimensional wake produced by a trapezoidal pitching panel, Journal of Fluid Mechanics 685, 2011.

[4] K. Mulleners and M. Raffel, The onset of dynamic stall revisited, Experiments in Fluids 3, Vol 52, 2012.

[5] M. P. Rockwood and M. A. Green, An Analysis of the Unsteady Wake Behind a Circular Cylinder using Lagrangian Coherent Structures, in AIAA SciTech, 2015.

MOTION OF A VORTEX PAIR AT HIGH AND LOW REYNOLDS NUMBERS

Yasuhide Fukumoto *[1] and Ummu Habibah[2]
[1]*Institute of Mathematics for Industry, Kyushu University, Fukuoka, Japan*
[2]*Graduate School of Mathematics, Kyushu University, Fukuoka, Japan*

Summary We establish a high- and a low-Reynolds-number asymptotics for the speed of a counter-rotating vortex pair, traveling in a viscous incompressible fluid. At a high Reynolds number, the solution of the Navier-Stokes equation is constructed by use of the matched asymptotic expansions in a small parameter, a measure of the core radius to the half distance between the vortices. The correction to the traveling speed, originating from finite-thickness effect, arises at fifth order. We drastically simplify it in a form including solely strength of the quadrupole field of second order. We derive a two-dimensional analogue, applicable in the entire range of the Reynolds number, of the Helmholtz-Lamb formula for an axisymmetric vortex ring. At a low Reynolds number, the vorticity field obeying the Stokes equation is substituted into this formula. Thereby we describe the whole life of the motion a vortex pair.

INTRODUCTION

Motion and stability of a counter-rotating vortex pair is a long-standing problem since the late 1960s when jet planes started their commercial flight. Finite-thickness effect of interacting vortex tubes has been intensively studied so far. Half a century ago, the method of matched asymptotic expansions was put forward for the two-dimensional motion, at high Reynolds numbers, of a viscous vortex embedded in an external flow [10]. This method has been highly developed for a curved vortex tube [6, 2], for a vortex ring [7] and for a helical vortex tube [9]. Compared with the axisymmetric problem, less developed are the asymptotic expansions for interaction of (anti-) parallel vortex tubes of distributed vorticity. For motion of point vortices, sophisticated methods are available from the Hamiltonian mechanics, while, for interaction of finite vortices with distributed vorticity, asymptotic methods remain to be matured, except for vortex patches, vortex tubes with uniform vorticity. For a planer problem, the effect of finite thickness of the core makes its appearance at a higher order in small parameter ε, a measure for the ratio of the core radius to the distance between the vortices, compared with a curved vortex tube.

We first establish, at a high Reynolds number, a general formula of the traveling speed of a counter-rotating vortex pair in an inviscid as well as a viscous fluids, for an arbitrary initial distribution of vorticity. We reach a surprisingly simple formula of the correction to the traveling velocity; the strength of quadrupole of $O(\varepsilon^2)$ suffices to calculate the $O(\varepsilon^5)$ correction.

The rest of paper is concerned with low-Reynolds-number motion. A vortex pair dies away. For an axisymmetric vortex ring, an initial-value problem valid over the whole time range is found at low Reynolds numbers [4] which enables us to view, in perspective, the early-time behavior and the decaying law. We adapt this method to the planer problem of a vortex pair. The key tool is a two-dimensional analogue of the Helmholtz-Lamb formula for the traveling velocity [8, 3].

HIGH-REYNOLDS-NUMBER MOTION OF A VORTEX PAIR

Inner and outer expansions

Consider a counter-rotating vortex pair with circulations $\pm\Gamma$ moving in an inviscid or a viscous fluid with the kinematic viscosity ν. The core radius σ of the two vortices is assumed to be much smaller than the distance $2d$ between the centroids of the two vortices. The outer solution is provided by the Biot-Savart law, though the distribution of vorticity remains to be obtained. The latter is found from the solution of the inner problem. The behavior of the Biot-Savart law valid near one of the vortex provides the matching condition on the inner solution.

Inner solution and traveling speed of a vortex pair

The inner solution is obtained by integrating the Navier-Stokes equation. We introduce the Cartesian coordinates (x, y), fixed in space, with the x axis parallel to the direction of the line connecting the centroids. At the same time, we introduce local polar coordinates (r, θ), centered at the centroid (X, Y) of one of the vortices, moving with it. The angle is measured from the direction parallel to the x-axis, and therefore the laboratory and the moving frames are related with each other through $x = X + r\cos\theta$ and $y = Y + r\sin\theta$ (Figure 1). The radial coordinate r is non-dimensionalized by εd where $\varepsilon = \sqrt{\nu/\Gamma}$ is a small parameter. The solution for the streamfunction ψ is sought in a power series in ε as

$$\psi = \psi^{(0)} + \varepsilon\psi^{(1)} + \varepsilon^2\psi^{(2)} + \varepsilon^3\psi^{(3)} + \varepsilon^4\psi^{(4)} + \varepsilon^5\psi^{(5)} \ldots . \tag{1}$$

*Corresponding author. Email: yasuhide@imi.kyushu-u.ac.jp

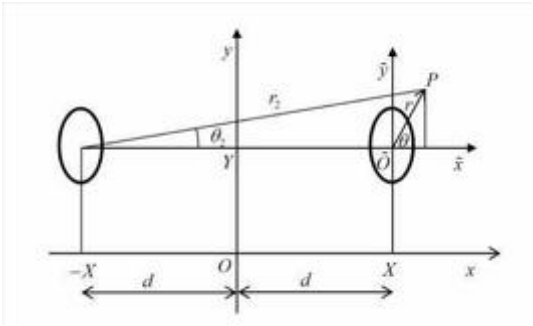

Figure 1: The Cartesian coordinates (x, y) fixed in space and the polar coordinates (r, θ) centered at (X, Y) in moving frame.

The Navier-Stokes equation and the matching condition at $O(\varepsilon^5)$ yields the correction $\dot{Y}^{(4)}$ of $O(\varepsilon^4)$, to the traveling speed. After some manipulation, we reach the eventual formula for the translation speed of a vortex pair, being written in dimensional form as

$$\dot{Y} \approx -\frac{\Gamma}{4\pi d}\left(1+\frac{2\pi}{\Gamma d^2}q\right); \quad \psi_{\rm right} = -\frac{\Gamma}{2\pi}\log r + q\frac{\cos 2\theta}{r^2} + \cdots; \quad q = \varepsilon^2 q_2. \tag{2}$$

Remarkably $\dot{Y}^{(4)}$ includes only the strength q_2 of the $O(\varepsilon^2)$ quadrupole field.

LOW-REYNOLDS-NUMBER MOTION OF A VORTEX PAIR

Identity for vorticity centroid

It is advantageous to derive the two-dimensional analogue of the Helmholtz-Lamb formula for axisymmetric vortex rings [8, 3]. Given the vorticity field $\omega = \omega(x, y, t)$, we invoke the hydrodynamic impulse $I_y = \int x\omega \mathrm{d}A$ to define the y component of the vorticity centroid Y_c. By use of the Navier-Stokes equation, its evolution, denoted with a dot, is found to be

$$Y_c = \frac{\int yx\omega \mathrm{d}A}{\int x\omega \mathrm{d}A}; \quad \dot{Y}_c = \frac{2\int yu\omega \mathrm{d}A}{\int x\omega \mathrm{d}A}, \tag{3}$$

where use has been made of the fact that I_y is constant even in the presence of viscosity.

Motion of vorticity centroid

To examine the motion of a vortex ring at a very low Reynolds number, we substitute, into (3), the solution of the Stokes equation. Given a point-vortex pair with the strength $\pm\Gamma_0$ at $(\pm d, 0)$ at the initial instant $t = 0$, the vorticity is

$$\omega = \frac{\Gamma_0}{4\pi\nu t}\left\{e^{-\frac{(x-d)^2+y^2}{4\nu t}} - e^{-\frac{(x+d)^2+y^2}{4\nu t}}\right\}. \tag{4}$$

The translation velocity $\dot{Y}_c$ of the vorticity centroid is written out, in terms of the error functions, in a tidy form. Its small- and large-time behavior is manipulated, with ease, as

$$\dot{Y}_c = -\frac{\Gamma_0}{4\pi d}\left\{1 - 2\frac{\nu t}{d^2} + O\Big(e^{-\frac{d^2}{\nu t}}\Big)\right\} \ \text{ for } \nu t \ll d^2, \quad \dot{Y}_c = -\frac{\Gamma_0 d}{16\pi\nu t}\left\{1 - \frac{1}{6}\frac{d^2}{\nu t} + O\left[\left(\frac{d^2}{\nu t}\right)^2\right]\right\} \ \text{ for } \nu t \gg d^2. \tag{5}$$

These results achieves an improvement in those of Cantwell & Rott [1] and van Dommelen & Shankar [11].

References

[1] Cantwell B., Rott N.: The decay of a viscous vortex pair. *Phys. Fluids* **31**: 3213-3224, 1988.
[2] Fukumoto Y.: Three-dimensional motion of a vortex filament and its relation to the localized induction hierarchy. *Euro. Phys. J. B.* **29**: 167–171, 2002.
[3] Fukumoto Y.: Global time evolution of viscous vortex rings. *Theor. Comput.Fluid Dyn.* **24**: 335–347, 2010.
[4] Fukumoto Y., Kaplanski F.: Global time evolution of an axisymmetric vortex ring at low Reynolds numbers. *Phys. Fluids* **20**: 053103, 2008.
[5] Fukumoto Y., Habibah U.: Finite thickness effect on speed of a counter-rotating vortex pair. submitted to *Fluid Dyn. Res.*, 2015.
[6] Fukumoto Y., Miyazaki T.: Three-dimensional distortions of a vortex filament with axial velocity. *J. Fluid Mech.* **222**: 369–416, 1991.
[7] Fukumoto Y., Moffatt H. K.: Motion and expansion of a viscous vortex ring. Part 1. A higher-order asymptotic formula for the velocity. *J. Fluid Mech.* **417**: 1–45, 2000.
[8] Fukumoto Y., Moffatt H. K.: Kinematic variational principle for motion of vortex rings. *Physica D* **237**: 2210-2217, 2010.
[9] Fukumoto Y., Okulov V. L.: The velocity field induced by a helical vortex tube. *Phys. Fluids* **17**: 107101, 2005.
[10] Ting L., Tung C.: Motion and decay of a vortex in a non-uniform stream. *Phys. Fluids* **17**: 1039-51, 1965.
[11] van Dommelen L., Shankar S.: Two counter-rotating diffusing vortices. *Phys. Fluids* **7**: 808-819, 1995.

MOTION OF A COMPRESSIBLE VORTEX PAIR

Stefan G. Llewellyn Smith*[1], Daniel V. Freilich[1], Vikas Krishnamurthy[2], and Darren G. Crowdy[2]

[1]*Department of Mechanical and Aerospace Engineering, UCSD, La Jolla, California, USA*
[2]*Department of Mathematics, Imperial College, London, United Kingdom*

Summary Two equal and opposite point vortices translate uniformly. The desingularization of this configuration to vortex patches and hollow vortices leads to a translation velocity that depends on the size of the vortices. The hollow case was first considered by Pocklington. We extend the hollow solution to the case with compressibility by employing the Imai-Lamla version of the Rayleigh-Janzen expansion. We find the $O(M^2)$ correction to the shape and velocity of the pair. The results are compared in the limit of small vortex size to the previous compressible calculations of Moore and Pullin and of Leppington.

INTRODUCTION

Obtaining exact solutions to model problems in vortex dynamics has a long history. The simplest possible two-dimensional solutions to vortex dynamics are point vortices, and configurations with one, two or three vortices in the plane are integrable. In particular, two equal and opposite vortices with circulation $\pm\Gamma$, separated by a distance d, propagate uniformly along the direction of the normal to the segment joining them at a velocity $U = \Gamma/(4\pi d)$. Point vortices are singular solutions of the equations of motion [6], and it is of some interest to understand their relation to obtain desingularized versions. Two common models to obtain desingularized solutions are vortex patches and hollow vortices. The former consist of finite regions with constant vorticity; then the vorticity equation is automatically satisfied and the evolution of the vortex can be obtained by tracking the motion of its boundary (this is contour dynamics). Hollow vortices are in fact closed vortex sheets separating two regions of irrotational fluid (they are called hollow because in the steady case, the inner region say can contain fluid at rest or in fact no fluid). Hollow vortices go back to Pocklington (1895) [8] who obtained steadily translating dipolar solution. Crowdy, Llewellyn Smith and Freilich (2013) [4] revisited Pocklington's solution using the prime function to examine its stability.

The above are solutions to incompressible fluid dynamics. This is an approximation for small fluid velocities compared to the speed of sound, whereas real fluids are all compressible to some extent. When the Mach number, $M \equiv U/c_0$, is small, the incompressible solution at $O(1)$ can be augmented by corrections at $O(M^2)$ and above. This is known as the Rayleigh–Janzen expansion. A compressible extension to the line array of hollow vortices of Baker, Saffman and Sheffield (1976) [2] was obtained by Ardalan, Meiron and Pullin (1995) [1].

We use the Imai–Lamla version of the Rayleigh–Janzen expansion as given by Barsony-Nagy, Er-El and Yungster (1987) [3], applied to the hollow vortex case. The incompressible solution is given as a conformal map from the outside of the vortex (or vortices) to the inside of the unit circle in the unit circle, and the kinematic and dynamic boundary condition specify the analytic part of the $O(M^2)$ potential. The mapping is also computed as a series in Mach number.

FORMULATION

We consider the motion of an irrotational fluid with non-zero Mach number. We denote the complex potential by $W(z, \bar{z})$, where z is the physical variable and define the complex velocity by $\partial W/\partial z$. Primes denote differentiation with respect to the argument of a function. We then consider a map $z(\zeta)$ from the outside of the vortex to the inside of the unit circle in the ζ-plane.

We now expand in Mach number, with $W = W_0 + M^2 W_1 + \cdots$ and $z = z_0 + M^2 z_1 + \cdots$ Then W_0 is a function of z_0 alone. As shown in [3], the $O(M^2)$ correction to the potential is

$$W_1(\zeta, \bar{\zeta}) = \frac{1}{4U^2} W_0'(z_0) \overline{\int^z (W_0'(z_0))^2 \, dz} + G(z) = \frac{1}{4U^2} \frac{W_0'(\zeta)}{z_0'(\zeta)} \overline{\int^\zeta R_0(\zeta) W_0'(\zeta) \, d\zeta} + G(\zeta), \tag{1}$$

where $G(\zeta)$ is an analytic function that is unknown at this stage. Hence the correction to the complex velocity is

$$R_1 = \frac{1}{z_0'} \left(\frac{\partial W_1}{\partial \zeta} + \frac{\partial W_1}{\partial \bar{\zeta}} \circ \; W_0'(z_0) z_1' \right). \tag{2}$$

*Corresponding author. Email: sgls@ucsd.edu

POCKLINGTON'S VORTEX PAIR

We start with the solution for Pocklington's vortex. The potential takes a simple form (which is not needed here), while its ζ-derivative satisfies

$$W_0'(\zeta) = \frac{B}{\zeta}\left\{\frac{P(\zeta/\alpha,\rho)P(\zeta\alpha,\rho)P(\zeta/\overline{\alpha},\rho)P(\zeta\overline{\alpha},\rho)}{P^2(\zeta/\sqrt{\rho},\rho)P^2(\zeta\sqrt{\rho},\rho)}\right\}, \tag{3}$$

where the Schottky-Klein prime function $P(\zeta,\rho)$ is defined by

$$P(\zeta,\rho) = (1\circ\ \zeta)\prod_{k=1}^{\infty}(1\circ\ \rho^{2k}\zeta)(1\circ\ \rho^{2k}\zeta^{-1}). \tag{4}$$

The function $P(\zeta,\rho)$ has a single zero at $\zeta = 1$. The fluid occupies the annulus $\rho < |\zeta| < 1$ in the mapped plane; α is a point in the annulus whose value is given by solving a transcendental equation. Each value ρ between 0 and 1 gives a member of the family of Pocklington pairs. The area of the vortices is a monotonically increasing function of ρ.

The complex velocity at $O(1)$ is

$$R_0(\zeta) = \frac{A}{\zeta}\left\{\frac{P(\zeta\alpha^{-1},\rho)P(\zeta\overline{\alpha}^{-1},\rho)}{P(\zeta\overline{\alpha},\rho)P(\zeta\alpha,\rho)}\right\}, \tag{5}$$

Combining (3) and (5) and using the chain rule leads to an equation for the shape at $O(1)$:

$$z_0'(\zeta) = \frac{\zeta W_0'(\zeta)}{\zeta R_0(\zeta)} = C\left\{\frac{P(\zeta\sqrt{\rho}e^{i\Theta},\rho)P(\zeta\sqrt{\rho}e^{-i\Theta},\rho)}{P(\zeta/\sqrt{\rho},\rho)P(\zeta\sqrt{\rho},\rho)}\right\}^2 \tag{6}$$

with $\alpha = \sqrt{\rho}e^{i\Theta}$. The quantity inside the integral in (1) is

$$R_0(\zeta)W_0'(\zeta) = \frac{AB}{\zeta^2}\left\{\frac{P(\zeta\alpha^{-1},\rho)P(\zeta\overline{\alpha}^{-1},\rho)^2}{P(\zeta/\sqrt{\rho},\rho)P(\zeta\sqrt{\rho},\rho)}\right\}^2, \tag{7}$$

The goal is now to obtain $G(\zeta)$ so that the conditions $\Im\ W = 0$ is satisfied on $|\zeta| = 1$. This can be rewritten as

$$\text{Im } G = \circ\ \frac{W_1 \circ\ \overline{W_1}}{2i} \tag{8}$$

on $\zeta = 1$.

We need another degree of freedom to satisfy the dynamic boundary condition $|R| = 1$ on $|\zeta| = 1$. We use the correction z_1 to satisfy the resulting condition Re $(\bar{z}_0 z_1) = 0$ on $|\zeta| = 1$.

Detailed calculations lead to a correction to the velocity U of the pair, as well as a change in shape.

CONCLUSIONS

We have computed the $O(M^2)$ correction to the Pocklington dipole pair. This is a free boundary-value problem in which the physical region with unknown boundary is obtained as a map from a double-connected region (an annulus). Using the Schottky-Klein prime function leads to explicit expressions for the correction to the potential and map.

The motion of a compressible vortex pair was investigated in the Rayleigh–Janzen limit by Moore and Pullin (1987) [7] and by Leppington (2006) [5]. The results disagree. While the latter seems correct, the singular nature of the solution motivates us to consider the limit of small vortex cores to recover the point vortex pair. The limit $\rho \to 0$ in the detailed results above, obtained from an exact solution to the equation of vortex dynamics, can be compared to the predictions of previous work.

Our work here complements the sister presentation "Analytical solutions for weakly compressible von Kármán vortex streets" by Krishnamurthy and Crowdy.

References

[1] Ardalan, K., Meiron, D.I., Pullin, D.I.: Steady compressible vortex flows: the hollow-core vortex array. J. Fluid Mech. 301:1-17, 1995.
[2] Baker, G.R., Saffman, P.G., Sheffield, J.S.: Structure of a linear array of hollow vortices of finite cross section. J. Fluid Mech. 74:469-476, 1976.
[3] Barsony-Nagy A., Er-El J., Yungster S.: Compressible flow past a contour and stationary vortices. J. Fluid Mech. 178:367-378, 1987.
[4] Crowdy D.G., Llewellyn Smith S. G., Freilich, D.V.: Translating hollow vortex pairs. Eur. J. Mech. B/Fluids 37:180-186, 2013.
[5] Leppington, F.G.: The field due to a pair of line vortices in a compressible fluid. J. Fluid Mech. 559:45-55, 2006.
[6] Llewellyn Smith, S.G.: How do singularities move in potential flow? Physica D 240: 1644-1651, 2011.
[7] Moore, D.W., Pullin, D.I.: The compressible vortex pair. J. Fluid Mech. 185:171-204, 1987.
[8] Pocklington H.C.: The configuration of a pair of equal and opposite hollow straight vortices of finite cross-section, moving steadily through fluid. Proc. Camb. Phil. Soc. 8:178-187, 1895.

WHAT TREFOIL RECONNECTION SAYS ABOUT NAVIER-STOKES REGULARITY

Robert M. Kerr[1]

[1]*Department of Mathematics, University of Warwick, United Kingdom*

Summary Scheeler et al. [1] have recently demonstrated that one can experimentally investigate helicity by imprinting high Reynolds number helical vortex knots into a fluid by yanking 3D-printed aerofoils covered with hydrogen bubbles out of a water tank. Some surprising claims were made based upon the evolution of the resulting vortex filaments. This contribution will address those claims by simulating the evolution and self-reconnection of a similarly perturbed trefoil vortex knot over a range of Reynolds numbers and core diameters. The surprisingly long time it takes for reconnection to begin is confirmed. However, the simulations suggest that the significance of the trefoil is not just in the initial preservation of helicity, but in how it is dissipated in a finite time once reconnection begins. This result implies that the trefoil's vortex dynamics is controlled primarily by the helicity, and not the energy, enstrophy or peak vorticity.

One of the fundamental, unanswered questions about turbulence is why every physical turbulent flow dissipates finite energy in a finite time. Which seems to be inconsistent with the best current mathematics, which indicates that no Navier-Stokes solution from any smooth initial condition can dissipate finite energy in a finite time as the viscosity goes to zero.

This presentation will use the unique properties of a trefoil vortex to address this paradox by taking a step back and asking what defines the evolution of the vortices in incompressible fluids. Is it the energy and enstrophy/dissipation? Or the topology and helicity of the configuration? And if it is the helicity, what is the limit as the diameter of the filament goes to zero?

The trefoil vortex knots that these simulations [2] and the earlier experiments have generated seem particularly well-suited for addressing these questions for the following reasons.

- First, the helicity of these simulations is roughly 1/4 the upper bound given by a single perfectly helical Fourier mode. The most helical I have seen.
- Second, to fully address the Navier-Stokes regularity problem one must have initial conditions whose major Sobolev and Lebesgue norms are finite in Whole (infinite) Space. Other initial conditions such as initially anti-parallel and orthogonal vortices do not have this property.
- Third, if one decreases the filament's diameter a while holding its circulation Γ fixed, its kinetic energy and enstrophy grow without bound, while the configuration's helicity $\mathcal{H} = \Gamma^2 \mathcal{L}$ remains constant. Γ is the circulation and the self-linking number is $\mathcal{L} = \mathcal{W} + \mathcal{T}$ (writhe+twist).

* These contrasting trends make it easy to see whether the timescales are governed by the circulation and helicity, or the energy, enstrophy and the maximum vorticity.

Two figures are given. Fig. 1 illustrates the contortions of the trefoil just as reconnection begins using a vorticity isosurface, three closed vortex loops and two particular points. One where reconnection is beginning and the other the maximum of vorticity. The closed trajectories allow one to make qualitative comparisons with the bubble trajectories in the experiments [1] and relate the topological changes to some recent theoretical work [3]. Which is that the topological changes up to this time are independent of the viscosity of the calculations and the thickness of the filament, there has been very little reconnection and the helicity has not changed. All consistent with the surprisingly long period of helicity preservation in the experiments.

Note that in a classical fluid, reconnection is not instantaneous, so one of the curves (green) follows its original trajectory, while the red and blue curves represent a portion that has reconnected. At this early time, following predictions [3], the red and blue together preserve the total linking number of the trefoil. By determining the writhe, twist and the self-linking directly, primarily using different forms of the Gauss-linking integral [2], it can be confirmed that the self-induced velocity along the filaments has three parts: The self-Biot-Savart term whose integral is the writhe, the traditional bi-normal self-induction, plus the torsion whose integral is the twist.

Fig. 2 illustrates how the helicity and related norms evolve in the period after reconnection begins for the five simulations [2] described in the caption. All dissipate approximately 1/3 of their helicity by $t = 65$. Over this period there is minimal energy loss, which decreases as the viscosity $\nu \to 0$. All three norms have been normalised to have the same units.

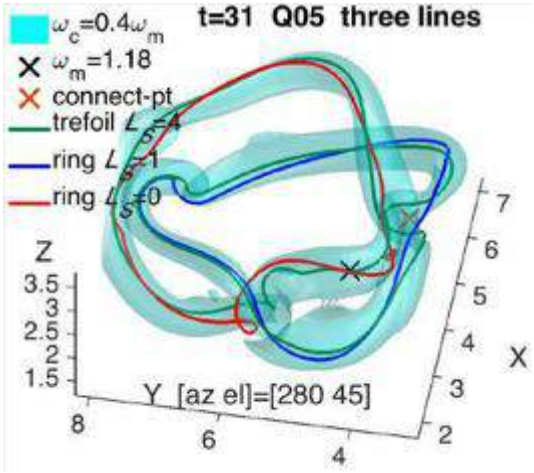

Figure 1: A single vorticity isosurface plus three closed vortex lines at $t = 31$. The green line follows a remaining trefoil trajectories seeded near ω_m, indicated by **X**. Its $\mathcal{L}_S = 4$, split into $\mathcal{W} + \mathcal{T} = 2.85 + 1.15 = 4$ The **orange cross** is the "reconnection point", the point between the closest approach of the trefoil's two loops and where, due to an extra twist, the loops are locally anti-parallel. The **Red** $\mathcal{L}_S = 0$ and **blue** $\mathcal{L}_S = 1$ lines originate on either side of the reconnection point and are linked, which gives a total linking of $\mathcal{L}_t = 2\mathcal{L}_{rb} + \mathcal{L}_{Sb} + \mathcal{L}_{Sr} = 2 + 1 + 0 = 3$, the linking of the original trefoil.

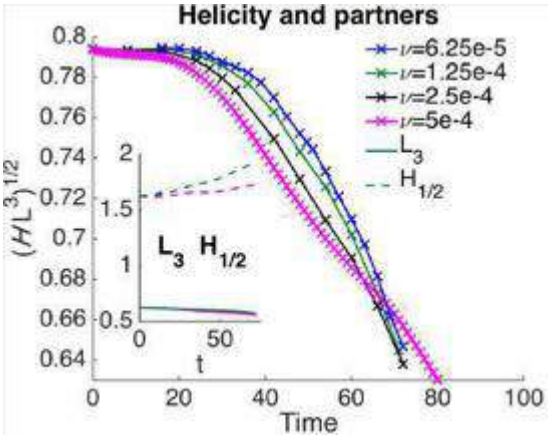

Figure 2: Time evolution of the normalised helicity $(\mathcal{H}L)^{1/2}$ for 5 cases. Four with radius $a = 0.25$ for the viscosities listed, and one with radius $a = 0.175$ and $\nu = 0.0005$ that lies on the $\nu = 0.00025$ case shown. By $t \approx 72$ all cases have roughly the same decrease in helicity. The inset shows normalised L_3 and $H^{(1/2)} = \|u\|_{\dot{H}^{1/2}}$ for two of the calculations. L_3, $H^{(1/2)}$ and $\mathcal{H}$ are all normalised to have the units of circulation. $H^{(1/2)}$ must bound both L_3 and $|\mathcal{H}|$ from above and increases slowly, as required by its upper bound of $\sqrt{2EZ}$. None of which prevents the strong decrease in $\mathcal{H}$.

If $L_3 = \|u\|_{L^3} < \infty$ then Navier-Stokes is regular. Here L_3 is controlled as it decays just a bit more slowly than L_2 (2×energy). $|\mathcal{H}| \leq H^{(1/2)}$ is an upper bound for helicity magnitude. Together these tell us why the energy spectrum [2] goes as k^{-4}. It is necessary for helicity dissipation.
How $a = 0.175$, $\nu = 0.0005$ lays on the $a = 0.25$, $\nu = 0.00025$ case suggests that as $a \to 0$:

A. It is the helicity, not the energy, that controls the dynamics.
B. The time between when reconnection begins and ends goes to zero.
C. If seems possible that there can be finite helicity dissipation in a finite time.
* None of this violates any mathematics related to fixed smooth initial conditions.

What these calculations don't tell us whether there could be finite energy dissipation in a finite time as $a \to 0$, even though a $\nu \to 0$ limit should not exist for fixed (that is a fixed) initial conditions.

References

[1] Scheeler, M. W., Kleckner, D., Proment, D., Kindlmann, G. L., & Irvine, W.T.M. (2014) *Helicity conservation by flow across scales in reconnecting vortex links and knots*. Proc. Nat. Acac. Sci. **111**, 1535015355.
[2] Kerr, R.M. (2015) *Simulated Navier-Stokes trefoil reconnection*. arXiv:1410.1259v1.
[3] Laing, C.E., Ricca, R.L. & Sumners, D.W.L (2015) *Conservation of writhe helicity under anti-parallel reconnection*. Sci. Rep. **5**, 9224.

COLLAPSE VORTICES AND FILAMENTS OF VORTICITY

Henryk Kudela *[1]

[1]*Faculty of Mechanical-Engineering, Wroclaw University of Technology, Wroclaw, Polnad*

Summary The system of a finite number of point vortices that are in self-similar motion, under suitable conditions that are related to the initial positions and circulations of the vortices, can collapse to the point with finite time. The initial positions that lead to the collapse can be found numerically. An explicit solution for collapsing trajectory is derived. The numerical evidence is presented that collapsing vortices may organized itself in vortex sheets. In the distribution of vortices one can clearly notices some regular structures. Examples of the collapsing configurations of vortices is presented.

INTRODUCTION

The collapse of the vortices belongs to one of the most interesting problems related to the dynamics of vortices. In [1, 9] proved that collapse three vortices (n=3) is possible. We will show that collapse vortices is possible for any number of the vortices, $n \geq 3$. The presence of the one or two strong vortices in the set of collapsing vortices lead to rising of filaments created by point vortices. That filaments are stable and take part in the collapsing process. It can be interpret as vortex sheets [7].

EQUATIONS OF MOTION AND THEIR INVARIANTS

The equations of motion of the system of n-point vortices on the plane with distinct positions $\mathbf{z} = (z_1, z_2, \ldots, z_n) \in \mathbb{C}^n$, $z_k = x_k + iy_k$, and circulations $\Gamma_1, \Gamma_2, \ldots, \Gamma_n$, each $\Gamma_j \in \mathbb{R} \setminus 0$ are

$$\frac{dz_k(t)}{dt} = \mathbf{v}_k(\mathbf{z}(t)) = \frac{i}{2\pi} \sum_{l=1, l\neq k}^{n} \Gamma_l \, \frac{z_k \circ z_l}{|z_k \circ z_l|^2} \tag{1}$$

It is well known that the systems (1) posses several invariants [1, 6, 8]

$$\begin{aligned} M_x = \sum_k^n \Gamma_k x_k, \quad M_y = \sum_k^n \Gamma_k y_k, \quad S = \sum_k^n \Gamma_k (x_k^2 + y_k^2), \quad V = \frac{1}{2\pi} \sum_{k>j} \Gamma_k \Gamma_j \\ L = (\sum_k \Gamma_k) S \circ M_x^2 \circ M_y^2, \quad H = \circ \frac{1}{4\pi} {\sum_{k,j}}' \Gamma_k \Gamma_j \ln r_{kj} \end{aligned} \tag{2}$$

SELF-SIMILAR MOTIONS AND COLLAPSE

The system of the n-vortices is in self similar collapsing motion if there exist complex function $\lambda(t) \in \mathbb{C}$, $\lambda(t) = \lambda_r(t) + i\lambda_i(t)$ that $Re(\lambda) = \lambda_r(t) < 0$ and $\lambda_i(t) \neq 0$, such that for all k we have

$$\frac{\mathrm{d}z_k}{\mathrm{d}t} = v_k = \lambda(t) z_k, \qquad k = 1, 2, \ldots, n \tag{3}$$

Introducing the new variables $(r(t), \varphi(t))$ and assuming that $z_k = z_k(0) r(t) e^{i\varphi(t)}$, $r(0) = 1, \quad \varphi(0) = 0$, one can find that the solution of (1),(3) has a form [3, 4]

$$z_k(t) = \sqrt{2\lambda_r(0)t + 1} e^{\left(i \frac{\lambda_i(0)}{2\lambda_r(0)} \ln(2\lambda_r(0)t+1) \right)} z_k(0) \tag{4}$$

Solution (4) represents the logarithmic spiral. The critical (collision) time $t \to T_c$ is $T_c = \circ \frac{1}{2\lambda_r(0)}$. If $\lambda_r(t) > 0$ then the vortices system expand. If the real part of $\lambda(t)$ equals to zero, $\lambda_r = 0$, the vortices are in relative equilibrium and the systems rotate as a solid body (the collapse time is infinite, $T_c = \infty$).
The Hamiltonian H in(2) during the self-similar motion will conserve, when the invariant V in (2) is equal zero, $V = 0$. With out loosing the generality we assumed that $M_x = 0$ and $M_y = 0$. So the vortex system collapsed to the beginning of

*Corresponding author. Email: henryk.kudela@pwr.edu.pl

the coordinate system. It can be proved that when $V = 0$, $M_x = 0$, $M_y = 0$ then also $S = 0$ and $L = 0$ in (2). From the similarity of the motion (3), we have the following algebraic system of equations [6, 4]

$$\mathbf{v}_1 z_k = \mathbf{v}_k z_1 \quad (k = 1, .., n \circ 3). \tag{5}$$

The collapsing positions of vortices can be determined by common zeros of the functions $V = 0$, $M_x = 0$, $M_y = 0$, $S = 0$ and 2(n-3) equations (5), $f_j = \mathbf{v}_1 z_{j+2} \circ \mathbf{v}_{j+2} z_1, j = 2, \ldots, n \circ 2$. To complete the systems to $2n$ equations, it was assumed that one of the vortex in the system e.g z_n has the fixed position, and it was included to the system of equation the identity $\sum_j \Gamma_j z_j^* \mathbf{v}_j = 0$ [3, 4]. The nonlinear algebraic system of equation was solved by the Newton method [3, 4]. For each collapsing positions it is possible to find the curves where vortices are distributed in the continuous way.The positions of the vortices on the curves are parameterized by the value of the Hamiltonian. Different Hamiltonian values results in different collision time T_c. The number of collapsing set of vortices are infinite.

NUMERICAL RESULTS

In Figure 1 A), B), C), D) was shown different cases of the collapsing systems of 72 vortices. In Figures 1 were shown the initial collapsing positions and only a few trajectories in order to preserve the readability and expose the vortex structures. The thick points represent the vortices with big intensities. The blue color is related to the negative intensity and red one to the positive. In Figure 1 A) intensities $\Gamma_{1\ to\ 71} = 1$ and only one vortex has dominat value $\Gamma_{72} = \circ\, 35$. Collision time was $T_c = 5.86232$, $H = 49.036$. In Figure 1 B) there were two strong vortices $\Gamma_{71,72} \approx 20.1502$,and $\Gamma_{1\ to\ 70} = \circ\, 1$. Collision time was $T_c = 32.72233$ and $H = 21.961502$. In Figure 1 C) there were also two strong vortices $\Gamma_{71,72} \approx 20.1502$, $\Gamma_{1\ to\ 70} = \circ\, 1$, and $H = 14.8442$ but collision time was very long $T_c \cong 63511.8$. One can noticed that vortices created the circle . In Figure 1 D) there were three strong vortices $\Gamma_{71,72} = \circ\, \Gamma_{70} = \approx 24.9663$,and $\Gamma_{1\ to\ 70} = 1$. The collision time time was $T_c = 31.0392$ and $H = 7.60762$.

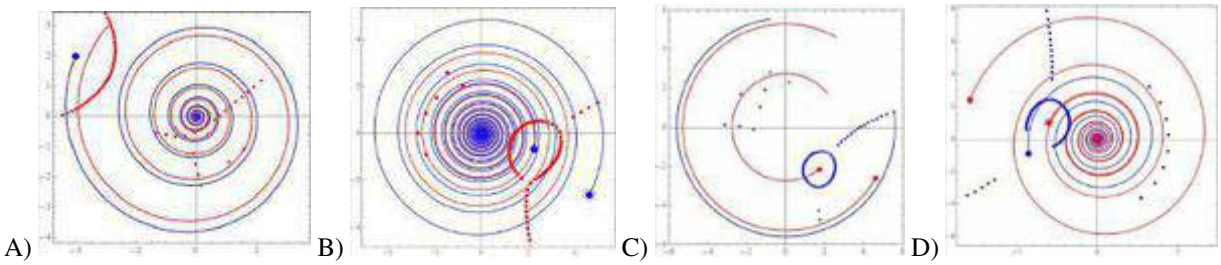

Figure 1: Examples of collapsing systems of 72 vortices; In order to keep the readability of the graph it was shown only a few trajectories. Bigger points mark the stronger vortices. The blue color related to negative intensity, the red color to the positive one.

CONCLUSIONS

From examples it is clear that the presence a few stronger vortices in the set of collapsing vortices caused that the vortices collect their self in the pieces curves that can be interpret as vortex sheets. They can crete a closed circle that take part in collapsing phenomenon. In the atmospheric physics, it seems that collapsing vortices have relevance to the meteorological phenomenon of a polar cyclone [4]. Spirals and filaments of vorticity are characteristic feature of two-dimensional turbulent flow [5, 2].

References

[1] Aref H.: Motion of three vortices. Phys. Fluids 22:393-400, 1979.
[2] Kevlahan N.K-R , Farge M.: Vorticity fiaments in two-dimensional turbulence: reation, stability and effect.J. Fluid Mech 346:49-76, 1997
[3] Kudela H.: Collapse of n–point vortices in self-similar motion. Fluid Dyn. Res. 46: 1-16, 2014
[4] Kudela H.: Self-Similar collapse of n point vorticies. J. Nonlinear Sci. 24: 913-933, 2014
[5] Moffat H.K.: Spiral structures in turbulent flow. New Approaches and Concepts in Turbulence. Brikhäuser, Monte Verità, 2014
[6] O'Neil K. A.: Stationary configurations of points vortices. Trnas. Amer. Math. Society 302: 383-425, 1987
[7] O'Neil K. A.: Relative equilibria of vortex sheets. Physica D 238:379-383, 2009
[8] Newton P. K.: The N-vortex problem. Analytical Techniques. Springer, 2001
[9] Novikov E. A.: Dynamics and statistics of a system of vortices. Zh. Eksp. Teor. Fiz. 68: 1868-1882, 1975

CURVATURE AND ELLIPTIC INSTABILITIES IN HELICAL VORTICES

Francisco J. Blanco-Rodríguez and Stéphane Le Dizès*
IRPHE, CNRS, Aix Marseille Université, Centrale Marseille, France

Summary Short-wavelength instabilities of helical vortices are analysed using a combined theoretical and numerical approach. The helical vortices are described using an asymptotic approach in the limit of small core size (compared to the pitch and the radius of the helix). Both the curvature instability induced by the local vortex curvature and the elliptic instability induced by the strain field deformation are considered for a vortex with Gaussian axial vorticity and axial velocity (Batchelor vortex). Theoretical predictions are obtained for the growth rate of each instability and used to analyse the competition between both instabilities. We show the crucial role of the axial flow component of the Batchelor vortex in the selection of the dominant instability. For weak axial flow, the elliptic instability is found to dominate the curvature instability, whereas it is the opposite when the axial flow is no longer negligible. The results are compared to recent experimental observations.

Horizontal-axis wind turbines generate helical vortices which are subject to a complex spatial evolution involving several instabilities. This evolution provides the characteristics of the wind-turbine far-wake which impacts other wind turbines placed downstream. This wake is a source of increased mechanical fatigue and it affects their efficiency. Understanding the physical mechanisms acting on the wake evolution is therefore a first step toward the prediction and control of wind turbine wakes, which constitutes a goal for increasing the efficiency and life-time of wind turbine farms.

The long-wavelength instability discovered by Widnall [1] is the first instability affecting helical vortices. This instability leads to a reorganisation of the vortex system through local pairing events but it does not seem to affect the global coherence of the vortices [2]. More promising are short-wavelength instabilities which are known to possibly lead to the destruction of the vortices [3]. Short-wavelength instabilities lead to the growth of perturbations within the vortex with a wavelength comparable to the core size. Two short-wavelength instabilities could develop in helical vortices: the curvature instability and the elliptic instability. In this work, we analyse the occurrence of both instabilities using a combination of asymptotic and numerical methods.

The helical system is described using asymptotical methods by assuming that the ratio of vortex core radius to the curvature radius is small. At leading order, the base flow is then a columnar vortex aligned along with the helix centreline. We assume that the axial velocity and vorticity of the vortex are both Gaussian (Batchelor vortex). Curvature corrections are obtained as first order corrections, while torsion and strain field corrections appears at second order [4, 5].

Both curvature and elliptic instability in a helical vortex can be analysed using the framework developed by Moore & Saffman (1975) [6] for the elliptic instability of a strained vortex. Both instabilities are interpreted as a resonance of two (Kelvin) modes of the Batchelor vortex with non-axisymmetric corrections. The curvature instability results from the coupling with the dipolar corrections associated with curvature. The condition of resonance for the curvature instability corresponds to the existence of two modes of azimuthal wavenumbers m and $m+1$ with identical axial wavenumber and frequency [7, 8]. The elliptic instability results from the coupling with the quadripolar corrections, which implies a similar condition of resonance between two modes of azimuthal wavenumber m and $m+2$ [6].

The first difficulty of the analysis is to find the resonant configurations for the Kelvin modes of a Batchelor vortex. Contrarily to the Rankine vortex (vortex with a uniform vorticity in its core and no vorticity outside), numerous Kelvin modes of the Batchelor vortex are now damped due the presence of a critical layer singularity [9]. This affects significantly the condition of resonance: they are found to systematically involve singular modes. The instability can therefore be present only if the growth associated with the resonant coupling can overcome the critical layer damping of the Kelvin mode. This is a strong constraint which selects very few possible resonant configurations. For the elliptic instability, Lacaze *et al.* [10] showed that this explains why the sinuous mode present without axial flow, is replaced, as the axial flow is increased, by other instability modes involving $m=0$ and $m=2$ Kelvin modes. The same sensibility with respect to the axial flow is observed for the curvature instability. For small axial flow, only Kelvin modes of azimuthal wavenumbers $m=0$ and $m=1$ with a high radial complexity are found to be possible. As the axial flow is increased, the radial complexity of the resonant modes becomes simpler.

The second difficulty of the analysis is the computation of the coupling terms. For the curvature instability, we can follow Moore & Saffman method and obtain coupling coefficients by a simple orthogonality condition at first order. For the elliptic instability, the problem is more involved as coupling occurs at second order. It implies additional terms coming from a double interaction with curvature corrections. Such terms were previously obtained for a Rankine vortex by Widnall & Tsai [11]. For the Batchelor vortex, their calculation requires a numerical computation of the curvature correction to each Kelvin mode.

For each resonant configuration, a formula for the growth rate is obtained as a function of the Reynolds number, the local curvature ratio, and a parameter characterizing the external strain field felt by the vortex. The stability results are then applied to helical vortices by expressing this strain parameter in terms of the geometrical parameters of the helix.

*Corresponding author. Email: ledizes@irphe.univ-mrs.fr

The competition between both instabilities is analyzed by comparing the growth rates of the various resonant configurations. We observe that the characteristic of the most unstable modes strongly varies with the value of axial jet.

Without axial flow, we show that the first sinuous mode of the elliptic instability is the dominant instability mode when the Reynolds number remains smaller than a critical value. In the presence of axial flow, this is no longer the case. The curvature instability is found to provide unstable modes with the largest growth rate even for moderate values of the Reynolds numbers.

The results are discussed in light of recent experimental results obtained for helical vortices [12].

Acknowledgements. Financial support from the french Agence Nationale de la Recherche (ANR Helix project ANR-12-BS09-0023-01; LABEX MEC Project ANR-11-LABX-0092) is kindly acknowledged.

References

[1] S. E. Widnall, "The stability of a helical vortex filament," J. Fluid Mech. **54,** 641–663 (1972).

[2] H. U. Quaranta, H. Bolnot, and T. Leweke, "Long-wave instability of a helical vortex," J. Fluid Mech. **780,** 687–716 (2015).

[3] N. Schaeffer and S. Le Dizès, "Nonlinear dynamics of the elliptic instability," J. Fluid Mech. **646,** 471–480 (2010).

[4] A. J. Callegari and L. Ting, "Motion of a curved vortex filament with decaying vortical core and axial velocity," SIAM Journal of Applied Mathematics **35,** 148–175 (1978).

[5] F. J. Blanco-Rodriguez, S. Le Dizès, C. Selçuk, I. Delbende, and M. Rossi, "Internal structure of vortex rings and helical vortices," J. Fluid Mech. **785,** 219–247 (2015).

[6] D. W. Moore and P. G. Saffman, "The instability of a straight vortex filament in a strain field," Proc. R. Soc. Lond. A. **346,** 413–425 (1975).

[7] Y. Fukumoto and Y. Hattori, "Curvature instability of a vortex ring," J. Fluid Mech. **526,** 77–115 (2005).

[8] Y. Hattori and Y. Fukumoto, "Modal stability analysis of a helical vortex tube with axial flow," J. Fluid Mech. **738,** 222–249 (2014).

[9] S. Le Dizès and L. Lacaze, "An asymptotic description of vortex Kelvin modes," J. Fluid Mech. **542,** 69–96 (2005).

[10] L. Lacaze, K. Ryan, and S. Le Dizès, "Elliptic instability in a strained Batchelor vortex," J. Fluid Mech. **577,** 341–361 (2007).

[11] S. E. Widnall and C.-Y. Tsai, "The instability of the thin vortex ring of constant vorticity," Phil. Trans. R. Soc. London *A* **287,** 273–305 (1977).

[12] T. Leweke, H. U. Quaranta, H. Bolnot, F. J. Blanco-Rodriguez, and S. Le Dizès, "Long- and short-wave instabilities in helical vortices," J. Phys.: Conf. Ser. **524,** 012154 (2014).

SIMULATIONS OF HELICAL VORTEX INSTABILITY

Ivan Delbende*[1,2], Can Selçuk[1,2], and Maurice Rossi[1,3]
[1]*Sorbonne Universités, UPMC Univ Paris 06, 75252 Paris CEDEX 05, France*
[2]*LIMSI, CNRS, Université Paris-Saclay, 91405 Orsay CEDEX, France*
[3]*CNRS, UMR 7190, Institut Jean Le Rond d'Alembert, 75252 Paris CEDEX 05, France*

Summary Using dedicated DNS codes, we simulate the linear growth of perturbations in the vicinity of helically symmetric vortex systems, and extract the dominant instability properties: long-wave displacement modes and short-wave modes emerging through elliptical instability. Nonlinear simulations also reveal the complex dynamics of interacting helical vortices: overtaking, leapfrogging, merging.

OBJECTIVES

The near wake behind rotating devices such as helicopter rotors, wind turbines and propellers is dominated by helical vortices. Investigating their stability properties is a necessary step to predict their dynamics. On one hand, instabilities in helical vortex systems have been studied theoretically by Widnall [1], Gupta & Loewy [2] and more recently by Okulov and Sørensen [3]. These studies describe the inviscid instability of thin vortices with respect to displacement modes. On the other hand, there has been much experimental and theoretical work on the elliptical instability, a situation where a pair of Kelvin waves resonate with an external strain field which elliptically deforms the vortex core. This phenomenon has been encountered in co- and counter-rotating rectilinear vortex pairs (see Leweke *et al.* [4] for a review) and has also been predicted in helical vortices. The present work has thus a twofold objective: by means of viscous linearized and nonlinear numerical simulations, we want to generalize the inviscid studies on displacement modes to more realistic vorticity profiles and arbitrary core sizes, and to simulate the growth of elliptical instabilities in the context of helical vortices.

HELICAL SYMMETRY AND BASE FLOW

The base flows considered here are helically symmetric: fields are invariant through combined axial translation of distance Δz and rotation of angle $\Delta\theta = \Delta z/L$ around the z-axis, where $2\pi L$ denotes the helix pitch. In this context, the field components depend solely on the radial distance r to the axis, on the variable $\varphi = \theta - z/L$ (a constant along helical lines) and on time. The dynamics is then governed by a system of two coupled dynamical equations for the components of velocity and vorticity tangent to the helical lines. These two helical components are linked to a streamfunction through a Poisson-like equation: the formulation extends the two-dimensional $\psi - \omega$ method to helical flows [5]. The numerical implementation (HELIX code) in a (r, φ) domain uses Fourier modes in the periodic φ-direction (typically 256) and finite differences in the radial direction (typically 512 grid points). The base flows are first computed using the HELIX code: they consist in one helical vortex or several helical vortices of same unit circulation Γ and same core size a, of pitch L, regularly spaced along the azimuth at a unit radial distance from the axis (see figure 1a for the $N = 2$ vortex case).

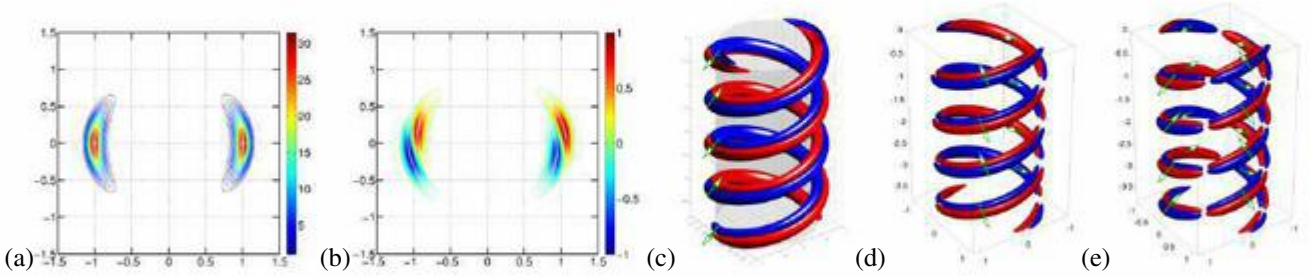

Figure 1: Two helical vortices with pitch $L = 0.3$ and core size $a = 0.1$. (a) Base flow: contours of helical vorticity in a plane orthogonal to the helix axis z. (b) Dominant Okulov mode: contours of the helical vorticity perturbation in the same plane as (a). (c) Three-dimensional representation of the Okulov mode: the arrows indicate the displacement that the perturbation induces on the base flow. (d)-(e) Long-wave subdominant modes at $k_z = 0.5$ and $k_z = 1$.

INSTABILITIES HAVING THE SAME HELICAL SYMMETRY AS THE BASE FLOW

We first perform a linear temporal stability analysis of these base flows using an Arnoldi procedure [6] coupled to a linearised version of the HELIX code. This procedure gives access to the instability modes having the same helical symmetry as the base flow, which generalize the Okulov modes. Instabilities are found to be dominated by displacement modes, the structure of which is illustrated in figure 1b-c. Cases where a hub vortex is involved are also investigated and linked to the findings of Felli *et al.* [7] in propeller wakes. We then compute the nonlinear dynamics of a basic flow perturbed with a linear mode of the above type, set at a small initial amplitude. This displacement mode is shown to be responsible for a complex dynamics with a sequence of overtaking events, leapfrogging and eventually merging, as shown in figure 2. The influence of the parameters (a, L, Re) on the growth rate and the nonlinear dynamics is investigated.

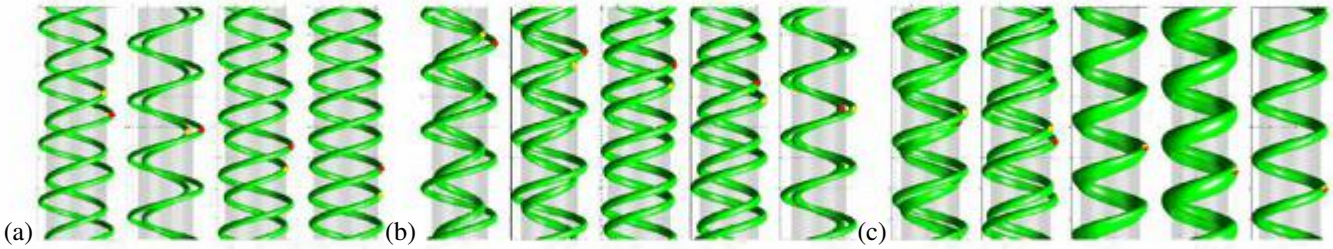

Figure 2: Nonlinear dynamics at $Re = \Gamma/\nu = 10^4$ of two helical vortices with pitch $L = 0.3$ and initial core size $a = 0.1$, initially perturbed by the mode of figure 1b-c. Successive snapshots of the helical vorticity isosurface at half-maximum level showing (a) overtaking, (b) leapfrogging, (c) merging. Color dots provide a visual help to follow vortices in time.

INSTABILITIES BREAKING THE SYMMETRY OF THE BASE FLOW

As the system is invariant along helical lines, the base flow components depend explicitly on r and $\varphi = \theta - z/L$, but not explicitly on z. More general eigenmodes can be found which vary along z as $f(r, \varphi)\mathrm{e}^{\mathrm{i}k_z z}$ ($k_z > 0$). Another numerical code has been developed that simulates the linearized temporal evolution of such modes that break the helical symmetry of the base flow (code HELIKZ). The complex Navier–Stokes equations relative to a given wavenumber k_z are discretized on the same grid as above. Primitive variables are used, and zero divergence is ensured by a projection step.

Two types of modes are investigated: *(i)* long-wave modes which generalize the modes obtained by Widnall and Gupta & Loewy (see figure 1d-e for a $N = 2$ case). The results we obtained for one vortex compare very well to those observed in recent experimental work [8]. Note that the nonlinear saturation of such modes has been simulated using a vortex method by Walther *et al.* [9] and using a grid method by Ivanell *et al.* [10]; *(ii)* modes with a wavelength smaller than the core size, arising from elliptical instability. This part of the work is in progress.

ACKNOWLEDGMENTS

Financial support from ANR HELIX project ANR-12-BS09-0023-01 is acknowledged, as well as the use of HPC resources from GENCI–IDRIS (grants 2015- and 2016-2a1386).

References

[1] Widnall S. E.: The stability of a helical vortex filament. J. Fluid Mech. 54:641-663, 1972.

[2] Gupta B. P., Loewy R. G.: Theoretical analysis of the aerodynamic stability of multiple, interdigitated helical vortices. AIAA J. 12(10):1381-1387, 1974.

[3] Okulov V. L., Sørensen J. N.: Stability of helical tip vortices in a rotor far wake. J. Fluid Mech. 576:1-25, 2007.

[4] Leweke Th., Le Dizès S., Williamson C. H. K.: Dynamics and instabilities of vortex pairs. Annu. Rev. Fluid Mech. 48:1-35, 2016.

[5] Delbende I., Rossi M. and Daube O.: DNS of flows with helical symmetry. Theo. Comp. Fluid Dyn. 26:148-175, 2012.

[6] Edwards W. S., Tuckerman L. S., Friesner R. A., Sorensen D. C.: Krylov methods for the incompressible Navier-Stokes equations. J. Comp. Phys. 110:82-102, 1994.

[7] Felli M., Camussi R., di Felice F.: Mechanisms of evolution of a propeller wake in the transition and far fields. J. Fluid Mech. 682:5-53, 2011.

[8] Quaranta H. U., Bolnot H., Leweke Th.: Long-wave instability of a helical vortex. J. Fluid Mech. 780:687-716, 2015.

[9] Walther J. H., Guénot M., Machefaux E., Rasmussen J. T., Chatelain P., Okulov V. L., Sørensen J. N., Bergdorf M., Koumoutsakos P.: A numerical study of the stability of helical vortices using vortex methods. J. Phys.: Conference Series 75:012034, 2007.

[10] Ivanell S., Mikkelsen R., Sørensen J. N., Henningson D.: Stability analysis of the tip vortices of a wind turbine. Wind Energ. 13:705-715, 2010.

THE USE OF HELICAL VORTEX SOLUTIONS IN WIND TURBINE PERFORMANCE ANALYSIS

D.H.Wood[1a], V.L. Okulov[2] and D. Bhattacharjee[3]
[1]Department of Mechanical and Manufacturing Engineering, University of Calgary, Calgary T2N 1N4, AB, Canada
[2]Department of Wind Energy, Technical University of Denmark, DK 2800, Lyngby, Denmark
Institute of Thermophysics, Siberian Branch of the Russian Academy of Sciences, 630090, Novosibirsk, Russia
[3]Department of Mechanical Engineering, University of Alberta, Edmonton T6G 1H9, AB, Canada

Summary The exact solutions for the velocities induced by helical line vortices are applied to two related aspects of wind turbine performance analysis. First it is shown that they allow the determination of the "tip loss factor" which relates the velocities at the blades to the average velocity at the same radius. The new calculation of tip loss is shown to be suitable for the computational modeling of wind turbine performance and is more accurate than the simple approximation due to Prandtl that is commonly used. Second, the conservation equations for momentum and angular momentum are nonlinear so the azimuthal variation of the induced velocities can be important. The exact solutions are used to determine the nonlinear terms in the torque and thrust equations. Approximate forms for the nonlinear terms are developed.

For wind turbines with a finite number of blades, N, the wind speed at the blades may differ from the average wind speed at the same radius. The difference is usually expressed as the tip loss factor, F, defined as the ratio of the average induced velocity to the induced velocity at the blade. Typically, F reduces the power output of a three-bladed turbine by around 5%, and must, therefore, be included when analyzing turbine power extraction. F is commonly evaluated using Prandtl's approximation which is computationally simple, see, for example, Chapter 6 of Hansen [1], but not necessarily accurate. Alternatively, F can be computed from the Kawada-Hardin equations for the velocity field due to a helical vortex of constant pitch and radius, Fukumoto et al. [2]. These equations contain infinite sums of products of Bessel functions and their derivatives and are not computationally attractive. However, Kawada [3] and Okulov [4] provide approximations that are much more easily computed.

In the first part of the presentation, Prandtl's approximation and the three methods of determining F described above, will be compared for optimal Betz-Goldstein (BG) rotors whose loading (bound vorticity) was determined by the method of Okulov & Sørensen [5]. For these rotors, the vortex pitch is constant across the wake and an independent and accurate estimate of F is available. Comparison is made for $N = 3$ and tip speed ratio, λ, from zero to 15. Typical results are shown in Figure 1.

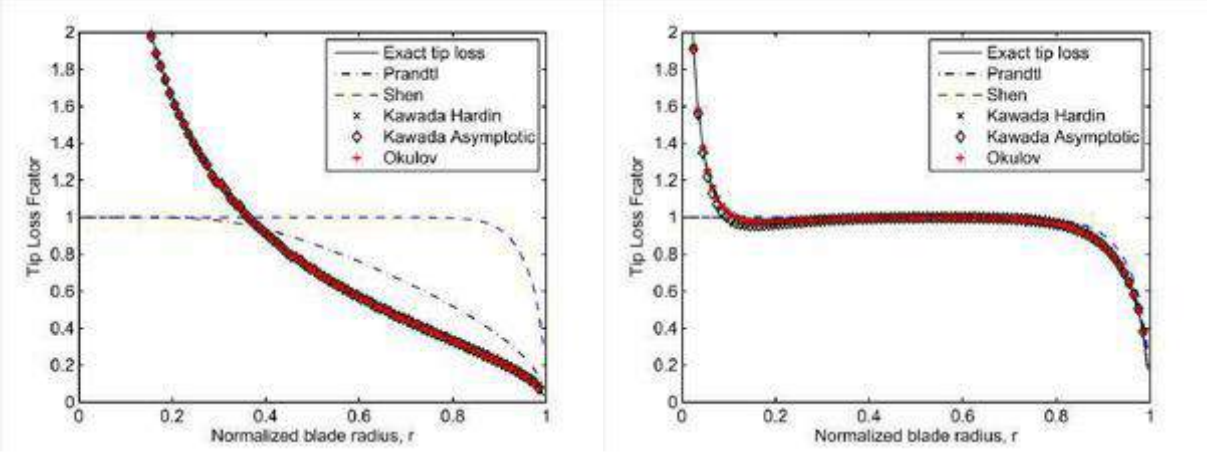

Figure 1: Tip loss factor for $N = 3$. $\lambda = 0.05$ (left) and $\lambda = 6.6$ (right)

It is clear that Prandtl's approximation works well at high λ, but only for the outer part of the blade. Near the hub, F exceeds unity which is the maximum possible value of Prandtl's approximation at all λ. Okulov's approximate equations are the most accurate of the three direct methods and it will be shown that they can be utilized in a wind turbine analysis program with only a small additional computational cost compared to Prandtl's approximation.

If F differs significantly from unity, there must be significant azimuthal variations in the velocities. Since all the conservation equations used in wind turbine analysis, apart from the mass equation, are nonlinear, the "quadratic" or "nonlinear" terms may be significant. For example, the conservation of angular momentum equation is usually written in terms of UW, the product of the average axial and circumferential velocities, but the deviations from the averages, u and w, may also contribute. For BG rotors, u and w are directly related so the nonlinear terms are reasonably straightforward to compute. They always reduce the angular momentum flux. In most turbine analyses, the nonlinear terms are accounted for in terms of F. It is shown, however, that they do not depend explicitly on F but are closely related to it, and go to zero as F approaches unity. So far, we have computed them

[a)] Corresponding author. Email: dhwood@ucalgary.ca

only from the Kawada-Hardin equations. Figure 2 shows the results for two values of λ, along with the blade torque determined from the Kutta-Joukowsky equation (see Equation (12) of Okulov & Sørensen (2008)) which must exactly balance the angular momentum flux. The quadratic terms are very important at the lower λ. At the higher λ, the quadratic terms are smaller in magnitude and are insufficient to reduce the average angular momentum flux to match the rotor torque.

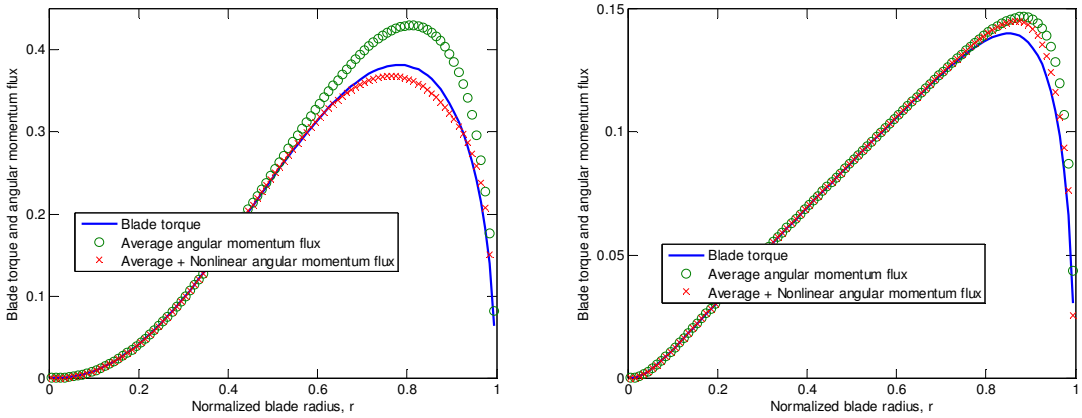

Figure 2: Torque and angular momentum for $N = 3$. $\lambda = 0.55$ (left) $\lambda = 6.6$ (right)

We are currently investigating these results further and will present the analysis of the nonlinear terms along with the implication for including F in the conservation equations for momentum and angular momentum in general wind turbine analysis.

References

[1] M.O.L. Hansen *Aerodynamics of Wind Turbines*, 2nd edition, Earthscan, 2008.

[2] Y. Fukumoto, V.L. Okulov, D.H.Wood, The contribution of Kawada to the analytical solution for the velocity induced by a helical vortex filament, *Applied Mechanics Reviews*, **67**, 060801-1., 2015. DOI: 10.1115/1.4031964.

[3] S. Kawada, Calculation of induced velocity by helical vortices and its application to propeller theory, Tech. Rep. 172, Aeronautical Research Institute, Tokyo Imperial University, 1939. **http://repository.tksc.jaxa.jp/pl/dr/IS4146951000/en**.

[4] V. L. Okulov, On the stability of multiple helical vortices, Journal of Fluid Mechanics, **521**, 319-342, 2004.

[5] V.L. Okulov and J. N. Sørensen, Refined Betz limit for rotors with a finite number of blades, Wind Energy, **11**, 415-426, 2008.

TOPOLOGICAL FLUID MECHANICS OF THE FORMATION OF THE KARMAN-VORTEX STREET

Matthias Heil*[1], Jordan Rosso[2], Andrew Hazel[1], and Morten Brøns[3]

[1]*School of Mathematics, University of Manchester, UK*

[2]*Ecole Centrale Lyon, France*

[3]*Department of Applied Mathematics and Computer Science, DTU, Denmark*

Summary We analyse the topology of the vorticity field downstream of a circular cylinder to show that the Karman vortex street develops at a large but finite distance downstream of the cylinder, and only when the Reynolds number is increased beyond a value $Re_{\rm K}$ which is slightly larger than the value $Re_{\rm crit}$ at which the steady base flow becomes unstable to time-dependent perturbations. In the region of validity of our analysis, that is, small values of $\epsilon \sim (Re - Re_{\rm crit})^{1/2}$, only a finite number of vortices exist. Moving downstream after their creation in a topological cusp bifurcation, the vortices later disappear in a similar but reversed event. However, the number of vortices and the length of the domain where they exist grow rapidly with ϵ.

The flow of a viscous fluid past a circular cylinder undergoes a symmetry-breaking, super-critical Hopf bifurcation at a critical Reynolds number, $Re_{\rm crit}$, of approximately 46 [1]. The key feature of the time-periodic unsteady flow that ultimately emerges is the periodic shedding of vortices which results in the formation of the famous Karman vortex street. The transition from steady to periodic flow and the transition of the shear layer in the wake of the cylinder into individual vortices are distinct events. Mathematically the former is a bifurcation in a function space of velocity fields while the latter is a topological change of the vorticity field in the physical space [2]. The purpose of the present study is to elucidate the connection between these two bifurcation phenomena and to show that they occur at two slightly different Reynolds numbers.

To facilitate the analysis, we exploit the fact that for Reynolds numbers close to $Re_{\rm crit}$, the flow can be described by the superposition of the steady, symmetric base flow, $\overline{\mathbf{u}}$, and the Navier-Stokes eigenfunction, $\widehat{\ }$, both evaluated at $Re_{\rm crit}$; see, e.g., [3]. Thus

$$\mathbf{u}(x,y,t;Re) \approx \overline{\mathbf{u}}(x,y;Re_{\rm crit}) + \epsilon\, \widehat{\mathbf{u}}(x,y;Re_{\rm crit})\exp({\rm i}\Omega t), \tag{1}$$

where $\epsilon \sim (Re - Re_{\rm crit})^{1/2}$ and Ω (the purely imaginary Navier-Stokes eigenvalue associated with $\widehat{\mathbf{u}}$) represents the frequency at which vortices are shed. Using our finite-element library `oomph-lib` [4], we compute the vorticity fields $\overline{\omega}$ and $\widehat{\omega}$ associated with the base flow and the eigenfunction, respectively, in a long but finite channel, imposing parallel, traction-free outflow at $x = X_{\rm right}$, and "tow-tank" boundary conditions at the sidewalls at $y = \pm H/2$. The time-periodic vorticity field associated with the flow defined by (1) is given by

$$\omega(x,y,t;Re) = \overline{\omega}(x,y;Re_{\rm crit}) + \epsilon\, \widehat{\ }(x,y;Re_{\rm crit})\exp({\rm i}\Omega t), \tag{2}$$

and we define a vortex as a local extremum in this vorticity field. Given that the steady base flow, $\overline{\mathbf{u}}$, does not contain any vortices downstream of the cylinder, we expect that the amplitude of the perturbation, ϵ, has to be nonzero for such vortices to develop in the time-periodic flow (1). Since $\epsilon \sim (Re - Re_{\rm crit})^{1/2}$ this would imply that the Karman vortex street develops at Reynolds number $Re_{\rm K} > Re_{\rm crit}$.

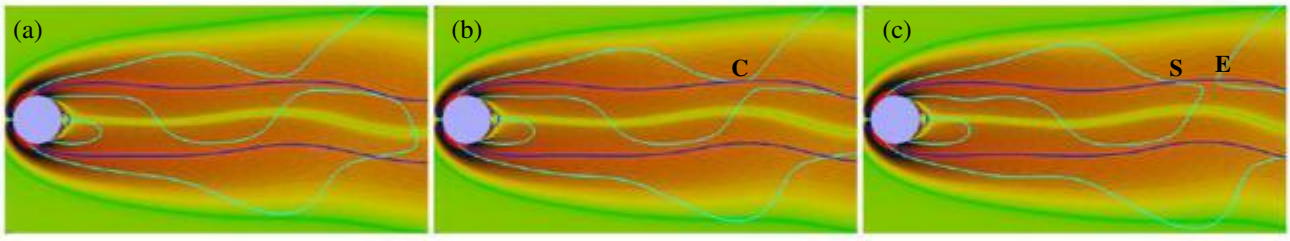

Figure 1: Three snapshots of the vorticity field (a) before, (b) close to, and (c) after the generation of a new vortex via a cusp bifurcation. Colours and the thin black isolines indicate logarithmic contours of the magnitude of the vorticity; the thick cyan and blue lines show zero levels of $\partial\omega/\partial x$ and $\partial\omega/\partial y$, respectively. The cyan and blue lines intersect at critical points of the vorticity; either at a cusp ("**C**"), a saddle ("**S**") or an extremum ("**E**").

*Corresponding author. Email: M.Heil@maths.manchester.ac.uk

We start by analysing how new vortices are generated in the flow field given by equation (1). For this purpose Fig. 1 shows three snapshots of the associated vorticity field (a) before, (b) close to, and (c) after the generation of a new vortex. The thick cyan and blue lines in these plots show the zero levels of $\partial\omega/\partial x$ and $\partial\omega/\partial y$, respectively. These lines intersect at positions where the vorticity has a critical point, $\nabla\omega = \mathbf{0}$. The sequence of snapshots shows that new vortices are formed via a cusp bifurcation in the vorticity field during which a saddle point (**S**) and an extremum (**E**) emerge from a degenerate critical point (**D**) at which the Hessian $\mathcal{H}$ of the vorticity vanishes. Given the vorticity field $\omega(x, y, t)$ from (2), we therefore determined the position $(X_{\rm cusp}, Y_{\rm cusp})$ and the time $T_{\rm cusp}$ at which a new vortex is created by solving the three equations

$$\partial\omega/\partial x = 0, \quad \partial\omega/\partial y = 0 \quad \text{and} \quad \mathcal{H} = \frac{\partial^2\omega}{\partial x^2}\,\frac{\partial^2\omega}{\partial y^2} \circ \left(\frac{\partial^2\omega}{\partial x \partial y}\right)^2 = 0 \tag{3}$$

for $X_{\rm cusp}, Y_{\rm cusp}$ and $T_{\rm cusp}$.

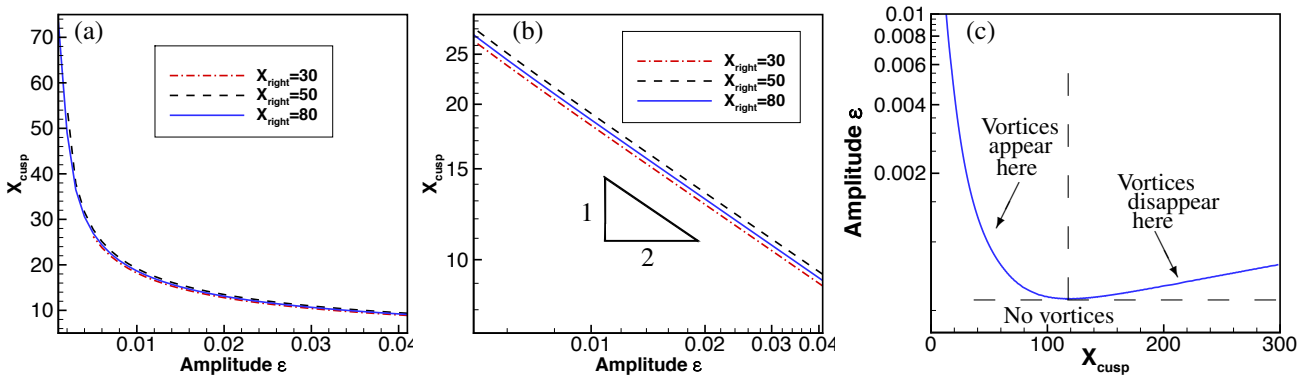

Figure 2: Dependence of the axial position of the cusp, $X_{\rm cusp}$, on the amplitude of the perturbation, ϵ for different channel lengths. (a,b): $X_{\rm right} = 30, 55, 80$; (c) $X_{\rm right} = 400$ (note the swapped axes).

Figs. 2(a,b) show how the axial position at which the vortex is created, $X_{\rm cusp}$, depends on the amplitude ϵ of the perturbation. Somewhat surprisingly, the plot suggests that a reduction in ϵ does not suppress the generation of new vortices but simply moves the position at which the vortices are created further and further downstream. The computations can, of course, only track $X_{\rm cusp}$ to the downstream end of the computational domain but Fig. 2(b) shows that, at least for channel lengths up to $X_{\rm right} = 80$ (which is much larger than the lengths considered in many other analyses of the Karman vortex street), this behaviour is independent of the domain length and, in fact, very well described by a power-law, $X_{\rm cusp} \sim \epsilon^{-1/2}$.

It is easy to show that this behaviour is only possible if the vorticity associated with the base flow, $\overline{\omega}$, decays more quickly in the streamwise direction than that associated with the perturbation, $\widehat{\omega}$. An inspection of the vorticity fields confirms that, for the domains considered in Figs. 2(a,b), this is indeed the case. However, computations in even longer domains (up to $X_{\rm right} = 400$) show that even further downstream the relative size of the decay rates is reversed so that, sufficiently far downstream, the vorticity associated with the perturbation decays more quickly than that associated with the base state, resulting in the behaviour shown in Fig. 2(c) (note the swapped axes). This plot shows that, as originally expected, there does indeed exist a minimum value of the amplitude, $\epsilon_{\rm min}$, below which no vortices are created. If ϵ exceeds this threshold, the vorticity field develops a cusp at two instances during the period of the oscillation: once when/where the vorticity associated with the base flow has decayed sufficiently for the perturbation to create a new vortex via the mechanism discussed above; and then again further downstream when/where the vorticity associated with the perturbation has become too weak to sustain the most downstream vortex, causing it to disappear via a reverse cusp bifurcation. In Fig. 2(c) the two solution branches identify the upstream/downstream boundaries of the region within which vortices exist. The two branches meet at $\epsilon_{\rm min}$; for this value each newly created vortex is immediately annihilated, implying that this point is characterised by the convergence of two cusp bifurcations. We exploited this observation to compute $\epsilon_{\rm min}$ directly from the two vorticity fields.

References

[1] Williamson, C. H. K. *Vortex dynamics in the cylinder wake*, Annu. Rev. Fluid Mech. **28**, 477–539 (1996).

[2] Brøns, M., Jakobsen, B., Niss, K., Bisgaard, A. V. & Voigth, L. K. *Streamline topology in the near wake of a circular cylinder at moderate Reynolds numbers*, J. Fluid Mech. **584**, 23–34 (2007).

[3] Mathis, C., Provansal, M. & Boyer, L. *The Benard-Von Karman instability: an experimental study near the threshold*, J. Physique Lett. **45**, L-483 – L-491 (1984).

[4] Heil, M. & Hazel, A. L. `oomph-lib` – *An Object-Oriented Multi-Physics Finite-Element Library.* In: Fluid-Structure Interaction, Editors: M. Schafer und H.-J. Bungartz. Springer (Lecture Notes on Computational Science and Engineering), pp. 19–49, (2006). `oomph-lib` is available as open-source software at `http://www.oomph-lib.org`.

AN ANALYSIS OF VORTICITY FORCE VERSUS PRESSURE-FRICTION FOR INCOMPRESSIBLE FLOW

Kuan-Ruei Lai[1], Chien-Cheng Chang[1,2,a)], Chin-Chou Chu[1,a)] & Meng-Tian Song[2]
[1]*Institute of Applied Mechanics and Centre of Advanced Studies in Theoretical Sciences, National Taiwan University, Taipei 106, Taiwan*
[2]*Colleges of Civil Engineering and Mechanical Engineering, Guangxi University, Nanning 530004, China*

Abstract. Over the years, we have proposed a force decomposition to quantify the contributions to the forces exerted on the plate in terms of all the fluid elements with nonzero vorticity. This presentation is aimed to illustrate the usefulness that the force element analysis complements the traditional analysis based on pressure and friction. An example of flow over a delta wing is provided to examine various contributions to the forces on an impulsively started finite plate from the perspective of a force-element representation. The present vorticity force analysis (VFA) was made parallel to the pressure force analysis (PFA) by examining the sectional force contributions along the wing span, but can further extend to include the outer regions of tip vortices.

Introduction. A vorticity force theory is most applicable to flow abundant in vortices. Counter-rotating tip vortices are an important aerodynamic feature of wings of finite span due to the pressure difference between the upper and lower wing surfaces. Tip vortices can cause undesirable noise and vibrations as well as induce downwash, which increases the drag force on the wing. In recent years, research in tip vortices has shifted into low-Reynolds-number flows for understanding of animal locomotion with applications to development in micro air vehicles (MAVs) and small unmanned aerial vehicles (UAVs). Because the wing geometry of animal wings and fins typically has a low aspect ratio (LAR), the induced flow is unsteady, and the influence of tip flow is obviously significant. As a model problem, impulsively started LAR plates at low Reynolds number can provide an in-depth research relevant to the design of small aircraft and the aerodynamics of animal locomotion.

In spite of the many important studies on LAR-plate aerodynamics, a quantitative analysis that can identify the primary aerodynamic forces and relate them to individual vortex structures is still lacking. In the literature, there are several useful force theories that shed light on different aspects of hydrodynamic or aerodynamic forces. Circulation theory was an early effort toward predicting lift, which provided insightful relationships between forces and inviscid models in terms of boundary layer separation, vortex shedding, and conservation of circulation. Subsequent studies were meant to provide exact means or theories for hydrodynamic forces through a rigorous analysis of the equation for viscous flow, in particular, ideas that validate a separation of hydrodynamic loadings into potential flow forces and vortex-flow forces. The applied force was deliberately explained as the rate of change of a momentum, defined by an absolutely convergent integral. In this study, we investigate the unsteady mechanisms of a LAR plate with different angle of attack at low Reynolds flows in terms of a diagnostic force theory (Chang 1992; Chang et al. 2008; Hsieh et al. 2010, Lee et al. 2012). The force representation theory for real viscous flow is used to separate potential forces such as added-mass and inertial forces and to distinguish the contributions of individual fluid elements to aerodynamic forces. The theory starts from the D'Alembert theorem that the incompressible potential flow predicts that no force will be exerted on a body if the incident flow is a constant uniform stream. Incompressible potential flow means that there is no single fluid element possessing nonzero vorticity or dilation. It is therefore considered that in a more realistic flow, any fluid element with nonzero vorticity or dilation may be considered a source of the hydrodynamic force.

Results & Discussion. There are four regions of distinguishable vortex structures (see Fig. 1 for illustration). Above all, it is noted that the LEV (leading-edge vortices) has a separation bubble in the x-y plane for sections near the middle span, and is connected to the tip vortices, the side edges where the roll-up structure contains a separation bubble above the plate in the y-z plane. First, the LEV contributes large positive lift elements, yet near the middle span, there are negative elements inside the separation bubble. Second, the part of each tip vortex above the extended plate contributes large positive lift elements, while along the downstream direction there is a developing region of negative elements inside each separation bubble. Third, we have strong positive elements in the two regions where the LEV and TiVs (tip vortices) interlink and rotate against each other. Fourth, the velocity field in the slender region just below the plate contributes substantially negative lift elements. The LEV, TiVs and TEV (trailing-edge vortices) are interwoven to form a complete vorticity-loop structure. As long as the loop structure is extending downstream the finite wing, its contribution to the lift is quickly diminished. The force-element approach is different from the classical aerodynamic theory. The latter considers the downwash flow of the tip vortices as the cause of reduction in the lift of a finite wing as compared to its 2D counterpart. The former, on the other hand, considers that, as there is no longer a genuinely 2D flow for a finite wing, it is more meaningful to examine directly the contribution from the TiVs to the lift. In other words, TiVs and LEV as sources of lift (and other force components) are considered on an equal basis; TiVs generated by the side edges, like LEV generated by the front edges, work collaboratively with LEV in

[a)] Corresponding author. Email: mechang@iam.ntu.edu.tw.

contributing lift. In the flow past a finite plate, not only is there spanwise (longitudinal) vorticity, but are also there vorticity components in the other two orthogonal (transverse) directions. In order to examine the three-dimensional effects, we provided two viewpoints: (i) sectional vorticity force distribution (C_{Dv}, C_{Lv}) contrasted with the traditional pressure force distribution (C_{Lp}, C_{Dp}), and (ii) the force credited to orthogonal (transverse) components (ω_x, ω_y, ω_z) contrasted with all of the total force (C_D, C_L) credited to all the vorticity components in the entire flow region as well as in the outer regions. It is noted that in the ideal case of two-dimensional flow, there are no outer regions, and C_{Lv}' and C_{Lp} are identical, and C_{Dv}' and C_{Dp} are identical. Both viewpoints based on the force element theory show distinguished differences at different AR and angles of attack, and between the early and later stages of flow development. Consider the lift force from viewpoint 1. At the lower AR=1, the sectionwise pressure force (SPF) is always larger than the sectionwise vorticity force (SVF) in the plate region. The deficit of SVF as compared to SPF in the plate region is made up by the positive SVF contribution in the outer regions. The difference between SPF and SVF is more conspicuous at large α. At the large AR=3, the SPF and SVF are usually small in the middle plate region; the discrepancy occurs near the outer edges of the plate. But the situation changes in the case of a large angle of attack (say, α=45°). In the initial transient, SVF may exceed SPF in the middle of the plate, and becomes much smaller towards the edges of the plate. In the nearly steady state, the difference is small in the middle region of the plate, and becomes large farther from this region. Consider the lift force from viewpoint 2. In the early stages just after the flow is started, the force component due to ω_z dominates other components in the plate region. But the other force components due to ωx and ω_y have also been developed in the outer region and may exceed the component of ω_z in magnitude. It is found that all the lift components due respectively to ω_x, ω_y and ω_z in the outer regions are positive, and the lift component due to ω_y is invariably the largest at the later time. At the larger AR=3, the lift components due to ω_x and ω_y are typically small in the middle plate region, but may exhibit negative contributions at the outer edges of the plate region. At a lower AR=1 but a larger α, the lift components due to ω_x and ω_y may become substantial in the plate region, though still small compared to that due to ω_z. It is reasonable to consider that ω_z is mainly contributed by the LEV, while ω_x and ω_y are contributed by the TiVs. The temporal variations of the relative importance of force contributions strongly depend on the interplay between the two vortex systems. (i) For the shorter plate (AR=1), the LEV is suppressed by the TiVs in the initial stage, and then develops gradually, extending its vorticity beyond the outer edges. (ii) For the longer plate (AR=3), the TiVs are initially suppressed by the strong LEV, but have more room for development in later stages as the LEV weakens in strength because of diffusion. As a final remark, the VFA for assessing the relative importance of individual force contributions can be pursued for all kinds of finite wings by relating the flow features directly to the aerodynamics forces that have no two-dimensional counterparts, such as those of a delta wing and of many natural flights.

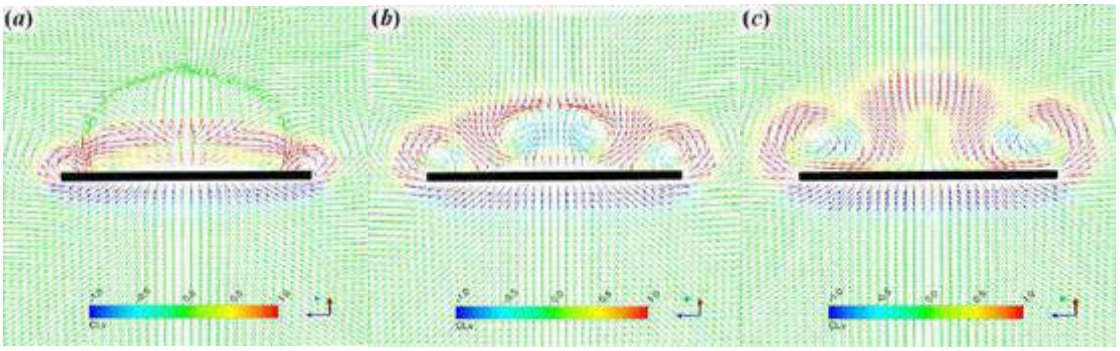

Figure 1. The scales are chosen to be the chord length L, and the time L/U, where L is the chord length and U the incoming flow velocity in the x-direction. The plots show the y-z plane velocity vectors colored by the volume lift elements at various chordwise locations for the AR=1 plate with α=45°, Re=300 at t=1.4: (a) x=0.14 (b) x=0.35 (c) x=0.57. First, the LEV contributes large positive lift elements, yet near the middle span, there are negative elements inside the separation bubble. Second, the part of each tip vortex above the extended plate contributes large positive lift elements, while along the downstream direction there is a developing region of negative elements inside each separation bubble. Third, we have strong positive elements in the two regions where the LEV and TiVs interlink and rotate against each other. Fourth, the velocity field in the slender region just below the plate contributes substantially negative lift elements. Note that at this low Reynolds number, although the contribution from the vorticity within the flow dominates, the surface vorticity contribution is not negligible, typically ranging from 10 to 30% contribution to the lift.

References

Chang, C.C. (1992) Potential flow and forces for incompressible viscous flow. *Proc. R. Soc. A-Math. Phys. Eng. Sci.* **437**, pp. 517-525.

Chang, C.C., Yang, S.H. & Chu, C.C. (2008) A many-body force decomposition with applications to flow about bluff bodies. *J. Fluid Mech.* **600**, pp. 95-104. .

Hsieh, C.T., Kung C.F., Chang, C.C. & Chu, C.C. (2010) Unsteady aerodynamics of dragonfly using a simple wing-wing model from the perspective of a force decomposition. *J. Fluid Mech.* **663**, pp. 233-252

Lee JJ, Hsieh CT, Chang CC & Chu CC (2012) Vorticity forces on an impulsively started finite plate. Journal of Fluid Mechanics 694, 464-492.

FREE SURFACE VORTEX INSTABILITY IN MAGNETICALLY DRIVEN LIQUID METAL SWIRLING FLOW

Sergio Cuevas[1a)], J. Carlos Domínguez-Lozoya[1] , Michel Rivero[2] & Eduardo Ramos[1]
[1] *Universidad Nacional Autónoma de México, Renewable Energy Institute, Temixco, Morelos, Mexico*
[2] *Instituto Tecnológico de la Laguna, División de Posgrado e Investigación, Torreón, Coahuila, Mexico*

Summary We describe experimental observations of a free surface vortex instability in a shallow liquid metal layer driven by different arrays of rotating magnetized bars located underneath the bottom of a cylindrical container. For layer thicknesses smaller than a certain threshold, the swirling vortex flow created by induced Lorentz forces reveals a spontaneous instability for specific magnet rotation frequencies, leading to the opening of the free surface and the formation of regular structures that rotate stably with a speed about one order of magnitude lower than the magnets. An ellipse and a triangle are observed for one and three rotating magnets. When four or five magnets are used, transient polygons with the same number of corners appear on the deformed surface at the initial stages of spin-up. It is suggested that the formation of the structures is a consequences of resonant interactions between gravity and centrifugal waves.

INTRODUCTION

Electromagnetic stirring offers a non-intrusive method for vortex flow generation in electrically conducting fluids. It consists in the production of driving Lorentz forces in a conducting fluid by the interaction of induced or applied electric currents with an external magnetic field. With this method, free surface vortex flows that resemble geophysical phenomena have been created in swirling liquid metal flows. For instance, the spin-up of a tornado-like vortex in a cylindrical liquid metal column has been generated by two flow-independent magnetic forces, produced by a combination of a rotating magnetic field and a vertical traveling magnetic field [1]. In the formation of vortex structures in swirling flows, the height of the fluid column is an important parameter. The question then arises as to how is the vortex flow structure changed by decreasing the fluid height. In fact, it has been reported that symmetry-breaking transitions can appear in swirling flows with a free surface. Experiments conducted in a cylindrical container with water and rotating bottom plate have shown that for certain fluid heights and rotation frequencies, a rotationally symmetric surface spontaneously deforms into a rotating polygonal structure [2-4]. The instability has been explained in terms of resonant interactions between gravity waves on the outer part of the surface and centrifugal waves on the inner part [5]. In the present contribution, instead of using rotating and traveling magnetic fields, liquid metal vortex flows are generated by different arrays of rotating magnetized bars located beneath the bottom of a cylindrical container. If the layer thickness is sufficiently small, the free surface of the induced vortex flow is drastically deformed for specific rotation frequencies giving place to regular shapes that rotate uniformly.

EXPERIMENTAL SETUP AND RESULTS

The experimental setup consists of a fixed acrylic cylindrical container (L=101 mm radius) with a shallow layer (6-9 mm thickness) of eutectic alloy GaInSn. Underneath the bottom wall of the cylinder an array of one, three, four, or five rectangular permanent magnets ($6\,\mathrm{cm} \times 1.27\,\mathrm{cm} \times 1.27\,\mathrm{cm}$) are placed radially and equidistantly on a rotating external acrylic disc coupled to an electric motor. The bars are uniformly magnetized perpendicularly to a pair of the faces of greater area. The Reynolds number based on the maximum rotation frequency of the magnets ($\Omega = 7\mathrm{Hz}$) is $\mathrm{Re} = \Omega L^2/\upsilon = 2\times10^4$, where υ is the kinematic viscosity, while the maximum Hartmann number is $\mathrm{Ha} = B_0 h\sqrt{\sigma/\rho\upsilon} = 22$, where B_0 is the maximum magnetic field strength and h is half the layer thickness. Experiments, performed with each magnet array for different layer thicknesses, started with the fluid at rest increasing the rotation frequency in the range 0-7.5 Hz until the appearance of the instability. Ultrasonic Doppler Velocimetry measurements were obtained previously to the emergence of the instability. The rotating magnetized bars acted as *magnetic blades,* producing initially a swirling flow and suddenly the free surface vortex touches the floor of the vessel and a region void of liquid metal is formed. To illustrate this phenomenon, we show in figure 1a) four snapshots taken with one magnet spinning at 7.5 Hz. It was observed that the liquid metal rotates with a frequency of 0.25 Hz. The images in the figure show a structure of an ellipse with waves of small amplitude running near the edge. Also, hysteresis was observed as the magnet spin velocity was increased or decreased. Actually, as the angular velocity of the magnets is decreased, a circular structure rotating eccentrically was observed. The dynamic behavior is summarized in figure 1b) and suggests that the phenomenon can be described as a subcritical bifurcation.

[a)] Corresponding author. Email: scg@ier.unam.mx.

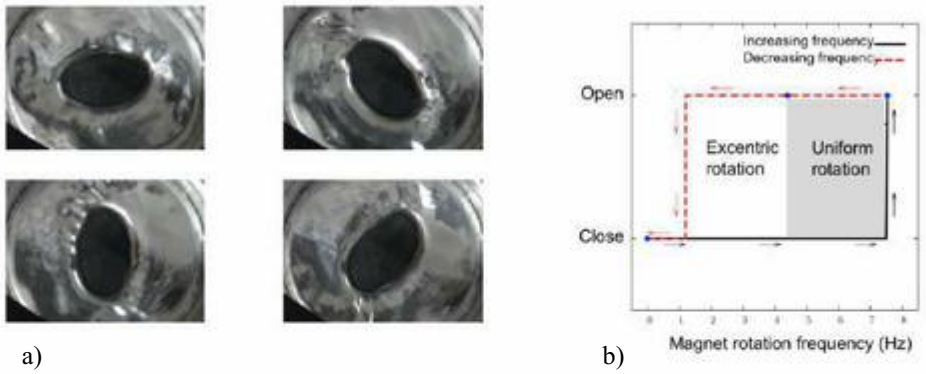

a) b)

Figure 1. a) Snapshots of ellipses formed with one rotating magnet at 6 Hz. b) Hysteresis as the rotation frequency increases or decreases.

Figure 2 shows snapshots of vortical flows formed with three, four, and five rotating magnets, respectively. The first corresponds to a stable rotating triangle. The formation of the polygonal structure on the free surface is not a smooth process; the structure appears in a small time scale compared to the rotation of magnets once the threshold of the magnet spin has been reached. With four and five magnets (figs. 2b-c), square and pentagon shapes are formed instantly on the free surface at the initial stages of the spin-up; these structures are unstable and eventually the open surface evolves towards a stable rotating triangular structure.



a) b) c)

Figure 2. Polygonal structures formed on the liquid metal free surface with three a), four b), and five c) rotating magnets.

CONCLUSIONS

In this contribution, we describe the formation of polygons in free surface flows similar to those observed before in water flows driven by rotating the bottom plate of a partially filled, fixed cylindrical container [2-4]. Although in the present study the rotation is promoted by a body force rather than by a rotating boundary, the physical effects that produce the polygon instability are closely related. In the present case, the azimuthal Lorentz force generates a swirling motion that in turn originates the free surface instability. Non-uniformity of the applied magnetic field seems to play a role in the appearance of the instability although, just as in the rotating boundaries case, the formation of polygons can be attributed to the resonance of gravity and centrifugal waves at the free surface [5].

Acknowledgment. Work supported by CONACYT, Mexico, under project 240785.

References

[1] Vogt T., Grants I., Eckert S., Gerbeth, G.: Spin-up of a magnetically driven tornado-like vortex. *J. Fluid Mech*. **736**: 641-662, 2013.

[2] Vatistas, G. H.: A note on liquid vortex sloshing and Kelvin's equilibria. *J. Fluid Mech*. **217**, 241,1990.

[3] Jansson T. R. N., Haspang M. P., Jensen K. H., Hersen P., Bohr T.: Polygons on a rotating fluid surface, *Phys. Rev. Lett.* **96**, 174502, 2006.

[4] Bergman R., Tophoj L., Homan T. A. M., Hersen P., Andersen A., Bohr T. Polygon formation and surface flow on a rotating fluid surface, *J. Fluid Mech*. **679**, 415-431 2011.

[5] Tophoj L., Mougel J., Bohr T., Fabre D.: Rotating polygon instability of a swirling free surface flow, *Phys. Rev. Lett*. **110**, 194502, 2013

ON THE INFLUENCE OF END EFFECTS FOR STATIONARY AND VIBRATING CIRCULAR CYLINDERS

Sina Daneshvar[1] & Chris Morton[1a)]
[1]*Department of Mechanical and Manufacturing Engineering, University of Calgary, Calgary, Alberta, Canada*

Summary The flow development over stationary and oscillating circular cylinders with two distinct end conditions has been investigated experimentally for $2100 \leq Re_D \leq 7000$. The end conditions employed correspond to a free surface and a free end. For both the stationary and oscillating cylinder, near the free surface the wake vortices are oriented parallel to the cylinder axis. Circulation is preserved in this region with vortices terminating at the free surface. Near the free end the vortices cannot end abruptly in the fluid, hence, they must either incline towards the cylinder and maintain a direct connection to the free end (observed for 2S type shedding pattern) or they must form half-loop connections with adjacent vortices of the opposite sign (observed for the 2P type shedding pattern). The apparent changes in vortex dynamics due to differing end conditions may significantly influence the unsteady loading characteristics.

INTRODUCTION

Vortex shedding from circular cylinders has been a topic of interest in fluid mechanics for over a century. For a stationary cylinder, Williamson [1] affirmed that vortex shedding occurs from a circular cylinder for Reynolds numbers ($Re = UD/\nu$) greater than about 50. Depending on the Reynolds number, the vortex shedding may be laminar and two-dimensional, laminar and three-dimensional, or turbulent [1]. In addition, the flow behaviour can be affected by such other parameters as the cylinder's aspect ratio, roughness, and end conditions. When a cylinder is free to move in either the transverse or free stream direction, the vortex shedding can lead to vortex-induced vibrations (VIV). According to Williamson [2], for low mass-damping ratio, there are two abrupt changes in the amplitude of the cylinder's vortex induced oscillatory motion resulting enabling the classification of three branches: initial, upper, and lower branch. While VIV has been the subject of numerous studies over the last several decades, few studies have been dedicated to identifying the effect of cylinder aspect ratio, roughness, or end conditions. The present study aims to address the effects of some commonly employed end conditions on vortex shedding and VIV.

EXPERIMENTAL SETUP

Experiments were carried out in a water tunnel facility at the University of Calgary. The free stream turbulence intensity was measured to be less than 1% and the flow uniformity is within 2% for the full range of flow speeds tested, $0.05 \leq U \leq 0.4$ [m/s]. An image of the experimental setup is shown in Fig.1. As shown in the figure, an acrylic cylinder is fixed directly to a system of two air bearings mounted to parallel stainless steel rails and springs, facilitating the free oscillatory movement of the cylinder in the transverse (y) direction. The system was validated by measuring its amplitude response ($A^* = A/D$) across a wide range of reduced velocities ($U^* = U/f_N D$, where f_N is the natural frequency of the cylinder), as shown in Fig. 2. The results were found to be in good agreement with Williamson [2] for low mass-damping ratio.

Hydrogen bubble flow visualization technique is used to trace the flow pattern and highlight wake vortices. The hydrogen bubble wire is placed upstream of the cylinder, at a position of $(x/D, y/D) = (-1, -0.25)$, so that the bubbles pass over only one side of the cylinder. Using a Photonics DM40 pulsed laser coupled with two consecutive cylindrical lenses, a conical expanding volume of light is generated, illuminating the near wake of the cylinder (Fig.1). Images and videos were obtained using a Nikon 1V3 camera. Two boundary conditions are employed: a free surface at the top, and a free end at the bottom. This configuration provides the opportunity to investigate the effects of these two boundary conditions on the vortex dynamics. The flow behaviour is observed in four different scenarios: (i) the stationary cylinder, (ii) initial excitation branch, (iii) the upper branch, and (iv) the lower branch, as depicted in Fig. 2.

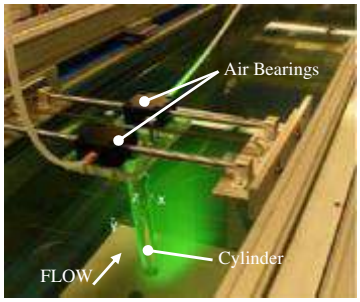

Fig. 1. Experimental setup. The cylinder aspect ratio is L/D = 16.

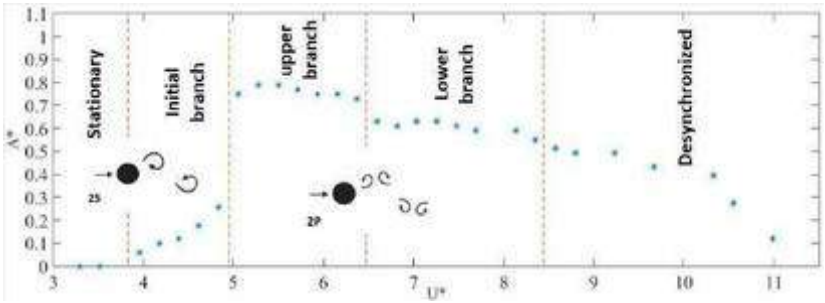

Fig. 2. Cylinder's amplitude response and vortex shedding modes in the wake versus flow's reduced velocity.

a) Corresponding author. Email: chris.morton@ucalgary.ca

DISCUSSION

The results are presented in Fig. 3 with instantaneous snapshots of flow visualizations. In all cases, the spanwise vortices form and are shed parallel to the cylinder axis near the free surface. In the vicinity of the free end, they tend to bend towards the cylinder and connect to the free end at formation. Downstream of formation the vortex connectivity is dependent on the nature of the vortex shedding pattern. For a stationary cylinder and in the initial branch of VIV (Fig. 2), the vortex shedding pattern is 2S (one single vortex is shed from each side of the cylinder periodically), while for upper and lower branch the vortex shedding pattern is 2P (pairs of opposite signed vortices are shed from each side of the cylinder periodically). The vortex patterns were confirmed via analysis of video records, and are in agreement with [2].

For the stationary cylinder (2S mode, Fig. 3a), the vortex shedding can be categorized into three main cells: (i) parallel shedding, which starts from the water level and continues to almost midspan. (ii) oblique shedding end cell, which terminates at the free end of the cylinder, and (iii) central cell, which joins the two aforementioned cells. The cellular vortex shedding is similar to that observed by Eisenlohr and Eckelmann [3], and has been attributed to the presence of the free end and its effect on the cylinders base pressure. It should be noted that the spanwise extent and vertical position of the central cell varies with time, and was observed to be linked to the relative phase alignment of the parallel shedding cell and end cell.

For the initial branch, (2S mode, Fig. 3b), parallel vortex shedding becomes more dominant along the cylinder span (cf. Figs. 3a and 3b). However, near the free end, in order to maintain the Helmholtz vortex theorems, the vortices must distort and stretch in order to connect to the free end. Subsequently shed vortices must either form looped connections with adjacent vortices on the opposite side of the wake, or connect directly to the free end. As shown in the visualization (Fig. 3b), the vortices appear to maintain connection to the free end, and rapidly break down due to the wake turbulence.

For the upper as well as lower branch (2P mode, Figs. 3c and 3d) the parallel vortex shedding continues with two vortices shed in close succession on one side of the wake, as depicted in Fig. 3c and 3d with vortices V1 and V2. Analysis of video records revealed that near the free end, each pair forms a half-loop connection to one another, which is depicted within the annotations in Fig. 3d. Moreover, no consistent secondary vortex connections were observed in video records, suggesting that for the cases studied the circulation of the vortices are similar in magnitude.

CONCLUSION

The vortex shedding from stationary and vibrating circular cylinders in the present study is highly three-dimensional due to the imposed free surface and free end boundary conditions. For a stationary cylinder, three vortex shedding cells form along the cylinder span. On the other hand, for a vibrating cylinder, a single cell forms, but near the free end there are significant changes in vortex dynamics. In particular, when a 2S mode of vortex shedding occurs from the cylinder (in either the stationary case or initial branch of VIV), the wake vortices connect to the free end of the cylinder, resulting in significant three-dimensional distortions of those vortices. When a 2P mode of vortex shedding occurs (in the upper and lower branch of VIV), vortices at the free end instead form half-loop connections in order to preserve circulation in the wake.

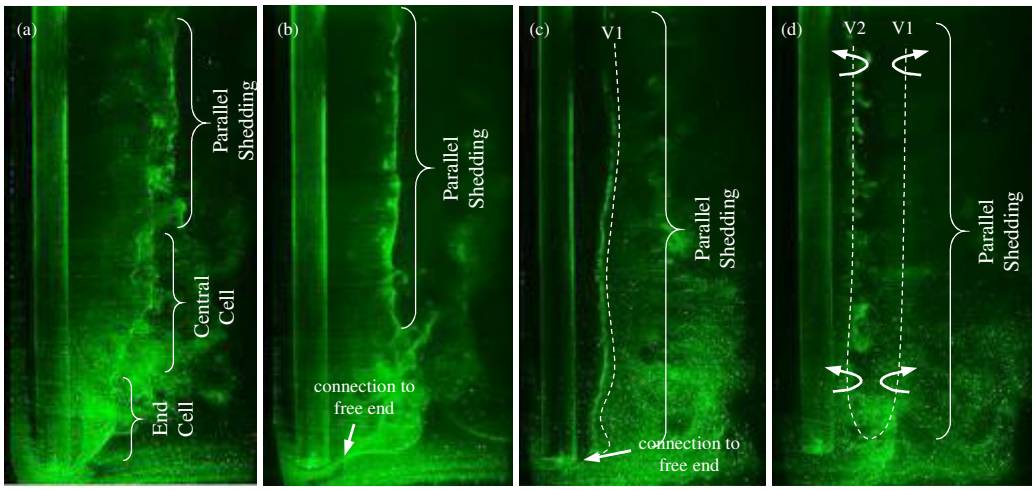

Fig. 3. (a) Stationary cylinder: three cells of vortices are observed, (b) Initial branch: near the free end, vortices bend in order to connect to the free end, (c) Upper/lower branch: connection of the vortex to the free end, (d) Upper/lower branch: looped connection between paired vortices.

References

[1] C.H.K Williamson. Vortex dynamics in the cylinder wake. Annu. Rev. Fluid. Mech. 28:477-539, 1996.

[2] C.H.K Williamson, R. Govardhan. Vortex-induced vibrations. Annu. Rev. Fluid Mech. 36:413–55, 2004.

[3] H. Eisenlohr, H. Eckelmann. Vortex splitting and its consequences in the vortex street wake of cylinders at low Reynolds number. Physics of Fluids A: Fluid Dynamics (1989-1993) 1, 189, 1989.

VORTEX STATISTICS FROM VORTICITY LOCAL PROPERTIES

José Hugo Elsas*[1] and L. Moriconi[1]

[1]*Instituto de Física, Universidade Federal do Rio de Janeiro*

Summary Systematic procedures for the identification of vortices/coherent structures have been proposed as a way to address their kinematical and dynamical roles in structural formulations of turbulence. We investigate how the known vortex identification criteria performs in controled numerical experiments, and pinpoint a number of relevant difficulties. These issues are addressed – and essentially solved – from the introduction of an alternative vortex identification criterion which is entirely based on local properties of the vorticity field.

INTRODUCTION

Turbulent flow is present in many natural and industrial systems, being prevalent in usual natural and industrial flows. Some examples include atmospheric, pipe and channel flow, which encompasses both free streaming and wall bounded flows. Furthermore, the question of whether or not organized structures exist in turbulent fluid remains open, despite long-standing discussions [1], and several arguments against turbulence as being merely a superposition of a sort of collored noise. A major problem in the study of such coherent structures arises in the difficulty in identifying them, which in turn restricts their usefulness as theoretical and practical tools.

We recently revised the main shortcomings of the swirling strength (Sw.St.) method, and have proposed an extension of this approach as an attempt to overcome current limitations of vortex identification methods. Here we explore the impacts of different procedures on the computed statistics of vortices on turbulent flows, as it would be necessary in the formulation of statistical models for the fluctuation of flow observables.

VORTEX IDENTIFICATION

Vortex identification methods that only rely on local information are limited, in a way or another, to the gradient of the velocity field. Three popular identification methods, the Okubo-Weiss Q-criterion [2], the Δ-criterion from Chong, Perry and Cantwell [3], and the λ_2-criterion from Jeong and Hussain [4], are equivalent for 2D incompressible flows. We chose to study, for simplicity, the Δ-criterion, or swirling strength, for bidimensional incompressible flows.

The starting point of the swirling strength is to analyse the eigenvalues of the velocity gradient $\nabla\mathbf{u}$, and to search for regions where its anti-symmetric part, which measures local rotation, dominates the symmetric, or shearing component, which appear when $\nabla\mathbf{u}$ has imaginary eigenvalues.

Swirling strength λ is the imaginary part of the eigenvalue of $\nabla\mathbf{u}$. For bidimensional incompressible flows, the eigenvalue equation reduces to:

$$\det(\nabla\mathbf{u} - \lambda) = \lambda^2 - \mathrm{Tr}(\nabla\mathbf{u})\lambda + \det(\nabla\mathbf{u}) = 0 \Rightarrow -\lambda^2 = \det(\nabla\mathbf{u}) \tag{1}$$

The usual swirling strength criterion identifies correctly a single vortex, but can greatly distort cases with multiple vortices, as in Fig. 1, or cases with vortices within background shear. Our modification, which we call "vorticity curvature criterion", consists in the calculation of the Sw.St. taking $\tilde{\mathbf{u}} = \nabla \times (\nabla \times \mathbf{u})$ instead of the real velocity field, and to correct the result by filtering spurious regions using the sign of $\omega \cdot \tilde{\omega} = -\,\omega \cdot \nabla^2\omega$, which should be positive only for the region over true vortices.

$$\lambda_\omega = \Theta(\omega \cdot \tilde{\omega})\Im(\sqrt{-\det \nabla\tilde{\mathbf{u}}});\;\; \Theta(x) = 1 \;\text{ if } x \geq 0 \;\text{ otherwise }\; 0 \tag{2}$$

*Corresponding author. Email: jhelsas@if.ufrj.br

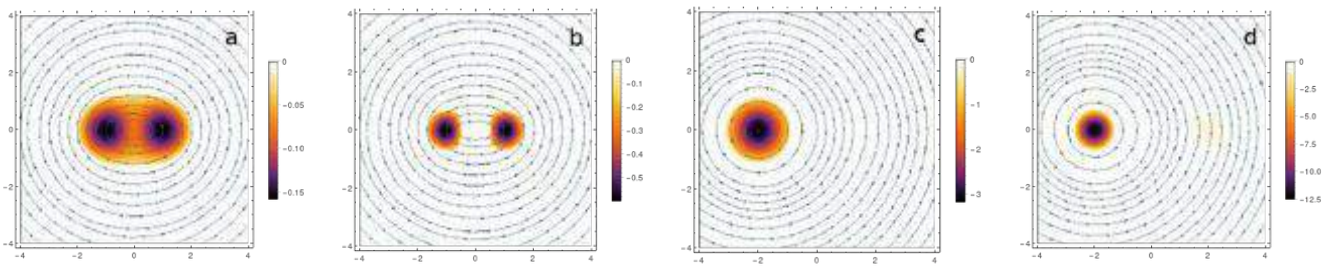

Figure 1: Streamlines of two Lamb-Oseen vortices, in different configurations, using the swirling strength λ and the vorticity curvature λ_ω in density plots. a) two close vortices, merged by λ; b) the same vortices as first, but resolved using λ_ω; c) two unequal vortices, $\Gamma_L/\Gamma_R = 20$, right vortex has zero λ, thus, it is not detected. d) same vortices as third, but with λ_ω, and both vortices are detected.

STATISTICS

Qualitative features of statistical observables in turbulent boundary layer can be recovered with a statistical model [5], in which, the detailed information on the flow is encoded in a probability distribution funcion (PDF) of vortices.

Our goal is to reliably retrieve this PDF from data, either through Direct Numerical Simulation (DNS) or Particle Image Velocimetry (PIV). To test for reliability, we compared these methods with Monte-Carlo tests, shown in Fig. 2. We compared the performance of the Sw.St. and of the vorticity curvature criterea with and without background shear.

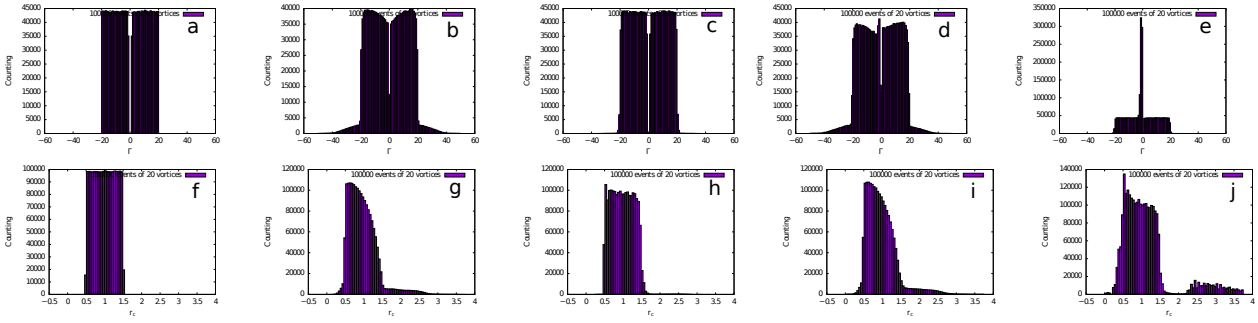

Figure 2: a) input circulations (circ.), b) output circ. from Sw.St., no shear, c) output circ. from V.C., no shear d) output circ. from Sw.St., weak shear, e) output circ. from V.C., weak shear, f) input radius, g) output radius from Sw.St., no shear, h) output radius from V.C., no shear, i) output radius from Sw.St., weak shear, j) output radius from V.C., weak shear

The first three columns show that vorticity curvature performs better than the original swirling strength for cases without background shear, but still has problems in presence of background shear, still making it inadequate for the treatment of boundary layer data.

References

[1] D.J.C. Dennis, Coherent structures in wall-bounded turbulence, Acad. Bras. Ciênc., 87, 2 (2015).
[2] A. Okubo, Deep-Sea Research, 1970, Vol. 17, pp. 445 to 454 (1969); J. Weiss Physica D 48 (1991) 273-294 (1990)
[3] M.S. Chong, A.E. Perry, and B.J. Cantwell, A general classification of threedimensional flow fields, Phys. of Fluids A 2, 765 (1990)
[4] J. Jeong and F. Hussain, On the identification of a vortex, J. Fluid Mech. (1995), vol. 285, pp. 69-94 (1995)
[5] L. Moriconi, Phys. Rev. E, 79, 046306 (2009).

ELLIPTICAL INSTABILITY OF THE MOORE-SAFFMAN MODEL FOR A TRAILING WINGTIP VORTEX

Jan Feys*[1] and Sherwin A. Maslowe [2]

[1]*Department of Mathematics and Statistics, McMaster University, Hamilton, Ontario, Canada*
[2]*Department of Mathematics, McGill University, Montreal, Quebec, Canada*

Summary In this study, the elliptical instability exhibited by two counter-rotating trailing vortices is considered. This type of vortex instability can be viewed as a resonance between two normal modes of a vortex and an externally imposed strain field. Recently, numerical investigations have extended earlier results that ignored axial flow to include models with a simple axial jet such as the similarity solution found by Batchelor [1]. Here, we present growth rates of elliptical instability for a family of velocity profiles found by Moore & Saffman [2]. These profiles involve a parameter n that depends on the wing loading, and are therefore capable of modelling both the jet-like and wake-like axial flow present in a trailing vortex at short and intermediate distances behind the wingtip. A direct numerical simulation is performed using an efficient spectral method in cylindrical coordinates developed by Matsushima & Marcus [3]. We compare our results to those for the Batchelor vortex.

INTRODUCTION

The recent introduction of large jetliners like the A380 has refocused attention on the study of the stability of the trailing wingtip vortex. In flight aircraft shed, from their wingtips, a counter-rotating pair of trailing vortices which represents a hazard to other air traffic, especially during take-off and landing. It is therefore important to understand the dynamics and stability of such vortex pairs. In this study we investigate the elliptical instability, which is a cooperative instability characterized by short wavelengths, for a realistic model of the trailing vortex described in Moore & Saffman [2].

Since Moore & Saffman [4], the mechanism underlying the elliptical instability is recognized to be one of resonance — see Kerswell [5] for a review. The vortical flows of interest here include an axial mean flow component $W(r)$ as well as a swirl component $V(r)$. Most investigations have made restrictive assumptions, such as a specific swirl profile and an absence of axial flow. An exception is the work by Lacaze et al. [6] that examines the model introduced by Batchelor [1]:

$$V(r) = \frac{1}{r}\left(1 \circ \exp\left(\circ\, r^2\right)\right), \quad W(r) = W_0 \exp\left(\circ\, r^2\right).$$

Batchelor's model, however, can not account for the diversity of axial flow present in trailing vortices; as Spalart [7] points out, the relative axial velocity in a trailing vortex can be directed towards the airplane (wake-like) or away from it (jet-like).

THE MOORE-SAFFMAN VORTEX

Moore & Saffman [2] employed the viscous light-loading approximation to estimate the effects of viscosity. Denoting the azimuthal and axial velocity profiles $V_n(\eta)$ and $W_n(\eta)$, outside of the viscous core

$$V \sim \beta r^{-n}, \quad \text{and} \quad W \sim \frac{\beta^2}{2W_\infty}\left(\frac{1}{n} \circ 1\right) r^{-2n} \text{ as } r \to 0.$$

The similarity variable $\eta = \circ\, r^2 U/4\nu z$, where U is the speed of the wing in a fixed frame. The parameter n is important, as it depends on the wing loading and, indirectly, on angle of attack. Varying n controls the amount of jet-like and wake-like flow (see figure 1). Special cases are $n = 0$ (a delta wing configuration), $n = 1/2$ (elliptic wing loading) and $n = 1$ (Batchelor profile). Feys & Maslowe [8] examined the linear inviscid stability of this model.

GOVERNING EQUATIONS AND NUMERICAL APPROACH

We consider a Moore-Saffman vortex deformed by an externally imposed stationary dipolar strain field of strength ε. The incompressible Navier-Stokes equations are linearized about this mean flow and solved numerically using a spectral method in cylindrical coordinates. In the axial direction, we perform a Fourier expansion into modes with axial wavenumber k. In the perpendicular plane, we employ a method due to Matsushima & Marcus [3] which involves expanding all perturbation quantities into associated Legendre polynomials. A random initial perturbation field is evolved in time and the growth rate ω_i of each azimuthal Fourier mode is obtained by tracking its energy.

*Corresponding author. Email: jan.feys@mail.mcgill.ca

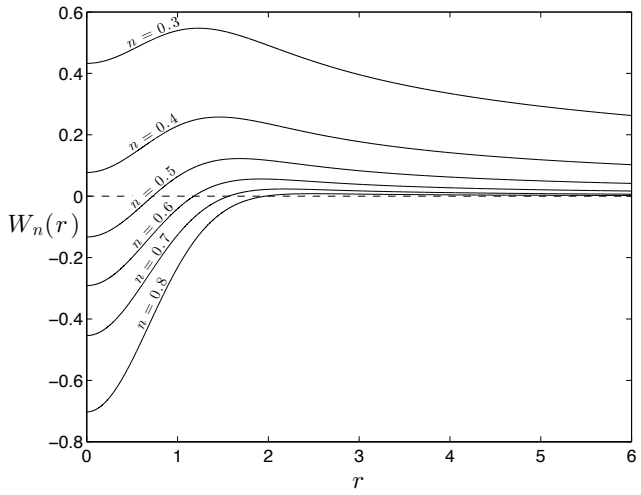

Figure 1: The axial velocity component $W_n(r)$ of the Moore-Saffman vortex.

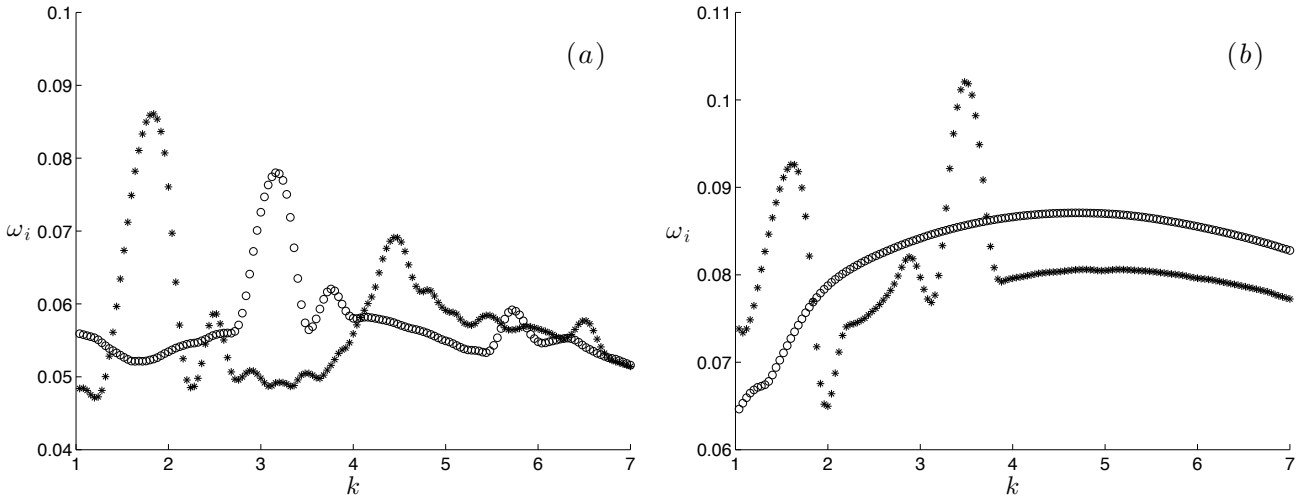

Figure 2: The growth rate ω_i as a function of the axial wavenumber k for the Moore-Saffman vortex with (a) $n = 0.95$ and (b) $n = 0.70$. The flow parameters are $\varepsilon = 0.0625$, $W_0 = 0.482$ and $Re = 3180$. Results for odd and even azimuthal wavenumbers are represented by stars and circles, respectively.

RESULTS AND CONCLUSIONS

The influence of n on ω_i is our primary point of interest. Figure 2 shows findings for a representative set of flow parameters. Several resonant parabolae are visible in (a), with peak amplification rates close to those for the Batchelor vortex. When n is decreased, in (b), the elliptical modes of instability are instead organized on a wide arc, i.e. a continuum of modes appears. Further, the growth rate of the unstable modes increases; we recover $n \simeq 0.44$ as being a particularly unstable value of the wing loading parameter. Finally, we find that varying n causes the dominant pair of azimuthal wavenumbers to shift from $(m_1, m_2) = (\circ\, 1, 1)$ to other modes such as $(\circ\, 2, 0)$ and $(\circ\, 3, \circ\, 1)$. The case $n = 0.50$ will be discussed further in the talk.

References

[1] Batchelor, G.K.: Axial flow in trailing line vortices. J. Fluid Mech. 20:645-658, 1964.

[2] Moore, D.W., Saffman, P.G.: Axial flow in laminar trailing vortices. Proc. R. Soc. London Ser. A 333:491-508, 1973.

[3] Matsushima, T., Marcus, P.S.: A spectral method for unbounded domains. J. Comput. Phys. 53:321-345, 1997.

[4] Moore, D.W., Saffman, P.G.: The instability of a straight vortex filament in a strain field. Proc. R. Soc. London Ser. A 346:413-425, 1975.

[5] Kerswell, R.R.: Elliptical instability. Ann. Rev. Fluid Mech. 34:83-113, 2002.

[6] Lacaze, L., Ryan, K., Le Dizès, S.: Elliptical instability in a strained Batchelor vortex. J. Fluid Mech. 577:341-361, 2007.

[7] Spalart, P.R.: Airplane trailing vortices. Ann. Rev. Fluid Mech. 30:107-138, 1998.

[8] Feys, J., Maslowe, S.A.: Linear stability of the Moore-Saffman model for a trailing wingtip vortex. Phys. Fluids 26:024108, 2014.

CHARACTERISTICS OF EIGEN-VORTICAL-AXIS LINES

Hideki Hasegawa[1] & Katsuyuki Nakayama[2a)]
[1]*Division of Mechanical Engineering, Graduate School of Mechanical Engineering, Aichi Institute of Technology, Toyota, Aichi, Japan*
[2]*Department of Mechanical Engineering, Aichi Institute of Technology, Toyota, Aichi, Japan*

Summary Characteristics of eigen-vortical-axis line defined as a vortical axis is investigated by tracing plural lines as a bundle in a vortical region and compared with the vorticity line. It shows that this line follows along a vortical core region with strong intensity of swirling or vorticity where the some vorticity lines may deviate from. On the other hand, in the outer area of the core region, eigen-vortical-axis line may deviate or be diffuse, whereas a bundle of the vorticity lines seem to have a similar feature in the direction. The orbit of eigen-vortical-axis line is robust in the vortical core region.

INTRODUCTION

Vortices are important subjects to be analysed in many turbulences. Since the universal definition of a vortex has not been established, several definition or identification methods have been proposed for a vortex and vortical axis in terms of a physical aspect of them. Identification of a vortical axis may be expected to follow the core region of a vortex and have a specific feature of vortices such as pressure minimum. The local flow topology specified by the velocity gradient tensor $\nabla \boldsymbol{v}$ has been used to categorize the invariant flow pattern (topology) in turbulences, and associated with several vortex definitions. A vortical axis where the tangent vector is parallel to the axis of the local vortical flow topology specified by $\nabla \boldsymbol{v}$ has been defined as "eigen-vortical-axis line" [1]. It has been shown that this line follows a core region of a vortex where the vorticity line deviates [1-3]. In addition, this line can follow the intense pressure minimum region [3] specified by the Q-definition or the integrated vortex definition of the Δ-, Q- and λ_2-definitions [4], whereas the pressure minimum axis derived from the eigenvector of the pressure Hessian in the λ_2-definition fails to follow this region [5]. On the other hand, the eigen-vortical-axis line is specified as a line that passes an arbitrary point in a vortical region where $\nabla \boldsymbol{v}$ has complex eigenvalues, and uncountable lines can exist such as vorticity line in the velocity field. The present study identifies plural eigen-vortical-axis lines in a vortical region as a bundle, and investigates its feature, comparing with that of the vorticity line.

EIGEN-VORTICAL-AXIS LINE

In three dimensional and instantaneous velocity field, if $\nabla \boldsymbol{v}$ has complex conjugate eigenvalues $\varepsilon_R \pm i\psi$ (i: imaginary number) and their eigenvectors $\boldsymbol{\xi}_{pl} \pm i\boldsymbol{\eta}_{pl}$, and a real eigenvalue ε_a and its eigenvector $\boldsymbol{\zeta}$, then the local flow orbit around the considered point can be represented as $\boldsymbol{x} = 2\exp(\varepsilon_R t)\{\cos(\psi t)\boldsymbol{\xi}_{pl} - \sin(\psi t)\boldsymbol{\eta}_{pl}\} + \exp(\varepsilon_a t)\boldsymbol{\zeta}$, which indicates that vortical flow swirls in the plane defined by $\boldsymbol{\xi}_{pl}$ and $\boldsymbol{\eta}_{pl}$ and proceeds along an axis $\boldsymbol{\zeta}$ [6]. Then $\boldsymbol{\zeta}$ represents the local axis direction of the vortical flow, and an eigen-vortical-axis line (referred to as EVAL hereafter) $\boldsymbol{\alpha} = [\alpha_i]$ (i = 1, 2, 3) can be defined from the following equation:

$$\frac{d\alpha_1}{\zeta_1} = \frac{d\alpha_2}{\zeta_2} = \frac{d\alpha_3}{\zeta_3} \tag{1}$$

EVAL can be defined in a vortical region where $\nabla \boldsymbol{v}$ has complex eigenvalues, and is traced along $\boldsymbol{\zeta}$ from a point in a region.

NUMERICAL ANALYSIS

Vortical axes are analysed in isotropic homogeneous decaying turbulence in DNS (Direct Numerical Simulation) where the pseudo-spectral method with the phase shifting method is applied [1, 3]. It is noted that all vorticity lines and EVALs are traced from (initial) points in vortical regions, and, from one point, both vorticity line and EVAL are traced so that these two lines pass through the same point. The tracing is terminated when they reach at non-vortical region. Figure 1 shows plural EVALs and vorticity lines in a sub-region in DNS where the Taylor Reynolds number $Re_\lambda = 35$. The color on axes denotes the contour of the swirlity φ [6] that indicates the uniformity and intensity of azimuthal flow in terms of the geometric mean (note $\varphi = \psi$), and φ is nondimensionalized by its root mean square value at the corresponding time.

Figure 2 shows a bundle of EVALs and vorticity lines in the same vortical region located in the sub-region in Fig. 1, with isosurface of φ =2. Both EVALs and vorticity lines are traced with the same points in the lower part of the vortical region. EVALs show that they follow the vortical core region with intense φ. The vorticity lines similarly follow the

a) Corresponding author. Email: nakayama@aitech.ac.jp.

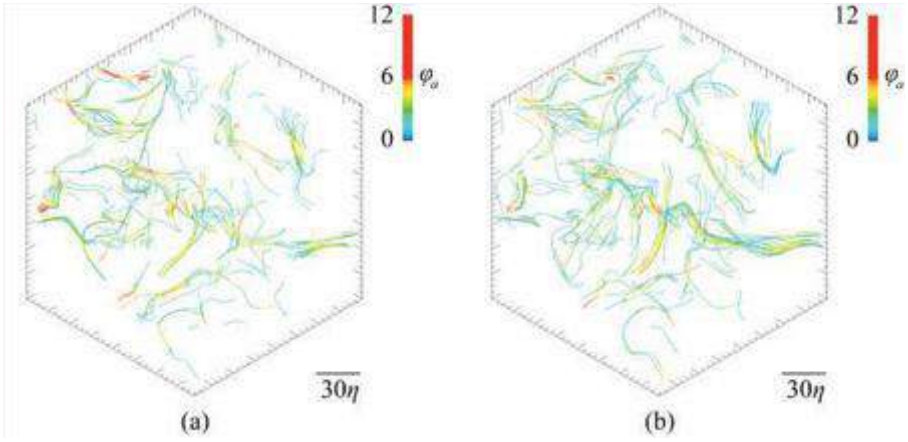

Fig. 1: (a) EVALs and (b) vorticity lines in a sub-region.

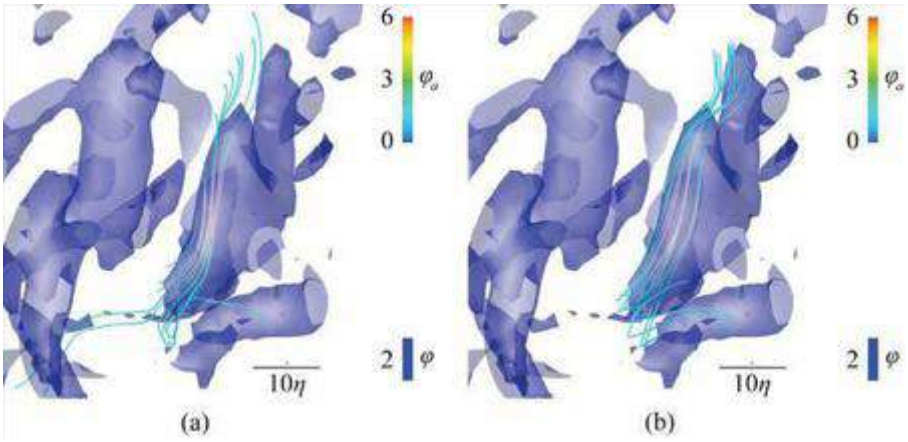

Fig. 2: Bundles of (a) EVALs and (b) vorticity lines in the same vortical region located in Fig. 1, with isosurface of φ =2.

core region, however, φ on the several lines is not as high as that on EVALs, and some line deviates from the isosurface of φ =2. Then (the bundle of) EVAL is robust in its characteristics, in the core region. On the other hand, both lines meander at the outside of the isosurface, and EVALs trace in several directions. It is noted that the direction of $\boldsymbol{\zeta}$ is influenced by vorticity components parallel to the swirl plane. In weak vortical region, vorticity vector may have diversity rather than a uniform feature in the core region, then the vorticity lines meander, and EVAL may be influenced more than the vorticity lines and then diffuse.

CONCLUSIONS

The eigen-vortical-axis line was investigated in terms of the feature of its bundle. The feature of the eigen-vortical-axis line as a vortical axis in the vortical core region is robust, and follows the intense swirlity region. On the other hand, in outer region of the core region, the characteristic of the eigen-vortical-axis line is not robust and may be diffuse.

References

[1] Nakayama, K., Hasegawa, H.: A numerical method of tracing a vortical axis along local topological axis line. *AIP Proc.* (ICNAAM2015), (in press).

[2] Nakayama, K., Hasegawa, H.: A Vortical Axis Tracing and its Feature in Isotropic Homogeneous Turbulence. *Proc. ICFD2015*, 2015.

[3] Nakayama, K., Hasegawa, H.: Relationships between eigen-vortical-axis line and vorticity line. *IUTAM symp. 2016 Venice*: (submitted).

[4] Nakayama, K., Sugiyama, K, Takagi, S.: A unified definition of a vortex derived from vortical flow and the resulting pressure minimum. *Fluid Dyn. Res.* **46**:055511, 2014.

[5] Hasegawa, H., Nakayama, K.: Pressure minimum feature of eigen-vortical-axis line in isotropic homogeneous turbulence. *Proc. 65th JSME Tokai*, (in press).

[6] Nakayama, K.: Physical properties corresponding to vortical flow geometry. *Fluid Dyn. Res.* **46**:055502, 2014.

FAR-FIELD WAKE BEHIND A ROTATING ELLIPSE AT A LOW REYNOLDS NUMBER

Ruifeng HU[1, a)]
[1]*School of Mechano-Electronic Engineering, Xidian University, Xi'an, China*

Summary Far-field wake pattern of flow past a rotating ellipse at a low Reynolds number Re = 200 was obtained by numerical computation. The effect of rotating speed was investigated over a wide range for the first time. Various different far-field wake patterns were observed. It is found that, at small rotating speeds, there exist apparent vortex sheet which is comprised of vortex dipoles or isolated vortices. At large rotating speeds, the shed vortices tend to strongly interact with each other and regular wake patterns no longer exist.

INTRODUCTION

The rotation of a thin foil around an axis perpendicular to inflow or plane of motion is widely existed in natural life or environment, e.g. freely falling plate or disk in tumble [1-3], autorotating wing [4], windborne debris [5], etc. However, so far we have little knowledge on the far-field wake patterns of flow past a rotating foil or wing. There are only several studies on this topic in the literature. Lugt & Ohring [6] computed two-dimensional flow past a rotating elliptic cylinder at α = 0.5 and α = 2.0 (where $\alpha=\omega c/2U$, ω is rotating speed, c is chord length and U is freestream velocity) and Reynolds number Re = 200. Lua *et al*. [7] performed an experimental measurement of the flow around a rotating elliptic foil using DPIV. In their experiment, the non-dimensional rotation speed α was set to be 0.417, 0.833, 1.667, and 2.5, and the Reynolds number was Re = 200 and 1000. Recently, the present author carried out computation of three-dimensional flow past a rotating wing at α = 0.417, 0.833 and 1.667, and the Reynolds number was Re = 200. None of the above studies provided detailed far-field wake patterns over a wide range of rotating speeds, but near wake evolutions at some selected conditions. Therefore, in this work, we made a much more comprehensive computational study on flow past a rotating ellipse at $\alpha \leq 1$ and Re = 200.

COMPUTATIONAL METHOD AND VALIDATION

The two-dimensional incompressible Navier-Stokes equation and the continuity equation were solved numerically by an opensource code Gerris [9]. Gerris adopts quadtree grid finite-volume method for spatial discretization in 2D. The fractional-step projection method is employed for time-advancing in Gerris. The numerical method was validated by computing the two-dimensional flow past a normal elliptical cylinder at Re = 200, and an appropriate grid setup for rotating ellipse problem was found. The aspect ratio of the normal elliptical cylinder is $\beta = b/a$ = 0.25, where b and a are the minor and major axis length of an ellipse, respectively. The computational domain extended between $-50 \leq x/a \leq 150$ and $-50 \leq y/a \leq 50$, of which the blockage was 1% to be small enough, the same as Thompson *et al*. [10]. Three tests of different maximum grid refinement level were carried out, namely 10, 11 and 12, and the refinement level at the solid surface was 13. Table 1 shows the computed mean and root-mean-squared values of aerodynamic coefficients and the Strouhal number at different maximum grid refinement level, as well as the computational result by Thompson *et al*. [10]. The differences between present computation and Thompson *et al*. [10] for the mean drag coefficient and the Strouhal number are less than 3% and 4%. Therefore, we adopted a maximum grid refinement level of 11 in present study, which was proved to be sufficient to give accurate results. Furthermore, we computed the two-dimensional flow past a rotating elliptical cylinder of β = 0.125 at α = 0.417 and α = 1.667, compared with the experimental measurement by Lua *et al*. [7] for validation. Excellent agreement between present computation and PIV measurement has been achieved (not given here due to space limitation). Thus, the numerical method and formulation used in present study were validated.

Table 1: Mean and root-mean-squared values of aerodynamic coefficients and the Strouhal number at different maximum refinement level.

Maximum refinement level	$C_{L,mean}$	$C_{D,mean}$	$C_{L,rms}$	$C_{D,rms}$	St
10	-0.0012	2.1366	0.3741	2.1397	0.1667
11	0.0017	2.2097	0.4096	2.2143	0.1613
12	-0.0003	2.1893	0.4133	2.1935	0.1613
Thompson *et al*. [10]	-	2.1615	-	-	0.1611

RESULTS

The computed wake vorticity fields of flows past a rotating ellipse with different rotating speeds at t^*=300 ($t^*=tU/a$) are displayed in figure 1. At the lowest non-dimensional rotating speed, i.e. α = 0.05, the wake is consisted of distinct vortex dipoles and isolated vortices, which are located below and above the centreline, respectively. There are also some weak vortices around the strong ones. A regular and approximately symmetric vortex street is observed at α = 0.10. Each side of the street is composed of vortex dipoles in a nearly staggered arrangement. When the non-dimensional rotating speed is

[a)] Corresponding author. Email: rfhu@xidian.edu.cn.

further increased to $\alpha = 0.15$, the vortex strength at the upper side of the street is apparently weakened. Moreover, the lower side of the vortex street tilts downwards from the centreline in a certain distance, or in other words the vortex street is not symmetric anymore. At $\alpha = 0.20$, similar wake pattern to that of $\alpha = 0.15$ is obtained, but the saturation distance for the tilt of the lower side street is obviously shorter. Another significant difference is that vortex dipole disappears while isolated vortices with the same sign arise at the upper side of the street. The wake tends to be irregular when the non-dimensional rotating speed is increased to $\alpha = 0.30$. At $\alpha = 0.40$ and 0.50, vortex streets arise again in the wakes and break up at some downstream distances. The critical broken up distance of $\alpha = 0.40$ is shorter than that of $\alpha = 0.50$. When the non-dimensional rotating speed is larger than 0.60, the vortices shed from the ellipse can hardly move downstream separately but strongly interact with each other, resulting in more and more complicated wake pattern, similarly as reported in a three-dimensional study by the present author [8].

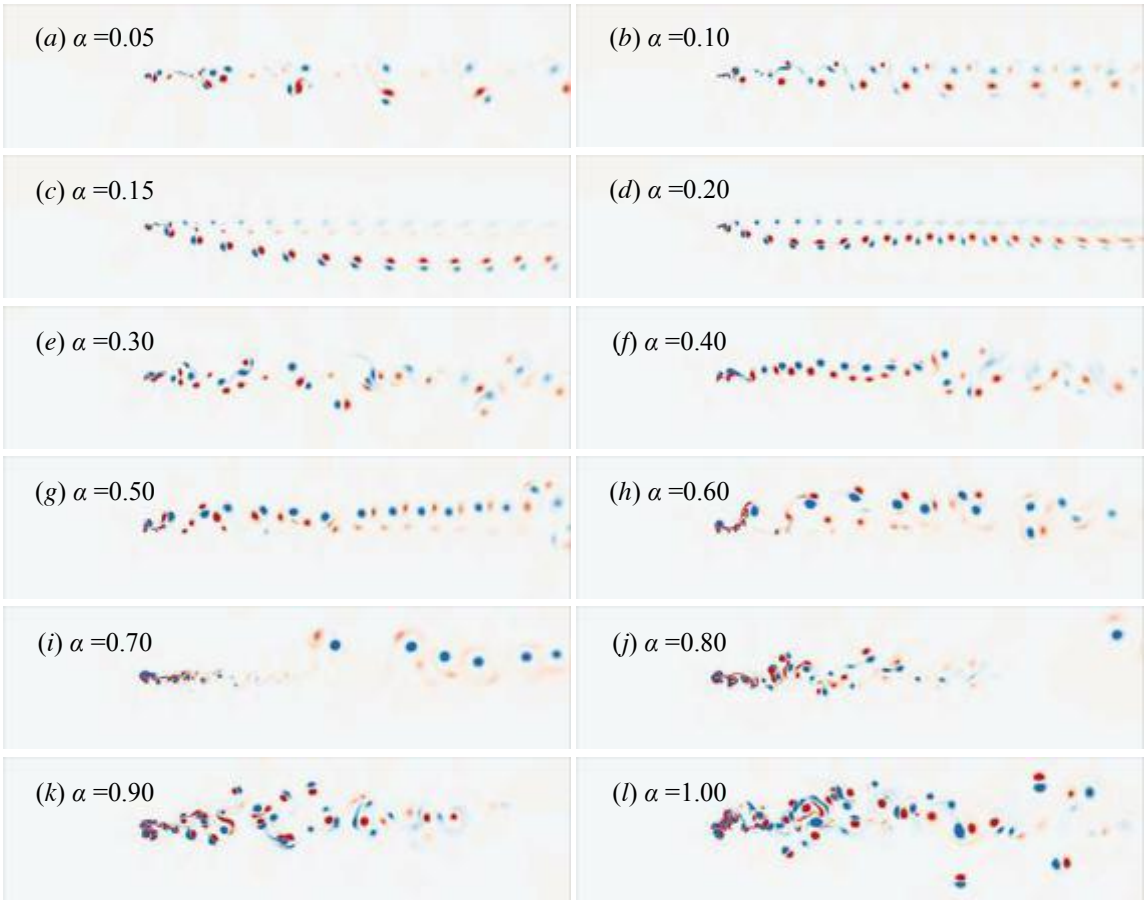

Figure 1: Wake vorticity fields at t^*=3.0

This work was supported by the National Science Foundation of China (Grant No. 11502185) and the Fundamental Research Funds for the Central Universities of China (Grant No. JB140418).

References

[1] Field S. B., Klaus M., Moore M. G., Nori F.: Chaotic dynamics of falling disks. *Nature* **388**: 252–254, 1997.
[2] Andersen A., Pesavento U., Wang Z. J.: Unsteady aerodynamics of fluttering and tumbling plates. *J. Fluid Mech.* **541**: 65–90, 2005.
[3] Wang W. B., Hu R. F., Xu S. J., Wu Z. N.: Influence of aspect ratio on tumbling plates. *J. Fluid Mech.* **733**: 650–79, 2013.
[4] Lugt H. J.: Autorotation. *Ann. Rev. Fluid Mech.* **15**: 123–147, 1983.
[5] Tachikawa M.: Trajectories of flat plates in uniform flow with application to wind-generated missiles. *J. Wind Eng. Ind. Aerodyn.* **14**: 443–453, 1983.
[6] Lugt H. J., Ohring S.: Rotating elliptic cylinders in a viscous fluid at rest or in a parallel stream. *J. Fluid Mech.* **79**: 127–156, 1977.
[7] Lua, K. B., Lim, T. T., Yeo, K. S.: A rotating elliptic airfoil in fluid at rest and in a parallel freestream. *Exp. Fluids* **49**: 1065–1084, 2010.
[8] Hu R. F.: Three-dimensional flow past rotating wing at low Reynolds number: a computational study. *Fluid Dyn. Res.* **47**: 045503, 2015.
[9] Popinet S.: Gerris: a tree-based adaptive solver for the incompressible Euler equations in complex geometries. *J. Comput. Phys.* **190**: 572–600, 2003.
[10] Thompson M. C., Radi A., Rao A., Sheridan J., Hourigan K.: Low-Reynolds-number wakes of elliptical cylinders: from the circular cylinder to the normal flat plate. *J. Fluid Mech.* **751**: 570–600, 2014.

SINGULAR-VALUE ANALYSES OF SYMMETRIC AND ASYMMETRIC PERTURBATIONES ON A CYLINDRICAL VORTEX SHHET

Toshihisa Itano[1]
[1]*Department of Earth and Ocean Sciences, National Defense Academy, Yokosuka, Kanagawa, Japan*

Summary The singular-value analyses of symmetric and asymmetric perturbations on a cylindrical vortex sheet is, instead of the eigenvalue analyses, investigated in order to reveal the form and growth rate of possible symmetric and asymmetric perturbations which give the maximum development during a finite evaluation time. Here, two types of norms are adopted: i.e. the *L*2 norm (the square root of the sum of amplitude squared) and the energy norm. The new formulation based on the precedent studies by Micalke & Timme (1967) and Rotunno (1978) enables us to obtain the singular-values and the following forward and backward singular-vectors analytically. The optimally-excited perturbations thus obtained indicate secure non-normal growth and significant norm dependency.

INTRODUCTION

Michalke & Timme [1] gave two types of models for a particular vortex, later known as a "multiple-vortex", where several secondary vortices are embedded in their parent vortex and revolve around its center. The first model is a vortex consisting of "ring-shaped" piecewise-constant vorticity regions. Especially, in their analysis, a solidly rotating core surrounding by a high vorticity ring is focused. Meanwhile, the second model is a cylindrical vortex sheet, where the vorticity is zero except at the cylindrical region of infinitesimal thickness whose vorticity is infinite. They performed linear stability analyses of the proposed models against symmetric and asymmetric perturbations to explain the destabilization of the parent vortices and possible formation of the multiple-vortex structure. As for the second model of Michalke & Timme, Rotunno [2] later added the axial flow inside and outside of the cylinder after correcting a fatal misunderstanding seen in their analysis. This revealed significant effects of updraft and downdraft on the stability of the cylindrical vortex sheet.

In order for considering the development of symmetric and asymmetric perturbations on such parent vortices, it is insufficient to examine the linear stability (i.e. eigenvalues) alone even if the focus is limited in the "linear" developing stage. This is because possible non-normality existing in the linear system prevents the most unstable eigenmode to develop most rapidly during a finite evaluation time [3][4]. In this respect, the present author [5] performed a singular-value analysis of the first model of Michalke & Timme, and revealed the form and growth rate of the optimally-excited perturbations on the axisymmetric vortex with piecewise-constant vorticity. On the other hand, the present study focuses on the optimal excitation of perturbations on the second model of Michalke & Timme, i.e. the cylindrical vortex sheet.

REFORMULATION

Theoretical setup is carried out here based on the formulation by Rotunno [2]. A cylindrical vortex sheet accompanying the axial flow, whose radius and length are R and infinite, respectively, is considered. The axial flow inside and outside of the cylinder is assumed to have constant speed of $W/2$ but point opposite directions. In the tangential direction, the angular velocity outside of the cylinder is constant ($=\Gamma$) whereas it is zero inside. Assumptions of constant density and zero vorticity (except exactly at the cylindrical region where vorticity is infinite) enable the introduction of the velocity potential ϕ to describe the velocity field due to symmetric or asymmetric perturbations on the cylindrical vortex sheet. Since the velocity potential is a solution of the Laplace's equation expressed in cylindrical coordinates (r, θ, z), it can be solved as

$$\phi = \begin{cases} A_1(t) I_m(kr) \exp[i(m\theta + kz)], & r < R + l(\theta, z, t) \\ A_2(t) K_m(kr) \exp[i(m\theta + kz)], & r > R + l(\theta, z, t) \end{cases} \tag{1}$$

under the boundary condition of $\phi=0$ at $r=0$ and ∞. Here, A_1 and A_2 denote the amplitudes, m and k the azimuthal and vertical wave numbers, respectively, and I_m and K_m the modified Bessel functions of the first and second kind, respectively. Meanwhile, l indicates the infinitesimal deformation of the cylindrical vortex sheet and is also assumed to take the sinusoidal structure, i.e. $l=L(t)exp[i(m\theta+kz)]$, where L indicates the magnitude of the deformation. It is natural to consider the tendency of the deformation equals the radial velocity across the cylindrical vortex sheet: i.e. $(\partial\phi/\partial r)_{r=R+l}=dl/dt$, which gives the relation among A_1, A_2, and L. Finally, the time evolution of the perturbations is determined by Bernoulli's theorem. Linearizing the theorem, equating either side of the pressure just across the cylinder, and substituting the equations derived above lead to the second-order ordinary differential equation on L as $d^2L/dt^2+2i\Omega dL/dt-BL=0$ where

$$\Omega = k(m+kS)K_m(k)I'_m(k) - kS/2, \qquad \mathrm{B} = k^2 I'_m(k)K'_m(k) + mk(m+kS)K_m(k)I'_m(k) + (kS/2)^2. \tag{2}$$

Note that scaling of variables are carried out in (2) following the conversion of $r/R \to r$, $L/R \to L$, $Rk \to k$, $(R^2/\Gamma)t \to t$, and $(A_1, A_2)/\Gamma \to (A_1, A_2)$. Thus, all variables are dimensionless hereafter. Also note that S ($=WR/\Gamma$) is a dimensionless number known as the "Swirl ratio", which is the most important parameter controlling the configuration of tornado-like vortices [6].

[a] Corresponding author. Email: itano@nda.ac.jp.

The formulation shown above is essentially same as that derived by Rotunno [2]. Here, as an alternative form of the governing equation, a set of the first-order simultaneous ordinary equations

$$\frac{d}{dt}\begin{pmatrix} A_1 \\ A_2 \end{pmatrix} + i\begin{pmatrix} \Omega+\Omega_d & -Q_K \\ Q_I & \Omega-\Omega_d \end{pmatrix}\begin{pmatrix} A_1 \\ A_2 \end{pmatrix} = 0, \quad \text{where} \quad Q_I = (m+kS)kI'_m(k)I_m(k) - \frac{k^2\{I'_m(k)\}^2}{m+kS}, \quad \Omega_d = -\frac{k^2 I'_m(k)K'_m(k)}{m+kS}, \tag{3}$$

$$Q_K = -(m+kS)kK'_m(k)K_m(k) - \frac{k^2\{K'_m(k)\}^2}{m+kS},$$

is obtained by changing the dependent variable from L to X [$=(A_1, A_2)^t$]. It is the fundamental equation for present analyses.

SINGULAR-VALUE ANALYSES

The equation (3) can be solved as an initial value problem. Symbolically, the solution is written as $X=MX_0$, where X_0 is the initial value of X and M the resolvent matrix. The singular-value under the $L2$ norm, λ_{L2}, is the square root of the eigenvalue of M^*M or MM^* (the suffix * indicates the Hermitian conjugate), and the forward and backward singular-vectors, f_F and f_B, are the eigenvectors of the former and latter matrices. They are given as

$$\lambda_{L2}^{\pm} = \sqrt{1+[\frac{1}{2}(Q_I+Q_K)\frac{\sinh(\sqrt{|D|}t)}{\sqrt{|D|}}]^2} \pm \frac{1}{2}|Q_I+Q_K|\frac{\sinh(\sqrt{|D|}t)}{\sqrt{|D|}}, \tag{4}$$

$$f_F^{\pm} \propto \begin{pmatrix} \pm\frac{|Q_I+Q_K|}{Q_I+Q_K}\sqrt{1+[\frac{Q_I+Q_K}{2}\frac{\sinh(\sqrt{|D|}t)}{\sqrt{|D|}}]^2} + \frac{Q_I-Q_K}{2}\frac{\sinh(\sqrt{|D|}t)}{\sqrt{|D|}} \\ \Omega_d\frac{\sinh(\sqrt{|D|}t)}{\sqrt{|D|}} + i\cosh(\sqrt{|D|}t) \end{pmatrix}, \tag{5}$$

$$f_B^{\pm} \propto \begin{pmatrix} \mp\frac{|Q_I+Q_K|}{Q_I+Q_K}\sqrt{1+[\frac{Q_I+Q_K}{2}\frac{\sinh(\sqrt{|D|}t)}{\sqrt{|D|}}]^2} + \frac{Q_I-Q_K}{2}\frac{\sinh(\sqrt{|D|}t)}{\sqrt{|D|}} \\ \Omega_d\frac{\sinh(\sqrt{|D|}t)}{\sqrt{|D|}} - i\cosh(\sqrt{|D|}t) \end{pmatrix}, \tag{6}$$

where the plus and minus signs indicate the growing and decaying modes, respectively.

The singular-values and corresponding vectors under the energy norm are obtained as follows: First, the kinetic energy E of a slice of the cylindrical vortex sheet per unit length is given as

$$E(=\frac{\pi}{2}e^*e) = \frac{1}{2}\int_0^\infty [|\frac{\partial\phi}{\partial r}|^2 + |\frac{1}{r}\frac{\partial\phi}{\partial\theta}|^2 + |\frac{\partial\phi}{\partial z}|^2](2\pi r)dr = \frac{\pi}{2}\begin{pmatrix} A_1^* & A_2^* \end{pmatrix}\begin{pmatrix} k\{|I_m(k)|^2\}' & 0 \\ 0 & -k\{|K_m(k)|^2\}' \end{pmatrix}\begin{pmatrix} A_1 \\ A_2 \end{pmatrix} = \frac{\pi}{2}X^*HX. \tag{7}$$

Here, if we set to $E=(\pi/2)e^*e$, comparison between both sides of (7) reveals $e=H^{1/2}X$. Since $X=MX_0$, the resolvent matrix which relates e and its initial value e_0 ($=H^{1/2}X_0$) as $e=M_E e_0$ turns out to be $M_E=H^{1/2}MH^{-1/2}$. The singular-value under the energy norm, λ_E, is the square root of the eigenvalue of $M_E^*M_E$ or $M_EM_E^*$, and the corresponding forward and backward singular-vectors, g_F and g_B, are the eigenvectors of the former and latter matrices, respectively. After some calculations, actual form and components of λ_E, g_F and g_B are proven to be those converting Q_I and Q_K appeared in (4), (5) and (6) into $\hat{Q}_I$ and $\hat{Q}_K$ as

$$Q_I \to \sqrt{-\frac{\{|K_m(k)|^2\}'}{\{|I_m(k)|^2\}'}}Q_I\ (\equiv\hat{Q}_I), \qquad Q_K \to \sqrt{-\frac{\{|I_m(k)|^2\}'}{\{|K_m(k)|^2\}'}}Q_K\ (\equiv\hat{Q}_K). \tag{8}$$

CONCLUSIONS

Equation (4) suggests the growing singular mode is larger whereas the decaying counterpart is smaller than unity. This means the non-normal growth or decay of the perturbations on the cylindrical vortex sheet. Such a feature is seen even under the energy norm though the growth rate and the wavenumber dependency are quite different. It is possible that such non-normal growth or decay crucially determine the occurrence and the dominant wavenumber of the multiple-vortex structure of tornado-like vortices.

References

[1] Michalke A., Timme A.: On the Inviscid Instability of Certain Two-Dimensional Vortex-Type Flows. *J. Fluid Mech* **29**:647-666, 1967.

[2] Rotunno R.: A Note on the Stability of a Cylindrical Vortex Sheet. *J. Fluid Mech* **87**:761-771, 1978.

[3] Farrell B.F.: The Initial Growth of Disturbances in a Baroclinic Flow. *J. Atmos Sci* **39**:1663-1686, 1982.

[4] Farrell B.F., Ioannou P.J.: Generalized Stability Theory. *J. Atmos Sci* **53**:2025-204-, 1996.

[5] Itano T.: Optimal Excitation of Asymmetric Perturbations on an Axisymmetric Barotropic Vortex. *J. Atmos Sci* **72**:1533-1550, 2015.

[6] Lewellen W.S.: A Solution for Three-Dimensional Vortex Flows with Strong Circulation. *J. Fluid Mech* **14**:420-432, 1962.

ANALYTICAL SOLUTIONS FOR WEAKLY COMPRESSIBLE VON KARMAN VORTEX STREETS

Vikas Krishnamurthy and Darren Crowdy
Department of Mathematics, Imperial College London, 180 Queen's Gate, London, SW7 2AZ, UK

Summary Vortex streets are a common feature of fluid flows at high Reynolds numbers and their study is now well developed for incompressible fluids. Much less is known, however, about compressible vortex streets. Recently Crowdy & Green presented analytical solutions describing a class of steady incompressible von Kármán vortex streets with distributed vorticity. To construct these they adopted the hollow vortex model where each vortex is modelled as a finite-area constant pressure region with non-zero circulation. For weakly compressible flows steady hollow vortex solutions are well known to be candidates for the leading order solution in a perturbative Rayleigh-Jansen expansion of a compressible flow. Here we give details of that expansion based on the vortex street solutions of Crowdy & Green. Physical properties of the compressible vortex streets are described. Our approach uses the Imai-Lamla method coupled with analytic function theory and conformal mapping.

INCOMPRESSIBLE HOLLOW VORTEX EQUILIBRIA

The *point vortex* is arguably the simplest and most widely used model of a two-dimensional vortex in an incompressible flow [1]. The basic idea is to model a vortex as a δ-function distribution of vorticity in which all vorticity is concentrated at a point. While this model has proved to be very useful in applications, not least because of its mathematical simplicity, it is nevertheless limited in scope. However, as soon as a vortex distribution is endowed with any spatial extent, the mathematical description of it becomes much more challenging.

There are various ways to desingularize the point vortex and devise more realistic models with distributed vorticity. A popular choice is to consider a *vortex patch* [1] where a centre of vorticity is approximated as a finite area region of uniform vorticity. A lesser known possibility is to employ a *hollow vortex* [1] model where vorticity is assumed to be concentrated on a closed vortex sheet enclosing a finite-area region at constant pressure. This paper focusses on the hollow vortex model.

In a classical work, Pocklington [4] studied the hollow vortex desingularization of the travelling point vortex pair. He used Schwarz-Christoffel mappings in a hodograph plane together with the machinery of elliptic functions to write down an analytical solution for the shapes of two hollow vortices, of equal size, translating steadily in a rectilinear motion. Recently, Pocklington's solutions have been rederived [8] using a novel approach based on use of the Schottky-Klein prime function for the annulus [6] (rather than elliptic function theory). Another contribution to the theory of hollow vortices was made by Baker, Saffman and Sheffield [5] who considered the hollow vortex desingularization of a single periodic point vortex row; they constructed the solutions using free streamline theory, again in a hodograph plane, and they also presented some partial stability results.

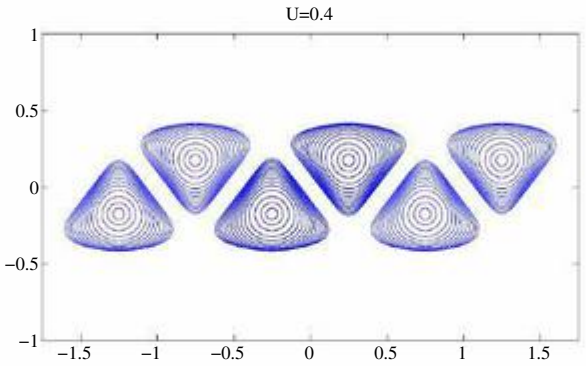

Figure 1: Von Kármán streets of hollow vortices with different areas; the solutions can be described in explicit form by the map (1) (see [3])

A VON KÁRMÁN STREET OF HOLLOW VORTICES

A new addition to this catalogue of analytical solutions for hollow vortex equilibria has been given recently by Crowdy & Green [3] who identified solutions for a von Kármán vortex street made up of hollow vortices. Such vortex streets are known to occur in a variety of fluid dynamical situations such as in the wake of flow past bluff bodies and in atmospheric flows. If the vortex configuration is modelled as a staggered array of hollow vortices travelling at a steady speed U it can be shown that a conformal mapping from the annulus $\rho < |\zeta| < 1$ in a parametric ζ-plane to the fluid region in a principal period window exterior to two typical hollow vortex members (in a co-travelling frame of reference) is given by the explicit formula

$$z(\zeta) = \int_{\zeta_0}^{\zeta} \left\{ \frac{BP^2(\zeta'\overline{\gamma_1}, \rho)P^2(\zeta'\overline{\gamma_2}, \rho)}{P(\zeta'/\alpha, \rho)P(\zeta'\overline{\alpha}, \rho)P(\zeta'/\beta, \rho)P(\zeta'\overline{\beta}, \rho)} \right\} d\zeta', \tag{1}$$

where the special function $P(\zeta, \rho)$ is defined by

$$P(\zeta, \rho) \equiv (1 \circ\ \zeta) \prod_{k=1}^{\infty} (1 \circ\ \rho^{2k}\zeta)(1 \circ\ \rho^{2k}\zeta^{-1}) \tag{2}$$

while α, β, γ_1 and γ_2 are some parameters. To within a normalization, the function $P(\zeta, \rho)$ is the aforementioned Schottky-Klein prime function for the annulus [6]. For appropriate choices of the parameters in (1), the formula encompasses both unstaggered and staggered vortex streets. Those parameters are uniquely determined by specifying the translational speed of the street configuration and the vortex size. Figure 1 shows a superposition of hollow vortex streets, with vortices of gradually increasing area superposed, all travelling at the same speed $U = 0.4$.

COMPRESSIBLE VORTICES: THE IMAI-LAMLA METHOD

So far, we have discussed hollow vortices in the incompressible case. However this model turns out to be of particular significance for the study of *compressible* vortices for which much fewer analytical results are available. The infinite pressures associated with singular point vortices preclude an extension of those models to the compressible case, but hollow vortices are ideally suited to compressible extension because they are essentially regularized point vortices (the infinite pressure is "cut off" by the hollow vortex region) and, moreover, the model is such that one retains control over the pressure inside the vortex (unlike, say, a vortex patch model where it is much more difficult to get information on the fluid pressure).

If the Mach number of the flow is assumed to be small everywhere then it is usual to perform a perturbation analysis about the incompressible state; this analysis produces what are known as Rayleigh-Jansen expansions. One approach to such a perturbation analysis is by an ingenious linearization of the governing nonlinear equations due to Chaplygin; Ardalan *et al* [7] used such a method, for example. An alternative mathematical approach is via the *Imai-Lamla method* which exploits a complex variable formulation of the compressible flow problem; it was used, for example, by Barsony-Nagy *et al* in studying the compressible Föppl vortex pair [9]. The latter method is natural for us given that the analytical solutions of Crowdy & Green [3] for the hollow vortex street are derived using free streamline and analytic function theory together with conformal mapping ideas. Here it becomes of great advantage that the incompressible hollow vortex equilibria are known in closed form (in particular, functional properties of the Schottky-Klein prime function (2) can be harnessed to facilitate the analysis).

CONCLUSION

We show how to carry out the weakly compressible Rayleigh-Jansen expansions of the von Kármán hollow vortex street solutions in [3] by a novel approach combining the Imai-Lamla method with elements of analytic function theory and conformal mapping. Properties of the compressible vortex streets are examined. Our work here complements the sister presentation "Motion of a compressible vortex pair" by S. Llewellyn Smith and co-authors.

References

[1] P.G. Saffman, Vortex dynamics, Cambridge University Press, Cambridge, (1992).
[2] S.G. Llewellyn Smith & D.G. Crowdy, Structure and stability of hollow vortex equilibria, *J. Fluid Mech.*, **691**, 170-200, (2012).
[3] D.G. Crowdy & C.C. Green, Analytical solutions for double von Kármán streets of hollow vortices, *Phys. Fluids*, **23**, 126602, (2011).
[4] H.C. Pocklington, The configuration of a pair of equal and opposite hollow straight vortices of finite cross-section moving steadily through fluid, *Phil. Trans. Roy. Soc. London*, , 178–187, (1894).
[5] G.R. Baker, P.G. Saffman & J.S. Sheffield, Structure of a linear array of hollow vortices of finite cross-section, *J. Fluid Mech.*, **74**, 469–476, (1976).
[6] D.G. Crowdy, A new calculus for two-dimensional vortex dynamics, *Theor. Comput. Fluid Dyn.*, **24**, 9-24, (2010).
[7] K. Ardalan, D. Meiron & D. Pullin, Steady compressible vortex flows: the hollow-core vortex array, *J. Fluid Mech.*, **301**, 1–17, (1995).
[8] D.G. Crowdy, S. Llewellyn Smith and D. Freilich, Translating hollow vortex pairs, *Eur. J. Mech B/Fluids*, **37**, 180-186, (2012).
[9] A. Barsony-Nagy, J. Er-El & S Yungster, Compressible flow past a contour and stationary vortices, *J. Fluid Mech.*, **178**, 367–378, (1987).

REPRESENTATION OF REAL FLOWS WITH DYNAMICALLY EQUIVALENT CONCENTRATED POINT VORTICES

Eric Limacher*[1], Chris Morton[1], and David Wood[1]
[1]*Mechanical & Manufacturing Engineering, University of Calgary, Calgary, Alberta, Canada*

Summary Unsteady inviscid point vortex models predict vortex locations and circulations as functions of time. In order to adequately predict forces on plates undergoing unsteady maneuvers, we assert that such models ought to predict the centroids of leading-edge (LE) and trailing-edge (TE) vorticity distributions in real flows. For a surging, nominally two-dimensional plate, we have used particle image velocimetry (PIV) to calculate LE and TE vorticity centroids and circulations at early dimensionless times. These measurements are used as inputs to a force formulation for an existing point vortex model. The instantaneous forces calculated in this way exhibit the same trend as the direct force measurements, but underpredict the magnitude. Further work will be completed to identify the source of the discrepancy, such that existing unsteady point vortex convection models can be validated.

INTRODUCTION

Low-order point vortex models have been used with some success to predict the forces on plates or wings undergoing unsteady motions, e.g. [1]. Typically, such models are validated against experimental results or high-fidelity simulations to show some level of agreement in the force histories. In the present work, we seek to validate existing point vortex models in a more comprehensive way. The force on a plate due to the shedding of leading- and trailing-edge vorticity is dependent on the circulation of the shed vorticity distributions, as well as the velocities of all fluid elements possessing vorticity.

Consider a two-dimensional fluid domain extending to infinity within which the total circulation sums to zero. If viscous skin friction on a submerged body is assumed to be negligible, the force, $\mathbf{F}$, on that body is given by the following [2]:

$$\mathbf{F} = \circ\, \rho \frac{d}{dt} \int_A \mathbf{x} \times \omega dA + \rho \frac{d}{dt} \oint_{S_b} \mathbf{x} \times (\hat{n} \times \mathbf{u}) dS, \tag{1}$$

where $\mathbf{x}$ is the position vector, $\mathbf{u}$ is velocity, $\hat{n}$ is the body surface normal pointing into the body, S_b is the body surface, A is the fluid volume outside the body, ρ is density and ω is plane-normal vorticity. To represent a vorticity distribution within a subdomain A_v with a single concentrated point vortex in a dynamically equivalent way, the impulse of that point vortex, i.e. its contribution to the first integral in equation (1), must equal the impulse of the true vorticity distribution at all points in time. This is achieved if the point vortex has equal circulation to the true vorticity distribution, Γ_v, and if its location lies at the centroid of the vorticity distribution, $\mathbf{x_c}$, defined as follows:

$$\mathbf{x_c} = \frac{\int_{A_v} \mathbf{x}\omega dV}{\Gamma_v}. \tag{2}$$

Wang and Eldredge [1] provide an expression for the force on an infinitesimally thin plate by conformally mapping the domain around the plate to a domain around a unit circle. With some manipulation, the force, $\tilde{F}$, can be expressed in a plate-fixed frame of reference in complex notation in terms of physical coordinates normalized by chord, c:

$$\tilde{F} = F_t + iF_n = \circ\, i\rho \frac{d}{dt} \left[\frac{\pi}{4} c^2 \tilde{V} \circ \sum_j c\Gamma_j \tilde{z_j} + \frac{1}{2} \sum_j c\Gamma_j g(\tilde{z_j}) \right] h, \tag{3}$$

where $\tilde{V}$ is plate-normal velocity, F_t and F_n are the plate-aligned and plate-normal forces, respectively, h is the submerged height of the plate, and $\tilde{z_j} = \tilde{x_j} + i\tilde{y_j}$ are the chord-normalized locations of vorticity centroids in a plate-fixed frame of reference (see figure 1b). The function $g(\tilde{z})$ is a real function of vortex position only. If one has knowledge of the leading- and trailing-edge vorticity centroids and circulations over a time interval of interest, and the plate kinematics are known, we hypothesize that equation (3) can be used to calculate the instantaneous force on the plate.

EXPERIMENTAL METHODS

In the present work, we seek to validate equation (3) experimentally. The chosen test case is a nominally two-dimensional flat plate surging in otherwise quiescent fluid at a fixed angle of attack of $\alpha = 60°$. A preliminary experiment has been conducted in the water tunnel at the University of Calgary. Particle image velocimetry (PIV) has been used to quantify the flow-field behind the plate at the midspan. The centroids of leading- and trailing-edge vorticity, as well as the circulations of

*Corresponding author. Email: ejlimach@ucalgary.ca

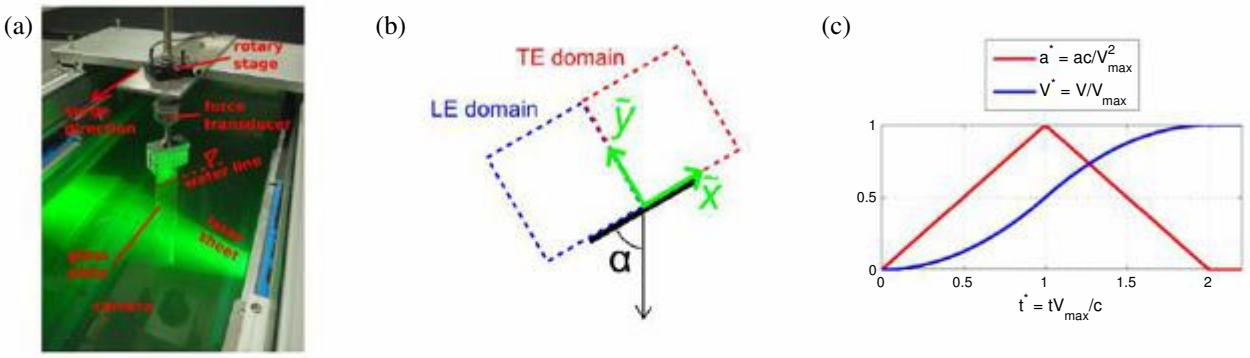

Figure 1: (a) Experimental apparatus. (b) Two-dimensional schematic of the measurement plane. Domains of integration for the leading-edge (LE) and trailing-edge (TE) vorticity distributions are shown approximately. (c) Programmed normalized acceleration and normalized velocity of surge motion over the time period investigated using PIV.

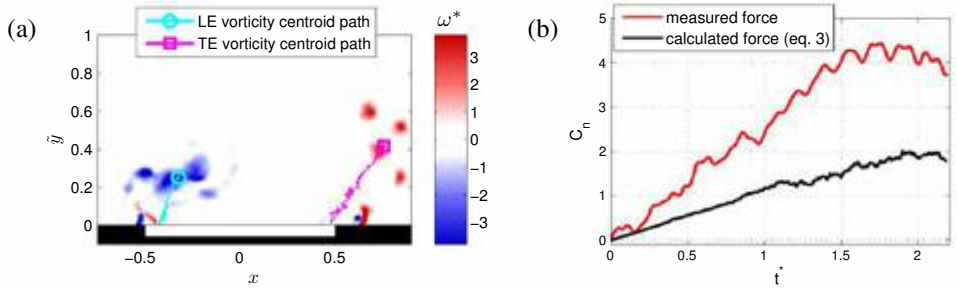

Figure 2: (a) Trajectories of leading-edge (LE) and trailing-edge (TE) vorticity centroids in a plate-fixed frame of reference, extracted from the PIV results. The markers at the end of the lines represent the calculated centroid locations in the final time-step of data, for which contours of normalized span-wise vorticity, $\omega^* = \omega c/V_{max}$, are also plotted. (b) Plate-normal force coefficient, $C_n = F_n/(1/2\rho chV^2_{max})$, versus time from direct force measurement (minus the known inertial force due to the mass of the apparatus) and calculated from experimentally obtained vorticity fields using equation (3).

these vorticity distributions, have been measured. Direct force measurements were also taken to compare to the calculated force based on the vorticity field.

The experimental setup and two-dimensional schematic of the measurement plane are shown in figure 1a and 1b. The plate was made of glass to minimize reflections at the plate surface. With a chord length of $c = 50$mm, and a maximum surge velocity of $V_{max} = 0.2$m/s, the Reynolds number is calculated to be $Re = 9950$. The plate thickness is 3mm, or $0.06c$. PIV data is available for a dimensionless time of $t^* = 2.2$ from the start of the surge motion (see figure 1c).

PRELIMINARY RESULTS AND SUBSEQUENT WORK

Figure 2a shows that the leading- and trailing-edge vorticity centroids depart from the plate over time, consistent with qualitative observations of the instantaneous vorticity fields. The associated plate-normal force calculated using equation (3) displays a similar trend to the measured force, but underpredicts the magnitude (see figure 2b). This suggests that the concentrated point vortex force formulation captures the relevant physics of the problem, but there may be fundamental experimental limitations, e.g. influence of the free surface and solid boundary at the plate ends, plate flexibility, missing vorticity data near plate edges due to optical access limitations, etc. The investigation and quantification of such sources of experimental bias will be the focus of future experiments.

In future work, a validated formulation that allows a real flow-field to be dynamically represented by concentrated point vortices will facilitate experimental validation of predictive point vortex models for canonical kinematic test cases. In particular, the vorticity centroid paths predicted by the Brown-Michael and impulse matching models [1] will be compared to experimental results.

References

[1] Wang C., Eldredge J. D.: Low-order phenomenological modeling of leading-edge vortex formation. Theor. and Comp. Fluid Dyn. 27:577-598, 2013.

[2] Noca, F.: On the evaluation of time-dependent fluid-dynamic forces on bluff bodies. PhD Thesis, California Institute of Technology, 1997.

CASCADE OF VORTEX KNOTS DETECTED BY HOMFLYPT POLYNOMIAL

Xin Liu*[1] and Renzo L. Ricca[2]
[1]*BDIC & Institute of Theoretical Physics, Beijing University of Technology, Beijing, P.R. China*
[2]*Department of Mathematics & Applications, U. Milano-Bicocca, Milano, Italy*

Summary Due to reconnection of neighboring strands superfluid vortex knots seem to undergo a cascade process that consistently reduces topological complexity by stepwise unlinking. Here, by using the HOMFLYPT polynomial recently introduced for fluid knots (Liu & Ricca, 2015), we prove that this cascade process follows a complexity-reducing path detected by a unique, monotonically decreasing sequence of HOMFLYPT numerical values. This result holds true for any sequence of $T(2, 2n + 1)$ torus knots and $T(2, 2n)$ torus links. By this result we demonstrate that the computation of this adapted HOMFLYPT polynomial provides a powerful tool to measure topological complexity of any physical system, and it is useful to investigate relationships between topological complexity and kinetic energy.

HOMFLYPT POLYNOMIAL FOR VORTEX KNOTS

Tangles of vortex filaments forming an intricate networks of thin tubes are generic features of quantum turbulence in superfluids and, under appropriate circumstances, characterize the decay of vortical flows in classical turbulence. These filaments may form knots and links, that decay rapidly through reconnections to form various loops, till final dissipation. Kinetic helicity is an appropriate measure of topological complexity, but it is known to suffer from some serious limitations. To overcome these difficulties Liu & Ricca have derived various knot polynomials (Kauffman bracket, Alexander–Conway, Jones and HOMFLYPT) for fluid knots as new invariants of ideal fluid mechanics. By applying knot theoretical techniques to vortex flows the HOMFLYPT polynomial $P = P_K$ has been derived [1] from the kinetic helicity H of vortex knots.

Theorem (Liu & Ricca, 2015). *Let K denote a physical knot. If the helicity of K is $H = H(K)$, then*

$$e^{H(K)} = e^{\oint_K \mathbf{u}\cdot \mathrm{d}\mathbf{l}}\,, \tag{1}$$

appropriately re-scaled, satisfies (with a plausible statistical hypothesis) the skein relations of the HOMFLYPT polynomial $P = P_K$.

Remark 1. If K is a vortex knot, then $\mathbf{u}$ is the self-induced velocity associated with its vorticity, aligned along the knot centerline of elementary line element $\mathrm{d}\mathbf{l}$. To make sense of $e^{H(K)}$, $H(K)$ must be normalized with respect to some reference value of vortex circulation Γ.

Remark 2. The derivation of the result above relies on a statistical hypothesis, that assumes equally probable state decomposition of the crossing sites in the minimal, 2D knot diagram. This is equivalent to the ergodic assumption that all possible (virtual) reconfiguration states of the given knot or link are equally admissible.

CASCADE OF VORTEX KNOTS BY STEPWISE UNLINKING DETECTED BY HOMFLYPT

Vortex filaments in classical and quantum fluids may interact and recombine through reconnection of neighboring strands [2]-[5]. While details of the process depend on specific local mechanisms that may differ from classical to quantum case, certain qualitative features — such as the preservation of the original strand orientation after reconnection — are generic and common to both systems. In the majority of cases orientation-preserving reconnections occur when neighboring strands tend to align (at the time of closest approach) in an anti-parallel fashion before transversal merging and final separation. In general, when two disjoint, closed tubes reconnect, the result is a single closed tube and when a single closed tube reconnects with itself, the result is two closed tubes [6]. Reconnections determine a change of topology often accompanied by a change in energy, and this mechanism may play a fundamental rôle in the energy transfer and dispersion in turbulent flows.

According to recent observations based on direct numerical simulations of decaying Bose-Einstein condensates [7]-[6] vortex knots and links seem to undergo a generic cascade process through an alternate sequence of $T(2, 2n + 1)$ torus knots and $T(2, 2n)$ torus links, as n (integer) decreases to 0. After every reconnection the knot/link gradually unties by removing a single crossing at a time, by reducing consistently topological complexity. Remarkably, the sequence of topological transitions seem to follow an identical topological decay pattern, irrespective of the physical context considered (consistent even with recombinant DNA plasmid reactions [9]). Here we show that HOMFLYPT polynomial not only detects topological differences between knots and links (as standard knot polynomials typically do), but it can be used to *quantify* topological differences between the various stages of the cascade process by a unique, monotonically decreasing sequence of numerical values. This

*Corresponding author. Email: xin.liu@bjut.edu.cn

result, anticipated by the recursive application of the HOMFLYPT skein relations on the 2D knot diagrams [10], can be proven analytically by direct application of the skein relations to a generic portion of torus knot/link diagram. Direct comparison of the decreasing sequence of numerical values of topological complexity with kinetic energy data of corresponding vortex knots [12] shows remarkable, intriguing similarities that will be explored in the near future.

References

[1] Liu, X., Ricca, R. L.: On the derivation of the HOMFLYPT polynomial invariant for fluid knots. J. Fluid Mech. 773: 34–48 2015.

[2] Kida, S., Takaoka, M.: Vortex reconnection. Ann. Rev. Fluid Mech. 26: 169–189 1994.

[3] Bewley, G., Paoletti, M. S., Sreenivasan, K. R., Lathrop, D. P.: Characterization of reconnecting vortices in superfluid helium. PNAS USA 105: 13707–13710 2008.

[4] van Rees, W., Hussain, F., Koumoutsakos, P.: Vortex tube reconnection at Re = 104. Phys. Fluids 24: 075105-1–14 2012.

[5] Zuccher, S., Caliari, M., Baggaley, A. W., Barenghi, C. F.: Quantum vortex reconnection. Phys. Fluids 24: 1251081–21 2012.

[6] Zuccher, S., Ricca, R.L.: Helicity conservation under quantum reconnection of vortex rings. Phys. Rev. E 92: 061001 2015.

[7] Kleckner, D., Irvine, W. T. M.: Creation and dynamics of knotted vortices. Nature Physics 9: 253–258 2013.

[8] Kleckner, D., Kauffman, L.H., Irvine, W. T. M.: How superfuid vortex knots untie. arXiv: 1507.07579v1 [physics.flu-dyn] 27 Jul. 2015.

[9] Shimokawa, K., Isihara, K., Grainge, I., Sherratt, D. J., Vazquez, M.: FtsK-dependent XerCD-dif recombination unlinks replication catenanes in a stepwise manner. PNAS USA 110: 20906–20911 2013.

[10] Ricca, R.L.: Vortex knot cascade in polynomial skein relations. In Numerical Analysis and Applied Mathematics ICNAAM 2015 AIP Conf. Proc.: in press.

[11] Liu, X., Ricca, R.L.: Knots cascade detected by a monotonically decreasing sequence of values. Submitted.

[12] Maggioni, F., Alamri, S. Z., Barenghi, C. F., Ricca, R. L.: Velocity, energy, and helicity of vortex knots and unknots. Phys. Rev. E 82: 26309-26317 2010.

UNSTEADY KUTTA CONDITION AND VORTEX-SHEET GENERATION

Xi Xia[1] and Kamran Mohseni [*1,2]
[1]*Department of Mechanical and Aerospace Engineering, University of Florida, Gainesville, FL, USA*
[2]*Department of Electrical and Computer Engineering, University of Florida, Gainesville, FL, USA*

Summary Vortex method has been widely used for low-Reynolds-number flights as it reduces the computation domain from the entire flow field to only finite vortical structures. An essential challenge of the vortex method lies in the prediction of the vortex sheets separated from the solid body. To tackle this problem, this study extends the classical Kutta condition to unsteady situations based on the physical sense that flow cannot turn around a sharp edge. This unsteady Kutta condition can be readily applied to an airfoil with cusped trailing edge, where the forming vortex sheet is known to be tangential to the trailing edge. For a finite-angle trailing edge, previous studies indicate that the direction of the forming vortex sheet is ambiguous. Therefore, this study proposes a novel analytical formulation to determine the angle of the trailing-edge vortex sheet based on momentum conservation in the direction normal to the forming vortex sheet.

INTRODUCTION

Natural flies are observed to be superior than man-made aerial vehicles in terms of aerodynamic performance, especially the high lift-generation mechanisms. Early experimental investigations suggested that the existence of an attached leading edge vortex (LEV) contributes to enhanced lift generation for flapping wings [2]. To understand the fundamental mechanism of the LEV, recent analytical studies have been extensively focused on using vortex method (diagram shown in Fig. 1) to solve the unsteady aerodynamics of a flat plate wing by means of tracking the wake vortices that are shed from the wing [7]. The fundamental question associated with vortex methods is how to decide the rate at which vorticity is being created at the leading or trailing edge. In reality, the generation of vorticity is caused by the interaction between fluid and solid boundary that forms the shear layer, which is essentially a viscous process. Since viscosity is ignored in the Euler equation, a typical solution to that is applying vorticity releasing conditions at the vortex shedding locations of the solid body, e.g. the steady-state Kutta condition at a sharp trailing edge, which requires a finite velocity at the trailing edge [5, 3]. For a Joukowski airfoil or a flat plate, the steady-state Kutta condition is realized by setting the trailing edge to be a stagnation point in the mapped cylinder plane. The effect of this implementation is that the flow from both sides of the trailing edge will be tangential to the edge, which guarantees the streamline emanating from this edge point to be inline with the plate, fulfilling the condition proposed in previous studies [1, 4]. In this study, the objective is to extend the steady-state Kutta condition to unsteady situations for cusped and finite-angle trailing edges.

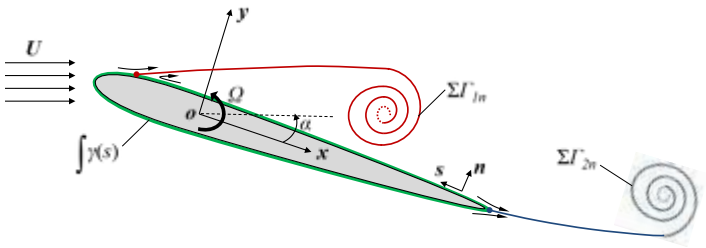

Figure 1: Diagram showing the unsteady aerodynamic model for a two-dimensional airfoil. The green contour line represents the bound vortex sheet surrounding the airfoil. The red and blue structures are the leading and trailing edge vortices, respectively.

UNSTEADY KUTTA CONDITION

The application of the steady-state Kutta condition for a flat plate or a Joukowski airfoil (with cusped trailing edge) has already been discussed in our previous work [7]. Basically, this condition is equivalent to enforcing a stagnation point at the trailing edge in the mapped cylinder plane. However, Xia & Mohseni [8] later pointed out that a stagnation point generally does not exist at the trailing edge of an unsteady flat plate that has rotary motion. To address this difficulty, they further proposed a modified Kutta condition which relaxes the trailing edge point from totally stagnant to only stagnant in the tangential direction of the surface in the cylinder plane. They have shown that this modified Kutta condition is consistent with the physical meaning of the classical Kutta condition that flow around the sharp edge should be prevented in a reference frame that is fixed to the flat plate. This condition can be generalized in the physical plane (the plane of the flat plate or airfoil) as

$$\boldsymbol{u}_g \cdot \boldsymbol{n} = 0, \tag{1}$$

where $\boldsymbol{u}_g$ denotes the de-singularized flow velocity at the trailing edge, and $\boldsymbol{n}$ represents the vector perpendicular to the trailing-edge tangential vector ($\boldsymbol{n} \cdot \boldsymbol{t} = 0$) as shown in Fig. 2.

*Corresponding author. Email: mohseni@ufl.edu

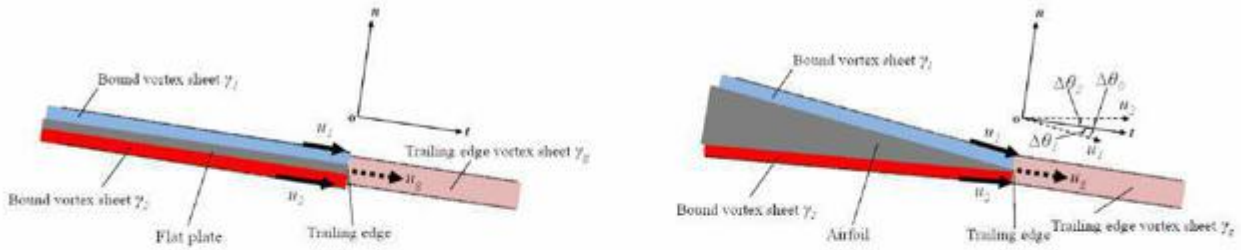

Figure 2: The formation of vortex sheet for a cusped trailing edge (left) and a finite-angle trailing edge (right).

The unsteady Kutta condition (Eq. 1) have been shown to yield promising results in estimating vortex-sheet formation at cusped trailing edges, yet, it was only validated for the situation where a flat plate or a Joukowski airfoil can be mapped to a circle. For a general airfoil, solving Eq. 1 might be challenging because of possible finite-angle trailing edge. As shown in Fig. 2, the two bound vortex sheets at a finite-angle trailing edge are at a certain angle to each other, which is different from the case of a flat plate or a cupsed airfoil where the two bound vortex sheets share the same tangent. This inconsistency of the flow direction at the trailing edge creates an ambiguity in deciding the angle of the streamline emanating from the trailing edge, especially for unsteady cases. In this study, we propose that the angle of the trailing-edge vortex sheet should be decided in a momentum conservation sense. As a result, the angle of the forming vortex sheet can be decided by

$$\gamma_2 \sin \Delta\theta_2 + \gamma_1 \sin \Delta\theta_1 = 0 \quad \text{with} \quad \Delta\theta_1 \cdot \Delta\theta_2 \geq 0, \tag{2}$$

and

$$\Delta\theta_1 + \Delta\theta_2 = \Delta\theta_0, \tag{3}$$

where $\Delta\theta_0$ is the finite angle of the trailing edge. The unsteady Kutta condition for an airfoil is validated through the simulation of a NACA 0012 airfoil with a combined pitching and heaving motion, the experiment of which was conducted by Schouveiler et al. [6]. The chord length, c, and the towing speed, U, are 0.1 m and 0.4 m/s, respectively. This corresponds to a Reynolds number of 4×10^4. The phase difference angle, ψ, between the pitching and heaving motions is set to 90° in all circumstances. Fig. 3 shows the comparison of the flow structures between this simulation and the flow visualization image of the original experiment for a sample case with $St = 0.45$ and $\alpha_{max} = 30°$. The good matching of the wake patterns provides qualitative support for the unsteady Kutta condition for a finite-angle trailing edge.

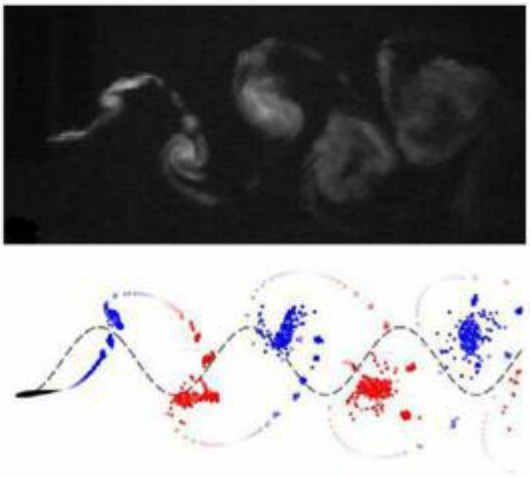

Figure 3: Comparison between flow visualization and simulation. The NACA 0012 airfoil is towed from right to left with $St = 0.45$ and $\alpha_{max} = 30°$. The flow visualization image is adapted from Schouveiler et al. [6].

CONCLUSIONS

The unsteady Kutta condition is extended from the classical Kutta condition to study the vortex sheet formation at a sharp edge. Applying the unsteady Kutta condition to an airfoil with finite-angle trailing edge is not straightforward, as the angle of the forming vortex sheet is ambiguous. This study proposes to determine this angle based on the momentum conservation in the direction normal to the forming vortex sheet. The good agreement between simulation and experiment confirms the validity of the proposed unsteady Kutta condition.

References

[1] S.H. Chen and C. M. Ho. Near wake of an unsteady symmetric airfoil. *Journal of Fluids and Structures*, 1:151–164, 1987.

[2] C.P. Ellington. The aerodynamics of hovering insect flight. iv. aerodynamic mechanisms. *Phil. Trans. R. Soc. Lond. B*, 305:79–113, 1984.

[3] M-K. Huang and C-Y. Chow. Trapping of a free vortex by joukowski airfoils. *AIAA*, 20(3), 1981.

[4] D.R. Poling and D.P. Telionis. The trailing edge of a pitching airfoil at high reduced frequency. *Journal of Fluid Engineering*, 109:410–414, 1987.

[5] P.G. Saffman and J.S. Sheffield. Flow over a wing with an attached free vortex. *Studies in Applied Mathematics*, 57:107–117, 1977.

[6] L. Schouveiler, F. S. Hover, and M. S. Triantafyllou. Performance of flapping foil propulsion. *Journal of Fluids and Structures*, 20(7):949959, 2005.

[7] X. Xia and K. Mohseni. Lift evaluation of a two-dimensional pitching flat plate. *Physics of Fluids*, 25(9):091901, 2013.

[8] X. Xia and K. Mohseni. A flat plate with unsteady motion: Effect of angle of attack on vortex shedding. AIAA paper 2014-0746, National Harbor, MD, Jan 13-17 2014.

INVARIANT LOCAL FLOW TOPOLOGY IN TRANSITION INTO A VORTEX AND PROPERTY OF ITS PREDICTION

K. Nakayama[1]

[1] *Department of Mechanical Engineering, Aichi Institute of Technology, Toyota, Aichi, Japan*

Summary Local flow topology specified by the velocity gradient tensor and features of corresponding physical properties are investigated in transition into a vortical flow. The swirlity that indicates the uniformity and intensity of azimuthal flow follows the transition process, and it shows that this property in the transition depends on two real eigenvalues of the tensor with the same sign, not on vorticity. Sourcity shows that the uniformity of the radial flow depends on both these eigenvalues and vorticity (shear) in the plane that becomes the swirl plane.

INTRODUCTION

The eigenvalues of the velocity gradient tensor $\nabla \boldsymbol{v}$ have contributed greatly to categorize the local flow geometry (topology or pattern) in turbulences that is Galilei invariant. They also derived the Δ-definition of a vortex [1] that specifies the swirling motion, and vortex definitions focused on the pressure minimum feature in terms of the flow kinematics, i.e., the Q- and λ_2- and their integrated definitions [2], are associated with $\nabla \boldsymbol{v}$ and its eigenvalues. Recently the physical interpretation of the complex eigenvalues of $\nabla \boldsymbol{v}$ has been clarified, and it has derived other invariant properties to specify the detail flow geometry, e.g. swirlity, sourcity, and property of flow symmetry [3]. The swirlity represents the uniformity and intensity of azimuthal flow, and can be applied to the prediction of generation of a vortex [4]. The sourcity specifies the above characteristics of the radial flow. These properties specify not only the detail flow geometry of a vortex, but also that before the generation of a vortex. The present study investigates features of the flow geometry before the generation of a vortex, and characteristics of the swirlity and sourcity.

REPRESENTATION OF VELOCITY GRADIENT TENSOR

The local flow geometry around a point x_i $(i = 1, 2, 3)$ in the velocity field v_i $(i = 1, 2, 3)$ can be expressed by $\nabla \boldsymbol{v}$, i.e., $dx_i/dt = (\partial v_i/\partial x_j)x_j$, where the summation convention is applied. In this local flow, the radial and azimuthal velocities in the x_1-x_2 plane, v_r and v_θ, are extracted as $v_r = {}^t\hat{\boldsymbol{x}}\boldsymbol{Q}_r\hat{\boldsymbol{x}}/\left|\hat{\boldsymbol{x}}\right|$ and $v_\theta = {}^t\hat{\boldsymbol{x}}\boldsymbol{Q}_\theta\hat{\boldsymbol{x}}/\left|\hat{\boldsymbol{x}}\right|$, respectively, where $\hat{\boldsymbol{x}} = (x_1, x_2)$ and $|\hat{\boldsymbol{x}}| = \sqrt{x_i x_i}$ $(i = 1, 2)$, and $\boldsymbol{Q}_r$ and $\boldsymbol{Q}_\theta$ denote the respective matrix of the quadratic forms. $\boldsymbol{Q}_r$ and $\boldsymbol{Q}_\theta$ are expressed as follows:

$$\boldsymbol{Q}_r = \begin{bmatrix} a_{11} & (a_{12}+a_{21})/2 \\ (a_{12}+a_{21})/2 & a_{22} \end{bmatrix}, \quad \boldsymbol{Q}_\theta = \begin{bmatrix} a_{21} & -(a_{11}-a_{22})/2 \\ -(a_{11}-a_{22})/2 & -a_{12} \end{bmatrix}. \tag{1}$$

The eigenvalues of these matrices specify the feature of v_r and v_θ.

Here we derive a representation of $\nabla \boldsymbol{v}$ that has three real eigenvalues λ_i $(i = 1, 2, 3)$. We assume that λ_1 and λ_2 have the same sign, and set an orthonormal coordinate system x_i with unit bases $\boldsymbol{e}_i$ $(i = 1, 2, 3)$ where the x_1-x_2 plane, referred to as P hereafter, is the eigenplane associated with λ_1 and λ_2, and $\boldsymbol{e}_1$ are parallel to the eigenvector of λ_1. Then $\boldsymbol{A} = \nabla \boldsymbol{v}$ $(= [a_{ij}] = [\partial v_i/\partial x_j]$ $(i, j = 1, 2, 3))$ can be expressed as:

$$\boldsymbol{A} = \begin{bmatrix} \lambda_1 & -\omega_3 & \omega_2 \\ 0 & \lambda_2 & -\omega_1 \\ 0 & 0 & \lambda_3 \end{bmatrix}, \tag{2}$$

where ω_i $(i = 1, 2, 3)$ denote components of the vorticity vector, and a_{12}, a_{13}, and a_{23} are expressed in terms of ω_i.

When $\nabla \boldsymbol{v}$ with λ_i becomes to have a pair of conjugate complex eigenvalues, λ_1 and λ_2 change to them, and then P becomes the swirl plane defined by the complex eigenvector of them [4]. Equation (2) is a general representation of $\nabla \boldsymbol{v}$ with three real eigenvalues, which is expressed as an upper triangular matrix. It shows that the vorticity component normal to P or shear in P is expressed by only one component of $\nabla \boldsymbol{v}$.

SWIRLITY AND SOURCITY, AND LOCAL TOPOLOGY IN A VORTEX TRANSITION

From Eq. (2), the eigenvalues λ_{θ_i} $(i = 1, 2; \lambda_{\theta_1} < \lambda_{\theta_2})$ of $\boldsymbol{Q}_\theta$ are expressed as $\lambda_{\theta_i} = \omega_3/2 \pm \sqrt{\omega_3^2 + 4\delta^2}/2$ where $\delta = (\lambda_1 - \lambda_2)/2$. We note that λ_{θ_1} and λ_{θ_2} have the different sign and the azimuthal flow has both clockwise and

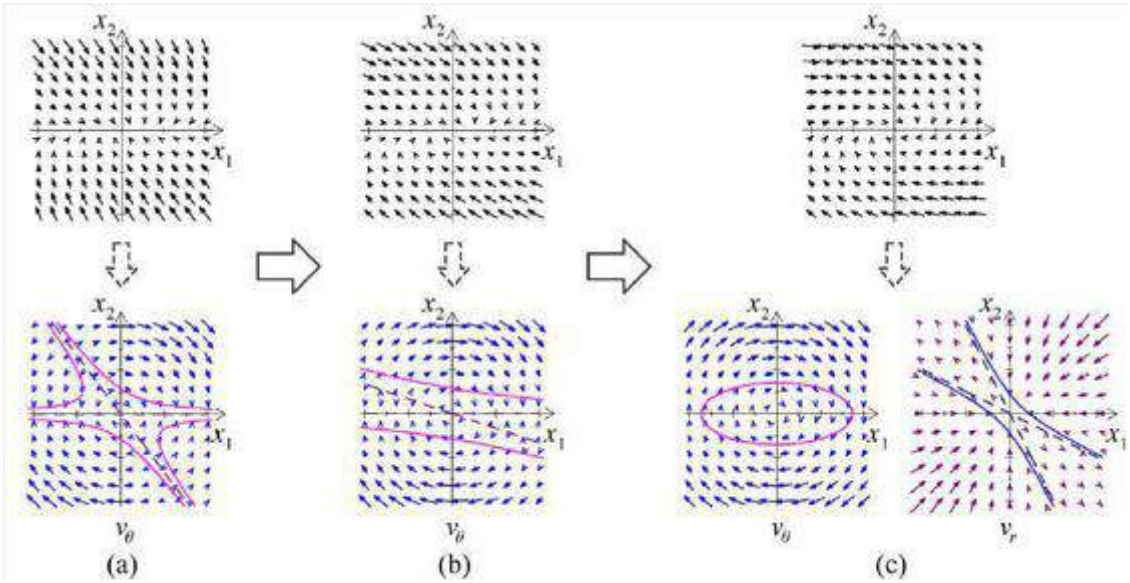

Fig. 1: Transition of flow geometry in P and decomposed flow of v_θ (and v_r in (c)) with contours of ${}^t\hat{\boldsymbol{x}}\boldsymbol{Q}_\theta\hat{\boldsymbol{x}}$ (and ${}^t\hat{\boldsymbol{x}}\boldsymbol{Q}_r\hat{\boldsymbol{x}}$) in transition into a vortex. Through (a) and (b), vortical flow is generated in (c). (a) $\phi = -2$, (b) $\phi = -1/2$, and (c) $\phi = \sqrt{3/2}$ and $\sigma = -3/4$. (Note that the vector lengths are adjusted in respective figures.)

counterclockwise directions in P, as shown in Fig. 1. The swirlity ϕ is given by $\phi = \mathrm{sgn}(\lambda_{\theta_1}\lambda_{\theta_2})\sqrt{|\lambda_{\theta_1}\lambda_{\theta_2}|}$, thus

$$\phi = -|\delta| < 0. \tag{3}$$

This feature is of great interest. The swirlity, that specifies the geometrical characteristic of azimuthal (swirling) flow, depends on not the vorticity component ω_3 but the eigenvalues associated rather with the radial flow. Figure 1 shows the transition of the flow geometry into a vortex followed by ϕ.

On the other hand, the eigenvalues λ_{r_i} $(i = 1, 2; \lambda_{r_1} < \lambda_{r_2})$ of $\boldsymbol{Q}_r$ are expressed as $\lambda_{r_i} = (\lambda_1 + \lambda_2)/2 \pm \sqrt{\omega_3^2 + 4\delta^2}/2$. The sourcity σ is defined as $\sigma = \mathrm{sgn}(\lambda_{r_1}\lambda_{r_2})\sqrt{|\lambda_{r_1}\lambda_{r_2}|}$, then σ in P becomes

$$\sigma = \lambda_1\lambda_2 - \frac{\omega_3^2}{4}. \tag{4}$$

Equation (4) shows that σ is positive while $\omega_3^2/4 < \lambda_1\lambda_2$, then the radial flow is inflow in all directions in P, if $\lambda_1, \lambda_2 < 0$. If $\omega_3^2/4$ exceeds $\lambda_1\lambda_2$, then the radial flow has both inflow and outflow (such as Fig. 1 (c)). The symmetry or uniformity of the radial flow depends on both intensities of $\lambda_1\lambda_2$ and ω_3. If ω_3 is small (and $\lambda_1, \lambda_2 < 0$), the generated vortex may be weak. However, as σ is positive, this vortex exhibits effective vortex stretching that have compression (inflow) from all directions in P and increases vorticity.

CONCLUSION

The general representation of the velocity gradient tensor and the local flow topology in the transition into a vortex were shown. The swirlity and the generation of a vortex depend on the two eigenvalues of the tensor with the same sign, not on the vorticity. The sourcity shows that the uniformity or symmetry of the radial flow depends on the two eigenvalues and the vorticity normal to the plane (shear in the plane) that becomes the swirl plane.

Acknowledgements. This study was supported by the 31st grant from The Nitto Foundation.

References

[1] Chong, M. S., Perry, A. E., Cantwell, B. J.: A general classification of three-dimensional flow fields.*Phys. Fluids* **A2**(5): 765–777, 1990.

[2] Nakayama, K., Sugiyama, K., Takagi, S.: A unified definition of a vortex derived from vortical flow and the resulting pressure minimum. *Fluid Dyn. Res.* 46: 055511, 2014.

[3] Nakayama, K.: Physical properties corresponding to vortical flow geometry. *Fluid Dyn. Res.* **46**: 055502, 2014.

[4] Nakayama, K., Mizushima, L. D.: Study of local flow topology in transition into vortical flow *Proc. ICFD2015*, 2015

DEFLECTION OF A VORTEX DIPOLE BY A FLAT PLATE

Monika Nitsche[1] and Ling Xu *[2]
[1]*Department of Mathematics and Statistics, University of New Mexico, Albuquerque, NM, USA*
[2]*Department of Mathematics, University of Michigan, Ann Arbor, MI, USA*

Summary We present inviscid and viscous simulations of the trajectory of a counterrotating pair of point vortices in the presence of a flat plate centered on the vortex path, at an angle β_p with the horizontal. We vary the plate length and the angle β_p. In the inviscid case, the observed dynamics are extremely rich. In particular, singularities are observed that correspond to topological discontinuities in the vortex path as a function of β_p. In the viscous case, wall vorticity alters the vortex trajectory dramatically. Most notably, the inviscid limit of the viscous flow does not equal the inviscid solution. We are currently planning outdoor experiments to study the effect of possible wall slip on the flow.

PROBLEM DESCRIPTION

This paper presents a study of a rather simple dynamical system, namely, the trajectory of a pair of counterrotating point vortices in the presence of a plate positioned in its path. The flow considered is illustrated in figure 1(a). Two counter-rotating point vortices with circulation $\pm\Gamma$ are initially positioned at distance D from each other on a horizontal plane. In the absence of a plate, the vortices travel with constant velocity downward, in direction normal to the horizontal. We consider the deflection of the vortex trajectory by a plate of length L, centered on the path of the dipole sufficiently far downstream from the initial vortex position, and at an angle β_p from the horizontal. We vary $0 \leq \beta_p \leq \pi/2$ and the ratio of plate to dipole lengths, L/D. The results presented are nondimensionalized with respect to the vortex circulation Γ and the distance D.

INVISCID FLOW

In the inviscid case, the observed dynamics are extremely rich. For all values of L/D and β_p, the vortices surround the plate and leave at a deflected angle β_v on the opposite side of the plate. Figure 1(b) shows a sample trajectory for $\beta_p = 35^o$ and $D/L = \pi/4$. In some regimes, small changes in the angle β_p lead to large changes in the outgoing angle β_v. The dynamics become more complex for smaller values of D/L, that is, for larger plate lengths L relative to D. Figure 2 plots the trajectories for a decreasing set of values of D/L, as indicated. For smaller D/L, the right vortex is seen to approach the plate more closely, and behaves more closely as if the second vortex were absent. It tends to rotate around the plate, until it eventually returns to pair up with the left vortex and leave the plate. However, it is evident from the figure that between $D/L = 0.5\pi/4$ and $0.45\pi/4$ a topological discontinuity has occured in the path of the right vortex: with $D/L = 0.5\pi/4$ the vortex leaves above the plate. With $D/L = 0.45\pi/4$ it leaves below the plate. We show that these bifurcations correspond in singularities in β_v as a function of β_p. As D/L decreases further to $0.25\pi/4$, another singularity occurs so that the vortex again leaves the plate from above. Furthermore, the number of singular values of β_p increases as D/L decreases.

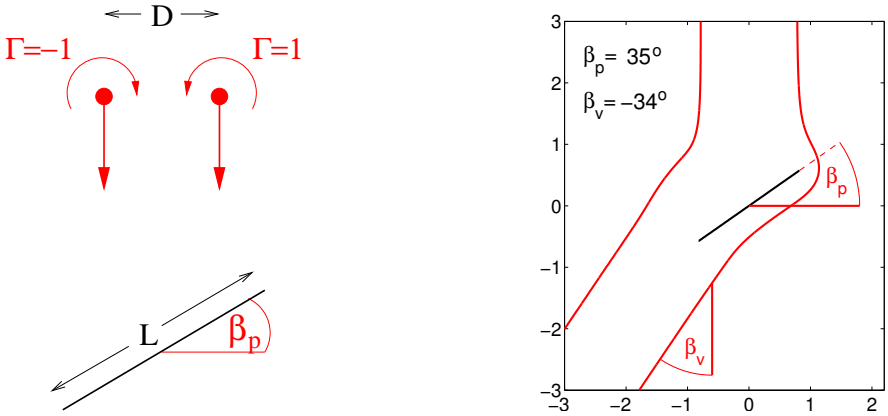

Figure 1: (a) (left) Initial configuration. (b) (right) sample trajectory and definitions.

*Corresponding author. Email: nitsche@math.unm.edu

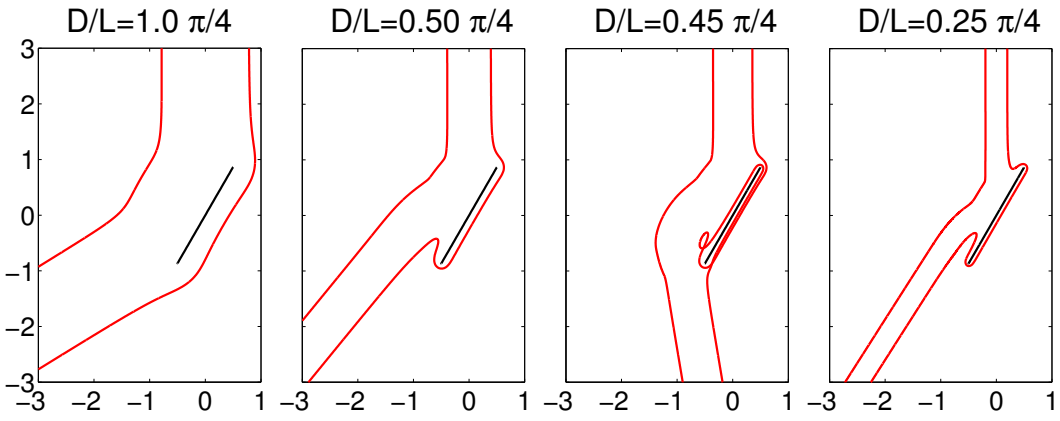

Figure 2: Vortex trajectories for decreasing values of $D/L = 1.0\pi/4, 0.5\pi/4, 0.45\pi/4, 0.25\pi/4$, as indicated.

VISCOUS FLOW

In the viscous case, we show that even in the simplest case of $\beta_p = \pi/2$ (vertical plate) the no-slip boundary condition creates a significant amount of opposite signed wall vorticity that merges with the vortices and alters the vortex trajectory dramatically. The amount of wall vorticity depends only on the dipole induced velocity at the wall, and not on fluid viscosity. Therefore, the change in trajectory does not vanish in the inviscid limit. The inviscid limit of the viscous Navier-Stokes flow therefore interestingly does not equal the inviscid Euler flow.

CONCLUSIONS

We have studied a simple point vortex system using inviscid and viscous simulations. In the inviscid case, this simple dynamical system has extremely rich structure. In the viscous case, the no-slip fluid velocity at the wall creates wall vorticity that effects the flow significantly, in a manner independent of fluid viscosity. We are planning to complement these simulations with outdoor experiments to study the effect of different surfaces with more or less slip at the wall on the vortex trajectory.

A VORTEX SHEET / POINT VORTEX DIPOLE

Kevin O'Neil [*1]

[1]*Department of Mathematics, The University of Tulsa, Tulsa Oklahoma USA*

Summary Few steady (weak) solutions of the 2D Euler equations involving vortex sheets are known. In this paper a distribution of vorticity is described analytically, consisting of one point vortex and one vortex sheet, that is an equilibrium in a uniformly translating frame. It can be considered a partial nonlocal desingularization of the +/- point vortex dipole. The vortex sheet is found as the limiting distribution of zeroes of a normalized modified Bessel function of the second kind, and can be described as the image under a conformal mapping of one half of the unit circle. The method used to find the solution, a two-step application of the "method of polynomials," may be more widely applicable.

Exact vortex sheet equilibria and vortex dipoles

Singular distributions of vorticity are commonly used as simplifications of the full 2D Euler equations; zero- and one-dimensional distributions are point vortices and vortex sheets, respectively. Many point vortex equilibria are known, including completely stationary configurations ("vortex crystals"), uniformly translating configurations, and relative (steadily rotating) equilibria. Many examples of the first two types have been found by the *method of polynomials*, where the vortex positions are represented as roots of polynomials that consequently satisfy differential equations [1]. This gives an analytic description of the complex potential of the flow. The well-known Adler-Moser and modified Adler-Moser polynomials are encountered in this context. However, only a few stationary configurations involving vortex sheets have been found analytically (other than the trivial parallel lines and concentric circles.) These include the straight line segment obtained as the limit of elliptical Kirchhoff vortices (a relative equilibrium) and the Prantdl-Munk vortex sheet [2] associated with elliptical lift distribution on a finite wing (a uniformly translating configuration.) Stationary vortex sheets in the presence of a flow due to fixed point vortices can be found exactly in some circumstances [3]. On the other hand, many stationary states have been found numerically, approximated by point vortex arrays, on the sphere as well as the plane [4,5]. These vorticity distributions can consist of only vortex sheets, or a hybrid of vortex sheets and point vortices. Some hybrid configurations shrink while rotating, resulting in rapid concentration of the one-dimensional vorticity [6].

In this paper a uniformly translating state consisting of one vortex sheet and one point vortex is described analytically. This vortex sheet/ point vortex configuration can be thought of as a partial desingularization of the simple $+1/\circ\ 1$ point vortex dipole that is nonlocal in the sense that the sheet extends over quite a long distance relative to its separation from the point vortex. Alternatively, in the presence of a uniform external flow the vorticity distribution will be stationary and the fluid velocity field can be interpreted as a separated flow past a one-dimensional barrier with a point vortex entrained in the flow.

The method of polynomials is used in two ways in the derivation of this flow. The vortex sheet appears as the limit of point vortex distributions related to Bessel polynomials. First, the (reverse) Bessel polynomials satisfy a differential equation related to uniformly translating point vortex configurations. Second, in the limit as the degree of the polynomials goes to infinity, the properties of this differential equation have been used to find the limiting positions and distribution of the roots of the polynomials. As a result the vortex sheet is described by a conformal mapping of the unit circle. It seems quite likely that generalizations of this process will yield other stationary vortex-sheet configurations.

Reverse Bessel polynomials

The Bessel polynomials

$$y_n(z) = \sum_{k=0}^{n} \frac{(n+k)!}{(n\circ\ k)!k!2^k}\, z^k, \quad n = 0,\, 1,\, 2,\, \ldots$$

are a well-known sequence of orthogonal polynomials related to the Bessel functions [7]. The zeroes of y_n are simple and have negative real part. The reverse Bessel polynomial $\theta_n(z) = z^n\, y_n(1/z)$ satisfies the second-order differential equation $z\theta_n''\circ\ 2(z+n)\theta_n' + 2n\theta_n = 0$. The zeroes of $\theta_n(z)$ are the reciprocals of the zeroes of y_n, and coincide with the zeroes of the modified Bessel function of the second kind, $K_{n+1/2}(z)$ [7]. Let $f_n(z) = \theta_n(nz)$ be the normalized reverse Bessel polynomial, so that f_n satisfies the equation $(z/n)f_n''\circ\ 2(z+1)f_n' + 2nf_n = 0$. Consequently the rational function

$$\frac{1}{n}\frac{f_n''}{2f_n}\circ\ (1+1/z)\frac{f_n'}{f_n} + \frac{n}{z},$$

which has simple poles at the zeroes $a_1, \ldots, a_n$ of f_n, is identically zero and every residue vanishes. Using the identities

$$\frac{f_n'(z)}{f_n(z)} = \sum_j \frac{1}{z\circ\ a_j}, \quad \frac{f_n''(a_j)}{2f_n'(a_j)} = \sum_{k\neq j} \frac{1}{a_j\circ\ a_k}$$

*Corresponding author. Email: koneil@utulsa.edu

to calculate the residue at $z = a_j$ then yields the relation

$$\sum_{k \neq j} \frac{1/n}{a_j \circ a_k} \circ (1 + 1/a_j) = 0.$$

Summing these relations over all j yields the additional relation $0 = n + \sum 1/a_j$. Taken together, these relations show that a configuration of point vortices consisting of one vortex of strength $1/n$ at each of the n points $z = a_j$ together with one vortex of strength $\circ\, 1$ at $z = 0$ will be at rest when in the presence of a constant external flow field. Without the external flow, the entire configuration moves uniformly in the fluid plane with a constant velocity $i/2\pi$.

Shape and density of the vortex sheet

The zeroes of f_n are the reciprocals of the zeroes of the normalized Bessel polynomial $y_n(z/n)$. In the limit $n \to \infty$ the zeroes of $y_n(z/n)$ are known to lie on a certain arc in the complex plane with a known limiting density [8, Theorem 7.1]. In terms of the the uniformly translating point vortex configurations mentioned above, the limit of the collection of n point vortices of strength $1/n$ is a vortex sheet Γ of total strength 1. The location and shape of the sheet and the corresponding linear vorticity density μ of the sheet can be derived from the information in [8], as follows. Let $\alpha(z) = \sqrt{1 + z^2}$ (principal branch) and $g(z) = z\, e^{\alpha}/(1 + \alpha)$. Then:

$$\Gamma = \{g^{-1}(\circ\, e^{it}),\ \circ\, \pi/2 \leq t \leq \pi/2\}, \quad \mu(z) = (1/\pi)\, |1 + z^{-2}|^{1/2}.$$

This curve extends from $\circ\, i$ to i to the left of the axis $\mathrm{Re(z)} = 0$, passing through the real axis at $z \approx \circ\, 0.663$. The sheet very nearly coincides with a circular arc. Indeed, the distance between any point on Γ and the nearest point on the circle with radius 1.086 and center 0.423 (that is, the circle that touches Γ at the center and two endpoints) is no greater than 0.024. (See also Figures 2,3 of [2] showing the reciprocal of Γ.) It is also significant that the vorticity density μ is bounded and goes to zero at the ends of the sheet, in contrast to the Prandtl-Munk vortex sheet [2]. The contribution of the vortex sheet to the velocity field of the fluid is computed using the Cauchy transform of μ [9] since, as $n \to \infty$,

$$\frac{1}{n} \frac{f_n'(z)}{f_n(z)} \to \int_\Gamma \frac{\mu(w)}{z \circ w}\, |dw|.$$

The magnitude of the discontinuity in the fluid velocity on either side of the sheet is proportional to μ, and the average of these velocities is the velocity of the sheet at that point. In this case every point of the sheet has the same velocity, so that when a uniform external flow is added to make the sheet motionless the fluid velocity on the two sides of the sheet are equal and opposite, with magnitude proportional to μ. Vanishing of μ at the ends of Γ means that the flow has stagnation points at the ends, i.e. satisfies a Kutta condition at both ends. If the vortex sheet is replaced by a barrier (a nearly circular arc extending from i to $\circ\, i$ to the left of the origin) the flow can be visualized as separated flow around the barrier with an entrained point vortex at the origin.

References

[1] Clarkson P.: Vortices and polynomials. Stud. Appl. Math. 123:37-62, 2009.

[2] Lopes Filho M.C., Nussenzveig Lopes H.J., and Souza M.O.: On the equation satisfied by a steady Prandtl-Munk vortex sheet. Comm. Math. Sci. 1:68-73, 2003.

[3] O'Neil K.A: Stationary vortex sheets in a stirring flow. Theor. Comp. Fluid Dyn. 27:777-785, 2013.

[4] O'Neil K.A: Stationary states of identical point vortices and vortex foam on the sphere. Proc. Royal Soc. A 469:20120622, 2012

[5] O'Neil K.A: Relative equilibria of vortex sheets. Physica D 238:379-383, 2009.

[6] O'Neil K.A: Collapse and concentration of vortex sheets in two-dimensional flow. Theor. Comp. Fluid Dyn. 24:39-44, 2009.

[7] Grosswald E.: Bessel Polynomials. Lecture Notes in Mathematics 698, Springer-Verlag, New York 1978.

[8] De Bruin M.G, Saff E.B. and Varga R.S.: On the zeros of generalized Bessel polynomials. Proc. (A) Amer. Math. Soc. 84:1-25, 1981.

[9] Hou T., Lowengrub J., Krasney R.: Convergence of a point vortex method for vortex sheets. SIAM J. Numer. Anal. 28:308-320, 1991.

HYBRID RANS-LES SIMULATION OF WINGTIP VORTICES OF AN AIRLINER

Dmitry Kolomenskiy[1] and Roberto Paoli*[2,3,4]
[1]*Graduate School of Engineering, Chiba University, Chiba, Japan*
[2]*Department of Mechanical and Industrial Engineering, University of Illinois at Chicago, Chicago, Illinois, USA*
[3]*Argonne National Laboratory, Argonne, Illinois, USA*
[4]*CERFACS, Toulouse, France*

Summary Numerical simulation of the wake of a realistic model of an airliner have been conducted using a hybrid RANS–LES approach. Dynamics of the trailing vortices is analyzed and a simple analytical model is proposed that accounts for the turbulence in the wake.

INTRODUCTION

Modeling of aircraft wakes is an important component of many research areas in the aviation sector, including the prediction of wake encounter hazard and the environmental impact of aviation. The latter has caught the attention of scientific community because of its contribution to the general problem of climate change produced by anthropogenic activity [1]. Contrails, the ice crystals forming behind jet engines by condensation of water vapor onto exhaust soot particles are the most uncertain contributors to the Earth radiative balance among all aircraft emissions. A good estimation of the radiative perturbation depends partly on the accurate description of the long-time development of contrails, which is related to the dynamics of trailing vortices past the wing tips [2]. Various hydrodynamic effects are involved in the process, such as generation of a vortex sheet from the boundary layers, its subsequent roll-up in a pair of vortices, interaction with the jets and hydrodynamic instabilities. In addition, chemical and micro-physics phenomena have to be considered such as formation and dispersion of soot particles, ice crystal growth, evolution of their optical properties etc. In this work, we focus on the dynamics of the near wake within the distance of about three wing spans downstream.

AIRLINER MODEL AND NUMERICAL METHOD

We consider a medium range twin-engine airliner and model its cruise flight at the altitude of 35000 feet, Mach number $M = 0.82$ and lift coefficient $c_L = 0.5$. The with wing span is $b = 57.6$ m, bilateral symmetry is assumed. Reynolds–Averaged Navier–Stokes (RANS) and Large Eddy Simulations (LES) computations are performed in sequence. Averaged quantities obtained form the RANS simulation are projected (using spline interpolation) on a uniform Cartesian grid at a cross-section downstream from the trailing edge (figure 1*a*). The location chosen corresponds to the inflow boundary of the LES domain. More information about our RANS–LES hybrid approach can be found in [3].

The LES simulations are performed using NTMIX [5], a research code developed for fundamental study of turbulent reactive two-phase flows. The LES domain is a rectangular box located downstream from the wing. It spans $L_y = 180$ m in the vertical direction, $L_z = 90$ m in the lateral direction and $L_x = 192\ m$ in the downstream direction. A Cartesian discretization grid is used that consists of $N_x \times N_y \times N_z = 1280 \times 620 \times 852$ points. It is stretched in the vertical and lateral directions, but the volume that encompasses the wake is discretized uniformly with grid step 0.036 m. In the downstream direction, the grid is uniform with step 0.15 m. The inflow boundary condition is supplied by a RANS computation (see figure 1*b*). Conservative variables are sampled on a plane past the wing tip and extended inside the fuselage.

DISCUSSION

Figure 2 shows a visualization of the wake. The surface of the aircraft is shown in grey, for reference. The two distinctive features clearly visible in this image are trailing vortices and turbulent jets. For the vortices, based on the results of our numerical simulation, we propose a generalized Moore–Saffman model adapted to the turbulent regime. It yields a similarity solution for the tangential velocity in a plane perpendicular to the inflow direction, in the laboratory reference frame,

$$v_\theta(r,\tau) = C_\theta \left(\nu^{-1}\tau^{\alpha-1}\right)^{\frac{1}{4}} V(\circ\ \frac{1}{4} r^2 \nu^{-1}\tau^{\alpha-1}), \tag{1}$$

where r is the distance to the vortex core, τ is the time variable, C_θ, ν and α are the parameters of the model. The self-similar profile is expressed in terms of the Kummer confluent hypergeometric function M as

$$V(\eta) = (\circ\ \eta)^{\frac{1}{2}} M\left(\frac{1}{2} + \frac{b}{\alpha \circ\ 1}, 2; (1 \circ\ \alpha)\eta\right). \tag{2}$$

*Corresponding author. Email: paoli@cerfacs.fr

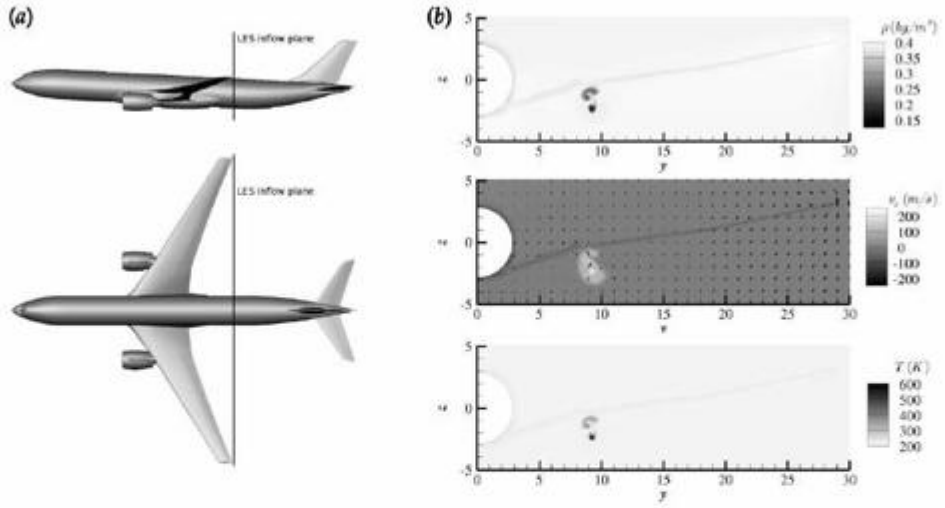

Figure 1: (*a*) Side and top views of the airliner. (*b*) Flow parameters at the RANS-LES interface.

The original Moore–Saffman model [6] for laminar vortices is recovered if $\alpha = 0$ and if ν is the kinematic viscosity of the fluid. In our turbulent case, however, the numerical simulation suggests that $\alpha = 0.707$ and $\nu = 0.00101$ m^2/s$^{0.293}$. Similarity solutions for the pressure deficit and for the axial velocity have also been obtained.

References

[1] Lee, D., D. W. Fahey, P. M. Foster , P. J. Newton, R. C. N. Wit, L. L. Lim, B. Owen, and R. Sausen: Aviation and global climate change in the 21th century. Atmos. Env., 43, 3520–3537, 2009.

[2] Paoli R. and K. Shariff: Contrail modeling and simulation. Annu Rev. FLuid Mech., 48: 393–427, 2016.

[3] Kolomenskiy D., Paoli R. and Boussuge, J.: Hybrid RANS-LES simulation of wingtip vortex dynamics. Proceedings of the ASME 2014 4th Joint US-European Fluids Engineering Division Summer Meeting and 12th International Conference on Nanochannels, Microchannels, and Minichannels. August 3-7, 2014, Chicago, Illinois, USA, 2014, FEDSM2014-21349.

[4] Cambier L., Heib S. and Plot S.: The ONERA elsA CFD software: input from research and feedback from industry. Mech. & Industry 14, 159-174, 2013.

[5] Stoessel A.: An efficient tool for the study of 3D turbulent combustion phenomena on MPP computers. Proceedings of the HPCN 95 Conference, Milan, Italy, 1995.

[6] Moore D. W. and Saffman P. G.: Axial flow in laminar trailing vortices. Proc. R. Soc. London, Ser. A 333, 491-508, 1973.

[7] Paoli R., Nybelen L., Picot J. and Cariolle D.: Effects of jet/vortex interaction on contrail formation in supersaturated conditions. Phys. Fluids 25, 053305, 2013.

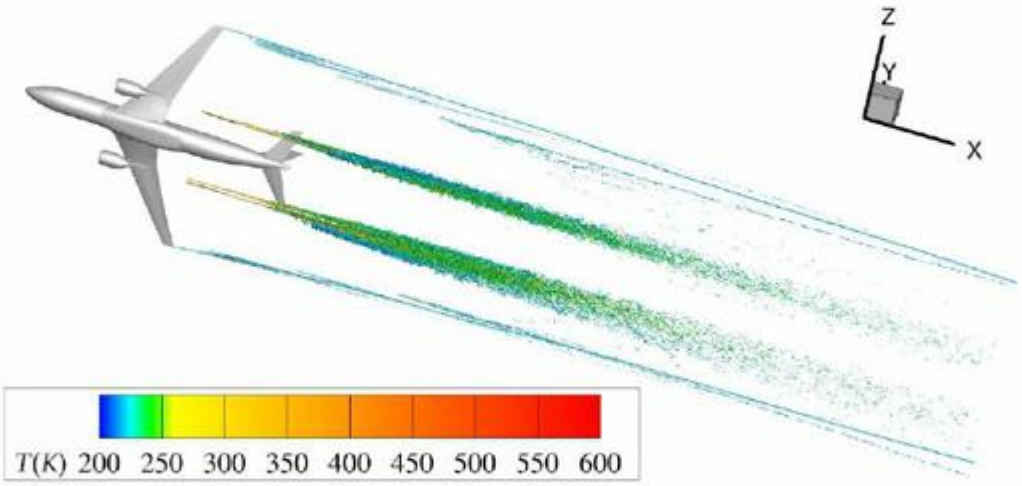

Figure 2: Isosurface of λ_2 criterion coloured with the temperature.

MOTION AND FLOW TOPOLOGY OF MULTIPLE HELICAL VORTICES

Oscar Velasco Fuentes *
Departamento de Oceanografía Física, CICESE, Ensenada, México

Summary A set of equal, coaxial, symmetrically-arranged helical vortices translate and rotate steadily while the vortices preserve their shape and relative position in an unbounded, ideal fluid (Joukowsky 1912). We obtained the corresponding linear and angular velocities (U and Ω, respectively) as the sum of the mutually induced velocities found by Okulov (2004) and the self-induced velocities found by Velasco Fuentes (2016). Numerical computation of the velocities with the Biot-Savart law, and numerical simulation of the vortex motion with a 3D vortex-in-cell method verified that our theoretical results are accurate for any number of vortices and over the whole range of values of the vortices' pitch and radius. An analysis of the flow topology in a reference system that translates with velocity U and rotates with angular velocity Ω served to determine the capacity of the vortices to carry fluid.

VORTEX MOTION

We study the motion of a system of N equal helical vortices in an unbounded, inviscid, incompressible fluid. Each vortex is an infinite tube whose centerline is a helix of pitch L and whose cross-section is a circle of radius a, where the vorticity is uniform and parallel to the centerline. The vortices' centerlines intersect any polar plane on the vertices of a regular polygon of N sides inscribed in a circle of radius R. Since the vortices' circulations are assumed to be equal (Γ), the flow evolution is determined by three non-dimensional parameters only: the number of vortices N, the vortex radius $\alpha = a/R$ and the vortex pitch $\tau = L/2\pi R$. Joukowsky (1912) deduced that this system translates and rotates steadily while the vortices preserve their form and relative position: he found the approximate velocity of a single vortex of large pitch but made no attempt to compute the motion of two or more vortices.

We determine the motion of the vortices by adding the self-induced velocity, defined as the velocity of the ith vortex in an otherwise quiescent fluid, to the mutually induced velocity, defined as the velocity induced by the remaining $N \circ 1$ vortices on the ith vortex. Therefore the set of vortices has linear velocity $U = U_S + U_M$ and angular velocity $\Omega = \Omega_S + \Omega_M$. To obtain U_S and Ω_S Velasco Fuentes (2016) assumed that the vortices have, to a first approximation, circular cross section and uniform vorticity, and evaluated the cylindrical components of the velocity field at two diametrically-opposed points on the vortex boundary using Boersma & Wood's (1999) approximation to Hardin's (1982) velocity field. The self-induced velocities (made dimensionless by dividing them by $\Gamma/4\pi R$ and $\Gamma/4\pi R^2$, respectively) are given as follows:

$$U_S^* = \frac{1}{(1+\tau^2)^{3/2}}\left(\ln(2/\epsilon) \circ \ln(\sqrt{1+\tau^2}) + (1+\tau^2)^{3/2} W(\tau)\right)$$

$$\Omega_S^* = \frac{\circ\ \tau}{(1+\tau^2)^{3/2}}\left(\ln(2/\epsilon) \circ \ln(\sqrt{1+\tau^2}) + (1+\tau^2)^{3/2}(W(\tau) \circ 2/\tau) + 2(1+\tau^2)\right)$$

where $\epsilon = a/R(1+\tau^2)$ and $W(\tau)$ is an integral that cannot be evaluated in closed form (Boersma & Wood 1999). These formulas are more accurate, over the whole range of values of the vortex' pitch and radius, than any of those published in one hundred years of research on the subject.

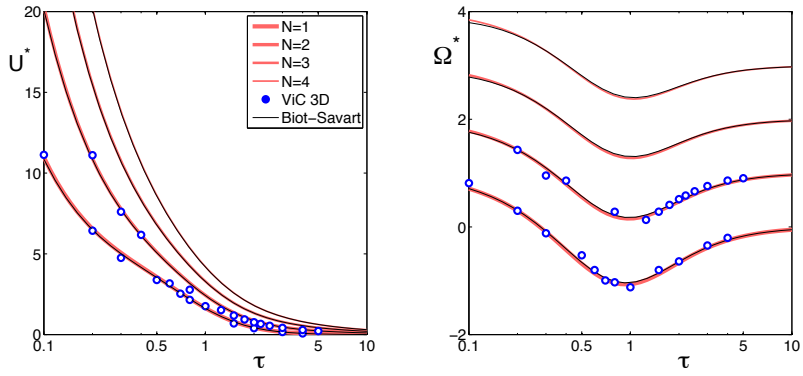

Figure 1: Linear and angular velocities (U and Ω, respectively) of a set of helical vortices as functions of the number of vortices (N) and the vortex pitch (τ), for a given vortex radius ($\alpha = 0.1$).

*Corresponding author. Email: ovelasco@cicese.mx

Okulov (2004) obtained U_M and Ω_M by a complicated but efficient evaluation procedure of the Kapteyn series appearing in Hardin's (1982) velocity field.

Thus, by adding the self- and mutually-induced velocities, we find that the set of helical vortices move with a linear velocity U that grows with the number of vortices (N) but decreases as their radius (α) and pitch (τ) increase, whereas the angular velocity Ω grows with N and α but has a minimum around $\tau = 1$ for fixed values of N and α. Figure 1 shows a comparison of the theoretical results with two numerical calculations: (a) the velocity evaluated at a single point using the Rosenhead-Moore approximation to the Biot-Savart integral and (b) the velocities obtained with a three-dimensional, vortex-in-cell model by computing the linear and angular displacements of fluid particles located within the vortex, dividing those displacements by the elapsed time and taking the average over all the particles used in the simulation.

FLOW TOPOLOGY

We determined the capacity of the vortices to carry fluid by analysing the topology of the helical stream function in a reference frame where the vortices are stationary; that is to say, in a frame that translates with linear velocity U and rotates with angular velocity Ω. The steady stream function Ψ is given as follows

$$\Psi(r,\phi) = \frac{1}{2}\left(\Omega \circ \frac{U}{l}\right) r^2 + \sum_{i=1}^{N} \psi_i(r,\phi)$$

where $l = L/2\pi$, (r,ϕ) are helical coordinates related to the cylindrical coordinates by $(r,\phi) = (r, \theta \circ z/l)$, and ψ_i is the stream function of the flow induced by the ith vortex (Hardin, 1982).

We found that for all N there are three qualitatively different flow geometries depending on the vortices radius and pitch (see figure 2, which shows the case $N = 3$): (I) large-pitch vortices move slowly but carry a large volume of fluid, (II) thin small-pitch vortices move fast and carry a small volume of fluid, (III) thick small-pitch vortices move at intermediate velocities, carry a moderate volume of fluid but push fluid forward along the helices' axis. Two vortices of intermediate pitch ($N = 2$, $1 < \tau < 4$) exhibit a fourth regime which is similar to regime I except for the flow relatively far from the vortices.

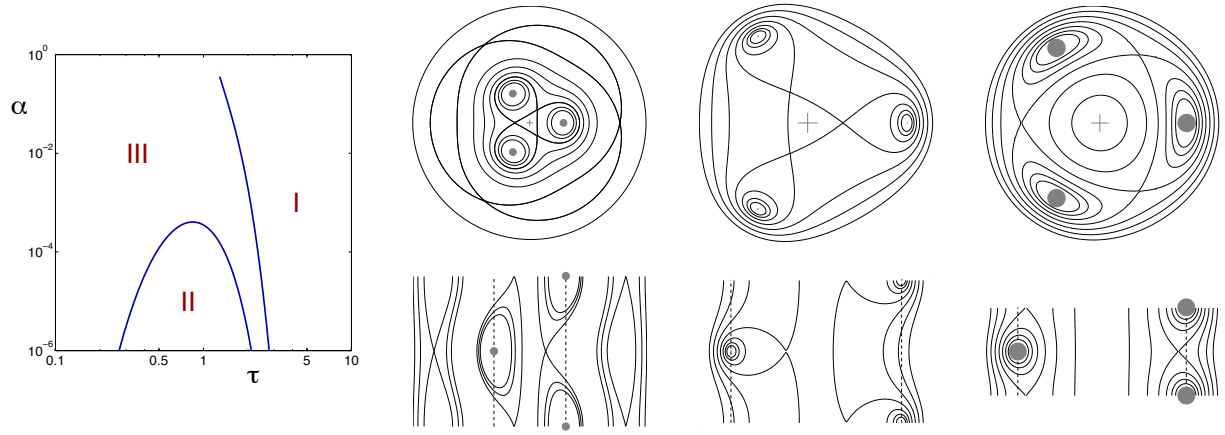

Figure 2: Left panel: The flow regimes for three helical vortices in the parameter plane (τ, α): (I) large-pitch helices, (II) thin small-pitch helices, and (III) thick small-pitch helices. Upper row: the helical stream function Ψ on the polar plane (r,θ) for representative cases of each regime (I to III from left to right). Lower row: the corresponding stream function on meridional planes (r,z)

References

[1] Boersma J., Wood D.: On the self-induced motion of a helical vortex. J. Fluid Mech. 384: 263-280, 1999.

[2] Hardin J.: The velocity field induced by a helical vortex filament. Phys. Fluids 25, 1949-1952, 1982.

[3] Joukowsky N.E.: Vihrevaja teorija grebnogo vinta, Trudy Otdeleniya Fizicheskikh Nauk Obshchestva Lubitelei Estestvoznaniya 16: 1–31, 1912. French translation in *Théorie tourbillonnaire de l'hélice propulsive* (Gauthier-Villars, Paris, 1929).

[4] Okulov V.L.: On the stability of multiple helical vortices, J. Fluid Mech. 521: 319–342, 2004.

[5] Velasco Fuentes O.: Motion of a helical vortex, submitted to Eur. J. Mech. B/fluids, 2016.

FM16 - Waves in Fluids

TS.FM16-1.01	Toledo, Yaron - A nonlinear triad interaction source term for wave forecasting models (INVITED)	1582
TS.FM16-1.02	Babanin, Alexander - Turbulence induced by surface water waves (INVITED)	1584
TS.FM16-1.03	Perrard, Stéphane - Surface waves on levitating liquid	1586
TS.FM16-1.04	Mizuta, Yo - Numerical and theoretical analyses on interface wave of magnetic fluids	1588
TS.FM16-1.05	Vogt, Tobias - Investiagtion of inertial waves inside a liquid metal column by means of electromagnetic fields	1590
TS.FM16-1.06	Steinrück, Herbert - Asymptotic analysis of a rotary wave in a cylindrical container	1592
TS.FM16-2.01	Kadri, Usama - Evolution of Faraday waves by resonant triad interactions of surface--compression waves	1594
TS.FM16-2.02	Christodoulides, Paul - Ocean waves and microseisms	1596
TS.FM16-2.03	Rajchenbach, Jean - Faraday waves revisited	1598
TS.FM16-2.04	Domino, Lucie - Faraday wave lattice as an elastic metamaterial	1600
TS.FM16-2.05	Funakoshi, Mitsuaki - Surface waves in a square container due to its resonant horizontal elliptic motion	1602
TS.FM16-2.06	McTavish, James - Nonlinear Acoustics in Brass Instruments	1604
TS.FM16-3.01	Ardhuin, Fabrice - Observing and understanding short gravity waves (INVITED)	1606
TS.FM16-3.02	Shrira, Victor - Spectral evolution of random wave fields: Kinetic equations vs. direct numerical simulations (INVITED)	1608
TS.FM16-3.03	Veron, Fabrice - Laboratory measurements of the inception and evolution of centimeter-scale Langmuir turbulence	1610
TS.FM16-3.04	Clamond, Didier - Dispersion-improved fully nonlinear shallow water model	1612
TS.FM16-3.05	Malecha, Ziemowit - Baroclinically-driven acoustic streaming	1614
TS.FM16-3.06	Albrecht, Thomas - Components of mean streaming flow in a precessing cylinder at small nuation angles	1616
TS.FM16-4.01	Grue, John - Nonlinear vs. linear supercritical dead water	1618
TS.FM16-4.02	Liu, Hua - Generation and runup of triple solitary waves on plane slope	1620
TS.FM16-4.03	Horne Iribarne, Ernesto - Transport of particles by internal waves	1622
TS.FM16-4.04	Lerisson, Gaétan - Internal Wave in the Ocean, Local, Global Stability and Transient Growth	1624
TS.FM16-4.05	Buckley, Marc - Structure of the airflow above surface gravity waves	1626
TS.FM16-4.06	Deike, Luc - Air entrainment and bubble statistics in three-dimensional breaking waves	1628
PO.FM16-1.01.184	Itay, Uri - A Kinematic Criterion for the Breaking of Shoaling Waves	1630
PO.FM16-1.02.185	Mangan, Niall - Optimal distribution of riverine turbines in a linear array with systematic flow manipulation	1632
PO.FM16-1.03.186	Pizzo, Nicholas - Wave modulation: the geometry, kinematics, and dynamics of surface-wave packets	1634
PO.FM16-1.04.187	Rzeznik, Andrew - Energy propagation and group speed for complex exponential waves	1636
PO.FM16-1.05.188	Müllner, Markus - Stationary solitary waves above bumps or ramps in turbulent	1638

	open channel flow	
PO.FM16-1.06.189	Shestakovskaya, Elena - Analytical solution of a shock wave in gas sphere in lagrangian coordinates	1640
PO.FM16-1.07.190	Zhao, Xi - Analysis of nearshore tsunami wave patterns: solitary waves, N-waves and undular bores.	1642

A NONLINEAR TRIAD INTERACTION SOURCE TERM FOR WAVE FORECASTING MODELS

Teodor Vrecica[1] and Yaron Toledo [*1]
[1]*School of Mechanical Engineering, Tel-Aviv University, Israel*

Summary Quasi-2D deterministic and non-local stochastic evolution equations are derived for water waves up to quadratic nonlinearity. The models include nonlinear shoaling and wave breaking effects. The work identifies that the stochastic model should be localized in two different manners in order to account for two nonlinear resoant mechanisms related to intermediate and shallow water regimes. The locallization process allows a 2D nonlinear triad source term (S_{3nl}) fitting for implementation in wave forecasting models to be formulated by locally using a quasi-2D approach. The derived formulation presents good agreements with deterministic ensembles, field measurements and laboratory experiments.

Nonlinear interactions between sea waves and the sea bottom are a main mechanism for energy transfer between the different wave frequencies in the near-shore region. Nevertheless, it is difficult to implement this phenomenon in stochastic wave forecasting models due to its mathematical complexity, which mostly consists of computing either the bi-spectral evolution or non-local shoaling coefficients. Such an implementation is of great importance as it will allow extending the wave forecast to the nearshore region.

In this work, quasi-2D stochastic energy evolution equations are derived for dispersive water waves up to quadratic nonlinearity based on the deterministic model of [1]. The bi-spectral evolution equations are formulated using the stochastic closure of [2]. They are solved analytically and substituted into the energy evolution equations to construct a stochastic model with non-local shoaling coefficients.

The nonlinear shoaling mechanism is investigated and shown to present two different behavior types. The first consists of a rapidly oscillating behavior transferring energy back-and-forth between wave harmonics in deep water. Due to the contribution of bottom components for closing the class III Bragg resonance conditions, this behavior includes mean energy transfer when waves reach intermediate water depths. The second behavior relates to 1D shoaling effects in shallow water depths. In contrast to the behavior in intermediate water depths, it is shown that the nonlinear shoaling coefficients refrain from their oscillatory nature while presenting an exponential energy transfer. It is explained through the 1D satisfaction of the resonance conditions by wave triads even without depth changes due to the non-dispersive propagation in this region. The energy evolution model is localized using a matching approach to account for both behavior types.

A common assumption in formulating bi-spectral evolution equations is of slow changes of the wave spectrum. This assumption causes very large discrepancies when the shoaling becomes significant or when breaking occurs. The present work avoids this assumption by utilizing a perturbation approach. It shows that the stochastic closure of [2] does hold in the above situation when and does not require the incorporation of additional nonlinear coefficients (i.e., to be extended to the closure of [3]). The solution of the full 2D nonlinear interaction problem is addressed by using the quasi-2D formulation locally in allignment with the local bathymetry gradient as a first approximation. This results in a nonlinear triad source term (i.e., a 2D S_{3nl}) that is fitting for implementation in wave forecasting models.

The derived formulation is evaluated with respect to deterministic ensembles, field measurements and laboratory experiments while performing well in modeling directional monochromatic super-harmonic self-interactions, infra-gravity wave generation from bi-chromatic waves and a realistic wave spectrum evolution. This lays physical and mathematical grounds for constructing a formulation that consistently accounts for 2D nonlinear energy transfers from deep to shallow water in stochastic wave forecasting models.

[*]Corresponding author. Email: toledo@tau.ac.il

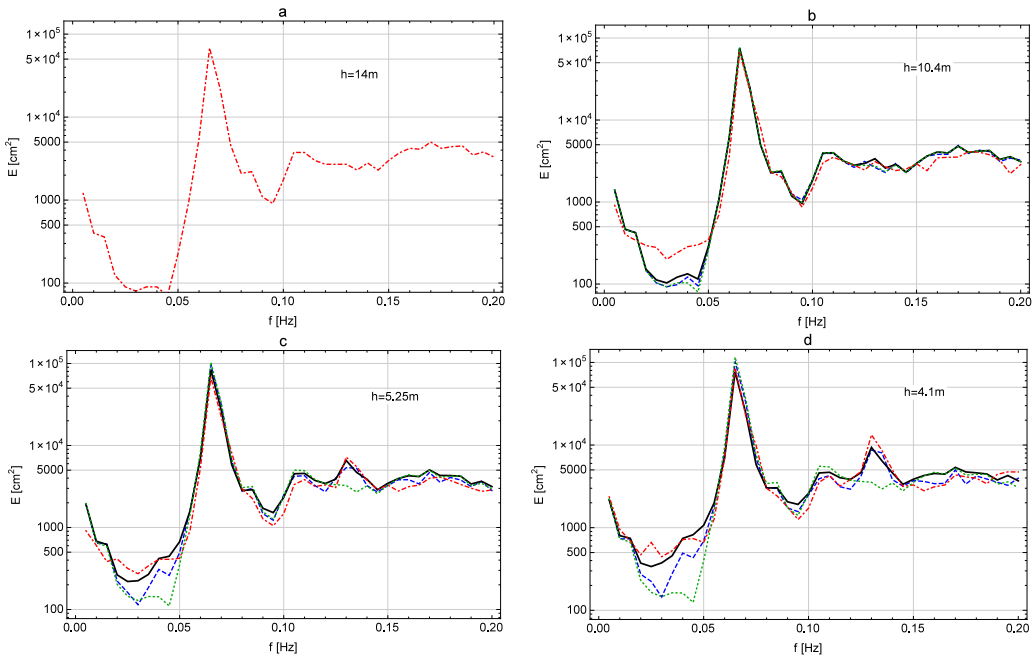

Figure 1: Evolution of a measured wave spectrum over a mildly sloping beach. The dot-dashed red line describes the field measurements results of [4]; The thick black line represents the current localized stochastic model; The dashed blue line describes the ensemble averaged results of the deterministic model of [1]; the dark green dotted line describes the linear stochastic model solution. Results are plotted for the depths of 14(a), 10.4(b), 5.25(c) and 4.1(d) meters.

References

[1] Bredmose H., Agnon Y., Madsen P.A., Schaffer H.A.: Wave transformation models with exact second-order transfer. European Journal of Mechanics - B/Fluids 24(6):659-682, 2005

[2] Benney D.J., Saffman P.G.: Nonlinear interaction of random waves. Proceedings of the Royal Society of London A 289:301-321

[3] Holloway G.: Oceanic internal waves are not weak waves. Journal of Physical Oceanography. 10:906-914

[4] Freilich M.H., Guza R.T.: Nonlinear effects on shoaling surface gravity waves. Philosophical Transactions of the Royal Society of London A311:1-41

TURBULENCE INDUCED BY SURFACE WATER WAVES

Alexander V Babanin[1],
[1]*The University of Melbourne, Melbourne, Australia*

Summary Turbulence produced by orbital motion of surface water waves will be discussed. While important across a broad range of ocean engineering, oceanographic and air-sea interaction applications, this is also an outstanding topic of the fluid mechanics. Its theory will be revisited, numerical and experimental results presented, field observations outlined.

INTRODUCTION

Breakthroughs in the potential wave theories in the 60s defined the development of analytical research and drove experimental research in water waves for decades to come. Series of spectacular works by Hasselmann, Zakharov, Benjamin and Feir, Longuet-Higgins, among other researches, allowed us to reveal and explain many details of wave dynamics such as resonant and quasi-resonant interactions, modulational instability; led to introducing and embracing the kinetic theory, Zakharov and Nonlinear Schrödinger Equations, concept of weak turbulence for surface waves.

In the meantime, rotational approaches and solutions for the waves have not been receiving such an attention or even forgotten. One can trace a setup of this problem back to 1920s [1], but Phillips [2], followed by an extended summary in the book [3], provided explicit solutions for infinitesimal one-dimensional surface waves in the water of non-zero viscosity. The solutions are rotational, but as the authors rightly foresaw the one-dimensional approach imposed limitations on their practical applicability.

Such applicability was greatly enhanced by the Benilov theory [4,5]. It describes instability of three-dimensional vortexes in response to forcing by one-dimensional orbital wave motion. The wave motion is regarded potential in this theory, and hence the turbulence has to be pre-existent. Then, it is unstable in the two planes perpendicular to the wave orbits, and this instability radically changes the outcomes by comparison with the Phillips theory which applied to the stable plane. The Phillips one-dimensional wave-induced turbulence, after being produced by the wave orbital motion, is constantly damped by viscosity, whereas the Benilov three-dimensional turbulence should grow on behalf of the wave energy.

The ocean is always turbulent and the turbulence away from thin boundary layers is always three-dimensional, and therefore in the oceanographic context it can be expected that the Benilov mechanism prevails. The Phillips mechanism, however, should not be disregarded as having only an academic value. Whatever is the source of turbulence generation in the ocean, for example, the popular these days Langmuir turbulence, any pre-existing turbulence will be enhanced in presence of the waves (see e.g. [6] for a review).

While being an input of energy for turbulence, the wave-turbulence interactions are a loss of energy for waves, and hence a dissipation mechanism which has to be taken into account in the ocean wave forecast, particularly in case of swell propagation. Extra source of turbulence is also of primary significance for the upper-ocean mixing and hence the large-scale air-sea interactions which can be altered essentially, for example, in case of tropical cyclones (large waves) or at climate scales.

THEORY, NUMERICAL SIMULATIONS AND EXPERIMENTS

Introduction above explains how the Phillips and Benilov theories are different, and this implies that turbulence production/dissipation rates and their dependences should be different between the two. Laboratory experiments [7] and numerical simulations [8], however, found both the intensity of the turbulence and its dependence on wave amplitude being similar in the two circumstances. Therefore, there may be a connection between the two mechanisms.

Here, we consider a similarity theory of isotropic turbulence induced by waves on the water with free surface. Scaling is obtained from observations of dissipation rates for swell propagation in the ocean, and then used to estimate the turbulent viscosity and spectrum of the locally-isotropic turbulence. The estimates are compared with measurements and modelling.

CONCLUSIONS

The paper discusses turbulence produced or enhanced by the orbital motion of surface water waves. Similarity theory is proposed based on the concept of Lomogorov-Obukhov locally isotropic turbulence and agrees well with estimates of the turbulence dissipation rates and estimates of the coefficient of turbulent viscosity for oceanic conditions.

[a)] Corresponding author. Email: ababanin@swin.edu.au

References

[1] Jeffreys, H.: On turbulence in the ocean. *The London, Edinburgh, and Dublin Philosophical Magazine and Journal of Science*, **39**:578–586, 1920.

[2] Phillips, O.M.: A note on the turbulence generated by gravity waves. *J. Geophys. Res*., **66**:2889–2893, 1961.

[3] Kinsman, B.: *Wind Waves: Their Generation and Propagation on the Ocean Surface*. Prentice Hall, Englewood Cliffs, N.J., 676p, 1965.

[4] Benilov, A.Y., T.G. McKee, and A.S. Safray: On the vortex instability of the linear surface wave. *Numerical Methods in Laminar and Turbulent Flow*, **8**, edited by C. Taylor, Pineridge, Swansea, U.K.:1323-1334, 1993.

[5] Benilov, A.Y:. On the turbulence generated by the potential surface waves. *J. Geophys. Res*., **117**:C00J30, 2012.

[6] Ghantous, M., and A.V. Babanin: Ocean mixing by wave orbital motion. *Acta Physica Slovaca*, **64**, 1-56, http://www.physics.sk/aps/pub.php?y=2014&pub=aps-14-01 , 2014.

[7] Babanin, A.V., and B.K Haus: On the existence of water turbulence induced by non-breaking surface waves. *J. Phys. Oceanogr.*, **39**, 2675-2679, 2009.

[8] Babanin, A.V., and D. Chalikov: Numerical investigation of turbulence generation in non-breaking potential waves. *J. Geophys. Res.*, **117**, doi:10.1029/2012JC007929, 14p, 2012.

SURFACES WAVES ON LEVITATING LIQUID

Stéphane Perrard *[1,2], Luc Deike[1,3], Charles Duchêne[1], and Chi-Tuong Pham[1,4]

[1]*MSC Laboratory, University Paris-Diderot, FR, EU*
[2]*current address : James Franck Institute, University of Chicago, IL, US*
[3]*current address : Scripps Institution of Oceanography, University of California at San Diego, CA, US*
[4]*LIMSI, University Paris-Orsay, FR, EU*

Summary Under earth conditions, water surface waves of wavelength larger than few centimeters are usually dominated by gravity. We present an experimental way to obtain steady levitated liquid puddles that can be used to observe quasi one-dimensional capillary waves at the centimeter scale. Two modes of waves are observed: first linear and non-linear gravity-capillary waves, including capillary solitons, as well as sloshing modes of the levitated puddle. Moreover, we show how various experimental geometry can be used to tune the influence of gravity on the wave propagation.

INTRODUCTION

When water is deposited on a surface hotter than 200°C, it breaks into small drops that roll over the substrate with very little friction. The evaporation process lasts for a much longer time than expected. This effect is named after J.G. Leidenfrost who discovered it in a spoon heated by a localized flame during the XVIII century. The presence of a thin vapour layer supports the liquid weight by lubrication forces and the evaporation is drastically limited by the poor thermal conductivity of the gas phase [1]. However, this Leidenfrost effect has long been limited to drop size, as larger volumes of liquid lead to the formation of large gas pockets beneath which violently disturbs the liquid surface [1]. A few years ago we showed that the drop size limitation can be circumvented by using a curved substrate to form a torus of liquid in levitation without any specific limitation in length and volume [2]. The evacuation of vapour is then directed along the transverse direction, while the length is no longer limited in the other direction. Using levitating liquids of larger dimensions, we study the propagation of waves at the free surface. Figure 1 shows the two experimental configurations that have been used. One corresponds to a linear channel (Figure 1a), the second is a toroidal channel (Figure 1c,d). In each geometrical configuration, we observe linear and non-linear waves that can be characterized both from an experimental and theoretical point of view.

LINEAR WAVES

Figure 1a shows the one dimensional channel experimental setup, made of a dural plate with a transverse section of the quarter pipe shape (figure1a and c). Once heated above 250°C, 60mL of water poured into the substrate forms a cylinder of water, levitating on its own vapor film. Using an external exciter, we observe the propagation of two types of gravity-capillary waves. Their dispersion relations are displayed in Figure1b. Type I corresponds to a deformation of one interface (left interface in Fig1a), and follow the usual gravity capillary wave dispersion relation :

$$\omega^2 = \tanh(kH_{eff})(g_{eff}k + \frac{\gamma}{\rho}k^3).$$

However, the usual water depth H and acceleration of gravity g are here replaced by effective depth H_{eff} and gravity g_{eff}, that can be derived theoretically from our particular geometry (solid line, Figure1b inset). In particular, we have $g_{eff} = g\sin\alpha$ where α is the angle between the substrate slope and the horizontal axis (defined either Fig1a of Fig1c). The angle α can therefore be changed by inclining the substrate more or less. The dispersion relation can thus be tuned from waves propagating on a horizontal interface as commonly encountered ($\alpha = 90°$), to an almost zero gravity situation for $\alpha \to 0$ (consequently, $g_{eff} \to 0$). One striking consequence is the variation of the minimum velocity of linear waves (Figure2b inset), that goes to 0 for $\alpha \to 0$. Close to $\alpha \approx 0$ quasi pure capillary waves are observed (dashed line) in a much larger range of wavelengths the effective capillary length l_c being greater than 1cm. Type II waves correspond to sloshing modes, associated to out of phase oscillations of same amplitude for both interface. Their dispersion relation presents a frequency cut-off also dependent on the geometry (*i.e.* α). Both dispersion relations can be rationalized by using a theoretical model based on a triangular shape of the section. It predicts a good agreement with all the observed dispersion relations for linear waves. Type I and II waves can also be observed in the toroidal geometry sketched in Figure1c. The linear channel has here been replaced by an annular channel with an equivalent section profile (side view sketch of Figure 1c can be applied to each geometry). In this case however the type I waves is amplified by a flow instability [2]. Indeed, a free surface toroidal flow turns out to be unstable on its inner perimeter and the selected wavelength can be well predicted from a full hydrodynamic calculation [3]. It leads to the formation of an asymmetric pattern, better describe by a non-linear wave equation (Figure 1d).

*Corresponding author. Email: sperrard@uchicago.edu

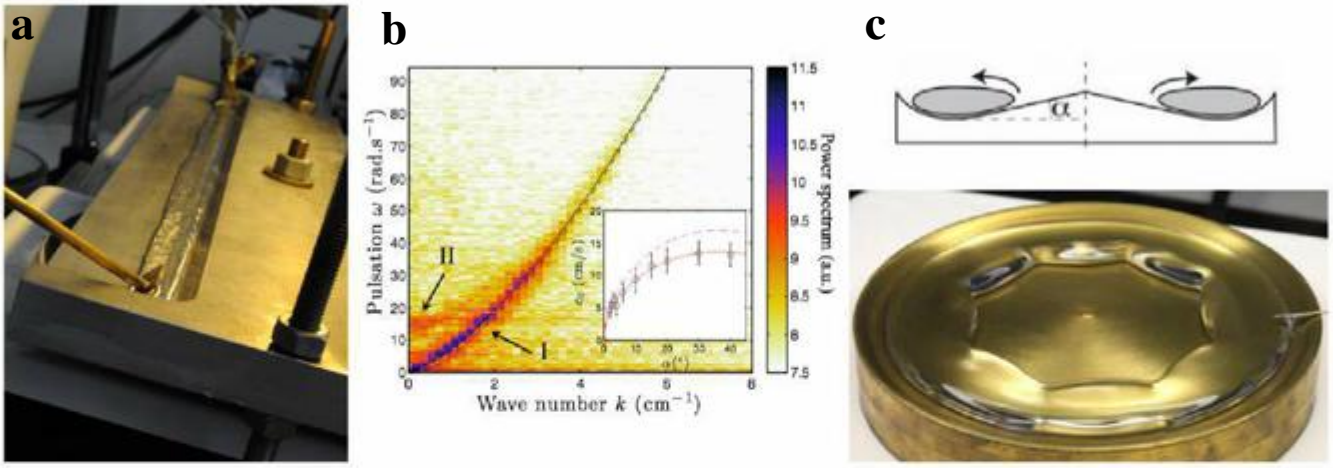

Figure 1: **Levitated liquid using Leidenfrost effect** Using curved substrate heated above 200°C, we generate levitating cylinder or torus of water. a) the substrate has a shape of a quarter pipe, so that only the left interface is free to move. Capillary waves generated by an external exciter (brass tube on the left bottom) are observed on the surface. They correspond to gravito-capillary waves with an effective gravity $g_{eff} = g \sin \alpha$ that can be tuned experimentally. The effective capillary length is 1.3cm, five times larger than the usual value. b) Relation dispersion of linear waves. Two branches type I and II are observed. Inset : minimum phase velocity of linear waves for various inclination angles. The limit $\alpha \to 0$ leads to $c_0 \to 0$. c) Sketch of toroidal substrate side view, with the same angle α that controls the effective gravity. Due to a symmetry breaking, a rotating flow inside the torus is observed. d) Spontaneous generation of a train of capillary solitons, triggered by an instability of the rotating flow inside the torus.

NON-LINEAR WAVES AND PATTERNS : DEPRESSION KDV SOLITONS AND POLYGONS

When the typical width of a localized wave is of the order or longer than the depth of fluids, there exist stationnary non-linear waves solutions called solitons. They are described by the Korteweg de Vries (KdV) equation [5] where the presence of both dispersive and non-linear term can balance to form a localized, stationary solution moving at constant speed. In the gravity dominated domain, they are of positive amplitude and above the minimum of phase velocity c_0. Due to our reduced effective gravity, we observe capillary driven solitons that correspond to negative amplitude and subsonic velocities. We present a full characterization of these solitons, and their shape, velocity, width and amplitude is well descrined by our modified KdV solitons theory for a non-uniform bottom and a reduced gravity term. In the annular geometry, they correspond to a train of solitons, that repel each other to form a periodic pattern.

CONCLUSION

We have revealed the propagation of a wide variety of waves in a quasi one dimensional system, ranging from linear capillary waves in a reduced gravity environnement, sloshing modes, individual capillary solitons, collective organized soliton state, and random soliton superposition. We model these various types of waves in a common theoretical framework by a modified KdV theory, taking into account our specific substrate geometry, the reduced gravity, and the first non-linear terms. The superposition of many individual solitons leads to a complex superposition where each localized structure can barely be followed. This statistical wave state may be assigned to soliton turbulence in quasi one dimension.

References

[1] Biance A.L., Clanet C. and Quéré D. : Leidenfrost drops. *Phys. of Fluids*, **15** 6 (2003)

[2] Perrard S., Couder Y., Fort E. and Limat L. : Leidenfrost levitated liquid tori. *EPL* **100** 54066 (2012)

[3] Labousse M. and Bush J.W.M. : Polygonal instabilities on interfacial vorticities. *Eur. Phys. J E*, **38** 113 (2015)

[4] Perrard S., L. Deike , E. Duchêne and Pham C.T. : Capilary solitons on a levitated medium. *PRE*, **92** 011002 (2015)

[5] Korteweg D. and de Vries G. *Philos. Mag. J. Sci.*, **39** 422 (1895)

NUMERICAL AND THEORETICAL ANALYSES ON INTERFACE WAVE OF MAGNETIC FLUIDS

Yo Mizuta *

Division of Applied Physics, Faculty of Engineering, Hokkaido University, Sapporo, Hokkaido, Japan

Summary Interface profile of magnetic fluid is known to change abruptly when the intensity of the applied magnetic field H_0 is increased. It is considered that during this transition process between interface profiles many modes are generated once but converge into one mode corresponding to the final regular profile. From this standpoint, this paper inspects the spectra for interfacial quantities changing in time, by use of the fluid and magnetic analyses which are applicable for arbitrary interface profiles and applied magnetic field distributions. As the time goes on, several prominent modes are generated other than the initial basic modes as the result of the nonlinear wave-wave interactions. Among various nonlinear processes, three-wave interaction is considered in this paper. When H_0 is close to the critical intensity $H_{\rm CL}$, modes with a triad of wavenumber vectors of the same size compose the interface profile of hexagonal lattice, as experimentally observed.

EQUATION FOR INTERFACE MOTION

When we analyze the free surface phenomena of irrotational and inviscid magnetic fluid with all nonlinear effects but with no limitations on the interface profile, we use the following **equation for interface motion** which is derived from Bernoulli's equation and the dynamic boundary condition on the interface [1]:

$$\rho\frac{\partial\varphi}{\partial t}+S+p_0=0,\quad S\equiv D+G+C+T,\quad T=-\left[\frac{1}{\mu_j}\right]\frac{\{\mu_1\mu_2(h_X^2+h_Y^2)+b_Z^2\}}{2},\tag{1}$$

where ρ, φ, D, G, C, T, p_0 are the fluid density, velocity potential, dynamic pressure, gravity potential, surface tension, magnetic stress difference and atmospheric pressure, respectively. In (1), φ is obtained from the vertical component of the fluid velocity v_z and the interface elevation ζ as $\varphi=\int_{-\infty}^{\zeta}\mathrm{d}zv_z$, Furthermore, T represents the action from the magnetic field to the fluid, where μ_j denotes the permeability of the fluid (j=1) or the vacuum (j=2), $[\cdots]$ the difference of the value across the interface (2−1), respectively. The tangential magnetic field $h_{X,Y}$ and the normal magnetic flux b_Z should be obtained rigorously as well as efficiently under arbitrary interface profiles and applied magnetic field distributions [2].

The interface elevation $\zeta(\boldsymbol{R})$ and the sum of interface stresses $S(\boldsymbol{R})$, as well as other interface quantities, are regarded as the functions of the interface coordinate parameter $\boldsymbol{R}=(X,Y)$, and they are expanded into series of periodic functions. We rewrite (1) by the column vectors $\tilde{\boldsymbol{\zeta}}\equiv\left(\tilde{\zeta}_\mu\right)$ and $\tilde{\boldsymbol{S}}\equiv\left(\tilde{S}_\mu\right)$ composed of the expansion coefficients $\tilde{\zeta}_\mu$, $\tilde{S}_\mu$ belonging to the wavenumber vector $\boldsymbol{k}_\mu$. Then, the temporal evolution equation for $\tilde{\boldsymbol{\zeta}}$ is derived.

TEMPORAL EVOLUTION OF WAVENUMBER SPECTRA

This section shows a temporal evolution of the spectra $|\tilde{\zeta}_\mu|^2$ and $|\tilde{S}_\mu|^2$ for the interface elevation and the sum of interface stresses. We prepare initially an interface profile with hexagonal lattice as shown in Fig.1(a) for the magnetic fluid with the density ρ=1.0 $\times10^3\,\mathrm{kg\,m^{-3}}$, capillary coefficient γ=2.6 $\times10^{-2}\,\mathrm{N\,m^{-1}}$, and relative permeability $\mu_1/\,\mu_0$=1.2 ($\mu_2/\,\mu_0$=1.0, $\mu_0=4\pi\times10^{-7}\,\mathrm{H/m}$). Three basic modes with the wavenumber vector $\boldsymbol{k}_\mu=m_\mu\boldsymbol{A}+n_\mu\boldsymbol{B}$, $(m_\mu,\,n_\mu)=(2,0),\,(0,2),\,(2,2)$ as shown by open circles in Fig.1(b) compose this profile, where $\boldsymbol{A}$, $\boldsymbol{B}$ are the basic vectors crossing each other with the angle of 120°. Amplitudes ζ_0=0.10 mm for these modes are same. The critical wavelength and the critical magnetic field intensity for infinitesimal ζ_0 are calculated as $\lambda_{\rm CL}=2\pi/\,k_{\rm CL}$=1.02 $\times10^{-2}$ m and $H_{\rm CL}$=3.75 $\times10^4\mathrm{A/m}$. The position of the critical wavenumber $k=k_{\rm CL}$ is represented by an arc in Fig.1(b). Applied magnetic field is vertical and homogeneous, and its intensity H_0 is $0.60H_{\rm CL}$ or $0.90H_{\rm CL}$ for the upper or lower row in Fig.2.

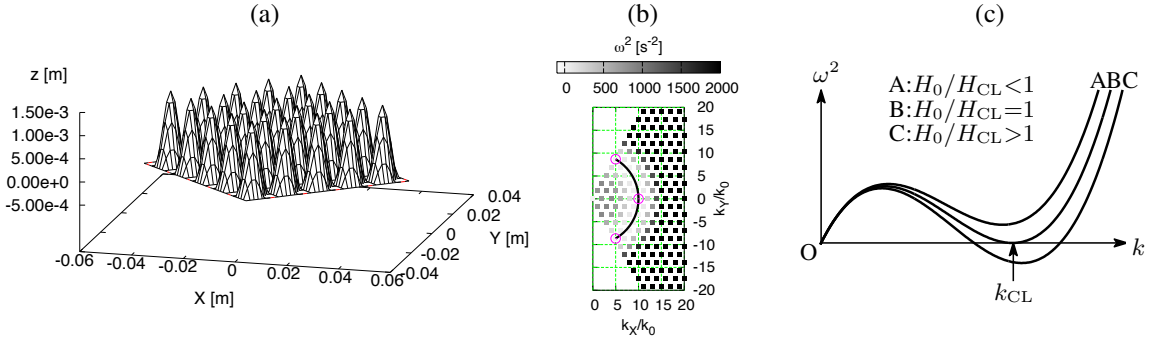

Figure 1: Interface profile of hexagonal lattice in (a) real space and (b) wavenumber space. (c) Dispersion relation for linear interface wave.

*Corresponding author. Email: yomizuta@eng.hokudai.ac.jp

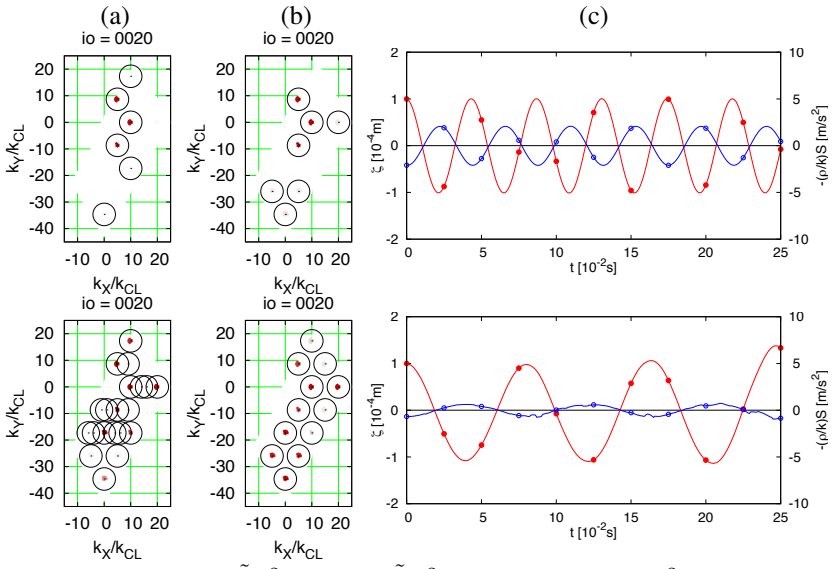

Figure 2: Spectrum $|\tilde{\zeta}_\mu|^2$ (a) and $|\tilde{S}_\mu|^2$ (b) after 20.0×10^{-2} s. Temporal change of $\tilde{\zeta}_\mu$ (red line in (c)) and $-(k_\mu/\rho)\,\tilde{S}_\mu$ (blue line in (c)) at basic modes. $H_0 = 0.60H_{\rm CL}$ (upper row) and $H_0 = 0.90H_{\rm CL}$ (lower row).

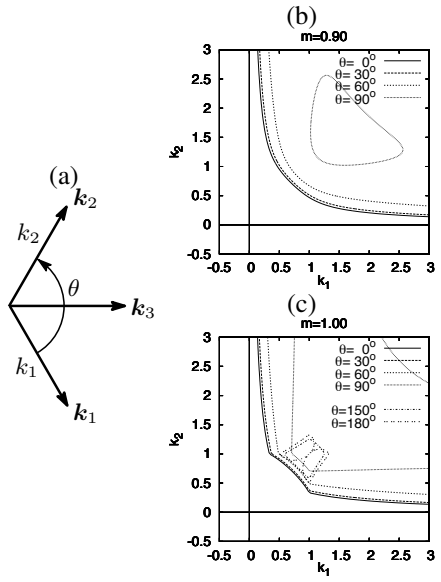

Figure 3: (a) Triad of wavenumber vectors for three-wave interaction. (b), (c) Their resonance curves.

As shown in Fig.1(c), the dispersion relation for linear wave (LNDS) is $\{\omega(k)\}^2{=}Gk{+}Ck^3{-}Mk^2$, where $k{=}|\boldsymbol{k}_\mu|$, ω is the angular frequency, and G, C, M are the gravity, capillary and magnetic coefficients, respectively. Shaded squares in Fig.1(b) show the value of $\{\omega(k)\}^2$ at $H_0{=}H_{\rm CL}$. Modes as many as $18{\times}18$ in the wavenumber space cover those generated by the nonlinearity of the surface tension and the magnetic stress difference.

Figure 2(a), (b) shows the wavenumber spectra after some time. Many spectral modes other than the initial basic modes are generated due to the nonlinearity in C and T of (1), where several prominent modes are shown encircled and weak continuous modes as hiding the basic plane. For the case of H_0 closer to $H_{\rm CL}$ (lower row in Fig.2), both of the prominent and continuous modes increase, but the latter more. In addition, the interface elevation $\tilde{\zeta}_\mu$ and the interface force $-(k_\mu/\rho)\,\tilde{S}_\mu$ change more slowly as in Fig.2(c) due to the close balance of the interface stresses around $H_{\rm CL}$, but their change become unstable gradually.

NONLINEAR WAVE-WAVE INTERACTION ON THE INTERFACE OF MAGNETIC FLUIDS

During the transition process between interface profiles, various nonlinear wave-wave interactions will occur. On the interface of magnetic fluids, three-wave interaction is anticipated since the magnetic stress difference is second order in the magnetic field. Three-wave interaction is known to exist for gravity-capillary waves though not for gravity waves in normal monolayer fluids [3].

For a triad of wavenumber vectors $\boldsymbol{k}_{1,2,3}$ as Fig.3(a), the resonance condition is $\boldsymbol{k}_3{=}\boldsymbol{k}_1{+}\boldsymbol{k}_2$ and $\omega(k_3){=}\omega(k_1){+}\omega(k_2)$, where $\omega(k)$ is given by the LNDS in the previous section with $k_{1,2,3}{=}|\boldsymbol{k}_{1,2,3}|$. These resonance condition and LNDS are expressed as

$$\bar{k}_3 = \sqrt{\bar{k}_1^2 + \bar{k}_2^2 + 2\bar{k}_1\bar{k}_2\cos\theta}, \quad \{\omega(k)\}^2/\sqrt{G^3/C} = \bar{k} + \bar{k}^3 - 2m\bar{k}^2 \tag{2}$$

by the wavenumber $\bar{k}{\equiv}\,k/\,k_{\rm CL}$ and the magnetic coefficient $m{\equiv}\,M/\,M_{\rm CL}$ which are nondimensionalized by $k_{\rm CL}{=}\sqrt{G/C}$ and $M_{\rm CL}{=}2\sqrt{CG}$. If $\bar{k}_3$ is eliminated between two equations in (2) as $F(\bar{k}_1,\bar{k}_2;m,\theta){=}0$, we can draw $\bar{k}_1$–$\bar{k}_2$ resonance curves with parameters m and θ, as in Fig.3(b),(c).

When $H_0{<}H_{\rm CL}$ ($m{<}1$) and $\bar{k}_1{=}\bar{k}_2$, θ increases with $\bar{k}_{1,2}$ but never exceeds 90°, like the gravity-capillary waves [3]. However, when $m{\le}1$, there appears the resonance with $\theta \ge 90°$. Especially when $m{=}1$, the resonance for $\theta{=}120°$ is at the spot $\bar{k}_{1,2}{=}1$ instead of on a line. In this case, $\bar{k}_3{=}\bar{k}_{1,2}{=}1$ from the first of (2), and $\omega(k_{1,2,3}){=}0$ from the second of (2).

The above discussion means that the modes with a triad of wavenumber vectors of the same size $k_{\rm CL}$, which compose the initial profile as Fig.1(a),(b), are resonant and static, as experimentally observed (note that each point in (b) represents a combination of modes symmetric with respect to the origin).

References

[1] Mizuta Y.: Stability Analysis on the Free Surface Phenomena of a Magnetic Fluid for General Use. *J. Magn. Magn. Mater.* **323**:1354–1359, 2011.
[2] Mizuta Y.: Interface Magnetic Field Analysis for Free Surface Phenomena of Magnetic Fluid. *Magnetohydrodynamics* **44**:155–165, 2008.
[3] McGoldrick L.F.: On the Dynamics of Unsteady Gravity Waves of Finite Amplitude. *J. Fluid Mech.* **9**:305–331, 1965.

INVESTIGATION OF INERTIAL WAVES INSIDE A LIQUID METAL COLUMN BY MEANS OF ELECTROMAGNETIC FIELDS

Tobias Vogt, Dirk Räbiger & Sven Eckert
Institute of Fluid Dynamics, HZDR, Dresden, Germany

Summary In this study, the dynamics of inertial waves inside a cylindrical vessel was studied experimentally. The liquid metal GaInSn was chosen as fluid in order to enable a contactless stimulation of the flow inside the cylinder by means of electromagnetic fields. A rotating magnetic field (RMF) generates a supercritical rotating motion of the liquid. The excitation of the inertial waves is realised by means of periodic field strength modulations and by means of short intense magnetic field pulses. Furthermore, the experiment demonstrates that inertial waves may be excited spontaneously by turbulent structures in the rotating flow. The ultrasound Doppler velocimetry was used to record the flow structure and to identify the inertial waves occurring in the setup

INTRODUCTION

Inertial waves are transversal mechanical waves which only occur in rotation fluids. The restoring force of inertial waves is the Coriolis force and their upper frequency limit is twice the rotation rate of the fluid. Due to the rotation of earth, one can find very large scale inertial waves for example in oceans [1], in the atmosphere [2] and also deep inside the earth in the liquid outer core [3]. Besides this, inertial waves can also be detected in a variety of technical applications. In all cases, the source for an inertial wave is a disorder in the centrifugal force balance of the rotating fluid. So far, the majority of experiments on inertial waves are performed with water inside spinning vessels. The excitation is typically realized mechanically by means of oscillating plates, inclined vessel walls or cylinders subjected to a precessional movement. We describe a new approach for studying inertial waves using a highly conducting liquid metal and electromagnetic fields that are used to induce a Lorentz force in the liquid metal. This study demonstrates that electromagnetic fields can be considered as an effective tool for generating a variety of inertial wave modes in a laboratory-scale set-up.

Forced inertial waves

Inertial waves can be excited in the present setup by distinct variations of the electromagnetic driving force. For instance, a pulsating RMF can be used to force particular inertial wave modes. Such a pulsating RMF implies periodic changes of the driving force. The fluid rotates because of inertia and the constant direction of the angular acceleration. We performed measurement series where the repetition frequency of the RMF pulses was varied in very fins steps. By this, the excitation of several inertial wave modes can be achieved. We analysed the spatial structures of the different wave modes by means 2D-FFT and compared the results to predictions of the linear inertial wave theory.

In a further series of experiments, the rotating flow was exposed to a strong, but very short duration, magnetic field pulses in either a vertical or azimuthal direction. These pulses generate a short-time propulsion of the fluid. The field strength of each pulse was set significantly higher than that of the RMF that continuously drives the background rotation of the fluid. The time duration of the pulses was chosen to be as short as possible in order to avoid a substantial change of the main rotating flow. Both the vertical and azimuthal pulses produce free inertial waves, which decay gradually.

Spontaneous occurrence of inertial waves

Surprisingly, we also observed inertial waves in our experimental setup during a stationary rotation even without any external perturbation. Figure 1 displays a section of a long-term measurement lasting over a period of about one hour. In this figure, the evolution of the vertical velocity (u_z) averaged along the axis of the liquid metal column is shown. An almost periodic oscillation of the mean axial velocity becomes visible collapsing from time to time. Because any external forcing was avoided here, the inertial wave must be triggered by the flow itself.

A typical feature of an RMF-driven flow at supercritical forcing is the formation of Taylor-Görtler (TG) vortices, which is a result of the instability of the side wall layers. These TG-vortices develop typically in the boundary layer at the side wall of the cylindrical vessel. After formation, the TG-vortices are conveyed by the secondary flow towards the horizontal end walls of the vessel, where they dissipate in the Bödewadt layers. The impingement of the TG-vortex on the Bödewadt layer provokes a temporary disturbance of the boundary layer. Velocity measurements made during an RMF-driven spin-up [4] showed how such a disturbance propagates inside the boundary layer and excites an inertial wave appearing in the center of the vessel. Such a vortex dissipation in the Bödewadt layer leads to a perturbation of the Ekman pumping resulting in the excitation of an inertial wave.

[a] Corresponding author. Email: ictam2016papers@legendconferences.com.

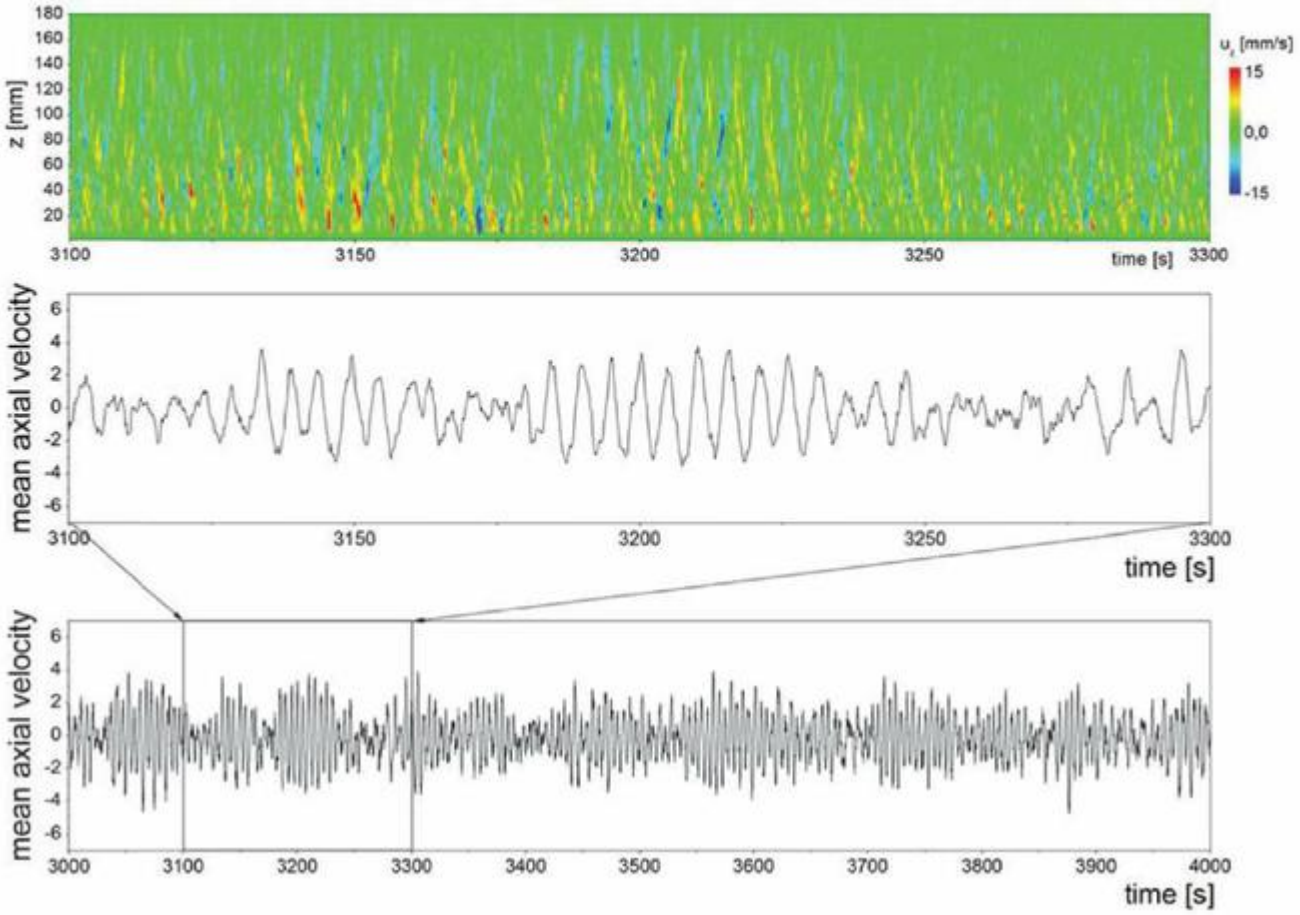

Figure 1, To : Free inertia wave along he axis of the rotating liquid metal colu n. Middle and below: Me n axial velocity averaged alo g the cylinder height [0 < < H_0]; recor ed during a l ng-term measurement wit out magnetic disturbance B_R = 1.3 mT; r/R_0 = 0

ONCLUSIONS

In this w rk, the occur ence of force and spontaneously excite inertial wav s was studied inside a cyli drical vessel. A rotating mag etic field (R F) was used herefore to generate a swirl ng motion in ide the liquid metal filled i the cylinder. A detailed description of the e perimental setup and the results can be found in [5]

References

[1] Fu, L.L. 19 0, Observations nd models of inertial waves in the eep ocean. PhD t esis, Massachusetts

[2] Thompson, R. 1978, Observation of inertial waves in the stratos here. Quarterly Journal of the Royal Meteorological ociety 104 (441), 691–698.Nygus .: Numerical nalysis Using Fi ite Element Met od. *PhD Thesis*, TU Mech. Eng. ept., Lagos, 198 .

[3] Aldridge, K.D. & Lumb, LI 1987 Inertial waves identified in the earth's fluid outer core. *Nature* 325, 421–423.

[4] Vogt, T. Grants, I. Räbiger, . Eckert, S. & Gerbeth, G. 2012 O the formation of Taylor–Görtler v rtices in RMF-driven spin-up flow . *Exp. Fluids* 52 (1), 1–10.

[5] Vogt, T. Räbiger, D. & Eckert, S. 2014 Inertial wave dynamics i a rotating liquid etal. *J. Fluid Mech.* 753, 472-498.

ASYMPTOTIC ANALYSIS OF A ROTARY WAVE IN A CYLINDRICAL TANK

Herbert Steinrück*[1] and Lorenz Gusner[2]

[1]*Institute of Fluid Mechanics and Heat Transfer, Technische Universität Wien, Vienna, Austria*

Summary The free surface flow in a vertical, cylindrical, rotating container will be considered when axis-symmetric angular and radial shear stress distributions are applied on the free surface. It is well known that in the inviscid case a rotary wave which can be described by a flow potential exists. We want to determine the stability limit of the axis-symmetric base state with respect to the rotary wave for small Ekman and Froude numbers. Under the above assumption, the critical flow conditions can be determined analytically. The results can be verified experimentally using a vertical, cylindrical container partially filled with water where the top lid rotates with a given angular velocity. Thus, the induced air flow will exert shear stresses in the angular and radial direction onto the water surface. Above a certain threshold, rotary waves can be observed.

PROBLEM FORMULATION

Using a Francis turbine in phase condenser mode, the rotor sets the air above the water level in the suction pipe into a rotation. If the angular speed of the rotor is above a critical value a rotary wave in the water forms. The angular wave speed is almost independent of the rotor speed, and the amplitude of the wave can be considerably large. Thus, we want to explain the excitation mechanism using asymptotic analysis of this wave. In particular, we want to determine critical conditions when the axial-symmetric surface of the water becomes unstable, and the rotary wave develops. Since we are interested in an analytical solution, we define a simplified model problem.

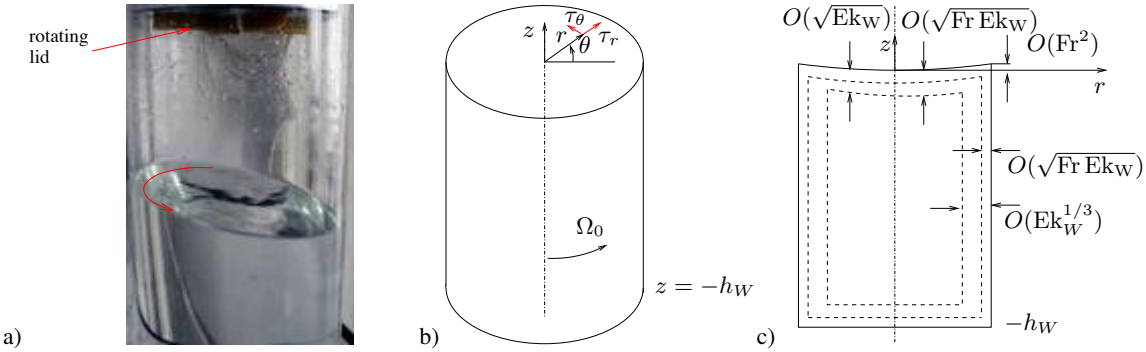

Figure 1: a) Rotatry wave in a vertical, cylindrical container induced by a rotating lid, b) coordinate system and applied shear stresses c) boundary-layers relevant for the stability analysis

Consider a vertical cylindrical tank with radius R partially filled with water. Assume that on the free surface shear stresses in azimuthal $\tau_\theta = \tau_{\theta,0} r/R$ and inward radial $\tau_r = \tau_{r,0} r/R$ direction are applied. These stresses model the action of the rotating air flow onto the water. The shear stress distributions are assumed to be axis-symmetric and depend linearly on the distance from the axis of the container.

For an inviscid fluid, the rotary gravity wave given by the flow potential $\phi = J_1(\mu_1 r)\sin(\theta - \omega_0 t)e^{\mu_1 z}$ is well known, see figure 1a, where J_1 is the Bessel function with index 1, μ_1 is the smallest zero of its derivative, ω_0 is the dimensionless angular wave speed, see [1]. Here and in the following, r and z denote the dimensionless radial and vertical coordinate. They are referred to the radius R of the container. The angular velocity is made dimensionless with $\sqrt{g/R}$, where, and g is the gravity acceleration. All other quantities like time, velocity are scaled accordingly. For the definition of the coordinate system and the boundary conditions, see figure 1b.

To facilitate a complete analytical solution, we assume that the container rotates with given angular velocity Ω_0.Thus, we define the following dimensionless numbers,

$$\mathrm{Ek}_W = \frac{\nu}{R^2\Omega_0}, \quad \mathrm{Fr} = \frac{\Omega_0}{\sqrt{g/R}} \quad \delta = \sqrt{\mathrm{Ek_W}}\frac{\tau_{\theta,0}}{\rho\nu\Omega_0}, \quad \tau = \frac{\tau_{r,0}}{\tau_{\theta,0}}.$$

where ρ, and ν are the density and the viscosity of the fluid, respectively. Assuming $\delta \ll 1$ and $\mathrm{Ek_W} \ll 1$ the base flow can be obtained by linearizing the Navier-Stokes equation around the solid body rotation with angular speed Ω_0. Thus, it is given

*Corresponding author. Email: herbert.steinrueck@tuwien.ac.at

by a solid body rotation in the core (with a perturbed angular speed) and boundary-layers of width $\sqrt{\mathrm{Ek_W}}$ at the free surface and the bottom of the container, see [2]

$$u_B = \mathrm{Fr}\,\delta r \hat{u}_B(\eta), \quad v_B = \mathrm{Fr}\, r(1+\delta(\bar{v}_B + \hat{v}_B(\eta))), \quad w_B = \mathrm{Fr}\,\delta\sqrt{\mathrm{Ek}_W}(\bar{w}_B + \hat{w}_B(\eta)), \qquad \eta = z/\sqrt{\mathrm{Ek}_W}.$$

Here, u_B, v_B, W_B denote the velocity components of the base flow in the radial, azimuthal, and vertical direction. Since the boundary-layer of the base flow along the container wall does not play a role in the following asymptotic stability analysis, the corresponding terms are omitted here.

ASYMPTOTIC STABILITY ANALYSIS

We linearize the governing equations (Navier-Stokes equations, the kinematic and dynamic boundary conditions, respectively) around the base flow. We are looking for a rotary eigensolution in the double limit

$\mathrm{Ek_W} \to 0$, $\mathrm{Fr} \to 0$, $\delta << 1$, $\tau = O(1)$. Thus, the asymptotic ansatz for the radial velocity component is of the form

$$u \sim \left[\left(u_0^{(s)} + \sqrt{\mathrm{Ek_W Fr}}u_G^{(s)} + \mathrm{Fr}\,u_1^{(s)} + \mathrm{Fr}^2\,u_2^{(s)}\right)\sin(\theta-\omega t) + \left(\sqrt{\mathrm{Ek_W Fr}}u_G^{(c)} + \mathrm{Fr}\,u_1^{(c)} + \mathrm{Fr}^2\,u_2^{(c)}\right)\cos(\theta-\omega t)\right] e^{g\,t}$$

with the dimensionless angular wave speed $\omega = \omega_0 + \sqrt{\mathrm{Ek_W Fr}}\omega_G + \mathrm{Fr}\omega_1 + ...$, and the dimensionless growth rate $g = -d\sqrt{\mathrm{Ek_W Fr}} + \mathrm{Fr}g_1 + \mathrm{Fr}^2 g_2 + ...$

Note that we have written in the ansatz only the order of magnitude of the terms needed for the discussion of the stability. The terms $u_G^{(s)}$, $u_1^{(s)}$, u_2 have to be expanded with respect to $\mathrm{Ek_W}$ and δ and they may have boundary-layers of thickness $\sqrt{\mathrm{Ek_W Fr}}$ and $\sqrt{\mathrm{Ek_W}}$, respectively. The leading order term is given by the inviscid rotary wave supplemented by boundary layers at the wall. In the following we will shortly discuss the role of the terms in the expansion.

The inviscid rotary wave does not satisfy the no-slip boundary conditions at the container wall and bottom. Thus, boundary-layers of thickness $\sqrt{\mathrm{Ek_W Fr}}$ will develop along the wall, see figure 1c, and the bottom causing a velocity component normal to the wall of the order $\sqrt{\mathrm{Ek_W Fr}}$ at the outer edge of the boundary layer. Thus, a secondary flow of the same order is induced in the core region. Applying the kinematic, and dynamic boundary condition in the normal direction at the free surface yields a condition for the decay rate d and the shift of the angular velocity ω_G.

At the free surface, the shear stresses are prescribed. The rotary wave displaces the free surface. Thus, a boundary-layer correction of the radial and azimuthal component of the rotary wave of the order $\delta\mathrm{Fr}^{3/2}/\sqrt{\mathrm{Ek_W}}$ is necessary. This, however, induces a vertical flow velocity of order $\mathrm{Fr}^2\delta$ and depending on the sign a growth or decay rate of the wave of the same order. A detailed analysis shows that this correction is positive (growth rate) if the radial component of the surface velocity is negative.

In the core region of the flow, the rotary wave interacts with the base flow causing an additional correction to the wave speed and the growth/decay rate. However, the corrections to the growth rate are only created in the boundary layer of the base flow (width $\sqrt{\mathrm{Ek_W}}$). It turns out that only the second order term g_2 is different from zero. The contribution of this terms of the same order $\delta\mathrm{Fr}$ as the correction of the growth rate induced by the dynamic boundary condition in the radial direction.

Under the above assumptions all this contributions to growth/decay rate can be evaluated analytically yielding our main result

$$g \sim -\sqrt{\mathrm{Fr\,Ek_W}}d(h_W) + \mathrm{Fr}\sqrt{\mathrm{Ek_W}}\tilde{g}_1 - \mathrm{Fr}^2\delta\hat{u}_B(0)\tilde{g}_2(h_W),$$

where d, and $\tilde{g_2}$ are positive constants depending only on the dimensionless water depth h_W. Setting the growth rate equal to zero, conditions for neutral stability are obtained. Thus, for neutral stability the radial surface velocity $\hat{u}_B(0)$ of the base flow has to be negative.

NON-ROTATING CONTAINER AND EXPERIMENTAL VERIFICATION

In the case of a non-rotating container, see figure 1a, the main ideas of the present analysis hold. However, the equations have to be solved numerically. Formally, we have to set $\delta = 1$ and set $\Omega_0 = (\tau_{\theta,0}^2/\rho^2\nu R^2)^{1/3}$, a scale for the angular velocity induced by the angular shear stress at the surface. The angular speed of the wave can be measured easily from a video. The angular velocity of the core region can be estimated by the time an immersed particle needs for a complete revolution. The ratio of the angular velocity of the flow in the core region to the angular wave speed is of the order Fr. In case of neutral stability, we have $\mathrm{Fr} \sim (\mathrm{Ek_W\,Fr})^{1/4} = (\frac{\nu}{\mathrm{R}^2\sqrt{\mathrm{g/R}}})^{1/4}$ which is in agreement with experimental observations.

References

[1] R. A. Ibrahim, Liquid Sloshing Dynamics, Cambridge Univ. Press, 2005.

[2] H. P. Greenspan, The Theory of Rotating Fluids, Cambridge Univ. Press, 1969.

EVOLUTION OF FARADAY WAVES BY RESONANT TRIAD INTERACTIONS OF SURFACE–COMPRESSION WAVES

Usama Kadri*[1]
[1]*Department of Mathematics, Massachusetts Institute of Technology, Cambridge, MA 02139, USA*

Summary The propagation of wave disturbances over a vertically oscillating liquid may form standing waves, known as Faraday waves. Here we present an alternative description of the generation and evolution of Faraday waves by nonlinear resonant triad interactions, accounting for gravity surface effects and the slight compressibility of the liquid. To this end, we analyse a triad comprising an infinitely long-crested compression mode and two oppositely propagating subharmonic surface waves.

INTRODUCTION

A surface wave disturbance over a fluid layer that is subject to sinusoidal vertical oscillation at frequency 2ω may excite subharmonic standing field of waves of frequency ω known as Faraday waves. The wavelength of these waves is prescribed by the standard dispersion relation [1]. For many applications the driven flow due to the interaction of the disturbance with the oscillating bath is attributed to parametric instability ([5]) (or parametric resonance). Here, we introduce an alternative approach to describe this energy share between the surface waves and the oscillating bath. We model the oscillating bath as an infinitely long-crested compression wave that exchanges energy with surface waves via resonant triad interactions.

Special triad interactions between surface wave disturbances and compression modes associated with resonances were noted by Longuet-Higgins [4]. More specifically, these comprise a standing compression mode at a cut-off frequency 2ω, and two subharmonic surface waves with frequency ω and opposite wavenumbers k. Here, we consider the interaction of a propagating radial surface wave disturbances and a standing compression mode in a deep fluid. Such resonance interaction depends on the small parameter $\mu = gh/c^2$, ($\mu \ll 1$) (see [3]) that governs the effects of gravity relative to compressibility, where g is the gravitational acceleration. Thus, free-surface wave disturbances feature vastly different spatial and/or temporal scales from the compression mode. Specifically, the surface wavelength λ is much shorter than the vertical compression lengthscale represented by the water depth ($\lambda \ll h$), whereas the gravity timescale $\tau \sim (\lambda/g)^{1/2}$ in keeping with the deep-water dispersion relation. Then, taking τ to be comparable to the acoustic timescale h/c implies $\lambda \sim \mu h$; hence, in the present setting, the parameter μ may be interpreted as the ratio of the gravity to the (vertical) compression mode lengthscale.

PRELIMINARIES

Based on irrotationality, the surface–compression wave problem is formulated in terms of the velocity potential $\varphi(r, z, t)$, where $\mathbf{u} = \nabla\varphi$ is the velocity field. Moreover, we shall use dimensionless variables, employing μh as lengthscale and h/c as timescale. We shall also assume radial motion ($\partial_\theta = 0$), far from the centre ($1/r \ll 1$); then the field equation obeys

$$\varphi_{tt} \circ \frac{1}{\mu^2}\left(\varphi_{rr} + \varphi_{zz}\right) + \varphi_z + |\nabla\varphi|_t^2 + \tfrac{1}{2}\mathbf{u}\cdot\nabla\left(|\nabla\varphi|^2\right) = 0. \tag{1}$$

On the free surface $z = \eta(r, t)$, we consider the standard dynamic and kinematic conditions. Finally, the boundary condition on the rigid bottom at $z = \circ\, 1/\mu$ reads

$$\varphi_z = 0 \qquad (z = \circ\, 1/\mu). \tag{2}$$

The velocity potential for the three interacting modes is expanded as follows

$$\varphi = \epsilon\, \mathrm{e}^{kz}\Big\{S_+(T)\mathrm{e}^{\mathrm{i}(kr-\omega t)} + S_-(T)\mathrm{e}^{-\mathrm{i}(kr+\omega t)} + \text{c.c.}\Big\} + \alpha\cos\omega(Z+1)\Big\{C(T)\mathrm{e}^{-2\mathrm{i}\omega} + \text{c.c.}\Big\} + \ldots. \tag{3}$$

The first terms in (3) represent the two surface waves while the last represents the compression mode, that is scaled in the vertical coordinate $Z = \mu z$. The surface wave amplitudes $S_\pm$ and the compression mode amplitude C depend on the 'slow' time $T = \mu t$, and space $R = \mu r$, where $\epsilon = \alpha\mu^{1/2}$ with $\alpha = O(1)$ ([3]).

*Corresponding author. Email: ukadri@mit.edu

EVOLUTION EQUATIONS

Upon substituting (3) in the surface–compression mode problem (1) and the boundary conditions, we focus on terms proportional to $\exp\{\mathrm{i}(kr-\omega t)\}$, $\exp\{-\mathrm{i}(kr+\omega t)\}$, and $\exp\{-2\mathrm{i}\omega t\}$. These terms cause secular behaviour at higher order in expansion (3) as they have the same spatial and temporal dependence as the three linear propagation modes at the leading order. To overcome this difficulty we impose solvability conditions on the problems governing higher-order corrections to these modes, which results in the desired evolution equations for the compression wave amplitude $C(T)$

$$\frac{\partial C}{\partial T} = -\frac{\mathrm{i}}{2\omega}\frac{\partial^2 C}{\partial R^2} - \frac{\mathrm{i}}{2\omega}C + \frac{1}{4}\omega^3\alpha S_+ S_-. \tag{4}$$

and the surface wave amplitudes $S_\pm(T)$

$$\frac{\mathrm{d}S_\pm}{\mathrm{d}T} = -\frac{1}{8}\omega^3\alpha C S_\mp^* - \frac{\mathrm{i}}{64}\omega^7\alpha^2\left(S_\pm^2 S_\pm^* - 4|S_\mp|^2 S_\pm\right), \tag{5}$$

where $*$ stands for complex conjugate. Note that equation (5) is a particular case of equation (5.9) derived by Kadri & Akylas [3].

RESULTS AND DISCUSSION

A qualitative comparison between experiments (presented in [2]) and the proposed mechanism are shown in figure 1 (a)-(d). The amplitude evolution of a surface wave is given in figure 1 (e). Note that in the given example, the prescribed surface waves are travelling in opposite directions and thus present a standing disturbance in analogy to a disturbance by a falling steel ball impacting the surface. Unlike parametric resonance, with the proposed mechanism we can also consider a moving disturbance, say due to a moving droplet (e.g. see [5]), resulting in a rigorous description of the evolution of the disturbance path memory.

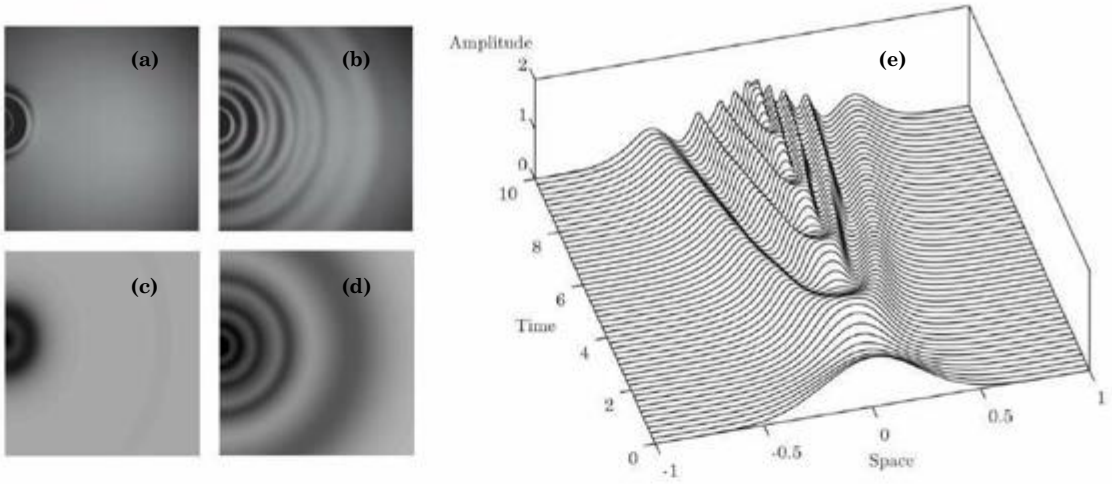

Figure 1: (a,b): Photographs of the wave field generated by a falling steel ball on a vertically oscillating liquid bath, at times t=51 ms (a) and t=173 ms (b) after the collision — (a,b) are presented in [2]. (c,d): Simulations of the wave field generated from nonlinear triad resonance of two surface waves propagating in opposite directions, and a compression mode oscillating in the vertical direction, at times $T = 17$ (c) and $T = 51$ (d). (e): Evolution of the surface wave amplitude during the resonant interaction.

References

[1] Benjamin, T. B., Ursell, F.: The stability of the plane free surface of a liquid in vertical periodic motion. Proc. R. Soc. Lond. A 225, 505–515, 1954.

[2] Eddi, A., Sultan, E., Moukhtar, J., Fort, E., Rossi, M., Couder, Y.: Information stored in Faraday waves: the origin of a path memory. J. Fluid Mech. 674, 433–463, 2011.

[3] Kadri, U., Akylas, T. R.: On resonant triad interactions of acoustic–gravity waves. J. Fluid Mech. 788, R1, doi:10.1017/jfm.2015.721, 2016.

[4] Longuet-Higgins, M. S.: A theory of the origin of microseisms. Phil. Trans. R. Soc. Lond. 243 1–35, 1950.

[5] Milewski, P. A., Galeano-Rios, C. A., Nachbin, A., Bush, J. W. M.: Faraday pilot-wave dynamics: modelling and computation. J. Fluid Mech. 778, 361–388, 2015.

OCEAN WAVES AND MICROSEISMS

Paul Christodoulides[1a)], Lauranne Pellet[2], Chris Bean[3], Sarah Donne[3] & Frederic Dias[4]
[1]*Faculty of Engineering and Technology, Cyprus University of Technology, Limassol, Cyprus*
[2]*Ecole Centrale Marseille, Marseille, France*
[3]*Seismology Laboratory, School of Geological Sciences, University College Dublin, Belfield Dublin 4, Ireland*
[4]*School of Mathematics and Statistics, University College Dublin, Belfield Dublin 4, Ireland*

Summary Ocean gravity waves generate pressure variations on the sea floor, which may lead to microseisms. Secondary microseisms are due to the interaction of surface waves with nearly equal frequencies but nearly opposite directions. A theoretical analysis with goal to quantify the degree of nearness that must be reached for the occurrence of such phenomena is presented. Based on a weakly nonlinear analysis expressions are obtained for the free surface elevation and pressure of interacting waves. Results are discussed for various regimes.

INTRODUCTION

Ocean microseisms have been observed from shallow water to deep water [1] and can be recorded as noise by coastal seismic stations either as primary or secondary. Various studies have been performed both on the origin and the propagation of microseisms [2–6]. The primary microseisms are generated by surface gravity waves incident on a sloped bottom in shallow water and have the same period as the incoming waves, while the secondary microseisms are due to the nonlinear interaction of a pair of linear surface gravity waves. Our interest here is in the secondary microseisms, which have a frequency twice that of the causative wave and amplitude independent of the depth. The main goal is to quantify the degree of nearness between the two frequencies needed to obtain a significant second-order pressure that extends all the way to the bottom of the ocean. From the records of coastal seismic stations, one can determine wave characteristics (period, height). So one needs to know the sea states that allow pressure variations large enough to generate microseisms, as well as to understand how pressure variations vary in space and time and how they are linked to the sea floor. We present the results obtained for the oceanic pressure in different cases, including both 2D and 3D regimes. We show the conditions on different parameters to obtain pressure variation able to generate microseisms. We also study the case of a train of freely TWs.

GOVERNING EQUATIONS

As compressible effects do not play a role for the conditions to generate a strong second-order pressure independent of depth, we consider the 3D, irrotational and periodic in the horizontal directions flow of an ideal, incompressible and homogeneous fluid, with gravity as the only driving force. The flow is bounded above by a free surface at $z = \eta(x, y, t)$ ($z = 0$ at rest) and below by a flat bottom at $z = -h$, and is governed by the continuity equation

$$\nabla^2\phi = 0 \tag{1}$$

subject to dynamic (Bernoulli equation) and kinematic conditions at the free surface (where $p = 0$) and bottom boundary condition, given respectively by

$$\frac{\partial\phi}{\partial t} + \frac{1}{2}|\nabla\phi|^2 + g\eta + \frac{p}{\rho} = 0, \qquad \frac{\partial\eta}{\partial t} + \frac{\partial\phi}{\partial x}\frac{\partial\phi}{\partial x} + \frac{\partial\phi}{\partial y}\frac{\partial\phi}{\partial y} = \frac{\partial\phi}{\partial z}, \qquad \frac{\partial\phi}{\partial z} = 0, \tag{2}$$

where ρ is the density, p is pressure and velocity $\mathbf{u} = \nabla\phi$, for velocity potential $\phi(x, y, z, t)$ with x and y the horizontal coordinates, z the vertical coordinate and t the time. We assume that the unknown quantities in the system under consideration (η, ϕ and p) can be decomposed as

$$\eta = \varepsilon\eta_1 + \varepsilon^2\eta_2 + O(\varepsilon^3), \qquad \phi = \varepsilon\phi_1 + \varepsilon^2\phi_2 + O(\varepsilon^3), \qquad p = \varepsilon p_1 + \varepsilon^2 p_2 + O(\varepsilon^3), \tag{3}$$

for a small parameter ε (typically the sea-surface slope).

WEAKLY NONLINEAR ANALYSIS

Applying decompositions (3) on system (1)–(2) we obtain first- and second-order expressions for the free-surface elevation η, the velocity potential ϕ (not presented here) and the pressure p, as explored for various regimes in the sequel.

First we look at several simplified cases of increasing complexity. The first one is an extension of the case studied by Longuet-Higgins [2] and deals with the superposition of two Traveling Waves (TWs) with opposite wave numbers of the same magnitude and with unequal amplitudes. The second one deals with the superposition of two TWs with different wavenumber vectors and not directly opposing.

Sum of two opposite TWs of the same wave number

For two opposite 2D TWs of the same wave number k (and frequency ω) and amplitudes A, B respectively we have

$$\eta_1 = Ae^{i(kx-\omega t)} - Be^{i(kx+\omega t)} + c.c., \qquad p_1 = \frac{\rho g\cosh(k(h+z))}{\cosh(kh)}(Ae^{i(kx-\omega t)} - Be^{i(kx+\omega t)} + c.c.), \tag{4}$$

$$p_2 = \rho g k\left(\frac{3\cosh(2k(h+z))}{2\sinh^3(kh)\cosh(kh)} - \frac{gk}{2\omega^2\cosh^2(kh)}\right)\left(A^2 e^{2i(k\cdot x-\omega t)} + B^2 e^{2i(kx+\omega t)} + c.c.\right) - \frac{\rho\,k^2\cosh(2k(h+z))}{\omega^2\cosh^2(kh)}\left(|A|^2 + |B|^2\right).$$
$$+\; g^2k^2\left(\frac{1+3\tanh^2(kh)}{\omega} - \frac{\cosh(k(h+z))}{2\omega^2\cosh^2(kh)}\right)\left(AB^* e^{-i\omega t} + c.c.\right) - \frac{\rho g^2 k^2}{2\omega^2\cosh^2(kh)}\left(B^2 e^{2ikx} + c.c.\right)$$

The expression for η_2 is not shown as it is not important for our discussion. We obtain a second-order pressure independent of the depth with twice the frequency of the carrier waves. For the limiting cases of k_1h, k_2h, $(k_1 + k_2)h \gg 1$, $z \to -h$ ($p_1 \to 0$), the period for the second-order pressure is half the period of the original waves, while the amplitude of the pressure wave increases when the period of the standing wave. An indicative case for p_2 is shown in Figure 1(a).

Sum of two TWs not directly opposing

For two 2D TWs of different wavevectors ($\mathbf{k_1}$ and $\mathbf{k_2}$) traveling in different not directly opposing) directions, for $|\mathbf{k_1}|h$, $|\mathbf{k_2}|h$, $|\mathbf{k_1} + \mathbf{k_2}|h \gg 1$, $z \to -h$ ($p_1 \to 0$), we obtain

$$\eta_1 \quad Ae^{i(\mathbf{k_1}\cdot x-\omega_1 t)} - \quad e^{i(\mathbf{k_2}\cdot x+\omega_2 t)} + c.c., \tag{5}$$

$$p_2 \quad 4\rho[g^2\mathbf{k_1}\cdot\mathbf{k_2}\;\omega_1^{-1}\omega_2^{-1}) + \;\omega_1\omega_2(\omega_1+\omega_2\;](\omega_1+\omega_2)\cos\;(|\mathbf{k_1}-\mathbf{k_2}|(h\quad z))}{[(\omega_1+\omega_2)^2 - g|\mathbf{k_1}-\mathbf{k_2}|\tanh(|\mathbf{k_1}-\mathbf{k_2}|h)]\cosh(|\;_1-\mathbf{k_2}|h)}\left(ABe^{i((\mathbf{k_1}-\;_2)\cdot\mathbf{x}-(\omega_1+\omega_2)t)} + c.\;.\right).$$

It is clear that the results above can be reduced (and modified) to accommodate the 2D cases for the sum of two TWs with wave numbers of different magnitudes and with unequal amplitudes traveling either in the same or in opposite directions. The second-order pressure is periodic in space ($k = 2\pi/|\mathbf{k_1} - \mathbf{k_2}|$) and time ($T = 2\pi/\,\omega_1 + \omega_2$)). The expression is independent of the depth with restrictive conditions on $|\beta|$ (β is the angle between the two waves) and $|\delta T| = |T_1 - T_2|$. The amplitude of the second-order pressure diminishes when $|\beta|$ and $|\,T|$ increase. This could explain why microseisms are so localized in space and time. Figure 1(b) illustrates the sensitivity of the expression on the angle of incidence of the interacting TWs. As the deviation from 180° angle of incidence increases the second-order pressure wave amplitude decreases exponentially. However longer period waves appear less sensitive to this effect.

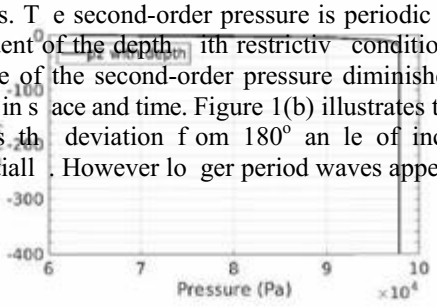

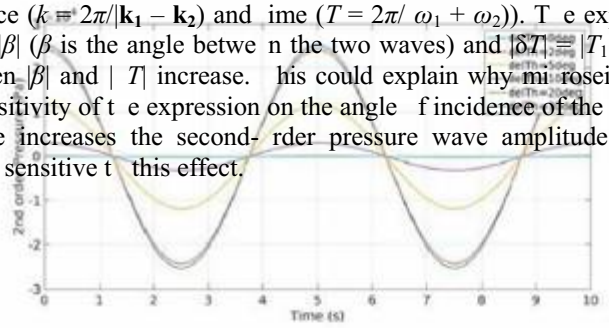

Fig. 1. (a) Second order pressure (p2) from two directly opposing TWs with periods 5s as a function of z at t = 2.5s. (b) The second-order pressure generated by the sum of TWs with the same wavenumbers, with $A = B$ = 1.5m, $T_1 = T_2$ = 10s, and not directly opposing as $|\;|$ ranges from 0 to 180° (0 to 30° only shown here as subsequent values produce negligible p_2).

DISCUSSION ON OTHER REGIMES

The superposition of several waves traveling in different directions has been considered by several authors (see for example [2, 7]). The results above for the superposition of 2 TWs are then generalized (the resulting formulas are not shown here), for a train of freely TWs, including the possibility for each wave of complex amplitude A_n to have a 'sister' wave of complex amplitude B_n with equal frequency but opposite direction. This fulfills the second objective –not less important– of this work to check, review, generalize, as well as unify the analytical expressions, already published, to describe the interaction of waves.

Finally other cases dealing with various situations encountered in the ocean (the west coast of Ireland being an example where such pressures can probably be found), such as coastal reflection, broad storm (single swell event), wind waves interacting with swell are also considered.

References

[1] Bromirski .: Earth vibration , *Science* **324**: 10 6-1027, 2009.

[2] Longuet-Higgins M.: A theory of the origin of icroseisms, *Phil sophical Transactions of the Royal Society of Londo A* **243**:1-35, 195 .

[3] Hasselman K.: Ocean wave sources of seismi noise, *Rev. Geo hys.* **1**:177-210, 1 63.

[4] Ardhuin F., Stutzmann E., Schimmel M., Mangeney A.: Ocea wave sources o seismic noise, *ournal of Geoph sical Research*: *Oceans (1978-2012)* **116**:C0900 , 2011.

[5] Ardhuin F., Herbers T.: Noise generation in th solid earth, ocean and atmosphere, from nonlinear interacting surface gravity waves in finite depth, *J. Fl id Mech.* **716**: 16-348, 2013.

[6] Ying Y., B an C., Bromirski P.: Propagation o microseisms fro the deep ocean to land, *Geophysical Research Lette s* **41(18)**:6374-6379, 2014.

FARADAY WAVES REVISITED

Jean Rajchenbach[1] and Didier Clamond[2]
[1] *Laboratoire de Physique de la Matière Condensée (CNRS UMR 7336),*
[2] *Laboratoire Jean-Alexandre Dieudonné (CNRS UMR 7351)*
Université de Nice-Sophia Antipolis, Parc Valrose, 06108 Nice Cedex 02

Summary We revisit the theoretical description of Faraday waves. We show that the relation of dispersion is not that of free unforced waves; the forcing amplitude and the viscosity play a significant role in the dispersion relation. We then determine the instability thresholds and the wavenumber selection in cases of both short and long waves. We also show that, depending on the depth, the instability leading to the formation can be either supercritical or subcritical, in agreement with experimental observations.

INTRODUCTION

Despite notable advances in the theoretical understanding of parametrically-forced water waves [1-3], some of their fundamental properties remain obscure. For instance, the dispersion relation (relating angular frequency ω and wave number $\boldsymbol{k}$) of Faraday waves has astonishingly not been explicitly established hitherto. Moreover, following of the seminal paper of Benjamin & Ursell [1], the wave number of Faraday waves is often supposed to be selected by the size and the shape of the vessel and correspond to eigenmodes, and their dispersion relation identified with that of free unforced waves, namely $\omega_o^2 = gk \tanh(kd)$ (g is the gravity constant and d is the depth). Both these hypotheses are actually incorrect and contradict experimental evidences. First, as can be seen in the movie given as supplemental materials in [4], the parametrically forced mode oscillates at half of the forcing frequency Ω, but corresponds there to two contra-propagative waves and not to an eigenmode of the tank. Then, the experimental determination of the dispersion relation of dispersion of parametrically-forced waves shows significant deviations compared to that of free unforced waves (see e.g. Fig. 7 in [5]). It is also worth noting that formation of patterns can actually be observed in shallow water, that is *inconsistent* with the dispersion relation $\omega_o = \sqrt{gd}\, k$ corresponding to free unforced waves in shallow water. Indeed, the formation and the symmetry of the surface patterns are determined by a multiwave resonant coupling mechanism, which requires the simultaneous fulfilment of $\boldsymbol{k}_1 + \boldsymbol{k}_2 + \boldsymbol{k}_3 = \boldsymbol{0}$ and $\omega_1 + \omega_2 + \omega_3 = 0$ ($\boldsymbol{k}_i$ and ω_i being the wave number and the angular frequency of the waves). Such relations require a *convex dispersion relatio*n, and this condition is obviously not fulfilled by pure gravity waves in shallow water at the leading linear order.

Furthermore, up to now, theoretical models predicted a supercritical (i.e. continuous) bifurcation from the rest state to the wavy state when increasing the forcing. If experiments conducted in deep water are consistent with this standpoint, recent experiments conducted in shallow water revealed rather a discontinuous, subcritical transition. At last, measurements of the instability threshold showed significant discrepancies with values proposed in the theoretical literature. Therefore, it turns out to be necessary to revisit the theoretical description of Faraday waves The first aim of this work is to establish the actual relation of dispersion of Faraday waves for *nonzero* forcing and dissipation. We have shown that dispersion relation of free, unforced waves is significantly altered in the case of parametrically-forced excitations: two different wavenumbers correspond then to the same angular frequency. We have then carried out their stability analysis and we have discussed the nature of the bifurcation giving rise to the wavy surface state from the rest state when the forcing is increased. Thus, the threshold of the Faraday instability is established as well as the selected wavenumbers in both cases of short and long waves. At last, it is shown that the transition can be either smooth (supercritical) or discontinuous and hysteretic (subcritical), depending on the thickness of the liquid layer.

RESULTS

As established by Benjamin & Ursell [1], a parametrically-driven surface mode of wavenumber $\boldsymbol{k}$ and of amplitude ζ obeys in the linear approximation a damped Mathieu equation

$$\zeta_{tt} + 2\,\sigma\,\zeta_t + \omega_o^2\,[1 + F\cos(\Omega t)]\,\zeta = 0$$

where $\sigma = \sigma(k)$ is the viscous attenuation and ω_o the angular frequency of linear waves without damping and without forcing.

It is well known that systems obeying a (damped) Mathieu equation with excitation angular frequency Ω exhibit a series of resonance conditions for response angular frequencies ω equal to $n\Omega/2$, n being an integer. These solutions are expressed in term of the Mathieu functions together with a dispersion relation involving the so-called Floquet exponent. Mathieu functions are transcendent and cannot be expressed in term of simple functions in closed form. In order to

understand qualitatively these solutions we consider approximations in the limit of small forcing and dissipation. Assuming $F << 1$ and $\sigma \sim 0(F)$, an approximate dispersion relation can be found for the sub-harmonic response $\omega=\Omega/2$. We obtain $\omega_o/\omega \approx 1 \pm \sqrt{(F/4)^2 - (\sigma/\omega)^2}$. We note that two wavenumbers $k^{\pm}$ correspond to the same angular frequency $\omega=\Omega/2$, and that *both forcing and dissipation intervene in the relation of dispersion*. Then, assuming $|kA| << 1$ and seeking an approximation in the form $\eta(t) = Re\{A(t)\}\cos(kx) + 0(A^2)$, an amplitude equation can be derived in the form [6] $\frac{dA}{dt} + (\sigma - i\omega_o) A + \frac{iF\Omega}{8} e^{i\Omega t} A^* + \frac{iK\Omega k^2}{2} |A|^2 A = 0$, with $K = \frac{2 - 6s - 9s^2 - 5s^3}{16(1+s)(1-s)^2}$ (where $s = \mathrm{sech}(2kd)$) [7]. *A important fact is that the sign of the nonlinear term* (via the sign of K) *depends on the depth*: we have $K>0$ for short waves and $K<0$ for long waves [7]. This plays a key role for the stability of the solutions. In order to deal with an autonomous amplitude equation, we define $B = A\exp(\frac{i\pi}{4} - \frac{i}{2}\Omega t)$ and the previous equation is recast into $\frac{dB}{dt} = (i\omega_o - \frac{i}{2}\Omega - \sigma) B + \frac{F\Omega}{8} B^* - \frac{iK\Omega k^2}{2} |B|^2 B$. Then, looking for solutions of the form $B=a\exp(i\pi/4 - i\delta)$, we obtain $\omega_o/\omega \approx 1 + (Ka)^2 \pm \sqrt{(F/4)^2 - (\sigma/\omega)^2}$. Clearly, only the rest solution $B=0$ can exist if $F<F_{\downarrow} = 4\sigma/\omega$. In the other hand, there are two possible nonzero solutions in the range $F_{\downarrow} < F < F_{\uparrow} = 4\omega^{-1}\sqrt{(\omega_o - \omega)^2 + \sigma^2}$. In order to study the stability of these solutions, we introduce a small perturbation into the stationary solutions of the above amplitude equation and we look for the eigenvalues of the linearized system of equations obeyed by the perturbation. The stability analysis that we conduct below resembles that carried out in [8] for the parametric pendulum. However, *major differences are that the eigenfrequency of a freely-oscillating pendulum is unique, whereas free, unforced, water waves exhibit a continuous spectrum of mode frequencies* and that *the sign of the nonlinear term depends here on the depth*. We finally find that, for short waves ($K>0$), the only stable solutions are the rest one if $F< F_{\uparrow}$, and a nonzero amplitude solution (with $\omega < \omega_o$) if $F > F_{\uparrow}$. The bifurcation is here surcritical. In the other hand, for long waves ($K < 0$), the only stable solution is the flat one if $F < F_{\downarrow}$, there are two stable solutions in the range $F_{\downarrow} < F < F_{\uparrow}$ (the rest solution, and a nonzero amplitude solution with $\omega < \omega_o$), and only one stable solution (a nonzero amplitude solution with $\omega < \omega_o$) if $F> F_{\uparrow}$. In the latter case of long waves, the range $F_{\downarrow} < F < F_{\uparrow}$ corresponds to a hysteretical region, with both the possibilities of having a zero or nonzero wave amplitude, according to the forcing history, and the bifurcation is subcritical [9].

We are now in position to determine the wave number selected at the instability onset. The minimal forcing required to destabilize the free surface is $F_{\uparrow} = 4\omega^{-1}\sqrt{(\omega_o - \omega)^2 + \sigma^2}$, with $\omega=\Omega/2$. The first wave to emerge from rest is the one requiring the smaller value of $F_{\uparrow}$, and corresponding to the wavenumber such that $\partial F_{\uparrow}/\partial k = 0$. In the limiting case of deep water (i.e. $d = \infty$, $\omega_o = \sqrt{gk}$, $\sigma = 2\upsilon k^2$, υ being the kinematic viscosity) the most unstable wavenumber k is given by $2\omega_o = \omega + \sqrt{\omega^2 - 16\sigma^2}$. In the opposite limit of long waves (i.e. $kd << 1$, $\omega_o = \sqrt{gd}\, k$, $\sigma = (gd)^{1/4} \sqrt{k\upsilon/8d^2}$), the most unstable wavenumber corresponds to $\omega_o = \omega - 16\upsilon/d^2$ [9].

CONCLUSIONS

We have shown that the dispersion relation of Faraday waves is modified compared to that of free, unforced waves: forcing and dissipation play a key role in the relation of dispersion. We have also studied the nature of the bifurcation at the instability onset, and we have shown that the transition is supercritical for short waves and subcritical for long waves. We have determined the instability threshold, and the selected wavenumber in the two limiting cases of short and long waves.

References

[1] T.B. Benjamin, & F. Ursell, Proc. R. Soc. Lond. A225, 505 (1954).

[2] S.T. Milner, J. Fluid Mech. 225, 81 (1992).

[3] K. Kumar, K. & L.S. Tuckerman, J. Fluid. Mech. 279, 49 (1994).

[4] J. Rajchenbach, D. Clamond & A. Leroux, Phys. Rev. Lett. 110, 094502 (2013).

[5] W.S. Edwards, S. Fauve, J. Fluid Mech. 278, 123 (1994).

[6] E. Meron, Phys. Rev. A 35, 4892 (1987).

[7] I. Tadjbakhsh, J.B. Keller, 1960. J. Fluid Mech. 3, 442, (1960).

[8] S. Fauve, in *Hydrodynamics and Nonlinear Instabilities*, p. 387 (C. Godrèche et P. Manneville Ed.), Cambridge University Press, 1998.

[9] J. Rajchenbach, D. Clamond, J. Fluid. Mech. 777, R2-1 (2015).

FARADAY WAVE LATTICE AS AN ELASTIC METAMATERIAL

Lucie Domino[1], Malo Tarpin[1], Sylvain Patinet[1], and Antonin Eddi *[1]
[1]*Laboratoire de Physique et Mécanique des Milieux Hétérogènes (PMMH), ESPCI, Paris, France*

Summary Metamaterials enable the emergence of novel physical properties due to the existence of an underlying structure. Here, we use the Faraday instability to shape the fluid-air interface with a regular pattern. This pattern undergoes an oscillating secondary instability and exhibits spontaneous vibrations that are analogous to transverse elastic waves. By locally forcing these waves, we fully characterize the dispersion relation of these waves and show that a Faraday pattern presents an effective shear elasticity. We propose a physical mechanism combining surface tension with the Faraday structured interface that quantitatively predicts the elastic wave phase speed, revealing that the liquid interface can be considered as a mechanical metamaterial.

INTRODUCTION

An artificial material made of organized functional building blocks is called a metamaterial [1] when it exhibits properties that differ greatly from that of the unit cell. These new physical properties are intrinsic of the presence of an underlying structure. Here we propose to use pattern formation in non-linear physics to produce the underlying structure of a metamaterial. For this purpose, the Faraday instability is often used as a model system. This hydrodynamic instability appears at the interface between two fluids (in our case an oil-air interface) subjected to a vertical oscillation [2]. Above a certain threshold of acceleration a_c, the surface shows a stationary deformation [Fig. 1(a)] that oscillates at half the excitation frequency. This pattern is both stable in time and regular in space, with a Faraday wavelength λ_F defined by the inviscid gravity-capillary wave dispersion relation $\omega_0^2 = (gk_F + \frac{\sigma}{\rho}k_F^3)\tanh(k_F h)$, where $k_F = (2\pi)/\lambda_F$ is the Faraday wavenumber, g is the acceleration of gravity, σ is the surface tension of the fluid, h the fluid depth and ρ its density. For a square vessel it is most often a square pattern that is obtained. It becomes unstable and oscillates [3] upon increasing the driving amplitude, and then destabilizes into a chaotic state.

EXPERIMENTAL SET-UP, VIBRATION OF THE PATTERN

Experimental set-up

Our experimental set-up consisted of a square vessel filled with a thin layer of silicone oil of thickness $h = 3$ mm. The vessel is mounted on a vibration exciter and we work with a sinusoidal acceleration $a\cos 2\pi f_0 t$ with frequency f_0 ranging from 72 Hz to 120 Hz. The pattern is about 25×25 Faraday wavelengths. A top view of the stable pattern obtained is shown in Fig. 1(a). Each white dot corresponds to an horizontal slope of the fluid interface, there are thus 4 white spots per Faraday unit cell.

Spontaneous

Upon increasing the driving amplitude to about twice the threshold value, spontaneous oscillations of the square lattice appear (Fig.1(d). These oscillations are in-plane modulations of the pattern along its two main directions. They exhibit a spatial periodicity $\lambda = 4\ \lambda_F$, corresponding to the white segment presented in this figure. We detect each point in-plane position $(x(t), y(t))$ using a custom Matlab algorithm. Fourier spectra of the periodic oscillations show a peaked signal at $f = 1.35$ Hz. These spontaneous oscillations of the pattern correspond to a supercritical Hopf bifurcation that takes place close to the threshold of transition to chaos. The spontaneous oscillations occur at a frequency f much lower than the Faraday frequency f_F whereas their spatial wavelength $\lambda \simeq 2.0$ cm is 4 times larger than λ_F. In our experimental conditions and at this frequency f, the gravito-capillary dispersion relation gives a wavelength of $\lambda_{gc} = 23.26$ cm much larger than λ. This means that the transverse standing wave responsible for the pattern oscillations is governed by a different physical mechanism that we identify by performing a new set of experiments.

Forced vibrations

We now investigate all the oscillating modes of the Faraday wave pattern by forcing the vibrations of stable square patterns. We add to the vessel a custom-made forcing device consisting of a comb dipping into the liquid to a small depth [Fig. 1(c)]. The comb is set in motion by a second vibration exciter to oscillate horizontally in the reference frame of the container at frequencies ranging from 0.5 Hz to 5 Hz. This allows us to generate a sinusoidal oscillation of the line of Faraday peaks located below the forcing comb. We observe a transversal wave that propagates away from the forcing device at the forcing frequency f. From the experimental data we extract its wavenumber k_T for each value of f. We do the same analysis to extract k_T for waves propagating in the perpendicular direction. Fig. 1(c) presents the dispersion relations $f(k_T)$ (blue triangles for y direction and red triangles for x direction) that we obtain for f ranging from 0.5 to 10 Hz. We observe a linear increase of f with k_T. A linear fit gives the phase speed of the transverse waves $v_\varphi = 4.60$ cm.s^{-1}.

*Corresponding authors. Email: lucie.domino@espci.fr, antonin.eddi@espci.fr

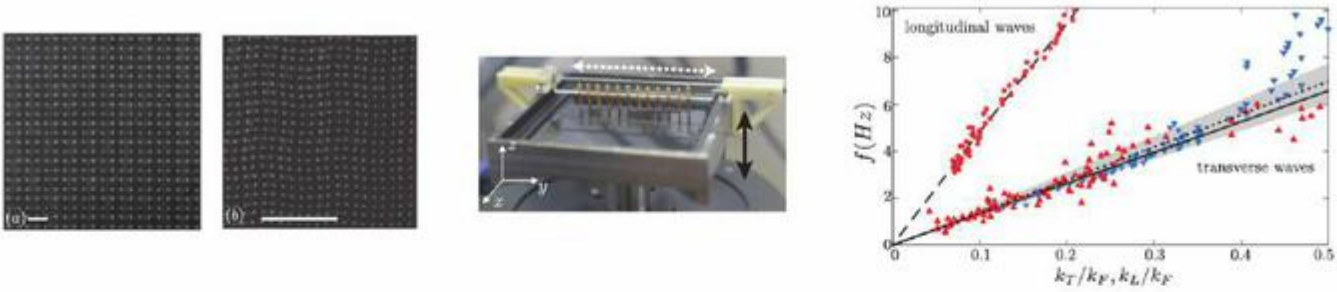

Figure 1: (a) Top view of the stable square pattern. The white segment has a length equal to λ_F. (b) Top view of the oscillating Faraday pattern. The white segment has a length equal to $4\lambda_F$, which is the wavelength of the spontaneous oscillations. (c) Device used to force the vibrations of the Faraday pattern. Plain black arrow shows the vertical motion of the whole vessel, dotted white arrow shows horizontal vibration of the comb. The width of the vessel is 12 cm. (d) Dispersion relation of the oscillations $f(k_T)$ and $f(k_L)$. Blue down triangles: transversal waves in the y direction. Red up triangles: transversal waves in the x direction. Open circles: longitudinal waves in the x direction. Plain dark line: linear fit. Dashed line: gravity-capillary wave dispersion relation. Dotted line and grey background: prediction and its associated uncertainty.

PHYSICAL MECHANISM

We consider a reference state for the surface defined as $z_0(x,y,t) = A(t)\cos\left(\frac{2\pi}{\lambda}x\right)\cos\left(\frac{2\pi}{\lambda}y\right)$, with $\lambda = \lambda_F\sqrt{2}$ and $A(t) = A_0\cos(2\pi f_F t)$ the amplitude of the stationary wave. Measurements with a high-speed camera give $A_0/\lambda_F = 13.5\% \pm 3.5\%$. This 2D function gives a succession of peaks and crests arranged in a square pattern tilted at $45°$. We apply a shear strain $\gamma = \tan\theta$ to this elementary cell and calculate analytically the surface area $S(\gamma)$. As γ and $-\gamma$ give the same area we can approximate for small deformations $S(\gamma) - S_0 = \Delta S = \frac{1}{2}\frac{\partial^2 S}{\partial\gamma^2}\Big|_{\gamma=0}\gamma^2 = \frac{1}{2}S_{\gamma\gamma}\gamma^2$. Due to surface tension there is an energy cost that depends on the applied shear deformation $\Delta E(\gamma) = \sigma\Delta S(\gamma)$. We then define the effective elastic energy density per unit area $W_S = \sigma\Delta S/\lambda^2$ and introduce the effective shear modulus μ_S of the Faraday wave pattern: $W_S = 2\mu_S(\frac{1}{2}\gamma)^2$. Following standard elasticity theory the transverse elastic wave phase velocity c_T in a 2D elastic medium is written

$$c_T = \sqrt{\frac{\mu_S}{\rho_S}} = \sqrt{\frac{\sigma S_{\gamma\gamma}}{\rho_S\lambda^2}}, \text{ with } \rho_S \text{ the density per unit area, defined as } \rho_S = \rho\mathcal{A}. \quad (1)$$

The velocity we obtain is $c_T = 4.90 \pm 0.63$ cm.s^{-1}, which is in excellent agreement with the experimental result of 4.60 cm.s^{-1}. We represent in Fig. 1(d) the estimated dispersion relation (dotted line), the grey background representing the uncertainty due to the uncertainty on A_0/λ_F.

CONCLUSION

In this work, we observe the emergence of a new physical property, namely an effective 2D elasticity, at the air-liquid interface. Our interpretation reveals that it is intimately related to the existence of a cellular pattern imprinted on the liquid interface. From this perspective, the Faraday pattern formed at the interface of a newtonian liquid creates a mechanical metamaterial at macroscopic scale. In the future, we would like to characterize the effect of the structure periodicity on the elastic waves and investigate in more detail the limit $k/k_F = 1/2$ that would correspond to the edge of the first Brillouin zone in a crystalline solid material. Another line of future research is to understand if there exists a second elastic constant for the medium that would correspond to the Poisson ratio of our meta-solid. More generally, other pattern formation instabilities known in non linear physics could be investigated as a way to form structures for metamaterials.

References

[1] Buckmann, R. Schittny, and M. Wegener, Reports on Progress in Physics 76, 126501 (2013)
[2] M. Faraday, Phil. Trans. R. Soc. London 121, 299 (1831); S. Douady, J. Fluid Mech. 221, 383 (1990)
[3] I. Shani, G. Cohen, and J. Fineberg, Phys. Rev. Lett. 104, 184507 (2010).

SURFACE WAVES IN A SQUARE CONTAINER DUE TO ITS RESONANT HORIZONTAL ELLIPTIC MOTION

Ai Hiramitsu[1] and Mitsuaki Funakoshi [*1]
[1] *Department of Applied Analysis and Complex Dynamical Systems, Graduate School of Informatics, Kyoto University, Yoshida-Honmachi, Sakyo-ku, Kyoto 606-8501, Japan*

Summary Surface waves in a square container due to its resonant horizontal elliptic motion are examined theoretically. The motion of the container is characterized by the ratio of the lengths of the major and minor axes of its elliptic orbit, and by the angle between the directions of the major axis and one of its sidewalls. Using the reductive perturbation method, nonlinear time evolution equations for the complex amplitudes of two degenerate modes excited by this motion are derived with the inclusion of linear damping. Solutions to these equations expressing regular co-rotating or counter-rotating waves and waves with periodic or chaotic variations in their amplitudes are obtained. Counter-rotating waves are not observed for the circular motion of the container. Chaotic waves are obtained frequently when the container's motion is close to linear.

DERIVATION OF MODEL EQUATIONS

Because of their interesting behavior as an example of nonlinear dynamical systems and their importance in many applications, surface waves due to the resonant oscillation of a container have been investigated theoretically and experimentally by many researchers[1, 2]. In the present study, surface waves due to the resonant horizontal elliptic motion (including linear motion as its special case) of a rectangular container with a square base are investigated, in which the frequency of the elliptic motion is assumed to be close to the natural frequency of two degenerate modes with the smallest natural frequency. The main purpose of this study is to examine the dependence of excited surface waves on the parameters characterizing this elliptic motion with a weakly nonlinear theory, because the waves due to this motion have not been examined before.

We consider three-dimensional surface waves in a rectangular container of square base with side length πL. In the following part, all variables are nondimensionalized by the length L and the time $\sqrt{L/g}$, where g is the gravitational acceleration. We first introduce the Cartesian coordinates ($\tilde{}$ $\tilde{}$ $\tilde{}$) of an inertial system, where $\tilde{}$ and $\tilde{}$ are horizontal coordinates. We assume that the horizontal displacement of the container is expressed as

$$\tilde{} = -a_0(\cos\phi\cos\theta\cos\Omega t - \sin\phi\sin\theta\sin\Omega t), \qquad y = -a_0(\cos\phi\sin\theta\cos\Omega t + \sin\phi\cos\theta\sin\Omega t), \tag{1}$$

where t is the time, a_0 is a positive constant, and θ and ϕ are constants satisfying $0° \le \theta \le 45°$ and $0° \le \phi \le 45°$. Therefore, the container moves with frequency Ω, and the orbit of its motion is elliptic, as illustrated in Fig. 1. Here θ is the angle between the major axis of the elliptic orbit and the x-axis. Since the lengths of the major and minor axes of the elliptic orbit are expressed as $2a_0\cos\phi$ and $2a_0\sin\phi$, respectively, the ratio of the length of the minor axis to the length of the major axis is $\tan\phi$. Next, we introduce Cartesian coordinates (x, y, z) fixed to the container, as illustrated in Fig. 2. Here, x and y are horizontal coordinates along the sidewalls of the container in which sidewalls are expressed as $x = 0,\ \pi$

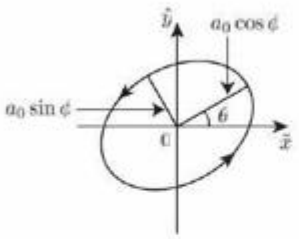

Figure 1. Orbit of container's motion.

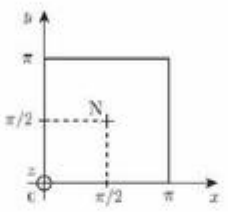

Figure 2. Cartesian coordinates fixed to a container.

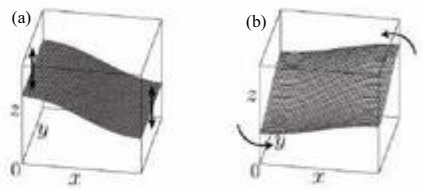

Figure 3. Schematic diagrams of excited surface waves. (a) Surface waves with $M = 0$ (and $B = 0$). (b) Surface waves with $M > 0$.

and $y = 0,\ \pi$, whereas z is the upward vertical coordinate in which a quiescent surface is defined by $z = 0$.

We assume the irrotational flow of an incompressible inviscid fluid of depth h. Therefore, using a velocity potential $\Phi(x, y, z, t)$, the x, y, and z components of fluid velocity $\boldsymbol{u}$ are expressed as $\boldsymbol{u} = \nabla\Phi$. The displacement of the free surface is expressed by $z = \eta(x, y, t)$. Φ and η satisfy governing equations of surface gravity waves including boundary conditions on the walls of the container.

Now we assume that $a_0\Omega^2 = \epsilon^3\pi$, where $\epsilon > 0$ satisfies $\epsilon \ll 1$. We then expand Φ and η as

$$\Phi = \epsilon\Phi_1 + \epsilon^2\Phi_2 + \epsilon^3\Phi_3 + \cdots, \quad \eta = \epsilon\eta_1 + \epsilon^2\eta_2 + \epsilon^3\eta_3 + \cdots. \tag{2}$$

We also assume that $\Omega - H = O(\epsilon^2)$, where $H = \sqrt{\tanh h}$ is the natural frequency of two degenerate modes of standing waves called the $(1, 0)$ and $(0, 1)$ modes , and write as $\Omega = H + \epsilon^2\delta$ with the detuning parameter δ. Moreover,

*Corresponding author. E-mail: mitsu@acs.i.kyoto-u.ac.jp

in order to describe the slow time evolution of amplitudes and phases of excited surface waves, we introduce the slow time variable $\tau = \epsilon^2 t$, and then assume that Φ and η depend on not only t but also τ. Under the above assumption for Ω, only the $(1,0)$ and $(0,1)$ modes are expected to be resonantly excited. Therefore, η_1 can be expressed as $\eta_1 = -\mathrm{i}H[a(\tau)\cos x + b(\tau)\cos y]\mathrm{e}^{\mathrm{i}Ht} + \mathrm{c.c.}$, where $a(\tau)$ and $b(\tau)$ are functions of τ, and $-\mathrm{i}Ha(\tau)$ and $-\mathrm{i}Hb(\tau)$ are the complex amplitudes of the $(1,0)$ and $(0,1)$ modes.

By using the reductive perturbation method, and including the effect of linear damping, we finally derive the following nonlinear time evolution equations from the governing equations of surface waves:

$$\begin{cases} \frac{\mathrm{d}A}{\mathrm{d}\tau} = -\alpha A - \mathrm{i}\delta A - \mathrm{i}R_1|A|^2A - \mathrm{i}R_2|B|^2A - \mathrm{i}R_3A^*B^2 + \cos\phi\cos\theta + \mathrm{i}\sin\phi\sin\theta, \\ \frac{\mathrm{d}B}{\mathrm{d}\tau} = -\alpha B - \mathrm{i}\delta B - \mathrm{i}R_1|B|^2B - \mathrm{i}R_2B|A|^2 - \mathrm{i}R_3A^2B^* + \cos\phi\sin\theta - \mathrm{i}\sin\phi\cos\theta, \end{cases} \tag{3}$$

where $A(\tau) = a(\tau)\mathrm{e}^{-\mathrm{i}\delta\tau}$ and $B(\tau) = b(\tau)\mathrm{e}^{-\mathrm{i}\delta\tau}$, α is the coefficient of linear damping, and $*$ denotes complex conjugate. R_1, R_2 and R_3 are constants depending only on h. To characterize the energy of excited surface wave, we introduce a variable E defined by $E = \frac{H^2}{2}(|A|^2 + |B|^2)$. $\sqrt{E}$ is a measure of amplitude of these waves. We also introduce $M = \frac{\mathrm{i}}{2}H^2(A^*B - AB^*)$ to characterize the rotation of the wave pattern. We can say that the pattern of excited waves rotates counterclockwise (clockwise) if $M > 0$ ($M < 0$). Schematic diagrams of excited surface waves with $M = 0$ and $M > 0$ are shown in Fig. 3.

RESULTS

For fixed values of α and h, response curves, expressing the dependence of $\sqrt{E}$ on δ, for stationary solutions to (3), are computed numerically for several θ and ϕ. An example of response curve is shown in Fig. 4. Stationary solutions are characterized by the value of M as well as the value of $\sqrt{E}$. Non-rotating waves with $M = 0$ are possible only for linear motions of the container with $\phi = 0^\circ$ along the direction of $\theta = 0^\circ$ or 45°. For other values of ϕ and θ satisfying $0^\circ < \phi \leq 45^\circ$ and $0^\circ < \theta < 45^\circ$, only rotating waves with $M = 0$ can be observed. Moreover, for the elliptic motion of the container with $\phi = 0^\circ$, these waves are classified into co-rotating waves of $M > 0$, whose direction of rotation is the same as that of the container, and counter-rotating waves of $M < 0$, whose direction of rotation is opposite to that of the container's motion. Response curves for such ϕ are composed of an unbounded branch extending to $\delta \to \pm\infty$, and a bounded branch of a closed curve observed within a finite range of δ not far from zero, if ϕ is sufficiently small. With increasing ϕ, this bounded branch shrinks, and the region of δ where stable counter-rotating waves are observed on an unbounded or bounded branch becomes smaller for any θ. If ϕ is sufficiently close to 45° corresponding to a nearly circular motion of the container, for any θ stable co-rotating waves are observed for all δ on an unbounded branch and no counter-rotating wave is observed.

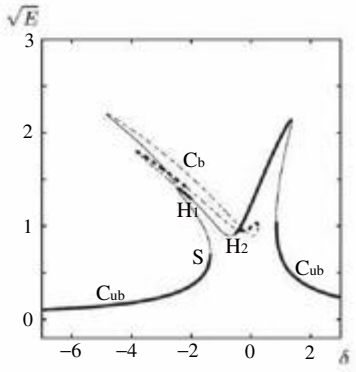

Figure 4. Response curves for $\alpha = 0.3$, $h = \pi$, $\theta = 0^\circ$, and $\phi = 20^\circ$. Solid lines are stationary solutions with $M > 0$. Broken lines are those with $M < 0$. Thick and thin lines denote stable and unstable solutions, respectively. $\mathrm{C_{ub}}$ and $\mathrm{C_b}$ are unbounded and bounded branches of response curves, respectively. S and H_j $(j = 1, 2)$ denote the points of saddle-node bifurcation and Hopf bifurcation, respectively.

For $\theta = 0^\circ$, non-stationary solutions with chaotic or periodic slow variations in the amplitude and phase of excited surface waves are observed for δ within the region of no stable stationary solutions. These solutions are either uni-directionally or bi-directionally rotating waves. Chaotic solutions are observed more frequently for smaller ϕ. Moreover, with increasing ϕ, the region of δ where chaotic or periodic solutions of bi-directionally rotating waves are observed tends to shrink and then disappears. Only periodic solutions of uni-directionally rotating waves are observed for all the δ within the region of no stable stationary solutions if ϕ is sufficiently large. Some of the transitions of non-stationary solutions associated with the variation in δ and the multiplicity of these solutions can be explained from a complicated branching of periodic solutions.

Finally, stable stationary and non-stationary solutions for the linear motion of the container with $\theta = 0^\circ$, 30° and 45° are compared with the experimental results by Ikeda et al.[3] The wave amplitudes at two measurement points and the rotation of the wave pattern for several forcing frequencies observed in this experiment agree fairly well with our results.

References

[1] Faltinsen O M and Timokha A N 2009 *Sloshing* (Cambridge: Cambridge University Press).

[2] Ibrahim R A 2005 *Liquid Sloshing Dynamics* (Cambridge: Cambridge University Press).

[3] Ikeda T, Ibrahim R A, Harata Y and Kuriyama T 2012 Nonlinear liquid sloshing in a square tank subjected to obliquely horizontal excitation. *J. Fluid Mech.* **700**, 304-328.

NONLINEAR ACOUSTICS IN BRASS INSTRUMENTS

James McTavish[1] and Edward Brambley *[1]
[1]*Department of Applied Mathematics and Theoretical Physics, University of Cambridge, Cambridge, United Kingdom*

Summary Since the work of Stokes in 1848 it has been well known that sound propagating over large distances begins to distort due to the accumulation of small nonlinear effects. It can be shown that plane sound waves in a straight duct will eventually steepen to form discontinuous shocks (in the absence of viscosity). More recently experiments have shown that this distortion and the resulting shock waves may be responsible for the characteristic "brassy" sound of trombones and trumpets - especially when played at louder volumes [1]. The mathematics however, describing this nonlinear behaviour in ducts with curvature - such as the trombone resonator - remains little understood. Our work extends the Multimodal Method of Félix and Pagneux [2] [3] with the introduction of a 'nonlinear admittance' term coupling pressure and velocity modes to give a description of nonlinear behaviour in ducts with curvature.

METHOD OUTLINE

Beginning with the compressible Euler equations, we consider small perturbations of pressure, density and velocity about a state of rest, where the perturbations are (in non-dimensional variables) of the order of the Mach number $M < 1$ which is assumed to be small but finite. The mass and momentum conservation equations are then expanded correct to order M^2 so that only quadratic nonlinearities are considered. A Taylor expansion of the equation of state at constant entropy is also considered, relating the pressure and density (also correct to $\mathcal{O}(M^2)$). This is used to eliminate density terms from the governing equations. The pressure and velocity perturbations are then expanded into a temporal Fourier series and a basis of the transverse duct modes of a *straight* duct

$$p' = \sum_{a=-\infty}^{\infty}\sum_{p=0}^{\infty} P_p^a(s)\psi_p(\mathbf{r}_\perp)e^{-ia\omega t}, \qquad \mathbf{u}' = \sum_{a=-\infty}^{\infty}\sum_{p=0}^{\infty} \mathbf{U}_p^a(s)\psi_p(\mathbf{r}_\perp)e^{-ia\omega t}$$

where we are using a coordinate system based on the arc-length s along the centreline of a general duct (including the possibility of varying curvature) and transverse components perpendicular to the longitudinal direction. The transverse duct modes satisfy the eigenvalue problem $\nabla_\perp^2\psi_p + a_p^2\psi_p = 0$ subject to the no penetration condition on the duct wall $\mathbf{n}\cdot\nabla_\perp\psi_p = 0$.

Following the work of Félix and Pagneux, the transverse velocity components are eliminated to obtain two equations - one for the pressure modal amplitudes and one for the longitudinal velocity modal amplitudes as they vary through the duct. Due to the presence of evanescent modes these equations are numerically unstable. To overcome this, a nonlinear relation between pressure and velocity modes is defined in terms of the linear admittance $Y_{pq}^a(s)$ of Félix and Pagneux and a new nonlinear admittance term $\mathcal{Y}_{pqr}^{ab}(s)$ representing the $\mathcal{O}(M^2)$ correction

$$U_p^a = \sum_{q=0}^{\infty} Y_{pq}^a(s)P_q^a + \sum_{b=-\infty}^{\infty}\sum_{q,r=0}^{\infty} P_q^{a-b}P_r^b\mathcal{Y}_{pqr}^{ab}$$

By taking derivatives, substituting the governing equations and considering orders of magnitude, separate equations for Y' and $\mathcal{Y}'$ can be found, and by applying a suitable boundary condition downstream the equations can be numerically solved to the inlet and the admittance found everywhere along the duct. Using the admittance and the governing equations, an equation for just the pressure can be found. By numerically integrating from a chosen source condition at the inlet, the pressure can be found throughout the duct.

RESULTS

Numerical results of the nonlinear multimodal method have shown good agreement with the analytical Blackstock solution [4] for a straight duct. Figure 1 shows a direct comparison of the modal amplitudes at various distances down the duct (normalised in terms of the shock formation distance $\sigma = x/x_{\text{shock}}$) for an initially sinusoidal planar waveform. Qualitative results are also in good agreement with the non-planar or angled planar waveforms observed by Fernando et. al. [5]. Figure 2 shows the characteristic straight but angled shock fronts of a planar wave propagated at 84° degrees to the normal, at the point of shock formation.

As an interesting aside, in certain cases the method may be used to tackle non-linear inverse problems. Figure 3 shows the modal amplitudes of a waveform which propagates into a sinusoidal waveform (all the harmonics transfer their energy to the fundamental) before steepening again. This initial waveform was found by applying the inverse method to a sinusoidal waveform.

*Corresponding author. Email: E.J.Brambley@damtp.cam.ac.uk

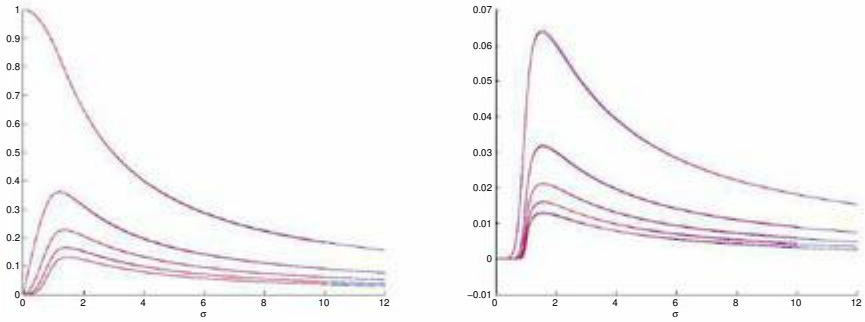

(a) Modes 1 to 5 (b) Modes 10, 20, 30, 40 ,50

Figure 1: Numerical solution using the nonlinear multimodal method (blue) against analytic Blackstock solution (red)

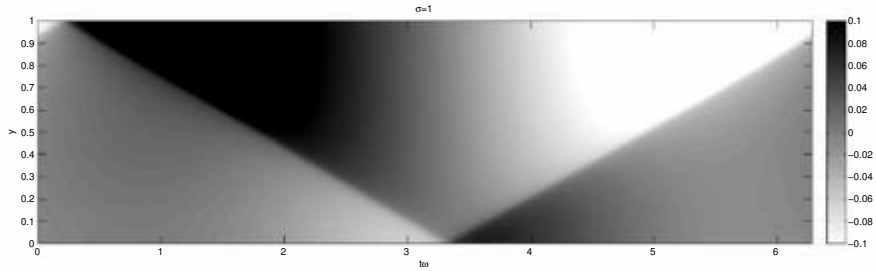

Figure 2: Pressure scan against time for a guided shock at the point of formation

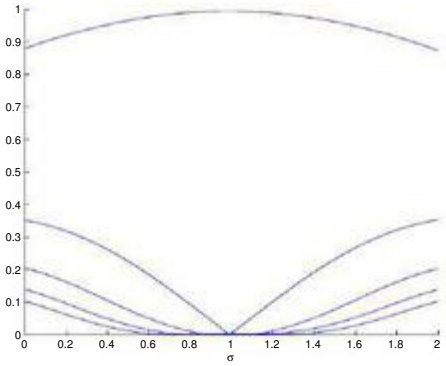

Figure 3: Modal amplitudes against propagation distance showing energy being transferred to the fundamental and back again

CONCLUSION

This method extends the work of Félix and Pagneux to the weakly nonlinear case as well as allowing for more general duct systems of non-constant curvature . It also has advantages over similar nonlinear methods for a straight duct (such as that by Fernando et. al.) in that it can solve for a nonlinear superposition of forwards and backwards propagating waves (determined by the radiation condition at the outlet) as well as being able to stably solve for evanescent waves.

References

[1] Hirschberg, A., Gilbert, J., Msallam, R., Wijnands, A. P. J.: Shock waves in trombones. J. Ac. Soc. Am. 99:1754-1758, 1996.

[2] Félix, S., Pagneux, V.: Sound propagation in bends: A multimodal approach. J. Ac. Soc. Am. 110:1329-13337, 2001

[3] Félix, S., Pagneux, V.: Multimodal analysis of acoustic propagation in three-dimensional bends. Wave Motion 36:157-168, 2002

[4] Blackstock, D.: Connection between the Fay and Fubini solutions for plane sound waves of finite amplitude. J. Ac. Soc. Am. 39:1019-1026, 1966

[5] Fernando, R., Druon, Y., Coulouvrat, F., Marchiano, R.: Nonlinear waves and shocks in a rigid acoustical guide. J. Ac. Soc. Am. 129:604-615, 2011

OBSERVING AND UNDERSTANDING SHORT GRAVITY WAVES

Fabrice Ardhuin *[1], Charles Peureux[1], Pedro V. Guimaraes[1,2], Alvise Benetazzo[3], Filipo Bergamasco[4], Fabien Leckler[5], and Vladimir Dulov[6]

[1]*Laboratoire d'Oceanographie Physique et Spatiale (LOPS), UBO, CNRS, Ifremer, IRD, IUEM, Brest, France*

[2]*Ecole Centrale de Nantes, France*

[3]*ISMAR, Venezia, Italy*

[4]*Universita Ca' Foscari, Venezia, Italy*

[5]*SHOM, Brest, France*

[6]*Marine Hydrophysics Institute, Sebastopol, Crimea, Russia*

Summary The energy level and its directional distribution are key observations for understanding the energy balance in the wind-wave spectrum between wind-wave generation, non-linear interactions and dissipation. Here, properties of gravity waves are investigated from a fixed platform in the Black sea, equipped with a stereo-video system that resolves waves with frequency f up to 1.6 Hz, and wavelengths from 0.3 to 12 m. We made observations during 3 experiments in 2009, 2011 and 2013, in conditions with wind speeds ranging from 2 to 17 m/s, from the deep water platform of Katsiveli, operated by the Sebastopol Marine Hydrophysics Institute, off the coast of Crimea in the Black sea. The observations allow a measurement of the full frequency-wavenumber spectrum, revealing a strong variability of the shape of the short wave spectrum. This variability is possibly related to the wind speed and effects of the dominant waves. Possible processes that could reduce the input of energy from the wind or enhance the dissipation may explain the data and are under investigation.

SHORT WAVES GO IN MANY - BUT NOT ALL - DIRECTIONS

We take advantage of recent improvements in stereo-video processing [5, 4, 3] to investigate the properties of short gravity waves, with wavelengths between 10 and 0.3 m, and young wave ages.

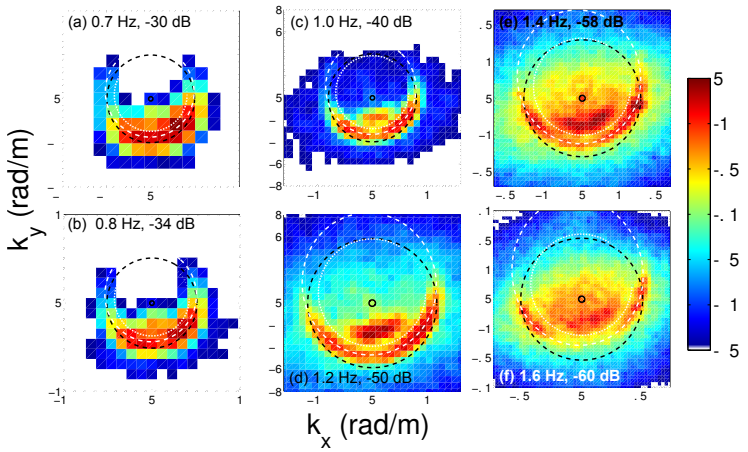

Figure 1: Case with wind speed of 13 m/s and a dominant wave frequency $f_p = 0.33$ Hz. Slices of the double-sided spectrum for positive apparent frequencies 0.7, 0.8, 1.0, 1.2, 1.4 and 1.6 Hz. The energy appears in the direction from where it is coming. For each panel the color scale spans 30 dB with the dark red corresponding to the power indicated on the figure (e.g. -30 dB) relative to 1 m^4/Hz. Note that 1.4 and 1.6 Hz are twice 0.7 and 0.8 Hz, so that the first harmonic of the components in (a) and (b) appear at approximately twice the wavenumbers in panels (e) and (f). In each panel, the linear dispersion relation without current is plotted in black, in white with a uniform current $U = 0.15$ m/s towards the trigonometric angle 99 degrees. The white dashed line marks approximately the separation between the linear part of the spectrum and the faster non-linear components.

The analysis of a first case recorded in 2011 was presented in [9] and illustrated in figure 1 revealed, as shown in figure 1, (1) a very strong bimodal distribution of the directional spectrum for frequencies above 3 times the dominant frequency (2) a deep gap in the wind direction at these high frequencies, with a spectral density less than 25% of the peaks at the same frequency (3) a significant amount of energy traveling in opposite directions, capable of generating acoustic and seismic waves [1] (4) at frequencies above 4 times the dominant frequency, the energy is mostly contained in second order harmonics that are well predicted by the full second order spectrum [7]

*Corresponding author. Email: ardhuin@ifremer.fr

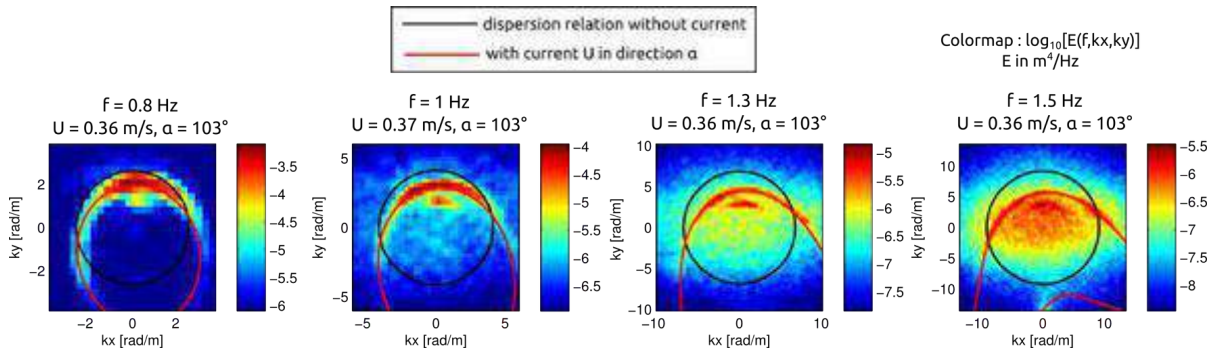

Figure 2: Sections of the 3D wave spectrum at frequencies 0.8 to 1.5 Hz and fitted linear dispersion relation with current (red lines), compared to dispersion relation without current (black). This other event was recorded on 29 September 2013.

WHY?

How general are these features and how can they be explained? A particularly puzzling pattern is the very low energy in the wind direction at high frequencies. Short waves can be influenced by longer waves in many ways. Banner and Phillips [2] had observed and explained that in the laboratory, the wind produces a strong shear of the current near the sea surface that can facilitate wave breaking and thus potentially reduce the energy in the downwind direction compared to other directions. Using or data we can estimate the current that advects the different frequencies and, using wave dispersion theory for random waves [8] we can estimate a likely vertical shear of the current.

Although the analysis is underway, preliminary results (figure 2) for cases with moderate winds (8 m/s and $f_p = 0.4$ Hz and measured in 2013) show that the current is almost constant for all wave frequencies, suggesting that there may actually be a vertical shear of the Eulerian mean current that opposes the shear of the Stokes drift to produce a Lagrangian mean current with nearly zero shear, yet the directional spectrum is again strongly bimodal. This may not be general and previous observations with coarser data concluded otherwise [3]. There can also be effects of the long waves on the short wave interactions with the wind, or short wave modulation by long waves. The spectrum is more narrow and less bimodal for strong wind cases (17 m/s).

CONCLUSIONS

Observations of the full frequency-wavenumber spectrum using stereo-video imagery are revealing new details on the shapes and statistical properties. In real sea conditions the current shear appears to be minimal, at least compared to extrapolation from laboratory experiments, probably due to wave-induced breaking which is more intense for the more developed waves found in field conditions. We are now looking for explanations for the very broad and strongly bimodal directional distributions observed at low to moderate wind speeds. Numerical simulations (not shown here) of the 4-wave interactions do produce a bimodal spectrum but the minimum in the wind direction is much less marked than in our field observations. We suspect that some yet-to-be-indentified process is either enhancing the dissipation in the wind direction or reducing the source of wind energy to the short waves.

References

[1] Ardhuin, F. and T. H. C. Herbers, 2013: Noise generation in the solid earth, oceans and atmosphere, from nonlinear interacting surface gravity waves in finite depth. *J. Fluid Mech.*, **716**, 316–348.

[2] Banner, M. L. and O. M. Phillips, 1974: On the incipient breaking of small scale waves. *J. Fluid Mech.*, **65**, 647–656.

[3] Benetazzo, A., F. Fedele, G. Gallego, P.-C. Shih, and A. Yezzi, 2012: Offshore stereo measurements of gravity waves. *Coastal Eng.*, **64**, 127–138.

[4] Fedele, F., A. Benetazzo, G. Gallego, P.-C. Shih, A. Yezzi, F. Barbariol, and F. Ardhuin, 2013: Space-time measurements of oceanic sea states. *Ocean Modelling*, **70**, 103–115.

[5] Gallego, G., A. Yezzi, F. Fedele, and A. Benetazzo, 2011: A variational stereo method for the three-dimensional reconstruction of ocean waves. *IEEE Trans. on Geosci. and Remote Sensing*, **49**, 4445–4457.

[6] Garrett, C. and J. Smith, 1976: On the interaction between long and short surface waves. *J. Phys. Oceanogr.*, **6**, 925–930.

[7] Janssen, P. A. E. M., 2009: On some consequences of the canonical transformation in the Hamiltonian theory of water waves. *J. Fluid Mech.*, **637**, 1–44.

[8] Kirby, J. T. and T.-M. Chen, 1989: Surface waves on vertically sheared flows: approximate dispersion relations. *J. Geophys. Res.*, **94 (C1)**, 1013–1027.

[9] Leckler, F., F. Ardhuin, C. Peureux, A. Benetazzo, F. Bergamasco and V. Dulov, 2015: Analysis and interpretation of frequency-wavenumber spectra of young wind waves. *J. Phys. Oceanogr.*, **45 (10)**, 2484–2496.

SPECTRAL EVOLUTION OF WEAKLY NONLINEAR RANDOM WAVE FIELDS: KINETIC EQUATIONS VS DIRECT NUMERICAL SIMULATIONS

Victor Shrira[1] and Sergei Annenkov *[1]

[1]*Department of Mathematics, Keele University, Newcastle under Lyme, UK*

Summary We examine how accurately the kinetic equations describe evolution of random weakly nonlinear waves in fluids and solids. To this end we simulate numerically long-term evolution of wave spectra without forcing using three different models: (i) the classical kinetic equation (KE); (ii) the generalised kinetic equation (gKE) valid also when the wave spectrum is changing rapidly; (iii) the DNS based on the Zakharov integrodifferential equation for water waves (DNS-ZE). (DNS-ZE does not rely on any statistical assumptions. As the initial conditions we choose two spectra with the same frequency distribution and different degrees of directionality. All three approaches demonstrate very close evolution of integral characteristics of spectra. However, there are notable systematic differences (e.g. the broadening of angular spectra is much faster for the kinetic equations), which suggests the presence and significance of coherent interactions not accounted for by the established closure for the kinetic equations.

INTRODUCTION

The challenge of describing wave turbulence, i.e. evolution of random weakly nonlinear dispersive waves in fluids (and solids) in various contexts is a major open fundamental problem despite being intensively studied theoretically and experimentally for more than fifty years, e.g. [Nazarenko (2011)]. In contrast to the classical hydrodynamic turbulence, there is a well-established general formalism for treating weakly nonlinear wave fields that exploits smallness of nonlinearity and subtle assumptions about quasi-Gaussianity of a statistically homogeneous wave field. This approach leads to a closed equation for the second statistical momenta of the field which we will refer to as the *kinetic equation* (KE). Although the theory based upon the KE has been able to predict the major features of wave field evolution (e.g. [Annenkov and Shrira (2006)]) and is widely used (e.g. [Zakharov et al 1992]). However the basic question — to what extent the theory corresponds to actual behaviour of physical systems — remains open. Here we address it by performing a detailed comparison of predictions of the KE and its generalization (gKE) with the results of direct numerical simulations (DNS) employing the algorithm specially designed for long term evolution of random weakly nonlinear wave fields [Annenkov and Shrira (2013)]. For certainty and without much loss of generality we perform these comparisons for weakly nonlinear water waves.

To make the comparisons maximally clean and simple and retain as much generality as possible we do the following. We take as the starting point the equation of motion in the form of the "four-wave" Zakharov equation

$$\mathrm{i}\frac{\partial b_0}{\partial t} \;=\; \omega_0 b_0 + \int T_{0123} b_1^* b_2 b_3 \delta_{0+1-2-3}\,\mathrm{d}\mathbf{k}_{123}\,, \tag{1}$$

where the wave field is expressed in terms of canonical variables $b(\mathbf{k})$ linked to the Fourier harmonics of the surface elevation $\zeta(\mathbf{k})$ and potential $\psi(\mathbf{k})$: $b(\mathbf{k}) = \frac{1}{\sqrt{2}}\left\{\sqrt{\frac{\omega(\mathbf{k})}{k}}\zeta(\mathbf{k}) + \mathrm{i}\sqrt{\frac{k}{\omega(\mathbf{k})}}\psi(\mathbf{k})\right\} + O(\varepsilon)$, here asterisk means complex conjugation, $\omega(\mathbf{k}) = \sqrt{g|\mathbf{k}|}$ is the linear dispersion relation, the compact notation used designates arguments by indices, e.g. $\omega_0 = \omega(\mathbf{k})$, $T_{0123} = T(\mathbf{k}, \mathbf{k}_1, \mathbf{k}_2, \mathbf{k}_3)$, $\delta_{0+1-2-3} = \delta(\mathbf{k} + \mathbf{k}_1 - \mathbf{k}_2 - \mathbf{k}_3)$. Equation (1) is a generic equation describing dynamics of weakly nonlinear waves with the fourth and higher order terms truncated. The specificity of each physical problem is only in the dispersion relation $\omega(\mathbf{k})$ and the interaction coefficient T_{0123}. We use the expressions for T_{0123} derived for water waves by [Krasitskii(1994)]. Note that $b(\mathbf{k})$ are not wave amplitudes in original variables, but appear as a result of a canonical transformation (see [Krasitskii(1994)]). The statistical theory for waves is most naturally formulated in terms of $b(\mathbf{k})$.

The wave field is taken to be statistically homogeneous in space, which implies $\langle b(\mathbf{k},t)b^*(\mathbf{k}_1,t)\rangle = n(\mathbf{k})\delta(\mathbf{k}-\mathbf{k}_1) \equiv n_{\mathbf{k}}\delta_{01}$; here $\langle b(\mathbf{k},t)b^*(\mathbf{k}_1,t)\rangle$ means ensemble averaging. Under the key assumptions that wave field remains quasi-Gaussian over the timescale of evolution the higher statistical moments can be expressed in terms of the spectra (the "closure hypothesis") and spectral evolution can be described by a closed kinetic equation

$$\frac{\partial n_0}{\partial t} = 4\pi \int T_{0123}^2 f_{0123}\delta_{0+1-2-3}\delta(\omega_0+\omega_1-\omega_2-\omega_3)\,\mathrm{d}\mathbf{k}_{123}, \tag{2}$$

where n_0 is the second-order correlator, $< b_0^* b_1 >= n_0\delta_{0-1}$, and $f_{0123} = n_2 n_3(n_0+n_1) - n_0 n_1(n_2+n_3)$. This classical kinetic equation (KE) in the derivation employs large time limit. The equation without this approximation allowing for much faster evolution, the *generalized kinetic equation* (gKE), reads (see [Annenkov and Shrira (2013)])

$$\frac{\partial n_0}{\partial t} = 4\mathrm{Re}\int\left\{T_{0123}^2\left[\int_0^t \mathrm{e}^{-\mathrm{i}\Delta\omega(\tau-t)} f_{0123}\,\mathrm{d}\tau\right] - \frac{\mathrm{i}}{2}T_{0123}J_{0123}^{(1)}(0)\mathrm{e}^{\mathrm{i}\Delta\omega t}\right\}\delta_{0+1-2-3}\,\mathrm{d}\mathbf{k}_{123}\,. \tag{3}$$

where $\Delta\omega = \omega_0+\omega_1-\omega_2-\omega_3$ and the correlator $J_{0123}^{(1)}(0) = \langle b_0^* b_1^* b_2 b_3\rangle$ is specified by the initial conditions.

*Corresponding author. Email: v.i.shrira@keele.ac.uk

SIMULATIONS AND RESULTS

We study numerically the long-term evolution of wave spectra without forcing using three different models. For the KE simulations we employ the WRT code kindly provided by G. van Vledder. For the gKE simulations we use a novel algorithm described in [Annenkov and Shrira (2015)]. The DNS based on the Zakharov equation with ensemble averaging (1) employs the algorithm described in [Annenkov and Shrira (2013)]. To examine the role of focussin/defocussing nonlinearity we consider two physical systems described by the the Zakharov equation (1) differing by the sign of the interaction coefficient only, i.e. with focussing and de-focussing nonlinearity.

For initial conditions we choose two narrow-banded spectra with the same frequency distribution (a JONSWAP spectrum with high peakedness $\gamma = 6$) and different degrees of directionality. These spectra are from the set of observations collected in a directional wave tank by Onorato et al (2009). Spectrum A is very narrow in angle (corresponding to $N = 840$ in the $\cos^N$ directional model). Spectrum B is initially wider in angle (corresponds to $N = 24$). Short-term evolution of both spectra ($O(10^2)$ wave periods) has been studied numerically by Xiao et al (2013) using two other approaches (broad-band modified nonlinear Schrödinger equation and direct numerical simulation based on the high-order spectral method). We use these results to validate the initial stage of our DNS-ZE simulations. The advantage of the DNS-ZE method is that it allows to study long-term spectral evolution (up to $O(10^4)$ periods), which was previously possible only with the KE.

In the first 150 periods, we find a nearly perfect agreement between our DNS-ZE results and simulations by Xiao et al (2013), both for the evolution of frequency spectra and for the directional spreading. Over larger times all three approaches demonstrate very close evolution of integral characteristics of spectra, approaching at large times the theoretical asymptotes of the self-similar stage of evolution. However, the detailed comparison of the spectral evolution shows certain notable differences. Both kinetic equations give virtually identical evolution of spectrum B, but in the case of initially nearly one-dimensional spectrum A the KE overestimates the amplitude of the spectral peak. The DNS-ZE results show considerably wider spectra with less pronounced peak. There is a striking difference for the rate of spectral broadening, which is much larger for the gKE and especially for the KE, than for the DNS-ZE. We show that the maximal rates of change of the spectra obtained with the DNS-ZE are proportional to the fourth power of nonlinearity, corresponding to the dynamical timescale of evolution, rather than the statistical timescale of both kinetic equations. The DNS shows that the spectral evolution does not depend on whether the nonlinearity is focussing or de-focussing.

CONCLUSIONS

The results show the presence and significance of coherent interactions not accounted for by the established closure for the kinetic equations, which implies that the fundamental issue of closure for random wave field has to be revisited.

References

[Annenkov and Shrira (2006)] Annenkov, S. Y. , Shrira V. I.:Direct numerical simulation of downshift and inverse cascade for water wave turbulence. Phys. Rev. Letters, 96, 204501, 2006.

[Annenkov and Shrira (2013)] Annenkov, S. Y. , Shrira V. I.:Towards a new picture of wave turbulence. Advances in wave turbulence. World Scientific, 2013.

[Annenkov and Shrira (2015)] Annenkov, S. Y. , Shrira V. I.:Modelling the Impact of Squall on Wind Waves with the Generalized Kinetic Equation. J. Phys. Oceanogr., 45, 807812, 2015.

[Krasitskii(1994)] Krasitskii, V. P. On reduced equations in the Hamiltonian theory of weakly nonlinear surface waves. J. Fluid Mech. 272, 1–20, 1994.

[Nazarenko (2011)] Nazarenko, S. V. Wave Turbulence. Lecture Notes in Physics, 825, Springer, 2011.

[Onorato et al 2008] norato, M., Cavaleri, L., Fouques, S., Gramstad, O., Janssen, P. A. E. M., Monbaliu, J., Osborne, A. R., Pakozdi, C., Serio, M., Stansberg, C. T., Toffoli, A. & Trulsen, K.: Statistical properties of mechanically generated surface gravity waves: a laboratory experiment in a three-dimensional wave basin. J. Fluid Mech. 627, 235257, 2009.

[Xiao et al 2013] Xiao, W., Liu, Y., Wu, G., and Yue, D. K. P.: Rogue wave occurrence and dynamics by direct simulations of nonlinear wave–field evolution. J. Fluid Mech. 720, 357392, 2013.

[Zakharov et al 1992] Zakharov, V. E., L'vov,V. S., Falkovich, G.: Kolmogorov Spectra of Turbulence I: Wave Turbulence. Springer Series in Nonlinear Dynamics, 1992.

LABORATORY MEASUREMENTS OF THE INCEPTION AND EVOLUTION OF CENTIMETER-SCALE LANGMUIR TURBULENCE

Fabrice Veron *[1], Yi Ma [1], Marc Buckley[1], Andres Tejada-Martinez[2], and Amine Hafsi[2]
[1]*University of Delaware, Delaware, USA*
[2]*University of South Florida, Florida, USA*

Summary When wind starts to blow over a quiescent air-sea interface, both currents and surface waves are initially generated. The interaction between the wind-driven waves and currents leads to the generation of Langmuir circulations (LC) consisting of counter rotating vortices aligned with the wind. Shortly thereafter, Langmuir turbulence (LT), that is multiple scales of LC, appear. In the field, LT length scales range from several centimeters when short capillary waves first appear up to tens of meters when the spectrum of waves broadens. We present results from a laboratory experiments where the evolution centimeter-scale LT are investigated. We present surface infrared imagery and subsurface Particle Image Velocimetry. We show that evolution from organized small scale LC to LT leads to intense surface mixing thereby disrupting the near surface molecular layers. Subsurface turbulence measurements are presented in the context of scalar (gas) flux through the air-water interface.

INTRODUCTION

Succinctly, when wind blows over an initially quiescent air-sea interface, it first generates surface currents, then short capillary waves which in time coexist with longer waves as part of a broad spectrum of waves. The interaction between the wind-driven waves and shear current leads to Langmuir turbulence characterized by a spectrum of Langmuir circulation (LC) consisting of counter rotating vortices roughly aligned in the direction of the wind. In the field, the typical length scale of the vortices ranges from several centimeters when short capillary waves first appear up to tens of meters when the spectrum of waves broadens. In this laboratory study, we focus on the centimeter-scale LC. These small scale LC are generated very quickly with the gustiness in the wind field (and disappear very quickly as well), thereby providing, over intermittent and repeated gust events, very intense turbulent bursts at the surface which may very well dominate the average surface renewal processes. These renewal events are critical to our understanding of air-sea scalar fluxes. To date, direct numerical simulations (DNS) of small scale LC and their evolution has not been made and measurements of surface renewal time scales and other parameters influenced by these coherent structures have not been performed.

The overarching goal of this study is to characterize the effect of small scale Langmuir turbulence on the thin molecular boundary layers beneath the air-sea interface. In this study, we are particularly interested in the effects of the LT on the thermal molecular layer (i.e. the cool skin) and on the fluxes of slightly soluble gases across the interface. Accordingly, we set out to perform a laboratory study to capture the growth stages of LC and transition to Langmuir turbulence during the wave growth process.

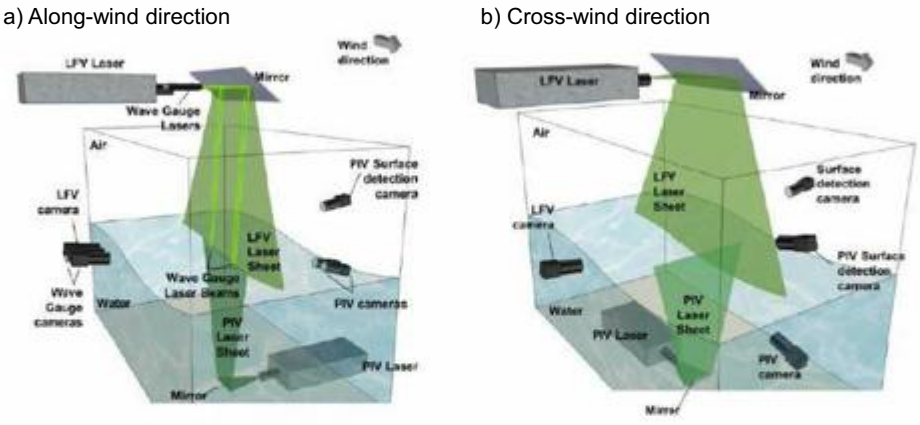

Figure 1: Sketch of the wind/wave imaging system, positioned at a fetch of 10 m, shown for both the along-wind and cross-wind setups. The PIV setup consists of PIV cameras recording underwater motion, a surface detection camera, and cameras for the optical wave gauge system. Illumination is provided by two flashed Nd-Yag lasers for the surface detection and the PIV. Both surface detection and optical wave gauge are using laser-induced fluorescence.

*Corresponding author. Email: fveron@udel.edu

RESULTS

The experiments were performed in the large wind wave tank of the University of Delaware. The tank's overall length is 42 m with a 37 m long working section. It is 1 m wide and 1.25 m high. Water depth was kept at 0.71 m to allow sufficient air space above the surface. The recirculating wind tunnel was computer-controlled and programmed to accelerate the wind from rest to a final value of 10 m/s over times ranging from 30 s to 60s. The main data acquisition system consisted of several imaging systems positioned at a fetch of 10 m (figure 1). The main Particle Image Velocimetry (PIV) setup consists of PIV cameras recording underwater velocity, a surface detection camera, and cameras for the optical wave gauge system. PIV and surface detection illumination was provided by two flashed Nd-Yag lasers. Both surface detection and optical wave gauges used laser-induced fluorescence. The overall system was similar to that used by [3]. The PIV system was also rotated 90° to measure cross-wind velocity fields (figure 1b). In that case, the camera was placed in a waterproof underwater housing. In addition, the surface motion was detected using an Infrared camera (not shown) along with a CO_2 laser which laid down thermal markers on the surface. This led to a direct measure of the Lagrangian velocity at the interface (see [1] and [2]).

We completed a series of experiments consisting of 4 different forcing conditions. In each case, following the start of the wind, (a) the surface accelerates and momentum is diffused in the water column under the effect of molecular viscosity; (b) surface waves are then generated and shortly thereafter (c) LC appear in the form of well organized counter rotating vortex pairs (figure 2); (d) the LC become unstable and the transition to LT occurs while the wave field is still growing. The LC (and subsequently LT) disrupt the near surface molecular diffusive processes. The infrared surface data showed that the surface cool skin is violently mixed while concurrently, the subsurface motion (measured with the PIV) becomes turbulent and the momentum originally confined to the near surface laminar (molecular) shear layer is mixed down into the water column.

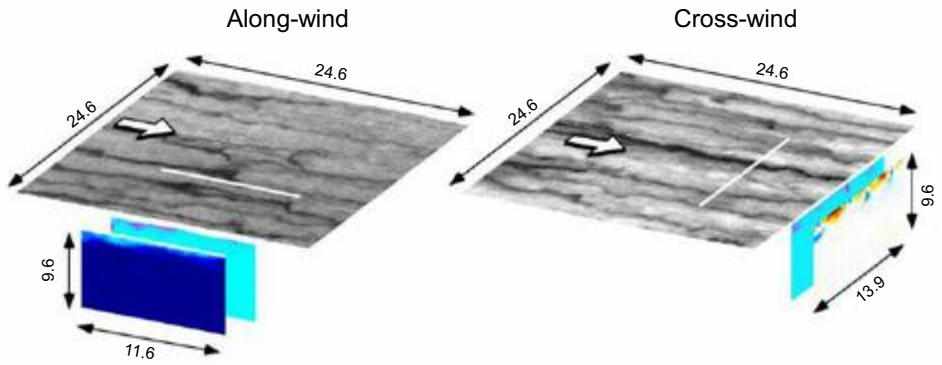

Figure 2: Composite image showing the surface infrared image (unscaled gray color - white is hot, black is cold) where the LC can clearly been seen, as well as fluorescent dye concentration (inner panel) and the velocity (outer panel) measured with the PIV system. The white line on the surface shows the location (on the surface) of the subsurface PIV measurements. Dimensions are shown in cm.

CONCLUSIONS

We have performed a comprehensive series of laboratory experiments on the generation of the LC, and their evolution into LT. In this presentation, we show that the initial generation of the LC disrupts the surface molecular layers of heat and momentum thereby providing an efficient and rapid near surface mixing mechanism. Surface infrared measurements confirm that the heat (and gas) air-water transfer velocity is greatly influenced by the presence of the LC. In turn, subsurface turbulence measurements reveal that the LC first appear in as downward jets (figure 2) which subsequently become unstable and evolve into fully developed LT. We will present results linking the sub-surface turbulence measurements with estimates of the surface fluxes and we will frame the results in the context of air-sea interactions.

References

[1] Veron, F., and W. K. Melville, 2001: Experiments on the stability and transition of wind driven water surfaces. *J. Fluid Mech.*, **446**, 25-65.

[2] Veron, F., W.K. Melville, and L. Lenain. 2008: Infrared techniques for measuring ocean surface processes. *J. Atmos. Oceanogr. Technol.*, **25** (2): 307-326.

[3] Buckley, M.P., and F. Veron. 2015: Structure of the airflow above wind waves *J. Phys. Oceanogr. Submitted*.

DISPERSION-IMPROVED FULLY NONLINEAR SHALLOW WATER MODEL

Didier Clamond*[1], Denys Dutykh[2], and Dimitrios Mitsotakis[3]
[1]*Université de Nice - Sophia Antipolis, Laboratoire J. A. Dieudonné, Parc Valrose, 06108 Nice cedex 2, France*
[2]*Université Savoie Mont Blanc, LAMA, Campus Scientifique, 73376 Le Bourget-du-Lac cedex, France*
[3]*Victoria University of Wellington, School of Mathematics, Statistics and Operations Research, PO Box 600, Wellington 6140, New Zealand*

Summary We propose a variant of the fully-nonlinear weakly-dispersive Serre–Green–Naghdi equations involving a free parameter that can be chosen to improve the dispersion properties. Contrary to other models of this kind found in the literature, the one proposed here conserves the energy, thanks to the approximation procedure based on a variational principle. In addition to improved dispersion properties, the new model admits limiting waves with angular crests. Numerical comparisons with the Euler equations show that the new model is substantially more accurate than the classical Serre equations, specially for long time simulations and for large amplitudes.

INTRODUCTION

Water waves in channels and oceans are usually described by the Euler equations. Due to their complexity, several approximate models have been derived in various wave regimes. In shallow water, the main restriction comes from the ratio between the characteristic wavelength and the mean water depth d. Many approximate equations have been derived for waves in shallow water, such as the Korteweg–deVries (KdV) equation for unidirectional waves, the Saint-Venant equations (SVE) for bidirectional non-dispersive waves and many variants of the Boussinesq equations (BE) for dispersive waves propagating in both directions [1]. Considering long waves propagating in shallow water but without assuming small amplitudes, Serre [2] derived a so-called *fully-nonlinear weakly dispersive* system of equations which, after further approximations, include the KdV, BE and SVE as special cases. For 2D (1D horizontal) gravity waves over a horizontal bottom, these equations are

$$h_t \,+\, \partial_x[\,h\,u\,] \,=\, 0, \qquad \partial_t[\,h\,u\,] \,+\, \partial_x\big[\,h\,u^2 \,+\, \tfrac{1}{2}\,g\,h^2 \,+\, \tfrac{1}{3}\,h^2\,\gamma\,\big] \,=\, 0, \tag{1}$$

where h is the total water depth (bottom to free surface), u is the depth-averaged horizontal velocity, g is the acceleration due to gravity and $\gamma = h(u_x^2 - u_{xt} - uu_{xx})$ is the fluid vertical acceleration at the free surface. Serre's equations represent a substantial improvement with respect to the Boussinesq theory, but many shallow water phenomena involve significant dispersive effects that are not well described by Serre's equations.

One possibility to improve the Serre model is by including higher-order terms. However, this modification yields higher-order derivatives in the model equations, making its numerical resolution (and thus its applicability) rather challenging. Actually, the numerical resolution of these high-order Boussinesq-like equations is slower (and less accurate) than that of the irrotational Euler equations, at least for simple (e.g. periodic) domains.

An alternative way of improving the classical model consists in introducing a free parameter into the model that can be appropriately chosen to improve some of the desired properties, in particular the dispersion relation. This can be achieved, for example, by replacing the depth-averaged velocity variable by the velocity of the fluid evaluated at a certain depth in the bulk of the fluid. Another possibility to introduce a free parameter is obtained from arbitrarily-weighted averages of different (but of same order) approximations of some quantities. All the improved models of this kind we are aware of (e.g. [3, 4, 5, 6]) have a common drawback: they do not conserve the energy. Thus, one may improve the dispersive properties of the model but, on the other hand, loses the energy conservation property. For many applications, specially in the case of long time simulations, the disadvantages can crucially override all the advantages. In the present work, we address this issue, proposing a method for deriving an improved version of the Serre equations that preserves the energy, like the original Serre model.

IMPROVED MODEL

The classical Serre equations can be obtained from a variational principle involving the Lagrangian density

$$\mathcal{L}_1 \,=\, \tfrac{1}{2}\,h\,u^2 \,+\, \tfrac{1}{6}\,h^3\,u_x^2 \,-\, \tfrac{1}{2}\,g\,h^2 \,+\, \{\,h_t \,+\, [\,h\,u\,]_x\,\}\,\phi, \tag{2}$$

where ϕ is a Lagrange multiplier introduced to enforce the mass conservation. To the same order of approximation, an alternative Lagrangian density can be introduced as [7]

$$\mathcal{L}_2 \,=\, \tfrac{1}{2}\,h\,u^2 \,+\, \big(\tfrac{1}{6} + \tfrac{1}{4}\beta\big)\,h^3\,u_x^2 \,-\, \tfrac{1}{2}\,g\,h^2\,\big(1 + \tfrac{1}{2}\beta\,h_x^2\big) \,+\, \{\,h_t \,+\, [\,h\,u\,]_x\,\}\,\phi, \tag{3}$$

*Corresponding author. Email: didierc@unice.fr

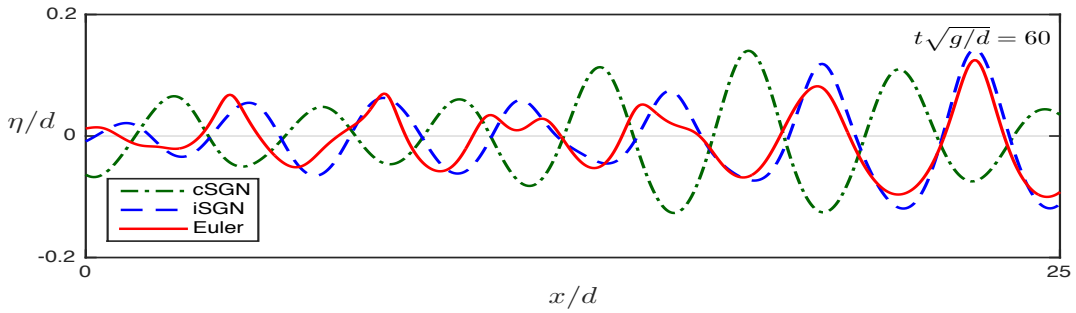

Figure 1: *Random wave field.*
'—': Euler; '− −': improved Serre equations ($\beta = 2/15$); '− · −': classical Serre equations ($\beta = 0$).

where β is a free parameter at our disposal. From $\mathcal{L}_2$, one can easily derive the improved Serre conservative equations

$$h_t + \partial_x[hu] = 0, \tag{4}$$

$$q_t + \partial_x\left[uq - \tfrac{1}{2}u^2 + gh - \left(\tfrac{1}{2} + \tfrac{3}{4}\beta\right)h^2u_x^2 - \tfrac{1}{2}\beta g(h^2h_{xx} + hh_x^2)\right] = 0, \tag{5}$$

$$\partial_t[hu] + \partial_x\left[hu^2 + \tfrac{1}{2}gh^2 + \tfrac{1}{3}h^2\Gamma\right] = 0, \tag{6}$$

$$\partial_t\left[\tfrac{1}{2}hu^2 + (\tfrac{1}{6} + \tfrac{1}{4}\beta)h^3u_x^2 + \tfrac{1}{2}gh^2\left(1 + \tfrac{1}{2}\beta h_x^2\right)\right] +$$
$$\partial_x\left[\left\{\tfrac{1}{2}u^2 + (\tfrac{1}{6} + \tfrac{1}{4}\beta)h^2u_x^2 + gh\left(1 + \tfrac{1}{4}\beta h_x^2\right) + \tfrac{1}{3}h\Gamma\right\}hu + \tfrac{1}{2}\beta gh^3h_xu_x\right] = 0, \tag{7}$$

where $q = \phi_x = u - \left(\frac{1}{3} + \frac{1}{2}\beta\right)h^{-1}\left[h^3u_x\right]_x$ and $\Gamma = \left(1 + \frac{3}{2}\beta\right)h\left[u_x^2 - u_{xt} - uu_{xx}\right] - \frac{3}{2}\beta g\left[hh_{xx} + \frac{1}{2}h_x^2\right]$. Thus, these modified Serre's equations conserve mass (4), tangential momentum at the free surface (5), momentum flux (6) and energy (7), for all values of the parameter β.

To the linear approximation, the dispersion relation of the improved Serre equation is

$$\frac{c^2}{g\,d} = \frac{2 + \beta\,(kd)^2}{2 + (\frac{2}{3} + \beta)\,(kd)^2} \approx 1 - \frac{(kd)^2}{3} + \begin{pmatrix}1\\3\end{pmatrix} + \frac{\beta}{2}\frac{(kd)^4}{3}, \tag{8}$$

that should be compared with the exact relation $c^2/gd = \tanh(kd)/kd = 1 - (1/3)(kd)^2 + (2/15)(kd)^4 + \cdots$, where c is the phase speed and k is the wavenumber. The parameter β can be chosen such that the dispersion relation matches the exact one up to the highest possible order in its expansion around $k = 0$. Thus, we have to take $\beta = 2/15$ to ensure that the two relation match up to k^4. This choice of β improves significantly the model, specially when high frequencies are involved (Figure 1) but also for large amplitudes.

CONCLUSIONS

An improved Serre-like equations model has been derived. In addition to better dispersion properties and energy conservation, these equations represents a mild modification of the classical model. Therefore, they can be easily incorporated into existing numerical codes.

Several properties of this new model will be discussed at the conference, as well as generalisations in 3D and varying bottom. It should be noted that our approach is rather general and thus not limited to model waves in shallow water.

References

[1] Wehausen, J. V. & Laitone, E. V.: Surface waves. Handbuch der Physik 9, 446–778, 1960.

[2] Serre, F.: Contribution l?tude des coulements permanents et variables dans les canaux. La Houille blanche 8, 374–388, 1953.

[3] Antunes Do Carmo, J. S.: Extended Serre Equations for Applications in Intermediate Water Depths. The Open Ocean Engineering Journal 6 (1), 16–25, 2013.

[4] Castro-Orgaz, O. & Hager, W. H.: Boussinesq- and Serre-type models with improved linear dispersion characteristics: applications. J. Hydraulic Res. 53 (2), 282–284, 2015.

[5] Dias, F. & Milewski, P.: On the fully-nonlinear shallow-water generalized Serre equations. Phys. Lett. A 374 (8), 1049–1053, 2010.

[6] Nwogu, O.: Alternative form of Boussinesq equations for nearshore wave propagation. J. Waterway, Port, Coastal and Ocean Engineering 119, 618–638, 1993.

[7] Clamond, D., Dutykh, D. & Mitsotakis, D.: Conservative modified Serre-Green-Naghdi equations with improved dispersion characteristics. arXiv:1511.07395, 2015.

BAROCLINICALLY-DRIVEN ACOUSTIC STREAMING

Ziemowit Malecha*[1] and Greg Chini[2]

[1]*Department of Cryogenic, Aeronautic & Process Engr. , Wroclaw University of Technology, Wroclaw, Poland*
[2]*Department of Mechanical Engineering, University of New Hampshire, Durham, NH, USA*

Summary A multiscale asymptotic theory is constructed to explain the occurrence of *strong* acoustic streaming – with time-mean flow velocities comparable to the instantaneous fluid velocities induced by a standing sound wave – as observed in high-intensity discharge lamps. Neither the magnitude nor the orientation of the streaming velocity field in these lamps is correctly predicted by classical theories. A new theory of acoustic streaming is developed here by analyzing two-dimensional flow of a density-stratified ideal gas in a channel in the asymptotic limit of high-frequency acoustic waves. The analysis yields a novel wave/mean-flow interaction system that correctly predicts the direction and magnitude of the streaming flow. The streaming is shown to be baroclinically rather than viscously driven.

INTRODUCTION

Acoustic streaming, the time-averaged, emergent Eulerian flow driven by time-periodic sound waves, is a classical topic in wave/mean-flow interaction theory with a long and distinguished history in fluid dynamics [1]. Streaming flows have been investigated extensively over the last century beginning with Rayleigh's seminal work [2] and are crucial to a variety of technologies ranging from the measurement of absorption coefficients in common fluids, to heat transfer enhancement to or from oscillating particles, to mass transport in biomedical devices. In all these applications, streaming speeds are much smaller than instantaneous velocities; i.e. the streaming is comparably weak. Indeed, in classical Rayleigh streaming theory, which describes the streaming induced by the viscous retardation of standing sound waves in thin boundary layers adjacent to channel walls, the ratio of the typical streaming speed to the maximum fluctuating wave-induced velocity is $O(S^{-1})$, where the Strouhal number $S \equiv a_*/U_* \gg 1$, a_* is the sound speed and U_* is a characteristic speed of a fluid parcel [3].

NON-CLASSICAL ACOUSTIC STREAMING IN HIGH-INTENSITY DISCHARGE LAMPS

Curiously, in high-intensity discharge (HID) lamps, *strong* acoustic streaming is observed. HID lamps are a highly energy-efficient type of electrical gas-discharge arc lamp. The arc heats and evaporates metal salts added to the gas, forming a plasma and thereby greatly reducing power consumption. Owing to the temperature variations within the gas, however, undesirable buoyancy-driven flows are induced. Sound waves, selectively excited by modulating the frequency of the current running through the gas, can nonlinearly interact to drive time-mean flows that are able to counteract the $O(50)$ cm/s buoyancy-driven flows – speeds that are *comparable* with the acoustic-wave velocity fluctuations. Crucially, Dreeben & Chini [4] demonstrate via numerical simulations and theoretical arguments that neither the magnitude nor the orientation of the cellular streaming in HID lamps is correctly predicted by classical (Rayleigh) theory.

A NOVEL WAVE/MEAN-FLOW INTERACTION ANALYSIS

To understand the fundamental mechanism governing acoustic streaming in HID lamps, an idealized system involving the two-dimensional flow of a density-stratified ideal gas in a channel geometry (with x parallel and Y normal to the channel walls) is investigated using multiple time-scale asymptotic analysis [5]. A time-independent, spatially-uniform volumetric heat source is imposed to crudely model the hot arc region associated with the gas near the channel (lamp) centerline. The compressible Navier–Stokes (NS) and energy equations are analyzed in the physically-relevant *distinguished limit* in which the Reynolds number $Re \equiv \rho_* U_*/(k_*\mu_*) = O(S)$, where ρ_* is a characteristic density , k_* is the x-wavenumber of the standing sound wave, and μ_* is the viscosity coefficient; the channel aspect-ratio $\delta \equiv k_* H_* = O(S^{-1/2})$, where H_* is the channel half-height; and the ratio of the difference between the centerline and wall temperatures to the wall temperature itself $\Gamma = O(1)$, as $S \to \infty$. Two time scales are introduced $\tau = t$ and $T = S^{-1}t$ so that generic dependent field $f(x, Y, t; S) \to f(x, Y, \tau, T; S)$, and a slow/fast decomposition is performed: $f(x, Y, \tau, T; S) = f(x, Y, T; S) + f'(x, Y, \tau, T; S)$. Finally, the following asymptotic expansions are posited for the velocity vector (u,V), pressure perturbation π, temperature perturbation Θ and density ρ:

$$(u, V) \sim S^{-1}(\bar{u}_1 + u_1', \bar{V}_1 + V_1') + \ldots, \quad \pi \sim S^{-1}\pi_1' + S^{-2}(\bar{\pi}_2 + \pi_2') + \ldots,$$
$$\Theta \sim \bar{\Theta}_0 + S^{-1}(\bar{\Theta}_1 + \Theta_1') + \ldots, \qquad \rho \sim \bar{\rho}_0 + S^{-1}(\bar{\rho}_1 + \rho_1') + \ldots$$

Substituting these expansions into the governing equations, collecting terms at various orders in S and parsing the results into mean and fluctuation components yields a novel set of PDEs governing the evolution of the fast (essentially linear and non-dissipative) acoustic waves and the slowly-evolving (possibly steady) streaming dynamics.

*Corresponding author. Email: ziemowit.malecha@pwr.edu.pl

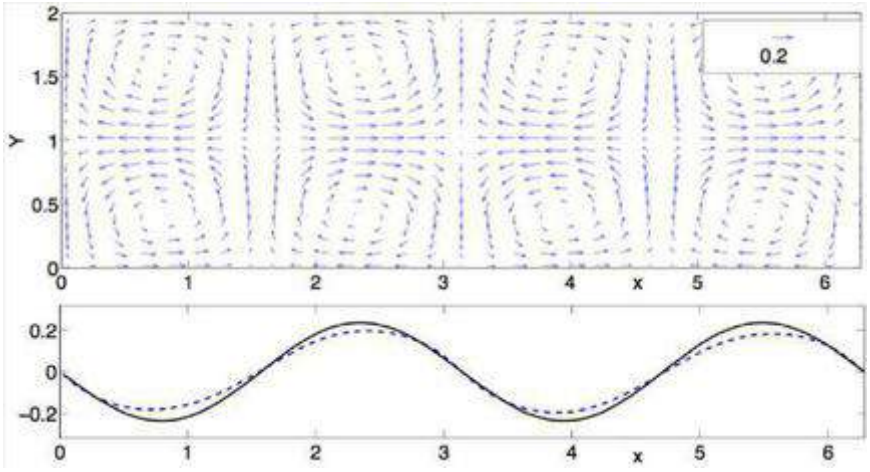

Figure 1: Upper plot: Theoretically predicted streaming velocity field for $\Gamma = 2$, $R = 10\sqrt{7}/3$, specific heat-ratio $\gamma = 3/2$ and Prandtl number $Pr \to 0$. (The streaming flow pattern obtained from DNS of the compressible NS equations, although not shown here, is closely similar.) Lower plot: Comparison of the centerline streaming velocity $\bar{u}_1(x,\mathrm{Y}=1)$ predicted from the asymptotic theory (solid curve) with the corresponding mean flow profile $\bar{u}(x,\mathrm{Y}=1)$ extracted from the DNS (dashed line), with $Pr = 0.1$ in the DNS.

RESULTS AND DISCUSSION

Unlike classical theories of acoustic streaming, the new wave/mean-flow interaction equations derived here exhibit fully *two-way coupling* between the acoustic waves and the streaming flow; that is, not only do the waves drive streaming flows but because the streaming is strong, the background temperature and density profiles induced by the imposed heat source are modified, in turn altering the acoustic wave dynamics (i.e. through the occurrence of $\bar{\Theta}_0$ and $\bar{\rho}_0$ in the fluctuation PDEs). To make further analytical progress, it is possible to consider a small Prandtl number limit, in which case $\Theta_0 = 0$, making the waves independent of the streaming. In this limit, the resulting streaming equations can be expressed as

$$\begin{aligned} \bar{\rho}_0\left(\bar{u}_1\partial_x\bar{u}_1 + \bar{V}_1\partial_Y\bar{u}_1\right) &= -\frac{1}{\gamma}\partial_x\bar{\pi}_2 - \partial_x\left(\bar{\rho}_0 u_1'^2\right) - \partial_Y\left(\bar{\rho}_0 u_1' V_1'\right) + \frac{1}{R}\partial_Y^2\bar{u}_1, \qquad \bar{\rho}_0 = \frac{1}{T_B(Y)}, \\ J(\bar{\Psi},\bar{\Omega}) - \begin{pmatrix} 1 \\ 2\bar{\rho}_0^2 \end{pmatrix}\partial_Y\bar{\rho}_0\partial_x[(\partial_Y\bar{\Psi})^2] &= \frac{\Gamma}{2}(1-Y)\sin(2x) + \frac{1}{R}\partial_Y^2\bar{\Omega}, \qquad \partial_Y\left[T_B(Y)\partial_Y\bar{\Psi}\right] = -\bar{\Omega}, \end{aligned}$$

where $\bar{\Omega} \equiv -\partial_Y\bar{u}_1$, $\bar{\rho}_0\bar{u}_1 \equiv \partial_Y\bar{\Psi}$ and $\bar{\rho}_0\bar{V}_1 \equiv -\partial_x\bar{\Psi}$. $T_B(Y) = 1 + \Gamma Y(2-Y)$ is the background temperature profile maintained by the imposed heat source, and $R \equiv Re/S$ is the 'streaming Reynolds number'. Note that the streaming vanishes as $\Gamma \to 0$; thus, the streaming is baroclinically driven. More specifically, *fluctuating baroclinic torques generated within the bulk of the fluid, rather than viscous torques arising in thin Stokes (oscillatory) boundary layers, are responsible for generating the vorticity fluctuations required to induce the strong streaming*. Indeed, Fig. 1, which compares the results of the new theory with those from DNS of the full compressible NS equations, confirms that the baroclinic mechanism is capable of correctly capturing the magnitude and the orientation of the induced streaming. We conclude by suggesting that beyond applications in lighting, there is the possibility that baroclinically-driven acoustic streaming may find future application in the quiet cooling of electronic components [6].

Acknowledgements The work has been partially supported by statutory funds from the Polish Ministry for Science and Higher Education, Statutory Funding 2014/2015, S40104/K0901.

References

[1] Lighthill M. J.: Acoustic Streaming. Journal of Sound and Vibration 61:391-418, 1978.
[2] Rayleigh: On the Circulation of Air Observed in Kundt's Tubes and Some Allied Acoustical Problems. Transactions of the Royal Society 75:1-21, 1883.
[3] Riley N.: Steady Streaming. Annual Review of Fluid Mechanics 33:43-65, 2001.
[4] Dreeben T. D., Chini G. P.: Two-Dimensional Streaming Flows in High-Intensity Discharge Lamps. Physics of Fluids 23:056101, 2011.
[5] Chini G. P., Malecha M. Z., Dreeben T. D.: Large-Amplitude Acoustic Streaming. Journal of Fluid Mechanics 744:329–351, 2014.
[6] Hyun S., Lee D. R., Loh B. G.: Investigation of Convective Heat Transfer Augmentation Using Acoustic Streaming Generated by Ultrasonic Vibrations. International Journal of Heat and Mass Transfer 48:703718, 2005.

COMPONENTS OF MEAN STREAMING FLOW IN A PRECESSING CYLINDER AT SMALL NUTATION ANGLES

T. Albrecht*[1], H. M. Blackburn[1], J. M. Lopez[2], R. Manasseh[3], and P. Meunier[4]
[1]*Department of Mech. and Aerospace Engineering, Monash University, VIC 3800, Australia*
[2]*School of Math. and Statistical Sciences, Arizona State University, Tempe, AZ 85287, USA*
[3]*Dep. of Mech. and Product Design Engineering, Swinburne University of Technology, VIC 3122, Australia*
[4]*IRPHE, CNRS, Aix–Marseille Université, 49 Rue Joliot-Curie, 13013 Marseille, France*

Summary Mean streaming is often observed in precessing cylinder flows, yet the exact mechanism of its creation remains obscure. By Reynolds-decomposition of the Navier–Stokes equation for a rotating frame of reference, we identify two forcing terms which, when applied to an axisymmetric simulation, generate a streaming flow identical to that obtained from a full three-dimensional simulation. These terms are (i), the usual Reynolds-stress term, and (ii), a term originating from the Coriolis term. The latter accounts for most of the energy of the streaming flow at small nutation angles.

Mean streaming flows (MSFs) are due to the quadratic nature of the nonlinear term in the momentum equation. When amplitudes are small, the nonlinear term is a second-order correction evaluated by substituting the linear solution into it. The time-average of a linear wave solution is zero, simply because the average of a sinusoidal function of time is zero. However, the nonlinear term is the square of a sinusoidal function, so its time average is nonzero. This provides a stress, effectively the Reynolds stress, that can drive time-mean flows at second order. The nonlinear term in contained rotating flows is known to lead to a variety of time-dependent phenomena explicable by triadic resonances [1, 2, 3, 4, 5]. However, the origin of the mean streaming remains unclear.

In rotating flows, inertial waves can exist which drive the streaming flow, as is regularly observed in experiments and simulations. Kelvin modes, the inviscid eigenmodes of solid body rotation flow, are usually considered a good approximation for inertial waves contained in a cylinder, however, prior theory [6] has been interpreted to suggest that Kelvin modes cannot create mean streaming. Our ultimate aim is to explain the observed streaming flow.

We use precession to excite inertial waves in a set-up shown in figure 1(a). Characterised by the Poincaré number $Po = \Omega_2/\Omega_1$, precession directly injects energy into a mode referred to as the forced mode. Certain combinations of forcing frequency and aspect ratio H/R enable energy transfer via triadic resonance from the forced mode to a pair of free modes. Triadic resonance represents the system's first bifurcation, found to be ubiquitous at low nutation angles α [5].

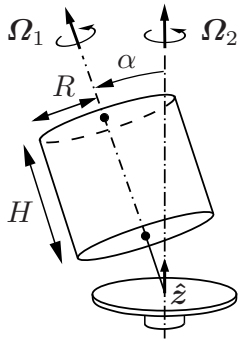

Figure 1: Schematic of the precessing flow.

In order to synthesise the streaming flow, we first integrate the full 3D problem. Once forced and axisymmetric modes are saturated, we extract the reference streaming flow and correlations from which we compute a number of forcing terms, details of which will be given shortly. These forcing terms are then used to drive an axisymmetric DNS, and we expect the resulting flow to match the reference MSF. Computing the isolated response to individual forcing terms provides further insight.

We compute the flow in the cylinder frame of reference, which has time-dependent angular velocity $\boldsymbol{\Omega} = [\Omega_z, \Omega_r, \Omega_\varphi] = [\Omega_1 + \Omega_2 \cos\alpha,\ \Omega_2 \sin\alpha \cos(-\Omega_1 t),\ \Omega_2 \sin\alpha \sin(-\Omega_1 t)]^T$. The rotating frame of reference is accounted for by Coriolis terms in the incompressible Navier–Stokes equation

$$\partial_t \boldsymbol{u} + \boldsymbol{u}\cdot\boldsymbol{\nabla}\boldsymbol{u} + 2\boldsymbol{\Omega}\times\boldsymbol{u} + \partial_t\boldsymbol{\Omega}\times\boldsymbol{x} = -\boldsymbol{\nabla}p + Re^{-1}\nabla^2\boldsymbol{u}, \qquad \boldsymbol{\nabla}\cdot\bar{\boldsymbol{u}} = 0, \tag{1}$$

where potential terms have been absorbed into the reduced pressure p, and the Reynolds number $Re = R\Omega_1/\nu$. The walls are at rest and the forced mode rotates at $-\Omega_1$. The streaming flow is defined as the time-averaged, axisymmetric component of the flow. A comparison of numerical and experimental results showed excellent agreement [7].

The forcing terms are obtained by Reynolds-averaging the Navier–Stokes equation (1): decomposition of linear and angular velocities and pressure into mean and fluctuating parts, $\boldsymbol{a} = \bar{\boldsymbol{a}} + \boldsymbol{a}'$, $\boldsymbol{a} = (\boldsymbol{u}, \boldsymbol{\Omega}, p)$, followed by averaging in time, produces two additional terms through which higher azimuthal modes can generate the $m = 0$ mean streaming flow, where m is the azimuthal wave number. First, the usual Reynolds-stress term $\boldsymbol{R} = \nabla\cdot(\overline{\boldsymbol{u}'\boldsymbol{u}'})$, and, second, a term resulting from the Coriolis force $\boldsymbol{C} = 2\overline{\boldsymbol{\Omega}'\times\boldsymbol{u}'}$. Their respective axisymmetric part is used to force a steady, axisymmetric flow that satisfies

$$\bar{\boldsymbol{u}}_0\cdot\boldsymbol{\nabla}\bar{\boldsymbol{u}}_0 + 2\bar{\boldsymbol{\Omega}}_0\times\bar{\boldsymbol{u}}_0 + [\nabla\cdot(\overline{\boldsymbol{u}'\boldsymbol{u}'})]_0 + [2\overline{\boldsymbol{\Omega}'\times\boldsymbol{u}'}]_0 = -\boldsymbol{\nabla}\bar{p}_0 + Re^{-1}\nabla^2\bar{\boldsymbol{u}}_0, \qquad \boldsymbol{\nabla}\cdot\bar{\boldsymbol{u}}_0 = 0, \tag{2}$$

and boundary conditions $\bar{\boldsymbol{u}}_0 = 0$, where subscript 0 indicates $m = 0$. The Reynolds-stress term can be computed using all azimuthal modes (referred to as $\boldsymbol{R}$), just the (leading) forced $m = 1$ mode ($\boldsymbol{R}_1$), or either of the free modes ($\boldsymbol{R}_5$, $\boldsymbol{R}_6$), which are known to participate in triadic resonances for these parameters [5].

*Corresponding author. Email: thomas.albrecht@monash.edu

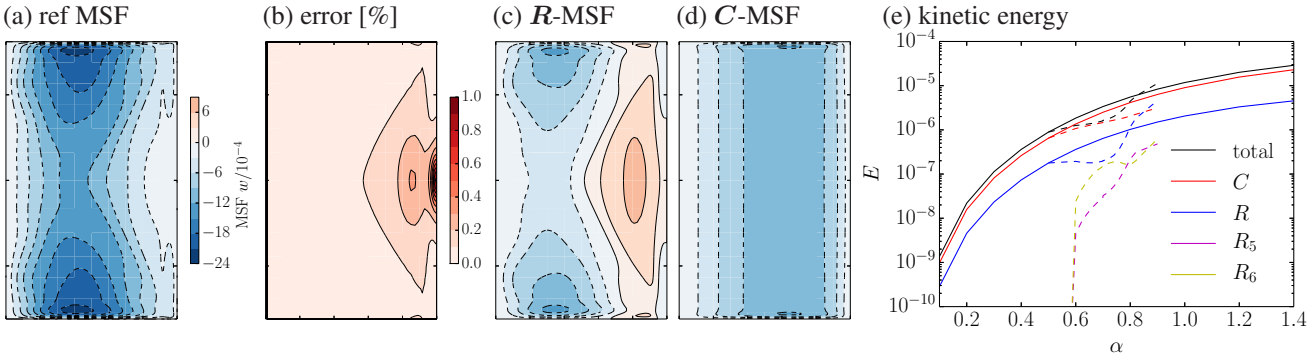

Figure 2: Contours of the streaming flow in a meridional semi-plane with the axis on the left, for a case below the threshold of triadic resonance: (a) reference MSF, (b) relative error ($w_{\rm syn}/w_{\rm ref} - 1$) of the total synthetic MSF, (c) synthetic MSF due to $\boldsymbol{R}$-forcing, only, and (d) ditto due to $\boldsymbol{C}$-forcing, only. All MSF plots use the contour levels given in (a). $H/R = 1.62, Re = 7670, Po = -0.153, \alpha = 0.4°$. (e) Kinetic energy of the total streaming flow, and of the response to individual forcing parts, vs. nutation angle.

Figure 2 shows results for a case where $\alpha = 0.4°$ is below the threshold α_c of triadic resonance instability (for the present aspect ratio, weakly nonlinear theory [3] predicts $\alpha_c = 0.63°$). Hence, the asymptotic state is quasi-steady and essentially consists of a rotating forced mode and the streaming flow. The Fourier kinetic energy E_m of any azimuthal mode is steady, with $E_1/E_0 \approx 141$ and $E_2/E_0 \approx 0.044$. Figure 2(a) shows the azimuthal velocity component w of the reference streaming flow. It is negative throughout the domain (i.e., it opposes the solid body rotation), has an hourglass-like structure with a maximum in the end wall layers, and is about an order of magnitude larger than the axial and radial components. Since a contour plot of the synthetic streaming flow would be indistinguishable from the reference in figure 2(a), we plotted the relative error $w_{\rm syn}/w_{\rm ref} - 1$ in figure 2(b). The error is well below 1% for most of the domain, confirming we identified all terms required for the production of the streaming flow. If we decompose the total forcing into $\boldsymbol{R}$- and $\boldsymbol{C}$-parts, we can compute the corresponding flow response individually, which is shown in (c) and (d). The hourglass-like structure is created by the $\boldsymbol{R}$-forcing, whereas $\boldsymbol{C}$-forcing produces a columnar structure. Also, $\boldsymbol{R}$-forcing creates a streaming flow which is *positive* in the outer region of the cylinder.

We applied this procedure to a range of nutation angles. In figure 2(e), we plotted the kinetic energy of the total synthetic streaming flow (black). It matches the reference to within 0.1%. Also shown are energies of the individual responses to $\boldsymbol{C}$-forcing, to $\boldsymbol{R}$-forcing, or to forcings due to the free modes ($\boldsymbol{R}_5$ and $\boldsymbol{R}_6$). Solid lines show results where triadic resonance is absent and the flow appears stable, either because it in fact is ($\alpha < \alpha_c$), or because it has not evolved for long enough for the free modes to accumulate significant energy. For these "stable" cases, $\boldsymbol{C}$- and $\boldsymbol{R}$-parts account for about 75% and 20% of the total energy, respectively (these figures do not have to add up, since the underlying decomposition is not orthogonal).

Once triadic resonance is active (dashed lines), the response to $\boldsymbol{R}_5$- and $\boldsymbol{R}_6$-forcing becomes significant. However, for tilt angles just above critical ($0.6° \le \alpha \le 0.8°$), the total streaming flow decreases as compared to the non-resonant flow, because the free modes drain energy from the forced mode which reduces the $\boldsymbol{C}$-response, and because parts of the $\boldsymbol{R}/\boldsymbol{R}_5/\boldsymbol{R}_6$-response is positive and opposes the main streaming flow.

In an attempt to explain the origin of mean streaming in a precessing cylinder flow, we identified all relevant forcing terms. When applied to axisymmetric simulations, these forcing terms create streaming flows virtually identical to those obtained from full three-dimensional simulations. The forcing can be decomposed into contributions from Coriolis and nonlinear (Reynolds stress) terms for cases below and slightly above the threshold of triadic resonance. For all cases $0.1° \le \alpha \le 1.4°$ we considered, the Coriolis forcing term creates the largest response, however, the effect of the Reynolds stress term grows quickly when triadic resonance becomes active.

References

[1] R. Lagrange, C. Eloy, F. Nadal, and P. Meunier. Instability of a fluid inside a precessing cylinder. *Phys. Fluids*, 20:081701, 2008.

[2] P. Meunier, C. Eloy, R. Lagrange, and F. Nadal. A rotating fluid cylinder subject to weak precession. *J. Fluid Mech.*, 599:405–440, 2008.

[3] R. Lagrange, P. Meunier, F. Nadal, and C. Eloy. Precessional instability of a fluid cylinder. *J. Fluid Mech.*, 666:104–145, 2011.

[4] F. Marques and J. M. Lopez. Precession of a rapidly rotating cylinder flow: traverse through the resonance. *J. Fluid Mech.*, 782:63–98, 2015.

[5] T. Albrecht, H. M. Blackburn, J. M. Lopez, R. Manasseh, and P. Meunier. Triadic resonances in precessing rapidly rotating cylinder flows. *J. Fluid Mech.*, 778:R1, 2015.

[6] H. P. Greenspan. On the non-linear interaction of inertial modes. *J. Fluid Mech.*, 36:257–264, 1969.

[7] T. Albrecht, H. M. Blackburn, P. Meunier, R. Mannaseh, and J. M. Lopez. PIV of a precessing cylinder flow at large tilt angles. In *Proc. 9th Int'l Symposium on Turbulence and Shear Flow Phenomena*, Melbourne, June 2015.

NONLINEAR VS. LINEAR SUPERCRITICAL DEAD WATER

John Grue [*1]
[1]*Mechanics Division, Department of Mathematics, University of Oslo, Oslo, Norway*

Summary Nonlinear calculations of the internal wave wake behind a moving ship – dead water – differ largely from the state-of-the-art linear calculations, where the ratio between the ship draught and surface layer depth constitutes the nonlinearity parameter. The fundamental differences come from the local finite excursions of the flow at the complex ship geometry. Assuming a two-layer model, it is shown that linear theory overpredicts the wave wake excursions by 50 per cent, when the ship draught is comparable to the surface layer depth. The nonlinear calculations fit with observations. The ship speed is supercritical. Evaluation of the surface velocity and strain rate may be used for observational interpretation.

INTRODUCTION

Accurate calculations of the internal wave wake behind a moving ship – dead water – have been actualized by some recent measurements in a Canadian sub-Arctic fjord (Bourgault, 2014, private communication). Improved modelling of internal wave wakes are relevant in relation to construction of new infrastructure such as submerged floating tunnels, where the wave loads should be accurately accounted for. Numerical predictions of the phenomenon are vital in relation to surveiance. We present novel nonlinear calculations at supercritical speed which significantly improve the existing linear methods, where the linear theory overpredicts the amplitudes of the wave wake by 50 per cent, for a ship draught comparable to the surface layer depth.

Ship generated internal wave wakes occur in coastal waters where a surface layer of brackish water is overlaying the salty sea water. The phenomenon is visible by its signature on the ocean surface, cause an additional resistance on the ship and may even affect the maneuverability. Existing methods for the prediction of ship generated internal wave wakes, where the actual geometry of the hull is accounted for, are linear, see e.g., Miloh et al. [1], Yeung and Nguyen [2]. Papers on simplified methods assuming generation by pressure or source distributions are found in the references in these papers. A nonlinear method assuming a pressure distribution was given by Parau et al. [3]. Requests for improved models of the wave wake and its generation, more specifically accounting for the effects of nonlinarity, were requested by Watson et al. [4], discussing observations carried out in the Loch Linnie experiment in UK. In the present paper, the internal wave wake at supercritical speeds is analyzed, generalizing the subcritical strongly nonlinear calculations by Grue [5].

STRONGLY NONLINEAR MODEL

A two-layer model is assumed where to fluids of different densities are separated by an interface. The fluid motion is driven by a ship moving at forward speed U along the upper boundary of the two-fluid system, where the Froude number is given by $Fr = U/c_0$, where c_0 denotes the linear long wave speed of the two-fluid system. The ratio between the ship draught (d_0) and thinner upper layer depth (h_0), i.e., d_0/h_0, defines the nonlinearity parameter and is varied up to $d_0/h_0 = 1.2$, where the interface in the supercritical conditions is pushed downward right below the ship geometry. Essential differences between the nonlinear and linear calculations stem from fundamental differences of the representation of the flow at the complex ship hull. The interfacial excursions are comparable to the thinner upper layer depth.

Laplacian potentials in each layer are obtained by integral equations involving the potentials and their normal derivatives along the interface and ship surface. Assuming a small density jump, the rigid lid condition at the free surface is justified. Inversion of the integral equations are obtained by the method of successive approximations. This leads to rapid convergence of the set of expansions. Use of Fourier transform, extensively applied in the inversion procedure, leads to fast evaluations of the integrals. The prognostic equations, obtained by the kinematic and dynamic boundary conditions along the interface, are used to integrate forward in time, the evolving interfacial wave system, driven by the ship geometry, starting from rest.

Results

Let (x_1, x_2) denote horizontal coordinates. The computational horizontal plane has length by width of L_1 by L_2 and is discretized by $0.5 \cdot 10^6$ points. The ship geometry is specified lengthwise and sideways by sixth order polynomials. In the computations, the ship length by width are 29.6 by 4 times the upper layer depth (h_0), corresponding to an actual observation of a large tanker causing an internal wave wake. Nonlinear and linear calculations show that the latter overpredict by 50 per cent, the amplitudes of the internal wave wake (figure 1a), when the draught is comparable to the upper layer depth, and $Fr = 4$ and 8, see figure 1c-d. The overprediction is about 20 per cent for a moderate draught of $d_0/h_0 = 0.5$ and $Fr = 4$ (figure 1b).

*Email: johng@math.uio.no

Bourgault (2014, personal communication, unpublished) measured, at a lateral distance of $133h_0$ from the ship track, a train of about 8 internal waves of height of 1-2 m, moving laterally, along a pycnocline localized at an average depth of $h_0 = 7.5$ m in the actual fjord. The nonlinear computations of the trough amplitudes in figure 2, for $Fr = 8$ and $d_0/h_0 = 1.2$, give wave heights of $0.2h_0 = 1.5$ m at $x_2 = 133h_0$, fitting very well to the observations. Linear calculations give wave heights of $0.3h_0 = 2.3$ m which exceed the observations. By the nonlinear calculations we evaluate other quantities like surface velocity and strain rate as requested by Watson et al. [4].

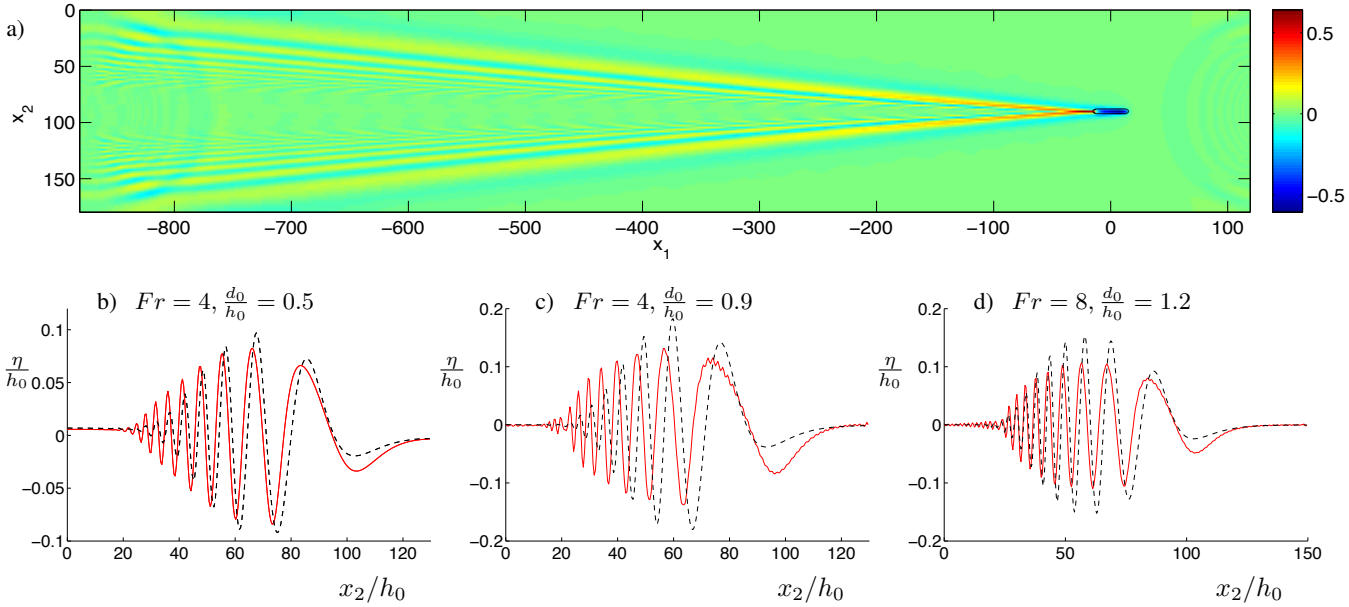

Figure 1: a) Nonlinear interfacial elevation η/h_0 of internal wave wake. $Fr = 8$. $d_0/h_0 = 1$. (x_1, x_2) scaled by h_0. b)-d) Nonlinear (red solid line) and linear (black dashed line) interfacial elevation η/h_0 as function of the lateral coordinate, x_2, at fixed downstream positions $x_1 - Ut$ in the wave wake, for increasing ship draught and Froude number. b)-c) $(x_1 - Ut)/h_0 = 370$, $Fr = 4$, ship draught $d_0/h_0 = 0.5, 0.9$. d) $(x_1 - Ut)/h_0 = 840$, $Fr = 8$, ship draught $d_0/h_0 = 1.2$. Ship model of length $l_0 = 29.4h_0$ and width $w_0 = 4h_0$.

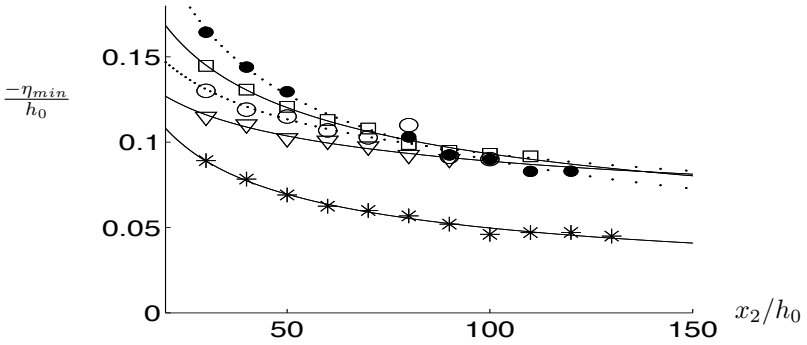

Figure 2: Amplitude of trough 1 ($*$), trough 2 ($\bullet$), trough 3 ($\square$), trough 4 ($\circ$), trough 5 (∇) vs. lateral coordinate x_2. Solid/dotted lines: fitted algebraic decay. $Fr = 8$, $d_0/h_0 = 1.2$.

References

[1] Miloh T., Tulin M.P., Zilman, G.: Dead-water effects on a ship moving in stratified seas. J. Offsh Mech Arctic Engng 115:105-110, 1993.

[2] Yeung R.W., Ngyuen T.C.: Waves generated by a moving source in a two-layer ocean of finite depth. J. Engng Math 35:85-107, 1999.

[3] Parau E.I., Vanden-Broeck J.-M., Cooker M.J.: Nonlinear three-dimensional interfacial flows with a free surface. J. Fluid Mech 591:481-494, 2007.

[4] Watson G., Chapman R.D., Apel J.R.: Measurements of the internal wave wake of a ship in a highly stratified sea loch. J. Geophys Res 97(C6):9689-9703, 1992.

[5] Grue J.: Nonlinear dead water resistance at subcritical speed. Phys. Fluids, 27(8):082103, 2015.

GENERATION AND RUNUP OF TRIPLE SOLITARY WAVES ON PLANE SLOPE

Yiyi Rong [1], Wei Wu[1] & Hua Liu[2a)],
[1] *School of NAOCE, Shanghai Jiao Tong University, Shanghai, China*
[2] *MOE Key Lab of Hydrodynamics, Shanghai Jiao Tong University, Shanghai, China*

Summary An experimental study on generation and runup of the wave train of three solitary waves (referring as Triple Solitary Waves, TSW) on a plane slope has been conducted in a wave flume. The modified Goring's method and the third order solution of a solitary wave are integrated to generate a wave train of three solitary waves with different distance between the crests of two successive solitary waves. Time series of the surface elevation and waterline movement are measured. With regard to a train of three solitary waves with same height, the runup amplification coefficient of the individual wave varies and the runup coefficient of the second wave is smallest among them. Details of experimental results and discussion on the details of velocity field and energy budget of TSW will be presented.

METHODOLOGY

Run-up and back-wash process of waves on a plane beach belong to one of the important hydrodynamic phenomena in coastal water. An experimental study on runup of the double solitary waves on a plane beach was carried out by Lo et al. (2013) and Pujala et al. (2015). Xuan et al. (2013) implemented the generation and runp of two successive solitary waves with different wave amplitudes in a wave flume. We carried out experiments on the runup characteristics of triple solitary waves in the wave flume of the MOE Key Laboratory of Hydrodynamics at Shanghai Jiao Tong University. The facility consists of a wave flume (65m long×1.8m deep×0.8m wide), a piston-type wave generation system and a wave elevation measurement system. A piston-type wave generator is installed at the left end of the wave flume and the paddle is moved horizontally in a prescribed trajectory by means of a hydraulic servo-system. At the right end of the wave flume, a slope beach is installed to eliminate the wave reflection. There are total 9 wave gauges along the wave flume, as shown in Fig. 1. The maximum wave runup is recorded by two high-speed cameras.

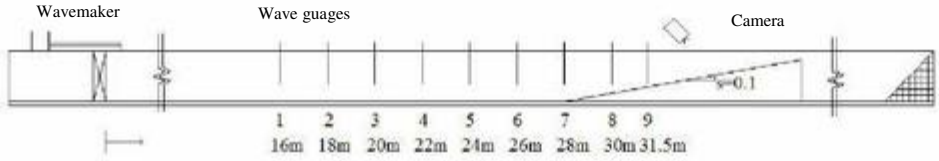

Figure 1 Experimental setup

The modified Goring's method (Goring, 1978), proposed by developed Malek-Mohammadi and Testik (2010), is used to generate a wave train of two successive solitary waves (referring as TSW). Using the third order solution of a solitary wave, the target wave train consisting of three solitary waves with different phase difference can be constructed and, then, the time series of the displacement of the wavemaker can be obtained. The time series of the surface elevation measured by the wave gauges, for the case of the relative wave amplitude H/d=0.1, are plotted in Fig. 2. The solid line represents the double solitary wave and the dashed line denotes the triple solitary wave and the parameter ε represents the phase difference among waves.

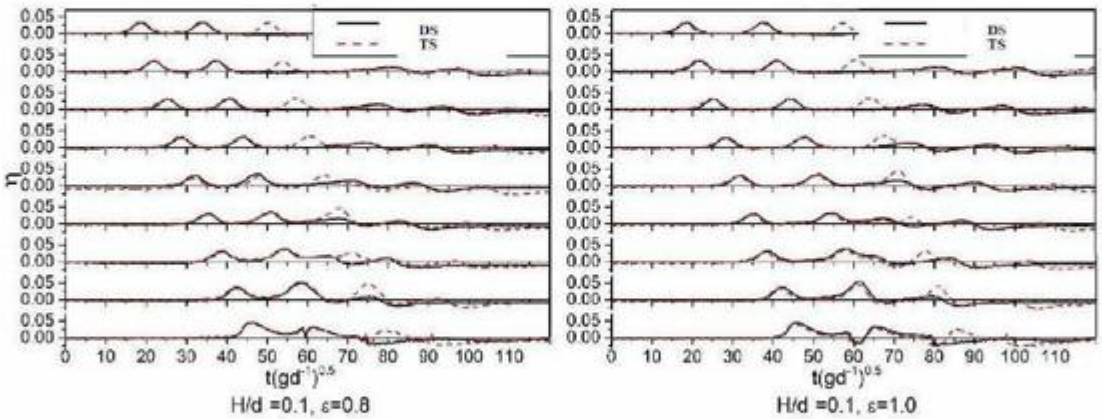

Figure 2 Time series of surface elevation of TSW

a) Corresponding author. Email: hliu@sjtu.edu.cn

RESULTS AND DISCUSSION

The runup amplification coefficient of a solitary is defined as the ratio of the maximum runup to the wave amplitude R/H. The distance between the peaks of two successive solitary waves δL is proportional to the phase difference parameter ε. For the case of TWS with identical amplitude, the same referred amplitude is adopted to calculate the runup amplification. The measured runup amplification coefficients for individuals are presented in Fig. 3.

It is found that influence of the leading solitary wave is obvious to the following wave due to strong swash current appearing in the stage of rundown of the first wave. The relationship between the runup amplification coefficient of the second waves and initial phase difference will change with the increase of the relative amplitude of incoming wave. However, the runup amplification coefficient of the third wave increases with the increase of initial phase difference and the relationship is independent of the relative amplitude of incoming wave. Basically, the runup amplification coefficient of the first waves is larger than that of the second wave, while the runup amplification coefficient of the third wave is larger than that of the second wave.

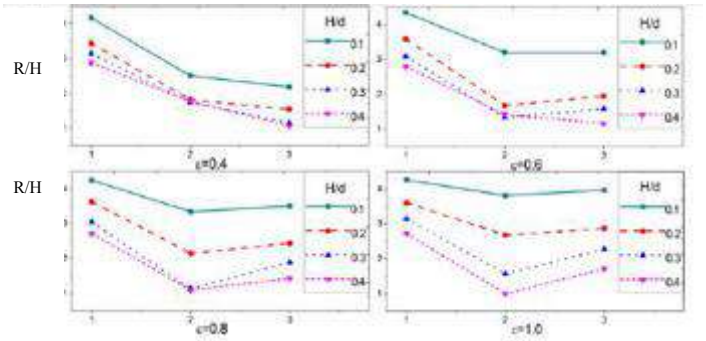

Figure 3 Runup amplification of TSW

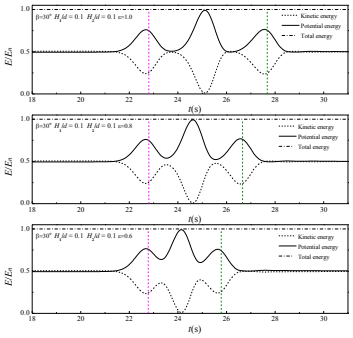

Figure 4 Energy budget during run-up of waves

In order to understand the mechanism of the variation of the runnup amplification of individual waves, numerical simulations of runup of two successive solitary waves are carried out. Based on the computed velocity field and the wave profile by the RANS equations based numerical model, the kinetic energy and potential energy of the water in the computational domain can be obtained. Fig.4 depicts the time series of the kinetic energy, potential energy and total energy of two successive solitary waves with identical amplitude during the period of runup and rundown on a plane slope. Three different phase difference of initial linear superposition of waves are considered. There are three peaks in the time series of the potential energy and three troughs in that of the kinetic energy. The first and third peaks of the potential energy appear at the time when the first solitary wave and second solitary wave reach the maximum runup respectively. The highest peak of the potential energy appears when the second solitary wave propagating from left to right meets the first reflected solitary wave from the beach. The kinetic energy is basically equal to zero at the head-on collision time. When the initial position of these two solitary waves separate with large distance between two peaks for cases of ε=1.0 and 0.8, the variation of the energy budge of these two solitary waves in the process of each runup are identical with each other, which means that the influence of the first runup and rundown on the second runup can be ignored. If we look at the bottom panel of Fig. 4 for the case of ε=0.6, where the distance between two peaks is seventeen times as large as water depth, it can be seen that these two runup processes of the two successive solitary waves overlap partly and the maximum potential energy for the second runup is smaller than that of the first runup.

ACKNOWLEDGEMENTS

The research has been supported by the National Basic Research Program of China (973 Program, No. 2014CB046200) and National Natural Science Foundation of China (No. 51379123).

References

[1] Goring D.G. : Tsunamis-the Propagation of Long Waves onto a Shelf. *Ph.D. Thesis*, California Institute of Technology, Pasadena, CA, 1978.

[2] Lo H.Y., Park Y.S., Liu P.: On the run-up and back-wash process of single and double solitary waves-An experimental study. *Coastal Engineering*, 80: 1-14, 2013.

[3] Malek-Mohammadi S, Testik F.Y.: New methodology for laboratory generation of solitary waves, *Journal of Waterway, Port, Coastal, and Ocean Engineering*, 36(5): 286-294, 2010.

[4] Pujala N., Liu P. L-F., Yeh H. H.: An experiment study of the interaction of two successive solitary waves in the swash: A strongly interacting case and a weakly interacting case. *Coastal Engineering*, 105: 66-74, 2015.

[5] Xuan R.T. Wu W., Liu H.: An experimental study on runup of two solitary waves on plane beaches. *Journal of Hydrodynamics*, 25(2), 317-320, 2013.

TRANSPORT OF PARTICLES BY INTERNAL WAVES

Ernesto Horne *[1,2], Diane Micard[1,2], Sylvain Joubaud[1], and Philippe Odier[1]
[1]*Laboratoire de Physique, Ecole Normale Supérieure de Lyon, Université de Lyon, CNRS, Lyon, France*
[2]*Laboratoire de Mecanique des Fluides et d'Acoustique, UMR 5509, CNRS, Ecole Centrale de Lyon, Université de Lyon, Ecully, France*

Summary We study experimentally the effect of internal waves on slowly settling particles in a stratified environment. The granular column formed by the particles oscillates around an equilibrium position due to the presence of the internal gravity waves. Depending on the frequency and the amplitude of the internal waves, the column can even be displaced as a whole. Surprisingly, this displacement is directed towards the source of the waves. A resonant behavior of this displacement with the frequency of the internal waves is observed. A theoretical approach based on the drift induced by internal waves is developed.

INTRODUCTION

The settling of organic particles from the upper layers of the ocean to the deep sea (known as oceanic snow) has an intense effect on global ocean properties. It is substantial for the development of diversified life in the benthic layer and it also sequesters large quantities of CO_2 from the atmosphere. The dispersion and concentration of these particles will be strongly attached to the dynamics of the ocean via its carrying fluid. Internal waves, omnipresent in the ocean, can act as a mechanism producing resuspension of particles lying in the boundary layers [1] and generate net transport of the oceanic snow that could play a role in the behavior of marine habitat [2].

Experimental and numerical efforts have been performed to understand the dynamics of a single body settling in a stratified environment [3], as well as the collective dynamics of particles settling in a stratified fluid [4]. In our work, we include an additional degree of complexity, by trying to study experimentally the main effects of an internal plane wave propagating through a column of slowly settling particles, in a stratified fluid.

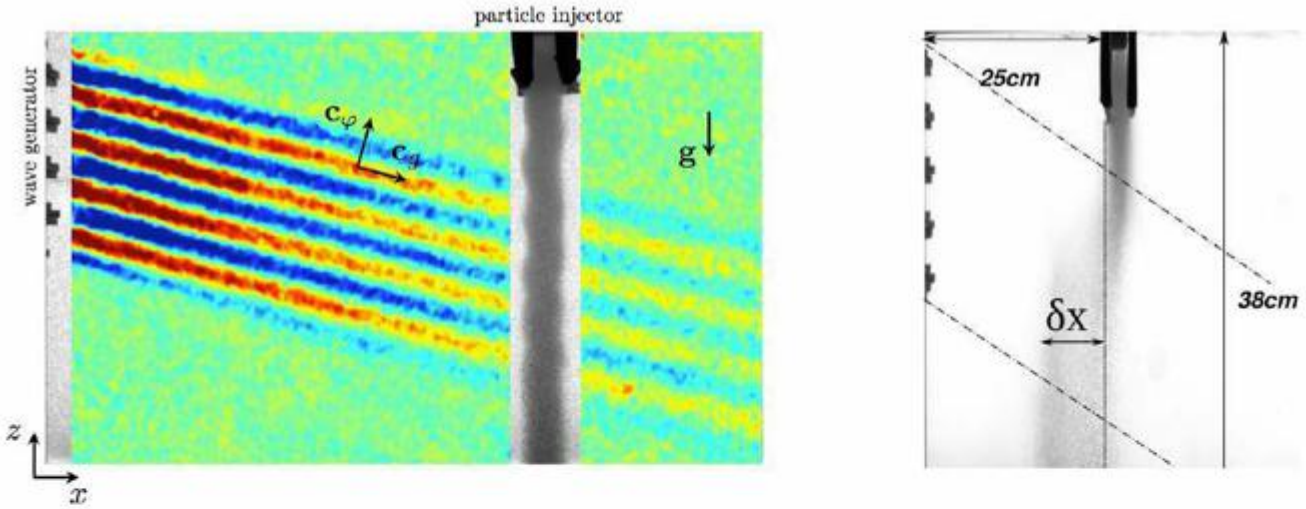

(a) (b)

Figure 1: (a) Snapshot of an internal wave beam passing through a column of settling particles. The column oscillates following the group velocity of the wave. The colormap indicates the intensity of the horizontal gradient of density. (b) Column displacement obtained for a particular set of control parameters. The value of the displacement after a given time is denoted δx. In both figures, the wave field is generated in the upper-left corner and propagates to the lower-right corner.

*Ernesto Horne. Email: ernesto.horne@ec-lyon.fr

EXPERIMENTAL SET-UP

A rectangular test tank of size $80 \times 17 \times 42.5$ cm^3 is filled with a linearly salt-stratified fluid with a buoyancy frequency $N \simeq 1$ rad·s^{-1}. Internal plane waves are introduced into the system by an internal wave generator, consisting of stacked moving plates. This wave maker is built so that the frequency, phase shift and amplitude of each plate can be controlled independently. The gradient of density of the wave field is then observed using Synthetic Schlieren technique.

A quasi-2D granular column is formed by injecting polystyrene grains ($d = 200$ μm , $\rho_p = 1.05$ g·cm^{-3}) at the surface. After some time, a stationary homogeneous column (width $d_c \simeq 3$ cm) is produced with a packing fraction $\phi \sim O(10^{-2})$.

RESULTS

For the particle concentrations explored we do not detect a difference in the amplitude of the waves between the cases with and without column of particles: the particles have no influence over the waves.

We observe that internal waves produce an oscillatory effect on the column as shown in figure 1(a). It oscillates with a phase velocity equal to the phase velocity of the waves. It is remarkable that oscillations are observed outside the wave beam as well. In addition, frequencies not contained in the wave spectra are measured within these oscillations, which could be consequence of non-linear effects of the waves in the column or because of collective effects of the particles.

The column can also be displaced as a whole (see figure 1(b)). This displacement is observed to be always towards the generator. It was measured for experiments presenting two different density gradients (in our case large density gradient implies small sedimentation velocity). For the largest sedimentation velocity (figure 2(a)), the displacement is very small for small amplitudes of the wave and is independent of the frequency. For larger amplitudes, it increases with the frequency. For the case with smaller sedimentation velocity and larger amplitude, we observe a resonant behavior of the displacement with the frequency (figure 2(b)).

CONCLUSIONS

We have developed a set-up capable of performing experiments to study the interaction between internal gravity waves and particles in suspension. We observed two main effects produced by internal waves over the column: it oscillates around an equilibrium position and it is displaced as a whole toward the source of the waves. The dependency of the displacement of the column has been measured as a function of the density gradient and amplitude of the waves for a range of frequencies of the incoming waves. In addition, a model which considers the drift produced by the internal waves [5] and the excursion time of the particles in the wave beam achieves to explain the direction of displacement of the column.

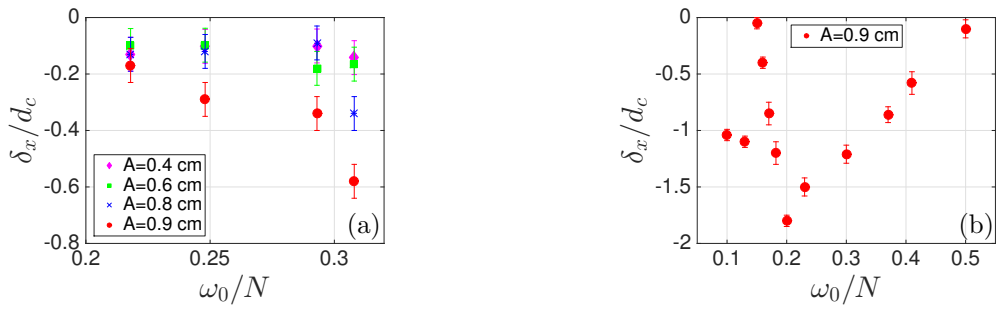

Figure 2: Displacement of the column after 500 seconds ($\delta x < 0$: the motion is towards the generator) normalized by the width of the column d_c as a function of the forcing frequency ω_0 normalized by the buoyancy frequency N. (a) $N = 0.8$ rad·s^{-1} (large sedimentation velocity) and $A = 0.4$ cm, 0.6 cm, 0.8 cm and 0.9 cm. (b) $N = 1.1$ rad·s^{-1} (small sedimentation velocity) and $A = 0.9$ cm.

References

[1] Hosegood P., Bonnin J., van Haren H.: Solibore-induced sediment resuspension in the Faeroe-Shetland Channel. Geophys. Res. Lett., 31(9), 2004.

[2] Pineda J., Starczak V., da Silva J. C. B., Helfrich K., Thompson M., & Wiley D.: Whales and waves: Humpback whale foraging response and the shoaling of internal waves at Stellwagen Bank. Journal of Geophysical Research: Oceans, 120(4):2555 2570, 2015.

[3] Yick K. Y., Torres C. R., Peacock T., Stocker R.: Enhanced drag of a sphere settling in a stratified fluid at small Reynolds number. J. Fluid Mech., 632:4968, 2009.

[4] Bush J. W. M., Thurber B. A., Blanchette F.: Particle clouds in homogeneous and stratified environments. J. Fluid Mech., 489, pp 29-54. 2003.

[5] Hazewinkel J.: Attractors in stratified fluid. PhD Thesis, University of Utrecht, 2010.

INTERNAL WAVE IN THE OCEAN, LOCAL, GLOBAL STABILITY AND TRANSIENT GROWTH

Gaétan Lerisson *[1], Jean-Marc Chomaz[1], and Sabine Ortiz[1]
[1]*LadHyX, Ecole polytechnique, Palaiseau, France*

Summary Internal gravity waves that exist in a continuously stratified fluid are particularly important in the ocean. They transport energy and are thought to generate turbulent mixing which contributes to the deep ocean circulation. Through fully non-linear and linear direct numerical simulations the stability of a gravity wave beam, we show that the stability properties and transient growth intensity strongly depend on the mean flow intensity. Small scale instabilities dominate for small mean flow as for internal tide. For lee waves or more generally strong mean flows, large scales lead the instability but small scales dominate the short time growth. Computing the linear impulse response of a monochromatic internal wave we propose an interpretation based on an extension of absolute and convective theory to 2D periodic base flow and make the connection with the classical triadic instability theory [1].

GLOBAL STABILITY

We compute in a two dimension domain the stability properties of an internal gravity wave beam solution of the non-linear Navier-Stokes equation under the Boussinesq approximation and a linear stratification. The wave is generated using a penalization localized in space that forces an internal gravity wave of specific horizontal wavelength and frequency propagating down as in the experiment [2]. In this case equivalent to a tidal wave where the tidal flow oscillates over a topography and generates a wave, experiment results of [2] are recovered. The beam destabilizes (see figure 1 (b)) and we show that the instability mechanism involves a small triadic resonance. To extend the results of [2], we consider the effect of a horizontal mean advection velocity U_∞. The forcing frequency ω' in the wave maker frame is $\omega' = \omega_0 + U_\infty k_{0x}$ where ω_0, the frequency in the fluid frame and $U_\infty k_{0x}$ the doppler effect. In all the computations ω_0 is kept constant in order to have locally in the fluide the same wave. A limit case appears when mean advection velocity of $U_\infty = -U_\phi$ where $U_\phi = \omega_0/k_{0x}$ then ω' decreases to zero: the forcing is stationary. This case is equivalent to a lee wave appearing when a stratified fluid flows over a topography.

We show that the stability property of beams made locally of the same gravity wave strongly depends on mean advection velocity. For small magnitude of advection velocity, small scale instabilities develop as in the tidal case. Then the beam stabilizes at intermediate advection velocity and destabilizes again when we keep increasing the advection. At this second threshold, down to the lee wave case, the instability is of much larger scale than for the tidal case reported by [2]. Increasing the Reynolds number or the beam size makes the stable domain to disappear but the instability scale selection stays the same with small scale instability in the tidal rgime with scale decreasing when increasing the Reynold number, and large scale instability in the lee rgime with scales indpendante on the Reynolds number or beam size.

We show that the instability may be interpreted using the triadic instability [1] and that scale selection corresponds to different branch of triadic resonance. We confirm the presence of a stability region for intermediate value of the mean advection velocity by computing the linear eigenmode as Floquet mode with an Arnoldi-Krylov technique and showing that the leading eigenmode has a negative growthrate.

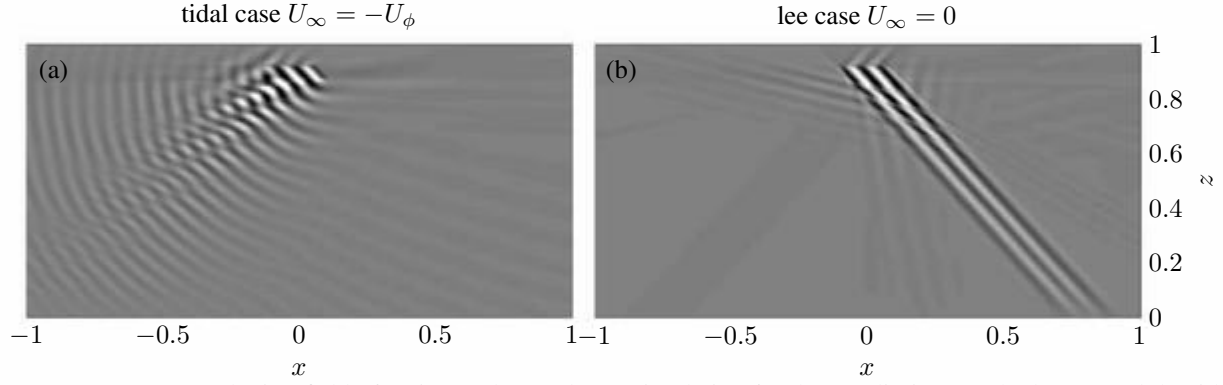

Figure 1: Buoyancy perturbation field of an internal wave beam simulation for the two limit case, the lee (a) and the tidal (b) case.

*Corresponding author. Email: gaetan.lerisson@ladhyx.polytechnique.fr

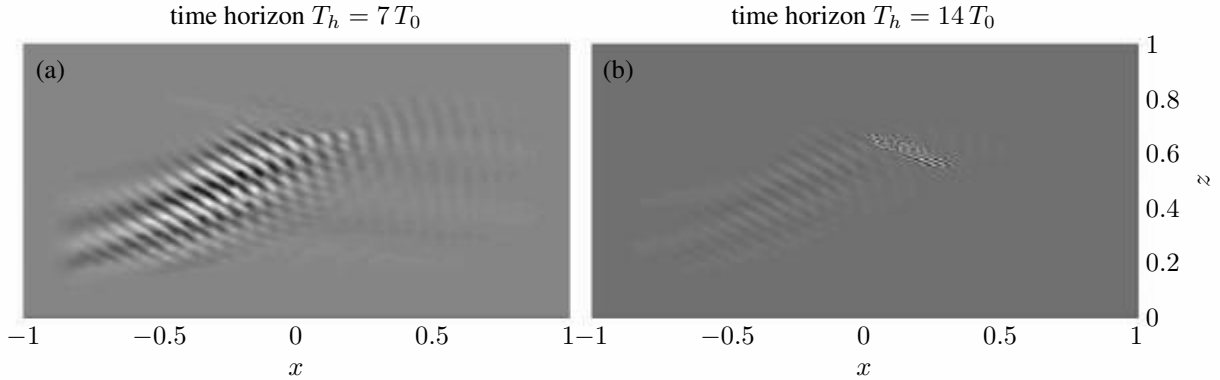

Figure 2: Buoyancy perturbation field of this optimal perturbation that maximize the total energy over a lee wave beam for two time horizon (a) $T_h = 7\,T_0$ and (b) $T_h = 7\,T_0$, where T_0 is the lee wave period $T_0 = 2\pi/\omega_0$.

LINEAR GLOBAL STABILITY AND TRANSIENT GROWTH

We confirm the presence of a stability region for intermediate value of the mean advection velocity by computing the linear eigenmode as Floquet mode with an Arnoldi-Krylov technique and show that the leading eigenmode has a negative growthrate. In the lee wave case the flow is unstable and a selective frequency damping method [3] is used to first compute the steady base flow solution. Then we implement a direct-adjoint method to access the optimal perturbation that maximize the total energy growth at different time horizon using a similar Arnoldi-Krylov technique. At short time horizon, the optimal perturbation is small scale and is advected by the flow while at large time, the perturbation switches to a large scale solution and converges to the perturbation characteristic observed through nonlinear simulation (previous section). Analyzing optimal perturbations and optimal responses in fourrier space seems to indicates that small scale short time transient corresponds to the small scale triadic instability advected by the flow whereas the long time large scale instability corresponds to large scale bra,nah of the triadic instability that is able to sustain the flow.

LINEAR LOCAL STABILITY

We propose an interpretation of the different instability selection in term of absolute and convective instability. We conjecture that, In the case of the lee wave, the large scale instability is absolute whereas the small scale instability is convective and leads short time transient growth because its local growth rate is larger. When the mean advection flow is varied the properties of small scale and large scale instabilities exchange and in the tidal case the short scale instability is absolute and the large scale convective. This conjecture is confirmed by computing the impulse response around a plane monochromatic internal gravity wave in an extended two dimension periodic domain. The spatiotemporal evolution of a localized in space and time perturbation (a multipolar gaussian vorticity perturbation) evidences the formation of three different wavepackets. From their fourrier space characteristic, we show that each of these wave packets corresponds to a different branch of triadic instability. Two of the wavepacket are small scale and have a small group velocity compared to the fluid while the third wave packet is large scale and has a much larger group velocity compared to the fluid. Using the triadic theory with finite detuning [4] we derive the group velocity at the maximum growthrate of the three different branches of triadic instability and find good agreement with the velocity of the three wave paquet maxima in the impulse response.

Analyzing the impulse response energy not versus space but along rays i.e. at x/t and z/t constant, we compute the absolute growth rate along all possible rays and show that our conjecture seems valid.

In the lee reference frame the large scale mode corresponding to the large scale triadic instability has a positive absolute growth rate and therefore the lee wave is absolutely unstable toward the large scale mode whereas in the tidal reference frame the small scale mode corresponding to the small scale triadic instability has a positive absolute growth rate and therefore the tidal wave is absolutely unstable toward the small scale mode.

References

[1] Phillips, O.M.: The dynamic of the upper ocean, 2nd edition, Cambridge University Press, 1967.

[2] Bourget, B. and Dauxois, T. and Joubaud, S. and Odier, P.: Experimental study of parametric subharmonic instability for internal plane waves, J. Fluid Mech. 2013.

[3] Akervik, E and Brandt, L and Henningson, D S and Hœpffner, J and Marxen, O and Schlatter, P: Steady solutions of the Navier-Stokes equations by selective frequency damping, Physics of Fluids 2006.

[4] McEwan, A.D. and Plumb, R.A.: Off-resonant amplification of finite internal wave packets, Dynamics of atmospheres and oceans 1977.

STRUCTURE OF THE AIRFLOW ABOVE SURFACE GRAVITY WAVES

Marc P Buckley*[1] and Fabrice Veron[2]

[1]*Institute of Coastal Research, Helmholtz Zentrum Geesthacht, Germany*
[2]*College of Earth, Ocean, & Environment, University of Delaware, Delaware, USA*

Summary The exchanges of momentum and scalars between the atmosphere and the oceans are influenced by the small-scale dynamics at the wavy air-sea interface. We present 2D PIV measurements of the kinematics in the airflow as low as 100 μm above the water surface for different wind-wave conditions (wave ages C_p/u_* between 1.4 and 66.7). Laboratory data were obtained at University of Delaware's (42-m long) wind-wave-current facility, using a multi-camera multi-laser setup that combines PIV with laser induced fluorescence. Field PIV measurements are also reported. We observe coherent turbulent structures in the airflow, including ejections of low velocity fluid away from the surface and downward sweeps of higher velocity fluid. Wave-phase-resolved quadrant analysis suggests that these events are modulated by the waves. Airflow separation occurs past young wave crests ($C_p/u_* < 3.7$), producing intense phase-locked turbulence. When C_p/u_* = 6.5, the mean wave-coherent airflow is qualitatively consistent with linear critical layer theory.

INTRODUCTION

Small-scale physics at the wavy air-sea interface strongly impact the coupled oceanic and atmospheric boundary layers, and have received increased interest in recent years [4, 5]. The fluxes of momentum, energy, heat, and mass depend upon a number of wind-wave parameters, including wave slope and wave age [4]. Wave age, generally defined as C_p/u_*, or C_p/U_{10}, where C_p, u_*, an U_{10} are respectively the peak wave velocity, air friction velocity, and 10-m wind speed, controls wind-wave coupling mechanisms [1, 3, 2] and air-sea momentum fluxes as a whole [4]. Recent fixed probe measurements at heights of $O(10)$ m above the ocean surface have confirmed the wave age dependence of wind-wave growth/attenuation, and shown evidence of a critical layer mechanism for wind-wave momentum fluxes [3]. In this study, we present direct measurements of the fine two-dimensional structure of the airflow, within the first 10 cm above the wavy water surface, and up to 100 μm from the air-water interface, for a wide range of wave ages ($1.4 < C_p/u_* < 66.7$). We are able to identify instantaneous viscous and turbulent characteristics of the airflow within the wave boundary layer, and, using phase-averaging and quadrant analysis techniques, understand how the waves influence the mean structure of the air-water momentum flux.

RESULTS

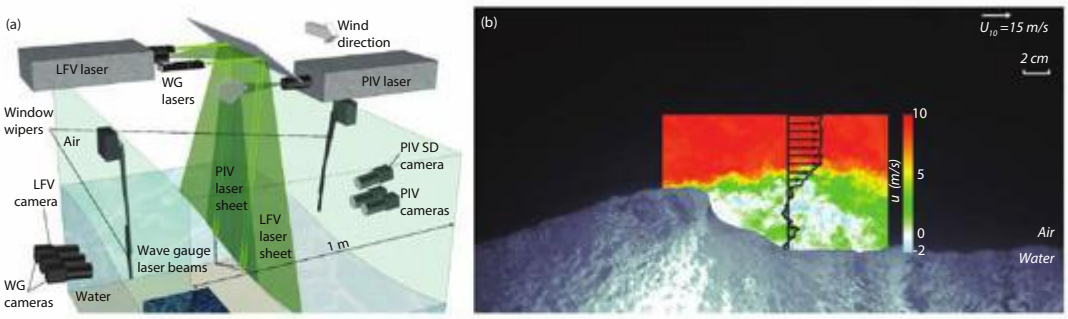

Figure 1: (a) Sketch of the wind/wave imaging system, positioned at a fetch of 22.7 m. Velocities in the airflow are measured by PIV, and the air-water interface is detected using laser-induced fluorescence (LIF). LIF is used for 3 types of measurements: large field of view images of the water surface for wave phase detection (LFV), PIV field of view images for surface detection on PIV images (PIV SD), and single point wave gauge data (WG).(b) Example of instantaneous horizontal velocity field in the air, obtained by PIV, above a wind-generated wave.

We present experimental results obtained in the large wind-wave-current tank at the Air-Sea Interaction Laboratory of University of Delaware. The tank is 42 m long, 1 m wide and 1.25 high. For this study, the water depth was 0.70 m, and the recirculating wind tunnel generated winds with 10-m speeds ranging from 0.9 to 16.6 m s^{-1}. In some cases, the waves were solely wind generated. In other cases, wind waves were combined with longer mechanically generated waves. The experimental setup, positioned at a fetch of 22.7 m, is sketched in figure 1(a). PIV and LIF techniques were combined, in

*Corresponding author. Email: mbuckley@udel.edu

order to simultaneously provide 2D airflow velocity fields (PIV), high resolution water surface profiles for the PIV images (PIV SD), large field of view water surface profiles (LFV), and single point wave gauge time series (WG). Data were acquired for 17 different wind-wave conditions, yielding thousands of airflow-velocity/wave-profile snapshots, such as the one plotted in figure 1(b), where we show an instantaneous 2D PIV velocity field above a young wind-generated wave (U_{10} = 15 m s^{-1}, C_p/U_{10} = 1.6). Airflow separation takes place past the crest of this steep wave, where important sheltering occurs, as suggested by the dramatic drop in airflow velocities downwind of the crest.

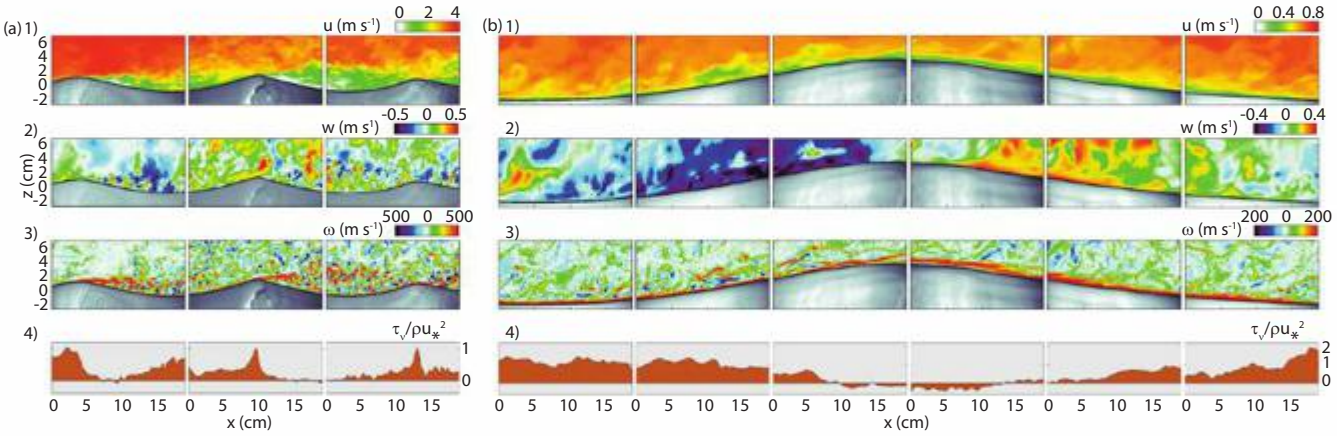

Figure 2: Instantaneous 2D velocity (u (m s^{-1}) and w (m s^{-1})) and vorticity (ω (s^{-1})) fields, and normalized along-surface viscous stress ($\tau_\nu/(\rho u_*^2)$), above segments of waves for 2 different experiments, with mean wave ages C_p/u_* = 3.7 (a), and 27.7 (b). Each row contains consecutive snapshots from one experiment.

Slightly older wind waves can also cause airflow separation, as depicted in figure 2a, where C_p/u_* = 3.7. We show the horizontal (panel 1) and vertical (2) components of the velocity field above the waves, the vorticity (3), and the along-surface viscous stress (4). Quadrant analysis and phase averaging of turbulent quantities (obtained by triple decomposition) show that the systematic drop in viscous stress past wave crests (panel a4), combined with the detachment of high vorticity layers past wave crests (see panel a3), leads, on average, to an enhancement of turbulent stresses downwind of crests, and important sheltering and boundary layer thickening effects on the phase-averaged airflow. These phase-locked mechanisms cause important fluxes of viscous, turbulent and wave-coherent momentum into the wave field. Older swells on the other hand (see figure 2a, where C_p/u_* = 27.7), show a very different airflow regime, whereby the vertical motions in the air (panel b2) are forced by the underwater orbital motions. In this case, ejections of high vorticity layers take place upwind of the crest, and the surface stress drops at the crest, which suggests that the waves are being attenuated by the wind.

CONCLUSIONS

Using a novel complex experimental system, we were able to measure the detailed two-dimensional structure of the airflow above wind-forced surface gravity waves, within the logarithmic, buffer and viscous layers of the airflow. Coherent turbulent structures in the airflow are organized by the waves, leading to phase-locked distributions of turbulence and momentum in the airflow. We observe 3 distinct regimes in the instantaneous and mean (wave-coherent) airflow properties, dependent upon wave age: Very young waves ($C_p/u_* < 4$) experience a large sheltering effect (generally accompanied by flow separation); over older wind waves (C_p/u_* = 6.5) a critical layer appears, below which the airflow is directly coupled with the underwater orbitals; finally old swells ($C_p/u_* > 27.7$) cause a reversed, upwind sheltering effect.

References

[1] Belcher, S. E. and Hunt, J. C. R. (1998). Turbulent flow over hills and waves. *Annu. Rev. Fluid Mech.*, 30:507–538.

[2] Buckley, M. P. and Veron, F. (submitted). Structure of the airflow above surface waves. *J. Phys. Oceanogr.*

[3] Grare, L., Lenain, L., and Melville, W. K. (2013). Wave-coherent airflow and critical layers over ocean waves. *J. Phys. Oceanogr.*, 43(10):2156–2172.

[4] Sullivan, P. P. and McWilliams, J. C. (2010). Dynamics of winds and currents coupled to surface waves. *Annu. Rev. Fluid Mech.*, 42:19–42.

[5] Veron, F. (2015). Ocean spray. *Annu. Rev. Fluid Mech.*, 47:507–538.

AIR ENTRAINMENT AND BUBBLE STATISTICS IN THREE-DIMENSIONAL BREAKING WAVES

Luc Deike*[1], W. Kendall Melville[1], and Stéphane Popinet[2]
[1]*Scripps Institution of Oceanography, University of California San Diego, La Jolla, California*
[2]*Sorbonne Universités, UPMC Univ Paris 06, CNRS, UMR 7190 Institut Jean Le Rond d'Alembert, F-75005 Paris, France.*

Summary We investigate air entrainment and bubble statistics in three-dimensional breaking waves through novel direct numerical simulations of the two-phase air-water flow. The dissipation due to breaking is found to be in good agreement with previous experimental observations and inertial-scaling arguments. For radii r larger than the Hinze scale, the time-averaged bubble size distribution is consistent with a $\bar{N}(r) \propto r^{-10/3}$ scaling, as observed experimentally. Moreover, we find that the time dependent and time averaged bubble size distribution scale linearly, respectively, with the time dependent and time averaged dissipation rate due to the breaking event. Based on these numerical results, existing laboratory data, earlier models, and the balance between mechanical dissipation and work done against buoyancy forces, we propose a phenomenological turbulent bubble break-up model, that describes both the bubble size distribution and the total volume of entrained air, as a function of the external wave parameters.

CONTEXT

Surface wave breaking plays an important role in the coupling between the atmosphere and the ocean from local weather to global-climate scales [1]. Wave breaking limits the height of surface waves, transfers momentum from waves to currents and significantly enhances the transfer of heat, moisture, marine aerosols and gases between the atmosphere and the ocean. Approximately 30% of the CO2 released into the atmosphere is taken up by the ocean, much from the entrainment and dissolution of bubbles by breaking and the associated mixing. Moreover, large bubbles entrained by breaking rise back to the surface and collapse, ejecting aerosols, which are transported into the atmosphere and ultimately evaporate leaving water vapour and salt crystals that affect the radiative balance of the atmosphere and form cloud condensation nuclei. Therefore, improvements in our understanding of the coupled ocean-atmosphere system and climate requires a detailed understanding of the physics of air entrainment and subsequent bubble generation. Due to the complex nature of the breaking process, a coupled two-phase turbulent flow, an understanding of the dynamical and statistical properties of the generated bubbles is still elusive.

RESULTS

We present novel Direct Numerical Simulations (DNS) of breaking waves by solving the three-dimensional two-phase air-water Navier-Stokes equations, using the open source solver Gerris [2]. These DNS resolve accurately the relevant length scales for the bubble formation problem: the capillary length and the Hinze scale (the scale at which surface tension prevents bubble break-up due to turbulence). These simulations permit tracking in space and time of both fluids, therefore accessing the bubble and droplets size distributions, together with the local turbulent properties of the flow.

The dissipation due to wave breaking is found to be in very good agreement with previous experimental observations, inertial-scaling arguments and with our previous two-dimensional DNS [3].

The air-entrainment properties and bubble-size statistics are investigated for various initial characteristic wave slopes. An example of a plunging breaker is shown in Figure 1. We observe air entrainment through different mechanisms: the entrapment of an air pocket when the jet reconnects with the water, entraining a large cavity and large bubbles; entrainment around the jet impact site entraining smaller bubbles; entrapment by the subsequent splash events, and finally, entrainment by the turbulent breakdown of the forward face of the wave. Entrainment of air also occurs when the jet impacts the surface, during the subsequent splashing, and when high velocity droplets fall back into the water.

The time-averaged bubble size distribution for radii larger than the Hinze scale (the bubble radius for which surface tension prevents break-up by turbulence, typically $r \sim 1$mm) is found to scale initially as $\bar{N}(r) \propto r^{-10/3}$, as observed experimentally [4], and in agreement with a turbulent break-up scaling argument [5]. Moreover, we find that the time-dependent bubble size distribution $N(r,t)$ is linearly dependent on $\epsilon(t)$, the time dependent turbulent dissipation rate, and that the time-averaged bubble size distribution $\bar{N}(r)$ scales with $\epsilon_l = \rho A \bar{\epsilon}(t)$, the wave dissipation rate per unit length of breaking crest, with $A = \pi h^2/4$, the area of the initial air pocket entrained by the breaking wave, and h the height at breaking. We propose an extension of the existing turbulent break-up model [5], constraining the entrained volume of air to be proportional to the dissipation rate.

*Corresponding author. Email: ldeike@ucsd.edu

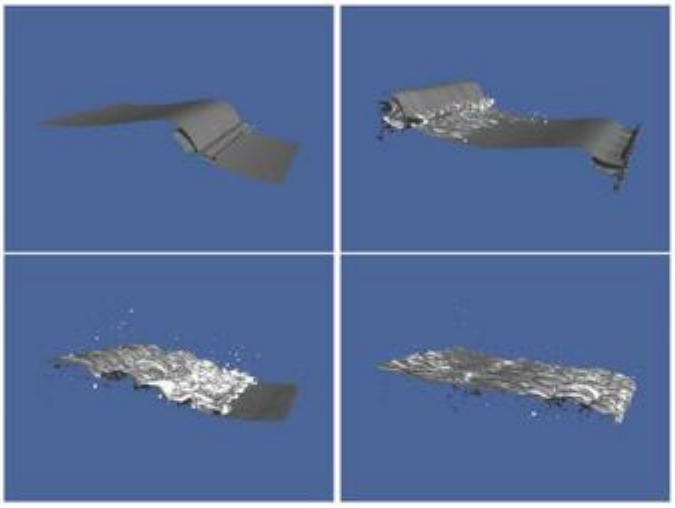

Figure 1: Interface of a breaking wave obtained by three-dimensional direct numerical simulations of the two-phase Navier Stokes equations, using the solver Gerris, showing the impact and entrainment of the initial air pocket (top left); splashing and fragmentation of the air pocket (top right); large dense bubble plume with numerous bubbles of various sizes in the water, together with droplets in the air.

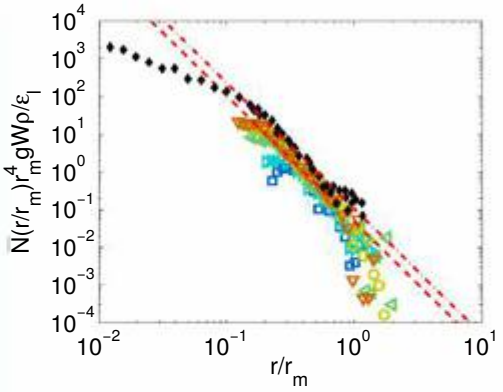

Figure 2: Rescaled bubble size distribution according to our theoretical model (Eq. 2), as a function of the rescaled radius r/r_m. Color symbols are DNS results for various initial slopes, black diamond are lab data from [4]. Dashed line shows the theoretical model, $B(r/r_m)^{-10/3}$, with $B = 0.05$ and dot-dashed line is $B(r/r_m)^{-10/3}$, with $B = 0.11$, which gives an estimation of the constant B. For $0.1 < r/r_m < 1$, our model, based on the bubble cascade idea, is compatible with the lab and DNS data.

This extended model describes the time evolution of the bubble cloud during the active breaking stage in that it relates the bubble size distribution to the instantaneous turbulent dissipation rate. In the same spirit, it describes the time-averaged bubble size distribution for one breaking event. In the end, for radii larger than the Hinze scale, our model describes the bubble size distribution by

$$N(r,t) = B\frac{3}{4\pi}\frac{\epsilon(t)}{Wg}r_m^{-2/3}r^{-10/3}V_0, \tag{1}$$

where r_m is the maximum bubble radius, $V_0 = AL_c$ the initial volume of air entrained with L_c the length of breaking crest, W is a weighted vertical velocity of the bubble plume and B a dimensionless constant. The time-averaged bubble size distribution is then given by

$$\bar{}(r) = B\frac{3}{4\pi}\frac{\epsilon_l L_c}{Wg\rho}r^{-10/3}r_m^{-2/3}. \tag{2}$$

Within the scatter of the data, the model is fully consistent with the DNS and the available experimental data, as shown in Fig. 2. It leads to an estimation of the constant B, which says that between 5 to 11% of the energy lost by the breaking event is due to entrainment of air. From the bubble size distribution, the total volume of air entrained can be physically scaled to the energy dissipated due to breaking and to the characteristic wave slope at breaking, and the averaged total volume of entrained air, $\bar{}$, is, $\bar{} = B(3/2)(\epsilon_l L_c/Wg\rho)$, which leads to a relationship to the slope, S, of $\bar{} \propto S^{5/2}$. Again, a reasonable agreement between the lab data, the DNS data and the model is observed.

This numerical modeling study of entrainment by breaking waves has led to a formulation of the amount of air entrained as a function of the external wave parameters. We foresee the possibility of using these results, along with field measurements of breaking to improve the models of air entrainment, and ultimately air-sea gas transfer. The work described in this abstract is in review in the Journal of Fluid Mechanics [6].

References

[1] Melville, W. K. The role of surface wave breaking in air-sea interaction. *Annu. Rev. Fluid Mech.* **28**, 279–321, 1996.

[2] Popinet, S. An accurate adaptative solver for surface-tension-driven interfacial flows. *Journal of Computational Physics* **228**, 5838–5866, 2009.

[3] Deike, L., Popinet, S., Melville, W.K.: Capillary effects on wave breaking. *J. Fluid Mech.* **769**, 541–569, 2015.

[4] Deane, G.B., Stokes, M.D.: Scale dependance of bubble creation mechanisms in breaking waves. *Nature* **418**, 839–844, 2002.

[5] Garrett, C., Li, M., Farmer, D.: The connection between bubble size spectra and energy dissipation rates in the upper ocean. *J. Phys. Oceanogr.* **30** (9), 2163–2171, 2000.

[6] Deike, L., Melville, W., Popinet, S.: Air entrainment and bubble statistics in breaking waves. *J. Fluid Mech.*, In Review, 2016.

A KINEMATIC CRITERION FOR THE BREAKING OF SHOALING WAVES

Uri Itay[1 a)], Dan Liberzon[1]
[1]*Department of Civil and Environmental Engineering, Technion- Israel Institute of Technology, Haifa, Israel*

Summary An experimental study was conducted with the aim of validating the kinematic criterion introduced for breaking of shoaling waves, based on approach by Shemer and Liberzon (2014) [2]. Special attention was dedicated to the relation between the instantaneous horizontal water velocity *U* and the instantaneous propagation speed of the crest on a verge of breaking. It was found that the inception of a breaker occurs when the monotonically increasing water particle velocity on the crest exceeds that of the slowing steep crest. Additionally, an objective method of breaking detection was developed utilizing the Phase-Time Method [1]. These results' main expected contributions are the formation of an applicable criterion, accompanied by wave breaking detection method independent of human decision. Incorporation of these into existing waves prediction models will contribute significantly to marine projects efficiency and eventually reduce design, construction and operational costs.

Introduction

The energy balance in the ocean is maintained partially due to the mechanism of waves breaking. Part of the energy being transferred throughout the ocean is accumulated in steepening waves to the point of breaking, resulting in energy dissipation and redistribution. The complete understanding of the mechanism of waves' breaking has numerous applications in various scientific and engineering concerns. Besides directly affecting the energy balance, breaking process involves production of sea spray and influences the boundary layer of the wind flow through the coupled wind-waves system close to water surface, hence directly governing wind waves' growth/decay rates. Near the shore, breaking is a part of sediment transport and coastline formation, therefore being of high significance in engineering considerations. A structure that is present at a site of breaking should be planned to absorb the impact of breaking. An engineering project, such as a harbor, that relies on specific near shore characteristics, such as water depth and coastline, should consider wave breaking and its effects on local features.

Hypothesis

The most common rule of thumb for the inception of a breaker relates to the wave's steepness, meaning its geometric characteristics, but the determination of such in actual breaking wave is nontrivial. First, the wave profile close to breaking is highly irregular, which introduces ambiguity in the definition of local wave's parameters. Second, breaking waves are highly unsteady and they deform rapidly. Even with accepted definitions, the timing for the determination of the wave parameters by a direct spatial measurement of the surface profile is problematic. Through the last decades, progress has been made in numerous numerical and experimental studies of the topic, and various geometric, dynamic and kinematic criteria for waves breaking has been suggested and examined. Nevertheless, an applicable universal method for determination of the conditions required for breaking occurrence in the open sea is not yet available.

Recently an applicable and potentially universal kinematic criterion was suggested [2]. Kinematic breaking criterion often involves the horizontal velocity on the crest *U*, while the phase or group speed (*c*) is taken to be constant along the examined wave, then wave breaking occurs when *U* exceeds *c*. However, application of such criterion should address the asymmetry of a nonlinear wave, hence the kinematic criterion for wave breaking should be applied to the relation between local instantaneous *U* and the instantaneous propagation speed of a steep crest on a verge of breaking. Such kinematic criterion addresses the high non-linearity of the near-breaking wave and therefore is a promising candidate to be universally valid for all types of breakers and breaking conditions (i.e. deep water waves groups, shoaling, and propagation over barriers, etc.).

Methods

A new kinematic criterion was recently suggested and tested for deep-water non-linear waves breakers [2], based on accurate measurements of Lagrangian water surface velocities at the wave's crest. Implementing similar methods, we have examined the feasibility of this kinematic criterion for the breaking of shoaling waves by staging measurements in a large wave tank. In order to simulate the process of shoaling, an artificial shore with changeable inclination angle was built and installed in the flume. Important parameters of mechanically generated waves, shoaling on the artificial beach, were obtained using a combination of flow visualization techniques (PTV) and traditional wave gauges. Comparing water surface velocity on the wave's crest with the instantaneous crest propagation speed up to and at the inception of a breaker allowed validating the kinematic criterion.

The experiments were performed in a large, 30 m long and 2.5 m wide, wave tank, holding water at depth of up to 1.25 m. An artificial, 6 m long shore, was built and installed at 15 m fetch, in order to allow mechanically generated waves to naturally shoal and break. Shore's frame allowed setting a desired inclination angle in the range between 2 and 20 degrees. To collect the experimental data acquiring both the velocities of the water parcels at waves' crests and the local near and breaking crest shapes a combination of several measuring instruments was used. Two fast 4 MPix resolution cameras were used. One camera was filming the motion of small buoyant particles on the water surface, following the motion of water parcels. Lagrangian velocity and acceleration values on the water surface were then obtained from these records by PTV. Simultaneously, the second camera filmed the motion of the wave profile, being pointed toward tank's wall.

[a)] Corresponding author. Email: **uriitay@campus.technion.ac.il**

Results

In the following images a record of a representative breaking wave is presented.

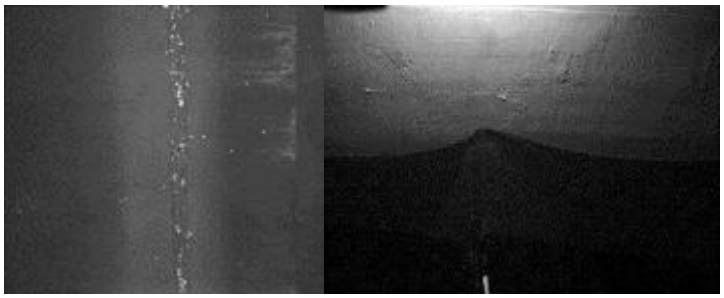

Figure 1- Images from both high speed cameras of a wave on the verge of breaking. Left image: particles floating on water surface, right image: instantaneous wave profile

Instantaneous fluctuations of water surface of the approaching and then shoaling waves' were recorded by several consecutive resistance type wave gauges, providing an independent measurement of various important waves' parameters such as height, steepness, and phase and group velocities. Besides the confirmation of waves' parameters along the flume, data acquired from the wave gauges were used to develop an objective method for breaking detection, based on the local frequency variations in the highly nonlinear wave. A PTM (Phase-Time Method) method of data processing, based on Hilbert transform [1], was implemented here to detect occurances of breakers. Deriving an expression for the instantaneous/local change in phase referred to as the local frequency, and examination of breaking waves' data allowed determining a specific pattern in the local frequency fluctuations associated with the appearance of a breaker. A linear pre-breaking part, and an exponential post-breaking part was recognized (Figs. 2 and 3), and an automatic algorithm for detection of breaking waves was developed.

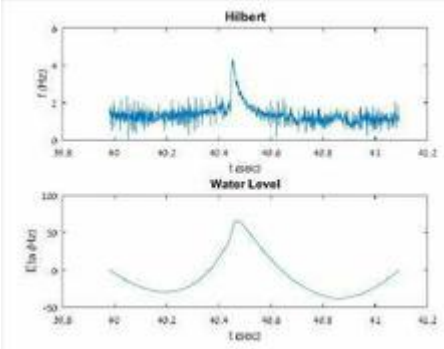

Figure 2- Hilbert frequency variation with relevant water level of breaking site

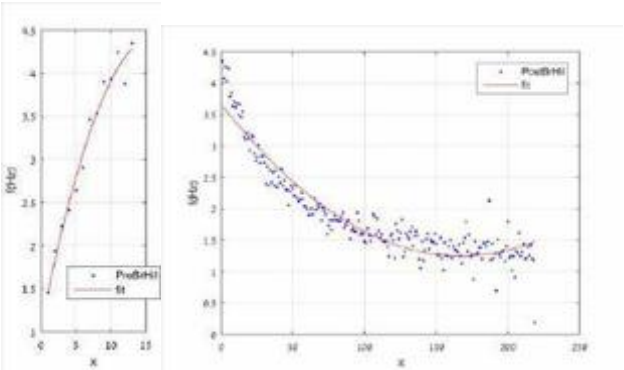

Figure 3- typical exponential fits for Hilbert frequency before and after wave breaking

References

[1] C.-A. Zimmermann and R. Seymour, “Detection of breaking in a deep water wave record,” *J. Waterw. port, coastal, Ocean Eng.*, vol. 128, no. 2, pp. 72–78, 2002.

[2] L. Shemer and D. Liberzon, “Lagrangian kinematics of steep waves up to the inception of a spilling breaker,” Phys. Fluids, vol. 26, no. May, 2014.

OPTIMAL DISTRIBUTION OF RIVERINE TURBINES IN A LINEAR ARRAY WITH SYSTEMATIC FLOW MANIPULATION

Niall Mangan[1] and Shreyas Mandre *[2]

[1]*Department of Applied Mathematics, University of Washington, Seattle, Washington, USA*
[2]*School of Engineering, Brown University, Providence, Rhode Island, USA*

Summary Hydrokinetic turbine arrays must be optimized not only to extract the maximum power from the fluid flow, but also to reduce navigational and environmental impacts. We recently showed that an array with minimal footprint, oriented in-line with the river flow, could extract an order of magnitude higher power by deflecting the flow through the array at angle α. Here we derive the optimal distribution of turbines along such an array. For small α, corresponding to weak deflection, we find the turbines should ideally be distributed uniformly between recirculation zones at the edge of the array. The size of the recirculation zones depends on the strength of deflection. For α above $\approx 45^\circ$, the distribution deviates from uniform, with the downstream turbines generating almost twice the power per unit length compared to those upstream.

OVERCOMING PRACTICAL LIMITATIONS ON ARRAY PLACEMENT THROUGH FLOW MANIPULATION

Practical considerations often constrain the placement of hydrokinetic turbines in an array away from the location where they could collectively extract maximum power. The ideal configuration of a tidal or riverine turbine array is in the form of a fence that spans the width and depth of the channel at its narrowest. However, navigation and environmental considerations prohibit construction of such arrays (see ref. [1] and references within). Any alternative array arrangements, besides the fence, suffer from a severe reduction in power conversion efficiency because placing turbines in the wakes of other turbines deteriorates their performance. We re-frame the problem from organizing the turbines in a configuration with maximum power to redirecting the flow to a the array, using deflectors within the array. Ultimately we would like to understand how to optimize turbine and deflector placement in the array to maximize power density.

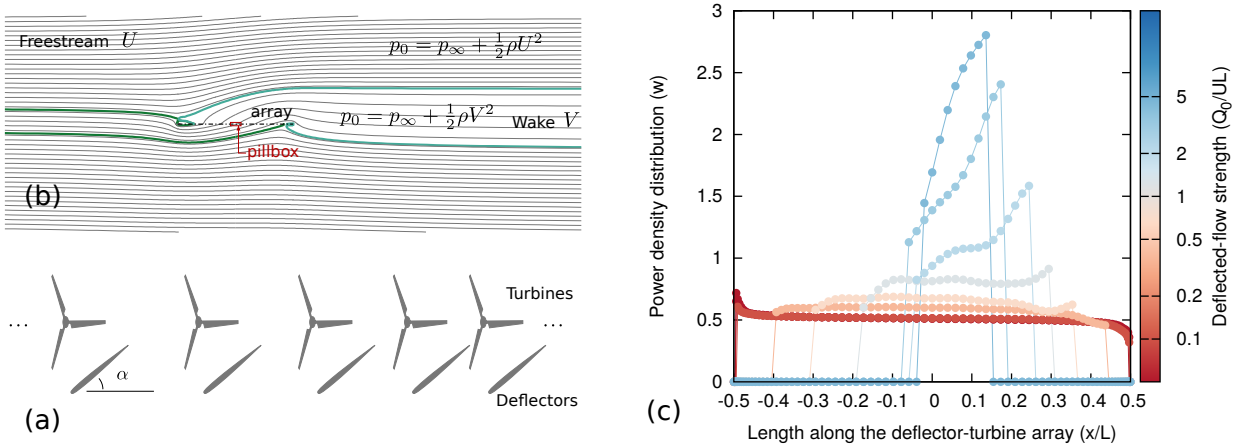

Figure 1: (a) Arrangement of hydrokinetic turbines and deflector plates in a linear array aligned with the freestream. The spacing between the turbines is non-uniform to maximize the extracted power. (b) The flow field resulting from optimal operation of a deflector-turbine array in the continuum limit for the case $\alpha = 63^\circ$. Light curves show streamlines, and the bold curves show the streamtube intercepted by the array. An extreme value of α is chosen for demonstration of the important features of the flow, namely the recirculation regions near the ends of the array. Also shown in red is a sample pillbox control volume for energy balance. (c) The profiles of the power coefficient per unit length w along the array for the optimal flow reduction factor as a function of the deflected-flow strength. The profiles are color coded with the deflected-flow strength Q_0/UL ranging from 0.02 to 20 depending on α.

Consider turbines placed along the centerline of a "river," such that the length L of the array is parallel to the freestream. Without flow redirection, there is negligible power incident on the turbines; the turbines are augmented with deflectors to redirect the flow. In a recent paper [2], we developed an inviscid fluid dynamics framework for analyzing the energy conversion by an idealized version of such a deflector-turbine array. Here we present results on the distribution of installed capacity in this array for a given flow deflection.

*Corresponding author. Email: shreyas_mandre@brown.edu

Background: Improving limits on array power using deflection

The flow around the array is described in terms of bound and free vorticity. The bound vorticity is chosen such that the fluid velocity $\boldsymbol{u}$ makes a constant angle α with the freestream at the array. The array also sheds free vorticity along the two extreme streamlines, in the form of a vortex sheet. The magnitude of this shed vortex sheet is chosen such that, for a given α, the power extracted by the array is maximized. The flow is solved by determining the shape of the vortex sheets, which according to inviscid fluid dynamics, coincides with streamlines.

Using this framework we determine an upper bound on the array power. We predict that we could increase the power from $1.2 \times 10^{-2}\rho U^3 L$ for an array relying on natural turbulent fluctuations for recovering the wake deficit to $0.3\rho U^3 L$ using state of the art deflectors, achieving $\alpha \approx 40^\circ$.

TURBINE DENSITY DISTRIBUTION WITHIN ARRAY TO MAXIMIZE POWER EXTRACTION

Next we wish to gain insight about how to arrange turbines in the array to realize this optimum array power conversion. To determine the arrangement of turbines, we calculate the power conversion per unit length as a function of the location along the array and the angle of deflected flow α. Due to the confounding factors of non-local influence of deflectors and the resistance offered to the flow by the turbines extracting power, the optimal profile of the power per unit length (and therefore the distribution of turbines) is non-obvious.

Calculating power density distribution from flow field

The fluid mechanical energy flux is $\boldsymbol{e} = \boldsymbol{u}p_0$, where p_0 is the stagnation pressure $p_\infty + \frac{1}{2}\rho|\boldsymbol{u}|^2$. The mechanical energy is conserved, and therefore it is divergence free, everywhere except on the array. On the array, the flux jumps discontinuously, by an amount equal to the power extracted by the array. Furthermore, the Bernoulli principle for inviscid flow imply that the stagnation pressure is one of two values; it is $p_\infty + \frac{1}{2}\rho U^2$ outside the wake, and $p_\infty + \frac{1}{2}\rho V^2$ within the wake. Therefore, the power converted in a small pillbox (see Figure 1 (a)) of length ΔL along the array is $W_{\text{array}} = \frac{1}{2}\rho(U^2 \circ V^2)\boldsymbol{u} \cdot \boldsymbol{n}\, \Delta L$.

Since the jump in the stagnation pressure is uniform across the array, the variation of the power density with location arises from the profile of normal component of the fluid velocity. We obtain the normal component from our calculations as described in [2], and determine the profile of power density.

We use the deflected flow rate Q_0, which occurs in the absence of any energy extraction, to non-dimensionalize the power density. The dimensionless version we define is

$$w = \frac{W_{\text{array}}}{\frac{1}{2L}\rho U^2 Q_0}. \tag{1}$$

CONCLUSIONS: NON-UNIFORM TURBINE DENSITY ENABLES OPTIMAL POWER EXTRACTION

The calculated power density distribution, w, is plotted in Figure 1, and shows the optimal distribution of turbines for deflected-flow strength ranging from weak to strong. For weaker deflection, from $0^\circ < \alpha < 45^\circ$ the normal velocity component of the fluid across the array is approximately uniform, and therefore the corresponding density of turbines is also uniform. However, with increasing deflected-flow strength, $\alpha > 45^\circ$ the normal component of the fluid velocity becomes larger at the far end of the array. The range along the deflector-turbine array where power density is significant (non-zero), also decreases dramatically at the highest deflection strengths. This decrease in array efficiency, due to increasing recirculation regions, is outweighed by the massive gain in increased flow strength.

The power density distribution for the highest deflection flow strength indicates an un-intuitive strategy for maximizing power conversion in this type of array. If such deflection strengths were attainable turbines should be placed in only 1/5th of the total array length at center of the array, and increase in density toward the back of the array. We estimate current airfoil technology can achieve angles of $\alpha \approx 40^\circ$ without flow separation [2], which corresponds to a deflected flow strength of 1 (grey data in Figure 1 c). Therefore, for existing deflector technology, the turbines should be placed in the inner 2/5ths of the array with slightly non-uniform optimal turbine distribution. To maintain the deflected flow strength, the deflectors will also need to be optimized across the array, which is a topic of future research.

References

[1] Vennell R., Funke S.W., Draper S. Stevens C., Divett T.: Designing large arrays of tidal turbines: A synthesis and review. Renewable and Sustainable Energy Reviews, 51:1461-1476, 2015.

[2] Mandre S., Mangan N. M.: Framework and limits on power density in wind and hydrokinetic device arrays using systematic flow manipulation. arXiv:1601.05462 [physics.flu-dyn], 2016.

WAVE MODULATION: THE GEOMETRY, KINEMATICS, AND DYNAMICS OF SURFACE-WAVE PACKETS

Nick Pizzo* and W.K. Melville

Scripps Institution of Oceanography, University of California, San Diego, La Jolla, California

Summary We derive a set of conserved quantities and moment evolution equations for the modified nonlinear Schrodinger equation (Dysthe 1979; MNLSE), with application to interpreting the geometry, kinematics, and dynamics of deep-water surface gravity wave packets. Our theory predicts modifications to the group velocity and explains the asymmetric leaning forward of the wave packet as focusing occurs.

The theory is examined numerically for dispersive focusing wave packets, and these results are compared to numerical simulations of the fully-nonlinear potential flow equations. It is found that the MNLSE models the bulk scale features of the focusing event, and that the numerical results are consistent with the theoretical predictions.

INTRODUCTION

This paper reports on a theoretical and numerical study of the properties of weakly nonlinear narrow-banded deep-water wave packets (i.e. compact wave groups). Weakly nonlinear Stokes waves are subject to the Benjamin-Feir instability (Benjamin & Feir 1967), so that the subsequent nonlinear evolution of the wave field is of considerable interest from both a mathematical and physical point of view.

Our model equation in this study is the spatial modified nonlinear Schrodinger equation (Dysthe 1979), subsequently derived by (Lo & Mei 1985), and given by

$$\frac{\partial A}{\partial \chi} + i\frac{\partial^2 A}{\partial \tau^2} + i|A|^2 A + \beta_0 |A|^2 \frac{\partial A}{\partial \tau} + i\alpha_0 A\mathcal{H}\left(|A|^2_\tau\right) = 0, \tag{1}$$

where $A = A(\epsilon^2\chi, \epsilon\tau)$ is a slowly varying complex valued function, related to the lowest order coefficient of the first mode of the velocity potential expansion, $\mathcal{H}$ is the Hilbert transform, $\chi = k_0 x$, $\tau = \omega_0(2k_0/\omega_0 x \circ\ t)$, $\beta_0 = 8\epsilon$, $\alpha_0 = \epsilon$ and $\epsilon = a_0 k_0$ is a small parameter for (a_0, ω_0, k_0) the characteristic amplitude, angular frequency and wavenumber, respectively.

Equation (1) governs weakly nonlinear narrow-banded surface gravity waves and has been shown (Lo & Mei 1985) to predict certain features of wave train evolution that are not apparent at lower order (i.e. for $\epsilon \downarrow 0$), including asymmetric wave envelope growth, a better prediction of the modulation instability growth rate (Dysthe 1979), asymmetric spectral growth, and the coupling of an Eulerian mean flow to the wave amplitude evolution. These asymmetries arise from the term in equation (1) with coefficient β_0, while the induced mean flow is related to the term with coefficient α_0.

RESULTS

By employing Whitham's method, we derive equation (1) from the Lagrangian for deep-water irrotational inviscid surface gravity waves, making the variational structure of the equation manifest. Through Noether's theorem, this allows us to deduce conserved quantities of the MNLSE, connected to the symmetries of the action.

The first of these conservation laws, associated with the phase-shift invariance of the action, is shown to be

$$\frac{\partial |A|^2}{\partial \chi} + \frac{\partial}{\partial \tau}\left(i\left(A^* A_\tau \circ\ A A^*_\tau\right) + \frac{\beta_0}{2}|A|^4\right) = 0. \tag{2}$$

Note, if $(A^* A_\tau \circ\ A A^*_\tau)$ is constant in τ, then equation (2) takes the form of the inviscid Burger's equation in the variable $|A|^2$. This explains the asymmetric leaning of the envelope, which is commonly observed in laboratory experiments.

An example of a focusing wave packet is shown in figure 1, where the forward leaning of the wave packet is evident. Here, dispersive focusing is used to induce wave packet focusing; that is, by generating longer waves before shorter waves, the packet converges . As the packet focuses, we see that the forward face of the wave group steepens. As this steepening occurs, dispersion begins to act more strongly, leading to a spreading out of the wave packet, arresting the self-steepening due to the nonlinear term in equation 2 (i.e. $\partial_\tau(\beta_0|A|^4/2)$).

*Corresponding author. Email: npizzo@ucsd.edu

Next, based on equation (2), we consider the evolution of the centroid of the energy density of a compact wave group. We define the centroid as $\mathcal{M} = \int_{-\infty}^{\infty} \tau |A|^2 \, d\tau / \int_{-\infty}^{\infty} |A|^2 \, d\tau$, which serves as an unambiguous marker of the packet location. Now, in the laboratory frame, the speed of the centroid, which we define as U, can be found via equation (2) to be

$$U = \frac{\omega_0}{2k_0} \left(1 \circ \frac{\epsilon}{2} \frac{d\mathcal{M}}{d\chi} \right)^{-1} = \frac{\omega_0}{2k_0} \left(1 \circ 2k_0^2 K \right)^{-1}, \tag{3}$$

where K is a measure of the concentration of the linear energy density, and is defined as $K = \int |B|^4 \, dt / \int |B|^2 \, dt$, where $B = a_0 A$. This equation says that changes in the speed of the centroid depend on the evolution of the distribution of linear energy density in the wave group, and in particular on the integral term $K = K(x)$. Recall, K is a measure of the focusing of the linear energy density, so we expect it to increase as the packet focuses. Hence, wave packets speed up as they focus.

To examine the applicability of this asymptotic result, the MNLSE and the fully nonlinear potential flow equations are integrated. The fully nonlinear equations are integrated using the scheme of Dold & Peregrine (1985: DP). Note, the initial conditions are the same as those considered in figure 1.

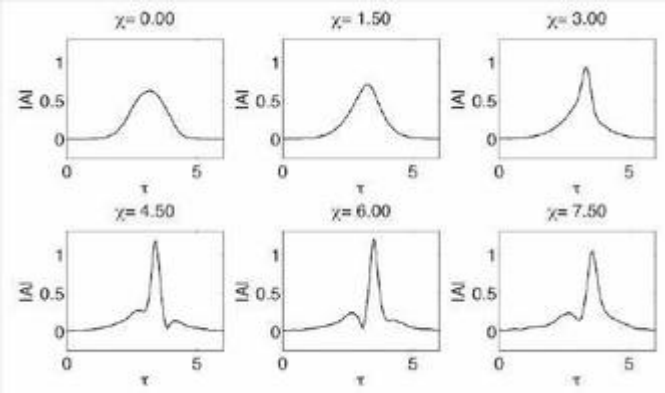

Figure 1: The evolution of the modulus of the wave envelope, $|A|$, in (χ, τ) coordinates. As the packet focuses, the envelope becomes asymmetric with the face at larger τ leaning forward.

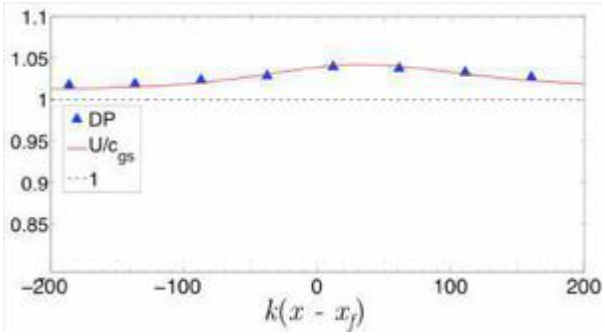

Figure 2: The evolution of the speed of the centroid of the potential flow theory (blue) and the MNLSE (red), normalized by the linear group velocity c_{gs}, versus downstream position, compared to theoretical model U, shown by the solid red line.

Figure 2 shows the normalized centroid velocity as predicted by the MNLSE, as well as the theory (equation 3). The prediction of the fully nonlinear model is shown by the blue triangles, while the linear prediction is shown by the black dashed line. There is good agreement between the predictions of the asymptotic model, i.e. the MNLSE, and the fully nonlinear potential flow equations. Both sets of equations predict that the packet accelerates as it focuses, with a magnitude that is around 4% larger than the linear prediction in the region of maximum focusing (which is denoted by x_f).

References

[1] Benjamin, T. B., and J. Feir (1967), The disintegration of wave trains on deep water part 1. Theory, J. Fluid Mech., 27 (03), 417430.

[2] Dysthe, K. B. (1979), Note on a modification to the nonlinear Schrodinger equation for application to deep water waves, Proc. Roy. Soc.of London. A., 369 (1736), 105-114.

[3] Lo, E., and C. C. Mei (1985), A numerical study of water-wave modulation based on a higher-order nonlinear Schrodinger equation, J. Fluid Mech., 150, 395-416.

[4] Dold, J., and D. Peregrine (1986), Water-wave modulation, Coast. Eng. Pro., 1(20).

ENERGY PROPAGATION AND GROUP SPEED FOR COMPLEX EXPONENTIAL WAVES

Andrew J. Rzeznik *[1], Lyubov G. Chumakova[2], Esteban G. Tabak[3], and Rodolfo R. Rosales[1]
[1]*Department of Mathematics, Massachusetts Institute of Technology, Cambridge, Massachusetts, USA*
[2]*School of Mathematics, University of Edinburgh, Edinburgh, Scotland, UK*
[3]*Courant Institute of Mathematical Sciences, New York University, New York City, New York, USA*

Summary In classical dispersive wave equations, the solution is specified by a superposition of plane waves of the form $\exp(i(\mathbf{k}\cdot\mathbf{x}-\omega t))$ (with $\mathbf{k}$ and ω real valued) along with a dispersion relation $G(\omega,\mathbf{k})=0$. However, in many problems one needs to consider solutions of the form $\exp(\mathbf{d}\cdot\mathbf{x}+st)$, where $\mathbf{d}$ and s are complex and correspondingly related by $G(is,-i\mathbf{d})=0$. In these cases the classical theory providing the speed and direction of the energy propagation no longer applies. In this paper we derive general energy propagation formulas for generic complex exponential wave solutions. We show that: parallel to the direction of the exponential spatial envelope, the energy propagation speed is $c_{e_\parallel}=-\mathrm{Re}(s)/\mathrm{Re}(d_\parallel)$, while in the orthogonal directions it is $c_{ei_\perp}=-\partial\mathrm{Im}(s)/\partial\mathrm{Im}(d_{i\perp})$. In the classical limit this is consistent with the standard group velocity.

BACKGROUND

Consider a linear, conservative, dispersive wave equation with classical dispersion relation $G(\omega,\mathbf{k})=0$. In many cases the need to consider more general complex exponential wave solutions arises. These generalizations occur often when the bulk medium is absorbing [1, 2], but can also be important for conservative media. These are solutions of the form $e^{\mathbf{d}\cdot\mathbf{x}+st}$, where s and $\mathbf{d}$ are complex valued and satisfy the generalized dispersion relation $G(is,\circ\, i\mathbf{d})=0$ — here G is the analytic extension of the classical dispersion relation. Examples of these type of solutions arise naturally in problems that include evanescent waves or absorbing boundaries [3], and through use of Laplace transforms.

THEORY

We present the derivation first for a one-dimensional problem, and then generalize it to the case of arbitrary dimension.

1D Group Velocity

In 1D the solutions of interest take the form e^{dx+st}, where d is a complex scalar and $G(is,\circ\, id)=0$. In the classical case, where $d=ik$ and $s=\circ\, i\omega$, the group velocity (and therefore the energy propagation speed) is given by $c_g=\circ\, G_k/G_\omega$ [4].

Now write d and s in terms of its real and imaginary parts, $d=m+ik$ and $s=\sigma\circ\, i\omega$ — where we use notation consistent with the classical theory for the imaginary parts. The energy for the wave can be written in the form

$$E=e^{2mx+2\sigma t}\Phi(x,t), \tag{1}$$

where Φ is an oscillatory function in x and t. This follows because, in general, the energy in a conservative linear field is quadratic in the field and its derivatives[4]. From this we see that the average velocity of the energy is given by

$$c_g=\circ\,\frac{\sigma}{m}=\circ\,\frac{\mathrm{Re}(s)}{\mathrm{Re}(d)}, \tag{2}$$

as long as $m\neq 0$. Next we note that $m=0$ with $\sigma\neq 0$ is not allowed for a conservative system, while $m=\sigma=0$ is the classical case given above. A simple calculation shows that (2) *yields the classical case in the limit* $m\to 0$. Note that, as should be expected, evanescent waves, $m\neq 0$ and $\sigma=0$, have zero velocity.

Multi-Dimensional Case

In multiple dimensions, where the waves have the form $e^{\mathbf{d}\cdot\mathbf{x}+st}$, we can always change coordinates so that the real part of the $\mathbf{d}$ vector is entirely in the first coordinate. Then the problem splits into calculating the group velocity in the envelope direction (first component) and the orthogonal directions. In the envelope direction the 1D result still applies. In the orthogonal directions (for a given σ and m) one can use either modulation theory or averaged Lagrangians [4], to show that a classical wave packet can be constructed, with velocity

$$c_{ei_\perp}=\frac{\circ\,\partial(\mathrm{Im}(s))}{\partial(\mathrm{Im}(d_{i\perp}))}=\frac{\partial\omega}{\partial k_{i\perp}}. \tag{3}$$

Where the real derivative is evaluated at complex values $\mathbf{d}, s$.

*Corresponding author. Email: rzeznik@mit.edu

APPLICATIONS

Evanescent Mountain Waves

As an interesting example, we investigate evanescent mountain waves, which are trapped modes of internal gravity waves created over obstacles [5, 6]. Consider a constant profile wind with velocity U in the horizontal direction x, and stratification N in the vertical direction z. Let the bottom boundary be a sinusoidal surface with wave number k_1 and small amplitude. The generated wave will have the form $\phi = Ae^{ik_1x+ik_2z-iUk_1t}$ where k_2 is given by the dispersion relation

$$k_2 = \pm k_1 \sqrt{\frac{N^2}{\omega^2} \circ\ 1} = \pm k_1 \sqrt{\frac{N^2}{U^2 k_1^2} \circ\ 1}. \tag{4}$$

When $Uk_1 > N$, k_2 is imaginary — since the solution must decay as $z \to \infty$, it must also be positive imaginary. We can now use the formula in (3) to calculate the group speed in the x direction. This yields

$$c_{gx} = U(1 \circ\ \frac{U^2k_1^2}{N^2}) \tag{5}$$

If $Uk_1/N > \sqrt{2}$ then $c_{gx} < \circ\, U$. Thus some trapped evanescent waves may travel upwind along the lower boundary.

Laplace Transform Solutions

In terms of Laplace transforms, the (general) solution to a linear wave equation has the form [7]

$$u(x,t) = \frac{1}{2\pi i} \int_\Gamma U(x,s)e^{st}ds \tag{6}$$

where $U(x,s)$ is the Laplace transform of u, and Γ is an appropriate contour in the complex plane. Here $U(x,s)$ can often be expressed as some integral over complex exponentials, resulting from solving the equation for U using Greens' functions. This results in u being expressed as a linear combination of waves of the form $e^{\kappa(s)x+st}$ where $\kappa(s) = d$ is given by some branch of the (complexified) dispersion relation. Which precise branch(es) should be used when solving for U, so that causality is not violated, can then be determined using the theory presented here.

CONCLUSIONS

The theory here gives a tool for determining the group velocity and direction of energy propagation for plane waves with complex-valued phase velocity and wave number. This is useful in itself for examining the energy propagation properties of non-standard waves, and also as a tool for performing more advanced mathematical operations like Laplace transforms on wave equations where energy propagation conditions matter. The results match up with intuition, and are shown to agree for simple cases with current theory, such as evanescent waves.

This material is based upon work supported by the National Science Foundation Graduate Research Fellowship under Grant No. 1122374, which funded A. Rzenzik. Any opinion, findings, and conclusions or recommendations expressed in this material are those of the authors and do not necessarily reflect the views of the National Science Foundation. This work was also partially supported by the NSF grant DMS-1318942, and by the Hertz Foundation.

References

[1] Gerasik V., Stastna M.:Complex group velocity and energy transport in absorbing media. Phys. Rev. E 81, 056602, 2010.
[2] Sonnenschein E., Rutkevich I., Censor D.: Wave packets, rays, and the role of real group velocity in absorbing media. Phys. Rev. E 57, 1005, 1998.
[3] Chumakova L.G., Rosales R.R., Tabak E.G.: Leaky Rigid Lid: New Dissipative Modes in the Troposphere. J. Atmos. Sci., 70, 31193127, 2013.
[4] Whitham G. B.: Linear and Nonlinear Waves. New York: Wiley, 1974.
[5] Holton J. R.: An Introduction to Dynamic Meteorology. New York: Academic Press, 1972.
[6] Durran, D.R.: Mountain Waves and Downslope Winds. In Atmospheric Processes over Complex Terrain. Meteorological Monographs, Vol 23, No. 45., 1990.
[7] Evans L. C.: Partial Differential Equations. Providence, R.I.: American Mathematical Society, 1998.

STATIONARY SOLITARY WAVES ABOVE BUMPS OR RAMPS IN TURBULENT OPEN CHANNEL FLOW

Wilhelm Schneider [a] & Markus Müllner
Institute of Fluid Mechanics and Heat Transfer, Technical University of Vienna, Vienna, Austria

Summary Steady two-dimensional turbulent free-surface flow in a channel is considered. The slope of the channel bottom is assumed to be small, and the bottom roughness is assumed to be constant. An unevenness of the bottom in the form of a bump or a ramp of large length, but very small height, is taken into account. Asymptotic expansions for large Reynolds numbers and Froude numbers close to the critical value 1, respectively, give a steady-state version of an extended Korteweg-deVries equation for the surface elevation. No turbulence modelling is required. In case of ramps, stationary solitary waves of the classical shape are obtained as particular solutions. For bumps, there are solutions that describe stationary solitary waves with a 'tail'.

INTRODUCTION

A simple momentum balance shows that stationary solitary waves cannot exist in two-dimensional steady turbulent open channel flow over a plane bottom of constant roughness. However, stationary solitary waves were predicted for a roughness that varies along the plane bottom [1], and the predictions were confirmed by measurements in a water tunnel [2]. In the present paper, it is investigated whether channel bottoms with bumps or ramps of small height may also give rise to stationary solitary waves.

GOVERNING EQUATIONS

The basic differential equations are the continuity and momentum equations, respectively, for the ensemble-averaged variables of steady two-dimensional flow. Flows that differ only slightly from fully developed flow are considered. For large Reynolds numbers the viscous wall layer is known to have universal properties [3]. Thus, it suffices to consider the turbulent bulk flow (defect layer), where the viscous stresses are negligible, whereas the Reynolds stresses are of essential importance. Non-dimensional variables are introduced, with the fully developed flow far upstream serving as the reference state. Thus, the averaged surface height in the fully developed flow is the reference length, while the volumetric mean velocity is chosen as the reference velocity. The near-critical flow conditions are characterized by a small parameter ε, which is defined by the relation

$$\mathrm{Fr} = 1 + \tfrac{3}{2}\varepsilon \quad (0 < \varepsilon \ll 1) \ , \tag{1}$$

where Fr is the Froude number. Cartesian coordinates X and Y are introduced. With the aim of considering long waves, the longitudinal coordinate X has been stretched with $3\sqrt{\varepsilon}$, while the lateral coordinate Y remains unstretched.

At the free surface, the conventional kinematic and dynamic boundary conditions are prescribed. Concerning the boundary conditions at the bottom, the shape of the bottom that exhibits a bump or a ramp is given as $Y = B(X)$. The tangential-flow condition is then applied at the bottom. Furthermore, matching of the defect layer and the viscous wall layer is accomplished by making use of the well-known logarithmic overlap law ("law of the wall") [3], modifying the procedure pursued in [1] as follows: The time-dependence is dropped, the roughness is taken as constant, and the matching conditions are applied for $Y \to B(X)$ instead of $Y \to 0$. This implies that the thickness of the viscous sublayer must be much smaller than the height of the bump/ramp, i.e. the Reynolds number in terms of the reference friction velocity, Re_τ, has to be sufficiently large to satisfy the condition $\varepsilon^{5/2}\mathrm{Re}_\tau \gg 1$.

ASYMPTOTIC EXPANSION FOR $\varepsilon \to 0$

It was observed in [1] that the analysis can be kept free of turbulence modelling if the slope of the (undisturbed, plane) bottom, α, is as small as ε^2. Furthermore, an analogous reasoning for the height of the bump or ramp leads to the condition that B ought to be of the order of $\varepsilon^{5/2}$ or, equivalently, $\alpha\varepsilon^{1/2}$. Thus, we introduce a bottom shape function $\psi(X)$ according to the relation

$$B = \alpha\varepsilon^{1/2}\psi(X) \ , \tag{2}$$

where $\psi(X) = \mathrm{O}(1)$ and satisfies the following conditions far upstream and far downstream, respectively:

$$\psi \to 0 \ \text{ as } \ X \to \pm\infty \ \text{ for a bump;} \tag{3a}$$

$$\psi \to 0 \ \text{ as } \ X \to -\infty \, , \ \psi' \to 0 \ \text{ as } \ X \to +\infty \ \text{ for a ramp.} \tag{3b}$$

The dependent variables are then expanded in terms of powers of ε. In particular, the non-dimensional, ensemble-averaged surface height, $\bar{}$, is expanded as follows:

$$\bar{}(X;\varepsilon) = 1 + \varepsilon H_1(X) + \varepsilon^2 H_2(X) + o(\varepsilon^2). \tag{4}$$

[a] Corresponding author. Email: wilhelm.schneider@tuwien.ac.at.

The expansion of the governing equations is performed following [1]. As the last step, a solvability condition for the second-order perturbation equations gives the following ordinary differential equation for the first-order surface elevation, $H_B(X)$:

$$H_B''' + (H_B - 1)H_B' = \beta(H_B - \psi') \ , \tag{5}$$

with $\beta = (1/3)\alpha\varepsilon^{-3/2}$. It can be shown that β is proportional to the square of the friction velocity, i.e. it characterizes dissipation. The limiting case $\beta = 0$ corresponds to inviscid flow, for which (5) reduces to the steady-state version of the Korteweg-deVries equation. For turbulent flow, however, $\beta \neq 0$, though it is quite small in cases of practical interest, cf. [2].

Eq.(5) is to be solved subject to the boundary conditions

$$H_B \to 0 \ \text{ as } \ X \to \pm\infty \ . \tag{6}$$

Integrating (5) from $-\infty$ to $+\infty$ and accounting for the boundary conditions (6), the following integral relation, representing the conservation of momentum, is obtained:

$$\int_{-\infty}^{+\infty}(H_B - \psi')\mathrm{d}X = 0 \ . \tag{7}$$

SOLUTIONS

For a ramp of the shape

$$\psi(X) = 6\,[1 + \tanh(X/2)] \tag{8}$$

an exact solution of (5) with boundary conditions (6) is

$$H_B = 3\,\mathrm{sech}^2(X/2) \ , \tag{9}$$

i.e. the classical solitary wave solution for inviscid flow. Since the right-hand side of (5) is identically zero in this particular case, the solution (9) has the remarkable property of being valid for any value of the dissipation parameter β.

In case of a bump, the boundary conditions (3a) apply, and it is obvious that the integral relation (7) cannot be satisfied with a solution resembling (9), i.e. a stationary solitary wave of the classical type. However, the integral relation can be satisfied for a stationary solitary wave with a tail. For small values of β, the negative surface elevation in the tail is of the order of β, while the length of the tail is as large as $1/\beta$. A simple example for a solitary wave with a tail is provided by a bump with triangular cross section, i.e. piecewise constant values of ψ', see Fig. 1. Note that the inclination angle of the flank of the bump is as small as ε^3. For inviscid flow, a bump with triangular cross section was considered in [4].

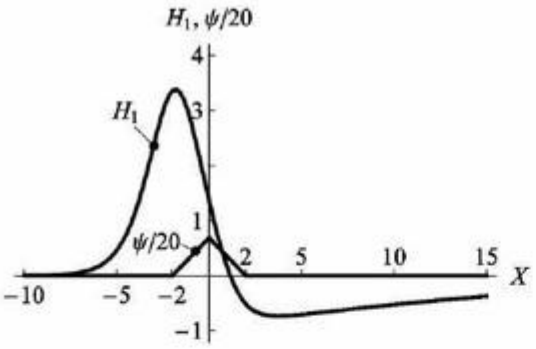

Fig. 1. A solitary wave with a tail above a symmetric triangular bump. The bump is in the region $-2 \le X \le +2$, while its maximum height is $B(0) = \alpha\varepsilon\ /\ \psi(0)$, with $\psi(0) = 13.8$. Numerical solution of (5) with boundary conditions (6), $\beta = 0.1$.

CONCLUSIONS

It has been shown that a very small unevenness in the channel bottom can produce much larger surface elevations in steady near-critical turbulent open channel flow. For a ramp of a particular shape, the shape of the surface elevation has been found to be that of the classical solitary wave of inviscid flow. In case of bumps, the solutions can be interpreted as stationary solitary waves with a tail. It will be of interest to compare the analytical results with numerical solutions of the full equations of motion with modelled Reynolds stresses, e.g. by applying the iteration method described in [5].

References

[1] Schneider W.: Solitary Waves in Turbulent Open-Channel Flow. J. Fluid Mech. **726**:137-159, 2013.

[2] Schneider W., Yasuda Y.: Stationary Solitary Waves in Turbulent Open-Channel Flow: Analysis and Experimental Verification. J. Hydr. Eng. **142**/1: 04015035, 2016.

[3] Schlichting H., Gersten K.: Boundary-Layer Theory. 8th Ed., Springer, Berlin-Heidelberg-New York 2000.

[4] Dias F., Vanden-Broeck J.-M.: Open channel flows with submerged obstructions. J. Fluid Mech. **206**:155-170, 1989.

[5] Schneider W., Jurisits R., Bae Y. S.: An asymptotic iteration method for the numerical analysis of near-critical free-surface flows. Int. J. Heat & Fluid Flow **31**: 1119-1124, 2010.

ANALYTICAL SOLUTION OF A SHOCK WAVE IN GAS SPHERE IN LAGRANGIAN COORDINATES

Valentin Kuropatenko[1,2] and Elena Shestakovskaya [*2]

[1] *Theoretical Department, Russian Federal Nuclear Center–Zababakhin All–Russia Research Institute of Technical Physics, Snezhinsk, Chelyabinsk region, Russian Federation*

[2] *Department of Computational Continuum Mechanics, South Ural State University (National Research University), Chelyabinsk, Russian Federation*

Summary An exact solution of the problem of a convergent shock wave and dynamic compression of the gas in a spherical vessel with an impermeable wall has been constructed in Lagrangian coordinates. At the initial time a negative velocity is set at the gas border; when $t > t_0$ the shock wave spreads in the gas. The boundary of the ball will move under the certain law, which is agreed with the motion of the shock wave. The trajectories of the gas particles in Lagrangian coordinates are straight lines. The equations determining the structure of the gas flow between the shock front and gas border have been found as a function of time and the Lagrangian coordinate; the dependence of the entropy on the speed of the shock wave has been found too. In Lagrangian coordinates the problem is solved for the first time, and it is fundamentally different from previously known formulations of the problem of the self-convergence of the shock wave to the center of symmetry and its reflection from the center, in which there is no boundary of the gas.

Attempts to construct analitical solutions in order to create the conditions for energy cumulation were made for more than half a century. The solutions were usually constructed for an infinite region in Euler coordinates. In contrast to [1-5], we consider the solution of the problem of dynamic compression of the gas sphere with finite size in Lagrangian coordinates in the following formulation. At the time t_0 in a spherical region with Lagrangian coordinate m_0 the cold ideal gas with parameters $\rho_0 = const$, $P_0 = 0$, $u_0 = 0$ is located (ρ_0 is the density, P is the pressure, u is the velocity). At the point $t = t_0$, $m = m_0$ a negative velocity of the ball boundary is given. When $t > t_0$ the shock wave spreads from this point to the gas.

The flow of gas between the shock wave and the boundary of the ball is determined by the equation of the trajectory, the law of mass conservation and the equation of motion:

$$\left(\frac{\partial r}{\partial t}\right)_m = u, \tag{1}$$

$$\left(\frac{\partial \rho}{\partial t}\right)_m + 4\pi\rho^2\frac{\partial(r^2u)}{\partial m} = 0, \tag{2}$$

$$\left(\frac{\partial u}{\partial t}\right)_m + 4\pi r^2\frac{\partial(F\rho^\gamma)}{\partial m} = 0. \tag{3}$$

The condition of constant entropy along the path is considered instead of the energy equation. We pass on from the old functions r, u, ρ to the new functions

$$R = r^3, \quad \rho, \quad C = r^2u. \tag{4}$$

In the new variables the equations (1) – (3) take the form:

$$\left(\frac{\partial R}{\partial t}\right)_m \circ\ 3C = 0, \tag{5}$$

$$\left(\frac{\partial \rho}{\partial t}\right)_m + 4\pi\rho^2\frac{\partial C}{\partial m} = 0, \tag{6}$$

$$\left(\frac{\partial C}{\partial t}\right)_m + 4\pi R^{\frac{4}{3}}\frac{\partial(F\rho^\gamma)}{\partial m} \circ\ 2C^2R^{-1} = 0. \tag{7}$$

Equations (5) – (7) are essential for finding the R, C, ρ in the area of integration: $0 \le m \le m_0$, $t_0 \le t \le t_f$.

To solve the problem we pass on from the variables t, m to the new variables t, $\xi(t, m)$. As a result of the transition we consider the following equation instead of equations (5) – (7)

$$\left(\frac{\partial R}{\partial t}\right)_\xi + \left(\frac{\partial R}{\partial \xi}\right)_t\left(\frac{\partial \xi}{\partial t}\right)_m \circ\ 3C = 0, \tag{8}$$

*Corresponding author. Email: leshest@list.ru

$$\left(\frac{\partial\rho}{\partial t}\right)_\xi + \left(\frac{\partial\rho}{\partial\xi}\right)_t \left(\frac{\partial\xi}{\partial t}\right)_m + 4\pi\rho^2 \left(\frac{\partial C}{\partial\xi}\right)_t \left(\frac{\partial\xi}{\partial m}\right)_t = 0, \tag{9}$$

$$\left(\frac{\partial C}{\partial t}\right)_\xi + \left(\frac{\partial C}{\partial\xi}\right)_t \left(\frac{\partial\xi}{\partial t}\right)_m \circ \frac{2C^2}{R} + 4\pi R^{\frac{4}{3}} \left[\rho^\gamma \left(\frac{\partial F}{\partial\xi}\right)_t \left(\frac{\partial\xi}{\partial m}\right)_t + \gamma F \rho^{\gamma-1} \left(\frac{\partial\rho}{\partial\xi}\right)_t \left(\frac{\partial\xi}{\partial m}\right)_t\right] = 0. \tag{10}$$

We define the relationship $\xi(t, m)$ so that it would be a constant across the shock wave. The easiest way is to take it in the form

$$\xi = \frac{m}{m_0} \left(\frac{t_f \circ t}{t_f \circ t_0}\right)^{-n}$$

To find the solution of (8) – (10) we use the method of separation of variables, which is based on the following representation of functions

$$\rho = \alpha_\rho(t)\delta(\xi), \quad R = \alpha_R(t)T(\xi), \quad C = \alpha_C(t)Z(\xi). \tag{11}$$

On the shock wave at $\xi = 1$ these functions are of the form

$$\begin{gathered} \alpha_\rho = \rho_0, \delta_w(1) = \frac{\gamma+1}{\gamma \circ 1}, \alpha_R = \left(\frac{t_f \circ t}{t_f \circ t_0}\right)^n, \\ T_w(1) = R_0, \alpha_C = \left(\frac{t_f \circ t}{t_f \circ t_0}\right)^{n-1}, Z_w(1) = C_0. \end{gathered} \tag{12}$$

Using relations (11), (12) we transform the system of equations (8) – (10) to the form

$$A_1 T' = A_4, \quad B_2 Z' + \xi B_3 \delta' = 0, \quad \xi C_2 Z' + C_3 \delta' = C_4, \tag{13}$$

where

$$\begin{gathered} A_1 = \xi, \quad A_4 = T \circ \frac{3Zm_0}{W_0}, \quad B_2 = 1, \quad B_3 = \circ \frac{W_0}{4\pi\rho_0\delta^2}, \\ C_2 = \circ \frac{W_0}{m_0}, \quad C_5 = \frac{4\pi\rho_0^\gamma F_0}{m_0}, \quad C_3 = C_5\gamma\xi^{\frac{2n-6}{3n}} T^{\frac{4}{3}} \delta^{\gamma-1}, \\ C_4 = \frac{2Z^2}{T} \circ \frac{(n \circ 1)W_0 Z}{m_0 n} \circ C_5 \left(\frac{2n \circ 6}{3n}\right) \xi^{\frac{-n-6}{3n}} T^{\frac{4}{3}} \delta^\gamma. \end{gathered}$$

Equations (13) are the system of linear inhomogeneous equations regarding to the T', δ', Z'. The determinant of the system is the following

$$\Delta = A_1(B_2C_3 \circ \xi^2 B_3 C_2) \neq 0.$$

We can write the solution of the system (13)

$$T' = \frac{A_4}{A_1}, \quad \delta' = \frac{B_2 C_4}{\Delta}, \quad Z' = \circ \frac{A_1 B_3 C_4}{\Delta}. \tag{14}$$

Functions $T(\xi)$, $\delta(\xi)$, $Z(\xi)$ are found by integrating the equations (14) in $1 \leq \xi \leq \infty$. Next, using the relations (11) and (4), the dimensional quantities can be found.

Thus, an analytical solution of the problem of converging shock wave in the collapsing gas has been constructed in Lagrangian coordinates.

References

[1] Krajko A.N.: Fast Cylindrically and Spherically Symmetric Strong Compression of an Ideal Gas. J. Applied Mathematics and Mechanics 5:744-760,2007.

[2] Landau L.D., Lifshitz E.M.: Theoretical Physics. Moscow, Russian Federation 1986.

[3] Stanyukovich K. P.: Unsteady Motion of a Continuous Medium. Moscow, Russian Federation 1971.

[4] Brushlinskij K.V., Kazhdan Ja.M.: Similar Solutions of Some Problems of Gas Dynamics. J. Russian Mathematical Surveys 2:3-23,1963.

[5] Guderley G.: Strong Spherical and Cylindrical Shock Waves Near the Center of the Sphere and the Cylinder Axis. J. Aviation Research 9:302-312,1942.

ANALYSIS OF NEARSHORE TSUNAMI WAVE PATTERNS: SOLITARY WAVES, N-WAVES AND UNDULAR BORES

Xi Zhao[1] and Hua Liu *[2]

[1]*Department of Engineering Mechanics, MOE Key Laboratory of Hydrodynamics, Shanghai Jiao Tong University, Shanghai, 200240, China*

[2]*Department of Engineering Mechanics, MOE Key Laboratory of Hydrodynamics, Shanghai Jiao Tong University, Shanghai, 200240, China*

Summary Numerical simulations of tsunami propagation on various sloping beaches are carried out based on the fully nonlinear and highly dispersive Boussinesq model. Different wave patterns near the shoreline are obtained. The characteristics of the nearshore tsunami waves including solitary waves, N-waves and undular bores are discussed. Scenarios of real and hypothetic tsunamis are simulated and different tsunami patterns in the nearshore regions are compared with the field observation. The impacts of the topographies on the nearshore tsunami waveforms are analyzed.

INTRODUCTION

Usually, the submarine earthquakes occur in the pressure zone of two plates, so a seabed deformation with an uplift zone and a subduction zone motivates an N-shape tsunami wave. This type of tsunami wave was observed in the recent tsunami events, for example, Chile tsunami[1] in 1960, Okushiri tsunami[2] in 1993 and Indian Ocean tsunami[3] in 2004, etc. It was shown that tsunami waves with N-shape are stable over transoceanic propagation distances in deep ocean. Models based on the KdV equations and the Boussinesq equations can well catch this specific phenomenon[4,5].

Though tsunami waves propagate long distance without deformation in the deep ocean, they will develop into different types of waveforms in the nearshore region. When they propagate on the shallow continental shelf, solitary waves or undular bores may emerge in the wave front. In this paper, the enhanced fully nonlinear and highly dispersive Boussinesq model is used. Numerical simulations of tsunami propagation on various sloping beaches are carried out. The tsunami waveforms near the shoreline are quite different on steep and mild sloping beaches, which could not be predicted by the analytical solution of the nonlinear shallow water equations. N-shape tsunami waves develop into long wave trains on the steep sloping beaches and form undular bores on the mild sloping beaches. Due to the emergence of undulations, the wave heights increase a lot, which is quite different comparing with the linear theory. Several scenarios of real and hypothetic tsunamis are presented. Different tsunami wave patterns in the nearshore regions are obtained. The impacts of the topographies on the nearshore tsunami waveforms are analyzed.

NUMERICAL SIMULATIONS

The tsunami propagation model used in this paper is based on the horizontal one-dimensional fully nonlinear and highly dispersive Boussinesq equations which developed by Madsen et al.[6]. In order to compute the fifth-derivatives numerically, seven points difference stencil is introduced. For time integration, the fifth-order Cash-Karp-Runge-Kutta scheme is used. The dispersion effect of the model makes it possible to describe the dispersive waves or the undulations well.

The numerical simulations are carried out on sloping beaches where the slopes are from 1:20 to 1:6000. It covers large scale of the real undersea slopes basically. For example, the continental shelf in the East China Sea is extremely gentle, the mean slope is only 1:6000 there. The slope of the seabed in the South China Sea is between 1:300 to 1:800.

Obvious differences of wave profiles near the shoreline can be found. Small undulations appear at the crests and the troughs of the N-shape waves in the numerical results on milder slopes. However, these undulations cannot be obtained by the analytical solution of the nonlinear shallow water equations. Because of the emergence of the undulations, the wave heights of the numerical results are larger than the analytical solution. When the slopes become steeper, the waves disperse into long dispersion waves. The wave trains extend much longer on the steep sloping beaches, which indicates that the dispersion effect is more obviously for the steeper sloping beaches.

NEAR SHORE TSUNAMI PATTERN ANALYSIS

The waveforms of tsunamis in the nearshore region may appear to be solitary waves, undular bores, N-shape waves and long wave trains. The tsunami waves have the chance to develop into leading solitons if the shoaling distance is long enough. Meanwhile, the water depth and the dispersion are also important factors. Wave shoaling on very shallow water leads to the

*Corresponding author. Email: hliu@sjtu.edu.cn

accumulation of dispersion. Proper numerical model with dispersive terms can perform the dispersion effect of wave shoaling. If the propagation distance of tsunami waves on the shallow and gentle sloping beach is not long enough, the undular bores may appear. Besides, if the epicenter is quite near the shore and the propagation distance of the tsunami wave is short. Maybe there is not enough time to form undulations. So a typical N-shape wave or long wave trains will be observed in the nearshore region.

SCENARIOS OF TSUNAMI ON REAL TOPOGRAPHIES

Several tsunamis are simulated by the numerical model. The real cases are Indian Ocean tsunami in 2004, Chile tsunami in 1960 and Sendai tsunami in 2011. The hypothetic tsunamis are from the Manila trench to the South China Sea and from the Okinawa trench to the East China Sea. The nearshore tsunami patterns are quite different due to the diverse topographies. It appears to be solitary waves, N-waves or undular bores. The numerical results are also compared with waveforms from the field observation. In the Indian Ocean tsunami, the tsunami waves are leading-depression N-waves near Banda Ache of Sumatra. However, undular bores are observed in the nearshore region of Thailand. The numerical simulations indicate that N-shape tsunami waves develop into solitary waves after shoaling on the long gentle continental shelf in the East China Sea and form undular bores in the South China Sea.

CONCLUSIONS

In this paper, we study the tsunami waveforms in the nearshore region after a distance of propagation numerically. The numerical model is the fully nonlinear and highly dispersive Boussinesq model which can perform the nonlinearity and dispersion characters of water waves quite well. The numerical simulations are carried out on various sloping beaches. N-shape tsunami waves will develop into long wave trains on the steep sloping beaches and form undular bores on the mild sloping beaches. As tsunamis propagate on the real topographies, different waveforms in the nearshore regions are obtained. The N-shape tsunami waves evolve into long wave trains, undular bores or solitons in the coastal area. The circumstances of formation of different waveforms are discussed.

References

[1] Report on the Chilean Tsunami of May 24, 1960, as observed along the coast of Japan. Committee for Field Investigation of the Chilean Tsunami of 1960, 1961, 397 p.

[2] Sato S.: Numerical simulation of 1993 southwest Hokkaido earthquake tsunami around Okushiri Island. J. Waterway, Port, Coastal and Ocean Engineering 122(5):209-215, 1996.

[3] Lay T., Kanamori H., Ammon C., Nettles M., Ward S., Aster R., Beck S., Bilek S., Brudzinski M., Bulter R., DeShon H., Ekstrom G., Satake K., Sipkin S.: The great Sumatra-Andaman earthquake of 26 December 2004. Science 308:1127-1133, 2005.

[4] Tadepalli S., Synolakis C. E.: Model for the leading waves of tsunami. Phys. Rev. Letts. 77:2141-2144, 1996.

[5] Zhao X., Wang B., Liu H.: Propagation and runup of tsunami waves with Boussinesq model. Proc. The 32nd International Conference on Coastal Engineering, 32, Shanghai, China, 2010.

[6] Madsen P. A., Bingham H., Liu H.: A new Boussinesq method for fully nonlinear waves from shallow to deep water. J. Fluid Mech. 462:1-30, 2002.

FM17 - Other Topics in Fluid Mechanics

PO.FM17-1.01.93	Balapanov, Daniyar - One-dimensional flow of heat conductive gas in homobaric approximation	1645
PO.FM17-1.02.94	Liu, Zhengliang - A Discrete Vortex Method for Flapping Foil Power Generator Modelling at Low Reynolds Numbers	1647
PO.FM17-1.03.95	Rinoshika, Hiroka - Passive control of flow structures around a low-aspect-ratio cylinder mounted on a flat plate	1649
PO.FM17-1.05.97	Weiss, Adam - Inviscid counterflow jets from aligned nozzles	1651
PO.FM17-1.06.98	Zandi, Sahab - Flows in channels with vibrating walls	1653

ONE-DIMENSIONAL FLOW OF HEAT CONDUCTIVE GAS IN HOMOBARIC APPROXIMATION

Daniyar Balapanov *[1] and Andrei Vedernikov[1]

[1]*Microgravity Research Centre, Université Libre de Bruxelles, Brussels, Belgium*

Summary One-dimensional mathematical model of a confined gas flow is developed on the basis of uniform pressure approximation. Compressibility, heat conduction, boundary displacement and mass sources are taken into account. General solution is obtained for perfect gas in case of negligible convective heat transfer thanks to decoupling of energy equation. Explicit analytic solutions are found for a set of particular statements in planar, axial and central symmetries. The validity of the obtained solutions is demonstrated by comparison to corresponding numerical solutions of the full system of conservation equations. The approach is efficient for obtaining exact and approximate analytic solutions in terms of integral calculus.

Due to compressibility, the confined gases can flow with velocity normal to the vessel boundaries, unlike confined non-compressible liquids forming circulating flows. One-dimensional gas flows frequently appear, for example, in microgravity experiments for measurement of particle transport properties in planar, cylindrical or spherical cells. We assume that the gas density perturbations are slow enough to consider the pressure uniform in the cell, in other words the flow Mach number is low. In one-dimensional geometry it excludes momentum equation from the consideration allowing obtaining velocity from the mass and energy conservation laws. This approximation excludes acoustic and thermoacoustic waves from the solution. In [1] numerical solutions are obtained for the processes where the gas compressibility plays important role causing significant convective heat transfer. In the present work we consider processes with negligible influence of the convective heat transfer. We found analytic solutions for the pressure and velocity in flows driven by possible boundary heating, boundary motion and mass sources: both boundary and distributed.

Consider an inert compressible gas confined between two boundaries $r_2(t) \geq r \geq r_1(t) \geq 0$, where t denotes time. The boundary motion laws $r_i(t)$ should be known as well as functions of distributed mass production rate $J(r,t)$ and matter fluxes $\mathbf{j}_i(t)$ at the boundaries. Combining total mass conservation law with the equation of state of perfect gas and factoring the pressure $p(t)$ out of the space integral, we get:

$$p = p_0 \left\{ \int_{r_{10}}^{r_{20}} \frac{\xi^n \mathrm{d}\xi}{T_0(\xi)} + \frac{R}{p_0} \int_0^t \left(\int_{r_1}^{r_2} J(\xi,\tau)\, \xi^n \mathrm{d}\xi + r_1^n j_1 \circ r_2^n j_2 \right) \mathrm{d}\tau \right\} \Bigg/ \int_{r_1}^{r_2} \frac{\xi^n \mathrm{d}\xi}{T(\xi,t)} \tag{1}$$

where n is the geometry-dependent exponent ($n = 0$ in planar, $n = 1$ in axial and $n = 2$ in central symmetry), R is the specific gas constant, $T(r,t)$ is the gas temperature, and $j_i(t)$ is r-projection of $\mathbf{j}_i(t)$. Subscript "0" stands for the initial value of a variable.

Integrating the continuity equation, the local gas velocity is found as the motion law of a virtual surface containing constant gas mass of the reference volume:

$$u = \frac{T}{T_1} \left(\frac{r_1}{r}\right)^n \dot{r}_1 + \frac{T}{r^n} \left[\int_{r_1}^{r} \frac{\partial T}{\partial t} \frac{\xi^n \mathrm{d}\xi}{T^2(\xi,t)} + \frac{R}{p} \left(r_1^n j_1 + \int_{r_1}^{r} J(\xi,t)\, \xi^n \mathrm{d}\xi \right) \circ \frac{\dot{p}}{p} \int_{r_1}^{r} \frac{\xi^n \mathrm{d}\xi}{T(\xi,t)} \right] \tag{2}$$

where T_i designates the temperature on the i-th boundary. Here the reference volume is confined between the first boundary $r = r_1(t)$ and the imaginary moving surface with coordinate r. The influence of the rest of the volume and of the second boundary is represented by the multiplier $\dot{p}/p$, which we did not expand for brevity.

The assumption of the negligible convective heat transfer allows writing partial differential equation with respect to the temperature in the form close to the standard heat equation:

$$\frac{\partial T}{\partial t} = \frac{\chi}{r^n} \frac{\partial}{\partial r} \left(r^n \frac{\partial T}{\partial r} \right) + Q + \frac{\gamma \circ 1}{\gamma}\, T \left(\int_{r_1}^{r_2} \frac{\partial T}{\partial t} \frac{\xi^n \mathrm{d}\xi}{T^2(\xi,t)} \right) \Bigg/ \int_{r_1}^{r_2} \frac{\xi^n \mathrm{d}\xi}{T(\xi,t)} \tag{3}$$

The heat diffusivity χ is taken constant, γ is the specific heat ratio and $Q(r,t)$ represents heat sources. Expression (3) differs from the heat equation by the integral containing term, which defines the pressure work. At high Fourier number $\mathrm{Fo} = \chi t \,/ (r_2 \circ r_1)^2 \ll 1$ this term as well as the term with time derivative can be omitted. In case of low Fourier number, neglecting the pressure work underestimates the temperature variation out of the region influenced by the heat diffusion.

*Corresponding author. Email: dbalapan@ulb.ac.be

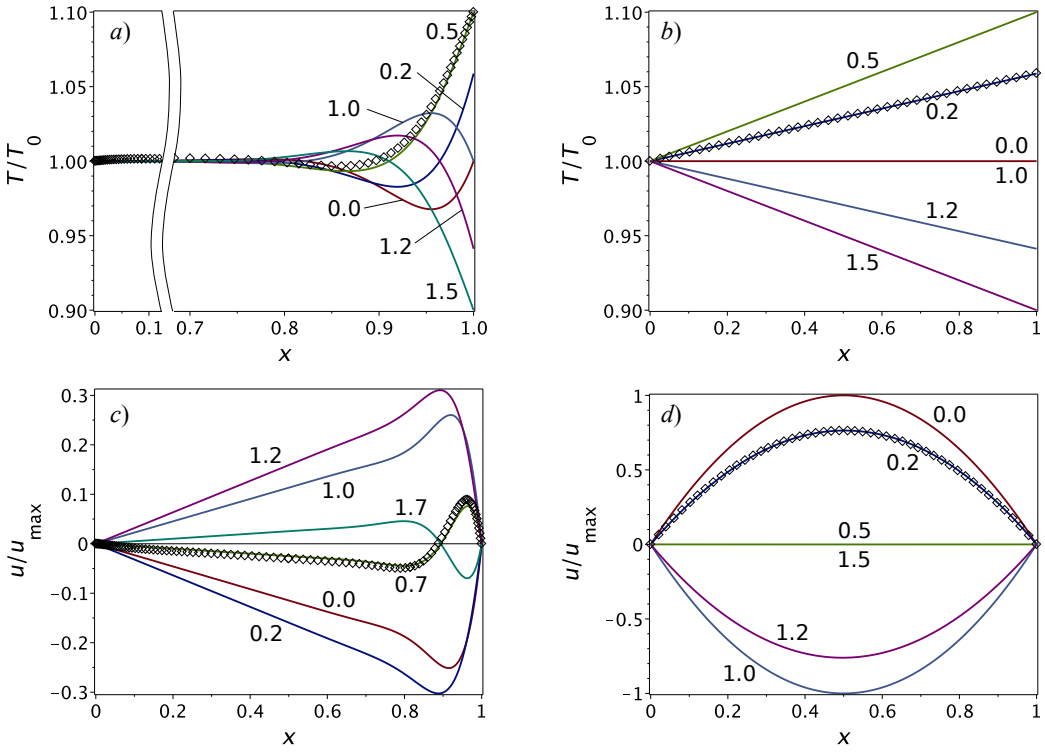

Figure 1: Example solution for a gas in a planar gap with periodic temperature variation on the right boundary. Dimensionless temperature and velocity profiles at $\mathrm{Fo} = 0.01$ (*a*, *c*) and $\mathrm{Fo} = 100$ (*b*, *d*). The oscillation phases are next to the curves in terms of $\omega t/\pi$. Analytic profiles are shown by solid lines; diamonds represent numerical solutions.

As an example, we consider here gas motion between two planar rigid non-moving walls at temperatures $T_1 = T_0$ and $T_2 = T_0 + A\sin(\omega t)$ and in absence of mass and heat sources, $J = 0, j_i = 0, Q = 0$. Known analytic solution [2] of (3) without the last term is used to find the velocity from (2). Calculations are done for N_2 at $T_0 = 300$K and two pressure values: $p_0 = 1$atm ($\mathrm{Fo} = 0.01$) and $p_0 = 10^{-4}$atm ($\mathrm{Fo} = 100$). Temperature oscillation parameters: $A/T_0 = 0.1$, $\omega/2\pi = 20$Hz. The velocity is normalized by maximal value $u_{\max} = A(r_2 \circ r_1)\omega/8T_0$ corresponding to $\mathrm{Fo} \to \infty$.

As it is seen on figure 1, the analytic solution well corresponds to the numerical solution of full conservation equation system. The numerical sulution is obtained by the ANSYS Fluent software. The discrepancies at low Fo are caused by neglecting pressure work term in (3). It was found that at $\mathrm{Fo} \gg 1$ no velocity zeroes appear in the domain, and at $\mathrm{Fo} < 1$ one velocity zero can appear as well as one inflection point. Generally, velocity extreme value drops with decreasing Fo.

Analytic solutions for the flows driven additionally by the motion of walls, boundary and distributed mass sources are also obtained and verified by comparison to numerical simulation. The results are generalized for all three type of symmetries when it is possible.

The analytic solutions obtained are applicable as reference solutions for validation of numerical methods in compressible fluid dynamics at low Mach number. A possibility to estimate gas creep at non-stationary thermal conditions is demanded for accurate processing of experimental measurements of the kinetic coefficients and particle transport properties. The results can be of interest for specialists in bubble dynamics, aerosol physics, condensation/evaporation experiments, especially in microgravity. Proposed methodology should be valuable in university coursework in fluid dynamics as it allows obtaining exact solutions and approximations for large variety of tasks using integral calculus.

European Space Agency PRODEX program and Belgian Federal Science Policy Office are kindly acknowledged for their support.

References

[1] Agafonov, D.V., Cherkasov, S.G.: The Effect of the Variability of Density on the Propagation of Heat in a Gas. High Temperature 40:571-576, 2002.

[2] Landau L.D., Lifshitz E.M.: Fluid Mechanics, Volume 6 (Course of Theoretical Physics S). Butterworth-Heinemann, 1987.

A DISCRETE VORTEX METHOD FOR FLAPPING FOIL POWER GENERATOR MODELLING AT LOW REYNOLDS NUMBERS

Zhengliang Liu*[1], Joseph C.S. Lai[1], John Young[1], and Fang-Bao Tian[1]

[1]*School of Engineering and Information Technology, The University of New South Wales, Canberra, Australian Capital Territory, Australia*

Summary Turbines harvesting energy from the motion of flapping foils have attracted significant research attention in the last 10 years. Several numerical and experimental studies have shown that a leading edge vortex (LEV) can provide lift enhancement and improve the performance of a flapping foil turbine. To overcome the obstacle for optimization and engineering design due to the substantial resources required for computational fluid dynamics (CFD) methods, a discrete vortex method (DVM) which incorporates motions of LEVs with computational time at least two orders of magnitude less than that for CFD is modified for flapping foil simulations. Semi-empirical functions are introduced to account for the effects of the trailing edge flow separation. Instantaneous power coefficients from the DVM with trailing edge flow separation corrections are compared against those from a dynamic stall model and CFD method. Results from the DVM shows good agreement with CFD simulations.

INTRODUCTION

Studies on flapping foil power generators indicate that the formation and evolution of the LEV plays a significant role in improving the performance of a flapping foil[1]. While advances in CFD methods have improved our understanding of vortex shedding, exploring the applications of reduced order models for predictions is worthwhile because of their low computational expenses.

Studies of unsteady aerodynamics accounting for the LEV formation are motivated by the phenomena of dynamic stall in the analysis of helicopter blades from 1970s. Some semi-empirical models, for example, Office National D'Etudes et de Recherches Aerospatiales (ONERA) and Leishman-Beddoes (LB) model[2] have been developed for analysing unsteady aerodynamic loads on helicopter blades. To extend the application of the ONERA model for flapping foil simulations, Bryant et al[3] have tuned constants with respect to unsteady effects using the CFD results of Kinsey and Dumas[4]. Another approach to model unsteady flows with LEV formation is the discrete vortex method (DVM) [5]. However, models based on the DVM assume that the flow separates at the leading edge, neglecting the influence of the trailing edge flow separation.

In this study, empirical functions used in the LB model are introduced into the DVM to account for the influence of the trailing edge flow separation. The aim of this study is to examine the feasibility of using a surrogate method to reduce the computational cost in the optimization and engineering design of a flapping foil power generator.

METHODOLOGY

Kinematics

In this study, a two-dimensional NACA0015 foil undergoing prescribed pitch and plunge motions in a uniform flow with velocity U is considered:

$$\theta(t) = \theta_0 \sin(2\pi f_0 t), h(t) = h_0 \sin(2\pi f_0 t + \varphi) \tag{1}$$

where $\theta(t)$ and $h(t)$ are the instantaneous angular and plunge positions respectively; θ_0 and h_0 are the angular and plunge amplitude; f_0 is the frequency; and φ is the phase angle between the pitch and plunge motion.

Dynamic Loads

In the LB model, Theodorsen's theory is used to predict the lift when the flow is fully attached to the foil. However, this classical method is limited by assumptions of planar wake and small amplitudes and is unsuitable for flapping foil motions. Here, the DVM developed by Katz and Plotkin[6] which eliminates small amplitude approximations is used.

To predict the initiation of the LEV formation, a leading edge suction parameter (LESP) determined by the aerofoil profile and Reynolds number (Re) regardless of kinematic parameters is introduced. LESP=0.19 (NACA0015 foil, $Re = 1100$) given by Ramesh et al[5] is used here. Since the separation point is fixed at the leading edge, the DVM with LESP cannot take into account the influence of the trailing edge flow separation. Here, Kirchhoff flow approximation is used for trailing edge flow separation corrections (TEFSC). This simple model has been extended for unsteady flow predictions in the LB model[2]. With the use of the DVM incorporating the TEFSC, the lift coefficient (C_L) is given as

*Corresponding author. Email: Zhengliang.Liu@student.adfa.edu.au

$$C_L = \frac{2}{U^2 c}\left[\left(1+\sqrt{f}\right)^2 \int_0^c \left(\dot{h}\sin\theta + U\cos\theta + \frac{\partial\phi}{\partial x}\right)\gamma(x)\,dx + \int_0^c \frac{\partial}{\partial t}\int_0^x \gamma(x_0)\,dx_0\cos\theta + \pi\left[\lim_{x=0}\gamma\sqrt{x}\right]^2\sqrt{f}\sin\theta\right] \quad (2)$$

where ϕ is the potential; γ is the chordwise circulation; x is the chordwise position; x_{piv} is the pivot location; and f represents the position of flow separation. The integrals for the moment coefficient (C_M) calculation are similar to those treated in Eq.(2).

RESULTS

The DVM with the TEFSC is validated against CFD results from Kinsey and Dumas' work[4] for non-dimensional plunge amplitude $h = h_0/c = 1$ and $\phi = 90°$. The dimensionless frequency f^* is defined as $f^* = f_0 c/U$, where c is the chord length. To evaluate the power extracted from the flow, the power coefficient $C_P = (C_L\dot{h} + C_M\dot{\theta}c)/U$ is used.

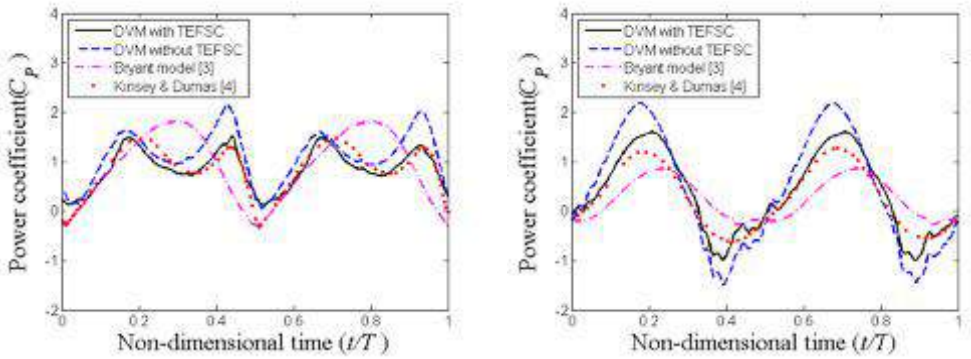

(a) (b)

Figure 1: Predictions of power coefficients with (a)$f^* = 0.14, \theta_0 = 76.3°$ and (b) $f^* = 0.18, \theta_0 = 60°$

To assess C_P predicted by the DVM, two cases are selected for comparison because strong LEVs are predicted in the first case ($f* = 0.14, \theta_0 = 76.3°$) and no LEV is observed in the second case ($f^* = 0.18, \theta_0 = 60°$)[4]. In the first case (Figure 1a), the time history of C_P predicted by the DVM with TEFSC agrees with the CFD results[4] much better than the DVM without TEFSC and Bryant model[3]. The averaged C_P for DEVM with TEFSC and without TEFSC are 0.86 and 1.12 respectively, compared with 0.86 of Kinsey & Dumas[4] and 0.87 of Bryant model[3]. In the second case (Figure 1b), although the time history of C_P predicted by the DVM without TEFSC follows similar trend as that of Kinsey & Dumas[4], its magnitude is almost double for most part of the cycle, but the results of the DVM with TEFSC are much closer to [4]. The averaged C_P for DEVM with TEFSC and without TEFSC are 0.37 and 0.41 respectively, compared with 0.27 of Kinsey & Dumas[4] and 0.24 of Bryant model[3]. In these two cases, the DVM provides better approximations of the time history to the CFD method compared with the Bryant model[3]. Furthermore, empirical constants used in the DVM with TEFSC are determined only by the flow condition and the foil profile, whereas constants tuned to match CFD results in the Bryant model[3] are determined by both the geometry and kinematic parameters which limit the application of the Bryant model[3].

CONCLUSIONS

In this paper, a reduced order model based on the Discrete Vortex Method (DVM) to capture the complex aerodynamic effects of a flapping foil power generator at a Reynolds number of 1100 has been presented. Results of the DVM incorporating the trailing edge flow separation correction show reasonable agreement with the CFD results in terms of the power coefficient amplitude, trend and phase. The computational time required is only 40 minutes compared to over 100 hours for the CFD method on a single P4/3.2-GHz processor [4]. This study demonstrates the potential of using DVM with TEFSC to explore the optimization and design of a flapping foil power generator.

References

[1] Young J., Lai J.C.S., Platzer M.F.: A Review of Progress and Challenges in Flapping Foil Power Generation. Progress in Aerospace Sciences 67: 2-28, 2014.

[2] Leishman J.G.: Principles of Helicopter Aerodynamics. Cambridge University Press, 2002.

[3] Bryant M., Gomez J.C., Garcia E.: Reduced-Order Aerodynamic Modelling of Flapping Wing Energy Harvesting at Low Reynolds Number. AIAA Journal 51(12): 2771-2782, 2013.

[4] Kinsey T., Dumas G.: Parametric Study of an Oscillating Airfoil in a Power-Extraction Regime. AIAA Journal 46(6): 1318-1330, 2008.

[5] Ramesh K., Gopalarathnam A., Granlund K., Ol M.V., Edwards, J.R.: Discrete-Vortex Method with Novel Shedding Criterion for Unsteady Aerofoil Flows with Intermittent Leading-Edge Vortex Shedding. Journal of Fluid Mechanics 751: 500-538, 2014.

[6] Katz J., Plotkin A.: Low-Speed Aerodynamics. Cambridge University Press, 2001.

PASSIVE CONTROL OF FLOW STRUCTURES AROUND A LOW-ASPECT-RATIO CYLINDER MOUNTED ON A FLAT PLATE

Hiroka Rinoshika, Shun Fujimoto & Akira Rinoshika[a)]
Department of Mechanical Systems Engineering, Yamagata University, Yamagata, Japan

Summary The present study proposed a passive control method to control and reduce the rear separation region and the vortex of the free-end surface around a low aspect ratio circular cylinder, by using a hole from the free-end surface to the side of the rear surface. High-speed PIV measurements were performed for comparing the flow structures between the controlling and no-controlling wakes. The Reynolds number based on the diameter of cylinder was 8,570. It is found that the fluid flows from the large rear recirculation zone to small recirculation zone on the free end surface through the hole. The size of rear recirculation zone becomes smaller than that of the standard cylinder due to the suction of the hole. Meanwhile, the Reynolds shear stress also decreases comparing with the standard cylinder.

INTRODUCTION

The flow around the base of the low aspect ratio cylinder and over the free end (or tip) of the cylinder causes a strongly three-dimensional complex flow field, which is different from "infinite" structure. It is encountered in many engineering applications, such as offshore structures, buildings, chimney stacks, automobile and so on. The wake structures of a low aspect ratio circular cylinder has been well studied [1]-[4], and are characterized by a pair of counter-rotating streamwise vortices (trailing vortices) originating from either side of the rear surface, denominated tip-vortices coming off the circumferential leading edge of the free end, and a horse shoe (or necklace) vortex forming upstream mat the cylinder-wall junction. However, fundamental works about controlling VIV (Vortex-induced vibration) of low aspect ratio cylinders are few in the literature, which is very important to reduce drag and noise in many engineering applications. Although some of flow passive control techniques have been well studied in "infinite" structure [5], less research focus on the control of vortices in the rear recirculation region and vortex appearing on the free end surface around a low-aspect-ratio cylinder, which motivates the present investigation.

To control and reduce the rear separation region of cylinder and the vortex on the free-end surface, the present study proposed a passive control method, in which a hole from the free-end surface to the side of the rear surface is made to generate both suction and blowing flows. The controlling wake structures of this low aspect ratio circular cylinder mounted normal to a ground plane were measured by PIV in a circulation water tunnel.

EXPERIMENTAL METHODS

The three-dimensional cylinder model, as shown in Fig.1, having an aspect ratio H/D = 1 with height H and diameter D of 70 mm, is mounted on a flat plate. The x, y, and z axes are in the streamwise, spanwise and transverse directions, respectively. To control the flow structures, a hole with a diameter of d = 10 mm, called the controlling hole (CH), is made from the free-end surface to the side of the rear surface with L = 30mm and h = 50mm (Fig.1).

The experiment was conducted in the circulating water channel, which has 400 (width)×200 (height)×1000(length) mm working section, and was performed at a constant free stream velocity of U = 0.16 m/s, corresponded to Reynolds number Re ($\equiv UD/\nu$) = 8,570. The turbulence intensity of the circulating water channel was less than 0.5% of the free stream velocity. As the PIV tracer particles, polystyrene particle which have an averaged diameter 68 μm are used. The flow field of downstream from experimental model is illuminated by a high-intensity laser light sheet with a thickness of 1.0 mm. A high-speed camera is used to capture the digital images by the flame rates of 250 fps (flame per second). The high-speed PIV measurements are carried out in the (x, y)-plane, (x, z)-plane and (y, z)-plane. 7,000 digital images are analyzed by PIV software and PIV interrogation window size is set as 32 pixels. This PIV measurement has the uncertainty of velocity estimated at $\pm$4% in the reliability of 95%.

RESULTS AND DISCUSSIONS

Figure 2(a) shows the time averaged streamlines and the distribution of the normalized Reynolds shear stress contours of $\overline{uv}/U^2$ around a standard low-aspect-ratio cylinder (no-hole) in the (x, y)-plane, calculated by the measured instantaneous velocity. The colour mappings have been assigned to the Reynolds shear stress values and the highest concentration is displayed as red and the lowest as blue, respectively. It is evident that a mean small recirculation region or vortex appears on the free end surface and its central position is about x_0 = 30 mm from the leading edge. A mean large rear recirculation region or vortex originating from side of the rear surface and leading edge of the free end is clearly observed and its height of central position is about y_0 = 50 mm.

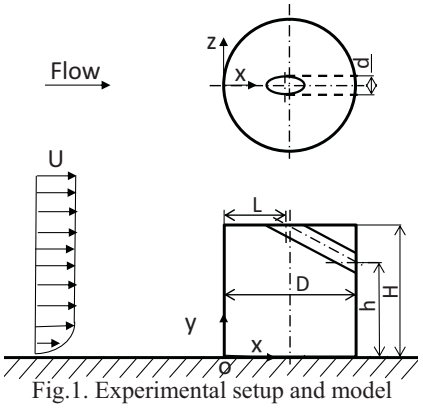

Fig.1. Experimental setup and model

[a)] Corresponding author. Email: rinosika@yz.yamagata-u.ac.jp.

To reduce the rear recirculation region, the controlling hole (CH) is used to connect the central locations of two recirculation region, i.e. from the free-end surface to the side of the rear surface with $L = x_0 = 30$mm and $h = y_0 = 50$mm (Fig.1). The role of the CH can be said as that the pressure difference between two recirculation regions drive the fluid to flow and generates suction and blowing to control the recirculation region.

The time averaged streamlines and the distribution of the normalized Reynolds shear stress contours of $\overline{uv}/U^2$ around a cylinder with CH in the (x, y)-plane are shown in Fig.2(b). It is interesting to find that the fluid flows from the large rear recirculation zone to small recirculation zone on the free end surface through the CH. It indicates that the pressure of the free end surface is lower than that of the rear surface side. As comparing with the standard cylinder (Fig.2a), the size of rear recirculation zone becomes smaller than that of the standard cylinder, since the CH generates suction flow to reduce the rear separation region. Due to the effect of suction and blowing of the CH, the Reynolds shear stress, as shown in Fig.2, decreases comparing with the standard cylinder.

The instantaneous streamlines and corresponding vorticity contours of ω_z in the (x, y)-plane are shown in Fig.3. The color mappings have been assigned to the vorticity values and the highest and lowest concentrations are respectively displayed as red and blue. It is clearly observed that the vortex of the CH on the free end surface becomes smaller than that of the standard cylinder due to the blowing flow. Several vortical structures appear behind the standard cylinder in the rear recirculation zone (Fig.3a). In the case of the CH, however, a relatively large-scale vortical structure can be identified and small vortices are sucked into the hole (Fig.3b). Therefore, the rear separation region can be reduced by the CH.

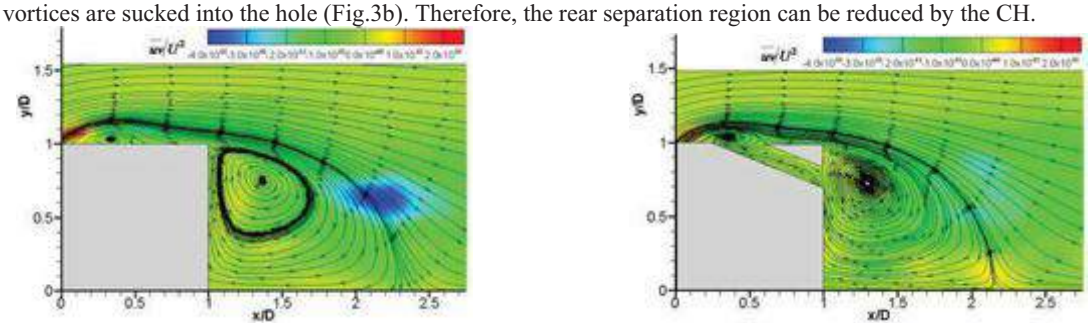

(a) Standard cylinder (b) Cylinder with CH

Fig.2 The time-averaged streamlines and Reynolds shear stress contours in the (x, y)-plane

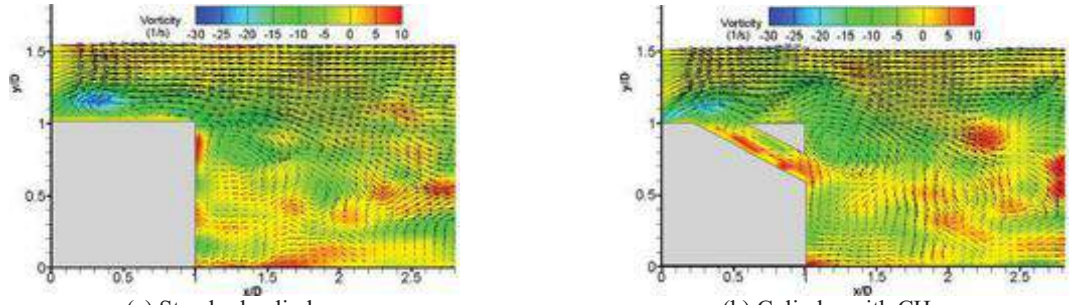

(a) Standard cylinder (b) Cylinder with CH

Fig.3 Instantaneous streamlines and corresponding vorticity contours in the (x, y)-plane

CONCLUSIONS

A passive control technique to control and reduce the rear separation region and the vortex on the free-end surface around a low aspect ratio circular cylinder is experimentally studied. The flow structures of the controlling and no-controlling wakes were measured and compared by using High-speed PIV. The following conclusions can be drawn.

(1) The fluid flows from the large rear recirculation zone to small recirculation zone on the free end surface through the hole.

(2) The size of rear recirculation zone becomes smaller than that of the standard cylinder due to the suction of the hole.

(3) The Reynolds shear stress also decreases comparing with the standard cylinder.

References

[1] Kawamura T., Hiwada M., Habino T., Mabuchi I., Kumada M.: Flow around a Finite Circular Cylinder on a Flat Plate. *Bull JSME* **27**: 2142-2150, 1984.

[2] Pattenden R.J., Turnock S.R., Zhang X.: Measurements of the flow over a low-aspect-ratio cylinder mounted on a ground plane. *Experiments in Fluids* **39**: 10-21, 2005.

[3] Rostamy N., Sumner D., Bergstrom D.J., Bugg J.D.: Local flow field of a surface-mounted finite circular cylinder. *Journal of Fluids and Structures* **34**: 105-122, 2012.

[4] Sumner D.: Flow above the free end of a surface-mounted finite-height circular cylinder: A review. *Journal of Fluids and Structures* **43**: 41-63, 2013.

[5] Choi H., Jeon W., Kim J.: Control of Flow Over a Bluff Body, *Annu. Rev. Fluid. Mech.* **40**: 113-139, 2008.

INVISCID COUNTERFLOW JETS FROM ALIGNED NOZZLES

Adam D. Weiss*, Stefan Llewellyn Smith, Antonio L. Sánchez[1]
[1]*Department of Mechanical and Aerospace Engineering, UCSD, USA*

Summary This paper examines the inviscid interaction of two planar counterflowing streams of different gases issuing from two aligned nozzles of equal radius R separated a distance H. The problem is relevant in connection with the counterflow burners used in laboratory experiments to characterize flame response to strain. The computation of the inviscid flow involves integration of the Euler equations, with the outer jet boundaries and the interface separating the two jets appearing as free surfaces, to be obtained as part of the solution. It is shown how introduction of a single density-weighted stream function facilitates the description. While conformal mapping can be used to determine the solution for irrotational flow, numerical integration is required in general, with simplified limiting solutions arising in the limiting cases $H/R \ll 1$ and $H/R \gg 1$.

A canonical problem of interest in connection with the high-Reynolds-number flows typically encountered in burners is that of counter-flowing jets. Counterflow structures that move with the mean velocity can be abstracted from the interface dynamics of shear and mixing layers [1]. Similarly, local counterflow configurations emerge in typical combustion chambers around the stagnation point that forms near the injector exit as a result of vortex breakdown of the swirling air-feed stream [2]. Both axisymmetric and planar counterflow configurations have been widely employed in laboratory experiments for studying reacting and non-reacting flows [3] as well as in numerical simulations to address the effects of strain on flames [4].

Consider the planar flow of two gaseous jets impinging from opposed aligned nozzles of semi-width R separated a distance $2H$, as sketched in Fig. 1(a), corresponding to a typical counterflow arrangement employed in combustion experiments. The velocity profiles in the feed streams are given by $v_x = (Q_1/R)U_1(y)$ and $v_x = \circ\,(Q_2/R)U_2(y)$. Here, $2Q_1$ and $2Q_2$ denote the volume fluxes for the two streams and $U_1(y)$ and $U_2(y)$ represent nondimensional shape functions, such that $\int_0^1 U_1 \mathrm{d}y = \int_0^1 U_2 \mathrm{d}y = 1$, with y being the distance from the center line scaled with R (i.e. $U = 1$, $U = 2(1 \circ |y|)$, and $U = \frac{3}{2}(1 \circ y^2)$ for uniform flow, Couette flow, and Poiseuille flow, respectively).

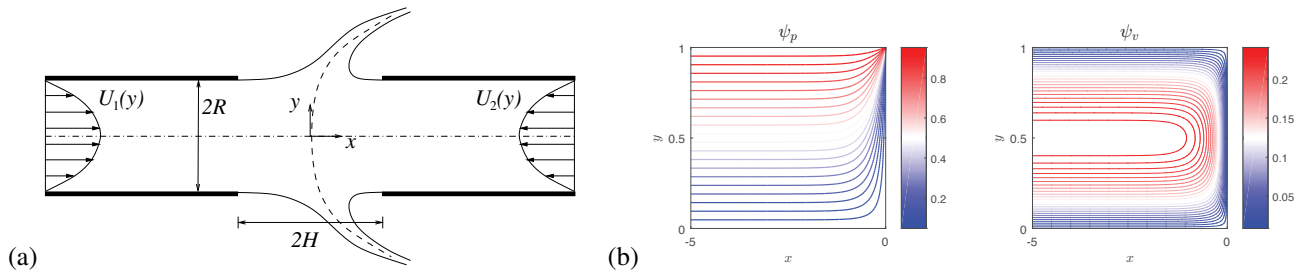

Figure 1: (a) Sketch of the counterflow configuration investigated here (b) sample distributions of stream function for Couette jets with $H/R \ll 1$ and $\Lambda = 1$.

In applications, the Reynolds numbers Q_1/ν_1 and Q_2/ν_2 based on the kinematic viscosities of the two fluids ν_1 and ν_2 are typically moderately large, so that the flow in the impinging region is laminar and inviscid. Since the Mach number is assumed to be small, the flow in each of the impinging jets is effectively incompressible, although the corresponding densities ρ_1 and ρ_2 are in general different. For this ideal planar flow, both the vorticity ω and the stagnation pressure remain constant along each stream line. In principle, the problem involves integration of the incompressible Euler equations for the two gas jets, including as free boundaries the vortex sheets separating the jets from the ambient stagnant air and the vortex sheet separating the two gases. Because of symmetry, only the semi-space $y \geq 0$ needs to be considered in the description.

The existence of two different fluids requires in principle introduction of two different stream functions ψ_1 and ψ_2 in the description, with the condition of equal pressure on both sides of the separating surface yielding $\rho_1|\nabla\psi_1|^2 = \rho_2|\nabla\psi_2|^2$, to be used as matching condition in determining the location of the separating surface. This last condition suggests that one can simplify the description, removing the need for treating the separating surface as a free boundary, by introducing a renormalization factor $(\rho_2/\rho_1)^{1/2}$ in the definition of new kinematic variables (i.e. velocity, vorticity, and stream function) for the gas of density ρ_2, resulting in a single stream function $\psi = \psi_1 = (\rho_2/\rho_1)^{1/2}\psi_2$ satisfying

$$\frac{\partial^2\psi}{\partial x^2} + \frac{\partial^2\psi}{\partial y^2} = \circ\,\omega(\psi), \tag{1}$$

*Corresponding author. Email: a2weiss@ucsd.edu

as follows from the definition of the vorticity, with R and Q_1/R used as length and velocity scales. The associated boundary distributions of stream function and vorticity in the feed streams are

$$\psi = \int_0^y U_1 \mathrm{d}y \quad \text{and} \quad \omega = \circ\, \frac{\mathrm{d}U_1}{\mathrm{d}y} \qquad \text{as} \quad x \to \circ\, \infty \quad \text{for} \quad 0 \le y \le 1 \tag{2}$$

and

$$\psi = \circ\, \Lambda \int_0^y U_2 \mathrm{d}y \quad \text{and} \quad \omega = \Lambda \frac{\mathrm{d}U_2}{\mathrm{d}y} \qquad \text{as} \quad x \to \infty \quad \text{for} \quad 0 \le y \le 1, \tag{3}$$

where $\Lambda = (\rho_2/\rho_1)^{1/2}\,(Q_2/Q_1)$ is a measure of the ratio of the momentum fluxes of both jets. The distribution of vorticity $\omega(\psi)$ is different in both jets (i.e. for $\psi > 0$ and for $\psi < 0$), with corresponding expressions following from the boundary values of ψ and ω given in (2) and (3). For example, for Poiseullie flow one obtains $\int_0^y U \mathrm{d}y = (3\circ\, y^2)y/2$ and $\mathrm{d}U/\mathrm{d}y = \circ\, 3y$, yielding

$$\psi = \frac{\omega}{6}\left[3 \circ\, \left(\frac{\omega}{3}\right)^2\right] \quad \text{for} \quad 0 \le \psi \le 1 \qquad \text{and} \qquad \psi = \frac{\omega}{6}\left[3 \circ\, \left(\frac{\omega}{3\Lambda}\right)^2\right] \quad \text{for} \quad \circ\, \Lambda \le \psi \le 0 \tag{4}$$

as an implicit representation for $\omega(\psi)$, whereas for Couette flow one finds

$$\omega = 2 \quad \text{for} \quad 0 \le \psi \le 1 \qquad \text{and} \qquad \omega = \circ\, 2\Lambda \quad \text{for} \quad \circ\, \Lambda \le \psi \le 0. \tag{5}$$

The problem reduces to that of integrating (1) with the boundary distribution given in (2) and (3) as $x \pm \infty$ and the additional boundary conditions $\psi = 0$ at $y = 0$ for $\circ\, \infty < x < +\infty$, $\psi = 1$ at $y = 1$ for $\circ\, \infty < x \le \circ\, H/R$, and $\psi = \circ\, \Lambda$ at $y = 1$ for $H/R \le x < +\infty$, with the condition of constant pressure on the jet surfaces $\psi = 1$ and $\psi = \circ\, \Lambda$ written in the form $(\partial\psi/\partial x)^2 + (\partial\psi/\partial y)^2 =$ constant.

It will be shown that, while conformal mapping can be employed to determine the solution for $U_1 = U_2 = 1$ [5], numerical integration is needed in general for rotational flow. Results will be obtained for different values of H/R and different profile shapes $U_1(y)$ and $U_2(y)$, with particular attention given to the important case of Poiseuille flow, corresponding to long injectors. The solution will be seen to simplify in the limit $H/R \gg 1$, when the collision region appears near the exit of the jet with lower momentum flux, the other stream approaching as a free jet of constant radius, and also in the limit $H/R \ll 1$, where the opening acts as an annular sink for the flow in the pipe. In the latter limit, the solution can be facilitated by expressing ψ as the sum of a potential stream function

$$\psi_p = y \circ\, \frac{1+\Lambda}{\pi} \arctan\left[\frac{e^{\pi x}\sin(\pi y)}{e^{\pi x}\cos(\pi y)+1}\right], \tag{6}$$

carrying the mass flux of the two streams, and a vortical stream function ψ_v, with associated zero mass flux, determined by integration of

$$\frac{\partial^2 \psi_v}{\partial x^2} + \frac{\partial^2 \psi_v}{\partial y^2} = \circ\, \omega(\psi) \tag{7}$$

with boundary conditions $\psi_v = 0$ at $y = 0, 1$ for $\circ\, \infty < x < \infty$ and far-field distributions for $0 \le y \le 1$ given by $\psi_v = \int_0^y (U_1 \circ\, 1)\mathrm{d}y$ as $x \to \circ\, \infty$ and by $\psi_v = \circ\, \Lambda \int_0^y (U_2 \circ\, 1)\mathrm{d}y$ as $x \to \infty$. The function $\omega(\psi)$ must be evaluated in terms of $\psi = \psi_p + \psi_v$ with ψ_p obtained from (6). Sample distributions of ψ_p and ψ_v obtained with $\Lambda = 1$ for the Couette vorticity distribution given in (5) are shown in Fig. 1(b).

References

[1] Corcos G.M., Sherman F.S.: Vorticity concentration and the dynamics of unstable free shear layers. J. Fluid Mech. 73:241–264, 1976

[2] Edwards C.F., Rudoff R.C.: Structure of a swirl-stabilized spray flame by imaging, laser doppler velocimetry, and phase doppler anemometry, Proc. Combust. Inst. 23:1353–1359, 1990.

[3] Niemann U., Seshadri K, Williams F.A.: Accuracies of laminar counterflow flame experiments, Comb. Flame 162:1540–1549, 2015.

[4] Williams F. A.: Progress in knowledge of flamelet structure and extinction. Progress in Energy and Combustion Science 26:657-682, 2000.

[5] Gurevich M.I.: Theory of Jets in Ideal Fluids. Academic Press, London 1965.

FLOWS IN CHANNELS WITH VIBRATING WALLS

Sahab Zandi[1a)] & Jerzy M. Floryan[1]
[1]*Department of Mechanical and Materials Engineering, Western University, London, Ontario, Canada*

Summary Analysis of flows in channels with vibrating walls has been carried out as a part of search for the new drag reducing strategies. Vibrations in the form of waves travelling up- and down-stream have been considered. Their effect is assessed by evaluating the pressure gradient correction required to maintain the same flow rate in the stationary and vibrating channels with the same mean opening. It is shown that drag reduction can be achieved using waves travelling in the downstream direction.

INTRODUCTION

It is known that deformed channel walls have significant effects on drag changes. It has been recognized that stationary transverse grooves always increase drag; however, some types of longitudinal grooves may result in drag reduction [1]. In this work effects of vibrating surfaces on channel flow are investigated. Vibrating boundaries can be found in many engineering and biological applications. Design of roller pumps for fluid pumping without pump components coming into contact with the fluid represents one example. Another example is the use of these boundaries to push urine from the kidney to the bladder. These boundaries also help to push food forward through the gullet. In addition, bile moving from the gall-bladder to the duodenum is caused by moving boundaries as well as ovum movement in the fallopian tube. In the present study, pressure losses in channels with vibrating walls have been analyzed. Surface vibrations were assumed to have the form of travelling waves. The spectrally accurate immersed boundary conditions (IBC) method based on the Fourier expansions in the flow direction and the Chebyshev expansions in the transverse direction has been developed [2]. The results show dependence of the pressure losses on the phase speed of the waves.

PROBLEM FORMULATION AND RESULTS

Consider steady, two-dimensional flow of a fluid confined in a channel bounded by two parallel walls extending to $\pm\infty$ in the X-direction and placed at a distance $2h$ apart as shown in Fig.1. The flow is driven in the positive X-direction by a pressure gradient. This flow is modified by wall vibrations in the form of travelling waves. The resulting time-dependent channel geometry is described as

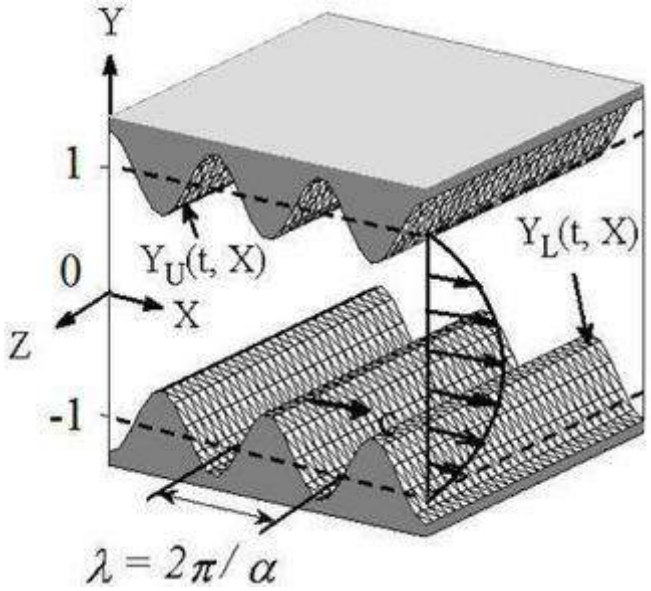

Figure 1. Physical domain with vibrating boundaries.

$$Y_{Us}(t,X) = 1 + h_U(X - ct), \qquad Y_{Ls}(t,X) = -1 + h_L(X - ct), \tag{1a,b}$$

where h_U and h_L describe the known wave shapes, the subscripts L and U refer to the lower and upper walls, respectively, and c denotes the wave phase speed. Our interests are in the waves that do not affect the mean channel

[a)] Corresponding author. Email: szandi@uwo.ca.

opening. The system response is described by the Navier-Stokes and continuity equations subject to boundary conditions of the form

$$u_T\big(t,X,Y_U(t,X)\big)=0,\quad v_T\big(t,X,Y_U(t,X)\big)=\frac{\partial Y_U(t,X)}{\partial t}=-ch'_U(X-ct), \tag{2a}$$

$$u_T\big(t,X,Y_L(t,X)\big)=0,\quad v_T\big(t,X,Y_L(t,X)\big)=\frac{\partial Y_L(t,X)}{\partial t}=-ch'_L(X-ct) \tag{2b}$$

where subscripts t, X and Y denote the arguments of partial differentiations and prime denotes differentiation with respect to the argument. The system is subject to the mass flow rate constraint of the form

$$Q(t,X)|_{mean}=\left(\int_{Y_L(t,x)}^{Y_U(t,x)}u(t,X,Y)\,dY\right)\Big|_{mean}=\frac{4}{3}, \tag{2c}$$

i.e. the flow rate through the vibrating channel must be the same as the flow rate through the stationary reference channel. The additional pressure gradient required to maintain such flow rate is represented in the form of

$$\frac{\partial p_T}{\partial X}\Big|_{mean}=\frac{-2}{Re}+\frac{\partial p_1}{\partial X}\Big|_{mean} \tag{3}$$

where p_T stands for the complete pressure and the second term on the right hand side represents the correction. Positive values of this correction signify the vibrations-induced drag reduction. Detailed results are presented for a sinusoidal wave propagating along the lower wall resulting in the shape of the flow domain of the form

$$Y_U=1,\quad Y_L=-1+A\cos[\alpha(X-ct)] \tag{4}$$

where A and α are the amplitude and the wave number of the wave, and c denotes its phase speed. An explicit solution determined in the limit of small wave amplitude $(A\to 0)$ demonstrates that drag change increases proportionally to A^2 [3]. Figure 2 illustrates variations of $(Re/A^2)*(dp_1/dx)$ as functions of the wave speed for selected wave and Reynolds numbers. In general, waves propagating in the downstream direction lead to drag reduction with its magnitude increasing with c. The trend is different for the short wavelength waves and depends on Re as such waves propagating in the upstream direction result in drag decrease if Re is large enough.

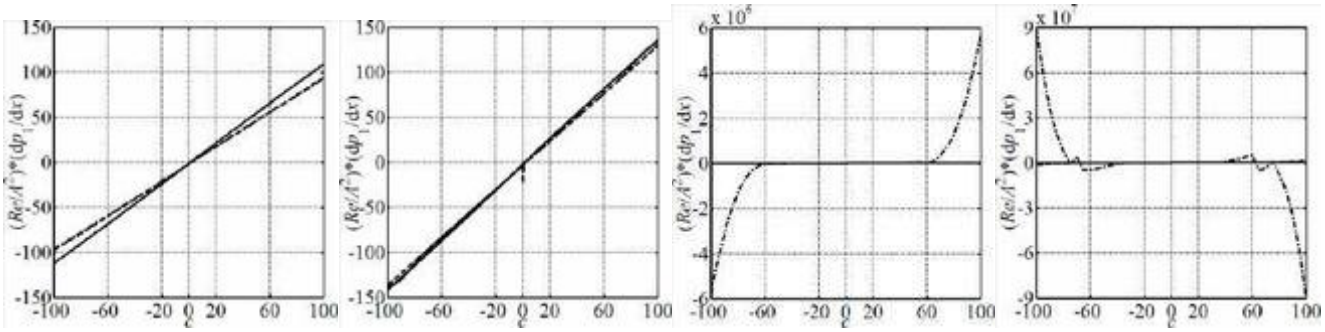

Figure 2. Variations of $(Re/A^2)*(dp_1/dx)$ for small-amplitude sinusoidal waves as functions of the wave speed c for: (A)$\alpha=0.1$; (B)$\alpha=1$; (C)$\alpha=5$; (D)$\alpha=10$. Solid, dashed and dash-dotted lines correspond to $Re=1$, $Re=100$, and $Re=500$, respectively.

CONCLUSIONS

The pressure losses in a pressure-driven flow in a vibrating channel have been analyzed. The results show dependence of the pressure losses on the phase speed of the waves, with the waves propagating in the downstream direction reducing these losses. This argument is not always correct in the limit of small wave amplitude. As it can be seen in Fig.2 (D) when α and Re are large enough, waves which propagate in downstream direction with the phase speeds higher than a certain critical speed result in a significant drag increase while similar waves propagating in upstream direction lead to drag reduction.

References

[1] Mohammadi A., Floryan J.M.: Pressure Losses in Grooved Channels. *J. Fluid Mech.* **725**:23-54, 2013.

[2] Zandi S., Mohammadi A., Floryan J.M.: Spectrally-Accurate Algorithm for the Analysis of Flows in Two-Dimensional Vibrating Channels. *J. Comp. Phys.* **301**:425-455, 2015.

[3] Zandi S., Mohammadi A., Floryan J.M.: On the Analysis of Flows in Vibrating Channel. *Bull. Am. Phys. Sci.* **60**:D17.00002, 2015.

SM01 - Biomechanics and Biomaterials

TS.SM01-1.01	McMeeking, Robert - Remodeling of cardiomyocytes in vitro (INVITED)	1657
TS.SM01-1.02	Holzapfel, Gerhard - Experimental and computational analysis of aortic dissection	1659
TS.SM01-1.03	Ehret, Alexander - Analysing the fracture behaviour of soft biological membranes	1661
TS.SM01-1.04	deBotton, Gal - Micromechanics motivated modeling of fibrous tissues	1663
TS.SM01-1.05	Marchi, Benjamin - The Importance of Physiologically and Anatomically Representative Ligaments in Knee Models	1665
TS.SM01-1.06	Xu, Xinpeng - Nonlinear elasticity of biopolymer gels under compression	1666
TS.SM01-2.01	Deshpande, Vikram - Fluctuations in experiments of cells on substrates (INVITED)	1668
TS.SM01-2.02	Sun, Cuiru - Carotid wall stress analysis based on in vivo intravascular optical coherence tomography imaging	1670
TS.SM01-2.03	Untaroiu, Costin - Modeling liver parenchyma tearing using a cohesive zone modeling approach	1672
TS.SM01-2.04	Epstein, Marcelo - A model for mechanically driven morphogenesis	1674
TS.SM01-2.05	Chai, Herzl - On deformation and fracture of tooth enamel	1676
TS.SM01-2.06	Bao, Gang - Force-induced internalization of magnetic nanoparticles for drug delivery and cell tracking	1678
TS.SM01-3.01	Weitz, Dave - Universal correlation between stiffness and volume for cells (INVITED)	1679
TS.SM01-3.02	Rubin, Miles - An eulerian formulation of soft tissue growth	1680
TS.SM01-3.03	Espinosa, Horacio - Cell-selective electroporation for novel single-cell applications	1682
TS.SM01-3.04	Crone, Wendy - Influence of Microscale Patterning and Substrate Stiffness on Cardiomyocyte Maturation	1684
TS.SM01-3.05	Zündel, Manuel - Mechanical considerations on traction force microscopy	1686
TS.SM01-4.01	Long, Mian - Biomechanics of hepatic cells and engineered construction of liver (INVITED)	1688
TS.SM01-4.02	Spector, Alexander - Mechanics of stem cell myogenesis	1689
TS.SM01-4.03	Belay, Tsegay - The role of line tension on budding formation induced by diffusion of proteins on lipid bilayer	1691
TS.SM01-4.04	Biria, Aisa - The conformational change of animal cells during cytokinesis	1693
TS.SM01-4.05	Franck, Christian - Mean deformation metrics for quantifying 3D cell-matrix interactions	1695
TS.SM01-5.01	Shearer, Tom - Sequential Straightening and Loading Viscoelasticity	1697
TS.SM01-5.02	Martini, Roberto - Design of bioinspired armor for optimum puncture resistance, stability and flexural compliance	1699
TS.SM01-5.03	Jasiuk, Iwona - Hierarchical modeling of plasticity and strength of trabecular bone	1701
TS.SM01-5.04	Kumar, Aloke - Nonlinear deformation and localized failure of bacterial streamers in creeping flows	1703
TS.SM01-5.05	Melancon, David - Mechanical response surfaces of a periodic porous biomaterial for orthopaedic implants	1705
PO.SM01-1.01.192	Breslavsky, Ivan - Dynamics of statically pre-loaded human aorta	1707
PO.SM01-1.02.193	Bronik, Kevin - Mechanical description and engineering analysis of cutting and needle insertion into Human skin	1709
PO.SM01-1.03.194	Formalskii, Alexander - Crutch walking: experiments, mathematical modeling	1711

PO.SM01-1.04.195	Hamashita, Yuki - Inverstigations on Fatigue Properties of Meshed Gum Metal Plates for Bone Graft Applications	1713
PO.SM01-1.05.196	Hamedzadeh, Amirhossein - Damage Model for Biological Tissues	1715
PO.SM01-1.06.197	Hashlamoun, Kotaybah - Effective Computation of Higher-Order Averaged Structure Tensors in Biomechanics	1717
PO.SM01-1.07.198	Hedrih, Andjelka - Zona pelucida as a mechano-responsive polymer	1719
PO.SM01-1.08.199	Huo, Bo - Mechanical status within cell monolayer decides the fusion of osteoclast precursors	1721
PO.SM01-1.09.200	Liu, Jinzhao - Measurement of piezoelectric voltage and streaming potential in wet bone	1723
PO.SM01-1.10.201	Luo, Yunhua - Yield-strain-energy is a better discriminator of hip fractures than BMD	1725
PO.SM01-2.01.100	Mak, Arthur - Damage of muscle cells under mechanical and oxidative stresses	1727
PO.SM01-2.02.101	Milewski, Grzegorz - Strength analysis of root fractures for endodontically treated lateral teeth	1729
PO.SM01-2.03.102	Nguyen, Khoi - Mechanics of fin stiffness in ray-finned fish	1731
PO.SM01-2.04.103	Ni, Yong - Toughening and strengthening bioinspired nanolaminates: Size effect and design insight	1733
PO.SM01-2.05.104	Ohara, Hitoshi - Evaluation on mechanical properties of 3d flexible meshed gum metal plate implants	1735
PO.SM01-2.06.105	Pak, Wansoo - Development and preliminary validation of a 5th percentile female pedestrian finite element model	1737
PO.SM01-2.07.106	Ramírez Torres, Ariel - Modeling avascular tumor growth via linear elasticity	1739
PO.SM01-2.08.107	Rodriguez, Marcel - Loading-rate dependent mechanical response of the human and porcine knee joints	1741
PO.SM01-2.09.108	Rohani, Seyed Alireza - Spatial non-uniformity in the young's modulus of the human eardrum	1743
PO.SM01-2.10.109	Soldatos, Konstantinos - Mass-growth at small strain and the human nail	1745
PO.SM01-2.11.110	Voronkova, Eva - Assessment of material and geometrical parameters influence on IOP changes after injections	1747
PO.SM01-2.12.111	Yuan, Hongyan - A cell migration model integrating mechanical stress with biochemical signals	1749
PO.SM01-2.13.112	Zhang, Lei - A study on imperfection sensitivity of pressured buckling of spherical virus shells	1751

REMODELING OF CARDIOMYOCYTES *IN VITRO*

Robert McMeeking[1,2a)], Mattia Bacca[1], Jeffrey Holmes[3] & Vikram Deshpande[4]
[1]*Materials & Mechanical Engineering Departments, University of California, Santa Barbara CA, USA*
[2]*School of Engineering, University of Aberdeen, United Kingdom*
[3]*Biomedical Engineering & Medicine, University of Virginia, Charlottesville VA, USA*
[4]*Cambridge University Engineering Department, Cambridge, United Kingdom*

Summary A feature of hypertrophy in heart disease is remodeling of cardiomyocytes. In hypertension, the heart wall tends to thicken as sarcomeres are added within cardiomyocytes in parallel, so that the heart can pump more effectively against high blood pressure. In volume overload, where the heart is called on to pump more blood, the heart tends to enlarge by adding sarcomeres within cardiomyocytes in series. This observation is duplicated *in vitro* in similar conditions imposed on excised animal myocardium. A model is presented for this response. Chemical kinetics accounts for the addition and subtraction of sarcomeres, while a contractile force is generated by an actomyosin simulator whose output also influences the chemical potentials driving remodeling. Results are presented for cyclic straining of myocardium subject to displacement boundary conditions to simulate volume overload, and force boundary conditions to simulate pressure overload. The results are consistent with the observation of remodeling *in vitro*.

INTRODUCTION

In conditions leading to congestive heart failure the heart wall tends to thicken when the heart is required to generate a higher pressure to pump blood against the higher resistance of the circulatory system associated with high blood pressure [1]. This thickening is associated with the addition of sarcomeres within cardiomyocytes where the new ones augment those already there in parallel with them, thereby enabling the heart to generate higher contractile force. When the heart is required to increase the volume of blood being pumped, such as when a faulty valve allows regurgitation, the myocytes tends to lengthen [1]. This remodeling occurs because sarcomeres within cardiomyocytes are added in series with those already there and the circumference of the heart grows. An example of *in vitro* remodeling in a rat papillary muscle is shown in Figure 1, taken from Guterl *et al.* [2]. The pair of images on the left shows the cross section of the muscle in a control sample in the same condition as extracted from the rate heart, whereas the pair of images on the right shows the cross section after remodeling in a stretched, electrically stimulated isometric condition after 36 hours. We note that the cardomyocytes have thickened in the isometric case, indicating the addition of sarcomeres in parallel to those already there.

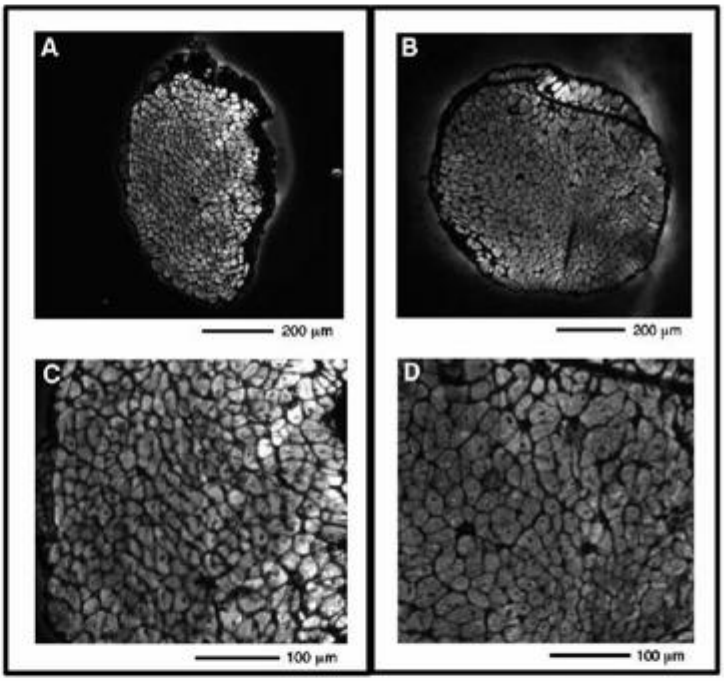

Figure 1 *A* Cross section of rat papillary muscle as extracted. *B* Cross section of rat papillary muscle after electrical stimulation *in vitro* in isometric conditions for 36 hours. *C* is a magnified image of *A* and *D* is a magnification of *B*.

We present a bio-chemo-mechanical model that is capable of predicting these phenomena as a result of changes to the thermodynamics and chemical kinetics of cardiomyocytes and their sarcomeres. Rate equations from chemical kinetics are considered to control the remodeling, but with the chemical potentials driving it being influenced by the contractile stress that the cardiomyocytes generate, thereby providing a feedback between mechanical conditions and remodeling. The simplest model for pressure overload is a force boundary condition applied to myocardium as it contracts and extends during the cardiac cycle, with the mean level of contractile load set to be higher than normal. Similarly, an elementary way of invoking volume overload is to impose a displacement boundary condition on the myocardium as it contracts and extends, with the mean extent of stretching involved being greater than normal. Such simulations are carried out with the model, and it is found that the results are consistent with the observations from experiments carried out *in vitro*. Since the results of *in vitro* experiments are consistent with *in vivo* behavior, we are encouraged that our results may have relevance to the conditions of hypertrophy.

[a)] Corresponding author. Email: rmcm@engineering.ucsb.edu.

THE BIO-CHEMO-MECHANICAL MODEL

We summarize the model as given by Vigliotti *et al.* [3] where the rate at which sarcomeres are added in parallel is given by

$$\dot{\xi} = \frac{n_u}{n}\omega_n \exp\left[-\frac{n(\mu_t - \mu_u)}{k_b T}\right] - \xi\omega_n \exp\left[-\frac{n(\mu_t - \mu_b)}{k_b T}\right] \tag{1}$$

where ξ is the number of parallel stress fibers in a cardiomyocyte, the superposed dot indicates differentiation with respect to time, n_u is the number of unbound sarcomeres collectively in the cytosol of the cardiomyocyte, ω_n is the frequency at which sarcomeres/stress-fibers attempt to cross the transition energy barrier, μ_b is the standard free energy of a sarcomere when bound in a stress-fiber, μ_u is the collective standard free energy of the proteins making up a sarcomere when they are unbound in the cytosol, μ_t is the standard free energy of a functional unit at the transition barrier, k_b is a Boltzmann's constant representative of a unit, and T is the absolute temperature. The standard free energy of a bound sarcomere is given by

$$\mu_b = \mu_{bo}\left(1 + \beta\varepsilon^2\right) - \sigma_f(1+\varepsilon)\Omega \tag{2}$$

where μ_{bo}, β and Ω are constants, ε is the strain of the myocardium and σ_f is the sarcomere stress, given by a Hill-like behavior that depends on strain and strain rate [4]. These equations are augmented by the rate at which sarcomeres are added in series, given by solving

$$\dot{n} = -\frac{\mu_{bo} n_u^2\left(1 + \beta\varepsilon^2\right)}{q\Omega\xi^2 n} \tag{3}$$

as long as $\dot{n} > 0$, and where q is a rate constant. We note that a different result is used when sarcomeres are being removed and $\dot{n} < 0$.

These 3 coupled equations, along with the expressions stating the Hill-like dependency of sarcomere stress on strain and strain rate [4], are integrated numerically in time subject to

$$\varepsilon(t) = \varepsilon^o + \Delta\varepsilon(t) \tag{4}$$

when displacement boundary conditions are imposed and subject to

$$\sigma_f(t) = \sigma_f^o + \Delta\sigma_f(t) \tag{5}$$

when traction boundary conditions are imposed. In each of these equations the superscript zero indicates a mean value and the term containing Δ is cyclic in time, with the simplest case being simply a sawtooth. Initial conditions are chosen to represent cardiomyocytes in normal, healthy condition. The outcome of the integration is then a prediction of how the myocardium thickens by increase of ξ or lengthens by increase of n.

References

[1] Grossman W, Jones D, McLaurin LP, Wall stress and patterns of hypertrophy in the human left ventricle, *J. Clin. Invest.* **56**, 56–64, 1975.

[2] Guterl AG, Haggart CR, Janssen PM, Holmes JW, Isometric contraction induces rapid myocyte remodeling in cultured rat right ventricular papillary muscle, *Am. J. Heart Circ. Physiol.* **293**, H3707-H3712, 2007.

[3] Vigliotti A, Ronan W, BaaijensFPT, Deshpande VS, A thermodynamically motivated model for stress-fiber reorganization, *Biomech. Model. Mechanobiol.* DOI 10.1007/s10237-015-0722-9, 1-29, 2015.

[4] Hill AV, The heat of shortening and the dynamic constants of muscle, *Proc. Roy. Soc. B,* **126**, 136-195. 1938.

EXPERIMENTAL AND COMPUTATIONAL ANALYSIS OF AORTIC DISSECTION

Gerhard A. Holzapfel *[1], Osman Gültekin[1], Selda Sherifova[1], Gerhard Sommer[1], and Boyce E. Griffith[2]

[1]*Institute of Biomechanics, Graz University of Technology, Stremayrgasse 16/II, A-8010 Graz*
[2]*Department of Mathematics, University of North Carolina, Chapel Hill, NC, USA*

Summary We elaborate on the mechanical strength of human thoracic aortas, in particular of harvested tissues in which a dissection occurred. Results suggest that the media has a much lower resistance to rupture under in-plane than under out-of-plane shear loading, while the tensile strength is lowest in the radial direction. A phase-field approach was used to computationally capture the obtained data, whereby an energy-based anisotropic failure criterion was developed to drive the crack phase-field. Finite element results of a simple shear test are shown and in favorable agreement with experimental data.

EXPERIMENTAL TESTS AND COMPUTATIONAL ANALYSIS OF HUMAN THORACIC AORTAS

Tissue dissection has been observed in several arterial branches including the thoracic aortas. Frequently, aortic dissection initiates from an intimal defect, may continue to propagate in the radial direction, then through the media, and may cause delamination of the aortic layers. One clinical consequence may be the creation of a false lumen (decrease of lumen and oxygen supply, see insert in Fig. 1(a)) that influences the hemodynamics with the consequence that the mechanical properties and the structural stability of the aortic wall might alter. Dissection is fatal when it propagates, in particular, by running to the adventitial side to cause an acute rupture of the aortic wall. For a review of the knowledge up to 2011 and available evidence surrounding some of the most important aspects of the disease see [1].

Mechanical strength of dissected human thoracic aortas

Among other diseased aortic tissues, in [2] we have investigated dissected human thoracic aortas using triaxial shear and uniaxial tensile tests; ultimate stress values were determined. One key finding is that the aortic media has a much lower resistance to rupture under in-plane than under out-of-plane shear loading, and under different shear loadings the aortic tissues revealed anisotropic failure properties with higher ultimate shear stresses and amounts of shear in the longitudinal than in the circumferential direction. In addition, the tensile strength is lowest in the radial direction. In-plane shear responses of dissected specimens are given in Fig. 1.

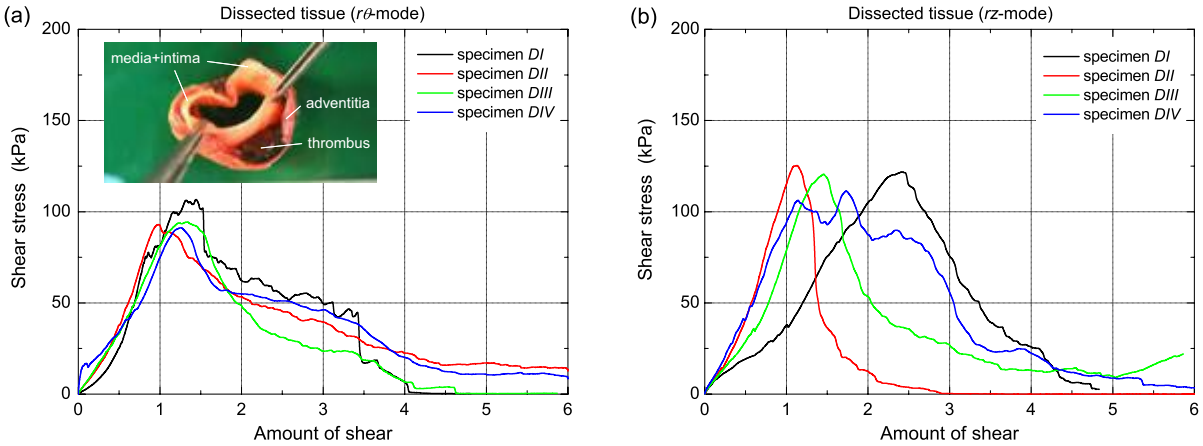

Figure 1: Cauchy shear stress vs amount of shear during 'in-plane' shear tests of dissected human thoracic aortic tissues: (a),(b) 'in-plane' shear behavior of dissected tissues tested in the circumferential and longitudinal directions, respectively [2].

A modeling approach to capture aortic failure

We use the phase-field approach to model aortic dissection. A regularized crack surface is used to overcome the problems inherent in a sharp crack discontinuity [3, 4]. In particular, to approximate the sharp crack topology we use an exponential function of the crack-field variable d according to

$$d(x) = e^{-|x|/l}, \tag{1}$$

with the conditions $d(0) = 1$ and $d(\pm\infty) = 0$, and the regularizing length-scale parameter l (sharp crack topology is restored with vanishing l), where $l \geq 2h$ for the crack zone to be resolved properly (h is the minimum finite element size) [3].

*Corresponding author. Email: holzapfel@tugraz.at

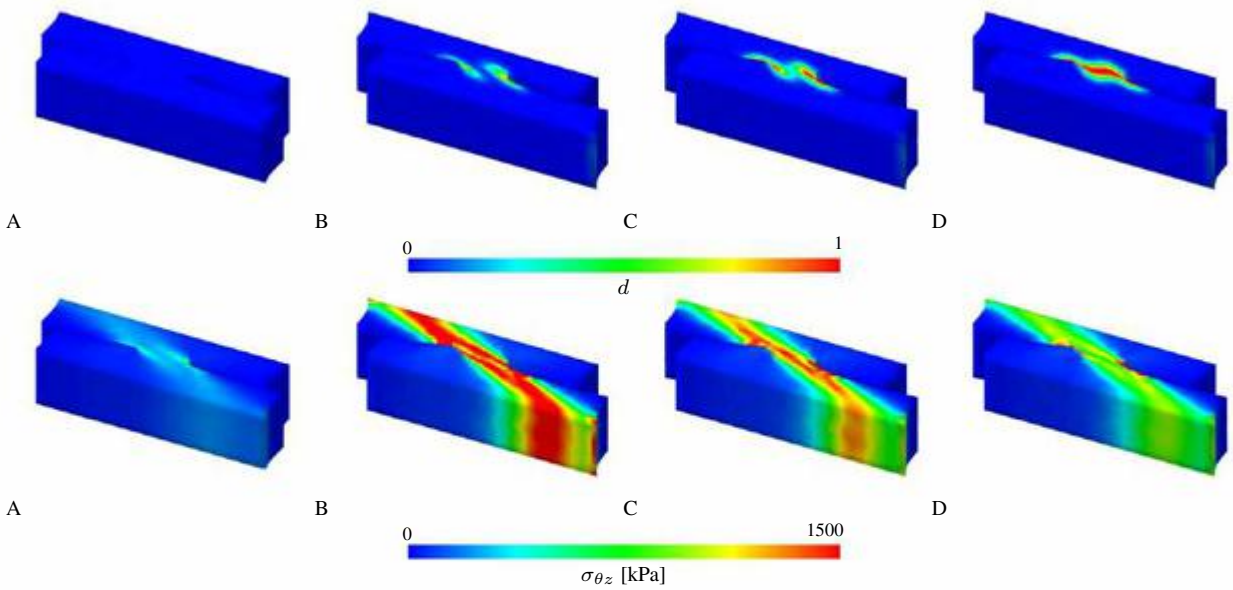

Figure 2: Distributions of the finite element results of simple shear in the longitudinal direction at four different deformation modes (A, B, C, D): (above) distribution of crack phase-field d; (below) corresponding Cauchy shear stress $\sigma_{\theta z}$ [4].

We consider an invariant-based anisotropic constitutive model expressed by the free-energy function Ψ, i.e.

$$\Psi(F, A_1, A_2; d) := g(d)\Psi_0(F, A_1, A_2), \tag{2}$$

where Ψ_0 is the effective free-energy function of the hypothetical intact tissue (for which we have taken the model in [5]), and $g(d) := (1-d)^2$ is a monotonically decreasing function describing the degradation of the tissues with the evolving d following the growth condition $g'(d) \leq 0$ with $g(0) = 1$, $g(1) = 0$ and $g'(1) = 0$. In (2), F is the deformation gradient and A_1, A_2 are tensors characterizing the two families of fibers in an aortic layer. We consider an energy-based anisotropic failure criterion which captures the evolution of d, and introduce a dimensionless crack driving function $\mathcal{H}$ which depends on two critical fracture energies relating to the ground matrix and the fiber contribution. Thus

$$\mathcal{H}(t) = \max_{s\in[0,t]} \left[\langle\, \bar{\mathcal{H}}(s) - 1 \,\rangle \right], \tag{3}$$

where $\langle\,(\bullet)\,\rangle$ is the Macaulay brackets. Hence, d does not evolve for $\bar{\mathcal{H}}(s) < 1$ and $\mathcal{H}(t)$ ensures the irreversibility of the crack evolution. The coupled problem is solved using an operator-splitting algorithm composed of a mechanical predictor step and a crack evolution step. A Galerkin procedure provides the weak forms, and spatial discretization the residual vectors and element matrices, after linearization.

Figure 2 shows the finite element results of the crack phase-field and the Cauchy shear stress of a specimen undergoing simple (out-of-plane) shear in the longitudinal direction at four different deformations states (A, B, C, D). The geometry of the specimen has incisions at both ends. The crack patterns meet in the middle where the complete failure phenomenon occurs, accompanied by a sudden loss of the load-bearing capacity. The numerical results agree with the experimental findings.

CONCLUSION

The rupture data of triaxial shear and uniaxial extension serve a basis for the development of more realistic models for tissue failure, as happening in aortic dissections; the phase-field approach has potential to model the separation of aortic layers.

Acknowledgement. We gratefully acknowledge the financial support of NIH, research grant no. NIH 7R01HL117063-03.

References

[1] Criado F.J.: Aortic dissection: a 250-year perspective. Tex Heart Inst J. 38:694-700, 2011.

[2] Sommer G., Sherifova S., Oberwalder P.J., Dapunt O.E., Ursomanno P.A., Griffith B.E., Holzapfel G.A.: Mechanical strength of aneurysmatic and dissected human thoracic aortas at different shear loading modes. J Biomech, in press.

[3] Miehe C., Welschinger F., Hofacker M.: Thermodynamically consistent phase-field models of fracture: Variational principles and multi-field FE implementations. Int J Numer Meth Engng, 83:1273-1311, 2010.

[4] Gültekin O., Dal H., Holzapfel G.A.: A phase-field approach to model fracture of arterial walls: theory and finite element analysis. Comput Meth Appl Mech Eng, in press.

[5] Holzapfel G.A., Gasser T.C., Ogden R.W.: A new constitutive framework for arterial wall mechanics and a comparative study of material model. J Elasticity, 61:1-48, 2000.

ANALYSING THE FRACTURE BEHAVIOUR OF SOFT BIOLOGICAL MEMBRANES

Alexander E. Ehret*[1,2], Alberto Stracuzzi[1], Kevin Bircher[1], and Edoardo Mazza[1,2]
[1]*ETH Zurich, Institute for Mechanical Systems, 8092 Zürich, Switzerland*
[2]*Empa, Swiss Federal Laboratories for Materials Science and Technology, 8600 Dübendorf, Switzerland*

Summary In the present contribution, the fracture characteristics, particularly the property known as 'fracture toughness' of soft collageneous membranes are analysed by means of experimental methods and theoretical models at different length-scales. Methods are proposed to overcome limitations that arise when adopting classical approaches for measuring tearing energy of non-linear materials to biological membranes. These methods are applied to different soft tissue membranes and the results are rationalized by simulations based on continuum as well as discrete network models with a focus on the localized behaviour in the near field of the crack.

FRACTURE CHARACTERISTICS OF SOFT TISSUES

The various soft collageneous membranes, including, for example, the capsules of visceral organs, the eardrum or the foetal membrane, play important physiological, structural and protective roles so that the ability to tolerate lesions or tears without catastrophic failure can literally become a 'vital' characteristic. It is widely known that soft biological tissues possess high fracture resistance and, lately, this behaviour has gained large interest [1, 2]. This property is frequently quantified in terms of the 'characteristic energy of tearing' defined in Rivlin and Thomas' seminal work on rubber [3]. Although the corresponding experimental procedures, based on testing specimens with long cuts, have been applied to soft tissues for several decades [4], their adoption is complicated by several factors. These include (i) the large sample-to-sample variability typical for biological material precluding a comparison of data between cut and uncut reference samples, (ii) the need for gentle clamping of the soft material so that slippage may occur, compromising strain measurements, and (iii) high tissue resistance to crack propagation rendering difficult the detection of the instant at which the crack grows. Moreover, (iv) for thin tissues acting in a membrane state, the significance of 'toughness' expressed in terms of energy per newly formed crack surface is questionable and the use of according (two-dimensional) membrane measures stands to reason. Finally, (v) the critical question must be posed whether absolute values of tearing energy are adequate measures to quantify the fracture resistance of soft tissues at all, cf. [5].

In addition to these experimental aspects, theoretical explanations for the observed resistance of collageneous tissues to fracture are needed and mechanisms based on the characteristics of both fibrils and networks have been identified, e.g., [1, 2]. In recent studies on the mechanical behaviour of the foetal membrane we have observed strong volume changes associated with out- and inflow of water [6, 7] and it is known that volume reduction in collagenous materials is often accompanied by strong reorientation and compaction of the collagen network, e.g., [8, 9]. Due to the small thickness, flow through the membrane surfaces is expected to dominate the water loss except for the regions which are close to the membrane's edges, where the distance to the free boundary is in the order of the thickness. Such free boundaries exist at cuts and lesions so that the reported bi-phasic behaviour is expected to be an important factor in the toughening mechanism of biological membranes. In the present contribution, this behaviour will be studied experimentally and in finite element (FE) simulations in order to better understand the fracture behaviour of biological membranes and to define appropriate measures for comparison among different tissues.

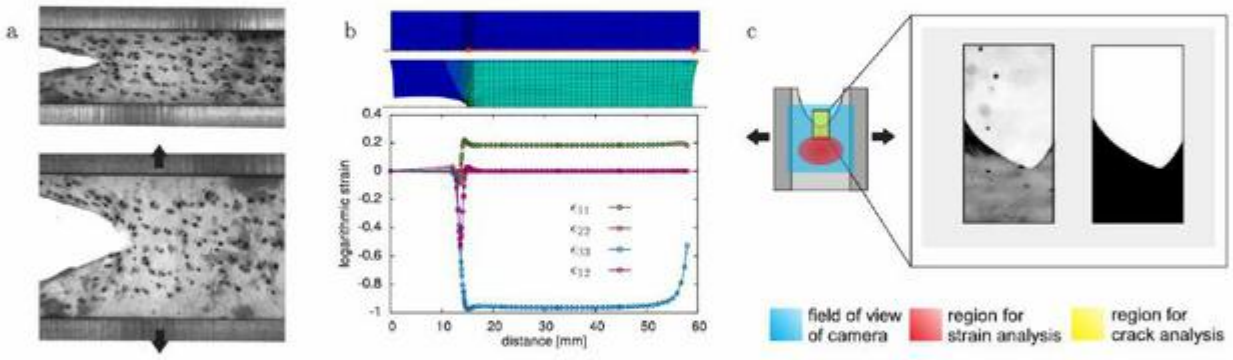

Figure 1: (a) Example of mode I tear test on bovine liver capsule. (b) Strain distribution in a FE model of a pre-cut strip-biaxial tension sample showing the rapid transition to a homogeneous state. (c) Illustration of the optical techniques used to quantify strain and the initiation of crack growth.

*Corresponding author. Email: ehret@imes.mavt.ethz.ch

EXPERIMENTAL AND THEORETICAL ANALYSES

To address the above mentioned problem of inter-sample variability a strategy is presented that allows quantifying the energy of tearing from a single, notched strip-biaxial tension sample in a mode I tear test by use of optical methods (Fig. 1a). FE simulations based on a recently proposed continuum model [10] indicated a very rapid transition to a state of plane strain with increasing distance from the tip of the cut (Fig. 1b). Strain is therefore quantified by image analysis in an appropriate region, and from the same pictures the initiation of crack growth close to the tip is detected by a custom algorithm (Fig. 1c). An analytical correction to account for sample slippage is included and the methodology is applied to different membranes including amnion and bovine liver capsule. These tissue-scale experiments are supplemented by in-situ investigations of pre-cut membranes under the multiphoton microscope, imaged by means of the second harmonic generation signal provided by collagen [9]. For the computational analysis a bi-phasic continuum model is used and combined with a discrete network approach [11] allowing for higher resolution in the vicinity of the cut and thus for investigations of the localized behaviour in this region. Eventually, based on the results provided by these experimental and theoretical tools, the fracture behaviour of different membranes is compared.

References

[1] Koh C. T., Oyen M. L.: Branching toughens fibrous networks. J. Mech. Behav. Biomed. Mater. 12:74-82, 2012.

[2] Yang W. et al.: On the tear resistance of skin. Nature Comm. 6:6649, 2015.

[3] Rivlin R. S., Thomas A. G.: Rupture of rubber. I. Characteristic energy for tearing. J. Polym. Sci. 10:291-318, 1953.

[4] Purslow P. P.: Measurement of the fracture toughness of extensible connective tissues. J. Mater. Sci. 18:3591-3598, 1983.

[5] Kendall K., Fuller K.N.G.: J-shaped stress/strain curves and crack resistance of biological materials J. Phys. D. Appl. Phys. 20:1596-1600, 1987.

[6] Mauri A et al: Time-dependent mechanical behavior of human amnion: Macroscopic and microscopic characterization. Acta Biomater. 11:314-323, 2015.

[7] Perrini M. et al.: Mechanical and microstructural investigation of the cyclic behavior of human amnion. J. Biomech. Eng. 137:061010, 2015.

[8] Lake S. P. et al.: Mechanics of a fiber network within a non-fibrillar matrix: model and comparison with collagen-agarose co-gels. Ann. Biomed. Eng. 40:2111-2121, 2012.

[9] Mauri A. et al.: Deformation mechanisms of human amnion: Quantitative studies based on second harmonic generation microscopy. J. Biomech. 48:1606-1613, 2015.

[10] Mauri A. et al.: A model for the compressible, viscoelastic behavior of human amnion addressing tissue variability through a single parameter. Biomech. Model. Mechanobiol., in press (doi:10.1007/s10237-015-0739-0), 2015.

[11] Mauri A. et al.: A discrete network model to represent the deformation behavior of human amnion. J. Mech. Behav. Biomed. Mater., in press (10.1016/j.jmbbm.2015.11.009), 2015.

MICROMECHANICS MOTIVATED MODELING OF FIBROUS TISSUES

Mor B. Frank[1], Gerhard A. Holzapfel[2], Gal deBotton[1]
[1]*Department of Biomedical Engineering, Ben-Gurion University of the Negev, Israel*
[2]*Institute of Biomechanics, Graz University of Technology, Austria*

Abstract *Investigation of the mechanical behavior of biological tissues requires efficient computational tools to provide a reliable prediction of their response. Hence there is a pressing need for models that based on realistic representation of tissues from their microstructure up to the macroscopic level. Presently, the number of models available in the literature which thoroughly capture the structure of biological tissues is fairly small. Here, we propose a novel micromechanically-based model for biological tissues that accounts for the properties of the constituting components, their spatial distribution and morphology. To this end, a 3D periodic representative volume element of the tissue is constructed and its average response is determined. The model reveals that crimped collagen fibers are recruited such that the mechanical response admits stiffening under tension versus a much softer response under compression. This model is useful to determine the mechanical response of tissues while reducing experimental labor.*

INTRODUCTION

Collagenous tissue is an abundant construction in various tissue types, e.g., blood vessels, skin, tendons, and ligaments and thus play a crucial role in physiological and pathological conditions. It is well known that the functionality of tissues and progress of diseases are affected by the mechanobiology at the ultrastructure tissue scale [1]. Moreover, many methods of clinical interventions rely on mechanical stimulus such as balloon angioplasty which enlarge a narrowed coronary artery. Taken together, there is a crucial need to investigate the mechanics of tissues and of a collagenous tissue in particular.

Recently it is commonly accepted that computational models of tissue microstructure are necessary to obtain a reliable description of the mechanical response, specifically when dealing with soft tissues. Broadly speaking, models of tissues belong to one of the classes: phenomenological or structural. In recent decades, most of the proposed models were phenomenological with the incorporation of several structural elements [2]. In order to reliably describe the material behavior these models require distinctive tuning and calibration against large sets of costly experimental measurements. To overcome this shortening, we propose here a micromechanically-based model of soft collagenous tissues [3] which is based on structural information from microscopic images of collagenous tissues (Fig.1). Image-based structural description of fibrous tissue microstructure further leads to a better understanding of the mechanical behavior by enabling information regarding the heterogeneous microstructure of the tissue.

Methods

In this study we examine the behavior of fibrous tissues by application of periodic homogenization using finite element method (FEM). We define 3D representative volume element (RVE) of collagenous tissue (Fig.2). Our model is based on geometrical and histological parameters of collagen fibers such as diameter, contour length, wave length, volume fracture, waviness, spatial distribution, amplitude etc. Numerical simulations using FEM are performed to analyze the recruitment process of crimped collagen fibers and to predict the overall mechanical behavior of fibrous biological tissues. Average energy and stresses are computed for the RVE in accordance with the periodic boundary conditions.

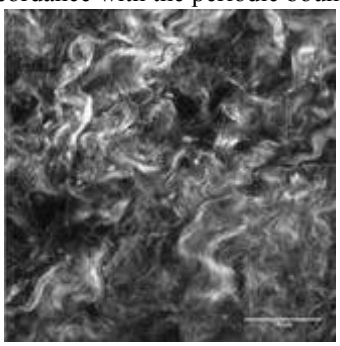

Figure 1. Crimped collagen fibers embedded in adventitial layer obtained from a human abdominal aorta. Courtesy: Institute of Biomechanics, TU Graz (JA Niestrawska).

[a)] Corresponding author. Email: morbeno@post.bgu.ac.il

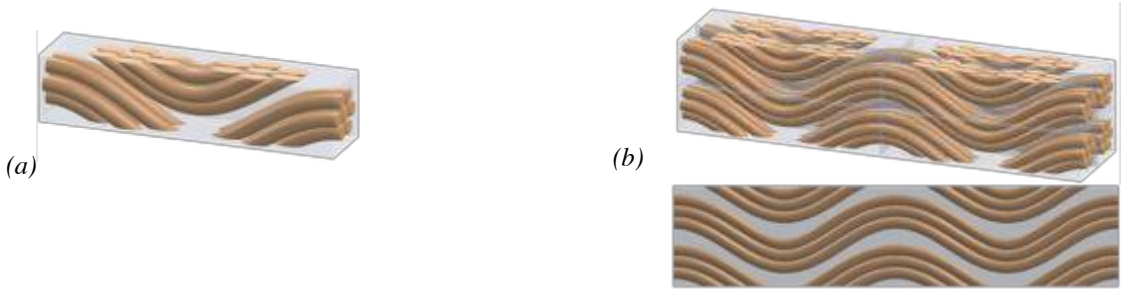

Figure 2. *(a)* 3D representative periodic RVE. *(b)* 3D periodic media of collagenous tissue; isometric view (top) and front view (bottom).

Results

Stored energy and stress in the fiber direction are computed and average quantities over the RVE are extracted (Fig.3, 4). We note that while simple neo-Hookean models were assigned to both the fibers and the matrix constituents, the overall response admits stiffening of the tissue under tensile loads versus a much softer response under compressive loads. This behavior stems from straightening of the fibers under tension.

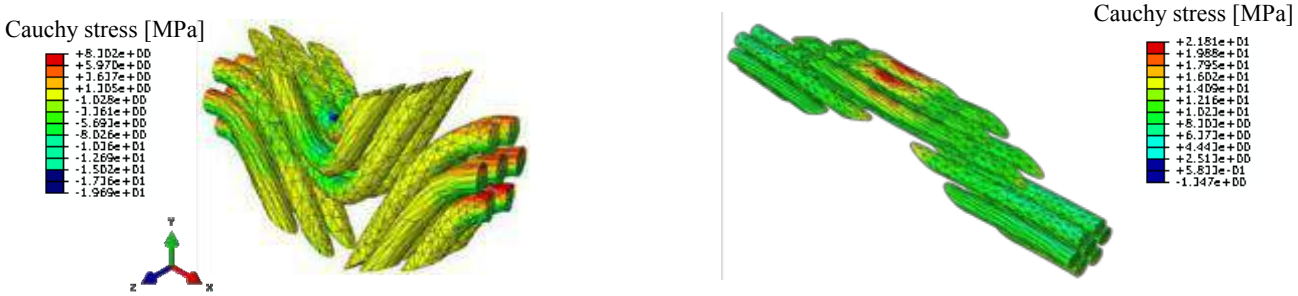

Figure 3. Deformed configuration at 30% compression (left) and tension (right) along the fibers.

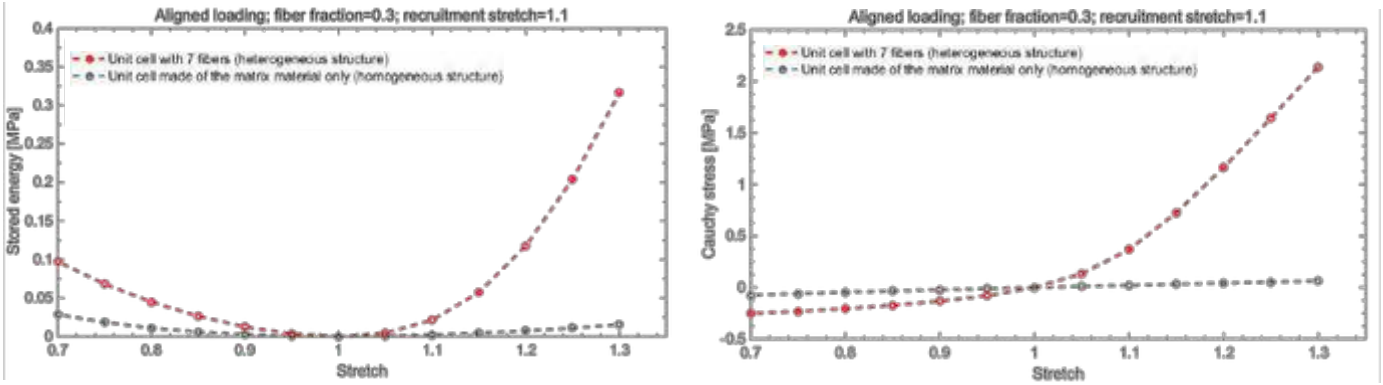

Figure 4. Stored energy (left) and Cauchy stress (right) versus stretch of a collagenous tissue RVE.

CONCLUSION

In summary, we propose a 3D micromechanically-based model which considers structural parameters of fibrous biological tissues and thus can predict the mechanical response of collagenous tissues. As expected, the crimped collagen fibers are recruited up to a pre-defined locking (recruitment) stretch. At this deformation state the collagen fibers start to exhibit linear stress-stretch relationship indicating overall stiffening of the tissue at the macroscale.

References

[1] Humphrey J. D.: Continuum biomechanics of soft biological tissues. Proc. R. Soc. Lond. A, 459:3-46, 2003.

[2] Holzapfel G.A., Ogden R.W.: Constitutive modelling of arteries. Proc. R. Soc. A, 466:1551–1597, 2010.

[3] deBotton G., Oren T.: Analytical and numerical analyses of the micromechanics of soft fibrous connective tissues. Biomech Model Mechanobiol, 12:151-166, 2013.

THE IMPORTANCE OF PHYSIOLOGICALLY AND ANATOMICALLY REPRESENTATIVE LIGAMENTS IN KNEE MODELS

Benjamin C. Marchi *[1] and Ellen M. Arruda[1,2,3]

[1]*Department of Mechanical Engineering, University of Michigan, Ann Arbor, Michigan, USA*
[2]*Department of Biomedical Engineering, University of Michigan, Ann Arbor, Michigan, USA*
[3]*Program in Macromolecular Science and Engineering, University of Michigan, Ann Arbor, Michigan, USA*

Summary The mechanical responses of soft tissues are complex, potentially incorporating components of nonlinearity, anisotropy, and viscoelasticity. The constitutive intricacies are augmented by challenges associated with the construction of accurate geometric representations of soft tissues, particularly in computational models of whole knee biomechanics. This work investigates the role of ligament structure and constitutive form in the evolution of strain within soft tissues during active joint motion including effects related to ligament prestrain.

ABSTRACT

The anterior cruciate ligmanet (ACL) is a critical lower limb stabilizing ligament. Its integrity is paramount in maintaining joint health and performance. Yet, ACL tears and ruptures are among the most common injuries in sport, contributing to over $200,000$ ligament reconstruction procedures annually just in the United States. While the high incidence of ACL injury is alone troubling, the frequency of rupture is markedly increasing [2]—the number of reconstructions is projected to increase by $4 \circ 5\%$ annually over the next 5 years—while the median age of those affected is decreasing [1]. This combination is particularly problematic due to the potentially significant long-term complications linked to surgical interventions involving ligament reconstruction. Osteoarthritis (OA) is a degenerative soft tissue disease that is characterized by declining articular cartilage integrity. OA, a tremendously prevalent and debilitating disease affecting over 15% of the adult American population [3], has been hypothesized to manifest from fundamental alternations in the biomechanics of the knee resulting from either ACL deficiency or reconstruction. Therefore, by understanding the role of the ACL in preserving the natural operating conditions of the joint and by determining the corresponding contribution of reconstructive procedures it is possible to construct individual-specific treatments optimized for positive patient outcomes, potentially reducing the risk of detrimental secondary effects like OA or graft failure.

This work explores the complex anatomy and constitutive behavior of the native ACL. Structurally the ACL is an aggregate of two independent fiber bundles, the anteromedial (AM) and posterolateral (PL); each of these fiber bundles has unique mechanical properties, which include elements of nonlinearity, viscoelasticity, and anisotropy, driven by the underlying macromolecular composition of the ACL—which is composed primarily of oriented collagen fibrils within a compliant extracellular matrix. While both the AM and PL bundles emanate proximately on the lateral femoral condyle and terminate distally on the anterior tibial plateau, the fiber bundles interact with each other and collateral tissues within the joint capsule to yield a geometrically complex, prestrained double bundle structure. This prestrained complex is characterized at the femoral enthesis by the AM bundle covering the PL bundle, attaching proximally on the femoral condyle, and along the ligament bulk by the AM bundle wrapping around the perimeter of the PL bundle in a slightly compressed configuration. Due to the substantial interaction between bundles and the spatial constraints imposed by the physics of normal joint motion there exists no physiological configuration in which the AM and PL bundles are stress free. Limitations imposed by traditional imaging and segmentation techniques further complicate modeling the interaction between fiber bundles, especially in the context of whole joint computational models. In this work we extract approximate representations of each fiber bundle by computationally manipulating the joint in a nonphysical manner to orient the joint such that the effects of the structural interaction between the bundles is minimized. Once the bundles are extracted, the deformations associated with the manipulations are removed and, starting from that stress free configuration, the joint is restored to its natural configuration. This operation yields unique, inhomogeneous strain distributions in each fiber bundle at every knee flexion angle. The effect of the *a priori* strain distributions was quantified by examining the response of the joint to both normal, everyday activities (gait) and potentially injury causes events (simulated landing).

References

[1] J. G. Ingram, S. K. Fields, E. E. Yard, and R. D. Comstock. Epidemiology of knee injuries among boys and girls in us high school athletics. The American journal of sports medicine, 36(6):11161122, 2008.

[2] S. Kim, J. Bosque, J. P. Meehan, A. Jamali, and R. Marder. Increase in outpatient knee arthroscopy in the united states: a comparison of national surveys of ambulatory surgery, 1996 and 2006. The Journal of bone and joint surgery. American volume, 93(11):9941000, 2011.

[3] R. C. Lawrence, D. T. Felson, C. G. Helmick, L. M. Arnold, H. Choi, R. A. Deyo, S. Gabriel, R. Hirsch, M. C. Hochberg, G. G. Hunder, et al. Estimates of the prevalence of arthritis and other rheumatic conditions in the united states: Part II. Arthritis & Rheumatism, 58(1):2635, 2008.

*Corresponding author. Email: bmarchi@umich.edu

NONLINEAR ELASTICITY OF BIOPOLYMER GELS UNDER COMPRESSION

Xinpeng Xu[a] & Samuel A. Safran[b]
Department of Materials and Interfaces, Weizmann Institute of Science, Rehovot, Israel

Summary Biopolymer gels, comprised of cross-linked semiflexible filaments, show nonlinear elasticity at small tensile strains (above some characteristic value) as well as softening for compressive strains. Here we predict an unusual elastic response to uniaxial compression. We focus on two competing mechanisms that contribute to the elasticity of biopolymer gels upon compression: (i) Stiffening, due to polymer densification by out-going water flow. (ii) Softening, due to polymer buckling under compression. We predict three generic types of behavior in different regions of the stress-strain curve: (1) Densification region at small strains, before the onset of polymer buckling, (2) Intermediate region where a fraction of the polymer segments are buckled which tends to counteract the densification effect, and (3) Buckled region where all the polymers are buckled and the modulus tends to very small values.

Biopolymer hydrogels comprise crosslinked, semiflexible filaments (e.g., actin, collagen, and fibrin) [1]. They are important constituents of both the cellular cytoskeleton and extracellular matrix of tissues [2]. Unlike most synthetic gels, biopolymer gels often exhibit highly nonlinear elastic responses to applied tensile forces above some small strain or compressive forces at small strain [1, 3-6], e.g., fibrin gels stiffen at small shear strains above 10% [1, 3] and soften at compressive strain about 5% [5, 6]. The strain stiffening nonlinearity of biopolymer gels has been identified to be of great biological importance [1, 3] since it impacts force transmission by cells in such gels and many studies have aimed to understand its physical origin [1, 3]. However, relatively less attention has been paid to the elastic responses of biopolymer gels under compression [6, 7]. This nonlinear elastic response is also critical for the physiological function of animal cells and some tissues [1, 4, 7, 8]. For example, in recent work [4], we have shown that the nonlinear (asymmetric) responses of biopolymer gels to both tension and compression can together significantly increase the range of force transmission and are hence critical for the long-range cell-cell and cell-matrix communication. Moreover, recently it has been shown [7] that the understanding of the elastic responses of biopolymer gels to compression is a key feature of the self-contraction dynamics of cellular cytoskeleton at subcellular scale. In this paper, we investigate the elastic responses of biopolymer gels to uniaxial compression. We propose that the balance of two competing mechanisms contribute to the nonlinear elasticity of biopolymer gels upon compression (as schematic shown in Fig. 1): (i) Stiffening due to polymer densification by out-going water flow: Compression applied to biopolymer gels induces water to flow out of the gels and hence increase the density of polymer segments within the gel. This densification results in an increase in the elastic modulus of the gel which scales with the energy per unit volume per crosslink. (ii) Softening due to polymer buckling: Compression can also induce the buckling [1, 5, 6] of the polymer segments between cross-linkers. The buckled polymers lose resistance to the applied forces and this tends to decrease the elastic modulus of the gel.

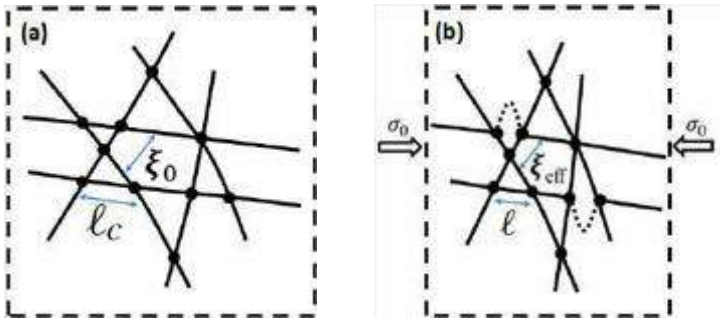

Fig. 1. Schematic illustration of the elastic responses of a biopolymer gel to uniaxial compression. (a) Reference state. ℓ_c denotes the contour length of polymer segments between cross-linkers. We take into account the polydispersity of the contour length by assuming a uniform distribution of ℓ_c over a range of values. ξ_0 denotes the mesh size of the gel, which scales with the polymer concentration c, as $c^{-1/2}$. (b) Deformed state. Some polymer segments buckles (for affine deformation, shorter ones buckle first, shown as dotted lines). ℓ denotes the deformed distance between cross-linkers. ξ_{eff} denotes the effective mesh size of the gel, which takes into account the polymer densification due to the flow of water out of the gel as it is compressed.

For simplicity, we first consider the case of affine deformations (strains), a uniform length distribution of the polymers, and zero Poisson ratio (due to water flow). We later briefly discuss the effects of various length distributions and that of non-affine deformation by considering the case where equal forces applied to each polymer segments. This is in contrast to most previous studies [1, 6, 7] where the lengths of polymer segments were assumed to be identical and the length polydispersity is neglected completely. Here we show how the polydispersity of the polymer length has an important effect on the elastic modulus of biopolymer gels under uniaxial compression. We have identified three limiting regimes that are functions of the concentration of semiflexible polymers and the degree of polydispersity (as schematic shown in Fig. 2a): (i) Dilute regime, where polymer segments are independently compressed and buckle when the force exceeds a critical value. (ii) Gas regime for large polydispersity, where the gels have high configurational entropy that is a function of the polymer concentration, analogous to the translational entropy of gases. (iii) Semidilute regime, where excluded volume interactions

[a]Email:xpxu2010@gmail.com
[b]Email: sam.safran@weizmann.ac.il

between the polymers becomes important. We predict that corresponding to each of the three regimes, there exist three regions in the stress-strain curve (as schematic shown in Fig. 2b) whose derivative yields the elastic modulus of the system: (1) Densification region where none of the polymers have yet buckled; here the elastic modulus increases with strain. (2) Intermediate region where a fraction of the polymer segments are buckled and the densification effect is moderated by the softening due to buckling and (3) Buckled region where all the polymers are buckled and the elastic modulus can be very small. We will relate these theoretical predictions to recent experiments [5-7].

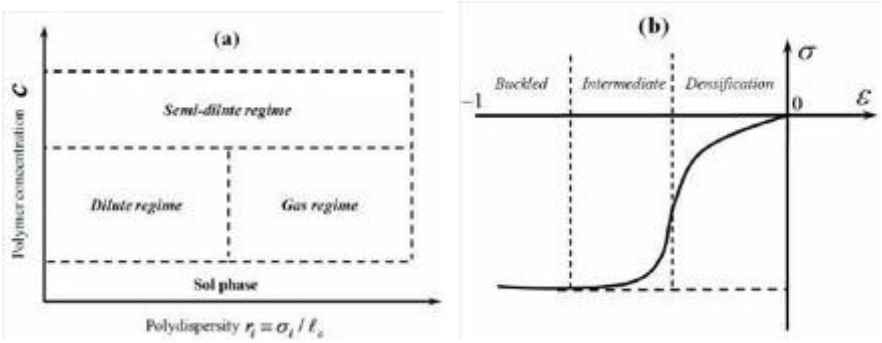

Fig. 2. (a) Schematic illustration of the regimes defined by the concentration of semiflexible polymers and the degree of polydispersity. For a fixed ratio of crosslinkers to polymer (monomers), the semiflexible polymer network undergoes a sol-gel transition when the polymer concentration exceeds a certain value. Here we have investigated three gel regimes: (i) Dilute regime. (ii) Gas regime for large polydispersity. (iii) Semidilute regime. (b) Schematic illustration of a typical stress-strain curve. Three regions can be identified: (1) Densification region at small strains, before the onset of polymer buckling, (2) Intermediate region where a fraction of the polymer segments are buckled, and (3) Buckled region where all the polymers are buckled.

References

[1] Broedersz, C. P.. and MacKintosh F. C.: Modeling semiflexible polymer networks. *Rev*. *Mod*. *Phys*. **86**:995, 2014.

[2] B. Alberts, A. Johnson, J. Lewis, M. Raff, K. Roberts, and P. Walter, Molecular Biology of the Cell, 5th ed. (Taylor & Francis, London, 2007).

[3] M. L. Gardel, J. H. Shin, F. C. MacKintosh, L. Mahadevan, P. Matsudaira, and D. A. Weitz, *Science* 304, 1301 (2004); C. Storm, J. J. Pastore, F. C. MacKintosh, T. C. Lubensky, and P. A. Janmey, *Nature***435**:191, 2005.

[4] Xu X. and Safran S. A.: Nonlinearities of biopolymer gels increase the range of force transmission.*Phys*. *Rev*. *E* **92**:032728, 2015.

[5] Kim O. V., Litvinov R. I., Weisel J. W., and Alber, M. S.: Structural basis for the nonlinear mechanics of fibrin networks under compression. *Biomaterials***35**:6739, 2014.

[6] Kim O. V., Liang, X., Litvinov R. I., Weisel J. W., Alber, M. S., and Purohit P. K.: Foam-like compression behaviour of fibrin networks. *Biomech*. *Model Mechanobiol*,2015.

[7] Ideses Y., Simon S., Kruse K., S. A. Safran, and Bernheim-Groswasser A.: The dynamics of buckling of active self-organizing contractile sheets.*in preparation*.

[8] Schwarz, U. S. and Safran, S. A.: Physics of adherent cells. *Rev*. *Mod*. *Phys*.**85**:1327, 2013.

FLUCTUATIONS IN EXPERIMENTS OF CELLS ON SUBSTRATES

Vikram Deshpande[1a)] & Andrea Vigliotti[2]
[1]*Cambridge University Engineering Department, Cambridge, United Kingdom*
[2]*Innovative Materials Laboratory, Italian Aerospace Research Centre, Capua, Italy.*

Summary We present a statistical mechanics framework to model the inherent variability observed in experiments of cells on a range of engineered substrates. The framework comprises two components. First, the probability of observing the cell in a particular state is estimated in terms of the free-energy of that state by invoking the concept of maximising Gibbs entropy. Second, a cytoskeletal protein model is presented for this free-energy of a given state. Predictions using this framework are discussed for a range of experimentally observed phenomena. These include: (i) the spreading of cells as a function of the stiffness and the substrate; (ii) durotaxis whereby cells tends to migrate guided by rigidity gradients on substrates and (iii) differentiation of stem cells guided by the stiffness of substrates.

INTRODUCTION

Substrate stiffness, topology and patterning of ligands on substrates are important factors in the response of many cell types. Observables in such experiments include cell shape, area, cytoskeletal protein arrangements etc. However, these observables typically exhibit significant variability between nominally identical experiments though statistics such as mean cell area, shape etc. over a large number of experiments is very consistent. This variability in inherent in terms of the bio-chemical processes occurring within cell but *deterministic* "cell mechanics" models neglect/ignore these critical phenomena. In order to redress this deficiency we take an alternative approach present a statistical mechanics viewpoint to analyse the response of cells in such in-vitro settings over a time-period of 1 week of so. Over this time-frame processes such as protein production, cell division etc. are not significant and thus we mainly concerned with the evolution of cell shape, cytoskeletal structure etc. In in-vitro experiments, the cell(s) is typically immersed in a medium (nutrient bath) that is maintained at a constant thermodynamic temperature and pressure by contact with the external atmosphere. Moreover, over the duration of the experiment further nutrients may be added to the medium in order to maintain the nutrient concentration. The experimental setup (i.e. substrate + cell + medium) is in contact with an isobaric-isothermal reservoir but it is difficult (and not desirable) to analyse this entire setup. We thus define the system as comprising the substrate + cell but absent any nutrient packets (i.e. glucose etc.). These nutrients are part of the thermo-nutrient reservoir (along with any other nutrients added to the medium). The equilibrium of this system is analysed by maximising Gibbs entropy.

Equilibrium of the system based on Gibbs entropy

To define equilibrium, we define two time-separated levels of micro-states: (i) molecular micro-states defined by the type, position and velocities of the molecules in the system and (ii) spread micro-states defined by the mapping of material points on the surface of the cell to substrate material points that the cell is in contact with. Then we define a Gibbs entropy function as

$$S_T = -\sum_J \sum_M P^{(m,j)} \ln P^{(m,j)}, \tag{1}$$

where $P^{(m,j)}$ is the joint probability of molecular micro-state 'm' and spread micro-state 'j'. The summations are over all possible molecular micro-states M and energy carrier micro-states J. The equilibrium probability distribution $P^{(m,j)}$ corresponds to the distribution that maximises S_T subject to appropriate constraints. It is convenient to recast (1) in terms of the conditional probability $P^{(m|j)}$ of molecular micro-state 'm' given a spread micro-state 'j' so that

$$S_T = -\sum_J P^{(j)} \sum_{M(j)} P^{(m|j)} \ln P^{(m|j)} + \sum_J P^{(j)} \ln P^{(j)}, \tag{2}$$

where $P^{(j)} = \sum_{M(j)} P^{(m,j)}$ is the probability of the spread-micro-state 'j' and $M(j)$ the number of molecular micro-states given spread micro-state 'j'. The fluctuation of the molecular micro-states is governed by the diffusion of molecules within the cell and thus occurs on the order to a few milli-seconds with the molecular macro-state (i.e. $P^{(m|j)}$) changing on the order of seconds. By contrast, the spread micro-state can change by processes such as actin treadmilling, dendritic nucleation etc. with the spread-macro-state $P^{(j)}$ changing on the order of minutes. We then use this separation of time-scales first examine equilibrium for a given spread micro-state. This gives the entropy $\tilde{S}_T$ at equilibrium for a given spread micro-state 'j' as

$$\tilde{S}_T = -\frac{1}{k_B T}\left[\sum_J P^{(j)} G^{(j)} + k_B T \sum_J P^{(j)} \ln P^{(j)}\right] + \frac{\bar{H}}{k_B T}, \tag{3}$$

[a)] Corresponding author. Email: vsd@eng.cam.ac.uk

where k_B and T are the Boltzmann's constant and thermodynamic temperature, respectively while $G^{(j)}$ is the equilibrium Gibbs free-energy of spread-micro-state 'j'. This expression is derived by maximising S_T subject to the enthalpy constraint $\bar{H} \equiv \sum_J P^{(j)} \sum_{M(j)} P^{(m|j)} H^{m(j)}$ with $H^{m(j)}$ the enthalpy of molecular micro-state 'm' given a spread micro-state 'j'. The equilibrium distribution of the spread micro-states is determined by maximising $\bar{S}_T$ subject to the constraint that complex bio-chemical processes within the cell attempt to maintain constant time-averaged concentrations of of proteins within the cell (i.e. *cellular homeostatis*). This then gives the probability $P^{(j)}$ in terms of a distribution constant β as

$$P^{(j)} = \frac{e^{-\beta G^{(j)}}}{\sum_J e^{-\beta G^{(j)}}} \tag{4}$$

with β determined from the known ensemble average free energy $\bar{G} \equiv \sum_J P^{(j)} G^{(j)}$. This probability distribution is calculated by employing the model of Vigliotti *et al*. [1] for the free-energy $G^{(j)}$ of a spread micro-state and then calculating the partition function $\sum_J e^{-\beta G^{(j)}}$ by performing a large number of finite element calculations for $G^{(j)}$ over the entire phase-space.

RESULTS

Here we present some selected results for the cell area A as a function of the Young's E_s of the substrate. In all cases, the cell area is normalised by the area A_∞ of the cell on an infinitely rigid ($E_s = \infty$) substrate. The probability distribution $p(\bar{A})$, where $\bar{A} \equiv A / A_\infty$, is plotted in figure 1A for selected values of substrate stiffness E_s. With increasing E_s, both the spread of the probability distribution as well as the mode of the distribution increases. The corresponding predictions of the mean cell area $< A >$ are included in figure 1B along with the measurements reported in [2]: the predictions are in excellent agreement with measurements. Moreover, Engler *et al*. [2] report that the standard error of the cell area also increases with increasing E_s. This is consistent with the prediction in figure 1A that the spread of the probability distribution increases with E_s.

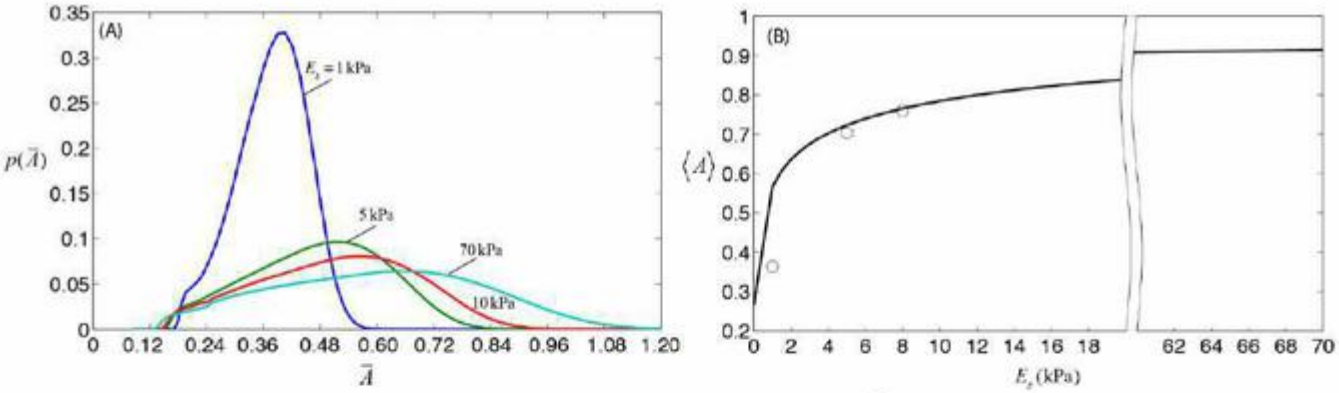

Figure 1: (a) Predictions of the probability distribution of normalised cell area $\bar{A} \equiv A / A_\infty$ for selected values of substrate stiffness E_s. (b) Comparison between predictions and measurements [2] of the mean cell area $< A >$ as function of the substrate stiffness E_s.

CONCLUSIONS

Comparisons between predictions of the mean cell area as a function of the substrate stiffness are shown here to be in excellent agreement with measurements. The observed variability in measurements (i.e. the reported standard error) is a natural outcome of the model suggesting that this variability is a result of the biochemical processes that results in cellular homeostatis.

References

[1] Vigliotti A., Ronan W., Baaijens F.P.T., Deshpande V.S.: A thermodynamically motivated model for stress-fiber reorganisation. *Biomech. Model. Mechaniobiology*, http://dx.doi.org/10.1007/s10237-015-0722-9, 1-29, 2015.

[2] Engler A., Bacakova L., Newman C., Hategan A., Griffin M., Discher D.: Substrate compliance versus ligand density in cell on gel responses, *Biophys J*., **86**, 617-628, 204.

CAROTID WALL STRESS ANALYSIS BASED ON *in vivo* INTRAVASCULAR OPTICAL COHERENCE TOMOGRAPHY IMAGING

Cuiru Sun[1], Guangwei Lu[1] , Victor Yang[2,3], Jinlong Chen[1]
[1] *Department of Mechanical Engineering, Tianjin University, Tianjin, China*
[2]*Department of Electrical and Computer Engineering, Ryerson University, Toronto, Ontario, Canada*
[3] *Division of Neurosurgery, Sunnybrook Health Sciences Centre, Toronto, Ontario, Canada*

Summary Biomechanical properties of arteries are strongly related to vascular disease. Theoretical analysis or numerical simulation based on simplified models can't provide accurate information about the deformation of the blood vessel. In this paper, high resolution intravascular optical coherence tomography (IVOCT) imaging is integrated with numerical simulation to study the transmural stress distribution of arteries. 3D structure and flow profile was obtained through imaging of a porcine carotid artery *in vivo*. 3D carotid model was created based on the images and the blood flow velocity was incorporated for simulation. Preliminary results show that the Von Mises stress distribution across the vascular wall thickness is circumferentially uniform. This is the first carotid wall stress analysis based on *in vivo* IVOCT imaging. It may pave the road for vascular mechanics studies by integrating high resolution imaging and numerical simulation, which will provide important information for the study, diagnosis and treatment of vascular diseases.

INTRODUCTION

Atherosclerosis-hardening and narrowing of the arteries is the main reason for vascular disease, for example, carotid atherosclerosis can cause strokes and lead to brain damage [1]. Hemodynamic factors in the carotid are important determinants of the development of the plaques [2]. Although great progress has been made in vascular mechanics by both solid and fluid theoretical and numerical analysis, most of the studies are based on idealized models and unverified assumptions. There is little work performed by employing real vascular anatomy and blood flow profile. Blood vessels stay in a complicated loading environment in human body. Subtle changes in geometry of blood vessels can affect the flow field significantly [3]. It is crucial to obtain realistic vascular models and blood flow profiles.

Intravascular optical coherence tomography (IVOCT)[4] has been playing an important role in coronary imaging since its approval by the US FDA (food and drug Administration) three years ago. IVOCT provides histological resolution images of the vascular wall, which is greatly facilitated atherosclerotic plaque imaging and stenting treatment. We have developed method to obtain the blood flow profile simultaneously with the vascular wall structure [5]. In this manuscript, *in vivo* IVOCT imaging of porcine carotid is integrated with biomechanical simulation to study the deformation and stress distribution within the wall thickness. The results will provide new insights to arterial mechanics and the development of atherosclerotic plaques.

METHODS

A porcine carotid artery was imaged by an intravascular OCT system (C7-XR, St. Jude Medical Inc. St. Paul, Minnesota, USA) *in vivo*[6]. As described in [5], an OCT imaging catheter was inserted through the femoral artery to the common carotid, where a pull-back of the catheter was run to obtain a series of images along the length of the artery. The structural images could be reconstructed to a 3D image of the carotid artery using image processing software. We developed algorithms to obtain the blood flow pattern simultaneously with the arterial wall structure [5]. The carotid structure and blood flow are then used for numerical simulation to study the carotid wall stress. Blood is modelled as an incompressible Newtonian fluid. The carotid vascular model is modelled as Neo-Hookean hyperelastic material. A 3-layer model of the blood vessel including the intima, media and adventitia is built in COMSOL (COMSOL 4.4, Stockholm, Sweden) based on the 3D IVOCT image. Blood is modelled as a Newtonian fluid with density ρ = 1050 kg/m3 and dynamic viscosity μ=2.68E-3 kg/ms. The blood flow waveform of a point shown as the * in Figure 1 c) and d) is plotted out with time and is shown in Figure 2 b), which is used for simulation. One way fluid-structure coupling is applied where the change of the shape of the vessel wall is assumed not to influence the blood flow to analyse the deformation and stress distribution of the carotid wall.

RESULTS

3D structure of the porcine carotid shown in Fig. 1 a) was constructed in Osirix by inputting a hundred frames of pull back OCT images. Fig. 1 b) is one frame of the OCT images of the cross-section of the porcine carotid, where the OCT imaging catheter and guide wire can be seen as circles and a bright curve with shadow behind. From Fig. 1 a) and b) the layers of intima, media and adventitia can be identified. Blood flow is imaged when the OCT catheter is parked at a position. Fig. 1 c) and d) are images of the Doppler phase change induced by blood flow at two different times. The Doppler phase change, which is in proportion to the blood flow velocity demonstrates the contour of the velocity. The carotid model created in COMSOL based on Fig. 1 a) and b) is shown in Fig. 2 a). Blood velocity waveform extracted from the point A shown on Fig. 1 c) and d) is plotted in Fig. 2 b). A quadratic curve fitting was applied to the velocity, which was then input to COMSOL for the fluid simulation. Three cross-sections of the velocity distribution at 0.5 s are plotted in Fig. 2 c), which show similar pattern as those in Fig. 1 c) and d). The vascular wall stress were then analysed. The Von Mises stress is

[a] Corresponding author. Email: carry_sun@tju.edu.cn

shown in Fig. 2 d) where the distribution is circumferentially uniform despite the eccentric annulus created by the IVOCT catheter.

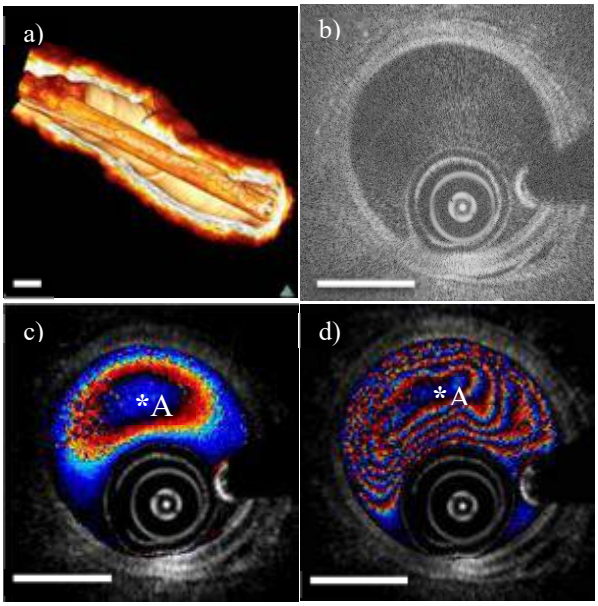

Fig. 1 OCT imaging of porcine carotid artery: a) OCT 3D image of the artery; b) OCT structural image of a cross-section of the artery; c) and d) blood flow profiles at two different times during flush. Scale bars represent 1 mm.

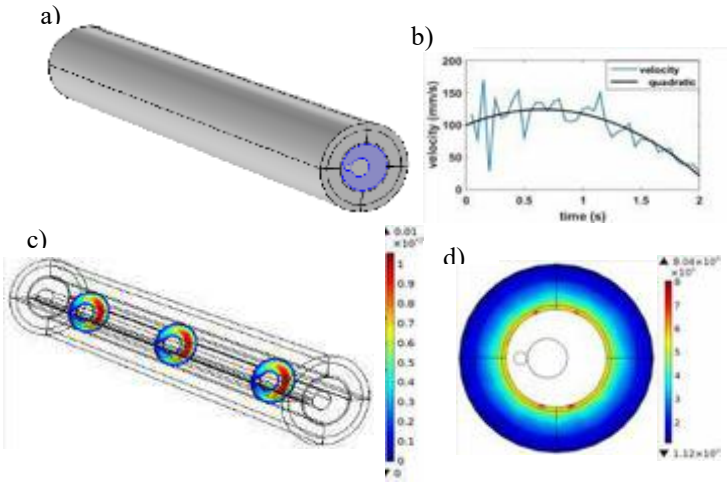

Fig. 2 Stress analysis by COMSOL simulation. a) geometrical model built based on Fig. 1 a); b) velocity profile based on Fig. 1 c); c) velocity wave form of point A in Fig. 1 c); d) von mises stress distribution of a cross-section

DISCUSSION AND CONCLUSIONS

Blood flow velocity and blood vessel structure with an eccentric catheter obtained through IVOCT are integrated with COMSOL simulation for carotid stress analysis. From Fig. 1 and 2, it can be seen the current simulated flow pattern matches well to the experimental results when the flow velocity is small as shown in Fig. 1 c). When the velocity becomes greater such as Fig. 1 d), umbilicate contour lines appear, which don't show in the simulation. Thus, the velocity profile obtained from IVOCT imaging, instead of the velocity of a point will be integrated with numerical simulation in our following studies. In addition, how the imaging catheter will influence the flow and the wall stress will be studied further. In conclusion, this is the first carotid wall stress analysis based on *in vivo* IVOCT imaging. This study demonstrated the possibility of integrating IVOCT images with numerical simulation to study vascular mechanics. Based on the high resolution *in vivo* images, the most realistic model up to date was created. Integrated with numerical simulation, the basic carotid wall stress was analysed. This study will pave the road for vascular mechanics studies by integrating high resolution imaging and numerical simulation, which will provide important information for the study, diagnosis and treatment of strokes and other vascular diseases.

References

1 Rosenfeld, M.E.: An overview of the evolution of the atherosclerotic plaque: from fatty streak to plaque rupture and thrombosis, *Z Kardiol*, **89**: 2-6, 2000

2 Malek, A.M., Alper, S.L., and Izumo, S.: Hemodynamic shear stress and its role in atherosclerosis, *Jama-J Am Med Assoc*, **282**, (21): 2035-2042, 1999

3 Perktold, K., and Resch, M.: Numerical Flow Studies in Human Carotid-Artery Bifurcations - Basic Discussion of the Geometric Factor in Atherogenesis, *J. Biomed. Eng.*, **12**, (2): 111-123, 1990

4 Suter, M., Nadkarni, S., Weisz, G., Tanaka, A., Jaffer, F., Bouma, B., and Tearney, G.: Intravascular optical imaging technology for investigating the coronary artery, *JACC. Cardiovascular imaging*, **4**, (9): 1022-1039, 2011

5 Sun, C., Nolte, F., Cheng, K.H.Y., Vuong, B., Lee, K.K.C., Standish, B.A., Courtney, B., Marotta, T.R., Mariampillai, A., and Yang, V.X.D.: In vivo feasibility of endovascular Doppler optical coherence tomography, *Biomed Opt Express*, **3**, (10): 2600-2610, 2012

6 Kenneth K. C. Lee, Adrian Mariampillai, Joe X. Z. Yu, David W. Cadotte, Brian C. Wilson, Beau A. Standish, and Yang, V.X.D.: Real-time speckle variance swept-source optical coherence tomography using a graphics processing unit, *Biomed. Opt. Express* **3**: 1557-1564, 2012

MODELING LIVER PARENCHYMA TEARING USING A COHESIVE ZONE MODELING APPROACH

Costin D. Untaroiu[1]
[1]*Department of Biomedical Engineering and Mechanics, Virginia Tech, Blacksburg, Virginia, United States*

Summary. The rapid advancement in computational power has made human finite element (FE) models one of the most efficient tools for assessing the risk of abdominal injuries in a crash event. In this study, specimen-specific FE models were employed to quantify material and failure properties of human liver parenchyma. First, the pre-tearing region of each coupon test was simulated and the parameters of a hyper-elastic material model were identified by FE optimization. Then, the tissue tearing was numerically simulated using a cohesive zone modeling (CZM) approach. The results show that the proposed approach is able to capture both the biomechanical and failure response, and accurately model the overall force- deflection response of liver parenchyma over a large range of tensile loadings rates.

INTRODUCTION

Liver injuries frequently caused by both frontal and side impact motor vehicle collisions are associated with high morbidity and mortality rates[1]. Human finite element (FE) models have the capability to simulate each time step during an impact event and calculate the stress/strain field within human organs that could be correlated with injuries. However, the FE predictions are highly dependent on the model geometries, the connections of its parts, and especially the assigned material properties. Therefore, to numerically investigate liver injuries, biofidelic material properties are needed over a large range of loading rates.

The primary goal of this study was to accurately model both the biomechanical and failure responses of human liver parenchyma under high-rate tensile loading. To identify the parameters of a non-linear material model assigned to liver parenchyma, specimen-specific FE models and a simulation-based optimization approach were employed as in other recent studies[2-4] To model the tear of the liver parenchyma, the Cohesive Zone Modeling (CZM) approach, implemented recently in most FE software packages, was utilized to model the pre- and post-failure behaviour of parenchyma coupon specimens. The data reported in the current study could be easily implemented in current human liver models. Then, a better understanding of injury mechanism of liver could be obtained using biofidelic human models in numerical impact simulations.

METHODS

"Dog-bone shape" specimens of liver parenchyma were prepared using the custom blade assembly, slicing jig, and stamp, described in previous studies[4, 5]. Then, over 20 uniaxial tensile tests were performed until complete failure at one of the following two high strain rates: 1 s^{-1}, or 10 s^{-1} (Fig. 1a). The time histories of displacement between grips and tensile force were measured using potentiometers attached to the linear stages, and load cells, respectively. The surfaces of the specimens were reconstructed from the point clouds recorded prior to testing with a FARO laser scanner. FE models were developed for each specimen and a first order Ogden material model, implemented in the FE software (LS-Dyna vers. 6.0, LSTC, Livermore, CA), was assigned to specimen-specific. Each tension test was simulated by prescribing the displacement-time histories, recorded during testing, to the specimen ends (Fig. 1b). The material parameters, μ_1 and α_1, were identified using a metamodel-based optimization, called the sequential response surface method (SRSM), implemented in LS-Opt software. Various traction-separation relationships have been proposed in the literature. A material model implemented in LS-Dyna (MAT_185, *MAT_COHESIVE_TH) with a normalized trapezoidal traction-separation relationship (Fig.1c) was used in the definition of the CZM part. In this material formulation, the peak traction (the force over area $-\sigma_{max}$) reached at a separation of λ_1 is kept constant (ductile behavior) until the separation reaches λ_2 . Then, a linear reduction of the traction (elastic softening response) is simulated until a separation of λ_{fail} is reached, which corresponds to when the damage is complete. An additional optimization was setup to match the experimental and numerical force time histories for both pre- and post-failure regimes. The CZM parameters, λ_1, λ_2, λ_{fail}, δ_n^c, and σ_{n_max}, were considered as input variables. Since the specimen is loaded primarily in tension, the tearing occurs as failure mode I.

[a] Corresponding author. Email: costin@vt.edu.

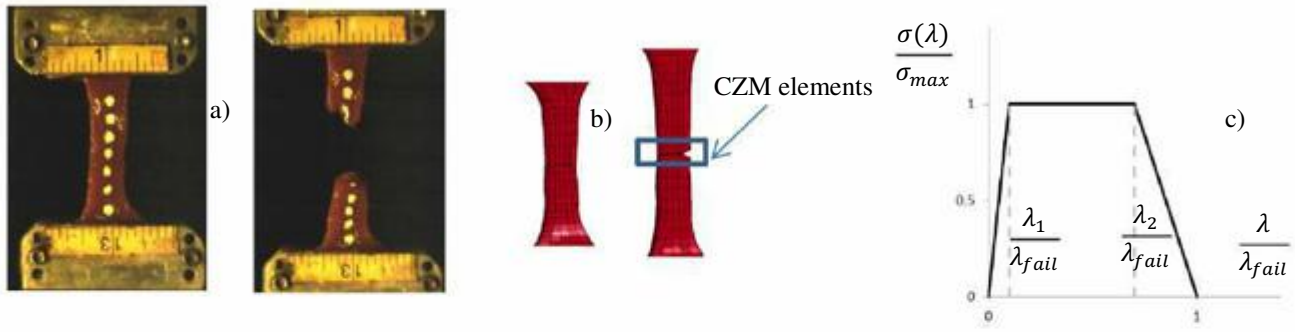

Figure 1. The specimen before and after/during tearing: physical test (a) FE simulation (b) Cohezive zone model: effective traction-separation relationship (c)

RESULTS AND DISCUSSION

A reasonable match to the test data was shown by the parenchyma models with CZM added at the tear location. The pre-failure region optimized previously was not affected by adding the CZM and it maintained a good fit with the test data (Fig. 2 a,b). The failure of CZM region generates a drop in the grip forces at almost the same time as the test data. The model force time histories reasonably followed the test data after the tear initiation. While there are some inherent variations in the identified values of maximum traction $(\sigma_{\max})$ and failure separation (λ_{fail}), some similarities are observed in the normalized traction-separation curves (Fig. 2c)

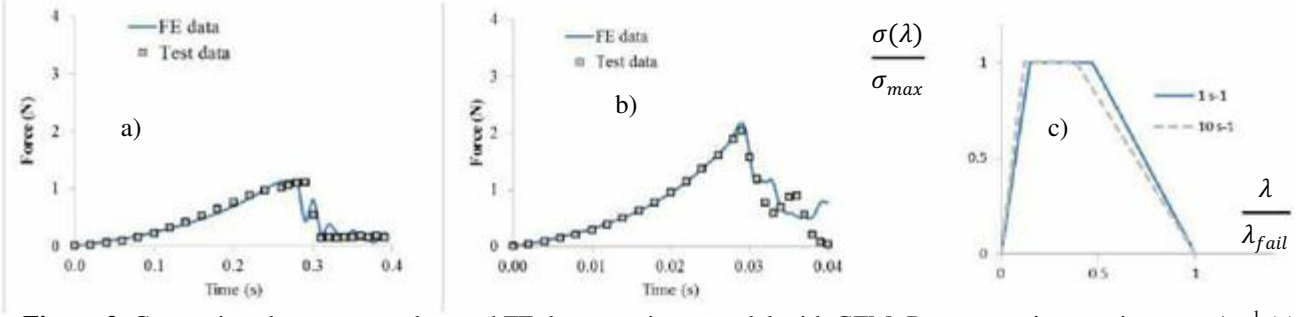

Figure 2. Comparison between test data and FE data: specimen model with CZM: Representative specimens at 1 s^{-1} (a) 10 s^{-1} (b), The identified traction-separation laws (c).

This study has some limitations. In the current work, as in previous studies that used CZM to model failure (Bhattacharjee et al., 2013), the path of the tear was assumed to be known. Therefore, the CZM elements were developed perpendicular to the direction of loading at tear location. However, for a liver model included in a full human body model, the tear location and propagation is not known *a priori*. Therefore, CZM elements should be developed in the whole liver FE model between all liver parenchyma elements. Based on our knowledge, an automatic methodology for the generation of these CZM elements is lacking in current software packages, and therefore should be developed in the future.

CONCLUSIONS

The cohesive zone modeling (CZM) approach, used to model tearing process, showed promising results in terms of modeling the post-failure force time history response at higher loading rates. Mechanical and failure data reported in this study could be easily implemented in human liver models to help identify the mechanisms of liver injuries during vehicle collisions, and possibly aid in the development of protective systems.

References

[1] A. M. Nahum and J. W. Melvin, *Accidental injury: biomechanics and prevention*, 2nd Edition ed.: Springer, 2002.

[2] J. Hu, K. D. Klinich, C. S. Miller, J. D. Rupp, G. Nazmi, M. D. Pearlman, *et al.*, "A stochastic visco-hyperelastic model of human placenta tissue for finite element crash simulations," *Ann Biomed Eng,* vol. 39, pp. 1074-83, Mar 2011.

[3] Y. C. Lu, A. R. Kemper, S. Gayzik, C. D. Untaroiu, and P. Beillas, "Statistical modeling of human liver incorporating the variations in shape, size, and material properties," *Stapp Car Crash J,* vol. 57, pp. 285-311, Nov 2013.

[4] C. D. Untaroiu and Y.-C. Lu, "Material characterization of liver parenchyma using specimen-specific finite element models," *Journal of the Mechanical Behavior of Biomedical Materials,* vol. 26, pp. 11-22, 10// 2013.

[5] Y. C. Lu, A. R. Kemper, and C. D. Untaroiu, "Effect of storage on tensile material properties of bovine liver," *Journal of the Mechanical Behavior of Biomedical Materials,* vol. 29, pp. 339-349, Jan 2014.

A MODEL FOR MECHANICALLY DRIVEN MORPHOGENESIS

Marcelo Epstein*[1]

[1]*Department of Mechanical and Manufacturing Engineering, University of Calgary, Alberta, Canada*

Summary After drawing a clear distinction between various kinds of processes of material evolution encountered in biological tissues, processes of morphogenesis are identified as those for which material symmetry breaking occurs. Assuming that long molecules embedded in an extracellular matrix have a degree of freedom so that they can interlock in at least two different arrangements, a bi-modal energy density can give rise to morphogenesis purely driven by histories of deformation.

MATERIAL EVOLUTION

Assume a solid material with a constitutive equation of the form

$$W = W(\mathbf{F}; t). \tag{1}$$

In this equation, W can be interpreted as the free-energy density per unit *spatial* volume. The deformation gradient $\mathbf{F}$ is measured with respect to a fixed reference configuration. For simplicity, we assign a zero energy to a natural state, assumed to exist and to be defined within an arbitrary rigid body rotation. The appearance of the time variable t will permit us to describe phenomena of *material evolution*. Naturally, although not explicitly shown by the notation, it is implicitly assumed that time is measured from some defining event such as a chemical reaction or a fabrication procedure that took place at $t = 0$.

The time dependence of the constitutive law (1) can be either explicitly stated or, more commonly, mediated by the presence of *internal variables*. In this case, the time evolution of these internal variables is governed by further *evolution equations* (usually, first-order ODEs) that provide a coupling with constitutive variables such as deformation and stress.

Processes of material evolution can be classified into various distinct categories, as done in detail in [2]. This classification is particularly relevant in biological applications[1, 4], particularly to determine whether a process of evolution can be canonically decomposed into remodeling, growth and aging components so as to attribute each component to a definite causal law. We say that a material point with constitutive law (1) undergoes a process of *remodeling* within a time interval T if, and only if, the time dependence is mediated by a non-singular time-dependent linear transformation $\mathbf{P}$ as follows

$$W = W(\mathbf{F}\mathbf{P}(t)). \tag{2}$$

An equivalent way to express the concept of pure remodeling is by saying that throughout a process of remodeling a material point remains *materially isomorphic*, a term introduced by Noll [5]. Indeed, if (without loss of generality) we impose the initial condition

$$\mathbf{P}(0) = \mathbf{I}, \tag{3}$$

where $\mathbf{I}$ is the identity tensor, we can write

$$W(\mathbf{F}; t) = W(\mathbf{F}\mathbf{P}(t); 0), \tag{4}$$

which means that the constitutive equation at any fixed time $t > 0$ can be regarded as identical to the constitutive equation at time $t = 0$, except for a change of local reference configuration, represented by $\mathbf{P}$. We may say that a small neighborhood of material at time $t = 0$ has been cut out, deformed by $\mathbf{P}$ and thereafter grafted back, as it were, at time t. We call this operation a *material transplant* [3]. This kind of material evolution is essentially the one considered in the pioneering paper by Rodriguez et al [6]. An intuitive way to visualize it is to imagine that the constitutive properties can be boiled down to a linear spring with stiffness k and rest length L_0. In a process of pure remodeling, the stiffness coefficient k remains constant, while the rest length L_0 changes with time.

Any material evolution process of the form (1) that is not expressible in the form (2) is, by definition, an *aging process*. This definition and the attendant terminology require some justification. Clearly, if the constitutive equation is not expressible by Equation (2), the instantaneous material response does not remain at all times materially isomorphic to its initial response, which means that some of its constitutive properties are changing in time. We refer to this fact by saying that the material has aged, although the term 'rejuvenation' would be equally acceptable.

*Corresponding author. Email:mepstein@ucalgary.ca

MORPHOGENESIS

A material point may undergo a radical process of aging by moderate or drastic changes of its properties, such as the modulus of elasticity in the case of a linear elastic isotropic material. A process of aging may result, for example, in the weakening of the stiffness of mineralized bone due to hormonal deficiencies. If, however, the weakened bone mineral is still isotropic, there has not been a *qualitative* change of material response. This observation leads us to identify an aging process as a process of *morphogenesis* if it entails a sudden change in the material symmetry type, as when the material changes from fully isotropic to orthotropic. The symmetry groups at different times in a morphogenetic process are no longer necessarily conjugate. This *symmetry breaking* is indeed considered as essential for pattern formation in plants and animals, as already envisioned in the epoch-making article by Turing [7]. Point-wise morphogenetic evolution can give rise to non-uniformity resulting in pattern formation.

In biological contexts, a situation of this kind may arise at early stages of development whereby long molecules are relatively free to move within a material matrix and to form branches and more or less stable cross-links before settling in a less permissive environment. Assume, for example, a thin membrane of isotropic matrix material in which identical long molecules or fibres are initially arranged in a regular orthogonal lattice, thus resulting in an initially transversely isotropic composite material. The molecules are assumed to be all parallel to the plane of the membrane. The corresponding free-energy density function will, accordingly, enjoy all the symmetries provided by the group of rotations about the axis normal to the plane of the membrane. We may assume, moreover, that there is a single alternative local arrangement of the molecules in which they are all mutually parallel, such as the case of two identical helices side by side. This arrangement will be assumed to be permanent once it has taken place, on the basis that the bond is stronger than in the original orthogonal counterpart. The free-energy density of the parallel arrangement will, naturally, enjoy less symmetries than the original. We obtain, in fact, an orthotropic material. In going from the orthogonal to the parallel arrangement there is, therefore, a symmetry breaking mechanism at play. Both alternative energy densities are functions of the local value of the deformation gradient (or strain). For a given state of strain the material will choose to transform itself to the lower energy mode, provided it was in the transversely isotropic mode. The reverse passage is forbidden, as already pointed out, due to the strength of the parallel bond. Naturally, the mechanism just described is a point-wise affair governed by the local value of the strain. The reorientation of the molecules in those parts where it has taken place will manifest itself macroscopically by a change in color or texture of the membrane and a pattern will emerge. Several examples will serve to illustrate this kind of purely mechanically driven pattern formation.

Acknowledgment: The financial support of the Natural Sciences and Engineering Research Council of Canada is gratefully acknowledged.

References

[1] Ambrosi D, Ateshian G A, Arruda E M, Cowin S C, Dumais J, Goriely A, Holzapfel G A, Humphrey J D, Kemkemer R, Kuhl E, Olberding J E, Taber L A and Garikipati K (2011), Perspectives on Biological Growth and Remodeling, *J of the Mechanics and Physics of Solids* **59**/4, 863-883.

[2] Epstein M (2015), Mathematical characterization and identification of remodeling, growth, aging and morphogenesis, *J of the Mechanics and Physics of Solids* **84**, 72-84

[3] Epstein M and Elżanowski M (2007), *Material Inhomogeneities and their Evolution*, Springer-Verlag.

[4] Menzel A and Kuhl E (2012), Frontiers in Growth and Remodeling, *Mechanics Rsearch Communications* **42**, 1-14.

[5] Noll W (1967) Materially Uniform Bodies with Inhomogeneities, *Archive for Rational Mechanics and Analysis* **27**, 1-32.

[6] Rodriguez E K, Hoger A and McCulloch A D (1994), Stress-dependent Finite Growth in Soft elastic Tissues, *J Biomechanics* **27**/4, 455-467.

[7] Turing A M (1952), The Chemical Basis of Morphogenesis, *Phil Trans Royal Society London* **B**237, 37-72.

ON DEFORMATION AND FRACTURE OF TOOTH ENAMEL

Herzl Chai[1]
[1]*School of Mechanical Engineering, Tel-Aviv University, Tel-Aviv, Israel*

Summary Tooth enamel, although having nominal material properties similar to glass, is able to sustain repeat contact loading under harsh conditions from food processing, a critical function for survival. To understand how individual material phases of enamel are combined to impart tooth resilience, a robust characterization of material properties under actual loading conditions and valid failure and fracture analyses need be conducted. In this work, some basic macro scale deformation and fracture characteristics of tooth enamel under occlusal loading are established. This information is then used in a fracture mechanics analysis to produce critical loads for tooth failure. The results show that the most critical strength factors are enamel thickness and enamel material nonlinearity.

Introduction

Tooth enamel, although having nominal material properties similar to glass, is able to sustain repeat contact loading under harsh conditions from food processing, a critical function for survival. This remarkable performance is accomplished by a unique, natural design of material microstructure and geometry [1]. Enamel is composed of rods made of crystallite platelets which are held together by thin layers of organic matrix. Rods are grouped into bundles called Hunter-Schreger bands (HSB) which orientations change in space. To understand how these individual characteristics combine to impart tooth resilience necessitates a robust characterization of material properties under actual working conditions and valid failure/fracture analyses. Most material characterization works on this subject are concerned with basic quantities such as elastic modulus, hardness, fracture toughness and stress-strain response, typically generated using nano or micro indentation testing techniques. It remains to be seen, however, how such properties are combined together to impart the unique fracture resistance of tooth enamel. The main purpose of this work is to establish the basic deformation and fracture characteristics for tooth enamel under occlusal loading in the macro scale and gain insight into how material architecture quantitatively affect the fracture resistance under such loading.

Testing and Analysis

Indentation tests using W/C balls of various radii are performed on extracted human molar teeth. The balls are placed at the tooth center or on the flat surfaces of polished prominent cusps and then they are pressed down to predetermined load values. After unloading, samples are sectioned transversely or longitudinally, and the internal as well as external damage observed and quantified with the aid of optical and scanning electron microscopy. Of special interest in these are the quantification of the stress-strain response and failure stress of enamel, and the initiation and growth of damage or cracks in the enamel. The stress-strain behaviour of enamel is established analytically with the aid of a FEA which makes use of experimental plots of mean stress vs. indentation strain. A fracture mechanics analysis in conjunction with the Finite Element (FEM) technique is employed to determine the load needed to initiate radial cracks at the dentin/enamel junction (DEJ) or to propagate median radial cracks under the contact to the DEJ.

Results

The indentation tests revealed that enamel is a highly nonlinear material exhibiting a pronounced strain hardening. This response is influenced by the damage induced by indentation, which is dependent on ball radius. It is found that the constitutive behavior of enamel is well represented by a Ramberg-Osgood constitutive law, obtained by a best fit to the experimental data, of the form

$$\varepsilon/\varepsilon_Y = \sigma/\sigma_Y + 0.12\,(\sigma/\sigma_Y)^{1.3},\ \sigma_Y = 330\ \text{MPa},$$

where σ_Y and ε_Y are the true yield stress and true yield strain in a uniaxial tension test.

Figure 1 shows a representative longitudinal section of a tooth loaded by a W/C ball placed at the central fossa. The plane of the cut intersects the tip of two diagonal tooth cusps. As shown, the enamel layer suffered considerable damage. The image plane in Fig. 1a contains two (I and II) contact spots. A few cracks marked R extend from these spots, typically normally to the occlusal surface, some of which reach the DEJ. This form of damage is consistent with a radial crack pattern on a surface intersecting a contact circle. Several small cracks also emanate from the DEJ, typically from tufts [1]. A relatively large one is seen in region III across from spot II. The magnified view of spot I shown at the right side reveals additional thin, surface normal cracks marked C that are confined to an annulus ring bounded by the contact circle. These cylindrical cracks, the analogue of shallow cone cracks in homogeneous materials, are constrained to grow in the weak interrod material between enamel rods [2].

[a] Corresponding author. Email: herzl@eng.tau.ac.il.

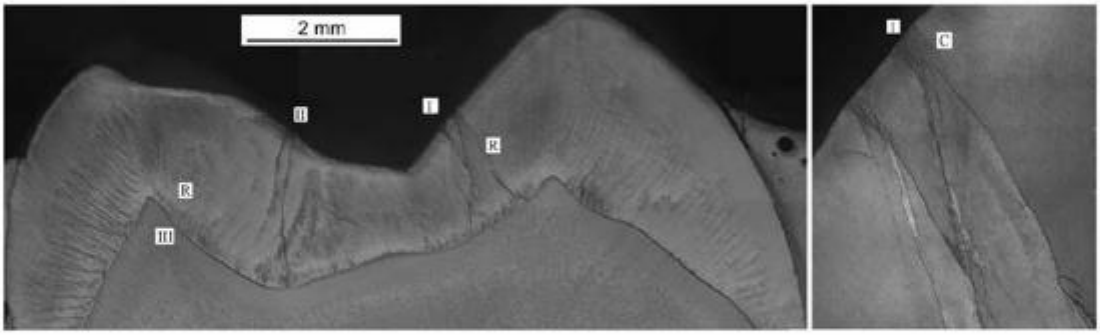

Figure 1: A longitudinal section of a molar tooth after unloading. The specimen was loaded by a 1.57 mm radius W/C ball at load P = 1004 N. The section intersects two contact spots I and II; the image on the right is a magnified view of spot I. Median radial cracks (R) and cylindrical cracks (C) grow from the contact surface, radial crack (R) grow from the DEJ at site III.

References

[1] Chai, H, Lee, JJ-W, Constantino, PJ, Lucas, PW, Lawn, BR. Remarkable resilience of teeth. *PNAS* **106**: 7289–93, 2009.

[2] Chai, H. On the mechanical properties of tooth enamel under spherical indentation. *Acta Biomaterialia* **10**: 4852-60, 2014.

FORCE-INDUCED INTERNALIZATION OF MAGNETIC NANOPARTICLES FOR DRUG DELIVERY AND CELL TRACKING

Linlin Zhang[1], Sheng Tong[1] and Gang Bao[1]
[1]*Department of Bioengineering, Rice University, Houston, TX, USA*

Summary We have systematically studied the use of applied magnetic force to facilitate the cellular internalization of magnetic nanoparticles. The magnetic nanoparticles have uniform core sizes and coated with phospholipid-PEG. We investigated the pathway of nanoparticle internalization into different cell types under an applied magnetic field and determined the dependence of cellular uptake on nanoparticle size and concentration, substrate stiffness, temperature, and changes of the cytoskeletal structure. Our results shed light on force-induced endocytosis of nanoparticles and provide a means to remotely control vascular permeability, thus having the potential to shift the paradigm of targeted drug delivery and open up new opportunities for the application of nanotherapeutics.

INTRODUCTION

Magnetic nanomaterials are being extensively exploited for magnetically guided delivery of therapeutic agents and cells, focused hyperthermia and remote triggering of molecular and cellular events. A process fundamental to these therapeutic paradigms is the cellular uptake of magnetic nanomaterials under an applied magnetic field. Here we dissect magnetically guided internalization of magnetic nanoparticles by primary cells and cancer cells in a semi-homogeneous magnetic force field. Our study indicates that the magnetic nanoparticle were internalized by cells through energy-dependent endocytic pathways. The rate of endocytosis increases with the magnetic force in a cell type-independent manner, but is not sensitive to the concentration of nanoparticles on cell surface.

RESULTS AND DISCUSSION

To obtain a mechanistic understanding, we quantified endocytosis of magnetic nanoparticles ranging from superparamagnetic to ferromagnetic regimes by cells grown on substrates with different stiffness. The magnetic nanoparticles have uniform core sizes of 10, 15, 25 and 40 nm respectively, coated with DSPE-PEG2000 copolymers, and their cellular internalization was quantified using HeLa, HUVEC and HDF cells at both 37°C and 4°C. We also determined the dose-dependence of nanoparticles and the effect of different drug concentrations in disrupting actin stress fibers.

We found that magnetic nanoparticles are internalized through endocytic pathways. The applied magnetic force increases the accumulation of magnetic nanoparticles on cell surface, and there is a clear dependence on nanoparticle core size and magnetization. Our experimental and modeling results suggest a vesicle packing model for the endocytosis of magnetic nanoparticles, whereas magnetic forces increase the packing density of nanoparticles in pre-formed endocytic vesicles on the cell surface, which promote the invagination of vesicles by overcoming membrane tension. Our studies also indicate that magnetic nanoparticles can be internalized into vascular endothelial cells under applied magnetic forces and accumulate in perinuclear lysosomes. We found that magnetic force applied to intracellular magnetic nanoparticles can induce the formation of actin stress fibers. Using a microfluidic device, we show that the intracellular magnetic force can induce rearrangements of stress fibers, which in turn leads to a reversible disruption of the tight junctions among endothelial cells.

CONCLUSIONS

Our studies shed light on the endocytosis of nanoparticles and provide a means to remotely control vascular permeability, thus having the potential to shift the paradigm of targeted drug delivery and open up new opportunities for nanotherapeutics

[a)] Corresponding author. Email: gang.bao@rice.edu.

UNIVERSAL CORRELATION BETWEEN STIFFNESS AND VOLUME FOR CELLS

D.A. Weitz
Dept. of Physics and SEAS, Harvard University, Cambridge MA, USA

Summary The stiffness of cells is commonly assumed to depend on the stiffness of their surrounding: bone cells are much stiffer than neurons, and each exists in surrounding tissue that matches the cell stiffness. In this talk, I will discuss new measurements of cell stiffness, and show that that cell stiffness is strongly correlated to cell volume. This affects both the mechanics and the gene expression in the cell, and even impacts the differentiation of stem cells. To probe the effects of gene expression, I will discuss lab-on-a-chip developments, using drop-based microfluidics, that provide a full gene expression analysis at the level of individual cells.

Email: weitz@seas.harvard.edu.

AN EULERIAN FORMULATION OF SOFT TISSUE GROWTH

MM Safadi[1], MB Rubin[2a)] & M Jabareen[3]
[1,2] *Faculty of Mechanical Engineering, Technion-Israel Institute of Technology, Haifa, Israel*
[3] *Faculty of Civil and Environmental Engineering, Technion-Israel Institute of Technology, Haifa, Israel*

Summary An Eulerian formulation of soft tissue growth has been developed. In contrast with standard Lagrangian formulations of growth that use multiplicative forms connecting total, elastic and growth deformation tensors, this Eulerian formulation uses evolution equations for elastic deformation measures. These evolution equations model homeostasis as an inelastic process causing the elastic deformation measures to approach their homeostatic values. An advantage of the Eulerian approach is that it is not influenced by unphysical arbitrariness of specifications of reference and intermediate configurations.

EVOLUTION EQUATIONS

An Eulerian formulation of growth in soft tissues is proposed which is based on the work in [1]. The tissue is modelled as a composite of a matrix and additional components that model the response to elastic stretching of the area of a material surface, the elastic stretching of material fibers and elastic shearing in a material direction in a material surface. These additional components introduce anisotropy in both the elastic and inelastic response of the tissue. The balance laws model an open system with a rate of mass supply and the constitutive equations are thermodynamically consistent. In contrast with other formulations, evolution equations are proposed directly for elastic deformation measures. This approach has the advantage that the material response is not influenced by arbitrariness of the choice of reference and intermediate configurations. Specifically, the elastic dilatation J_e and a symmetric positive-definite unimodular second order tensor $\boldsymbol{B}'_e$ $(\det \boldsymbol{B}'_e = 1)$ that characterizes elastic distortions of the tissue are determined by the evolution equations

$$\frac{\dot{J}_e}{J_e} = \boldsymbol{D}\cdot\boldsymbol{I} - \Gamma_m \ln\left(\frac{J_e}{J_h}\right) ,$$

$$\dot{\boldsymbol{B}}'_e = \boldsymbol{L}\boldsymbol{B}'_e + \boldsymbol{B}'_e\boldsymbol{L}^T - \frac{2}{3}(\boldsymbol{D}\cdot\boldsymbol{I})\boldsymbol{B}'_e - \Gamma\left[\boldsymbol{B}'_e - \left(\frac{3}{\boldsymbol{B}'^{-1}_e\cdot\boldsymbol{H}'}\right)\boldsymbol{H}'\right] .$$

In these equations, $\boldsymbol{L}$ is the velocity gradient, $\boldsymbol{D} = (\boldsymbol{L}+\boldsymbol{L}^T)/2$ is the total deformation rate, $\boldsymbol{I}$ is the unit tensor, $\boldsymbol{A}\cdot\boldsymbol{B} = \mathrm{tr}(\boldsymbol{A}\boldsymbol{B}^T)$ denotes the inner product between the second order tensors $\{\boldsymbol{A},\boldsymbol{B}\}$ and a superposed dot denotes material time differentiation. Also, $\{\Gamma_m,\Gamma\}$ are non-negative scalar-valued functions that characterize the rate of homeostasis, which is the inelastic process causing $\{J_e,\boldsymbol{B}'_e\}$ to approach their homeostatic values $\{J_h,\boldsymbol{H}'\}$, with $\boldsymbol{H}'$ being a symmetric positive-definite unimodular tensor. The constitutive equations for the Cauchy stress tensor $\boldsymbol{T}$ are defined so that $\boldsymbol{T}$ vanishes when the elastic dilatation J_e equals 1 and the elastic distortional deformation tensor $\boldsymbol{B}'_e$ equals $\boldsymbol{I}$. Since $\{J_h,\boldsymbol{H}'\}$ can be different from $\{1,\boldsymbol{I}\}$, the homeostatic state of the tissue can have non-zero residual stresses.

When the homeostasis rates $\{\Gamma_m,\Gamma\}$ are positive, homeostasis occurs simultaneously with loading $\{\boldsymbol{L}\neq 0\}$ and nonzero stress. When $\{\Gamma_m,\Gamma\}$ are positive and loading vanishes $\{\boldsymbol{L}=0\}$, the elastic deformation measures $\{J_e,\boldsymbol{B}'_e\}$ approach their homeostatic values $\{J_h,\boldsymbol{H}'\}$ with non-zero stress. To model growth at zero stress it is convenient to take $\boldsymbol{H}'$ in the form

$$\boldsymbol{H}' = \det(\boldsymbol{H})^{-1/3}\boldsymbol{H} \ , \ \boldsymbol{H} = \boldsymbol{I}+\boldsymbol{H}'' \ , \ \boldsymbol{H}''\cdot\boldsymbol{I} = 0 \ ,$$

where $\boldsymbol{H}''$ is a symmetric deviatoric tensor which is restricted by the condition that $\boldsymbol{H}$ is positive definite. It then follows that homeostasis can cause growth at zero stress with

$$\boldsymbol{L} = \boldsymbol{D} = -\frac{1}{3}\Gamma_m \ln(J_h)\,\boldsymbol{I} - \frac{1}{2}\Gamma\,\boldsymbol{H}'' \ , \ \boldsymbol{D}\cdot\boldsymbol{I} = -\Gamma_m \ln(J_h) \ , \ \boldsymbol{D}'' = -\frac{1}{2}\Gamma\,\boldsymbol{H}'' \ ,$$

$$\text{for } \boldsymbol{T}=0 \text{ with } J_e = 1 \text{ and } \boldsymbol{B}'_e = \boldsymbol{I} \ ,$$

where $\boldsymbol{D}''$ is the deviatoric part of $\boldsymbol{D}$. Thus, for zero stress, the logarithmic rate of total volume growth is determined by the product $\{\Gamma_m \ln(J_h)\}$ and the rate of total distortional deformation is determined by the product $\{\Gamma\,\boldsymbol{H}''\}$, which emphasizes the importance of the deviatoric tensor $\{\boldsymbol{H}''\}$. Consequently, within the context of this theory, it is possible to control the rate of growth due to homeostasis with the scalars $\{\Gamma_m,\Gamma\}$ separately from the value of the stress in the homeostatic state of the tissue with the homeostatic values $\{J_h,\boldsymbol{H}'\}$.

[a)] Corresponding author. Email: mbrubin@tx.technion.ac.il

Most formulations of finite growth of tissues are based on a Lagrangian model [2], which is an adaptation of models for finite deformation plasticity, with the total deformation gradient $\boldsymbol{F}$ expressed in a multiplicative form using an elastic deformation tensor $\boldsymbol{F}_e$ and a growth tensor $\boldsymbol{F}_g$

$$\boldsymbol{F} = \boldsymbol{F}_e \boldsymbol{F}_g \ .$$

A model using multiplicative forms of a number of deformation tensors from the reference configuration and a number of intermediate configurations was proposed for residual stresses in biomaterials in [3]. Removal of unphysical arbitrariness of multiplicative formulations of these kind has been discussed in [4]. In contrast with these formulations, the proposed Eulerian formulation does not introduce a total deformation or a growth tensor and does not have unphysical arbitrariness.

EXAMPLES

Shi et al. [5] have studied the morphogenetic process of c-looping of the heart using a simplified model of an inhomogeneous circular cylindrical tube as well as using realistic anatomically based geometry of the heart tube. Specifically, they used a multiplicative model similar to that described in [2] and specified the growth deformation tensor by a series of growth mechanisms which characterize the c-looping process.

A robust, strongly objective numerical integration algorithm for the evolution equations in the Eulerian formulation of soft tissue growth has been developed and is being implemented into ABAQUS together with a consistent tangent stiffness. Examples of the c-looping growth process of the heart are considered using the simplified circular cylindrical tube model. Differences between the growth process in the Eulerian model [1] and that in the Lagrangian model [2] used in [5] will be discussed.

References

[1] Rubin M.B., Safadi M.M., Jabareen M.: A unified theoretical structure for modelling interstitial growth and muscle activation in soft tissues. *Int. J. Engng. Sci.* **90**:1-26, 2015.

[2] Rodrigez E.K., Hoger A., McCulloch A.D.: Stress-dependent finite growth in soft elastic tissues. *J. Biomechanics* **27**:455-467, 1994.

[3] Hoger A., Van Dyke T.J., Lubarda V.A.: Symmeterization of the growth deformation and velocity gradients in residually stressed biomaterials. *Z. anges. Math. Phys.* **55**:848-860, 2004.

[4] Rubin M.B.: Removal of unphysical arbitrariness in constitutive equations for elastically anisotropic nonlinear elastic-viscoplastic solids. *Int. J. Engng. Sci.* **53**:38-45, 2012.

[5] Shi Y, Yao J, Xu G, Taber LA: Bending of the looping heart: differential growth revisited. . *J. of Biomechanical Engng.* **136**:081002-1-15, 2014.

CELL-SELECTIVE ELECTROPORATION FOR NOVEL SINGLE-CELL APPLICATIONS

Horacio Espinosa[1a,2], Rebecca McNaughton[1,2] & Ruiguo Yang[1,2]
[1]*Department of Mechanical Engineering, Northwestern University, Evanston, Illinois, USA*
[2]*Infinitesimal LLC, Skokie, Illinois, USA*

Summary A robust method for single cell access to deliver genes and molecules into adhered cells is needed to enable novel capabilities for temporal biological studies and new approaches to *in vitro* cell analysis, cell cloning, and gene editing. To realize this goal, we developed a microfluidic nanofountain probe (NFP) technology for localized electroporation of individual cells via automated positioning of the probe in contact with the target cell. Our recent development has increased ease-of-use and throughput for single-cell transfection.

SIGNIFICANCE

Biological studies at the single-cell level are increasing exponentially to allow researchers to investigate and compensate for significant cell heterogeneity within a population. Most of these studies involve single-cell analysis of a lysed or fixed cell via quantitative polymerase chain reaction (PCR), microarrays, or fluorescent in situ hybridization (FISH). These techniques limit the data collected to discrete points in the lifecycle of the cell and prevent dynamic cell analyses. Furthermore, a single-cell approach to the introduction of genes or other molecules into a cell is not common despite the advantages that it offers for temporal and spatial precision, as well as the preservation of monoclonality and capability for non-destructive *in vitro* analysis of live cells. Our nanofountain probe electroporation (NFP-E) technique is a convenient method for precise single-cell transfection that can provide these experimental advantages [1].

NANOFOUNTAIN PROBE ELECTROPORATION

The NFP-E system is comprised of a microfabricated nanofountain probe chip packaged with a wire electrode and mounted onto a micromanipulator, and a custom-built electronics unit and software (Figure 1). The tip of the NFP is positioned in contact with the cell membrane of a target cell, and an electric pulse is applied to induce electroporation that is localized near the region of contact. The localized electroporation creates temporary pores on the cell membrane and facilitates entry of molecules into the cell cytosol. To assist and/or automate positioning of the NFP tip, the onset of probe-cell contact is detected by continuous monitoring of the electric circuit to detect a sudden increase in electrical resistance. Further details about the working principle for NFP-E and automated positioning of the probe have been published elsewhere.

During development, we have demonstrated using NFP-E to transfect various cell types (HeLa, HT1080, HEK293, A431, murine embryonic fibroblasts) with a wide range of molecules (small molecules (70 kDa dextran and PI); proteins (BSA, Cas9); plasmids (20 MDa GFP); nucleic acids (gRNA, DNA- and RNA-based molecular beacons))[2]. Furthermore, we have shown that qualitative dosage control of the transfected molecules is possible by modifying the duration of the applied electric pulse. With these capabilities, the NFP-E system has potential to enable novel biological studies including: single cell analysis (gene expression studies, time-dependent cell biology, protein interaction studies, and drug toxicity and response), monoclonal cell line development, and temporal stem cell reprogramming/differentiation. For example, recent advances have allowed us to demonstrate applications such as temporal gene expression analysis using molecular beacons and gene editing using CRISPR/Cas9.

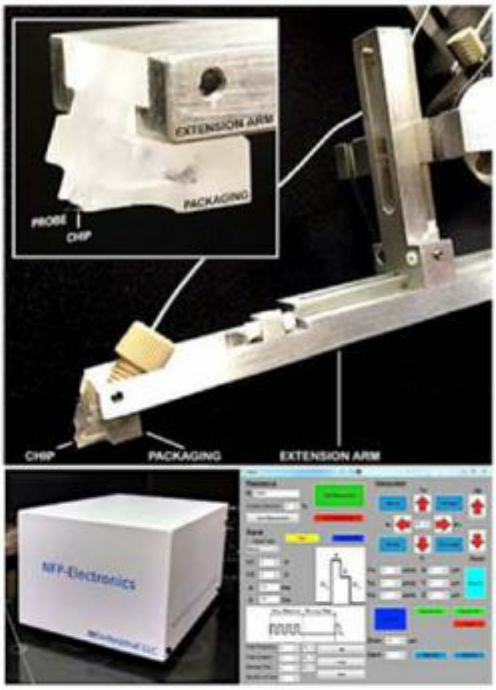

Figure 1. The nanofountain probe electroporation system. The microfabricated probe is packaged with a wire electrode (inset) and mounted on an adjustable extension arm connected to a micromanipulator (top). The electric pulse needed to induce electroporation, and resistance-based positioning control, is supplied by custom-built electronics and software (bottom).

[a)] Corresponding author. Email: espinosa@northwestern.edu

RECENT APPLICATIONS

Temporal gene expression analysis using molecular beacons

We used NFP-E to transfect molecular beacons, oligonucleotides that emit fluorescence upon binding to an mRNA target, as a demonstration for spatial and temporal studies of live cells enabled by single-cell transfection [3]. Specifically, we transfected into HT1080 cells a DNA-based beacon that detects glyceraldehyde 3-phosphate dehydrogenase (GAPDH) and an RNA-based beacon that detects a sequence cloned in the green fluorescence protein mRNA. Immediate imaging analysis after transfection allows mRNA detection within seconds after transfection without suspending the adhered cell. In addition, we showed potential for time-dependent detection of mRNA expression by transfecting the same cell at different time points (different days in this case; Figure 2) by using different color fluorophores for subsequent transfection. This technique could be particularly useful for studies of cell differentiation, where several measurements of mRNA expression are required over time.

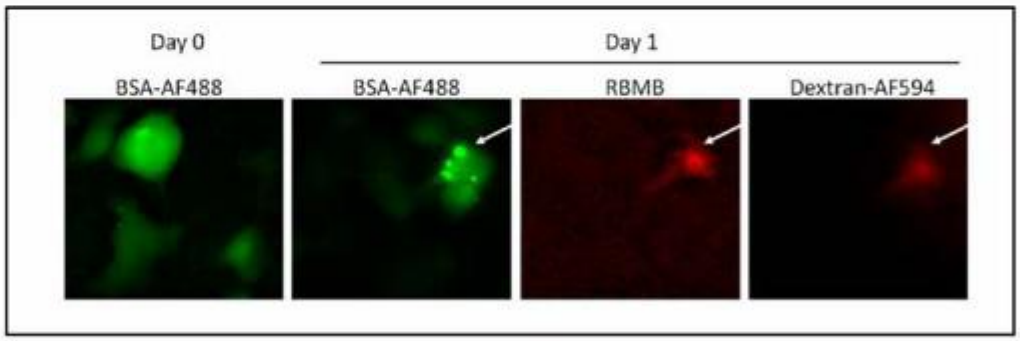

Figure 2. Example of temporal transfection by NFP-E. HT1080 cells were transfected on day 0 with green fluorophore-tagged (AF488) bovine serum albumin (BSA) and incubated overnight. The following day, Day 1, those cells showed BSA-AF488 localized within an organelle of the cell. Also on day 1, one cell from this group (white arrow) was transfected again with a solution of the RNA-based beacon and red fluorophore-tagged dextran-AF594 (positive control).

Knock-down of green fluorescent protein expression with CRISPR

To demonstrate and explore the best approach to single-cell gene editing using CRISPR/Cas9, we generated a HEK293 cell line expressing a single copy of green fluorescent protein (GFP) by standard cell cloning practices. We tested three approaches to GFP knock-down: (1) transfecting a CRISPR/Cas9 plasmid, (2) transfecting Cas9 protein with guide RNA, and (3) transfecting Cas9 expressing mRNA with the guide RNA. Each approach produced knock-down of the GFP expression in transfected cells. An example of successful knock-down is shown in Figure 3 using approach (2). A comprehensive study of the efficiency of transfection relative to the efficiency of knock-down is ongoing.

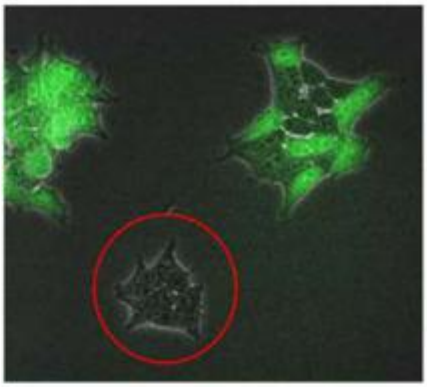

Figure 3. Demonstration of knock-down of GFP expression in HEK293 GFP+ cells by NFP-E transfection of a mixture of Cas9 protein with guide RNA. Each cell in the red circle was transfected and the image was taken 24 hours after transfection.

CONCLUSIONS

The NFP-E system has unprecedented capabilities for precise transfection such as single-cell selectivity, qualitative dosage control, high efficiency, and high cell viability. The demonstrations presented in this paper show examples of new capabilities for single-cell experiments in gene analysis and editing. We are currently optimizing the automated positioning algorithm to enable increased throughput of NFP-E and the ability to transfect cells patterned in arrays or isolated in microwells. This automation will greatly increase the throughput and robustness of the NFP-E system and make it an extremely useful new biotool.

References

[1] Kang, W., R.L. McNaughton, F. Yavari, M. Minary-Jolandan, A. Safi, and H.D. Espinosa, Microfluidic Parallel Patterning and Cellular Delivery of Molecules with a Nanofountain Probe. Journal of Laboratory Automation, 2014, 19, 100-109.

[2] W. Kang, F. Yavari, M. Minary-Jolandan, J.P. Giraldo-Vela, A. Safi, R. L. McNaughton, and H. D. Espinosa, “Nanofountain Probe Electroporation (NFP-E) of Single Cells,” Nano Letters, 2013, 13, 2448−2457.

[3] J. P. Giraldo-Vela, W. Kang, R. L. McNaughton, X. Zhang, B.M. Wile, A. Tsourkas, G. Bao, H. D. Espinosa, "Single-Cell Detection of mRNA Expression Using Nanofountain-Probe Electroporated Molecular Beacons," Small, 2015, 11(20), 2386-2391 (cover article).

INFLUENCE OF MICROSCALE PATTERNING AND SUBSTRATE STIFFNESS ON CARDIOMYOCYTE MATURATION

Brett N. Napiwocki[1,2], Max R. Salick[1,3], Timothy J. Kamp[1,4], Randolph S. Ashton[1,2], Wendy C. Crone[1,2,3,5 a)]
[1] *Wisconsin Institute for Discovery, University of Wisconsin – Madison, Madison, WI, USA*
[2] *Department of Biomedical Engineering, University of Wisconsin – Madison, Madison, WI, USA*
[3] *Materials Science Program, University of Wisconsin – Madison, Madison, WI, USA*
[4] *Depts. of Medicine and Cell & Regenerative Biology, University of Wisconsin – Madison, Madison, WI, USA*
[5] *Department of Engineering Physics, University of Wisconsin – Madison, Madison, WI, USA*

Summary Recent advancements in methods of deriving immature human cardiomyocytes from pluripotent stem cells now facilitates the potential of these cells to develop into mature, fully-functional adult cardiomyocytes - the next step towards producing useful drug screening models. Differentiation protocols are now able to achieve both high yield and purity of stem cell derived cardiomyocytes. However, biochemical signaling alone is insufficient to produce well-aligned, mature cardiomyocytes that recapitulate adult cell functionality. Our work using hESCs explores the use of micropatterned substrates and substrate stiffness to improve the cytoskeletal organization of the immature cardiomyocytes to improve maturation. We show that pattern widths ranging from 30-80μm promote significant increases in nuclear alignment and enhanced myofilament structure due to the feature geometries. Results for immature CMs cultured on patterned PDMS substrates are presented, in comparison to our prior work on glass, showing the portability of this technique between substrates.

BACKGROUND

While methods for deriving contracting cardiomyocytes from pluripotent stem cells in large quantity has improved significantly in recent years, a remaining challenge is the maturation of these immature cardiomyocytes toward a functional, adult phenotype needed for applications in regenerative medicine or drug discovery. A range of methods using biochemical, electrical and mechanical cues have been explored to induce maturity [1-2]. Measures of maturation include sarcomere structure, multinucleation, gap junction distribution, electrophysiological properties, and contractile force [3]. Most studies involving micropatterned cardiomyocytes have utilized rat and mouse neonatal ventricular cardiomyocytes as their model, and show that these cells form improved cell-cell junctions, contractile strength, and sarcomere organization [4-6], as well as trends between cell shape, sarcomere formation, and α-catenin expression [7-8]. The research presented here uses immature cardiomyocytes differentiated from human embryonic stem cells (hESCs) and demonstrates micropattern techniques used previously on glass [9] can be applied to PDMS substrates in order to control cytoskeletal organization within cardiomyocytes.

RESEARCH METHODS

Microcontact printing designs created in AutoCAD were sent to the Stanford Microfluidics Foundry for fabrication of a high-resolution photomask Si wafer master stamp (Stanford University, Santa Clara County, CA). These master stamps were then used to produce reusable polydimethylsiloxane (PDMS) (Sylgard, 184 Kit) stamps for the microcontact printing. In the experiments reported here the pattern design incorporated long lanes with widths ranging from 40-240μm [10].

PDMS substrates with different mechanical properties were created by blending Sylgard 184 with Sylgard 527 (Dow Corning) combined in different mass ratios to create specific elastic moduli across a physiological stiffness range. On stiffer substrates the stamping to PDMS can be done directly, but on softer substrates a sacrificial polyvinyl alcohol (PVA) film was used as an intermediate step. After lanes were created, the remaining substrate areas not coated with ECM proteins are backfilled with Pluronics F127, followed by an additional PBS wash. Afterwards, the PDMS substrate now containing lanes of Matrigel was seeded with hESC-CMs.

As described in detail elsewhere [9], cardiomyocytes were derived from an engineered H9 human embryonic stem cell (hESC) line containing a cardiac troponin T GFP (cTnT-GFP) promoter with resistance to the antibiotic Zeocin along with cardiac troponin T expression indicated by the presence of GFP which allows for the purification of cTnT-expressing cells. Following the work of Lian et al. [11], a modified version of the small molecule Wnt-agonist method of differentiation was used to produce immature cardiomyocytes and further purified with Zeocin [9]. The dissociated cells were seeded onto the PDMS substrate containing lanes of Matrigel at a density of 30,000 cells/cm^2.

RESULTS

Cell shape greatly influences cell behavior and cytoskeleton conformation as shown by our prior work. Forcing immature hESCs-derived cardiomyocytes into an aligned, elongated cell shape leads to a more mature-like phenotype [9]. Experiments using varying pattern shapes have shown that patterns with widths of less than 100μm induce an increase in nuclear alignment for hESC-CMs. In contrast to standard two-dimensional cultures of cardiomyocytes where cells form cell-cell junctions in all

[a)] Corresponding author. Email: wendy.crone@wisc.edu.

directions, these patterned cells repeatability form extremely polarized structures which produce synchronous contraction. However, while sarcomere formation and cell alignment (Fig. 1) were dramatically improved within the thin feature widths, there was no significant difference in gap junction plaque expression and calcium propagation rate among the micropattern lane widths explored on glass substrates [9].

In addition to glass substrates, experiments were conducted with immature cardiomyocytes using PDMS substrates with 1.72MPa stiffness [10] and now 50 and 5 kPa stiffness. The lowest stiffness is in the physiological range of the heart [12]. When the width of the lane pattern is less than 100µm, the cardiomyocytes form highly aligned structures within the features (Fig. 2), as opposed to the pleomorphic cell shape observed in cells on unpatterned substrates. Patterns with widths of 36µm continued to be ideal for producing connected, highly structured, one-cell-wide lanes of hESC-CMs that exhibit synchronous contraction on PDMS over a wide range of substrate stiffnesses. However, results to date continue to show signs of immaturity in cell-cell junction organization.

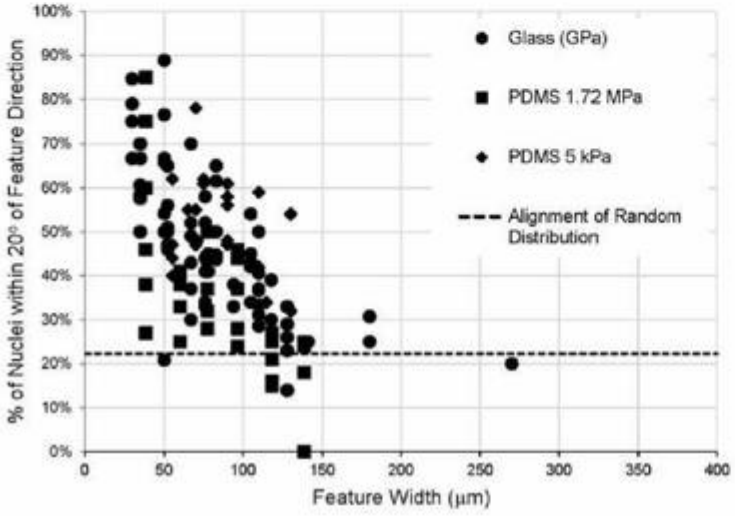

Fig. 1: Percentage of aligned nuclei aligned with respect to feature axis within +/-10°. Results on 5kPa PDMS are compared with 1.72 MPa PDMS [10] and those of Salick et al. [4] on glass substrates. In a system in which the cells are randomly oriented, an alignment of 22% would be expected (dotted horizontal line).

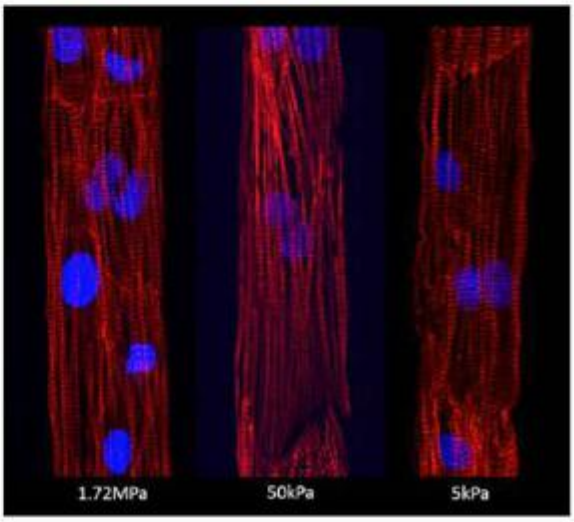

Fig. 2: Micropattern lanes of 36µm width on PDMS substrates of 1.72 MPa, 50 kPa, and 5 kPa stiffness. DAPI (blue) and α-actinin (red) images of hESC-CMs on day 5 after seeding.

CONCLUSION

A critical challenge facing cardioregenerative biology is the achievement of a more mature phenotype that will allow for more accurate modeling of native myocardium for pharmacological studies. By providing a highly-organized substrate with physiological stiffness, we aim to accelerate the processes of cardiomyocyte maturation which will ultimately display adult physiological response.

References

[1] Higuchi A, Ling QD, Kumar SS, Chang Y, Alarfaj AA, Munusamy MA, Murugan K, Hsu ST, Umezawa A.: Journal of Materials Chemistry B. 2015;3(41):8032-58.

[2] Stoppel WL, Kaplan DL, Black LD.: Advanced drug delivery reviews. 2015 Jul 30.

[3] Yang X, Pabon L, Murry CE.: Circulation research. 2014 Jan 31;114(3):511-23.

[4] Cimetta E, Pizzato S, Bollini S, Serena E, Coppi P, Elvassore N.: Biomed Microdevices 2009;11(2):389e400.

[5] McDevitt TC, Angello JC, Whitney ML, Reinecke H, Hauschka SD, Murry CE, et al.:. J Biomed Mater Res 2002;60(3):472e9.

[6] Feinberg AW, Alford PW, Jin H, Ripplinger CM, Werdich AA, Sheehy SP, et al.: Biomaterials 2012;33(23):5732e41.

[7] Bray MA, Sheehy SP, Parker KK.:. Cell Motil Cytoskeleton 2008;65(8):641e51.

[8] Chopra A, Patel A, Shieh AC, Janmey PA, Kresh JY.: PLoS ONE 2012;7(10):e47592.

[9] Salick MR, Napiwocki BN, Sha J, Knight GT, Chindhy SA, Kamp TJ, Ashton RS, Crone WC.: Biomaterials. 2014;35(15):4454-64.

[10] Napiwocki BN, Salick MR, Ashton RS, Crone WC. Polydimethylsiloxane Lanes Enhance Sarcomere Organization in Human ESC-Derived Cardiomyocytes. In Mechanics of Biological Systems and Materials, Volume 6 2016 (pp. 105-111). Springer International Publishing.

[11] Lian X, Hsiao C, Wilson G, Zhu K, Hazeltine LB, Azarin SM, Raval KK, Zhang J, Kamp TJ, Palecek SP.: Proceedings of the National Academy of Sciences. 2012 Jul 3;109(27):E1848-57.

[12] Bhana B, Iyer RK, Chen WL, Zhao R, Sider KL, Likhitpanichkul M, Simmons CA, Radisic M.: Biotechnol Bioeng. 2010;105:1148-1160

MECHANICAL CONSIDERATIONS ON TRACTION FORCE MICROSCOPY

Manuel Zündel*[1], Alexander E. Ehret[1,2], and Edoardo Mazza[1,2]
[1]*ETH Zürich, Institute of Mechanical Systems, Switzerland*
[2]*EMPA. Materials Science and Technology, Dübendorf , Switzerland*

Summary In the present contribution we present a study on critical factors that should be considered to fully exploit the great potential provided by non-linear traction force microscopy approaches. To this end, various influencing factors are studied numerically in benchmark examples based on experimentally observed cellular traction fields using a custom, finite element based framework to analyze traction force microscopy experiments on highly deformable substrates.

TRACTION FORCE MICROSCOPY

Mechanical stimuli play an important role for cell differentiation and the regulation of cellular processes [1, 2]. The quantification of the mechanical interactions between cells and their environment is thus an important topic in the field of mechanobiology. Traction Force Microscopy (TFM) refers to a set of methods that base on inferring the forces exerted by cells from the observed motion of a deformable substrate with known material properties [3]. This includes, for example, the use of very thin films allowing the reconstruction of cellular tractions by analysing the induced wrinkling pattern [4], or structured substrates such as nano-pillar arrays. The latter bend upon cellular loads, so that the forces can be calculated from measuring tip displacements and beam theory [5]. While the mechanical problem is straightforward, the method does not allow quantifying out-of-plane forces and, moreover, the particular substrate topology is known to affect the cell behaviour [6]. The latter can be circumvented by placing the cells on continuous and deformable substrates equipped with fluorescent markers inside or on the surface of the material [7]. Tracking these markers in a laser microscope provides the displacements in two or even three dimensions caused by the cells' tractions on the surface, and with the material properties of the substrate given, these tractions result from solving the inverse mechanical problem [8]. For the solution of this inverse problem, different approaches have been developed in the past based on the Boussinesq-Green solution for the elastic half-space [9]. Since these methods invoke the principle of superposition, their applicability is limited to materially and geometrically linear cell-substrate systems, i.e. with small deformations and linear-elastic substrates. While the former requirement limits the sensitivity of the method, the latter significantly restricts the choice of the substrate materials. To overcome these limitations TFM approaches were proposed that use finite element analysis (FEA) to compute the inverse problem. Such non-linear approaches bear great potential but they come along with a number of challenges relating to the discretisation of the substrate domain into a finite element mesh, the according interpolation of the displacement field, the handling of experimental noise and a thorough characterization of the substrate material. In the present contribution these essential aspects are studied by use of benchmark examples along with relevant questions related to the interpretation of numerical TFM results.

NUMERICAL ANALYSES

Applying a newly developed FEA-based TFM approach for the three-dimensional analysis of cellular traction forces on continuous, highly deformable substrates to benchmark test-cases, we discuss the influence of resolution and noise of the displacement field, the quality of the finite element discretization, the type of interpolation scheme and the choice of the substrate material law on the accuracy of the computational traction field reconstruction. The benchmark test-cases are based on traction fields observed from the TFM analysis of different cells (HeLa cells and Fibroblasts) on very soft silicone substrates with an equivalent elastic modulus of 10-15 kPa.

RESULTS

The regularisation strategies used to account for noise in the Green-Boussinesq approaches to TFM, see e.g. [10] are not directly applicable to the non-linear framework. In addition, since the majority of elastomeric substrates are characterised by incompressible behavior, already very small inaccuracies in the experimentally determined displacements can lead to spurious behavior if these errors violate the volumetric constraint.

While a finite element discretization that is finer than the grid of measurement points improves the quality of the numerical calculation and is in many cases mandatory to obtain convergent solutions, it brings about the necessity to interpolate between these points, and it is shown that both the refinement of the mesh but also the method for interpolation strongly affect the result if not appropriately interpreted. The influence of the interpolation on the traction field reconstruction of a simple benchmark example is shown in figure 1.

*Corresponding author. Email: zuendel@imes.mavt.ethz.ch

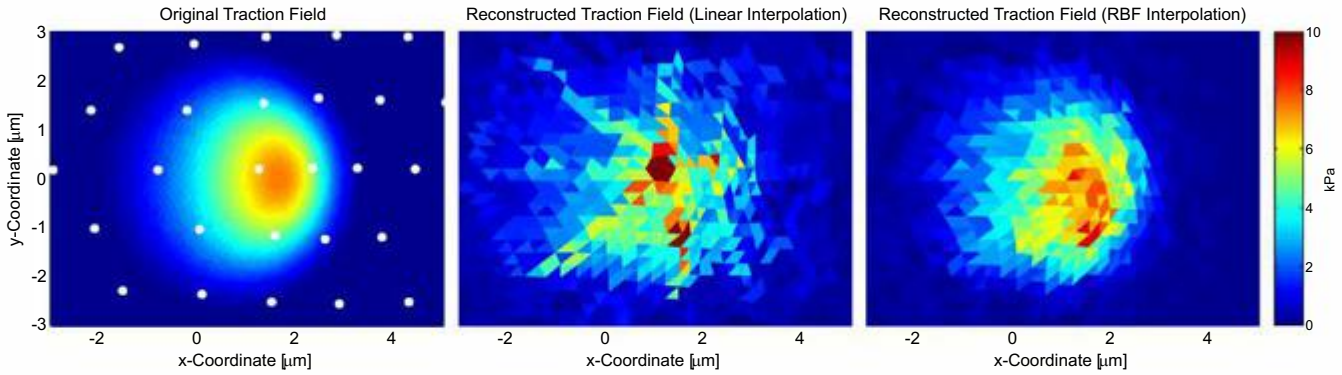

Figure 1: The figure on the left reports the traction field which was applied on the substrates surface as a benchmark. After computing the traction induced substrate deformations, the displacements were extracted in discrete locations on the surface (marked by white dots) and used for the reconstruction of the traction fields with the proposed nonlinear TFM framework using two different displacement field interpolation approaches: a linear interpolation scheme (center) and an interpolation based on Radial Basis Functions (right). All figures show the deformed configuration.

Moreover, the benchmark examples are used to study the consequences of disregarding geometric and material nonlinearities, particularly the nonlinear stress-strain behavior typical for elastomeric materials at high strains, as well as the influence of potential substrate inhomogeneity as a result of substrate preparation for TFM. To this end, monotonic and cyclic experiments in uniaxial and multiaxial stress states were performed on soft silicone-based materials, and the corresponding model equations were used in the FEA algorithms.

CONCLUSIONS

In summary, the results suggest that the consideration of large displacements in TFM bears great potentials for the analysis of cell traction forces. However, the additional complexity induced by the nonlinear characteristics require the use of an accurate material model for the substrate, an appropriate interpolation scheme for the displacements and methods to quantify measurement errors and their influence on cell traction forces determination.

References

[1] Prendergast P.J., Huiskes R., Soballe K.: .Biophysical stimuli on cells during tissue differentiation at implant interfaces. J. Biomech. 30:539-548, 1997.

[2] Vogel V.: Mechanotransduction involving multimodular proteins: converting force into biochemical signals. Annu. Rev. Biophys. Biomol. 35:459-488, 2006

[3] Schwarz, U.S. and Soin, J.R.: Traction force microscopy on soft elastic substrates: A guide to recent computational advances. Biochimica et Biophysica Acta (BBA)-Molecular Cell Research, 2015

[4] Harris, A.K., Wild, P. and Stopak, D.: Silicone rubber substrata: a new wrinkle in the study of cell locomotion. Science, 208(4440), 1980

[5] Fu, Jianping, et al.: Mechanical regulation of cell function with geometrically modulated elastomeric substrates. Nature methods 7.9 , 2010

[6] Lehnert D, Wehrle-Haller B, David C, Weiland U, Ballestrem C, Imhof BA, et al.: Cell behaviour on micropatterned substrata: limits of extracellular matrix geometry for spreading and adhesion. J Cell Sci, 2004

[7] Dembo M, Oliver T, Ishihara A, Jacobson K.: Imaging the traction stresses exerted by locomoting cells with the elastic substratum method. Biophys J. 1996

[8] Sabass, B., Gardel, M.L., Waterman, C.M. and Schwarz, U.S.: High resolution traction force microscopy based on experimental and computational advances. Biophysical Journal, 2008

[9] Butler, J.P., Toli-Nrrelykke, I.M., Fabry, B. and Fredberg, J.J.: Traction fields, moments, and strain energy that cells exert on their surroundings. American Journal of Physiology-Cell Physiology, 282(3), 2002

[10] S. V. Plotnikov et al.: Methods in Cell Biology Vol. 123, Chap. 20, pp. 367-394, 2014

BIOMECHANICS OF HEPATIC CELLS AND ENGINEERED CONSTRUCTION OF LIVER

Mian Long[a)], Ning Li, Yan Zhang, Dongyuan Lü, and Shouqin Lü
Center of Biomechanics and Bioengineering and Key Laboratory of Microgravity (National Microgravity Laboratory), and Beijing Key Laboratory of Engineered Construction and Mechanobiology, Institute of Mechanics, Chinese Academy of Sciences, Beijing 100190, China.

Summary Based on the unique sinusoidal structure of liver microcirculation and its essential biological function, we evaluated systematically the multi-scale biomechanics and mechanobiology of liver at molecular, cellular, or tissue level, which included the contribution of β2-integrin-ICAM-1 ligand interactions to the cell-cell adhesion, flow-induced crawling of mouse PMN on LSEC monolayer, the impact of substrate stiffness and microtopography on hepatic differentiation of embryonic stem cells (ESCs) , as well as the impact of a in-house built 3D *in vitro* sinusoidal model and engineered liver bioreactor in implementing hepatic functions. This work provides an insight for quantifying the intrinsic binding kinetics and the blood flow-induced crawling features of hepatic cells, and also proposes a novel 3D supporting system for liver function with well defined blood hemodynamics.

Liver microcirculation is unique due to its complexity of sinusoidal structure, in which multiple types of hepatic and/or hemapoietic cells interact with each other under blood flow in a three-dimensional (3D) environment. Adhesion of flowing leukocytes to liver sinusoidal endothelial cells (LSECs) or Kupffer cells (KCs) is crucial in liver immune responses. While it is known that two β2-integrins LFA-1 and Mac-1 play distinct roles in the most of organ-specific microcirculations, Mac-1 seems to be predominant in neutrophil (PMN) adhesion and crawling in localized inflammation while the role of LFA-1 is controversial in liver.

We combined the probabilistic model of small system kinetics with the mechano-chemical coupling theory to quantify the cell-cell adhesion mediated by β2-integrin-ICAM-1 ligand interactions. Upon these models, we compared experimentally the binding kinetics of LFA-1 and Mac-1 to ICAM-1s on mouse LSECs or KCs and found that the binding kinetics between these two integrin molecules is different when ICAM-1s were expressed on distinct cells, supporting that Mac-1 predominantly mediates the adhesion between leukocytes and LSECs and KCs. Next, we tested the flow-induced crawling of mouse PMNs on LSEC monolayer and indicated that PMNs tend to migrate along the direction of shear flow and yield high crawling velocity and moving displacement than those under static case, mainly mediated by LFA-1. We also quantified the impact of substrate stiffness and microtopography on hepatic differentiation of embryonic stem cells (ESCs) and demonstrated that substrate microtopography (grooved, pillar, or hexagonal configuration) works cooperatively with its stiffness to manipulate ESC stemness and hepatic differentiation. Finally, a 3D *in vitro* sinusoidal model and engineered liver bioreactor were in-house built, in which physiologically-mimicking microenvironment is critical for implementing hepatic functions.

Multi-scale biomechanics and mechanobiology of liver at molecular, cellular, or tissue level were systematically evaluated, which provides an insight for quantifying the intrinsic binding kinetics and the blood flow-induced crawling features of hepatic cells. This work also proposes a novel 3D supporting system for liver function with well defined blood hemodynamics.

This work was supported by National Natural Science Foundation of China grants 31230027 and 31110103918 and Strategic Priority Research Program of Chinese Academy of Sciences grant XDA01030102.

[a)]Corresponding author. Email: mlong@imech.ac.cn

MECHANICS OF STEM CELL MYOGENESIS

Alexander Spector[1a)], Rajiv Deshpande[2] & Warren Grayson[2]
[1] *Departments of Biomedical Engineering and Mechanical Engineering, Johns Hopkins University, Baltimore, Maryland, USA*
[2] *Department of Biomedical Engineering, Johns Hopkins University, Baltimore, Maryland. USA*

Abstract Myogenesis of stem cells is the process of their conversion into skeletal muscle cells. The mechanical factors play a key role in this process, and they can be used to maximize the stem cell myogenic output. Our goal here is a better understanding and use of this effect. We interpret stem cell myogenesis as a progression through several key stages where each of them is characterized by the expression of specific proteins (myogenic factors). The cell stage-to-stage progression is affected by the magnitude and time course of the applied strain through the intracellular signalling. The model of this mechanism is described in terms of nonlinear ODEs and applied to the analysis of stem cell myogenesis under the action of cyclic uniaxial strain. The model parameters are adjusted based on a parallel experiment, and the results are used for the optimization of the amplitude, frequency, and duration of the applied strain.

INTRODUCTION

Under physiological conditions, skeletal muscle regeneration is provided by specialized stem cells, called satellite cells whose differentiation has typical stages of expression particular proteins and morphological transformations. This mechanism fails under pathological conditions, such as muscular dystrophy, ageing, or severe muscle trauma. Other stem cells are now used in muscle therapies, and these cells (if transplanted) should follow the time course of satellite stem cell differentiation, it is, however, associated with a number of limitations. One medically promising approach is related to adipose-derived stem cells that are easily accessible in the patient's body and demonstrate potential of differentiation into skeletal muscle cells. The output of this differentiation is low, but it has been recently shown in the experiment that the results can be significantly improved by the application of mechanical strains [1]. The time course of application of such strains (cyclic following periods of rest) is similar to that experienced by the muscle cells under physiological conditions. The mechanism of the strain effect on cell differentiation has not been fully understood: such mechanism was actively studied in other adherent (non-stem) cells but in stem cell myogenesis it has different features, such as cell fusion. The goal of our study is to develop a model to better understand the mechanism of strain effect on stem cell myogenesis with a further purpose to estimate the optimal parameters of the applied strain.

KINETIC MODEL

We follow four key factors of stem cell myogenesis and define five major stages of this process, starting from the original stem cells where neither factor is expressed through the final ("mature") stage of muscle-like cells where all (but one) factors are expressed. The expression of this exceptional factor (PAX7) increases to push stem cells out of its initial state and then decreases because the factor becomes an obstacle to the late stages of cell differentiation. After the definition of the main stages, we specify the biological mechanisms of cell progression from stage to stage. One such mechanism is asymmetric cell division where cells in a particular stage partially reproduce the parent cells (self-renew) and partially express a new factor (move to the next stage). This concept has been supported by our experiment showing that stem cells do divide in the early stages of their myogenesis [2]. Such a mechanism of differentiation changes in the late stages when the late factors are expressed by transcription without cell division. Thus, in each stage, cells self-renew, differentiate (either through division or directly) and dye with certain rates which are characteristics of our model. These rates are affected by the applied strain resulting in the strain-dependent stem cell kinetics. How to determine the strain dependence of the model rates? For the late stages of differentiation by the transcription mechanism, the strain dependence of the differentiation rate can be derived by assuming that the strain effect occurs via a signalling molecule which binds the transcription factor as its activator. This binding occurs much faster than the protein production which simplifies the kinetic equations and results in a sigmoidal (saturating for large strains) multiplicative term [3] in the differentiation rate. Then, we use a similar sigmoidal terms for the strain dependence of the rates in the early stages. In addition to the signalling associated with the strain effect (which is due to the cell-extracellular matrix interaction), we also introduce a feedback signalling which is due to the cell-cell interaction. It is characterized by a feedback factor dependent on the cell density and expressed in terms of the total cell number. These and other features make the problem nonlinear. Computationally, the problem reduces to a system of nonlinear ODE's which is integrated assuming that initially all cells are the original stem cells, and cells in other stages are absent.

[a)] Corresponding author. Email: ictam2016papers@legendconferences.com.

EXPERIMENT

In the experiment, adipose-derived stem cells are seeded on a flexible membrane substrate subjected to uniaxial strain (the Flexcell system). The daily-applied strain consists of a cyclic (tensile) component following by a period of rest. Such dynamic conditions are compared with control static (no-strain) condition of myogenesis. The myogenic markers are analysed by using immunofluorescent staining, and the brightness of images is converted into the numbers of cells expressing particular factors. We also estimate the number of proliferating (dividing) cells at different times.

RESULTS

We compute the numbers of cells in each of the five stages of myogenesis as functions of time for the dynamic and static conditions. We use a particular dynamic case (strain amplitude of 10%) to adjust the model parameters, and the resulting kinetics is presented in Fig. 1 along with the data for the static case. The number of the original stem cells is not shown but

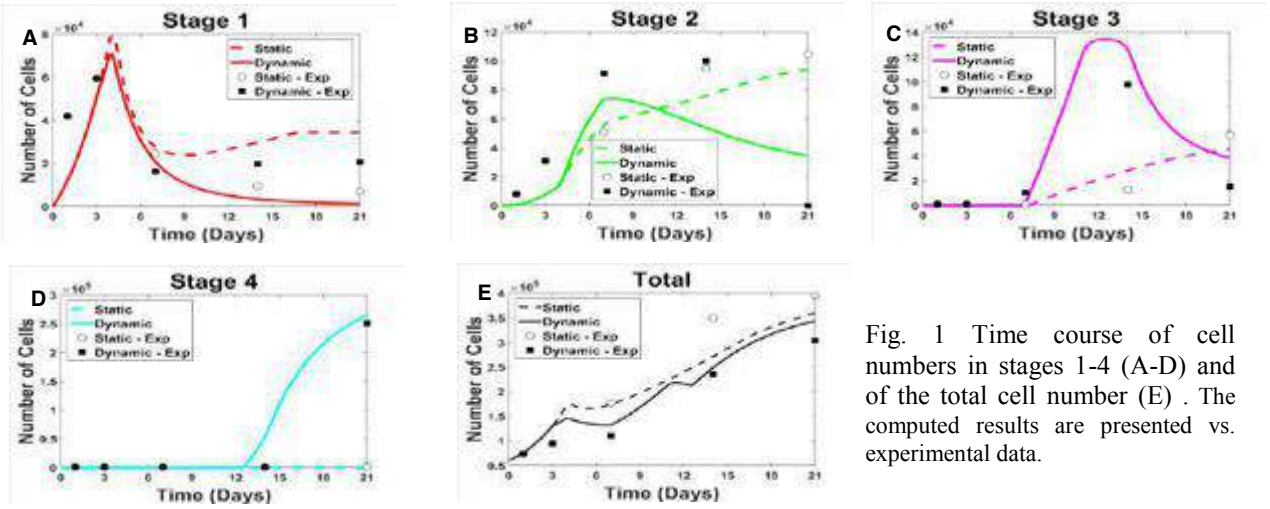

Fig. 1 Time course of cell numbers in stages 1-4 (A-D) and of the total cell number (E) . The computed results are presented vs. experimental data.

it can be extracted based on the data for the total number of cells (Fig. 1E). We use the model with the adjusted parameters to predict the kinetics of stem cell myogenesis for strains of other amplitudes. We found that the dynamic-case myogenesis follows a path where the original stem cells gradually disappear and are replaced with the cells expressing the late myogenic factors. This is opposite to the static case where the number of stem cells continues to rise, and the late factors are not expressed during the time of the experiment. Interestingly, there is a border-line case of the strain amplitude of about 2% where a transition between the dynamic and static patterns of kinetics occurs. Next, we consider the effect of the time course of the applied strain. We assume that the process of stem cell myogenesis depends on a "signal" reflecting the time course of the strain. The signal is considered as constant during the part of the day when the strain is applied. This constant is determined by the amplitudes of the strain and strain rate (strain frequency). During the rest of the day, the signal exponentially relaxes. We re-computed the kinetics of myogenesis taking into account the time course of the strain. Finally, we apply our model to the optimization of the strain daily time course varying the strain amplitude, frequency, and duration. The proposed model can be applied to different stem cells, it can also be extended to take into account 3-D spatiotemporal conditions, and the obtained results can lead to a better understanding of stem cell myogenesis

References

[1] Huri P.Y., Cook C.A., Hutton D.L., Goh B.C., Gimble J.M., DiGirolamo D.J., et al. Biophysical Cues Enhance Myogenesis of Human Adipose Derived Stem Cells. *Biochem Biophys Res Commun.* **438**: 180-185, 2013.
[2] Huri P.Y., Wang A., Spector A.A, Grayson W.L. Multistage Adipose-Derived Stem Cell Myogenesis: An Experimental and Modeling Study. *Cell Mol Bioeng.* 7: 497–509, 2014
[3] Alon U. An Introduction to Systems Biology: Design Principles of Biological Circuits. 1st ed. Chapman & Hall/CRC Press; 2006.

THE ROLE OF LINE TENSION ON BUDDING FORMATION INDUCED BY DIFFUSION OF PROTEINS ON LIPID BILAYER

Tsegay Belay[1], Chun IL Kim [*2], and Peter Schiavone[3]

[1,2,3]*Department of Mechanical Engineering, University Of Alberta, Edmonton, Alberta, T6G 1H9,Canada*

Summary We investigate the effects of line tension at the lipid-protein domain interface on membrane budding formation which is assumed to be induced by surface diffusion of the trans-membrane proteins. The theoretical model for the mechanics of membrane shape transformation is described by a modified formulation of the Helfrich model in order to accommodate any nonlinear response of the membrane due to the diffusion of the trans-membrane proteins. The resulting shape equation is numerically solved for Non-Monge or general membrane surface representation. Our results show that line tension at the domain interface makes a significant contribution on a spherical-shape-like budding formation on weakly curved or flat lipid membrane. We show numerically that increasing the line tension facilitates the reduction of the interface diameter between the flat membrane and generated spherical bud, thus increasing the potential to pinch off the bud. Full details can be found in [1].

INTRODUCTION

Lipid bilayer membranes are negligibly thin (typically 5-10nm) but they represent a critically important interface within biological cells mediating all interactions between cells and their surrounding environment through the involvement of a variety of proteins. These proteins can aggregate into clusters or domains on the membrane surface. In particular, so-called 'trans-membrane proteins' domain can induce local curvature [2] and hence assist morphological aspects of cellular processes such as fission, fusion and budding [3, 4, 5] regulated by membrane forces. Specifically, membrane budding, which are spherical protrusions emerging out of a flat or curved bilayer membrane, is one particular phenomena and is an important step in cellular exocytosis and endocytosis processes. Consequently, extensive studies have been made on the influence of trans-membrane proteins on membrane budding formation (see [6] and references therein). However, in most cases, the derived shape equations of the membrane are solved by linear geometric approximation in the Monge representation of the membrane surface. The work described here is motivated by the approach in [6] to consider the use of surface diffusion of trans-membrane proteins on the membrane as one possible driving mechanism for the membrane budding. However, line tension is suppressed in [6]. Here we find the effect of line tension at the domain interface to be non-negligible but making a significant contribution to the shape transformation (budding formation) of the lipid membrane.

PROBLEM FORMULATION

In the absence of lateral pressure, the membrane shape equation is obtained as [1, 6]

$$L' = 2r[H(k(H-C)^2 + (\alpha\sigma - \beta)^2 + \lambda) - k(H-C)(H^2 + (H - \sin\psi(s)/r)^2)], \tag{1}$$

where

$$L = kr(H' - \mu\varphi\sigma'), \tag{2}$$

is a transverse shear force. Here, r measures the radial distance of a point from the axis of symmetry of an axisymmetric membrane surface, k is bending rigidity which pertain to lipid membranes with nonuniform properties, H is the mean curvature of the membrane surface ω, σ is protein density and $\psi(s)$ is an angle that the membrane makes from the horizontal axis. The spontaneous curvature ,$C = (\mu\varphi)\sigma$, is proposed in order to account for the asymmetry of the bilayer induced by the diffusion of the trans-membrane proteins on the lipid bilayer membrane surface [6]. In this proposal, $(\mu\varphi)$ is a constant of proportionality where μ being a positive constant and φ the angle made by the meridian of the protein geometry (in this case assumed as a conical shape) with the surface normal $\mathbf{n}$. In addition, α and β are positive constants which conforms to the conventional theory of bending elasticity in the absence of protein diffusion. The Lagrange multiplier λ in Eq. (1) satisfies [6]

$$\lambda' = 2[k\mu\varphi(H-C) - \alpha(\alpha\sigma - \beta)]\sigma'. \tag{3}$$

The edge conditions (e.g. boundary forces $\mathbf{f}$ and moments M on a smooth boundary $\partial\omega$) are obtained as

$$\mathbf{f} = F_\upsilon \boldsymbol{\upsilon} + F_t\mathbf{t} + F_n\mathbf{n}, \quad M = k(H-C), \tag{4}$$

$$\text{where} \quad F_\upsilon = (\alpha\sigma-\beta)^2 + k[H-C]^2 + \lambda - \psi' M + \gamma\frac{\cos\psi(s)}{r}, \quad F_t = 0, \quad F_n = -\frac{L}{r} + \gamma\frac{\sin\psi(s)}{r}, \tag{5}$$

*Corresponding author. Email: cikim@ualberta.ca

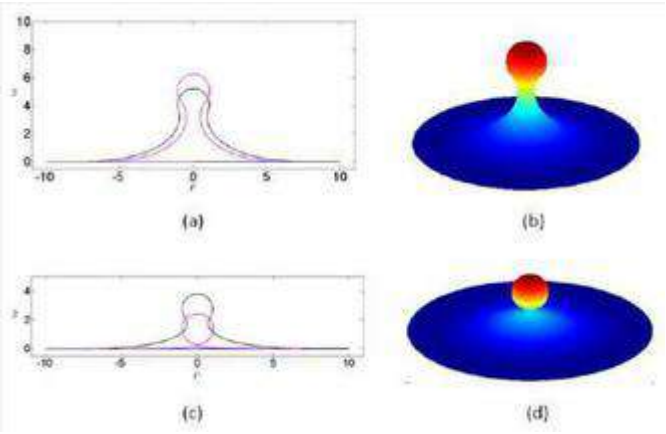

Figure 1: (**a**) Sequence of membrane shape-changes as the protein diffuses into the domain with $(\gamma = 0)$, and weak membrane tension of $(f = 0.001)$, (**b**) sequence of membrane shape-changes as the protein diffuses into the domain with $(\gamma = 0.1)$, and weak membrane tension of $(f = 0.001)$, (**c**) 3D contour plot of membrane budding formation without the effect of line tension at the interface domain, (**d**) 3D contour plot of membrane budding formation with the effect of line tension at the interface domain.

are, respectively, the $\boldsymbol{\upsilon}$-,$\mathbf{t}$- and $\mathbf{n}$-components of distributed forces per unit length applied to $\partial\omega$ and γ is line tension at the domain interface. (We note here the use of the primes to also denote the partial differentiation with respect to an arclength surface coordinates s , i.e. $(\cdot)' = \frac{\partial(\cdot)}{\partial s}$). The force applied to the membrane at the ith corner of $\partial\omega$ is zero. Finally, the normal and tangential velocities of the surface as well as the trans-membrane protein diffusion law are given below [6]

$$u\mathbf{n} = \mathbf{r}_t, \quad (rv)' = 2Hu, \quad \sigma_t + v\sigma' = \frac{2c}{r}[r((\alpha^2 + k\mu^2\varphi^2)\sigma' - k\mu\varphi H')]'. \tag{6}$$

NUMERICAL EXAMPLES AND CONCLUSIONS

We non-dimensionalize all the equations by introducing suitable reference scales. Finally, the Matlab routine $bvp4c$ [7] was used to solve the boundary value problem by applying suitable boundary conditions from the derived edge conditions. Figures (1a) and (1c) indicate that the membrane shape-changes at a succession of times starting with a planar configuration. The succession of shape-changes in the membrane is characterized by a gradual increase in protein concentration over the domain. It should be noted that the protein diffusion destabilizes the weakly curved or flat membrane and as a result, the sequence of shapes is seen to become more curved as time advances due to gradual increase in protein concentration over the domain. Hence, this process leads to the formation of budding on the membrane. However, as clearly indicated in Figs. (1b) and (1d), increasing the line tension facilitates the reduction of the interface diameter between the flat membrane and generated spherical bud, thus increasing the potential to pinch off the bud. This suggests that the contribution of line tension energy in the membrane budding formation is very significant and therefore can not be ignored. It also suggested that the membrane cells may utilize the membrane line tension energies to control the budding process.

References

[1] Belay T., Kim C.I. and Schiavone P.:The Effect of Line Tension on Membrane Budding Formation Induced by Surface Diffusion of Trans-membrane Proteins on Lipid Bilayers. (Submitted).

[2] Review How proteins produce cellular membrane curvature. Zimmerberg J, Kozlov MM Nat. Rev. Mol. Cell Biol. 2006 Jan; 7(1):9-19.

[3] Chernomrdik, L. and Kozlov, M. (2008) *Mechanics of membrane fusion.* Nat. Struct Mol Biol. **15:** 675-683.

[4] Lenz, M., Morlot, S. and Roux A. (2009) *Mechanical requirements for membrane fission: Common facts from various examples.* FEBS Lett **583:** 3839-3846.

[5] Razani, B. and Lisanti, M. P. Caveolins and caveolae. (2001) *Molecular and functional relationships.* Exp Cell Res, **271(1):** 36-44.

[6] Agrawal A. and Steigmann D.J.: A Model For Surface Diffusion of Transmembrane Proteins on Lipid Bilayers. Z. Angew. Math. Phys. 62 (2011), 549-563.

[7] Shampine L.F., Gladwell I., and Thompson S.: Solving ODEs with Matlab, Cambridge Univ. Press, New York, 2003.

THE CONFORMATIONAL CHANGE OF ANIMAL CELLS DURING CYTOKINESIS

Aisa Biria*[1] and Luc Mongeau[2]
[1]*Department of Mechanical Engineering and Materials Science, Yale University, New Haven, Connecticut, USA*
[2]*Department of Mechanical Engineerin, McGill University, Montreal, Quebec, Canada*

Summary Cytokinesis is the last stage of eukaryotic cell devision. During this process, an actin-myosin contractile ring constricts the cell membrane at the equator, until the cell partitions in two. We study this process by modeling the cell membrane as a two-dimensional, inextensible fluid membrane, with curvature elasticity, and subject to a contractile force field distributed along an equatorial curve. The membrane dynamics equilibrates the dissipative and energetic forces subject to an inextensibility constraint. The theory enables us to estimate the energy consumed for conformational change of the cells during cytokinesis process. A numerical simulation of the process is developed based on this theory.

Introduction

Cytokinesis is the mechanical process that finalizes cell division by cleaving the mother cell into two daughter cells. At the onset of this process, the cell rounds up into a nearly spherical shape and a thin (0.10.2 ?m) layer of cross-linked protein filaments assemble a contractile ring around the cell equator and beneath the plasma membrane. Afterwards, this actomyosin ring contracts plasma membrane in a string-purse effect. We provide a simple mechanical theory to model this process. There is a long literature on modelling the cell membranes as 2D inextensible fluid membranes. We build on that frame work, and obtain insight on the energies required for cytokinesis and the dynamics of the process. We start by considering an arbitrary geometry for the cell and the contractile ring and develop the general form of governing equations. Next, motivated by experiments, numerical solutions are obtained for the case of a spherical-shaped cell, contracted along an equatorial circle.

FORMULATION

Consider an evolving fluid membrane to be identified by a smooth, orientable surface $\mathcal{S}_t$ and let $\boldsymbol{x}_t$ present an arbitrary parametrization of it at a given instant t. For simplicity we drop the dependence of all quantities on time from now on. Denote the total area of surface $\mathcal{S}$ by A and define the velocity field $\boldsymbol{v} = \dot{\boldsymbol{x}}$ on $\mathcal{S}$, where a superposed dot denotes the material time-derivative. The elastic energy ψ of the system is given by integrating the Helfrich-Canham functional on the surface:

$$\psi = \int_{\mathcal{S}} \tfrac{1}{2}\mu(H \circ \ H_\circ)^2 + \bar{\mu}K, \tag{1}$$

with H and $H_\circ$ being the mean curvature and spontaneous mean curvature, K the Gaussian curvature, and where μ and $\bar{\mu}$ represent the splay and saddle-splay modulus respectively. Consider there is a closed curve $\mathcal{C}$ on surface $\mathcal{S}$, on which a uniform force field $\boldsymbol{f}$ normal to the surface is distributed. The power P expended by this force is

$$P = \int_{\mathcal{C}} \boldsymbol{f}.\boldsymbol{v} \tag{2}$$

By the principle of virtual power, the power expended on the system equates the energy release rate and the dissipative energy rate. The system evolves such that this balance holds, subject to the volume and areal inextensibility constraints, according to

$$\dot{\psi} = P + \dot{D} + \sigma\dot{A}, \tag{3}$$

where $\dot{D}$ is the dissipative energy rate, and P and σ are the Lagrange multipliers associated with the volume and area inextensibility constraints. The explicit forms of quantities $\dot{\psi}$ and $\dot{A}$ are given by Biria et. al. [1], while $\dot{D}$ is provided by Arroyo and DeSimone [2]. Substituting those explicit forms in (3) leads to Euler–Lagrange equations for the membrane.

RESULTS

REQUIRED ENERGY FOR CELL DEFORMATION DURING CYTOKINESIS

As experiments suggest, the cells round up into a spherical shape in the beginning of cytokinesis. For a spherical conformation, the elastic energy of the plasma membrane given by (1) is $8\pi\mu + 4\pi\bar{\mu}$. Notice that this energy is independent of the size of the cell, and so, as the cell divides in two almost-identical daughter cells, the elastic energy of the system increases by $8\pi\mu + 4\pi\bar{\mu}$. This is the minimum required energy that has been expended by the protein motors of the cell. The actual energy expense can be more due to dissipative effects, and any resistant to conformational change by the cytoplasm.

*Corresponding author. Email: aisa.biria@yale.edu

NUMERICAL RESULTS

Numerical simulations were performed starting with a spherical membrane, in the absence of dissipation and assuming a saddle-splay modulus of zero. By increasing the contractile force, the cell starts elongating and narrowing in the equator. At a threshold force of $fR^2/\mu = 2.2$, the capsule-shaped configuration becomes unstable, and the mother-cell buckles into a dumble-like shape, with two connected spherical daughter-cells. With this transition, the increasing surface tension of the membrane is suddenly released. Our calculations predict that the cell volume slightly decreases during cytokinesis.

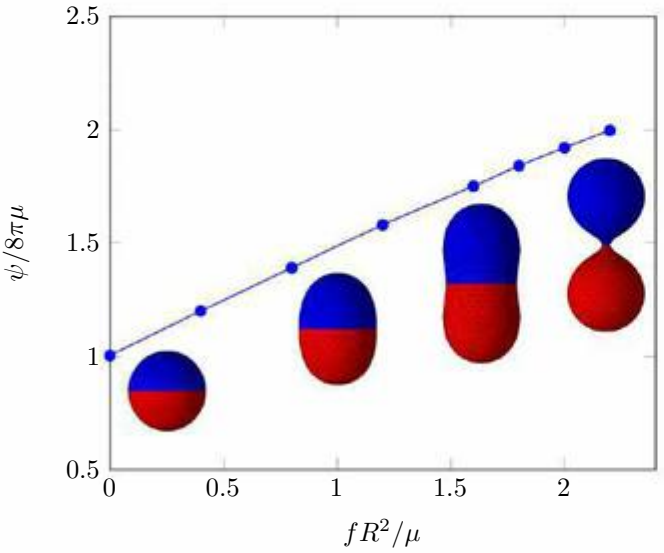

(a) The change in elastic energy of the cell with increasing contractile force

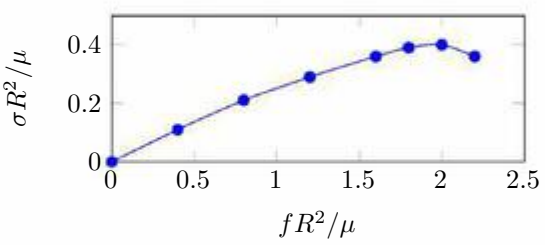

(b) The change of surface tension with increasing contractile force

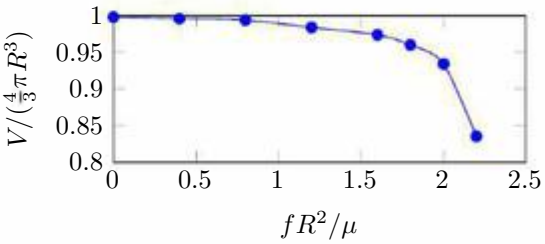

(c) The change of cell volume during cytokinesis

CONCLUSIONS

A theory is developed, which is capable of explaining the conformational changes of cells during cytokinesis. Our results confirmed the previous predictions [3] that cell elasticity plays an important role in shape regulations during cell division. For simplification, the effects of dissipation and resistance to Gaussian curvature were neglected in the numerical calculations. Accounting for these effects has been postponed to a future work. Also, as suggested by experiments [4], the cortex contraction has been assumed to be concentrated at the cell equator in the present work. A generalization can be attained by considering a smooth contractility gradient across the cell membrane.

[1] Biria, A., Maleki, M., & Fried, E.: Continuum theory for the edge of an open lipid bilayer. Adv. Appl. Mech 21:1-78, 2013.

[2] Arroyo, M., DeSimone, A.: Relaxation dynamics of fluid membranes. Physical Review E, 79: 031915, 2010.

[3] Sedzinski, J., Biro, M., Oswald, A., Tinevez, J. Y., Salbreux, G., & Paluch, E.: Polar actomyosin contractility destabilizes the position of the cytokinetic furrow. Nature 476:462-466, 2011.

[4] Bray D., White J.G: Cortical flow in animal cells. Science 239:883-888, 1988.

MEAN DEFORMATION METRICS FOR QUANTIFYING 3D CELL-MATRIX INTERACTIONS

David A. Stout[1], Eyal Bar-Kochba[2], Jonathan B. Estrada[2], Jennet Toyjanova[2], Haneesh Kesari[2], Jonathan S. Reichner[3] & Christian Franck[2, a)]

[1]*Department of Mechanical and Aerospace Engineering, California State University, Long Beach, CA, USA*

[2]*School of Engineering, Brown University, Providence, RI, USA*

[3]*Department of Surgery, Rhode Island Hospital, Providence, RI, USA*

Summary Investigations in mechanobiology rely in large part on correlation of cellular processes with mechanical signals, such as matrix stiffness and cell tractions. Almost all cell traction and force quantification methodologies require knowledge of the underlying mechanical properties of the extracellular matrix to convert displacement data into corresponding traction data. This restricts the use of these techniques to material systems for which the user can accurately determine material properties. To overcome this hurdle, we present a new approach that does not require any knowledge of the underlying matrix properties but rather makes use of the intrinsically recorded kinematic displacement data. We show through rigorous validation and an application to a neutrophil disease model that such an approach produces both accurate and biologically significant information similar to traditional force-focused approaches.

INTRODUCTION

Quantification of cellular force generation has received much attention over the last two decades since the physical interactions of cells with their surrounding matrix material constitutes an important component of the development of biological organisms and disease states [1]. Among several experimental techniques, traction force microscopy (TFM) has been extensively used for single and multi-cell studies in a variety of in-vitro material platforms. In TFM, cell-generated material displacement fields are converted via the material's constitutive equations to their respective stress and traction fields. While our group and others have developed several mathematical frameworks with various levels of complexity for calculating cellular tractions, the requirement of supplying the constitutive properties of the underlying matrix material has limited the use of TFM to relatively simple, mostly isotropic and homogenous material systems [2,3]. Yet, with the emergence of 3D printing and nanoscribing capabilities, biomaterials with increasingly sophisticated architectures, including spatial hierarchies and material heterogeneities are being developed and deployed for use in cellular investigations. To provide an experimental technique that can hold pace with the development of new advanced material systems, we developed a new approach that is capable of quantifying cell-matrix interactions without requiring the user to supply any information about the material's constitutive behaviour. Our technique, call the Mean Deformation Metrics (MDM) approach deduces all of its measures from the original kinematic displacement field. The advantage is that this technique is immediately applicable to any material system from which displacement information can be derived. The limitation is that, due to its kinematic nature, the MDM approach cannot discern differences due to changes in the stiffness of the material. Here, we present both the formalism of our MDM technique and an application to a neutrophil disease model in a 3D collagen gel.

3D DISPLACEMENT FIELDS & MEAN DEFORMATION METRICS

Cell-induced material deformations are described according to standard continuum mechanics formulations, i.e., $\boldsymbol{x}(\boldsymbol{X},t) = \boldsymbol{u}(\boldsymbol{X},t) + \boldsymbol{X}$, where $\boldsymbol{X}$ is the material's point position vector in the undeformed reference configuration, and $\boldsymbol{x}$ is the material's point position vector in a deformed state at time t undergoing a displacement $\boldsymbol{u}$. Next, we derive the material's deformation gradient tensor $\boldsymbol{F}(\boldsymbol{X},t) = \nabla \boldsymbol{x}(\boldsymbol{X},t)$, which is defined point-wise throughout the matrix. Following a similar formalism described by Hill [4] for addressing the effective mechanical behaviour in composites and heterogeneous media, we define a mean deformation gradient tensor $<\boldsymbol{F}>$ as,

$$< \boldsymbol{F} > = \frac{1}{V_0} \int_{V_0} \boldsymbol{F}\, dV.$$

Using the divergence theorem, $<\boldsymbol{F}>$ can be rewritten as,

$$< \boldsymbol{F} > = \boldsymbol{I} + \frac{1}{V_0} \int_{\partial V_0} \boldsymbol{u} \otimes \boldsymbol{n}\, dA,$$

where $\boldsymbol{u}$ denotes the matrix displacement field along the boundary of the cell, ∂V_0, and $\boldsymbol{n}$ denotes the cell's surface normal. This final expression of $<\boldsymbol{F}>$, allows computation of the mean deformation gradient tensor directly from the matrix displacement data, $\boldsymbol{u}$, and the cell surface data ($\boldsymbol{n}$) without invoking any spatial derivatives, which is a significant benefit for

a) Corresponding author. Email: franck@brown.edu

working with experimental data in the presence of noise. Once <$\boldsymbol{F}$> is determined, any other kinematic quantity can be derived using standard continuum mechanics approaches.

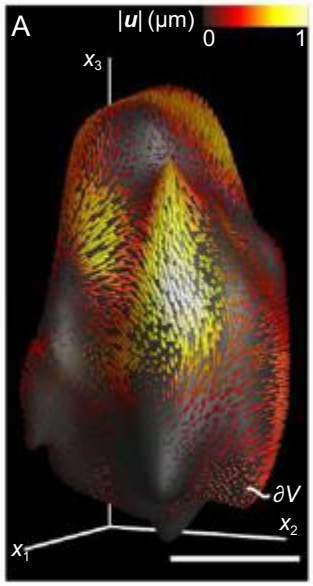

Figure 1. Displacement field along the surface of a migrating human neutrophil through a 3D collagen gel.

RESULTS & DISCUSSION

We illustrate the power of our MDM technique by investigating the biophysical characteristics of human neutrophils moving through a 3D collagen matrix. Briefly, we induce chemotaxis by establishing a uniform planar diffusion gradient within a 3D collagen gel [5], which causes neutrophils to respond and migrate along the gradient. Using laser scanning confocal microscopy we reconstruct the 3D neutrophil induced collagen deformation fields using our previously published FIDVC technique [6]. An example of a typical deformation field around a migrating human neutrophil is shown in Fig. 1. Here, the 3D matrix displacement field ($\boldsymbol{u}$) adjacent to the cell is mapped onto the cell boundary, ∂V. Next, using the above-derived formulation for the mean deformation gradient, <$\boldsymbol{F}$>, we compute the mean volume change, <J>, and the principal stretches<λ_i> of migrating neutrophils, shown in Fig. 2. Specifically, we discern differences in the compressibility (Fig.2, left) and contractility (Fig.2, right) of healthy naïve neutrophils (T-N) vs. neutrophils treated with lipopolysaccharide (LPS) (T-L), a common disease model for sepsis. Our findings show that LPS-treated neutrophils become increasingly compressible and contractile compared to their naïve counterparts. These findings are biologically significant as they allow quantitative phenotyping of human cells without the need to fluorescently label the cells. In short, the biophysical mean characteristic, or phenotype, of the given cell can be derived from just the matrix deformations alone. Along with Figs. 1 and 2, this talk will explore other kinematic measures derived from <F> and demonstrate their usefulness as a means for a mechanics-based clinical assay.

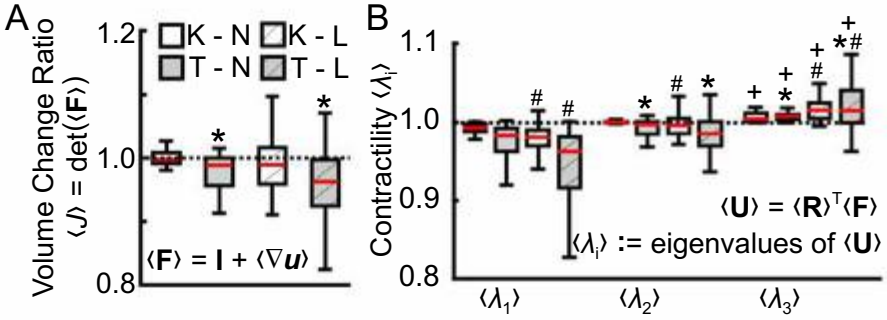

Figure 2. Mean cellular compressibility (left) and contractility (right) of migrating

CONCLUSIONS

In this talk we present a new 3D cell-matrix quantification methodology that is purely based on the deformation kinematics of the extracellular matrix. Specifically, we present a rigorous approach of how to effectively use matrix displacement data to characterize different cellular phenotypes, differentiate between healthy and disease cells, and quantify the physical interaction with the extracellular matrix without the need to prescribe material constitutive information as is required in conventional traction force microscopy. Furthermore, we show that even when the mechanical properties of the underlying matrix material are known, our MDM approach can provide unique biophysical descriptions, e.g., cell rotation, that are not usually captured by TFM, thus making it a great complement to traditional force reconstruction techniques.

References

[1] Chen, C.S.: Mechanotransduction – a field pulling together. *J. Cell Sci* **121**:3285-3292, 2008.

[2] Schwarz, U.S., Soine, J.R.D.: Traction force microscopy on soft elastic substrates: A guide to recent computational advances. *BBA – Mol Cell Res* **1853**:3095-3104, 2015.

[3] Toyjanova, J. et al.: 3D Viscoelastic traction force microscopy. *Soft Matter* **10**:8095-106, 2014.

[4] Hill, R.: On constitutive macro-variables for heterogeneous solids at finite strain. *P Roy Soc Lond A Mat* **326**:131-147, 1972.

[5] Stout, D.A., Toyjanova, J., Franck, C.: Planar gradient diffusion system to investigate chemotaxis in a 3D collagen gel. *J. Vis. Exp.* E52948, 2015.

[6] Bar-Kochba, E. et al.: A fast iterative digital volume correlation algorithm for large deformations. *Exp. Mech.* **55**:261-274, 2015.

SEQUENTIAL STRAIGHTENING AND LOADING VISCOELASTICITY

Tom Shearer *[1], William J. Parnell[1], Barbara Lynch[2], Jean-Marc Allain[2], and I. David Abrahams[1]
[1]*School of Mathematics, University of Manchester, Oxford Road, Manchester M13 9PL, UK*
[2]*Solid Mechanics Laboratory, Ecole Polytechnique, Centre National de la Recherche Scientifique, Institut National de la Santé et de la Recherche Medicale U696, Palaiseau Cedex, France*

Summary Collagenous soft tissues exhibit complex viscoelastic behaviour, such as strain-rate dependence, hysteresis and strain-dependent relaxation. Many existing theories, such as quasi-linear viscoelasticity, fail to capture some of these features. In this paper, a model for soft tissue viscoelasticity that is based on the notion of "sequential straightening and loading", whereby fibrils contribute to tissue stiffness only when taut, is presented. Each fibril is modelled as linear viscoelastic and has an associated critical strain at which it becomes taut. We show that, even given such simple constitutive behaviour, all of the desired viscoelastic features occur as a consequence of there being a distribution of such critical strains. The model is used to fit mechanical tests on three different rat tail tendon fascicles and we show that they can be reproduced with a single set of constitutive parameters, with the only difference being the distribution of the critical strains in each case.

THE MODEL

Configuration and parameters

We model the fascicle as a two-phase inhomogeneous medium consisting of a background extracollagenous matrix and a large number of individual fibrils, each of which is initially crimped in the rest state of the fascicle. Our approach is based on the ideas of Kastelic *et al.* (1980) and their "sequential straightening and loading" (SSL) model and the low density crosslink (LDCL) model described by Lanir (1980). As the fascicle is stretched, the shortest fibrils are the first to become taut and start contributing to its stiffness. As the stretching continues, more fibrils straighten, and the stiffness of the fascicle increases, accounting for its exponential-shaped stress-strain curve. In our model, we additionally take into account the contribution to the macroscopic stress of the matrix phase. The fibrils are assumed to reside within the matrix and it is assumed that it is their interactions with each other and with the matrix that cause the effective viscosity in each phase. We write the total volume fraction of (crimped and uncrimped) fibrils as ϕ so that the volume fraction of the matrix phase is $1 \circ \ \phi$. We model both the fibrils and the matrix as linear viscoelastic. In addition to the fibril volume fraction we also need the following parameters: the instantaneous and long-time fibril Young's moduli, E_0 and E_∞, the fibril relaxation time τ_r and the corresponding matrix parameters: E_0^m, E_∞^m and τ_r^m. We define the *fibril* and *matrix* stress and strain as σ_f, e_f and σ_m, e_m respectively. We also denote the imposed *macroscopic* (fascicle) strain as e and the resulting macroscopic (fascicle) stress as σ.

Matrix response

First we consider the response of the extracollagenous matrix to an applied fascicle load. The matrix strain is equal to the applied fascicle strain and we model the matrix as a linear viscoelastic material, so that we have:

$$e_m(t) = e(t), \qquad \sigma_m(t) = E(0)e_m(t) + \int_0^t E_m'(t \circ \ s)e_m(s)ds, \qquad E_m(t) = E_\infty^m + (E_0^m \circ \ E_\infty^m)e^{-t/\tau_r^m}, \tag{1}$$

where E_0^m and E_∞^m can be identified as the instantaneous and long-time Young's moduli of the matrix, respectively, and τ_r^m is its relaxation time.

Single fibril response

Next, we consider the response of a single fibril to an applied fascicle strain. The strain in a given fibril depends on the critical fascicle stretch e_c at which it first becomes taut:

$$e_f^t(t) = \frac{1}{1+e_c}(e(t) \circ \ e_c). \tag{2}$$

As with the extracollagenous matrix, the fibril will be modelled as linear viscoelastic so that

$$\sigma_f(t) = E(0)e_f(t) + \int_0^t E'(t \circ \ s)e_f(s)ds, \qquad E(t) = E_\infty + (E_0 \circ \ E_\infty)e^{-t/\tau_r}, \tag{3}$$

where E_0 and E_∞ can be identified as the instantaneous and long-time Young's moduli of the fibril, respectively, and τ_r is its relaxation time.

*Corresponding author. Email: tom.shearer@manchester.ac.uk

Total fascicle response

Now that we have expressions for the stresses in the matrix and in a fibril that tautens at critical fascicle strain e_c, it is simple to obtain the homogenised response of a fascicle containing fibrils with a range of crimp lengths. The total fascicle stress is equal to the average of the stresses in the fibrils and matrix in proportion to their volume fractions; i.e. $(1 \circ \ \phi)$ times the matrix stress plus ϕ times the average fibril stress. Since each fibril has its own associated critical strain, the average fibril stress is determined by integrating over the individual fibril stresses multiplied by a critical strain distribution function. Considering a unit volume of fascicle we have

$$\sigma(t) = (1 \circ \ \phi)\sigma_m(t) + \phi \int_0^\infty p(e_c)\sigma_f(e(t), e_c)de_c, \qquad t \in [0, \infty), \tag{4}$$

where $p(e_c)$ is the initial distribution of critical strains and the notation $\sigma_f(e(t), e_c)$ is used to emphasise the fact that the stress in each individual fibril is dependent on both the imposed fascicle strain, $e(t)$, and the critical fascicle strain, e_c, at which that fibril first becomes taut. We note that any continuous function may be chosen for the imposed fascicle strain, provided it satisfies $e(0) = 0$.

EXPERIMENTS AND MODEL PREDICTIONS

To test the model, we used it to fit three experiments on rat tail tendon fascicles: two relaxation tests and a cycle test. The constitutive parameters were kept the same when modelling each experiment:

$$E_0 = 1 \text{ GPa}, \qquad E_\infty = 250 \text{ MPa}, \qquad \tau_r = 90 \text{ s}, \qquad \phi = 0.8, \tag{5}$$

$$E_0^m = 30 \text{ MPa}, \qquad E_\infty^m = 10 \text{ MPa}, \qquad \tau_r^m = 6000 \text{ s}, \tag{6}$$

and the only difference between the three fascicles being modelled was their assumed critical strain distribution. A beta distribution was used for all three experiments:

$$p(e_c) = \frac{(e_c)^{\alpha-1}(1 \circ \ e_c)^{\beta-1}}{\mathrm{B}(\alpha, \beta)}, \tag{7}$$

where α and β are the distribution parameters (which both must be greater than 0), and $\mathrm{B}(\alpha, \beta)$ is the beta function; however, the distribution parameters were allowed to vary in each case. The results and the critical strain distributions used are plotted in the figures below.

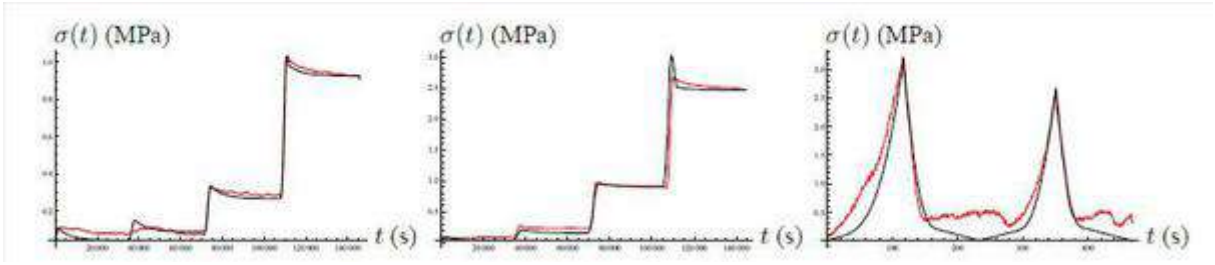

Theoretical (black) and experimental (red) fascicle stress as a function of time. Distribution parameters: left - $\alpha = 12$*,* $\beta = 135$*, middle -* $\alpha = 12$*,* $\beta = 200$*, right -* $\alpha = 4$*,* $\beta = 41$*.*

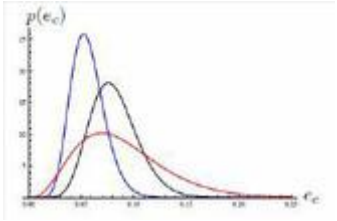

Critical strain distributions used to model Relaxation Test 1 (black), Relaxation Test 2 (blue) and the Cycle Test (red).

References

[1] Kastelic J., Palley I., Baer E. A structural mechanical model for tendon crimping. J. Biomech. 13:887-893, 1980.

[2] Lanir, Y. Structure-strength relations in mammalian tendon. J. Biomech. 16:1-12, 1978.

DESIGN OF BIOINSPIRED ARMOR FOR OPTIMUM PUNCTURE RESISTANCE, STABILITY AND FLEXURAL COMPLIANCE.

Roberto Martini and Francois Barthelat [a)]
Department of Mechanical Engineering, McGill University, Montreal, Quebec, Canada

Summary: Flexible natural armors from fish or snakes are attracting an increasing amount of attention from their unique combination of hardness, flexibility and light weight. In particular, the extreme contrast of stiffness between the hard scales and the surrounding soft tissues give rise to unusual and attractive mechanisms, which now serve as model for the design of bio-inspired armors. There is however little guidelines as to the choice of materials, optimum thickness, size, shape and arrangement for the protective scales. In this paper, we present recent experiments and models to explore and characterize the different failure modes of flexible skins reinforced by hard scales and subjected to puncture: flexural and contact fracture, unstable tilt, interactions between scales. We optimized the size, shape and arrangement of the scales which govern these mechanisms to produce synthetic bioinspired armor with optimum combination of resistance to sharp puncture and flexural compliance.

INTRODUCTION

Over millions of years of evolution, high-performance protecting materials and systems have emerged from an "arm's race" between predators and preys. These natural armors, which include mollusk shells, testudines carapace and arthropods exoskeleton, display a wide range of compositions, architectures and sizes to resist a variety of threat including sharp puncture, laceration or crushing. The armor of animals with fast locomotion presents particularly interesting features. These protective materials must be hard to resist puncture and lacerations, yet sufficiently compliant and light to allow unimpeded movement. In natural organisms this design contradiction is often resolved by segmentation of the hard protective layer into scales of finite size (Fig.1). Typical examples of segmented armors include the scaled skins of fishes and snakes or the osteoderms of armadillos and crocodiles. These natural dermal armors are light, locally hard to resist puncture, yet flexible at larger length scales to allow for motion [1]. A characteristic common to these natural protective systems is the extreme contrast of stiffness between the protective material and the soft underlying tissues. For example, teleost fish scales are five orders of magnitude stiffer than the underlying skin (stratum compactum) and the soft underlying tissues (muscles, other organs) [2]. In terms of mechanics, large contrasts of stiffness between the scales and their substrate lead to a rich set of deformation and failure modes, which we explore and characterize in details in this work. The findings can inspire and guide the design of better synthetic protective systems, which we also discuss.

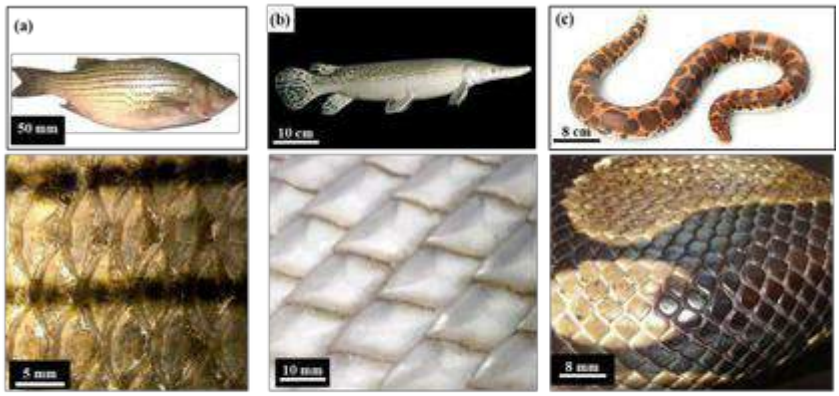

Fig. 1: Examples of natural compliant armor with overlapping scales: (a) Teleost scales (striped bass *Morone saxatilis*) (b) ganoid scales (alligator gar *Atractosteus spatula*), (c) snake scales (sand boa *Gongylophis colubrinus*).

MECHANICS OF HARD SCALES ON SOFT SUBSTRATES

Depending on the relative stiffness of a hard plate (scale) and its substrate, sharp indentation on a stiff scale resting on a soft substrate may lead to ring cracks initiated by contact stresses, or radial cracks initiated by flexural stresses. The transition between the two modes is of high importance for a variety of applications, and can be captured using relatively simple models [3]. For high contrast of stiffness between scales and substrate and for the case where the failure of the scales is governed by flexural stresses, we found that segmented scales increase the resistance to puncture compared to continuous coatings of the same materials (Fig. 2). It therefore appears, interestingly, that segmenting the hard layer not only makes the system more compliant in flexion, but also increases the resistance to sharp puncture. Our experiments of sharp puncture on segmented glass plates on elastomeric substrates also highlighted a third failure mode [4] where the tablet suddenly tilts, leading to the sliding of the indenter onto its surface and into the substrate (Fig. 2). This failure mode does not involve any damage to the tablet, but it is highly detrimental, since the unstable tilting of the tablet exposes the soft and fragile substrate to the tip of the indenter. This failure mode was also observed on the hard and bony scales of gar fish indented with a sharp needle. Individual

[a)] Corresponding author. Email: francois.barthelat@mcgill.ca

scales do not fracture. Instead, at a critical puncture force the indented scale suddenly tilts, the needle slides on their surface finds its way between the scales and into the softer skin and other soft underlying tissues. Using stress analysis, finite elements and contact mechanics, we constructed a failure map for stiff scales on soft substrates which captures the effects of material properties and geometry of the scales on failure mode transitions between contact fracture, flexural fracture and unstable tilting.

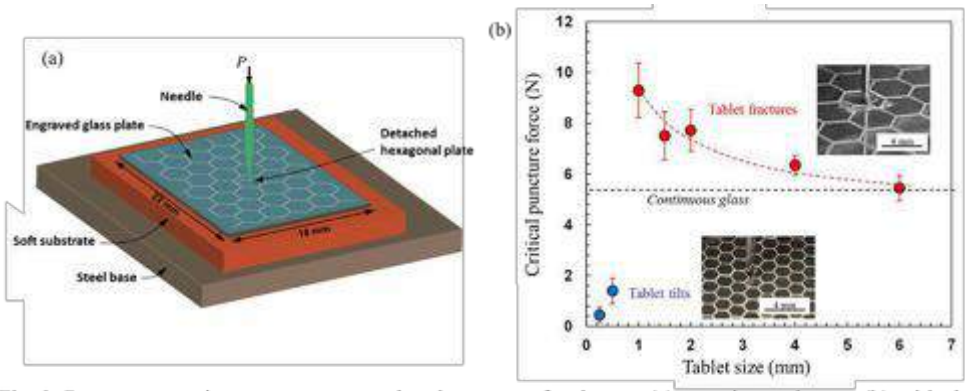

Fig. 2: Puncture experiments on segment glass layer on soft substrate (a) experimental setup (b) critical puncture force as function of tablet size: the critical puncture force increases when the tablet size is reduces, but below a critical threshold (~0.75 mm) the force is much lower because the tablet tilts.

Direct interaction between adjacent scales can also increase their stability. To explore this aspect of the design we 3D printed stiff scales of ABS on a silicone substrate. Enriching the geometry of the scale by incorporating slanted sides and other features can generate overlaps and interlocking between scales, which greatly increases their stability while maintaining a high flexural compliance.

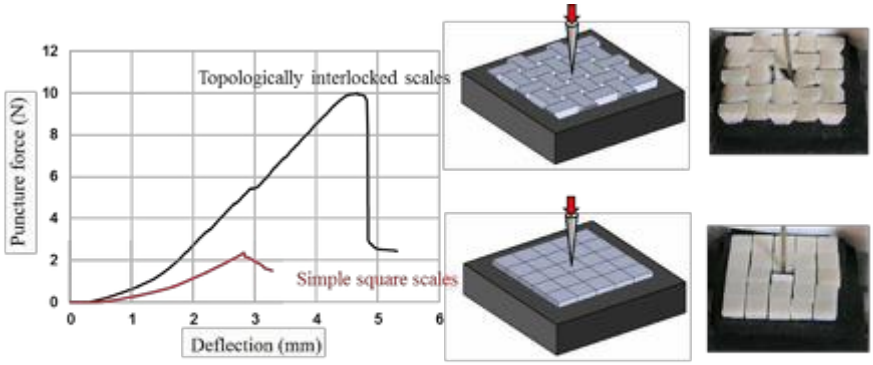

Fig. 3: Stability of 3D printed ABS scales on soft silicone substrate. The scales are defeated by unstable tilting. Slanted sides generate topological interlocking between the scales, which delays instability and increases the puncture resistance fourfold

BIOINSPIRED FLEXIBLE ARMOR

The main outcome of this work is a rigorous set of guidelines for the design and optimization of bioinspired flexible armors. Here we also report a new technique to fabricate fish skin-inspired flexible protective layers. We demonstrated that the scalation pattern can be easily and accurately controlled through a simple combination of laser engraving and stretchable tape transfer process. This approach can produce scaled structures with high morphological control over the shape, arrangement and overlap of the scales (Fig. 4). The as-produced protective system presents a specific puncture resistance higher than the one of the continuous ceramic plate, yet preserving a high compliance. The approach is versatile since it can be adapted to form scaled structures with different materials and on different flexible substrates. Extended surfaces can be covered with a staggered configuration of scales that allows the protective system to bend in different directions, for various applications.

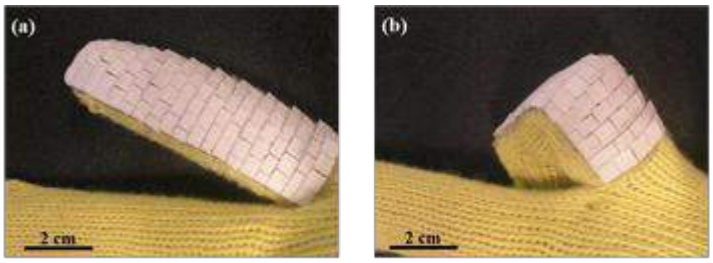

Fig. 4: Kevlar glove partially covered with bio-inspired ceramic scales in (a) extended and (b) bent position

References

[1] Vernerey F., Barthelat F.: On the Mechanics of Fish Scale Structure. *Int. J. Solids Struct. Solids* **47**:2268-2275, 2010.

[2] Zhu D., Ortega C. F., Motamedi R., Szewciw L., Vernerey F., Barthelat F.: Structure and Mechanical Performance of a "Modern" Fish Scale. *Adv. Eng. Mater.* **14**:B185-B194, 2012

[3] Lawn B. R., Deng Y., Miranda P., Pajares A. Chai H., Kim D. K.: Overview: Damage in Brittle Layer Structures from Concentrated Loads. *J. Mater. Res.* **17**:3019 –3036, 2002.

[4] Chintapalli R. K., Barhelat F.: Fabrication, Testing and Modeling of a New Flexible Armor Inspired from Natural Fish Scales and Osteoderms. *Bioinspir. Biomim.* **9**:036005, 2014

HIERARCHICAL MODELING OF PLASTICITY AND STRENGTH OF TRABECULAR BONE

Iwona Jasiuk [a)], Fereshteh Sabet, Diab W. Abueidda, Elham Hamed, Ouli Jin & Seid Koric
Department of Mechanical Science and Engineering, University of Illinois at Urbana-Champaign, Urbana, Illinois, USA

Summary We study computationally, using a finite element method, plastic deformations and strength of trabecular bone. We represent the trabecular bone as a material with hierarchical structure and consider four structural scales: the nanoscale (mineralized collagen fibril), the sub-microscale (single lamella consisting of mineralized collagen fibrils), the microscale (trabecular bone tissue), and the mesoscale (trabecular cellular network). At each scale we model the elastic and inelastic responses of bone until failure. We account for the experimentally observed failure mechanisms. Theoretical results are in good agreement with experiments conducted on cylindrical porcine trabecular bone samples.

INTRODUCTION

Bone consists of a *cortical* (dense) bone forming an outer shell and *trabecular* (spongy) bone filling space within bone. Such structure is optimized so bone can effectively resist loads while being lightweight. The cortical bone provides resistance to axial as well as bending and torsional loads while the trabecular bone redistributes loads and absorbs energy. Bone has excellent mechanical properties, including high strength and fracture toughness, when healthy. However, bone diseases such as osteoporosis make bones brittle and prone to fracture. Bone fractures often take place in regions dominated by trabecular bone such as in femoral neck. Thus, study of plasticity and fracture of trabecular bone is of high clinical importance. Predictions of the trabecular bone strength can be used as inputs for models of whole bone, which can provide patient specific predictions of bone quality and its susceptibility to fracture.

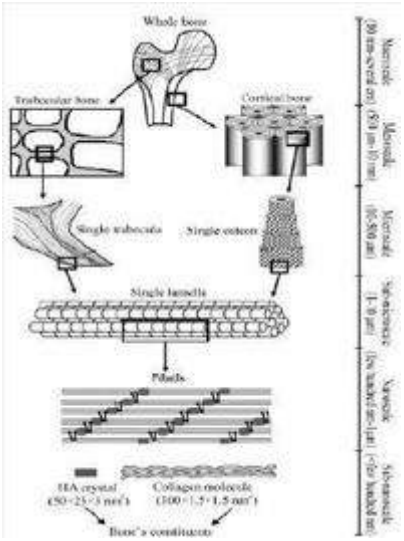

Fig. 1 Hierarchical structure of bone [1].

Bone is a biological composite material in which soft and deformable proteins (mainly collagen), stiff but brittle hydroxyapatite (HA) minerals, and fluids fillings pore spaces, are combined together. Proteins and minerals self-assemble to form a complex structure of bone spanning from the atomic level to the macroscale. Superior properties of bone are due to this composite, spatially heterogeneous, and hierarchical structure. The apatite crystals are in the shape of irregular platelets, 20-50 nm in length and width and few nm in thickness. Cross-linked collagen molecules, which are triple helical protein chains about 1.5 nm in diameter and 300 nm in length with 40 nm gaps between ends, are staggered to form collagen fibrils about 50-100 nm in diameter. Crystals are located both within and around collagen fibrils but their exact arrangement is still not fully understood. The fibrils reinforced by crystals form a mineralized collagen fibril which is a building block of bone. These mineralized collagen fibrils are preferentially aligned and arranged into lamellar sheets (3-7 μm in thickness). These are stacked at different orientations in crescent-like trabecular pockets which form a complex network of cylindrical (or platelike) struts called trabeculae, which are about 0.1 mm in diameter and 1 mm long. This gives trabecular bone a porous appearance. Porosity of trabecular bone ranges from 70 to over 90%. In osteoporotic bone this porosity is higher than in healthy bone and some struts are missing connectivity. Thus, the trabecular bone has a complex hierarchical structure in which different geometrical features occur on different length scales. We identify these scales as follows: a) nanoscale (mineralized collagen fibril), b) sub-microscale (single lamella level), c) microscale (trabecular pockets, single trabecula level), and d) mesoscale (random network of struts or plates). The next structural level, macroscale, represents the whole bone, which includes both trabecular (porous) and cortical (solid) bone types. Bone's hierarchical structure is illustrated in Figure 1 [1].

In this paper we model bone plasticity and strength at these different structural scales. Inelastic behaviour and failure of bone has been studied computationally by many researchers but there are limited multiscale models of bone plasticity and strength [2].

METHODS

We model bone at the nanoscale by considering several different geometric configurations of collagen and crystals. They include geometries when crystals are forming an interpenetrating phase, following the experimental observations reported in [3]. Other arrangements are also considered including the one proposed in [4] which assumes that the HA phase is embedded in the collagen and not interpenetrating. The volume fraction of HA is assumed to be around 45% in both cases. The analysis is performed using a finite element method and assigning cohesive laws between different interfaces. Modeling of bone at the sub-microscale (single lamella level) and the microscale (trabecular bone tissue level) is summarized in our recent study [1].

[a)] Corresponding author. Email: ijasiuk@illinois.edu.

Modeling of bone at the mesoscale level (trabecular network) is based on micro-computed tomography (CT) images of porcine trabecular bone (6 months) which are used to create a finite element mesh. Several different yield criteria have been used in the literature to model trabecular bone such as eccentric von Mises, principal strain-based, Drucker-Prager, cast iron, and Drucker-Lode [5-9]. Although it is well agreed that the behavior is un-symmetric under tension and compression, a consensus has not been yet reached yet on which constitutive model is best [6]. In this study a bi-linear elastic-plastic law is used based on Niebur et al. [10] with a Drucker-Prager yield criterion [6] to capture the un-symmetric behavior of the trabecular bone tissue. Elastic modulus and Poisson's ratio of tissue level are taken as 12 GPa and 0.3 [6, 10], respectively. As mechanical properties of porcine bone at a bone tissue level are not available, the strain at onset of plasticity and hardening modulus are calibrated to match experimentally obtained stress-strain curve at the mesoscale.

RESULTS

Von Mises stress distribution under compressive load is shown in Fig. 2-a while Fig. 2-b shows a comparison between experimental and finite element stress-strain curves for a representative trabecular bone sample at the mesoscale. Good agreement was found between experimental and computational results.

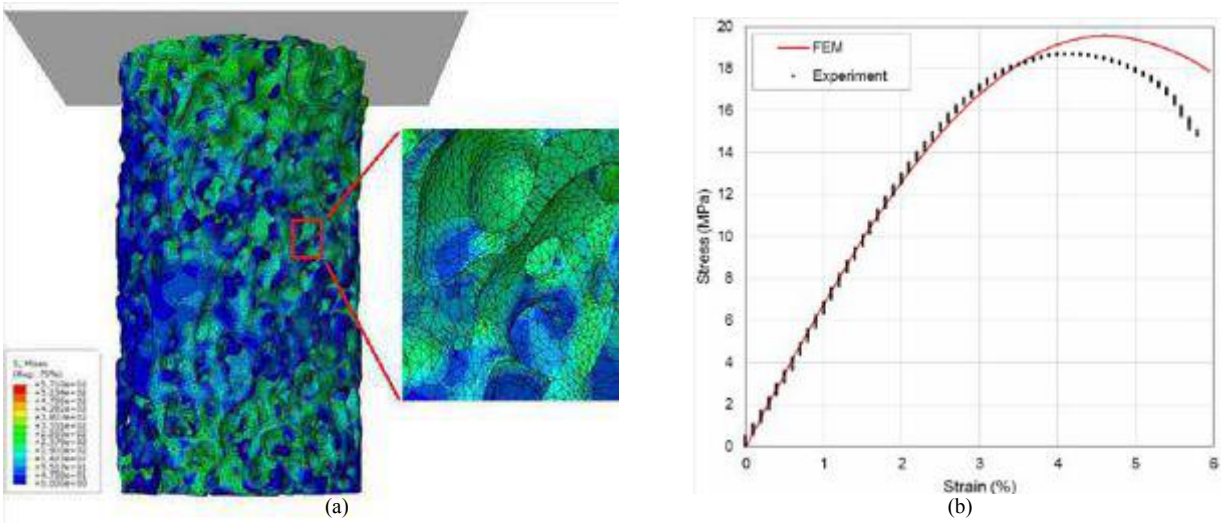

(a) (b)

Fig. 2 – a) Mises stress distribution in a representative trabecular bone sample (mesoscale level), b) Stress-strain curve obtained from micro-CT finite element simulations (solid line) compared with experimental results (dashed line).

References

[1] Hamed, E., Jasiuk, I.: Multiscale damage and strength of lamellar bone modelled by cohesive finite elements. *J Mech Behav Biomed Mater* **28**:94-110, 2013.

[2] Sabet, F., Najafi Raeisi, A., Hamed, E., Jasiuk, I.: Modeling of bone fracture and strength at different scales: a review. *Interface Focus* **6**:20150055, 2016.

[3] Hamed, E., Novitskaya, E., Li, J., Jasiuk, I., McKittrick, J. Experimentally-based multiscale model of the elastic modulus of trabecular bone and its constituents. *Materials Science and Engineering C – Materials for Biological Applications* **54**: 207-216, 2015.

[4] Jäger I, Fratzl P. Mineralized Collagen Fibrils: A Mechanical Model with a Staggered Arrangement of Mineral Particles. Biophysical Journal **79**(4):1737-1746, 2000.

[5] Sanyal, A., Gupta, A., Bayraktar, H. H., Kwon, R. Y., Keaveny, T.M. Shear strength behavior of human trabecular bone. *J Biomechanics* 45:2513-1519, 2012.

[6] Schwiedrzik, J., Gross, T., Bina, M., Pretterklieber, M., Zysset, P., Pahr, D. Experimental validation of a nonlinear μFE model based on cogesive-frictional plasticity for trabecular bone. *International J Numerical Methods in Biomedical Engineering*, (2015); e02739, DOI: 10.1002/cnm.2739

[7] Shi, X., Liu, X. S., Wang, X., Guo, X. E., Niebur, G. L. Effects of trabecular type and orientation on microdamage susceptibility in trabecular bone. *Bone* **46**: 1260–1266, 2010.

[8] Wolfram, U., Gross, T., Pahr, D. H., Schwiedrzik, J., Wilke, H-J., Zysset, P. Fabric-based Tsai-Wu yield criterion for vertebral trabecular bone in stress and strain spaces. J Mech Behav Biomed Mater **15**: 218-228, 2015.

[9] Kelly, N., McGarry, J. P. Experimental and numerical characterization of the elasto-plastic properties of bovine. *Behav Biomed Mater* **9**: 184–197, 2012.

[10] Niebur, G. L., Feldstein, M.J., Yuen, J. C., Chen, T.J., Keaveny, T. M. High-resolution finite element models with tissue strength asymmetry accurately predict failure of trabecular bone. J Biomechanics **33**: 1575-1583, 2000.

NONLINEAR DEFORMATION AND LOCALIZED FAILURE OF BACTERIAL STREAMERS IN CREEPING FLOWS

Ishita Biswas[1], Ranajay Ghosh[2], Mohtada Sadrzadeh[1] & Aloke Kumar[1a)]
[1]*Department of Mechanical Engineering, University of Alberta, Edmonton, Alberta, Canada*
[2]*Department of Mechanical and Industrial Engineering, Northeastern University, Boston, MA, USA*

Summary We investigate nonlinear deformation and localized failure of filamentous bacterial biomass known as streamers in a microfluidic device. *In-situ* quantification of streamer deformation and failure behaviour is made possible by the use of 200 nm fluorescent polystyrene beads which firmly embed in the extra cellular polymeric substance (EPS) and act as tracers. The streamers, which form soon after the commencement of flow begin to deviate from an apparently quiescent fully formed state in spite of steady background flow and limited mass accretion indicating significant mechanical nonlinearity. This nonlinear behaviour shows distinct phases of deformation with mutually different characteristic times and comes to an end with a distinct localized failure of the streamer far from the walls.

INTRODUCTION

Bacterial streamers, which are microscopically slender filamentous aggregates primarily comprising of bacterial cells encased in matrix of self-secreted EPS [1] and formed typically under sustained hydrodynamic flow. More importantly, their filamentous structure can extend significantly with flow [2-4], which makes colonization rapid, pervasive and resistant to erosion with flow [5, 6]. Das and Kumar [7] carried out a theoretical investigation on the formation and disintegration of biofilm streamers treating them as liquid jets. A lack of clear experimental evidence and study exists for such systems as *ex-situ* characterization of such biomass is very difficult. Here, we report an *in-situ* quantitative study and direct observation of the ultimate failure and instability of bacterial streamers formed from bacterial flocs [6] using a microfluidic platform. A silicon master mold was prepared to make the microfluidic device. Polydimethylsiloxane (PDMS) (Sylgard 184, Dow Corning) was used to prepare the device, which contains an array of pillars (diameter of 50 μm and were spaced 10 μm apart) in a staggered grid pattern. The height of the pillars is 50 μm in z direction and the total width of the chip is 436 μm. PDMS and glass slides were exposed to the oxygen plasma for 30 s for bonding. The device was then annealed at 70ºC for 10 minute to seal the channel. *Pseudomonas fluorescens* CHA0 (wild type) bacteria strain from -80ºC collection was incubated overnight in the Luria – Bertani (LB) agar plate at 30ºC. A single colony from the agar plate was poured in Luria – Bertani (LB) broth and incubated for 14 hours in shaking incubator (Fisher Scientific) at 30ºC and 150 rpm. The microfluidic device was placed on the stage of an inverted optical microscope (Nikon Eclipse Ti). A syringe pump was used to inject the solution into the microfluidic device (Fig. 1a). Epi-florescence capability of the microscope was utilized to image using either a Nikon GFP Green filter cube or Nikon Texas Red filter cube. Tracking was performed by using the measurement tracking module of the NIS Element AR software interface.

RESULTS AND DISCUSSION

Bacterial flocs laden fluid was injected in the device and the fluid flow rate (Q) was maintained in the creeping flow regime ($Re \ll 1$). Streamers formed in the device after approximately 20 minutes of starting the experiment. In Fig. 1b, only bacterial cells are visible with both the encapsulating EPS and liquid media appearing dark. The experiments show the evidence of far from wall failure and instability; however it is less useful in quantifying the failure process due to the invisibility of the EPS. We perform these experiments with 200 nm red fluorescent amine-coated polystyrene micro-spheres, which are of different color, much smaller and numerous thereby making quantification and visualization of instability much easier and more accurate. This method allows for *in-situ* characterization and we depict a streamer undergoing axial failure (Fig. 1c) by keeping the background velocity scale constant at $U = 8.92 \times 10^{-4}$ m/s. The first - formation stage occurs almost as soon (t_{form}) as the flow stabilizes, which is typically in seconds. The streamers thus formed continue to retain their shape and size, remaining apparently static against a steady background flow till about time $t_0 \gg t_{form}$ when the deformation begins again. The time between t and t_0 when the streamer formation is complete but the next stage of deformation is not yet perceptible can last for several minutes. After t_0, streamers begin to deform perceptibly, resembling a creep type deformation over a much larger time scale ($t_{cr} \gg t_{form}$). This creep stage ends rather abruptly through a short region of increasing deformation culminating in a distinct sharply defined instability after which the streamer suffers terminal failure through a final catastrophic large deformation stage occurring over a much smaller time scale $t_{fail} \ll t_{cr}$. The deformation is quantified using a non-dimensional measured 'stretch ratio', $\lambda_{mes} = |dx|/|dX|$, where $|dX|$ is the distance between the two points at time t_0 and $|dx|$ is the distance between the two points at any given time t ($t_0 > t$) (Fig. 1d). $\lambda_{mes} = 1$ corresponds to the time when the streamer formation and initial deformation in response to the fluidic loading is complete and thus the beginning of the creep stage. In this regards, observing that the background flow is steady with little mass addition in this phase, Fig. 1c, we conclude that the creep type deformation has origins in the material

a) Corresponding author. Email: aloke.kumar@ualberta.ca.

constitution. Within the creep stage, we find three distinct deformation regimes beginning first with a rather rapid strain rate regime, which then decreases significantly indicating substantial hardening of the material, stabilizing to almost a constant strain rate. This continues for some time till the strain rate begins to increase again and the streamer deformation accelerates, transitioning after a critical stretch ratio λ_c into the terminal failure stage. The ultimate failure process observed through microscope shows significant localization, with the streamer structure left almost entirely intact at either side of instability resembling a necking route to failure of solids under axial loading.

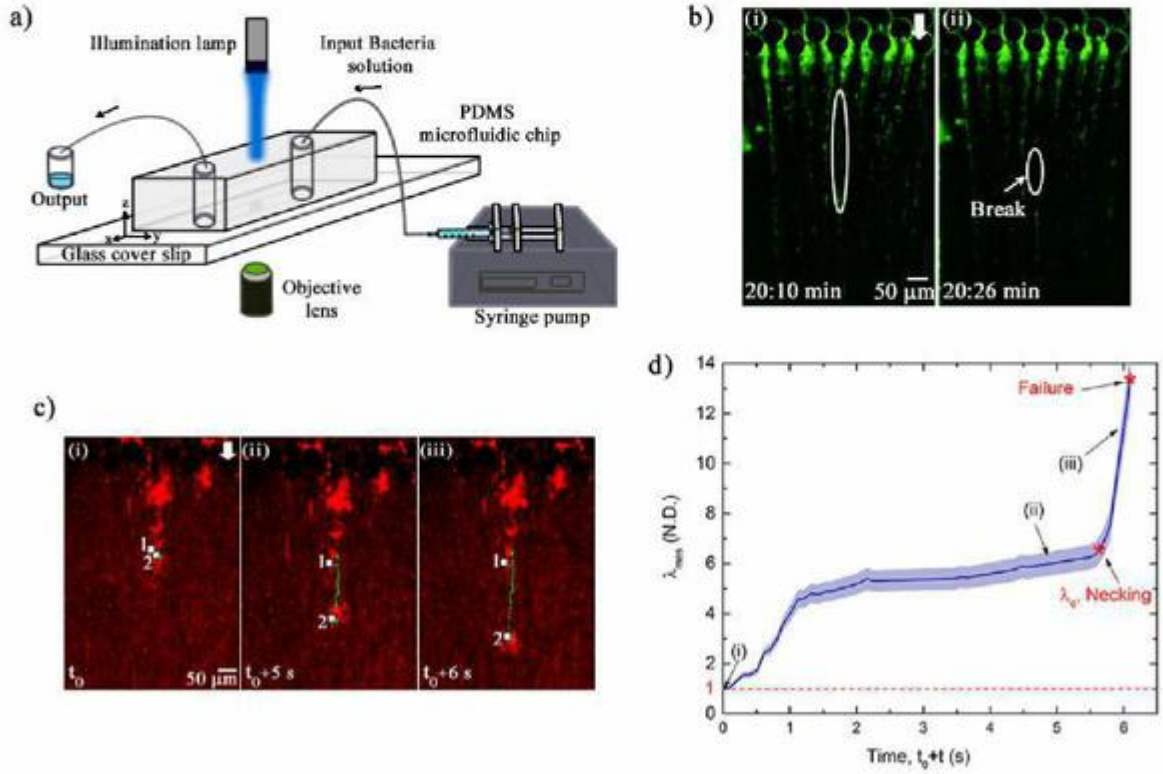

Figure 1: a) Schematic of experimental set-up under pressure driven flow, b) (i) stretching of one streamer with time and (ii) final breaking point. The arrow is showing flow, c) Temporal behavior of two points ('1' & '2'), which lie inside a streamer, culminating in the failure of streamer, t_0= 30.34 minute, d) Stretch ratio for the same streamer as a function of time. Data points corresponding to the experimental conditions ((i)-(iii)) are depicted on the curve. The blue shaded region denotes the estimated 8% tracking error envelope applicable for any observed streamer.

CONCLUSIONS

The apparent stability of the formed streamers transitioned slowly into complex creep like deformation regimes with their own characteristic time scales in spite of stable background flow conditions. The final stages of deformation were characterized by high strains over relatively small time scales leading to failure of the streamers. However, unlike previously believed fluid like models which could account for the creep as well as terminal failure of the streamers through a global hydrodynamic instability, we discovered highly localized failure of the streamers in our current experiments.

References

[1] Karimi A., Karig D., Kumar A., Ardekani A. M.: Interplay of physical mechanisms and biofilm processes: review of microfluidic methods. Lab on a Chip, **15**, 23-42, 2015

[2] Marty A., Causserand C., Roques C., Bacchin P.: Impact of tortuous flow on bacteria streamer development in microfluidic system during filtration, Biomicrofluidics, **8**, 2014.

[3] Rusconi R., Lecuyer S., Guglielmini L., Stone H. A.: Laminar flow around corners triggers the formation of biofilm streamers, J. R. Soc. Interface, **7**, 1293–1299, 2010.

[4] Valiei A., Kumar A., Mukherjee P. P., Liu Y., Thundat T.: A web of streamers: biofilm formation in a porous microfluidic device, Lab on a Chip, **12**, 2012.

[5] Drescher K., Shen Y., Bassler B. L., Stone H. A.: Biofilm streamers cause catastrophic disruption of flow with consequences for environmental and medical systems, P Natl Acad Sci USA, **110**, 4345–4350, 2013.

[6] Hassanpourfard M., Nikakhtari Z., Ghosh R., Das S., Thundat T., Liu Y., Kumar A.: Bacterial floc mediated rapid streamer formation in creeping flows, Scientific Reports, **5**, 2015.

[7] Das S., Kumar A.: Formation and post-formation dynamics of bacterial biofilm streamers as highly viscous liquid jets, Scientific Reports, **4**, 2014.

MECHANICAL RESPONSE SURFACES OF A PERIODIC POROUS BIOMATERIAL FOR ORTHOPAEDIC IMPLANTS : AN EXPERIMENTAL AND COMPUTATIONAL STUDY

Z. Shaghayegh Bagheri[1], David Melancon[1], and Damiano Pasini *[1]

[1]*Department of Mechanical Engineering, McGill University, Montreal, Quebec, Canada*

Summary A previous study on high strength porous biomaterials proposed a methodology to systematically elucidate the interplay between their morphological parameters and mechanobiological properties. This work extends that method to investigate the impact of manufacturing errors on the mechanical properties of Ti-6Al-4V Octet lattice for use as load-bearing orthopaedic material. Via a combined approach of experiments and simulations, we generate response surfaces that illustrate the mechanical properties as a function of the geometric parameters defining the unit cell of the Octet cell. The results reveal the impact of manufacturing imperfections on the compressive elastic modulus of as-manufactured samples when compared to their as-designed counterpart. This study contributes to forge essential tools to systematically design porous orthopaedic implants.

INTRODUCTION

High-strength porous biomaterials, through Additive Manufacturing (AM), are particularly suited for orthopaedic applications that impose severe load-bearing requirements [1]. One of their advantages is that their morphological parameters can be tailored to maintain high mechanical performance, without compromising their ability to meet bone ingrowth requirements and provide effective stiffness locally close to that of the surrounding bone tissue. Morphological parameters that control their mechanobiological response include topology, pore size, porosity, strut thickness and cell size. In a previous work [2], we proposed a methodology to systematically elucidate the relation among the parameters of the unit cell and the constraints that enables bone ingrowth and allow additive manufacturing. This paper further extends that methodology to generate properties response maps that show the impact of manufacturing deviations on the mechanical properties (elastic modulus, yield strength and first maximum strength) of periodic porous biomaterials with Octet-truss cell topology.

METHODS

Figure 1 shows a map illustrating the main geometric relationships among the parameters defining the Octet cell topology. The x-axis and y-axis represent respectively pore size and strut thickness, while the cell size and porosity are represented by isoperformance lines. From the chart, a triangular domain, namely the admissible design space, emerges bounded by bold lines defining the requirements imposed by bone ingrowth (pore size between 50-650 μm and porosity above 50%) and manufacturing constraints (minimum manufacturable strut thickness of 200 μm).

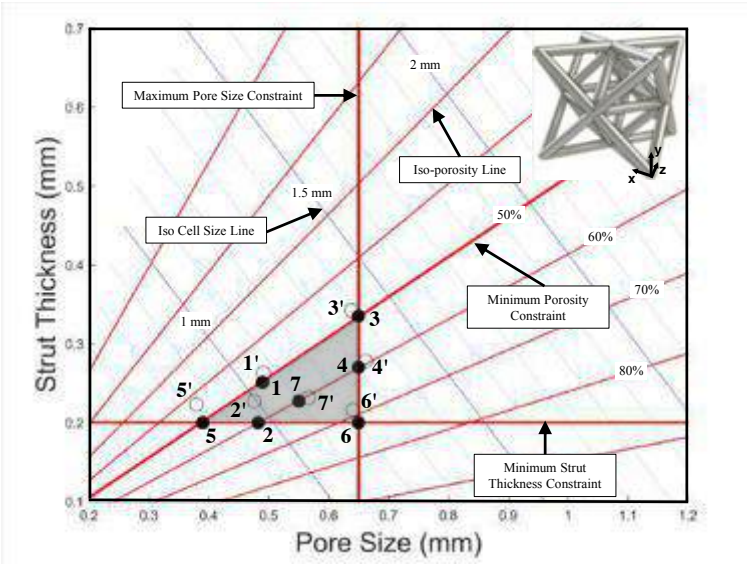

Figure 1: Design space (dark gray) for Octet-truss topology, with imposed constraints of manufacturing, pore size, and porosity. Solid and hollow points represent respectively designed and manufactured samples of this study.

*Corresponding author. Email: damiano.pasini@mcgill.ca

Across the design domain, we selected seven representative samples and manufactured them out of Ti-6Al-4V via Selective Laser Melting (SLM), with x, y and z periodicity equals to 10, 15 and 10, according to ISO 13314 [3]. The deviations between the morphological parameters of the manufactured *vs.* as-designed is represented in Figure 1 with solid and hollow bullets. The mechanical characterization of the lattice samples is obtained via experiments and simulations. In particular, uniaxial compression test is performed at a constant strain rate of 0.01 s^{-1} with five replicates at each point. In parallel, a fully detailed Finite Element Analysis of the as-designed lattices is completed to identify the impact of the manufacturing errors on the tested mechanical properties. The results from both experiments and simulations are used to generate response surfaces, one from the testing of the as-manufactured samples and the other from the detailed simulations of the as-designed samples, which capture the properties trend that the Octet lattice biomaterial exhibits within its admissible domain.

RESULTS

Figure 2 shows the response surfaces of the compressive elastic modulus for the Octet-truss, overlaid on its triangular design domain. The response surfaces are generated from the experimental and computational data using a second-order quadratic polynomial model. For low porosities, i.e. 50%, the compressive elastic modulus shows dependency on porosity only, as it stays almost constant for all the values of the geometric parameters of the unit cell. However, for porosities above 60%, we observe that the pore size and the strut thickness have an additional impact, since thinner struts and smaller pore sizes result in higher stiffness with constant porosity. Moreover, compared to the experimental results, the computational analysis overestimates the compressive elastic modulus at high porosities, whereas underestimates it at low porosities. This leads to a noticeable shift in the response surface of the as-manufactured samples with respect to their as-designed counterparts, a factor that can be attributed to the role of manufacturing defects in the failure mechanisms of the samples.

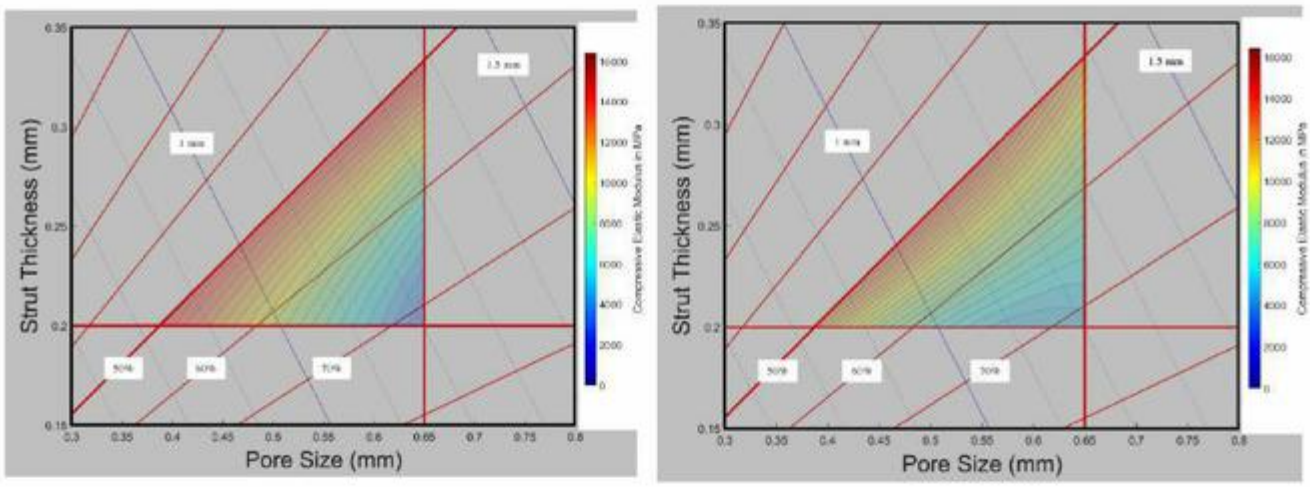

(a) Experimental response surface.

(b) Numerically simulated response surface.

Figure 2: Compressive elastic modulus response surfaces using second-order polynomial approximation.

CONCLUSIONS

This study contributes to further elucidate the interplay between mechanical properties, morphological parameters and manufacturing defects. The scheme here adopted resorts to the generation of response surfaces that capture the mechanical properties of a given porous biomaterial within the geometric domain of a cell topology that is relevant for orthopaedic applications. As example, our focus has been on the Octet-truss, for which we obtain its stiffness properties for both as-manufactured and as-designed samples over its own design domain. This work provides a holistic understanding of the mechanical response of a periodic porous biomaterial as a function of the design variables defining the geometry of its unit cell. The results contribute to provide tools for the design of porous biomaterials for sturdy orthopaedic implants.

References

[1] Murr L., et al.: Next Generation Orthopaedic Implants by Additive Manufacturing Using Electron Beam Melting. International Journal of Biomaterials 368:1999-2032, 2010.

[2] Arabnejad S., et al.: High-Strength Porous Biomaterials for Bone Replacement: a strategy to assess the interplay between cell morphology, mechanical properties, bone ingrowth and manufacturing constraints. Acta Biomaterialia, 30:345-356, 2016.

[3] Normalisation OId, Standardization IOf. ISO 13314: ISO, 2011.

DYNAMICS OF STATICALLY PRE-LOADED HUMAN AORTA

Ivan D. Breslavsky [1a)], Marco Amabili[1], Mathias Legrand[1], Annie Ruimi[2]
[1]*Department of Mechanical Engineering, McGill University, Montreal, Quebec, Canada*
[2]*Department of Mechanical Engineering, Texas A&M University at Qatar, Doha, Qatar*

Summary The response of human aortic segment under static and dynamic pressure is investigated. The aortic segment is modelled as three-layered hyperelastic circular cylindrical shell. Both geometrical and physical nonlinearities are taken into account. The effect of internal fluid is also taken into account. The results are presented in the form of pressure-deflection curves and frequency responses of forced vibrations.

PROBLEM DESCRIPTION

Static and dynamic analysis of circular cylindrical shell that models a segment of human aorta is carried out in this study. The shell is assumed to be three-layered, with each layer being hyperelastic, fiber-reinforced, viscoelastic material. Following the paper [1], we chose a material model in form of combination of Neo-Hookean and Fung models. The strain energy density for this case has the following form:

$$W = W_{NH} + W_F, \tag{1}$$

$$W_{NH} = \frac{E}{6}(I_1 - 3), \tag{2}$$

$$W_F = C(Exp(c_{11}\varepsilon_x^2 + c_{12}\varepsilon_x\varepsilon_\theta + c_{22}\varepsilon_\theta^2) - 1), \tag{3}$$

where E is the Young's modulus of the shell material; I_1 is the first invariant of the right Cauchy-Green deformation tensor $\mathbf{C} = \mathbf{2E} + \mathbf{I}$, and $\mathbf{E}$ is Green-Lagrange strain tensor. The material (1-3) is anisotropic material due to Fung term, which is included to describe anisotropic response of the fibers and their sharp increase in stiffness. Neo-Hookean term describes the isotropic part of the tissue response. The geometrical nonlinearity is described with the higher-order shear deformation theory [2].

The viscoelasticity is taken into account through employment of Kelvin-Voigt model [3].
The shell is filled with quiescent fluid [4]. Since we deal with large deflections and large strains, the displacement-dependent expression for pressure is used [5]. Such load is proportional to the area of the deformed surface and is orthogonal to it.

Strain energy density in the form (1-3) is not polynomial in strain components, which significantly complicates the investigation of the dynamics. The analysis is simplified by expansion of strain energy density into truncated after order 4 series in strain components. Such model is able to describe the behavior of the vessel only locally, in the vicinity of a given configuration of interest around which the expansion is made. To reach highly deformed configurations, a sequence of successive local models has to be built.

NUMERICAL EXAMPLE

We consider the shell with geometrical parameters that are similar to the parameters of the straight thoracic aortic segment of human aorta. The geometrical parameters are [6]: radius $R = 0.01575$ m, length $L = 0.126$ m. Thicknesses for three layers are: for intima, the internal layer, $h_i = 0.00033$ m, for media, the medium layer, $h_m = 0.00132$ m, for adventitia, the external layer, $h_a = 0.00096$ m. The material parameters are partially determined based on experimental data from [1], partially adopted from [1]. It is assumed that all three layers have the same density $\rho = 1200$ kg/m^3, the contained fluid density is taken $\rho_F = 1060$ kg/m^3.

The shell is simply supported at the ends. The boundary conditions, including the natural nonlinear boundary condition of zero stress resultant, are identically satisfied by the trigonometric functions of special form as shown in [2]. The convergence study has been carried out and it is concluded that the 29 degrees-of-freedom system provides good approximation of the solution.

Initially, the static problem of inflation of the shell under the pressure load was studied. The pressure-defection curve is shown in Fig. 1. As can be seen, the stiffness drastically increases after certain strain threshold is reached.

Afterwards we analyzed free and forced vibrations around pre-loaded state of the entire artery as a composite shell and also single-layered shell to understand the contribution of different layers. For the three-layered artery model the configuration in the middle of physiological range (12.5 kPa pressure) was chosen for the expansion of the strain energy density around it. Vibrations with dominant first axisymmetric bending mode and with dominant mode with two half-waves in circumferential direction of the empty and fluid-filled shells are studied. The frequency response for the empty shell made of adventitial material is shown in Fig. 2. We can see that the nonlinearity is weak enough for this case, however, in the case of fluid-filled shell it is stronger.

[a)] Corresponding author. Email: ivan.breslavskyi@mcgill.ca

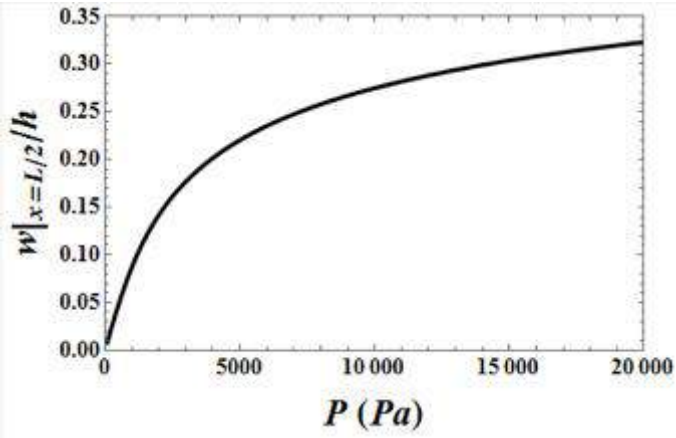

Figure 1. Static pressure-deflection curve. The abscissa shows central deflection.

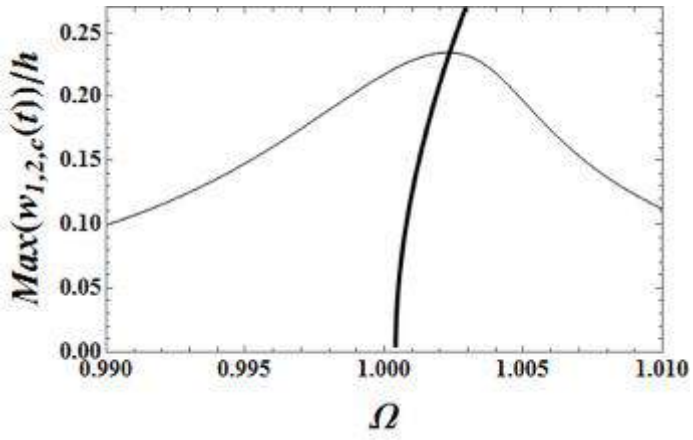

Figure 2. Frequency response of empty shell vibrations around pre-loaded configuration (adventitial material). Principal bending mode amplitude vs. frequency. Frequency response (thin line) and backbone curve (thick line).

CONCLUSIONS

The method for the analysis of nonlinear vibrations of arteries is presented. The method is able to deal with hyperelastic, viscoelastic, multilayered, fiber-reinforced shells that model blood vessels. The method is tested on the human aortic segment model. Under the static pressure initially soft shell becomes much stiffer with the pressure growth, which is the common feature for soft biological tissues. The dynamic nonlinearity is not very strong, but still nonlinear effects, like change in stiffening type, are observed.

ACKNOWLEDGEMENTS

The authors acknowledge the financial support of the NSERC Discovery Grant, Canada Research Chair and the Qatar National Research Fund NPRP 7-032-2-016.

References

[1] Holzapfel G. A.: Determination of material models for arterial walls from uniaxial extension tests and histological structure. *J. Theor. Biol.* **238**:290-302, 2006.

[2] Amabili M., Reddy, J. N.: A new non-linear higher-order shear deformation theory for large-amplitude vibrations of laminated doubly curved shells. *Int. J. Non-linear Mech.* **45(4)**:409-418, 2010.

[3] Lakes R.: Viscoelastic Materials. New York, USA 2009.

[4] Amabili M.: Nonlinear vibrations and stability of shells and plates. New York, USA 2008.

[5] Amabili M., Breslavsky I. D.: Displacement dependent pressure load for finite deflection of shells and plates. *Int. J. Non-linear Mech.* **77**:265-273, 2015.

[6] Amabili M., Karazis K., Mongrain R., Païdoussis M. P., Cartier R.: A three-layer model for buckling of a human aortic segment under specific flow-pressure conditions. *Int. J. Numer. Methods Biomed. Eng.* **28(5)**:495-512, 2012.

MECHANICAL DESCRIPTION AND ENGINEERING ANALYSIS OF CUTTING AND (STERILE) NEEDLE INSERTION INTO HUMAN SKIN

*Kevin Bronik[1], Prof Sam L Evans[2] and Dr Pierre Kerfriden[3]
[1]*Mechanical engineering department, School of Engineering ,Cardiff University, United Kingdom*
[2] *Director, School of Engineering, Cardiff University, United Kingdom*
[3]*Mechanical engineering department, School of Engineering ,Cardiff University, United Kingdom*

Abstract Understanding the total complexity of biomechanical/mechanical properties of the human skin and developing an advance computational model (e.g. the Finite element skin models) that do not differ (or not so much differ!) from experimental data would provide information which could be very useful for surgical training and practical use (special in this project, the goal is to inform the development of optimized device which can be used for effective and reproducible skin penetration in the clinical setting. This project will also provide clear definition of underlying mechanisms of penetration and cutting and make it possible of generating a robust computational and physical model and an excellent technique for measuring skin deformation and in combination with advanced computational/mechanical methods it will offer many possibilities for in vivo measurements).

INTRODUCTION/LITERATURE REVIEW

Various theoretical and numerical formulation of the Cutting and needle insertion have been widely studied and applied for the different problem classes using the (traditional) finite element methods.

Using a combination of digital image correlation and advanced Finite element modeling and explicitly taken into consideration the complexities of the algorithms due to the complexity of non-linear mechanical behavior of human skin, after a series of Experimental Measurements on human skin and related computational modeling, S Evans and C A Holt [4] found evidence to suggest the application of stochastic optimization algorithms (due to the reduction of the errors).

In other study, in order to design optimised micro-needle device which completely depends on understanding of human skin biomechanics under small deformations, after doing a series of optimized laboratory developed tests and using much more precise model (considering the skin as a multilayer composite) by applying multilayer finite element model (with the results of which show a remarkable degree of success), R.B. Grovesa, S.A. Coulmanb, J.C. Birchallb and S.L. Evans[2,3] argue that, the problem with the precise approach and optimum development of numerical-experimental procedure and modelling of very complex mechanical behaviour of human skin would require first the perfect understanding of dependency and in-dependency of parts or elements of skin combined with mechanical description which can be used later for computational modelling.

Naturally all these studies were carried out in laboratory conditions with parallel load (Evans and Holt 2009) and perpendicular load (Grovesa, Coulmanb, Birchallb and Evans 2011) to the human skin surface.

At this point it is worth adding that, there were two main studies which aim to help us develop this project. The first one was the study by Oliver A.Shergold and Norman A. Fleck[1] about the development of the deep penetration of a soft solid by a flat-bottomed and by a sharp-tipped cylindrical punch with application of one term Ogden strain energy function and consideration the skin as an in-compressible hyper-elastic isotropic solid. The second one was the study by Vincent Hayward and Mohsen Mahvash[5] about the development of the haptic-rendering of cutting with the clarification of the geometry and the mechanism of the interaction of the tools and the sample.

Without being affected by the complex nature of soft solid penetration, it is worth noting that the existing literature unfortunately provides little insight into Underlying Mechanisms of the penetration and cutting. Generally they indicate the deep penetration involves deformation and cracks and in most case without taking the existence of (sliding) friction into account. Therefore, this Project goals keep the focus on what is most important; namely mathematical and physical clarification of the mechanisms of the penetration and cutting processes following the related algorithms and computational implementation of the theory.

*Corresponding author. Email: kbronik@gmail.com or BronikK@cardiff.ac.uk

METHODOLOGY

In order to process the development of this project, the first step was the classification of computational and mechanical-mathematical problems related to modelling which were clearly separated into those with the implementation of the clarified underlying theory and those problems with optimization using advanced computational and mechanical optimization algorithms and methods. Then the accuracy of the implemented algorithms has been practically and experimentally verified.

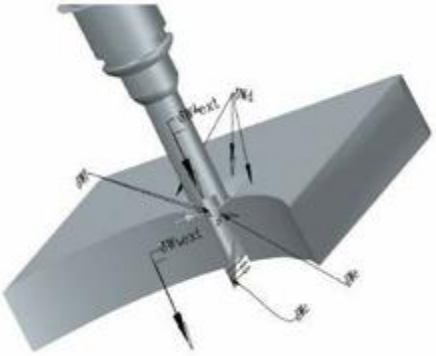

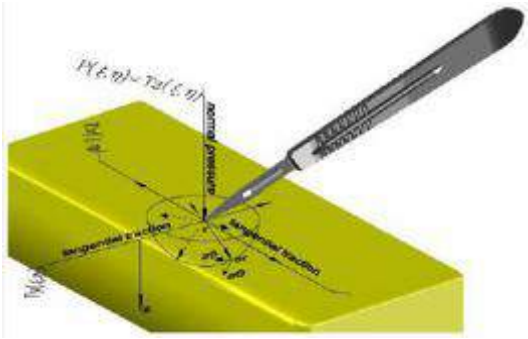

The numerical computation part done by using the algorithm of modified contact, optimized with inequality constraints: the Kuhn-Tucker conditions which enforces the contact constrains within a strong Mixed Mode Cohesive Law formulation by clearly taking the place of the classical contact constrains formulation and in the case of the physical requirement of impenetrability and compressive interaction between two bodies, enforces the classical contact constrains. The numerical implementation of the theories (the theoretical framework used in this project) has been performed in the open source code FEBio (Non-linear finite element solver for biomechanical applications http://febio.org/febio/) by the modification of the existing contact algorithm.

CONCLUSION

In this study it has been shown that the development of computation model, in this way, by using the Modified Contact fulfils the strong condition of the cohesive zone law and additionally supports the physical ideas and mathematical structures of the Classical Contact, allowing us a significant degree of flexibility and success in the deployment of robust models for engineering analysis.

ACKNOWLEDGEMENT

The developer of this project would like to thank HPC Wales teams for setting up the facility supercomputing in order to perform high performance computing from which this study totally benefited. Additionally, he would like to extend his sincere gratitude and thankfulness to Fujitsu the Funder of the project.

References

[1] Oliver A.Shergold and Norman A. Fleck. Mechanisms of deep penetration of soft solids, with application to the injection and wounding of skin. 2004.

[2] R.B. Groves , S.A. Coulmanb, J.C. Birchallb and S.L. Evans. Quantifying the mechanical properties of human skin to optimise future microneedle device design. *Computational Methods Biomechanical Biomedical Engineering*, 15(1):73–82, 2012

[3] R.B. Groves , S.A. Coulmanb, J.C. Birchallb and S.L. Evans. An anisotropic, hyperelastic model for skin: experimental measurements, finite element modelling and identification of parameters for human and murine skin. *Journal of Mechanical Biomechanical Engineering*, 2013

[4] S Evans and C A Holt. Measuring the mechanical properties of human skin in vivo using digital image correlation and finite element modeling. *The Journal of Strain Analysis for Engineering Design*, 44(5):337–345, 2009.

[5] Vincent Hayward, Mohsen Mahvash. Haptic rendering of cutting: A fracture mechanics approach. 2001.

CRUTCH WALKING: EXPERIMENTS, MATHEMATICAL MODELING

Alexander Formalskii[a)], Andrei Ivanov
Institute of Mechanics, Lomonosov Moscow State University, Moscow, Russia

Summary Using a motion capture system, a human walking with the crutches can be registered. After this, using obtained trajectories, the variations of the angles in the joints of human as functions of time can be calculated. We use also the force platforms to measure the support reactions applied to the human's feet and the coordinates of the points, where these forces are applied. A planar mechanism with five heavy links – body, two thighs and two shins – and attached weightless feet and weightless crutches is studied as the mathematical model of the human with crutches. By solving the inverse dynamics problem, we find the torques developed at the joints and creating power torques. They can be used for choosing actuators for the joints of medical exoskeleton. The inter-link angles obtained experimentally can be used as tracked programmed trajectories for the organization of the motion of an exoskeleton put on a paraplegic.

INTRODUCTION

A difficult problem of modern society is the rehabilitation of wheelchair-bound disabled persons who partially or completely lost the ability to walk. In last two decades, devices combining the functions of rehabilitation and motion started to be developed – these are medical exoskeletons. The idea of creating a medical exoskeleton appeared much earlier – it was proposed by M. Vukobratovic [1]. By the present time, such medical exoskeletons as "ReWalk" [2], "Indego" [3], "Rex" [4], "Exobionics" [5] have been created. The aim of these devices is to give to such disabled persons the ability to walk. Even though the first exoskeletons are already on sale, there are a lot of issues that need improvement and modification.

A key issue in the development of medical exoskeleton is the specification of programmed motions and the creation of a control system. Programmed motions provide a basis for the organization of walking in the exoskeleton. In the general case, this problem can have many solutions because the gaits of even healthy people are considerably different. An ideal solution would be the organization of walking that reproduces a gait of a healthy person. The construction of walk of a medical exoskeleton is a very difficult problem and the resulting gait can be unsafe to the exoskeleton user due to the instability of the system "person-exoskeleton". An approach that received widespread use assumes that the person in exoskeleton uses crutches. In this case, the exoskeleton user can actively participate in maintaining the equilibrium. The resulting gait is more stable due to four supporting points of which two are controlled by the walker.

The exoskeleton user cannot move his (her) lower extremities on one's own – this is done by the exoskeleton, which actually moves the person's legs. Therefore, the exoskeleton must be able to execute programmed motions that must realize the walking of the human-exoskeleton man-machine system. The first step in the construction of programmed motions is the study of crutch walking. It is hardly possible to construct such a motion with the help of a paraplegic. Therefore, here we propose to construct the programmed motion using the gait of a healthy person walking on crutches. This person must adhere to some rules:

to maintain equilibrium, he or she must use not only the legs, but also the crutches;
the motions in the frontal plane must be small because the side motions of the legs are supposed to be limited.

SPECIFIC FEATURES OF CRUTCH WALKING

The walk of a healthy person consists of two alternating phases – single-support and double-support ones. The single-support phase is much easier to model than the double-support phase. There are a lot of problems related to the double-support phase modeling caused by dynamic indeterminacy. The solution of the inverse dynamics problem and the determination of the forces and torques at the human's joints and reactions of the support are impossible for double-support phase without introducing additional constraints or making additional measurements.

A distinctive feature of crutch walking is the complete or almost complete absence of the single-support phase and the presence of double-, triple-, and quadruple-support phases. Therefore, the approaches used for the study of ordinary walk cannot be directly applied and must be modified for the study of crutch walking.

KINEMATICS. MOTION PHASES

It is reasonable to begin the study of crutch walking by dividing the step cycle into phases. The division is based on the experimental data obtained using the motion capture system "Vicon" [6] and two three-component force platforms "AMTI" [7] placed one after the other. The output data of "Vicon" are the trajectories of the hip and ankle joints needed to reconstruct the legs' motion, the trajectories of the shoulder joints, and the crutches' support points needed to calculate the body and crutches angles of inclination. The force platforms provide the reaction forces for each leg and the location of the zero moment point [1]. The second author of this paper took part in the experiments described below (his mass is 70 kg and his height is 170 cm). Based on the experimental data, the gait diagram (stick diagram) of crutch walking (sequence of

[a)] Corresponding author. Email: formal@imec.msu.ru.

configurations) was composed. In the gait considered here, the crutches move synchronously, for this reason, they are treated as a single crutch (with the arm holding it). Figure shows the gait diagram of crutch walking in the course of a half step from the time when one foot looses contact with the support until the time when the other foot looses the support.

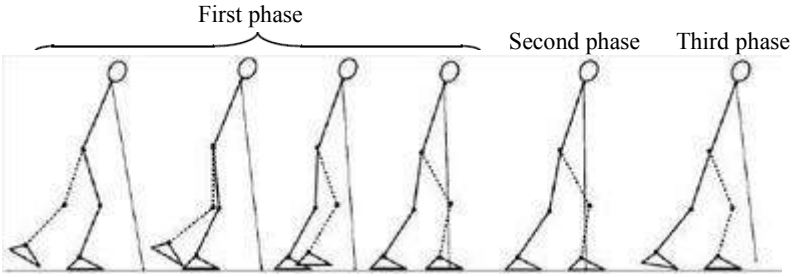

The first phase is the leg transfer. The second phase is the full stance. The third phase is the crutch transfer.

EQUATIONS OF MOTION

The model of a crutch walker can be considered as a planar mechanism with five heavy links, two weightless feet, and a weightless crutch (see Figure). We use the motion equations from [8, 9] as a mathematical model of our mechanism; only the forces applied at the shoulder-joint where the crutch is fastened to the body and the torque created at this joint must be added. This model also must be complemented with equilibrium conditions of the weightless feet and crutch.

SOLUTION OF INVERSE PROBLEM OF DYNAMICS

After calculation variations of the angles in the human inter-link joints and their first and second derivatives we substitute them in the motion equations in order to find the torques applied in these joints, solving the inverse problem of dynamics.

Considering the first phase (leg transfer), we obtain nine non-autonomous linear equations with eight unknowns (two torques in the hips, two in the knees, one torque in the ankle of the stance leg, one in the shoulder-joint, and two components of the ground reaction, applied to the crutch). Thus, this system of nine equations is over-determined. We solve this system at each instant by the least squares method, using the pseudo-inverse matrix.

For the second phase (full stance), we obtain ten equations with nine unknowns (two torques in the hips, two in the knees, two in the ankles, one torque in the shoulder-joint, and two components of the ground reaction, applied to the crutch). We solve this over-determined system, also using the least squares method.

For the third phase (crutch transfer), we obtain seven equations with six unknowns, these are two torques in the hips, two in the knees, and two torques in the ankles. Again, we solve this system, using the least squares method.

CONCLUSIONS

A procedure for the experimental determination of angles in the leg joints of a crutch walker is considered, which can be used for constructing the programmed motion of an exoskeleton. A mathematical model of the crutch walker is constructed. An approach for estimating the torques that must be developed by the exoskeleton actuators for the realization of the desired programmed trajectories is proposed. To realize the gait considered in this paper in a real-life exoskeleton, the actuators in its hinges must develop the torque and power not less than 39 $N{\cdot}m$ and 23 W at the ankle joint, 46 $N{\cdot}m$ and 22 W at the knee joint, 44 $N{\cdot}m$ and 27 W at the hip joint.

References

[1] Vukobratovic M.: Legged Locomotion Robots and Anthropomorphic Mechanisms. Mihailo Pupin Institute, Belgrade, 1975.
[2] **http://rewalk.com/**
[3] **http://indego.com/**
[4] **www.rexbionics.com/**
[5] **http://eksobionics.com/**
[6] **www.vicon.com/**
[7] **www.amti.biz/**
[8] Beletskii V.V.: Biped Walking. Nauka, Moscow 1984 [in Russian].
[9] Formalskii Alexander M.: Ballistic Walking Design via Impulsive Control. *J. of Aerospace Engineering*, 129-138, 2010.

INVESTIGATIONS ON FATIGUE PROPERTIES OF MESHED GUM METAL PLATES FOR BONE GRAFT APPLICATIONS

Yuki Hamashita[1] & Jianmei He[1]
[1]*Kogakuin University, Mechanical Engineering, 1-24-2, Nishi-shinjuku, Shinjuku-ku, Tokyo, Japan*

SUMMARY

Meshed titanium plates for bone graft applications have improved with excellent three dimensional flexibility, lower elastic modulus and higher strength in previous studies. In this study, mesh structure application on gum metal plates with high biocompatibility was carried out and the fatigue properties of such meshed gum metal plates were investigated through experimental and analytical approach for bone graft applications like the intervertebral disc defections. Based on two kind of designed mesh shape, sample meshed gum metal plates were made by laser cutting process for experimental and analytical approaches on the fatigue property evaluations and the results are reported here.

INTRODUCTION

Meshed titanium plates having higher 3-dimensional flexibility were designed with different fundamental mesh shapes and line-up patterns using 3D CAD tool from the light-weight, higher flexibility and durability view points [1]. In this study, mesh structure applications on gum metal plates with high biocompatibility are carried out and the tensile fatigue properties of such meshed gum metal plates are investigated through experimental and analytical approach for bone graft applications like the case of intervertebral disc defections as shown in Fig.1.

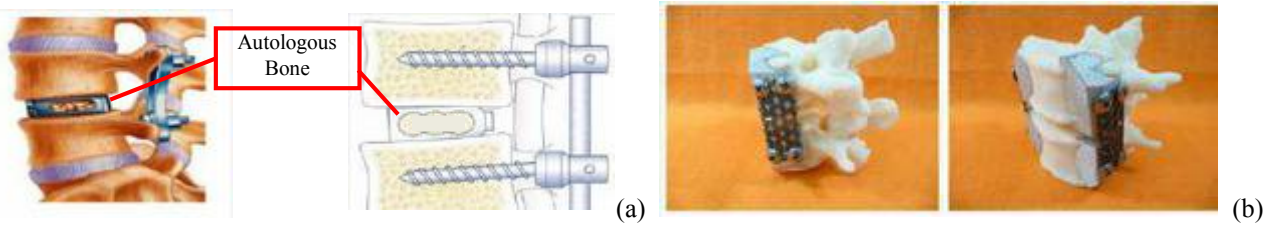

(a) (b)

Fig.1 Fixation methods on spine for hernia of intervertebral disk (a: current implants; b: meshed gum metal plates)

Based on two kinds of designed mesh shape, sample meshed gum metal plates are made by laser cutting process for experimental approaches on the tensile fatigue property evaluations. On the other hand, analytical approach on the static tensile property evaluation of sample meshed gum metal plates are also executed based finite element analysis method [2] to compare with the fatigue experimental results.

FUNDAMENTAL MESH SHAPE DESIGNS FOR MESHED GUM METAL PLATES

Fundamental mesh shapes are considered under the following structural design conceptions.

(1) Single fundamental mesh shape construction for simplification of manufacturing processing and cost-down purpose
(2) Higher three-dimensional flexibilities including expansion/contraction, bending and torsion for possibility of handily shape changes during surgery
(3) Easy-controllable mechanical properties like elastic modulus, bending stiffness etc. for approachability to natural-bone's mechanical properties
(4) Uniform mesh line width and non-angle smooth shape desired to avoid the stress concentrations and lead for higher strengths and longer operating life
(5) Ensured optional spaces for screw fixing

Based on the above mentioned design conceptions, two basic mesh shapes are designed as shown in Fig.2. Then 3-deimensional meshed plate models using the designed mesh shapes with mesh line width of 0.8 mm are obtained and the CAD models are shown in Fig.3. From these models, one can see that the meshed plates have uniformed mesh line widths and smooth shapes just along the requirements of design conceptions. Then sample meshed gum metal plate specimens with 0.6 mm plate thickness are fabricated for experimental evaluations by laser cutting process as shown in Fig.3.



90° axisymmetric 60° axisymmetric

Fig.2 Basic mesh shapes with 0.8 mm mesh line width

[a] Corresponding author. Email: am15049@ns.kogakuin.ac.jp

TENSILE FATIGUE TEST OF MESHED GUM METAL PLATES

Tensile fatigue tests of sample meshed gum metal plate specimens shown in Fig.3 are executed based on the JIS Z 2273 [3] standard testing method. Fig.4 shows the experimental results of two kinds meshed gum metal plate specimens.



(a) CAD models (b) Sample specimens

Fig.3 Meshed plate models and sample specimens

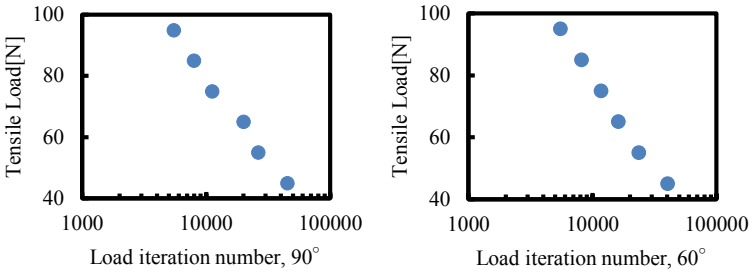



Fig.4 Experimental results of two sample meshed gum metal plate specimens (Left: tensile load; Right: fractured specimen)

ANALYTICAL APPROACH ON TENSILE TESTS OF SAMPLE MESHED GUM METAL PLATES

Because of the mesh structure configuration, cross-sectional area changes very well and it is difficult to evaluate the tensile stresses from experimental evaluation. Here analytical approaches on tensile tests of sample meshed gum metal plates are carried out using Solidworks CAD software and ANSYS finite element analysis code. 3D meshed plate models with the same shapes and sizes of specimens on tensile fatigue tests are modeled and material properties of gum metal plate shown in Table 1 are used for analytical inputs. Fig.5 shows the analytical results of two kinds meshed gum metal plate specimens. Fig.6 shows the analytical stress results with the maximum stress locations coincident with experimental fractural locations as shown in Fig.4. endurance.

Table 1 Material property input for analysis

Material	Elastic modulus (GPa)	Poison's ratio	Density (kg/mm^3)
Gum metal	75	0.32	5.6

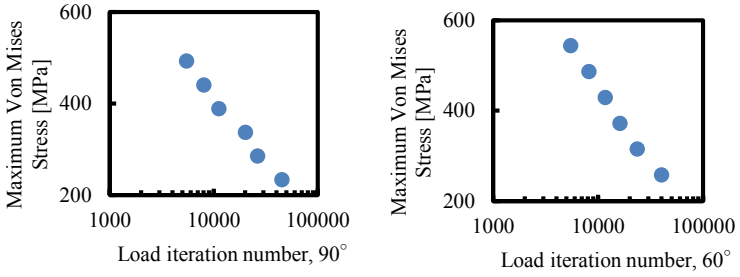

Fig.5 Analytical results of two sample meshed gum metal plate specimens

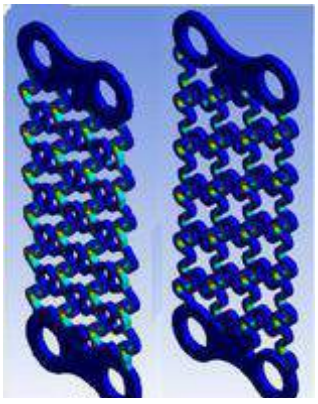

Fig.6 Stress results of meshed specimens

CONCLUSION

From the tensile fatigue property evaluation of sample meshed gum metal plates,

(1) 90° axisymmetric meshed specimens have more endurance than 60°axisymmetric specimens. Further experiments on the same specimens with same and lower tensile loading could be done.

(2) Same behaviors between experimental and analytical results are obtained and Goodman fatigue analysis could be used to predict both the location and fatigue life of the meshed plate in the future study.

References

[1] H. Takeyama and J. He, EVALUATION ON MECHANICAL PROPERTIES OF 3D FLEXIBLE MESHED TITANIUM PLATES FOR BONE IMPLANT APPLICATIONS, The 5th TSME International Conference on Mechanical Engineering, AMM020, 2014/12

[2] Toshiro Miyoshi: Finite Element Method Introduction. Baifukan, 1995

[3] Japanese Industrial Standards: JIS Z 2273, 1974

DAMAGE MODEL FOR BIOLOGICAL TISSUES

Amir Hamedzadeh[1], T. Christian Gasser[2], and Salvatore Federico*[3]
[1]*Graduate Programme in Mechanical Engineering, The University of Calgary, Alberta, Canada*
[2]*Department of Solid Mechanics, Royal Institute of Technology (KTH), Stockholm, Sweden*
[3]*Department of Mechanical and Manufacturing Engineering, The University of Calgary, Alberta, Canada*

Summary The mechanical behaviour of soft biological tissues is heavily influenced by the presence of the collagen fibres. In this study, we introduced a constitutive damage model for a single fibre. The model is based on the progressive recruitment and failure of the fibrils of which the fibre is mainly comprised. We employed distribution functions to model the progressive recruitment and failure of the fibrils. The recruitment-damage model has been implemented into Finite Elements (FE) and was able to reproduce several aspects of the experimentally observed behaviour of soft biological tissues.

INTRODUCTION

From the perspective of mechanics, biological tissues are non-linear, anisotropic, inhomogeneous, time-dependent materials which are responsive to external stimuli such as mechanical forces. The unique behaviour of biological tissues stems from their hierarchical structure. Collagen fibres are one of the main constituents of biological tissues [1]. Collagen fibres are comprised of bundles of collagen fibrils. The failure and damage mechanisms of soft biological tissues strongly depend on the tissues microstructure, but the irreversible phenomena related to the failure of soft tissue have not been fully understood. In this paper we introduced a constitutive damage model for a single fibre based on [2].

GENERAL ASSUMPTIONS

We assume that: a) the non-collagenous matrix and the collagen fibres are both non-linearly elastic; b) each fibre is a one-dimensional element bearing only tension along its axis; c) each fibre is comprised of bundle of fibrils that are connected by means of proteoglycan (PG) cross-bridges. These bridges transmit the load between fibrils, forming an integrated structure, which can elongate significantly. The fibrils are crimped in the reference configuration and each of them is recruited at different stretch denoted λ_s (see Figure 1).

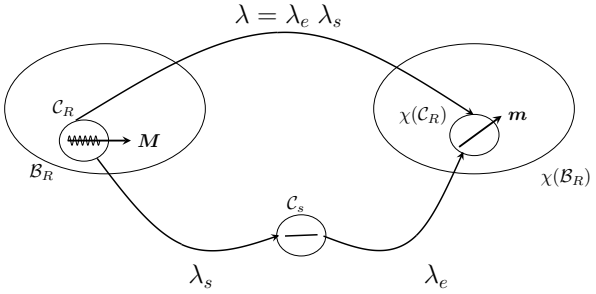

Figure 1: Intermediate Configuration for a Single Fibril [2]

All fibrils are assumed to fail at the same stretch λ_f calculated with respect to the straightened configuration $\mathcal{C}_s$, so that, with respect to the reference configuration, the failure stretch of each fibril is $\lambda_s\lambda_f$ (See Figure 2).

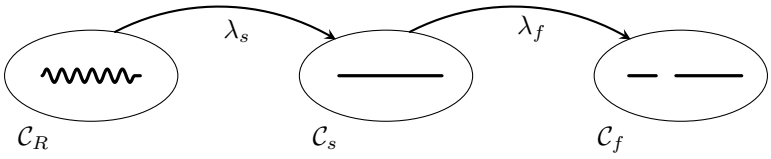

Figure 2: Recruitment and failure of a typical fibril; $\mathcal{C}_f$ is the configuration at which the fibril fails

*Corresponding author. Email: salvatore.federico@ucalgary.ca

CONSTITUTIVE EQUATIONS FOR A SINGLE FIBRE

In order to describe progressive recruitment and failure in a fibre, we use a triangular distribution function [2], and derive an expression for both recruitment and damage processes (Figure 1). To find the first Piola-Kirchhoff (P-K) stress in the fibre, we adopt a linear constitutive relation for each fibril between the first (P-K) stress and the logarithmic strain. Using this constitutive relation, we can find the stress in the fibre by integration over the distribution functions (See Figure 3). For the unloading part, we neglect the portion of fibrils that have already failed and integrate over the remaining portion of the probability distribution functions. Figure 4 shows a typical stress-stretch curve for a single fibre, as well as the unloading profiles for different unloading stretches (λ_u). The theoretical model has been implemented into the Finite Element package FEAP, including the unloading feature. Despite the simple assumptions at the collagen fibril level, the macroscopic tissue properties showed many typical properties observed from experimental tissue testing [1]. Most interestingly, although no plastic deformation mechanisms were introduced at the micro-scale, macroscopic plastic-like effects could clearly be observed.

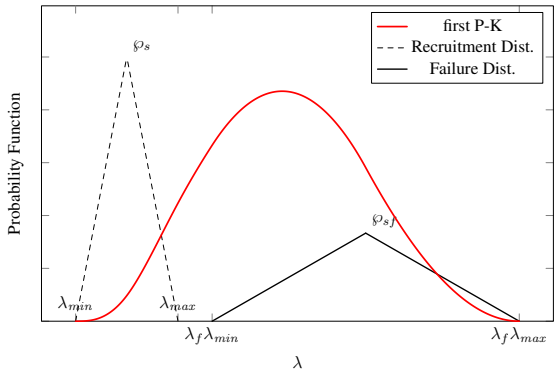

Figure 3: Probability Functions for Recruitment and Damage, First P-K stress

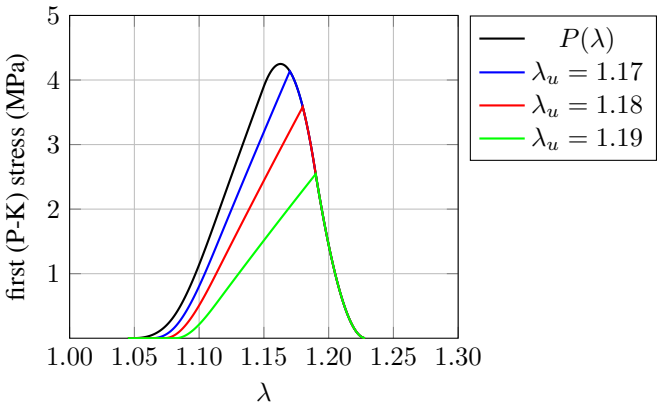

Figure 4: Stress-stretch curve for $P(\lambda)$ and $P_u(\lambda, \lambda_u)$

SUMMARY

We proposed a one-dimensional constitutive model for a single fibre using triangular probability distribution functions in order to account for the progressive recruitment and damage of individual fibrils.

References

[1] Peter Fratzl. *Collagen: structure and mechanics*. Springer Science & Business Media, 2008.

[2] G. Martufi and T. C. Gasser. A constitutive model for vascular tissue that integrates fibril, fiber and continuum levels with application to the isotropic and passive properties of the infrarenal aorta. *Journal of Biomechanics*, 44(14):2544–2550, 2011.

EFFECTIVE COMPUTATION OF HIGHER-ORDER AVERAGED STRUCTURE TENSORS IN BIOMECHANICS

Kotaybah Hashlamoun[1] and Salvatore Federico *[2]

[1]*Graduate Programme in Biomedical Engineering, The University of Calgary, Alberta, Canada*
[2]*Department of Mechanical and Manufacturing Engineering, The University of Calgary, Alberta, Canada*

Summary For biological tissues reinforced by statistically oriented collagen fibres (such as articular cartilage), a probability distribution function is used to describe the orientation of the fibres. In evaluating the material response, the overall effect of the fibres is accounted for via the evaluation of averaging integrals over all possible directions in space. The averaging integral of the structure tensor (tensor product of the unit vector describing the fibre direction by itself), or the averaged structure tensor, is of high significance. Higher-order averaged structure tensors feature in several models and carry similarly important information. However, the computational cost associated with their evaluation is very high. This work proposes to introduce mathematical techniques to minimise the computational cost associated with the evaluation of higher order averaged structure tensors, for the case of a transversely isotropic distribution of orientation. Tensor and component expressions are presented.

INTRODUCTION

For a given direction, described by the unit vector $\boldsymbol{M}$, the structure tensor is defined as $\boldsymbol{A} = \boldsymbol{M} \otimes \boldsymbol{M}$. The averaged structure tensor is defined as the weighted average of the structure tensor associated with each fibre family, and the weight is the probability distribution function $\Psi(\boldsymbol{M})$, i.e., the probability of finding a fibre in direction $\boldsymbol{M}$. The integral is evaluated over the set of referential unit vectors, the "material unit sphere" $\mathbb{S}^2\mathcal{B}$, and, in our notation, it reads

$$\mathbb{H}_1 \equiv \boldsymbol{H} = \int_{\mathbb{S}^2\mathcal{B}} \Psi(\boldsymbol{M})\, \boldsymbol{A}. \tag{1}$$

This integral was introduced by Gasser et al. [1] (who called it *generalised structure tensor* and denoted it by $\boldsymbol{H}$) for the evaluation of the overall effect of the fibres. Vasta et al. [2] introduced a representation involving the average of the fourth-order tensor $\boldsymbol{A} \otimes \boldsymbol{A} = \boldsymbol{M} \otimes \boldsymbol{M} \otimes \boldsymbol{M} \otimes \boldsymbol{M}$, which, in our notation, reads

$$\mathbb{H}_2 = \int_{\mathbb{S}^2\mathcal{B}} \Psi(\boldsymbol{M})\, \boldsymbol{A} \otimes \boldsymbol{A}. \tag{2}$$

In a recently proposed scheme [3], a constitutive function for a biological tissue can in general be represented by a polynomial in $\boldsymbol{A}$, and therefore contains terms of the type $\boldsymbol{A} \otimes ... \otimes \boldsymbol{A}$ (k times), which, once averaged, give rise to the averaged structure tensors of order $2k$:

$$\mathbb{H}_k = \int_{\mathbb{S}^2\mathcal{B}} \Psi(\boldsymbol{M})\, \boldsymbol{A}^{\otimes k}. \tag{3}$$

In general, the determination of the components of the averaged structure tensor $\mathbb{H}_k$ of order $2k$ requires the evaluation of 3^{2k} integrals.

For a probability distribution Ψ which is transversely isotropic with respect to a given direction $\boldsymbol{M}_0$, i.e., $\varrho(\Theta) = \Psi(\boldsymbol{M}(\Theta, \Phi))$ (where Θ is the co-latitude angle with respect to $\boldsymbol{M}_0$ and Φ is the longitude angle), the integrals in Equation (3) will also be transversely isotropic with respect to $\boldsymbol{M}_0$, and will also be completely symmetric, i.e., symmetric with respect to any permutation of the indices.

Gasser et al. [1] showed that, for a transversely isotropic probability distribution, the average $\boldsymbol{H}$ of the structure tensor $\boldsymbol{A}$ is given (in our notation) by

$$\boldsymbol{H} \equiv \mathbb{H}_1 = \kappa_1\, \boldsymbol{G}^{-1} + (1 \circ\ 3\kappa_1)\boldsymbol{A}_0, \tag{4}$$

where $\boldsymbol{A}_0 = \boldsymbol{M}_0 \otimes \boldsymbol{M}_0$ is the structure tensor associated with the axis of symmetry $\boldsymbol{M}_0$, $\boldsymbol{G}^{-1}$ is the material inverse metric tensor (i.e., the "contravariant identity tensor") and

$$\kappa_1 = \pi \int_0^{\pi} \varrho(\Theta) \sin^3\Theta\, d\Theta \tag{5}$$

is the dispersion about the axis of transverse isotropy. Only one integral is required to evaluate the components of $\mathbb{H}_1$.

*Corresponding author. Email: salvatore.federico@ucalgary.ca

OBJECTIVE

For the case of fibres obeying a transversely isotropic probability distribution, we aim at minimising the computations necessary to determine the higher-order averaged structure tensors $\mathbb{H}_k$ by introducing higher-order dispersion parameters κ_k.

METHODS

If we define a higher-order dispersion parameter κ_k as

$$\kappa_k = \frac{\pi}{4^{(k-1)}} \int_0^\pi \varrho(\Theta) \sin^{(2k+1)} \Theta \; d\Theta, \tag{6}$$

we want to represent a higher-order averaged structure tensor $\mathbb{H}_k$ in terms of the dispersions κ_k.

We take advantage of the full symmetry of averaged structure tensors to write a general expression for any component by using only 3 parameters (the dimension of the physical space). Let p, q, and r indicate the number of repetitions of the values 1, 2 and 3 respectively, where $p + q + r = 2k$ and let $\mathbb{H}_k|_{p,q,r}$ refer to all entries with these repetitions. Since the probability distribution is independent of Φ we can write components of $\mathbb{H}_k$ as the product of an integral in Θ and an integral in Φ, i.e.,

$$\mathbb{H}_k|_{p,q,r} = \int_0^\pi \varrho(\Theta) \; \sin^{(q+r+1)} \Theta \; \cos^p \Theta \; d\Theta \int_0^{2\pi} \sin^r \Phi \; \cos^q \Phi \; d\Phi. \tag{7}$$

We also propose to express the averaged structure tensors in terms of the second-order basis tensors for transverse isotropy with respect to $\boldsymbol{M}_0$, i.e., the tensors $\{\boldsymbol{T}_0, \boldsymbol{A}_0\}$, where $\boldsymbol{T}_0 = \boldsymbol{G}^{-1} \circ \boldsymbol{A}_0$ is the projection tensor (see, e.g., [3]). Here, we also take advantage of the full symmetry of averaged structure tensors, and rewrite them using fully-symmetric basis tensors, which are expressed in terms of the fully-symmetric parts of all the possible tensor products of the second-order basis tensors for transverse isotropy.

RESULTS

After some manipulations in Equation (7), we obtain the expression

$$\mathbb{H}_k|_{p,q,r} = \alpha_{qr} \sum_{i=0}^{p/2} \binom{p/2}{i} \frac{(\circ\, 1)^i \; 4^{k+i-p/2-1}}{\pi} \; \kappa_{k+i-p/2}, \tag{8}$$

where α_{qr} are constants obtained by induction with α_{20} and α_{02} known. Moreover, a general expression for $\mathbb{H}_k$ is

$$\mathbb{H}_k = \beta_l \; \frac{(2k)!}{2(2l)!((k \circ \; l)!)^2} \; \mathrm{sym}(\boldsymbol{T}_0^{\otimes(k-l)} \otimes \boldsymbol{A}_0^{\otimes l}) + \beta_k \boldsymbol{A}_0^{\otimes k}, \tag{9}$$

where

$$\beta_l = \sum_{i=0}^{l} \binom{l}{i} (\circ\, 1)^i 4^i \kappa_{(i+k-l)}. \tag{10}$$

CONCLUSION

Our goal was to minimise the computational cost of the evaluation of the higher-order averaged structure tensors for the case of transverse isotropy. The averaged structure tensors $\mathbb{H}_k$ were expressed in terms of the dispersion parameters and each $\mathbb{H}_k$ has k independent parameters $\{\kappa\}_{i=1}^k$ and $k + 1$ independent components. Component expressions and component-free expressions were provided.

References

[1] Gasser, T. C., Ogden, R. W., Holzapfel, G. A. Hyperelastic modelling of arterial layers with distributed collagen fbre orientations. Journal of the Royal Society Interface, 3:1535, 2006.

[2] Vasta, M., Gizzi, A., and Pandolfi, A. On three- and two-dimensional fiber distributed models of biological tissues. Probabilistic Engineering Mechanics, 37:170-179, 2014.

[3] Federico, S. Porous materials with statistically oriented reinforcing fibres. In Dorfmann, L. and Ogden, R. W., editors, Nonlinear Mechanics of Soft Fibrous Materials, pp. 49-120. Springer, Berlin, Germany, 2015. CISM Courses and Lectures No. 559, International Centre for Mechanical Sciences, 2015.

ZONA PELUCIDA AS A MECHANO-RESPONSIVE POLYMER

Andjelka Hedrih[1] a)

[1] *Department for Biomedical Science, State University of Novi Pazar, Serbia*

Summary Zona pelucida (ZP) is the most outer structure of mammalian oocytes and is important for gamete recognition, fertilization and integrity of the embryo. ZP is highly sulfated and glycosylated polymer gel that exhibit visco-elastic properties. Temperature, pH, ionic strength influences its biological function and aggregate state. We consider ZP as mechano-responsive polymer and proposed a new theory of fertilization based on coupled chemical—electrical fields and modeled ZP as a non-linear oscillatory reactive system. Analysis of its oscillatory states regarding external force is discussed.

INTRODUCTION

The ZP can be considered as an oscillatory structure that exhibits transition in oscillatory behavior before and after fertilization [1, 2, 3]. Fertilization is a process of reunion of a single oocyte and single sperm cell. The process requires certain amount of functionally capable spermatozooa, although only one sperm will fertilized the oocyte ensuring the constant quantity of genetic material in each generation. In in vivo conditions there are constant decline of sperm number from the moment when they enter the female reproductive tract. In *in vitro* conditions the huge amount of spermatozooa are also required, partially due to huge differences in cell masses between spermatozoa and oocyte (in range of 10^7). In this system oocyte is reacting as inert body. Fertilization on the cellular level begins with receptor recognition but still some details of the fertilization process remain unknown. From the oscillatory theory of fertilzation [4] ZP changes its oscillatory states after fertilization [1, 2] as well as mechanical properties [4]. Changing in mechanical and electrical properties after fertilization allows attaching of silicon nano chip [5]. ZP is a polymer with highly sulfated glycoproteins interconnected with non covalent bonds, so it is easily dissolved by mild heating, low pH, low ionic strength [6].

BASIC CONCEPT OF THE MODEL

In this model ZP is considered as a mechano-responceive but also electroactive – polymer analog to [7, 8]. Using phenomenological mapping [9,10], concept of controlling chemical oscillations in mechano reactive gels [11,12] and consequent rhythmical soluble-insoluble changes of the gel [13] the new mechano-chemical fertilization concept is proposed. The system (ZP) is considered to be incompressible.

Oscillations in chemical reactions are possible to control via mechanical strain [11, 12].

Basic assumptions: Sperm penetration area is determined by local parameters acting upon ZP surface. ZP surface is negatively charged due to content of sulfated glycoproteins. Numerous sperms with different velocities and different sperm impact angles act upon ZP surface in a form of periodic impulsive forces transferring a part of their kinetic energy to the ZP structure. This external mechanical influence (time dependent force intensity and pressure changings) of spermatozoa cause changing in chemical reaction (analog to [11,12] that change local pH of ZP causing local changes of its aggregate state (analog to [13]) from solubile to insoluble or causing the state of plastic flow of ZP. The area of ZP where the plastic flow persists long enough will be the “week spot/area” for sperm penetration. The spermatozoon that is in range of this area could easily swim trough ZP. By changing the local parameters of external mechanical force (stress intensity, pressure, sperm arrangement…) it is possible to control local chemical oscillatory processes [11]. Further, receptor recognition between sperm and oocyte changes locale potential of cell membranes. According to proposed model of fertilization process, ZP has area of coupled mechano-elekttro-chemical fields. The approximation is that this phenomenon has a local character and that it is not uniform through the entire ZP.

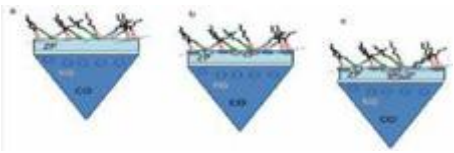

Figure 1.Part of the oocyte with a. spermatozoa acting upon ZP b. Changing the local electro-mechanical properties of ZP c. Sperm penetration in the area of local change of aggregate stat. CG-cortical granules. Co-cytoplasm of the oocyte.

The changes of oscillatory states of ZP as a gel polymer could be described by gel energy density. The gel energy density could be described by equation:

$$u = u_{el} + u_{FH} + u_{ion} \tag{1}$$

Where u_{el} is rubber elasticity of cross linked polymer chains contribution to the gel energy density, u_{FH} -contribution from interaction between the polymer and solvent units, u_{ion} - contribution to gel energy density that comes from ions [9]. The basic equation that couples mechanical stress and strain in ZP polymer could be in form:

a) Corresponding author. Email: handjelka@hm.co.rs

$$\hat{\sigma} = -P(\phi)\hat{I} + c_0 v_0 \phi_0^{-1} \phi \hat{B} \quad (2)$$

Where $\hat{\sigma}$ is stress tensor, $P(\phi)$ -pressure, $\hat{I}$ - is unit tensor, c_0 - crosslink density-the number density of elastic strands in undeformed polymer network, v_0 -velocity of the polymer network at the given network deformation, ϕ_0 -volume fraction of the polymer, ϕ, $\hat{B}$ -strain tensor in the swollen polymer gel. (taken from [9]). When the "chosen spermatozoa" swim through ZP, and its plasma membrane merge with oocyte plasma membrane, oocyte plasma membrane change its electrical potential and the cortical granules (CG) release will occur. According to the biochemical theory CG release is followed by structural changes and changes of mechanical properties of ZP resulting in polyspermy block. The exact roles of the content of CG are still not known. In light of coupled field theory we suggest possible role of CG: content of CG (mostly enzymes) are acting like catalyst to chemical reactions in sense they change pH of the local environment. Changed pH than change the conformation of the ZP glycoproteins and disclosed additional bounding sides on ZP glycoproteins leading to its structural reorganization.

CONCLUSIONS

Using mathematical analogies and phenomenological mapping ZP was considered as an responsive gel that respond on external mechano-electrical stimuli that originate of numerous spermatozoa impacting its surface in process of fertilization. Oscillatory changing of external mechano-electrical stimuli upon ZP surface lead to local oscillatory phenomenon of rhythmical soluble-insoluble changes of ZP resulting in sperm spermatozoa penetration via mechanism of oscillations of relaxation if the soluble ZP state lasts long enough. Local chemical oscillations of ZP gel could be control via external mechanical strain. The proposed model brings new light to understanding the process of fertilization.

Acknowledgments: Part of this research was supported by the Ministry of Education, Sciences and Technology of Republic of Serbia Grant ON174001, coordinated through Mathematical Institute SANU and realized through State University of NoviPazar.

References

[1] Hedrih A. Transition in oscillatory behavior in mouse oocyte and mouse embryo trough oscillatory spherical net model of mouse Zona Pellucida" ch in *Applied Non-Linear Dynamical Systems*, Springer Proceedings in Mathematics & Statistics 93, J. Awrejcewicz (ed.), **93**: 295-303. Springer International Publishing Switzerland, 2014.

[2] Hedrih A. Modeling oscillations of zona pelucida before and after fertilization EUROMECH Newsletter, Young Scientist Prize Paper. ENOC 2011 Young Scientist Prize, awarded at the 7th European Nonlinear Dynamics Conference held in Rome, Italy, July, 2011. Europian Mechanics Society, 40, pp. 6-14.

[3] Hedrih A. Frequency analysis of knot mass particles in oscillatory spherical net model of mouse *zona pellucida*. Lecture Session, Short Paper, Abstract book of 23rd IUTAM ICTAM Beijing 2012, SM01-049, pp. 209. ISBN 978-988-16022-3-7

[4] Murayama Y., Mizuno J., Kamakura H., Fueta Y,, Nakamura H., Akaishi K., Anzai K., Watanabe A., Inui H., Omata S. Mouse zona pellucida dynamically changes its elasticity during oocyte maturation, fertilization and early embryo development. *Human Cell* **19**:119–125, 2006.

[5] Durán, S. et al. Silicon-nanowire based attachment of silicon chips for mouse embryo labelling. *Lab Chip* **15**:1508–1514, 2015.

[6] Wasserman P. Zona Pellucida Glycoproteins. *Ann Rev Biochem* 57:415-442 1988.

[7] Hara Y. Function and Autonomous Behavior of Self-Oscillating Polymer Systems. *Polymers* **6:**1958-1971, 2014.

[8] Yashin V.V., and Balazs C.A. Pattern Formation and Shape Changes in Self-Oscillating Polymer Gels. *Science* 314: 798, 2006.

[9] (Stevanović) Hedrih R.K., Hedrih A.N. Phenomenological mapping and dynamical absorptions in chain systems with multiple degrees of freedom. *J Vib Cont* **22(1):**18–36, 2016.

[10] Hedrih N.A., Machado J.T., (Stevanović) Hedrih R. K. Electromechanical analogy and generalized function of fractional order energy dissipation in spherical net discrete continuum model of mouse zona pelucida. Proceedings of 5th International Congress of Serbian Society of Mechanics, Jun15-17th 2015, Arandjelovac, Serbia. Published by Serbian Society of Mechanics and Faculty of Technical Sciences Novi Sad, Editors: Spasić T.D, Lazarević M, Grahovac N, Žigić M. ISBN 978-86-7892-715-7, COBISS.SR-ID 296997639.

[11] Yashin V.V., Kuksenok O., Dayal P., Balazs A.C. Mechano-chemical oscillations and waves in reactive gels. *Rep Prog Phys*. 75: 6, 066601, 2012. doi: 10.1088/0034-4885/75/6/066601.

[12] Yashin, V.V., Van Vliet K.J., and Balazs, C.A. Controlling chemical oscillations in heterogeneous Belousov-Zhabotinsky gels via mechanical strain. *Physical Review E* 79 (2009), 046214 _2009.

[13] Yoshida R., Sakai T., Ito S., Yamaguchi T. Self-Oscillation of Polymer Chains with Rhythmical Soluble-Insoluble Changes. *J Am Chem Soc*. 124:8095-8098 9 8095, 2002.

MECHANICAL STATUS WITHIN CIRCULARLY MICROPATTERNED CELL MONOLAYER DECIDES THE FUSION OF OSTEOCLAST PRECURSORS

Bo Huo[a], Chenglin Liu, Xue Bai
Department of Mechanics, School of Aerospace Engineering, Beijing Institute of Technology, Beijing, China

Summary It is always a confusing issue why bone resorption occurs at the site of microdamage within bone, where osteoclast precursors aggregate and finally fuse into osteoclasts. We hypothesize that the mechanical status within cell monolayer correlating with its morphology decides the cell fusion. In this study, the micro-contact printing technology was adopted to build multicellular monolayer with circular pattern. Traction force observations showed that the cell-substrate interaction reached its maximum value at the outer edge, interestingly, where the expression of force-transferring proteins, F-actin (intracelluar tension), vinculin (cell-substrate interaction), β-catenin and E-cadherin (cell-cell connections), were also highest. Probably responding to this high-level in-plane shear stress, the cell fusion was lowest at the outer edge of circular patterns. These results indicate that the mechanical microenvironment within the cell monolayer plays an important role in the fusion of osteoclast precursors and provide insight into the molecular mechanism.

INTRODUCTION

Osteoclasts are highly specialized multinucleated cells that are uniquely capable of resorbing bone matrix. The formation of mature osteoclasts is characterized by the fusion of mononuclear phagocytes (i.e. osteoclast precursors) originating from hematopoietic stem cells. There are lots of microdamages within bone due to fatigue. It has been found that bone resorption usually occurs around microdamage, especially at the leading edge of the cutting zone, which is called targeted bone resorption or bone remodelling [1]. But it is still unknown how mononuclear osteoclast precursors locating in this specific area fuse into multinucleated osteoclasts. By using the micropatterning technique, a large number of studies demonstrated that adhesion morphologies regulates the differentiation of stem cells through cell-matrix interactions. For example, one study found that after having been cultured on circular patterns, the human mesenchymal stem cells locating at the edges tended into osteogenesis, whereas those at the center differentiated into adipocytes [2]. The traction force analysis revealed that the regions of high cell-matrix shear stress resulted in osteogenesis, while stem cells in the regions of low shear stress differentiated into adipocytes. Nelson et al. found that cell proliferation occurred at the edge of a circular pattern or the corner regions of a rectangular pattern, where high traction stress was generated within the cell sheet [3]. When the cell-cell interaction was inhibited by blocking the binding of E-cadherin to β-catenin, the concentrated proliferation was substantially reduced. The above studies indicated that cell adhesion may influence the cell-matrix interaction or cell-cell interaction, and in turn regulate the differentiation of stem cells, but few studies focused on osteoclasts. In the present work, we analyzed the effect of cell monolayer morphology on the fusion of osteoclast precursors RAW264.7 monocytes.

MATERIALS AND METHODS

Micropatterned cell monolayer. The micropatterned substrate was made by using the technology of soft photolithography. Briefly, a mask with designed geometric features was first fabricated, which were replicated on the layer of photoresist and then on the PDMS stamp. This stamp with the comb-polymer inadhesive to proteins was immediately impressed onto a slide with pre-coated type I collagen. The mononuclear RAW264.7 cells were seeded on the micropatterned substrate and induced for 4 d or 6 d to fuse or differentiate into multinucleated osteoclasts with the 1:1 mixture of fresh DMEM medium with the conditioned medium from osteoblast-like MC3T3-E1 cells.

Traction force. The cells were seeded on the gel surface and cultured for 24 h until they get confluent. For a specific location, a phase contrast image of the cells on the substrate surface and a fluorescent image of the beads embedded within the substrate were recorded. Then the cell layer was dissociated from the gel substrate with trypsin and another fluorescence image for the beads were recorded again. Basing on two fluorescent images, the displacement fields in the substrate were calculated using digital image correlation method, and the corresponding traction stress field was computed using Fourier transform traction microscopy.

Inhibition and fluorescent staining. To block the calcium-dependent cell-cell connection, DMEM medium was replaced by calcium-free DMEM medium or anti-E-cadherin antibody was kept in the induction medium. In addition, the force-transferring proteins, i.e. F-actin (intracelluar tension), Vinculin (cell-substrate interaction), β-catenin and E-cadherin (cell-cell connections), were fluorescently stained by using phalloidin or the corresponding immunohistochemistry assays.

Identification of cell fusion. Cells were washed with PBS twice after removing the culture medium, and fixed with citrate-acetone solution for 30 s at room temperature. The cells were incubated with TRAP staining kit reaction solution at 37°C for 1 h. The cells were washed with deionized water three times, and incubated with 0.2 mM Hoechst for 10 min, followed by being washed with PBS twice.

Statistical analysis. All experiments were performed at least six times, and more than 1500 cells were measured for each group. The data were presented as mean ± standard deviation (SD) if not specifically claimed. One-way analysis of

[a] Corresponding author. Email: huobo@bit.edu.cn.

variance (ANOVA) with Bonferroni's post hoc analysis was performed to determine the statistical significance of the differences between the mean values of different groups ($p < 0.05$).

RESULTS

The fusion of osteoclast precursors depends on the location in cell monolayer

RAW264.7 monocytes were seeded on the circular adhesive pattern and gradually formed a cell monolayer, then some cells fused as multinucleated ones, which revealed TRAP-positive staining and were regarded as osteoclasts. The proportion of multinucleated cells in the center region was 7.1%-8.3%, which is significantly higher than 4.8% in the outer region. The average density of multinucleated cells showed a region-dependent manner after 4-d culture. For cells with 2-4 nuclei, the density (167-183 cells/mm^2) is larger than that at the outer edge (77-104 cells/mm^2); for cells with 5-7 nuclei, the density exhibits a same region-dependent behaviour, i.e., the density is 57-77 cells/mm^2 in the middle region, while that at the edge is 17-20 cells/mm^2. Interestingly it was found that nuclear density, i.e. the number of nuclei per unit area, did not reveal significant difference within the entire region in the pattern for 4-d or 6-d culture. This result suggests that the higher fusion ratio of osteoclasts in the center region is not due to the overcrowding of cells, but due to the local mechanical status of this region in cell monolayer which is different from that in the outer edge.

Cadherin-related cell-cell interactions regulate the region-dependent fusion

The low calcium medium was prepared using calcium free DMEM medium 1:1 mixed with the conditioned medium from MC3T3-E1 osteoblasts. After RAW264.7 monocytes were seeded on the circular pattern for 4 d with this low calcium induction medium, the percentage of multinucleated cells was greatly decreased, but that in the center region was still higher than the outer edge. The multinucleated cells density with 2-4 nuclei was suppressed to about 50-100 cells/mm^2, which was significantly lower than the control group of about 100-200 cells/mm^2. The multinucleated cells density with 5-7 nuclei decreased to 10-20 cells/mm^2. When maintaining 1 μg/ml anti-E-cadherin antibody in the induction medium during 4-d culture, the data showed that the percentage of multinucleated cells was greatly decreased, and the region-dependent fusion vanished. The multinucleated cells density with 2-4 nuclei was suppressed to about 50-100 cells/mm^2 and that with 5-7 nuclei decreased to 6-16 cells/mm^2. If there was no conditioned medium added in the culture medium, only less than 1% multinucleated cells formed, and no significant difference along the radial direction was found. The analysis of nuclear number showed that the multinucleated cells density with 2-4 nuclei was significantly suppressed to about 20-40 cells/mm^2 and that with 5-7 nuclei decreased to less than 10 cells/mm^2.

Force distribution within cell monolayer is consistent with the region-dependent fusion

The in-plane stresses were obtained based on the measured traction force. The results showed that the traction force was generally along the radial direction, and its radial component increased as a function of the distance to the pattern center. There was generally a linear relationship between the traction force and the distance to the ring center for the soft substrate, whereas the traction force concentrated at the outer edge. The distribution of the traction force is consistent with theoretical predictions in this work and with those of our previous study. The maximal principal stress was in general along the circumferential direction, and the minimal principal stress was along the radial direction. The in-plane maximal shear stress on the pattern localized at the outer edge. This measurement of the in-plane principal stress and maximal shear stress was also consistent with our observation on the expression of force-transferring proteins, i.e. F-actin (intracelluar tension), Vinculin (cell-substrate interaction), β-catenin and E-cadherin (cell-cell connections). The results showed that the fluorescent intensity of these four types of proteins were significantly higher than those in the center regions.

CONCLUSIONS

Our present study suggests that the pattern of substrate on which cell monolayer adheres may influence the organization of cytoskeleton and the cell-cell connection, which then leads to the region-dependent fusion phenomenon of osteoclast precursors. But the detailed mechanism about the force transmitting between cell-substrate, cell-cell and intracellular cytoskeleton still needs further investigations. The corresponding studies are ongoing in our lab..

References

[1] Robling A.G., Castillo A.B., Turner C.H.: Biomechanical and molecular regulation of bone remodeling. *Annu Rev Biomed Eng* **8**:455-98, 2006.

[2] Ruiz S.A., Chen C.S.: Emergence of patterned stem cell differentiation within multicellular structures. *Stem Cells* **26**:2921-7, 2008.

[3] Nelson C.M., et al.: Emergent patterns of growth controlled by multicellular form and mechanics. *PNAS* **102**:11594-9, 2005.

AN EXPERIMENTAL TECHNIQUE FOR MEASURING THE PIEZOELECTRIC VOLTAGE AND STREAMING POTENTIAL IN WET BOVINE BONE

Jinzhao Liu, Zhende Hou[a], Lianyun Xu, Cheng Yu
Department of Mechanics, School of Mechanical Engineering, Tianjin University, Tianjin, China

Summary. The electromechanical properties of bone refer to piezoelectricity and streaming potential which are induced by external loads acting on human body, which the electric signals induced can affect the growth of bone. The purpose of the study is to investigate the coupling effect between the piezoelectricity and streaming potentials in wet bone. We developed an experiment technique that can be used to measure synchronously the piezoelectric voltage and streaming potential of wet bone. The coupling effect between the streaming potentials and piezo-voltages in bone is observed using the setup developed.

MANUSCRIPT PREPARATION

The electromechanical properties of bone refer to piezoelectricity [1] and streaming potential[2] which are induced by external loads acting on human body. Bone can change its structure, shape and density to adapt itself to the external loads, known as remodelling, which is the core of Wolf's Law[3]. A significant fact is that the piezoelectricity and streaming potentials, also called stress generated potentials (SGPs), may affect the growth of bone, which providing the motivation for studying the electromechanical behavior of bone.

The piezoelectric property arises from the collagens the organic component of bone when they are subjected to shear stresses. Both dry and wet bone have piezoelectric properties [1] [4].

The streaming potential of bone is generated by relative flow between the tissue fluid and the surfaces of solid matrix inside the microchannels of bone (Haversian canal or bone canaliculus) [2][5], which reflects the amplitude of an electric potential known as the zeta potential on the solid surface. It is the electric fields, produced by the zeta potential, surrounding the bone cells that can affect their growing.

This paper aims to investigate the coupling effect between the piezoelectricity and the streaming potential in wet bone. We developed an experiment technique that can measure synchronously the piezoelectric voltage and streaming potential of wet bone. The coupling effect between the streaming potential and piezo-voltage in bone is observed using the setup developed.

MATERIALS AND METHODS

The experimental setup developed is shown in Fig.1. A circular thin plate bone specimen used (Fig.2) was harvested from the mid-diaphysis of bovine (age2–3 years) tibias. Its dimension is 0.8 mm in thickness and 7 mm in diameter and it was fixed in the plexiglass U-shape container containing phosphate-buffered saline solution (0.145 M, pH 7.3). The specimen was immersed in the solution and its edge was sealed off by a rubber ring to prevent the liquid flowing through the gap between container wall and the edge of the specimen.

An Instron test machine (Instron E10000) was used to apply a compressive force to the upper surface center of the specimen via a loading bar made of plexiglass. When the compressive force bends the plate specimen, the shear stresses in the specimen induce a piezoelectric voltage between the upper and lower surfaces of the specimen. The ions in the buffer solution gave the solution weak conductivity; hence the two platinum/iridium (pt-ir) electrodes could sense or test the voltage without touching the bone.

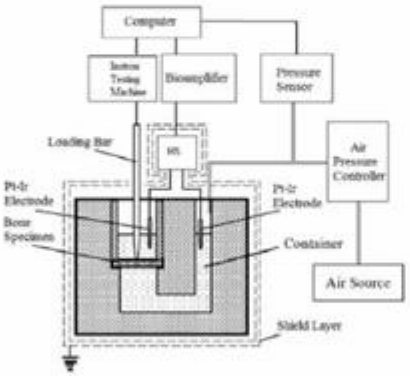

Fig. 1. Schematic diagram of the measurement setup

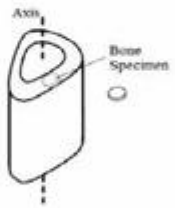

Fig.2 Specimen and its location

[a]Corresponding author. Email: hou@tju.edu.cn

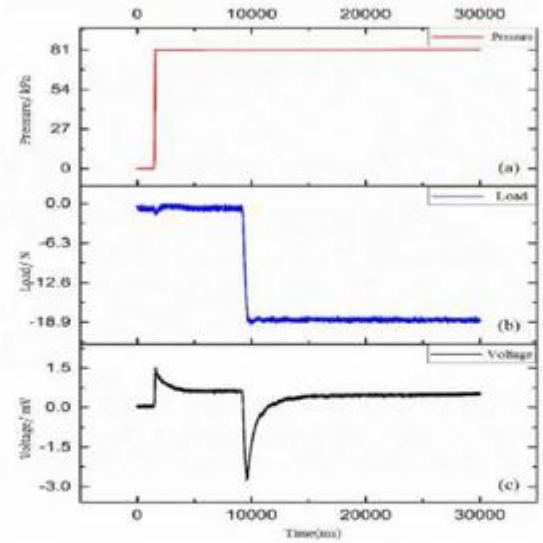

Fig.3 Waveform Loadings and the measured voltages

The left inlet of the U container is sealed. When the air pressure generated by the air controller is inputted into the container, it can be maintained and drives the solution to flow. Once the buffer solution flows from the lower surface to the upper surface through the microchannels of the specimen, the streaming potential is generated between the two surfaces, which can also be detected by the two electrodes.

The measured voltage signals between the pair of Pt-Ir electrodes are input into a bioamplifier (BMA- 931, CWE Inc., USA) via an ultra-high-input impedance (over 10^{12} Ω) head stage (Super Z, CWE Inc., USA). The amplified voltage signals are recorded by the computer in the measurement setup.

The solution container and the head stage were enclosed in a double electromagnetic shield with the outer shield connecting to earth and the inner to the head stage common terminal. This arrangement kept the electric field constant around the specimen.

RESULTS

The experimental procedure was as follows. A step air pressure of 80 kPa (the red curve in Fig. 3(a)) was first applied to the inside of the container and leading the solution to flow through the specimen from the lower surface to the upper surface. Consequently, the streaming potentials were measured. The first part of the curve in Fig3 (c) is the corresponding streaming potential. This part starts with a peak corresponding to rising edge of the pressure and tends to a constant value V_1 during the pressure holding constant, which is a typical feature of the streaming potential in bone [5].

After about 1.5 second, a step concentrated force of 19N as illustrated in Fig.3(b) was applied to the specimen and the piezo-voltage occurred between the two surfaces of the specimen. The second part of the curve in Fig3 (c) is the measured piezo-voltages. This part also starts with a peak corresponding to the rising edge of the forces loaded and then tends to a constant value V_2 and V_2 is not equal to V_1. The typical feature of the piezo-voltage in bone is that it tends to zero during the force loaded remaining unchanged [4]. So, V_2 does not only depend on the piezoelectricity. The difference of V_1 and V_2 may represent the coupling between the streaming potential and piezo-voltage in bone.

Acknowledgment

The work was supported by the National Natural Science Foundation of China under Grant No. 11372218

References

[1] Fukada E.Yasuda I.: On the piezoelectric effect of bone. J Phys Soc Jpn **12**:1158-1162, 1957

[2] Beck B.R. Qin,Y X.:On the relationship between streaming potential and strain in an in vivo bone preparation. Calcif Tissue Int **71**:335-343, 2002

[3] Ahn A C. Grodzinsky A J.: Relevance of collagen piezoelectricity to "Wolff's Law":a critical review. Med.Eng.Phy **31**:733-741, 2009

[4] Xu LY. Hou Z D.: Stretched exponential relaxation of piezovoltages in wet bovine bone, J Mech Behav Biomed Mater **41**,115-123, 2015

[5] Xu LY, Hou, Z D.: Investigation of pressure loading rates on streaming potentials in bone. Sci China Tech Sci 54:1376-1381, 2011

YIELD-STRAIN-ENERGY IS A BETTER DISCRIMINATOR OF HIP FRACTURES THAN BMD

Yunhua Luo[1, 2, a)]
[1]*Department of Mechanical Engineering, University of Manitoba, Winnipeg, Manitoba, Canada*
[2]*Department of Biomedical Engineering, University of Manitoba, Winnipeg, Manitoba, Canada*

Summary Osteoporotic fracture is a major cause of suffering and disability for old people over the world. Accurate discrimination of high-risk patients is necessary to prevent osteoporotic fractures. Bone mineral density (BMD) measured by hip dual energy X-ray absorptiometry (DXA) is the gold standard reference recommended by the World Health Organization for screening osteoporosis, but it has limited accuracy in predict fracture risk. Clinicians are thus looking for more accurate tools such as biomechanical models. We proposed to use yield-strain-energy at the narrowest femoral neck (NFN-YSE) as a discriminator of hip fracture risk. NFN-YSE can be calculated from the subject's hip DXA image using mechanical methods. A clinical cohort consisting of 195 hip fracture cases and 592 controls with matched sex and age was used to study the discrimination accuracy. The results show that NFN-YSE was more accurate than BMD in discriminating fractures from controls.

INTRODUCTION

Osteoporosis has become an epidemic disease among old people over the world [1], and osteoporotic fractures are a major cause of suffering, disability and death in older women and men. In Canada, the prevalence of osteoporosis is reported to be 26% in women and 7% in men over age 50. Over 30,000 hip fractures occur each year in Canada [2]. By the year 2041, the number of hip fractures in Canada is expected to quadruple [3]. The annual cost of hip fractures alone in Canada was estimated at $650 million in 1993 and is expected to increase to $2.4 billion by 2041; the total cost burden from all osteoporotic fractures is far greater [4, 5]. According to a report recently released by the US National Osteoporosis Foundation (NOF) (http://nof.org/news/2948), about 54 million Americans are affected by osteoporosis and low bone mass.

Osteoporosis is a 'silent disease' as it has no symptom until the patient's first-time fracture. It is very desirable that high-risk patients can be timely and accurately identified so that the incidents of first-time fracture can be prevented or at least be reduced. Bone mineral density (BMD) measured by hip DXA (dual energy X-ray absorptiometry) is the gold standard reference recommended by the World Health Organization (WHO) to screen osteoporosis, and it has also been widely used as a surrogate for predicting fracture risk. The BMD measured from an old individual is compared to the mean BMD of young people of the same ethnic group. The results is expressed as a T-score, which is a standard deviation (SD) from the mean BMD. The WHO defines osteoporosis as T-score<-2.5 and it indicates high risk of fracture. However, the majority of clinical fractures occurred with T-score above -2.5. From the view point of material mechanics, a bone fractures when the applied force exceeds its strength. The force causing fracture is usually induced in accident fall, which is random and difficult to predict. Therefore, bone strength is the only reliable parameter available for assessing fracture risk. Bone strength is jointly determined by bone quality and bone geometry. BMD measured by clinical DXA is an average areal BMD over a region of interest. It can only partly represents bone quality. Bone geometry information is missing in the BMD based tool. To improve prediction accuracy of fracture risk, we proposed to use femur cross-sectional yield-strain-energy to represent bone strength.

MATERIALS AND METHODS

In mechanics of materials [6], yield strain energy density represents the maximum amount of mechanical energy that the material can absorb without developing plastic deformation. The yield or ultimate strain energy density has been frequently used in development of failure theories. Material failure criteria based on strain energy density have theoretical advantages, for example, they consider both stresses and strains, which is necessary to accommodate both stress and strain controlled material failure; they are able to integrate all the six stress and strain components, which is necessary for describing material failure in a multiaxial stress state. Therefore, we developed a criterion based on cross-sectional yield-strain-energy to evaluate hip fracture risk. Clinical studies have shown that the narrowest femoral neck, as shown in Figure 1(a), is usually the weakest cross-section on the femur, as hip fractures frequently occurred at the location. Therefore, it is rational to use the yield-strain-energy at the narrowest femoral neck (NFN-YSE) to represent femur strength in assessing hip fracture. NFN-YSE can be calculated from the subject's hip DXA image [Figure 1(b)] using correlations between bone density and bone mechanical properties. The profile of areal BMD (aBMD) at the narrowest femoral neck, Figure 1(c), is extracted from the subject's hip DXA. The aBMD (ρ_A, g/cm^2) at each point across the narrowest femoral neck was converted into volumetric BMD (ρ_V, g/cm^3) [7],

$$\rho_V = 0.0347 + 0.3096\rho_A \qquad (1)$$

[a)] Corresponding author. Email:Yunhua.Luo@umanitoba.ca.



(a) (b) (c)

Figure 1 (a) Femoral neck fracture; (b) hip DXA image; (c) femoral neck cross-sectional BMD profile

Elasticity modulus is calculated from volumetric BMD (ρ_V) using empirical functions established by experiments [8, 9],

$$E = \begin{cases} 33.9\rho_V^{2.20} \ (GPa) & (\rho_V \le 0.28 \frac{g}{cm^3}) \\ 10.5\rho_V^{2.29} \ (GPa) & (\rho_V > 0.28 \frac{g}{cm^3}) \end{cases} \quad (2)$$

Yield stress is estimated from elasticity modulus [10],

$$\sigma_Y = \begin{cases} -0.41 + 0.0062E \ (MPa) & (Compressive) \\ 0.33 + 0.0039E \ (MPa) & (densile) \end{cases} \quad (3)$$

YSE at the narrowest femoral neck is obtained by integration,

$$\pi_{AB} = \frac{1}{2}\int_A^B \frac{\sigma_Y^2}{E} dx \quad (4)$$

To investigate the accuracy of NFN-YSE in discriminating hip fracture cases from controls, a clinical cohort consisting 195 women with prior hip fracture (mean age 75.2) and 592 women without fracture (mean age 74.8) were obtained from a community clinic centre. The discrimination accuracy and ability are measured by the area under the ROC (receiver operating characteristic) curve, or AUC in short, and odds ratio (OR). The results are compared with those of femoral neck BMD.

RESULTS AND DISCUSSION

The discrimination accuracy and ability of NFN-YSE and femoral neck BMD are given in Table 1. Compared to femoral neck BMD, the AUC of NFN-YSE was improved by 11.9% and the OR was increased by 29.0%, indicating that NFN-YSE has a significantly higher accuracy and stronger ability in discriminating fracture cases. The improvement is mainly attributed to the inclusion of more information in NFN-YSE than in BMD, especially bone yield stress that is directly related to bone strength.

Table 1 AUC and odds ratio of NFN-YSE and femoral neck BMD in discriminating clinical hip fracture cases

	AUC	OR (95% CI), p-value
FCS-YSE	0.783	2.94 (2.16 – 3.99), p<0.001
Femoral Neck BMD	0.706	2.28 (1.73 – 3.01), p<0.001

CONCLUSIONS

NFN-YSE has been demonstrated a better discriminator of hip fractures than BMD. The input required for calculating NFN-YSE is the subject's hip DXA image. Therefore, the proposed method can be easily implemented in clinic and used by clinicians.

References

[1] J.Y. Reginster and N. Burlet. Osteoporosis: a still increasing prevalence. *Bone*, 38(2 Suppl 1):S4–9, 2006.
[2] W.D. Leslie, S. O'Donnell, S. Jean, and et al. Trends in hip fracture rates in Canada. *JAMA*, 302:883–9, 2009.
[3] E.A. Papadimitropoulos, P.C. Coyte, R.G. Josse, and C.E. Greenwood. Current and projected rates of hip fracture in Canada. *CMAJ*, 157:1357–63, 1997.
[4] M.E. Wiktorowicz, R. Goeree, A. Papaioannou, J.D. Adachi, and E. Papadimitropoulos. Economic implications of hip fracture: health service use, institutional care and cost in Canada. *Osteoporos Int*, 12:271–8, 2001.
[5] R. Goeree, B. O'Brien, D. Pettit, L. Cuddy, M. Ferraz, and J.D. Adachi. An assessment of the burden of illness due to osteoporosis in Canada. *Journal of the Society of Obstetricians and Gynaecologists of Canada*, 18:15–24, 1996.
[6] G.C. Sih. Strain energy density theory applied to plate-bending and shell problems. In G.C. Sih, editor, *Mechanics of Fracture Initiation and Propagation*, pages 57–98. Kluwer Academic Publishers, Dordrecht, Netherlands, 1991.
[7] Y. Luo and H. Yang. Correlation between areal and volumetric BMD established by QCT Pro. Technical Report 2015-04, Department of Mechanical Engineering, University of Manitoba, 2015.
[8] J.H. Keyak, I.Y. Lee, and H.B. Skinner. Correlations between orthogonal mechanical properties and density of trabecular bone: Use of different densitometric measures. *J Biomed Mater Res*, 28:1329–1336, 1994.
[9] T.S. Keller. Predicting the compressive mechanical behavior of bone. *J Biomech*, 27:1159–1168, 1994.
[10] E.F. Morgan and T.M. Keaveny. Dependence of yield strain of human trabecular bone on anatomic site. *J Biomech*, 34:569 – 577, 2001.

DAMAGE OF MUSCLE CELLS UNDER MECHANICAL AND OXIDATIVE STRESSES

Singwan Wong, Yifei Yao, Julia Y Hong, Bruce PT Pang, Brian CH Cheung and Arthur FT Mak
Division of Biomedical Engineering, The Chinese University of Hong Kong, Shatin, Hong Kong

Summary Deep tissue injury due to prolonged excessive loadings can lead to clinical pressure ulcers. We assess the duration-dependent damage thresholds of muscle cells in compression and shear using myoblasts in-vitro, and study the effects of oxidative stress on such thresholds. We study the effects of oxidative stress on cytoskeletal polymerization and use AFM to study the corresponding changes in cell stiffness. We use femtosecond laser to evaluate how oxidative stress affects the pre-tension in the cytoskeletal fibers and the ability of cells to repair submicron-pores on their plasma membranes. Our findings suggest interesting implications of damage vulnerability under prolonged oxidative exposures, such as during chronic inflammation. Using a mouse model, we examine the damages incurred by a prolonged exposure to epidermal pressure and how a surfactant cell membrane stabilizer poloxamer-188 and intermittent vibration may alleviate these damages.

MYOBLAST COMPRESSIVE & SHEAR DAMAGE THRESHOLDS IN-VITRO

Spherical indentation was applied onto a 3mm thick agarose gel covering a monolayer of C2C12 myoblasts. Cell damage was recognized using propidium iodide (PI). The spatial profile of the measured percentage cell death was correlated with the radially varying stress field as determined by finite element analysis to estimate the compressive stress threshold for cell death (Yao et al., 2015). To measure the damage threshold in shear, a flat plate was used to apply a uniform compressive strain and a radially increasing shear strain on discs of GelMA hydrogel with myoblasts encapsulated within. The percentages of cells damaged were estimated with PI and calcein AM staining. Results suggested that cell damage depended on both the level and duration of the applied strains. There seemed to be a non-linear coupling between compression and shear. The experiments were conducted on myoblasts after oxidative exposure of various intensities and durations, as compared to the control in regular culture media. Results supported the hypothesis that chronic exposure to high-dosage oxidative stress could compromise the capability of muscle cells to withstand compressive and shear damages, while short exposure to low-dosage oxidative stress could enhance such capability.

ACTIN CYTOSKELETON IN OXIDATIVE ENVIRONMENTS

H_2O_2 was applied as an extrinsic oxidant to C2C12 myotubes. Atomic force microscopy results showed that short exposures to H_2O_2 apparently increased the stiffness of myotubes, but that long exposures made the cells softer. The turning point seemed to take place somewhere between 1hr and 2hrs of H_2O_2 exposure. We found that the stiffness change was probably due to actin filaments being favoured for depolymerization after prolong H_2O_2 treatments, especially when the exposure duration exceeded 1 hour and the exposure concentration reached 1.0mM. Such depolymerization effect was associated with the down-regulation of thymosin beta 4, as well as the up-regulation of both cofilin2 and profilin1 after prolong H_2O_2 treatments (Wong et al, 2015). Utilizing a femtosecond (fs) laser to sever single stress fibres (SF) inside living C2C12 myoblasts, we investigated the retraction rheology of the severed single SF to probe into the mechanical conditions of the cells and the effect of H_2O_2 on them. The initial gap between the two severed ends of the SF immediately after fs laser severing was larger in the H_2O_2-treated groups, suggesting that H_2O_2 exposure could promote the pre-stress in individual SF (Ma et al., 2015). The results were consistent with cell stiffness measured on single myoblasts under oxidative stress. A confocal-based cell specific finite element model was built to study the effects of stress fiber density, fiber cross-sectional area, tensile pre-strain in the fibers, elastic moduli of SF, actin cortex, actin cytoskeleton (including both actin SF and actin cortex), nucleus and cytoplasm. The results supported that a decrease in actin cytoskeletal elastic modulus could increase the average tensile strain on the actin cortex-membrane structure and reduce the elastic modulus of the cell. Assuming the cell would die when a certain percentage of membrane elements was strained beyond a threshold, lower elastic modulus of actin cytoskeleton would compromise the compressive resistance of a myoblast and lead to cell death more readily.

CELL MEMBRANE REPAIR AFTER FEMTOSECOND LASER POTOPORATION

A femtosecond (fs) laser mounted on a confocal microscopic platform was used to generate a highly focused hole at a targeted site of the myoblast plasma membrane. With the same laser power and irradiation duration, photoporation invoked bigger holes in the myoblasts after oxidative treatments than those in the control. Myoblasts showed difficulty in repairing holes with initial size beyond certain threshold. Within the threshold, holes could apparently be resealed within 100 seconds under the normal condition; while in oxidative condition, the resealing process even if successful could take 100-300s. A significantly higher percentage of myoblasts in chronic oxidative conditions could not have their holes resealed within the entire period of observation. It is interesting to note that brief exposure to oxidative stress apparently could promote resealing in myoblasts (Duan et al., 2015).

Corresponding author: Arthur FT Mak. Email: arthurmak@cuhk.edu.hk.

POLOXAMER-188 TO PROTECT MUSCLE CELLS AGAINST DAMAGES

We investigated the preventive effect of poloxamer 188 (P188) on muscle cells against extrinsic oxidative challenges. It was found that with 1mM P188 pre-treatment for 1 hour, skeletal muscle cells could maintain their compressive damage threshold, actin polymerization dynamics, and membrane sealing ability after H_2O_2 insults. These findings suggested that P188 pre-treatment can help skeletal muscle cells retain their normal mechanical integrity in oxidative environments, adding a potential clinical use of P188 against the combined challenge of mechanical-oxidative stresses. We used a mouse model to investigate the protective effect of P188 on muscle compressive injury in-vivo. Three concentrations of P88 (200mg/kg, 400mg/kg and 800mg/kg) were administered to the mice through intraperitoneal injection. 100mmHg static pressure was delivered to the mice's biceps femoris for 6 hours. Extracted tissues were examined using creatine kinase (CK-MM) ELISA and immunohistochemistry (IHC) analysis. Preliminary results showed that the P188 treatment groups reduced the CK-MM level in mice serum as well as the amount of TNF-alpha in the muscle tissue sample after compression.

MECHANICAL VIBRATION TO ALLEVIATE MUSCLE DAMAGES FROM STATIC COMPRESSION

We tested the hypothesis that intermittent vibrations (iV) can reduce apoptosis in tissues under prolonged compression. Senescence accelerated (SAMP8) mice were subjected to static loading on the biceps femoris of the right limb for 6 hrs. A 10-minute of iV at 0.25g and 35Hz was applied vertically to the loading site once every 30 minutes throughout the compression period. iV and the compression force were real-time monitored using a single axial accelerometer and a three-axial force transducer respectively. The compressed tissues were collected for immuno-histochemical analysis, creatine kinase-MM (CK-MM) ELISA and western blot analysis. Up-regulations of cleaved caspase-3 and TNFα in the compressed group validated our compression protocol in inducing tissue injury. Preliminary findings suggested that these apoptotic factors were evidently down-regulated in the vibration group when compared with the group under only static compression group. This suggested that apoptotic activity might be reduced with iV applied on the compressed tissue.

CONCLUSIONS

Muscle cells in-vivo need to serve their biomechanical functions even in challenging conditions such as in oxidative stresses under chronic inflammatory situations. We have provided in-vitro and in-silico evidences that under prolonged oxidative environment, the capacity of muscle cells to resist and repair physical damages could be significantly compromised. We hypothesize that oxidative stresses and/or a compromised anti-oxidative defence could be involved in the development of deep tissue ulcers. Preliminary findings on the use of P188 and intermittent vibration were encouraging with regard to alleviating the apoptotic factors associated with the damaging processes.

Acknowledgements

This presentation builds on our recently published work as referenced below, with contributions also from LM Bian, KT Chan, CC Cheng, T Cheng, M Cho, Xinxing Duan, YC Hsu, KKH Lee, Zili Ma, S Sun, YQ Wu, and ZT Xiao. The work was supported by The Hong Kong Research Grants Council through its General Research Fund (CUHK415413).

References

[1] XIAO ZT, WU YQ, MAK AFT. Accumulation of Loading and Unloading Reperfusion Injury – Modeling for the Propagation of Deep Tissue Ulcers. Journal of Biomechanics. 47(2014): 1658-1664. 2014.

[2] SUN S, WONG SW, MAK AFT, CHO M. Impact of Oxidative Stress on Cellular Biomechanics and Rho Signaling in C2C12 Myoblasts. Journal of Biomechanics, 47(2014): 3650-3656. 2014.

[3] YAO YF, XIAO ZT, WONG SW, HSU YC, CHENG T, CHANG CC, BIAN LM, MAK AFT. The Effects of Oxidative Stress on the Compressive Damage Thresholds of C2C12 Mouse Myoblasts: Implications for Deep Tissue Injury. Annals of Biomedical Engineering. 43(2): 287-296. 2015.

[4] WONG SW, SUN S, CHO M, LEE KKH, MAK AFT. H2O2 Exposure Affects Myotube Stiffness and Actin Filament Polymerization. Annals of Biomedical Engineering. 43(5):1178-1188. 2015.

[5] DUAN XX, CHAN KT, LEE KKH, MAK AFT. Oxidative Stress and Plasma Membrane Repair in Single Myoblasts after Femtosecond Laser Photoporation. Annals of Biomedical Engineering. 43(11): 2735-2744, 2015.

[6] MA ZL, WU YQ, MAK AFT. Rheological Behavior of Actin Stress Fibers in Myoblasts after Nanodissection: Effects of Oxidative Stress. Biorheology. 52:225-234. 2015.

STRENGTH ANALYSIS OF CATASTROPHIC ROOT FRACTURES FOR ENDODONTICALLY TREATED LATERAL TEETH

Grzegorz Milewski[1a)], Agnieszka Chojnacka-Brożek[1]
[1]*Institute of Applied Mechanics, Cracow University of Technology, Cracow, Poland*

Summary The paper deals with the strength aspects of catastrophic vertical root fractures, which is the most common reason of tooth loss after the endodontic treatment, what with regards to the American Association of Endodontists is described with the term Cracked Tooth Syndrome. Numerical strength analyses were done for the two basic clinical cases: MOD (mesial-occlusal-distal) reconstruction and total crown overlay. In conclusion, the reconstructions with variant number of post of different material and depth of insertion were chosen to play a protective role in preventing the root and the whole crown against catastrophic fractures.

INTRODUCTION

Cracks formed in the teeth are considered as one of the biggest problems in modern dentistry; They are recognized as the third leading cause of tooth loss after the dental caries and periodontal diseases [1]. The case of a particularly importance is the so-called catastrophic, irreparable fracture, which is one of the most common cause of tooth loss after endodontic treatment. Biomechanical features of teeth after endodontic treatment are considered by majority of dentists as weaker when comparing with so called health teeth. Their experience prove that those teeth become more stiff and seem to be more susceptible to break or fracture what essentially influence their further reconstruction. The worst catastrophic fractures, which result in serious teeth mechanical strength weakening, are in particular vertical root fractures. They always lead to the tooth extraction. The case of the partial or total vertical root fracture in majority concern the teeth after endodontic treatment. The way of the destruction always starts at the area of the apical part of the root channel or alternatively at the bifurcation roots area and then comes to the tooth crown – Fig. 1. Those features become the most often factors of teeth loss after endodontic treatment and statistically concern 2 – 5% of all cases [2].

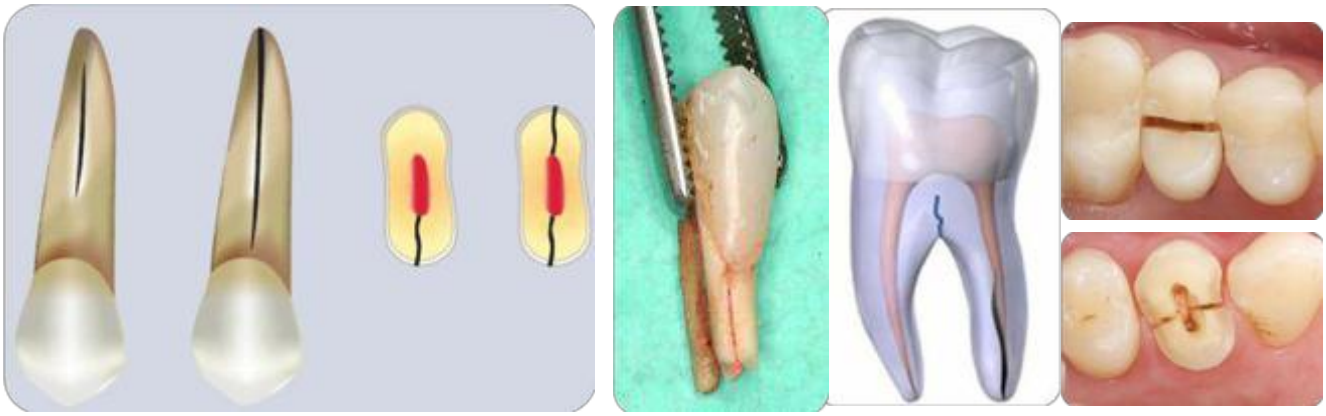

Fig. 1. Vertical root fractures schemes and their respective clinical cases

The total and partial root cracks are generally difficult to diagnose in the early stages, and therefore they become a serious problem for both the dentist and the patient. When properly recognized, usually extraction is the only solution.

The aim of the paper was to check and analyze, from the strength point of view, the influence of the number and depth of posts insertion in the root channels on the risk of catastrophic vertical root fractures in lateral teeth after endodontic treatment.

METHODS

Numerical strength analyses were done for the following basic clinical cases: MOD (mesial-occlusal-distal) reconstruction and a total crown overlay, for three models simulated root canal treated teeth followed by reconstruction with the use: only the composite material, the composite material and one glass-polymeric post inserted in a buccal root channel, the composite material and two glass-polymeric posts inserted in both (buccal and lingual) root channels. Additional variant numerical simulations were also done for the cases of the tooth reconstructions with one post inserted in the lingual channel and two posts with mutually different insertion depth in both buccal and lingual root channels. The strength analyses were done with regards to the various post materials (stainless steel, titanium alloy, ceramic and glass fiber reinforced polymer). Numerical modeling and stress analyses were done in a CAD CATIA and FEM ANSYS programs [3]. The model of tooth was

a) milewski@mech.pk.edu.pl

embedded in a periodontium, surrounded by bone structure. A special attention was paid to the areas of stress concentration within the area of the roots bifurcation, around the apical region of a root and in the area of the gingival line.

RESULTS

The numerical calculations were done for normal occlusion of the value 150 [N] for all materials of the structure taken as elastic and isotropic. As an example Fig. 2 presents the von Mises reduced stress distributions in roots bifurcation area for one glass fiber reinforced polymer post in buccal root channel for the various depth of insertion.

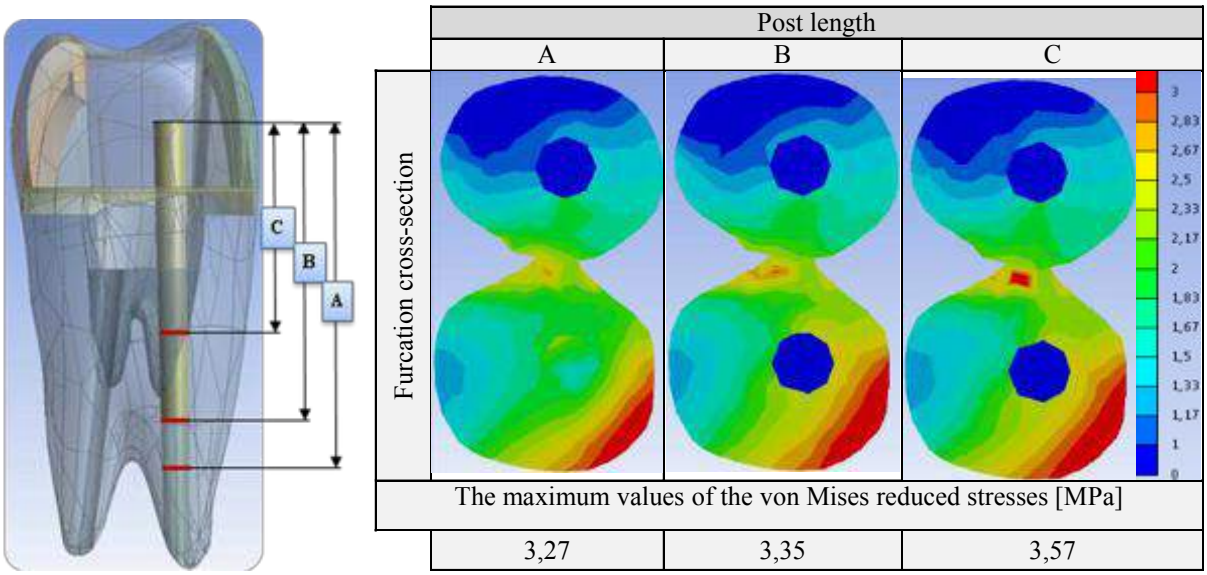

Fig. 2. The risk of the vertical root fracture with regards to the von Mises reduced stress distributions in roots bifurcation area for one glass fiber reinforced polymer post in buccal root channel for the various depth of insertion in MOD case reconstruction

CONCLUSIONS

The main conclusions which can be withdrawn from the number of simulations and calculations can be formulated as following:

- the posts with the higher elastic modulus, taking over the biggest loads, produce the stress concentration in the dentin around the apical top of the root; this can lead to the catastrophic fracture of the whole tooth structure,
- in the case of two post application in MOD cavities, von Mises stress analysis revealed more favorable stress distribution in roots bifurcation area, which can play protective role in preventing the root fracture,
- for the total overlay of crown reconstruction the application of one root post seems to be the most advantageous; in this case the maximal stress effort in the dentine at the bifurcation area was about 14% less when comparing with the reconstruction with the use of two posts,
- assessment of the posts depth insertion, for both the MOD and overlay reconstruction cases, proves that decreasing insertion depth increases the stress concentration in the root dentine at the bifurcation area, respectively by 9 and 17%, what may also result in vertical root fracture.

ACKNOWLEDGEMENTS

Special thanks to Dr Maciej Żarow from the Dental Clinic and Postgraduate Course Centre “DENTIST” in Cracow, Poland for the countless number of hours devoted to clinical aspects of teeth reconstruction after endodontic treatment.

References

[1] Tronstad L..: Clinical Endodontics, *PZWL*, Warsaw, Poland, 2004
[2] Caplan D. J., et al.: Factors related to loss of root canal filled teeth, *J.Public Health Dentistry*, 57(1). 1997, 31-39
[3] Chojnacka-Brożek A.: Strength analysis of teeth reconstructions for endodontically treated premolars, *PhD thesis*, Cracow, 2013

MECHANICS OF FIN STIFFNESS IN RAY-FINNED FISH

Khoi Nguyen[1], Ning Yu[2], Mahesh Bandi[1], Madhusudhan Venkadesan[3], and Shreyas Mandre [*2]

[1]*Okinawa Institute of Science and Technology, Okinawa, Japan*
[2]*School of Engineering, Brown University, Providence, Rhode Island, USA*
[3]*School of Engineering and Applied Science, Yale University, New Haven, Connecticut, USA*

Summary The fin of ray-finned fish is a composite structure consisting of rays (bony supports) connected by membranes. The elastic stiffness of a transversely curved fin is higher than for a flat fin because the curvature geometrically couples ray bending with membrane stretching. We present a fin model of two rays, jointed by a single membrane, as a simplified analysis for the coupled mechanics between rays and membranes. The stiffness interpolates between two limits. In the first limit, the membranes are infinitely extensible and the fin simply takes the stiffness of individual rays. In the opposite limit, the membranes are inextensible and rays are restricted to bend along a single direction. The fin takes a higher stiffness which increases monotonically with curvature.

INTRODUCTION

The flapping locomotion of ray-finned fish, or simply fish, depends on the elastic stiffness of their fins which, in turn, depends on fin material and geometry. Studies on fin mechanics have historically focused on properties of individual rays (bony rod-like supports) [1, 2], musculature controls of these rays [3], and coupled fin-fluid dynamics [4, 5]. We present another aspect of fin mechanics in treating the fin as a composite structure consisting of both rays and their connective membranes and in analyzing the coupled mechanics of rays and membranes. The fin, rays, and membranes are depicted in Figure 1a and our focus is on the elastic stiffness for a fin curved away from the figure's plane. To the best of our knowledge, the coupled mechanics of rays and membranes are not yet modeled.

MODEL

To model the coupled mechanics between rays and membranes in a fish fin, we present a simplified analysis for two identical rays of length L, aligned symmetrically and connected by a single membrane at their centroids. The principal axes of bending for each ray are rotated away from the membrane by an angle θ. For nonzero values of θ, the membrane acts as an additional resistance against bending of rays. In response to an applied force, the rays bend along the principal axes with values $w(x)$ and $v(x)$ and the membrane stretch with value $\epsilon(x)$ where x is the distance from the fin base. A schematic for this model is shown in Figure 1b.

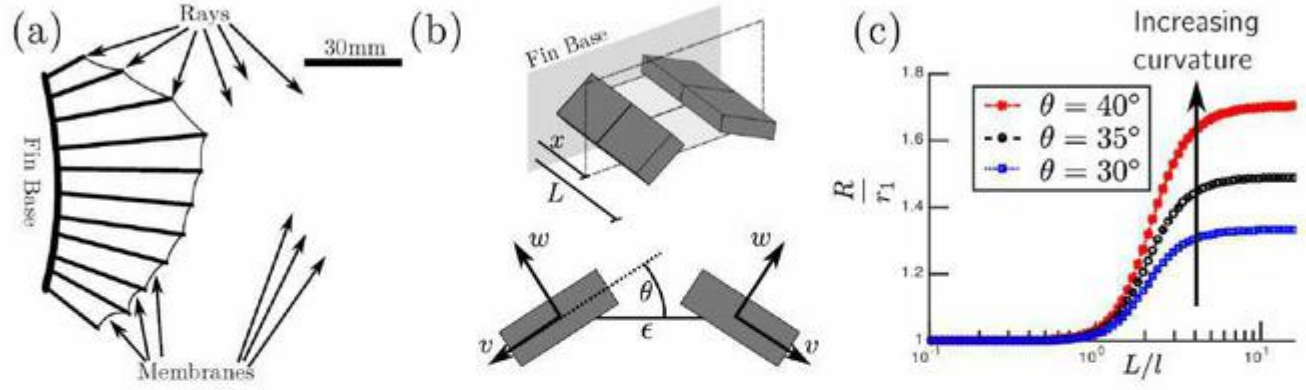

Figure 1: (a) Schematic and picture of a fish pectoral fin (*Aprion virescens*). The protypical fish fin consists of multiple bony structures, known as rays, extruding from the fin base and connected by tissue membranes. (b) Schematic of a symmetric 2-ray fin and a cross sectional view for a distance x from the base. The dark rectangular beams and gray strip represent fin rays and the membrane, respectively, and are all of equal length L. In the cross-sectional view, the ray bendings along their principal axes are w and v while the membrane stretching is ϵ. θ is the angle between v and the membrane. (c) The nondimensional scaling of stiffness R for a 2-ray fin under symmetric normal loadings. R is normalized by its value zero curvature ($\theta = 0$), $r_1 = 3B_n/L^3$. L/l is the nondimensional fin length where l is a length scale arising from the balance between ray and membrane elastic forces.

*Corresponding author. Email: shreyas_mandre@brown.edu

The coupling mechanism serves to modulate the fin's elastic stiffness as a function of θ. As an intuitive guideline to show this relation, we apply point-force loadings F at the tip of each ray, along w, and define the stiffness to be $R = F/w$ evaluated $x = L$. By treating the rays as elastic beams and membranes as one-dimensional springs, the governing equations for the coupling mechanism are the Euler-Bernoulli equations and are given as

$$B_n w'''' = ksin\theta\epsilon, \quad B_t v'''' = kcos\theta\epsilon, \tag{1}$$

$$\epsilon = 2cos\theta w + 2sin\theta v \tag{2}$$

where the primes are derivatives with respect to x, k is the membrane spring constant, and where B_n and B_t are the bending moments along w and v, respectively. We imposed clamped conditions at the fin base and point-force loadings on the opposite end; these are boundary conditions for which (1 - 2) have analytical solution and show how R, fin stiffness, modulates with θ, the geometric constraint.

$$r_1 = \frac{3B_n}{L^3}, \quad r_2 = \frac{3B_n}{L^3}\left(1 + \frac{B_t sin^2\theta}{B_n cos^2\theta}\right) \tag{3}$$

$$\frac{1}{l^4} = \left(\frac{2ksin^2\theta}{B_n} + \frac{2kcos^2\theta}{B_t}\right) \tag{4}$$

R interpolates between the two limits shown in (3). In one limit, the ray stiffness, r_1, dominates over the membrane stiffness, k, and R takes the stiffness of individual rays. In the opposite limit, the membrane stiffness dominates and the rays are restricted to bend entirely normal to the membrane. Here, R takes a higher, θ-dependent value, r_2. Between the limits, R depends on the ratio of ray and membrane stiffnesses. This is captured with L/l, where L is the ray length and where l is a length scale given in (4) and arises from nondimensionalizing (1-2). We plot the nondimensional scaling of R/r_1 with L/l in Figure 1c for different values of θ. It shows the stiffness of a 2-ray fin increases with θ but only appreciably if L/l is at least unity.

CONCLUSIONS

Intuitively, a transversely curved fin is stiffer than a flat fin because the curved geometry adds the membrane as an additional elastic force to resist ray bending. To show this geometric coupling quantitatively, we use a simplified model of beams and springs to approximate the fin rays and membranes. We show that the intuition is correct for a 2-ray fin system, ***i.e***, the fin stiffness increases with curvature. In future works, we will show that this result is essentially valid for a discrete N-ray system and for a continuous fin surface.

References

[1] Alben, Silas, Peter G. Madden, and George V. Lauder. "The mechanics of active fin-shape control in ray-finned fishes." Journal of The Royal Society Interface 4.13 (2007): 243-256.

[2] McCutchen, C. W. "The trout tail fin: a self-cambering hydrofoil." Journal of biomechanics 3.3 (1970): 271-281.

[3] Thorsen, Dean H., and Mark W. Westneat. "Diversity of pectoral fin structure and function in fishes with labriform propulsion." Journal of Morphology 263.2 (2005): 133-150.

[4] Dong, H., et al. "Computational modelling and analysis of the hydrodynamics of a highly deformable fish pectoral fin." Journal of Fluid Mechanics 645 (2010): 345-373.

[5] Flammang, Brooke E., et al. "Functional morphology of the fin rays of teleost fishes." Journal of morphology 274.9 (2013): 1044-1059.

TOUGHENING AND STRENGTHENING BIOINSPIRED NANOLAMINATES: SIZE EFFECT AND DESIGN INSIGHT

Yong Ni[a)], Zhaoqiang Song & Linghui He
Department of Modern Mechanics, CAS Key Laboratory of Mechanical Behavior and Design of Materials,University of Science and Technology of China, Hefei, Anhui 230026, P. R. China

Summary Understanding how bioinspired nanolaminate design efficiently mitigates the strength-ductility tradeoff in brittle materials via arresting the crack at the interface followed by controllable interface failure is important to fabricate biomimetic laminates with high strength and toughness. By using the nonlinear shear-lag model, the effects of the interface plasticity and the overlapping length between adjacent platelets on the stress field and the failure mode in the laminate are discussed. The size dependent failure modes are identified. They could explain the non-monotonic size-dependent mechanical properties observed in various laminate composites and provide guideline for rational design of strong and tough bioinspired laminates.

Laminar composite design becomes an efficient way to mitigate the strength-ductility tradeoff in brittle materials. Extremely high work-of-failure without much sacrifice of strength can be achieved by designing weak interface. The role of the low interface strength in crack deflection by interface delamination has been identified in previous studies. Such laminar composites that usually result in a step-like or saw-tooth load-displacement response exhibit a well-known graceful failure process. Biological materials, i.e. nacre and bone are good examples to achieve excellent mechanical performance by controlling interface failure via delicate hybrid discontinuous laminate design, a so called brick-and-mortar microstructure. A lot of efforts are taken to fabricate biomimetic discontinuously laminated composites towards superb mechanical properties. Recent studies show that there are significant size-dependent mechanical properties in these discontinuously laminated composites under uniaxial stretch[1]. It is known that the aspect ratio of the platelet in nacre has a characteristic value, at which the platelet and the interface simultaneously undergo uniform failure[2]. In contrast, the polymer/nanoclay nacre-mimetics exhibit high toughness and interface failure with low aspect ratio nanoplatelets, while they exhibit superior stiffness and strength with large aspect ratio nanoplatelets, in accompany with the failure mode changing from interface failure to platelet fracture[3]. A non-monotonic size-dependency of the mechanical response is observed in the case of even no platelet fracture. The stiffness, strength, failure strain and toughness can be synergistically increased with the increase of the overlapping length in discontinuously overlapped ply carbon/epoxy composites, and they show a ductile behavior wherein the interface fails progressively although their components are brittle[4]. However in 3D-printed laminated composites under uniaxial stretch the measured failure strain is found to decrease with the increase of the overlapping length, and they exhibit a brittle behavior wherein the propagation of the interface failure is catastrophic[5]. These experimental data seems contradictory. A unified explanation about the size effect of the interface failure in such structures is needed.

In this paper, we aim to theoretically elucidate the size effect of the interface failure in such structures mentioned in the literatures. We use a shear lag model to calculate the stress field in the discontinuously laminated composite under uniaxial stretch. The followed interface failure zone is considered as a debonding zone wherein the shear stress drops to zero when the failure criterion is met. We then adopt a stress-based criterion to characterize the condition of the interface failure instead of the energy-based criterion usually used in the interfacial fracture mechanics. The failure mode transition depends on where the maximum stress first reaches the failure point. We have revealed that the overlapping length and the interfacial elasto-plasticity influence the nonuniformity of the shear stress and the stress-transfer efficiency. There are two characteristic lengths at which strength and toughness are optimized respectively. Simultaneous optimization of the strength and toughness of nacreous composites is achieved by matching these lengths as close as possible. Since these lengths are expressed as a function of geometrical and mechanical parameters of the brick and interface, the current model in fact provides a parametric selection guideline for optimal strength and toughness of nacreous composites. This parameter selection outlines the integration of design strategies including component selection, size and arrangement tailoring of building blocks, and interface design[6]. In addition, our analytical results indicate that propagation of the interface failure can be unstable or stable when the interfacial shear stress between laminae is uniform or highly localized, respectively. A dimensionless key parameter defined by the ratio of two characteristic lengths governs the transition between the two interface-failure modes, which can explain the non-monotonic size-dependent mechanical properties observed in various laminate composites[7]. The size-dependent mechanical response in the randomly staggered laminates is also discussed. The staggering randomness is found to suppress the single-sided interface failure on the interface with short overlapping length and to promote the double-sided interface failure which significantly increases the failure strain and the work of failure. The calculated step-like stress-strain response that exhibits the feature of "graceful failure" in these randomly staggered laminates is obtained. Its formation can be roughly explained as the result of superposition of propagation of interface failure involving different overlapping lengths.

[a)] Corresponding author. Email: yni@ustc.edu.cn.

References

[1] Espinosa H. D., Rim J. E., Barthelat F. & Buehler M. J. Merger of Structure and Material in Nacre and Bone-Perspectives on de novo Biomimetic Materials. *Prog. Mater. Sci.* 54, 1059-1100, 2009.

[2] Gao H., Ji B., Jäger I. L., Arzt E. & Fratzl P., Materials Become Insensitive to Flaws at Nanoscale: Lessons from Nature. *Proc. Natl. Acad. Sci. USA* 100, 5597-5600, 2003.

[3] Das P. et al., Nacre-mimetics with Synthetic Nanoclays up to Ultrahigh Aspect Ratios. *Nat. Commun.* 6, 5967, 2015.

[4] Czél G., Pimenta S., Wisnom M. R. & Robinson P. Demonstration of Pseudo-Ductility in Unidirectional Discontinuous Carbon Fibre/Epoxy Prepreg Composites. *Compos. Sci. Technol.* 106, 110-119,2015.

[5] Sakhavand, N. & Shahsavari R. Universal Composition-Structure-Property Maps for Natural and Biomimetic Platelet-Matrix Composites and Stacked Heterostructures. *Nat. Commun.* 6, 6523, 2015.

[6] Song Z.Q., Ni Y., Peng L.M., Liang H.Y., He L.H., Optimization Design of Strong and Tough Nacreous Nanocomposites through Tuning Characteristic Lengths,. *J. Mech. Phys. Solids* 81, 41-57, 2015.

[7] Ni Y., Song Z.Q., Jiang H.Y, Yu S.H., & He L.H., Interface Failure Modes Explain Non-monotonic Size-dependent Mechanical Properties in Bioinspired Nanolaminates. submitted.

EVALUATION ON MECHANICAL PROPERTIES OF 3D FLEXIBLE MESHED GUM METAL PLATE IMPLANTS

Hitoshi Ohara[1], Kazutomo Imai[1] & Jianmei He[1]
[1]*Kogakuin University, 1-24-2, Nishi-shinjuku, Shinjuku-ku, Tokyo, 163-8677 Japan*
E-mail; am15016@ns.kogakuin.ac.jp, Tel/Fax +81-3-3340-2646

ABSTRACT

Present metal-alloy artificial bones for bone grafts like herniated intervertebral disc applications have the problems like too heavy, excessive elastic modulus and stiffness compared with natural bones. In our study, meshed gum metal plates are introduced having light-weight and high three-dimensional flexibility in order to solve such kind of problems. Different basic mesh shapes were designed using 3D-CAD tools from the viewpoints of light-weight, higher flexibility and durability. Evaluations of mechanical properties on such meshed gum metal plates were executed experimentally and analytically by comparisons with the natural bones' mechanical properties and the results are reported in this study.

Keyword: Meshed gum metal plates, Mechanical properties, 3D flexibility, Experimental and analytical approaches

INTRODUCTION

Present titanium implants for bone graft applications like hernia of intervertebral disc shown in Fig.1 have the problems like too heavy, mismatch-elasticity and excessive-strength compared with natural bones [1]-[4]. In this study, meshed gum metal plates with higher 3-dimensional flexibility [5] were interested to solve such kind of problems. Gum metal is one kind of titanium alloy with higher biocompatibility, lower elastic modulus and excellent elastic deformability [6].



Fig.1 Fixation methods on spine for hernia of intervertebral disks using titanium implants

Fundamental mesh shapes were designed using three dimensional CAD tool from the light-weight, higher flexibility and longer life viewpoints. Based on the designed mesh shapes, sample specimens of the meshed titanium plates having different plate thickness and line-up patterns were manufactured through the laser beam machining. Mechanical properties of sample manufactured meshed titanium plate specimens like volume density, tensile and compressional elasticity and bending stiffness were experimentally evaluated. On the other hand, analytical approaches on mechanical properties of meshed titanium plates are also carried out using ANSYS finite element analysis code. Comparisons between experimental and analytical results are used to validate the analytical approach method.

BASIC MESH SHAPE DESIGN FOR MESHED GUM METAL PLATE APPLICATION

Design concepts of basic mash shapes

Basic mesh shape designs are carried out under the following design conceptions.

(1) Single fundamental mesh shape construction for simplification of manufacturing processing and cost-down purpose
(2) Higher three-dimensional flexibilities including expansion/contraction, bending and torsion for possibility of handily shape changes during surgery
(3) Uniform mesh line width and non-angle smooth shape desired to decrease stress concentrations and lead for higher strengths and longer operating life
(4) Ensured optional spaces for screw fixation

Meshed plates with different basic mesh shapes for sample experimental investigations

3-dimensional meshed plate models using the designed basic mesh shapes with 1.0 mm mesh line widths are obtained and CAD models for sample meshed gum metal plates are shown in Fig.2 with the specimen size.



120° axisymmetric specimen 90° axisymmetric specimen 60° axisymmetric specimen

Fig.2 Meshed plate shape models for sample specimen evaluations

[a] Corresponding author. Email: am15016@ns.kogakuin.ac.jp

EVALUATION ON MECHANICAL PROPERTIES OF SAMPLE MESHED GUM METAL PLATES

Tensile, compressional and bending property characteristics of sample meshed gum metal plates

Based on the mesh shapes shown in Fig.2, sample meshed gum metal plates with 1.0 mm thickness are fabricated by laser cutting process for experimental evaluations and specimen photos are shown in Fig.3. Based on JIS Z 2241, JIS K 7076 and JIS Z 2248 [7], tensile, compression and bending experiments are executed for mechanical property evaluation of these sample meshed gum metal plates. Table 1 shows the experimental results of mechanical properties of sample meshed gum metal plates.

Table 1 Experimental results of mechanical properties of sample meshed gum metal plates

Mechanical properties	Elastic stiffness			Approximated elastic modulus [MPa]			Volume density [kg/mm^3]		
	120°	90°	60°	120°	90°	60°	120°	90°	60°
Tensile [N/mm]	483.0	204.0	191.6	1067.4	409.0	394.3	2.35	3.13	2.92
Compression[N/mm]	645.0	527.0	455.3	1823	1183	1062			
Bending[N・mm^2]	10734.5	13189.8	9373.2						

Analytical approaches on mechanical property evaluation of sample meshed gum metal plates

Analytical approaches on mechanical properties of meshed gum metal plates are carried out here using 3D Solidworks CAD software and ANSYS finite element analysis code. 3D meshed plate models with the same shapes and sizes of specimens on experimental evaluations are modeled as shown in Fig.4 and material properties of gum metal plate shown in Table 2 are used for analytical inputs.

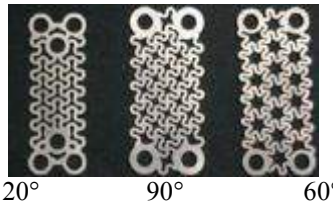

Fig.3 Meshed gum metal Specimens

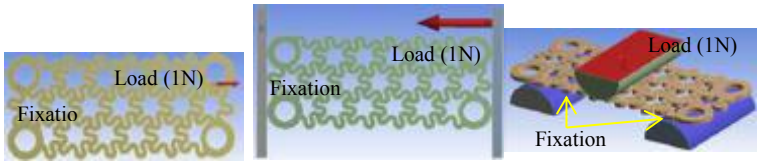

Fig.4 3D model of tensile, compression and bending tests

Table 2 Material property input for analysis

Material	Elastic modulus (GPa)	Poison's ratio	Density (kg/mm^3)
Gum metal	75.0	0.32	5.6

Table 2 Analytical results of mechanical properties of sample meshed gum metal plates

Mechanical properties	Elastic stiffness [N/mm]			Approximated elastic modulus [MPa]			Deviation from experimental results [%]		
	120°	90°	60°	120°	90°	60°	120°	90°	60°
Tensile [N/mm]	370.9	195.8	175.6	1048.5	439.4	409.7	-0.99	-0.48	-1.81
Compression [N/mm]	624.0	506.5	449.63	1764.1	1136.7	1049.0	3.36	4.05	1.26
Bending [N・mm^2]	8707.4	12122.8	8458.6				-2.30	-0.85	-4.73

CONCLUSIONS

Tensile, compression and bending properties of sample meshed gum metal plate specimens were experimentally and analytically evaluated with designed basic mesh shapes under light-weight, high flexibility and durability viewpoints. From the experimental and analytical approaches, the following conclusions are obtained.

(1) Experimental results indicated first that volume densities of the meshed gum metal plates can be controlled to close to natural bone's densities.

(2) From three basic mesh shapes, 60° axisymmetric specimen shows the most flexibility from tensile, compression and bending performances.

(3) Analytical approach methods for mechanical property evaluations are introduced and the comparisons between experimental and analytical results indicate that analytical approach method is valid.

References

[1] Satoh K., Murata J., Tomioka M., Seino Y., Yokota M., Mizuki H., Miura H.(2011), Postsurgical stability following sagittal split ramus osteotomy with biodegradable Poly-L-lactide bone mini plate fixation, Dental journal of Iwate Medical University, Vol.36, No.1, pp.46-52 (in Japanese).

[2] Wakui D., Nagashima G., Ueda T., Takada T., Tanaka Y., Hashimoto T. (2012), Three Cases of Scalp Rupture and Cosmetic Deformity caused by a Fixation Plate after Craniotomy, Japanese journal of neurosurgery, Vol. 21, No. 2, pp.138~142 (in Japanese).

[3] Seki Y., Bessho K., Sugatani T., Kageyama T., Inui M., Tagawa T.(1994), Clinicopathological study on titanium miniplates, Japanese Journal of Oral and Maxillofacial Surgery, Vol.40, pp.892-896 (in Japanese).

[4] Stryker Japan K.K., Meshed Plate (Approved documents of medical instruments), URL: http://www.info.pmda.go.jp/downfiles/md/pdf/730093_16200BZY01088000_A_LB_06.pdf, access on 16th Jan. 2014.

[5] Abiko R., Zama K., Sinoda T., Suzuki S., He J. (2011), A Primary Study on the Titanium mesh plate Structures for Reinforcement of Tricalcium Phosphate Bone Implants, International Conference on Advanced Technology in Experimental Mechanics 2011 (ATEM'11, 2011), Kobe, Japan.

[6] Introduction of GUM METAL, http://www.nissey-sabae.co.jp/wp/wp-content/uploads/gummetal.pdf

[7] Japanese Industrial Standards JIS Z 2241 (1952), JIS Z 2248 (1952), JIS K 7076 (1991)

DEVELOPMENT AND PRELIMINARY VALIDATION OF A 5th PERCENTILE FEMALE PEDESTRIAN FINITE ELEMENT MODEL

Wansoo Pak[1], Costin D. Untaroiu[1]
[1]*Department of Biomedical Engineering and Mechanics, Virginia Tech, Blacksburg, Virginia, USA*

Summary Pedestrians represent one of the most vulnerable road users. Impact simulations using finite element (FE) pedestrian models could help to better understand the injuries recorded in pedestrian accidents and design pedestrian-friendly vehicles. A high biofidelity finite element pedestrian model corresponding to anthropometry of a 5th percentile female (F05) in standing posture was developed and preliminarily validated in this study. The model was validated at component level and then verified in a car-to-pedestrian simulation. Overall, the model showed promising results and a good capability to predict the injury risk of the pedestrian during lateral car impact.

INTRODUCTION

Pedestrians represent one of the most vulnerable road users and comprise nearly 22 percent of the road crash related fatalities in the world [1]. Therefore, protection of pedestrians in car-to-pedestrian collisions (CPC) has recently generated increased attention with vehicle regulations (in Europe, Asia, and recently US) which involve three subsystem tests for adult pedestrian protection (leg, thigh and head impact tests). In addition to these physical tests, the development of finite element pedestrian models could be a complementary alternative that characterizes the pedestrian's whole-body response during CPC impact and assesses more specifically the risk of pedestrian injuries.

The primary goal of this study was to develop and preliminarily validate a finite element model corresponding to a 5th percentile female anthropometry. This new pedestrian FE model could be useful to evaluate pedestrian injuries in lateral vehicle accident.

METHODS

The mesh of pedestrian finite element model have been developed by morphing the mesh of a 50th percentile male pedestrian FE model [2] on the scanned surface of a 5th percentile female having 149.9 cm height and 48.6 kg weight [3]. The material properties were defined as the same material properties of 50th percentile male FE model. To validate the FE model at a component level, impact simulations were performed on knee joint, lower extremity and upper body based on literature data [4-6]. Simulation setups for each impact test were modelled and implemented in the FE software (LS-Dyna, LSTC, Livermore, CA). The lower extremity was impacted by a 6.25 kg impactor under the knee joint in the shearing test and near the ankle bone for the bending test (Figure 1. a). Upper body validations were also performed by impact simulations to the abdomen, pelvis and thorax. Then, the whole body FE model was verified in a CPC simulation (Figure 1. b) [7]. The kinematic trajectories of head's centre of gravity (CG), first thoracic vertebra (T1) and sacrum relative to the car were recorded in a CPC simulation and compared to the Post Mortem Human Surrogate (PMHS) test data.

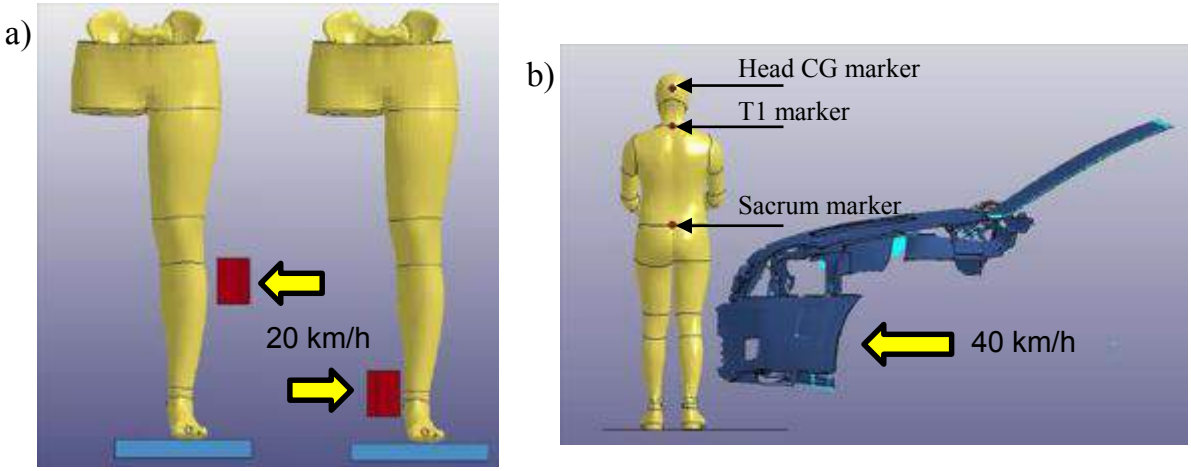

Figure 1. Schematic simulation setups of a) lower extremity and b) full body validation.

[a] Corresponding author. Email: wspak@vt.edu.

RESULTS AND DISCUSSION

Overall, the model showed promising results and a good capability to predict the injury risk of pedestrians during lateral car impact. Due to the lack of PMHS data for 5th percentile female, the impact responses of the pedestrian model were compared to scaled test corridors corresponding to 50th percentile male. Therefore, the force time histories predicted by the FE model were usually close to the lower boundaries of test corridors (Figure 2. a). Similarly, the trajectory of F05 head CG, obtained from the CPC simulation, was close to the trajectories recorded on shorter PMHS (Figure 2. b). In terms of injury predictions, the model predicted initial MCL/ACL ruptures in the right knee (the first one impacted by the car) followed by LCL/ACL ruptures in the left knee. These types of injuries were observed in the PMHS impacted in CPC tests. Future work will be focused on improving the model's responses and on adding more details to the current model.

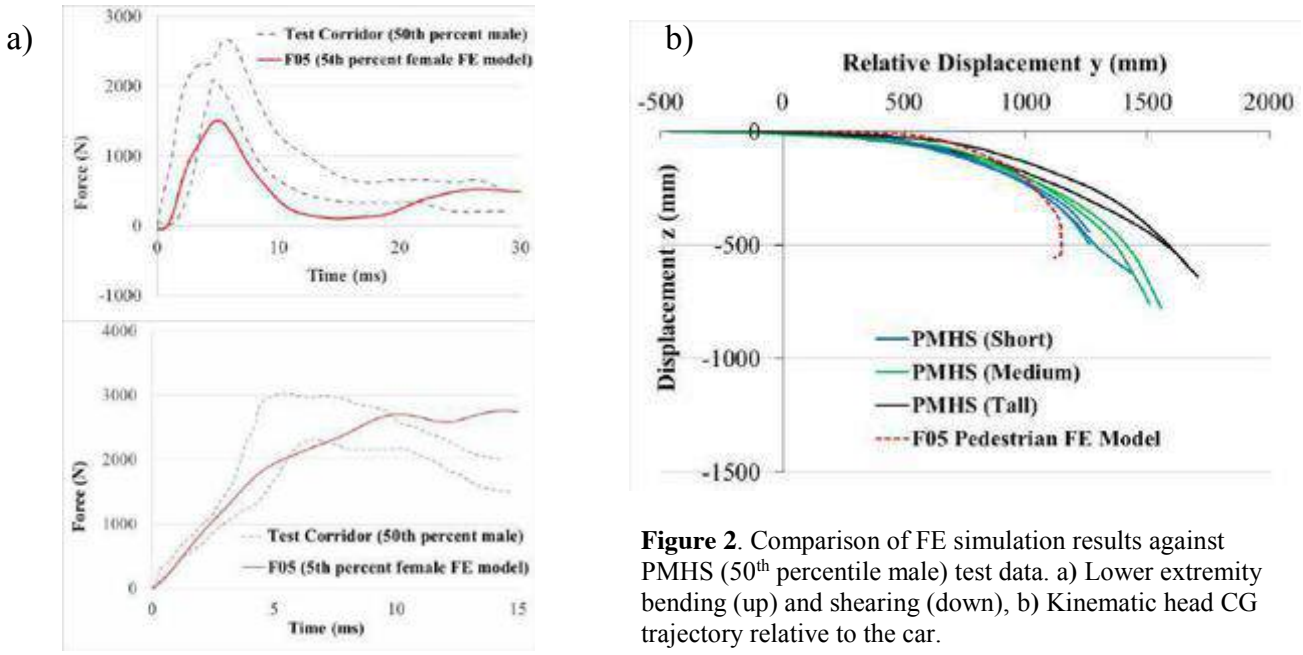

Figure 2. Comparison of FE simulation results against PMHS (50th percentile male) test data. a) Lower extremity bending (up) and shearing (down), b) Kinematic head CG trajectory relative to the car.

CONCLUSIONS

A 5th percentile female pedestrian finite element model was developed and preliminarily validated in this study. The model showed relatively accurate results against PMHS test data recorded in components and CPC tests. Generally, the validated pedestrian model will be used by safety researchers in the design of front ends of new vehicles in order to increase pedestrian protection.

ACKNOWLEDGEMENT

This study was funded by the Global Human Body Models Consortium (GHBMC).

References

[1] (2013). *Pedestrian safety: a road safety manual for decision makers and practitioners*. Available: http://apps.who.int/iris/bitstream/10665/79753/1/9789241505352_eng.pdf?ua=1

[2] C. D. P. Untaroiu, J.B.; Schap, J.; Davis; Gayzik, F.S., "Development and preliminary validation of a 50th percentile finite elemnt model," presented at the ASME IDETC conference, Buffalo, NY, USA, 2015.

[3] M. L. Davis, B. C. Allen, C. P. Geer, J. D. Stitzel, and F. S. Gayzik, "A Multi-Modality Image Set for the Development of a 5th Percentile Female Finite Element Model," *IRCOBI Conference*, 2014.

[4] D. Bose, K. S. Bhalla, C. D. Untaroiu, B. J. Ivarsson, J. R. Crandall, and S. Hurwitz, "Injury tolerance and moment response of the knee joint to combined valgus bending and shear loading," *J Biomech Eng*, vol. 130, p. 031008, Jun 2008.

[5] J. Kajzer, G. Schroeder, H. I. a. Y. Matsui, and U. Bosch, "Shearing and bending effects at the knee join at high speed lateral loading," *Society of Automotive Engineers*, 1997.

[6] D. C. Viano, "Biomechanical responses and injuries in blunt lateral impact."

[7] J. R. Kerrigan, J. R. Crandall, and B. Deng, "Pedestrian Kinematic Response to Mid-sized Vehicle Impact," *International Journal of Vehicle Safety*, vol. 2, 2007.

MODELING AVASCULAR TUMOR GROWTH VIA LINEAR ELASTICITY

Ariel Ramírez Torres[1], Fernando Valdés Ravelo[2], Reinaldo Rodríguez Ramos*[3],
Julián Bravo Castillero[3], Raúl Guinovart Díaz[3], and Federico J. Sabina[4]
[1]*Centro de Estudios Matemáticos (CEMAT), Instituto Superior Politécnico "José Antonio Echeverría" (ISPJAE), Marianao, Havana, Cuba.*
[2]*Centro de Inmunología Molecular (CIM), Playa, Havana, Cuba.*
[3]*Departamento de Matemáticas, Facultad de Matemática y Computación, Universidad de La Habana, Vedado, Havana, Cuba.*
[4]*Instituto de Investigaciones en Matemáticas Aplicadas y en Sistemas, Universidad Nacional Autónoma de México, Delegación de Álvaro Obregón, D.F., México.*

Summary Cancer represents one the most challenging problems in medicine and biology nowadays. Recently, it has been shown that stresses affect tumor patho-physiology. In fact, we believe that a better understanding of the state of stress present in growing tumors is needed to develop new therapies and further improvement in treatments. This work represents an extension of the study made by Ngwa and Agyngi 2012 [3] in three major aspects: the introduction of anisotropic growth, the construction of a growth law depending of the stress levels and the effect of the parameters representing these contributions in stress and growth.

BACKGROUND

Tumor growth involves the generation of mechanical forces both within the tumor and between the tumor and the host tissue. These mechanical forces, coupled with neovascularization, induce abnormal solid and fluid stresses that facilitate tumor progression and hinder response to various treatments (Jain et al. 2014 [2]). In the way of looking for a solution, mathematical models arise as a tool in order to understand this phenomenon. In particular, some works are focused on the macroscopic scale using a mechanical approach. For example, Araujo and McElwain 2005 [1] and Ngwa and Agyngi 2012 [3], assumed a constitutive equation from linear elasticity theory in order to relate growth with deformation. The present paper is based on a previously reported simpler model by Ngwa and Agyngi 2012 [3], where the authors modeled the evolution of growth-induced stresses in an spherical growing tumor surrounded by an external medium and exhibiting isotropic properties. Following their analysis, we extend the model by incorporating the effect of anisotropic growth and an improved growth law depending on stresses. Furthermore, it is explored the effect of the parameters representing anisotropy and growth-stress dependence, in the tumor evolution.

MODEL FORMULATION

In the following, we assume that tumor cells form a homogeneous population which is considered as a continuum; moreover, the tumor is modeled as a sphere and its spherical symmetry is maintained at all times; in particular, the tumor material is supposed incompressible and responds to stress in a purely elastic and isotropic form. Furthermore, the nutrient concentration variation is determined by nutrient diffusion through the tumor boundary and its consumption by tumor cells in the interior. Additionally, there is a constant nutrient concentration in the tumor boundary and it is assumed the existence of an elastic, isotropic and incompressible external medium. Now, according to Araujo and McElwain 2005 [1], linear elasticity models which just consider isotropic growth are insufficient to describe the stresses evolution in a growing tissue, because it does not reflects the stresses relaxation effect. In this sense, we incorporate the effect of anisotropic growth to the model proposed by Ngwa and Agyngi 2012 [3] following the ideas of Araujo and McElwain 2005 [1]. Specifically,

$$e_{ij} = g(\delta_{1i}\gamma_r + (\delta_{2i} + \delta_{3i})\gamma_\theta)\delta_{ij} + \frac{1+\nu}{E}\sigma_{ij} - \frac{\nu}{E}\delta_{ij}\sigma_{kk}, \text{ with } i,j,k = r,\theta,\phi, \tag{1}$$

where e_{ij} represents the material strain, δ_{ij} is the Kronecker delta, σ_{ij} denotes the Cauchy stress tensor, ν is the Poisson ratio, E the Young modulus, g is the growing factor and the constants $\gamma_r, \gamma_\theta \in \mathbb{R}^*_+$ with the constraint $\gamma_r + 2\gamma_\theta = 1$, promote the anisotropic behavior. Now, like it was mentioned above, from a mechanical point of view, the stresses are a determining factor in the regulation of cellular proliferation and death. In this sense, we propose the following law

$$\frac{\partial \rho}{\partial t} + \nabla \cdot (\boldsymbol{v}\rho) = \alpha c \rho (1 + \eta_1 tr(\boldsymbol{\sigma})) - k\rho(1 - \eta_2 tr(\boldsymbol{\sigma})), \tag{2}$$

where $\boldsymbol{v}$ is the tumor cell displacement velocity, ρ is the cell density, c symbolizes the nutrient concentration, α and k are positive numbers representing proliferation and death rates, respectively and $\eta_1, \eta_2 \in \mathbb{R}_+$ are constants representing the dependence of cellular proliferation and death from stresses. The positive sign in η_1 is for that in the presence of compressive stresses (negative stresses) the cellular division is inhibited, and the negative sign of η_2 means that compressive forces promote cellular death. In particular, we take η_2 depending on η_1.

*Corresponding author. Email: reinaldo@matcom.uh.cu

Mathematical model

To summarize, the dimensionless model equations are given by

$$\frac{dR(r,t)}{dt} = v_r(R,t), \tag{3}$$

$$\frac{\partial v_r}{\partial r}(r,t) = \frac{R\sinh(r)}{r\sinh(R)}[1+\eta_1 E(3\sigma_{rr}(r,t)-2\beta(r,t))] - \epsilon[1+\eta_2 E(2\beta(r,t)-3\sigma_{rr}(r,t))] - 2\frac{v_r(r,t)}{r}, \tag{4}$$

$$\frac{\partial \sigma_{rr}}{\partial r}(r,t) = -\frac{2\beta}{r}, \tag{5}$$

$$\left(\frac{\partial}{\partial t} + v_r(r,t)\frac{\partial}{\partial r}\right)\beta(r,t) = 2\gamma_\theta\left(\frac{R\sinh(r)}{r\sinh(R)}[1+\eta_1 E(3\sigma_{rr}(r,t)-2\beta(r,t))] - \epsilon\left[1+\eta_2 E(2\beta(r,t)-3\sigma_{rr}(r,t))\right]\right) + + \frac{\partial v_r(r,t)}{\partial r}, \tag{6}$$

where $r \in [0,R)$, $t \in \mathbb{R}_+^*$, R is the tumor radius, v_r is the radial component of $\boldsymbol{v}$ and $\beta = \sigma_{rr} - \sigma_{\theta\theta}$.

RESULTS

In the following, it is shown the relevance of the new parameters γ_θ (contributes to the anisotropy) and η_1 (contributes to the growth-stress dependence) in the solutions of the mathematical model.

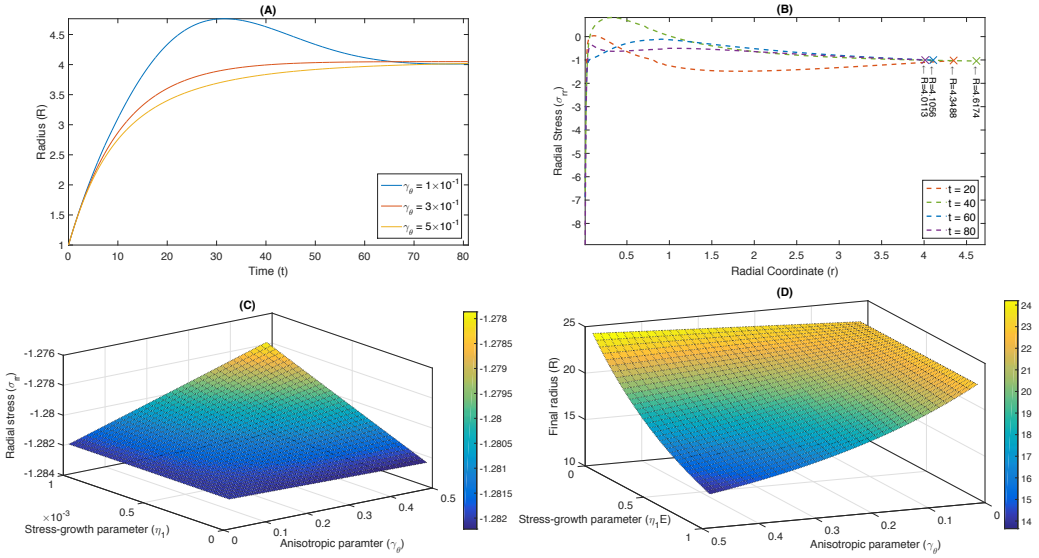

Figure 1: Influence of the anisotropy parameter in the growth pattern (A). Radial stress distribution at different time instants for the radius associated to $\gamma_\theta = 0.1$ (B). Dependence of the final radial stress on parameters γ_θ and η_1 (C). Dependence of the final tumor radius on parameters γ_θ and $\eta_1 E$ (D).

ACKNOWLEDGEMENTS

Ariel Ramírez Torres gratefully acknowledges the Program of Postdoctoral Scholarships from UNAM, Mexico.

CONCLUSIONS

The presented model is considered an extension of the work of Ngwa and Agyngi 2012 [3]. With the considerations of anisotropic growth and the dependence of the growth from the stresses. Given the fact that the actual treatment situation still needs to develop. A systematic theoretical study of mathematical models modeling tumor growth will contribute to the generation of new approaches for cancer diagnosis and therapies.

References

[1] Araujo, R.P., McElwain, D.L.S.: The nature of the stresses induced during tissue growth. Appl. Math. Lett. 18:1081-1088, 2005.

[2] Jain, R. K., Martin, J. D., Stylianopoulos, T.: The role of mechanical forces in tumor growth and therapy. Annu. Rev. Biomed. Eng. 16:321346, 2014.

[3] Ngwa, M., Agyngi, E.: Effect of an External Medium on Tumor Growth-induced Strees. IAENG Int. J. Appl. Math. 42:4, 2012.

LOADING-RATE DEPENDENT MECHANICAL RESPONSE OF THE HUMAN AND PORCINE KNEE JOINTS

Marcel Rodriguez[a)], LePing Li
Department of Mechanical and Manufacturing Engineering, University of Calgary, Calgary, Alberta, Canada

Summary The knee joints are subjected to changing loads during daily activities. The understanding of loading mechanisms within the joint may contribute to the prevention, diagnosis, and treatment of injury and disease. The load response of soft tissues, cartilages and menisci, depends on the loading-rate, showing different levels of fluid pressure load support at different loading rates. This response has been investigated with tissue discs, but not sufficiently examined within the entire joint. Computational simulation is an effective tool for studying this response, taking into account realistic contact conditions. The objective of the present study is to quantify the compression-rate dependence in the knee joint, which is thought to be mainly contributed by the fluid pressurization in the tissues. Computer simulations are being validated against laboratory tests. Results revealed a similar nonlinear compressive loading-rate-dependent mechanical response of the human and porcine knee joints.

INTRODUCTION

The knowledge of joint mechanics is essential for understanding the mechanism of joint injury and disease. Applications of this knowledge include joint reconstruction and replacement. The load response of articular cartilage is compression rate dependent. For a given compression magnitude, the reaction force is substantially greater if the compression is applied at a greater rate. This response is well known in cartilage disk, but has not been sufficiently investigated for the complex geometry of the whole joint. Knee joint modeling represents a challenging process due to the geometric, kinematic, material and contact issues involved in the process. The finite element method has allowed the development of several knee joint models for biomechanical applications with different levels of complexity [1,2]. The commercial software ABAQUS (Simulia Inc., Providence, RI, USA) is widely used for 3D finite element modeling allowing a realistic joint geometry, whose influence on the joint contact mechanics is undeniable. Models have been developed for studying consequences of injuries or defects in the knee, surgical procedure, healthy and osteoarthritic knee. The objective of this study is to quantify the compressive loading-rate dependent mechanical behavior of the knee joint and the creep and relaxation of the joint with the dissipation of the fluid pressure in the joint. Our interest is the poromechanical response of the human knee joint, but as porcine joints have anatomy similarities and are easily available, they have been used for testing. Human knee joint compression will be obtained with dual fluoroscopy.

MATERIALS AND METHODS

Two approaches were followed on this research: computational simulations and mechanical tests. For simulations, the knee joint geometry was obtained from a healthy male subject using MRI techniques and converted to a computational model. The commercial software ABAQUS was employed in a poromechanical analysis subjected to large deformation at several compression rates. Mechanical tests were performed on a 858 Mini Bionix® II Biomaterial Testing System (MTS, Minnesota, USA), with a 10 kN force transducer (MTS-661.19F-02). Fresh porcine stifle joints with intact joint capsules were purchased within 24 hours of slaughter. The ankle joint was mostly retained to keep the tibia and fibula together. The top of the femur and the bottom of the tibia and fibula were fixed in hollow metal cylinders with dental cement (Fastray™ LC, Bosworth). The natural angle of the joint (~ 40º) was kept with cementing. Sample preconditioning was done to ensure a repeatable reference state [3]. An 800-µm ramp compression was applied at several rates followed by a 1200 seconds relaxation period. In other tests, 200 N of compression was applied followed by 2000 seconds of creep. Tissue hydration was ensured by keeping wet gauzes covering the joint.

RESULTS

For computational results, the reaction force is plotted against joint compression (Figure 1). The maximum reaction force for the fastest compression is about ten times that of static compression. These results show a remarkable rate dependence as well as nonlinear behavior, particularly for the faster compressions. This is because the fluid tends to be trapped in the tissues to form a higher fluid pressure, as compression rate becomes higher. This effect makes that peak force attain an asymptotic value when the rate of compression is sufficiently high (Figure 2, results from Figure 1). In the case of laboratory tests, the peak reaction force for the fastest compression is about 1.5 times that of the slowest compression (~75N @ 10 µm/s and ~125 N @ 2000 µm/s, Figure 3). Note that very slow compressions were not tested because the force transducer does not have high enough resolution for slow, small force measurements. After the loading phase, fluid exudation makes the reaction force decrease until equilibrium is reached. The fluid pressure in cartilage and menisci caused a difference between peak and equilibrium load (no more fluid flow), evidencing the role of fluid load support in the

[a)] Corresponding author. Email: mlrodrig@ucalgary.ca

mechanical response of the knee under compression. The repeatability of laboratory tests and the influence of the test sequence were also verified, obtaining less than 5 % of fluctuations in both cases. For creep tests, the equilibrium should be reached when fluid exudation stops, and the compression approaches a constant value (Figure 4). However, we obviously need longer time to observe the equilibrium in our case.

DISCUSSION

Preliminary results revealed the feasibility of using a geometrically accurate model for large deformations. A significant nonlinear compression rate and load rate dependent load response for laboratory tests is also noticed. Fluid pressurization plays an important role in the load support of knee joint as shown in both computational simulations and laboratory tests. The differences between the peak and equilibrium loads are contributed by the fluid pressure within the tissues. In our case, the fluid pressure supports 60-70% of the total loading in most pig knee joints for a fast compression. The mechanical response of the knee joint is also influenced by the geometry of contacting areas and the interplay between tissues on the load support, as up to 90% fluid pressure load support was found in a cartilage disk and this is also seen in the human knee joint simulation.

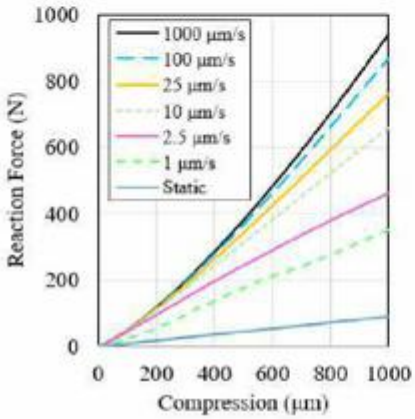

Figure 1. Human joint simulation results, loading phase.

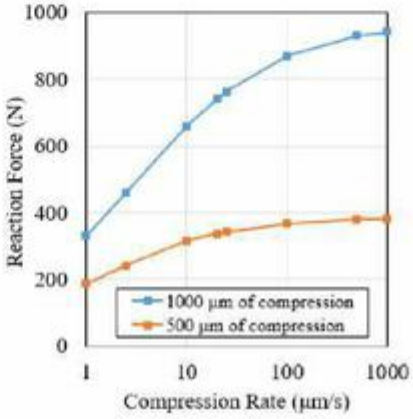

Figure 2. Reaction force vs. compression rate.

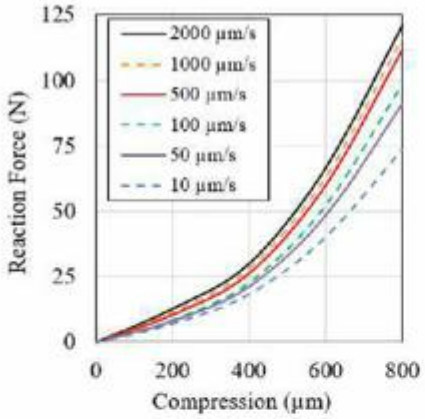

Figure 3. Porcine joint test results, loading phase.

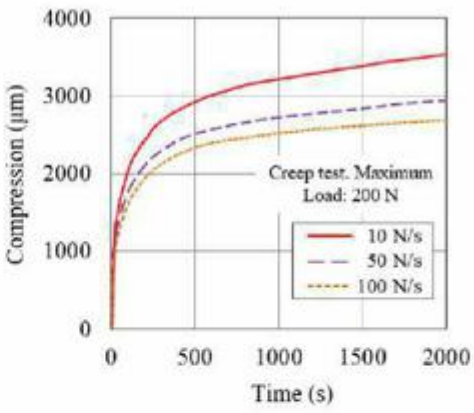

Figure 4. Porcine joint test results, creep response.

References

[1] Halonen K., Mononen M., Jurvelin J., Töyräs J., Salo J., Korhonen R.: Deformation of articular cartilage during static loading of a knee joint - Experimental and finite element analysis. *J Biomech*. 2014;47(10):2467-2474.

[2] Kazemi M., Li LP, Savard P, Buschmann M.D.: Creep behavior of the intact and meniscectomy knee joints. *J Mech Behav Biomed Mater*. 2011;4(7):1351-1358.

[3] Cheng S, Clarke EC, Bilston LE.: The effects of preconditioning strain on measured tissue properties. *J Biomech*. 2009;42(9):1360-1362.

SPATIAL NON-UNIFORMITY IN THE YOUNG'S MODULUS OF THE HUMAN EARDRUM

S. Alireza Rohani[1a)], Soroush Ghomashchi[2], Sumit K. Agrawal[3] & Hanif M. Ladak[1, 2, 3]
[1]*Biomedical Engineering, Western University, London, Ontario, Canada*
[2]*Medical Biophysics, Western University, London, Ontario, Canada*
[3]*Otolaryngology - Head & Neck Surgery, Western University, London, Ontario, Canada*

Summary The eardrum plays an important role in transferring sound energy to the cochlea. Several recent studies have used inverse finite element (FE) methods to estimate the mechanical properties of the eardrum. However, the non-uniformity of the mechanical properties over the surface of the eardrum has not yet been reported. Our objective was to develop an approach to investigate the spatial non-uniformity of the Young's modulus (E) of the eardrum. In this work, the shape of the eardrum before and after pressurization was imaged and compared with FE model simulations for optimization purposes. A modified Nelder-Mead optimization technique was used in this study. The effects of two types of eardrum partitioning on the optimization were studied and compared. Results showed that partitioning of the eardrum into 4 quadrants produces a closer match between simulated and experimentally measured deformations compared with the assumption of uniformity or with partitioning into concentric regions.

INTRODUCTION

The eardrum has a significant role in hearing. Sound in the environment is collected by the auricle (outer visible part of the ear) and is focused down the ear canal where it vibrates the eardrum, a thin conical membrane. Vibration of the eardrum causes a chain of three tiny bones (malleus, incus and stapes) to vibrate and transfer the sound energy to the inner ear, specifically the cochlea, where mechanical vibrations of the cochlear fluids are transduced to sensorineural signals for processing and perception. Common hearing tests, such as tympanometry, involve measurement of the acoustic properties of the air in the ear canal under specific conditions including both static pressurization and dynamic acoustic stimulation. Finite element (FE) modelling of these tests could potentially improve the diagnosis and treatment of hearing diseases[1].

Accurate values for the mechanical properties of the eardrum are crucial for FE modelling. For physiological sound pressure levels, a linear elastic material model characterized by the Young's modulus (E) can be used. In current models, it is assumed that E is either constant over the eardrum's surface or E changes concentrically over the surface. The objective of this work is to develop and evaluate an approach to estimate the spatial non-uniformity in Young's modulus of the human eardrum with the aim of improving the accuracy of FE models.

MATERIALS AND METHODS

Previously, we introduced an *in situ* estimation technique in which an FE model was optimized to match experimental data acquired during eardrum pressurization in a rat model[2]. We have adapted this approach and applied it to a freshly frozen cadaveric human ear. The middle-ear cavity was pressurized to 500 Pa and the deformed shape of the eardrum after pressurization was imaged using a Fourier transform profilometer (FTP). To simulate the pressurization experiment, a specimen-specific FE model of the eardrum at rest was defined from a 3D micro-computed tomography (micro-CT) image (Figure 1a). E was then estimated using Nelder-Mead optimization, by minimising the cost function comparing the deformed FE model shape to the measured shape after pressurization. The cost function is based on the differences in measured and simulated eardrum height values (Z) relative to the XY-plane defined by the plane of the eardrum boundary at multiple points over the eardrum. Figure 2 shows a schematic representation of the optimization technique.

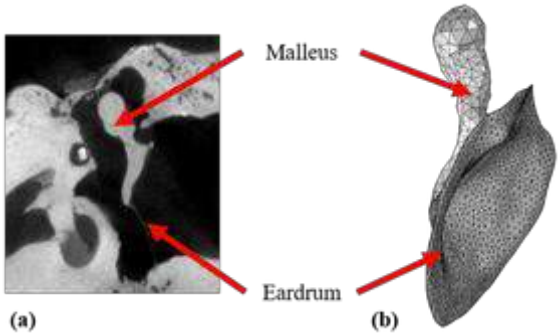

Figure 1 – Imaging and modeling of the eardrum. **(a)** 3D micro-CT image of human middle ear. **(b)** FE mesh of the eardrum and malleus.

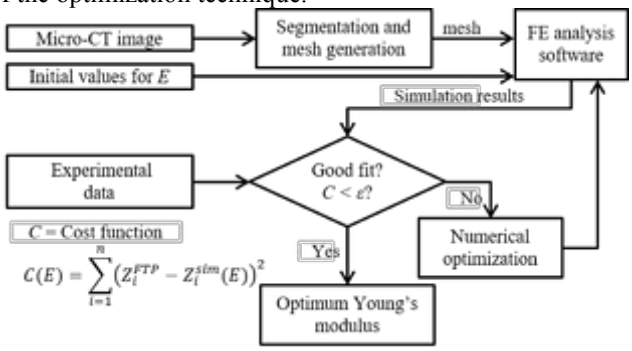

Figure 2 – Flowchart of the estimation algorithm. C is the cost function to be minimized in which Z_i^{FTP} and Z_i^{sim} denote the measured and simulated Z coordinates, respectively, for point i.

[a)] Corresponding author. Email: srohani4@uwo.ca.

In this work, we assumed a uniform thickness of 110 um for the eardrum. The eardrum was modelled using triangular shell elements, and the malleus was modelled using tetrahedral solid elements. All FE modelling was performed in COMSOL Multiphysics® (Version 5.1) and optimizations were performed in MATLAB® (Release 2015a). In order to investigate the spatial non-uniformity of E over the surface of the eardrum, results from two types of partitioning of the eardrum were compared with results from the uniform E assumption. The two types of partitioning considered in this study included dividing the eardrum into 4 quadrants or into 4 concentric regions; the values of E were permitted to vary from quadrant to quadrant or from region to region when performing optimization, thus simulating non-uniformity.

RESULTS

Optimal E values for this specimen were obtained under the asumption of a single uniform E value and the two types of partitioning and are summarized in Table 1. Figures 3a-c show the difference (i.e., error) between the simulated and measured shapes at a pressure of 500 Pa when using the optimal E values for the simulations.

Table 1 – E estimates for each partitioning type. E_PI, E_PS, E_AI and E_AS are the values of E in each quadrant shown in Figure 3b. Similarly, E_1, E_2, E_3 and E_4 are E values in each concentric region shown in Figure 3c.

	Partitioning Type				
	Single	**Quadrants**		**Concentric**	
E (MPa)	5.39	E_PI	9.7	E_1	16.5
		E_PS	5.4	E_2	6.7
		E_AI	2.4	E_3	3.6
		E_AS	4.3	E_4	3.5
Cost Function	0.96	0.79		0.89	

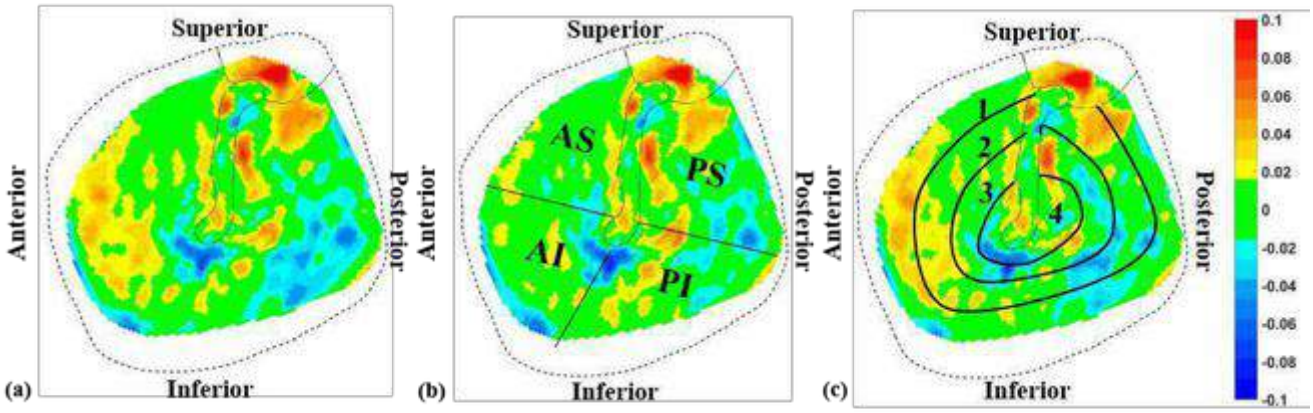

Figure 3 – Error maps between simulated and measured shape at a pressure of 500 Pa with simulations done using optimal E values from Table 1. Dotted line represents the boundary of the entire eardrum obtained from micro-CT image. Colored areas are regions within the field of view of the FTP apparatus. Simulations were performed under the following assumptions: **(a)** uniform mechanical properties, **(b)** properties varying over 4 quadrants, and **(c)** properties varying over 4 concentric regions.

DISCUSSION AND CONCLUSION

Estimation of E using a pressurization technique has the advantage of being non-destructive and is easier to model compared with tensile testing on eardrum strips or indentation testing. Results from the single-E assumption are comparable to recent literature using indentation techniques[3]. The cost function decreases by 18% after partitioning into 4 quadrants, while the reduction was only 7% with concentric region partitioning. Therefore, partitioning of the eardrum into four quadrants and allowing E to vary from quadrant to quadrant improves the match between simulated and measured deformations.

References

[1] Daniel S. et al.: Clinical Application of a Finite-Element Model of the Human Middle Ear. *J. Otolaryngology* 30(6):340-345, 2001.

[2] Ghadarghadar N. et al.: Estimation of the Quasi-Static Young's Modulus of the Eardrum Using a Pressurization Technique." *Comput Meth Prog Bio* 110(3):231-239, 2013.

[3] Aernouts J. et al.: Mechanical Properties of Human Tympanic Membrane in the Quasi-Static Regime From *in situ* Point Indentation Measurements. *Hearing Res* 290(1):45-54, 2012.

SMALL STRAIN GROWTH AND THE HUMAN NAIL

Kostas P. Soldatos[1a)]
[1]*School of Mathematical Sciences, University of Nottingham, Nottingham, NG7 2RD, UK*

Summary The nail apparatus comprises the living soft tissue nail matrix and the hard, dead tissue nail plate. This paper models the nail matrix germinal activity by combining the constitutive equations of hyper-elastic mass-growth detailed in [1] with the concept of incompressible, small strain growth. Full details of the outlined modelling and analytical development have just appeared in [2], where details are also provided of the manner in which the obtained analytical solution forms the basic approximation of its slight or moderately incompressible mass-growth counterpart.

INTRODUCTION

The nail apparatus comprises the soft nail matrix and the hard nail plate (e.g., [3]). The first of those plate-like structures is made of living soft tissue that grows and causes elongation of the nail by pushing forward the second, partially visible nail plate. The latter is made of hard, dead tissue which is unable to grow and is mainly produced, and added to the nail plate by germinal activity of the matrix. Nevertheless, the living germinal matrix is confined within physical boundaries which have seemingly no reason and/or ability to deform substantially.

The nail plate is formed by layers of identical keratinous material, which are compacted together. This fact is here perceived as evidence of temporary interruption in the nail elongation process, which thus seems to be periodic rather than continuous in time. The occasional appearance of the so-called Beau's lines (e.g., [4]) is also interpreted as clinical evidence of the nail ability to grow in a discontinuous manner.

These observations support the feeling that the implied "push forward" mechanism is activated periodically, at specific time instances, when the small strain accumulated within the nail matrix enables the stress state at the soft-hard tissue interface to reach some critical intensity level, $\boldsymbol{\sigma}^{cr}$. The latter negates the resultant of all frictions met at the edges and lateral supports of the hard nail plate. It is thus considered either experimentally or theoretically measurable and, therefore, known. When reached within the nail matrix, it enables the latter to push the nail plate forward, and add fresh keratinous tissue into it.

This paper models the nail matrix germinal activity by combining the constitutive equations of hyper-elastic mass-growth developed in [1] with the concepts of small strain growth and incompressible mass-growth. The efficiency of the model is tested in an example application, which leads to an exact analytical solution of the obtained governing differential equations. Full details of the outlined modelling and analysis are available in [2], where details are also provided of the manner in which slight or moderately incompressible mass growth can be treated.

MATHEMATICAL MODEL AND BASIC EQUATIONS

In a Cartesian co-ordinate system Ox_i consider a solid continuum whose mass grows elastically according to

$$\dot{\rho} + \rho v_{i,i} = r_g \,, \tag{1}$$

where the mass density, ρ, and the mass-growth rate, r_g, are in general functions of x_i and the time t, $v_i = \dot{u}_i$ and u_i are the components of the velocity and displacement vector, respectively, and a dot denotes differentiation with respect to time. Stress equilibrium prevails at all times and is described by the quasi-static version of the equations of motion,

$$\sigma_{ij,i} = 0 \,, \tag{2}$$

where $\boldsymbol{\sigma}$ is the Cauchy stress tensor. In can be shown [2] that, for incompressible mass-growth of infinitesimally small magnitude, the relevant hyper-elasticity constitutive equation obtained in [1] is adequately approximated by the Hooke's law met is conventional linear elasticity. In that case, (2) is reduced into its classical Navier form

$$(\lambda + \mu) u_{k,ki} + \mu u_{i,jj} = 0 \,, \tag{3}$$

where λ and μ are the Lame elastic moduli. Use is also made of the indicial summation convention, form which a suffix "g" is the only exception.

Because ρ is time independent when mass-growth is incompressible ($\rho = \rho_0$), (1) simplifies and converts (3) into the set of uncoupled Poisson's equations

$$u_{i,jj} = -\frac{(1+\lambda/\mu)}{\rho_0} \int_{t_0}^{t} \frac{\partial r_g}{\partial x_i} dt \,. \tag{4}$$

In a specific mass-growth boundary value problem where the form of the mass-growth rate, r_g, is known, each one of equations (4) may thus be solved independently for the corresponding displacement component, u_i.

a) Corresponding author. Email: kostas.soldatos@nottingham.ac.uk

APPLICATION: THE HUMAN NAIL ELONGATION PROCESS

Certain simplifying considerations, which are justified in [2], enable a human nail specimen to be geometrically represented in the manner shown in Figure 1, where ℓ is the matrix length in the longitudinal x_1-direction, and t_0 is an appropriate time of reference. These include also the choice of the mass-growth rate

$$r_g = g\left(1 - x_1/\hat{m}\right)\left(t_0/t\right), \quad g << \rho_0/t_0, \quad \hat{m} > \ell \ , \tag{5}$$

where the positive parameters g and $\hat{m}$ are considered known or due to be determined experimentally or theoretically. The implied considerations and symmetries allow mass-growth of the nail matrix to be treated as a linearly elastic, plane strain process which converts (4) into

$$u_{1,jj} = \frac{\left(1+\lambda/\mu\right)gt_0}{\rho_0\hat{m}} \ln(t/t_0), \quad u_{2,jj} = u_{3,jj} = 0, \tag{6}$$

and leads to the exact analytical solution

$$u_1 = \frac{\left(1+\lambda/\mu\right)gt_0}{2\rho_0\hat{m}} x_1\left(x_1 - \ell\right)\ln(t/t_0), \quad u_2 = \frac{gt_0}{2\rho_0\hat{m}}\left\{-2\left(2+\frac{\lambda}{\mu}\right)x_1x_2 + \left(3 - 2\frac{\hat{m}}{\ell} + \frac{\lambda}{\mu}\right)h_\ell x_1 + \left(1 + 2\frac{\hat{m}}{\ell} + \frac{\lambda}{\mu}\right)\ell x_2\right\}\ln(t/t_0), \ u_3 = 0. \tag{7}$$

The corresponding stress field predicts [2] that, on the tissue transition plane $x_1 = \ell$, σ_{11} is constant, positive and increasing in time. Because it is thus tensile within the matrix part of the nail, it indeed pushes the nail plate forward, and at

$$t^{cr} = t_0 \exp\left\{\frac{\rho_0}{\left(\lambda + \mu\ell/\hat{m}\right)gt_0}\sigma_{11}^{cr}\right\} > t_0, \tag{8}$$

reaches the critical stress value σ_{11}^{cr} which, as already mentioned, is considered independent of the matrix growth process, measurable and, therefore, known. By releasing the energy stored within it, the grown nail matrix then bounces at $t = t^{cr}$ into a new, unstressed and unstrained state, thus enabling the length of the whole nail apparatus, L, to increase and become

$$\hat{L} = L + \frac{\sigma_{11}^{cr}}{4\mu\left(\lambda+\mu\right)}\left[\left(\lambda + 2\mu\right)\ell - \lambda h_\ell^2/2\ell\right]. \tag{9}$$

The outlined nail mass-growth and elongation process is then set to be repeated in a periodic manner, after t_0 and L are replaced by t^{cr} and $\hat{L}$, respectively.

CONCLUDING REMARKS

There is considerable lack of detailed clinical evidence regarding the status and activity of several of the mass-growth functions, parameters and concepts considered in the described human nail model. Wherever this lack required implementation of assumptions in an essentially speculative manner, those were selected in a manner that serves mathematical simplicity. However, as is detailed in [2], the current version of this human nail model can be refined and, hence, lead to considerably improved predictions as soon as new experimental or clinical evidence becomes available.

References

[1] Soldatos, K.P.: Modelling framework for mass-growth. Mech. Res. Comm. **50**, 50-57, 2013.

[2] Soldatos, K.P.: Small strain growth and the human nail. J. Elasticity, online (DOI 10.1007/s10659-015-9561-2) 2016.

[3] Baran, R., Dawber, R.P.R., Haneke, E., Tosti, A., Bristow, I.: A Text Atlas of Nail Disorders. 3rd Edn., Taylor & Francis, London, 2002.

[4] Bodman, M.A.**:** Nail dystrophies. Clin. Podiatr. Med. Surg. **21**(4), 663-87, 2004.

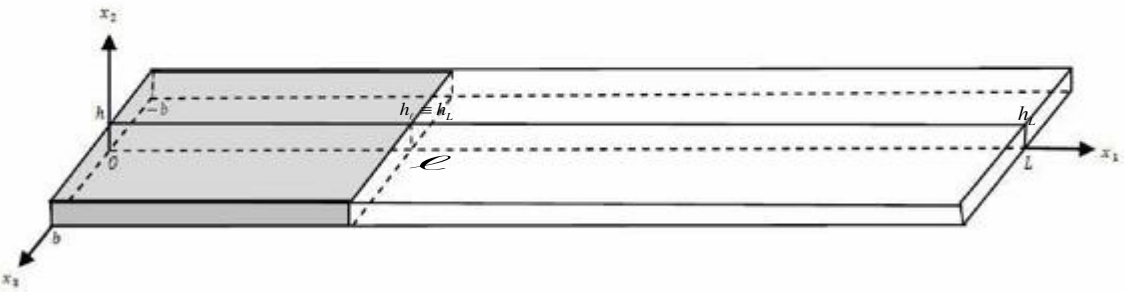

Figure 1: Simple geometrical representation and nomenclature of a specimen of the human nail apparatus. The shaded and unshaded parts represent the nail matrix (left) and the nail plate (right), respectively; see [2] for full details.

ASSESSMENT OF MATERIAL AND GEOMETRICAL PARAMETERS INFLUENCE ON IOP CHANGES AFTER INJECTIONS

Eva B. Voronkova * [1], Svetlana M. Bauer[2], Daria I. Zhuravleva[1], and Konstantin E. Kotliar[3]
[1]*St. Petersburg State University, Department of Mathematical Modelling of Energetic Systems, St. Petersburg, Russia*
[2]*St. Petersburg State University, Department of Theoretical and Applied Mechanics, St. Petersburg, Russia*
[3]*FH Aachen — University of Applied Sciences, Faculty of Biomedical Engineering and Technomathematics, Aachen, Germany*

Summary In this work we present mathematical models for the intraocular pressure (IOP) simulations after intravitreal injections. We developed models of IOP changes for the ellipsoidal form of the eye, considering its coat to be transversally isotropic. We simulated the relationship between the IOP and the inner volume of the eye with the help of the refined theory of thin shells and using Comsol Multiphysics FEM package. Global sensitivity analysis was performed to quantify the relative importance of material and geometrical parameters of the eyeball on the IOP elevation. The results showed that the axial length and elastic modulus affect the IOP changes significantly and the effects of Poisson's ratios are almost neglectable. However, when we introduced the relative volume, it became the most influential parameter: the magnitude of its effect was 50% of the total response.

INTRODUCTION

Intravitreal injections are performed for a variety of ocular diseases by adding the amount of fluid (drug) into the eye. Due to a short-time increase of the inner volume of the eye, the intraocular pressure (IOP) elevates after such an injection and can cause undesired effects [1]. From mechanical point of view this is the problem of estimation of the internal pressure changes in a closed shell filled with an incompressible fluid when an additional volume of incompressible fluid is introduced into the shell cavity. The change in pressure causes the deformation of the eyeball shell and the new inner volume can be calculated from a biomechanical simulations $\Delta p = \Phi(\Delta V, V_0, E, \nu)$, where ΔV is a volume of a medicament; V_0, V are the inner volumes of the eyeball before and after the injection, respectively; Δp – the change in IOP; and E, ν are parameters related to the properties of the eyeball tissues.

Natural variations in the model input parameters, e.g., stiffness of the eye tissues, the diameter and the length of the anterior-posterior axis (APA), can affect the model output. Global sensitivity analysis (GSA) has been performed to determine the effect of variation of each input model parameter on the assigned output variable [2].

MATHEMATICAL MODELS OF THE IOP CHANGE

The sclera composes more than 90% of the external coat of the eye and it is the principal load-bearing tissue of the eye. People with normal vision have nearly spherical shape of the eyeball, while for people with refractive errors (short- or longsighted) the eyeball shape is close to ellipsoidal one.

The first model adopted in this paragraph was introduced and discussed in [3]. We modeled the corneoscleral shell of the eye as an axisymmetric ellipsoidal shell of revolution subjected to inner pressure and treated the sclera as an transversally isotropic material with principal axes in meridional and circumferential directions. The aspherical geometry of the corneoscleral shell can be expressed, for example, by the following equation $r^2 + z^2/\kappa^2 \circ\ \kappa^2 R_0^2 = 0$, where the z-axis is the axis of revolution of ellipsoid as well as the optical axis of the eye, r is the radial distance from the APA axis, and $R_0 = R_a^2/R_b$ is the apical radius of curvature. A value of shape parameter $\kappa = R_b/R_a < 1$ corresponds to a prolate ellipsoidal shape modelling the hyperopic eye, $\kappa > 1$ — to an oblate ellipsoidal shape (the myopic eye), $\kappa = 1$ — to a spherical surface (the eye with normal vision). Here we denote the length of the optical axis as $2R_b$, and $2R_a$ is the eyeball diameter at the equator.

We calculated the displacements of the shell subjected to the inner pressure p with the help of a linear high-order theory of anisotropic shells presented in [4]. To find all quantities of interest, i.e. strains, stresses and deformations, the expansions into series in the thickness directions were used.

Assuming that after deformation the shell keeps the ellipsoidal shape, the change of the inner volume can be written

$$\Delta V = \frac{4}{3}\pi(R_a + u_a)^2(R_b + u_b) \circ\ \frac{4}{3}\pi R_a^2 R_b, \quad u_a = \Delta p \left(\frac{R_0^2(1 \circ\ \nu_{12})}{2E_1 h} + \frac{R_0 \nu_{13}}{2E_1} + \frac{h}{4E_{33}} \right), \tag{1}$$

$$u_b = \Delta p \left(\kappa^2 \frac{R_0^2(2 \circ\ \nu_{12} \circ\ 1/\kappa^2)}{2E_1 h} + \kappa \frac{R_0 \nu_{13}(2 \circ\ 1/\kappa^2)}{2E_1} + \frac{h}{4E_{33}} \right), \quad E_{33} = \frac{E_1 E_3 (1 \circ\ \nu_{12}^2)}{(1+\nu_{12})(E_1(1 \circ\ \nu_{12}) \circ\ 2E_3 \nu_{13}^2)},$$

*Corresponding author. Email: e.voronkova@spbu.ru

and a relationship between Δp and ΔV can be derived. Here, $E_i, i = 1, 2, 3$ — moduli of elasticity, ν_{ij} — Poisson's ratios.

We also generated the finite element model (FEM) of the eye using Comsol Multiphysics software (v. 5.0). To simulate the enclosed inner volume containing the fluid, we added an additional equation for the pressure needed to maintain a volume change. The differential pressure was computed and applied as a load to the interior of the simulated eyeball.

We conducted a GSA to assess the effect of each model parameters using Sobol' approach [2]. The global sensitivity indices S_y were calculated using ANOVA-decomposition of the function $f(x)$ describing the mathematical model. If S_y is close to zero we can consider that $f(x)$ does not depend on the variables from the y subset. The function $f(x)$ mainly depend on y variables if S_y is almost equal to 1. Since $f(x)$ is not always analytically integrable, a quasi-Monte-Carlo algorithm is chosen for numerical evaluation of the Sobol' indices.

RESULTS AND DISCUSSION

The model response was investigated to the material (E_1, E_3, ν_{12}, ν_{13}), geometrical (R_1^a, R_1^b, h) parameter variations and to the absolute ΔV and relative $\Delta V/V_0$ injection volume fluctuations. Parameters regions and distributions were taken from the literature and the data of the clinical trials.

Results for the ellipsoidal model (Eqs. 1) are presented in Fig. 1. One can see that the impact of the axial length (R_b) and Young's modulus E_1 were comparable: Sobol' indices differ only by about 10% from each other. At the same time dependence of the IOP changes on the equatorial radius R_a is smaller that dependence on the axial length.

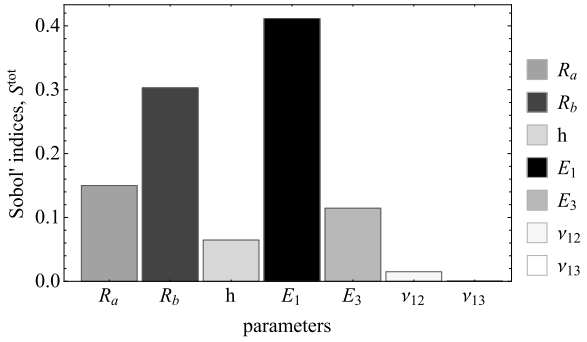

Figure 1: Sensitivity indices for the ellipsoidal model with fixed value of $\Delta V = 0.1$ ml

This study is subject to several limitations. Representation of the eye as an ellipsoidal shell of uniform thickness with linear material properties for the tissues is a significant simplification from physiological reality. However, these simplest models can help to find unessential parameters and fix them in future studies.

CONCLUSION

We have developed models of IOP changes for the ellipsoidal form of the eye, considering its coat to be transversally isotropic. The results showed that the axial length R_a and elastic modulus E_1 affect the IOP changes significantly and the effects of Poisson's ratios ν_{12} and ν_{13} are almost neglectable. However, when we introduced the relative volume, it became the most influential parameter: the magnitude of its effect was 50% of the total response.

The two region shell and nonlinear material properties can be incorporated into future models.

ACKNOWLEDGMENT

The reported study was partially supported by RFBR research project No. 15-01-06311 and was performed at the Observatory of environmental safety of St. Petersburg State University.

References

[1] Fuest M., Kotliar K., Walter P., Plange N.: Monitoring intraocular pressure changes after intravitreal ranibizumab injection using rebound tonometry. Ophthalmic and Physiological Optics 34:438-444, 2014.

[2] Sobol' I. M.: Global sensitivity indices for nonlinear mathematical models and their Monte Carlo estimates. Mathematics and Computers in Simulation 55:271-280, 2001.

[3] Bauer S. M., Voronkova E. B.: Models of shells and plates in the problems of ophthalmology. Vestnik St. Petersb. Univ. Math. 47:123-139, 2014.

[4] Rodionova V. A.,Titaev V. F., Chernykh K. F.: Applied Theory of Anisotropic Plares and Shells. St. Petersburg, Russia 1996, (in Russian).

A CELL MIGRATION MODEL INTEGRATING THE MECHANICAL STRESS GENERATION AND SENSING WITH BIOCHEMICAL SIGNALS

Hongyan Yuan[1a)]

[1] *Department of Mechanical, Industrial and Systems Engineering, University of Rhode Island, Kingston, RI, United States*

Summary In the present work, a mathematical model for cell migration has been developed to study how the mechanical stresses experienced by a cell are integrated with biochemical activities for cell migration.

INTRODUCTION

Cell migration plays an essential role in many biological processes such as tissue morphogenesis, tumor metastasis, angiogenesis, and wound healing. In recent experiments, mechanical stresses generated by cytoskeleton contraction have been shown to not only move the cell body forward but also play an active role in regulating other components of cell migration such as protrusion, cell-matrix and cell-cell adhesions, and cytoskeletal organization [1-3]. Our understanding of the biochemical aspects of cell migration has advanced greatly over the past decades. However, we know little about how mechanical and biochemical signals are integrated spatially and temporarily across the cell. In the present work, a mathematical model for cell migration has been developed to study how the mechanical stresses experienced by a cell are integrated with biochemical activities for cell migration.

METHODS

We have formulated mathematical equations to describe various cell activities including cell contraction, cell protrusion and retraction, cell-matrix and cell-cell interactions. Continuum mechanics theory and finite element method are used for calculating cellular stress and traction stress (see Figure 1). Numerical algorithm similar to cellular automaton is used to simulate cell protrusion and retraction. Reaction-diffusion equations are used to describe spatiotemporal evolution of protrusion and retraction signals, and rate equations are used to describe the dynamic remodeling of mechanical properties of cytoskeleton and cell-matrix and cell-cell adhesions. Mechanobiochemical integration will be implemented by coupling the parameters in these equations (see Figure 2).

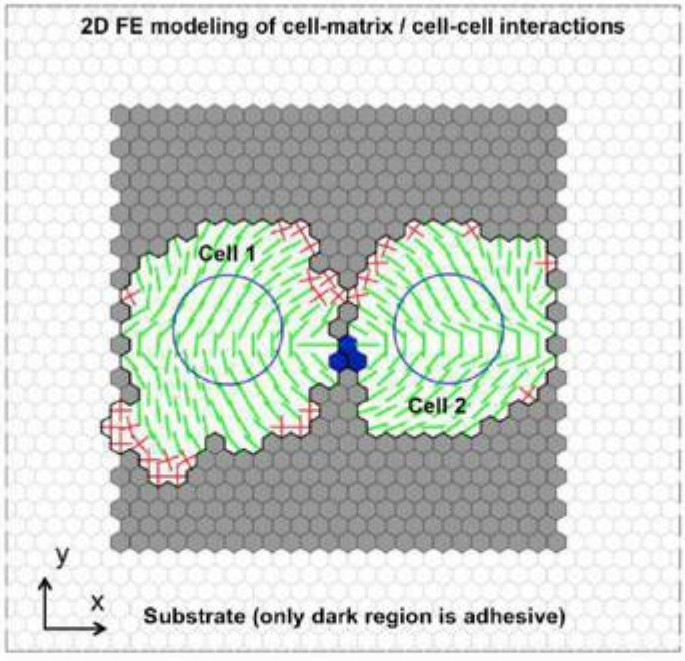

Figure 1: Finite element model of 2D cell migration in a multicellular environment.

[a)] Corresponding author. Email: Hongyan_yuan@uri.edu.

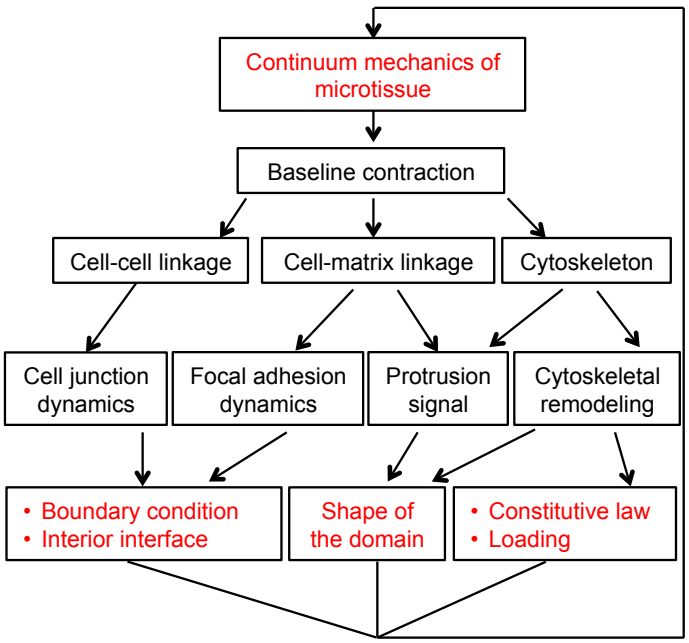

Figure 2: A flow diagram showing the assumptions of mechanobiochemical coupling and integration in cell migration.

RESULTS AND DISCUSSION

The finite element simulation results show that the mechanical stresses alone are sufficient to initiate the spatial pattern formation for actomyosin stress fiber organizations, focal adhesion distributions, and lamellipodia extension from an isotropic and homogeneous initial condition. The simulation results suggest that mechanobiochemical couplings at the whole-cell level enable cells to sense their shape. It has been demonstrated that this model can simulate durotaxis in which cell migration direction is guided by the rigidity of the substrate. Furthermore, by adding a cell-cell adhesion component to the single-cell migration model, cell-pair morphogenesis when the shape of the microtissue is constrained was simulated and compared with previous experiments involving cardiac microtissues.

This whole-cell level model for cell migration can help understand how the interior activities of a cell are merged with active sensing of mechanical cues of the external microenvironment. It can be used to study the effect of mechanical microenvironments in many biological problems such as tissue formation, cancer metastasis, would healing.

References

[1] Parker, K. K. et al. Directional control of lamellipodia extension by constraining cell shape and orienting cell tractional forces. Faseb J 16, 1195–1204 (2002).

[2] Parker, K. K., Tan, J., Chen, C. S. & Tung, L. Myofibrillar architecture in engineered cardiac myocytes. Circ Res 103, 340–342 (2008).

[3] Grosberg, A. et al. Self-Organization of Muscle Cell Structure and Function. PLoS Comput Biol 7, e1001088 (2011).

A STUDY ON IMPERFECTION SENSITIVITY OF PRESSURED BUCKLING OF SPHERICAL VIRUS SHELLS

Lei Zhang[1a)], C Q Ru[2]
[1]*Department of Mechanical Engineering, University of Alberta, Edmonton, Alberta T6G 2G8, Canada*
[2]*Department of Mechanical Engineering, University of Alberta, Edmonton, Alberta T6G 2G8, Canada*

Abstract Motivated by the geometric heterogeneity inherent in spherical viruses, an imperfection sensitivity analysis is conducted based on a refined elastic shell model recently developed for spherical virus shells of high structural heterogeneity. The influence of key parameters of the refined model on imperfection sensitivity is examined. Our results show that the ratio of effective bending thickness to average shell thickness has a major effect, while the ratio of transverse shear modulus to in-plane shear modulus has a negligible influence on the imperfection sensitivity. In particular, with relevant parameters for typical imperfect spherical virus shells, the predicted buckling pressure could be roughly reduced to 55-65% of that of a prefect spherical virus shell.

INTRODUCTION

A nano-sized spherical virus is essentially spherical shell (known as "capsid") that encloses viral genetic material (RNA or DNA) [1]. It is of great significance to study buckling instability of spherical virus shells under external radial pressure and the influence of such pressured buckling on their biological functioning (e.g. protect, deliver and release genetic materials [1]). A common key feature of virus spherical shells is their high geometric heterogeneity. For example, Wan [1] shows that the existence of geometrical defects in spherical crystalline shells affect the shells' ability to sustain external hydrostatic pressure. Therefore, no doubt, the study on the effect of geometrical imperfection on pressured buckling behavior of virus spherical shells is vital in understanding some of their biological functions. The present work aims to examine imperfection sensitivity of geometrically heterogeneous spherical virus shells using the refined elastic shell model developed in [3]. The methods developed in previous seminal works on buckling of elastic shells, e.g. by Koiter [4] for spherical shells, are employed to study the imperfection sensitivity of geometrically heterogeneous spherical virus shells defined by the refined model [3] (the detailed formulation and analysis are omitted in the present abstract).

THE REFINED SHELL MODEL

In view of the fact that virus spherical shells are characterized by high geometrical heterogeneity and thickness non-uniformity, a refined elastic spherical shell model was developed in [3] which was recently used to study the rupture of ultrasound contrasts agents (UCAs) by Chitnis et al. [5]. The effect of geometrical heterogeneity and thickness non-uniformity on the critical pressure P_{cr} for buckling of a prefect spherical virus shell is given by

$$P_{cr}=\left(\frac{2E}{\sqrt{3\left(1-v^2\right)}}\right)\left(\frac{h_0}{h}\right)^{\frac{3}{2}}\left(\frac{h}{R}\right)^2-\left(\frac{E}{3\left(1-v\right)k_s}\right)\left(\frac{h_0}{h}\right)^3\left(\frac{h}{R}\right)^2\left(\frac{G}{G^*}\right) \tag{1}$$

where E is Young's modulus, v is Poisson's ratio of the viral shell, k_s is the shear coefficient, R is the average radius, G^* is the transverse shear modulus, G is the in-plane shear modulus, h_0 is the effective bending thickness and h is the average thickness. It is known that for microtubules transverse shear modulus can be lower than in-plane shear modulus, and transverse shear becomes significant for shorter-wavelength deformation. For spherical viral shells, because wavelengths are always shorter as compared to the diameter, it is expected that the transverse shear could be relevant for viral shells. In particular, in view of similar thickness non-uniformity and structural heterogeneity of microtubules and viral shells, it is assumed here that transverse shear modulus of viral shells G^* could be lower than the in-plane shear modulus G and h_0 can be different from h. Therefore, the physically realistic range of G^*/G for spherical virus shells could be smaller than one.

In this work, the effect of these three key parameters on the imperfection sensitivity is examined within the framework Koiter's general theory of post-buckling of pressured elastic spherical shells. Some numerical results are obtained with the aid of Mathematica software, as shown below.

NUMERICAL RESULTS AND CONCLUSIONS

First of all, a comparison of the present results with the well-known Koiter's results is demonstrated in fig.1-a) for classical elastic spherical shells (with $G^*/G=\infty$, $h_0/h=1$). Furthermore, how the three key parameters (R/h, G^*/G and h_0/h) influence the imperfection sensitivity of an imperfect spherical virus shell is shown in fig.1-a), b) and c). And fig 1-d) shows the imperfection sensitivity with relevant parameters for some typical imperfect spherical virus which are listed in table 1 and obtained from [6]. Here the knockdown factor λ is defined by the ratio of the maximum pressure of an imperfect virus

[a)] Contact person. Email: lzhang@ualberta.ca

shell to the maximum pressure of a perfect virus shell (the latter is actually given by Eq. (1)), and μ is dimensionless imperfection amplitude normalized by the average thickness h. It is concluded from figure 1 that:

1) From fig 1 a), our results are validated by the well-known Koiter's results of imperfection sensitivity for the classical spherical shells (with $G^*/G=\infty$, $h_0/h=1$, for which the present refined model reduces to the classical model). In this classical case, it is seen from fig.1-a) that the knockdown factor λ decreases with the increasing ratio of radius to average shell thickness.
2) From fig 1 b), it is concluded that the effect of transvers shear modulus of a spherical virus shell on the imperfection sensitivity is negligible when the ratio G^*/G varies within a physically realistic range for spherical virus shells.
3) From fig 1 c), it is concluded that the knockdown factor λ decreases quickly with decreasing ratio of the effective bending thickness to the average shell thickness, which predicts that the effective bending thickness has a greater effect on the imperfection sensitivity and the thickness non-uniformity of spherical virus shells could be mainly responsible for the imperfection sensitivity.
4) From fig 1 d), it is concluded that with the relevant parameters for some typical imperfect spherical virus shells, the maximum pressure of an imperfect spherical virus shell could reduce to 55-65% of the maximum pressure of a perfect spherical virus shell with the ratio R/h ranging from 3 to 5, h_0/h ranging from 1.15 to 1.45 and the dimensionless imperfection amplitude μ ranging from 0.08 to 0.21. As stated above, the ratio G^*/G has negligible effect on the imperfection sensitivity when it varies within a physically realistic range.

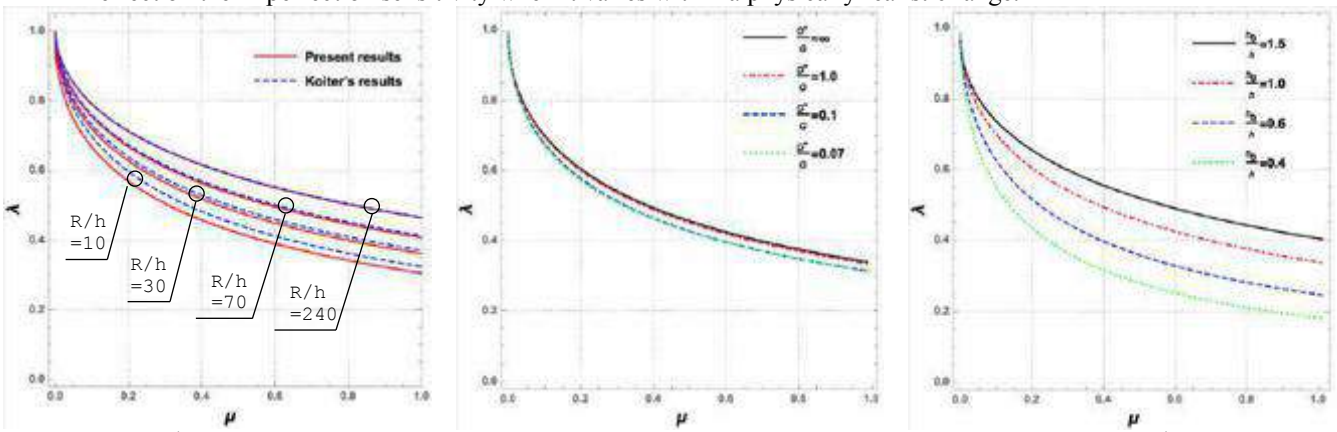

a) $G^*/G=\infty$ $h_0/h=1$ b) $R/h=15$ $h_0/h=1$ c) $R/h=15$ $G^*/G=\infty$

Table 1 (unit: nm)

No.	Virus	R	h	h_0	R/h	h_0/h	G^*/G	$\mu=\lvert h_0-h\rvert/2h$
1	cowpea chlorotic mottle virus	11.8	2.9	4.2	4	1.45	0.5	0.21
2	tobacco necrosis virus	12.9	2.5	3.1	5	1.25	0.5	0.11
3	flockhouse virus	13.7	4.3	5.2	3	1.21	0.5	0.12
4	norwalk virus	15.8	6.2	7.1	3	1.15	0.5	0.08

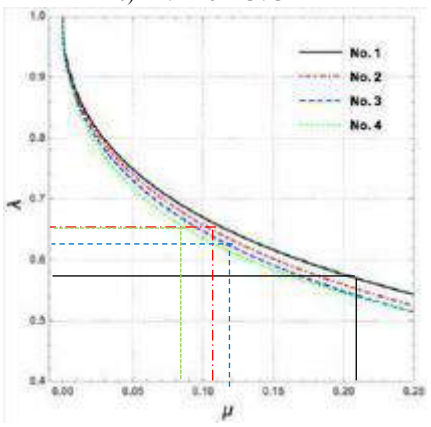

d) typical spherical viruses

Fig. 1 The dependence of the knock down factor λ on the dimensionless imperfection amplitude μ

Acknowledgement: Financial support of the Natural Science and Engineering Research Council (NSERC) of Canada (Grant No. RGPIN 204992) is gratefully acknowledged.

References

[1] Zandi R., Reguera D.: Mechanical properties of viral capsids. *Phys Rev E* **72**, 021917, 2005.
[2] Wan D., Bowick M. J., Sknepnek R.: Effects of scars on icosahedral crystalline shell stability under external pressure. *Phys Rev E*, **91**: 033205, 2015.
[3] Ru C. Q.: Buckling of empty spherical viruses under external pressure. *J. Appl Phys* **105**: 124701, 2009.
[4] Koiter W. T.: The Nonlinear Buckling Problem of a Complete Spherical Shell Under Uniform External Pressure. *Proc R Netherlands Acad Sci*, *B* **72**: 40123, 1969.
[5] Chitnis P. V., Koppolu S., Mamou J., Chlon C., and Ketterling J. A.: Influence of shell properties on high-frequency ultrasound imaging and drug delivery using polymer-shelled microbubbles. *IEEE Trans Ultrason Ferroelectr Freq Control*, **60**: 53–64, 2013.
[6] May E. R., Brooks C. L. III.: On the morphology of viral capsids: elastic properties and buckling transitions. *J Phys Chem B*, **116**:8604–8609, 2012.

SM02 - Contact and Friction

TS.SM02-1.01	Fineberg, Jay - Slippery but tough - the rapid fracture of lubricated frictional interfaces (INVITED)	1754
TS.SM02-1.02	Barber, James - slip-weakening laws and apparent static friction coefficient	1756
TS.SM02-1.03	Cabboi, Alessandro - Unlocking Dynamic Friction: the Frictional Frequency Response	1758
TS.SM02-1.04	Yang, Jun - Nanotribology Study With T-shape Probe by Atomic Force Microscopy	1760
TS.SM02-1.05	Vasu, Thamarai Selvan - Surface loading of layer-substrate system under plane-strain condition with surface effects	1762
TS.SM02-1.06	Aizikovich, Sergey - Analytical solutions of contact problems for bodies with functionally graded coatings	1764
TS.SM02-2.01	Hills, David - Characterisation of edge conditions in general incomplete contacts (INVITED)	1766
TS.SM02-2.02	Adams, George - Determination of frictional slip zone from a perfect bond solution	1768
TS.SM02-2.03	McKay, Andrew - Unifying different measurements of dynamic friction	1770
TS.SM02-2.04	Kolesnikov, Alexey - An initially cylindrical elastic membrane wrapped around a rigid cylinder	1772
TS.SM02-2.05	Jin, Fan - A two-dimensional double-hertz model for adhesive contact between elastic cylinders	1774
TS.SM02-3.01	Yastrebov, Vladislav - Contact between rough surfaces: mechanical and transport phenomena at small scales (INVITED)	1776
TS.SM02-3.02	Goryacheva, Irina - The system of indenters sliding over the viscoelastic half-space	1778
TS.SM02-3.03	Proppe, Carsten - Multiscale modelling of dynamical systems with friction between randomly rough surfaces	1780
TS.SM02-3.04	Diop, Thierno - Frictional Contact, Numerical Approximation and Algorithms	1782
TS.SM02-3.05	Perez Rafols, Francesc - An LCP based approach for the contact mechanics of elastic half spaces	1784
TS.SM02-4.01	Babehsko, Vladimir - Action of the two semi-infinite plates on the elastic layer (INVITED)	1786
TS.SM02-4.02	Cocou, Marius - A class of slip depending surface interactions	1788
TS.SM02-4.03	Huang, Gan-Yun - Model for friction in small-sized adhesive particles	1790
PO.SM02-1.01.114	Adamowicz, Adam - Numerical modeling of the coupling between the temperature and velocity in braking systems	1792
PO.SM02-1.02.115	Bartosh, Ilona - A new formulation for re-centering friction-based isolation systems	1794
PO.SM02-1.03.116	Fedotenkov, Grigory - Elastic Semi-space Impacted with Elastic Filled Shell	1796
PO.SM02-1.04.117	Jiang, Yuxi - The Dual Domain Decomposition Parallel Contact Algorithm in CHAP3D Code	1798
PO.SM02-1.05.118	Kuciej, Michal - Nonlinear analytical – numerical models of solving frictional heat problems	1800
PO.SM02-1.06.119	Nuzhdin, Kirill - Modelling of external dynamic of the friction engagement	1802

SLIPPERY BUT TOUGH - THE RAPID FRACTURE OF LUBRICATED FRICTIONAL INTERFACES

Jay Fineberg, Elsa Bayart & Ilya Svetlizky
The Racah Institute of Physics, The Hebrew University of Jerusalem,Jerusalem, 91904, Israel

Summary We study the onset of friction for contacting blocks whose rough, spatially extended interface is coated with a thin lubrication layer. High speed measurements of the real contact area and stress fields adjacent to the interface reveal that propagating shear cracks mediate lubricated frictional motion. While lubricants reduce interface strengths, surprisingly, they significantly increase the fracture energy (amount of dissipated energy) during rupture. Moreover, lubricant viscosity affects the onset of friction but has *no* effect on the fracture energy. These results suggest a new view of lubricated friction.

Frictional processes entail the rupture of the ensemble of discrete contacts defining a frictional interface. There are a variety of views on how best to describe the onset of frictional motion. These range from modeling friction with a single degree of freedom, a 'friction coefficient', to theoretical treatments using dynamic fracture to account for spatial and temporal dynamics along the interface. We investigate the onset of dry and lubricated frictional motion by performing simultaneous high-speed measurements of the real contact area and the strain fields adjacent to the rough interface separating two spatially extended blocks. We show that the transition from static to dynamic sliding is mediated by earthquake-like rupture fronts that propagate along the interface, while dissipating energy by fracturing the discrete contacts along the interface. In the region surrounding the propagating rupture we first demonstrate that the transition from 'static' to 'dynamic' friction is quantitatively described by classical singular solutions described by Linear Elastic Fracture Mechanics for the motion of a rapid shear crack. We find that these singular solutions, originally derived to describe brittle fracture, are in excellent agreement with experiments [1,2]. The singular solution for the strain tensor variations, $\Delta\varepsilon_{ij}(r,\theta)$, in Eq. 1 provides us with a quantitative measurement of the fracture energy, Γ, (the amount of energy dissipated per unit rupture extension) at the interface:

$$\Delta\varepsilon_{ij} \propto \frac{K}{\sqrt{r}} \Sigma_{ij}(\theta, c_f) \qquad (1)$$

where K is the stress intensity factor for shear (Mode II) fracture and Σ_{ij} a known universal function [3] of the rupture velocity, c_f. In the experiments the fracture energy, $\Gamma \propto K^2/E$, where E is the material's Young's modulus and is nearly constant with rupture velocity.

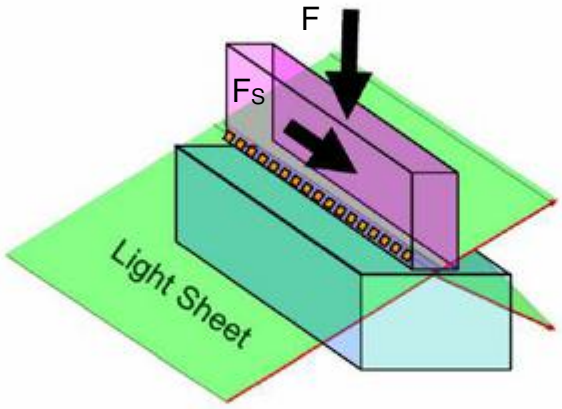

Figure 1. The experimental system. The real contact area $A(x,t)$ is measured by light transmission along a rough 200x100x6mm mm frictional interface while all 3 components of the strain tensor are measured at 14 locations adjacent to the interface (orange squares). $A(x,t)$ is measured at 580000 frames/sec (@ spatial resolution of 1280 x 8 pixels) while, in parallel, each of the strain components are measured at 10^6 samples/sec.

[a] Corresponding author. Email: jay@mail..huji.ac.il

We now turn to a study of how boundary lubrication acts to weaken a frictional interface. By performing stick-slip experiments where the contacting surfaces are covered by a thin lubricating layer, we show that fracture mechanics also describes the measured strain fields when rupture of a lubricated interface takes place. Surprisingly, although reducing the frictional strength of the interface (friction coefficient), lubricants actually significantly increase the fracture energy (amount of dissipated energy) during rupture. Thus surface lubrication, while strongly reducing the residual stresses in the wake of rupture propagation, actually toughens the contacting surfaces.

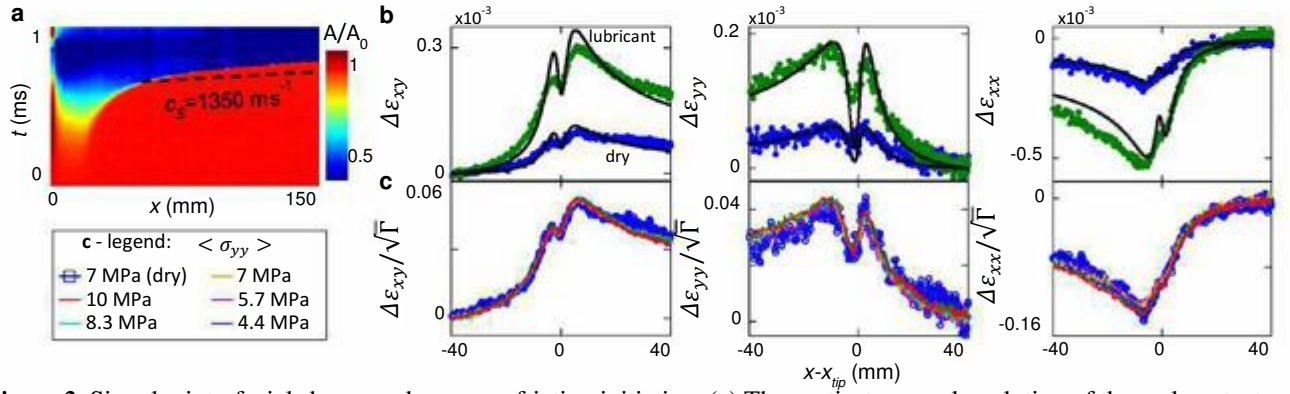

Figure 2. Singular interfacial shear cracks govern friction initiation. (a) The spatio-temporal evolution of the real contact area A(x,t) of a typical lubricated interface with a hydrocarbon lubricant during a typical transition from stick to slip (note that the transition takes place over ~200μs, the time required for a rupture front to traverse the entire 150mm long frictional interface. Only when a front traverses the entire interface will macroscopic frictional motion take place. Each line is a snapshot in time of A(x,t) normalized by A_0= A(x,0) for t=0 immediately prior to the event. Here, a rupture accelerates to a propagation velocity c_f=0.92c_R, where c_R is the Rayleigh wave speed in PMMA. The rupture tip, $x_{tip}(t)$ is the location where A(x,t) drops sharply. (b) Variation of the strain field $\Delta\varepsilon_{ij}(x\text{-}x_{tip})$ with the distance from $x_{tip}(t)$ for ruptures propagating along dry (blue line) and lubricated (oiled, green line, rupture presented in (a)) interfaces. In both, the applied normal stress was 7MPa for , c_f=0.3c_R and strains were measured at x=77mm. Black solid lines are fits to the singular LEFM solution. The only fitting parameter is the fracture energy; Γ= 2.6±0.3J/m^2 for the dry and Γ=23±3 J/m^2 for the lubricated interfaces. (c) Comparison of $\Delta\varepsilon_{ij}(x\text{-}x_{tip})$ for dry and lubricated experiments, when normalized by √Γ. Superimposed are the dry experiment in (b) and 5 lubricated experiments where c_f~0.3c_R with mean normal stresses, $<\sigma_{yy},>$ of 4.4, 5.7, 7, 8.3 and 10 MPa yielding fracture energies of Γ =2.6 and 12.3, 18.2, 23, 25 and 29.5 J/m^2.

The coupling between friction and fracture demonstrated in this work is important to our fundamental understanding of both frictional motion and related processes, such as earthquake dynamics. We show that fracture mechanics provide a new way to view the otherwise hidden complex dynamics of the lubrication layer

References

[1] Svetlizky, I. & Fineberg, J.: Classical shear cracks drive the onset of dry frictional motion. Nature *509*, 205-208, 2014.
[2] Bayart, E., Svetlizky, I. & Fineberg J.: Fracture mechanics determine the lengths of interface ruptures that mediate frictional motion. Nature Physics to appear 2016.
[3] Freund, L. B.:,Dynamic Fracture Mechanics (Cambridge,NewYork,1990).

SLIP-WEAKENING LAWS AND APPARENT STATIC FRICTION COEFFICIENT

A. Papangelo[1], M. Ciavarella[1], and J. R. Barber [*2]
[1]*Department of Mechanics, Mathematics and Management, Politecnico di Bari, Bari, Italy.*
[2]*Department of Mechanical Engineering, University of Michigan, Ann Arbor, U.S.A.*

Summary Solutions are described for tangentially loaded contact problems in which the coefficient of friction transitions from a static to a dynamic value over some small but finite slip displacement. Numerical and analytical result for a Hertzian geometry show that the maximum tangential force occurs before all the contact slips, and that the maximum macroscopic friction coefficient is lower than the pointwise value. If the transition occurs over a small slip distance, the assumed behaviour is mathematically analogous to a mode II fracture criterion.

FRICTION LAWS

It has been observed in many contexts that the force required to initiate relative tangential motion at a frictional interface exceeds that required to perpetuate motion [1]. This is often characterized by defining a static coefficient of friction f_s and a dynamic, or kinetic, coefficient f_d such that $f_s > f_d$. However, this distinction is lost if the friction law is applied in a pointwise sense to a typical elastic contact problem. For example, suppose two elastic bodies that can be modelled by half spaces are pressed together by a normal force P after which a tangential force Q_x is gradually applied in the x-direction. If the materials of the two bodies are the same, the normal tractions $p(x,y)$ and the extent of the contact area $\mathcal{A}$ are independent of Q_x, so the tangential contact problem is defined by the boundary conditions

$$\begin{aligned} u_x(x,y) &= 0\ ; \quad q_x(x,y) < f_s p(x,y)\ ; \quad (x,y) \in \mathcal{S} \\ q_x(x,y) &= f_d p(x,y)\ ; \qquad\qquad\qquad (x,y) \in (\mathcal{A}-\mathcal{S})\ , \\ \iint_{\mathcal{A}} q_x(x,y)dxdy &= Q_x \end{aligned}$$

where q_x, u_x are the tangential traction and the slip displacement respectively, and $\mathcal{S}$ is the 'stick' area. Intuitively, we would expect that increasing f_s should increase $\mathcal{S}$ for a given Q_x, but any such assumption can be shown to lead to a singular traction at the boundary of $\mathcal{S}$. Thus, the only solution of the problem is identical to that which would be obtained were f_s equal to f_d. Furthermore, it is easily shown that the maximum value of Q_x occurs at incipient sliding, and hence that the resulting macroscopic friction force is predicted by a simple Coulomb law with only the dynamic coefficient of friction f_d.

SLIP WEAKENING

A more realistic friction law would recognize that the transition from f_s to f_d should occur over a finite slip displacement, rather than instantaneously. In other words,

$$q_x = \{f_d + F(u_x)\}p$$

where $F(0) = f_s - f_d$ and $F(u) \to 0$ as $u \to \infty$. Such a law can be regarded as a special case of the rate-state law [2] and is also related to the shear failure law proposed by Abercrombie & Rice [3]. Rabinowicz [1] describes some elegant experiments designed to determine the function $F(u)$, but the results are based the macroscopic tangential force Q_x and rigid-body tangential displacement and hence we might anticipate significant differences from the conditions that apply to the pointwise tractions, where microslip occurs.

In a recent paper [4], laws of this form have been applied to the two-dimensional Hertzian contact geometry in which a cylindrical body of radius R is first pressed into a half plane, establishing a contact area of width $2a$ and then sheared. Numerical results were obtained by the finite element method, using the ramp function $F(u_x) = (f_s - f_d)(1 - u_x/\Delta)$ for $0 < u_x < \Delta$ and $F(u_x) = 0$ for $u_x > \Delta$, where Δ defines a slip-displacement length scale over which the transition occurs from static to dynamic friction. The traction distributions showed generally good agreement with an approximate analytical solution based on the superposition of two Cattaneo-Mindlin traction distributions [5].

In these solutions, we can distinguish three regions in the contact area, a central stick region $|x| < c$ in which there is no slip displacement and $q_x < f_s p$, a transition region $c < |x| < b$ in which the slip displacement $u_x < \Delta$ and hence $q_x > f_d p$, and if the applied force Q_x is sufficiently large, a region $b < |x| < a$ in which $u_x > \Delta$ and the dynamic friction coefficient is fully established. When $Q_x = 0$ the entire contact area is in a state of stick, so $c = a$, but as Q_x is increased, c decreases monotonically. Figure 1 shows a plot of Q_x as a function of c for various values of the dimensionless parameter

$$\Psi = \left(\frac{f_s}{f_d} - 1\right)\chi \quad \text{where} \quad \chi = \frac{R\Delta}{f_d a^2}\ .$$

[*]Corresponding author. Email: jbarber@umich.edu

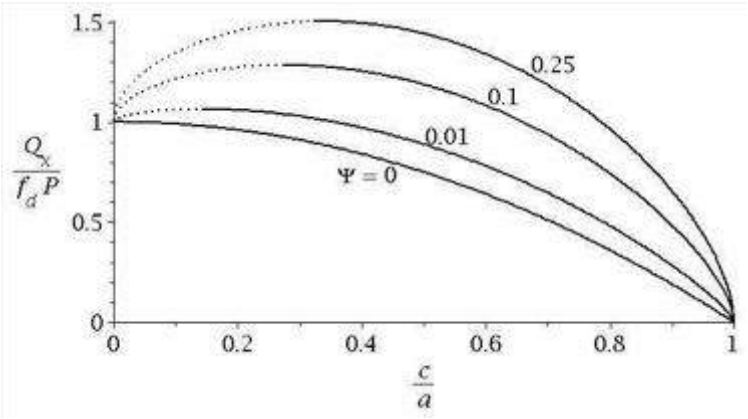

Figure 1: Dimensionless tangential force Q_x/f_dP as a function of the semi-width of the stick zone c.

Notice that in general a maximum value is achieved before the stick zone has shrunk to zero. Under force control, the system would then jump from this maximum to a state of sliding with $Q_x = f_dP$. More significantly, experiments conducted on such a system would predict a ratio f_s/f_d equal to the maximum in the figure. This is always smaller than the pointwise ratio and often very significantly smaller, as shown in Figure 2.

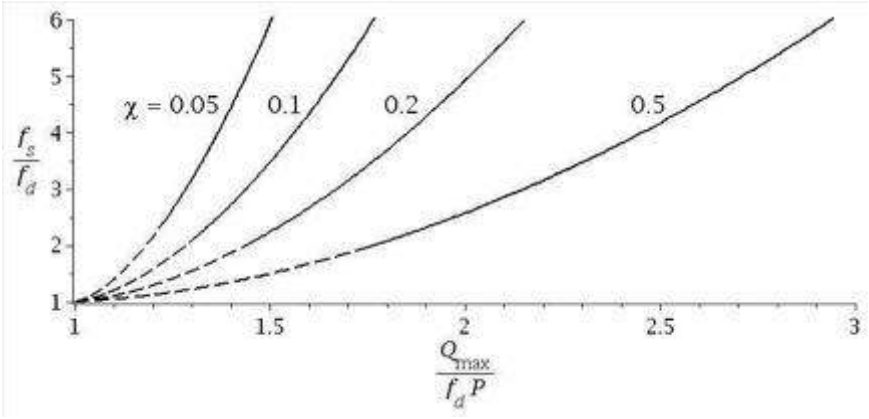

Figure 2: The apparent static friction coefficient.

When $\chi \ll 1$, the transition zone $c < |x| < b$ is a small proportion of the contact area and the solution in the limit tends to a state where the shear tractions exhibit a singularity at the stick-slip boundary analogous to that in mode II fracture problems. In this case, the equivalent of the fracture energy release rate is

$$W = \int_0^\infty F(u_x) p du$$

Mathematically, the tangential contact problem then has the same form as the classical JKR solution for adhesive forces under normal contact, with W playing the rôle of the surface energy γ. Notice however that W is proportional to the contact pressure local to the transition from stick to slip.

CONCLUSIONS

A slip weakening friction law is shown to be equivalent in a certain limit to a fracture-based shear criterion. Also, the static coefficient of friction can be significantly underestimated from experiments based on macroscopic geometries.

References

[1] Rabinowicz E.: The nature of the static and kinetic coefficients of friction, J. Appl. Phys. 22: 1373-1379, 1951.

[2] Ruina, A. Slip instability and state variable friction laws, J. Geophys. Res. 88 (B12): 10359-10370, 1983.

[3] Abercrombie R. E., Rice J. R. Can observations of earthquake scaling constrain slip weakening? Geophys. J. Int. 162: 406-424, 2005.

[4] Papangelo A., Ciavarella M., Barber J. R.: Fracture Mechanics implications for apparent static friction coefficient in contact problems involving slip-weakening laws, Proc. Roy. Soc (London): A 471 Issue: 2180: Article Number: 20150271, (2015).

[5] Ciavarella M.: The generalized Cattaneo partial slip plane contact problem. I-Theory, II-Examples, Int. J. Solids Struct. 35: 2349–2378, (1998).

UNLOCKING DYNAMIC FRICTION: THE FRICTIONAL FREQUENCY RESPONSE

Alessandro Cabboi[1a)], Thibaut Putelat[2] & Jim Woodhouse [1]
[1]*Department of Engineering, University of Cambridge, Cambridge, UK*
[2]*Department of Engineering Mathematics, University of Bristol, Bristol, UK*

Summary Constitutive laws for dynamic friction are discussed, by following two interconnected routes. The first route is experimental, based on systematic measurements of the frictional frequency response function up to mid-high frequencies, which is the required input to perform stability analysis of mechanical systems under steady sliding. It is worth mentioning that previous efforts to explain such measurements from a theoretical model have failed. The second route describes an enhanced rate-and-state model that takes the contact stiffness into account. The described results show that the model can predict the measured dynamic frictional response remarkably well for a range of sliding speeds, normal forces and frequencies, and a systematic methodology to identify the model parameters is described.

PROBLEM STATEMENT AND NEW MEASUREMENTS OF DYNAMIC FRICTION

The prediction of self-excited vibration requires an accurate description of the frictional interface, where the level of such accuracy is driven by the required target. For example, the quickest method to predict friction-induced vibration relies on a linearised stability threshold analysis, for which the friction force needs to be described by a linearised constitutive law of dynamic friction. The most common friction laws used are usually deduced from tribological tests that involve measuring the friction force under different velocities and normal loads. Naively, such identified velocity-dependent laws are then used to predict the dynamic friction behaviour at mid-high frequencies where friction-induced vibration commonly occurs. This approach often leads to erroneous results and has been challenged in previous works [1-3]. In fact, it has been shown in [1,3] that the actual frictional response measured by inducing a small velocity fluctuation at a given frequency highlights a deep difference in the physics, compared to the one predicted by using only velocity-dependent dynamic friction laws. The new measurement takes the form of a *frequency response function*, $\beta(\omega)$ (Fig. 1b), constructed by measuring the perturbation in the frictional force F' divided by the perturbation of the sliding speed v' as a function of frequency. The measurements so far are found to be complex and to vary with frequency as shown in Fig. 1c and Fig. 2.

The test machine is a pin-on-disc device (Fig. 1a). A piezo actuator is used to superimpose a small fluctuation in sliding speed. The disc is made of glass and three different sample pins are used: nylon, polycarbonate and tufnol. The pin is held by a dynamometer unit that hosts a package of sensors close to the contact region, allowing force and velocity to be measured in the frictional and normal directions. The actuator is driven with band-limited random noise.

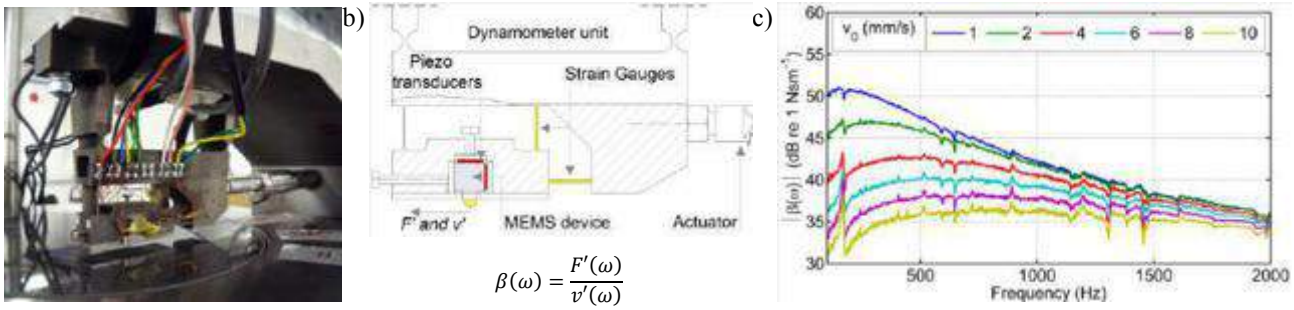

Fig. 1 - a) Pin-on-disc device ; b) dynamometer unit scheme and measured quantities; c) typical $\beta(\omega)$ measurement obtained for a Nylon pin on a glass disc; the normal force was kept constant at 30 N and the sliding speed was varied between 1, 2, 4, 6, 8 and 10 mm/s.

CONSTITUTIVE FRICTION LAW: ENHANCED RATE -AND-STATE MODEL

In [3, 4] it has been found that a dynamic model of the rate-and-state type, enhanced to take into account the contact stiffness, can fit the $\beta(\omega)$ measurements remarkably well. A model of this kind can be generally defined by a pair of equations (1), which after linearization leads to the expression (2) for the frictional frequency response function $\beta(\omega)$:

$$F = f\left(v - \dot{F}/k_t, \phi\right) \qquad \dot{\phi} = -g(v, \phi) \tag{1}$$

$$\beta(\omega) = -\left[\frac{g_{,\phi} f'_{ss} + i\omega f_{,v}}{g_{,\phi} + i\omega}\right]\left[\frac{1}{1 + i\omega\, f_{,v}/k_t}\right] \tag{2}$$

in which v is the interfacial slip rate, f'_{ss} is the slope of the steady-state frictional force, ϕ is the internal state variable, and $f_{,v}$ and $g_{,\phi}$ are the partial derivatives of the frictional force and state evolution law with respect to the slip rate and state variable, respectively. The contact stiffness k_t is modelled by using a power law of the normal force. In order to get the

[a)] Corresponding author. Email: ac932@cam.ac.uk.

partial derivatives, a mathematical expression for the frictional force and the state evolution law is needed. In [3], a systematic optimization methodology is presented to identify the model parameter values and discriminate among possible variants of enhanced rate-and-state models of the Dieterich-Ruina type. This provides "the best" model for the measured data.

IDENTIFICATION OF FRICTION MODEL PARAMETERS FROM THE β(ω) MEASUREMENTS

Compared to the previous work [3], a further set of material combination have been systematically tested in order to investigate the application range of the proposed model. In Fig. 2, some samples of these new $\beta(\omega)$ measurements are shown. Specifically, sets of Nyquist plots for three material combinations are plotted: a) Nylon-Glass; b) Polycarbonate-Glass; c) Tufnol-Glass (see caption in Fig. 2 for more details). The proposed model in [3] succeeds well in reproducing the effect of variation of the normal load. Further measurements have been performed by changing also the sliding speed. The fitting methodology proposed in [3] has been used then to systematically identify all the model parameters. In this context, special attention has been devoted to the identification of the contact stiffness, which needs to be treated somewhat differently from the other fitting parameters. Concurrently, the larger data set has allowed more detailed investigation of some peaks, corresponding to system antiresonances, that often appear in the measurement results.

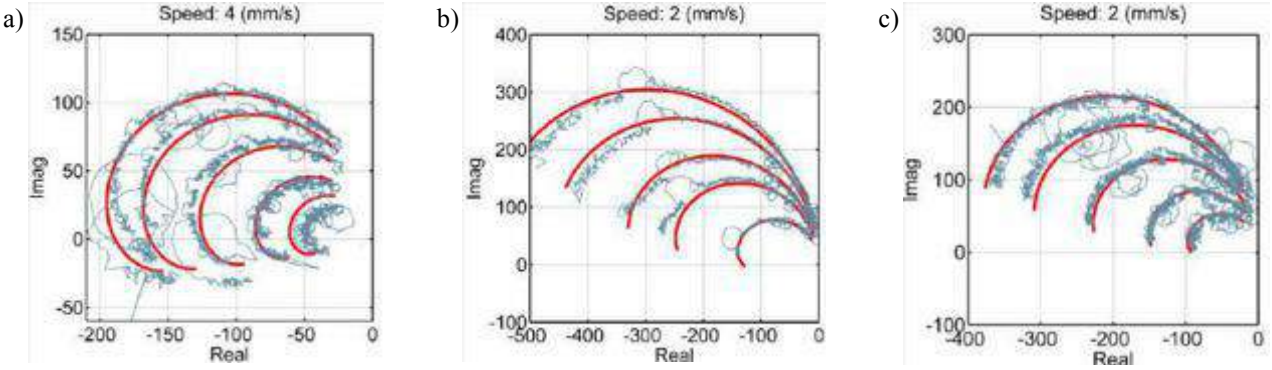

Fig. 2 - Measurement of $\beta(\omega)$ and fitting performance of the rate-and-state model: a) Nylon-Glass; b) Polycarbonate-Glass; c) Tufnol-Glass. The Nyquist curves increase by increasing the normal force that are assumed to be approximately: 10-20-30-40-50 (N).

CONCLUSIONS

It is shown that the frictional frequency response reveals new dynamic features of the frictional interface for a perturbed steady-sliding contact. A measurement of this type turns out to be the required input for predicting friction-induced vibration by using linearised stability analysis. Concurrently, a rate-and-state model that takes into account the contact stiffness has been shown to give excellent agreement with the measurements. The application range of this type of friction model has been successfully tested by comparing the prediction performance with a range of material combinations. The results suggest that the validity range of the enhanced rate-and-state model can be extended up to mid-high frequencies.

References

[1] Wang S., Woodhouse J.: The Frequency Response of Dynamic Friction: A New View of Sliding Interfaces. *Journal of the Mechanics and Physics of Solids* **59(5)**:1020-1030, 2011.

[2] Butlin T., Woodhouse J.: Friction-induced Vibration: Model Development and Comparison with Large-scale Experimental Tests. *Journal of Sound and Vibration* **332(21)**:5302-5321, 2013.

[3] Cabboi A., Putelat T., Woodhouse J.: The Frequency Response of Dynamic Friction: Enhanced Rate-and-State Models. **Under review**, 2016.

[4] Bureau, L., Baumberger, T., Caroli, C.: Non-Amontons Behavior of Friction in Single Contacts. *European Physical Journal E* **19 (2)**:163-169, 2006.

Acknowledgements

The authors would like to thank Neil Houghton for his crucial contribution to design and construction of the test rig. Alessandro Cabboi and Thibaut Putelat both acknowledge support from the EPSRC programme grant "Engineering Nonlinearity" (ref. EP/K003836/1).

NANOTRIBOLOGY STUDY WITH T-SHAPE PROBE BY ATOMIC FORCE MICROSCOPY

Qiuquan Guo[1,2], Xiaobing Cai[1] & Jun Yang [1,2a]
[1]*Mechanical & Materials Engineering, The University of Western Ontario, London, Ontario, Canada*
[2]*Biomedical Engineering Program, The University of Western Ontario, London, Ontario, Canada*

Summary With the continuous development of materials science, microscopic material design and microstructure build-up are essential to realize desired properties which has attracted more and more attention. Other than the bulk properties of the material, the properties on the microscopic surface of the material, particularly the friction and adhesion properties, have played a crucial role in the design of materials, especially for the development of biomimetic materials. In this study, taking cartilage as a model sample, we employed a facile atomic force microscopy based nanotribology method with T-shape probe to investigate the friction coefficient of materials at nanoscale. Compared to other methods, the complicated force calibration processes are eliminated with this new method, thus the process is more practical and the results are more accurate.

INTRODUCTION

Although macroscale coefficients of friction can be assessed using the surface force apparatus, the results can barely reflect the design of microstructure and the development of the material at microscale. Nanotribology is the study of friction phenomena at nanometer scale, which plays a significant role in many scientific and technological areas. It originates from the short-range molecular forces. Although different techniques have been developed for friction measurement at microscale, the simplicity of the process and accuracy of the results are still a main issue. Atomic force microscopy (AFM) is employed as a highly accurate technique to perform nanotribology study. In literature, a few other AFM based measurement techniques were also introduced. However, they often require the complex process of force calibration or need the assistance of other ancillary equipment of finish the measurement, which further complicates the process.

Base on technology development, measurement of the frictional response of articular cartilage at the microscale even nanoscale became possible. Our group has developed a new method with T-shape probe, which eliminates the requirements of force calibration . Not only the process is simple, the results are more accurate which could provide as credible data for both scientists and engineers to design the implantable materials. With the development of biomaterials, more and more biomimetic materials are being introduced as implants. Artificial joints, one of the most popular implantable materials, attracts great attention from scientists and engineers, and artificial joint cartilage plays the main role for load and friction transmission. The high reliability and durability of the artificial cartilage is crucial. Among the various properties to consider, one of the important properties is the friction, which has been studied for decades.

For cartilage materials, understanding of the friction coefficient will directly determine the success of the implant. The functional lifetime of articular cartilage is dependent on minimizing friction and wear. Therefore, degradation of either part of articular cartilage leads to increased friction, wear and reduction of mobility that may lead to joint pain. Thus, the measurement of friction at nanoscale is of significant importance.

MATERIALS AND METHOD

Materials and Apparatus

Porcine articular cartilage, purchased from grocery store and kept in the fridge at 4°C, was used within 2 days from purchased. Dulbeccco's Phosphate-buffered saline (PBS) was used as rinsing solution. Highly oriented pyrolytic graphite (HOPG) was used as calibration sample. Polydimethylsiloxane (PDMS) was used as substrate to fix the sample. Atomic Force Microscope (Veeco, Dimension 3100) and T-shaped cantilever (HMX-10, Veeco Inc.) were used to conduct the measurement.

Friction Coefficient Theory

In literature, there are two AFM methods being proposed for friction coefficient measurements, both of which require high accurate ancillary equipment or accessories to conduct the measurement. In order to simply the measurement process, a T-shaped AFM cantilever was employed into this measurement. In contact mode, the change in normal voltage signal ΔVn on the AFM photodetector is proportional to the normal loading force Fn. Applying T-shape cantilever method, normal voltage signal and the lateral voltage signal is only needed for friction coefficient measurement.

$$\Delta V_{Ln} = C_0 F_n = C_0 k_c S_n \Delta V_n = C'_0 \Delta V_n \tag{1}$$

$$\Delta V_{Lf} = C_1 F_f = C_0 F'_n \tag{2}$$

$$F'_n = \frac{F_f H}{D}. \quad \Rightarrow \quad F_f = \frac{\Delta V_{Lf} D}{C_0 H} \tag{3}$$

$$\Rightarrow \quad \mu = \frac{F_f}{F_n} = \frac{\Delta V_{Lf}}{C_0 F_n} \frac{D}{H} = \frac{\Delta V_{Lf} D}{C_0 k_c S_n \Delta V_n H} = \frac{\Delta V_{Lf}}{C'_0 \Delta V_n} \frac{D}{H}. \tag{4}$$

Where ΔV_{Ln} is lateral voltage signal, ΔV_{Lf} is lateral voltage change, ΔV_n is normal voltage change, C_0 and C'_0 are coefficients, F_n is normal force, S_n is deflection sensitivity, F_f is friction force, F'_n is equivalent normal force of F_f, k_c is stiffness of the cantilever, H is the height of the tip, D is the distance from the tip to the longitudinal axis of the cantilever, μ is friction

[a)] Corresponding author. Email: jyang@eng.uwo.ca.

coefficient. From equation (4), friction coefficient is determined by the coefficient C_0', D/H, lateral voltage change ΔV_{Lf} and ΔV_n is normal voltage change. The plausible part is the C_0' can be obtained from equation (1), without complex calibration process. D/H can be obtained from scanning electron microscopy (SEM) images, which can precisely determine the geometry parameters. D and H were often provided by the manufacturer as well.

Calibrations

From equation (4), the calibration of coefficient C_0' is essential in friction coefficient measurement. In order to achieve calibration coefficient, the normal voltage ΔV_n increases as the increasing of normal load without commencing scan and the relation. However, it should be noted that, during the calibration, the tip tends to move sideways if the normal load is too big. In order to avoid this problem, we should make sure the collected calibration data are in good linearity.

EXPERIMENTAL AND RESULTS

Calibration of coefficient C_0'

Fig. 1 shows the relation between the resultant lateral voltage signal ΔV_{Ln} and the normal voltage ΔV_n when an increasing normal load. The calibration of the coefficient C_0', 0.0968, is obtained by the linear relationship between normal voltage change and lateral voltage change when an increasing normal load applied to the tip without scanning.

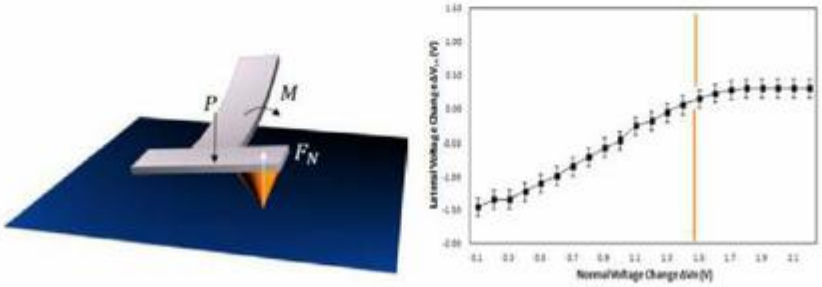

Figure 1. Left: schematic of loading; Right: calibration of the coefficient C_0' according to the linear relationship between ΔV_{Ln} and ΔV_n (data on the left of the right line was used only) when an increasing normal load applied to the tip without scanning.

Friction Coefficient Measurement

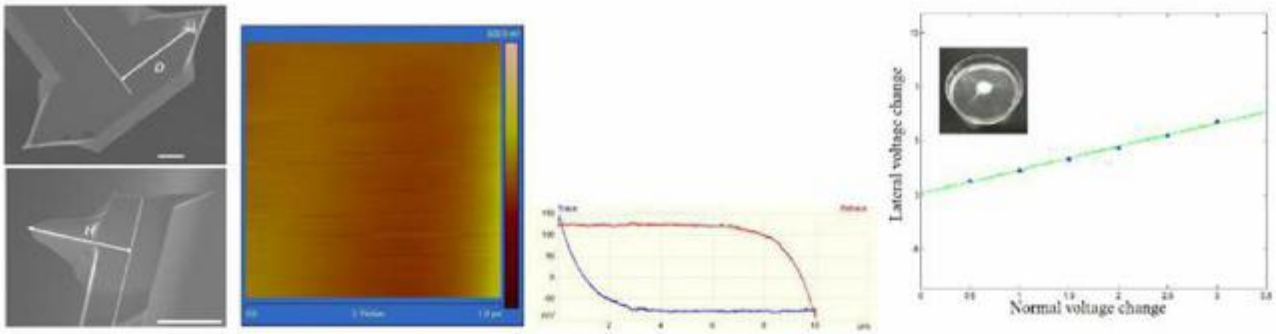

Figure 2. Left to right: (a) SEM images for determining D and H, scale bar 5μm; (b) friction mapping; (c) typical friction profile for each measurement line; (d) the relation between lateral voltage change (mV) and normal voltage change (V).

Simply applying SEM to scan the images of a T-shaped cantilever. From Fig. 2, the cantilever we used in this research was with tip height (H) of 5.54 μm and tip offset (D) of 18.5 μm, D/H = 3.34. Fig 2c is a typical friction measurement profile, which was used to calculate the lateral voltage change at certain normal voltage applied. Images of articular cartilage friction (Fig. 2b) mapping were obtained at a scanning rate of 0.5 Hz in PBS buffer solution and scan size was 1 μm and 5 μm. The friction coefficients of cartilage in PBS solution was measured to be 0.284, which fell in the range of 0.02 ~0.16 .

CONCLUSIONS

A facile AFM based nanotribology method was applied to investigate the friction coefficient of cartilage material under its biological condition. The measured friction coefficient is well consistent with results from literature. More importantly, without complex calibration processes, the technique is practical for repeatable and accurate measurement.

References

[1] Chizhik, Sergei A, Krzysztof Wierzcholski, Anastasia V Trushko, Mariya A Zhytkova and Andrzej Miszczak. "Properties of Cartilage on Micro- and Nanolevel." Advances in Tribology 8, (2010).

[2] Liu, E., B. Blanpain and J. P. Celis. "Calibration Procedures for Frictional Measurements with a Lateral Force Microscope." Wear 192, no. s 1–2 (1996): 141-150.

[3] Liu, Yu, Kar Man Leung, Heng-yong Nie, Woon Ming Lau and Jun Yang. "A New AFM Nanotribology Method Using a T-Shape Cantilever with an Off-Axis Tip for Friction Coefficient Measurement with Minimized Abbé Error." Tribology Letters 41, no. 1 (2010): 313-318.

SURFACE LOADING OF LAYER-SUBSTRATE SYSTEM UNDER PLANE-STRAIN CONDITION WITH SURFACE EFFECTS

Thamarai Selvan Vasu and Tanmay K Bhandakkar *

Department of Mechanical Engineering, Indian Institute of Technology, Powai, Mumbai, India

Summary Layered-substrate system subjected to arbitrary normal and tangential surface loading with surface effects based on Gurtin-Murdoch model is solved semi-analytically through the combination of Airy stress function and Fourier integral transforms under plane strain condition. The obtained solution is applied to study the influence of layer thickness, modulus mismatch between layer and substrate, surface parameters on stresses in layer-substrate system. Lastly a map is presented which indicates whether a layer-substrate system analysis is required or a homogeneous analysis based on layer properties is enough for a given shear modulus mismatch ratio and layer thickness.

INTRODUCTION

Recent years have seen tremendous improvement in material processing and fabrication methods leading to development of layered coatings made up of various combination of materials and having thickness in the range of micrometer to nanometer[1]. Nano-indentation is one of the important process of practical interest, which is used to obtain the elastic properties of thin layer materials. The very first step involved in modeling an indentation problem is to obtain the Green's function relating surface displacement to contact pressure in the contact region by solving the boundary value problem where stresses and displacement are calculated when a known specified load is acting on a given part of surface. In the present study, the problem of elastic layer bonded to an elastic substrate subjected to specified normal and tangential load at the surface under plane-strain condition with surface effects represented using Gurtin-Murdoch (GM) model is solved through the combination of Airy stress function approach and method of Fourier integral transforms.

MODELING AND SOLUTION

Figure 1 shows the schematic of layer-substrate system with the layer having thickness t and adhering perfectly to the substrate. The part $|y| \leq y_0$ of the surface $x = 0$ is subjected to quasi-static normal load $p(y)$ and tangential load $q(y)$ which are assumed to be symmetric about x-axis. The deformation in the layer-substrate system is assumed to be infinitesimal and obeying plane strain condition. The layer and substrate are modeled as a linear elastic isotropic material with Lame's constants μ_n and λ_n with subscript *n* taking values of 1 and 0 for layer and substrate respectively. This subscript representation will be used here onwards to differentiate whether any material property or field variable like displacement or stress corresponds to layer or substrate. The component of displacement along x and y direction in the bulk are denoted by u_{xn} and u_{yn} respectively while the normal and shear component of stresses are represented as σ_{an} and τ_{abn} respectively where a and b can denote x, y or z co-ordinates and $a \neq b$. The surface equilibrium conditions relating the surface and bulk stresses with the applied loading is as follows [2],

$$\sigma_{x1} + \tau^s u_{x1,yy} + p(y) = 0, \;\; \tau_{xy1} + \kappa^s u_{y1,yy} + q(y) = 0, \;\; |y| \leq y_0, \tag{1}$$

where, τ^s and $\kappa^s = 2\mu^s + \lambda^s$ are residual surface energy parameter and surface elasticity parameter respectively. The perfect bonding between the layer and substrate interface ($x = t$) provides the continuity of displacements and tractions,

$$u_{x1}(t,y) = u_{x0}(t,y); \; u_{y1}(t,y) = u_{y0}(t,y); \; \sigma_{x1}(t,y) = \sigma_{x0}(t,y); \; \tau_{xy1}(t,y) = \tau_{xy0}(t,y). \tag{2}$$

The stresses and displacements are represented in terms of Airy stress function and the method of Fourier integral transform is applied to the boundary and interface conditions in Equations (1-2) along with the condition that the stresses and displacements in the substrate should vanish far away from the loaded region ($x \to \infty$), leading to the six simultaneous equations needed to be solved for the six unknowns A_0, B_0, A_1, B_1, C_1 and D_1 as given below,

$$\begin{bmatrix} \circ\, e\xi \circ\ 2 & \circ\, ea & e\xi \circ\ 2 & \circ\, ea & 0 & 0 \\ \xi(f\xi+2) & (bf\xi+2) & \circ\, \xi(f\xi \circ\ 2) & (\circ\, bf\xi+2) & 0 & 0 \\ \xi e^{-2\xi t} & (\xi t \circ\ b)\, e^{-2\xi t} & \xi & \xi t+b & \circ\, \xi\alpha e^{-2\xi t} & \circ\, \alpha(\xi t \circ\ d)\, e^{-2\xi t} \\ \xi e^{-2\xi t} & (\xi t+a)\, e^{-2\xi t} & \circ\, \xi & \circ\, \xi t+a & \circ\, \xi\alpha e^{-2\xi t} & \circ\, \alpha(\xi t \circ\ c)\, e^{-2\xi t} \\ e^{-2\xi t} & te^{-2\xi t} & 1 & t & \circ\, e^{-2\xi t} & \circ\, te^{-2\xi t} \\ \circ\, \xi e^{-2\xi t} & (1 \circ\ \xi t)\, e^{-2\xi t} & \xi & \xi t+1 & \xi e^{-2\xi t} & (\xi t \circ\ 1)\, e^{-2\xi t} \end{bmatrix} \begin{bmatrix} A_1 \\ B_1 \\ C_1 \\ D_1 \\ A_0 \\ B_0 \end{bmatrix} = \begin{bmatrix} 2\bar{p}(\xi)/\xi^2 \\ \circ\, 2i\bar{q}(\xi)/\xi \\ 0 \\ 0 \\ 0 \\ 0 \end{bmatrix} \tag{3}$$

*Corresponding author. Email: tbhanda2@iitb.ac.in

where, $\bar{p}(\xi)$ and $\bar{q}(\xi)$ are the Fourier transform of the applied traction $p(y)$ and $q(y)$ respectively in the loading region and

$$\alpha = \frac{\mu_1}{\mu_0};\ \ a = \frac{\mu_1}{\mu_1 + \lambda_1};\ \ b = \frac{2\mu_1 + \lambda_1}{\mu_1 + \lambda_1};\ \ c = \frac{\mu_0}{\mu_0 + \lambda_0};\ \ d = \frac{2\mu_0 + \lambda_0}{\mu_0 + \lambda_0};\ \ e = \frac{\tau^s}{\mu_1};\ \ f = \frac{\kappa^s}{\mu_1}, \tag{4}$$

α is the shear modulus ratio and along with the ratio λ_n/μ_n represent the mismatch in elastic properties of layer and substrate in the present formulation. *e* and *f* denote the ratio of surface to bulk elastic constants and provide an inbuilt length scale in the present problem. The unknowns A_1, B_1, C_1, D_1, A_0 and B_0 are found by solving Equation (3) in Maple© and the solution for stresses and displacements in layer and substrate can be obtained using the Airy stress function based on these constants.

RESULTS AND CONCLUSIONS

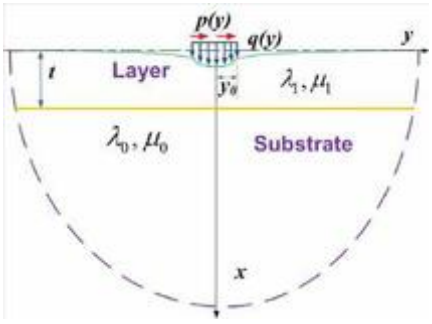

Figure 1: Schematic of layer-substrate system subjected to prescribed normal load $p(y)$ and tangential load $q(y)$ acting in the region $|y| \leq y_0$ under plane-strain condition, where y_0 is referred to be semi-loading length.

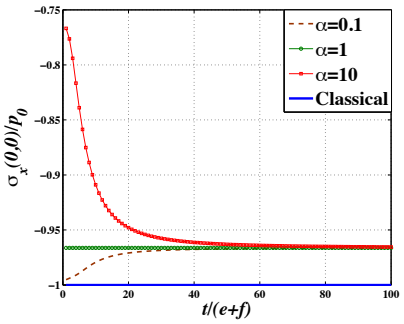

Figure 2: Effect of layer thickness 't' on the bulk normal stress component σ_x at the origin $(x = 0, y = 0)$ with $y_0/(e + f) = 10$ and normalized surface parameters $e/(e + f) = f/(e + f) = 0.5$.

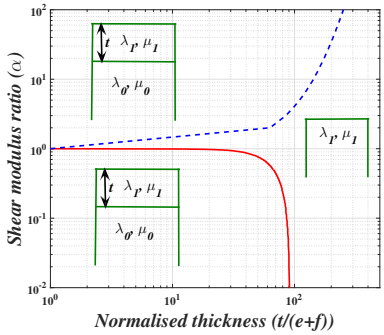

Figure 3: Map of shear modulus ratio α and normalized thickness $t/(e+f)$ with normalized semi-loading length $y_0/(e+f) = 10$.

The obtained solution is used to analyze the combined effect of mismatch in elastic properties of layer with respect to substrate, layer thickness and the surface parameters on the stress and displacement fields in layer and substrate by considering the normal load $p(y) = (p_0\sqrt{y_0^2 \circ\ y^2})/y_0$ and tangential load $q(y) = 0$. Without loss of generality, in all of the numerical results presented in this study, the ratio between the Lame's constants λ_n/μ_n of layer and substrate is taken same and equal to 1.5 and in fact the mismatch in the ratio λ_n/μ_n doesn't affect the results significantly. The loading length y_0 is chosen equal to $10(e + f)$ just to study the results effectively. From the study it's observed that in the presence of surface effects, higher the value of shear modulus ratio α, greater is the deviation of stresses from the classical result where surface effects are not considered. It can be seen from Figure 2 through normal stress component σ_x (0,0), that for smaller layer thickness, the deviation in stresses closer to the surface in the presence of surface effects increases compared to the classical solution (no surface effects), as the layer becomes more and more stiffer compared to the substrate. Further the study is used to propose a map as shown in Figure 3 which identifies combination of shear modulus ratio of layer and substrate and layer thickness where the homogeneous analysis based on the layer elastic properties is not sufficient and layer and substrate both should be modeled as done in the present work. The Green's function relating surface displacement to contact pressure is one of the important outcome of present study, which can be used to solve the contact problem.

References

[1] Subramanian C., Strafford K.N.: Review of multicomponent and multilayer coatings for tribological applications. Wear 165:85-95, 1993.

[2] Zhou S., Gao X.L.: Solutions of half-space and half-plane contact problems based on surface elasticity. Zeitschrift fr angewandte Mathematik und Physik 64:145-166, 2013.

ANALYTICAL SOLUTIONS OF CONTACT PROBLEMS FOR BODIES WITH FUNCTIONALLY GRADED COATINGS

Sergey Aizikovich [1 a)], Andrey Vasiliev [2] & Andrey Petrov [1]
[1] *Research and Education Center "Materials", Don State Technical University, Rostov-on-Don, Russia*
[2] *Research Institute of Mechanics, University of Nizhni Novgorod, Nizhny Novgorod, Russia*

Summary We suggest a solution method for some plane and axisymmetric contact problems of linear elasticity, thermoelasticity and electroelasticity involving half-infinite bodies with functionally graded isotropic or transversally isotropic coatings. The method is based on analytical approximation of kernel transforms of integral equations of corresponding problems. By using this method, approximate analytical solutions can be obtained, effective for a wide range of values of physical and geometric parameters of such problems.

INTRODUCTION

Tribological characteristics of friction units depends on a stress-strain state at a contact interface and in thin subsurface layers. Localization of external friction in subsurface layers stipulates wide usage of functional coatings. Coating deposition can be performed by various methods and for different purposes. Substantial amount of modern functional coatings have inhomogeneous structure. Investigation of stress-strain state of coated bodies is carried out within framework of elastic contact problems. Most of analytical solution methods for contact problems are based on 1950-60th results and are effective only in limited ranges of geometrical and physical parameters [1-4].

Well-known solutions to contact problems are obtained mainly for particular cases of inhomogeneity, allowing to construct exact analytic solutions for systems of differential equations [5,6]. Very few authors considered arbitrary variations of elastic properties by depth of the coating. For example, Wang and Ke et al. used partially linear functions approximation for arbitrary variation of elastic properties by coating depth, but they solved obtained integral equations numerically by collocation method [7].

We constructed and further developed bilateral asymptotic method for solution of dual integral equations, to which wide class of mixed boundary value problems of continuum mechanics can be reduced. Important advantage of the method is its applicability for modeling coatings of any thickness; solutions are proven to be asymptotically exact both for thin and thick coatings. Method can be applied to problems for functionally graded or layered, soft or rigid coatings. Here softness means significant difference in elastic moduli of coating and substrate at their interface; cases of up to 1000 times difference were considered.

BILATERAL ASYMPTOTIC METHOD AND ANALYTICAL SOLUTIONS OF SOME CONTACT PROBLEMS

It is known that some plane and axisymmetric static contact problems of elasticity for inhomogeneous coatings by using integral transforms method are reduced to dual integral equations of a kind

$$\begin{cases} \int_0^\infty T(\gamma)L(\lambda\gamma)R_1(l\gamma)d\gamma = \Theta(0)f(l), \ l \le 1 \\ \int_0^\infty T(\gamma)R_0(r\gamma)d\gamma = 0, \ l > 1 \end{cases} \tag{1}$$

where $L(\lambda\gamma)$ is a kernel transform of the integral equation; $T(\gamma)$ is an image of integral transform for unknown function of contact stresses; $R_0(x\gamma)=\cos(x\gamma)$, $R_1(x\gamma)=\cos(x\gamma)/\gamma$ for the plane punch indentation problem, $R_0(x\gamma)=\gamma J_0(r\gamma)$, $R_1(r\gamma)=J_0(r\gamma)$ for the axisymmetric punch indentation problem; $f(l)$ defines elastic displacements of the surface under the punch; $\lambda = H/a$ is the dimensionless geometric parameter of the problem, where H is thickness of the inhomogeneous coating, a is half-width or radius of the contact area; $\Theta(0)$ is real constant dependent on values of elastic moduli on the coating surface.

In general case, kernel transforms of such integral equation can be constructed only numerically. Study of properties of kernel transforms for continuously inhomogeneous half-space and half-plane shown [8] that if elastic moduli don't turn to zero in any point inside the media and kernel transforms have following properties

$$L(\gamma) = A + B|\gamma| + Cu^2 + \mathrm{O}\left(|\gamma|^3\right) \quad \text{for } \gamma \to 0 \quad \text{and} \quad L(\gamma) = 1 + \frac{D}{|\gamma|} + \frac{E}{\gamma^2} + \mathrm{O}\left(|\gamma|^{-3}\right) \quad \text{for } \gamma \to \infty \tag{2}$$

then the kernel transforms can be approximated with high accuracy by analytic expressions of the following form:

[a)] Corresponding author. Email: saizikovich@gmail.com.

$$L(\gamma) \approx L_N(\gamma) = \prod_{i=1}^{N} \left(\gamma^2 + A_i^2\right) \Big/ \left(\gamma^2 + B_i^2\right),\ A_i,\ B_i \in C \tag{3}$$

Substituting (3) into the initial dual integral equation (1) one can construct analytic expression for the corresponding right-hand side.

Below we provide solutions for some axisymmetric and plane punch indentation problems:

1. Plane problem on a flat punch indentation into an inhomogeneous elastic strip on a homogeneous elastic half-plane:

$$\tau(x) = \frac{P}{a}\left(\frac{1}{\pi\sqrt{1-x^2}} + \sum_{i=1}^{N} C_i \left(\frac{I_1(A_i\lambda^{-1})}{\sqrt{1-x^2}} - A_i\lambda^{-1} \int_x^1 \frac{tI_0(A_i\lambda^{-1})\cosh(A_i\lambda^{-1}(t-x)) - I_1(A_i\lambda^{-1})\sinh(A_i\lambda^{-1}(t-x))}{\sqrt{1-t^2}} dt \right) \right)$$

2. Plane problem on a parabolic punch indentation into an inhomogeneous elastic strip on a homogeneous elastic half-plane:

$$\tau(x) = \left(2\frac{P}{a\pi} + \sum_{i=1}^{N} 2C_i I_1(A_i\lambda^{-1}) \right)\sqrt{1-x^2} - \sum_{i=1}^{N} C_i A_i \lambda^{-1} \int_x^1 \frac{tI_0(A_i\lambda^{-1})\cosh(A_i\lambda^{-1}(t-x)) - I_1(A_i\lambda^{-1})\sinh(A_i\lambda^{-1}(t-x))}{\sqrt{1-t^2}} dt$$

3. Axisymmetric problem on a parabolic (spherical) punch indentation into an inhomogeneous elastic layer lying on an elastic half-space:

$$\tau(r) = \frac{2a\Theta(0)}{\pi R}\left[2L_N^{-1}(0)\sqrt{1-r^2} + \sum_{i=1}^{N} C_i A_i \lambda^{-1} \int_r^1 \frac{\sinh\left(A_i\lambda^{-1}t\right)}{\sqrt{t^2-r^2}} dt \right]$$

In the obtained solutions, constants C_i are determined from the conditions of satisfying solutions to initial dual integral equation (1), P is the indentation force, R is the radius of punch curvature.

Method was also applied to solution of thermoelasticity problems (e.g. hot punch indentation [9]) and electroelasticity problems (for piezoelectric bodies and coatings [10]).

Solutions in analytic form allow to conduct qualitative analysis of different applied problems of tribology, including lubrication theory [11,12]. Numeric examples are given.

The authors acknowledge financial support of the Russian Science Foundation (grant 15-19-10056).

References

[1] Vorovich I.I., Ustinov Iu. A.: Pressure of a Die on an Elastic Layer of Finite Thickness. *J. Appl. Math. Mech* **23**: 637-650, 1959.

[2] Aleksandrov V.M., Vorovich I.I.: Contact Problems for the Elastic Layer of Small Thickness. *J. Appl. Math. Mech* **28**: 425-427, 1964.

[3] Popov G.Ya.: On the Method Of Orthogonal Polynomials In Contact Problems Of The Theory Of Elasticity. *J. Appl. Math. Mech* **33**: 503-517, 1969.

[4] Kalandiya A.I.: Mathematical methods in two-dimensional theory of elasticity. Moscow, USSR 1973.

[5] Guler M.A., Erdogan F.: The frictional sliding contact problems of rigid parabolic and cylindrical stamps on graded coatings. *Int. J. Mech. Sci* **49**: 161-182, 2007.

[6] Awojobi A.O.: On the Hyperbolic Variation of Elastic Modulus in a Non–Homogeneous Stratum. *Int. J. Solids Struct* **11**: 639-748, 1976.

[7] Ke L.-L., Wang Y.-S.: Two-Dimensional Sliding Frictional Contact of Functionally Graded Materials. *Eur. J. Mech. A/Solids* **26**: 171-188, 2007.

[8] Aizikovich S.M., Aleksandrov V.M.: On the Properties of Compliance Functions Corresponding to Polylayered and Continuously Inhomogeneous Half-space. *Soviet. Phys. Dokl* **27**: 40-43, 1982.

[9] Krenev, L.I., Aizikovich, S.M., Tokovyy, Y.V., Wang, Y.-C.: Axisymmetric Problem on Indentation of a Hot Circular Punch into an Arbitrarily Inhomogeneous Half-Space. *Int. J. Solids Struct* **59**: 18-28, 2015.

[10] Vasiliev A.S., Volkov S. S., Aizikovich S.M.: Normal Point Force and Point Electric Charge in a Piezoelectric Transversely Isotropic Functionally Graded Half-Space. *Acta Mech*: DOI 10.1007/s00707-015-1414-3 (published online 14 October 2015).

[11] Kudish I.I., Volkov S.S., Vasiliev A.S., Aizikovich S.M.: Some Criteria for Coating Effectiveness in Heavily Loaded Line Elastohydrodynamically Lubricated Contacts — Part I: Dry Contacts. *J. Tribol* **138**(2): 021504, 2015.

[12] Kudish I.I., Volkov S.S., Vasiliev A.S., Aizikovich S.M.: Some Criteria for Coating Effectiveness in Heavily Loaded Line Elastohydrodynamically Lubricated Contacts — Part II: Lubricated Contacts. *J. Tribol* **138**(2): 021505, 2015

CHARACTERISATION OF EDGE CONDITIONS IN GENERAL INCOMPLETE CONTACTS

David A. Hills[1a)], Rodolfo M. N. Fleury[1]
[1]*Department of Engineering Science, University of Oxford, Oxford, UK*

Summary We use edge asymptotes to describe the stresses very close to the edge of incomplete contacts under cyclic loading, but with constant normal force. The solution allows us to match identically the conditions very close to the contact edge, where cracks initiate, of significantly different problems and correlate, for example, fatigue lives of laboratory experiments with complex prototypical geometries.

INTRODUCTION

The three most commonly occurring contacts are; incomplete, complete and receding. Examples of each are widespread and may be subject to general oscillatory loading in the form of varying normal load, tangential load and differential remote bulk tension. The characterisation of the edge behaviour of each type of contact are necessary to correlate the lives of laboratory specimens with those arising in prototypical geometries. This is easiest for complete contacts because, unless the normal load is reduced to the point where gross separation occurs the contact patch size remains fixed, and this simplifies things greatly. With both receding and incomplete contacts the problem is much more complicated because the contact edge position moves if the normal load changes. An attempt to track out partial slip problems for a Hertzian contact under generally varying normal and tangential loads has been successful [1]. The problem of a rigid flat indenter with rounded edges using edge asymptotes has been solved with the asymptotic approach in [2]. We have also solved the problem for the elastics incomplete contacts (e.g. Hertzian, flat and rounded) using edge asymptotes [3], however the flat and rounded solution there is only true if the one body is rigid and the elastic body is incompressible. A numerical calibration has been done recently for the elastic flat and rounded punch pressed onto an elastically similar half-plane problem, using a three-quarter plane model as an asymptote to the problem [4,5]. Although different aspects of partial slip problems for incomplete contacts have already been tackled, the tractions for the cyclic load under constant normal load has not yet been fully derived in terms of the edge asymptotes. We present here a discussion on the use of edge asymptotes for incomplete contacts under periodic loading, but with constant normal load, as well as the limitations of the assumptions used in the approach. The variation of the shear traction asymptote as a function of the phase angle between the periodic loadings is also presented, which may be helpful in the design of new fretting tests where the state of stress on each edge of the contact is controlled.

ASYMPTOTIC FORM OF INCOMPLETE CONTACTS

Consider the contact shown in Figure 1a. If the coefficient of friction is sufficiently high for all slip to be prevented, the shear traction, $q(x)$, due to an applied shear load, Q, and a bulk tension, $\sigma_0 = \sigma_2$-σ_1, are given by

$$q(x) = \frac{Q}{\pi\sqrt{a^2 - x^2}} \quad \text{and} \quad q(x) = \frac{\sigma_0 x}{\sqrt{a^2 - x^2}}. \tag{1}$$

If $q(s) = K_T/\sqrt{s}$, where K_T is the singular edge asymptote scaling factor and s is the coordinate from the edge of the contact inwards (Figure 1b), then in the presence of both shear traction and bulk tension K_T is given by

$$K_T = \frac{Q}{\pi\sqrt{2a}} + \frac{\sigma_0}{4}\sqrt{\frac{a}{2}} \tag{2}$$

Near the edge of the contact, the contact pressure is given by $p(s) = K_N\sqrt{s}$ (Figure 1b) and K_N is geometry dependent and for simple geometries it may be written in closed form. For a Hertzian contact, for example, K_N is given by

$$K_N = p_0\sqrt{\frac{2}{a}} \equiv \sqrt[4]{\frac{P}{\pi}\left(\frac{E^*}{R}\right)^3}. \tag{3}$$

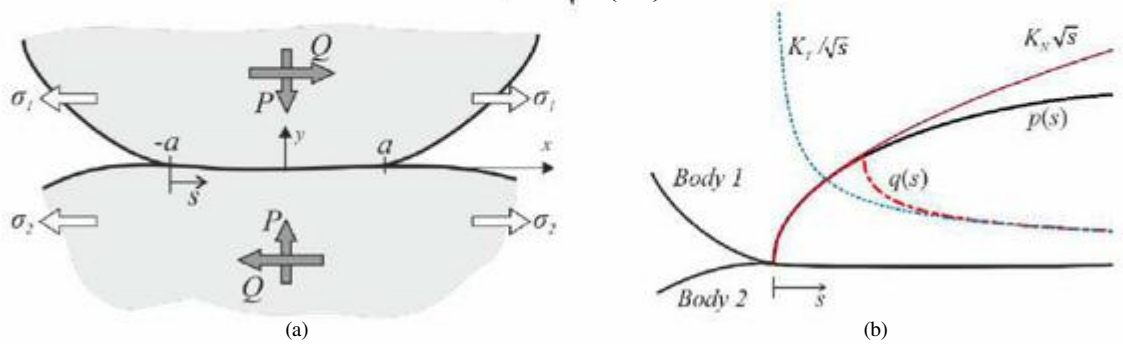

(a) (b)

Figure 1: a) Fretting problem of two elastic bodies subjected to normal and tangential forces and remote bulk tension; b) Square root bounded and square root singular edge asymptotes for the normal and tangential tractions.

[a)] Corresponding author. Email: david.hills@eng.ox.ac.uk

In a cyclic loading problem, unless the applied loading is fully reversing, some frictional shakedown will always occur with the first cycle, so that the steady state extend of the slip zone size, d, is independent of the mean value of Q, σ_0 and K_T. The range ΔK_T is what will determine the size of the slip zone [3], which is given in the 'steady' state of the cyclic loading by

$$fd = \frac{\Delta K_T}{K_N} \tag{4}$$

If the cyclic loading is periodic, i.e. $Q(\mathrm{t}) = Q_m + Q_a \sin \omega t$ and $\sigma(t) = \sigma_m + \sigma_a \sin(\omega t - \phi)$, the range ΔK_T may be written as a function of the shear force amplitude, Q_a, the bulk tension amplitude, σ_a, and the phase angle, ϕ, in a normalised form at the left hand side (L.H.S.) of the contact as

$$\frac{\Delta K_T \sqrt{a}}{Q_a} = \sqrt{\frac{2}{\pi^2} + \frac{1}{8}\left(\frac{\sigma_a^2 a}{Q_a}\right)^2 + \frac{\cos\phi}{\pi}\frac{\sigma_a a}{Q_a}}\,. \tag{5}$$

Equation (5) gives the strength of the variation of the normalised singular asymptote multiplier as a function of the loading amplitude and the phase angle. The results are displayed in Figure 2. The variation of ΔK_T at right hand side of the contact is shifted by an angle π from the behaviour of the left hand side of contact. We also note that when $\phi = \pm\pi$ the edge of contact experience no variation in K_T and both edges experience the same ΔK_T when $\phi = \pm\pi/2$.

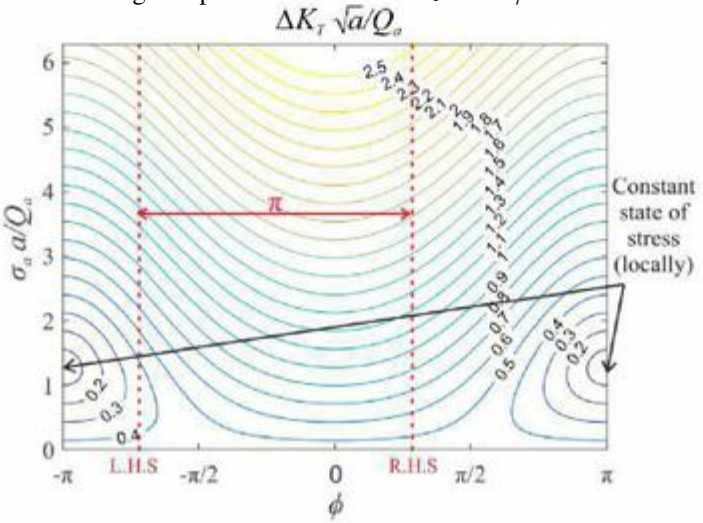

Figure 2: Contour lines of constant ΔK_T at the L.H.S. edge of contact as a function of the dimensionless load parameter $\sigma_a\, a/Q_a$ and the phase angle φ.

CONCLUSIONS

Nucleation of cracks is controlled by the state of stress and slip displacement in the neighbourhoods of the contact edge. We propose that one element of this is the magnitude of ΔK_T, and the relative distributions of shear and bulk tension do not matter. The formulation obtained of ΔK_T for different problems may be used to design new fretting fatigue tests where the conditions at both edges of the contact are controlled. This allows for the design of tests where, for example, the probability of failure on both edges of contact are identical, i.e. same ΔK_T, or having similar crack initiation times between tests but with varying crack propagation time. The work developed so far is only valid if the normal load is constant throughout the test. Hence, K_N and the contact size also remain constant. The remaining challenge is to apply asymptotic methods when the normal load is varying as well. The underlying reason for the difficulty is that the asymptotes are attached to the contact edge and tracking out the moving origin means that the contact law must also be incorporated in some form. If this can be done, it potentially means that laboratory calibrations for fretting fatigue strength for any kind of incomplete contact, and subject to any load history may then be correlated with complex prototypes. We will then have a comprehensive procedure for establishing true material properties which are fretting fatigue strengths, and which is the objective of the research taken as a whole.

References

[1] Barber, J.R., Davies, M., Hills, D.A., Friction elastic contact with periodic loading, Intl. J. Solids Struct., 48, (2011), 2041-2047.

[2] Mugadu, A., Hills, D. A. Barber, J.R. and Sackfield, A., The application of asymptotic forms to characterising the process zone in almost complete frictional contacts. Intl. Jnl. Solids Struct., 42, (2004), 385-397.

[3] Dini, D. and Hills, D. A., Bounded asymptotic solutions for incomplete contacts in partial slip, Intl. Jnl. Solids Struct., 41, (2004), 7049-7062.

[4] Fleury, R.M.N., Hills, D.A., Barber, J.R., Flat punch with rounded edges-part I: basic contact characteristics in terms of Williams notch intensity factors, Intl. J. Solids Struct., *in print*.

[5] Fleury, R.M.N., Hills, D.A., Barber, J.R., Flat punch with rounded edges-part II: near edge asymptotes and the effect of shear, Intl. J. Solids Struct., *in print*.

DETERMINATION OF FRICTIONAL SLIP ZONE FROM A PERFECT BOND SOLUTION

George G. Adams[a)]
Mechanical Engineering, Northeastern University, Boston, MA, USA

Summary A variety of solutions exist for stress fields on perfectly bonded interfaces. Such solutions are often singular near the edge of contact. However these stress fields are not relevant for a frictional interface if the ratio of shear to the magnitude of the normal stress exceeds the coefficient of friction. The determination of the corresponding friction solution with stick and slip zones can be quite complicated, although some solutions have been obtained for special cases. In this paper a method is developed which allows the length of the frictional slip zone as well as the magnitudes of the stresses in the slip zones to be determined from the solution for a perfect bond without the need to re-solve the complete friction problem.

INTRODUCTION

Many solutions exist for the stresses along perfectly bonded interfaces. However the determination of the stress field and corresponding slip zone(s) for friction boundary conditions can be quite complicated. One relatively simple classical example is the Catteneo-Mindlin problem (e.g. [1]) in which a slightly curved elastic half-space is pressed against a flat elastic half-space while also applying a tangential force (Fig. 1). This problem was considered without including the effect of normal/shear stresses on relative tangential/normal displacements. At the edges of the contact, the perfect bond solution is singular in the shear stress but bounded in the normal stresses. Thus frictional slip is inevitable and in this case; an exact solution was obtained using a "corrective" solution.

Other configurations, however, do not readily allow a corrective frictional slip solution to be obtained. Consider for example a rigid indenter pressed against and bonded to an elastic half space. The perfect bond solution is given in [2] with oscillating singularities at both ends. The corresponding problem with friction was solved by Spence [3], but the solution is quite complicated.

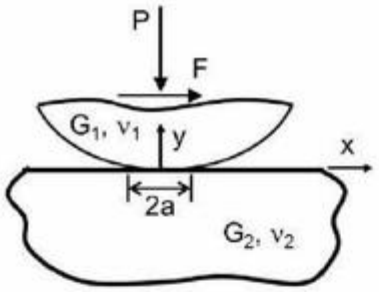

Figure 1. Catteneo-Mindlin Problem where G is the shear modulus and ν is Poisson's ratio.

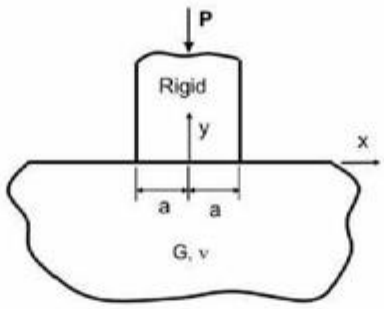

Figure 2. Rigid punch bonded to an elastic half-plane.

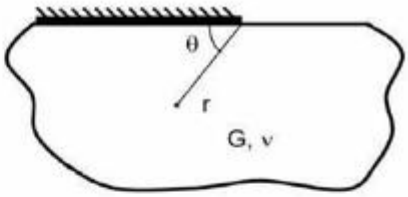

Figure 3. Region near the $x = a$ corner in Figures 1 and 2.

PROBLEM FORMULATION

As a representative case consider the rigid punch problem of width *2a* perfectly bonded to and pressed against a rigid base (Fig. 2). The existing solution in the literature [2] is denoted here as the bonded solution (τ_{ij}^{B}). We seek a correction solution (τ_{ij}) such that the sum ($\tau_{ij}^{f} = \tau_{ij} + \tau_{ij}^{B}$) satisfies the appropriate equations of plane strain linear elasticity as well as the conditions of Amontons-Coulomb friction, i.e.

$$\tau_{xy} + \tau_{xy}^{B} = -\mathrm{sgn}(x)\mu(\tau_{yy} + \tau_{yy}^{B}) \text{ and } \mathrm{sgn}(x)u_x < 0, \text{ for } b < |x| < a \tag{1}$$

where $\mathrm{sgn}(x)$ is equal to +1 if $x > 0$ and equal to -1 if $x < 0$, the stick zone is denoted by $-b < x < b$, and μ represents the coefficient of friction.

The Mellin transform of a suitably regular function *f(r)* on $0 < r < \infty$ is given by

[a)] Corresponding author. Email: adams@coe.neu.edu.

$$\hat{f}(s)=\int_0^{\infty} f(r)r^{s-1}dr \quad \text{and its inverse by} \quad f(r)=\frac{1}{2\pi i}\int_{c-i\infty}^{c+i\infty}\hat{f}(s)r^{-s}ds \tag{2}$$

and has been shown in [4] to be useful in analyzes near singular corners. Its advantage over the simpler asymptotic method ([5]) is that it also allows the stresses and displacements to be determined away from the immediate region of the wedge tip.

It is well-known that the stresses and displacements can be found from Airy stress function which is a solution of the biharmonic equation. Application of the Mellin transform proceeds as in [6],[7] and enables a solution to be obtained in terms of a finite series of terms representing the slip displacements along the frictional interface, i.e.

$$u_r(r,0)=\sum_{m=1}^{M} f_m r_0^{-(m-1/2)} r^{m-1}(r_0-r)^{3/2}+\sum_{n=1}^{N} g_n r_0^{-(n-\lambda+1/2)} r^{n-\lambda}(r_0-r)^{3/2} \tag{3}$$

where λ represents the order of the stress singularity of the bonded problem i.e. $\tau_{ij}\to Q_k r^{-\lambda}$ as $r\to 0$. Further details of the analysis parallel that used in [6] and [7] for different problems.

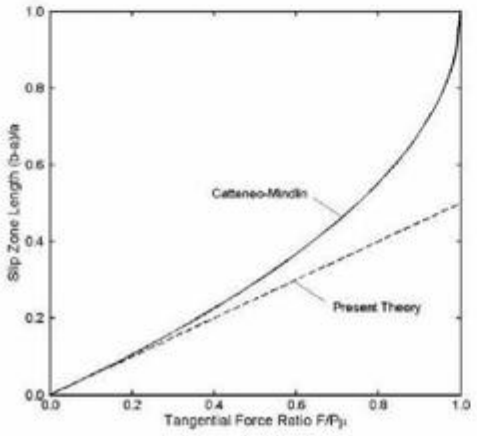

Figure 4. Slip zone length vs. ratio of tangential force to available friction force for Catteneo-Mindlin problem and for present theory.

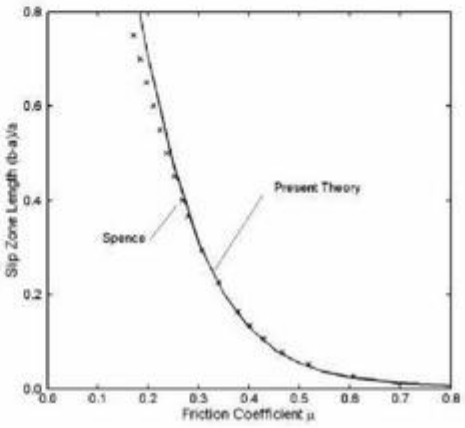

Figure 5. Slip zone length vs. coefficient of friction for a rigid punch. Solution from Spence is shown with crosses.

RESULTS AND DISCUSSION

In Figure 4 is shown the variation of the slip length with the ratio of the tangential force to the available friction force for the exact Catteneo-Mindlin problem along with the present theory. The agreement is very good up to a slip length of about 20% of the contact half-width. Figure 5 shows the variation of the slip zone length with the friction coefficient from Spence and also for the present theory, both with $\nu = 0.3$. In this case the agreement is excellent even for slip zones greater than half of the punch half-width.

CONCLUSIONS

A method based upon Mellin transforms has been developed to allow the determination of the slip zone length and the stresses in the slip zone from a known solution for a perfectly bonded interface. This method has been applied to the Catteneo-Mindlin problem and to the indentation of an elastic half-plane by a rigid punch with perfect bonding. It both cases it was shown to give solutions accurately. It is also being applied to other problems such as that of a semi-infinite elastic strip pressed against a rigid base.

References

[1] Barber, J.R.: Elasticity, 2nd edition, Kluwer Academic Publishers, 2002.

[2] Muskhelishvilli, N.I.: Some Basic Problems of the Mathematical Theory of Elasticity, P. Noordhoff Ltd., 1953.

[3] Spence, D.A.: An eigenvalue problem for elastic contact with finite friction. *Proc. Camb. Phil. Soc.* **73**:249-268, 1973.

[4] Tranter, C.J.: The use of Mellin Transforms in finding the stress distribution in an infinite wedge. *Q. J. Appl. Math.* **1**:125-130, 1948.

[5] Williams, M.L.: Stress singularities resultring from various boundary conditions in angular corners of plates in extension. *J. Appl. Mech.* **19**:526-528, 1952.

[6] Adams, G.G.: Adhesion and pull-off force of an elastic indenter from an elastic half-space. *Proc. Royal Soc. A* **470**:20140317, 2014

[7] Adams, G.G.: Critical value of the generalized stress intensity factor for a crack perpendicular to an interface. *Proc. Royal Soc. A* **471**:20150571, 2015.

UNIFYING DIFFERENT MEASUREMENTS OF DYNAMIC FRICTION

Andrew McKay[1a)], Alessandro Cabboi[1] & Jim Woodhouse[1]
[1]*Department of Engineering, University of Cambridge, Cambridge, UK*

Summary A regularised version of the Dieterich-Ruina rate and state friction law gives promising results towards a general constitutive law of dynamic friction. A pin-on-disc rig for producing a frictional frequency response is used in this work to reproduce a number of different frictional measurements. The regularised rate and state law provides a good fit to these results and the model parameters show sensitivity in accordance with their physical interpretations.

DEVELOPMENT OF RATE AND STATE FRICTION LAWS

A general constitutive model of friction is a longstanding problem that has been tackled in many fields such as tribology, position control, vibration and rock mechanics. A hierarchy of difficulty of frictional problems is proposed in [1] that suggests different levels of model complexity may be required for each problem. A Stribeck law is a commonly used model where the steady friction force is measured for a range of speeds to create a friction-velocity curve. However, many tests reveal that friction depends on more than sliding velocity. Rate and state friction models were proposed in [2], with a dependence on the rate of sliding but also a dependence on an unobservable state variable ϕ that is used to describe the state of the interface. The general form of these laws is

$$\mu = F(v, \phi); \qquad \dot{\phi} = -G(v, \phi) \tag{1}$$

where μ is the coefficient of friction, v is the relative sliding velocity and ϕ is the state variable. The law used in the following work is a regularised version of the Dieterich-Ruina law as described in [3]. The regularisation includes removal of the logarithmic dependence on velocity by making the approximation $2\sinh(\mu/a) \approx \exp(\mu/a)$, a residual interfacial strength at high velocity and bounded interfacial healing. Incorporating an interfacial stiffness k the friction force is finally obtained from the coupled ODEs

$$\dot{\tau} = k\left\{v - 2V_* \sinh(\tau/a\sigma)\exp(-\mu_*/a)\left(=+\phi\right)^{-b/a}\right\}; \qquad \dot{\phi} = (a-\phi)/t_{**} - |v|\phi/L \tag{2}$$

where τ and σ are the friction and normal force, μ_*, V_*, L, a and b are parameters present in the Dieterich-Ruina law and $=$ and t_{**} are parameters introduced to control the residual strength at high velocities and the timescale of interfacial healing respectively.

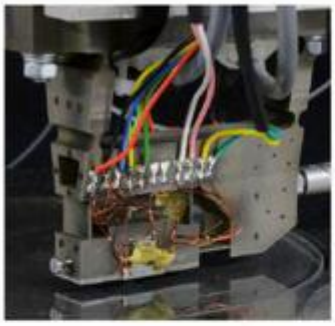

Fig. 1: Sensor head of pin-on-disc rig

Recent success has been had with this law to describe the result of a type of frictional frequency response function where the dynamometer head of a pin-on-disc rig (fig.1) is perturbed by band limited random noise to superpose a velocity fluctuation $v'(\omega)$. The resulting fluctuation in friction force $f'(\omega)$ can then be used to calculate a transfer function $\beta(\omega) = f'(\omega) / v'(\omega)$. The frictional frequency response function $\beta(\omega)$ is found to be a complex function of frequency and (2) provides an excellent fit to the results. Further details of the results as well as an investigation of different state evolution laws can be found in [4].

The aim of the research described in this paper is to build upon the success of the fit to the $\beta(\omega)$ measurements and use the same law to fit other results produced by the same pin-on-disc rig. The rig is capable of performing a number of friction tests all under the same contact conditions. This will allow fitting of the model across all the tests and will reveal the sensitivity of different model parameters to different tests.

IDENTIFICATION AND SENSITIVITY OF THE MODEL PARAMETERS

Fig. 2 shows some of the tests that can be performed on the pin-on-disc rig. The dynamometer head of the rig (fig. 1) is instrumented with strain gauges, piezo sensors and MEMs accelerometers in the normal and frictional directions. The experimental data shown in fig. 2a,b,c is from the piezo sensor and 2d is from the MEMs accelerometer. The results show that the regularised law can provide a good fit to different types of experiment and different model parameters were found to be sensitive to different tests.

Fig. 2a shows the classic Stribeck curve, which can be described in the rate and state framework as the result of ϕ decaying to its velocity dependent steady state i.e. $\mu_{ss} = F(v, \phi_{ss}\ v))$. A local minimum is revealed; in the regularised law

[a)] Corresponding author. Email: am2198@cam.ac.uk.

(2) the position and presence of this local minimum are heavily influenced by the parameter $=$ and the fit is found to be highly sensitive to it. Equation 2 with a non-zero value of $=$ predicts an N shaped steady-state curve and at very low velocities it can be seen that the experimental results start to turn. The experiment also showed a turning point at high velocities; this is not captured by the regularised law and may suggest a requirement for an extra state variable such as interfacial temperature. The Dieterich-Ruina law is included to highlight that for the same parameters as $v \to 0,\ \mu \to +\infty$.

Fig. 2b shows speed jumps where a rapid jump in disc velocity produces a rapid jump in friction followed by a slow relaxation to the higher steady state level. This new level corresponds to the velocity strengthening seen for these velocities in figure 1a. The fit to the results is very sensitive to the parameter L: the length scale associated with the renewal of the population of contacting asperities.

Fig. 2c shows the result of sinusoidal reciprocating motion of the disc. When the friction force is plotted against disc displacement an asymmetric loop is observed. Approaching zero velocity the friction force is lower than after passing through zero. As commonly observed – the static coefficient of friction increases with the period of rest. In the regularised law the rate of this interfacial healing is controlled by the parameter t_{**} and in the reciprocating test when passing through zero the interface strengthens and this strength persists over the length L. This is reflected in a sensitivity to these parameters during fitting.

Finally, one result from [4] is shown in figure 2. The Nyquist plot of the $\beta(\omega)$ measurement shows that it is a complex function of frequency and that (2) again provides a good fit.

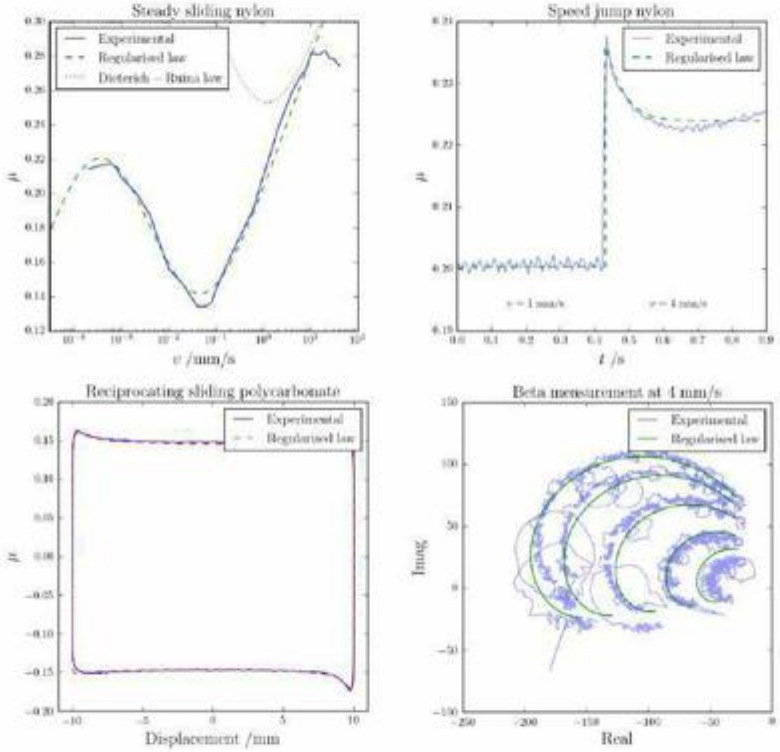

Fig. 2- a) Steady sliding ; b) Speed jump; c) Reciprocating sliding: amplitude of 10 mm at 0.8 Hz; d) *β(ω)* measurement for 10, 20, 30, 40 and 50 N

CONCLUSIONS

The regularised Dieterich-Ruina law is shown to provide an excellent fit to a range of experiments performed on a pin-on-disc rig. The removal of the singularity at $v = 0$ is validated by both the steady sliding and the reciprocating tests. The different tests reveal different parameter sensitivities that agree with the expected microphysics of the contacting asperities such as the interfacial healing at very low velocities and the memory length. The different parameter sensitivities to different tests may help explain the lack of convergence from different fields on a single friction law. By performing more types of tests and with a range of materials we hope to provide further validation of this model.

References

[1] Woodhouse J., Putelat T., McKay A.: Are there reliable constitutive laws for dynamic friction?, Phil. Trans. R. Soc. A, 373: 2051, 2015

[2] Ruina A.I.: Slip instability and state variable friction laws. J. Geophys. Res., 88: 10359-10370, 1983

[3] Putelat T., Dawes J.H.P, Willis J.R.: Sliding interactions of two frictional interfaces, J. Mech. Phys. Solids, 55: 2073-2105, 2007

[4] Cabboi A., Putelat T., Woodhouse J.: The Frequency Response of Dynamic Friction: An Improved Rate-and-State Model, **under review**

AN INITIALLY CYLINDRICAL ELASTIC MEMBRANE WRAPPED AROUND A RIGID CYLINDER

Alexey M. Kolesnikov *
Institute of Mathematics, Mechanics and Computer Science, Southern Federal University, Rostov-na-Donu, Russian Federation

Summary We consider finite axisymmetric deformations of an initially cylindrical membrane made of an incompressible, homogeneous, isotropic elastic material. We use a strain energy function of Bartenev–Khazanovich (Varga). A part of the membrane is placed over an end of a fixed rigid cylinder. The other end of the membrane is free or is subjected to a tensile force. We use Coulomb's friction law of dry friction in a contact area. We study a length of the membrane wrapped around the rigid cylinder, which is needed for the equilibrium of the membrane.

FORMULATION

Shells and membranes often interact with solid bodies. For hyperelastic membranes, such studies are few. In his pioneer work Kydoniefs [2] studied the finite axisymmetric static deformations of a cylindrical membrane that contains a rigid body. Using similar approach the dynamics of a rigid body was simulated in the work [3]. The contact problem of the balance and movement of a rigid body into an elastic tube has applications in biomechanics [5, 6, 7]. Other contact problem of the interaction a rigid body and an elastic cylindrical membrane is investigated in [4, 8]. In these works a rigid tube contains an inflated cylindrical membrane. In the works [2, 4, 5] the contact problem of a membrane with a rigid frictionless body has been considered. In [8] an adhesive and frictionless contact has been considered. The adhesive contact was modelled as a perfectly sticking contact without slip. In [6, 7] dry and viscous frictions has been considered.

In this work we study the equilibrium of a thin-walled elastic tube wrapped around a rigid cylinder (Fig. 1). The tube is modeled by a semi-infinity cylindrical membrane of initial radius r_0 with uniform thickness h (Fig. 1*a*). Let $R_0 > r_0$ be a radius of the rigid cylinder (Fig. 1*b*). The end of the membrane is placed over the rigid cylinder (Fig. 1*c, d*). We assume that Coulomb's law holds for the frictional stresses between the membrane and the cylinder. We denote by f the coefficient of static friction. Also note that the equilibrium of the membrane wrapped around the rigid cylinder is impossible for a frictionless contact. It is clear that there is a minimum length L at which the membrane does not slide off the rigid cylinder. The main goal of this study is the calculation of this minimal length L. We consider two problems. In the first problem the membrane is free at infinity (Fig. 1*c*). In the second problem the membrane is subjected to a tensile force at infinity (Fig. 1*d*).

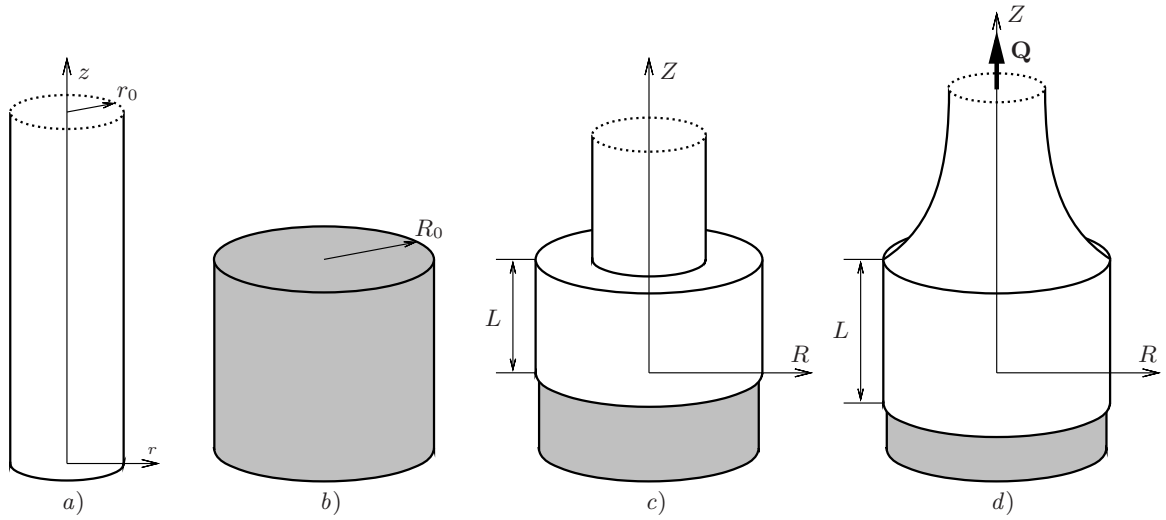

Figure 1: *a*) The initially cylindrical membrane with radius r_0, *b*) the rigid cylinder with radius R_0, *c*) the membrane wrapped around the rigid cylinder, *d*) the membrane wrapped around the rigid cylinder and subjected to a tensile force.

*Corresponding author. Email: Alexey.M.Kolesnikov@gmail.com

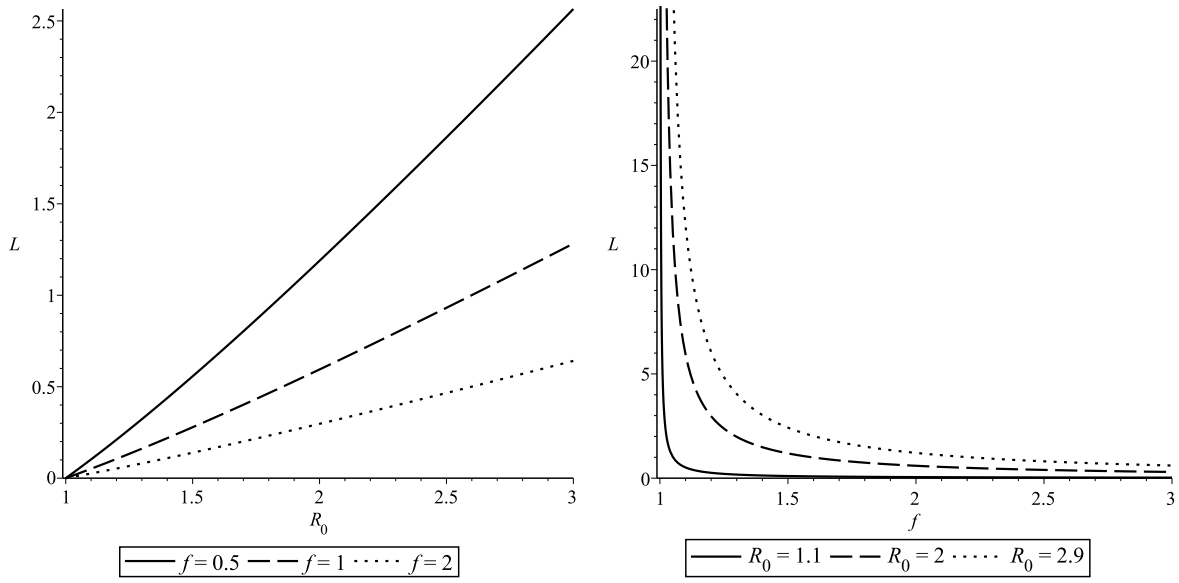

Figure 2: The minimal length L of the membrane wrapped around the rigid cylinder, which is needed for the equilibrium of the membrane, vs *a*) the radius R_0 of the rigid cylinder for different friction coefficients f *b*) the friction coefficient f for different radii R_0 of the rigid cylinder.

RESULTS

Here, we present a solution of the first problem. Using the equilibrium equations of elastic membranes [1] it can be shown that the deformed membrane has the shape presented in Fig. 1c. The first part of the membrane is stretched over a side surface of the cylinder. The second part of membrane is a circular annulus. The third part is undeformed.

For the membrane made of Bartenev–Khazanovich material we have a solution in explicit form. We obtain the minimal length L as the function of r_0, R_0 and f in the following form

$$L = \frac{2r_0\rho_0}{f} \ln\left(\frac{3\rho_0\,(\rho_0 \circ 1)}{2\left(\rho_0^2 \circ \sqrt{\rho_0}\right)}\right), \quad \rho_0 = \frac{R_0}{r_0}.$$

The dependence of f on L is inversely proportional. The effect of the friction coefficient f on the minimal length L is observed for $r_0 = 1$ and for the different radii R_0 of the rigid cylinder in Fig. 2b. It is clear that if $f \to 0$ then $L \to \infty$.

The dependence of R_0 on L is more complex. But it is close to linear law. The effect of the radius R_0 of the rigid cylinder on the minimal length L is observed for $r_0 = 1$ and for the different friction coefficients f in Fig. 2a. Increasing the radius R_0 leads to growth of the length L.

Acknowledgements

The work was supported by the Ministry of Education and Science of Russian Federation (the state contract No. 9.665.2014/K).

References

[1] Green A. E. and Adkins J. E.: Large elastic deformations and non-linear continuum mechanics. Clarendon Press, Oxford, 1960.

[2] Kydoniefs A. D.: Finite deformation of an initially cylindrical elastic membrane enclosing of a rigid body. Quart. Journ. Meck, and Applied Math. XXII, Pt. 3: 319-331, 1969.

[3] Bertuzzi, A., Martinelli, R., Ronzoni, G., Salinari, S.: Peristaltic transport of a solid bolus. Journal of Biomechanics. 16: 459464, 1983.

[4] Khayat R. E., Derdouri A., Garcia-Rejon A.: Multiple contact and axisymmetric inflation of hyperelastic cylindrical membranes. Proceedings of the Institution of Mechanical Engineers, Part C: Journal of Mechanical Engineering Science. 207: 175-183, 1993.

[5] Eftaxiopoulos D. A., Atkinson C.: A nonlinear, anisotropic and axisymmetric model for balloon angioplasty. Proc. R. Soc. A. 461: 1097-1128, 2005.

[6] Miftahof R., Fedotov E.: Intestinal propultion of a solid non-deformable bolus. Journal of Theoretical Biology. 235: 57-70, 2005.

[7] Miftahof R., Akhmadeev N.: Dynamics of intestinal propulsion. Journal of Theoretical Biology. 246: 377-393, 2007.

[8] Patil A., Nordmark A., Eriksson A.: Free and constrained inflation of a pre-stretched cylindrical membrane. Proc. R. Soc. A. 470: 1-6, 2015.

A TWO-DIMENSIONAL DOUBLE-HERTZ MODEL FOR ADHESIVE CONTACT BETWEEN ELASTIC CYLINDERS

Fan Jin[1, a], Xu Guo[2]
[1]*Institute of Systems Engineering, China Academy of Engineering Physics, Mianyang, Sichuan, PR China*
[2]*Department of Engineering Mechanics, Dalian University of Technology, Dalian, PR China*

Summary This report provides a cohesive zone model for two-dimensional (2D) adhesive cylindrical contact by extending the classical double-Hertz model of elastic spheres [1]. This is achieved by describing the adhesive force in terms of the difference between two Hertzian pressures corresponding to different contact widths. Closed-form analytical solutions are obtained for the interfacial traction, deformation field and the equilibrium relation among applied load, contact half-width and the size of cohesive zone. Based on these results, a complete transition between the JKR and the Hertz type contact models is captured by defining a dimensionless transition parameter, which governs the range of applicability of different models. JKR and Hertz type solutions are included as two limiting cases of the present model. The present model can serve as an alternative cohesive zone solution to the 2D Maugis-Dugdale solution [2], [3].

TWO-DIMENSIONAL DOUBLE-HERTZ MODEL

Fig. 1 shows a rigid cylinder of radius R in frictionless adhesive contact on an elastic half-plane with a Young's modulus E and a Poisson radio ν. A normal load P is prescribed with unit N/m, which is negative when tensile. Contact occurs over a rectangular region of width 2a. The distribution of surface traction consists of two terms: the Hertz pressure p_H acting on a contact region of width $2a$ and the adhesive tension p_A acting on an interaction zone of width $2c$. The noncontact regions bounded by half-widths a and c (i.e., $a \le |x| \le c,\ z = 0$) are known as the cohesive zones.

According to Greenwood and Johnson (1998), the essential idea behind the proposed two-dimensional double-Hertz model is to represent the adhesive tensile traction by resorting to the difference of two Hertzian pressure distributions, which scaled by an arbitrary factor $\lambda(>0)$ is then employed to model the adhesive tensile traction over $a \le |x| \le c$, resulting in the final distribution of surface traction when combined with an original unscaled Hertzian pressure.

By introducing the following nondimensional parameters:

$$a^* = \frac{a}{\eta},\quad c^* = \frac{c}{\eta},\qquad P^* = \frac{P}{(\pi R E^* \Delta\gamma^2)^{/}} \qquad \text{with} \qquad \eta = 2\left(\frac{R^2\Delta\gamma}{\pi E^*}\right)^{/},$$

the equilibrium equations in a dimensionless form are derived as

$$P^* = a^{*2} - \lambda\left(c^{*2} - a^{*2}\right),\qquad \frac{4\lambda(1+\lambda)}{3\pi}\left[c^*\left(c^{*2}+a^{*2}\right)E\left(\frac{\sqrt{c^{*2}-a^{*2}}}{c^*}\right) - 2c^*a^{*2}K\left(\frac{\sqrt{c^{*2}-a^{*2}}}{c^*}\right)\right] = 1,$$

where $K(\cdot)$ and $E(\cdot)$ are the complete elliptic integral of the first and second kinds, respectively. To determine λ, a transition parameter similar to the Tabor parameter is introduced as

$$\mu = 4\left(\frac{R\Delta\gamma^2}{\pi^2 E^{*2} z_0^3}\right)^{/} = \frac{4\lambda}{\pi}\left(c^{*2}-a^{*2}\right)^{1/2}.$$

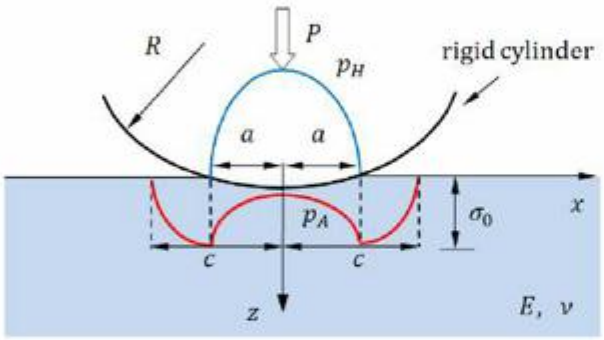

Fig. 1 Adhesive contact of a rigid cylinder on an elastic half-plane

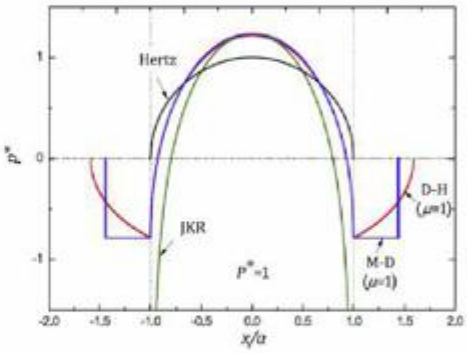

Fig. 2 Interfacial traction predicted by different models

Comparison of the interfacial traction distributions for the case of $P^* = 1$ predicted by different contact models is illustrated in Fig. 2. It can be observed that the interfacial tractions within the contact region are almost the same in the double Hertz (D-H) and the Maugis-Dugdale (M-D) models in spite of different adhesive traction forms within the cohesive zone.

[a] Corresponding author. Email: jinfan2046@163.com.

Fig. 3 displays the equilibrium $P-a$ curves in the present D-H model under various values of μ. The corresponding Hertz, JKR and M-D solutions are also included for comparison. It can be seen that the D-H curves nearly coincide with the M-D solution and they approach the Hertz solution as μ is reduced to zero. For sufficiently large μ, the JKR curve is readily approached.

The pull-off force as a function of the transition parameter μ is shown in Fig. 4, together with the corresponding M-D curve. It can be seen that the magnitude of the pull-off forces predicted by these two cohesive zone models increase smoothly from zero for small μ to the JKR value for large μ. As a consequence, the Hertz and JKR models for cylindrical contacts are unified in the present double-Hertz model.

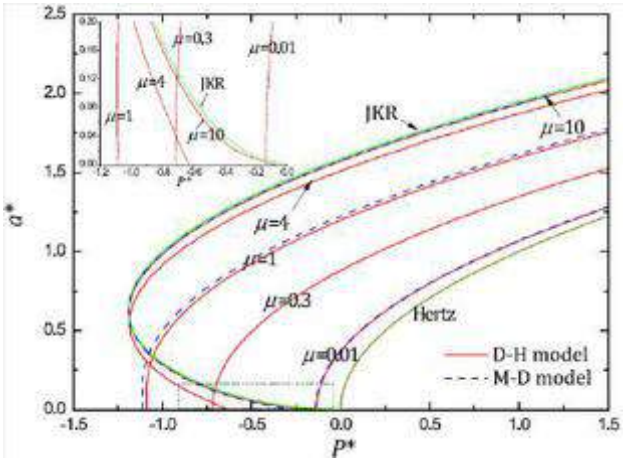

Fig. 3 Equilibrium $P-a$ curves for various values of μ.

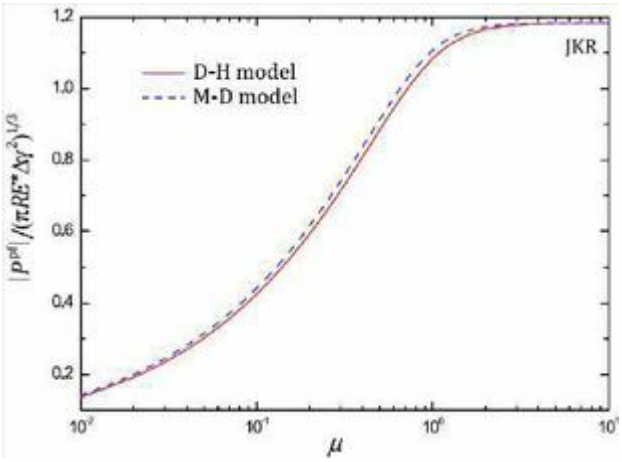

Fig. 4 Pull-off forces predicted by the D-H and M-D models

CONCLUSIONS

A cohesive zone model for two-dimensional adhesive contact between elastic cylinders is developed by extending the classical double-Hertz model. Closed-form analytical solutions are obtained for the interfacial traction, deformation field and the equilibrium relation among applied load, contact half-width and the size of cohesive zone. Based on these results, a complete transition between the JKR and the Hertz type contact models is captured by defining a dimensionless transition parameter.

References

[1] Greenwood J.A., Johnson, K.L.: *J. Phys. D: Appl. Phys.* 31, 3279-3290, 1998.

[2] Johnson K.L., Greenwood J.A.: *J. Phys. D: Appl. Phys.* 41, 155315-1-6, 2008.

[3] Baney J.M., Hui C.Y.: *J. Adhesion Sci. Technol.* 11, 393–406, 1997.

CONTACT BETWEEN ROUGH SURFACES: MECHANICAL AND TRANSPORT PHENOMENA AT SMALL SCALES

Vladislav A. Yastrebov*[1], Guillaume Anciaux[2], Georges Cailletaud[1], and Jean-François Molinari[2]
[1]*MINES ParisTech, PSL Research University, Centre des Matériaux, CNRS UMR 7633, Evry, France*
[2]*Laboratoire de Simulation en Mecanique des Solides, Ecole Polytechnique Fédérale de Lausanne, Lausanne, Switzerland*

Summary Normal contact between solids with rough self-affine surfaces is studied. Elastic and elastic-plastic solids are considered in the framework of classical and generalized continua. The following questions were investigated: evolution of the contact area and its morphology, fluid flow through the contact interface and the near-percolation behavior, energy transfer across the contact interface is also considered. Numerical results obtained using the finite and the boundary element methods are compared with analytical and semi-analytical models.

INTRODUCTION

Engineering and natural surfaces are inevitably rough, and this roughness, evolving due to mechanical loads, aging and environmental effects, influences many mechanical and physical phenomena: light scattering, catalysis, initiation of fatigue cracks, oxidation and corrosion, fluid-structure interaction, in particular, boundary layer separation and transition to turbulence. What is more important, when solids with rough surfaces are brought in mechanical contact, their roughness fully determine almost all micro- and macroscopic interface processes: mechano-metallurgical (stress concentration, flash heating, near surface phase-transformation), tribological (complex frictional behavior, wear, adhesion and lubrication), and multi-physical (electric contact resistance, sealing properties, heat conduction, permeability of fractured media). The complex nature of surface roughness spanning many spatial scales and evolving due to many factors presents a very challenging fundamental and engineering problem and poses many questions: How to describe properly the roughness? Is continuous description able to capture all essential macroscopic phenomena? How can their physical properties be predicted based on certain parameters of materials and of rough surfaces? In this talk we plan to address these important questions by considering normal mechanical contact between rough elastic and elastic-plastic solids in the framework of computational models incorporating synthesized and real roughness. The objective of this presentation is to establish (or refine) models for (1) evolution of the contact area under an increasing normal load, (2) evolution of the contact interface transmissivity for incompressible viscous fluid, (3) evolution of the electric contact resistance between rough surface for weak currents.

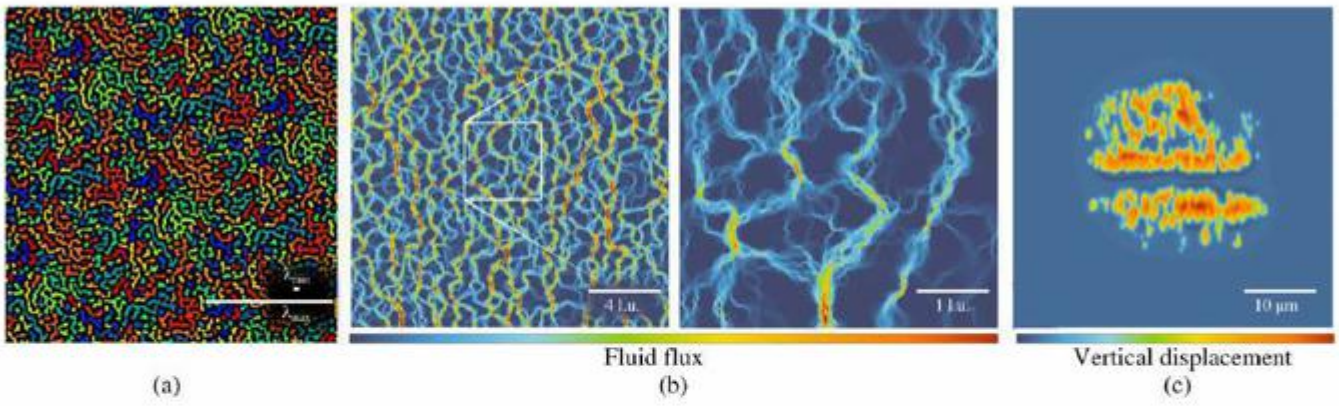

Figure 1: (a) Analysis of contact clusters' morphology (scales represent the minimal $\lambda_{\min}$ and maximal $\lambda_{\max}$ wavelengths present in the surface spectrum); (b) scale effect in fluid transport in the interface between two rough surfaces brought in contact: left figure for the period $L = 16\lambda_{\min}$, right one for $L = 4\lambda_{\min}$; (c) spherical indentation on a rough elastic-plastic multi-layered solid (CuzN plated with 1 μm of Ni and 1 μm of gold) (mechanical and electro-static finite element analysis).

*Corresponding author. Email: vladislav.yastrebov@mines-paristech.fr

METHODS

To study the effect of roughness, we use synthesized [1] self-affine surfaces with truncated spectra and controlled Gaussianity, isotropy and fractal dimension. Some results are presented for engineering surfaces, metallic surfaces used in metal-to-metal water seals [3] and electroplated surfaces for electric applications [2]. To solve the mechanical contact problem for two linearly elastic half-space with periodic roughness, we use an FFT-based boundary element method [4]. To solve the linear transport problem (viscous flow of incompressible fluid and electro-static problem) as well as the geometrically nonlinear elastic-plastic mechanical contact problem, a finite element method was used: penalty, augmented Lagrangian and Partial Dirichlet-Neumann methods were used to incorporate contact terms in variational framework [5]. The finite element method was also used to simulate contact interaction for the Cosserat continuum. To represent large surface spectra, fine mesh discretizations were used (up to 4096×4096 surface nodes in FFT-based methods and up to 1024×1024 surface elements in finite element simulations). All considered problems are three-dimensional. Low level multi-threading and FETI-based domain decomposition strategy were used to solve large nonlinear finite element problems on distributed memory parallel architectures.

RESULTS

A link between geometrical characteristics of the effective roughness (lower, upper wavelength cutoffs in the surface spectrum, fractal dimension and standard deviation of the surface gradient), elastic properties and the contact area was established for the entire range of pressures: from the infinitesimal to full contact [6] (see Fig. 1,a). This rather universal result was compared with predictions of asperity based models [7, 8] for small contact areas and with Persson's model [9] for the entire range. Particularities due to elastic-plastic material behavior were also investigated. In addition, the effect of introducing characteristic length via the Cosserat continuum was studied for the indentation of elastic-plastic contact, which enables to take into account size dependent rough contact behavior.

Free interface volume between contacting surfaces, extracted from mechanical simulations, was used to study the sealing properties with the objective to establish a link between mechanical, roughness and fluid properties and the contact transmissivity (see Fig. 1,b) which is of great importance for the sealing engineering as well as for natural and engineering geophysical problems. In the finite element framework, this coupled fluid-solid problem was enhanced to account for strong coupling, i.e. the hydrostatic fluid pressure influences the mechanical solution and vice versa.

Electro-mechanical contact problem for a sphere-plane setup is solved for a synthesized and real roughness under assumption of weak currents (no Joule heating) (see Fig. 1,c). A weak coupling was used for elastic-plastic mechanical model for a plated solid and for electro-static problem. These results are compared with simplified models [2].

CONCLUSIONS

The discussed results, being in good agreement with analytical models and also, for some of them, with experimental data, cannot be considered general as in reality the macroscopic behavior emerges from the interplay of multiple microscale phenomena. Further extensions and improvements of mathematical and computational models will be considered in this light.

References

[1] Hu Y.Z., Tonder K.: Simulation of 3-D random rough surface by 2-D digital filter and Fourier analysis. Int J Mach Tool Manu 32:83-90, 1992.

[2] Yastrebov V.A., Cailletaud G., Proudhon H., Mballa Mballa F.S., Noël S., Testé P., Houzé F.: Three-level multi-scale modeling of electrical contacts sensitivity study and experimental validation. In proceedings of IEEE 61st Holm Conference on electrical contacts, 414-422, 2015.

[3] Yastrebov V.A., Durand J., Proudhon H., Cailletaud, G.: Rough surface contact analysis by means of the Finite Element Method and of a new reduced model. CR Mecanique 339(7):473-490, 2011.

[4] Stanley H. M., Kato T.: An FFT-based method for rough surface contact. J Tribol-T ASME 119:481-485, 1997.

[5] Yastrebov, V. A. Numerical methods in contact mechanics. John Wiley & Sons, 2013.

[6] Yastrebov V.A., Anciaux G., Molinari J.F.: From infinitesimal to full contact between rough surfaces: evolution of the contact area. Int J Solids Struct 52:83-102, 2015.

[7] Bush A.W., Gibson R.D., Thomas T.R.: The elastic contact of a rough surface. Wear 35:87-111, 1975.

[8] Greenwood J.A.: A simplified elliptic model of rough surface contact. Wear 261:191-200, 2006.

[9] Persson B.N.J.: Theory of rubber friction and contact mechanics. J Chem Phys 115:3840-3861, 2001.

THE SYSTEM OF INDENTERS SLIDING OVER THE VISCOELASTIC HALF-SPACE

Irina Goryacheva[1a)] & Feodor Stepanov[2]
[1,2] *Ishlinsky Institute for Problems in Mechanics, Russian Academy of Sciences, Moscow*

Summary Sliding contacts of a system of indenters, or the indenter in the presence of additional loads outside of the contact regions, over a viscoelastic half space are considered. The solutions of the formulated 3-D contact problems are based on BEM and iteration procedure. The results of numerical calculations are used to analyse the influence of the distance between the contact sports and sliding velocity on pressure distribution and on the friction force.

PROBLEM FORMULATION

In studies of contact characteristics and friction of bodies with rough surfaces it is very important to take into account the mutual effect of contact spots. Solutions of the contact problems for a system of indenters and periodic contact problems are widely used to analyse this effect [1].
This paper presents two types of 3-D contact problems for the viscoelastic half-space taken into account the interaction between indenters. The mechanical behavior of the viscoelastic half-space for both cases is described by the following constitutive equation:

$$\gamma(t)=\frac{1}{G}\tau_{xz}(t)+\frac{1}{G}\int_{-\infty}^{t}\tau_{xz}(t)K(t-\tau)d\tau;\quad K(t')=k\exp\left(-\frac{t'}{\lambda}\right)$$

Here, $\gamma(t)$ and $\sigma(t)$ are the shear deformation and shear stress components, respectively, G is the instantaneous shear modulus, λ is the retardation time and k is the return value of relaxation time.

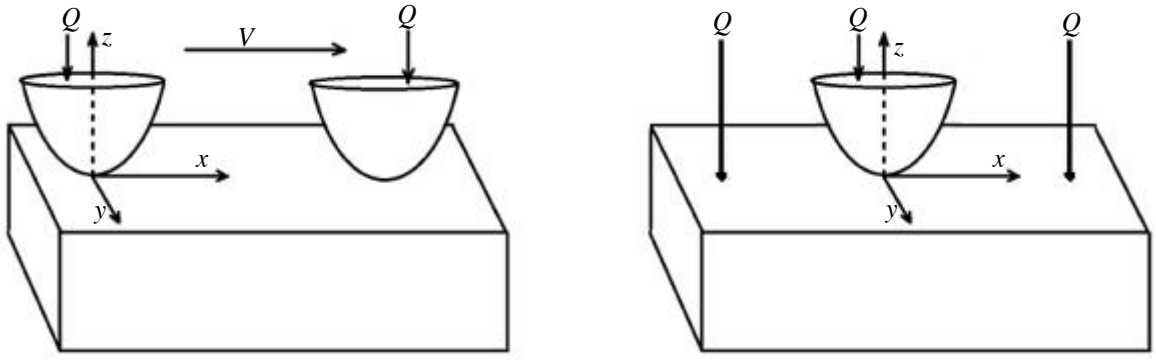

Fig.1 Schemes of the contacts.

Problem 1.
Two solid indenters with fixed distance l between them slide with a constant velocity V over the viscoelastic half-space in direction of the 0x-axis (Fig.1 left side). The line between centers of indenters is parallel to 0x. The indenters are of the same shape described by the given smooth function $f(x,y)$. Both sliders are loaded with vertical force Q; the shear stress within the contact region is described by Amonton law. The coordinate system is associated with the rear moving indenter.
Problem 2.
One solid indenter of the given shape $f(x,y)$, loaded by the vertical force Q, and two concentrated normal loads Q located ahead and behind the indenter at the fixed distances along the axis Ox, move with a constant velocity V over the viscoelastic half space in direction of the 0x-axis (Fig.1 write side).

METHOD OF SOLUTION

Both problems are solved with the BEM method. The mesh of square elements covers the unknown contact region. The pressure is assumed to be constant in each element. A normal displacement of the surface in the centre of an arbitrary element is obtained by summation of displacements caused by the pressure applied to each element (influence coefficients).
The influence coefficients are determined from the solution of the problem for one concentration force moving along the boundary of the viscoelastic half-space with a constant velocity V [2]. For problem 1 it's necessary to obtain contact area and pressure distribution for the case of isolated slider (for example the front slider) using method described in [3]. Then the function $\psi_1(x.y)$ of normal displacements under the rear slider caused by the front one is calculated. Boundary and

[a)] I.G. Goryacheva. Email: goryache@ipmnet.ru

equilibrium conditions for the rear slider are written below using influence coefficients k_i^j and normal displacements $\psi_1(x.y)$:

$$\begin{bmatrix} \Delta^2 & \cdots & \Delta^2 & 0 \\ k_1^1 & \cdots & k_N^1 & -1 \\ \vdots & \ddots & \vdots & \vdots \\ k_1^N & \cdots & k_N^N & -1 \end{bmatrix} \cdot \begin{bmatrix} p_{1,1} \\ \vdots \\ p_{1,N} \\ D_1 \end{bmatrix} = \begin{bmatrix} Q \\ f_{1,1} + \psi_{1,1} \\ \vdots \\ f_{1,N} + \psi_{1,N} \end{bmatrix} \qquad (1)$$

Here $p_{1,i}$ is the pressure in the element i, Δ is the size of element, D_1 is the indentation depth of the rear indenter. Contact area and pressure distribution is found with iterative procedure that solves system (1) and excludes elements that appear to have negative pressure in each step. Therefore the normal displacements caused by the rear indenter under the front one may be calculated. This two-level iterative procedure continues until the changes in contact areas and pressure distributions for both sliders become insignificant. Problem 2 is solved with one level iterative procedure.

RESULTS AND DISCUSSION

The calculations were performed in the dimensionless variables and functions. Fig.2 represents the pressure distributions under the indenters described in problem 1. The results indicate that if the distance between indenters decreases two local maxima of pressure arise under the rear indenter. It was established that contact region under the rear indenter may be separated into two sub regions under certain conditions. It was estimated that sliding velocity and distance between indenters (problem 1) or an indenter and additional loads (problem 2) effect sufficiently on contact characteristics, and therefore on the mechanical component of the friction force. The mutual effect of indenters leads to a decrease of mechanical component of the friction force for the rear indenter and an increase for the front one.

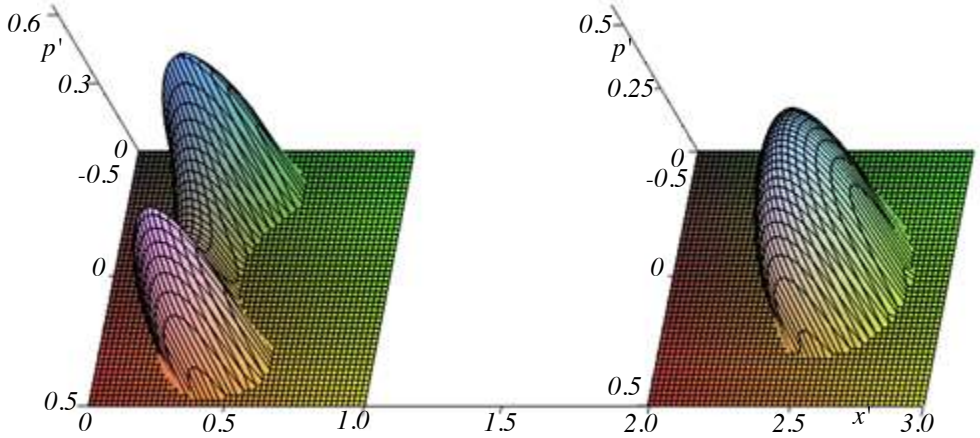

Fig.2 Pressure distributions for the front and rear indenters.

CONCLUSIONS

The elaborated solution method is suitable for a large number of contact problems considering indenters with different shapes sliding on viscoelastic half space.The presented results may be used for estimation of contact characteristics and mechanical component of the friction force in sliding contact of elastomers and bodies with rough surfaces.

Acknowledgements This work is financially supported by Russian Scientific Foundation (grant 14-29-00198).

References

[1] Goryacheva I.G. Mechanics of friction interaction - Moscow: Nauka, 2001. – 478p.

[2] Alexandrov V.M., Goryacheva I.G., Torskaya E.V. Sliding contact of a smooth indenter and a viscoelastic half-space (3D problem)"//*Doklady Physics*, **55**(2), 77-80, 2010

[3] Goryacheva I.G., Stepanov F.I., Torskaya E.V. Effect of friction in sliding contact of a sphere over a viscoelastic half-space //Mathematical Modeling and Optimization of Complex Structures. Jyväskylä. Springer. 2016. P. 93-103. (Ser. Computational methods in applied sciences)

MULTISCALE MODELLING OF DYNAMICAL SYSTEMS WITH FRICTION BETWEEN RANDOMLY ROUGH SURFACES

Carsten Proppe*[1]

[1]*Institute of Engineering Mechanics, Karlsruhe Institute of Technology, Karlsruhe, Germany*

Summary Friction induced vibrations are present in many engineering systems, e.g. in brakes and cam follower systems. In these systems, self-excited oscillations may occur. Surface roughness is an important source of uncertainty in friction systems.

We present a multi-scale approach to the modeling and simulation of dynamical systems with friction between randomly rough surfaces. In a first step, a stochastic model for the rough surface is identified based on observations obtained directly by a white light interferometer, from which statistical characteristics such as the probability density function, the correlation function and the spectral density of the surface heights are estimated. From these characteristics, sample surfaces can be simulated by Karhunen-Loève expansion or a spectral approach.

In a second step, the normal contact problem for samples of the rough surface is solved, where the contact pressure is represented by a polynomial chaos expansion. By repeated solution of the normal contact problem, the coefficients of the the polynomial chaos expansion can be estimated by regression.

From the polynomial chaos expansion of the contact pressure and area, a stochastic friction coefficient can be identified by application of the Bowden-Tabor approach. In this way, a stochastic process for the friction coefficient is obtained from the statistical properties of the surface roughness.

Finally, on a structural level, vibration systems with friction between randomly rough surfaces are studied, where the classical friction coefficient is replaced by the stochastic process that has been identified previously. As an example, the classical mass on a belt system is considered, where stick-slip vibrations occur. The influence of the stochastic process for the friction coefficient on the limit cycle is studied.

STOCHASTIC DESCRIPTION OF THE ROUGH SURFACE

A rough surface can be represented by a random field $z(x,\theta)$. In general, two stochastic descriptions of rough surfaces are widely used in the literature:

- A fractal approach, where $z(x,\theta)$ is represented by the Weierstrass-Mandelbrot function

$$z(x,\theta) = \sum_{j=-\infty}^{\infty} \gamma^{(D-2)j} \left(\cos\xi_j(\theta) - \cos\left(\gamma^j \boldsymbol{x} + \xi_j(\theta)\right)\right), \tag{1}$$

  where $1 < D < 2$ denotes the fractal dimension of the surface, γ determines the density of frequencies and the random variables $\xi_j(\theta)$ represent random phase shifts.

- A Karhunen-Loève expansion

$$z(x,\theta) = \mathrm{E}\left[z(x,\theta)\right] + \sum_{j=1}^{\infty} \xi_j(\theta)\sqrt{\lambda_j}\varphi_j(x) \tag{2}$$

  where $(\lambda_j, \varphi_j(x))$ are the eigenvalues and eigenvectors of the covariance function of $z(x,\theta)$. In practice, this series is truncated at a given order M. If z is Gaussian, $\xi_j(\theta)$ will be independent standard Gaussian random variables. If the random field does not follow a Gaussian distribution, an isoprobabilistic transformation can be used to transform the Gaussian field into another field which follows a given probability density function.

Both descriptions can be generalized to the multivariate case.

SOLUTION OF THE STOCHASTIC NORMAL CONTACT PROBLEM

The resulting pressure field is a random field whose characteristics have to be determined from a stochastic normal contact problem.

In principle, its properties could be determined by Monte Carlo simulation. To this end, the series representation of the surface roughness is truncated and sample surfaces are generated from samples of the random variables ξ_j, $j = 1,\ldots,M$. Then, the elasto-plastic normal contact problem is solved for each sample surface to determine the pressure field. However, in

*Corresponding author. Email: proppe@kit.edu

order to describe precisely the cumulative density function of the pressure, a huge number of Monte Carlo simulations has to be performed. This is not suitable for large size problems.

In the following, an approach based on regression and polynomial chaos expansion is introduced that permits to approximate the cumulative density function without drastically increasing the problem size. To simplify the explanation, we limit our approach to the determination of the pressure field at a given position x which is a random variable $\tilde{p}_x(\theta)$. The approach can be easily extended to the determination of the complete pressure field. We will distinguish the pressure when contact occurs (*i.e.* when $\tilde{p}_x(\theta) > 0$, denoted $p_x(\theta)$) and probability of contact at a position $\boldsymbol{x}$ which is given by $1 - \rho_{\tilde{p}}(0)$ where $\rho_{\tilde{p}}$ is the cumulative density function of $\tilde{p}_x(\theta)$.

We seek to express the pressure using a PC basis:

$$p_x(\theta) = \left(\sum_{i=1}^{P} p_i^x \Gamma_i(\boldsymbol{\xi}(\theta)) \right)^+ \tag{3}$$

where $\Gamma_i(\boldsymbol{\xi}(\theta))$ are multi-dimensional orthogonal polynomials and where $(\bullet)^+$ denotes the strictly positive part. As the functions Γ_i and the M random variables $\boldsymbol{\xi}(\theta) = \{\xi_i(\theta)\}_{i=1..M}$ are known, the solution is fully determined by the coefficients p_i^x.

The regression approach [1] consists of estimating the unknowns from a minimization of least square error between polynomial representation and realizations of the field. The coefficients p_i^x is estimated by minimizing:

$$\Delta(p^x) = \sum_{k=1}^{K_t} \left[p_x^{(k)} - \sum_{i=1}^{P} p_i^x \Gamma_i \left(\boldsymbol{\xi}^{(k)}(\theta) \right) \right]^2 \tag{4}$$

where K_t denotes the total number of observation points, $p_x^{(k)}$ is the pressure obtained solving the deterministic problem between the smooth rigid plane and the rough surface defined by $z(x, \boldsymbol{\xi}^{(k)}(\theta))$. Keeping only K realizations which induce a strictly positive pressure $p_x^{(k)}$, the coefficients read:

$$\{\boldsymbol{p_i^x}\} = \left(\boldsymbol{\Gamma}^T \boldsymbol{\Gamma} \right)^{-1} \boldsymbol{\Gamma}^T \boldsymbol{U_i} \tag{5}$$

where $\boldsymbol{\Gamma}$ is a $P \times K$ matrix such that $(\boldsymbol{\Gamma})_{ij} = \Gamma_i(\boldsymbol{\xi}^{(j)})$. To ensure the well-posedness of the problem, the number of realizations K has to be greater than P. By selecting a Latin Hypercube Sampling scheme, one needs few realizations to estimate the unknown coefficients.

After estimating the unknowns p_i^x, the cumulative density function ρ_p of the pressure field when contact occurs can be represented. Given a large number N_t of initial realizations for $\boldsymbol{\xi}(\theta)$, we keep only those which lead to a strictly positive pressure $p_x(\theta)$ (N_p realizations). From this, we are able to construct N_t realizations of $\tilde{p}_x$ whose N_p realizations are those obtained previously, whereas the remainder are let at zero. From this final set of N_t realizations, the cumulative density function $\rho_{\tilde{p}}$ can be estimated, as well as the probability of contact at position $\boldsymbol{x}$.

COMPUTATION OF A STOCHASTIC FRICTION COEFFICIENT

From the random pressure field, the Bowden Tabor approach allows to determine a stochastic processes for the friction coefficient μ. For a given test surface and under assumption of a shear dominated friction force, the friction ooefficient is computed from $\mu = A_c \tau_{max}/N$, where τ_{max} is the shear strength of the material. The contact area A_c and the normal force N are obtained by averaging the pressure field on the test surface. The autocorrelation function of μ can be obtained by comparing the results for two test surfaces centered at different coordinates. The properties of the stochastic process for μ depends on the size of the test surface and become invariant, if the size of the test surface is large.

MACROSCOPIC LEVEL

On a structural level, vibration systems with friction between randomly rough surfaces are studied, where the classical friction coefficient is replaced by the stochastic process that has been identified previously. As an example, the classical mass on a belt system is considered, where stick-slip vibrations occur. The influence of the stochastic process for the friction coefficient on the limit cycle is studied.

References

[1] Blatman, G., Sudret B.: Sparse polynomial chaos expansions and adaptive stochastic finite elements using a regression approach, C.R. Mecanique 336:518-523, 2008.

FRICTIONAL CONTACT, NUMERICAL APPROXIMATION AND ALGORITHMS

Thierno Diop *[1], Michel Fortin[1], and Jean Deteix[1]

[1]*GIREF, Department of Mathematics and Statistics, Laval University, Quebec, Quebec, Canada*

Summary In this presentation we will propose an iterative approach for solving three-dimensional frictional contact problems, that is frictional contact between elastic bodies, including contact with a rigid body, contact between two or more bodies and also self contact. Since the precise formulation of the elastic part is irrelevant for the description of the algorithm we shall consider a generic case. In practice, however, we will have to deal with a non linear material (for instance Mooney-Rivlin model).

INTRODUCTION

We are interested in solving a finite element discretization of the problem, leading to large-scale non linear discrete problem. Solving large-scale problem means dealing with large linear systems and ultimately calculations needing iterative methods. This also implies that penalty methods, and therefore augmented Lagrangian method, are to be banned because of their negative effect on the condition number of the underlying discrete systems and thus on the convergence of iterative methods. This is in rupture to the mainstream of methods for contact in which augmented Lagrangian is the principal tool. We shall first present the problem and its discretisation, this will lead us to describe a general solution algorithm relying on a preconditionner for saddle-point problems which we shall describe in some detail as it is not entirely standard.

THE CONTACT PROBLEM ANS ITS DISCRETISATION

The discrete problem employs a Lagrange multiplier for the contact condition. We denote $\underline{\lambda}_n$ and $\underline{\lambda}_T$ its normal and tangential part. In practice, we use quadratic elements for the displacement and linear elements for the multipliers. The quasi-static formulation leads to a saddle-point problem, with a Tresca friction condition, coupled with an equation for the threshold s to obtain the Coulomb law. We impose the constraints $\underline{\lambda}_n \geq 0$ and $|\underline{\lambda}_T| \leq s$ at the nodes and we denote these Tresca conditions by $\lambda \in \mathcal{T} \subseteq \Lambda$. We thus solve the problem

$$\inf_{\underline{v}\in V} \sup_{\underline{\lambda}\in\mathcal{T}} \mathcal{L}(\underline{v},\underline{\lambda}) = \frac{1}{2}\langle A\underline{v},\ \underline{v}\rangle + I(\lambda_n, \hat{v}_n \circ\ \hat{g}_n) + I(\underline{\lambda}_T, \hat{\underline{v}}_T \circ\ \hat{\underline{g}}_T) \circ\ \langle \underline{f},\ \underline{v}\rangle, \tag{1}$$

$$s = \mu\lambda_n,$$

where $I(\cdot,\cdot)$ denotes some numerical integration and where $\hat{v}$ is a projection of $\underline{v}$ on the space of multipliers. We can then write the optimality conditions on the multipliers.

- For the normal part, we have the Kuhn-Tucker conditions.

$$\lambda_n \geq 0, \langle \mu_n, \hat{u}_n \circ\ \hat{g}_n\rangle \leq 0 \quad \forall \mu_n \geq 0, \langle \lambda_n, \hat{u}_n \circ\ \hat{g}_n\rangle = 0. \tag{2}$$

- For the tangential part, we impose $|\underline{\lambda}_T| \leq s$ and we have for adherent nodes

$$B_T\underline{u} \circ\ \underline{g}_T = 0 \quad \text{if} \quad |\underline{\lambda}_T| < s, \tag{3}$$

  while for sliding nodes we have the non linear condition

$$(\hat{\underline{u}}_T \circ\ \hat{\underline{g}}_T)^{\perp} = 0, \langle \hat{\underline{u}}_T \circ\ \hat{\underline{g}}_T, \underline{\lambda}_T\rangle \geq 0, \tag{4}$$

  where, for $\underline{r} \in \Lambda$ we define, pointwise, the *angular component* as

$$\underline{r}_T^{\perp} = \underline{r}_T \circ\ \frac{\langle \underline{r}_T, \underline{\lambda}_T\rangle}{|\underline{\lambda}_T|^2}\underline{\lambda}_T. \tag{5}$$

For two-dimensional problems, the condition on the angular component disappears and only the second condition of (4) remains, leading to a much simpler problem.

*Corresponding author. Email: thierno.diop.1@ulaval.ca

THE ALGORITHM

The algorithm that we introduce contains three imbedded iteration :

1. A Newton method more precisely a sequential quadratic programming method in $\underline{u}$ to take into account the eventual non linearity of the material, and the change in geometry, that is the normals and the gaps.
2. Given a displacement and the associated geometry, we solve for the multiplier $\underline{\lambda}$, solving the non linear condition (4) by a Newton method.
3. A preconditioned solver for solving the linearised equation in $\underline{\lambda}$.

In our implementation, we use a GCR (Generalized Conjugate Residual) iteration to solve the linearised equation in $\underline{\lambda}$. The condition $s = \mu\lambda_n$ is imposed exactly by the preconditionner, avoiding another iteration on the Tresca treshhold which is often present in algorithms for frictional contact.

Finally, for the displacements component of the system, the GCR algorithm could use a direct method (leading a factoring of the tangent matrix) but this becomes impossible for large problems. Therefore we rely on an iterative methods for this part also, leading to a flexible and powerful solver for large-scale frictional contact problem.

CONCLUSIONS

The purpose of this presentation is to introduce the algorithm and present some numerical results.

AN LCP BASED APPROACH FOR THE CONTACT MECHANICS OF ELASTIC HALF SPACES

Andreas Almqvist* and Francesc Perez Rafols
Machine Elements, Luleå University of Technology, Luleå, Sweden

Summary The Contact Mechanics (CM) problem can be considered a complementarity problem. If assuming linearly elasticity of the contacting bodies, the discretised system of equations as a Linear Complementarity Problem (LCP). The contact mechanics model is first formulated in continuous form by posing a complementarity relation between the gap of the deformed surfaces and the contact pressure. The LCP is then obtained after a linearisation and discretisation of the equations. An advantage of posing the CM problem as a strict LCP formulation, is that this allows for the application of well-established numerical solution techniques, such as Lemke's pivoting algorithm. In addition, Lemke's pivoting algorithm has the advantage that it finds the numerically exact solution, within a finite number of iterations. This type of LCP based contact mechanics approach is applied here to solve the Hertzian line contact problem, with and without the addition of surface roughness, to demonstrate it's applicability.

INTRODUCTION

The Contact Mechanics (CM) problem can be formulated in at least two different ways. It can for instance be as variational problem expressing the total complementary potential energy, see Kalker [1] for the linear elastic case and Almqvist et al. [2] for a later development including a linear elastic – perfectly plastic material model. Another way of formulating the CM problem is by considering it as a complementarity problem, e.g., as presented in Sahlin et al. [3]. If the material of the contacting bodies is assumed to behave linearly elastically, it is possible to state the discretised system of equations as a Linear Complementarity Problem (LCP), see e.g. the book by Cottle et al. [4]. In this particular case, the complementarity originates in that contact (between two bodies) means that at locations where the contact pressure is positive (non-zero) the gap must be zero and vice versa. The contact mechanics model is first formulated in continuous form through mathematically modelling of the aforementioned complementarity relation. The LCP can then be obtained after linearisation and discretisation of the continuous model. An advantage of posing the CM problem as a strict LCP formulation, is that it lends itself to the application of well-established numerical solution techniques such as Lemke's pivoting algorithm. This particular numerical solution procedure also has the advantage that it within a finite number of iterations, finds the numerically exact solution. An implementation of a contact mechanics model problem in MATLAB code is made available for the reader, see [5]. In the present work, this LCP based contact mechanics solution procedure is applied to solve the Hertzian line contact problem. The numerical solution is validated against the analytical Hertzian solution for the line contact problem between two perfectly smooth cylinders. In addition, surface roughness is included in order to demonstrate the applicability of the proposed method.

METHOD

The gap between the (deformed) surfaces, h, includes three parts. That is,

$$h = h_0 + g + u, \tag{1}$$

where h_0 the rigid body separation, g the geometry/topography of the contact (cylinder and roughness) and u the elastic deformation/deflection. In continuous form, the contact mechanics model expressing the complementarity relation between the gap h and the contact pressure p may be stated as

$$\begin{array}{ll} h = 0, & p \geq 0, \\ h \geq 0, & p = 0. \end{array} \tag{2}$$

If the contacting bodies are approximated as linear elastic half spaces, the Boussinesq-Cerruti integral equation solution can be applied to express the deformation (u) as a function of the contact pressure (p), i.e.,

$$u = \int_{-\infty}^{\infty} K\left(x - s\right) p(s) ds, \tag{3}$$

where

$$K = \frac{4}{\pi E'} \ln \left| x - s \right|, \tag{4}$$

*Corresponding author. Email: andreas.almqvist@ltu.se

in 1D and

$$K = \frac{2}{\pi E'} \frac{1}{\sqrt{(x_1 - s_1)^2 + (x_2 - s_2)^2}}, \tag{5}$$

in 2D and where $2/E' = (1 - \nu_1^2)/E_1 + (1 - \nu_2^2)/E_2$.

This means that a discretisation of the linear elastic contact mechanics problem may be posed on the form of a standard linear complementarity problem reading

$$\begin{aligned} \mathbf{h} &= \mathbf{h_0} + \mathbf{g} + \mathbf{C}\mathbf{p}, \\ \mathbf{h} \cdot \mathbf{p} &= \mathbf{0}, \;\; \mathbf{p} \geq \mathbf{0}, \;\; \mathbf{h} \geq \mathbf{0}, \end{aligned} \tag{6}$$

where $\mathbf{C}$ is a matrix, whose elements are so called influence coefficients relating the contact pressure and the deformation.

The strict LCP formulation of the CM problem presented in (6), allows for direct application of well-established numerical solution techniques such as Lemke's pivoting algorithm. The Lemke algorithm has the advantage that it finds the numerically exact solution within a finite number of iterations. In this work the MATLAB implementation presented by Almqvist in [5] is employed to solve the problem numerically.

NUMERICAL EXAMPLES

The LCP based contact mechanics solution procedure was applied to solve the Hertzian line contact problem. In Fig. 2, the dimensionless numerical solution for the smooth Hertzian problem (left) and for the same case but with the addition of surface roughness (right) are presented. The surface roughness signal added to the smooth cylinder is depicted in Fig. 1 (in dimensionless form). In the case of smooth cylinders the problem was discretised using 512 grid nodes and the relative error in Hertzian contact radius; $b = \sqrt{8WR/(\pi E')}$, where W is the applied load (in N/m) and R is the reduced radius of the two contacting cylinders, was $< 9 \times 10^{-4}$. In terms of the Hertzian pressure; $p_h = \sqrt{WE'/(2\pi R)}$ the relative error was found to be $< 4 \times 10^{-6}$. The dimensionless rigid body separation $h_0/(b^2/R)$ was specified as -5.06 and the case including surface roughness was resolved using 1024 grid nodes.

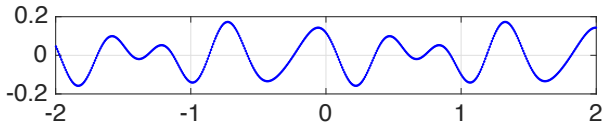

Figure 1: The surface roughness signal added to the smooth cylinder to achieve the solution depicted in Fig. 2 (right).

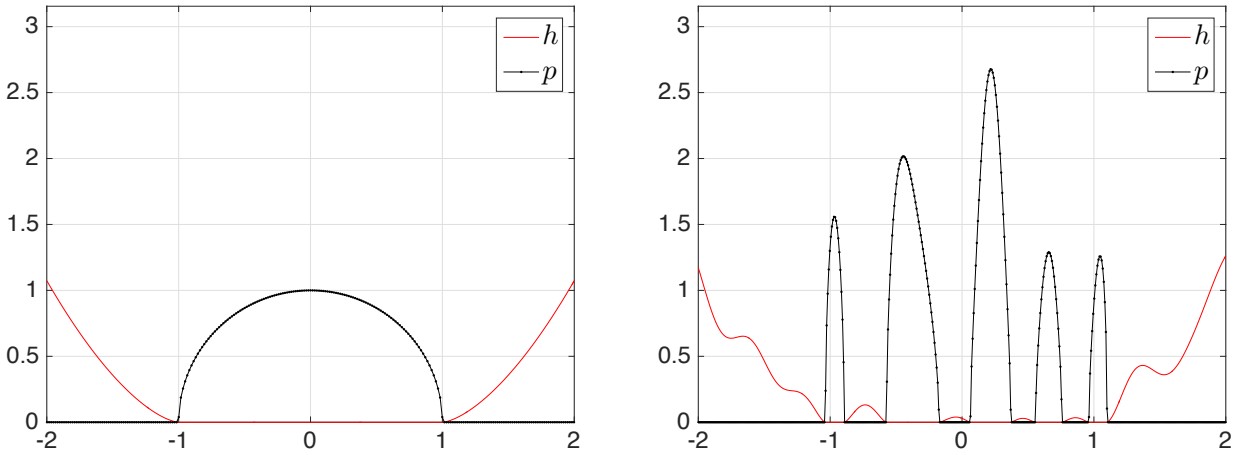

Figure 2: Smooth problem (left), Including surface roughness (right).

References

[1] J. J. Kalker and Y. Van Randen. Minimum principle for frictionless elastic contact with application to non-hertzian half-space contact problems. *Journal of Engineering Mathematics*, 6(2):193 – 206, 1972.

[2] A. Almqvist, F. Sahlin, R. Larsson, and S. Glavatskih. On the dry elasto-plastic contact of nominally flat surfaces. *Tribology International*, 40(4):574 – 579, 2007.

[3] F. Sahlin, R. Larsson, P. Marklund, P. M. Lugt, and A. Almqvist. A mixed lubrication model incorporating measured surface topography. part 1: theory of flow factors. *Proceedings of the Institution of Mechanical Engineers, Part J: Journal of Engineering Tribology*, 224(4):335–351, 2010.

[4] R. W. Cottle, J. S. Pang, and R. E. Stone. *The linear complementarity problem*. Number 60. Society for Industrial Mathematics, 2009.

[5] A. Almqvist. An lcp solution of the linear elastic contact mechanics problem. http://www.mathworks.com/matlabcentral/fileexchange/43216, 2013.

ACTION OF THE SEMI-INFINITE PLATES ON THE ELASTIC LAYER

Vladimir Babeshko [*], Olga Evdokimova [1] and Olga Babeshko [2],
[1] *Department of Mechanic, Southern Scientific Center RAS, Rostov-on-Don, Russia*
[2] *Department of Mechanic, Kuban State University, Krasnodar, Russia*

Summary The contact problem of acting of the two semi-infinite Kirchhoff plates on the elastic layer is considered. The vertical static stresses acts on the plates. The problem is to study the contact stresses concentrations between the plates and the layer in this block structure. It was proved that the contact stresses concentrations in the end-walls of the plats are the same as in the end-walls of the rigid stamps acted on the layer if the distance between the end-walls of the plates is not equal to zero and is equal the square of this stresses if this distance is equal to zero. It can induce the destruction of the materials in engineering or appearance of the earthquake in seismology.
Parts of this study were supported by the Presidium of the Russian Academy of Sciences, Program 33 and the Russian Foundation for Basic Research, Project 14-08-404.

INTRODUCTION

The conducted research is based on the theory of hidden defects worked out in [1] and other authors' publications. Let us use the schemes made for describing concealed defects in environments with coverings [1] assuming that the coverings are half-plates with parallel boarders with the distance of θ between them, placed on some linear deformed foundation. Lithospheric plates are shaped by the Kirchhoff plates. Let us assume that the space between the plates of different types is hollow and on the butt-ends the outside powers are acting, which are directed according to the rule of outward vectors in a local system of coordinates $x\,x\,x$ with the beginning in the plane $x\,x$ coinciding with the middle plane of the plate, with the axis ox_3 directed upward normally to the plate, with the axis ox_1 directed along the tangent to the fault zone edge, with the axis ox_2 normally to its edge. The area occupied by the left plate is marked by λ and described by the correlations $|x_1| \le \infty \quad x_2 \le -\theta$, and the area occupied by the right one is marked by the index r and coordinates $|x_1| \le \infty \quad \theta \le x_2$. We will proceed from the fact that the lithospheric plates move extremely slow. The speed is about tens of millimeters annually, that is why the boarder task can be examined in static variant. Kirchhoff's equation for fragments of b cover, $b = \lambda, r$, which occupy interval Ω_b with borders $\partial\Omega_b$ at vertical static exertion impacts t_{3b} from above and g_{3b} from below, looks like

$$\mathbf{R}_b\,\partial_1\,\partial_2\,u_{3b} + \varepsilon_{53b}(t_{3b} - g_{3b}) \equiv \left(\frac{\partial}{\partial_1^4} + 2\frac{\partial^2}{\partial_1^2}\frac{\partial^2}{\partial_2^2} + \frac{\partial^4}{\partial x_2^4}\right)u_{3b} + \varepsilon_{53b}(t_{3b} - g_{3b}) = 0, \quad \mathbf{R}_b(-\alpha_1, -\alpha_2)U_{3b} \equiv R_b(-\alpha_1, -\alpha_2)U_{3b} \equiv (\alpha_1^2 + \alpha_2)\,U_{3b},$$

$$U_{3b} = \mathbf{F}_2 u_{3b}, \quad G_{3b} = \mathbf{F}_2 g_{3b}, \quad T_{3b} = \mathbf{F}_2 t_{3b} \quad b = \lambda, r \quad M_b = -D_{b1}\left(\frac{\partial^2 u_{3b}}{\partial x_2^2} + \nu_b \frac{\partial^2 u_{3b}}{\partial x_1^2}\right), \quad D_{b1} = \frac{D_b}{H^2}, \quad D_{b2} = \frac{D_b}{H^3}, \quad D_b = \frac{E\,h^3}{(1 - \nu_b^2)},$$

$$Q_b = -D_{b2}\left(\frac{\partial^3 u_{3b}}{\partial x_2^3} + (2 - \nu_b)\frac{\partial^3 u_{3b}}{\partial_1 \partial_2}\right) = f_{4b}(\partial\Omega_b), \quad \varepsilon_{53b} = \frac{(1 - \nu_b^2)12H^4}{E\,h^3} \quad u_{3b} = f_{1b}(\partial\Omega_b), \quad \frac{\partial u_{3b}}{H\partial x_2} = f_{2b}(\partial\Omega_b), \quad \varepsilon_6^{-1} = \frac{(1 - \nu)H}{\mu}$$

The connection between boundary stress and surface displacement of elastic earth, where plates are situated looks like

$$u_{3m}(x_1\,x) = \varepsilon_6^{-1}\sum_{n=1}^{2}\iint_{\Omega_n} k(x_1 - \xi_1, x_2 - \xi_2)\,g_{3n}(\xi_1\,\xi)\,d\xi_1\,d\xi_2, \quad x_1\,x_2 \in \Omega_m, m = \lambda \quad \theta$$

$$\Omega_\lambda(|x_1| \le \infty; \quad x_2 \le -\theta), \quad \Omega_r(|x_1| \le \infty \quad \theta \le x_2), \quad \Omega_\theta(|x_1| \le \infty; \quad -\theta \le x_2 \le \theta), \quad n = \lambda, r$$

M_b and Q_b are bending moment and sharing force in the system of axis $x_1 o x_2$; h_b - is plate thicknesses, H is dimensional parameter of base material, for example, layer thickness. The designation is borrowed from [1]. $\mathbf{F}_2 \quad \mathbf{F}_2\,\alpha_1\,\alpha_2$ and $\mathbf{F}_1 \quad \mathbf{F}_1\,\alpha_1$ are two-dimensional and one-dimensional Fourier-transform operators, apparently.

TOPOLOGICAL METHOD

Functional equations of boundary-value problems can be represented as [1-4]

$$R_b(-\alpha_1, -\alpha_2)U_{3b} \equiv (\alpha_1^2 + \alpha_2)\,U_{3b} = -\int_{\partial\Omega_b} \omega_b \quad \varepsilon_{53b}S_{3b}(\alpha_1\,\alpha_2), \quad S_{3b}(\alpha_1\,\alpha_2) = \mathbf{F}_2(\alpha_1\,\alpha_2)(t_{3b} - g_{3b}), \quad b = \lambda, r$$

==========

*) Corresponding author. Email:babeshko41@mail.ru

Here we can see that ω_b are exterior forms, participating in performance and looking like

$$\omega_b = e^{\langle\alpha\ \rangle}\{\ -[\ \frac{\partial^3 u_{3b}}{\partial x_2^3} - i\alpha_2\frac{\partial^2 u_{3b}}{\partial x_2^2} - \alpha_2^2\frac{\partial u_{3b}}{\partial x_2} + \alpha_2^3\ _{3b} + 2\frac{\partial^3 u_{3b}}{\partial\ _1\partial\ _2} - 2i\alpha_2\frac{\partial^2 u_{3b}}{\partial x_1^2}\ ]dx_1 + [\ \frac{\partial^3 u_{3b}}{\partial x_1^3} - i\alpha_1\frac{\partial^2 u_{3b}}{\partial x_1^2} - \alpha_1^2\frac{\partial u_{3b}}{\partial x_1} + \alpha_1^3\ _{3b}\quad dx_2\ \},\quad b=\lambda,r$$

Calculating Leray's residue forms, including two-fold and pseudodifferential equations of boundary-value problems and taking into account agreed notations we can introduce for plates $b=\lambda$. as

$$\mathbf{F}_1^{-1}\ \xi_1^\lambda\ \langle\ -\int\limits_{\partial\Omega_\lambda}\left\{iD_{\lambda 1}^{-1}M_\lambda - 2\alpha_{2-}\frac{\partial u_{3\lambda}}{\partial x_2} + i[\ 3\alpha_{2-}^2 + (2-\nu_\lambda\ \alpha_1^2\ ]u_{3\lambda}\right\}^{\ \alpha_1\ 1}dx_1 + \varepsilon_{53\lambda}\quad_{3\lambda}\ \alpha_1\ \alpha_{2-}\ \rangle = 0,$$

$$\mathbf{F}_1^{-1}\ \xi_1^\lambda\ \langle\ -\int\limits_{\partial\Omega_\lambda}\{\ i\alpha_{2-}D_{\lambda 1}^{-1}M_\lambda - D_{\lambda 2}^{-1}Q_\lambda - \alpha_{2-}^2 + \nu_\lambda\alpha_1^2)\frac{\partial u_{3\lambda}}{\partial x_2} + i\alpha_{2-}[\ \alpha_{2-}^2 + (2-\nu_\lambda\ \alpha_1^2\ ]u_{3\lambda}\ \}e^{\alpha_1\ 1}dx_1$$

$$+\varepsilon_{53\lambda}S_{3\lambda}(\alpha_1\ \alpha_{2-})\ \rangle = 0,\quad \xi_1^\lambda\in\partial\Omega_\lambda,\quad \partial\Omega_\lambda = -\infty\le x_1\le\infty,\quad x_2=-\theta\ ,\quad \alpha_{2-}=-i\sqrt{\alpha_1^2},\quad \xi_1^\lambda\in\partial\Omega_\lambda$$

It exist the similar pseudodifferential equations for the right plate. The derivative is calculated from parameter α_2. Let's introduce the next system of notations on basis pseudodifferential equations.

$$\mathbf{Y}_\lambda = \{y_{1\lambda}, y_{2\lambda}\},\quad \mathbf{Z}_\lambda = \{z_{1\lambda}, z_{2\lambda}\},\quad \mathbf{Y}_\mathbf{r} = \{y_{1r}, y_{2r}\},\quad \mathbf{Z}_\mathbf{r} = \{z_{1r}, z_{2r}\},\quad \mathbf{F}_1 g = \mathbf{F}_1(\alpha_1)g,\quad \mathbf{F}_2 g = \mathbf{F}_2\ \alpha_1\ \alpha_2$$

$$y_{1\lambda} = \ _\lambda^{-1}\mathbf{F}_1 M_\lambda,\quad y_{2\lambda} = D_\lambda^{-1}\mathbf{F}_1 Q_\lambda,\quad y_{1r} = \ _r^{-1}\mathbf{F}_1 M_r,\quad y_{2r} = \ _r^{-1}\mathbf{F}_1 Q_r,\quad z_{1\lambda} = \mathbf{F}_1\frac{\partial u_\lambda}{\partial x_2^\lambda},\quad z_{2\lambda} = \mathbf{F}_1 u_\lambda,\quad z_{1r} = \mathbf{F}_1\frac{\partial u_r}{\partial x_2^r},\quad z_{2r} = \mathbf{F}_1 u_r,$$

$$\mathbf{K}_\lambda = k_{1\lambda}, k_{2\lambda}\ ,\quad \mathbf{K}_\mathbf{r} = k_{1r}, k_{2r}\ ,\quad k_{1\lambda} = \varepsilon_{53\lambda}\mathbf{F}_2\ \alpha_1\ \alpha_{2-}\quad _\lambda - \ _\lambda = \varepsilon\ _\lambda S\ _\lambda(\alpha_1\ \alpha_{2-}),$$

$$k_{2\lambda} = \varepsilon_{53\lambda}S'_{3\lambda}(\alpha_1\ \alpha_{2-}),\quad k_{1r} = \varepsilon_{53r}\mathbf{F}_2\ \alpha_1\ \alpha_{2+}\quad _\lambda - \ _\lambda = \varepsilon_{53r}S\ _r(\alpha_1\ \alpha_{2+}),\quad k_{2r} = \varepsilon_{53r}S'_{3r}(\alpha_1\ \alpha_{2+})$$

As the result pseudodifferential equations for this case can be rewritten as a system of algebraic equations

$$-\alpha_{2-}\ _{1\lambda} + \ _{2\lambda} + (\alpha_{2-}^2 + \nu_\lambda\alpha_1^2)z_{1\lambda} - \alpha_{2-}[\ \alpha_{2-}^2 + (2-\nu_\lambda\ \alpha_1^2\ ]z_{2\lambda} + k_{1\lambda} = 0;\quad -iy_{1\lambda} + 2\alpha_{2-}z\ _\lambda - [\ 3\alpha_{2-}^2 + (2-\nu_\lambda\ \alpha_1^2\ ]z_{2\lambda} + k_{2\lambda} = 0$$

$$-\alpha_{2+}\ _{1r} + \ _{2r} + \alpha_{2+}^2 + \nu_r\alpha_1^2)z_{1r} - \alpha_{2+}[\ \alpha_{2+}^2 + (2-\nu_r\ \alpha_1^2\ ]z_{2r} + \ _{1r} = 0;\quad -iy_{1r} + 2\alpha_{2+}z\ _r - [\ 3\alpha_{2+}^2 + (2-\nu_r\ \alpha_1^2\ ]z_{2r} + \ _{2r} = 0$$

Having continued to apply the topological method the next functional equations can be received [1,2]

$$[\ \varepsilon_{53r}(\alpha_1^2+\alpha_2^2)^- + \varepsilon_6^{-1}\ _1\ \alpha_1\ \alpha_2\quad ^+\ \alpha_1\ \alpha_2\ = -[\ \varepsilon_{53\lambda}(\alpha_1^2+\alpha_2^2)^- + \varepsilon_6^{-1}\ _1\ \alpha_1\ \alpha_2\quad ^-\ \alpha_1\ \alpha_2\ +\ _{3\theta}\ \alpha_1\ \alpha_2\ +$$

$$+(\alpha_1^2+\alpha_2^2)^-[\ A_\lambda k_{1\lambda} + B_\lambda k_{2\lambda} + \ _r\ _r + \ _r\ _r + \varepsilon_{53\lambda}\ ^+\ \alpha_1\ \alpha_2\ + \varepsilon_{53r}\quad \alpha_1\ \alpha\quad _{3\theta}\ \alpha_1\ \alpha_2\ = \int\limits_{-\infty}^{\infty}\int\limits_{-\theta}^{\theta}u_3(x_1, x\ )e^{\langle\alpha\ \rangle}dx_1dx\ ,\quad \theta>0,$$

$$[\ \varepsilon_{53r}(\alpha_1^2+\alpha_2^2)^- + \varepsilon_6^{-1}\ _1\ \alpha_1\ \alpha\quad ^+\ \alpha_1\ \alpha_2\ = -[\ \varepsilon_{53\lambda}(\alpha_1^2+\alpha_2^2)^- + \varepsilon_6^{-1}\ _1\ \alpha_1\ \alpha\quad ^-\ \alpha_1\ \alpha_2\ +$$

$$+(\alpha_1^2+\alpha_2^2)^-[\ A_\lambda k_{1\lambda} + B_\lambda k_{2\lambda} + \ _r\ _r + \ _r\ _r + \varepsilon_{53\lambda}\ ^+\ \alpha_1\ \alpha_2\ + \varepsilon_{53r}\quad \alpha_1\ \alpha_2\quad \theta = 0$$

Having solved these functional equations it can receive the contact stresses in the form

$$g_{3\lambda}(x_1,x_2) = \sigma_{1\lambda}(x_1,x_2)(-x_2-\theta)^{-1/2},\quad x_2<-\theta;\quad g_{3r}(x_1,x_2) = \sigma_{1r}(x_1,x_2)(x_2-\theta)^{-1/2},\quad x_2>\theta;\quad \theta>0$$

$$g_{3\lambda}(x\ ,x\ )\to\sigma_{2\lambda}(x_1,x\ )x_2^{-1} + \sigma_{3\lambda}(x_1,x\ )ln|x_2|;\quad g_{3r}(x\ ,x\ )\to\sigma_{2r}(x\ ,x\ )x_2^{-1} + \sigma_{3r}(x\ ,x\ )ln|x_2|;\quad \theta=0$$

CONCLUSION

The functions , $\sigma_{nb}(x\ ,x\ ),\ b=\lambda,r;\ \ n=2,3$ are continuous at the both parameters. Proceeding from the position that last correlations prove that there is detection of the new type of earthquake, let us describe its common factors.

At $\theta>0$ the plates act upon layer as simple stamps with right angles at borders [2]. If the edges break, then the facilities at edges disappear. This can induce a slight earthquake. When the plates approached, $\theta=0$, but did not combine, preserving specified boundary conditions on edges, and Newton's third law hasn't been there yet, then the irregularities between them occur. For mechanics this is absolutely clear situation, described in many works and frequent, for example, in studies of solidity of metal angle, welded onto foundation. For some values of angular solution of angle there is the growth of exertion factors in vicinity of an angle.

Reference

[1]. Babeshko V.A., Evdokimova O.V., Babeshko O.M. *Doklady Physics. – 2014. – V. 59. – No.7 . – P. 313-317.*

[2] Babeshko V.A., Evdokimova O.V., Babeshko O.M. *Ecolojical Bulletin of Research Centers of the Black Sea Economic Cjjperetion, 2015, №2, C. 8-13*

[3] Babeshko V.A., Evdokimova O.V., Babeshko O.M. *Doklady Physics. – 2014. – V. 59. – No.8 . – P. 379-384.*

[4] Babeshko V.A., Evdokimova O.V., Babeshko O.M. *Doklady Physics. – 2014. – V. 59. – No.1 . – P. 30-34.*

A CLASS OF SLIP DEPENDING SURFACE INTERACTIONS

Marius Cocou *
LMA, Aix-Marseille University, CNRS, UPR 7051, Centrale Marseille, France

Summary The aim of this work is to study a class of nonsmooth dynamic viscoelastic contact problems that constitutes a unified approach to describe some complex interface behaviors, including relaxed unilateral contact, adhesion and slip depending Coulomb friction. The classical formulations of the problems are presented and the variational formulations are given as two and three-field problems. Based on some approximation results, we analyze these variational formulations, written as evolution implicit variational inequalities. Finally, several examples are presented to illustrate the capability of the proposed model.

INTRODUCTION

This work is concerned with the study of some nonsmooth dynamic contact problems which describe various interactions between the boundaries of two Kelvin-Voigt viscoelastic bodies, including some relaxed unilateral contact, adhesion or pointwise friction.

Quasistatic elastic problems with unilateral contact conditions and Coulomb friction law have been analyzed in [1, 14] and in [13, 5], where an adhesion law based on the evolution of the intensity of adhesion was also proposed.

The normal compliance model, which is a particular regularization of Signorini's conditions, has been investigated by several authors, see e.g. [8, 15] and references therein. A recent unified approach, which can be applied to various quasistatic problems, including unilateral and bilateral contact with nonlocal friction, or normal compliance conditions, has been considered in [2].

Dynamic viscoelastic problems with nonlocal friction laws, obtained by suitable regularizations of the normal component of the stress vector appearing in the Coulomb friction law, were analyzed in [9, 6] and dynamic problems coupling unilateral contact, recoverable adhesion and nonlocal friction were studied in [7].

A static contact problem with relaxed unilateral conditions and Coulomb friction was studied in [12], based on new formulations and on a fixed point method. The extension of these results to dynamic viscoelastic contact problems with Coulomb friction was investigated in [3, 4].

The results presented here constitute a generalization of the contact condition considered in [3, 4] to the case of a contact condition that contains not only the gap function but also the normal velocity.

Using the Clarke subdifferential, the variational formulations of these contact problems can be given as hemivariational inequalities, see [10, 11], but our results enable a direct and simpler approach to study some complex surface interactions, including normal compliance, adhesion, local and nonlocal friction laws.

CLASSICAL AND VARIATIONAL FORMULATIONS

Let Ω^α be the reference domains of $\mathbb{R}^d,\ d=2$ or 3, occupied by two viscoelastic bodies, characterized by a Kelvin-Voigt constitutive law. Suppose that the bodies have Lipschitz boundaries $\Gamma^\alpha = \partial\Omega^\alpha$, $\alpha = 1, 2$, and let $\Gamma_U^\alpha,\ \Gamma_F^\alpha$ and Γ_C^α be three disjoint parts of Γ^α such that $\Gamma^\alpha = \overline{\Gamma}_U^\alpha \cup \overline{\Gamma}_F^\alpha \cup \overline{\Gamma}_C^\alpha,\ \alpha = 1, 2$. Let $\boldsymbol{f}_1 = (\boldsymbol{f}_1^1, \boldsymbol{f}_1^2)$ denote the given body forces in $\Omega^1 \cup \Omega^2$ and $\boldsymbol{f}_2 = (\boldsymbol{f}_2^1, \boldsymbol{f}_2^2)$ denote the tractions on $\Gamma_F^1 \cup \Gamma_F^2$. Let $\boldsymbol{\sigma}^\alpha$ and $\boldsymbol{\varepsilon}(\boldsymbol{u}^\alpha)$ be the stress tensor and the infinitesimal strain tensor corresponding to the displacement vector field $\boldsymbol{u}^\alpha$ in Ω^α, $\alpha = 1, 2$. Suppose that the solids can be in contact between the potential contact surfaces Γ_C^1 and Γ_C^2 which are parametrized by two C^1 functions defined on a subset Ξ of $\mathbb{R}^{d-1}$.

We consider the following dynamic viscoelastic contact problem.

Problem $\boldsymbol{P_c}$: Find the displacement vector $\boldsymbol{u} = (\boldsymbol{u}^1, \boldsymbol{u}^2)$ such that $\boldsymbol{u}(0) = \boldsymbol{u}_0$, $\dot{\boldsymbol{u}}(0) = \boldsymbol{u}_1$ and, for all $t \in (0, T)$,

$$
\begin{aligned}
&\ddot{\boldsymbol{u}}^\alpha \circ \operatorname{div} \boldsymbol{\sigma}^\alpha(\boldsymbol{u}^\alpha, \dot{\boldsymbol{u}}^\alpha) = \boldsymbol{f}_1^\alpha,\ \ \boldsymbol{\sigma}^\alpha(\boldsymbol{u}^\alpha, \dot{\boldsymbol{u}}^\alpha) = \boldsymbol{\mathcal{A}}^\alpha \boldsymbol{\varepsilon}(\boldsymbol{u}^\alpha) + \boldsymbol{\mathcal{B}}^\alpha \boldsymbol{\varepsilon}(\dot{\boldsymbol{u}}^\alpha) \ \text{ in } \ \Omega^\alpha,\ \ \alpha = 1, 2,\\
&\boldsymbol{u}^\alpha = \boldsymbol{0} \ \text{ on } \ \Gamma_U^\alpha,\ \boldsymbol{\sigma}^\alpha \boldsymbol{n}^\alpha = \boldsymbol{f}_2^\alpha \ \text{ on } \ \Gamma_F^\alpha,\ \alpha = 1, 2,\ \ \boldsymbol{\sigma}^1 \boldsymbol{n}^1 + \boldsymbol{\sigma}^2 \boldsymbol{n}^2 = \boldsymbol{0} \ \text{ in } \ \Xi,\\
&\underline{\kappa}([u_N], \dot{u}_N) \le \sigma_N^1 \le \overline{\kappa}([u_N], \dot{u}_N) \ \text{ in } \ \Xi,\\
&|\boldsymbol{\sigma}_T^1| \le \mu(\dot{\boldsymbol{u}}_T)\, |\sigma_N^1| \ \text{ and } \ \dot{\boldsymbol{u}}_T \ne \boldsymbol{0} \Rightarrow \boldsymbol{\sigma}_T^1 = \circ\, \mu(\dot{\boldsymbol{u}}_T) |\sigma_N^1| \frac{\dot{\boldsymbol{u}}_T}{|\dot{\boldsymbol{u}}_T|} \ \text{ in } \ \Xi,
\end{aligned}
$$

where u_N, $\boldsymbol{u}_T$, σ_N^1, $\boldsymbol{\sigma}_T^1$ denote the normal and tangential components of the relative displacement field and of the stress vector $\boldsymbol{\sigma}^1 \boldsymbol{n}^1$, respectively, $[u_N]$ is the corresponding gap, $\underline{\kappa}$, $\overline{\kappa}$ are two given mappings depending on the gap and on the normal velocity, and $\mu = \mu(\dot{\boldsymbol{u}}_T)$ is the slip dependent coefficient of friction.

The variational formulation is a two-field problems that consists in an evolution implicit variational inequality having as unknowns the displacement field and a Lagrange multiplier corresponding to σ_N^1.

*Email: cocou@lma.cnrs-mrs.fr

ANALYSIS OF THE VARIATIONAL PROBLEM

We focus on an equivalent three-field variational problem, obtained by an appropriate decomposition of the initial Lagrange multiplier.

A more general evolution variational inequality is analyzed by using an equivalent fixed point problem, some auxiliary approximation results and a fixed point method for set-valued mappings.

These results enable to prove the existence of variational solutions of the dynamic contact problems.

Using some established estimates of the variational solutions we compare different particular cases, including the relaxed contact formulation, the normal compliance and the unilateral contact conditions with friction.

Finally, several examples are presented to illustrate the generality and the capability of this surface interaction model.

References

[1] Andersson L.E.: Existence results for quasistatic contact problems with Coulomb friction. Appl. Math. Optim. 42:169-202, 2000.

[2] Badea L., Cocou M.: Internal and subspace correction approximations of implicit variational inequalities. Mathematics and Mechanics of Solids 20:1026-1048, 2015.

[3] Cocou M.: A class of dynamic contact problems with Coulomb friction in viscoelasticity. Nonlinear Analysis: Real World Applications 22:508-519, 2015.

[4] Cocou M.: A variational analysis of a class of dynamic problems with slip dependent friction. Annals of the University of Bucharest (mathematical series) 5 (LXIII):279-297, 2014.

[5] Cocou M, Rocca R.: Existence results for unilateral quasistatic contact problems with friction and adhesion. Math. Modelling and Num. Analysis 34:981-1001, 2000.

[6] Cocou M., Scarella G.: Analysis of a dynamic unilateral contact problem for a cracked viscoelastic body. Z. Angew. Math. Phys. 57:523-546, 2006.

[7] Cocou M., Schryve M., Raous M.: A dynamic unilateral contact problem with adhesion and friction in viscoelasticity. Z. Angew. Math. Phys. 61:721-743, 2010.

[8] Kikuchi N., Oden J.: Contact Problems in Elasticity : A Study of Variational Inequalities and Finite Element Methods, SIAM Studies in Applied Mathematics. SIAM, Philadelphia, 1988.

[9] Kuttler K.L., Shillor M.: Dynamic bilateral contact with discontinuous friction coefficient. Nonlinear Analysis: Theory, Methods & Applications 45:309-327, 2001.

[10] Migórski S., Ochal A., Sofonea M.: Nonlinear Inclusions and Hemivariational Inequalities. Springer, New York, 2013.

[11] Panagiotopoulos P.D.: Hemivariational Inequalities: Applications in Mechanics and Engineering. Springer, Berlin, 1993.

[12] Rabier P.J., Savin O.V.: Fixed points of multi-valued maps and static Coulomb friction problems. J. Elasticity 58:155-176, 2000.

[13] Raous M., Cangémi L., Cocou M.: A consistent model coupling adhesion, friction, and unilateral contact. Comput. Meth. Appl. Mech. Engrg. 177:383-399, 1999.

[14] Rocca R., Cocou M.: Existence and approximation of a solution to quasistatic Signorini problem with local friction. Int. J. Engrg. Sci. 39:1233-1255, 2001.

[15] Shillor M., Sofonea M., Telega J.J.: Models and Analysis of Quasistatic Contact, Lect. Notes Phys. 655. Springer, Berlin, Heidelberg, 2004.

MODEL FOR FRICTION IN SMALL-SIZED ADHESIVE PARTICLES

Gan-Yun Huang[1a)], Xiang-Long Peng[1]
[1]*Department of Mechanics, School of Mechanical Engineering, Tianjin University, Tianjin, 300072, PR China*

Abstract: In the present work, a model for sliding and rolling friction in adhesive particles has been developed by extending the JKR model. The results predicted by the model are consistent with experiments. It has been found the friction duality in particles may arise from the different modes of motion onset and under proper conditions rolling friction may be larger than sliding friction, which is contrary to what has been found at macroscopic level.

INTRODUCTION

Nanotribology has become a field of growing interest in the recent years due to the requirement for understanding the basic physical laws of friction and the challenges involved in MEMS and NEMS technology. In particular, friction behaviour of small sized particles has been probed experimentally[1-3], which reveals some poorly understood peculiar behaviours such as friction duality or inconsistent scaling between friction force and the particle's radius. In spite of the possible mechanisms involved, the interaction modes between probes and the particles may be variable that may result in different modes of motion onset, e.g., by sliding or rolling. In the present work, it is attempted to develop models for friction of rolling and sliding in adhesive particles of spherical shape.

MODEL DEVELOPMENT AND RESULTS

For small sized particles under a normal force P and a tangential force T, the non-slipping adhesive contact can be well characterized by extending the JKR model[4, 5]. So the contact tractions at the interface may be expressed as

$$p(r)=2E^*(a^2-r^2)^{1/2}/\pi R-(P_1-P)/[2\pi a(a^2-r^2)^{1/2}],\quad \tau(r)=T/[2\pi a(a^2-r^2)^{1/2}] \tag{1}$$

where $P_1=4E^*a^3/3R$, E^* is the composite modulus for the contacting bodies, R the effective radius for the two contacting bodies, a the contact radius. Since the stresses are singular of square root at the contact edge, one may define stress intensity factors as

$$K_I=(P_1-P)/[2a\sqrt{\pi a}],\quad K_{II}=\sqrt{(2-\nu)/(2-2\nu)}T/[2a\sqrt{\pi a}] \tag{2}$$

with ν being the Poisson's ratio. By analogy with fracture mechanics theory, i.e., the equilibrium contact size is governed by equating the energy release rate $G=K_I^2+K_{II}^2$ to the work of adhesion w, one may obtain the relationship between the contact size and the applied force as follows

$$4E^*a^3/3R=P+P_c+\sqrt{2PP_c+P_c^2-(2-\nu)T^2/(2-2\nu)} \tag{3}$$

with $P_c=3\pi wR/2$. From Eq.(3), it is found that the tangential force reduces the contact radius as compared to that under purely normal forces. Such an effect has been referred to as shear induced peeling. Nevertheless, for Eq.(3) to be valid, $2PP_c+P_c^2-(2-\nu)T^2/(2-2\nu)\ge 0$ should be satisfied. What happens otherwise remains controversial. Some researchers argued that when $T=T_c=\sqrt{(2-2\nu)/(2-\nu)}\sqrt{2PP_c+P_c^2}$, the onset of sliding may occur, which lacks physical implications. Here we assume that the sliding onset may take place through nucleation of a dislocation loop which by analogy with that in crack problem can be determined by $K_{II}^2=\gamma_{us}E^*$[6]. Here, γ_{us} is the unstable stacking fault energy. Thus, one can obtain the friction force as

$$T_s/P_c=\sqrt{2\beta(2-2\nu)/(2-\nu)}\sqrt{P/P_c+1-\beta+\sqrt{(2P/P_c+1-\beta)(1-\beta)}},\quad \beta=\gamma_{us}/w. \tag{4}$$

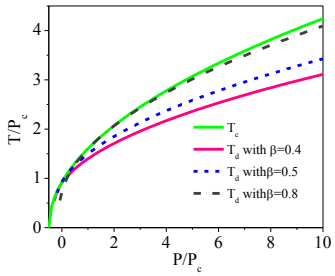

Fig.1 Sliding friction as a function of the normal force

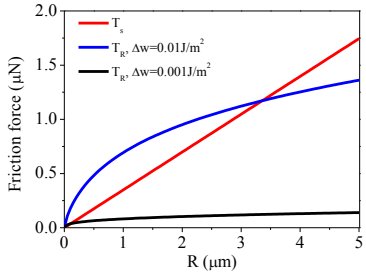

Fig.2 Sliding and rolling friction as a function of R

a) Corresponding author. Email: gyhuang@tju.edu.cn.

By taking $v = 0.25$ and different values of β, T_c and T_s as functions of P have been plotted Fig.1a. It can be seen they behave similarly but T_s is smaller than T_c. Since Thorton once found that some experimental results on friction can be approximated by T_c [4], one may expect that the present T_c can predict the friction well.

On the other hand, if the tangential force is applied after the normal force and acts such that a moment $M = nTR$ is induced at the interface, one may expect the possibility of relative motion through rolling. In such context, we take the assumption by Krijt et al [7] to obtain the critical tangential force. Specifically, the moment is balanced by the normal traction whose distribution can be written as

$$p(r) = E^*(a_1^2 - 2r^2 + R\delta)/(a_1^2 - r^2)^{1/2}, \quad p(r) = E^*(a_2^2 - 2r^2 + R\delta)/(a_2^2 - r^2)^{1/2} \tag{5}$$

at which δ is the indentation depth, a_1 and a_2 respectively the radius of the left half and the right half circular areas. It is assumed they are only slightly different from the equilibrium radius a before the tangential force is applied. Hence a can be obtained by setting T to zero in Eq.(3). The tangential traction in the two half circles is obtained by replacing a by a_1 and a_2 in Eq.(1). The normal force and the moment can be related to a_1 and a_2 as

$$P = E^*[R\delta(a_1 + a_2) - (a_1^3 + a_2^3)/3]/R, \quad M = E^*[(a_1^2 - R\delta)^2 - (a_2^2 - R\delta)^2]/4R \approx \eta(4E^* a^3/3R - P) \tag{6}$$

with $\eta = (a_2 - a_1)/2$. And the energy release rate at the trailing and the leading edges can be written as

$$G_1 = E^*(a_1^2 - R\delta)^2/2\pi a_1 R^2 + T^2/4\pi E^* a_1^3, \quad G_2 = E^*(a_2^2 - R\delta)^2/2\pi a_2 R^2 + T^2/4\pi E^* a_2^3 \tag{7}$$

For the rolling initiation, $G_1 = w_1$ and $G_2 = w_2$ should be satisfied. Here w_1 is larger than w_2, which implies that rolling depends on the adhesion hysteresis $\Delta w = w_1 - w_2$. In the case of vanishing normal force, one may explicitly obtain the critical tangential force for rolling onset as

$$T_R/2P_c = [2^{-1}(\bar{a} + \sqrt{4 + \bar{a}^2})]^{1/3} - [2(\bar{a} + \sqrt{4 + \bar{a}^2})^{-1}]^{1/3}, \quad \bar{a} = \Delta w a/2nwR \tag{8}$$

Taking $v = 0.25$, $E^* = 10\text{MPa}$, $w = 0.1\text{J/m}^2$ and $n = 1$, we have calculated the friction force due to rolling as a function of R for Δw equal to 0.01 and 0.001 J/m^2, respectively. The results are presented in Fig.2. The friction due to sliding for $\beta = 0.8$ has also been demonstrated in the figure. One can find that the scaling between friction and the radius is different for sliding and rolling. If the adhesion hysteresis is very small, behaviour of the rolling friction and the sliding friction is very similar to the friction duality observed in small-sized particles. Thus the friction duality may also arise from different modes of motion onset. In addition, one can also see that rolling friction may be larger than the sliding friction if the size of the particles is small enough, which is contrary to that at macroscopic level. Such a prediction depends on the adhesion hysteresis, and is interesting for further experimental verification.

CONCLUDING REMARKS

In summary, we have proposed models for sliding and rolling friction in small sized particles where adhesive interaction has been taken into account by extending the JKR model. The results thus predicted are consistent with experiments. In addition, a novel finding is that it may be easier slide than to roll for some small sized particles which nevertheless remain for future verification.

Acknowledgement -The work is partially supported by the National Natural Science Foundation of China (NSFC) under Grant No.11572216 and the National Key Basic Research Scheme of China under Grant No. 2012CB937500.

References

[1] Dietzel D., Ritter C.,Möninghoff T., Fuchs H., Schirmeisen A, Schwarz U. D.:. Friction duality observed during nanoparticle sliding. *Phys. Rev. Lett.* **101**: 125505, 2008

[2] Ritter C.; Heyde M.; Schwarz U. D.; Rademann K.: Controlled translational manipulation of small latex spheres by dynamic force microscopy. *Langmuir*, **18**: 7798−7803, 2002.

[3] Guo D., Li J., Chang L., Luo J.: Measurement of the friction between single polystyrene nanospheres and silicon surface using atomic force microscopy. *Langmuir*, **29**: 6920-6925, 2013.

[4] Thornton C.: Interparticle sliding in the presence of adhesion. *J. Phys. D: Appl. Phys.* **24**, 1942-1946, 1991.

[5] Rice, J.R.: Dislocation nucleation from a crack tip: an analysis based on Peierls concept. *J. Phys. Mech. Solids.* **40**, 239-272, 1992.

[6] Savkoor A.R., Briggs, G. A. D.: The effect of tangential force on the contact of elastic solids in adhesion. *Proc. R. Soc. Lond. A.* **356**, 103-114, 1977.

[7] Krijt S., Dominik C., Tielens A. G. G. M.: Rolling friction of adhesive microspheres. *J. Phys. D: Appl. Phys.*, **47**: 175302 1-9, 2014.

NUMERICAL MODELING OF THE COUPLING BETWEEN THE TEMPERATURE AND VELOCITY IN BRAKING SYSTEMS

Piotr Grzes, Adam Adamowicz & Aleksander Yevtushenko
Faculty of Mechanical Engineering, Bialystok University of Technology, Bialystok, Poland

Summary The numerical analysis of temperature fields in a pad-disc braking system at the coupling of temperature-dependent coefficient and velocity was carried out. The computations are obtained from the solution of HDFW (heat dynamics of friction and wear) system of equations by means of the finite element method (FEM). The proposed methodology, unlike analytical methods, allow to combine a feedback between the velocity, applied load and moment of braking force using complex geometrical objects. The parameters of the process are interdependent and vary according to frictional, mechanical, thermophysical properties of materials of the friction pair, construction of a brake. It was concluded that in order to satisfy the requirements resulting from the conditions of exploitation of the machines and durability of the materials of the friction pair, it is necessary to take into account the mathematical description of the process comprised in HDFW system of equations.

INTRODUCTION

Frictional heating in braking systems is a complex relationship between the velocity, applied load, moment of braking force, frictional, mechanical, thermophysical properties of materials of the friction pair, construction of a brake, etc. The integral quantity combining these parameters is the temperature due to generated heat on the interfaces of the working components of a braking system [1, 2]. It reflects a specific power of friction $q = fpV$, where f – is the coefficient of friction, p – is the contact pressure, V – is the velocity. The temperature has a decisive influence on the magnitude and character of fluctuations of the coefficient of friction f during braking. Despite the fact that under the influence of temperature, intensity of thermomechanical processes on the friction surface varies, which in turn leads to changes in thermal and mechanical properties of materials and may result in instability of the coefficient of friction during braking. Robust dependence of the characteristics of friction and wear of the materials on temperature is well known and reported by many researchers [3-5]. In order to take into account these factors in the analysis, the HDFW system of equations should be incorporated. There are different variants of the HDFW systems describing the change in the coefficient of friction, velocity, load, temperature and wear depending on the initial values of the parameters of the braking process, dimensions, thermophysical and frictional characteristics of the materials of the friction pair. The main idea at the development of HDFW systems of equations is an assumption of the functional relationship of the coefficient of friction f and the maximum temperature $T_{\max} = T_m + T_f$, where T_m – mean temperature of the nominal contact, T_f – flash temperature of the real contact area. The dependencies of the coefficient of friction use the data in regard to thermal stability of friction, obtained during investigations of the specimens for friction and wear according to standard methodology. Typical HDFW system of equations during single braking consists of: law of change in contact pressure with time, equation of motion of the brake disc, experimental dependencies of the coefficients of friction and thermomechanical wear of the considered friction pair on the maximum temperature, experimental dependencies of hardness and thermophysical properties of materials of the friction pair on the temperature, thermal problem of friction for the pad-disc system to determine the mean temperature of the nominal contact area, the problem of assessment of the flash temperature taking into account spatial distribution and migration of spots of the real contact and micro geometry, the law of change of the coefficient of wear of the friction surfaces with time. In case of a multiple braking the given scheme should be completed with the problem of calculation of the bulk temperature of the braking system.

Solutions of the HDFW systems of equations give mathematical description of the braking process, taking into account mutual influence of load, velocity, braking time, coefficient of friction, mean temperature of the surfaces, flash temperature and thermomechanical wear. The fundamental components of the sets are the initial problems for equations of motion and thermal problems of friction during braking. The common factors of both questions are the contact pressure and the coefficient of friction. Spatial distribution and change in the contact pressure with time, the most often are known a priori, and the coefficient of friction during braking can be constant or temperature-dependent.

So far use of HDFW modeling of frictional heating in braking systems concerned mainly the development of simplified one-dimensional models of calculation of the mean temperature of the friction surface [6]. None comparative analysis was carried out of the flash temperature for the given friction pair, found using different theoretical solutions with the experimental data.

In this study spatial models on calculation of the maximum temperature taking into account mutual relationship of the sliding velocity, temperature and thermal sensitivity of the materials of the pad and the disc have been examined. The known numerical solutions for 2D and 3D problems are extended to thermally nonlinear materials and time-dependent contact pressure [7-9]. The data connected with the magnitude of the mass wear of the friction components in the braking process, are obtained by calculation, and taking into account dependencies of the coefficients of intensity of wear and friction on the maximum temperature.

[a] Corresponding author. Email: p.grzes@pb.edu.pl.

FINITE ELEMENT ANALYSIS

Simulations of a single braking process were carried out using 2D and 3D finite element models of a disc brake system for automotive application. In order to incorporate a feedback between the transient temperature fields of the sliding components, velocity, applied load, moment of braking force as well as thermal nonlinearity of the materials, the calculations were based on the HDFW system of equations. According to the theory of HDFW, the maximum temperature was calculated as a sum of the flash and the mean temperature from the solution of equation of motion and the formulated thermal problem of friction. It was assumed that the perfect contact conditions take place within the friction surfaces, namely the sum of heat flux densities directed into the pad and the disc was equal the specific power of friction as well as the temperatures of these surfaces at the corresponding points were equal. On the free surfaces convective conditions were applied. The computations were performed using FE based software COMSOL Multiphysics. Thermal nonlinearity of the materials, dependencies of the coefficients of friction and wear rate were included in the models. The obtained temperature evolutions on the contact surface of the brake disc at different radii: 66 mm – inner radius of the disc, 76.5 mm – inner radius of the pad, 96.2 mm – equivalent radius of the rubbing path and 113.5 mm – outer radius of the disc are shown Fig. 1.

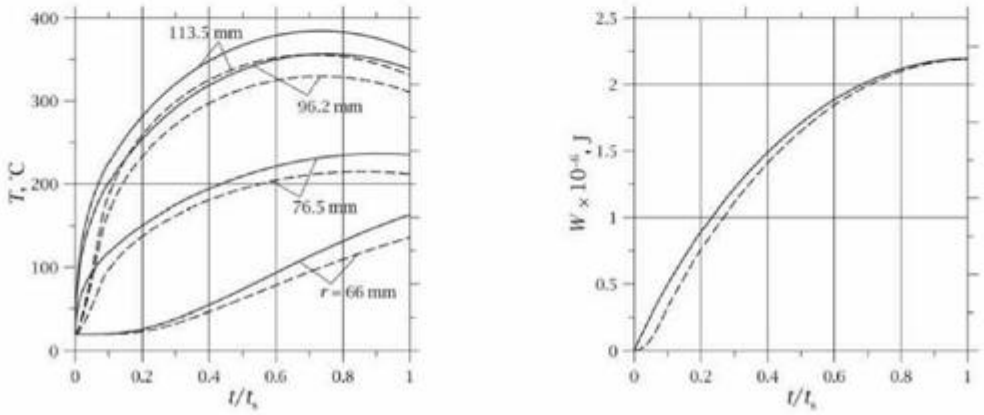

Fig. 1. Changes in the mean temperature T on the contact surface of a disc and work done during braking W obtained using 2D FE model at constant (solid lines) and temperature-dependent (dashed lines) coefficient of friction, p = 1.47 MPa

CONCLUSIONS

The carried out studies of transient temperature fields in braking system using 2D and 3D FE models indicate that in order to obtain comprehensive thermal behavior of the analyzed friction pair, HDFW system of equations should be taken into account. It requires parallel solution of equation of motion and thermal problem of friction. In the proposed FE modeling of problems of heating in braking systems, temperature-dependent coefficients of friction, wear rate, thermophysical properties of materials, hardness and time-dependent contact pressure were interdependent and included. The comparative analysis performed allow to state that the operating characteristics of braking (time, braking distance, evolution of contact temperature, wear) vary from those, where the constant parameters (coefficient of friction, properties of materials) were used (Fig. 1). The obtained results are the basis for the further analysis of transient temperature fields in sliding components of a brake during multiple braking.

References

[1] Newcomb T. P.: Temperatures reached in disc brakes. *J. Mech Eng Sci* **2**:167-177, 1960.

[2] Day A.J., Braking of road vehicles. Oxford, UK 2014.

[3] Chichinadze A. V.: Processes in heat dynamics and modelling of friction and wear (dry and boundary friction). *Trib Int* **28**:55-58, 1995.

[4] Yevtushenko A., Adamowicz A., Grzes P., Yevtushenko O., Kuciej M., Och E.: Analytical and numerical modeling of process of transient heat generation in friction components of brake systems. Bialystok, Poland 2014.

[5] Yevtushenko A. A., Grzes P.: 3D FE model of frictional heating and wear with a mutual influence of the sliding velocity and temperature in a disc brake. *Int Commun Heat Mass Transfer* **62**:37-44, 2015.

[6] Yevtushenko A. A., Kuciej M.: One-dimensional thermal problem of friction during braking: The history of development and actual state. *Int J. Heat Mass Transfer* **55**:4148-4153, 2012.

[7] Adamowicz A., Grzes P.: Analysis of disc brake temperature distribution during single braking under non-axisymmetric load. *Appl Therm Eng* **31**:1003-1012, 2011.

[8] Yevtushenko A. A., Grzes P.: Maximum temperature in a three-disc thermally nonlinear braking system. *Int Commun Heat Mass Transfer* **68**:291-298, 2015.

[9] Yevtushenko A. A., Grzes P.: Mutual influence of the sliding velocity and temperature in frictional heating of the thermally nonlinear disc brake. *Int J. Therm Sci* **102**:254-262, 2016.

A NEW FORMULATION FOR RE-CENTERING FRICTION-BASED ISOLATION SYSTEMS

Ilona Bartosh [1] and Najib Bouaanani [a) 1]
[1]*Departement of Civil, Geological and Mining Engineering, Polytechnique Montréal, Montréal, Québec, Canada*

Summary This paper proposes novel analytical formulation and its numerical solution to evaluate the 3D nonlinear response of re-centering friction-based isolation systems subjected to multi-component dynamic excitations. The fundamental equations of the formulation are first presented, and then programmed to obtain multi-directional nonlinear response solutions of the isolated structure incrementally at each time step of the dynamic excitation representing multi-component ground motions. Simple case studies are provided to illustrate the performance and efficiency of the proposed technique and highlight its advantages over conventional finite element solutions.

INTRODUCTION

Seismic isolation is widely used to mitigate earthquake damaging effects on structures [1,2]. Isolators are often placed at the base of a structure, or between a bridge deck and its piers, decoupling the ground motion from the motion of the structure. This prevents damage by causing the superstructure to move as a rigid body or by minimising dynamic amplification. Friction-based isolation systems are popular for their decoupling capacity as well as their ability to dissipate energy through friction. To accurately predict the behaviour of friction-based isolators for design or evaluation purposes, robust nonlinear time-history analyses are required. These analyses are often performed using finite elements, which can be time consuming due to the size of the models, complexity of the analyses, and their large number when optimization or fragility assessments are required. In this paper, a new analytical formulation is proposed to considerably enhance such nonlinear dynamic analyses.

PROPOSED FORMULATION

A friction-based isolator can be modelled as the two sliding interfaces shown in Fig. 1. Isolator restrainers for re-centring capacity can be modeled as springs linking both sliding interfaces. The upper block, representing the isolated structure, is characterized by a mass m, initially at rest on a sliding surface characterized by friction coefficient μ. If the applied acceleration is sufficient to initiate sliding motion, the block may slide and/or rock on the surface, detach entirely in a pure uplift mode, or demonstrate a combination of these modes. If the vertical acceleration of the block is less than a unit gravity acceleration, i.e. $1g$, the block will not detach entirely but may rock. Provided the dimensions of the block satisfy the rocking equilibrium [3], then the block will not rock but enter a stick-slip mode. Under these conditions and using the notation described in Fig. 1, the equations governing the bidirectional dynamic response of the isolator under a harmonic ground motion with frequency ω_g can be written as

$$\ddot{u} + \omega_n^2 u + \mathrm{sgn}(\dot{u})\ddot{u}_f = -\ddot{u}_g \quad \text{and} \quad \ddot{v} + \omega_n^2 v + \mathrm{sgn}(\dot{v})\ddot{v}_f = -\ddot{v}_g \tag{1}$$

where sgn denotes the signum function, corresponding to 1 and -1 when the block moves along positive and negative directions, respectively, and

$$\ddot{u}_f = \mu|\cos\theta|g + \mu|\cos\theta|\ddot{w}_g, \quad \ddot{v}_f = \mu|\sin\theta|g + \mu|\sin\theta|\ddot{w}_g \quad \text{and} \quad \theta = \mathrm{atan}\left(\dot{v}_g/\dot{u}_g\right) \tag{2}$$

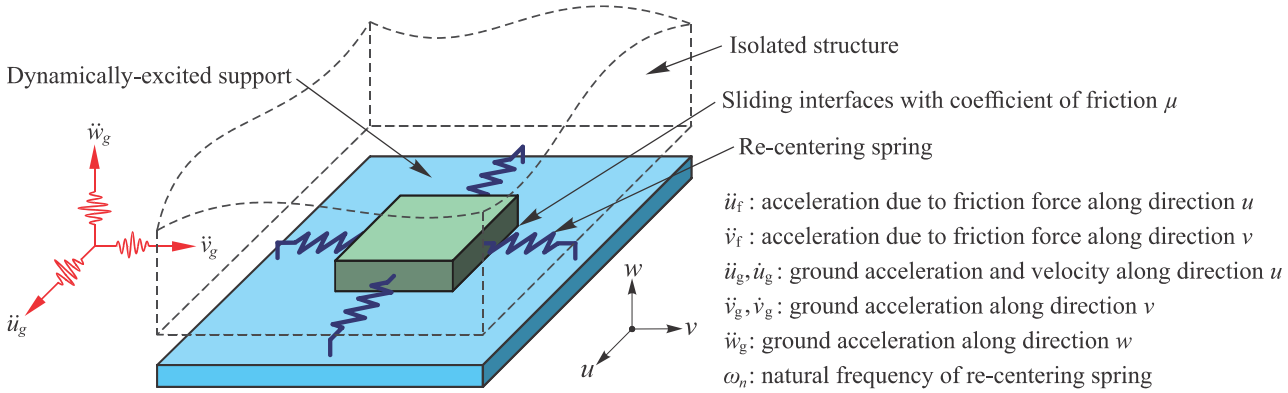

Figure 1. Model of the studied friction-based isolation system with re-centering springs.

Assuming initial displacements and velocities u_0, $\dot{u}_0$, v_0 and $\dot{v}_0$, along axes u and v, respectively, we show that the closed-form analytical solutions of the acceleration of the isolated block are given by following equations (3) and (4) when the block slides along positive and negative direction u, respectively

[a)] Corresponding author. Email: najib.bouaanani@polymtl.ca

$$\ddot{u} = -\sin(\omega_n t)\,\dot{u}_0\,\omega_n - \cos(\omega_n t)\,\omega_n^2\,u_0 - \cos(\omega_n t)\,\ddot{u}_{\mathrm{f}} - \cos(\omega_n t)\,\ddot{u}_{\mathrm{g}} \quad (3)$$

$$\ddot{u} = -\sin(\omega_n t)\,\dot{u}_0\,\omega_n - \cos(\omega_n t)\,\omega_n^2\,u_0 + \cos(\omega_n t)\,\ddot{u}_{\mathrm{f}} - \cos(\omega_n t)\,\ddot{u}_{\mathrm{g}} \quad (4)$$

Similar relations can be obtained for acceleration $\ddot{v}$ by replacing $\dot{u}_0$, u_0, $\ddot{u}_{\mathrm{f}}$ and $\ddot{u}_{\mathrm{g}}$ in Eq. (3) by $\dot{v}_0$, v_0, $\ddot{v}_{\mathrm{f}}$ and $\ddot{v}_{\mathrm{g}}$, respectively. The bidirectional dynamic response of the isolated structure can then be obtained incrementally at each time step. For this purpose, the previous equations were programmed in MATLAB [4].

ILLUSTRATIVE RESULTS

To illustrate the proposed formulation, we consider a re-centering friction-based isolator, subjected to 5 cycles of a 3D sinusoidal ground accelerations taken as $\ddot{u}_{\mathrm{g}} = 0.75g\,\sin(\omega_{\mathrm{g}} t)$, $\ddot{v}_{\mathrm{g}} = 0.5g\,\sin(\omega_{\mathrm{g}} t)$, $\ddot{w}_{\mathrm{g}} = 0.6g\,\sin(\omega_{\mathrm{g}} t)$, where $\omega_{\mathrm{g}} = 10\pi$. The natural frequency of the re-centring spring is $\omega_n = \pi$. Fig. 2(a) illustrates the response of the isolation system considering a friction coefficient μ = 0.1. For verification purposes, a finite element model using contact elements is developed in ADINA [5]. Fig. 2(a) shows the excellent agreement between the results obtained using the proposed formulation and those from finite elements. Fig. 2(b) illustrates how the technique can be efficiently used to predict the effects of variations in friction coefficient μ for design or optimization purposes. Such analyses are indeed required to assess the high sensitivity of this type of friction-based isolators to friction, re-centring system and characteristics of multi-component dynamic excitation.

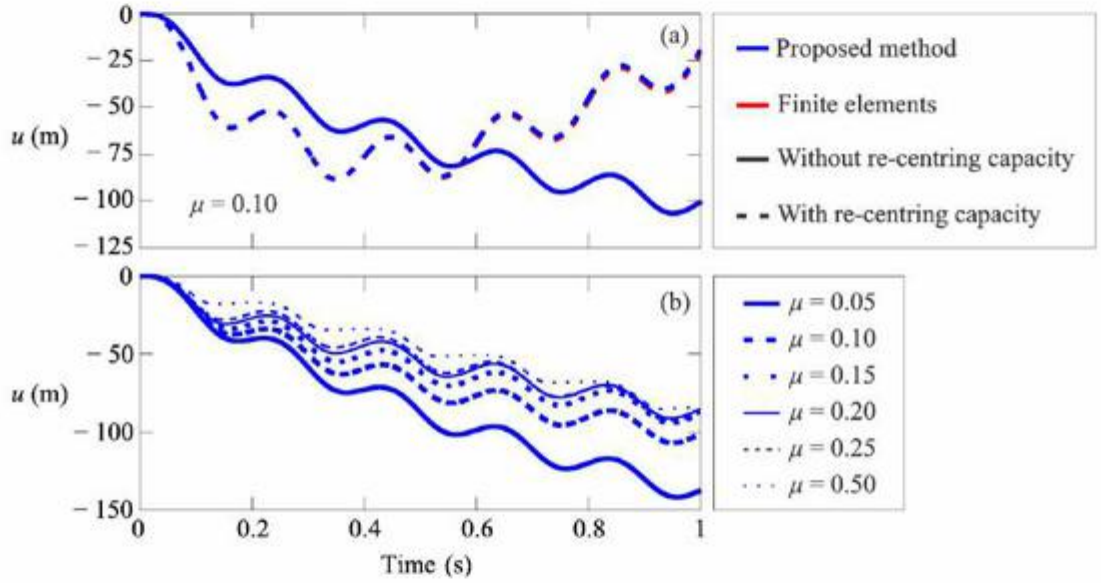

Figure 2. Illustrative results: (a) Comparison of the results with those from finite elements; (b) Effects of friction coefficient.

CONCLUSIONS

This paper proposed an efficient analytical formulation to account for the highly nonlinear 3D dynamic response of re-centring friction-based isolation systems. The proposed formulation can be easily programmed and used to perform extensive parametric studies required for optimized design of friction-based isolation devices or safety evaluation of isolated structures. The rapidity of the proposed method, in terms of programming and execution times, was found to be highly advantageous when compared to conventional finite element modelling, even for simple cases. The robustness of the technique was verified through a large number of case studies, considering harmonic and seismic dynamic excitations.

References

[1] Buckle I. G., Mayes, R. L.: Seismic isolation: history, application, and performance-a world view. *Earthquake spectra* 6(2): 161-201, 1990.

[2] Mokha A. S., Amin N., Constantinou M. C., Zayas V.: Seismic isolation retrofit of large historic building. *Journal of Structural Engineering*, 122(3), 298-308, 1996.

[3] Lopez Garcia D., Soong, T. T.: Sliding fragility of block-type non-structural components. Part 1: Unrestrained components. *Earthquake engineering structural dynamics*, 32(1), 111-129, 2003.

[4] MATLAB: The Mathworks, Inc., Natick, MA, USA, 2011.

[5] ADINA: Theory and modeling guide. Report ARD 06-7. ADINA R & D Inc., 2014.

[a)] Corresponding author. Email: najib.bouaanani@polymtl.ca

ELASTIC SEMI-SPACE IMPACTED WITH ELASTIC FILLED SHELL

Dmitry Tarlakovskii[1a)], Grigory Fedotenkov[2], Georgy Sapozhnikov[2]
[1]*Institute of Mechanics Lomonosov Moscow State University, Laboratory of dynamic tests, Moscow, Russia*
[2]*Moscow Aviation Institute (National Research University), Department of Applied Mechanics, Moscow, Russia*

Summary a solution is found to a non-stationary contact problem of impact of a thin-walled elastic round cylindrical shell filled with elastic medium on elastic semi-space. By virtue of principle of superposition and boundary conditions the problem is converted into a system of functional resolving equations. In order to resolve such system, a numerical and analytical quadrature-based algorithm was developed.

PROBLEM DESCRIPTION

At an initial moment $\tau = 0$ a thin elastic round cylindrical shell of radius R and of h thickness filled with homogeneous elastic medium, at V_0 of initial velocity, contacts elastic semi-space $z \ge 0$ with its element of cylinder. Assuming that the contact between the shell and semi-space as well as between the shell and the filling is friction free. The shell is described by Timoshenko model equations in displacements [1]. In a cylindrical coordinate system with center at shell axis and polar angle $\alpha \in (-\pi, \pi]$ they are represented as follows (hereinafter dots above a value mark time derivatives):

$$\ddot{\mathbf{w}} = \mathbf{L}\mathbf{w} + \mathbf{p},\ \mathbf{w} = (u, w, \chi)^T,\ \mathbf{L} = \left(L_{ij}\right)_{3\times 3},\ \mathbf{p} = (0, p, 0)^T, \tag{1}$$

$$L_{11} = \frac{\partial^2}{\partial\alpha^2} - \eta^2 k^2,\ L_{12} = -L_{21} = \left(1 + \eta^2 k^2\right)\frac{\partial}{\partial\alpha},\ L_{13} = -\gamma^2\frac{\partial^2}{\partial\alpha^2} + \eta^2 k^2,\ L_{22} = \eta^2 k^2\frac{\partial^2}{\partial\alpha^2} - 1,$$

$$L_{23} = \eta^2 k^2\frac{\partial}{\partial\alpha},\ L_{31} = -L_{33} = \gamma^{-2}L_{13},\ L_{32} = -\eta^2 k^2\gamma^{-2}\frac{\partial}{\partial\alpha},\ k^2 = \frac{5}{6}.$$

Here u, w are tangent and normal displacements of shell; χ is angle of rotation from normal to middle surface until deformation of fiber due to shear deformation, p is contact pressure.

The motion of elastic mediums (semi-space and filling) is described by equations of motion of plain theory of elasticity in potentials of elastic displacements (hereinafter the values with index $k = 0$ belong to semi-space while $k = 1$, to filling):

$$\ddot{\varphi}_k = \beta_k^2\Delta_k\varphi_k,\ \ddot{\psi}_k = \eta_k^2\Delta_k\psi_k\ (k = 0,1),\ \Delta_0 = \frac{\partial^2}{\partial x^2} + \frac{\partial^2}{\partial y^2},\ \Delta_1 = \frac{\partial^2}{\partial r^2} + \frac{1}{r}\frac{\partial}{\partial r} + \frac{1}{r^2}\frac{\partial^2}{\partial\alpha^2}. \tag{2}$$

Here φ_k, ψ_k are scalar and non-zero component of vector potential. The motion of the medium which the semi-space is filled with is considered in relation to rectangular Cartesian coordinate system Oxz, the motion of the filling, polar coordinate system $O_1 r\alpha$ with the center at the axis of the shell.

The links of displacements with elastic potentials are defined by the following equations:

$$u_0 = \frac{\partial\varphi_0}{\partial x} - \frac{\partial\psi_0}{\partial z},\ w_0 = \frac{\partial\varphi_0}{\partial z} + \frac{\partial\psi_0}{\partial x},\ u_r = \frac{\partial\varphi_1}{\partial r} + \frac{1}{r}\frac{\partial\psi_1}{\partial\alpha},\ u_\alpha = \frac{1}{r}\frac{\partial\varphi_1}{\partial\alpha} - \frac{\partial\psi_1}{\partial r}, \tag{3}$$

where u, w are displacements of the semi-place along axes Ox and Oz; u_r, u_α are radial and angle displacements of the filling.

Non-zero components of the semi-space deformation tensor $\varepsilon_{\xi\zeta}$ $(\xi, \zeta = x, z)$ and the filling $\varepsilon_{\xi\zeta}$ $(\xi, \zeta = \alpha, r)$ are connected with the displacements by Cauchy equations:

$$\varepsilon_{xx} = \frac{\partial u_0}{\partial x},\ \varepsilon_{zz} = \frac{\partial w_0}{\partial z},\ \varepsilon_{xz} = \frac{1}{2}\left(\frac{\partial u_0}{\partial z} + \frac{\partial w_0}{\partial x}\right),\ \varepsilon_{rr} = \frac{\partial u_r}{\partial r},\ \varepsilon_{\alpha\alpha} = \frac{1}{r}\frac{\partial u_\alpha}{\partial\alpha} + \frac{u_r}{r},\ \varepsilon_{r\alpha} = \frac{1}{2}\left(\frac{\partial u_\alpha}{\partial r} + \frac{1}{r}\frac{\partial u_r}{\partial\alpha} - \frac{u_\alpha}{r}\right). \tag{4}$$

Non-zero components of the semi-space deformation tensor $\sigma_{\xi\zeta}$ $(\xi, \zeta = x, z)$ and the fillings $\sigma_{\xi\zeta}$ $(\xi, \zeta = \alpha, r)$ are connected with deformations by the Hook's law:

$$\sigma_{\xi\xi} = \left(\lambda_k + 2\mu_k\right)\varepsilon_{\xi\xi} + \lambda_k\varepsilon_{\zeta\zeta},\ \sigma_{\zeta\zeta} = \left(\lambda_k + 2\mu_k\right)\varepsilon_{\zeta\zeta} + \lambda_k\varepsilon_{\xi\xi},\ \sigma_{\xi\zeta} = 2\mu_k\varepsilon_{\xi\zeta}\ (k = 0,\ \xi, \zeta = x, z;\ k = 1,\ \xi, \zeta = \alpha, \beta). \tag{5}$$

The area of contact is changing in the course of the interaction, and it is described by semi-width $b(\tau)$ which in zero approximation is defined by condition of crossing of non-deformed boundaries of the semi-space with the shell:

$$b = \sin\alpha_* = \sqrt{w_s\left(2 - w_s\right)}, \tag{6}$$

a) Corresponding author. Email: tdvhome@mail.ru

where w_s is the depth of penetration of the shell as perfectly solid body defined by the solution of the Cauchy problem

$$m\ddot{w}_s = P(\tau) + R_1(\tau),\ P(\tau) = \int\limits_{-\alpha_*(\tau)}^{\alpha_*(\tau)} p(\sin\alpha, \tau)\, d\alpha = \int\limits_{-b(\tau)}^{b(\tau)} \frac{p(\xi, \tau)}{\sqrt{1-\xi^2}}\, d\xi,$$
$$R_1(\tau) = \int\limits_{-\pi}^{\pi} \sigma_r(\alpha, \tau)\, d\alpha,\ \sigma_r(\alpha, \tau) = \sigma_{rr}\big|_{r=1},\ w_s(0) = 0,\ \dot{w}_s(0) = V_0. \tag{7}$$

where P is the resultant of contact pressure p; R_1 is response of the elastic filling; m bulk weight of the shell.

The boundary conditions are represented as follows:

$$\sigma_{xz}\big|_{z=0} = 0\ \left(x \in (-\infty, \infty)\right),\ \sigma_{zz}\big|_{z=0} = 0\ \left(|x| > b(\tau)\right),$$
$$\sigma_{zz}\big|_{z=0} = p(x, \tau),\ w_0\big|_{z=0} = w + \sqrt{1 - x^2} - 1\ \left(|x| \le b(\tau),\ |\alpha| \le \alpha_*(\tau)\right), \tag{8}$$
$$u_r\big|_{r=1} = w\ \left(\alpha \in (-\pi, \pi]\right),\ \sigma_{r\alpha}\big|_{r=1} = 0\ \left(\alpha \in (-\pi, \pi]\right).$$

Supposedly, at the center of the impact and at an infinity point of the semi-space perturbations are limited.

Initial conditions:

$$\varphi_0\big|_{\tau=0} = \dot{\varphi}_0\big|_{\tau=0} = \psi_0\big|_{\tau=0} = \dot{\psi}_0\big|_{\tau=0} = 0,$$
$$\varphi_1\big|_{\tau=0} = \psi_1\big|_{\tau=0} = \dot{\psi}_1\big|_{\tau=0} = 0,\ \dot{\varphi}_1\big|_{\tau=0} = V_0 r\cos\alpha, \tag{9}$$
$$u\big|_{\tau=0} = w\big|_{\tau=0} = \chi\big|_{\tau=0} = 0,\ \dot{\chi}\big|_{\tau=0} = 0,\ \dot{u}\big|_{\tau=0} = -V_0\sin\alpha,\ \dot{w}\big|_{\tau=0} = V_0\cos\alpha.$$

All values and parameters have a dimensionless form.

SOLUTION EQUATIONS AND METHOD

Boundary conditions (8) and the principle of superposition and reduction of initial conditions (9) to zero result into the following integral equation:

$$\int\limits_0^\tau \int\limits_{-b(t)}^{b(t)} G_0(x-\xi, \tau-t)\, p(\xi, t)\, d\xi dt = \int\limits_0^\tau \int\limits_{-b(t)}^{b(t)} G(x-\xi, \tau-t)\, p(\xi, t)\, d\xi dt + \int\limits_0^\tau \int\limits_{-\pi}^{\pi} G(\alpha-\xi, \tau-t)\, \sigma_r(\xi, t)\, d\xi dt + \sqrt{1 - x^2} - 1. \tag{10}$$

where the koernels of integral operators $G(x, \tau)$, $G_0(x, \tau)$ represent dominant functions for the shell and semi-space [1, 2].

It turns into a closed system by problem (7) and kinematic proportion (6).

The dominant function for the shell with the filling is the solution of problem (1) – (5) (if $k = 1$) with zero initial conditions and pressure $p = \delta(\alpha)\delta(\tau) - \sigma_r(\alpha, \tau)$, where $\delta(z)$ is Dirac delta-function. This dominant function is constructed by use of Fourier expansions and integral Laplace time transformation.

For finding solutions of the system of resolving equations an original quadrature based algorithm was developed. In doing so, integrals (10) and (7) are substituted with their numerical analogues by making use of special quadrature formulas adapted for specificities of kernels of integral operators

This study was performed with financial support of the Russian Foundation for Basic Research (project 14-49-00091).

References

[1] Tarlakovskii D.V., Fedotenkov G.V.: TwoDimensional Nonstationary Contact of Elastic Cylindrical or Spherical Shells *Journal of Machinery Manufacture and Reliability*, **43**(2):145–152, 2014.

[2] Gorshkov A.G., Tarlakovskii D.V., Fedotenkov G.V.: Plane problem of a vertical cylindrical shell hit on elastic half-space *Mechanics of Solids*, **5**:151-158, 2000.

THE DUAL DOMAIN DECOMPOSITION PARALLEL CONTACT ALGORITHM IN CHAP3D CODE

Yuxi Jiang[1a)], Haibing Zhou[1], Jun Xiong[1] & Shudao Zhang[1]
[1]*Institute of Applied Physics and Computational Mathematics, Beijing, China*

Summary CHAP3D code is a three-dimensional Lagrangian program developed by IAPCM. The parallel contact algorithm used in this program for the Clusters of Multi-Processors computers is introduced in this paper. The dual domain decomposition method is applied and two methods of the contact surfaces decomposition are provided in this parallel contact algorithm. One is to distribute a whole contact surface to a processor and the other is to divide the master surface into each processor. In each processor, the contact search methods are adopted to determine whether and where the nodes are contact with a surface segment, and the distributed parameter method and penalty method are optional to calculate the contact constrains. The numerical example illustrates that CHAP3D has the ability to simulate the different types of contact problems such as contact with sliding only interfaces, sliding with closure and separation interfaces, contact with tied interfaces and self-contact.

THE INTRODUCTION TO CHAP3D

CHAP3D (Compatible Hydrodynamics Analysis Program 3D) code is a three-dimensional Lagrangian program developed by IAPCM. It is based on Compatible Lagrangian hydrodynamics numerical method [1], [2], which preserves total energy conservation by compatible differential operator discretization. So CHAP3D code is fit for the numerical simulation of the problems that request the accurate calculations of the energy transition and the total energy conservation such as high velocity impact, explosion and implosion.

.

THE PARALLEL CONTACT ALGORITHM

Contact between moving surfaces and/or moving bodies is one of the most crucial parts of the whole simulation in Lagrangian formulations. The parallel contact algorithm is one of the most important parts of CHAP3D code. The dual domain decomposition method is adopted by the parallel contact algorithm in CHAP3D code.

The essential idea of the parallel contact algorithm is to divide a large contact problem into some smaller subsets such that the computation of each subset will be conducted on a single computer processor. The METIS [3] is used as the tool to decompose the computational domain for the Clusters of Multi-Processors computers. However the computational domain decomposition will divide the whole contact surface into several processors, and the computation of this contact surface need lots of communications between processors. So another decomposition of the contact domain is appealed to reduce the communications and promote the efficiency. This is called “Dual Domain Decomposition”.

The strategy of the parallel contact algorithm with dual domain decomposition is:

1. “The first domain decomposition”: divide the main computational domain into processors.
2. “The second domain decomposition”: divide the contact computational domain into processors.
3. Parallel calculate the node force.
4. Parallel calculate the nod contact force.
5. Update the acceleration, velocity, coordinate of node
6. Return to 3.

In the second domain decomposition, two methods of contact surface division are provided in CHAP3D. One is to distribute a whole contact surface (include the master surface and the slave surface) to a single processor. This contact surface could be calculated by using the serial contact algorithm in a processor, and there is not any communication in calculation. This method is likely to make some processors to be vacant. The other method is to divide the master surface into the all processors and distribute the whole slave surface to every processor. A part of contact surface could be calculated in a processor by using the serial contact algorithm. The communication is only recalled to get the whole contact surface when the calculations in all the processors are finished.

THE CONTACT SEARCH ALGORITHM

In each processor, the contact search process in CHAP3D is categorized into the global contact searching and the local contact searching. The global search is about to find all the possible candidate surface segments of a particular node. The bucket-sorting algorithm [4] is the main global search method and the face-tracking algorithm and the brute force search method are the supplementary ones. The local search is used to determine precisely whether and where the node is in contact. The node-to-segment algorithm, one of the most popular methods, is employed in CHAP3D. The Newton-Raphson

a) Corresponding author. Email: Jiang_yuxi@iapcm.ac.cn

iteration is usually used to solve the contact point parameter coordinates. Moreover the inside-outside search algorithm [5] is introduced in CHAP3D as the complementary one.

THE CONTACT ALGORITHM

The distributed parameter method [4] and the penalty method [4] are applied to calculate the contact constrains on the contact nodes. The distributed parameter method is used for contact pressure in the megabar regime such as sliding explosive and the penalty method is used for the impact-contact problems.

NUMERICAL EXAMPLE

The Fig. 1- Fig.2 are the results of the numerical simulation of the HR-2 steel tube expansion induced by inside head-on hitting two detonation waves[6]. The simulated contours of deformed HR-2 steel tubes are in agreement with the results measured by flash X-ray cineradiography.

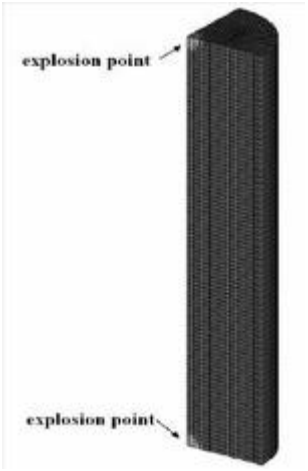

Fig. 1 The model of calculation

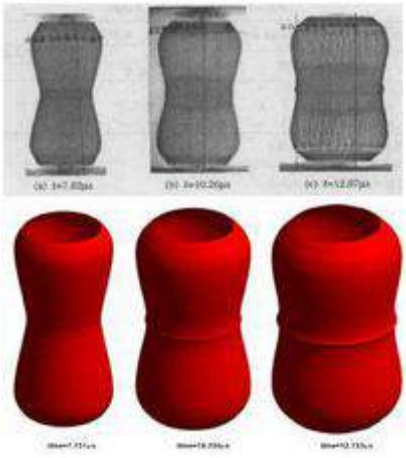

Fig. 2 the contours of the metallic tubes by numerical simulation and flash X-ray cineradiography

CONCLUSIONS

CHAP3D has the ability to simulation the different types of contact problems such as contact with sliding only interfaces, with closure and separation interfaces, with tied interfaces and with self-contact interfaces

References

[1] Caramana E. J., Burton D. E., Shashkov M. J., Whalen P. P.: The Construction of Compatible Hydrodynamics Algorithms Utilizing Conservation of Total Energy. *J. Compt. Phys.* **146**:227-262, 1998.

[2] Caramana E. J., Rousculp C. L., Burton D. E.: A Compatible, Energy and Symmetry Preserving Lagrangian Hydrodynamics Algorithm in Three-dimensional Cartesian Geometry. *J. Compt. Phys.* **157**:89-119, 2001.

[3] Karypis G., Kumar V.: METIS: Unstructured Graph Partitioning and Sparse Matrix Ordering System. Version 1.0, University of Minnesota, Department of Computer Science, 1995.

[4] Hallquist J. O.: LS-Dyna Theoretical Manual. Livermore Software Technology Corporation, Livermore, 1998

[5] Wang S. P., Nakamachi E.: The Inside-Outside Contact Search Algorithm for Finite Element Analysis. *International Journal for Numerical Methods in Engineering*, 40(19): 3665-3685, 1997.

[6] Zhang S. W., Hua J. S., Liu C. L., Han C. S.: A numerical simulation of the metallic tube expansion induced by inside head-on hitting two detonation wave. Explosion and Shock Wave, 24(3): 219-225, 2004.

NONLINEAR ANALYTICAL – NUMERICAL MODELS OF SOLVING FRICTIONAL HEAT PROBLEMS

Aleksander Yevtushenko, Michal Kuciej, Ewa Och
Faculty of Mechanical Engineering, Bialystok University of Technology, Bialystok, Poland

Summary The nonlinear thermal problems of friction have been formulated for two semi-spaces, compressed by time dependent pressure and sliding with a speed that changes in time. Due to friction at the contact surface the heat is generated. It is assumed that the thermal contact of the bodies is imperfect, and the materials are thermal-sensitive, i.e. their thermophysical properties are temperature dependent. This problem allows to determine temperature fields in such elements of brakes, as a pad and a disk. As a consequence of the assumption, linearization of a corresponding boundary-value heat conduction problem using the Kirchhoff transformation has been incompleted. Depending on the type of nonlinearity of friction bodies material (simple or arbitrary), the various methods of linearizing the final task have been suggested. The effectiveness of these methods has been illustrated by the numerical analysis of the friction materials for couples with a linear or nonlinear temperature dependence of thermal properties.

INTRODUCTION

Analytical models of frictional heating of heavily loaded friction nodes in many cases should take into account the change in temperature of the thermal properties (coefficient of heat conductivity and diffusivity, specific heat) of materials they are made from. When in the formulation of the frictional heat problem we take into consideration the change of these properties with temperature, the problem becomes nonlinear. One of techniques used for solving nonlinear problems is to reduce those problems to linear ones, using the substitution methods. The most common substitution method is Kirchhoff [1] integral transformation. It either linearizes the problems fully (after substitution to the basic equations and to the boundary conditions), or reduces to a nonlinear equations of such a class which methods of solutions are known. Reviews of the application of substitutions methods used to solve the nonlinear boundary-value heat conduction problems are in the monographs [2, 3]. The review of analytical methods of solving the thermal problems of friction have been presented in paper [4].

A solution to the thermal problem of friction during braking with a constant retardation, when thermosensitive materials of a pad and a disk have simple nonlinearity (materials in which coefficients of heat conduction and specific heat depend on the temperature, and their ratio – a coefficient of thermal diffusivity – is constant), have been obtained by means of the step-by-step linearization method or method of linearizing parameters in articles [5, 6]. A solution to the arbitrary (i.e. with the coefficients changing independently of each other) nonlinear thermal problems of friction for two semi-spaces in case of sliding with a constant speed has been obtained by method of successive approximations in the article [7], and the same iterative scheme for solving thermal problems of friction at braking has been proposed in the paper [8].

The main aim of this article is to obtain, using different analytical and numerical methods, solutions to the thermal problems of friction for the two semi-spaces with materials characterized simply or arbitrary nonlinearities, and with taking into account thermal resistance of bodies, increase in time contact pressure and nonlinear velocity of sliding.

DESCRIPTION OF NONLINEAR MODELS AND NUMERICAL ANALYSIS

In this paper the solutions to nonlinear boundary-value problems of thermal conductivity have been presented for the two semi-infinite (semi-spaces) bodies. Materials of the bodies are thermosensitive, ie. their coefficients of thermal conductivity and specific heat change with temperature. Thermosensitive materials are divided into two types; one with simple nonlinearity, when coefficients of thermal conductivity and specific heat depend on the temperature, and their ratio – a coefficient of thermal diffusivity – is constant. Another type is the one with an arbitrary nonlinearity, when the thermal coefficients change with temperature independently of each other.

Semi-spaces, in the most general case that has been considered, are pressed at infinity by pressure increasing in time from zero to nominal value. At the time adopted as the initial ($t = 0$) the bodies begin to slide relatively to each other at a speed decreasing with time. In another considered case, with the constant pressure, when the time of increase of pressure to the nominal value tends to zero, the sliding velocity decreases linearly (braking with uniform delay). Under the influence of the friction forces on the contact surface the heat is generated, which warms both bodies. It is assumed that the thermal contact between bodies is imperfect, ie. the heat transfer takes place with a constant coefficient of thermal conductivity of contact.

In accordance with the above assumptions, the nonlinear boundary-values heat conduction problems have been formulated. In order to obtain analytical solutions the problems must be linearized. As a first step, the Kirchhoff substitution has been used, but only the partial linearization of problems was achieved. The boundary condition of imperfect thermal contact was nonlinear.

[a)] Corresponding author. Email: m.kuciej@pb.edu.pl.

In order to complete linearization of problems, depending on the type of material with simple or arbitrary nonlinearity, various methods for the final linearization have been applied.

For a simple nonlinearity of materials:

- expansion of the nonlinear function in a power series,
- linearizing parameters method,
- spline-approximation method,

and for arbitrary nonlinearity of materials:

- method of successive approximations,
- method of lines.

On the basis of the obtained solutions numerical analysis has been carried out for various frictional pairs made from such materials, that its thermal properties' changes with temperature are characterized by simple or arbitrary nonlinearity. We have examined how the thermosensitivity of material influences the evolution and the temperature distributions in the frictional systems. The results have been compared with calculations of temperature conducted at the constant thermal properties. The effect of pressure increase and oscillations, sliding velocity and thermal resistance of contact on the evolutions of the temperature on the frictional elements working surfaces have been investigated, too. Additionally, the results of temperature calculations obtained by linearizing methods described above, have been compared as well. The calculation results are presented in graphs and tables.

References

[1] Kirchhoff G.R.: Vorlesungen über die Theorie der Wärme, B.G. Teubner, Leipzig, 1894.

[2] Kushnir R.M., Popovych V.S.: Heat conduction problems of thermosensitive solids under complex heat exchange. In: Heat conduction – Basic Research, V. Vikhrenko Ed., In Tech, Croatia, 2011, pp. 131–154.

[3] Kozdoba L.A.: Methods of solving non-linear problems of heat conduction, Nauka, Moscow, 1975 (in Russian).

[4] Yevtushenko A., Kuciej M.: One-dimensional thermal problem of friction during braking: The history of development and actual state. *Int. J. Heat Mass Transf.* 55: 4148-4153, 2012.

[5] Yevtushenko A., Kuciej M., Och E.: Effect of thermal sensitivity of materials of tribojoint on friction temperature. *Journal of Friction and Wear* 35: 105-113, 2014.

[6] Yevtushenko A.A., Kuciej M., Och E.: Influence of thermal sensitivity of the pad and disc materials on the temperature during braking. *Int. Comm. Heat Mass Transf.* 55: 84-92, 2014.

[7] Yevtushenko A.A., Kuciej M., Och. E.: Some methods for calculating the temperature during friction of the thermosensitive materials. *Numerical Heat Transfer, Part A.* 67: 696-718, 2015.

[8] Yevtushenko A.A., Kuciej M., Och. E.: Temperature in thermally nonlinear pad-disk brake system. *Int. Comm. Heat Mass Transf.* 57: 274-281, 2014.

MODELLING OF EXTERNAL DYNAMIC OF THE FRICTION ENGAGEMENT

Kirill Nuzhdin[1a)], Victor Musalimov[1] & Andrei Tyurin[1]
[1]*Department of Computer Technologies and Control Systems, Chair of Mechatronics, ITMO University, Saint Petersburg, Russian Federation*

Summary Evolution of tribocontact, forecasting of friction and wear of tribopair materials are one of the main tasks of the tribology.
In this paper the problems of external friction dynamics were explored, in particular investigations of dynamic characteristics of tribological objects. In the context of automatic control theory, the system of this type is object of parametric identification, wherein in the simplest case, the parameters are damping coefficient and unit speed of rotation.
This approach allows to use amplitude-frequency characteristics for evaluating the dynamic coefficients of friction interaction. The proposed method is the basis of the investigations of processes of evolution tribological characteristics. The suggested approach provides the measuring instrument Tribal-T, whereon the investigated tribopairs, which have a slip-step scheme of friction process, are fixed.

DESCRIPTION OF THE INSTRUMENT TRIBAL-T AND HOW IT WORKS

The experimental device "Tribal-T" for determining the tribological and mechanical properties of materials was developed on the basis of Chair of Mechatronics of ITMO University. As an analogy was used device for rub testing, which was described in the inventor's certificate [1]. The idea of reciprocating motion of testing samples relative to each other was applied in this machine [2].
In Fig. 1 shown the exterior of the measuring instrument Tribal-T and its main components.

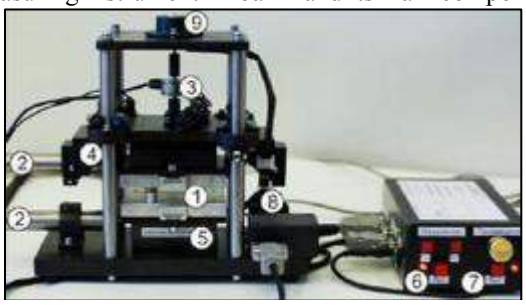

Figure 1 - The measuring instrument Tribal-T:
1 - specimens; 2 - displacement sensor; 3,4 - sensors of normal load and circumferential load; 5 - precision guideways; 6,7 - equipment control board of load and velocity; 8 - actuator of cyclic displacement; 9 - actuator of load

Driven by the external actuator, one of the tribopairs is in cyclic reciprocating motion. Due to impact of frictional force, the second tribopair is in cyclic constrained motion. The device is equipped with sensors of displacement and pressure, which allow to track the absolute movement of tribopairs, and the measured signals are the inputs and outputs of the system.

IDENTIFICATION MODEL

In the paper, as test specimens was selected a friction couple Aluminum - Aluminum.

At the first stage of research tribological characteristics of dynamic objects have been carried out a series of experiments using the Tribal-T. In the course of the experiment were obtained signals characterizing the absolute displacement of the lower pattern (input signal) and the top of the sample (output signal).

Then, a discrete model in the state space (which describes the behavior of dynamic systems of tribological pair) was received by dint of the MATLAB application package. The following (in Fig. 3) is model parameters in the initial moment of experiment.

Discrete-time identified state-space model:

$$x(t+Ts) = Ax(t) + Bu(t) + Ke(t), \quad y(t) = Cx(t) + Du(t) + e(t)$$

$$A=\begin{bmatrix} 0 & 1 \\ -0.568 & 1.439 \end{bmatrix}, \; B=\begin{bmatrix} -0.421 \\ -0.2572 \end{bmatrix}, \; C=[1 \;\; 0], \; D=[0], \; K=\begin{bmatrix} 0.7427 \\ 0.429 \end{bmatrix}, \; x(0)=\begin{bmatrix} 0 \\ 0 \end{bmatrix}$$

A – a coefficients vector in state of space; C – a vector of offset coefficients; K – matrix of noises;
B – a coefficients vector in control matrix; D – a vector of feedback coefficients; x(0) – initial conditions.

Fig. 3 - Model parameters in the initial moment

[a)]Corresponding author. Email: nkirill74@gmail.com.

STEP RESPONSE

Dynamic properties of linear mechanical objects and automatic control systems can be described by equations and characteristics curve. In automatic control theory it is used two types of characteristics - transient characteristic and frequency.

These characteristics can be calculated from the experimentally obtained data in the generation of equation of a dynamic object. Furthermore, these characteristics help to define the object response to any impact arbitrary species. Thus, transient and frequency characteristics are uniquely related to the equation of dynamic object and at the same time they are a comprehensive description of the dynamic properties of the friction process [3].

The transition function (or transient response) is a time based historical graph of output value of the dynamic object, at the time of action input step disturbance.

Reaction of the output when action such an impact - this is the transition function (shown in Fig. 4). We used the function step in MATLAB for determining of transition function.

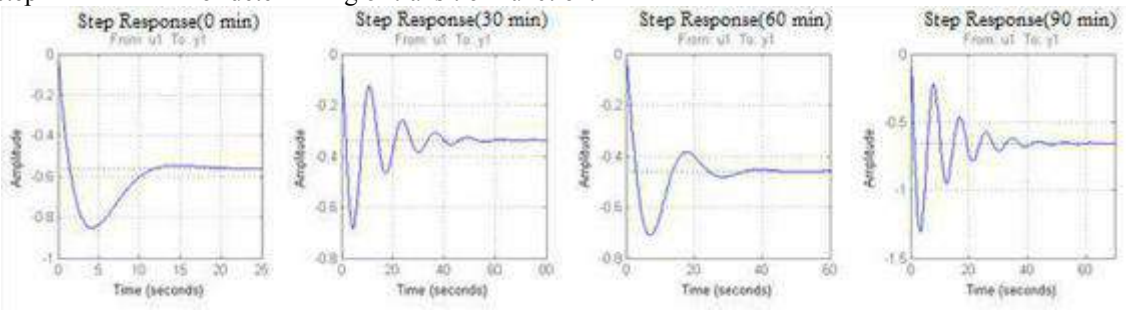

Fig. 4 – Transition function curves for different moments of experiment

FREQUENCY RESPONSE

The most important characteristic of a dynamic object is frequency transfer function. Frequency characteristics describe the steady-state oscillations at the output of the object caused by harmonic influence on input [4].

If amplitude of input vibrations is detented then amplitude and phase of the output waveform depends on the frequency.

For estimation of phase-frequency characteristic and frequency-response characteristic we used Bode function, which provides logarithmic frequency response. Graphs of the phase-frequency characteristic (right) and frequency-response characteristic (left) are shown in Fig. 5.

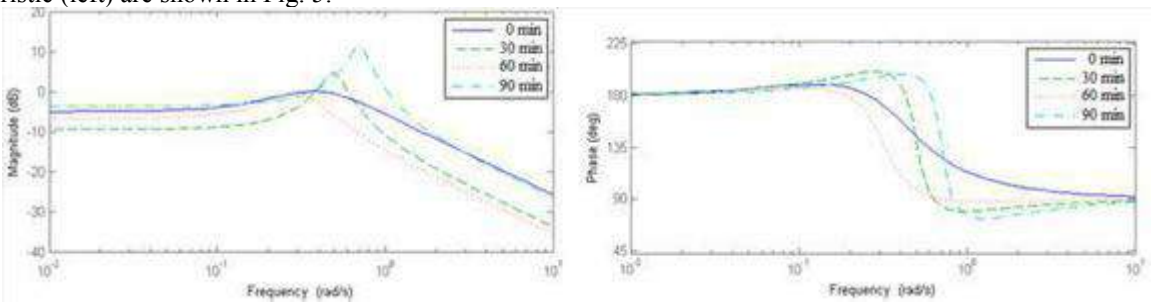

Fig. 5 – Dependencies of frequency-response characteristic and phase-frequency characteristic

CONCLUSIONS

In the paper it was reviewed and used the method for estimate of dynamic coefficients of friction interaction and monitoring of the evolution of tribological characteristics in friction process.

In operation, the identification model, which describes the dynamic processes of friction was built based on the input - output data obtained experimentally by dint of the machine Tribal-T.

References

[1] Izmailov G.M., Sokhanev B.V., Musalimov V.M., Shiyanov V.D.: The apparatus for rub testing of materials. Inventor's certificate №1821689, USSR 1993.

[2] Buzunov D.A., Buzunov R.A., Sizova A.A.: Modernization of the tribometric system “Tribal”. *Paper*, V-th Conference for Young Scientists, SPb, Russia 2007.

[3] Musalimov V.M., Valetov V.A.: Dynamic of frictional engagement. ITMO University, SPb, Russia 2006.

[4] Musalimov V.M., Sizova A.A., Ivanov E. K., Krylov N.A., Tkachev A.L.: Foundations of tribonics. ITMO University, SPb, Russia 2009.

SM03 - Damage Mechanics

TS.SM03-1.01	Hild, François - In situ observations of strained bands and ductile damage in thin aluminum alloy sheets (INVITED)	1806
TS.SM03-1.02	Pandolfi, Anna - A model of poro-mechanical damaging material (INVITED)	1808
TS.SM03-1.03	Brünig, Michael - Biaxial experiments and numerical analysis of stress-state-dependent damage and failure	1810
TS.SM03-1.04	Chen, Naigeng - Experimental determination of non-woven bond strength distributions.	1812
TS.SM03-1.05	De Geus, Tom - Systematic analysis of fracture in two-phase materials at all stages	1814
TS.SM03-1.06	Fan, Zhengxuan - Atomistic simulation of surface cyclic slip irreversibility in FCC metals	1816
TS.SM03-2.01	Poh, Leong Hien - A gradient damage formulation with transient nonlocal interaction (INVITED)	1818
TS.SM03-2.02	Gurses, Ercan - Experimental and numerical investigation of impact induced damage progression in CFRP composites	1820
TS.SM03-2.03	Kouhia, Reijo - Modelling of anisotropic fatigue	1822
TS.SM03-2.04	Kuna, Meinhard - Damage Model of a Particle Reinforced TRIP-Steel Matrix Composite	1824
TS.SM03-2.05	Larsson, Ragnar - Damage growth in compressive loaded fibre reinforced composites	1826
TS.SM03-2.06	Liang, Bowen - An automated multiscale simulation of the failure response of adhesive-bonded structural joints	1828
TS.SM03-3.01	Sun, Lizhi - Dynamic Viscoelastic Modeling of Interfacial Debonding for Magnetorheological Nanocomposites (INVITED)	1830
TS.SM03-3.02	Longère, Patrice - Modelling of shear failure caused by adiabatic shear banding and subsequent microvoiding	1832
TS.SM03-3.03	Matous, Karel - Virtual materials testing	1834
TS.SM03-3.04	Revil-Baudard, Benoit - Modeling plasticity-damage coupling in anisotropic titanium & validation by XCMT	1836
TS.SM03-3.05	Turteltaub, Sergio - Multiscale traction-separation relations for fiber-reinforced composites	1838
TS.SM03-3.06	Welemane, Hélène - A micromechanical damage model for initially anisotropic materials	1840
PO.SM03-1.01.203	Abed, Farid - Coupled damage-plasticity modeling of the inelastic behavior of C45 steel at high temperatures	1842
PO.SM03-1.02.204	Chen, Zengtao - Molecular dynamics insights into the coalescence of closely-packed voids	1844
PO.SM03-1.03.205	Graham-Brady, Lori - Predicting dynamic failure in armor ceramic using efficient initial flaw statistics	1846
PO.SM03-1.04.206	Gundlach, Janto - Numerical two-scale simulations with application towards refractories	1848
PO.SM03-1.05.207	Hao, Shengwang - Localization pattern evolution of rock under uniaxial compression experiments	1850
PO.SM03-1.06.208	Hure, Jeremy - Void growth and coalescence in irradiated materials	1852

PO.SM03-1.07.209	Jespersen, Kristine - 3D X-ray CT of fatigue damage in fibre composite	1854
PO.SM03-1.08.210	Kondori, Babak - Micromechanical modeling of damage and fracture in magnesium alloys	1856
PO.SM03-1.09.211	Kurek, Andrzej - Low Cycle Fatigue Of 16Mo3 Steel In Strain Controled Cyclic Bending	1858
PO.SM03-1.10.212	Kuwazuru, Osamu - Microscopic corrosion electric field analysis with damaged passive film of stainless steel	1860
PO.SM03-1.11.213	Lavoie, Shawn - A rate-dependent damage model for elastomers at large strain	1862
PO.SM03-2.01.121	Behdinan, Kamran - Effect of Mg impurities on sapphire's strength: a multiscale simulation approach	1864
PO.SM03-2.02.122	Mishra, Ashish - A fully nonlinear model of a damaged unidirectional metal matrix composite	1866
PO.SM03-2.03.123	Morada, Ghodratollah - Numerical Analysis on Compression Failure Mechanisms of Impacted Ncf Reinforced Composites	1868
PO.SM03-2.04.124	Pathak, Nikky - Role of the microstructure on sheared edge fracture of advanced high strength steel	1870
PO.SM03-2.05.125	Ryś, Maciej - Total Energy Equivalence in Constitutive Modelling of Multidissipative Materials	1672
PO.SM03-2.06.126	Saeedi, Navid - Damage-plasticity simulation of a premature failure in FRP strengthened RC beams	1874
PO.SM03-2.07.127	Simons, Erik - Mesh-independent damage-plasticity model for ceramics in ballistic protection	1876
PO.SM03-2.08.128	Wei, Yueguang - Characterization of damage and failure for nanocrystalline materials	1877
PO.SM03-2.09.129	Yang, Li - Quantitative Assessment of Failure in Tbcs Based on Frequency Spectrum of Acoustic Emission	1879
PO.SM03-2.10.130	Yu, Feng - Stress triaxiality effect on damage evolution of high-strength steels	1881
PO.SM03-2.11.131	Zhang, Yi - Effects of compressive loading history on mechanical properties of HDPE	1883

IN SITU OBSERVATIONS OF STRAINED BANDS AND DUCTILE DAMAGE IN THIN ALUMINUM ALLOY SHEETS

Ante Buljac[1,2], Thibault Taillandier-Thomas[1,2], Thilo F. Morgeneyer[2], Lukas Helfen[3,4], Stéphane Roux[1], and François Hild*[1]

[1]*LMT, ENS Cachan/CNRS/University Paris-Saclay, Cachan, France*
[2]*MINES ParisTech, PSL Research University, MAT-Centre des matériaux, CNRS UMR 7633, Evry, France*
[3]*ANKA/Institute for Photon Science and Synchrotron Radiation, Karlsruhe Institute of Technology (KIT), Karlsruhe, Germany*
[4]*European Synchrotron Radiation Facility (ESRF), Grenoble, France*

Summary Up to now, when the fracture of ductile sheet materials is studied, the interaction between plasticity and damage (*e.g.* flat-to-slant transition) is still a matter of active debate. The fundamental question can be phrased as: Which mechanism is responsible for localized phenomena leading to the final failure? To address this issue, mechanical tests have been conducted on notched plates made of 2198 T8 aluminum alloy and imaged via synchrotron laminography at micrometer resolution. Ductile damage is analyzed via the reconstructed volumes and the correlation residuals associated with digital volume correlation. The latter allows displacement fields to be measured and strain fields to be estimated in the bulk of the material during the test. The development of plasticity and damage can therefore be studied during the loading history.

While ductile fracture of metallic engineering materials at high stress triaxiality is fairly well-established, failure at lower levels of stress triaxiality (*i.e.* below 1) is less understood. An example of poorly understood localized failure phenomena is the flat-to-slant crack transition. During this process, fracture typically initiates at crack-like features with an initial flat crack forming normal to the loading direction, which evolves into a slant crack by so-called localized "fast-shear" decohesion (*i.e.* flat-to-slant transition). These phenomena are also found in thick specimens close to their external surface in the form of "shear lips."

In this work, high-resolution *in-situ* synchrotron X-ray laminography [1] combined with global digital volume correlation (*i.e.* C8-DVC [2]) is used to measure the damage and plastic strain fields ahead of a notch introduced within a 2198 Al-Cu-Li alloy sheet. Synchrotron laminography is a technique specifically developed for three-dimensional (3D) imaging of laterally extended sheet specimens with micrometer resolution. DVC is carried out by registering the 3D image contrast caused by iron-rich intermetallic particles present in the alloy. The alloy is recrystallized and tested in T8 artificial ageing condition involving relatively low work hardening.

Incremental loading steps are especially interesting in terms of plastic activity. Sections normal to the crack propagation direction (L) of von Mises equivalent strain fields for loading step (0)-(1) are shown in Figure 1. Starting from 110 μm ahead of the notch root, the section planes are chosen as regularly spaced with a mutual distance of 140 μm. The magnitude of the equivalent strain close to the notch root is significantly higher than in the remainder of the analyzed region. To capture interesting features, the color bar range is limited to 0.1 for all displayed sections. Strained bands are observed starting at a distance of 250 μm from the notch root.

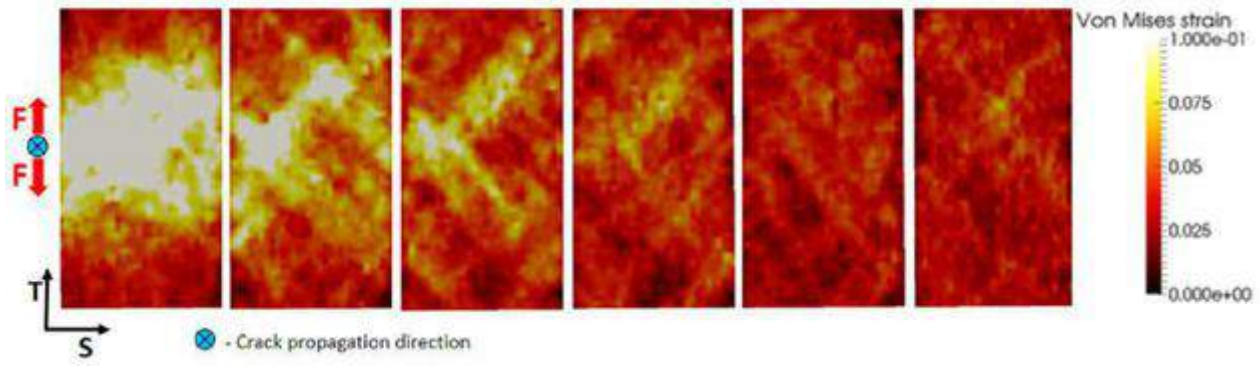

Figure 1: Sections normal to the crack propagation direction showing von Mises equivalent strain maps for loading step (0)-(1)

Figure 2 shows isometric views of the microstructure voids (obtained by thresholding gray levels) inside the same region of interest and corresponding equivalent incremental strain fields. Strained bands occur from the very beginning of the loading

*Corresponding author. Email: hild@lmt.ens-cachan.fr

process. The undeformed microstructure state (0) shows very small amounts of porosity without any pattern distribution. The first loading step (1) already reveals strained bands (Figure 1). This localized strain pattern did not cause explicit damage growth inside the bands, which is seen for microstructure state (1). Void nucleation and growth are very limited, except for loading step (2)-(3), where the damage activity is more developed mainly in the zone close to the notch root due to higher strain and stress levels. Significant damage does not occur immediately after the onset of heterogeneous plastic flow, which appears to be the prevalent mechanism explaining the flat-to-slant transition in the studied aluminum alloy. During the loading process very high plastic strains develop within the bands and in the bulk, which induce at a later stage damage nucleation and limited growth leading to the final failure. The final fracture path is explained by the measured incremental strain patterns. Therefore, in an area close to the notch root the onset and development of slanted strain bands precede damage. The activity of the different strained bands at the notch root is alternating between different locations over the loading history [3]. However, the band leading to final rupture is always active.

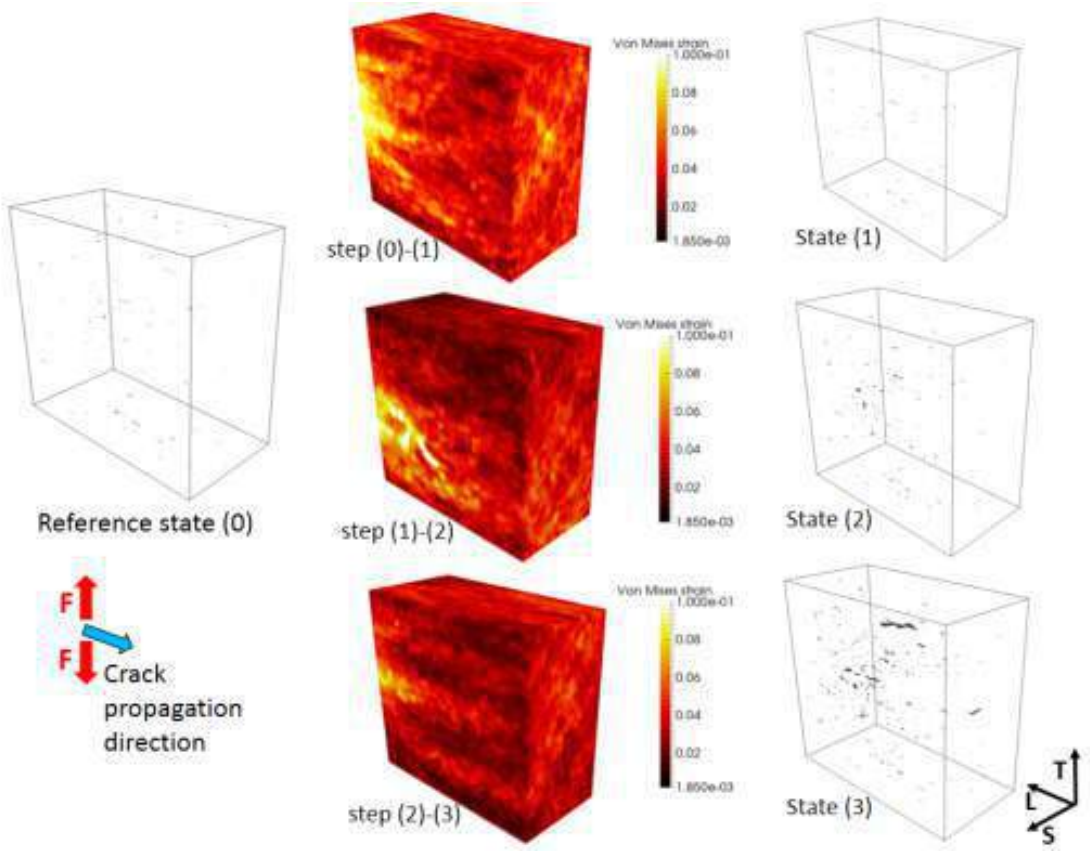

Figure 2: Isometric views of the void (damage) distribution together with the von Mises equivalent strain distribution for the evaluated incremental loading steps

Less numerous inclined strained bands also develop 800 μm from the notch prior to the onset of damage [4]. Damage in this region mainly results from the nucleation of voids on micrometer intermetallic particles and occurs at an even later stage of deformation, again followed by very limited void growth.

References

[1] Helfen L., Baumbach T., Mikulík P., Kiel D., Pernot P., Cloetens P., Baruchel J.: High-resolution three-dimensional imaging of flat objects by synchrotron-radiation computed laminography. Appl. Phys. Lett., 86:071915, 2005.

[2] Roux S., Hild F., Viot P., Bernard D.: Three dimensional image correlation from X-Ray computed tomography of solid foam. Comp. Part A, 39:1253-1265, 2008.

[3] Buljac A., Taillandier-Thomas T., Morgeneyer T.F., Helfen L., Roux S., Hild F.: Slant strained band development during flat to slant crack transition in AA 2198 T8 sheet: in situ 3D measurements. Int J. Fract. in press, DOI:10.1007/s10704-015-0052-z, 2016.

[4] Morgeneyer T.F., Taillandier-Thomas T., Helfen L., Baumbach T., Sinclair I., Roux S., Hild F.: In situ 3D observation of early strain localisation during failure of thin Al alloy (2198) sheet. Acta Mat. 69:78-91, 2014.

A MODEL OF PORO-MECHANICAL DAMAGING MATERIAL

Anna Pandolfi[1], Maria Laura De Bellis[2], Gabriele Della Vecchia[1]& Michael Ortiz[3]
[1]*Civil and Environmental Engineering Department, Politecnico di Milano, Milano, Italy*
[2]*Department of Innovation, University of Lecce, Italy*
[3]*Engineering and Applied Sciences Division, Caltech, CA USA*

Summary A poro-mechanical model of a damaging material under overall compression state is presented. The damage is characterized by the formation of microstructures in the form of equi-distant parallel faults and characterizes the evolution of the permeability of the material. The model is particularly suitable for engineering applications in soil and rock mechanics.

INTRODUCTION

Deterioration of mechanical and hydraulic properties of rock masses and subsequent problems are closely related to changes in the stress state, formation of new cracks, and increase of permeability in porous media saturated with freely moving fluids. In fully saturated rocks, fluid and solid phases are interconnected and the interaction between fluid and rock is characterized by coupled diffusion-deformation mechanisms that convey an apparent time-dependent character to the mechanical properties of the rock. The two governing equations of the coupled problem are the linear momentum balance and the continuity equation (mass conservation). The kinematic quantities that characterize this picture are the solid displacement and the rate of fluid volume per unit area. Hydro-mechanical coupling arises from the influence of the mechanical variables (stress, strain and displacement) on the continuity equation, where the primary variable is the fluid pressure, and from the influence of the hydraulic variables (pore pressure and seepage velocity) on the equilibrium equations, where the primary variables are the displacements. In the present talk, we describe a coupled approach to model damage induced by hydro-mechanical processes in low permeability solids. Classic methods can be applied to describe the porous-mechanical behaviour of the solid to estimate the flow of fluids across the medium according to the presence of a fluid pressure gradient.

THE BRITTLE DAMAGE MODEL OF DRY SOIL

We describe the solid as an anisotropic brittle continuum where the damage is characterized by the formation of nested microstructures in the form of equidistant parallel faults [1], characterized by distinct orientation $\boldsymbol{N}^{\mathrm{k}}$ and spacing L^k. Faults bound otherwise elastic matrix material. We refer to this mode of deformation as recursive faulting, and the resulting microstructures as recursive faults. The assumption of faulting separates the requisite constitutive relations into two independent components: the behaviour of the matrix, assumed to be elastic for simplicity; and the behaviour of the faults, governed by a cohesive relation in the fault initiation stage, and by Coulomb friction and contact henceforth. The faulting construction can be applied recursively in order to generate complex fault patterns; moreover, to model more realistic materials, the elasticity of the matrix can be replaced by other dissipative behaviours, such as viscoplasticity.

ANALYTICAL EXPRESSION OF DAMAGE INDUCED POROSITY AND PERMEABILIY

The fractured medium can be regarded as an anisotropic porous material. Pores in the form of planar parallel voids form when faults undergo a normal opening displacement $\Delta_{\boldsymbol{k}}^{\boldsymbol{N}}$. The particular geometry of the faults allows for the analytical derivation of the porosity of the medium, as the sum of the original porosity n^{matrix} of the matrix and of the contribution of the Q sets of faults,

$$n = n^{\mathrm{matrix}} + \sum_{k=1}^{Q} \frac{\Delta_{\boldsymbol{k}}^{\boldsymbol{N}}}{L^k}$$

and the analytical derivation of the anisotropic permeability $\boldsymbol{K}$ of the medium, as sum of the original permeability of the matrix $\boldsymbol{K}^{\mathrm{matrix}}$ and of the contribution of the Q sets of faults,

$$\boldsymbol{K} = \boldsymbol{K}^{\mathrm{matrix}} + \sum_{k=1}^{Q} \frac{\Delta_{\boldsymbol{k}}^{\boldsymbol{N}}}{L^k} \frac{(\Delta_{\boldsymbol{k}}^{\boldsymbol{N}})^2}{12} (\boldsymbol{I} - \boldsymbol{N}^{\mathrm{k}} \times \boldsymbol{N}^{\mathrm{k}})$$

COUPLED PROBLEM

According to standard approaches used in poro-mechanical problems, upon space discretization the continuity and equilibrium equations assume the following matrix form:

$$\boldsymbol{H}^T \dot{\boldsymbol{U}} + \boldsymbol{K}\boldsymbol{P} = \boldsymbol{Q}^{ext}(t)$$
$$\boldsymbol{H}\boldsymbol{P} + \boldsymbol{F}^{int}(\boldsymbol{U}) = \boldsymbol{F}^{ext}(t)$$

Where the array $\dot{\boldsymbol{U}}$ collects the unknown discrete velocities and $\boldsymbol{P}$ the unknown discrete pore pressures. $\boldsymbol{Q}^{ext}(t)$ contains the discrete external (imposed and known) fluxes, and $\boldsymbol{K}$ represents the hydraulic conductivity matrix. $\boldsymbol{F}^{ext}(t)$ contains the discrete external forces (imposed and known) and $\boldsymbol{F}^{int}(\boldsymbol{U})$ contains the discrete internal forces, dependent on the unknown displacements through the constitutive law of the material. Finally, the rectangular matrix $\boldsymbol{H}$ is a coupling matrix, dependent only on the shape functions used for the discretization of the domain. The solution of the coupled system can be achieved through a staggered approach, by alternating the solution of first and second systems.

APPLICATIONS

The material model has been validated against experimental triaxial tests conducted in permeable rocks [2]. The coupled approach can be used for a wide range of engineering problems, ranging from the prevention of water or gas outburst into underground mines to the prediction of the integrity of reservoirs for underground CO2 sequestration or hazardous waste storage. As an example of application of the dry model, we consider the progressive damaging induced in a rock mass by the drilling of a borehole with an increasing diameter. The initial stress state of the rock mass anisotropic, and the material surrounding the borehole fail creating a typical fracture pattern that is nicely reproduced by the numerical simulations, see Fig. 1.

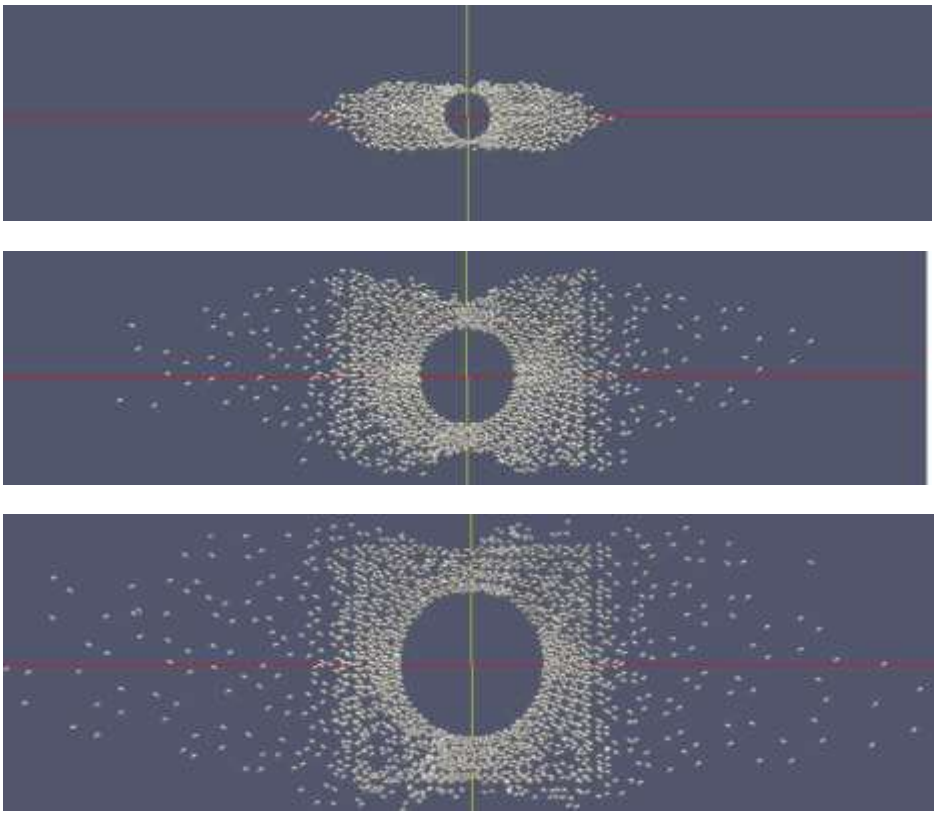

Fig. 1. Distribution of faults around a borehole drilled in a rock mass characterized by an anisotropic stress state. Three different stages corresponding to different diameters of the borehole.

References

[1] Pandolfi A., Conti S., Ortiz M. A recursive-faulting model of distributed damage in confined brittle materials. *Journal of the Mechanics and Physics of Solids* **54**:1972-2003, 2006.

[2] De Bellis ML, Della Vecchia G, Ortiz M, Pandolfi A. A multiscale model of distributed fracture and permeability in solids in all-round compression, Submitted, 2015.

BIAXIAL EXPERIMENTS AND NUMERICAL ANALYSIS OF STRESS-STATE-DEPENDENT DAMAGE AND FAILURE

Michael Brünig*[1], Steffen Gerke[1], and Marco Schmidt[1]

[1]*Institute of Engineering Mechanics and Structural Analysis, University BW Munich, 85577 Neubiberg, Germany*

Summary The paper deals with an anisotropic continuum damage and failure model for ductile metals. The approach takes into account the effect of stress state on damage and failure criteria. Different branches of these conditions are considered corresponding to various microscopic mechanisms depending on stress states. To validate the proposed framework experiments with biaxially loaded specimens and corresponding numerical simulations have been performed. Geometries of different specimens are discussed to analyze a wide range of stress triaxialities and Lode parameters. Digital image correlation technique has been used to analyze current strain states in critical regions of the specimens. Combination of experiments and numerical simulations greatly enriches understanding of damage and fracture processes of ductile metals.

CONTINUUM DAMAGE AND FAILURE MODEL

Caused by fast technological developments damage and failure prediction is one of the most important issues in analysis and design of metal forming processes. Therefore, a thermodynamically consistent anisotropic damage and failure model is presented. It is based on kinematic definition of damage leading to definition of damage strain tensors [1]. These tensors take into account isotropic as well as anisotropic effects providing realistic representation of ductile material degradation. The phenomenological approach is based on free energy functions defined in damaged and corresponding fictitious undamaged configurations, respectively, leading to elastic material laws which are affected by increasing damage. In addition, a hydrostatic-stress-dependent yield condition and a non-associated flow rule are introduced in the undamaged configurations adequately describing the plastic behavior of ductile metals. Furthermore, considering the damaged configurations a damage condition and a damage rule are formulated in stress space characterizing onset and evolution of damage. They are based on experimental observations and mainly on various numerical calculations on the micro-level studying the deformation and failure behavior of void-containing unit cells [2]. Different branches of the damage criteria are considered corresponding to different damage and failure mechanisms acting on the micro-scale depending on stress triaxiality and the Lode parameter: for high positive stress triaxialities damage is mainly caused by nucleation, growth and coalescence of micro-voids and for small positive or negative ones the prevailing damage mechanism is formation and growth of micro-shear-cracks whereas combination of both mechanisms is active for moderate positive stress triaxialities [3, 4, 5].

EXPERIMENTS AND NUMERICAL SIMULATIONS

An experimental program will be presented analyzing the effect of stress state on inelastic behavior, damage and fracture in ductile metals. The experiments are performed using a biaxial test machine allowing individual loadings in two different directions. Digital image correlation technique has been used to analyze current strain states in critical regions of the specimens. Corresponding numerical simulations are carried out to get detailed information on amounts and distributions of stress and strain measures especially in critical regions of the specimens where localized inelastic deformations and failure will occur.

Ideas for development of geometries of suitable specimens covering a wide range of stress triaxialies and Lode parameters are discussed. For example, two possible geometries and loading conditions of flat specimens are shown in Fig. 1. During the experiments, the specimens are simultaneously loaded in horizontal and vertical direction by F_1 and F_2. The load F_2 leads to shear mechanisms in the center of the specimen whereas F_1 leads to superimposed tension or compression modes. Therefore, with variation of load ratios and of geometries in the critical parts different combined shear-tension and shear-compression modes and corresponding failure mechanisms will occur.

Furthermore, performing numerical calculations of the respective experiments allows detailed analysis of stress and strain quantities especially in the critical parts of the specimens. For example, the stress invariants I_1 and $\sqrt{J_2}$ as well as the stress triaxiality η characterize the state of stress (Fig. 2). This corresponds to different damage modes like void growth (1), occurrence of micro-shear-cracks (3) or mixed modes (2). Their distributions are shown in Fig. 2 in the central part of the specimen (Fig. 1(a)) for the load ratio $F_1 : F_2 = \circ\, 1 : 1$. In addition, the numerically predicted equivalent

*Corresponding author. Email: michael.bruenig@unibw.de

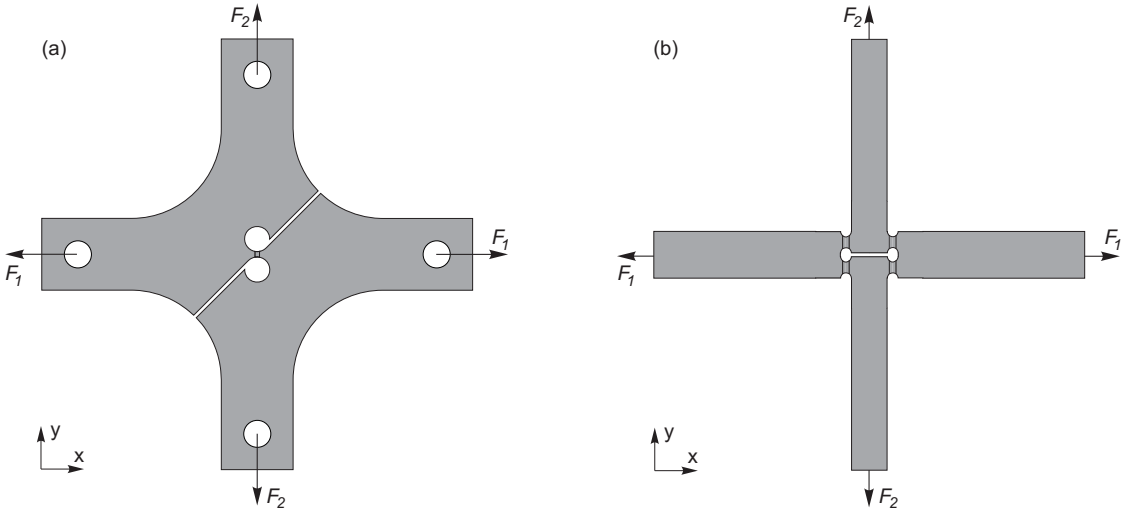

Figure 1: Specimens and loading conditions

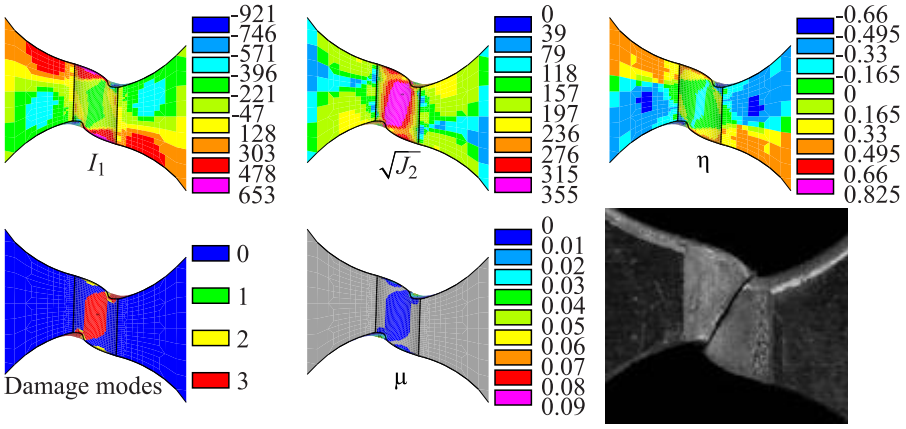

Figure 2: First stress invariant I_1 [MPa], second deviatoric stress invariant $\sqrt{J_2}$ [MPa], stress triaxiality η, damage mode, equivalent damage strain μ, experimental fracture line ($F_1 : F_2 = \circ\, 1 : 1$) for the specimen shown in Fig. 1(a)

damage strain measure μ is visualized. The band of moderate equivalent damage strain indicating the weakest points of the material corresponds to the fracture line of the tested specimen. Further results for other specimens will demonstrate the efficiency of the experimental program and the corresponding numerical simulations.

CONCLUSIONS

The presented experimental program allows biaxial loading of different specimens covering a wide range of stress states even in the shear-tension and shear compression regime. Combination of experiments and numerical simulations allows validation of the proposed continuum damage and failure model and has greatly enriched understanding of damage and fracture processes of ductile metals.

References

[1] Brünig M.: An anisotropic ductile damage model based on irreversible thermodynamics. Int. J. Plasticity 19:1679-1713, 2003.

[2] Brünig M., Gerke S., Hagenbrock, V.: Micromechanical studies on the effect of the stress triaxiality and the Lode parameter on ductile damage. Int. J. Plasticity 50:49-65, 2013.

[3] Bao Y., Wierzbicki T.: On the fracture locus in the equivalent strain and stress triaxiality space. Int. J. Mech. Sci. 46:81-98, 2004.

[4] Lou Y., Yoon J., Huh H.: Modeling of shear ductile fracture considering a changeable cut-off-value. Int. J. Plasticity 54:56-80, 2014.

[5] Brünig M., Brenner D., Gerke S.: Stress state dependence of ductile damage and fracture behavior: Experiments and numerical simulations. Eng. Fract. Mech. 141:152-169, 2015.

EXPERIMENTAL DETERMINATION OF NON-WOVEN BOND STRENGTH DISTRIBUTIONS

Naigeng Chen[1], Margaret K. A. Koker[2], and Meredith N. Silberstein *[1]

[1]*Sibley School of Mechanical and Aerospace Engineering, Cornell University, Ithaca, NY, USA*
[2]*Cornell High Energy Synchrotron Source, Cornell University, Ithaca, NY, USA*

Summary Bond fracture greatly affects the strength and damage progression of many non-wovens. Here we present a novel combined experimental and simulation approach to extract the bond strength of a particular non-woven. The approach was implemented for a commercial polyprolylene non-woven. A small non-woven specimen was imaged by micro computed tomography (μCT) and then subjected to uniaxial tensile loading through complete failure. The geometry of the non-woven was imported from the μCT data into a discrete finite element model. Using known fiber properties, the bond properties were then determined by comparing the simulated load-displacement curve with the experimental load-displacement curve. The sensitivity of the load-displacement curve to bond strength distribution will also be presented.

INTRODUCTION

Non-wovens are fibrous materials manufactured without a weaving or knitting process. Due to versatile manufacturing methods, high porosity and high damage tolerance, non-wovens constitute a rapidly growing portion of the textile industry. A typical non-woven consists of a set of randomly oriented fibers bonded at fiber-fiber crosslinks. The deformation of non-wovens at finite strain is complex, including fiber stretching, fiber bending, structural change, and bond fracture. Bond fracture is a key material property since it directly contributes to material degradation [1] and leads to a change of network connectivity. Experimental determination of bond strength distribution within a non-woven remains a difficult task. Individual fiber-fiber bonds can be prepared and then tested (for example, by atomic force microscopy [2]), but the bonding conditions within the non-woven may not be accurately replicated and these experiments are time and labor intensive. Here we present a method that combines experimental characterization and numerical simulation to determine bond strength throughout a non-woven. This approach carries the dual advantage of characterizing actual bonds within a non-woven and characterizing dozens to hundreds of bonds simultaneously.

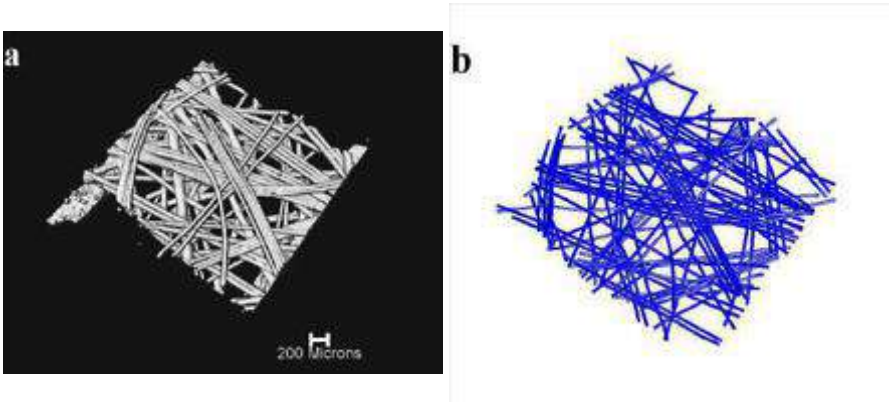

Figure 1: (a) The 3D microstructure of one non-woven specimen. (b) The corresponding extracted fiber network.

EXPERIMENTAL AND NUMERICAL METHODS

A commercial polypropylene-based non-woven (Dupont Typar series) is used for this investigation. The fibers in this non-woven are bonded into a sheet by simultaneously application of pressure and heat. To create specimen for testing, a 2 mm wide strip is cut from a bulk sheet, and attached to a sample holder spanning across a 2 mm gage length. The microstructure of the specimen is imaged using micro computed tomography (μCT). The specimen is then tested under uniaxial tensile loading until failure while the load-displacement curve is recorded.

The reconstructed 3D image from the μCT of the specimen is used to extract fiber coordinates and bond locations using the software FNXCT [3]. The network geometry is discretized and imported into the finite element software ABAQUS. Both

*Corresponding author. Email: ms2682@cornell.edu

fibers and bonds are explicitly represented in the model, with fiber properties constitutively prescribed according to prior single fiber experiments. The bonds are modeled as connector elements with a failure criterion. Each bond strength value is an independent parameter and a change of its value affects the overall damage propagation process and the macroscopic mechanical response. Individual bond strengths are tuned so the simulated load-displacement curve fits to the experimental one. This multivariable optimization problem is solved by gradient decent method.

RESULTS AND DISCUSSION

The 3D microstructure of one non-woven specimen is shown in Figure 1a. The constituent filaments are much longer than the specimen size. The corresponding extracted fiber network is shown in Figure 1b. Good agreement is achieved between these two geometries. The experimental load-displacement data (blue line in Figure 2a) shows that the non-woven has a short elastic region followed by a gradual roll over yield region. The curve becomes jagged at around the peak load indicating significant damage. Such damage is a combination of bond fracture and fiber fracture. Three simulated load-displacement curves are overlaid on the experimental results in Figure 2a. In the simulations used to produce this plot, all bonds were assumed the same and the strength values were assigned to infinity (rigid bond), 0.5N and 0.001N. The network with rigid bonds has the highest macroscopic strength (peak load) among the three. The damage comes solely from fiber fractures and the damage progression is more drastic and occurs at smaller strains than the other two cases. The network with really weak bonds ($b = 10^{-3}$N) has a smooth curve. The shape of the curve is similar to that of a single fiber under uniaxial tension. This shape similarity is consistent with our expectation since most of the bonds break at small strains and only the longitudinal fibers connected to both ends of the grips carry the load. The simulation with 0.5N bond strength has the best fit of these three cases, however the fit is still poor ($R^2 = 0.20$) indicating that a bond stregth distribution exists in the network. The percentage of fractured bonds with deformation (Figure 2b) shows that bond fracture initiates at the beginning of the test and increases monotonically since no healing is allowed. The drops in the load-displacment curve are associated with large numbers of bond fracture. Moreover, not all bonds are broken before the end of the test even for the weakest bonds, indicating that some bonds do not participate in the load transmission throughout the network. These strength of these non-transmitting bonds cannot be obtained through this experimental methods.

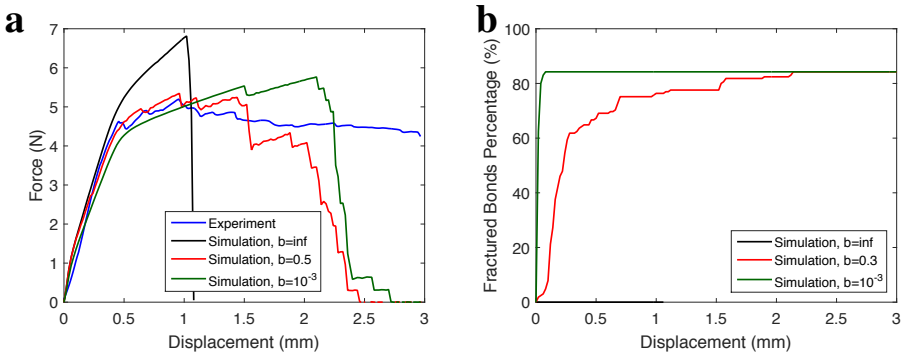

Figure 2: (a) Experimental and simulated load-displacement curves. b is the bond strength. (b) Percentage of fractured bonds with deformation.

CONCLUSIONS

A method to determine non-woven bond properties is presented. The microstructure and macroscopic behavior of a non-woven specimen is first characterized through experiments. A finite element model is then applied to fit individual bond strengths. The presented method prevails in its efficiency in dealing with scattered bond strength distribution, and also is able to provide insights on the damage progression process of non-wovens.

References

[1] Ridruejo, A., Gonzalez, C., and LLorca, J.: Micromechanisms of deformation and fracture of polypropylene nonwoven fabrics. International Journal of Solids and Structures 48(1): 153-162, 2011.

[2] Wernersson, E. L. G., Borodulina, S., Kulachenko, A., and Borgefors, G.: Characterisations of fibre networks in paper using micro computed tomography images. Nord Pulp Pap Res J 29(3): 468-475, 2014.

[3] Schmied, F. J., Teichert, C., Kappel, L., Hirn, U., and Schennach, R.: Joint strength measurements of individual fiber-fiber bonds: an atomic force microscopy based method. Review of Scientific Instruments 83(7): 073902, 2012.

SYSTEMATIC ANALYSIS OF FRACTURE IN TWO-PHASE MATERIALS AT ALL STAGES

Tom de Geus*[1], Ron Peerlings[1], and Marc Geers[1]
[1]*Eindhoven University of Technology, Department of Mechanical Engineering, Eindhoven, The Netherlands*
[2]*Materials innovation institute (M2i), Delft, The Netherlands*

Summary Although multi-phase materials are widely used, the micro-mechanisms dominating fracture are only partially understood. This paper systematically investigates this topic using computational models. An idealized microstructure is employed wherein a brittle hard phase and a ductile soft phase are randomly distributed. The idealization facilitates transparent analyses with well controlled variations. Three topics are considered: the competition between fracture initiation in either of the phases, and the effect of the local phase distribution on fracture initiation and on propagation. The results indicate that, depending on the macroscopic stress state, one of the phases dominates the fracture initiation. The local phase distribution determines where fracture initiates. Regions of hard phase in the tensile direction intersected by bands of the soft phase in the shear directions promote damage for both mechanisms. Voids then link-up through the soft phase, strongly influenced by the amount of hard phase and the phase contrast.

COMPETITION BETWEEN DUCTILE AND BRITTLE FRACTURE

A simple microstructural model is employed in which the microstructure is modeled using a periodic volume element comprising square cells representing individual grains or particles. Each cell is randomly assigned the properties of the hard or the soft phase according to a certain volume fraction of hard phase – which is also varied. To obtain a statistically representative set, a large ensemble of random volume elements is used. The two phases are modeled using isotropic elasto-plasticity, whereby damage indicators signal fracture initiation in the individual cells. For the hard phase the quasi-brittle Rankine criterion is used, whereas for the soft phase the ductile Johnson-Cook criterion is used. Macroscopic fracture is predicted once 1% of the cells have failed. Because of all these idealizations the computations remain cheap, allowing an extensive parameter study.

The predicted macroscopic fracture initiation strain, $\langle \varepsilon_{\mathrm{f}} \rangle$, as a function of applied stress triaxiality η is shown in Figure 1(a) using a black curve. As observed the fracture strain decreases with increasing triaxiality, as is common for ductile materials. However, around a critical triaxiality of approximately 0.5 a sharp decrease in fracture strain is observed. This is understood by considering fracture in the soft phase only (blue curve) and in the hard phase only (red curve). At low triaxiality the fracture is dominated by the soft phase while above the critical value it is dominated by the hard phase. Around the critical value the two mechanisms are in competition. It is found that the transition point, is a function of the hard phase volume fraction and the contrast in mechanical properties between the phases (not shown).

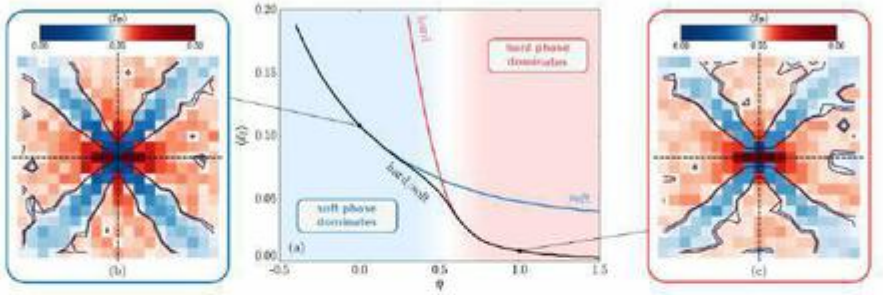

Figure 1. (a) Predicted macroscopic fracture initiation strain, $\langle \varepsilon_{\mathrm{f}} \rangle$, as a function of applied stress triaxiality, η, for fracture in both phases (black), in the soft (blue) or hard (red) phase only. (b,c) Hard phase probability around fracture initiation, $\langle \mathcal{I}_{\mathcal{D}} \rangle$, for two values of applied triaxiality; the colors may be interpreted as an elevated probability of the soft phase (blue) and of that of the hard phase (red). Pure shear is applied: horizontal extension and vertical compression.

INFLUENCE OF LOCAL MICROSTRUCTURE ON FRACTURE INITIATION

The influence of the arrangement of the phases on fracture initiation is quantified using the hard phase probability as a function of position relative to the fractured cells [1]. As the microstructure consists of only two phases, the soft phase probability is contained in this quantity. For two values of applied triaxiality, $\eta = 0$ and 1, the results are shown in Figures 1(b,c). To interpret the result, the hard phase probability, $\langle \mathcal{I}_{\mathcal{D}} \rangle$, must be compared to the hard phase volume fraction, in this case $\varphi^{\mathrm{hard}} = 0.25$. A value $\langle \mathcal{I}_{\mathcal{D}} \rangle > \varphi^{\mathrm{hard}}$ (red in the figures) corresponds to an elevated probability of the hard phase, and $\langle \mathcal{I}_{\mathcal{D}} \rangle < \varphi^{\mathrm{hard}}$ (blue) to that of the soft phase. Both figures are for loading in plane strain pure shear, with extension in

*Corresponding author. Email: T.W.J.d.Geus@tue.nl

horizontal direction and compression in vertical direction. Each cell in the diagram corresponds to a position relative to the fracture initiation sites in the center.

From Figure 1(b), in the regime where fracture in the soft phase dominates, bands of hard phase are observed in horizontal direction, the direction in which the extension is applied. Under ± 45 degree angles with respect to this axis, bands of soft phase are observed that interrupt the band of hard phase in the fracture initiation sites. By simple mechanical arguments it can be understood that the band of hard phase provides a high hydrostatic tensile stress, while the bands of soft phase provide significant plastic deformation, which are together critical for fracture. Remarkably, Figure 1(c) – taken in the regime where hard phase fracture dominates – is qualitatively very similar to Figure 1(b) outside the fractured cell in the center. This means that the microstructural features that are responsible for the initiation of fracture are identical, regardless whether fracture initiates in the hard phase or in the soft phase.

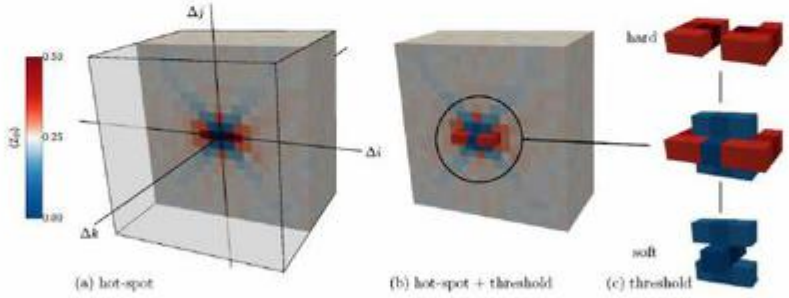

Figure 2. Hard phase probability around fracture initiation, $\langle \mathcal{I}_{\mathcal{D}} \rangle$. From left to right: (a) a cross-section perpendicular to the plain strain direction, (b) the same cross-section with an applied threshold, and (c) the isolated thresholded result.

This is further investigated by extending the analysis to three-dimensions [2]. To overcome computational limitations a solution scheme that uses the Fast Fourier Transform is employed. Different loading paths are considered from which only one result, in pure shear, is included in Figure 2 – which shows the arrangement of phases around fracture initiation. It is observed that the basic features are the same as predicted by the 2-D analysis.

PROPAGATION OF FRACTURE

The analysis is extended beyond regime of fracture initiation. In the spirit of the idealized model used above, propagation is modeled using a simple a cell erosion technique. Once the damage indicator in a cell has exceeded a critical value it is completely removed and thus no longer carries load. This corresponds to a non-local damage criterion as the underlying numerical discretization is finer than the cells. A typical result is shown in Figure 3, the homogenized macroscopic response in (a) and the local incremental damage indicator in (b). As observed, fracture initiates in a couple of locations in which the local arrangement of phases is similar to Figure 1(b). Above a threshold, initiation sites start to link up along a shear band, macroscopically observed as fracture. These observations are confirmed by a statistical analysis. Furthermore it is observed that fracture is accelerated for higher hard phase volume fraction, whereby the microstructure has a stronger influence on both void nucleation and the localization path.

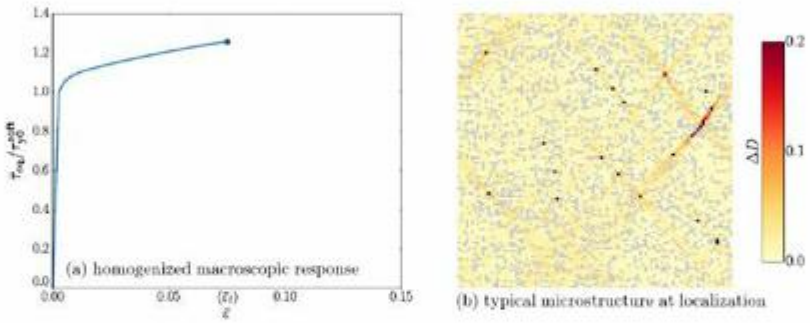

Figure 3. Fracture propagation: (a) the homogenized macroscopic equivalent stress τ_{eq} as a function of (applied) equivalent strain $\bar{}$ based on 100 random volume elements, and (b) the incremental damage indicator a typical volume element.

References

[1] T. W. J. de Geus, R. H. J. Peerlings, and M. G. D. Geers. Microstructural topology effects on the onset of ductile failure in multi-phase materials A systematic computational approach. *Int. J. Solids Struct.*, 67-68:326–339, 2015. doi: 10.1016/j.ijsolstr.2015.04.035.

[2] T. W. J. de Geus, M. Cottura, B. Appolaire, R. H. J. Peerlings, and M. G. D. Geers. Fracture initiation in multi-phase materials: a systematic three-dimensional approach using a FFT-based solver Mechanics of Materials. *Mech. Mater.*, Accepted, 2016.

ATOMISTIC SIMULATION OF SURFACE CYCLIC SLIP IRREVERSIBILITY IN FCC METALS

Zhengxuan Fan[1,2a)], Olivier Hardouin Duparc[1], Maxime Sauzay[2] & Boubakar Diawara[3]
[1]*Laboratoire des Solides Irradiés, École Polytechnique, Palaiseau, France*
[2]*Laboratoire d'étude du Comportement Mécanique des Matériaux, Commissariat à Energie Atomique et aux énergies alternatives, Gif sur Yvette, France*
[3]*Laboratoire de Physico-Chimie des Surfaces, Ecole Nationale Supérieure de Chimie de Paris, Paris, France*

Summary The mechanical behaviour of surface steps created by the emergence at the free surface of gliding dislocations, subjected to cyclic loading is examined using molecular dynamics simulations. Different face centred cubic metals, Al, Cu, Ag and Ni are analysed. An atomistic reconstruction phenomenon is observed at these surface steps which can induce strong irreversibility. The irreversibility cumulates and a micro-notch is produced whose depth increases cyclically. A rough estimation of surface irreversibility for pure edge dislocations gives an irreversibility fraction between 0.5 and 0.75 in copper. An analysis coupling surface mechanisms with the classical EGM bulk slip irreversibility model gives an irreversibility fraction of 0.62 in copper for pure screw dislocations, contrary to many sketches proposed in the past. It seems that oxygen molecules cannot lead to higher irreversibility as they have no major influence on different mechanisms linked to surface relief evolution.

INTRODUCTION AND SIMULATION TECHNIQUES

Fatigue is one of the major damage mechanisms of metals. Fatigue damage generally starts at free surfaces from the accumulation of unreversed slip steps. And cyclic micro-plasticity based on the glide of dislocations is one of the mechanisms responsible for the fatigue phenomena in single phase fcc metals and alloys. The slip irreversibility can be characterized by the fraction p of irreversible plastic shear strain per cycle compared to the total plastic shear strain ($p=\Delta\gamma_{plirr}/\Delta\gamma_{pl}$). The EGM II model describes the evolution of the surface roughness based on the dislocation production and annihilation in the bulk [1]. This EGM model only considers bulk mechanisms and neglects the surface slips mechanisms and environment effect. The aim of this work is to evaluate random surface step irreversibility by atomistic analyses of surface step evolution mechanisms in order to complete the EGM (part II) model by explicitly taking into account the mechanics of surface steps. b=a<110>/2 edge dislocations are inserted in the bulk and then glide to free surfaces and create surface steps. Molecular dynamics simulations are carried out in this work to follow the atom movements from the very first steps created at a free surface until their accumulation, and from the very first cycle to several cycles.

N-body embedded atom model (EAM) like potentials are used for simulations in vacuum. ReaxFF (reactive force field) potentials are used for simulations in oxygen environment. All these potentials give fairly correct estimations of different physical properties of the materials analyzed. The crystallographic orientations of the three axes are x: [-131], y: [714] and z: [11-2]. Contraction-dilation (compression/extension) cycles will be applied along the y: [714] direction. This choice of orientations has several advantages: it corresponds to a large Schmid factor value equal to 0.445, it makes the slip plane and the surface steps easy to visualize, and it is oriented for single slip in agreement with older studies. There are nearly 12,500 atoms in the box and periodic boundary condition is used along the z-direction. The time step used in the simulations with EAM potentials and ReaxFF potentials are respectively 1 fs and 0.5 fs, small enough to ensure its stability.

MAIN RESULTS

A surface step reconstruction phenomenon is observed when an inserted dislocation glides out of the surface and creates a surface step. The geometry of the surface step changes afterwards. Some atoms on the surface step 'fall' down to the lower surface as illustrated by arrows in Figs 1a and 1b, the atoms of the column position M will move to N and the concave shape of the surface step thus turns into a convex geometry. By doing this move, the step atoms get more neighbours, optimize their cohesive energies and thus minimize the surface step energy. This phenomenon is observed for all geometries of surface steps. Three different types of mechanisms can be identified for the reconstruction depending on both the nature of the step and the temperature: the quasi-instantaneous reconstruction which occurs at all temperature in only a few picoseconds in case of larger surface steps, the thermal vibration assisted reconstruction whose rate depends on temperature and time, the surface diffusion assisted reconstruction which only takes place at higher temperatures and requires surface atomic diffusion and longer time, in the order of magnitude of 0.1 nanoseconds. The reconstruction can be achieved via just one mechanism or by the combination of two or three mechanisms. At room temperature, nearly all steps reconstruct, but at lower temperatures, non-reconstructed steps exist.

Reversibility of created surface steps are analyzed during opposite loading cycle and one full loading cycle is thus achieved. It is observed that when there is no arrival of opposite sign dislocations during the opposite loading, previously created and not reconstructed surface steps can be reversible although a critical resolved shear stress larger than one GPa is

[a)] Corresponding author. Email: zhengxuan.fan@polytechnique.edu

required for the reversion. This value is much larger than the usual stresses applied during experimental cyclic loadings which are only from several to hundreds of MPa. If the previously created steps are reconstructed, they are not reversible, even under a shear stress of at least 2GPa or more. When there are arrivals of opposite sign dislocations located in direct neighbor plane with respect to the previous dislocations, it is obvious that non-reconstructed surface steps can be erased. A reconstructed step cannot be fully erased by an opposite sign dislocation at low temperature and there is a remaining surface hole defect. Yet, if the temperature is high enough and the 'surface diffusion activated reconstruction' can take place, diffusing surface atoms can eventually fill the small hole of the surface and the step is finally completely erased. It is possible of course that opposite sign dislocations do not appear at immediate neighbouring planes. Simulations are thus carried out for cases where there is one, two, three or four atomic planes between the planes of insertion of the opposite sign dislocations. It is observed that in these cases, surface steps cannot be fully erased and a micro-notch is initiated and grows deeper cycle by cycle, as shown in Figs. 1c.

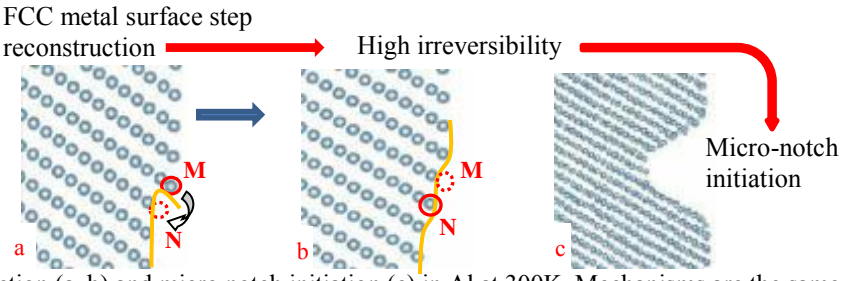

Fig.1. Surface step reconstruction (a, b) and micro notch initiation (c) in Al at 300K. Mechanisms are the same in Cu, Ag and Ni.

Similar simulations are carried out in oxygen environment. Oxygen molecules are adsorbed on metal surface and dissociate into oxygen atoms which are absorbed. This locally generates high-temperature areas. The temperature and the oxygen gas pressure have effects on the surface oxygen diffusion depth. Yet, probably because oxygen atoms are very lightweight compared to metal atoms, absorption of oxygen has no significant effect on the surface step reconstruction and does not impede the gliding of dislocations towards the surface as shown in Figs. 2. Oxygen will thus not increase the step irreversibility and has no major effect on the surface roughness. This holds only for surface relief evolution and agrees with experimental observations [3].



Fig.2. Oxygen effect for the gliding of dislocations towards the surface at 300K in Ni.

DISCUSSIONS

The atomistic simulations carried out in this work show a strong irreversibility of surface slips. A simple estimation of the irreversibility gives an irreversibility fraction between 0.5 and 0.75 in copper for pure edge dislocations and this value is 0.62 for screw dislocations combining bulk and surface mechanisms. The value of p that we evaluated is much larger than the value estimated by the EGM II model where a value of 0.4 was found considering pure screw dislocations, and even smaller for edge dislocations. Our value is much closer to the experimental AFM carried out on nickel in air where p is about 0.8 [2].

The irreversibility factor p estimated in this MD study in inert environment is almost at its maximum value and it is observed that oxygen environment does not increase surface irreversibility in nickel and copper. This is indeed in agreement with observations made by several workers who found that the PSB surface relief is the same for fatigue in inert environment and in air [3]. This shows that old sketches proposed in literature concerning effect of adsorbed atoms on slip irreversibility [4] are not valid for Ni and oxygen. Two more questions remains: how is surface slip irreversibility affected as surface crystalline oxide film is formed and how may we explain the large effects of environment on cyclic propagation [4]. Computations are in progress for answering questions.

References

[1] Differt K., Essmann U., Mughrabi H.: A model of extrusions and intrusions in fatigued metals. Part II: Surface roughening by random irreversible slip. Phil. Mag. A **54**: 237-258, 1986.

[2] Weidner A., Sauzay M., Skrotzki W.: Experimental evaluation of the cyclic slip irreversibility factor. Key Eng. Mat. **465** : 223-226, 2011.

[3] Basinski Z.S., Basinski S.J.: Fundamental aspects of low amplitude cyclic deformation in face-centred cubic crystals. Progr. Mat. Sci. **36**: 89-148, 1992.

[4] Suresh S.: Fatigue of Materials. Cambridge, England 1998.

A GRADIENT DAMAGE MODEL WITH TRANSIENT NONLOCAL INTERACTION

Leong Hien Poh[a)]
Department of Civil and Environmental Engineering, National University of Singapore, Singapore

Summary The "implicit" gradient enhancement is widely used in literature to regularize the material response during strain softening. The conventional approach with a constant length scale parameter, however, may result in spurious damage growth at high deformation levels. This partial regularization phenomenon is also encountered with the integral averaging method. In this contribution, a gradient damage model is formulated based on the generalized micromorphic framework, with only the undamaged regions contributing to the micro-macro coupling driving the damage mechanisms. The resulting governing balance equation recovers a similar form as the implicit gradient equation, albeit with a nonlocal interaction that is of a transient nature. It is shown that a fully regularized solution is obtained during strain softening, with the damaged region localizing towards a macroscopic crack.

INTRODUCTION

It is well documented that standard damage models become ill-posed during strain softening, leading to numerical results which are mesh dependent. One remedy is to adopt the so-called implicit gradient enhancement to regularize the softening behavior, with the associated length scale parameter collectively characterizing the various micro-processes underlying the localized deformation. The conventional approach adopts a constant length scale parameter, which may result in spurious damage growth at high deformation levels. Instead of localizing into a single crack, the damage region expands with deformation, as shown in Fig 1.

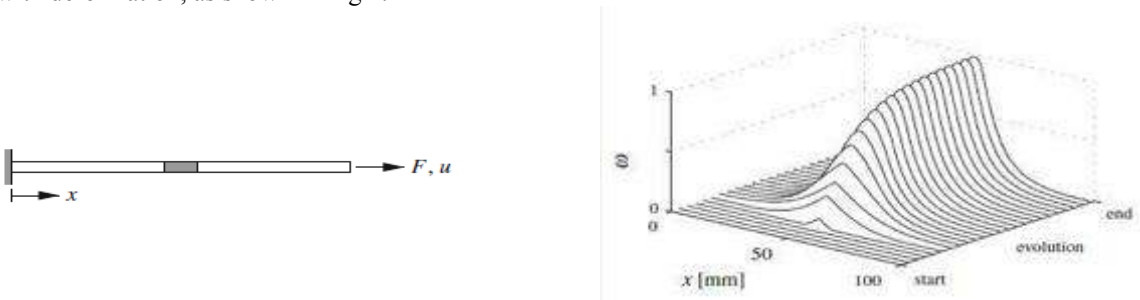

Fig 1: (left) 1D problem with imperfection at the shaded region; (right) Damage evolution profile along the bar with the conventional implicit gradient damage enhancement. At complete structural failure, the damaged region spreads throughout the entire bar, a non-physical behavior. Figure from [1].

In view of this anomaly, a strain-based transient gradient damage model was proposed in [1], where the nonlocal interaction is controlled by a gradient activity parameter through a proposed evolution law. However, it was reported that at large deformations (e.g. with exponential type damage evolution law) the spurious damage growth is delayed, but not fully eliminated, with the strain-based transient damage model [2].

GRADIENT DAMAGE MODEL WITH TRANSIENT NONLOCAL INTERACTIONS

In this contribution, a higher-order damage model is formulated within the generalized micromorphic framework in [3]. Departing from the standard framework, the energy exchange between the micro and macro RVEs are limited only to the undamaged material. The governing equations and constitutive relations are next extracted as per standard thermodynamics procedure. The resulting micro-macro force balance equation resembles closely the Helmholtz expression in conventional implicit gradient models, though the nonlocal interaction is now of a transient nature, which vanishes when the material is fully damaged. A 1D spectral analysis reveals that the softening response is well-regularized, with a vanishing localized bandwidth at complete failure.

The full regularization property of the damage model is further demonstrated by considering the same uniaxial tension problem in Fig 1. At the structural level, the softening response converges upon mesh refinement as depicted in Fig 3, despite the localizing damage profile at failure. It is also easily observed from Fig 4 that non-local damage strain localizes with deformation, hence remedying the spurious damage growth encountered in conventional gradient models.

[a)] Corresponding author. Email: leonghien@nus.edu.sg

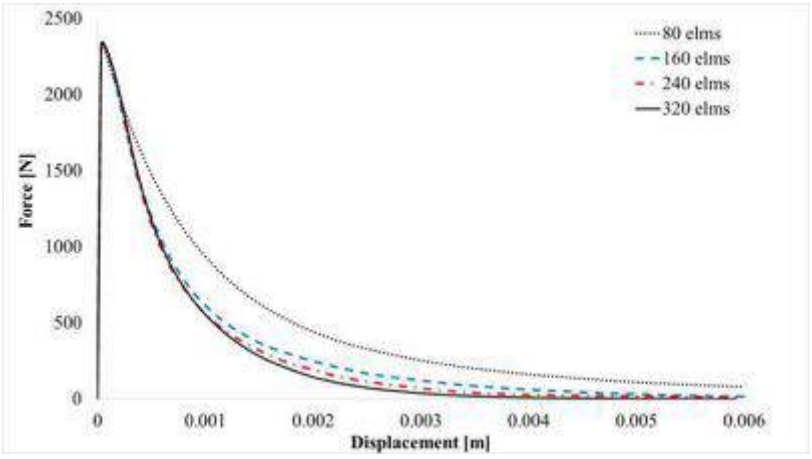

Fig 3: Convergence of the force displacement curve with respect to mesh refinement.

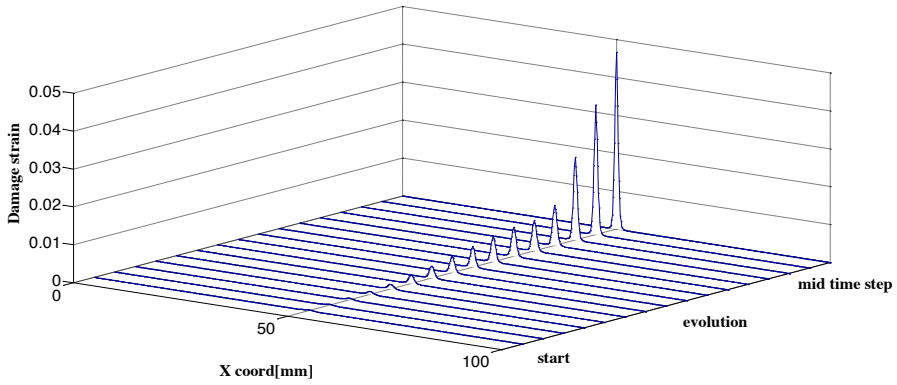

Fig 4: The non-local damage strain localizes at complete structural failure, which remedies the non-physical response obtained in conventional gradient damage models.

References

[1] Geers M.G.D., de Borst R., Brekelmans W.A.M., Peerlings R.H.J.: Strain-based transient-gradient damage model for failure analyses. *Computer Methods in applied mechanics and engineering* **160**, 133-153, 1998.

[2] Saroukhani S., Vafadari R., Simone A.: A simplified implementation of a gradient-enhanced damage model with transient length scale effects. *Comput Mech* **51**, 899-909, 2013.

[3] Forest S.: Micromorphic approach for gradient elasticity, viscoplasticity and damage. *J Eng Mech* **135**, 117-131.

EXPERIMENTAL AND NUMERICAL INVESTIGATION OF IMPACT INDUCED DAMAGE PROGRESSION IN FIBER REINFORCED COMPOSITES

Ercan Gurses[1a)], O. Tanay Topac[1,2] & Demirkan Coker[1]
[1] *Department of Aerospace Engineering, Middle East Technical University, Ankara, Turkey*
[2] *Turkish Aerospace Industries (TAI), Ankara, Turkey*

Summary Damage process in composites subjected to low-velocity impact is investigated both experimentally and numerically. Drop-weight impact experiments are carried out, in which a model unidirectional $[0/90]_s$ carbon fiber reinforced polymer (CFRP) laminate beam is impacted by a cylindrical head creating an almost uniform two-dimensional loading condition. Damage sequence is visualized in real-time via ultra-high-speed camera and the resulting final failure patterns are characterized by a digital microscope. In the computational part, a three-dimensional finite element analysis is performed in ABAQUS/Explicit with the intraply matrix and delamination models. Damage initiation time, location and the interaction of failure modes are compared with the experimental data. A very good overall agreement between experimental and numerical results is observed.

INTRODUCTION

Impacts occurring at speeds 1 to 10 m/s are usually produced by accidental stepping, hail storm and tool drops, and are classified as low-velocity impact (LVI) [1]. Under LVI, barely visible impact damage (BVID) that creates internal delamination without any noticeable damage on the surface is the primary damage form. In literature, damage mechanism of $[0/90]_s$ laminates is studied both experimentally and numerically [2]. The failure sequence is predicted to be unstable shear matrix cracks, leading to delamination, however this sequence has not been fully verified by experiments. In the current study, a 2D line-loading impact proposed by [3] is applied on a simple beam laminate. During the event, progression of damage is captured from the side of the specimen at 60,000 frame per second. This high-speed camera footage is then quantified by a Digital Image Correlation (DIC) analysis. Furthermore, the characteristics of failure are studied in detail by microscopy of post-mortem specimens. The strain history and failure sequence is compared to finite element simulations and the effect of inherent asymmetry on the computational model is further discussed.

RESULTS

Finite element simulations are conducted in ABAQUS/Explicit in which intralaminar ply damage in middle 90° layer and interlaminar delamination damage in cohesive layers are considered. LaRC04 failure criterion proposed by [4] is employed for the intralaminar ply damage and a cohesive zone method (CZM) with a triangular bilinear response is used for the interlaminar damage (delamination). Digital image correlation (DIC) analysis on high-speed camera imaging revealed a close correlation between experiments and the simulations for undamaged elastic loading state as seen in Figure 1(a) and (b).

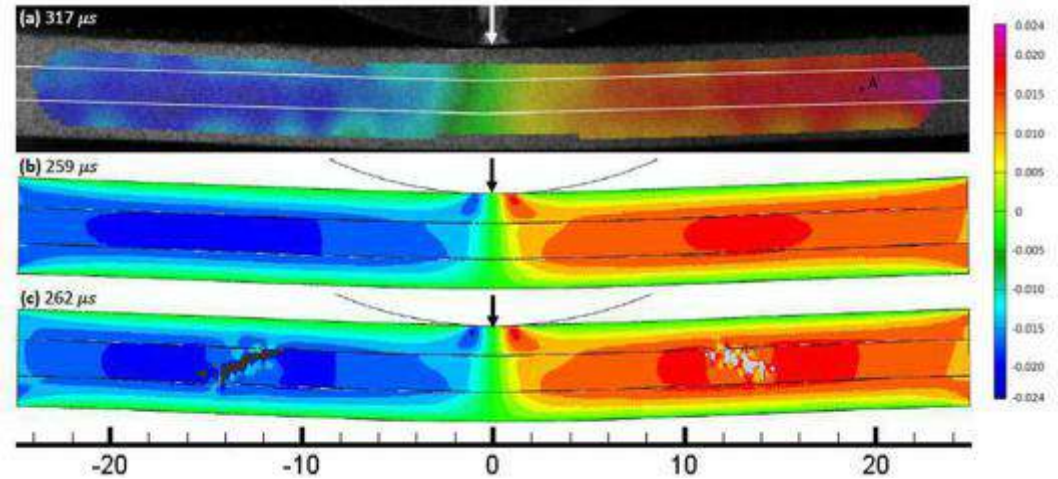

Figure 1 Transverse shear strain contours obtained from (a) DIC analysis just before the initiation of failure (b) FE simulations just before the initiation of failure, (c) FE simulations just after the initiation of failure. Scale is in mm.

[a)] Corresponding author. Email: gurses@metu.edu.tr.

A similar correlation is achieved in terms of initiation and progression of damage as seen in Figure 2. The pictures obtained from simulations are presented on the left side of Figure 2. At 262 μs, a clear picture of the initial formation of diagonal matrix damage in middle 90° layer can be seen followed by its progression to delamination at 267 μs. The experimental high-speed camera pictures for specimen at two different times are shown on the right side of Figure 2. At time 217 μs, a diagonal line forms near the left end of the picture giving a conclusive evidence for matrix crack initiation under impact loading. At time 233 μs, which is the next frame time, clear evidence of delamination from the tips of the matrix crack at the top and bottom 0/90 interfaces is presented. The mechanism is clearly observed in experiments and simulations to be the initiation of matrix creaks, propagating towards the interface and creating a delamination. The whole failure event occurs at less than 16μs.

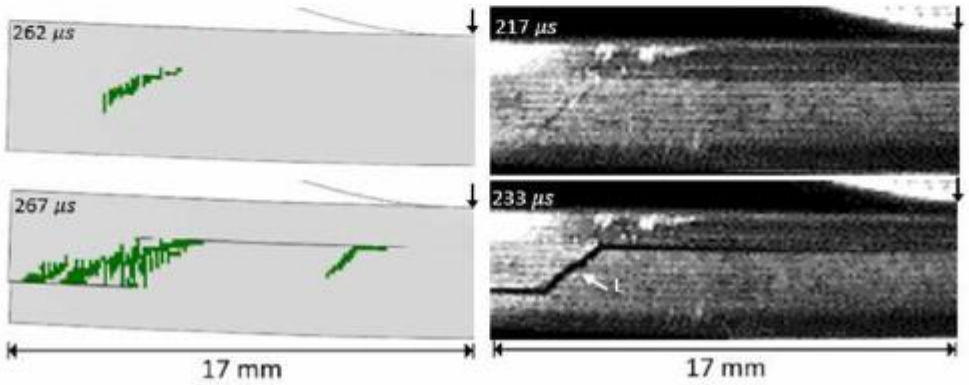

Figure 2 Crack initiation and progression mechanism predicted by (a) finite element simulations and (b) experiments

CONCLUSIONS

The dynamic failure process of composite laminates under low-velocity impact is studied using a combined experimental and numerical approach. Impact experiments are conducted on a thick $[0_5/90_3]_s$ CFRP beam laminate and damage process is studied by a high-speed camera imaging, Digital Image Correlation (DIC) analysis and microscopy. In explicit FE simulations intraply matrix cracking is considered in a 3D Continuum Damage Mechanics (CDM) framework and delamination is considered through cohesive elements. Our main conclusions are summarized as follows:

• First experimental evidence of the failure sequence in 0/90/0 laminates is presented consisting of diagonal matrix cracks followed by delamination. The right and left matrix cracks are shown to occur sequentially. Simultaneous formation of two symmetric matrix cracks is never observed in the experiments.

• Experimental scatter in the location of first major matrix crack is attributed to the inhomogeneity of material properties and the dynamic translation of stress fields. This behavior is also captured in our FE simulations.

References

[1] Cantwell W.W.J, Morton J. The impact resistance of composite materials a review. Composites **22**:34762, 1991.

[2] Richardson M.O.W, Wisheart M.J. Review of low-velocity impact properties of composite materials. Compos Part A Appl Sci Manuf 27:112333, 1996.

[3] Choi, H. Y., Wu, H.-Y. T. and Chang, F.-K. A new approach toward understanding damage mechanisms and mechanics of laminated composites due to low-velocity impact: Part II—Analysis, *J. Compos. Mater.*, **25**:1012–1038, 1991.

[4] Pinho S. T., Dàvila C. G., Camanho P. P., Iannucci L., Robinson P. Failure models and criteria for FRP under in-plane or three-dimensional stress states including shear non-linearity. Technical Report, NASA/TM-2005-213530, 2005.

MODELLING OF ANISOTROPIC FATIGUE

Sami Holopainen[1], Reijo Kouhia [*1], Niels Saabye Ottosen[2], Matti Ristinmaa[2], and Timo Saksala[1]

[1]*Dep. of Mechanical Engineering and Industrial Design, Tampere University of Technology, Tampere, Finland*
[2]*Div. of Solid Mechanics, Lund University, Lund, Sweden*

Summary A continuum approach for anisotropic fatigue is described. The approach is based on the idea of a moving endurance surface in the stress space where the movement is described by a back-stress type tensor. The evolution associated with the movement is described by a rate type equation. In addition, damage accumulation is governed by a rate type evolution equation, thus facilitating its use under arbitrary complex loading conditions. The main emphasis of this paper is to discuss the possible forms of the endurance surface and pertinent evolution equations to model high-cycle anisotropic fatigue. Suggestions towards a unified model capturing the low-cycle regime are also given.

INTRODUCTION

Fatigue of materials under variable loads is a complicated physical process which can even result in catastrophic failure of engineering components. It is characterized by nucleation, coalescence and stable growth of cracks. Nucleation of cracks starts from stress concentrations near persistent slip bands, grain interfaces and inclusions [1, 2, 3].

In high-cycle fatigue, the macroscopic behavior of the material is primarily elastic, while in the low-cycle fatigue regime considerable macroscopic plastic deformations take place. Transition between low- and high-cycle fatigue occurs between $10^3 - 10^4$ cycles. In recent years, it has been observed that fatigue failures may occur for very large fatigue cycles in the order of $10^9 - 10^{10}$ cycles, i.e. below the previously assumed fatigue limits.

Main emphasis is here given to high-cycle fatigue modelling. Many different approaches have been proposed which can roughly be classified into stress invariant, or average stress based and critical plane approaches. In these approaches, damage accumulation is usually based on cycle-counting, which makes their use questionable under complex load histories [4, 5].

A different strategy for high-cycle fatigue modelling was proposed by Ottosen et al. [4]. In this approach, which could be classified as evolutionary, the concept of a moving endurance surface in the stress space is postulated together with a damage evolution equation. The endurance surface is expressed in terms of the first stress invariant and the second invariant of the reduced deviatoric stress tensor where the center of the surface in the deviatoric plane is defined by a deviatoric back stress tensor, as is done similarly in kinematic plasticity models. Therefore, the load history is memorized by the back-stress tensor. In this model, arbitrary stress states are treated in a unified manner for different loading histories, thus avoiding cycle-counting techniques.

EVOLUTION EQUATION BASED CONTINUUM FATIGUE MODELS

The key ingedients of the continuum based fatigue model are the assumption of the existence of an endurance surface defined in the stress space and the evolution equations describing the development of damage and internal variables needed in the model. A function β that depends on the stress tensor and some internal variables is established and the endurance surface is then defined as

$$\beta(\boldsymbol{\sigma}, \{\boldsymbol{\alpha}\}; \text{parameters}) = 0, \tag{1}$$

where $\boldsymbol{\sigma}$ is the stress tensor and $\{\boldsymbol{\alpha}\}$ denotes the set of internal variables. Evolution of the internal variables and the damage are described by the evolution equations

$$\{\dot{\alpha}\} = \{\boldsymbol{G}\}(\boldsymbol{\sigma}, \{\boldsymbol{\alpha}\})^{\cdot} \qquad \text{and} \qquad \dot{D} = g(\beta, D)^{\cdot} \tag{2}$$

The form of the functions $\boldsymbol{G}$ and g are important for modelling the finite life durability, while the endurance surface dictates the infinite life resistance. In contrast to plasticity the stress state can lie outside the endurance surface and the evolution of the internal variables and the damage take place only when $\beta \geq 0$ and $\dot{\beta} > 0$.

Isotropic fatigue

The original version of the model was developed for isotropic high-cycle fatigue [4] where the endurance surface was given in terms of two stress invariants: $I_1 = \operatorname{tr} \boldsymbol{\sigma}$ and $\sigma = \sqrt{3J_2(\boldsymbol{s} - \boldsymbol{\alpha})} = \sqrt{(3/2)(\boldsymbol{s} - \boldsymbol{\alpha}) : (\boldsymbol{s} - \boldsymbol{\alpha})}$. For the back stress evolution, the Ziegler type model was chosen and for the damage evolution equation the function g proportional to $\exp(\beta)$ has proven to be successfull. The endurance surface contains only two material parameters, which can be determined from two fatigue tests for infinite life. In the evolution laws three additional material parameters are needed.

An alternative formulation utilizing the idea of [4] for the endurance surface was presented by Brighenti et al. [6] containing all the three stress invariants of the isotropy group.

*Corresponding author. Email: reijo.kouhia@tut.fi

Transversally isotropic fatigue

For transverse isotropy, the unit vector $\boldsymbol{b}$ designates the privileged longitudinal direction. The integrity basis of a scalar function depending on a symmetric second order tensor and a vector contains six invariants. Since the vector $\boldsymbol{b}$ is a unit vector, the integity basis contains the following invariants

$$I_1 = \mathrm{tr}\,\boldsymbol{\sigma}, \quad I_2 = \tfrac{1}{2}\mathrm{tr}\,\boldsymbol{\sigma}^2, \quad I_3 = \tfrac{1}{3}\mathrm{tr}\,\boldsymbol{\sigma}^3, \quad I_4 = \mathrm{tr}\,(\boldsymbol{\sigma}\boldsymbol{B}), \quad I_5 = \mathrm{tr}\,(\boldsymbol{\sigma}^2\boldsymbol{B}), \tag{3}$$

where $\boldsymbol{B} = \boldsymbol{b} \otimes \boldsymbol{b}$ is the structural tensor for transverse isotropy. In terms of the stress deviator $\boldsymbol{s}$ the invariants 2,4 and 5 are defined as

$$J_2 = \tfrac{1}{2}\mathrm{tr}\,(\boldsymbol{s}^2), \quad J_4 = \mathrm{tr}\,(\boldsymbol{s}\boldsymbol{B}), \quad J_5 = \mathrm{tr}\,(\boldsymbol{s}^2\boldsymbol{B}). \tag{4}$$

In the model proposed in [7], the key idea is to split the stress tensor into the longitudinal and transverse parts $\boldsymbol{\sigma} = \boldsymbol{\sigma}_\mathrm{L} + \boldsymbol{\sigma}_\mathrm{T}$, where the transverse component is obtained from

$$\boldsymbol{\sigma}_\mathrm{T} = \boldsymbol{P}\boldsymbol{\sigma}\boldsymbol{P} = \boldsymbol{\sigma} - \boldsymbol{\sigma}\boldsymbol{B} - \boldsymbol{B}\boldsymbol{\sigma} + I_4\boldsymbol{B}, \tag{5}$$

where $\boldsymbol{P}$ is the projection tensor, $\boldsymbol{P} = \boldsymbol{I} - \boldsymbol{B}$.

It is known that fatigue failure is also dependent on the maximum shear stresses occurring in the longitudinal planes and in the transverse isotropy plane. These quantities can be expressed in terms of the deviatoric invariants J_2, J_4, and J_5 as

$$\tau_\mathrm{L}^2 = J_5 - J_4^2, \qquad \tau_\mathrm{T}^2 = J_2 + \tfrac{1}{4}J_4^2 - J_5. \tag{6}$$

The endurance surface for transversely isotropic fatigue given in [7] can be considered as the simplest possible extension of the evolution equation based fatigue model to transversally isotropic case. Only two additional parameters are needed in comparison to the isotropic model in [4].

In this paper different forms of the endurance surface in terms of invariants $I_1, \ldots I_5$ or I_1, I_3, J_2, J_4 and J_5 or $I_1, I_3, \tau_\mathrm{L}, \tau_\mathrm{T}$ are discussed. Special emphasis is given to the ease of determining the material parameters.

Orthotropic fatigue

In the case of orthotropic symmetry group, the integrity basis contains seven invariants, for example $\mathrm{tr}\,(\boldsymbol{\sigma}\boldsymbol{B}_1)$, $\mathrm{tr}\,(\boldsymbol{\sigma}\boldsymbol{B}_2)$, $\mathrm{tr}\,(\boldsymbol{\sigma}\boldsymbol{B}_3)$, $\mathrm{tr}\,(\boldsymbol{\sigma}^2\boldsymbol{B}_1)$, $\mathrm{tr}\,(\boldsymbol{\sigma}^2\boldsymbol{B}_2)$, $\mathrm{tr}\,(\boldsymbol{\sigma}^2\boldsymbol{B}_3)$ and $\mathrm{tr}\,(\boldsymbol{\sigma}^3)$, where $\boldsymbol{B}_i = \boldsymbol{b}_i \otimes \boldsymbol{b}_i$ are the structural tensors or orthotropic symmetry group. Also the necessity to have an anisotropic description for the damage variable is discussed.

Low-cycle fatigue

Extension of the evolution equation based continuum fatigue model to the low-cycle regime inevitably couples the constitutive model into the fatigue model [8]. Here, the modifications in the endurance surface and the evolution equations are briefly discussed.

CONCLUSIONS

Different forms of endurance surfaces and pertinent evolution equations for various symmetries when modelling high-cycle fatigue are discussed. Behaviour of these models have been investigated. Special emphasis is given to simplicity and minimality in the number of material parameters, which is of paramount importance in fatigue analysis due to the expense of fatigue testing.

References

[1] Suresh, S. *Fatigue of Materials* (Cambridge University Press, 1998), 2nd edn.

[2] Bolotin, V. *Mechanics of Fatigue*. CRC Mechanical Engineering Series (CRC Press, Boca Raton, 1999).

[3] Socie, D. & Marquis, G. *Multiaxial Fatigue* (Society of Automotive Engineers, Inc., Warrendale, Pa, 2000).

[4] Ottosen, N., Stenström, R. & Ristinmaa, M. Continuum approach to high-cycle fatigue modeling. *International Journal of Fatigue* **30**, 996–1006 (2008).

[5] Lemaitre, J. & Desmorat, R. *Engineering Damage Mechanics, Ductile, Creep, Fatigue and Brittle Failures* (Springer-Verlag, Berlin, Heidelberg, 2005).

[6] Brighenti, R., Carpinteri, A. & Vantadori, S. Continuum approach for modeling transversely isotropic high-cycle fatigue (2012). *Fatigue & Fracture of Engineering Materials & Structures* **35**, 141–153.

[7] Holopainen, S., Kouhia, R. & Saksala, T. Continuum approach for modeling transversely isotropic high-cycle fatigue (2015). Submitted for publication.

[8] Holopainen, S., Barriere, T. & Cheng, G. & Kouhia, R. Continuum approach for modeling fatigue in amorphous glassy polymers. Applications to the investigation of damage mechanisms in polycarbonate (2016). Manuscript in preparation.

DAMAGE MODEL OF A PARTICLE REINFORCED TRIP-STEEL MATRIX COMPOSITE

Andreas Seupel[1] and Meinhard Kuna [*1]

[1]*TU Bergakademie Freiberg, Institute of Mechanics and Fluid Dynamics, Freiberg, Germany*

Summary The paper considers a particle reinforced metal matrix composite based on a steel exhibiting TRansformation Induced Plasticity (TRIP-effect). The main focus is on deriving a macroscopic, phenomenological model for the material. On the one hand, strain hardening mechanisms due to particle reinforcement and TRIP-effect have to be included. Otherwise, different damage mechanisms are primary influencing factors on the material's performance. With help of cell model simulations, the influence of stress state on the mentioned mechanisms is investigated. The resulting data sets are used to specify and calibrate the proposed macroscopic damage model. A good agreement between the cell model simulation and the calibrated macroscopic model is found in terms of macroscopic stress-strain response.

INTRODUCTION

TRansformation Induced Plasticity (TRIP-effect) is a deformation mechanism due to mechanical induced martensite formation observed for metastable austenitic steels. These TRIP-steels exhibit special deformation and strain hardening mechanisms leading to excellent mechanical properties. Recently, highly alloyed TRIP-steels have been proposed as basis of particle reinforced Metal Matrix Composites (MMC) [1]. The MMCs are used to process honeycomb structures, e.g. for crash absorption applications [1]. From experiments, a strongly asymmetric plastic flow behavior is found for the material, see [1]. This phenomenon is due to particle based damage mechanisms (particle cracking, interface failure) and their impact on the composite's overall plastic flow behavior. The present paper is devoted to the phenomenological modeling of TRIP-matrix composites in the continuum mechanics framework. The aim is to incorporate the effects of damage mechanisms and martensitic transformation. But primarily, the model should be able to describe the overall stress-strain response of the composite.

MODELING APPROACH

Starting point of the MMC's material modeling is the proposal of Seupel and Kuna [2], which was initially developed to describe TRIP-steels undergoing ductile damage due to growth and coalescence of preexisting microvoids. Therein, Rousselier's model [3] for ductile damage of metals is extended by a criterion to capture martensitic phase transformation originally proposed by Hallberg et al. [4]. The macroscale TRIP-MMC model rests on the idea of considering failed particles as effective voids (effective void volume fraction f_{eff}), which later on grow by plastic deformation. The general structure of the model is explained in [2]. In the following, important new features for the desired MMC application are discussed in detail.

The final yield function y of the elastoplastic material response and the martensite transformation function p read

$$y = \tau_{\text{eq}}^{\text{y}}\left(J_2, J_3\right) + f_{\text{eff}} K_1 \exp\left[\frac{I_1}{3\sigma_1}\right] \circ \; R\left(\varepsilon_{\text{eq}}\right) \circ \; \tau_{\text{z}}\left(z\right) \leq 0, \tag{1}$$

$$p = M\tau_{\text{eq}}^{\text{p}}\left(J_2, J_3\right) + \frac{1}{3}\Delta_{\text{v}} I_1 \circ \; \bar{T}\left(z\right) \leq 0. \tag{2}$$

To proceed a step further, a dependency of the plastic yield function y on the third invariant J_3 of the Kirchhoff-stress deviator τ is added to take the observed tension-compression asymmetry of the TRIP-steel into account (see experimental results in [1]). One recognizes, that all three invariants of the Kirchhoff-stress tensor (I_1, J_2, J_3) are now included in the yield function y as well as in the transformation function p. The damage influence is controlled by the exponential term containing the hydrostatic stress state I_1 and the effective void volume fraction, where K_1 and σ_1 denote model parameters. The particle reinforcement effect on strain hardening is cast into an overall isotropic hardening function $R\left(\varepsilon_{\text{eq}}\right)$ driven by the equivalent strain of deviatoric plastic deformation ε_{eq}. The hardening contribution of the evolving martensite volume fraction z is also considered as a phenomenological term $\tau_{\text{z}}\left(z\right)$. The martensite evolution is coupled to the criterion p, where $\bar{T}\left(z\right)$ denotes a barrier function against transformation. M as well as Δ_{v} are additional model parameters to be determined.

The effective void volume fraction develops due to void growth $\dot{f}_{\text{growth}}$ and nucleation of effective voids $\dot{f}_{\text{nuc}}$:

$$\dot{f}_{\text{eff}} = \dot{f}_{\text{growth}} + \dot{f}_{\text{nuc}} = \left(1 \circ \; f_{\text{eff}}\right) \text{tr}\left[\boldsymbol{d}_{\text{pl}}\right] + c_{\text{p}} \dot{d}\left(\varepsilon_{\text{eq}}\right). \tag{3}$$

The void nucleation is assumed to be mainly driven by plastic deformation. Therefore, an indicator function $d\,(0 \leq d \leq 1)$ is introduced representing the progress of particle based damage, e.g. averaged interface debonding. The nucleation shall be limited by the initial particle volume fraction c_{p}. The following evolution for the microdamage d is proposed:

$$\dot{d} = \left(1 \circ \; d\right) \left(\frac{\varepsilon_{\text{eq}}}{P_{\text{n}}}\right)^{s_{\text{n}}} \frac{s_{\text{n}}}{\varepsilon_{\text{eq}}} \dot{\varepsilon}_{\text{eq}}, \quad d\left(0\right) = 0. \tag{4}$$

*Corresponding author. Email: Meinhard.Kuna@imfd.tu-freiberg.de

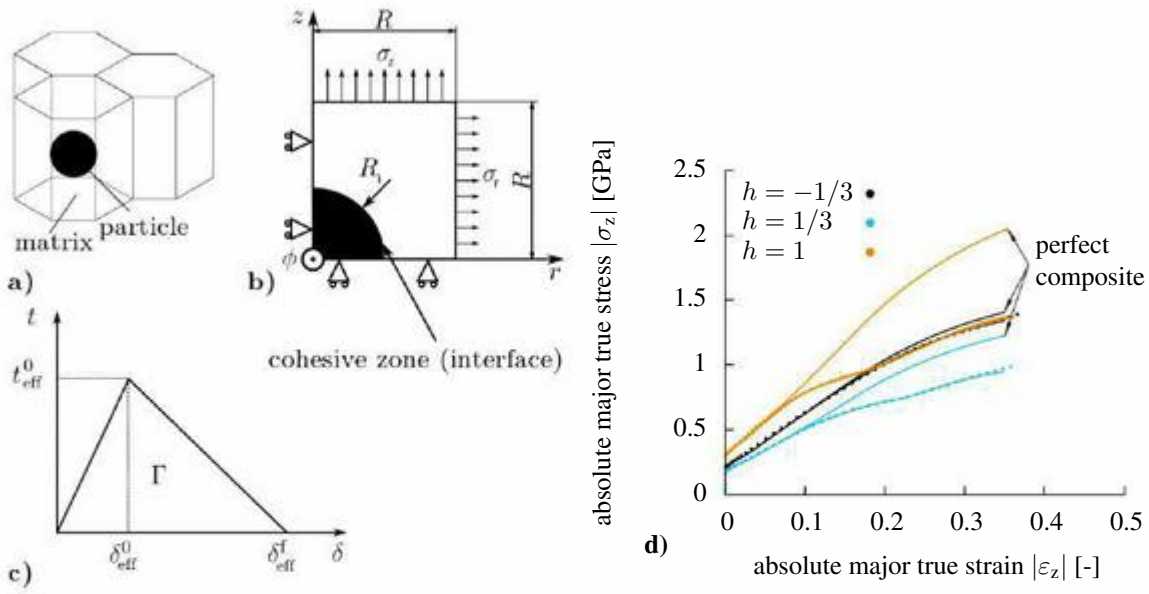

Figure 1: Considered microstructure (a), cell model with boundary conditions (b) and illustrated cohesive law (c). Parameters: R_i =3 µm, $t_0^\mathrm{eff} = 650$ MPa, $\Gamma = t_0^\mathrm{eff}\delta_\mathrm{f}^\mathrm{eff}/2 = 100$ Jm^{-2}, $\xi = \delta_0^\mathrm{eff}/\delta_\mathrm{f}^\mathrm{eff} = 0.01$. Macroscopic stress-strain curves (d) of a composite with particle volume fraction $c_\mathrm{p} = 0.1$ undergoing interface damage: cell model (solid line) and the calibrated phenomenological model response (dots) for three triaxialities h, the perfect composite behavior is also shown as comparison (highlighted by arrows).

The described macroscopic model is calibrated and tested with help of results generated by simple cell model simulations. As schematically illustrated in Fig. 1a, a periodic microstructure of the MMC is considered containing equally sized particle reinforcements of spherical shape. As damage mechanism, interface failure is considered by a cohesive zone obeying a bilinear cohesive law (see Fig. 1c). FE simulations of axisymmetrical unit cells are performed keeping a constant macroscopic stress triaxiality $h = I_1/\left(3\sqrt{3J_2}\right)$ (boundary conditions according to Fig 1b, h is controlled by the ratio $\sigma_\mathrm{r}/\sigma_\mathrm{z}$). Macroscopic stress-strain behavior, an averaged microscopic damage progress and averaged martensite evolution in the matrix are extracted from the cell simulation results. These data sets are subsequently used to calibrate the macroscopic damage model.

RESULTS AND CONCLUSION

As an example, cell model and calibration results of a TRIP-MMC with a particle volume fraction of $c_\mathrm{p} = 0.1$ are presented. The interface properties are given in Fig. 1c. Isotropic elastic properties are assigned to the particle, which are typical for Mg-partially stabilized zirconia used as reinforcement material [1]. The TRIP-steel matrix is described by the J_3 extended model of Seupel and Kuna [2] deactivating damage influence. In order to generate realistic results, the matrix model is calibrated with help of quasi-static, uniaxial tension and compression experiments of a high alloyed TRIP-steel. The following stress states are prescribed during deformation: uniaxial and multiaxial tension ($h = 1/3, 1$ with $\sigma_\mathrm{z} > \sigma_\mathrm{r}$) and uniaxial compression ($h = -1/3$ with $\sigma_\mathrm{z} < \sigma_\mathrm{r}$).

With the cell simulation results at hand, the proposed macroscopic model is calibrated using a specially developed strategy. The parameters P_n and s_n in Eq. (4) are found to depend on the stress triaxiality h. Implementing these dependencies, a good agreement can be concluded for all considered stress states in terms of the stress-strain response (Fig. 1d). The transition from undamaged to damaged behavior caused by progressive interface failure is well captured. Especially the experimentally observed tension-compression asymmetry for uniaxial loading can be described. Additionally to the shown results, it should be mentioned that the evolution of martensitic volume fraction z, void growth f_growth and microdamage d are also in qualitative accordance with the cell model results.

References

[1] Ehinger D., Krüger L., Martin U., Weigelt C., Aneziris C.G. Int. J. Solids and Struct. 66 (2015) 207-217
[2] Seupel A., Kuna M. Appl. Mech. Mater. 784 (2015) 484-491
[3] Rousselier G. J. Mech. Phys. Solids 49 (2001) 1727-1746
[4] Hallberg H., Hakansson P., Ristinmaa M. Int. J. Plast. 23 (2007) 1213-1239

DAMAGE GROWTH IN COMPRESSIVE LOADED FIBRE REINFORCED COMPOSITES

Ragnar Larsson*[1], Renaud Gutkin[2], and Mohammad Rouhi[2]

[1]*Dept of Applied Mechanics, Chalmers University of Technology, S-412 96 Göteborg, Sweden*
[2]*Swerea SICOMP, P.O. Box 104, 431 22 Mölndal, Sweden*

Summary We propose a new and computationally efficient continuum damage based model that is able to predict the compressive response in the fibre direction. Instead of invoking the geometric instability into the material model, a key feature is to consider the geometrical fibre kinking instability on the macro-level based on a finite strain formulation. To represent the proper energy dissipation, an elastic damage model is formulated in the invariants of fibre shear and fibre compression. As opposed to the rotating crack modeling commonly used for this problem, we propose a different approach to the UD–ply fracture based on continuum gradient damage, cf. [1]. Two models are defined; one model based on the non–local continuum damage theory and another local one, cf. ref. [2]. The numerical results indicate the predictive capabilities of the modeling.

INTRODUCTION

Bearing failure and crash simulations involving structural polymeric composites are a few examples where it is crucial to account for the longitudinal compressive response of Carbon Fibre Reinforced Plastics (CFRP). The ultimate goal our activity in this field is to facilitate the predictive modeling/simulation of 3D structural composites; a major issue is to account for the intra-laminar failure mechanisms within a UD–ply, used to form a laminate as a stacked sequence of plies. Our knowledge of the mechanisms behind longitudinal compressive failure has been under development for quite some time. In particular, the failure mechanisms in compression are difficult to model, since they involve both matrix-shear induced failure combined with fibre crushing and kink-band formation within the same failure scenario.

The behavior of a UD-ply at fibre shearing under compression has been considered based on micromechanically motivated models. In particular, micro-buckling (or fibre kink) phenomena has been studied, cf. ref. [3] with simplified the matrix and fibre response. It has been realized [4] that the compressive failure mechanism is attributed to geometrical instability combined with fibre shearing under compression as induced by misaligned fibres; hence, the importance of modeling the degrading ply behavior under fibre shearing is underlined. However, for computational efficiency in the context of 3D laminates failure modeling and simulation, phenomenological models that are micromechanically motivated are needed. Recently, Gutkin et al. [5] presented a model accounting for fibre kinking in a mechanistic fashion directly in the material model describing a fixed crack band.

REPRESENTATION OF INTRA-LAMINAR DAMAGE DEGRADATION IN COMPRESSION

A continuum damage model with special emphasis on the representing degradation in compression is proposed upon introducing an isotropic damage variable α with respect to intra-laminar damage evolution. We then introduce the damage function $f[\alpha]$ for the degradation of the matrix and fibre shear responses and the function $g[\alpha]$ representing the compressive fibre response due to crushing. These functions are defined in terms of a degradation "$1 \circ \alpha$" raised to the exponents β^f and β^g defined as $f[\alpha] = (1 \circ \alpha)^{\beta^f}$ and $g = (1 \circ \alpha)^{\beta^g}$. Please note that the rate of the degradation becomes different depending on the $\beta^f \circ$ and β^g–exponents. In particular, the rate of damage degradation is much faster in the matrix and fibre shear responses as compared to the fibre crushing in the beginning of the damage progression. In view of the discussed scenario for the degradation of the UD fibre reinforced material, we formulate the degraded free energy function as

$$\psi = f[\alpha]\left(\hat{\psi}^{\text{dev}} + \hat{\psi}^{\text{vol}}_{+} + \hat{\psi}^{\text{fs}}\right) + g[\alpha]\hat{\psi}^{f} + \hat{\psi}^{\text{vol}}_{-} \Rightarrow \boldsymbol{S} = \frac{\partial \psi}{\partial \boldsymbol{E}} = f[\alpha]\left(\hat{\boldsymbol{S}}^{\text{dev}} + \hat{\boldsymbol{S}}^{\text{vol}}_{+} + \hat{\boldsymbol{S}}^{\text{fs}}\right) + g[\alpha]\hat{\boldsymbol{S}}^{f} + \hat{\boldsymbol{S}}^{\text{vol}}_{-} \tag{1}$$

whereby the rate of energy dissipation per unit volume becomes

$$\mathcal{D} = A\dot{\alpha} \geq 0 \text{ with } A = \circ\, f'[\alpha]\left(\hat{\psi}^{\text{dev}} + \hat{\psi}^{\text{vol}}_{+} + \psi^{\text{fs}}\right) \circ\, g'[\alpha]\psi^{f} \tag{2}$$

In view of the reduced dissipation (2), the *non-local damage evolution model* is obtained from a maximum dissipation principle in terms of a damage threshold defined as

$$\phi_\alpha[A, \alpha, \Delta\alpha] = A \circ \frac{g_c}{l}\left(\alpha \circ\, l^2 \Delta\alpha\right) \Rightarrow \mathcal{D} = \sup_{A,\,\mu} A\dot{\alpha} \circ\, \mu\phi_\alpha \geq 0 = g_c \frac{\partial \gamma}{\partial \alpha}\dot{\alpha} \geq 0 \tag{3}$$

*Corresponding author. Email: ragnar@chalmers.se

corresponding to $\mu = \dot{}$ and the non-local Kuhn–Tucker conditions $\dot{\alpha} \geq 0, \phi_\alpha \leq 0, \alpha\phi_\alpha = 0$.

In the present context, the *local damage evolution model* is readily obtained from the dissipation due to localized damage, where we consider a simple local damage loading function $\phi_\alpha[A, \alpha] \leq 0$ from the non-local one in the previous sub-section. We now write the loading function as

$$\phi_\alpha[A, \alpha] = A - \frac{g_c}{l}\alpha \Rightarrow \mathcal{D} = \sup_{A,\,\mu} A\dot{\alpha} - \mu\phi_\alpha = \frac{g_c}{l}\alpha\dot{\alpha} \geq 0 \tag{4}$$

corresponding to the Kuhn-Tucker conditions (3) using the local $\phi_\alpha[A, \alpha]$ damage loading function. We may, in fact, now directly associate the fracture dissipation with the continuum dissipation leading to $\frac{d_e}{l} = 2$. Note that the progressive damage model is now associated with an assumed localized damage field, cf. [2], which in the finite element application is confined to the size of one element diameter, i.e. we have that $l \to \frac{d_e}{2}$.

NUMERICAL RESULTS

The damage models are applied to a Non-Crimp Fabric (NCF) composite and compared to a state of the art model based on kinking theory [5]. The evolution of the damage variable is found from in-plane shear tests performed on a unidirectional laminate. A calibration procedure yields the material parameters pertinent to the effective elastic stress response as: $E_1 = 128000\frac{N}{mm^2}$, $E_2 = 79000\frac{N}{mm^2}$, $G_{12} = 3000\frac{N}{mm^2}$, $\nu_{12} = .3$, $\nu_{21} = \nu_{12}\frac{E_2}{E_1}$, and for the damage response: $g_c = 118\frac{N}{mm}$, $l = 4mm$, $\beta^g = 1$, $\beta^f = 9$. The models are compared in uniaxial compression for range for fibre angles relative to the loading direction. The response from the proposed model generally yields a higher peak stress, especially for small of-axis kinking, as compared to ref [5]. The non-local and local models are also compared from the FE–fracture analysis of a 20×20mm clamped plane strain plate under compression. The preliminary results are as shown in Fig. 1b. It may be observed that the non-local damage model corresponds to more smooth and slightly more ductile behavior as compared to the local damage model.

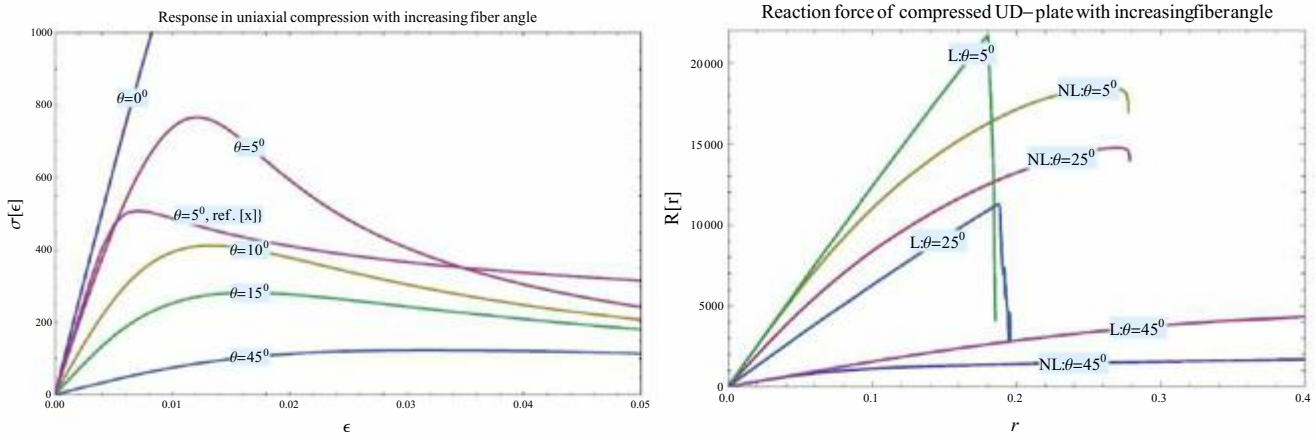

Figure 1: a) Uniaxial compressive response for different fibre kinking of the present model compared to a kinking model developed in [5]. b) Reaction force R versus prescribed displacement r for a 20×20mm clamped plane strain plate under compression; a range of fibre angles, $\theta = 5^0 - 45^0$, relative to the loading direction are considered. Notation N means the local damage model whereas NL means the non–local damage model.

References

[1] C. Miehe, F. Welschinger and M. Hofacker, Thermodynamically consistent phase-field models of fracture: Variational principles and multi-field FE implementations, *Int. J. Numer. Meth. Engng.*, 83:1273–1311 (2010).

[2] R. Larsson, S. Razanica, B. L. Josefson, Mesh objective continuum damage models for ductile fracture, *Int. J. Numer. Meth. Engng.*, DOI: 10.1002/nme.5152, (2015).

[3] Fleck NA, Deng L, Budiansky B, Prediction of kink width in Compressed Fiber Composites, *Journal of Applied Mechanics*, 62(2):329-337, (1995).

[4] S. Pimenta, R. Gutkin , S.T. Pinho and P. Robinson, A micromechanical model for kink-band formation: Parts I-II, *Composites Science and Technology*, 69(7-8):948955, (2009).

[5] R. Gutkin, S. Costa, R. Olsson. A physically based constitutive model for kink-band growth and longitudinal crushing of composites under 3D stress states. Submitted (2016).

AN AUTOMATED MULTISCALE SIMULATION OF THE FAILURE RESPONSE OF ADHESIVE-BONDED STRUCTURAL JOINTS

Bowen Liang[1,3] and Soheil Soghrati *[1,2,3]

[1]*Department of Mechanical and Aerospace Engineering, The Ohio State University, Columbus, OH, USA*
[2]*Department of Materials Science and Engineering, The Ohio State University, Columbus, OH, USA*
[3]*Simulation Innovation and Modeling Center (SIMCenter), Columbus, OH, USA*

Summary Adhesive bonding is one of the key components for the development of lightweight structures in industries such as the aerospace and automotive. However, predicting the failure response of the adhesive layer, which has small thickness and complex microstructure, could be a challenging task. In this work, we implement a computational cohesive model to quantify the impact of microstructural uncertainties such as pre-existing flaws and adherends surface roughness on the failure response of heterogeneous adhesives. A hierarchical interface-enriched finite element method (HIFEM) is employed to simulate the damage initiation and propagation in the adhesive layer. This mesh-independent method allows for using simple structured meshes to discretize the domain, which considerably facilitates the modeling process. A new virtual prototyping algorithm is also introduced and integrated with the HIFEM to automatically generate realistic models of the adhesive microstructure based on imaging data.

METHODOLOGY

There has been a significant increase in the application of adhesive-bonded joints in the automotive and aerospace industries as a key component for the design of lightweight structures. Adhesive bonding offers several benefits over more conventional fastening techniques (e.g., welding), including a smooth exterior, reduced local stress concentrations, and ease of joining thin and dissimilar materials. Thus, a clear understanding of the impact of microstructural features such as the type, volume fraction, and morphology of embedded particles in structural adhesives is crucial for the accurate prediction of the failure response of the joint. While several researchers have implemented numerical techniques such as the finite element method (FEM) to quantify these effects, only a handful of studies have incorporated the realistic microstructure of the adhesive layer in simulating its multiscale damage response.

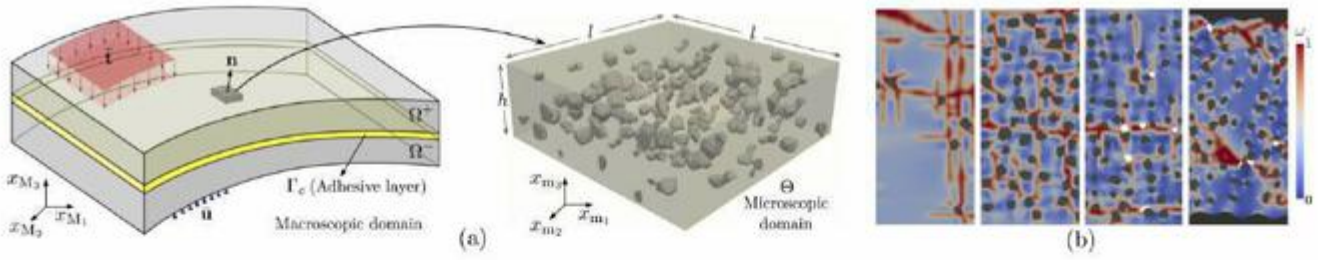

Figure 1: (a) Schematic of the two-scale adhesive-bonded structure. The macroscopic domain Ω contains a thin heterogeneous adhesive layer Γ_c with the representative unit cell (RUC) Θ at each macroscopic point; (b) HIFEM simulation of the multiscale damage response of multiple RUCs of the adhesive with different microstructural features (ω indicates the extent of the damage in the material).

There are two main challenges involved in simulating the failure response of adhesive joints: (i) small thickness of the adhesive layer and (ii) its complex microstructure. While the cohesive zone modeling (CZM) has been introduced and widely used to avoid modeling the small thickness of the adhesive layer, the reliability of the simulations depends on the traction-separation (cohesive) law used for describing the failure response. In this manuscript, we implement a multiscale computational approach to evaluate the cohesive law of heterogeneous adhesives taking into account the impact of the realistic microstructure of the adhesive layer on the initiation and propagation of damage. As shown in Figure 1a, a periodic representative unit cell (RUC) is assigned to each macroscopic point of the adhesive in this multiscale cohesive model. The first-order homogenization theorem together with an energy-based continuum brittle damage model [1] is then implemented to simulate the damage evolution at the micro scale and link that to the macroscopic behavior of the structure. The viscous regularization scheme is also employed to alleviate the mesh-dependency issues associated with using the continuum damage model.

While a multiscale approach can efficiently resolve the difficulties associated with the mismatch between the length scales of the adhesive and the adherends, high fidelity simulation of the damage process in the adhesive layer requires incorporating its realistic microstructure in the microscopic RUCs. However, the laborious and time-consuming process of creating geometrical models of the adhesive heterostructure on one hand and the difficulties associated with creating conforming (matching)

*Corresponding author. Email: soghrati.1@osu.edu

finite element meshes on the other hand prohibit the straightforward application of the standard FEM for modeling this problem. Note that quantifying the impact of microstructural uncertainties such as pre-existing flaws on the mechanical strength of the adhesive layer requires performing multiple damage simulations, which is practically unfeasible using such conventional modeling techniques. To resolve the challenge associated with discretizing the microscopic models, we implement a hierarchical interface-enriched FEM (HIFEM) [2, 3] to simulate the damage process in the adhesive layer. This advanced mesh-independent method uses a hierarchical enrichment scheme to capture stress discontinuities along the embedded particles and the matrix in nonconforming elements, which thus enables the use of simple structured meshes for discretizing the domain without sacrificing the accuracy. Figure 1b illustrates the application of this method for simulating the damage pattern in several 2D RUCs of a heterogeneous adhesive with embedded glass particles [4].

To enable simulating the failure response of 3D adhesive RUCs with various microstructural features, we also introduce a new microstructure quantification algorithm for creating realistic heterogeneous models of the adhesive layer based on micro-computed tomography (micro-CT) imaging data. As shown in Figure 2, after performing the required image processing steps including segmentation and noise filtration, the morphology of embedded particles is transformed to Non-Uniform Rational B-Splines (NURBS) parametric shape functions. Due to the complexity of the adhesive heterostructure, it is not possible to properly characterize the morphology of all particles and thus only a small set of the resulting closed NURBS surfaces can appropriately represent the embedded particles. These NURBS functions are then used in a synthetic microstructure generation algorithm relying on the Random Sequential Adsorption (RSA) algorithm to determine the spatial distribution of particles in the virtual RUC, while their morphologies are described using feasible NURBS surfaces extracted from the micro-CT images. Integrating the proposed RSA-NURBS algorithm with the mesh-independent modeling capability of the HIFEM provides an automated computational framework for evaluating the failure response of several adhesive RUCs with different volume fractions of embedded particles and pre-existing flaws. Figure 2 illustrates the application of this automated modeling pipeline for simulating the damage pattern in two RUCs of an epoxy-based adhesive with embedded silica particles subject to in-plane (shear) and out-of-plane (tensile) loads. More comprehensive results will be presented to study the impact of pre-existing voids and surface roughness of adherends on the mechanical behavior of this heterogeneous adhesive.

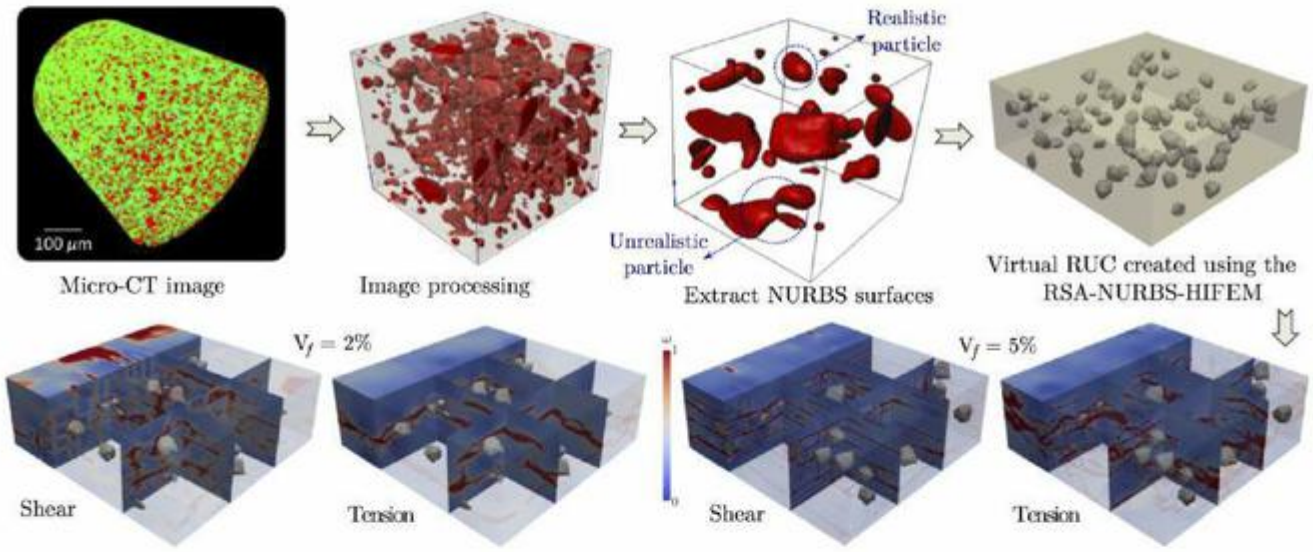

Figure 2: Application of the RSA-NURBS-HIFEM automated pipeline for creating realistic models of a heterogeneous adhesive with embedded silica particles based on micro-CT images. The bottom row shows the simulated damage patterns in two RUCs with different volume fractions subjected to shear and tensile loads (ω indicates the extent of the damage in the material).

References

[1] Kulkarni MG, Matous K, and Geubelle PH. Coupled multi-scale cohesive modeling of failure in heterogeneous adhesives. *International Journal for Numerical Methods in Engineering*, 84:916–964, 2010.

[2] Soghrati S. Hierarchical interface-enriched finite element method: An automated technique for mesh-independent simulations. *Journal of Computational Physics*, 275:41–52, 2014.

[3] Soghrati S and Ahmadian H. 3D hierarchical interface-enriched finite element method: Implementation and applications. *Journal of Computational Physics*, 299:45–55, 2015.

[4] Soghrati S and Liang B. Automated analysis of microstructural effects on the failure response of heterogeneous adhesives. *International Journal of Solids and Structures*, 2015.

DYNAMIC VISCOELASTIC MODELING OF INTERFACIAL DEBONDING FOR MAGNETORHEOLOGICAL NANOCOMPOSITES

Rui Li and Lizhi Sun[a)]
Department of Civil and Environmental Engineering, University of California, Irvine, CA 92697-2175, USA

Summary A dynamic viscoelastic interface model is proposed to study the effective magneto-mechanical responses of magnetorheological nanocomposites filled with carbon nanotubes. It is incorporated with the Eshelby's micromechanics and the elastic-viscoelastic correspondence principles. The effective dynamic stiffness and damping of randomly-dispersed, chain-structured nanocomposites are investigated with the consideration of imperfect interfacial condition between the filler and matrix. Comparisons are performed between the model-based simulation and the experimental data for a specific type of multi-walled carbon nanotube reinforced elastomer nanocomposites to demonstrate the potential of the proposed framework.

INTRODUCTION

Interfacial bonding condition between the inhomogeneities and matrix plays an important role in determining the overall mechanical properties of composite materials. Imperfect interfaces may arise for various reasons such as thin coating layers, interfacial debonding, and surface chemical reactions. Mathematically speaking, for a perfect interface the displacement and traction fields are both continuous across the boundary of two phases, while for an imperfect interface this is not the case. Generally the modeling efforts which account for the effect of imperfect interfaces can be divided into two major categories. The first category of models assumes interfaces where the displacement or traction field is discontinuous with no thickness, and is usually referred to as interface models. The other category of models describes the interface as a layer of a certain thickness whose properties are different from those of either matrix or inhomogeneities, and is usually referred to as interphase models [1]. For the above models to be successful, appropriately assigning the interface/interphase parameters is the key factor, and commonly a difficult task which requires precise experimental characterization.

Elastic interface models have been extended to viscoelastic interface models by replacing the interfacial linear spring with its viscoelastic counterpart, which is time and frequency dependent. Hashin [2] has studied the creep and relaxation behavior of unidirectional fiber composites with viscoelastic interfaces and analytical solutions have been given. Carbon nanotube (CNT) reinforced nanocomposites have proved to demonstrate improved mechanical performance including stiffness, strength, and damping when compared with neat matrix materials [3, 4] due to the extraordinary properties of CNTs including nanometer size, high aspect ratio, and high modulus. Good dispersion of CNTs and bonding between CNTs and matrix remain challenging tasks. CNT clustering and poor bonding often lead to less efficient reinforcement in stiffness and strength. Nevertheless, imperfect interfaces within nanocomposites allow for interfacial slippage and friction which are among the major sources of energy dissipation, and thus increase the damping capability under dynamic loads. Both interphase and interface models have been adopted to investigate the influence of interfacial bonding condition on the overall stiffness and damping of nanocomposites. For example, Liu and Brinson [5] applied a hybrid interphase method incorporating Mori-Tanaka approach and finite element technique to predict the viscoelastic behavior of nanotube and nanoplatelet reinforced polymer composites. Esteva and Spanos [6] assumed elastic interfacial bonds and studied the effective moduli of polymer nanocomposites filled with randomly oriented single-walled nanotubes. Chen et al. [7] examined the interface energy effect on damage evolution for viscoelastic nanocomposites.

Interface models are applicable when interphases cannot be defined or identified since they are also mathematically simpler and more transparent. While previous works involving viscoelastic interfaces focus on the creep and relaxation behavior of composites, in the present paper a micromechanics-based model for composites with both viscoelastic phases and interfaces is developed, which directly addresses the effect of imperfect interfaces on the dynamic viscoelastic behavior of composites; i.e., dynamic stiffness and damping, under dynamic loads. The proposed model is applied to randomly oriented magnetorheological (MR) nanocomposites and simulation results are compared with experimental data.

CONSTITUTIVE RELATION WITH VISCOELASTIC INTERFACES

A micromechanics-based constitutive model is proposed to predict the dynamic viscoelastic behavior of multi-phase composites with viscoelastic imperfect interfaces. With the incorporation of the classic dipole-dipole magnetic interaction model, the scope of the proposed model has been extended to cover as well the magnetic-field-induced changes in dynamic stiffness and damping of MR nanocomposites.

We apply the Fourier transform to the interfacial displacement jump-stress relation so that we can express the complex interfacial compliance in the frequency ω domain as $(\ ) = \prime - i\ \prime\prime(\ )$. The corresponding displacement jump at the interface reads $\Delta u_i\ \omega = \alpha\ \omega\ \delta_{ij} - n\, n\ \sigma_{jk}\ \omega\ n_k$. The developed smart MR nanocomposites are in essential three-phase viscoelastic composites, within which viscoelastic silicone rubber is the matrix phase and elastic CNTs and iron particles are

[a)] Corresponding author. Email: lsun@uci.edu.

the inhomogeneities. While CNTs are fiber-like and randomly oriented in the composites, spherical iron particles are aligned by the applied magnetic fields during the curing process to form chain-like structures, which render the MR nanocomposites macroscopically transversely isotropic. To model the dynamic viscoelastic properties of MR nanocomposites, a two-step homogenization method has been used. In the first step, the matrix silicone rubber and CNTs are treated as a two-phase nanocomposite with overall isotropic viscoelastic properties. The imperfect interfaces between CNTs and silicone rubber matrix are represented by the first set of appropriate interfacial parameters in this step. In the next step, the homogenized nanocomposite is regarded the new matrix, and the three-phase MR nanocomposite is consequently modeled as a two-phase composite with chain-like iron particle structures embedded in the new matrix, which shows overall transverse isotropy. The second set of interfacial parameters has been used to characterize the imperfect interfaces between the new matrix and iron particle chains.

RESULTS, DISCUSSION AND CONCLUSIONS

Given the complex shear modulus of matrix silicone rubber and the elastic constants, volume fraction, and aspect-ratio of CNTs, in combination with interfacial parameters, the complex stiffness tensor of the MR nanocomposites reinforced with randomly oriented CNTs is calculated. The dipole-dipole magnetic interaction model is utilized here to simulate the MR effect on the dynamic shear stiffness. Numerical simulations have been performed to take advantage of the proposed model, and the results are compared with the experimental data we conducted [8, 9]. Figs. 1 and 2 show the comparisons between model predictions and experimental data for the MR effect on dynamic viscoelastic behavior of MR nanocomposites. Similar trends are found here for MR nanocomposites and MREs, in that both the interfacial storage compliance and loss factor are increased when external magnetic fields are applied. This observation further supports the explanation that the applied magnetic fields disturb the stress field at the interfaces between particle aggregates and the matrix, which lead to weaker overall bonding however higher viscosity at the interfaces.

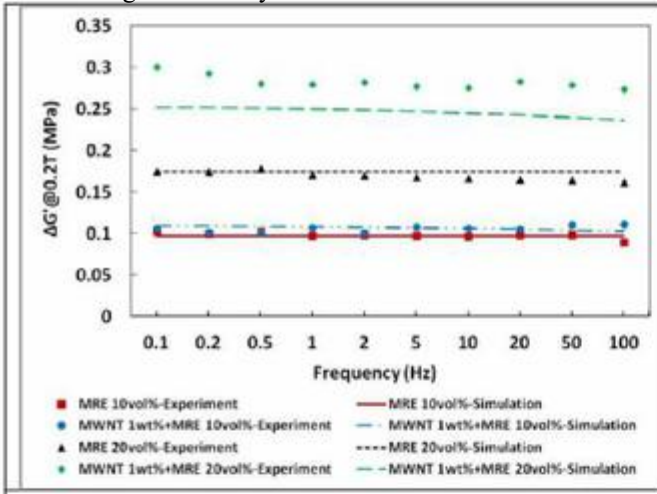

Fig. 1. Comparisons between model predictions and experimental data for the MR effect on storage shear modulus of MR nanocomposites.

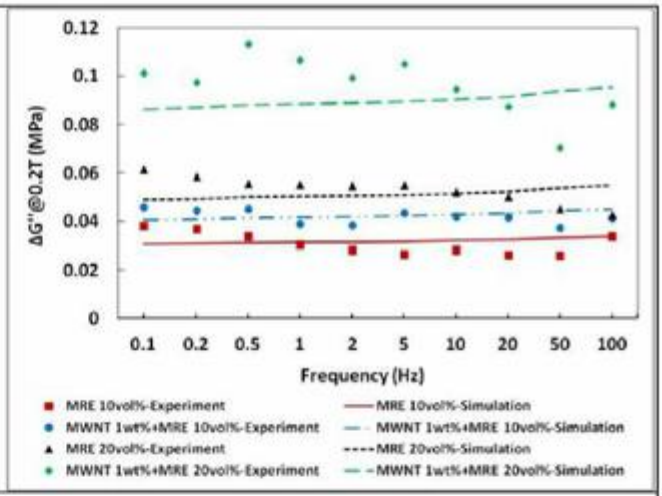

Fig. 2. Comparisons between model predictions and experimental data for the MR effect on loss shear modulus of MR nanocomposites.

References

[1] Hashin, Z.: Thin Interphase/Imperfect Interface in Elasticity with Application to Coated Fiber Composites. *J. Mech. Phys. Solids*, **50**: 2509-2537, 2002.

[2] Hashin, Z.: Thermoelastic Properties of Particulate Composites with Imperfect Interface. *J. Mech. Phys. Solids*, **39**: 745-762, 1991.

[3] Schandler, L.S., Brinson, L.C. and Sawyer, W.G.: Polymer Nanocomposites: A Small Part of the Story, *JOM*, **59**: 53-60, 2007.

[4] Sun, L., Gibson, R.F., Gordaninejad, F. and Suhr, J.: Energy Absorption Capability of Nanocomposites: A Review, *Composites Science and Technology*, **69**: 2392-2409, 2009.

[5] Liu, H. and Brinson, L.C.: A Hybrid Numerical-Analytical Method for Modeling the Viscoelastic Properties of Polymer Nanocomposites, *Journal of Applied Mechanics-Transactions of the ASME*, **73**: 758-768, 2006.

[6] Esteva, M. and Spanos, P.D.: Effective Elastic Properties of Nanotube Reinforced Composites with Slightly Weakened Interfaces, *Journal of Mechanics of Materials and Structures*, **4**: 887-900, 2009.

[7] Chen, J.K., Wang, W.C. and and Huang, Z.P.: Surface Energy Effect on Damage Evolution in a Viscoelastic Nanocomposite, *International Journal of Damage Mechanics*, 19: 949-970, 2010.

[8] Li, R. and Sun, L.Z.: "Dynamic Mechanical Behavior of Magnetorheological Nanocomposites Filled with Carbon Nanotubes", *Applied Physics Letters*, **99**, 131912-1-3, 2011.

[9] Li, R. and Sun, L.Z.: "Dynamic Viscoelastic Behavior of Multi-Walled-Carbon-Nanotube-Reinforced Magnetorheological Nanocomposites", *ASCE Journal of Nanomechanics and Micromechanics*, 4, A4013014-1-7, 2014.

XXIV ICTAM, 21-26 August 2016, Montreal, Canada
Session on Damage Mechanics SM03

MODELLING OF SHEAR FAILURE CAUSED BY ADIABATIC SHEAR BANDING AND SUBSEQUENT MICROVOIDING

Patrice Longère [1a)], André Dragon [2] & Dorothy Hannah-Lois [1]
[1] *Université de Toulouse, ISAE-SUPAERO, ICA (UMR CNRS 5312), Toulouse, France*
[2] *CNRS-Institut Pprime (UPR CNRS 3346), ISAE/ENSMA- Futuroscope - Chasseneuil du Poitou, France*

Summary An enlarged finite strain modelling is presented aiming at reproducing the loss of structural material resistance induced by the formation and growth of dynamic strain localisation bands known as adiabatic shear bands. In the modelling at stake, the adiabatic shear bands are embedded within the representative volume element and their kinematic and material effects are described using a specific velocity gradient and an anisotropic damage-like state variable, respectively. Criteria for adiabatic shear banding occurrence are discussed regarding the nature of the viscoplastic materials considered. At an advanced stage of deformation, micro-voids develop and grow within the adiabatic shear bands leading to the formation of micro-void sheets in the wake of the adiabatic shear bands. The kinematic consequences of this second softening mechanism – the first one being the adiabatic shear banding properly speaking - are accounted for by modifying the yield function/plastic potential within a unified large deformation modelling.

INTRODUCTION

Strain localisation provokes a local material softening resulting in a global structural resistance loss making accordingly premature the failure of the whole structure. Whereas during the past decades strain localisation in ductile materials has been considered as a consequence of advanced microvoiding-induced softening (due notably to microvoid coalescence), recent experimental works [1] have shown that strain localisation may actually precede microvoiding and that the latter may thus result from an advanced stage of strain localisation – and not the opposite. We are here interested in the second scenario.

While the approach developed further may apply to any strain localisation-induced post-microvoiding failure, we are here focusing on strain localisation occurring under dynamic loading involving (quasi) adiabatic conditions in the form of adiabatic shear bands, see Fig.1 and [2]. Generally speaking, materials with high strength and/or low thermal conductivity and/or low hardening capability, are more susceptible to adiabatic shear banding, including a wide class of structural materials such as steels, aluminium alloys, titanium alloys, and so on.

An enlarged finite strain modelling is presented herein aiming at reproducing the loss of structural material resistance induced by the formation and growth of adiabatic shear bands. In the modelling at stake, the adiabatic shear bands are embedded within the representative volume element and their kinematic and material effects are described using a specific velocity gradient and an anisotropic damage-like state variable, respectively. Criteria for adiabatic shear banding occurrence are discussed regarding the nature of the viscoplastic materials considered. At an advanced stage of deformation, micro-voids develop and grow within the adiabatic shear bands leading to the formation of micro-void sheets in the wake of the adiabatic shear bands. The kinematic consequences of this second softening mechanism – the first one being the adiabatic shear banding itself - are accounted for by modifying the yield function/plastic potential within a unified large deformation modelling.

METHODOLOGY

In the approach developed, instead of a fine description involving a small representative volume element (RVE), whose length scale would have been lower than the bandwidth ($l<\lambda$), a more global insight is preferred, employing a 'large' RVE, i.e. the one whose length scale is greater than the bandwidth ($l>>\lambda$). To distinguish the dissipation process relevant strictly to the band deformation mechanism from the process non-relevant to the bands (relative to adjacent sound material), the first is henceforth called 'singular' while the second is called 'regular' one. In this aim in view, all the set of singular variables V_{sing} and respective dissipation effects are incorporated in the density d^{α} of the 2nd order damage-like state variable $\mathbf{D}$ introduced in (1) below, $\mathbf{n}$ representing the band orientation and α a family of bands with the same orientation. The evolution of Tr$\mathbf{D}$ along the shearing process is schematically plotted in Fig.2. The kinematic consequences of the presence of the shear band pattern are viewed as those of a 'super-dislocation' (or a super-gliding system). By generalizing, for the RVE considered, the kinematics of the crystalline plasticity, an ASB-induced supplementary velocity gradient $\mathbf{L}^{d}$ in addition to the one relevant to regular plastic deformation outside the band, designated $\mathbf{L}^{p}$, is introduced as the result of the glide velocity $\dot{\gamma}^{\alpha}$ in the direction of a unit vector $\mathbf{g}^{\alpha}$ relative to the band pattern α of the normal $\mathbf{n}^{\alpha}$, see (2).

$$\mathbf{D} = \sum_{\alpha} d^{\alpha}\mathbf{N}^{\alpha}\ ;\ d^{\alpha} = d^{\alpha}\left(\lambda, V_{\text{sing}}\right) = d^{\alpha}\left(\lambda, T^{*}, \kappa^{*}, \xi^{*}, \delta^{*}, ...\right);\ \mathbf{N}^{\alpha} = \mathbf{n}^{\alpha} \otimes \mathbf{n}^{\alpha} \tag{1}$$

$$\mathbf{L}^{in} = \mathbf{L}^{dp} = \mathbf{L}^{p} + \mathbf{L}^{d}\ ;\ \mathbf{L}^{d} \propto \sum_{\alpha} \dot{\gamma}^{\alpha}\mathbf{g}^{\alpha} \otimes \mathbf{n}^{\alpha}\ ;\ \mathbf{d}^{d} = sym\mathbf{L}^{d} \propto \sum_{\alpha} \dot{\gamma}^{\alpha}\mathbf{M}^{\alpha}\ ;\ \mathbf{M}^{\alpha} = sym\left[\mathbf{g}^{\alpha} \otimes \mathbf{n}^{\alpha}\right] \tag{2}$$

[a)] Corresponding author. Email: patrice.longere@isae.fr

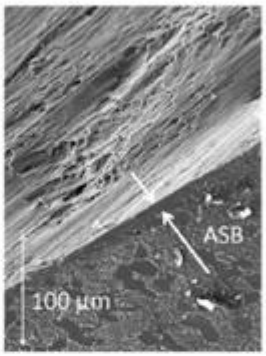

FIG.1: Experimental evidence of adiabatic shear banding (ASB) as precursor of shear failure of the material, from [2].

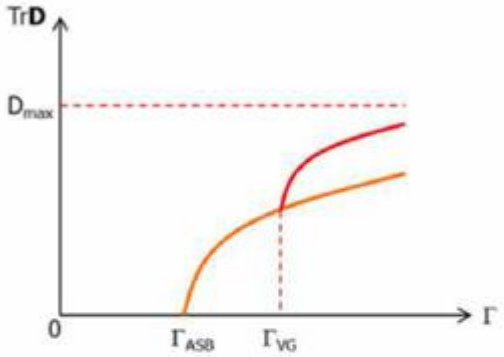

FIG.2: Representation of the influence of the successive failure modes on the damage like state variable **D** along the shearing process

A criterion for adiabatic shear banding occurrence is deduced from the linear perturbation method, see [3], involving the ASB/resolved shear stress $\tau = \mathbf{s}:\mathbf{M}$, with $\mathbf{s}$ the deviatoric part of the Kirchhoff stress tensor τ (α=1), the isotropic hardening force r and its derivative with respect to strain κ (strain hardening) and temperature T (thermal softening), and the strain rate induced overstress $Y\dot{\kappa}^{1/n}$, see (3). Depending on the material considered (steel, titanium alloy, etc), the origin of strain hardening/softening and thermal softening is discussed.

$$\mathrm{J}\left(\boldsymbol{\tau}, r, \dot{\kappa}; \frac{\partial r}{\partial \kappa}, \frac{\partial r}{\partial T}\right) = 3\tau - \left(r - \frac{1}{n} Y\dot{\kappa}^{1/n} + \rho_0 c_0 \left(\frac{\partial r}{\partial \kappa} \Big/ \left(-\frac{\partial r}{\partial T}\right)\right)\right) \geq 0 \tag{3}$$

The model is built within the irreversible thermodynamics framework. As ASB and microvoiding, successive sources of material anisotropic deterioration, affect elastic and plastic properties, the damage like variable **D** degrades both the elastic stiffness and isotropic hardening force. Those two contributions are thus present in the **D**-driving force **G** (the energy release rate wrt **D**). In the context of the normality rule, the two contributions of the inelastic strain rate in (2) and the internal variables (κ; **D**) kinetics are derived from the tentative unified yield function/plastic potential (4), where the energy release rate **G** intervenes via 'effective' values $\Delta G_X = G - G_X$, with X representing the deterioration mechanism at stake (ASB, VG for void growth), G the current value of **G:N** and G_X the value of **G:N** at X-occurrence.

$$\mathrm{F}_{\mathrm{VG}}^{\mathrm{ASB}}(\boldsymbol{\tau}, r, \mathbf{G}; \mathbf{M}, \mathbf{N}) = f\left(\sigma_{eq}, \tau, \Delta G_{ASB}, \Delta G_{VG}\right) + 3\beta \Delta G_{VG} \exp\left(\frac{\sigma_m}{\sigma}\right) - (R_0 + r) \geq 0 \; ; \; \sigma_{eq} = \sqrt{\frac{3}{2}\mathbf{s}:\mathbf{s}} \; ; \; \sigma_m = \frac{Tr\boldsymbol{\tau}}{3} \tag{4}$$

During a monotonically increasing loading, the yield direction of the sound viscoplastic material $\left(\Delta G_{ASB} = \Delta G_{VG} = 0\right)$ is thus progressively deviated first by the adiabatic shear banding $\left(\Delta G_{ASB} > 0 \; ; \; \Delta G_{VG} = 0\right)$ then by the microvoiding in ASB wake $\left(\Delta G_{ASB} = \text{constant} \; ; \; \Delta G_{VG} > 0\right)$.

This model completes the approach developed in [4] containing an intrinsic length scale and so some affinity with nonlocal modelling, see e.g. [5]. It has been implemented in the engineering finite element computation code LS-DYNA. Its performances are evaluated considering different initial-boundary value problems.

CONCLUSIONS

An enlarged finite strain modelling including void-sheet post-localization mechanism is advanced in this work on the basis of experimental observations. It is being done by completing the form of yield/deterioration function and related viscoplatic/deterioration potentials by inserting genuine energy terms corresponding to the mechanisms at stake.

References

[1] Morgeneyer, T.F., Taillandier-Thomas, T., Helfen, L., Baumbach, T., Sinclair, I., Roux, S., Hild, F., 2014. In situ 3-D observation of early strain localization during failure of thin Al alloy (2198) sheet. Acta Mater. 69, 78–91.

[2] Longère P., Dragon A., 2015, Dynamic vs. quasi-static shear failure of high strength metallic alloys: experimental issues, Mech. Mater., 80, pp.203–218.

[3] Longère, P., Dragon, A., Trumel, H., de Resseguier, T., Deprince, X., and Petitpas, E., 2003, Modelling Adiabatic Shear Banding Via Damage Mechanics Approach, Arch. Mech., 55, pp. 3–38.

[4] Longère, P., Dragon, A., Deprince, X., 2009. Numerical study of impact penetration shearing employing finite strain viscoplasticity model incorporating adiabatic shear banding. J. Eng. Mater. Technol. ASME 131, 011105.1-14

[5] Voyiadjis G. Z., Abu Al-Rub R. K., 2006, A Finite Strain Plastic-Damage Model for High Velocity Impacts using Combined Viscosity and Gradient

VIRTUAL MATERIALS TESTING

Karel Matouš *[1], Matthew Mosby[1], and Andrew Gillman[1]
[1]*Department of Aerospace and Mechanical Engineering, University of Notre Dame, Notre Dame, Indiana, USA*

Summary We present extreme multiscale simulations in terms of both physical length scales and computational resources. In this paper, we delineate a hierarchically parallel computational homogenization (CH) solver that employs hundreds of thousands of computing cores and resolves material length scales from $\mathcal{O}$(cm) to $\mathcal{O}$(100 nm). Simulations of this kind are important in understanding multiscale behavior of many natural and synthetically made materials. When combined with image-based modeling concepts and co-designed simulations and experiments, these predictive computations are an important step towards *Virtual Materials Testing* and can aid in development of new material formulations.

INTRODUCTION

With concentrated efforts from the material science community to develop new multifunctional materials using unique processing conditions, the need for modeling tools that accurately describe the physical phenomena at each length scale has only further been emphasized. For example, additive manufacturing and shock synthesis lead to unique material morphologies that need to be understood for reliable engineering analysis and product safety assessments. Considering these material complexities, Direct Numerical Modeling (DNM) is accessible only for moderate system sizes. Thus, a multiscale strategy must recognize that just a relatively small part of the material will typically be instantaneously exposed to rapid material transformations. The rest of the material may be adequately described by macroscopic constitutive models, obtained from homogenization of the complex but slowly-varying microstructure [5, 6]. Nonlinear model reduction, pattern recognition and data-mining are key to future on-the-fly modeling and rapid decision making [8].

IMAGE-BASED MULTISCALE MODELING

To address these challenges, we present an image-based (data-driven) multiscale framework for modeling the chemo-thermo-mechanical behavior of heterogeneous materials while capturing the large range of spatial and temporal scales [2]. This integrated computational approach for predicting the behavior of complex heterogeneous systems combines macro- and micro-continuum representations with statistical techniques, nonlinear model reduction and high performance computing. Our approach exploits knowledge of the instantaneous localization to decide where more advanced computations are required. Simulations involving a wide range of scales, $\mathcal{O}(10^6)$ from nm to mm, and billions of computational/discretization cells (e.g. finite elements) are inherently expensive, requiring the use of high-performance computing. Therefore, we have developed a hierarchically parallel high performance computational framework that executes on hundreds of thousands of processing cores with exceptional scaling performance [1, 3].

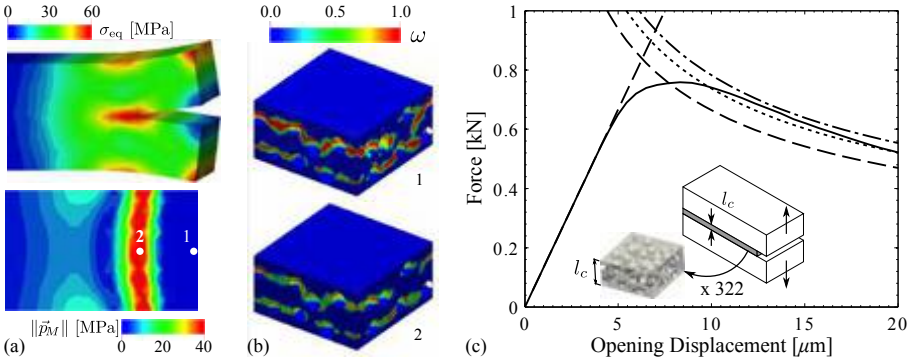

Figure 1: Fully coupled multiscale simulation of progressive mode-I failure of a DCB. The material cells are each discretized with 249k finite elements, and the total multiscale simulation contains 80M finite elements and 42.5M nonlinear degrees of freedom. (a) The macroscale response. (b) Extent of damage in the microscale at the marked points in (a). (c) Multiscale force-displacement curves. Broken lines denote the LFM theory response for $G_c^{\min} = 141$ J/m^2 (dashed), $G_c^{\max} = 175$ J/m^2 (dash-dot), and $G_c^{\text{mean}} = 162$ J/m^2 (dotted).

*Corresponding author. Email: kmatous@nd.edu

To demonstrate the ability of the CH solver to predict multiscale failure, we compute the response of a dual cantilever beam (DCB) using an isotropic viscous damage model at the microscale [3]. Figure 1(a) shows the non-planar progressive failure of the interface governed by the microscale damage as well as the crack tunneling. The extent of damage in the microscale at the marked points along the macroscale interface (point 1 and point 2) is displayed in Figure 1(b). The CH solver predicts that the fracture toughness of the interface is $G_c \in [141,\ 175]$ J/m^2 due to varying local strain rates. The mean toughness of the interface is $G_c^{\text{mean}} = 162$ J/m^2. The critical interface traction is predicted as $t_c = \max \|\vec{t}_M\| \in [61,\ 68.2]$ MPa, with $t_c^{\text{mean}} = 65.6$ MPa. Figure 1(c) shows that the multiscale response of the DCB, loaded in mode-I, is bounded by the Linear Fracture Mechanics (LFM) theory (broken lines). The multiscale response is computed using up to 128k cores on the Mira supercomputer at Argonne National Laboratory.

MATERIAL MORPHOLOGY

Any serious attempt to model a heterogeneous system must also include a strategy for constructing a complex computational domain. This work follows the concept of data-driven (image-based) modeling. We will delineate a procedure based on topology optimization and machine learning to construct a Representative Unit Cell (RUC) with the same statistics (n-point probability functions) to that of the original material [7]. Our imaging sources come from micro-computed-tomography (micro-CT), focused ion beam (FIB) sectioning, and advanced photon source nano-tomography at the Argonne National Laboratory. We show that fully coupled computational homogenization of these statistically meaningful RUCs is possible utilizing high-performance computing. With this framework, well-resolved microstructure-statistics-property (MSP) relationships can be obtained [4].

MULTISCALE MODEL VALIDATION, VERIFICATION AND UNCERTAINTY QUANTIFICATION

Finally, the integrated V&V/UQ program with co-designed simulations and experiments provides a platform for computational model verification, validation and propagation of uncertainties.

CONCLUSIONS

We present extreme scale computations, in terms of both physical scales and computing resources. Our image-based modeling concept is applied to construct statistically Representative Unit Cells of heterogeneous materials. We show that statistically optimal unit cells yield improved predictions of material response. This leads to smaller standard deviations for physical quantities as compared to previous studies. Results in this presentation show the impact of extreme scale simulations in predicting and better understanding mechanics across vast spatial scales during the complex rate-dependent physical processes. With co-designed experiments and properly validated constitutive models, such large predictive simulations can be the basis of *Virtual Materials Testing* standards, and aid in development of new material formulations.

Acknowledgment

This work was supported in part by the Department of Energy, National Nuclear Security Administration, under Award Number DE-NA0002377 as part of the Predictive Science Academic Alliance Program II. We would also like to acknowledge computational resources from the 2015 ASCR Leadership Computing Challenge (ALCC) under project number CSC188.

References

[1] Mosby M., Matouš K.: Hierarchically parallel coupled finite strain multiscale solver for modeling of heterogeneous layers. Int. J. Numer. Meth. Engng., 102:748-765, 2015.

[2] Mosby M., Matouš K.: On mechanics and material length scales of failure in heterogeneous interfaces using a finite strain high performance solver. Modelling Simul. Mater. Sci. Eng., 23:085014, 2015.

[3] Mosby M., Matouš K.: Computational homogenization at extreme scales, 6:68-74, 2016.

[4] Gillman A., Matouš K., Atkinson S.: Microstructure-statistics-property relations of anisotropic polydisperse particulate composites using tomography. Physical Review E, 87: 022208, 2013.

[5] Gillman A., Amadio G., Matouš K., Jackson TL.: Third-order thermo-mechanical properties for packs of Platonic solids using statistical micromechanics. Proc. R. Soc. A, 471: 20150060, 2015.

[6] Gillman A., Matouš K.: Third-order model of thermal conductivity for random polydisperse particulate materials using well-resolved statistical descriptions from tomography. Physics Letters A, 378:3070-3073, 2014.

[7] Lee H., Brandyberry M., Tudor A., Matouš K.: Three-dimensional reconstruction of statistically optimal unit cells of polydisperse particulate composites from microtomography. Physical Review E, 80: 061301, 2009.

[8] Bhattacharjee S., Matouš K.: A Nonlinear Manifold-based Reduced Order Model for Multiscale Analysis of Heterogeneous Hyperelastic Materials. J. Computational Physics: in press, 2016.

MODELING PLASTICITY-DAMAGE COUPLING IN ANISOTROPIC TITANIUM & VALIDATION BY XCMT

Benoit Revil-Baudard *[1], Oana Cazacu [1], and Nitin Chandola[1]
[1]*Department of Mechanical and Aerospace Engineering, University of Florida/REEF, Shalimar, FL, USA.*

Summary A comprehensive experimental study on plastic deformation and damage in titanium was conducted. The ex-situ and in-situ X-ray tomography measurements conducted reveal that damage distribution and its evolution in titanium is markedly different than in a typical FCC material such as copper. Theoretically, it is shown that only by modeling both the anisotropy and the tension-compression asymmetry in plastic behavior it is possible to realistically predict Ti behavior. Specifically, for a smooth axisymmetric specimen subject to uniaxial tension, the model developed predicts that damage initiates at the center of the specimen, and is diffuse; the level of damage close to failure being very low. On the other hand, for a notched specimen subject to the same loading the model predicts that damage initiates at the outer surface of the specimen, and further grows from the outer surface to the center of the specimen, which corroborates with the in-situ tomography data.

Significant progress has been made in understanding and modeling the micro-mechanics of ductile fracture in porous polycrystalline materials. Most of the available theories of dilatational plasticity and viscoplasticity make use of the assumption that the matrix (void-free material) is incompressible and displays the same response in tension and compression. However, titanium materials are strongly anisotropic [1]. Indeed, the mechanical tests on a Ti plate, which were done as part of the study reported here, reveal a strong anisotropy in Lankford coefficients, with the r-value along the rolling direction (RD) being much larger than in the 45°and 90°orientations from RD. It was also found a marked difference between the stress-strain response in the normal direction (ND) and that in the in-plane directions of the plate. Furthermore, irrespective of the loading orientation, the material studied is harder in compression than in tension (for these test results, see [2]). To account for the influence of these particular features of the plastic behavior on damage, the following plastic potential, which depends on the mean stress and the mixed invariants of stress and symmetry tensors associated with orthotropy, namely $\boldsymbol{M}_i = \boldsymbol{x}_i \otimes \boldsymbol{x}_i$,$i = \overline{1,3}$, $\boldsymbol{x}_i$ being the orthotropy axes, is considered:

$$\phi(\boldsymbol{\sigma}, f) = m^2 \frac{\sum_{i=1}^{3} (|\tilde{\sigma}_i| \circ \ k\sigma_i)^2}{\bar{\sigma}_x^T} + \bar{\sigma}_x^T \left(2f \cosh\left(\frac{3\sigma_m}{h\bar{\sigma}_x^T} \right) \circ \ \left(1 + f^2\right) \right) = 0, \tag{1}$$

where k is a parameter describing the tension-compression asymmetry of the matrix; f is the void volume fraction, and $\tilde{\sigma}_i$ are the principal values of the transformed stress tensor $\tilde{\boldsymbol{\sigma}} = \boldsymbol{L} : \boldsymbol{\sigma}'$, $\boldsymbol{\sigma}'$ being the deviator of the Cauchy stress tensor and $\boldsymbol{L}$ a fourth-order symmetric tensor describing the anisotropy of the matrix. Specifically, the two constants m amd h depends on the anisotropy coefficients L_{ij} (for more details, the reader is referred to [3]). Note that all the parameters involved in the criterion have a clear physical significance, being related to plastic properties. These parameters were identified based on data from a few mechanical characterization tests: uniaxial tension tests on specimens of rectangular cross-section for three orientations, and uniaxial compression tests. In this paper, we present only model predictions for loading conditions that were not used for parameter identification. These validation tests are uniaxial tensile tests on smooth and notched specimens of circular cross-section.

Moreover, to further the understanding of the plasticity-damage couplings of the material, and assess the predictive capabilities of the model, both ex-situ and in-situ XCMT measurements were done. The XCMT measurements on axisymmetric smooth specimens reveal the drastic difference in damage evolution between the hcp α-Ti material studied and a typical copper material for which the plastic deformation is governed by von Mises criterion. Note that for the same axial displacement and similar levels of plastic deformation, the copper material is very damaged while the titanium material shows very little damage (see Fig.1).

Fig.2 shows a comparison between the XCMT data on Ti and the F.E. isocontours of the void volume fraction of a smooth specimen corresponding to the same axial displacement. Note that both the anisotropy of plastic deformation (i.e. ellipticity of the deformed cross-section) and damage distribution are correctly described. Specifically, it is predicted that for a smooth axisymmetric specimen subject to uniaxial tension, damage initiates at the center of the specimen and is diffuse; the level of damage close to failure is very low.

The average porosity in the minimal cross-section (root of the neck) is of 0.25%. It is worth noting that the Stewart and Cazacu [3] model also predicts that in the minimal cross-section the maximum void volume fraction is of 0.22% (see Fig. 2a). Likewise, for the other views, most of the voids observed by XCMT are inside the region of maximum void volume fraction

*Corresponding author. Email: revil@ufl.edu



Figure 1: Post-test X-ray computed micro-tomography (XCMT) scans of smooth axisymmetric specimens of circular cross-sections that were subjected to uniaxial tension to large plastic deformations (close to failure): (a) hcp-titanium material studied ; (b) isotropic copper material.

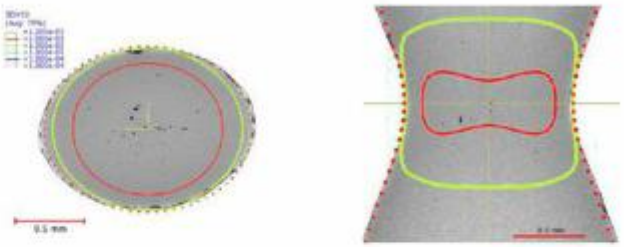

Figure 2: Comparison between the F.E. cross-sections and isocontours of void volume fraction of a smooth axisymmetric specimen of hcp-titanium subjected to uniaxial tension along RD, according to the Stewart and Cazacu (2011) model and XCMT data.

predicted by the model. Furthermore, in Fig.2, the F.E. predictions of the geometry of the specimen for the respective axial displacement (red points) are superposed on the different experimental cut views. It is to be noted that the Stewart and Cazacu [3] model correctly predicts the section geometry in all the planes.

On the other hand, for a notched specimen subject to uniaxial tension the model predicts that damage initiates at the outer surface of the specimen, and further grows from the outer surface to the center of the specimen, which corroborates with the in-situ XCMT data (see Fig.3). This is contrary with the generally held belief that damage evolution in Ti can be predicted using models and damage evolution laws originally developed for materials for which the plastic behavior is governed by either von Mises or Hill (1948) criterion.

CONCLUSIONS

In this paper, it was shown that only by modeling both the anisotropy and the tension-compression asymmetry in plastic behavior it is possible to realistically predict Ti behavior. If the tension-compression asymmetry is neglected, the maximum void volume fraction is located at the center of the specimen, while if the model accounts for both anisotropy and tension-compression asymmetry, the zone of maximum damage shifts toward the outside surface (see Fig.4).

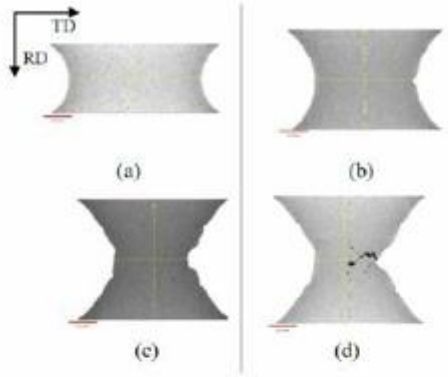

Figure 3: X-ray micro-tomography in-situ scans of the hcp-titanium notched specimen subject to uniaxial tension along rolling direction (RD) showing the (TD, ND) view, (RD-TD) view, and (RD, ND) views, respectively corresponding to a notch displacement of : (a) 0.24 mm (b) 0.73 mm (c) 1.02 mm, (d) 1.2 mm.

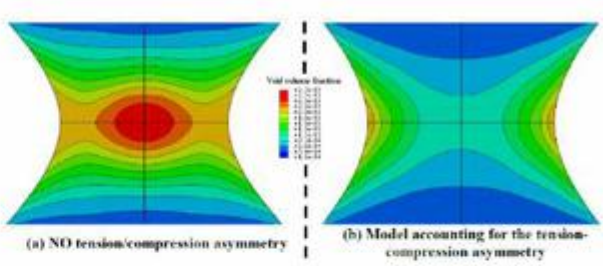

Figure 4: Importance of accounting for the tension-compression asymmetry of the plastic behavior of an hcp-titanium. Comparison of the isocontours of the void volume fraction in the (RD-TD) section of the notched specimen for an axial notch displacement of 1.2 mm, respectively according with: (a) anisotropic model with no tension-compression asymmetry (k=0), (b) Stewart and Cazacu (2011) model which accounts for both anisotropy and tension-compression asymmetry.

References

[1] Nixon M. E., Cazacu O., Lebensohn R.A.: Int. J. Plasticity 26:510532.
[2] Revil-Baudard B., Cazacu O., Flater P., Chandola N., Alves J.L.: J. Mech. Phys. Solids, doi:10.1016/j.jmps.2016.01.003, 2016.
[3] Stewart J. B., Cazacu O.: Int. J. Solids Struct. 48:357-373, 2011.

MULTISCALE TRACTION-SEPARATION RELATIONS FOR FIBER-REINFORCED COMPOSITES

Niels van Hoorn[1], Sergio Turteltaub *[1], and Javad Fatemi[1,2]

[1]*Faculty of Aerospace Engineering, Delft University of Technology, Delft, The Netherlands*
[2]*Airbus Defence and Space Netherlands, Leiden, The Netherlands*

Summary An effective traction-separation relation (cohesive law) for fiber-reinforced composites is developed with the aim of incorporating microscopic fracture mechanisms under various mode mixity loading conditions in a unified, simple expression that is useful for analysis and design purposes. The relation is based on an extensive parametric study carried out to correlate the constituents' fracture properties, their adhesion strength and microstructural characteristics to the macroscopic fracture properties. It is shown that this procedure provides a viable alternative to the fully-coupled multiscale framework.

INTRODUCTION

Failure analysis of composite materials, such as fiber-reinforced laminates, requires establishing a relevant connection between the macroscopic response behavior and the microscale fracture mechanisms of the material. The growth of cracks observable at larger length scales (i.e., macrocracks) is controlled by the distinct fracture mechanism that may be activated at the microscale, such as matrix cracking, fiber cracking, debonding or combinations thereof [1]. In turn, the nucleation and growth of microcracks depend on the applied loads, the microstructural characteristics (e.g., volume fractions), the fracture properties of the constituents and their bonding strength and adhesion fracture energy.

A popular approach in the area of multiscale fracture mechanics is the so-called finite element-squared framework (FE^2), where a traction-separation law or a distributed damage evolution relation for a macroscopic finite element simulation is computed from a lower length scale finite element simulation [2,3]. One practical limitation of this approach is its high computational cost since the macroscopic fracture response requires a large number of microscale simulations, which need to be repeated every time the characteristics of the microstructure and/or the properties of the components are changed.

In the present contribution, the goal is to develop simple bilinear macroscopic traction-separation relations for unidirectional Carbon-Fiber Reinforced Plastics (CFRP). The bilinear relations capture in an averaged sense the initiation and evolution of the cracks occurring at the microscale. In this approach, the computational effort is concentrated in an a-priori calibration of the macroscopic traction-separation relations for arbitrary loading conditions and for a wide range of combinations of material properties. These relations can subsequently be used in single-scale macroscopic simulations for general loading conditions and for composites of distinct characteristics, which is useful for design purposes. The overall computational gain is achieved by reducing the total number of microscale simulations since these are replaced by effective traction-separation relations.

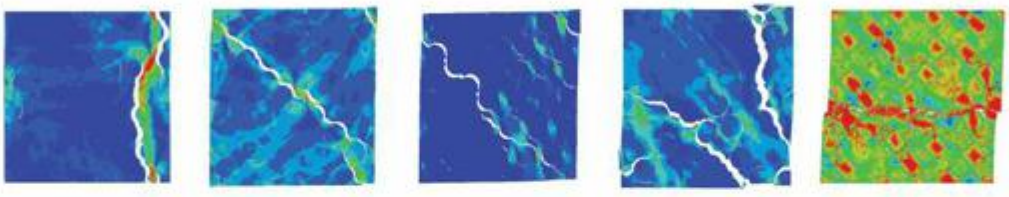

Figure 1: Distinct load cases for a given microstructural configuration and material properties

MICROSCALE SIMULATIONS

The microscale fracture behavior of a CFRP is obtained from simulations that explicitly account for the different phases (matrix and fibers). The phases are treated as homogeneous and their fracture properties are incorporated using traction-separation relations implemented via cohesive elements, which are inserted along the boundaries of all bulk elements. The interface between fibers and matrix is modeled with a separate traction-separation relation that characterizes the bonding strength and adhesion fracture energy. Simulations are conducted on volume elements of increasing size until a representative volume element (RVE) is identified, based on convergence of the effective traction-separation relation to within a reasonable

*Corresponding author. Email: s.r.turteltaub@tudelft.nl

tolerance. The effect of five variables was studied: interface cohesive strength, fiber cohesive strength, interface fracture energy, fiber fracture energy and fiber volume fraction. The study also includes different loading conditions ranging from a macroscopic pure mode I to pure mode II. Typical simulations are shown in Fig. 1, which illustrate the formation of microcracks that eventually generate a macroscopic crack.

MACROSCOPIC CRACK NUCLEATION, ORIENTATION AND TRACTION-SEPARATION RELATION

For each combination of fracture properties, fiber volume fraction and loading conditions, an effective traction-separation relation was obtained by averaging the material response over the RVE. In addition, an effective crack orientation was obtained by averaging the micro-crack orientations. A typical effective traction-separation relation is shown in Fig. 2a. In order to mitigate the error due to the discreteness of the volume element (particularly for the fracture energy), the effective traction-separation relation was obtained as the average of four different realizations, i.e. fiber distributions, as shown in Fig. 2b. The procedure was repeated for distinct material properties, volume fractions and loading conditions. For each case, an equivalent bilinear relation was used to approximate the corresponding effective traction-separation response [4]. Furthermore, a functional relation was established between the effective crack normal vector and the average separation of the RVE. The parameters for the bilinear traction-separation relation, both for the normal and tangential components, consist of an initial slope K, a cohesive strength t_{u} and a fracture energy G_{f}. A further correlation was carried out to establish the dependency of K, t_{u} and G_{f} on the fracture properties of the phases, the bonding strength, the fiber volume fraction and the mode mixity. As a result of this procedure, simple closed-form expressions can be established to compute the effective fracture properties using the basic microscale properties as input. In addition, a criterion can also be established to predict the crack orientation based on macroscopic quantities, which is useful for implementations using the extended finite element method. The validity of these expressions, which essentially predict the response for cases not included in the calibration procedure, was tested by carrying out an independent set of simulations. The agreement with the effective strength was validated while the interpolated fracture energy was predicted within an acceptable discrepancy.

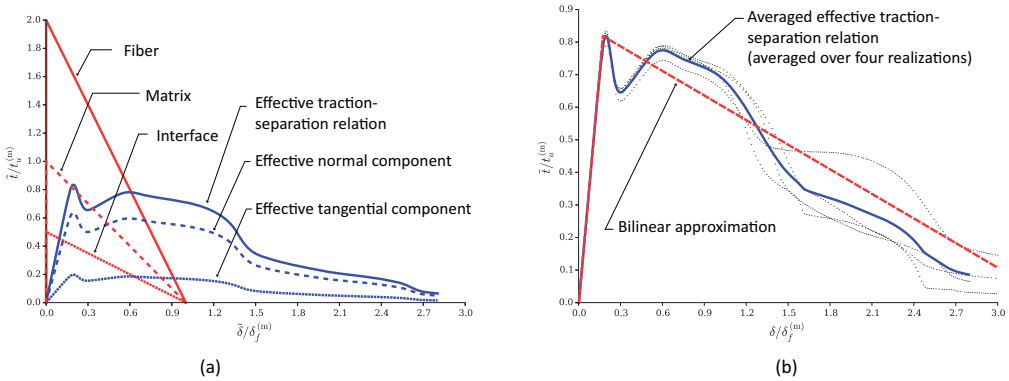

Figure 2: (a) Effective traction-separation relation. (b) Bilinear approximation of effective relation

CONCLUSIONS

The methodology developed in the present contribution demonstrates that it possible to obtain simple macroscopic models that implicitly account for complex microscale fracture behavior. The relevant macroscopic fracture properties can be expressed as simple functions of the constituent's properties, which is particularly useful for design purposes in structures that employ CRFPs. The procedure is a computationally-attractive alternative to fully-coupled multiscale simulations.

References

[1] Ponnusami, SA, Turteltaub, S, van der Zwaag, S: Cohesive-zone modelling of crack nucleation and propagation in particulate composites, Eng. Frac. Mech., 149: 170-190, 2015.

[2] Remmers, JC, Gutierrez, MA, de Borst, R: Computational homogenization for adhesive and cohesive failure in quasi-brittle solids, Int. J. Num. Meth. Eng. 83(8-9):1155-1179, 2010

[3] Nguyen, VP, Lloberas-Valls, O, Stroeven, M, Sluys, LJ: Homogenization-based multiscale crack modelling: From micro-diffusive damage to macro-cracks, Comp. Meth. App. Mech. Eng., 200(9-12): 1220-1236, 2011

[4] Hille T, Turteltaub S, Suiker AS: Microcrack nucleation in thermal barrier coating systems, Eng. Frac. Mech., 76(6) SI:813-825, 2009

A MICROMECHANICAL DAMAGE MODEL FOR INITIALLY ANISOTROPIC MATERIALS

Hélène Welemane[1a)], Cristina Goidescu[1], Vincent Pensée[2] & Djimédo Kondo[3]
[1]*Université de Toulouse, Ecole Nationale d'Ingénieurs de Tarbes, INP/ENIT, LGP EA 1905, Tarbes, France*
[2]*Université Paris-Est, Laboratoire Modélisation et Simulation Multi Echelle, MSME UMR 8208 CNRS, Marne-La-Vallée, France*
[3]*Sorbonne Universités, UPMC Univ Paris 06, CNRS, UMR 7190, Paris, France*

Summary We propose a new model of brittle damage for initially orthotropic materials. The proposed strain energy-based formulation allows to account for the interaction between initial and induced anisotropies and to address the very challenging issue of opening-closure effects (unilateral behaviour). In order to derive the complete model including the damage growth, we take advantage of micromechanical developments suitably combined with the thermodynamics framework of the standard generalized materials. The model has been implemented within the finite-element code ABAQUS and various numerical simulations have been carried out to illustrate its predictive capabilities. In particular, emphasis is put on the evolution of the material symmetry and the influence of microcracks opening-closure states on the damage process.

CONTEXT AND ISSUES

Several experimental studies have shown that microcracking governs the mechanical behavior of various engineering materials. Some of the main macroscopic consequences induced by these microcracks are degradation elastic properties, load-induced anisotropy and microcracks opening-closure effects (also called unilateral effects). For many industrial applications, an appropriate modelling of such degradation process is required to derive a reliable evaluation of mechanical systems. Continuum Damage Mechanics offers an appropriate theoretical framework to account for the inelastic response associated to these features. Accounting for these phenomena in the context of initially anisotropic materials such as composites or sedimentary rocks constitutes a very challenging issue. The interaction between primary anisotropy and damage-induced one is itself a difficult task [1,2]. Addressing the additional representation of damage activation–deactivation effects is then most often restricted to damage in some given specific directions [3]. The present study intends to present a new model for brittle damage for initially anisotropic materials based on results obtained in Goidescu et al. [4]. The resulting analytical 2D micromechanical model (see [5]) avoids inconsistencies often associated to the description of the unilateral behavior [6,7], while exhibiting a physical motivation of the deactivation representation.

CONSTITUTIVE LAW

Small strain, rate independent and isothermal conditions are considered. Dilute concentration of frictionless microcracks is assumed. Following micromechanical arguments [4], a discrete approach, consisting in a finite number of microcracks systems, is considered for the damage description based on the set of scalar microcracks density parameters $\mathbf{d}=(d_i)_{i=1,N}$, with d_i the microcrack density of the ith microcrack system. Orientations $\mathbf{n}_i$ (unit normal) of microcracks are regularly distributed and not restricted to initial structural axes.

In the virgin state (without damage), the material is assumed to exhibit an orthotropic elastic linear behaviour defined by the orthonormal basis $(\mathbf{e}_1,\mathbf{e}_2)$ ($W_0(\varepsilon,\mathbf{A})$ denotes the virgin free energy where second tensor $\mathbf{A}=\mathbf{e}_1\otimes\mathbf{e}_1$ accounts for initial anisotropy). The macroscopic free energy corresponding to such a material weakened by arbitrarily oriented microcracks systems is essentially derived from standard micromechanical analysis, with the help of Hill lemma in the context of cracked bodies and the use of crack displacements expressions in the context of anisotropic elasticity [4]. The thermodynamic potential comes thus to the following form:

$$W(\varepsilon,\mathbf{d})=W_0(\varepsilon,\mathbf{A})+\sum_{i=1}^{N} d_i \begin{cases} h_{\,open}(\varepsilon,\mathbf{A})+h'_{\,open}\,(\varepsilon,\mathbf{n}_i)+h''_{\,open}\,(\varepsilon,\mathbf{A},\mathbf{n}_i), & if\ \ g(\varepsilon,\mathbf{A},\mathbf{n}_i)>0 \\ h_{\,clos}(\varepsilon,\mathbf{A})\ +h'_{\,clos}(\varepsilon,\mathbf{n}_i)\ +h''_{\,clos}(\varepsilon,\mathbf{A},\mathbf{n}_i), & if\ \ g(\varepsilon,\mathbf{A},\mathbf{n}_i)\le 0 \end{cases}$$

Such formulation accounts for the different behaviour of microcracks according to their status (open or closed) defined by the opening-closure criterion g. Moreover, for both situations, elementary free energy contributions may represent various interaction modes between initial and induced anisotropies: h addresses isotropic-like damage effect that keeps the initial symmetry of the material, h' introduces weak-coupling with a directional dependence similar to the one derived in the isotropic context, whereas h'' accounts for strong interaction between initial and damage induced anisotropies that may lead to a complex resulting elasticity. It is to note that appropriate mathematical conditions are satisfied, especially the objectivity and the continuity of class C^1 of W (that ensures the existence and continuity of the stress-strain response and of the thermodynamic forces) and the piecewise continuity of class C^∞ of the tangent operator. Moreover, micromechanics provides a physical justification to the representation of activation-deactivation effects, regarding both the complex recovery

a) Corresponding author. Email: Helene.Welemane@enit.fr.

phenomenon occurring at the closure of defects and the opening-closure criterion that derives from the cancellation of the normal jump displacement of microcracks.

The framework of generalized standard materials is chosen to easy the satisfaction of the thermodynamical admissibility of the formulation. Following classical form, damage evolution is formulated for each system independently (see [8] for instance):

$$f(F^{d_i}, d_i) = F^{d_i} - k_0 (1 + \eta\, d_i), \quad with \quad F^{d_i} = -\partial W / \partial d_i$$

Dealing with a reduced number of coefficients (4 elastic coefficients of the virgin medium and 2 parameters related to the damage evolution, k_0 and η), such formulation may take into account very complex damage growth. Indeed, since the damage thermodynamic force F^{d_i} is considered as the driving force of the damage process, the damage evolution depends also on the opening and closure of microcracks and on the interaction between anisotropies.

APPLICATIONS TO A CERAMIC COMPOSITE

The mechanical response of a ceramic composite (SiC-SiC) under uniaxial tension load followed by compression is studied. Axis and off-axis loads have been investigated. Considering a sufficiently large number N of systems provides a relevant representation of microcracks density distribution obtained in such a case. Fig. 1 shows first that the model is able to describe the specific asymmetric behavior between tensile and compressive loads of brittle materials. The different opening-closure state between these two situations explains the differences in the yield stress and in the damage evolution: all microcracks are open during tensile load and some of them get closed during compression. Such a test highlights also the influence of unilateral effects on elastic properties. As shown by the evolution of Young modulus E(**y**) in the axial direction **y**, elastic properties recover to some extent their initial value (partial damage deactivation) when compressive load induces the closure of some microcracks. Finite element simulations on structure case studies (notched samples) also illustrate these features. Note finally, that such model provides a suitable basis for the consideration of a supplementary dissipative mechanism such as the friction on the closed microcracks lips.

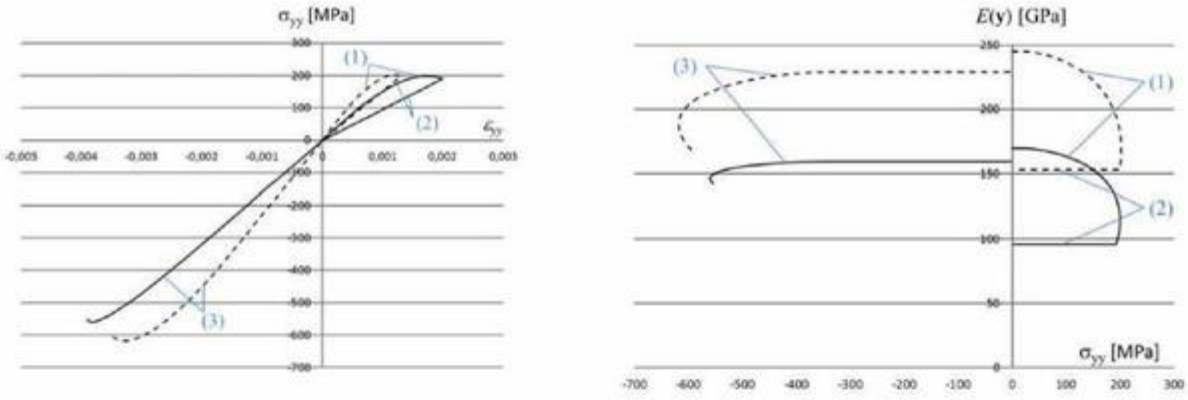

Axial stress-strain response — Axial Young modulus E(**y**) according to the axial stress

Fig. 1. Uniaxial tension load (1) followed by unloading (2) and then compression (3) along unit axis **y** on a ceramic composite (full line corresponds to axis load along a structural axis of the material, dashed line denotes an off-axis loading case).

References

[1] Mauge C., Kachanov M., Effective elastic properties of anisotropic materials with arbitrarily oriented cracks, J. Mech. Phys. Solids **42**, 1-24, 1994.

[2] Cazacu O., Soare S., Kondo D., On modeling the interaction between initial and damage-induced anisotropy in transversely isotropic solids, Math. Mech. Solids **12**:305–318, 2007.

[3] Chaboche J.L., Lesne P.M., Maire J.F., Continuum damage mechanics, anisotropy and damage deactivation for brittle materials like concrete and ceramic composites, Int. J. Damage Mech. **4**:5–22, 1995.

[4] Goidescu C., Welemane H., Kondo D., Gruescu C., Microcracks closure effects in initially orthotropic materials, Eur. J. Mech. A/Solids **37**:172-184, 2013.

[5] Goidescu C., Welemane H., Pantalé O., Karama M., Kondo D., Anisotropic unilateral damage with initial orthotropy: A micromechanics-based approach, Int. J. Damage Mech. **24**:313-337, 2015.

[6] Chaboche J.L., On the difficulties associated with the active/passive unilateral condition, Int. J. Damage Mech. **1**:148-171, 1992.

[7] Cormery F., Welemane H., A critical review of some damage models with unilateral effect, Mech. Res. Comm. **29**:391-395, 2002.

[8] Marigo J.J., Modelling of brittle and fatigue damage for elastic material by growth of microvoids, Engng Frac. Mech. **21**:861-874, 1985.

COUPLED DAMAGE-PLASTICITY MODELING OF THE INELASTIC BEHAVIOR OF C45 STEEL AT HIGH TEMPERATURES

Farid Abed[1a)] & Mohammad Saffarini [1]
[1]*Department of Civil Engineering, American University of Sharjah, Sharjah, UAE*

Summary A series of tensile tests are conducted on C45 steel at a range of temperatures between 298 °K and 923 °K and strain rates up to $0.15s^{-1}$. Scanning electron microscopy images are also taken to quantify the density of cracks and voids of each fractured specimens which are then utilized to define the evolution of internal defects. A microstructure-based yield surface and an energy-based damage model were utilized and incorporated into a thermodynamic consistent formulation to accurately describe the coupled damage-plasticity behavior of C45 steel at high temperatures. Good correlation was observed between the model predictions and the experiments.

INTRODUCTION

The understanding of the mechanical behavior of these materials over a wide range of temperatures and strain rates has been the subject of extensive studies in the past few decades, both experimentally and theoretically [1-3].This research aims to describe the behavior of C45 structural steel that is increasingly used in the oil and gas industry in environment where high temperatures and strain rates are applied. The primary goal is to introduce a systematic understanding of the thermo-mechanical ductile failure that occurs due to accumulation of micro-cracks and voids along with plastic deformation to enable proper structural design; and hence provide better serviceability.

EXPERIMENTAL PROGRAM AND RESULTS

The experimental program conducted in this research provides important results regarding the thermomechanical behavior for C45 steel at different loading conditions. The program includes tensile tests and scanning electron microscope images to characterize the microstructure behavior of this alloy at elevated temperatures.

Tensile tests at room and high temperatures

The tensile test specimens were fabricated according to ASTM standards with a slight modification in the gauge length that was shortened to achieve higher strain rates. The room temperature experiments were conducted at three strain rates of 0.0015s-1, 0.015s-1, and 0.15s-1. The thermo-mechanical tests were conducted by surrounding the UTM with a high temperature furnace that was controlled independently. Specimens were then tested at a combination of three various temperatures of 523°K, 723°CK and 923°K, and at two velocities equivalent to strain rates of $0.0015s^{-1}$ and $0.15s^{-1}$. The temperature was maintained within ± 1°C of the test temperature over the specimen gauge length using a universal 3-zone furnace controller. Figure 1 presents samples of the true stress-true strain results at selected temperatures and strain rates.

Scanning Electron Microscope (SEM)

One important step towards understanding the thermo-mechanical behavior of metals is to study the microstructure of the material and to evaluate the internal damage caused by the complex loadings. Scanning electron microscopic images were produced on each tested specimen to characterize the microstructure behavior of C45 steel at different levels of temperatures and loading rates. Damage measurements were performed by processing SEM images of 1000X magnifications to determine the void fractions. Figure 2 shows a sample SEM image for a fractured specimen.

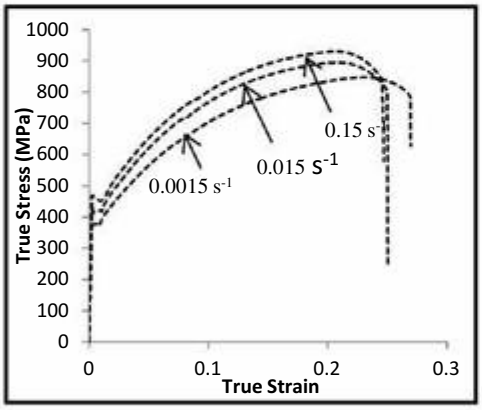

Figure 1 Samples of stress-strain results for C45 steel at different temperatures and strain rates

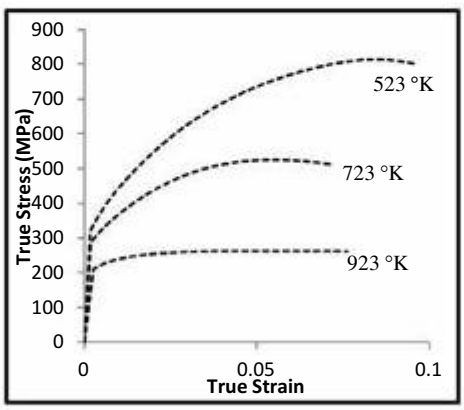

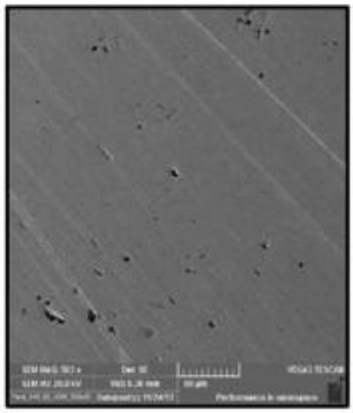

Figure 2 Samples of SEM images

[a)] Corresponding author. Email: fabed@aus.edu

COUPLED DAMAGE-PLASTICITY CONSTITUTIVE MODELING

A general consistent thermodynamic framework for thermo-viscoplastic and damage deformations of C45 steel is developed by utilizing a microstructure-based yield surface coupled with an energy-based isotropic damage definition. This coupled model is capable of capturing the evolution of damage throughout the deformation process and describing the degradation of the steel alloy. The deformation behavior is defined using a thermodynamic potential to describe the present state using Helmoltz free energy and the dissipative potential to describe the irreversible evolution behavior. The determination of internal state variables is achieved by using the fundamental laws of thermodynamics; the conservation of mass, balancing laws, linear and angular momenta, the conservation of energy, and the second law of thermodynamics. The dynamic yield surface for C45 steel is defined as follows:

$$f = \sqrt{\frac{3\tau_{ij}\tau_{ij}}{-\phi^{\ 2}}} - {}_1 - {}_2{}^{\ c_3} - {}_4 - -c_5 T \ln\frac{\dot{p}}{\dot{p}_o})^{q}\ )^{q_2} \qquad (1)$$

The material parameters c_1-c_5 appeared in the above constitutive relations are related to the microstructure physical quantities (see, for more details, Ref. [3]).

Energy-based damage model

Damage is usually characterized by void nucleation, growth, and coalescence that is concentrated in regions near the fracture surface where plastic strains and their associated stresses are maximum. Abed et al. [4] developed an energy based model that is capable of describing the damage evolution in steel using the principles of continuum damage mechanics. The proposed model treats damage, φ, as an increase in the dissipated energy of the material and consequently a reduction in its ability to absorb further energy prior to failure. It defines damage at a certain level as the ratio between the dissipated energy at that level and the dissipated energy at failure as given below:

$$\phi = \left(\frac{\Pi}{\Pi^T}\right)^{\alpha}\phi_f \qquad \text{where} \qquad \Pi = \sigma\ \varepsilon^p - Rp - q\,T \quad T \geq 0 \qquad (2)$$

where φ_f is the critical damage at fracture, q is the heat flux vector, and R represents the thermodynamic conjugate force associated with the flux of the plastic internal state variable p. Figure 3 presents samples of stress strain comparisons between experiments and the coupled damage-plasticity model. Also, Figure 4 illustrates the capability of the energy-based damage model of capturing the internal damage evolution with strain at different level of strain rates and temperatures.

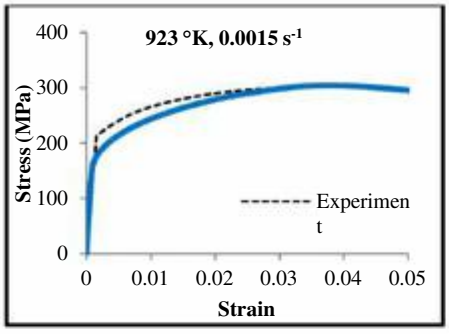

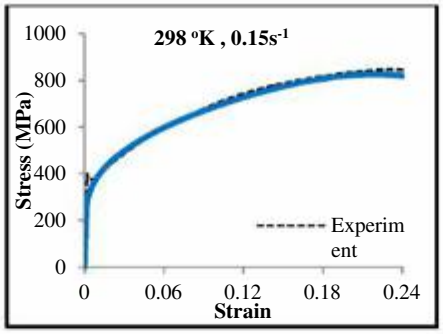

Figure 3 Samples of comparisons between model predictions and experiments

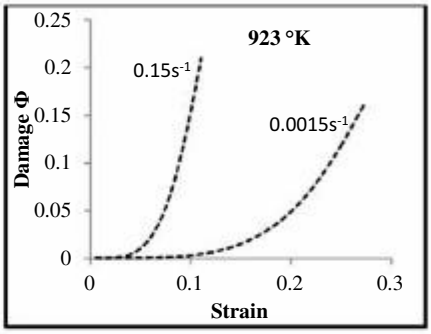

Figure 4 Damage evolutions with strain

CONCLUSIONS

The tests results at high temperatures revealed the typical degradation trend of the thermal stresses with temperature increase except in regions where dynamic strain aging is active. The energy-based damage model successfully captured the damage evolution within the microstructure of the material and the failure mode beyond the ultimate point. The coupled damage-plasticity model was also successful in predicting the flow stress of C45 steel at elevated temperatures.

References

[1] Nemat-Nasser S., Guo W.: Thermomechanical response of HSLA-65 steel plates: experiments and modeling. *Mech Mate* 37: 379–405, 2005.

[2] Abed, F.H., Voyiadjis, G. Z.: Plastic deformation modeling of AL-6XN stainless steel. *Int. J. of Plasticity*, 21: 1618-1639, 2005.

[3] Abed, F.H., Ranganathan, S.I., Serry, M.A.: Constitutive modeling of nitrogen-alloyed austenitic stainless steel at low and high strain rates and temperatures. Mech Mater **77**: 142-157, 2014.

[4] Abed, F.H., Al-Tamimi, A.K.., Alhimairee, R.M..: Characterization and modeling of ductile damage in structural steel at low and intermediate strain rates. *ASCE J. Eng Mech*, **138**: 1186-1194, 2012.

MOLECULAR DYNAMICS INSIGHTS INTO THE COALESCENCE OF CLOSELY-PACKED VOIDS

Yi Cui, Zengtao Chen [a)]
Department of Mechanical Engineering, University of Alberta, Edmonton, AB T6G 1H9, Canada

Summary Both the void clustering effects with fixed-size voids and changing-size voids under uniaxial load are studied via molecular dynamics (MD) method. Large nanovoids up to 50 nm in diameter are focused in this study. The total number of atoms in the system ranges from 0.32 million to 95.4 million. The corresponding stress-strain relation and void volume fraction are monitored during the microstructure evolution of the specimens. For the larger changing-size voids inside the fixed-size simulation box, the critical strain to trigger dislocation shows a very weak dependence on the void size. The dislocation emission pattern is highly subject to the initial intervoid ligament distance (ILD) with a strong clustering effect. For the void cluster, larger voids with short initial ILD tend to reach larger coalescence porosity. The highlands on the void surface, formed due to the presence of dislocation structure, cause the local breakdown of the intervoid ligament.

INTRODUCTION

For void formation in irradiated FCC and BCC metals, not only a large density of voids but also void ordering into complete or partial superlattice was observed [1, 2]. For these highly ordered voids, a periodic cell can significantly reduce the computation cost without much loss of the physical representation. For less orderly-arranged nanovoids, clusters with closely-packed voids are more important since their shorter intervoid ligaments facilitate the void coalescence. Three-dimensional finite element analysis, which based on constitutive model and without the consideration of size effect, draws a general conclusion that void clustering accelerates the damage accumulation and intensifies the interaction among neighboring voids [3, 4].

MODELS, RESULTS AND DISCUSSION

Fig. 1 illustrated the forming of the periodical simulation box which physically represents a cluster of closely-packed voids. During the continued loading, the void interacts and finally coalesces through the periodical boundary with “other” voids. The atomistic interaction is modeled by the embedded atom method (EAM) potential. Applied uniaxial loading is strain-controlled.

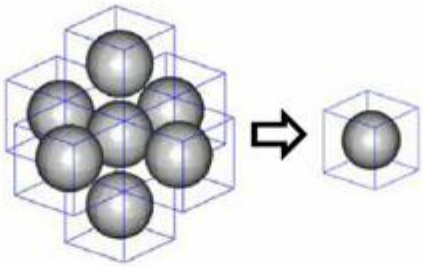

Fig. 1 Periodical simulation box with void inside FCC copper

Fixed-size void inside changing-size simulation box

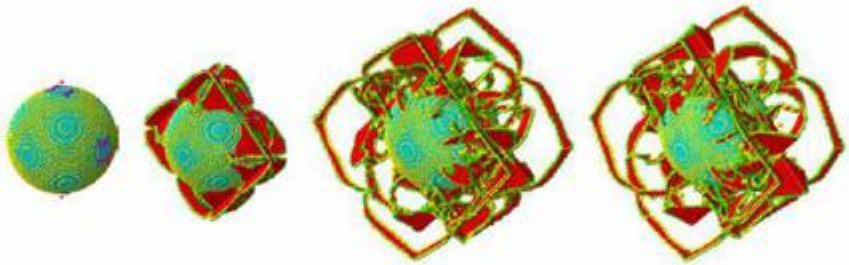

V_{fr}=27% V_{fr}=8% V_{fr}=1% V_{fr}=0.125%

Fig. 2 Fixed-size void (d=14nm) embedded in differently-sized simulation box at a strain of 0.06 (add a coordinate system)

At a uniaxial strain of 0.06, the voids with 1% and 0.125% initial volume fraction show very little difference in their developed dislocation structure. These two developed dislocation networks, which have slip systems common to FCC metals, contain quadrangular-frustum structures in the loading direction (*x*-axis) and some prismatic structure in the lateral

[a)] Corresponding author. Email: zengtao.chen@ualberta.ca (ZT Chen).

direction (*y*- and *z*-axes). It appears that void of this size can be considered as isolated once its initial volume fraction is below 1% from Fig. 2.

Changing-size void inside fixed-size simulation box

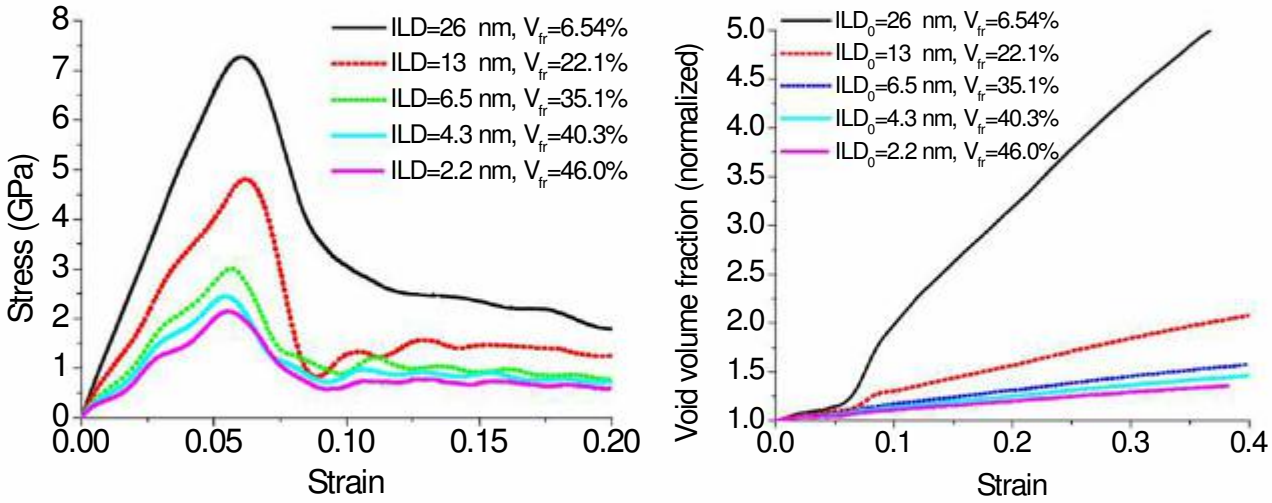

Fig. 3 Stress-strain relations and normalized void volume fraction curves under different initial ILD

As predicted by the continuum theory [5], the increasing porosity lowers the effective Young's modulus of the composite material in a similar way shown in Fig. 3. The changing slope of the stress curve before a strain of 0.05 can be associated with the changing void volume fraction in this range.

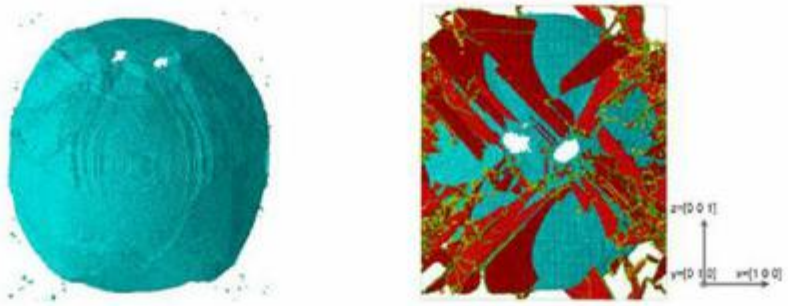

(a) The surface of the coalesced void (b) The corresponding local dislocation structure

Fig. 4 Dislocation structure and forming of the highlands (arrowed) to facilitate the void coalescence

The two highlands on the void surface in Fig. 4(a) are formed by the nearby dislocation structure as spotted in Fig. 4(b). The forming of the highlands on the void surface, in other words, is the faster consumption sites of the intervoid ligament.

CONCLUSIONS

For fixed-size void inside the changing-size simulation box, the critical strain to trigger the dislocation emission decreases as the simulation size increases. For porosity below 1%, further enlarging the simulation size makes virtually no difference to this critical strain. Therefore, void with the size and other conditions concerned here can be viewed as isolated once its initial volume fraction is below 1%. For the larger changing-size void inside the fixed-size simulation box, the critical strain to trigger dislocation shows a very weak dependence on the void size. The dislocation emission pattern is highly subject to the initial ILD with a strong clustering effect. Both the ultimate strength and the effective Young's modulus are lowered by the enlarging void size. For the void cluster, larger void with short initial ILD tends to reach larger coalescence porosity. The highlands on the void surface, formed by nearby dislocation structures, cause the local breakdown of the intervoid ligament.

References

[1] S.J. Zinkle, K. Farrell, J. Nucl. Mater. 168 (1989) 262-267.
[2] N.M. Ghoniem, D. Walgraef, S.J. Zinkle, J. Comput-aided Mater. 8 (2001) 1-38.
[3] C. Thomson, M.J. Worswick, A.k. Pilkey, D.J. Lloyd, G. Burger, J. Mech. Phys. Solids. 47 (1998) 1-26.
[4] X. Gao, T. Wang, J. Kim, Int. J. Solids Struct. 42 (2005) 5097-5117.
[5] R.M. Christensen, Proc. Math. Phys. Sci. 440 (1993) 461-473.

PREDICTING DYNAMIC FAILURE IN ARMOR CERAMIC USING EFFICIENT INITIAL FLAW STATISTICS

F. Huq[1] and L. Graham-Brady *[2]

[1]*Department of Civil Engineering, Johns Hopkins University, Baltimore, MD, USA*
[2]*Department of Civil Engineering, Johns Hopkins University, Baltimore, MD, USA*

Summary The failure process in armor ceramic under an impact event is fundamentally linked to the type and distribution of subscale defect population in the material. For many armor ceramics the controlling defects that causes significant microcracking are crack-like defects or flaws. The current modeling framework uses micromechanics damage models with an input statistical samplings from the parent flaw distribution of the material to represent the subscale processes (e.g. microcracking) and a conventional continuum mechanics code is used for the macro-scale problem. The initial input flaw statistics is divided into a smaller number of groups or bins and each bin has its characteristic flaw size and fraction of flaws associated with it. An efficient numerical method has been used to obtain the characteristic flaw size and flaw fraction associated with each group or bin in order to increase the computational efficiency while retaining the desired level of accuracy.

INTRODUCTION

The failure of armor ceramic which are mostly brittle in nature under an impact event is a complex phenomenon. There are a number of physical processes (microcracking, granular flow, pore collapse etc.) that occur within the material specimen under dynamic loading. One major mechanism that is observed in brittle ceramics under high strain rate loading is microcracking from preexisting crack-like defects or flaws. The microcracks continue to grow and intersect with each other creating numerous fragments at some stage of loading. This existing multi-scale Tonge-Ramesh (T-R) material model incorporates a number of microscale mechanisms along with the key microcracking mechanism. To capture the effect of micro-scale cracking micromechanics-based analytical damage models are used here. This micromechanics model incorporates a distribution of crack-like flaws as the key microstructural feature. The distribution of crack-like flaws also represents the inherent statistical nature of the brittle ceramic. The point-to-point variability in the material is described by assigning a local flaw population at each point in a discretized material domain. At each material point, the damage evolution for the local flaw population is calculated using the micromechanics model. The flaw population have flaws with both size and orientation distribution. For this work, only the flaw size distribution is considered. For a three dimensional material domain, the damage is defined within each discretization volume V_o as the sum of the cubed flaw sizes s_i over all N flaws in the volume V_o divided by V_o:

$$\Omega = \frac{1}{V_o} \sum_{i=1}^{N} s_i^3 \tag{1}$$

For a large flaw population, computing the damage Ω for all the flaws and also repeating the procedure of damage calculation for each material point is computationally extensive. To reduce the computational burden, the flaw population for a material point is divided into smaller number of groups or bins. Each bin is characterized by a characteristic size and a fraction of flaw population associated with that bin. The damage is then calculated for those selected flaw sizes representing each bin. The damage for each bin is calculated as:

$$\Omega = \sum_{k=1}^{N_b} \frac{N_k}{V_o} s_k^3 \tag{2}$$

where N_b is the number of bins, N_k is the number of flaws within each bin and s_k is the representative flaw size of that bin. The details of the damage model is descibed in [1]. To select the critical characteristic flaw size and the fraction of flaws associated with each bin, a novel binning technique is developed in [2]. The binning technique is used in the current T-R model to predict the constitutive response of the armor ceramic under different loading scenario.

BINNING METHODOLOGY

The current T-R multi-scale framework incorporated various binning techniques to increase the computational efficiency in calculating the damage due to microcracking. To enhance the capability of the current model, another generalized binning technique is integrated into the current unified model framework. This novel binning technique can take any random bounded or unbounded flaw size distribution as an input. The binning is done using the probability space (ranging between $0 \sim 1$) to

*Corresponding author. Email: lori@jhu.edu

ensure binning in a finite space and capture the upper bin (larger flaw size) accurately. To select the characteristic flaw sizes for each bin, a one dimensional grid is laid out in probability space. Uniformly distributed random numbers representing the flaw sizes are generated on the probability space. These random numbers are transferred to nodes and associated Gauss points of the probability space. The locations of the Gauss points are the bin locations which represent the characteristic flaw size (in realization space) for the bins and the weights associated with each Gauss points are the fraction of the flaws associated with each bin. The actual flaw size is then obtained through an inverse mapping from the probability space to the flaw size space. In addition, different mesh density on the probability space is used to obtain the optimal number of bins. This mesh density is obtained by using a zooming function which is developed based on the criterion that each bin contributes equally to the damage.

RESULT

An example problem with efficient binning scheme and T-R binning scheme is provided here. The loading condition for the simulation problem is uniaxial strain with a rate of $10^3 s^{-1}$. The axial stress (stress in 11 direction) is compared with axial strain (strain in 11 direction) for both efficient binning and an existing binning technique against a solution that has a population of 500 cracks. The T-R binning scheme and the efficient binning scheme tracks the 500 crack solution accurately

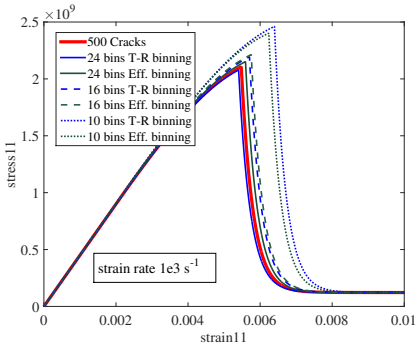

Figure 1: Stress-strain comparison for different number of bins for each binning scheme. The T-R binning represents the existing binning scheme in the Tonge-Ramesh multiscale model which requires random sampling within each bin. Both the binning schemes suggests non-uniform bin width in flaw size space.

using 24 bins. The same trend is observed in case of using 16 bins. The efficient binning scheme shows better results in case of 10 bins.

CONCLUSION

The micromechanics based damage model with an efficient statistical input flaw sizes incorporates the physically based variability into the constitutive response. In addition to that, the spatial variability also provides localized initiation sites for damage to predict realistic fragmentation of the material. Selection of efficient initial flaw statistics is very important in capturing the damage and fragmentation in the material. The efficient flaw statistics is obtained by the characteristic flaw size and fraction of flaws for each bin. This is achieved by implementing the efficient binning scheme into the T-R model. The binning scheme captures the constitutive response accurately with the same number of bins as suggested by T-R binning scheme. The efficient binning scheme shows better result over T-R binning scheme with a relatively low margin of errors when compared with 500 crack (assumed to be exact solution) solution. In addition to that, the efficient binning scheme eliminates the need for random selection of flaw sizes in each bin as suggested by the existing T-R binning scheme. The efficient binning scheme can also use any bounded or unbounded flaw size distribution and capture the largest flaw size (upper bound) without the prior knowledge on the upper bound of the flaw sizes which was the limitation of the T-R binning scheme.

References

[1] Tonge, A. L., and Ramesh, K. T. : Multi-scale defect interactions in high-rate brittle material failure. Part I: Model formulation and application to ALON. Journal of the Mechanics and Physics of Solids. 86:117-149, 2016.

[2] Huq, F., Brannon, R., and Graham-Brady, L.: An efficint binning scheme with application to statistical crack mechanics. International Journal for Nummerical Methods in Engineering. 105:33-62, 2016.

NUMERICAL TWO-SCALE SIMULATIONS WITH APPLICATION TOWARDS REFRACTORIES

Janto Gundlach *[1] and Andreas Ricoeur[1]
[1]*Chair of Engineering Mechanics/Continuum Mechanics, Institute of Mechanics, University of Kassel, Germany*

Summary Numerical results of damage evolution are reported of thermoshock processes on refractory ceramics. Damage patterns have been generated using a two-scale approach for brittle materials, implemented in a finite element framework. For this purpose, so-called cell models are employed, incorporating either microcracks or cohesive grain boundaries on a microscopic level. The impact of these discontinuities on macroscopic material properties and damage evolution is determined with the help of homogenization techniques. Finally, the potential of the numerical tool is demonstrated by means of refractory bricks, being imposed by thermomechanical loading.

INTRODUCTION

Refractory materials are commonly used to protect metallic structures against high input of heat, which is for instance the case in iron and steel industry. A thermoshock, where the surface of a structure is subjected to high temperature loads within a very short time span, is considered as the most critical event in possible processes. In addition to typical thermomechanical material properties such as strength, density, thermal conductivity, and thermal expansion behavior, the resistance to temperature changes depends on the characteristics of the microstructure. After fabrication, refractory materials contain voids, microcracks, grain boundaries, and inclusions of other phases. These heterogeneities have an impact on the damage evolution during instantaneous thermoshocks and affect the material properties, moreover.

In this investigation, both effects are reproduced within a two-level continuum damage approach. Cell models are developed, taking microstructural features into account. Both models crystallize in an internal damage variable which is directly related to the effective stiffness of the brittle material.

TWO-SCALE MODELING AND IMPLEMENTATION

In general, the solution is sought for the thermomechanical initial boundary value problem governed by

$$\sigma_{ij,j} = 0, \tag{1}$$

$$\rho c \dot{\theta} = \lambda \theta_{,ii}, \tag{2}$$

with prescribed temperatures $\overline{\theta}$, displacements $\overline{u}_i$, stresses $\overline{t}_i$ and heat fluxes $\overline{q}_i$ as suitable boundary conditions. The parameters of the energy balance, i. e. mass density ρ, specific heat capacity c, and thermal conductivity λ, are allowed to be temperature dependent. The stresses σ_{ij} and the temperatures in equations (1) and (2) are valid on the macroscopic level of the two-scale concept displayed in Fig. 1. The microscopic level is defined by a Representative Volume Element (RVE) which is intended to describe the properties of the particular microstructure and is associated with a point $\mathcal{P}$ at a macroscopic coordinate x_i^m. On the one hand, an RVE is required to be sufficiently small in order to allow this punctual allocation, on the other hand, it must be large compared to the dimensions of the microstructural features: $l \ll d \ll L$. For ceramics, an appropriate choice is $d \approx 0.1\,\mathrm{mm}$. The heterogeneities taken into account in this study are either microcracks of arbitrary orientation or grain boundaries in a polycrystal. Owing to these discontinuities, both stresses and strains are field variables, depending on the microscopic coordinate x_i. In the process of homogenization, these fields are averaged within the respective volume V of the RVE. A constitutive law in this thermomechanical framework relates macroscopic values according to Hooke's law including thermal expansion:

$$\langle \sigma_{ij} \rangle = C^*_{ijkl} \left(\langle \epsilon_{kl} \rangle \circ \ \alpha \delta_{kl} \Delta\Theta \right), \tag{3}$$

where the brackets $\langle \cdot \rangle$ indicate volume averaged quantities henceforth. In a state of plane stress, assuming a dilute microcrack distribution in a linear elastic matrix, an appropriate expression of the effective stiffness C^*_{ijkl} is derivable analytically [1]:

$$\begin{bmatrix} \langle \epsilon_{11} \rangle \\ \langle \epsilon_{22} \rangle \\ 2\langle \epsilon_{12} \rangle \end{bmatrix} = \frac{1}{E} \begin{bmatrix} 1 + \frac{f_0 \pi}{4} & \circ\ \nu & 0 \\ \circ\ \nu & 1 + \frac{f_0 \pi}{4} & 0 \\ 0 & 0 & 2(1+\nu) + \frac{f_0 \pi}{2} \end{bmatrix} \begin{bmatrix} \langle \sigma_{11} \rangle \\ \langle \sigma_{22} \rangle \\ \langle \sigma_{12} \rangle \end{bmatrix} \tag{4}$$

reflects an isotropic behavior according to a distribution of arbitrarily oriented cracks and is used as the starting point in simulations, whereas

$$\begin{bmatrix} \langle \epsilon_{11} \rangle \\ \langle \epsilon_{22} \rangle \\ 2\langle \epsilon_{12} \rangle \end{bmatrix} = \frac{1}{E} \begin{bmatrix} 1 & \circ\ \nu & 0 \\ \circ\ \nu & 1 + \frac{f \pi}{2} & 0 \\ 0 & 0 & 2(1+\nu) + \frac{f \pi}{2} \end{bmatrix} \begin{bmatrix} \langle \sigma_{11} \rangle \\ \langle \sigma_{22} \rangle \\ \langle \sigma_{12} \rangle \end{bmatrix} \tag{5}$$

*Corresponding author. Email: gundlach@uni-kassel.de

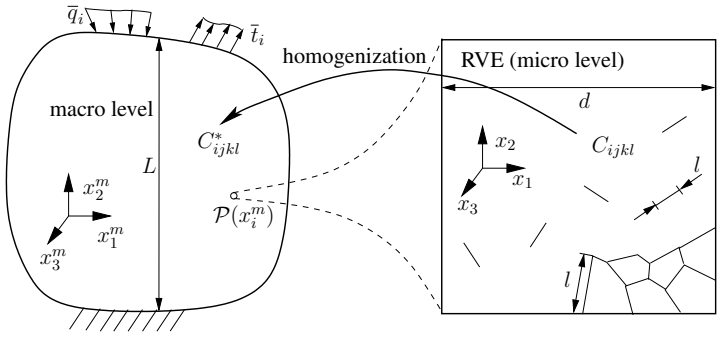

Figure 1: Thermomechanical two-scale problem and concept of homogenization.

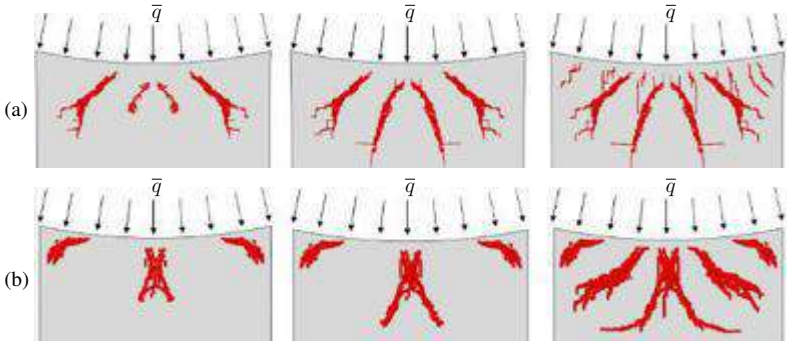

Figure 2: Refractory bricks exposed to cyclic thermoshocks. In (a) the analytical microcrack-based cell model is applied, (b) represents the numerical model incorporating grain boundaries.

corresponds to an RVE which is already damaged and therefore more compliant perpendicular to the particular crack face orientation. In expressions (4) and (5), E denotes Young's modulus, ν Poisson's ratio, and $f = \frac{4a^2}{A}$ represents, as ratio between quadratic crack length and size of the RVE, the internal damage variable. If f reaches unity, a crack has proceeded through the entire volume element. Considering grain boundaries, the damage is evaluated numerically, regarding the interaction between grains which are connected with a bilinear cohesive law (cf. [2]).

NUMERICAL EXAMPLE

The model in Fig. 2(a) displays the typical shape of a refractory brick with a concavely curved top edge, exposed to a thermal shock heat flux $\bar{q} = 30$ MW/m^2. Width and height of the model have been chosen as 100×80 mm, the bottom edge is mechanically supported allowing for unconstrained extension and the three edges (only a shortened extract of the whole brick is shown), not being exposed to the heat flux, are adiabatic. Simulations for three thermal load cycles, as depicted in the plot, are presented, each with a heat flux kept constant for 30 seconds, intercepted by 10 seconds of rest. The damage zones or cracks, outlined in red, are shown at the ends of the heating periods and indicate a damage value of $f = 1$. A network of cracks develops, nucleating underneath the surface and growing with increasing number of thermal shocks. The largest effect on the damage is observed for the first two shocks, while the crack pattern moderately develops with further load cycles.

In Fig. 2(b) the geometry and boundary conditions are the same as in (a) including an identical thermal loading scheme and results taken at the same instants of time. The simulations, however, are based on the numerical cell model accounting for grain boundaries and intercrystalline crack growth. Comparing both results, the damage patterns are similar, showing four to six isolated branches, which could be interpreted as macroscopic cracks or crack networks. All of them tend to diverge from the axis of symmetry, both with analytical and numerical cell models. The relative areas of damaged zones are slightly larger for the polycrystalline two-scale FE approach than for the analytical crack model.

References

[1] Henneberg, D., Ricoeur, A., Judt, P.: Multiscale Modeling for the Simulation of Damage Processes at Refractory Materials under Thermal Shock. *Comput. Mater. Sci.*, **70**, 187-195, (2013).

[2] Henneberg, D., Ricoeur, A.: Numerical Two-Scale Simulations of Damage Evolution at Refractory Materials. *J. Ceram. Sci. Tech.*, **5**, 83-92, (2014).

LOCALIZATION PATTERN EVOLUTION OF ROCK UNDER UNIAXIAL COMPRESSION EXPERIMENTS

Shengwang Hao[1,2a)], Ping Wang[1], Guojun Du[1] & Yuda Hu[1]
[1]*School of Civil Engineering and Mechanics, Yanshan University, Qinhuangdao, China*
[2]*State Key Laboratory of Nonlinear Mechanics (LNM), Institute of Mechanics, Chinese Academy of Sciences, Beijing 100190, China*

Summary We report three modes of the localized zone evolution observed in uniaxial compression experiments of rock. A single rupture surface formed in three samples, but the strain patterns are obviously different. For marble 1 sample, only one high strain zone was observed and the eventual rupture surface formed in the high strain zone. However, two high strain zones appeared in marble 2 and granite 1. Interestingly, in granite 1, two high strain zones presented a process of competition and selection. During this process, one high strain finally withdraws the competition and the rupture surface formed in the other high strain zone. For marble 2, two high strain zones evolved simultaneously but the growth of one high strain zone became turned in a new direction along the other high strain zone, finally these two high strain zones connected and induced eventual rupture.

INTRODUCTION

Strain localization is a very common phenomenon in geological materials and serve as an effective precursor of catastrophic rupture[1,2]. After localization, the sample bifurcated into a two-part continuum consisting of less-deformation zone plus a highly deformed band which is named as localized zone[3-5].

It is documented that as soon as the elastic energy stored in the testing system and(or) outside localized zone, becomes greater than the fracture energy of the localized zone, the catastrophic rupture will occur[5]. So, localization is a cause inducing catastrophic rupture and thus the unknown of the size of localized zone results in the uncertainty of catastrophic rupture[5]. The knowledge about the evolution properties of localized zone is definitely significant to clarify the mechanism of catastrophic rupture and its prediction.

EXPERIMENT METHOD AND MATERIAL

The uniaxial compressive experiments were conducted on granite and marble prismatic blocks cut to 16mm× 20mm× 40 mm. The specimens were loaded along the direction of 40 mm height at a constant rate of 0.02mm/min.

To investigate the characteristics of deformation pattern evolution, the digital speckle correlation method was used to measure the spatiotemporal pattern of the surface deformation fields of rock specimens. The digital image, acquired by a charge-coupled-device camera, was immediately transmitted to image capturing board on a personal computer and recorded on a hard disk. After the experiment, the deformation fields of each test were calculated by the image analysis software.

RESULTS

The strain patterns for three samples are shown in figures 1-3 and it is clear that the strain accumulation appeared before the eventual rupture. It should be pointed out that figures 1, 2 and 3 represent three pattern evolution modes of high strain zones. It can be seen that only one high strain zone appeared in marble 1 sample (as shown in figure 1), but the other two samples, marble 2 and granite 1 both presented two high strain zones (figures 2, 3) respectively but they exhibited two different evolution modes as described follow.

The series of images in figure 1 illustrate the process that the high strain zone formed and evolved in marble 1. It is shown that a high strain zone initiated at left down corner of the sample (figure 1a). Then it propagated upwards to the right corner (figure 1b-c). Finally, this high strain zone became an inclined localized band (figure 1d-e) and induced the macroscopic rupture. The rupture photo shown in figure 1f indicates that the eventual rupture surface formed in the high strain zone.

For marble 2 shown in figure 2, a high strain zone first initiated in the left-up corner of sample (figure 2b) following the early stage characterized by random strain fluctuation (figure 2a). Then the other high strain zone also appeared in the right-up corner (figure 2c). Afterwards, these two high strain zones located in two conjugate directions evolved together (figure 2d). The eventual rupture surface is shown in figure 2f. Figure 2e illustrates the schematic of the evolution ways about these two high strain zones. It can be seen that the second high strain zone became curved and turned to the conjugate direction. Then it connected with the first high strain zone and led to the eventual catastrophic rupture.

The granite 1 sample (figure 3) exhibited an interest pattern. After the early stage that the strain fields are randomly fluctuation (shown in figure 3a), two high strain zones appeared almost synchronously in two conjugated direction of left- and right-bottom corners (shown in figure 3b), which is very different from the mode exhibited by marble 2 (figure 2) where the two high strain zones initiated one by one in sequence. Moreover, the way that the deformation of granite 1 sample evolved to induce the eventual macroscopic rupture was also different from marble 2.

There are usually multiple high strain zones observed in rock experiments. But, the eventual rupture surface formed mostlyin one high strain zones. In this paper, three modes of localization evolution have been observed in our rock

[a)]Corresponding author. Email: hsw@ysu.edu.cn.

experiments. he results present a deep insight into the complex mec anism of localization inducing macroscopic rupture and the localization pattern evolution.

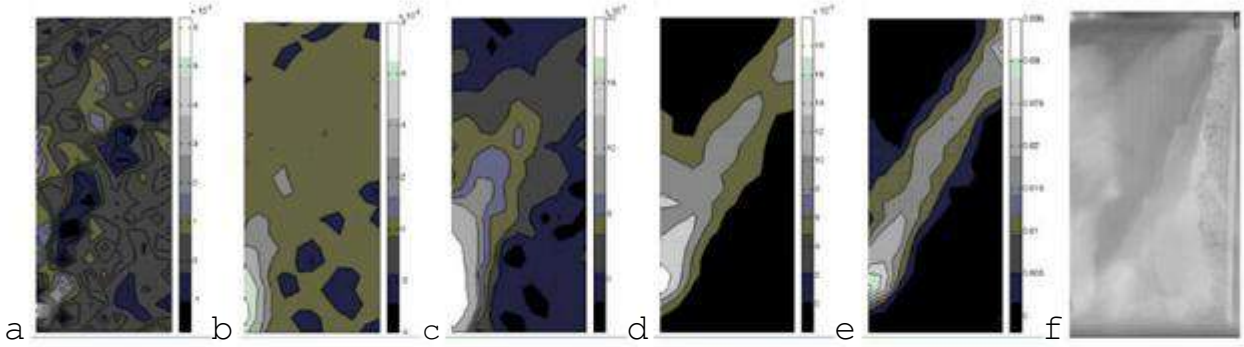

Figure 1 Strain patterns of Marble 1 and its eventual rupture mode

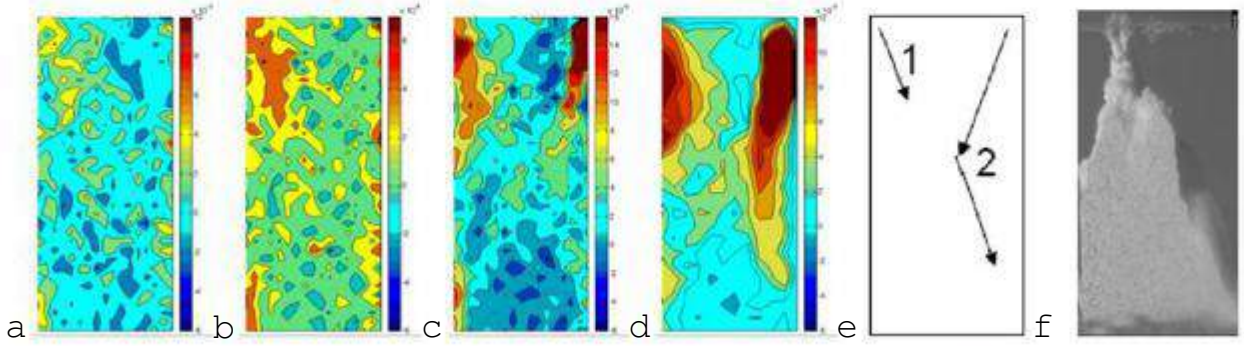

Figure 2 Strain patterns of Marble and its eventual rupture mode

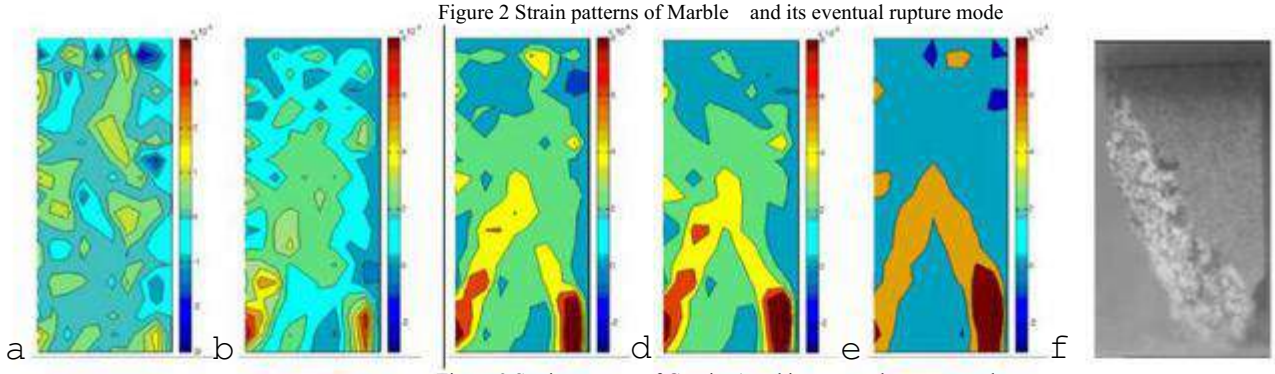

Figure 3 Strain p tterns of Granite 1 and its eventual rupture mode

CO CLUSIONS

wo conjugate high strain zones somet mes appear in rock experiments. But they might exhibit various evolution echanisms. uring the co peting process of two hig strain zones, one scenario might appear that the first ucleating igh strain zo e will fail in he competition although it et priority to ropagation a d the eventua rupture surface formed n the second high strain z ne. The other case observe in our rock experiments is that two high strain zones appeared almost simultaneously. Finally these two h gh strain zones connected a d induced cat strophic rupture.

cknowledge ents

his work wa supported by the Natural Science Found tion of Hebei province, Chi a (D2015203 98), the Nati nal Basic esearch Pro ram of Chin (Grant No. 013CB83410), and the O ening Fund f State Key aboratory of Nonlinear echanics, In titute of Mec anics, Chines Academy of Science.

eferences

[1] Rudnicki J. ., Rice J.R.: Conditions for the locali ation of deformation in pressure-sen itive dilatant mate ials. *J. Mech. Phy . Solids***23**:371-39 , 1975.

[2] Bai Y.L. *et a* : Statistical meso echanics of solid, liking coupled multiple space and time scales. Appl. Mech. Rev**58**:372-388, 2005

[3] Olsson W. A., Holcomb D. J.: ompaction localization in porous roc . *Geophys. Res. L tt***27**:3537-3540, 2000.

[4] Lockner, D. . *et al*: Quasi-stati fault growth and shear fracture ener y in granite. Natu e**350**:39-42, 1991.

[5] Hao S.W., Xia, M. F., Ke, F. J., Bai, Y. L.: Evolution of Localized D mage Zone in Heterogeneous Media. *Int. J. damage Mech***19**: 787-804, 2010.

VOID GROWTH AND COALESCENCE IN IRRADIATED MATERIALS

Jérémy Hure*[1], Pierre-Olivier Barrioz[1], and Benoît Tanguy[1]

[1]*CEA, Université Paris-Saclay, DEN, Service d'Études des Matériaux Irradiés, 91191 Gif-sur-Yvette cedex, France*

Summary Irradiation with high energy particles induces crystalline defects in metallic materials. These microstructural changes strongly modify the mechanical properties, leading in particular to significant hardening and strain localization at the grain scale. The effects of irradiation on the mechanisms of ductile fracture - void growth and coalescence - are assessed in this study based on model experiments. Pure copper thin tensile samples have been irradiated with ions, showing a strong increase of hardness. Micron-scale holes drilled through the thickness of these samples subjecting to uniaxial loading conditions allow a detailed description of void growth and coalescence. Results are compared to those obtained on unirradiated materials, as well as to theoretical and numerical predictions.

BACKGROUND

Materials used in the nuclear field undergo significant microstructural changes due to ballistic damages of high energy particles such as neutrons, ultimately leading to the formation of crystalline defects [1]. Typically observed defects are faulted dislocation loops, cavities and stacking fault tetrahedron. These microstructural changes lead to the degradation of mechanical properties such as increase of yield stress and decrease of strain hardening capabilities at the macroscopic scale, but also changes in deformation modes at the microscopic (grain) scale - from rather homogeneous deformation to localization in bands. One key ingredient for structural analysis of nuclear power plant core components is the fracture behavior of the materials. The aim of this study is thus to assess the ductile fracture mechanisms of irradiated metallic materials, based on model experiments of void growth and coalescence.

MATERIALS AND METHODS

Pure copper films (75 μm thick) are used in this study as a model material to study the effect of irradiation on ductile behavior, both at the unirradiated and irradiated states. Proton-irradiation have been performed to emulate neutron irradiation at the JANNuS facility [2], leading to the formation of crystalline defects. Increase of yield stress and decrease of strain-hardening capabilities have been quantified post to irradiation. 20 μm diameter voids were drilled through the thickness of tensile samples machined from the thin films using Focused Ion Beam (FIB) atomic milling (Fig. 1). Tensile samples were subjected to uniaxial loading conditions, and the evolution of the voids dimensions was measured using Scanning Electron Microscope (SEM) as a function of applied strain (Fig. 2). Such model experiment - first proposed in [3] - allows a detailed characterisation of the ductile fracture mechanisms of void growth and coalescence.

RESULTS AND DISCUSSION

For both unirradiated and irradiated materials, the evolution of voids dimensions and coalescence strains are shown to be in rather good agreement with theoretical predictions (McClintock growth model, Coalescence models) and in very good agreement with finite element simulations accounting for the evolution of mechanical properties with irradiation. Irradiated material exhibits a higher void growth rate compared to unirradiated material. For the void size used in this study, only the increase of yield stress and the decrease of strain-hardening capabilities - and not the change in deformation modes promoting localization - are thus sufficient to describe the effect of irradiation of the ductile behavior of irradiated materials. Lower void sizes are finally used to assess the potential effect of localized bands on void growth and coalescence.

References

[1] Was G: Fundamentals of Radiation Materials Science, Springer-Verlag Berlin Heidelberg, 2007

[2] Beck L, Serruys Y, Miro S, Trocellier P, Bordas E, Leprêtre F, Brimbal D, Loussouarn T, Martin H, Vaubaillon S, Pellegrino S, Bachiller-Perea D: Ion irradiation and radiation effect characterization at the JANNUS-Saclay triple beam facility, J. Mater. Res. 30:1183-1194, 2015

[3] Weck A, Wilkinson D.S.: Experimental investigation of void coalescence in metallic sheets containing laser drilled holes, Acta Mat. 56:1774-1784, 2008

*Corresponding author. Email: jeremy.hure@cea.fr

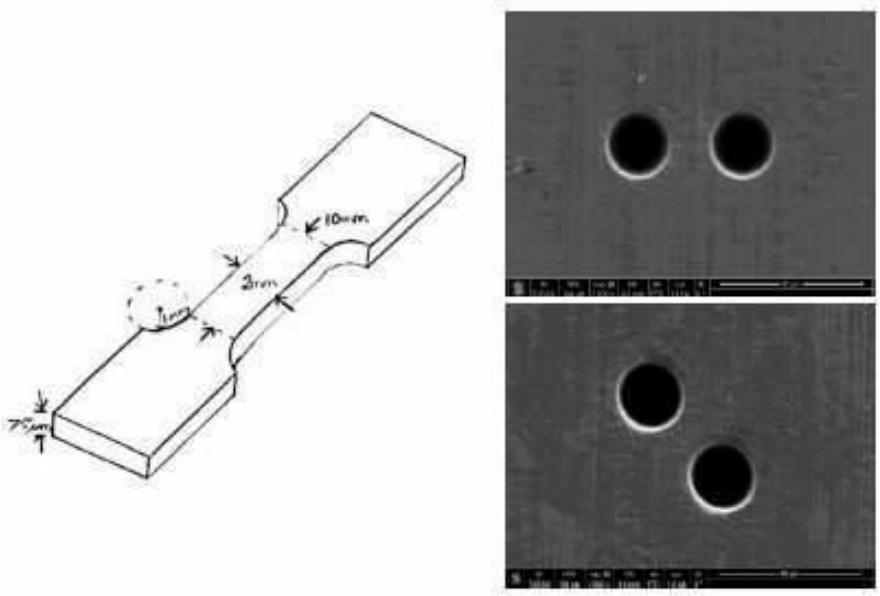

Figure 1: Tensile sample geometry and holes (20 μm diameter) drilled by FIB (Focused Ion Beam) through the thickness of the samples to assess void growth and coalescence.

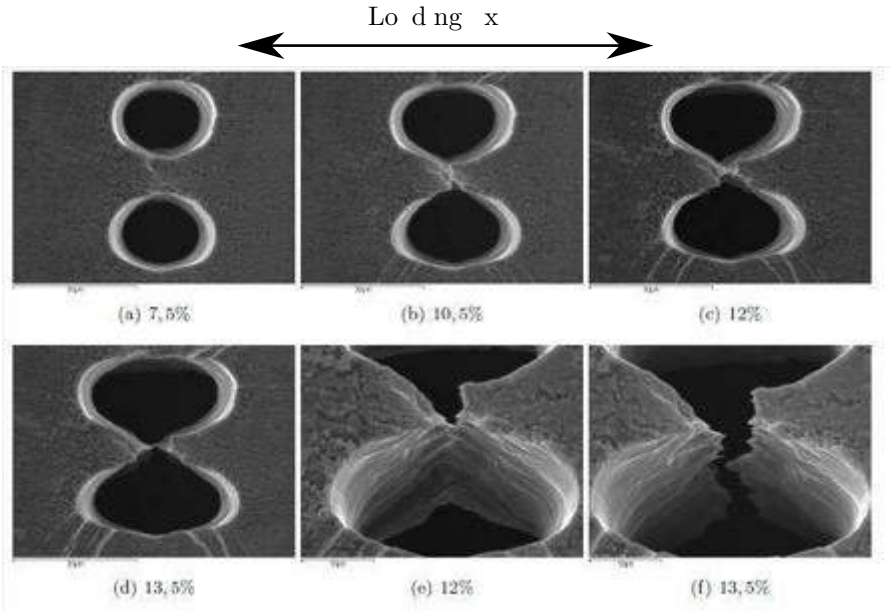

Figure 2: Typical SEM (Scanning Electron Microscope) observations of void growth and coalescence in pure copper in uniaxial loading conditions, as a function of macroscopic plastic strain.

3D X-RAY CT OF FATIGUE DAMAGE IN FIBRE COMPOSITE

Kristine M. Jespersen[1 a)], Jens Zangenberg[2], Philip J. Withers[3], Tristan Lowe[3] & Lars P. Mikkelsen[1]
[1]*Department of Wind Energy, Technical University of Denmark, Roskilde, Denmark*
[2]*LM Wind Power Blades, Composites Mechanics, Kolding, Denmark*
[3]*School of Materials, University of Manchester, Manchester, United Kingdom*

Summary In this study, 3D X-ray CT was used to investigate the fatigue damage in a uni-directional (UD) glass fibre composite made from a non-crimp fabric at different stages of the fatigue life. The damage was found to appear as local UD fibre fracture regions close to the so called supporting backing layer, which seemed to have an important role in the location of the damage initiation. Furthermore, the damage appeared as 3D regions containing both clusters and chains of fibre fractures, and it was concluded that considering this problem in 3D seemed to be important in order to obtain realistic results.

INTRODUCTION AND MOTIVATION

Over the years, composite materials have been replacing conventional materials in more and more applications such as in airplanes, cars, wind turbines, sports equipment and much more. In the case of wind turbines, modern blades consist of fibre composites and sandwich materials chosen carefully to match the present loads and form the aerodynamic shape of the blade. During the 20-30 years of life time of a wind turbine, the blades are subjected to fatigue loads in the order of 10^8-10^9 cycles resulting from the variation in the wind and gravitational loads [1]. This is much higher than for most other industrial applications and consequently fatigue is one of the main limiting factors when designing the blades. The laminate carrying the main bending fatigue loads in the blade are mainly uni-directional (UD) glass fibre composites made from non-crimp fabrics (NCF). The fatigue damage for this type of material is not well understood and understanding how the damage evolves on a microstructural level could make it possible to design closer to the limit and make fatigue resistant designs.

One way to understand how the fatigue damage evolves is to perform non-destructive examinations at different stages of the life-time during fatigue testing. Because of recent technology advances within X-ray CT, making it possible to obtain pixel sizes down to the nanoscale, 3D X-ray Computed Tomography (CT) has become an interesting technique for use in material science and mechanics. Since X-ray CT is non-destructive, it opens for the possibility of performing over-time studies providing 3D visualisations of how the damage evolves within the material. If this is accomplished, not only will it be possible to understand how to improve the fatigue properties of the material, but also make it easier to do realistic life-time predictions. For fibre composites, damage mechanics related numerical simulations easily become complex with high calculation times. If the nature of the damage mechanism is understood through experiments, it will make it easier to make realistic assumptions for simplifying the models. Furthermore, it can serve as a good validation base for microstructural simulations. The current study examines the tension-tension fatigue damage of a fibre composite similar to that used for wind turbine blades by means of 3D X-ray CT.

MATERIAL SYSTEM

The composite material considered in this study is a UD glass fibre/polyester matrix composite similar to that used to carry the main loads in a wind turbine blade. The composite consists of four layers of non-crimp fabrics (NCF) which are stacked on top of each other and infused with resin using the vacuum assisted resin transfer moulding (VARTM) technique. For each layer of fabric a layer of parallel UD bundles of glass fibres is stitched to a thin layer of ±80° supporting backing fibre bundles. The considered composite has the stacking sequence $[0/b,0/b]_s$ where "0" indicates the location of the UD layer and "b" the backing layer for each layer of fabric.

FATIGUE TESTING AND X-RAY COMPUTED TOMOGRAPHY

Tension-tension ($\sigma_{min}/\sigma_{max}$ =0.1) fatigue tests were carried out on 410 mm long butterfly shaped test specimens using a hydraulic Instron machine. The tests were conducted in load control mode with a test frequency of 5Hz. The butterfly test geometry is a special geometry optimized for testing UD materials, as standard plane test specimens tend to fail prematurely in the tap region (see [2] for more information). Rectangular samples with cross-sections of ~4x4mm were cut out from the tested butterfly specimens and examined using X-ray CT. The X-ray CT experiments were carried out using a Zeiss Xradia Versa 520 scanner with a 4X detector (2000×2000 pixels) and a source-to-sample distance of 11mm along with a detector-to-sample distance of 20mm resulting in a pixel size of 1.2µm and a field of view (FOV) of 2.4×2.4mm. The software AVIZO 9.0 by FEI was used for segmentation and visualisation.

[a)] Corresponding author. Email: kmun@dtu.dk.

RESULTS AND DISCUSSIONS

To investigate how the damage progressed during fatigue, fatigue tests were interrupted at different stages of the fatigue life and cut-out samples were scanned using X-ray CT. One test was stopped during the initial stiffness drop region at only a few thousand cycles (S1), two tests were stopped during the stable stiffness degradation regime (S2 and S3), and one test was interrupted around the point where the stiffness decreases drastically, close to final failure (S4). For each of the scanned samples the backing bundles and individual UD fibre fractures were manually segmented in 3D. Fig. 1 shows the segmented damage for sample S4, and similar segmentations can be found in [3] for S2 and S3. For sample S1, it was not possible to locate any damage in the performed scans. Matrix cracks are believed to be present in the backing bundles, however, since they might cause the initial stiffness drop [4]. Therefore, it is likely that the resolution was insufficient to visualise these cracks. Damage regions were observed in both the S2, S3, and S4 scans, and if assuming an average bundle thickness of 0.9mm the observed damage regions had a maximum penetration depth of ~14%, ~34%, and ~41% percent respectively (S1<S2<S3). This could indicate that the damage regions in the samples grow in the depth direction as a function of the cycles, until a certain point at which the increases load on the remaining fibres will cause final failure.

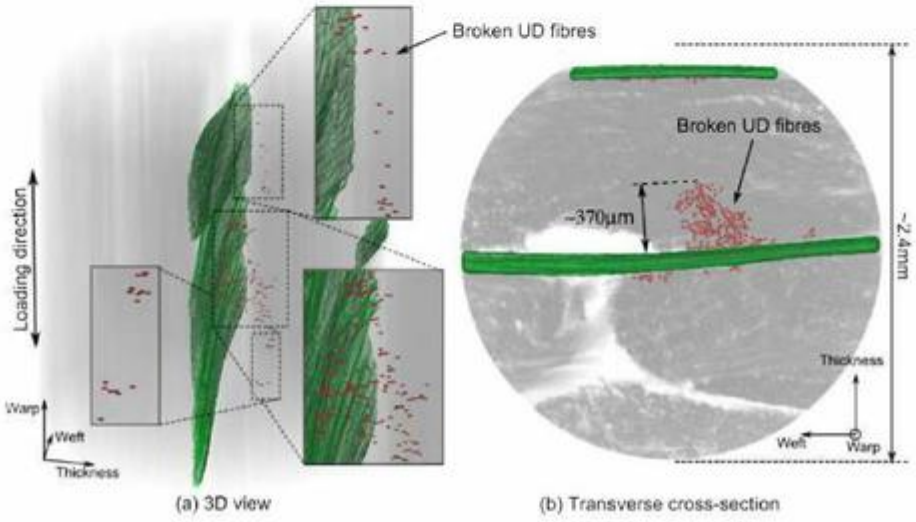

Fig. 1 3D segmentation of individual UD fibre fractures for S4. The backing bundles are marked by green, and the broken UD fibres are shown as red discs. The UD fibres are rendered opaque for clarification and appear light grey.

From Fig. 1, it is seen that the damage appears as a local phenomenon close to the backing layer, and this was the case for all the observed damage regions. UD fibre fracture regions were only observed near locations where the backing bundles cross over each other (intersect) and at the same are in close contact with the UD bundles. Furthermore, close to the backing the UD fibre fractures were observed to align with the backing fibre direction, which could indicate initiation from a matrix crack in the backing bundle. Further away from the backing, the fractures are seen to spread out more and form clusters or chains rather than fracture planes. It is seen that the fatigue damage for this material is a 3D phenomenon, and that a 2D examination would be highly dependent on the location of the cut plane. Furthermore, it is seen that it would be very conservative to assume that the full UD bundle width (weft direction) would have the same penetration depth (thickness direction) in the entire bundle, as might be assumed in a 2D analysis. The reason for this is that UD bundle width significantly larger than the width of the damage zone.

CONCLUSIONS

3D X-ray CT was used to examine fatigue damage evolution in a glass fibre composite on a microstructural level at different stages of the fatigue life. Regions with UD fibre fractures were observed to be highly related to the presence of the supporting thin backing layers. Furthermore, the damage mechanism was seen to be a 3D phenomenon and considering the problem in 2D might give overly conservative and/or misleading results.

References

[1] Nijssen R.: Fatigue life prediction and strength degradation of wind turbine rotor blade composites, *PhD Thesis*, TUDelft, Fac. of Aero., Netherlands, 2006

[2] Hansen, J. Z.: The effects of fibre architecture on fatigue life-time of composite materials, PhD Thesis, DTU, Dept. of Wind Energy, Denmark, 2013

[3] Jespersen, K. M. et. al: Fatigue damage assessment of glass/polyester composite using x-ray computed tomography, J. Comp Sci Tech, 2016 (In preparation)

[4] Zangenberg, J. et. al: Fatigue damage propagation in unidirectional glass fibre reinforced composites made of a non-crimp fabric, *J. Comp. Mat.*, 48(2):2711-2727, 2014

MICROMECHANICAL MODELING OF DAMAGE AND FRACTURE IN MAGNESIUM ALLOYS

Babak Kondori *[1] and A. Amine Benzerga[1,2]
[1]*Department of Materials Science & Engineering, Texas A&M University, College Station, TX*
[2]*Department of Aerospace Engineering, Texas A&M University, College Station, TX*

Summary Processes of damage and fracture in magnesium alloys are modeled using a micromechanics-based framework. The formulation has two main components (i) a void growth model; and (ii) a criterion for the onset of void/crack coalescence. Application to two magnesium alloys shows that their fracture loci are well predicted using only one fitting parameter. The analysis suggests that the ductile fracture of magnesium alloys involves limited void opening/blunting and is controlled by void coalescence. The results provide the groundwork for understanding the effects of microstructural and loading variables on damage and fracture in these materials.

BACKGROUND

Fundamental understanding of the processes of damage and fracture in Mg alloys over a wide range of stress states is still lacking. Recent notched bar experiments revealed that unlike most materials, magnesium (Mg) AZ31 notched bars with pronounced rolling texture exhibit higher ductility than their uniaxial bars, an unconventional dependence to stress triaxiality. Also, the damage initiation mechanism in this alloy changed from deformation twin related cracks to void nucleation at second phase particles upon going from uniaxial to triaxial loadings [1]. On the contrary, the ductility of isotropic WE43 Mg alloy dropped significantly as the acuity of the notch increased (higher triaxiality) [2]. This is while both alloys have comparable strain to failure under uniaxial loading. Identification of the mechanisms controlling the ductility in Mg alloys across a wide range of stress states is key to understanding their overall mechanical behavior. Here, a micromechanics-based continuum damage model is used to rationalize the main experimental trends in [1, 2] and correlate the macroscopic behavior with microscopic variables.

GENERAL FRAMEWORK

The formulation, which is in the spirit of the local approach [3] and top-down approaches [4] to fracture, relies on three-dimensional finite strain constitutive relations in which anisotropic plasticity is coupled with anisotropic damage. The matrix is assumed to contain pre-existing voids. This is a reasonable assumption considering the fact that brittle second phase particles in Mg are susceptible to breaking after limited plastic strain. To account for relevant ductile fracture mechanisms, the model evaluates criteria for growth and coalescence of voids inside an anisotropic matrix. Void growth is described using a Gurson-like model that accounts for both void shape and anisotropy of the matrix [5]. Evolution laws of internal parameters (porosity, void shape and orientation) represent the microstructural evolution relevant to fracture. The rate of change of void shape is heuristically modified using a multiplicative factor k, which is used as a fitting parameter. Void coalescence is described using recently developed criteria for plastically isotropic materials [6, 7]. The implementation used here uses a co-rotational formulation with a hypoelastic law, power-law strain hardening and a Hill-type plastic anisotropy. Obviously, such representation is not ideal for Mg but is shown to be adequate for the purposes of modeling damage accumulation to fracture.

A triaxiality range close to that accessible via notched bar experiments is explored here ($0.3 < T < 1.5$). In each calculation, the stress triaxiality is kept constant. At each loading step, both yield criteria for void growth and coalescence are evaluated and an increment of plastic strain is calculated utilizing the normality rule for one material point. Using the evolution laws, the change in microstructural variables, corresponding to the plastic strain increment, is determined. The loading continues up to the point where the yield function for coalescence is equal to that of void growth. This point, which corresponds to the onset of micro-scale localization, is identified as the failure criterion. An equivalent measure ε_f of the accumulated strain at the onset of coalescence is identified as the strain to fracture.

RESULTS

The proposed framework for void growth and coalescence, supplied with a characterization of plastic anisotropy and proper material parameters (initial values of the internal variables, extracted from metallography and image analysis) is employed to predict the fracture loci of AZ31 and WE43. Figure 1 compares the experimentally measured fracture loci with their corresponding predictions. When a single fitting parameter $k = 0.43$ is used to modify the evolution of void shape, a close

*Corresponding author. Email: bkondori.13034@tamu.edu

match with the experimental results of the two alloys is achieved. There can be a scatter in the predictions if alternative assumptions are made or different material parameters are chosen. Our sensitivity analysis shows that experimental results reside in this scatter range. The mismatch between predictions and experimental results is more significant in the case of AZ31. It should be noted that these predictions are not solutions for a boundary value problem (BVP) and therefore do not account for spatial variations in the mechanical and internal variables.

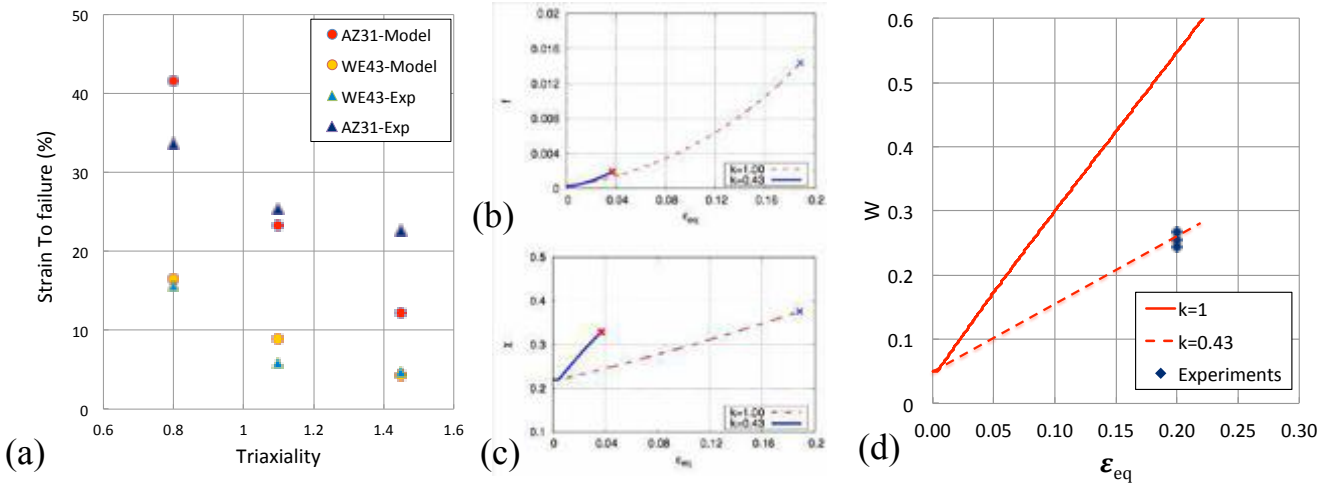

Figure 1: (a) Comparison between the experimentally measured fracture loci of AZ31 and WE43 against model predictions. (b) The heuristic parameter, $k = 0.43$, does not affect the evolution of porosity, f whereas it significantly changed the ligament ratio, χ as presented in (c). The predicted void aspect ratio matches perfectly with the experimentally acquired ones using traditional metallography and high resolution tomography (shown by blue diamonds).

The parameter k controls the rate at which voids open up during loading. The value of $k = 0.43$ indicates that fracture in both Mg alloys is controlled by limited void opening. In case of WE43, the limited void opening along with the spatial arrangement of second phase particles lead to early coalescence of voids at high triaxialities. Figure 1b and c illustrate that while introduction of the heuristic parameter k does not affected the evolution of porosity, it significantly alters the ligament ratio. This influence of limited void opening over the evolution of ligament ratio controls the fracture loci of Mg alloys in this study. Finally, the void shape data from metallography of the interrupted specimens and high resolution micro-tomography of deformed AZ31 specimens showed that the predicted void shapes match the experimental ones with good accuracy, see Figure 1d.

CONCLUSION

A micromechanics-based framework was used to model damage and fracture in Mg alloys and predict their fracture loci. Using only one fitting parameter, k, and pertinent materials properties, the fracture loci of two alloys were predicted with good accuracy. It was concluded that limited void growth and early coalescence of voids control the fracture loci of Mg alloys.

References

[1] B. Kondori, A. A. Benzerga, Effect of stress triaxiality on the flow and fracture of Mg alloy AZ31, Metallurgical and Materials Transactions A. 45 (2014) 3292–3307.

[2] B. Kondori, A. A. Benzerga, On the notch ductility of a magnesium-rare earth alloy, Materials Science and Engineering: A. 647 (2015) 74–83.

[3] A. Pineau, A. A. Benzerga, T. Pardoen, Failure of metals I. Brittle and Ductile Fracture, Acta Materialia (2016) In press. doi:10.1016/j.actamat.2015.12.034

[4] J. W. Hutchinson, A. G. Evans, Mechanics of materials: Top-down approaches to fracture, Acta Materialia 48 (2000) 125–135.

[5] S. M. Keralavarma, A. A. Benzerga, A constitutive model for plastically anisotropic solids with non-spherical voids, Journal of the Mechanics and Physics of Solids 58 (2010) 874–901.

[6] A. Benzerga, J.-B. Leblond, Effective yield criterion accounting for microvoid coalescence, Journal of Applied Mechanics 81 (2014) 031009.

[7] M. E. Torki, A. A. Benzerga, J.-B. Leblond, On void coalescence under combined tension and shear, Journal of Applied Mechanics 82 (2015) 071005.

TEMPLATE FOR ICTAM2016 SHORT PAPER (MAXIMUM 2 PAGES)

Andrzej Kurek[1a], Tadeusz łagoda[1]
[1]*Opole University of Technology, Poland*

Summary The paper presents a comparison of the fatigue life curves based on test of 15Mo3 steel under cyclic, pendulum bending and tension-compression. These studies were analysed in terms of a large and small number of cycles where strain amplitude is dependent on the fatigue life. It has been shown that commonly used Manson-Coffin-Basquin model cannot be used for tests under cyclic bending due to the impossibility of separating elastic and plastic strains. For this purpose, some well-known models of Langer and Kandil and one new model of authors, where strain amplitude is dependent on the number of cycles, were proposed. Comparing the results of bending with tension-compression it was shown that for smaller strain amplitudes the fatigue life for both test methods were similar, for higher strain amplitudes fatigue life for bending tests was greater than for tension-compression.

INTRODUCTION

Most often fatigue tests for a range of low number of cycles (Low Cycle Fatigue) are performed at a controlled strain and the high range of cycles (High Cycle Fatigue) tests are characterized by a study in strength-controlled environment. Such tests are carried out for tension-compression and torsion of thin specimens. However, in the case of bending or torsion of full specimens, as is the case of many experimental studies, the torque causing bending or torsion is controlled and therefore the tests are conducted in terms of large number of cycles In the literature to describe the fatigue test results for tension-compression both stress and strain models are used. However there is a significant amount of fatigue tests for bending, often pendulum rather than rotary. It turns out that for bending, due to the stress (strain) gradient, those two types of models are not equal. There aren't many studies comparing stress and strain fatigue curves (models). For stress curves some comparison might be found in [2, 9, 11]. While in [10] authors prove that changes in bending plane has an effect on fatigue strength relative to the constant surface bending (pendulum bending). Results from these comparisons show that on the level of fatigue limit the loading method does not affect fatigue life. However for higher stress levels fatigue strength obtained from bending tests is higher than corresponding push-pull results. There is no comparison of this kind for strain curves.
Therefore, the present study compares the fatigue life curves of 15Mo3 steel obtained from new test stand capable of conducting pendulum bending with controlled strain amplitude with push-pull results. The results for push-pull tests were taken from the literature [1].

STRAIN-LIFE CURVES

The most well-known equation allowing to describe fatigue properties from strain-controlled tests is proposed by Manson-Coffin-Basquin (MCB) for the strain-life curve (ε_a-N_f):

$$\varepsilon_{at} = \varepsilon_{ap} + \varepsilon_{ae} = \varepsilon' f \left(2N_f\right)^c + \frac{\sigma' f}{E}\left(2N_f\right)^b, \tag{1}$$

where: E - Young's modulus, ε'_f, c - coefficient and exponent of the plastic strain, respectively, σ'_f, b - coefficient and exponent of the fatigue strength, respectively.
This model (1) can only be used when it is possible to distinguish elastic ε_{ae} and plastic ε_{ap} parts of the strain amplitude ε_{at}.

Different authors have proposed different empiric models subordinating total strain amplitude on the number of cycles.
Langer's (1962) [5] proposal can be one of the examples. It is commonly used in many studies and is prompted by Manson (1965, 1979) [6, 7]and Chopra (1999) [8].

$$log N_f = A - B\, log(\varepsilon_{at} - C), \tag{2}$$

where: *A, B, C* - material constants.

Another model was proposed by Kandil (2000) [3] and Gorash and Chen (2013) [4]:

$$log\varepsilon_{at} = A - B\, log\left(N_f\right) + C\, log^2(N_f), \tag{3}$$

where: *A, B, C* - material constants.
As in the case of cyclic bending tests where there is no possibility to distinguish elastic and plastic parts of total strain amplitude the MCB model (1) cannot be used. However both (2) and (3) or any other empirical form of strain-life model can be used. It can be for example combination of (2) and (3) (Authors model):

$$log(\varepsilon_{at} - D) = A - B\, log\left(N_f\right) + C\, log^2(N_f), \tag{4}$$

where: *A, B, C, D* - material constants.

[a)] Corresponding author. Email: **a.kurek@po.opole.pl**

COMPARISON OF FATIGUE LIFE CURVES

Authors developed new test stand for fatigue tests under bending and capable of experimental studies with controlled strain in the range of a small number of cycles (LCF). Operation of the machine was verified on the basis of experimental tests on specimens made of steel commonly used in the power industry - 15Mo3 (16Mo3, 1.5415) [1]. Finally the strain controlled experimental data for tension-compression and pendulum bending was compared.
The idea behind this machine is that using the screw on the eccentric we can set the deflection of machine arm acting on the specimen, that deflection is set as constant and controlled by the micrometer. This way we obtain a constant strain amplitude on specimen
Additionally, during the test, bending torque is monitored. At the time, when this torque drops significantly, the initiation of fatigue crack occurs but further tests allow us to obtain total fatigue life of the tested specimen.

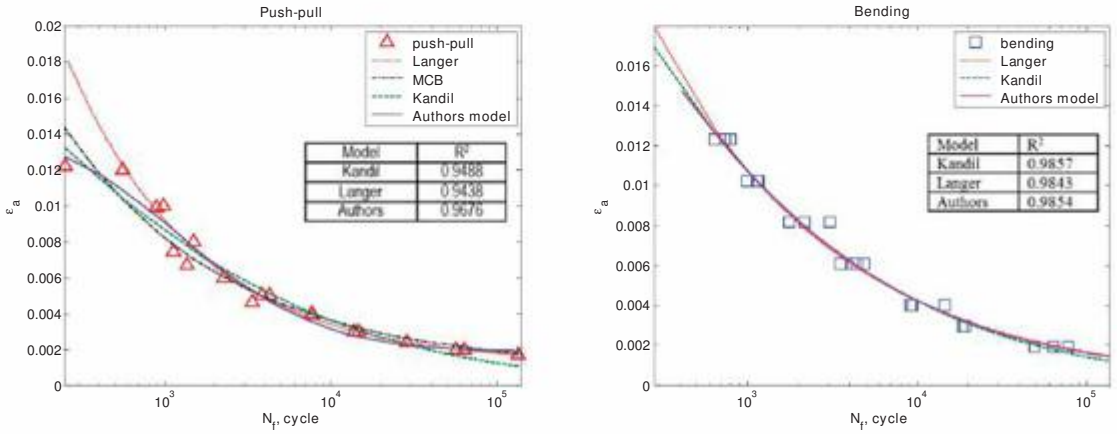

Fig. 1. Strain-life curves for push-pull and bending tests
The study determined the fatigue life both to the initiation point and total fatigue life. At the fatigue crack initiation point there is a sharp drop of the bending moment acting on specimen which correlate with the appearance of visible cracks on a specimen of a size of less than 1 mm.

CONCLUSIONS

1. The newly designed and built test stand is capable of experimental studies with controlled strain for bending in the range of a small number of cycles (LCF).
2. Preliminary experimental studies of pendulum bending, with controlled strain amplitude, have shown that fatigue life for bending is close to tension-compression tests for small loading and lager for high strain.
3. Further verification of the correlation between the bending fatigue curves for other materials is necessary.
4. In the future strain-controlled test for pure torsion and combination of bending and torsion should be performed.

References

[1] Boller C., Seeger T.: Materials Data for Cyclic Loading, *Materials Science*, Monographs, 42, Elsevier Publisher, 1987
[2] Manson S.S., Muralidharan U.: Fatigue life prediction in bending from axial fatigue information, *Fatigue & Fracture Engineering Materials & Structures*, Vol. 9, No. 5, 357-372, 1987
[3] Kandil F.A.: The Determination of Uncertainties in Low Cycle Fatigue Testing, Standards Measurement & Testing Project No. SMT4-CT97-2165, Issue 1, 1-26, 2000
[4] Gorash Y., Chen H.: On creep-fatigue endurance of TIG-dressed weldments using the linear matching method, *Enineering Failure Analysis*, Vol.34, 308-323, 2013
[5] Langer B.F.: *Design of Pressure Vessels for Low-Cycle Fatigue*, ASME Journal of Basic Engineering, Vol. 84, 389-402, 1962
[6] Manson S.S: Inversion of the strain-life and strain-stress relationships for use in metal fatigue analysis, *Fatigue of Engineering Matarials and Structures*, Vol. 1, 37-57, 1979
[7] Manson S.S.: Fatigue: A complex subject-some simple approximations, *Experimental Mechanics*, Vol. 5(4), 193-226, 1965
[8] Chopra O.K.: *Effects of LWR coolant environments of fatigue design curves of austenitic stainless steels*, U.S. Nuclear Regulatory Commission, NUREG/CR-5704, ANL-98/31, 1998
[9] Troschenko V.: High-cycle fatigue and Inelasticity of Metals, Multiaxial and Fatigue Design, ESIS 21, (Edited by A. Pinueau, G. Cailletaud and T. C .Lindley), *Mechanical Engineering Publications*, London, 335-348, 1996
[10] Krzyżak D., Kurek M., Łagoda T. Sówka D: Influence of changes of the bending plane position on the fatigue life, *Materialwissenschaft und Werkstofftechnik*, Vol. 45, No. 11, 1018-1029, 2014
[11] Megahed M.M.: Prediction of bending fatigue behaviour by the reference stress approach, *Fatigue & Fracture of Engineering Materials & Structures*, Vol. 13, No. 4, 361-374, 1990

MICROSCOPIC CORROSION ELECTRIC FIELD ANALYSIS WITH DAMAGED PASSIVE FILM OF STAINLESS STEEL

Osamu Kuwazuru[1a)], Makoto Yamada[1], Kazuhiro Ode[1] & Wenli Liu[1]
[1]*Department of Nuclear Power & Energy Safety Engineering, University of Fukui, Fukui, Japan*

Summary The electrochemical property of stainless steel subjected to a stress in a corrosive environment is addressed through the experimental and numerical investigations. The polarization curves of stainless steel under some constant tensile stresses were measured by the potentio-galvanostat. To clarify the effect of stress on the polarization curve, the electric field around the damaged passive film was simulated by the boundary element method. The passive film is broken by the plastic strain and defect surface appears. However its electrochemical property was unknown in general, so approximately replaced by the property of carbon steel. The defect area fraction can be associated with the plastic strain. From such viewpoint, the defect area fraction was fixed at some levels, and the macroscopic polarization curve was estimated by the microscopic electrostatic analysis. The numerical results were compared with the experimental results, and the effect of plastic strain was examined.

INTRODUCTION

The stress-affected corrosion is a theoretically unresolved problem. The mechanism of stress corrosion cracking has been elucidated by experimental approaches [1], however its quantitative evaluation such as corrosion rate or cracking life is still impossible due to the lack of mathematical models for corrosion. In this study, we tried to make a numerical method to evaluate the microscopic electric field around the damaged passive film of stainless steel in a sodium chloride solution. This simulation reveals the current density distribution on the material surface which leads to the dissolution rate of metallic ions into the solution. Focused here is the effect of broken passive film on the macroscopic polarization curve. The damaged passive film by external stress is represented by the intact part and defect part. The defect part is considered to be newly generated by the local plastic strain and exposed without the passive film. These two types of surface lead to the local galvanic corrosion. The boundary element method (BEM) is used for the electrostatic simulation since it is advantageous to the rearrangement of mesh following to the metal dissolution corresponding to the current density [2]. The relationship between the area fraction of defect surface and the macroscopic polarization curve is examined by the BEM electrostatic simulation, and the result is compared to the experimental results. From this comparison, we discuss the validity of damaged passive film model of stainless steel.

EXPERIMENTAL AND NUMERICAL METHODS

Materials and environment

The material used is 304 austenitic stainless steel. The damaged passive film model consists of intact part and defect part. The electrochemical property of the intact passive film was obtained from the experiment of the stainless steel without stress. On the other hand, it is difficult to measure the electrochemical property of the defect part, so we use the property of a JIS S50C carbon steel. The NaCl solution of 0.1 mass% is employed as the corrosive environment.

Measurement of polarization curve

We have developed a mechanical and electrochemical measurement system consisting of the hydraulic fatigue test machine with the corrosion chamber. For electrochemical measurement, the counter and reference electrodes are inserted to the chamber. The working electrode is the tensile specimen, which is coated by a nail polish except for the corrosion window of 3×3 mm^2 located on the center of specimen. Polarization curves were measured for both the stainless and carbon steels in unstressed state. For the electrostatic simulation, the obtained polarization curves were approximated by the empirical formula as follows,

$$p = p_0 + Rq + \frac{D}{1+\exp\left[-(q-q_0)/B\right]} \tag{1}$$

where p_0, R, D, and B are the fitting parameters which is determined by the least squares method. Next, the polarization curves in stressed state were measured for the stainless steel at several levels of constant tensile stress.

Corrosion electric field analysis

The analysis domain Ω is illustrated in Fig. 1, where Γ_p is the constant potential boundary, Γ_q is the constant current density boundary, and Γ_A and Γ_C are the anodic and cathodic boundaries corresponding to the defect surface and intact passive film, respectively. In the after-mentioned simulations, the repetitive arrangement of intact and defect surfaces are assumed. The galvanic corrosion is a simple potential problem described by the Laplace equation:

[a)] Corresponding author. Email: kuwa@u-fukui.ac.jp.

$$\nabla^2 p = 0 \tag{2}$$

where p is the electric potential. By using the Green's second identity and a fundamental solution, the boundary integral equation can be obtained and subsequently discretized by the boundary elements as follows,

$$\mathbf{HP} \quad \mathbf{GQ} \tag{3}$$

where **P** and **Q** are the nodal potential and nodal current density vectors, and **H** and **G** are the coefficient matrices, respectively. The **P** includes the polarization curves. The discontinuous linear element is used to represent the discontinuity of potential and current density at the switching point between intact and defect surfaces. After imposing the boundary conditions to Eq.(3), it can be solved by the Newton-Raphson iterative procedure, since the metallic surfaces give the nonlinear relationship between potential and current density [3]. The polarization curves and its regression curves are shown in Fig. 2. The experimental curves (solid curves) are highly nonlinear, therefore the regression curves are slightly different from the actual responses.

To examine the effect of plastic strain, the area ratio of defect surface to the intact surface is changed systematically. The enforced current $\overline{q}$ is applied on Γ_q boundary which is sufficiently far from the metal surface, then the averaged potential $\overline{p}$ on the overall metal surfaces is calculated and regarded as the macroscopic potential of the material. By changing $\overline{q}$, the relationship between $\overline{p}$ and $\overline{q}$ is obtained as the macroscopic polarization curve. This numerically evaluated polarization curve is obtained for some levels of defect area fraction. This results show the effect of defect fraction ratio on the macroscopic polarization curve and compared to the experimental results.

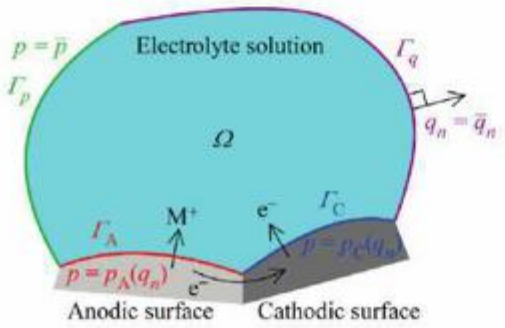

Fig. 1 Galvanic corrosion electric field problem

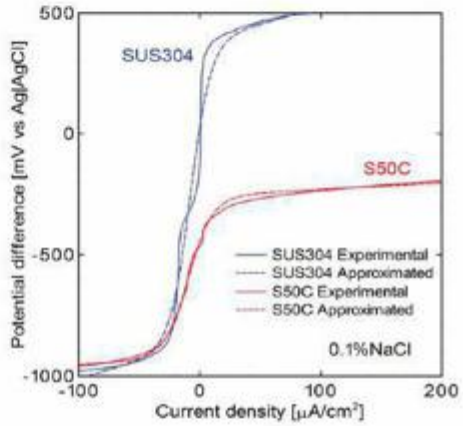

Fig. 2 Polarization curves of steels

RESULTS

The experimental results showed that the spontaneous potential slightly decreased as the applied stress increased until the proof stress. Exceeding the proof stress, the spontaneous potential became constant. This trend is consistent with the experimental result of corrosion tensile test [4]. Three defect area fractions of 0.0, 0.5 and 1.0 % are simulated, and its effect on the numerically evaluated macroscopic polarization curve is discussed. The comparison between the effect of stress in the experiments and the effect of defect area fraction in the simulations will clarify the validity of our proposed damaged passive film model.

CONCLUSIONS

From the comparison between the mechanical-electrochemical tests and BEM electrostatic simulations, validity of the damaged passive film model of stainless steel is examined, and the availability of BEM simulation will be demonstrated.

References

[1] Gorman J. A.: Stress Corrosion Cracking and Nuclear Power. *Corrosion* **74**: 1414-1433, 2015.

[2] Butler B. M., Kassab A. J., Chopra M. B., Chaitanya V.: Boundary Element Modeling of Electrochemical Dissolution with Geometric Non-linearities. *Eng. Analysis with Bound. Elem.* **34**: 714-720, 2010.

[3] Aoki S., Kishimoto K.: Prediction of Galvanic Corrosion Rates by the Boundary Element Method. *Math. Comput. Model.* 15: 11-22, 1991.

[4] Orlikowski J., Darowicki, K.: Electrochemical Investigations of Al-Mg Alloy Subjected to Tensile Test. *J. Solid State Electrochem.* 13: 1659-1667, 2009.

A RATE-DEPENDENT DAMAGE MODEL FOR ELASTOMERS AT LARGE STRAIN

Shawn R. Lavoie[1], Rong Long[2] & Tian Tang [1a)]
[1]*Department of Mechanical Engineering, University of Alberta, Edmonton, AB, Canada T6G 2G8*
[2]*Department of Mechanical Engineering, University of Colorado Boulder, Boulder, CO, USA 80309*

Summary The fracture toughness of elastomers is known to depend on the rate of crack propagation. It has been proposed that rate dependent chain scission, where bonds on the polymer chains are ruptured under mechanical stress, is a contributing factor to this rate dependence. To model this process we introduce chain scission, predicted using concepts of mechanochemistry, into a hyperelastic constitutive model (Arruda-Boyce as an example). The result is a model capable of handling large strain and rate dependent damage. Additionally, polydispersity is incorporated by considering a distribution of chain lengths, which gives the model the capability to predict progressive material damage. To demonstrate the application of the model, uniaxial tensile deformation with constant extension rates is examined. The tensile stress is found to first reach a peak and then decrease due to scission, and faster rates of deformation result in larger peak stress. The model has also been implemented in a finite element subroutine to demonstrate its application to crack initiation.

INTRODUCTION

Elastomers exhibit rate dependent fracture behavior which is not yet fully understood [1]. The kinetics of "scission," rupture of polymer chains, contributes to this rate dependency. Previously, this process has been modelled by using "Mechanochemistry" to predict the rate of rupture of covalent bonds under tensile stress, on chains in a cohesive zone [2]. However, recent experiments have mapped bond rupture events using light emitting photophores [3] and have shown that the scission is not localized to fracture plane, as is assumed in cohesive zone modelling. To capture such behavior it is necessary to model damage due to scission in the material model.

Numerous models exist in the literature to describe damage of elastomers. A classical family of these models consider the Mullin's effect, see for example Ogden and Roxburgh [4]; these models are rate independent since their damage functions depend only on the maximum deformation previously experienced by the material. Another family of models treats damage as a rate dependent process where the volume fraction of undamaged material evolves temporally instead of being determined by deformation; the application of these models to describe elastomers undergoing scission has been reviewed by Wineman [5]. In all these damage theories, the actual stress sustained by the damaged elastomer network is calculated by multiplying the volume fraction of undamaged material by the stress in the undamaged virgin network under the same deformation as the damaged network. However, these damage functions must be determined empirically. We propose that these damage functions can be determined by using mechanochemistry to predict the rate of scission in the material. This scission model can be readily incorporated into hyperelastic models that are based on a polymer chain force-extension relationship and volumetric density of chains. We demonstrate the procedure using the Arruda-Boyce model [6].

Also important is the effect of non-uniform polymer chain lengths within the material. The single characteristic chain length in the Arruda-Boyce model [6], is approximate and does not completely reflect the nature of real polymers where there should exist a distribution of chain lengths (polydispersity). For small deformations without damage a characteristic chain length is often adequate to characterize the mechanical response of the material. Mechanochemistry predicts accelerated rupture of bonds when they are activated by large tension forces, and if all chains were the same length this would result in catastrophic rates of scission within a small range of chain extension. This is inconsistent with experimental observations [3] that scission occurs over a larger range of deformations. Introducing a distribution of chain lengths allows for the model to accommodate this observation since chains of different lengths will experience different tensile forces for the same macroscopic deformation.

METHODOLOGY

Reinterpreting the mechanochemistry based models for scission of chains in a polymeric interface [2] for volumetric scission the following rate equation can be written:

$$-\frac{dN}{dt} = \frac{n_m N}{\tau_-} e^{L_a F / k_B T}, \qquad (1)$$

where N is the number of surviving load-bearing chains per unit volume, τ_- and L_a are fixed parameters respectively representing the relaxation time and activation length for bond dissociation, F is the tensile force on a polymer chain, k_B is the Boltzmann constant and T is the absolute temperature. The number of monomers per chain, n_m, appears here since rupture of a single bond on the chain's backbone is sufficient to break the chain.

Numerous models exist which relate the tensile force of a polymer chain F, to its fractional extension r/L_c where r is the end to end distance of a chain and L_c is the contour (fully extended) length of the chain. To demonstrate how to introduce scission we consider the Arruda-Boyce constitutive model which is based on Langevin chain statistics [6]; the tensile force on a polymer chain is given by $F = k_B T\beta/A$, where A is the Kuhn length the polymer chains. β is the inverse Langevin function defined so that $r/L_c = \coth\beta - \beta^{-1}$, $L_c = nA$ is the contour length of the polymer chains, n is the number of Kuhn segments per polymer chain. The force (F) - fractional extension (r/L_c) relationship is highly nonlinear because the stiffness

[a)] Corresponding author. Email: tian.tang@ualberta.ca.

of the chain dramatically increases as the fractional extension approaches unity. Integrating F with respect to extension gives the stored energy in a single chain and multiplying by N, the number of load bearing polymer chains per unit volume, gives the strain energy density [6]

$$U\left(\frac{r}{L_c}\right) = Nk_BT\left[n\left(\frac{r}{L_c}\beta + \ln\left(\frac{\beta}{\sinh\beta}\right)\right) - c\right], \quad (2)$$

where c is a constant to ensure that the strain energy is zero at undeformed state. Assuming an affine network implies that the deformation of a chain is the same as the macroscopic deformation of the material which gives $r/L_c = \sqrt{I_1/3n}$ [6], where I_1 is the first invariant of the left Cauchy-Green deformation tensor.

To implement this model the decrease in chain density is calculated using Eq. (1) which decreases the strain energy (Eq. (2)) and results in a loss in both stress and stiffness compared with an undamaged material. In addition polydispersity is considered by allowing the strain energy to be determined as the sum of strain energies from a distribution of chains of different lengths.

RESULTS

Uniaxial Extension

Eqs. (1) and (2) are used to evaluate the stress for uniaxial extension under a variety of different stretching rates (R). The stress is plotted against the stretch (λ) in Figure 1a). In each case the stress increases, reaches a peak and decreases due the accumulation of damage. Faster rates of extension result in larger peak stresses; since scission is a rate process on average faster deformation results in chains achieving larger extensions before rupture. The distribution of chain lengths results in the gradual decline in stress in Figure 1a).

Crack Initiation

The model presented was implemented in an Abaqus user material subroutine. This user subroutine has been applied to study crack initiation for a hyperelastic region with a circular hole. The calculated dissipation is shown in Figure 1b). Here the concentration of deformation at the edge of the hole results in increased scission and hence dissipation. The dissipation in Figure 1b) occurs in a finite sized region in stark contrast to the idealization of a cohesive zone model.

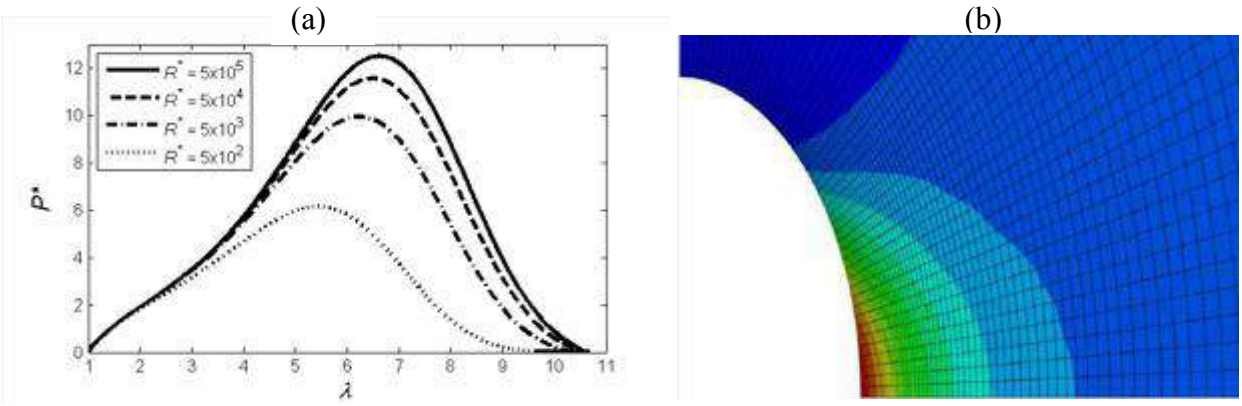

Figure 1. a) Nominal stress, $P^* = P/N(0)k_BT$, obtained by varying the stretch λ while holding γ_L = 1/3. A Maxwell-Boltzmann distribution with n_{avg} = 17.42 specified the initial chain length distribution. Each curve represents a different stretching rate ($R^* = R\tau_-$). b) Preliminary FEA results showing calculated dissipation for crack initiation at a circular hole.

References

(1) Gent, A.N. Adhesion and Strength of Viscoelastic Solids. Is there a Relationship between Adhesion and Bulk Properties? *Langmuir*, 1996, 12, pp 4492–4496

(2) Ghatak, A.; Vorvolakos, K.; She, H.; Malotky, D.L.; Chaudhury, M.K. Interfacial Rate Processes in Adhesion and Friction. *J. Phys. Chem. B.*, 2000, 104, pp 4018–4030

(3) Ducrot, E., Chen, Y., Butlers, M., Sijbesma, R.P., Creton, C. Toughening Elastomers with Sacrificial Bonds and Watching them Break. *Science* **2014**, 344, 186-189

(4) Ogden, R.W., Roxburgh, D.G, A pseudo-elastic model for the Mullins effect in filled rubber. *Proc. R. Soc. Lond. A* **1999**, 455, 2861-2877

(5) Wineman, A. On the Mechanics of Elastomers Undergoing Scission and Cross-linking *Int. J. Adv. Eng. Sci. Appl. Math.* **2009**, *1*, 123–131

(6) Arruda, E.M, Boyce, M.C. A Three-Dimensional Constitutive Model For The Large Stretch Behavior of Rubber Elastic Materials. *J. Mech. Phys. Solids.*, **1993**, *41*(2), 389-412

EFFECT OF MG IMPURITIES ON **SAPPHIRE'S** *STRENGTH: A MULTISCALE SIMULATION APPROACH*

Seyed Mohammad Mahdi Zamani[1], Kamran Behdinan[1a)]
[1]Advanced Research Laboratory for Multifunctional Light Weight Structures, Department of Mechanical and Industrial Engineering, University of Toronto, Toronto, Ontario, Canada

Summary This paper presents a study on the effect of Mg impurities on the mechanical properties of sapphire using a multi-scale simulation approach called bridging cell method (BCM). BCM performs a finite element framework throughout the system where it decomposes the problem into atomistic, bridging and continuum domains to develop macro scale models capable of accounting for nanoscale defects within the atomistic domain. The most resistant crystal plane of sapphire, C-plane, is selected for this study, and the stress distribution and the variations of ultimate tensile strength (UTS) of the material is investigated in presence of biaxial loads at two finite temperatures of 300K and 1600K. Results showed symmetric stress distribution for the selected orientations, and the magnitude of stresses increased as the temperature elevated. However, C-plane retained most of its initial UTS at high temperatures and in presence of Mg impurities.

INTRODUCTION

Alumina is one of the most common ceramic materials used at high temperatures and aerospace applications, due to its excellent mechanical and thermal properties including high elasticity, melting point and strength [1], [2]. The single crystal of alumina called sapphire, has even better structural properties with higher elasticity- about 500GPa at most - and tensile strength – about 1025 MPa at most -, made it more appropriate for high temperature applications in the recent years [3]. However, structural defects such as voids, cracks and impurities which are mainly of Mg type for alumina, can significantly affect alumina's functionality [1]. Thus, investigating the mechanical and thermal response of alumina and sapphire in presence of defects has been interesting for researchers, either experimentally or through simulation techniques [3]–[5]. In this essence, most simulation studies on alumina have incorporated purely atomistic models where minimal time scales and small size of the model are the common limitations. In contrast, multi-scale modelling approaches which divide the whole system to three domains of atomistic, transition and continuum domains can address the scale limits and sometimes the time limit. This study applies the BCM multiscale technique to investigate the effect of Mg impurities in the crystalline structure of C-plane sapphire on stress distribution and material strength at two finite temperatures. Section 2 provides the methodology, formulation of BCM, and the model description; and Section 3 presents the simulation results followed by a discussion of the material's mechanical response.

METHODOLOGY

BCM, performs a finite element (FE) framework throughout the three atomistic, bridging and continuum domains of the model, and relies on energy minimization and temperature-dependant calculations which make it independent of small time steps and suitable for simulations at finite temperatures. The displacements of the atoms are mapped into the displacements of the nodes in the bridging domain so that the two atomistic and continuum domains are coupled seamlessly. Temperature-dependent calculations are implemented in this method based on quasi static free energy minimization by considering temperature as the atomistic vibrations about the primary structure; and an iterative approach is used to minimize the free energy of the system [6], [7].

Formulation

The BCM technique divides the domain into three domains of continuum, Ω^C, bridging, Ω^B, and atomistic, Ω^A; where energy of the different domains are calculated through equations (1) to (5) as follows:

$$E_A = U_{tot} = \sum_{i<j}^{n_a} U(r_{ij}) \quad (1)$$

$$U(r_{ij}) = \frac{q_i q_j}{r_{ij}} + A\exp[B(\alpha - r_{ij})] - \frac{C}{r_{ij}^6} \quad (2)$$

where E_A is the atomistic domain total energy, n_a is the number of atoms in the atomistic domain and $U(r_{ij})$ is the interatomic potential between atom i and j at a distance of r_{ij} from each other; q_i and q_j are atom charges and α is the repulsive radii, B is the softness parameter, and A and C are coefficients [8].

$$E_C = \sum_{e=1}^{n_t}\left(\int_{\Omega^C}\psi(F_e)dV_e - \int_{\partial\Omega^C} t_e . u_C dA_e\right) \quad (3)$$

where E_C is the continuum domain total energy, n_t is the total number of elements, ψ is the strain energy and F_e, V_e, A_e and t_e are deformation gradient, volume, area and traction of element e, respectively. And

$$E_B = \sum_{c=1}^{n_c}[w_c.\psi(F_c).V_c + \sum_{i\in\Omega^B}^{n_a}\sum_{j\in\Omega^B\cap\Omega^A} U(r_{ij})]; \quad (4)$$

$$w_c = 1 - \frac{\sum_i R_{ij}U(r_{ij})}{W(F_c).V_c} \quad (5)$$

a) Corresponding author. Email: behdinan@mie.utoronto.ca

where E_B is the bridging domain total energy; n_c is the number of cells in the bridging domain, R_{ij} is the ratio of the distance between atom i and j within the cell, and w_c is a weighting function. Having all the energy contributions calculated, the stiffness matrix of each domain is achieved by getting the second derivative of the energy with respect to displacements, and the general finite element framework is implemented to find the forces as a product of the stiffness and displacement.

BCM Model Description

The effect of the Mg impurities was investigated for C-plane or <0001>, containing 124904 atoms, by substituting 5ppm Mg atoms with Al atoms. The dimension of the model was 200x80x200Å. Z direction represents [0-110] orientation, and X direction represents [-2110] orientation. Biaxial tensile load was exerted in the X and Z directions at 300K and 1400K and results in terms of stress distribution and tensile strength were used to investigate the effect of the Mg impurities.

RESULTS

Figure 1 shows the stress distribution and resulted stress-strain plot of the C-plane sapphire in presence of Mg impurities in the structure, at 300K and 1600K. As shown in Figure 1a and 1b, the atomistic domain is under stresses higher than 15GPa at 300K, where the graphs of the stress distribution in the Z direction (SZ) or [0-110] orientation, and X direction (SX) or [-2110] orientation are symmetric. These stresses are considerably increased throughout the domain at 1600K as shown in Figure 1c and 1d, especially around the Mg impurities; which is in agreement with Schmid [2] and Zhang [3]'s experimental results.

Figure 1e shows the stress-strain plots at 300K and 1600K. The UTS of the C-plane in presence of Mg impurities at 300K is 23GPa, occurring at relatively high strains of 6.25%; and as the temperature rises to 1600K, the failure strain decreases to 6% and the strength drops to 20GPa. In addition, the initial calculated UTS of the defect-free C-plane of this model is about 28GPa. Thus, while the UTS of C-plane decreases as the temperature elevates, it is only dropped 18% compared to the defect-free UTS of C-plane sapphire showing that C-plane is so resistant to the structural defects and does not easily lose its strength even at high temperatures; which is consistent with previous works in literature [2], [3].

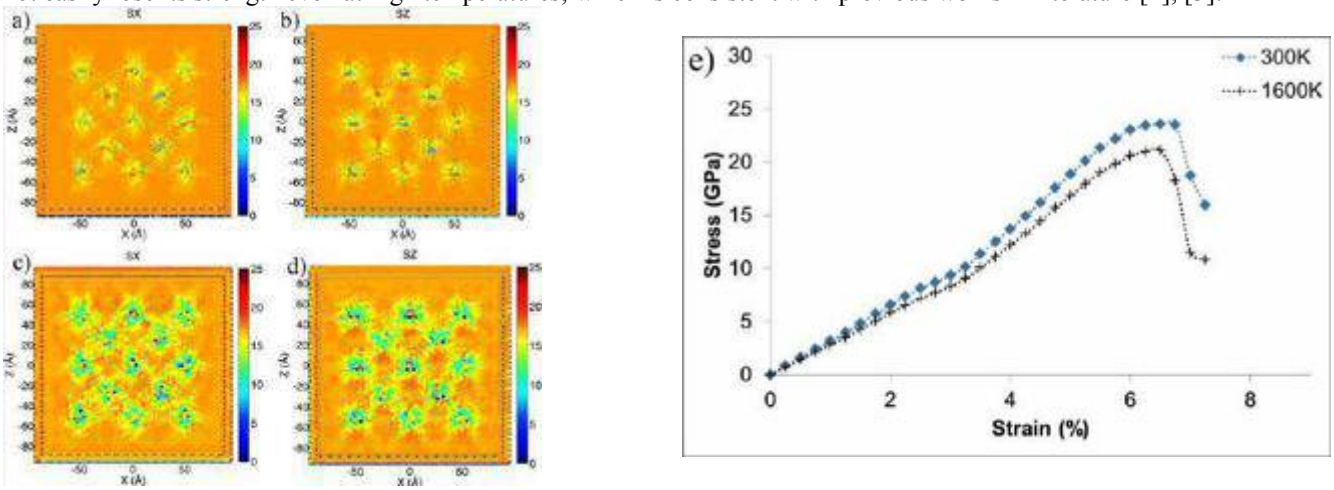

Figure 1. Stress distribution for C-plane with Mg impurities – a) in X direction or [-2110] orientation at 300K, b) in Z direction or [0-110] orientation at 300K, c) in X direction at 1400K, d) in Z direction at 1600K; e) Stress-strain plot

CONCLUSIONS

BCM was successfully applied to simulate the effect of Mg impurities in C-plane sapphire structure at two finite temperatures. Results showed that temperature elevation increases the critical stress concentration areas around the Mg impurities within the structure, and reduces the UTS of the system. However, the overall reduction in UTS of C-plane which is less than 20%, confirms that it is resistant against structural nanodefects.

References

[1] J. F. Shackelford and R. H. Doremus, *Ceramic and glass materials*, vol. 71. Springer, 2008, pp. 317–322.
[2] F. Schmid and D. C. Harris, "Effects of crystal orientation and temperature on the strength of sapphire," *J. Am. Ceram. Soc.*, vol. 81, no. 4, pp. 885–893, 1998.
[3] H. L. Zhang, M. F. Zhang, Z. G. Hu, J. C. Han, H. X. Guo, and C. H. Xu, "Mechanical characteristics of sapphire before and after neutron irradiation," *Phys. B Condens. Matter*, vol. 408, pp. 34–38, 2013.
[4] A. Tewari, U. Aschauer, and P. Bowen, "Atomistic Modeling of Effect of Mg on Oxygen Vacancy Diffusion in α-Alumina," *J. Am. Ceram. Soc.*, vol. 97, no. 8, pp. 2596–2601, 2014.
[5] J. Houska, "Pathway for a low-temperature deposition of α-Al 2 O 3: A molecular dynamics study," *Surf. Coatings Technol.*, vol. 235, pp. 333–341, 2013.
[6] V. Iacobellis and K. Behdinan, "Multiscale coupling using a finite element framework at finite temperature," *Int. J. Numer. Methods Eng.*, vol. 92, pp. 652–670, 2012.
[7] V. Iacobellis and K. Behdinan, "Comparison of Concurrent Multiscale Methods in the Application of Fracture in Nickel," *J. Appl. Mech.*, vol. 80, no. 5, p. 51003, 2013.
[8] J. Sun, T. Stirner, W. E. Hagston, A. Leyland, and A. Matthews, "A simple transferable interatomic potential model for binary oxides applied to bulk α-Al2O3 and the (0001) α-Al2O3 surface," *J. Cryst. Growth*, vol. 290, no. 1, pp. 235–240, 2006.

A FULLY NONLINEAR MODEL OF A DAMAGED UNIDIRECTIONAL METAL MATRIX COMPOSITE

Ashish Mishra[1] and S Mahesh *[1]

[1]*Department of Aerospace Engineering, Indian Institute of Technology Madras, Chennai 600036 India.*

Summary A fully non-linear shear-lag model of a unidirectional metal-matrix composite, which accounts for fibre and matrix breakage, matrix plasticity, and fibre-matrix interfacial debonding and slippage has been developed in a deformation theory framework. A computationally light solution procedure based on the pseudospectral method has been developed. This approach allows the analysis of realistically sized composites. One such specimen level analysis of the Ti/SiC composite material studied by Hanan et al. [2] has been performed. The present model predictions accurately match the load recovery and stress distribution measured using neutron diffraction near a small crack.

INTRODUCTION

Metal matrix composites (MMCs) made of high temperature titanium (Ti) alloy reinforced with continuous unidirectional silicon carbide (SiC) fibres are potential weight-saving replacements for conventional alloys in jet engines. Ti/SiC possess excellent strength, stiffness and damage resistance when loaded along fibre direction. However, unlike monolithic materials the damage and failure modes in MMCs are quite complex. Damage starts at the microscopic fibre length scale in form of fibre breaks, matrix crack, fibre-matrix interfacial slippage. Under monotonically increasing load, damage propagates until the point of the composite rupture. A reliable model for simulating this process must account for the non-linearities intrinsic to the damage modes. A number of presently available models are based on restrictive assumptions on the type of non-linearity allowed, or on linear superposition of non-linear elastostatic solutions around a small number of breaks. The present work aims to develop a model of the composite, which can not only fully capture the nonlinearity of the failure modes, and material constitutive response, but also be amenable to quick computational solution.

SHEAR LAG MODEL

MMC geometry is idealised as shown in Fig. 1. Model elements are fibres, tensile matrix, shear matrix, and interfacial sliders. The physical matrix bay is subdivided into tensile and shear matrices. Fibres, and tensile matrices are assumed to deform in axial tension, while the shear matrix is assumed to deform in simple shear. The interfacial sliding element is assumed to undergo frictional sliding.

Fibres are assumed linear elastic and brittle. The tensile matrix is assumed to follow the law

$$\sigma_{\mathrm{tm}} = \sigma_{\mathrm{Y}} \tanh\left(\frac{(E_1 - E_2)\varepsilon_{\mathrm{tm}}}{\sigma_{\mathrm{Y}}}\right) + E_2\varepsilon_{\mathrm{tm}}. \tag{1}$$

Here, σ_{tm} and $\varepsilon_{\mathrm{tm}}$ denote the stress and strain at a point in the tensile matrix. σ_{Y} denotes its yield strain, E_1 its Young's modulus, and E_2 its hardening modulus. A similar law applies to the shear matrix. The frictional sliding elements are taken to satisfy

$$w_{\mathrm{s}} = w_{\mathrm{s0}}\left(\frac{\tau_{\mathrm{s}}}{\tau^*}\right)^{2n+1}. \tag{2}$$

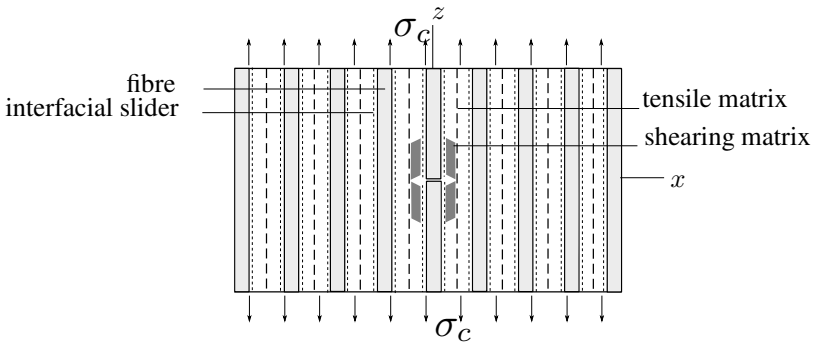

Figure 1: The model metal matrix composite. Fibres are shown shaded dark. The matrix domain is divided into two parts: The 'shear matrix' is assumed to deform exclusively by shear, and the 'tensile matrix' in tension (dashed lines). Sliding displacements at the fibre matrix interface is permitted (dotted lines). A fibre break and matrix shears around it are schematically shown.

*Corresponding author. Email: smahesh@iitm.ac.in

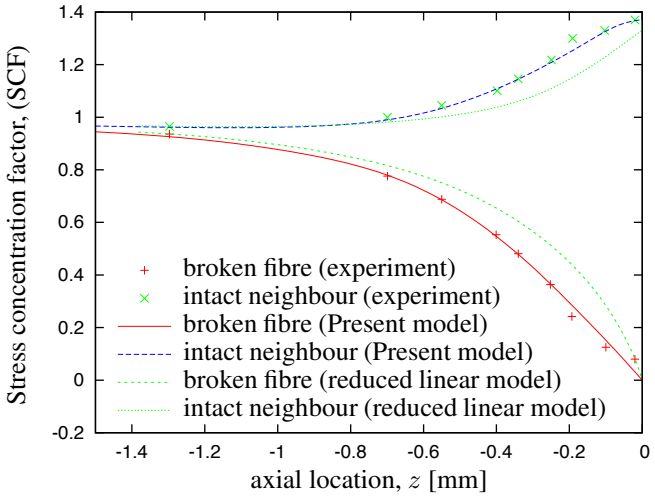

Figure 2: Stress concentration predicted by model (solid lines) compared with the experimental data reported by [2] in a Ti/SiC composite. Reduced linear form of the present model (dashed lines) are also plotted to show the effect of non-linearity in the model.

Here, $w_{\rm s}$ and $\tau_{\rm s}$ denote the sliding displacement, and shear stress at a slider element, respectively. τ^* denotes the slipping threshold, a material parameter. The governing equations of the model are obtained from equilibrium considerations of the various axial elements. They turn out to be second order non-linear differential equations.

SOLUTION STRATEGY AND RESULTS

Finite difference method based solutions schemes are found to be grossly inadequate to provide accurate solutions for the present model. A pseudo-spectral scheme is therefore employed. The formulated differential and algebraic equations are first non-dimensionalised and consolidated in terms of five independent characteristic constants. The governing differential equations are then converted into non linear algebraic equations discretised on Chebyshev grid points. Differentiation matrices are used to approximate derivatives in the governing equations [1]. The discretised equations are non-linear algebraic equations, which are solved using a trust-region method.

Hanan et al. [2] used neutron diffraction to measure the stress state in a metal matrix composite comprised of 29 fibres with guage length of 26 mm. Two fibres and the in-between tensile matrix bay were broken in a plane normal to the fibre direction in their composite. They measured the load recovery in the broken fibres and the overload in the next adjacent fibre.

The present model was employed to simulate the stress state in this specimen at far-field load 850 MPa. Fig(2) compares the presently predicted values of the stress concentration factor (SCF) near first intact fibre and in one of the broken fibre with the experimental value [2]. The good comparison indicates that the present model is capable of capturing all the significant mechanical and material aspects of load transfer near the fibre breaks. Lines corresponding to the "reduced linear model" suggests that accounting for non-linear effects is important for accurately capturing load transfer near fibre break clusters.

CONCLUSIONS

We have briefly described a fully non-linear, realistic and computationally light model of a metal matrix composite. We expect to use this model in reliability studied of MMCs in the future.

References

[1] B. Fornberg. *A Practical Guide to Pseudospectral Methods*. Cambridge Monographs on Applied and Computational Mathematics. Cambridge University Press, 1998.

[2] J. C. Hanan, E. Üstündag, I. J. Beyerlein, G. A. Swift, J. D. Almer, U. Lienert, and D. R. Haeffner. Microscale damage evolution and stress redistribution in ti–sic fiber composites. *Acta materialia*, 51(14):4239–4250, 2003.

NUMERICAL ANALYSIS ON COMPRESSION FAILURE MECHANISMS OF IMPACTED NON-CRIMP FABRIC REINFORCED COMPOSITES

G. Morada[1], A. Marouene[1], A. Vadean[1], R. Boukhili[1]
[1]*Department of Mechanical Engineering, Polytechnic Montreal, Montreal, Quebec, H3C 3A7, Canada*

Summary This study investigates the compression-after-impact (CAI) failure in non-crimp fabric (NCF) reinforced composites. A numerical damage model based on continuum damage mechanics was applied to simulate the failure mechanisms of impacted NCF glass/epoxy composite subjected to compressive loading and to estimate the residual CAI strength.

INTRODUCTION

Non-crimp fabrics (NCF) are textile preforms increasingly used as reinforcement in composite materials. Compared to the uni-directional laminates, NCF offer an attractive alternative especially in terms of low-cost manufacturing processes [1]. One major concern with composite structures consists on the low damage tolerance. Many researchers have addressed issues related to the CAI behaviour and numerous damage models have been proposed to estimate the CAI strength of the composite laminates. Furthermore, there exist some studies dealing with the failure mechanisms leading to the ultimate failure of structures. Some researchers reported that the residual compressive strength of an impacted composite is strongly governed by the delamination growth [2, 3]. Whereas, others highlight two phenomena that play an essential role in the final failure: delamination growth and crack growth besides the impact point [4, 5]. Rivallant et al. [5] have reported that it is crucial to consider the crack growth in numerical simulations to accurately predict the CAI strength. Edgren et al. [1] demonstrated that the propagation of kink-bands was the main failure mechanism responsible for collapse of the NCF laminate under compression. There was not clear consensus on the failure mechanisms responsible for the final failure of composite structures in CAI test.

This paper focuses on CAI test simulations performed on a NCF glass/epoxy laminate impacted at 30J impact energy. A physically based damage model was developed to predict the failure mechanisms such as: matrix cracking, fiber failure and delamination growth. The impact-induced damages were introduced in the numerical model through considering the presence of artificial delaminations and matrix cracks inside the impacted zone. The damage propagation in the NCF composite laminate was analysed for a better comprehension of the mechanisms of failure under compressive loading.

NUMERICAL MODELING OF CAI

The specimen geometry, boundary conditions and impact-induced damage considered into the numerical analyses are shown in Fig. 1. A 150 mm × 100 mm × 4 mm rectangular plate impacted with 30J was modelled to investigate damage tolerance in six layers NCF glass/epoxy laminates. Then, the damage morphologies of delamination and matrix cracks induced by a low-velocity impact were considered in the CAI model. A longitudinal compression displacement was applied on the upper plate while the bottom plate was clamped as shown in Fig. 1. An anti-buckling knife-edges condition was reproduced on both longitudinal sides of the plate.

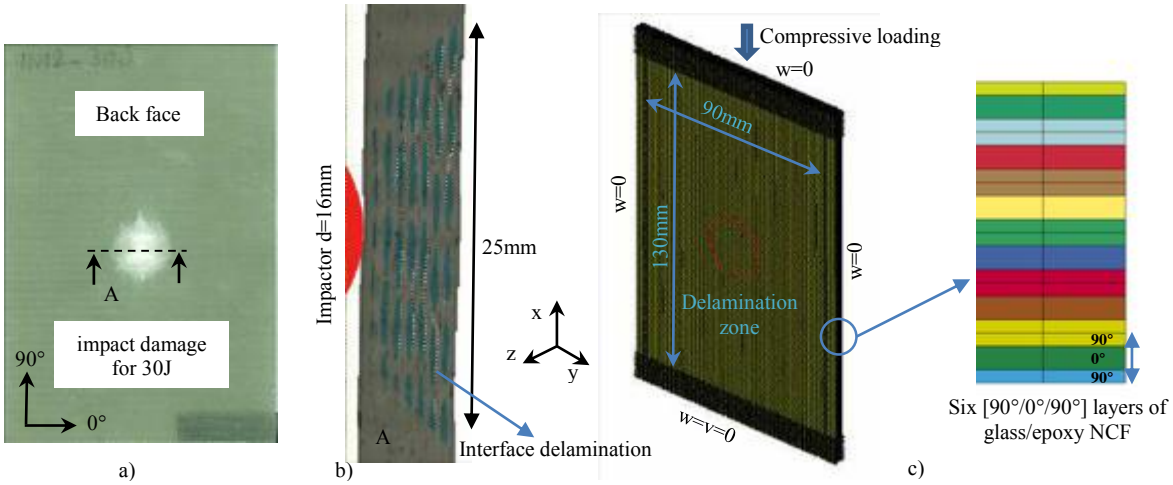

Fig. 1. a) Impact-induced damage, b) Impact delamination through-the-thickness, c) FEM model and boundary conditions

The zone of the impact-induced delamination is approximately of circular shape[3]. The delamination zone between the three bottom plies interfaces is larger than that at the upper plies interfaces. Therefore, delamination was considered only between the three bottom plies interfaces. Further than delamination, the matrix cracking was observed in the damage zone

[a] Corresponding author. Email: g.morada@polymtl.ca.

as shown in Fig. 1b. In this paper, it was assumed that the plies, in the conical damage zone, have negligible residual transverse strength. The intra-laminar damage in each ply were simulated using a physically-based constitutive damage model which is developed based on Donadon work [6] and implemented via UMAT in LS-DYNA/Explicit finite element software. The maximum stress criterion was adopted to predict the fiber failure combined to the Puck failure criterion to simulate matrix cracking and crushing. The inter-laminar damage initiation and propagation was modelled here using the cohesive zone model where cohesive elements were introduced between two neighboring plies with different fiber orientations. The elastic material properties used in the FE simulation are as following: E_{11}=34.4 GPa, E_{22}=E_{33}=6.98 GPa, v_{12}=v_{23}=v_{13}=0.28, G_{12}=G_{23}=G_{13}=3.2 GPa and the interfacial properties are as following: G_{IC}=800J/m^2, G_{IIC}=1200J/m^2, N=30 MPa, S=T=45 MPa, k_I=13.93GPa/mm, k_{II}=1.43GPa/mm, η=1.4 [3].

RESULTS AND DISCUSSIONS

Fig. 2 illustrates the stress-strain response of NCF laminates under compression loading. This figure depicts the numerical results for three studied cases: (1) a plate without impact damage, (2) a plate with impact-induced delamination, and (3) a plate with both impact-induced delamination and matrix cracks in conical zone. The slope of the strain-stress curve of the undamaged and damaged plate is the same which means that the presence of impact-induced damage does not have effect on the plate membrane stiffness. However, as expected, the compressive strength is sensitive to impact damage. The results show that compared with the undamaged plate, the CAI strength of an impacted plate decreases by 27% at 30J impact energy. For all the studied cases, the numerical results reveal that the buckling is the main mechanism responsible for the compressive failure of NCF laminates. Nevertheless, it was found that the buckling mode is different from one case to another. Indeed, for a plate with impact-induced delamination, it is found that the local buckling of the sub-laminates around the impact point leads to structural instability and thus the final failure of the plate. However, for the two other cases, the global buckling triggers structural collapse. Finally, a comparison between the two impact-induced damage scenarios shows that the matrix cracks in the conical damage zone have a little effect on the CAI strength, however, the initiation and propagation of delamination plays a primary role in the CAI strength reduction.

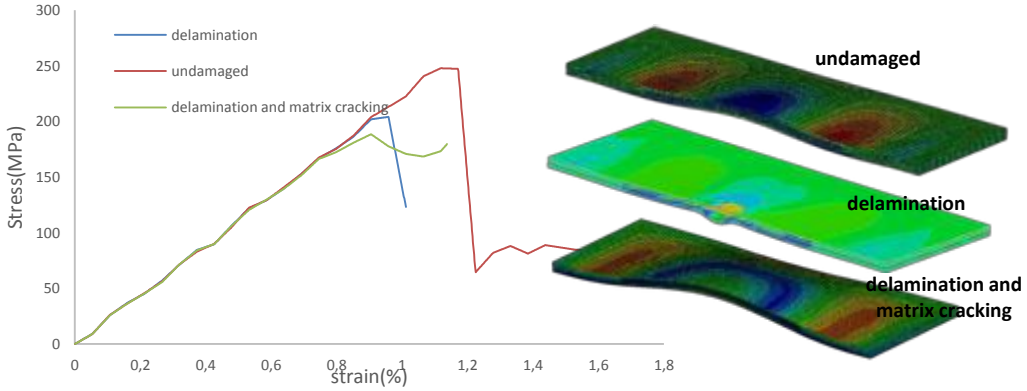

Fig. 2. The stress-strain response of NCF under compressive loading

CONCLUSION

This paper presents a numerical analysis aimed at understanding the failure mechanisms responsible for the compressive failure of impact damaged NFC glass/epoxy laminates. To this end, two CAI damage models were developed: (i) a CAI model with only impact induced delamination and (ii) a CAI model with both impact-induced delamination and matrix cracks. The obtained results show that the matrix cracks inside the conical damaged zone have a little effect on the residual compressive strength of the impacted NCF laminates. However, the local and global buckling appeared to be the main phenomena which cause structural instability and collapse. Moreover, it is found that the delamination growth occurred before matrix cracking and fiber failure.

References

[1] Edgren, F., Soutis, C., and Asp, L. E., 2008, "Damage tolerance analysis of NCF composite sandwich panels," Composites Science and Technology, 68(13), pp. 2635-2645.
[2] Suemasu, H., Sasaki, W., Ishikawa, T., and Aoki, Y., 2008, "A numerical study on compressive behavior of composite plates with multiple circular delaminations considering delamination propagation," Composites Science and Technology, 68(12), pp. 2562-2567.
[3] Yan, H., Oskay, C., Krishnan, A., and Xu, L. R., 2010, "Compression-after-impact response of woven fiber-reinforced composites," Composites Science and Technology, 70(14), pp. 2128-2136.
[4] Rivallant, S., Bouvet, C., Abi Abdallah, E., Broll, B., and Barrau, J.-J., 2014, "Experimental analysis of CFRP laminates subjected to compression after impact: The role of impact-induced cracks in failure," Composite Structures, 111, pp. 147-157.
[5] Rivallant, S., Bouvet, C., and Hongkarnjanakul, N., 2013, "Failure analysis of CFRP laminates subjected to compression after impact: FE simulation using discrete interface elements," Composites Part A: Applied Science and Manufacturing, 55, pp. 83-93.
[6] Donadon, M. V., Iannucci, L., Falzon, B. G., Hodgkinson, J. M., and de Almeida, S. F. M., 2008, "A progressive failure model for composite laminates subjected to low velocity impact damage," Computers & Structures, 86(11-12), pp. 1232-1252.

Role of the Microstructure on Sheared Edge Fracture of Advanced High Strength Steel

Nikky Pathak[1], Cliff Butcher[1], Michael Worswick[1], Erika Bellhouse[2] and Jeff Gao[2]
[1]*Mechanical and Mechatronics Engineering, University of Waterloo, Waterloo, Ontario, Canada*
[2]*Research and Development, ArcelorMittal Dofasco, Hamilton, Ontario, Canada*

Summary In this work, an experimental investigation of the fracture mechanism of advanced high strength steels (AHSS) during the edge stretching was conducted to identify the microstructural parameters influencing formability. To account for the sheared edge condition, the accumulated void damage and work hardening due to the shearing process was determined. The relevant microstructural paramaeters were implemented into a damage-based model to predict sheared edge fracture.

INTRODUCTION

Advanced high strength steels (AHSS) such as ferritic-martensitic dual-phase (DP) steels are gaining importance in the automotive industry due to their combination of high strength and good formability. In the automotive industry, shearing operations are widely used for blank trimming and for the introduction of holes and feature cutouts. However, the shearing process introduces severe work-hardening and nucleates voids within the so-called shear-affected zone (SAZ) behind the sheared edge [1]. This residual damage leads to abrupt and premature failure at the sheared edge during a subsequent forming operation. Advanced high strength steels are especially prone to sheared edge cracking due to the large strength differential between the constituent phases [2]. Consequently, this limitation has led to the development of ferritic-bainitic stretch-flangeable (SF) steels with a minor fraction of martensite to enhance the performance of AHSS in forming operations requiring good local formability as in stretch flanging and tight radius bending. The performance of a sheared edge in stretch-flanging operations is strongly related to the microstructure of material. For a material designer seeking to optimize the microstructure and thermal processing/chemistry, further insight into the mechanism controlling the fracture process is necessary. Therefore, the overall objective of this work was to characterize damage evolution and the fracture mechanism during edge stretching to develop a micromechanics-based model that can predict failure in simulations of sheet metal forming operations. A fracture study on interrupted hole tension specimens with different edge conditions was conducted to characterize the void shape, nucleation and distribution. To characterize the sheared edge, several experimental techniques are proposed to estimate the work-hardening and damage within the SAZ. The estimated shear strain and damage distribution behind the sheared edge coupled with the microstructural measurements is implemented in finite element modeling to predict fracture in different edge conditions. The experiments and simulations show that void evolution within the SAZ are strongly related to the microstructure and strength differential between the constituent phases.

DAMAGE CHARACTERIZATION DURING EDGE STRETCHABILITY

Traditionally, hole expansion tests are used to characterize edge failure and consist of expanding a hole with a conical punch until failure. The hole expansion test poses challenges for relating the damage mechanism to the microstructure since it has tooling contact and friction, is sensitive to the punch geometry and burr orientation and cannot directly account anisotropy. As an alternative to the hole expansion test, a hole tensile test specimen was employed in the present work to evaluate the edge sensitivity of stretch-flangeable and dual phase steels with similar ultimate tensile strengths of 800 MPa. Hole tensile specimens are simply tensile specimens with a hole processed in the center of the sample and avoids the sensitivities of the hole expansion test. Void initation and evolution within the SF and DP steels were systematically characterized during the edge stretching by interrupting the hole tension experiments at different strain levels. The DIC was used to measure the strains at six different sections along the edge as shown in Figure 1. The interrupted samples were observed under a scanning electron microscope (SEM) to observe the ductile fracture mechanism in the SF and DP steels. To quantify void nucleation and evolution, the void morphology was characterized at the different strain levels and edge conditions using the void density, area fraction, spacing and aspect ratio. Void nucleation was measured using the void density and is strongly related to the edge condition as shown in Figure 2. A procedure for quantifying damage during the edge stretching of SF and DP steels was developed to identify the microstructural parameters governing void nucleation and coalescence in an advanced damage-based constitutive model. In addition to characterizing void evolution in these steels, the residual strain field

within the SAZ must also be characterized as these residual strains drive void nucleation and fracture in subsequent edge stretching operations.

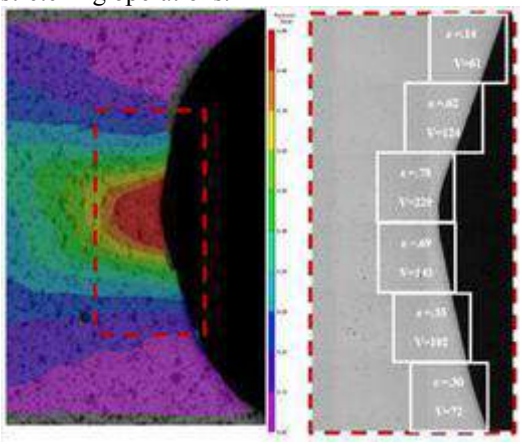

Figure 1: Contour plot of the equivalent strain and divided into six different strain levels along corresponding optical image

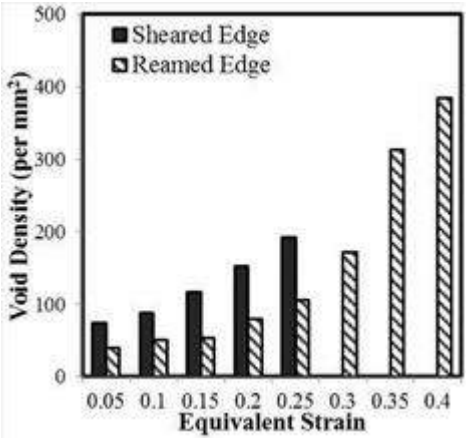

Figure 2: The plot of void density versus equivalent strain for the DP780 reamed and sheared edges

SHEARED EDGE CHARACTERIZATION

The evaluation of the sheared edge formability of a material is not straight-forward due to the shearing process that alters the local microstructure. A sheared edge stretching operation is essentially a two-stage non-proportional forming operation where through-thickness shearing is followed by in-plane uniaxial tension. To characterize the residual strains and work hardening within the SAZ, a novel experimental technique was developed involving micro-hardness measurements and interrupted shear tests. Correlations were established between the microhardness and plastic strain in shear deformation. With these correlations, hardness measurements from the SAZ can be converted to plastic strains and then mapped into a finite-element model to account for work hardening and void damage to accurately predict edge fracture in a forming operation.

CONCLUSION

An experimental investigation of the fracture mechanism of SF and DP steels was conducted using the reamed and sheared to identify the relevant microstructural parameters influencing void nucleation and edge fracture. It was found that the work-hardening introduced during the shear process significantly alters the void nucleation rate in the secondary stretching operation. The residual strain and void distributions at the sheared edges can be mapped into the finite-element models to simulate sheared edge fracture.

References

[1] Levy, B. and Van Tyne, C. (2012b). Review of the Shearing Process for Sheet Steels and Its Effect on Sheared-Edge Stretching. Journal of materials engineering and performance, 21(7), pp.1205--1213.

[2] Hasegawa, K., Kawamura, K., Urabe, T. and Hosoya, Y. (2004). Effects of Microstructure on Stretch-flange-formability of 980 MPa Grade Cold-rolled Ultra High Strength Steel Sheets. ISIJ International, 44(3), pp.603-609.

TOTAL ENERGY EQUIVALENCE IN CONSTITUTIVE MODELLING OF MULTIDISSIPATIVE MATERIALS

Halina Egner[1] & Maciej Ryś [1a)]
[1]*Institute of Applied Mechanics, Cracow University of Technology, Cracow, Poland*

Summary In the present work damage evolution in two – phase material is considered where the volume fraction of each phase exhibits different mechanical properties, and also the volume fraction of each phase in the representative volume of the material is subjected to evolution. The model is derived within the framework of thermodynamics of irreversible processes with internal state variables and continuum damage mechanics, where the concept of total energy equivalence, classically used to describe damage evolution in constitutive model, is generalized also to other dissipative phenomena. A numerical algorithm is also proposed in order to implement the constitutive model in the finite element software Abaqus/Explicit by means of the user subroutine VUMAT. A uniaxial tension test was simulated in Abaqus/Explicit to compare experimental and numerical results.

INTRODUCTION

In Continuum Damage Mechanics the phenomenon of damage softening is described by the use of so-called effective state variables of a pseudo-undamaged quasicontinuum. To define these damage-effective state variables various equivalence hypotheses are formulated: (a) strain equivalence hypothesis, (b) stress equivalence hypothesis, (c) strain energy or complementary energy equivalence hypotheses, or finally, (d) total energy equivalence hypothesis. According to these hypotheses, the effective state variables are defined in such a way that respectively strains, stresses, strain energy or complementary strain energy, or total energy for both real (damaged) and fictitious (pseudo-undamaged) materials are the same.

In the present work we consider a material that is subjected not only to damage, but also to other dissipative phenomena, for example: plastic slips, phase transformation from the primary ductile matrix material to the secondary brittle inclusion material, and damage development in both phases [1,2]. The constitutive description of such multidissipative material will be derived on the basis of total energy equivalence hypothesis, extended to all the dissipative phenomena regarded.

CONSTITUTIVE MODEL

The rearrangements of a material microstructure affect its global mechanical properties either causing softening (damage) or hardening (transformation from soft to hard phase). This means that material behavior (both elastic and inelastic) is influenced by the microstructural mechanisms. To account for the influence of the dissipative phenomena on the global mechanical properties the so-called effective state variables can be used in the state and dissipation potentials, instead of the classical state variables. The definitions of effective state variables are related to different fictitious configurations introduced in the model (see Fig. 1). Let's consider a real, discontinuous and heterogeneous configuration (R) of elastic-plastic-damage two phase material, subjected to ductile damage of matrix and brittle damage of inclusions. Its mechanical state is represented by couples of state variables and conjugated forces. We introduce a fictitious quasi-continuous configuration (F), characterized by the couples of effective state variables and effective thermodynamic forces defined on the basis of the total energy equivalence hypothesis. The total energy equivalence hypothesis (H1) we formulate in the following way [3]: *At any time (t), to an RVE in its real (deformed, damaged and phase transformed) configuration, described by the set of state variable pairs, we associate a safe (undamaged) and untransformed equivalent fictive configuration, the state of which is described by the effective state variables – in such a manner that the total energy defined over the two (real and fictive) configurations is the same*.

Mapping from configuration (R) to (F) may be equivalently performed with the use of two intermediate configurations: (UT), which is idealized undamaged but phase transformed, and (DU), which is damaged but idealized untransformed configuration (see Fig. 1). Each intermediate configuration is characterized by the proper pairs of effective variables, defined on the basis of the total energy equivalence applied to the real configuration (R) and the intermediate configuration considered.

To derive state and evolution equations we adopt another hypothesis (H2) [3]: *The mechanical behavior of the damaged medium may be derived from the same state and dissipation potentials as a fictitious undamaged untransformed medium in which the state variables are replaced by the effective variables*.

[a)] Corresponding author. Email: maciej_rys@o2.pl

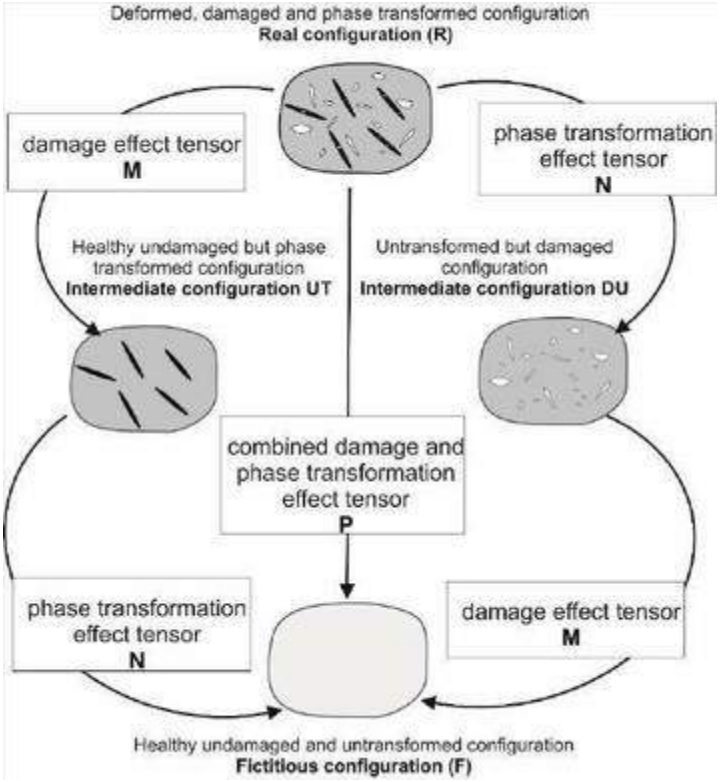

Figure 1. Schematic representation of the total energy equivalence concept.

PARAMETRIC STUDIES

Numerical algorithm is proposed where the Newton-Raphson scheme is employed to solve the set of nonlinear differential equations, while backward Euler method was used to numerically integrate the equations. The numerical procedure was also built with the use of AceGen program. AceGen was used to generate highly optimized and efficient compiled code in FORTRAN language what allowed to build user subroutine VUMAT. In the next step VUMAT procedure was used in Abaqus/Explicit to simulate uniaxial tension tests in order to validate the model (see Fig. 2).

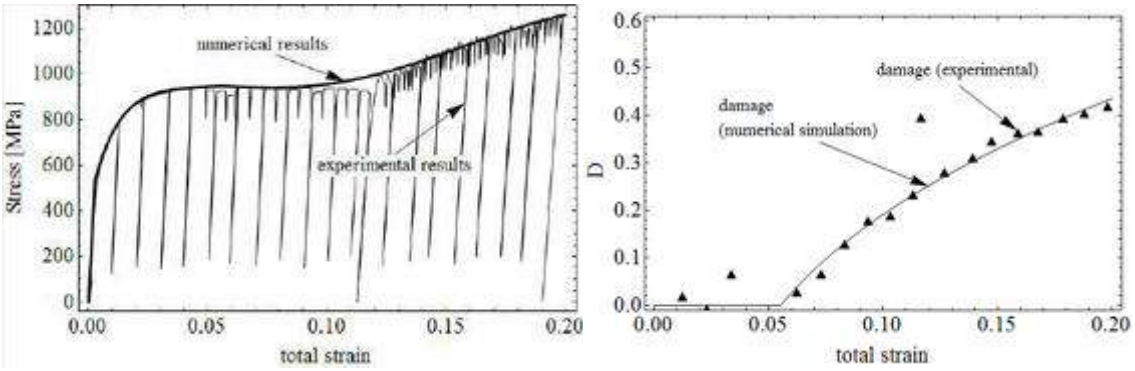

Figure 2. Experimental and numerical results of stress – strain relations and damage evolution

Acknowledgements
UMO-2013/11/B/ST8/00332, 2015/17/N/ST8/01169

References

[1] Egner, H. and Skoczeń, B., Ductile damage development in two-phase materials applied at cryogenic temperatures, *Int. J. Plasticity*, 26, pp. 488-506, 2010.

[2] Egner, H., Skoczeń, B. and Ryś, M., Constitutive and numerical modeling of coupled dissipative phenomena in 316L stainless steel at cryogenic temperatures, *Int. J. Plasticity*, 64, pp. 113-133, 2015.

[3] Saanouni, K., *Damage Mechanics in Metal Forming: Advanced modeling and numerical simulation*, ISTE/Wiley, London, 2012.

DAMAGE-PLASTICITY SIMULATION OF A PREMATURE FAILURE IN FRP STRENGTHENED RC BEAMS

Navid Saeedi[1]
[1]*Solid Mechanics Department, IFP Energies nouvelles, Rueil-Malmaison, France*

Abstract This work is concerned with numerical modeling of "Peeling-off" or "Concrete cover separation" which is a premature failure mode in FRP strengthened reinforced concrete (RC) beams. 3D Finite element simulations are made using the commercial program Abaqus. Four-point bending loading is applied on non-strengthened and FRP strengthened beams. A damaged plasticity constitutive law is used for the modeling of concrete. The asymmetric behavior of concrete in compression and tension, and the tension stiffening phenomenon are taken into account. The results of the numerical simulations are compared with some experimental results available in the literature. The flexural and the Peeling-off failure modes are well obtained in the simulations. Comparisons between the numerical predictions and test results illustrate a very good agreement and it is found that the proposed model is able to closely predict the ultimate load, the beam behavior and its failure mode.

INTRODUCTION

An efficient solution to rehabilitate civil engineering structures is the use of Fiber Reinforced Polymers (FRP) sheets which can be bonded onto external surfaces. The main advantages of FRP plates are their high tension strength to density ratio, low sensitivity to corrosion and a long fatigue life. As a simple application, the flexural strength of reinforced concrete beams can be increased by bonding a FRP sheet to their tension faces. Although this method increases considerably the flexural capacity of the strengthened beam, it may cause a premature failure mode called "Peeling-off" or "Concrete cover separation" (Figure 1). This work tries to model this premature failure mode via a damage-plasticity finite element approach.

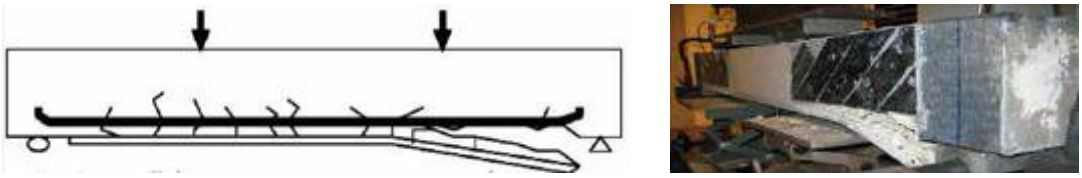

Figure 1: Concrete cover separation (Peeling-off)

BEAMS CONFIGURATION AND EXPERIMENTS

A series of FRP strengthened and non-strengthened reinforced concrete beams were tested to failure under four-point bending load tests [1]. All of the beams have a length of 1000mm, a width of 100mm and a height of 150mm. The failure mode of normal beams was flexural cracking while all of the beams strengthened with FRP sheets at the bottom collapsed by Peeling-off. It is noted that mechanical characteristics of concrete, steel and FRP have been identified by experiments.

FINITE ELEMENT MODELING

Three dimensional finite element (3D-FE) non-linear simulations have been done by means of the commercial program Abaqus. The steel rebars are modeled by beam (1D) elements with an elasto-plastic behavior. For the concrete part, quadratic tetrahedral solid (3D) elements are used with a damage-plasticity formulation based on Lubliner's and Lee's formulations [2, 3]. The asymmetric behavior of concrete in compression and tension are taken into account. The post cracking softening behavior of concrete in tension is modeled with tension stiffening taking into account the effects of the reinforcement interaction with concrete. In order to avoid the mesh dependency problems, the Hillerborg's fracture energy proposal [4] is adapted and the post-failure behavior is characterized by a stress-displacement response rather than a stress-strain response. Concerning the FRP flexural sheet, consist of carbon epoxy composite laminates, shell elements (2D) with an orthotropic elastic behavior are used. In order to reduce the size of the model, the two symmetry planes of the problem were applied to model just a quarter of the specimens.

Figure 2 illustrates the damage patterns for a normal RC beam (left) and a strengthened FRP one (right). For the normal RC beam, the flexural cracks in the region of maximum bending moment lead to the failure of the beam (bending failure mode). However, if the beam is strengthened by a FRP sheet on its bottom face, the failure mode will be different. The failure of such a beam does not occur at bending and its ultimate capacity is very superior. We will have several small bending cracks in the concrete cover region (i.e. between the bottom face of the beam and the rebar position). These cracks are not sufficient to produce a failure. By increasing the applied load, a relatively brittle crack starting from the bonded FRP edge appears. The coalescence of this crack and the existing small flexural cracks leads to a large crack located at the

[a] Corresponding author. Email: navid.saeedi@ifpen.fr

reinforcement layer position. The propagation of this crack is relatively fast and causes the concrete cover separation which leads to the total failure of the beam.

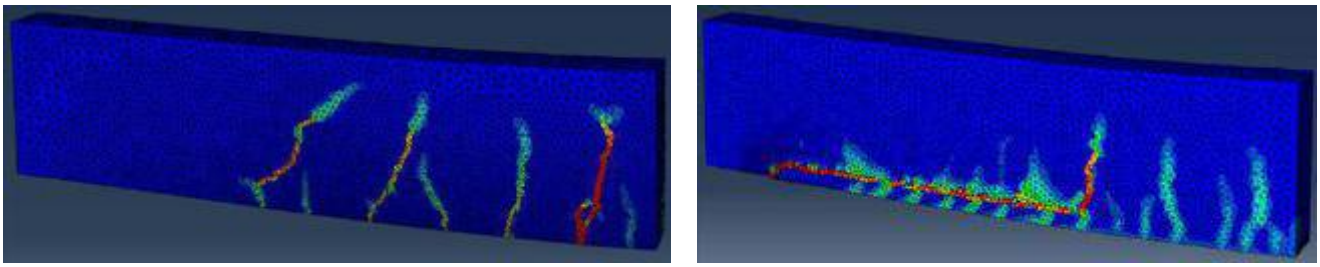

Figure 2: Flexural failure (Left) - Peeling-off failure (Right)

Figure 3 plots the total applied load versus the midspan deflection for the both normal and strengthened configurations. The rigidity of the reinforced beam in the propagation phase (corresponding to the second slope of the curve) is much higher than the normal beam. As seen, the presence of FRP sheet increases the ultimate load capacity by about 100% (50kN against 25 kN). However, the concrete cover separation is a premature mode of failure in the FRP strengthened beam and does not allow us to use all the bending capacity of the beam. It is noted that the failure mode of the normal beam is ductile and there is third phase before the failure which corresponds to the plasticity of steel rebars. By contrast, the failure mode of the FRP reinforced beam (i.e. concrete cover separation) is brittle without any steel plasticity phase.

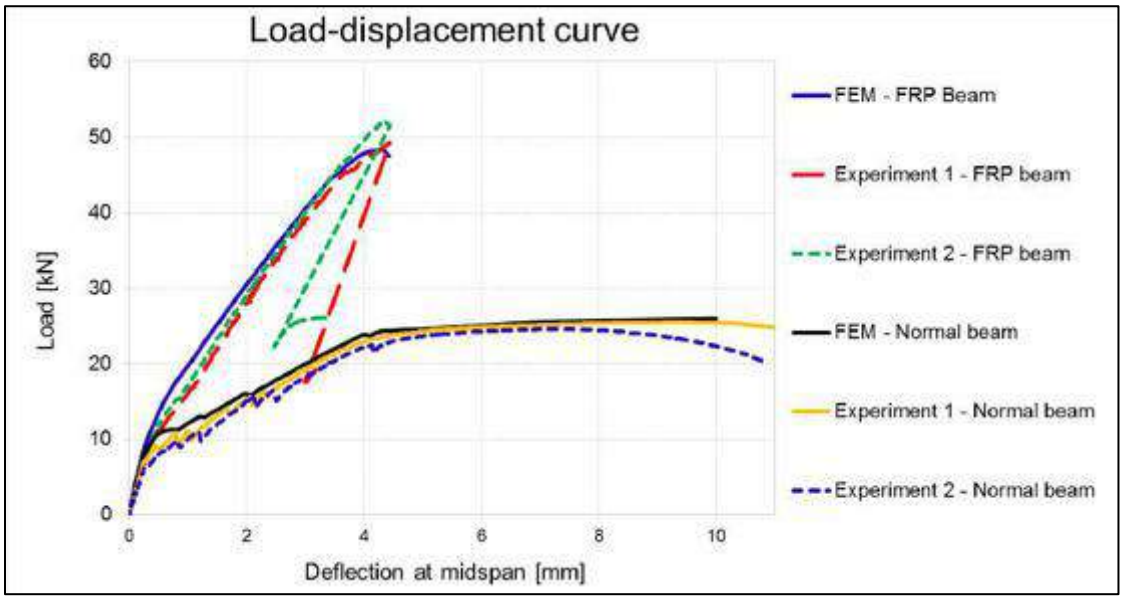

Figure 3: Comparison between FE model and experiments – Normal and FRP strengthened beams

CONCLUSIONS

The nonlinear damage-plasticity FE model proposed herein can be used by researchers and designers as a computational tool for FRP strengthened beams. Comparisons between the FE and experimental results illustrate that the model is capable of predicting the behavior of FRP strengthened RC beams. Very good agreements are found between the FE model and experiments in terms of crack zones, failure mode and ultimate failure load. Consequently, the proposed model can be used to improve the design procedure of FRP plated RC beam and find a better repair/strengthening scheme.

References

[1] Radfar S., Foret G., Saeedi N. and Sab K., Simulation of concrete cover separation failure in FRP plated RC beams, *Construction and Building Materials, vol. 37, 791-800, 2012*

[2] Lubliner J., Oliver J., Oller S., and Oñate E., "A Plastic-Damage Model for Concrete," International Journal of Solids and Structures, vol. 25, 299-329, 1989.

[3] Lee J. and Fenves G. L., "Plastic-Damage Model for Cyclic Loading of Concrete Structures," Journal of Engineering Mechanics, vol. 124, 892–900, 1998.

[4] Hillerborg A., Modeer M. and Petersson P. E., "Analysis of Crack Formation and Crack Growth in Concrete by Means of Fracture Mechanics and Finite Elements," Cement and Concrete Research, vol. 6, 773-782, 1976.

MESH-INDEPENDENT DAMAGE-PLASTICITY MODEL FOR CERAMICS IN BALLISTIC PROTECTION

Erik Cornelis Simons*[1], Jaap Weerheijm[1,2], and Lambertus Johannes Sluys[2]
[1]*Delft University of Technology, Delft, The Netherlands*
[2]*TNO, Rijswijk, The Netherlands*

Summary Ceramics are hard, relatively light and brittle materials which are used in armour systems. Design of these armour systems typically requires a high number of ballistic experiments to be performed. Finite Element (FE) simulation of ballistic loading on ceramics provides an alternative and reduces the required number of experiments. Unfortunately current material models fail to properly capture behaviour of ceramic materials. A number of improvements on current material models are proposed.

In FE simulations on ballistic impact the Johnson-Holmquist (JH) material models [1, 2] are often used to model ceramic materials. These (softening) plasticity models (Figure 1) require calibration through impact experiments. Model properties related to intact material strength can directly be obtained from experiments. Other properties such as softening related material properties can currently only be obtained through inverse modelling.

A promising experimental technique to study damage in ceramic materials is quasi-static indentation. Under indentation a ceramic will experience 'controlled' failure, allowing to calibrate damage or softening related quantities for material models. This requires a ceramic material model suited for quasi-static FE simulations of damaging or softening material under indentation. The current JH models predict the ceramic material behaviour in the so called 'quasi-plastic' zone directly underneath the indentor relatively well. Using the JH models for indentation simulations does however introduce three problems. The first problem is mesh-sensitivity, an inherent property of softening-plasticity models such as the JH models. A second problem is that the current model formulations are not suited for quasi-static simulations. As a third problem the JH models fail to properly capture intergranular cracking/sliding in the 'quasi-plasticity' zone and the models fail to properly capture brittle tensile failure.

A modification of the JH material models is proposed, addressing the three previously mentioned problems. The modified model includes a damage formulation to the existing plasticity formulation and an adequate regularization for mesh-objective failure prediction. Furthermore, the new formulation allows for quasi-static FE simulation. Future work will contain validation of the new model to quasi-static and dynamic indentation experiments.

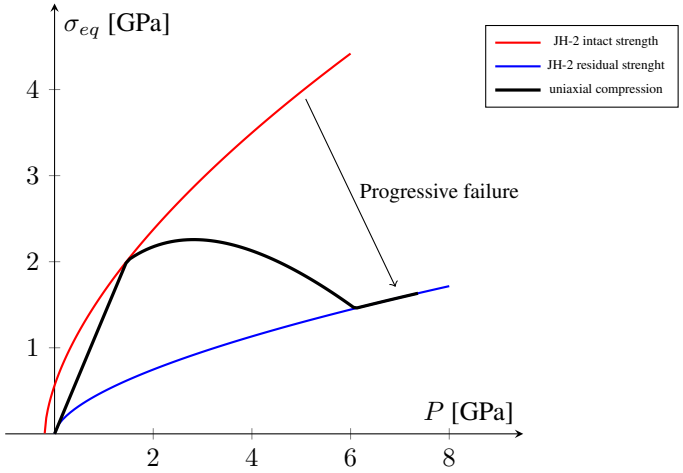

Figure 1: Johnson-Holmquist material model, pressure-equivalent stress relation for intact and residual strength.

References

[1] G.R. Johnson and T.J. Holmquist, *A computational constitutive model for brittle materials subjected to large strains, high strain rates and high pressures*, Shock Wave and High-Strain-Rate Phenomena in Materials, 1992, p1075-1081.

[2] G.R. Johnson and T.J. Holmquist, *An improved computational constitutive model for brittle materials*, Highpressure science and technology-1993. Vol. 309. No. 1. AIP Publishing, 1994.

CHARACTERIZATION OF DAMAGE AND FAILURE FOR NANO-CRYSTALLINE MATERIALS

Yueguang Wei[1a)], Yunlong Li[1] & Li Chen[1]
[1]*State Key Laboratory of Nonlinear Mechanics, Institute of Mechanics, Chinese Academy of Sciences, Beijing, China*

Summary In the present research, mechanical behaviors of the nanocrystalline materials considering the damage developing on the grain boundaries are investigated systematically. A mixed-mode cohesive interface model is used to describe the damage and failure process of the materials. Based on the mixed-mode cohesive interface model, the grain boundary damage are defined and characterized. In order to describe the size effect, the strain gradient plasticity theory is used for grain materials and the interface energy effect is considered along grain boundary. In the present results, the overall stress-strain relations and corresponding damage evolution curves are obtained and as the functions of several independent parameters. The present results show that both the overall strength and ductility of the nanocrystalline materials are closely depended on the grain boundary damage evolution and the overall stress-strain curve displays a catastrophic feature. Further discussions on the cell representativity and damage of nanoscale particle-reinforced materials are carried out.

INTRODUCTION

Investigations on the mechanical behaviors of polycrystalline materials with grain sizes typically less than 100 nm (nanocrystalline (nc) metals) or within 100-1000 nm (ultra-fine crystalline (ufc) metals) have been the key subjects worldwide over the past two decades [1]. The nc/ufc metals exhibit the higher yield strength, tensile strength, and hardness, but the lower tensile ductility relative to their bulk counterparts. In the present research, the strain gradient plasticity theory [2] is used to describe the size effects of the inelastic deformation in grain interiors, and a cohesive interface model is used to describe the damage of the grain boundary. Particular attention is focused on the influence of damage on the overall strength and ductility of the nc/ufc metals. Further discussions on the cell representativity and damage of nanoscale particle-reinforced materials are carried out.

MODEL AND DESCRIPTIONS

To particularly study the mechanical behaviors of the nc/ufc materials, and to investigate how the competition of grain-boundary damage with that of grain interior determines the observed overall stress-strain response and the overall ductility of polycrystalline aggregates by various properties of grain boundary and grain interiors, a regular quasi-three-dimensional representative volume element with taking into account of three dimensional effects is presented here. Fig. 1 shows the schematic figure of representative calculation model. The calculation model is consisted of twelve regular hexagon grains. The diameter of grain, d is the diameter of the circumcircle of regular hexagon.

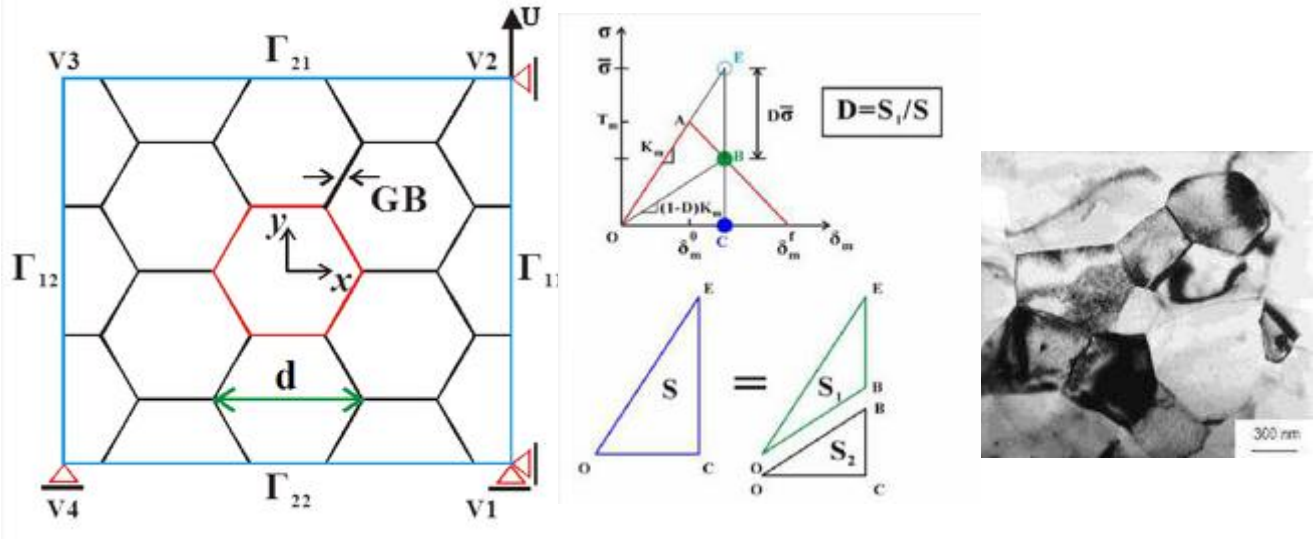

(a) (b) (c)

Fig. 1 Representative cell model (a) for nano- or ultra-fine polycrystalline metal (c)[1] with periodic boundary conditions of *xy* plane and *z* direction. (b) Damage definition on GB based on cohesive model [3].

[a)] Corresponding author. Email: ywei@LNM.imech.ac.cn.

As displayed in Fig. 1, periodic boundary conditions are enforced along the four sides in *xy* coordinate plane [4]:

$$\vec{\mathbf{u}}_{12}-\vec{\mathbf{u}}_{V4}=\vec{\mathbf{u}}_{11}-\vec{\mathbf{u}}_{V1} \tag{1}$$

$$\vec{\mathbf{u}}_{22}-\vec{\mathbf{u}}_{V1}=\vec{\mathbf{u}}_{21}-\vec{\mathbf{u}}_{V2} \tag{2}$$

$$\vec{\mathbf{u}}_{V3}-\vec{\mathbf{u}}_{V2}=\vec{\mathbf{u}}_{V4}-\vec{\mathbf{u}}_{V1} \tag{3}$$

where $\vec{\mathbf{u}}_{ij}$ is the displacement vector for any material point on the corresponding boundary Γ_{ij}, and $\vec{\mathbf{u}}_{Vi}$ is the displacement vector for each vertex Vi. The intergranular fracture process of grains is described by the cohesive zone (CZ) model.

A comparative parameter study for overall strength and ductility of polycrystalline aggregates affected by the material parameters of grain boundaries and grain interiors with different grain sizes is performed. The overall stress-strain relation and the grain boundary damage of the nanostructured materials with parameter dependence normalized by the initial yield stress σ_Y and intrinsic material length l can be expressed respectively as follows

$$\frac{\sigma}{\sigma_Y}=f\left(\varepsilon;\ \underbrace{\frac{E}{\sigma_Y},\ \ \nu,\ \ N,\ \ \frac{d}{l}}_{\text{intragranular parameters}},\ \underbrace{\frac{T_1}{\sigma_Y},\ \frac{T_S}{T_1},\ \frac{G_{IC}}{\sigma_Y l},\ \frac{G_{SC}}{G_{IC}},\ \frac{K_c}{\sigma_Y}}_{\text{interfacial parameters}}\right) \tag{4}$$

$$D=g\left(\varepsilon;\ \underbrace{\frac{E}{\sigma_Y},\ \ \nu,\ \ N,\ \ \frac{d}{l}}_{\text{intragranular parameters}},\ \underbrace{\frac{T_1}{\sigma_Y},\ \frac{T_S}{T_1},\ \frac{G_{IC}}{\sigma_Y l},\ \frac{G_{SC}}{G_{IC}},\ \frac{K_c}{\sigma_Y}}_{\text{interfacial parameters}}\right) \tag{5}$$

where the intragranular parameters are Young modulus E, Poisson's ratio ν, initial yield stress σ_Y, strain hardening exponent N, grain diameter d, respectively. The interfacial parameters of grain boundary are maximum separation strength T_1 and T_S, mode I and shear mode fracture toughness G_{IC} and G_{SC}, effective initial separation modulus $K_c=T_1/\left(\delta_m^0/l\right)$ in CZ model.

RESULTS AND BRIEF DISCUSSIONS

A typical computational result for overall stress-strain relations of the nc/ufc metal related to the grain boundary damage evolution is shown in Fig.2. From Fig.2, the feature and catastrophic of the overall stress-strain relations are closely dominated by the properties of grain boundary damage, and the stress turning points of stress strain relation correspond to grain boundary damage turning points. The failure characteristic of stress strain curves is a catastrophic process at strength point which can be described by the grain boundary damage.

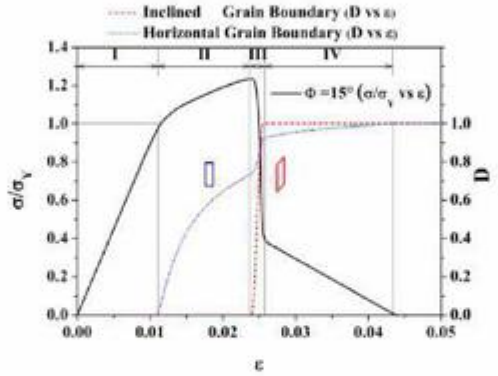

Fig. 2. Overall stress–strain curves related to the grain boundary damage evolution.

References

[1] Wei YG, Shu SQ, Du Y, Zhu C. International Journal of Plasticity **21**(11):2089-2106, 2005.
[2] Wei YG, Hutchinson JW, Journal of the Mechanics and Physics of Solids **45**(8):1253-1273, 1997.
[3] Chen L, Wei YG, International Journal of Damage Mechanics **23**(1):25-42, 2014.
[4] van der Sluis O, Schreurs PJG, Meijer HEH. Mechanics of Materials **33**(9):499-522,2001.

QUANTITATIVE ASSESSMENT OF FAILURE IN TBCS BASED ON FREQUENCY SPECTRUM OF ACOUSTIC EMISSION

Li Yang[1a)], Yichun Zhou[1], Wang Zhu[1]
[1]*Key Laboratory of Key Film Materials & Application for Equipment (Hunan province), School of Materials Science and Engineering, Xiangtan University, Xiangtan, Hunan 411105, China*

Summary Fracture behavior of thermal barrier coatings (TBCs) subjected to thermal and/or mechanical loading is investigated using an acoustic emission (AE) method. The crack mode is only dependent on frequency spectrum of AE signal, which phenomena is proved by clustering analysis of AE parameters. Based on this result, intelligent discrimination of crack modes are realized by using wavelet packet transformation and neural network analysis of AE. The quantitative correlations of damage in TBCs and AE parameters are established, including surface crack density and interface crack length, which are well agreement with experimental results.

INTRODUCTION

The application of thermal barrier coatings (TBCs) has facilitated a steep increase of the turbine entry temperature and the associated increase in performance and efficiency of gas turbine [1]. Unfortunately, the complex shape, structure, and harsh operating conditions make the failure behavior of TBCs much more complicated than that in metallic, ceramic components or other coating systems, and thus the failure assessment of TBCs is very difficult by using traditional strength theories or experimental mechanics methods [2]. There has been a growing interest in bringing together experiments under destructive load with ideas from in-situ or real time nondestructive tests [2-3], such as acoustic emission (AE) [2]. However, crack mode discrimination, quantitative assessment of damage evolution in TBCs are challenges in AE monitoring, which are necessary for the real time testing of TBC failure. In this study, an acoustic emission method to realtimely monitor failure behavior is built up to intelligently distinguish crack mode, quantitatively assess damage evolution, and predict ultimate spallation. The main process of investigation comprise: first, AE behavior of TBCs is recorded under loading, which can form main failure types at service condition. Then, all AE parameters are analyzed by clustering to find key parameter of crack mode, and four crack types of TBCs as well as their AE character are obtained. Third, intelligent discrimination method is established by combinating wavelet packet transform and neural network, the fracture behavior, therefore, can be understood through the distribution feature of different failure modes in TBCs. Finally, surface crack density, interface crack length are theoretically calculated to establish quantitative correlation with AE, which can be used to estimate damage degree of TBCs under service condition.

RESULTS AND DISCUSSION

Although TBCs are generally operated under thermal loading, the main factor on their failure is tensile/compressive stress in coatings or at interface due to thermal and mechanical mismatch. Therefore, tension and compression tests are separately applied at room temperature by an RG2000 universal machine with a loading rate of 0.3 mm/min, 250 N/min, respectively. TBCs failure processes were monitored by an AE system (PCI-2) with the threshold of 38 dB, pre-amplifier of 40 dB, and sampling frequency of 2 MHz, respectively. TBC specimens were made by typical atmospheric plasma spraying, including a Ni-based superalloy GH3030 substrate, a 100 μm CoNiAlY bonding and a 200 μm ZrO2-8%Y2O3 ceramic coatings. The thickness of substrate is 3 mm in tension and 5 mm in compression. The length and width of TBC specimens in tension are 80 and 8 mm, and those in compression are 20 and 5 mm, respectively.

The distributions of four clusters of AE signals (labeled as A, B, C and D, respectively) form tension in various parameter spaces are shown in Fig. 1. AE signals of clusters A, B and C are hard to classify from their amplitudes (see Fig. 1(a)), duration and rise time (see Fig. 1(b)), showing nearly same ranges, i.e, 38-65 dB in amplitude, 0 to 500 μs in duration . However, clusters A, B and C present their distinct frequency bands in the range of 260−350, 170−250 and 40−150 kHz, respectively. Similar clustering analysis is conducted to compressive fracture behavior of TBCs, presenting five clusters. Only in peak frequency, five clusters can be separated from each other, with their frequency bands in the range of 260−350, 170−250, 0−150 and 400−450 kHz, respectively. Combination with microstructure observation, cluster A(A'), B(B'), C(C'), E' are indentified as sliding interface crack, surface crack, substrate deformation and opening interface crack, respectively. It is worth noting that cluster D and D' with higher amplitudes and longer durations, but no obvious frequency band, is from ultimate spallation of coating.

Based on key parameter of frequency, AE signals are analyzed by wavelet packet transformation and a back-propagation neural network. By using the energy coefficient vector as input, the back-propagation neural network exhibits a powerful self-learning ability to cluster signals with the same order features. Four classes of AE signals, corresponding to the four types of failure mechanisms in TBCs, can be successfully identified. Then failure mechanisms of TBC are clearly understood by distribution of four clusters AE signals with loading. The fracture process of TBCs under tension is divided

[a)] Corresponding author. Email: Lyang@xtu.edu.cn, Zhouyc@xtu.edu.cn.

into surface cracking, sliding cracking and spallation, that for compression is opening interface cracking, surface cracking and sliding interface cracking. These are in good agreement with experimental result.

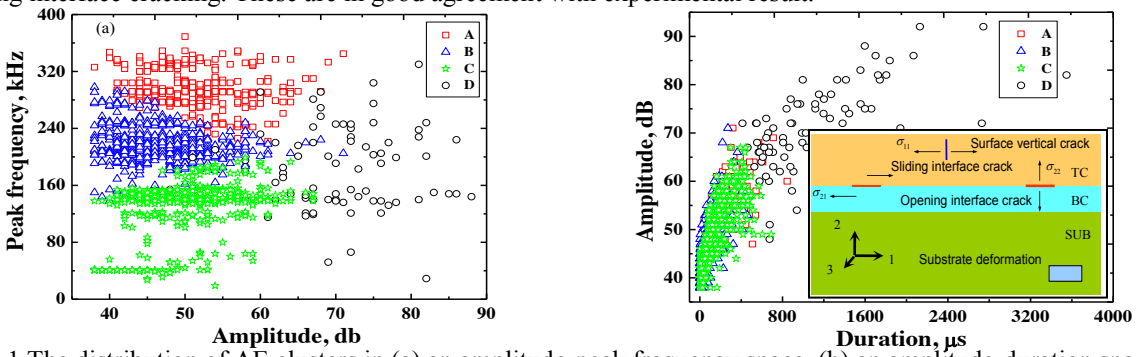

Fig. 1 The distribution of AE clusters in (a) an amplitude-peak frequency space, (b) an amplitude-duration space

For a brittle film on a ductile substrate under tensile loading, a traditional shear-lag model [4] is commonly accepted to evaluate the surface crack density ρ, which is defined as the ratio of multiple crack numbers to the length of a specimen. The model includes an elastic-plastic interlayer, in which the load transfer from thick ductile substrate to thin brittle film can be described. The structure of TBCs is consistent with the shear-lag model except that coating is thicker than that in the model. Therefore, such a model is modified by considering the strain gradient in coating, and if substrate is in the elastic-plastic state, the crack density ρ of coating can be expressed as $\rho = \frac{\tau_b K}{2}[d_1\sigma_b K + M - \sqrt{M^2+\tau_b^2} + \tau_b ar\sinh\frac{\tau_b}{M}]^{-1}$, the parameters can be referred to reference [4].

Naturally, AE is the release of strain energy of cracking, so there is a proportional relationship between the AE energy and the released energy from cracking. Therefore, the interface energy release rate for interface crack is calculated, and then linearly correlated with AE energy as, $E_{AE} = \frac{2w}{\alpha}\left[\frac{(1-\nu_c^2)\sigma^2 h}{2E_c}(b-b_0) - \frac{\pi^4 E_c h^5}{288(1-\nu_c^2)}\left(\frac{1}{b^3}-\frac{1}{b_0^3}\right) - \frac{\pi^2 h^3\sigma}{12}\left(\frac{1}{b}-\frac{1}{b_0}\right)\right]$

the parameters can be referred to reference [4].

Figs. 2 and 3 show the correlation of surface crack and interface crack length with AE, respectively. Obviously, a linear relationship presents between surface crack density and the logarithm of AE events, which well coincides with experimental results. Fig. 3 showed that the maximum error of AE energy between Eq. (2) and experimental results is about 20%, indicating the theoretical results are well consistent with those from experiment. Obviously, the AE energy increases with the increase of crack half length.

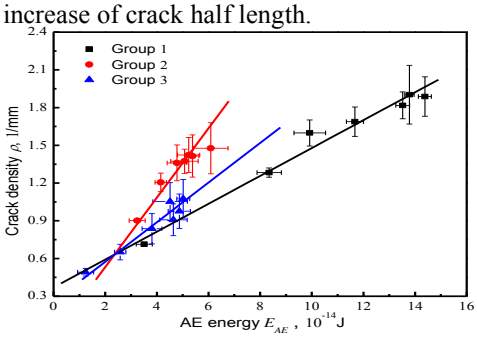

Fig.2 The correlation of surface crack density and AE

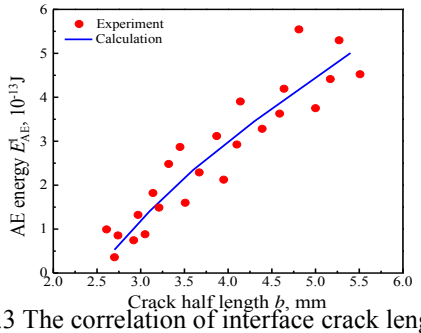

Fig.3 The correlation of interface crack length with AE

CONCLUSIONS

In this paper, a real-time acoustic emission testing method has been established to distinguish crack mode, quantitatively assess damage evolution in TBCs. The main results can be summarized as follows: (1) frequency is the key parameter to crack mode discrimination. (2) fracture mechanism can be clearly understood according to intelligent crack mode discrimination results of AE behavior. (3) The surface crack density show a linear relationship with the logarithm of AE events, that for interface crack is also indentified.

References

[1] R.A. Miller, J. Therm. *Spray Technol*.6: 35-42, 1997.

[2] L. Yang, Y. C. Zhou, C. Lu. *Acta Mater*.59: 6519-6529, 2011.

[3] L. Yang, H. S. Kang, Y. C. Zhou, W. Zhu, C. Lu. *Surf. Coat. Technol*., 2015, 264: 97-104.

[4] L. Yang*, H. S. Kang, Y. C. Zhou, L. M. He, C. Lu. *Exp. Mech*., 2015, 55: 321-330.

STRESS TRIAXIALITY EFFECT ON DAMAGE EVOLUTION OF HIGH-STRENGTH STEELS

Feng Yu[1a)], P.-Y. Ben Jar[1] & Michael T. Hendry[2]
[1]*Department of Mechanical Engineering, University of Alberta, Edmonton, Alberta, Canada*
[2]*Department of Civil and Environmental Engineering, University of Alberta, Edmonton, Alberta, Canada*

Summary The damage evolution of three high strength steels was characterized at two levels of stress triaxiality, 0.4 and 1.2, using both smooth and short gauge tensile specimens, respectively, where the value of stress triaxiality was determined using finite element modelling. With the aid of numerical simulation, the degradation of elastic modulus for the smooth tensile specimens was first characterized by eliminating the influence of geometry on the unloading modulus measured from cyclic tensile tests. The approach was also applied to the short gauge tensile specimens to further explore the damage evolution. A theoretical model describing the dependence of damage parameter on the stress triaxiality was then used to show the difference in the damage evolution between the two types of tensile specimens.

INTRODUCTION

Based on the concept of continuum damage mechanics (CDM), indentation technique is being considered as an alternative approach to predict fracture toughness of ductile materials with the assumption that the crack tip and indenter tip are subjected to similar stress triaxiality [1]. The critical damage parameter, D_{cr}, is a material parameter which based on the results from in-situ X-ray analysis, may vary with the stress triaxiality [2]. Celentano and Chaboche [3] and Bonora et al. [4] reported values for the damage parameter in the triaxial loading conditions. The former, with the aid of numerical simulation, eliminated the effect of the specimen geometry on elastic modulus measurement due to the necking-induced non-uniform deformation. The latter used notched tensile specimens to study the dependence of damage evolution on stress triaxiality from 0.33 to 0.7. In this paper, the preliminary results of the effect of stress triaxiality on damage evolution for three high strength steels are presented. These results characterized damage evolution and D_{cr} values at two different loading conditions, using both smooth and short gauge tensile specimens. This study will be extended to predict D_{cr} at a sharp crack tip and the ultimate goal is to predict fracture toughness in high strength steels using indentation technique, with the D_{cr} value determined from the crack tip to identify the characteristic indentation depth to represent fracture initiation.

MATERIALS AND EXPERIMENTAL PROCEDURE

Monotonic and cyclic tensile tests were performed at room temperature using an Instron hydraulic universal testing machine at a constant crosshead speed of 0.004 mm/s. High strength steels were sampled from three rail steels, named as JP, EV, and CZ which were provided by Canadian National Railway Company (CN). The smooth and short gauge tensile specimens were designed to generate different levels of stress triaxiality. The shape and dimensions of the two types of tensile specimens are provided in Fig. 1a, along with the variation of the true stress versus logarithmic strain curves for the three rail steels measured from the monotonic tensile testing. Fig. 1b and 1c show the typical true stress-logarithmic strain curves obtained from experimental loading-unloading tensile tests of smooth and short gauge tensile specimens, respectively, for characterizing damage response of the three materials by measuring values of the axial load and the gauge section diameter during the test.

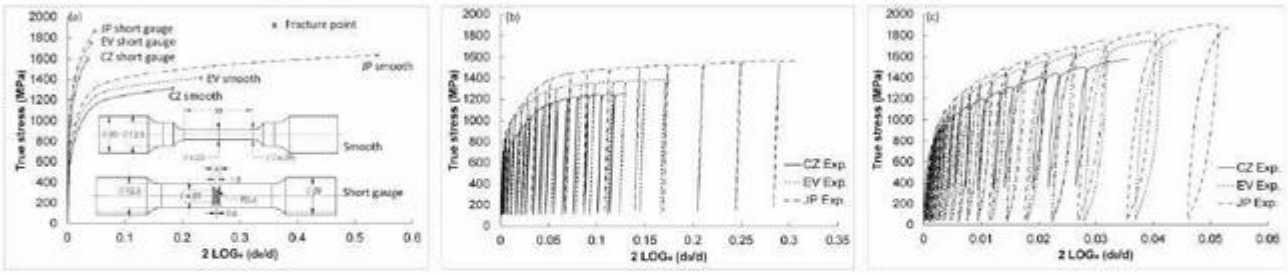

Fig.1. Experimental test results: (a) monotonic tensile tests for smooth and short gauge tensile specimens; (b) cyclic tensile tests of smooth tensile specimens; (c) cyclic tensile tests of short gauge tensile specimens

RESULTS AND ANALYSIS

Axisymmetric FE modelling for smooth and short gauge tensile tests was performed using ABAQUS standard solver v6.13. Fig. 2 shows the FEM analysis of monotonic and cyclic tensile tests for the two types of specimens to determine variation of the stress triaxiality and also correction factors to eliminate geometry effect on the elastic modulus measurement. By mimicking the load-elongation and cross-section reduction curves from the monotonic smooth tensile test

[a)] Corresponding author. Email: fyu@ualberta.ca

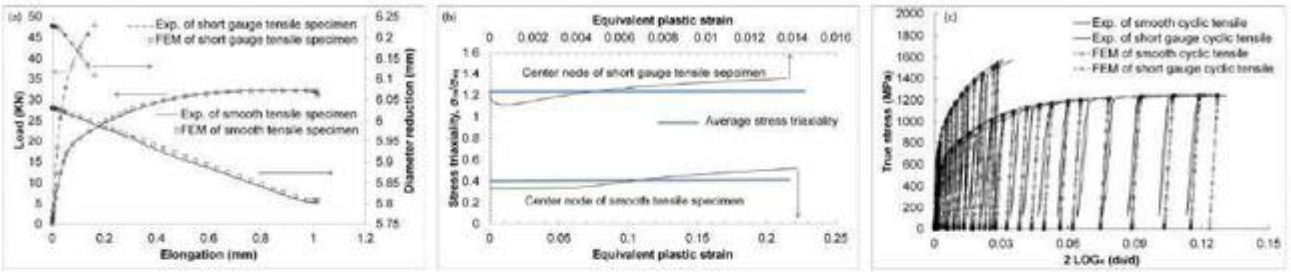

Fig.2. FEM analysis of smooth and short gauge tensile specimens: (a) monotonic tensile tests; (b) stress triaxiality evolution; (c) cyclic tensile tests; (here, only curves for CZ steel are presented)

using FE modelling, as shown in Fig. 2a, the constitutive equations for the three high strength rail steels are established phenomenologically. To quantify the damage evolution in the short gauge tensile specimen, the constitutive equation from smooth tensile specimen is applied to the FEM modelling where the simulation results fit the two experimental data of the short gauge tensile specimen (Fig. 2a). Fig. 2b shows the evolution of stress triaxiality at the centre of the smooth and short gauge tensile specimens during the simulation, where the averaged stress triaxiality is 0.4 and 1.2, respectively. Numerical simulation of cyclic tensile tests for smooth and short gauge tensile specimens were performed for the purpose of quantifying variation of the unloading modulus due to the geometry effect and calibrating a correction factor by comparing the calculated unloading modulus with the pre-specified Young's modulus (Fig. 2c). The correction factor was then used to eliminate the geometrical influence on elastic modulus measured from the experimental data.

Fig. 3 shows the corrected experimental results of elastic modulus deterioration of the two types of tensile specimens for all of the three high strength rail steels. The theoretical model describing the dependence of damage evolution on the stress triaxiality is shown in Fig. 3, which verifies the experimental data at stress triaxiality of both 0.4 and 1.2 [5]. As the modulus degrades at a very early stage, the onset of damage initiation is assumed to occur at the yield point for both types of tensile specimens. The fitting parameter D_c was used to represent the value of the critical damage parameter at a stress triaxiality of 0.4. The other parameters i.e. fracture strain for smooth tensile (ε_f) and short gauge tensile (p_f) specimens, and Young's modulus E_0, were all determined experimentally. As shown in the figure, the model fits well to the degradation of corrected elastic modulus, and depicts the difference in modulus degradation at the two levels of stress triaxiality. The corresponding D_{cr} values calculated at stress triaxiality of 1.2 for CZ, EV, and JP are 0.60, 0.67, and 0.65, respectively; these values are notably larger than the D_c values determined for the stress triaxiality of 0.4.

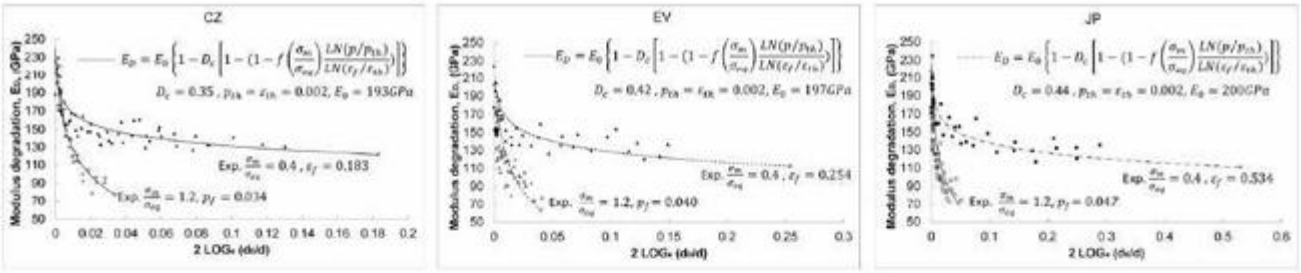

Fig.3. Stress triaxiality effect on damage evolution of three high strength steels: (a) steel CZ; (b) steel EV; (c) steel JP

DISCUSSION AND CONCLUSION

The effect of stress triaxiality on plastic deformation and damage is apparent from the experimental test results. Since the same constitutive equation can describe the deformation behaviour for both types of tensile specimens, the obtained constitutive equation is a combination of both elastic-plastic and damage mechanisms. The damage evolution and D_{cr} value are shown to be dependent on stress triaxiality.

References

[1] Lee J.S., Jang J.I., Lee B.W., Choi Y., Lee SG., Kwon D.: An instrumented indentation technique for estimating fracture toughness of ductile materials: A critical indentation energy model based on continuum damage mechanics. *Acta Mater* **54**:1101-9, 2006.

[2] Maire E., Zhou S., Adrien J., Dimichiel M.: Damage quantification in aluminium alloys using in situ tensile tests in X-ray tomography. *Eng Fract Mech* **78(15)**:2679-90, 2011.

[3] Celentano D.J., Chaboche J.L.: Experimental and numerical characterization of damage evolution in steels. *Int J Plasticity* **23**:1739-62, 2007.

[4] Bonora N., Gentile D., Pirondi A., Newaz G.: Ductile damage evolution under triaxial state of stress: theory and experiments. *Int J Plasticity* **21**:981-1007, 2005

[5] Bonora N.: A nonlinear CDM model for ductile failure. *Eng Fract Mech* **58(1)**:11-28, 1997.

EFFECTS OF COMPRESSIVE LOADING HISTORY ON MECHANICAL PROPERTIES OF HDPE

Yi Zhang[a] & P.-Y. Ben Jar
Department of Mechanical Engineering, University of Alberta, Edmonton, Alberta, Canada

Abstract This paper examines the influence of compressive loading history on mechanical properties of high-density polyethylene (HDPE) using specimens prepared from HDPE pipe. The examination consists of two tests. Compressive loading history was introduced in the first test, to generate five prestrain levels at crosshead speeds of 0.01, 1 and 50mm/min, corresponding to strain rates of 1.85×10^{-5}, 1.85×10^{-3} and 9.26×10^{-2} respectively. The second compressive test was carried out two months later, to characterize mechanical properties of specimens including elastic modulus and yield stress, at crosshead speed of 0.01mm/min. Variation of the elastic modulus is used to establish the damage evolution under the compressive loading condition. The results indicate that both yield stress and elastic modulus decrease with the increase of the prestrain. The results also suggest that the extent of decrease of yield stress and elastic modulus, thus the damage evolution, depend on the crosshead speed applied in the first test.

INTRODUCTION

Semi-crystalline polymers are increasingly used in a broad range of applications such as pressure tubing, pipeline systems and parts in nuclear power plant. Nowadays, majority of low-pressure natural gas pipes with a 50-year service life are made of polyethylene (PE). However, there are many loading scenarios [1, 2] in which the pipelines can be subjected to plastic deformation. This loading history affects further load-carrying capability of the pipe, and thus its lifetime is affected. Although several experimental investigations have been conducted to evaluate the effect of loading history on mechanical properties of HDPE [3-5], none of them was focused on the damage characterization based on compressive loading history. In addition, our recent test results suggest degradation of mechanical properties for HDPE, generated during a squeeze-off process for pipe maintenance, is surprisingly insensitive to deformation speed. As a result, a preliminary investigation has been conducted on the possibility of generating compressive damage in HDPE, with a focus on the effects of strain rate (by varying the crosshead speed). This paper summarizes the results obtained from the study.

EXPERIMENTAL DETAILS

Materials

All specimens used in this study were prepared from commercial PE4710, Cell classification 445576C HDPE pipe of 2 inches in diameter. Resin for the HDPE pipe is known as PE-80 which is for a grade of PE which has to have the Minimum Required Strength (MRS) of 8MPa. Dimensions of arc-shaped specimens, loading direction and compressive test setup are shown in Fig. 1.

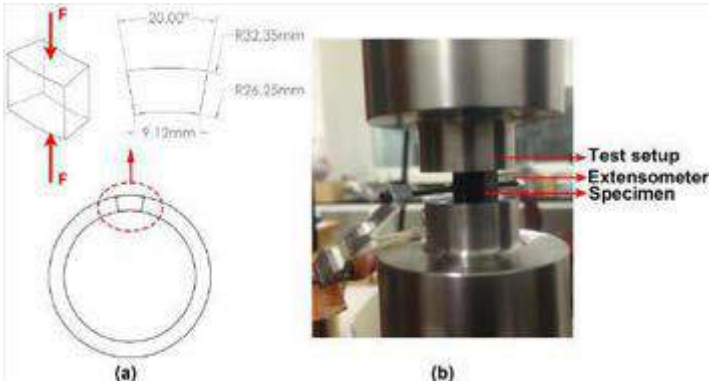

Figure 1 Arc-shaped specimens (a) and compressive test setup (b)

Test Conditions

The strain was determined based on the variation of thickness along the radial direction, measured using an extensometer made in-house. Load is applied in the longitudinal direction of the pipe, as shown in Fig. 1. A preliminary test to minimize the end constrain on the test result has suggested that most of the friction at the contact point can be removed by applying lubricating grease between specimen and test fixture. The first tests were to apply monotonic compressive loading to five prestrain levels (10%, 20%, 30%, 40% and 45%) at crosshead speeds of 0.01, 1 or 50mm/min. In contrast, condition used for the second test was monotonic compressive loading at the crosshead speed of 0.01mm/min. Yield stress and elastic modulus were determined from the second tests, to evaluate influence of the prestrain level and crosshead speed applied in the first tests on variation of their values.

[a] Corresponding author. Email: yz4@ualberta.ca.

RESULTS AND DISCUSSION

Yield stress and elastic modulus determined from the second tests are summarized in Fig. 2(a) and 2(b), respectively, as a function of prestrain introduced in the first tests. Note that values for specimens without any loading history are also included in the figures, at prestrain of 0. The figures suggest that yield stress increases slightly with small prestrains and then decreases with further increase of the prestrain, while elastic modulus decreases monotonically with the increase of the prestrain. Damage parameter (D) is determined based on the variation of elastic modulus, as shown below [6]:

$$D = 1 - \frac{\tilde{E}}{E_0} \tag{1}$$

where $\tilde{E}$ and E_0 are elastic moduli of the specimens with and without the prestrain, respectively.

Fig. 2(c) presents variation of D value as a function of the prestrain introduced in the first test. The figure also includes curves generated using Equation (2) [7], with values for A and B determined by fitting the curves to the trend of change of measured values. Fig. 2(c) indicates that both prestrain and crosshead speed have a significant effect on the change of D values.

$$D = A\left[1 - \exp\left(-B\varepsilon\right)\right] \tag{2}$$

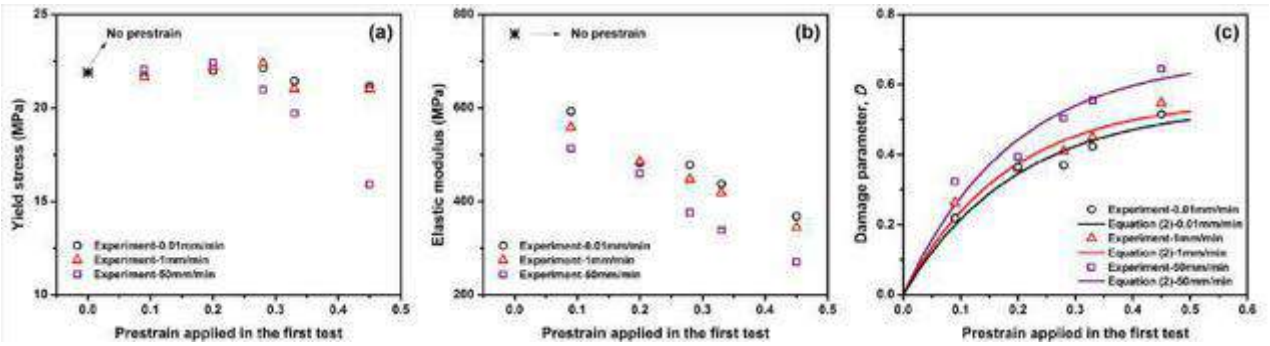

Figure 2 Effects of prestrain applied in the first test on the yield stress (a), elastic modulus (b) and the damage parameter D determined based on the variation of elastic modulus (c)

CONCLUSIONS

Effects of compressive loading history on mechanical properties of HDPE have been assessed using the two-test method, on specimens prepared from the HDPE pipe. The results show that mechanical properties of HDPE are strongly affected by the loading conditions used in the first test. In particular, elastic modulus from the second test, measured at the strain of 0.5%, decreases significantly with the increase of prestrain applied in the first test. Damage evolution in the first test is established using a phenomenological damage model based on the variation of the elastic modulus measured from the second test. The results suggest that increase of the crosshead speed, i.e., increase of the strain rate, causes acceleration of the damage evolution, thus increasing the extent of damage in the HDPE pipe. Further investigation will be conducted to ascertain the existence of the compressive damage in HDPE, and the results will be presented in the conference.

ACKNOWLEDGEMENT

The work was supported by Natural Sciences and Engineering Research Council of Canada (NSERC) and China Scholarship Council (CSC). Sincere appreciation is due to technical staff in the Department of Mechanical Engineering, at the University of Alberta, particularly, Campbell, Waege and Bubenko for specimen preparation and Faulkner for fabrication of the extensometer.

References

[1] Yayla, P. and Bilgin, Y.: Squeeze-off of polyethylene pressure pipes: Experimental analysis. Polymer Testing: 132-141, 2007.
[2] Palermo, G.: Correlating Aldyl "A" and Century PE Pipe Rate Process Method Projections with Actual Field Performance. Milan, Italy 2004.
[3] Jar, P.Y.B.: Effect of tensile loading history on mechanical properties for polyethylene. Polymer Engineering & Science, 2014.
[4] Jar, P.Y.B: Effect of Loading History on Elastic Modulus of HDPE. In ASME 2015 Pressure Vessels and Piping Conference.
[5] Zhang, Y. and Jar, P.Y.B: Quantitative assessment of deformation-induced damage in polyethylene pressure pipe. Polymer Testing, 42-50, 2015.
[6] Lemaitre, J: A continuous damage mechanics model for ductile fracture. Journal of Engineering Materials and Technology, 83-89, 1985.
[7] Detrez F, Cantournet S, Seguela R: Plasticity/damage coupling in semi-crystalline polymers prior to yielding: Micromechanisms and damage law identification. Polymer, 1998-2008, 2011.

SM04 - Elasticity

TS.SM04-1.01	Ashida, Fumihiro - Control of complicated stress oscillations in FGPM thin plates (INVITED)	1888
TS.SM04-1.02	Banerjee, Amartya - A framework for frequently occurring non-generic degeneracies	1890
TS.SM04-1.03	Dai, Hui-Hui - On a consistent shell theory based on finite elasticity	1892
TS.SM04-1.04	Kapuria, Santosh - Accurate prediction of free edge effect in piezolaminated panels	1894
TS.SM04-1.05	Liu, Liping - Geometrically nonlinear theories for curved beams and shells	1896
TS.SM04-1.06	Weller, Thibaut - Mathematical modeling of thin linearly quasicrystalline plates	1898
TS.SM04-2.01	Chen, Changqing - Elastic properties of origami-inspired reconfigurable metamaterials (INVITED)	1900
TS.SM04-2.02	Desmorat, Boris - Application of the tensorial polar decomposition to 2D medium with open and closed cracks	1902
TS.SM04-2.03	Nie, Guohua - Bi-stability of FGM Cylindrical Shells with Piezoelectric Surface Layers	1904
TS.SM04-2.04	Chen, Shaohua - A new elastic theory for nanomaterials and its application	1906
TS.SM04-2.05	Chen, Weiqiu - theory of nanoindentation for multiferroic materials	1908
TS.SM04-2.06	Mauthe, Steffen - Minimization principles in poro-hydro-elasticity at fracture and their exploitation	1910
TS.SM04-3.01	Miehe, Christian - Variational phase field models for ductile fracture at finite strain (INVITED)	1912
TS.SM04-3.02	Berdichevsky, Victor - The variational principle for probabilistic measure, Hashin-Shtrikman bounds and beyond	1914
TS.SM04-3.03	Buryachenko, Valeriy - Random structure composites with nonlocal thermoelastic properties of constituents	1915
TS.SM04-3.04	Rudykh, Stephan - Micromechanics of magneto- and electro-active soft composites	1917
TS.SM04-3.05	Podolskaya, Ekaterina - Elastic fields and effective properties of triangular lattice with vacancies	1919
TS.SM04-3.06	Bleiler, Christian - A novel microstructurally-based material model to describe passive skeletal muscle tissue	1921
TS.SM04-4.01	Triantafyllidis, Nicolas - Freedericksz Instability for the Twisted Nematic Device; A 3D Analysis (INVITED)	1923
TS.SM04-4.02	Bellis, Cédric - Converting strain maps into elasticity maps for materials with small contrast	1925
TS.SM04-4.03	Shifrin, Efim - Identification of small inhomogeneities in 3D thermoelasticity	1927
TS.SM04-4.04	Peerlings, Ron - Hygro-Mechanical Structure-Property Relations for Paper Sheets	1929
TS.SM04-4.05	Shmuel, Gal - The universality of the band structure of layered composites	1931
TS.SM04-4.06	Matlack, Kathryn - Controlling band gaps with geometry in composite elastic meta-structures	1933
TS.SM04-5.01	Segev, Reuven - On the relation between generalized stress theory and electrodynamics	1935
TS.SM04-5.02	Pence, Thomas - Swelling induced burst in hyperelastic spheres and cylinders	1937

TS.SM04-5.03	Man, Chi-Sing - Remarks on isotropic extension of anisotropic constitutive functions via structural tensors	1939
TS.SM04-5.04	Itskov, Mikhail - Mechanics of nano-particles filled elastomers based on polymer chain length statistics	1941
TS.SM04-5.05	Dorfmann, Luis - Modeling of Residually Stressed Materials	1943
TS.SM04-5.06	Weil, Gidon - Finite shear of thin-wall composite spheres	1944
PO.SM04-1.02.216	Chu, Haijian - Elastic Response Due To Dislocation Arrays With Core Spreading In Multilayered Materials	1946
PO.SM04-1.03.217	Dai, Ming - Stress field around an elliptical hole with surface tension in an anisotropic half-plane	1948
PO.SM04-1.04.218	Domanskaia, Tatiana - Bi-material plane of John's harmonic material with a point force at interface	1950
PO.SM04-1.05.219	Dyer, Tom - Intercalation of carbon nanotubes into a graphene sheet	1952
PO.SM04-1.06.220	Grigor'Ev, Yuri - Regular Quaternionic Functions and their Applications in Three-dimensional Elasticity	1954
PO.SM04-1.07.221	Jaiani, George - On Cusped (Tapered) Prismatic Shells	1956
PO.SM04-1.08.222	Karyakin, Mikhail - Discontinuous solutions of the nonlinear theory of Volterra dislocations	1958
PO.SM04-1.09.223	Koguchi, Hideo - Analysis for arbitrary misfit dislocations considering interface property	1960
PO.SM04-1.10.224	Kossa, Attila - On the constitutive modelling of elastomeric foams	1962
PO.SM04-1.11.225	Lambadi, Harish - Modeling of biaxial response of Polyvinyledene Fluoride (PVDF)	1964
PO.SM04-1.12.226	Li, Zhengwei - Mechanics and Optics of Artificial Compound Eye Camera	1966
PO.SM04-1.13.227	Liu, Li-Wei - A general solution for three-dimensional problems of anisotropic elasticity	1968
PO.SM04-1.14.228	McArthur, Dan - A circular inclusion with inhomogeneous imperfect interface in harmonic materials	1970
PO.SM04-1.15.229	Mei, Yue - Parameter identification via a modified constrained minimization procedure	1972
PO.SM04-1.16.230	Schneider, Patrick - Mathematically justified refined theories for thin structures	1974
PO.SM04-1.17.231	Tóth, Balázs - Dual-mixed principles in elastodynamics - an application to cylindrical shells	1976
PO.SM04-1.18.232	Van Pham, Phe - A complementary strain energy solution for higher order beam theory	1978
PO.SM04-1.19.233	Vannucci, Paolo - Some recent theoretical results in plane anisotropic elasticity	1980
PO.SM04-1.20.234	Vu, Khiem - Micromechanical modeling of rubber-like materials based on analytical network averaging	1982
PO.SM04-1.21.235	Wang, Ji - Thickness-shear vibrations of circular quartz crystal plates	1984
PO.SM04-1.22.236	Wang, Linjuan - Generalized thermoelasticity in framework of peridynamics	1986
PO.SM04-1.23.237	Ye, Zhiming - Finite element numerical simulation of bi-modulus beams	1988
PO.SM04-1.24.238	Zhang, Lele - Rayleigh waves in a layered piezoelectric nanostructure with surface effects	1990
PO.SM04-1.25.239	Zhang, Li - An arbitrarily oriented crack problem for a functionally graded coating-substrate structure	1992

PO.SM04-1.26.240	Zhao, Jia-Min - Standardized compliance matrices for general anisotropic materials	1994
PO.SM04-1.27.241	Zhao, Yingtao - Polynomial Stress Functions for Piezoelectric Problems and Their Application in ATF Method	1996
PO.SM04-1.28.242	Zhavoronok, Sergey - High-order shell theory based on the analytical continuum dynamics formalism	1998
PO.SM04-1.29.243	Zhou, Shenjie - A strain gradient elasticity theory with independent length scale parameters	2000
PO.SM04-1.30.244	Zou, Wennan - An elasticity theory with defects	2002

CONTROL OF COMPLICATED STRESS OSCILLATIONS IN FGPM THIN PLATES

Fumihiro Ashida[1a)], Takuya Morimoto[1] & Hidenori Ozaki[2]
[1]*Department of Mechanical, Electrical, and Electronic Engineering, Shimane University, Matsue, Shimane, Japan*
[2]*OPTON Co. Ltd., Seto, Aichi, Japan*

Summary One-dimensional electro-elastodynamic problems in functionally graded piezoelectric material (FGPM) thin plates subjected to uniform impact pressures are analyzed and exact analytical solutions are presented. Numerical results show that the behavior of stress oscillation obtained under electric charge-free boundary conditions is different from it derived under prescribed electric potential boundary conditions. The applied voltages which completely suppress the complicated stress oscillations are determined from the analytical solutions.

INTRODUCTION

Many papers dealt with dynamic problems in various functionally graded material (FGM) solids subjected to harmonic loadings, but a few papers investigated stress oscillations induced in FGM solids by elastic wave propagations. The first author et al. revealed that the mechanical impedance governed the behavior of stress oscillation in an FGM thin plate [1].

This paper addresses a one-dimensional electro-elastodynamic problem in an FGPM thin plate subjected to uniform impact pressure when electric charges are free on both surfaces of the thin plate and that when electric potentials are prescribed on both surfaces. Employing techniques of the space-variable transformation and Laplace transform, the analytical solutions are respectively derived for the case where nonhomogeneous material properties vary exponentially in the thickness direction. Numerical results obtained under the electric charge-free conditions show that the stress oscillation is periodic when the mechanical impedance is independent of the space-variable, whereas it is complicated when the impedance depends on the space-variable. The stress oscillations derived under the prescribed electric potential conditions are complicated for both cases of mechanical impedance. The complicated stress oscillations can be controlled by applying appropriate voltages.

PROBLEM STATEMENT AND ANALYTICAL SOLUTIONS

It is assumed that an FGPM thin plate depicted in Fig. 1 is initially in stress-free state, one surface is subjected to an impact pressure $\sigma_0 H(t)$, and the other surface is fixed to a flat rigid body. The initial and elastic boundary conditions are

$$u_z = u_{z,t} = 0 \ \text{ at } \ t = 0, \ u_z = 0 \ \text{ on } \ z = 0, \ \sigma_{zz} = -\sigma_0 H(t) \ \text{ on } \ z = l \tag{1}$$

where $u_z(z,t)$ is the displacement, $\sigma_{zz}(z,t)$ is the stress, $H(t)$ is Heaviside's unit step function, t is time, l is the thickness of the plate, and $u_{z,t} = \partial u_z / \partial t$. For the electric field of the thin plate, it is assumed that the electric charges are free or the electric potentials are prescribed on the top and bottom surfaces:

$$D_z = 0 \ \text{ on } \ z = 0, l \quad \text{or} \quad \Phi = 0 \ \text{ on } \ z = 0, \ \Phi = V_l \ \text{ on } \ z = l \tag{2}$$

where $D_z(z,t)$ is the dielectric flux density, $\Phi(z,t)$ is the electric potential, and V_l is an applied voltage. The constitutive and governing equations are

$$\sigma_{zz} = c_{33}(z)\, u_{z,z} + e_3(z)\Phi_{,z}, \ \ \sigma_{zz,z} = \rho(z) u_{z,tt} \tag{3}$$

$$D_z = e_3(z)\, u_{z,z} - \eta_3(z)\Phi_{,z}, \ \ D_{z,zt} = 0 \tag{4}$$

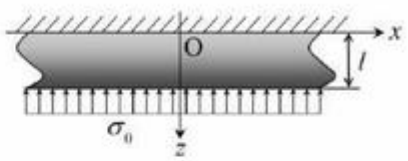

Fig.1 Geometry of an FGPM thin plate

where $c_{33}(z)$ is the elastic modulus, $\rho(z)$ is the density, $e_3(z)$ is the piezoelectric constant, and $\eta_3(z)$ is the dielectric permittivity. They are assumed to be expressed as $c_{33}(z) = c_{330} e^{pz}$, $\rho(z) = \rho_0 e^{qz}$, $e_3(z) = e_{30} e^{az}$, and $\eta_3(z) = \eta_{30} e^{bz}$.

Employing techniques of the space-variable transformation defined as $\zeta = e^{\delta z}$ and the Laplace transform, the exact analytical solutions are obtained when the nonhomogeneous parameters are taken to be $a = b = p$ and $q - p = 2\delta$.

When the electric charges are free on the top and bottom surfaces of the thin plate, the stresses are given by

$$\sigma_{zz} = -\sigma_0 + 2\sigma_0 \sum_{n=1}^{\infty} \frac{\cos\{\alpha_n(\zeta - 1)\}\cos(\delta v_{e0} \alpha_n t)}{\alpha_n(\zeta_l - 1)\sin\{\alpha_n(\zeta_l - 1)\}} \ \text{ for } \ p = -\delta, q = \delta \tag{5}$$

$$\sigma_{zz} = -\sigma_0 - 2\sigma_0 \sum_{n=1}^{\infty} \frac{[\beta_n \zeta \cos\{\beta_n(\zeta - 1)\} - \sin\{\beta_n(\zeta - 1)\}]\cos(\delta v_{e0} \beta_n t)}{\beta_n[\cos\{\beta_n(\zeta_l - 1)\} - \beta_n(\zeta_l - 1)\zeta_l \sin\{\beta_n(\zeta_l - 1)\}]} \ \text{ for } \ p = \delta, q = 3\delta \tag{6}$$

When the electric potentials are prescribed on the top and bottom surfaces of the thin plate, the stresses are expressed by

$$\sigma_{zz} = -\sigma_0 - 2(\sigma_0 + \phi V_l) \sum_{n=1}^{\infty} \frac{[\delta Y_0 \gamma_n \cos\{\gamma_n(\zeta - 1)\} - \psi \sin\{\gamma_n(\zeta_l - 1)\}]\cos(\delta v_{e0} \gamma_n t)}{\gamma_n[\{\delta Y_0 - \psi(\zeta_l - 1)\}\cos\{\gamma_n(\zeta_l - 1)\} - \delta Y_0 \gamma_n(\zeta_l - 1)\sin\{\gamma_n(\zeta_l - 1)\}]} \ \text{ for } \ p = -\delta, q = \delta \tag{7}$$

$$\sigma_{zz} = -\sigma_0 - 2(\sigma_0 + \zeta_l \phi V_0) \sum_{n=1}^{\infty} \frac{\langle \delta Y_0[\varepsilon_n \zeta \cos\{\varepsilon_n(\zeta - 1)\} - \sin\{\varepsilon_n(\zeta - 1)\}] - \psi \sin\{\varepsilon_n(\zeta_l - 1)\} \rangle \cos(\delta v_0 \varepsilon_n t)}{\varepsilon_n[\{\delta Y_0 - \psi(\zeta_l - 1)\}\cos\{\varepsilon_n(\zeta_l - 1)\} - \delta Y_0 \varepsilon_n \zeta_l(\zeta_l - 1)\sin\{\varepsilon_n(\zeta_l - 1)\}]} \ \text{ for } \ p = \delta, q = 3\delta \tag{8}$$

a) Fumihiro Ashida. Email: ashida@ecs.shimane-u.ac.jp

Here, the mechanical impedance is expressed by $Z(z)=Z_0$ in the case of $p=-\delta$ and $q=\delta$, while it is given by $Z(z)=Z_0 e^{2\delta z}$ in the case of $p=\delta$ and $q=3\delta$. The coefficients in the above equations are

$$Y_0=c_{330}+\frac{e_{30}^2}{\eta_{30}},\ v_{e0}=\sqrt{\frac{Y_0}{\rho_0}},\ Z_0=\sqrt{Y_0\rho_0},\ \zeta_l=e^{\delta l},\ \phi=\frac{\delta e_{30}}{\zeta_l-1},\ \psi=\frac{e_{30}\phi_1}{\eta_{30}} \quad (9)$$

$$\alpha_n=\frac{(2n-1)\pi}{2(\zeta_l-1)},\ \sin\{\beta_n(\zeta_l-1)\}-\zeta_l\beta_n\cos\{\beta_n(\zeta_l-1)\}=0 \quad (10)$$

$$\psi\sin\{\gamma_n(\zeta_l-1)\}-\delta Y_0\gamma_n\cos\{\gamma_n(\zeta_l-1)\}=0 \quad (11)$$

$$(\delta Y_0+\psi)\sin\{\varepsilon_n(\zeta_l-1)\}-\delta Y_0\zeta_l\varepsilon_n\cos\{\varepsilon_n(\zeta_l-1)\}=0 \quad (12)$$

NUMERICAL RESULTS

For convenience in presentation of numerical results, the following nondimensional quantities are introduced.

$$\bar{z}=\frac{z}{l},\ \bar{t}=\frac{v_{e0}t}{l},\ \bar{\sigma}_{zz}=\frac{\sigma_{zz}}{\sigma_0},\ \bar{V}_l=\frac{e_{30}V_l}{\sigma_0 l},\ \bar{Z}=\frac{Z}{Z_0},\ \bar{\delta}=\delta l,\ \bar{p}=pl,\ \bar{q}=ql$$

The material on the top surface of the thin plate is assumed to be PZT-4.

Numerical results derived under the electric charge-free conditions are illustrated in Figs. 2, where the arbitrary constant of the space-variable transformation is taken to be $\bar{\delta}=0.4$. It is seen that the stress oscillation is periodic and monotonic when the mechanical impedance is independent of the space-variable $(\bar{Z}(\bar{z})=1)$, while it is complicated when the impedance depends on the space-variable $(\bar{Z}(\bar{z})=e^{2\bar{\delta}\bar{z}})$.

Numerical results obtained under the prescribed electric potential conditions are illustrated in Figs. 3, where the mechanical impedance is given by $\bar{Z}(\bar{z})=e^{2\bar{\delta}\bar{z}}$ and the arbitrary constant is taken to be $\bar{\delta}=0.4$ and $\bar{\delta}=-0.302$. Applying the voltage $\bar{V}_l=-0.824$ which is determined from the condition of $\sigma_0+\zeta_l\phi V_0=0$ in Eq. (8), the complicated stress oscillation is completely suppressed. When the arbitrary constant is taken to be $\bar{\delta}=-0.302$ in order to satisfy the condition of $\delta Y_0+\psi=0$ in Eq. (12), the stress oscillation is periodic. Although the figure is omitted here for brevity, numerical results obtained for the case of $\bar{Z}(\bar{z})=1$ and $\bar{\delta}=0.4$ are similar to those depicted in Fig. 3 (a), in which case the stress oscillation is completely suppressed by applying $\bar{V}_l=-1.230$. It follows that the stress oscillation for the case of $\bar{Z}(\bar{z})=e^{2\bar{\delta}\bar{z}}$ and $\bar{V}_l=0$ in Fig. 3 (a) is similar to that illustrated in Fig. 2 (b), while the stress oscillation for the case of $\bar{Z}(\bar{z})=1$ and $\bar{V}_l=0$ is different from that illustrated in Fig. 2 (a). Therefore, the behavior of stress oscillation depends on the setting of electric boundary conditions and the complicated stress oscillations can be controlled by applying appropriate voltages.

CONCLUSIONS

In this study, the analytical solutions to the one-dimensional electro-elastodynamic problems of the FGPM thin plates subjected to uniform impact pressures are obtained. Numerical results show that the behavior of stress oscillation depends on the setting of electric boundary conditions. The complicated stress oscillations are controlled by applying appropriate voltages and suppressed completely when the specified voltages determined from the analytical solutions are applied.

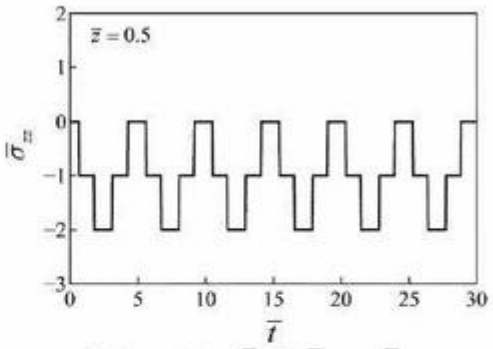

(a) $\bar{Z}(\bar{z})=1\ (\bar{p}=-\bar{\delta},\bar{q}=\bar{\delta})$ and $\bar{\delta}=0.4$

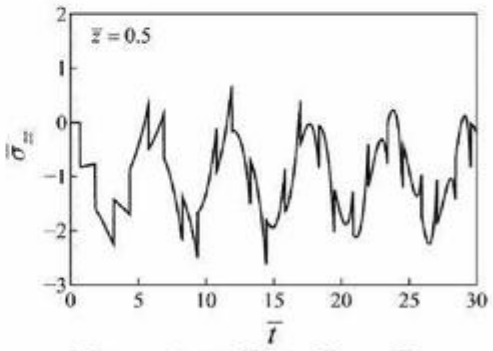

(b) $\bar{Z}(\bar{z})=e^{2\bar{\delta}\bar{z}}\ (\bar{p}=\bar{\delta},\bar{q}=3\bar{\delta})$ and $\bar{\delta}=0.4$

Figs. 2 Numerical results derived under electric charge-free conditions

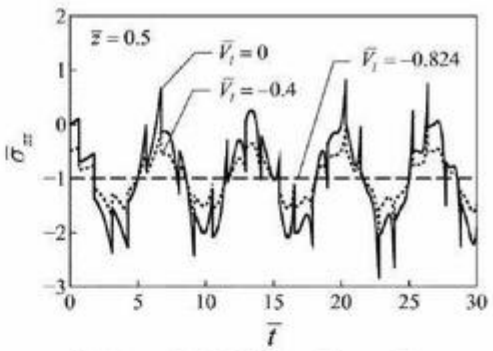

(a) $\bar{Z}(\bar{z})=e^{2\bar{\delta}\bar{z}}\ (\bar{p}=\bar{\delta},\bar{q}=3\bar{\delta})$ and $\bar{\delta}=0.4$

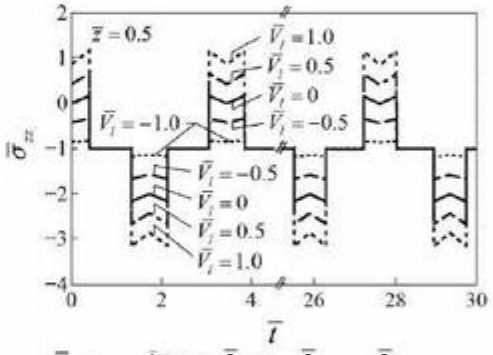

(b) $\bar{Z}(\bar{z})=e^{2\bar{\delta}\bar{z}}\ (\bar{p}=\bar{\delta},\bar{q}=3\bar{\delta})$ and $\bar{\delta}=-0.302$

Figs. 3 Numerical results derived under prescribed electric potential conditions

References

[1] Ashida F., et al.: Analysis of Complicated One-dimensional Stress Oscillation Behaviour in a Functionally Graded Material Plate. *ZAMM* **95**: 184-192, 2015.

A FRAMEWORK FOR FREQUENTLY OCCURRING NON-GENERIC DEGENERACIES

Amartya S. Banerjee[1,2] and Ryan S. Elliott *[2]

[1]*Computational Research Division, Lawrence Berkeley National Laboratory, Berkeley, CA 94720, U.S.A.*
[2]*Department of Aerospace Engineering and Mechanics, University of Minnesota, Minneapolis, MN 55455, U.S.A.*

Summary The occurrence of generic degeneracies in physical systems is closely related to underlying symmetries of the governing equations. The occurrence of additional non-generic degeneracies which cannot be accounted for by symmetry arguments is usually termed *accidental*. In this work, we develop a framework that helps identify and investigate a particular class of degeneracies associated with equivariant systems under certain common symmetry groups. We show that the existence of a first-integral for such systems (i.e., a potential function or energy functional) guarantees generically that non-generic degeneracies in the spectrum of the Jacobian (and other system properties) occur. We describe concrete examples of physical systems exhibiting these types of degeneracies and comment on the ramifications.

INTRODUCTION

Symmetry plays a very important role in the formulation of physical theories in different branches of science and engineering. In the mechanics of materials for example, the presence of symmetry is usually associated with the occurrence of interesting material properties, or sometimes, symmetry provides an explanation for the lack of such properties. The most widely studied structures in materials science and solid state physics are crystals, whose wide variety of interesting material properties are usually directly related to their underlying space group symmetries [6, 3]. Indeed, physical symmetry alone has been used to motivate and inform the search for novel materials and structures possessing unprecedented properties, with anticipated applications of such materials in various branches of science and engineering [1].

The presence of symmetry in physical systems often manifests itself through the occurrence of degeneracies. Specifically, the governing equations of physical systems often exhibit the mathematical property of *equivariance* from which, for example, the occurrence of multiple solutions (corresponding to degenerate physical states) or low dimensional parameterizations of the solution space can be inferred [2, 8, 3, 7, 5]. In practice, this mathematical procedure is almost always used in conjunction with the additional assumption of *generic behavior* – this says that the observation of degeneracies in a physical system are always due to the underlying symmetries – and to repeatedly use this assumption in the derivation and proof of theorems for such systems [7, 3]. Indeed, the results of equivariant bifurcation theory [4, 2] for example, are based on the assumption that the Jacobian of the equilibrium equations will generically have exactly the degenerate spectrum that is dictated by the symmetry of the governing equations. In particular, the *generic behavior* argument is used to explicitly exclude the possibility of additional *non-generic* (or *accidental*) degeneracies in the spectrum of the Jacobian.

In this work, we formulate a framework which helps identify and investigate a particular class of degeneracies. This class of degeneracies cannot be expected to occur based on physical symmetry arguments alone (and so, these degeneracies might be considered accidental) but nevertheless they occur generically enough in the sense that numerous examples of their occurrence in various branches of science and engineering can be identified through this framework. Specifically, we show that for equivariant systems under certain common symmetry groups, the existence of a first-integral for the system (i.e., a potential function or energy functional) guarantees generically that non-generic degeneracy of the Jacobian (and other properties of the system) occurs. We apply our theory to common physical systems and show that it successfully explains the *accidental* degeneracy found in problems involving truss structures with cyclic symmetry, periodic crystals without inversion symmetry and the well-known degeneracies of the elastic constants matrix in the theory of linear elasticity.

THEORETICAL FRAMEWORK

From a mechanics perspective, it is natural to describe a physical system as a subset $\mathfrak{B} \subseteq \mathbb{R}^m$, with $m \in \{1, 2, 3\}$ and to ascribe to it a *degree of freedom field* by means of a map of the form $\mathfrak{F} \ni y : \mathfrak{B} \to \mathfrak{S}_F \subseteq \mathbb{R}^{n_F}$ ($n_F \in \mathbb{Z}^+$). The degree of freedom field $y \in \mathfrak{F}$ induces an appropriate response $\mathcal{M} \ni \chi : \mathfrak{B} \to \mathfrak{S}_R \subseteq \mathbb{R}^{n_R}$ ($n_R \in \mathbb{Z}^+$) over the body. The degree of freedom field and its associated response are linked via a *constitutive relation* $\Xi : \mathfrak{F} \to \mathcal{M}$. An example from classical continuum mechanics would consider a material body B and associate the set $\mathfrak{B}$ with a domain in $\mathbb{R}^m$: the *reference configuration*. The degree of freedom field would be a *deformation mapping* of the reference configuration into the *current configuration* $\mathfrak{S}_F$. The stress field resulting from the deformation would be identified as a response field.

An energy functional for the body $\mathfrak{B}$ is simply a map $\mathcal{E}_{\mathfrak{B}} : \mathfrak{F} \times \mathcal{M} \to \mathbb{R}$. This definition sets up the degree of freedom field and its associated response field as *energy conjugates*. If the functional $\mathcal{E}_{\mathfrak{B}}$ has an integral representation, then $f \in \mathfrak{F}$ and $\chi \in \mathcal{M}$ can possibly be related as functional derivatives. The search for zeros of suitable response functions $G_{\mathfrak{B}} : \mathfrak{F} \to S$ can be interpreted as solving the *governing equations* for the physical system. For systems with energy functionals, one can arrive at governing equations by using the principle of stationary potential energy.

*Corresponding author. Email: relliott@umn.edu

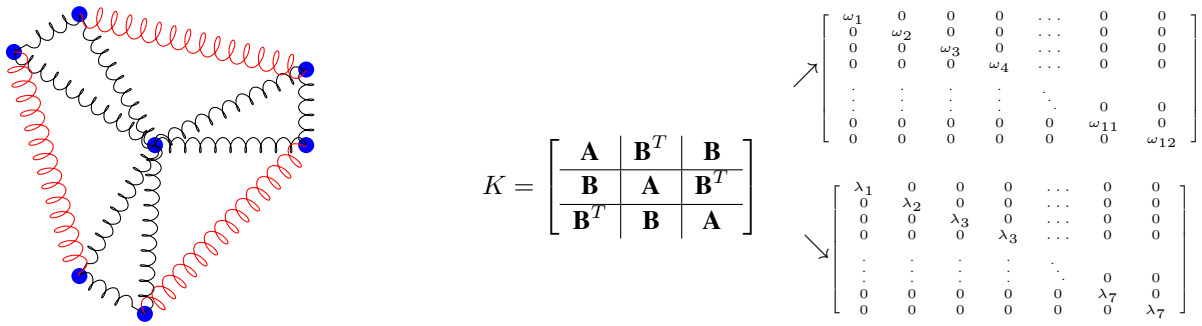

(a) Truss structure with three fold cyclic symmetry. The center node is assumed fixed. The energy functional for this system is invariant under the group C_3.

(b) The truss structure's block circulant stiffness matrix (left) is expected to diagonalize with all distinct eigenvalues due to cyclic symmetry (top-right), but it is actually found to contain unexpected degeneracies (bottom-right).

Figure 1: Non-generic degeneracies arising in a elastic truss system with cyclic symmetries

In order to bring symmetry into this framework, we suppose that a group $\mathcal{G}$ acts on the physical system and that the group action on points in $\mathfrak{B}$ is denoted as . For $g \in \mathcal{G}$, we introduce the notation g $\mathfrak{B}$ to denote the set $\{g \quad p : p \in \mathfrak{B}\}$. Then, $\mathcal{G}$ is a *geometric symmetry group* of $\mathfrak{B}$ provided that for each $g \in \mathcal{G}$, we have g $\mathfrak{B} = \mathfrak{B}$. The notion of physical symmetry is associated with the governing equations of the physical system and it is usually expressed through *equivariance*: A governing response function $G_{\mathfrak{B}} : \mathfrak{F} \to S$ is *equivariant* for every $g \in \mathcal{G}$ and every $f \in \mathfrak{F}$, if we have: $G_{\mathfrak{B}}(f) = g \quad G_{\mathfrak{B}}(g^{-1} \bullet f)$, i.e., $G_{\mathfrak{B}}(g \bullet f) = g \quad G_{\mathfrak{B}}(f)$. Here, the action of the group $\mathcal{G}$ on $\mathfrak{F}$ and S have been denoted as $\bullet$ and respectively.

Invariance of the energy functional is the condition $\hat{\mathcal{E}}_{\mathfrak{B}}(f) = \hat{\mathcal{E}}_{\mathfrak{B}}(g \bullet f)$ for every $f \in \mathfrak{F}$ and $g \in \mathcal{G}$. If we suppose the action of $\mathcal{G}$ on $\mathfrak{F}$ can be characterized using unitary representations then energy invariance can be used to imply equivariance of the first derivative of the energy. Further, we can show that the second derivative of the energy (the *stiffness* operator; also the Jacobian of the governing equations) commutes with unitary representations of the group $\mathcal{G}$. Under some hypotheses on $\mathcal{G}$ this can be used to further imply that the stiffness operator admits a block diagonal structure commensurate with the irreducible subspaces of $\mathcal{G}$. However, we can show that under certain circumstances, additional operators commuting with the stiffness operator may be found as a result of which non-generic degeneracies are observed frequently in practice.

EXAMPLE SYSTEMS

We consider first, the case of the truss structure shown in Fig. 1a. We may choose the set $\mathfrak{B}$ to be the collection of six nodal positions $\{x_i \in \mathbb{R}^2 : i = 1, 2, \ldots, 6\}$ of the truss and we can let $\mathfrak{S}_F = \{u_i \in \mathbb{R}^2 : i = 1, 2, \ldots, 6\}$ denote the corresponding set of nodal displacement vectors. It is easy to check that the system has an energy invariant under the three-fold cyclic symmetry group C_3. The stiffness matrix however admits a representation commensurate with a larger symmetry group D_3 (Fig. 1b). The existence of these *accidental degeneracies* in the structure of the stiffness matrix is naturally explained by our framework. Two further examples are as follows: First, for the single electron model of a periodic solid, the action of the translation group can be used to justify the fact that the eigenstates of the Hamiltonian can be decomposed in terms of Bloch states. The fact that this calculation deals with the Hamiltonian (which has an energy structure) results in extra degeneracies for the Bloch states, i.e., degeneracies which cannot be expected based on the translation symmetry alone. Secondly, the elastic constants matrix in the theory of linear elasticity often shows additional degeneracies – for example, the 11 crystallographic Laue groups produce only eight distinct forms for the stiffness matrix, so that some Laue groups lead to non-generic degenerate stiffness matrices. These examples are discussed in detail in a forthcoming paper by the authors.

ACKNOWLEDGMENTS

ASB received support at the Lawrence Berkeley National Laboratory through the Scientific Discovery through Advanced Computing (SciDAC) program funded by U.S. Department of Energy, Office of Science. ASB acknowledges support from the following grants at the University of Minnesota: AFOSR FA9550-15-1-0207, NSF-PIRE OISE-0967140, ONR N00014-14-1-0714 and the MURI project FA9550-12-1-0458 (administered by AFOSR). RSE acknowledges the support of the National Science Foundation (NSF) grant CMMI-1462826. Both authors acknowledge support by the Minnesota Supercomputing Institute.

References

[1] A. S. Banerjee. *Density Functional Methods for Objective Structures: Theory and Simulation Schemes*. PhD thesis, University of Minnesota, Minneapolis, 2013.

[2] M. Golubitsky and I. Stewart. *The Symmetry Perspective: From Equilibrium to Chaos in Phase Space and Physical Space*, volume 200 of *Progress in mathematics*. Birkhäuser, first edition, 2002.

[3] M. Hammermesh. *Group Theory and Its Application to Physical Problems*. Dover, first edition, 1989.

[4] T. J. Healey. A group-theoretic approach to computational bifurcation problems with symmetry. *Computer Methods in Applied Mechanics and Engineering*, 67(3):257–295, 1988.

[5] T. J. Healey. Symmetry and equivariance in nonlinear elastostatics, Part I. *Archive for Rational Mechanics and Analysis*, 105(3):205–228, 1989.

[6] M. Lax. *Symmetry Principles in Solid State and Molecular Physics*. Dover Publications, 2001.

[7] R. McWeeny. *Symmetry:An Introduction to Group Theory and Its Applications*. Dover, first edition, 2002.

[8] W. Miller. *Symmetry Groups and Their Applications*, volume 50 of *Pure and Applied Mathematics Series*. Elsevier Science & Technology Books, 1972.

ON A CONSISTENT SHELL THEORY BASED ON FINITE ELASTICITY

Zilong Song[1] and Hui-Hui Dai *[1]

[1]*Department of Mathematics, City University of Hong Kong, Kowloon Tong, Hong Kong*

Summary This paper presents a finite-strain shell theory, which is consistent with the principle of stationary three-dimensional (3-D) potential energy. Based on 3-D finite elasticity and by a series expansion, we deduce a vector shell equation with three unknowns. The success relies on deriving exact recursion relations for the expansion coefficients from the 3-D system. Appropriate 2-D boundary conditions and associated 2-D weak formulations are also proposed. As an example, the axisymmetric deformation of a spherical shell is considered, and the shell theory produces second-order correct results by comparison with the exact solution. The advantages of the present shell theory include consistency, high accuracy, without higher-order stress resultants and its applicability to general loadings.

INTRODUCTION

Shell theory is a classical research field, which can be dated back at least 120 years ago. Early attempts on shell theories relied on *a priori* hypotheses, mostly motivated by engineering intuition. The well-known shell theories include Kirchhoff-Love (1888), Reissner (1974), Koiter (1966) and Donnell (1976) theories, and we refer to [1] for a more detailed review. Although these theories have found a huge success in engineering applications, due to the hypotheses involved their consistency with the 3-D theory cannot be expected under general loadings.

In recent decades, some consistent mathematical methods, such as asymptotic method and method of Gamma convergence, have been employed to derive or justify the above theories. Many works are able to establish certain convergence results, but they rely on *a priori* scalings between applied loads and shell thickness, which restricts the wide application of such theories. Recently Steigmann [2] derived a shell theory which incorporates both bending and stretching effects, nevertheless he mainly focused on the traction-free case. This work intends to generalize previous plate theory [3] to a finite-strain shell theory, which is consistent with the 3-D weak formulation and with no special restrictions on applied loads.

THE 3-D FORMULATION

We consider a homogeneous thin shell of constant thickness $2h$ composed of a hyperelastic material. A material point in the reference configuration $\Omega \times [0, 2h]$ is denoted by $\mathbf{X}$. Curvilinear coordinates θ^α ($\alpha = 1, 2$) are used to parameterize the base surface Ω.The deformed position is denoted by $\mathbf{x} = \mathbf{x}(\theta^\alpha, Z)$. Accordingly, the deformation gradient is given by

$$\mathbf{F} = \frac{\partial \mathbf{x}}{\partial \mathbf{X}} = (\nabla \mathbf{x})(\mathbf{1} - Z\boldsymbol{\kappa})^{-1} + \frac{\partial \mathbf{x}}{\partial Z} \otimes \mathbf{n}, \tag{1}$$

where ∇ is the in-plane (surface) 2-D gradient, $\boldsymbol{\kappa}$ is the curvature tensor, $\mathbf{1}$ is the 2-D identity tensor within the tangent plane, and $\mathbf{n}$ is the unit outward normal to Ω. The nominal stress $\mathbf{S}$ can be readily obtained from the energy function $\Psi(\mathbf{F})$ by the formula $\mathbf{S} = \partial\Psi/\partial\mathbf{F}$. For the case of dead-loading and in the absence of body forces, the 3-D differential system dictates

$$\begin{aligned} &\mathrm{Div}\mathbf{S} = \mathbf{0}, \quad \text{in} \quad \Omega \times [0, 2h], \quad \mathbf{S}^T\mathbf{n}\big|_{Z=0} = -\mathbf{q}^-, \quad \mathbf{S}^T\mathbf{n}\big|_{Z=2h} = \mathbf{q}^+, \quad \text{in} \quad \Omega \\ &\mathbf{x} = \mathbf{b}(s, Z), \qquad \text{on} \quad \partial\Omega_0 \times [0, 2h], \quad \mathbf{S}^T\mathbf{N} = \mathbf{q}(s, Z), \quad \text{on} \quad \partial\Omega_q \times [0, 2h], \end{aligned} \tag{2}$$

where $\mathbf{q}^\pm$, $\mathbf{q}$ and $\mathbf{b}$ are the prescribed data on the 3-D boundaries, and $\mathbf{N}$ is the unit outward normal to the edge.

THE 2-D SHELL THEORY

Derivation of vector shell equation

First, we adopt a series expansion of the deformed position from the bottom surface

$$\mathbf{x}(\theta^\alpha, Z) = \sum_{n=0}^{4} \frac{1}{n!} Z^n \mathbf{x}^{(n)}(\theta^\alpha) + \frac{1}{5!} Z^5 \mathbf{x}^{(5)}(\theta^\alpha, Z^*), \quad 0 \le Z \le 2h, \quad \mathbf{x}^{(n)}(\mathbf{r}) = \left.\frac{\partial^n \mathbf{x}}{\partial Z^n}\right|_{Z=0}. \tag{3}$$

Similarly, $\mathbf{F}$ and $\mathbf{S}$ can be expanded in series like (3). It follows from (1) and the definition of $\mathbf{S}$ that the expansion coefficients $\mathbf{F}^{(n)}$ and $\mathbf{S}^{(n)}$ are linked up to $\mathbf{x}^{(n+1)}$, and depend linearly on $\mathbf{x}^{(n+1)}$. Note that the above general series is expanded from the bottom surface rather than from the middle surface of the shell as in classical shell theories. Based on such a new expansion

*Corresponding author. Email: mahhdai@cityu.edu.hk

and together with strong-ellipticity condition, the coefficient $\mathbf{x}^{(1)}$ can be uniquely solved in terms of $\mathbf{x}^{(0)}$ from the bottom traction condition $(2)_2$. Furthermore, substituting these expansions into the field equation $(2)_1$, we obtain a sequence of equations. The first three can be utilized to derive the recursion relations for $\mathbf{x}^{(n)}$ $(n = 2, 3, 4)$. In brief, all these coefficients are expressible in terms of $\mathbf{x}^{(0)}$. Finally, the top traction condition $(2)_3$ furnishes the 2-D vector shell equation in the form

$$\nabla \cdot (\mathbf{1}\tilde{\mathbf{S}} + h\boldsymbol{\kappa}\hat{\mathbf{S}}) + h(\mathbf{1}\hat{\mathbf{S}})^T[2\nabla H - \nabla \cdot \boldsymbol{\kappa}] = -\tilde{\mathbf{q}}, \quad \tilde{\mathbf{q}} = \frac{1}{2h}\left[(1 - 4hH + 4h^2K)\mathbf{q}^+ + \mathbf{q}^-\right], \tag{4}$$

where H and K are the mean and Gaussian curvatures, and

$$\tilde{\mathbf{S}} = (1 - 2hH)\mathbf{S}^{(0)} + h(1 - \frac{8}{3}hH)\mathbf{S}^{(1)} + \frac{2}{3}h^2\mathbf{S}^{(2)}, \quad \hat{\mathbf{S}} = \mathbf{S}^{(0)} + \frac{4}{3}h\mathbf{S}^{(1)}. \tag{5}$$

This system is a fourth-order differential equation for the vector $\mathbf{x}^{(0)}$. We point out that the previous plate equation in [3] can be recovered by setting $\boldsymbol{\kappa} = \mathbf{0}$, and this shell equation contains certain extra balancing effects due to the presence of curvature.

The 2-D boundary conditions and weak formulations

To complete the shell theory, two boundary conditions concerning $\mathbf{x}^{(0)}$ or its derivatives are needed either on position boundary $\partial\Omega_0$ or the traction boundary $\partial\Omega_q$. We propose them in an average sense, i.e,

$$\mathbf{x}^{(0)} = \mathbf{b}^{(0)}, \quad \frac{1}{2h}\int_0^{2h} \mathbf{x} dZ = \bar{\mathbf{b}}, \quad \text{on} \quad \partial\Omega_0, \quad \frac{1}{2h}\int_0^{2h} \{1, Z - h\}\mathbf{S}^T\mathbf{N}\sqrt{g_\tau} dZ = \{\mathbf{q}_0, \mathbf{m}\} \quad \text{on} \quad \partial\Omega_q, \tag{6}$$

where $\bar{\mathbf{b}}, \mathbf{q}_0, \mathbf{m}$ are the averaged position, traction and moment vectors, and $\sqrt{g_\tau}$ is a factor related to the local curvatures. It can be shown that the 2-D shell equation (4) and boundary conditions (6) are consistent with the 3-D variational principle.

The associated 2-D weak formulation can be derived by multiplying $(4)_1$ by $\boldsymbol{\xi} = \delta\mathbf{x}^{(0)}$ and integration by parts,

$$\int_\Omega (\mathcal{W} - \tilde{\mathbf{q}} \cdot \boldsymbol{\xi})\, \mathrm{dA} = \int_{\partial\Omega_q} (\mathbf{q}_0 \cdot \boldsymbol{\xi} - 2\mathbf{m} \cdot \boldsymbol{\eta})\, \mathrm{ds}, \quad \text{or} \quad \int_\Omega (\mathcal{W} - \tilde{\mathbf{q}} \cdot \boldsymbol{\xi})\, \mathrm{dA} = \int_{\partial\Omega} (\hat{\mathbf{q}} \cdot \boldsymbol{\xi} + \hat{\mathbf{m}} \cdot \boldsymbol{\xi}_{,\nu})\, \mathrm{ds}, \tag{7}$$

where $\boldsymbol{\eta} = \delta\mathbf{x}^{(1)}$, $\mathcal{W}$ involves $\mathbf{S}^{(n)}$, and $\hat{\mathbf{q}}, \hat{\mathbf{m}}$ are generalized traction and moment vectors. The former one is suitable for the boundary conditions (6), while the latter one can accommodate various practical edge conditions (e.g. clamped edge).

AN EXAMPLE: AXISYMMETRIC DEFORMATION OF A SPHERICAL SHELL

In this section, we examine the axisymmetric deformations of a spherical shell (cf. [4]), with the strain-energy function for harmonic materials $\Psi = \frac{2}{27}\nu I_1^3 - \nu I_2 + \nu$ where I_1, I_2 are the first two principal invariants of the stretch tensor, and $\nu \geq 0$ is a material constant. The deformation is determined by scalar function $r(R)$ according to $\mathbf{x} = r\mathbf{e}_R$. As an example, we set $\mathbf{q}^- = \mathbf{0}, \mathbf{q}^+ = q^+\mathbf{e}_R$, and the exact solution given in [4] is:

$$r(R) = \frac{1}{2}\left(1 + \sqrt{(B^3(2q^+ + \nu) - A^3\nu)/(B^3 - A^3)\,\nu}\right)R + A^3B^3q^+/[2\left(B^3 - A^3\right)\nu R^2], \quad A \leq R \leq B. \tag{8}$$

In our shell theory with $Z = R - A$, we first expand $r(R)$ as $r = \sum_{n=0}^{4} \frac{1}{n!} r_n Z^n + \cdots$. From recursion relations, coefficients r_n $(n = 1, .., 4)$ can be expressed by r_0. The shell equation reduces to an algebraic equation of r_0, which yields

$$r_0 = \frac{1}{4}A\left[1 + \sqrt{1 + A(A + 2h)^2q^+/(4h^3 + 3A^2h)\,\nu}\right]^2. \tag{9}$$

By using Taylor expansions (with scale $q^+ = O(h\nu/A)$ for finite deformations), one can easily verify that all the coefficients r_n are correct to $O(h^2)$, and hence the shell theory produces an $O(h^2)$-correct solution for $r(R)$. This conclusion is also true for the general dead-load case and the internally pressurized case.

CONCLUSIONS

In this paper, a consistent finite-strain shell theory is developed with no special restrictions on external loadings (like scalings with thickness), thus can be potentially applied to various practical situations.

References

[1] Wan, F. Y. M., and Weinitschke, H. J. : On Shells of Revolution with the Love-Kirchhoff Hypotheses, J. Eng. Math., 22, 285-334, 1988.

[2] Steigmann D.J. : Koiter's Shell Theory from the Perspective of Three-dimensional Nonlinear Elasticity, J. Elast., 111: 91107, 2013.

[3] Dai H-H, Song Z.: On a Consistent Finite-strain Plate Theory Based on Three-dimensional Energy Principle, Proc. R. Soc. A, 470(2171), 2014.

[4] Ogden, R. W.: Non-linear Elastic Deformations, Courier Corporation, 1997.

ACCURATE PREDICTION OF FREE EDGE EFFECT IN PIEZOLAMINATED PANELS

N. Dhanesh[1] and Santosh Kapuria*[1,2]

[1]*Department of Applied Mechanics, Indian Institute of Technology Delhi, New Delhi 110016, India*
[2]*CSIR-Structural Engineering Research Centre, Chennai 600113, India*

Summary An accurate analytical three-dimensional piezoelasticity solution is presented for the free edge stress field in smart piezoelectric laminated plates, using the recently developed mixed-field multiterm extended Kantorovich method (MMEKM). The formulation considers the two-way electromechanical coupling, and the solution satisfies all traction-free boundary conditions and interlaminar continuity conditions exactly and point-wise. The solution is employed to accurately determine the transverse shear and peel stresses developed at the actuator-host plate interfaces, and to predict the actuation potential required to control the free edge stresses caused by extension loading.

INTRODUCTION

The well known *free edge effect* [1] in composite laminated structures becomes further complex in case of hybrid laminates featuring integrated piezoelectric layers, due to electromechanical coupling. The development of localized three dimensional (3D) interlaminar stresses near the free edges in laminates subjected to various loadings is known to be the main cause for initiation of delamination damage in such laminates. In smart laminates, these stresses may be controlled by the application of electric field across the piezoelectric layers. Compared to elastic laminates, the prediction of free edge stress field in hybrid laminates has been less attempted due to its inherent complexity. Recently, Huang and Kim [2] have proposed a stress function based approach for the free edge stress analysis of symmetric piezo-bonded laminates, without considering the full electromechanical coupling. Being a stress based approach, it fails to satisfy the point-wise interlaminar displacement continuity conditions and showed unwanted oscillations of the stress variations across the thickness. In the present work, the mixed-field multiterm extended Kantorvich method (MMEKM) developed recently by the authors' group for the 3D elasticity solution of free edge stresses in elastic laminates [3] is extended to analyze hybrid laminates under electromechanical loading.

GOVERNING EQUATIONS FOR PIEZOLAMINATED PANEL

Consider an infinitely long (y-direction) hybrid angle-ply laminated panel with free edges at $x = 0$ and $x = a$, and thickness h along z-direction. Some of the layers can be of monolithic piezoelectric or piezoelectric fibre reinforced composite (PFRC) materials with poling along the thickness direction. The panel is subjected to uniform axial strain ε_0 along the y-direction. At the bottom and top surfaces ($z = \mp h/2$), either electric potential ϕ_i or charge D_i is prescribed. The problem falls under the state of generalized plane deformation as the stresses and strains are independent of y-coordinate. The Reissner-type variational principle for such problem with no body force and internal charge source can be expressed as [4]

$$\int_V [\sigma_{ij,j}\delta u_i + D_{i,j}\delta\phi + (\varepsilon_{ij} - \varepsilon_{ij}^G)\delta\sigma_{ij} - (E_i - E_i^G)\delta D_i]\,\mathrm{d}V - \int_{A_T}(T_i^n - \bar{T}_i^n)\delta u_i \mathrm{d}A$$
$$- \int_{A_u} T_i^n \delta u_i\,\mathrm{d}A - \int_{A_D}(D_n - \bar{D}_n)\delta\phi\,\mathrm{d}A - \int_{A_\phi} D_n\delta\phi\,\mathrm{d}A = 0, \quad \forall\ \delta u_i,\ \delta\sigma_{ij},\ \delta\phi,\ \delta D_i \tag{1}$$

where V denotes the volume per unit length. A subscript comma denotes partial differentiation. ε_{ij} and E_i denote the strain and electric field components respectively, obtained from the constitute equations, and superscript G is used to denote the same when obtained from the strain-displacement and electric field-potential relations, respectively. Substituting $\varepsilon_y = \varepsilon_0$ in the corresponding constitutive equation, σ_y can be eliminated from all other strain components in Eq. (1). The area integrals in Eq. (1) vanish as all surface boundary conditions are sought be to satisfied exactly. Apart from the traction free boundary conditions, the following continuity conditions also are to be satisfied at any kth interface:

$$[(u,\, v,\, w,\, \sigma_z,\, \tau_{yz},\, \tau_{zx},\, \phi,\, D_z)|_{z=z_k}^{(k)} = [(u,\, v,\, w,\, \sigma_z,\, \tau_{yz},\, \tau_{zx},\, \phi,\, D_z)|_{z=z_k}^{(k+1)} \tag{2}$$

except for D_z for the interfaces between piezoelectric and elastic layers, where it is grounded ($\phi = 0$) for effective actuation.

MMEKM SOLUTION

In the MMEKM, both displacements/electric potential and stress/electric displacement variables are taken as primary variables. The solution for $\mathbf{X} = [\,u \quad v \quad w \quad \sigma_x \quad \sigma_z \quad \tau_{xy} \quad \tau_{yz} \quad \tau_{zx} \quad \phi \quad D_x \quad D_z\,]^{\mathrm{T}}$ is expressed as an n-term series of the product of separable functions in the inplane and thickness directions as $X_l(\xi,\zeta) = \sum_{i=1}^{n} f_l(\xi)^i g_l^i(\zeta) + \delta_{l9}\bar{g}_9 \quad \text{for} \quad l \in [1, 11]$, where $\delta_{l9} = 1$ for $l = 9$ and else $\delta_{l9} = 0$, $\bar{g}_9 = \phi_1(1-\zeta)$ for $k = 1$ and $\bar{g}_9 = \phi_2(\zeta)$ for $k = L$. Here ξ and ζ are the normalized inplane and local thickness coordinates, varying from 0 to 1. Functions $f_l^i(\xi)$ and $g_l^i(\zeta)$ are determined iteratively.

*Corresponding author. Email: kapuria@am.iitd.ac.in

In the first step of any iteration, functions $f_l^i(\xi)$ from the previous iteration are considered to be known. By substituting the variables X_l and its variations δX_l in the variational equation (1), integrating over ξ-direction, and equating the coefficients of δg_l^i individually to zero, a system of first order ordinary differential (ODEs) and algebraic equations are obtained for g_l^i:

$$\mathbf{M}\bar{\mathbf{G}}_{,\zeta} = \bar{\mathbf{A}}\bar{\mathbf{G}} + \hat{\mathbf{A}}\hat{\mathbf{G}} + \bar{\mathbf{Q}}_\mathbf{e}; \qquad \mathbf{K}\hat{\mathbf{G}} = \tilde{\mathbf{A}}\bar{\mathbf{G}} + \tilde{\mathbf{Q}}_\mathbf{e} \tag{3}$$

where $\bar{\mathbf{G}}$ is a column vector containing g_l^i's corresponding to the eight variables which appear in the boundary and continuity conditions in z direction [Eq. (2)] and $\hat{\mathbf{G}}$ consists of those for the remaining three variables.The elements of the coefficient matrices and electromechanical load vectors $\bar{\mathbf{Q}}_\mathbf{e}$ and $\tilde{\mathbf{Q}}_\mathbf{e}$ are evaluated in closed-form, and the ODEs are solved analytically [3]. In the second step, the last determined $g_l^i(\zeta)$ are considered as known, and a system of differential-algebraic equations are obtained for $f_l^i(\xi)$ and solved analytically. The iterations over the two directions are continued until the desired convergence is achieved. The mixed-field approach allows for the exact satisfaction of all the boundary and interlaminar conditions and also ensures the same order of accuracy for all variables. A quadruple precision (128 bit) program has been used to obtain the numerical results, considering the singular nature of free edge stress field.

NUMERICAL RESULTS

Numerical results are presented for a cross-ply composite panel integrated with PFRC actuator layers (Fig. 1a). The material properties of the elastic substrate and PFRC layers are taken from [3] and [4], respectively. The convergence of the series solution for uniform actuation potential loading (ϕ_1=$-\phi_0$, ϕ_2=ϕ_0) is shown in Fig. 1b. The longitudinal distributions of τ_{zx} and σ_z show fast convergence within four to five terms, and are in good agreement with full-field 3D finite element (FE) solution. The solution captures the singularity in τ_{zx} (peak increases with n). It is shown in Figure 1c that the free edge interlaminar stresses in the laminate caused by uniform extension ($\bar{E}_z = 0$ case) can be reduced to the desired level by the proper application of an electric field to the actuators.

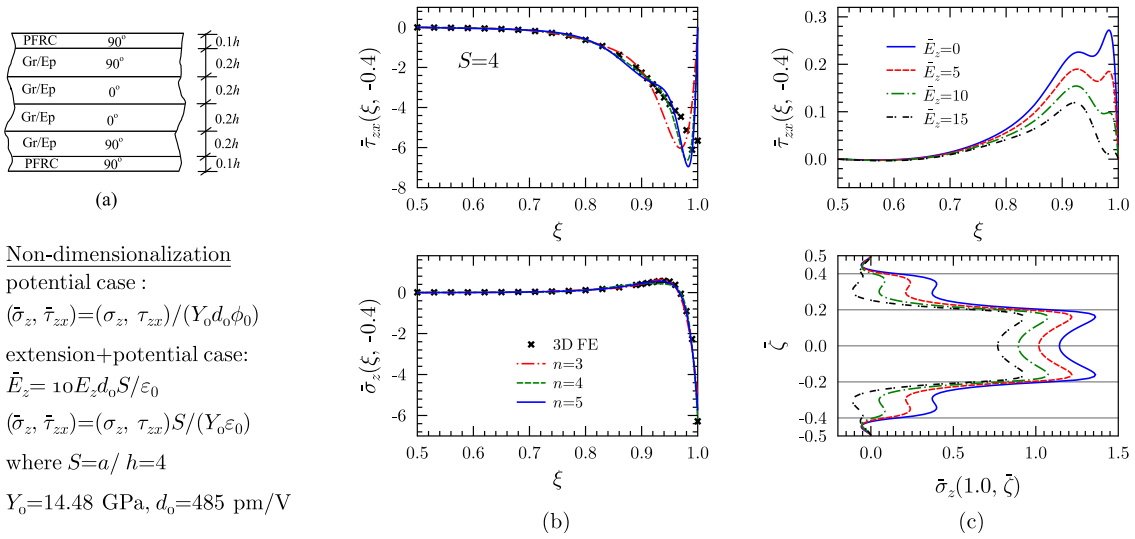

Figure 1: (a) Laminate configuration, (b) distributions of interlaminar stresses under electric potential loading, (c) control of stresses through actuation

CONCLUSIONS

The analytical series solution based on 3D piezoelasticity presented here employing the MMEKM for the free edge stress field in hybrid panels under electromechanical loading shows rapid convergence and good agreement with 3D FE results, and also captures the stress singularity. The solution is useful not only for accurate prediction of free edge interfacial stresses, but also in determining the actuation potential required for controlling the stresses caused by mechanical loading.

References

[1] Mittelstedt C., Becker W.: Free-edge Effects in Composite Laminates. Appl. Mech. Rev. 60:217–244, 2007.

[2] Huang B., Kim H. S.: Control of Free-edge Interlaminar Stresses in Composite Laminates Using Piezoelectric Actuators. Smart Mater. Struct. 23:074002, 2014.

[3] Dhanesh N., Kapuria S., Achary G. G. S.: Accurate Prediction of Three-dimensional Free Edge Stress Field in Composite Laminates Using Mixed-field Multiterm Extended Kantorovich Method. Acta Mech. In press, 2015.

[4] Kapuria S., Kumari P.: Extended Kantorovich Method for Coupled Piezoelasticity Solution of Piezolaminated Plates Showing Edge Effects. Proc. R. Soc. A 469:20120565, 2013.

GEOMETRICALLY NONLINEAR THEORIES FOR CURVED BEAMS AND SHELLS

Wei Wang[1], Liping Liu [*2, 1], and Nanshu Lu[3]

[1] *Department of Mechanical Aerospace Engineering, Rutgers University, NJ 08854*
[2] *Department of Mathematics, Rutgers University, NJ 08854*
[3] *Department of Aerospace Engineering and Engineering Mechanics, University of Texas, Austin, TX 78712*

Summary We outline a variational procedure to derive geometrically nonlinear theories for lower dimensional elastic bodies. We emphasize a geometric viewpoint and employ general curvilinear coordinates for describing the reference (or undeformed) and current (or deformed) configurations. It is observed that the local *elastic strain* (or change of length of an infinitesimal segment) is precisely characterized by the *metric tensors* of two configurations induced by the ambient 3D Euclidean space. Upon assuming small *elastic strains* and linear stress-strain laws, we immediately obtain the strain energy associated with deformations. The equilibrium configuration can then be found as the energy-minimizing state of the total free energy. This framework recovers a number of classic simplified theories for beams and shells if appropriate kinematic assumptions are made.

It is of great interest to study lower-dimensional structures such as 1D rods and 2D shells because of their adaptivity to geometric constraints and ease of deformation. Most of classic theories for beams and shells are based on some *a priori* kinematic assumptions: the kinematic variables, typically, the displacements, are assumed to be small and admit a certain ansartz, from which the elastic strain can be directly computed [1, 2]. Such approach in general cannot be used to address structures undergoing *large deformations*, which motivates our variational approach to geometrically nonlinear theories for curved beams and shells. We consider 1D space curved beams and 2D shells in the subsequent two sections, respectively.

A geometrically nonlinear theory for space curved bemas

Consider a space curved beam. In the reference configuration $\mathcal{B}_0$ (resp. deformed or current configuration $\mathcal{B}$), the centroid line of the beam is a space curve with arc-length parameterization given by $\{\mathbf{c}_0(\xi^1) : 0 \le \xi^1 \le L\} \subset \mathbb{R}^3$ (resp. $\{\mathbf{c}(\xi^1) : 0 \le \xi^1 \le L\} \subset \mathbb{R}^3$). For simplicity, we assume the centroid curve remains to be of C^3-class. Let (ξ^1, ξ^2, ξ^3) be the coordinates such that a material point $\mathbf{x} \in \mathcal{B}_0$ can be represented as $\mathbf{x} = \mathbf{c}_0(\xi^1) + \xi^2\tilde{\mathbf{e}}_2 + \xi^3\tilde{\mathbf{e}}_3$, where $\tilde{\mathbf{e}}_1(\xi^1) = \mathbf{c}_0{}'(\xi^1)$, $\tilde{\mathbf{e}}_2(\xi^1) = \frac{\mathbf{c}_0{}''(\xi^1)}{|\mathbf{c}_0{}''(\xi^1)|}$ and $\tilde{\mathbf{e}}_3(\xi^1) = \tilde{\mathbf{e}}_1(\xi^1) \times \tilde{\mathbf{e}}_2(\xi^1)$ are the local Frenet frame associated with the centroid curve $\mathbf{c}_0$. Then the distance between two material points (ξ^1, ξ^2, ξ^3) and $(\xi^1, \xi^2, \xi^3) + d(\xi^1, \xi^2, \xi^3)$ in the *reference configuration* is given by

$$ds_0^2 = \tilde{g}_{ij} d\xi^i d\xi^j, \qquad \tilde{g}_{ij} = \frac{\partial \mathbf{x}}{\partial \xi^i} \cdot \frac{\partial \mathbf{x}}{\partial \xi^j} = \begin{bmatrix} |1 \circ \kappa_0\xi^2|^2 + |\xi^2\tau_0|^2 + |\xi^3\tau_0|^2 & \circ\, \xi^3\tau_0 & \tau_0\xi^2 \\ \circ\, \xi^3\tau_0 & 1 & 0 \\ \tau_0\xi^2 & 0 & 1 \end{bmatrix}, \tag{1}$$

where $\kappa_0(\xi^1) = \tilde{\mathbf{e}}_2(\xi^1) \cdot \tilde{\mathbf{e}}_1'(\xi^1)$ and $\tau_0(\xi^1) = \tilde{\mathbf{e}}_2' \cdot \tilde{\mathbf{e}}_3(\xi^1)$ is the curvature and torsion of the undeformed centroid curve $\mathbf{c}_0$, respectively, and $\tilde{g}_{ij}$ is referred to as the *metric tensor* associated with the undeformed configuration. In addition to the deformed centroid curve $\mathbf{c} = \mathbf{c}(\xi^1)$, we introduce the *relative twist angle* $\varphi : (0, L) \to \mathbb{R}$ to describe the deformed configuration $\mathcal{B}$. Then according to the *Bernoulli-Euler* kinematics, the deformation $\mathbf{y} : \mathcal{B}_0 \to \mathcal{B}$ is given by $\mathbf{y} = \mathbf{c}(\xi^1) + \mathbf{Q}(\xi^2\tilde{\mathbf{e}}_2 + \xi^3\tilde{\mathbf{e}}_3)$, where $\mathbf{e}_1(\xi^1) = \frac{\mathbf{c}'(\xi^1)}{|\mathbf{c}'(\xi^1)|}$, $\mathbf{e}_2(\xi^1) = \frac{\mathbf{e}_1'(\xi^1)}{|\mathbf{e}_1'(\xi^1)|}$ and $\mathbf{e}_3(\xi^1) = \mathbf{e}_1(\xi^1) \times \mathbf{e}_2(\xi^1)$ are the local Frenet frame associated with the deformed centroid curve $\mathbf{c}(\xi^1)$, and the rigid rotation matrix $\mathbf{Q}$ is determined by $\mathbf{Q}\tilde{\mathbf{e}}_1 = \mathbf{e}_1$, $\mathbf{Q}\tilde{\mathbf{e}}_2 = \cos\varphi\mathbf{e}_2 + \sin\varphi\mathbf{e}_3$, and $\mathbf{Q}\tilde{\mathbf{e}}_3 = \circ\, \sin\varphi\mathbf{e}_2 + \cos\varphi\mathbf{e}_3$. Therefore, the distance between the two material points (ξ^1, ξ^2, ξ^3) and $(\xi^1, \xi^2, \xi^3) + d(\xi^1, \xi^2, \xi^3)$ in the *deformed configuration* is given by

$$ds^2 = g_{ij} d\xi^i d\xi^j, \qquad [g_{ij}] = [\frac{\partial \mathbf{y}}{\partial \xi^i} \cdot \frac{\partial \mathbf{y}}{\partial \xi^j}] = \begin{bmatrix} \zeta_1^2 + \zeta_2^2 + \zeta_3^2 & \zeta_2\cos\varphi + \zeta_3\sin\varphi & \circ\, \zeta_2\sin\varphi + \zeta_3\cos\varphi \\ \zeta_2\cos\varphi + \zeta_3\sin\varphi & 1 & 0 \\ \circ\, \zeta_2\sin\varphi + \zeta_3\cos\varphi & 0 & 1 \end{bmatrix}, \tag{2}$$

where $\gamma' = |\mathbf{c}'|$, $\zeta_1 = \gamma'(1 \circ\, \xi^2\kappa\cos\varphi + \xi^3\kappa\sin\varphi)$, $\zeta_2 = (\varphi' + \tau\gamma')(\circ\, \xi^2\sin\varphi \circ\, \xi^3\cos\varphi)$ and $\zeta_3 = (\varphi' + \tau\gamma')(\xi^2\cos\varphi \circ\, \xi^3\sin\varphi)$. Therefore, we find that $\frac{ds - ds_0}{ds_0} \approx \frac{ds^2 - ds_0^2}{2|ds_0|^2} = \frac{1}{2}(g_{ij} \circ\, \tilde{g}_{ij})\frac{d\xi^i}{ds_0}\frac{d\xi^j}{ds_0} \approx \epsilon_{ij}(\xi^1, \xi^2, \xi^3)\frac{d\xi^i}{ds_0}\frac{d\xi^j}{ds_0}$, where the linearized strain tensor is given by

$$\epsilon_{ij} = \begin{bmatrix} \epsilon_{11} & \xi^3(\tau_0 \circ\, \varphi' \circ\, \tau\gamma')/2 & \xi^2(\varphi' + \tau\gamma' \circ\, \tau_0)/2 \\ \xi^3(\tau_0 \circ\, \varphi' \circ\, \tau\gamma')/2 & 0 & 0 \\ \xi^2(\varphi' + \tau\gamma' \circ\, \tau_0)/2 & 0 & 0 \end{bmatrix}, \tag{3}$$
$$\epsilon_{11} = \gamma' \circ\, 1 + \xi^2(\circ\, \kappa\gamma'\cos\varphi + \kappa_0) + \xi^3\kappa\gamma'\sin\varphi.$$

*Corresponding author. Email: liu.liping@rutgers.edu

For isotropic materials with Young's modulus E and Poisson's ration ν (shear modulus $G = \frac{E}{2(1+\nu)}$), we obtain the strain energy associated with the deformation $\mathbf{y} : \mathcal{B}_0 \to \mathcal{B}$ as a functional of kinematic variables $(\mathbf{c}, \varphi)$ as

$$U_e[\mathbf{c}, \varphi; \mathbf{c}_0] = \frac{1}{2}\int_0^L \Big\{ EA(\gamma' \circ\ 1)^2 + GJ(\varphi' + \tau\gamma' \circ\ \tau_0)^2 + \frac{EI_3}{2}(\circ\ \kappa\gamma' \cos\varphi + \kappa_0)^2 + \frac{EI_2}{2}(\kappa\gamma' \sin\varphi)^2 d\xi^1. \tag{4}$$

Let $P[\mathbf{c}, \varphi; \mathbf{c}_0]$ be the potential energy functional due to external loadings and $\mathcal{C}$ be the admissible space of the kinematic variables $(\mathbf{c}, \varphi)$. Then the equilibrium configuration can be determined by the principle of minimum free energy:

$$\min\Big\{ F[\mathbf{c}, \varphi; \mathbf{c}_0] \equiv U_e[\mathbf{c}, \varphi; \mathbf{c}_0] + P[\mathbf{c}, \varphi; \mathbf{c}_0] : (\mathbf{c}, \varphi) \in \mathcal{C} \Big\}, \tag{5}$$

which completes the geometrically nonlinear theory for space curved beams. The interested reader is referred to [3] for full details.

A geometrically nonlinear theory for elastic shells

We consider a shell of thickness h and mid-surface $\mathcal{S}_0$. Let $(\xi^1, \xi^2) : \mathcal{S}_0 \to \mathbb{R}^2$ be a local parametrization of $\mathcal{S}_0$ and $\xi^3 \in (\circ\ h/2, h/2)$ so that a point in the reference (or undeformed) shell $\mathcal{B}_0$ can be represented as $\mathbf{x} = \xi^3\tilde{\mathbf{n}} + \tilde{\mathbf{r}}(\xi^1, \xi^2)$, where $\tilde{\mathbf{n}}(\xi^1, \xi^2) = \frac{\tilde{\mathbf{r}}_{,\xi^1} \times \tilde{\mathbf{r}}_{,\xi^2}}{|\tilde{\mathbf{r}}_{,\xi^1} \times \tilde{\mathbf{r}}_{,\xi^2}|}$. Then the distance between two material points (ξ^1, ξ^2, ξ^3) and $(\xi^1, \xi^2, \xi^3) + d(\xi^1, \xi^2, \xi^3)$ in the *reference configuration* is given by ($\tilde{g}_{\alpha\beta} = \tilde{\mathbf{r}}_{,\alpha} \cdot \tilde{\mathbf{r}}_{,\beta}$; $\tilde{\mathbf{n}}_{,\alpha} = \tilde{h}^\nu_\alpha \tilde{\mathbf{r}}_{,\nu}$, $\tilde{h}_{\alpha\beta} = \tilde{h}^\nu_\alpha \tilde{g}_{\nu\beta}$)

$$ds_0^2 = \tilde{g}_{ij} d\xi^i d\xi^j, \qquad \tilde{g}_{ij} = \frac{\partial \mathbf{x}}{\partial \xi^i} \cdot \frac{\partial \mathbf{x}}{\partial \xi^j} = \begin{bmatrix} \tilde{g}_{\alpha\beta} + \xi^3(\tilde{h}_{\alpha\beta} + \tilde{h}_{\beta\alpha}) + (\xi^3)^2 \tilde{h}^\nu_\alpha \tilde{h}^\mu_\beta \tilde{g}_{\nu\mu} & 0 \\ 0 & 1 \end{bmatrix}. \tag{6}$$

To describe the deformed configuration $\mathcal{B}$, we denote the deformation of mid-surface by $\boldsymbol{\varphi} : \mathcal{S}_0 \to \mathcal{S}$ and the induced parametrization of $\mathcal{S}$ by $\mathbf{r}(\xi^1, \xi^2) = \boldsymbol{\varphi}(\tilde{\mathbf{r}}(\xi^1, \xi^2))$. Let $\mathbf{n}(\xi^1, \xi^2) = \frac{\mathbf{r}_{,\xi^1} \times \mathbf{r}_{,\xi^2}}{|\mathbf{r}_{,\xi^1} \times \mathbf{r}_{,\xi^2}|}$ be the unit normal. Then the deformation $\mathbf{y} : \mathcal{B}_0 \to \mathcal{B}$ is given by $\mathbf{y} = \mathbf{r}(\xi^1, \xi^2) + \xi^3 \mathbf{n}(\xi^1, \xi^2)$, and hence the distance between the two material points (ξ^1, ξ^2, ξ^3) and $(\xi^1, \xi^2, \xi^3) + d(\xi^1, \xi^2, \xi^3)$ in the *deformed configuration* is given by ($g_{\alpha\beta} = \mathbf{r}_{,\alpha} \cdot \mathbf{r}_{,\beta}$; $\mathbf{n}_{,\alpha} = h^\nu_\alpha \mathbf{r}_{,\nu}$, $h_{\alpha\beta} = h^\nu_\alpha g_{\nu\beta}$)

$$ds^2 = g_{ij} d\xi^i d\xi^j, \qquad g_{ij} = \frac{\partial \mathbf{y}}{\partial \xi^i} \cdot \frac{\partial \mathbf{y}}{\partial \xi^j} = \begin{bmatrix} g_{\alpha\beta} + \xi^3(h_{\alpha\beta} + h_{\beta\alpha}) + (\xi^3)^2 h^\nu_\alpha h^\mu_\beta g_{\nu\mu} & 0 \\ 0 & 1 \end{bmatrix}. \tag{7}$$

Therefore, we find that $\frac{ds - ds_0}{ds_0} \approx \frac{ds^2 - ds_0^2}{2|ds_0|^2} = \frac{1}{2}(g_{ij} \circ\ \tilde{g}_{ij}) \frac{d\xi^i}{ds_0}\frac{d\xi^j}{ds_0} \approx \epsilon_{ij}(\xi^1, \xi^2, \xi^3)\frac{d\xi^i}{ds_0}\frac{d\xi^j}{ds_0}$, where the linearized strain tensor is given by $\epsilon_{\alpha\beta} = \frac{1}{2}[g_{\alpha\beta} \circ\ \tilde{g}_{\alpha\beta} + \xi^3(h_{\alpha\beta} + h_{\beta\alpha} \circ\ \tilde{h}_{\alpha\beta} \circ\ \tilde{h}_{\beta\alpha}) + (\xi^3)^2(h^\nu_\alpha h^\mu_\beta g_{\nu\mu} \circ\ \tilde{h}^\nu_\alpha \tilde{h}^\mu_\beta \tilde{g}_{\nu\mu})]$. By the constitutive relations, the strain energy associated with mid-surface deformation $\boldsymbol{\varphi}$ is given by ($C^{\alpha\beta\nu\mu}$ is the stiffness tensor)

$$U_e[\boldsymbol{\varphi}; \tilde{\mathbf{r}}] = \frac{1}{2}\int_{\mathcal{S}_0}\int_{-h/2}^{h/2} C^{\alpha\beta\nu\mu}\epsilon_{\alpha\beta}\epsilon_{\nu\mu} d\xi^3 dS \approx \frac{1}{8}\int_{\mathcal{S}_0} C^{\alpha\beta\nu\mu}\Big[h \triangle g_{\alpha\beta} \triangle g_{\nu\mu} + \frac{h^3}{12}(2\triangle g_{\alpha\beta}\triangle m_{\nu\mu} + \triangle h_{\alpha\beta}\triangle h_{\nu\mu})\Big] dS, \tag{8}$$

where $\triangle g_{\alpha\beta} = g_{\alpha\beta} \circ\ \tilde{g}_{\alpha\beta}$, $\triangle h_{\alpha\beta} = h_{\alpha\beta} \circ\ \tilde{h}_{\alpha\beta}$, and $\triangle m_{\alpha\beta} = h^\nu_\alpha h^\mu_\beta g_{\nu\mu} \circ\ \tilde{h}^\nu_\alpha \tilde{h}^\mu_\beta \tilde{g}_{\nu\mu}$. Let $P[\boldsymbol{\varphi}; \tilde{\mathbf{r}}]$ be the potential energy functional due to external loadings and $\mathcal{D}$ be the admissible space of the kinematic variables $\boldsymbol{\varphi}$. By the principle of minimum free energy, the equilibrium configuration of the shell is determined by

$$\min\Big\{ F[\boldsymbol{\varphi}; \tilde{\mathbf{r}}] \equiv U_e[\boldsymbol{\varphi}; \tilde{\mathbf{r}}] + P[\boldsymbol{\varphi}; \tilde{\mathbf{r}}] : \boldsymbol{\varphi} \in \mathcal{D} \Big\}, \tag{9}$$

which completes the geometrically nonlinear theory for space curved beams. In particular, we can obtain: (i) the classic membrane theory if the second term in (8) is neglected, (ii) the Love-Kirchhoff plate/shell theory if the constraint $\triangle g = 0$ is enforced, and (iii) the Von Kármán plate theory if both terms in (8) are kept and $\tilde{g} = \tilde{h} \equiv 0$ (i.e., the reference configuration is planar).

References

[1] S. S. Antman. Linear theories of elasticity and thermoelasticity; linear and nonlinear theories of rods, plates, and shells (Ed.: C. Truesdell). pages 641–703, 1973.

[2] A. E. H. Love. *A Treatise on the Mathematical Theory of Elasticity (4th Ed.)*. Dove, 1944.

[3] L.P. Liu and N. Lu. Variational formulations, instabilities and critical loadings of space curved beams *Int. J. Solids Struct.*, In review.

MATHEMATICAL MODELING OF THIN LINEARLY QUASICRYSTALLINE PLATES

Thibaut Weller*[1] and Christian Licht[2]
[1,2]*Laboratoire de Mécanique et Génie Civil, UMR 5508 CNRS, Université Montpellier, c.c. 048, Place Eugène Bataillon, 34095 Montpellier cedex 5, France*

Summary We derive a theory of thin linearly quasicrystalline plates by studying the limit behavior of a three-dimensional flat body as its thickness tends to zero. We exhibit the existence of a surprisingly high number of models, each of them linked to a specific set of boundary conditions. As such, these results show that quasicrystals behave as smart materials.

INTRODUCTION

Here we perform an asymptotic modeling of linear quasicrystalline plates by regarding its thickness as a small parameter denoted by ε. We study the behavior of the solution of the physical problem when ε tends to 0. We show that depending on the type of boundary conditions, 26 different models indexed by a triplet $p = (p_1, p_2, p_3) \in \{0, 1, 2\}^3$ appear at the limit. Comparing to our previous studies devoted to the mathematical modeling of thin plates in the framework of multi-physical couplings [1]-[3], this number is stunning. This multiplication of models, however, has its roots in the very structure of quasicrystals. As shown in [4], the constitutive law of quasicrystalline media present a coupling between two different kinds of displacement fields: the *phonon* field, denoted by u, and the *phason* field, denoted by w (see (1) below). Whereas phonons are related to translation of atoms and therefore to classical elastic displacements, phasons are associated with atomic rearrangements and appear in the constitutive equations only through their (noon symmetrized) gradients. This is the main cause of the huge amount of models we obtain for a single quasicrystalline thin plate. Provided that we manage to control and/or measure the phason fields, quasicrystals may be used to design new kinds of smart structures.

SETTING THE PROBLEM

We will denote phonon fields by the letters u, v and v' while the phason fields will be denoted by w, ψ and ψ'. Depending on the nature of our formulation, these letters and some other symbols may be indexed by ε which stands for the thickness of the plate, seen as a parameter. The reference configuration of a linearly quasicrystalline thin plate is the closure in $\mathbb{R}^3$ of the set $\Omega^\varepsilon = \omega \times (\circ\, \varepsilon, \varepsilon)$ whose outward unit normal is n^ε and where ω is a bounded domain of $\mathbb{R}^2$ with a Lipschitz boundary $\partial\omega$. Used as indices, letters i and j take their values in $\{1, 2, 3\}$ while α and β take their values in $\{1, 2\}$. With classical notations and a suitable partition of the plate (see [5] and [6]), the equations determining the physical state $s^\varepsilon = (u^\varepsilon, w^\varepsilon)$ at equilibrium are:

$$\mathcal{P}(\Omega^\varepsilon)\ \begin{cases} \text{div}\,\sigma^\varepsilon + f^\varepsilon = 0 \text{ in } \Omega^\varepsilon, \quad \sigma^\varepsilon n^\varepsilon = F^\varepsilon \text{ on } \Gamma^\varepsilon_{uN}, \quad u^\varepsilon = 0 \text{ on } \Gamma^\varepsilon_{uD}, \\ \text{div}\,\tau^\varepsilon + g^\varepsilon = 0 \text{ in } \Omega^\varepsilon, \quad \tau^\varepsilon_{ij} n^\varepsilon_j = G^\varepsilon_i \text{ on } \Gamma^\varepsilon_{wN,i}, \quad w^\varepsilon_i = w^\varepsilon_{0_i} \text{ on } \Gamma^\varepsilon_{wD,i}, \quad i = 1, 2, 3, \\ (\sigma^\varepsilon, \tau^\varepsilon) = Q^\varepsilon(x)(e(u^\varepsilon), \nabla w^\varepsilon) \text{ in } \Omega^\varepsilon, \end{cases}$$

where u^ε, w^ε, σ^ε and τ^ε respectively stand for the phonon field, the phason field, the phonon stress tensor and the phason stress tensor and where the operator Q^ε is such that:

$$\sigma^\varepsilon_{ij} = C^\varepsilon_{ijkl}\, e_{kl}(u^\varepsilon) + R^\varepsilon_{ijkl}\, (\nabla w^\varepsilon)_{kl}, \quad \tau^\varepsilon_{ij} = R^\varepsilon_{klij}\, e_{kl}(u^\varepsilon) + K^\varepsilon_{ijkl}\, (\nabla w^\varepsilon)_{kl}. \tag{1}$$

In these constitutive equations, C^ε_{ijkl}, K^ε_{ijkl} and R^ε_{ijkl} stand for the phonon, phason and phonon-phason coupling coefficients, respectively.

Without specifying the functional framework, we introduce a bilinear form m^ε:

$$m^\varepsilon(\xi, \zeta) = m^\varepsilon((v, \psi), (v', \psi')) = \int_{\Omega^\varepsilon} Q^\varepsilon(e(v), \nabla\psi) \cdot (e(v'), \nabla\psi')\, dx^\varepsilon, \tag{2}$$

and a linear form L^ε:

$$L^\varepsilon(\xi) = L^\varepsilon((v, \psi)) = \int_{\Omega^\varepsilon} (f^\varepsilon \cdot v + g^\varepsilon \cdot \psi)\, dx^\varepsilon + \int_{\Gamma^\varepsilon_{uN}} F^\varepsilon \cdot v\, ds^\varepsilon + \sum_{i=1}^{3} \int_{\Gamma^\varepsilon_{wN,i}} G^\varepsilon_i\, \psi_i\, ds^\varepsilon. \tag{3}$$

*Corresponding author. Email: thibaut.weller@umontpellier.fr

The coupled physical problem then takes the form

$$\mathcal{P}(\Omega^\varepsilon) \quad : \quad \text{Find } s^\varepsilon = (u^\varepsilon, w^\varepsilon) \text{ such that } m^\varepsilon(s^\varepsilon, \xi) \,=\, L^\varepsilon(\xi), \quad \forall\, \xi.$$

With the classical assumptions of regularity of the loading and of uniform ellipticity and boundedness of elastic operators, it is possible to show that this problem has a unique solution. To derive simplified and accurate models, the true question is to study the behavior of s^ε when ε, *regarded as a parameter*, tends to zero.

THE MODELS

It is possible to show that 26 different limit behaviors (indexed by a triplet $p = (p_1, p_2, p_3)$ of $\{1,2,3\}^3 \setminus \{0,0,0\}$) appear, according to both the type and magnitude of the boundary conditions in $\mathcal{P}(\Omega^\varepsilon)$. Classicaly (see [7]) we come down to a fixed open set $\Omega = \omega \times (\circ\, 1, 1)$ through the mapping π^ε:

$$x = (x_1, x_2, x_3) \in \overline{\Omega} \;\mapsto\; \pi^\varepsilon x = (x_1, x_2, \varepsilon x_3) \in \overline{\Omega}^\varepsilon. \tag{4}$$

To get physically meaningful results, we have to make various kinds of assumptions. The more significant deals with the magnitude of the electromechanical loading:

$$\begin{cases} f^\varepsilon_\alpha(\pi^\varepsilon x) = \varepsilon\, f_\alpha(x),\; f^\varepsilon_3(\pi^\varepsilon x) = \varepsilon^2\, f_3(x),\; \forall\, x \in \Omega, \\ F^\varepsilon_\alpha(\pi^\varepsilon x) = \varepsilon^2\, F_\alpha(x),\; F^\varepsilon_3(\pi^\varepsilon x) = \varepsilon^3\, F_3(x),\; \forall\, x \in \Gamma_{uN} \cap \Gamma_\pm, \\ F^\varepsilon_\alpha(\pi^\varepsilon x) = \varepsilon\, F_\alpha(x),\; F^\varepsilon_3(\pi^\varepsilon x) = \varepsilon^2\, F_3(x),\; \forall\, x \in \Gamma_{uN} \cap \Gamma_{lat} \\ g^\varepsilon_i(\pi^\varepsilon x) = \varepsilon^{2-p_i}\, g_i(x),\; \forall\, x \in \Omega, \\ G^\varepsilon_i(\pi^\varepsilon x) = \varepsilon^{3-p_i}\, G_i(x),\; \forall\, x \in \Gamma_{wN,i} \cap \Gamma_\pm, \\ G^\varepsilon_i(\pi^\varepsilon x) = \varepsilon^{2-p_i}\, G_i(x),\; \forall\, x \in \Gamma_{wN,i} \cap \Gamma_{lat} \\ w^\varepsilon_{0_i}(\pi^\varepsilon x) = \varepsilon^{p_i}\, w_{0_i}(x),\; \forall\, x \in \Omega. \end{cases}$$

Also, with the true physical state $s^\varepsilon = (u^\varepsilon, w^\varepsilon)$ defined on Ω^ε, we associate a *scaled* physical state $s_p(\varepsilon) = (u(\varepsilon), w_p(\varepsilon))$ defined on Ω by:

$$u^\varepsilon_\alpha(x^\varepsilon) = \varepsilon\, u(\varepsilon)_\alpha(x), \quad u^\varepsilon_3(x^\varepsilon) = u(\varepsilon)_3(x), \quad w^\varepsilon_i(x^\varepsilon) = \varepsilon^{p_i}\, w_p(\varepsilon)_i(x), \quad \forall\, x^\varepsilon = \pi^\varepsilon x \in \overline{\Omega}^\varepsilon, \tag{5}$$

We therefore build a family of variational problems indexed by ε. The asymptotic analysis of this family is processed classically: a priori estimates, week convergence, strong convergence. Without spelling out the topology, one of the main strong convergence result of this analysis is:

$$s_p(\varepsilon) \underset{\varepsilon \to 0}{\circ\!\!\to} \overline{s}_p. \tag{6}$$

To get physically meaningful results it is necessary to define a physical state $\overline{s}^\varepsilon_p$ over the genuine plate Ω^ε through the descaling $\overline{s}^\varepsilon_p(\pi^\varepsilon x) = \overline{s}_p(x)$, for all x in Ω. This physical state living in the genuine quasicrystalline plate is the unique solution of a problem posed over the reference configuration, namely:

$$\overline{\mathcal{P}}(\Omega^\varepsilon)_p : \text{Find } \overline{s}^\varepsilon_p \text{ such that } \int_{\Omega^\varepsilon} \widetilde{Q}^\varepsilon_p(x)\, k(\overline{s}^\varepsilon_p)^0_p \cdot k(\xi)^0_p\, dx = L^\varepsilon(\xi),\; \forall\, \xi.$$

The detailed definition of $k(\overline{s}^\varepsilon_p)^0_p$ cannot be given here. However, it corresponds to the effective components of the linearized tensor of small phononic strains and of the gradient of the phason field. The algebraic operations that are associated with these components lead to the explicit expression of $\widetilde{Q}^\varepsilon_p$ which gives the limit constitutive law.

References

[1] T. Weller, C. Licht, Asymptotic modeling of thin piezoelectric plates, Ann. Solid Struct. Mech. 1 (2010) 173-188.

[2] T. Weller, C. Licht, Mathematical modeling of piezomagnetoelectric thin plates, European Journal of Mechanics A/Solids 29 (2010) 928-937.

[3] T. Weller, C. Licht, Asymptotic modeling of piezoelectric plates with electric field gradient, C. R. Mecanique 340 (2012) 405-410.

[4] D. H. Ding, W. G. Yang, C. Z. Hu, R. Wang. Generalized elasticity theory of quasicrystals. Phys. Rev. B, 48 (1993) 7003-7010.

[5] T. Weller, C. Licht, Asymptotic modeling of thin linearly quasicrystalline plates, C. R. Mecanique 341 (2013) 793-798.

[6] T. Fan, Mathematical Theory of Elasticity of Quasicrystals and Its Applications, 2011, Springer.

[7] P.G. Ciarlet, Mathematical Elasticity, vol. II, North-Holland, 1997.

ELASTIC PROPERTIES OF ORIGAMI-INSPIRED RECONFIGURABLE METAMATERIALS

Fei Wang, Changqing Chen [a)]
Department of Engineering Mechanics and Centre for Nano and Micro Mechanics, AML
Tsinghua University, Beijing 100084, China

Abstract Origami structures have enriched mechanical metamaterials with the ability of converting morphologies between two dimensional (2D) thin sheets and three dimensional (3D) spatial structures. In this study, we analyse the kinematics and elastic properties of multiple assembled origami morphologies on the basis of various origami folding techniques. By modifying Miura-ori pattern, mechanical metamaterials such as curved origami shell and large-scale bendable elastic structures are developed. The concept of in-plane Poisson's ratio is extended to the curved shell structures and the existence of a critical folding state is presented by analysing the geometric characteristics. An analytical model is adopted to study the mechanical properties of the assembled structures and elastic behaviors such as load softening and snap-through are obtained. By introducing origami assemblages, we extend the design space of mechanical metamaterials and provide benchmarks for their practical applications in science and engineering.

GEOMETRY AND MECHANICS OF ORIGAMI-BASED CYLINDRCAL SHELLS

Origami, an art of folding a piece of thin sheet into 3D structures, has recently received extensive attention in science and engineering [1, 2]. Miura-folded origami is one of the simplest folding patterns. With a single degree of freedom (DOF), it is easy to control the kinematics and mechanics of Miura-ori. With one more independent geometric parameter added in the Miura pattern, a modified origami configuration also having a single DOF is proposed (shown in Fig. 1a). Upon folding/unfolding, the vertices locate regularly on two concentric cylindrical surfaces, resulting an origami based open cylindrical shell (Origami-based cylindrical shell, OCS). Moreover, as the periodically repeated units shrink/expand, the structure is able to vary the central angles and radii. An extended concept of Poisson's ratio $\nu_{z\theta} = -\varepsilon_\theta / \varepsilon_z$ which couples the structural strains in the axial and circumferential directions, is proposed to demonstrate the auxetic properties of OCS. An analytical model [3] of rigid plates connected by linear elastic hinges is employed to describe the mechanics of rigid folding/unfolding of the origami shell with finite number of periodic units. We demonstrate that under particular initial angles and different isometric loads, the origami shell shows novel mechanical responses such as load softening, snap-through [4] and critical folding states, which means that the folding/unfolding process is in fact limited by a specified folding angle no matter how large a force is exerted in the elastic limit. Numerical simulations (Finite Element Method, FEM) are also conducted, showing excellent agreement with the analytical results. Figure 1b and c show the predicted radial and axial balanced force versus folding angle ψ (ψ=180°$-\theta$, shown in Fig. 1a) under particular geometric conditions, respectively. Dependence of the existence of a critical folding state or load softening upon the geometric parameters (for example, the constant angles α_1 and α_2) is also studied, in which it is pointed out that the tangent stiffness of the elastic origami shell determines the load softening properties. Moreover, the counterparts of the finite-thickness and elastic-plate models of the origami shell are studied, respectively. Geometric constraints to maintain the completeness and compatibility of the thick curved shell are obtained. The local deformation behaviour of the elastic shells under line force, with multistage characteristics, are also studied, showing that the origami shell has a good potential in load bearing structures.

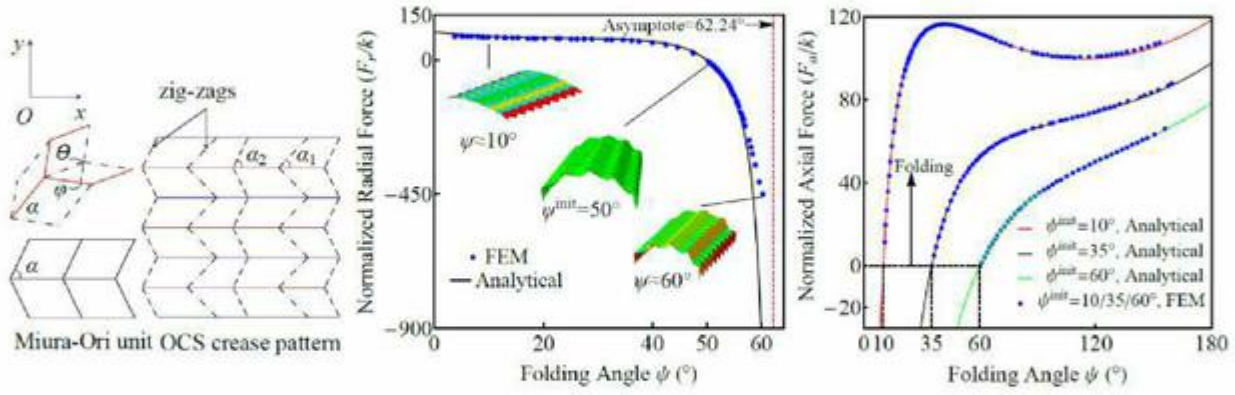

(a) (b) (c)

Figure 1. Crease pattern and elastic responses of the origami cylindrical shell (OCS). (a) One unit of Miura-Ori and a 3×2 pattern of OCS, α_1 and α_2 are the constant line angles that influence the pattern and corresponding elastic properties. (b) Analytical and FEM predicted force-displacement curves under radial loading (α_1=45°, α_2=60° and the initial folding angle $\psi^{\text{init}} = 50°$). The critical state is at about

[a)] Corresponding author. Email: chencq@tsinghua.edu.cn

$\psi \approx 62.24°$. (c) Analytical and FEM predicted force-displacement curve under axial loading for α_1=45°, α_2=60° and $\psi^{init} = 10°$, 35° and 60°, respectively. Load softening appears at small initial folding angles.

MIURA-INSPIRED ORIGAMI ASSEMBLAGES

Rigid-foldable Miura-ori possesses only one deformation mode, which is in-plane compression (folding) or tension (unfolding), and the exerting forces are often in-plane or out-of-plane isometric loadings. While in many practical engineering problems such as micro/nano functional devices, large scale bending or other out-of-plane deformations are needed. Based on the geometric characteristics of Miura pattern and its derivatives [5], a class of origami structures is proposed to realise morphological assemblages in 3D space. One of the assemblages is the auxetic cylindrical shells, as mentioned above. Figure 2 shows the tunable elastic properties of a large-scale bendable origami structure with varying radius of the connection arc. Analytically, we present the elastic deformation characteristics with multiple varying geometric parameters. The existence of the critical folding state φ_c (φ in Fig. 1a is used as the folding angle.) is dictated by m_1, m_2, α and β. Combined with other parameters, the elastic behavior is fully tunable. Besides, a class of origami-inspired reconfigurable structures are also studied and developed, in which different kinematics and mechanics can be realized for specific applications. Note that although relatively complex morphological transformation is conducted, the DOF of the system is limited according to the geometric compatibility. As a result, the difficulty of controlling the assemblages' mobility and mechanics is decreased. On the other hand, in the conceptual design of our origami-inspired reconfigurable metamaterials, stiffness of the plates is much higher than that of the elastic hinges, so the structural kinematics are decoupled from deformation of the plates.

Mechanics of origami structures is experiencing a rapid development, in the aspects from mathematic modeling such as curved creases and thick origami, to more practical engineering applications such as multi-stability, architecture and micro assembly [6]. Our study of origami-inspired morphological assemblages broaden the research points and design space of mechanical metamaterials. It is expected that such structures may provide a wide range of applications in science and engineering.

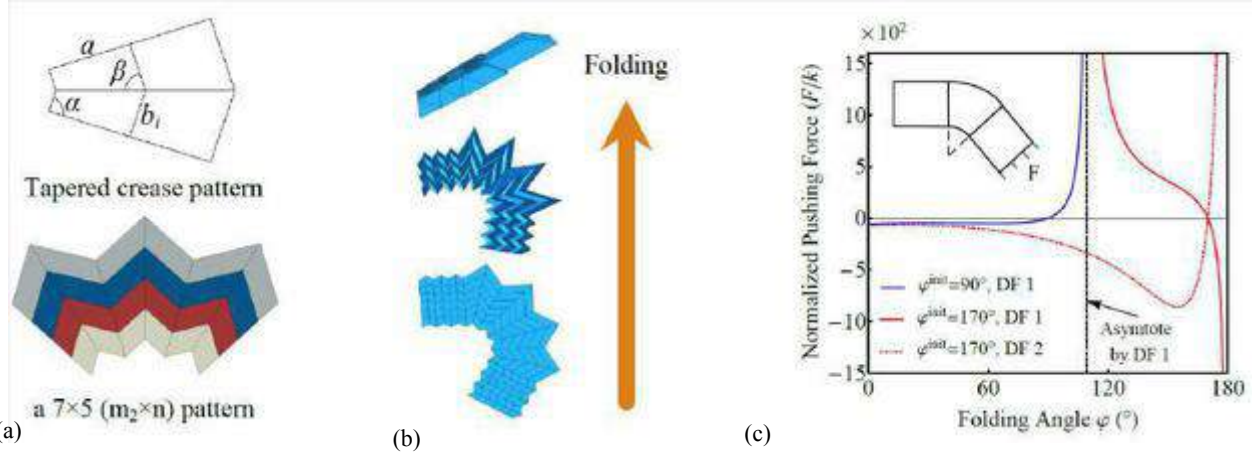

Figure 2. Crease pattern and tunable elastic responses of the assembled bendable structure. (a) Crease pattern of the tapered connection arc. We character the structure with 3 odd numbers m_1, m_2 and n, where m_1 and m_2 are the number of straight lines of the Miura and tapered pattern, respectively; n is the number of zig-zag lines of the 2 patterns [5]. (b) Illustration of the folding process of the structure, in which 2 same Miura-ori are connected by a tapered pattern to realize bending. (c) Tunable elastic properties of the bendable structure, with 2 set of determining factors (DF). i.e., DF 1: $m_1 = 5$, $m_2 = 7$, $\alpha = 70°$ and $\beta = 40°$ and DF 2: $m_1 = 11$, $m_2 = 5$, $\alpha = 70°$ and $\beta = 40°$. In DF 1, there exists a critical folding state despite of the initial folding angles φ^{init}, while in DF 2 there does not.

References

[1] Silverberg J. L. *et al*.: Using origami design principles to fold reprogrammable mechanical metamaterials. *Science* **345,** 647–650, 2014.

[2] Magleby S. P., Lang R. J. & Howell L. L.: Force–Deflection Modeling for Generalized Origami Waterbomb-Base Mechanisms. *J. Appl. Mech.* **82(8)**, 081001, 2015

[3] Wei Z. Y. *et al*.: Geometric Mechanics of Periodic Pleated Origami. *Phys. Rev. Lett.* **110**, 2013.

[4] Yasuda H. & Yang J.: Reentrant Origami-Based Metamaterials with Negative Poisson's Ratio and Bistability. *Phys. Rev. Lett.* **114**, 2015.

[5] Gattas J. M., Wu W. & You Z.: Miura-Base Rigid Origami: Parameterizations of First-Level Derivative and Piecewise Geometries. *J. Mech. Des.* **135**, 111011, 2013.

[6] Xu S. *et al*.: Assembly of micro/nanomaterials into complex, three-dimensional architectures by compressive buckling. *Science* **347**, 154–159, 2015.

APPLICATION OF THE TENSORIAL POLAR DECOMPOSITION TO 2D MEDIUM WITH OPEN AND CLOSED CRACKS

Boris Desmorat *[1] and Rodrigue Desmorat[2]
[1]*Sorbonne Universités, UPMC Univ Paris 06, CNRS, Institut Jean Le Rond d'Alembert, F-75005, Paris, France*
[2]*LMT-Cachan (ENS Cachan, CNRS, Université Paris Saclay), 94235 Cachan, France*

Summary Using the recently published tensorial polar decomposition, we investigate the induced anisotropy due to the presence of (non-interacting) cracks in an initially isotropic linear elastic material. Three new results are presented in the case of closed cracks: the micro-cracking state is represented by a single 2nd order crack density tensor, the compliance tensor is square symmetric, and two cracks arrays allow to represent the effects of any arbitrary closed microcracks systems, the angle made by the two cracks arrays being $\frac{\pi}{4}$.

TENSORIAL POLAR DECOMPOSITION

Considering the structure of 2D symmetric fourth-order tensors, i.e. having both minor and major indicial symmetries, Verchery polar decomposition [1, 2] is rewritten in a tensorial form entitled Tensorial Polar Decomposition [3]. The main result is that any 2D symmetric fourth-order tensor $\mathbb{T}$ can be written in terms of second-order tensors only in the form

$$\mathbb{T} = 2t_0\mathbb{J} + 2t_1\mathbf{1}\otimes\mathbf{1} + 2r_0\left[\mathbf{R}'_0\otimes\mathbf{R}'_0\circ\,\mathbb{J}\right] + 2r_1\left(\mathbf{1}\,\overline{\otimes}\,\mathbf{R}'_1 + \mathbf{R}'_1\,\overline{\otimes}\,\mathbf{1}\right) \tag{1}$$

in which $\mathbf{R}'_0$ and $\mathbf{R}'_1$ are deviatoric second order tensors of unit J2-norm ($(.)'$ denotes the deviatoric part of a second order tensor). This decomposition that makes explicitly appear invariants t_0, t_1, r_0, r_1 and $\mathbf{R}'_0 : \mathbf{R}'_1$, and symmetry classes as orthotropy is $\mathbf{R}'_0 : \mathbf{R}'_1 = \pm 1$ or 0, r_0-orthotropy is $r_0 = 0$, square symmetry is $r_1 = 0$ and isotropy is $r_0 = r_1 = 0$.

SYMMETRY ANALYSIS OF OPEN AND CLOSED CRACKS CONTRIBUTIONS

Considering a 2D isotropic uncracked material with a compliance tensor $\mathbb{S}_0$, the induced anisotropy in the 2D cracked material will result from anisotropy of the change of compliance tensors with open cracks $\hat{\mathbb{S}}_{\text{open}}$, closed cracks $\hat{\mathbb{S}}_{\text{closed}}$ or with both open and closed cracks. We investigate the type of induced anisotropy using the polar method in the standard framework of elastic effective properties of solids with non-interacting cracks expressed in terms of compliance tensor [4], so that the effective compliance tensor $\mathbb{S}$ reads:

$$\mathbb{S} = \mathbb{S}_0 + \hat{\mathbb{S}}_{\text{open}} + \hat{\mathbb{S}}_{\text{closed}} \tag{2}$$

The polar parameters of the change of compliance tensor defined for open cracks $\hat{\mathbb{S}}_{\text{open}}$ are found to be

$$\begin{aligned} &\hat{t}_0^{\,o} = \frac{1}{2E_0}\sum_{\text{open } p} d^{(p)} \qquad \hat{r}_0^{\,o} = 0 \\ &\hat{t}_1^{\,o} = \frac{1}{4E_0}\sum_{\text{open } p} d^{(p)} \qquad \hat{r}_1^{\,o} = \frac{1}{4E_0}\left|\sum_{\text{open } p} d^{(p)} e^{2i\varphi^{(p)}}\right| \qquad \hat{\varphi}_1^{\,o} = \frac{1}{2}\arg\left(\sum_{\text{open } p} d^{(p)} e^{2i\varphi^{(p)}}\right) \end{aligned} \tag{3}$$

Previous equation shows that the change in compliance tensor for open cracks is $r_0\circ$ orthotropic. This symmetry presents all the properties already discussed in [4] for cracked media.

The polar parameters of the change of compliance tensor defined for closed cracks $\hat{\mathbb{S}}_{\text{closed}}$ are found to be

$$\begin{aligned} &\hat{t}_0^{\,c} = \frac{1}{4E_0}\sum_{\text{closed } p} d^{(p)} \qquad \hat{r}_0^{\,c} = \frac{1}{4E_0}\left|\sum_{\text{closed } p} d^{(p)} e^{4i\varphi^{(p)}}\right| \qquad \hat{\varphi}_0^{\,c} = \frac{1}{4}\arg\left(\sum_{\text{closed } p} d^{(p)} e^{4i\varphi^{(p)}}\right) + \frac{\pi}{4} \\ &\hat{t}_1^{\,c} = 0 \qquad\qquad \hat{r}_1^{\,c} = 0 \end{aligned} \tag{4}$$

Previous equation (4) shows that the change in compliance $\hat{\mathbb{S}}_{\text{closed}}$ in the case of multiple arrays of closed cracks is square symmetric.

*Corresponding author. Email: boris.desmorat@upmc.fr

REWRITING WITH SECOND ORDER CLOSED CRACK DENSITY TENSOR

In case of open cracks, the fact that the knowledge of only one second order crack density tensor is needed to represent for the effects of any arbitrary open microcracks systems is a standard result [4].

For closed cracks, we proove that such a result is also true. Rewriting equation (4) using the tensorial polar decomposition (1), the change in compliance tensor for closed cracks $\hat{\mathbb{S}}_{\text{closed}}$ reads

$$\hat{\mathbb{S}}_{\text{closed}} = \frac{1}{E_0}\left[\delta_m^c \mathbb{J} + \delta_{eq}^c \left(\frac{\boldsymbol{\delta}^{c\prime}}{\delta_{eq}^c} \otimes \frac{\boldsymbol{\delta}^{c\prime}}{\delta_{eq}^c} \circ \mathbb{J}\right)\right] \tag{5}$$

with $\delta_m^c = 2E_0\hat{t}_0^c$, $\delta_{eq}^c = 2E_0\hat{r}_0^c$, $\boldsymbol{\delta}^{c\prime}/\delta_{eq}^c = 2(\mathrm{N}_\delta^c \otimes \mathrm{N}_\delta^c)'$ and $\mathrm{N}_\delta^c = \cos(\hat{\varphi}_0^c)\,\mathrm{e}_1 + \sin(\hat{\varphi}_0^c)\,\mathrm{e}_2$. This allows for the definition of second order closed crack density tensor

$$\boldsymbol{\delta}^c = \frac{1}{2}\,\mathrm{tr}\,\boldsymbol{\delta}^c\,\mathbf{1} + \boldsymbol{\delta}^{c\prime} \qquad \begin{cases} \delta_m^c = \frac{1}{2}\,\mathrm{tr}\,\boldsymbol{\delta}^c \\ \delta_{eq}^c = \sqrt{\frac{1}{2}\boldsymbol{\delta}^{c\prime} : \boldsymbol{\delta}^{c\prime}} \end{cases} \tag{6}$$

REPRESENTATION OF ANY ARBITRARY CLOSED CRACKS SYSTEM BY TWO NON ORTHOGONAL FAMILIES OF MICROCRACKS

In case of open cracks, the fact that only two arrays of open cracks are needed to represent for the effects of any arbitrary open microcracks systems is a standard result [4].

Let us consider multiple arrays of closed cracks. The non zero polar parameters of the change in compliance tensor are $\hat{t}_0^c$, $\hat{r}_0^c$ and $\hat{\varphi}_0^c$, see equation (4). Let us then consider two unknown arrays of closed cracks with densities $d^{(1)}$ and $d^{(2)}$ and angles $\varphi^{(1)}$ and $\varphi^{(2)}$. In order to retrieve the same change in compliance tensor by means of only those two arrays of closed cracks, one has to solve

$$\frac{1}{4E_0}\left(d^{(1)} + d^{(2)}\right) = \hat{t}_0^c \qquad \frac{1}{4E_0}\left(d^{(1)}e^{4i(\varphi^{(1)}+\frac{\pi}{4})} + d^{(2)}e^{4i(\varphi^{(2)}+\frac{\pi}{4})}\right) = \hat{r}_0^c \mathrm{e}^{4i\hat{\varphi}_0^c} \tag{7}$$

with unknowns $d^{(1)}$, $d^{(2)}$, $\varphi^{(1)}$ and $\varphi^{(2)}$ at given values $\hat{t}_0^c$, $\hat{r}_0^c$ and $\hat{\varphi}_0^c$. By doing so, one shows that two arrays of closed cracks with densities and angles

$$d^{(1)} = 2E_0(\hat{t}_0^c \circ\ \hat{r}_0^c) \qquad \varphi^{(1)} = \hat{\varphi}_0^c \qquad d^{(2)} = 2E_0(\hat{t}_0^c + \hat{r}_0^c) \qquad \varphi^{(2)} = \hat{\varphi}_0^c + \frac{\pi}{4} \tag{8}$$

allow to represent the effects of any arbitrary closed microcracks systems. The angle between the to equivalent families of closed cracks is not $\frac{\pi}{2}$ as in the open cracks case, it is $\varphi^{(2)} \circ\ \varphi^{(1)} = \frac{\pi}{4}$.

CONCLUSIONS

The main conclusions of the present work are:

- with open cracks only , the microcracking state is represented by a single 2nd order crack density tensor do and the compliance tensor is (r0-) orthotropic (standard results),
- with closed cracks only , the microcracking state is represented by a single 2nd order crack density tensor and the compliance tensor is square symmetric (new result),
- with open and closed cracks, the microcracking state is represented by the two second order tensors and the compliance tensor can be fully anisotropic (new result),
- two families of cracks allow to represent the effects of any arbitrary open or closed microcracks systems, the angle made by the two families of cracks being $\frac{\pi}{2}$ for open cracks (standard result) and $\frac{\pi}{4}$ for closed cracks (new result).

References

[1] Verchery G., Les invariants des tenseurs d'ordre 4 du type de l'élasticité. In: Proceedings of Euromech 115, Villard-de-Lans. Published by Editions du CNRS, Paris 1982, pp. 93-104, 1979.

[2] Vannucci P., Plane anisotropy by the polar method, Meccanica, 40:437-454, 2005.

[3] Desmorat B., Desmorat R., Tensorial Polar Decomposition of 2D fourth order tensors, C. R. Mecanique, 343:471–475, 2015.

[4] Kachanov M., Elastic effective properties of cracked solids: critical review of some basic concepts, Appl. Mech. Rev., 45:304-335, 1992.

BI-STABILITY OF FGM CYLINDRICAL SHELLS WITH PIEZOELECTRIC SURFACE LAYERS

Guohua Nie[1a)], Bin Wang[1]
[1]*Institute of Applied Mechanics, School of Aerospace Engineering and Applied Mechanics, Tongji University, Shanghai 200092, China*

Summary The condition for existence of bi-stability of FGM cylindrical shells with piezoelectric surface layers is formulated and analytical expressions for the rolled-up radii of the stable shells are derived by using the principle of minimum potential energy for the elastic shell system. The solution indicates that the system may have two stable states besides its initial state under an actuating electric field when the direction of polarization is along the direction of thickness of the piezoelectric layers. The magnitude in the electric field determines the number of the stable states. The present prediction for the bi-stable states is verified by FEM simulation. The results indicate that a larger magnitude in the electric field will cause a larger rolled-up radius for the first stable state and smaller one for the second stable state. However, a change in the constituent volume fraction exponent has no remarkable effect on the rolled-up radii.

INTRODUCTION

Deployable structures have a wide application prospect in space and mechanical engineering. A bi-stability cylindrical shell owns two stable states, i.e., a coiled state in which the structure is folded along its length and an extended state in which the structure is unfolded. In general the initial state of the shell is regarded as the first stable state, and the second stable state corresponds to a local equilibrium position during rolled-up without twisting deformation. Recently related studies show that laminated cylindrical shells with anti-symmetrical lay-up with respect to the mid-plane present better behaviours of bi-stability. For isotropic cylindrical shells, it has been proven that they do not have bi-stability [1]. However, the existing initial stresses may produce the bi-stable states, but one corresponding to its initial state [2]. This paper is aimed at analysis of existence of bi-stability of FGM (Functionally Graded Material) cylindrical shells with piezoelectric surface layers.

ANALYSIS AND RESULTS

The elastic shell system is formed by a FGM elastic cylindrical shell and its two attached surface anisotropic piezoelectric layers. The geometry of the shell is shown in Fig.1. The FGM is assumed to be constituted by two materials. The effective material parameters (elastic modulus, shear modulus, Poisson's ratio, etc.), can be written by $P_{\text{eff}} = {}_{\text{PK}} + {}_{\text{PP}}(1-V_{\text{PK}}\ z$ where $V_{\text{PK}}\ z = \ z+h\ \ h)^n$ is constituent volume fraction, and $n\ \ (0< \ <\infty)$ is volume fraction exponent [3]. For the piezoelectric surface layers, it is assumed that the direction of polarization is only along the direction of thickness, i.e., $E_3 \neq 0$, $E_1 = E_2 = 0$. For every material, the resultant internal forces and moments can be obtained by integration with respect to the thickness based on the corresponding constitutive equations. Suppose that the effect of mid-plane strains on bending deformation of the shell is neglected, Gaussian curvature will be zero for a possible stable shell corresponding to an equilibrium position for the minimum potential energy. Accordingly, a deformed shell can be characterized by the curvature of the shell, C, and the angle θ indicating a change in orientation of coordinate axes along 1- and 2-directions (i.e. axial and transverse directions of the shell). The variance of curvatures of the deformed shell is expressed by $\chi_{11} = C(1-\cos 2\theta)/2$, $\chi_{22} = C\ + \ \ \theta\ \ - K_{02}$, $\chi_{12} = C\ \ \ \theta\ \ $. The strain energy for the shell system, U, can be expressed by $U = \alpha Lu\ \ K_{02}$ in which $u = \{\ \}\left[D_{sys}\right]\{\ \}^T/2 - \{\ \}\{G\ G\ 0\}^T E_3$ where $\chi\ = \chi\ \ \chi\ \ \chi_{12}\}$, and $\left[D\ \right]$ is $\times$ stiffness matrix with its elements $D_{\text{ij}} = 2D_{\text{pij}} + {}_{\text{fij}}$ $(\text{i,j} = 1,2,6)$, $D_{\text{fij}} = \int_{-h/2}^{h/2} G\ z\ dz$, $D_{\text{pij}} = \int_{t/2}^{t/2+t_1} Q\ z^2\ z$, $G = \int_{t/2}^{t/2+t_1} e'\ z\ z$, $Q_{\text{ij}} = \text{C}_{\text{ij}} - \text{C}\ \ \text{C}\ \ /\text{C}\ \ \ \ = \ \ \ )$, $e'_{3i} = \text{e}_{3i} - \text{C}\ \ \text{e}\ \ /\text{C}\ \ .$

The condition for extreme values of the function, $U = U\ \ C,\theta)$ indicates there are two equilibrium positions for the shell system, i.e., $\theta_1 = 0, C_1 = GE_3\ \ D_{11} + K_{02}$ and $\theta_2 = \ \ /2, C_2 = GE_3 + D\ \ K_{02}\ \ D_{11}$. The magnitude of two corresponding rolled-up radii is given by $R_1 = \left|\ \ C_1\right|\ R_2 = \left|1/C_2\right|$. The results show that the first equilibrium position is stable if the condition equation $\left(GE_3 + D_{11}K_{02}\right)\left[(D_{12} + 2D_{66} - D_{11}\ GE_3 + 2D\ D\ \ K\ \right] > 0$ is satisfied while the second equilibrium position is stable if the inequality $\left(GE_3 + D\ \ K_{02}\right)\left[(D_{12} + 2D_{66} - D_{11}\ GE_3 + \ D_{12}^2 - \ \ ^2 + 2D\ \ D\ \ \ K_{02}\right] > 0$ holds. It is concluded that there exist two stable states if the two resulting conditions related to geometrical and material properties of the shell system are all satisfied. As an example, the PEEK and PP are chosen in computation as two constituent materials with $E = \ \ \times \ \ ^9\,\text{Pa}, \nu = 0.4$ and $E = \ \ \times \ \ ^9\,\text{Pa}, \nu = 0.35$, respectively. The thickness of for the FGM shell is $h = \ \ \times \ \ ^{-3}$. The geometrical parameters

a)Corresponding author. Email: ghnie@tongji.edu.cn

for the shell and the piezoelectric material property for the surface layers are listed in Ref.[2]. To verify theoretical prediction, a FEM model is constructed using S4R shell element based on ABAQUS code. The process for the rolled-up of the shell under the actuating electric field $E_3 = -\quad \times \quad ^7$ (V/m) is presented in Fig.3. The first stable state, corresponding to the first equilibrium position under the action, is shown in Fig.3(a). Flattening of the shell is shown in Fig.3(b). In this stage, the shell extends and the rolled-up around the "1" direction disappears gradually while an anti-directional rolled-up around the "2" direction begins. A state of anti-directional rolled-up is displayed in Fig.3(c). Finally, the shell deforms to its second stable state corresponding to the second equilibrium position, as shown in Fig.3(d). A comparison of the theoretical prediction with the FEM simulation is listed in Table 1. A good agreement is observed and shows validity of the present model. The results show that a larger magnitude in the electric field will cause a larger rolled-up radius for the first stable state and smaller rolled-up radius for the second stable state. In addition, changes in the rolled-up radii with the constituent volume fraction exponent are displayed in Fig.2. It is seen that an increase in the exponent results in a larger rolled-up radius for the first stable state and a smaller radius for the second stable state when the value of exponent is small. However, the resulting change in the radii is small. The exponent does not produce a remarkable effect on the rolled-up radii.

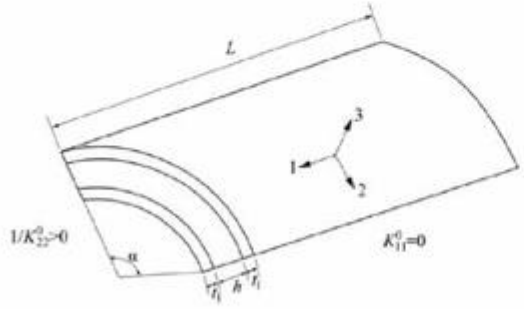

Fig. 1. Geometry of the shell system

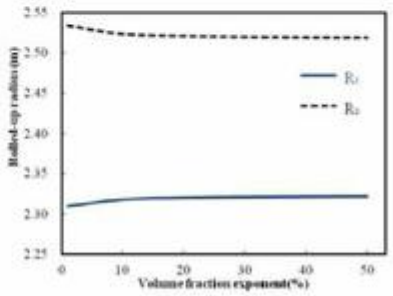

Fig.2. Effect of constituent volume fraction exponent of FGM on the rolled-up radii of the stable shell

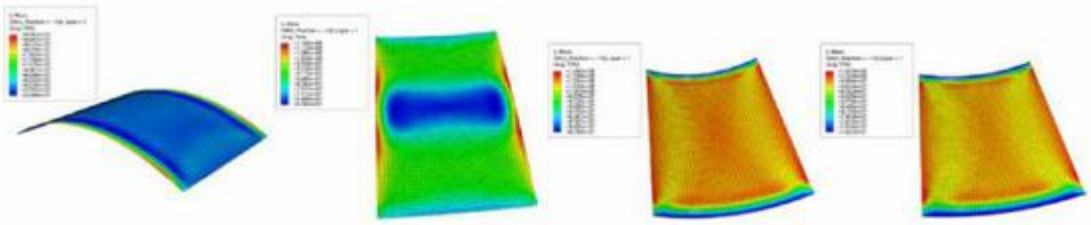

(a) (b) (c) (d)

Fig. 3. Simulation of process for the rolled-up of the shell

Table 1 Comparison of the rolled-up radii of the stable shell (n=1)

E_3/(*10^7V/m)	R_1/m (present)	R_1/m (FEM)	R_2/m (present)	R_2/m (FEM)
-0.9	1.7201	1.7436	4.0635	4.1586
-1.1	2.3106	2.2847	2.5337	2.5010
-1.3	3.5186	3.5736	1.8407	1.8200

CONCLUSIONS

The condition equations for existence of bi-stability of FGM cylindrical shells with piezoelectric surface layers are presented by using the principle of minimum potential energy for the elastic shell system. The analytical expressions for the rolled-up radii of the stable shells are given and verified by FEM. The result indicates that the system may have two stable states besides its initial state. The magnitude in the electric field determines the number of the stable states. The computational results show that a larger magnitude in the electric field will cause a larger rolled-up radius for the first stable state and smaller one for the second stable state. A change in the constituent volume fraction exponent has no remarkable effect on the rolled-up radii of the stable shell.

References

[1] Guest S.D., Pellegrino S.: Analytical Models for Bi-stable Cylindrical Shells. *Proc R Soc A* **462**:839-854, 2006.

[2] Wang B., Nie G.H.: Bi-stable States of Initially Stressed Elastic Cylindrical Shell Structures with Two Piezoelectric Surface Layers. *Acta Mechanica Sinica* **31**:653-659, 2015.

[3] Reddy J.N.: Analysis of Functionally Graded Plates. *Int J Numer Meth Eng* **47**:663-684, 2000.

A NEW ELASTIC THEORY FOR NANOMATERIALS AND ITS APPLICATION

Shaohua Chen[a)], Yin Yao & Yaochi Wei
LNM, Institute of Mechanics, Chinese Academy of Sciences, Beijing, 100190, China

Summary Within the framework of continuum mechanics, a new theory for nanomaterials based on surface-energy density is proposed to predict size effect (surface effect) of nanomaterials. In contrast to previous theories, the linearly elastic constitutive relationship that is usually adopted to describe the surface layer of nanomaterials is not invoked. The surface elastic constants, which is difficult to determine experimentally, are no longer needed in the new theory. Instead, a surface-induced traction to characterize the surface effect in nanomaterials is derived. Only the surface-energy density of bulk materials and the surface-relaxation parameter are needed in the new theory. It is further used to characterize the elastic property of several kinds of nanomaterials or nanostructures, the theoretical predictions agree very well with existing numerical or experimental ones.

INTRODUCTION

Many experiments have explored the surface effect in nanomaterials, including characterizing surface atomic structures by using electron diffraction and scanning-probe microscopy. The experimental findings provide a convincing demonstration that surface effect (size effect) plays an important role in mechanical property of nanomaterials. The energy of each atom in the surface region deviates significantly from those in the interior of a nanomaterial, and this discrepancy has been identified as the main cause of size effects associated with the mechanical behaviors of nanoscale materials. The classical elastic theory has no relations with the scale, which can not predict the mechanical property of nanomaterials. Recently, based on the surface elastic theory, a large number of theoretical models have been created to analyze size effects in nanomaterials. However, the involved surface elastic constants in the models can not be measured experimentally till now, which are also much difficult to determine even using molecular dynamics (MD) calculation.

AN ELASTIC THEORY FOR NANOMATERIALS

As we know that size effect of nanomaterials is essentially induced by the increasing ratio of surface to volume. A typically physical parameter to describe the surface of nanomaterials is the surface energy density. Based on the surface energy density of nanomaterials, a new elastic theory to characterize size effect in nanomaterials has been proposed by Chen and Yao (2014). Consider a nano-solid with an initial (or reference) configuration in a three-dimensional Euclidean space, which transforms into a current configuration under an external loading.

Relation between the Eulerian surface-energy density ϕ in the current configuration and the Lagrangian surface energy density ϕ_0 in the reference configuration satisfies $= {}_0/\mathrm{J}_s$, where J_s is a Jacobean determinant characterizing the surface deformation from the reference configuration to the current one.

In the current configuration, the potential energy function Π of nano-solids can be written as

$$\Pi\ \boldsymbol{u}\ = \int_{\mathrm{V-S}} \psi\ \boldsymbol{\varepsilon}\ \mathrm{dV} + \int_{\mathrm{S}} \phi \mathrm{dS} - \int_{\mathrm{V-S}} \boldsymbol{f}\ \ \boldsymbol{u} \mathrm{dV} - \int_{\mathrm{S_p}} \boldsymbol{p}\ \ \boldsymbol{u} \mathrm{dS}$$

where ψ is the elastic strain energy density, $\boldsymbol{f}$ and $\boldsymbol{p}$ are the body force and external surface traction; $\boldsymbol{u}$ and $\boldsymbol{\varepsilon}$ are the displacement and strain induced by $\boldsymbol{f}$ and $\boldsymbol{p}$. Variational analysis of the potential energy yields the equilibrium equation and stress boundary conditions,

$$\begin{cases} \boldsymbol{\sigma}\cdot\nabla + \boldsymbol{f} = \quad (\quad \mathrm{V-S}) \\ \boldsymbol{n}\ \boldsymbol{\sigma}\ \boldsymbol{n}\quad \boldsymbol{p}\ \boldsymbol{n}\quad \gamma_{\mathrm{n}}\boldsymbol{n}\quad (\text{on S}) \\ (\boldsymbol{I}\quad \boldsymbol{n}\quad \boldsymbol{n})\ \boldsymbol{\sigma}\ \boldsymbol{n}\quad (\boldsymbol{I}\quad \boldsymbol{n}\quad \boldsymbol{n}\quad \boldsymbol{p}\quad \gamma_{\mathrm{t}}\quad (\text{on S}) \end{cases}$$

where $\boldsymbol{\sigma}$ is the bulk Cauchy stress tensor, $\boldsymbol{n}$ is the unit normal vector perpendicular to the boundary surface S of the nano-solid, $\boldsymbol{I}$ is a unit tensor; γ_{n} and γ_{t} are the normal and tangential components of an additional surface-induced traction vector, respectively, which characterizes the force disturbance at boundaries due to the surface effect. Based on an infinitesimal element, the principle of virtual work yields the surface-induced traction, which is related to the surface energy density, $\gamma_{\mathrm{t}} = \nabla_{\mathrm{s}}\phi \quad \gamma_{\mathrm{n}}\boldsymbol{n} = \phi(\boldsymbol{n}\cdot\nabla_{\mathrm{s}})\boldsymbol{n}$. ∇_{s} is a surface gradient operator. Then, the boundary condition of the new theory can be rewritten as,

$$\begin{cases} \boldsymbol{n}\ \boldsymbol{\sigma}\ \boldsymbol{n}\quad \boldsymbol{p}\ \boldsymbol{n}\quad \dfrac{\phi_0(\boldsymbol{n}\cdot\nabla_{\mathrm{s}})}{\mathrm{J}_{\mathrm{s}}} \quad (\text{in the normal directionon of S}) \\ (\boldsymbol{I}\quad \boldsymbol{n}\quad \boldsymbol{n})\ \boldsymbol{\sigma}\ \boldsymbol{n}\quad (\boldsymbol{I}\quad \boldsymbol{n}\quad \boldsymbol{n}\quad \boldsymbol{p}\quad \dfrac{\phi_0(\nabla_{\mathrm{s}}\mathrm{J}_{\mathrm{s}})}{\mathrm{J}_{\mathrm{s}}^2} - \dfrac{\nabla_{\mathrm{s}}\phi_0}{\mathrm{J}_{\mathrm{s}}} \quad (\text{in the tangential directions of S}) \end{cases}$$

[a)]Corresponding author. Email: shchen@LNM.imech.ac.cn

In contrast to G-M theory (Gurtin and Murdoch, 1975), the new theory no longer requires the surface elastic constants. The Lagrangian surface-energy density ϕ_0 in the reference configuration serves as a unique quantity characterizing the surface effect of nanomaterials, which depends on the surface-energy density of the corresponding bulk material and the relaxation parameter (Chen and Yao, 2014). Both Parameters have clearly physical meanings and are very easy to determine through experiment and simple MD simulation.

APPLICATION OF THE NEW THEORY

The new theory is further used to characterize the elastic property of fcc metallic nanofilms under biaxial tension and nanowires under bending. It is found that the biaxial modulus of the nanofilm increases with the decreasing nanofilm thickness and the theoretical prediction agrees very well with the MD simulation given by Streitz et al. (1994) as shown Fig. 1(a). The deflection of a fixed-fixed nanowire predicted by the new theory is consistent with the experimental results given by Chen et al. (2006) and the theoretical one achieved by He and Lilley (2008) with the Y-L model as shown in Fig. 1(b). The results predicted by the classical beam theory without surface effect deviate obviously with the experimental one.

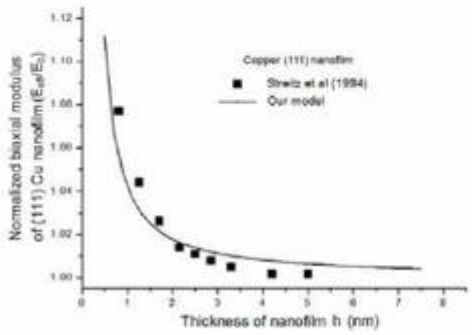

Fig. 1(a) Surface effects in nanofilms under biaxial tension

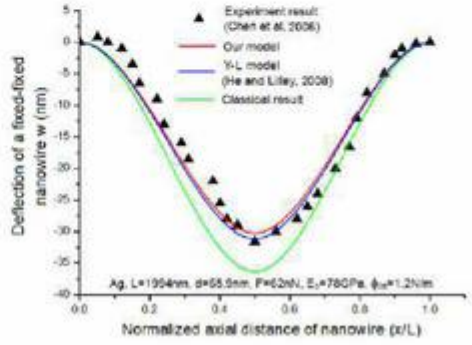

Fig. 1(b) Surface effect in nanowires under bending

Combining molecular dynamics simulation, the new theory is further used to predict size effect of the surface energy density of nanoparticles. It is found that the parameter in the well-known Tolman equation will influence the size effect variation trend of the surface energy density of nanoparticles (Yao, et al., (2015); Wei and Chen, (2015)).

An interesting finding is that the whole property of nanomaterials may exhibit nonlinearly elastic due to the nonlinear boundary conditions on the surface of nanomaterials, though the inside of nanomaterials is linearly elastic. Furthermore, it is found that the stiffening or softening behavior of nanofilms results essentially from the competition between the residual surface strain induced by the surface relaxation and the excess surface strain caused by an external loading.

CONCLUSIONS

A new theory to describe surface effect in nanomaterials is developed, in which only the surface energy density of bulk-materials and the surface relaxation parameter are involved. The present theory is demonstrated to be much convenient for predicting the mechanical behavior of nanomaterials since the involved parameters are easy to ascertain.

ACKNOWLEDGEMENTS

The work is supported by NSFC (11372317 and 11532013) and the Nano-project (2012CB937500).

References

[1] Chen S.H., Yao Y.: Elastic theory of nanomaterials based on surface energy density. *ASME: J. Appl. Mech.* **81**:121002, 2014.

[2] Chen Y.X., Dorgan B.L., Mcllroy D.N., Aston D.E.: On the importance of boundary conditions on nanomechanical bending behavior and elastic modulus determination of silver nanowires. *J. Appl. Phys.* **100**:104301, 2006.

[3] He J., Lilley C.M.: Surface Effect on the elastic behavior of static bending nanowires. *Nano Lett.* **8**:1798, 2008.

[4] Streitz F.H., Cammarata R.C., Sieradzki K.: Surface-stress effects on elastic properties I. Thin metal films. *Phy. Rev. B* **49**:10699, 1994.

[5] Wei Y.C., Chen S.H.: Size-dependent surface energy density of spherical fcc metallic nanoparticles. *J. Nanosci. Nanotecnol.* **15**:9457-9463, 2015.

[6] Yao Y., Wei Y.C., Chen S.H.: Size effect of the surface energy density of nanoparticles. *Surf. Sci.* **636**:19-24, 2015.

[7] Yao Y., Chen S.H.: Surface effect on resonant properties of nanowires predicted by an elastic theory for nanomaterials. *J. Appl. Phys.* **118**:044303, 2015.

[8] Gurtin M.E., Murdoch A.I.: A Continuum Theory of Elastic Material Surfaces. *Arch. Ration. Mech. Anal.* **57**:291–323, 1975.

[9] Wang G. F., Feng X. Q.: Surface Effects on Buckling of Nanowires Under Uniaxial Compression. *Appl. Phys. Lett.***94**:141913, 2009.

[10] Wang J.X., Huang Z.P., Duan H.L., Yu S.W., Feng X.Q., Wang G.F., Zhang W.X., Wang T.J.: Surface Stress Effect in Mechanics of Nanostructured Materials. *Acta Mech. Solida. Sin.***24**: 52–82, 2011.

THEORY OF NANOINDENTATION FOR MULTIFERROIC MATERIALS

Weiqiu Chen[1,2,3a)]
[1]*Department of Engineering Mechanics, Zhejiang University, Hangzhou 310027, China*
[2]*Soft Matter Research Center, Zhejiang University, Hangzhou 310027, China*
[3]*Key Laboratory of Soft Machines and Smart Devices of Zhejiang Province, Zhejiang University, Hangzhou 310027, China*

Summary Materials at small scales may exhibit different properties than their macroscopic counterpart, and new techniques need to be developed and used for the characterization of micro/nano materials. Nanoindentation is such a new technique, which has been widely employed since its development. The technique heavily relies on the classical Hertz contact theory for elastic materials. It has been extended to piezoelectric materials and multiferroic materials as well. In this work, we further take the surface energy into the analysis by extending the JKR contact theory for elastic materials. Thus, an exact adhesive contact theory for materials with multi-field couplings is established, which may serve the base of the nanoindentation technique for multiferroic materials.

INTRODUCTION

Instrumented indentation technique, in which the load and indentation depth are continuously measured and recorded, has become one type of the most useful and convenient methods to characterize mechanical properties of conventional as well as advanced materials. They are particularly useful when the tested materials are at a microscale or nanoscale, which may exhibit different properties than their macroscopic counterpart. The success of the technique relies on the classical theory of elastic contact established by Hertz, plus a few necessary modifications [1].

Indentation theories for some advanced multifunctional materials have also been developed. Giannakopoulos and Suresh derived analytical contact relations for typical circular rigid indenters contacting with piezoelectric materials using Hankel transform [2]. Almost simultaneously, Chen et al. [3,4] obtained exact three-dimensional contact solutions for piezoelectric materials by making use of the new results in potential theory. In their solutions, the exact expression for any physical quantity at any point in the piezoelectric half-space is analytically given in terms of elementary functions. The method was further extended to materials with mutual couplings between electric, magnetic, and elastic fields to establish the indentation theory for multiferroic composite materials [5]. A recent survey on the method is given in Ref. [6]

When the materials are at a micro/nanoscale, their properties may be different from that measured at a microscale. The nanoindentation behaviour of small-scaled materials may to a large extent also become different. In this study, we take the effect of surface energy into consideration, in addition to the multi-field coupling characteristic that is intrinsic for multiferroic materials. The work is an extension of the well-known JKR adhesive contact theory for elastic solids [7] and the Chen-Yu theory for piezoelectric materials [8].

GENERAL SOLUTION

We base on our analysis on potential theory and employ the following general solution for multiferroic media:

$$u_x = \frac{\partial \Psi_0}{\partial y} - \sum_{i=1}^{4} \frac{\partial \Psi_i}{\partial x},\ u_y = -\frac{\partial \Psi_0}{\partial x} - \sum_{i=1}^{4} \frac{\partial \Psi_i}{\partial y},$$
$$w_k = \sum_{i=1}^{4} \beta_{ik} \frac{\partial \Psi_i}{\partial z_i},\ (k = 1, 2, 3), \tag{1}$$

where u_i are displacement components, $w_1=u_z$, $w_2=\phi$, and $w_3=\psi$, with ϕ and ψ being the electric and magnetic potentials respectively, β_{ik} are related to material constants of the multiferroic material, and Ψ_i (i=0,1, …, 4) are (quasi-) harmonic functions satisfying:

$$\left(\Delta + \frac{\partial^2}{\partial z_i^2}\right)\Psi_i = 0 \quad (i = 0, 1, \cdots, 4), \tag{2}$$

where $z_i=s_iz$, with s_i being the characteristic material indices solely determined by the material properties.

The above general solution, expressed in terms of harmonic functions, could be obtained from a more general one with thermal effect [9]. It is valid for multiferroic solids with transverse isotropy (the material axis perpendicular to the x-y plane) when the material indices s_i (i=1,2, 3, 4) are distinct from each other. For more details, the reader is referred to Ref. [9].

POTENTIAL THEORY METHOD

For a circular rigid indenter contacting with a multiferroic half-space with surface z=0, we may assume

a) Corresponding author. Email: chenwq@zju.edu.cn.

$$\Psi_0 = 0,\ \ \Psi_i(z) = \sum_{k=1}^{3} c_{ik} H_k(z_i) \quad (i = 1,2,3,4)\,, \tag{3}$$

where c_{ik} are constants to be determined, and $H_k(\rho,\phi,z) = \iint_S \ln[R(M,N)+z]\sigma_k(N)\,\mathrm{d}S$ are potentials, with R being the distance between any interior point M and a surface point N within the contact area S, σ_1=σ_z, σ_2=D_z, and σ_3=B_z. Here σ_z, D_z and B_z are the normal stress, electric displacement and magnetic induction, respectively, all being in the z-direction.

Substituting Eq. (3) into Eq. (1), making use of the constitutive relations, we can obtain all physical quantities in terms of the three potentials H_k. From the contact conditions on S and the boundary conditions outside S at z=0, we can determine the constants c_{ik} in Eq. (3) as well as derive the following integral equations

$$w_k(N_0) = \sum_{l=1}^{3} g_{lk} \iint_S \frac{\sigma_l(N)}{R(N_0,N)}\,\mathrm{d}S \quad (k = 1,2,3)\,, \tag{4}$$

where $g_{lk} = \sum_{i=1}^{4} c_{il}\beta_{ik}$ $(l,k = 1,2,3)$. The mathematical structure of the above integral equations is identical to that for elastic contact, and hence we can readily obtain the exact solutions of $\sigma_k(N)$ $(k = 1,2,3)$ for three typical circular indenters (i.e. spherical, flat-ended, and conical). Moreover, by substituting $\sigma_k(N)$ back into the potentials in Eq. (3), we can obtain analytical expressions of the four harmonic functions all in terms of elementary functions [6].

ADHESIVE CONTACT ANALYSIS OF A SPHERICAL INDENTER

To show the procedure of adhesive contact analysis, we consider for illustration an electrically and magnetically conducting spherical indenter with zero electric and magnetic potentials prescribed on it. Assuming the contact radius is a, we can obtain the energy release rate G at the contact edge as

$$G = \lim_{\Delta a \to 0} \frac{1}{\Delta a} \int_0^{\Delta a} \frac{1}{2}\sigma_1[w_1]\,\mathrm{d}x = -\frac{\pi\eta}{2\eta_{11}} K_1^2\,, \tag{5}$$

where $K_1 = \lim_{\rho \to a}[\sqrt{2\pi(a-\rho)}\sigma_1(\rho,\phi,0)]$ which can be obtained from the analytical expression of σ_1=σ_z, and η and η_{11} can be determined from the material properties [9]. According to the JKR theory, we should set

$$-\pi\eta K_1^2 / (2\eta_{11}) = \eta_0\,, \tag{6}$$

where η_0 is the surface energy. Equation (6) plus the following relation

$$P = -\frac{2\eta_{11} a}{\pi\eta}\left(\delta - \frac{a^2}{3R_0}\right), \tag{7}$$

where R_0 is the radius of the spherical indenter, completely determine the relation between the load P and the indentation depth δ or that between P and the contact radius a. Note that Eq. (7) is obtained by integrating σ_1 over the contact area.

With the exact contact relations thus obtained, the adhesive contact theory of multiferroic materials is completely established. It is worth strengthening that all results are given in terms of elementary functions by our analysis.

ACKNOWLEDGEMENTS

The work was supported by the National Natural Science Foundation of China (No. 11321202) and the Specialized Research Fund for the Doctoral Program of Higher Education (No. 20130101110120).

References

[1] Oliver W.C., Pharr G.M.: Improved Technique for Determining Hardness and Elastic Modulus Using Load and Displacement Sensing Indentation Experiments. *J. Mater. Res.* **7**: 1564-1583, 1992.

[2] Giannakopoulos A.E., Suresh S.: Theory of Indentation of Piezoelectric Materials. *Acta Materialia* **47**: 2153-2164, 1999.

[3] Chen W.Q., Ding H.J.: Indentation of a Transversely Isotropic Piezoelectric Half-Space by a Rigid Sphere. *Acta Mech. Solida Sin.* **12**: 114-120, 1999.

[4] Chen W.Q., Shioya T., Ding H.J.: The Elasto-Electric Field for a Rigid Conical Punch on a Transversely Isotropic Piezoelectric Half-Space. *J. Appl. Mech.* 66(3): 764-771, 1999.

[5] Chen W.Q., Pan E.N., Wang H.M., Zhang C.Z.: Theory of Indentation on Multiferroic Composite Materials. *J. Mech. Phys. Solids* **58**: 1524-1551, 2010.

[6] Chen W.Q.: Some Recent Advances in 3D Crack and Contact Analysis of Elastic Solids with Transverse Isotropy and Multi-field Coupling. *Acta Mech. Sin.* **31**: 601-626, 2015.

[7] Johnson K.L., Kendall K., Roberts A.D.: Surface Energy and the Contact of Elastic Solids. *Proc. Royal Soc. Lond.* **A324**: 301-313, 1971.

[8] Chen Z.R., Yu S.W.: Micro-Scale Adhesive Contact of a Spherical Rigid Punch on a Piezoelectric Half-Space. *Compos. Sci. Tech.* **65**: 1372-1381, 2005.

[9] Chen W.Q., Lee K.Y., Ding H.J.: General Solution for Transversely Isotropic Magneto-Electro-Thermo-Elasticity and the Potential Theory Method. *Int. J. Eng. Sci.* **42**: 1361-1379, 2004.

MINIMIZATION PRINCIPLES IN PORO-HYDRO-ELASTICITY AT FRACTURE AND THEIR EXPLOITATION

S. Mauthe, S. Teichtmeister, C. Miehe*[1]
[1]*Institute of Applied Mechanics (CE), University of Stuttgart, Stuttgart, Germany*

Summary The goal of this work is twofold. First, a minimization principle for the evolution problem of Biot-type poro-hydro-elasticity is developed [5]. It does not only have the advantage of a compact canonical notation that emphasizes symmetries. The displacement-flux principle obtained can be exploited by a new *unconstrained stable finite element design*, while space discretizations of standard displacement-pressure saddle point principle are constrained by the LBB condition. Second goal is the coupling of the variational model for poro-hydro-elasticity with fracture. This is done by a recently developed phase field approach [1, 5] that regularizes sharp crack discontinuity. In this multi-physics scenario, specific attention has to be paid to the crack growth function as well as extra treatment of fluid flow inside of cracks.

MINIMIZER IN PORO-HYDRO-ELASTICITY

Following conceptually the recent work Miehe et al. [3], new minimization and saddle point principles are developed for coupled multi-physics problems. For the model problem of Darcy-Biot-type fluid transport in porous media, it is shown that the quasi-static problem of elastically deforming, fluid-saturated porous media is related to a *minimization principle for the evolution problem*. This two-field principle determines the rate of deformation of the solid as well as the fluid mass flux vector. It provides a canonically compact model structure, where the stress equilibrium and the *inverse* Darcy's law appear as the Euler equations of a variational statement

$$\{\dot{\boldsymbol{\varphi}}, \dot{\mathbb{h}}\} = \arg\{\inf_{\boldsymbol{\varphi}} \inf_{\mathbb{h}} \Pi(\dot{\boldsymbol{\varphi}}, \dot{\mathbb{h}})\} \tag{1}$$

A partial Legendre transformation of the dissipation potential relates the minimization principle to a characteristic *three field saddle point principle*, the Euler equations of which determine the evolution of deformation, the fluid content as well as Darcy's law. Since for the model problem of Darcy-Biot-type fluid transport the fluid content equation is an ordinary differential equation and hence can be evaluated locally, the saddle point principle turns out to be the classical displacement-pressure formulation.

The existence of these variational principles underlines inherent *symmetries* of Darcy-Biot theories of porous media. This can be exploited in the numerical implementation by the construction of time- and space-discrete variational principles, which fully determine the update problems of typical time stepping schemes. Here, the proposed minimization principle for the coupled problem is advantageous with regard to a *new unconstrained stable finite element design*, while space discretizations of the saddle point principles are constrained by the LBB condition, see Miehe et al. [5]. The non-standard variational structure of the minimization principle demands for a conforming finite element discretization the fluid mass flux to be approximated by a Raviart-Thomas space. Alternatively, we show that using a standard nodal-based finite element formulation in combination with a reduced integration technique of the coupling term does also lead to stable results.

MINIMIZER IN PORO-HYDRO-ELASTICITY AT FRACTURE

Next, this formulation is coupled to a phase-field approach for fracture, characterized by a regularization that converges for vanishing length-scale parameter to a sharp crack. In contrast to formulations with a sharp-crack discontinuities, the proposed regularized approach has the main advantage of a straight-forward continuum modeling of complex crack patterns including branching. The phase field regularization can be regarded as a specific gradient damage modeling approach with geometric features rooted in fracture mechanics, see Miehe et al. [2].

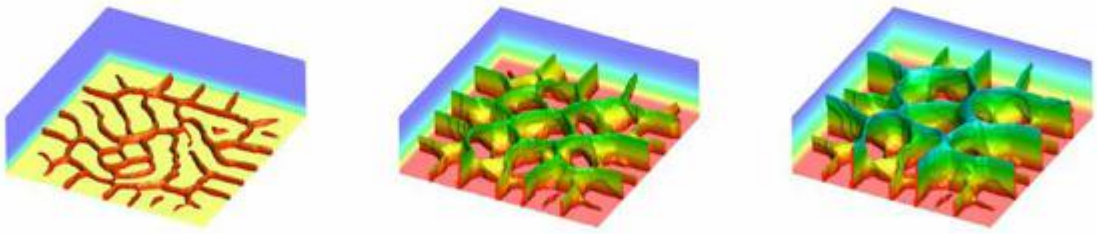

Figure 1. Crack formation and evolution of a drying process in soils.

*Corresponding author. Email: cm@mechbau.uni-stuttgart.de

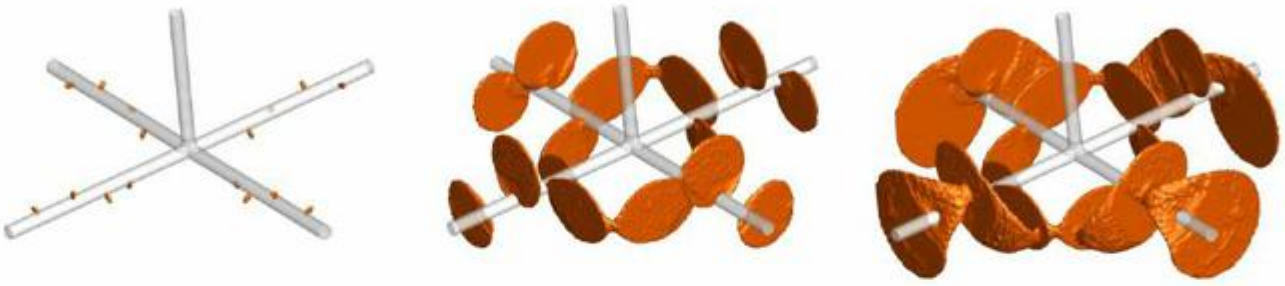

Figure 2. Crack formation in a hydraulic fracturing process.

In this work, we extend the general concepts of phase field fracture modeling to the coupled problem of Biot-Darcy-type poro-hydro-elasticity at fracture. The quasi-static coupled problem is shown to be related to a *three-field minimization principle for the evolution problem*, that in addition to the rate of deformation of the solid and the fluid mass flux vector determines the evolution of the crack phase field variable.

$$\{\boldsymbol{\varphi}, \dot{\boldsymbol{h}}, \dot{d}\} = \arg\{\inf_{\boldsymbol{\varphi}} \inf_{\boldsymbol{h}} \inf_{d} \Pi(\dot{\boldsymbol{\varphi}}, \dot{\boldsymbol{h}}, \dot{d})\} \, . \tag{2}$$

Taking the variation of this potential provides the Euler equations

$$\begin{array}{lll}
1. & \textit{Stress equilibrium} & -\mathrm{Div}[\partial_{\boldsymbol{F}}\widehat{\psi}] - (m_0 + m)\bar{\boldsymbol{g}} = \boldsymbol{0} \text{ in } \mathcal{B}_0 \\
2. & \textit{Inverse Darcy law} & \nabla[\partial_m \widehat{\psi} - \bar{\boldsymbol{g}} \cdot \boldsymbol{\varphi}] + \partial_{\boldsymbol{H}}\widehat{\phi} = \boldsymbol{0} \text{ in } \mathcal{B}_0 \\
3. & \textit{Phase field evolution} & \partial_d \widehat{\psi} - \mathrm{Div}[\partial_{\nabla d}\widehat{\psi}] + \partial_d \widehat{\phi} \ni 0 \text{ in } \mathcal{B}_0 \\
4. & \textit{Prescribed tractions} & \partial_{\boldsymbol{F}}\widehat{\psi} \cdot \boldsymbol{n}_0 - \boldsymbol{t}_0 = \boldsymbol{0} \text{ on } \partial\mathcal{B}_0^{\boldsymbol{t}} \\
5. & \textit{Prescribed fluid potential} & -\partial_m \widehat{\psi} + {}^{-} = 0 \text{ on } \partial\mathcal{B}_0^{\mu} \\
6. & \textit{Phase field outflux} & \partial_{\nabla d}\widehat{\psi} \cdot \boldsymbol{n}_0 = 0 \text{ on } \partial\mathcal{B}_0
\end{array} \tag{3}$$

Following Miehe et al. [4], different phase field growth functions appropriate for porous media at fracture at large strains are investigated, which allow for crack evolution in tension and account for the local irreversibility of crach growth.

Computational implementations of the minimization problem are applied to two model problems: (i) Drying processes in soils and (ii) hydraulic fracturing processes, see Figures 1 and 2. For the problem of hydraulic fracturing in soils, a crucial point is the description of the fluid flow inside the crack. This includes a transition from an isotropic Darcy-type fluid flow in the unbroken bulk material to an anisotropic Poiseuille-type fluid flow within a crack. To do so, appropriate transition rules considered in Miehe et al. [1, 5] are discussed.

Recent Publications

[1] C. Miehe and S. Mauthe. Phase field modeling of fracture in multi-physics problems. Part III. Crack driving forces in hydro-poro-elasticity and hydraulic fracturing of fluid-saturated porous media. Computer Methods in Applied Mechanics and Engineering, 2015. doi: http://dx.doi.org/10.1016/j.cma.2015.09.021.

[2] C. Miehe, F. Welschinger, and M. Hofacker. Thermodynamically consistent phase-field models of fracture: Variational principles and multi-field fe implementations. International Journal for Numerical Methods in Engineering, 83:1273 1311, 2010.

[3] C. Miehe, S. Mauthe, and H. Ulmer. Formulation and numerical exploitation of mixed variational principles for coupled problems of Cahn-Hilliard-type and standard diffusion in elastic solids. International Journal for Numerical Methods in Engineering, 99(10):737762, 2014.

[4] C. Miehe, M. Hofacker, L.-M. Schanzel, and F. Aldakheel. Phase field modeling of fracture in multi-physics problems. Part II. Brittle-to-ductile failure mode transition and crack propagation in thermo-elastic-plastic solids. ComputerMethods in Applied Mechanics and Engineering, 294:486522, 2015.

[5] C. Miehe, S. Mauthe, and S. Teichtmeister. Minimization principles for the coupled problem of darcy-biot-type fluid transport in porous media linked to phase field modeling of fracture. Journal of the Mechanics and Physics of Solids, 82: 186217, 2015.

VARIATIONAL PHASE FIELD MODELS FOR DUCTILE FRACTURE AT FINITE STRAIN: A GRADIENT-EXTENDED PLASTICITY-DAMAGE THEORY AND ITS MICROMORPHIC REGULARIZATION

C. Miehe*, S. Teichtmeister, F. Aldakheel [1]
[1] *Institute of Applied Mechanics (CE), University of Stuttgart, Stuttgart, Germany*

Summary A novel variational-based theory [7, 9] for the phase field modeling of ductile fracture in elastic-plastic solids at large strains is outlined. The phase field approach, which regularizes sharp crack surfaces within a pure continuum setting by a specific gradient damage modeling, is linked to a formulation of gradient plasticity. The framework includes two independent length scales which regularize both the plastic response as well as the crack discontinuities. This ensures that the damage zones of ductile fracture develop inside of plastic zones, and guarantees on the computational side mesh objectivity in postcritical ranges.

DIFFERENT PHASE FIELD APPROACHES TO FRACTURE

Ductile fracture is a phenomenon that couples at the macroscopic level plastic deformations with the accumulation of damage and crack propagation. Damage is caused by deformation mechanisms at the microscopic level, such as void nucleation, growth and coalescence, the formation of micro-shear-bands and micro-cracks. A large number of phenomenological and micro-mechanically approaches exists for the continuum modeling of ductile fracture, see e.g. Besson [3] for an overview.

From a computational point of view, the *tracking of sharp crack surfaces* provides substantial difficulties and is often restricted to simple crack topologies. This difficulty can be overcome by recently developed *phase field approaches* to fracture, which *regularize sharp crack discontinuities* within a pure continuum formulation. This geometrically motivated *diffusive crack modeling* allows the resolution of complex failure patterns. For Griffith-type brittle fracture, a Γ-convergent variational structure based on the Mumford-Shah functional steming from image segmentation is presented in Bourdin et al. [4]. For this model, a typical temporal development of the fracture phase field is depicted in Figure 1a). Here, irreversibility of the cracking process is modeled by *evolving Dirichlet-type boundary conditions* and does not constrain the fracture phase field locally. The phase field approach presented by Miehe et al. [6] is a gradient damage theory with constitutive structures rooted in fracture mechanics, which bases on the incorporation of a regularized crack surface density function motivated by geometric considerations. Here, a *local irreversibility constraint* on the fracture phase field is included, which, in contrast to the first mentioned formulation, allows the phase field variable only to grow. Figure 1b) depicts a typical evolution of the fracture phase field for a *gradient damage theory with threshold*, as considered in Pham et al. [10] and Miehe et al. [8]. Note, that both approaches result in a distribution of the phase field with a non-differentiable point at the cracked point and are hence suitable to reproduce a sharp crack limit for a vanishing length scale.

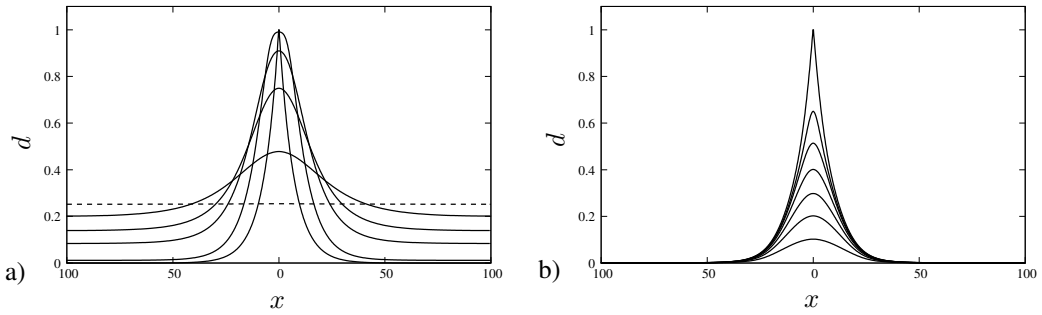

Figure 1. Evolution of the fracture phase field d for formulations a) without and b) with local irreversibility.

COUPLING OF GRADIENT PLASTICITY AND GRADIENT DAMAGE

Extensions to the phase field modeling of ductile fracture are exclusively related to the second approch, representing conceptually a coupling of gradient damage mechanics with models of elasto-plasticity, see Alessi et al. [1] and Ambati et al. [2]. However, these settings combine models of *local* plasticity *without inherent length scales* to the gradient-damage-type phase field modeling of fracture. This does not meet the demand of related plastic and damage length scales, keeping regularized fracture zones inside of plastic zones, and does not guarantee on the computational side mesh objectivity in postcritical ranges. This is achieved in the recent work Miehe et al. [7] that couples gradient plasticity to gradient damage. A characteristic computational result is depicted in Figure 2.

*Corresponding author. Email: cm@mechbau.uni-stuttgart.de

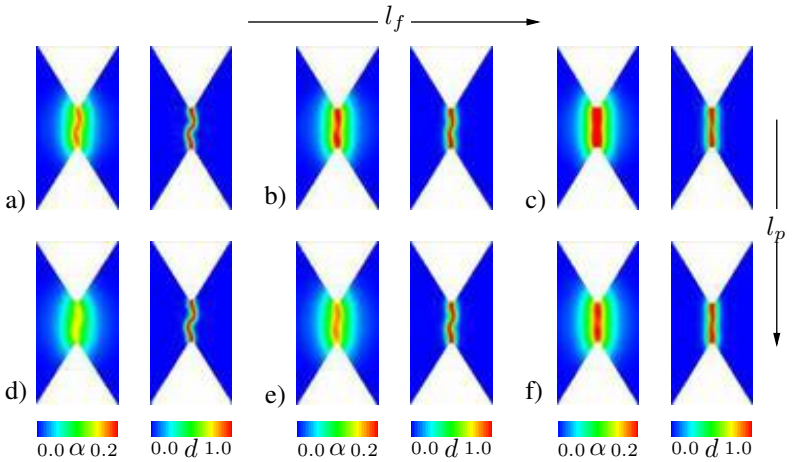

Figure 2. Ductile fracture of a V-notch bar in tension. Contours of equivalent plastic strain α and fracture phase field d for different combinations of fracture l_f and plastic length scale $l_p > l_f$.

However, the implementation of coupled gradient plasticity-damage by the finite element method is demanding. Especially on the plastic side, the realization of sharp plastic boundary induces substantial difficulties. An alternative is conceptually provided by the micromorphic approach to gradient-extended models in the sense of Forest [5], which was applied in Miehe et al. [9] as a *regularization of the canonical theory* developed above. Here, the key idea is the introduction of *dual local-global field variables* $\{\bar{d}, d\}$ and $\{\bar{\alpha}, \alpha\}$ linked via a penalty method, where only the global fields α and d are restricted by boundary conditions. With these extensions at hand the evolution problem of gradient damage coupled with gradient plasticity is shown to be governed by the pure minimization principle

$$\{\dot{\boldsymbol{\varphi}}, \dot{\alpha}, \dot{d}, \dot{\bar{\alpha}}, \dot{\bar{d}}, \dot{\boldsymbol{\varepsilon}}^p\} = \text{Arg}\{ \inf_{\dot{\boldsymbol{\varphi}}, \dot{\alpha}, \dot{d}, \dot{\bar{\alpha}}, \dot{\bar{d}}, \dot{\boldsymbol{\varepsilon}}^p} \Pi(\dot{\boldsymbol{\varphi}}, \dot{\alpha}, \dot{d}, \dot{\bar{\alpha}}, \dot{\bar{d}}, \dot{\boldsymbol{\varepsilon}}^p) \} ,$$

the existence of which accounts for inherent symmetries of the coupled problem.

In summary, the basic ingredients of the proposed formulation are three aspects: (i) A phase field model for ductile fracture that *combines ingredients of gradient plasticity and gradient damage*. (ii) A thermodynamic framework that is fully variational in nature, based on a split of a *work density function* W into energetic and dissipative parts, and a *dissipation function* V with separate thresholds for plasticity and damage. (iii) The *micromorphic regularization* of the variational principle of gradient-enhanced plasticity-damage, allowing a convenient and robust numerical implementation. The modeling capacity of the formulation is underlined by representative numerical simulations.

References

[1] R. Alessi, J.-J. Marigo, and S. Vidoli. Gradient damage models coupled with plasticity: Variational formulation and main properties. Mech Mater, 80:351–367, 2015.

[2] M. Ambati, T. Gerasimov, and L. De Lorenzis. Phase-field modeling of ductile fracture. Comput Mech, 55: 1017–1040, 2015.

[3] J. Besson. Continuum models of ductile fracture: A review. Int J Damage Mech, 19:3–52, 2010.

[4] B. Bourdin, G.A. Francfort, and J.-J. Marigo. The Variational Approach to Fracture. Springer, 2008.

[5] S. Forest. Micromorphic approach for gradient elasticity, viscoplasticity, and damage. J Eng Mech, 135:117–131, 2009.

[6] C. Miehe, F. Welschinger, and M. Hofacker. Thermodynamically consistent phase-field models of fracture: Variational principles and multi-field FE implementations. Int J Numer Meth Eng, 83:1273–1311, 2010.

[7] C. Miehe, M. Hofacker, L.M. Schänzel, and F. Aldakheel. Phase field modeling of fracture in multi-physics problems. Part II. Coupled brittle-to-ductile failure criteria and crack propagation in thermo-elastic-plastic solids. Comput Method Appl M, 294:486–522, 2015.

[8] C. Miehe, L. Schänzel, and H. Ulmer. Phase field modeling of fracture in multi-physics problems. Part I. Balance of crack surface and failure criteria for brittle crack propagation in thermo-elastic solids. Comput Method Appl M, 294:449–485, 2015.

[9] C. Miehe, S. Teichtmeister, and F. Aldakheel. Variational phase field modeling of ductile fracture. A gradient-extended plasticity-damage theory and its micromorphic regularization. Philos T R Soc A, in press.

[10] K. Pham, H. Amor, J. Marigo, and C. Maurini. Gradient damage models and their use to approximate brittle fracture. Int J Damage Mech, 20(4):618–652, 2011.

THE VARIATIONAL PRINCIPLE FOR PROBABILISTIC MEASURE, HASHIN-SHTRIKMAN BOUNDS AND BEYOND

Victor L. Berdichevsky[1a], David Ostberg[1]
[1]*Mechanical Engineering Department, Wayne State University, MI 48202, USA*

Summary Numerical studies reveal the enormous complexity of local fields in composites with random microstructures. There is no doubt that the local fields can be described adequately only in probabilistic terms. Such description is needed not only for characterization of the state of a composite, but also for prediction of microstructure evolution due to plasticity, fatigue, or fracture, where the path of evolution is controlled by the local fields. At the moment, the probabilistic characteristics of local fields are sought by statistical analysis of a huge number of numerical simulations conducted for different realizations of microstructures. Apparently, a more practical way is desirable. In this talk it is discussed the possibility of using for such purposes the variational principle for probabilistic measure constructed in (Berdichevsky, J. Appl. Math. Mech., 1987). We derive classical results of homogenization theory and obtain statistical characteristics of local fields which were not available previously.

Numerical studies reveal the enormous complexity of local fields in composites with random microstructures. There is no doubt that the local fields can be described adequately only in probabilistic terms. Such description is needed not only for characterization of the state of a composite, but also for prediction of the evolution of microstructures due to plasticity, fatigue, or fracture, where the path of evolution is controlled by the local fields. At the moment, the probabilistic characteristics of local fields are sought by statistical analysis of a huge number of numerical simulations conducted for different realizations of microstructures. Apparently, a more practical way is desirable. In this talk the possibility of using for such purposes the variational principle for probabilistic measure [1-3] is discussed.

The variational principle for probabilistic measure states that the true probabilistic characteristics of local fields u give minimum value to the mathematical expectation of energy,

$$\mathbb{I}(f) = \int \Lambda(a,u) f(a,u) da du,$$

where a denotes the set of material characteristics, u the set of field gradients (electric field, strains, etc), $\Lambda(a,u)$ energy density, $f(a,u)$ one-point joint probability density of material characteristics a and field gradients u. The admissible functions $f(a,u)$ satisfy an infinite chain of constraints, which include all n-point probability densities of fields a and u. The variational principle was proved in [1] and discussed in detail in [2]. The major difficulty in applications of the variational principle is to understand how to properly truncate the infinite chain of constraints. The first advancement in this direction was made in [3], where approximate solutions for probabilistic characteristics of local fields were obtained for lognormal composites and some two-phase composites. In this talk it will be shown that

1) the basic approximations of probability density for two-phase composites with random microstructures (Reuss, Hashin-Shtrikman) correspond to δ-functions concentrated at two points; the corresponding fields u are not potential,

2) if probability density is concentrated at a number of points, then the minimum number of points that are necessary to satisfy the potentiality condition is three,

3) the approximate solutions for probability density concentrated at three points and obeying the potentiality constraint are obtained for heat conduction and elasticity of two-phase composites; the corresponding effective moduli are within Hashin-Shtrikman bounds while local fields get more accurate description,

4) an iteration procedure is developed for further rectification of the local field description.

References

[1] Berdichevsky V.L.: The problem of averaging of random structures in items of distribution functions. *J. Appl Math Mech (PMM)* **51**:704-710, 1987.
[2] Berdichevsky V.L.: Variational principles of continuum mechanics. Springer-Verlag, 2009.
[3] Berdichevsky V.L.: Homogenization in probabilistic terms: the variational principle and some approximate solutions. *JMPS*, **87**:86-114, 2016.

[a)] Corresponding author. Email: vberd@eng.wayne.edu.

RANDOM STRUCTURE COMPOSITES WITH NONLOCAL THERMOELASTIC PROPERTIES OF CONSTITUENTS

Valeriy Buryachenko *
Micromechanics & Composites LLC, Dayton, Ohio 45459, USA

Summary A theory of thermoelastic composite materials (CMs) with nonlocal properties (either strongly nonlocal or peristatic) of constituents is analyzed for multiphase statistically homogeneous elastic solids of arbitrary geometry and material symmetry subjected to the homogeneous boundary conditions. One obtains the new representation of the effective modulus and compliance through the mechanical influence function which does not explicitly depend (as opposed to its local counterpart) on the elastic operators of constituents. A generalization of the Hill's [1] equality to the composites with nonlocal properties (either strongly nonlocal or peristatic) is proved. However, the representations of the effective eigenfields through the mechanical influence functions generalizing Levin's [2] representation does not in general hold for thermoperistatic CMs. The general integral equations (GIEs) connecting the displacement fields in the point being considered and the surrounding points are proposed without any auxiliary assumptions which are implicitly exploited in the known centering methods.

CM WITH NONLOCAL THERMOELASTIC PROPERTIES OF CONSTITUENTS

The current interest in nonlocal simulation is driven largely by a practical need in the design, fabrication and characterization of nanocomposites containing heterogeneities with at least one size of nano length scale. The general results establishing the links between the effective properties (effective elastic moduli, effective thermal expansion, and effective specific heat) and the corresponding mechanical and transformation influence functions are worthy of notice. The works of this general direction were inspired by Hill [1] and Levin [2], who obtained the classical representations of effective elastic moduli and thermal expansion through the mechanical influence functions. In the current presentation, we formulate a theory of thermoelastic composites with nonlocal properties of constituents at the similar level of generality as [1, 2] whose micromechanical theories for composites contain only constituents with local elastic properties. We restrict our consideration to thermostatics, so that we analyze systems at uniform temperature. Due to their generality, we will use the nonlocal integral models because the gradient models are usually derived as approximations of corresponding integral models in the immediate (infinitely closed) vicinity of the point being considered. One explores a simplified theory for linear elasticity ("strongly nonlocal", see for references), which differs from the classical local theory in the stress-strain constitutive relation only $\boldsymbol{\sigma}(\mathbf{x})\boldsymbol{\mathcal{L}} * \boldsymbol{\varepsilon}(\mathbf{x}) + \boldsymbol{\alpha}(\mathbf{x})$, whereas the equilibrium and compatibility equations remain unaltered; here the elastic integral operator $\boldsymbol{\mathcal{L}}$ is defined by the kernel $\boldsymbol{\mathcal{L}}(\mathbf{x}, \mathbf{y})$ depending on the scalar attenuation function $\boldsymbol{\mathcal{L}}(\mathbf{x}, \mathbf{y}) = \mathbf{L}(\mathbf{x})\lambda(\mathbf{x}, \mathbf{y})$.

One [3] obtains the new representations of the effective modulus and compliance through the mechanical influence function which does not explicitly depend (as opposed to its local counterpart) on the elastic operators of constituents. These representations yield the symmetry of local effective properties $\mathbf{K}^*$ [$\mathbf{K}^* = \mathbf{L}^*, \mathbf{M}^* = (\mathbf{L}^*)^{-1}$] inside the index pairs. The symmetry of $\mathbf{K}^*$ between the index pairs $(\mathbf{K}^*)^\top = \mathbf{K}^*$ was prowed from the new energetic representations of $\mathbf{K}^*$. One also prowed that the effective elastic operator (which is the tensor $\mathbf{L}^*$ in our case) is self-adjoint if the nonlocal elastic operator at the fine scale is self-adjoint. The representations for the effective eigenstrains and eigenstresses through either the mechanical influence functions or transformation influence functions are presented. The effective strain energy and potential energy are expressed in terms of only average values of the state variables and the effective properties. Representations of both the first and second statistical moments of stress and strain fields in the constituents are also performed. Many of the results were obtained as the straightforward generalizations of their local counterparts because the methods used for obtaining the mentioned results widely exploit the Hill's [1] condition which holds for any compatible strain field and equilibrium stress field not necessarily related to each other by a specific stress-strain relation.

In spite of a variety of nonlocal models for a single heterogeneity in an infinite matrix (first problem), these solutions are usually incorporated in a generalized Mori-Tanaka scheme (second problem) although the use of any other micromechanical method based on the effective field hypothesis (EFH, see for references [4]) presents no difficulties. However, the Mori-Tanaka scheme is just a particular case of a one particle version of the effective field method (EFM) which is based on both the hypothesis of effective field homogeneity and quasi-crystalline approximation (see for details [4]). However, the nonlocal nature of constitutive law necessarily leads to inhomogeneity of stress distribution inside homogeneous ellipsoidal inclusion that in turn leads to a drastic inhomogeneity of the effective fields (it will be qualitatively demonstrated in the current presentation) that makes validity of the classical micromechanical approaches to be questionable. A solution of a volume integral equation for one heterogeneity inside an infinite matrix is presented by the iteration method. The operator representation of this solution is incorporated into the new general integral equations (GIE, see [5-7]) of micromechanics proposed without exploiting basic hypotheses of classical micromechanics such as the EFH and the "*ellipsoidal symmetry*"

*Corresponding author. Email: buryach@yahoo.com

assumption. New GIEs present in fact the new (second) background of multiscale analysis offering the opportunities for a fundamental jump in multiscale research of random heterogeneous media with drastically improved accuracy of local field estimations (with possible change of sign of predicted local fields). These new GIEs are obtained by centering procedure of subtraction from both sides of a new initial integral equation their statistical averages obtained without any auxiliary assumptions which are implicitly exploited in the known centering methods. Numerical results are presented in [8].

TERMOPERISTATIC COMPOSITES

In contrast to the classical local and nonlocal theories, the peridynamic equilibrium equation introduced by Silling [9] is free of any spatial derivatives of displacement and presented in the form of a Fredholm equation of second kind (bond-based approach, see for the notations and details [1]): $\hat{\boldsymbol{\mathcal{L}}}(\mathbf{u})(\mathbf{x}) + \mathbf{b}(\mathbf{x}) = \mathbf{0}$, where $\hat{\boldsymbol{\mathcal{L}}}(\mathbf{u})(\mathbf{x}) = \int \mathbf{f}(\mathbf{u}(\hat{\mathbf{x}}) - \mathbf{u}(\mathbf{x}), \hat{\mathbf{x}} - \mathbf{x}, \mathbf{x}) d\hat{\mathbf{x}}$ and $\mathbf{f}$ is a pairwise force function (called also a *bond force*). In opposite to micromechanics of thermoelastic composite materials (CM, [1, 2]), the general theory of peristatic CM is not nearly developed. Because of this even the background concepts of micromechanics (see for details, e.g., [10, 11]) such as the effective moduli and effective eigenfields are not yet defined in the theory of random structure peristaltic CMs. The current work is dedicated to closing this gap between micromechanical approaches and perydynamic models and to generalization of the mentioned general results for thermoelastic CMs to its peristatic counterparts.

For statistically homogemneous thermoperistatic media subjected to homogeneous volumetric boundary loading, one proved that the effective behaviour of this media is governing by conventional effective constitutive equation which is intrinsic to the local thermoelasticity theory. A generalization of the Hill's equality to the peristatic composites is proved. The general results establishing the links between the effective properties (effective elastic moduli, effective thermal expansion) and the corresponding mechanical and transformation influence functions are obtained by the use of decomposition of local fields into the load and residual fields. A detected similarity of results for both the locally elastic and peristaltic composites is explained by the fundamental reasons because the methods used for obtaining of the mentioned results widely exploit the Hill's [1] condition (generalized to the peristatic CMs in this work) and the self-adjointness of the stress operator $\boldsymbol{\mathcal{L}}^{\sigma}$ defined by the equation $\boldsymbol{\sigma}(\mathbf{x}) = \boldsymbol{\mathcal{L}}^{\sigma}(\mathbf{u})(\mathbf{x})$, $\boldsymbol{\mathcal{L}}^{\sigma}(\mathbf{u})(\mathbf{x}) := \boldsymbol{\mathcal{L}}^{\sigma}(\mathbf{C}, \boldsymbol{\alpha}, \mathbf{u})(\mathbf{x})$. Effective moduli $\mathbf{L}^{*}$ end effective eigenstrain $\boldsymbol{\beta}^{*}$ of termoperistatic CM are expressed through the introduced new concept of the local stress polarisation tensor $\boldsymbol{\tau}(\mathbf{x}) = \boldsymbol{\mathcal{L}}^{\sigma}(\mathbf{C}_1, \boldsymbol{\alpha}_1, \mathbf{u})(\mathbf{x})$ averaged over the extended inclusion phase rather than in an entire space. Here $\mathbf{C}_1$ and $\boldsymbol{\alpha}_1$ are the jump of the micromodulus and microeigenstress, respectively, inside the inclusion with respect to the matrix. pectations. However, the representations of the effective eigenfields through the mechanical influence functions generalizing Levin's [2] representation does not in general hold for thermoperistatic CMs (see for references and details [11]).

For thermoperistatic CMs, the new general integral equations (GIE) connecting the displacement fields in the point being considered and the surrounding points is proposed in the operator form of perturbators expressed through the local stress polarisation tensor $\boldsymbol{\tau}(\mathbf{x})$ and generalizing their thermoelastic counterpart [10]. The mentioned analogy instills confidence in ease of straightforward generalizations of well known methods of micromechanics of thermoelastic media (see for references [6, 7]) to its thermoperistatic counterparts. The numerical results are presented in [10, 12, 13] for 1D examples demonstrate a convergence of effective properties estimations obtained for peristatic composite bar to the corresponding exact evaluations for the local thermoelastic theory.

The author acknowledges the support of the US Office of Naval Research.

References

[1] Hill R.: Elastic properties of reinforced solids: some theoretical principles. J Mech Phys Solids, 11: 357–372, 1963.

[2] Levin V.M.: Thermal expansion coefficient of heterogeneous materials. Izv AN SSSR, Mekh Tverd Tela, 2, 88–94, 1967 (In Russian. Engl Transl. Mech Solids, 2: 58–61, 1967)

[3] Buryachenko V. A.: On thermoelastostatics of composites with nonlocal properties of constituents. I. General representations for effective material and field parameters. Int. J. Solids and Structures 48: 1818–1828, 2011.

[4] Buryachenko V.: Micromechanics of Heterogeneous Materials. Springer, NY, 2007.

[5] Buryachenko V. New Background of Micromechanics. iMechanica; http://imechanica.org/node/17650). Posted 12.14.2014, 1600 visitors on 01.15.2016.

[6] Buryachenko V.: Solution of general integral equations of micromechanics of heterogeneous materials. J. Solids and Structures. 51: 3823-3843, 2014.

[7] Buryachenko V.: General integral equations of micromechanics of heterogeneous materials. J. Multiscale Comput. Enging., 13: 11–53, 2015.

[8] Buryachenko V. A.: On thermoelastostatics of composites with nonlocal properties of constituents. II. Estimation of effective material and field parameters. Int. J. Solids and Structures 48: 1829–1845, 2011.

[9] Silling S.: Reformulation of elasticity theory for discontinuities and long-range forces. J. Mech. Physics of Solids, 48: 175–209, 2000.

[10] Buryachenko V. A.: Some general representations in thermoperistatics of random composites. Int. J. Multiscale Comput. Enging., 13: 331-350, 2015.

[11] Buryachenko V.A.: Thermoperistatics of random structure composites: some background principles. Math. Mech. of Solids. 21, 2016 (in press).

[12] Buryachenko V.: Effective elastic modulus of heterogeneous peristatic bar of random structure. J. Solids and Structures 51: 2940–2948, 2014.

[13] Buryachenko V. A.: Effective thermoelastic properties of heterogeneous thermoperistatic bar of random structure. J. Multiscale Comput. Enging. 13: 55–71, 2015.

MICROMECHANICS OF MAGNETO- AND ELECTRO-ACTIVE SOFT COMPOSITES

Stephan Rudykh*
Department of Aerospace Engineering, Technion – Israel Institute of Technology, Haifa, Israel

Summary In this work, we analyze the nonlinear coupled behavior of magnetoactive elastomer (MAE) composites undergoing finite deformations in the presence of a magnetic field. The responses of MAEs with periodically distributed active particles embedded in a soft matrix are determined numerically. These numerical results together with analytical estimates for random distributions of particles illustrate the strong sensitivity of the magnetomechanical coupling to changes in microstructures. Based on an exact solution for magneto-active laminates, we propose a model for anisotropic MAEs with chain-like structures induced during the curing process in a magnetic field. Next, stability of the anisotropic MAEs is analyzed, and explicit expressions for critical magnetic field are derived in terms of constituents' volume fractions and material properties. Finally, a new distinct mode of instabilities is found for the composites with high concentrations of the active phase. Thanks to the mathematical analogy, the findings also apply to dielectric elastomer composites.

INTRODUCTION

Magneto-active elastomers (MAE) are soft responsive materials that can change their effective stiffness and undergo finite deformations when subjected to an external magnetic field. Thanks to MAEs' abilities to remotely, rapidly and reversible change their properties and shape, many potential applications have been proposed ranging from vibration and acoustic control devices to actuators and biomedical applications. These active composite materials usually comprise magnetizable particles embedded in a soft elastomeric magnetically inactive matrix. Thus, the magneto-active properties are due to the interactions of the magnetizable particles, while the ability to deform is provided by the soft magnetically inactive matrix. The distribution of the active particles can be characterized by different statistics, however, it depends on the MAE fabrication process. For example, an application of a magnetic field during the curing process leads to the alignment of the particles with the applied magnetic field, forming the so-called chain-like structures. Indeed, the effect depends strongly on the intensity of the applied field. Moreover, recent advances in fabrication (including additive manufacturing and 3D printing) may allow realizations of highly structured composites. Motivated by this, in this work, we examine the influence of various microstructures of MAEs on the magneto-mechanical coupling and actuation. The heterogeneity can be an origin for MAEs' instabilities, reminiscent of the purely elastic bifurcations. Here, we analyze this important aspect of MAEs behavior, and make use of the obtained effective properties to estimate the onset of instability on the macroscopic level. However, coupled instabilities may develop earlier at a smaller length-scales. To predict these so-called microscopic instabilities the Bloch-Floquet analysis is utilized as described below.

MODELING COUPLED BEHAVIOR OF MAGNETO-ACTIVE ELASTOMERS

To analyse the magnetomechanical coupling in MAEs with periodic microstructures, we employ the finite element (FE) method. We construct representative volume elements (RVE) and apply the corresponding periodic boundary conditions. The magneto-static problem is solved separately in the deformed configuration provided by the solution of the equilibrium state. The resulting magnetic field is used to calculate the magnetically induced stress tensor, which is added to the equilibrium equations. Thus, the two-way magnetomechanical coupling is established in the numerical solver.

We examine the periodic structures with rectangular and hexagonal RVEs subjected to finite strains in the presence of a magnetic field. To analyse the behavior of these periodic composites, we defined the effective magneto-mechanical coupling coefficient and calculate the actuation strain in response to a magnetic excitation. These quantities are found to be very sensitive to variations of the concentrations and shape of the active particles. For example, the magnetomechanical coupling can be of different sign for the hexagonal and rectangular periodic MAEs with identical volume fractions and shapes of the particles. As a result, these composites exhibit very different actuations [1].

We compare the responses of the periodic composites and MAEs with random distribution of the particles. The estimates for MAEs characterized by random distributions are obtained from the model of Ponte-Castañeda and Galipeau [2]. We find that periodic and random MAEs exhibit a very similar behavior in the range of small strains and weak (particle shape induced) anisotropy. However, the magnetomechanical coupling becomes rather different for large strains and more complicated shapes of inclusions. This sensitivity allows us to enhance the magnetomechanical coupling and actuation by tailoring the microstructure of the periodic MAEs according to the range of operational strains and magnetic fields.

Finally, we introduce a compact model for anisotropic MAEs with chain-like structures induced during the curing process [3]. The model is based on an exact analytical solution for layered MAEs. Thanks to the built-in anisotropy, the idealized model allows the modeling of MAEs with chain-like structures aligned along a preferable direction. The availability of such solutions can be used to estimate and predict the onset of instabilities in the corresponding MAEs, as described next.

*Corresponding author. Email: rudykh@technion.ac.il

MACROSCOPIC AND MICROSCOPIC MAGNETO-MECHANICAL INSTABILITIES

To analyze the macroscopic instabilities, we derive a condition based on the effective magneto-elastic moduli for the general 3D magnetomechanical loadings. The macroscopic stability criterion is further specialized for 2D problems, and it is written in terms of sixth order polynomial with coefficients comprising combinations of magneto-mechanical moduli. Then, we apply this condition to study the stability of anisotropic MAEs characterized by the idealized laminate model. We identify the corresponding stable and unstable domains in terms of magneto-mechanical loadings, volume fractions and contrasts in the material properties of the constituents [3, 4]. Remarkably, compact explicit expressions are derived for critical magneto-mechanical loadings in terms of the volume fractions and material properties of the consentient.

To identify the onset of possible instabilities on smaller length-scales, we employ the Bloch-Floquet technique for the instability analysis superimposed on the finitely deformed state in the presence of a magnetic field. For the finitely deformed state, we utilize the exact analytical solution obtained for the active laminates. We find that for a large range of moderate volume fractions and magneto-mechanical loadings, the microscopic and macroscopic instabilities appears at very close levels of magneto-mechanical loadings. However, for small concentrations of the active phase, the microscopic instabilities occur first and they are significantly different from the macroscopic ones. This is similar to the elastic instabilities reported for purely mechanically loaded laminates [5]. Remarkably, at high concentrations of the active phase, the analysis predicts the existence of a distinct mode of coupled instabilities [6], which does not appear in the purely mechanical case.

CONCLUSIONS

We studied the behavior of MAE undergoing finite deformations in the presence of a magnetic field. Through the FE based numerical simulations, we find that MAE composites with similar microstructures (periodic hexagonal and rectangular arrangements of active particles) and identical volume fractions and particle shapes exhibit very different magneto-mechanical behavior for various ranges of magnetomechanical loadings. Moreover, the comparison with the analytical estimate of Ponte-Castañeda and Galipeau for isotropic MAE with random distributions of particles shows that the periodic microstructures can be tailored to enhance the magnetomechanical coupling. The behavior of the anisotropic MAEs with chain-like alignments of the particles was analyzed by means of the compact analytical model based on an exact solution for soft magneto-active laminates. This solution is used to analyze the stability of the magnetoactive composites on macroscopic and microscopic length-scales. A new distinct type of coupled instabilities, which does not appear in the purely mechanical case, is revealed in composites with high concentration of the active phase. Thanks to the mathematical analogy, the findings also apply to another class of soft active materials, namely, dielectric elastomer composites.

References

[1] Galipeau E., Rudykh, S., deBotton, G., Ponte-Castañeda, P.: Magnetoactive elastomers with periodic and random microstructures. Int. J. Solids Struct., 51, 3012–3024, 2014.

[2] Ponte-Castañeda, P., Galipeau, E.: Homogenization-based constitutive models for magnetorheological elastomers at finite strain. J. Mech. Phys. Solids, 59, 194–215, 2011.

[3] Rudykh, S., Bertoldi, K.: Stability of Anisotropic Magnetorheological Elastomers in Finite Deformations: A Micromechanical Approach. J. Mech. Phys. Solids, 61, 949–967, 2013.

[4] Rudykh, S., deBotton, G.: Stability of Anisotropic Electroactive Polymers with Application to Layered Media. Z. Angew. Math. Phys.(ZAMP), 62, 1131–1142 2011.

[5] Li, Y., Kaynia, N., Rudykh, S., Boyce, M. C.: Wrinkling of Interfacial Layers in Stratified Composites. Adv. Eng. Mater., 15 (10), 921–926, 2013.

[6] Rudykh, S., Bhattacharya, K., deBotton, G.: Multiscale Instabilities in Soft Heterogeneous Dielectric Elastomers. Proc. Royal Soc. A 470, 20130618, 2014.

ELASTIC FIELDS AND EFFECTIVE PROPERTIES OF TRIANGULAR LATTICE WITH VACANCIES

Ekaterina Podolskaya *[1,2], Vitaly Kuzkin[1,2], Anton Krivtsov[1,2], and Mark Kachanov[2,3]

[1]*Institute for Problems in Mechanical Engineering, St. Petersburg, Russia*
[2]*Peter the Great St. Petersburg Polytechnic University, St. Petersburg, Russia*
[3]*Department of Mechanical Engineering, Tufts University, Medford, Massachusetts, USA*

Summary We consider linear elastic deformation of the two-dimensional triangular lattice with multiple vacancies. For the lattice with doubly periodic system of vacancies we derive closed-form analytical expressions for displacement field, and calculate effective elastic moduli. Molecular dynamics simulations of a lattice with random distribution of vacancies are carried out, and we compare the obtained elastic moduli with the analytical results. If the vacancy concentration is less than 4%, random and periodic distributions of vacancies produce the same effect on elastic moduli. We examine the possibilities and limitations of modeling of the lattice with vacancies by an elastic continuum with holes. We conclude that it is possible to model the effective elastic properties adequately, if the shape of the holes is chosen appropriately. Nevertheless, the strain field, in particular, strain concentration differs significantly.

The influence of point defects on physical properties of crystals is a long-standing problem in mechanics and physics of solids. Foundations of continuum theory of lattice defects have been developed in pioneering works of Eshelby [1, 2]. In continuum mechanics, such defects are modeled as pores in a homogeneous elastic medium, and continuum mechanics tools are used for calculation of displacement fields, elastic interaction of defects, effective properties of imperfect crystals, etc. Although the continuum mechanics modeling is expected to be appropriate for the effective properties, it may become inadequate at microscale, in particular, near vacancies, where the discreteness plays important role [3, 4].

One of the first attempts to solve the problem in the discrete formulation was made by Kanzaki [5], where foundations of the so-called lattice statics method have been developed. The effect of vacancy is simulated by applying forces to atoms that simulate interatomic interactions with both the nearest and farther lying atoms. Then equations of lattice statics in harmonic approximation are solved using discrete Fourier transform. An alternative discrete approach based on lattice Green's function has been proposed by Tewary [6] who showed that this approach is equivalent to Kanzaki one, but is computationally simpler.

The two dimensional modeling taken in the present work is relevant for a variety of 2-D materials that have become available due to recent advances in technology, such as graphene, 2-D colloids, etc. Displacement fields caused by point defects in two-dimensional colloidal crystals were studied in [7, 8]. Authors have adopted Ewald summation technique for solution of continuum elasticity problems with periodic boundary conditions. It has been demonstrated that the continuum theory looses accuracy in close vicinity of defects. However, displacement fields around vacancies have not been given.

The present work focuses on elastic deformation of a triangular lattice with periodic array of vacancies. Firstly, the displacements of all particles are expressed in terms of a mean strain; secondly, using Hooke's law and defining the mean traction as the mean force acting on the cell boundary (that, in turn, is a function of displacements), the effective moduli are calculated that can be used further to find the relation between displacements and stresses applied at infinity. This approach differs from Kanzaki and lattice Green's function approaches, where the displacements are expressed in terms of interatomic forces. Note that our approach constitutes a discrete analog of doubly periodic problem in continuum elasticity [9, 10, 11]. Analytical treatment of the *discrete doubly periodic problem* is based on the exact solution of corresponding partial difference equations. Closed form expressions for particle displacements in the mentioned discrete doubly periodic problem are obtained by the use of discrete Fourier transform.

We examine the following issue: "to what extent a vacancy in triangular lattice can be modeled by a pore (hole) in elastic continuum media and what the pore shape should be?" The equivalence is considered from two points of view: (i) displacement field around a vacancy and (ii) effective elastic properties of a lattice with vacancies. Effective elastic moduli of a triangular lattice with doubly-periodic system of vacancies are calculated analytically. Afterwards, the results are compared with molecular dynamics simulations for a crystal with random distribution of vacancies. Then, the effective elastic moduli obtained in the discrete formulation are compared with prediction of continuum elasticity theory for porous medium, and the question of the pore shape is discussed. Figure 1a shows that, from the viewpoint of the effective elastic properties, a lattice with vacancies can be modeled in the framework of 2-D elasticity (plate with holes). In continuum elasticity models, the effective elastic moduli depend on pore shapes, with the circular shape being the stiffest one among all shapes of given area. However, in this case the circular pore shape assumption results in poor agreement with discrete models: the discrete system is softer. The difference between circular and best-fit shapes is even larger for the effective Poisson's ratio. Note that hole shape factors required for the best fit are substantially different from the ones for a circle, and the geometrical shape corresponding to the mentioned shape factors is not easily identifiable (and may even be non-unique).

*Corresponding author. Email: katepodolskaya@gmail.com

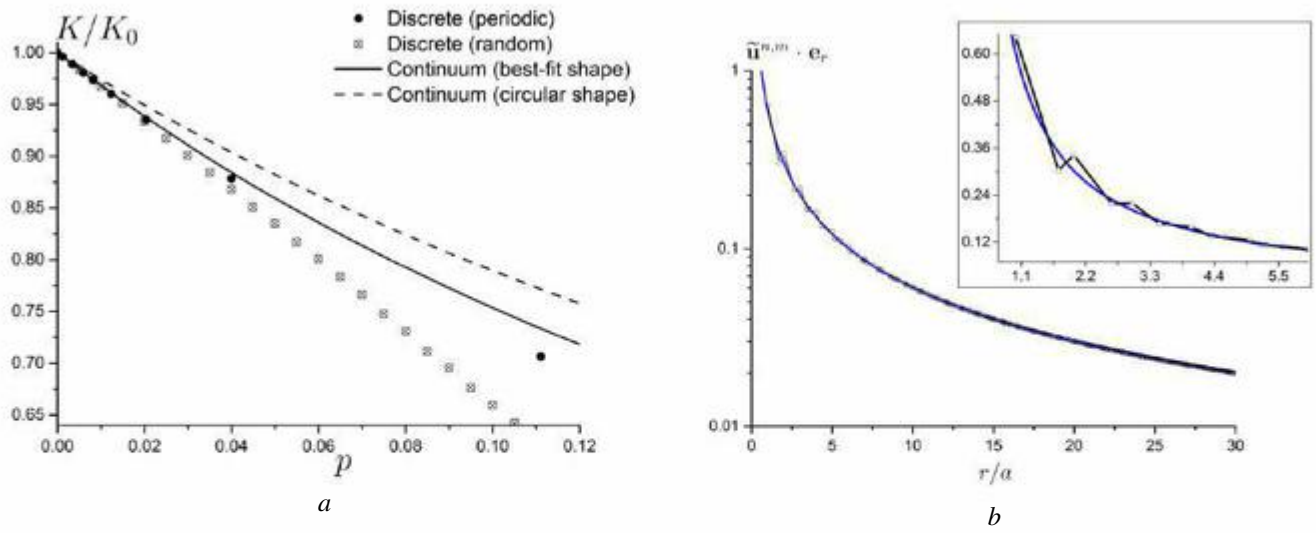

a *b*

Figure 1: (a) The porosity dependence of the effective bulk modulus of a triangular lattice with periodic and random distributions of vacancies. The moduli are normalized to their values in absence of vacancies. Comparison with the continuum results [12] for best-fit shape factors (solid line) and for circular pores (dashed line). (b) The radial displacement as a function of the dimensionless distance from the vacancy. Volumetric strain.

However, the strength characteristics and local fields — in particular, strain concentrations near vacancies — cannot be adequately modeled in the continuum elasticity framework. One of the crucial differences between the discrete and continuum solutions is demonstrated in the off-set figure in Figure 1b. In the vicinity of vacancy the dependence of radial component of particle displacements on distance is *non-monotonic*. In an elastic plate with a hole, the presence of the hole leads to concentration of stresses. The stress concentration factor for a circular hole under imposed volumetric strain is equal to 2 at all points of the boundary; for other shapes, the maximal, around the boundary, concentration factor is higher. Vacancy causes similar effect, however calculation of stress concentration factor is not straightforward, since stresses in discrete media are defined somewhat ambiguously [13]. We define and compute, the strain concentration factor, k, as the ratio of the maximal deformation of the bonds adjacent to the vacancy to the deformations of bonds at infinity. In the case of volumetric deformation, the maximum elongation is reached in the bonds that surround the vacancy $k_{vol} = 1.642$ that is substantially smaller than the value of 2 for the circular hole; the difference with non-circular shapes providing the best fit for the effective moduli will be larger, as well as for other modes of loading. Consider, for example, two cases of uniaxial loading along orthogonal axes x and y, with y being parallel to one of the lattice vectors. The strain concentration factors calculated using displacement field are $k_x = 1.449$ and $k_y = 1.283$ that is much smaller than the factor of 3 in the continuum Kirsch problem for a circular hole (that is even higher for non-circular shapes).

To sum up, we conclude that the effective properties of discrete media can be described by continuum theory, whereas local fields and their concentrations, specifically, strain concentration, are qualitatively different.

References

[1] Eshelby J. D.: Distortion of a crystal by point imperfections. J. Appl. Phys. 25:255-261, 1954.

[2] Eshelby J. D.: The continuum theory of lattice defects. Solid State Phys. 3:79-144, 1956.

[3] Krivtsov A. M., Morozov N. F.: On mechanical characteristics of nanocrystals. Phys. Solid State 44:2260-2265, 2002.

[4] Goldstein R. V., Morozov N. F.: Mechanics of deformation and fracture of nanomaterials and nanotechnology. Phys. Mesomech. 10:235246, 2007.

[5] Kanzaki H. Point defects in face-centred cubic lattice — I distortion around defects. J. Phys. Chem. Solids 2:24-36, 1957.

[6] Tewary V. K. Green-function method for lattice statics. Adv. Phys. 22:757-810, 1973.

[7] Lechner W., Scholl-Paschinger E., Dellago, C.: Displacement fields of point defects in two-dimensional colloidal crystals. J. Phys.-Condens. Mat. 20:404202, 2008.

[8] Lechner W., Dellago C.: Point defects in two-dimensional colloidal crystals: simulation vs. elasticity theory. Soft Matter 5:646-659, 2009.

[9] Muskhelishvili N. I.: Some Basic Problems of the Mathematical Theory of Elasticity. Noordhoff, Netherlands, 1953.

[10] Linkov A. M.: Boundary Integral Equations in Elasticity Theory. Dordrecht-Boston-London, Kluwer Academic Publishers, 2002.

[11] Karihaloo B. L., Wang J.: On the solution of doubly periodic array of cracks. Mech. Mater. 26:209-212, 1997.

[12] Kachanov M., Tsukrov I., Shafiro B. Effective moduli of solids with cavities of various shapes. Appl. Mech. Rev. 47:S151-S174, 1994.

[13] Kuzkin V. A., Krivtsov A. M., Jones R. E., Zimmerman J. A. Material frame representation of equivalent stress tensor for discrete solids. Phys. Mesomech. 18:13-23, 2015.

A NOVEL MICROSTRUCTURALLY-BASED MATERIAL MODEL TO DESCRIBE PASSIVE SKELETAL MUSCLE TISSUE

Christian Bleiler*[1,2], Pedro Ponte Castañeda[3], and Oliver Röhrle[1,2]
[1]*Institute of Applied Mechanics (CE), University of Stuttgart, Germany*
[2]*Stuttgart Research Centre for Simulation Technology, Germany*
[3]*Department of Mechanical Engineering and Applied Mechanics, University of Pennsylvania, Philadelphia, USA*

Summary Like for many biological materials, the elastic properties of skeletal muscle tissue can vary quite significantly between different specimen, for example, from person to person or due to different muscle fibre types. This is mainly due to alterations of the properties or the arrangement of microstructural elements, such as, for example, sarcomeres or connective tissue. Further, these microstructural variations also influence the anisotropic properties of the material. Current state-of-the-art muscle models often lack the ability to take into account such variations in a natural way. They assume a phenomenological behaviour for the overall material properties. To overcome this issue, we propose a novel, homogenised material model, which predicts the anisotropic behaviour of muscle tissue by incorporating the arrangement of the underlying microstructures.

MOTIVATION

Inside the strictly hierarchically organised microstructure of skeletal muscle tissue, there are two parts that can be identified to be responsible for the overall mechanical properties: the muscle fibres and the extracellular matrix. Muscle fibres contain the contractile units (sarcomeres) and therefore mainly account for the active behaviour of the muscle and only contribute little to the material's passive elasticity. Skeletal muscle's elastic stiffness is mainly due to the existence of collagen fibres inside the extracellular matrix. As illustrated in Figure 1, the collagenous structures are arranged around the muscle fibre in a helical fashion, which is typical for fibre reinforcements in biological tissue. Therefore, the alignment of muscle fibres in preferred direction $\boldsymbol{a}_0$ also constitutes the transversely isotropic behaviour of the overall muscle. State-of-the-art phenomenological

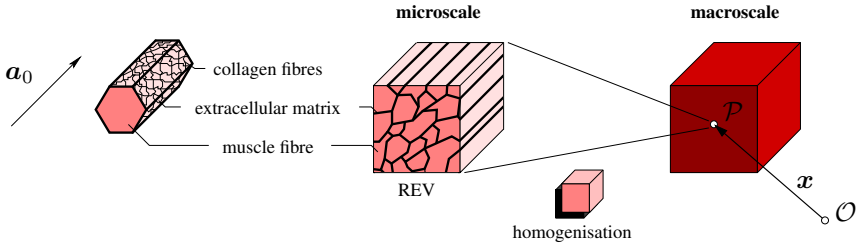

Figure 1: Illustration of the collagenous structure around the muscle fibre and the representative elementary volume (REV) for the homogenised material model.

muscle models, which consider only fibre reinforcement during tension in the preferred direction, are not able to appropriately describe the mechanical response of such a microstructure. For instance, the transversely isotropic effects of muscle tissue during compression in direction $\boldsymbol{a}_0$ cannot be appropriately addressed with phenomenological material models, see [2]. Thus, the arrangement of the decisive collagenous structures, which govern the direction-dependent properties of skeletal muscle tissue, should be incorporated in an appropriate material model.

MODELLING AND METHODS

We propose a novel material model to describe the elastic behaviour of skeletal muscle tissue based on an analytical, second-order homogenisation method (cf., e. g., [4]), consisting of two constituents: (i) muscle fibre φ^F and (ii) extracellular matrix φ^M. The two constituents are superpositioned in the macroscopic material point $\mathcal{P}$ and constitute an effective overall material

$$\varphi = \bigcup_{\alpha} \varphi^{\alpha} \quad \text{with} \quad \alpha \in \{F, M\}\,. \tag{1}$$

The microstructure is considered via the hyperelastic strain energies $\mathcal{W}^{\alpha}$ of the constituents and statistical quantities, such as, for example, the volume fractions n^{α}. The homogenisation procedure leads to a transversely isotropic formulation with an effective strain-energy function

$$\widetilde{\mathcal{W}} = \underset{\boldsymbol{F}\in\mathcal{K}(\bar{\boldsymbol{F}})}{\text{stat}} \left\{ n^F \langle \mathcal{W}^F(\boldsymbol{F}) \rangle^F + n^M \langle \mathcal{W}^M(\boldsymbol{F}) \rangle^M \right\} \tag{2}$$

*Corresponding author. Email: christian.bleiler@mechbau.uni-stuttgart.de

for the overall muscle material φ. This is achieved by applying the principle of stationary energy with respect to a set $\mathcal{K}$ of kinematically admissible deformation gradients and assuming statistical uniformity of the microstructure and the separation of length scales. In (2), the operation $\langle\cdot\rangle^\alpha$ denotes the average over the constituent's volume and $\bar{\boldsymbol{F}}$ is the macroscopic deformation gradient. The overall muscle material is considered as incompressible, hence, $\det \bar{\boldsymbol{F}} = 1$. The average first Piola-Kirchhoff stress is derived by

$$\bar{\boldsymbol{P}} = \frac{\partial \widetilde{\mathcal{W}}}{\partial \bar{\boldsymbol{F}}} \,. \tag{3}$$

Microstructural data about the shape of the constituents inside the overall material is included into the model during the evaluation of the variational statement (2). Here, the model accounts for the transversely isotropic structure of the muscle fibres φ^F and the surrounding matrix φ^M. The strain energies of the constituents are composed of an isotropic, an anisotropic, and a volumetric part and take the general form

$$\mathcal{W}^\alpha = \mathcal{W}^\alpha_{\mathrm{iso}}(I_1^\alpha) + \mathcal{W}^\alpha_{\mathrm{aniso}}(I_1^\alpha, J_4^\alpha) + \mathcal{W}^\alpha_{\mathrm{vol}}(J^\alpha)\,, \tag{4}$$

with the first strain invariant $I_1^\alpha = \mathrm{tr}[\boldsymbol{F}_\alpha^T \boldsymbol{F}_\alpha]$, the Jacobian $J^\alpha = \det \boldsymbol{F}_\alpha$, and the mixed invariant $J_4^\alpha = \mathrm{tr}[(\boldsymbol{a}_0 \otimes \boldsymbol{a}_0)\boldsymbol{F}_\alpha^T \boldsymbol{F}_\alpha]$. Further, $\boldsymbol{F}_\alpha$ denotes the partial deformation gradient. The preferred direction $\boldsymbol{a}_0$ is the same for both of the constituents as well as for the overall muscle material. Carrying out the homogenisation, the volumetric part $\mathcal{W}^\alpha_{\mathrm{vol}}$ is further decomposed to derive an incompressible formulation of the effective energy $\widetilde{\mathcal{W}}$, see [1]. The general, transversely isotropic form (4) for the constituent's strain energies allows to describe the mechanical behaviour of the constituents in a very detailed manner. For instance, the arrangement of the collagen fibres in the extracellular-matrix-constituent φ^M is included by introducing an orientation distribution function $\mathfrak{p}_\theta(\theta_0)$ (cf., e. g., [3]), which describes the distribution of the collagen fibres around a mean angle θ_0 with respect to the preferred direction $\boldsymbol{a}_0$ (cf., e. g., [5]). The anisotropic strain-energy part of the matrix-constituent φ^M is then given by

$$\mathcal{W}^M_{\mathrm{aniso}}(I_1^M, J_4^M) = \int_0^\pi \mathfrak{p}_\theta \, \mathcal{W}_f(I_1^M, J_4^M) \, \sin\theta \, \mathrm{d}\theta \,, \tag{5}$$

where $\mathcal{W}_f$ is associated with the strain energy of the collagen fibres. This energy can be obtained by directly adopting data of collagenous tissue and using suitable strain-energy approaches. Another possibility is to consider a further upscaling step from the level of single collagen fibres to the level of collagenous tissue, leading to an even more detailed model for the overall muscle behaviour. Some of the ingredients and the basic idea of the homogenisation-based material model can be schematically depicted as follows:

- elastic properties of muscle fibres $\rightarrow \mathcal{W}^F$
- elastic properties of collagen, distribution of collagen fibres $\rightarrow \mathcal{W}^M$
- composition of the muscle material $\rightarrow n^F, n^M$

$\rightarrow \widetilde{\mathcal{W}} \quad \Rightarrow$ overall muscle model.

Concluding, this study presents a novel, hyperelastic muscle model, which includes microstructural data in order to obtain the effective response of the overall muscle tissue. The direction-dependent properties of the macroscopic tissue are direct consequences of the arrangement and the mechanical properties of the micro-constituents. This is in contrast to standard continuum-mechanical muscle models, which require that experimentally observed material behaviour is included phenomenologically into the model. Thus, the novel model provides deeper insights into the mechanical behaviour of skeletal muscles and helps us to understand the elastic characteristics of muscle tissue. Further note that the presented model serves as a general framework and can be modified or extended for further needs. For instance, the description of the muscle-fibre constituent φ^F can be extended by incorporating the active behaviour of the sarcomeres and electro-chemo-mechanical effects, see, for example, [6].

References

[1] Avazmohammadi R., Ponte Castañeda P.: Tangent Second-Order Estimates for the Large-Strain, Macroscopic Response of Particle-Reinforced Elastomers. J Elasticity 112:139-183, 2013.

[2] Böl M., Ehret A. E., Leichsenring K., Weichert C., Kruse R.: On the anisotropy of skeletal muscle tissue under compression. Acta Biomater 10:3225-3234, 2014.

[3] Lanir Y.: Constitutive equations for fibrous connective tissues. J Biomech 16:1-12, 1983.

[4] Ponte Castañeda P., Tiberio E.: A second-order homogenization method in finite elasticity and applications to black-filled elastomers. J Mech Phys Solids 48:1389-1411, 2000.

[5] Purslow P. P., Trotter J. A.: The morphology and mechanical properties of endomysium in series-fibred muscles: variations with muscle length. J Muscle Res Cell M 15:299-308, 1994.

[6] Röhrle O., Davidson J. B., Pullan A. J.: Bridging scales: A three-dimensional electromechanical finite element model of skeletal muscle. Siam J Sci Comput 30:2882–2904, 2008.

FREEDERICKSZ INSTABILITY FOR THE TWISTED NEMATIC DEVICE; A 3D ANALYSIS

N. Triantafyllidis*[1,2,3], G. I. Sfyris[1], K. Danas[1], and G. Wen[1]

[1]*Laboratoire de Mecanique des Solides, C.N.R.S. UMR7649*
Ecole Polytechnique, FRANCE
[2]*Département de Mecanique, Ecole Polytechnique, FRANCE*
[3]*Aerospace Engineering Department & Mechanical Engineering Department (emeritus)*
The University of Michigan, USA

Summary Of interest here is the three-dimensional analysis of the Freedericksz transition for the Twisted Nematic Device (TND), which is widely used in Liquid Crystal Display (LCD) monitors. Using a coupled mechanical-electromagnetic variational formulation, we study a finite thickness liquid crystal layer, anchored between two infinite parallel plates relatively rotated with respect to each other by a given angle and subjected to a transverse uniform electric field. For small values of this field, all directors lie in planes parallel to the boundary. Above a critical electric field, this solution becomes unstable, while a new bifurcated solution, which has directors with an out-of-plane component, emerges. By scanning a wide range of the liquid crystal's material parameter space, we establish whether the Freedericksz transition corresponds to a global mode (depending solely on the layer thickness coordinate), or to a local one, with finite wavelengths in one or both directions parallel to the plate.

BACKGROUND

Liquid crystals, are materials with elongated rod-like molecules that have preferred local average direction, which are modeled as directors; they exhibit important multi-physics coupling properties between their director orientation and externally applied mechanical, electric, magnetic or thermal fields. In addition to their theoretical interest, they are of tremendous importance to applications which have revolutionized the display technology in the form of LCD's (Liquid Crystal Displays).

The Twisted Nematic Device (TND) is the most widely used fundamental building block of LCD and the object of the present investigation, consists of a liquid crystal layer anchored between two parallel plates. One of the plates is rotated with respect to the other by an angle $\Delta\phi$: 90° for a typical TND or 270° for a Super Twisted Nematic Device (STND). In the absence of a transverse (i.e. normal to the bounding plates) electric field, all the directors are parallel to the bounding planes and form helices that rotate the light by $\Delta\phi$, allowing its passing through the two polarized end plates (their polarization directions differ also by $\Delta\phi$). When the applied transverse electric field exceeds a critical value, the directors suddenly acquire a transverse component. This phenomenon, termed *Freedericksz transition* is responsible for the change of polarization direction in the light, which prevents its passage through the device.

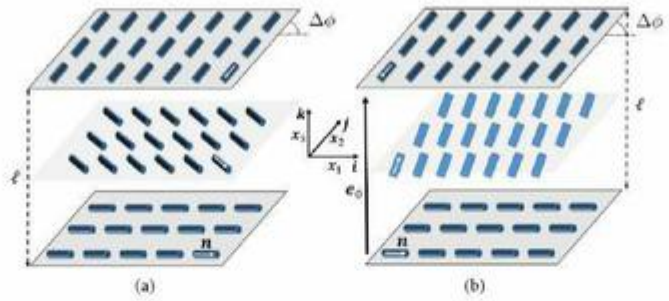

Figure 1: A typical twisted nematic device with 90° twist. In (a) the strength of the electric field is below its critical value and the nematic molecules in each x_3=const plane are parallel to the bounding plates, while in (b) the strength of the electric field is above its critical value and the molecules in each x_3 =const plane rotate out of their plane, tending to align with the externally applied electric field.

The present work is motivated by the fact that modeling the Freedericksz transition problem in liquid crystals' literature is often based on a 1D analysis that uses director fields depending solely on the layer thickness coordinate. Special cases have been shown by [1] to exist with finite, with respect the plate-parallel coordinates, wavelength eigenmodes, termed *periodic Freedericksz transitions*. However, no systematic, general investigation of the Freedericksz transition problem for the TND has been presented, to the best of the authors knowledge, that considers all possible eigenmodes in order to select the critical one (corresponding to the lowest electric field) and to thus establish whether this mode is global, i.e. dependent solely on the thickness coordinate (and thus captured by a 1D analysis) or local, i.e. has finite wavelengths with respect to one or both in-plane coordinate directions (and thus requiring a full 3D modeling).

*Corresponding author. Email: nick@lms.polytechnique.fr

PROBLEM SETTING AND RESULTS

The Freedericksz transition in a fully anchored TND is modeled here as a bifurcation problem for the finite thickness liquid crystal with a Frank-Oseen energy, where the loading parameter is the magnitude of the applied transverse electric field (dimensionless parameter ζ). The continuum mechanics model uses a novel coupled electromechanical variational principle for nematic elastomers proposed by [2], where the Euler-Lagrange equations are the mechanical equilibrium equations plus the Faraday law for the electric field. The stability of the TND is based on the loss of positive definiteness of the second functional derivative of the energy evaluated on the principal solution.

For the special case of zero twist angle, we derive the analytical solution for the the fully 3D boundary value problem and use this solution as a highly nontrivial check for the numerical algorithm developed for the general case. For arbitrary values of the TND's twist angle, no analytical solution can be found and a mixed analytical/numerical technique, combining an FEM discretization for the thickness coordinate with a Fourier transform for the remaining coordinates (wavenumbers ω_1, ω_2 respectively). By scanning a wide range of the liquid crystal's material parameter space (the splay k_1, bend k_2 and twist k_3 constants of the Frank-Oseen energy plus the electric susceptibility constants χ and χ_n – perpendicular and parallel to the director direction), we establish whether the Freedericksz transition corresponds to a global mode ($(\omega_1, \omega_2) = (0,\ 0)$, with an eigenmode depending solely on the layer thickness coordinate, or to a local one (termed periodic Freedericksz transition), with an eigenmode that has finite wavelengths ($(\omega_1, \omega_2) \neq (0,\ 0)$ in one or both directions parallel to the plate.

Our calculations show that a device with a global critical mode for low values of twist, invariably shows a local critical mode once the twist exceeds a certain level, depending on constitutive parameters of the liquid crystal. Also a monotonically increasing critical electric field as a function of the twist angle is not always the case, as our calculations have shown for liquid crystals with low twist Frank-Oseen constant.

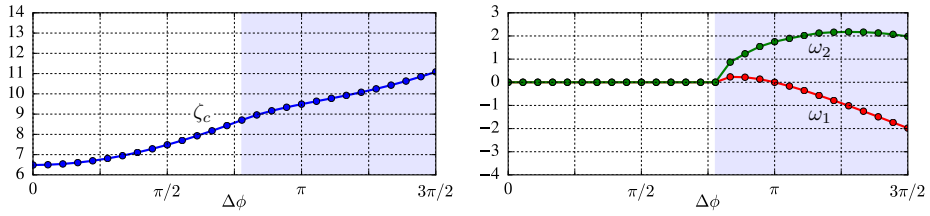

Figure 2: Dependence of the dimensionless critical electric field ζ_c (left) and the corresponding dimensionless eigenmode wavenumbers $\omega_1,\ \omega_2$ (right) on the twist angle $\Delta\phi$. Notice that above a certain value of $\Delta\phi$, the critical eigenmode changes from global to local (from infinite to finite wavelengths) for the base case of 5CB liquid crystal

.

The systematic investigation, based on 3D analysis, presented above for the influence of the Frank-Oseen and electric susceptibility constants of TND's on the critical (lowest) electric field and corresponding eigenmode gives the range of these parameters where the onset of bifurcation in these devices (Freedericksz transition) is global or local in nature and calculates the associated wavelengths for the latter case. These results could be useful in guiding liquid crystal selection for applications, since lowering the critical electric field reduces the energy consumption of the device, but the presence of a short wavelength mode might need to be taken into account in the design. Moreover, the continuum mechanics-based methodology introduced here is applicable to a wider class of problems involving the stability of devices involving liquid crystals (methodology that can be generalized to include nematic elastomers, see [2]), problems that besides their theoretical interest are at the heart of exciting new technological developments.

References

[1] F. Lonberg and R. B. Meyer. New ground state for the splay-freedericksz transition in a polymer nematic liquid crystal. *Physical Review Letters*, 55(7):718 – 721, 1985.

[2] G. Pampolini and N. Triantafyllidis. Continuum Electromechanical Theory for Nematic Continua with Application to Freedericksz Instability. *Under review*, 2015.

CONVERTING STRAIN MAPS INTO ELASTICITY MAPS FOR MATERIALS WITH SMALL CONTRAST

Cédric Bellis* and Pierre Suquet
Laboratory of Mechanics and Acoustics, CNRS, Marseille, France

Summary This study focuses on the quantitative reconstruction of heterogeneous distributions of isotropic elastic moduli from full strain field data. A local reconstruction procedure is developed here for materials with small contrast. Within the framework of the integral formulation of the linear elasticity problem, first-order asymptotics are investigated. Properties of the featured infinite-body Green's operator are studied to characterize its local and non-local contributions to the volume integral equations considered. On this basis, the combination of multiple strain field solutions corresponding to well-chosen applied macroscopic strains yields a set of local and uncoupled equations relating, respectively, bulk and shear moduli to the spherical and deviatoric components of the strain fields. Valid for any material configuration at first-order in the small contrast limit, such relations permit pointwise conversions of strain maps into elasticity maps. A set of examples illustrates the use of these local equations for parameters identification from full-field data.

CONTEXT AND MOTIVATIONS

Imaging the mechanical properties of a solid body from displacement or strain field measurements is an ill-posed inverse problem with applications to material characterization, non-destructive testing or medical diagnosis. Motivated by the flourishing development of kinematic full-field measurement techniques [1, 2], the starting point for this study is the availability of full strain field measurements from which we aim at inferring quantitatively bulk and shear modulus distributions.

The approach investigated in this paper revolves around explicit reconstruction formulae which derivation is sought based on the integral formulation framework of the linear elasticity problem. The latter allows to express a given strain field as the solution of a volume integral equation commonly referred to as the Lippmann-Schwinger equation [3]. Focusing on materials with small contrast then the governing integral equations are expressed in terms of the Green's operator for the infinite medium and expanded at the first-order in the material parameter perturbations. Upon characterizing the geometrical properties of the featured Green's tensor it is shown that specific experiments, associated with either purely hydrostatic or deviatoric applied macroscopic strains, can be combined to yield pointwise identities relating the sought moduli to the corresponding strain field solutions. Thus, it is demonstrated that explicit formulae can be obtained at the first-order for a set of well-chosen experiments so that it makes it possible to reconstruct the unknown elastic moduli at a given point from strain field data at this point.

INTEGRAL FORMULATION

Consider a heterogeneous linear elastic medium $\mathcal{V} \subset \mathbb{R}^d$, with $d = 2$ or 3. The static governing equations reads

$$\boldsymbol{\varepsilon}(\boldsymbol{x}) = \big[\boldsymbol{\nabla}\boldsymbol{u} + (\boldsymbol{\nabla}\boldsymbol{u})^t\big]/2, \qquad \boldsymbol{\sigma}(\boldsymbol{x}) = \boldsymbol{\mathcal{L}}(\boldsymbol{x}) : \boldsymbol{\varepsilon}(\boldsymbol{x}), \qquad \boldsymbol{\nabla}\cdot\boldsymbol{\sigma}(\boldsymbol{x}) = \boldsymbol{0},$$

with displacement field $\boldsymbol{u}$, second-order strain and stress fields $\boldsymbol{\varepsilon}$, $\boldsymbol{\sigma}$ and isotropic constitutive elasticity tensor field $\boldsymbol{\mathcal{L}}$ given by bulk and shear modulus distributions κ, $\mu \in L^\infty(\mathcal{V}, \mathbb{R}^*_+)$ as $\boldsymbol{\mathcal{L}}(\boldsymbol{x}) = d\kappa(\boldsymbol{x})\boldsymbol{\mathcal{J}} + 2\mu(\boldsymbol{x})\boldsymbol{\mathcal{K}}$ where $\boldsymbol{\mathcal{J}}$, $\boldsymbol{\mathcal{K}} \in \overset{2}{\otimes}_{\rm s}\big(\overset{2}{\otimes}_{\rm s}\mathbb{R}^d\big)$. The characteristic length-scale of the inhomogeneities are considered to be small compared to this of the domain $\mathcal{V}$. The mechanical loading applied on $\partial\mathcal{V}$ is assumed to be compatible with a uniform macroscopic strain $\bar{\boldsymbol{\varepsilon}} \in \overset{2}{\otimes}_{\rm s}\mathbb{R}^d$, i.e. $\langle\boldsymbol{\varepsilon}\rangle = \bar{\boldsymbol{\varepsilon}}$. Introducing a reference homogeneous elasticity tensor $\boldsymbol{\mathcal{L}}_0$ and owing to a perturbation approach, then the solution $\boldsymbol{\varepsilon}$ to the elasticity problem considered is known to satisfy the following Lippmann-Schwinger equation [3, 4]:

$$\boldsymbol{\varepsilon}(\boldsymbol{x}) = \bar{\boldsymbol{\varepsilon}} \circ \big[\boldsymbol{\Gamma}\left(\delta\boldsymbol{\mathcal{L}} : \boldsymbol{\varepsilon}\right)\big](\boldsymbol{x}) \tag{1}$$

where $\delta\boldsymbol{\mathcal{L}} = \boldsymbol{\mathcal{L}} \circ \boldsymbol{\mathcal{L}}_0$ and $\boldsymbol{\Gamma}$ is the linear integral operator such that $\boldsymbol{\varepsilon}' = \boldsymbol{\Gamma}\boldsymbol{\tau}$ is a compatible strain field solution in $\mathcal{V}$ associated with zero displacements over $\partial\mathcal{V}$ and such that the divergence of the stress field defined as $\boldsymbol{\sigma}' = \boldsymbol{\mathcal{L}}_0 : \boldsymbol{\varepsilon}' + \boldsymbol{\tau}$ is zero. Assuming that $\mathcal{V}$ is large compared to the length-scale of the inhomogeneities, we henceforth make the translation-invariant approximation in (1) for $\boldsymbol{x}$ distant from $\partial\mathcal{V}$:

$$\big[\boldsymbol{\Gamma}\boldsymbol{\tau}\big](\boldsymbol{x}) = \int_{\mathbb{R}^d} \boldsymbol{\Gamma}_0^\infty(\boldsymbol{x} \circ \boldsymbol{y}) : \big[\boldsymbol{\tau}(\boldsymbol{y}) \circ \langle\boldsymbol{\tau}\rangle\big]\,{\rm d}\boldsymbol{y}$$

with $\boldsymbol{\Gamma}_0^\infty : \mathcal{V} \to \overset{2}{\otimes}_{\rm s}\big(\overset{2}{\otimes}_{\rm s}\mathbb{R}^d\big)$ being the fourth-order infinite-body Green's tensor associated with $\boldsymbol{\mathcal{L}}_0$ and vanishing displacements at infinity. The results presented in this paper are based on key properties of the tensor $\boldsymbol{\Gamma}_0^\infty$, namely, that the Green's operator $\boldsymbol{\Gamma}$ can be decomposed into a local part and a non-local operator as

$$\big[\boldsymbol{\Gamma}\boldsymbol{\tau}\big](\boldsymbol{x}) = \boldsymbol{\Lambda}_0 : \boldsymbol{\tau}(\boldsymbol{x}) + \big[\boldsymbol{\Pi}_0 \underline{\underline{*}}\, \boldsymbol{\tau}\big](\boldsymbol{x}),$$

*Corresponding author. Email: bellis@lma.cnrs-mrs.fr

where the operation $\underline{\underline{*}}$ denotes the combination of space convolution and double inner product. It will be shown that the fourth-order tensor $\boldsymbol{\Lambda}_0$ coincides with the isotropic component of the Fourier transform $\boldsymbol{\Gamma}_0^\infty(\boldsymbol{\xi})$, so that it reads $\boldsymbol{\Lambda}_0 = \lambda_{\scriptscriptstyle J}\,\boldsymbol{\mathcal{J}} + \lambda_{\scriptscriptstyle K}\,\boldsymbol{\mathcal{K}}$ with $\lambda_{\scriptscriptstyle J}\,,\ \lambda_{\scriptscriptstyle K}\ \in \mathbb{R}$, while the non-local component $\boldsymbol{\Pi}_0$ is orthogonal to the space of isotropic tensors.

LOCAL RECONSTRUCTION FORMULAE

Inverting the fundamental integral equation (1) and expanding at first order in $\|\delta\boldsymbol{\mathcal{L}}\| = o(\|\boldsymbol{\mathcal{L}}_0\|)$ entails

$$\boldsymbol{\varepsilon}(\boldsymbol{x}) = \boldsymbol{\varepsilon} - \big[\boldsymbol{\Gamma}\,(\delta\boldsymbol{\mathcal{L}} \quad \boldsymbol{\varepsilon})\big](\boldsymbol{x}) + o\big(\|\delta\boldsymbol{\mathcal{L}}\|\big).$$

When applying the inner product with $\boldsymbol{\varepsilon}$ in the above equation one has to deal with the non-local term $\big[\boldsymbol{\varepsilon} : \boldsymbol{\Gamma}\,(\delta\boldsymbol{\mathcal{L}} \quad \boldsymbol{\varepsilon})\big](\boldsymbol{x})$. As a consequence, for an arbitrary chosen macroscopic strain $\boldsymbol{\varepsilon}$, the corresponding strain field $\boldsymbol{\varepsilon}(\boldsymbol{x})$ depends on the constitutive moduli in a non-local fashion. However, given the described properties of the Green's tensor, then multiple experiments can be combined in order to retain only the contribution of the constant isotropic component $\boldsymbol{\Lambda}_0$ of the Green's tensor $\boldsymbol{\Gamma}_0^\infty$. Doing so yields a local equation relating strain fields and elastic moduli. A simple way to achieve this is to consider macroscopic strains that constitute an orthogonal eigentensor basis of the fourth-order projection tensors $\boldsymbol{\mathcal{J}}$ and $\boldsymbol{\mathcal{K}}$. Therefore, one obtains the following results:

(1) Let $\boldsymbol{\varepsilon}$ denote a purely spherical macroscopic strain with associated strain field solution $\boldsymbol{\varepsilon}(\boldsymbol{x})$. The latter satisfies, at the first order, the following local equation:

$$\kappa(\boldsymbol{x}) = \kappa_0 + \frac{1}{d\,\lambda_{\scriptscriptstyle J}}\left[1 - \frac{\mathrm{tr}[\boldsymbol{\varepsilon}(\boldsymbol{x})]\,\mathrm{tr}[\bar{\boldsymbol{\varepsilon}}]}{d\|\boldsymbol{\varepsilon}\|^2}\right] + o\big(\|\delta\boldsymbol{\mathcal{L}}\|\big). \tag{2}$$

(2) Consider a set of purely deviatoric and orthogonal strains $\boldsymbol{\varepsilon}^{(i)}$, for $i = 1, \ldots, n_{\scriptscriptstyle K}$ with $n_{\scriptscriptstyle K} = d(d+1)/2 - 1$, such that

$$\boldsymbol{\mathcal{K}} = \sum_{i=1}^{n_{\scriptscriptstyle K}} \frac{\boldsymbol{\varepsilon}^{(i)} \otimes \boldsymbol{\varepsilon}^{(i)}}{\|\boldsymbol{\varepsilon}^{(i)}\|^2} \quad \text{with} \quad \boldsymbol{\varepsilon}^{(i)} \ \ \boldsymbol{\varepsilon}^{(j)} = \|\boldsymbol{\varepsilon}^{(i)}\|\,\|\boldsymbol{\varepsilon}^{(j)}\|\,\delta_{ij}.$$

Then, at the first order, the associated strain field solutions $\boldsymbol{\varepsilon}^{(i)}(\boldsymbol{x})$ satisfy the local identity:

$$\mu(\boldsymbol{x}) = \mu_0 + \frac{n_{\scriptscriptstyle K}}{2\,\lambda_{\scriptscriptstyle K}}\left[n_{\scriptscriptstyle K} - \sum_{i=1}^{n_{\scriptscriptstyle K}} \frac{\mathbf{dev}[\boldsymbol{\varepsilon}^{(i)}(\boldsymbol{x})] : \mathbf{dev}\ \boldsymbol{\varepsilon}^{(i)}]}{\|\boldsymbol{\varepsilon}^{(i)}\|^2}\right] + o\big(\|\delta\boldsymbol{\mathcal{L}}\|\big). \tag{3}$$

For materials with small contrasts, the closed form identities, such as (2) and (3), derived in this study allow to convert locally strain field maps into elasticity maps. For a generic material configuration in 2D and 3D then only one strain map is sufficient to reconstruct the bulk modulus while the computation of the shear modulus requires the combination of either 2 or 5 strain field measurements respectively. Furthermore, provided that the material considered satisfies additional geometrical properties then it will be shown that only one measurement is actually sufficient to reconstruct either one of the parameters.

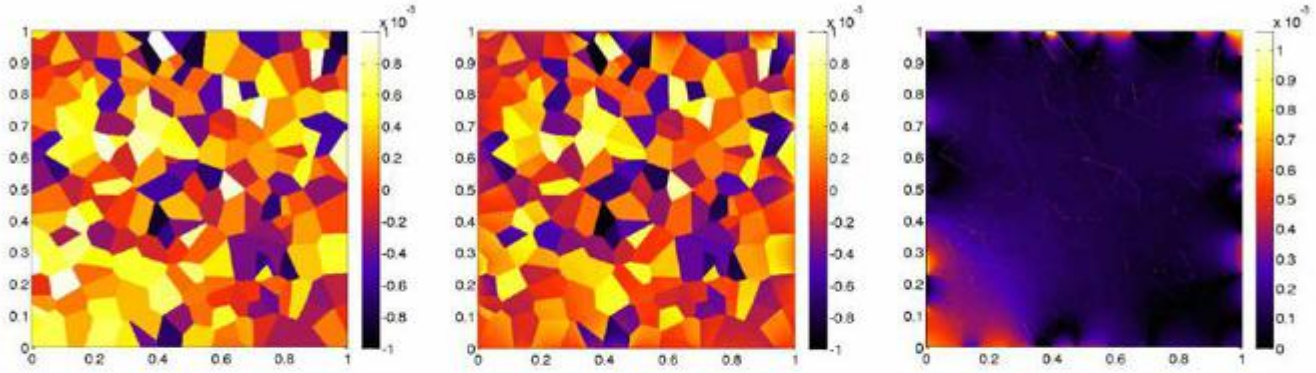

(a) Reference elasticity map $\mu_{\text{ref}}(\boldsymbol{x}) - \mu_0$ (b) Reconstruction $\mu_{\text{id}}(\boldsymbol{x}) - \mu_0$ (c) Relative error $|\mu_{\text{ref}}(\boldsymbol{x}) - \mu_{\text{id}}(\boldsymbol{x})|/\mu_{\text{ref}}(\boldsymbol{x})$

Figure 1: Numerical example: The reconstruction μ_{id} of the objective elasticity map μ_{ref} is performed using Eqn. (3) based on the knowledge of two associated synthetic strain fields which correspond to purely deviatoric macroscopic strains.

References

[1] M. Grédiac and F. Hild, editors. *Full-Field Measurements and Identification in Solid Mechanics*. John Wiley & Sons, Inc., 2013.

[2] J.-Y. Buffière and E. Maire, editors. *Imagerie 3D en mécanique des matériaux*. Hermès, 2014.

[3] J. R. Willis. Variational and related methods for the overall properties of composites. *Advances in Applied Mechanics*, 21:1 – 78, 1981.

[4] G. W. Milton. *The Theory of Composites*. Cambridge University Press, 2002.

IDENTIFICATION OF SMALL INHOMOGENEITIES IN 3D THERMOELASTICITY

Efim I. Shifrin[1a)], Alexander V. Kaptsov[1] & Alexander L. Levitin [1]
[1]*A.Yu. Ishlinsky Institute for Problems in Mechanics, Russian Academy of Sciences, Moscow, Russia*

Summary A geometrical inverse thermoelastic problem is considered. It is assumed that a finite number of defects (cavities, cracks, inclusions) are located inside a linearly elastic, mechanically and thermally isotropic 3D body. It is assumed also that mechanical and steady-state thermal loads are applied to the external boundary of the body in a single experiment. As a result of the experiment the displacements and the applied mechanical loads are measured on the boundary. A method for identification of the number and locations of defects, which are considered as point defects, is developed. It is important to stress that the identification method is based only on the knowledge of the displacements and the applied mechanical loads, if any, on the external boundary of the body. The knowledge of the thermal conditions on the boundary and the conditions of heat exchange between the matrix and inclusions are not assumed. Numerical examples are considered.

INTRODUCTION

To date, methods for solving geometric, inverse, thermoelastic problems are not developed enough. Among the publications in this area, it is possible to note the papers [1] and [2] where the problems of identification of one and two cavities in 2D thermoelastic bodies were solved by the level set method and the method of fundamental solutions, respectively. In the papers [3,4] it was developed a method for the identification of small, multiple defects in both 3D isotropic and anisotropic linearly elastic bodies, by means of the boundary data. The method is based on the use of the reciprocity gap functional. The purpose of the paper to extend the method to solve the 3D inverse problems of thermoelasticity.

STATEMENT OF THE PROBLEM

Let $V \subset R^3$ be a bounded simply connected domain with a boundary ∂V. $G_k \subset V$, $k = 1,2,\cdots,n$ are simply connected subdomains. We suppose that $\overline{G}_i \cap \overline{G}_j = \varnothing$, $i \neq j$, $\overline{G} = \bigcup_{k=1}^{n} \overline{G}_k \subset V$, where $\overline{G}_k$ is a closure of the subdomain G_k. Let us suppose that a linearly elastic, mechanically and thermally isotropic body occupies the domain $\Omega = V \setminus \overline{G}$. Introduce some notation for the thermal and mechanical characteristics of the body, which occupies the domain Ω. The thermal characteristics are as follows: α_M is the coefficient of thermal expansion, κ_M is the heat conductivity, h_M is the convective heat transfer coefficient. The elastic properties are: μ_M is the shear modulus and ν_M is the Poisson ratio. The defects G_k can be cavities or inclusions (rigid or linear elastic). If G_k is a cavity we suppose that its boundary ∂G_k is free of mechanical loads. If G_k is an inclusion, it is supposed complete mechanical bonding between the matrix and inclusion. Below we consider the case of linear elastic inclusions because the cavities and rigid inclusions can be considered as particular cases when the shear modulus tends to zero and infinity, respectively. The thermal and elastic characteristics of the inclusion G_k we denote by the index Ik: α_{Ik}, κ_{Ik}, μ_{Ik}, ν_{Ik}. The temperature, displacements, strains and stresses in the body Ω we will mark with the superscript d: T^d is the temperature, $\mathbf{u}^d = \left(u_1^d, u_2^d, u_3^d\right)$ is the displacements vector, e_{ij}^d is the strain tensor and σ_{ij}^d is the stress tensor. The similar values in the inclusion G_k we will mark with the superscript Ik: T^{Ik}, $\mathbf{u}^{Ik} = \left(u_1^{Ik}, u_2^{Ik}, u_3^{Ik}\right)$, e_{ij}^{Ik}, σ_{ij}^{Ik}. Here and below, we suppose that some Cartesian coordinates $Ox_1x_2x_3$ are introduced and all values are considered in these coordinates. We suppose that static mechanical loads and steady-state thermal loads are applied to the external boundary of the body in a single experiment. We assume also that as a result of the experiment the applied mechanical loads $t_i^d = \sigma_{ij}^d n_j$ and displacements $\mathbf{u}^d$ are measured on the boundary of the body. Here $n = \left(n_1, n_2, n_3\right)$ is a unit outward normal to the boundary ∂V. We assume that typical sizes of the defects have the same order. Denote the typical size l. Assume also that the typical distances between the defects have the same order and denote the typical distance L. We assume that the defects are small and well-separated in the following sense: $l \ll L$. The problem is to determine the number of defects and their locations, using the known mechanical loads and displacements on ∂V.

The elastostatic fields in the body V without defects we call regular elastic fields and mark by a superscript r $\left(\sigma_{ij}^r, e_{ij}^r, u_i^r\right)$ in case, if the fields satisfy the condition $\sum_{k=1}^{3} e_{kk}^r = 0$. Construct a reciprocity gap functional depending on the

a) Corresponding author. Email: shifrin@ipmnet.ru

given thermoelastic field with a superscript d and regular elastostatic field with superscript r. The functional is defined as follows:

$$RG(d,r)=\int_{\partial V}\left(t_i^d u_i^r - t_i^r u_i^d\right)dS,\quad t_i^r=\sigma_{ij}^r n_j \tag{1}$$

Because the functions t_i^d and u_i^d are known, the values $RG(d,r)$ can be calculated for all regular elastic fields r. So, the problem of the defects reconstruction will be solved if we express the parameters of the domains G_k by means of the values $RG(d,r)$. The expression (1) can be reduced to the following form:

$$RG(d,r)=\sum_{k=1}^{n}2\left(\mu_{Ik}-\mu_M\right)\int_{G_k}e_{ij}^{Ik}e_{ij}^r\,dx \tag{2}$$

SOLUTION OF THE PROBLEM

We suppose that the diameters of the defects are small. Using this supposition we will consider the defects as points and determine the projections of the points on an arbitrary plane. Let us determine, for example, the projections of point defects on the plane x_1x_2. To determine the projections we take as the regular elastic fields, the elastic fields corresponding to plane strain state. We consider the regular elastic fields of two types with the following strains: $e_{13}^r=e_{23}^r=e_{33}^r=0$, $e_{11}^r+e_{22}^r=0$, $e_{22}^r-e_{11}^r+2ie_{12}^r=-2H(z)$, $e_{13}^\rho=e_{23}^\rho=e_{33}^\rho=0$, $e_{11}^\rho+e_{22}^\rho=0$, $e_{22}^\rho-e_{11}^\rho+2ie_{12}^\rho=-2iH(z)$. Here $z=x_1+ix_2$, $H(z)$ is an arbitrary holomorphic function. Eq. (2) for the introduced regular elastic fields can be reduced to the form

$$RG(d,r)-iRG(d,\rho)=\sum_{k=1}^{n}2\left(\mu_{Ik}-\mu_M\right)\int_{G_k}\left[\left(e_{11}^{Ik}-e_{22}^{Ik}\right)+2ie_{12}^{Ik}\right]H\,dx \tag{3}$$

Let us take $H(z)=H_m(z)=w^m(z)$, $m=0,1,2,\cdots$. Denote r_m and ρ_m the regular elastic fields corresponding to the holomorphic function $w^m(z)$. Denote also the centers of the defects G_k by $x^k=\left(x_1^k,x_2^k,x_3^k\right)$ and the volumes of the domains G_k by $|G_k|$. Using Eq. (3) we obtain a system of equations

$$RG(d,r_m)-iRG(d,\rho_m)=\sum_{k=1}^{n}2\left(\mu_{Ik}-\mu_M\right)\int_{G_k}\left[\left(e_{11}^{Ik}-e_{22}^{Ik}\right)+2ie_{12}^{Ik}\right]w^m(z)\,dx \tag{4}$$

Now we use the assumption that the domains G_k are small and approximate the integrals in Eq. (4) by the principle term of the asymptotic expansion, provided that $l/L\to 0$.

$$RG(d,r_m)-iRG(d,\rho_m)=\sum_{k=1}^{n}2\left(\mu_{Ik}-\mu_M\right)\left[\left(e_{11}^{Ik}(x^k)-e_{22}^{Ik}(x^k)\right)+2ie_{12}^{Ik}(x^k)\right]w^m(z_k)|G_k| \tag{5}$$

Here $z_k=x_1^k+ix_2^k$. The system of Eq. (5) has the following form:

$$\sum_{k=1}^{n}A_k w_k^m=b_m,\quad m=0,1,2,\cdots,\quad w_k=w(z_k) \tag{6}$$

Eq. (6) coincide with the equations arising in the problem of simple poles of a meromorphic function identification and can be solved by the known methods. The projections z_k can be obtained from the values w_k.

Acknowledgements

The support of RFBR grant 16-01-00149 is gratefully acknowledged.

References

[1] Ben Ameur, H., Burger, M., Hackl, B.: Cavity identification in linear elasticity and thermoelasticity. *Math. Meth. Appl. Sci.* **30**: 625-647, 2007.

[2] Karageorghis, A., Lesnic, D., Marin, L.: A moving pseudo-boundary MFS for void detection in two-dimensional thermoelasticity. *International Journal of Mechanical Sciences*. **88**: 276-288, 2014.

[3] Shifrin, E.I., P.S. Shushpannikov, P.S.: Identification of small well-separated defects in an isotropic elastic body using boundary measurements. *International Journal of Solids and Structures*. **50**: 3707-3716, 2013.

[4] Shifrin, E.I., Shushpannikov, P.S.: Identification of finitely many small defects in an anisotropic linearly elastic body from a single static test. *Mechanics of Solids*. **50**: 421-431, 2015.

HYGRO-MECHANICAL STRUCTURE–PROPERTY RELATIONS FOR PAPER SHEETS

Ron H.J. Peerlings*[1], Emanuela Bosco[1,2], and Marc G.D. Geers[1]

[1]*Department of Mechanical Engineering, Eindhoven University of Technology, Eindhoven, Netherlands*
[2]*Materials innovation institute M2i, Delft, Netherlands*

Summary Our objective is to establish models which allow one to predict the hygro-mechanical properties of paper sheets based on the properties of the underlying fibrous network. Asymptotic homogenisation is used to determine rigorous effective properties of random networks numerically. The trend predicted by these random networks is however captured quite reasonably by a much simpler analytical model which assumes a regular network of perpendicular fibres. The latter model is fully analytical and is thus a much more powerful tool for developing understanding and designing materials. Predictions made by it compare well with measured hygro-expansivities reported in the literature.

INTRODUCTION AND OBJECTIVES

Significant dimensional variations may occur in paper sheets when they are subjected to changes in moisture content. Gradients of the moisture content in the plane of the sheet, in particular, may result in instabilities and out-of plane deformation of the sheet, which are problematic in e.g. digital printing devices.

Moisture induced deformations are ultimately governed by the swelling of individual fibres, which is transferred through inter-fibre bonds within the fibrous network. The fibres' swelling is highly anisotropic and as a result complex interactions between mechanical and hygro-expansive properties take place in the bonding areas, affecting the overall material response. Matters are further complicated by the fact that the fibre orientation distribution is anisotropic as well and internal stresses may be 'dried in' during paper production [1].

Our objectives are (i) to understand how the hygro-mechanical properties of individual fibres, via the bonds and network, determine the sheet-level hygro-expansion of paper sheets and (ii) based on this understanding, to formulate structure–property relations which allow one to predict the sheet-level hygro-expansivity as a function of microstructural parameters such as single-fibre properties and fibre orientation distribution.

METHODOLOGY

We address the issue by developing microstructural, i.e. network-level, models which incorporate the relevant effects. We then study the overall response of these models and its dependence on the characteristics of the network and fibres. The models are so far of a two-dimensional nature and assume a perfect bonding between fibres where they overlap. In this contribution we focus on the reversible hygro-mechanical response – although progress has also been made on the issue of dried-in stress and strain.

Within this scope, we follow two approaches:

1. Unit cells comprising periodic, but otherwise random fibre networks are generated according to a certain orientation distribution, see Figure 1 (left) for an example. Their overall mechanical and hygroscopic properties are computed by rigorous, asymptotic homogenisation. This involves discretising the networks by finite elements and solving a set

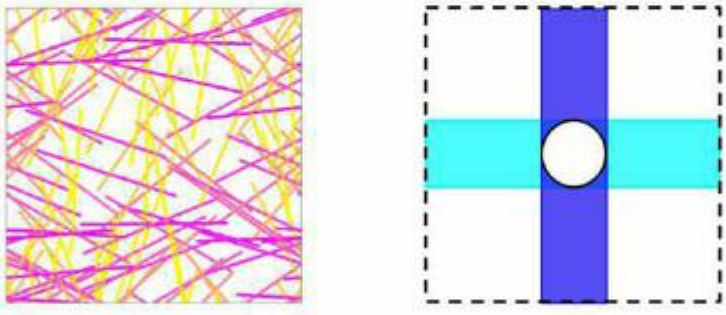

Figure 1: Sketches of the two types of microstructural models used: (left) unit cell with random fibre distribution and (right) idealised unit cell with two fibre families.

*Corresponding author. Email: R.H.J.Peerlings@tue.nl

of boundary value problems which deliver the network-level displacement fluctuations due to mechanical as well as hygroscopic loading. Equivalent, homogenised elastic moduli and hygro-expansivities can finally be computed from these fluctuation functions.

2. An extremely idealized model is considered, in which the fibrous network is assumed to consist of infinitely long fibres which are organised in a square, periodic pattern – see the sketch in Figure 1 (right) for a unit cell of this periodic pattern. Crucially, the model does distinguish between free-standing fibre parts and bonded areas. The anisotropy of the network is reflected in the fact that the 'fibre bundles' in the two directions have a different thickness. The ratio of these thicknesses is established by lumping the fibre orientation distribution into two perpendicular contributions. The model can be solved analytically, allowing one to determine its anisotropic hygro-mechanical response as an explicit function of its parameters [1, 2].

RESULTS AND CONCLUSIONS

Comparison of results obtained by the two models (not shown here) demonstrates that the analytical, highly idealised model qualitatively captures the trends predicted by the more detailed numerical model. In fact, a good quantitative agreement is also observed in the range of realistic parameters values.

Figure 2 shows a comparison of predictions made by the simple, analytical model with experimental data reported by Uesaka [3]. Shown are the hygro-expansive coefficients in machine direction and cross direction as a function of the degree of anisotropy of the fibre orientation distribution. The latter is characterised by the ratio of the elastic moduli in machine direction and cross direction – which were measured in the experiments and are obtained as a by-product of the model. The solid and dashed curves represent the model prediction for the two different paper grades considered in the experiments and the square and circular markers indicate the respective corresponding experimental data. The trends exhibited by the experimental data are captured quite accurately by the model – despite the fact that no effort was made to fit the model specifically to this data set. In the model, the dependence on the fibre network's anisotropy can be traced back to the fibre bonds, which are thus shown to play a crucial role.

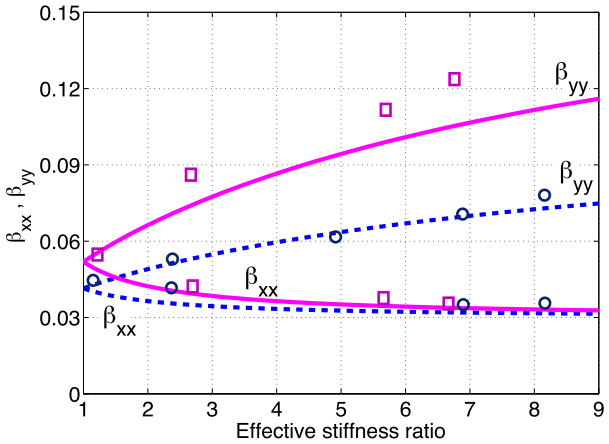

Figure 2: Hygro-expansive coefficients in machine direction, β_{xx}, and cross direction, β_{yy}, as a function of the degree of (mechanical) anisotropy. The curves represent the prediction of the simplified model for two paper grades; the markers are the experimental data for these grades as reported in [3].

References

[1] Bosco, E., Bastawrous, M.V., Peerlings, R.H.J., Hoefnagels, J.P.M., Geers, M.G.D.: Bridging network properties to the effective hygroexpansivity of paper: experiments and modelling, Philosophical Magazine 95:28-30, 2015.

[2] Bosco, E., Peerlings, R.H.J., Geers, M.G.D.: Predicting hygro-elastic properties of paper sheets based on an idealized model of the underlying fibrous network, International Journal of Solids and Structures Structures 5657: 4352, 2015.

[3] Uesaka, T.: General formula for hygroexpansion of paper. Journal of Materials Science 29:2373-2377, 1994.

THE UNIVERSALITY OF THE BAND STRUCTURE OF LAYERED COMPOSITES

Gal Shmuel [*1] and Ram Band[2]
[1]*Faculty of Mechanical Engineering, Technion–Israel Institute of Technology, Haifa, Israel*
[2]*Department of Mathematics, Technion–Israel Institute of Technology, Haifa, Israel*

Summary We find that the frequency spectra of layered phononic and photonic composites admit a universal structure, independent of the geometry of the periodic-cell and the specific physical properties [1]. In certain cases, this representation extends to highly deformable and multi-physical materials of tunable spectra. The structure is employed to establish universal properties of the corresponding band-gaps, and to rigorously determine their statistical and optimal characteristics. Specifically, we investigate the density of the gaps, their maximal width and expected value. As a result, rules for tailoring the laminate according to desired spectra properties follow. Our representation further facilitates characterizing the tunability of the band-structure of soft and multi-physical materials.

Wave propagation in heterogeneous media has fascinated the scientific community for decades. The inhomogeneity causes multiple scattering, and, in turn, wave interferences that give rise to intriguing phenomena in various fields. Of particular interest are the transition of conducting to isolating behavior of electronic crystals, localization of electromagnetic waves in dielectrics, and attenuation of mechanical motions in elastic media [2]. Layered media have been extensively studied by virtue of their relative simplicity of fabrication and theoretical modeling. In what follows, we provide new insights on the relation between their geometry, physical properties, and frequency spectrum. We find a universal representation for the spectrum, *independent* of the unit-cell geometry and specific constituents properties. This structure reveals a universal property of the gaps-density, namely, its invariance under the change of various geometric and physical properties. We utilize this representation to determine exactly the density of the gaps, and their expected and maximal widths. These results are identified with classes of compositions, hence provide rules for tailoring the laminate according to desired spectra characteristics.

The canvas upon which the analysis is presented is of phononic crystals. The conclusions we draw, however, extend to additional systems. By virtue of the similarity between electromagnetic and elastodynamics wave equations for the considered geometry, our insights apply to one-dimensional (1D) photonic crystals as well. Our analysis further applies in certain cases to soft non-linear media and multi-physical composites, whose physical properties are changed upon application of external stimuli.

We begin by considering a 1D crystal made out of two alternating layers. We denote the layers with 1 and 2, and their associated quantities with superscript (p), $p = 1$ and 2, respectively. The dispersion relation governing the propagation of waves in the crystal is [3]

$$\eta = \cos k_B h, \tag{1}$$

where

$$\eta = \cos\frac{\omega h^{(1)}}{c^{(1)}}\cos\frac{\omega h^{(2)}}{c^{(2)}} - \gamma\sin\frac{\omega h^{(1)}}{c^{(1)}}\sin\frac{\omega h^{(2)}}{c^{(2)}}. \tag{2}$$

In the above, ω is the frequency, k_B is the Bloch-parameter, $h^{(p)}$ is the thickness, and $h = h^{(1)} + h^{(2)}$. The parameter $c^{(p)}$ corresponds to different velocities, depending on the type of media and waves considered. Specifically, when the crystal is photonic, $c^{(p)}$ is the velocity of light in the layer; when the crystal is phononic, $c^{(p)}$ is the velocity of either transverse waves or longitudinal waves, propagating in a bulk. The parameter $\gamma = \frac{1}{2}\left(\alpha c^{(1)}/c^{(2)} + \alpha^{-1}c^{(2)}/c^{(1)}\right)$ quantifies the contrast between the constituents impedance, where $\alpha = 1$ in the photonic case, and $\alpha = \rho^{(1)}/\rho^{(2)}$ in the phononic case, $\rho^{(p)}$ being the mass density. The frequency spectrum is obtained by solving Eq. (1) for values of k_B in the irreducible 1st Brillouin zone $0 \le k_B h \le \pi$. *Band-gaps* correspond to ranges of frequencies of attenuating waves, for which $|\eta| > 1$.

Upon defining the variables

$$\zeta^{(p)} \coloneqq \frac{\omega h^{(p)}}{c^{(p)}}, \tag{3}$$

one can write η as a doubly 2π-periodic function of $\zeta^{(1)}$ and $\zeta^{(2)}$, namely

$$\eta\left(\zeta^{(1)}, \zeta^{(2)};\, \gamma\right) \coloneqq \cos\zeta^{(1)}\cos\zeta^{(2)} - \gamma\sin\zeta^{(1)}\sin\zeta^{(2)}. \tag{4}$$

Fixing γ, we consider η as a function defined on a 2D torus of edge length 2π, characterized by the coordinates $\left\{\zeta^{(1)}, \zeta^{(2)}\right\}$. The absolute value $|\eta|$ is invariant under the transformations $\zeta^{(p)} \to \zeta^{(p)} + \pi$. This symmetry allows to make a further reduction, and fold the torus into a π-periodic torus; we denote the new torus by $\mathbb{T}$, and denote by $\mathbb{D}$ its subdomain where

*Corresponding author. Email: meshmuel@tx.technion.ac.il

$|\eta| > 1$, *i.e.*, where Eq. (1) is solved with imaginary k_B. We now interpret Eq. (3) as one which defines the following flow on $\mathbb{T}$

$$\vec{\zeta}(\omega) = \omega \cdot \left(\frac{h^{(1)}}{c^{(1)}}, \frac{h^{(2)}}{c^{(2)}} \right) \mod \pi, \tag{5}$$

where ω has the role of a time-like parameter. Band-gaps are identified with values of ω for which the flow $\vec{\zeta}(\omega)$ coincides with $\mathbb{D}$. We denote the lower and upper curves bounding $\mathbb{D}$ by $\mathcal{C}_l$ and $\mathcal{C}_u$, respectively. We find that $\eta = -1$ on these curves; plugging this value into Eq. (4) provides the following expressions for the curves

$$\zeta^{(2)} = \pi - \arccos \left[\frac{\cos \zeta^{(1)} \pm \gamma \sqrt{\gamma^2 - 1} \sin^2 \zeta^{(1)}}{1 + (\gamma^2 - 1) \sin^2 \zeta^{(1)}} \right], \tag{6}$$

where the upper (resp. lower) curve $\mathcal{C}_u$ (resp. $\mathcal{C}_l$), corresponds to the plus (resp. minus) sign in the numerator.

The direction of the flow on the torus is given by the ratio

$$a = \frac{h^{(2)}}{h^{(1)}} \frac{c^{(1)}}{c^{(2)}}. \tag{7}$$

The irrationality of the ratio, on account of the physical nature of the parameters involved, implies that the flow covers the torus ergodically, with a uniform measure. Using the ergodicity of the flow, we may replace spectral averages by averaging over the torus. Hence, the density of the gaps is simply the relative area of $\mathbb{D}$ in $\mathbb{T}$, which can be calculated via the integral of the *closed-form* expression

$$1 - \frac{2}{\pi^2} \int_0^\pi \mathcal{C}_l \mathrm{d}\zeta^{(1)}. \tag{8}$$

The widths of the gaps are investigated next. We recognize that these widths, which we denote by $\Delta\omega$, are related to lengths of intervals directed along the flow, which we denote by $\Delta\zeta$, whose endpoints lie on $\mathcal{C}_u$ and $\mathcal{C}_l$, via

$$\Delta\omega = \Delta\zeta \frac{\kappa^{(1)}}{\sqrt{1 + a^2}}, \tag{9}$$

where $\kappa^{(p)} = c^{(p)}/h^{(p)}$. We associate each length $\Delta\zeta$ with the parameters a and b which characterize the line equation of its corresponding flow interval

$$\zeta^{(2)} = a\zeta^{(1)} + b. \tag{10}$$

These observations, together with the derived expressions for the curves $\mathcal{C}_u$ and $\mathcal{C}_l$, enable determining the width of the gaps, and relating it to the physical and geometrical properties of the crystal. As the whole spectrum is encapsulated in the torus, we are able, in turn, to formulate optimization problems rigorously.

By way of example, consider the 1st gap, whose width maximization is of practical importance, being the one which is most often realized experimentally. We would like to know: given two materials, what is the microstructure which maximizes the 1st gap? The problem is interpreted as a search for an optimal $h^{(2)}/h^{(1)}$ at fixed $c^{(p)}$. Over the torus, the 1st gap is identified with the flow line emanating from the origin. Therefore, we seek the slope a which maximizes the right-hand side of Eq. (9), at $b = 0$.

References

[1] G. Shmuel and R. Band. Universality and optimality of band-gaps in laminated media *Submitted*, 2016.

[2] M. S. Kushwaha, P. Halevi, L. Dobrzynski, and B. Djafari-Rouhani. Acoustic band structure of periodic elastic composites. *Phys. Rev. Lett.*, 71(13): 2022–2025, 1993.

[3] P. Yeh, A. Yariv, and C.-S. Hong. Electromagnetic propagation in periodic stratified media. i. general theory. *J. Opt. Soc. Am.*, 67(4):423–438, 1977. 10.1364/JOSA.67.000423. URL http://www.osapublishing.org/abstract.cfm?URI=josa-67-4-423.

CONTROLLING BAND GAPS WITH GEOMETRY IN COMPOSITE ELASTIC META-STRUCTURES

Kathryn Matlack[1a)], Antonio Palermo[1,2], Sebastian Krödel[1], Anton Bauhofer[1], & Chiara Daraio [1]
[1]*Department of Mechanical and Process Engineering, ETH Zürich, Zürich, Switzerland*
[2]*Department of Civil, Chemical, Environmental and Materials Engineering - DICAM, University of Bologna, Bologna, Italy*

Summary Architected materials can obtain enhanced elastic wave propagation properties not found in natural materials, such as low frequency or broadband vibration and sound absorption. Recent research has shown that composite elastic meta-structures present a way of simultaneously obtaining wide band gaps at low frequencies, by using resonating elements to broaden and lower Bragg gaps. These meta-structures combine embedded particles and an architected lattice, and are fabricated with novel 3D printing techniques. We demonstrate how tuning the lattice geometry of these meta-structures can control locally resonant modes of the embedded particles to achieve wider band gaps at lower frequencies, while keeping the total mass constant.

BACKGROUND

Both phononic crystals and acoustic metamaterials have shown to be effective in controlling elastic wave propagation. Phononic crystals refer to materials characterized by some type of periodicity in e.g. material properties, geometry, or arrangement of components. These materials can form band gaps, induced by Bragg scattering mechanisms, at frequencies whose wavelengths are roughly equal to the unit cell dimension, such that low frequency band gaps require large structures, e.g. [1] and the references therein. Acoustic metamaterials are structures that include heavy masses and soft springs such that their resonant frequencies are low. As acoustic or elastic waves propagate through these metamaterials, the energy is transferred to the resonances, forming a low frequency but narrow band gap, e.g. [2-3]. In earlier work [4], we showed, both numerically and experimentally, that composite elastic meta-structures present a way to tune Bragg-induced band gaps with local resonances, to produce wide band gaps at low frequencies. This approach allows us to overcome the drawbacks of traditional phononic crystals and acoustic metamaterials. The current work further illustrates how the geometry can control the band gaps, by studying iso-mass meta-structure designs.

METHODS

The unit cell design consists of a polymeric lattice surrounding a locally resonant embedded steel cube particle. The lattice serves as both a structural support to the resonant particles and as a means to control the particle's resonant modes. The basic design is shown in Figure 1a, where periodicity is along the *x*-axis. Finite element modelling (FEM) with COMSOL is used to analyze the dispersion relation of the three-dimensional unit cell by means of periodic Bloch boundary conditions along the *x*-direction. The wavenumber is varied in the reciprocal space of the periodic dimension to extract the elastic modes of the meta-structure. A photograph of a 3D-printed six-unit cell meta-structure sample is shown in Figure 1b, and the fabrication process is described in [4]. The lattice geometry within the meta-structure is used to control the locally resonant modes of the steel particles and thus the center frequency and the width of the band gaps. To demonstrate the ability to tune the band gaps of the structure, we analyse three different meta-structure designs with the same number of beams connecting the steel particle to the surrounding exterior lattice and thus the same mass, see Figure 2.



(a) (b)

Figure 1: (a) Meta-structure unit cell with polycarbonate lattice (gray) and embedded steel particle (purple), with arrows indicating planes for corresponding cross sections in Figure 2. (b) 3D printed six-unit cell meta-structure.

RESULTS

We analyse the dispersion relation focusing on the longitudinal mode of the elastic meta-structure, shown in the mode shapes plotted at the band edge as indicated by the star points in the dispersion relations in Figure 2. For this mode the structure behaves as a 1D mass (the steel particle) and spring (surrounding lattice) system, where the spring stiffness stems from the stiffness of the beams acting under axial deformation (beams aligned along the *x*-axis) and bending deformation (beams aligned along the y and z axes). Since the collective stiffness of the longitudinal mode depends on location and

[a)] Corresponding author. Email: matlackk@ethz.ch

orientation of the individual beams with respect to the resonators, we can engineer the band gaps in the meta-structures by varying the positions and number of beams under axial and bending deformation. For example, the unit cell in Figure 2a contains 24 beams under axial loading and 48 beams under bending, while the unit cells in Figure 2b and 2c contain 8 beams under axial loading and 64 beams under bending deformation. These meta-structures have band gaps with center frequency and width of (a) 6442 Hz and 21%, (b) 6026 Hz and 36%, and (c) 5291 Hz and 51%, respectively. The lower and wider band gap in structure (b) compared to structure (a) results from decreasing the stiffness of the longitudinal mode by replacing 16 axially loaded beams with the same number of beams in bending deformation. The wider band gap in (c) compared to (b) stems from moving the beams along the *z*-axis from the edge to the center of the resonator, which lowers the stiffness of the flexural mode that is the lower bound of the band gap in (b).

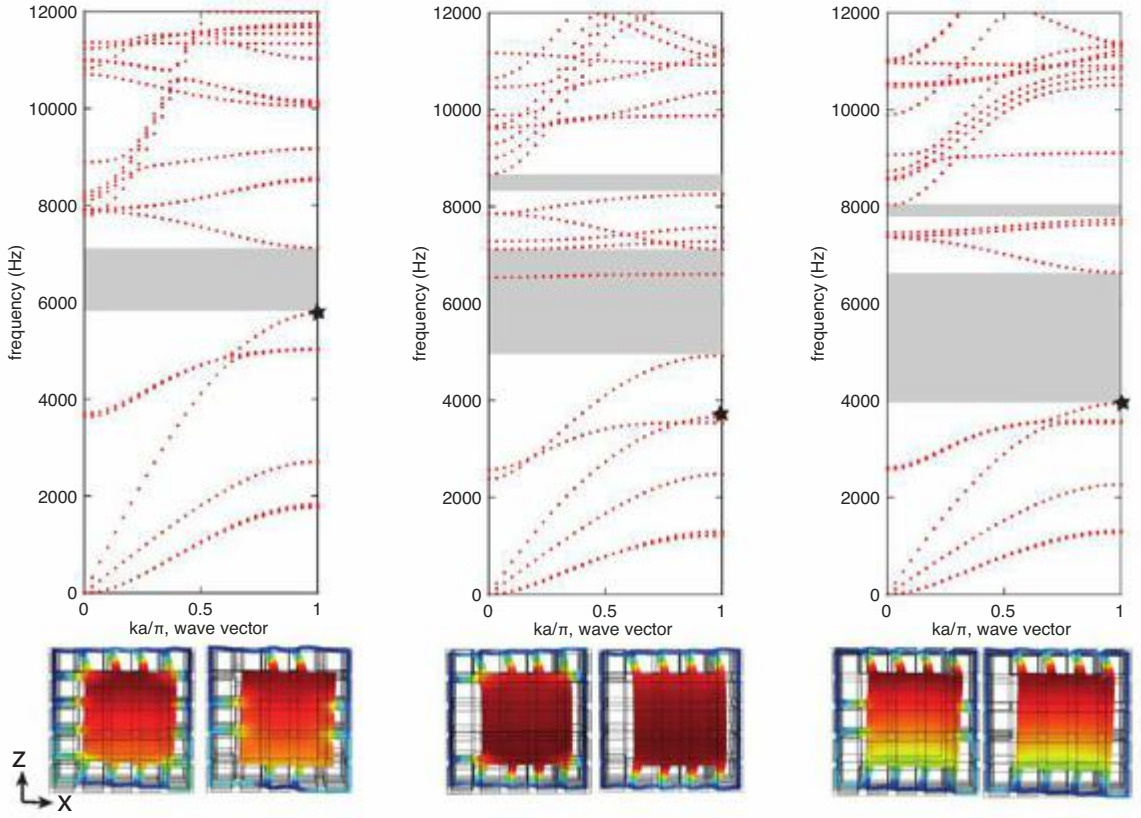

Figure 2: Dispersion curves of 3 iso-mass meta-structures with varying beam positions. Two cross sections (locations indicated in Figure 1a) of each design are plotted as normalized displacements of the longitudinal mode, and star data points indicate where the mode shape is calculated. Beams along the *y*-axis have the same configuration as those along the *z*-axis.

CONCLUSIONS

This work illustrates how tuning the lattice geometry in meta-structures can selectively control their band gap sizes and widths. While we have explored a cubic lattice geometry, there is a large design space of lattice geometries to explore for the design of meta-structures with potentially even wider band gaps at lower frequencies. This research informs the design of tailored materials that can effectively control elastic wave propagation, with applications in vibration immune structural components, robust and lightweight sound absorbers for buildings, and protection of MEMS devices from harmful impacts.

ACKNOWLEDGEMENTS

This work was partially supported by an ETH Postdoctoral Fellowship to the first author.

References

[1] Hussein M.I., Leamy M.J., Ruzzene M.: Dynamics of Phononic Materials and Structures: Historical Origins, Recent Progress and Future Outlook. *Applied Mechanics Review*, **66**(4):040802, 2014.

[2] Liu Z., et al.: Locally resonant sonic materials. *Science* **289**(5485):1734-1736, 2000.

[3] Fang N,. et al.:Ultrasonic metamaterials with negative modulus. *Nature Materials,* **5**(6):452–6, 2006.

[4] Matlack K., et. al: Composite 3D-printed meta-structures for low frequency and broadband vibration absorption. arXiv:1511.09465 [cond-mat.mtrl-sci].

ON THE RELATION BETWEEN GENERALIZED STRESS THEORY AND ELECTRODYNAMICS

Reuven Segev *[1]

[1]*Mechanical Engineering, Ben-Gurion University of the Negev, Beer-Sheva, Israel*

Summary A mathematical formulation of continuum mechanics is proposed which includes an extension of the basic equations of electrodynamics as a special case. In the continuum mechanics context, we present a weak Eulerian formulation of the fundamentals of continuum mechanics on differentiable manifolds. Forces and stresses are considered in the framework of the theory of de Rham currents and some extensions thereof. In particular, stresses maybe as irregular as Borel measures. Considering generalized velocities represented by differential forms and interpreting such a form as generalized potential field, we present a weak formulation of pre-metric, p-form electrodynamics as a natural example of the foregoing theory in which the current density may be the distributional derivative of a measure. Finally, it is shown that the assumptions leading to p-form electrodynamics may be replaced by the condition that the force functional is continuous with respect to the flat topology.

INTRODUCTION

In this work we propose a general setting of continuum mechanics which includes an extension of the basic equations of electrodynamic, a generalization of Maxwell's equations, as a special case.

Stress theory of continuum mechanics is formulated here from a Eulerian approach, that is, without any reference to material points and a material body. Allowing growth, the basic notion considered is a virtual velocity field which is a differentiable vector valued field in an n-dimensional physical space that vanishes outside a compact subset. The nature of the particular vector or tensor field depends on the particular physical theory considered. The physical space, which may also be interpreted as space-time, is described by an n-dimensional differentiable manifold. Neither a metric structure nor a connection are assumed on the space manifold. A generalized force is defined to be a linear functional on the space of virtual velocity fields which is continuous relative to the C^1-topology. Thus, a force is a vector valued distribution of order one on a manifold. This implies mathematically that there are measures valued in a specified vector bundle, stresses, that represent a force non-uniquely through an analog of Cauchy's formula and the principle of virtual work.

For the case of electrodynamics, the vector fields under consideration are completely antisymmetric tensor fields of order p that generalize the four-dimensional vector potential of the standard theory. The resulting theory extends the formulation of Maxwell's equations for four dimensional spacetime to p-form electrodynamics (see [1]) in any dimension. The equations are independent of any Riemannian or semi-Riemannian metric and allow current density fields that can be as irregular as the distributional derivatives of measures.

AN EXAMPLE

In this section, we present, as an example, the simplest relation between stress theory in continuum mechanics and a restricted version of Maxwell's equations. We recall that for classical continuum mechanics, one assumes that the forces on a body $\mathscr{R} \subset \mathbb{R}^3$ are given in terms of a vector field $\mathbf{b}$ defined in the physical space and a surface force $\mathbf{t}_{\mathscr{R}}$ defined on the boundary $\partial\mathscr{R}$ of $\mathscr{R}$. The virtual power of the forces on $\mathscr{R}$ for a virtual velocity field w is given by

$$P_{\mathscr{R}} = \int_{\mathscr{R}} \mathbf{b} \cdot w \, \mathrm{d}V + \int_{\partial\mathscr{R}} \mathbf{t}_{\mathscr{R}} \cdot w \, \mathrm{d}A. \tag{1}$$

It is further recalled that if the dependence of $\mathbf{t}_{\mathscr{R}}$ on the body $\mathscr{R}$ satisfies Cauchy's postulates, then, there is a 3×3 tensor field, the Cauchy stress field σ, such that $\mathbf{t}_{\mathscr{R}}(x) = \sigma(x)(\mathbf{n}(x))$ where $\mathbf{n}(x)$ is the outwards pointing normal to the boundary of $\mathscr{R}$ at $x \in \partial\mathscr{R}$. Thus, one has

$$P_{\mathscr{R}} = \int_{\mathscr{R}} \mathbf{b} \cdot w \, \mathrm{d}V + \int_{\partial\mathscr{R}} \sigma^{\mathsf{T}}(w) \cdot \mathbf{n} \, \mathrm{d}A \tag{2}$$

where the standard definition of the transpose has been used.

It is also noted that balance of moment of momentum implies traditionally that the stress tensor σ is symmetric. However, we want to examine the case where σ is skew symmetric. In this case, using the Levi-Civita symbol, we may define a vector field $\mathfrak{g}$ whose components are given by

$$\mathfrak{g}_p = \frac{1}{2}\varepsilon_{pjk}\sigma_{jk}, \tag{3}$$

*Corresponding author. Email: rsegev@bgu.ac.il

such that $\sigma^{\mathsf{T}}(w) = \mathfrak{g} \times w$. Thus, assuming that $\mathbf{b} = 0$, one has

$$P_{\mathscr{R}} = \int_{\partial \mathscr{R}} (\mathfrak{g} \times w) \cdot \mathbf{n} \, \mathrm{d}A. \tag{4}$$

Using Gauss's theorem and the identity $\nabla \cdot (\mathfrak{g} \times w) = (\nabla \times \mathfrak{g}) \cdot w - \mathfrak{g} \cdot (\nabla \times w)$, we have

$$P_{\mathscr{R}} = \int_{\mathscr{R}} (\nabla \times \mathfrak{g}) \cdot w \, \mathrm{d}V - \int_{\mathscr{R}} \mathfrak{g} \cdot (\nabla \times w) \, \mathrm{d}V. \tag{5}$$

Setting

$$\mathfrak{F} = \nabla \times \mathfrak{g}, \qquad \mathfrak{f} = \nabla \times w, \tag{6}$$

so that

$$\nabla \cdot \mathfrak{F} = 0, \qquad \nabla \cdot \mathfrak{f} = 0, \tag{7}$$

the power may be written in the form

$$P_{\mathscr{R}} = \int_{\mathscr{R}} \mathfrak{F} \cdot w \, \mathrm{d}V - \int_{\mathscr{R}} \mathfrak{g} \cdot \mathfrak{f} \, \mathrm{d}V. \tag{8}$$

We finally observe that in case we interpret w as the vector potential of magneto-statics, interpret $\mathfrak{g}$ as the magnetic field intensity, interpret $\mathfrak{f}$ as the magnetic field and interpret $\mathfrak{F}$ as the current density, Equations (6, 7) are simply the restriction of Maxwell's equations to magneto-statics.

ON THE MATHEMATICAL SETTING

The mathematical framework uses the theory of de Rham currents as in [2], and generalized sections of vector bundles (see [3]). We consider a vector bundle $\pi : W \to \mathcal{S}$ over the space or space-time manifold $\mathcal{S}$. Virtual velocity fields are differentiable sections of W having compact supports and so the set of virtual velocities is a topological vector space denoted as $C_0^1(W)$. Generalized forces are elements of the dual space $C_0^1(W)^*$ and their actions on virtual displacements are interpreted as producing virtual power. It is also convenient to view forces as elements of $C^{-1}\big(W^* \otimes \bigwedge^n T^*\mathcal{S}\big)$—currents of order one valued in the vector bundle $W^* \otimes \bigwedge^n T^*\mathcal{S}$. This is a special case of defining vector valued p-currents of order r as elements of $C^{-r}(W^* \otimes \bigwedge^{n-p} T^*\mathcal{S}) := C_0^r\big(W \otimes \bigwedge^p T^*\mathcal{S}\big)^*$. Forces are shown to be represented by elements $S \in C_0^0(J^1W)^* = C^{-0}\big((J^1W)^* \otimes \bigwedge^n T^*\mathcal{S}\big)$, to which we refer as variational stress measures, through the principle of virtual work $F(w) = S(j^1 w)$. Here, J^1W is the jet bundle of W and j^1 is the jet extension mapping. A variational stress measure induces a unique element $\sigma = p_\sigma(S) \in C^{-0}\big(W^* \otimes \bigwedge^{n-1} T^*\mathcal{S}\big)$ to which we refer as a traction stress. Surface forces result from composing σ with the restriction of $(n-1)$-forms to the boundaries of regions. In addition, defining a general divergence operator $\partial\mathrm{iv}$ with $\partial\mathrm{iv}\, S \in C^{-0}\big(W^* \otimes \bigwedge^n T^*\mathcal{S}\big)$, and setting $\mathbf{b} = -\partial\mathrm{iv}\, S$ as the induced body force, we obtain the principle of virtual work in a form analogous to the traditional one.

The generalization of Maxwell's equations is obtained when one takes the vector bundle W to be the vector bundle of p-forms $\bigwedge^p T^*\mathcal{S}$ and setting $\mathbf{b} = 0$. The main assumption is that the traction stress is given in terms of a $(p+1)$-current of order zero $g \in C^{-0}\big(\bigwedge^{n-p-1} T^*\mathcal{S}\big) = C_0^0\big(\bigwedge^{p+1} T^*\mathcal{S}\big)^*$ so that for each test p-form α, the one-current $\sigma \cdot \alpha$ is given by

$$(\sigma \cdot \alpha)(\varphi) = g(\alpha \wedge \varphi) = \int g \wedge \alpha \wedge \varphi \tag{9}$$

for each test 1-form φ. Finally, it is shown that the last assumption may be replaced by the requirement that the force functional is continuous with respect to the flat topology on the space of differential forms (see [4]). It is noted that this topology is sensitive only the exterior derivative of a form and not the whole jet.

For further details, see [5].

References

[1] Henneaux M., Teitelboim C.: p-Form Electrodynamics. Found. Phys., 16:593–613, 1986

[2] de Rham G.: Differentiable Manifolds. Springer, 1984.

[3] Guillemin V., Sternberg S.: Geometric Asymptotics. American Mathematical Society, 1977.

[4] Federer H.: Geometric Measure Theory, Springer, 1969.

[5] Segev R.: Continuum Mechanics, Stresses, Currents and Electrodynamics. Phil. Trans. R. Soc. A, Accepted, 2015.

SWELLING INDUCED BURST IN HYPERELASTIC SPHERES AND CYLINDERS

Thomas J. Pence*[1] and Vahid Zamani[1]
[1]*Department of Mechanical Engineering, Michigan State University, East Lansing, MI, USA*

Summary The conventional theory of hyperelasticity is easily generalized to include a swelling effect. The resulting theory can be viewed as giving a finite strain version of the well known eigenstrain problem in linear elasticity. We use this theory to study an abrupt inflation instability in pressurized shells. At fixed pressure, a slowly changing amount of swelling can suddenly cause a finite jump in the shell radius.

HYPERELASTIC MODEL WITH SWELLING

Material swelling in highly elastic materials can occur by a variety of mechanisms, perhaps the most common of which is fluid absorption. In such a case, if a comprehensive study of the absorption phenomenon is itself of primary interest – such as how the fluid is transported within the otherwise solid material and on what timescales steady state distributions are obtained – then it is typically necessary to pursue a relatively detailed poroelastic development. If, however, the mechanical consequences of otherwise known fluid distributions are of primary interest, then it is useful to consider more direct treatments in which the swelling is regarded as a specified field quantity, i.e., $v = v(\mathbf{X})$ where $\mathbf{X}$ are locations in the chosen reference configuration.

Such treatments need not be tied to a particular swelling mechanism. Indeed, classical eigenstrain analysis procedures in linear elasticity can be viewed in this light, where the eigenstrains are stress-free strains that may arise from a variety of causes. Such concepts then generalize to the large strain setting [7] where they can lead to a variety of interesting mechanical deformation modes (flexure [2], torsion [6]) and instability phenomena (e.g., cavitation [5], microchannel formation [4]). Processes of biomechanical growth, while enormously more complicated than a simple fluid induced swelling, can also be modeled by a similar framework [3].

Let $\mathbf{x} = \chi(\mathbf{X})$ denote locations in the deformed configuration and let $\mathbf{F} = \partial\mathbf{x}/\partial\mathbf{X}$ be the deformation gradient tensor. The swelling is described in terms of the volume constraint $det\mathbf{F} = v$ which is an obvious generalization of the conventional incompressible theory. In conventional isotropic incompressible hyperelasticity, i.e., the theory with no swelling, the material constitutive behavior is specified by means of the stored energy density $W = W(I_1, I_2)$ where I_1 and I_2 are the usual invariants of $\mathbf{C} = \mathbf{F}^T\mathbf{F}$. In the most straight forward generalization so as to include the effect of swelling the stored energy will also depend upon v so that $W = W(I_1, I_2, v)$. The Cauchy stress tensor continues to have a hydrostatic pressure p, but now it is associated with the more general swelling constraint. Forms for W can be considered such that W reduces to standard models from the conventional incompressible theory when $v = 1$. Here we focus attention on a constitutive model that generalizes the well known Mooney-Rivlin model, namely

$$W(I_1, I_2, v) = A_1\Big(I_1 \circ\ 3v^{2/3}\Big) + A_2\Big(I_2 \circ\ 3v^{4/3}\Big) \tag{1}$$

where $A_1 = A_1(v) \geq 0$, $A_2 = A_2(v) \geq 0$ and $A_1 + A_2 > 0$.

ABRUPT EXPANSION OF A SPHERICAL SHELL

Consider a sphere with outer and inner radii $R_o > R_i > 0$ prior to any loading or swelling. Spherical symmetry will hold for simple pressure boundary conditions and a radially symmetric swelling field $v = v(R)$. Employing (R, Θ, Φ) and (r, θ, ϕ) for the reference and deformed spherical geometry coordinates, the deformation is then described by $r = r(R), \theta = \Theta$ and $\phi = \Phi$. The volume constraint becomes $v = det\mathbf{F} = r'r^2/R^2$, which gives integrals

$$r^3 = r_i^3 + 3\int_{R_i}^{R} v(R)R^2dR, \quad \text{and in particular} \quad r_o^3 = r_i^3 + 3\int_{R_i}^{R_o} v(R)R^2dR,$$

using $r_i = r(R_i)$ and $r_o = r(R_o)$. Consequently, for any swelling field $v(R)$, the unknown function of radial expansion $r = r(R)$ is completely determined by the mapping $R_i \to r_i$.

In the absence of swelling ($v \equiv 1$) problems of this kind have a long history in the hyperelasticity literature, and elegant treatment methods are described in [1]. These methods are easily generalized for the case of uniform swelling, i.e., $v(R)$ a positive constant. In this uniform swelling case, and taking the stored energy W to be given by (1), one is led to the following relation between the amount of swelling v, the pressure difference $\Delta P = P_i \circ\ P_o$, and the deformed inner radius location r_i:

*Corresponding author. Email: pence@egr.msu.edu

$$\Delta P = \int_{r_i/R_i}^{r_o/R_o} \frac{4}{v \circ s^3}\left[A_1(v)\left(s \circ \frac{v^2}{s^5}\right) + A_2(v)\left(s^3 \circ \frac{v^2}{s^3}\right)\right] ds, \quad \text{where} \quad r_o^3 = r_i^3 + v(R_o^3 \circ R_i^3).$$

In order to illustrate, take $A_1(v)$ and $A_2(v)$ in (1) to be

$$A_1(v) = \tfrac{1}{2}\mu\alpha v^{a_1} \qquad \text{and} \qquad A_2(v) = \tfrac{1}{2}\mu(1 \circ \alpha)v^{a_2}, \tag{2}$$

where $0 \leq \alpha \leq 1$. Then $\mu > 0$ is the infinitesimal shear modulus in the absence of swelling. Taking specific and reasonable parameter choices for the sphere's undeformed geometry in terms of R_i/R_o and the material constitutive parameters (α, a_1, a_2), the left figure shows the inflation graph (normalized pressurization ΔP vs. normalized radius r_i) at three values of v. For no swelling ($v = 1$) the graph is monotonically increasing and, as expected, gives $r_i = R_i$ when $\Delta P = 0$. Keeping $\Delta P = 0$ and increasing v then shows a small increase in r_i. At a moderately higher pressure, because the inflation graphs have started to move apart, increasing v causes the radius to increase somewhat more rapidly with v. This increase remains smooth for relatively small values of pressurization. However, as we describe in the paragraph after the figure, because the inflation graphs exhibit a transition from monotonic to nonmonotonic as v increases, it follows that swelling alone can cause an abrupt change in the shell radius when ΔP is sufficiently large.

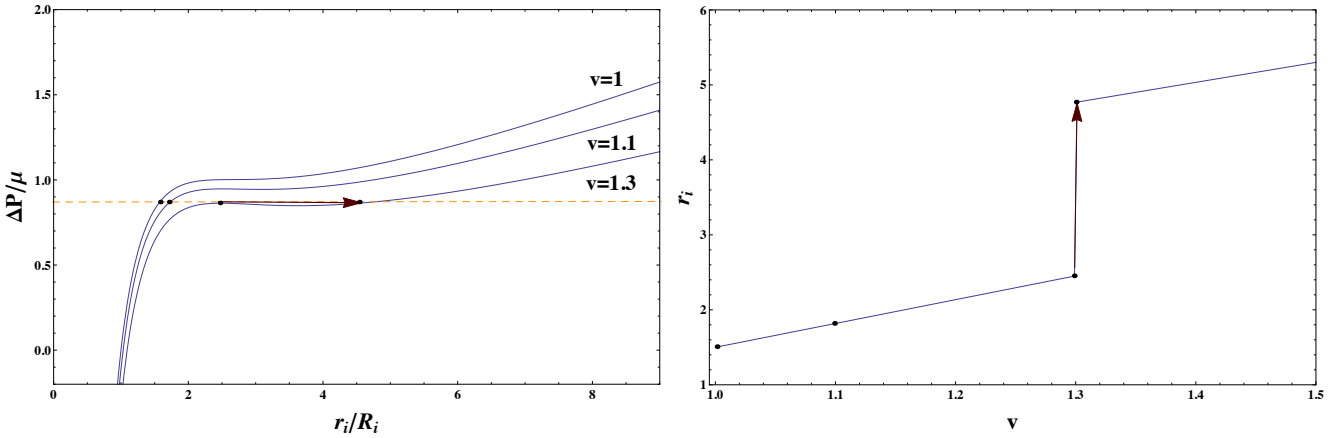

Figure 1: Swelling induced burst due to a uniform increase in swelling. In this example: $R_o = 2R_i$, $\alpha = 0.85$, $a_1 = 0$, and $a_2 = -4/3$. At fixed pressure $\Delta P/\mu = 0.86$ there is an abrupt jump in r_i as v passes through the value $v = 1.3$.

The example in the figure corresponds to a pressurization ΔP that, first of all, slowly increases from 0 to 0.86μ before there is any swelling ($v = 1$). This results in r_i/R_i increasing smoothly from 1 to 1.6 on the $v = 1$ graph. Now holding $\Delta P/\mu = 0.86$ let v increase (dashed orange line on left). Then r_i will first increase smoothly with v. However, because of the eventual loss of monotonicity in the inflation graphs, r_i is unable to increase smoothly with v when v reaches the value 1.3. The form of the inflation graph at $v = 1.3$ causes an abrupt change in the value of r_i, as indicated by the arrows in each panel. In this example, because the inflation graph for $v = 1.3$ has a second increasing branch, the inflation is able to once again proceed smoothly by following the associated second branch curves on the various inflation graphs for $v > 1.3$. However, if W depends upon v in ways other than indicated by (1) and (2) then more intricate types of jumping phenomena may arise.

ACKNOWLEDGMENT

This work was supported in part by NPRP grant no. 4-1333-1-214 from the Qatar National Research Fund (a member of Qatar Foundation). The statements made herein are solely the responsibility of the authors.

References

[1] Carroll M. M.: Pressure maximum behavior in inflation of incompressible elastic hollow spheres and cylinders. Quarterly of Applied Mathematics 45.1: 141-154, 1987.
[2] Tsai H., Pence T.J., Kirkinis E.: Swelling induced finite strain flexure in a rectangular block of an isotropic elastic material, J. Elasticity 75: 69-89, 2004.
[3] Amar M. B., Goriely A.: Growth and instability in elastic tissues. Journal of the Mechanics and Physics of Solids 53(10), 2284-2319, 2005.
[4] Pence T. J., Tsai H.: Swelling-induced microchannel formation in nonlinear elasticity. IMA Journal of Applied Mathematics 70.1: 173-189, 2005.
[5] Pence T. J., Tsai H.: Swelling-induced cavitation of elastic spheres. Mathematics and mechanics of solids 11.5: 527-551, 2006.
[6] Demirkoparan H., Pence T.J.: Torsional swelling of a hyperelastic tube with helically wound reinforcement. Journal of Elasticity 92: 61-90, 2008
[7] Yavari A., Goriely A.: Nonlinear elastic inclusions in isotropic solids. Proc. Royal Soc. London, A 469: 20130415

REMARKS ON ISOTROPIC EXTENSION OF ANISOTROPIC CONSTITUTIVE FUNCTIONS VIA STRUCTURAL TENSORS

Chi-Sing Man*
Department of Mathematics, University of Kentucky, Lexington, KY 40506-0027, USA

Summary In their original formulation of the method of isotropic extension via structural tensors, which is meant for applications to the derivation of coordinate-free representation formulas for anisotropic constitutive functions, both Boehler and Liu started with the assumption (*) that the invariant group of structural tensors is the symmetry group that defines the anisotropy of the constitutive function in question. As a result, the method (with structural tensors of order not higher than two) is applicable only when the anisotropy is characterized by a cylindrical group or belongs to the triclinic, monoclinic, or rhombic crystal classes. In this talk we present a reformulation of the method in which assumption (*) is relaxed and show by examples in anisotropic linear and finite elasticity that the method of isotropic extension via structural tensors could be applicable beyond the original limitations.

INTRODUCTION

To derive coordinate-free representation formulas for anisotropic constitutive functions, Boehler [1] and Liu [2] independently proposed the same method that appeals to the general representation theorems for isotropic tensor functions [3, 4] available. As illustration, let us consider the class $\mathcal{A}$ of second-order-tensor-valued anisotropic constitutive functions $\boldsymbol{S}(\overset{\ominus}{\boldsymbol{v}}, \overset{\ominus}{\boldsymbol{A}})$, where $\overset{\ominus}{\boldsymbol{v}} := (\boldsymbol{v}_1, ..., \boldsymbol{v}_p)$, $\overset{\ominus}{\boldsymbol{A}} := (\boldsymbol{A}_1, ..., \boldsymbol{A}_q)$, $\boldsymbol{v}_i$ $(i = 1, ..., p)$ are vectors, and $\boldsymbol{A}_j$ $(j = 1, ..., q)$ are second-order tensors. Let O(3) denote the group of orthogonal transformations on V, the translation space of the 3-dimensional physical space. For $\boldsymbol{Q} \in$ O(3) let

$$\boldsymbol{Q}\overset{\ominus}{\boldsymbol{v}} := (\boldsymbol{Q}\boldsymbol{v}_1, ..., \boldsymbol{Q}\boldsymbol{v}_p), \qquad \boldsymbol{Q}\overset{\ominus}{\boldsymbol{A}}\boldsymbol{Q}^T := (\boldsymbol{Q}\boldsymbol{A}_1\boldsymbol{Q}^T, ..., \boldsymbol{Q}\boldsymbol{A}_q\boldsymbol{Q}^T). \tag{1}$$

Let the anisotropy of tensor functions $\boldsymbol{S}(\overset{\ominus}{\boldsymbol{v}}, \overset{\ominus}{\boldsymbol{A}})$ be characterized by a subgroup $\mathcal{G}$ of O(3), i.e. $\boldsymbol{S}$ satisfies

$$\boldsymbol{Q}\boldsymbol{S}(\overset{\ominus}{\boldsymbol{v}}, \overset{\ominus}{\boldsymbol{A}})\boldsymbol{Q}^T = \boldsymbol{S}(\boldsymbol{Q}\overset{\ominus}{\boldsymbol{v}}, \boldsymbol{Q}\overset{\ominus}{\boldsymbol{A}}\boldsymbol{Q}^T) \qquad \text{for each } \boldsymbol{Q} \in \mathcal{G}. \tag{2}$$

The method that Boehler [1] and Liu [2] proposed is to seek (i) a set of "structural tensors" (say, $\overset{\oplus}{\boldsymbol{m}} := (\boldsymbol{m}_1, ..., \boldsymbol{m}_r)$, $\overset{\ominus}{\boldsymbol{M}} := (\boldsymbol{M}_1, ..., \boldsymbol{M}_s)$, where $\boldsymbol{m}_k$ $(k = 1, ..., r)$ are unit vectors and $\boldsymbol{M}_l$ $(l = 1, ..., s)$ are second-order tensors) which characterize the anisotropy of the class $\mathcal{A}$ in the sense that

$$\mathcal{G} = \{\boldsymbol{Q} \in \text{O(3)} : \boldsymbol{Q}\overset{\oplus}{\boldsymbol{m}} = \overset{\oplus}{\boldsymbol{m}}, \boldsymbol{Q}\overset{\ominus}{\boldsymbol{M}}\boldsymbol{Q}^T = \overset{\ominus}{\boldsymbol{M}}\}, \tag{3}$$

and (ii) a class Ext of constitutive functions $\hat{\boldsymbol{S}}(\overset{\ominus}{\boldsymbol{v}}, \overset{\ominus}{\boldsymbol{A}}, \overset{\oplus}{\boldsymbol{m}}, \overset{\ominus}{\boldsymbol{M}})$ such that for each $\boldsymbol{S} \in \mathcal{A}$, there is an $\hat{\boldsymbol{S}} \in$ Ext which satisfies

$$\boldsymbol{S}(\overset{\ominus}{\boldsymbol{v}}, \overset{\ominus}{\boldsymbol{A}}) = \hat{\boldsymbol{S}}(\overset{\ominus}{\boldsymbol{v}}, \overset{\ominus}{\boldsymbol{A}}, \overset{\oplus}{\boldsymbol{m}}, \overset{\ominus}{\boldsymbol{M}}) \tag{4}$$

for each $(\overset{\ominus}{\boldsymbol{v}}, \overset{\ominus}{\boldsymbol{A}})$ in the domain of $\boldsymbol{S}$. As pointed out by Boehler, material frame-indifference requires that the function $\hat{\boldsymbol{S}}$ be isotropic, i.e., $\hat{\boldsymbol{S}}$ satisfies

$$\boldsymbol{Q}\hat{\boldsymbol{S}}(\overset{\ominus}{\boldsymbol{v}}, \overset{\ominus}{\boldsymbol{A}}, \overset{\oplus}{\boldsymbol{m}}, \overset{\ominus}{\boldsymbol{M}})\boldsymbol{Q}^T = \hat{\boldsymbol{S}}(\boldsymbol{Q}\overset{\ominus}{\boldsymbol{v}}, \boldsymbol{Q}\overset{\ominus}{\boldsymbol{A}}\boldsymbol{Q}^T, \boldsymbol{Q}\overset{\oplus}{\boldsymbol{m}}, \boldsymbol{Q}\overset{\ominus}{\boldsymbol{M}}\boldsymbol{Q}^T) \qquad \text{for each } \boldsymbol{Q} \in \text{O(3)}. \tag{5}$$

Then we may appeal to representation theorems for isotropic functions to obtain a representation formula for $\hat{\boldsymbol{S}}$ and, *a fortiori*, for the anisotropic $\boldsymbol{S}$. Moreover, it follows immediately from (3), (4) and (5) that the constitutive function $\boldsymbol{S}$, as given by (4), satisfies (2). What we have outlined above is the method of isotropic extension of anisotropic constitution functions via structural tensors as formulated by Boehler and by Liu.

The method of Boehler and Liu, however, has its limitations. Liu [2] remarked that "[o]bviously, not every anisotropic material can be specified by symmetry group of the type" (3), but he did not elaborate on what to him might have seemed obvious. Later in the same paper he gave a list ("which does not mean to be exhaustive") of groups $\mathcal{G} \subset$ O(3) that are characterized by some set $\{\overset{\oplus}{\boldsymbol{m}}, \overset{\ominus}{\boldsymbol{M}}\}$ of structural tensors in the sense specified by (3). Besides transverse isotropy, Liu's list includes groups pertaining to crystal classes in the triclinic, monoclinic, and rhombic systems. More recently, Xiao et al. [5] proved that "any number of vectors and second order tensors can merely characterize and represent one of the cylindrical groups and the triclinic, monoclinic, rhombic crystal classes."

*Corresponding author. Email: cman@uky.edu

REFORMULATION OF THE METHOD

We contend that the aforementioned limitations of the method of isotropic extension via structural tensors arise from an oversight in the original formulation of Boehler and of Liu. Given a symmetry group $\mathcal{G} \subset \mathrm{O}(3)$ defined by the constitutive function $\boldsymbol{S}$ through (2), the crucial requirement for the method of isotropic extension to work is that the extended function $\hat{\boldsymbol{S}}(\overset{\ominus}{\boldsymbol{v}}, \overset{\ominus}{\boldsymbol{A}}, \overset{\ominus}{\boldsymbol{m}}, \overset{\ominus}{\boldsymbol{M}})$ satisfies

$$\hat{\boldsymbol{S}}(\overset{\ominus}{\boldsymbol{v}}, \overset{\ominus}{\boldsymbol{A}}, \boldsymbol{Q}\boldsymbol{m}_1, \cdots, \boldsymbol{Q}\boldsymbol{m}_r, \boldsymbol{Q}\boldsymbol{M}_1\boldsymbol{Q}^T, \cdots \boldsymbol{Q}\boldsymbol{M}_s\boldsymbol{Q}^T) = \hat{\boldsymbol{S}}(\overset{\ominus}{\boldsymbol{v}}, \overset{\ominus}{\boldsymbol{A}}, \boldsymbol{m}_1, \cdots \boldsymbol{m}_r, \boldsymbol{M}_1, \cdots, \boldsymbol{M}_s) \tag{6}$$

for each $(\overset{\ominus}{\boldsymbol{v}}, \overset{\ominus}{\boldsymbol{A}})$ in the domain of $\boldsymbol{S}$ and for each $\boldsymbol{Q} \in \mathcal{G}$. While the assumption (3) that $\mathcal{G}$ be "the invariance group of the structural tensors" [6] is certainly sufficient for (6) to be valid, it is far from necessary. For example, (6) will remain valid if $\hat{\boldsymbol{S}}$ is symmetric in the variables $\boldsymbol{m}_k$ $(k = 1, \cdots, r)$ and in $\boldsymbol{M}_l$ $(l = 1, \cdots, s)$ and if each $\boldsymbol{Q} \in \mathcal{G}$ leads only to a permutation of the $\boldsymbol{m}_k$'s and $\boldsymbol{M}_l$'s. As illustrated by the following example, once requirement (3) is relaxed, it may become possible to represent anisotropic constitutive functions, beyond the classes indicated by Xiao et al. [5], by the method of isotropic extension (with structural tensors of order not higher than two).

A Simple Example

Let a Cartesian coordinate system with orthonormal basis $\boldsymbol{e}_i$ $(i = 1, 2, 3)$ be chosen. Let $\boldsymbol{R}(\boldsymbol{n}, \omega)$ denote the rotation of angle ω about the unit vector $\boldsymbol{n}$. Consider a tetragonal linearly-elastic material, the symmetry group of which is $\mathcal{G} = D_4$ with generators $\boldsymbol{R}(\boldsymbol{e}_3, \pi/2)$, $\boldsymbol{R}(\boldsymbol{e}_2, \pi)$. Let $\boldsymbol{T} = \boldsymbol{T}(\boldsymbol{E})$, where $\boldsymbol{T}$ is the Cauchy stress and $\boldsymbol{E}$ the infinitesimal strain, be the stress-strain relation of the anisotropic material.

What follows is an isotropic extension of $\boldsymbol{T}(\boldsymbol{E})$ with three structural tensors $\boldsymbol{M}_1 := \boldsymbol{e}_1 \otimes \boldsymbol{e}_1$, $\boldsymbol{M}_2 := \boldsymbol{e}_2 \otimes \boldsymbol{e}_2$, and $\boldsymbol{M}_3 := \boldsymbol{e}_3 \otimes \boldsymbol{e}_3$:

$$\begin{aligned}
\boldsymbol{T}(\boldsymbol{E}) &= \hat{\boldsymbol{T}}(\boldsymbol{E}, \boldsymbol{M}_1, \boldsymbol{M}_2, \boldsymbol{M}_3) \\
&:= \big(\alpha_1 \mathrm{tr}(\boldsymbol{M}_1\boldsymbol{E}) + \alpha_2 \mathrm{tr}(\boldsymbol{M}_2\boldsymbol{E}) + \alpha_3 \mathrm{tr}(\boldsymbol{M}_3\boldsymbol{E})\big)\boldsymbol{M}_1 \\
&\quad + \big(\alpha_2 \mathrm{tr}(\boldsymbol{M}_1\boldsymbol{E}) + \alpha_1 \mathrm{tr}(\boldsymbol{M}_2\boldsymbol{E}) + \alpha_3 \mathrm{tr}(\boldsymbol{M}_3\boldsymbol{E})\big)\boldsymbol{M}_2 \\
&\quad + \big(\alpha_3 (\mathrm{tr}(\boldsymbol{M}_1\boldsymbol{E}) + \alpha_3 \mathrm{tr}(\boldsymbol{M}_2\boldsymbol{E})) + \alpha_4 \mathrm{tr}(\boldsymbol{M}_3\boldsymbol{E})\big)\boldsymbol{M}_3 \\
&\quad + \alpha_5\big((\boldsymbol{M}_1 + \boldsymbol{M}_2)\boldsymbol{E} + \boldsymbol{E}(\boldsymbol{M}_1 + \boldsymbol{M}_2)\big) + \alpha_6\big(\boldsymbol{M}_3\boldsymbol{E} + \boldsymbol{E}\boldsymbol{M}_3\big),
\end{aligned} \tag{7}$$

where α_i $(i = 1, 2, \cdots, 6)$ are undetermined elastic constants. Note that $\hat{\boldsymbol{T}}$ is symmetric in $\boldsymbol{M}_1$ and $\boldsymbol{M}_2$, i.e. it satisfies $\hat{\boldsymbol{T}}(\boldsymbol{E}, \boldsymbol{M}_1, \boldsymbol{M}_2, \boldsymbol{M}_3) = \hat{\boldsymbol{T}}(\boldsymbol{E}, \boldsymbol{M}_2, \boldsymbol{M}_1, \boldsymbol{M}_3)$. It is straightforward to verify that the function $\hat{\boldsymbol{T}}(\boldsymbol{E}, \boldsymbol{M}_1, \boldsymbol{M}_2, \boldsymbol{M}_3)$ is isotropic and

$$\hat{\boldsymbol{T}}(\boldsymbol{E}, \boldsymbol{Q}\boldsymbol{M}_1\boldsymbol{Q}^T, \boldsymbol{Q}\boldsymbol{M}_2\boldsymbol{Q}^T, \boldsymbol{Q}\boldsymbol{M}_3\boldsymbol{Q}^T) = \hat{\boldsymbol{T}}(\boldsymbol{E}, \boldsymbol{M}_1, \boldsymbol{M}_2, \boldsymbol{M}_3) \qquad \text{for each } \boldsymbol{Q} \in \mathcal{G}, \tag{8}$$

which together with $(7)_1$ imply that

$$\boldsymbol{T}(\boldsymbol{Q}\boldsymbol{E}\boldsymbol{Q}^T) = \boldsymbol{Q}\boldsymbol{T}(\boldsymbol{E})\boldsymbol{Q}^T \qquad \text{for each } \boldsymbol{Q} \in \mathcal{G}. \tag{9}$$

Moreover, by rewriting (7) in matrix form under the Kelvin notation [7], it is clear that every constitutive function $\boldsymbol{T}$ that satisfies (9) has an isotropic extension $\hat{\boldsymbol{T}}$ given by (7). Hence $\hat{\boldsymbol{T}}(\boldsymbol{E}, \boldsymbol{M}_1, \boldsymbol{M}_2, \boldsymbol{M}_3)$ is a perfectly fine isotropic extension of the anisotropic $\boldsymbol{T}(\boldsymbol{E})$ via the structural tensors $\boldsymbol{M}_1$, $\boldsymbol{M}_2$, and $\boldsymbol{M}_3$. It should be emphasized that the symmetry group $\mathcal{G}$ of the material in question does not belong to the type (3) required in the original formulation of Boehler and Liu.

In the talk based on this paper, a reformulation of the method of isotropic extensions, with further applications to anisotropic linear and finite elasticity, will also be presented. This presentation reports joint work with J.D. Goddard (University of California at San Diego, USA).

References

[1] Boehler J.-P.: A Simple Derivation of Representations for Non-Polynomial Constitutive Equations in Some Cases of Anisotropy. Z. Angew. Math. Mech. 59: 157–167, 1979.

[2] Liu I.-S.: On Representations of Anisotropic Invariants. Int. J. Engng Sci. 20: 1099–1109, 1982.

[3] Wang, C.-C.: A New Representation Theorem for Isotropic Functions, Part I and II. Arch. Rational Mech. Anal. 36: 166–197, 198–223, 1970; Corrigendum, ibid. 43: 392–395, 1971.

[4] Smith G.F.: On Isotropic Functions of Symmetric Tensors, Skew-Symmetric Tensors and Vectors. Int. J. Engng Sci. 9: 899–916, 1971.

[5] Xiao H., Bruhns O.T., Meyers A.: On Isotropic Extension of Anisotropic Constitutive Functions via Structural Tensors. Z. Angew. Math. Mech. 86: 151–161, 2006.

[6] Boehler J.P. (ed.): Applications of Tensor Functions in Solid Mechanics. Springer, Wien, 1987, p. 41.

[7] Mehrabadi M.M., Cowin S.C.: Eigentensors of Linear Anisotropic Elastic Materials. Q. J. Mech. Appl. Math. 43: 15–41, 1990.

MECHANICS OF NANO-PARTICLES FILLED ELASTOMERS BASED ON POLYMER CHAIN LENGTH STATISTICS

Mikhail Itskov [*1]
[1]*Department of Continuum Mechanics, RWTH Aachen University, Aachen, Germany*

Summary The present contribution deals with the constitutive modeling of carbon nanotube (CNT) reinforced rubbers on the basis of the polymer chain length statistics. Rubbers both with conventional fillers like silica or carbon black (hybrid system) and without them are considered. The reinforcement by CNTs is explained by additional cross-linking which influences the probability density function of polymer chain lengths. The change in the probability density function is statistically reasoned and incorporated into a full network model based on the numerical integration over the unit sphere. This full network model is able to describe typical inelastic effects of filled rubbers like the Mullins effect, strain induced anisotropy and permanent set. The so obtained model demonstrates good agreement with experimental data on CNT blended rubbers available in literature.

INTRODUCTION

Polymer chain length statistics as it results from the polymerization process has long been known in chemistry but, to the best of our knowledge, has not so far been applied to mechanics of elastomers. Accordingly, the probability that a linear polymer molecule is composed of exactly k segments is given by the expression [1]: $P(k) = p^{k-1}(1-p)$, $k = 1, 2, \dots$, known as the geometric probability density function, where $0 < p < 1$ denotes the probability of the chain propagation while $1-p$ represents then the probability of the chain termination. These are exactly the events that the polymer chain connects to a free radical (monomer) with either two or one active end, respectively. The above representation is based on the assumption of the classical polymerization theory that p remains constant over the whole polymerization process. The chain length statistics assumes the minimal number of chain segments available in the distribution to be 1 but can be generalized to an arbitrary minimal number of chain segments n with the following probability density function [3]: $P(k) = p^{k-n}(1-p)$, $k = n, n+1, \dots$ a priori satisfying the normalization condition for any n. The continuous counterpart of this probability density function is of the form

$$P(u) = \frac{1}{\Delta} e^{\frac{n-u}{\Delta}}, \tag{1}$$

where u is a real valued number of segments.

This chain length statistics should be distinguished form the classical non-Gaussian or Gaussian statistics for freely joint chains. For example, according to the latter statistics for a freely jointed chain with a fixed number k of segments each of the length l the probability of the end-to-end distance to be between r and $r + dr$ is given in three-dimensional space by [4]

$$P(r,k)\,dr = \left(\frac{3\alpha}{2\pi k l^2}\right)^{3/2} e^{-\frac{3\alpha r^2}{2kl^2}} r^2 dr, \tag{2}$$

where α is a constant defined by the valence angle. Conversely, considering a subset of polymer chains with the same r one obtains a distribution of k. This statistics is bases on the random walk theory and has thus nothing in common with the polymerization process. In Fig. 1 both the probability density function (1) for various values of Δ and the Gaussian distribution function (2) for $r = 2$, $l = 1$ and $\alpha = 1$ are plotted. In comparison to the Gaussian distribution the probability density function (1) is always monotone decreasing.

EFFECT OF CARBON NANOTUBES

CNTs form additional cross-links for the polymer chains (see Fig. 2) and thus influence the chain length probability density function discussed above. The placement of these CNT cross-links within a polymer chain is random. Thus, from the point of view of the chain length statistics a chain with u segments transforms into two (or one) chains with the number of segments either $0/u$ or $1/u-1, \dots$ or $u-1/1$. The probabilities of these events are equal and can thus be expressed as $1/u$. The new chain length probability density function resulting from this cross-linking can be expressed by (1) as (see Ref. [2] for details)

$$D(u) = \int_u^\infty \frac{P(\bar{u})}{\bar{u}} d\bar{u} = \frac{1}{\Delta} \int_u^\infty \frac{e^{\frac{n-\bar{u}}{\Delta}}}{\bar{u}} d\bar{u}. \tag{3}$$

*Corresponding author. Email: itskov@km.rwth-aachen.de

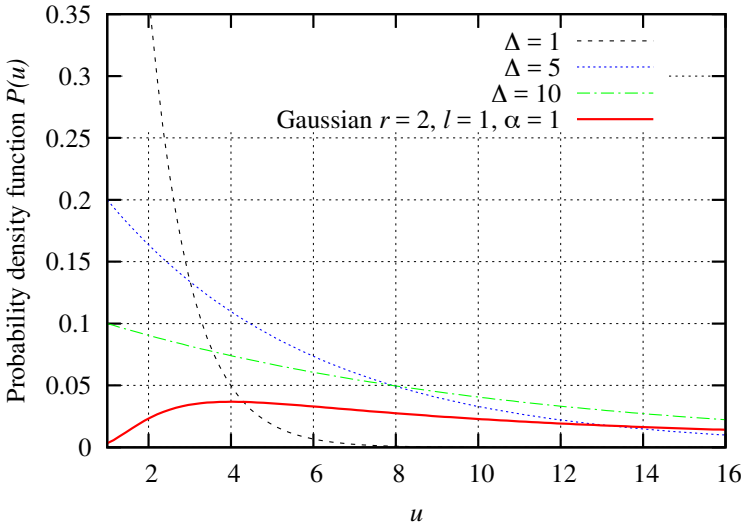

Figure 1: Illustration of the probability density function (1) for various values of Δ versus the Gaussian distribution function (2) for $r = 2$, $l = 1$ and $\alpha = 1$

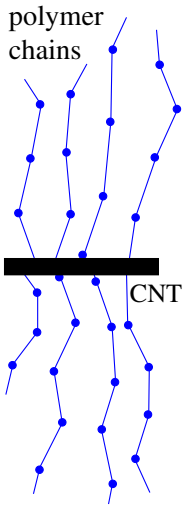

Figure 2: Illustration of polymer chains cross-links by CNT

AN ANISOTROPIC SOFTENING MODEL

According to the non-Gaussian chain statistics the chain force tends to infinity as the chain length tends to its maximal value at the fully stretched straight state. Thus, for any material direction the above model is restricted by the condition

$$\lambda_{max} < \sqrt{n}, \tag{4}$$

where λ_{max} denotes the maximal stretch ever reached in the loading history. In order to satisfy this condition for every material direction we adopt a deformation driven evolution of the minimal number of chain segments such that the condition (4) always satisfies. This evolution can be expressed by

$$n\left(\boldsymbol{d}\right) = \nu^2 \lambda_{max}^2\left(\boldsymbol{d}\right), \tag{5}$$

where $\boldsymbol{d}$ denotes a unit vector specifying a material direction. $\nu > 1$ is a material constant which can be referred to as sliding ratio. It expresses the ratio of the chain contour length kl to the length at break or debonding from the filler aggregate. Further, we assume that the broken/debonded segments still contribute to the entropic energy of the network. The softening is only due to the evolution of the chain length distribution. In order to describe the softening as a continuous process we further apply the continuous distribution function (3) and assume that $\Delta = const$ although $n\left(\boldsymbol{d}\right)$ increases with increasing $\lambda_{max}\left(\boldsymbol{d}\right)$ according to (5). This means that the form of the distribution function remains unchanged, it only shifts parallel to the u-axis to higher values of u. The free energy of all chains in a direction specified by a unit vector $\boldsymbol{d}$ can thus be given by

$$\psi\left(\boldsymbol{d}\right) = \int\limits_{\nu^2 \lambda_{max}^2\left(\boldsymbol{d}\right)}^{\infty} \tilde{w}\left(\lambda, u\right) D\left(u\right) du, \tag{6}$$

where $D\left(u\right)$ is given by (3). The constitutive model described by (6) is one-dimensional and can be generalized to three dimensions within the concept of the full network model mentioned above. Accordingly, the free energy of chains in one spatial direction is integrated over the unit sphere. To this end, a numerical cubature is applied. The so obtained 3D model includes very few physically motivated material constants and shows good agreement with experimental data on both unfilled and filled rubbers. In the latter case predictions of the models were compared to a hybrid elastomer composite with various amounts of CNTs and a classical filler like silica.

References

[1] Flory P. J.: Principles of Polymer Chemistry. Baker lectures 1948. Cornell University Press, 1953.

[2] Itskov M., Darabi E.: Constitutive modeling of carbon nanotube rubber composites on the basis of chain length statistics. Composites B: Eng., published online, doi:10.1016/j.compositesb.2015.12.002.

[3] Itskov M., Knyazeva A.: A rubber elasticity and softening model based on chain length statistics. Int. J. Solids & Struct. 80, 512-519, 2016.

[4] Kuhn W, and Grün F.: Beziehungen zwischen elastischen Konstanten und Dehnungsdoppelbrechung hochelastischer Stoffe. Kolloid-Zeitschrift, 101:248-271, 1942.

MODELING OF RESIDUALLY STRESSED MATERIALS

Touhid Ahamed[1], Luis Dorfmann [*2], and Ray Ogden[3]
[1]*Department of Civil Engineering & Engineering Mechanics, The University of Arizona, Tucson, AZ, USA*
[2]*Department of Civil and Environmental Engineering,Tufts University, Medford, MA, USA*
[3]*School of Mathematics and Statistics , University of Glasgow, Glasgow, UK*

Summary Stresses that are present in a material body in the absence of any applied loads (either body forces or surface tractions) are referred to as residual stresses. To effectively model the elastic response, relative to a residually stressed configuration, the residual stresses need to be incorporated into the constitutive equations. In this talk we provide an overview of the basic equations required to present a general elastic, invariant-based anisotropic constitutive formulation that includes residual stress. We summarize a three-dimensional incremental formulation appropriate for the implementation of the theory in a nonlinear finite element code. For numerical purposes the general constitutive formulation is specialized to a simple prototype model and a simple representation of the residual stress distribution is adopted. As well as possessing anisotropy associated with residual stresses in its unloaded (reference) configuration, the considered material has anisotropy corresponding to two preferred directions that are identified with the orientations of two families of fibers. To validate the theory and its implementation the wall stress distribution in an abdominal aortic aneurysm (AAA) using patient specific geometry and material model parameters is evaluated. The method presented in this talk is general and can be used, by specifying appropriate energy functions, to investigate other residually stressed biological systems.

References

[1] Ahamed T., Dorfmann L., Ogden R.W.: Modelling of residually stressed materials with application to AAA, in review.
[2] Dorfmann A., Wilson C., Edgar E.S., Peattie R.A.: Evaluating patient-specific abdominal aortic aneurysm wall stress based on flow-induced loading. Biomech. Model. Mechanobiol. 9:127–139, 2010.
[3] Merodio J., Ogden R.W.: Extension, inflation and torsion of a residually stressed circular cylindrical tube. Continuum Mech. Thermodyn. 28:157174, 2016.
[4] Merodio, J., Ogden, R.W., Rodríguez, J.: The influence of residual stress on finite deformation elastic response. Int. J. Non-Linear Mech. 56, 43–49, 2013.
[5] Pancheri F.Q.: Experimental and analytical aspects of biological and engineering materials subject to planar biaxial loading. Ph.D. Thesis, Tufts University, Medford, USA, 2014.

[*]Corresponding author. Email: luis.dorfmann@tufts.edu

FINITE SHEAR OF THIN-WALL COMPOSITE SPHERES

Gidon Weil *and Gal deBotton
Department of Mechanical Engineering, Ben-Gurion University, Beer-Sheva, Israel

Summary We examine the mechanical response of a thin-wall composite sphere (TWCS) to moderate level of shear, within the framework of finite deformation elasticity. Results show very good correspondence between our proposed analytical solution and a numerical simulation carried out by FE method.

TWCSs are very common structures in nature. For example, cells prior to division (Fig. 1A) which can be approximated as TWCS subjected to uniaxial tension, globular cells such as the single-cell Chlorella algae (Fig. 1B), enveloped viruses which are commonly modeled as spherical (Fig. 1C), many types of fruit (Fig. 1D) and others. TWCSs are very common also in man-made structures. For example, gold nanoshells for cancer treatment (Fig. 1E), coated hydrogel capsules for targeted drug delivery applications, golf balls (Fig. 1F) and many more.

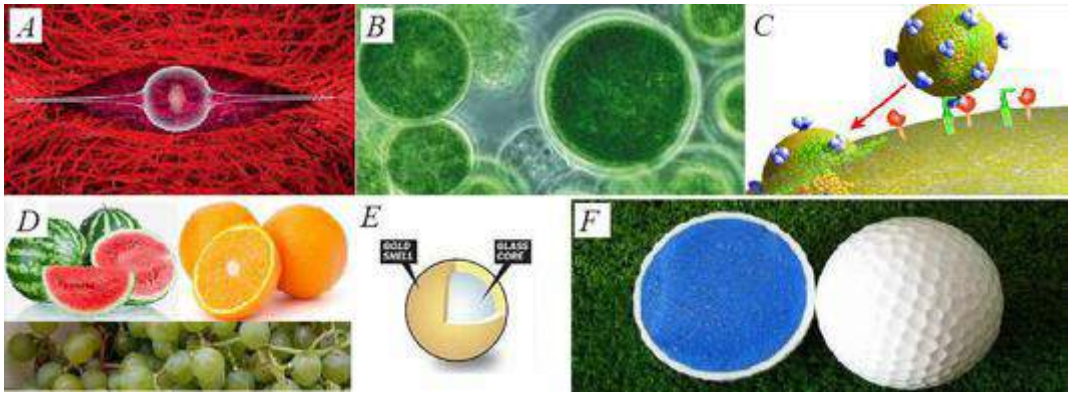

Figure 1: TWCS examples

Studies of the mechanical response of composite spheres consisting of two phases in the limit of infinitesimal deformation elasticity are available in the literature, but when dealing, for example, with cells which undergo large deformations, finite deformations must be accounted for. Within this framework the topic was barely dealt with and only the relatively simple case of inflation/compression was discussed. To the best of our knowledge there are currently no published solutions to the problem of hyperelastic TWCS under non-spherical loading within the frameworks of finite deformation elasticity.

We consider the case of TWCS with incompressible neo-Hookean phases subjected to homogeneous shear loading. The homogeneous deformation gradient and nominal stress associated with this deformation are

$$\boldsymbol{F}^{(h)}=\begin{pmatrix}1&\gamma&0\\0&1&0\\0&0&1\end{pmatrix},\boldsymbol{P}^{(h)}=\begin{pmatrix}0&\tau&0\\\tau&0&0\\0&0&0\end{pmatrix},$$

where γ is the shear strain and τ is the shear load, respectively.

We determine the form of the displacement and the pressure fields in terms of a power series about the shear strain (displacement BC) or shear load (traction BC) and a function of the referential spherical coordinate system $\{r,\theta,\phi\}$, up to the first order in the shell volume fraction c_s. We develop an exact form for the solution up to constant coefficients that are determined using the incompressibility constraint and the equilibrium equations in both phases and the continuity of the displacement and the traction at the interface. In addition the appropriate boundary conditions are used. Specifically, we begin the analysis with the shell and determine the displacement (displacement BC) or traction (traction BC) at the interface. Then we move on to the core and determine the traction (displacement BC) or displacement (traction BC) at the interface, completing the solution in the core, before moving back to the shell and completing the solution for the TWCS. We start with the linear term in γ or in τ, and once the solution is completed we use it and repeat the same procedure for the quadratic term. The higher order terms are determined by repeating these steps.

*Corresponding author. Email: weilg@post.bgu.ac.il

We compared the analytical solution to numerical simulations carried out with the commercial finite elements code ABAQUS. An example for the FE simulation can be seen in Fig. 2. The cases of stiffer or softer core were examined. In order to examine the range of the validity of the thin shell assumption we modeled TWCSs with c_s=5% and 10%. We compared the principal Cauchy stresses along the principal directions of the strain for different shear strains and loads. In Fig. 3 an example is shown for amounts of γ and τ which correspond to stretch ratio of about 150%. In addition, we compared the analytical and numerical average principal Cauchy stress and strain energy as a functions of γ or τ, where the average is defined by integration over the sphere's volume, normalized by the sphere's volume.

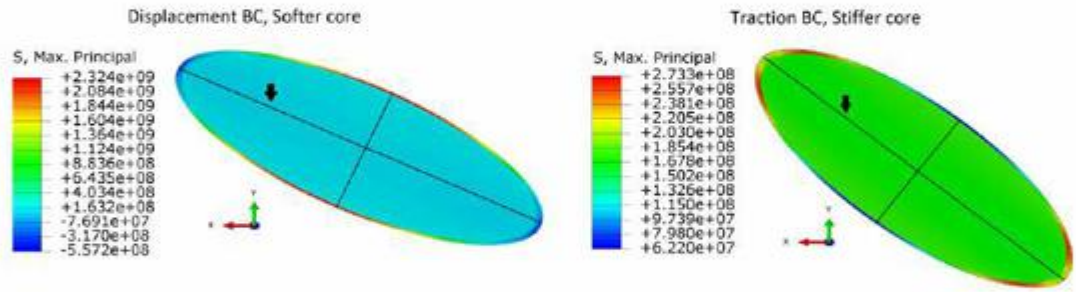

Figure 2: Maximal principle stresses according to FE simulation for TWCSs under displacement BC with softer core (left) and TWCSs under traction BC with stiffer core (right)

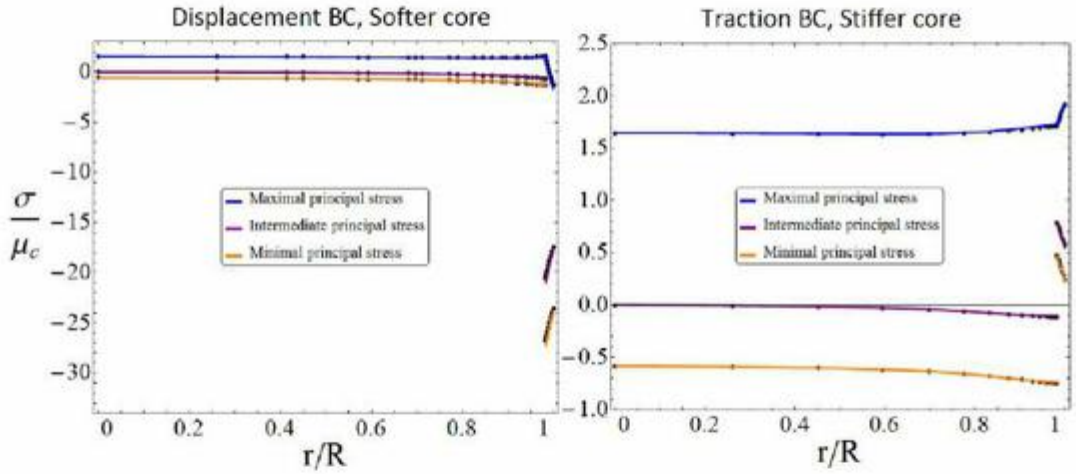

Figure 3: Comparisons between the normalized principle stresses along the maximal stretch direction according to the analytical results (curves) and the FE simulations (dots) for TWCSs under displacement BC with softer core (left) and TWCSs under traction BC with stiffer core (right).

We found that if we impose the same average shear in both displacement and traction boundary conditions we end up with identical amount of average shear stress, first invariant of the average Cauchy-Green deformation tensor and average strain energy. We note that differences do exist between the cases, for example the second invariant isn't identical. Therefore, as opposed to the case of displacement boundary condition, when exerting traction boundary condition the deformation is not planar.

CONCLUSIONS

We developed an analytical solution for a hyperelastic TWCS subjected to simple shear BC in the frameworks of finite deformation elasticity. Correspondence between the analytical proposed solution and the numerical simulations for the local stresses up to stretch ratios of about 150% for a thinner shell occupying 5% of the volume was excellent for the cases of softer core under displacement BC and stiffer core under traction BC, and was fair for the two opposite cases. For the average stresses and strain energy the correspondence was excellent for all cases, with relative errors of up to 5%.

Elastic Response Due To Dislocation Arrays With Core Spreading In Multilayered Materials

Haijian Chu [1,2], Yuheng Zhang[3] & Jie Liu [3], Jian Wang[4]
[1] *Department of Mechanics, Shanghai University, Shanghai, PR China*
[2] *Shanghai Key Laboratory of Mechanics in Energy Engineering, Shanghai University, Shanghai, PR China*
[3] *Shanghai Institute of Applied Mathematics and Mechanics, Shanghai University, Shanghai, PR China*
[4] *Mechanical & Materials Engineering, University of Nebraska-Lincoln, Lincoln, NE 68588-0526, USA*

Abstract The effect of core spreading of interface dislocation arrays on the elastic field and related properties is explored in this paper. Employing the Green's function for a single compact dislocation, we derived the expressions for the elastic fields associated with core-spreading dislocation arrays in multilayer anisotropic materials. It is found that core spreading would significantly reduce stress/strain concentration of the dislocation at the interface. The accuracy of the results is validated by the continuity of traction across the interfaces. Numerical results show that: (1) after core spreading, the stress singularity of the dislocation with condensed core is eliminated and the stress intensity near the cores region is reduced; (2) the region influenced by the dislocations is expanded for the core spreading model. Besides, Peach-Kohler Force with respect to the distance between two adjacent dislocations is analyzed, which may influence the strength of the multilayer material.

Keywords: Dislocation array; Core spreading; Multilayered anisotropic material; Green's function

ELASTIC FIELDS OF DISLOCATION ARRAYS CORE SPREADING IN ANISOTROPIC MATERIAL

When an interface shows a weak shear resistance, such as Cu/Nb metallic multilayers and metal/amorphous interfaces, interface dislocations show a spreading core at the interface. For instance, Dholabha et al. (2014) found an edge dislocation spreads at STO/MgO interface with the width of ~2nm. Regarding to the multilayer material with a few nanometers, the core dimension is comparable to the layer thickness, which may have a great effect on the dislocation nucleation and propagation. Therefore, it is necessary to study the elastic response of the core spreading.

The dislocation arrays at interfaces in a multilayered anisotropic material are given in Fig.1(a). For simplicity, the elastic constants of the different materials are assumed to be the same. The layer thickness is denoted by h and the distance between two adjacent dislocations at the interface L. The dislocation has a spreading core with a width of w at the interface.

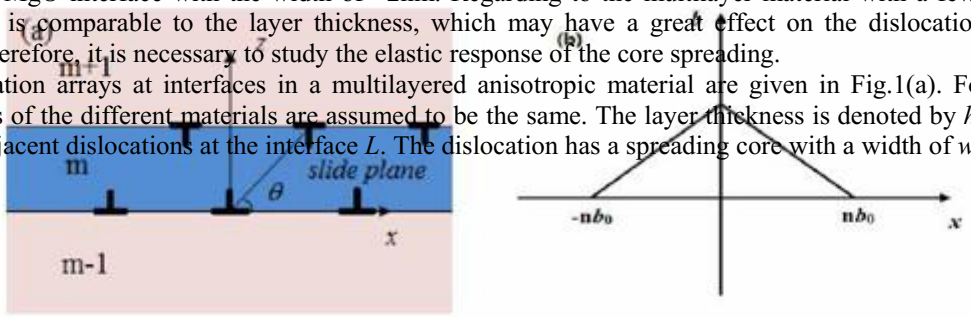

Fig.1. Dislocation core spreads in a width of w in a multilayered anisotropic material (a), and the distribution of Burgers vector along the core spreading region (b)

For a dislocation with a spreading core, Eshelby (1949) suggested to treat the spread-out dislocation as an array of infinitesimal dislocations. The Burgers vector of the single dislocation in every array is denoted by $\boldsymbol{b}_0$. The distributed Burgers vector in the spreading region is denoted by $\boldsymbol{b}$ which is a function of the source position (X, Z). The width of the spreading core is assigned to be $2nb_0$, and the distribution of the Burgers vector at the core region is assumed as a linear distribution along the interface as shown in Fig. 1(b), i.e.

$$\boldsymbol{b} = \begin{cases} (-1)^{m+1}\left[a\ \ X + nb_0 - X_0\right]\boldsymbol{b}_0, & X \le X_0 \\ (-1)^{m}\left\lfloor a\ \ X - nb_0 - X_0\right\rfloor\boldsymbol{b}_0, & X \ge X_0 \end{cases}, \quad \text{with} \quad a = \frac{1}{n\ b_0} \tag{1}$$

The coordinate (X_0, Z_0) is the position of the dislocation and the parameter m denote the layer number of the interface. According to Stroh formulism, we can derive the elastic field due to the dislocation with core spreading at the interface as follows:

$$\boldsymbol{u}_{,i} = \frac{(-1)^{m+1}}{L}\,\mathrm{Im}\left\{\boldsymbol{A}\boldsymbol{q}^{\infty}\quad(\delta_{i1}+p_*\delta_{i3})\sum_{m=1}^{k}\int_0^{nb_0}\begin{bmatrix} aX\cot\left(\pi\dfrac{z_*-X+nb_0-h\ \ m-1)(p_*+\cot\theta)}{L}\right)\\ -a\ \ X-nb_0)\cot\left(\pi\dfrac{z_*-X-h\ \ m-1)(p_*+\cot\theta)}{L}\right)\end{bmatrix}dX\right\} \tag{2}$$

where $\boldsymbol{A}$ and $\boldsymbol{q}^{\infty}$ are determined by the material constants, and $z_* =\ \ +\ \ _*$.

NUMERICAL EXAMPLE

The stress fields induced by dislocation arrays with core spreading at the interfaces in multilayer anisotropic materials are numerically evaluated. The elastic constants of the materials are assumed to be the same but the glide plane and glide direction are different with each other. Fig.2 is the contour of the stress field σ_{11} (GPa) for the dislocation arrays with core spreading (a) and unspreading (b). We can find that: (1) with core spreading, the stress singularity of the dislocation arrays is eliminated and the stress intensity near the cores of the dislocation arrays is reduced greatly, compared with the dislocation arrays with condensed cores; (2) at the same point outside of the core regions, the stress for the core spreading model is larger than the compact dislocation arrays model, which means that the region influenced by the dislocations is expanded for the core spreading model.

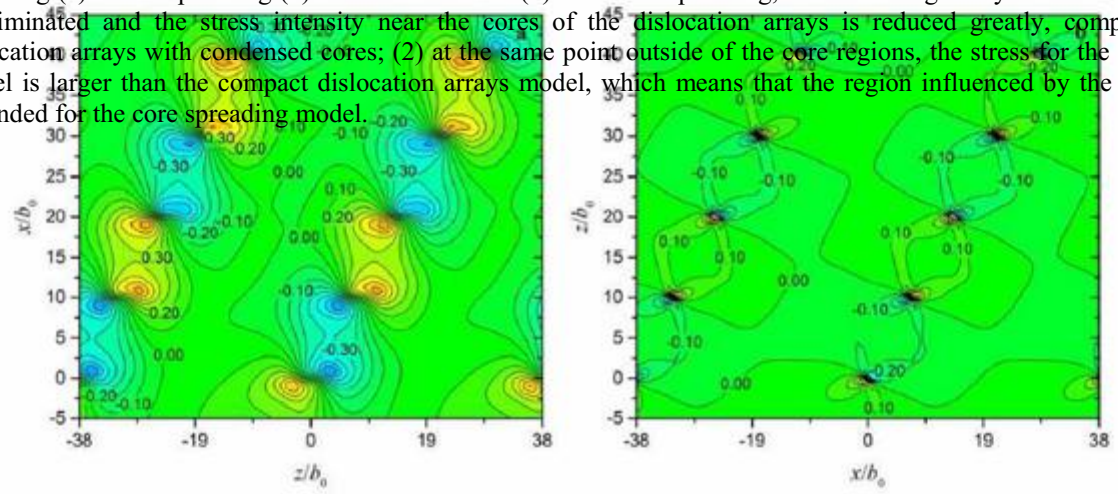

Fig.2. The contour of the stress field σ_{11} (GPa) for the dislocation arrays with core spreading (a) and unspreading (b).

The influence of interface dislocation arrays with core spreading on the dislocation slide is a key process of the plastic deformation propagation in the layered composites. The interaction force (i.e., Peach-Koehler (P-K) force) may provide extra resistance force to the dislocation glide, and consequently strengthen the material. The influences of the dislocation space L and the layer thickness are explored systematically. We found that the P-K force is sensitive to the core spreading and generally P-K force for the core spreading case is larger than that for the compact dislocation.

CONCLUSIONS AND DISSCUSSION

The expressions for the elastic fields due to dislocation arrays with core spreading in multilayered anisotropic materials were derived. It is found that dislocation core spreading has a great influence on the displacement and stress fields in the core region, and the stress singularity in the conventional compact model can be eliminated in the core-spreading models. The analysis of the P-K force on the approaching dislocation shows that the spreading model has a relative large influence region, compared with the compact model. The findings from this work seem more important to nanolayered multilayers since the core spreading width of dislocations is comparable to the layer thickness, and thus provide new insights into understanding the role of interfaces in determining materials strength and plastic deformation.

References

[1] Chu, H.J., Pan, E.,2014. Elastic fields due to dislocation arrays in anisotropic bimaterials. International Journal of Solids and Structures 51(10), 1954-1961.

[2] Stroh, A.N., 1958. Dislocations and cracks in anisotropic elasticity. Philosophical Magazine 3, 625-646.

[3] Stroh, A.N., 1962. Steady state problems in anisotropic elasticity. Journal of Mathematical Physics 41, 77-102.

[4] Eshelby, J.D., 1949. Edge dislocations in anisotropic materials. Philosophical Magazine 40, 903-912.

Stress field around an elliptical hole with surface tension in an anisotropic half-plane

Ming Dai[1,2], Peter Schiavone[2a)]
[1]*State Key Laboratory of Mechanics and Control of Mechanical Structures, Nanjing University of Aeronautics and Astronautics, Nanjing 210016, China*
[2]*Department of Mechanical Engineering, University of Alberta, Edmonton, Alberta T6G 1H9, Canada*

Abstract We examine the surface tension-induced stress concentration around an elliptical hole inside an anisotropic half-plane with traction-free surface. Using conformal mapping techniques, the corresponding complex potential in the half-plane is expressed in a series whose unknown coefficients are determined numerically. Our results indicate that surface tension makes a significant contribution to the stress concentration around the hole as the size of the hole approaches the nanoscale. In particular, we find that, with decreasing distance between the hole and the free surface, the hoop stress can switch from compressive to tensile at certain points on the hole's boundary and from tensile to compressive at others. This phenomenon is absent in the case of an elliptical or even circular hole with surface tension in an isotropic half-plane. (this work forms part of a paper recently submitted for publication [1])

INTRODUCTION

In recent years, nano-structures and nano-composites have been widely used in mechanical and biomedical engineering applications because of their unique physical and mechanical properties. In an effort to accurately predict stress distributions in such structures and composites, surface/interface effects induced by the contributions of surface/interface energy and surface/interface tension have been incorporated into the models of deformation around, for example, inner nanosized holes or inclusions. Most investigations involving nanosized holes/inclusions incorporating surface/interface effects, however, have been restricted to the simple case where the matrix surrounding the holes/inclusions is assumed to be isotropic (see, for example, [2-5]). This essentially prevents the analysis of cases involving most ceramic-matrix nano-structures and nano-composites in which the matrix appears to be highly anisotropic. In view of this deficiency, we present in this paper an efficient method to deal with the problem of stress concentration around an elliptical hole in an anisotropic matrix subjected to plane deformations when surface tension is included on the boundary of the hole. This assumption is reasonable for problems involving small strain. In fact, in certain technological applications, the effect of deformation-dependent surface elasticity has been found to be small compared to that of surface tension [6, 7]. In our approach, the matrix is modelled specifically as a half-plane to incorporate the interaction between the hole and the edge of the matrix.

PROBLEM FORMULATION

We refer to the *xy*-coordinate system and consider an anisotropic lower half-plane containing an elliptical hole. As noted above, we consider only the contribution of surface tension T and disregard the deformation-dependent surface elasticity on the boundary of the hole. This assumption is reasonable for problems involving small strain [6, 7]. The stress distribution in the anisotropic half-plane can be expressed in terms of two complex potentials $\varphi_i(z_i)$ ($z_i = x+\mu_i y,\ i=1,2$) by [8]

$$\sigma_{xx} = 2\,\mathrm{Re}\left[\mu_1^2\varphi_1'(z_1)+\mu_2^2\varphi_2'(z_2)\right],\ \sigma_{yy} = 2\,\mathrm{Re}\left[\varphi_1'(z_1)+\varphi_2'(z_2)\right],\ \sigma_{xy} = 2\,\mathrm{Re}\left[\mu_1\varphi_1'(z_1)+\mu_2\varphi_2'(z_2)\right], \tag{1}$$

where μ_1 and μ_2 are two distinct complex roots with positive imaginary parts each determined by the following fourth-order equation in μ,

$$a_{11}\mu^4 - 2a_{13}\mu^3 + (2a_{12}+a_{33})\mu^2 - 2a_{23}\mu + a_{22} = 0. \tag{2}$$

Here, the constants a_{ij} (i,j=1,2,3) are the compliance coefficients of the anisotropic material occupying the half-plane. The traction boundary conditions on the hole's boundary L and the free surface L' of the half-plane are described in terms of $\varphi_1(z_1)$ and $\varphi_2(z_2)$ as [8]

$$\left.\begin{aligned} 2\,\mathrm{Re}\left[\varphi_1(z_1)+\varphi_2(z_2)\right] &= T\sin\beta + A \\ 2\,\mathrm{Re}\left[\mu_1\varphi_1(z_1)+\mu_2\varphi_2(z_2)\right] &= -T\cos\beta + B \end{aligned}\right\}(\text{on } L),\quad \left.\begin{aligned} 2\,\mathrm{Re}\left[\varphi_1(z_1)+\varphi_2(z_2)\right] &= C \\ 2\,\mathrm{Re}\left[\mu_1\varphi_1(z_1)+\mu_2\varphi_2(z_2)\right] &= D \end{aligned}\right\}(\text{on } L'), \tag{3}$$

where β is the angle between the positive x-axis and the tangent to the boundary L, while A, B, C and D are real constants to be determined. The complex potentials $\varphi_1(z_1)$ and $\varphi_2(z_2)$ can be determined from conditions (3) using conformal mapping techniques and Fourier expansion methods. Numerical examples for surface tension-induced stress concentrations around elliptical holes in an anisotropic half-plane are given in the next Section.

NUMERICAL EXAMPLES AND CONCLUSIONS

The following figures show the hoop stresses σ_{tt} around circular and elliptical holes with surface tension in an anisotropic half-plane with increasing distance between the hole and the free surface of the half-plane.

[a)] Corresponding author. Email: P.Schiavone@ualberta.ca

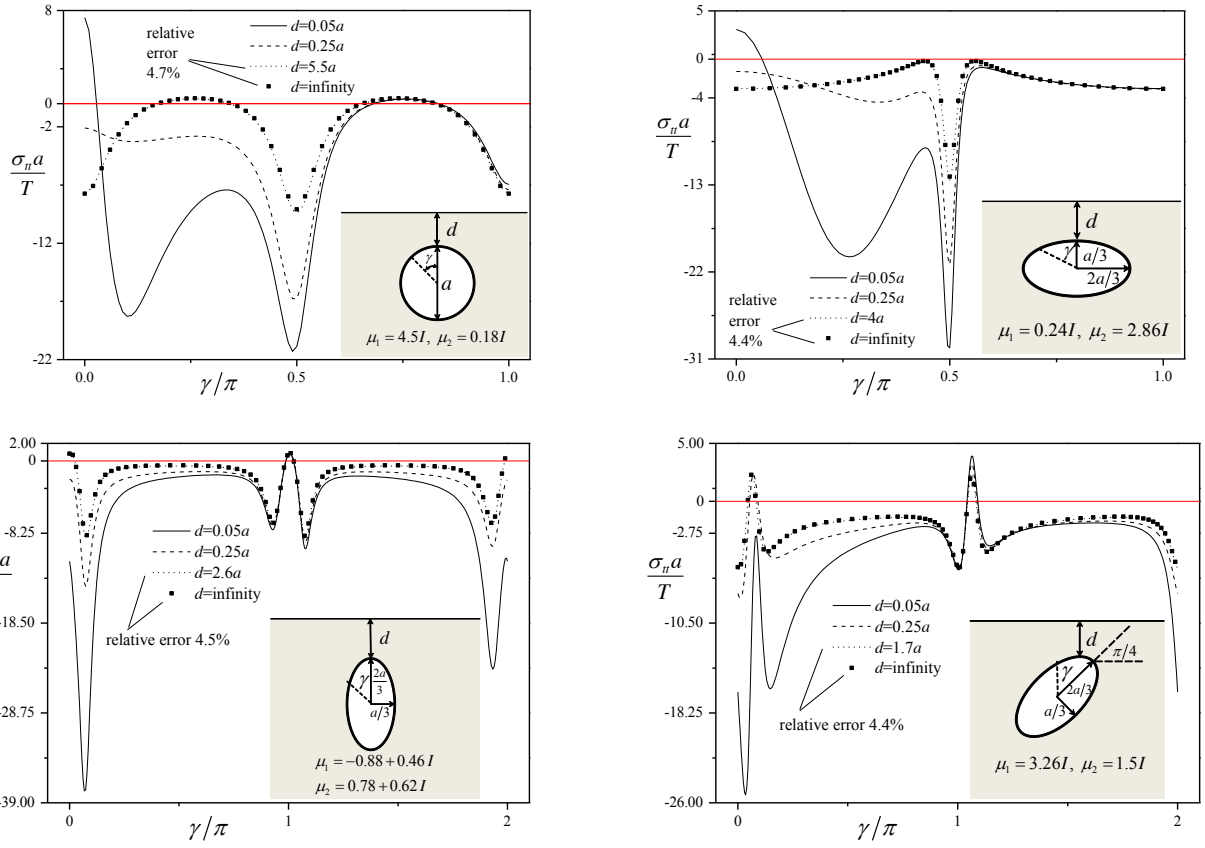

From the above results, we conclude that:

(1) Surface tension makes a significant contribution to the stress concentration around the hole in a half-plane as the size of the hole approaches the nanoscale.

(2) The maximum hoop stress around the hole increases significantly with decreasing distance between the hole and the free surface of the half-plane. The maximum hoop stress usually appears in the vicinity of the point of maximum curvature on the hole's boundary.

(3) For an elliptical or even for a circular hole in an anisotropic whole plane, positive surface tension may induce tensile hoop stress at certain points around the hole, which is in sharp contrast to the case of a circular or elliptical hole with positive surface tension in an isotropic whole plane (see [9] for the case of isotropic whole plane).

(4) For an elliptical or even circular hole (with surface tension) in a half-plane, compressive hoop stress at certain points around the hole may become tensile while simultaneously tensile hoop stress at certain other points around the hole may become compressive as the hole approaches the free surface of the half-plane. This, of course, is true only if the half-plane is anisotropic and not isotropic (see [5] for the case of an isotropic half-plane).

References

[1] Dai M., Schiavone P., Gao C.F.: Surface Tension-induced Stress Concentration Around an Elliptical Hole in an Anisotropic Half-plane (submitted Dec. 2015)

[2] Wang G.F., Wang T.J.: Deformation Around a Nanosized Elliptical Hole with Surface Effect. *Appl Phys Lett* **89**:161901-161901-3, 2006.

[3] Tian L., Rajapakse R.K.N.D.: Elastic Field of an Isotropic Matrix with a Nanoscale Elliptical Inhomogeneity. *Int J. Solids Struct* **44**:7988-8005, 2007.

[4] Miri A.K., Avazmohammadi R., Yang F.: Effect of Surface Stress on the Deformation of an Elastic Half-plane Containing a Nano-cylindrical Hole under a Surface Loading. *J. Comput Theor Nanosci* **8**:231-236, 2011.

[5] Dai M., Gao C.F., Ru C.Q.: Surface Tension-induced Stress Concentration Around a Nanosized Hole of Arbitrary Shape in an Elastic Half-plane. *Meccanica* **49**:2847-2859, 2014.

[6] Sharma P., Wheeler L.T.: Size-Dependent Elastic State of Ellipsoidal Nano-Inclusions Incorporating Surface/Interface Tension. *ASME J. Appl Mech* **74**:447-454, 2007.

[7] Hui T., Chen Y.H.: The M-integral Analysis for a Nano-inclusion in Plane Elastic Materials under Uni-axial or Bi-axial Loadings. *ASME J. Appl Mech* **77**:021019, 2010.

[8] Lekhnitskii S.G.: Theory of Elasticity of an Anisotropic Elastic Body. Moscow, Russia 1950.

[9] Wang S., Dai M., Ru C.Q., Gao C.F.: Stress Field Around an Arbitrarily Shaped Nanosized Hole with Surface Tension. *Acta Mech* **225**:3453-3462, 2014.

BI-MATERIAL PLANE OF JOHN'S HARMONIC MATERIAL WITH A POINT FORCE AT INTERFACE

Tatiana Domanskaia *[1], Venyamin Malkov[1], and Yulia Malkova[1]
[1]*Faculty of Applied Mathematics and Control Processes, Saint Petersburg State University, Saint Petersburg, Russia*

Summary The analytical solution of a nonlinear problem of elasticity (plain strain) for a bi-material plane, consisting of two half-planes, is obtained under action of a point force at an interface. Mechanical properties of half-planes are described by a model of John's harmonic material. The problem is solved by methods of functions of a complex variable, the stresses and displacements are expressed through two analytical functions, which are found from boundary conditions. Based on the global solutions the asymptotic expansions are constructed for stresses and displacements in a vicinity of a point force. The solution of a problem for half-plane loaded by point force on a border is found.

INTRODUCTION

The considered model of an elastic material is proposed by F. John in work [1]. The complex formulation to the equations of nonlinear plane problems is given in [2]. The further development of a complex method is made in [3], where the problem about an interface crack for John's material is solved. The new form of complex equations is received in work [4]. Problems an interface crack and a point force on an interface are solved using a method of jumps of stresses and displacements. The case of an interface crack loaded by pressure is studied in work [5]. For the first time it is shown, that there is the critical pressure which excess leads to loss of the material stability as well as large deformations and stresses.

PROBLEM SOLUTION

Consider John's elastic potential (strain energy density) [3]

$$\Phi = 2\mu[F\,(I) \circ\ J], \quad I = \lambda_1 + \lambda_2,\ J = \lambda_1\lambda_2,$$

$$8\mu b F'(I) = I + \sqrt{I^2 \circ\ 16bc},$$

where λ_1, λ_2 are principal stretches; the constants b, c are defined by transition to Hookean law under small deformations: $4\mu b = 1 + \mu/(\lambda + 2\mu)$, $c = 2\mu(1 \circ\ 2\mu b)$.

The equilibrium and compatibility equations of a plane problem in cartesian coordinates are

$$\begin{gathered}(s_{11} + is_{12})'_1 + i(s_{22} \circ\ is_{21})'_2 = 0,\\ (g_{22} \circ\ ig_{12})'_1 + i(g_{11} + ig_{21})'_2 = 0,\end{gathered} \tag{1}$$

$s_{ij} = \partial\Phi/\partial g_{ji}$ are nominal stresses, g_{ij} — components of deformation gradient. Let's $z = x_1 + ix_2$, $\zeta = \xi_1 + i\xi_2$ are the complex variables of undeformed and deformed states, σ is a stress function. The equations (1) are identically satisfied at substitution of expressions

$$\begin{gathered}s_{11} + is_{12} = \frac{\partial\sigma}{\partial z} \circ\ \frac{\partial\sigma}{\partial\overline{z}}, \quad s_{22} \circ\ is_{21} = \frac{\partial\sigma}{\partial z} + \frac{\partial\sigma}{\partial\overline{z}},\\ g_{11} + ig_{21} = \frac{\partial\zeta}{\partial z} + \frac{\partial\zeta}{\partial\overline{z}}, \quad g_{22} \circ\ ig_{12} = \frac{\partial\zeta}{\partial z} \circ\ \frac{\partial\zeta}{\partial\overline{z}}.\end{gathered} \tag{2}$$

The functions ζ and σ are received from the elasticity law and formulas (2)

$$\begin{gathered}\zeta = b\varphi(z) + \overline{\psi(z)} + \frac{cz}{\overline{\varphi'(z)}},\\ \sigma = (1 \circ\ 2\mu b)\varphi(z) \circ\ 2\mu\overline{\psi(z)} \circ\ 2\mu\frac{cz}{\overline{\varphi'(z)}},\end{gathered} \tag{3}$$

$\varphi(z)$, $\psi(z)$ are analytic functions. The boundary conditions at interface

$$[s_{22} \circ\ is_{21}]^+ \circ\ [s_{22} \circ\ is_{21}]^- = \Delta\, s(t), \quad [g_{11} + ig_{21}]^+ \circ\ [g_{11} + ig_{21}]^- = \Delta\, g(t), \tag{4}$$

*Corresponding author. Email: tanyath57@gmail.com

the functions $\Delta\, s(t)$, $\Delta\, g(t)$ are the jumps of stresses and strains. For point force F, applied at interface in $z = 0$, the jumps are $\Delta\, s(t) = \circ\, iF\delta(t), \quad \Delta\, g(t) = 0$.

We introduce functions $h(z)$ and $k(z)$, which holomorphic in all plane, except interface, then equations (4) and their solutions will become [4], [6]

$$[h(z)]^+ \circ\ [h(z)]^- = \Delta\, s(t), \quad [k(z)]^+ \circ\ [k(z)]^- = \Delta\, g(t),$$

$$h(z) = \circ\, \frac{F}{2\pi}\, \frac{1}{z} + h(\infty), \quad k(z) = k(\infty).$$

Constants $h(\infty)$, $k(\infty)$ are defined from conditions $s_{ij} \to 0$ at $|z| \to \infty$.

The asymptotic expansions of nominal stresses and displacements for upper half-plane S_2 at $r \to 0$ are:

$$\begin{gathered} s_{11} + is_{12} = \circ\, \left[\frac{1 \circ\ 2\mu_2 b_2}{b_2} p_2 e^{-i\theta} + 2\mu_2 p_1 e^{i\theta}\right] \frac{F}{2\pi r} + O(1), \\ s_{22} \circ\ is_{21} = \circ\, \left[\frac{1 \circ\ 2\mu_2 b_2}{b_2} p_2 e^{-i\theta} \circ\ 2\mu_2 p_1 e^{i\theta}\right] \frac{F}{2\pi r}, \\ u_1 + iu_2 = \circ\, (p_1 + p_2) \frac{F}{2\pi} \ln r + O(1), \end{gathered} \tag{5}$$

where $z = re^{i\theta}$,

$$p_1 = \frac{b_1}{1 + 2b_1(\mu_2 \circ\ \mu_1)}, \quad p_2 = \frac{b_2}{1 + 2b_2(\mu_1 \circ\ \mu_2)}.$$

The Cauchy stresses are calculated under formulas

$$t_{11} + it_{12} = \frac{s_{11} + is_{12}}{\sqrt{g_{22}^2 + g_{12}^2}}, \quad t_{22} \circ\ it_{21} = \frac{s_{22} \circ\ is_{21}}{\sqrt{g_{11}^2 + g_{21}^2}}.$$

The asymptotic expansions of Cauchy stresses for upper half-plane at $r \to 0$

$$\begin{gathered} t_{11} + it_{12} = \circ\, \sqrt{\frac{F}{\overline{F}}} \frac{(1 \circ\ 2\mu_2 b_2) p_2 e^{-i\theta} + 2\mu_2 b_2 p_1\, e^{i\theta}}{b_2 \sqrt{p_1^2 \circ\ 2p_1 p_2 \cos 2\theta + p_2^2}} + O(r), \\ t_{22} \circ\ it_{21} = \circ\, \sqrt{\frac{F}{\overline{F}}} \frac{(1 \circ\ 2\mu_2 b_2) p_2 e^{-i\theta} \circ\ 2\mu_2 b_2 p_1\, e^{i\theta}}{b_2 \sqrt{p_1^2 + 2p_1 p_2 \cos 2\theta + p_2^2}} + O(r). \end{gathered} \tag{6}$$

The expansions for lower half-plane S_1 are obtained by cyclic replacing of indexes $(1 \leftrightarrow 2)$ in the right parts of (5), (6).

CONCLUSIONS

The nominal stresses have singularities $1/r$ at $r \to 0$ in vicinity of point force, the displacements have singularity $\ln r$, while the Cauchy stresses have no singularity. The stresses and displacements of single half-plane problem (S_1 or S_2) under action of point force on border we receive from above-described results when one of modules μ equal zero.

References

[1] John F. Comm. Pure and Appl. Math. 1960. Vol. XIII.

[2] Varley E., Cumberbatch E. J. of Elasticity. 1980. Vol. 10, No 4.

[3] Ru C. Q. Acta Mechanica. 2002. Vol. 156, No 3–4.

[4] Malkov V. M., Malkova Y. V. Vestnik Saint Petersburg State University. Ser. 1. Issue 3. 2008.

[5] Malkov V. M., Malkova Y. V, Stepanova V. A. Vestnik Saint Petersburg State University. Ser. 1. Issue 3. 2013.

[6] Malkov V. M. Introduction in nonlinear elasticity. Saint Petersburg, Russia. 2010.

INTERCALATION OF CARBON NANOTUBES INTO A GRAPHENE SHEET

Tom Dyer[1], Ngamta Thamwattana[1], Barry Cox[2], and James McCoy[1]

[1]*School of Mathematics and Applied Statistics, University of Wollongong, NSW, Australia*
[2]*School of Mathematics Sciences, University of Adelaide, SA, Australia*

Summary Folding graphitic materials have the potential to create complex structures with new properties. Intercalating molecules into these folds is an interesting method of one-dimensional functionalisation of a graphene sheet. We investigate the incorporation of a single-walled carbon nanotube into folded graphene structures and between sheets of graphene. The optimal curved structure caused by both the elastic and van der Waals energies is examined using variational calculus. Results are shown to match with molecular dynamics simulations.

INTRODUCTION

Graphene sheets are materials known to be able to withstand immense stress [1]. However, it is much simpler to move graphene out of the plane creating folded structures of graphene known as grafolds [2]. In comparison to graphene, grafolds have been shown to have enhanced mechanical properties under compressive forces [1, 3] and increased chemical reactivity [4]. One of the more novel applications of these folds is the intercalation of small molecules into the structure. This creates a one-dimensional functionalisation of the graphene sheets allowing us to experiment with the mechanical, electrical and optical properties affected by the interlayer interaction. Experiments involving intercalation into folds have been performed before with C_{60} fullerences [2]. Here, we investigate a similar structure formed by the intercalation of a single-walled carbon nanotube into a fold. Due to the isotropic nature of this structure along the axis of the nanotube, the problem can be reduced to two dimensions and we examine a cross-section of the system. Simulations are conducted and a comparison is made between the equilibrium state of an MD simulation of the system and the mathematical model of the structure formulated by variational calculus.

MODELLING

We construct a model to determine the optimal geometric structure of a graphene sheets wrapped around a single-walled nanotube. The dominant forces are assumed to be the van der Waals (vdW) interaction energy and the elastic bending energy involved in the bending of the sheet. The vdW energy is taken to dominate as the sheet wraps around the nanotube and so we represent this curve as a perfectly circular arc. When the edges of the folded sheets are a sufficient distance from the tube, the elastic force rapidly decreases and the sheets stack in a horizontal fashion as in graphene. Furthermore, we assume the graphene-graphene and SWNT-graphene van der Waals interaction are equal and denote the resulting equilibrium distance as 2δ Å . The SWNT is fixed at a radius of r Å .

Invariance of the structure along the length of the nanotube allows us to reduce the problem into two dimensions as shown in Fig. 1. We assume reflective symmetry around the x-axis and so can independantly consider the upper section. The curve is split into three distinct sections denoted by C_1, C_2 and C_3. We define C_1 as a circular arc of radius $R = r + 2\delta$ and C_3 is defined as a horizontal line bounded on the left. Our interest is in the formation of the central curve C_2 bounded by the points $P_1 = (x_0, y_0)$ and $P_2 = (x_1, \delta)$.

The elastic energy, E_e, uses Euler's formulation of the potential energy of an ideal elastic line and the vdW energy, E_v, is modelled as a Heaviside step function. Additionally, we assume the curve section C_2 is dominated by the elastic force and thus C_1 and C_3 are the sections of the curve affected by the vdW force. Our total energy E is then

$$E = E_e + E_v = \int_C (\gamma\kappa^2 \circ \epsilon u(x_1 \circ x) \circ \epsilon u(x \circ x_2))\, ds,$$

where κ is the strictly negative line curvature and γ is a constant denoting the bending rigidity of graphene. Additionally, u represents the heaviside function and ϵ is a scaling constant denoting the vdW energy per area length.

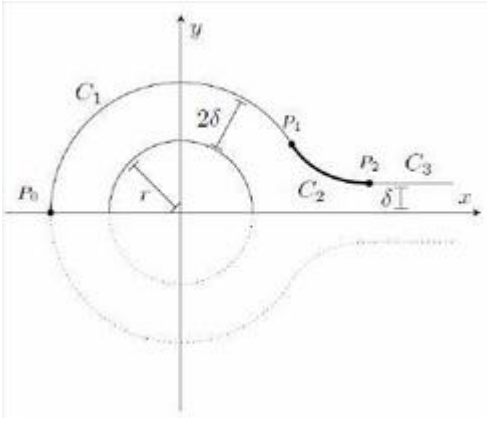

Figure 1: Representation of a graphene sheet wrapped around a carbon nanotube.

We aim to minimise the energy together with an isoperimetric constraint on the total arclength, $\int_C ds = L$, which we incorporate in our functional by multiplying by a Lagrange multiplier λ.

$$\begin{aligned} E &= \int_C (\gamma\kappa^2 \circ \epsilon u(x_0 \circ x) \circ \epsilon u(x \circ x_2) + \lambda)\, ds \\ &= \frac{\gamma L_1}{R^2} + \int_{C_2} (\kappa^2 + \alpha)\, ds + (\lambda \circ \epsilon) L, \end{aligned}$$

where we have defined $\alpha = \epsilon/\gamma$.

The general parametric solution for the minimal energy curve is given in Cox et. al. [5]

$$x(\phi) = c_1 \circ \frac{2(\alpha+\beta)^{1/2}}{\beta}\left(1 \circ k^2 \sin^2\phi\right), \qquad y(\phi) = c_2 \circ \frac{2(\alpha+\beta)^{1/2}}{\beta}\left(E(\phi,k) \circ \frac{\alpha}{\alpha+\beta}F(\phi,k)\right),$$

where $k = \left(\frac{2\beta}{\alpha+\beta}\right)^{1/2}$ and E and F are, respectively, the incomplete elliptic integrals of the first and seconds kinds.

Using the boundary conditions defined for a second order variational problem, we can find our constants

$$c_1 = \frac{2 + 2(R^2\alpha + 2)^{1/2}}{R\beta}, \qquad c_2 = \frac{(R^4\beta^2 \circ 4)^{1/2}}{R\beta} + \frac{2(\alpha+\beta)^{1/2}}{\beta}\left(E(\phi_0,k) \circ \frac{\alpha}{\alpha+\beta}F(\phi_0,k)\right).$$

The van der Waals energy is taken as $\epsilon = 0.0214\,\text{eV}\,\text{Å}^{-2}$ and the bending energy as $\gamma = 1\,\text{eV}\,\text{Å}^{-2}$ [5]. The remaining constant β is determined numerically for each case.

RESULTS

Several MD simulations were run for a number of different sized nanotubes ranging from (6,6) to (10,10) armchair nanotubes. The resulting structure was overlayed with the curve defined by the mathematical model for nanotubes of an equivalent radius as shown in Fig. 2. This alternate modelling method gives a curve that reasonably approximates the curved structure of the model. We do however note that the nanotube has been slightly compressed forming an elliptical rather than a perfectly circular structure which gives a possible further extension to the model.

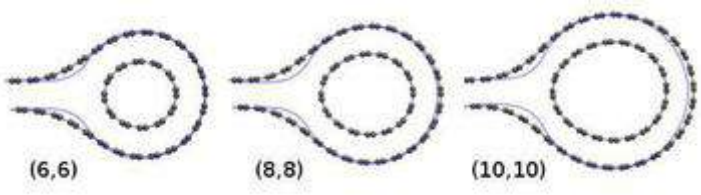

Figure 2: Comparison of mathematical model and MD simulation equilibrium structure for (6,6), (8,8) and (10,10) armchair nanotubes wrapped by a graphene sheet. The simulation is represented by the dotted line.

MOLECULAR DYNAMICS

Molecular dynamics (MD) simulations were performed using the LAMMPS MD simulator. A folded sheet of graphene around a single-walled carbon nanotube was modelled in a 10nm $\times$ 10nm simulation box. This system was repeated periodically along the axis of the nanotube. All interactions were modelled using the AIREBO forcefield. The simulation was equilibriated under the NPT ensemble at a temperature of 300 K and pressure of 1 bar. Temperature and pressure control were managed using the Nose-Hoover thermostat and barostat. The system was first minimised using the conjugate gradient (CG) algorithm and was then run at a timestep of 0.5 femtoseconds.

References

[1] J. H. Warner, *Graphene: Fundamentals and emergent applications*. Elsevier, 2012.

[2] K. Kim, Z. Lee, B. D. Malone, K. T. Chan, B. Alemán, W. Regan, W. Gannett, M. F. Crommie, M. L. Cohen, and A. Zettl, "Multiply folded graphene," *Phys. Rev. B*, vol. 83, p. 245433, Jun 2011.

[3] Y. Zheng, N. Wei, Z. Fan, L. Xu, and Z. Huang, "Mechanical properties of grafold: a demonstration of strengthened graphene," *Nanotechnology*, vol. 22, no. 40, p. 405701, 2011.

[4] M. Chhikara, E. Pavlica, and G. Bratina, "Grafold-driven nucleation of pentacene on graphene," *Surface Science*, vol. 609, pp. L5 – L8, 2013.

[5] B. J. Cox, D. Baowan, W. Bacsa, and J. M. Hill, "Relating elasticity and graphene folding conformation," *RSC Adv.*, vol. 5, pp. 57515–57520, 2015.

REGULAR QUATERNIONIC FUNCTIONS AND THEIR APPLICATIONS IN THREE–DIMENSIONAL ELASTICITY

Yuri Grigor'ev *
North-Eastern Federal University, Academy of Sciences of Republic Sakha (Yakutia), Yakutsk, Russia

Summary In the plane elasticity an effective method of using the holomorphic complex function theory is based on Kolosov-Muskhelishvili formulae. For three–dimensional problems monogenic Clifford functions or regular quaternionic functions of a reduced quaternion variable are used. We present some variants of three–dimensional Kolosov-Muskhelishvili formulae where elastic displacements and stresses are expressed in terms of two arbitrary regular quaternionic functions. It is shown that in particular cases of plane and axially symmetric deformations these representations go into the Kolosov–Muskhelishvili and Solov'ev formulae expressed in terms of two complex functions. Some applications of quaternionic representations for elastic equilibrium problems are shown.

INTRODUCTION

In two-dimensional problems of the theory of elasticity the methods of complex variable theory are effectively used. In plane problems the basis of this is the representation of the general solution of the equilibrium equations in terms of two arbitrary analytic functions called the Kolosov–Muskhelishvili formulae. In axially symmetric problems different classes of generalized analytic functions of complex variable are used. As a generalization of the method of complex functions in multidimensional problems the method of hypercomplex functions are developed (see [1, 4] etc.). For three-dimensional problems of mathematical physics such an apparatus is the Moisil–Theodoresco system theory, which is developed as the theory of regular quaternion functions of reduced quaternion variable (see [3]). In [2, 5] one can find short reviews about some results in using of hypercomplex functions in the three-dimensional elasticity. In this report we present the basis of the theory of regular quaternionic functions of a reduced quaternion variable. Some variants of the quaternion Kolosov-Muskhelishvili formulae with the expressions for stresses are obtained. It is shown that in particular cases of plane and axially symmetric deformations these representation goes into the Kolosov–Muskhelishvili and Solovyov formulae expressed in terms of two complex functions. Some applications of quaternion representations for elastic equilibrium problems are shown.

THEORY OF QUATERNIONIC FUNCTIONS

Let $\mathbf{i}$, $\mathbf{j}$, $\mathbf{k}$ be the basic quaternions obeying the following rules of multiplication: $\mathbf{i}^2 = \mathbf{j}^2 = \mathbf{k}^2 = \circ\, \mathbf{1}$, $\mathbf{ij} = \circ\, \mathbf{ji} = \mathbf{k}$, $\mathbf{jk} = \circ\, \mathbf{kj} = \mathbf{i}$, $\mathbf{ki} = \circ\, \mathbf{ik} = \mathbf{j}$. An element q of the quaternion algebra $\mathbb{H}$ we write in the form $q = q_0 + \mathbf{i}q_x + \mathbf{j}q_y + \mathbf{k}q_z = q_0 + \mathbf{q}$, q_0 is the scalar part of a quaternion, $\mathbf{q} = \mathbf{i}q_x + \mathbf{j}q_y + \mathbf{k}q_z$ is the vector part of a quaternion q. The quaternion conjugation is denoted as $\tilde{q} = q_0 \circ\ \mathbf{q}$. Let x, y, z be the Cartesian coordinates in the Euclidean space $\mathbb{R}^3$. A quaternion-valued function f of a reduced quaternion variable $\mathbf{r} = \mathbf{i}x + \mathbf{j}y + \mathbf{k}z \in \mathbb{R}^3$ is a mapping $f : \Omega \circ\!\to \mathbb{H}$ such that $f(\mathbf{r}) = f_0(\mathbf{r}) + \mathbf{f}(\mathbf{r}) = f_0(x, y, z) + \mathbf{i}f_x(x, y, z) + \mathbf{j}f_y(x, y, z) + \mathbf{k}f_z(x, y, z)$. The differential operator $\nabla = \mathbf{i}\partial_x + \mathbf{j}\partial_y + \mathbf{k}\partial_z$ is called the generalized Cauchy– Riemann operator. A function f is called (left) regular if $\nabla f = 0$. With the vector notations the regularity condition is given as follows: $\nabla f(\mathbf{r}) = \circ\, \nabla \cdot \mathbf{f}(\mathbf{r}) + \nabla f_0(\mathbf{r}) + \nabla \times \mathbf{f}(\mathbf{r}) = 0$, where $\nabla f_0,\ \nabla \cdot \mathbf{f},\ \nabla \times \mathbf{f}$ are the usual gradient, divergence and curl, respectively. This system in the Cartesian coordinates is called the Moisil–Theodoresco system (MTS) and is a spatial generalization of the Cauchy-Riemann system. For quaternion functions analogues of the main properties of the holomorphic complex functions have been established (see [1]–[4]).

The quaternion function F is called a primitive of a regular function f if $\nabla F = f$. Because of a regular function f is a harmonic function then a primitive function F is also harmonic and the function F is also called as a harmonic primitive.

THREE–DIMENSIONAL ANALOGUES OF THE KOLOSOV–MUSKHELISHVILI FORMULAE

The equation of elastic equilibrium is called the Lame equation and has the next form

$$L\mathbf{u} \equiv (\lambda + 2\mu)\nabla(\nabla \cdot \mathbf{u}) \circ\ \mu\nabla \times (\nabla \times \mathbf{u}) = 0. \tag{1}$$

If we introduce the next scalar function f_0 and vector function $\mathbf{f}$:

$$(\lambda + 2\mu)\nabla \cdot\ \mathbf{u} = f_0, \quad \circ\, \mu\nabla \times \mathbf{u} = \mathbf{f}, \tag{2}$$

then the Lame equation (1) is transformed into the MTS, thus, the quaternion function $f = f_0 + \mathbf{f}$ is regular.

*Email: grigyum@yandex.ru

The three-dimensional analogue of the Kolosov–Muskhelishvili formulae for a displacement is obtained in the next form

$$2\mu\mathbf{u}(\mathbf{r}) = \varkappa\Phi(\mathbf{r}) \circ \widetilde{\mathbf{r}\varphi(\mathbf{r})} \circ \widetilde{\psi(\mathbf{r})},\ \varkappa = \circ\ \frac{3\lambda+7\mu}{\lambda+\mu} = \circ\ 7+8\nu, \tag{3}$$

where as Φ one can take any primitive of function φ, having subordinated ψ to the condition $\varkappa\Phi_0 = \mathbf{r}\cdot\boldsymbol{\varphi}+\psi_0$; ν is a Poisson's ratio. Thus, the vector of elastic displacement is represented in terms of two arbitrary regular functions φ, ψ and a harmonic primitive Φ of a function φ. It is proved that the quaternion representation (3) is a general solution of the Lame equation (1) in the cases of star–shaped domains or simply connected domains with a smooth boundary. Components of a stress tensor are also expressed in terms of regular functions φ, ψ and a harmonic primitive Φ.

In the case of star–shaped regions we have other form of a quaternion representation:

$$\mathbf{u}(\mathbf{r}) = \frac{\mathbf{r}}{\mu} \times I^1\mathbf{f} + \nabla\left\{r^2\left[\frac{3\lambda+7\mu}{4\mu(\lambda+2\mu)}I^{1/2} \circ\ \frac{1}{\mu}I^1\right]f_0\right\} + \nabla g_0, \quad I^\alpha f = \int_0^1 t^\alpha f(\mathbf{r}t)dt, \tag{4}$$

where the regular function f is from (2); g_0 is an arbitrary scalar harmonic function thus ∇g_0 is a pure vector regular function. It is shown that quaternion representations (3) and (4) are equivalent. It can be shown that in particular cases of plane and axially symmetric deformations these representations goes into the Kolosov–Muskhelishvili and Solov'ev formulae expressed in terms of two complex functions.

APPLICATIONS

From the quaternion representation (4) the new representation of a general solution of the Lame equation expressed in terms of three harmonic functions is obtained. With the help of that representation solutions of each of four main problems about an elastic ball's equilibrium are expressed through solutions of three independent Dirichlet and Neumann problems for the harmonic functions. Thus the solutions of these elastic problems are obtained in closed forms in quadratures and these quadratures are expressed in terms of the Appell hypergeometric functions. For the solution of the first main problem of an elastic equilibrium of an arbitrary body the three dimensional quaternion analogue of the Muskhelishvili integral equation is obtained by means of the representation (3). Basics of the quaternionic boundary element method with the numerical example are presented. The system of polynomial solutions of the Lame equation is obtained by means of the representation (4). As application of an approximation theorem for the MTS the theorem about a polynomial approximation for the Lame equation is established.

When it is necessary to reconstruct a stress field in a body from measurement data on a part of a boundary we must solve the Cauchy problem for the Lame equation. In this case we have overdetermined data on a part of a boundary (all components of the displacement and the stress vector) and unknown boundary conditions on the remaining part of a boundary. It is shown that this problem is equivalent to the problem of an analytical continuation of a regular quaternion function from a part of a boundary.

CONCLUSIONS

In this paper the theory of Moisil-Theodoresco system in terms of regular quaternion functions of reduced quaternion variable is used. Two variants of a quaternion representation of the Lame equation solution are presented. One of them was obtained in star–shaped regions with using radial integration operators, another one – in simply connected domains with a smooth boundary. These two representations in star–shaped domains are equivalence. It is shown that the quaternion representation in the case of plane deformation goes into the general Kolosov–Muskhelishvili solution and in the case of axially symmetric deformation goes into the general Yu.I. Solov'ev solution. Applications of these representations for solving three–dimensional elastic problems are shown.

This work was supported by RFBR grant 15-41-05081.

References

[1] F. Brackx, R. Delanghe, F. Sommen: Clifford Analysis. Research Notes in Mathematics No. 76, Pitman, London, 1982.

[2] Yu. Grigor'ev:Three–dimensional Quaternionic Analogue of the KolosovMuskhelishvili Formulae. Hypercomplex Analysis: New perspectives and applications, Trends in Mathematics, (Eds. S. Bernstein, U. Kaehler, I. Sabadini, F. Sommen), Birkhauser, Basel: 145-166, 2014, DOI 10.1007/978-3-319-08771-9-10.

[3] Yu. Grigoriev: Radial integration method in quaternion function theory and its applications. AIP Conference Proceedings, **1648**: 440003, 2015, DOI: 10.1063/1.4912654

[4] K. Gürlebeck, W. Sprößig: Holomorphic functions in the plane and n-dimensional space. Birkhauser-Verlag, 2008.

[5] D. Weisz–Patrault, S. Bock, K. Gürlebeck: Three–dimensional elasticity based on quaternion–valued potentials. International Journal of Solids and Structures, **51**: 3422-3430, 2014. DOI: 10.1016/j.ijsolstr.2014.06.002

ON CUSPED (TAPERED) PRISMATIC SHELLS

George Jaiani[1]

[1]*I.Vekua Institute of Applied Mathematics & Chair of Mechanics, I.Javakhishvili Tbilisi State University, Georgia*

Summary Well-posedeness of boundary value (BVP) and initial boundary value problems for elastic cusped (tapered) prismatic shells (i.e. for shells with vanishing thickness at the boundary) claims non-classical setting of boundary conditions (BC). The present paper is devoted to a concise up-dated exploratory survey of results within the framework of various models of prismatic shells, in particular, plates of variable thickness (Kirchoff-love model, hierarchical models, multi-layer models, etc.). It also contains the non-published results of the author concerning micropolar and classical (with microtemperatures) elastic cusped prismatic shells.

DEFINITION OF CUSPED PRISMATIC SHELLS

Let $Ox_1x_2x_3$ be an anticlockwise-oriented rectangular Cartesian frame. We conditionally assume the x_3-axis vertical. The elastic body is called a prismatic shell if it is bounded above and below by, respectively, the face surfaces $x_3 = \overset{(+)}{h}(x_1, x_2)$ and $x_3 = \overset{(-)}{h}(x_1, x_2)$, laterally by a cylindrical surface of generatrix parallel to the x_3-axis and its vertical dimension is sufficiently small compared with other dimensions of the body [1]: $\Omega := \big\{(x_1, x_2, x_3) \in \mathbb{R}^3 : (x_1, x_2) \in \omega, \overset{(-)}{h}(x_1, x_2) < x_3 < \overset{(+)}{h}(x_1, x_2)\big\}$, where $\overline{\omega} := \omega \cup \partial\omega$ is the so-called projection of the prismatic shell $\overline{\Omega} := \Omega \cup \partial\Omega$, the thickness $2h(x_1, x_2) := \overset{(+)}{h}(x_1, x_2) - \overset{(-)}{h}(x_1, x_2) > 0$ for $(x_1, x_2) \in \omega$, and $2h(x_1, x_2) \geq 0 \quad \text{for} \quad (x_1, x_2) \in \partial\omega$. Let $x_3 = \widetilde{h}(x_1, x_2)$ denote the middle surface of the prismatic shell, then $2\widetilde{h}(x_1, x_2) := \overset{(+)}{h}(x_1, x_2) + \overset{(-)}{h}(x_1, x_2)$. In the symmetric case of the prismatic shells (i.e., $\overset{(-)}{h}(x_1, x_2) = -\overset{(+)}{h}(x_1, x_2)$, therefore, $2\widetilde{h}(x_1, x_2) = 0$) we have to do with plates of variable thickness $2h(x_1, x_2)$ and a middle plane ω (see Figures 1, 2). Prismatic shells are called cusped ones if a set γ_0, consisting of $(x_1, x_2) \in \partial\omega$ for which $2h(x_1, x_2) = 0$, is not empty.

GOVERNING EQUATIONS

The governing equations of cusped prismatic shells are equations and systems of partial differential equations (PDE) with the order degeneration on γ_0. The order degeneration involves essentially different from the classical setting of BCs. Degeneration of governing systems is caused by the complexity of the geometry of the 3D body (e.g., cusps, cuspidal edges).

Let us give as examples: (i) Kirchoff-Love bending equation (see [2], Chap. V, Sec. 40 and also [3])

$$Bw := (Dw_{,11})_{,11} + (Dw_{,22})_{,22} + \nu(Dw_{,22})_{,11} + \nu(Dw_{,11})_{,22} + 2(1-\nu)(Dw_{,12})_{,12} = q(x_1, x_2), \tag{1}$$

where w is the deflection, $D := \frac{2Eh^3}{3(1-\nu^2)}$ is the flexural rigidity of the plate, q is the lateral load, E is Young's modulus, ν is Poisson's ration (indices after comma mean differentiation with respect to the corresponding variables, displacements $u_3(x_1, x_2, x_3) = w(x_1, x_2)$, $u_\beta(x_1, x_2, x_3) = -x_3 w_{,\beta}$, $\beta = 1, 2$); (ii) the bending system of $N = 1$ approximation of I. Vekua's hierarchical models [4] (see also [1]):

$$\mu(hv_{30,\alpha})_{,\alpha} + 3\mu(hv_{\alpha 1})_{,\alpha} = -\overset{0}{X}_3, \quad \mu\Big[(h^3 v_{\alpha 1,\beta})_{,\alpha} + (h^3 v_{\beta 1,\alpha})_{,\alpha}\Big] + \lambda\big(h^3 v_{\gamma 1,\gamma}\big)_{,\beta} - \mu h(v_{30,\beta} + 3v_{\beta 1}) = -h\overset{1}{X}_\beta, \quad \beta = 1, 2, \tag{2}$$

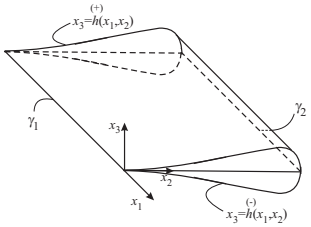

Figure 1: A cusped plate with sharp γ_1 and blunt γ_2 edges, $\gamma_0 = \gamma_1 \cup \gamma_2$. $\partial\Omega$ is a non-Lipschitz boundary

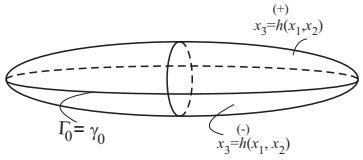

Figure 2: A blunt cusped plate with the edge γ_0. $\partial\Omega$ is a Lipschitz boundary

where Einstein's summation (Greek indices take values 1,2) convention is used, λ and μ are Lamé's constants (for symmetric shells $u_3(x_1,x_2,x_3) \cong \frac{1}{2}v_{30}(x_1,x_2)$, $u_\beta(x_1,x_2,x_3) \cong \frac{3}{2}x_3v_{\beta 1}(x_1,x_2)$, $\beta = 1,2,$); (iii) governing system of $N = 0$ approximation

$$\mu\big[(hv_{\alpha 0,\beta})_{,\alpha}+(hv_{\beta 0,\alpha})_{,\alpha}\big]+\lambda(hv_{\gamma 0,\gamma})_{,\beta}=-\overset{0}{X}_\beta,\ \beta=1,2,\ \ \mu(hv_{30,\alpha})_{,\alpha}=-\overset{0}{X}_3, \tag{3}$$

(displacements $u_i(x_1,x_2,x_3) \cong \frac{1}{2}v_{i0}(x_1,x_2)$, $i = 1,2,3$), unknowns v_{i0}, $i = 1,2,3$, $v_{\beta 1}$, $\beta = 1,2$, are so called weighted moments; $\overset{0}{X}_i$ $= 1,2,3$, $\overset{1}{X}_\beta$, $\beta = 1,2$, are expressed by tractions applied at face surfaces and by volume forces. Evidently, equations (1)-(3) have the order degeneration on γ_0.

We consider both the single-layer and multi-layered cusped prismatic shells within the framework of classical and micropolar theories of elasticity and thermoelasticity without or with microtemperatures. Some principal results obtained are stated in Conclusions.

CONCLUSIONS

1. Cusped bodies, in particular, cusped shells, plates, and bars are not possible to be fully investigated within the framework of 3D Elasticity Theory, since its methods fail for bodies with non-Lipschitz boundaries.
2. Only by means of 2D and 1D models can be revealed the peculiarities of setting BCs for cusped bodies [1,3].
3. Within the framework of 2D models for cusped bodies (the presence of cusped edges implies order degeneration of the governing 2D PDEs, see [1,3,5,6]): (i) both the cases of Lipschitz and non-Lipschitz 2D boundaries can be studied; (ii) BVPs which fall outside the framework of 3D model can be set and solved; (iii) the sequence ($N = 0, 1, 2, ...$) of approximate solutions can be considered as a solution of the corresponding 3D BVPs (in particular, in the case of the Lipschitz 2D boundary the above sequence can be replaced by its H^1 limit [5]).
4. If at cusped edges concentrated along a cusped edge (i.e., along a line) forces are applied then stresses become infinite (since the area of loading equals zero) but integrated stress vectors are finite at the cusped edge.
5. In $N = 0$ approximation, when the cusped prismatic shell-like body projection is a half-plane $x_2 \geq 0$, the thickness $2h = h_0x_2^\kappa$, κ, $h_0 = \text{const} \geq 0$, and at the edge $x_2 = 0$ integrated stress vector (either distributed but concentrated along the cusped edge or concentrated at point of the cusped edge load) is applied, the problem is solved in the explicit form (in quadratures). For $\kappa > 0$ prismatic shell-like body is cusped one; for $\kappa = 0$ we have the plate of a constant thickness. The Flamant, Ceruti, and Carothers type problems are solved in the explicit form, which contain as particular cases the classical Flamant, Ceruti, and Carothers formulas [1] (see also [7]). Cusped edges cannot be clamped (fixed) or be simply supported in all the cases of sharpening; e.g., let ω lies in $x_2 \geq 0$ and γ_0 is a segment of the x_1-axis, then (see [1,3]) (i) in $N = 0$ approximation γ_0 can be fixed only if $\kappa < 1$ (blunt edge), while by $\kappa \geq 1$ (cusped edge) γ_0 should be free; (ii) for Kirchhoff-Love and I. Vekua $N = 1$ models at γ_0: w and v_{30} can be prescribed only if $\kappa < 2/3$, while $w_{,2}$ and $v_{\alpha 1}$, $\alpha = 1,2$, can be prescribed only if $\kappa < 1/3$. If $\kappa \geq 2/3$ ($\kappa > 1/3$), then BC on γ_0 should be replaced by the boundedness of w, v_{30} ($w_{,2}$, $v_{\beta 1}$, $\beta = 1,2$) in right neighbourhood of γ_0. On $\partial\omega\backslash\gamma_0$ all the classical BCs can be prescribed.
6. In the case of geometrically non-linear (von-Kármán-Föppl type) model in contrast to linear model shearing forces and bending moments cannot be always correctly applied. The corresponding criteria are established [8].
7. Considering hierarchical models for cusped elastic prismatic shells with microtemeratures in addition to peculiarities of setting BCs at cusped edges (see Point 5 of Conclusions) for displacement vector weighted moments the similar peculiarities arise also for microtemperature vector weighted moments. The same is true for weighted moments of displacements and microrotations in the case of hierarchical models of micropolar elastic cusped prismatic shells.

References

[1] Jaiani G.: Cusped Shell-like Structures, SpringerBriefs in Applied Science and Technology, Springer-Heidelberg-Dordrecht-London-New York 2011.

[2] Timoshenko S., Woinowsky-Krieger S.: Theory of Plates and Shells. McGraw-Hill Book Company, New York-Totonto-London 1959.

[3] Jaiani G.V.: Theory of Cusped Euler-Bernoulli Beams and Kirchoff-Love Plates. Lect. Notes TICMI 3, 2002.

[4] Vekua I.N.: Shell Theory: General Methods of Construction. Pitman Advanced Publishing Program, Boston-London-Melbourne 1985.

[5] Jaiani G., Kharibegashvili S., Natroshvili D., Wendland W.L.: Two-dimensional Hierarchical Models for Prismatic Shells with Thickness Vanishing at the Boundary, Journal of Elasticity 77(2):95-122, 2004 (Sringer 2005).

[6] Chinchaladze N., Gilbert R., Jaiani G., Kharibegashvili S., Natroshvili D.: Existence and uniqueness theorems for cusped prismatic shells in the N-th hierarchical model. Math. Methods Appl. Sci. 31(11):1345-1367, 2008.

[7] Chinchaladze N., Jaiani G., Maistrenko B., and Podio-Guidugli P.: Concentrated contact interactions in cuspidate prismatic shell-like bodies, Archive of Applied Mechanics 81(10):1487-1505, 2011.

[8] Chinchaladze N., Jaiani G.: Cylindrical Bending of a Cusped Plate with Big Deflections, Journal of Mathematical Sciences 157(1):52-69, 2009.

DISCONTINUOUS SOLUTIONS OF THE NONLINEAR THEORY OF VOLTERRA DISLOCATIONS

Mikhail Karyakin[a] & Olga Pustovalova
I.I.Vorovich Institute of Mathematics, Mechanics and Computer Science,
Southern Federal University, Rostov-on-Don, Russia

Summary The paper studies different aspects of the cavity formation along the axis of screw dislocation and wedge disclination within the framework of nonlinear elasticity of incompressible media. For some classes of elastic energy functions the necessary conditions for the existence of discontinuous solutions were determined. Several boundary value problems on the formation of a cavity in a nonlinear elastic body with isolated defects were resolved taking into account the microstructure of the material. For this purposes the theory of Cosserat continuum has been used. It was shown that account of microstructure typically reduces the radius of the cavity until its complete elimination.

INTRODUCTION

Though the hole model of the dislocation core have been using in physics and mechanics of crystals since the concept of dislocation was invented, real observations of cavities connected with dislocations were done much later [1]. Disclination structures containing cavities were found in the cobalt nanowires in 2008 [2]. As to the mathematical modelling of cavitation in solids the pioneer work of J. Ball [3] should be mentioned. He showed that the problem of the expansion of the isotropic sphere can have a solution that describes the formation of a cavity in the center of the ball. The existence of discontinuous solutions of the problems of the formation of dislocation and disclination in nonlinear elastic bodies was for the first time shown in the works of L. Zubov et al [4–5].

The studying of mechanical fields of the isolated defects is based in this work upon the semi-inverse representations describing the dependence of the radius-vector of the body point in the deformed state upon its position in the reference (non-deformed) configuration:

$$R = P(r),\ \Phi = \varphi,\ Z = a\varphi + z \tag{1}$$

for screw dislocation with Burgers vector of the length $2\pi a$, and

$$R = P(r),\ \Phi = \kappa\varphi,\ Z = z \tag{2}$$

for wedge disclination with Frank vector proportional to $\kappa - 1$.

CLASSICAL CONTINUUM

General equilibrium equations and boundary conditions

Boundary value problem for the cylinder with isolated defect consists of equilibrium equations $\operatorname{div}\mathbf{D} = 0$ for Piola stress tensor $\mathbf{D}$, boundary conditions on free surface $\mathbf{n}\cdot\mathbf{D} = 0$ and constitutive relations $\mathbf{D} = -p\mathbf{F}^{-1} + \mathbf{S}^{\mathrm{T}}$, where $\mathbf{F}$ – deformation gradient, and $\mathbf{S}$ can be expressed in terms of potential energy function W by $\mathbf{S} = \partial W / \partial \mathbf{F}$. Existence of dislocations can be accounted by some extra relations [4] or in the semi-inverse representation of the solution (1) or (2). In latter case boundary conditions on the ends of the cylinder are satisfied in the integral (Saint-Venant) sense.

For compressible materials the problem above is reduced to the nonlinearly (generally speaking) second order boundary problem relative to $P(r)$ function describing the radius of the cylinder in the deformed configuration. In the case of incompressible materials this function can be determined analytically from the incompressibility condition $\det\mathbf{F} = 1$:

$$P(r) = \kappa^{-\frac{1}{2}}\sqrt{r^2 + A^2}\ . \tag{3}$$

Discontinuous solutions

The cavity formation near the defect line corresponds to discontinuous solution for solid cylinder when constant A in (3) is not equal to zero. The equation for this constant can be obtained by direct analysis of boundary value problem when solid cylinder is considering as a limiting case of the hollow one, or by energy approach thus calculating extreme value of potential strain energy with respect to "cavity" parameter A. Both approaches lead to the same equation

$$\int_0^{r_1} \frac{1}{\sqrt{r^2 + A^2}}(-P'^2 S_{rR} + S_{\varphi\Phi})dr = 0 \tag{4}$$

Conditions of the existence of nontrivial solutions of Eq. (4) are in turn the necessary conditions of existence of the discontinuous solutions of the original problems. In particular for strain energy function depending upon primary invariants of Cauchy-Green strain measure I_1, I_2 these conditions can be written as $W < \text{const}\, I_1^{1-\beta}$, $I_1 \to \infty$; $W < \text{const}\, I_2^{1-\beta}$,

[a] Corresponding author. Email: karyakin@sfedu.ru.

$I_2 \to \infty;\ \beta > 0$. The state with the hole is preferred from energetic point of view. In can be shown both numerically and analytically that the total energy of the cylinder with the cavity is always less than the energy of the solid cylinder. That means that the hole formation is energetically advantageous.

CONTINUUM WITH MICROSTRUCTURE

In the model of Cosserat's continuum [6–7] each particle of the media has the degrees of freedom of absolutely rigid body. The particle's position in deformed configuration is described by radius-vector $\mathbf{R}$ and properly orthogonal tensor $\mathbf{H}$ (tensor of micro-rotation). The elastic potential W is the function of two tensors of the second range – measure of deformation $\mathbf{Y} = \mathbf{F}^{\mathrm{T}} \cdot \mathbf{H}^{\mathrm{T}}$ and the tensor of bending strain $\mathbf{L}$, determining from the equation $\operatorname{div}\left(\mathbf{H} \cdot \mathbf{H}^{\mathrm{T}}\right) = -\mathbf{L} \times \mathbf{I}$. To analyse the problems of dislocations and disclinations one should add one extra assumption to the semi-inverse representations (1) or (2), namely the presentation of $\mathbf{H}$ tensor. For the problem of disclination following form is suitable:

$$\mathbf{H} = \cos\chi(\mathbf{e}_r\mathbf{e}_R + \mathbf{e}_\varphi\mathbf{e}_\Phi) + \sin\chi(\mathbf{e}_r\mathbf{e}_\Phi + \mathbf{e}_\varphi\mathbf{e}_R) + \mathbf{e}_z\mathbf{e}_Z$$

where $\chi(r)$ – angle function that describes the proper rotation of the particle, not associated with the strain of the continuum; for the problem of dislocation this presentation is similar.

To study the possibility of the hole formation in the Cosserat media energy approach is more suitable and the equation for determining the radius of the cavity similar to (4) can be obtained. The results of its numerical investigation in the case of dislocation for the energy function $W = 2\mu\,\mathrm{tr}(\mathbf{Y} - \mathbf{I}) + \eta m^{-1}\left|\mathrm{tr}\,\mathbf{L}\right|^m$ are presented at the figures below where dependence of the hole radius upon the dislocation parameters is depicted (solid line corresponds to the classical nonlinear elasticity).

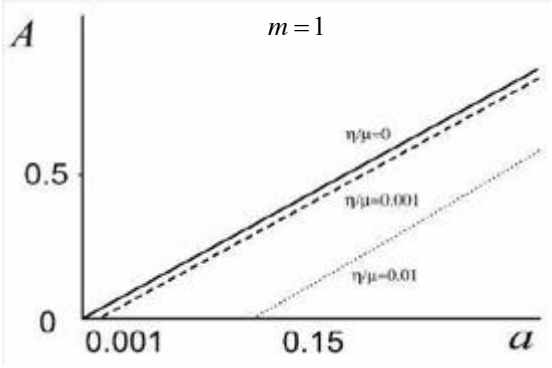

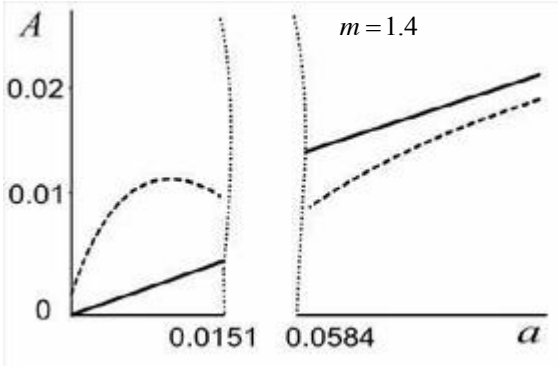

CONCLUSIONS

In the framework of the nonlinear theory of elasticity for incompressible media an equation for determining the radius of the cavity which can be formed around the axis of the wedge disclination and screw dislocation was formulated. Necessary conditions of the cavity existence were obtained as the limit relations of specific potential energy function. It was shown that the state with the cavity (in the case of its existence) is energetically favourable. It was shown that this existence or non-existence is not related with well-known Hadamard inequality of nonlinear elasticity. For an incompressible nonlinear elastic Cosserat continuum it was shown that for a screw dislocation microstructure effect of accounting is not univalent. Typically, this consideration leads to a decrease in the radius of the cavity up to its complete elimination. At the same time there are models of materials and range of material and geometric parameters for which the radius of the cavity in the Cosserat medium surpasses the similar value of the classical theory of elasticity.

References

[1] Tanaka H. Observations of holes around dislocation core in SiC crystal. *Journal of Crystal Growth*: **53**(3): 630-632, 1981.

[2] Zhou K., Wu M.S., Nazarov A.A.: Relaxation of a disclinated tricrystalline nanowire. *Acta Materialia* **56**: 5828–5836, 2008.

[3] Ball J. M.: Discontinuous equilibrium solutions and cavitaton in nonlinear elasticity. *Phil. Trans. R. Soc. Lond.* **306**: 557-611, 1982.

[4] Zubov L.M.: Nonlinear Theory of Dislocations and Disclinations in Elastic Bodies. Springer, 2001.

[5] Eremeev V. A., Zubov L. M., Karyakin M. I., Chernega N. Ya.: Formation of cavities in nonlinearly elastic bodies with dislocations and disclinations. *Dokl. Ross. Akad. Nauk*. **326**: 968-971, 1992.

[6] Toupin R.A: Theories of elasticities with the couple-stresses. *Arch. Ration Mech. and Analysis*. **17**: 85-112, 1964.

[7] Shkutin L.I.: Nonlinear models of deformable media with couple-stresses. *Journal of Applied Mechanics and Technical Physics.* **21** (6): 826-831,1980.

ANALYSIS FOR ARBITRARY MISFIT DISLOCATIONS CONSIDERING INTERFACE PROPERTY

Hideo Koguchi[1]
[1]*Department of Mechanical Engineering, Nagaoka University of Technology, Nagaoka, Niigata, Japan*

Summary Misfit dislocations occur at the interface under a combination of materials with different lattice lengths. When a external force is applied to materials, and Burger's vector of the misfit dislocation varies. Then, a solution for an arbitrary misfit dislocation is needed. For this problem, a model for incoherent interface is proposed and equations for the displacement and stress fields around the misfit dislocation are derived incorporating the interface stress and the interface elasticity. The stress distribution along the interface is investigated precisely. The effect of the interface properties, such as the interface stress and the interface elasticity, on the singular stress field around the misfit dislocation is clarified.

INTRODUCTION

Recent advanced electro-mechanical system and electronic devices are manufactured using nanotechnology. A nano-scaled bump or wire can be built on a substrate using such as atomic layer epitaxy and molecular beam epitaxy technologies. When the crystal structure in the bump is different from that in the substrate, mismatch dislocation occurs at the interface. It is known that interface stress generally exists at the interface like the surface stress. In a nanoscale, the interface properties, such as interface stresses and interface elasticity, influence on the stress and displacement field near the interface. In the present paper, an arbitrary misfit dislocation is introduced to a coherent interface to calculate the stress and displacement distributions in an incoherent interface. The stress and displacement fields are analytically derived and the influence of interface properties on the stress fields near the interface is discussed.

ANALYSIS METHOD

Anisotropic elastic material is considered, and a rectangular Cartesian coordinate system is used.

A model for analysis is two half-anisotropic materials joined at $x_3 = 0$. The upper region ($0 \le x_3$) is material 1 and the lower region ($x_3 < 0$) is material 2. Here, solutions for two regions considering the conditions for $\mathbf{u} = \mathbf{0}$ and $\mathbf{t} = \mathbf{0}$ as $x_3 \to \infty$ and misfit dislocation are set at the interface as:

1) $0 \le x_3$ for material 1

$$\tilde{\mathbf{u}}^{(1)}\left(\eta_1,\eta_2,x_3\right) = \overline{\mathbf{A}}^{(1)}\left\langle e^{-\overline{ip}_\alpha^{(1)}\rho x_3}\right\rangle \overline{\mathbf{q}}^{(1)}, \quad \tilde{\mathbf{t}}^{(1)}\left(\eta_1,\eta_2,x_3\right) = -i\rho\overline{\mathbf{B}}^{(1)}\left\langle e^{-\overline{ip}_\alpha^{(1)}\rho x_3}\right\rangle \overline{\mathbf{q}}^{(1)} \tag{1}$$

2) $x_3 < 0$ for material 2

$$\tilde{\mathbf{u}}^{(2)}\left(\eta_1,\eta_2,x_3\right) = -\mathbf{A}^{(2)}\left\langle e^{-\overline{ip}_\alpha^{(2)}\rho x_3}\right\rangle \mathbf{q}^{(2)}, \quad \tilde{\mathbf{t}}^{(2)}\left(\eta_1,\eta_2,x_3\right) = i\rho\mathbf{B}^{(2)}\left\langle e^{-ip_\alpha^{(2)}\rho x_3}\right\rangle \mathbf{q}^{(2)} \tag{2}$$

Here, the superscripts (1) and (2) for $\mathbf{A}$, $\mathbf{B}$ and p_α denote materials 1 and 2, $\overline{\mathbf{q}}^{(1)}$ and $\mathbf{q}^{(2)}$ are unknown vectors to be determined from the boundary conditions.

Boundary condition for interface

A model for interface is proposed to incorporate the interface properties. Here, a region referred to as an interface zone is supposed between materials 1 and 2. The positions of atoms at the interface do not match in materials 1 and 2. So, the traction vector acting on each material may be mismatch as shown in Fig.1. Now, a traction vector $\mathbf{t}^{(\mathrm{int})}$ is introduced as a traction in the interface zone. This traction originated from atomic structures near the interface is different from the traction in bulk and depends on the interface properties in a view of continuum mechanics. Then, an equilibrium condition at the interface zone is derived. The unknown vectors, $\overline{\mathbf{q}}^{(1)}$ and $\mathbf{q}^{(2)}$, are determined using the following Eqs.(3) and (4).

1) Boundary condition of misfit dislocation

$$\tilde{\mathbf{u}}^{(1)} - \tilde{\mathbf{u}}^{(2)} = \overline{\mathbf{A}}^{(1)}\overline{\mathbf{q}}^{(1)} + \mathbf{A}^{(2)}\mathbf{q}^{(2)} = \Delta\tilde{\mathbf{u}}_{dis} \tag{3}$$

2) Boundary condition of traction

$$\tilde{\mathbf{t}}^{(1)} - \tilde{\mathbf{t}}^{(2)} - \rho^2\left(\mathbf{F}_1\tilde{\mathbf{u}}^{(1)} + \mathbf{F}_2\tilde{\mathbf{u}}^{(2)}\right) = -i\rho\left(\overline{\mathbf{B}}^{(1)} + i\rho\mathbf{F}_1\overline{\mathbf{A}}^{(1)}\right)\overline{\mathbf{q}}^{(1)} - i\rho\left(\mathbf{B}^{(2)} + i\rho\mathbf{F}_2\mathbf{A}^{(2)}\right)\mathbf{q}^{(2)} = \mathbf{0} \tag{4}$$

where $\Delta\tilde{\mathbf{u}}_{dis}$ represents the Fourier transformed misfit dislocation, and matrices, $\mathbf{F}_1$ and $\mathbf{F}_2$, are consisted of the interface properties in materials 1 and 2.

[1)] Hideo Koguchi. Email: Koguchi@mech.nagaokaut.ac.jp.

Solutions

Here, an arbitrary misfit dislocation is considered. Furthermore, an oblique coordinate system, $(\hat{x}_1,\hat{x}_2)$, is introduced at the interface to express a network of dislocation. The coordinates are related to Cartesian coordinates following a relationship.

$$\hat{x}_1 = h_{11}x_1 + h_{12}x_2, \quad \hat{x}_2 = h_{21}x_1 + h_{22}x_2 \tag{5}$$

The arbitrary misfit dislocation can be expressed within a range of period, L, as:

$$\Delta\mathbf{u}_{dis}(\hat{x}_1,\hat{x}_2) = \mathbf{a}_0 + \sum_{n=1}^{\infty}\left(\mathbf{a}_n \cos \ell_{1n}\hat{x}_1 + \mathbf{b}_n \sin \ell_{1n}\hat{x}_1\right) + \sum_{m=1}^{\infty}\left(\mathbf{c}_m \cos \ell_{2m}\hat{x}_2 + \mathbf{d}_m \sin \ell_{2m}\hat{x}_2\right) \tag{6}$$

where $\ell_{1n} = n\pi/L_1$ and $\ell_{2m} = m\pi/L_2$.

The displacements and stresses in a real space are derived by applying the inverse Fourier transform to the equations of Eqs.(1) through (2), into which the relationship of Eq.(6) are substituted.

1) $0 \le x_3$ for material 1

$$u_j^{(\,)} = \frac{\overline{A}_{jk}^{(\,)}\hat{W}_{Dkl}}{2\pi}\left\{a_{0l}e^{-2\pi i\overline{p}_k^{(\,)}x_3} + \sum_{n=1}^{\infty}\left[a_{nl}e^{-2\pi i\overline{p}_k^{(\,)}x_3}\cos k_{1n} + b_{nl}e^{-2\pi i\overline{p}_k^{(\,)}x_3}\sin k_{1n}\right] + \sum_{m=1}^{\infty}\left[c_{ml}e^{-2\pi i\overline{p}_k^{(\,)}x_3}\cos k_{2m} + d_{ml}e^{-2\pi i\overline{p}_k^{(\,)}x_3}\sin k_{2m}\right]\right\} \tag{7}$$

where $k_{1n} = (h_{11}x_1 + h_{12}x_2)n\pi/L_1$ and $k_{2m} = (h_{21}x_1 + h_{22}x_2)m\pi/L_2$.

2) $x_3 < 0$ for material 2

$$u_j^{(\,)} = -\frac{\overline{A}_{jk}^{(\,)}\hat{S}_{Dkl}}{2\pi}\left\{a_{0l}e^{-2\pi ip_k^{(\,)}x_3} + \sum_{n=1}^{\infty}\left[a_{nl}e^{-2\pi ip_k^{(\,)}x_3}\cos k_{1n} + b_{nl}e^{-2\pi ip_k^{(\,)}x_3}\sin k_{1n}\right] + \sum_{m=1}^{\infty}\left[c_{ml}e^{-2\pi ip_k^{(\,)}x_3}\cos k_{2m} + d_{ml}e^{-2\pi ip_k^{(\,)}x_3}\sin k_{2m}\right]\right\} \tag{8}$$

where $\hat{\mathbf{W}} = \left\{\left(\mathbf{A}^{(\,)}\right)^{-1}\overline{\mathbf{A}}^{(\,)} - \left(\mathbf{B}^{(\,)} + 2\pi i\mathbf{F}_2\mathbf{A}^{(\,)}\right)^{-1}\left(\overline{\mathbf{B}}^{(\,)} + 2\pi i\mathbf{F}_1\overline{\mathbf{A}}^{(\,)}\right)\right\}^{-1}$, $\hat{\mathbf{W}}_{\mathbf{D}} = \hat{\ }\left(\ \ ^{(\,)}\right)^{-1}$,

$\hat{\mathbf{S}} = \left\{\left(\overline{\mathbf{A}}^{(\,)}\right)^{-1}\mathbf{A}^{(\,)} - \left(\overline{\mathbf{B}}^{(\,)} + 2\pi i\mathbf{F}_1\overline{\mathbf{A}}^{(\,)}\right)^{-1}\left(\mathbf{B}^{(\,)} + 2\pi i\mathbf{F}_2\mathbf{A}^{(\,)}\right)\right\}^{-1}$ and $\mathbf{S}_{\mathbf{D}} = \left(\ \ ^{-(\,)}\right)^{-1}$.

Expressions for stress fields can be derived in the same way as the displacement fields.

Results

Material properties used in the calculation of displacement and stress fields are obtained from the MD analysis. Figs.1(b) and 1(c) demonstrate the distributions of the displacement, u_x, along the x-coordinate at z=-0.40 nm in Cu and z =0.40 nm in Au. Curves for different magnification of the interface properties are plotted. For instance, dotted line represents the result for classical boundary condition. Blue line indicates the distribution for a magnification of 2. The displacement, u_x, in Cu increases with the increase of the magnification. At lower magnification, the direction of displacements in Cu and Au is opposite, however, as the magnification increases, displacements are the same direction. This is attributed to the increase of stiffness in the interface.

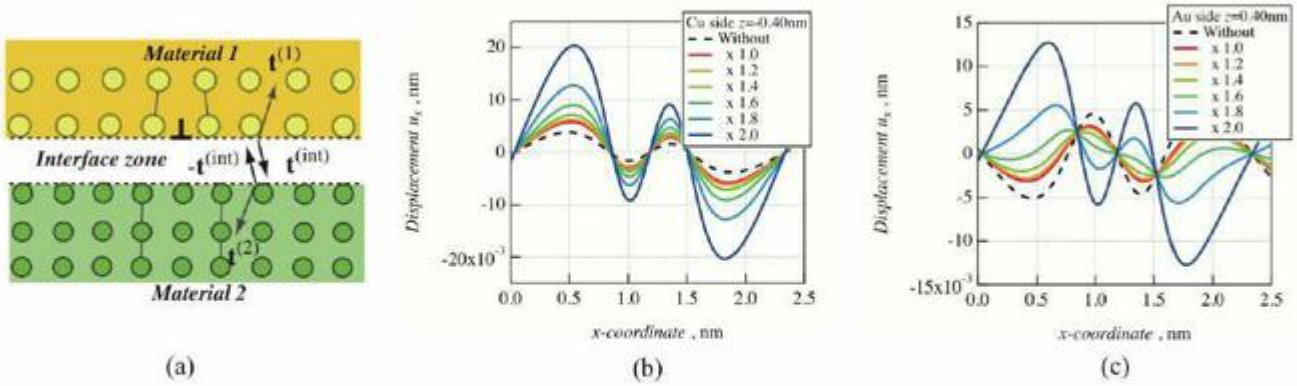

(a) (b) (c)

Figure 1: **A model of interface zone in two-phase materials (a), results of analysis (b) and (c)**

CONCLUSIONS

In the present paper, the expressions for displacement and stress fields near an interface with arbitrary misfit dislocations were derived using Stroh's formalism and the boundary condition with the interface properties, such as the interface stresses and the interface elasticity. It was found that the displacements and the stresses increase with the increase of the interface properties.

ON THE CONSTITUTIVE MODELLING OF ELASTOMERIC FOAMS

Attila Kossa [a)]
Budapest University of Technology and Economics
Department of Applied Mechanics
Budapest, Hungary

Summary. Accurate modelling technique of the mechanical behaviour of elastomeric foams is presented. The finite strain elastic behaviour is represented using the Ogden-Hill's compressible hyperelastic material model. A novel biaxial compression fixture was developed in order to capture the material behaviour in equibiaxial compression. A new accurate algorithm is proposed for the parameter fitting process.

1. INTRODUCTION

Polymeric foams are highly compressible materials due to their cellular (either open-celled or closed-celled) structure. An effective approach to model the material behaviour of these foams is the application of a suitable hyperelastic material model proposed for highly compressible (in volumetric sense) materials. The most widely-used hyperelastic foam material model is the Ogden—Hill's compressible foam material, which is termed as "hyperfoam" model in the commercial finite element software ABAQUS [1]. Hill [2] proposed a volumetric strain energy function for the Ogden's compressible hyperelastic model [3]. A generalized representation of this combined model was presented by Storåkers [4]. A slightly modified version of this model is the hyperfoam model in ABAQUS. However, it should be noted that in [4] the strain energy function is written in a series form, where the material parameter related to the volumetric deformation is the same for each term in the series representation. The strain energy function implemented in ABAQUS allows to use multiple material parameters (β_i) for the volumetric term:

$$W = \sum_{i=1}^{N} \frac{2\mu_i}{\alpha_i^2}\left(\lambda_1^{N_i} + \lambda_2^{N_i} + \lambda_3^{N_i} - 3\right) + \sum_{i=1}^{N} \frac{2\mu_i}{\alpha_i^2 \beta_i}\left(J^{-N_i\beta_i} - 1\right)$$

where α_i, β_i, μ_i are material parameters, N is the model order, whereas J defines the volume ratio. The principal stretches are denoted by $\lambda_1, \lambda_2, \lambda_3$. In order to obtain material parameters, which accurately represent the material behavior, various test experiments should be performed, such as the uniaxial tension/compression test, simple/pure shear tests, biaxial tension/compression test, volumetric compression test. Among these tests, the biaxial compression test is a crucial one for the parameter fitting process. A new biaxial compression fixture was developed to perform this type of test. The device is illustrated in Figure 1 [5].

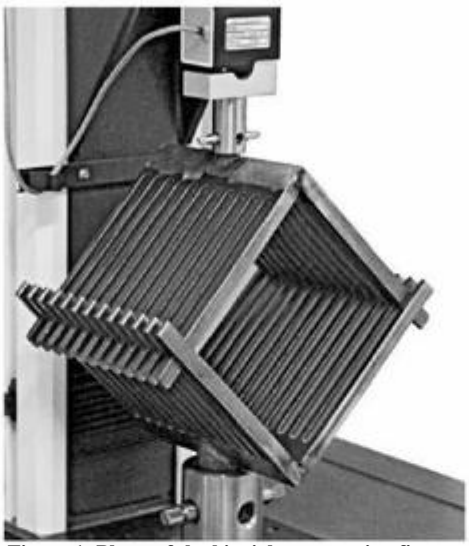

Figure 1: Photo of the biaxial compression fixture

2. STRETCH – STRESS RELATIONSHIPS

The principal nominal (engineering or 1st Piola-Kirchhoff) stresses (P_1, P_2, P_3) can be easily obtained from the strain energy potential (W) as

[a)] Corresponding author. Email: kossa@mm.bme.hu.

$$P_k = \frac{\partial W}{\partial \lambda_k} = \sum_{i=1}^{N} \frac{2\mu_i}{\alpha_i}\left(\lambda_k^{\alpha_i - 1} - \lambda_k^{-1} J^{-\alpha_i \beta_i}\right).$$

For isotropic uniaxial extension the volume ratio equals to $J = \lambda\lambda_T^2$, where λ is the stretch along the loading direction, whereas λ_T represents the transverse stretch. In case of biaxial expression, $J = \lambda^2\lambda_T$. Therefore, the nominal stress solutions can be expressed as

$$P^{UA} = \frac{1}{\lambda}\sum_{i=1}^{N} \frac{2\mu_i}{\alpha_i}\left(\lambda^{\alpha_i} - (\lambda\lambda_T^2)^{-\alpha_i\beta_i}\right), \qquad P_T^{UA} = \frac{1}{\lambda_T}\sum_{i=1}^{N} \frac{2\mu_i}{\alpha_i}\left(\lambda_T^{\alpha_i} - (\lambda\lambda_T^2)^{-\alpha_i\beta_i}\right),$$

$$P^{BA} = \frac{1}{\lambda}\sum_{i=1}^{N} \frac{2\mu_i}{\alpha_i}\left(\lambda^{\alpha_i} - (\lambda^2\lambda_T)^{-\alpha_i\beta_i}\right), \qquad P_T^{BA} = \frac{1}{\lambda_T}\sum_{i=1}^{N} \frac{2\mu_i}{\alpha_i}\left(\lambda_T^{\alpha_i} - (\lambda^2\lambda_T)^{-\alpha_i\beta_i}\right).$$

In the above expressions, superscript *UA* refers to the uniaxial extension, whereas *BA* refers to the biaxial extension. Subscript T indicates the transverse direction. Due to the stress-free boundary the transverse stress must be zero, $P_T = 0$. It is very important to emphasize that the transverse stretch cannot be eliminated from these expressions if the model order is greater than $N = 1$. Consequently, the stresses are functions of the stretches along the loading (λ) and along the transverse (λ_T) directions. If the material would be incompressible, then the transverse stretch could be eliminated using the incompressibility constraint $J = 1$. However elastomeric foams exhibit large volumetric change during the deformation, thus $J \neq 1$.

3. PARAMETER FITTING

The uniaxial and biaxial extension tests provide the experimental data pairs $\left(\lambda_q^{UAexp}, P_q^{UAexp}\right)$ and $\left(\lambda_r^{BAexp}, P_r^{BAexp}\right)$, where $q = 1,2,3 \ldots Q$ and $r = 1,2,3 \ldots R$ are the captured data points. In order to fit the stress solutions to the experimental data, the transverse stretches (λ_T) must be provided for the optimization routine. The most simple approach to take into account the transverse stretches is to neglect them, thus letting $\lambda_T = 0$ (see [6,7] for instance). In this case, the constraint $P_T = 0$ is automatically satisfied. This method can be used only for foam materials, where the transverse deformations are negligible (mostly open-cell elastomeric foams). A more realistic approach is to determine the lateral stretches from the zero lateral stress constraint (see [8,9] for instance). This method involves the solution of a nonlinear equation (to obtain λ_T from $P_T = 0$) at every iteration steps in the minimization algorithm. Using this method may result that the predicted lateral stretches have poor accuracy compared to the test data.

Here, a new algorithm is proposed, where the measured transverse stretch values are used in the error function. The proposed error function is defined as

$$\Phi = \frac{1}{Q}\sum_{q=1}^{Q}\left(P_q^{UAexp} - P_q^{UAmod}\right)^2 + \frac{1}{Q}\sum_{q=1}^{Q}\left(P_{Tq}^{UAmod}\right)^2 + \frac{1}{R}\sum_{r=1}^{R}\left(P_r^{BAexp} - P_r^{BAmod}\right)^2 + \frac{1}{R}\sum_{r=1}^{R}(P_{Tr}^{BAmod})^2$$

In the expression above superscript *mod* refers to model response. Consequently, the zero transverse stress constraint is enforced via the error function, which has to be minimized to find the material parameters.

Acknowledgements

This research has been supported by the Hungarian Scientific Research Fund, Hungary (Project Identifier: PD 108691). This research has been supported by the HAESF (Hungarian-American Enterprise Scholarship Fund's) Senior Leaders and Scholars Fellowship program. These supports are gratefully acknowledged.

References

[1] ABAQUS (2011) Theory Manual, Dassault Systèmes, Providence, RI, USA.

[2] Hill, R.: Aspects of invariance in solid mechanics. *Advances in Applied Mechanics* 18, 1-75, 1978.

[3] Ogden, R.W.: Large Deformation Isotropic Elasticity: On the Correlation of Theory and Experiment for Compressible Rubberlike Solids. *Proceedings of the Royal Society of London. Series A, Mathematical and Physical Sciences* 328, 567-583, 1972.

[4] Storåkers, B.: On material representation and consitutive branching in finite compressible elasticity. *J. Mech. Phys. Solids* 34, 125-145, 1986.

[5] Kossa, A.: A new biaxial compression fixture for polymeric foams. *Polymer Testing* 45, 2015.

[6] Briody, C., Duignan, B., Jerrams, S., Tiernan, J.: The implementation of a visco-hyperelastic numerical material model for simulating the behaviour of polymer foam materials. *Computational Materials Science* 64., 47-51, 2012.

[7] Mills, N.: Polymer foams handbook. Elsevier, Oxford, 2007.

[8] Petre, M.T., Erdemir, A., Cavanagh, P.R.: Determination of elastomeric foam parameters for simulations of complex loading. *Computer Methods in Biomechanics and Biomedcal Engineering* 9., 231-242, 2006.

[9] Silber, G., Then, C.: Preventive Biomechanics. Springer, Berlin, 2013.

MODELING OF BIAXIAL RESPONSE OF POLYVINYLEDENE FLUORIDE (PVDF)

Harish Lambadi[1], Lakshmana Rao C[2]
[1,2] *Department of Applied Mechanics, Indian Institute of Technology Madras*

Summary Polyvinylidene Fluoride (PVDF) is a piezo polymer and exhibits both sensor and actuator effects for different potential applications in industries. In this study the experimental and modelling results of monotonic biaxial response of PVDF will be presented. A non contact speckle monitoring method was used to monitor point wise finite deformation in the specimen. A hyper elastic constitutive model using four invariants was used to capture the anisotropy in the mechanical response. A paper reports a good correlation between the proposed model and the observed experimental data.

INTRODUCTION

Polyvinylidene Fluoride has a basic building block of $-CH_2-CF_2-$ monomer. The microstructure of the PVDF is semi crystalline. In the manufacturing process, the PVDF polymers have been stretched in one direction and a high electric field is applied in the thickness direction to amplify the polling and improve the piezoelectricity to the PVDF. The PVDF film sheets are transparent have silver coating on top and bottom of the film to capture and transmit the conduction of electric charges across the material. The mechanical behavior of the PVDF film sheets has been addressed in literature using conventional tensile test setup to see mechanical response. Vinogradov et al. [1] have observed the mechanical anisotropic on to the PVDF film. Due to a mechanical stretch applied at the time of manufacture time, the PVDF has been observed to have a high strength in that direction compared to orthogonal (unstretched) direction. Due to semi crystalline nature and alignment of fiber in direction of stretch, we assume PVDF as a transversely isotropic in the direction perpendicular to the poling direction. A detailed investigation of the nature of anisotropy in finite deformation and its modeling is attempted in this paper.

In this study, 128μm thin metalized PVDF sheets were used to do biaxial tests. The samples were cut into cruiceform shape to do biaxial static tests and a black speckle was markers on these white films to track the displacements locally. The biaxial test setup has been used to carry out the experiment and measure the strains locally using a stingray digital camera, which is fixed in a direction orthogonally to the testing sample. The stress-strain plots which were observed from the image displacements were observed to yield better estimates of the stress-strain plots compared to the plots that are generated by using data from cross head movement of the test setup. In this study we attempt to do constitutive model of the nonlinear elastic response using a transversely isotropic finite deformation constitutive model.

BIAXIAL TESTING

The Bi-axial monotonic static tests were carried out using a biaxial test machine. Cruciform shaped samples are cut as per the dimensions shown in Figure1 (a). Black speckle mark points are applied on the sample to monitor the displacements using a non contact optical measurement technique as shown in the figure 1(b). A low speed camera has been used to capture the images while conducting the experiment at 15fps (frames per second). The black mark dots on the captured images are tracked using a MATLAB code that was written for this purpose. Strains and stretches are calculated by measuring the displacements of the markers. Nominal stress was calculated from the loads by using the cross sectional area of the specimens. The stress-strain plots were made for the biaxial experiment (under equi biaxial loading) at a cross-head displacement rate of 0.5mm/sec. The stress-strain curves obtained using the speckle method yield a more accurate point wise strains, in comparison to the average strain estimates that were obtained by many researchers [1] using cross-head movement data. The stress-strain plots of the material are plotted in Figures 2(a) and (b). The difference between the two graphs clearly establishes the anisotropy in the mechanical response at finite strains in this material.

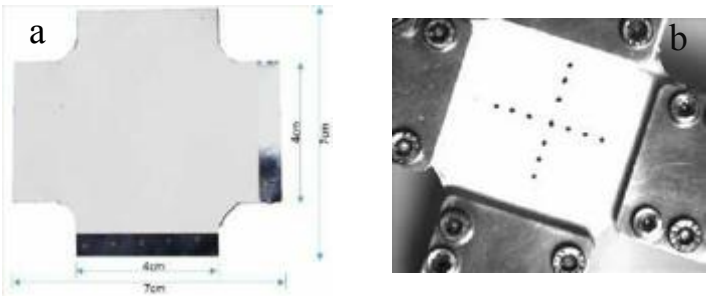

Figure 1: (a) PVDF cruciform specimen and corresponding dimensions (b) One of the captured image to measure the strains using black marks.

[a] Corresponding author. Email: harish06117@gmail.com

CONSTITUTIVE MODELLING

Usually PVDF will undergo moderate to large deformation (finite deformation) which also vary non-linearly with stresses, as observed in other uniaxial or biaxial tests. Hence a hyper elastic model was used to capture the mechanical response under monotonic loading of the material. With the transversely isotropic assumption and incompressibility constraints, we can choose a polynomial expansion for the strain energy density function, as suggested Humphrey [2] for transversely isotropic materials undergoing finite deformations. The strain energy function is proposed by Humphrey to be a function of the strain invariants I_1 and I_4 and is of the form given below.

$$W(I_1, I_4) = C_1\left(\sqrt{I_4} - 1\right)^2 + C_2\left(\sqrt{I_4} - 1\right)^3 + C_3\left(I_1 - 3\right) + C_4\left(I_1 - 3\right)\left(\sqrt{I_4} - 1\right) + C_5\left(I_1 - 3\right)^2$$

Where I_1 is trace of the stretch ratios in the three directions, and I_4 is square of the stretch ratio in the polling of stretch direction, C_1 to C_5 are the parameters which can be found using optimization of the experimental data and modal stress components.

From the continuum literature [4], stress tensor is a partial derivative of strain energy function with respect to right Cauchy green deformation tensor (**C**). After simplification and using the chain rule of the derivative the following stress strain relations were derived by Humphrey[2] for transversely isotropic materials.

$$\boldsymbol{\sigma} = -p\boldsymbol{I} + 2W_1\boldsymbol{B} + 2W_4\boldsymbol{F}e \otimes e\boldsymbol{F}^T$$

Where p is a Lagrangian multiplier, W_1 and W_4 are partial derivative of W with respect to I_1 and I_4 invariants, bold letters refers to second order tensor, e is a unit vector in the polling of stretched direction.

RESULTS

Levenberg-Marquardt algorithm [3] has been used to optimise the parameters. Differences between model and experimental stresses are found as an error and sum of the squares of the error is considered as an objective function to carry out this optimization. The optimised parameters obtained using the above algorithm, stress- stretch curves are obtained and are plotted as shown in the figure 2(a) and 2(b). The optimised parameters are given below.

$C_1 = 1.6 \times 10^5, C_2 = -2.1 \times 10^5, C_3 = 684, C_4 = -43808, C_5 = 40590,$

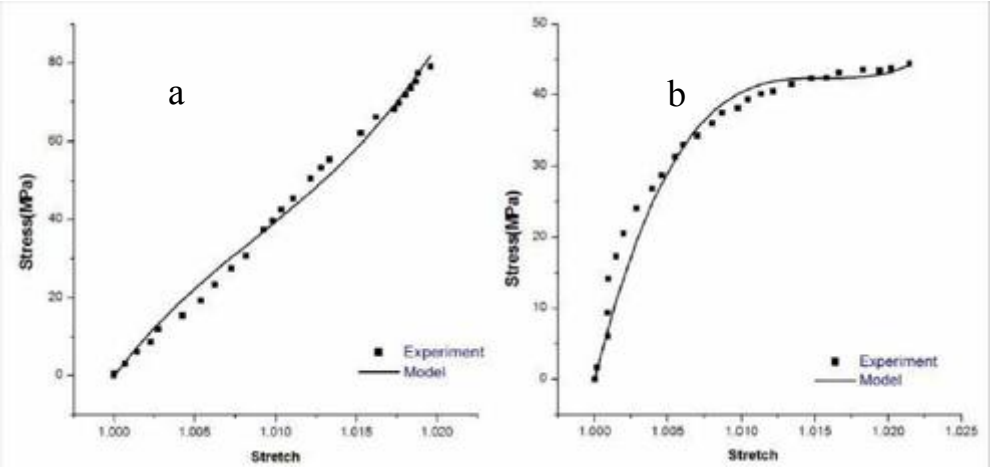

Figure 1: Biaxial test plot (a) in a polling of stretched direction (b) in an orthogonal direction or longitudinal direction

References

[1] Vinogradov, Aleksandra, and Frank Holloway. "Electro-mechanical properties of the piezoelectric polymer PVDF." *Ferroelectrics* 226.1 (1999): 169-181.

[2] Humphrey, J. D., R. K. Strumpf, and F. C. P. Yin. "Determination of a constitutive relation for passive myocardium: I. A new functional form."*Journal of biomechanical engineering* 112.3 (1990): 333-339.

[3] Moré, Jorge J. "The Levenberg-Marquardt algorithm: implementation and theory." *Numerical analysis*. Springer Berlin Heidelberg, 1978. 105-116.

[4] Lakshmana rao C., Abhijit P Deshpande., *Modeling of engineering materials*. Ane Books Pvt. Ltd.

MECHANICS AND OPTICS OF ARTIFICIAL COMPOUND EYE CAMERA

Zhengwei Li and Jianliang Xiao[a)]
Department of Mechanical Engineering, University of Colorado Boulder, Boulder, Colorado, USA

Abstract Compound eye-inspired imaging devices can find vast applications due to their remarkable imaging characteristics, such as extremely large field of view angle, low aberrations, high acuity to motion and infinite depth of field. Recently, researchers have successfully developed a digital camera that resembles the structure and functions of apposition compound eyes of arthropod, by combining an elastic array of microlenses with a stretchable array of photodetectors. Designing an elastomeric microlens array that can be mechanically stretched to very large extent without deteriorating the optical performance is critical to this development. In this work, mechanics and optics of the stretchable microlens array is studied. The results show that proper designs are critically important to meet both mechanical and optical requirements simultaneously. This study solved critically important designing issues of artificial compound eye cameras, and the results can have very important implications in developments that require stretchable optical elements.

INTRODUCTION

The in-depth understanding of light-sensing organs in biology provides opportunities for the development of digital cameras with operational features beyond the existing technologies [1-2]. For example, compound eyes, commonly seen in insects has attracted great interest, due to their unique imaging characteristics that are very different from vertebrate eyes and existing commercial cameras, such as extremely large field of view angle, low aberrations, acute sensitivity to motion and infinite depth of field [3-5]. These features can have huge potential in medical, industrial and military applications.

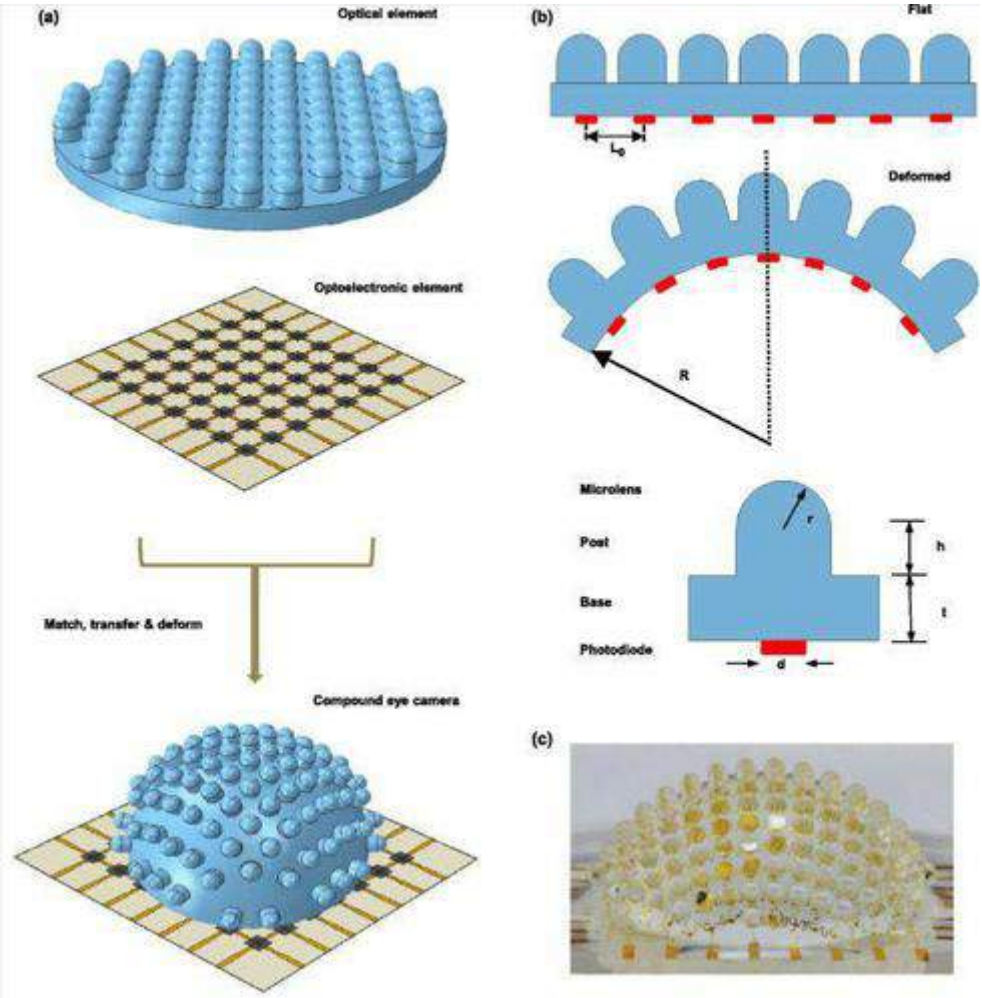

Figure 1. Schematic illustration of stretchable microlens array for artificial compound eye camera [1].

[a)] Corresponding author. Email: Jianliang.Xiao@Colorado.edu

Recently, Song *et al*. [2] have successfully developed a digital camera that resembles the structure and functions of apposition compound eyes of arthropods. Figure 1a schematically illustrates the fabrication processes. To fulfill such a digital camera, they firstly combined an array of elastic microlenses and a stretchable array of photodetectors into a two-layer design, and then transformed both layers into a hemispherical shape by hydraulic actuation. Figure 1c shows an optical picture of the artificial compound eye camera. Figure 1b shows cross-sectional view of the compound eye camera before and after deformation, with key parameters illustrated. During the geometrical transformation, very large strains are introduced into both the optical and optoelectronic elements. Therefore it's critically important to design both systems such that the strains don't deteriorating their optical and electronic performances, respectively. In this study, we analyze the strain and deformation of the microlens under both uniaxial and equibiaxial strains by using finite element simulations. Effects of different ratios of supporting post height versus the base membrane thickness are studied. The influence of microlens deformation on the optical performance is also investigated by optical ray tracing simulations.

RESULTS AND DISCUSSION

When the microlens array is deformed from flat geometry to hemispherical shape, microlenses at the periphery are subject to uniaxial strains due to the constraint from the circular fixture, microlenses at the center are subject to equibiaxial strains, and the other microlenses are subject to biaxial strains. Therefore, in this study, uniaxial and equibiaxial strains are applied to microlenses to investigate the mechanics of stretchable microlens array. Finite element analysis (FEA) is adopted to simulate microlens deformation. A unit cell (an artificial ommatidium) that contains a microlens, supporting post and base membrane, as shown in the bottom frame of Fig. 1b, is chosen for FEA simulation, and periodic boundary conditions are applied to the side walls of the base membrane. Eight-node, hexahedral brick elements are used to discretize the geometry. The results show that the strain and deformation of the microlens can be dramatically reduced when the supporting post is introduced between the microlens and the base membrane. As the height ratio, i.e. supporting post height versus membrane thickness increases, the strain and deformation in the microlens reduces rapidly. Once the height ratio reaches 1, the effect of strain in the microlens is negligible. In addition, the surface profile of the microlens is also studied since it directly affects the optics of the microlens. Results show that as supporting post is introduced, the influence of the stretching in the base membrane on the surface profile of the microlens is greatly reduced. When the height ratio h/t reaches 1, this influence is negligible.

The optics of the microlens unit cell subject to strain is also studied by optical ray-tracing simulation. Herein, the light beam is kept parallel to the optical axis. And we use collimated light beam of radius 0.3mm for the optical simulations. Our optical results show that when the supporting post is introduced, the focal length decreases rapidly with increasing height ratio. Once when the height ratio reaches 1, the focal length is equal that of the undeformed microlens. In addition, the image spot shape and size are also studied, which can be important for designing the photodetector. Under equibiaxial tension, tensile strain stretches the microlens uniformly in horizontal plane, the shape of microlens keeps hemispherical; therefore, the shape of the image spot also keeps circular. But spot size is much larger since the microlens becomes oblate. However, under uniaxial tension with height ratio 0, i.e., no supporting post, the microlens is deformed to an ellipsoid. This shape change is also reflected in the image spot shape. The majority of the light rays are focused into an ellipse. When the height ratio reaches 1, the spot shape changes to be a circle which is equal to that of the undeformed lens.

CONCLUSIONS

The mechanics and optics of the stretchable elastomeric microlens array under uniaxial and equibiaxial tension are studied. The results show that the strain and deformation of the microlens can be dramatically reduced when the supporting post is introduced between the microlens and the base membrane. As the ratio of the supporting post height to the base membrane thickness increases, the strain and deformation in the microlens reduces rapidly. Once the height ratio reaches 1, the effect of strain in the microlens is negligible. Ray tracing simulations illustrate how the deformation in the microlens affect the optical properties of the microlens, such as focal length, spot shape and size. This study provides critical information for designing artificial compound eye cameras or other systems that require microlens arrays to be mechanically stretchable without affecting the optical properties. The results could also have important implications on applications that require tuning of optics through mechanical means.

References

[1] Z. Li, J. Xiao, Mechanics and optics of stretchable elastomeric microlens array for artificial compound eye camera, J. Appl. Phys. 117 (2015) 014904.

[2] Y.M. Song, Y. Xie, V. Malyarchuk, et al., Digital cameras with designs inspired by the arthropod eye, Nature 497 (2013) 95–99.

[3] E. Warrant, D.E. Nillson, Invertebrate Vision, Cambridge Univ. Press, 2006.

[4] R. Dudley, The Biomechanics of Insect Flight: Form, Function, Evolution, Princeton Univ. Press, 2000.

[5] D. Floreano, J.C. Zufferey, M.V. Srinivasan, et al., Flying Insects and Robot, Springer, New York, 2009.

A GENERAL SOLUTION FOR THREE-DIMENSIONAL PROBLEMS OF ANISOTROPIC ELASTICITY

Li-Wei Liu*[1] and Hong-Ki Hong[2]
[1,2]*Department of Civil Engineering, National Taiwan University, Taipei 10617, Taiwan*

Summary Clifford algebra and Clifford analysis, which are the m-dimensional extensions of complex algebra and complex analysis are applied to solve three-dimensional problems of anisotropic elasticity. Using the coordinate transformation as what is done in the Lekhnitskii formalism or the Stroh formalism for two-dimensional problems, we convert the governing equations of three-dimensional elasticity of anisotropic materials into eigenvalue problems taking values of Clifford numbers. After solving the eigenvalue problems with the aid of Clifford analysis, we obtain a truly three-dimensional general solution of anisotropic elasticity.

INTRODUCTION

Due to the developments of composite materials and smart materials, anisotropic elasticity attracts attention of scholars and engineers more and more recently . In two dimensional problems, the Lekhnitskii formalism [1] and the Stroh formalism [2] are two well-documented approaches to solve all material symmetries (anisotropic, orthotropic, transversely isotropic, cubic, isotropic) or all crystal systems (triclinic, monoclinic, orthorhombic, trigonal, tetragonal, hexagonal, cubic) systematically. Both approaches convert a problem of finding solution for partial differential equations into an eigenvalue problem with a sixth order characteristic equation. They can be recognized as certain methods of coordinate transformation in two dimensional spaces.

There exist a small number of three-dimensional problems such as an infinity domain containing a concentrated point force or a dislocation or a half-space including a surface concentrated force for which the transformation domain is two dimensional are solved [3, 4, 5]. For the half-space problems with the traction varying linearly in one surface coordinate, the solution can be constructed by a sequence of partial integrations [6].

In the approaches, the theory of complex algebra and complex analysis provides a powerful tool and enables one to attack two-dimensional problems. However, it is not comfortable for complex analysis to treat three-dimensional problems. A more natural way to treat three-dimensional problems is the usage of Clifford analysis [7, 8, 9, 10, 11, 12, 13]. The authors [14] used Clifford analysis to find the general solutions of isotropic elasticity in three-dimensional problems. In this paper, we apply Clifford analysis to solve three-dimensional elasticity of generally anisotropic material.

CLIFFORD ALGEBRA AND CLIFFORD ANALYSIS

Consider m-dimensional Euclidean space $\mathbb{R}^m$ with orthonormal base vectors e_1, e_2, ..., e_m, and further define the Clifford algebra multiplication rule of the base vectors:

$$e_k e_l + e_l e_k = 2\delta_{kl}, \quad k, l = 1, 2, \ldots, m.$$

In this paper we take three-dimensional spaces into consideration. Let e_1, e_2, and e_3 be orthonormal base vectors and define the multiplication rule of base vectors

$$e_1^2 = e_2^2 = e_3^2 = 1, e_1 e_2 = \circ\, e_2 e_1, e_1 e_3 = \circ\, e_3 e_1, e_2 e_3 = \circ\, e_3 e_2.$$

Then the basis $\{e_\alpha\}$ of Clifford algebra $\mathrm{C}\ell_3(\mathbb{R})$ can be constructed as follows:

$$e_\phi, e_1, e_2, e_3, e_1 e_2, e_1 e_3, e_2 e_3, e_1 e_2 e_3.$$

The 0-vector e_ϕ is the scalar basis which is identified with and hence plays the role of the unit element $e_0 \equiv 1$. The 1-vectors e_1, e_2, and e_3 are the orthonormal base vectors. The 2-vectors $e_1 e_2 =: e_{12}$, $e_1 e_3 =: e_{13}$, and $e_2 e_3 =: e_{23}$ are the base bivectors which are geometric product of e_i and e_j representing a unitary oriented area of square with sides e_i and e_j where $i, j = 1, 2, 3,\ i \neq j$. The 3-vector $e_1 e_2 e_3 =: e_{123}$ is a pseudo-scalar which $e_{123} e_{123} = \circ\, 1$. Thus an element (multivector) a of Clifford algebra $\mathrm{C}\ell_3(\mathbb{R})$ is represented as follows:

$$a = a_0 + a_1 e_1 + a_2 e_2 + a_{12} e_{12} + a_{13} e_{13} + a_{23} e_{23} + a_{123} e_{123}.$$

Also, the Clifford-valued $\mathrm{C}\ell_3$ function can be represented as follows:

$$f = f_0 + f_1 e_1 + f_2 e_2 + f_{12} e_{12} + f_{13} e_{13} + f_{23} e_{23} + f_{123} e_{123}.$$

*Corresponding author. Email: liweiliu@ntu.edu.tw

ANISOTROPIC ELASTICITY AND ITS GENERAL SOLUTIONS

Three-dimensional problems of anisotropic elasticity are governed by the following equations.

$$0 = \sum_{j=1}^{3}\sum_{k=1}^{3}\sum_{l=1}^{3} C_{ijkl}\frac{\partial}{\partial x_l}\frac{\partial}{\partial x_j}u_k, \quad i = 1, \cdots, 3, \tag{1}$$

where u_k denotes the displacement field and the elasticity tensor C_{ijkl} satisfies the symmetry conditions $C_{ijkl} = C_{klij}$, and $C_{ijkl} = C_{jikl}$.

Via conducting the coordinate transformation as what were done in the Lekhnitskii formalism and the Stroh formalism and the derivation, we convert the governing equation into an eigenvalue problem as follows:

$$\left(\begin{bmatrix} \mathbf{C}_{11} & \mathbf{0} & \mathbf{0} \\ \mathbf{C}_{21} & \circ\,\mathbf{I} & \mathbf{0} \\ \mathbf{C}_{31} & \mathbf{0} & \circ\,\mathbf{I} \end{bmatrix} + P_{12} \begin{bmatrix} \mathbf{C}_{12} & \mathbf{I} & \mathbf{0} \\ \mathbf{C}_{22} & \mathbf{0} & \mathbf{0} \\ \mathbf{C}_{32} & \mathbf{0} & \mathbf{0} \end{bmatrix} + P_{13} \begin{bmatrix} \mathbf{C}_{13} & \mathbf{0} & \mathbf{I} \\ \mathbf{C}_{23} & \mathbf{0} & \mathbf{0} \\ \mathbf{C}_{33} & \mathbf{0} & \mathbf{0} \end{bmatrix} \right) \begin{bmatrix} \mathbf{a} \\ \mathbf{b} \\ \mathbf{c} \end{bmatrix} = \mathbf{0}, \tag{2}$$

where $\mathbf{a}$, $\mathbf{b}$, and $\mathbf{c}$ denote three vectors, P_{12} and P_{13} are Clifford algebra valued, and the matrices

$$\begin{aligned} (\mathbf{C}_{11})_{ik} &= C_{i1k1}, \quad (\mathbf{C}_{12})_{ik} = C_{i1k2}, \quad (\mathbf{C}_{13})_{ik} = C_{i1k3}, \\ (\mathbf{C}_{21})_{ik} &= C_{i2k1}, \quad (\mathbf{C}_{22})_{ik} = C_{i2k2}, \quad (\mathbf{C}_{23})_{ik} = C_{i2k3}, \\ (\mathbf{C}_{31})_{ik} &= C_{i3k1}, \quad (\mathbf{C}_{32})_{ik} = C_{i3k2}, \quad (\mathbf{C}_{33})_{ik} = C_{i3k3}. \end{aligned}$$

After solving the Clifford algebra valued eigenvalue problem, we can obtain a general solution for three-dimensional elasticity of anisotropic materials in the following.

$$\mathbf{u} = \mathbf{\Phi}_{\mathrm{I}}^{a}\mathbf{f}_{\mathrm{I}}\boldsymbol{\xi}_{\mathrm{I}} + \mathbf{\Phi}_{\mathrm{II}}^{a}\mathbf{f}_{\mathrm{II}}\boldsymbol{\xi}_{\mathrm{II}}, \tag{3}$$

where the matrices $\mathbf{\Phi}_{\mathrm{I}}^{a}$ and $\mathbf{\Phi}_{\mathrm{II}}^{a}$ are related to the eigenvectors or the generalized eigenvectors of the problem (2), the vectors $\mathbf{f}_{\mathrm{I}}$ and $\mathbf{f}_{\mathrm{II}}$ consist of the complex functions whose independent variables are related to the eigenvalues, and $\boldsymbol{\xi}_{\mathrm{I}} = \frac{1}{2}(1 + e_3)$ and $\boldsymbol{\xi}_{\mathrm{II}} = \frac{1}{2}(1 \circ e_3)$. This general solution can be used to solve the problems whose domain can not be transformed into two-dimensional spaces.

ACKNOWLEDGEMENT

This research was supported by the Ministry of Science and Technology in Taiwan through Grants MOST 103-2218-E-002-018, MOST 104-2218-E-002-026-MY3, and MOST 103-2221-E-002-283-MY3.

References

[1] Lekhnitskii S. G.: Theory of Elasticity of an Anisotropic Body, MIR Publishers, Moscow, 1977.

[2] Stroh A. N.: Dislocations and cracks in anisotropic elasticity, Philosophical Magazine 3:625-646, 1958.

[3] Sveklo V. A.: Boussinesq type problems for the anisotropic half-space, Journal of Applied Mathematics and Mechanics 28:1099-1105, 1964.

[4] Willis J. R.: Hertzian contact if anisotropic bodies, Journal of the Mechanics and Physics of Solids 14:163-176, 1966.

[5] Wu K. C.: Generalization of the Stroh formalism to 3-dimensional aniostropic elasticity, Journal of Elasticity 51:213-225, 1998.

[6] Barber J. R., Ting T. C. T.: Three-dimensional solutions for general anisotropy, Journal of the Mechanics and Physics of Solids 55:1993-2006, 2007.

[7] Brackx F., Delanghe R., Sommen F.: Clifford Analysis, Pitman, London, 1982.

[8] Hestenes D., Sobczyk G.: Clifford Algebra to Geometric Calculus: A Unified Language for Mathematics and Physics, Reidel, Dordrecht, The Netherlands, 1984.

[9] Gürlebeck K., Sprößig W.: Quaternionic Analysis and Elliptic Boundary Value Problems, Birkhäuser Verlag, 1990.

[10] Gilbert J. E., Murray M. A. M.: Clifford Algebras and Dirac Operators in Harmonic Analysis, Cambridge University Press, Cambridge, England, 1991.

[11] Delanghe R., Sommen F., Souček V., Brackx F., Constales D.: Clifford Algebras and Spinor-Valued Functions, a Function Theory for the Dirac Operator, Kluwer, Dordrecht, The Netherlands, 1992.

[12] Ryan J., Sprößig W. (Eds.): Clifford Algebras and Their Applications in Mathematical Physics, Vol. 2: Clifford Analysis, Birkhäuser, Basel, Switzerland, 2000.

[13] Lounesto P.: Clifford Algebras and Spinors, Cambridge University Press, Cambridge, England, 2001.

[14] Liu L.-W., Hong H.-K.: A Clifford algebra formulation of Navier-Cauchy equation, Procedia Engineering 79:184-188, 2014.

A CIRCULAR INCLUSION WITH CIRCUMFERENTIALLY INHOMOGENEOUS IMPERFECT INTERFACE IN HARMONIC MATERIALS

D.R.McArthur[1], L.J.Sudak[1a)]
[1] *Department of Mechanical Engineering, University of Calgary, Alberta, Canada*

Summary Complex variable methods have been employed extensively to model inclusions in linear elasticity but have not yet seen a similar degree of success in the finite regime. With the advent of Fritz's harmonic materials [1] and more recently the work of Ru [2], a concise framework has been established for approaching inclusion problems using complex variable techniques in finite elasticity. From these foundations, a number of inclusion problems in finite elasticity have been studied in recent years including but not exclusive to; elliptical inclusions with uniform stress fields, partially de-bonded circular inclusions, three phase circular inclusions, and a circular inclusion with homogeneously imperfect interface. Of these works, none have incorporated the concept of a circumferentially inhomogeneous imperfect interface. This is an important distinction because in general, interfacial damage does not occur homogeneously and it is thought that this could have a significant impact on the stress fields within the inclusion.

FUNDAMENTAL EQUATIONS OF HARMONIC MATERIALS

In the following analysis it is assumed that the matrix, given by an infinite domain D_2 , and inclusion, given by a simply connected finite domain D_1 which is embedded in the matrix D_2 , are a particular class of harmonic materials characterized by the following

$$W(I,J) = 2\mu[F(I) - J], F_{ij} = \frac{\partial y_\mu}{\partial x_j}, F'(I) = \frac{1}{4\alpha}\left[I + \sqrt{(I^2 - 16\alpha\beta)}\right], \tag{1}$$

where $W$is the strain energy function, F_{ij} are the components of the deformation gradient tensor, α, β are material constants and I and J are the scalar invariants of FF^T given by

$$I = \lambda_1 + \lambda_2 = \sqrt{F_{ij}F_{ij} + 2J}, J = \lambda_1\lambda_2 = \det[\boldsymbol{F}], \tag{2}$$

and λ_1, λ_2 are the principal stretches. According to Ru [2], the deformation map and Piola stress function can be given in terms of two complex potential functions $\phi_k(z)$ and $\psi_k(z)$, $k = 1,2$ (where subscripts 1,2 refer to the inclusion and matrix, respectively) as follows

$$iw_k(z,\overline{z}) = \alpha_k\phi_k(z) + i\bar{\psi}\ z\ + \frac{\beta_k z}{\phi_k'(z)}, \tag{3}$$

$$\chi_k(z,\overline{z}) = 2i\mu_k\ \mu(\alpha_k - 1)\phi_k(z) + i\overline{\psi_k(z)} + \frac{\beta_k z}{\phi_k'(z)}\Big] , k = 1,2. \tag{4}$$

It can be shown that (3), (4) gives rise to the following rectilinear expressions for the Piola stress and displacement

$$w_k(z,\overline{z}) - z = (u_1 + iu_2)_k , \chi_k(z,\overline{z}),_2 = (-\sigma_{21} + i\sigma_{11})_k , \chi_k(z,\overline{z}),_1 = (\sigma_{22} - i\sigma_{12})_k , k = 1,2. \tag{5}$$

In order to facilitate the problem into a tractable form, let us consider the case where the first Piola stress is symmetric. In this way, equation (5) takes the following polar form for stress and displacement

$$\frac{R}{z}w_k(z,\overline{z}) - R = (u_r + iu_\theta)_k , \chi_k'(z,\overline{z}) = (\sigma_{rr} + i\sigma_{\theta r})_k , k = 1,2, \tag{6}$$

where a ($'$) prime denotes differentiation with respect to z.

FORMULATION

We assume that the interface is inhomogeneously imperfectly bonded and adopt the following imperfect interfacial boundary conditions

$$\left|\left|\sigma_{rr} + i\sigma_{r\theta}\right|\right| = 0 , z \in \partial L, \tag{7}$$

a) Corresponding author. Email: Lsudak@ucalgary.ca

(8) $$\sigma_{rr} = m(\theta)||u_r||, \sigma_{\theta r} = n(\theta)||u_\theta||, z \in \partial L,$$

where $m(\theta)$ and $n(\theta)$ are two non- negative imperfect interface parameters and $||.|| = (\mathrm{s})_2 - (\mathrm{s})_1$ represents the jump across the interface. Through the use of the technique of analytic continuation, and by limiting the analysis to the case of an interface where $m(\theta) = n(\theta)$ two ordinary differential equations with variable coefficients are developed for the potentials $\phi_k(z)$, $k = 1,2$ from which the following expressions are obtained for a specific class of interface

(9) $$s\phi_1(z) = \frac{2}{b_m}\left[\left(\frac{z}{R}\right)^m - \rho^*\right]^{\frac{\gamma\lambda}{m}}\left[\left(\frac{z}{R}\right)^m - \frac{1}{\rho^*}\right]^{-\frac{\gamma\lambda}{m}} \int_{R\rho^*}^{z} \left(\frac{t}{R}\right)^m G(t)\left[\left(\frac{t}{R}\right)^m - \rho^*\right]^{-\frac{\gamma\lambda}{m}-1}\left[\left(\frac{t}{R}\right)^m - \frac{1}{\rho^*}\right]^{\frac{\gamma\lambda}{m}-1} dt, z \in D_1,$$

(10) $$s\phi_2(z) = \frac{2}{b_m}\left[\left(\frac{z}{R}\right)^m - \rho^*\right]^{\frac{\eta\lambda}{m}}\left[\left(\frac{z}{R}\right)^m - \frac{1}{\rho^*}\right]^{-\frac{\eta\lambda}{m}} \int_{\frac{R}{\rho^*}}^{z} \left(\frac{t}{R}\right)^m F(t)\left[\left(\frac{t}{R}\right)^m - \rho^*\right]^{\frac{\eta\lambda}{m}-1}\left[\left(\frac{t}{R}\right)^m - \frac{1}{\rho^*}\right]^{\frac{-\eta\lambda}{m}-1} dt, z \in D_2.$$

In (9) and (10) $F(t)$ and $G(t)$ are artifacts of the analytic continuation process, γ, η are exponents comprised of material parameters and are strictly positive, ρ^* characterizes the degree of interface imperfection and λ is a function of $\rho^*$and the other interface parameters. We may then present an example for a specific case of the exponents $m = \gamma = \eta = 1, \lambda = -1$ and study the ratio of the inhomogeneous to homogeneous imperfect interface mean stress

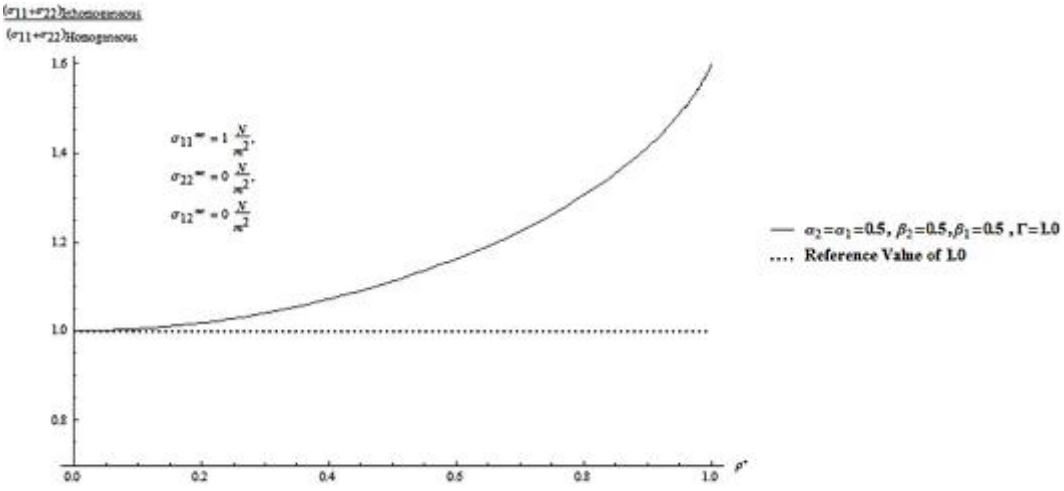

Figure1. Mean stress ratio for a circular inclusion with various values of the inhomogeneous interface parameter ρ^* subject to remote loading $\sigma_{11}^{\infty} = 1$s $\sigma_{12}^{\infty} = 0, \sigma_{22}^{\infty} = 0$.

CONCLUSIONS

Figure 1 clearly shows that the circumferential inhomogeneous interface parameter ρ^* has a pronounced effect on the estimation of the mean stress inside the inclusion and, at its peak, the discrepancy between the inhomogeneous mean stress and homogeneous counterpart reaches 60 percent. This signifies, for the first time in finite elasticity, that in circumstances where the inclusion interface may have circumferentially non-homogeneous imperfections, the homogeneously imperfect interface model is insufficient in determining the mean stress.

References

[1] Fritz, J.: Plane strain problems for a perfectly elastic material of harmonic type. Comm. Pure Appl. Math. **XIII**, 239-290 (1960)

[2] Ru, C.Q.: On complex-variable formulation for finite plane elastostatics of harmonic materials. Acta Mech. **156**, 219-234 (2002)

PARAMETER IDENTIFICATION VIA A MODIFIED CONSTRAINED MINIMIZATION PROCEDURE

Yue Mei[1], Sevan Goenezen[1a)]
[1]*Department of Mechanical Engineering, Texas A&M University, College Station, TX, USA*

Summary This paper introduces a modified formulation of the objective function to solve the inverse problem in elasticity posed as a constrained and regularized minimization method. Hereby, the displacement correlation term in the modified version of the objective function is weighted spatially with a strain dependent function and the regularization term is post adjusted from the prior solution. We test this novel procedure using a well-chosen 2D numerical example and compare it with the solution from the conventional formulation. We observe that the modified formulation has significantly reduced sensitivity towards altered boundary conditions and the shear modulus contrast improves drastically while preserving overall smoothness. The problem is then generalized and analyzed with a 1D analogue, elucidating the observations in the 2D continuum problem.

INTRODUCTION

Characterizing non-homogenous material properties of soft tissues has importance in biomedical imaging. For instance, breast tumors, prostate cancer, skin cancer, etc. could be detected by their stiffness contrast. To determine the non-homogeneous elastic property distribution it is essential to measure the deformation field from imaging techniques such as ultrasound, MRI, or CT scan. The inverse problem here is posed as a minimization problem under the constraint of the equilibrium equations in elasticity. The conventional objective function for this optimization problem is given in Eq.(1) and has been thoroughly discussed in[1, 2]. In this paper, we introduce a modified objective function (Eq.(2)), weighted by a strain field and a prior computed shear modulus distribution, and show that it reduces sensitivity to varying boundary conditions and improves the reconstructed contrast.

METHODS

To simplify the analysis, the objective function is shown for only 1 acquired displacement field in Eq.(1) and (2) for the conventional and modified objective function, respectively.

$$F_{conv} = \frac{1}{2}\left\| \left(u_y^m - u_y^i\right) \right\|_2^2 + \frac{1}{2}\alpha \int_\Omega \sqrt{\left(\nabla\mu\right)^2 + c^2}\, d\Omega \tag{1}$$

$$F_{new} = \frac{1}{2}\left\| \left(u_y^m - u_y^i\right) / \varepsilon_{yy} \right\|_2^2 + \frac{1}{2}\alpha \int_\Omega \sqrt{\left(\nabla\mu\right)^2 + c^2}\, d\Omega \tag{2}$$

The shear modulus is denoted by μ and is introduced as nodal unknowns in the finite element mesh. The first term in the objective function is the displacement correlation term, where u_y^m is the measured displacement field and is the computed displacement field, obtained by solving the forward problem for the current estimate of μ .We assume we only know y displacement component. The displacement correlation term in Eq.(2) is weighed by the strain field [3]. The second term is the regularization term to penalize oscillations in the reconstructed solution. Further, α is the regularization factor that controls the smoothness of the final solution and is selected based on Morozov's discrepancy principle or a smoothness criteria, and c is a small constant to avoid singularities. Note that α in previous works was chosen to be a constant. In Eq.(2), however, a spatially varying regularization factor $\overline{\alpha}$ is introduced with $\overline{\alpha} = \alpha \ \ \mu$. The optimization problem is solved using the limited BFGS method and the reader is referred to references in [1, 2] for more details on the solution process.

RESULTS AND DISCUSSIONS

In this paper, the measured displacement fields are acquired by solving the finite element forward problem with a target shear modulus distribution shown in Figure 1(a), where the circular inclusions represent two theoretical breast tumors of similar stiffness and the soft background represents normal tissue. The stiffness ratio between tumor and normal tissue is 5:1. We apply a linearly changing displacement boundary on the top and restrict the vertical motion of the bottom edge. To avoid rigid motion, we fix the center node of the bottom edge. The 2D model is in plane strain and the tissue is assumed to be incompressible. To mimic experimental data, we add 3% white Gauss noise to the simulated data and only minimize the vertical displacement field [1, 3]. We observe that the conventional approach results in ambiguous reconstructions in that the left inclusion appears to be softer than the right inclusion (Figure 1(b), while the spatially weighted displacement correlation addresses this issue (Figure 1(c)). The reconstructions of μ using the spatially weighted displacement correlation term and the spatially varying regularization factor further improve the overall contrast while avoiding oscillations due to noise. To understand these observations, we consider in Figure 1(e) a simplified one-dimensional model to represent the 2D continuum model. In particular, two elastic bars are modeled in parallel and coupled by a rigid plate. The grey part in the bars represents the inclusions and the white surrounding denotes the background. The relationship between the reconstructed shear modulus value of the left and right inclusions can be obtained by fundamental physics and calculus [3].

[a)] Corresponding author. Email: sgoenezen@tamu.edu.

We then define a measure of error and compute the error for the reconstructed shear modulus in the left inclusion over the exact modulus reconstruction in the right inclusion $\bar{\mu}_{in}^{2}$ while fixing the exact shear modulus in the left inclusion $\bar{\mu}_{in}^{1}$ for values ranging from 3 to 10 for both the conventional (Figure 2(a)) and new approach (Figure 2(b)). We obverse that the reconstruction error with the new approach is significantly smaller than with the conventional method.

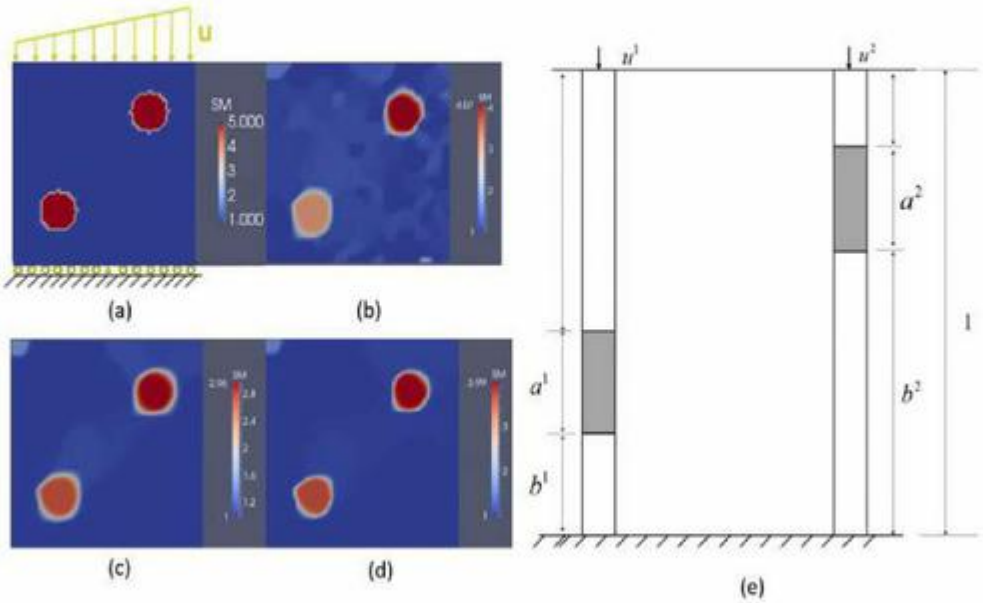

Figure 1(a) Target (exact) shear modulus distribution; (b) Reconstruction with the conventional mthod; (c) Reconstruction with the spatially weighted displacement correlation term; (d) Reconstruction with the spatially weighted displacement correlation term and spaially varying regularization factor; (e) The schematic of a 1D simplified model.

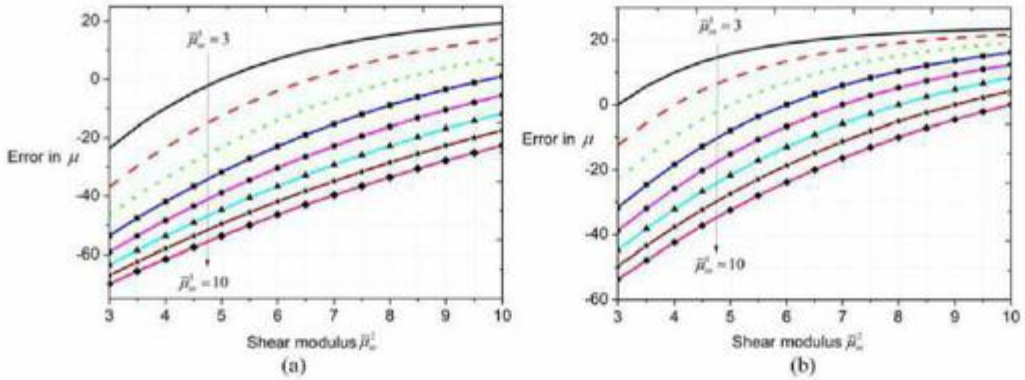

Figure 2 Error plot of the reconstructed shear modulus in the left inclusion over the prescribed shear modulus in the right inclusion ;(a) conventional method; (b) spatially weighted method.

CONCLUSIONS

We have presented a modified objective function to solve the inverse problem in elasticity, where the displacement correlation term is weighted by a strain dependent function and the regularization factor is weighted from a prior computed shear modulus distribution. We have successfully shown that the new method reduces ambiguity in the reconstructed results and significantly improves the overall contrast. Finally, we have developed a 1D simplified analogous model to analyze mathematically the observations with the 2D model and to validate this model for a wide range of target shear modulus values.

References

[1] Goenezen S.: Inverse problem: An Application to Imaging the Nonlinear Elastic Properties of Soft Tissues. PhD Thesis, RPI, 2011

[2] Goenezen S., Barbone P., and Oberai A.A.: Solution of the Nonlinear Elasticity Imaging Inverse Problem: The incompressible case. *Computer Methods in Applied Mechanics and Engineering*, 2011. 200(13-16): p. 1406-1420.

[3] Mei Y., Kuznetsov S., Goenezen S.:. Reduced Boundary Sensitivity and Improved Contrast of the Regularized Inverse Problem Solution in Elasticity. SME Journal of Applied Mechanics, 2015, 031001-10.

MATHEMATICALLY JUSTIFIED REFINED THEORIES FOR THIN STRUCTURES

Patrick Schneider*[1] and Reinhold Kienzler[1]
[1]*Department of Production Engineering, University of Bremen, Bremen, Germany*

Summary The uniform approximation approach is a dimension reduction procedure. It can be applied to derive analytical theories for thin structures from the settled theory of three-dimensional linear elasticity without the use of a-priori assumptions. In the talk, we show how the approach can be extended by arguments from duality theory, in order to proof its approximation property, which provides the mathematical justification for the approach. We treat the specific example of an isotropic, linear elastic beam with constant rectangular cross-section. The first-order approximation coincides with the Euler-Bernoulli beam theory, whereas the second-order approximation is new. Timoshenko´s beam theory can be transformed to an equivalent theory, if a specific shear-correction factor is used.

INTRODUCTION

Classical theories for thin structures like the Euler-Bernoulli beam and the Kirchhoff plate theory were developed by the use of disputable a-priori assumptions already in the 18th and 19th Century. They provide reasonable results for practical applications, if the structure under consideration is sufficiently thin. In the present century, rigorous mathematical justifications for these theories are available as well. These justifications make use of comparatively new mathematical tools like, e.g., Γ-convergence, which proof the classical theories to appear as a limit of the three-dimensional theory of elasticity, if the thickness of the structure tends to zero.

Driven by practical needs of the engineering community, the development of refined theories, i.e., theories for moderately thick structures, or higher precision, started long before the classical theories were justified already in the middle of the 20th century. Nowadays refined theories are still an open topic which is under intensive development. Mathematical justifications for refined theories are missing - even for the most established theories like the Reissner-Mindlin plate theory.

THE UNIFORM APPROXIMATION APPROACH

The uniform approximation approach for the a-priori assumption free derivation of theories for thin structures from the three-dimensional theory of linear elasticity goes back to pioneer treaties of Naghdi [4] and Koiter [3]. Kienzler [2] interprets the approach as a truncation of the elastic energy after a maximum power of a characteristic parameter that describes the relative thickness of the structure. We extend his ideas by truncating the associated dual energy as well, in order to provide a mathematical justification for refined theories by the use of arguments from the duality theory of functional analysis.

By extending a standard result from duality theory towards general anisotropy, the square error of an arbitrary admissible displacement field v from the (weak) solution of three-dimensional elasticity can be estimated via

$$\frac{1}{2}\lambda_{\min} c_{\text{Korn}} \left\| v \circ u \right\|_X^2 \leq E_{\text{pot}}(v) \circ E_{\text{pot}}(u) \circ \left(E_{\text{dual}}(\mu) \circ E_{\text{dual}}(\sigma) \right),$$

where $\lambda_{\min}$ is the minimum eigenvalue of the stiffness tensor, c_{Korn} is the constant from the classical Korn inequality, σ denotes the stress-field solution of the dual problem $(E_{\text{dual}}(\sigma) = E_{\text{pot}}(u))$ and μ is an arbitrary admissible stress field.

By using a dimensionless formulation and series expansions in thickness direction for the displacement field, the potential and dual energy appear as infinite power series in parameters describing the relative thickness of the structure. When truncating both series after a certain power, a finite set of field equations and stress-boundary conditions can be derived from the Euler-Lagrange equations of the potential energy, whereas the dual energy's Euler-Lagrange equations deliver matching displacement-boundary conditions. This generates a hierarchy of theories with regard to the truncation power. By virtue of the mentioned theorem, the error of the Nth-order approximation theory decreases like the $(N+1)$th power of the characteristic parameter. Therefore, any solution of an Nth-order theory converges to the three-dimensional solution, if the thickness tends to zero. Furthermore, a considerable gain of accuracy is achieved by increasing the approximation order, which finally proofs the approximation property of the approach.

If smooth solutions are available, one is enabled to reduce the number of unknown displacement coefficients in a certain theory by successive elimination. This leads to the classical theories for thin structures for first-order approximations and to new refined theories for higher-order approximations.

We already applied the approach for the derivation of a refined monoclin plate theory, cf. [9], which turns out to be equivalent to the Reissner-Mindlin theory for the special case of an isotropic material. For a comparison to other established higher-order theories we refer to [6].

*Corresponding author. Email: pasch@uni-bremen.de

REFINED BEAM THEORY

In the talk we illustrated the approach by deriving theories for an isotropic, linear elastic beam (length l) with constant rectangular cross-section (width b, height h). The error of the Nth-order approximation decreases like

$$k \left\| v_N \circ u \right\|_X^2 \leq O\left(\max\left\{ \frac{b}{\sqrt{12}l}, \frac{h}{\sqrt{12}l} \right\}^{2(N+1)} \right).$$

It should be noted that in general, a refined definition is needed for the beam load case, in order to be able to decompose arbitrary three-dimensional load cases on a quasi one-dimensional structure into independent subproblems, cf. [7]. For the simple case of the classical beam load, i.e., symmetric pressure in hight direction, the first-order approximation equals the Euler-Bernoulli beam theory. This is not surprising with regard to other results from literature derived by the use of Γ-convergence. However, the second-order beam theory for the classical beam load case only coincides with the most established beam theory, i.e., Timoshenko's beam theory, if the shear correction factor in this theory is chosen as

$$K = \underbrace{\frac{3}{20}\frac{5\nu+8}{1+\nu}}_{\text{Olsson, [5]}} \circ \beta^2 \frac{\nu}{1+\nu}\left[\frac{1}{4} + \frac{\beta^2}{\beta^2+5}\frac{\nu}{1+\nu}\right],$$

where $\beta = \frac{b}{h}$ denotes the cross-section aspect ratio and ν denotes Poisson's ratio. Indeed the limit value for $\beta = 0$ is a known shear-correction factor. The (most probably) most cited paper on shear correction factors [1] dedicates the factor to Olsson, cf. [5]. However, in this article Olsson states that he "concluded" the factor from the work of [10]. The factor for $\beta \neq 0$ is not known from literature to our best knowledge. It covers weakening from shear deformations as well as stiffening effects for plate-like beams.

It has to be noted, again, that the uniform second-order approach does not introduce any correction factors nor any others a-priori assumptions - The shear correction factor is derived by a vis-a-vis comparison of the resulting ordinary differential field equation with Timoshenko´s equation.

Peer-reviewed papers with the presented results are in preparation. In the meantime, we refer the interested reader to [8].

References

[1] Kaneko, T. (1975). On Timoshenko's correction for shear in vibrating beams. *Journal of Physics D: Applied Physics*, 8(16), 1927–1936. http://dx.doi.org/10.1088/0022-3727/8/16/003.

[2] Kienzler, R. (2002). On consistent plate theories. *Archive of Applied Mechanics*, 72, 229–247. http://dx.doi.org/10.1007/s00419-002-0220-2.

[3] Koiter, W. (1970). On the mathematical foundation of shell theory. In *Proc. Int. Congr. of Mathematics, Nice*, volume 3 (pp. 123–130).

[4] Naghdi, P. M. (1963). Foundations of elastic shell theory. In I. Sneddon & R. Hill (Eds.), *Progress in solid mech.*, volume 4 (pp. 1–90). Amsterdam: North-Holland.

[5] Olsson, R. G. (1935). Zur Berechnung der Frequenz der Transversalschwingung des prismatischen Stabes. *ZAMM - Journal of Applied Mathematics and Mechanics / Zeitschrift für Angewandte Mathematik und Mechanik*, 15, 245. http://dx.doi.org/10.1002/zamm.19350150410.

[6] Schneider, P. & Kienzler, R. (2014b). Comparison of various linear plate theories in the light of a consistent second-order approximation. *Mathematics and Mechanics of Solids*. http://dx.doi.org/10.1177/1081286514554352.

[7] Schneider, P. & Kienzler, R. (2015). On exact rod/beam/shaft-theories and the coupling among them due to arbitrary material anisotropies. *International Journal of Solids and Structures*, 56–57, 265–279. http://dx.doi.org/10.1016/j.ijsolstr.2014.10.022.

[8] Schneider, P. (2015). On the mathematical justification of the consistent-approximation approach and the derivation of a shear-correction-factor free refined beam theory. *Dissertation, Universität Bremen.* http://nbn-resolving.de/urn:nbn:de:gbv:46-00104458-18.

[9] Schneider, P., Kienzler, R., & Böhm, M. (2014). Modeling of consistent second-order plate theories for anisotropic materials. *ZAMM - Journal of Applied Mathematics and Mechanics / Zeitschrift für Angewandte Mathematik und Mechanik*, 94(1-2), 21–42, doi:10.1002/zamm.201100033. http://dx.doi.org/10.1002/zamm.201100033.

[10] v. Kármán, T. & Seewald, F. (1927). *Abhandlungen aus dem Aerodynamischen Institut der Technischen Hochschule Aachen*, volume 7. Berlin.

DUAL-MIXED PRINCIPLES IN ELASTODYNAMICS – AN APPLICATION TO CYLINDRICAL SHELLS

Balázs Tóth*
Institute of Applied Mechanics, University of Miskolc, Miskolc, Hungary

Summary The commercial finite elements suffer from several kind of numerical difficulties. These problems occur in such a way that the finite element solution for the unknowns deteriorates as the mesh become refined step by step, namely the convergence for the relative errors of variables is very slow. This is the numerical locking effect. These low-order, primal and primal-mixed structural finite elements suffer from the most serious convergence problems. One of the most efficient strategies, to avoid the numerical locking phenomenon, is the use of multi-field dual-mixed variational principles for development of finite element models. Accordingly three, new multi-field dual-mixed energy principles using non-symmetric stresses are presented for linear elastodynamic problems. One of them provides a theoretical basis for construction of a new hp-version cylindrical shell finite element which is tested through benchmark problems, and the numerical results are compared to computed ones by the models appearing in the literature.

ABOUT SOME LOCKING PHENOMENA

One of the most common numerical techniques, to model phenomena in continuum physics, is the finite element method and its extended versions. The finite element solution for problems in mechanics is usually based on different kind of variational formulations. For example in case of elasticity problems the commercial, widely-used, built-in finite elements are usually based on the principle of virtual work which fulfills weakly the translational equation of motion (or equilibrium equation in static case) and the traction boundary condition, namely the fundamental variable is the displacement field. However, these standard finite element softwares can often suffer from several types of numerical problems.

Numerical convergence problems mentioned appear in the relative errors of displacements and stresses computed when the deformation of incompressible materials is investigated, i.e., the value of the Poisson ratio achieves the incompressibility limit of 0.5. This is named as incompressibility locking effect [1]. Besides these standard finite element models can give low convergence rates and accuracy in the calculated stress field which has more importance in engineering practice than the displacement field. However, higher convergence rates can be achieved by the application of the p-type approximation technique. In this case the coarse finite element mesh kept fixed while the polynomial degree p of the displacement approximations is increasing simultaneously on each element. The combination of the p-version and the mesh-refining techniques (labeled as h-version) called hp-type approximation method. Although the higher-order displacement-based finite elements provide optimal accuracy for the displacements, the stresses recovered numerically by postprocessing from the displacement field are not free from the incompressibility locking, see the details in [1].

The standard low-order structural finite elements (beam and shell elements) can suffer from several, additional numerical difficulties. These numerical problems arise from the very small value of one of the characteristic structural lengths, i.e., for example when the shell becomes extremely thin. The standard low-order h-version shell and beam elements with Naghdi-type (or Timoshenko-type) kinematics have the most serious locking phenomena such as the shear- and membrane locking, as well as the boundary layer effect which are exhibited, see for example in [2]. To attempt the removal of these kind of locking effects, numerous primal- and primal-mixed shell, solid-shell and solid finite elements were elaborated, see some test results for shells for example in [2]. Some of these convergence problems can be avoided by the use of p-version approximation technique. Although these elements are free from locking in the energy norm computations in case of general shells, the computational results obtained for the stress field are not free from locking, see, for instance, [3]. The lack of general locking-free shell elements motivate the research work in this direction.

PROPOSED METHODS AND AN APPLICATION

The use of the multi-field dual-mixed variational principles is one of the reliable and efficient ways to avoid numerical convergence problems in the case of structural finite elements. However the development of the finite element model based on this approach is much more difficult task than that is possible with the use of primal and primal-mixed variational formulation. The difficulty arises from the complexity of the related theoretical background and the selection of the appropriate polynomial approximation spaces of the independent unknowns.

Accordingly three types of multi-field dual-mixed energy principles using *a priori* non-symmetric stress tensor will be presented on the basis of [4] for linear elastodynamic problems. Firstly it is shown how a new four-field dual-mixed functional can be derived using the Lagrangian multiplier method. The fundamental variables of this functional is the displacement- and impulse vector, as well as the non-symmetric stress and skew-symmetric rotation tensor. Secondly after having modified the

*Email: mechtb@uni-miskolc.hu

four-field functional with the use of the Legendre transformation, we obtain a new five-field dual-mixed functional allowing the impulse- and velocity field to be varied independently. Thirdly a complementary energy-based three-field dual-mixed variational principle is derived by the elimination of the impulse- and velocity vector from the five-field functional. In this context we present how to handle correctly the six different kind of initial conditions weakly and/or strongly by adding a new integral expression to the functionals.

Then a new hp-version cylindrical shell finite element model based on a multi-field dual-mixed variational formulation will be presented. The computational performance of this element is tested through the comparisons of the numerical results to the computed ones by the models appearing in the literature. It is verified that the h- and p-version cylindrical shell finite elements are robust and reliable, namely this finite element application provides incompressibility- and shear locking-free results for all of unknown fields, see the early results in [5, 6].

References

[1] Szabó B., Babuška I.: Finite Element Analysis. John Wiley & Sons, New York, 1991.

[2] Wiśniewski K.: Finite Rotation Shells. Springer Netherlands, 2010.

[3] Chapelle D., Bathe K.-J.: Fundamental Considerations for the Finite Element Analysis of Shell Structures. Comput Struct 66:19-36, 1998.

[4] Tóth B.: Multi-field Dual-Mixed Variational Principles Using Non-symmetric Stress Field in Linear Elastodyanamics. J. Elasticity 122:113-130, 2016.

[5] Tóth B.: Three-field Dual-Mixed Variational Formulation and hp Finite Element Model for Elastodynamic Analysis of Axisymmetric Shells. PhD Thesis, Department of Mechanics, University of Miskolc, Miskolc, 2013.

[6] Tóth B., Kocsán L.G.: Comparison of Dual-Mixed h- and p-version Finite Element Models for Cylindrical Shells. Finite Elem Anal Des 65:50-62, 2013.

COMPLEMENTARY STRAIN ENERGY SOLUTION FOR HIGHER ORDER BEAM THEORY

Phe Van Pham[1a)], Magdi Mohareb[1] & Amir Fam[2]

[1]*Department of Civil Engineering, University of Ottawa, Ottawa, Ontario, Canada*
[2]*Department of Civil Engineering, Queen's University, Kingston, Ontario, Canada*

Summary: The study develops a higher order beam theory based on the principle of stationary complementary energy. The theory successfully captures transverse shear stresses and transverse and longitudinal normal stresses. The predicted displacements and stresses are shown to agree well with the theory of elasticity solution and 3D FEA analysis.

INTRODUCTION

Beam theories have been widely developed based on the commonly used principle of stationary potential energy (Conventional Treatment) [e.g., 1]. Less common is the principle of stationary complementary strain energy [e.g., 2]. A description of both methodologies is depicted in Fig. 1. The present theory adopts the stationary complementary strain energy principle to develop a higher order beam theory. While the conventional treatment overestimates the stiffness of the beam, the present treatment has the desirable conservative feature of underestimating the stiffness while converging to the elasticity solution when enough higher order terms are taken.

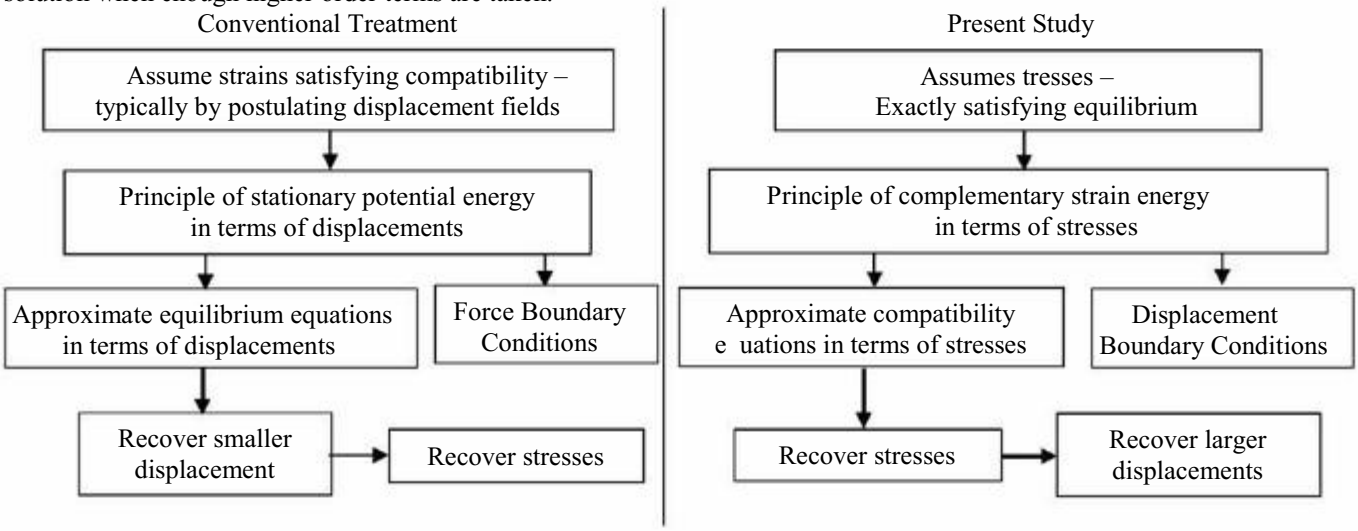

Figure 1. Comparison of present methodology and conventional treatment.

FORMULATION

The longitudinal normal stresses are assumed to take the form $\sigma_z\ y\ z = \sum_{i=1}^{n} y^{i-1} F_i\ z\ \ldots\ 1$ where $F_i\ z$ are unknown functions. As an example, the formulation is presented here for a simply supported beam with a rectangular cross-section for the simplest case $n = 3$ (Fig. 2). The beam is subjected to a transverse uniform traction on top surface $\bar{\sigma}(\ _1) = \bar{\sigma}$ and $\bar{\tau}\ h_1\ = \bar{\sigma}(h_2) = \bar{\tau}(h_2) = 0$ at top and bottom surfaces. Given the symmetry of the structure, only half of the beam is considered. From Eq. (1), by substituting into two equilibrium equations $\partial\tau_{yz}/\partial\ + \partial\sigma_z/\partial\ =\ _z$, $\partial\sigma_y/\partial\ + \partial\tau_{yz}/\partial\ =\ _y$ where $p_z\ y\ z)$ and $p_y\ y\ z)$ are longitudinal and transverse body forces, respectively, and enforcing the traction boundary conditions at top and bottom surfaces, the expressions for the three transverse shear and normal stresses can be shown to take the form:

$$\tau_{yz}(y\ z) = \left(-\ +\ y^3/h^2\ \ F_1'\ z\ + 6\sigma z\ \ h^2/4 - y^2\ \right)/h^3 +\ Q\ \ \left(h^2/4 - y^2\ \right)/bh^3$$

$$\sigma_y(y\ z) = \left(-h^2/16 + y^2/2 - y^4/h^2\ \ F_1''\ \ z\ + 2\ 1 - 3y/h +\ \ y^3/h^3\right)\bar{\sigma} \qquad (2a\text{-}c)$$

$$\sigma_z(y\ z) = \left(1 - 12y^2/h^2\ \ F_1\ \ z\ + 12\ \lfloor\ \ \ 0\ + zQ\ \ 0\ + M\ \ 0\ \rfloor/bh^3 + \left(6yz^2/h^3\right)\bar{\sigma}$$

in which $N\ \ 0\ = \int_A \sigma_z\ y\ \ dA\ \ Q\ \ 0\ = \int_A \tau_{yz}\ y\ \ dA\ \ M\ \ 0\ = \int_A y\sigma_z\ y\ \ dA$ are stress resultants at $z = 0$. Given the stress-strain relations $\varepsilon_z = \left(\sigma_z - \mu\sigma_y\right)/E$, $\varepsilon_y = \left(\sigma_y - \mu\sigma_z\right)/E$, $\gamma_{zy} = \tau_{zy}/G$, in which E, G and μ are elastic modulus, shear

a) Corresponding author. E-mail:MagdiEmile.Mohareb@uottawa.ca

modulus and Poisson's ratio, respectively, the total complementary strain energy of the system is expressed in term of $F_1\ z$ and the stationarity conditions are evoked to recover the compatibility equation

$$a\,F''''\ z\ +\quad''\quad +a\,F\ z\ -a_4 N\ 0\ =\tag{3}$$

in which $a_1 = bh^5/630E$; $a_2 = 2bh^3(2\mu\ -\ )/105EG$ $a_3 = 4bh/\ E$ $a_4 = 4/5E$; and b and h are width and depth of the cross-sectional section. Also, the following seven boundary equations are recovered.

$F_1\ 0\ =\ \ldots\ 4$; $M\ 0\ =\ \ldots\ 5$; $_1'\ \ /2)=\ \ldots\ 6$; $\quad'\ \ /2)+a\,F'''(L/2)=0\ldots 7$; $a\,F''\ 0\ +a\,F\ \ 0\ +a_8 N\ 0$

$-\sigma/240EI=0\ldots\ 8$; $\int_0^{L/2}\left[a\,F\ \ z\ +\quad''\quad +a_9 N\ 0\ \right]dz+(3\mu\sigma L/\ E)-\lfloor W\ 0\ +W\ \ L/2)\rfloor=0\ldots\ 9$;

$\int_0^{L/2}\left[\left(z^2/EI+6/5Gbh\ \ Q\ 0\ +(z/EI\ \ M\quad -\sigma z(\mu/5\quad +\ ^2/\ \ ^3+1/5\quad\right]\ -\lfloor V\ 0\ +V\ \ L/2)+\ \ \theta\quad\ /2)\rfloor=0\ldots\ 10)$

where $W\ z_0),V\ \ z_0),\theta(z_0)$ ($z_0=0$ or $L/2$) are the longitudinal and transverse displacements and rotation, respectively (Fig. 2) and coefficients $a_6 = 8I(\mu\ -\ )/35EG$ $a_7 = 8\mu I/\ \ G$ $a_8 = \mu h^2/\ \ E$ $a_9 = 9/5Ebh$ $I = bh^3/12$ have been defined.

EXAMPLE

Consider the case $h=1\,m$, $h/b=100$, $L/h=2$, $\bar{\sigma}=10\ MPa$, $E=\ 200\ GPa$ and $\mu=0.3$. The deflection at mid-span is presented in Table 1 and comparisons are provided with the conventional Euler-Bernoulli beam (EB), Timoshenko beam (TB), theory of elasticity (Timoshenko and Goodier 1970) [3]. Solutions based on the present study are presented for $n=3,4,5$. The deflection based on EB solution underestimates the deflection by 36.2% compared to the converged value. The TB solutions without a shear correction are 3.6% smaller. When using a shear factor of 5/6, the difference reduces to 3.1%. The longitudinal stresses (Fig. 3) based on $n=3$ is linear in manner consistent with EB or TB. When $n\geq 4$, the longitudinal stress profile is cubic in a manner consistent with the theory of elasticity solution. Unlike the EB and TB theories, the vertical normal stresses (Fig. 4) are nonzero and resemble those based on the elasticity solution.

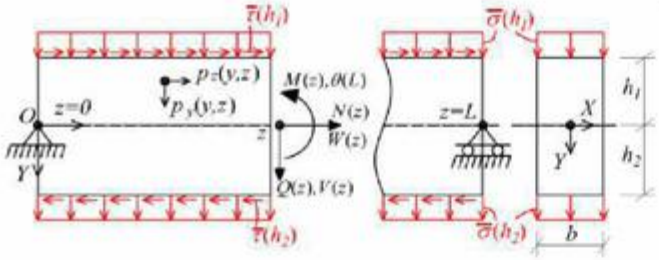

Figure 2. Beam profile and cross-section

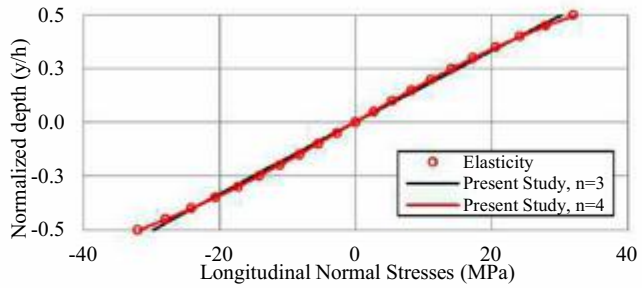

Figure 3. Longitudinal normal stresses at mid-span

Table 1. Deflection at mid-span

Solution		Deflection (mm)	Difference (%)***
Present Study	n=3	0.198	1.0
	n=4	0.196	0.0
	n=5	0.196	0.0
Elasticity		0.196	0.0
EB*		0.125	36.2
TB*		0.190	3.1
TB*+		0.203	3.6

* Conventional Treatment; +Shear correction factor 5/6 is applied;
*** % Difference of a solution is compared to converged value (0.196 mm)

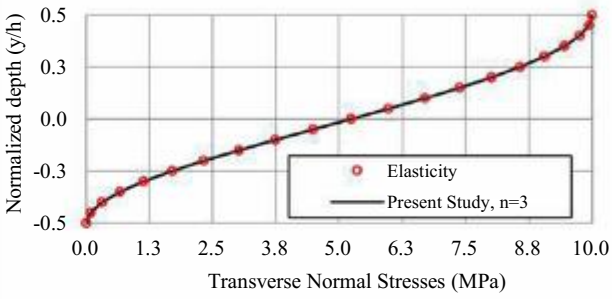

Figure 4.Vertical normal stresses at any cross-section

CONCLUSIONS

A higher order theory which captures transverse shear and vertical normal deformations was developed based on the principle of stationary complementary strain energy. Deformations obtained from present study are higher than the exact solution.

ACKNOWWLEGMENTS

The authors gratefully acknowledge scholarship support from the University of Ottawa to the first author and research funding from the Natural Sciences and Engineering Research Council (NSERC) of Canada to the second and third authors.

References

[1] Jha, D., K., Kant, T., and Singh, R., K., (2013), Stress analysis of transversely loaded functionally graded plates with a higher order shear and normal deformation theory ,J. of engineering mechanics, 139(12), 1663-1680

[2] Erkmen, R., E., and Mohareb, M., (2006), Torsion analysis of thin-walled beams including shear deformation effects, Journal of thin walled structures, 44(10), 1096-1108.

[3] Timoshenko, S. P. and Goodier, J., N. (1970), theory of elasticity (McGwaw-Hill, New York).

SOME RECENT THEORETICAL RESULTS IN PLANE ANISOTROPIC ELASTICITY

Paolo Vannucci [*1]

[1] *University Paris-Saclay - Laboratoire de Mathématiques de Versailles, UMR8100, Versailles, France*

Summary Some recent theoretical results, obtained using the polar formalism and concerning special orthotropies, anisotropy of planar damage, anisotropy of special materials, anisotropic rari-constant materials and interaction between geometry and anisotropy, are briefly presented.

GENERALITIES ABOUT THE POLAR FORMALISM

The use of anisotropic materials is one of the ways to tackle some modern problems of structural engineering. Their use is today almost compulsory in aircraft design or in the fabrication of sport devices etc. The most attractive property in the use of anisotropic materials is to dispose of stiffness and strength where it is needed; the idea, tacitly understood, is that in doing so, the structure will be lighter.

The mechanics of anisotropic materials, this is the price to pay for the designers, is much more cumbersome than that of classical isotropic, e.g. metallic, materials, which renders the whole process of design sometimes a true puzzle for engineers. There is a simple reason for that: the Cartesian representation of anisotropic elasticity is not effective when elastic moduli are frame-dependent.

The use of an alternative formalism for anisotropic elasticity should hence be interesting *per se* and for applications, especially for design purposes.

In the planar case, this is possible thanks to the *polar formalism*, [1], [2]; originally, this is just an algebraic method, based upon a complex variable transformation, to find all the invariants of a planar tensor of any rank.

In the polar formalism, the elastic tensor $\mathbb{C}$ is represented using exclusively invariants and angles, which can be very helpful in some situations, typically, for design problems and for theoretical developments:

$$\begin{cases} \mathbb{C}_{xxxx}(\theta)=T_0+2T_1+R_0\cos 4\left(\Phi_0-\theta\right)+4R_1\cos 2\left(\Phi_1-\theta\right) \\ \mathbb{C}_{xxxy}(\theta)=R_0\sin 4\left(\Phi_0-\theta\right)+2R_1\sin 2\left(\Phi_1-\theta\right) \\ \mathbb{C}_{xxyy}(\theta)=-T_0+2T_1-R_0\cos 4\left(\Phi_0-\theta\right) \\ \mathbb{C}_{xyxy}(\theta)=T_0-R_0\cos 4\left(\Phi_0-\theta\right) \\ \mathbb{C}_{xyyy}(\theta)=-R_0\sin 4\left(\Phi_0-\theta\right)+2R_1\sin 2\left(\Phi_1-\theta\right) \\ \mathbb{C}_{yyyy}(\theta)=T_0+2T_1+R_0\cos 4\left(\Phi_0-\theta\right)-4R_1\cos 2\left(\Phi_1-\theta\right) \end{cases} \tag{1}$$

In fact, the very characteristics of anisotropy is the dependence, for all the quantities, upon the direction: no Cartesian component is a constant and their dependence upon he direction is cumbersome (it depends actually upon the tensor's rank). So, disposing of a representation of elasticity using only invariants and angles, that appear explicitly in the equations, like in eq. (1), can be very helpful.

In the above equation, the invariants of $\mathbb{C}$ are the moduli T_0, T_1, R_0, R_1 and the difference of the two polar angles $\Phi_0 - \Phi_1$. It is apparent that T_0 and T_1 are the isotropy invariants, while R_0, R_1 and $\Phi_0 - \Phi_1$ are the anisotropy invariants: in the polar formalism, the representation of elasticity is naturally split into its isotropic and anisotropic part, which is very useful in different theoretical and design problems. In addition, it can be proved that T_0 and T_1 actually are a generalization of the classical shear and bulk moduli of isotropic elasticity.

The polar formalism puts in a new light all the theory of anisotropic bodies. Namely, another, more general, algebraically based classification of anisotropy, comprehending also particular cases never seen before, can be given; in such a classification, six algebraically distinct plane orthotropies can be enumerated, all of them corresponding with a particular value taken by one of the polar invariants, [3], [4].

Thanks to the polar formalism, a deep and new insight can be given into the anisotropy of specially elastic layers, i.e. layers whose elastic tensor has a different set of index symmetries. In particular, the cases of elastic materials not possessing the major or minor symmetries have been considered; in such a case, we can see the link existing between the index symmetries, i.e. the algebraic structure of the elastic tensor, and the material symmetries, namely, the number and types of orthotropies, [5].

Also, the old, long-lasting debated case of rari-constant materials has been considered and some new results found; in particular, it has been shown that there are two mutually exclusive cases of rari-constant materials, [6]. A simple way to realize such rari-constant materials is also given.

*Corresponding author. Email: paolo.vannucci@uvsq.fr

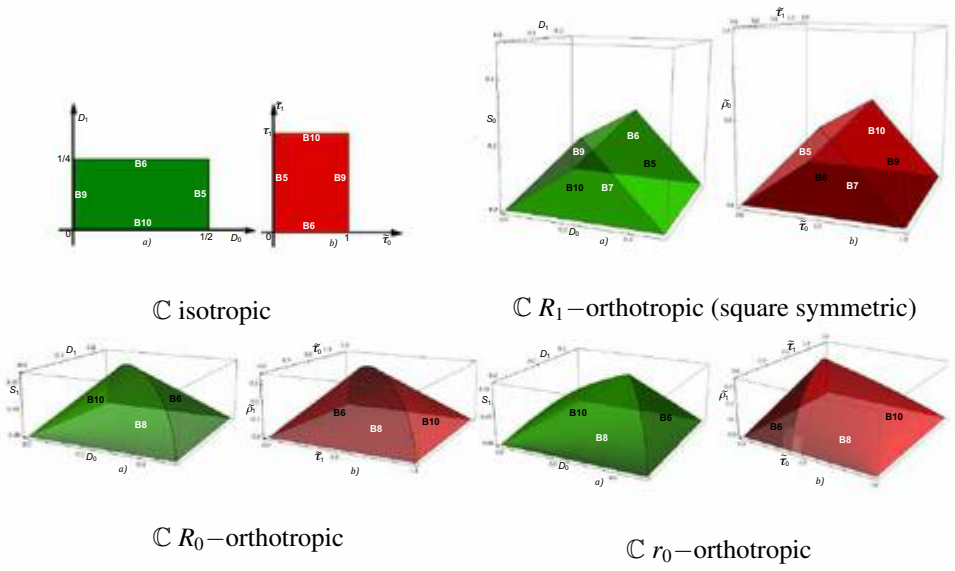

Figure 1: Bounds for the damaged elastic tensor $\mathbb{C}$ and for the damage tensor $\mathbb{D}$.

Some physical effects, coupling in a strange way geometry and elasticity, can be found thanks to the polar formalism, showing that in some cases an anisotropic structure can behave like an isotropic one, [7].

The use of the planar formalism has also allowed to solve another theoretical problem: what are the bounds on the elastic properties for a layer that, being initially isotropic, becomes anisotropic because of the damage induced by the applied loads? Using a classical representation of damage, described by a fourth-rank tensor $\mathbb{D}$ having the symmetries of elasticity, it has been possible to find an analytical expression of the bounds for the damaged elastic tensor $\mathbb{C}$ and for $\mathbb{D}$, see Fig. 1, [8].

CONCLUSIONS

The polar formalism is an effective algebraic representation of anisotropy based upon the use of tensor invariants and angles; some classical and more recent results, concerning special orthotropies, interaction between geometry and anisotropy, specially elastic materials, rari-constant materials and damaged anisotropic materials are briefly presented in this communication.

References

[1] Verchery G.: Les invariants des tenseurs d'ordre 4 du type de l'élasticité. Proc. of Colloque Euromech 115, Editions du CNRS, Villard-de-Lans, France 1979.

[2] Vannucci P.: Plane anisotropy by the polar method. Meccanica, 40: 437–454, 2005.

[3] Vannucci P.: A special planar orthotropic material. J Elast 67: 81–96, 2002.

[4] Vannucci P.: On special orthotropy of paper. J Elas 99: 75–83, 2010.

[5] Vannucci P., Verchery G.: Anisotropy of plane complex elastic bodies. International Journal of Solids and Structures, 47: 1154–1166, 2010.

[6] Vannucci P., Desmorat B.: Plane anisotropic rari-constant materials. To appear in Mathematical Methods in the Applied Sciences, 2015 (DOI: 10.1002/mma.3770).

[7] Vannucci P.: Strange laminates. Mathematical Methods in the Applied Sciences, 35: 1532-1546, 2012.

[8] Vannucci P., Desmorat B.: Analytical bounds for damage induced planar anisotropy. International Journal of Solids and Structures, 60-61: 96-106, 2015.

MICROMECHANICAL MODELING OF RUBBER-LIKE MATERIALS BASED ON ANALYTICAL NETWORK AVERAGING

Vu Ngoc Khiêm [*1] and Mikhail Itskov[1]

[1]*Department of Continuum Mechanics, RWTH Aachen University, Kackertstr. 9, 52072 Aachen, Germany*

Summary In this contribution, a micromechanical model is proposed to capture quasi-static response of all types of rubber-like materials. Accordingly, the rubber composite is decomposed into a pure rubber network considered to contribute to the deformation-induced network rearrangement, and a polymer particle network in charge of the network damage. The numerical integration over the unit sphere is avoided by using a generalized analytical network-averaging concept. The free energy of polymer chains is developed on the basis of a closed-form of Rayleigh's exact non-Gaussian distribution function. The inelastic effects in filled rubbers are elucidated by three deformation-induced mechanisms: network damage, network recovery, and network rearrangement. The proposed model includes very few physically motivated material constants and demonstrates good agreement with multi-dimensional experimental data of both unfilled and filled rubbers. The result confirms that the concept of numerical integration over the unit sphere is not crucial for both isotropic and anisotropic constitutive modeling.

NETWORK DECOMPOSITION

In the general case of filler reinforced elastomers, the rubber composite is decomposed into an elastic rubber network (CC) containing polymer subnetworks with cross-links at both ends, and an inelastic polymer particle network (PP) containing polymer subnetworks attached to two filler particles [2]. Accordingly, the strain energy of the whole composite is written as $\Psi = \Psi_{CC} + \Psi_{PP}$. Recent wide-angle X-ray experimental studies revealed a pronounced alignment of polymer chains in the stretching direction. Thus, in contrast to the previous works (see e.g. [2]), the CC network is considered in our model to contribute to the deformation-induced network anisotropic rearrangement, and the PP network is responsible for the network damage.

MOLECULAR STATISTICAL BASIS OF A POLYMER NETWORK

The pure rubber network is considered as a composition of several one-dimensional subnetworks dispersed in different directions in a unit sphere. The conformational probability density function of a polymer chain with n segments and normalized end-to-end distance r can be considered as a non-Gaussian probability of a random walk chain. By means of quantum mechanics, a closed-form $P_{\mathrm{c}}(n, r)$ of Rayleigh's exact distribution function [1] for non-Gaussian chains can be derived. Thus, the non-Gaussian free energy $\psi_{\mathrm{c}}(r)$ can be obtained.

GENERALIZED NETWORK-AVERAGING

A probability distribution of the polymer subnetworks in space is developed, taking the deformation-induced spatial alignment of polymer molecules into account (Fig.1)

$$\rho(\boldsymbol{u}) = \underset{\tau \in (-\infty, t]}{\mathcal{P}} \left[\mathbf{F}(\tau)\right], \tag{1}$$

where $\boldsymbol{u}$ is an arbitrary direction, the response function $\mathcal{P}$ denotes a mapping the deformation history into the spatial distribution of polymer chains, $\mathbf{F}$ is the deformation gradient, τ denotes a point of time in the past, and t is the current time.

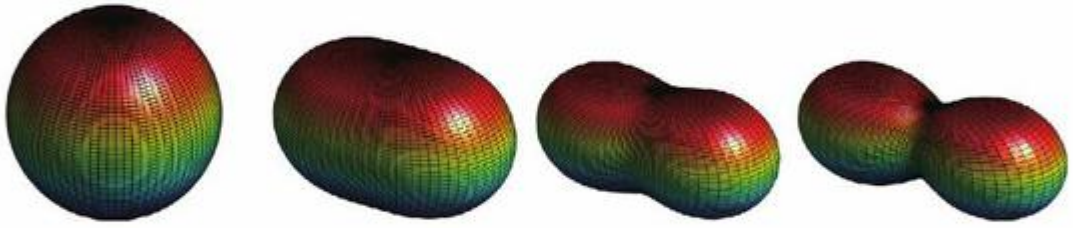

Figure 1: Rearrangement of the spatial distribution of polymer chains during a uniaxial tension.

The energy of the full network is evaluated from the mean field free energy of the subnetworks over the unit sphere by means of a generalized network averaging concept. In our model, the mean field quantity can be derived analytically, so numerical integration over the unit sphere is not applied here.

*Corresponding author. Email: vu@km.rwth-aachen.de

MECHANISMS OF THE MULLINS EFFECT AND HYSTERESIS

We assume that there exist two types of adsorption sites (areas for the adsorption of polymer chains on the filler particles) on the aggregate surface: irreversible adsorption and reversible adsorption sites. Polymer chains connected to irreversible adsorption and reversible adsorption sites are referred to as irreversible and reversible chains, respectively. The stress softening between the initial loading and the subsequent reloading can be explained by permanent debonding of molecular chains from the irreversible adsorption area. The hysteresis is elucidated by failure and recovery of polymer chains connected to the reversible adsorption sites. By means of statistical mechanics, the number of irreversible chains N_{PP}^{ir} and reversible chains N_{PP}^{rv} can be calculated. Thus, the free energy of the PP network can be obtained as $\Psi_{PP} = N_{PP}^{\mathrm{ir}}\psi_c(r) + N_{PP}^{\mathrm{rv}}\psi_c(r)$.

RESULTS

In this section, we first validate the performance of the proposed model by comparing it to various sets of multi-dimensional experimental data of unfilled rubber [3, 4] (see Fig.2). In the next step, the model is further compared to uniaxial tension

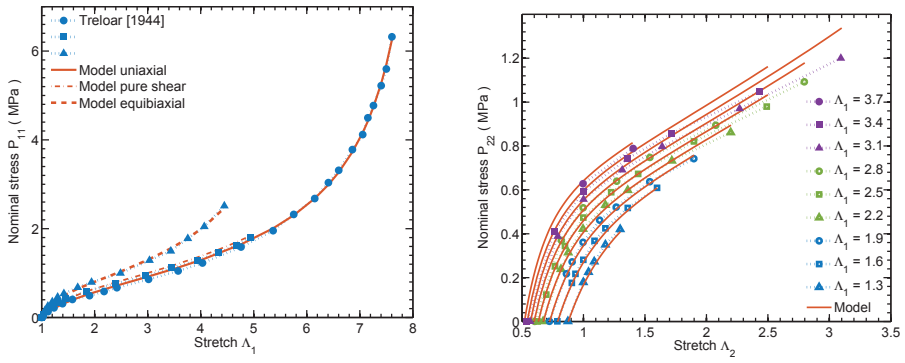

Figure 2: Prediction of the proposed model in comparison with the multi-dimensional experimental data of unfilled rubber: in uniaxial tension, pure shear and equibiaxial tension [3] (left), and in a series of biaxial tensions [4] (right).

experimental data of 50phr carbon black filled polychloroprene (Fig.3).

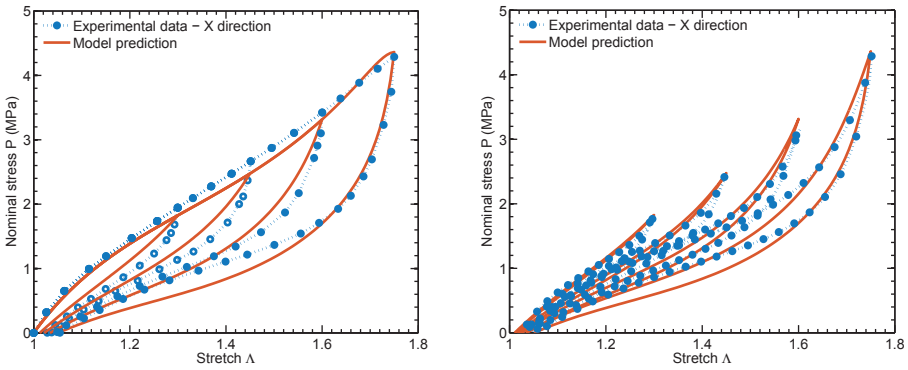

Figure 3: Comparison of the model predictions with experimental data of the cyclic uniaxial tension at different stretch ratios: the Mullins effect (left), and the hysteresis (right).

References

[1] Lord Rayleigh, J. W. S., 1919. On the problem of random vibrations, and of random flights in one, two, or three dimensions. Philosophical Magazine 37 (6), 321–347.

[2] Govindjee, S., Simo, J., 1991. A micro-mechanically based continuum damage model for carbon black-filled rubbers incorporating Mullins' effect. Journal of the Mechanics and Physics of Solids 39, 87–112.

[3] Treloar, L. R. G., 1944. Stress-strain data for vulcanised rubber under various types of deformation. Transactions of the Faraday Society 40, 59–70.

[4] Kawabata, S., Matsuda, M., Tei, K., Hawai, H., 1981. Experimental survey of the strain energy density function of isoprene rubber vulcanizate. Macromolecules 14, 154–162.

THICKNESS-SHEAR VIBRATIONS OF CIRCULAR QUARTZ CRYSTAL PLATES

Ji Wang[a)], Chen Hao, Hui Chen, Jianke Du, Bin Huang, Lijun Yi
Piezoelectric Device Laboratory, School of Mechanical Engineering & Mechanics, Ningbo University, 818 Fenghua Road, Ningbo, Zhejiang 315211, China

Summary The thickness-shear vibrations of quartz crystal plates are of interests in the analysis and design of quartz crystal resonators which usually have complications because of structural configuration. Due to the material anisotropy, vibrations of circular plates of quartz crystal are no longer axisymmetric and solutions are not available from analytical solutions. By approximating the equations for the thickness-shear vibrations with the reduced couplings with the flexural mode only, we obtained the simplified equations of the only fundamental harmonics terms of angular dependence. The differential equations are solved by the Frobenius method with solutions in infinite power series for the thickness-shear and flexural mode shapes and frequency spectra.

INTRODUCTION

Vibrations of elastic plates have been the major topic of structural analysis with a long and rich history. Earlier efforts have been on the analysis of flexural vibrations of thin plates with the classical plate theory which considers the flexural mode only at relatively lower vibration frequency. However, even in simple cases like isotropic plates, analytical solutions are only scarcely available and the finite element analysis also tends to be difficult due to the higher frequency of the thickness-shear mode and the refined mesh which result in a larger eigenvalue problem.

With the objective to establish systematic equations of vibrations of circular elastic plates at the thickness-shear mode, we start with the derivation of the Mindlin plate equations in the polar coordinate for circular plates. By following the procedure demonstrated by Mindlin for rectangular plates in Cartesian coordinates, we obtained similar equations in polar coordinates and some results for infinite plates to validate the equations are obtained as before [1, 2]. Then, equations with truncation are used for the coupled vibrations of thickness-shear and flexure of isotropic finite circular plates. The results from this analysis are used for the in-depth understanding of thickness-shear vibrations in finite plates [2]. For anisotropic materials like quartz crystals, the equations are even more strongly coupled, and solutions will no longer be axisymmetric for further simplification due to the angular dependence of elastic constants. The simplification has to be done with all complications considered. Our study of quartz crystal plates vibrating in the vicinity of thickness-shear mode starts from the calculation of elastic constants to obtain their expressions including the angular variable. It is natural to expect that the solution should also have trigonometric terms, but the way to obtain such solutions have to be explored. The accurate solution can often be obtained from such differential equations with the Frobenius method for power series solutions.

GENERAL EQUATIONS FOR THICKNESS-SHEAR VIBRATIONS OF QUARTZ CRYSTAL PLATES

By following the standard procedure for the development of Mindlin plate equations based on the power series expansion of displacements with both Cartesian and polar coordinates, we have derived the Mindlin plate equations for circular plates of isotropic and anisotropic materials [2]. As we know, the Mindlin plate equations are a set of differential equations with infinite number of vibrations modes with couplings through material anisotropy. For applications, the equations have to be truncated based on targeted modes and frequencies [3]. For example, quartz crystal resonators of overtone modes such as the fifth have to be studied with the fifth-order Mindlin plate equations [3]. Upon simplification and truncation, the Mindlin plate equations for the thickness-shear vibrations with the normalized frequency Ω

$$\Omega = \frac{\omega}{\omega_0}, \omega_0 = \frac{\pi}{2b}\sqrt{\frac{c_{66}}{\rho}}, \tag{1}$$

and the truncated vibration equations of the flexural ($u_z^{(0)}$) and thickness-shear ($u_r^{(1)}$) modes are

$$\begin{aligned} &C_1 u_{z,rr}^{(0)} + C_2 \frac{1}{r} u_{z,r}^{(0)} + \frac{\pi^2}{4b^2}\Omega^2 u_z^{(0)} + C_1 u_{r,r}^{(1)} + C_2 \frac{1}{r} u_r^{(1)} = 0, \\ &C_3 u_{r,rr}^{(1)} + C_4 \frac{1}{r} u_{r,r}^{(1)} + \left(\frac{\pi^2}{4b^2}\Omega^2 - C_5 \frac{1}{r^2} - C_1 \frac{3}{b^2}\right) u_r^{(1)} - C_1 \frac{3}{b^2} u_{z,r}^{(0)} = 0, \end{aligned} \tag{2}$$

with the assumption that displacements are axisymmetric. This is obviously not true because material constants in above equations are angular dependent and so are the displacements. However, a careful examination of the constants revealed that terms associated with the angular variable $\cos 2\theta$ are generally much smaller than constant terms, and their effect on the angular distribution of displacements can be better represented with the combinations of two terms. For demonstration, the elastic constants of AT-cut quartz crystal with the consideration of angular dependence are

$$C_1 = 1.17 - 0.17\cos 2\theta, C_2 = 1.17 - 0.5\cos 2\theta, C_3 = 4.46 - 0.28\cos 2\theta, C_4 = 6.87 - 0.56\cos 2\theta, C_5 = 6.87 + 0.56\cos 2\theta. \tag{3}$$

By eliminating $u_z^{(0)}$ from Eq. (2), we obtain the fourth-order differential equation for the thickness-shear vibration as

[a)] Corresponding author. Email: wangji@nbu.edu.cn.

$$u'''' + A\frac{1}{r}u''' + \left(B\frac{1}{r^2} + C\right)u'' + \left(D\frac{1}{r^3} + E\frac{1}{r}\right)u' + \left(F\frac{1}{r^4} + G\frac{1}{r^2} + H\right)u = 0, \quad (4)$$

where

$$u = u_r^{(1)}, A = 2.54 - 0.31\cos 2\theta, B = \approx -4.08 - 0.35\cos 2\theta, C = \frac{\pi^2\Omega^2}{b^2}(0.27 + 0.03\cos 2\theta),$$
$$D = 4.62 + 1.98\cos 2\theta, E = \frac{\pi^2\Omega^2}{b^2}(0.39 + 0.03cos2\theta), F = -4.62 - 1.98\cos 2\theta, G = -\frac{\pi^2\Omega^2}{b^2}(0.39 + 0.08\cos 2\theta), \quad (5)$$
$$H = \frac{0.01\pi^4\Omega^4 - 0.14\pi^2\Omega^2}{b^4} + \frac{0.002\pi^4\Omega^4 - 0.01\pi^2\Omega^2}{b^4}\cos 2\theta.$$

Now the task is to solve this fourth-order differential equation and obtain both thickness-shear and flexural deformation for the calculation of frequency and mode shapes.

APPROXIMATION AND SOLUTIONS

For analytical solutions of equations given in the above section, further approximation and simplification are needed. First of all, we need to assume the vibrations are still axisymmetric even the material itself may not be axisymmetric in terms of material elastic constants. This is to suggest that we can eliminate the angular depended for the axisymmetric solutions, and effects of angular variables will not the neglected completely because parameters containing angular variable are still there to affect the solutions which are still angular dependent.

With above assumption, Eq. (5) can be further separated into two parts as

$$L_0(u) + \cos 2\theta\, L_1(u) = 0, \quad (6)$$

Then it is natural to assume the solutions will be in the form of

$$u = u_0 + u_1\cos 2\theta, \quad (7)$$

where u_0 and u_1 are the displacements from $L_0(u)$ and $L_1(u)$, respectively. With actual equation, solutions can only be obtained with the Frobenius method as functions in infinite power series, as we do for Bessel functions and other transcendental solutions and functions of similar equations. The boundary conditions will also be decomposed to a form similar to Eq. (7) and further approximation can be made accordingly.

EXAMPLES AND NUMERICAL RESULTS

With the Frobenius solutions in infinite power series, we can evaluate these solutions and utilize the boundary conditions to obtain frequency and mode shape solutions. For quartz crystal resonators, usual boundary conditions are traction-free, which are used to realize and maximize the energy trapping effect. With solutions outlined above, we found the thickness-shear vibration frequency of relatively larger plates is approaching to the thickness-shear frequency of infinite plates. This is a reasonable validation of the approximate equations and solutions. The results are shown with spectra (frequency versus radius) and mode shapes. These results usually are needed for the design of quartz crystal resonators.

CONCLUSIONS

With approximation and simplification regarding the Mindlin plate equations for thickness-shear vibrations of circular quartz crystal plates, we have obtained vibration solutions of the strongly coupled thickness-shear and flexural vibrations. The frequency and mode shapes are important in the analysis and design of quartz crystal resonators of circular types. Although the solutions are from the simplified equations with assumptions like the axisymmetric solutions, they can offer simple and quick results needed in the design evaluation. It is always a good start of the design process of complicated devices like quartz crystal resonators which challenge the vibration analysis with features like higher vibration frequency and coupled vibration modes involving finite elastic solids of anisotropic materials.

Acknowledgment

This research is supported by the Natural Science Foundation of China through Grant 11372145. Additional support is through the Zhejiang Provincial Key Field Program of Mechanics at Ningbo University.

References

[1] Chen H., Wang L., Ma T., Yi L., Du J., Wang J.: An Analysis of Thickness-shear Vibrations of an Annular Plate with the Mindlin Plate Equations. *Proceedings of 2015 IEEE International Frequency Control Symposium and European Frequency and Time Forum*, 402-405,. [DOI: 10.1109/FCS.2015.7138867]

[2] Chen H., Wang J., Ma T., Du J.: An Analysis of Free Vibrations of Isotropic, Circular Plates with the Mindlin Plate Theory. *Proceedings of the 2014 Symposium on Piezoelectricity, Acoustic Waves, and Device Applications*, 397-400. [DOI: 10.1109/SPAWDA.2014.6998608]

[3] Wang J., Wu R., Yang L., Ma T., Du J.: The Fifth-order Overtone Vibrations of Quartz Crystal Plates with Corrected Higher-order Mindlin Plate Equations, *IEEE Trans. Ultrason., Ferroelect, and Freq. Contr.*, **59**(10):2278-2291, 2012. [DOI: 10.1109/TUFFC.2012.2453]

GENERALIZED THERMOELASTICITY IN FRAMEWORK OF PERIDYNAMICS

Linjuan Wang[1], Jifeng Xu[2], Jianxiang Wang[1a)]
[1]*State Key Laboratory for Turbulence and Complex Systems, Department of Mechanics and Engineering Science, College of Engineering, Peking University, Beijing 100871, P. R. China*
[2]*Beijing Aeronautical Science and Technology Research Institute, Beijing 100083, P. R. China*

Summary Nonlocality may arise in modelling the overall thermomechanical properties of heterogeneous media or in solving thermomechanical problems at small scales. This paper presents the nonlocal peridynamic equations of generalized thermoelasticity that couples together the ordinary state-based peridynamic non-Fourier heat conduction theory and the peridynamic equation of motion. Based on irreversible thermodynamics, the equations are derived by introducing the concept of phase lags of time into the peidynamic framework, which considers nonlocal mechanical effect and non-Fourier heat conduction simultaneously. Numerical procedures are proposed to solve the integro-differential equations, and the results are in good agreement with available experimental data of two examples. Compared with classical generalized thermoelasticity, the peridyanmic generalized thermoelasticity can be easily applied to multidimensional media containing discontinuities.

INTRODUCTION

Heat is found to propagate at a finite speed in more and more cases, such as self-heating in micro-electronic devices and the situations at very low temperature near absolute zero, whilst the diffusive parabolic heat conduction equation based on the Fourier law results in an infinite speed of heat propagation. The simulation of non-Fourier heat conduction has attracted much attention. Many models of non-Fourier heat conduction have been proposed, such as the wave model with a hyperbolic heat conduction equation[1], the two-process model[2], the Dual-Phase-Lag (DPL) model[3] and so on. Following these non-Fourier models, some generalized thermoelastic theories are developed, such as the L-S theory proposed by Lord and Shulman[4], and the G-L theory proposed by Green and Lindsay[5]. These models including non-Fourier heat conduction give a finite heat propagation speed, but do not address the nonlocal effect.

Nonlocality is inherent in the transfer of thermal energy, since heat conduction requires sufficient collisions among energy carries, such as phonons and electrons, which collide with each other and bring energy from one point to another. In the last decades, invalidity of local formulation has been found in more and more situations, for instance, emergency cooling and rapid transient heating in modern industry, and heat conduction in nanostructures. As the characteristic length is comparable to, or less than, the mean free path of the carriers, the nonlocality needs to be taken into account. On the mechanical side, the peridynamic theory [6] replaces the conventional differential equation of motion with an integral formula, leading to a strongly nonlocal theory that accounts for long range interactions among material points. Thus, the peridynamic framework provides a unified platform that includes the mechanical nonlocality and the nonlocal heat conduction.

Considering the above developments, we present a non-Fourier heat conduction model and a framework of generalized thermoelasticity based on state-based peridynamics, which considers the mechanical nonlocal effect and non-Fourier heat conduction simultaneously.

THEORETICAL MODEL

Based on the framework of stated-based peridynamic thermal diffusion[7], peridynamic non-Fourier heat conduction equations are derived by introducing the phase lags τ_q and τ_T which are proposed in the DPL model[3] as follows

$$\underline{q}\left[\mathbf{x}, t+\tau_q\right] = \underline{q}\left(\underline{\Theta}\left[\mathbf{x}, t+\tau_T\right]\right) \tag{1}$$

where $\underline{q}$ is the peridynamic heat flow state and $\underline{\Theta}$ is the temperature state, and $\mathbf{x}$ and t represent the position of a material point and the moment of time, respectively. This model includes the effect of finite relaxation time through the phase lags in the heat flow state and temperature state, where the time lag τ_q is caused by micro-structural interactions such as phonon scattering, and the τ_T is interpreted as the relaxation time due to fast-transient effects of thermal inertia. In addition, with the assumption of bond-based peridynamics, bond-based peridynamic heat conduction equations can be obtained.

The previously developed fully coupled peridynamic thermomechanics[8] utilizes a thermal equation based on the Fourier law which may become invalid in many cases as discussed in the introduction. The PD-DPL model provides a method to overcome this problem. Then the coupled thermomechanical theories that admit a finite speed of heat propagation are developed in this paper, and these theories are referred to as peridynamic generalized thermoelasticity. The derivations of state-based peridynamic generalized thermoelasticity equations are based on irreversible thermodynamics. In view of the widespread application of the classical L-S theory and the G-L theory, we develop two kinds of peridynamic

[a)]Corresponding author. Email: jxwang@pku.edu.cn.

generalized thermoelasticity, i.e., the peridynamic L-S theory and the peridynamic G-L theory. Derivations are briefly summarized as follows.

First, the equations of the peridynamic L-S theory are derived by introducing only one relaxation parameter τ_0 into the heat conduction equation (1), which leads to

$$\rho c_v(\dot{\Theta}+\tau_0\ddot{\Theta}) = \bar{Q} - \Theta\underline{\mathbf{B}}\cdot(\dot{\underline{\mathbf{Y}}}+\tau_0\ddot{\underline{\mathbf{Y}}}) + \rho(s_b+\tau_0\dot{s}_b) \tag{2}$$

where ρ, c_v and s_b represent the mass density, the specific heat capacity and the prescribed volumetric heat generation per unit mass, respectively. $\underline{\mathbf{B}}$ is the thermal modulus state, $\underline{\mathbf{Y}}$ is the deformation state, and $\bar{Q} = \int_H (\underline{h}(\mathbf{x}',t)\langle \mathbf{x}'-\mathbf{x}\rangle - \underline{h}(\mathbf{x},t)\langle \mathbf{x}-\mathbf{x}'\rangle)dV'$ is the rate of heat energy in which $\underline{h}$ is the heat flow scalar state and H is a neighbourhood determined by the peridynamic horizon. The heat conduction equation (2) is a special case of the PD-DPL model. For the deformation field, the equation of motion of the peridynamic L-S theory is the same as that of the fully coupled peridynamic thermomechanics.

Then, the derivation of the peridynamic G-L theory is obtained as follows. As in the classical G-L theory, by introducing a relaxation parameter τ_1 into the heat conduction equation and with a series of derivation, we obtain the heat conduction equation of the peridyanmic G-L theory

$$\rho c_v(\dot{\Theta}+\tau_1\ddot{\Theta}) = \bar{Q} - \Theta\underline{\mathbf{B}}\cdot\dot{\underline{\mathbf{Y}}} + \rho s_b$$

On the other hand, introducing a relaxation parameter τ_2 into the equation of motion leads to the peridynamic force state $\underline{\mathbf{T}}$ of the peidynamic G-L theory as

$$\underline{\mathbf{T}} = \underline{\mathbf{T}}_s - \underline{\mathbf{B}}(\Theta+\tau_2\dot{\Theta})$$

The part of the force state $\underline{\mathbf{T}}_s$ includes only the structural deformation. The equation of motion of the peridynamic G-L theory can be finally expressed as

$$\rho\ddot{\mathbf{u}}(\mathbf{x},t) = \int_H \left[\underline{\mathbf{T}}(\mathbf{x}',t)\langle \mathbf{x}'-\mathbf{x}\rangle - \underline{\mathbf{T}}(\mathbf{x},t)\langle \mathbf{x}'-\mathbf{x}\rangle\right]dV + \mathbf{b}(\mathbf{x},t) \tag{3}$$

where $\mathbf{u}(\mathbf{x},t)$ and $\mathbf{b}(\mathbf{x},t)$ represent the displacement and body force fields at time t. We also obtained and discussed the bond-based peridynamic generalized thermoelasticity and the numerical procedure.

RESULTS

The PD-DPL model is used to investigate the temperature field of a thin metal film irradiated by an ultrashort-pulse laser. The results are compared with the available experimental data. For two values of the thickness of the film, the results of the PD-DPL model agree well with the experimental data[9]. Furthermore, the PD-DPL model is applied to problems with discontinuities, such as cracks and composite materials. Then, the bond-based peridynamic L-S theory and G-L theory are used to solve a one-dimensional thermoelasticity problem of a semi-infinite bar subjected to a thermal shock at the end. The temperature field and displacement field are calculated. It is shown that the two kinds of generalized thermoelasticity predict the characteristics of wave propagation, with the positions of the wave front and the turning points of the displacement field being clearly captured.

References

[1] Joseph D.D., Preziosi L.: Heat Waves. *Reviews of Modern Physics* **62**: 375-391, 1990.

[2] Qiu T.Q., Tien C.L.: Short-Pulse Laser-Heating on Metals. *International Journal of Heat and Mass Transfer* **35**: 719-726, 1992.

[3] Tzou D.Y.: A Unified Field Approach for Heat Conduction from Macro- to Micro-scales. Transactions of the ASME *Journal of Heat Transfer* **117**: 8-16, 1995.

[4] Lord H.W., Shulman Y.: A Generalized Dynamical Theory of Thermoelasticity. *Journal of the Mechanics and Physics of Solids* 1**5**: 299-309, 1967.

[5] Green A.E, Lindsay K.A.: Thermoelasticity. *Journal of Elasticity* **2**: 1-7, 1972.

[6] Silling S.A., Lehoucq R.B.: Peridyanmic Theory of Solid Mechanics. *Advances in Applied Mechanics* **44**: 73-168, 2010.

[7] Oterkus S., Madenci E., Agwai A.: Peridynamic Thermal Diffusion. *Journal of Computational Physics* **265**: 71-96, 2014.

[8] Oterkus S., Madenci E., Agwai A.: Fully Coupled Peridynamic Thermomechanics. *Journal of the Mechanics and Physics of Solids* **64**: 1-23, 2014..

[9] Ho C.Y., Wen M.Y, Chen B.C., Tsai Y.H.: Non-Fourier Two-Temperature Heat Conduction Model Used to Analyze Ultrashort-Pulse Laser Processing of Nanoscale Metal Film. *Journal of Nanoscience and Nanotechnology* **14**: 5581-5586, 2014.

FINITE ELEMENT NUMERICAL SIMULATION OF BI-MODULUS BEAMS

Zhiming Ye[1,2], Huiling Zhao[1a)]
[1] *Department of Civil Engineering, Shanghai University, China*
[2] *Shanghai Institute of Applied Mathematics and Mechanics, China*

Summary This paper improves the bi-modulus elastic constitutive equation employed in the bi-modulus finite element numerical method (FEM). The new elastic matrix model is proposed based on Ye's principal strain criterion with the assumption that the Poisson ratio maintain constant whenever in tension or in compression, and the elastic matrix is symmetric by equivalent transmitting. The shear modulus expression of this elastic matrix model is derived to enable the elastic matrix completely and improve the convergence of the FEM calculation. The statically indeterminate bi-modulus beam is analysed by means of FEM employing the proposed elastic matrix model. The effects of the tensile modulus to compressive modulus ratio and the boundary condition on the stress and deflection of the bi-modulus beam is studied.

INTRODUCTION

Bi-modulus materials exhibit the different modulus in tension and compression. The value of elastic modulus and Poisson ratio of every point in the bi-modulus elastic body not only depend on the material itself, but also the stress state and the strain state of the point. The uncertainty and nonlinearity of the elastic constitutive relation result in that the bi-modulus elastic problem is the complicated nonlinear problem. Due to difference between tensile and compressive elastic modulus, the line is not smoothness in mathematically. The relationship curve presents continue but not smooth at origin point. This point gives much trouble at investigation on the mechanical behaviour of structures made of this kind of material [Yao 2004].

Most of structures are complex and indeterminate. Bi-modulus finite element numerical method is a good solution to structural analysis [He 2009, Yang 2014]. Ambartsumyan[1965] put forward finite element method of bi-modulus elasticity early stages. The value and positive-negative sign of elastic modulus of every point in the bi-modulus elastic body depends on the material itself, but also the boundary conditions and loads [Ye 2001]. Criterion for elastic modulus positive-negative signs and values of elastic matrix model is the focus of bi-modulus finite element method.

Johns[1977] and Vijayakumar[1987] modified the relationship between constants of elastic matrix to improve the finite element method. Ye[1997] proposed the modified elastic matrix based on the criteria of principal strain.

THE CRITERIA OF PRINCIPAL STRAIN

As for the elastic matrix of FEM for bi-modulus elasticity, in order to obtain symmetry of elastic matrix, the assumption $\mu^t / E^t = \mu^c / E^c$ was given. However, this assumption is not necessarily proper for all the bi-modulus materials. Ye[2001] proposed "the criteria of principal strain", based on which a new elastic matrix was given. The assumption $\mu^t / E^t = \mu^c / E^c$ was abandoned and a new assumption was proposed that the Poisson ratio for compression and tension is the same, kept as $\mu = \left(\mu^t + \mu^c\right)/2$, which is more correspond with the actual.

Ye[2001] proposed "the criteria of principal strain" to judge the elastic coefficients of elastic matrix model are tensile or compressive, shown as eq.(1):

$$\begin{Bmatrix} \sigma_\alpha \\ \sigma_\beta \\ \sigma_\gamma \end{Bmatrix} = \begin{bmatrix} d_{11} & d_{12} & d_{13} \\ d_{21} & d_{22} & d_{23} \\ d_{31} & d_{32} & d_{33} \end{bmatrix} \begin{Bmatrix} \varepsilon_\alpha \\ \varepsilon_\beta \\ \varepsilon_\gamma \end{Bmatrix} \qquad \text{eq.(1)}$$

where, if $\varepsilon_i > 0$, $d_{il} = d_{il}^+$, contrary $d_{il} = d_{il}^-$. Whether the elastic coefficient is tensile or compressive depends on the principal strain is tensile or compressive.

IMPROVEMENT OF ELASTIC MATRIX MODEL

As seen in eq.(4), the elastic matrix model is unsymmetrical. In order to obtain symmetry of elastic matrix, the method of equivalence is used as follows.

$$[\overline{D}_I] = ([D_I] + [D_I]^T)/2 \qquad \text{eq. (2)}$$

By completeness, the improved bi-modulus elastic matrix expressing the relation of principal stress and strain is as eq. (3)

$$\widetilde{\boldsymbol{D}}_I = \begin{bmatrix} d_{11} & d_{12} & 0 \\ d_{21} & d_{22} & 0 \\ 0 & 0 & d_{33} \end{bmatrix} \qquad \text{eq. (3).}$$

[a)] Corresponding author. Email: hlzhao@shu.edu.cn

The expression of element d_{33} of the bi-modulus elastic matrix, refers to bi-modulus shear modulus G_{xy} can be expressed as eq. (4).

$$\begin{aligned} G_{xy} &= \frac{\mu^2\left(E^t+E^c\right)^2-4E^tE^c}{4\left(\mu^2-1\right)}\frac{\sigma_1-\sigma_2}{\left[(2+\mu)E^c+\mu E^t\right]\sigma_1-\left[(2+\mu)E^t+\mu E^c\right]\sigma_2} \\ &= \frac{\mu^2\left(E^t+E^c\right)^2-4E^tE^c}{4\left(\mu^2-1\right)}\frac{|\sigma_1|+|\sigma_2|}{\left[(2+\mu)E^c+\mu E^t\right]|\sigma_1|+\left[(2+\mu)E^t+\mu E^c\right]|\sigma_2|} \\ &= \frac{\mu^2\left(E^t+E^c\right)^2-4E^tE^c}{4\left(\mu^2-1\right)}\frac{1}{\left[(2+\mu)E^c+\mu E^t\right]\eta'+\left[(2+\mu)E^t+\mu E^c\right](1-\eta')} \end{aligned} \qquad \text{eq. (4)}$$

where, η' is called accelerating convergence factor, and $\eta'=\dfrac{|\sigma_1|}{|\sigma_1|+|\sigma_2|}$. When $E^t=E^c$, the expression of bi-modulus shear modulus $G_{xy}=\dfrac{E}{2(1+\mu)}$.

As for the bi-modulus elastic matrix with completeness, when $E^t=E^c$, it is the same as the Classical elastic matrix. It can be seen that regression test is passed.

As for the computation of FEM of bi-modulus structures, the flow chart can be given. Initially, the first calculation is conducted under the consideration of the same modulus. Tensile and compressive areas are obtained attentively. E^t, μ^t and E^c, μ^c are used for the 1st kind of areas where all the principal strain are tensile and compressive, respectively. As for the 2nd kind of area, $E=\overline{E}=(E^t+E^c)/2$ and $\mu=\overline{\mu}=(\mu^t+\mu^c)/2$ are used temporarily. The stiffness matrix of each element is obtained based on these elastic constants. And then, the calculation results can be treated as the initial stress, strain, and displacement of the structure.

Consequently, according to the principal stress and strain of each node, new elastic matrix of each node, with symmetricity and completeness by equivalent modification and shear modulus introduction as previous section stated, can be obtained. And then the iterating calculation continues by this rule until the difference between adjacent iterations satisfies the precision requirement.

CONCLUSIONS

According to the finite element numerical simulation of the bi-modulus beans, the deflection errors for three boundary conditions are larger than zero when $n<1$, and they increase as n decreases, which indicates that the deflections obtained by classical elasticity are smaller than the real results and the errors increase as n decreases when $n<1$. The deflections obtained by classical elasticity are larger than the real results and the errors increase as n increases when $n>1$. Deflection errors by classical elasticity of simply-supported, fixed-freely supported, and clamped-clamped beam are exceed 5% when n <0.9, 0.88, 0.86 or n >1.12, 1.13, and 1.3. More attention should be paid to these situations.

References

[1] Yao W. J., Ye Z. M.: Analytical solution for bending beam subject to lateral force with different modulus. *Applied Mathematics and Mechanics (English Edition)*, 25(10): 1107-1117, 2004.

[2] He X., Zheng Z., Sun J.: Convergence analysis of a finite element method based on different moduli in tension and compression. *International Journal of Solids and Structures*, 46: 3734-3740, 2009.

[3] Yang Q., Zheng B. L., Zhang K. and et al.: Elastic solutions of a functionally graded cantilever beam with different modulus in tension and compression under bending loads. *Applied Mathematical Modelling*, 27(2): 1403-1416, 2014.

[4] Ambartsumyan S. A. Elasticity Theory of Different Moduli (Trans. by Wu, R. F. and Zhang, Y. Z.). China Railway Publishing House, Beijing, China, 1986.

[5] Ye Z. M., Yu H. R., Yao W. J. A new elasticity and finite element formulation for different Young's modulus when tension and compression loading. *Journal of Shanghai University (English Edition)*, 5(2): 89-92, 2001.

[6] Johns R.M. Stress-strain relations for materials with different moduli in tension and compression. *AIAA Journal*, 15(1): 16-23, 1977.

[7] Vijayakumar K., Rao K.P. Stress-strain relation for composites with different stiffness in tension and compression-a new model. *Int. J. of Computational Mechanics*, 1(2):167-175, 1987.

[8] Ye Z. M. A new finite element formulation for planar elastic deformation. *International Journal for Numerical Methods in Engineering*, 40: 2579-2591, 1997.

RAYLEIGH WAVES IN A LAYERED PIEZOELECTRIC NANOSTRUCTURE WITH SURFACE EFFECTS

Lele Zhang[1a)], Jinxi Liu[1], Xianglin Liu[1] & Guoquan Nie[1]
[1]*Department of Engineering Mechanics, Shijiazhuang Tiedao University, Shijiazhuang, P.R. China*

Summary Based on the surface piezoelectricity model, surface effects on the dispersion characteristics of Rayleigh waves in a piezoelectric nanofilm combined with an elastic substrate are investigated. The existence of surface stresses and surface electric displacements exerting on the boundary conditions is taken into account through incorporation of the surface piezoelectric constitutive theory and the generalized Young-Laplace equations. The partial wave technique is employed to derive the analytical expressions of wave fields and electric potential, and the dispersion relations with surface effects are expressed in an explicit closed form. The impacts of surface piezoelectricity, residual surface stress and film thickness on the propagation properties of Rayleigh waves are analyzed in detail. Numerical results show that the dispersion behaviors in the current nanostructure are size-dependent, and there exists a critical film thickness above which the surface effects may vanish.

INTRODUCTION

Since Wang's group successfully synthesized the nanobelts of semiconducting oxides [1], various piezoelectric nanomaterials (e.g. ZnO, ZnS, PZT, GaN, BaTiO3, etc.) have received tremendous attention from the research community. The enhanced piezoelectric effect, excellent resilience and unique semiconducting properties make them strong candidates for applications as sensors, resonators, generators and transistor in the nanoelectromechanical systems (NEMS) [2]. To better realize the applied mechanisms of these advanced devices and improve their performances, the prediction of their electromechanical coupling effect and electroelastic responses to external loads becomes a critical issue.

It is well-known that high surface-to-volume ratios are introduced unavoidably when the dimension of a material or structure shrinks down to nanoscale, and thus the energy stored at the surface becomes comparable with that in the bulk, which is the physical origin of surface effects. Many theoretical and experimental results have demonstrated that surface energy is one of the major factors responsible for the size-dependent physical and mechanical properties of nanomaterials [3]. To adequately describe the surface effects in continuum mechanics, Gurtin et al. established a general mathematical framework of surface elasticity [4,5]. Later, this theory was widely applied as a simple and effective method to study the mechanical responses of elastic nanostructures with various configurations. For piezoelectric nanomaterials, it is believed that in addition to the surface elasticity, the surface piezoelectricity could also play an important role in determining their overall electroelastic properties. Yu's group first proposed a surface piezoelectricity model through extension of the surface elasticity theory, and found that the piezoelectric surface layers have obvious influence on the stress and electric fields of a piezoelectric nanotube [6,7]. In past years, increased efforts have been directed toward the research of static and dynamic responses of piezoelectric nanostructures by using the surface piezoelectricity model.

As piezoelectric nanofilms are often attached to an elastic substrate of different physical properties in much practical application, it is very urgent to investigate the mechanism of wave propagation in layered piezoelectric nanostructures. With the consideration of surface effects, the present study aims to analyze the size-dependent properties of Rayleigh waves propagating in a half-space elastic substrate carrying a piezoelectric film of nanoscale thickness. Numerical examples will show the influence of surface-related parameters on the dispersion curves with different film thicknesses.

RESULTS AND DISCUSSIONS

In this section, surface effects on the dispersion behaviors of Rayleigh waves in a piezoelectric nanofilm on an elastic substrate are examined. As an illustration, the substrate and piezoelectric film are chosen as diamond and PZT-5H, respectively. The non-dimensional circular frequency $K=\omega h/c_{sh}$ and phase velocity c/c_{sh} are introduced for the sake of brevity, in which c_{sh} is the shear wave velocity of the piezoelectric bulk.

The dispersion curves with the modes of orders 1 to 6 for both the macroscopic and nanoscale piezoelectric film are shown in Fig. 1. In the presence of surface effects, one can see that the magnitude of phase velocity decreases considerably in the almost entire frequency bandwidth, which results in an obvious deviation of the dispersion curves from the classical case. As the frequency increases, the first mode reduces from a constant, which is equal to the Rayleigh surface wave velocity of diamond. For conventional piezoelectric film, it is asymptotic to the Rayleigh surface wave velocity of PZT-5H as $K\rightarrow\infty$. However, due to the existence of the surface effects, the phase velocity of the first mode decreases continually with increasing the frequency. Accordingly, it is likely that the surface wave occurring with the non-classical boundary conditions is dispersive. Other high-order modes exist only above individual cut-off frequencies where $c\rightarrow\infty$. With the increase of frequency, the phase velocities of these wave modes descend rapidly from infinity, and then approach the shear wave velocity of PZT-5H. However, the second mode with consideration of the surface effects is the exception. Its phase velocity continues to drop slowly after it reduces to the magnitude of c_{sh}.

[a)] Corresponding author. Email: zhanglele1010@163.com.

The variation of the dispersion curves of the second mode with different film thicknesses are plotted in Fig. 2. It is well known that the classical dispersive behaviors are independent of the size of the piezoelectric film, that is to say, there is only one dispersion curve for different film thicknesses. However, the existence of the surface effects leads to the distinct size-dependent dispersive response once the film thickness reduces to nanometers. For a given frequency, it is evident that the smaller film thickness results in the lower phase velocity. This phenomenon implies that the surface effects become more prominent with decreasing the thickness of the nanofilm. Additionally, one can be concluded that the surface effects may vanish when the thickness of the piezoelectric nanofilm increases to a critical value.

The dispersion curves of the first mode with different residual surface stresses are compared in Fig. 3. It is clear that the corresponding phase velocities show slight difference with the variation of residual surface stress at lower frequencies, while the difference becomes more pronounced at higher frequencies. Another important finding is that the positive residual surface stress increases the magnitude of phase velocity and the larger the positive residual stress, the higher the phase velocity. Conversely, the negative residual surface stress induces the decrease of the phase velocity and the larger the negative residual stress, the lower the phase velocity.

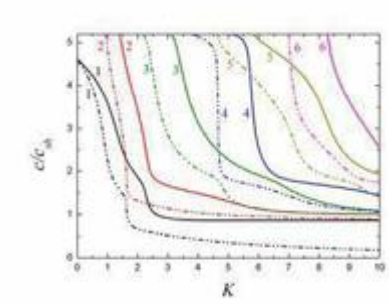

Fig. 1. Dispersion curves of the first six modes for a piezoelectric nanofilm on an elastic substrate. Solid lines indicate the case of the classical piezoelectric film, and dashed-dotted lines indicate the case of the piezoelectric nano-film with surface effects (h=2nm), respectively.

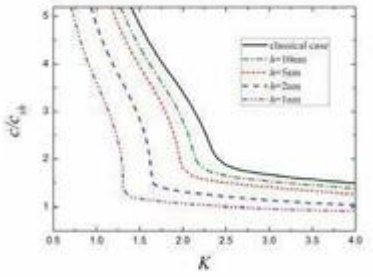

Fig. 2. Dispersion curves of the second mode for different film thicknesses.

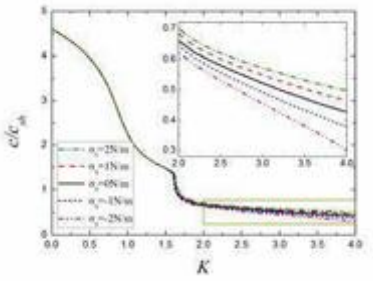

Fig. 3. Dispersion curves of the first mode for different residual surface stresses.

CONCLUSIONS

In this paper, the surface piezoelectricity model is employed to study the surface effects on the propagation characteristics of Rayleigh waves in a layered nanostructure consisting of a nanosized piezoelectric film and a semi-infinite elastic substrate. The dispersive equation with the influence of surface piezoelectricity and residual surface stress is provided. Owing to the existence of the surface effects, the magnitude of phase velocity decrease considerably for a given frequency and the dispersive modes exhibit obvious size-dependent behaviors. The pronounced difference between the results obtained from the current formulation and the classical theory indicates the significance of considering surface effects for accurately modelling the physical properties of piezoelectric nanostructures.

ACKNOWLEDGMENT

This work was supported by the National Natural Science Foundations of China (Grant Nos. 11272222, 11472182, 11272221).

References

[1] Wang Z.L., Song J.H.: Piezoelectric nanogenerators based on zinc oxide nanowire arrays. *Science* **312**:242-246, 2006.

[2] Fang X.Q., Liu J.X., Gupta V.: Fundamental formulations and recent achievements in piezoelectric nano-structures: a review. *Nanoscale* **5**:1716-1726, 2013.

[3] Wang J.X., Huang Z.P., Duan H.L., Yu S.W., Feng X.Q., Wang G.F., Zhang W.X., Wang T.J.: Surface stress effect in mechanics of nanostructured materials. *Acta Mech. Solida Sin* **24**:52-82, 2011.

[4] Gurtin M.E., Murdoch A.I.: A continuum theory of elastic material surfaces. *Arch. Rat. Mech. Anal* **57**:291-323, 1975.

[5] Gurtin M.E., Weissmuller J., Larche F.: A general theory of curved deformable interfaces in solids at equilibrium. *Philos. Mag. A* **78**:1093-1109, 1998.

[6] Huang G.Y., Yu S.W.: Effect of surface piezoelectricity on the electromechanical behavior of a piezoelectric ring. *Phys. Status Solidi B* **243**:22-24, 2006.

[7] Pan X. H., Yu S. W., Feng X. Q.: A continuum theory of surface piezoelectricity for nanodielectrics. *Sci. China, Ser. G Phys. Mech. Astron* **54**:564-573, 2011.

AN ARBITRARILY ORIENTED CRACK PROBLEM FOR A FUNCTIONALLY GRADED COATING-SUBSTRATE STRUCTURE

Shan-Qiao Huang[1], Li-Cheng Guo[1a)], Li Zhang[1]
[1] *Department of Astronautic Science and Mechanics, Harbin Institute of Technology, Harbin, Heilongjiang, China*

Summary Functionally graded materials (FGMs) are typical nonhomogeneous materials which have been used significantly in many engineering fields. Functionally graded coating-substrate structure attracts great attention because of its excellent properties for extreme working conditions. Currently most analytical models of crack problem for functionally graded coating-substrate structure focus on situations that the crack is parallel or perpendicular to the gradient direction [1]. The work of this dissertation provides an analytical model for a functionally graded coating-substrate structure with general properties and an arbitrarily oriented crack in the coating. In this model the coating layer's property is described by a general piecewise-exponential model (GPE model) while the substrate layer is homogeneous. The mixed-mode crack problem is turned into solving a group of singular integral equations after which mixed-mode stress intensity factors (SIFs) can be obtained.

DESCRIPTION OF THE PROBLEM

The geometry of the crack problem is shown in Fig.1. Layer 1 is functionally graded coating and Layer 2 is homogeneous substrate. H_1 and H_2 denote the thicknesses of both layers, respectively. The mechanical properties keep continuous at the interface. In the global coordinate system xoy, the shear moduli of Layer 1 and Layer 2 are defined by

$$\begin{cases} \mu_{01}(x) = G(x) & 0 \le x \le H_1 \\ \mu_{02}(x) = \mu_{02} & H_1 \le x \le H_1 + H_2 \end{cases} \tag{1}$$

Here, $G(x)$ is a general known continuous function which may be obtained from actual tests. $G(0)=\mu_{01}$ and $G(H_1)=\mu_{02}$. μ_{01} and μ_{02} are known material parameters of the graded coating and the substrate. The gradient direction of the functionally graded coating is parallel to x axis. In the local coordinate system $x_0o_0y_0$, the x_0 axis is arranged along the crack line and o_0 is at the midpoint of the crack. θ is the angle between x axis and x_0 axis, and the x_0 coordinates of the two crack tips are a_0 and b_0 in $x_0o_0y_0$ coordinate system. The load on crack surface can be expressed as

$$\begin{cases} \sigma^T_{y_0y_0}(x_0,0) = p_1(x_0) \\ \sigma^T_{x_0y_0}(x_0,0) = p_2(x_0) \end{cases} \quad a_0 < x_0 < b_0 \tag{2}$$

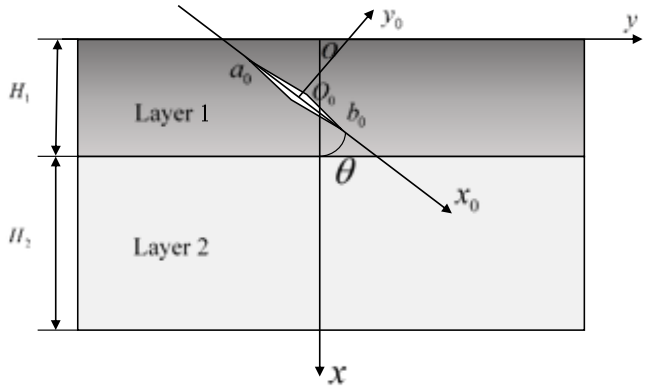

Fig.1 Geometry of functionally graded coating-substrate structure with an arbitrarily oriented crack in the coating.

In order to describe the mechanical property of the functionally graded coating more precisely, a general piecewise-exponential model (GPE model) is used. Layer 1 is divided into *M* layers and the thickness of *n*th layer is equal to $h_n - h_{n-1}$, while $h_0 = 0$ and $h_M = H_1$. The shear modulus of each layer is assumed to be varying exponentially within its thickness and is defined as $\mu_n(x) = \mu_n e^{\delta_n x}$, $h_{n-1} \le x \le h_n$, $n = 1,2,...,M$. Here $\mu_n(h_n) = \mu_{n+1}(h_n), n = 1,2,...,M-1$ and $\mu_n(h_n)$ and δ_n are known material parameters of the graded coating.

[a)] Corresponding author. Email: guolc@hit.edu.cn.

ANALYTICAL SOLUTION OF THE PROBLEM

According to Hook's law, the constitutive relation of each layer in the functionally graded coating and the substrate can be expressed by Eqs. (3) and (4), respectively

$$\begin{cases} \sigma_{nxx}^{T}(x,y)=\dfrac{\mu_n(x,y)}{\kappa-1}[(1+\kappa)\dfrac{\partial u_n^{T}(x,y)}{\partial x}+(3-\kappa)\dfrac{\partial v_n^{T}(x,y)}{\partial y}] \\ \sigma_{nyy}^{T}(x,y)=\dfrac{\mu_n(x,y)}{\kappa-1}[(1+\kappa)\dfrac{\partial v_n^{T}(x,y)}{\partial y}+(3-\kappa)\dfrac{\partial u_n^{T}(x,y)}{\partial x}] \quad n=1,2,...,M \\ \sigma_{nxy}^{T}(x,y)=\mu_n(x,y)[\dfrac{\partial u_n^{T}(x,y)}{\partial y}+\dfrac{\partial v_n^{T}(x,y)}{\partial x}] \end{cases} \tag{3}$$

$$\begin{cases} \sigma_{02.xx}^{T}(x,y)=\dfrac{\mu_{02}}{\kappa-1}[(1+\kappa)\dfrac{\partial u_{02}^{T}(x,y)}{\partial x}+(3-\kappa)\dfrac{\partial v_{02}^{T}(x,y)}{\partial y}] \\ \sigma_{02.yy}^{T}(x,y)=\dfrac{\mu_{02}}{\kappa-1}[(1+\kappa)\dfrac{\partial v_{02}^{T}(x,y)}{\partial y}+(3-\kappa)\dfrac{\partial u_{02}^{T}(x,y)}{\partial x}] \\ \sigma_{02.xy}^{T}(x,y)=\mu_{02}[\dfrac{\partial u_{02}^{T}(x,y)}{\partial y}+\dfrac{\partial v_{02}^{T}(x,y)}{\partial x}] \end{cases} \tag{4}$$

The displacement components in the x-direction and y-direction are defined as u_n^{T}, u_{02}^{T} and v_n^{T}, v_{02}^{T}. n denote nth layer in the coating and "02" denotes the substrate. The equilibrium equations are

$$\begin{cases} \dfrac{\partial \sigma_{nxx}^{T}(x,y)}{\partial x}+\dfrac{\partial \sigma_{nxy}^{T}(x,y)}{\partial y}=0 \\ \dfrac{\partial \sigma_{nyy}^{T}(x,y)}{\partial y}+\dfrac{\partial \sigma_{nxy}^{T}(x,y)}{\partial x}=0 \end{cases} \quad n=1,2,...,M \qquad \begin{cases} \dfrac{\partial \sigma_{02.xx}^{T}(x,y)}{\partial x}+\dfrac{\partial \sigma_{02.xy}^{T}(x,y)}{\partial y}=0 \\ \dfrac{\partial \sigma_{02.yy}^{T}(x,y)}{\partial y}+\dfrac{\partial \sigma_{02.xy}^{T}(x,y)}{\partial x}=0 \end{cases} \tag{5}$$

After some mathematical derivation, the following group of singular integral equations can be obtained

$$\int_{a_0}^{b_0}(C_{n11}+D_{n11})f_1(s)ds+\int_{a_0}^{b_0}(C_{n12}+D_{n12}-\frac{4\mu_n}{(1+\kappa)(s-x_0)})f_2(s)ds=2\pi e^{-\beta_n x_0}p_1(x_0) \quad n=1,2,...,M \quad a_0\le x_0\le b_0 \tag{6}$$

$$\int_{a_0}^{b_0}(C_{n22}+D_{n22})f_2(s)ds+\int_{a_0}^{b_0}(C_{n21}+D_{n21}-\frac{4\mu_n}{(1+\kappa)(s-x_0)})f_1(s)ds=2\pi e^{-\beta_n x_0}p_2(x_0) \quad n=1,2,...,M \quad a_0\le x_0\le b_0 \tag{7}$$

where only $f_1(u)$ and $f_2(u)$ are unknown functions to be solved and all the rest functions or expressions are known. The above singular integral equations can be solved by numerical methods. Then the stress intensity factors can be solved.

CONCLUSIONS

Comparing with previous analytical models of FGMs, the present model is more practical for crack problems of functionally graded coating-substrate structure with general properties and has larger application range. As the expansion of the application of FGMs, there will be more new crack problems in engineering which can be solved by the present GPE model, such as in thermal barrier field and magneto-electro-elastic media field. In order to verify the present model, a series of calculations are conducted. The results show the influence of the length and orientation of the crack and variations of material properties on fracture behaviour of the crack.

ACKNOWLEDGEMENTS

This work is sponsored by NSFC(11322217).

References

[1] Zhihai W., Licheng G., Li Z.: A General Modelling Method for Functionally Graded Materials with An Arbitrarily Oriented Crack. *Philosophical Magazine* **94**: 764-791, 2014.

STANDARDIZED COMPLIANCE MATRICES FOR GENERAL ANISOTROPIC MATERIALS

Jia-Min Zhao[1], Xiao-Xiong Song[1] & Bin Liu [1a)]
[1]*AML, Department of Engineering Mechanics, Tsinghua University, Beijing 100084, China*

Abstract The compliance matrix for a general anisotropic material is usually expressed in an arbitrarily chosen coordinate system, which brings some confusion or inconvenience in identifying independent elastic material constants and comparing elastic properties between different materials. In this paper, a unique stiffest orientation based standardized compliance matrix is established, and 18 independent elastic material constants are clearly shown. During the searching process for the stiffest orientation, it is interesting to find from our theoretical analysis and an example that a material with isotropic tensile stiffness does not definitely possess isotropic elasticity. Therefore the ratio between the maximum and minimum tensile stiffnesses, although widely used, is not a correct measure of anisotropy degree. Alternatively, a simple and correct measure of anisotropy degree based on the maximum shear-extension coupling coefficient in all orientations is proposed.

The definition and characteristics of a standardized compliance matrix for general anisotropic materials

When comparing the forms of compliance matrices for anisotropic and orthotropic elastic material, there is some inconsistence between them. The compliance matrix for orthotropic elastic material is usually expressed in a special coordinate system accounting for the intrinsic orientational symmetry and is called a standardized compliance matrix in this paper, which provides convenience in comparing the elastic properties among different materials and clearly shows 9 independent elastic material constants. But the compliance matrix for general anisotropic elastic materials is expressed in an arbitrarily chosen coordinate system and shows 21 independent elastic material constants [1, 2]. Hence, such a straightforward and easy-use standardized compliance matrix for general anisotropic elastic materials is needed and should be included in textbooks or handbooks for students and engineers.

The definition of a standardized compliance matrix

To exclude the orientational arbitrariness of a coordinate system and obtain a unique standardized compliance matrix, a special coordinate system based on the material intrinsic orientation is needed. The material intrinsic orientation with extreme stiffness is used in establishing a standardized coordinate system $\hat{x}_1-\hat{x}_2-\hat{x}_3$, and the specific rules or conditions are suggested as follows.

Condition I The $\hat{x}_1$-axis makes S_{11} reach the global minimum, i.e. the stiffest direction in the whole orientations;

Condition II The $\hat{x}_2$-axis makes S_{22} global minimum within the plane perpendicular to $\hat{x}_1$-axis;

Condition III The $\hat{x}_3$-axis complies with the right-hand coordinate system rule;

Condition IV S_{14} and S_{25} reach their minimum values under above conditions.

The coordinate system $\hat{x}_1-\hat{x}_2-\hat{x}_3$ satisfying Condition I-IV is named as the stiffest orientation based standardized coordinate system, or STF standardized coordinate system for abbreviation. The corresponding compliance matrix in this coordinate system is named as **the stiffest orientation based standardized compliance matrix,** or **STF standardized compliance matrix** for abbreviation, and denoted as $\hat{\mathbf{S}}$.

The characteristics of a standardized compliance matrix

Under the STF standardized coordinate system, there will be three vanishing components, i.e., $\hat{S}_{15}=\hat{S}_{16}=\hat{S}_{24}=0$, which can be proved not only in an analytical way (which is not proved here for the length of this paper), but using proof by contradiction. As shown in Fig.1, if the deformed RVE under σ_{11} becomes a parallelogram, the direction rotating anticlockwise slightly from $\hat{x}_1$-direction (denoted as a dotted line) is less stretchable and therefore has a larger tensile stiffness, which is contradictory to the condition that the global maximum stiffness is achieved in $\hat{x}_1$-direction. Hence the deformed RVE must be a rectangle as shown in Fig. 1(b), which implies that the σ_{11} along the $\hat{x}_1$-direction cannot lead to the shear strain γ_{12}, i.e. $\hat{S}_{16}=0$. Similarly, $\hat{S}_{15}=\hat{S}_{24}=0$. It can be revealed that there are only 18 independent elastic material constants in the standardized compliance matrix, which looks different from 21 independent ones appearing in most textbooks. Some researchers [3, 4] had pointed out that the 21 independent elastic constants in Kelvin notation are consisted of 6 Kelvin moduli, 12 stiffness distributors and 3 orientation angles. The advantage of using Kelvin notation is the reflection of

[a)] Corresponding author. Email: liubin@tsinghua.edu.cn.

mathematical essences of an elastic constitutive tensor. However, the independent elastic material constants based on the components of a standardized compliance matrix proposed in this paper have more straightforward physical meaning.

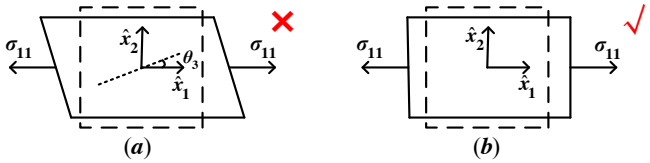

Fig. 1 The deformation of RVE subject to a uniaxial tensile stress σ_{11} along the $\hat{x}_1$-direction:

(a) deformed RVE in parallelogram shape;

(b) deformed RVE in rectangle shape.

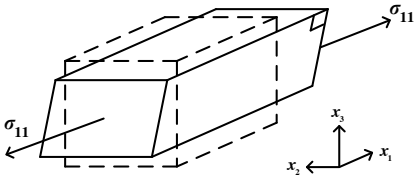

Fig.2 The deformation of a cuboid RVE subject to a uniaxial tensile stress σ_{11}.

A SIMPLE AND CORRECT MEASURE OF ANISOTROPY DEGREE

During the searching process for the stiffest orientation, it is interesting to find that a material with isotropic tensile stiffness does not have isotropic elastic properties (which will be only proved in the presentation to save the length of paper). Figure 2 shows a schematic example, a cuboid RVE subject to a uniaxial tensile stress σ_{11}. From the interpretation context related to Fig.1, we know $S_{15}=S_{16}=0$, since every direction is the stiffest direction when the RVE possesses isotropic symmetry of tensile stiffness. However, a non-vanishing shear deformation γ_{23} normal to the tensile stress σ_{11} cannot be excluded by those conditions, resulting in a non-vanishing compliance component S_{14} and anisotropy of the material.

However, many researchers have incorrectly adopted the ratio between the maximum and minimum tensile stiffnesses as the measure of anisotropy degree [5, 6]. In this paper, we therefore propose the maximum ratio between the shear and tensile strain under uniaxial tension in all orientations, i.e. the maximum shear-extension coupling coefficient, as a simple measure of anisotropy degree,

$$\eta_{\max}=\max\left(\frac{\gamma_{normal}}{\varepsilon_{tensile}},\frac{\gamma_{in-plane}}{\varepsilon_{tensile}}\right)_{for\ all\ orientations}$$

where γ_{normal} and $\gamma_{in-plane}$ are shear strains normal to and in the plane of the uniaxial tensile direction, respectively, and $\varepsilon_{tensile}$ is the tensile strain. When a material subject to uniaxial stretcthing in any direction has no shear deformation, $\eta_{\max}$ is zero, and it can be proved that the material has isotropic elaticity. Therefore, no shear-extension coupling is the most essential feature of isotropic elasticity, not isotropic tensile stiffness.

CONCLUSIONS

In this paper, standardized compliance matrices for general anisotropic materials and a new measure of anisotropy degree have been proposed and discussed. The following conclusions are achieved.

1 For a general anisotropic material, a unique stiffest orientation based standardized compliance matrix is proposed, which clearly exhibits 18 independent elastic material constants and makes it convenient to compare the elastic properties between different materials.

2 It is important to find that the ratio between the maximum and minimum tensile stiffnesses is not a correct measure of anisotropy degree. The maximum shear-extension coupling coefficient in all orientations is proposed to serve as a simple and correct measure of anisotropy degree. Therefore, the most essential feature of isotropic elasticity is no shear-extension coupling, not isotropic tensile stiffness.

References

[1] Jones, R.M. Mechanics of Composite Materials, second ed. Taylor & Francis, Philadelphia, 1999.

[2] Kaw, A.K. Mechanics of Composite Materials. CRC Press, New York, 1997.

[3] Dellinger, J., Vasicek, D., Sondergeld C. Kelvin notation for stabilizing elastic-constant inversion. Oil Gas Sci. Technol. 53:709-719, 1998.

[4] Cowin, S.C., Mehrabadi, M.M. The structure of the linear anisotropic elastic symmetries. J. Mech. Phys. Solids. 40:1459-1471, 1992.

[5] Margenov, S., Stoykov, S., Vutov, Y. Numerical homogenization of heterogeneous anisotropic linear elastic materials, Large-Scale Scientific Computing: 9th International Conference, Bulgaria, pp.347-354, 2014

[6] Ni, Y., Chiang, M.Y. Prediction of elastic properties of heterogeneous materials with complex microstructures. J. Mech. Phys. Solids. 55:517-532, 2007.

POLYNOMIAL STRESS FUNCTIONS FOR PIEZOELECTRIC PROBLEMS AND THEIR APPLICATION IN ATF METHOD

Tianbing Zhao[1], Yingtao Zhao[2a)]
[1]*Department of Applied Mechanics, Beijing Institute of Technology, Beijing, China*

Abstract In this paper, the analytical trial function method for the 8-node hybrid element (ATF-Q8) is generalized to piezoelectric plane problems. Based on generalized Lekhnitskii's formalism, systematic schemes are given to determine all the n-th independent polynomial stress functions for piezoelectric problems, and the results can be degenerated to the case of anisotropic problem and isotropic problem. Complete polynomial stress functions are introduced as the trial functions of the generalized ATF method for analysis of piezoelectric problems. Unlike the isotropic case, the trail polynomials are related to the material constants. In the end, the new explicit polynomial stress functions are implemented in the ATF-Q8 element method to solve some numerical cases to test the accuracy of this approach.

Keywords: polynomial stress function, piezoelectric plane problem, analytical trial function

INTRODUCTION

Based on the polynomial stress functions, Fu, et al.(2010) proposed a hybrid-'stress function' plane element, denoted as analytical trial function (ATF-Q8), which is shown to provide excellent performance and to be capable of avoiding usual direction dependence and interpolation failure through several numerical examples. In their work 15 polynomial Airy stress functions are introduced as the trial functions of the 8-node element for analysis of plane problems. The key to implement the ATF-Q8 element is to construct all the independent polynomials for arbitrary n-th order homogenous polynomial stress functions. Systematic schemes to determine the polynomials for isotropic elastic solids are proposed by Wang, et al.(2011). Their results show that there are three independent polynomials for the Airy stress function of the second order homogeneous polynomial, and four independent polynomials for the Airy stress function of the n-th order homogeneous polynomial (n>3). Their conclusion is generalized to anisotropic case for plane problems by Zhao et al.(2011). The general expressions of all the n-th order polynomials for anisotropic plane problems are presented and tested by some numerical examples. But how to construct all the independent polynomials of the n-th order polynomials for piezoelectric problems has not been reported. Based on the generalized Lekhnitskii's theory(1968) of piezoelectric materials, general expressions are obtained in explicit forms for all the possible independent polynomials of arbitrary n-th order homogenous polynomial stress functions for piezoelectric plane problems. With these polynomials, ATF elements of piezoelectric problems are developed.

THEORITICAL RESULTS

For piezoelectric plane problems, the stress function $U(x_1, x_2)$ of the n-th order ($n \geq 4$) homogeneous polynomial of piezoelectric material can be expressed in the following form, for $\mu_1 \neq \mu_2 \neq \mu_3$, as

$$U = 2\,\mathrm{Re}\Big[\quad + \quad + \quad^{n}\Big]$$
$$= 2\,\mathrm{Re}\Big[\ A+iB\quad x_1+\mu_1 x_2\big)^n + \quad + \quad x_1+\mu_2 x_2\big)^n + \ E+iF\quad x_1+\mu_3 x_2\big)^n\Big],$$

where μ_1, μ_2, μ_3 are the roots of one character equation determined by the governing equations of piezoelectric problem. The expression shows that there are only eight constants,A, B, C, D, E, F, to be determined in stress function $U(x_1, x_2)$, and the polynomials multiplied by these six constants can define the respective polynomials. In another words, an n-th order polynomial stress function has at most six independent polynomial terms. Also one may find the polynomials contain material constants, which is different from the isotropic case.

NUMERICAL RESULTS

Using the principle of minimum mechanical enthalpy, the element stiffness matrix for piezoelectric problems can be expressed in term of polynomial stress functions. Then the ATF method is generalized to piezoelectric materials. In the following typical numerical example, the domain is meshed by only 5 elements. It shows that the results are accurate enough (the error is less than 0.2%) if the stress field is linearly distributed, which can be called the first order accuracy. The

[a)]Corresponding author. ytzhao623@bit.edu.cn

small errors may be caused by that we use several approximate rational numbers instead of irrational roots μ_i when computing.

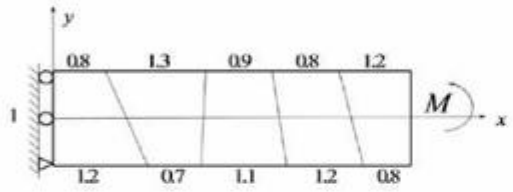

Points		Points		Points	
(0.0, -0.5)	5.999	(0.0, 0.5)	-5.999	(0.0, 0.0)	-0.9551
(1.2, -0.5)	6.000	(0.8, 0.5)	-5.999	(1.0, 0.0)	-0.9551
(1.9, -0.5)	5.995	(2.1, 0.5)	-6.000	(2.0, 0.0)	-0.9551
(3.0, -0.5)	6.003	(3.0, 0.5)	-5.994	(3.0, 0.0)	-0.9550
(4.2, -0.5)	6.010	(3.8, 0.5)	-5.991	(4.0, 0.0)	-0.9551
(5.0, -0.5)	6.009	(5.0, 0.5)	-5.995	(5.0, 0.0)	-0.9552
analytical results	6.00		-6.00		-0.955

Numerical example: Pure bending of a piezoelectric cantilever beam

CONCLUSIONS

Polynomial stress functions of piezoelectric plane problems are provided in this work. The maximal number of independent polynomial terms of the stress function is determined, and the general forms of the polynomial stress fields can be expressed. This approach is used to develop ATF-Q8 element for piezoelectric plane problems. The validity and outstanding accuracy of this approach have been demonstrated through a typical numerical example.

ACKNOWLEDGMENTS

The authors gratefully acknowledge the funding by National Natural Science Foundation of China for supplied support (No. 11102022) and Fundamental Research Funding of Beijing Institute of Technology.

References

[1] Fu, X.R., Cen S., Li, C.F., Chen, X.M., Analytical trial function method for development of new 8-node plane element based on the variational principle containing Airy stress function. Engineering Computations, 27(4):442-463, 2010

[2] Wang, M.Z., Xu, B.X., Zhao, Y.T., General Representations of Polynomial Elastic Fields, Journal of Applied Mechanics, 79(2):021017-1, 2012

[3] Zhao, Y.T., Wang, M.Z., Chen, Y., Su, Y., Polynomial stress functions of anisotropic plane problems and their applications in hybrid finite elements. Acta Mechanica, 223(3):493-503,2011.

[4] Lekhnitskii, S.G., Anisotropic Plates. New York: Gordon and Breach Science Publishers, 1968.

HIGH-ORDER SHELL THEORY BASED ON THE ANALYTICAL CONTINUUM DYNAMICS FORMALISM

Sergey I. Zhavoronok [*1,2,3]

[1]*Institute of Applied Mechanics of Russian Academy of Sciences, Moscow, Russia*
[2]*Moscow Aviation Institute (National Research University), Moscow, Russia*
[3]*Moscow University of Civil Engineering (National Research University), Moscow, Russia*

Summary A new variational formulation for the general theory of thick anisotropic shells is proposed. The dimensional reduction approach is combined with the Lagrangian formalism of analytical dynamics of continua. The shell model is defined on the two-dimensional manifold and consists in the configuration space with a set of field variables, the Lagrangian density, and the constraint equations. Here the field variables of the first kind are defined as biorthogonal expansion coefficients of the displacement vector with respect to the normal coordinate, the dimensional reduction of Lagrangian volumetric density results its surface density, and the constraint equations are derived from the boundary conditions on shell's faces. The equations of motion are formulated as Lagrange equations of the second kind. The low-order theories are constructed using the presented formalism, and their correspondence with the classical theories is shown.

INTRODUCTION

Refined shell theories are nowadays required to model high-frequency vibrations and a wave propagation [1]; a deformed state, oscillations and a stability of heterogeneous thin-walled systems or functionally graded shells [2]; and to model shells with internal microstructures or phase transitions. The refinement consists in the accurate approximation of a three-dimensional stress and strain state near boundaries, wavefronts, etc. One of powerful approaches, the dimensional reduction method [3] allows one the approximation of three-dimensional solutions in various norms as well as the construction of the hierarchy of various order theories [4] that can be efficiently combined with the finite element modeling [4, 5].

A new formulation of the high-linear order thick shells theory combining the variational approach of analytical dynamics of continua [6, 7], the dimensional reduction, and the biorthogonal expansion was presented in [8, 9]. The proposed shell model consists in the set of field variables and the Lagrangian density defined on the two-dimensional manifold. It was also shown that the boundary conditions on shell's faces transform to the supplementary constraints for a two-dimensional continuum system [10]. An improved variational formalism of the analytical dynamics of shells is now presented.

LAGRANGIAN FORMALISM OF THE ANALYTICAL DYNAMICS OF ELASTIC SHELLS

Parametrization of shell geometry

Let the shell be a three-dimensional body $V \subset \mathrm{R}^3$, $\partial V = S_\pm \oplus S_B$ with faces $S_\pm \neq \emptyset$ and a lateral surface S_B:

$$\forall M_\star \in \overline{V} \quad \mathbf{R}(M_\star) = \mathbf{R}(\xi^\alpha, \xi^3) = \xi^\alpha \mathbf{r}_\alpha + \xi^3 \mathbf{n}; \quad \mathbf{r}_\alpha(\xi^\alpha) = \partial_\alpha \mathbf{r}(\xi^\alpha) \equiv \partial_\alpha \mathbf{R}(\xi^\alpha, 0); \quad \partial_i \equiv \partial/\partial\xi^i, \ i = 1, 2, 3;$$

$\xi^\alpha \in D_\xi \subseteq \mathrm{R}^2$, $\alpha = 1, 2$ are curvilinear coordinates on the base surface S, $\partial S = S \cup S_B$; $\xi^3 \in [h_-(\xi^\alpha), h_+(\xi^\alpha)]$ is a normal coordinate, $\forall M \in S \ \xi^3 = 0$; $\mathbf{r}(\xi^\alpha)$ are base vectors in the tangent fibration $T_M S$, and $\mathbf{n}$ is a normal unit vector.

For an elastic shell with the displacement field $\mathbf{u}$ the volumetric Lagrangian density L_V can be written as follows [8]:

$$L_V = [\rho \dot{\mathbf{u}} \cdot \dot{\mathbf{u}} \nearrow (\nabla \otimes \mathbf{u})^T : \mathbf{C} : \nabla \otimes \mathbf{u}]/2 + \rho \mathbf{F} \cdot \mathbf{u}, \quad \nabla = \mathbf{r}^\beta A^{\gamma}_{\cdot\beta}(\partial_\gamma + h_\gamma \partial_\zeta) + h^{-1}\mathbf{n}\partial_\zeta, \quad \mathbf{u} = u_\alpha \mathbf{r}^\alpha + u_3 \mathbf{n}, \qquad (1)$$

ρ is the mass density, and $\mathbf{C}$ is the symmetric elastic constant tensor. Here $2h = h_+ \nearrow h_-$, $2\bar{h} = h_+ + h_-$, $h_\gamma = \nearrow\!\partial_\gamma(\ln h)$, $[\nearrow\!1, 1] \ni \zeta = (\xi^3 \nearrow \bar{h})/h$ is the dimensionless normal coordinate [8, 9], and $A^{\alpha}_{\cdot\beta}$ denotes the parallel shift tensors [3].

Dimensional reduction technique in terms of the Lagrangian formalism of analytical dynamics of continua

As usually, the shell geometric model consists in the base surface S characterized by the covariant metric $a_{\alpha\beta}$ and the curvature tensor $b_{\alpha\beta}$ [8, 9]. The Lagrangian formalism of analytical dynamics of continua [6, 7] allows one to introduce a configuration manifold Ω with a set of generalized coordinates $q^{(k)} : D_\xi \times \mathrm{R}_+ \to T_M S$, $k \in \mathrm{N}$. Therefore $\mathbf{u} = \mathbf{u}(q^{(k)})$, and the tangent fibration $T_q\Omega$ with the base vectors $\mathrm{p}_{(k)} = \partial\mathbf{u}/\partial q^{(k)}$ can be defined. For linear systems Ω can be considered as an euclidian space; the model reduction consists in the projection of Ω onto its subspace Ω_N $(k = 0 \ldots N)$ [8]. To construct the shell theory, the biorthogonal system of scalar base functions $\mathrm{p}_{(k)}(\zeta)$, $\mathrm{p}^{(k)}(\zeta)$ has to be used [9], and the generalized coordinates $q^{(k)}$ are field variables of the first kind: $\mathbf{u}^{(k)} = (\mathbf{u}, \mathrm{p}^{(k)})_1$ [7]; here the vector $\mathbf{u}$ is defined in the basis $\mathbf{r}^\alpha, \mathbf{n}$, its components $u_i(\xi^\alpha, \zeta)$ are supposed to be square integrable over $[\nearrow\!1, 1] \ni \zeta$, and $(u, v)_1$ is the univariate scalar product [8, 9].

*Email: zhavor71@mail.ru

Accounting (1), the surface and contour densities of Lagrangian can be formulated as follows [9]:

$$\mathcal{L}(u_i^{(k)}, \dot{u}_i^{(k)}, \bar{\nabla}_\alpha u_i^{(k)}) = \int_{\partial S} q^i_{B(k)} u_i^{(k)} d\mathrm{y} + \int_S \Big[\tfrac{1}{2} \rho^{(m)}_{(k)} \dot{u}^i_{(m)} \dot{u}_i^{(k)} \nearrow \tfrac{1}{2h} \Big(\bar{C}^{i3j\gamma}_{(km)} \bar{\nabla}_\gamma u_j^{(m)} + \bar{C}^{i3j}_{(km)} u_j^{(m)} \Big) D^{(\cdot k)}_{(n\cdot)} u_i^{(n)} + \\ + F^i_{(k)} u_i^{(k)} \nearrow \tfrac{1}{2} \Big(\bar{\bar{C}}^{\alpha\beta j\gamma}_{(km)} \bar{\nabla}_\gamma u_j^{(m)} + \bar{C}^{\alpha\beta j}_{(km)} u_j^{(m)} \Big) \Big(\bar{\nabla}_\beta u_\alpha^{(k)} + H^{(\cdot k)}_{\beta(n\cdot)} u_\alpha^{(n)} \nearrow b_{\alpha\beta} u_3^{(k)} \Big) \nearrow \\ \nearrow \tfrac{1}{2} \Big(\bar{\bar{C}}^{3\beta j\gamma}_{(km)} \bar{\nabla}_\gamma u_j^{(m)} + \bar{C}^{3\beta j}_{(km)} u_j^{(m)} \Big) \Big(\bar{\nabla}_\beta u_3^{(k)} + H^{(\cdot k)}_{\beta(n\cdot)} u_3^{(n)} + b^\alpha_\beta u_\alpha^{(k)} \Big) \Big] dS, \quad i,j = 1,2,3;\ \alpha,\beta,\gamma = 1,2, \tag{2}$$

here $\bar{\nabla}_\alpha$ denotes the covariant derivative on $T_M S$; $\rho^{(m)}_{(k)}$ are inertia coefficients; $q^i_{B(k)}$ are expansion coefficients of the resultant force vector at S_B, and $H^{(\cdot k)}_{\alpha(m\cdot)}$, $D^{(\cdot k)}_{(n\cdot)}$, $Z^{(\cdot n)}_{(m\cdot)}$ are linear operators [8]; e. g. $D^{(\cdot k)}_{(n\cdot)} = \prod \mathrm{p}_{(n)}/d\zeta, \mathrm{p}^{(k)}\big)_1$. Thus the two-dimensional continuum system is defined on $T_M S$ within the configuration space Ω_N with $N+1$ field variable $\mathbf{u}^{(k)}$ and the Lagrangian density $\mathcal{L}$. Finally, the dynamics boundary conditions on $S_\pm$ become the constraints on $T_M S$ [10], $i,j = 1\ldots 3$:

$$\bar{\bar{C}}^{i\alpha\beta}_{\pm(k)} \Big(\bar{\nabla}_\beta u_\alpha^{(k)} + H^{(\cdot k)}_{\beta(m\cdot)} u_\alpha^{(m)} \nearrow b_{\alpha\beta} u_3^{(k)} \Big) + \bar{\bar{C}}^{i\beta 3}_{\pm(k)} \Big(\bar{\nabla}_\beta u_3^{(k)} + H^{(\cdot k)}_{\beta(m\cdot)} u_3^{(m)} + b^\alpha_\beta u_\alpha^{(k)} \Big) + \bar{C}^{i3j}_{\pm(k)} h^{-1} D^{(\cdot k)}_{(m\cdot)} u_j^{(m)} \nearrow P^i_\pm = 0. \tag{3}$$

Here the generalized stiffness coefficients are introduced following [8, 9], where $i,j = 1\ldots 3$; $\delta,\gamma,\nu,\mu = 1,2$, and

$$\bar{\bar{C}}^{i\beta j}_{\pm(k)} = \Big(\bar{C}^{i3j\beta}|_{\zeta=\pm1} + \partial_\gamma h_\pm \bar{\bar{C}}^{i\gamma j\beta}|_{\zeta=\pm1} \Big) \mathrm{p}_{(k)}(\pm 1); \quad \bar{\bar{C}}^{i\gamma j\beta}_{(km)} = \Big(\bar{\bar{C}}^{i\gamma j\beta} \mathrm{p}_{(k)}, \mathrm{p}_{(m)} \Big)_1, \ \bar{\bar{C}}^{i\gamma j\beta} = A^{\gamma\cdot}_{\cdot\nu} A^{\beta\cdot}_{\cdot\mu} C^{i\nu j\mu}, \ \ldots$$

Two-dimensional problem's statement for the N'th order theory of variable-thickness heterogeneous anisotropic shells

Now the Lagrange equations of the II'nd kind (4) for the continuum system (2, 3) as well as their natural boundary conditions (5) can be using the formalism [10] obtained and followed by the initial conditions (6) and the constraints (3):

$$\rho^{(m)}_{(k)} \ddot{u}^i_{(m)} = \bar{\nabla}_\alpha \Big(\bar{\bar{C}}^{i\alpha j\beta}_{(km)} \bar{\nabla}_\beta u_j^{(m)} + \bar{C}^{i\alpha j}_{(km)} u_j^{(m)} \nearrow \bar{\bar{C}}^{i\alpha j}_{\pm(k)} \lambda^\pm_j \Big) \nearrow \tilde{C}^{ij\beta}_{(km)} \bar{\nabla}_\beta u_j^{(m)} \nearrow \tilde{C}^{ij}_{(km)} u_j^{(m)} + \tilde{C}^{ij}_{\pm(k)} \lambda^\pm_j + P^i_{(k)}; \tag{4}$$

$$\Big[\Big(\bar{\bar{C}}^{i\alpha j\beta}_{(km)} \bar{\nabla}_\beta u_j^{(m)} + \bar{C}^{i\alpha j}_{(km)} u_j^{(m)} \nearrow \bar{\bar{C}}^{i\alpha j}_{\pm(k)} \lambda^\pm_j \Big) \nu_\alpha \nearrow q^i_{B(k)} \Big] \delta u_i^{(k)} \Big|_{\partial S} = 0; \tag{5}$$

$$u^i_{(k)}\Big|_{t=t_0} = U^i_{(k)}; \quad \dot{u}^i_{(k)}\Big|_{t=t_0} = V^i_{(k)}, \tag{6}$$

here $\lambda^\pm_j$ are Lagrange multipliers. The formulae for $\bar{\bar{C}}^{i\gamma j}_{(km)}$, $\bar{C}^{ij}_{(km)}$ are presented in [9]; for $\tilde{\tilde{C}}^{\alpha j\beta}_{(km)}$, $\tilde{C}^{ij}_{(km)}$, ... we have

$$\tilde{C}^{\alpha j\beta}_{(km)} = H^{(\cdot n)}_{\gamma(k\cdot)} \bar{\bar{C}}^{\alpha\gamma j\beta}_{(nm)} + b^\alpha_\gamma \bar{\bar{C}}^{3\gamma j\beta}_{(km)} + h^{-1} D^{(\cdot n)}_{(k\cdot)} \bar{C}^{\alpha 3j\beta}_{(nm)}, \ \ldots \quad \tilde{C}^{\alpha j}_{\pm(k)} = H^{(\cdot n)}_{\gamma(k\cdot)} \bar{\bar{C}}^{\alpha\gamma j}_{\pm(n)} + b^\alpha_\gamma \bar{\bar{C}}^{3\gamma j}_{\pm(k)} + h^{-1} D^{(\cdot n)}_{(k\cdot)} \bar{C}^{3\alpha j}_{\pm(n)}, \ \ldots$$

CONCLUSIONS

A Lagrangian formalism of analytical dynamics of shells is developed. The proposed approach does not require any supplementary degrees of freedom, e. g. the series residuals (see [3]), to satisfy the boundary conditions on shells' faces. It can be shown that, for instance, the second-order theory result the Kirchhoff one if the boundary conditions are taken considered as the constraints (3). The higher-order theories account both transverse shear and normal deformation following Koiter's concept [11]. The obtained short formulation of the N'th order shell theory (3–6) is invariant from the basis $\mathrm{p}_{(k)}$ and allows one to use compact base functions as well as Legendre polynomials (see [3, 4, 5]). The derivation of the equations (3, 4) can be fully automated using computer algebra software. Some solutions of dynamical problems obtained using the proposed formalism are presented, their accuracy is analyzed, and various high-order theories' applications are shown.

Author is supported by the Russian Foundation for Basic Researches under grant No.16-01-00751-a.

References

[1] Eremeyev V., Pietraszkiewicz W.: Refined theories of plates and shells. ZAMM 94(1-2):5-6, 2014.

[2] Thai H-T., Kim S-E.: A review of theories for the modeling and analysis of functionally graded plates and shells. Composite Struct. 2015, http://dx.doi.org/10.1016/j.compstruct.2015.03.010.

[3] Vekua I. N.: Shell Theory: General Methods of Construction. Pitman Adv. Pub. Program. Boston. 1986.

[4] Schwab C., Wright S.: Boundary layers in hierarchical beam and plate models. J. Elast. 38:1-40, 1995.

[5] Zozulya V.V.: A higher order theory for shells, plates and rods. Int. J. Mech. Sci. 2015, http://dx.doi.org/10.1016/j.ijmecsci.2015.08.025

[6] Leech J. W.: Classical Mechanics. Wiley & Sons Inc. N. Y., 1958.

[7] Kil'chevskiy N. A., Kil'chinskaya G. A., and Tkachenko N. E.: Analytical Mechanics of Continuum Systems. Naukova Dumka, Kiev, 1979.

[8] Zhavoronok S. I.: A Vekua-type linear theory of thick elastic shells. ZAMM 94(1-2):164-184, 2014.

[9] Zhavoronok S. I.: Variational formulations of Vekua-type shell theories and some their applications. Shell Structures: Theory and Applications. Vol. 3, 341-344. CRC Press / Balkema, Taylor & Francis Gr., Leiden, 2014.

[10] Zhavoronok S. I.: On the variational formulation of the extended thick anisotropic shells theory of I.N.Vekua type. Procedia Engng, 111:888-895, 2015.

[11] Koiter W. T.: A consistent first approximations in the general theory of thin elastic shells: Proc. Symp. on the Theory of Thin Elastic Shells. 1959, North Holland, Amsterdam. 12-23.

A STRAIN GRADIENT ELASTICITY THEORY WITH INDEPENDENT LENGTH SCALE PARAMETERS

Shenjie Zhou [1a)], Anqing Li [1], Binglei Wang [2], Guangyang Fu [1]
[1] *School of Mechanical Engineering, Shandong University, Jinan, Shandong, China*
[2] *School of Civil Engineering, Shandong University, Jinan, Shandong, China*

Summary A general isotropic strain gradient theory with independent material length-scale parameters (MLSPs) is presented that differs from the established models. The strain gradient theory is reformulated by introducing two different orthogonal decompositions of higher-order metrics to characterize strain gradient behaviors. Just by reformulating constitutive relations, no extra conditions needed, the number of independent MLSPs is theoretically proved to be only three for isotropic linear elastic materials. The new theory can be directly reduced to the established models when some of the components of strain gradients are ignored. The analytically solutions of several simple problems reveal the availability of the present theory with independent multi-MLSPs to describe size effects in microstructures.

INTRODUCTION

Many experiments have shown the size-dependent deformation behaviors in micro scale structures. Classical elasticity theories fair to describe such a behaviors in microstructures. Strain gradient elasticity theories, such as, the general model [1], the modified model [2], the simple model [3], and the geometrically nonlinear model [4], which introduce MLSPs into constitutive relations, have been used to predict the size effects of microstructures. The both general theory and nonlinear model involve five MLSPs in the strain energy density for isotropic materials besides Lame constants. We can recognize that the five MLSPs are not independent due to the energy density relation contains cross terms for strain gradients. Although the modified model removes the cross terms and reduces MLSPs to three from five by applying the equilibrium conditions for a moment of couple vectors, the mechanics effect of conditions is unable to be comprehended for the free character of couple vectors. Up to now, it is unclear that the number of independent MLSPs is theoretically needed for isotropic materials within strain gradient elasticity (SGE).

The purpose of this work is to discuss the number of independent MLSPs needed for isotropic materials within SGE and to reformulate the general isotropic SGE theory with independent MLSPs.

DEVELOPMENT OF INDEPENDENT HIGHER-ORDER METRICS

In order to remove cross terms for strain gradients in the strain energy density, two sets of independent higher-order metrics are developed by introducing two different orthogonal decompositions of a strain gradient tensor, of which one is based on a symmetric/anti-symmetric splitting, the other on a hydrostatic/deviatoric splitting. For the symmetric/anti-symmetric splitting, the strain gradient tensor η_{ijk} is decomposed into a set of four components by splitting the tensor into symmetric and anti-symmetric parts η^s_{ijk} and η^a_{ijk}, and then splitting the symmetric and anti-symmetric parts into a trace part $\eta^{(0)}_{ijk}$ and a traceless part $\eta^{(1)}_{ijk}$ and into the symmetric and anti-symmetric parts η^{as}_{ijk} and η^{aa}_{ijk}, respectively. While, for the hydrostatic/deviatoric splitting, the strain gradient tensor is decomposed into different set of four components by splitting the tensor into the hydrostatic part η^h_{ijk} and the deviatoric part η'_{ijk}, and then splitting the deviatoric part into three parts following the strategy of Fleck et al [5]. The two sets of independent components have

$$\eta_{ijk}=\eta^s_{ijk}+\eta^a_{ijk}=\eta^{(0)}_{ijk}+\eta^{(1)}_{ijk}+\eta^{as}_{ijk}+\eta^{aa}_{ijk},\quad \eta_{ijk}=\eta^h_{ijk}+\eta'_{ijk}=\eta^h_{ijk}+\eta'^{(1)}_{ijk}+\eta'^{as}_{ijk}+\eta'^{(2)}_{ijk} \tag{1}$$

The first term and fourth term in the first relation are associated with the hydrostatic strain; the first term in the second relation is dependent only on the hydrostatic strain. The relationships $\eta^{(1)}_{ijk}=\eta'^{(1)}_{ijk}$, $\eta^{as}_{ijk}=\eta'^{as}_{ijk}$ and $\eta^{(0)}_{ijk}+\eta^{aa}_{ijk}=\eta^h_{ijk}+\eta'^{(2)}_{ijk}$ between these components can be confirmed. The higher-order stresses work-conjugated to these components can be correspondingly defined. The expressions of the components can be obtained based on their decomposing relations.

REFORMULATION OF CONSTITUTIVE RELATIONS

For linear elastic isotropic materials, the strain energy density *w* depends on both strains and strain gradients in manner

$$w=\tfrac{1}{2}C_{ijkl}\varepsilon_{ij}\varepsilon_{kl}+\tfrac{1}{2}F_{ijkpqr}\eta_{ijk}\eta_{pqr} \tag{2}$$

where C_{ijkl} is the four-order isotropic elasticity tensor (IET), F_{ijkpqr} is a six-order IET obeying the symmetry $F_{ijkpqr}=F_{pqrijk}$ and $F_{ijkpqr}=F_{ikjpqr}=F_{ijkqpr}$. The part for strain gradients in the strain energy density (2) also can be expressed in terms of two sets of independent components, respectively, as

$$w_h=\tfrac{1}{2}F^s_{ijkpqr}\eta^s_{ijk}\eta^s_{pqr}+\tfrac{1}{2}F^a_{ijkpqr}\eta^a_{ijk}\eta^a_{pqr} \tag{3}$$

$$w_h=\tfrac{1}{2}F^h_{ijkpqr}\eta^h_{ijk}\eta^h_{pqr}+\tfrac{1}{2}F'_{ijkpqr}\eta'_{ijk}\eta'_{pqr} \tag{4}$$

a) Corresponding author. Email: zhousj@sdu.edu.cn.

Here, F^s_{ijkpqr} and F^a_{ijkpqr} obey the major symmetry $F^s_{ijkpqr}=F^s_{kijpqr}=F^s_{jkipqr}$ and the major anti-symmetry $F^a_{ijkpqr}+F^a_{kijpqr}+F^a_{jkipqr}=0$, respectively, while F^h_{ijkpqr} is symmetric in indices (j, k) depending on δ_{jk}, and F^d_{ijkpqr} has a property $F^d_{ijkpqr}=0$, in addition, they have the same symmetry as F_{ijkpqr}. These IETs can be read as linear combinations of their basic tensors, which are derived from a general sixth-order isotropic tensor by applying their symmetric conditions [6]. We have results of that F_{ijkpqr} needs five basic tensors involving five constants, F^s_{ijkpqr} and F^a_{ijkpqr} require different two basic tensors containing two constants, respectively, while F^h_{ijkpqr} needs only one basic tensor and one constant, and F^d_{ijkpqr} has three basic tensors and three constants. The constitutive relations of higher-order metrics can be obtained from Eqs. (2)-(4), respectively, as

$$\tau_{ijk}=F_{ijkpqr}\eta_{pqr},\quad \tau^s_{ijk}=F^s_{ijkpqr}\eta^s_{pqr},\quad \tau^a_{ijk}=F^a_{ijkpqr}\eta^a_{pqr},\quad \tau^h_{ijk}=F^h_{ijkpqr}\eta^h_{pqr},\quad \tau'_{ijk}=F^d_{ijkpqr}\eta'_{pqr} \tag{5}$$

Applying the decomposing relations and orthogonal properties of higher-order tensors, we have the results

$$F_{ijkpqr}=F^s_{ijkpqr}+F^a_{ijkpqr}=F^h_{ijkpqr}+F^d_{ijkpqr} \tag{6}$$

From the above relations, the restriction relationships between constants involved in the constitutive relations Eq. (5) can be obtained. Applying these relationships, we prove that there are only three independent MLSPs in the constitutive relations expressed in terms of whether the strain gradient tensor or its independent components. The constitutive relations is expressed in the form of the components as

$$\tau_{ijk}=2\mu[l_0^2(\eta^h_{ijk}+\eta'^{(2)}_{ijk})+l_1^2\eta^{(1)}_{ijk}+l_2^2\eta^{as}_{ijk}],\quad \tau_{ijk}=2\mu[l_0^2(\eta^h_{ijk}+\eta^{aa}_{ijk})+l_1^2\eta^{(1)}_{ijk}+l_2^2\eta^{as}_{ijk}] \tag{7}$$

where l0, l1, l2 are three MLSPs introduced. The first relation in Eq. (7) can be reduced to that of incompressible materials by assuming the term η^h_{ijk} associated with the hydrostatic strain to be zero; while the second relation in Eq. (7) can be reduced to that of couple stresses by ignoring the terms $\eta^{(0)}_{ijk}$ and $\eta^{(1)}_{ijk}$ associated with the symmetric part of strain gradients. The equilibrium equation and boundary conditions in the form of independent components will be obtained by virtual work principles.

SOLUTIONS TO SIMPLE PROBLEMS AND DISCUSSION

The size-dependent model of a plane-strain cantilever beam with an applied force at the free-end is developed based on the present theory. The model is compared with other theory models and experimental results. Fitting the experimental data [2] of epoxy polymeric beams to the present model gives a MLSP 6μm when assuming l_0=l_1=l_2, while, the modified model under same assuming and the simple model give 8μm and 9μm, respectively. When taking the same MLSPs for each theory, the predicting deflection at the free-end of cantilever from large to small is orderly by the simple model, the modified model and the model of the present theory. Results indicate that those theories ignoring some components of strain gradients will underestimate size effects from strain gradients.

Further, three simple problems, such as torsion of bars, shearing of fixed-end layers, and pure bending of micro-beams, are analyzed using the present theory and the simple theory with one length-scale parameter l, respectively. In order to facilitate comparison between two theories, we introduce an equivalent scale parameter (ESP), which is defined as the scale parameter under identical gradient effects from two theories. In the torsion problem, the ESPs of l_2 and $1/3l$ are obtained for the new theory and the simple version, respectively. This result shows that identical gradient effects from two theories would be expected by l=$3l_2$. Nevertheless, the factor is difference in both shearing and bending problems. For instance, in the shearing problem, the new theory ESP is $(\frac{9}{10}l_0^2+\frac{8}{15}l_1^2+\frac{1}{2}l_2^2)^{0.5}$, while the simple version is l. The problem-dependence of factor indicates the necessity of using the multiple parameter theory to predict size effects in microstructures.

CONCLUSIONS

Two sets of independent components of the strain gradient tensor are developed by applying two different orthogonal decompositions. It is theoretically proved that there are only three MLSPs needed in the general isotropic SGE theory. The general SGE theory with three independent MLSPs is proposed for isotropic materials. The new theory can be reduced to that of incompressible materials and the couple stress model by assuming the terms associated with the hydrostatic strain and by ignoring the symmetric parts of strain gradients, respectively. Analytically solutions of simple problems reveal the availability of the new theory with independent MLSPs to describe size effects in micron scales; while the existed theories underestimate the effects.

References

[1] Mindlin R., Eshel N.: On first strain-gradient theories in linear elasticity. *Int. J. Solids Struct.* 4: 109-124, 1968.
[2] Lam D.C.C., Yang F., Chong A.C.M.: Experiments and theory in strain gradient elasticity. *J.Mech. Phys. Solids* 51:1477-1508, 2003.
[3] Aifantis, E.: On the role of gradients in the localization of deformation and fracture. *Int. J. Eng. Scien.*30:1279–1299, 1992.
[4] Dell'lsola F., Sciarra G., Vidoli, S.: Generalized Hooke's law for isotropic second gradient materials. *Proc. R. Sor. A* 465:2177-2196, 2009.
[5] Fleck N. A., Huntchinson J. W.: A reformulation of strain gradient plasticity, J. Mech. Phys. Solids 49:2245-2271, 2001.
[6] Suiker A. S. J., Chang C. S.: Application of higher-order tensor theory for formulating enhanced continuum models. Acta Mech.142:223-234, 2000.

AN ELASTICITY THEORY WITH DEFECTS

Wennan Zou[1]
[1] *Institute for Advanced Study, Nanchang University, Nanchang, P.R. China, 330031*

Abstract: Defect, scale effect and couple stress are obviously different but all inevitable in extending the classical theory of elasticity, just like different aspects of a thing. In this paper, based on the "micro-finite element" model of continua, an elasticity theory with defects is constructed through some relaxation of geometric constraints in deformation. The equilibrium equations are derived from the virtual work principle.

INTRODUCTION

In the previous paper[1], the constituent *micro-finite element*, instead of *material particle*, was proposed to model the continuous media. Thus, the intrinsic state of the microelement, including the internal deformation and external motion, are described by *stretch* **V** or *mass measure* $=$ $^{-1}$ and *velocity* **v**, respectively. And on the body as a differential manifold, the *space-time connection* Γ_i^j, defined by $D\mathbf{e}_i = \Gamma_i^j \mathbf{e}_j$ with $\Gamma_i^j = \Gamma_{ik}^j dx^k + \Omega_i^j dt$, is necessary to indicate the isomorphism relation between adjacent microelements. The change between two arbitrary line-elements on the same microelement can be determined from the *metric tensor* **G**, given by $\mathbf{G} = g_{ij}\ ^i \otimes\ ^j$ $g_{ij} =$ $_i \cdot\ _j = b\ b$. The *relative rotation* compatible to the stretch is expressed by $w_k^i = \varepsilon_{ips} V_{qs} \left(\partial_q b_{pk} - \partial_k b_{pq} \right) + \frac{1}{2}\varepsilon$ $b\ V\ V\ \partial\ b$, whose *attitude rotation* is then calculated with the Homotopy operation as $R_{pq} = \exp\left\{ \varepsilon_{ipq} \int_0^1 \left(x_k - x_k^0 \right) w_k^i \lfloor \mathbf{r}_0 + \lambda \left(\quad - \ _0 \right) \rfloor \right\}$.

Some auxiliary properties are available if no defect exists or forms during the inhomogeneous elastic deformation. Since two adjacent microelements could be overlapping, the *rotation* **R** other than the rigid rotation must be introduced to keep the geometrical compatibility between adjacent microelements such that it is realizable to past these microelements together. Then a general unloading transformation is indicated by $\mathbf{e}_i \to \mathbf{g}_i =$ $R\ b$, where the base $\mathbf{e}_i$ is used as the representation of the line element along the direction $\mathbf{e}_i$ at the present state. Combination of **V** and **R** yields the *deformation tensor* $=$. If the connection is completely determined by the metric tensor and curvature-free, the rotation **R** is equally the attitude rotation such that $\mathbf{w}^i = w_k dx_k = \frac{1}{2}\varepsilon_{ipq} R_{lp} dR_{lq}$ and the isomorphism relation is exactly expressed by $\Gamma_i^j = F\ dF_{ni}^{-1}$. The completely compatible deformation also implies that the 1-form vector $F^{-1} dx_j$ is a perfect differential, capable of indicating unstressed line-elements. Such an understanding gives the differential formula of the velocity as $_i =$ $^{-1}$ $_j$.

All properties in this paper are referred to fixed Cartesian system, which is attached to the real body until Section 2.1 and hereafter to the virtual body.

STATE DESCRIPTION OF ELASTIC BODY WITH DEFECTS

Three sources of defects

Real materials are complex and their deformations may be inelastic or irreversible. Prior to the elastic process that the body can restore it to its original state if the external force is no longer applied, some constraints must be prescribed. The connection has three sources. (1) The *Q-tensor*, defined by $-\mathbf{Q} = D\mathbf{G} = \left(dg_{ij} - \ _{il}\Gamma_j^l - g_{jl}\Gamma_i^l \right)\ ^i \otimes\ ^j$, indicates the distribution property of inner product of directional line-elements. The materials with null Q-tensor, namely the invariance of inner product, are called *simple media*, which are homogeneous in the state free of loading, and such a simplicity is in general heritable during the deformation. (2) The dislocation can be measured by the closeness of the four line-elements: two line-elements $\mathbf{e}_j$ and $\mathbf{e}_k$ from a point and their isomorphism counterparts from each other's ends. Such a property is called the *torsion tensor* T_{jk}^i, expressed by $T_{jk}^i = \Gamma^i\ - \Gamma_{jk}^i$. (3) The third source of the connection is the metric tensor. Using $\phi_{jki} = g_{il}\phi_{jk}$ and the Schouten notation $\phi_{ijk\}} = \phi_{jki} + \phi_{kij} - \phi_{ijk}$, we can derive the decomposition of the connection[2] as $\Gamma_{ijk} = \frac{1}{2}\left(g_{\{ij\ k\}} + T_{\{kij\}} + Q_{\{ijk\}} \right)$.

According to differential geometry[3], the connection itself is not a tensor, e.g. one can always construct a transformation (deformation) to make the connection vanish at a point. The topological property of the connection is characterized by the *curvature tensor* $S_i^l = D\Gamma_i^l$, where $S_{ijk}^l = \partial\ \Gamma\ \ - \partial\ \Gamma\ + \Gamma\ \ \Gamma\ \ - \Gamma\ \ \Gamma^m$. If the curvature tensor vanishes, the elastic body can be represented by the Euclidean domain, and the displacement description becomes available.

Local unstressed state

[a]Corresponding author. Email: zouwn@ncu.edu.cn.

In the present state, the connection is expressed as a mixture of the stretch and the objective defects. In order to clarify different factors, we first assume that the solid bodies mentioned below are simple (initially homogeneous). Then imaged that every microelement in the body is unstressed, namely experiencing a unloading deformation **b**, to restore it to its natural state, a virtual state of the body occupying the same space is called its *local unstressed state*. Obviously, the overlapping microelements are in general incompatible to each other if the stretch is inhomogeneous.

Now, moving the Cartesian coordinate system from the real body to the virtual one, we harvest the following properties: (1) The metric tensor becomes $\mathbf{G} = \delta_{ij}\ ^i \otimes\ ^j$ while the connection has expression $\Gamma_i^j = \mathbf{W}^\alpha \gamma_{\alpha i}^j$, $\mathbf{W}^\alpha = A_k^\alpha dx_k + \Phi^\alpha dt$, where $\gamma_{\alpha j}^i$ is the generator of SO(3). (2) The curvature tensor has expression $\mathbf{S}_i^j = D\Gamma_i^j = \left(B_k^\alpha da_k + H_k^\alpha dx_k \wedge dt\right)\gamma_{\alpha i}^j$, with $B_k^\alpha = \varepsilon_{lmk}\left(\partial_l A_m^\alpha + \frac{1}{2}\kappa_{\beta\gamma}^\alpha A_l^\beta A_m^\gamma\right)$ and $H_k^\alpha = \partial_k \Phi\ - \partial_t A_k^\alpha + \kappa_{\beta\gamma}^\alpha A_k^\beta \Phi^\gamma$ where $\kappa_{\beta\gamma}^\alpha$ is the structural constants of SO(3): $\kappa^\alpha\ \gamma_{\alpha i}^j = \gamma^j\ \gamma_\gamma^l\ - \gamma_\gamma^j\ \gamma_{\beta i}^l$. (3) The mass measure **b** can be recognized as a 1-form vector field attached on the virtual body $= b\ dx_j$, where $\mathbf{e}_i$ is associated with the line-element of the virtual body in reason.

Defects associated with the stretch

One should realize that the inelastic process accompanies the topological change and the one-to-one correspondence of microelements is destroyed. Based on the local unstressed state, we may build up a description instead of the two-configuration one. From the 1-form variable **b**, the covariant exterior-differentials $\alpha = D\ = {}_i\left(\partial_k b_{ij} + A_k^\alpha \gamma_\alpha^l b\right.\ dx_k \wedge dx_j$ and $\chi = DD\ =\ \gamma_\alpha^p b\ \ B^\alpha dx_1 \wedge dx_2 \wedge dx_3$ are referred to as the 2-form (*dislocation*) and 3-form (*disclination*) variables. Hence we obtain the following four categories: (1) $\alpha =\ \ \chi = \mathbf{0}$, (2) $\alpha =\ \ \chi \neq \mathbf{0}$, (3) $\alpha \neq \mathbf{0}, \chi = \mathbf{0}$, (4) $\alpha \neq \mathbf{0}, \chi \neq \mathbf{0}$. Case (1) is just the classical elastic deformation. Considering that the case (3) is a special case and the case (4) is rather complex, we will confine ourselves to the case (2), where the stretch is somehow the only inwardness.

The velocity **v** and the angular velocity Φ will be used as virtual qualities attached to the present body in equilibrium. The differentials of b_{ij} and A_k^α with respect to the time could be associated with virtual qualities in such a way: $D_t\mathbf{b} =\ \ \Rightarrow dv_i = -V\ \ \dot{b}_{kj} + \Phi^\alpha \gamma_{\alpha k}^l b_{lj}\ dx_j$, and $H_k^\alpha =\ \ \Rightarrow \dot{A}_k^\alpha = \partial_k \Phi\ + \kappa_{\beta\gamma}^\alpha A_k^\beta \Phi^\gamma$.

EQUILIBRIUM EQUATIONS

The equilibrium equations of elastic bodies can be derived through the *principle of virtual work*. We now consider that any part of the elastic body occupies at the present state the region *V* with the closed surface *S*, denoting by **X** the body force referred to unit mass and by **Y** the body moment; the surface force and moment on a unit area with normal **n** are given by **p** and **m**, respectively. Let ρ be the density and *e* the stored energy of the elasticity per unit volume, the virtual work principle can be expressed by $\dot{E} = \int_V \rho \dot{e} dV = \int_V \rho\left(\ _i\ _i + \ _i\Phi^i\right)dV + \int_{S_\sigma}\left(\ _i\ _i + \ _i\Phi^i\right)dS$. Then the variation with respect to virtual qualities results in the equilibrium equations $\partial_j\left(b_{ik}\Sigma_{ij}^0 + \gamma_\alpha^i\ b\ B_j^\alpha \Sigma_q^2\right) = \rho X_k$, $-\gamma_{\alpha i}^l b_{lj} \gamma_{\beta q}^i B_j^\beta \Sigma_q^2 = \rho Y_\alpha$, and the boundaries $-\ _j\left(\ _{ik}\Sigma_{ij}^0 + \gamma_{\alpha q}^i b_{ik} B_j^\alpha \Sigma_q^2\right) = p_k$, $0 = m_\alpha$, respectively, where $\Sigma^0 = \rho\partial\ _0 / \partial\ _{ij}$, $\Sigma_i^2 = \rho\partial e_2 / \partial\chi_i$. Together with the continuity equation $\rho = \rho_0 \det\mathbf{b}$, we are able to solve the stretch. Finally, comparing with the definition of Cauchy stress, we get its formula in the frame of the new theory as $\sigma = -\rho\mathbf{b}\cdot\left(de_0 / d\mathbf{b}\right) = -\mathbf{b}\cdot\Sigma_0$.

CONCLUDING REMARKS

Based on the "micro-finite element" model of continua, a general frame of elasticity theory with defects is proposed. For the special case with deformation-compatible defects, the virtual work principle is used to derive the equilibrium equations where the couple stress and scale parameter could be naturally expected to emerge. The difference between the present theory and the previous theories is quite obvious[4], though the former could be equivalent with the latter in the context of the classical elasticity[1]. Starting from the present frame, more complex theories involved irreversible processes are also expectable in the future study.

References

[1] Zou WN. Recasting theory of elasticity with micro-finite elements. *Acta Mechanica Sinica*, 2015, 31(**5):** 679-684.

[2] Wang ZQ. *Foundation of Rational Mechanics* (in Chinese). Science Press, 2000.

[3] Chern SS, Chen WH, Lam KS. *Lectures on Differential Geometry*. World Scientific Pub., Singapore, 1999.

[4] Kadic A., Edelen DGB. *A gauge theory of dislocations and disclinations*. Springer, 1983.

SM05 - Fracture Mechanics

TS.SM05-1.01	Heyden, Stefanie - Towards a one-parameter fracture model in soft matter mechanics (INVITED)	2007
TS.SM05-1.02	Moulinet, Sébastien - Fracture patterns in exploding balloons	2009
TS.SM05-1.03	Kroon, Martin - Dynamic crack propagation in rubber	2011
TS.SM05-1.04	Bouklas, Nikolaos - Effect of Solvent Diffusion on Fracture of Hydrogels	2013
TS.SM05-1.05	Liu, Zhanli - Hydraulic fracture in porous media	2015
TS.SM05-1.06	Barthelat, Francois - Overcoming brittleness through bio-inspiration and microarchitecture	2017
TS.SM05-10.01	Kysar, Jeff - Fracture and indentation in single metal crystals (INVITED)	2019
TS.SM05-10.02	Srivastava, Ankit - Ductile fracture of controlled microstructures	2021
TS.SM05-10.03	Benzerga, Amine - Micromechanical modeling of void coalescence in ductile solids	2023
TS.SM05-10.04	Liu, Zhigang - On the transition from void collapse to void coalescence	2025
TS.SM05-10.05	Felter, Christian - Crack tip flipping under Mode I/III tearing	2027
TS.SM05-2.01	Larsen, Chris - Mathematical difficulties in cohesive fracture evolution	2029
TS.SM05-2.02	Landis, Chad - A phase-field model for fluid driven cracks in porous media	2030
TS.SM05-2.03	Bobaru, Florin - Peridynamic modelling of dynamic fracture and fatigue cracking	2032
TS.SM05-2.04	Delaume, Eric - Local adaptive refinement method for the fracture of heterogeneous materials	2034
TS.SM05-2.05	Jain, Shruti - Interface Strength Versus Fracture Energy Driven Fracture in Thin Film Transfer	2036
TS.SM05-2.06	Shen, Yongxing - Universal meshes for a crack with triple junctions	2038
TS.SM05-3.01	Antipov, Yuri - Crack growth at nonuniform speed beneath the boundary of a half-plane	2040
TS.SM05-3.02	Unger, David - Linear elastic solutions for slotted plates revisited	2042
TS.SM05-3.03	Coré, Arthur - Experimental and numerical investigation of hollow spheres subjected to fracture	2044
TS.SM05-3.04	Walton, Jay - Plane Strain Fracture with Surface Mechanics: Non-Local Boundary Regularization	2046
TS.SM05-3.05	Roman, Benoit - Intertwined spiraling crack path in perforated sheets	2048
TS.SM05-3.06	Curtin, William - Crack tip blunting and cleavage under dynamic conditions	2050
TS.SM05-4.01	Ponson, Laurent - Cracking the crack: What do we learn from the statistical properties of fracture surfaces? (INVITED)	2052
TS.SM05-4.02	Woelke, Pawel - Investigation of fracture in large ductile plates	2054
TS.SM05-4.03	Zikry, Mohammed - Dynamic fracture and orientation relations of h.c.p.-f.c.c. systems	2056
TS.SM05-4.04	Baxevanis, Theocharis - Thermomechanical Fracture in Shape Memory Alloys	2058
TS.SM05-4.05	Hoshide, Toshihiko - Statistical Simulation of Biaxial Fatigue Behaviour Affected by Microstructure	2060
TS.SM05-4.06	Li, Yan - Prediction of fracture toughness scatter of composite materials as function of microstructure	2062
TS.SM05-5.01	Ariza, Pilar - Nanovoid cavitation in Aluminum	2064

TS.SM05-5.02	Li, Jiaoyan - Topological Design of Graphene with Enhances Fracture Toughness	2066
TS.SM05-5.03	Khosrownejad, Mostafa - Crack propagation mechanisms in amorphous LiSi alloys: Insights from molecular dynamics	2068
TS.SM05-5.04	Guin, Laurent - Molecular dynamics based cohesive zone model for polycrystalline graphene	2070
TS.SM05-5.05	Yang, Hui - Fracture toughness of LixSi alloys in lithium ion battery	2072
TS.SM05-5.06	Ding, Bin - Atomistic mechanisms of fracture in amorphous lithiated silicon	2074
TS.SM05-6.01	Begley, Matthew - Cohesive zone modeling of crack kinking out of an interface	2076
TS.SM05-6.02	Iacobellis, Vincent - Multiscale cohesive zone model of a composite microstructure	2078
TS.SM05-6.03	Hoefnagels, Johan - Stretchable electronics: solving metal-matrix debonding by removing the matrix	2080
TS.SM05-6.04	Juan, Pierre-Alexandre - Mechanics of finite crack considering interfacial elasticity	2082
TS.SM05-6.05	Lu, Wei - Interaction of delamination and electrochemical processes	2084
TS.SM05-6.06	Massabo, Roberta - A homogenized approach for delamination fracture in laminated structures	2086
TS.SM05-7.01	Palvadi, Naga Sundeep - Extracting rate dependent traction separation relations for interfaces	2088
TS.SM05-7.02	Perelmuter, Mikhail - Modelling and analysis of bridging effect for interface cracks	2090
TS.SM05-7.03	Pan, Kui - Particle dynamics modeling of buckle-delamination of thin film materials	2092
TS.SM05-7.04	Sehr, Stephen - Analysis of cracking in candidate environmental barrier coatings	2094
TS.SM05-7.05	Morini, Lorenzo - Integral identities for thermodiffusive interfacial cracks	2096
TS.SM05-7.06	Banks-Sills, Leslie - Reassessment of the virtual crack closure technique for interface cracks	2098
TS.SM05-8.01	Narasimhan, R. - Brittle-ductile transition in notched nanoscale metallic glass specimens (INVITED)	2100
TS.SM05-8.02	Korkolis, Yannis - Failure of an austenitic stainless steel under linear and non-linear loading paths	2102
TS.SM05-8.03	Liu, Yinghua - T-stress and mismatch constraint for a blunted creep crack	2104
TS.SM05-8.04	Sartori, Cédric - Micromechanical Model for Ductile Porous Material under Dynamic Loading	2106
TS.SM05-8.05	Rodríguez-Martínez, José - Multiple necking during biaxial loading of thermoviscoplastic plates	2108
TS.SM05-9.01	Ravi-Chandar, Ravi - Emergence of echelon cracks under mixed-mode I + III loading	2109
TS.SM05-9.02	Kolvin, Itamar - Crack front dynamics	2111
TS.SM05-9.03	Sherman, Dov - Crack dynamics in brittle crystals at the low energy speed regime	2113
TS.SM05-9.04	Kaliske, Michael - Approaches for dynamic fracture simulation: r-adaptive material force and phase-field method	2115
TS.SM05-9.05	Vandenberghe, Nicolas - Fragmentation as an aggregation process	2117
PO.SM05-1.01.246	Bbosa, Lawrence - Modelling impact damage and breakage of a particle bed using SPH and DEM	2119

PO.SM05-1.02.247	El Abdi, Rochdi - Strength measurement of fluoride fiber by bending and tensile test	2121
PO.SM05-1.03.248	Hou, Junling - Fracture toughness analysis by the material configurational forces in transformable materials	2123
PO.SM05-1.04.249	Huang, Yifan - Impacts of residual stress on J-integral for clamped SE(T) specimen	2125
PO.SM05-1.05.250	Keer, Leon - A micromechanical damage model for solder joints with an intermetallic compound layer	2127
PO.SM05-1.06.251	Liu, Junjie - Plastic Zone around a Moving Crack Tip in Viscoplastic Polymers	2129
PO.SM05-1.07.252	Mamaghani, Mohammadhossein - Nonlinear finite element analysis of adobe structures strengthened by synthetic nylons	2131
PO.SM05-1.08.253	Piat, Romana - Transverse cracking in metal-ceramic composites with lamellar microstructure	2133
PO.SM05-1.09.254	Pro, John - GPU-based simulations of fracture in bio-inspired brick & mortar composites	2135
PO.SM05-1.10.255	Singh, Gaurav - Dependence of timescale on crack velocity during diffusion-controlled crack growth	2137
PO.SM05-1.11.256	Stamoulis, Georgios - Influence of material non-linearity in the fracture properties of structural adhesives	2139
PO.SM05-1.12.257	Wolf, Johannes - Numerical modelling of the damage-to-crack transition in a Gurson-type material	2141

TOWARDS A ONE-PARAMETER FRACTURE MODEL IN SOFT MATTER MECHANICS

Stefanie Heyden*[1], Bo Li[2], Sergio Conti[3], and Michael Ortiz[4]
[1]*Department of Aerospace, California Institute of Technology, Pasadena, California, USA*
[2]*Department of Mechanical & Aerospace Engineering, CWRU, Cleveland, Ohio, USA*
[3]*Institute for Applied Mathematics, University of Bonn, Bonn, North Rhine-Westphalia, Germany*
[4]*Department of Aerospace, California Institute of Technology, Pasadena, California, USA*

Summary We present a simple one-parameter macroscopic model of distributed damage and fracture of soft matter that is amenable to a straightforward and efficient numerical implementation as introduced in [6]. The failure model is motivated by post-mortem fractographic observations of void nucleation, growth and coalescence in an elastomeric polymer stretched to failure, and accounts for the specific fracture energy per unit area attendant to rupture of the material. Furthermore, it is shown that the macroscopic model can be rigorously derived, in the sense of optimal scaling, from a micromechanical model of chain elasticity and failure regularized by means of fractional strain-gradient elasticity. In addition, the scope and fidelity of the model is demonstrated by means of an example of application, namely Taylor-impact experiments of polyurea rods. Hereby, optimal transportation meshfree approximation schemes using maximum-entropy interpolation functions are employed.

INTRODUCTION

The use of polymers as structural materials is critically limited by their tendency to degrade by distributed damage or to fail by fracture, sometimes in a brittle manner. Damage in polymers deformed under tensile loading often takes the form of distributed voids [2, 1]. Voids nucleate heterogeneously from flaws or inclusions, Fig. 1a, and subsequently grow under tension, Fig. 1b, resulting in softening – or loss of bearing capacity – of the material. Likewise, fracture in polymers can often be traced to the formation of crazes, which are thin layers of highly localized tensile deformation. The craze surfaces are bridged by numerous fine fibrils, themselves consisting of highly oriented chains, separated by connected voids. Crazes undergo several stages along their formation, including nucleation, growth and final breakdown, resulting in the formation of a traction-free crack, or fracture. Craze initiation is likely the result of heterogeneous cavitation at flaws loaded under conditions of high triaxiality. Craze propagation has been linked to a meniscus instability resulting in the formation of fibrils. This analogy is immediately suggestive of some role played by surface energy or other similar physical properties not accounted for by bulk behavior. Eventually, crazes break down to form cracks. Owing to its engineering importance, polymer damage and fracture have been the focus of extensive modeling. The connection between micromechanical properties and polymer fracture however, and specifically any scaling laws thereof, has defied rigorous analytical treatment and characterization. Of special interest is the identification of optimal scaling laws relating the macroscopic behavior to micromechanical and loading parameters. Such optimal scaling laws are established by producing upper and lower bounds of a power-law type with matching exponents for all parameters in both bounds. Optimal scaling methods were pioneered by [7] as part of their seminal work on branched structures in martensite, and have been since successfully applied to a number of related problems, including shape-memory alloys, micromagnetics, crystal plasticity, and others.

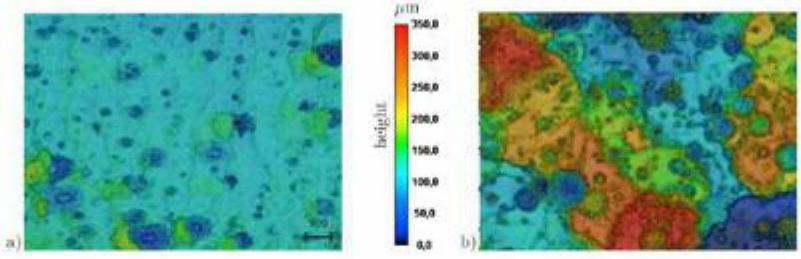

Figure 1: Surface profiles (height measured from the deepest point) of a polyurea specimen tested in uniaxial tension [1]. a) Initial profile showing initial porosity. b) Profile after fracture showing proliferation of voids.

*Corresponding author. Email: heyden@caltech.edu

OPTIMAL SCALING ANALYSIS AND TAYLOR-IMPACT SIMULATIONS

In the present work, we posit that fracture in polymers results from a competition between distributed damage, due to progressive chain failure, and fractional strain-gradient elasticity. Thus, we assume that the material behavior has two components, *local* and *nonlocal*. The local behavior is characteristic of large material samples deforming uniformly and it represents the configurational statistics of a polymeric chain network in the thermodynamic limit. A principal aim of the present work is to derive rigorous optimal scaling laws for the macroscopic fracture energy from the micromechanical model just described. Such optimal scaling laws are established producing upper and lower bounds of a power-law type with matching exponents for all parameters in both bounds. In order to facilitate the analysis, we assume that the effective deformation-theoretical energy is additive in the first and second deformation-gradients, with zero growth of the former and linear growth of the latter. The specific problem considered concerns a material sample in the form of an infinite slab of finite thickness subjected to prescribed opening displacements on its two surfaces. Under these conditions, we derive optimal scaling laws for the dependence of the effective energy on cross-sectional area, micromechanical parameters, opening displacement and intrinsic length of the material as

$$c_L k_L \ell^{\frac{\sigma}{1+\sigma}} \delta_c^{\frac{1}{1+\sigma}} \leq G_c \leq c_U k_U \ell^{\frac{\sigma}{1+\sigma}} \delta_c^{\frac{1}{1+\sigma}}. \tag{1}$$

In particular, the upper bound is obtained by means of a construction that mimics, in a particular simple manner, the crazing mechanism. The scaling laws thus derived supply a rigorous link between micromechanical properties and macroscopic fracture properties of polymers. In particular, they reveal the relative roles that surface energy and chain elasticity and damage play as contributors to the specific fracture energy of the material. The macroscopic fracture model that results from the optimal scaling analysis is characterized by a single parameter, namely, the critical energy-release rate G_c. This simple structure greatly facilitates material characterization. By way of illustration, and in order to calibrate subsequent calculations, we estimate G_c for polyurea 1000 from the uniaxial-tension test data of [1]. Another appealing aspect of the macroscopic fracture model is that it is amenable to a straightforward numerical implementation based on material-point erosion [4, 3]. We demonstrate the scope of the resulting numerical model by means of an example of application: The Taylor-impact experiments of Mock *et al.* on polyurea 1000 specimens [5]. Figure 2 depicts snapshots of a Taylor-impact simulation and the state of damage in the recovered specimen at high impact velocity as computed and as observed post-mortem in tests. The experimental figure shows the recovered specimen after impact, wherein the extent and distribution of damage can be clearly discerned optically. These simulations additionally furnish a modicum of validation of the fidelity of the failure and fracture model.

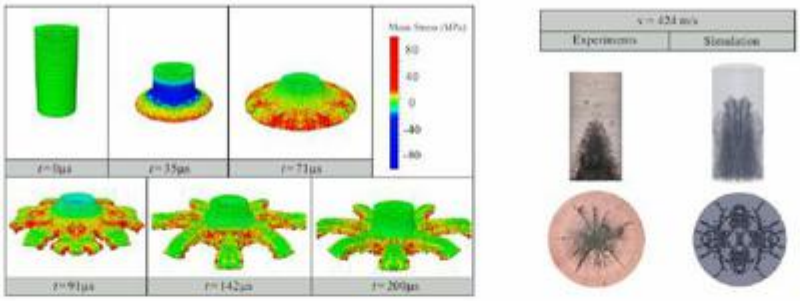

Figure 2: Snapshots of a Taylor-impact simulation at $v = 424$ m/s impact velocity (left) and comparison of the recovered target after shot btw. experiments and simulations (right)

References

[1] Reppel, T. and Dally, T. and Weinberg, K.: On the elastic modeling of highly extensible polyurea, Technische Mechanik 33(1):19-33, 2012.

[2] Jiao, T. and Clifton, R. J. and Grunschel, S. E.: Pressure-Sensitivity and Consititutive Modeling of an Elastomer at High Strain Rates, Shock Compression of Condensed Matter 1195:1229-1232, 2009.

[3] Pandolfi, A. and Ortiz, M.: An eigenerosion approach to brittle fracture, International Journal for Numerical Methods in Engineering 92(8):694-714, 2012.

[4] Li, B. and Kidane, A. and Ravichandran, G. and Ortiz, M.: Verification and validation of the Optimal Transportation Meshfree (OTM) simulation of terminal ballistics, International Journal of Impact Engineering 42:25-36, 2012.

[5] Mock, W. and Drotar, J.: Penetration Protection Experiments Using Polymer Materials, ONR Workshop, St. Michael's, Maryland, 2006.

[6] S. Heyden and K. Weinberg and S. Conti and B. Li and M. Ortiz: A micromechanical damage and fracture model for polymers based on fractional strain-gradient elasticity, Journal of the Mechanics and Physics of Solids 74:175195, 2015.

[7] R. V. Kohn and S. Müller: Branching of twins near an austenite-twinned-martensite interface, Phil. Mag. A 66:697-715, 1992.

FRACTURE PATTERNS IN EXPLODING BALLOONS

Sébastien Moulinet*[1] and Mokhtar Adda-Bedia[1]
[1]*Laboratoire de Physique Statistique, Ecole Normale Supérieure, UPMC Paris 6, Université Paris Diderot, CNRS*

Summary In this paper, we describe the formation of different fracture patterns observed in exploding rubber balloons. Thanks to a device using latex sheets, the patterns are obtained in a controlled manner. High-speed video allows monitoring the trajectory of the crack as well as the deformation of the stretched membrane. The first pattern is a tree-like crack network that yields the fragmentation of the balloon. Such a network develops through a succession of crack tip-splitting when the crack tips reach a limiting velocity. The second pattern is the occurrence of abrupt 90° turns in the crack trajectory. The phenomenon is observed when the cracks propagate perpendicularly to the retraction of the membrane. The turns occur when the membrane stretch become locally isotropic. Our observations indicate that the cracks maintain a trajectory perpendicular to the direction of the strongest stretch.

PATTERN FORMATION IN EXPLODING BALLOON

By examining the fragments of a toy balloon after it had exploded, one can see a large variety of shapes. In some situations, the membrane has split in two, while in others, it has turned into numerous elongated shreds. Sometime, some fragments display oscillating cracks. Other fragments reveal that a crack had made an abrupt 90° turn during its propagation. Two dimensional pattern formation due to fracture is well understood when the dynamic is quasi-static, i.e. when the stress field can be considered anytime as at equilibrium. For a bursting balloon, this assumption is wrong as the crack velocity can be compared to the sound celerity and as the surrounding material is relaxing with characteristic velocity comparable to the speed of the crack itself. In this paper, we will show how we have reproduced this phenomenology in a controlled manner. We demonstrate that the pattern formation is governed by dynamical aspects of the crack propagation.

In order to work with a more controlled system than toy balloon, we developed a setup to burst latex sheets of known thickness (from 350 to 1100 μm). The initially flat membrane is clamped to a circular frame (Fig. 1.a). The front side of the frame is opened to allow the expansion of the membrane while the closed rear side is connected to a compressed air inlet. When air is injected, the sheet stretches, taking the form of a growing axisymmetric balloon, until it hits an acute indenter (X-ACTO blade) that triggers the explosion. By choosing the position of the indenter, we define the inflation state of the ballon when it explodes, as well as the initial puncture position of the membrane. Using a fast camera (Photron APX RS) the explosion of the membrane is recorded at a frequency of 30 000 fps or 60 000 fps.

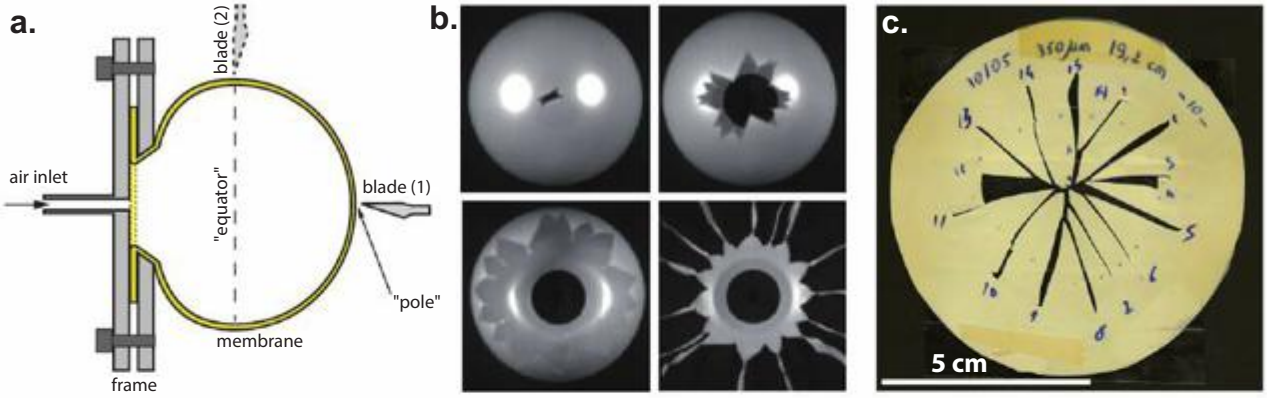

Figure 1: **a.** Cross-section of the experimental setup. The dotted line represents the initial flat state of the latex sheet before its inflation. The two positions of the blade correspond to (1) fragmentation experiment and (2) "Pac-Man" experiment. **b.** Axial views of the balloon fragmentation at different stages. The duration between the first and the last image is 300 ms. The dark disc in the center of the images is the circular frame, its inner diameter (52 mm) sets the scale. **c.** Example of *post-mortem* sample.

*Corresponding author. Email: moulinet@lps.ens.fr

FRAGMENTATION

If the blade is placed on the axes of the balloon (position 1 in fig. 1.a), two situations are observed. For a moderate tension of the membrane, a single crack splits the balloon into two large fragments. By increasing the distance between the the blade and the frame, we intensify the tension of the membrane at time it explodes. As a result, the velocity of the cracks increases as well. Although, if the blade is far enough, or if the balloon explodes spontaneously, the tensile stress in the membrane exceed a threshold value and the balloon fragmentizes into elongated shreds. The final number of cracks then increases with the membrane tension. As seen on the *post-mortem* sample, fig. 1.c, the cracks form a tree-like network that originate from a single seed-crack. The Y-shape of the junctions indicates that new branches are created through the splitting of the crack tip. During the growth of the network, the cracks propagate at a limiting velocity $v_l = 570 \pm 15\,\mathrm{m/s}$, proving that the branchings are a consequence of a dynamical instability [1].

THE "PAC-MAN" FRAGMENTS

A different kind of pattern is observed when the blade hits the balloons near its "equator" (position 2 in fig. 1.a). As depicted in fig 2.a, after the puncture, two cracks propagate on the membrane parallel to the frame. Then after having cut approximately five sixths of the perimeter, the cracks suddenly turn toward the "pole". Eventually, the two cracks meet, yielding the separation of a fragment. Fig. 2.b shows the resulting fragments whose shape ressembles the video game character Pac-Man, the two corners of the mouth resulting of the swift turns.

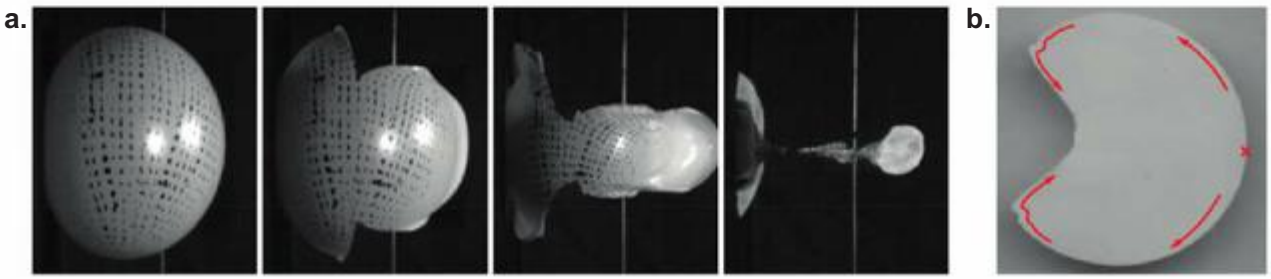

Figure 2: **a.** Side view of successive steps in the formation of a "Pac-Man" fragment. In chronological order : $t = 0$: the fracture is initiated on the other side of the balloon, $t = 0.47\,\mathrm{ms}$ the cracks are about to turn, $t = 0.67\,\mathrm{ms}$: the turns have happened and $t = 0.97\,\mathrm{ms}$: the cracks meet and a fragment is detached. The balloon has an initial diameter of $152\,\mathrm{mm}$. **b.** *Post-mortem* fragment (from a different experiment without ink spots). The diameter is $23\,\mathrm{mm}$. The cross indicates the position of the initial puncture, the arrows illustrate the crack trajectories.

In order to understand how the trajectory of the cracks are coupled to the relaxation of the membrane, we have deposited ink spots as tracers on the membrane. We used them to monitor the evolution of the membrane's stretch, with a specific focus on the points where the turns occur. Initially the longitudinal stretch is higher than the transversal stretch. This can be understood as an intermediate situation between the pole of the balloon where the stretching is isotropic, and the clamping where it is uniaxial. Even before the turn, the retraction of the membrane is visible: the cracks are propagating inside a relaxing medium. The turn coincides with the moment when the two stretch components become equal. Another observation confirmes that the turns occurs when the membrane become isotropically stretched: prior to the turn, a crack path oscillates with increasing amplitude and wavelength. According ref. [2], anisotropic stretch is needed to maintain a straight crack, otherwise the crack oscillates with diverging amplitude and wavelength as the ratio of the components tends to 1. One good rule of thumb to understand the crack patterns for quasi-static fracture is "a crack propagates perpendicularly to direction of the strongest stress". Surprisingly, the rule appears to apply for dynamic cracks in a relaxing medium as well.

Dynamic fragmentation and fracture of relaxing medium are not specific to rubber membranes, they can occur in a large variety of material such as glasses, minerals, ceramics... The large deformations it can withstand and its relatively low sound celerities makes the latex membrane an excellent model system to study dynamical fracture. The mechanisms of pattern formation we have described might be applied to other brittle materials.

References

[1] Moulinet S., Adda-Bedia M. : Physical review Letters 115:184301, 2015.
[2] Deegan R.D., Petersan P.J., Marder M., Swinney H.L. : Physical Review Letters 88:014304, 2002.

DYNAMIC CRACK PROPAGATION IN RUBBER

Martin Kroon[1]
[1]Malmoe University, Malmoe, Sweden

Summary The dynamic energy release rates in rubber are investigated by use of a numerical model. The model is calibrated by use of experimental results, and the dynamic crack tip energy release rate is calculated. The outcome is found to be in good agreement with previous experimental results.

INTRODUCTION

Rubbers may be characterized as viscoelastic, which means that viscoelastic dissipation contributes to the total fracture toughness of the material. Hence, there are at least two different sources for energy consumption at an advancing crack tip in rubber. The first source is associated with the innermost region at the crack tip, where cavities form, polymer chains are pulled out, and polymer chain bonds are broken. This process is mainly governed by the basic molecular structure and strength of the material. The second source is the viscoelastic dissipation in the polymer in front of the crack tip. Possibly some amount of damage may also be involved. On the basis of these observations, it is to be expected that the tearing energy of rubber will depend strongly on both temperature and crack velocity. In the present work, a computational framework is proposed for analyzing high-speed crack propagation in biaxially stretched rubber sheets under conditions of steady-state and plane stress. The main purpose of the study is to shed some more light on the contributions from local surface energy at the crack tip and bulk viscoelasticity and possible damage processes to the total work of fracture required to propagate a crack.

OBJECTIVES AND METHODOLOGY

The problem that is analyzed is illustrated in Figure 1 [1]. Consider a crack that propagates through a rubber solid at a constant speed and under steady-state conditions. The problem is analyzed using the FE method.

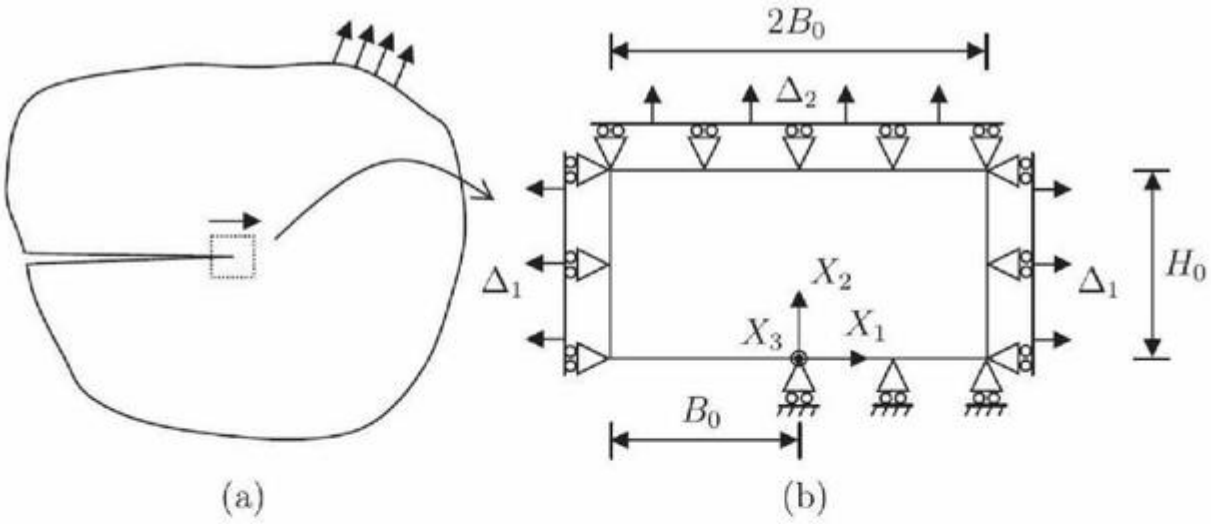

Fig.1. Problem to be analyzed.

RESULTS AND ANALYSIS

[a] Corresponding author. Email: martin.kroon@mah.se

The model is calibrated using experimental results, and the dynamic energy release rates are predicted, see Figure 2. The open symbols in Figure 2 denote experimental results from other studies, and the filled symbols denote the numerical predictions from the present study. As can be seen, the present predictions are well in line with previous results.

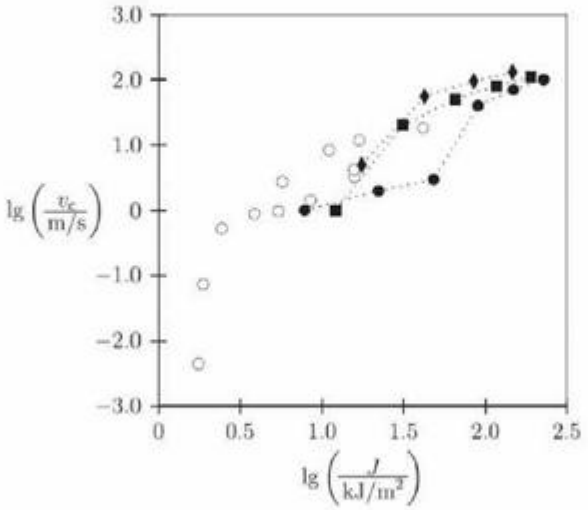

Fig.2. Predicted energy release rates vs. crack velocity.

CONCLUSIONS

The dynamic energy release rates in rubber has been assessed numerically, and the results were found to agree well with experimental findings.

References

[1] M. Kroon. Energy release rates in rubber during dynamic crack propagation. *International Journal of Solids and Structures*, 51:4419-4426.

EFFECT OF SOLVENT DIFFUSION ON FRACTURE OF HYDROGELS

Nikolaos Bouklas,[a] Chad M. Landis & Rui Huang
Department of Aerospace Engineering & Engineering Mechanics, University of Texas, Austin, TX 78712, USA

Summary This paper presents a thermodynamically consistent method for calculating the transient energy release rate for crack growth in hydrogels based on a modified path-independent J-integral. The transient energy release rate takes into account the effect of solvent diffusion, separating the energy lost in diffusion from the energy available to drive crack growth. Numerical simulations are performed using a nonlinear transient finite element method for center-cracked hydrogel specimens, subject to remote tension under generalized plane strain conditions. The transient energy release rate is predicted as a function of time for two types of chemical boundary conditions with distinct behaviours due to solvent diffusion. It is found that the stress singularity near the crack tip depends on both the far-field strain and the local solvent diffusion.

INTRODUCTION

Mechanical properties of hydrogel-like soft materials are important for many applications, ranging from biomedical devices to soft robotics. Fracture of hydrogels has been studied by many, both for understanding the fracture mechanisms and for characterizing the fracture properties such as toughness. The reported fracture toughness values for hydrogel-like soft materials range widely from ~ 1 J/m2 for gelatin gels [1] to ~1000 J/m2 for cartilage [2] and ~9000 J/m2 for a hybrid alginate–polyacrylamide gel [3]. Several studies have noted the rate dependence of the fracture toughness, suggesting kinetic processes associated with fracture of hydrogels. Two primary suspects for the kinetic processes in hydrogel-like soft materials are polymer viscoelasticity and solvent diffusion. While fracture mechanics of viscoelastic materials has been studied extensively, the effects of solvent diffusion on fracture of hydrogels have received little attention until recently [4-7]. In this paper, we focus on the effects of solvent diffusion on fracture of hydrogels and ignore the effects of viscoelasticity.

THEORY AND FORMULATION

Hydrogels in their simplest form consist of two components, long crosslinked polymer chains that form a three dimensional network structure and small solvent molecules that can migrate within the network. The nonlinear transient behaviour of hydrogels with coupled deformation and solvent diffusion has been studied by many. The general formulation by Hong et al. [8] is adopted in this study. There are two ways to do work to the hydrogel aggregate. One is by the application of mechanical forces, including body forces and surface tractions. The second is the exchange of solvent molecules through the source or the surface flux. The total potential energy of the aggregate system can be written as a sum of the internal stored energy and the work of the external mechanisms, and then the rate of the total potential energy is

$$\frac{d\Pi}{dt}=\int_{V_0}\frac{dU}{dt}dV-\int_{V_0}b_i\frac{dx_i}{dt}dV-\int_{S_0}T_i\frac{dx_i}{dt}dS-\int_{V_0}\mu r dV-\int_{S_0}\mu i dS \tag{1}$$

The rate of energy dissipation associated with solvent diffusion can be written as

$$\frac{d\Sigma}{dt}=-\int_{V_0}J_K\frac{\partial\mu}{\partial X_K}dV \tag{2}$$

where J_K is the nominal flux of solvent and μ is the chemical potential.

Define the total energy of the system as: $\Psi=\Pi+\Sigma$. By this definition, the total energy is conserved throughout the transient stage (without crack growth for the moment).

Next we derive the energy release rate for quasistatic crack growth in a hydrogel, where the inertial effect is negligible and the crack growth is slow in terms of the time scale of solvent diffusion. Growth of a crack in the hydrogel is accompanied by deformation of the polymer network and migration of the solvent molecules. As a result, the change of total potential energy includes a conservative part and a dissipative part. The driving force for crack growth is the release of the total energy Ψ, which is the conservative part of the potential energy. Following a standard procedure [7], we obtain the transient energy release rate in form of a modified J-integral as

$$J^*=\int_{S_1}\left(\hat{U}N_1-s_{iJ}N_J\frac{\partial x_i}{\partial X_1}\right)dS+\int_{V_0}\frac{\partial\mu}{\partial X_1}CdV \tag{3}$$

where $\hat{U}(\mathbf{F},\mu)=U(\mathbf{F},C)-\mu C$. It can be shown that, for a domain containing a crack tip, the modified J-integral is path-independent, whereas the standard J-integral is path-dependent for hydrogels.

For an accurate numerical calculation of the J-integral, it is advantageous to convert the surface integral to a volume integral by the domain integral method [9]. A specific material model [8] is employed for the hydrogels, and a nonlinear finite element method is developed to solve initial boundary value problems, similar to that in a previous study [10].

[a] Corresponding author. Email: nbouklas@utexas.edu.

RESULTS AND DISCUSSION

We consider a hydrogel specimen with a center crack (Fig. 1a), subject to remote tension by Mode I displacement controlled loading under generalized plane strain conditions. Different boundary conditions are used to simulate hydrogels either immersed in a solvent or not-immersed. By symmetry, only a quarter of the rectangular domain is modelled with a two-dimensional finite element mesh. A sharp crack model is used for the cases with infinitesimal to moderately large far-field strains, whereas a rounded notch model is used for the cases with large far-field strains.

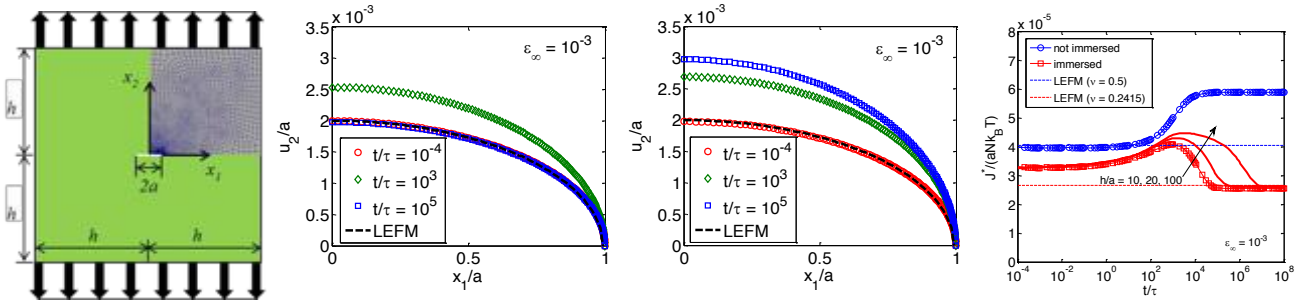

Figure 1. (a) Schematic of a hydrogel specimen with a center crack. (b, c) Temporal evolution of crack opening profiles for immersed and not-immersed hydrogel specimens subject to a small remote strain ($\varepsilon_\infty = 0.001$). (d) J^* as a function of time.

Subject to a small far field strain, the stress field around the crack tip can be compared to linear elastic fracture mechanics (LEFM). The numerical results confirmed the square root stress singularity ($\sim r^{1/2}$) near the crack tip for a small far-field strain ($\varepsilon_\infty = 0.001$). The crack opening displacements are shown in Fig. 1. The instantaneous opening profiles for both cases agree closely with LEFM. For the immersed case (Fig. 1b), the crack first opens up and then gradually closes in. For the not-immersed case (Fig. 1c), the crack opens up continuously and attains an equilibrium profile different from the LEFM prediction. Figure 1d shows the evolution of J^*. While the J-integral increases monotonically with time for the not-immersed specimen, it increases and then decreases for the immersed case. This behaviour is similar to crack opening. In addition, the effect of the specimen size is shown for the immersed case, where the peak J^* increases with increasing specimen size. After a long time, the J-integral saturates at an equilibrium value, which is lower than the instantaneous limit for the immersed specimen but higher for the not-immersed specimen. The monotonic increase of J^* for the not-immersed case could lead to delayed fracture of gels as observed in experiments [5].

Under a relatively large far-field strain ($\varepsilon_\infty = 0.5$), the stress field near the crack tip is no longer square-root singular. The instantaneous response is similar to that of a hyperelastic material, for which a stronger singularity ($\sim r^{1}$) has been predicted previously [11]. The numerical result at a very short time shows a transition from the square-root singularity to the stronger singularity. Furthermore, another transition is revealed at a smaller distance, where the stress singularity becomes much weaker. This may be explained as a result of solvent diffusion [7]. Therefore, the stress distribution near the crack tip under a relatively large far-field strain is influenced by both hyperelasticity and solvent diffusion in the hydrogel specimen. The evolution of the modified J-integral is qualitatively similar to the small strain behavior, but the calculated J^* is considerably lower than the LEFM prediction for both the immersed and not-immersed specimens.

CONCLUSIONS

A modified J-integral is derived for calculating the transient energy release rate for crack growth in hydrogels. Numerical simulations show that the transient energy release rate is a function of time for hydrogel specimens due to solvent diffusion. It is found that the stress singularity near the crack tip depends on both the far-field strain and the local solvent diffusion. Ongoing work of this study includes development of a methodology for the experimental evaluation of the critical energy release rate. Further study is also underway to consider steady state crack growth in hydrogels.

References

[1] Forte, A.E., D'Amico, F., Charalambides, M.N., Dini, D., Williams, J.G., Food Hydrocolloids **46**, 180-190 (2015).
[2] Simha, N. K., Carlson, C. S., Lewis, J. L., Journal of Materials Science: Materials in Medicine **14**, 631–639 (2003).
[3] Sun, J.-Y., Zhao, X., Illeperuma, W. R. K., Chaudhuri, O., Oh, K. H., Mooney, D. J., Vlassak, J. J., Suo, Z., Nature **489**, 133-136 (2012).
[4] Hui, C. Y., Long, R., Ning, J., Journal of Applied Mechanics **80**, 021014 (2013).
[5] Wang, X., Hong, W., Soft Matter **8**, 8171-8178 (2012).
[6] Zhang, J., An, Y., Yazzie, K., Chawla, N., Jiang, H., Soft Matter **8**, 8107-8112 (2012).
[7] Bouklas, N., Landis, C.M., Huang, R., Journal of Applied Mechanics **82**, 081007 (2015).
[8] Hong, W., Zhao, X., Zhou, J., Suo, Z., Journal of the Mechanics and Physics of Solids **56**, 1779-1793 (2008).
[9] Li, F. Z., Shih, C. F., Needleman, A., Engineering Fracture Mechanics **21**, 405-421 (1985).
[10] Bouklas, N., Landis, C.M., Huang, R., Journal of the Mechanics and Physics of Solids **79**, 21-43 (2015).
[11] Bouchbinder, E., Livne, A., Fineberg, J., Journal of the Mechanics and Physics of Solids **57**, 1568–1577 (2009).

HYDRAULIC FRACTURE IN POROUS MEDIA

Tao Wang, Zhanli Liu[a] & Zhuo Zhuang
Applied Mechanics Lab., School of Aerospace Engineering, Tsinghua University, Beijing, China

Summary Hydraulic fracture in porous media which involves fluid flow/diffusion and solid deformation is a complex multi-physic process frequently observed in the nature world and engineering application. In this paper the coupled extended finite element method (CXFEM) is developed to study the hydraulic fracture in permeable rocks. In CXFEM, the fluid flow in the fracture and interstitial flow in the medium are solved in a unified framework by assuming that the fracture is a special type of porous media and introducing Poiseuille-type fluid flow inside the fracture. The biggest advantage of this computational model is that it is very convenient to deal with the fluid flow inside the complex fracture network. The dynamic effect and the influence of the permeability on the hydraulic driven fracture problems are studied.

INTRODUCTION

The hydraulic driven fractures in porous media needs consider (i) the mechanical behaviors of the solid skeleton, fluid bulk phases and their interaction; (ii) the fracture propagation on arbitrary paths; (iii) the extra fluid flow in the developed fractures. The fluid flow in a deforming porous medium was first studied by Terzaghi [1] for one-dimensional consolidation problems, which is called Terzaghi one-dimensional consolidation theory, and extended to a three-dimensional consolidation theory that includes Darcy's law of fluid transport by M.A. Biot [2]. Since these pioneering works, it has attracted many researchers' interests due to its abundant practical applications. The fundamentals and applications of the mechanics of porous medium have been illustrated by many researchers. The Darcy-Biot approach to porous media may be deemed to an extension of the standard materials, especially for soils and rocks, attributed to H. Ziegler et.al [3] and M.A. Biot el.al, to the coupled problems of fluid transport in deforming solids.

In this work, the fluid flow in the fracture and interstitial flow in the medium are solved in a unified framework by assuming that the fracture is a special type of porous media and introducing Poiseuille-type fluid flow inside the fracture. The biggest advantage of this computational hydraulic fracture model is that it is very convenient to deal with the fluid flow inside the complex fracture network and the porous matrix. Based on this idea, a fully coupled hydraulic fracture problem is solved by coupling the traditional extend finite element method and the Biot theory of the porous medium..

COMPUTATIONAL HYDRAULIC FRACTURE MODEL

Hydraulic fracture in porous media is a strong coupled problem between the deformation of solid and the fluid flow. The interaction between solid and fluid contains the following several aspects: (i) the pore pressure in the medium can cause the expansion or contraction of solid; (ii) the fluid in the fracture can open or propagate the fracture; (iii) the deformation of solid can affect the interstitial flow in the medium; (iv) the fracture opening can affect the fluid flow in the fracture. In order to solve this strong coupled problem, some basic assumptions are introduced: (i) the media is permeable, elastic and brittle, which is governed by the Biot constitutive relation and characterized by fracture toughness, Young's modulus, Poisson's ratio, Biot constant and undrained poisson's ratio; (ii) the driving fluid is incompressible and has a constant dynamic viscosity; (iii) the fracture is a special type of porous media and the fluid flow inside the fracture obeys Poiseuille-type flow; (iv) the fluid transport in the interstitial space can be described by the well-known Darcy's law; (v) gravity is neglected in the fluid transport equation.

The coupled hydraulic fracture model proposed in this paper is the combination of extend finite element method with Biot constitutive relation and the interstitial flow in the porous medium (including the fracture), as shown in Fig. 1.

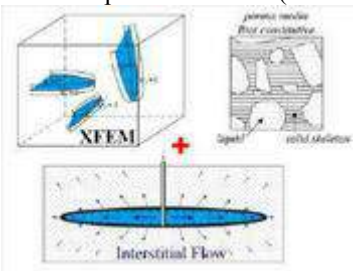

Fig. 1 Schematic of the hydraulic fracture in porous media

PERMEABILITY EFFECT ON THE HYDRAULIC FRACTURE

[a] Corresponding author. Email: liuzhanli@tsinghua.edu.cn.

Consider a square domain which is shown in Fig. 2 with a = 8 m. The domain has a notch of length a in its center [4]. A constant fluid volume flux $Q_0 = 4\times10^{-4} m^3/s$ is injected into the fracture. The deformation at all sides is fixed, and the sides are assumed to be permeable, i.e. p = 0 Pa.

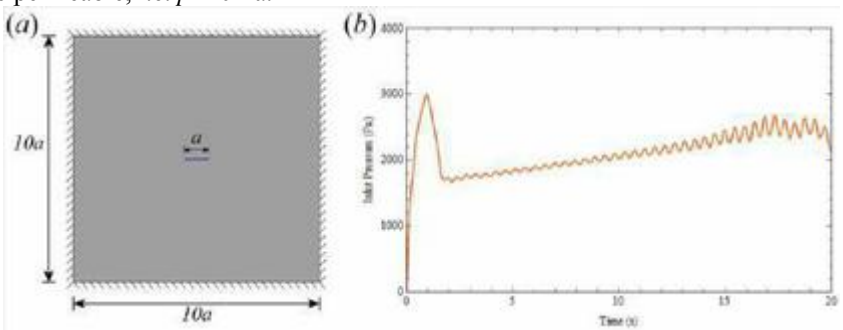

Fig. 2 Hydraulically induced fracture driven by fluid volume injection. (a) All sides are mechanically constrained and are assumed to be permeable (p = 0 Pa). (b) Inlet fluid pressure p in the fracture over the total injected time

Next, let us consider the effect of the permeability of the medium on the hydraulic fracture process. Fig. 3 shows the fracture surface and the contour of pore pressure under different medium permeability at time t = 5s. We can find that if the permeability is large enough, the fracture will not propagate under a given injection rate, as shown in Fig. 3(a). If the permeability is small enough, the fluid is almost inside the fracture, as shown in Fig. 3(d). Furthermore, if the permeability is appropriate, the fracture will propagate for some time, and then may arrest when the fluid leak-off rate is equal to the injection rate as the infiltrating area becomes larger.

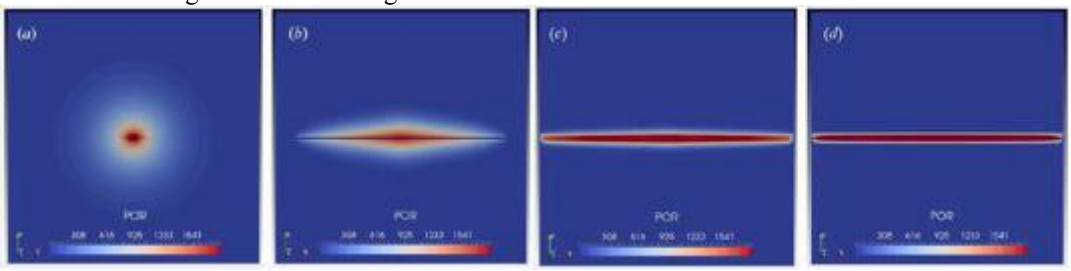

Fig. 3 Hydraulically induced fracture driven by fluid volume injection under different medium permeability at time t=5s: (a)-(d), the permeability of the medium is [2.0e5, 2.0e4, 2.0e3, 0.2]md

CONCLUSIONS

In this paper the coupled extended finite element method (CXFEM) is developed to study the hydraulic fracture in permeable rocks. In CXFEM, the fluid flow in the fracture and interstitial flow in the medium are solved in a unified framework by assuming that the fracture is a special type of porous media and introducing Poiseuille-type fluid flow inside the fracture. The influence of the permeability on the hydraulic driven fracture problems are studied.

References

[1] Terzaghi K.: Erdbaumechanik auf bodenphysikalischer Grundlage, 1925.

[2] Biot M.A.: General Theory of Three‐Dimensional Consolidation. Journal of Applied Physics. 12:155-164, 1941.

[3] Ziegler H.: Some extremum principles in irreversible thermodynamics, with application to continuum mechanics. Swiss Federal Institute of Technology, 1962

[4] Miehe C., Mauthe S., Teichtmeister S.: Minimization principles for the coupled problem of Darcy–Biot-type fluid transport in porous media linked to phase field modeling of fracture. Journal of the Mechanics and Physics of Solids 82:186-217, 2015.

OVERCOMING BRITTLENESS THROUGH BIO-INSPIRATION AND MICROARCHITECTURE

Francois Barthelat [a)]
Department of Mechanical Engineering, McGill University, Montreal, Quebec, Canada

Summary: Architectured materials contain specific structural features which are larger than what is typically considered microstructure but smaller than the size of the component. More specifically dense architectured materials are made of stiff blocks which can slide, rotate, separate or interlock collectively, provide a wealth of tunable mechanisms mediated by the interfaces between the blocks. This strategy is also observed in hard biological materials such as bone, teeth or mollusk shells, which now serve as models for new materials with superior properties. To explore these concepts in synthetic materials we used a three-dimensional laser-engraver to carve arrays of microcracks with well-defined geometries and toughness within the bulk of glass. This bio-inspired glass not only shows how the powerful toughening mechanisms observed in nature can be harnessed in synthetic materials, but it also shows a pathways to making bio-inspired composite materials by "fabricating" weak interfaces within stiff materials.

OVERVIEW

Ever increasing requirements for structural performance are driving the research and the development of stronger, tougher and lighter materials. Specific microstructures, heterogeneities or hybrid compositions are now used in modern materials to generate high performance structures [1]. The structural performance of hybrid materials (stiffness, strength, toughness) is governed by their mechanics of deformation and failure, which in turn is largely governed by their microstructure. Optimized performance can therefore be attained with tight control over the size, topology, arrangement of the microstructure, an idea which can be exploited to the extreme in architectured materials. To introduce and define "Architecture" in materials [2] it is useful to consider Fig. 1, which shows different levels of structural elements with their characteristic length scales (i.e. the size of their main geometrical features) and the degree of control and geometrical fidelity that current fabrication techniques provide. "Architectural" features bridge component and microstructure and have an intermediate length scale, which allows a very high control over the morphology and a high dimensional fidelity. Interestingly, structures and mechanisms at intermediate length scales are prevalent in biological materials, and in particular in high-performance structural materials such as bone, mollusc shells or wood [3].

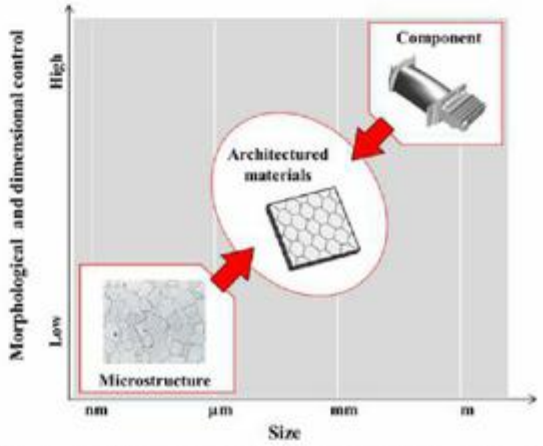

Fig. 1: Architectured materials bridge the length scales of microstructures to the larger length scales at the component size. At these intermediate length scales the morphological control is high.

THE MECHANICS OF DENSE ARCHITECTURED MATERIALS

The examination of engineered and natural architectured materials reveals common characteristics in terms of structure, mechanics and performance. In dense architectured materials, the building blocks are made of stiff and hard materials: rigid polymers, metals, engineering ceramics or biominerals. The deformation of individual blocks remains small and within the limits of linear elasticity, even in the case of large deformations and extreme loadings. The shape and arrangements of the building blocks vary from simple multilayered to layered-segmented to more complex three-dimensional arrangements. Fig. 2a shows a

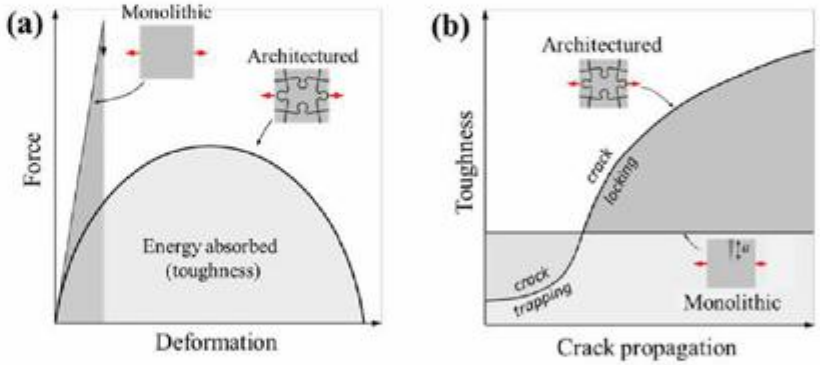

Fig. 2: Key concepts in architectured materials: (a) Deformation: Interfaces in architectured materials profoundly change the way inherently brittle material deform. In particular, large deformations and energy absorption become possible; (b) Fracture: cracks are trapped onto weaker interfaces where they are channeled into toughening configurations, resulting in a rising crack resistance curve

[a)] Corresponding author. Email: francois.barthelat@mcgill.ca

generic force-deformation curve for a brittle monolithic material and for an architectured material based on the same constituent. In architectured materials individual blocks do not deform significantly. Instead, large deformations are generated by the collective motion of the blocks relative to each other, in a fashion similar to grain boundary sliding in polycrystalline metals. The mechanical response is therefore largely governed by the structure, composition and mechanics of the interfaces. Architectured materials can also give rise to powerful toughening mechanisms, and a critical requirement to trigger these mechanisms is that the crack must follow the interfaces instead of propagating through the building blocks. Once the cracks are "trapped" into the weaker interfaces, they can trigger a second line of toughening mechanisms which can involve crack deflection, interlocking, friction, pullout or a combination of the above. As the crack progresses along the interfaces, the architecture of the material therefore forces the cracks into configuration where further propagation is more difficult. As a result, the overall toughness of the materials can rise to levels which can be significantly greater than the monolithic materials (Fig. 2b).

EXAMPLES OF BIOINSPIRED, ARCHITECTURED MATERIALS

To explore the concepts of architecture and weak interfaces in synthetic materials we used a three-dimensional laser-engraver to carve arrays of microcracks with well-defined geometries and toughness within the bulk of borosilicate glass slides. The microcracks, positioned along specific surfaces within the material, coalesce upon application of an external load and guide large cracks following the concept of "stamp holes". Using this approach we engraved curved interfaces with re-entrant features ahead of an incident crack in glass, defining jigsaw-like building blocks (Fig. 3a) [4]. After initial crack propagation along the weak interface, the jigsaw features produced a tremendous amount of toughness by pullout and interlocking, dissipating energy by friction. This powerful nonlinear failure mechanism, inspired by natural nacre, amplified the toughness of glass 100 times. Infiltrating the interfaces with polyurethane generated additional toughening mechanisms by ligament bridging, similar to the mechanics of proteins in hard biological materials [5]. This additional step led to a material made of about 95% of glass but 200 times tougher, as stiff as plain glass but displaying non-linear deformations and failing at strains in excess of 3%. Another bio-inspired architectured materials we fabricated and tested is a laminated glass augmented with nacre-like laser engraving in each of the glass layer (Fig. 3b) [6]. Specific arrangements of the patterns across layers generates a nacre-like staggered arrangement of glass tablets bonded by a soft adhesive. This bio-inspired architecture profoundly changed the mechanisms of deformation and failure of the material. Architecture in materials therefore offers a powerful pathway to tailoring mechanical behaviour and to combine mutually exclusive properties. Nature is far ahead of engineers in this respect, and therefore materials like bone, nacre or wood can continue to inspire new designs for high-performance structural materials in years to come.

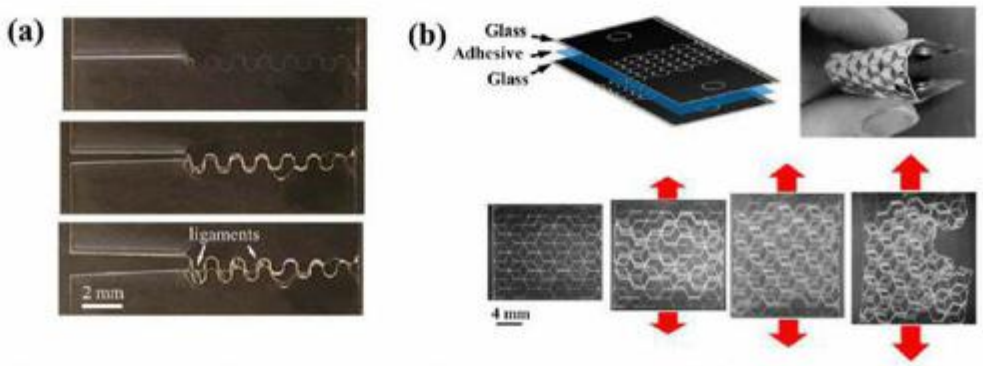

Fig. 3: (a) A bio-inspired laser engraved glass. Jigsaw –like sutures generate frictional pullout and toughening. The interfaces are infiltrated with polyurethane, providing an additional source of toughness. (b) A nacre-like glass-PDMS composite. The material can be bent; it shows large deformation and progressive failure

References

[1] Ashby MF. Hybrids to fill holes in material property space. Philosophical Magazine 2005;85:3235-57.
[2] Bouaziz O, Brechet Y, Embury JD. Heterogeneous and architectured materials: A possible strategy for design of structural materials. Adv Eng Mater 2008;10:24-36.
[3] Barthelat F. Architectured materials in engineering and biology: fabrication, structure, mechanics and performance. International Materials Reviews 2015;to appear.
[4] Mirkhalaf M, Dastjerdi AK, Barthelat F. Overcoming the brittleness of glass through bio-inspiration and micro-architecture. Nature Communications 2014;5.
[5] Barthelat F, Yin Z, Buehler MJ. Structure and mechanics of interfaces in biological materials. Nature Reviews Materials 2016;in press.
[6] Chintapalli RK, Breton S, Dastjerdi AK, Barthelat F. Strain rate hardening: A hidden but critical mechanism for biological composites? Acta Biomaterialia 2014;10:5064-73.

FRACTURE AND INDENTATION IN SINGLE METAL CRYSTALS

Jeffrey W. Kysar *[1]

[1]*Department of Mechanical Engineering, Columbia University, New York City, New York, USA*

Summary Cracks in elastic-plastic single crystals offer an opportunity to develop a fundamental understanding of plasticity under the extreme conditions of high plastic strain and plastic strain gradients. The asymptotic deformation fields near a crack tip in an elastic-plastic single crystal adopt an angular sector structure centered at the tip that are strikingly different for stationary and quasistatically growing cracks. Herein we extend Prandtl's analogy between a flat punch and a stationary crack to an angled indenter and quasistatically moving crack. Specifically, the angled indenter impinging into a material can be modeled asymptotically as a quasistatically closing crack. We present analytical asymptotic solutions to this boundary value problem and demonstrate that they are consistent with the predicted deformation state associated with the overall indentation deformation fields. Finally, we show that the predicted deformation state is consistent with experimental results of lattice rotation fields and associated densities of geometrically necessary dislocations.

INTRODUCTION

In one of the earliest studies of fracture mechanics in plastically deforming materials, Prandtl [1] employed plane strain slip-line theory and an analogy between a stationary crack and a flat punch impinging into a surface to predict the deformation state near a crack tip within a rigid-ideally plastic isotropic material. This type of analysis predicts that the stress and deformation fields near a stationary crack tip exhibit a "centered-fan" type of field whereby one family of slip lines consists of straight lines emanating radially from the crack tip (or analogously from the corner of the punch) and the other family of slip lines necessarily consists of concentric circular arcs. The analysis of the asymptotic fields of a quasistatically growing crack, however, is complicated by the necessary presence (i.e. [2]) of an elastic unloading angular sector centered at the crack tip. In order to account for the unloading sector, Rice [3] extended the theory of conventional isotropic slip line theory for a rigid-ideally plastic material to an elastic-ideally plastic isotropic material, which Drugan et al. [4] employed to derive the asymptotic fields for a quasistatically growing plane strain crack under pure Mode I conditions.

Rice [5] as well as Booker & Davis [6] extended isotropic rigid-ideally plastic slip line theory to account for rigid-ideally plastic materials with arbitrary anisotropy under plane strain conditions. Rice [5] applied this theory to derive the slip line fields beneath a flat punch impinging into a material with a polygonal yield surface such as that associated with a single crystal NaCl-type ionic crystal. Just as for isotropic materials, the asymptotic fields consist of angular sectors for which slip lines extend radially from the stationary singular point (i.e. the punch corner or analogously the crack tip). However it is important to note that in single crystals the slip lines correspond to physical slip systems. Thus there is a finite number of slip lines that intersect the singular point, each of which coincides with either a unit vector in the direction of plastic slip or a unit normal vector to the slip plane. These radial slip lines serve as the boundaries between the angular sectors and correspond in stress space to the edges of the polygonal yield surface. The stress state within a plastically deforming angular sector is at a vertex of the polygonal yield surface. Hence, in general two plastic slip systems are activated within each angular sector. In going from one angular sector to another, the stress state must traverse an edge of the polygon thus introducing a stress discontinuity across sector boundaries. Rice [7] noted that asymptotic fields associated with a stationary crack tip are the identical—except for sign—to those of the flat punch in the same anisotropic rigid-ideally plastic material.

In order to analyze quasistatically growing cracks in single crystals, Rice [7] extended anisotropic rigid-ideally plastic slip line theory to account for an elastic-ideally plastic anisotropic material necessary to include elastically-unloading angular sectors in the asymptotic solution. Rice [7] demonstrated that the asymptotic deformation fields of a quasistatically moving crack tip consists of a combination of plastically-deforming angular sectors and elastically unloading angular sectors. Importantly, for quasistatically propagating cracks an angular sector boundary corresponds physically to a ray of plastic deformation emanating from the crack tip. Furthermore, the stress state varies smoothly across a sector boundary, but it does admit a velocity discontinuity in a radial direction. Rice [7] employed the general framework to derive the elastic-plastic asymptotic fields for quasistatically growing Mode I cracks in specially oriented face-centered cubic (fcc) and body-centered cubic (bcc) elastic plastic metals.

Shield & Kim [8] examined the deformation fields near the tip of a crack in an iron-silicon single crystal and Kysar & Briant [9] measured the lattice rotation fields near the crack tip of an aluminum bicrystal. Their experiments confirmed the existence of many of the key predictions by Rice [7] regarding the structure of the deformation fields. However no experiments to date have investigated directly the asymptotic fields associated with a growing crack tip in a single crystal.

*Email: jk2079@columbia.edu

INDENTATION EXPERIMENTS AS AN ANALOG TO QUASISTATIC FRACTURE EXPERIMENTS

The Prandtl [1] analogy relates the boundary value problems of a stationary crack to a flat punch. This analogy breaks down for angular indenters (such as a wedge indenter under plane strain conditions) because the singular point where the indenter first comes into contact with the surface moves quasistatically along the surface as the indenter impinges further into the material. Thus Prandtl's analogy can be extended to relate the boundary value problems of a quasistatically *closing* crack with that of an angled indenter. Herein we focus on this extended analogy to treat the problem of quasistatic crack growth in a single crystal from both an analytical as well as experimental perspective.

DISCUSSION

We discuss the analytical solutions for the asymptotic deformation fields near the singular point of a wedge indenter impinging into specially oriented single fcc and bcc crystals under plane strain deformation conditions. We demonstrate [10] that the solution consists solely of angular sectors separated by rays of plastic deformation for the case of a nearly flat wedge for which lattice rotation can be neglected. Furthermore, we demonstrate [11] that the asymptotic deformation field near the singular point dictates the form of the deformation field throughout the overall deformation field under the wedge indenter, and that the overall structure of the deformation field is maintained even when the indenter induces large lattice rotations.

We present detailed experimental measurements using the methodology in [12] that characterize the deformation fields under a wedge indenter in a nickel single crystal. The lattice rotation accompanying the elastic-plastic deformation is measured using High-Resolution Electron Backscatter Diffraction (HR-EBSD) from which we infer a multiple length scale description of the spatially-resolved Geometrically Necessary Dislocation (GND) density—fully characterizing both the edge and screw components of the GND density on individual slip systems. We demonstrate that the aforementioned predictions of the asymptotic singular and overall indentation deformation fields are consistent with the experimental measurements.

CONCLUSIONS

We investigated indirectly the asymptotic deformation fields of a quasistatically growing crack in an elastic-plastic single crystal by focusing on the analogous fields in the material under a wedge indenter. The experimental results demonstrate unambiguously that elastically deforming regions separated by instantaneously plastically deforming rays sweep through the crystal in a geometrically similar manner. Analytical predictions of the deformation state based upon a slip line theory for elastic-ideally plastic anisotropic single crystals undergoing plane strain deformation are consistent with the experimental measurements. Furthermore we demonstrate that some of the features of the measured deformation fields are sensitive to the plastic work hardening rate, and that the experiments provide a sensitive means of experimentally validating single crystal elastic-plastic constitutive relationships.

References

[1] Prandtl, L., Über die härte plastischer körper, Nachtrichten von de Gesellschaft der Wissenschaften zu Göttingen, Mathematisch-Physikalische Klasse, 1920, pp. 74–85.

[2] Rice, J. R., W. J. Drugan and T. L. Sham, "Elastic-Plastic Analysis of Growing Cracks", in Fracture Mechanics: Twelfth Conference (ed. P. C. Paris), Special Technical Publication 700, ASTM, Philadelphia, 1980, pp. 189–221.

[3] Rice, J. R., "Elastic-Plastic Crack Growth", in Mechanics of Solids: The Rodney Hill 60th Anniversary Volume (ed. H.G. Hopkins and M.J. Sewell), Pergamon Press, Oxford and New York, 1982, pp. 539–562.

[4] Drugan, W. J., J. R. Rice and T.-L. Sham, "Asymptotic Analysis of Growing Plane Strain Tensile Cracks in Elastic-Ideally Plastic Solids", Journal of the Mechanics and Physics of Solids, 30, 1982, pp. 447–473; erratum, 31, 1983, p. 191.

[5] Rice, J. R., "Plane Strain Slip Line Theory for Anisotropic Rigid/Plastic Materials", Journal of the Mechanics and Physics of Solids, 21, 1973, pp. 63–74.

[6] Booker, J.R and Davis, E.H., "A General Treatment of Plastic Anisotropy under Conditions of Plane Strain", Journal of the Mechanics and Physics of Solids, 20, 1972, pp. 239–250.

[7] Rice, J. R., "Tensile Crack Tip Fields in Elastic-Ideally Plastic Crystals", Mechanics of Materials, 6, 1987, pp. 317-335.

[8] Shield T. W. and K.-S. Kim, "Experimental measurement of the near-tip strain field in an iron-silicon single-crystal", Journal of the Mechanics and Physics of Solids, 42, 1994, pp. 845–873.

[9] Kysar, J. W. and C. L. Briant, "Crack Tip Deformation Fields in Ductile Single Crystals" Acta Materialia, 50, 2002, pp. 2367–2380.

[10] Saito, Y. and J. W. Kysar, "Wedge Indentation into Elastic?Plastic Single Crystals, 1: Asymptotic Fields for Nearly-Flat Wedge", International Journal of Plasticity, 27, 2011, pp. 1640-1657.

[11] Saito, Y., M. S. Öztop, and J. W. Kysar, "Wedge Indentation into Elastic?Plastic Single Crystals, 2: Simulations for Face-Centered Cubic Crystals", International Journal of Plasticity, 28, 2012, pp. 70–87.

[12] Kysar, J. W. , Y. Saito, M. S. Öztop, D. Lee, and W. T. Huh. "Experimental lower bounds on geometrically necessary dislocation density", International Journal of Plasticity, 26, 2010, pp. 1097–1123.

DUCTILE FRACTURE OF CONTROLLED MICROSTRUCTURES

Ankit Srivastava[1], Shmulik Osovski[2], and Alan Needleman *[1]
[1]*Department of Materials Science & Engineering, Texas A & M University, College Station, TX, USA*
[2]*Faculty of Mechanical Engineering, Technion - Israel Institute of Technology, Haifa, Israel*

Summary The aim of this work is to develop a framework to engineer crack paths by controlling the distribution of second phase particles in a manner so as to increase the materials ductile crack growth resistance. We carry out analyses of ductile crack growth with voids nucleating from discretely modeled particles so as to introduce a characteristic length. Crack growth resistance curves and fracture surface roughness measures are computed for various distributions. The results indicate that by suitably designing the particle distribution, a material's ductile crack growth resistance can be significantly increased.

BACKGROUND

Ductile fracture limits the performance, safety, reliability and manufacturability of a variety of engineering components and structures; for example, the crash worthiness of automobiles, the integrity of pipelines, the blast resistance of ships and airplane cargo holds, and the manufacturability of sheet metal components. The mechanism of ductile fracture in engineering metals and alloys involves the nucleation, growth and coalescence of micron scale voids. An engineering possibility that stems from quantifying the relation between a microstructural effects on porosity evolution and ductile crack growth resistance is the use of this knowledge to design more fracture resistant materials. Furthermore, these same microstructural effects manifest themselves in the fracture surface roughness, which suggests that there is the possibility of a direct relation between fracture surface roughness and ductile crack growth resistance.

The microstructure of a variety of structural alloys, can be idealized as involving two size scales of void nucleating particles: larger particles that nucleate voids at relatively small strains and smaller particles that nucleate voids at larger strains. Microstructures with randomly distributed void nucleating particles (as in ferrous and aluminum alloys) has been modeled in a variety of 2D and 3D ductile fracture analyses. In particular, in recent work, [1, 2], ductile crack growth in this type of microstructure was computed to a sufficient extent and detail to characterize the crack growth resistance in terms of both J_{Ic} (a measure of crack initiation toughness) and T_R (the tearing modulus) as well as to quantify the fracture surface roughness statistics. The theoretical framework used in [1, 2] was based on the modified Gurson constitutive framework for progressively cavitating ductile solids generally referred to as the GTN relation. Predicting fracture requires a theory that incorporates a length scale and a Gurson-type constitutive relation incorporated does not contain a length scale. However, discretely modeling the microstructure as in [1, 2] introduces a length scale.

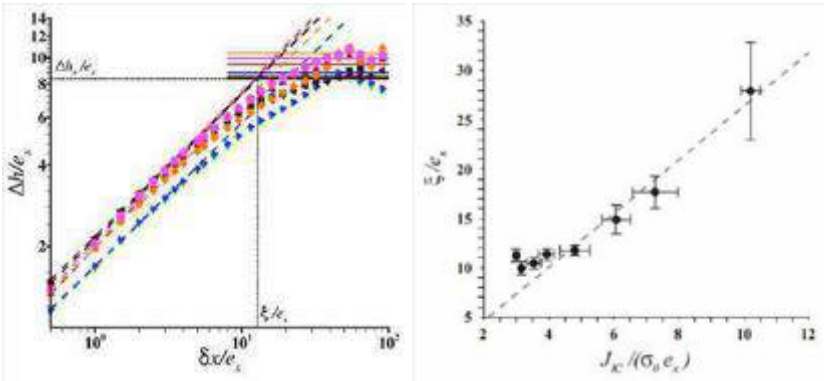

(a) (b)

Figure 1: (a) Height-height correlation functions of the fracture surface roughness for seven realizations with particle volume fraction of 2.4%. (b) Variation of J_{Ic} with the cut-off length ξ for particle volume fraction varying from 1.2% - 19%. From [1].

Advances in the description of complex scale invariant geometries have made quantitative statistical fractography possible. The hope since than has been to relate the roughness of fracture surfaces via the exponents characterizing their scale invariance properties to the materials crack growth resistance. However, it has been suggested that the value of the roughness exponent

*Corresponding author. Email: needle.tamu@gmail.com

is not only independent of the materials crack growth resistance but also of the material considered, as long as the failure mechanism remains the same, e.g. [3, 4]. The fracture surfaces obtained in [1, 2] were analyzed using a similar procedure to that in [3, 4]. The statistics of the fracture surface roughness were calculated in the direction of crack growth. Fig. 1a shows log-log plots of the correlation function $\Delta h(\delta x)$ for seven realizations with a 2.4% volume fraction of discretely modeled particles. The Hurst exponent β was determined by fitting a straight line through the log-log plot of the correlation function in Fig. 1a. The average value of β for the computed fracture surfaces was found to be essentially universal and was in very good agreement with experimental results. Power law behavior was found to hold for nearly two orders of magnitude of size scale and then to break down for $\delta x = \xi$ with a saturation value of Δh_s. It was found that ξ serves a characteristic length that, in certain circumstances, can be quantitatively related to J_{Ic} as seen in Fig. 1b.

CURRENT WORK

The aim of our analyses is to isolate the key features of a distribution of void nucleating particles and to quantify the effects on the material's fracture surface roughness and crack growth resistance.

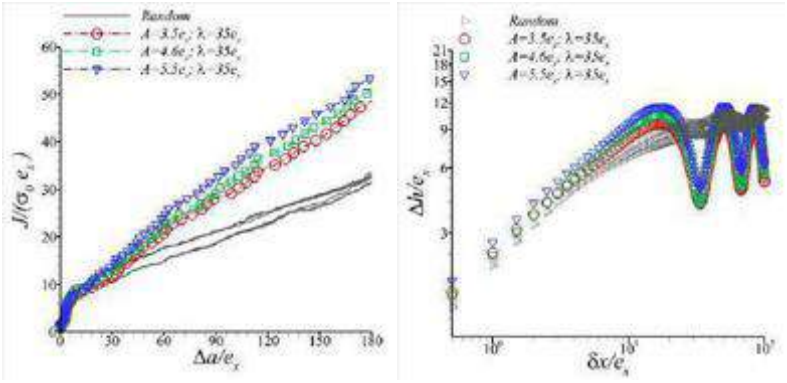

(a) (b)

Figure 2: (a) Comparison of curves of J versus Δa and (b) comparison of height-height correlation functions of the fracture surface roughness for random distribution of particles from [1] and sinusoidal distribution of particles with mean particle spacing $l_0 = 8.41e_x$.

The scaling of the crack growth resistance measures and fracture surface roughness measures in [1] suggests that for a random distribution of particles ξ is a characteristic length scale (of course with statistical variation). In order to clearly identify the key length scales and, in turn, key microstructural parameters calculations of ductile crack growth in microstructures with controlled distributions of particles are being carried out. Sinusoidal distributions (characterized by amplitude, A, and wavelength, λ) of particles are being analyzed. Initial calculations are for a mean particle spacing of $l_0 = 8.41e_x$ corresponding to $\approx 2.4\%$ volume fraction (e_x is a length unit). The values of A are chosen to be close to $\Delta h_s/2$ and λ is taken to be $\approx 2 \times \xi$. For a random distribution with $l_0 = 8.41e_x$ in [1], Δh_s was $\approx 9.2e_x$ and ξ was $\approx 17.5e_x$. The results for $l_0 = 8.41e_x$ together with the results of a random distribution of particles are shown in Fig. 2. As seen in Fig. 2a, the value of J at crack initiation is the same for the random and the controlled distributions, but the slope of the J versus Δa curve for the controlled distribution is much greater than the random distribution. As noted in [1], Δh_s and ξ can be related to the amplitude and the wave length of the larger zig-zag excursions of the crack path and by controlling these excursions (sinusoidal in this case), Fig. 2b, the crack growth resistance can increase significantly.

Our results indicate that by suitably designing the particle distribution one can significantly increase a material's crack growth resistance. Developments in material processing, in particular additive manufacturing, may make it possible to control such distributions in engineering materials.

References

[1] Srivastava A., Ponson L., Osovski S., Bouchaud E., Tvergaard V., Needleman A., 2014. Effect of inclusion density on ductile fracture toughness and roughness. J. Mech. Phys. Solids 63:62-79.

[2] Osovski S., Srivastava A., Ponson L., Bouchaud E., Tvergaard V., Ravi-Chandar K., Needleman A., 2015. The effect of loading rate on ductile fracture toughness and fracture surface roughness. J. Mech. Phys. Solids 76:20-46.

[3] Bonamy D., Bouchaud E., 2011. Failure of heterogeneous materials: a dynamic phase transition? Physics Reports, 498:1-44.

[4] Bouchaud E., 1997. Scaling properties of cracks. Journal of Physics: Condensed Matter, 9:4319-4344.

MICROMECHANICAL MODELING OF VOID COALESCENCE IN DUCTILE SOLIDS

Léo Morin[1], Mohammad Torki[2], Jean-Baptiste Leblond[1], and Amine Benzerga *[2]

[1]*Institut Jean Le Rond d'Alembert, Sorbonne Universités, UPMC Univ Paris 06, CNRS, UMR 7190, France*
[2]*Department of Aerospace Engineering, Texas A&M University, College Station, TX, USA*

Summary Recent extensions of an analytical micromechanics-based model for the coalescence of micron scale cavities in ductile materials are reported. For predominately tensile loading, two improved upper-bound models are obtained by considering alternative velocity fields in the limit analysis approach. For combined tension and shear loading, an extension of the original model employing a discontinuous velocity field is presented. Finally, a framework is laid out to develop macroscopic yield criteria for porous ductile solids accounting simultaneously for void growth and coalescence. Here again, solutions are obtained for axially symmetric tensile as well as non-axisymmetric loadings. In all cases, model predictions are compared with supposedly exact results obtained by an efficient method of finite-element based limit analysis.

INTRODUCTION

Benzerga and Leblond developed a closed-form solution to the problem of void coalescence in the form of an associated yield criterion [1]. Their limit analysis solution is valid for axisymmetric loadings and mimics the post localized response of an elementary cylindrical unit cell [2]. It also presents the first rigorous analytical solution to the problem initially posed by Thomason [3]. In doing so, the authors in [1] used kinematically admissible velocity fields that were discontinuous within the elementary volume, Fig. 1a. A void coalescence state is defined as one where the deformation of the unit cell has shifted to pure uniaxial extension due to the formation of rigid zones above and below the cavity. Such zones correspond to regions of elastic unloading in actual finite element (FE) cell calculations as in [2]. In the model developed by Benzerga and Leblond [1], the (tangential) discontinuity occurs precisely at the rigid-plastic interface.

Here, several extensions of the criterion in [1] are presented. In the first, see [4], attention is limited to tensile axisymmetric loadings. Two theoretical estimates of the limit load required for internal necking are obtained using two new sets of velocity fields. A family of generalized discontinuous fields is developed which considers the shape of the plastic/rigid interface as a parameter, Fig. 1b. A second family of continuous velocity fields is also used, Fig. 1c. The objective is to assess the improvements brought by these more refined velocity fields. In the second proposed extension, see [5], non-axisymmetric loadings are considered and a continuous shear velocity field is superposed onto that of Fig. 1a. The resulting criterion is also an elaboration of a recent model [6] where the microscopic velocity fields responsible for void expansion were not explicitly specified. Finally, a yield criterion is presented which unifies void growth and coalescence theories. Conventional void growth theory assumes that plastic flow is diffuse within the elementary cell. On the other hand, void coalescence theory assumes states of post-localized plasticity wherein flow is restricted to intervoid ligaments. The new theory accommodates both scenarios through some appropriate choice of velocity fields. Here again, solutions are obtained for both axially symmetric tensile loadings [7] and for non-axisymmetric loadings [8]. An important implication for actual evolution problems is a seamless transition from void growth to void coalescence. This is in contrast with previous "hybrid" approaches, e.g. [9], whereby abrupt transitions are associated with the presence of unavoidable corners in the effective yield surface.

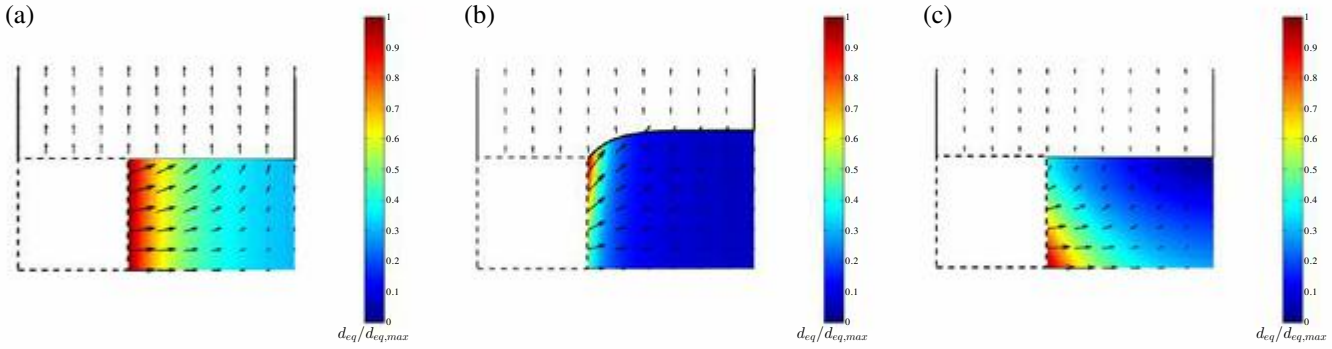

Figure 1: Trial velocity fields (arrows) and their associated equivalent strain rate (colors) (a) Benzerga and Leblond's [1], (b) generalized discontinuous [4], (c) continuous [4]. The non-axisymmetric model [5] as well as the unified models [7, 8] build on the field in (a).

*Corresponding author. Email: benzerga@tamu.edu

GENERAL FRAMEWORK

The elementary cell Ω used in the micromechanical analyses consists of a cylinder about the x_3 axis containing a coaxial cylindrical void of finite height. It is characterized by the void aspect ratio, W, the ligament parameter, χ, and the cell aspect ratio, λ. The matrix is modeled as rigid, ideally plastic obeying the associated von Mises criterion with yield stress $\bar{\sigma}$. The classical inequality of limit analysis reads:

$$\forall\, \mathbf{D}, \quad \mathbf{\Sigma} : \mathbf{D} \leq \Pi(\mathbf{D})\,, \qquad \Pi(\mathbf{D}) = \inf_{\mathbf{v}\in\mathcal{K}(\mathbf{D})} \langle \sup_{\boldsymbol{\sigma}^*\in\mathcal{C}} \sigma^*_{ij}\, d_{ij} \rangle_\Omega \tag{1}$$

where $\mathbf{\Sigma}$ and $\mathbf{D}$ are the macroscopic stress and rate of deformation tensors, defined as the volume averages of their microscopic counterparts $\boldsymbol{\sigma}$ and $\mathbf{d}$, and $\Pi(\mathbf{D})$ is the effective plastic dissipation, $\langle\cdot\rangle_\Omega$ stands for averaging over Ω, $\mathcal{C}$ is the microscopic reversibility domain, and $\mathcal{K}(\mathbf{D})$ is the set of kinematically admissible incompressible velocity fields. If the velocity field is discontinuous across the rigid-plastic interface S then a surface term must be added to $(1)_2$, see [5]. In that case, the effective yield criterion cannot be obtained using the usual parametric form by differentiation of $\Pi(\mathbf{D})$. Graphical solutions to inequality $(1)_1$ can then be used [5, 7]. Boundary conditions of the coalescence type mean $D_{11} = D_{22} = D_{12} = 0$. Trial velocity fields that satisfy these for use in $(1)_2$ are shown in Fig. 1 in the axisymmetric case.

RESULTS

Fig. 2a shows quasi-exact FE solutions to (1) for axisymmetric loadings without imposing the coalescence boundary conditions. The inclined flat parts correspond to coalescence and are well modeled using the criterion in [1] or variants thereof [4]. Fig. 2b shows the comparison of the coalescence model under combined tension and shear with FE results. Details may be found in [7] and [5], respectively.

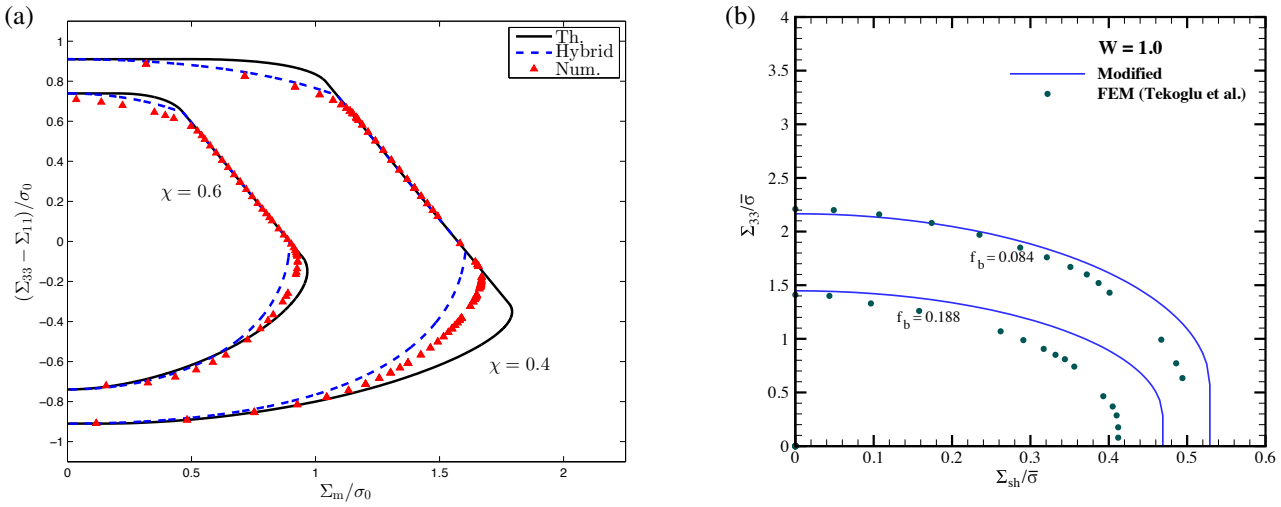

Figure 2: Effective yield loci under (a) axisymmetric loading for $W = 1$ and $\lambda = 1$ and two values of χ: unified model (solid), hybrid model (dashed) and FE results from [4] (points) after [7]; and (b) combined tension and shear loading for $W = 1$ and two values of $f_b \equiv \chi^2$: coalescence model (solid) and FE results from [6] (points) after [5]. Note $\sigma_0 = \bar{\sigma}$.

CONCLUSIONS

The availability of an anlytical solution to the problem of void coalescence by internal necking [1] has enabled several improvements. When supplemented with evolution equations for the microstructural variables, the results can be used in simulations of ductile fracture that are more physically based with fewer parameters than currently practiced.

AAB acknowledges NSF support under grants CMMI-1405226 and DMR-0844082.

References

[1] A. A. Benzerga and J.-B. Leblond. Effective Yield Criterion Accounting for Microvoid Coalescence. *J. Appl. Mech.*, 81:031009, 2014.

[2] J. Koplik and A. Needleman. Void growth and coalescence in porous plastic solids. *Int. J. Solids Struct.*, 24:835–853, 1988.

[3] P. F. Thomason. Three–dimensional models for the plastic limit–loads at incipient failure. *Acta Metall.*, 33:1079–1085, 1985.

[4] L. Morin, J.-B. Leblond, and A. A. Benzerga. Coalescence of voids by internal necking: theoretical estimates and numerical results. *J. Mech. Phys. Solids*, 75:140–158, 2015.

[5] M. E. Torki, A. A. Benzerga, and J.-B. Leblond. On Void Coalescence under Combined Tension and Shear. *J. Appl. Mech.*, 82(7):071005, 2015.

[6] C. Tekoglu, J.-B. Leblond, and T. Pardoen. A criterion for the onset of void coalescence under combined tension and shear. *J. Mech. Phys. Solids*, 60:1363–1381, 2012.

[7] L. Morin, J.-B. Leblond, A. A. Benzerga, and D. Kondo. A unified criterion for the growth and coalescence of microvoids. *J. Mech. Phys. Solids*, 2016.

[8] M. E. Torki, C. Tekoglu, A. A. Benzerga, and J.-B. Leblond. . *Int. J. Plast.*, 2016. In Preparation.

[9] A. A. Benzerga. Micromechanics of Coalescence in Ductile Fracture. *J. Mech. Phys. Solids*, 50:1331–1362, 2002.

On the transition from void collapse to void coalescence

Zhigang Liu[1], WeiHin Wong[1], Sridhar Narayanaswamy[1], and Tianfu Guo*[1]

[1]*Institute of High Performance Computing, A*STAR, Singapore*

Summary Void behavior of a ductile solid subjected to deformations with low or negative triaxiality (void collapse) is different from that with high triaxiality (void coalescence). We examine the critical strain-to-onset of void collapse and void coalescence via homogenization-based micromechanics analyses. Cells are subjected to a full range of the Lode parameter L and triaxiality T are obtained. Numerical results show that the loci are discontinuous functions of T, with the existences of transition zone separating loci of strain-to-onset of void collapse and that of void coalescence; within the zones neither of the two void behaviors is predicted at low triaxiality. Stress state dependence of void collapse and void coalescence are investigated and presented in the form of charts, analogous to phase diagrams; they illustrate and distinguish clearly, in the $T - L$ space, regions in which void collapse, void coalescence and neither of the two are possible.

MICROMECHANICS MODEL

Following the works of many researchers [1–7], A material body is subjected to three principal macroscopic stresses, characterized by the isotropically invariant stress triaxiality T and Lode parameter L. Preexisting voids are assumed to be present in the body and the process of void nucleation is not considered in this study. From statistical averaging, we assume that the voids are uniformly dispersed in the material, thereby allowing us to describe the microstructure using a periodic array of unit cells, each containing a centrallylocated spherical void of initial radius R_0. In this study, we confine the analysis to a planar layer of such cells. The cell has dimensions $2\ell \times 2\ell \times 2\ell$ and is subjected to macroscopic principal stresses on its deformed boundaries. A Cartesian coordinate system (X_1, X_2, X_3) is adopted in which the origin is located at the center of the void. The cell has an initial void volume fraction $f_0 = \pi {R_0}^3/6\ell^3$. The matrix material is taken to be voidfree, and its plastic response is characterized by a finite strain J_2 flow theory with isotropic hardening.

On the numerical aspects, the micromechanics and the numerical frameworks implemented in this work are analogous to those in Wong and Guo [8]. Boundary conditions of a cubic representative volume element (RVE) or unit cell are prescribed under proportional stressings such that the macroscopic stress ratios, $\phi_1 = \Sigma_1/\Sigma_3$ and $\phi_2 = \Sigma_2/\Sigma_3$ where Σ_1, Σ_2 and Σ_3 are the macroscopic principal stresses, remain constant throughout the loading history. Both ϕ_1 and ϕ_2 parametrize the isotropically invariant stress triaxiality T and the Lode parameter L. In order to uniquely define a stress state for any given T and L, a constraint of ordered macroscopic principal stresses is imposed such that$\Sigma_1 \geq \Sigma_2 \geq \Sigma_3$. Formulation and numerical implementation of proportional stressings are applied via a homogenization-based unimodular transformation matrix.

TRANSITION ZONE BETWEEN VOID COLLAPSE AND VOID COALESCENCE

We employ the energetics behind void coalescence and void collapse and present an energybased criteria for the determination of the onsets of these events. The motivation for examining void coalescence (and void collapse) from the energetics perspective stems from the phenomenological descriptions of coalescence mechanisms by Pardoen and Hutchinson [6], where the mechanisms have been described as the localization of plastic deformation between neighboring voids within a band, with material off this band undergoing elastic unloading. Using these criterion, we systematically examine the effects of stress triaxiality T, Lode parameter L, and the initial void volume fraction f_0 on these critical strains. We use E_e^* to denote collectively the critical strains E_e^v and E_e^c in the figures where applicable.

Fig. 1a plots the variation of critical macroscopic strain E_e^* over a range of T for $L = 0$ and $f_0 = 0.01$. In effect, the figure displays the loci of E_e^v and E_e^c in a single plot. The filled circles denote the critical macroscopic strains for onset of void collapse E_e^v, while the open circles for the onset of void coalescence E_e^c. For the range of T considered, E_e^* (specifically E_e^v) increases with increasing T for $0.33 \leq T \leq 0.43$, and E_e^* (specifically E_e^c) decreases with increasing T, for $0.52 \leq T \leq 2$. This display of non-monotonic dependence of E_e^* on T bears semblance to the straintofailure results of experimental works [1, 2]. However, a noticeable difference stands out between the current results and of those cited. While the latter results have reported the presence of cusps in the strain-to-failure responses of the different materials concerned, results in Fig. 1a have shown otherwise; the loci of E_e^v and E_e^c is not continuous and do not culminate to a cusp. Instead a finite "gap" exists in the region $0.43 < T < 0.52$ which separates the loci of E_e^v and E_e^c,as represented by the hatched area. We term this gap as "transition zone".

Focusing on the transition zones displayed by each level of L considered, it is apparent that the Lode parameter greatly influences the transition zones. In order to demonstrate this influence and gain insights to the stress state dependence of void

*Corresponding author. Email: guotf@ihpc.a-star.edu.sg (T.F. Guo)

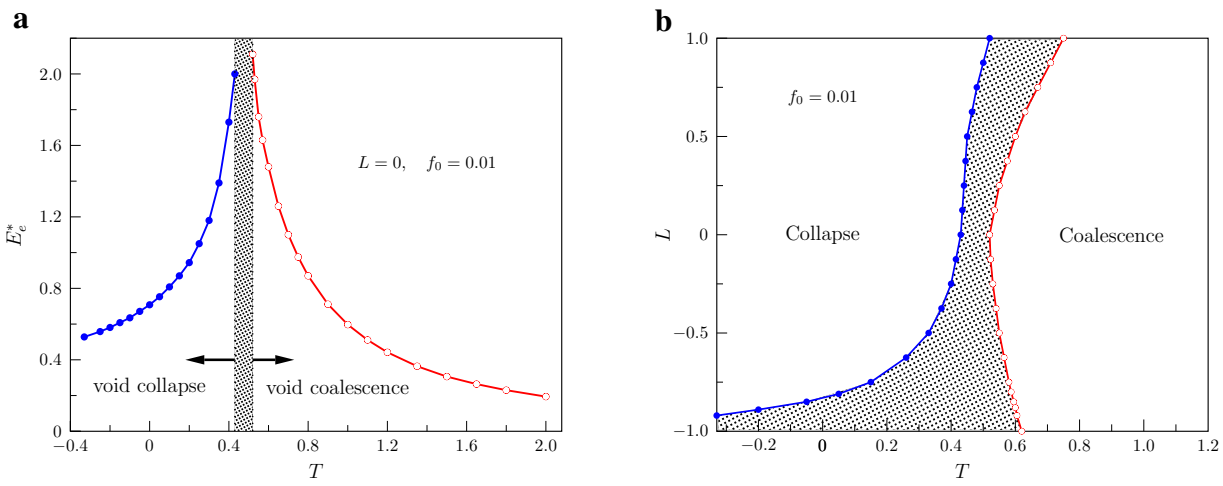

Fig.1 (a) Plot of critical macroscopic effective strain E_e^* versus stress triaxiality T for $L = 0$ and $f0 = 0.01$. Transition zone between void collapse and void coalescence is represented by the hatched region. (b) Stress state dependence of void collapse and void coalescence in $T - L$ space for $f_0 = 0.01$. The hatched region represents the transition zone for which neither void collapse nor void coalescence occurs.

collapse and void coalescence, we present Fig. 1b. It charts, in the $T-L$ space, the demarcated regions for which void collapse and void coalescence is possible for any given stress state described by the range of T and L considered. The hatched region clearly separates the two regions of void collapse and void coalescence, as shown demarcated by the blue and red boundaries respectively, and it represents the stress states for which neither void collapse nor void coalescence is present. Defining the span or width of the hatched region as the difference between the maximum and minimum values of T for which void collapse and void coalescence respectively are possible, one can see that it varies with L. The span is widest at $L = 1$, narrowing as L increases and at $L = 0$, at its narrowest. It widens again as L increases beyond zero. In short, for a dominant tensile state of stress ($L = 1$), void collapse is not anticipated. From Fig. 1b, it would appear then that if the span is zero, it is conceivable that a cusplike feature will emerge in the corresponding E_e^* versus T. This leads to the question of what may result in the narrowing of the span. It is well-known that, in addition to material properties, microstructural variations such as initial void size, initial void spacing etc, have significant effects on the macroscopic and voids response to loads [4]. For tractability and to keep within the scope of this paper, we have also examined the effects of initial void size on the transition zone in this work.

References

[1] Bao, Y., Wierzbicki, T., 2004. On the fracture locus in the equivalent strain and stress triaxiality space. Int. J. Mech. Sci. 46, 81–98.

[2] Barsoum, I., Faleskog, J., 2007. Rupture mechanisms in combined tension and shear–Experiments. Int. J. Solids Struct. 44, 1768–1786.

[3] Barsoum, I., Faleskog, J., 2007. Rupture mechanisms in combined tension and shear–Micromechanics. Int. J. Solids Struct. 44, 5481–5498.

[4] Benzerga, A. A., Leblond, J. B., 2010. Ductile fracture by void growth and coalescence. Adv. Appl. Mech. 44, 169–305.

[5] Koplik, J., Needleman, A., 1988. Void growth and coalescence in porous plastic solids. Int. J. Solids Struct. 24, 835–853.

[6] Pardoen, T., Hutchinson, J. W., 2000. An extended model for void growth and coalescence. J. Mech. Phys. Solids 48, 2467–2512.

[7] Tvergaard, V., 2009. Behaviour of voids in a shear field. Int. J. Fract. 158, 41–49.

[8] Wong, W. H., Guo, T. F., 2015. On the energetics of tensile and shear void coalescences. J. Mech. Phys. Solids, 82, 259–286.

CRACK TIP FLIPPING UNDER MODE I/III TEARING

Christian Lotz Felter *[1], Lasse Specht Jensen[2], and Kim Lau Nielsen[1]
[1]*Department of Mechanical Engineering, Solid Mechanics, Technical University of Denmark, DK-2800 Kgs. Lyngby, Denmark*
[2]*Mechanical Engineering Division, Burmeister & Wain Energy A/S, DK-2800 Kgs. Lyngby, Denmark*

Summary Crack tip flipping, where the fracture surface alternates from side to side in 45° shear bands, seems to be an overlooked propagation mode in Mode I sheet tearing often disregarded as "transitional" or tied to randomness in the material. In fact, such observations rarely make it to the literature. However, crack tip flipping is a true propagation mode, but unlike those already established: i) it never settles in a steady-state as the near tip stress/strain field continuously change, and ii) the mechanism governing failure evolves behind the leading crack tip. Recent research has revealed new insight into this intriguing behavior of a crack propagating by the void nucleation and growth mechanism, and the work presented compiles both published and unpublished experimental and numerical findings. E.g. in a recent attempt to gain control of the flipping crack a slight Mode III was imposed with interesting results.

INTRODUCTION

The fracture surface morphology that results from Mode I tearing of ductile thin sheet metals depends heavily on both the elastic-plastic material properties and the micro-structure. Low strength/low strain hardening metals typically display severe tunneling of the advancing crack, and favor a cup-cup (bath-tub like) propagation mode, whereas tearing of high strength sheet metals is governed by the shear band failure mechanism (slanting). However, most fracture surfaces display a mixture of morphologies. Slant crack propagation can be accompanied by large shear lips near the free sheet surface or a complete shear band switch – seemingly distributed randomly on the fracture surface (Rivalin et al., 2001; Simonsen and Törnqvist, 2004; Gruben et al., 2013). However, it has become clear that the occasionally observed shear band switch of Mode I slant cracks, in relation to ductile thin sheet tearing, is far from random as the crack can flip systematically from one side to the other in roughly 45 degree shear bands (El-Naaman and Nielsen, 2013). The "flipping" action of a slanted crack remains to be fully understood and the work presented serves to share details on the phenomenon – partly through unpublished experimental observations, and partly from detailed numerical modeling. Nielsen and Gundlach (2016) recently exploited X-ray tomography scanning to access the sheet interior and study the very tip of a slanted crack where a flip is underway. From their study it has become clear that the crack tip flipping initiates by the formation of shear-lips near the outer surface behind the leading tip.

What sets the formation of such shear-lips remains to be fully understood. However, it is obvious that once plastic flow localizes into a single shear band, and the crack propagates in a slanted manner, the symmetry of the system is lost. Thus, an asymmetry in the near tip stress/strain field arises, and a slight Mode III loading develops. It is this out-of-plane action which the authors believe to set of the crack tip flipping. *So why not deliberately induce a small Mode III loading to investigate its effect?* By doing so, one might even be able to provoke a flip! The present work focuses on ductile tearing in double edge notch tension specimens (DENTs), but with an added torque (see Fig. 1b).

EXPERIMENTAL PROCEDURE AND FINDINGS

Samples that primarily display slant crack propagation to one side only, under Mode I loading, was first created so that any flip later on can be tied to the applied Mode III. This was achieve by cutting DENT samples from 3 mm rolled 6082-T6 aluminum sheets (the rolling direction was found to have no significance), and through repeated heat treatments develop a material with the striven behavior (heated at 180°C for 16 hours from the super-saturated solid solution state and quenched). Standard tensile testing was then performed for DENT samples, both with/without a slight torque to induce a Mode III on the crack tip. The experimental set-up essentially mimics the out-of-plane behavior that is expected to set of the crack tip flipping.

Test results for monotonic proportionally increasing tension/torque are displayed in Fig. 1a. By applying the torque clock-wise (CW) on the lower part consistent slant crack propagation to one side is obtained, as depicted on the figure, whereas it was found that by altering the direction of the torque slanting occurs to the opposite side. What is important is that only a very small change in the twist of the sample is needed to alter the direction of the shear localization. This has also been confirmed in a simplified 2D plane strain Gurson type model (Gurson, 1977), along the lines of Nielsen and Hutchinson (2013), which easily captures the shift in localization. These modeling results indicate good reason to believe that a full 3D Gurson type model will capture the provoked flipping behavior.

Subsequently, experiments were performed by changing the direction of the introduced torque mid-way through the test, see Fig. 1b. This particular test is carried out by: i) initially adding loading through tension (1 mm/min) and clock-wise torque (1°/min), while, ii) a counter-clock-wise torque (3°/min) is started after crack propagation has initiated (final axial strain of

*Corresponding author. Email: clfe@mek.dtu.dk

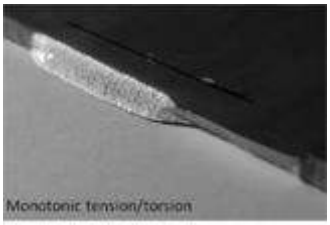

(a)

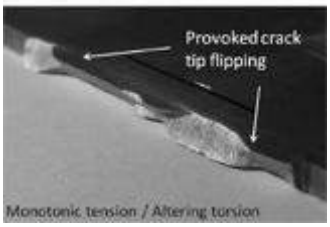

(b)

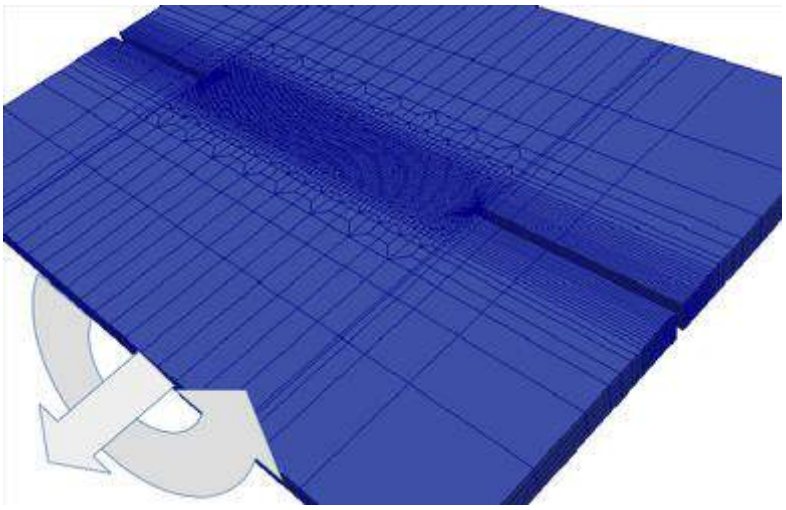

(c)

Figure 1: Axial displacement 1 mm/min. (a) $1^\circ/\text{min}$ CW twist, (b) $1^\circ/\text{min}$ CW twist followed by $3^\circ/\text{min}$ CCW twist, (c) Mesh for numerical analysis at initial condition indicating axial displacement and clock-wise (CW) twist of lower part.

0.02). Clearly, the change in the torque (hence the change in Mode III) gives rise to a provoked flip of the crack face. In fact, by simply observing the fracture surfaces it is hard to tell the difference between this artificially flip and a "natural" one – leading the authors to believe that both have been triggered by the out-of-plane action.

MODELING EFFORTS

The modeling effort aims at accurately describing the full sequence of events that comes with the ductile tearing process in thin sheet metals. Here, employing the micro-mechanics based Gurson material model that rests on void nucleation and growth to coalescence. The computational task is by no means trivial as the Gurson model outputs a mesh dependent result, and hence an accurate resolution of the fracture process itself requires the mesh to scale with the dominant void spacing (e.g. $50 \nearrow 100$ micron). That is, an accurate model requires on the order of 50 elements through the plate thickness (Nielsen and Hutchinson, 2012). To approach the challenge, an in-house explicit finite element program has been developed and is massively parallelized using the Message Parsing Interface (MPI) library. The program allows for 3D transient analysis and takes into account finite strains/displacements with the use of 20-node iso-parametric elements using reduced Gauss integration. Eventually, the individual elements may reach a critical level of damage after which it is removed completely by an element erosion technique. A schematic of the model set-up in Fig. 1c.

ACKNOWLEDGMENT

The work is financially supported by the VILLUM FOUNDATION Young Investigator Programme in the project "A New Phenomenon Yet to be Resolved in ductile PLATE tearing", grant VKR023451.

References

[1] El-Naaman, S.A., Nielsen, K.L. : Observations on Mode I ductile tearing in sheet metals, Europ. J. Mech. A/Solids, 42:54-62, 2013.

[2] Gruben, G., Hopperstad, O.S., Brvik, T. : Simulation of ductile crack propagation in dual-phase steel, Int. J. Frac., 180:1-22, 2013.

[3] Gurson, A.L. : Continuum Theory of ductile rupture by void nucleation and growth Part I. Yield criteria and ow rules for porous ductile media, J. Engrg. Mat. Tech., 99:215, 1977.

[4] Nielsen, K.L., Gundlach, C. : Crack Tip Flipping under Mode I Tearing: Investigated by X-Ray Tomography, (submitted for publication), 2016.

[5] Nielsen, K.L., Hutchinson, J.W. : Cohesive traction-separation laws for tearing of ductile metal plates, Int. J. Impact Eng., 48:15-23, 2012.

[6] Rivalin, F., Pineau, A., Di Fant, M., Besson, J. : Ductile tearing of pipeline-steel wide plates - I. dynamic and quasi-static experiments, Eng. Frac. Mech., 68:329-345, 2001.

[7] Simonsen, B.C., Törnqvist, R. : Experimental and numerical modelling of ductile crack propagation in large-scale shell structures, Marine Structures, 17:1-27, 2004.

MATHEMATICAL DIFFICULTIES IN COHESIVE FRACTURE EVOLUTION

Christopher J. Larsen*[1]

[1]*Mathematical Sciences, Worcester Polytechnic Institute, Worcester, MA, USA*

Summary There has been significant success over the past fifteen years in the mathematical analysis of models for Griffith fracture evolution (though the main questions are still open). However, for cohesive (Barenblatt) models, there are actually no existence results on models that predict the crack path. In this talk, I will explain why cohesive fracture is much more difficult, as well as some recent progress in overcoming these difficulties.

THE MAIN ISSUE: STABILITY OF UNILATERAL MINIMALITY

The main difficulty in showing existence for quasi-static (globally minimizing) Griffith fracture evolution was to show that for sequences of displacements that are unilateral minimizers for the Griffith fracture energy, if they converge to some limiting displacement, then that limiting displacement is also a unilateral minimizer. Showing the corresponding result for cohesive fracture has been the main sticking point in proving analogous existence results in that setting. In fact, this result turns out to be false. I will explain exactly (and simply) what the essential difference is between Griffith and cohesive. I will also give an explicit example of a sequence of unilateral minimizers that converges to a displacement that is not a unilateral minimizer. However, there is a weaker version of unilateral minimality that holds for these limits, and the proof will be outlined. Finally, I will also explain why there is still hope for existence for quasi-static cohesive fracture evolution.

*Corresponding author. Email: cjlarsen@wpi.edu

A PHASE-FIELD MODEL FOR FLUID DRIVEN CRACKS IN POROUS MEDIA

Chad M. Landis*[1] and Zachary A. Wilson[1]
[1]*Aerospace Engineering and Engineering Mechanics, The University of Texas at Austin, Austin, Texas, United States*

Summary Over the last two decades, the phase-field approach to fracture has been shown to be a useful tool for modeling complex crack evolution. This work demonstrates how phase-field methods can be applied to the problem of hydraulic fracture. The application of hydraulic fracturing involves the injection of fluid into a perforated wellbore with the intention of fracturing the surrounding reservoir and stimulating its overall production. This process involves the coupling of fluid flow with material failure. A continuum framework for fluid flow through a damaging porous medium able to represent the processes and interactions that occur during hydraulic fracturing will be presented. Several benchmark solutions will be discussed to verify the expected behavior and accuracy of the method and a few interesting problems will be presented in order to demonstrate the ability of the method to respond to various complexities.

ITRODUCTION

The propagation of fractures by hydraulically pressurized fluids is prevalent in many engineering applications, most of which reside in the field of geology. The most notable of these is the stimulation of oil and gas wells. The advent of massive hydraulic fracturing and horizontal drilling in recent decades has made the extraction of oil and gas from unconventional reservoirs, particularly shale, economically viable. Conventional modeling approaches to hydraulically fractured systems assume symmetric, planar, bi-wing crack geometries. Analytical 2D models were developed in the 1960s that made simplifying assumptions based on fracture height. Later, planar three-dimensional and pseudo-three-dimensional computational models were developed that incorporate anisotropic fracture properties of rock layers to predict more complex fracture height, length, and width growth and several commercial production codes in use today are based on these ideas. More recently, additional works, most notably by Detournay and co-workers, have carefully investigated the crack tip behavior and propagation regimes of hydraulic fractures for the KGD and penny-shaped fracture geometries. These asymptotic analyses provide valuable insights into some of the fundamental behaviors of fluid driven fractures[1].

Recently, however, research efforts have largely shifted towards the modeling of more complex fracture geometries. In particular, induced hydraulic fractures interact with pre-existing natural fractures and other anisotropies and inhomogeneities in the rock. Additionally, the implementation of horizontal drilling and the propagation of several fractures, either in sequence or simultaneously from a single well bore have added more complexity to the evolution and shapes of hydraulic fractures. Non-planar propagation can have numerous adverse effects on the desired outcomes of the fracture operation. Due to the low permeability of unconventional reservoirs, a proper understanding of fracture evolution is paramount in evaluating and ensuring the desired production of the well.

THE PHASE-FIELD APPROACH TO HYDRAULIC FRACTURE

A number of different methods have been developed and used to predict complex fracture propagation. Two of the more prevalent approaches are boundary element methods and the extended finite element method. One commonality of several of these works is that cracks are treated as discrete lines or planes which requires growth laws for crack propagation and potentially extra constitutive rules for other topology changes like crack branching or intersection. In order to address, and in fact avoid, some of the difficulties that can arise in the development constitutive rules for crack growth, this work enhances the phase-field or variational approach to fracture[2-3] by coupling the physics of flow through porous media and cracks with the mechanics of fracture. Instead of treating the cracks as a sharp discontinuity in the displacement field, as is done in the boundary element methods or in XFEM, the phase-field approach treats the crack as a diffuse zone of damage wherein the crack faces and crack tips are not explicitly tracked or identified. The method has been shown to recover Griffiths theory for brittle fracture. The modeling challenge addressed in this work is on how to allow for the flow of fluid and the pressure of said fluid within the diffuse representation for the cracks.

We have developed a continuum thermodynamics framework for fluid flow through a damaging porous medium that is able to represent the processes and interactions that occur during hydraulic fracturing. In the absence of phase-field fracture, the model reduces to the classic mixture theory developed by Coussy[4]. The model presented is capable of simulating both Stokesian flow through cracks and Darcy flow through the porous medium. The flow is coupled to the deformation of the bulk solid medium and the evolution of cracks within the material. Additionally, a finite deformation framework is utilized in order to capture the opening of the fractures, which can have substantial effects on the pressure profile within the material. A fully coupled non-linear finite element formulation is developed that utilizes the displacements of the bulk, the fluid pressure and

*Corresponding author. Email: landis@utexas.edu

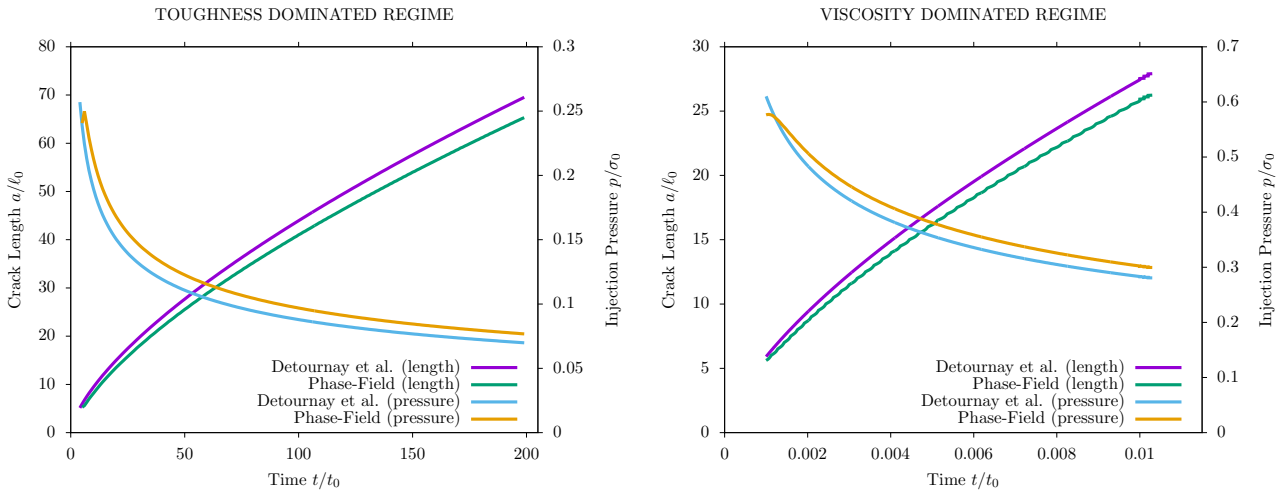

Figure 1: Comparisons between the phase-field model presented and the analytical solutions developed by Detournay et al. of the time-dependent crack growth and injection pressure variations for a plane strain center crack in an isotropic, linearly elastic, impermeable material. The phase-field simulation was conducted with an initial center crack of half-length $5\ell_0$. The left plot has material constants and injection rate such that the crack propagates in the toughness dominated regime. The right plot has material constants and injection rate within the viscosity dominated regime. The crack lengths shown are normalized by the phase-field length scale parameter ℓ_0 and the pressure is normalized by the characteristic stress, which is related to the fracture surface energy, the length scale parameter, and the elastic modulus as $\sigma_0 = \sqrt{G_c E/\ell_0}$.

velocity relative to the bulk, and the phase-field order parameter as nodal degrees of freedom. Several benchmark solutions will be presented to verify the expected behavior and accuracy of the method. The most encapsulating study, shown in Figure 1, compares the model to analytical results for the plane strain KGD fracture geometry of an impermeable medium. This problem illustrates the two major dissipative mechanisms involved in the hydraulic fracture problem. The first is the growth of cracks and the creation of new surfaces. This is typically referred to as the large toughness regime of propagation and is characterized by small injection rates, small viscosities, and short cracks. The pressure profile along the length of the crack is nearly uniform and cracks propagate according to the linear elastic fracture mechanics solution for a uniformly pressurized center crack. The second mechanism of dissipation is the viscous flow of the fluid in the crack. This regime, referred to as the viscosity dominated regime, is characterized by high injection rates, highly viscous fluid, and long cracks. Figure 1 demonstrates that the model compares favorably with the time-dependent analytical results for the two dominant propagation regimes. It is worthwhile to mention that this result, particularly for the viscosity dominated regime, would not be possible without accurately modeling the flow profile within the crack and its proper dependence on crack opening displacement. Additionally, a few interesting problems have been investigated that demonstrate the ability of the method to respond to various complexities like multiple cracks interacting with one another.

CONCLUSIONS

The phase-field or variational approach to fracture can be utilized to accurately represent the processes and interactions that occur during hydraulic fracture. Due to the generality and simplicity of the approach, the model has the potential to provide insight into how hydraulic fractures behave in complex three-dimensional settings.

References

[1] Detournay E.: Propagation Regimes of Fluid-Driven Fractures in Impermeable Rocks. International Journal of Geomechanics 4:35-45, 2004.

[2] Francfort G.A. and Marigo J-J.: Revisiting Brittle Fracture as an Energy Minimization Problem. J. Mech. Phys. Solids 46:1319-1342, 1998.

[3] Borden M.J., Verhoosel C.V., Scott M.A., Hughes T.J.R., and Landis C.M.: A Phase-Field Description of Dynamic Brittle Fracture. Comput. Methods Appl. Mech. Eng. 217-220:77-95, 2012.

[4] Coussy O.: Poromechanics. John Wiley & Sons, 1994.

PERIDYNAMIC MODELLING OF DYNAMIC FRACTURE AND FATIGUE CRACKING

Florin Bobaru[1a)], Yenan Wang[1], Guanfeng Zhang [1], Ziguang Chen [1] & Quang Le[1]
[1]*Department of Mechanical and Materials Engineering, University of Nebraska-Lincoln, Lincoln, Nebraska, USA*

Summary We discuss peridynamic formulations for dynamic brittle fracture problems and fatigue facture. In particular, we focus on dynamic fracture in Functionally Graded Materials (FGMs) where we show how the crack path is influenced by the dynamic loading conditions. Results compare well with those from experimental tests found in the literature. For fatigue cracking, we validate the peridynamic formulation for a modified compact tension test which leads to curved crack paths that sink in a hole or avoid it depending on the location of where the hole is placed. The model is then applied to simulate fatigue crack growth in a two-phase composite with multiple crack initiation points and cracks that interact in complex ways. We emphasize the role nonlocality plays in the peridynamic modelling of damage evolution.

DYNAMIC BRITTLE FRACTURE IN FUNCTIONALLY GRADED MATERIALS

Elastic deformations in Functionally Graded Materials (FGMs) have been studied in the past using homogenization methods. The success of such methods for modelling fracture is not guaranteed, because fracture is inherently a nonlinear phenomenon while homogenization methods are usually based on arguments of linearity. In [1] we have shown that a locally-homogenized peridynamic model for FGMs in which the inclusions are spherical and small relative to the sample size, is able to correctly predict fine details of the dynamic fracture behaviour reported in the experiment reported in [2,3]. The bond-based peridynamic formulation introduced is based on computing the bond properties by averaging the elastic modulus and the fracture energy at the two end-points of the bond. The density is a nodal quantity and does not require any changes. The model is valid as long as the nonlocal region size used (the peridynamic horizon) is small relative to how fast the effective properties change in the FGM. We study the dynamic fracture behaviour by using a test with asymmetric dynamic loading described by the experiments in [2,3]. The functionally graded plate has a monotonically varying volume fraction of reinforcement and the mixed-mode loading is imparted by eccentric impact relative to a pre-crack. We study the influence of material gradients, elastic waves, and of contact time and magnitude of impact loading on the fracture behaviour in terms of crack path geometry and crack propagation speed. The peridynamic simulations agree very well, through full failure, with the experiments in [2,3]. While the experiments in [2,3] provide only partial information of the conditions in which the experiments were conducted, our investigation allows us to determine some of these conditions by conducting a number of loading scenarios and observing the crack paths and their crack propagation speed. For a certain loading contact time, these computational outputs match extremely well those presented in the experiments (see Fig. 1). We discuss advantages offered by the peridynamic model in dynamic fracture of FGMs compared with, for example, FEM-based models.

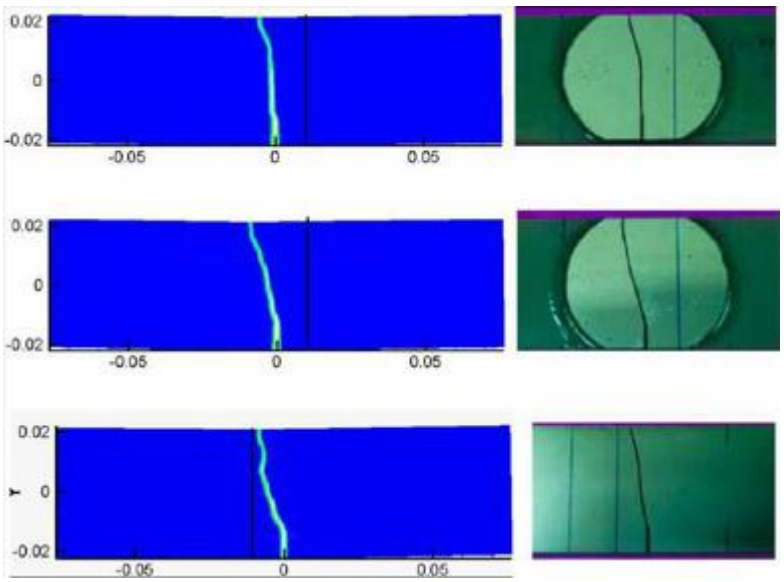

Figure 1. Damage maps (left column) show crack paths for different variations of material gradation (bottom row is for homogeneous sample) (from [1]) and corresponding experimental results (right column), reproduced from [2].

[a)] Corresponding author. Email: fbobaru2@unl.edu.

PERIDYNAMIC MODEL FOR FATIGUE CRACKING

While most applications of peridynamics have been to dynamic brittle fracture problems, the model holds promise in fatigue cracking as well, especially for difficult cases in which the crack paths are complex, or the microstructure leads to a multitude of crack initiation points and subsequent coalescence of cracks. We extend the peridynamic fatigue model introduced in [4] by introducing a set of two critical damage parameters that improve computational efficiency and maintain stability in the numerical solution process. The range for these parameters is determined via convergence studies of fatigue crack growth for a standard compact tension (CT) test. We then test the peridynamic fatigue crack model for curved fatigue crack growth by using some modified CT tests that have been employed in the literature (see [5]). In these modified CT tests, the location of a hole determines whether the fatigue crack sinks into it or by-passes it. The peridynamic model replicates the sensitivity of the experimental tests to the location of the extra hole in the sample (see [6]). We further formulate a peridynamic fatigue crack growth for a two-phase composite in which several crack initiation points exist due to the material heterogeneity. The peridynamic approach, because it does not require tracking of cracks and does not need to distinguish between localized crack and diffuse damage, is able to resolve the evolution of damage and cracks in such material systems (see Fig. 2) without an increase in algorithmic or computational complexity compared with the case of a single crack in a homogeneous material.

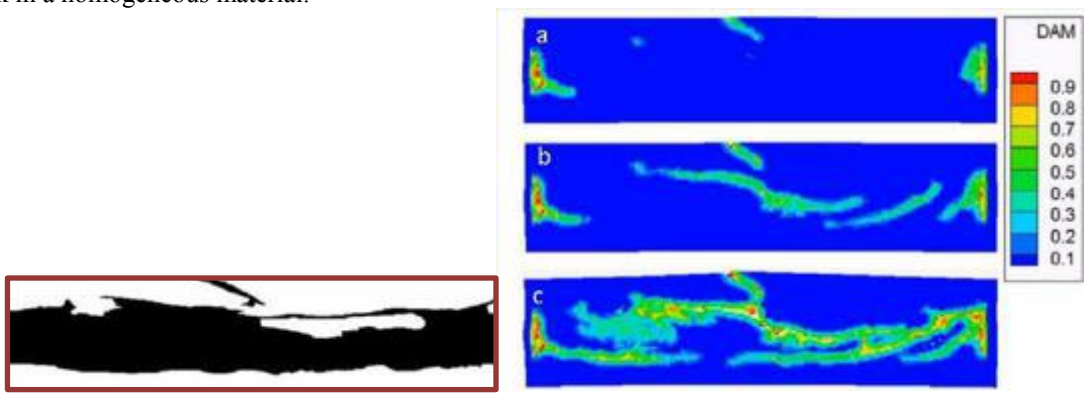

Figure 2. Damage maps showing the evolution of fatigue cracks in a two-phase composite with a microstructure shown to the left (reproduced from [6]).

CONCLUSIONS

The peridynamic approach to modelling of damage and fracture evolution under dynamic or fatigue-type conditions offers significant benefits compared to classical approaches. There is no conceptual difference in the peridynamic treatment of a single crack, or of a combination between a multitude of cracks and diffusive damage.

ACKNOWLEDGEMENTS

This work was supported in part by was supported in part by grants from ARO/ARL (program managers: Dr. Asher Rubinstein and Dr. Chian-Fong Yen), from an AFOSR MURI award (program managers: Dr. David Stargel, Dr. Ali Sayir and Dr. Fariba Fahroo), and by GE Research Center (Drs. Adrian Loghin and Arun Subramanian). The computational work was completed utilizing the Holland Computing Center of the University of Nebraska.

References

[1] Cheng Z., Zhang G., Wang Y., Bobaru F.: A peridynamic model for dynamic fracture in functionally graded materials. Composite Structures **133**:529 - 546, 2015.

[2] Kirugulige M.S., Tippur H.V.: Mixed-mode dynamic crack growth in functionally graded glass-filled epoxy. *Exp Mech* 46(2):269–281, 2006.

[3] Kirugulige M.S., Tippur H.V.: Mixed-mode dynamic crack growth in a functionally graded particulate composite: experimental measurement and finite element simulations. *J Appl Mech* **75**(5):051102, 2008.

[4] Silling S.A., Askari, A.: Peridynamic model for fatigue cracking. Tech. Rep. no. sand2014-0017j, Sandia National Laboratories, Albuquerque, New Mexico, USA, 2014.

[5] Miranda A., Meggiolaro M., Castro J., Martha L., Bittencourt T.: Fatigue life and crack path predictions in generic 2d structural components. *Engineering Fracture Mechanics* **70** (10): 1259–1279, 2003.

[6] Zhang G., Le Q., Loghin A., Subramaniyan A., Bobaru F.: Validation of a peridynamic model for fatigue cracking. (submitted) 2016.

LOCAL ADAPTIVE REFINEMENT METHOD FOR THE FRACTURE OF HETEROGENEOUS MATERIALS

Eric Delaume[1, 3], Loïc Daridon [*2, 3], Frédéric Dubois[2, 3], Yann Monerie[2, 3], and Frédéric Perales[1, 3]
[1]*Institut de Radioprotection et de Sûreté Nucléaire (IRSN), Saint-Paul-lez-Durance, France*
[2]*Laboratoire de Mécanique et Génie Civil, Université de Montpellier, Montpellier, France*
[3]*Laboratoire de Micromécanique et Intégrité des STructures, IRSN - CNRS - Université de Montpellier, France*

Summary In the frame of nuclear safety research program of the french 'Institut de Radioprotection et de Sûreté Nucléaire' (IRSN), a micromechanical approach is developed to predict the fracture of concrete containment structures in nuclear power plants. A problem in studying crack propagation within these structures is the computational cost related to spatial discretization of each relevant scale. A way to reduce the computational cost without any significant loss of accuracy is to perform local adaptive refinement. The refinement method presented in this paper is called CHARMS, and is based on the splitting of elements in a region of interest of an existing mesh. This refinement method is applied to the recent 'Eigen-Erosion' method allowing crack propagation based on a killing element-type method with respect to the Griffith's criterion.

Adaptive mesh refinement devoted to crack propagation problems rely on an adjustment of the spatial resolution in the region of interest of the discretized domain in order to achieve higher accuracy. Two main issues arise from such a spatial refinement: increase of the computational cost and possible decrease of the shape quality of some elements located in the coarse-to-fine transition region. A solution consists in adjusting the density of the mesh by performing local *refinement* (resp. unrefinement) of an existing mesh. In this work, the CHARMS method (Conforming Hierarchical Adaptive Refinement MethodS [1]) is investigated to perform such a refinement and coupled to the recent 'Eigen-Erosion' method proposed by Pandolfi and al. [2] to simulate crack propagation.

The refinement method (CHARMS) is based on the refinement (resp. unrefinement) of the basis functions rather than the refinement of the finite elements and thus allows non conformities. These non conformities are geometrical and not linked to spatial discretization: the approximation spaces remain H^1-conform. The fundamental property of this method is, given that the approximation spaces are nested, $X_J \subset X_{J+1}$ with $J \geq 0$, any basis function in the approximation space basis B_j, $j \in [\![1, J]\!]$, can be written as a linear combination of finer basis functions in B_{j+1} (see Figure 1). These linear combinations define child-parent relationships between basis functions of two consecutive refinement levels.

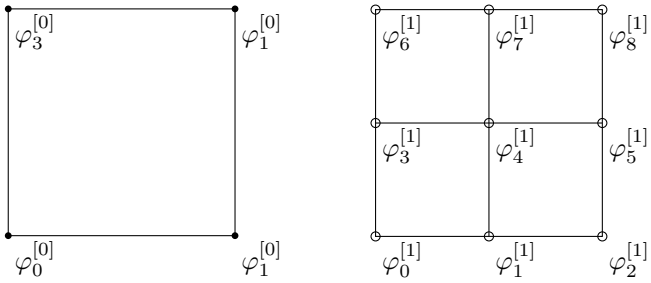

$$\begin{aligned}
\varphi_0^{[0]} &= \varphi_0^{[1]} + \tfrac{1}{2}\varphi_1^{[1]} + \tfrac{1}{2}\varphi_3^{[1]} + \tfrac{1}{4}\varphi_4^{[1]} \\
\varphi_1^{[0]} &= \varphi_2^{[1]} + \tfrac{1}{2}\varphi_1^{[1]} + \tfrac{1}{2}\varphi_5^{[1]} + \tfrac{1}{4}\varphi_4^{[1]} \\
\varphi_2^{[0]} &= \varphi_8^{[1]} + \tfrac{1}{2}\varphi_5^{[1]} + \tfrac{1}{2}\varphi_7^{[1]} + \tfrac{1}{4}\varphi_4^{[1]} \\
\varphi_3^{[0]} &= \varphi_6^{[1]} + \tfrac{1}{2}\varphi_3^{[1]} + \tfrac{1}{2}\varphi_7^{[1]} + \tfrac{1}{4}\varphi_4^{[1]}
\end{aligned}$$

Figure 1: Example of refinement equations for a linear $\mathbb{Q}_1$ element, φ represents the basis functions of refinement level [0] and [1].

The 'Eigen-Erosion' method is based on energetics criteria and enables to simulate crack propagation using an accurate killing-element technic. This method relies on a variational approach of fracture mechanics and offers two main advantages: a low computational cost and a mesh independent crack path [3].

The CHARMS method and the 'Eigen-Erosion' method have been implemented in the software Xper [4] and enable to simulate the crack propagation in refined regions. The test case presented in Figure 2 has been performed by using a simple geometrical criteron to refine the region of interest. Other refinement criteria may be used.

Figure 4(a) shows that the cracks obtained with a fine uniform mesh (blue crack) and with a refined mesh (red crack) are similar, and both cracks are comparable to the one obtained by the experiment in Figure 4(b). The difference between the two simulations is the computational cost.

*Corresponding author. Email: loic.daridon@umontpellier.fr

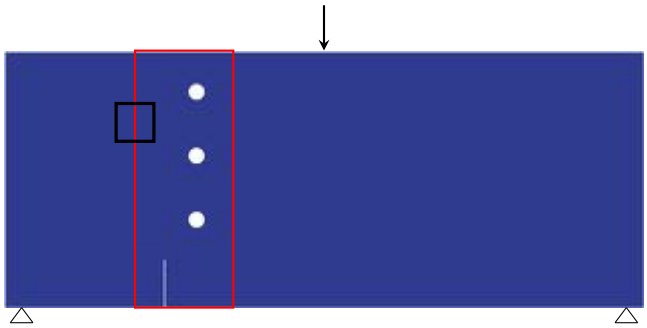

Figure 2: Example of a three holes bending beam proposed by [5] and using a geometrical criterion for refinement. The red rectangle is the region selected for refinement and where the crack will propagate and the black one shows the transition region for each meshes in Figure 3.

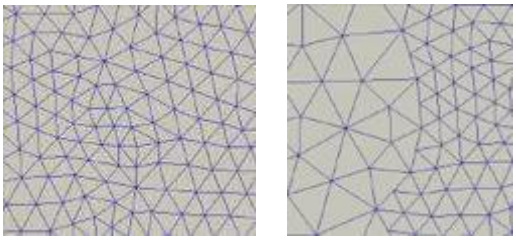

(a) (b)

Figure 3: Transition regions for (a) the fine uniform mesh and (b) the refined mesh where we can see the geometrical non-conformities.

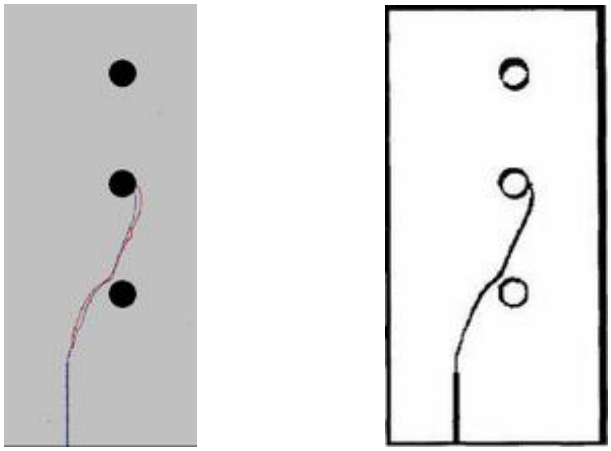

(a) (b)

Figure 4: Cracks obtained by (a) the simulation and (b) the experiment in [5]. In (a), the blue crack is obtained with a fine uniform mesh in 14H (1 087 710 cells) and the red one with a refined mesh in 1H (195 976cells). The element size of the fine uniform mesh is the same than the one of the refined region.

References

[1] Krysl P., Grinspun E., Schröder P.: Natural hierarchical refinement for finite element methods. International Journal for Numerical Methods in Engineering, 56, pp. 1109-1124, 2003.

[2] Pandolfi A., Ortiz M.: An eigenerosion approach to brittle fracture. International Journal for Numerical Methods in Engineering, 92, pp. 694-714, 2012.

[3] Bichet L., Dubois F., Monerie Y., Pelissou C., Perales F.: Une méthode d'Eigenerosion pour les matériaux hétérogènes. Application aux matériaux cimentaires. Matériaux & Techniques, 103, 2015.

[4] Perales F., Dubois F., Monerie Y., Piar B., Stainier L.: A non smooth Contact Dynamics-based multi-domain solver. Code coupling (Xper) and application to fracture. European Journal of Computatinal Mechanics, 19, pp. 389-417, 2010.

[5] Bittencourt T. N., Wawrzybek P. A., Ingraffea J. L., Sousa: Quasi-automatic simulation of crack propagation for 2D LEFM problems. Engineering Fracture Mechanics, 55, pp. 321-334, 1996.

INTERFACE STRENGTH VERSUS FRACTURE ENERGY DRIVEN FRACTURE IN THIN FILM TRANSFER

Shruti Jain[1], Seung R. Na[2], Kenneth M. Liechti[2] & Roger T. Bonnecaze [1a)]
[1]*Department of Chemical Engineering, The University of Texas at Austin, Austin, Texas, USA*
[2]*Department of Aerospace Engineering and Engineering Mechanics, Center for Mechanics of Solids, Structures and Materials, The University of Texas at Austin, Austin, Texas, USA*

Abstract The work presented here explores the fracture mechanics of very thin films and 2D materials when transferred from one substrate to another by dry transfer. Finite element simulations in ABAQUS as well as beam theory models are developed to study the role of material properties and traction separation relations in determining the interface of crack propagation. For mode-independent transfer of 2D materials, the results indicate that interface selection is strength driven. We explore the effect of shear to understand the shift from strength driven to fracture energy driven fracture under mixed-mode conditions. In the case of thin films (thinner than the substrates), simulations indicate a shift from fracture energy driven behavior to interface strength driven mechanics based on initial crack lengths, elastic modulus of the thin film as well as its thickness.

INTRODUCTION

Transfer printing is a fabrication technique for microelectronics and other applications where a patterned or printable layer is transferred from a host substrate to a target device substrate by taking advantage of the difference in adhesion of the thin layer to the two substrates. This technique has been studied for the case of few microns thick layers [1] and has also been demonstrated to work for transferring 2D materials like graphene [2]. Transfer printing has the potential to enable low cost manufacturing of flexible electronics and understanding the mechanics of this process is critical to improve the manufacturing methods.

Tucker, Hines and Li [1] performed ABAQUS simulations to study the effect of interface crack lengths and device substrate's elastic modulus on competing fracture in thin films. They identified the regions of successful and unsuccessful transfer based on these parameters. Kim-Lee et. al [3] also analysed the effect of thin film geometry on transfer and compared their simulation results with experimental data. Fracture toughness, energy release rates, crack lengths and device substrate's elastic modulus were the parameters discussed in these works. We have extended their analysis to include cohesive zone modelling for selective delamination, and we look at the effect of elastic modulus of the thin film as well as traction-separation relation parameters (interaction strength and range) in addition to crack lengths. We have also developed models for 2D material transfer to understand the underlying mechanics of dry transfer of graphene which are different from micron-thin film separation.

METHOD

Cohesive zone models are used to describe interface interactions in finite element simulations and beam theory models. The finite element model schematics for thin film separation and graphene transfer are shown in Fig. 1. We use cohesive elements for the two interfaces (polymer-thin film and thin film-copper) between the layers. Since 2D materials are one atom thick, we do not have an intermediate layer for the case of graphene transfer in Fig 1b. Beam theory models are developed for both systems by considering the interactions as distributed stresses along the polymer layer similar to the approach developed in [1] and [4].

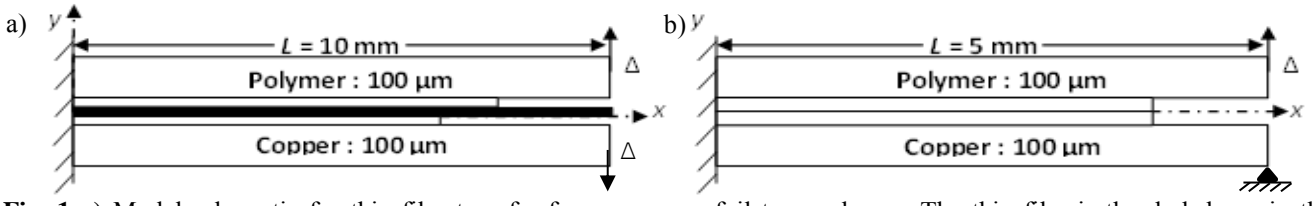

Fig. 1 a) Model schematic for thin film transfer from a copper foil to a polymer. The thin film is the dark layer in the middle. The layers immediately above and below represent the cohesive zones, which are much thinner than any of the layers but enlarged here. **b)** Model schematic for graphene transfer. The graphene is an infinitesimally thin layer sandwiched between the two cohesive zones.

Thin Film Transfer

We varied the film-copper crack length while keeping polymer-film interface crack fixed at 1mm. Both polymer and copper are displaced at the end by Δ=0.3 mm. A bi-linear traction separation relation (TSR) reported by Na, et al.[5] is used for the interaction between the film and copper and the TSR for the polymer-film interface is varied to understand mode-

[a)] Corresponding author. Email: rtb@che.utexas.edu.

independent fracture. In the simulations, Young's modulus and Poisson's ratio of the polymer are E_P = 2.5 GPa and υ_P = 0.34, respectively, and those of the copper layer are E_P = 110 GPa and υ_P = 0.32, respectively. For the thin film with varying Young's modulus, E_T = 2.5 GPa, 110 GPa and υ_T = 0.2. Finite element simulations in ABAQUS are performed under plane strain to study the effect of varying crack lengths, thin film modulus and TSR parameters. All materials are considered isotropic.

Graphene Transfer

Plane strain ABAQUS simulations are performed with model geometry as shown in Fig. 1b. Mixed-mode transfer is simulated to understand the effect of relative interface TSR parameters on the success of graphene transfer. It has been observed for mode-independent transfer that success of graphene transfer depends only on the relative strengths of the interfaces (Fig. 2a). We will study the effect of mixed-mode transfer mechanics on success of graphene transfer in ABAQUS as well as develop a beam theory model for the same.

PRELIMINARY RESULTS

For a fixed TSR of both interfaces where subscript t is used for top interface and subscript b is used for bottom interface, fracture energy (Γ) ratio is Γ_t/Γ_b = 0.67 and interface strength (σ) ratio is σ_t/σ_b = 2. Even though the fracture energy ratio favors crack propagation along the top interface, some of the simulations show fracture along the bottom interface suggesting strength driven fracture in certain cases. The effect of variation in notch length L_b (for fixed L_t = 1 mm), thin film thickness (h) and thin film elastic modulus E_T on fracture has been studied.

For a thin film thickness h = 10 μm and E_T=2.5GPa, simulations show fracture along the top interface for $L_b/L_t < 1$ and fracture at the bottom interface for $L_b/L_t \geq 1$. This indicates a transition between fracture energy driven and strength driven mechanics at L_b/L_t = 1. As the thickness of the thin film increases, this transition point shifts to higher values of L_b/L_t. A fracture map summarizing these observations is shown in Fig. 2b.

a)

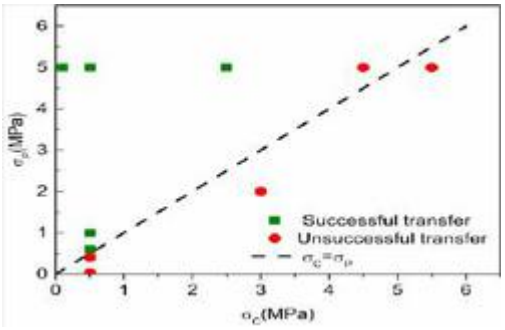

b)

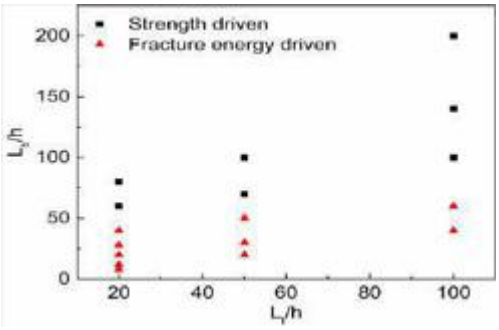

Fig. 2 a) Fracture map for graphene transfer where σ_P is the interface strength of polymer-graphene interface and σ_C is the interface strength of copper-graphene interface. **b)** Fracture map for thin film transfer for E_T=2.5 GPa, Γ_t/Γ_b = 0.67 and σ_t/σ_b = 2. There is a clear linear separation between strength driven and fracture driven fracture.

Simulations for variation in thin film elastic modulus indicate that there is a critical elastic modulus above which competing fracture is always fracture energy driven. For E_T = 110 GPa, cracks always propagated along the top interface. We will run more simulations to find the critical elastic modulus at which the transitioning behaviour occurs.

CONCLUSIONS

Thin film transfer simulations indicate that for a 2D material like graphene, interface fracture is predominantly governed by interface strength and not fracture energy. Mixed-mode transfer could introduce some deviations from this behaviour and results will be presented. However, for thin films with thickness of the order of microns, there is a clear shift from strength driven fracture to fracture energy driven crack propagation based on film thickness, film elastic modulus as well as initial crack lengths.

References

[1] Tucker M. B., Hanes D. R., Li T.: A Quality Map of Transfer Printing. *J. Appl. Phy* **106**:103504, 2009.

[2] Campos N., Perez-Mas A. M., Alvarez P., Menendez R., Gomez D.: Surface treatment ofpolyimide substrates for the transfer and multitransfer of graphene films. *Applied Surface Science* **349**:101-107, 2015.

[3] Kim-Lee H. J., Carlson A., Grierson D. S., Rogers J. A., Turner K. T.: Interface mechanics of adhesiveless microtransfer printing processes. *J. Appl. Phy* **115**:143513, 2014.

[4] Stigh U.: *Int. J. Fracture*, **37**, pp R13-R18, 1988.

[5] Na S. R., Suk J. W., Tao L., Akinwande D., Ruoff R. S., Huang R., Liechti K. M.: *ACS Nano*, **9**, 1325-1335, 2015.

UNIVERSAL MESHES FOR A CRACK WITH TRIPLE JUNCTIONS

Yongxing Shen*[1] and Can Wu[1]

[1] *University of Michigan-Shanghai Jiao Tong University Joint Institute, Shanghai Jiao Tong University, Shanghai, China*

Summary The universal meshes is an efficient way to handle problems with evolving domains or discontinuities by only perturbing a fraction of vertices of a fixed background (universal) mesh at every time step. In particular, it was adapted to problems with a simple propagating crack in an earlier contribution. In this work, we have generalized the formulation to the case of a branched crack with one or multiple triple junctions. This generalization will be useful for simulating dynamic crack propagation such as that generated by an impact.

INTRODUCTION

One of the challenges to simulate crack evolution with the finite element method is the need for a conforming mesh to the evolving geometry, since the brute-force way of generating a new mesh for each crack propagation step is costly. The *universal meshes* method was proposed by Rangarajan and Lew [1] for a closed domain and then adapted to crack problems with a simple crack by Rangarajan *et al.* [2] This method avoids both the costly step of mesh re-generation and the cumbersome evaluation of enrichments in enrichment techniques such as the extended finite element method. In this contribution, we extended the method in [2] to the case of a crack with one or multiple triple junctions.

THE PROCEDURE

The case of one junction This section devotes to introducing the main idea of the algorithm for the case in which the crack has exactly one junction, such as the example shown in Figure 1a. The algorithm includes three steps:

1. Move nodes to coincide with the junction and tips. For the junction and both crack tips, we find the nearest node (in case of multiple nodes, we pick any one) and move it to coincide with the junction (crack tip). To maintain the quality of the mesh, we also move the nodes within a certain radius ($2h$ in our example, where h denotes the mesh size), see Figure 1.

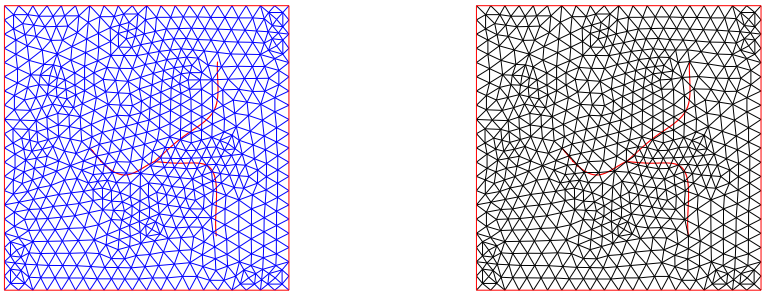

(a) (b)

Figure 1: (a) The original mesh (fixed for each stage of crack propagation). (b) The mesh after step 1.

2. Determine a specific set of nodes to be projected to their respective closest points on the crack. This step has two sub-steps: (a) Determine, among the neighboring nodes of the junction node, which three should be moved to the crack (each to each branch). The principle is to minimize the angles of rotation of the relevant edges resulting from such movement, see Figure 2a. (b) Determine more nodes to be projected for each branch, until the crack tip. The main idea is to, for each branch, first choose nodes only on one side, so that they form a series of edges topologically equivalent to the branch of interest. Then we adjust some of the chosen nodes to reduce element distortion, according to the criterion and procedure given in Rangarajan and Lew [3]. Finally we will ensure no triangle whose all nodes are chosen. The finally chosen nodes are shown in Figure 2b.

3. Project nodes onto the branched crack and relax the neighboring nodes. We project the nodes onto their closest point in the crack and simultaneously relax the neighboring nodes to get the final mesh, see Figure 2c.

*Corresponding author. Email: yongxing.shen@sjtu.edu.cn

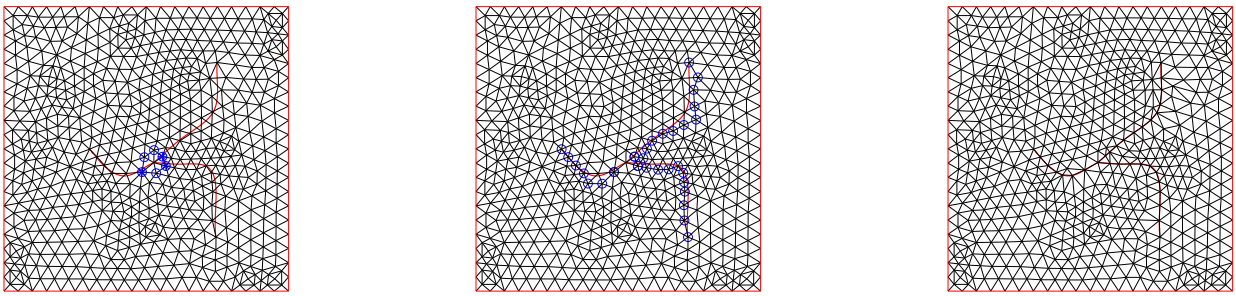

(a) (b) (c)

Figure 2: (a) The neighboring nodes of the junction marked with circles and the chosen nodes marked with stars to be projected to the three crack branches. (b) All nodes to be projected to their closest points on the crack marked with circles. (c) The final mesh after projecting the chosen nodes and relaxing their neighboring nodes.

The case of multiple junctions The method can be generalized to the case of multiple triple junctions. An example is shown in Figure 3.

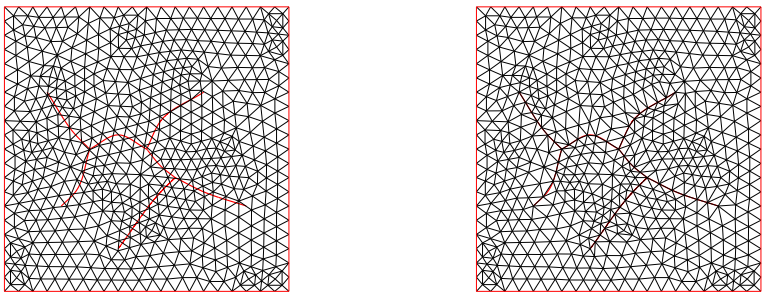

(a) (b)

Figure 3: Example with multiple triple junctions: (a) The crack and the original mesh (fixed for each stage of crack propagation). (b) The final mesh.

CONCLUSIONS

A method to obtain a conforming mesh from an evolving crack with triple junctions is developed. This method can be used to simulate problems such as dynamic crack propagation under impact.

ACKNOWLEDGMENT

This work is supported by the Natural Science Foundation of China grant #11402146 and the Young Thousand Talent Program of China.

References

[1] Rangarajan R., Lew A.J.: Universal meshes: A method for triangulating planar curved domains immersed in nonconforming meshes. Int. J. Numer. Meth. Engng 98(4):236–264, 2014.

[2] Rangarajan R., Chiaramonte M.M., Hunsweck M.J., Shen Y., Lew A.J.: Simulating curvilinear crack propagation in two dimensions with universal meshes. Int. J. Numer. Meth. Engng 102(3–4):632–670, 2015.

[3] Rangarajan R., Lew A.J.: Parameterization of planar curves immersed in triangulations with application to finite elements. Int. J. Numer. Meth. Engng 88(6):556–585, 2011.

CRACK GROWTH AT NONUNIFORM SPEED BENEATH THE BOUNDARY OF A HALF-PLANE

Yuri Antipov*[1] and Aleksandr Smirnov[1]

[1]*Department of Mathematics, Louisiana State University, Baton Rouge, United States*

Summary A semi-infinite crack propagates at sub-Rayleigh piece-wise constant speed in a homogeneous isotropic half-plane in the direction parallel to the half-plane boundary. Freund's approximate algorithm for the problem on a semi-infinite crack propagating in the whole plane is generalized for the half-plane case. The implementation of the method requires successive solution of two coupled Volterra convolution equations admitting a closed-form solution. The kernels of the system are the four weight functions of the transient problem on a semi-infinite crack propagating at constant speed parallel to the boundary and subjected to certain loading. By the Fourier and Laplace transforms the model problem reduces to an order-2 vector Riemann-Hilbert problem. A method of partial factorization and convolution integral equations for its numerical solution is proposed. The dynamic Griffith criterion for the determination of the piece-wise speed is applied.

PIECE-WISE CONSTANT SPEED

The elastic medium $\Pi=\{|x_1|<\infty,\ \nearrow\!\infty<x_2<\delta\}$ through which the crack propagates comprises an infinite strip $\{|x_1|<\infty,\ 0<x_2<\delta\}$ and a half-plane $\{|x_1|<\infty,\ \nearrow\!\infty<x_2<0\}$ bonded together. The bonding is not perfect, and it is assumed that along the interface there is a semi-infinite crack. The faces of the crack are subjected to plane strain loading, while the boundary of the body Π, $\{|x_1|<\infty,\ x_2=\delta\}$, is free of traction. The Lamé constants λ and μ and the density ρ of the strip and the half-plane are assumed to be the same. Under the action of the loads applied at time $t=0$ the crack starts moving, and its position at time t is described by $l(t)$, a continuously differentiable, nondecreasing function such that speed of propagation is less than the Rayleigh speed, $V(t)=l'(t)<c_R$. The presence of the weak interface encourages the crack to propagate parallel to the boundary $\{|x_1|<\infty, x_2=\delta\}$ rather than deviate towards it (Fig.1). The ultimate goal of this study is to analyze propagation of a semi-infinite crack in a half-plane at nonuniform speed in the direction parallel to the boundary, determine the propagation speed and study the boundary effects. The steady-state model problem for a semi-infinite crack propagating at constant speed beneath the half-plane boundary was solved by the authors earlier [1].

Following the Freund scheme [2] developed for nonuniform growth of a semi-infinite crack in a whole plane we approximate the curve $l(t)$ by a polygonal line with the vertices (t_k,l_k), $l_k=l(t_k)$, $t_0=0$, $l_0=0$, and denote $V_k=(l_{k+1}\nearrow l_k)/(t_{k+1}\nearrow t_k)$ the corresponding constant speed during the time $t_k<t<t_{k+1}$. Initially, as $0<t<t_1$, the crack extends at speed $V_0=const$ by negating stresses $\sigma^0_{12}(x_1,0)$ and $\sigma^0_{22}(x_1,0)$ for $x_1>0$. They are determined from the solution of the static problem, P_{-1}, on a semi-infinite crack parallel to the boundary of a half-plane. This problem provides the starting point for a complete description of the nonuniform motion of the crack. A method of matrix Wiener-Hopf factorization for a homogenous static problem was presented in [3]. On employing their method it is possible to derive the exact solution of the inhomogeneous static problem for general loading and determine the stresses everywhere in the body including the line $x_2=0$ ahead of the crack. It is accepted that the solution to Problem P_{-1} is already available.

The next step of the procedure is solving the problem on a moving crack that suddenly stops at time $t=t_1$ at the point $x_1=l_1, x_2=0$. Some stresses, $\tilde\sigma^1_{12}(x_1,0)$ and $\tilde\sigma^1_{22}(x_1,0)$, are radiated out along the line $x_2=0$, $x_1>l_1$. These stresses are unknown *a priori* and must be determined. To continue its motion, the crack negates these unknown stresses and results in vanishing the SIFs when $x_1=V_0t>l_1$,

$$K_I(t;V_0)=0,\quad K_{II}(t;V_0)=0,\quad V_0t>l_1, \tag{1}$$

and a necessity of solving a transient problem, P_0, arises. For this problem $V\equiv V_0=const$ and the boundary conditions on the faces of the crack read

$$\sigma_{j2}=\nearrow\!\sigma^0_{j2}(x_1,0)\chi_{(0,l_1)}(x_1)+\tilde\sigma^1_{j2}(x_1,0)\chi_{(l_1,V_0t)}(x_1),\quad \nearrow\!\infty<x_1<V_0t,\quad x_2=0^{\pm},$$

where $\chi_{(a,b)}(x)=1$ if $x\in(a,b)$ and vanishes otherwise; $\tilde\sigma^1_{j2}(x_1,0)$ are be recovered from equations (1) as follows. On solving and analyzing the solution of the transient model P_0 it is possible to prove the remarkable property of the transient weight functions for a semi-infinite crack propagating beneath the half-plane boundary at constant speed V, $W_{i,j}(x_0,t;V)=W_{i,j}(0,t\nearrow x_0/V;V)$, $i,j=I,II$, and eventually represent the SIFs in the form

$$K_I(t;V_0)=\nearrow\!K'(t;V_0)+\int_{l_1}^{V_0t}[W_{I,I}(0,t\nearrow x_1/V_0;V_0)\tilde\sigma^1_{22}(x_1,0)+W_{I,II}(0,t\nearrow x_1/V_0;V_0)\tilde\sigma^1_{12}(x_1,0)]dx_1,$$

*Corresponding author. Email: antipov@math.lsu.edu

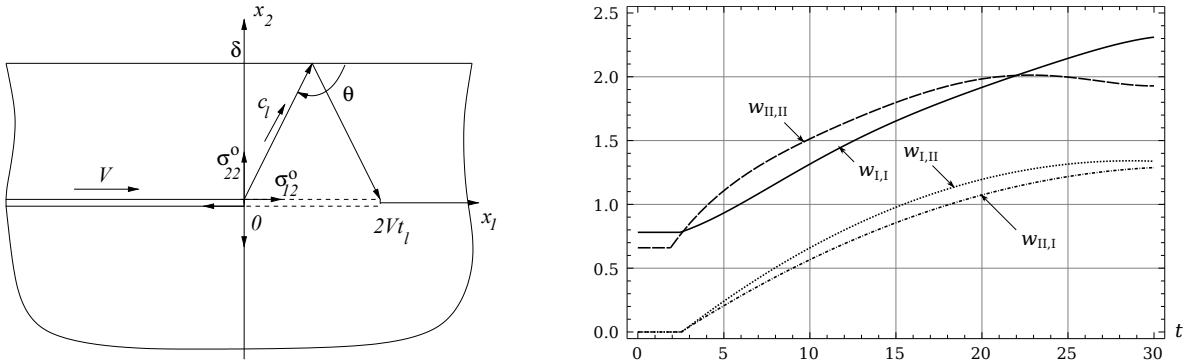

Figure 1: A semi-infinite crack propagating parallel to the boundary and the functions $w_{i,j}(0,t) = \sqrt{\frac{1}{2}\pi V t} W_{i,j}(0,t)$ $(i,j = I, II)$ versus time t when $\nu = 0.3$, $\delta = 1$ m, $V = 0.5 c_R$ m/s, $c_l = 1$ m/s ($c_s \approx 0.53\ \ 5$ m/s, $c_R \approx 0.\ \ 95\ \ $ m/s).

$$K_{II}(t;V_0) = \nearrow K''(t;V_0) + \int_{l_1}^{V_0 t} [W_{II,I}(0,t \nearrow x_1/V_0;V_0)\tilde{\sigma}^1_{22}(x_1,0) + W_{II,II}(0,t \nearrow x_1/V_0;V_0)\tilde{\sigma}^1_{12}(x_1,0)]dx_1,$$

where $K'(t;V_0)$ and $K''(t;V_0)$ are known functions. These relations, when substituted into the conditions (1), yield a system of two Volterra convolution equations solvable by the Laplace transform in closed form.

In addition to nullifying the stresses $\tilde{\sigma}^1_{j2}(x_1,0)$, $j = 1,2$, the solution for a suddenly stopped crack has to generate zero displacement jumps through the line $x_2 = 0$ on the segment $l_1 < x_1 < V_0 t$. In contrast to the whole plane problem, when this is possible to verify analytically for the sub-Rayleigh speeds [2] and for the transonic regime [4], in the case of a half-plane, it is not visible how it can be done without deploying computer based computations. That is why this condition needs to be tested numerically when the algorithm is applied. Following the pattern established above, this procedure can be continued further up to any period of time (t_k, t_{k+1}). It gives an approximate solution of the problem on motion of a semi-infinite crack beneath the boundary at piecewise constant speed $V = V_i$, $t \in (t_i, t_i + 1)$, $i = 0, 1, \ldots, k$, that approximates the original smooth function $V(t)$. The solution of this model problem, P, is obtained by summing up the solutions of all Problems P_i $(i = \nearrow 1, 0, 1, \ldots, k)$. As for the speeds V_i themselves, they are determined by applying the dynamic Griffith criterion and solving a certain transcendental equation associated with each step of the algorithm.

CONSTANT SPEED: THE WEIGHT FUNCTIONS FOR THE TRANSIENT PROBLEM

The procedure for nonuniform growth of a semi-infinite crack parallel to the boundary of a half-plane requires the knowledge of the weight functions associated with the transient problem for the crack propagating at constant speed V when the upper boundary $\{|x_1| < \infty, x_2 = \delta\}$ of the half-plane is free of traction, and the crack faces are subjected to general time-independent loading. By the Laplace and Fourier transforms with respect to t and $x = x_1 \nearrow Vt$, respectively, the model problem reduces to a vector Riemann-Hilbert problem on the real axis not solvable in closed form by the methods available in the literature. We propose a new approximate method based on splitting of the matrix coefficient into a discontinuous diagonal matrix and a continuous matrix, factorization of the discontinuous part and rewriting the vector Riemann-Hilbert problem as a system of two convolution equations on the segment $\nearrow \infty < x < 0$. We derive the Laplace transforms of the weight functions needed for the problem on nonuniform crack growth in terms of the solution of the convolution equations at the point $x = 0$. The Laplace transform is inverted numerically. We have obtained numerical results for the SIFs when concentrated loads are applied to the crack faces (at time $t = 0$ at the crack tip). This model problem generates four weight functions $W_{i,j}$, $i,j = I, II$. It is discovered that during a certain initial period of time, $0 < t < 2t_l$, before the longitudinal wave reflected from the boundary strikes the crack, the off-diagonal weight functions $W_{i,j}$, $i \neq j$, approximately equal zero, and the diagonal functions do not change their values (Fig.1). When the first longitudinal wave reflected from the half-plane boundary reaches the crack surface moving at speed $V(t) < c_R$, the boundary substantially affects the weight functions.

References

[1] Antipov Y.A., Smirnov A.V.: Subsonic propagation of a crack parallel to the boundary of a half-plane, Math. Mech. Solids, 18: 153-167, 2013.

[2] Freund L.B.: Dynamic Fracture Mechanics, Cambridge University Press, Cambridge, 1990.

[3] Zlatin A.N. Khrapkov A.A.: A semi-infinite crack that is parallel to the boundary of an elastic half-plane, Dokl. Akad. Nauk SSSR, 291, no. 4: 810-813, 1986.

[4] Huang Y., Gao H.: Intersonic crack propagation - Part II: Suddenly stopping crack, J. Appl. Mech., 69: 76-80, 2002.

LINEAR ELASTIC SOLUTIONS FOR SLOTTED PLATES REVISITED

David J. Unger[1a)]
[1]*Department of Mechanical and Civil Engineering, University of Evansville, Evansville, Indiana, 47722, USA*

Summary. Under plane stress loading conditions, the stress concentration factor determined from a finite element analysis of a plate with a slot having rounded ends in the shape of a Riabouchinsky roulette is compared to an analytical expression for the stress concentration factor obtained by a complex variable method. Good agreement is obtained between the two analyses for uniaxial tensile loads applied at infinity in a direction perpendicular to the longitudinal slot axis. When the maximum stress of this particular slot solution is further compared to two analogous hole problems, the elliptical and ovaloid holes, the new stress concentration factor is shown to be lower for identical aspect ratios of principal axes. This would indicate that when stress is critical in a component requiring a slot, this special shape may prove useful.

INTRODUCTON

The linear elastic solution for a crack in a plate [1] subject to a remote uniaxial tension was originally obtained as a limiting case of an elliptical hole problem [2] where the eccentricity of the ellipse approaches one. Similarly, rounded crack tip problems often rely on the same elliptical geometry or some slight perturbation of it such as a parabola (M. Creager, P.C. Paris in [3]) for analytical solutions near the crack tip. Naturally, the machining of an infinitesimally thin line crack in a plate is impossible physically and experimentalists must consequently rely on some variation of a slotted plate as an initial geometry for their test specimens. However, in terms of mathematical analyses, the differences between a linear elastic solution for an elliptical hole and a corresponding solution for a rounded slot may be quite large. Nevertheless, finding an exact mathematical solution of a true slot problem having flat and parallel surfaces with rounded ends has proven elusive. This difficulty arises in part because the most powerful solution scheme for plane elasticity problems, the Kolosov-Muskhelishvili [4] method, is restricted to use of conformal mapping functions that are rational functions of the complex variable. Further, most functions that will map a slotted plane geometry onto a circle to facilitate solution are transcendental functions, most notably, elliptic integrals. These integrals will typically appear whenever the Schwarz-Christoffel transformation is used in mapping a straight-edge boundary onto a circle.

The shape of the slot geometry shown in the insert in Figure 1 was originally derived in a fluid flow context by D. Riabouchinsky, see [5], in regard to free streamlines around two flat plates perpendicular to a uniform flow at infinity. In [6] it was recognized that the free streamline problem in hydrodynamics is analogous to the linear elastic-perfectly plastic antiplane slot problem provided the plastic zone is confined to the curved portions of the slot, whose boundary is entirely traction-free, and where the remote load is applied in the direction of the uniform flow. However, the antiplane problem involves solution of Laplace's equation; whereas, the plane problems in elasticity theory require solution of the higher-order biharmonic equation [7], which places severe restrictions on the mapping function in order to guarantee solution.

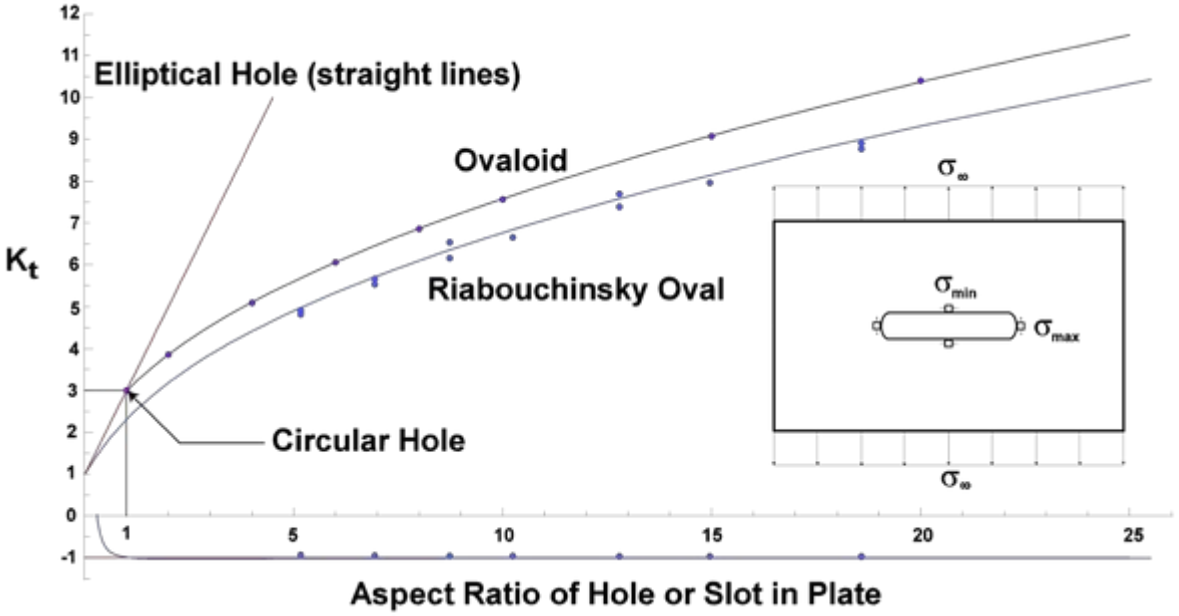

Figure 1. Comparison of Stress Concentration Factors for Various Openings in Plate.

[a)] Corresponding author. Email: du2@evansville.edu

An alternative representation of the mapping function presented in [6] is given by

$$z=\omega(\zeta)=\frac{a}{2}\left\{-(1-k')\frac{1+\zeta^2}{2\zeta}+\operatorname{sgn}\left(\operatorname{Re}(\zeta)\right)\left[k'K\left(m_1\right)-E\left(m_1\right)\right]\right.$$
$$\left.+i(1+k')\left[E\left(\sin^{-1}\frac{i}{k_1}\frac{1-\zeta^2}{2\zeta},k_1{}^2\right)-\frac{(1-k')^2}{(1+k')^2}F\left(\sin^{-1}\frac{i}{k_1}\frac{1-\zeta^2}{2\zeta},k_1{}^2\right)\right]\right\}. \tag{1}$$

This particular function maps the Riabouchinsky oval onto the interior of a circle. Upon the introduction of polar coordinates, $\zeta=\rho\exp i\vartheta$, the boundary of the slot maps onto the circular boundary, $\rho=1$.

Using residue theory, an integral (79.7) of [8] is evaluated to determine the complex potential $\Phi(\zeta)$ of [4, 8]. Because the mapping function (1) is not a rational function of ζ singularities are discovered in the solution. However, it is still possible to glean useful information away from these singularities to determine an approximate solution for the stress concentration factor K_t, which corresponds to the locations of $\sigma_{\max}$ in the insert of Figure 1. The stress concentration factor $\sigma_{\max}/\sigma_\infty$ for the Riabouchinsky oval is found in this manner to be

$$K_t=\frac{1}{2m_1^{1/4}(1+m_1)^2}\left\{3+m_1^{1/4}-3\sqrt{m_1}-m_1^{3/4}+8m_1+m_1^{5/4}-3m_1^{3/2}-m_1^{7/4}+3m_1^{2}\right.$$
$$\left.+\left(m_1^{1/4}-\sqrt{m_1}+m_1+m_1^{5/4}\right)\left[\mathrm{E}(m)-\sqrt{m_1}\,\mathrm{K}(m)\right]\right\}, \tag{2}$$

where the aspect ratio *AR* and various parameters related to the modulus of the elliptic integrals [9] employed in (1) are given by

$$AR=\frac{1-\sqrt{m_1}\left(K(m)+1\right)+E(m)}{2\left[E(\mathrm{m}_1)-\left(1-\sqrt{m_1}\right)K(\mathrm{m}_1)\right]},\ \text{where } m=1-m_1,k'=\sqrt{m_1},k_1=\frac{2\sqrt{k'}}{1+k'}. \tag{3}$$

Note that an additional relationship for the stress concentration factor that corresponds to $\sigma_{\min}$ is also plotted in Figure 1 for the Riabouchinsky oval. This particular result agrees well with the corresponding stress concentration factor for the elliptical hole, which is plotted and is exactly -1 for all aspect ratios. Data points obtained from finite element solutions of the Riabouchinsky slotted plate using the software Ansys® 14.5 are also shown for various aspect ratios with circular markers.

To further test the validity of (2) this relationship is compared with the analysis of [10] for the ovaloid. The ovaloid is defined here as a slotted hole with semi-circular ends. Bowie and Freese performed a detailed hybrid of analytical and numerical analyses to obtain solutions for the ovaloid. A curve fitting their data points by the present author using a simple parabolic relationship is also displayed. One finds that a design based on the Riabouchinsky oval would be conservative relative to the ovaloid as the stress concentration factor is always lower. This is anticipated as the ovaloid has a smaller radius of curvature than does the Riabouchinsky at the location of maximum stress, while having parallel faces similar to those of the Riabouchinsky oval.

CONCLUSION

The analytical expressions derived in this work (2)-(3) may serve as a useful guide for determining maximum stresses in slotted plates subject to remote tensile tractions.

References

[1] Griffith, A.A.: The Phenomena of Rupture and Flow in Solids, *Trans. R. Soc. London*, **221A**,163-197, 1920.
[2] Inglis, C.E.: Stresses in a Plate Due to the Presence of Cracks and Sharp Corners, *Trans. Inst. Naval Architects*, **55**, 219-241, 1913.
[3] Tada, H., Paris, P.C., Irwin, G.R.: The Stress Analysis of Cracks Handbook, 3rd edn, 8-10, ASME Press, New York, 2000.
[4] Muskhelishvili, N.I.: Some Basic Problems of the Mathematical Theory of Elasticity, Kluwer, Dordrecht, 1977.
[5] Milne-Thomson, L.M.: Theoretical Hydrodynamics, 5th edn., 322-324, Dover, Mineola, NY, 1996.
[6] Unger, D.J.: Linear Elastic Solutions for Slotted Plates. *J. Elast.* **108**: 67-82, 2012.
[7] Unger, D.J.: Analytical Fracture Mechanics, Dover, Mineola, NY, 2011.
[8] Sokolnikoff, I.S.: Mathematical Theory of Elasticity, 2nd edn., p. 293, McGraw-Hill, New York, 1956.
[9] Ambramowitz, M., Stegun, I.A.: Handbook of Mathematical Functions with Formulas, Graphs and Mathematical Tables, NBS, Series **55**, U.S. Government Printing Office, Washington, DC, 1964.
[10] Bowie, O.L., Freese, C.E.: Analysis of Notches Using Conformal Mapping, Mechanics of Fracture **5**, Stress Analysis of Notch Problems, ed. Sih, G.C., Noordhoff, Alphen aan den Rijn, 69-134, 1978.

EXPERIMENTAL AND NUMERICAL INVESTIGATION OF HOLLOW SPHERES SUBJECTED TO FRACTURE

Arthur Coré *, Jean-Benoît Kopp, Philippe Viot, Jean-Luc Charles, and Frédéric Dau
Arts et Métiers ParisTech, I2M-DuMAS, UMR 5295 CNRS F-33405, Talence, France

Summary This paper deals with the characterization and the numerical modeling of a new core structure developed to absorb energy during a bird strike on an airplane cockpit. This technology is based on the inclusion of composite hollow spheres in a sandwich structure. An experimental crushing analysis is conducted on a single hollow sphere to quantify the energy dissipated by dynamic fracture. A numerical model based on the Discrete Element Method (DEM) is investigated to take into account the brittle behavior of the constitutive material. The DEM used shows an original approach to correctly describe the dynamic fracture of a spherical and thin structure.

INTRODUCTION

Hollow sphere structure (HSS) belongs to cellular solids that have been studied recently for its multiples properties [1]. In our case, HSS aims to absorb soft impacts energy on an airliner cockpit. HSS is investigated through the SAMBA (Shock Absorber Material for Bird-shield Application) project because of its promises in term of specific energy dissipated (J.kg^{-1}) during impact. Hollow spheres can easily fill a sandwich structure to be placed in front of the plane. Hollow spheres studied in this study are made of epoxy resin and are subjected to dynamic fracture. The formalism of Linear Elastic Fracture Mechanics (L.E.F.M.) is therefore used to estimate the dynamic energy release rate G_{ID_C}. In the interest of studying the rapid crack propagation (RCP) on polymer hollow spheres, a numerical model is investigated. It is based on the Discrete Element Method. It reveals to be an interesting way to model the mechanical behavior of brittle materials.

DYNAMIC CRUSHING OF A SINGLE COMPOSITE HOLLOW SPHERE

Experimental investigation

First of all, quasi-static to dynamic ($v = 5$ mm.s^{-1} to $v = 2$ m.s^{-1}) compression tests are conducted at room temperature on a single sphere ($\phi = 30\ mm$). The material of the sphere appears to behave in a brittle manner. In fact, RCP is observed to be predominant at macroscopic scale, see Fig. 1. The elastic energy stored in the structure at failure is evaluated. This energy reported to the surface (typically the width b times the crack length Δa) is known as the quasi-static energy release rate G_{I0}. The crack tip location is measured during the crack propagation using a high speed camera (60,000 frames per second). The critical dynamic energy release rate G_{IDc} is finally estimated with taking into account inertial effects [2, 3]. Both fracture energies at quasi-static and dynamic ($v = 5$ mm.s^{-1} and $v = 2$ m.s^{-1}) solicitations are deduced and compared.

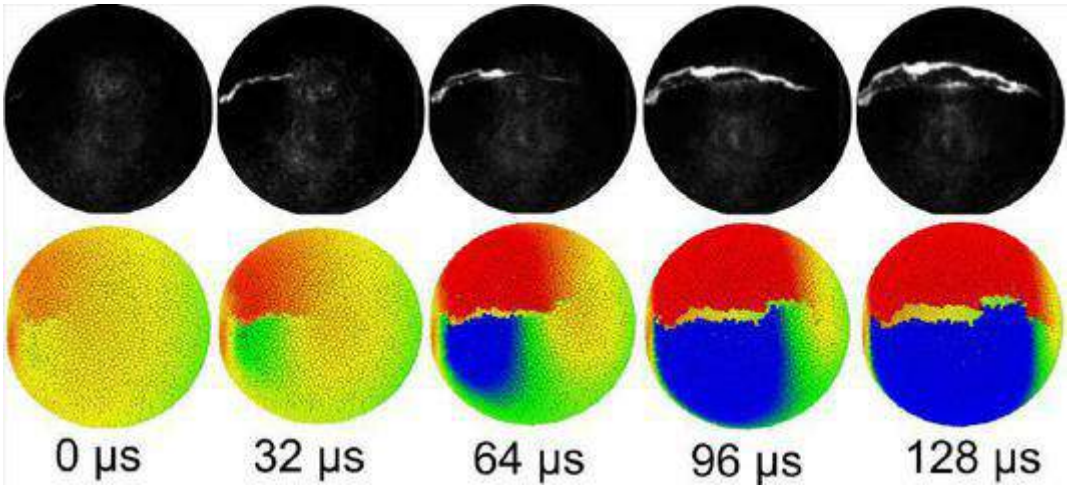

Figure 1: Dynamic compressive test on a hollow sphere (top) and the DEM model (bottom). Captures of the crack propagation versus time

*Corresponding author. Email: arthur.core@ensam.eu

Discrete Element Method

A model based on the discrete element method (DEM) is chosen to simulate the single sphere crushing. This method is well adapted for high strain, dynamic solicitations and fracture. Indeed, the DEM simulates naturally the propagation of cracks by breaking the bonds between each element. 3D simple Bernoulli beams are used as bonds to reproduce the behavior of continuous materials [4]. The principal stress criterion is applied for the crack initiation and propagation. The geometry of the hollow sphere is created by ensuring that the number of discrete element is adequate to represent a continuous material, typically more than 10 000 elements. The numerical sphere is then compressed at different velocities ($v = 1$ m.s^{-1} to $v = 100$ m.s^{-1}). Numerical results are confronted to the previous experiments of crushing spheres, see the force displacement curve in Fig. 2 and the crack initiation and propagation in Fig. 1.

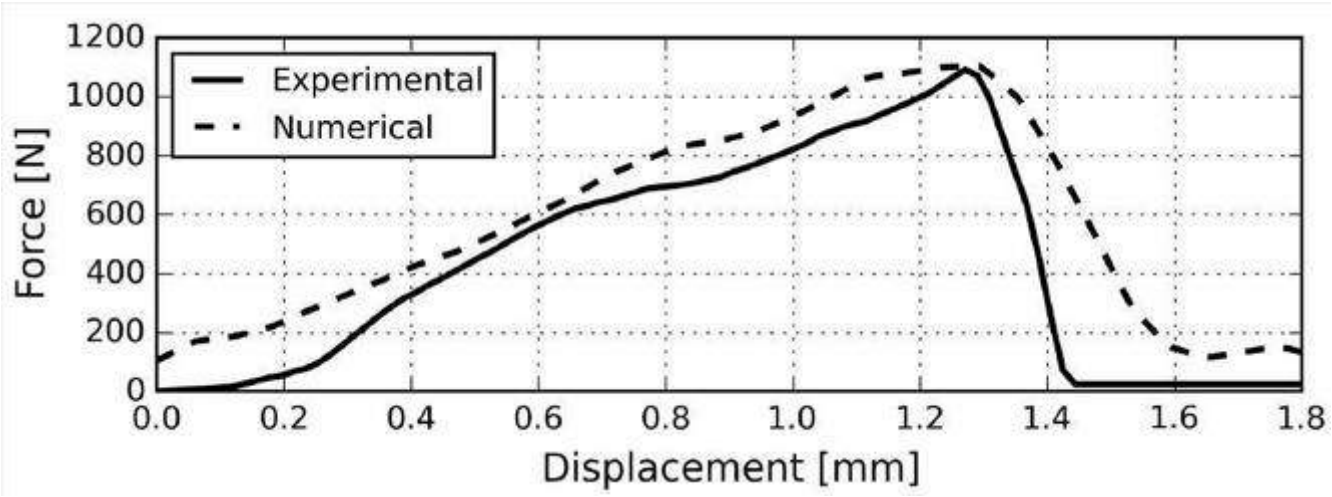

Figure 2: Dynamic compressive test on a composite hollow sphere at $v \approx 2$ m.s^{-1}. Comparison between experimental and numerical results

CONCLUSIONS

The fracture behavior of hollow sphere under quasi-static and dynamic compression tests were investigated using an experimental and a numerical approach. Experiments have been conducted at room temperature and at different compressive velocities (quasi-static to dynamic regime). For the studied material the more the impact velocity the more the crack tip velocity. And the more the crack tip velocity the more the critical energy release rate. G_{IDc} values have been estimated with experimental data to vary from 2.5 ± 0.2 kJ/m^2 in quasi-static to $.2 \pm 1.2$ kJ/m^2 in dynamic. The numerical model using DEM that has been developed to simulate the brittle behavior of the hollow sphere is in good agreement with the experimental data. The crack tip velocity computed is 182 m.s^{-1} with the DEM compared to 21 ± 9 m.s^{-1} measured experimentally. The fracture energy values are both estimated experimentally ($G_{IDc} = .2 \pm 1.2$ kJ/m^2) and numerically ($G_{IDc} = 6.15$ kJ/m^2). The Discrete Element Method used shows an original approach to correctly describe the dynamic fracture of a spherical and thin structure and can be applied to study the interaction between two or more hollow spheres.

References

[1] Augustin, C.: Multifunctional metallic hollow sphere structures: manufacturing, properties and application. Springer Science Business Media, 2009

[2] Broberg KB. The propagation of a brittle crack. *Arkiv Fysik* 1960;18:159

[3] Kopp, J. B., Schmittbuhl, J., Noel, O., Lin, J., Fond, C. (2014). Fluctuations of the dynamic fracture energy values related to the amount of created fracture surface. *Engineering Fracture Mechanics*, 126, 178-189.

[4] André, D., Iordanoff, I., Charles, J. L., Nauport, J. (2012). Discrete element method to simulate continuous material by using the cohesive beam model. *Computer Methods in Applied Mechanics and Engineering*, 213, 113-125.

PLANE STRAIN FRACTURE WITH SURFACE MECHANICS: NON-LOCAL BOUNDARY REGULARIZATION

Jay R. Walton*[1] and Mallikarjunaiah Muddamallappa[2]

[1]*Department of Mathematics, Texas A&M University, College Station, TX, USA*
[2]*Department of Mathematical Sciences, Worcester Polytechnic Institute, Worcester, MA, USA*

Summary The subject of this talk is a classical fracture problem: a single, finite plane strain crack subjected to combined mode I (out-of-plane) and mode II (in-plane shear) loading in the setting of linearized elasticity. It is now well understood that the square-root crack-tip singularities in stress and strain predicted by the classical solution can be removed by augmenting the boundary value problem with a higher-gradient surface mechanics model. However, naive implementation of the resulting boundary condition into standard weak formulations leads to unstable numerical algorithms. It is shown that the boundary value problem can be reformulated using non-local boundary operators to produce a numerically stable weak formulation.

INTRODUCTION

Classical Linear Elastic Fracture Mechanics (LEFM) is arguably one of the most successful theories in applied mechanics despite its well-known logical inconsistency by which it predicts strain singularities at crack edges while being a first-order asymptotic approximation to finite elasticity predicated upon infinitesimally small strains. It has been long understood that this logical inconsistency is due to the failure of classical LEFM to take proper account of nano-scale processes (bond breaking, crazing, dislocation motion, etc) at work near fracture edges. More generally, classical LEFM ignores the complex physical behavior associated with material interfaces even though recognition of its importance in understanding the mechanics of material bodies goes back at least to pioneering work of Gibbs [3] who modeled interfacial mechanics through the notion of a dividing surface endowed with *excess* physical properties (mass, momentum, internal energy, entropy, stress, etc) that separates distinct material phases.

One of the first and still most popular modeling strategies for augmenting LEFM to prevent crack-edge strain singularity predictions is the notion of *cohesive zone* as articulated by Barenblatt [1]. The cohesive zone model, in effect, modifies the traction-free boundary conditions on crack surfaces assumed in classical LEFM. More specifically, a fracture surface is viewed as consisting of two portions—a fully separated section on which traction-free boundary conditions are imposed and a damaged section on which cohesive tractions are imposed.

More recently there has been increasing interest given to augmenting classical LEFM by viewing fracture surfaces as dividing surfaces (in the sense of Gibbs [3]). One of the most popular approaches to modeling the mechanics of fracture surfaces has been the *surface elasticity* paradigm proposed by Gurtin and Murdoch [4]. A key feature of this approach to fracture is that the classical LEFM traction-free boundary condition on fracture surfaces must be replaced by one resulting from the *jump momentum balance* relation that holds on dividing surfaces. Several of the early studies making use of the Gurtin-Murdoch surface elasticity theory to model fracture asserted that the resulted boundary value problems predicted bounded crack-tip strains. However, it was shown in [6] that while the Gurtin-Murdoch surface elasticity model does prevent the strong, square-root, strain singularity at crack-edges predicted by classical LEFM, it still predicts a weak, logarithmic strain singularity.

In a different approach to modeling the mechanics of fracture surfaces [5], the surface stress tensor is assumed to be *Eulerian*, consisting only of (scalar) *surface tension*. However, surface tension is modeled constitutively to be a function of the surface deformation. More specifically, it was shown in [5] that for pure mode I loading (plane-strain, opening mode) of a classical Griffith crack, modeling surface tension to have a linear dependence on linearized (deformed) crack-surface curvature gives a theory that predicts bounded crack-tip strains and stresses. It was subsequently shown [9] that for the corresponding plane-strain problem for a curvilinear crack, this surface tension model, in certain cases, predicts the same weak logarithmic strain singularity at the crack-edge seen with use of the Gurtin-Murdoch theory. More generally, it was shown in [7] that the feature leading to the weak logarithmic strain singularity at a crack edge is whether it is subjected to mixed mode I/mode II loading. When mixed-mode loading occurs at a crack-edge, it was shown in [7] that strain and stress remain bounded at the crack-edge if the surface tension has a linear dependence upon both linearized (deformation based) curvature of the fracture surface and higher-tangential-gradients of the (tangential) crack-surface strain tensor. An analogous result for the simpler anti-plane strain (mode III) crack problem was shown in [2] in which the out-of-plane crack-surface curvature plays no role; surface tension on the crack-surface need only depend upon the (surface) gradient of the (surface) strain tensor within the fracture surface.

*Corresponding author. Email: jwalton@math.tamu.edu

WEAK FORMULATION AND DIRECT NUMERICAL SIMULATION

This talk addresses the issue of implementing the surface mechanics models studied for plane-strain fracture studied in [5]and [7] into finite element based direct numerical simulations. A central challenge encountered to that end is the well-posedness of the weak-form of the fracture boundary value problem corresponding to the surface tension models discussed above. In particular, the surface tension models depending upon higher tangential gradients of the fracture-surface strain tensor give rise to weak formulations of the boundary value problems that include tangential gradients of the crack-surface trace of the bulk strain tensor. The theory developed in [5] and [7] includes regularity results guaranteeing that the boundary traces of the bulk strain tensor has the required tangential smoothness for the weak formulation to make sense. However, it is evident from attempts to do finite element numerical simulations based upon these weak formulations that the standard finite element algorithms are not stable. A way forward was first studied in the simpler setting of a finite-length anti-plane shear crack [2].

Anti-Plane Shear Fracture with Surface Tension

The model studied in [2] models considers a single, anti-plane shear crack lying along the interval $-1 \leq x_1 \leq 1$. Surface tension is modeled by:

$$\tilde{\gamma}(x_1) = \gamma_0 + \gamma_1 u_{3,11}(x_1, 0+), \quad -1 \leq x_1 \leq 1 \tag{1}$$

in which $u_3(x_1, 0+)$ is the out-of-plane displacement of the upper crack surface and $u_{3,11}(x_1, 0+)$ denotes its second-order tangential derivative. The jump-momentum balance on the upper crack surface leads to the boundary condition:

$$u_{3,2}(x_1, 0+) = -\gamma_1 u_{3,111}(x_1, 0+) - \sigma_{23}^{\infty}, \quad -1 \leq x_1 \leq 1 \tag{2}$$

with σ_{23}^{∞} denoting the far-field anti-plane shear loading. The third-order derivative in (2) leads to a direct implementation of (2) based upon the associated weak formulation that is numerically unstable. It was shown in [2] that appealing to the anti-plane shear Dirichlet-to-Neumann map and making use of a particular surface Green's function, one can transform the boundary condition (2) into an equivalent (surface) non-local form:

$$u_{3,2}(x_1, 0+) = \frac{1}{\gamma_1}\left(\int_0^1 k(x_1, q) u_{3,2}(q, 0+)\, dq + \sigma_{23}^{\infty} g(x_1)\right), \quad 0 \leq x_1 \leq 1 \tag{3}$$

in which $k(x_1, q)$ are $g(x_1)$ are explicitly given functions. It was then shown that the non-local boundary condition (3) leads to a stable finite element numerical scheme.

Plane Strain, Mixed-Mode Loading

In [7], it was shown that the following model for surface tension leads to solutions of the fracture problem with bounded crack-tip strains and stresses:

$$\tilde{\gamma}(x_1) = \gamma_0 + \gamma_1 u_{2,11}(x_1, 0+) + \gamma_2 u_{1,1}(x_1, 0+) + \gamma 3 u_{1,111}(x_1, 0+). \tag{4}$$

The associated (linearized) boundary conditions are:

$$\sigma_{22}(x_1, 0+) = -\gamma_0 \sigma_{22}^{\infty} \tag{5}$$

$$\sigma_{12}(x_1, 0+) = -\gamma_2 u_{1,11}(x_1, 0+) - \gamma_3 u_{1,1111}(x_1, 0+) - \gamma_1 u_{2,111}(x_1, 0+) - \sigma_{12}^{\infty}. \tag{6}$$

Generalizing the strategy leading to (3) for the anti-plane shear problem leads to boundary conditions replacing (5) and (6) by a system of non-local integral operators and results a stable finite element algorithm.

References

[1] Barenblatt G. I.: The Mathematical Theory of Equilibrium Cracks in Brittle Fracture, In: Argon A. S. (ed.): Advances in Applied Mechanics. 7:55-129, Academic Press, San Diego, 1962.

[2] Ferguson L., Muddamallappa M., Walton J. R.: Numerical Simulation of Mode-III Fracture Incorporating Surface Mechanics, Int. J. Frac., 192:47-56, 2015.

[3] Gibbs J. W.: Collected Works Vol. 1. Longmans, New York, 1928.

[4] Gurtin M. E., Murdoch A. I.: A Continuum Theory of Elastic Material Surfaces. Arch. Ration. Mech. Anal. 57:291-323, 1975.

[5] Sendova T., Walton J. R.: A New Approach to the Modeling and Analysis of Fracture through Extension os Continuum Mechanics to the Nanoscale. Math. Mech. Solids. 15:368-413, 2010.

[6] Walton J. R.: A Note on Fracture Models Incorporating Surface Elasticity. J. Elast. 109:95-102, 2012.

[7] Walton J. R.: Plane-Strain Fracture with Curvature-Dependent Surface Tension: Mixed-Mode Loading. J. Elast. 114:127-142, 2014.

[8] Walton J. R., Zemlyanova A. Y. : A Rigid Stamp Indentation into a Semi-Plane with a Curvature-Dependent Surface Tension on the Boundary, in press, Int. J. Frac., 2015.

[9] Zemlyanova A. Y., Walton J. R.: Modeling of a Curvilinear Planar Crack with a Curvature-Dependent Surface Tension, SIAM J. Appl. Math., 72:1474-1492, 2012.

INTERTWINED SPIRALING CRACK PATH IN PERFORATED SHEETS

Benoît Roman *[1], Juan-Francisco Fuentealba[2], and Eugenio Hamm[2]
[1]*Physique et Mecanique des Milieux Hétérogènes - UMR 7636 CNRS/ESPCI/Paris6/Paris7, 10 rue Vauquelin 75231 Paris CEDEX 05, France*
[2]*Departamento de Física Universidad de Santiago de Chile, Avenida Ecuador 3493, 9170124 Estación Central, Santiago, Chile.*

Summary When a brittle sheet is indented by a rigid cone, a radial fracture pattern is usually observed ("petalling"). We show experimentally here that when the number n of cracks is smaller than 4, a spiraling pattern is observed instead of the petalling mode. In the limit of very thin and very brittle sheet, we do find solutions where the crack path are intertwined logarithmic spirals, and compute the corresponding perforation force. Both the geometry and the force agree well with experiments.

We study experimentally and theoretically the crack patterns arising from the quasi-static perforation of a thin brittle sheet by a rigid cone. We use polypropylene sheets, in which crack initiation and splitting are not possible for the typical stresses that develop during perforation. Starting from a large number n of initial radial notches, cracks are observed to propagate

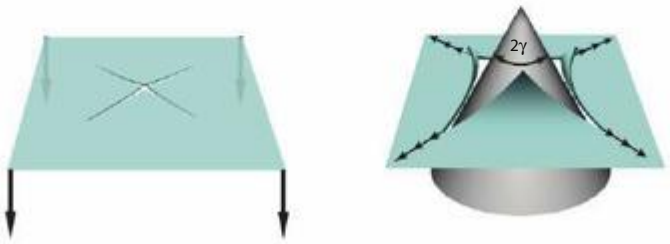

Figure 1: Indentation of a brittel thin sheet by a rigid cone.

along straight radial lines. But for a sufficiently small number n, we observe tears that spontaneously swirl one around each other.

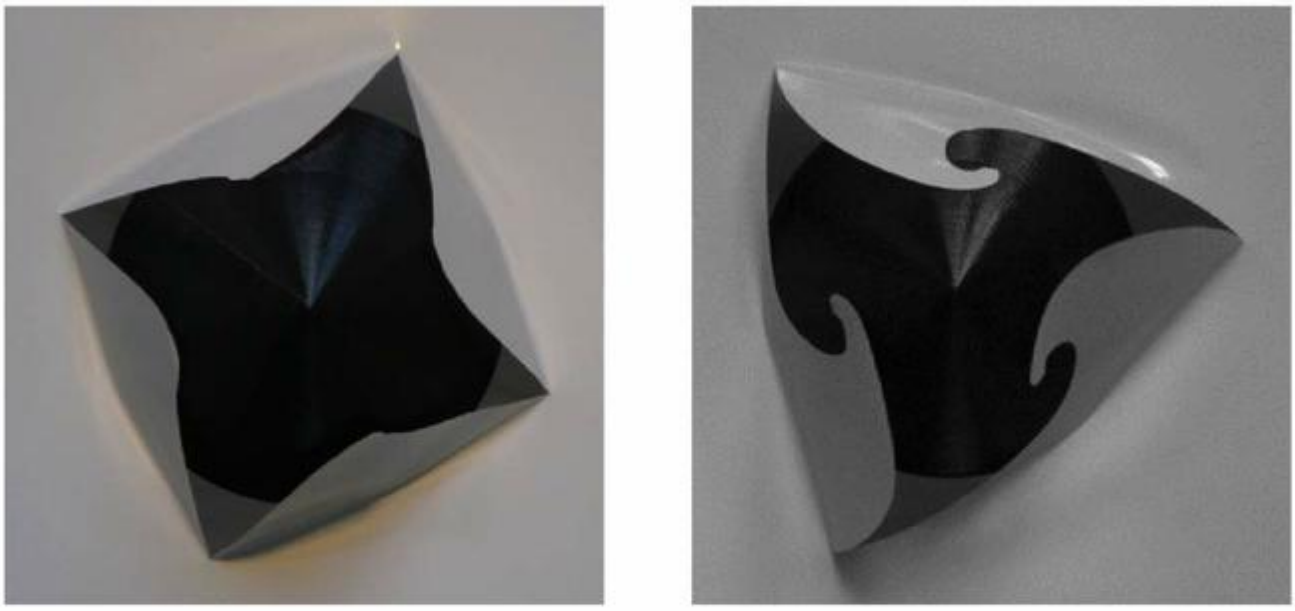

Figure 2: Top view of experiment. Four cracks leads to radial propagation (left); three cracks: intertwined spirals (right).

The same pattern has been reported by Vermorel [1] but not studied so far. This unexpected behaviour challenges numerical and theoretical modeling which usually assume that cracks propagate radially leading to petalling patterns [2]. We also observe a similar multiple spiral pattern when pulling the flaps of material perpendicularly away from the sheet, as in [3].

*Corresponding author. Email: benoit.roman@espci.fr

Although spiral fracture patterns have been observed in coatings under residual tensile stresses [4, 5, 6, 7] the spirals reported here are of a very different nature, since they involve the interaction of several cracks through large out-of-plane bending.

We give a theoretical description of the crack path based on basic principles of fracture mechanics in very thin brittle sheets [8]. This leads us to a purely geometrical problem where the existence and shape of multiple spiral cracks can be explained in terms of a delayed crack interaction. We examine the maximum number of spiral arms, and compare the measured and predicted tearing forces for the spiral and radial modes [9].

We find that spiral mode cannot develop for a number of crack larger than 4, which suggest that only the radial solution exists in these cases. For $n <$, radial as well as spiral patterns may compete, and it remains to be explained why the radial solution is unstable in this case.

References

[1] N. Vandenberghe, R. Vermorel, and E. Villermaux, Phys Rev Lett 110, 174302 (2013).

[2] Y.-W. Lee and T. Wierzbicki, Int J Impact Eng 31, 1277 (2005).

[3] V. Romero, B. Roman, E. Hamm, and E. Cerda, Soft Matter 9, 8282 (2013).

[4] J. Marthelot, J. Bico, F. Melo, and B. Roman, J Mech Phys Solids 84, 214 (2015), ISSN 0022-5096.

[5] M. Sendova and K. Willis, Applied Physics A: Materials Science and Processing 76, 957 (2003).

[6] Z. Neda, K. t. Leung, L. Jozsa, and M. Ravasz, Phys Rev Lett 88 (2002).

[7] V. Lazarus and L. Pauchard, Soft Matter 7, 2552 (2011).

[8] B. Roman, Int J Fracture 182, 1 (2013)

[9] J-F. Fuentealba , E. Hamm , and B. Roman, to be submitted (2016)

CRACK TIP BLUNTING AND CLEAVAGE UNDER DYNAMIC CONDITIONS

Varun P. Rajan *[1] and William A. Curtin[1]
[1]*Institute of Mechanical Engineering, EPFL, Lausanne, Vaud, Switzerland*

Summary Because many structural materials comprise two or more phases, fracture often involves growth of cracks from one phase to another. Researchers have hypothesized that dynamic effects are important in these processes, and can promote brittle failure in engineering alloys. We assess this hypothesis of "dynamic embrittlement" using molecular dynamics (MD) simulations. We focus on whether dynamics affects the energy barriers for crack tip dislocation emission or cleavage, and what happens in the dynamically overloaded situation, when both processes are energetically possible. In the MD simulations, we employ a novel potential, with a tunable energy barrier for dislocation emission, and a novel simulation technique, termed a "dynamic cleavage test." Our simulation results indicate that the competition between cleavage and emission—i.e., the intrinsic ductility of the material—is unaffected by dynamics. Finally, we discuss the implications of this finding for understanding the micromechanisms of fracture in engineering alloys.

INTRODUCTION

Tough structural metals are often composed of a ductile matrix phase and brittle inclusions or precipitates. Cracks initiate in the brittle phase and should be arrested when they encounter the ductile phase. Since such cracks run dynamically in the brittle phase after initiating from pre-existing flaws, the dynamic response of the system may govern the macroscopic "quasi-static" toughness. One important example is mild steel, where cracks develop within grain boundary carbides and propagate dynamically toward the primary α-ferrite grains. At sufficiently low temperatures, these cracks are often observed to cleave through the ferrite, resulting in an undesirable, low-toughness, transgranular mode of failure [Lin et al.(1987)]. One model for this process postulates that brittle failure arises because of dynamics, which suppresses dislocation emission and crack blunting, thereby causing the crack tip to remain atomically sharp [Lin and Thomson(1986), Lin et al.(1987)]. In this work, we assess this hypothesis. We pose two questions. First, how does dynamics affect the competition between brittle (cleavage) and ductile (dislocation emission) modes of crack tip deformation (i.e., the "intrinsic ductility" of a material)? Second, is it possible that cleavage is preferred over dislocation emission in an "overloaded" dynamic condition, where G exceeds both the Griffith cleavage value (G_{Ic}) and the dislocation emission value (G_{Ie}), even though dislocation emission is preferred under quasistatic conditions?

This paper is organized as follows. We describe a set of molecular dynamic simulations, termed "dynamic cleavage tests," in which a crack initiates within a brittle material and runs dynamically into a second material (typically ductile). In these simulations, we employ a novel set of interatomic potentials, for which the (quasistatic) intrinsic ductility can be tuned while leaving the surface energy and elastic constants unchanged, to avoid effects of elastic mismatch. The simulations reveal that dynamics *cannot* embrittle a ductile material; that is, if a crack tip at rest emits dislocations, then the same crack tip in motion will also emit dislocations. Finally, we explore the implications of this finding for understanding brittle failure in engineering alloys.

SIMULATION OF DYNAMIC CLEAVAGE

We conduct dynamic cleavage simulations in both 2D (hexagonal lattice) and 3D (FCC lattice) using molecular dynamics (MD). The simulation, illustrated schematically in Figure 1, uses a bi-material strip geometry. One part of the strip (Material 1), containing the initial crack, is described using the most brittle material (highest G_{Ie}/G_{Ic}) while the other part of the strip (Material 2) contains a more ductile material into which the initial crack will be driven. Using the strip geometry, a prescribed energy release rate (G) can be delivered to the crack. To describe interatomic interactions, we use a new flexible pair potential, developed for both 2D (hexagonal) crystals and 3D (FCC/HCP) crystals [Rajan et al.(in press)]. In these potentials, the unstable stacking fault energy can be changed independently of the surface energy or elastic constants. Therefore, these potentials differ only in the value of G_{Ie}, which can be tuned over a wide range, spanning the transition between brittle ($G_{Ie} > G_{Ic}$) and ductile ($G_{Ie} < G_{Ic}$) materials.

RESULTS

In 2D, dynamic cleavage tests were run at an applied load of $G/G_{Ic} = 1.61$. The normalized crack velocity v/c_R vs. crack position is shown in Figure 2. As seen, dynamic cracks encountering the more brittle materials ($G_{Ie}/G_{Ic} = 1.72$, 2.10, 2.53) grow dynamically into the second material while remaining atomically sharp. Dynamic cracks encountering the more ductile materials ($G_{Ie}/G_{Ic} \leq 1.37$) emit one or more dislocations, and then blunt and arrest at the interface. Thus, the critical

*Corresponding author. Email: varun.rajan@epfl.ch

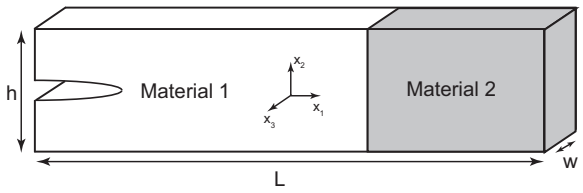

Figure 1: Strip geometry for dynamic cleavage test.

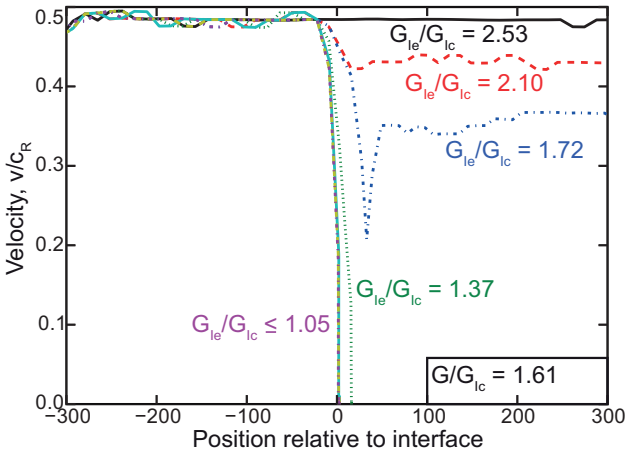

Figure 2: Crack velocity in 2D dynamic cleavage test. The second material has varying ductility ($G_{Ie}/G_{Ic} = 0.56 - 2.53$). Applied load is $G/G_{Ic} = 1.61$.

energy release rate for dynamic dislocation emission appears to be close to that in the quasistatic case, G_{Ie}; dynamics does not appear to affect the energetics of this process. In the overloaded case, even if cleavage is kinetically favorable relative to dislocation emission, ductile crack tip behavior will ultimately prevail as long as a *single* emission event can occur. This is because such an event irrevocably changes the competition between brittle and ductile crack tip behavior, arresting the crack and causing it to blunt. Subsequent behavior of the crack then depends on the critical *quasistatic* G_{Ie} and G_{Ic} in the *blunted* configuration, which generally also favors dislocation emission, at least for intrinsically ductile materials. We also find similar results for 3D FCC and HCP crystals (see [Rajan et al.(submitted)]).

CONCLUSIONS

Our central conclusion is that there is no evidence that dynamic effects can embrittle a material, at least in terms of altering the local crack tip behavior. The energy barrier for dislocation emission is unchanged by dynamics, and, in the overloaded situation, ductile crack tip behavior ultimately prevails. Thus, explanations for (semi-)brittle fracture in engineering materials should not rely on the dynamic embrittlement hypothesis. A fruitful path for further investigation may be provided by multi-scale methods that couple atoms to dislocations, enabling both micro-scale (dislocation elasticity) and atomic-scale (crack tip deformation) phenomena to be taken into account. Regardless, the present study points to the importance of understanding the small-scale mechanisms of fracture in semi-brittle materials. These will help to elucidate the role of dynamics in embrittlement, and may ultimately hold the key to designing tougher steels and other engineering alloys.

References

[Lin et al.(1987)] T. Lin, A. G. Evans, and R. O. Ritchie. Stochastic modeling of the independent roles of particle size and grain size in transgranular cleavage fracture. *Metallurgical Transactions A*, 18(5):641–651, 1987.

[Lin and Thomson(1986)] I.-H. Lin and R. M. Thomson. Dynamic cleavage in ductile materials. *Journal of Materials Research*, 1(01):73–80, 1986.

[Rajan et al.(in press)] V. P. Rajan, D. H. Warner, and W. A. Curtin. A novel interatomic potential with tunable intrinsic ductility. *In Press, Modelling and Simulation in Materials Science and Engineering*.

[Rajan et al.(submitted)] V. P. Rajan and W. A. Curtin. Crack tip blunting and cleavage under dynamic conditions *Submitted, Journal of the Mechanics and Physics of Solids*.

CRACKING THE CRACK: WHAT DO WE LEARN ABOUT THE STATISTICAL PROPERTIES OF FRACTURE SURFACES?

Laurent Ponson[1a)], Stéphane Vernède[2] & Jean-Philipe Bouchaud[3]
[1]*Institut Jean le Rond d'Alembert, CNRS – Université Pierre et Marie Curie, Paris, France*
[2]*Tortoise Analytics, Paris, France*
[3]*Captital Fund Management, Paris, France*

Summary Fracture surfaces have been a preferred field of investigation for understanding material failure as their roughness encodes the crack growth mechanisms. But the challenge is to decipher this information in terms of failure processes. Here, we analyze the roughness of several fractured materials like concrete, ceramics and metallic alloy and show that they share the same statistical structure: Below some length scale ξ, the slope amplitudes are uncorrelated and the surface is mono-affine while above ξ, long-range spatial correlations lead to a multifractal behavior, reminiscent of turbulent flows. These features reveal a common growth mechanism of cracks that propagate through damage coalescence at small scale and resembles to an elastic line at large scale. The crossover length ξ characterizes the extent of the crack tip damaged zone. Its measurement from the statistical analysis of fracture surfaces provides a way to measure the toughness of a material after its failure.

INTRODUCTION

After thirty years of research, it is now well established that fracture surfaces exhibit robust, universal fractal statistical properties [1]. For purely brittle failure, the roughness exponent is reported to be $\zeta \approx 0.45$ whereas for materials that undergo damage during failure, $\zeta \approx 0.75$. It has been conjectured that these exponents are signatures of the fracture mechanism above and below the process zone size [2]. We address here the question of the co-existence of these two regimes on fracture surfaces and provide tools that highlight their differences beyond the value of the roughness exponent.

THE COMMON STATISTICAL STRUCTURE OF FRACTURE SURFACES

Three materials are considered, an aluminum allow, a mortar and a ceramic, representative of different failure behaviors to elicit roughness properties common to a large range of materials. The topography $h(\mathbf{x})=h(x,z)$ of the fracture surface is shown on Fig. 1 together with the distribution $P_{\delta r}$ of height variations $\delta h = h(\mathbf{x}+\delta\mathbf{x}) - h(\mathbf{x})$ where the sampling is done on all admissible positions $\mathbf{x}$ and $\delta\mathbf{x}$ such as $\delta r = |\delta\mathbf{x}|$. We focus here on the height variations at different scales δr and treat fracture surfaces as isotropic maps. An interesting property of the family of distributions $P_{\delta r}$ is that they follow a Gaussian behavior at large scales $\delta r >> \xi$ while they exhibit fat tail statistics at small scales $\delta r << \xi$ as evidenced from the comparison with parabolas characteristic of Gaussian distributions in the semi-logarithmic representation of Fig. 1.

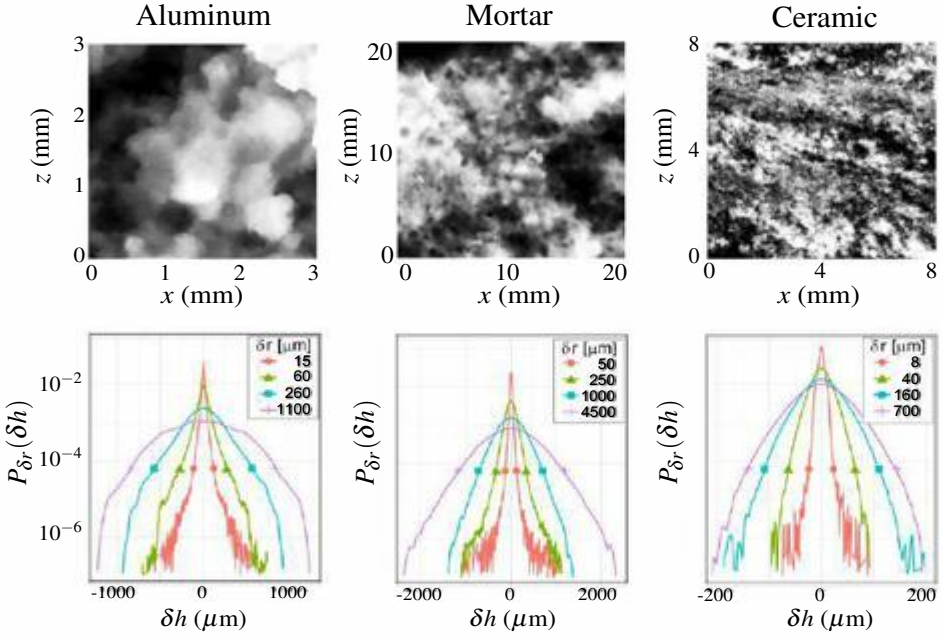

Figure 1: The top panels show the height maps of three fracture surfaces characteristic of three main failure mechanisms, namely ductile failure (aluminum alloy), quasi-brittle failure (mortar) and brittle failure (ceramics). The bottom panels show their distributions of height variations computed at different scales $\delta r=|\delta\mathbf{x}|$: It shows a Gaussian behavior for $\delta r >> \xi$ against fat tail behavior for $\delta r << \xi$ where ξ is a material dependent length scale measured in Fig. 2.

To measure the crossover length scale ξ between fat tail and Gaussian statistics, we introduce the following operator

$$\omega(\mathbf{x}) = 1/2 < \log(\delta h(\mathbf{x}, \delta\mathbf{x})^2 >_{|\delta\mathbf{x}|=\varepsilon} - \Omega_\varepsilon. \quad (1)$$

It transforms the original height map $h(\mathbf{x})$ into a map $\omega(\mathbf{x})$ of the local roughness amplitude that is defined from an average of the height variations over a circle of radius ε centered in $\mathbf{x}$. The constant Ω_ε is chosen such that $<\omega(\mathbf{x})>_{\mathbf{x}} = 0$. The fields ω

a) Corresponding author. Email: laurent.ponson@upmc.fr - Website: www.laurentponson.com

computed for the three fracture surfaces considered are shown in Fig.2. The patterns that emerge on the fracture surfaces through this transformation correspond to steep cliffs and reveal complex correlations of the height variations. Their characteristic size is reminiscent of the length scale ξ evidenced from the variations of $P_{\delta r}$ with δr.

The spatial correlations of ω are studied through the function $C(\delta r) = \langle \omega(\mathbf{x})\omega(\mathbf{x}+\delta\mathbf{x})\rangle_{\mathbf{x},|\delta\mathbf{x}|=\delta r}$ that is represented in Fig. 2 as a function of δr for different values of ε; C(δr) is independent of ε whenever ε << δr. For the three materials considered, we observe two regimes: At small δr, ω shows strong spatial correlations which decay logarithmically as C(δr) ~ -log(δr/ ξ) and extrapolates to zero for δr = ξ. For larger distances, these correlations are zero within statistical noise. ξ corresponds to the characteristics size of the patterns of the ω-fields shown in Fig.2.

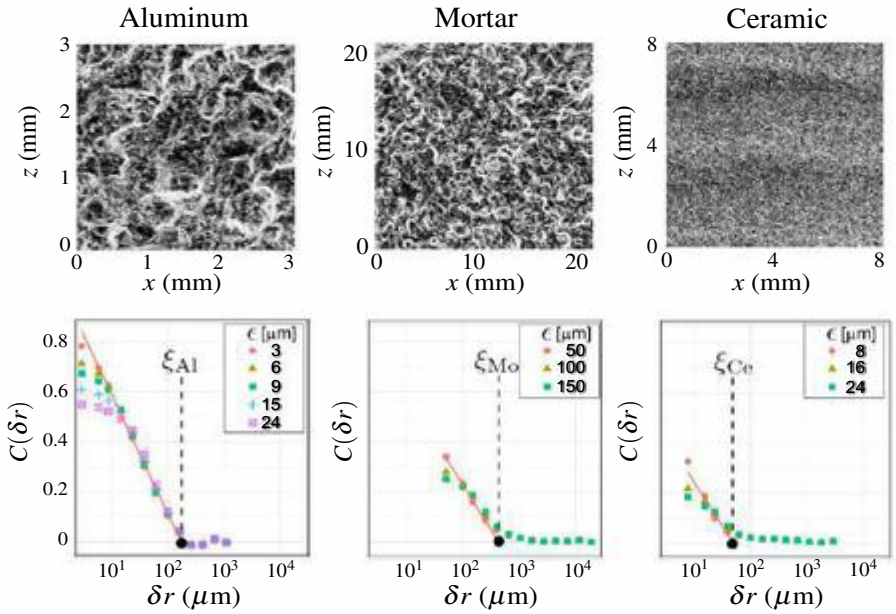

Figure 2: Fracture surfaces shown in Fig. 1 processed through Eq. (1) to highlight the steepest cliffs that are shown in white. The characteristic size ξ of the patterns visible on these maps is obtained from the variations of their correlation function C(δr) ~ -log(δr / ξ) and gives ξ = 170 μm, 430 μm and 170 μm for the aluminum alloy, the mortar and the ceramics fracture surface, respectively.

The presence of two ranges of length scales with distinct statistical properties on the surfaces of these materials is clear: For δr << ξ, the height fluctuations are strongly correlated and display non-Gaussian statistics while for δr >> ξ, the roughness follows a Gaussian behavior with no spatial correlation of the ω-field. The presence of these regimes is confirmed by the value of the roughness exponent that characterizes the scaling properties of the fracture height map h(**x**): For δr << ξ, the surface is multi-affine and ζ ≈ 0.75 while at larger scales δr >> ξ, the surface is mono-affine and ζ ≈ 0.45 [3].

THE STATISTICS OF FRACTURE SURFACES AS A PARADIGM FOR CRACK GROWTH PHENOMENA?

What is the physical interpretation of these observations? We believe that the presence of spatially correlated steep cliffs on short length scales δr << ξ is a strong indication that at these scales, fracture proceeds through the nucleation and coalescence of microcracks. On the contrary, for scales larger than ξ, the mechanism of crack growth is essentially brittle, and the surface is the trace left by an elastic line propagating in a random medium. As a result, the statistical properties of fracture surfaces recover the traditional text-book picture for crack propagation: Damage localizes at the crack tip vicinity while Linear Elastic Fracture Mechanics applies at larger distances from the crack tip where the material behaves elastically. But it actually goes beyond this classical description as fracture surfaces do display universal statistical features at small scale too. This suggests that the process of damage coalescence taking place within the process zone is common to many materials.

Within this scenario, the length ξ is a measurement of the extent of the damaged region near the crack tip where dissipation takes place. This observation paves the way to the measurement of the toughness of materials from the analysis of their fracture surfaces. We will show the various benefits of this approach as it allows the *post-mortem* characterization of the material failure properties that is relevant in failure analysis [4]. We will also illustrate how this approach can be used to achieve an improved characterization of the material failure properties, at it provides not only the material resistance at the structure scale, but also its toughness at the local scale, like for example at the microstructure scale.

References

[1] D. Bonamy and E. Bouchaud, 'Failure of heterogeneous materials: A dynamic phase transition?', *Phys. Rep.* **498**, 1-44, 2011.

[2] D. Bonamy and L. Ponson and S. Prades and E. Bouchaud and C. Guillot, 'Scaling exponents for fracture surfaces in homogeneous glass and glassy ceramics ', *Phys. Rev. Lett.* **97**, 135504, 2006.

[3] S. Vernède, L. Ponson and J.P. Bouchaud, 'Turbulent fracture surfaces: A footprint of damage percolation?', *Phys. Rev. Lett.* **114**, 215501, 2015.

[4] S. Vernède and L. Ponson, 'Procédé de caractérisation de la fissuration d'un matériau à partir de sa surface de rupture', *French patent* 1459525, 2014.

INVESTIGATION OF FRACTURE IN LARGE DUCTILE PLATES

Pawel Woelke[1a] & John W. Hutchinson[2]
[1]*Thornton Tomasetti – Weidlinger Applied Science, New York, USA*
[2]*School of Engineering and Applied Sciences, Harvard University, Cambridge, MA, USA*

Summary: Fracture investigation for plate structures is important for many industrial applications (e.g. marine, automotive, aerospace, oil & gas). Quantification of the energy dissipated during the fracture process can lead to not only better predictive capabilities but also to possible improvements in the material processing and joining technology, e.g. welding. This is especially relevant for undermatched welds, where the weld metal and/or heat affected zone are significantly weaker than the parent metal (e.g. aluminum welds, some high strength steels). This strength reduction, caused by welding, results in localization of plastic deformation in the weld and HAZ which negatively affects structural performance. A comparative study of energy dissipated during ductile fracture of two aluminum plates, one welded and one unwelded is presented here. The analysis results show that the effect of welding can be very significant for the energy of fracture both in the fracture process zone and away from the crack.

INTRODUCTION

We investigate fracture in two large scale aluminum plates subjected to mode I tensile loading. A numerical, comparative study of the unwelded Al6080-H116 and friction stir welded Al6061-T6 is conducted using shell finite elements with cohesive zone representing the details of the fracture process that cannot be reliably captured by the discretization level that is realistic for structural applications. A brief discussion of the cohesive zone calibration method is provided. The presented study indicates that while welding in considered Al6061 plate causes significant strength reduction of the heat affected zone (HAZ) material, it also leads to significant ductility increase. This results in very high relative toughness of the HAZ material in reference to the parent metal. A comparative study between the welded and unwelded plates also shows that, in the unwelded plate, significant energy dissipation occurs outside of the fracture process zone while plastic dissipation in the welded plate is confined to the weld and heat affected zone.

EXPERIMENTAL SETUP AND ANALYSES RESULTS

Mode I fracture in two aluminium plates is investigated here. The first plate under consideration is a pre-notched, 10mm thick, unwelded Al5083-H116 plate tested by Simonsen and Tornqvist [5]. The notch tip is blunt which was accomplished by drilling a 5mm diameter hole at the initial tip. The plate was tested under mode I tensile loading with a force-displacement response measured during the test, as shown in Figure 1 (left side). The plate was modelled using shell elements with in-plane dimension larger than thickness. A significantly more detailed discretization level, involving 3D elements with an advanced constitutive model, such as shear-modified Gurson model [2] is prohibitive for large scale structural applications. Cohesive zone model was used to represent the details of the fracture process which cannot be captured by shell elements. The cohesive zone calibration methodology was based on detailed plane-strain strip simulation performed by Nielsen and Hutchinson [4] as discussed in greater detail by Woelke et al. [13]. The calibrated, position-dependent cohesive traction-separation relationship allowed capturing not only the measured force-displacement response and overall behaviour of the plate, but also the crack growth resistance curve (R-curve). The results of the analyses indicate that only about 30% of the total energy dissipated during the plate deformation, was dissipated in the cohesive zone (i.e. the fracture process zone). Nearly 70% of the plastic dissipation occurred outside the cohesive zone, i.e. in the plate away from the crack, which indicates a large scale plasticity, as shown in Figure 1.

The second plate discussed here is an extruded, friction stir welded Al6061-T6 plate subjected to mode I tension. The extrusion walls were 3mm thick, as was the weld thickness joining the two sides together. Welding aluminium is problematic, since the heat introduced into the material during welding basically removes the effects of hardening returning the metal (in the weld/HAZ zone) to nearly annealed condition (low strength and high ductility state). This effect is especially pronounced for heat-treatable aluminium alloys, such as 6xxx series. Thus, we expect that the weld and HAZ zone areas will be significantly weaker than the parent metal, which will affect the energy dissipation. As previously, a shell finite element model was developed to represent the plate behaviour, with cohesive zone representing the weld and HAZ. The cohesive zone was calibrated based on the coupon level tensile test performed by Zheng et al. [14]. The simulated response matched very well the overall plate behaviour as well as the measured force displacement response. The investigation of the energy dissipation indicates that the heat affected zone is significantly more ductile than the parent metal. The steady-state toughness of the weld/HAZ, achieved after the crack has propagated several thicknesses is significantly higher than the parent metal away from the weld. It is also significantly higher than the corresponding steady-state toughness calculated for the unwelded Al5083-H116 plate discussed above. This is quite remarkable considering the fact that the nominal plane strain toughness of unwelded Al5083-H116 is more than twice that of unwelded Al6061-T6 ($\Gamma_{Ic-5083-h116} = 27kJ/m^2$ vs. $\Gamma_{Ic-6061-t6} = 12kJ/m^2$). In the same time, the HAZ is also significantly weaker than the parent metal which results in localization of plasticity in the weld and HAZ, limiting plastic dissipation outside of cohesive zone. A comparison of the plastic strain contours in the unwelded Al5083-H116 and welded Al6061-T6 plates, given in Figure 1 clearly show significant reduction of the overall plastic dissipation in the case of the welded plate.

[a)] Corresponding author. Email: pwoelke@thorntonttomasetti.com

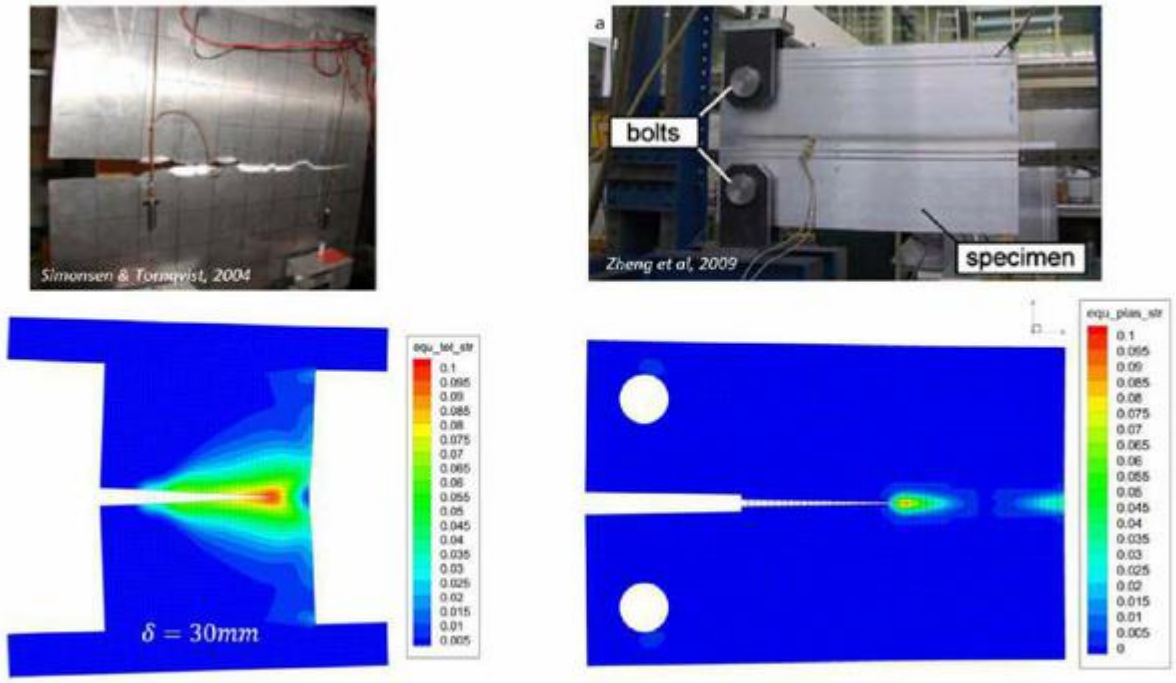

Figure 1 – Mode I ductile tearing of large plates: a) Al5083-H116 plate tested by Simonsen and Tornqvist [5] with corresponding finite element solution, and b) Al6061-T6 welded extrusion tested by Zheng et al. [14] with corresponding finite element solution

CONCLUSIONS

The presented study shows that the ductile fracture behaviour of large plates can be successfully represented by carefully calibrated cohesive zone model. This modelling approach allows approximate quantification of the energy dissipation in considered plates both in the fracture process zone and away from the crack. The analyses results presented here show that, for considered materials, strength reduction associated with welding aluminium is accompanied by significant ductility increase. Unfortunately, lower strength of the HAZ leads to localization of plasticity in that zone. This suggest that careful optimization of the size of the HAZ formed during welding can result in significant overall performance improvement for structures with undermatched welds.

References

[1] Li, W., & Siegmund, T. (2002). An analysis of crack growth in thin-sheet metal via cohesive zone model. *Engineering Fracture Mechanics, 69*, 2073-2093.

[2] Nahshon, K., & Hutchinson, J. W. (2008). Modification of the Gurson Model for shear failure. *European Journal of Mechanics A. / Solids*, 1-17.

[3] Nielsen, K.L. (2010). Predicting failure response of spot welded joints using recent extensions to the Gurson model. *Computational Materials Science.* 48, 71–82.

[4] Nielsen, K. L., & Hutchinson, J. W. (2011). Cohesive traction-separation laws for tearing of ductile metal plates. *International Journal of Impact Engineering*, 48, 15-23.

[5] Simonsen, B. C., & Törnqvist, R. (2004). Experimental and numerical modelling of ductile crack propagation in large-scale shell structures. *Marine Structures, 17*, 1-27.

[6] Tvergaard, V., & Hutchinson, J. W. (1992). The relation between crack growth resistance and fracture process parameters in elastic-plastic solids. *Journal of the Mechanics and Physics of Solids, 40*, 1377-1397.

[7] Voyiadjis, G.Z. and Woelke, P. (2005). General non-linear finite element analysis of thick plates and shells. *Int. J. Solids Structures*; Vol. 43; Issue 7-8, 1; p. 2209-2242

[8] Voyiadjis, G.Z. and Woelke, P. (2006), "Elasto-Plastic and Damage Analysis of Plates and Shells", 2008 Springer-Verlag.

[9] Wang, T., Hopperstad, O.S., Larson, P.K., and Lademo, O.-G. (2006). Evaluation of a finite element modeling approach for welded aluminum structures. *Computers and Structures*. 84, 2016-3032.

[10] Woelke, P., Abboud, N. (2012). "Modeling fracture in large scale shell structures" *J. Mechanics and Physics of Solids*, 60, (12), 2044-2063.

[11] Woelke, P., Shields, M.D., Abboud, N.N., and Hutchinson, J.W. (2013). "Simulations of ductile fracture in the idealized ship grounding scenario using phenomenological damage and cohesive zone models". *Computational Material Science*, 80; 79-95

[12] Woelke, P., Voyiadjis, G.Z. and Perzyna, P. (2006) "Elasto-plastic finite element analysis of shells with damage due to microvoids". *Int. J. Num. Meth. Eng.*, Vol. 68, (3), pp. 338 – 380.

[13] Woelke, P.B., Shields, M.D. and Hutchinson, J.W. (2015). Cohesive zone modeling and calibration for mode I tearing of large ductile plates. *Engineering Fracture Mechanics*, 147; 293-305

[14] Zheng, L., Petry, D., Rapp, H., and Wierzbicki, T. (2009). Characterization of material and fracture of AA6061 butt weld. *Thin-Walled Structures*. 47, 431-441.

DYNAMIC FRACTURE AND ORIENTATION RELATIONS OF H.C.P.-F.C.C. SYSTEMS

S. Ziaei[1] & M. A. Zikry[1a]
[1] *Department of Mechanical and Aerospace Engineering, North Carolina State University, Raleigh, NC, USA*

Summary We investigated how coherent interfaces, between f.c.c./h.c.p. systems, affect large strain deformation and fracture modes in h.c.p. zircaloy aggregates with f.c.c. hydrides. We derived 36 unique transformations related to coherent interfaces between f.c.c. and h.c.p. systems. We then used these ORs with a dislocation-density crystalline plasticity formulation, a non-linear finite-element and a fracture approach that account for crack nucleation and propagation. We investigated how these ORs affect crack nucleation and propagation, dislocation density and inelastic slip evolution, stress accumulation, lattice rotation, and adiabatic heating. The predictions indicate that the physical representation of ORs affect local deformation and fracture behavior, and are, therefore, essential for accurate predictions of behavior at different physical scales in heterogeneous crystalline systems.

MULTIPLE-SLIP CRYSTAL PLASTICITY DISLOCATION-DENSITY BASED FORMULATION

The multiple-slip crystal plasticity rate-dependent constitutive formulation and the derivation of the mobile and immobile dislocation-densities are briefly outlined. The dislocation-density crystal plasticity constitutive framework used in this study is based on the formulation developed by Zikry [1, 2]. It is assumed that the velocity gradient is decomposed into a symmetric deformation rate tensor, D_{ij}, and an anti-symmetric spin tensor W_{ij}. D_{ij} and W_{ij} can then be additively decomposed into elastic and inelastic components and the inelastic parts can be defined in terms of the crystallographic slip-rates. These slip rates can be then related to immobile and mobile dislocation densities, and it is assumed that, for a given deformed state of the material, the total dislocation-density, $\rho^{(\alpha)}$ can be additively decomposed into a mobile and an immobile dislocation-density, $\rho_m^{(\alpha)}$ and $\rho_{im}^{(\alpha)}$. Furthermore, the mobile and immobile dislocation-density rates can be coupled through the formation and destruction of junctions as the stored immobile dislocations act as obstacles for evolving mobile dislocations.

ORIENTATION RELATIONS (ORS) BETWEEN F.C.C. AND H.C.P. PHASES

The polycrystalline zircaloy-2 aggregate consists of the h.c.p. matrix and the f.c.c. hydrides. Hence, For 24 slip systems in h.c.p. and 12 slip systems in f.c.c., ORs are needed to account for the coherency between the crystalline phases. The lattice parameters of these two phases are such that the $(111)_{\text{f.c.c.}}$ plane is identical to the $(0001)_{\text{h.c.p.}}$ plane [4]. When the two crystalline phases are along their close packed planes and directions, the resultant interface is fully coherent. This coherency results in an ORs between the two crystalline phases, such that the slip planes and directions are parallel for the systems of $(111)_\alpha // (0001)_\kappa$ and $[\bar{1}10]_\alpha // [11\bar{2}0]_\kappa$, where α denotes an f.c.c. system and κ denotes an h.c.p. system [3,4,5]. Based on this, 36 unique ORs can be obtained for the parallel directions and planes between the f.c.c. and h.c.p. phases. Furthermore, the hydride f.c.c. orientations have to be related to the global orientation, and, therefore, two transformations are needed. The first transformation, $[T]_1$, relates the hydride f.c.c. (α) OR to the parent h.c.p. (κ) Euler grain orientations. The second transformation, $[T]_2$, relates the h.c.p. Euler grain orientation to the global coordinates. These transformations are given by $[X]_{\text{Global}} = [T]_2\,[T]_1 * [X]_\kappa$.

COMPUTATIONAL APPROACH

The total deformation rate tensor D_{ij} and the plastic deformation rate tensor D_{ij}^p, are needed to update the material stress state. The method used here is that developed by Zikry [1] for rate-dependent crystalline plasticity formulations, and only a brief outline will be presented here. For quasi-static deformations, an implicit FE method with BFGS iteration is used to obtain the total deformation rate tensor D_{ij}. To overcome numerical instabilities associated with stiffness a hybrid explicit-implicit method is used to obtain the plastic deformation rate tensor D_{ij}^p. The hybrid approach is based on using explicit Runge-Kutta, and an implicit Euler method, when numerical stiffness is encountered. Numerical stiffness can be encountered when due to different rate changes along slip systems, slip-rates, resolved shear–stresses, and dislocation-densities can vary widely.

RESULTS AND DISCUSSION

The multiple-slip dislocation-density-based crystal plasticity formulation, and the overlap fracture method were used to investigate the microstructural failure behavior of zircaloy-2. The parent h.c.p. zircaloy-2 grains and the f.c.c. hydrides are assumed to have random low angle misorientations, where the maximum misorientation was assumed to be less than 5°. In this investigation, it is assumed that the hydride volume fraction is approximately 3%, which is physically representative of zircaloys [6-9]. A convergent plane strain FE mesh of 6000 elements, with a model size of 4mm×5mm, with symmetric boundary conditions, was subjected to tensile loading for a dynamic nominal strain rate of 5000 s^{-1} .

[a] Corresponding author. Email: zikry@ncsu.edu.

We then investigated how a crack in an aggregate subjected to a nominal strain-rate of 5000/s. We, again, examined two cases, one case with the ORs and one case without the ORs. The crack length was taken as a/w=0.1, and it is an edge crack. As noted earlier, the crack would dynamically propagate when the maximum fracture stress is exceeded on one of the cleavage basal planes.

At a nominal strain of 4%, the maximum lattice, with and without the ORs are shown. As it can be clearly seen, the fracture behavior is different for both cases. For the case with ORs, the propagating crack is non-planar, and it deviated around the hydrides. Furthermore, cracks also nucleated at the bottom and at the top for both cases, and these cracks nucleate due to the reflecting inelastic waves. For the case without the ORs, the crack is planar, and the lattice rotations were significantly higher by approximately 60%. These higher lattice rotations were due to not physically representing ORs. Furthermore, the deviation of the cracks, for the case with ORs, is consistent with experimental observations pertaining to zircaloys with hydrides that show that cracks deviate around the hydrides. Hence, these results clearly indicate the necessity of accurately accounting for f.c.c./h.c.p. interfaces. (Figures 1 a-b)

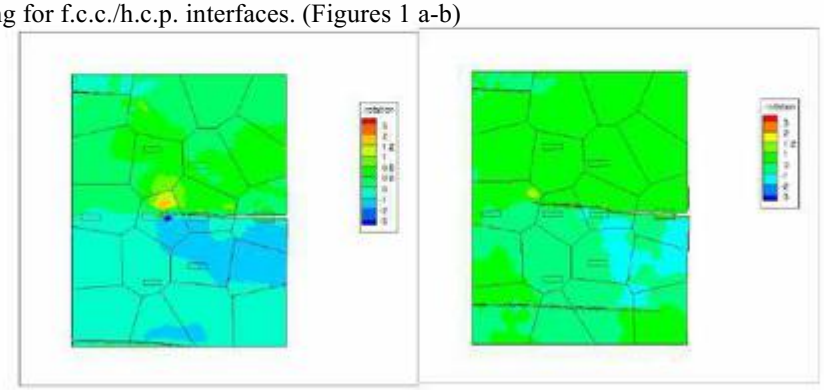

(a) (b)

Fig. 1: Lattice rotation at 20% (a) no ORs (b) with ORs at 4% nominal strain

CONCLUSIONS

We have presented a dislocation density based multiple slip crystal plasticity formulation that accounts for ORs between f.c.c. and h.c.p. systems. We investigated the effects of ORs for an aggregate with and without cracks subjected to dynamic loading conditions. We obtained 36 unique ORs between parallel directions and planes between the relevant f.c.c. and h.c.p. systems. The ORs significantly affected local behavior, in aggregates without cracks, such as shear slip accumulation, dislocation-density evolution, lattice rotation, thermal and stress buildup. For the case with a preexisting crack, the ORs had a significant effect on crack paths and orientations. The edge crack curved around the hydrides for the aggregate with ORs, and for the cases without ORs, the crack path was planar. This crack deviation and nonplanar behavior was due to the ORs and the higher stresses ahead of the crack front. For the aggregates with ORs, there was higher dislocation-density accumulation along the pyramidal plane due to lattice rotation in comparison with the case without ORs. These crack orientations are also consistent with experimental observations. This study underscores the need to represent the coherency between f.c.c. and h.c.p. interfaces in heterogeneous crystalline systems for accurate predictions of local behavior.

REFERENCES

[1] Zikry MA. Comput.Struct. 1994; 50:337.

[2] Wu Q, Shanthraj P, Zikry MA. Int. J. Fract. 2013; 184:241.

[4] Porter DA, Easterling KE, Sherif M. CRC press 2009; Textbook - 520 Pages.

[5] Pilania G, Thijsse BJ, Hoagland RG, Lazic I, Valone SM, Liu X. Sci.Rep. 2014; 4.

[6] Zhang M-, Chen S-, Ren H-, Kelly PM. Metallurgical and Materials Transactions A-Physical Metallurgy and Materials Science 2008; 39A:1077.

[7] Chen CQ, Li SX, Zheng H, Wang LB, Lu K. Acta Materialia 2004; 52:3697.

[8] Alam AM, Hellwig C. Zirconium in the Nuclear Industry: 15th International Symposium 2009; 1505:635.

[9] Arsene S, Bai JB, Bompard P. Metallurgical and Materials Transactions A 2003; 34:553.

THERMOMECHANICAL FRACTURE IN SHAPE MEMORY ALLOYS

Theocharis Baxevanis*[1], Sameer Jape[1], Antonino Parrinello[2], and Dimitris C. Lagoudas[1,3]
[1]*Department of Aerospace Engineering, Texas A&M University, College Station, TX 77843-3409, USA*
[2]*Department of Engineering Science, University of Oxford, Oxford, OX1 3PJ, UK*
[3]*Department of Materials Science & Engineering,, Texas A&M University, College Station, TX 77843-3409, USA*

Summary The effect of thermomechanically-induced phase transformation on the fracture response of Shape Memory Alloys (SMAs) is investigated by means of the finite element method. The prototype center-crack problem is analyzed numerically during thermal cycling under isobaric loading conditions. This thermomechanical loading path is an idealization of typical loading paths that utilize SMAs as actuators. Results show that during cooling under constant load, the driving force for crack growth can increase drastically, an order of magnitude for specific material systems, and stable crack growth may be triggered resulting eventually in SMA actuators' ultimate failure, in accordance with experimental evidence.

INTRODUCTION

The forthcoming commercial use of SMA actuators in aeronautics, automotive, and energy conversion and storage is expected to drastically increase the technological importance of fracture in SMAs under combined thermomechanical loading. As of today, most studies on the fracture resonse of SMAs, as reviewed in [1], are devoted to isothermal fracture of SMAs and little to no evidence is provided regarding non-isothermal fracture.

Owing to their unique thermomechanical properties, fracture response of SMAs is more complex than that of traditional structural metals and metallic alloys due to reversible phase transformation, detwinning and reorientation of martensitic variants, transformation-induced plasticity, and the strong thermomechanical coupling.

The present work is a first attempt to explore the fracture of SMAs during actuation, *i.e.*, under thermomechanical loading. As recently observed U-notched NiTi specimens may fail during cooling under a constant applied tensile load that is lower than the isothermal strength at the beginning of cooling [1]. For the U-shape notched specimens tested, failure by the formation of an unstable crack during cooling was observed for bias load levels as low as 50% of the isothermal bias load needed for failure at the beginning of cooling. This is an intriguing response that, from an energetic point of view, seems in disagreement with the general view of dissipative processes such as phase transformation resulting in an enhancement of fracture toughness.

FINITE ELEMENT ANALYSIS OF ACTUATION-INDUCED FRACTURE IN SMAS

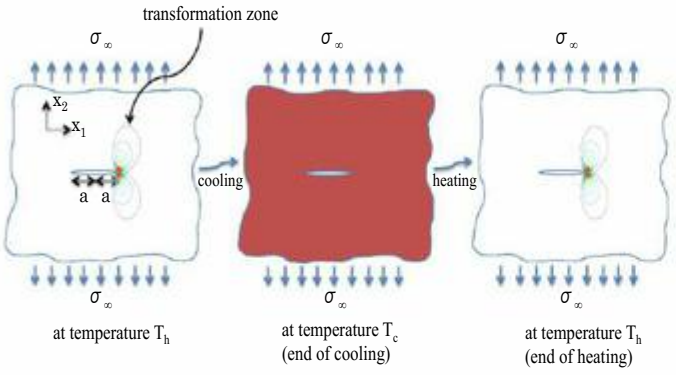

Figure 1: Boundary value problem for an infinite center-cracked SMA plate in initial austenite phase subjected to a constant far-field uniaxial tensile loading and thermal cycling. Martensite regions are shown in red color and austenite ones in blue.

An infinite center-cracked SMA plate subjected to thermal cycling under plane strain constant applied loading is assumed. The SMA plate is subjected to far-field in-plane uniform uniaxial tensile load, in the direction normal the crack line as shown in Fig. 1. The load is applied at a nominal temperature higher than the austenitic-finish temperature, A_f, and a region of transformed material is formed near the crack tip. Maintaining the tensile load at the boundary constant, the entire cracked SMA specimen is then subjected to thermal cycling, *i.e.*, alternate cooling and heating between the high temperature at which the mechanical load is applied and a low temperature that is smaller than M_f (to ensure that the bulk of the specimen completely transforms between pure austenite and martensite).

The incremental response of the material inside the fully transformed zone surrounding the crack tip is linear elastic at all times, and the fields are characterized by a crack-tip energy release rate, G_I. A finite element mesh of 8-node, isoparametric quadrilateral elements is constructed in ABAQUS to represent the center-cracked SMA specimen with a finer mesh density in front of the the crack-tip. The VCCT capability of ABAQUS, which is an extension of the classical crack-closure technique based on Irwin's crack closure integral is employed to calculate G_I.

*Corresponding author. Email: theocharis@tamu.edu

Driving force for crack growth prior to crack advance

During cooling, the thermomechanically-induced "global" scale phase transformation, *i.e.*, transformation extending to infinity, results in stress redistribution near the crack that substantially increases the crack-tip energy release rate, an order of magnitude for some material systems [2]. The evolution of normalized crack-tip energy release rate, G_I/G_∞, during a thermal cycle is shown in Fig. 2 under the assumption that the critical crack-tip energy release rate value required for crack growth is never reached, where G_∞ represents the energy release rate resulting from the applied mechanical load prior to thermal cycling. G_I/G_∞ first increases during cooling owing to "global" phase transformation occurring in a fan ahead of the crack tip where the transformation strains have an anti-shielding effect and reaches a peak. It then decreases, as a result of phase transformation occurring in regions behind the crack tip, before attaining a constant value at temperature $T = M_f$, at which the entire SMA specimen has fully transformed into martensite. During heating, the energy release rate starts increasing at $T = A_s$, which marks the beginning of reverse phase transformation behind the crack tip, reaches a peak, and decreases before attaining a constant value.

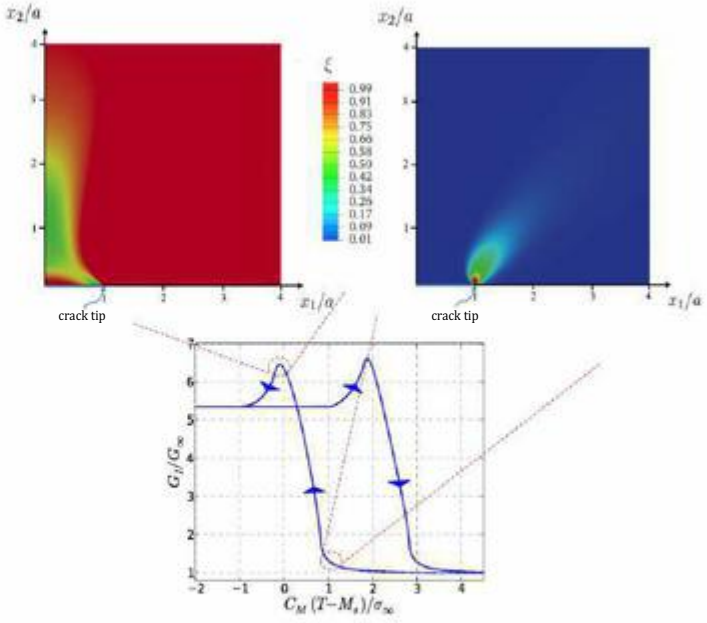

Figure 2: Normalized energy release rate, G_I/G_∞, versus normalized temperature, $C_M(T - M_s)/\sigma_\infty$, and martensite volume fraction, ξ, during cooling. The martensite volume fraction distribution during heating is similar to the one during cooling for the same values of G_I/G_∞.

Toughness enhancement associated with crack advance

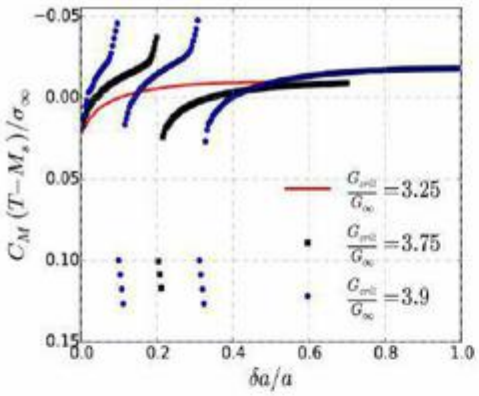

Figure 3: Normalized temperature, $C_M(T - M_S)/\sigma_\infty$, vs. normalized crack growth, $\delta a/a$, for varying bias loads, G_{crit}/G_∞.

Crack growth is assumed to occur when the crack tip energy release rate reaches during cooling the material specific critical value. Stable crack growth arises due to stress redistribution caused by the transformation deformations left in the wake of the growing crack that shields the crack and thus further cooling is required for maintaining a critical stress field at the advancing crack tip [3]. Eventually, once the crack advances a distance comparable to its initial length, the increment of the loading parameter, *i.e.*, temperature, needed to achieve a given increment of growth diminishes and the crack approaches nominally steady-state growth at a constant temperature. In Fig. 3, temperature vs crack growth results are plotted for different bias load levels, σ_∞, resulting in G_{crit}/G_∞ equal to 3.25, 3.75, and 3.9. For sufficiently high values of G_{crit}/G_∞ (= 3.75 and 3.9), *i.e.*, sufficiently low bias loads, the material is capable of sustaining multiple cooling/heating cycles before crack growth reaches nominally steady state conditions.

CONCLUSIONS

A numerical analysis of static and advancing cracks in SMA actuators during thermal cycling under constant bias load levels is performed. The numerical results show that during cooling "global"-scale forward phase transformation produces an anti-shielding effect on the crack, raising the driving force for crack growth at the tip. Stable crack growth is numerically observed due to transformation toughening, which is quite similar to the one observed in pseudoelastic SMAs or other dissipative material systems, and can extend over several heating-cooling cycles before resulting to structural failure.

References

[1] Baxevanis, T. and Lagoudas, D.C.: Fracture mechanics of shape memory alloys: review and perspectives. Int. J. Fract. 191: 191-213, 2015.

[2] Baxevanis, T., Parrinello, A. and Lagoudas, D.C.: On the driving force for crack growth during thermal actuation of shape memory alloys. J. Mech. Phys. Solids. In press.

[3] Jape, S., Baxevanis, T. and Lagoudas, D.C.: Stable crack growth during thermal actuation of shape memory alloys. Shape Mem. Superelasticity. In press.

STATISTICAL SIMULATION OF BIAXIAL FATIGUE BEHAVIOUR AFFECTED BY MICROSTRUCTURE

Toshihiko Hoshide [1a)] & Yuta Hitotsugi [2]
[1]Department of Energy Conversion Science, Kyoto University, Kyoto, Japan
[2]Graduate School of Energy Science, Kyoto University, Kyoto, Japan

Summary In this work, a modelling procedure was developed so that it should be applicable to the analysis of crack growth in materials with various microstructures under biaxial fatigue. Microstructures of two different polycrystalline materials were modelled by using Voronoi-polygons as grains. Then, the crack initiation was analysed as the slip plane separation in an individual grain, and the number of cycles required for the separation was calculated by using a dislocation pile-up model. In the crack propagation stage, the crack growth was analysed as a competition between the growth by crack coalescence during crack initiation and propagation stages and the propagation of a dominant crack as a single crack. Cracking morphologies and failure lives simulated by using the proposed model were compared with experimental results, and it was found that good correspondences were seen between them.

INTRODUCTION

It is recognized that crack growth in low cycle fatigue is affected by two factors; i.e., material microstructure and stress state. By considering difficulty in conducting experiments for various combinations of these factors, some theoretical approaches incorporating the two factors with themselves are required in order to describe crack growth behaviour, which determines fatigue life influenced by such factors. However, any appropriate procedure is not established. In this work, a simulation procedure based on theoretical model are developed, and simulated fatigue life are discussed statistically.

THEORETICAL MODELING AND SIMULARION PROCEDURE

Theoretical modelling is developed so that it should be applicable to the analysis of crack growth in materials with various microstructures under biaxial fatigue. Microstructures on component surface are modelled with Voronoi-polygons. Figure 1 presents examples of modelled microstructures with different morphologies, in which a grain is expressed as one Voronoi-polygon. In the modelled microstructure, the crack initiation is analysed as the slip plane separation in an individual grain having the slip-band length d which is equivalent to the length 2a of a crack initiated in the grain. It is assumed that a crack is initiated when a resolved shear stress $\tau_{\xi\eta}$ exceeds the critical shear stress τ_c to make a slip active and the number of cycles passes up to N_i to be required for the separation as follows.

$$\tau_{\xi\eta} > \tau_c \quad \text{and} \quad N_i = \frac{2\,G\,W_c}{\pi\,(1-\nu)\,d\,(\tau_{\xi\eta}-\tau_c)^2}$$

N_i is calculated by using a dislocation pile-up model [1], and G, ν and W_c are respectively the shear elastic modulus, Poisson's ratio and the fracture surface-energy, all of which are material constants.

The crack growth is analysed as a competition between the growth by crack linkage during crack initiation and propagation stages, and the propagation as a single crack which is expressed as a power function of J-integral range ΔJ as

$$da/dN = C\,(\Delta J)^m$$

A schematic illustration of the crack growth model proposed in this work is shown in Fig. 2. In the present study, simulations are iterated fifty times for a material under a given condition of loading by using different series of random numbers. The fatigue life is defined as the number of cycles at which a dominant crack grows to have a specified length. Consequently, fifty different cracking patterns and fatigue lives are obtained for the material under the loading condition.

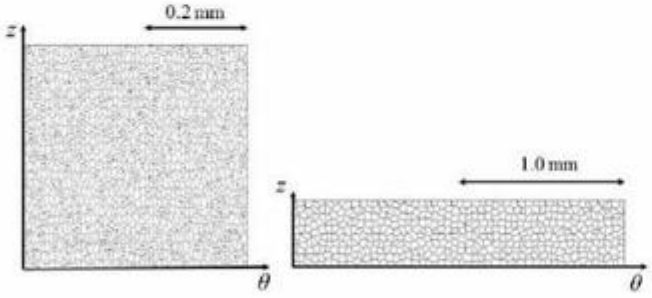

(a) (α+β) Ti-alloy (b) β Ti-alloy

Fig. 1. Examples of modelled microstructures

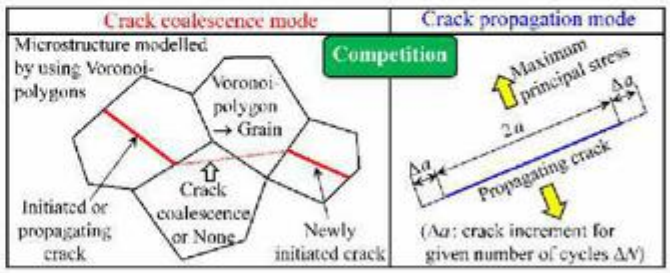

Fig. 2. Competition modelling for fatigue crack growth.

a) Corresponding author. Email: hoshide.toshihiko.5c@kyoto-u.ac.jp

ANALYTICAL RESULTS AND DISCUSSIONS

Analytical results simulated by using the developed model were compared with experimental results in fatigue tests which had been carried out by using notched specimens of (α+β) and β titanium (Ti) alloys [2]. Simulations were conducted for two Ti alloys. Examples of simulated cracking morphologies in (α+β) Ti alloy are depicted in Fig. 3, in which bold lines represent dominant cracks. It is clarified that the results shown in Fig. 3 almost coincides with experimental observations.

In Fig. 4, the experimentally observed fatigue lives are compared with scatter-bands of simulated lives, which are depicted as error-bars. The actual fatigue lives under axial and combined loading are almost covered within a scatter of factor of 3. Under torsional loading, however, the simulated fatigue life has a large dispersion, and the actual lives are almost covered within a scatter of factor of 10, which is larger than the scatter under the other two loading modes.

Table 1 summarises statistical parameters presenting the scatter in simulated lives, in which $N_{f,ave}$ and CV are respectively average lives and coefficient of variation. Parameters, α, $N_{f,S}$ and $N_{f,L}$, are respectively shape, scale and location parameters, which constitute Weibull distribution function. Since larger CV or smaller α imply larger scatter, it is confirmed that the largest dispersion appears in fatigue life distribution under torsional loading mode especially.

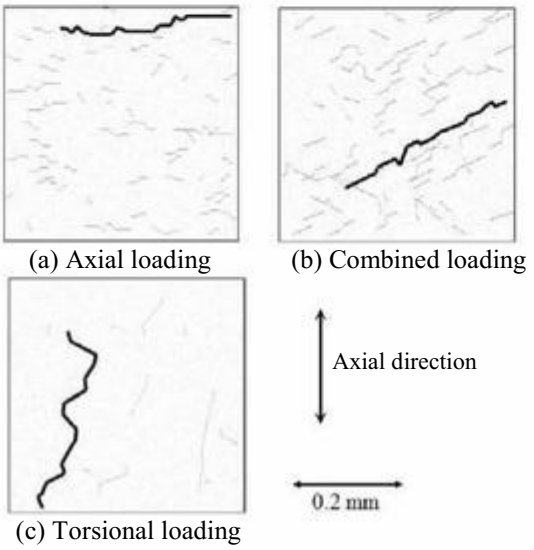

Fig. 3. Simulated cracking morphologies in (α+β) Ti alloy.

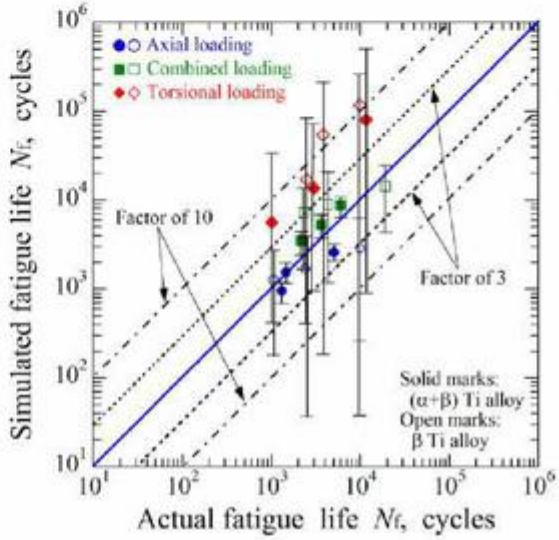

Fig. 4. Comparison between actual and simulated lives.

Table 1. Statistical characteristics of fatigue lives simulated for middle level of applied stress.

Material	Loading mode	Statistical parameters		Two-parameter Weibull dist. function		Three-parameter Weibull dist. function		
		$N_{f,ave}$	CV	α	$N_{f,S}$	α	$N_{f,S}$	$N_{f,L}$
(α+β) Ti alloy	Axial loading	1560	0.1147	10.43	1635	3.203	625.5	1000
	Combined loading	5356	0.1486	8.030	5678	2.851	2490	3140
	Torsional loading	13650	1.835	1.095	10850	0.6978	9373	939.2
β Ti alloy	Axial loading	1699	0.5094	2.199	1898	1.566	1565	298.5
	Combined loading	9013	0.5435	1.902	10160	1.878	10090	60.45
	Torsional loading	54570	0.9555	0.6929	50320	0.7348	50590	-200.2

CONCLUSIONS

In this work, microstructures of two different polycrystalline materials were modelled by using Voronoi-polygons, and a theoretical procedure for analysing crack growth in a modelled microstructure was proposed. By comparing simulated and experimental results, good coincidences were seen between them. It may be concluded that the proposed procedure is applicable to the analysis of crack growth affected by microstructural variation and stress biaxiality.

References

[1] Tanaka K., Mura T.: Dislocation model for fatigue crack initiation, *Trans. ASME, J. Appl. Mech.* **48**, 97-103, 1981.

[2] Hoshide T., Hirota T., and Inoue T.: Fatigue behavior in notched component of (α+β) and β titanium alloys under combined axial-torsional loading, *Mater. Sci. Res. Int.* **1**, 169–174, 1995.

PREDICTION OF FRACTURE TOUGHNESS SCATTER OF COMPOSITE MATERIALS AS FUNCTION OF MICROSTRUCTURE

Yan Li[1(a)] & Min Zhou[2]

[1]*Department of Mechanical and Aerospace Engineering, California State University, Long Beach, CA, 90840, USA*
[2]*The George W. Woodruff School of Mechanical Engineering, School of Materials Science and Engineering Georgia Institute of Technology, Atlanta, GA 30332, USA*

Summary Weibull distribution has been widely used to determine the probability of material fracture. However, its role has been primarily confined to fitting fracture toughness data rather than providing predictive insight of material fracture toughness and its magnitude of scatter. Besides, the Weibull parameters which are obtained through curve fitting carry little physical significance. In this paper, a multiscale framework is developed to predict material fracture toughness of composite materials in a statistical sense. The Weibull distribution parameters are correlated with the statistical measures of microstructure characteristics and the statistical characterization of the competition between crack deflection and crack penetration at matrix/reinforcement interfaces. The established correlations are useful for material sensitive design.

INTRODUCTION

Fracture toughness of a composite material is not a deterministic property. This is primarily due to the stochastic nature of its microstructure as well as the activation of different fracture mechanisms during the crack-microstructure interactions [1-3]. Prediction of material fracture toughness as well as its scatter is one of the biggest challenges in material sensitive design. The crack interactions with microstructure can result in different failure mechanisms which ultimately determine the variation of fracture toughness [4, 5]. Most of the existing probabilistic models for fracture toughness prediction only consider near crack-tip stress states [6-8]. Information regarding microstructure characteristics and failure mechanisms associated with the crack propagation process is not explicitly included in the model formulations. This is due to the fact that the material heterogeneities at the microstructure level and the interaction of a propagating crack with phases in a microstructure are hard to quantify. Both of them are very random and complicated. Li and Zhou [5] developed a semi-empirical model which allows fracture toughness of Al_2O_3/TiB_2 ceramic composites to be predicted. Although this quantification lends itself to the establishment of relations between the statistical attributes of microstructure, fracture mechanism and the fracture toughness of the material, the material fracture toughness is predicted in an average sense from the CFEM (Cohesive Finite Element Method) simulations in Li and Zhou [2]. Based on the previous work, a modified multiscale model is introduced which allows the possible range of fracture toughness values to be predicted as function of microstructure. The Weibull distribution parameters are directly correlated to the two-point correlation functions as well as the quantification of fracture mechanisms. These relations can be used for material reliability design by controlling the fracture toughness scatter through microstructure tailoring.

MODEL FORMULATION

For Al_2O_3/TiB_2 ceramic composites, a crack can propagate into Al_2O_3 matrix, TiB_2 reinforcements or along the interface in between. Our attention is primarily focused on the last two scenarios since they are the two competing fracture mechanisms when a crack interacts with reinforcements. He and Hutchinson [9, 10] first proposed an energy based criterion which quantifies the competition between crack deflection and crack penetration when a semi-infinite crack is perpendicular to an infinite planar interface. This criterion is only valid for isotropic bi-material which is symmetrically loaded. Based on the previous work, Li and Zhou [5] further extend He and Hutchinson's criterion by including the effects of finite reinforcement size s, reinforcement shape $\bar{\rho}$ and distribution in a two-phase composite material. The criterion is parameterized by

$$U = \frac{1-\beta^2}{a_0\left(1-\alpha\right)}\left[\left|c\right|^2+\left|h\right|^2+2R_e\left(ch\right)\right]\bar{\rho}^{a_1}e^{\left(\frac{a_2}{s}\right)}-\frac{\Phi_{in}}{\Phi_p}, \tag{1}$$

to determine the activation of the two competing failure mechanisms. Specifically, interface debonding, which is activated by crack deflection, is predicted when $U>0$. Otherwise, crack penetration induced reinforcement cracking will be activated instead.

Two-point correlation functions are employed to statistically parameterize the probability of crack interactions with randomly distributed particles in the microstructure. For example, $\mathrm{P}_{01}\left(D\right)$ quantifies the probability of a crack which is

[a)] Corresponding author. Email: Yan.Li@csulb.com.

initially in the matrix phase 0 to encounter the reinforcement phase 1 within propagation distance D. Based on the physical implications of two-point correlation functions, the crack length associated with interface debonding, matrix cracking and particle cracking, which are denoted as L_{in}, L_p and L_m, are calculated by considering the crack-microstructure interactions in a statistical sense.

Fracture toughness K_{IC} is predicted through the calculation of energy release rate J_{IC}, which is a function of L_{in}, L_p and L_m. Microstructures with non-overlapping circular reinforcements are considered in this study. The probability of fracture P_f is calculated as

$$P_f = 1 - \exp\left[-\left(\frac{K}{K_0} \right)^m \right]. \tag{2}$$

Here, K and K_0 are the fracture toughness value predicted using the developed model and the normalization factor, respectively. m is the shape factor which quantifies the magnitude of fracture toughness scatter. Calculations carried out here consider microstructures with systematically varied particle radius ($R = 20\,\mu\text{m}$, $30\,\mu\text{m}$ and $40\,\mu\text{m}$) and volume fraction ($f =$ 10%, 15%, 20% and 25%). m is predicted for each combination of particle size and volume fraction. It is found that the most effective way to improve the fracture toughness of two-phase composite material is to increase crack tortuosity by promoting interface debonding. This can be achieved by introducing refined second-phase reinforcements with adequate volume fraction. It should be noted that the decrease in reinforcement size and increase in volume fraction also enhance the sensitivity of the material system as larger fracture toughness scatter is observed at the same time.

CONCLUSIONS

A multiscale model is developed to predict the scatter of fracture toughness of two-phase composite material as functions of microstructure attributes and fracture mechanisms involved during the failure process. The Weibull parameter m, which quantifies the scatter of fracture toughness is quantitatively correlated to the geometric attributes of the microstructure as well as the proportion of interface debonding and particle cracking associated with the entire crack path. It is found that increase of interface debonding can result in higher fracture toughness. This fracture mechanism can be promoted by decreasing the reinforcement size and increasing its volume fraction in the dilute situation ($f < 35\%$). Although this type of microstructure tailoring can lead to improved fracture toughness, the material system becomes more sensitive as a larger fracture toughness scatter is observed. The upper and lower bound of fracture toughness scatter predicted here can provide insight to selection of materials and microstructure tailoring without doing repeated testing. The approach allows the upper and lower limit of fracture toughness to be predicted by considering microstructure attributes and fracture mechanisms involved in the failure process.

References

[1] K. Strecker, S. Ribeiro, R. Oberacker, and M. J. Hoffmann, "Influence of microstructural variation on fracture toughness of LPS-SiC ceramics," *International Journal of Refractory Metals & Hard Materials*, vol. 22, pp. 169-175, 2004.

[2] Y. Li and M. Zhou, "Prediction of fracture toughness of ceramic composites as function of microstructure: I. Numerical simulations," *Journal of the Mechanics and Physics of Solids*, vol. 61, pp. 472-488, Feb 2013.

[3] S. Lee, T. H. Kim, and D. Kwon, "Microstructural Analysis of Fracture-Toughness Variation in 2xxx-Series Aluminum-Alloy Composites Reinforced with Sic Whiskers," *Metallurgical and Materials Transactions a-Physical Metallurgy and Materials Science*, vol. 25, pp. 2213-2223, Oct 1994.

[4] S. Kumar and W. A. Curtin, "Crack interaction with microstructure," *Materials Today*, vol. 10, pp. 34-44, Sep 2007.

[5] Y. Li and M. Zhou, "Prediction of fracturess toughness of ceramic composites as function of microstructure: II. analytical model," *Journal of the Mechanics and Physics of Solids*, vol. 61, pp. 489-503, 2// 2013.

[6] T. L. Becker, R. M. Cannon, and R. O. Ritchie, "Statistical fracture modeling: crack path and fracture criteria with application to homogeneous and functionally graded materials," *Engineering Fracture Mechanics*, vol. 69, pp. 1521-1555, Sep 2002.

[7] B. Z. Margolin, A. G. Gulenko, and V. A. Shvetsova, "Probabilistic model for fracture toughness prediction based on the new local fracture criteria," *International Journal of Pressure Vessels and Piping*, vol. 75, pp. 307-320, Apr 1998.

[8] A. Valiente, J. Ruiz, and M. Elices, "A probabilistic model for the pearlite-induced cleavage of a plain carbon structural steel," *Engineering Fracture Mechanics*, vol. 72, pp. 709-728, Mar 2005.

NANOVOID CAVITATION IN ALUMINUM

M.P. Ariza [*1], M. Ponga[2], and M. Ortiz[3]
[1]*Escuela Técnica Superior de Ingeniería, Universidad de Sevilla, Sevilla, Spain.*
[2]*Department of Mechanical Engineering, The University of British Columbia, Vancouver, BC, Canada.*
[3]*Division of Engineering and Applied Science, California Institute of Technology, Pasadena, CA, USA.*

Summary The transition paths during nanovoid growth in Aluminum (Al) single crystals under triaxial load at different strain rates and finite temperature have been studied using the HotQC method. Our analysis reveals that after an initial plastic regime, dislocations interact between each other and promote a strain hardening regime that increases the peak stress during the simulation. This behavior is of remarkable importance since it might help to increase the spall strength of pure Al under high velocity impacts.

INTRODUCTION

Spallation is a failure mechanism that is observed in materials subject to dynamic loads typically applied at very high velocities, like in high energy impacts and explosions [1, 2]. Therefore, understanding the mechanisms that dominate this catastrophic failure mode is of great interest for many applications including defense applications, nuclear reactors, aerospace, etc.. Spallation happens when two release waves collide together after a shock compression load. The collision of the waves promotes a tensile stress that increases very quickly in a narrow plane, usually called the spall plane, inside the material. The tensile stress acts on defects like vacancies or cluster of vacancies and promotes nucleation, growth and coalescence of nanovoids that end-up with a macroscopic crack in the material that compromises the structural integrity of the specimen [3, 4, 5]. In this work we have applied the HotQC method [6, 7] to the study of void growth by dislocation emission in Al to shed light on the mechanisms that dominate dynamic failure driven by nanovoids growth and coalescence.

METHODOLOGY AND RESULTS

HotQC [6, 8, 7] is a nonequilibrium finite temperature multiscale modeling technique that provides coarse-grained description of atomistic systems in both time and length scales. The time coarse-graining is achieved using the maximum-entropy principle [9] and mean-field approximations [7] to generate temperature-dependent thermodynamic potentials. By treating the atomic thermal oscillations in a statistical sense, HotQC makes possible to perform spatial coarse-graining using the cluster version of the Quasi-Continuum (QC) technique [10]. Finally, in applications where the inertial effects are important the HotQC method solves the meso-dynamic equations of motion (the evolution of macroscopic positions and momenta) by using a explicit Newmark method. This allows larger time steps than MD making possible to access strain rates that can be achieved experimentally [11].

Our simulations consist in a single Al-crystal of $432a_0 \times 432a_0 \times 432a_0$, (where $a_0 = 4.032$ A is the lattice parameter of Al) or $0.17\mu m^3$. The material is simulated using the interatomic potential developed by Mishin *et al.* [12]. An initial full atomistic zone of $16a_0 \times 16a_0 \times 16a_0$ is provided at the center of the computational cell and then, the atomic description is coarsen with the distance to the center of the computational cell obtaining 36,000 repatoms in the initial stage. A nanovoid of diameter $12a_0$ (4.8 nm) is initially generated. A Finite Element (FE) mesh is performed over the repatoms and it is adaptively refined using the second invariant of the Lagrangian strain tensor as a metric of the distortion of the elements. At the final stage of our simulations, the samples contained about 1,000,000 repatoms near the center of the cell providing enough resolution to describe all dislocations emitted from the void.

The simulation cell is initially relaxed at 300K by minimizing the canonical free energy with respect to the atomic position and frequencies. Then, the meso-dynamic of the system is integrated using an explicit Newmark method for strain rates between $\epsilon = 10^7 - 10^{10} s^{-1}$. For $\epsilon = 10^5 s^{-1}$ the inertia effects are not important and the equilibrium configurations are

Table 1: Simulated strain rates, critical volumetric deformation and stress for void cavitation.

	Sim. 1	Sim. 2	Sim. 3	Sim. 4
ϵ [s^{-1}]	10^5	10^7	10^8	10^{10}
ϵ_{vol_c} [%]	13.4	13.6	13.2	18.46
σ_c [GPa]	13.1	13.7	15.1	18.55

*Corresponding author. Email: mpariza@us.es

found by energy minimization followed by a heat conduction step. The heat conduction introduces a time scale that allows for larger time steps compared to the dynamic cases. The load is applied by using a homogeneous deformation gradient to impose a hydrostatic tension. We carried out simulations at different strain rates specified in Table 1.

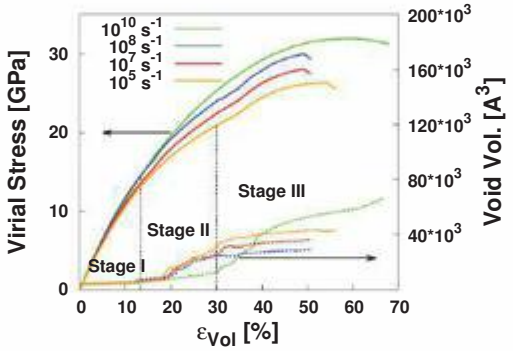

Figure 1: Virial stress and void volume as function of volumetric deformation ϵ_{vol} for different strain rates.

We now proceed to describe the evolution of the virial stress and the void volume as a function of the volumetric deformation evaluated as $\epsilon_{vol} = V(t)/V(t=0) - 1$, where $V(t)$ means the volume of the sample at a time t. The evolution is shown in Figure 1. For all simulations we have observed three different stages. For convenience, the three stages have been delimited by vertical dashed lines in Figure 1 only for the strain rate of $\epsilon = 10^5 s^{-1}$. A first stage (stage I) is observed where the deformation is purely elastic, no dislocations are observed and the deformation is reversible. The void fraction increases linearly with the volumetric deformation. This elastic range extends until ϵ_{vol_c} indicated on Table 1 for different strain rates. When the deformation reaches ϵ_{vol_c}, the void starts the cavitation process, then, a second stage (stage II) of plastic deformation is followed. Dislocations are emitted from the void surface to accommodate the deformation and the void increases its volume at a very high rate. The virial stress curve grows monotonically with the volumetric deformation, but at a much smaller slope than in the elastic regime. After the initial plastic regime, a secondary plastic regime (stage III) is observed due to deformation hardening, and consequently, the virial stress increases until the peak stress is reached. Once the peak stress is reached, the void grows quickly and a crack propagates almost instantaneously ending with the failure of the specimen.

CONCLUSIONS

In conclusion, we have studied the stress-strain deformation path attendant to nanovoid growth in Al. Our study reveals that there are three main stages in the process of nanovoid growth, an initial reversible linear elastic regime (stage I), a primary plastic stage where dislocations are emitted and the deformation is not longer reversible (stage II) and finally, a secondary strain hardening plastic regime where dislocations interact between each others and promote an increase in the peak stress. This behavior has been observed for all strain rates and is a clear evidence of the nonlinear mechanic behavior of the material under dynamic loads.

References

[1] A. L. Stevens, L. Davison, and W. E. Warren. Spall fracture in aluminum monocrystals: a dislocation-dynamics approach. *Journal of Applied Physics*, 43(12):4922–4927, 1972.

[2] M. A. Meyers and C. T. Aimone. Dynamic fracture (spalling) of metals. *Progress in Materials Science*, 28(1):1–96, 1983.

[3] V. Tvergaard. On localization in ductile materials containing spherical voids. *International Journal of Fracture*, 18:237–252, 1982.

[4] V. Tvergaard. Material failure by void growth to coalescence. 27:83 – 151, 1989.

[5] A. Heller. How metals fails. *Science and Technology Review*, pages 13–20, 2002.

[6] Y. Kulkarni, J. Knap, and M. Ortiz. A variational approach to coarse graining of equilibrium and non-equilibrium atomistic description at finite temperature. *Journal of the Mechanics and Physics of Solids*, 56:1417–1449", 2008.

[7] G. Venturini, K. Wang, I. Romero, M.P. Ariza, and M. Ortiz. Atomistic long-term simulation of heat and mass transport. *Journal of the Mechanics and Physics of Solids*, 73:242 – 268, 2014.

[8] M.P. Ariza, I. Romero, M. Ponga, and M. Ortiz. Hotqc simulation of nanovoid growth under tension in copper. *Int. Journal of Fracture*, 2011.

[9] E. Jaynes. Information theory and statistical mechanics. *Physical Review*, 106:620–630, 1957.

[10] J. Knap and M. Ortiz. An analysis of the quasicontinuum method. *Journal of the Mechanics and Physics of Solids*, 49:1899–1923", 2001.

[11] M. Ponga, M. Ortiz, and M.P. Ariza. Finite-temperature non-equilibrium quasi-continuum analysis of nanovoid growth in copper at low and high strain rates. *Mechanics of Materials*, 90:253 – 267, 2015.

[12] Y. Mishin, D. Farkas, M. J. Mehl, and D. A. Papaconstantopoulos. Interatomic potentials for monoatomic metals from experimental data and *ab initio* calculations. *Phys. Rev. B*, 59:3393–3407, Feb 1999.

TOPOLOGICAL DESIGN OF GRAPHENE WITH ENHANCED FRACTURE TOUGHNESS

Jiaoyan Li[1], Bo Ni[1], and Huajian Gao *[1]

[1]*School of Engineering, Brown University, Providence, RI, USA*

Summary Graphene has exhibited ultra-high Young's modulus and tensile strength, but very low fracture toughness which is close to that of an ideally brittle solid. As a typical example of 2D materials, the feature of the atomic thin thickness of graphene preserves flexibility for out-of-plane topological design so as to improve its mechanical and physical properties, such as fracture toughness. Here, we propose a novel methodology based on phase field crystal method to construct a curved graphene which conforms to a targeted arbitrary 3D surface, and in which topological defects (pentagon-heptagon pairs) are generated spontaneously to comply the surface curvature. Aiming at improving fracture toughness by introducing effective energy dissipation mechanisms, two patterns (strip and blister) are systematically designed and studied. The results show that (i) the fracture toughness of the designed graphene is increased significantly, and (ii) the underlying toughening mechanisms come from crack tip blunting/trapping, daughter crack bridging, and dislocation sheltering.

INTRODUCTION

Graphene has been attracting remarkable attention over the last decade due to its outstanding mechanical and physical properties, as well as its representation for the studies of two dimensional (2D) materials. Although the elastic modulus and theoretical strength of graphene have been reported as high as $1TPa$ and $130GPa$ respectively [1], the fracture toughness has been recently measured as low as $1\ J/m^2$ [2]. The intrinsically brittle nature of graphene has highlighted fracture as one of the most prominent concerns for practical applications. The most promising and inexpensive approach for deposition of reasonably high quality graphene is chemical vapor deposition (CVD), yet randomly distributed defects including dislocations and grain boundaries are still inevitable. These distributed defects have been found to play a crucial role in improving and/or altering mechanical and physical properties of graphene [3,4], and result in wrinkled configurations as validated by both simulation and experiment [5]. These results suggest that the distributed defects can be utilized to control the 3D geometrical configuration and further tune the properties of graphene sheet. Then, fundamental questions arise as: (i) Can fracture toughness be enhanced by introducing desired topological defects? (ii) How to introduce toughening mechanisms to toughen brittle graphene? (iii) Is it possible to design a curved graphene with arbitrary topological features? In this work, phase field crystal (PFC) method and atomistic simulations are integrated dynamically for the topological design of graphene with enhanced fracture toughness.

METHODS

Previous studies have employed geometrical methods and Monte Carlo simulations to search for the positions of atoms on a curved surface, which are unfortunately difficult to apply for a large system with complicated geometry feature. Recently, phase field crystal (PFC) method has been developed to model self-organization and pattern formation in crystalline materials with over-damped conservative/diffusive dynamics. As a case study, a sinusoidal graphene ruga has been successfully built using PFC method and leads to twice increment of fracture toughness compared with flat defect-free graphene [6]. The formulation of PFC model starts from the free-energy functional in the well-known $Swift \nearrow Hohenberg(SH)$ form:

$$F = \int [\frac{\phi}{2}(\nearrow\epsilon + (1+\Delta)^2)\phi + \frac{1}{-}\phi^4]d\mathbf{x}, \tag{1}$$

where $\Delta = \frac{\partial^2}{\partial x^2} + \frac{\partial^2}{\partial y^2}$ is the Laplace operator in 2D, ϕ is the reduced density and ϵ is the reduced temperature. If the dynamics of density evolution is assumed to be dissipative, the governing equation can be derived as:

$$\frac{\partial \phi}{\partial t} = \Delta\{(\nearrow\epsilon + (1+\Delta)^2)\phi + \phi^3\}, \tag{2}$$

The above high-order partial differential equation can be solved by Finite Element Method (FEM). The numerical scheme is based on a mixed formulation of FEM, with the introduction of two new variables to reduce the highest order in the spatial derivative. The software platform FEniCS is used for the implementation of PFC. Figure 1 describes the basic procedure of using PFC to build the full-atom configuration of a wrinkled graphene with designed topological features. First, PFC was performed on a given manifold surface (Fig 1a) to search for density distribution pattern with minimum energy. Identifying wave crests as vertices converts the density pattern (Fig 1b) to a discrete triangular lattice network (Fig 1c). Then, full-atom configuration (Fig 1d) is extracted from Voronoi construction on the triangular lattice, and it will serve as a building block for the preparation of large testing sample (Fig 1e) where an area of two assembled unit cells (Fig 1f) is enlarged. MD simulations were carried out via Large-scale Atomic/Molecular Massively Parallel Simulator (LAMMPS).

*Corresponding author. Email: Huajian_Gao@brown.edu

RESULTS AND CONCLUSIONS

The strip pattern (as shown in Fig 1e) and blister pattern (as shown in Fig 2) are systematically designed and studied. For the strip pattern, the design variables include ratio of length between flat part and wavy part (κ), height of the wavy part (H_{wavy}), and width of the unit cell (W_{cell}). The fracture toughness can be improved to $96J/m^2$, six times of the pristine case, when $\kappa = 0.8$, $H_{wavy} = 18$Å, and $W_{cell} = 50$Å. For the blister pattern, the design variables are even more, including radius of the representative blister, packing density of blisters, blister shape (circular, ellipse, etc.), and combination type of different blisters, as shown in Figure 2b (type I to type V). Figure 2a plots the stress-strain curves of a $80nm * 160nm$ specimen with a $36nm$ edge crack under uni-axial tension loading, packing with small, medium and large blisters respectively. It can be seen that the critical strain is effectively increased in blister graphene cases compared with pristine case (black line in Fig. 2a), while the Young's modulus are decreasing as the increasing of blister radius. The main toughening mechanisms are crack-tip blunting/trapping, daughter crack bridging, and dislocation sheltering. More results and underlying mechanisms will be discussed further during the talk. The proposed methodology has a great potential to be extended to the studies of broader 2D materials, and the resulting conclusions may shed a light on the fabrications of 2D materials with enhanced mechanical and physical properties.

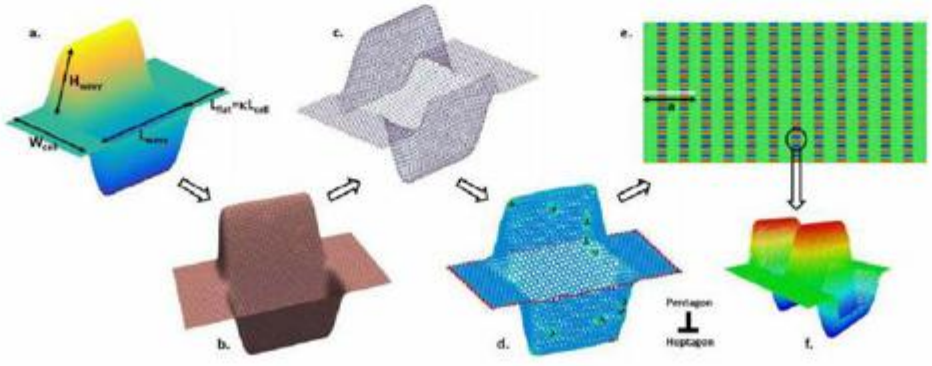

Figure 1: Basic procedure of using PFC to build the full-atom configuration of wrinkled graphene.

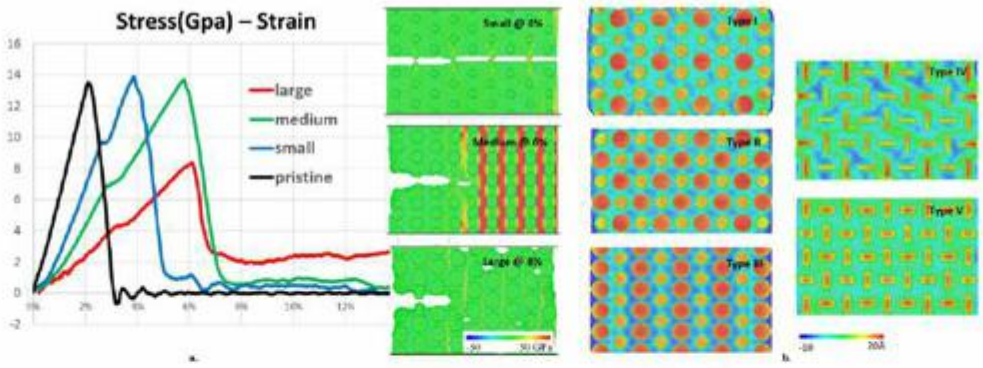

Figure 2: Blister graphene: (a) uniaxial tension tests of blister graphene with edge crack; (b) design patterns.

References

[1] Lee C., Wei X., Kysar J.W., Hone J.: Measurement of the Elastic Properties and Intrinsic Strength of Monolayer Graphene. Science 321: 385-388, 2008.

[2] Zhang P., Ma L.L., Fan F.F., Zeng Z., Peng C., Loya P.E., Liu Z., Gong Y.J., Zhang J.N., Zhang X.X., Ajayan P.M., Zhu T., Lou J.: Fracture Toughness of Graphene. Nat. Commun. 5(3782): 1-7, 2014.

[3] Grantab R., Shenoy V.B., Ruoff R.S.: Anomalous strength characteristics of tilt grain boundaries in graphene. Science 330: 946-948, 2010.

[4] Yazyev O.V., Louie S.G.: Electronic transport in polycrystalline graphene. Nature materials 9: 806-809, 2010.

[5] Zhang T., Li X.Y., Gao H.J.: Defects controlled wrinkling and topological design in graphene. Journal of Mechanics and Physics of Solids 67: 2-13, 2014.

[6] Zhang T., Li X.Y., Gao H.J.: Designing Graphene Structures With Controlled Distributions of Topological Defects: A Case Study of Toughness Enhancement in Graphene Ruga. Extreme Mech. Lett. 1(1): 3-8, 2014.

CRACK PROPAGATION MECHANISMS IN AMORPHOUS LiSi ALLOYS: INSIGHTS FROM MOLECULAR DYNAMICS

S. Mostafa Khosrownejad[1a] & William A. Curtin[1]
[1] *Laboratory for Multiscale Mechanics Modeling, EPFL, Lausanne, Switzerland*

Summary Despite apparent promise of silicon as anode material for lithium-ion batteries, the fracture characteristics of lithiated Si are largely unknown. Here, we report an atomistic study of the fracture toughness of lithiated Si for Li_xSi compositions of $x = 0.5, 1.0, 1.5$. We measure similar near-steady-state fracture toughness for all compositions, with void nucleation and coalescence observed to be the main mechanism of crack growth. With increasing Li content, the plastic flow stress decreases but the material becomes more susceptible to void nucleation and growth. To gain more insight, simulations of plane-strain expansion of uncracked samples provide complementary information on the void nucleation and growth, consistent with the fracture simulations. We also investigate the effect of discharging and show that the increased structural disorder generated by discharging decreases the flow stresses but expedites void nucleation and growth, indicating that the flow and fracture of lithiated silicon depends on the history of charging/discharging.

INTRODUCTION

Silicon is among the highest Li-storing anode materials in Li-ion batteries, but the large capacity is accompanied by large volume expansion that causes mechanical failure. Recent experimental studies have been performed on the fracture of lithiated silicon, with conflicting results [1,2]. However, at present, there is no mechanistic model for the fracture of these materials, which motivates our systematic atomistic simulation of fracture in lithiated silicon. In pure K fracture tests, we observe plastic flow around the crack tip followed by void nucleation and growth, leading to crack extension, with the development of an R-curve over 100s of Angstroms of crack growth. The fracture toughness does not vary significantly with lithium composition Li_xSi for $x = 0.5, 1.0, 1.5$, due to two competing effects. Increased lithium decreases the flow stress of the material but makes the material more susceptible to void nucleation and growth. To complete the direct crack propagation simulations, we perform simulations of plane-strain expansion, which corroborates the evolution observed ahead of the crack tip as a function of alloy composition. We then study materials that have been discharged from higher x to lower x. Recently, we have proposed a theory for plasticity in amorphous lithiated silicon which accounts for history of loading and charging/discharging, and leads to a history dependence of the flow stress in terms of excess internal energy relative to the initial relaxed material at the same composition (as quenched material) [3]. In the plane-strain tests on discharged materials, we find both decreasing flow stress and increasing susceptibility for void nucleation with increasing degree of discharging, indicating that the fracture toughness in lithiated silicon will be a function of the charging/discharging history of the material as well as the loading rates (imposed or induced by volumetric expansion/contraction).

SIMULATION RESULTS

Fracture toughness simulations

In order to model fracture in atomistic simulation we use a box of the size $x = 970, y = 20, 0 = 650\ A^o$. The sample is periodic along the line of the crack in the y direction in order to model plane strain conditions. The sample size in x and 0 is large enough to accommodate the full plastic zone development around the crack tip inside the sample and away from the boundaries, so that small-scale yielding remains valid. Samples are created by quenching the desired Li-Si composition from the melting point to 0^oK at a rate of $3000^oK/ns$. To model fracture, we apply displacement boundary conditions corresponding to the desired mode-I K field on the boundaries of the MD cell, increasing K_I in increments of $0.01\ MPa\sqrt{m}$. After each loading step, the boundary atoms are fixed and other atoms are relaxed in MD at $T = 1^oK$ for sufficient time to achieve near-equilibrium, i.e. convergence of the total energy.

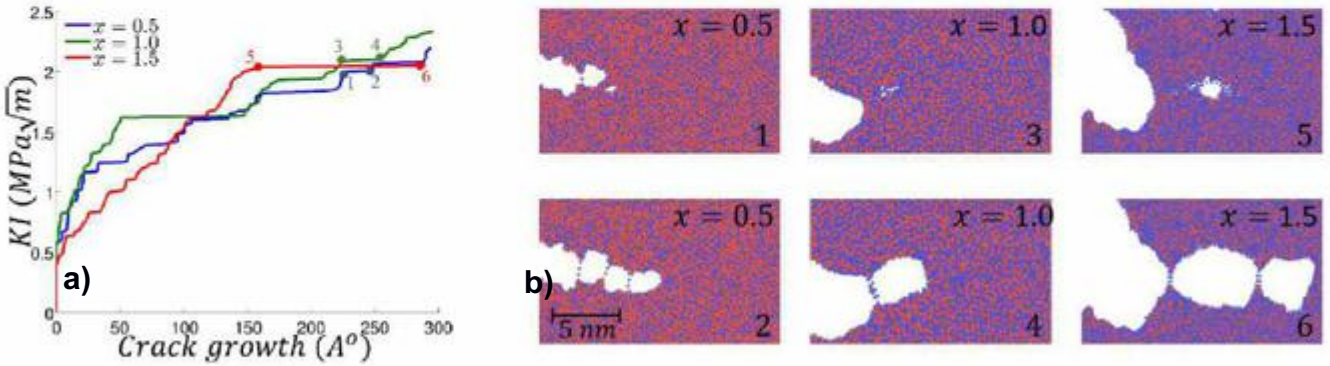

Figure 1: a) Crack growth versus applied load in the specimen, b) Mechanism of crack growth in different compositions.

[a)] Corresponding author. Email: mostafa.khosrownejad@epfl.ch.

Fig. 1a shows the crack growth versus applied K-field for three different compositions (Li_xSi with $x = 0.5, 1.0, 1.5$). As seen in the figure, the critical K values for different compositions are not very different, although their yield stress is quite different. Figure 1b shows the crack growth mechanism of void nucleation, growth, and coalescence with the main crack occurring in all three compositions, but with increasing void size/spacing with increasing Li composition that is associated with the lower plastic flow stress for higher Li compositions.

Plane-strain expansion simulations

As shown in our direct simulations, the main mechanism of crack growth in lithiated silicon is void nucleation and growth. Thus, we set up plane-strain expansion simulations for a complete range of compositions. For as-quenched materials (i.e. fully relaxed on the timescale of MD), the plane-strain stress-strain curves are shown in Figure 2a, which show the onset of plastic flow and then abrupt at a critical strain due to void nucleation and growth (not shown). The material with higher Li content shows much lower flow stress, and high failure strain, while the intermediate composition shows intermediate flow stress and failure strain. These variations correlate with the fracture toughness, although a more detailed analysis using ductile fracture theory remains to be done. We also study material that have been discharged from an initial high Li content to a final lower Li content, which leads to final materials with more excess energy and lower flow stress than the as-quenched material at the same composition. Fig. 2b shows the volumetric loading for samples with final composition $x = 0.5$ but prepared by removing atoms from samples with initial concentrations $x_\infty = 1.5$ and 1.0 in an incremental process of removal and relaxation that simulates fast discharging of the battery. The effects of charging/discharging on plasticity are discussed in our recent work [3]. Results in Fig. 2b show that the discharging history decreases both the flow stress and the failure strain, which should result in lower fracture toughness of the discharged materials. If the discharged samples were relaxed for a long time before testing, however, they would relax to the state of the as-quenched material and the flow stress and failure strain would be increased. Thus, crack propagation and fracture toughness in lithiated silicon are both composition and history-dependent processes, in general. There exists a dynamic competition between the changing in composition, the relaxation time of the glassy material, the rate of charging/discharging, and the rate of loading. With our new model for plastic flow [2] and guidance from simulations on the critical failure processes as a function of composition and discharging, we will apply ductile failure models such as the Gurson model [4] to establish a theory for lithiated silicon fracture.

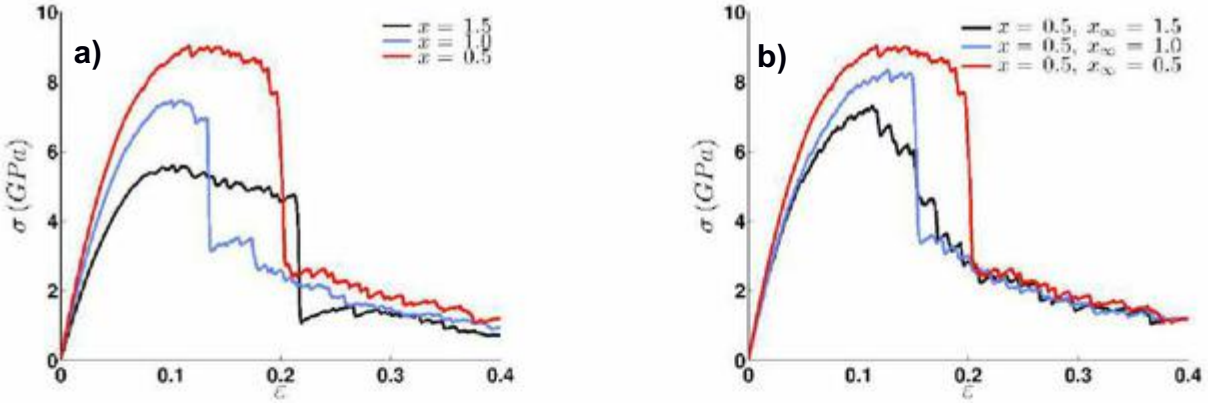

Figure 2: Volumetric stress versus strain for a) as quenched relaxed structure samples, b) samples with $x = 0.5$, but discharged from relaxed material at higher compositions x_∞.

CONCLUSIONS

In this research we have performed systematic atomistic simulation of crack propagation in lithiated silicon. Unexpectedly, despite of vastly different yield stresses, the critical fracture toughness is relatively constant for different compositions. In order to clarify this point, we analysed the mechanism of fracture which was shown to be void nucleation and coalescence for all compositions. To complete the analysis, we performed series of plane-strain expansion tests in which volumetric stress versus strains show expedited instability for higher concentrations. Thus although the yield stress of higher compositions is higher and we do expect further fracture resistance, the material became unstable sooner in front of the crack under high volumetric stress. Charging/discharging history also has the same effect. We conclude that the fracture of lithiated silicon is happening based on a dynamic competition between change of composition, loading and speed of charging/discharging.

References

[1] Pharr M., Suo Z. & Vlassak, J. J.: *Nano Lett.* **13**: 5570-7, 2013.

[2] Wang X. et. al.: *Nat. Commun.* **6**: 8417, 2015.

[3] Khosrownejad, S. M., Curtin W. A.: *J. Mech. Phys. Solids*: submitted, 2016.

[4] Gurson A. L.: *J. Eng. Mat. Tech.* **99**: 2-15, 1977

MOLECULAR DYNAMICS BASED COHESIVE ZONE MODEL FOR POLYCRYSTALLINE GRAPHENE

Laurent Guin*[1,2], Jean Raphanel[1], and Jeffrey W. Kysar[2]

[1]*Laboratoire de Mecanique des Solides, CNRS, Ecole Polytechnique, Université Paris-Saclay, Palaiseau, France*
[2]*Department of Mechanical Engineering, Columbia University, New York, New York, United States*

Summary Current continuum models of graphene do not specifically include grain boundaries properties. Through molecular dynamics simulations of graphene bicrystals we develop cohesive zone models of graphene grain boundaries. This atomistic to continuum scale bridging, based on local averages of atomic quantities raises issues regarding the quantitative aspect of the derived laws due to the influence of the size of the volume elements. We address this issue and deal with the energetic consistency of the derived law by estimating the fracture toughness of the grain boundaries through a global energetic analysis. The two high angle grain boundaries investigated show fracture properties comparable to that of pristine graphene.

INTRODUCTION

In a previous work [1], a continuum constitutive law of pristine graphene has been developed and validated against nanoindentation experiments on graphene membranes. For the purpose of extending that continuum model to polycrystalline graphene we develop cohesive zone models (CZM) for some idealized grain boundaries (GB). Since intergranular fracture takes place at the nanometer scale, we perform molecular dynamics (MD) simulations to compute the GBs' CZMs. To derive the continuum traction-separation laws (TSL) from atomistic quantities, we use a method [2] of local average over elementary volumes encompassing a few atoms.

MOLECULAR DYNAMICS TO COHESIVE ZONE MODEL

We focus our study on two high angle GBs (with tilt angles of 27.8° and 30.0°) that have been experimentally observed in chemical vapor deposited polycrystalline graphene. As a reference, we also consider fracture in the bulk of pristine graphene. To derive the traction-separation laws of the GBs, we perform MD simulations of crack propagation along a GB such as depicted on Figure 1. To achieve a controlled crack propagation, opposite vertical displacements are prescribed on the left end and fixed boundary conditions are applied on the right end.

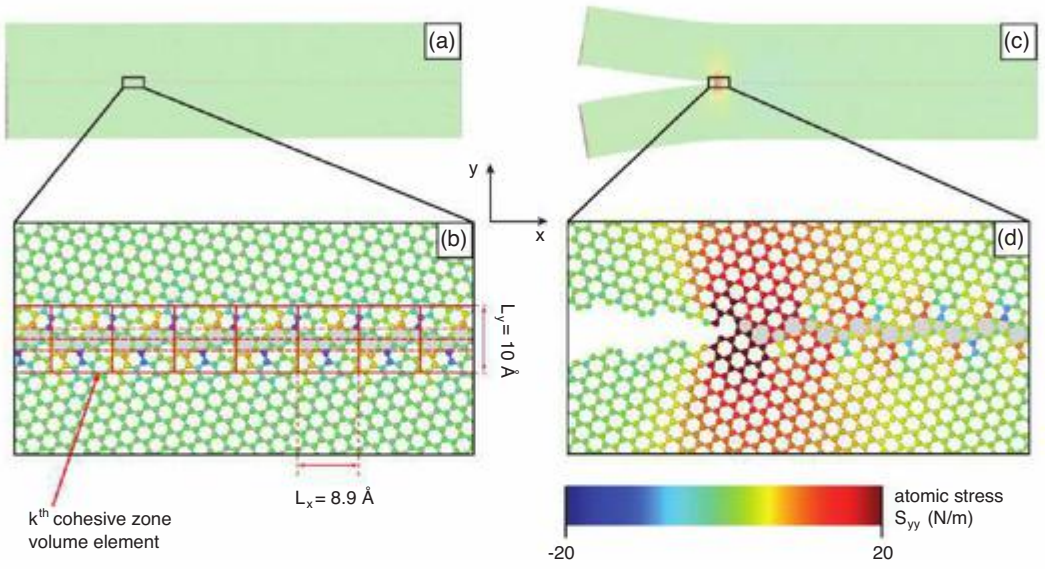

Figure 1: Double cantilever beam simulation domain for the computation of the traction-separation law. (a) and (b): relaxed configuration. (c) and (d): during crack propagation

*Corresponding author. Email: laurent.guin@polytechnique.edu

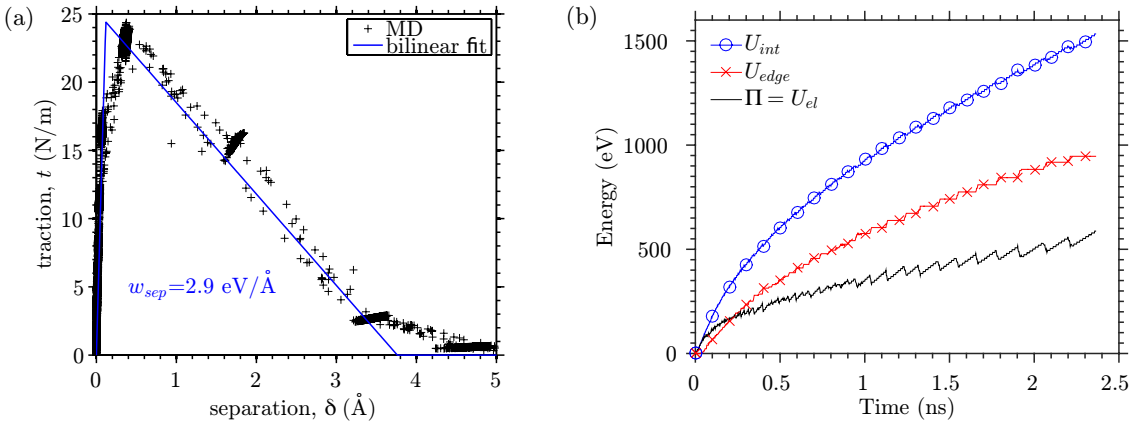

Figure 2: GB with tilt angle 27.8°: (a) Traction-separation MD computations and bilinear TSL fit. (b) Global energetic quantities evolution along the crack propagation.

Carbon-carbon interactions are modeled with the REBO2+S interatomic potential of Pastewka *et al.* [3]. During the crack propagation we compute the edge separation and interfacial traction by averaging over volume elements the atomic positions and atomic stresses respectively. To this end, we use the Virial definition of atomic stress. Figure 2(a) reports a bilinear traction-separation law fit to MD computation for the 27.8° tilt angle GB that is suitable for incorporation in a finite element method simulation. The work of separation w_{sep} corresponds to the area under the bilinear fit.

QUANTITATIVE ANALYSES OF THE LAWS

Energetic consistency

The energetic consistency of the traction-separation laws lies in the equality of the work of separation and the fracture toughness of the grain boundary. Unlike the local approach used for the TSLs, we perform a global computation to derive the fracture toughness of the GBs. In the Griffith approach to fracture, fracture toughness corresponds to the critical energy release rate G_c that equals the energy release rate G in the case of equilibrium crack propagation. We compute G from the knowledge of the potential mechanical energy Π of the system that is equal to the elastic energy $U_{el} = U_{int} \nearrow U_{edge}$, with U_{int} the internal energy and U_{edge} the edge energy associated to crack extension as obtained from MD (Figure 2(b)). The TSL's work of separation and the globally computed fracture toughness are in good agreement, which demonstrates internal consistency of the derived TSL.

Determination of the volume element size

As one may guess from Figure 1(b), the size of the volume elements where quantities are averaged affects the quantitative aspect of the traction-separation law. To determine the appropriate size of the volume elements we compare the peak traction of the TSL (which is strongly dependent on the averaging size) to the intrinsic strength of the GB as computed from uniform tensile simulations of flawless bicrystals.

CONCLUSION

In the present work, we have computed from molecular dynamics simulations, traction-separation laws that describe the cohesive zone model of some graphene grain boundaries. The consistency of the TSLs has been validated by comparing the work of separation dissipated by the TSL to the fracture toughness of the GB. Size effects have been addressed through a comparison of the peak traction to the intrinsic strength of the GB. Our results show little difference between the fracture properties of the high angle GBs and pristine graphene.

References

[1] Wei X., Kysar J. W.: Experimental validation of multiscale modeling of indentation of suspended circular graphene membranes. Int J. Solids Struct 49:3201-3209, 2012.

[2] Yamakov V., Saether E., Phillips D. R., Glaessgen E. H.: Molecular-dynamics simulation-based cohesive zone representation of intergranular fracture processes in aluminum. J. Mech Phys Solids 54:1899–1928, 2006.

[3] Pastewka L., Pou P., Pérez R., Gumbsch P., Moseler M.: Describing bond-breaking processes by reactive potentials: Importance of an environment-dependent interaction range. Phys Rev B 78:161402, 2008.

FRACTURE TOUGHNESS OF LI_XSI ALLOYS IN LITHIUM ION BATTERY

Hui Yang[1] & Jianmin Qu[1a)]
[1]*Department of Mechanical Engineering, Tufts University, Medford, Massachusetts, USA*

Summary A fundamental understanding of the fracture toughness of the Li_xSi alloys is crucial for the rational design of Si based high-capacity and failure-resistant electrodes. In this study, a chemo-mechanical model, which involves the bi-directional strong coupling between lithiation kinetics and stress, is adopted to demonstrate that the classic Rice's *J*-integral becomes path-dependent when both chemical and mechanical driving forces are present concurrently. However, our newly proposed electro-chemo-mechanical *J*-integral is shown to be path-independent under such combined multiple driving forces when the electrodes undergo large lithiation-induced elasto-plastic deformation. Based on the algorithm of the path-independent electro-chemo-mechanical *J*-integral, molecular dynamics (MD) simulations are conduced to investigate the fracture toughness of Li_xSi alloys. Good agreement is achieved between the obtained results and the limited published data derived from the experimental measurements. According to the calculated fracture toughness, the critical sizes of different Si anode nanostructures are finally discussed.

INTRODUCTION

Rechargeable lithium-ion batteries (LIBs), due to their high energy density and design flexibility, are widely used as power sources in portable electronics and electric vehicles. Currently, the commercialized LIBs widely adopt graphite as anode material. However, graphite suffers low specific charge capacity (372 $mAhg^{-1}$), which will obviously hinder the application of LIBs in new generation electronic devices. It is well-known that silicon (Si) stands as the leading candidate anode material owing to its highest theoretical capacity (4200 $mAhg^{-1}$). Nevertheless, inherent to the high-capacity electrodes, lithium (Li) insertion-extraction cycling induces huge volumetric change and stress inside the Si anode, leading to fracture, pulverization, electrical disconnectivity, and ultimately capacity loss. Therefore, a fundamental understanding of the degradation mechanisms in the Si anode during lithiation-delithiation cycling, especially the mechanics of damage initiation and propagation in the Si anode, is crucial for the rational design of next-generation failure-resistant Si based electrodes. Currently, the fracture toughness of Li_xSi alloys, which is essential to assess the damage initiation and propagation in the Si anode, is rarely investigated experimentally. This might be due to the difficult to prepare the Li_xSi alloy specimens with various Li concentrations based on currently available experimental techniques. Computationally, due to the large amount of atoms involving in the cracking initiation and propagation simulation, the first-principle based approach is also not feasible due to the huge computational cost. Consequently, the molecular dynamics (MD) simulation with a robust interatomic potential is emerged as an appropriate method to assess the fracture properties of Li_xSi alloys. In addition, as Li insertion/extraction always induces large elasto-plastic deformations in the Si anode, a reliable non-linear fracture mechanics based algorithm should be adopted to derive the fracture properties of Li_xSi alloys from the pertinent MD simulation results.

CHEMO-MECHANICAL MODEL & MD SIMULATIONS

The previously developed finite strain chemo-mechanical model is adopted in this study [1, 2]. In this model, the concurrent chemical reaction and diffusion processes are simulated in a unified manner by a non-linear diffusion model, despite the difference in interfacial reaction and bulk diffusion. Therefore, the classical diffusion equation is used to describe Li transport in the Si anode:

$$\frac{\partial c}{\partial t} \qquad \mathbf{J}_F \qquad \mathbf{J}_F = - \quad \nabla \qquad \mathbf{F}\ c\ = \mu_0\ c\ + \tau\ \mathbf{F}\ c \tag{1}$$

where, c is the Li concentration, D is a diffusion constant, $\mathbf{J}_F$ if the Li flux, which is related to the chemical potential of Li, μ, in Si. The $\mu_0\ c$ and $\tau(\ ,c)$ are the stress-independent and stress-dependent parts of the chemical potential, respectively, and $\mathbf{F}$ is the deformation gradient. It should note that the electrostatic potential in this study is assumed to be 0, therefore, its effect on the chemical potential is ignored here. For the mechanics part of the model, the following equilibrium equation

$$\sigma \quad 0 \tag{2}$$

is solved with corresponding boundary conditions. All the material properties are Li concentration dependent. Using the implicit coupled temperature-displacement procedure in ABAQUS/Standard with user subroutines, the corresponding Li concentration and stress-strain fields are updated incrementally. Meanwhile, contour integrations are conducted for both the classic Rice's *J*-integral and the electro-chemo-mechanical *J*-integral [3].

In the MD simulations, a second nearest neighbor MEAM (2NN MEAM) of Li_xSi alloy [4] is used to simulate the single edge crack propagation in the specimens with different Li concentrations under tension loading. The stress

[a)]Corresponding author. Email: Jianmin.Qu@tufts.edu.

distribution information at the critical moment that the crack starts to propagate is used to calculate the fracture toughness based on the electro-chemo-mechanical *J*-integral algorithm.

RESULTS

As shown in Fig. 1, a Li_xSi alloy specimen with an edge crack is adopted for the chemo-mechanical modelling. Initially, Li is uniformly distributed in the specimen, which is indicated by the uniform color in Fig. 1(a). During the simulation, uniaxial tensile loading is applied along the vertical direction, leading to the stress concentration and subsequently stress gradient around the crack tip. The stress gradient will further act as a dominant driving force for Li to migrate from far field to the crack tip till the new equilibrium state is reached [5], as shown in Fig. 1(b), where, the red color indicates high concentration, blue low concentration. Integrations of the classic Rice's *J*-integral and the electro-chemo-mechanical *J*-integral are conducted along three different contours around the crack tip. The classic Rice's *J*-integral, which is shown in Fig. 1(c), becomes path-dependent when both chemical and mechanical driving forces are present concurrently. However, the curves in Fig. 1(d), which are generated from our newly proposed electro-chemo-mechanical *J*-integral, are almost overlapping with each other, showing that the electro-chemo-mechanical *J*-integral is path-independent under such combined multiple driving forces when the electrodes undergo large lithiation-induced elasto-plastic deformations.

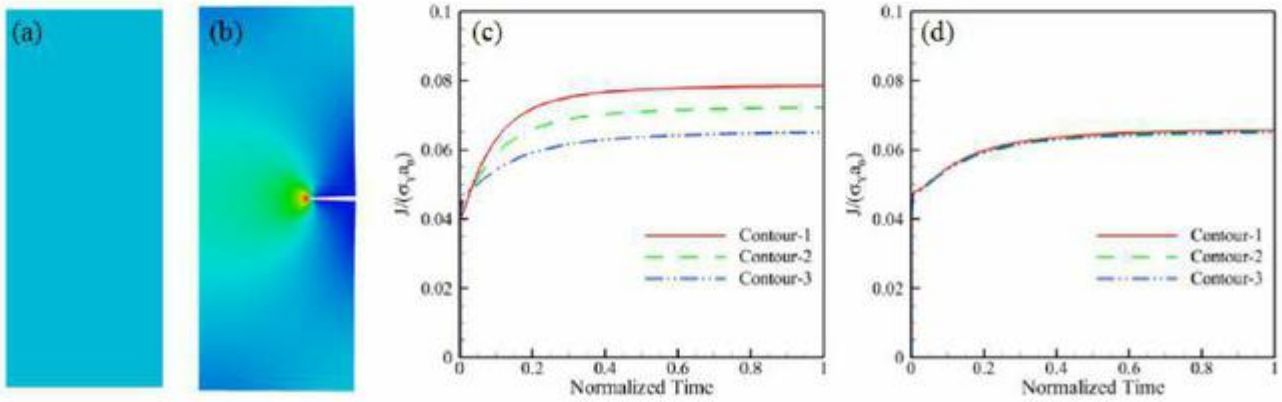

Figure 1. Chemo-mechanical simulations of a Li_xSi alloy specimen with an edge crack under tensile loading along the vertical direction. (a) Li distribution before loading; (b) Li re-distribution driven by the stress gradient around the crack tip; (c) Integrations of the classic Rice's *J*-integral along three different contours around the crack tip; (d) Integrations of the electro-chemo-mechanical *J*-integral along the contours around the crack tip.

CONCLUSIONS

In this study, a chemo-mechanical model, which involves the bi-directional strong coupling between lithiation kinetics and stress, is adopted to demonstrate that the classic Rice's *J*-Integral becomes path-dependent when both chemical and mechanical driving forces are present concurrently. However, our newly proposed electro-chemo-mechanical *J*-integral is shown to be path-independent under such combined multiple driving forces when the electrodes undergo large lithiation-induced elasto-plastic deformations. Based on the algorithm of the path-independent electro-chemo-mechanical *J*-integral, MD simulations are conduced to investigate the fracture toughness of Li_xSi alloys. Good agreement is achieved between the obtained results and the limited published data derived from the experimental measurements. According to the calculated fracture toughness, the critical sizes of different Si anode nanostructures are finally discussed.

References

[1] Yang H., Fan F., Liang W., Guo X., Zhu T., Zhang S.: A chemo-mechanical model of lithiation in silicon. *J. Mech. Phys. Solids* 70: 349-361, 2014.

[2] Yang H., Liang W., Guo X., Wang C.-M., Zhang S.: Strong kinetics-stress coupling in lithiation of Si and Ge anodes. *Extreme Mech. Lett.* 2: 1-6, 2015.

[3] Haftbaradaran H., Qu J.: A path-independent integral for fracture of solids under combined electrochemical and mechanical loadings. *J. Mech. Phys. Solids* 71: 1-14, 2014.

[4] Cui Z., Gao F., Cui Z., Qu J.: A second nearest-neighbor embedded atom method interatomic potential for Li-Si alloys. *J. Power Sources* 207: 150-159, 2012.

[5] Yang H., Huang X., Liang W., van Duin A. C. T., Raju M., Zhang S.: Self-weakening in lithiated graphene electrodes. *Chem. Phys. Lett.* 563: 58-62, 2013.

ATOMISTIC MECHANISMS OF FRACTURE IN AMORPHOUS LITHIATED SILICON

Bin Ding[1], Xiaoyan Li[1, 2] & Huajian Gao[2a)]
[1]*Centre for Advanced Mechanics and Materials, CNMM, Applied Mechanics Laboratory, Department of Engineering Mechanics, Tsinghua University, Beijing, China*
[2]*School of Engineering, Brown University, Providence, Rohde Island, USA*

Summary In the process of lithiation and delithiation, the destruction of silicon electrode in lithium ion battery always begins with the crack initiation. We performed atomistic simulations for the crack propagation in amorphous Li_xSi alloy, and found that fracture mechanism changes from intrinsic nanoscale cavitation to shear bandings in front of the crack tip. The observed mechanism transition can be understood from changing ratio between critical stresses for cavitation and plastic yield as lithium concentration increases.

INTRODUCTION

As an anode material, the silicon has a theoretical charge capacity of 4200 $mAhg^{-1}$, much higher than the conventional anodes used currently. However, silicon suffers ~280% volumetric expansion during lithiation-delithiation process, which significantly fades the capacity and eventually destroys the battery after hundreds of cycles. To mitigate this adverse effect, nanostructured silicon have been used since they have nano-sized structures which enables fast Li transport and rapid strain relaxation[1]. During cyclic charge-discharge, the fracture of nanostructured silicon electrode is the most common failure mode, which significantly reduces the battery life. Therefore, there have recently been numerous studies on deformation and fracture mechanisms during lithiation of nanostructured silicon, mostly from experimental and theoretical aspect. In this paper we investigate to the fracture behaviours of lithiated silicon by using molecular dynamics (MD) simulations. The results from MD simulations show that there exists a brittle-to-ductile transition with the variation of lithium concentration.

Methodology and results

All MD simulations are carried out via LAMMPS. After the first lithiation, the silicon electrode becomes amorphous, so all simulated samples are set as amorphous phases. Six types of Li-Si mixtures are picked. Interatomic interaction is described by a modified embedded atom method (MEAM) potential[2].
The initial lithiated silicon models go through a melting-and-quenching process to reach amorphous state. The simulated samples have the same size of ~200 nm × 122 nm × 2 nm but different Li concentrations, containing about 3 million atoms. An edge crack with length of 60 nm is created in the middle of samples. Mode I loading is applied to the samples with a constant strain rate of $\sim 5 \times 10^8\ s^{-1}$.[3]

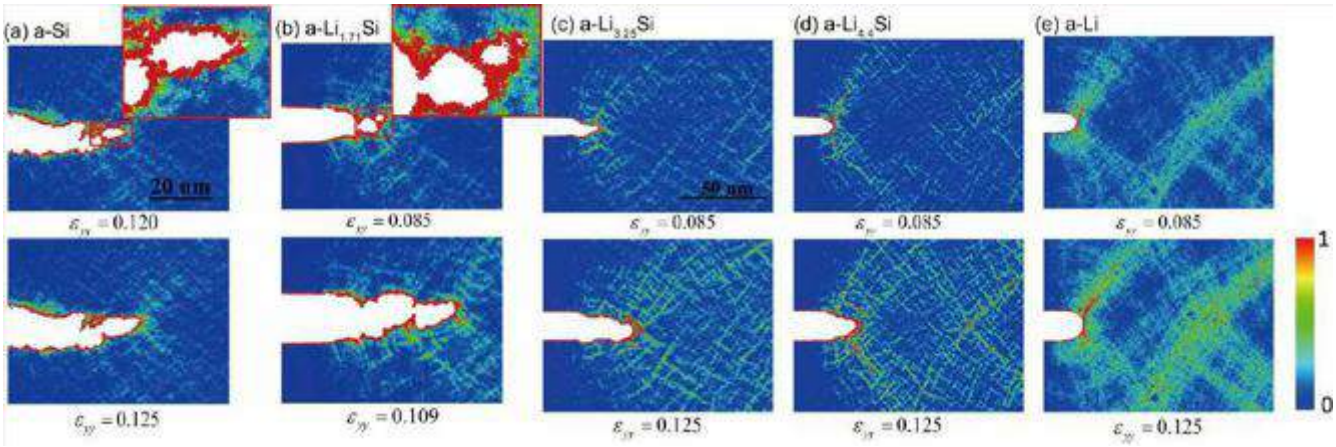

Figure 1. Snapshots of crack propagation

Figure 1 show the details of crack propagation at atomic scale in different samples. The atoms are painted by von Mises strain, which is averaged in the range of cut-off radius. In samples with lower lithium concentrations, nanosized voids spontaneously nucleate ahead of the crack tip, then gradually grow and eventually coalesce with the main crack, as illustrated by Figures 1a-1b. The coalescence of these nanovoids leads to fast crack propagation. In contrast, for samples with higher lithium concentrations, no cavitation is observed throughout the simulations, rather some shear bands are seen to form near the crack tip, as shown in Figures 1c-1e. As the applied strain increases, the crack tip becomes blunt due to extensive shear banding around the crack tip. The simulation results shown in Fig. 1 indicate that as the lithium concentration increases, there exists a brittle-to-ductile transition in lithiated silicon at a critical lithium concentration, due

[a)] Corresponding author. Email: Huajian_Gao@brown.edu.

to a switching of fracture mechanism from nanoscale void nucleation to extensive shear banding. The cavitation will form if the local hydrostatic stress reaches the cavitation stress. We obtained the range of cavitation stress by conducting hydrostatic-dilatation simulations. The maximum and minimum values of cavitation stress are shown in Figure 2 and indicated by two red lines. We also compute the local hydrostatic stress in front of crack tip at the moment when the first cavitation is about to nucleate. It can be seen from Figure 2 that the maximum crack-tip hydrostatic stress falls within the range of cavitation stress at relatively low lithium concentrations, suggesting an activation of nanoscale cavitation instabilities ahead of the crack tip. In contrast, at higher lithium concentrations, the local hydrostatic stress falls always below the minimum cavitation stress, in which case cavitation is suppressed.

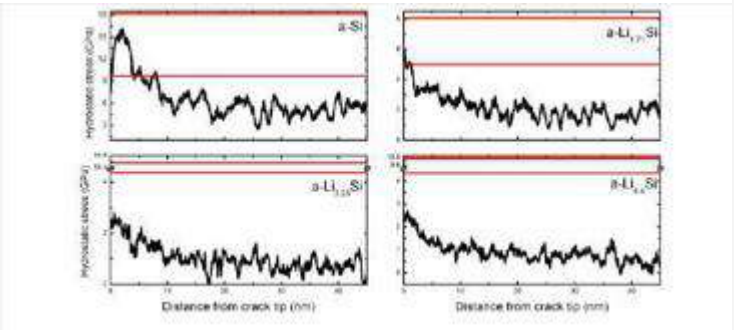

Figure 2. Variation of local hydrostatic stress

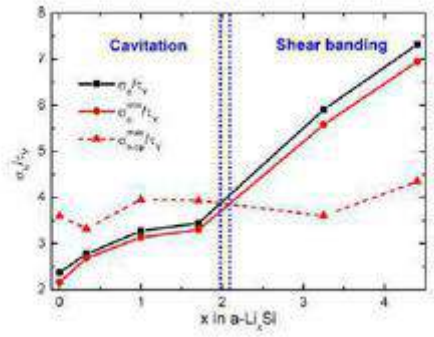

Figure 3. Ratios of cavitation stress to shear strength

To further complement our simulations, we conducted a theoretical analysis on the competition between cavitation and plastic deformation ahead of a crack tip in amorphous lithiated silicon. Based on the small-scale yield hypothesis, the maximum hydrostatic stress can be expressed as $\sigma_{h\text{-tip}}^{\max} = \alpha(\nu, \varepsilon_Y, N)\tau_Y$.[4] We assume a simple stress-based criterion that the void nucleates only when the hydrostatic stress is beyond the critical cavitation stress, i.e. $\sigma_h \geq \sigma_c$. The cavitation criterion can be re-written as $\sigma_c / \tau_Y \leq \alpha(\nu, \varepsilon_Y, N)$. The classical Prandtl slip-line theory shows $\alpha = 1+\pi$. We subsequently calculated α using the maximum crack-tip hydrostatic stress from MD simulations, as Figure 3 shows. This prediction is consistent with the observations of fracture-mechanism transition from our atomistic simulations, indicating that the transition from brittle fracture induced by nanoscale cavitation to ductile fracture due to plastic deformation in amorphous lithiated silicon can be characterized by the ratio of cavitation stress to shear yield stress.

CONCLUSIONS

In summary, we have revealed atomistic mechanisms of fracture in amorphous lithiated silicon with different lithium concentrations using large-scale MD simulations. At relatively low lithium concentrations, brittle fracture occurs due to spontaneous nucleation and coalescence of nanovoids ahead of the crack tip. However, at high lithium concentrations, plastic deformation contributes to the fracture process by the crack-tip blunting through extensive shear banding. Such fracture-mechanism transition can be determined by a ratio of cavitation stress to shear yield stress of materials.

References

[1] Armand, M.; Tarascon, J. M. *Nature* **451**, 652-657, 2008

[2] Z. Cui, F Gao, Z Cui, et al. *Journal of Power Sources*, **207**, 150-159,2012.

[3] P. Murali, T. F. Guo, Y. W. Zhang, et al. *Physical review letters*, **107**, 215501, 2011.

[4] Mcmeeking, R. M. *J. Mech. Phys. Solids*, **25**, 357-381, 1977

COHESIVE ZONE MODELING OF CRACK KINKING OUT OF AN INTERFACE

Matthew Begley[1,3a], William Pro[1], Stephen Sehr[1], Rone Kwei Lim[2], Linda Petzold[1,2]
[1]*Department of Mechanical Engineering, University of California at Santa Barbara, Santa Barbara, CA*
[2]*Department of Computer Science, University of California at Santa Barbara, Santa Barbara, CA*
[3]*Materials Department, University of California at Santa Barbara, Santa Barbara, CA*

Summary: This paper examines a modified cohesive zone approach to model crack kinking out of an interface. Here, for the first time, cohesive zone models are shown to accurately predict crack kinking without any assumption of crack growth direction. Key dimensionless mesh parameters are identified that control the critical initiation of a simulated crack, and the results are shown to be in excellent agreement with the results of He and Hutchinson [1] in the limit of a refined mesh. The simulation results correctly predict both the kink angle and critical ERR of the parent crack in the case of homogeneous bulk/interface toughness. However, the simulations predict a different transition between kinking and interface delamination for a non-homogeneous bulk & interface toughness. The method is applied to simulate the response of a film/substrate system subjected to a femtosecond laser pulse, with the resulting failure mechanisms a natural outcome of the simulation.

INTRODUCTION & SIMULATION APPROACH

The transition between interface delamination and crack kinking has been a long standing problem in interfacial fracture mechanics, and is highly relevant for brittle high temperature coating systems where multiple interacting failure mechanisms are possible. The analysis of He and Hutchinson has provided much insight on the conditions for crack kinking out of a brittle interface in terms of the material mismatch parameters and applied mode mixity and has been widely accepted. Here we extend these concepts and show that they can be reproduced using a cohesive zone approach, a method previously thought to be capable of analysing cracks where the crack path is known in advance [2]. It has also been shown that the accuracy of the solution depends largely on the dimensionless mesh parameter controlling the number of elements per unit length of the cohesive zone. We extend this concept and confirm it to be true for spontaneous crack paths as well, and demonstrate the utility of the method through dynamic simulations of an oscillating film on a substrate.

To fully reproduce the mixed-mode loading conditions analysed in [1], we adapt a methodology similar to that of Zavatierri and Bower [3]. A large disk is simulated, whose radius is much larger than any other characteristic length in the problem, and the known LEFM Mode I and Mode II displacements are applied to the outer boundary of the disk as shown in Fig. 1. Cohesive zones are placed in between every element pair. Explicit time stepping (dynamic) is used to avoid non-linear root finding, but quasi-static conditions are enforced by slowly loading the specimen and selecting appropriate damping parameters. A Delaunay triangulation is utilized for the mesh as it very well minimizes the tortuosity between any two mesh nodes. The critical initiation energy release rate (G_c) is defined as the applied ERR of the parent crack that first causes at least one cohesive zone to rupture. The dimensionless mesh density ($E\Gamma_i/\sigma_0^2 h_e$) is controlled within a focused region ahead of the crack tip, and is the main variable modulated in the parameter study.

RESULTS

The results for critical ERR (relative to the bulk toughness Γ_b) of the parent crack are shown in Fig. 2. In the limit of a highly refined mesh, the results are in excellent agreement with the maximum energy release rate established by He and Hutchinson over a wide range of applied mode mixity (defined through the phase angle ψ) for $\Gamma_i = \Gamma_b$. The average kinking angle (not shown here) is also in excellent agreement with the results predicted by He and Hutchinson, and agrees within 2% for the range of phase angles presented. Results are also shown for the non-homogeneous case where $\Gamma_i \neq \Gamma_b$ in Fig. 3. In this case, the simulation results overpredict the theoretical results of He and Hutchinson, but recover the correct initiation ERR in the limit where $\Gamma_i >> \Gamma_b$ and $\Gamma_i << \Gamma_b$. This can likely be explained by a non-linear interaction between the cohesive zones along the interface and in the bulk near the transition region. Lastly, Fig. 4 shows a basic failure mechanism map for a film under dynamic loading conditions where the crack is free to delaminate or kink into the film; the basic transition boundaries are then identified as a function of system properties.

[a)] Corresponding author. Email: begley@engr.ucsb.edu.

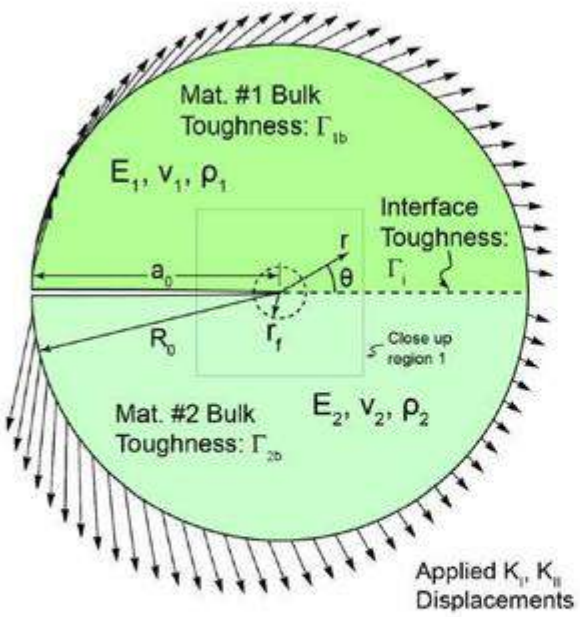

Figure 1 - Schematic of virtual specimen used to simulate kinking. Mode I and II displacements are applied along outer boundary.

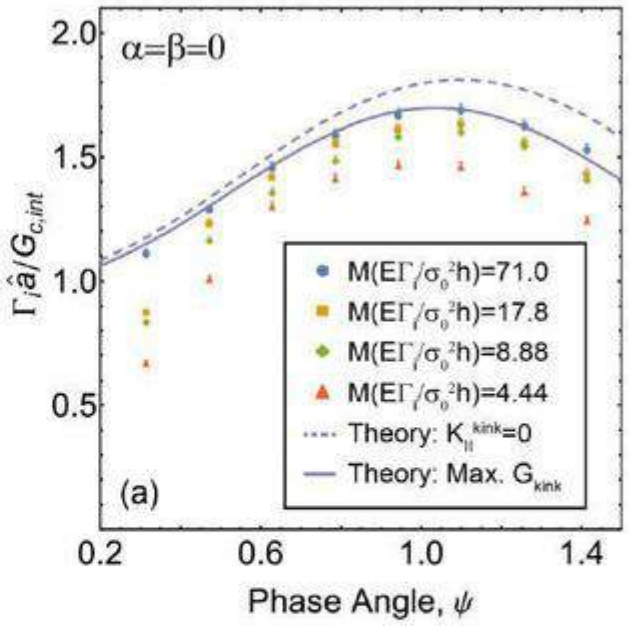

Figure 2 - Critical energy release rate of parent crack as a function of mesh density in focused region r_f

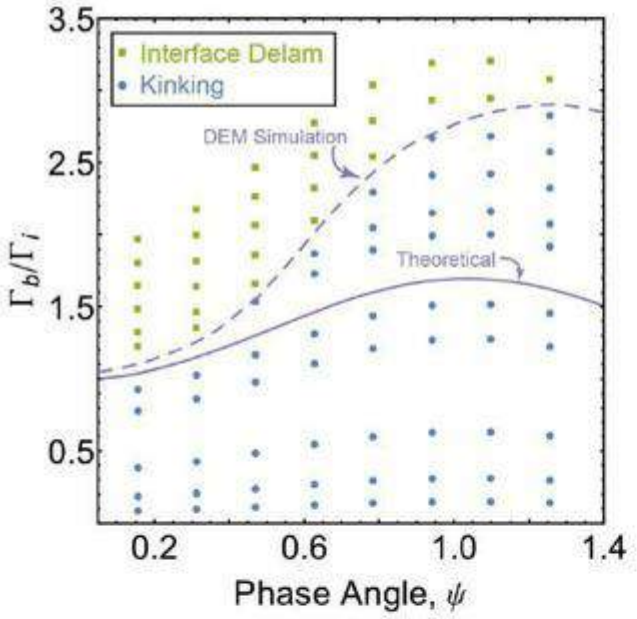

Figure 3 – Transition between interface delamination and bulk kinking as a function of the phase angle, with the toughness ratio plotted on the vertical axis

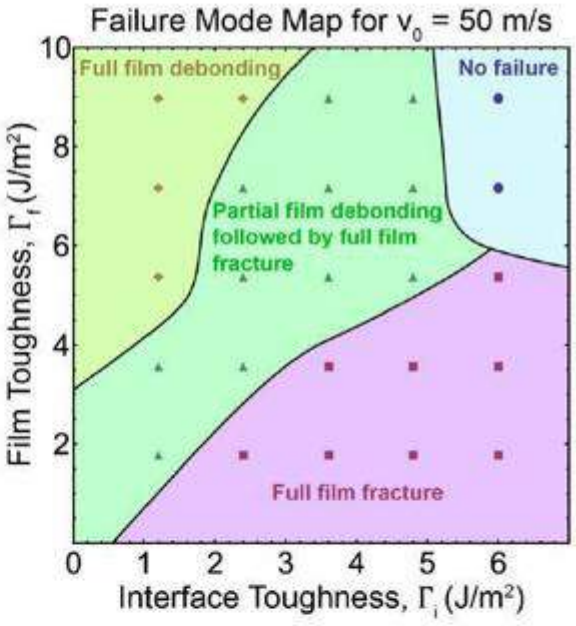

Figure 4 – Transition between various failure mechanisms in dynamic oscillating film simulations

References

[1] He, Ming-Yuan, and John W. Hutchinson. "Kinking of a crack out of an interface." Journal of Applied Mechanics 56.2 (1989): 270-278.

[2] De Borst, René. "Numerical aspects of cohesive-zone models." Engineering fracture mechanics 70.14 (2003): 1743-1757.

[3] Zavattieri, Pablo D., Louis G. Hector, and Allan F. Bower. "Cohesive zone simulations of crack growth along a rough interface between two elastic–plastic solids." Engineering Fracture Mechanics 75.15 (2008): 4309-4332.

MULTISCALE COHESIVE ZONE MODEL OF A COMPOSITE MICROSTRUCTURE

Vincent Iacobellis[1,a], Kamran Behdinan[2]
[1]*Advanced Research Lab for Multifunctional Lightweight Structures, Department of Mechanical and Industrial Engineering, University of Toronto, Toronto, Ontario, Canada*
[2]*Advanced Research Lab for Multifunctional Lightweight Structures, Department of Mechanical and Industrial Engineering, University of Toronto, Toronto, Ontario, Canada*

Summary A finite element analysis of a polyimide matrix-carbon fibre microstructure has been carried out. Cohesive zone elements were used to model the interface between fibre and matrix with the cohesive parameters obtained from previous research involving the atomistic-to-continuum level modelling of the fibre-matrix interface. The microstructure model underwent transverse loading with the stiffness, strength, and stress distribution calculated and compared to experimental results in the literature. The model was effective at predicting both stiffness and strength with respect to changes in temperature and showed the validity of using cohesive parameters obtained from atomistic based multiscale simulations.

INTRODUCTION

The transverse strength of composite materials is one of the limiting design criteria in composite structures. Fracture due to transverse loading is often the result of fibre-matrix debonding where the fibre-matrix interface is subjected to high local stress levels that increase the tendency for damage nucleation to occur near the bonding site. The incorporation of cohesive zone elements into a finite element model of the composite microstructure in order to capture the fibre-matrix debonding is increasingly being used [1]. The cohesive zone parameters are often obtained from experimental data fitting, however this approach to calculating interfacial strength and fracture toughness are extremely time-consuming and expensive. Thus, the ability to predict the interfacial strength of material interfaces has been a long desired goal. In the research presented here, a finite element cohesive zone model is used to predict the temperature dependent material properties of a polyimide matrix composite with unidirectional carbon fibre arrangement. The cohesive zone parameters have been obtained from previous research [2] involving an atomistic-to-continuum multiscale simulation of the fibre-matrix interface using the bridging cell multiscale method [3].

The cohesive parameters from this simulation were used to inform a cohesive zone model of the composite microstructure. A microscale representative unit cell (RUC) was used to predict the properties of the macroscale composite, including stiffness and strength, with respect to changes in temperature. The goal of the research presented here was to both investigate the effect that temperature change has on the composite behaviour as well as to validate the use of cohesive parameters obtained from atomistic-to-continuum multiscale modelling to predict fibre-matrix interfacial cracking.

MULTISCALE COHESIVE ZONE MODEL

The cohesive zone model approximates a traction-displacement relationship along a material interface by being embedded into zero-thickness cohesive zone elements. In this study, a mixed-mode bilinear form of the cohesive zone model is used. The mixed-mode bilinear model incorporates both normal and tangential cohesive tractions, with a region of linear elastic loading followed by a linear softening region. To obtain the cohesive parameters, the previously developed bridging cell method [3] is used to model the polyimide/graphite interface. As outlined in [2], the multiscale system was deformed to produce both normal and tangential separation at the polymer/graphite interface. The cohesive zone parameters obtained from the simulation are shown in Table 1.

Table 1. Cohesive zone parameters obtained from coupled atomistic-to-continuum simulation

Temp. (˚C)	Max Interfacial Normal Stress (MPa)	Max Interfacial Shear Stress (MPa)	Work of Adhesion (mJ/m^2)
21	46.82	40.10	120.50
204	35.29	34.09	100.35
316	25.84	24.22	78.55

MICROMECHANICS MODEL OF COMPOSITE MICROSTRUCTURE

The microstructure was represented by a periodic RUC of the unidirectional fibre reinforced composite. To produce the finite element model of the RUC a random fibre distribution was created with a fibre volume fraction of 56% and fibre diameter of 3 μm. The RUC, shown in Fig. 1(a), was modelled in ANSYS [4] with the matrix and fibre meshed using 10-node tetrahedral elements (SOLID187). Between the matrix and fibre were 15-node cohesive elements (INTER204) based on a bilinear traction-separation law. The polyimide matrix properties were nonlinear as obtained from experimental results

[a)] Corresponding author. Email: vincent.iacobellis@mail.utoronto.ca.

in [5]. The R C was defor ed in the transverse direction by displacing the top face of the RUC hile keeping the bottom face fixed.

ESULTS

From stress contour plot shown in Fig. 1(b), it as apparent that the micr scopic stress distribution is strongly dependent on the arrangement of fibres within the microstructure. This was a result of high locali ed stresses occurring in regions where the interfibre distance was the shortest with respect to the direction of loading. It as observed that crack initiation due to debonding between fibre nd matrix occ rred in the vicinity of areas with a high fi re concentration. It was also observed that the stress concentration shifted around the fibres to the location of the interfaci l crack tip as a result of the fibre and atrix becoming completely debonded. R sults for transverse stiffnes were close t those from experiment [5] for both lo and high te peratures, as hown in Fig. (a). With res ect to change in temperature, a decrease in stiffness was observed ith an increase in temperat re, which was expected lar ely due to the decrease in s iffness of the polyimide matrix. The st ength of the composite, sho n in Fig. 2(b), was also ob ained. Simila to the stiffne s, there was a reduction in strength as the temperature increased. his was attri uted to the l wer maximu normal and shear stress as obtained from the multiscale cohesive zone model. esults agreed with experimental values; however the lo er strength a 21 ˚C, as measured in [ ], can also be attributed to he specimen reaking at the grip as oppo ed to at the gauge location during the tensile tests. hen comparing the strength to the experimental data fit rovided in [5], the strength alculated fro the RUC agrees well.

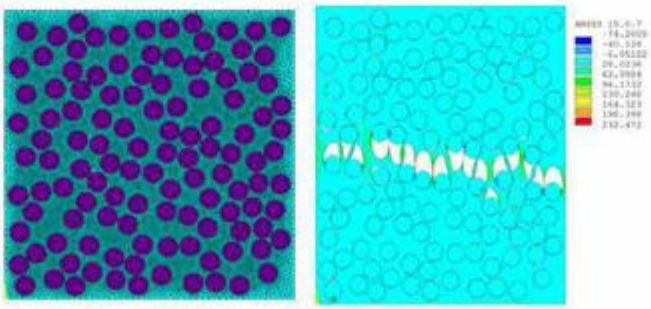

Fig. 1 (a) inite element model of com osite RUC, ( ) stress conto r of RUC at failure.

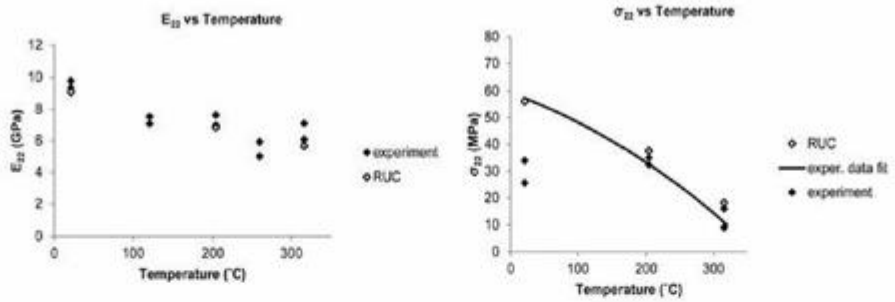

ig. 2 (a) Transverse stiffness, (b) transverse strength co pared to experimental values from [5].

CO CLUSIONS

Good ag eement was f und between the microscale RUC model and experimental results for stress-strain response and stiffness at lo and high te peratures. Examination of t e deformatio of the composite through localized crac initiation at the fibre-m trix interface also agreed with experimental observations of similar phenomena [5]. With respect to material strength, the values obtaine at each temperature agree with the experimental data fit. Overall, the potential of using an atomistic-to-c ntinuum simulation to obtai viable cohes ve zone para eters for microstructural models was dem nstrated.

References

[1] M Romanowicz, Comp. P. A: pp. Sci. and Manufact, 2010; 41(12): 1829-38.
[2] V Iacobellis, K Behdinan, Proc. of IMECE Houston, 2015; IMECE2 15-50682.
[3] V Iacobellis, K Behdinan, Int J umer Methods E g, 2012; 92(7): 652-70.
[4] ANSYS® A ademic Research, Release 15.0.
[5] G Odegard, Kumosa, Comp sites Sci Technol, 000; 60(16): 2979-2988.

STRETCHABLE ELECTRONICS: SOLVING METAL-MATRIX DEBONDING BY REMOVING THE MATRIX

Johan Hoefnagels[1], Jan Neggers[1], Salman Shafqat[1], Olaf van der Sluis[1,2], Angel Savov[2], Shivani Joshi[2], Ronald Dekker[2], Marc Geers[1]

[1]*Department of Mechanical Engineering, Eindhoven University of Technology, Eindhoven, the Netherlands*
[2]*Philips Research, Eindhoven, the Netherlands*

Summary Stretchable electronics holds the promise of futuristic electronic devices close to or inside human bodies. Stretchable electronics devices will be of hybrid nature, containing stiff application-specific integrated circuits embedded within a soft highly-stretchable matrix. However, stretchability-induced interface failure limits device reliability. Here, first, a multi-scale experimental analysis is presented that unravels how the microscopic delamination mechanisms result in the macroscopic fracture toughness. With this, a remarkably high fracture toughness has been achieved, however, stretchability-induced interface failure puts a limit to stretchable electronic technology relying on metal-substrate interfaces. It was realized, therefore, that the way to leap forward is to completely remove the substrate underneath the metal interconnects. A novel micro-fabrication process for completely free-standing interconnect structures was developed and interconnect structures were designed for maximum reversible stretchability. An unprecedentedly high reversible stretchability is achieved, opening up a realm of advanced future applications.

INTRODUCTION

Close integration of electronic devices with biological tissue enables a realm of ground-breaking (in-body) applications, from surgical and diagnostic implements that naturally integrate with the human body, such as eye-implanted retina-shaped photosensor arrays, electrode array probes for deep brain, heart, or nerve stimulation, and chips and sensors on the tip of minimally invasive instruments, to numerous ex-vivo applications, such as sensory skin for robotics and prostheses.

The main challenge of such devices is to match their shape and mechanical properties such as flexibility, stretchability and texture as closely as possible to that of the tissue. However, biological systems are soft, deformable, curved, whereas electronic devices are hard, brittle, flat. This apparently intrinsic incompatibility is at the verge of disappearing. The near future will see flexible devices such as bendable displays and rollable solar cells. Further into the future, electronics may even become stretchable. Thus far though, as argued below, proposed solutions in literature are fundamentally limited in mechanical reliability, manufacturability, and maximum stretchability. This calls for a paradigm shift in the approach towards stretchable electronics.

MULTI-SCALE EXPERIMENTAL ANALYSIS OF METAL–ELASTOMER INTERFACES

Stretchable electronics devices will be of hybrid nature, containing stiff application-specific integrated circuits (ASICs), such as sensors, actuators, and microprocessors, embedded within a soft highly-stretchable matrix (e.g. silicone rubber). Conductor wires connecting the microelectronic components are relatively stiff and brittle, but can be made stretchable with inventive mechanisms that can convert small local strains in large global stretch. However, stretchability-induced interface failure is a key reliability concern that limits device stretchability.[1] Surprisingly, early interface failure also occurs for large elastic-mismatch interfaces that exhibit a remarkable high fracture toughness (G_c>2 kJ/m2).[2] Therefore, a multi-scale experimental-numerical analysis was set up to bridge the gap between macroscopic fracture toughness to the microscopic delamination mechanisms.

T-peel and shear-peel delamination tests, at a wide range of peel rates, were conducted on elastomer-copper interface types, with different copper roughness (Ra ≈: 0.5/1.9 µm) and elastomer (TPU/PDMS), under *in-situ* optical and environmental scanning electron microscopic observation to unravel the characteristic features of the mesoscopic and microscopic peel front, see Fig. 1. Interface characterization at the macro-meso scale was achieved by matching optical deformation movies to FEM crack propagation simulations (employing a cohesive zone interface model), showing a notably low (macroscopic) mode angle dependency for both roughness types.[3] Real-time *in-situ* high-resolution ESEM movies revealed that 30µm-long fibrils are formed at the microscopic peel front, and detailed analysis of the fibril shape/distribution/evolution showed that fibril nucleation is caused by mechanical interlocking of the fibril basis in the copper roughness 'valleys', combined with cavitation at the roughness peaks, as can be seen in Figure 1.

A multi-scale rate-dependent energy dissipation analysis was conducted, including a study of fibril debonding versus rupture and post-mortem analysis (with a novel quasi-3D global DIC technique) that revealed permanent fibril deformation to be negligible.[4,5] The high macroscopic fracture toughness was found to originate from dynamical release of elastically stored energy in the fracture process zone upon fibril rupture. These insights give guide-lines for engineering interfaces with high macroscopic toughness, by enhancing the microscopic heterogeneity of interface loads to initiate a fibrillation process.

[a)] Corresponding author. Email: j.p.m.hoefnagels@tue.nl.

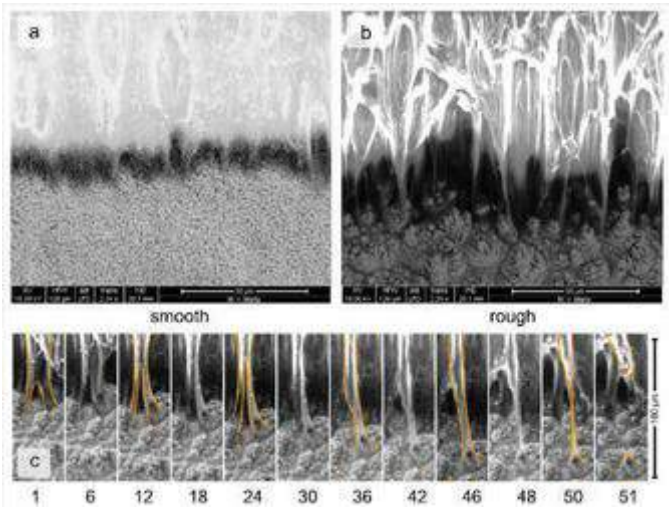

Fig.1. In-situ ESEM visualization of a delaminating peel front, showing a distinct difference in the micromechanisms between a smooth and rough copper interface. The lower image strip shows the evolution of a fibril up to failure from the rough copper. The numbers denote the image frame numbers, recorded at 1 frame per second. Guidelines have been added to mark the outline of the fibril and the original adhesion point. Figure reproduced from [5].

From this detailed multi-scale experimental analysis of metal-elastomer interfaces it was concluded that stretchable electronic technology relying on metal-rubber interfaces approaches its limits. It was realized, therefore, that the way forward is to completely remove the substrate underneath the metal interconnects.

FREE-STANDING INTERCONNECT STRUCTURES

A novel fabraction process for completely free-standing interconnect structures was developed. Figure 2 shows an examples of free-standing structures connecting the ASIC islands, which demonstrates that the production process has been succesfully implemented. In an elaborate FEM campaign, interconnect structures were designed for maximum elastic, i.e. reversible, stretchability. Preliminary results show that, using an interconnect design other than the one shown in Fig. 2, a huge elastic stretchability is achieved, roughly an order of magnitude higher than wat is reported in literature. This opens up a realm of advanced future applications in and outside the human body. The succesful interconnect design and the micro-mechanical origin of this huge elastic stretchability will be discussed at the ICTAM 2016 conference.

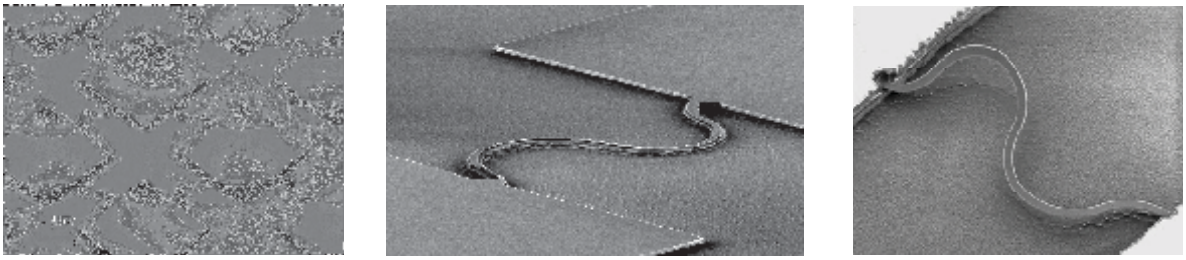

(a) *(b)* *(c)*

Fig.2. SEM images of successfully micro-fabricated free-standing interconnect structures, connecting ASIC islands.

References

[1] O. van der Sluis, Y.-Y. Hsu, P. H. M. Timmermans, M. Gonzalez, J. P. M. Hoefnagels, *Stretching-induced interconnect delamination in stretchable electronic circuits*, J. Phys. D **44**, 034008 (2011)

[2] J. P. M. Hoefnagels, J. Neggers, P. H. M. Timmermans, O. van der Sluis, M. G. D. Geers, *Copper-rubber interface delamination in stretchable electronics*, Scripta Mater. **63**, 875–878 (2010).

[3] J. Neggers, J.P.M. Hoefnagels, O. van der Sluis, O. Sedaghat, M.G.D. Geers, *Analysis of the dissipative mechanisms in metal–elastomer interfaces*, Engng. Frac. Mech. **149**, 412–424 (2015)

[4] B.G. Vossen, O. van der Sluis, P.J.G. Schreurs, M.G.D. Geers, J. Neggers, J.P.M. Hoefnagels, *On the role of fibril mechanics in the work of separation of fibrillating interfaces*, Mech. Mater. **88**, 1-11 (2015).

[5] J. Neggers, J.P.M. Hoefnagels, O. van der Sluis, M.G.D. Geers, *Multi-scale experimental analysis of rate dependent metal-elastomer interface mechanics*, Journal of the Mechanics and Physics of Solids **80**, 26–36 (2015).

Mechanics of finite crack considering interfacial elasticity

Pierre-Alexandre Juan [*1] and Rémi Dingreville[1]
[1]*Sandia National Laboratories, Albuquerque, NM 87185, USA*

Summary In this work we consider delamination and debonding phenomena in bi-material interfaces through a general formulation for two-dimensional (2-D) anisotropic elasticity while accounting for the interfacial structure by means of an interfacial elasticity paradigm. The elasticity formulation considers the necessary and sufficient conditions for a non-oscillatory, 2-D crack-tip stress field based on the Stroh formalism, while the interfacial mechanics is incorporated by employing a generalized interfacial elasticity formulation for coherent and incoherent interfaces. This general formulation provides an insight on the physical significance and the obvious coupling between the interface structure and the associated mechanical fields in the vicinity of the crack tip. The singularity of the crack-tip stress field will be discussed in terms of the interface properties.

Many engineering materials ranging from metal matrix composites, cast aluminum alloys, or oxide dispersed strengthened (ODS) steels all contain bi-material interfaces. Under certain loading conditions, delamination is most likely to occur along these interfaces. The structural and chemical characteristics of the interface separating both phases greatly affect the delamination process. The corollary of such an assertion is then that any theoretical framework describing interface crack problems shall strongly depend on the interface representation. So far, classical theoretical fracture mechanics studies considering the two-dimensional (2-D) problem of a finite crack lying on an interface between two distinct semi-infinite media [1, 2, 3, 4, 5, 6] neglect the effects of interfacial elasticity on the fracture of bi-materials. More recently, several studies have incorporated an interfacial model consisting of an interfacial constitutive behavior linking the interfacial strain to the interface surface stress [7, 8] into the classical fracture formulation. However these theories based on such a 2-D framework cannot account for the interface flexural stiffness nor can they describe the transverse behavior of real bi-material interfaces or account for the interfacial mismatch.

The purpose of the present work is not a discussion of the capabilities of the pre-cited mathematical formalisms but to consider, by using the same 2-D finite crack configuration, a more physical description of the interface mechanics [9] that accounts for the three-dimensional (3-D) nature of the interface and its state of coherency. The present formulation consists of three components: (i) the first component is based the Stroh formalism and considers the resolution of the Navier-type equation associated with the 2-crack problem in anisotropic elasticity; (ii) the second component describes the elastic behavior of coherent and incoherent interfaces under general loading conditions based on the Gibbs dividing surface concept; and (iii) the last component describes the boundary conditions at the interface while accounting for surface stresses.

(i) 2-D anisotropic elasticity formulation: Considering the 2-D crack problem schematically represented in Fig. 1, the displacement vector $\boldsymbol{u}\left(x_1, x_2\right)$ is the solution of the following Navier equation:

$$\underline{\underline{\mathbb{C}}} : \nabla.\nabla \mathbf{u}\left(\mathbf{x}\right) = \underline{\underline{\mathbb{C}}} : \nabla \boldsymbol{\epsilon}^{*,\mathbf{S}}\left(\mathbf{x}\right) \ , \tag{1}$$

where the second order eigenstrain tensor $\boldsymbol{\epsilon}^{*,S}$ is defined as the interfacial structure eigenstrain tensor only defined in medium "↗" [9]. This tensor associated where the interface represents the interface components of the strain of medium "↗" relative

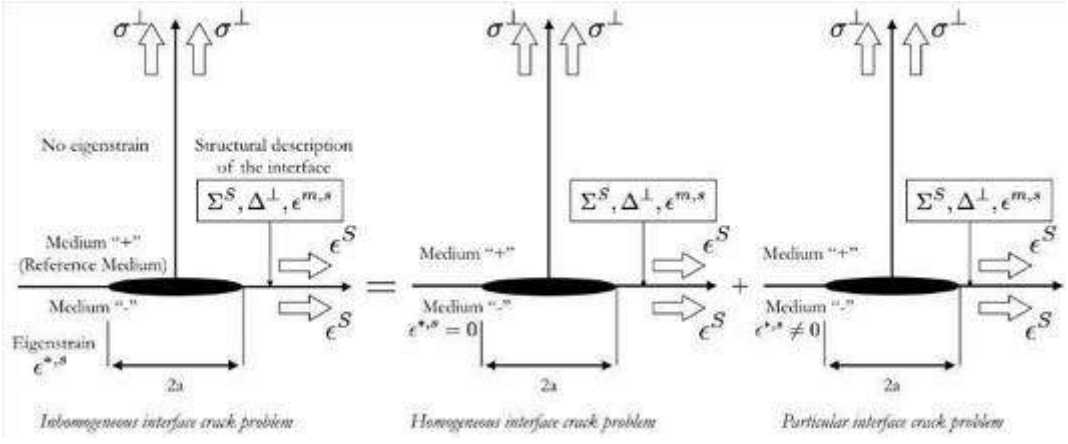

Figure 1: Interface crack between two anisotropic media

*Corresponding author. Email: pjuan@sandia.gov

to medium "+". It can be decomposed such that $\boldsymbol{\epsilon}^{*,S}(\mathbf{x}) = \boldsymbol{\epsilon}^{0,S} + \boldsymbol{\epsilon}^{m,s} g(\mathbf{x})$, where the strain tensor $\boldsymbol{\epsilon}^{0,S}$ is an eigenstrain related to stress free configuration corresponding to the change in molar volume between medium "+" and medium "$\nearrow$" and the spatial function g corresponds to the variation of the structural mismatch $\boldsymbol{\epsilon}^{m,S}$ over a few atomic layers and vanishes far from the interface.

(ii) Interfacial constitutive behavior: A generalized continuum framework describing the elastic behavior of coherent and incoherent interfaces [9] under general loading conditions based on the Gibbs dividing surface concept combined with the so-called "T-decomposition" is used to describe the uncracked part of the interface such that:

$$\boldsymbol{\Sigma}^S = \boldsymbol{\Gamma}^{(1)} \nearrow \underline{\underline{\boldsymbol{\Upsilon}}}^{(2)} : \boldsymbol{\epsilon}^{m,S} + \underline{\underline{\boldsymbol{\Gamma}}}^{(2)} : \boldsymbol{\epsilon}^S + \boldsymbol{\sigma}^\perp \cdot \underline{\underline{\mathbb{H}}}\,, \tag{2}$$

$$\boldsymbol{\Delta}^\perp = \boldsymbol{\Lambda}^{(1)} + \boldsymbol{\Lambda}^{(2)} \cdot \boldsymbol{\sigma}^\perp \nearrow \underline{\underline{\mathbb{H}}} : \boldsymbol{\epsilon}^S + \underline{\underline{\mathbb{K}}} : \boldsymbol{\epsilon}^{m,S}\,. \tag{3}$$

The interfacial tensors $\boldsymbol{\Sigma}^S$ and $\boldsymbol{\Delta}^\perp$are the coherent surface stress and the transverse excess strain, respectively. They represent the thermodynamic driving forces of stretching the interface and can be expressed as a function of the interfacial in-plane strain tensor, $\boldsymbol{\epsilon}^S$, the structural mismatch $\boldsymbol{\epsilon}^{m,S}$, and the transverse stress, $\boldsymbol{\sigma}^\perp$. The transverse stress and in-plane strain tensors are both applied remotely. The quantities $\boldsymbol{\Gamma}^{(1)}$, $\underline{\underline{\boldsymbol{\Upsilon}}}^{(2)}$, $\underline{\underline{\boldsymbol{\Gamma}}}^{(2)}$, $\underline{\underline{\mathbb{H}}}$, $\boldsymbol{\Lambda}^{(1)}$, $\boldsymbol{\Lambda}^{(2)}$ and $\underline{\underline{\mathbb{K}}}$ correspond to the residual surface stress, the interface in-plane coherency stiffness tensor, the interface in-plane elastic stiffness tensor, the interfacial Poisson's effect tensor, the residual transverse interfacial deformation, the interface transverse compliance tensor and the interface transverse structural interfacial mismatch tensor, respectively.

(iii) Boundary conditions with interface properties: While the boundary condition associated with the cracked region is similar to the one considered by [4, 2, 6], i.e. $\boldsymbol{\sigma}^\perp_+(x_1, 0^+) = \boldsymbol{\sigma}^\perp_-(x_1, 0^-) = \boldsymbol{t}(x_1)$, boundary conditions related to the uncracked part and listed hereafter differ significantly such that:

$$[\![\mathbf{u}]\!] = \boldsymbol{\Delta}^\perp\,, \tag{4}$$

$$\mathbf{n} \cdot [\![\boldsymbol{\sigma}]\!] \cdot \mathbf{n} = 0\,, \tag{5}$$

$$\mathbf{P} \cdot [\![\boldsymbol{\sigma}]\!] \cdot \mathbf{n} = \nearrow \nabla^S \boldsymbol{\Sigma}^S\,. \tag{6}$$

The resolution of the Navier-type equation is then conducted by combining the Stroh formalism [10] with so-called "T-decomposition" [4, 2]. It is noteworthy to mention that the displacement field obtained for the medium "$\nearrow$" consists of the sum of a particular solution resulting from the presence of the eigenstrain and a homogeneous solution whose expression depends directly on the structural characteristics of the interface. Through the resolution of this formulation, the singularity of the crack-tip stress field will be discussed in terms of the interface properties.

ACKNOWLEDGMENTS

Sandia is a multiprogram laboratory operated by Sandia Corporation, a Lockheed Martin Company, for the United States Department of Energy, under Contract No. DE-AC04-94AL85000.

References

[1] T. Ting, "Explicit solution and invariance of the singularities at an interface in anisotropic media," *International Journal of Solids and Structures*, vol. 22, no. 9, pp. 965–983, 1986.

[2] J. Bassani and J. Qu, "Finite crack on bimaterial and bicrystal interfaces," *Journal of the Mechanics and Physics of Solids*, vol. 37, no. 4, pp. 435–453, 1989.

[3] J. Bassani and J. Qu, "On elasticity solutions for cracks on bimaterial and bicrystal interfaces," *Materials Science and Engineering, A*, vol. 107, pp. 177–184, 1989.

[4] J. Qu and J. Bassani, "Interfacial fracture mechanics for anisotropic bimaterials," *Journal of Mechanics and Physics of Solids*, vol. 37, no. 4, pp. 417–433, 1989.

[5] Z. Suo, "Singularities, interfaces and cracks in dissimilar anisotropic media," *Proceedings of the Royal Society of London. Series A, Mathematical and Physical*, vol. 427, no. 1873, pp. 331–358, 1990.

[6] L. Ni and S. Nemat-Nasser, "Interface cracks in anisotropic dissimilar materials: an analytic solution," *Journal of the Mechanics and Physics of Solids*, vol. 29, no. 1, pp. 113–144, 1991.

[7] C. I. Kim, P. Schiavone, and C.-Q. Ru, "Effect of surface elasticity on an interface crack in plane deformations," *Proceedings of the Royal Society of London A: Mathematical, Physical and Engineering Sciences*, vol. 467, pp. 3530–3549, 2011.

[8] H. Nan and B. Wang, "Effect of residual surface stress on the fracture of nanoscale materials," *Mechanics Research Communications*, vol. 44, pp. 30–34, 2012.

[9] R. Dingreville, A. Hallil, and S. Berbenni, "From coherent to incoherent mismatched interfaces: A generalized continuum formulation of surface stresses," *Journal of the Mechanics and Physics of Solids*, vol. 72, pp. 40–60, 2014.

[10] A. Stroh, "Dislocations and cracks in anisotropic elasticity," *Philosophical Magazine*, vol. 3, pp. 625–649, 1958.

INTERACTION OF DELAMINATION AND ELECTROCHEMICAL PROCESSES

Wei Lu[a)]
Department of Mechanical Engineering, University of Michigan, Ann Arbor, Michigan, USA

Summary Inter-particle fracture, specifically debonding between the active particle and binder, is a major cause of capacity fade in Li-ion batteries. We integrated the electrochemical-mechanical model and cohesive zone model to investigate the interfacial debonding during lithium intercalation. We found that the mechanism of facture at the particle/binder interface is different from that inside a particle. The debonding at the interface is caused by the expansion of the particle that is closely related to the total amount of lithium intercalation, while the fracture inside a particle is caused by the gradient of lithium concentration. As a result, debonding at the interface is more likely to occur as the particle size and C-rate decrease, which is opposite to the trend of fracture inside a particle that is more likely to occur as the particle size and C-rate increase. This understanding of debonding mechanism can guide the development of more robust electrodes.

INTRODUCTION

Fracture in the electrode is known as one of the major causes for degradation in Li-ion batteries. The effects include loss of electric contact, isolation of active materials from the conductive matrix, and increased cell internal resistance. Fracture also increases the exposure of active materials to the electrolyte, accelerating side-reactions and capacity fade. The fracture behavior inside a single particle has been addressed by several works. However, inter-particle fracture in electrode materials has rarely been addressed in theoretical studies. In an electrode, particles are connected together by the binder. Two scenarios can possibly happen for inter-particle fracture depending on the locations: fracture in the middle of binder or at the particle/binder interface. With atomistic simulations we have shown that the cohesive strength at the interface is weaker than that inside the binder, suggesting that inter-particle fracture is more likely to happen at the particle/binder interface [1].

Here we report a study on the debonding behavior between a graphite particle and a PVDF (polyvinylindene fluoride) binder associated with the electrochemical-mechanical processes during the operation of a Li-ion battery. Graphite particles and PVDF are commonly used as the anode material and the binder in current commercial batteries. To capture fracture at the interface, we have developed an electrochemical-mechanical model that incorporates the cohesive zone approach. First, diffusion-induced stresses are calculated by the electrochemical-mechanical model. Then, the lithium concentration profile is exported to the cohesive zone model by thermal stress analogy. Since the cohesive zone model can describe crack initiation and its propagation, the simulation results can provide quantitative insight into the debonding process during lithium intercalation and capture the creation of new interfaces that are exposed to the electrolyte.

MODELLING OF COUPLED ELECTROCHEMICAL PROCESS AND DELAMINATION

An iterative two-step method is used to study the interfacial debonding due to lithium intercalation. We first calculate the diffusion-induced stress in the particle by coupling the stress field and Li-ion diffusion, and then export the calculated lithium concentration profile at any specific State of Charge (SOC) and apply it to the cohesive zone model to examine debonding.

Electrochemical-mechanical model: The stress-strain relation in the particle is $\varepsilon_{ij} = \left[(1+\nu)\sigma_{ij} - \nu\sigma_{kk}\delta_{ij}\right]/E + c\Omega\delta_{ij}/3$, where ε_{ij} are strain components, E is Young's modulus, ν is Poisson's ratio, σ_{ij} are stress components, δ_{ij} is the Kronecker delta, c is the Li-ion concentration and Ω is partial molar volume of Li-ions [2]. In the binder region the regular stress-strain relation is applied. The mechanical boundary condition is given by constraining the displacements at the bottom of the binder, as shown in Fig. 1. The gradient of chemical potential drives Li-ion diffusion. Both concentration and stress contribute to the chemical potential, leading to a diffusion flux of $\mathbf{J} = -D\left(\nabla c - \Omega c \nabla\sigma_h / RT\right)$, where D is the diffusion coefficient of Li-ion, R is gas constant, T is absolute temperature, and σ_h is the hydrostatic stress given by $\sigma_h = \left(\sigma_{11}+\sigma_{22}+\sigma_{33}\right)/3$. The time-dependent lithium concentration is given by $\partial c/\partial t + \nabla\cdot\mathbf{J} = 0$, with boundary conditions of $\mathbf{J}\cdot\mathbf{n} = i_n/F$, where $\mathbf{n}$ is the normal vector of the particle surface, i_n is the current density and F is Faraday's constant. The current density at the particle surface covered by the binder is set to zero. The current density at other regions on the particle surface is determined by the charge/discharge C-rate. Simulations are performed with COMSOL multiphysics [3].

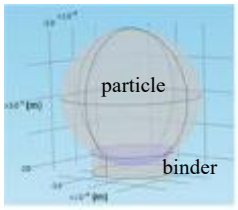

Fig. 1. A particle with binder at the bottom.

Cohesive zone model: The cohesive zone model is developed using ABAQUS, which is equipped with cohesive elements that COMSOL lacks [4]. We adapt a bilinear traction-separation law, where the governing parameters are the maximum stress and the fracture energy. The fracture process occurs on the cohesive surfaces as follows. The traction stress between two cohesive surfaces changes with the external loading. When the traction stress reaches the maximum stress, delamination of surfaces or fracture initiates. Then the crack evolves until all of the fracture energy is dissipated and

[a)] Corresponding author. Email: weilu@umich.edu

eventually, th fracture pro ess is compl ted with the appearance of new surfaces, i.e. an adva ce of the cr ck. Crack growth is captured by tracking the crack dvance step by step with the evolution o the external loading. In th cohesive zone model, t e parameters of the traction-separation la are critical. n this study, ore accurate prediction is enabled by using the para eters obtained from molec lar dynamics simulations [1]. The lithium concentration profile from COMSOL is loaded as a 'temperature' field in AB QUS. Cohesive elements re placed at the interface between the p rticle and binder. The cohesive behavi r is defined b two ingredie ts: "damage initiation" and "damage evol tion". For the criteria of "damage initi tion", the ma imum nomin l stress is prescribed in the ormal and shear direction. or "damage evolution", the fracture energy and a lin ar degradatio model with uncoupled nor al/shear mod s are prescrib d.

ESULTS

Figure 2 shows the ev lution of lithium concentration profile during charging. In the early stage when lit ium ions start to diffuse into the particle, the concentration gradient is fairly large. After the part cle is filled ith more ions, the concentration gradient becomes smaller. For an isolated sphe ical particle in the electr lyte without any binder, the lithium concentration distribution is spherically is tropic with th lowest concentration at the particle center. In contrast, for the system studied here the lithium flux from the surrounding electrolyte is blocked by the binder at the particle/binde interface. T e location of the lowest c ncentration a pears at the bottom of th particle, rather than at t e center. After t=1400s, a zone with high lithium concentration begins to app ar near the e ge of the bin er due to stress concentrati n. The stress concent ation is developed due to geometric disconti uity at the edge, which drives local lithium ccumulation. Our simulatio s (Fig. 3) show that debonding begins to occur at 85% SOC with a small mount of debonding near t e edge of the bin er. As SOC increases, the debonding ar a is graduall enlarged toward he center. When the SOC reaches 95%, the binder is separated entirely.

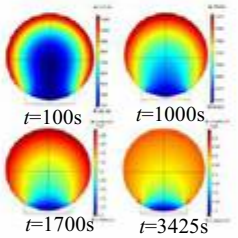

Fig. 2 Evol tion of Li concentration (particle radius: 5μm, 1C-rate).

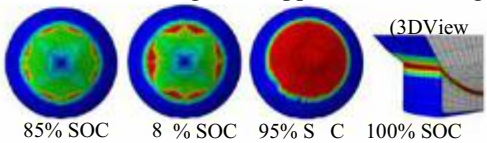

Fig. 3 Debonding areas (red c lor) at differen SOCs. View from bottom. (5μm, 1C-rate).

We investigated the effe t of C-rate and particle size on the debonding behavior. Figure 4 shows the debondi g area for the fully char ed state at di ferent C-rates and particle s zes. For the particle radius of 5μm, an entire separation occurs at 1C-rate. How ver, at 5C-rat only a small portion of separation is observed near the edge of the binder. When t e particle size increases from 5μm to 10 μm, an entire separation also occurs at 1C-rate. However, no debo ding is obser ed at 5C-rate. These results show that interface deb nding is more likely to hap en at a smaller particle size and a lower C-rate. This trend is opposite to the fract re behavior inside a particle, where fracture is more likely to happen at a larger pa ticle size and a higher C-rate. We attribute the distinct fracture behaviors at the particle/binder interface and inside a particle to different mechanisms of stress generation. For interface debonding, the stress at the inter ace mainly c mes from the expansion of the particle during lithium intercalation relative to the binder. As the C-rate decreases, it takes longer time for the concentration on the article surface to reach sto chiometry or a certain SOC. Thus there is enough tim for lithium i ns to diffuse eeply inside t e particle, and the concentration inside the particle is ore uniform. As a result, t e total amount of lithium ions intercalate is larger at a lower C-rate, leading to a larger volume expansion and strain at the interface. As the particle size increases, more space is available for lithium ions o fill, which leads to a smaller volume expansion. Therefore, a lar er volume expansion at a low C-rate with a smaller article size causes a large stress at the interface, which leads to interface fractur more likely to occur. In contrast, the mechanical stress inside a particle is related o the gradient of lithium co centration.

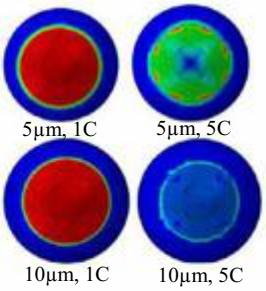

Fig. 4 Debon ing areas at 100% S C with different particle radii and C-rates.

CO CLUSIONS

Debonding at the particle/binder interfac was simulate using an inte rated electroc emical-mechanical model and cohesive zone model. T e simulations show that frac ure at the inte face occurs more likely at a smaller particl size and a lo er C-rate, which is opposite to the tendency of fracture inside a particle. The reason is that the inte face debondin is caused by the overall expansion of t e particle, whi e fracture insi e a particle is aused by the concentration g adient.

References

[1] Lee S., Park ., Yang J., Lu W.: *J. Electrochem. Soc.* **161**: A1218-A1 23, 2014.
[2] Park J., Lu ., Sastry A. M.:, *J. Electrochem. Soc.* **158**: A201-A206, 2011.
[3] Shalev O., Biswas S., Yang Y., Eddir T., Lu W., Clarke R., Shtein M.: *Nature Commun.* **5**, 5204, 2014.
[4] Lee S., Yang J., Lu W.: *Extrem Mech. Lett.* **6**: 37-44, 2016.

A HOMOGENIZED APPROACH FOR DELAMINATION FRACTURE IN LAMINATED STRUCTURES

Roberta Massabò
[1]*Department of Civil, Chemical and Environmental Engineering, University of Genova, Genova, Italy*

Summary Progressive damage in multi-layered structures is dominated by delamination fracture at the layer interfaces. Current modeling relies on cumbersome and computationally expensive discrete-layer models which represent the structures as an assembly of layers joined by cohesive interfaces and where the number of variables depend on the number of layers and may be very large. In this paper, fracture of laminated plates will be studied using a novel multi-scale homogenized model which has been recently formulated by the author. The model depends on a limited number of global variables, equal to those of classical single layer theories, and account for the small-scale fields, e.g. zig-zag displacements, jumps at the layer interfaces, through a homogenization technique. The model accurately predicts stresses and displacements in multi-layered plates with continuous imperfect interfaces and delaminations subjected to thermo-mechanical loading. Here the accuracy of the approach in deriving fracture parameters will be verified using some simple reference problems.

MULTISCALE HOMOGENIZED APPROACH

In this paper the potential of a novel homogenized structural theory to study fracture of multi-layered plates will be investigated.The theory was recently formulated in [1,2] and based on the original works in [3,4].
The theory uses a multiscale approach and a homogenization technique and couples an equivalent single layer theory and a detailed discrete-layer cohesive-interface model, in order to obtain efficient homogenized field equations while accounting for the inhomogeneous material structure and for the presence of imperfect interfaces and cohesive or traction-free delaminations. The equations depend on a reduced number of variables, which is independent of the numbers of layers or imperfections and coincides with that of the coarse grained model (four in wide plates and beams; six in general plates), Fig.1. The homogenized theory allows closed form solution of problems that would otherwise require numerical solutions if treated using classical discrete-layer approaches. Global displacements and force and moment resultants are obtained through the solution of the homogenized equations using solution techniques previously developed for homogeneous structures, while the local fields, in the layers and at the layer interfaces, can be easily evaluated a-posteriori. The accuracy and efficacy of the theory for the analysis of laminated wide plates and beams with imperfect sliding interfaces and delaminations subjected to thermo-mechanical loads has been demonstrated in [5]. Figure 2 shows stress and displacement fields in a thick highly anisotropic wide plate with imperfectly bonded layers and fully delaminated layers; the results are compared with exact elasticity solutions.

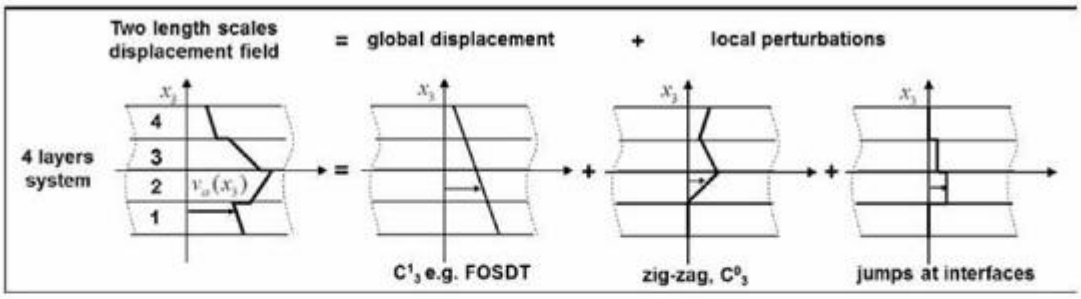

Figure 1: Global displacements (single layer theory) and local perturbations in the two length-scales displacement field assumed in the model in [1]. The local perturbations are derived, as functions of the global variables, through a homogenization technique.

FRACTURE ANALYSIS

The model in [2] will be used to define the fracture parameters in simple reference problems, e.g. beams with finite length delaminations under mixed-mode conditions, in order to verify its accuracy in predicting crack tip force resultants and local stress fields both for cohesive and traction free cracks. This verification is preliminary to the application of the approach for delamination damage progression analyses.

Acknowledgements: Support by U.S. Office of Naval Research no. N00014-14-1-0229, administered by Dr. Y.D.S. Rajapakse is gratefully acknowledged.

[a)] Corresponding author. Email: roberta.massabo@unige.it

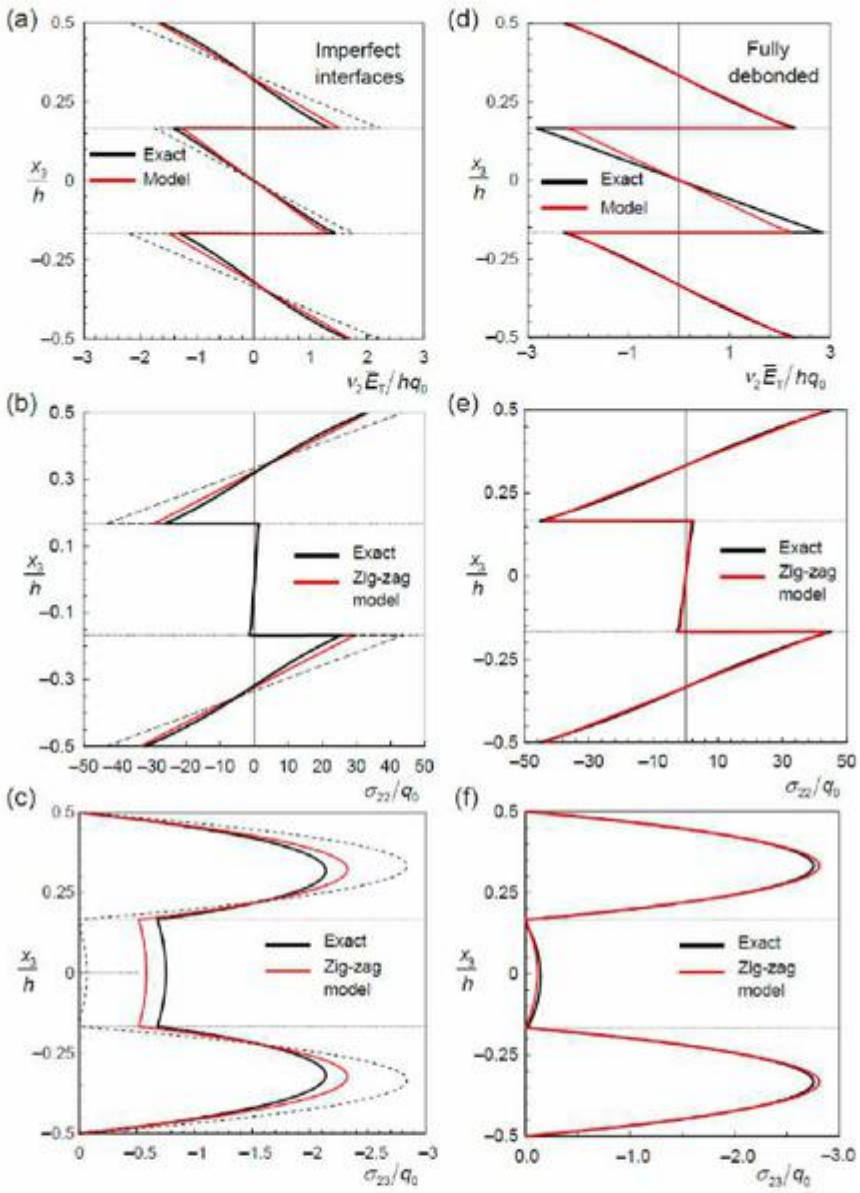

Figure 2: Longitudinal displacements, transverse shear (at plate end) and bending stresses (at mid-span) shown through thickness for a highly anisotropic simply supported thick, L = 4h, plate with three layers [0,90,0] subjected to a sinusoidal transverse load,and deforming in cylindrical bending. The first column refers to a plate with partially bonded layers joined by linearly elastic sliding-only interfaces with stiffness $K_S h \ \ \bar{E}_T = 0.25$. The second column to a fully delaminated plate. Elastic constants: $E_T \quad E_L / 25$, $G_{LT} = E_L / 50$, $G_{TT} = E_L / 125$, $\nu_{LT} = \nu_{TT} = 0.25$, $\bar{E}_T \quad E_T / (1 - \nu_{LT}\nu_{TL})$. (dashed curves refer to early solutions based on the homogenized approach which were not energetically consistent)

References

[1] Massabò R., Campi F., Assessment and correction of theories for multilayered plates with imperfect interfaces, *Meccanica*, (2015), DOI10.1007/s11012-014-9994-x

[2] Massabò R., Campi F., An efficient approach for multilayered beams and wide plates with imperfect interfaces and delaminations, Compos Struct (2014), 116, 311-324

[3] Di Sciuva, M., (1997) Geometrically nonlinear theory of multilayered plates with interlayer slips, *AIAA Journal*, 35 (11), 1753-1759

[4] Librescu, L., and Schmidt, R., (2001) A general theory of laminated composite shells featuring interlaminar bonding imperfections, *Int. J. Solids and Structures*, 3355-3375

[5] Pelassa M., and Massabò, R., (2015), Explicit solutions for multi-layered wide plates and beams with perfect and imperfect bonding and delaminations under thermo-mechanical loading, Meccanica, 50, 2497-2524.

EXTRACTING RATE DEPENDENT TRACTION SEPARATION RELATIONS FOR INTERFACES

S. Palvadi[1], K.M.Liechti[1] & N. Lu[1]
[1]*Center for the Mechanics of Solids, Structures and Materials*
Aerospace Engineering and Engineering Mechanics
The University of Texas at Austin, Austin, Texas, U.S.A

Summary Extracting traction-separation relationships for cracks/interfaces in both viscoelastic and elastic media can be equivalently described as solving a Cauchy inverse boundary value problem. In this work, for a given far field loading condition, a framework is proposed to independently solve for the tractions and displacements governing the interactions between elastic media. The proposed framework combines the field projection method [1] and an iterative method to solve Cauchy problems [2, 3], to obtain an optimization scheme that can be utilized to measure tractions and displacements. An attractive feature of this framework is that it only utilizes the displacement and load measurements made on a very small accessible part of the boundary, close to the loading point and far away from the crack-tip. Both numerical and physical experiments were performed to conclusively demonstrate the efficiency of the proposed framework.

OBJECTIVES

Current work elicits a methodology to extract traction separation relationships from load-displacement and end rotation data, measured from a delamination experiment carried out using a double cantilever beam type geometry as shown in Figure 1. It has to be emphasized that this framework does not make any major a *priori* assumptions on the functional form relating interfacial tractions and displacement quantities; this in turn enables the user to apply a similar framework to characterize rate dependent traction separation relations as well.

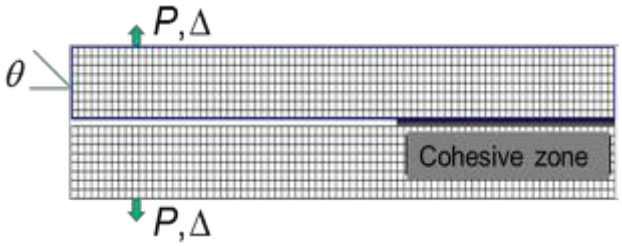

Figure1. Double cantilever beam, measured P,Δ,θ

METHODOLOGY

In order to represent the current problem as a Cauchy problem, analysis is restricted to the elastic adherent, highlighted by blue contour in Figure 1, with the effect of the cohesive zone now visible as unknown boundary conditions. This part of the boundary can now be effectively marked as being under constrained and characterizing these unknown boundary conditions constitute the immediate objective of this work.

As mentioned earlier, a nonlinear optimization was designed to solve this Cauchy problem and a complete statement for a non-linear optimization scheme usually consists of three main components: a) objective function generation b) linear/nonlinear constraints generation c) development of an initial guess. Briefly put, the objective function is developed in such a way that a solution field, satisfying all the constraints, will lie at the minimum and represent the unknown quantities, in this case tractions and displacements. The objective function was obtained by combining a condensation scheme [2, 3] with the results from field projection concepts [1]. The resulting objective function was

$$\left\| \mathrm{I}.\left[\frac{\mathrm{du}}{\mathrm{dx}}\right] + \mathrm{E}^{\mathrm{net}}\left[\mathrm{u}\right] - \mathrm{F}^{\mathrm{net}}\mathrm{P} - \mathrm{D}^{\mathrm{net}}\Delta - \mathrm{T}^{\mathrm{net}}\theta \right\| = 0 \qquad (1)$$

Where u is the nodal displacement vector in the cohesive zone, $P\Delta$ and θ are the measured/applied forces, displacement and end rotation. $\underrightarrow{F}^{net}, \underrightarrow{D}^{net}, \underrightarrow{T}^{net}$ and E^{net} are known vectors/array that remain constant for a particular geometry, and elastic properties. In other words nodal displacement values corresponding to actual displacement values will minimize Equation 1. Despite creating an objective function which has a minimum corresponding to the actual solution, it can be established, through trial and error, that there exist multiple local minima and the true solution exists at the global minimum. In order to reach the global minimum using any search algorithm, additional qualitative information regarding the traction separation relation has to be imposed as constraints for the system. In that vein, two sets of linear constraints involving the general form of all traction-separation relations were formulated and imposed. The final component of this optimization scheme was generating the initial guess. As a starting point, a linear traction-separation relationship is assumed and the initial stiffness K is obtained through a simple linear iterative scheme which will be omitted here.

RESULTS AND ANALYSIS

[a] Corresponding author. Email: p.n.sundeep@gmail.com

Owing to the theoretical nature of this work, numerical experiments were carried out using ABAQUS and other custom built finite element codes first to validate the scheme .Two different input traction-separation relations were chosen and were back predicted using the current algorithm as shown in Figure 3:

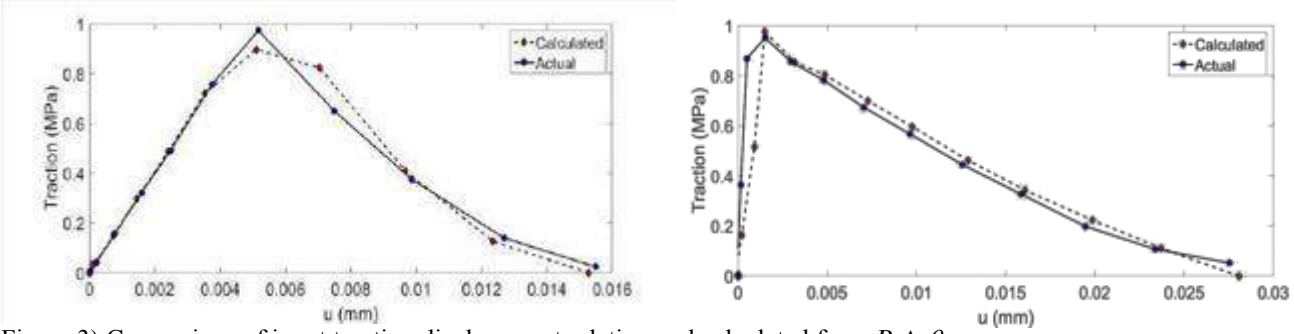

Figure 3) Comparison of input traction displacement relation and calculated from P, Δ, θ

As seen above, the agreement in the calculated and actual traction separation relationship is in reasonable agreement, which demonstrated that the current scheme can also be utilized in an experimental setting. Experiments were carried out using a custom built loading device as shown below in Figure 4. Two polystyrene adherends were used with a PDMS interlayer as the adhesive and the traction separation profile was characterized using the load, displacement and rotation values measured while applying a step displacement. The crack front is tracked through the microscope and the crack length is given as an additional input to the optimization scheme. Preliminary results from this set up are as shown below in Figure 5. Two immediate inferences can be established from experimental results; 1) Rate dependence can be very clearly observed by tracking the maximum traction value and 2) the faster the rate of crack propagation, the "stiffer" the traction separation relation.

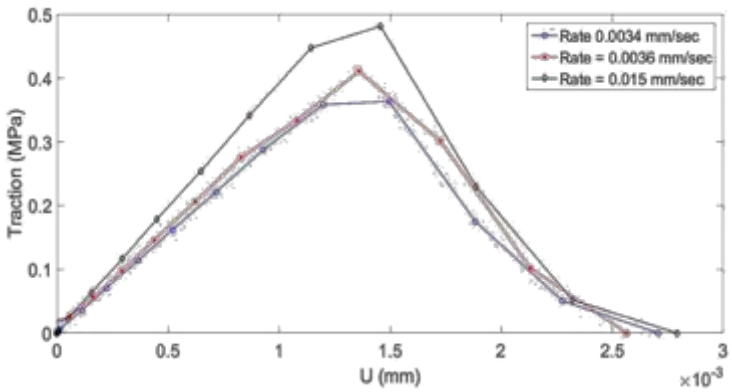

Figure5: Rate dependent traction separation relationship

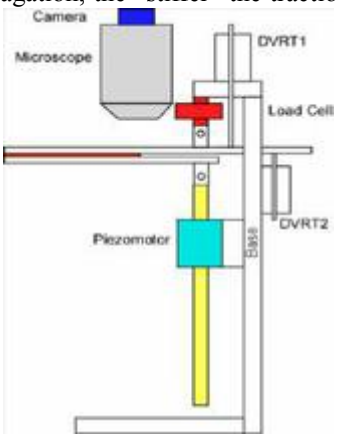

Figure 4: Loading device

CONCLUSIONS

A viable scheme based on the field projection method was developed to calculate traction separation relationships from far field quantities. The proposed scheme converts the problem into Cauchy value problem and an optimization scheme is established which shows good agreement with numerical experiments. In addition, experiments were performed to analyse the interface of polystyrene and PDMS using the optimization scheme

.

ACKNOWLEDGEMENTS

The authors gratefully acknowledge financial support of this work by the National Science Foundation through Grant No. 301335. Any opinions, findings and conclusions or recommendations expressed in this material are those of the author(s) and do not necessarily reflect the views of the National Science Foundation.

REFERENCES

[1] Hong S, Kim K-S. JMPS , 51(2003), p.1267
[2] A Cimetière et al. 2001 Inverse Problems 17 553
[3] F Delvare et al. 2010, Computer Methods in Applied Mechanics and Engineering, Volume 199
[4] Rice, J.R J. Appl. Mech., 35 (1968), p. 379

MODELLING AND ANALYSIS OF BRIDGING EFFECT FOR INTERFACE CRACKS

Robert Goldstein and Mikhail Perelmuter *
Institute for Problems in Mechanics of RAS, Prospect Vernadskogo 101-1, 119526, Moscow, Russia

Summary The multilevel model of bridged cracks for analysis of bridging effect for interface cracks is proposed and used. It's assumed: there are bonds of the different levels between jointed materials (the interface layer); a zone of weakened bonds in this layer is considered as an interfacial crack with distributed nonlinear spring-like bonds between the surfaces of a crack (the bridged zone); the size of the interface crack bridged zone is comparable to the whole crack size. The quantitative analysis of the bridging effect for interfacial cracks is performed accounting for the influence of the boundary conditions of structures and gradation of mechanical properties of jointed materials.

INTRODUCTION

Models of a crack with interaction of its surfaces make it possible to combine approaches of mechanics, physics and chemistry of fracture while analyzing a crack growth. Zones of crack surfaces interaction adjoin crack tips and they are commonly related to crack parts where cohesion forces are applied to the crack surfaces and suppress the crack opening. Different versions of such models (cohesive or bridged) for analyzing brittle, elastic-plastic and viscoelastic fracture were proposed. In this paper to model the bridging effect and fracture toughness of interfacial junctions the multilevel crack bridging concept is proposed and used. It is assumed within the concept: there are bonds of the different levels (intermolecular forces, molecular bundles, fibers, particles) between joined materials (the interfacial adhesion layer); a zone of weakened bonds in this layer is considered as the interfacial crack with distributed nonlinear spring-like bonds between the crack surfaces (bridged zone). The bonds properties on the different material levels define the stress state at the crack bridged zone and, hence, the fracture toughness of the interface junction. In the general case, the size of the interface crack bridged zone is comparable to the whole crack length. In the case of the crack bridged zone of large scale the conditions of the limit equilibrium and quasi-static growth of cracks must be reconsidered to model quantitatively the bridging effects. The quantitative analysis of the bridging effect for interfacial cracks consists of the following main steps: 1) development of the bond deformation law; 2) evaluation of stresses along the crack bridged zone; 3) application of the non-local crack growth criterion to analyze the fracture parameters of the interface junction taking into account fracture toughness of interface itself. Modelling the bridging effects leads to new methods for adjusting the adhesion fracture resistance.

INTERFACE CRACK: BRIDGED MODEL AND CRACK GROWTH ANALYSIS

Interface crack bridged model. It is assumed within the model, that the fracture process zone can contain ligaments of several levels acting on various scales of the crack length. For given crack length the total contribution to the fracture toughness of ligaments of all levels, except of the last (largest), is constant, and the region of their influence is small, compared to the whole crack size and the influence zone of the last level bonds, see Fig.1, two level ligaments. The total stress intensity factors due to external loading and bonds traction are not assumed equal to zero. The notations "bonds" and "bridged zone" refer only to bonds of the last level. This last level region (bridged zone) modelling is based on the following assumptions: 1) fracture process is localized at the crack bridged zone, which is treated as a crack part and can be comparable with the whole crack length; 2) distributed bridging traction depending on a crack opening are imposed to a crack surface in the bridged zone; 3) materials behind crack tip are considered as linearly-elastic and they are deformed together with fibers (or adhesion layer) without loss of their continuity.

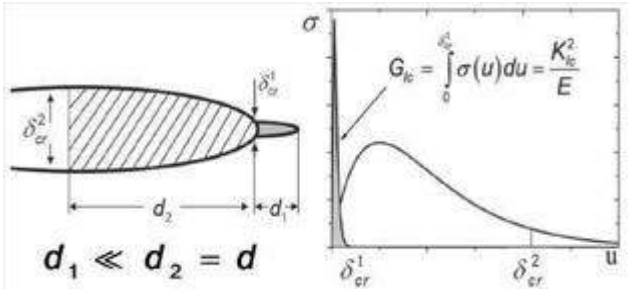

Figure 1: Two level ligaments, contribution of zone d_1 to fracture toughness is constant and $\delta_{cr}^1 \ll \delta_{cr}^2 = \delta_{cr}$ - COD.

To describe mathematically the interaction between the crack surfaces, we assume that there exist bonds with nonlinear deformation law between the surfaces of the crack at the bridging zone [1]. The traction appeared in the bonds between the interface crack surfaces under the external loads action have the normal q_n and tangential q_τ components, $\sigma = \sqrt{q_n^2 + q_\tau^2}$ is the modulus of the traction vector. The surfaces of the crack are loaded by the normal and tangential stresses, which are numerically equal to these components of the traction. Experimental determining of bonds deformation law for materials junction is labor-consuming task. The combined approach to determining such curves consists in phenomenological or micromechanical

*Corresponding author. Email: perelm@ipmnet.ru

definition of functional dependence between a crack opening and bridging stress for some groups or pairs materials and the experimental determination of some parameters for stressed bonds to describe the curve mathematically [2].

Stresses analysis. The stresses at the interfacial crack bridged zone are analyzed for the given nonlinear bond deformation law and accounting for the kinetic destruction of bonds due to elevated temperature and aggressive agent. The bonds kinetic model is the union of the Zhurkov fluctuation model of bonds destruction and the interface crack bridged model [3]. The mathematical background of the modelling is based on the singular integral-differential equations (SIDE) [1] and the boundary element methods (BEM) [4]. The relations between bond tractions and displacements difference of the upper and lower crack surfaces at the crack bridged zone are used in the following generalized form [1] $q_{n,\tau}(x) = \kappa_{n,\tau}(x,\sigma)\ u_{n,\tau}(x)$ where $q_{n,\tau}$ and $u_{n,\tau}$ are the components of tractions vector and crack opening in the local coordinate system connected with the normal n and tangential τ directions to the crack surface and $\kappa_{n,\tau}\,(x,\sigma)$ are the stiffness of bonds depending on distance from the crack tip, σ is the tractions vector modulus at the current point x.

In the frames of the SIDE a straight crack with bridged zone between two semi-infinite plates under the external normal and shear loading is considered. The size of the bridged zone can be comparable to the whole length of the crack. The BEM approach is developed on the basis on the multi-regions technique and is used for modelling of arbitrary interfacial bridged cracks in finite size structures with accounting influence of the structure boundary conditions and gradation of mechanical properties of jointed materials. The supplement conditions of displacements continuity and tractions equilibrium along the sub-regions boundaries without crack are used. If there is the temperature loading on the structure then the first step of the problem solution is the consideration of the steady state or transient thermal problem. The special crack boundary elements for modelling of displacements and stresses asymptotics are used near of the crack tips and the stress intensity factors are computed. The values of the displacements of the crack surfaces are considered as unknown parameters at the bridged zone. For nonlinear bond deformation law the iterative procedure is used. In the case of the bonds kinetics at each time step the bonds compliance is assumed to be proportional to the density of unbroken bonds.

Nonlocal criterion of bridged crack growth. The non-local fracture criterion [1, 5] is used in the frames of the bridged crack model to evaluate the fracture toughness and the critical external loading at the crack limit equilibrium state:

$$G_{tip}(d,\ell) = G_{bond}(d,\ell),\ u(x_0) = ([u_x(x_0)]^2 + [u_y(x_0)]^2)^{1/2} = \delta_{cr} \tag{1}$$

where $G_{tip}\,(d,\ell)$ is the strain energy release rate at creation of a new crack surface and $G_{bond}\,(d,\ell)$ is the rate of the energy absorption at the crack bridging zone, respectively. Within the model the rate of the energy absorption depends on the bridging zone size and bond characteristics. The equilibrium bridging zone size is not assumed to be constant. The first equation in (1) is necessary condition (this is insufficient for searching for a limit equilibrium state of the crack tip and the bridging zone) and the second equation in (1) the sufficient condition of bonds limit stretching at the trailing edge of the bridging zone x_0 (δ_{cr} is the bond rupture length). Based on these two fracture conditions the regimes of the bridged zone and the crack tip equilibrium and growth are formulated and considered [5]: 1) the crack tip propagates and the size of the bridged zone increases without rupture of the bonds if $G_{tip}(d,\ell) \geq G_{bond}(d,\ell)$ and $u(\ell - d) < \delta_{cr}$, where $u(\ell - d)$ is the crack opening at the trailing edge of the bridged zone; 2) the size of the bridged zone decreases due to rupture of the bond without the crack tip propagation if $G_{tip}(d,\ell) < G_{bond}(d,\ell)$ and $u(\ell - d) \geq \delta_{cr}$; 3) the crack tip propagates with simultaneous bond rupture at the trailing edge of the bridged zone if $G_{tip}(d,\ell) \geq G_{bond}(d,\ell)$ and $u(\ell - d) \geq \delta_{cr}$. The last case corresponds to quasi-static crack growth if equality for the both fracture conditions are fulfilled. The critical external loads, the bridged zone size and the adhesion fracture resistance versus of the crack length can be determined from these conditions for quasistatic cracks growth.

CLOSING COMMENTS

The main features of the criterion (1) are the accounting of energy consumed by bonds during cracks growth and the analysis on this ground of non self-similar cracks growth. This criterion implemented in the frames of the bridged crack model with assumption of singularity at the crack tip, but it includes the cohesive model as the special case for a long crack.

The application of the proposed model for stress state and fracture problems of the interface bridged cracks are presented and discussed. Possibilities for improving the adhesion fracture resistance by adjusting the bonding characteristics are considered. The case of the two-scale bridging is considered in details. Work was supported by **Russian Science Foundation**, the project number is 14-11-00844.

References

[1] Goldstein, R.V., Perelmuter, M.N.: Modelling of bonding at an interface crack, *Int. J. of Fracture*, **99**: 53-79, 1999
[2] Perelmuter, M.N.: An interface crack with non-linear bonds in a bridged zone, *J. of Appl. Math. and Mech.(PMM)* **75**, 1: 106-118, 2011
[3] Goldstein R. V., Perelmuter M. N.: Kinetics of crack formation and growth on the material interface, *Mech. Solids* **47**, 4: 400-414, 2012
[4] Perelmuter M.:Boundary element analysis of structures with bridged interfacial cracks, *Comput. Mechanics*, **51**, 4: 523-534, 2013
[5] Perelmuter M.N.: A criterion for the growth of cracks with bonds in the end zone, *J. Appl. Math. Mech. (PMM)*, **71**, 1: 137-153, 2007

PARTICLE DYNAMICS MODELING OF BUCKLE-DELAMINATION OF THIN FILM MATERIALS

Kui Pan[1], A. Srikantha, Phani*[1], and Sheldon Green[1]

[1]*Department of Mechanical Engineering, University of British Columbia, Vancouver, British Columbia, Canada.*

Summary A one-dimensional particle dynamics model has been developed to study the dynamic buckle-delamination process of compressed thin films on substrates. The simulation results of the maximum dynamic buckling deflection agree with the previous analytical solution. It is also found that the delamination propagation speed increases when the interfacial fracture energy is decreased and that the dynamic delamination is more likely to propagate than in the quasi-static buckle-delamination process.

INTRODUCTION

Buckle-delamination has been widely observed in compressed thin film/substrate systems. Most of previous studies assume that the buckle-delamination occurs in a quasi-static manner and thus neglect the inertial effects of the film. For a compressed thin film bonded onto a substrate with an initial interfacial defect, once the pre-strain exceeds the critical strain the subsequent buckling process is inherently dynamic. By assuming that the dynamic buckling deflection has the same sinusoidal form as the quasi-static buckling solution, Lee and Freund determined the maximum buckling deflection and found the energy release rate of dynamic buckle-delamination is much larger than that of the quasi-static case, thus resulting in a larger arrested delamination length [1]. The same problem was later studied by Chen and Leib and they found higher order buckling-mode functions should be included in the post buckling deflection to obtain an accurate solution [2]. However, it is difficult to decide which buckling-mode should be incorporated in the dynamic buckling deformation. In this paper, a one-dimensional particle dynamics model has been developed to study the dynamic buckle-delamination process without any ad-hoc assumption about the buckling deformation.

THEORETICAL MODEL

Fig. 1(a)-(c) show the buckling-driven delamination process of a compressed thin film on a rigid substrate with a pre-existing delamination zone $2b_0$. Here the film is uniformly discretized into a series of particles that are connected by axial and rotational spring-damper elements [3], shown in Fig. 1(d). When the film is not under compression, the spacing between two adjacent particles is $a_0 = L_0/(N-1)$ and the mass of each particle is $m = \rho a_0 hw$, where N is the total number of particles, L_0 is the natural length of the film, w is the width and ρ is the density. The initial spacing is set as $(1-\varepsilon_0)a_0$ to represent the pre-strain ε_0. Each particle is subject to axial elastic force $\boldsymbol{f}_a$ and damping force $\boldsymbol{f}_d$, as well as bending force $\boldsymbol{f}_b$ and viscous bending force $\boldsymbol{f}_v$, shown in Fig. 1(e) and Fig. 1(f). In this paper we adopt a bilinear cohesive zone model and incorporate it into the current discrete particle system [4]. For each particle we introduce a substrate node i and connect it to the corresponding particle i through a nonlinear spring which satisfies the cohesive law. Thus, the normal and tangential cohesive forces $\boldsymbol{f}_{c\perp}$ and $\boldsymbol{f}_{c\parallel}$ applied on the particle are dependent on the relative separation distance between the particle and the substrate node.

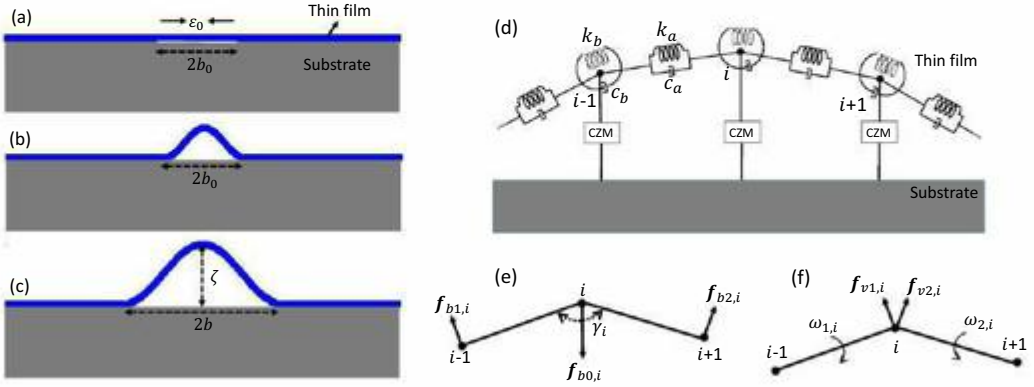

Fig. 1: Schematic of buckle-delamination process (a-c) and discrete particle model (d-f).

* Corresponding author. Email: skpa@mail.ubc.ca

The forces applied on the particles can be calculated based on their locations and velocities. We use Newton's equation of motion to evolve the particle system:

$$\boldsymbol{f}_{tot} = \boldsymbol{f}_a + \boldsymbol{f}_d + \boldsymbol{f}_b + \boldsymbol{f}_v + \boldsymbol{f}_{c\perp} + \boldsymbol{f}_{c\parallel} = m\boldsymbol{a}. \quad (1)$$

Here we adopt the Semi-implicit Euler iterative algorithm for the advancement in time. Given the particle's position vector N_i^t and velocity N_i^t at time t, the total force $\boldsymbol{f}_{tot_i}{}^t$ applied on the particle i can be calculated, which directly gives the acceleration $N_i^t = \boldsymbol{f}_{tot_i}{}^t/m$. Then the particle's velocity and position at time $N+\Delta N$are:

$$N_i^{t+\Delta t} = N_i^t + N_i^t \Delta N \quad (2)$$

$$N_i^{t+\Delta t} = N_i^t + N_i^{t+\Delta t} \Delta N \quad (3)$$

where $\Delta N$is time step. The semi-implicit Euler algorithm converges quickly and shows good stability at low computational cost. This algorithm also conserves the system's energy.

Results and Discussion

The one-dimensional buckle-delamination process is simulated by the current model. The parameters are chosen as $L_0 = 100h$, $b_0 = 10h$, $N = 501$ and $a_0 = 0.2h$. We have shown that when the particle spacing a_0 is reduced to $0.2h$, the numerical results are independent of the mesh size. Random deflections of the order of $10^{-6}h$ are added to the particles to facilitate the onset of buckling. When the compressive strain ε_0 exceeds the Euler strain $\varepsilon_E = \pi^2 h^2/12b_0^2$, the particles within the debonded region become unstable and move to relax the strain energy. Here we remove the damping in the system to neglect the viscosity. As a result, after buckling the film vibrate about the equilibrium position. Fig. 2(a) shows the maximum dynamic buckling deflection as a function of the pre-strain. Our simulation results are in close agreement with the analytical solution [1]:

$$\zeta = h\sqrt{\frac{8}{3}\left(\frac{\varepsilon_0}{\varepsilon_E} - 1\right)} \quad (4)$$

Fig. 2(b) shows the behavior of the potential energy in the film during the dynamic buckling process. There is a slight discrepancy between the simulation result and the previous analytical solution. This is because the dynamic buckling shape does not match the buckling form $\frac{1}{2}\zeta\left[1 + \cos(\frac{\pi x}{b})\right]$ assumed in the analytical solution, as shown in the inserted figure.

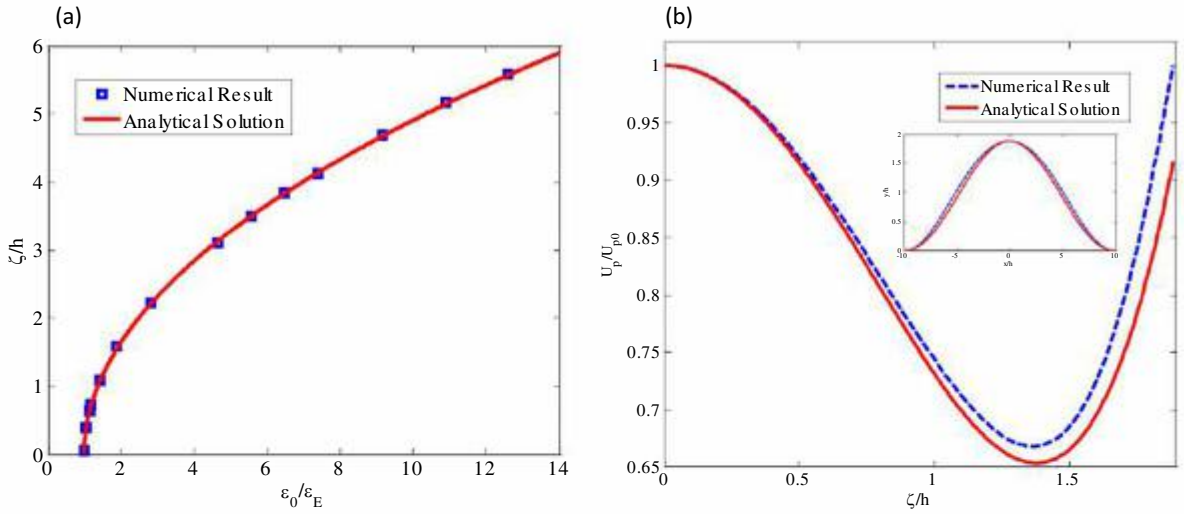

Fig. 2: (a) Maximum dynamic buckling deflection as a function of strain. (b) Behavior of potential energy of film during buckling.

References

[1] Lee Y.J., Freund L.B.: Dynamic buckling delamination of a bonded thin film under residual compression. Acta Mech. 3, 147-160, 1992.

[2] Chen H.P., Leib D.: Dynamic delamination growth in laminated composite structures. Compos Sci Technol, 46 (4), 325-333, 1993.

[3] Edvardsson S., and Uesaka T.: System dynamics of the open-draw with web adhesion: particle approach. J. Appl. Mech. 77 (2), 021009, 2010.

[4] Xie D., Waas A.M.: Discrete cohesive zone model for mixed-mode fracture using finite element analysis. Eng. Fract. Mech. 73 (13), 1783-1796, 2006.

ANALYSIS OF CRACKING IN CANDIDATE ENVIRONMENTAL BARRIER COATINGS

Stephen Sehr[1], Will Pro[1], Foucault de Franqueville[3], and Matthew Begley*[1,2]

[1]*Department of Mechanical Engineering, University of California, Santa Barbara*
[2]*Department of Materials, University of California, Santa Barbara*
[3]*ENS Cachan, Cachan, France*

Summary The desire to increase the operating temperatures of turbine engines has led to the exploration of silicon carbide composites as a replacement for nickel based superalloys. The combustion environment is very harsh and will lead to failure if parts are not protected. This protection comes from a multilayer environmental barrier coating (EBC) which must provide resistance against corrosive species and be compatible with the substrate. In some candidate EBC systems, vertical channel cracks have been observed bifurcating and turning into horizontal delamination cracks in multiple material systems. This complex cracking phenomena has been studied using a high throughput FEA tool to model the likelihood of crack advancement. A discrete element approach was also used to model crack growth after initiation. The property ranges for a coating system that are resistant to this type of cracking behavior are shown.

HIGH THROUGHPUT FINITE ELEMENT ANALYSIS

The coating systems needed to protect silicon carbide composites are quite complex and have multiple layers as shown in the schematic of Figure 1. Each layer serves a different function from protection against foreign species or mechanical compatibility. The varying properties of this coating system can lead to various failure methods. One of the most common is a through-thickness channel crack forming after cooling due the residual stresses in the layers. In multiple systems, channel cracks have been observed turning into horizontal delamination cracks as well as branching. In order to study this specific phenomena, a high-throughput finite element analysis has been designed which calculates the energy release rate for a channel crack of any depth with a kink of any angle. The tool is automated so that the layer system can be changed in order to test the effects of different layer dimensions and properties. The code runs through the thousands of combinations quickly, producing a large dataset consisting of the energy release rate and mode mixity at the crack tip. An output of the code can be shown in Figure 2. This is a map of the energy release rate for different depths and angles of a double kink crack. It shows there is a high likelihood of a channel crack to kink at a certain depth and angle. However, this method does not allow the study of crack growth.

DISCRETE ELEMENT MODELS OF FRACTURE

To study crack growth, a discrete element model was used. In this method, conventional elastic finite elements were tied together with cohesive elements. These cohesive elements are governed by a traction-separation law and can model fracture progression as well as initiation without any a priori assumptions. In this study, a channel crack was slanted an angle θ from vertical in a simple two layer coating with tensile stress in the top layer and compressive stress in the bottom layer. It was placed on a stress free substrate. The discrete element method was able to capture the crack turning as well as branching, shown in Figure 3. A full range of initial crack tip depths and angles were run and the results allow the construction of a failure mechanism map, shown in Figure 4. This map was created by running simulations at each slant angle and depth and then looking at the behavior of the crack at the end of the simulation. The plotted behavior was what was seen a set distance along the crack path. Cases that did not reach this growth distance were marked as not advancing. The map shows that if the initial crack is deep enough and the crack close to vertical, it is less likely to grow. Likewise, if the slant angle is high, the crack will not grow either. Of particular interest is the behavior in the middle where a crack with either turn horizontal or grow up. There is a specific depth, controlled by the layer thicknesses and residual stresses, that the cracks want to grow towards. Incidentally, this depth coincides with the depth at which the energy release rate for a delamination crack becomes greater than that of a channel crack.

*Corresponding author. Email: ictam2016papers@legendconferences.com

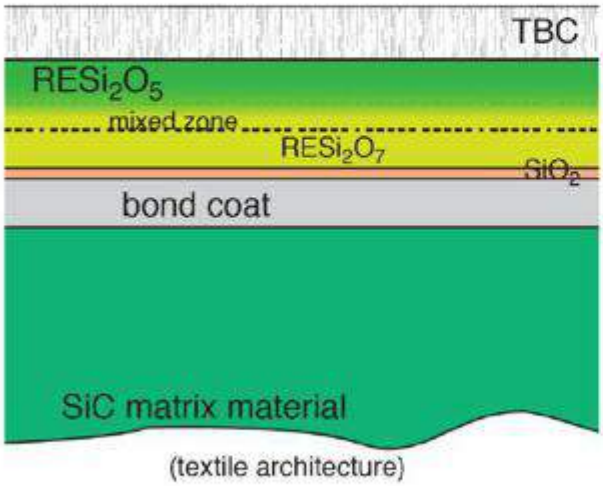

Fig. 1. Schematic of a typical EBC system.

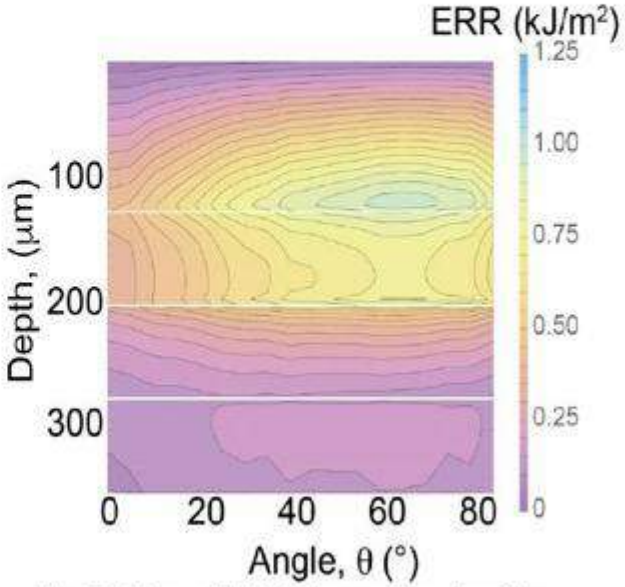

Fig. 2. Map of ERR for various depths and kink angles.

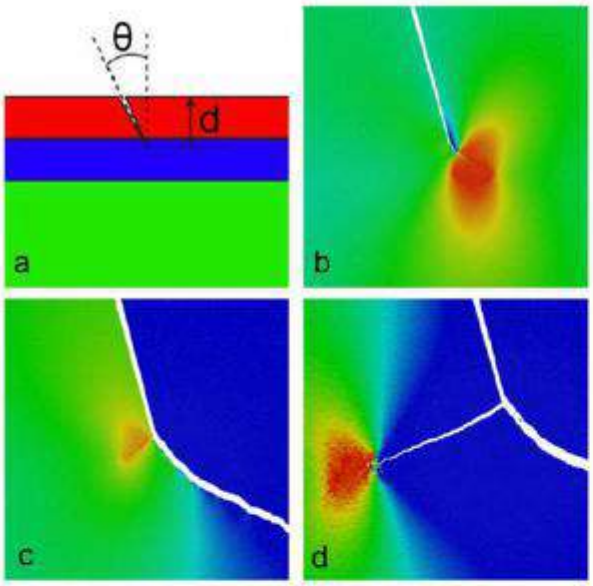

Fig. 3. Schematic of discrete element tests (a) and snapshots of the stress fields before main advance (b), prior to bifurcation (c) and after bifurcation (d).

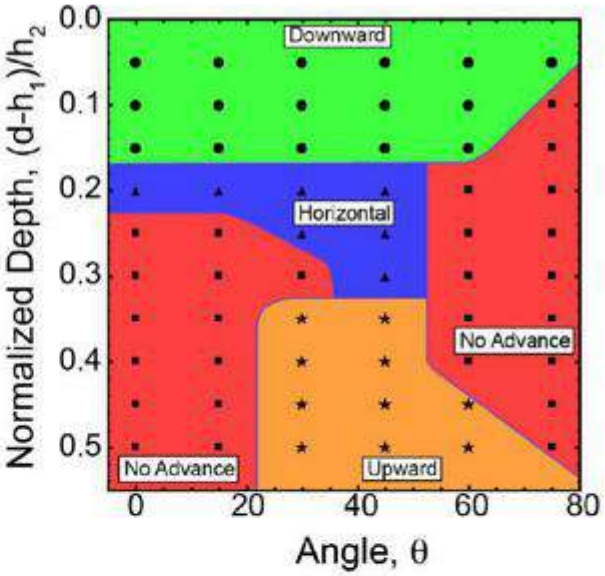

Fig. 4. Map of the different failure modes for the slanted channel crack tests.

INTEGRAL IDENTITIES FOR THERMODIFFUSIVE INTERFACIAL CRACKS

Lorenzo Morini*[1,2] and Andrea Piccolroaz[1]

[1]*Department of Civil, Environmental and Mechanical Engineering, University of Trento, Trento, Italy*
[2]*IMT Institute for Advanced Studies, Lucca, Italy*

Summary The problem of a crack at the interface between dissimilar materials in presence of thermodiffusion is formulated in terms of boundary integral equations by means of an original approach based on generalized Betti's theorem and weight functions. Integral identities relating the applied loading, the temperature, mass concentration, heat and mass fluxes on the fracture surfaces and the resulting crack opening are derived and accompanied by some examples of applications. The proposed approach can represent a powerful tool for studying the effects of temperature and heat flux distributions on fracture processes at the interface between different components in energy devices possessing multi-layered structures, such as solid oxide fuel cells.

GEOMETRY OF THE MODEL

A static semi-infinite crack between two dissimilar isotropic linear elastic materials in presence of thermodiffusion is condidered, the geometry of the system is shown in Fig.1. No body forces, heat and mass sources are assumed. The crack is situated in the half-plane $\mathbb{R}^2_- = \{\boldsymbol{x} = (x_1, x_2, x_3) \in \mathbb{R}^3 : x_1 < 0, x_2 = 0\}$, general non-symmetric loading applied to the crack faces is assumed, and perfect interface conditions ahead of the crack tip are considered.

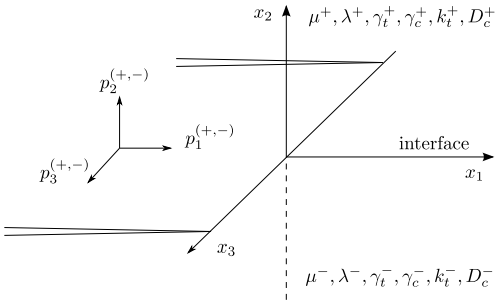

Figure 1: Geometry of the model.

RECIPROCITY THEOREM AND WEIGHT FUNCTIONS

In absence of body forces, heat and mass sources, the static Betti's reciprocity formula for linear thermodiffusive solids takes the form:

$$\int_{\partial V} \left(\boldsymbol{\sigma}^{(1)}\boldsymbol{n}\cdot\boldsymbol{u}^{(2)} \nearrow \boldsymbol{\sigma}^{(2)}\boldsymbol{n}\cdot\boldsymbol{u}^{(1)}\right) dS + \int_V \left(\boldsymbol{b}^{(1)}\cdot\boldsymbol{u}^{(2)} \nearrow \boldsymbol{b}^{(2)}\cdot\boldsymbol{u}^{(1)}\right) dV +$$
$$+\gamma_t \int_V \left(\theta^{(1)}\nabla\cdot\boldsymbol{u}^{(2)} \nearrow \theta^{(2)}\nabla\cdot\boldsymbol{u}^{(1)}\right) dV + \gamma_c \int_V \left(\chi^{(1)}\nabla\cdot\boldsymbol{u}^{(2)} \nearrow \chi^{(2)}\nabla\cdot\boldsymbol{u}^{(1)}\right) dV = 0, \tag{1}$$

where ∂V is any surface enclosing a region V within which both the sets of fields $\{\boldsymbol{u}^{(1)}, \theta^{(1)}, \chi^{(1)}\}$ and $\{\boldsymbol{u}^{(2)}, \theta^{(2)}, \chi^{(2)}\}$ satisfy the uncoupled governing equations of a static linear thermodiffusive medium, with corresponding stress states $\boldsymbol{\sigma}^{(1)}$ and $\boldsymbol{\sigma}^{(2)}$, and $\boldsymbol{n}$ denotes the outward normal to ∂V.

We assume that $\boldsymbol{u}^{(1)} = \boldsymbol{u}$ and $\boldsymbol{\sigma}^{(1)} = \boldsymbol{\sigma}$ are respectively the physical displacement and stress fields, associated with the crack loaded at its surface, whereas $\theta^{(1)} = \theta$ and $\chi^{(1)} = \chi$ represent the physical temperature and mass concentration fields. Similarly to the approach proposed in several boundary element formulations of thermoelasticity, for the auxiliary solutions system we assume $\theta^{(2)} = \chi^{(2)} = 0$. The displacement field $\boldsymbol{u}^{(2)}$ is represented by the non-trivial singular solution of the homogeneous traction-free crack problem, commonly known as the weight function [1], defined as $\boldsymbol{u}^{(2)} = \boldsymbol{R}\boldsymbol{U}$, and the stress tension $\boldsymbol{\Sigma}$ associated with $\boldsymbol{U}$ is given by $\boldsymbol{\sigma}^{(2)} = \boldsymbol{R}\boldsymbol{\Sigma}\boldsymbol{R}$, where $\boldsymbol{R}$ is the rotation matrix. In order to trasform the volume terms contained in the reciprocity identity (1) into surface integrals, the weight function is expressed using the

*Corresponding author. Email: lorenzo.morini@unitn.it

Helmholtz's decomposition theorem (see reference [1] for details). Applying the Betti's identity (1) to both the upper and lower thermodiffusive elastic half-spaces illustrated in Fig.1 and subtracting the derived integral expressions, we obtain

$$\begin{aligned}
&\boldsymbol{R}[\![\boldsymbol{U}]\!] \circledast \langle \boldsymbol{\sigma}_2 \rangle^{(+)} \nearrow \boldsymbol{R}\langle \boldsymbol{\Sigma}_2 \rangle \circledast [\![\boldsymbol{u}]\!]^{(-)} = \nearrow \boldsymbol{R}[\![\boldsymbol{U}]\!] \circledast \langle \boldsymbol{p} \rangle \nearrow \boldsymbol{R}\langle \boldsymbol{U} \rangle \circledast [\![\boldsymbol{p}]\!] \\
\nearrow \ &\left\langle \frac{\partial \Phi_{\gamma t}}{\partial x_2} \right\rangle \circledast [\![\theta]\!] \nearrow \left[\!\!\left[\frac{\partial \Phi_{\gamma t}}{\partial x_2} \right]\!\!\right] \circledast \langle \theta \rangle \nearrow \langle \Phi_{\beta t} \rangle \circledast [\![q_1]\!] \nearrow [\![\Phi_{\beta t}]\!] \circledast \langle q_2 \rangle \\
\nearrow \ &\left\langle \frac{\partial \Phi_{\gamma c}}{\partial x_2} \right\rangle \circledast [\![\chi]\!] \nearrow \left[\!\!\left[\frac{\partial \Phi_{\gamma c}}{\partial x_2} \right]\!\!\right] \circledast \langle \chi \rangle \nearrow \langle \Phi_{\beta c} \rangle \circledast [\![j_2]\!] \nearrow [\![\Phi_{\beta c}]\!] \circledast \langle j_2 \rangle \,,
\end{aligned} \tag{2}$$

where the symbol $\circledast$ denotes the convolution with respect to both x_1 and x_3, and we used standard notations to denote the average, $\langle f \rangle = \frac{1}{2}[f(x_1, 0^+, x_3) + f(x_1, 0^-, x_3)]$, and the jump, $[\![f]\!] = f(x_1, 0^+, x_3) \nearrow f(x_1, 0^-, x_3)$ of a function f across the plane containing the crack, $x_2 = 0$. The notation $\langle \boldsymbol{\sigma}_2 \rangle^{(-)} = \langle \boldsymbol{p} \rangle$ and $[\![\boldsymbol{\sigma}_2]\!]^{(-)} = [\![\boldsymbol{p}]\!]$, indicates the symmetrical and skew-symmetrical components of the mechanical load applied at the crack faces, q_2 and j_2 are the normal components of the heat and mass fluxes, and $\Phi_{\gamma t} = \gamma_t \Phi, \Phi_{\gamma c} = \gamma_c \Phi, \Phi_{\beta t} = \beta_t \Phi, \Phi_{\beta c} = \beta_c \Phi$ are the normalized potentials in the weight fuctions space where $\boldsymbol{U} = \nabla \Phi$. Finally, $[\![\boldsymbol{u}]\!]^{(-)}$ and $\langle \boldsymbol{\sigma}_2 \rangle^{(+)}$ are respectively the crack opening and the traction fields ahead of the tip associate to the loading distribution and to the temperature, concentration, heat and mass flux profiles on the crack surface. $[\![\boldsymbol{u}]\!]^{(-)}$ and $\langle \boldsymbol{\sigma}_2 \rangle^{(+)}$ are the two unknown physical quantities that we want to determine by means of the integral equation (2).

INTEGRAL IDENTITIES

Considering the case of plane strain deformations and substituting the weight functions matrices determined by Piccolroaz *et al.* [3] and the corresponding Lamé potentials in equation (2), by means of a procedure based on Fourier transform, we finally obtain the integral identities (see reference [1] for details):

$$\begin{aligned}
&\langle \boldsymbol{p} \rangle + \boldsymbol{\mathcal{A}}^{(s)} [\![\boldsymbol{p}]\!] + \boldsymbol{\mathcal{G}}_{1t}^{(s-)} [\![\theta]\!] + \boldsymbol{\mathcal{G}}_{2t}^{(s-)} \langle \theta \rangle + \boldsymbol{\mathcal{D}}_{1t}^{(s-)} [\![q_2]\!] + \boldsymbol{\mathcal{D}}_{2t}^{(s-)} \langle q_2 \rangle \\
&+ \boldsymbol{\mathcal{G}}_{1c}^{(s-)} [\![\chi]\!] + \boldsymbol{\mathcal{G}}_{2c}^{(s-)} \langle \chi \rangle + \boldsymbol{\mathcal{D}}_{1c}^{(s-)} [\![j_2]\!] + \boldsymbol{\mathcal{D}}_{2c}^{(s-)} \langle j_2 \rangle = \boldsymbol{\mathcal{B}}^{(s)} \frac{\partial [\![\boldsymbol{u}]\!]^{(-)}}{\partial x_1}, \quad x_1 < 0,
\end{aligned} \tag{3}$$

$$\begin{aligned}
&\langle \boldsymbol{\sigma}_2 \rangle^{(+)} + \boldsymbol{\mathcal{A}}^{(c)} [\![\boldsymbol{p}]\!] + \boldsymbol{\mathcal{G}}_{1t}^{(s+)} [\![\theta]\!] + \boldsymbol{\mathcal{G}}_{2t}^{(s+)} \langle \theta \rangle + \boldsymbol{\mathcal{D}}_{1t}^{(s+)} [\![q_2]\!] + \boldsymbol{\mathcal{D}}_{2t}^{(s+)} \langle q_2 \rangle \\
&+ \boldsymbol{\mathcal{G}}_{1c}^{(c)} [\![\chi]\!]^{(-)} + \boldsymbol{\mathcal{G}}_{2c}^{(s+)} \langle \chi \rangle + \boldsymbol{\mathcal{D}}_{1c}^{(s+)} [\![j_2]\!] + \boldsymbol{\mathcal{D}}_{2c}^{(s+)} \langle j_2 \rangle = \boldsymbol{\mathcal{B}}^{(c)} \frac{\partial [\![\boldsymbol{u}]\!]^{(-)}}{\partial x_1}, \quad x_1 > 0,
\end{aligned} \tag{4}$$

where $\boldsymbol{\mathcal{G}}_{1t}^{(s+),(s-)}, \boldsymbol{\mathcal{G}}_{2t}^{(s+),(s-)}, \boldsymbol{\mathcal{G}}_{1c}^{(s+),(s-)}, \boldsymbol{\mathcal{G}}_{2c}^{(s+),(s-)}, \boldsymbol{\mathcal{D}}_{1t}^{(s+),(s-)}, \boldsymbol{\mathcal{D}}_{2t}^{(s+),(s-)}, \boldsymbol{\mathcal{D}}_{1c}^{(s+),(s-)}, \boldsymbol{\mathcal{D}}_{2c}^{(s+),(s-)}$ are vectorial singular operators, whereas $\boldsymbol{\mathcal{A}}^{(s)}, \boldsymbol{\mathcal{B}}^{(s)}$ and $\boldsymbol{\mathcal{A}}^{(c)}, \boldsymbol{\mathcal{B}}^{(c)}$ are respectively singular and compact matrix operators depending by the standard integral operator of Cauchy type [4, 5]. The solution of (3) by the inversion of the matrix operator $\boldsymbol{\mathcal{B}}^{(s)}$ provides crack opening that corresponds to arbitrary loading configurations acting on the faces and arbitrary profiles of the thermodiffusive quantities. The obtained expressions for $[\![\boldsymbol{u}]\!]^{(-)}$ can then be used in (4) for evaluating the traction ahead of the crack tip.

CONCLUSIONS

Explicit integral identities relating the applied mechanical loading, the temperature, mass density, heat and mass flux distributions at the interface and the resulting crack opening have been obtained for plane strain interfacial fracture problems in thermodiffusive bimaterials. The solution of this system of singular integral equations provides explicit expressions for the crack opening and the stress fields associate to any arbitrary harmonic temperature and mass density profile and self-balanced heat or mass flux distribution at the interface. This original approach can have various relevant applications, expecially in the modelling of fracture processes induced by thermal and diffusive stresses at the interface between different components of multi-layered electrochemical devices such as solid oxide fuel cells.

References

[1] Morini L. and Piccolroaz A.: Boundary integral formulation for interfacial cracks in thermodiffusive bimaterials, Proc. R. Soc. A, 471:20150284, 2015.

[2] Willis J. R. and Movchan A. B.: Dynamic weight function for a moving crack. I. Mode I loading, J. Mech. Phys. Solids, 43:319–341, 1995.

[3] Morini L., Radi E., Movchan A. B. and Movchan N. V.: Stroh formalism in analysis of skew-symmetric and symmetric weight functions for interfacial cracks, Math. Mech. Solids, 18:135-153, 2013.

[4] Piccolroaz A., Mishuris G. and Movchan A. B.: Symmetric and skew symmetric weight functions in 2D perturbation models for semi-infinite interfacial cracks, J. Mech. Phys. Solids, 57:1657-1682, 2009.

[5] Morini L., Piccolroaz A., Mishuris G. and Radi E.: Integral identities for a semi-infinite interfacial crack in anisotropic elastic bimaterials, Int. J. Solids. Struct., , 50:1437-1448, 2013.

REASSESSMENT OF THE VIRTUAL CRACK CLOSURE TECHNIQUE FOR INTERFACE CRACKS

Leslie Banks-Sills*[1] and Elad Farkash[1]

[1]*Dreszer Fracture Mechanics Laboratory, School of Mechanical Engineering, Tel Aviv University, Ramat Aviv, Israel*

Summary The Virtual Crack Closure Technique (VCCT) was first presented in 1977 for cracks in linear elastic, homogeneous and isotropic material. It was extended to cracks along an interface between two linear elastic, homogeneous and isotropic materials. In that case, the modes I and II energy release rates were seen to depend upon the size of the virtual crack extension. Some attempts have been made to remove this dependence. Nevertheless, in most cases, the accuracy of both the energy release rates and stress intensity factors was not consistently good. In this study, the dependence of the energy release rates on the size of the virtual crack extension for interface cracks is analytically accounted for so that the stress intensity factors may be accurately obtained when fine finite element meshes are used, together with a virtual crack extension consisting of more than one element.

INTRODUCTION

The modes I and II energy release rates may be obtained from the Irwin (1958) crack closure integral. To calculate the energy release rates for particular problems by means of the finite element method, a virtual crack extension is used. The Virtual Crack Closure Technique (VCCT) was first presented by Rybicki and Kanninen (1977). In that study, one finite element analysis was carried out with a crack of length $a + \Delta a$ and four noded elements. The nodal force was taken from the crack tip. This will be larger than that for a crack of length a. The displacement was taken from the nodal point directly behind the crack tip. Two problems were solved with a relative virtual crack extension of $\Delta a/a = 0.1$. Stress intensity factors differed by less than 0.5% with those obtained by means of the line J-integral.

Unfortunately, for interface cracks between linear elastic materials, it has been shown that the values of the energy release rates $\mathcal{G}_I$ and $\mathcal{G}_{II}$ depend on the size of the virtual crack extension Δa (see Sun and Jih 1987; Raju et al. 1988; Toya 1992; Dattaguru et al. 1994; Mantič and París 2004; Kruger 2004; Hemanth et al. 2005). This affects the accuracy of the obtained stress intensity factors. Agrawal and Karlsson (2006) continued the work of Beuth (1996) seeking a dependable method for extracting an energy release rate mode mixity for interface cracks. Many expressions were developed for various mode mixity measures. It was shown that different expressions presented by previous investigators (Toya 1992; Chow and Atluri 1995; Beuth 1996; Sun and Qian 1997; Bjerkén and Persson 2001) which look different are equivalent. It may be seen in Agrawal and Karlsson (2006) that the difference between the mode mixity as calculated by the finite element technique with VCCT and that obtained analytically was above 13%. Hence, Oneida et al. (2015) sought to improve on the methods previously presented and extend them for treating cracks which also impinge on an interface. For calculating the modes I and II energy release rates, as well as an interaction energy release rate, expressions were taken from Toya (1992), Chow and Atluri (1995) and Agrawal and Karlsson (2006). One of the important contributions of Oneida et al. (2015) consists of the suggestion to use many very small elements as part of the virtual crack extension Δa.

In the next section, the basic equations related to an interface crack are presented. Those expressions for calculating the energy release rates by means of VCCT are rederived so that all relations are analytic as opposed to most previous investigations. Moreover, only two pairs of stress intensity factors are found. From the problems solved, it is concluded that the VCCT may be used to accurately obtain stress intensity factors by means of fine meshes and virtual crack extensions consisting of more than one element.

INTERFACE CRACK

The interface energy release rate is denoted as $\mathcal{G}_i$ where the subscript i represents interface. By means of Irwin's crack closure integral (Irwin 1958), it may be shown for plane problems that the energy release rate of an interface crack is given in the form

$$\mathcal{G}_i = \frac{1}{H_1}\left(K_1^2 + K_2^2\right) \tag{1}$$

where H_1 is a Young's modulus like parameter. For finite element analyses, the modes I and II energy release rates may be written as

$$\mathcal{G}_I = \frac{1}{2\Delta a}\sum_{m=1}^{N} F_{ym}\Delta u_{ym'} \tag{2}$$

*Corresponding author. Email: banks@tau.ac.il

$$\mathcal{G}_{II} = \frac{1}{2\Delta a} \sum_{m=1}^{N} F_{xm} \Delta u_{xm'} \tag{3}$$

where F_{xm} and F_{ym} are the nodal point forces in the x and y-directions, respectively, at node m ahead of the crack tip. The displacement jumps $\Delta u_{xm'}$ and $\Delta u_{ym'}$ in the x and y-directions, respectively, are taken from node m' behind the crack tip and N is the total number of nodes which participate in the calculation.

It is possible to show that

$$K_1 = \pm\sqrt{H_1 \mathcal{G}_i} \cos\omega \tag{4}$$

$$K_2 = K_1 \tan\omega \tag{5}$$

where

$$\omega = \frac{1}{2}\cos^{-1}\left(\frac{1}{C}\frac{1-g}{1+g}\right) - \frac{1}{2}\tan^{-1}\left(\frac{P_I}{P_R}\right) - \varepsilon \ln \Delta a \ . \tag{6}$$

Thus, with eqs. (4) and (5) there are only two pairs of soluttions. In eq. (6)

$$g \equiv \frac{\mathcal{G}_{II}}{\mathcal{G}_I} \tag{7}$$

and is found by the finite element method from eqs. (2) and (3),

$$C = \frac{\cosh \pi\varepsilon}{\pi}\sqrt{P_R^2 + P_I^2} \tag{8}$$

$$P = \frac{\Gamma\left(\frac{1}{2} + i\varepsilon\right)\Gamma\left(\frac{1}{2} + i\varepsilon\right)}{\Gamma\left(2 + 2i\varepsilon\right)} \tag{9}$$

and ε is the oscillatory parameter. To obtain the correct K_1 - K_2 pair, the criterion $\Delta u_y > 0$ is imposed.

Several problems with known solutions were solved with stress intensity factor results within 0.5% of the analytical solution.

CONCLUSIONS

The equations used for calculating the stress intensity factors for an interface crack between two linear elastic, isotropic and homogeneous media have been rederived. All expressions are analytic and in a simpler form than expressions presented by previous investigators. Most investigators present expressions in which numerical integration is required. Only two stress intensity factor pairs are found with one eliminated on physical grounds. The key to obtaining accurate results is use of several small elements as part of the virtual crack extension (Oneida et al. 2015).

References

[1] Agrawal A., Karlsson A.M. Obtaining Mode Mixity for a Bimaterial Interface Crack Using the Virtual Crack Closure Technique. Int J Fract 141:75–98, 2006.

[2] Beuth J.L. Separation of Crack Extension Modes in Orthotropic Delamination Models. Int J Fract 77:305–321, 1996.

[3] Bjerkén C., Persson C. A Numerical Method for Calculating Stress Intensity Factors for Interface Cracks in Bimaterials. Eng Fract Mech 68:235–246, 2001.

[4] Chow W.T., Atluri S.N. Finite Element Calculation of Stress Intensity Factors for Interfacial Crack Using Virtual Crack Closure Integral. Comput Mech 16:417–425, 1995.

[5] Dattaguru B., Venkatesha K.S., Ramamurthy T.S., Buchholz F.G. Finite Element Estimates of Strain Energy Release Rate Components at the Tip on an Interface Crack under Mode I Loading. Eng Fract Mech 49:451–463, 1994.

[6] Hemanth D., Shivakumar Aradhya K.S., Rama Murthy T.S., Govinda Raju N. Strain Energy Release Rates for an Interface Crack in Orthotropic Media – a Finite Element Investigation. Eng Fract Mech 72:759–772, 2005.

[7] Irwin G.R. Fracture. In: Flugge S. (ed.) Encyclopedia of Physics, Vol. IV. Springer, Germany, pp. 551–590, 1958.

[8] Krueger R. Virtual Crack Closure Technique: History, Approach, and Applications. Appl Mech Rev 57:109–143, 2004.

[9] Mantič V., París F. Relation Between SIF and ERR Base Measures of Facture Mode Mixity in Interface Cracks. Int J Fract 130:557–569, 2004.

[10] Oneida E.K., van der Meulen M.C.H., Ingraffea A.R. Methods for Calculating G, G_I and G_{II} to Simulate Crack Growth in 2D, Multiple-Material Structures. Eng Fract Mech 140:106–126, 2015.

[11] Raju I.S., Crews Jr. J.H., Aminpour M.A. Conversgence of Strain Energy Release Rate Components for Edge-Delaminated Composite Laminates. Eng Fract Mech 30:383–396, 1988.

[12] Rybicki E.F., Kanninen M.F. (1977) A Finite Element Calculation of Stress Intensity Factors by a Modified Crack Closure Integral. Eng Fract Mech 9:931–938, 1977.

[13] Sun C.T., Jih C.J. On Strain Energy Release Rates for Interfacial Cracks in Bi-material Media. Eng Fract Mech 28:13–20, 1987.

[14] Sun C.T., Qian W. The Use of Finite Extension Strain Energy Release Rates in Fracture of Interfacial Cracks. Int J Solids Struct 34:2595–2609, 1997.

[15] Toya M. On Mode I and Mode II Eenergy Rrelease Rates of an Interface Crack. Int J Fract 56:345–352, 1992.

BRITTLE-DUCTILE TRANSITION IN NOTCHED NANOSCALE METALLIC GLASS SPECIMENS

R. Narasimhan & I. Singh
Department of Mechanical Engineering, Indian Institute of Science, Bangalore 560012, India

Summary Tension tests on nano-sized metallic glass (MG) specimens have reported large ductility including considerable homogeneous deformation followed by necking as opposed to failure by shear banding which is seen in bulk samples. The necking is triggered by shallow notches present on the specimen surface. In this work, finite element simulations of tensile loading of nano-sized notched MG specimens are performed using a non-local plasticity model to understand the deformation behavior from a mechanics perspective. It is found that plastic zone size in front of the notch attains a saturation level at the stage when a dominant shear band (SB) forms. This size scales with an intrinsic material length associated with the interaction stress between flow defects. Further, the ratio of the saturation plastic zone size to uncracked ligament length governs the brittle-to-ductile transition.

INTRODUCTION

MGs have wide potential applications including micro/nano electro-mechanical systems owing to their attractive mechanical properties such as high strength and good corrosion resistance. Plastic deformation in MGs occurs by operation of shear transformation zones (STZs). The major drawback of MGs is their lack of tensile ductility due to unconstrained propagation of a single dominant SB. However, MG samples with initial size below some critical dimension of the order of 100 nm have shown large tensile ductility in the range of 27-45% [1]. Guo et al. [1] reported that failure occurs in these samples either by stable shear banding or necking. On the surface of specimens which failed by necking, they noticed presence of shallow notches which served as stress concentrators and triggered necking. Li and Li [2] also noted necking from their atomistic simulations of tensile loading on externally notched cylindrical and double-notched rectangular Ni-Zr MG specimens. They observed that transition in deformation behaviour from quasi-brittle to ductile occurs when the uncracked ligament length falls below a critical size governed by SB nucleus. In such a situation, plastic deformation expands over entire ligament and no dominant SB forms. In this study, continuum simulations of tensile deformations of nano-sized notched MG samples are performed to understand the mechanistic origin for the brittle-ductile transition and the role of relevant length parameters.

MODELING ASPECTS

A rectangular plane strain tension specimen (48×96 nm), containing a semi-circular edge notch with depth D and radius R is discretized using four-noded quadrilateral elements, and subjected to uniaxial stretching along the longitudinal direction at a constant strain rate of 2×10^{-3} s^{-1}. The material is assumed to follow the thermodynamically consistent finite strain non-local plasticity model of Thamburaja [3] for MGs. The model has been shown to be capable of capturing length scale effects on the mechanical response of MGs at temperatures well below the glass transition temperature [3]. It accounts for free volume production due to plastic shearing and hydrostatic stress, diffusion and annihilation. The plastic shearing rate, $\dot{\gamma}$, is given by:

$$\dot{\gamma} = \begin{cases} \dot{\gamma}_o \left(\dfrac{f^p}{c}\right)^{\frac{1}{a}} & (f^p = \bar{\ } - {}_{int} - \zeta({}_2(- {}_T) \ \bar{\ }) \ 0), \text{ where } \tau_{int} = -\zeta s_1 \nabla^2 \xi \\ 0 & (f^p \le 0) \end{cases} \quad (1)$$

Here, $\dot{\gamma}_o$ is a reference strain rate, a strain rate sensitivity parameter and ξ free volume concentration. Also, ζ, ξ_T, s_1 and s_2 are material constants. Further, in eq. (1), $\bar{\tau}$ is the equivalent stress, while rest of the terms in f^p constitute a back stress. In particular, τ_{int} signifies the stress field arising due to the interaction between flow defects such as STZs. Furthermore, $\bar{p}$ is hydrostatic stress, and c cohesion which is assumed to drop exponentially after commencement of plastic yielding. A material length $l_c = \sqrt{s_1 \ s_2}$ enters into the model which characterizes τ_{int} and scales the shear band width [4]. The values of constants appearing in the model are taken from the work of Thamburaja [3]. Also, in order to trigger SBs, initial cohesion is spatially perturbed by 1% around its mean value of 1 GPa. Various values of l_c = 0, 3.25, 4.5, 7.3 and 12 nm are considered.

RESULT AND DISCUSSION

Fig. 1(a)-(d) display contour plots of free volume, ξ, corresponding to macroscopic nominal strain of 0.024 for fixed R = 8 nm, but decreasing ligament length B. These plots pertains to l_c = 3.25 nm. A dominant band of ξ with noticeable shear offset can be perceived for B = 32 - 12 nm in Figs. 1(a)-(c), respectively. On the other hand, Fig.1(d) shows that the entire

a) Corresponding author. Email: narasi@mecheng.iisc.ernet.in.

ligament experiences plastic deformation and undergoes necking in the specimen with deeper notch (B = 6 nm). However, another simulation of tensile loading performed by setting $l_c = 0$ for the same sample exhibits a distinct band (Fig. 1(e)). Thus, the present continuum simulations suggest that B and l_c are the important length scales which control brittle-to-ductile transition in nano-sized MG samples.

In order to understand the mechanistic origin for the above transition, evolution of ξ and interaction stress τ_{int} are examined. It is observed that ξ (or STZ concentration) begins to develop in a semi-circular region at the notch root during initial stage of loading. Subsequently, it begins to spread along two lobes (or incipient bands) emanating at $\pm 45^{\text{o}}$ to the loading axis from the above embryonic plastic zone. The spatially varying free volume concentration gives rise to the interaction stress which is positive within the plastic zone at the notch root and the inclined lobes, but negative farther ahead on the ligament. It can be seen from eq. (1) that while $\tau_{\text{int}} > 0$ resists further plastic deformation, $\tau_{\text{int}} < 0$ assist it. Thus, positive-valued τ_{int} prevailing inside the inclined lobes retards strain localization. On the other hand, negative τ_{int} ahead of the notch tip plastic zone helps in advancing it along the ligament. As loading progresses further, the inclined lobes continue to grow up to the farther edge of the specimen. Eventually, ξ gets localized in one of the lobes resulting in formation of a dominant SB in the specimen with sufficiently large B (Fig. 1(a)-(c)). It is noticed that the SB propagates concurrently with the expansion of the plastic zone along the ligament. Once a dominant SB forms, elastic unloading takes place in the ligament and further plastic strain is accommodated primarily inside the SB. This causes plastic zones size ahead of the notch root to attain a saturation level r_s^p .

Further, when l_c is enhanced, magnitude of τ_{int} as well as the size of the region of negative τ_{int} farther ahead of the notch tip increases [4]. In other words, increase in l_c delays shear localization in a dominant SB and promotes the expansion of plastic deformation along the ligament, thereby enhancing r_s^p . Indeed, r_s^p scales with l_c, and is around 2.15 l_c ($\approx$ 7 nm for l_c = 3.25 nm) corresponding to R = 8 nm. It is important to note that while B > r_s^p in Fig. 1(a)-(c), it falls below r_s^p in Fig. 1(d). Thus, plastic deformation expands over entire ligament ahead of the notch tip resulting in necking before ξ begins to localize in a dominant band (Fig. 1(d)). However, in the absence of an intrinsic material length that scales r_s^p , a distinct band of ξ forms in Fig. 1(e) resulting in brittle response.

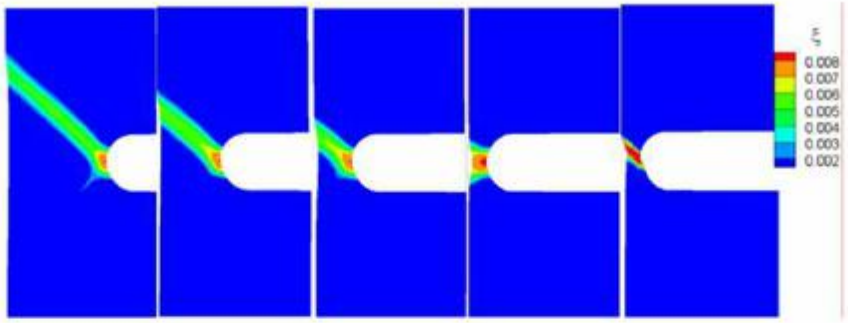

(a) (b) (c) (d) (e)

Fig. 1. Contour plots of free volume, ξ , pertaining to macroscopic nominal strain of 0.024 corresponding to R = 8 nm with (a) ligament length B = 32 nm, (b) B = 28 nm, (c) B = 12 nm, (d) B = 6 nm for l_c = 3.25 nm and (e) B = 6 nm for l_c = 0.

CONCLUSIONS

The present continuum simulations of tensile loading on nano-sized notched MG specimen have shown that interaction stress between flow defects plays a central role on the evolution of plastic strain. Also, at the stage when a dominant SB forms, the plastic zone ahead of the notch tip attains a saturation level r_s^p which scales with an intrinsic material length l_c associated with interaction stress. Finally, the ratio of the ligament length B to r_s^p governs the transition from shear banding to necking.

References

[1] Guo, H., Yan, P. F., Wang, Y. B., Tan, J., Zhang, Z. F., Sui, M. L., and Ma, E. *Nat. Mater.*,**6**: 735 – 739, 2007.

[2] Li, Q.-K. and Li, M. *Appl. Phys. Lett.*, **91**:231905 ,2007.

[3] Thamburaja, P. *J. Mech. Phys. Solids* , **59**:1552 – 1575, 2011.

[4] I. Singh and R. Narasimhan. *J. Mech. Phys. Solids* , **86**:53–69, 2016

FAILURE OF AN AUSTENITIC STAINLESS STEEL UNDER LINEAR AND NON-LINEAR LOADING PATHS

Yannis P. Korkolis[1a)], Peter W. Ripley[1] & Paul Knysh[1]
[1]*Department of Mechanical Engineering, University of New Hampshire, Durham, NH, USA*

Summary The failure limits of 304L austenitic stainless steel are measured under linear and non-linear loading paths. The experiments involve inflation of microtubes under axial load and internal pressure. Depending on whether the axial or the hoop stress is greater, the tubes fail by an axial or a circumferential rupture, respectively. The limits of uniform elongation were seen to exhibit significant anisotropy. The non-linear loading paths probed the path-dependence of failure, which was clearly found to be present not only for the strains, but also for the stresses at failure. The results can be used to inform numerical analyses of tube forming processes.

INTRODUCTION

The accurate numerical modelling of material forming processes requires the use of appropriate material models for the plasticity and failure (necking, fracture, bursting, etc.). Since the plastic deformation is path-dependent, the same can be expected for the failure. Hence these models need to be informed from both linear (aka radial or proportional) and non-linear loading paths. In this short paper, we report some first results from linear and non-linear paths on microtubes from the 304L austenitic stainless steel. It is seen that the tubular geometry plays a role in which instabilities are allowed to develop, and hence in the failure limits observed. Furthermore, the path-dependence of the failure limits is assessed.

EXPERIMENTS

The experiments were performed on microtubes from the austenitic stainless steel SS-304L. The tubes were received in the annealed state and had an outside diameter of 2.38 mm and a (nominal) wall thickness of 0.16 mm. Using standard metallographic techniques, it was determined that the average grain size was approximately 10-12 μm, so that there were approximately 12-15 grains through the tube-thickness [1]. When tested in uniaxial tension, the material exhibits a yield stress of about 470 MPa, a UTS of about 660 MPa and a uniform elongation of over 45%.

The experiments were performed on the custom axial load – internal pressure apparatus that was developed by the authors [2]. The apparatus consists of a mesoscale tensile stage of 2 kN load capacity and 50 mm of stroke and a high-pressure pump of 1,390 bar pressure capacity and with 67 ml of pressurized fluid available. The two systems are fully coupled, so that arbitrary paths on the nominal stress space (axial-hoop) can be realized, as described below.

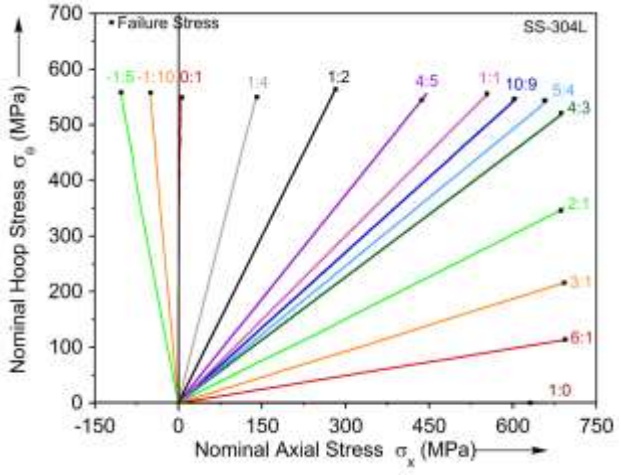

Figure 1: Linear paths prescribed in the nominal stress space.

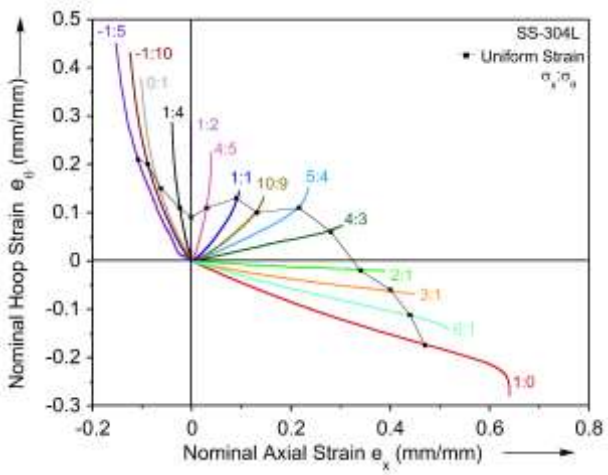

Figure 2: Induced nominal strain paths. Identified is the limit of uniform deformation.

The experiments reported here fall under two extreme categories: radial tests and corner tests. The fact that the apparatus can perform these tests is an indication that any other multilinear path in between them can be implemented, too. For the radial paths, to maintain the axial and hoop nominal stresses proportional throughout the experiment, the ratio of internal pressure to axial load must be maintained constant. On the other hand, it is advantageous for the experiments to be performed

a) Corresponding author. Email: yannis.korkolis@unh.edu

under volume-control. In that sense, the response of the tubes past the pressure maximum can be observed and recorded. In the apparatus developed, the inflation occurs under volume-control, the induced pressure is measured with a pressure transducer, and that signal is used as the input to the mesoscale tensile stage, which is run under force-control. A comparison of this approach vs. the pressure- and displacement-control is discussed in [2].

The corner experiments performed here fall under two categories. In the first, the microtubes are loaded in uniaxial tension up to a prescribed axial nominal stress. Then, the tubes are inflated so that a hoop stress develops, while keeping the axial stress constant. The inflation continues until failure. In the second category, the tubes are inflated under pure hoop tension, i.e., no axial stress is allowed to develop. After reaching the preset hoop stress, the tubes are loaded axially to failure, while keeping the hoop nominal stress constant.

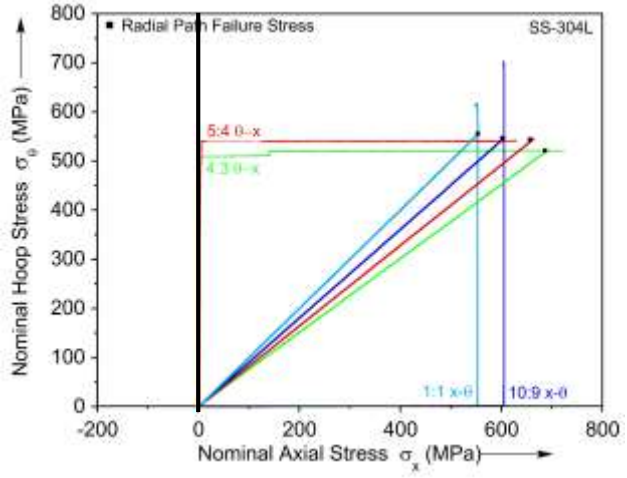

Figure 3: Corner paths prescribed in the nominal stress space

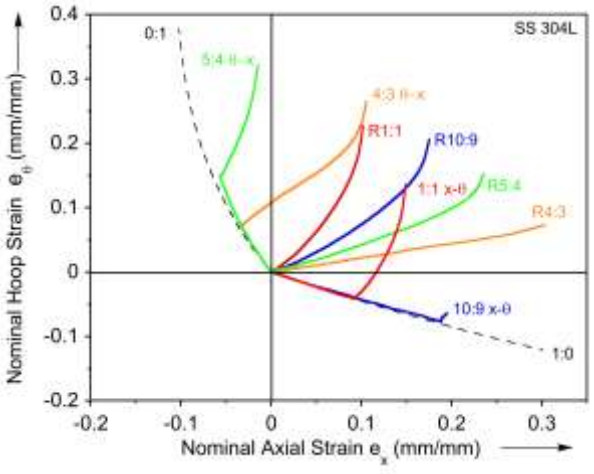

Figure 4: Induced nominal strain paths. Identified is the limit of uniform deformation.

Due to the size of the specimens, the full-strain-field was acquired during the experiments using the non-contact 3D Digital Image Correlation (DIC). The DIC system used was VIC-3D from Correlated Solutions, Inc. To facilitate these measurements, the microtubes were painted with a random pattern of black speckles on a white background. Two 2.0 Megapixel digital cameras (Point Grey Research, Inc., Vancouver, BC) with 17 mm Schneider-Kreuznach Xenoplan lenses were used for the 3D DIC.

RESULTS AND DISCUSSION

The radial paths that were performed are shown in Fig. 1. It can be seen that the paths are exactly linear, which validates the performance of the apparatus that was developed. The corresponding strain paths in Fig. 2 are slightly curved, which indicates that the material has deformation-induced anisotropy. Also marked on this figure are the strain at the pressure maximum, which correspond to the limit of uniform deformation during the inflation. These limits are seen to be quite anisotropic, which is attributed to the tubular geometry of the tubes [3], as well as the fact that the tubes fail in two different modes (axial or circumferential rupture), depending on which stress (hoop or axial, respectively) is greater. The corner path experiments revealed that not only the strains, but also the stresses at failure are path-dependent.

CONCLUSIONS

Experiments on 304L austenitic stainless steel using microtubes inflated under axial load and internal pressure, and following both linear and non-linear paths, revealed that: a) the strains at the limit of uniform deformation are anisotropic, and b) the stresses and strains at failure are path-dependent.

References

[1] Ripley, P.W., Biaxial stress testing of SS-304L microtubes by axial load and internal pressure, MS Thesis, UNH Mech. Eng. Dept., Durham, NH, 2015

[2] Ripley, P.W and Korkolis, Y.P. Multiaxial Deformation Apparatus for Testing of Microtubes Under Combined Axial-Force and Internal-Pressure. *Exp.Mech.*, (in press).

[3] Korkolis, Y.P. and Kyriakides, S. Inflation and burst of anisotropic aluminium tubes for hydroforming applications. *Int'l J Plast*. **24**:509-543, 2008

T-STRESS AND MISMATCH CONSTRAINT FOR A BLUNTED CREEP CRACK

Yanwei Dai[1], Yinghua Liu[1a)]
[1]*Department of Engineering Mechanics, AML, Tsinghua University, Beijing 100084, China*

Summary A mismatch modified boundary layer (MBL) model with a blunted creep crack is established in this paper. With the mismatch MBL model, the *T*-stresses within creeping regime under different mismatching factors are discussed. The generalized *T*-stress is almost independent of radial distance according to the analysis. The stress field of the blunted creep crack in the mismatched MBL is studied. The mismatch constraint effect of the blunted creep crack is also presented. The mismatch constraint parameter for the blunted creep crack is independent of radial distance when the mismatching factor is in a suitable range.

INTRODUCTION

The mismatch effect plays a crucial role for the safety of weldments. Zhang et al. [1] presented a fusion line crack at the interface between the HAZ and base metal in the MBL model, and proposed the $J-M$ two parameters to characterize the material constraint effect of elastoplastic weldments. Noticing that the MBL model for mode I crack was widely used in the constraint effect characterization of elastoplastic solids, Matvienko et al. [2] extended the MBL model to the creep regime, and presented the variation of *T*-stress at different creep time which can be calculated by $T=\sigma_{xx}-\sigma_{yy}$. Dai et al. [3] used the MBL model to study the mismatch constraint effect of a sharp creep crack which can be presented as

$$M^{*}=\frac{\sigma_{yy}^{\mathrm{M}}-\sigma_{yy}^{\mathrm{H}}}{\sigma_{0}} \tag{1}$$

where σ_{yy}^{M} and σ_{yy}^{H} are respectively the open stresses under mismatching and homogeneous conditions. In fact, there are some differences of stress field between the sharp crack and blunted crack [4-5], and the discussions on the blunted creep crack under mismatching condition have not been found yet in the available literatures. In this paper, the influence of mismatch effect on the *T*-stress and material constraint for the blunted creep crack will be discussed in a numerical way. The material properties of P92 type steel at 650°C is used [5], and the materials for base metal and weld metal satisfy the power law creep equation, i.e. $\dot{\varepsilon}^{c}=A_{b}\sigma^{n}$ for base metal and $\dot{\varepsilon}^{c}=A_{w}\sigma^{n}$ for weld metal. The mismatch factor is defined by $m=\left(A_{w}/A_{b}\right)^{1/n}$. The finite element code ABAQUS is adopted here to perform the numerical simulation. A blunted creep crack in a mismatch MBL model is shown in Fig. 1. For the statement of brevity, the detailed information on boundary conditions and geometry sizes can be referred to [6].

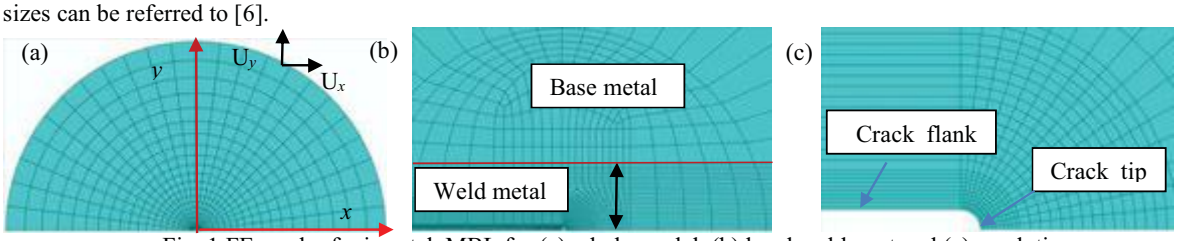

Fig. 1 FE mesh of mismatch MBL for (a) whole model, (b) local weldment and (c) crack tip

T-STRESS OF A BLUNTED CREEP CRACK WITHIN MISMATCH MBL MODEL

Considering the mode I crack, the calculation formula for *T*-stress can be obtained by $T=\sigma_{xx}-\sigma_{yy}$ at θ=0°. Herein, the variations of *T*-stress under two different mismatch factors, i.e. *m*=2.46 of overmatch and *m*=0.41 of undermatch, are presented in Fig. 2. A transition time of $t_{\mathrm{T}}=\left(1-\nu^{2}\right)K^{2}\Big/\left[(n+1)EC^{*}\right]$ is used to denote the creep time. It can be seen that the calculated *T*-stresses for *m*=2.46 and *m*=0.41 under the boundary condition of *T*=0 coincide very well with those under the boundary condition of *T*≠0 if the distance from crack tip is less than 0.1 mm for *m*=2.46 and 1 mm for *m*=0.41. The *T*-stress at the near crack tip field is governed by the applied *T*-stress of boundary conditions. In detail, the predicted *T*=-2.88, -0.87, 0.13, 1.12, 3.11 on the boundary of creep zone approach to the applied *T*=-3, -1, 0, 1 and 3 of far field for *m*=2.46, respectively. It can be shown that our numerical model is accurate as the *T*-stress of near crack tip can be approximated by the applied *T*-stress of far field. Further investigations on stress field analysis of creep crack tip can verify that the stress field of near crack tip in the mismatch MBL model still obeys the HRR type singularity, however, the open stress of crack tip is deviated from the HRR field greatly due to the influence of material mismatch. It implies that the material mismatch is a dominant factor which affects the creep crack tip. The comparisons of *T*-stress for different mismatch factors with sharp and blunted creep cracks are

a) Corresponding author. Email: yhliu@tsinghua.edu.cn

presented in Fig. 2. The boundary conditions and material properties for the MBL model of sharp crack are the same as those for the blunted crack. Clearly, the *T*-stresses are totally different for these two types of cracks. The *T*-stress for sharp crack is obviously path-dependent under both overmatch and undermatch conditions.

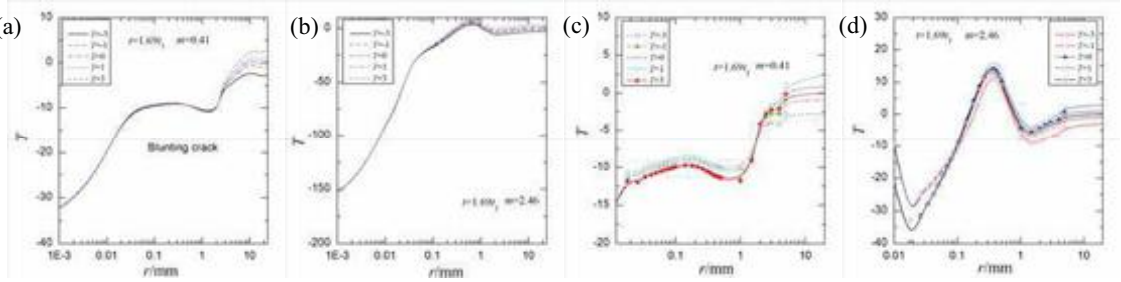

Fig. 2 *T*-stress for blunted creep crack (a) *m*=0.41, (b) *m*=2.46 and *T*-stress for sharp creep crack (c) *m*=0.41, (d) *m*=2.46

MISMATCH CONSTRAINT EFFECT OF BLUNTED CREEP CRACK

$M^*=\left(\sigma_{yy}^{\mathrm{M}}-\sigma_{yy}^{\mathrm{H}}\right)\big/\sigma_0$ is proposed to characterize the mismatch constraint effect of blunted creep crack. A normalized distance from creep crack tip is presented as $\bar{r}=\alpha r\big/\left(C(t)\big/\sigma_0\dot{\varepsilon}_0\right)$. α is a dimensionless scaled factor and the selection of α can be referred to [6]. Fig. 3 (a) presents the variation of open stress under different mismatch factors. It can be seen that the open stresses under the higher mismatch factors are much higher than those under the lower mismatch factors. Further results presented in Fig. 3 (b) show that the mismatch constraint effect is slightly dependent on normalized distance if $6<\bar{r}<10$ for $m<2$. On the other hand, the mismatch constraint under undermatch condition is less than zero, which is contrary to the conclusion under overmatch condition. The open stress and mismatch constraint effect are obtained at the creep time of $1.69t_{\mathrm{T}}$.

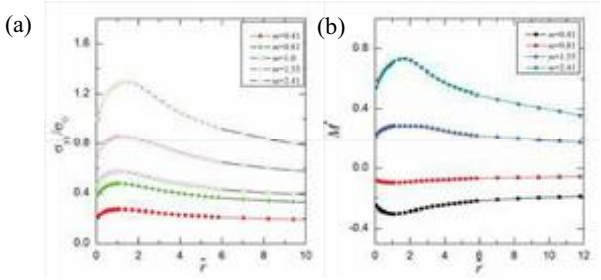

Fig. 3 The influence of mismatch on (a) open stress and (b) constraint effect

CONCLUSIONS

The mismatch MBL model with a blunted crack is established in this paper. With the mismatch MBL model, the *T*-stresses within creeping regime under different mismatching factors are studied. It can be found that *T*-stress of the blunted creep crack is influenced by mismatch factor, and the variations of *T*-stress under different mismatch factors are totally different. For a small *T*-stress of far field, the *T*-stress in creep region is independent of load for blunted creep crack in creep zone, compared with that for sharp crack. The creep crack type, i.e. blunted or sharp crack, can affect the tendency of *T*-stress in creep regime though the far *K*-field is the same. The stress filed of mismatch blunted creep crack is deviated from HRR field significantly because of material mismatch. The proposed M^*-parameter is path-independent if $m<2$ with the given normalized distance $6<\bar{r}<10$.

References

[1] Zhang ZL, Hauge M, Thaulow C.: Two-parameter characterization of the near-tip stress fields for a bi-material elastic-plastic interface crack. *Int. J. Fract.* 79: 65-83, 1996.

[2] Matvienko YG, Shlyannikov V, Boychenko N.: In plane and out of plane constraint parameters along a three - dimensional crack front stress field under creep loading. *Fatigue Fract. Eng. Mater. Struct.* 36: 14-24, 2013.

[3] Dai YW, Liu DH, Liu YH.: Mismatch constraint effect of creep crack with modified boundary layer model. *J. Appl. Mech.-Trans.* ASME 83: 031008, 2015.

[4] Wang X.: Two-parameter characterization of elastic–plastic crack front fields: Surface cracked plates under tensile loading. *Eng. Fract. Mech.* 76:958-82, 2009.

[5] English SA, Arakere NK.: Effects of the strain-hardening exponent on two-parameter characterizations of surface-cracks under large-scale yielding. *Int. J. Plast.* 27: 920-39, 2011.

[6] Dai YW, Liu DH, Liu YH, Chen HF.: Characterization of mismatch constraint effect and creep zone in creeping weldment: non-blunting and blunting crack. *Int. J. Solids Struct.* in preparation, 2016.

MICROMECHANICAL MODEL FOR DUCTILE POROUS MATERIAL UNDER DYNAMIC LOADING

Cédric Sartori[1], Sébastien Mercier[1a)], Nicolas Jacques[2] & Alain Molinari[1]
[1]*LEM3, Université de Lorraine UMR CNRS 7239, Metz, France*
[2]*LBMS, ENSTA Bretagne, Brest, France*

Summary The goal of this research is to propose a constitutive model to describe the behavior of porous ductile materials at high loading rates. This model accounts for void shape and micro-inertia effects. The proposed modeling is based on a multiscale. It will be shown that analytical results compare favorably to finite element calculations for porous materials containing spheroidal voids subjected to axisymmetric loading.
The effect of dynamic loading is observed to generate drastic changes in the flow surface. This effect is enhanced at large stress triaxiality. A key point of the present work is that the model is able to handle prolate and oblate voids. Void shape was previously illustrated in the literature only for quasi static conditions.
Based on the present work, we can conclude that micro inertia and void shape effects are crucial aspects to be accounted for when modeling damage evolution in porous materials subjected to dynamic loading.

INTRODUCTION

For many applications, related to the aeronautics, automotive or military industries, a precise understanding and description of the fracture mechanisms of engineering materials is necessary. In the present study, we focus on ductile materials. One of the first works on the modelling of ductile damage is the Gurson theory [1]. In this approach, the author proposed to model the growth of a spherical void embedded in a rigid matrix. From this seminal study, many works have investigated the void growth process to describe ductile fracture. It has been shown that void growth is dependent on different parameters. Among them, the shape of the voids and the loading rate have to be considered. The influence of the loading rate can be related either on the intrinsic strain-rate sensitivity of the matrix material (viscoplastic effect) or to inertia effects caused by the acceleration of the material in the vicinity of the surface of the growing voids (micro-inertia effects). Unfortunately, very few studies in the literature have proposed a model which integrates the combined contributions of void shape and micro-inertia. The development of such model is the goal of the present work. The theory and some results for porous material with prolate voids can be found in the recent work of Sartori et al. [2]. New results for oblate voids will be presented.

MODEL DEVELOPMENT

The modelling is based on the averaging method proposed by Molinari and Mercier [3]. The representative volume element (RVE) is composed by two confocal spheroids, as in Gologanu et al. [4]. The inner spheroid represents the void surface. Homogeneous strain rate boundary conditions are prescribed at the outer spheroid of the RVE.

The matrix is assumed rigid perfectly plastic (the yield stress is denoted by k_0). As in Molinari and Mercier [3] (where only the dynamic mechanical response of a porous material containing spherical void was considered), micro inertia effect is included in the model. The macrostress is defined as:

$$\underline{\underline{\Sigma}} = \langle \underline{\underline{\sigma}} \rangle + \langle \rho \underline{\gamma} \otimes \underline{x} \rangle \qquad \textbf{(1)}$$

where $\langle \blacksquare \rangle = \frac{1}{|\Omega|} \int_{\Omega} \blacksquare \, dv$ stands for the volume average operator, $|\Omega|$ being the volume of the RVE domain. ρ is the mass density of the material ($\rho = 0$ in the void). $\underline{x}$ and $\underline{\gamma}$ are respectively the position vector and the acceleration of any point within the RVE. $\underline{\underline{\sigma}}$ denotes the Cauchy stress tensor, solution of the dynamic problem. Such definition is not well appropriate for analytical derivation. So as in Molinari and Mercier [3], the use of the virtual work principle is proposed and is seen to be very convenient for an analytical characterization of the macrostress. Indeed, an approximation expression for the macrostress can be obtained by using an admissible velocity field. In the present work, the trial velocity field of Gologanu et al. [4] suitable for both prolate and oblate shapes is adopted.

As in Molinari and Mercier [3], the macroscopic stress is the sum of a static contribution and a dynamic contribution. The static contribution is derived from the work of Gologanu et al. [4]. Via the use of the trial velocity field, a semi analytical formulation of the dynamic contribution is finally proposed for oblate and prolate voids:

[a)] Corresponding author. Email: sebastien.mercier@univ-lorraine.fr.

$$\Sigma_{XX}^{(D)} = \rho \frac{c^5}{a_2 b_2^2} \left(D_{XX}^2 \Delta_1 + D_{ZZ}^2 \Delta_2 + D_{XX} D_{ZZ} . \Delta_3 + \dot{D}_{XX} \Delta_4 + \dot{D}_{ZZ} \Delta_5 \right) \quad \textbf{(2)}$$

$$\Sigma_{ZZ}^{(D)} = \rho \frac{c^5}{a_2 b_2^2} \left(D_{XX}^2 \Delta_6 + D_{ZZ}^2 \Delta_7 + D_{XX} D_{ZZ} . \Delta_8 + \dot{D}_{XX} \Delta_9 + \dot{D}_{ZZ} \Delta_{10} \right) \quad \textbf{(3)}$$

The coefficients Δ_i are defined as simple integral term which depends on the geometry of the RVE, see [2] for a precise definition. The dynamic part of the macroscopic stress is a quadratic function of the strain rate $\left(\underline{\underline{D}}\right)$ and a linear function of the time derivative of the strain rate $\left(\underline{\underline{\dot{D}}}\right)$. The matching of the dynamic stress obtained for spheroidal voids with previous results for spherical voids has been checked. As a consequence, the model is able to capture void evolution from prolate shape to oblate shape.

MODEL VALIDATION AND ANALYSIS

The model has been validated by comparison with finite element computations, carried out with Abaqus/Explicit software. Flow surfaces predicted by the model and by numerical simulations are plotted in Fig. 1, in the normalized mean stress $\left(\frac{\Sigma_m}{k_0}\right)$ versus the normalized deviatoric stress $\left(\frac{\Sigma_{ZZ}-\Sigma_{XX}}{k_0}\right)$ plane. Validation is decomposed in two stages: (i) validation of the linear part of the dynamic macroscopic stress ($\underline{\underline{D}} = \underline{\underline{0}}$, Fig. 1a) (ii) validation of the quadratic part of the dynamic macroscopic stress ($\underline{\underline{\dot{D}}} = \underline{\underline{0}}$, see Fig. 1b). A good agreement between model and numerical results is shown. Under loading at constant time derivative of the strain rate (Fig 1a), a dilatation of the flow surface is observed as the loading magnitude increases. Under loading at constant strain rate, a lack of convexity of the flow surfaces is observed for large triaxiality loading, in both compression and tension. It is shown that this phenomenon is due to a transfer of microscale kinetic energy which promotes void growth in tension or equivalently reduces the stress necessary to activate void growth. The reverse trend is observed in compression.

In the present talk, a comprehensive parametric study is further presented with a particular attention paid to the effects of porosity and void shape. The problem of the evolution of the porosity under dynamic loading will be also discussed.

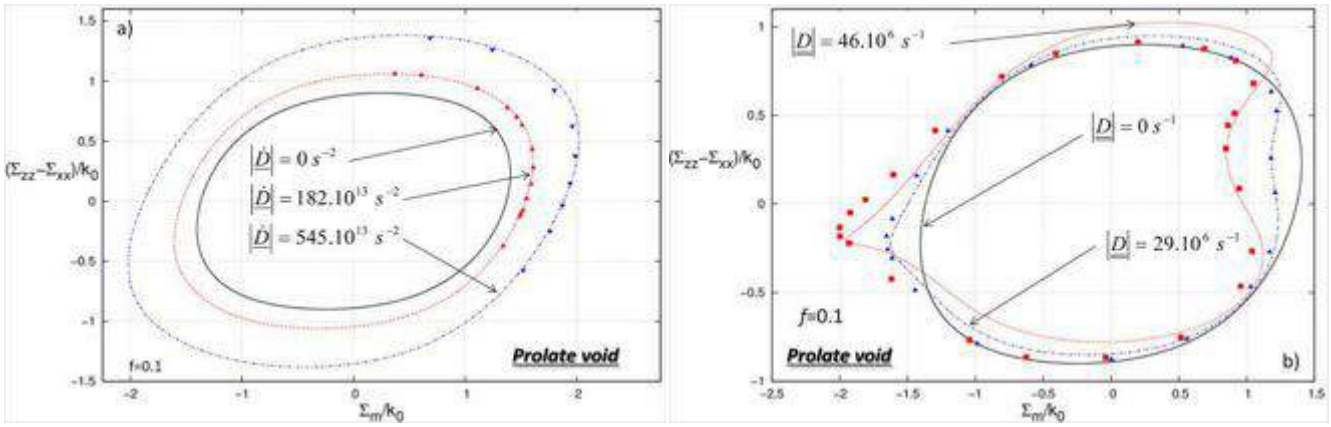

FIG. 1 - Flow surfaces for various dynamic loadings, from Sartori et al [2]. Porous materials containing prolate voids with an aspect ratio of 5 are considered. The porosity is set to $f = 0.1$, mass density of the matrix is $\rho = 7800\ kg/m^3$, the yield stress is $k_0 = 500\ MPa$. a) Dynamic loadings with $\underline{\underline{D}} = \underline{\underline{0}}$ and $\underline{\underline{\dot{D}}} \neq \underline{\underline{0}}$. b) Dynamic loadings with $\underline{\underline{D}} \neq \underline{\underline{0}}$ and $\underline{\underline{\dot{D}}} = \underline{\underline{0}}$.

References

[1] Gurson A. L.: Continuum theory of ductile rupture by void nucleation and growth: Part I - yield criteria and flow rules for porous ductile media. ASME Journal of Engineering Materials and Technology 99: 2-15, 1977.

[2] Sartori C., Mercier S., Jacques N., Molinari A.: Constitutive behavior of porous ductile materials accounting for micro-inertia and void shape. Mechanics of materials 80, part B: 324-339, 2015.

[3] Molinari A., Mercier S.: Micromechanical modeling of porous materials under dynamic loading. Journal of the Mechanics and Physics of Solids 41: 1723-1759, 2001.

[4] Gologanu M., Leblond J.-B., Perrin G., Devaux J.: Recent extensions of Gurson's model for porous ductile metals. Continuum Micromechanics, CISM Courses and lectures 377 P. Suquet, ed., Springer-Verlag:: 61-130, 1997.

MULTIPLE NECKING DURING BIAXIAL LOADING OF THERMOVISCOPLASTIC PLATES

J. A. Rodríguez-Martínez *[1], R. Zaera[1], G. Vadillo[1], J. Fernández-Sáez[1], and A. Molinari[2]
[1]*Department of Continuum Mechanics and Structural Analysis, University Carlos III of Madrid, Leganés, Madrid, Spain*
[2]*Laboratoire d'Etudes des Microstructures et de Mécanique des Matériaux, Université de Lorraine, Metz, Lorraine, France*

Summary In this work we have investigated the inception and development of necking bands in ductile plates subjected to dynamic (in-plane) biaxial loading. For that task we have developed two different methodologies (1) a 2D linear stability analysis accounting for stress triaxiality effects and (2) finite element simulations.

ABSTRACT

Diffuse or localized dynamic necking of a sheet metal is a major issue in high speed forming processes, leading to unacceptable thinning and even failure if fully developed, or in the dynamic behaviour of metallic structural elements of small thickness used for energy absorption purposes. This process is frequently related to the collective development of localization bands resulting in a necking pattern which depends on the sheet properties and the loading conditions.

In this work we have investigated the inception and development of necking bands in ductile plates subjected to dynamic (in-plane) biaxial loading. For that task we have developed two different methodologies. The first one is a linear stability analysis, following the original methodology proposed by Dudzinski and Molinari [1, 2] now including inertial effects and stress triaxiality due to strain localization, which permits to identify a dominant instability mode whose wavelength is related to the necking-band spacing. The second is a fully 3D finite element model aiming to systematically verify and complement the outcomes of the aforementioned theoretical approach. In agreement with the stability analysis, the loading conditions are constant velocities applied at the edges of the plate. In order to avoid the spurious propagation of waves along the plate, specific initial conditions consistent with the boundary conditions were imposed. The calculations have shown that multiple necking bands are formed and developed in the plate, following the orientations predicted by the linear stability analysis.

The loading path has been shown to play a major role in the necking pattern, with unevenly spaced necking bands with variability in their rate of development as this path deviates from plane strain conditions. Likewise, the effects of material properties (strain rate sensitivity, material density), sheet geometry (thickness) and thermal coupling on the stability of the deformation process and on the distance between necking bands have been examined. The calculations predicted a strong delay in the onset of necking with increasing *material rate sensitivity* for all the loading paths investigated. Both the linear stability analysis and the finite elements have been used to show that increasing the rate sensitivity enlarges the neck spacing and helps to develop more regular localization patterns. Increasing the *plate thickness* retards plastic localization for all the loading paths explored. Further, the necks spacing is diminished as the plate thickness decreases. Regarding *density*, the analysis predicted that increasing its value leads to a slight delay in the necking inception, whereas neck spacing is largely insensitive to this material property. Finally both methodologies demonstrated that the *thermal coupling* shorten the neck spacing, also leading to a substantial decrease in the necking strain, irrespective of the loading path considered.

The systematic confrontation and combination of results obtained from the linear perturbation analysis and the finite element calculations has allowed to provide new insights into the specific localization patterns that emerge under dynamic biaxial loading. We claim that this investigation sets a theoretical framework that can be used for design and optimization of high speed metal forming operations, with the ultimate aim of predicting the limits in material ductility which impose important restrictions to this type of industrial processes.

ACKNOWLEDGEMENT

JFS, RZ, GV and JARM are indebted to the Ministerio de Economía y Competitividad de España (Projects DPI2014-57989-P and EUIN2015-62556) for the financial support which permitted to conduct this work.

AM and JARM acknowledge the support by the French State through the program Investment in the future operated by the National Research Agency (ANR) and referenced by ANR-11-LABX-0008-01 (LabEx DAMAS).

References

[1] Dudzinski D., Molinari A.: Instability of visco-plastic deformation in biaxial loading. Comptes Rendues Academie Science Paris. 307:1315-1321, 1988.
[2] Dudzinski D., Molinari A.: Perturbation analysis of thermoviscoplastic instabilities in biaxial loading. International Journal of Solids and Structures. 27:601-628, 1991.

EMERGENCE OF ECHELON CRACKS UNDER MIXED-MODE I + III LOADING

Khai-Hong Pham[1] & Krishnaswamy Ravi-Chandar[2a)]
[1]*Massachussetts Institute of Technology, Cambridge, MA, USA*
[2]*Center for Mechanics of Solids, Structures and Materials, University of Texas at Austin, Austin, TX, USA*

Summary The development of echelon crack patterns under mixed-mode I + III loading conditions is examined first through carefully designed experiments performed on transparent specimens. These experiments present a direct visual evidence of the mechanisms involved in the formation of the echelon pattern of cracks and aid in the development of a model for their formation. This model is finally established through direct numerical simulations of mixed-mode I + III within the framework of phase-field methodology for fracture.

INTRODUCTION

Mixed-mode I+III fracture in brittle materials presents spectacular, scale-independent pattern formation in nature and engineering applications [1-3]; and it is one of the last remaining puzzles in *linear elastic fracture mechanics*. This problem has received much attention in the literature over the past few decades both from experiments [4-7] and analysis [8-11], but there are still open challenges that remain. Specifically, the existence of a threshold ratio of mode III to mode I loading below which fragmentation of the crack front (formation of daughter cracks) does not occur, and the length scale associated with the spacing of the fragments when they do occur are still under debate. We approach this problem through carefully designed experiments to examine the physical aspects of crack initiation and growth. Based on these experiments, a model for the formation of the echelon cracks is established. Finally, direct numerical simulation of crack initiation and growth is explored using a phase-field model.

EXPERIMENTALLY DERIVED MODEL FOR ECHELON CRACK FORMATION

The growth of cracks under mixed-mode loading I+III has been examined experimentally. Specially designed specimen configuration were used in order to examine the nucleation and growth of daughter cracks from a mixed mode I + III crack in a brittle polymer. A combination of confining pressure and a wedge load allowed generating mixed mode crack growth, but with significant confining compression in one orientation that allowed opening mode cracks to nucleate and grow. Microscopic examination was used to identify the structure of the nucleated daughter cracks. Another set of experiments was performed on a gelatin based hydrogel; the transparency of this material allowed good visualization of the development of the daughter cracks, both during nucleation and growth. Based on these experiments we show that

- Daughter cracks (type A) oriented perpendicular to the direction of maximum tension are nucleated from the parent crack when a critical loading condition is attained and are not formed through the growth of unstable modes from a smooth extension of the parent crack.
- Daughter cracks (type B) perpendicular to the minor principal axis are not nucleated under the confined compression-shear loading or the edge-cracked tension experiments.
- Coarsening of the spacing between the type A cracks occurs through elastic shielding.
- Final failure that occurs through break-up of the bridging regions between the type A cracks.

Based on the collection of experiments, the sequence of events that govern the initiation and growth of cracks under mixed-mode I + III is now clearly revealed to be composed of the following steps, illustrated in Figure 1:

- First, type A daughter cracks are nucleated from random defects in the vicinity of the parent crack (see Figure 1a); the spacing between the daughter cracks is governed by the characteristic dimension of the parent crack.
- Second, fluctuations and elastic interactions result in shielding of some subset of the nucleated daughter cracks; these daughter cracks are arrested (see Figure 1b).
- As the surviving daughter cracks grow farther, the parent crack, pinned at the original position, experiences increased stress intensity factor and the bridging regions begin to crack and the parent crack front advances towards the daughter cracks (see Figure 1c).

It is now possible to set up a new structure, where the leading edge is formed by the fragmented type A daughter cracks, while the trailing edge is created by the fracture of the bridging regions between the type A daughter cracks. In the absence of any mode II, there is no driving force to alter this picture, and the process can sustain itself and break the entire specimen creating a system of echelon cracks under the combined mode I + III loading. It is required to incorporate this mechanism in the analysis or simulation of crack growth under mixed-mode I + III conditions in order to generate a complete accounting of the energy associated with crack growth and to capture the correct pattern generation.

[a)] Corresponding author. Email: ravi@utexas.edu

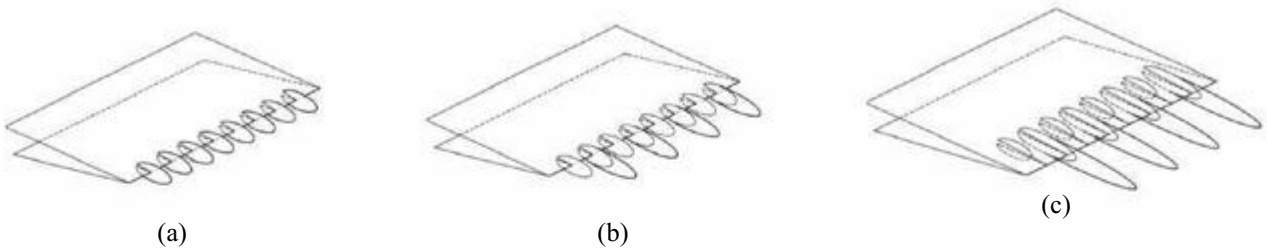

Figure 1. Illustration for the model of crack growth under mixed-mode I+III loading: (a) Type A daughter cracks are nucleated from random defects in the vicinity of the parent crack; (b) Growth and shielding of daughter cracks result in fewer daughter cracks growing; (c) Steady state growth where the leading edge is formed by the fragmented type A daughter cracks, while the trailing edge is created by the fracture of the bridging regions between the type A daughter cracks is established.



Figure 2. Phase-field simulation of formation of echelon cracks under pure mode III loading; formation is triggered by introducing defects in the vicinity of the crack.

PHASE-FIELD SIMULATION OF FRACTURE

The phase-field model of fracture has been implemented in a parallel simulation framework for simulation of three-dimensional linear-elastic fracture problems. The numerical code was verified for stationary crack problems by comparison of the crack opening displacement with the analytical linear elastic singular solution and the Dugdale-Barenblatt cohesive model solution. Validation of the numerical model was established through comparison to two-dimensional experiments. The phase-field model was then used in the simulation for mixed-mode I+III problems. It was shown that the phase-field model will predict the flat mode I crack path for mixed-mode I+III loading as well, since the energy release is maximum along this path. But the failure mechanism for specific materials places an energy barrier which does not allow for such crack path. Thus, we explored the introduction of defects and discrete nucleation in these problems. This allows the echelon cracks to nucleate and grow, and coarsening as we observed in the experiments through elastic shielding. An example of the phase field simulation of the formation of an echelon crack is shown in Figure 2.

CONCLUSIONS

Mixed-mode I + III crack initiation and growth is considered. It is shown through experiments on a brittle polymer and a hydrogel that crack initiation occurs through the nucleation of daughter cracks, and further growth occurs through a sequential development of coarsened daughter cracks and an eventual fracture of the parent cracks to reach a steady state. This model is implemented in a phase-field numerical simulation.

References

[1] Sommer E.: Formation of fracture ‘lances’ in glass. Eng Fract Mech, 1:539-546, 1969.

[2] Knauss W.G.: An observation of crack propagation in anti-plane shear. Int J Fract, 6:183-187, 1970.

[3] Younes A.I., and Engelder T.: Fringe cracks: Key structures for the interpretation of the progressive Alleghanian deformation of the Appalachian plateau. GSA Bulletin, 111: 219-239, 1999.

[4] Hull D.: The effect of mixed mode I/III on crack evolution in brittle solids. Int J Fract, 70, 59-79, 1995.

[5] Lazarus V., Buchholz F-G., Fulland M., Wiebesiek J.: Comparison of predictions by mode II or mode III criteria on crack front twisting in three or four point bending experiments, Int J Fract, 153:141-151, 2008.

[6] Lin B., Mear M.E., Ravi-Chandar K.: Criterion for initiation of cracks under mixedmode I+III loading. Int J Fract, 165:175-188, 2010.

[7] Goldstein R.V., Osipenko N.M.: Fracture structure near a longitudinal shear macrorupture. Mech of Solids, 47:505-516, 2012.

[8] Xu G., Bower A.F., Ortiz M.: An analysis of non-planar crack growth under mixed mode loading. Int J Solids Struct 31:2167–2193, 1994.

[9] Pons A.J., Karma A.: Helical crack-front instability in mixed-mode fracture, Nature, 464:85-89, 2010.

[10] Leblond J.B., Karma A., Lazarus V.: Theoretical analysis of crack front instability in mode I+III. J Mech Phys Solids, 59:1872-1887, 2011.

[11] Leblond J.B., Lazarus V., Karma A.: Multiscale cohesive zone model for propagation of segmented crack fronts in mode I+III fracture. Int J Fract, 191:167-189, 2015.

CRACK FRONT DYNAMICS [1]

Itamar Kolvin[1a)], Gil Cohen[1] & Jay Fineberg[1]
[1]*Racah Institute of Physics, The Hebrew University of Jerusalem, Jerusalem, Israel*

Summary Nominal toughness of materials is determined by structure and material composition, but actual toughness is strongly affected by macroscopic three-dimensional instabilities of cracks. We will present novel experiments in brittle gels, probing the dynamics of crack fronts as the fronts become unstable. By comparing the surface area created by unstable cracks to local velocity and curvature of the propagating crack fronts that created the fracture surface, we test the validity of planar front perturbation theory to bulk 3D fracture.

INTRODUCTION

Catastrophic failure via dynamic propagation of cracks is the main mechanics for failure of materials and structures [2]. The nucleation and subsequent dynamics of the crack is conventionally understood in the context of 2D Fracture Mechanics. In this description, fracture ensues from discrete cracks whose length exceeds a critical dimension determined by the stress distribution in the sample. Crack motion is then determined by an energy balance between the elastic energy flux into the crack tip and the intrinsic fracture energy needed for creating the new surfaces.

However, this 2D description is still a significant idealization of the actual fracture process. Real cracks break 3D materials and their singular crack fronts generically possess non-trivial local structure due to either dynamic instabilities [3-4] of the crack front or interaction with imperfections within a material. For example, the micro-branching instability is manifested by the nucleation and growth of localized microscopic cracks that branch off of the main crack front. These instabilities increase the surface area created by the crack, thereby enhancing the effective toughness of the material.

In recent decades 2D Fracture Mechanics have been extended to 3D settings where the crack front is confined to a single plane. A central result [5] provides the local stress intensity factor along a perturbed front

$$K(z) = K_0\left(1 + \frac{1}{\pi}P\int\frac{x'(z')}{z'-z}dz'\right)$$

for a front propagating in the x direction and confined within the (xz) plane. This result has been confirmed for fracture at interfaces, leading to surprising discoveries of anisotropic toughness in patterned interfaces. However, the relevance of the planar description to fully 3D fracture is still unclear.

EXPERIMENT

To investigate crack dynamics in 3D we visualize the crack front directly during propagation. We perform our experiments by initiating Mode I fracture under uniform tension in brittle polyacrylamide gels (14% w/v AAm, 2.6% MBAA, c_R = 5.2 m/s - the Rayleigh velocity). Gels are soft materials in which sound velocities are reduced by 2-3 orders of magnitude compared to more conventional materials. In our setup drawn in Fig. 1, the transparent gel sample is illuminated via collimated light directed parallel to the tensile (*y)* axis. Fracture of the sample ensues via a propagating crack front traversing the mid-plane. By imaging the fracture plane *during propagation* using a high-speed camera (~48,000 fps), we obtain shadow images of the propagating leading edge of the crack front in real time. After the fracture test we map out the resulting fracture surface using an optical profilometer.

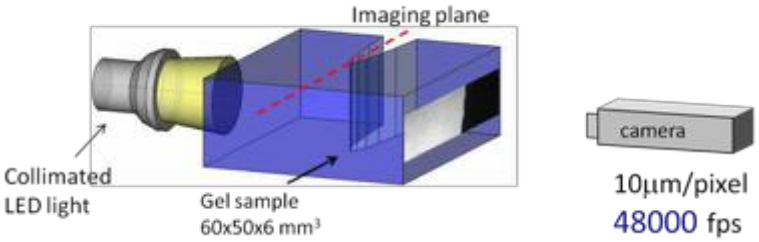

Fig. 1 Collimated light is shined through the gel sample along the tensile axis. The strong curvature at the crack tip diverts any rays impinging on it from reaching the high speed camera. This produces a shadowgraph image of the leading edge of the propagating crack front as it traverses the fracture plane.

When increasing the crack velocity we observe a transition of fracture dominated by the cross-hatching [6], or faceting instability to fracture dominated by the micro-branching instability. As seen in Fig. 2 the fracture surface at low velocities

a) Corresponding author. Email: itamar.kolvin@mail.huji.ac.il

appears to be composed of facets separated by discontinuous steps which propagate at ~40^0 angle to the crack propagation direction. As the mean crack velocity increases above ~$0.1c_R$ micro-branches begin to appear, nucleating in chain-like succession to form lines of directed micro-branches called *branch-lines*.

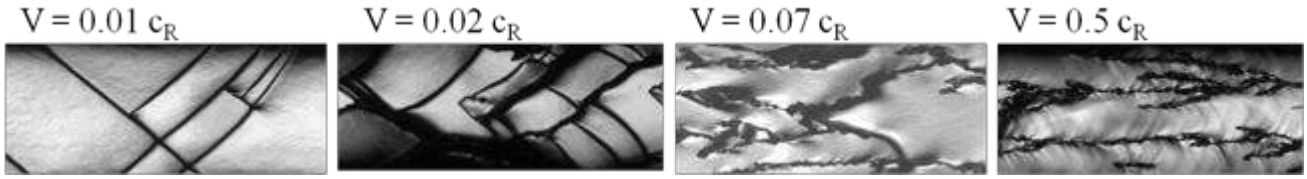

Fig. 2 Fracture surfaces formed by fronts with increasing velocity. Panel width is 10mm.

CRACK FRONT DYNAMICS DURING THE MICROBRANCHING INSTABILITY

As micro-branching unfolds the front develops a localized region of high curvature which exhibits rapid dynamics. The front initially locally decelerates and curves due to the increase in energy dissipation associated with micro-branch formation. The fronts then develop a cusp singularity in finite time which leads to micro-branch "death". Micro-branch deaths release the elastic energy stored by the front curvature and result in spatially local prominent velocity overshoots. These overshoots are shown to be well-correlated with $K(z)$ along the front.

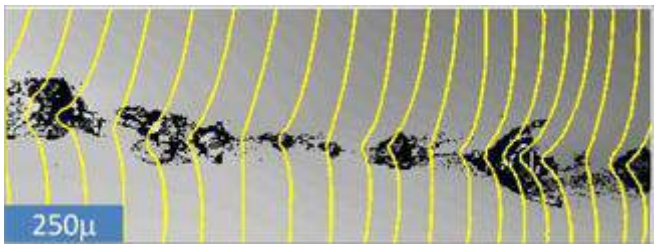

Fig. 3 Edge-detected fronts overlaid on top of the corresponding fracture surface. On the surface is a branch line consisting of six-seven microbranches.

CRACK FRONT DYNAMICS DURING THE FACETING INSTABILITY

At very slow velocities cracks can support single steps. Fig. 4 shows an example of a single step crossing the fracture surface for crack velocity of $v = 0.005c_R = 24$ mm/s. While both surface height and local velocity are discontinuous across the step, the two discontinuities are virtually constant during crack propagation. These remarkably stable steps can divide the crack into segments that propagate at different speeds, and their angle of propagation appear to be indifferent to perturbations that slow down the crack.

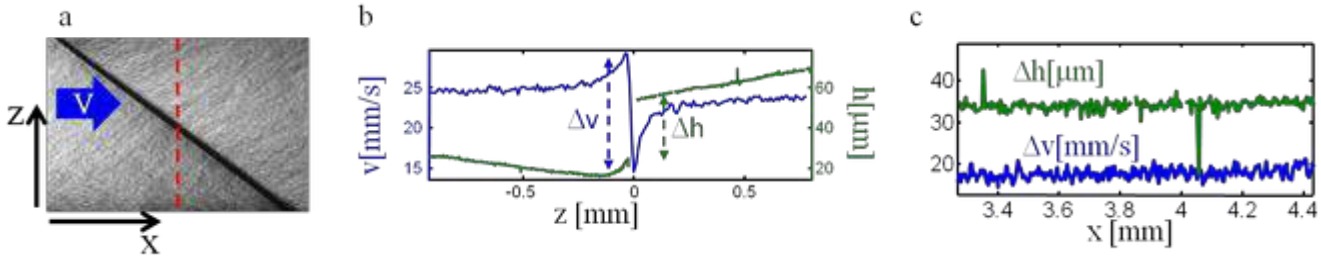

Fig. 4 Stability of a faceted crack front propagating at $v = 0.005c_R$. (a) The fracture surface. Panel width is 3 mm. (b) The velocity profile and the height profile along the red dashed line in (a). Both profiles show a discontinuity at the step. (c) The two discontiuities appear to be constant during crack propagation.

References

[1] Kolvin I. et al.: Crack front dynamics: the interplay of singular geometry and crack instabilities. *Phys. Rev. Lett.* **114** 17 (2015) 175501.

[2] Sun, S. et al.: Potential-dependent dynamic fracture of nanoporous gold. *Nature materials* **14** 9 (2015) 894-898.

[3] Fineberg, J. and Bouchbinder, E.: Recent developments in dynamic fracture: some perspectives. *Int. J. Fract.* (2015).

[4] Chen, C.-H. et al.: Crack front segmentation and facet coarsening in mixed-mode fracture. *Phys. Rev. Lett.* **115** 26 (2015) 265503.

[5] Rice, J. R.: First-order variation in elastic fields due to variation in location of a planar crack front. *J. App. Mech.* **52** 3 (1985) 571-579.

[6] Ronsin, O. et al.: Crack front échelon instability in mixed mode fracture of a strongly nonlinear elastic solid. *Europhysics Letters* **105** 3 (2014) 34001.

CRACK DYNAMICS IN BRITLE CRYSTALS AT THE LOW ENERGY-SPEED REGIME

Anna Gleizer[1], Guy Kovel[1], Fouad Atrash[1] Dov Sherman[2a)]
[1]*Department of Materials Science & Engineering, Technion, Haifa, Israel*
[2]*School of Mechanical Engineering, Tel-Aviv University, Tel-Aviv, Israel*

Summary We performed a set of cleavage fracture experiments of brittle silicon crystal specimens and compared the energy-speed relationship with continuum-based Freund equation of motion and atomistic simulations. Surprisingly, the continuum-based theory well described the energy-speed relationship at the low energy speed regime. We further performed new set of molecular dynamics simulations and explain why atomistic simulations are still inadequate to describe this relationship. Finally, we suggest a new approach for better atomistic simulations.

It is generally believed that cracks in brittle crystals initiate at high energy and high speed. Atomistic-based theoretical studies and massive atomistic simulations at all levels are in accord with this intuition, as they show that over 60% of the theoretical Griffith barrier of $2\gamma s$ is required to initiate a crack, followed by crack 'bursting' to a speed of 2000 m/sec [1]. The atomistic simulations suggest a 'lattice trapping' effect [2]: the atoms along the crack front are presumably trapped in the potential-well and require higher energy to overcome the barrier and to initiate. This behaviour has been confirmed by past cleavage fracture experiments [3,4].

Freund equation of motion (FEqM) of cracks [5] is continuum-based theory for a solid containing a crack loaded by time independent stresses; the energies in the solid are at equilibrium. The theory relates between the quasi-static strain energy release rate (SERR), G_0, and the resultant crack speed, V. The solution does not include crack wave reflections. Denoting G(V) as the dynamic energy release rate, the accepted energy-speed relationship is:

$$G(V) = G_0\left(1 - \frac{V}{C_R}\right), \qquad (1)$$

where C_R is the Rayleigh free surface wave speed, the upper bound for crack speed. In the most general form, crack initiation and propagation take place when $G(V)=\Gamma(V)$, where $\Gamma(V)$ is the velocity-dependent material resistance for crack initiation and propagation. For ideal brittle crystals $\Gamma(V)=2\gamma s$ (Eq. 1), hence:

$$\frac{V}{C_R} = \left(1 - \frac{2\gamma_s}{G_0}\right) \qquad (2)$$

The fundamental aspects arise from Eq. (2) are that cracks initiate at the Griffith barrier of $2\gamma_s$ and can propagate at speeds $0<V<C_R$.

We employed our coefficient of thermal expansion mismatch experimental method [6]. Briefly, the specimens were glued to an aluminum loading-frame by two thin layers of epoxy resin. These layers serve as a compliant agent that reduces energy flux rate to the crack tip. The SERR, G_0, was calculated by quasi-static finite element analysis (FEA), and crack speed was evaluated by the Wallner-lines technique. Silicon crystal specimens served here as a model material.

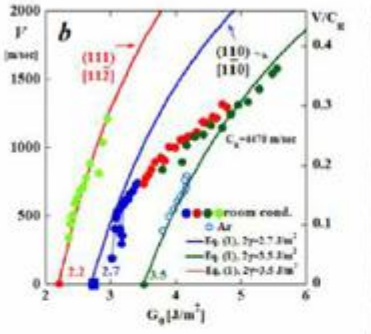

Fig. 1.

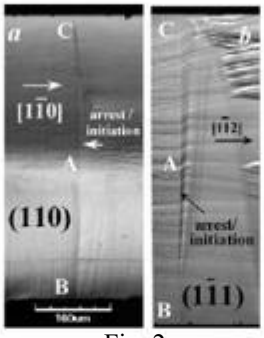

Fig. 2.



Fig. 3.

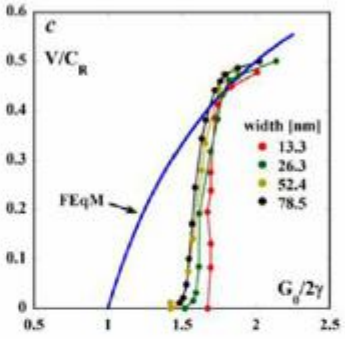

Fig. 4.

The nominal energy-speed relationship (**Fig. 1**) demonstrates that cracks can propagate at much lower energies and speeds than predicted by atomistic calculations; FEqM well describes the energy-speed relationship at the labelled speeds; the kinetic energy is the most significant energy consumption mechanism up to the measured speeds; reflected stress wave is less significant than expected, presumably since the external stresses are slowly applied, their magnitude is low (~10 MPa), and V<0.35CR.

We then studied the fracture surfaces of our cleaved silicon specimens by optical confocal microscope; these clearly show surface markings depicting curved crack front patterns (**Fig. 2**), generated during cycles of initiation, propagation, and nearly arrest. The only topological rationale for the curved profile is that of planner atomistic steps in form of numerous

a) Corresponding author. Email: dovsherman@post.tau.ac.il

kinks. The numerus kinks existing along the curved front raise the question how much energy is required for kink advance. This issue was recently analysed [7], and it was shown that when kinks are considered, the trapping effect becomes only about 20% in energy followed by crack bursting to nearly 1,000 m/sec, and is mainly due to kink formation. This is still higher than our experiments show.

We turned to a new class of MD calculations; the typical cracked long strip specimen model contained 70 atoms through the thickness, where the periodic boundary conditions were removed. The MD model consists of up to 12 million atoms. A modified Stillinger-Weber interatomic potential was used. Snapshot of the crack front is shown in **Fig. 3**, exposing the curvature. We examined farther the effect of free surfaces and curved crack front on the energy-speed relationship by analysing four different atomistic models, with fixed specimen height and length of 24.6 and 123 nm, respectively, and various thicknesses. While thickness has a certain effect on the energy-speed relationship, and the energy is reduced for a prescribed speed, the effect is still small (**Fig. 4**).

Our experiments reveal a different view of 'how brittle crystals break': crack front is curved and composed of enormous planar atomic-scale steps, or kinks; atoms along the crack front break by kinking mechanisms; cracks initiate near the Griffith barrier and can propagate at low speeds; and cracks are 3D in nature. The most significant conclusion is that atomistic models must follow the physical problem at hand, with no assumptions made, as in fracture mechanics theory. Non-physical boundary conditions may change the energy scheme required to stretch the atomic bonds along the crack front to failure. We therefore suggest using multiscale modelling in the form of quasicontinuum modeling [8], where very large models are to be constructed of atoms along the entire crack front and vicinity and continuum elements as the rest of the body. These issues and more will be discussed in the talk.

References

[1] M. J. Buehler, et al., *Phys. Rev. Lett.* **99**, 165502 (2007).
[2] J. C. H. Spence Y. M Huang, O. Sankey O, *Acta metall. Mater.* **41**, 15-2824 (1993).
[3] J. Hauch et al., *Phys. Rev. Lett.* **82**, 3823-3826 (1999).
[4] T. Cramer, A. Wanner, P. Gumbsch, *Phys. Rev. Lett.* **85**, 788-791 (2000).
[5] L. B. Freund, Dynamic fracture mechanics. Cambridge University Press, Cambridge (1998).
[6] A. Gleizer, D. Sherman, *Int. J. Frac.* **187**, 1-14 (2014).
[7] J. R. Kermode, et al., *Phys. Rev. Let.* **115**, 135501 (2015).
[8] E. B. Tadmor, R. E. Miller, Modeling Materials: Continuum, Atomistic, and Multiscale Techniques. Cambridge University Press (2011).

APPROACHES FOR DYNAMIC FRACTURE SIMULATION: R-ADAPTIVE MATERIAL FORCE AND PHASE-FIELD METHOD

Michael Kaliske[1], Christian Steinke[1] & Kaan Özenç[2]
[1] *Institute for Structural Analysis, Technische Universität Dresden, Dresden, Germany*
[2] *ANSYS Inc., Otterfing, Germany*

Summary The numerical crack approximation in finite element simulations may be categorized in discrete and smeared approaches. The discrete approach models a crack as free edges in the meshing with an actual separation of the elements along the crack surface. The smeared approach represents the crack by a modification of the relation of stresses and strains in the elements in the vicinity of the crack. This contribution presents the application of state of the art approaches of each category to dynamic fracture simulations and a detailed comparison of both methods by evaluation of the simulation results. In respect of the discrete approaches, an r-adaptive node duplication technique triggered by the evaluation of the "material force" at the crack tip is introduced. The smeared approach employs the phase-field method. Both methods are presented and applied to characteristic dynamic fracture examples for evaluation and comparison of their capabilities.

INTRODUCTION

The first and major step to a comprehensive theory of fracture mechanics was the linking of the formation of a crack Γ to the dissipation of strain energy by [3]. Furthermore, the knowledge of the material dependent amount of energy necessary for the formation of a crack allowed the evaluation of strain states of structures in respect of the propagation of cracks and led to the development of the theory of "material forces" and their interpretation as a driving force for crack propagation. With the criterion for crack propagation at hand, the modification of the spatial discretization led to discrete crack approximation approaches for finite element simulations as described e.g. in [4].

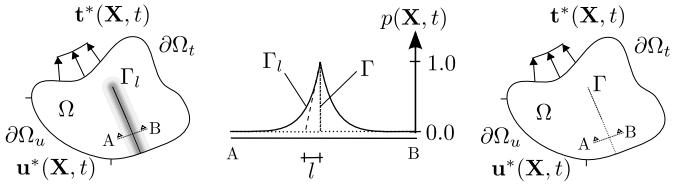

Figure 1: Continuum Ω with smeared crack approximation Γ_l and sharp crack Γ

Another approach emerged recently out of the pioneering work of [2]. The formation of cracks, including initiation, propagation and branching, is embedded into the framework of energy minimization. The additional field parameter "phase-field" $p(\mathbf{X},t)$ is introduced and interpreted as the regularized approximation of the crack's surface Γ_l. The relation of the surface energy to the regularized size of the surface of the crack allows the consideration of an additional dissipative contribution in a general energetic description of the problem. A comprehensive overview on the existing formulations of the phase-field method is given e.g. in [1].

GOVERNING EQUATIONS

Phase-field method

The main ingredient of the phase-field method is the definition of the part of the strain energy, that is available for the dissipation into crack surface formation. In this contribution, the spectral decomposition

$$\psi_S = \frac{\lambda}{2} \cdot \langle \boldsymbol{\varepsilon} : \mathbf{1} \rangle_+^{\,2} + \mu \cdot \boldsymbol{\varepsilon}^{+2} : \mathbf{1} \tag{1}$$

is employed. Here, the LAMÉ constants λ and μ, the strain tensor $\boldsymbol{\varepsilon}$, the bracket operator $\langle x \rangle_+ = \frac{x+|x|}{2}$ and the tensile part of the spectrally decomposed strain tensor $\boldsymbol{\varepsilon}^+ = \sum_i \langle \varepsilon_i \rangle^+ \, \mathbf{n}_i \otimes \mathbf{n}_i$ are utilized. The irreversibility of the crack evolution is ensured by the use of a history variable for the crack driving force.

Material force approach

The material forces are evaluated at the nodes of the finite element discretization and present a criterion for the propagation of the crack. They are evolved from the local form of the simplified material momentum balance

$$\nabla_{\mathbf{X}} \cdot \boldsymbol{\Sigma} = (\nabla_{\mathbf{X}} \boldsymbol{u}^T)^T \boldsymbol{b}_0 - \rho (\nabla_{\mathbf{X}} \boldsymbol{u}^T)^T \mathbf{u} - \rho (\nabla_{\mathbf{X}} \dot{\boldsymbol{u}}^T)^T \mathbf{u} - \frac{1}{2} \mathbf{u} \cdot \mathbf{u} \nabla_{\mathbf{X}} \rho + \frac{\partial \psi_{lin}}{\partial \boldsymbol{X}} \Big|_{exp} \tag{2}$$

in a small strain formulation with the material gradient $\nabla_{\mathbf{X}}(\bullet)$, the material divergence operator $\nabla_{\mathbf{X}} \cdot (\bullet)$, the partial time derivative operator $\dot{(\bullet)}$, the displacement vector $\mathbf{u}$, the ESHELBY stress tensor $\boldsymbol{\Sigma}$, the body forces $\boldsymbol{b}_0$, the density ρ and the free HELMHOLTZ energy density ψ_{lin}.

NUMERICAL EXAMPLES

The first numerical example evaluates an experiment on a thin PMMA specimen. In a special setup, the crack propagation velocity is recorded and can be compared to simulated results.

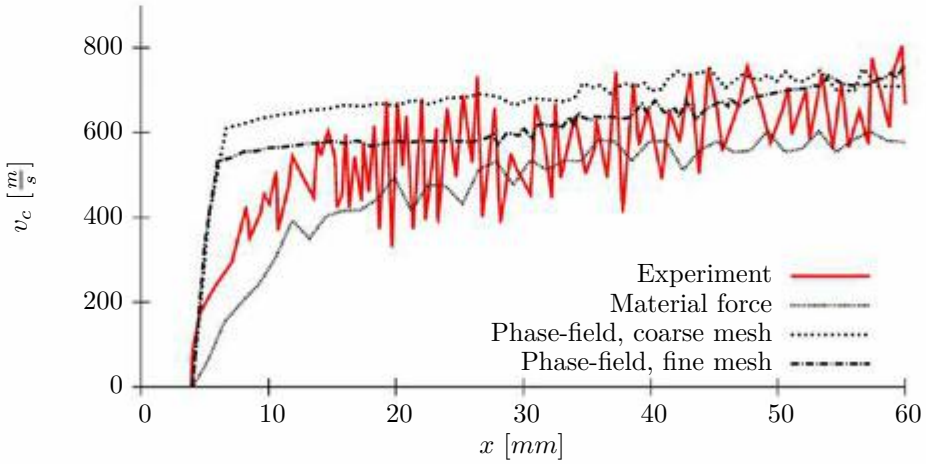

Figure 2: Velocity of crack propagation with respect to the crack length

The second simulation is a purely numerical crack branching benchmark in 2D. A specimen with a pre-existing crack under two-axial transient loading is studied with both approaches.

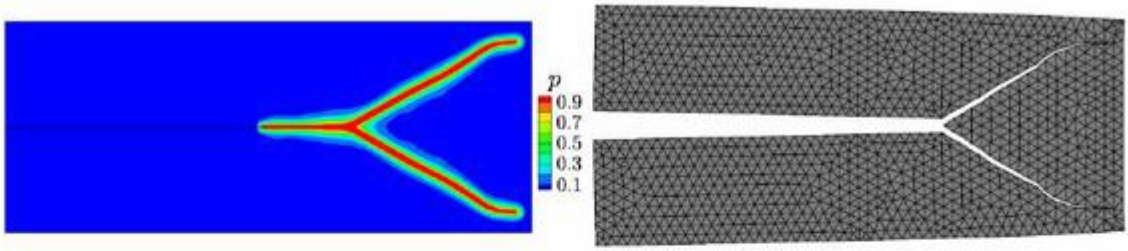

(a) Phase-field (b) Material force

Figure 3: Final path of the crack

CONCLUSION

The presented simulations investigate and compare in depth the characteristics of both approaches in respect of a realistic approximation of dynamic fracture.

References

[1] Ambati, M., Gerasimov, T., Lorenzis, L.D.: A review on phase-field models of brittle fracture and a new fast hybrid formulation. Computational Mechanics **55**, 383–405 (2015)

[2] Francfort, G.A., Marigo, J.J.: Revisiting brittle fracture as an energy minimization problem. Journal of the Mechanics and Physics of Solids **46**, 1319–1342 (1998)

[3] Griffith, A.A.: The phenomena of rupture and flow in solids. Philosophical Transactions of the Royal Society of London. Series A **221**, 163–198 (1921)

[4] Maugin, G.A.: Configurational Forces: Thermomechanics, Physics, Mathematics, and Numerics. CRC Press, Boca Raton (2010)

FRAGMENTATION AS AN AGGREGATION PROCESS

Nicolas Vandenberghe*[1], Alexandre Vledouts[1], and Emmanuel Villermaux[1]

[1]*Aix-Marseille Université, CNRS, Centrale Marseille, IRPHE, 13384 Marseille, France*

Summary The fragmentation of a ring in radial expansion is a benchmark experiment to test our understanding of solid fragmentation. We study a discrete version of it, using necklaces of cohesive spheres as an experimental model. After being communicated an initial radial impulse, the ring breaks and the spheres separate from each other. The attractive forces between the spheres drive an aggregation dynamics that proceed until a final state is reached. The time resolved observation of the fragment size distribution reveals that the process is self similar. This study combines experiments and modeling to offer a new approach to fragmentation dynamics when fracture energy is a relevant quantity and proposes the selection of the fragment size distribution as the results of the aggregation dynamics. The role of inhomogeneities (i.e. material flaws) is also addressed as well as the energetics of the process.

INTRODUCTION

When severely impacted a sample of a solid material breaks into fragment. Fragmentation is ubiquitous in natural processes such as the disruption of asteroids or meteorite impact cratering and in industrial processes ranging from the mining industry to crushing and grinding. Yet the complete description of the fragmentation of a 3-dimensional object remains a task of considerable difficulty. Simplifications of the geometry and material properties are mandatory to make progress in the field. The radial expansion of a ring has been proposed by Mott as a an experimental paradigm to study the fragmentation of solid materials [1, 2]. It offers a great simplification because the stress field is uniform (before breakage) and because the complexity associated with crack extension and branching is not present. Yet it reveals a rich dynamics.

We study the fragmentation of a necklace of N rigid spheres of mass m and diameter a linked together by attractive forces (magnetic or capillary), see figure 1. For spherical magnets the attractive force between two spheres separated by z (center-to-center distance) writes $F(z) = F(a)(a/z)^4$. The necklace is initially communicated a radial speed and the spheres separate from each other. The uniform extension is unstable and the spheres start to aggregate and to form fragments. Consequently, an aggregation dynamics proceed until the fragment size distribution is frozen.

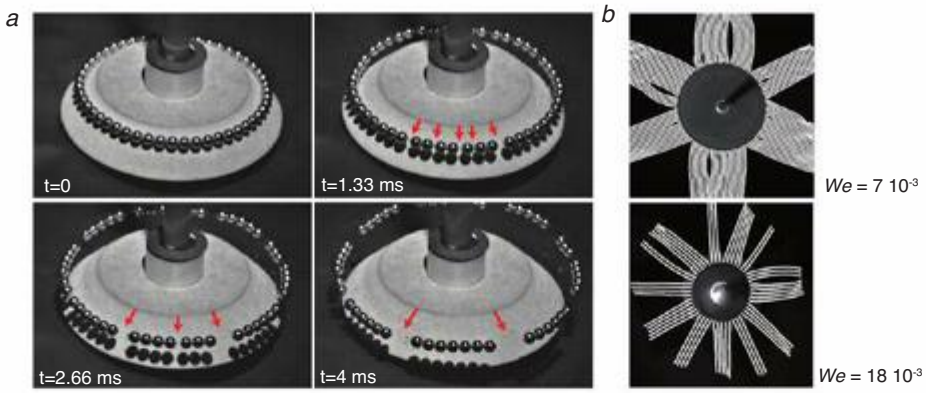

Figure 1: *a*. A necklace of spherical magnets of mass $m = 0.50$ g, diameter $a = 5$ mm with a contact force $F(a) = 4.6$ N stand on a cone which we let fall. When the cone hits the ground, each sphere is communicated a radial speed and the ring expands. The spheres separate from each other and start to aggregate, driven by the attractive magnetic force. *b*. The aggregation proceeds until the final mean fragment size n_∞ is reached. n_∞ increases for increasing Weber number.

The position of each sphere is extracted from movies of the experiment, and repeating the experiment, we obtain the fragment size distribution (Figure 2). At the beginning of the dynamics, the fragments are small and the distribution is narrow. As time goes, the mean fragment size increases and the distribution broadens. When plotted in units of the mean size $\langle n \rangle$ the fragment size distributions at successive times collapse indicating a self similar process.

*Corresponding author. Email: nicolas.vandenberghe@univ-amu.fr

RESULTS

The Weber number $We = 3mU^2/2aF(a)$ where U is the divergence speed related to the radial speed V through $U = 2\pi V/N$ measures the ratio between the initial kinetic energy and the cohesion energy. To gain insight into the dynamics we proceed as follows.

1. We consider that after initial rearrangements that occur concomitantly with the initial instability, the system is mixed and fragments interact by pair. The fate of two fragments of size p and q can be determined by Newton's equation for the distance between the two fragments. This yields an aggregation time $t_a(p,q)$ that depends on the initial divergence velocity $U(p,q)$ and the fragment sizes: the aggregation time increases with increasing fragment sizes.

2. The evolution of the fragment size distribution can be computed through Smoluchovski's model of aggregation [4] that describes the evolution of the fragment size distribution when aggregation results from random encounter of fragments. In the present case, the typical aggregation time between two fragments is $t_a(p,q)$ and the model can be solved with the assumption that aggregation occurs for small fragments (*i.e.* light fragments for which the aggregation time is shorter). It results in a self similar aggregation as observed in the experiments and the scaled measured p.d.f. $f(x = n/\langle n\rangle) = \mathcal{N}(n)\langle n\rangle^2/N$ where $\mathcal{N}(n)$ is the number of fragments of size n, is well approximated by a Gamma distribution [5]

$$f(x) = \frac{\nu^\nu}{\Gamma(\nu)} x^{\nu-1} \mathrm{e}^{-\nu x} \tag{1}$$

3. The aggregation time diverges as the fragments grow (and become more massive) and their divergence increases (because their number decreases). For two fragments of size n initially in contact ($z(0) = a$) and with a divergence velocity nU, conservation of energy yields $mn\dot{z}^2/4 - aF(a)(a/z)^3/3 = mn(nU)^2/4 - aF(a)/3$ and the final fragment size obtained for $z \to \infty$ and $\dot{z} \to 0$ is $n_\infty = (2/We)^{1/3}$ in agreement with experiments and the classical law proposed by Grady [3].

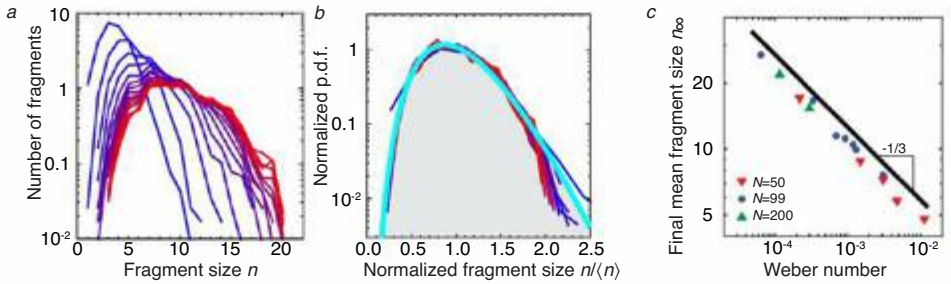

Figure 2: *a* Number of fragments $\mathcal{N}(n)$ of size n versus time (curves from left to right from $t = 2$ ms to 17 ms) at $We = 6.15 \times 10^{-4}$. At short times, the distribution is narrow and centerd on small sizes. As time increases, the mean fragment size increases and the fragment size distribution broadens. *b* The normalized probability density functions $f(x) =$ for the same times collapse, indicating a self similar process. The p.d.f. are well fitted by a gamma distribution of order $\nu = 8$. *c* The mean final fragment size agrees with Grady's law $n_\infty \sim We^{-1/3}$.

DISCUSSION

The present study addresses the mechanism by which the fragment size distribution builds up in the limit of energy-limited fragmentation (in Grady's terminology) for which the energy required to break the sample is not negligible. In this case the fragment size distribution is the result of an aggregation dynamics driven by the cohesive forces between the fragments. The fragment size distribution is independent of the distribution of flaws in the material because the Gamma distribution is attractive for the dynamics. The present model can be modified to account for material flaws for example by using a distribution of interaction forces [6], leading to a broadening of the fragment size distribution.

References

[1] Mott, N. F.: Fragmentation of shell cases. Proc. Royal Soc. London A 189, 300, 1947.
[2] Zhang, H., Ravi-Chandar, K: On the dynamics of necking and fragmentation I. . Int. J. Fracture 142, 183 (2007).
[3] Grady, D. E.: Local inertial effects in dynamic fragmentation. J. App. Phys. 53, 322 (1982).
[4] Smoluchovski, M.V.: Drei Vortrage über Diffusion, brownsche Bewegung und Koagulation von Kolloidteilchen. Z. Phys. 17, 557 (1916).
[5] Vledouts, A., Vandenberghe, N. Villermaux, E.: Fragmentation as an aggregation process. Proc. R. Soc. A 471, 20150678 (2015).
[6] Vledouts, A., Vandenberghe, N. Villermaux, E.: Fragmentation as an aggregation process: the role of defects. Proc. R. Soc. A submitted (2016).

MODELLING IMPACT DAMAGE AND BREAKAGE OF A PARTICLE BED USING SPH AND DEM

Lawrence Bbosa[1a)]
[1]*Centre for Minerals Research, Department of Chemical Engineering, University of Cape Town, South Africa*

Abstract This work aims to elucidate the impact breakage of a bed of particles in an environment similar to that found in comminution devices. Smoothed Particle Hydrodynamics (SPH) and the Discrete Element Method (DEM) are used to simulate the impact of rigid steel spheres on the particle bed. With SPH, continuum damage mechanics is used to simulate the extent of damage and (brittle) failure in the bed. For DEM, a Mohr-Coulomb law is applied to represent cohesive inter-particle forces and calculate the relevant failure criteria. The numerical simulations are conducted concurrently with laboratory experiments in which the stress and energy absorbed during the impact event is measured by a load cell. The rock progeny are also measured to assess the level of breakage. The SPH and DEM simulations are calibrated against experiment and subsequently demonstrated to be a valuable means of studying the stress distributions which initiate crack propagation and failure.

PROJECT SUMMARY

It is a well-known challenge currently facing the mining industry that current practices are not sustainable in the long term, largely due to increased constraints around energy requirements coupled with declining grades in ore bodies. Crushing and grinding of ore, or comminution, typically utilizes the majority of the supplied energy to processing plants and is often quoted[1] to be highly inefficient in its use. Fundamental research in the area of breakage is the most likely source from which existing comminution devices can be further optimized, or groundbreaking new technologies can be developed.

The impact breakage of ore bodies under confinement is a common size reduction mechanism in many comminution devices. Such devices are routinely characterized by aggressive internal environments which renders any meaningful measurement of particle interaction and fracture impractical if not impossible. Breakage characterization tests at the laboratory scale have thus been largely used as a means of studying the fundamental mechanisms of fracture[2]. A limitation of most experimental techniques is that they do not capture the micro-scale fracture behavior of the ore particles such that any notable trends can be exploited to improve traditional comminution devices.

In the last few decades, computational modelling has emerged as a valuable tool to glean new insights into the design and operation of the systems used in various comminution processes. Such simulations have been able to examine how the micro-scale response of different materials under stress leads to the creation and evolution of cracks and eventual fracture[3].

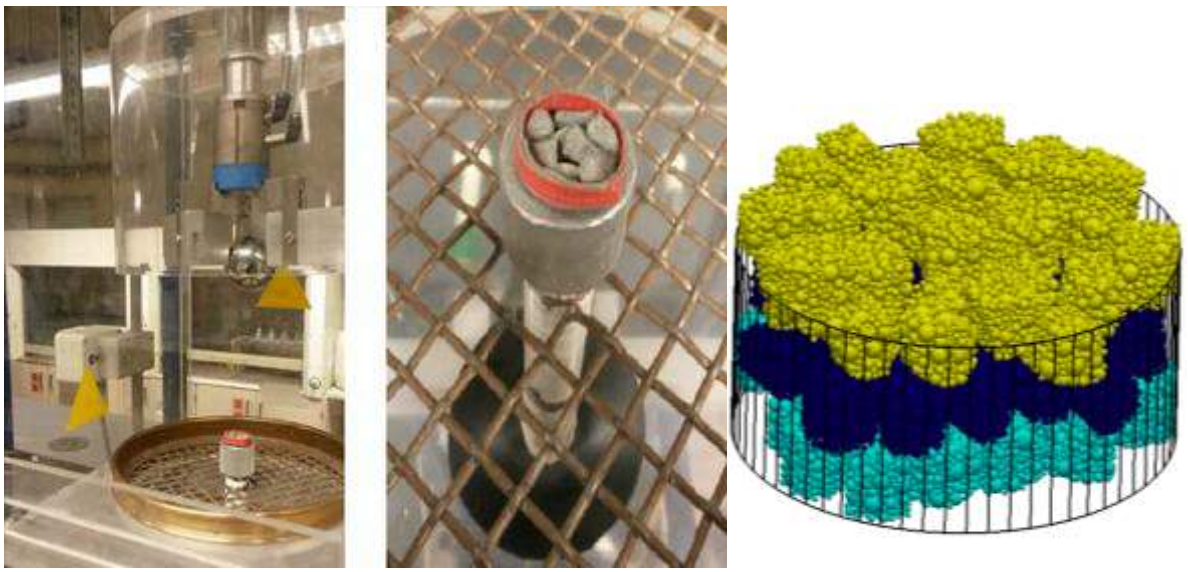

Figure 1: A picture of the SILC breakage apparatus (left), along with an example of a particle bed used for experiments (center) and a typical arrangement used for computational simulations (right)

[a)] Corresponding author. Email: lawrence.bbosa@uct.ac.za

In this paper, computational simulations of a typical bed breakage test are used to investigate the effect of steel ball diameter, drop height and bed depth on the strain energy absorbed and degree of crack propagation and failure. Experiments are conducted with a Short Impact Load Cell (SILC) and designed to represent an environment common to comminution devices. With the SILC, a steel ball of known mass is released by a pneumatic mechanism and falls vertically under gravity on a bed of particles from a fixed height. The device consists of a long steel rod on which the particle bed rests and is fitted with strain gauges to measure the load response, from which particle strength parameters and the amount of impact energy absorbed can be determined[4]. A homogenous basalt ore and UG2 platinum ore are used for the tests, and particles are constrained using rings of duct tape. A picture of the device and setup as described is given in Figure 1.

Simulations using both SPH and DEM are compared against SILC experiments. With either technique, ore particles are assumed to take simple polygonal shapes. For SPH simulations, a continuum damage model is used to predict the rock damage based on the local stress history and flaw distribution. For DEM simulations, each ore particle is modelled as an assembly of indivisible spherical particles with adjacent particles connected by cylindrical linear elastic beams. These cohesive bonds are broken when the inter-particle stress exceeds a specified limit.

Stress vs. Time plots generated from SILC experiments are compared against the numerical simulations which show good agreement. The key physical behavior observed from both computational techniques is then used to study the utilization of the impact energy in causing breakage. It is found that generally the energy absorbed by the particle bed is very low relative to the impact energy (less than 10%). The bulk of the available impact energy is dissipated as kinetic energy in the movement of particles rather than initiating crack propagation. The degree of breakage is found to increase with steel ball diameter, largely because the increased epicenter of the impact zone leads to a wider distribution of stress into the particle bed and thus greater propagation of micro-cracks. Increasing the impact energy by altering the drop height does not achieve as profound an effect, and it is notable that the relative energy absorbed tends to decrease at higher drop heights. The energy absorbed and degree of breakage are found to decrease with increasing bed depth. This is attributed to the increasing role played by the porosity of the bed as particle layers increase. A greater number of particle layers leads to the dissipation of the impact energy largely by rearranging of the particle bed rather than initiation and transmission of cracks through the bed.

References

[1] Powell, M., Govender, I., McBride, A. T.,: Applying DEM outputs to the unified comminution model. *Miner Eng*, 21 744-750, 2008

[2] Bbosa, L. S., Powell, M., & Cloete, T. J.: An investigation of impact breakage of rocks using the split Hopkinson pressure bar. *J. SAIMM 106*(4), 291-296, 2006

[3] Das, R., Cleary, P. W.,: Effect of rock shapes on brittle fracture using Smoothed Particle Hydrodynamics, *Theor. Appl. Fract. Mec.*, (53) 47-60, 2010 .

[4] Tavares, L. M., King, R. P.,: Measurement of the load-deformation response from impact breakage of particles. *Int. J. Miner. Process*. 74S S267-S277, 2004

STRENGTH MEASUREMENT OF FLUORIDE FIBER BY BENDING AND TENSILE TEST

Rochdi El Abdi [1a)], Alexandru Dumitrache Rujinski [2] and Marcel Poulain [3]
[1] *Université de Rennes1, IPR, Département Mécanique &Verres–CS74205-35042 Rennes, France*
[2] *Universitatea Politehnica din Bucuresti, Splaiul Independentei, 313, IMST, 060042 Bucarest, Romania*
[3] *Université de Rennes1, Lab. Matériaux Photoniques – CS 74205 - 35042 Rennes, France*

Summary Mechanical dynamic tests were performed on fluoride glass fibers and silica optical fibers to examine the mechanical strength on ambient atmosphere and after aging in a vacuum desiccator with silica gel used as the desiccant. The tensile tests showed that fluoride fiber elongation decreased with increasing velocity and the strength of silica fiber is nine times greater than that of fluoride fiber and eight times greater in the case of bending tests. Aging in a desiccator decreases the residual water content and improves the fluoride fiber strength.

INTRODUCTION

Fluoride glass fibers were first intensively developed for long distance telecommunication applications due to their ultra-low theoretical optical loss (0.001 dB/km). The specific material used for this research was a fluorozirconate glass, which is a subset of the Heavy Metal Fluoride Glasses family known as ZBLAN (ZrF_4, BaF_2, LaF_3, AlF_3, NaF). Such fibers can be doped with a number of rare earth ions for application in fiber lasers and amplifiers.

The main problem with this fiber is its poor mechanical strength. Degradation may be due to attack by atmospheric moisture or stresses and cracks introduced into the fiber during drawing and spooling or to damage which was not removed after drilling. The intrinsic strength of a core fiber, its real strength, depends on minor flaws. Considerable effort was made to remove scratches.

Many studies were undertaken concerning optical and chemical properties of fluoride fibers, but very few studies have been carried out on their mechanical behavior when subjected to bending or tensile tests due to their poor mechanical strength.

In this work, tensile and two point bending tests were performed on fluoride and silica fibers for different displacement velocities. Some fibers were aged in a desiccator before undergoing mechanical tests.

OPTICAL FIBERS USED

The multimode fluoride fiber of compositions (mol%) $53ZrF_4$-$20BaF_2$-$4LaF_3$-$3AlF_3$-20NaF (Fig.1a) has an operating wavelength between 0.3 μm and 4.3 μm. The combined coating diameter is 220 μm with a diameter clad of 150 μm and a core diameter of 100 μm. The operating temperature is from -180°C to 150°C. This fiber has a numerical aperture of 0.2 (NA value). Attenuation was ≤ 0.1 dB/m [3.4 - 3.6(μm].

The used multimode silica optical fiber has two acrylate coatings (primary and outer coatings) (Fig. 1b). This fiber has a numerical aperture of 0.2 (NA value) with an operating wavelength of 850/1300 nm. The combined coating diameter is 245 μm, the silica core has a diameter of 50 μm and the clad diameter is 125(μm.

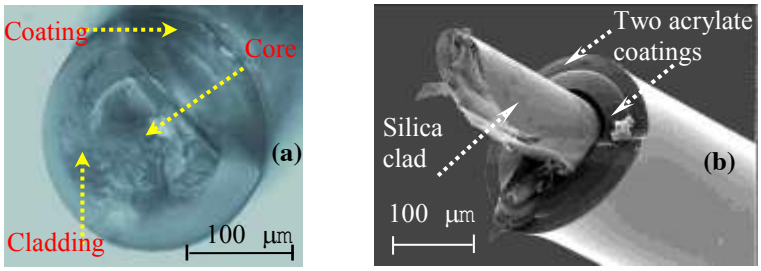

Fig. 1. Used optical fibers: a) Fluoride fiber; b) Silica fiber

TEST BENCHES USED

A two points bending bench is made up of a displacement plate which is mounted on an aluminium plate. A first thrust block is movable and mounted on the displacement plate, while the second thrust block is fixed on a force sensor. The optical fiber is positioned between the two thrust blocks in such a way that it forms a "U". To avoid slipping, the fiber is positioned in the grooves of the thrust blocks.

A dynamic tensile test consists of subjecting fibers to a deformation under a constant velocity until rupture. The fiber is

[a)] Corresponding author. Email: relabdi@univ-rennes1.fr

rolled three times around two pulleys; the lower pulley is fixed and the upper pulley is movable with different velocities. During the test, the tensile load was measured using a dynamometric cell (load sensor) while the fiber deformation was deduced from the displacement between the fixed lower pulley and the mobile higher pulley.

RESULTS and DISCUSSION

Bending tests- Figure 2a shows the change of the failure load between the plates when the fluoride fiber was subjected to the two point bending test for different faceplate velocities.

It is noted that the failure load between the two plates decreases according to their velocity. Indeed, the fluoride fiber is very brittle and breaks for large curvature radii when placed between the two plates.

When placing the fluoride fibers in the desiccator for one week in order to maintain them in a dry atmosphere, some residual water was removed and this leads to partial micro-crack closures. This allows the fiber to bend more and a smaller failure distance between the plates was obtained. Thus, the failure fiber force for the desiccated fiber was a little higher than that of an 'as-received fiber' (Fig. 2a). On the other hand, silica fiber can endure smaller curvature radii than the fluoride fiber and therefore will break for loads which are 8 times higher (Fig. 2b).

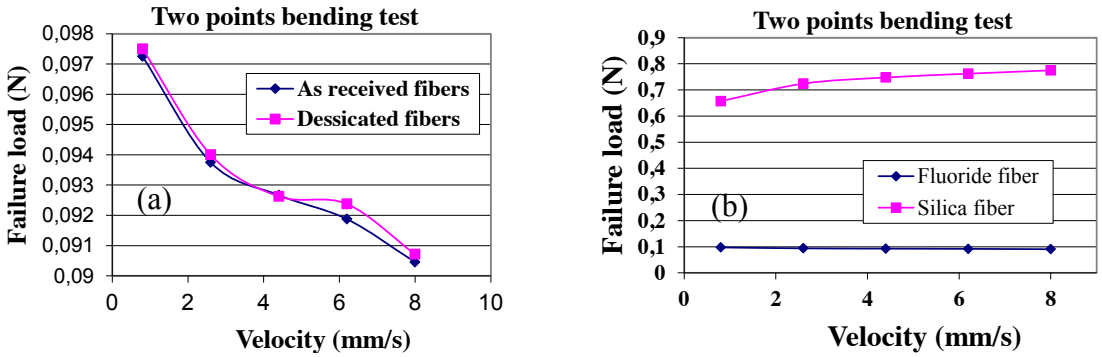

Fig. 2. Failure load for a): As received and dessicated fluoride fibers; b): Silica and fluoride fibers for different velocities

Tensile tests- Figure 3 compares the failure forces for silica and fluoride fibers submitted to tensile tests. The failure strength of silica fibers was higher than that of fluoride fibers, even if the cladding diameter of fluoride fiber was greater than that of the silica fiber. The failure load for the silica fiber was, on average, 9 times higher than that of the fluoride fiber (Fig. 3): Young's modulus of silica fibers was higher than that of the fluoride fibers.

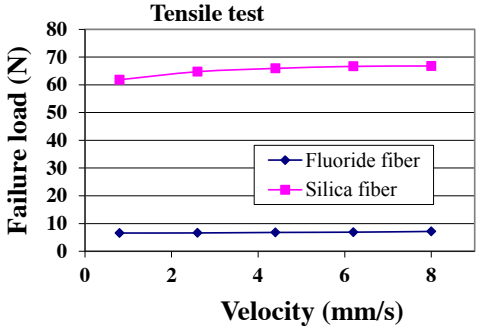

Fig. 3. Failure load for silica and fluoride fibers for different velocities during tensile test

CONCLUSION

The difficulty for testing fluoride fibers was due to their fragility and their cost. Indeed, the fluoride fibers are more expensive than silica fibers and one must take a lot of care to minimize sample losses during testing. Furthermore, their fragility involves frequent breaking before the beginning of bending or tensile tests. Although the pulley diameters for the traction bench were quite large, the winding of fluoride fiber around the pulley must be done slowly to avoid handling or compression of another portion of the fiber already wound around the pulley. In addition, fluoride fibers have many intrinsic defects that are not uniformly distributed. The number of testing experiments was quite high because many fiber failures occur around the pulley and not in the middle of the part of fiber between the two pulleys during the tensile test. The silica fiber, which is more flexible than the fluoride fiber, was easier to test. Finally, the tensile tests showed that fluoride fiber elongation decreased with increasing velocity and their failure loads remained much lower than that of silica optical fibers.

FRACTURE TOUGHNESS ANALYSIS BY THE MATERIAL CONFIGURATIONAL FORCES IN TRANSFORMABLE MATERIALS

Junling Hou[1], Qun Li[1)], Hong Zuo[1a)]
[1]*State Key Laboratory for Strength and Vibration of Mechanical Structures, School of Aerospace, Xi'an Jiaotong University, Xi'an, China*

Summary In the present paper, the crack-tip shielding from the residual strains which develop following transformable particles dispersed near the crack tip is estimated from the reduction of the crack tip *J*-integral associated with the material configurational forces. Numerical results show that the crack-tip shielding is dependent of the location and size of particles, and the radio of shear strain transformation and dilatant transformation. Moreover, the crack deflection angle in inhomogenous materials induced by the phase transformation can be claimed that the crack initiates along the direction which the potential energy release rate possesses a stationary (maximum) value in terms of the crack tip J_k-integral. The results show a significant non-symmetric stress distribution locally at the crack tip, causing the crack to deflect.

INTRODUCTION

It has been discovered that a second phase constituent which undergoes a stress-induced phase transformation could be used to toughen composites[1]. The contribution of phase transformation on the fracture toughness can be demonstrated by the material configurational forces associated with the J_k-integral. Recently, the configurational forces emerge as a strong tool to deal with crack problems associated with damage evolution, or phase transformation. The significant of the material forces is indeed to deal with material inhomogeneity such as dislocations, cracks, inclusions, cavities and non-homogeneities, which, under suitable conditions, can move or be displaced within the deformable material body in which they find themselves. In material space, the material forces are of specific interest as they are valuable to assess the failure of structures in the present of defects. The material configurational theory seems to be an effective and reliable technique to provide an accurate result for fracture toughness analysis induced by the transformable particles.

THE J_K-INTEGRAL ELUCIDATED BY THE CONFIGURATIONAL FORCES

The material configurational stress tensor b_{ji} is introduced[2],

$$b_{j\,i} = \quad \delta_{\ j\,\overline{i}}\,\sigma \quad u \tag{1}$$

where, W denotes the strain energy density of the elasticity system; δ_{ji} is the Kronecker delta; σ_{jk} is the Cauchy stress tensor; $u_{k,i}$ are the first derivatives of the displacement. The corresponding material configurational forces g_i, which originates from the material inhomogeneity,

$$g_i = -\ \partial W / \partial\ _i)_{\text{expl}} \tag{2}$$

$(\partial W/\partial x_i)_{\text{expl}}$ denotes the explicit dependence of W on x_i, and the equations of equilibrium are $b_{ji,j} + g_i = 0$.

Since the well-known J_k-integral integrating over a path enclosing the crack tip can be defined by the material configuration theory,

$$= \ _1 = \bigcirc_{\Gamma} b_{j1} n\ ds = \bigcirc_{\Gamma} \left(W n_1 - \sigma\ \ u\ \ n\ \ \right) ds, \tag{3}$$

$$J_2 = \bigcirc_{\Gamma} b\ _2 n\ ds = \bigcirc_{\Gamma} \left(W n_2 - \sigma\ \ u\ \ n\ \ \right) ds \tag{4}$$

see Fig. 1, where Γ is an integral contour beginning at the lower crack surface and ending at the upper surface and n_j refers to the outside normal of the contour Γ. A new parameter named J_{ktip}-integral, computed around the crack tip along a vanishing small contour Γ_ε as shown in Fig.1,

$$J_{ktip} = \lim_{\varepsilon \to 0} \int_{\Gamma_\varepsilon} b\ n\ ds = \int_{\Gamma} b\ n\ ds - \int_{A} b\ n\ dA = \boxed{\int_{\Gamma} \left(b\ n\ \ \right) ds} - \boxed{\int_{A} g_k dA}\ \ J_{k\infty} - G_k \tag{5}$$

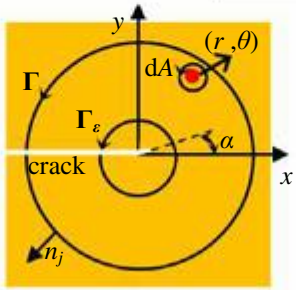

Fig.1. The geometric model of transformable materials

[a)]Corresponding author. Email: zuohong@mail.xjtu.edu.cn.

where $J_{k\infty}$ denotes the remote J_k-integral in terms of the remote stress intensity factors as follows, dA is the differential element of inhomogeneity and G_k (k=1, 2) denotes the total component of configurational forces given by integration of increment value over the area of transformation zone A.

Moreover, claiming that if the crack has advanced under an angle α with respect to its plane as depicted in Fig. 1, the direction of crack deflection can be claimed that the crack initiates in the direction along which the potential energy release G(α) possesses a stationary (maximum) value, i.e., the crack deflection angle can be formulated as,

$$\alpha = \arctan\left(\frac{G_y + J_{2\infty}}{G_x + J_{1\infty}}\right) \tag{6}$$

NUMERICAL ANALYSIS RESULTS

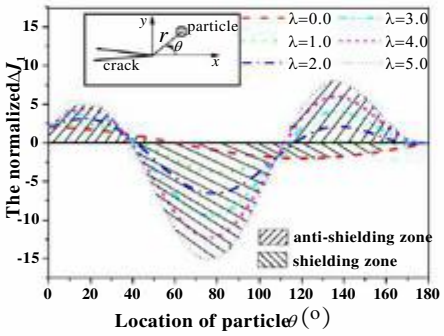

Fig.2. The variable tendency of ΔJ_1 against the location angle of one individual particle near the crack tip influenced by transformation strain.

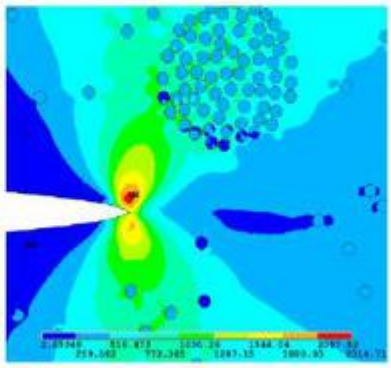

Fig.3. Non-symmetric stress contour with respect to the crack surface by a cluster of particles in non-homogeneous composites.

Considering the phase transformation which involves a dilatation strain e^T and a shear strain e_{12}^T, then the crack-tip J_1-integral disturbed by one transformable particle can be calculated by

$$G_x = \Delta J_1 = \pi R^2 e^T \cdot \frac{r^{-\frac{3}{2}}}{2\sqrt{2\pi}} \left\{ \left[2\cos\frac{3\theta}{2} + \lambda \quad \theta \quad \frac{5\theta}{2} \right] K_I - \left[2\sin\frac{3\theta}{2} + \lambda \left(\quad \theta \quad \frac{5\theta}{2} - 2\cos\frac{3\theta}{2} \right) \right] K_{II} \right\} \tag{7}$$

The tendency of ΔJ_1 normalized by $r^{-3/2} e^T \sqrt{\pi} R^2 K_I$ against the variable location of particle is plotted in Fig.2, where the ratio of e_{12}^T / e^T changes from 0 to 5.0 and the specimen is subjected to the pure Mode I loading. It can be concluded from Eq. (7) that the crack-tip shielding effect will be only dependence of the location angle of particle with respect to the crack face, and the ratio between the transformation shear and dilation strain. It is shown from Fig.2 that there are some critical angles of crack-tip shielding or anti-shielding. For instance, it can be illustrated as the particle has a shielding effect on the fracture toughness when the location angle of particle in the extent of (40°, 110°) for λ=4.0 in Fig.2 accounting for one zirconia (ZrO_2) particle with a shear strain of about 16% and a dilatation of 4% dispersed in composites[3].

The phenomenon of crack deflection due to the transformation of dispersed particles can also be predicted and explained by the non-symmetrical stress distribution around the crack tip. By FEM method, a strong non-symmetric stress distribution with respect to the crack surface is found in Fig.3 as the transformable particle around the crack tip is non-symmetric with respect to the crack plane by a cluster of particles in non-homogeneous composites. The present study is in the view of energy to get some indication of how crack deflects as the crack may find a path which is energetically more favorable.

CONCLUSIONS

The theoretical framework given in this paper could provide a useful tool to deal with problems associated with the fracture toughening and crack deflection occurred in the transformable material. The most important conclusion from the analysis is that the crack-tip shielding effect is mainly determined by the location and size of the particle, and the ratio between the shear and dilatation transformation strain components. A finite element approach is proposed to solve the problem of multiple particles with non-uniform distribution embedded in composites.

References

[1] Hu, J. Q., Zhang, Y., et al.: Phase transformation behaviors of TiNi fibers embedded in an aluminum matrix. J. Alloy. Compd. **589**, 491-497 (2014)

[2] Budiansky, B., Rice, J.R.: Conservation laws and energy release rates. J. Appl. Mech. **40**, 201-203 (1973)

[3] Budiansky, B., Hutchinson, J.W., Lambropoulos, J.C.: Continuum theory of dilatant transformation toughening in ceramics. Int. J. Solids Struc. **19**, 337-355 (1983)

IMPACTS OF RESIDUAL STRESS ON J-INTEGRAL FOR CLAMPED SE(T) SPECIMEN

Yifan Huang [1a)] & Wenxing Zhou [1]
[1]*Civil and Environmental Engineering, University of Western Ontario, London, Ontario, Canada*

Summary Three-dimensional (3D) finite element analyses (FEA) are performed on clamped single-edge notched tension (SE(T)) specimens to investigate the impact of residual stresses on the average *J*-integral (*J*) evaluated over the crack front. The residual stresses are introduced by two mechanical pre-loadings including tension and compression. The average *J*-integral corresponding to the specimens containing residual stresses are evaluated and compared with those corresponding to residual stress-free specimens.

INTRODUCTION

As a key input to the structural integrity assessment of metallic structures such as pressure vessels and energy pipelines, the fracture toughness resistance curve, e.g. the *J*-integral resistance (*J*-*R*) curve, is typically obtained from the single-edge bend (SE(B)) or compact tension (C(T)) specimen as standardized in ASTM E1820-13 [1], BS7448-4 [2]. Recently, the use of the shallow-cracked single-edge (notched) tension (SE(T) or SENT) specimen to determine the *J*-*R* curve has gained significant research interests [e.g. 3, 4] in the energy pipeline industry largely as a result of the development of the strain-based design and assessment methodologies. Figure 1(a) schematically depicts the configuration of a typical SE(T) specimen including the width (*W*), thickness (*B*), crack length (*a*) and the daylight distance (distance between the clamped surfaces, *H*) of the specimen. The fabrication and construction processes of pipeline inevitably introduce residual stresses [5]. It is generally acknoledged the presence of residual stresses directly influences the evaluation of the *J* integral using SE(B) specimens [5]. The present study focuses on this topic with respect to the clamped SE(T) specimen.

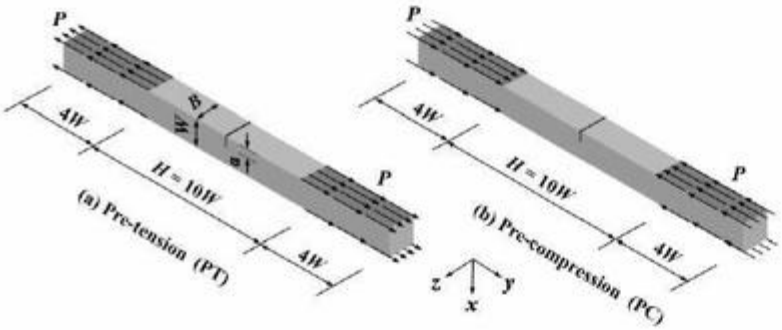

Figure 1. Schematics of SE(T) specimen and pre-loading techniques

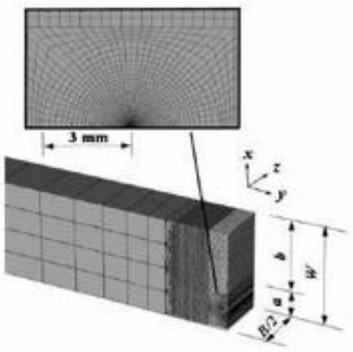

Figure 2. Configuration of a typical FE model

FINITE ELEMENT ANALYSES

Three-dimensional (3D) finite element analyses (FEA) are performed on the SE(T) specimen with W = 20 mm, H/W = 10, a/W = 0.2 and B/W = 1. Because of symmetry, only one quarter of the specimen with appropriate constraints imposed on the remaining ligament is modelled. A typical FE model is schematically shown in Fig. 2. Both specimens with and without residual stresses are analyzed. To generate the near-tip residual stresses, pre-loadings, e.g. pre-tension (PT) and pre-compression (PC) as shown in Figs. (1a) and (1b), are applied to the specimen prior to the primary tension loading, whereas the primary loading is directly applied to the residual stress-free specimens. The commercial software ABAQUS 6.13 [6] is employed to carry out the FEA. The 8-node 3D hexahedral elements with reduced integration (C3D8R) are used in the analysis. Stationary cracks are assumed. A sharp crack tip is incorporated and the surfaces of the hexahedral elements are collapsed to a line at the crack tip (see Fig. 2) to simulate the singularity condition. A spider-web mesh around the crack tip is established with 40 concentric semicircles (i.e. domains) surrounding the crack tip. The radii of the smallest and largest domain around the crack-tip are 0.01 and 3 mm, respectively. The model is equally divided into 20 layers over the half thickness (B/2). An elastic-plastic constitutive model based on the incremental theory of plasticity as well as the small-strain formulation [6] is adopted in FEA. The true stress (σ) and true strain (ε) relationship of the materials is characterized by the following equation:

$$\frac{\sigma}{\sigma_0} = \begin{cases} \frac{\sigma}{\sigma_{YS}} & , \varepsilon \le \varepsilon_0 \\ \left(\frac{\sigma}{\sigma_{YS}}\right)^n & , \varepsilon > \varepsilon_0 \end{cases} \qquad (1)$$

[a)] Corresponding author. Email: yhuan95@uwo.ca.

where σ_{YS} is the yield strength; $\varepsilon_0 = \sigma_{YS}/E$ with E denoting elastic modulus, and n is the strain hardening exponent. The loading level is cherecterized by the reference load ($P_Y = B(W - a)(\sigma_{YS} + \sigma_{UTS})/2$) where σ_{UTS} is the ultimate tensile strength. In the present study, σ_{YS}, σ_{UTS}, E, Poisson's ratio and n are assumed to be 510 MPa, 615 MPa, 207 GPa, 0.3 and 13 respectively. The load is applied based on the displacement control condition. The load P is calculated as the total reactions of the nodes on the clamped surface. For PT and PC, three levels of pre-loadings corresponding to $P/P_Y = 0.35$, 0.5 and 0.8 are defined and denoted as (I), (II) and (III), respectively. The primary loading in the FEA is identical to PT. The final applied displacement corresponding to $P/P_Y = 1.0 - 1.3$ is reached in each simulation. At each loading step, the values of J in each layer along the thickness direction are calculated using the domain integral method [6] corresponding to the 40th domain. Practical path-independence of the weighted average J value over the entire crack front is observed.

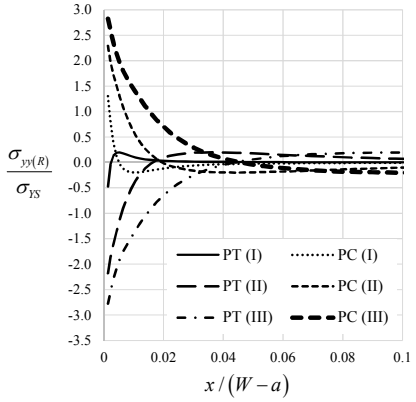

Figure 3. Distribution of $\sigma_{yy(R)}/\sigma_{YS}$ ahead of crack tip at specimen mid-thickness

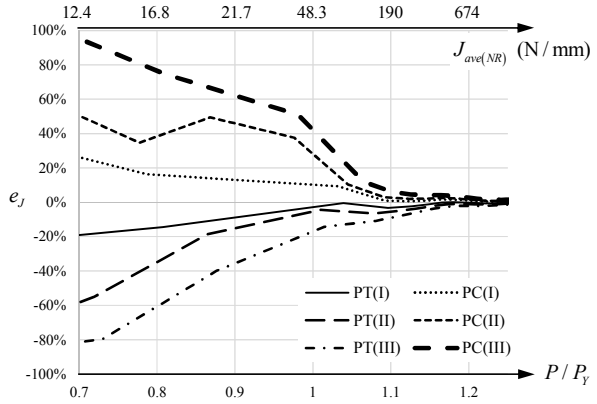

Figure 4. Variation of e_J with P/P_Y and $J_{ave(NR)}$

RESULTS AND DISCUSSIONS

Figure 3 shows the line distribution of the opening residual stress, $\sigma_{yy(R)}$ (generalized by σ_{YS}), within $0 \le x/(W - a) \le 0.1$ at the specimen mid thickness. According to the figure, PT generally leads to compressive $\sigma_{yy(R)}$ at the crack tip whereas PC yields tensile near-tip $\sigma_{yy(R)}$. The magnitude of the near-tip $\sigma_{yy(R)}$ increase as the level of the pre-loading increases. At each level of the primary loading characterized by P/P_Y, the difference between the average J obtained from a specimen containing residual stress (J_{ave}) and the average J ($J_{ave(NR)}$) obtained from the corresponding residual stress-free specimen is defined as $e_J = (J_{ave} - J_{ave(NR)})/J_{ave(NR)}$. Figure 4 shows e_J values plotted against P/P_Y for specimens with different residual stress states. Loading levels in terms of $J_{ave(NR)}$ are also indicated in the figure. The figure suggests that e_J depends strongly on P/P_Y. The absolute value of e_J generally decreases as P/P_Y increases. e_J is sensitive to the the near-tip $\sigma_{yy(R)}$ only when $P/P_Y \le 1.1$. It is observed that tensile near-tip $\sigma_{yy(R)}$ leads to positive e_J and vice versa. $|e_J|$ generally increases as near-tip $|\sigma_{yy(R)}|$ increases. e_J is approaching zero and is insensitive to the near-tip $\sigma_{yy(R)}$ for $P/P_Y > 1.1$.

CONCLUSIONS

Three-dimensional finite element analyses are performed to simulate pre-tension and pre-compression. PT and PC generally produces compressive and tensile near-tip $\sigma_{yy(R)}$, respectively. The magnitude of the near-tip $\sigma_{yy(R)}$ increase as the level of the pre-loading increases. A parameter, e_J, is evaluated to quantify the residual stress impacts on the average J. It is found that e_J depends strongly on P/P_Y. e_J is sensitive to the near-tip $\sigma_{yy(R)}$ for $P/P_Y \le 1.1$ and shows independence of $\sigma_{yy(R)}$ for $P/P_Y > 1.1$.

References

[1] ASTM: ASTM E1820-15: Standard Test Method for Measurement of Fracture Toughness. ASTM International. West Conshohocken, USA 2015.

[2] BSI: BS7448-4: Method for Determination of Fracture Resistance Curves and Initiation Values for Stable Crack Extension in Metallic Materials, British Standards Institution. London, UK 1997

[3] Huang Y., and Zhou W.: Investigation of Plastic Eta Factors for Clamped SE(T) Specimens Based on Three-dimensional Finite Element Analyses. *Eng Fract Mech* **132**:120-135, 2014.

[4] Huang Y., and Zhou W.: J-CTOD Relationship for Clamped SE(T) Specimens Based on Three-dimensional Finite Element Analyses. *Eng Fract Mech* **131**:643-655, 2014.

[5] Zerbst U., Ainsworth R.A., Beier H.T., Pisarski H., Zhang Z.L., Nikbin K., Nitschke-Pagel T., Münstermann S., Kucharczyk P., Klingbeil D.: Review on Fracture and Crack Propagation in Weldments–A Fracture Mechanics Perspective. *Eng Fract Mech* **132**:200-276, 2014.

[6] Dassault Systémes Simulia Corporation: ABAQUS/Standard Version 6.12-2.: Analysis User's manual. USA 2013

A MICROMECHANICAL DAMAGE MODEL FOR SOLDER JOINTS WITH AN INTERMETALLIC COMPOUND LAYER USING THE EQUIVALENT INCLUSION METHOD

Yuexing Wang[1], Yao Yao[1a)], Leon M. Keer[2a)]
[1]*School of Mechanics, Civil Engineering and Architecture, Northwestern Polytechnical University, Xi'an 710072, People's Republic of China*
[2]*Department of Civil Engineering, Northwestern University, 2145 Sheridan Rd., Evanston, IL 60208, USA*

Summary Intermetallic compound formation is critical to the reliability of microelectronic interconnections, especially for flip chip solder joints. It is well known that the presence of an intermetallic compound layer will significantly affect the mechanical behavior of solder joints due to its brittleness, while the solder joints generally exhibit ductile behavior. On the other hand, the thermal expansion coefficients of the intermetallic compound and solder materials are different. In this research, a micromechanical damage model is developed to study the solder joints combined with intermetallic compound layers based on the equivalent inclusion method. Taking the intermetallic compound layer as an inclusion and the solder joints as the matrix, the relationship between these two portions can be obtained by treating the intermetallic compound in this manner. The plastic strain, misfit strain and thermal strain can be determined and are included in the developed model, as eigenstrains.

INTRODUCTION

Solder joint integrity is recognized as a key issue in the reliability of electronic devices. In the past decades, SnAgCu eutectic based solders are replacing SnPb eutectic solders in the electronics industry. Although the Pb-free solder is usually regarded as having a higher melting temperature compared with traditional Pb-Sn eutectic solder, solder joints were generally operated at a high homologous temperature, and exhibit complex failure mechanism under coupled loading. Previously, the prevalent failure mode in a solder joint was the ductile thermo-mechanical fracture of solder material due to repeated thermal cycling. In addition to this mode of failure, the solder joints were also found to fail by brittle fracture near the solder-intermetallic interface. In this paper, we focus on fracture mechanics feature of the interface between the solder joint and the intermetallic. A micromechanical damage model is developed to analyze the failure evolution caused by joule heating associated with micro-damages. The disturbed stress field caused by the different coefficients of thermal expansion between the solder joint and intermetallic is investigated. An analytical enhancement of interface crack-tip intensity factor is proposed considering that voids exist in the intermetallic layer.

THE DISTURBED STRESS FIELD CAUSED BY THE JOULE HEATING

It is well known that a different thermal expansion coefficient between the solder joint and intermetallic is one of the main reasons for interface shear failure. In the current work, we assume the intermetallic as one inclusion in the half-space and define the thermal strain as the eigenstrain (stress free transformation strains) based on the Eshelby theory [1]; the disturbance of the strain field can be expressed as:

$$\varepsilon_{ij} = S_{ijkl}\varepsilon^{*}_{ij} \tag{1}$$

where ε_{ij} is the disturbed strain field; ε^{*}_{ij} is eigenstrain; S is the Eshelby tensor. The main problem is to solve the Eshelby tensor for an arbitrary inclusion in the half space. It is noted that the final formulation for the solution is given in a complicated form and the analytical solution is difficult to obtain. The Fast Fourier Transform (FFT) algorithms [2] are adopted to obtain a numerical result, which enables efficient and accurate computation.

ENHANCEMENT OF INTERFACE CRACK-TIP STRESS INTENSITY FACTOR CAUSED BY THE VOIDS AROUND THE CRACK TIP

In this part, the interaction between the interface crack and inclusion around the crack tip is studied. Many experiments have shown that intermetallic layer is not stable under high current density. The height will continue to grow and the voids or other inclusions will initiate, which will decrease the fracture strength to some extent. Based on the result of part1 and transformation toughing theory [3] and Eshelby equivalent inclusion method [1], an

a)Corresponding author. Email: yaoy@nwpu.edu.cn; l-keer@northwestern.edu

analytical description for the crack tip stress intensity factor increment under the effect of the voids around is given. The final analytic result for the crack tip stress intensity factor is expressed as follows:

$$\mathrm{dk}^{\mathrm{tip}} = \frac{1}{16\sqrt{2\pi}} \frac{E_m}{1-\nu^2} r^{-3/2} - e_{11}^T (5\sin\frac{3\theta}{2} + 3\sin\frac{7\theta}{2}) + 2e_{12}^T (3\cos\frac{7\theta}{2} + \cos(\frac{3\theta}{2})) + 3e_{22}^T (\sin\frac{7\theta}{2} - \sin\frac{3\theta}{2}) dA \quad (2)$$

Based on the Eshelby equivalent inclusion approach and thermal strain induced by the joule heating in the intermetallics layer, the equivalent transformation strain e^T is given by:

$$e^T = [(C_i - C_m)S + C_m]^{-1}(C_m - C_i)(e^A + e^*) \quad (3)$$

where C_i and C_m are the elastic constants of the inclusion and matrix, respectively. For the void problem, $C_i = 0$. e^A is the elastic strain caused by the crack which can be obtained from the classic solution; e^* is the strain caused by the disturbance of the intermetallic layer which obtained by using FFT method. The complete solution will need a statistic algorithms such as Monte Carlo simulation, by which the quantity and distribution of the voids is taken into account. In the current work, one unit void in front of the crack tip is studied, the average $dK^{tip}=1.23$. For two voids $dK^{tip}=1.30$, which means that the void will give an enhancement of the stress strength factor and shows that the Intermatellic layer becomes easier to fracture. It shows that the developed model is able to predict intermetallic layer fracture with voids exist inducing by electromigraiton, compared with the experimental observations [4-7].

CONCLUSIONS

A micromechanical damage model is developed for solder joints with an intermetallic compound layer by using the equivalent inclusion method. The proposed analytical method could predict how the voids in the intermetallic affect the fracture toughening of the interface between intermetallic and solder joints. The fast Fourier transform method is utilized to solve effectively the nonlinear problem. Case studies are conducted to explore the effects of the modulus, yield strength and thickness of the intermetallic compound layer. Reasonable prediction is obtained compared with experimental observations.

References

[1] Eshelby J.D.: The determination of the elastic fields of an ellipsoidal inclusion and related problems. *Proc R Soc London*. 376-96. 1957

[2] Chen W., Zhou K., Keer L.M., Wang Q.: Modeling elasto-plastic indentation on layered materials using the equivalent inclusion method. *Int J Solids Struct*., 2841-2854. 2010

[3] Lambropoulos J.C.: Shear, Shape and orientation effects in transformation toughening in ceramics, *Int J Solids Struct*., 83/86. 1984

[4] Ren F., Nah J.W., Tu K.N., Xiong B., Xu L.: Electromigration induced ductile-to-brittle transition in lead-free solder joints. *Applied Physics Letters*. 141914. 2006

[5] Yao Y., Wang Y.X., Keer L.M., Fine M.E.: An analytical method to predict electromigration-induced finger-shaped void growth in SnAgCu solder interconnect, *Scripta Materialia*, v95, 2, 7-10, 2015

[6] Yao Y, Keer L.M., Fine M.E.: Modeling the Failure of Intermetallic/Solder Interfaces, *Intermetallics*, v18, I8, 1603-1611, 2010

[7] Yao Y., Keer L.M., Fine M.E.: Electromigration Effect on Pancake Type Void Propagation near the Interface of Bulk Solder and Intermetallic Compound, *J. Applied Physics*, 105, 063710, 2009

PLASTIC ZONE AROUND A MOVING CRACK TIP IN VISCOPLASTIC POLYMERS

Junjie Liu[1], Xiaoding Wei[1a)]
[1] *LTCS and Department of Mechanics and Engineering Science, Peking University, Beijing, China*

Summary The plastic zone around a mode I moving crack tip in viscoplastic polymers is studied. A dynamic photo-elastic experiment system is constructed to capture images during crack propagation. The plastic zone wake is observed by the optical microscope from the fractured samples. A dynamic plastic zone model considering the viscoplastic effect is established to estimate the plastic zone size. Compared with the rate-independent model, this model modifies the effect which overrates the plastic zone size in the rate-independent model and agrees with experimental results well. A systematic study on the plastic zone is performed according to our model, which shows that the crack velocity has an essential influence on the plastic zone.

INTRODUCTION

For most materials, fracture often initiates at small defects. Around these defects, high stress localization results in a plastic zone although a lot of polymers fracture in a brittle manner. Strain gradient is high and the damage accumulation takes place in this region[1]. A large number of microdefects are activated here and control the crack path and stability[2]. But it is difficult to analyze the deformation field and stress distribution around a moving crack tip. The viscoplasticity of polymers will be distinct under the dynamic conditions[3]. In the present work, we established a plastic zone model considering viscoplastic effect to calculate the instantaneous plastic zone size of a propagating crack.

METHOD

The material used in the present investigation is polycarbonate (PC), which is a typical viscoplastic amorphous polymer. The rate-dependent constitutive model of PC can be written as[4]

$$\sigma_s(\dot{\varepsilon}^p) = \sigma_0 \left[1 + A \sinh^{-1} \left(\frac{\dot{\varepsilon}^p}{\dot{\varepsilon}_0} \right)^q \right]$$

By fitting the dynamic tensile experimental results at strain rates vary from10^{-1} s^{-1} to 10^3 s^{-1}, the quasi-static yield stress σ_0 =46.01 MPa, the reference strain rate $\dot{\varepsilon}_0$=17.22s^{-1}, and two undetermined coefficients A=0.47 and q=0.18.

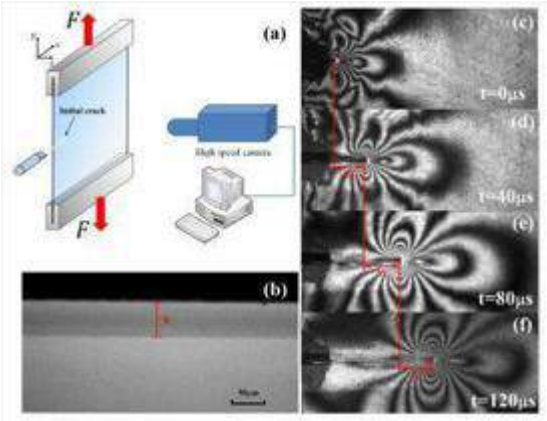

FIG. 1 (a) a schematic view of dynamic photo-elastic experiment. Samples are placed in a circularly polarized green laser field. (b) an image of a plastic wake obtained by the optical microscope from the fractured samples. (c)-(f) photo elastic images.

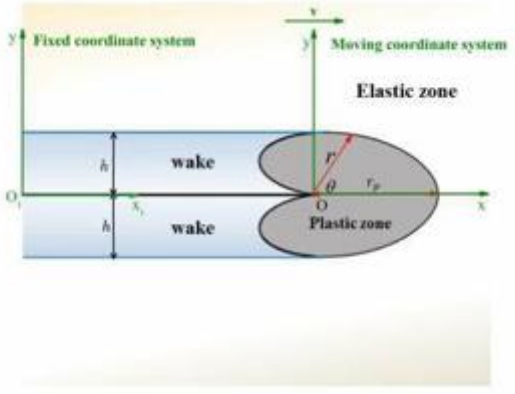

FIG. 2 Schematic view of the plastic zone and its wake. After the crack propagation, a plastic wake will be left. The wake width h is just a half of the plastic zone. r_p is the length of the plastic zone ahead of the crack tip.

Dynamic photo-elastic experiments(**FIG. 1**) were performed to capture the procedure of crack propagation. We obtained the average crack velocity v of the time interval 40 μs and the dynamic stress intensity factor K_I^D. The actual plastic wake(**FIG. 2**) was obtained by observing the fractured samples using an optical microscope. In order to establish a viscoplastic plastic zone model, we estimated the average strain rate in a moving polar coordinate(**FIG. 2**) at the crack tip as

a) Corresponding author. Email: xdwei@pku.edu.cn

$\dot{\varepsilon}^p = \varepsilon_c^p v/r_p$, in which r_p is the length of the plastic zone, ε_c^p is the failure plastic strain and v is the crack velocity. Under the small scale yielding conditions, according to the analysis of linear elastic dynamic fracture mechanics[5], we can get an equation

$$[\frac{K_I^D}{\sqrt{2\pi r D\ v}}]^2[(\eta_+ - \eta_-)^2 + \eta_+^2 + \eta_-^2 - \sigma_s^2\ r_p\ v\ =$$

to describe the plastic zone size, where η_+ and η_- are functions of crack velocity and coordinates.

RESULTS AND DISCUSSION

The predicted value of plastic wake according to our viscoplasitc plastic zone model and results from observation are shown in **FIG. 3**. Yield stress in rate-independent model is the value at the strain rate 0 s^{-1} and keeps in constant. Values of the rate-dependent model are much closer to the experimental results than that of the rate-independent model.

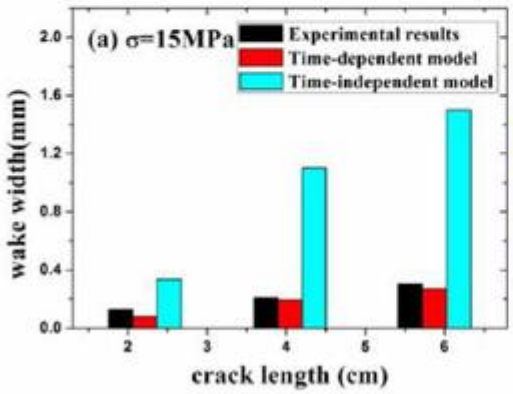

FIG. 3 Comparison between experimental results, time-dependent model and time-independent model.

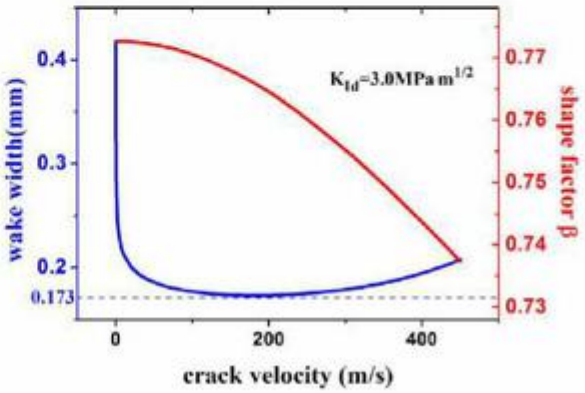

FIG. 4 Influence of the crack velocity on the plastic zone. A shape factor $\beta=r_p/h$ is defined to describe the plastic zone's shape.

A further discussion based on our model suggests that the plastic zone size of PC strongly relies on the viscoplastic property. This property becomes more distinct with the increase of the crack velocity, which presents a significant discrepancy of the plastic zone between rate-dependent model and rate-independent model. Furthermore, the shape and the size of the plastic zone are all functions of the crack velocity(**FIG. 4**). The plastic zone's profile changes with the increase of the crack velocity and the head of the plastic zone tends to be smooth. A minimum value of the plastic wake is found as increasing the crack velocity. It is a result of a competition between the mechanism which shrinks the plastic zone by improving the yield stress and another mechanism which expands the plastic zone by enhancing the crack tip fields.

CONCLUSIONS

In order to analyze the plastic zone around a moving crack tip for polymers, a viscoplastic plastic zone model is constructed to predict the plastic zone size, which is accurate sufficiently compared with the experiment results. The viscoplasticity effect is significant in polymers, which affects both the shape and the size of the plastic zone deeply. As the microdefects are activated at this point, the plastic zone plays an important part in understanding the fracture behavior and the energy dissipation of polymers. Predicting the plastic zone accurately is meaningful for studying the stability of a dynamic crack[6].

References

[1] Kujawski D, Ellyin F. On the size of plastic zone ahead of crack tip[J]. *Eng. Fract. Mech*, 1986, 25(2): 229-236.

[2] Ravi-Chandar K, Knauss W G. An experimental investigation into dynamic fracture: III. On steady-state crack propagation and crack branching[J]. *Int. J. Fract*, 1984, 26(2): 141-154.

[3] Ghorbel E. A viscoplastic constitutive model for polymeric materials[J]. Int. J. Plasticity, 2008, 24(11): 2032-2058.

[4] Chen Y T, Liu K X. Crack propagation in viscoplastic polymers: Heat generation in near-tip zone and viscoplastic cohesive model[J]. App. Phys. Lett., 2015, 106(6): 061908.

[5] Freund L B. Dynamic fracture mechanics[M]. Cambridge university press, 1998.

[6] Scheibert J, Guerra C, Célarié F, et al. Brittle-quasibrittle transition in dynamic fracture: An energetic signature[J]. Phys. Rev. Lett., 2010, 104(4): 045501.

NONLINEAR FINITE ELEMENT ANALYSIS OF ADOBE STRUCTURES STRENGTHENED BY SYNTHETIC NYLONS

Mohammadhossein Mamaghani[1], Hossein Ataei[1], Shobha K. Bhatia[1], Eric M. Lui[1]
[1]Department of Civil and Environmental Engineering, Syracuse University, Syracuse, NY, USA

Summary Adobe (or air-dried mud) brick is one of the earliest construction materials used around the world. It is still being used quite extensively in some developing countries. Adobe structures are relatively simple and often designed only for gravity loads. When subject to high shear force from settlement or earthquake effect, shear cracks often develop, thereby severely compromising the integrity of the structure. This paper presents several methodologies for strengthening adobe structures. Nonlinear finite element used in conjunction with a pushover analysis is employed to assess the behavior of these strengthened structural systems. The effectiveness of these strengthening schemes is then compared and discussed. It is found that a strengthening system that makes use of both sheet and strap reinforcements is the most effective. However, other strengthening schemes are also quite promising in increasing the lateral load and energy absorbing capacities of adobe structures.

PROBLEM STATEMENT

Adobe structures are commonly used for conventional residential construction in developing countries, and for construction in rural and remote areas in some developed countries. They are considered sustainable structures and carry high traditional value. However, unreinforced adobe structures are relatively weak when subject to settlement and lateral load, and are quite vulnerable to cracking and brittle failure as shown in Figure1.



Figure 1 – Cracking failure of Adobe Walls

Illampas et al. (2014), Varum et al. (2014) and Vint & Neumann (2005) have performed vulnerability assessment of unreinforced adobe houses in their research [1-3]. The applicable experimental work involved static tilt testing on house modules, displacement-controlled cyclic tests on *I*-shaped adobe walls as well as shake table tests on single story model buildings. In all these cases, the response associated with the unreinforced model buildings was compared with those reinforced by cane rods, geogrids, steel wire, fiber-reinforced polymer strips, tire straps, etc. It was shown that the introduction of reinforcement noticeably enhanced the structural integrity of the adobe houses.

PROPOSED METHODOLOGY

In this paper four relatively simple strengthening methods for adobe structures are proposed and investigated. They are: (1) adding a horizontal layer of synthetic nylon sheet in every 3 layers of adobe blocks; (2) vertically-tying the adobe wall with straps made from these synthetic nylons [4]; (3) adding stanchions in the form of corner columns to strengthen the wall, and (4) using both vertical straps and horizontal inter-layer synthetic nylon sheets. Figure 2 shows the model of a typical adobe wall with openings as well as how the four proposed strengthening schemes are implemented.

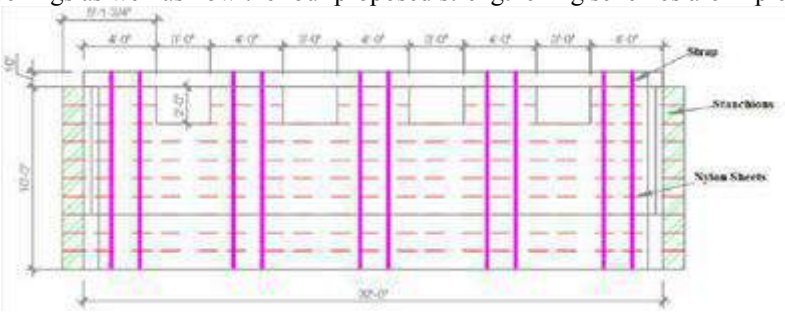

Figure 2 - Adobe Wall Model Showing the Different Strengthening Schemes

ABODE WALL MODEL PROPERTIES

A high fidelity finite element model of the above adobe wall was created using ABAQUS [5] and nonlinear pushover analysis was performed to determine the response of the strengthen structure. A damaged plasticity constitutive law was

---

Corresponding author: Email: hataei@syr.edu

adopted and experimentally-derived material data were used as input parameters [3]. To model the brittle behavior of the adobe bricks, the concrete damaged plasticity constitutive model, which is a continuum, plasticity-based, isotropic damage model that considers tensile cracking and compressive crushing as the main failure mechanisms was used. As shown in Figure 3(a) and (b), each adobe block was modeled using 4 hexahedral 8-node linear brick element with reduced integration (*C3D8R*) and the nylon sheets and straps were modeled using 4-node shell elements with reduced integration (*S4R*). A total number of 4148 elements was used for modeling one-half of the adobe structure as illustrated in Figure 3(c). In the tangential direction, finite-sliding formulation based on Coulomb friction theory with a friction coefficient of 0.7 was used at the interface between the adobe and the ring beam. To simulate the described behavior, a hard contact pressure–overclosure relationship was defined in the normal direction. When the contact pressure becomes zero, separation of the surfaces takes place and no transfer of the tensile stresses will occur across the interfaces.

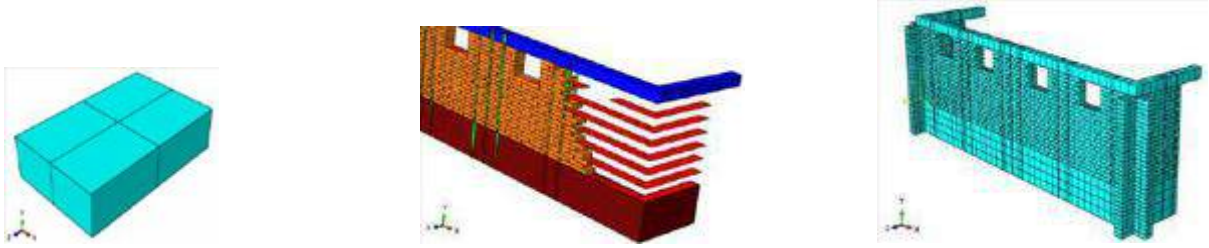

(a) **(b)** **(c)**

Figure 3 – Characteristics and Details of the Finite Element Adobe Wall Model

FINITE ELEMENT ANALYSIS RESULTS AND CONCLUSIONS

The maximum principal stresses (that correlate with the failure mode of the Adobe wall) calculated for an unreinforced and a reinforced adobe wall using strengthening scheme (4) are compared in Figure 4. It can be seen that the use of synthetic nylon sheets and straps help redistributes stresses in critical locations, thereby making the structure more resistant to lateral load.

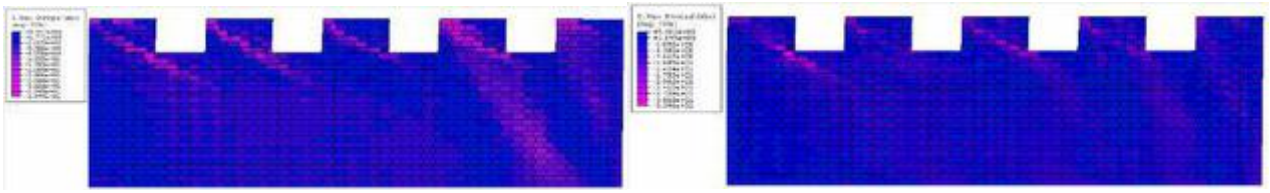

(a) **(b)**

Figure 4 – Maximum Principal Stress Contours (psi) for (a) Unreinforced Wall, and (b) Reinforced (Straps + Sheets) Wall (1 psi = 48 N/m^2)

In Figure 5, the pushover curve for an unreinforced adobe wall is compared with those using the four strengthening schemes. It can be seen there is a noticeable increase in the lateral load capacity (as depicted by the peak point of the curve) and energy dissipation (as measured by the area under each curve) of the wall using any one of the proposed strengthening schemes.

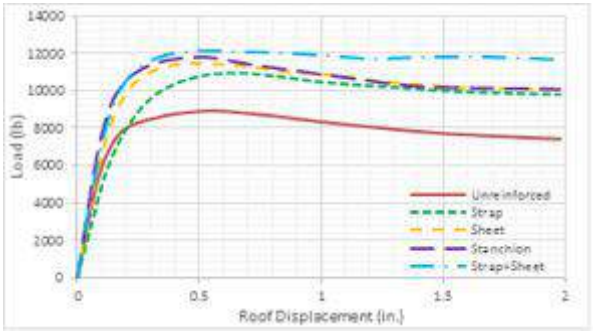

Figure 5 – Pushover Curves for Unreinforced and Reinforced Adobe Walls (1 lb = 4.45 N, 1 in. = 2.54 cm)

REFERENCES

[1] R. Illampas, D. C. Charmpis, , I. Ioannou, Laboratory testing and finite element simulation of the structural response of an adobe masonry building under horizontal loading, Engineering Structures, 80, 362–376, 2014.

[2] H. Varum, N. Tarque, D. Silveira, G. Camata, B. Lobo, M. Blondet, A. Figueiredo, M. M. Rafi, C. Oliveira and A. Costa, Structural Behaviour and Retrofitting of Adobe Masonry Buildings, Springer-Verlag Berlin Heidelberg, 2014.

[3] B. Vint and C. Neumann, Southwest Housing Traditions Design, Materials, Performance, May 2005.

[4] American Wire Rope and Sling catalog, Synthetic Web Sling, www.arsling.com

[5] ABAQUS 6.14-1 User Manual, 2009, SIMULIA, Dassault Systèmes, Providence, RI.

TRANSVERSE CRACKING IN METAL-CERAMIC COMPOSITES WITH LAMELLAR MICROSTRUCTURE

Romana Piat[1a)], Maria Kashtalyan[2], Igor Guz [2]
[1]*Faculty of Mathematics and Natural Sciences, Darmstadt University of Applied Sciences, Germany*
[2]*Centre for Micro- and Nanomechanics (CEMINACS), School of Engineering, University of Aberdeen, Scotland UK*

Summary Metal-ceramic composites with lamellar microstructure are a novel class of composites produced by infiltration of freeze-cast or ice-templated ceramic preforms with molten aluminium alloy. Due to the cost-effectiveness of production and relatively high ceramic content they are attractive for automotive, aerospace and biomedical engineering applications. A hierarchical lamellar microstructure, with randomly orientated domains in which all ceramic and metallic lamellae are parallel to each other, is the result of the ice crystal formation during freeze casting or ice-templating of preforms from water-ceramic suspensions. In this paper, a single-domain sample of metal-ceramic composite with lamellar microstructure is modelled theoretically using a combination of analytical and computational means. Stress field in the ceramic layer containing multiple transverse cracks is determined using a modified 2-D shear lag approach and a finite element method. Degradation of stiffness properties of the sample due to multiple transverse cracking is predicted using the equivalent constraint model.

INTRODUCTION

Metal-ceramic interpenetrating phase composites, in which ceramic preforms with open porosity are infiltrated with molten metal or alloy to produce composites with two three-dimensionally interpenetrating constituents, possess production-dependent ceramic content and exhibit highly sophisticated internal microstructures that depend on the preform fabrication method. Several innovative methods have been developed to produce open-pore ceramic preforms. One of them – freeze-casting – involves controlled directional freezing and subsequent freeze-drying of concentrated water-ceramic suspension [1-3]. The resulting ceramic preforms exhibit a lamellar microstructure, with thin parallel and connected layers. Damage mechanisms in metal/ceramic composites with lamellar microstructures have not been studied in depth yet. Initiation and accumulation of damage within the ceramic lamellae, mainly in the form of transverse cracking (Fig. 1a), has been observed under compressive loading [4, 5]. It is also expected to occur under tensile loading due to failure strain of ceramics being less than that of the metal. In this paper, a single-domain sample of MMC with lamellar microstructure is modeled theoretically using a combination of analytical and computational means.

THEORETICAL MODELLING

Consider a MMC sample consisting of a ceramic layer of thickness $2h_c$ fully bonded between two metal layers of thickness h_m. Ceramic layer contains multiple tunneling cracks, assumed to be spaced uniformly with crack spacing $S = 2s$, spanning the full thickness of the ceramic layer and depth of the sample. The sample is referred to the co-ordinate system $x_1x_2x_3$, with x_1 axis parallel to the cracks (Fig. 1b) and subjected to biaxial tension $\overline{\sigma}_{11}, \overline{\sigma}_{22}$ and in-plane shear loading $\overline{\sigma}_{12}$. Due to periodicity of damage and symmetry of the sample, only a quarter of the representative segment bounded by two cracks needs to be considered (Fig. 1c).

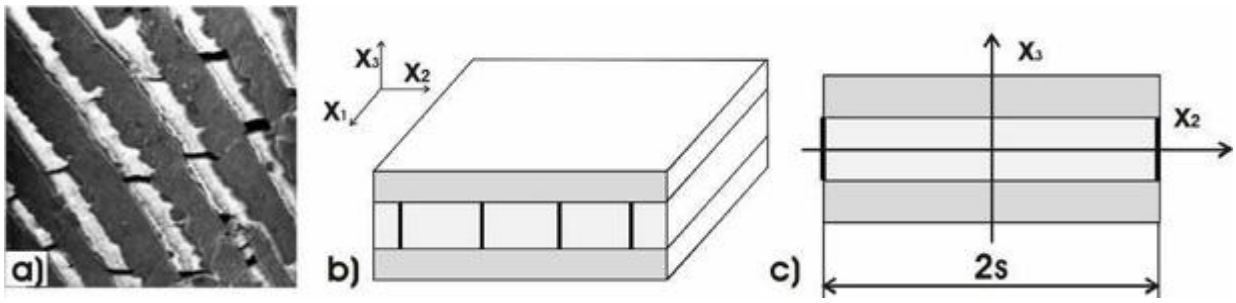

Fig. 1: a) Transverse cracks in ceramic layer of MMC with lamellar microstructure; b) Schematics of a composite sample with multiple tunnelling cracks in the ceramic layer; c) representative segment bounded by two cracks.

Stress field in the sample containing multiple transverse cracks in the ceramic layer is determined analytically using a modified 2-D shear lag approach [6-8] and a finite element method. The Equivalent Constraint Model is then applied to predict reduction of elastic properties of the sample due to multiple transverse cracking.

[a)] Corresponding author. Email: romana.piat@h-da.de

RESULTS AND DISCUSSION

Finite modeling of the metal-ceramic composite reveals that as crack spacing becomes smaller, a region of compressive stress in the ceramic layer emerges (Fig. 2a). From the distribution of shear stress σ_{23}, shear layer thickness can be estimated (Fig. 2b) and used as an input in the analytical model.

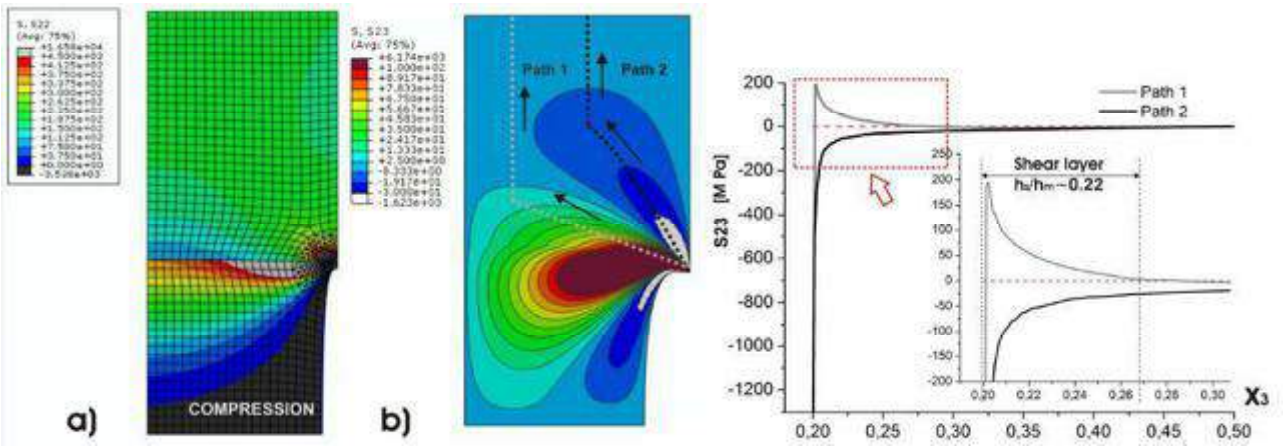

Fig. 2: Variation of: a) axial stresses; b) transverse shear stresses stresses.

Predicted reduction of in-plane elastic properties of the composite is shown in Fig. 3. The values of stiffness properties for the composite with cracks are normalised by their respective values for the undamaged composite and are plotted as reduction ratios against the relative crack density. Multiple cracking significantly reduces not only composite's Young's modulus E_2 (i.e. modulus in the direction normal to the cracks), but also shear modulus G_{12} and Poisson's ratio ν_{21}.

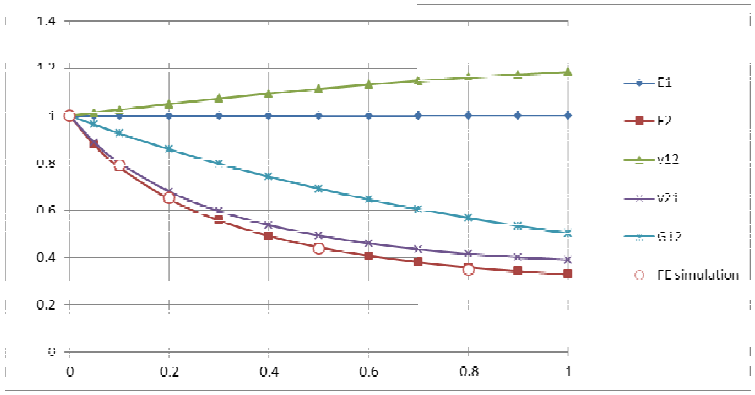

Material properties of the constituents:

Aluminium alloy Al-12Si
Young's modulus 80 GPa,
Poisson's ratio 0.33

Alumina Al_2O_3
Young's modulus 390 GPa
Poisson's ratio 0.24

Ceramic content 40%

Fig 3: Reduction of elastic properties of the metal-ceramic composite as a function of the relative crack density $D = h_c / s$.

CONCLUSIONS

The cracked microstructure of single domain MMC sample is modeled by analytical and computational approaches. Stress field is determined using a modified 2-D shear lag approach and a finite element method. Using FE modeling the shear layer thickness for different crack spacings was calculated and used as input in the analytical model. The Equivalent Constraint Model can be applied to predict degradation of stiffness properties of the sample due to multiple transverse cracking.

References

[1] Roy S, Wanner A. Composites Science and Technology **68**: 1136-1143, 2008.
[2] Roy S, Butz B, Wanner A. Acta Materialia **58**: 2300-2312, 2010.
[3] Ziegler T., Neubrand A., Piat R. Composites Science and Technology **70:** 664-670, 2010.
[4] Roy S, Gebert J-M, Stasiuk G, Piat R, Weidermann KA. Materials Science and Engineering A **528**: 8226-8235, 2011
[5] Sinchuk Y, Roy S, Gibmeier J, Piat R, Wanner A. Materials Science and Engineering A **585**, 10-16, 2013.
[6] Kashtalyan M, Soutis S. Applied Composite Materials, **18**: 31-43, 2011
[7] Katerelos DTG, Kashtalyan M, Soutis C, Galiotis C. Composites Science and Technology **68**: 2310-2317, 2008.
[8] Kashtalyan M, Sinchuk Y, Piat R, Guz I. Archive of Applied Mechanics **86**, 2016 (in press).

GPU-BASED SIMULATIONS OF FRACTURE IN BIO-INSPIRED BRICK & MORTAR COMPOSITES

Will Pro[1], Rone Kwei Lim[2], Linda Petzold[1,2], Marcel Utz[3], & Matthew Begley[1,4a)]
[1]*Department of Mechanical Engineering, University of California at Santa Barbara, Santa Barbara, CA*
[2]*Department of Computer Science, University of California at Santa Barbara, Santa Barbara, CA*
[3]*School of Chemistry, University of Southampton, Southampton, UK*
[4]*Materials Department, University of California at Santa Barbara, Santa Barbara, CA*

Summary: This paper examines the effect of microstructure on the macroscopic fracture properties of idealized brick and mortar composites, which consist of rigid bricks bonded with elastic-plastic mortar that ruptures at finite strain. Specifically, the effect of brick aspect ratio and non-uniform microstructures is studied. A simulation tool that harnesses the parallel processing power of graphics processing units (GPUs) was used to simulate fracture in large virtual specimens, whose microstructures were created by sampling a probability distribution of brick sizes. Quantitative connections between the statistical parameters defining heterogeneous brick distributions and the statistics of initiation toughness are presented. The results offer quantitative insights that can be used to identify microstructural targets for process development, notably specific brick size distributions that still provide macroscopic toughening. Moreover, the simulation approach aids in the development of bio-inspired composites by providing a virtual testing tool to connect microstructure to performance.

INTRODUCTION & SIMULATION APPROACH

Bio-inspired ‘brick and mortar’ composites offer promising pathways to high-strength and high-toughness synthetic materials. Similar to their natural counterparts (e.g., nacreous abalone shell), these composites boast material properties (namely fracture toughness) that are much higher than that of their constituents; a trait that can be attributed to their intricate ordered microstructure. The ability to connect local microstructural features with macroscopic mechanical properties is a central challenge in materials development, as such connections effectively define `processing targets' associated with acceptable levels of heterogeneity. This challenge is particularly acute for quasi-brittle composites that exploit ordering of microstructural features, as local disruptions to ordering can serve as defects that limit global performance [1]. Bio-inspired `brick and mortar' composites are an excellent example of this [2,3], where the ideal microstructure has perfectly aligned stiff features and achieves toughness through perfectly overlapping features that spread damage over large length scales. However, the physical reality is that most high through-put processing routes invariably introduce heterogeneous distributions of brick size and therefore overlap distances, which limit the effectiveness of the microstructure. The objective of this work is to elucidate the statistical characteristics of macroscopic fracture properties that result from variations in local microstructural features.

As illustrated in Fig 1b, the material is modelled using an idealized microstructure consisting of an overlapping grid of comparatively stiff bricks bonded together by thin, compliant mortar sections (modelled with cohesive zones). Heterogeneity is introduced by assigning a random width to each brick in the system and stacking them into a virtual fracture specimen with a macroscopically applied energy release rate (Fig 1a). Quasi-static conditions are assumed, and the governing equations are solved via parallel direct search energy minimization using the GPU. The critical ERR at crack advance is defined as the initiation fracture toughness. The specific population sample of bricks sizes is controlled by a microstructure seed, as shown in Fig. 1d. For a given average aspect ratio, several different microstructure seeds were analysed and the resulting statistics in the fracture toughness were tabulated.

RESULTS

Fig. 2 shows the resulting stress and damage fields for two different levels of heterogeneity, as dictated by the standard deviation in brick sizes. The equilibrium stress patterns are quite complex, but suggest a substantially lowered composite strength as variability into the microstructure is introduced. Fig. 3 shows the averaged fracture toughness over several microstructure seeds, for different average brick aspect ratios. As shown, there is a substantial reduction in average toughness (nearly 50%) for realistic values of brick size variance. Fig. 4 shows the effect of the brick size standard deviation on the resulting variability in toughness. As illustrated, the toughness standard deviation is maximized at about 1% deviation in brick size. Combined with the results of Fig. 3, this implies that a trade-off exists between toughness and the variability of the toughness. Above 1% deviation in brick sizes, higher toughness cannot be achieved without also increasing the variability in toughness. For less than 1% deviation in brick sizes, no trade-off between toughness and its variability exist, and both high toughness and low variability (both desirable traits) seem to be obtained simultaneously.

[a)] Corresponding author. Email: begley@engr.ucsb.edu.

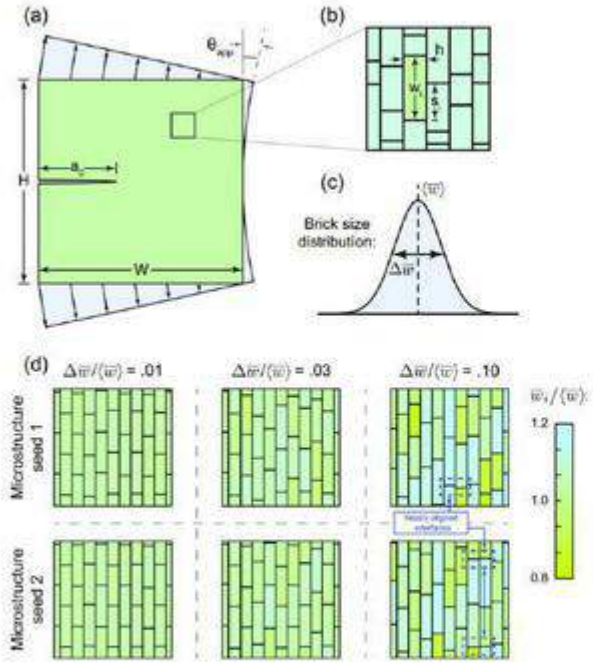

Figure 1 - Schematic of (a) Macroscopic Specimen and loading; (b) brick parameters; (c) Probability density function of brick size generation, and (d) example brick layouts for various brick distributions

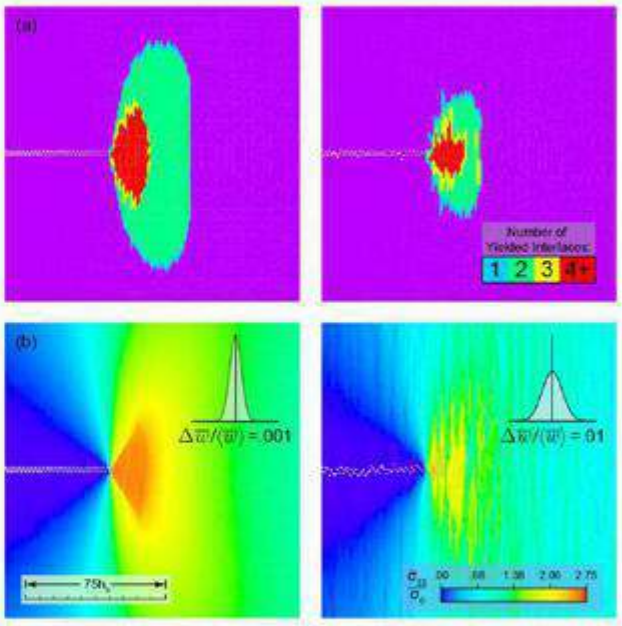

Figure 2 – (a) Damage zone contours ahead of dominant pre-crack for various brick size standard deviations and (b) Vertical brick stresses ahead of initial pre-crack

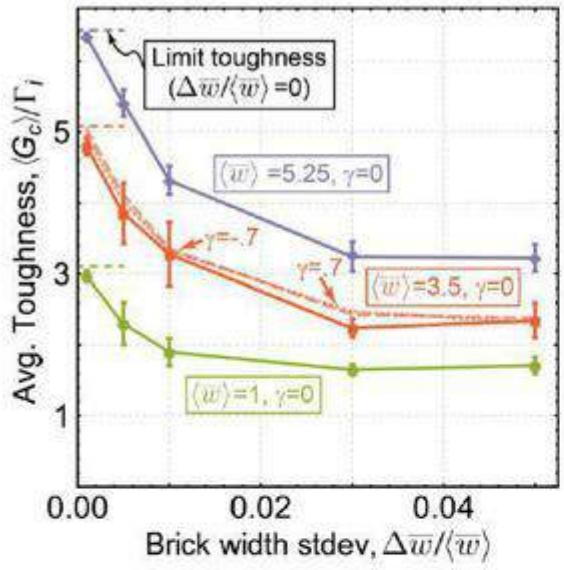

Figure 3 – Effect of brick width standard deviation on the average fracture initiation toughness for various average brick aspect ratios

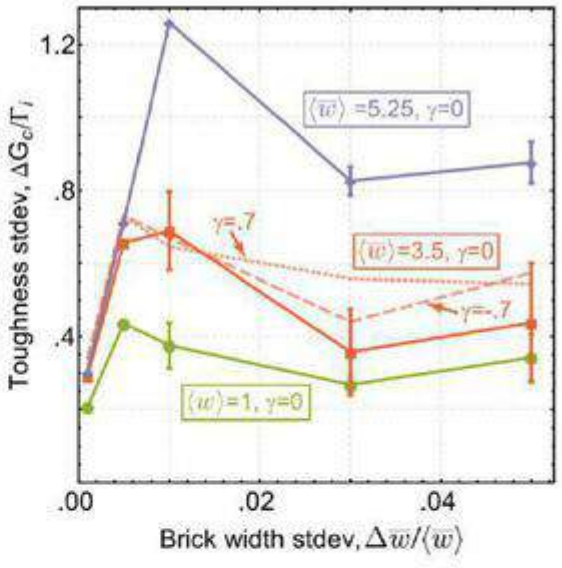

Figure 4 - Toughness standard deviation as a function of brick size standard deviation, for several different average brick aspect ratios

References

[1] Z. Zhang, Y.-W. Zhang, and H. Gao: On optimal hierarchy of load-bearing biological materials, Proc. of the Royal Society B: Biological Sciences, 2010

[2] E. Munch, M. E. Launey, D. H. Alsem, E. Saiz, A. P. Tomsia, & R. O. Ritchie: Tough, bio-inspired hybrid materials, Science, vol. 322, no. 5907, p. 1516-1520, 2008.

[3] F. Barthelat and D. Zhu, A novel biomimetic material duplicating the structure and mechanics of natural nacre: Journal of Materials Research, vol. 26, no. 10, pp. 1203-1215, 2011.

DEPENDENCE OF TIMESCALE ON CRACK VELOCITY DURING DIFFUSION CONTROLLED CRACK GROWTH

Gaurav Singh*
Mechanical Engineering, Birla Institute of Technology & Science, Pilani - KK Birla Goa Campus, Goa, India

Summary During hydrogen cracking, diffusion and crack growth simultaneously occur at different timescales - diffusion being a much slower process. In this paper, it is shown that the crack growth rate is underestimated due to the timescale difference.

INTRODUCTION

As a natural phenomena, hydrogen cracking is a complex process, however fractographic studies have given some insight into the process. This has lead to several diffusion-based models of hydrogen cracking [1, 2, 3] due to hydride formation [4].

Assume that the crack has begun to grow under the application of a physical load (remote or localized/pressurized) in an atmosphere of hydrogen. The two simultaneous process (at different timescales) happening are (a) crack growth and (b) hydrogen diffusion into the metal. If the process of diffusion (timescale t_d) happens at a longer timescale than that of crack growth (timescale t_c), then

$$t_d = g(t_c) > t_c \tag{1}$$

where g is the timescale function. This timescale difference can also be represented on a space-time graph in Figure 1(a). In the following section, a transient diffusion model will be discussed through a moving crack-tip surface boundary.

HYDROGEN DIFFUSION THROUGH MOVING CRACK-TIP SURFACE BOUNDARY

A general analysis of diffusion through a moving boundary has been given in [5]. In the present analysis, it is assumed that only hydrogen diffuses into the metal through the moving crack-tip (assumed to be a flat surface) while no metal diffuses into the hydrogen atmosphere. The process of diffusion takes place only in the direction perpendicular to the crack-tip surface as shown in Figure 1(b). Due to the instantaneous hydride formation and breakdown (following diffusion), the crack-tip surface is a moving boundary.

As shown in Figure 1(b), consider the hydrogen and metal medium separated by the crack-tip surface boundary. The x-coordinate system is at rest. The hydrogen and metal media are separated at time t_c by the crack-tip surface $x = X(t_c)$ which was initially located at $x = 0$. The hydrogen occupies all the space in $-\infty < x < X(t_c)$ while it is diffusing into $x > X(t_c)$ through the boundary. The concentration of the diffusing substance at time t_d is denoted by c at $x > X(t_c)$. In this situation, the following equation is obeyed

$$\frac{\partial c}{\partial t_d} = D\frac{\partial^2 c}{\partial x^2} \tag{2}$$

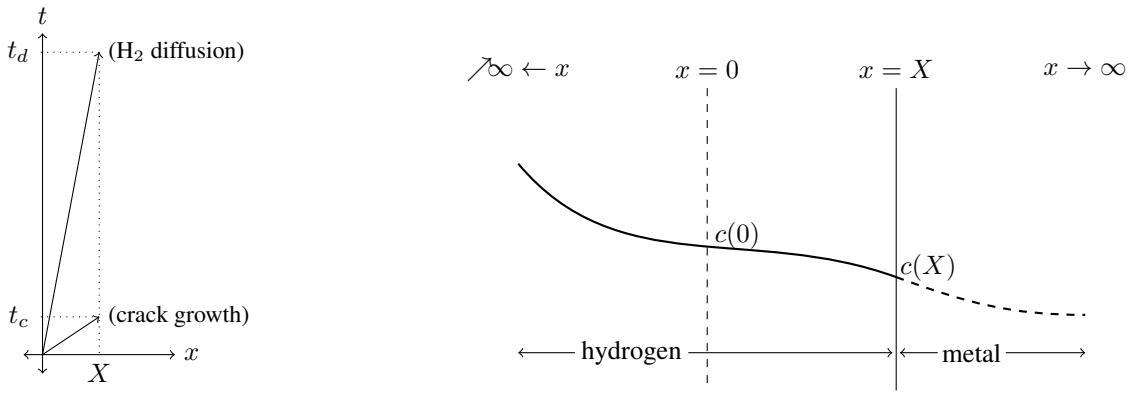

Figure 1: (a) Space-time representation of timescale issue during hydrogen cracking (b) Representation of hydrogen diffusion from the atmosphere into the metal through a moving (crack surface) boundary

*Corresponding author. Email: gauravs@goa.bits-pilani.ac.in

where the diffusion coefficient D is independent of the concentration c and time t_d. The diffusion rate of hydrogen at the crack-tip surface is equal to

$$\dot{H} = D\left(\frac{\partial c}{\partial x}\right)_{x=X} + c(X)\frac{X(t_c)}{t_c} \tag{3}$$

at the moving boundary $x = X(t_c)$. For an infinite medium where Equation (2) holds, the solution takes the form

$$\frac{c(\infty) \nearrow c}{c(\infty) \nearrow c(0)} = 1 \nearrow \ \mathrm{f}\frac{x}{\sqrt{\ Dt_d}} \tag{4}$$

where $c(\infty)$ is the hydrogen concentration in the metal at $t_d = 0$ (initial condition) and $c(0)$ is the ambient constant hydrogen concentration for all times (boundary condition). The hydrogen atmosphere extends through $\nearrow\infty < x < X(t_c)$ at any given time. The magnitude $|X(t_c)|$ is assumed to be proportional to the amount of diffusing hydrogen into the metal through the crack-tip surface boundary. This is justified as the hydrogen diffusing in, instantaneously forms hydride which breaks down (again, immediately). Using Equation (3), this proportionality as a derivative of time maybe written as

$$\underset{\mathrm{c}}{\frac{X(t_c)}{}} = S\left[D\left(\frac{\partial c}{\partial x}\right)_{x=X} + c(X)\frac{X(t_c)}{t_c}\right] \tag{5}$$

where S is the constant of proportionality. Combining the above equation with the partial derivative of c in Equation 4 at $x = X$ gives

$$\underset{\mathrm{c}}{\frac{X(t_c)}{}}\left[\frac{1}{S} \nearrow c(X(t_c))\right] = [c(\infty) \nearrow c(0)]\sqrt{\frac{D}{\pi t_d}}e^{-X^2/4Dt_d} \tag{6}$$

Now put $x = X(t_c)$ and $c = c(X(t_c))$ in Equation (4) to rewrite it as

$$c(X(t_c)) = c(0) + (c(\infty) \nearrow c(0)) \ \ \mathrm{f}\frac{X(t_c)}{\sqrt{\ Dt_d}} \tag{7}$$

Substituting t_d and t_c in terms of g from Equation (1) and using $t = t_c$, the Equations (6)-(7) can be written as

$$\underset{\mathrm{c}}{\frac{X(t)}{}}\left[\frac{1}{S} \nearrow c(X(t)\right] = [c(\infty) \nearrow c(0)]\sqrt{\frac{D}{\pi g(t)}}e^{-X^2/4Dg(t)}; \qquad c(X(t)) = c(0) + (c(\infty) \nearrow c(0)) \ \ \mathrm{f}\frac{X(t)}{\sqrt{\ Dg(t)}} \tag{8}$$

The above two Equations (8) are simultaneously satisfied for all values of t, only when $X(t)/\sqrt{\ Dg(t)}$ is a constant. Therefore, defining the constant k such that

$$X(t) = k\sqrt{\ Dg(t)} \tag{9}$$

which will yield the crack-tip surface velocity when a time-derivative is taken. The crack growth velocity can be written as

$$\frac{X(t)}{t} = k\sqrt{\frac{D}{g(t)}}g'(t) \tag{10}$$

RESULT AND DISCUSSION

As can be seen from Equation (10), for all $g'(t) > 1$ (always true in the described model), the predicted crack velocity will be under-estimated if the timescale difference between the crack growth and diffusion is neglected. For example, if $g(t) = \alpha t$, then the actual crack-growth rate will be $\sqrt{\alpha}$ times more. In physical terms, this example is a case when diffusion occurs α times slower than the crack growth. In this case $\frac{\mathrm{d}X(t)}{\mathrm{d}t} = k\sqrt{\frac{4D}{t}}\sqrt{\alpha}$ which also implies that the crack velocity should decrease with time. This has been experimentally suggested by the hydrogen induced crack growth phenomena in titanium [6] where the velocity drops with an increasing crack length (and crack length increases with time).

References

[1] Unger DJ. 1995 *Analytical fracture mechanics*. New York, Dover Publications.

[2] Taha A and Sofronis P. 2001 *A micromechanics approach to the study of hydrogen transport and embrittlement*. Engineering Fracture Mechanics, 68(6), 803-837.

[3] Wei RP. 2010 *Fracture mechanics: Integration of mechanics, materials science and chemistry*. New York, Cambridge University Press.

[4] Northwood D O and Kosasih U. 1983 *Hydrides and delayed hydrogen cracking in zirconium and its alloys*. International Metals Reviews, 28(1), 92-121.

[5] Crank J. 1975 *The mathematics of diffusion*. Oxford, Clarendon Press.

[6] Nelson HG. 1976 *A film-rupture model of hydrogen-induced, slow crack growth in acicular alpha-beta titanium*. Metallurgical Transactions A, 7(5), 621-627.

INFLUENCE OF MATERIAL NON-LINEARITY IN THE FRACTURE PROPERTIES OF STRUCTURAL ADHESIVES

Georgios Stamoulis[1] & Nicolas Carrere[2]
[1] *Université de Bretagne Occidentale, FRE CNRS 3744 IRDL, 29238 Brest, France*
[2] *ENSTA Bretagne, FRE CNRS 3744 IRDL, F-29200 Brest, France*

Summary: The influence of the non-linear behaviour of a crash optimized adhesive in its fracture properties is discussed. The adhesive has been previously analysed by means of standardized TDCB (Tapered Double Cantilever Beam) and MMB (Mixed Mode Bending) tests, which are based on the LEFM (Linear Elastic Fracture Mechanics) theory. In the present study, these tests were modelled numerically. The non-linearity of the adhesive was integrated in the simulations using a spectral viscoelastic law. Crack initiation and propagation were described using the Cohesive Zone Model (CZM) technique. Comparing with the standardized analysis, the results of the simulations showed small decrease of the value of the fracture toughness (G_C) when under mode I load and considerable decrease while reaching the mode II load case. These results of the simulations for G_C were also used to predict the break force of specially designed specimens tested by means of the Arcan fixture.

INTRODUCTION

Adhesive bonding technology has several advantages over conventional types of mechanical joints based on riveting, welding or screwing. Hence, adhesives are very frequently preferred in many joining situations. The strength of the bonded structure can be predicted by measuring the G_C of the adhesive based on the load state at the end of the crack tip: the tensile opening mode (mode I), the in-plane shear mode (mode II) and the mixed mode I/II case. This can be realized by means of standardized tests [1-5], whose evaluation relies on the LEFM theory assuming that the adhesive material (as well as the substrates too) behaves as a linear elastic and isotropic solid. Although this hypothesis is correct for brittle adhesives, it turns out to be insufficient for a certain number of structural adhesives, as for example the crash optimized ones. For this type of adhesives a large zone of micro-fibrillation is formed ahead of the crack tip, and the use of the standardized procedures to calculate G_C results to extremely high values when moving towards the mode II load state.

MAIN PART

In the present study, the fracture properties of the crash optimized adhesive SikaPower®-498 are examined. This adhesive has been previously tested in [6] by means of the TDCB test for the mode I load case (following the ISO 2517 standard [2]) and by means of the MMB test in the mixed mode I/II plane (following the ASTM D6671 standard [4]). The MMB test was performed at four different mode ratios G_{II}/G_I: 0.2, 0.4, 0.6 and 0.8 (with G_I and G_{II} being the energy release rates under mode I and II respectively). It has been shown in [6] that the evolution of the G_C of the SikaPower®-498 adhesive in the mixed mode I/II plane can be adequately described by the Benzeggagh-Kenane failure criterion, with the fracture toughness under mode I (G_{IC}) measured at about 3 N/mm and under mode II (G_{IIC}) at about 11 N/mm. Taking into account these results and considering also the low yield strength found for this adhesive (at about 17 MPa see [7]), it can be concluded that the calculated G_C by means of the LEFM theory should include an important amount of the dissipated potential energy due to plasticity of the adhesive layer rather than only to crack propagation, and this especially when moving towards the mode II load state.

The previous standardized TDCB and MMB tests were modelled numerically here using the Abaqus™ Ver.6.12-1 software. The substrates were simulated as linear elastic and isotropic solids. The non-linearity of the SikaPower®-498 adhesive was represented by means of a spectral viscoelastic law, whose parameters have been previously identified using Arcan tests [7]. Progressive damage and failure of the adhesive were simulated by means of the CZM approach, which first requires the definition of the crack propagation path. For the model used here, this path was set in the middle of the adhesive layer thickness and it was discretized by a thin layer of cohesive elements. Their constitutive response was described using the bi-linear traction-separation law, which was preferred here due to its simplicity. The onset and propagation of damage were simulated by means of the quadratic nominal stress and the 1st order power law criterions respectively. The approximation of the experimental curves was realized at the part describing the crack propagation for both the TDCB and MMB tests. The results of the simulations showed a slight decrease of the G_{IC} of the SikaPower®-498 adhesive (at about 2.5 N/mm) and a considerable decrease of G_{IIC} (at less than 6 N/mm) compared to the corresponding values issued by the standardized tests.

In order to validate the previous results, two types of alternative tests (based on the Arcan test device), which were also realized on the SikaPower®-498 adhesive, are used. The first type is the tests presented in [8], for which the

[1)] Corresponding author. Email: **georgios.stamoulis@univ-brest.fr**

specimen geometry has been specially designed to allow for crack propagation inside the adhesive layer, by fabricating substrates of increased width in their middle comparing to their two extremities. Hence, the specimens were tested at different phase angles in the mixed mode I/II plane, and the evaluation of the results by means of the LEFM theory showed good accordance with those issued by the standardized TDCB and MMB tests. The second type of Arcan tests was realized using the specimen configuration shown in figure 1.

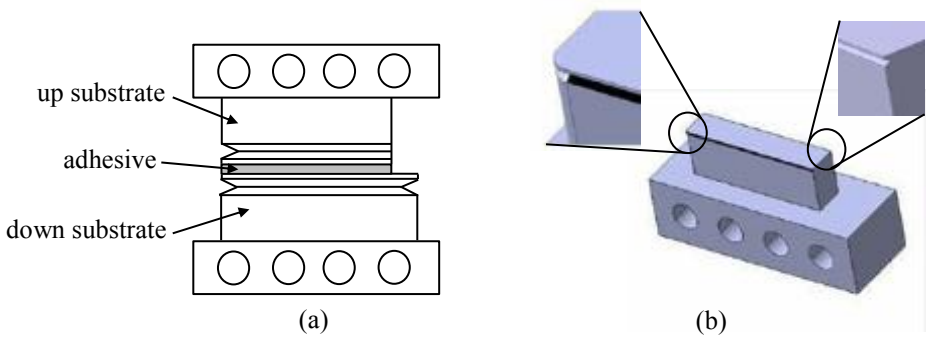

Figure 1: a) Specimen geometry used for the second type of Arcan tests, b) 3D detail of the "up" substrate

The substrates had a special geometry with a beak on all four sides in order to compensate for the edge effects (see also [9]). The up substrate (see figure 1a) was cut on one extremity in order to impose a stress singularity on one end of the joint. These specimens were also tested at different phase angles in the mixed mode I/II plane. Both types of Arcan tests were modelled using the same technique as the one described above for the TDCB and MMB tests. The values of the G_C that have been previously calculated after subtraction of the energy dissipated due to plasticity of the adhesive layer were used to predict the break force. At this point, it must be mentioned that, for all the experiments performed here, the adhesive layer thickness was set at 0.5 mm. In addition, all substrates used were made of aluminium except for the case of the MMB test where high limit of elasticity steel material was used.

CONCLUSIONS

In the present research the fracture behaviour of the SikaPower®-498 adhesive in the mixed mode I/II plane was examined, by taking into account the energy dissipated due to its plasticity when performing the standardized TDCB and MMB tests. The results showed considerable decrease of the G_C while moving towards the mode II load case. These results were used to predict the break force of alternative tests (Arcan type). In order to pursue with the current study, the influence of several other parameters than only material non-linearity must be examined in the computations for the G_C, as for example: the friction between the crack faces when under mode II load, possible deviations of the crack path from the mid-line of the adhesive layer thickness or even interface cracks.

References

[1] ASTM D3433-99. Annual book of ASTM standards, adhesives section 15. Philadelphia, PA: ASTM; 2012.

[2] ISO 25217:2009; 2009.

[3] BS 7991:2001; 2001.

[4] ASTM D6671/D6671M-13e1. Annual book of ASTM standards, Composite Materials section 15. Philadelphia, PA: ASTM; 2013.

[5] ISO/DIS 15114:2014; 2014.

[6] Stamoulis G, Carrere N, Cognard JY, Davies P, Badulescu C, On the experimental mixed-mode failure of adhesively bonded metallic joints, Int J Adhes Adhes 2014;51:148-58.

[7] Badulescu C, Germain C, Cognard JY & Carrere N, Characterization and modelling of the viscous behaviour of adhesives using the modified Arcan device, J Adhes Sci Technol 2015;29(5):443-61.

[8] Stamoulis G, Carrere N, Cognard JY, Davies P, Badulescu C, Investigating the fracture behavior of adhesively bonded metallic joints using the Arcan fixture, Int J Adhes Adhes, IN PRESS; http://dx.doi.org/10.1016/j.ijadhadh.2016.01.001.

[9] Cognard JY, Davies P, Sohier L, Créac'hcadec R, A study of the non-linear behaviour of adhesively-bonded composite assemblies, Compos Part A-Appl S 2006;76:34-46.

[1)] Corresponding author. Email: **georgios.stamoulis@univ-brest.fr**

NUMERICAL MODELLING OF THE DAMAGE-TO-CRACK TRANSITION IN A GURSON-TYPE MATERIAL

Johannes Wolf [1a)], Patrice Longère [1], Jean-Marc Cadou [2] & Jean-Philippe Crété [3]
[1] *Université de Toulouse, ISAE-SUPAERO, ICA (UMR CNRS 5312), Toulouse, France*
[2] *Université Européenne de Bretagne, UBS, LIMATB (EA 4250), Lorient, France*
[3] *Institut Polytechnique Grand Paris, SUPMECA, QUARTZ (EA 7393), Saint-Ouen, France*

Summary The present work aims at the numerical treatment of the crack propagation in engineering materials whose failure results from void initiation, growth and coalescence. With this aim in view, the objective is to describe the intermediate stage between more or less diffuse damage and the initiation of a macroscopic crack. This transient stage of damage induced deformation localisation in a narrow band necessitates a specific numerical treatment. An adapted extended finite element framework and its embedding into the existing formulation is presented and tested in fundamental numerical tests.

INTRODUCTION

Nowadays, ductile materials are deployed in many industrial applications as e.g. metal-forming, the improvement of automotive crash-worthiness or generally in the aerospace sector. When such metallic structures are subjected to large plastic deformations, micro-voids start to form, grow and coalesce leading finally to the formation of a crack (see fig. 1). As a result of damage evolution through void nucleation, growth and coalescence, the material resistance is subjected to continuous degradation and subsequent softening leading to strain localisation. In the post-localisation stage, the finite element analysis suffers from pathologic mesh dependency induced by the loss of uniqueness of the governing partial differential equations. Non-local regularisation techniques can be applied to attenuate the pathology, but accurate results require a very fine mesh at the scale of the microscopic localisation mechanisms. Particularly with regard to large engineering structures, we rather aim at using large finite elements and embed the band of highly localised deformation into the element formulation.

METHODOLOGY

The micromechanics-based Gurson-Tveergard-Needleman (GTN) widely used to reproduce the consequences of ductile damage-plasticity coupling has been applied herein to describe the behaviour of the material in the pre-localisation stage. Previous works (see Longère et al. [1]) have shown the interest of modifying the GTN constitutive model in order to reproduce the void growth induced damage in shear loading, in addition to the combined effects of strain hardening, thermal softening and viscoplasticity. This strongly non-linear model was implemented as user material (UMAT) within the engineering finite element computation code Abaqus using an implicit integration scheme.

A modified eXtended Finite Element (X-FE) formulation has been retained to describe the strong discontinuity kinematics of the crack which is the ultimate step of the localisation mechanism. Recent works have shown the feasibility of a coupling between the Gurson-type damage-plasticity model and the X-FE method relying on an averaging of quantities over an area (patch) located at the crack tip. In order to account for the history-dependent, strongly non-linear material, the numerical integration in the enriched elements is performed by using 64 Gauss points – instead of using the integration by sub-triangulation. The X-FEM and the coupling method were implemented as user subroutine (UEL) in Abaqus (see Crété et al. [2]).

The localisation stage which is the transition phase between diffuse damage and cracking is described using an X-FE method as well. A physics-based deformation profile can be represented with regularised enrichment functions allowing for dealing with the strain-localisation induced weak discontinuity (see e.g. Benvenuti et al. [3] and Areias et al. [4] for similar approaches). The characteristic length scale of the highly localized deformation band provides a regularization of the post-localisation response and thus reduces the inherent mesh dependency. The orientation of the band of highly localised deformation is determined by a bifurcation analysis (see Rice [5]) and involves considering quantities averaged over a patch which is positioned within the localisation band/at the crack tip.

The entire model is implemented in a two-dimensional formulation assuming small deformations and plane strain conditions.

The performance of the methodology is finally evaluated by numerical simulations of the tension loading of a notched plate and compared with experimental data.

[a)] Corresponding author. Email: Johannes.Wolf@isae.fr

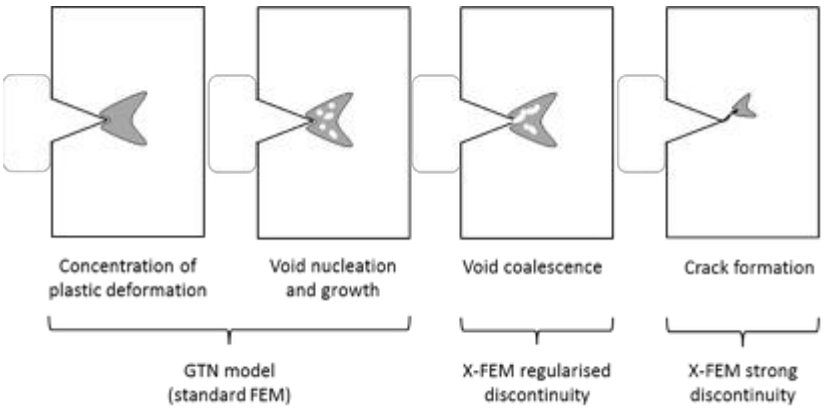

Fig. 1: Numerical methods for the stages of ductile failure

References

[1] P. Longère, A.G. Geffroy, B. Leblé and A. Dragon, 2012, Modelling the transition between dense metal and damaged (micro-porous) metal viscoplasticity. Int. J. Dam. Mech., 21:1020-1063

[2] J.P. Créte, P. Longère and J.M. Cadou, 2014, Numerical modelling of crack propagation in ductile materials combining the GTN model and X-FEM. Comp. Methods Appl. Mech. Eng., 275:204-233

[3] E. Benvenuti, A. Tralli, and G. Ventura, 2008, A regularized XFEM model for the transition from continuous to discontinuous displacements, International Journal for Numerical Methods in Engineering, 74:911-944

[4] P.M.A Areias and T. Belytschko, 2006, Two-scale shear band evolution by local partition of unity, International Journal for Numerical Methods in Engineering, 66:878

[5] J.R. Rice, 1976, The localization of plastic deformation, in W.T. Koiter ed., Theoretical and Applied Mechanics, Koiter, 207-220

[6] A.E. Huespe, A. Needleman, J. Oliver, P.J. Sanchez, 2009, A finite thickness band method for ductile fracture analysis, International Journal of Plasticity 25: 2349-2365

SM06 - Geophysics and Geomechanics

TS.SM06-1.01	Fialko, Yuri - Velocity-weakening behavior of granite and gabbro at temperature up to 600 degrees C (INVITED)	2144
TS.SM06-1.02	Jiang, Junle - Variability of earthquake slip and arresting depths in fault models	2146
TS.SM06-1.03	Higgins, Natalie - Exploring models of foreshock sources using rate-and-state friction	2148
TS.SM06-1.04	Kotov, Vasiliy - Experimental studies and mathematical modeling for dynamic deformation of soils	2150
TS.SM06-1.05	Lui, Semechah K. Y. - Physics-based elastodynamic modeling of interacting frictional shear cracks	2152
TS.SM06-1.06	Creyts, Timothy - Recirculating Ice Eddies in Subglacial Valleys	2154
TS.SM06-2.01	Hatano, Takahiro - Rate and state friction law as derived from atomistic processes at asperities (INVITED)	2156
TS.SM06-2.02	Perry, Stephen - Reproducing magnitude-invariant stress drops in fault models with thermal pressurization	2158
TS.SM06-2.03	Putelat, Thibaut - Nonlinear dynamics of frictional slip localization	2160
TS.SM06-2.04	Remij, Ernst - Hydraulic fracture propagation under the influence of natural fractures	2162
TS.SM06-2.05	Rivas, Endrina - Shear dilation using the extended finite element method	2164
TS.SM06-2.06	Rubino, Vito - Dynamic visualization of supershear ruptures	2166
TS.SM06-3.01	Rice, James - Thermo-hydro-mechanical processes stabilizing antarctic ice stream margins (INVITED)	2168
TS.SM06-3.02	Shigeno, Naoyuki - Dynamic impact-induced fracture development in ice spheres	2170
TS.SM06-3.03	Svetlizky, Ilya - Shear stress peak radiated ahead of rapidly accelerating frictional rupture	2172
TS.SM06-3.04	Touhei, Terumi - Near-field Equation for Quantitative Evaluation of Fluctuations	2174
TS.SM06-3.05	Vilotte, Jean-Pierre - Rupture dynamics along bimaterial interfaces	2176
TS.SM06-3.06	York, Jason - On the effects of plasticity in hydraulic fractures	2178
PO.SM06-1.01.259	Baimukhametov, Abay - Driving mechanisms of deep geodynamic processes	2180
PO.SM06-1.02.260	Turgumbayev, Arman - Movements of Earth's Surface in a Source Zones of Lithosphere by Satellite Data	2182
PO.SM06-1.03.261	Sharan, Shailendra - Elastoplastic analysis of circular openings in the generalized Hoek-Brown rock	2184
PO.SM06-1.04.262	Yu, Guangming - Analysis on the strength of rock mass based on fracture fractal evolution	2186

VELOCITY-WEAKENING BEHAVIOR OF GRANITE AND GABBRO AT TEMPERATURE UP TO 600 DEGREES C

Yuri Fialko *[1], Erica Mitchell[1], and Kevin Brown[1]
[1]*Institute of Geophysics and Planetary Physics, Scripps Institution of Oceanography, University of California, San Diego, La Jolla, CA 92093, USA*

Summary The depth extend of seismicity in the Earth's crust is believed to be controlled by a temperature-dependent transition from velocity-weakening to velocity-strengthening friction. Available experimental data on granite suggest a transition from unstable slip to steady creep at temperature about 350 °C. We present results of unconfined experiments on granite and gabbro at both dry and hydrated conditions that show increasingly unstable slip (velocity-weakening behavior) at temperatures up to 600 °C. We estimate the rate-state friction parameters using velocity-stepping tests and by fitting the data to predictions of a 1-D spring-slider model. We find that the "evolution" parameter b increases with temperature at a higher rate than the "direct effect" parameter a. We also find that the aging law provides a better fit to our experimental data compared to the slip law. Obtained results may help explain anomalously deep crustal seismicity in regions of active extension and convergence.

TEMPERATURE DEPENDENCE OF FRICTION AND SEISMICITY

The depth distribution of seismicity in the lithosphere is usually attributed to a transition from velocity-weakening to velocity-strengthening friction [9, 4]. Indeed, laboratory measurements of the rate parameter $(a \nearrow b)$ of rate-state friction[2, 7] for Westerly granite showed a transition from negative $(a \nearrow b)$ (velocity-weakening behavior, conditionally unstable slip) to positive $(a \nearrow b)$ (velocity-strengthening behavior, stable creep) at temperatures above 300-350 °C [8, 1]. Assuming a reasonable geotherm, this transition is expected to occur at depth of ∼15 km, in good agreement with the depth distribution of earthquakes in California [1]. The temperature dependence of the $(a \nearrow b)$ parameter is believed to control the depth range of seismicity, as earthquakes would not be able to nucleate under velocity-strengthening conditions. This view, however, is based on a relatively small number of experiments that were all done on the same type of experimental apparatus, the triaxial machine [8, 3, 1]. In addition, seismologic observations indicate that earthquakes do occur in the lower continental crust in various tectonic settings including regions of active extension and convergence in the temperature range at which existing laboratory data imply stable creep. To investigate the transition from unstable seismogenic slip to creep we performed a series of experiments on granite and gabbro using a heated direct shear apparatus.

EXPERIMENTAL SETUP

A direct shear apparatus consists of two steel sample holders that contain rock specimens with a total contact area of 2.64×10^3 square millimeters. The temperature of the samples is controlled using electric strip heaters connected to the sample holders. Normal stress is applied to the top sample holder by a ram with a PID-controlled hydraulic pump. The specimens are sheared at a constant velocity using a stepper motor. Experiments were conducted over a wide range of conditions including temperatures between 20-600 °C, load-point velocities 10^{-5} – 3×10^{-2} mm/s, normal stresses 5-40 MPa, on bare surfaces and simulated gouge, and at both dry and hydrated conditions. Direct-shear experiments can achieve large total displacements upon re-setting the sample multiple times. In case of stable slip, we performed velocity-stepping tests and directly measured the rate-state friction parameters a, b, D_c, and μ_o. In case of time-dependent (unstable) slip, we applied a constant load-point velocity and recorded the shear stress and sample displacement histories. The rate-state friction parameters were evaluated by fitting predictions of a one-dimensional spring-slider model incorporating rate-state friction to the stress timeseries.

NUMERICAL MODELING

We assume the classic rate-state constitutive equation at the sliding interface [2, 7],

$$\mu = \mu_o + a \ln\left(\frac{V}{V_o}\right) + b \ln\left(\frac{V_o\theta}{D_c}\right) \tag{1}$$

where μ is the coefficient of friction, V is the slip velocity, μ_o is the coefficient of friction at reference velocity V_o, a is the direct velocity effect, b is the evolution effect, θ is the state variable, and D_c is the slip weakening distance. We have used several evolution laws for the state variable θ, including the aging law [2], and the slip law [7]:

$$\dot\theta = 1 \nearrow \frac{V\theta}{D_c},\ \text{Aging}\ ; \dot\theta = \nearrow \frac{V\theta}{D_c} \ln\left(\frac{V\theta}{D_c}\right),\ \text{Slip} \tag{2}$$

The rate of change in shear stress $\dot{\tau}$ is given by

$$\dot{\tau} = k(V^* \nearrow V) \tag{3}$$

where k is the spring stiffness and V^* is the driving velocity. The best-fitting parameter values were chosen to be those that rendered the smallest misfit between the data and the model predictions. This process was repeated for data from experiments conducted at different temperatures. At high temperatures the best fit is obtained using the aging law. It reproduces the relatively constant displacement during "stick" intervals, as well as large stress drops during slip events. This model does a good job of reproducing the abruptness of slip events, although at the highest temperatures it still under-predicts the velocity during slip events. The model incorporating the slip law, on the other hand, over-predicts creep during "stick" intervals and under-predicts stress drops during slip events. The slip events predicted by this model are much less abrupt than those predicted by the model incorporating the aging law.

EFFECT OF WATER ON SLIP STABILITY

One could argue that the presence of water may help stabilize slip at high temperature by enhancing creep rate at the scale of micro-asperities[1]. Temperature and water content are expected to have similar effects on friction, as both factors contribute to lowering the effective viscosity of the asperity contacts. However, there may be a competition between a possible reduction in shear strength of the asperities, and an increase in the asperity size (and the true area of contact) [5]. To investigate the effects of water, we performed a series of tests in which water was injected into the bottom sample holder at a constant flow rate. We found that the injection of water into gouge samples at high temperature (300 and 500 °C) promotes stick-slip behavior. Slip events under hydrated conditions become notably larger compared to those under dry conditions.

MICRO-MECHANICAL INTERPRETATION

According to adhesion theory, the macroscopic friction coefficient is controlled by the area and the shear strength of microscopic contact asperities. Contact area may increase at higher temperatures due to enhanced creep and flattening of asperities [5, 6]. Modeling of stress histories associated with unstable slip using rate-state friction theory reveals that the observed decrease in $(a \nearrow b)$ with temperature occurs primarily at the expense of an increase in the "evolution" parameter b. Parameter b characterizes the rate of healing of a slip interface, often attributed to a time-dependent increase in real contact area due to creep at microscopic asperities [2]. Higher temperatures are expected to enhance frictional healing, resulting in greater values of b[5, 6]. The observed tendency for more unstable slip at greater temperature indicates that the parameter b is increasing with temperature at a greater rate than the parameter a. The effect of water on viscous flattening of the asperity contacts is expected to be similar to that of temperature: both processes result in higher rates of creep at the contacts and the concomitant frictional healing.

CONCLUSIONS

New high-temperature data on velocity dependence of granite and gabbro provide experimental evidence that friction of common crustal rocks can be velocity-weakening over a wider depth range than previously believed, in particular under dry conditions or low water fugacity. We note that these data are also relevant to the dynamics of earthquake ruptures. Our results suggest that frictional heating during rapid coseismic slip will result in the enhanced velocity-weakening due to decreases in the $(a \nearrow b)$ paramater. Temperature dependence of $(a \nearrow b)$ may thus contribute to dynamic weakening during seismic slip, in addition to a number of mechanisms predicted by theoretical studies and inferred from high-speed rock friction experiments.

References

[1] Blanpied M. L. , D. A. Lockner, and J. D. Byerlee: Fault stability inferred from granite silding experiments at hydrothermal conditions, Geophys. Res. Lett., 18(4):609, 1991.

[2] Dieterich. J. H.: Time-dependent friction and the mechanics of stick-slip, Pure and Applied Geophysics, 116:790-806, 1978.

[3] Lockner D. A., R. Summers, and J. D. Byerlee: Effects of temperature and sliding rate on frictional strength of granite, Pure and Applied Geophysics, 124: 445-469, 1986.

[4] Marone C.: Laboratory-derived friction laws and their application to seismic faulting, Annu. Rev. Earth Planet. Sci., 26: 643-696, 1998.

[5] Mitchell EK, Y Fialko, and KM Brown: Temperature dependence of frictional healing of Westerly granite: Experimental observations and numerical simulations, Geochemistry, Geophysics, Geosystems, 14: 567-582, 2013.

[6] Mitchell EK, Y Fialko, and KM Brown: Frictional properties of gabbro at conditions corresponding to slow slip events in subduction zones, Geochemistry, Geophysics, Geosystems, 16: 4006-4020, 2015.

[7] Ruina A.: Slip instability and state variable friction laws, J. Geophys. Res., 88:10359-10370, 1983.

[8] Stesky R. M.: Mechanisms of high temperature frictional sliding in Westerly granite, Canadian Journal of Earth Sciences, 15: 361-375, 1978.

[9] Tse S. T. and J. R. Rice: Crustal Earthquake Instability in Relation to the Depth Variation of Frictional Slip Properties: J. Geophys. Res., 91: 9452-9472, 1986.

VARIABILITY OF EARTHQUAKE SLIP AND ARRESTING DEPTHS IN FAULT MODELS

Junle Jiang[1a)] & Nadia Lapusta[1,2]
[1]*Division of Geological and Planetary Sciences, California Institute of Technology, Pasadena, CA, USA.*
[2]*Division of Engineering and Applied Science, California Institute of Technology, Pasadena, CA, USA.*

Summary Using rate-and-state fault models with temperature and pore pressure evolution, we explore the effect of depth-dependent fault properties, including permeability and shear-zone width, on earthquake slip and arresting depths as well as their variability which arise in the long-term fault behavior. Our fault models are susceptible to enhanced co-seismic weakening at high slip rates due to flash heating of micro-contacts and thermal pressurization of pore fluids. During large events, the along-depth behavior of dynamic earthquake rupture affects their along-strike development, due to the positive feedback loop between the rupture and weakening processes, even though fault properties are uniform along the strike. The non-uniform slip during one event leads to spatio-temporal complexity in subsequent events, including large variations of depth extent with time. These characteristics suggest that dynamic effects during earthquake ruptures are important factors which contribute to the complexity of earthquake slip and event patterns.

LONG-TERM FAULT MODELS WITH DEPTH-DEPENDENT PROPERTIES

Tectonic faults are characterized by depth-dependent frictional, hydraulic, and structural properties. Observationally, faults are separated into seismogenic layers (SL) and deeper creeping regions based on either microseismicity or inferred locking depth. Slip in large earthquakes is often assumed to be limited to the SL. Physically, this separation can be explained by conventional rate-and-state friction laws [1], which interpret the shallower interseismic locked zone as areas of velocity-weakening (VW) properties which allow for earthquake nucleation and the deeper creeping fault extensions as areas of velocity-strengthening (VS) properties which inhibit earthquake slip. The transition from VW to VS fault behavior could be associated with the onset of crystalline plasticity and the transition from brittle to semi-brittle deformation mechanisms as proposed in conceptual shear-zone models [2]. Recently, laboratory and theoretical studies [3,4] have revealed that enhanced dynamic weakening (DW) is a common phenomenon for rock friction at high slip rates. DW would presumably work in highly localized shear zones appropriate for mid-seismogenic depths, and could also be potentially active for the deeper VS fault extensions under conditions of high slip/strain rates, turning the stable fault areas into 'seismic' ones.

To study the long-term behavior of seismogenic faults, we develop 3D rate-and-state fault models [5] that incorporate evolution of temperature and pore pressure with depth-dependent frictional properties, permeability, and shear-zone width. Our fault models are governed by standard rate-and-state friction at low slip rates [1] and enhanced dynamic weakening at high slip rates, including two common mechanisms: flash heating (FH) of micro-contacts and thermal pressurization (TP) of pore fluids [4]. FH is effectively active only within the VW regions due to its inefficiency with the increase in ambient temperature [6] and more pronounced slip partitioning in the deeper shear zone, while TP is potentially active throughout the fault zone assuming that pore fluid is ubiquitous. The permeability on the fault decreases with depth as observed in the laboratory experiments (e.g., [7]), which favors thermal pressurization; the width of shearing zone increases below certain depth (as would be appropriate for delocalization caused by gradual transition from purely elastic to visco-elasto-plastic behavior) [8] which lowers the temperature rise due to earthquake-induced shear heating and hence makes thermal pressurization less efficient. Competition between the two properties, together with earthquake characteristics such as slip and slip rate, determines the depth dependence of co-seismic weakening, and hence the arresting of earthquakes at depth.

SIMULATED EARTHQUAKE SEQUENCES AND EVENT COMPLEXITY

We explore the characteristics of earthquake rupture and arrest processes in the long-term behavior of these fault models. We find that large earthquake ruptures can indeed penetrate below the conventionally defined seismogenic zone, into the "stable" fault regions, in models with reasonable fault properties. As shown in Figure 1, the simulated earthquake sequence in one of the models is characterized by large earthquakes that propagate across the fault with distance penetrating into the deeper VS regions, and smaller events which occur predominantly at the two ends of the fault due to concentrated loading from nearby creeping regions. There is variability in the arresting depths during large events, as dynamic rupture develops along the strike and interacts with shear-heating mechanisms, setting up a positive feedback loop between the dynamic process and fault weakening (Figure 1A). The complexity of single events leads to the spatio-temporal complexity throughout the sequence including large variations of earthquake depth extent with time, even though the frictional properties are uniform along the strike (Figure 1B).

Comparisons between the small and large earthquakes suggest that smaller ones fail to propagate over much of the weakly-stressed VW region, while large events occur at a higher overall stress levels. For large events, with the increase of event magnitude and associated slip, the penetration distance below the VW region increases in a nearly linear fashion,

[a)] Corresponding author. Email: jjle@gps.caltech.edu.

which is expected for the case of a near-constant stress drop. While the maximum local stress drop is ~50 MPa for most events, the energy-based slip-weighted estimates of stress drop produce smaller values (3-20 MPa), because a significant fraction of slip occurs in the VS regions of negative stress drop (stress increase) when earthquake penetrates deeper. These estimates are comparable to those of small events in the simulation and consistent with the range observed in seismology.

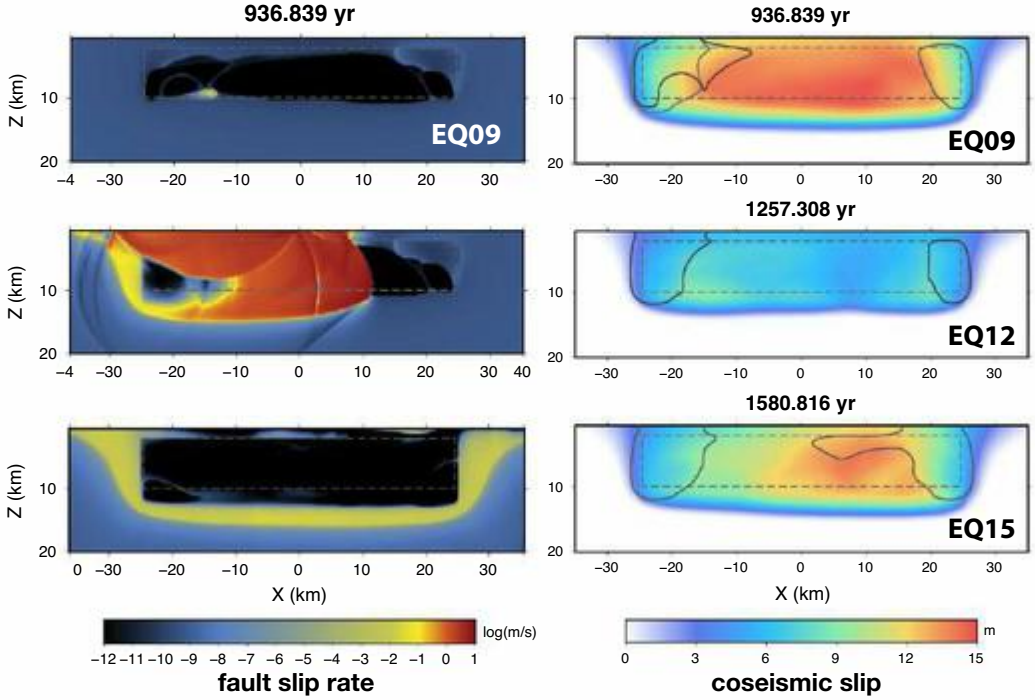

Figure 1. Variability in earthquake slip and arresting depths in models with depth-dependent permeability and shear-zone width. (Left) Snapshots of a large earthquake rupture (Event 9) with the slip rate in color on the logarithmic scale. (Right) Spatial distributions of coseismic slip are shown for three consecutive earthquakes. The spatial extent of smaller earthquakes that occur between the larger events (Event 9, 12 and 15) are indicated by black lines. The fault properties are the same throughout the simulation. At depths of 10-20 km, the model features a hydraulic diffusivity of 10^{-4} m^2s (proportional to permeability) and a shear zone width which transitions exponentially from 10 mm (10 km) to 1 m (20 km).

CONCLUSION

To study earthquake rupture and arrest at depth, we develop 3D rate-and-state fault models that incorporate enhanced dynamic weakening mechanisms – flash heating and thermal pressurization of pore fluids and feature depth-dependent fault properties based on laboratory experiments or motivated by geological studies. In our models, dynamic earthquake rupture couples with thermal pressurization, forming a positive feedback loop that enables penetration into the deeper VS regions, suggesting that physical models with realistic fault properties can indeed produce deeper penetration of large earthquake rupture. Our study demonstrates that dynamic processes during earthquake rupture can contribute significantly to slip heterogeneity and event complexity. In future studies, such physical models can be used to investigate the relative roles of fault property heterogeneity and earthquake dynamics in determining complexity of earthquake slip and patterns, and to reproduce physics-based earthquake scaling relations of slip, length and depth over a range of event sizes.

References

[1] Dieterich J.: Applications of Rate- and State-Dependent Friction to Models of Fault-Slip and Earthquake Occurrence, *Treatise on Geophysics (Second Edition)*, G. Schubert, ed. (Elsevier, Oxford, 2007), 2011.

[2] Scholz C. H.: The Mechanics of Earthquakes and Faulting, 2002.

[3] Di Toro G., et al.: Fault lubrication during earthquakes, *Nature*, **471**(7339): 494–498, 2011.

[4] Rice J. R.: Heating and weakening of faults during earthquake slip, *J. Geophys. Res*., **111**(B5), 2006.

[5] Noda, H., Lapusta N.: Three-dimensional earthquake sequence simulations with evolving temperature and pore pressure due to shear heating: Effect of heterogeneous hydraulic diffusivity, *J. Geophys. Res*., **115**(B12), 2010.

[6] Passelegue F.X., Goldsby D.L.: The influence of ambient fault temperature on flash-heating phenomena, *Geophys. Res. Lett*, **41**: 828–835, 2014.

[7] Mizoguchi K., et al.: Internal structure and permeability of the Nojima fault, southwest Japan, *J. Struct. Geol*., **30**(4):513–524, 2008.

[8] Cole J., et al.: Localized ductile shear below the seismogenic zone: Structural analysis of an exhumed strike-slip fault, Austrian Alps, *J. Geophys. Res.: Solid Earth*, **112**(B12), 2007.

EXPLORING MODELS OF FORESHOCK SOURCES USING RATE-AND-STATE FRICTION

Natalie Higgins[1a)] & Nadia Lapusta[1, 2]
[1]*Division of Engineering and Applied Science, California Institute of Technology, Pasadena, CA, USA*
[2]*Division of Geology and Planetary Science, California Institute of Technology, Pasadena, CA, USA*

Summary Many large earthquakes are preceded by foreshocks, which are understood to occur within the nucleating region of the mainshock. How are these precursory events able to occur without immediately triggering the larger event? In this study, earthquake nucleation is investigated numerically via simulations of earthquake cycles with foreshocks occurring on a rate-and-state fault. Inspired by the asperity interpretation of foreshock sources from laboratory observations, the models presented here have heterogeneous fault properties with patches that are under higher compression and/or smoother. In this unique model, mainshocks occur in the larger-scale velocity-weakening region and foreshocks can occur on the embedded patches. The results show that the rate-and-state models of foreshock sources are suitable for producing isolated foreshocks under the right conditions of scale separation. In addition, despite the wide variation in patch parameters implemented, remarkably, stress drops of the foreshocks are consistent with laboratory and field observations and are approximately constant.

MOTIVATION

On both natural and laboratory faults, many large earthquakes are preceded by foreshocks (e.g., [1]), which are hypothesized to occur within the nucleating region of the mainshock. However, the question remains: how are these precursory events able to occur in such a region without immediately triggering the larger event? The overarching goal of this project is to understand the physics of foreshocks and their relation to the nucleation of the mainshock. Investigation of how earthquakes initiate is a fascinating problem that also has powerful implications for earthquake forecasting. In this study, earthquake nucleation is explored by creating mechanical models of earthquake sources and numerically simulating their behaviour over time.

METHODOLOGY

Frictional instability and nucleation

The simulated fault interface is governed by the Dieterich-Ruina rate-and-state friction law:

$$\tau = \sigma\left[f_0 + a\ln\left(\frac{V}{V_0}\right) + b\ln\left(\frac{V_0\theta}{L}\right)\right] \quad \text{with} \quad \dot{\theta} = 1 - \frac{V\theta}{L}; \quad \text{and} \quad \bar{h}^*_{3D} = \frac{\pi}{2}\frac{\mu b L}{(b-a)^2\sigma} \tag{1}$$

where the shear resistance τ is related to the effective normal stress σ through a friction coefficient that depends on slip rate V and the "state" of the interface θ via parameters a, b, f_0, V_0 and characteristic slip L. For a constant slip velocity V, the state variable θ evolves to a steady-state value of L/V, thereby identifying the quantity $(a-b)$ as the one governing the rate dependence of the modeled interface. A velocity-weakening (VW) dependence, with $(a-b) < 0$, is required for spontaneous slip instabilities (earthquakes) to develop, whereas a velocity-strengthening (VS) dependence, with $(a-b) > 0$, results in stable slip in response to slow tectonic loading. For dynamic instability, in addition to the VW dependence, the size of the nucleating region needs to be large enough. This critical minimum size for dynamic rupture to develop has been estimated using 2D theoretical stability analysis of a quasi-static crack [2], and its 3D extension is given in (1) as $\bar{h}^*_{3D}$, where μ is the shear modulus. As the estimate shows, the nucleation size h^* depends on the effective normal stress and the fault frictional properties from the rate-and-state law. Furthermore, numerical studies have shown that there are additional factors that can affect the nucleation size, such as the loading rate.

Model setup and approach

Inspired by the unique laboratory-scale earthquake proxy experiments of [3], here, we develop numerical simulations of earthquake cycles with foreshocks using laboratory-relevant parameters. Due to the persistent locations of foreshock sources in the experiments, these small seismic events are inferred to be occurring at asperities, i.e. bumps, on the fault interface. In line with this asperity concept, the mechanical models of foreshock sources developed here consist of a larger-scale seismogenic region (with corresponding nucleation size h^*_{main}) with embedded patches of elevated normal stress σ (higher compression) and/or lower characteristic slip L (smoother interface) (Figure 1). Both a higher σ and lower L contribute to decreasing the nucleation size on the patch, h^*_{patch}. In order to produce isolated smaller-scale events, i.e. foreshocks that do not immediately trigger the mainshock, the two nucleation sizes in the model, h^*_{main} and h^*_{patch}, must be sufficiently separated. Our simulation code enables the elastodynamic analysis of a 2D planar fault, with the aforementioned heterogeneous properties, enclosed in a 3D homogeneous elastic bulk [4].

[a)] Corresponding author. Email: nhiggins@caltech.edu.

RESULTS AND DISCUSSION

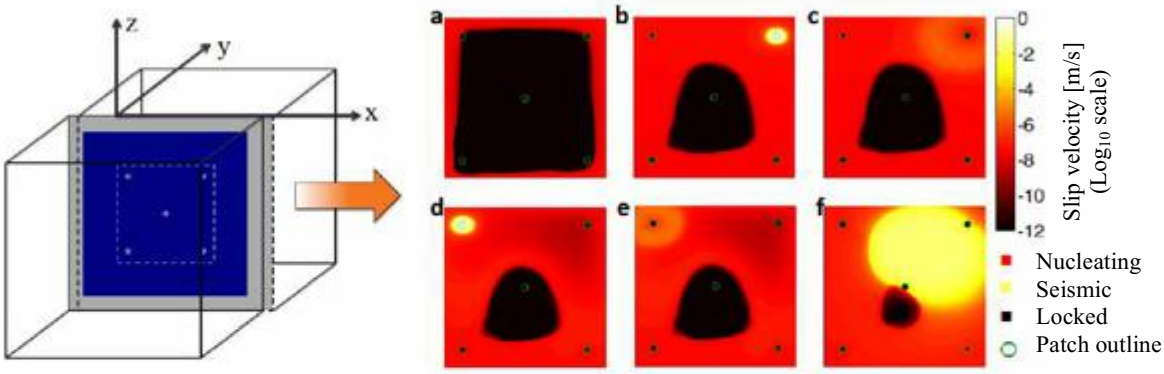

Figure 1: Diagram of simulation process. (Left) 3D problem with a heterogeneous distribution of normal stress on the fault interface. (Right) Representative snapshots of the slip velocity distribution in the seismogenic region, showing (a) mostly locked (black) fault zone; (b,d) small events (bright yellow) occurring on highly compressed patches driven by the nucleation (red) of the large-scale event; (c, e) postseismic effects of the small events; and (f) nucleation (yellow) of a larger-scale event.

Our simulations indeed produce isolated small events occurring within the larger-scale nucleation (Figure 1). For the model to produce such isolated smaller-scale events, the nucleation sizes h^*_{main} and h^*_{patch} must be substantially different. This factor of scale separation is at least 10 in the simulations so far, and potentially much more in future examples. This separation of scales can be achieved by assigning high levels of compression on the patches. However, one would expect unrealistically large stress drops for events on such patches, since friction and hence changes in friction scale with the compressive stress. Remarkably, in this model, stress drops are approximately constant, despite a wide variation in patch compression (Figure 2a). This is mostly due to dynamic rupture exiting from the patch into the surrounding low-stress-drop region (Figure 2b). The resulting stress drops are consistent with inferences for both laboratory and natural faults.

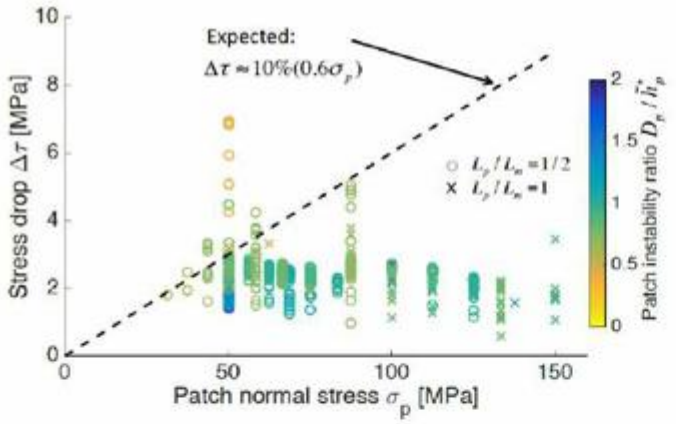

(a) Stress drops of patch-hosted events for varied simulations

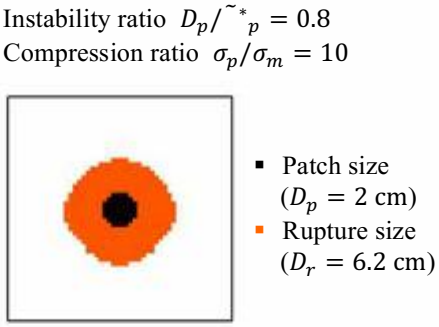

(b) Exemplary comparison of rupture area to patch size

Figure 2: Summary of trends in stress drops from simulations

Current work is directed towards exploring whether the smaller events, occurring on highly compressed patches due to nucleation-induced creep, have any observable differences from other seismic events, and hence whether they can be identified as foreshocks before the mainshock event.

References

[1] Bouchon, M., V. Durand, D. Marsan, H. Karabulut, and J. Schmittbuhl, The long precursory phase of most large interplate earthquakes, *Nature Geoscience, 6*, 299-302, 2013. doi: 10.1038/NGEO1770.

[2] Rubin, A. M., and J. P. Ampuero, Earthquake nucleation on (aging) rate and state faults, *Journal of Geophysical Research*, *110*(B1), B11312, 2005. doi:10.1029/2005JB003686.

[3] McLaskey, G. C., and B. D. Kilgore, Foreshocks during the nucleation of stick-slip instability, *Journal of Geophysical Research: Solid Earth, 118*, 2982–2997, 2013. doi:10.1002/jgrb.50232.

[4] Lapusta, N., and Y. Liu, Three-dimensional boundary integral modeling of spontaneous earthquake sequences and aseismic slip, *Journal of Geophysical Research, 114*, B09303, 2009. doi:10.1029/2008JB005934.

EXPERIMENTAL STUDIES AND MATHEMATICAL MODELING FOR DYNAMIC DEFORMATION OF SOILS

Anatoliy Bragov[1], Vladimir Balandin[1], Leonid Igumnov[1], Vasiliy Kotov[1a)], Alexandr Konstantinov[1] Andrey Lomunov[1], and William Proud[2]
[1]*Research Institute for Mechanics, Lobachevsky State University, Nizhny Novgorod, Russia*
[2]*Imperial College, London, UK*

Summary A complex experimental-theoretical approach to studying the problem of high-rate strain of soft soil media is presented. This approach combines the following contemporary methods of dynamical tests: the modified Hopkinson–Kolsky method applied to medium specimens contained in holders and the method of plane wave shock experiments. The following dynamic characteristics of sand soils are obtained: shock adiabatic curves, bulk compressibility curves, and shear resistance curves. The obtained experimental data are used to study the high-rate strain process in the system of a split pressure bar, and the constitutive relations of Grigoryan's mathematical model of soft soil medium are verified by comparing the results of computational and natural test experiments of impact and penetration to sand and clay.

INTRODUCTION

The dynamic properties of soft soils have been studied by many authors [1–2], but the range of pressures (< 50MPa) and strain rates (<10^2 s^{-1}) considered in these studies is insufficiently high. Only isolated attempts were made to study the dynamic compressibility in the intermediate range of loads (50–500MPa) and strain rates (10^2–10^4 s^{-1}). These attempts are related to the modified Kolsky method with the use of split Hopkinson pressure bars (SHPB) and a confining holder. But the possibility of using this method [3] to study the compressibility and plastic properties of soil media is restricted by the elastic limit of the pressure bar and holder materials, and the range of considered loads does not exceed 0.5GPa. Higher values of load amplitudes are attained under shock wave loading [4–8]. For the pressure ranges up to several gigapascals, there are no experimental data of the shock compressibility because of severe methodological difficulties in measurements of two components of the stress tensor. Plane wave shock or explosion experiments used in the field permit reliably determining only the shock adiabatic (SA). Thus, at present there are no sufficiently developed efficient methods for studying the physical-mechanical properties of soil media in a wide pressure range. It seems very promising to develop a complex experimental-theoretical approach [9] to the study of the properties of soils under dynamic loading and plane wave tests in combination with the data obtained by the modified SHPB method with the use of well-known soil models.

EXPERIMENTAL STUDIES OF DYNAMIC COMPRESSIBILITY OF SOIL MEDIA

The dynamic compressibility of soft soils can be studied experimentally in a wide range of strain rates by the following two complementary methods. The modified Kolsky method combined with the use of the split Hopkinson pressure bar (SHPB) is used for the strain rates 10^3 s^{-1} and loads up to 500MPa, and the plane wave shock experiment is used for higher strain rates (greater than 10^4 s^{-1} and loads greater than 500MPa). In both methods, the same type of stress–strain states of the specimen takes place, i.e., the one-dimensional strain ε_z and the bulk stress state with different stress tensor components σ_z and σ_r. This approach [10] permits one to obtain data for the dynamic compressibility in the pressure range from dozens of megapascals to several gigapascals.

The modified SHPB method allows one, in a single experiment, to determine the principal components of the stress tensor and obtain the uniaxial strain σ_z–ε_z curves, the bulk compressibility p–ρ curves, the τ–p dependence of the shear resistance on the pressure, and the lateral earth pressure coefficient $\xi = \sigma_r/\sigma_z$.

Figure 1 illustrates the averaged data obtained in nine tests with sand of air humidity and density 1.5 g/cm^3 by the modified Kolsky method at various load levels. The markers show the shock compressibility (*a*) and shear resistance (*b*) curves in GPa, and the solid lines are the approximating dependencies.

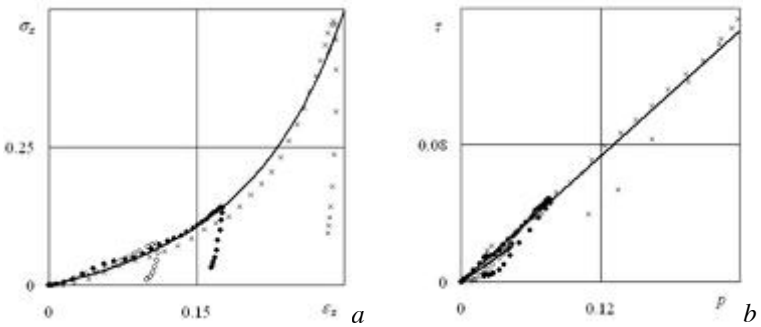

a *b*

Fig. 1

The experiments aimed at determining the shock compressibility of soils are based on the reflection method. Tests performed at various impact velocities allow one to obtain a SA for the material [5].

As was previously mentioned, the use of two complementary methods with the same type of the stress–strain state allows one to construct unified σ_z–ε_z curves under the uniaxial strain conditions in a wide range of loading parameters.

a) Corresponding author. Email: vkotov@inbox.ru

In Fig. 2, the dark and light points present the results of plane wave and reversed experiments in the form of stress (*GPa*) dependence on the density; the solid and dashed lines present the approximating dependencies for the initial densities of sand ρ_0 = 1.5 and 1.72 g/cm^3 respectively. The unified shock compressibility curve (solid line) of sand soil with the density 1.5 g/cm^3 (also see Fig. 1 *a*) agrees well with the earlier obtained results [6] for sand of nearly the same density. We also note that the SA curves of sand with various initial densities approach each other for pressures greater than 1 GPa.

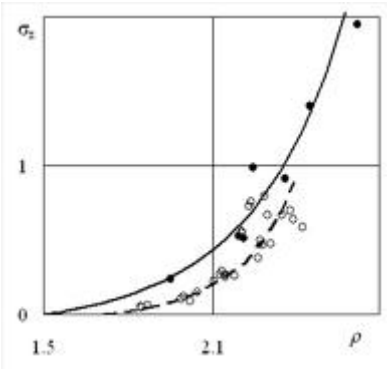

Fig. 2

NUMERICAL VERIFICATION

The numerical calculations were carried out using the mathematical model of dynamics of the Grigoryan soil medium [1], which is written in the cylindrical system of coordinates in the form of the set of differential equations expressing the laws of conservation of mass, pulse, and maximal density achieved during the active loading of the soil, and also the equations of the theory of plastic flow with the von Mises condition of plasticity. The set is closed by the finite relations determining the dynamic compressibility and resistance to shift of the soil medium. The contact algorithm of "impermeability" along the normal with "sliding along tangent with dry friction" is formulated according to the modified friction law.

Consider the problem of penetration of a cylindrical impactor with plane end surface into sand soil with a constant velocity. Figure 3 illustrates the dependence of the force (*kN*) of resistance to the impactor penetration with plane end surface into sand at the quasistationary stage on the impactor velocity (*m*/*s*). The dark markers correspond to experimental results, the light markers correspond to the impact velocities V_0 = 48, 100, 180, 275, 335 m/s and were obtained as averaged over five tests, and the intervals show the error with the confidence probability equal to 0.95.

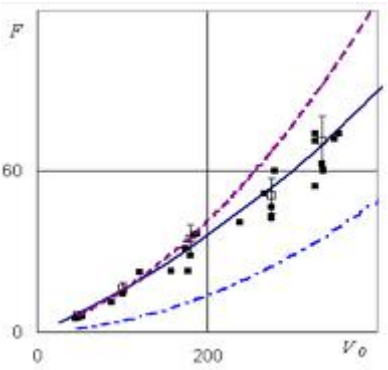

Fig. 3

The solid, dashed, and dash-pointed lines correspond to the computation results obtained by using the nonlinear and linear dependencies and of the yield point on the pressure and in the hydrodynamic approximation.

CONCLUSION

The paper deals with the complex experimental-theoretical approach to solving the problem of high rate strain of soft soil media, which combines the contemporary method of dynamical tests, the study of the impact deformation processes and obtaining the dynamical properties of soils on this basis, the choice of contemporary mathematical models and their constitutive relations which adequately describe the basic effects of high-rate strain, the identification of the constitutive relations by using experimentally obtained data, and their verification by comparing the results of computational and nature test experiments on impact and penetration. The common experimental and computational studies permit significantly increasing the reliability of the obtained results, which opens broad prospects in complex studies of nonlinear effects and laws of dynamical deformation of soft soil media.

Experimental research was supported by the Russian Science Foundation (grant No. 14-19-01096), numerical simulation was supported by RFBR (grants 16-01-00524, 16-08-00825).

Referencies

[1] Grigoryan S.S.: About the basic conceptions of the mechanics of soils. *Prikl Mat Mekh* **24** 1057–1072, 1960 [in Russian].
[2] Omidvar M., Iskander M., Bless S.: Stress-Strain Behavior of Sand at High Strain Rates. *Int. J. Impact Engng* **49** 192–213, 2012.
[3] Bragov A.M., Grushevskii G.M., Lomunov A.K.: Use of the Kolsky Method for Confined Tests of Soft Soils. *Exper. Mech.* **36(3)** 237–242, 1996.
[4] Lagunov V.A., Stepanov V.A.: Measurements of the Dynamic Compressibility of Sand under High Pressures. *Zh. Prikl.Mekh. Tekhn. Fiz.*, **1** 88–96, 1963.
[5] Kanel G.I., Razorenov S.V., Utkin L.V., Fortov V.E.: *Shock Wave Phenomena in Condensed Media,* Yanus-K, Moscow, 1996.
[6] Dianov M.D., Zlatin N.A., Mochalov S.M., et al.: Shock Compressibility of Dry and Water-Saturated Sand. *Tech. Phys. Lett.* **2** 207–208, 1977.
[7] Bragov A.M., Grushevskii G.M.: Influence of the Moisture Content and Granulometric Composition on the Shock Compressibility of Sand. *Tech. Phys. Lett.* **19** 385–386, 1993.
[8] Bragov A.M., V. V. Balandin, A. K. Lomunov, and A. R. Filippov: Determining the Impact Compressibility of Soft Soils from Reversed Test Results. *Tech. Phys. Lett.* **32(6)** 487–488, 2006.
[9] Bazhenov V.G., Bragov A.M., Kotov V.L.: Experimental-Theoretical Study of the Penetration of Rigid Projectiles and Identification of Soil Properties. *J. Appl. Mech. Tech. Phys.* **50(6)** 1011–1019, 2009.
[10] Bragov A.M., Lomunov A.K., Sergeichev I.V., et al.: Determination of Physicomechanical Properties of Soft Soils from Medium to High Strain Rates. *Int. J. Impact Engng* **35** 967–976, 2008.

PHYSICS-BASED ELASTODYNAMIC MODELING OF INTERACTING FRICTIONAL SHEAR CRACKS

Semechah K. Y. Lui[1a)] & Nadia Lapusta[1,2]
1. Division of Geological and Planetary Sciences, California Institute of Technology, Pasadena, CA, USA.
2. Division of Engineering and Applied Science, California Institute of Technology, Pasadena, CA, USA.

Summary Earthquake sources are frictional shear cracks inside the earth. They often interact by triggering one another. These interactions and their governing physical mechanisms can be studied through physics-based elastodynamic modeling. Here we model the interaction of repeating earthquakes in the framework of rate-and-state fault models using state-of-the-art simulation methods that reproduce both realistic seismic events and long-term earthquake sequences. Our simulations enable comparison among several types of stress transfer that occur between the repeating events. Our major finding is that postseismic creep dominates the interaction. Our findings open a possibility of using interaction of repeating sequences to estimate friction properties of creeping segments. As we refine our model and incorporate enhanced dynamic weakening mechanisms, we are able to reproduce realistic repeating earthquake sequences observed at Parkfield, California.

INTRODUCTION

Interaction of frictional shear cracks is important for uncovering fault physics and quantifying seismic hazard. Most explanations attribute this interaction to either static or dynamic stress changes caused by coseismic slip, although other mechanisms of interaction exist, and the governing physical mechanisms remain unclear [1]. Repeating microearthquake sequences are highly suited for studies of earthquake interaction due to their short recurrence time and known locations. For example, the "San Francisco" (SF) and "Los Angeles" (LA) repeating sequences on the creeping section of the San Andreas Fault in Parkfield, California are located close to each other and appear to interact. Here we aim at quantifying earthquake interactions through small repeaters and applying our model to explain field observations.

METHOD

Our numerical simulations are based on a model of a fault surface embedded into an elastodynamic medium, which is governed by laboratory-derived rater-and-state friction laws that have been successful in reproducing a number of earthquake phenomena [2]. At steady state, when slip velocity (V) is constant, the shear strength (τ_{ss}) is given by:

$$\tau_{ss} = \bar{\sigma}[f_0 + (a-b)\ln\frac{V}{V_0}]$$

where $\bar{\sigma}$ is the effective normal stress, f_0 is the reference friction coefficient at the reference slip velocity V_0, a and b are rate-and-state parameters. An interface with $a-b<0$ has friction being velocity weakening (VW), while $a-b>0$ indicates velocity strengthening (VS). In our fault model, two VW patches are surrounded by VS areas (Fig 1); outside, the long-term slip rate (V_{pl}) is imposed. Stresses, slips, and slip rates within the VW and VS regions are computed by equating the fault shear stress given by elastodynamic relations with the fault strength given by the friction law [3]. Our simulations produce realistic fault responses, including stick-slip behavior of the patches with aseismic nucleation processes, seismic events, and postseismic slip. This model allows us to compare effects of static stress changes due to coseismic and postseismic slip, as well as dynamic stress changes due to seismic waves.

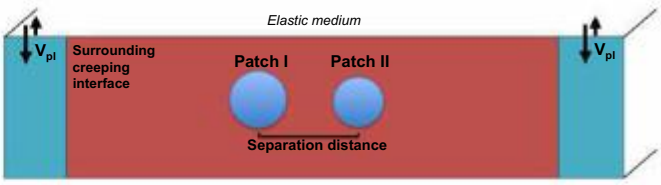

Fig 1. Fault model set up

To use the model to study earthquake interaction, we set up a quantitative measure of the interaction by assigning specific initial conditions on the fault, such that the two VW patches, if not interacting, produce earthquakes as far in time from each other as possible, i.e. half of their recurrence interval T_r apart. If interaction exists, events on the two patches occur closer in time. The difference ζ between the simulated inter-event time ΔT_{sim} and the non-interacting inter-event time $0.5T_r$, normalized by $0.5T_r$, can serve as the measure of the degree of interaction:

$$\zeta = \frac{|\Delta T_{sim} - 0.5T_r|}{0.5T_r}$$

RESULTS

As expected based on intuition and prior studies, the two seismogenic VW patches behave independently when they are far apart and rupture together if they are right next to each other. In the intermediate range of distances, ruptures on the two patches cluster in time. Importantly, interaction exists at distances as large as 7 patch diameters, which is unexpected given

a) Corresponding author. Email: klui@caltech.edu

the typical interaction distances of 1 to 2 rupture diameters [1]. Our simulation reveals several types of stress transfer that occur between the VW patches which host the repeating sequences. (i) As patch I ruptures, dynamic wave-mediated stress changes occur, which do not seem to have any appreciable effect in our model. (ii) Right after the end of the seismic event, patch II receives a positive jump of static stress due to the coseismic slip on patch I. (iii) Such static stress increase is experienced by other points on the fault, thus causing the stressing rate in the VS area adjacent to patch II to increase. (iv) A traveling postseismic front, which arrives at patch II slightly later in time, brings with it even larger stressing rate increases. Comparing the extent of interaction in our simulation and that in the Coulomb failure model and Dieterich aftershock model which only accounts for the effect of (ii) [4,5], the difference is as large as 75%, as marked in Fig 2 by orange arrows. These results indicate that earthquake triggering in our simulations is primarily due to the effect of (iv) – the accelerated postseismic creep.

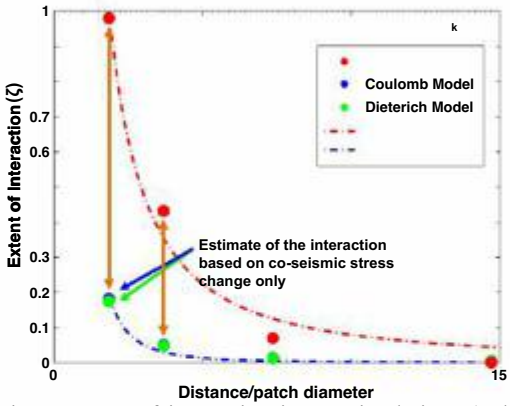

Fig 2. Extent of interaction in our simulations (red VS patches. Estimates of the interaction based on the coseismic stress changes only for the Coulomb and Dieterich models are shown as blue and green dots, respectively.

Our finding that the interaction of earthquakes on creeping segments is dominated by their postseismic slip opens the possibility of estimating fault friction properties based on modeling the interaction. Our results indicate that more VS faults, i.e. faults with larger values of $(a-b)_{\mathrm{VS}}$, suppress propagating creep fronts and reduce interaction. Further, triggering time is determined by the propagation speed of postseismic creep, which depends on the frictional properties and the coseismic stress increase on the creeping area. This latter parameter is related to the stress drop of the seismic event and can be estimated from coseismic slip distribution in the ruptured region. Therefore, with known stress drops and triggering mechanisms, it is possible to infer the frictional properties of the creeping region.

Next we model the interaction of the SF and LA repeaters at Parkfield, focusing on some intriguing observations, which include the inferred stress drops of these repeaters higher than the typical range and these sequences' irregular interaction before the 2004 Mw 6.0 event. To explain these phenomena, we incorporate in our model enhanced dynamic weakening of the VW patches with thermal pressurization [6]. We are able to reproduce similar seismic events as the SF and LA sequences, with comparable moment magnitude, recurrence time, triggering time, and high stress drop (Fig 3). The inferred frictional properties of the creeping segment, namely $(a-b)_{\mathrm{VS}}$, are also consistent with studies of laboratory friction and postseismic slip.

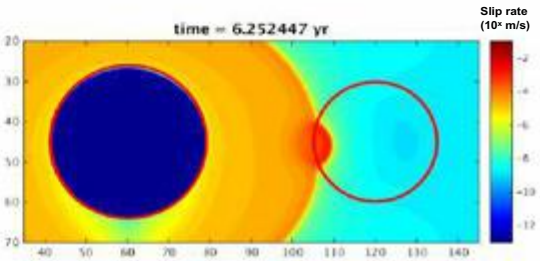

Fig 3. Slip-rate snapshot demonstrates the interaction between the SF and LA repeating sequences. Red circles indicate the two velocity-weakening patches. The left (SF) patch, which is now locked, has just experienced a seismic event. The (traveling) postseismic slip (orange) has just arrived at the LA patch, initiating near-seismic slip there (red).

CONCLUSIONS AND OUTLOOK

To summarize, the interaction of frictional shear cracks is studied using an elastodynamic fault model. Results show that static stress changes due to postseismic slip may dominate the interaction of repeating earthquakes on creeping segments. The associated propagating stress front causes the interaction to extend much farther than would be expected based on static stress changes from coseismic slip alone. This finding allows using interaction of repeating earthquakes to determine friction properties of the surrounding creeping regions. Our refined fault model with dynamic weakening can reproduce field observation of the repeating sequences at Parkfield. Current work focuses on exploring the extent of heterogeneity needed in our fault model in order to reproduce the irregular patterns observed at Parkfield, as well as fault models with repeaters occurring on VW patches with higher normal stress.

References

[1] Freed, A. M.: Earthquake triggering by static, dynamic, and postseismic stress transfer. *Annu. Rev. Earth Planet. Sci.* **33**: 335-367, 2005.

[2] Dieterich, J. H.: Modeling of rock friction: 1. Experimental results and constitutive equations. *J. Geophys. Res.* **84(B5)**: 2161-2168, 1979.

[3] Lapusta, N, & Liu, Y.: Three-dimensional boundary integral modeling of spontaneous earthquake sequences and aseismic slip. *J. Geophys. Res.* **114**: doi:10.1029/2008JB005934, 2009.

[4] Gomberg, J., Beeler, N., & Blanpied, M.: On rate-state and Coulomb failure models. *J. Geophys. Res.* **105(14)**: 7857-7872, 2000.

[5] Dieterich, J. H.: A constitutive law for rate of earthquake production and its application to earthquake clustering. *J. Geophys. Res.* **99**: 2601-2601, 94.

[6] Noda, H., & Lapusta, N.: Three-dimensional earthquake sequence simulations with evolving temperature and pore pressure due to shear heating: Effect of heterogeneous hydraulic diffusivity. *J. Geophys. Res*, **115**(B12), 2010.

RECIRCULATING ICE EDDIES IN SUBGLACIAL VALLEYS

Colin R. Meyer *[1], Timothy T. Creyts[2], and James R. Rice[1,3]

[1]*John A. Paulson School of Engineering and Applied Sciences, Harvard University, MA, USA*
[2]*Lamont-Doherty Earth Observatory, Columbia University, NY, USA*
[3]*Department of Earth and Planetary Science, Harvard University, MA, USA*

Summary In many locations beneath both Greenland and Antarctica, ice flows across deep valleys, potentially forming viscous eddies that can lead to stratigraphic folds. We use a set up analogous to Moffatt [1], where our domain is a subglacial valley. We numerically solve the non-Newtonian Stokes equations with a shear-thinning power-law rheology to determine the critical valley angle for the eddies to form. Shear-thinning fluids allows for greater shear localization and, therefore, ice requires smaller valley angles (steeper slopes) to form eddies than a Newtonian fluid. Due to the significant variation of temperature from the warm base to the cold surface of the ice, we analyze eddy formation when the rheology is temperature dependent. The warmer basal ice is less viscous and eddies form in larger valley angles (shallower slopes). Finally, we solve for the ice flow over topography from the Gamburtsev subglacial mountains and show Moffatt eddies in the subglacial valleys.

INTRODUCTION

Complex structures that include large stratigraphic folds and basal freeze-on ice affect ice cores by contaminating the horizontal layering [2, 3]. Long climate records can be recovered from deep ice if the original horizontal signature of deposition is preserved. For extensive overturning, reconstruction of climate records may not be possible. Here, we examine the development of Moffatt (recirculation) eddies at the base of ice sheets.

The creep of ice over long periods of time can be described by the flow of a viscous fluid with a non-Newtonian rheology. The most commonly used rheology in glaciology is a shear-thinning power-law rheology called Glen's law [4]

$$\dot{\epsilon}_E = A\tau_E^n, \tag{1}$$

where A is the ice softness, $\tau_E = \sqrt{\sigma'_{ij}\sigma'_{ij}/2}$ and $\dot{\epsilon}_E = \sqrt{\dot{\epsilon}_{ij}\dot{\epsilon}_{ij}/2}$ are the second invariants of the deviatoric stress $\sigma'_{ij} = \sigma_{ij} + p\delta_{ij}$ and strain rate $\dot{\epsilon}_{ij} = \left[(\partial u_i/\partial x_j) + (\partial u_j/\partial x_i)\right]/2$ tensors respectively. The parameter n is the rheological exponent and typically chosen to be 3 [4]. Moffatt eddies have been demonstrated in a power-law fluid [5, 6].

CRITICAL CORNER ANGLES IN ICE

In Moffatt's formulation for corner eddies [1], a Newtonian fluid flows across a wedge and the onset of recirculation is governed by a critical wedge angle α_c. If the wedge angle is shallower than the critical angle, no recirculation occurs, while if the wedge angle greater than the critical angle, then fluid recirculates indefinitely. For a fluid with a power-law rheology, the two control parameters are the wedge angle α and the rheological exponent n. We determine α_c as a function of n by solving the non-Newtonian Stokes equations in a wedge with no slip boundary conditions applied along the base (Figure 1). For ice, $n = 3$ [4] and, therefore, $\alpha_c = 13\ ^\circ$. Using this value, we examine radar data from the Gamburtsevs subglacial mountains and determine valleys where slopes may be steep enough to form Moffatt eddies. We then model the flow over these valleys using finite element simulations.

THERMOMECHANICAL EDDY SIMULATIONS

We use a temperature-dependent ice rheology in the non-Newtonian Stokes equations to examine the formation of valley eddies in the Gamburtsev subglacial mountains. The ice softness A from Glen's law (Equation (1)) is strongly temperature dependent and commonly modeled as an Arrhenius exponential. We solve the internal energy and momentum equations

$$Pe\ \underline{u}\cdot\nabla T = \nabla\cdot(\kappa\nabla T) + BrA^{-\frac{1}{n}}\dot{\epsilon}_E^{\frac{1}{n}+1}, \tag{2}$$

$$\nabla\cdot\left(A^{-\frac{1}{n}}\ \dot{\epsilon}_E^{\frac{1}{n}-1}\underline{\underline{\dot{\epsilon}}}\right) = \nabla p, \tag{3}$$

where Pe is the Péclet number, $\underline{u}$ is the velocity, T is the temperature, κ is the diffusivity, Br is the Brinkman number, and p is the pressure. Figure 2 shows the result of a COMSOL simulation of these equations over the Gamburtsev subglacial mountains, with no slip and fixed melting temperature boundary conditions along the base. Moffatt eddies can be seen in the three deepest valleys.

*Corresponding author. Email: colinrmeyer@gmail.com

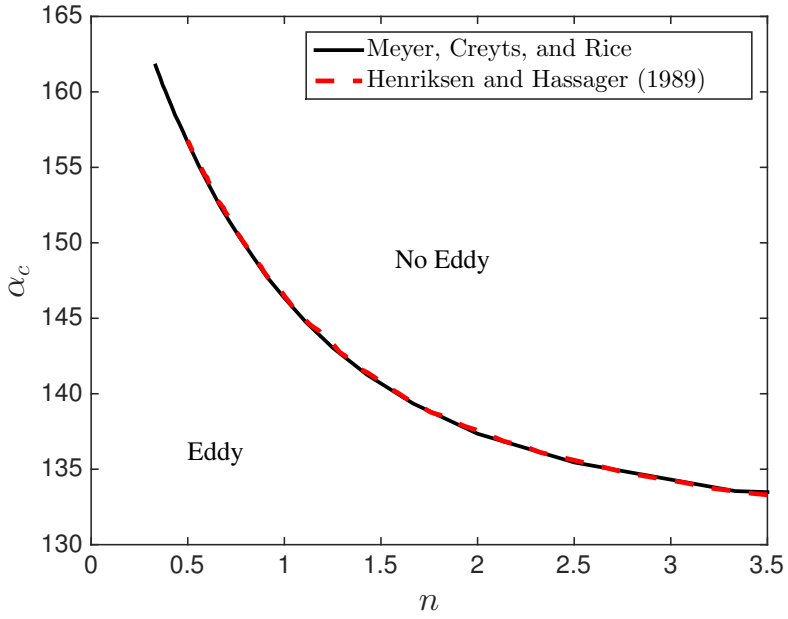

Figure 1: Critical corner angle α_c at which eddies first appear with viscosity exponent n. Red dashed line is simulation results from [5].



Figure 2: Comsol simulation of horizontal velocity over line 330 with temperature dependence: melting temperature and no slip at base.

CONCLUSIONS

In this paper, we determine the critical angle for Moffatt eddy formation in ice and use this critical angle to determine locations where Moffatt eddies may exist in the Gamburtsev subglacial mountains. We then model these locations using finite element simulations and show Moffatt eddies in subglacial valleys.

References

[1] Moffatt, K. H. (1964), Viscous and resistive eddies near a sharp corner, *J. Fluid Mech.*, *18*, 1–18.

[2] Bell, R. E., F. Ferraccioli, T. T. Creyts, D. Braaten, H. Corr, I. Das, D. Damaske, N. Frearson, T. Jordan, K. Rose, M. Studinger, and M. Wolovick (2011), Widespread persistent thickening of the east antarctic ice sheet by freezing from the base, *Science*, *331*(6024), 1592–1595.

[3] Alley, R. B., A. J. Gow, D. A. Meese, J. J. Fitzpatrick, E. D. Waddington, and J. F. Bolzan (1997), Grain-scale processes, folding, and stratigraphic disturbance in the GISP2 ice core, *J. Geophys. Res.*, *102*(C12), 26819–26830.

[4] Glen, J. W. (1955), The creep of polycrystalline ice, *Proc. R. Soc. Lond. Ser. A*, *228*(1175), 519–538.

[5] Henriksen, P., and O. Hassager (1989), Corner flow of power law fluid, *J. Rheology*, *33*(6), 865–879.

[6] Gudmundsson, G. H. (1997), Basal-flow characteristics of a non-linear flow sliding frictionless over strongly undulating bedrock, *J. Glaciol.*, *43*(143), 80–89.

RATE AND STATE FRICTION LAW AS DERIVED FROM ATOMISTIC PROCESSES AT ASPERITIES

Takahiro Hatano [*1]
[1] *Earthquake Research Institute, University of Tokyo, Tokyo, Japan*

Summary The RSF law describes rock friction quantitatively and therefore it is commonly used to model earthquakes and the related phenomena. But the RSF law is rather empirical and the theoretical basis has not been very clear. Here we derive the RSF law starting from constitutive laws for asperities, and give the atomistic expressions for the empirical RSF parameters. In particular, we show that both the length constant and the state variable are given as the 0th weighted power means of the corresponding microscopic quantities: a linear dimension and the contact duration of each asperity. As a result, evolution laws for the state variable can be derived systematically. We demonstrate that the aging and the slip laws can be derived and clarify the approximations behind these two major evolution laws. Additionally, the scaling properties of the length constant are clarified for fractal distribution of asperities.

BACKGROUND

The rate and state friction (RSF) law describes rock friction quantitatively [1] and therefore it is commonly used to model earthquakes and the related phenomena. But the RSF law is rather empirical and the theoretical basis has not been very clear. Particularly, the RSF law contains three empirical parameters, which dominate the degree of frictional stability/instability [2] Due to the empirical nature of the RSF law, however, these parameters should be given only empirically but cannot be inferred theoretically.

Among these parameters, the only dimensional parameter is the length constant L. The length constant is particularly important because it scales the critical nucleation size prior to unstable rupture propagation. Conventionally, L is interpreted as the typical size of asperity. This means that the RSF law could be scale-dependent, as the asperity size may depend on the size of the frictional surface. But there have been no experimental study that addresses the scale dependence of L by preparing samples of different size; there has not been any theoretical definition either.

Additionally, the definition of "typical" is problematic if the size of asperity is distributed over a wide range. Actually, the size distribution of asperity is a power law for rough brittle surfaces. Let us assume that the asperity size distribution $\rho(l)$ is proportional to $l^{-\alpha}$ with the lower and the upper cutoffs being $L_{\min}$ and $L_{\max}$, respectively. These cutoff length constants may be candidates of the typical length, but one cannot choose one and discard the other with legitimate reasoning because there has not been a mathematical expression for the typical length. If $1 < \alpha < 2$, the arithmetic average is proportional to $L_{\min}^{\alpha-1} L_{\max}^{2-\alpha}$ and very sensitive to the value of α; it ranges from $L_{\min}$ ($\alpha \nearrow 2$) to $L_{\max}$ ($\alpha \searrow 1$). As the exponent α may depend on the details of topography and may be time-dependent due to abrasion and healing, L may fluctuate in a very wide range between $L_{\min}$ and $L_{\max}$ (i.e., from microscopic to macroscopic scales). If L were such a volatile quantity, one could hardly expect that L is a good phenomenological parameter. Namely, there is a potential paradox if one interpret L as the arithmetic average of a linear dimension of asperities. To resolve this paradoxical situation, we need a clear mathematical expression for L.

To clarify the mathematical definition of L and to resolve the scale-dependent nature, one must derive the RSF law theoretically and establish the connection between the empirical friction law and the microscopic physical processes. In doing so, one can clarify the physical origin and the scaling properties of the parameters and provide them with the theoretical basis.

RESULTS

Throughout this paper, we assume that the covalent-bond reconnection at the asperities is a thermal activation process and the rate of reconnection is described by the Arrhenius law. Additionally, we assume that the local shear rate at asperity is proportional to the bond-reconnection rate.

Another essential assumption is aging of asperities. This is responsible not only for time-dependent increase of static friction but also for the negative velocity dependence of dynamic friction. We assume here that the number of covalent bond at asperity increases with time and adopt the logarithmic dependence.

By assuming several additional properties regarding atomistic parameters, we are led to atomistic expressions for the parameters a, b, and L. We confirm that the expressions for a and b are consistent with the previously obtained ones [3, 4, 5] However, they are not identical: our expressions may give the previous expressions only in a certain range of atomistic parameters. Namely, our theory provides a constraint on atomistic parameters for the RSF law to be valid: particularly the activation energy and the activation volume. We estimate that the activation energy E must range from 180 to 230 kJ/mol, and the activation volume must be 4×10^{-29} m^3 [3, 4].

*Corresponding author. Email: hatano@eri.u-tokyo.ac.jp

We also obtain an expression for the length constant:

$$L = \prod_i L_i^{\xi_i},$$

where L_i is the linear dimension of asperity i. The exponential weight ξ_i is given as

$$\xi_i = \frac{A_i}{\sum_i A_i},$$

where A_i is the area of asperity i. From this expression we can discuss the scale dependence of L.

In a similar manner, we are also led to an microscopic expression for the state variable θ.

$$\theta = \prod_i \theta_i^{\xi_i},$$

where θ_i is the contact duration of the asperity. From this expression we can derive evolution laws systematically: we will demonstrate that the slowness law can be derived easily.

References

[1] Dieterich, J. H.: Modeling of Rock Friction 1. Experimental Results and Constitutive Equations. J. Geophys. Res. 84: 2161–2168, 1979.

[2] Ruina, A. L.: Slip instability and state variable friction laws. J. Geophys. Res. 88(B12): 10359–10370, 1983.

[3] Nakatani, M.: Conceptual and physical clarification of rate and state friction: Frictional sliding as a thermally activated rheology. J. Geophys. Res.106(B7): 13347–13380, 2001.

[4] Rice, J. R., Lapusta, N., & Ranjith, K.: Rate and state dependent friction and the stability of sliding between elastically deformable solids. J. Mech. Phys. Solids 49(9): 1865–1898, 2001.

[5] Bar-Sinai, Y., Spatschek, R., Brener, E. A., & Bouchbinder, E.: on the velocity-strengthening behavior of dry friction. J. Geophys. Res. Solid Earth 119: 1738–1748, 2014.

REPRODUCING MAGNITUDE-INVARIANT STRESS DROPS IN FAULT MODELS WITH THERMAL PRESSURIZATION

Stephen Perry[1a)] & Nadia Lapusta [1,2]
[1]*Seismological Laboratory, Division of Geological and Planetary Sciences, Caltech, Pasadena, California, USA*
[2]*Mechanical & Civil Engineering, Division of Engineering & Applied Science, Caltech, Pasadena, California, USA*

Summary We use fully dynamic simulations of long-term earthquake sequences on rate-and-state governed faults to investigate the observed trend of magnitude-invariant stress drops in natural earthquakes as well as increasing breakdown energy with increasing event size. We add in thermal pressurization as a dynamic weakening mechanism that allows events to continue to weaken as they generate slip. We find that this mechanism is able to explain the magnitude-invariance of stress drops by allowing large events to nucleate at lower average levels of prestress and then weaken further to lower final stresses, thus keeping the stress drops roughly constant through a range of event sizes.

INTRODUCTION

Stress drops, a key characteristic used to describe natural earthquakes, have been observed to be magnitude-invariant across events of all sizes [1]. In addition, theoretical studies and lab experiments indicate that dynamic weakening, such as thermal pressurization, may be present on natural faults [2]. At first glance, one's intuition may suggest that these two observations are incompatible. We expect earthquakes to nucleate at similar levels of prestress, but larger earthquakes will dynamically weaken more and should thus have lower final stresses. This would lead to a trend of increasing stress drop with increasing event size, a trend that has not been observed. We hypothesize that dynamic weakening can be reconciled with magnitude-invariant stress drops due to larger events having lower average prestress when compared to smaller events (illustrated on the left side of Figure 1). Large events rupture a much larger area than small events and due to their greater dynamic weakening, are more likely to encompass points with lower prestresses. When we average the prestress over the entire ruptured area, larger events may have lower *average* prestresses than smaller events. The additional weakening would thus allow both the average initial and final stresses to be lower, but the stress drops may be similar.

MODEL

To explore this hypothesis, we study long-term earthquake sequences on a rate-and-state fault segment using a fully dynamic simulation approach [3]. Our seismogenic segment uses the aging form of rate and state friction and its properties are uniform. Outside of this region, we impose velocity-strengthening properties that promote stable creep. We force the edges of our model at the tectonic plate rate and allow creep to penetrate the velocity-strengthening regions. This loads the seismogenic zone, leading to the spontaneous nucleation of seismogenic events (Figure 1, right).

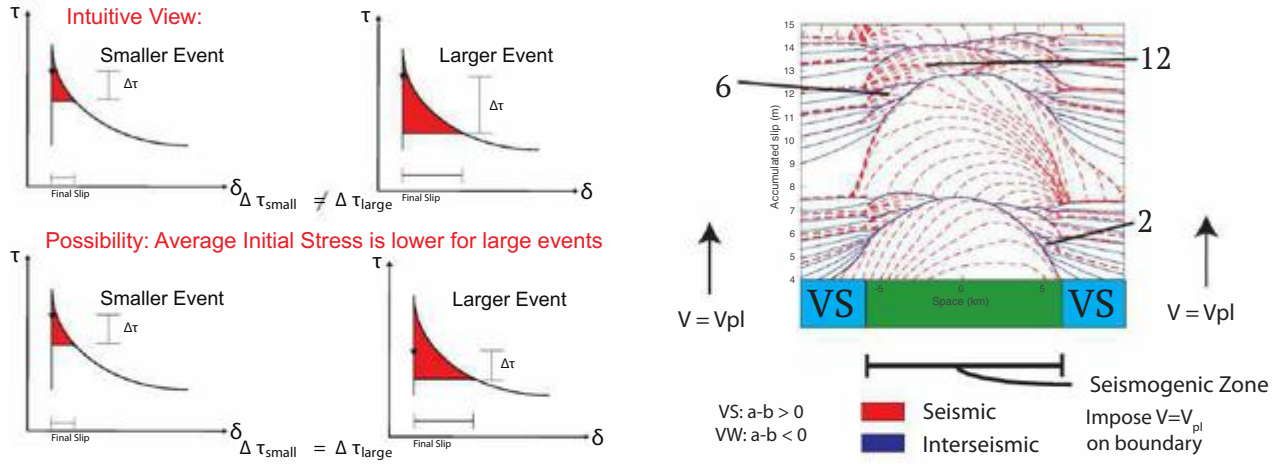

Figure 1: (Left) Illustration showing the intuitive view of the effect of dynamic weakening on stress drop (top) and our hypothesis that larger events have lower initial prestresses which may lead to constant stress drops across events of all sizes (bottom). (Right) Our model setup is shown with the seismogenic zone in green and the stable creeping regions in blue. An example of an earthquake sequence is shown with accumulated slip along the vertical axis. The red dotted lines signify seismic events and the blue lines signify slip accumulated during the interseismic periods.

[a)] Corresponding author. Email: sperry@caltech.edu.

RESULTS AND CONCLUSION

Our results show that such models can explain both the stress drop magnitude invariance and observationally inferred breakdown energy increase for a range of event sizes. Smaller events indeed have larger initial stresses than medium-sized events, and we get approximately constant stress drops for events spanning up to five orders of magnitude in moment. These events also have increases in breakdown energy consistent with observations. The variations in prestresses and final stresses that lead to magnitude invariant stress drops are illustrated in Figure 2.

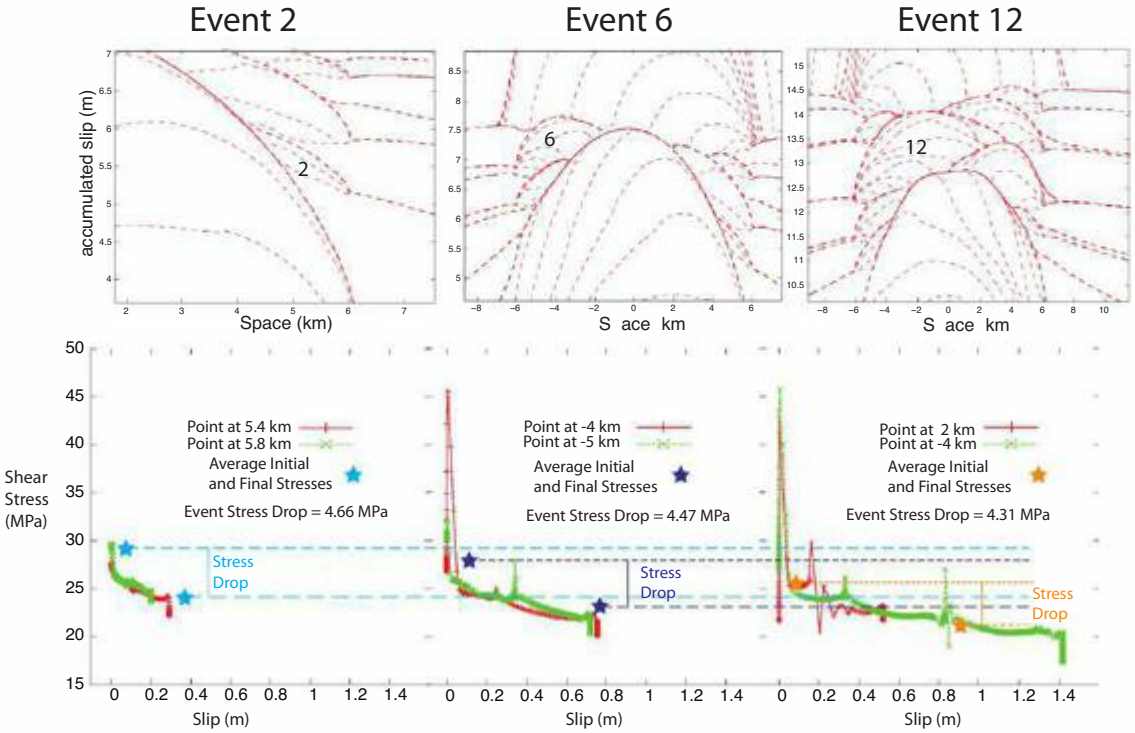

Figure 2: Accumulated slip profiles and stress drops for 3 events of different sizes. The top three plots show accumulated slip for a small, medium, and large event from a single earthquake sequence. The bottom three plots show average initial and final stresses (colored stars) as well as the shear stress evolution with slip for 2 illustrative points in the ruptured areas. We see that the smallest event has the highest initial shear stress but weakens less and thus also has the highest final stress. The largest event has the lowest initial shear stress and weakens the most. However, the stress drops for all three events are almost identical.

FUTURE WORK

We are working toward quantifying the robustness of these findings by exploring a range of fault properties, including the efficiency of dynamic weakening. Note, however, that our largest, segment-spanning events tend to have larger stress drops, possibly due to being contained by velocity-strengthening regions of the models rather than arresting due to insufficient prestress. An important next step is to consider models of heterogeneous faults that eliminate frequent model-spanning events and may extend the magnitude-invariant stress drops to the largest events simulated.

References

[1] Ide, S., and G. C. Beroza (2001), Does apparent stress vary with earthquake size? *Geophysical Research Letters*, 28(17), 3349-3352.

[2] Rice J.R. (2006), Heating and weakening of faults during earthquake slip, *J. Geophys. Res*., 111, B05311, doi:10.1029/2005JB004006.

[3] Noda, H., and N. Lapusta (2010), Three-dimensional earthquake sequence simulations with evolving temperature and pore pressure due to shear heating: Effect of heterogeneous hydraulic diffusivity, *J. Geophys. Res*., 115(B12), B12314, doi:10.1029/2010JB007780.

NONLINEAR DYNAMICS OF FRICTIONAL SLIP LOCALIZATION

Thibaut Putelat*[1], Jonathan H.P. Dawes[2], and Alan R. Champney[1]
[1]*Department of Engineering Mathematics, University of Bristol, Bristol BS8 1UB, UK*
[2]*Department of Mathematical Sciences, University of Bath, Bath BA2 7AY, UK*

Summary. An explanation is proposed of the origins of travelling waves of stick and slip that have been observed between frictional sliding surfaces. Such waves, at very different lengthscales, are thought to underlie both earthquakes' source and the performance of mechanical brakes and dampers. An idealised situation is studied of a long thin elastic plate, subject to uniform shear stress and frictional interaction with a rigid flat surface. Seeking deformation that is uniform in the transverse direction, a nonlinear wave equation is constructed under a long-wave assumption. Appearing from global homoclinic or heteroclinic bifurcations and under non-monotonic rate-and-state friction, a rich variety of solution types is discovered at intermediate shear stress between pure uniform stick and uniform slip, including: periodic stick-slip wave-trains, isolated pulses of stick or slip and detachment or attachment fronts. Careful consideration of the choice of the friction model and interfacial state kinetics is necessary to capture the full richness of wave types.

PROBLEM FORMULATION

Inhomogeneous frictional sliding between solid bodies is ubiquitous and characterised by multiple spatio-temporal scales. Practical and compelling examples include brake squeal and earthquake mechanics. The particular problem studied here is motivated by the intricate nature and diversity of earthquakes which have been recorded over the past decade ranging from aseismic events, episodic tremors, slow and fast earthquakes (e.g. [6, 5]). Another motivation comes from experimental monitoring of friction rupture fronts controlling the onset of frictional slip [3] and the simulations of a brake pad in steady sliding [1], in which various regimes of stick-slip travelling waves were observed for different values of normal load and sliding speed.

Specifically, we consider a canonical problem of a thin elastic plate of arbritrary wide extent (thickness h, density ρ, Young's modulus E, Poisson's ratio ν) and subjected to a uniform pressure $\bar{\sigma}$, which is driven by a constant shear stress $\bar{\tau} := \bar{\mu}\bar{\sigma}$ applied at its top and whose base slides on a flat and horizontal rigid foundation. Provided the wavelength of the elastic longitudinal wave propagating in the plate is large compared to its thickness, the distribution of the longitudinal stress and displacement components can be assumed uniform across the plate's cross-section. The equation of motion of the plate can then be derived from considering the balance of forces applied to a cross-section of infinitesimal width. Coupled with rate-and-state friction [8], a 'shallow layer' approximation to the full three-dimensional elasto-dynamic equations is derived as

$$\zeta(u_{tt} \nearrow u_{xx}) + \mu(u_{,t}, \phi) = \bar{\mu}, \qquad \phi_{,t} = \nearrow rG(u_{,t}, \phi), \tag{1}$$

where $u(x,t)$ is the plate horizontal displacement and ϕ is an internal state variable which quantifies the interface resistance to slip and whose time evolution is determined by some empirical state evolution law $(1)_2$ relaxing over a timescale t_*. The slab's longitudinal wavespeed reads $c^2 = E/[\rho(1 \nearrow \nu^2)]$. Nondimensionlisation reveals the key dimensionless parameters,

$$\zeta = (\rho c)/(\bar{\sigma}/V_*), \quad r = (h/c)/t_* \tag{2}$$

which characterise the interplay between the bulk elastic wave and frictional waves. Typically $r \ll 1$ represents the ratio of the perturbation propagation characteristic timescale over the characteristic interface rejuvenation timescale, whereas $\zeta \propto \bar{\sigma}^{-1}$ is the ratio of the mechanical and interfacial impedances. We interpret the impedance $\bar{\sigma}/V_*$ as the order of magnitude of the friction stress that is required so that the interfacial slip rate is V_*.

Within the travelling coordinate system $z := r(t + x/V)$ and denoting $v := rdu/dz$, the travelling-wave reduction of (1) leads to the multiple timescale two-dimensional dynamical system

$$\gamma\, dv/dz = \mu(v, \phi) \nearrow \bar{\mu}, \qquad d\phi/dz = \nearrow G(v, \phi), \tag{3}$$

whose bifurcation structure is sketched below as the key parameters, the applied shear stress $\bar{\mu}$ and the travelling wavespeed parameter $\gamma = r\zeta(1 \nearrow V^2)/V^2$, are varied. A linear stability analysis about different possible uniform sliding states shows that the wavelength of linear waves is consistent with the long-wave approximation.

*Corresponding author. Email: t.putelat@bristol.ac.uk

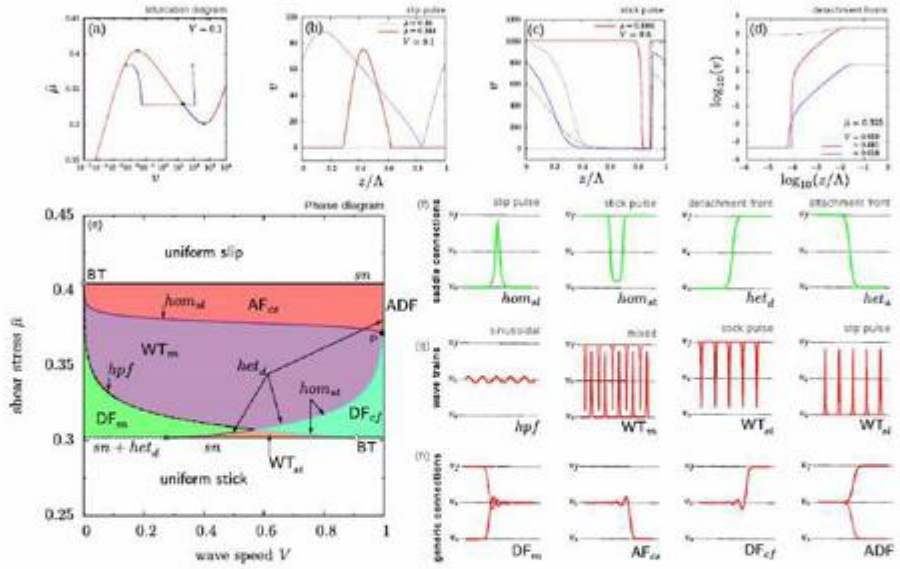

Figure 1: Numerical results for the spinodal friction law [7] of saddle-saddle connections (red line): (a) bifurcation diagram showing the growth of wave-trains from a Hopf bifurcation (■) leading to the homoclinic orbit (•) of slip pulse (b); examples of stick pulse (c) and detachment fronts (d). ($\Lambda \gg 1$ is the period). (e) Phase diagram of travelling wave patterns whose wave forms are summarised in (f-g). Nomenclature: loci of slip pulses (hom_{sl}), stick pulses (hom_{st}), detachment fronts (het_d), attachment fronts (het_a); Hopf bifurcation locus (hpf); saddle-node bifurcation loci at the local extrema of friction (sn); Stick-slip wave-trains (WT). Generic detachment (DF) and attachment (AF) fronts. Takens-Bogdanov bifurcation point (BT). Uniform slab slip rates (v_s, v_c, v_f) solutions of $\mu_{ss}(v) \equiv \mu(v, \phi_{ss}(v)) = \bar{\mu}$, $G(v, \phi_{ss}(v)) = 0$.

BIFURCATION STRUCTURE

Considering a friction model with non-monotonic velocity dependence [7], varying the applied shear stress between the local extrema of the steady-state friction law, we find the occurrence of travelling self-healing 'slip pulses', reminiscent of the pulses described by Heaton [4], arising from a homoclinic bifurcation of travelling periodic slip patterns born in a Hopf bifurcation promoted by velocity-weakening friction. Such slip pulses are anchored at the equilibrium saddle point lying on the low-velocity-strengthening branch of the steady-state friction curve. Interestingly, the existence of a high velocity strengthening branch of the friction curve also allows the existence of 'stick pulse' which corresponds to a narrow travelling 'stick' zone. Along the bifurcated branch, travelling wave-trains of slip pulses develop from a canard explosion, which can lead either to wave-trains of slip or stick pulses. Finally, heteroclinic connections corresponding to travelling 'detachment' (similar to [3, 2]) or 'attachment' fronts promoting the slab acceleration or deceleration are also possible. These saddle-saddle connections exist on lines within a (V, μ) phase diagram (Fig. 1) and delineate domains of generic travelling fronts and wave-trains of different types. The precise topology of this bifurcation structure strongly depends on the mathematical details of the friction model, in particular the state evolution equation. By contrast the classic monotonic Dieterich-Ruina laws [8] only predict wave trains of slip-pulse solutions in a window of the applied shear stress μ that is exponentially narrow.

CONCLUSIONS

This work shows how introducing a smooth rate-and-state interfacial friction model can explain the origin of slip pulses, stick pulses, travelling wave-trains, detachment fronts and attachment fronts, all in the same mathematical formulation of regional contact. Careful consideration of the choice of the non-monotonic friction law and the type of interfacial state kinetics is necessary to capture the full richness of wave types. This plethora of behaviours strongly depends on the analytical details of the friction model and may shed new light on the dynamics of earthquake ruptures, in particular with respect to the recent field evidence that suggests seismic slip localizes along a fault patch that is partially locked during the interseismic period [9]. Might a locked fault patch be a slow stick pulse? Finally we emphasise that this study shows that these slip patterns can exist over a wide range of speeds of travelling wave. This may explain the large variability of earthquake duration and frequency spectrum [6, 5]. Future work will study the stability of these localized slip structures and their physical selection.

References

[1] Behrendt J. et al., J. Sound Vib., **330**:636–651, (2011).
[2] Bouchbinder E. et al., Phys. Rev. Lett., **107**:235501, (2011).
[3] Ben-David O. et al., Science, **330**:211–214 (2010).
[4] Heaton T.H., Phys. Earth Planet Int., **64**:1–20, (1990).
[5] Ide S., Proc Jpn Acad Ser B Phys Biol Sci. **90**:259–277, (2014).
[6] Peng Z. & Gomberg J., Nature Geosci., **3**:599–607, (2010).
[7] Putelat T. & Dawes J.H.P., J. Mech. Phys. Solids, **78**:70–93, (2015).
[8] Ruina A.L., J. Geophys. Res., **88**:10,359–10,370, (1983).
[9] Thomas M.Y. et al., J. Geophys. Res., **119**: 5114–5139, (2014).

HYDRAULIC FRACTURE PROPAGATION UNDER THE INFLUENCE OF NATURAL FRACTURES

Ernst W. Remij*[1], Joris J.C. Remmers[1], Jacques M. Huyghe[1], and David J.M. Smeulders[1]

[1]*Department of Mechanical Engineering, Eindhoven University of Technology, PO BOX 513, 5600 MB Eindhoven*

Summary We developed a partition of unity based numerical model for hydraulic fracturing. The discontinuity in the displacement field due to the fracture is incorporated with the traditional Heaviside enrichment used in X-FEM. Poro-elastic effects are included by using Biot's theory. The pressure in the fracture is calculated by an additional degree of freedom that describes mass balance in the fracture. Fluid leakage is incorporated with an analytical solution based on Terzaghi's consolidation equation. The fracture process is governed by a cohesive traction separation law. In this contribution we show recent advancements we made in investigating the influence of natural fracture networks on the advancements of hydraulic fractures.

INTRODUCTION

Hydraulic fracturing is the process in which a fracture propagates by applying a high pressure inside the fracture. In geo-mechanics this process is used to stimulate oil and gas reservoirs by fracturing the underground rock formation. The induced fractures remain open, due to the addition of a proppant to the fracturing fluid, and therefore greatly enhance the permeability in the formation. Numerical models can be used to obtain more insight in the fracture process and may eventually be used to optimize the fracture process [1]. We developed the Enhanced Local Pressure (ELP) model to simulate hydraulic fracture patterns [2].

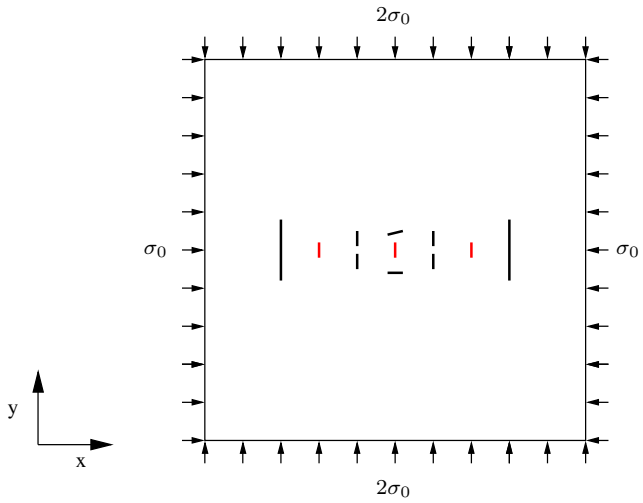

Figure 1: Scheme for the hydraulic fracturing example.

METHOD

The ELP is an X-FEM model based on the partition of unity property of finite element shape functions [3]. By exploiting this property the discontinuous behavior of a fracture can then be incorporated in a finite element mesh by adding additional degrees of freedom to the finite element nodes surrounding the discontinuity. The total displacement field of the solid skeleton can, at any time t, be described by a regular displacement field $\hat{\mathbf{u}}(\mathbf{x},t)$ and an additional displacement field $\tilde{\mathbf{u}}(\mathbf{x},t)$. For m fractures we can write the displacement field as:

$$\mathbf{u}(\mathbf{x},t) = \hat{\mathbf{u}}(\mathbf{x},t) + \sum_{j=1}^{m} \mathcal{H}_{\Gamma_{\mathrm{d}_j}}(\mathbf{x})\tilde{\mathbf{u}}_j(\mathbf{x},t), \tag{1}$$

where $\mathbf{x}$ is the position of a material point and $\mathcal{H}_{\Gamma_{\mathrm{d}_j}}$ is the Heaviside step function associated with fracture $\mathrm{y}_{\mathrm{d}_j}$

*Corresponding author. Email: e.w.remij@tue.nl

$$\mathcal{H}_{\Gamma_{\mathrm{d}_j}} = \begin{cases} 1 & \text{if} \quad \mathbf{x} \in \Omega_j^+ \\ 0 & \text{if} \quad \mathbf{x} \in \Omega_j^- \end{cases} \tag{2}$$

The pressure inside an opening fracture is different from the pressure inside the surrounding formation. The gradient of this pressure difference quantifies the interaction of fluid flow between the fracture and the formation. We therefore assume the pressure to be discontinuous across the fracture:

$$p(\mathbf{x}, t) = \hat{p}(\mathbf{x}, t) + \mathcal{H}_{\Gamma_{\mathrm{d}_j}}(\mathbf{x})\tilde{p}_j(\mathbf{x}, t). \tag{3}$$

The pressure in the fracture is described by an independent variable p_{d}

$$p_{\mathrm{d}} = p \quad \mathbf{x} \in \mathrm{y}_{\mathrm{d}_j}. \tag{4}$$

The three variational forms for, the displacement field, the pressure field, and the pressure in the fracture are discretized following the Bubnov-Galerkin approach. The pressure gradient due to leakage near the fracture surface is reconstructed analytically, based on Terzaghi's consolidation solution. With this numerical formulation we ensure that all externally applied fluid flow goes exclusively in the fracture and avoid the necessity to use a fine mesh near the fracture to capture the pressure gradient. The fracture surfaces are tracked by using two level sets for each surface.

EXAMPLE

We consider the propagation of three hydraulic fractures as shown in red in Figure 1. The hydraulic fractures are surrounded by natural fractures shown in black. The confining stress is 5 MPa in x-direction and 10 MPa in y-direction. Fluid is injected separately in the center of each hydraulic fracture under a constant rate. The result after 150 s of fluid injection is shown in Figure 2. The average stress criterion that we use for fracture propagation shows, as expected, growth in the direction of highest confining stress (y-direction). The central hydraulic fracture interacted with two natural fractures. The growth of the two hydraulic fractures at the sides was not influenced by the natural fractures. However, during fluid injection the propagation of the central fracture in the positive y-direction inhibited fracture growth in this direction of the two fractures at the side. Growing only in the negative y-direction than took over to be the favorable direction for these two fractures.

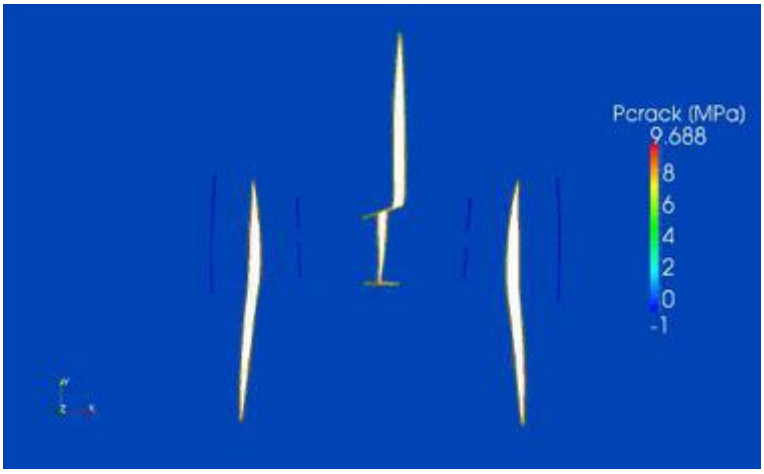

Figure 2: Result after 150 s of fluid injection. The pressure in the fractures is shown in the contour. We made the pressure in the natural fractures -1 in the post-processing to visualize them. The deformed configuration is magnified 200 times.

References

[1] J. Adachi, E. Siebrits, A. Peirce and J. Desroches. Computer simulation of hydraulic fractures. International Journal of Rock Mechanics and Mining Sciences, 44(5),739–757,2007.

[2] E.W. Remij, J.J.C. Remmers, J.M. Huyghe and D.M.J. Smeulders. The enhanced local pressure model for the accurate analysis of fluid pressure driven fracture in porous materials. Computer Methods in Applied Mechanics and Engineering,286,293-312,2015.

[3] Babuška, I. and J.M. Melenk. The partition of unity method. Int. J. Numer. Methods Eng. 40 (4), 727–758, 1997.

[4] J.J.C. Remmers, R. de Borst, and A.Needleman. The simulation of dynamic crack propagation using the cohesive segments method. Journal of the Mechanics and Physics of Solids, 56(1), 70-92,2008.

SHEAR DILATION USING THE EXTENDED FINITE ELEMENT METHOD

Endrina Rivas[a)], Robert Gracie
Civil Engineering, University of Waterloo, Waterloo, Ontario, Canada

Summary Microseismic monitoring is a tool used to determine the extent of the fracture network created by underground fracture treatments. Shearing of natural fractures is thought to be the main source of microseismic emissions. Shear dilation models have been implemented using the finite element method and discrete element methods, but not yet in the extended finite element method. In this talk, a two-dimensional model of shear dilation along a natural fracture is implemented in the extended finite element method. The simulations generated will model the formation and propagation of a shear discontinuity along natural fractures and the propagation of the resulting p- and s-waves in the surrounding medium to deepen the understanding of how microseismic emissions are generated.

BACKGROUND

The information provided from microseismic data is valuable in the design of fracture treatments and optimization of reservoir productivity. Interpretation of the microseismic signals continues to be vague in the industry due to a need for the understanding of how the microseisms are generated [1]. Shearing of natural fractures or other pre-existing planes of weakness is assumed to be the major source of seismicity [2]. Shearing of discontinuities in rocks is accompanied by shear dilation, or normal displacement that occurs along fracture surfaces. This mechanism is caused by surface roughness of the joints, as depicted in Figure 1. Models such as the empirical model by Barton and Bandis [3] and simplified linear models have been implemented in the traditional finite element method and discrete element method.

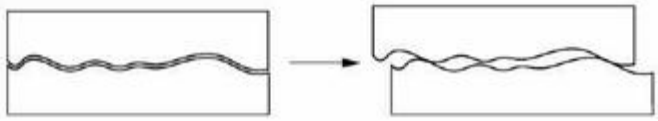

Figure 1. Fracture surface before and after shearing occurs.

The extended finite element method is an extension of the traditional finite element method which allows for discontinuous deformations within an element by adding enrichments to the nodes surrounding the crack [4]. It has been used to model multi-body physics, such as various types of contact and friction [5], but has not yet been implemented with shear dilation.

METHODOLOGY

To understand the mechanism that generates microseisms, a two-dimensional simulation of a shear discontinuity along natural fractures is performed using the XFEM.

Consider the equilibrium of a body Ω in motion, with a crack within its domain. Let Γ denote the boundary of Ω and Γ^{C+} and Γ^{C-} denote the two sides of the crack surface. It is assumed that the body behaves according to a linear constitutive law of the form $\boldsymbol{\sigma} = \mathbf{C}:\boldsymbol{\varepsilon}$ in which C is the fourth order elasticity tensor and ε is the infinitesimal strain. The dynamic motion of the body is modelled using an explicit time integration algorithm.

Using the XFEM, the body is discretized spatially into elements and the approximation is given by

$$\mathbf{u}(\mathbf{x},t) = \sum_{I} \mathbf{N}_I(\mathbf{x})\mathbf{u}_I(t) + \sum_{J} \mathbf{N}_J(\mathbf{x})\boldsymbol{\psi}(\mathbf{x})\mathbf{a}_J(t) \tag{1}$$

where I is the set of nodes in the domain, J is the set of nodes of elements located on the discontinuity, N_I are the standard finite element shape functions, $\boldsymbol{\psi}(x)$ is the enrichment function, u_I are the standard finite element nodal displacements, and a_J are the additional degrees of freedom at the discontinuity corresponding to the enrichment function.

[a)] Endrina Rivas. Email: endrina.rivas@uwaterloo.ca.

Contact, friction, and dilation are modelled along the crack surface, and are satisfied by imposing constraints on the standard finite element weak form for dynamic motion using a penalty method. The locations of discontinuities in the medium are known *a priori*, which is consistent with the physical model of pre-existing natural fractures in a rock. A node-to-node contact algorithm is implemented under the assumption of small displacements, such that the contact search is limited to predefined node pairs.

Contact and shear dilation imposes the constraint along the discontinuity that

$$[\![\mathbf{u}]\!] \cdot \mathbf{n} \geq w^s(\mathbf{x}, t) \tag{2}$$

where w^s denotes shear dilation at point **x** on the crack at time *t*, and **n** is the normal to the crack surface.

Figure 2 shows a two-dimensional frictionless domain that is sheared, with no dilation on the left, and a fixed dilation on the right. Dilation introduces a normal displacement at the crack surface.

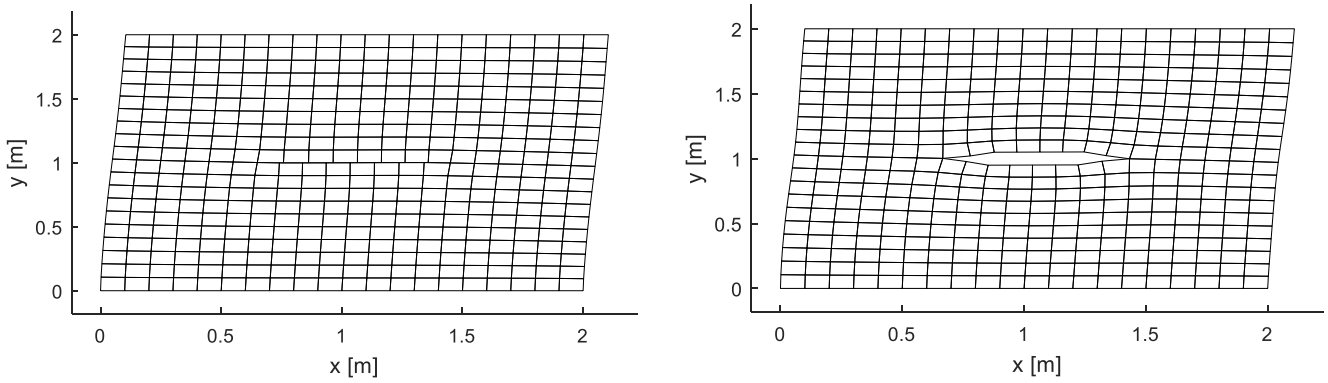

Figure 2. Shearing without dilation (left) and with dilation (right)

Frictional forces are applied along the discontinuity using a Coulomb friction model which states that

$$\tau \leq \mu\sigma_n \tag{3}$$

where τ is the shear force acting on the discontinuity, μ is the coefficient of friction, and σ_n is the normal force acting on the contact interface.

CONCLUSIONS

Using the model described in the previous section, the formation and propagation of a shear discontinuity along natural fractures will be simulated. The ensuing wave propagation in the surrounding medium will also be simulated and analysed to understand the microseismic emissions from shear dilation along a natural fracture.

References

[1] N. Warpinski, "Microseismic Monitoring: Inside and Out," *J. Pet. Technol.*, 2009.

[2] K. Agarwal, M. J. Mayerhofer, and N. R. Warpinski, "Impact of Geomechanics on Microseismicity," presented at the SPE/EAGE European Unconventional Resources Conference and Exhibition, 2012.

[3] N. Barton, S. Bandis, and K. Bakhtar, "Strength, deformation and conductivity coupling of rock joints," *Int. J. Rock Mech. Min. Sci. Geomech. Abstr.*, vol. 22, no. 3, pp. 121–140, Jun. 1985.

[4] N. Moës, J. Dolbow, and T. Belytschko, "A finite element method for crack growth without remeshing," *Int. J. Numer. Methods Eng.*, vol. 46, no. 1, pp. 131–150, Sep. 1999.

[5] J. Dolbow, N. Moës, and T. Belytschko, "An extended finite element method for modeling crack growth with frictional contact," *Comput. Methods Appl. Mech. Eng.*, vol. 190, no. 51–52, pp. 6825–6846, Oct. 2001.

DYNAMIC VISUALIZATION OF SUPERSHEAR RUPTURES

Vito Rubino[1a)], Ares J. Rosakis[1] & Nadia Lapusta[2,3]
[1]*Graduate Aerospace Laboratories, California Institute of Technology, Pasadena, USA*
[2]*Division of Engineering and Applied Science, California Institute of Technology, Pasadena, USA*
[3]*Division of Geology and Planetary Science, California Institute of Technology, Pasadena, USA*

Summary We report on unprecedented full-field measurements of spontaneous dynamic ruptures in a unique laboratory earthquake setup. These measurements are enabled by the development of a new technique, which combines ultra-high-speed photography with the digital image correlation method. Earthquakes are mimicked in the laboratory by dynamic rupture propagating along the inclined frictional interface of an analog material, prestressed in compression and shear. This experimental setup has been successfully used in the past to study key rupture features but the previous diagnostics was not capable of quantifying the full-field rupture behavior. In this paper, we discuss our experimental measurements of full-field displacements, velocities, strains and stresses,obtained by using our novel methodology. One important application of this technique is to image the evolution of dynamic friction and study its dependence on slip or slip velocity.

BACKGROUND

Earthquakes occur as dynamic frictional ruptures along pre-existing interfaces (or faults) in the Earth's crust. Seismic inversions together with other field observations have enhanced our understanding of earthquake physics. But detailed inversions are often impossible due to limited data availability or limited knowledge of the structure and properties of the crust. Numerical modeling of earthquakes helps to identify potential rupture scenarios but, in turn, requires a number of still uncertain inputs.

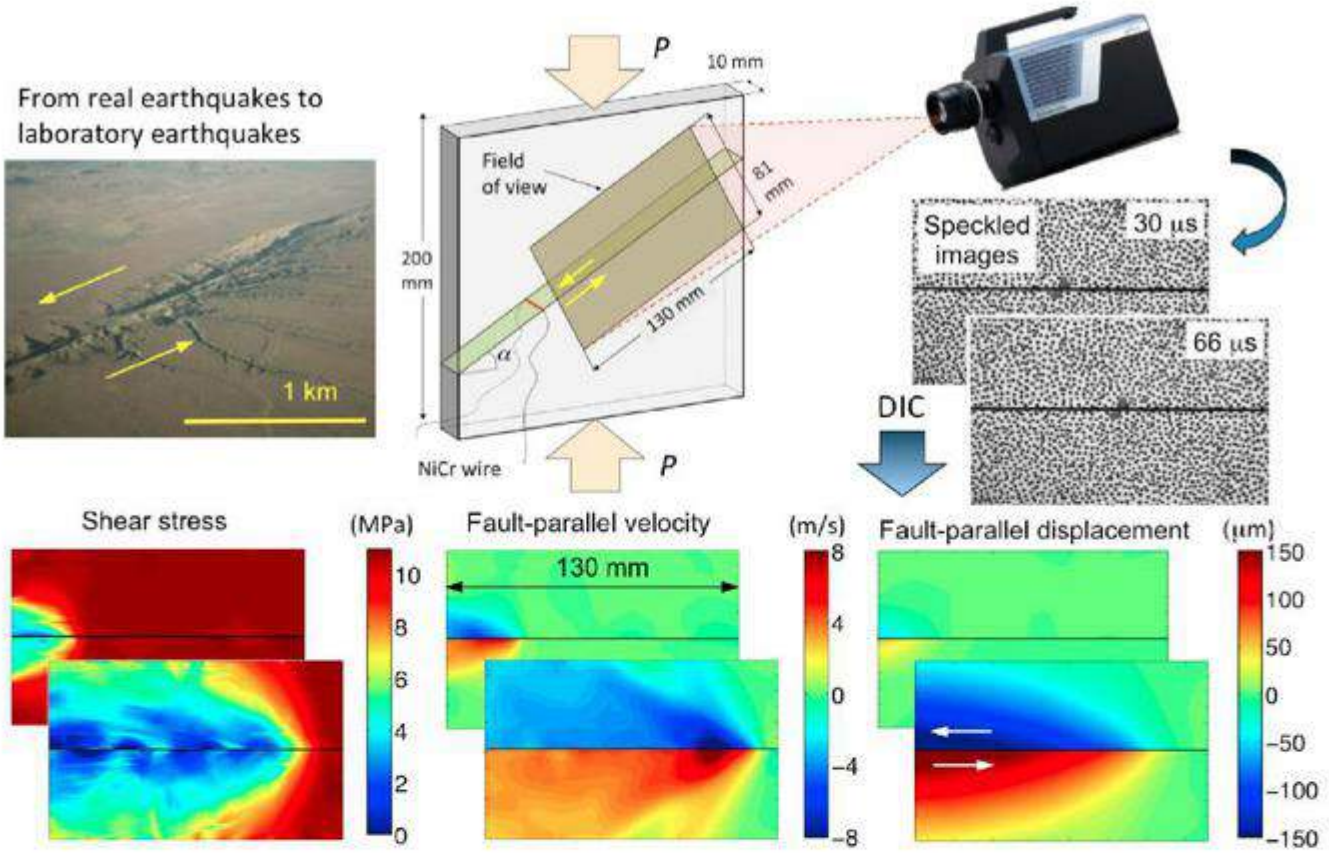

Figure 1. Dynamic imaging of supershear laboratory earthquakes. Top left: Picture of San Andreas Fault (modified from [7]**).** Top right: Schematics of the laboratory earthquake setup featuring a sample with an interface that mimics a crustal fault prestressed both in compression and shear, and the ultra-high-speed camera system, whose images are processed with the digital image correlation (DIC) method. Bottom row (right to left): Full-field maps at selected snapshots of the fault-parallel displacement, fault-parallel velocity, and the shear stress for the case of a supershear rupture (P = 25 MPa, α = 29).

[a)] Corresponding author. Email: vito.rubino@caltech.edu

This reality highlights the need for laboratory experiments that reproduce some of the basic physics governing rupture dynamics while preserving enough simplicity so that clear conclusions can be obtained. Studies of dynamic ruptures in our highly instrumented experimental setup have addressed a number of important issues in earthquake dynamics, confirming the possibility of supershear transition, demonstrating the change of rupture mode from crack-like to pulse-like with decreasing fault prestress, investigating the importance of the bimaterial effect for rupture directivity, and studying off-fault attenuation and damage [1-5]. These studies, however, were not able to obtain a spatially continuously mapping of displacement, velocities, strains and stresses. Our first step in this direction was to obtain static measurements of dynamic ruptures [6]. In this paper, we present the development of a new experimental technique that allows us to quantify the temporal evolution of full-field displacements, velocities, strains and stresses.

PRODUCING AND IMAGING EARTHQUAKES IN THE LAB

Earthquakes are simulated in the laboratory by dynamic rupture propagating along the frictional interface of two Homalite quadrilateral plates (Figure 1). The specimen's interface mimics a fault in the Earth's crust prestressed both in compression and shear. The far-field loading P, together with the interface inclination angle α, determines the level of resolved shear and normal stress along the interface. Dynamic ruptures are nucleated by the sudden local pressure release produced by the electrical discharge of a NiCr wire embedded in the interface.

Earlier versions of this setup have been successfully used to study a number of key rupture features [1-5], as mentioned in the preceding section. In those studies, the diagnostics used to capture the rupture behavior was based on high-speed photoelasticity, a full-field technique to measure maximum shear stress, and on laser velocimetry, a pointwise technique to measure particle velocity. While photoelasticity enables us to study rupture features by monitoring the evolution of the maximum shear stress, it does not allow us to quantify individual stress components. Laser velocimetry provides a fine temporal resolution of particle velocity components at selected locations but it has a sparse spatial resolution (up to three measurement locations in one experiment).

A major innovation of this setup is the development of a full-field technique to image dynamic ruptures. The new technique is based on a combination of ultra-high-speed photography and the digital image correlation (DIC) method. The specimen is first coated by a white paint and is then decorated by a black speckle pattern to produce a characteristic texture on the surface to be imaged. Typically, images are acquired at 1-2 million frame/sec. The images are processed with pattern matching algorithms [8] to produce a sequence of displacement maps. The velocity and strain fields are obtained from the displacement fields by temporal and spatial differentiation, respectively. The stress fields are computed from the strains by using the known linear-elastic constitutive properties for the Homalite material.

To illustrate the potential of this new experimental technique, Figure 1 (bottom row) shows two snapshots of the fault-parallel displacement, fault-parallel velocity and shear stress maps, produced by a supershear rupture. The fault-parallel displacement and velocity maps are characterized by a discontinuity across the fault line, which shows the purely shear (mode II) nature of the rupture. We have verified our full-field measurements by comparing particle velocities at selected locations with simultaneous independent measurements produced by well-characterized laser velocimeters. Excellent agreement between the measurements indicates the reliability of the ultra-high-speed DIC method. The stress fields also provide an important characterization of the rupture behavior. For example, the shear and normal stress measurements along the interface can be used to compute the evolution of frictional strength.

CONCLUSIONS

Our measurements produce unprecedented visualization and quantification of dynamic ruptures, which have been, until now, possible only with numerical simulations. We have verified these measurements against well-established diagnostics, such as laser velocimetry. Our ongoing and future work is aimed at quantifying the evolution of dynamic friction and exploring its dependence with controlling variables such as slip and slip rate.

References

[1] Xia, K., Rosakis A. J., Kanamori H.: Laboratory Earthquakes. The Sub-Rayleigh-to-Supershear Rupture Transition. *Science* **303**: 1859-1861, 2004.

[2] Xia, K., Rosakis A. J., Kanamory H., Rice J. R.: Laboratory Earthquakes Along Inhomogeneus Faults. Directionality and Supershear *Science* **308**:681-684, 2005.

[3] Lu, X., Lapusta N., Rosakis A. J.: Pulse-like and crack-like ruptures in experiments mimicking crustal earthquakes. *PNAS* **104**:18931-18936, 2007.

[4] Bhat, H. S., Biegel R. L., Sammis C. G., Rosakis A. J.: The effect of asymmetric damage on dynamic shear rupture propagation II: With mismatch in bulk elasticity. *Tectonophysics* **493**:263-271, 2010.

[5] Mello M., Bhat H.S., Rosakis A.J., Kanamori H.: Reproducing the supershear portion of the 2002 Denali earthquake rupture in laboratory. *Earth Planet. Sc. Lett.*, 387:89-96, 2014.

[6] Rubino, V., Lapusta N., Rosakis A. J., Leprince S., Avouac J. P.: Static Laboratory Earthquake Measurements with the Digital Image Correlation Method. *Exp. Mech.* **55**:77-94, 2015.

[7] Lynch D.K, web site http//:www.sanandreasfault.org.

[8] Sutton, M. A., Orteu J.-J., Schreier H. W.: Image Correlation for Shape, Motion, and Deformation Measurements. Springer, 2007.

THERMO-HYDRO-MECHANICAL PROCESSES STABILIZING ANTARCTIC ICE STREAM MARGINS

James R. Rice[1] [1]*Harvard University, Cambridge, MA, USA*

Summary Creeping flow of the Western Antarctic Ice Sheet is distinctly heterogeneous in a vast region bordering the Ross Sea. In that region the sheet is of order 1 km thick. Broad streaks of the ice, called "ice streams" and having horizontal width ranging up to several 10s of km, slide over their bed (which was seafloor in the last inter-glacial period) at > 100 m/yr, whereas they are bordered laterally by ice ridges flowing at < 10 m/yr. Major issues addressed, in studies with Thibaut Perol, John Platt and Jenny Suckale, are those of why does this flow streak morphology form, and what does it mean for the overall rate of ice loss to the ocean. The paper reports studies on these issues. Our work shows how shear heating of the ice, consequent formation of temperate ice zones that produce melt as they continuously deform, and subglacial hydrological processes associated with Rothlisberger channels, can select the shear margin location, leading to a smooth transition from a slipping to a locked bed at the base of the ice stream.

Creeping flow of the Western Antarctic Ice Sheet (WAIS) along the Siple Coast, bordering the Ross Sea, is strongly heterogeneous in a vast region (of order10^3 km scale). The WAIS discharges into that sea as a floating ice shelf, which ultimately melts or disintegrates into the surrounding Arctic ocean.

Flow of the WAIS in that region localizes into fast-flowing ice streams of 20-80 km width, moving at speeds of 100s of m/yr as the streams approach the sea [1]. The streams, whose beds where sampled [2] are typically at the pressure melting point, are bordered by notably colder ridges of nearly stagnant ice that is apparently frozen to its bed. No topographic feature in the ice sheet bed (which was seafloor in the last inter-glacial period) has been identified as guiding that width, which instead seems to be chosen dynamically.

This paper summarizes studies with present Harvard co-worker Thibaut Perol, and with former coworkers John D. Platt (now at Carnegie Institution of Science, Washington D.C.) and Jenny Suckale (now at Dept. of Geophys., Stanford Univ.) on understanding the origin of this flow morphology.

Using theoretical thermo-mechanical modeling ranging from simplified thickness-averaged flow models [3, 4] to large scale 2D antiplane flow models [5,6] in which distributions of downstream velocity and temperature are solved for, we are seeking to understand the mechanical, hydrologic and thermal processes active within the ice streams, and the origin of the stream morphology, in particular, to understand what controls the margin locations of the fast-flowing ice. Such understanding may ultimately help to understand how ice discharge from the West Antarctic Ice Sheet will respond to possible alterations in atmospheric and ocean temperatures and precipitation.

Our thickness-averaged flow models [3,4], when fit to near-margin deformation rate data inferred for a large group of WAIS ice streams [1], suggest that nearly all the ice stream margins studied have substantial temperate zones, i.e., that the ice is at the melting point for several dozens to hundreds of meters above the bed. (Ice at the melting point retains strength. E.g., based on data summarized in [7], the stress needed to enforce a given strain rate on temperate ice at 0 deg C is about half of that needed at to enforce the same strain rate at –13 deg C -- thought to be a representative average through-thickness temperature of ice in the streams). Thus, deforming that marginal temperate ice requires work which, because the ice is temperate, cannot raise its temperature and instead must generate melt which percolates through the (low-permeability) ice.

These concepts from the 1D model were verified and refined by the 2D thermo-mechanical modeling of Suckale et al. [5] and later Perol et al. [6], who focused on a particularly well-characterized ice stream margin (that of Whillans stream B2), in that unusually deatailed surface deformation data is available for it [8,9]. The feature added to the modeling in [6] is that the effect on the stress field due to meltwater collection in a Rothisberger channel is explicitly modeled. The R channel operates at a fluid pressure much below the ice overburden pressure, which frictionally strengthens the interface, an effect that extends well outside the channel according to the hydrologic modeling developed for the interface zone, and allows the ice to frictionally lock to the bed, thus forming the margin.

The studies were supported by the NSF- Office of Polar Programs, Award 1341499.

References:

[1] Joughin, I., S. Tulaczyk, R. Bindschadler, and S. F. Price (2002), Changes in West Antarctic Ice

Stream velocities: Observation and analysis, *J. Geophys. Res.*, 107(B11), 2289, doi:10.1029/2001JB001029.
[2] Kamb, B. (2001), Basal zone of the West Antarctic Ice Streams and its role in lubrication of their rapid motion, in *The West Antarctic Ice Sheet: Behavior and Environment*, vol. 77, edited by R. B. Alley and R. A. Bindschadler, pp. 157–199, AGU, Washington, D. C., doi:10.1029/AR077p0157.
[3] Perol, T., and J. R. Rice, Control of the width of West Antarctic ice streams by internal melting in the ice sheet near the margins, abstract C11B-0677, 2011 Fall Meeting, AGU, San Francisco, Calif., 5-9 Dec., 2011.
[4] Perol, T., and J. R. Rice, Shear heating and weakening of the margins of West Antarctic ice streams, Geophys. Res. Lett., doi:10.1002/2015GL063638, 2015.
[5] Suckale, J., J. D. Platt, T. Perol, and J. R. Rice, Deformation induced melting in the margins of the West Antarctic ice streams, J. Geophys. Res. Earth Surf., 119, doi:10.1002/2013JF003008, 2014.
[6] Perol, T., J. R. Rice, J. D. Platt, and J. Suckale, Subglacial hydrology and ice stream margin locations, J. Geophys. Res. Earth Surf., 120, doi:10.1002/2015JF003542, 2015.
[7] Cuffey, K., and W. Paterson (2010), The Physics of Glaciers, 4th ed., Elsevier, Butterworth Heinemann, London, U. K.
[8] Echelmeyer, K., W. Harrison, C. Larsen, and J. Mitchell, The role of the margins in the dynamics of an active ice stream, *J. Glaciol,* 40(136), 527- 538, 1994.
[9] Echelmeyer, K., and W. Harrison, Ongoing margin migration of Ice Stream B, Antarctica, *J. Glaciol.* 45(150), 361-369, 1999.

DYNAMIC IMPACT-INDUCED FRACTURE DEVELOPMENT IN ICE SPHERES

Koji Uenishi[1a)], Naoyuki Shigeno[1], Shintaro Sakaguchi[1], Ryosuke Yano[2] & Kojiro Suzuki[2]
[1]*Department of Aeronautics and Astronautics, The University of Tokyo, Bunkyo, Tokyo, Japan*
[2]*Department of Advanced Energy, The University of Tokyo, Kashiwa, Chiba, Japan*

Summary Ice may be commonly observed in our daily life, but its dynamic properties, especially those associated with inelastic collision and fracture, have not been thoroughly clarified. Therefore, in our previous study, utilising a high-speed digital video camera system in our laboratory and the numerical ED (Event-Driven) method, we have investigated the mechanical motion of ice spheres that impinge upon a plate of ice and based on the observations, we have quantitatively evaluated the scale effect of the relative impact velocity on the collisional behaviour of (a collection of) icy bodies as a granular material. In this contribution, we further perform laboratory experiments and three-dimensional numerical simulations to mechanically understand the collision of ice spheres against a flat plate, now with much higher impact energy, and try to comprehend the dynamic fracture process of ice spheres subjected to mechanical impact (dynamic collision).

INTRODUCTION

Icy bodies can be found at small scales as well as at larger scales, e.g. glaciers on the Earth and in the rings of Saturn in space. In a ring system, energy loss during collisions of ice particles may determinate the mean free path between collisions, the physical properties of the ring, the cooling rate in the system, etc., and quantitative information about the coefficient of restitution is definitely needed for more precise estimation of such energy loss [1]. The coefficient of restitution depends considerably on the relative impact velocity, but because of the inadequate amount of data sets related to this velocity dependency, the coefficient is often presumed to be constant regardless of the impact velocity in the analyses of inelastic collisions, energy loss and cooling in the system [2]. Hence, in our earlier investigation [3], we have studied the mechanical properties of ice as a solid / granular material and also the scaling effect of impact velocity by observing free fall of ice spheres (diameter 25 or 50 mm) impinging upon a plate of ice (thickness 60 mm) with a high-speed digital video camera (Photron FASTCAM SA5) at a frame rate of 7,000 fps (frames per second). We have set 17 different falling distances between 40 and 450 mm, without any rotation and fracture of the spheres, and from the experimentally recorded photographs before and after the collisions of the spheres, we have plotted the variation of the normal restitution coefficient and its fluctuations. Then, using the obtained data sets and the numerical ED (Event-Driven) method, we have simulated the cooling process associated with collisions of 3,000 ice spheres in a two-dimensional square. The results have shown, for example, that if we consider not only the velocity-dependent restitution coefficient but also its fluctuations, the final temperature in the system becomes some 4 % lower than that without taking the fluctuations into account.

EXPERIMENTAL OBSERVATIONS OF FRACTURE IN ICE SPHERES

In the second series of our laboratory experiments, fracture of the impinging ice spheres is involved. Cracks may be easily generated in icy bodies if they are abruptly immersed in warm water (due to thermal shock), but here, we have treated only fracture induced by mechanical impact with the falling distances of ice spheres (diameter 50 mm) being between 2.15 and 2.7 m (7 different distances). We have recorded collisions of 200 ice spheres against a flat polycarbonate plate (thickness 10 mm) by the same high-speed digital video camera, but at a frame rate of 150,000 fps. Figure 1 indicates the two representative fracture patterns observed. In Fig. 1 (top), as briefly reported in [2] for ice sphere-ice plate collisions with much smaller falling distance (700 mm), upon collision against the transparent polycarbonate plate, the sphere is divided mainly into three or four large segments of similar size (like segments of oranges; here called “orange segments” fracture pattern). On the contrary, in the sphere in Fig. 1 (bottom), prepared under the same (temperature etc.) conditions, only the sections near the free surface in the lower hemisphere are fragmented upon collision and the relatively large top-shaped part remains unbroken (“top” fracture pattern). We have recognised both fracture patterns repeatedly during the experiments, and now we are trying to numerically visualise the dynamic wave-fracture interaction process occurring inside the linear elastic spheres by employing our finite difference technique (Fig. 2) as well as ray-tracing (caustics) calculations and find the physical reasons for the generation of the two distinct fracture patterns found in this series of experiments.

CONCLUSIONS

We have shown two representative fracture patterns - “orange segments” and “top” - related to the collision of an ice sphere against a flat plate. In order to understand the fracture mechanics behind the generation of these fracture patterns and incorporate fracture effect in the simulations of the cooling process of a granular system, for instance, more quantitative data about the relation between the impact energy of the sphere and the distributions of sizes and masses of the fragmented segments and pieces of ice as well as more rigorous evaluation of the wave propagation and reflection, crack development, etc., i.e. the time-dependent evolution of stresses and deformations in the sphere, is required.

[a)] Corresponding author. Email: uenishi@dyn.t.u-tokyo.ac.jp.

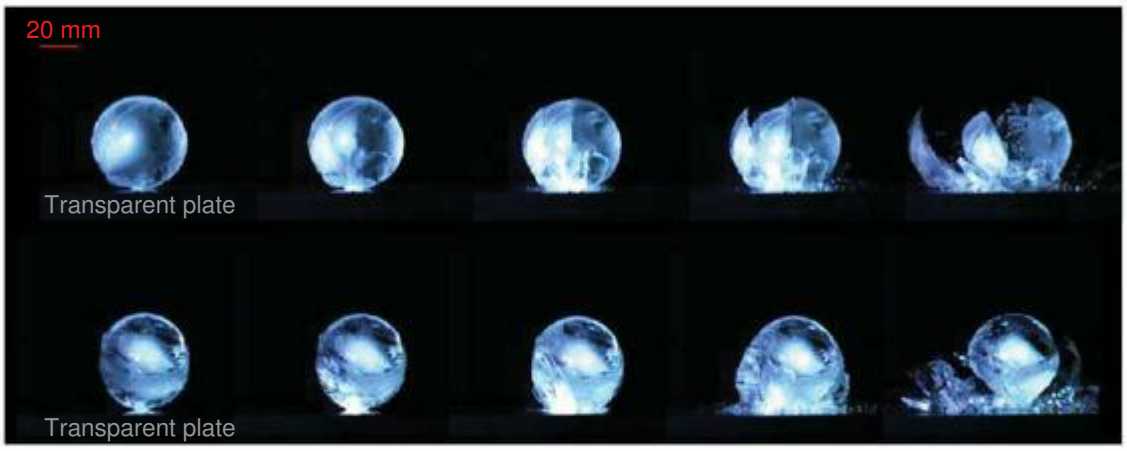

Fig. 1 Experimentally taken photographs illustrate representative dynamic fracture development in ice spheres (diameter 50 mm) upon collision against a transparent polycarbonate plate (side view). Although both ice spheres have been prepared under the same conditions, the sphere shown on the top is split into several segments of comparable size ("orange segments" fracture pattern) while that at the bottom is fractured only near the lower surface and the large part of the sphere is not broken ("top" fracture pattern). The free-falling distance of the spheres is 2.3 m, and the leftmost pictures correspond to the stage just after collision. The time elapsed after these leftmost pictures is 0.04, 0.5, 2 and 8 ms, respectively.

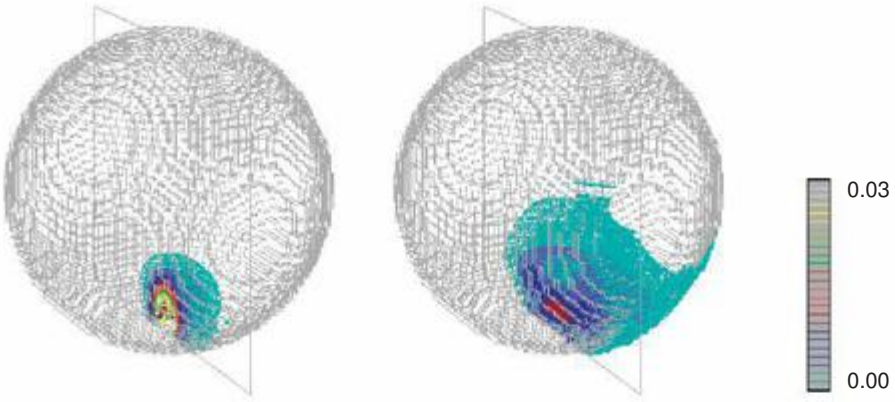

Fig. 2 We are currently investigating histories of stresses and deformations in modelled linear elastic ice spheres and tracing wave and fracture propagation using our finite difference scheme. Here, typical contours of normalised octahedral shear stress (stress / maximum pressure generated due to collision) associated with a collision at the bottom of an ice sphere are indicated. The normalised time (P wave speed × time / sphere diameter) after collision (normalised duration 0.8) is 0.4 (left) and 0.8 (right), respectively, and here due to the symmetry of the problem only contours in the right half parts are shown (preliminary results; no fracture involved).

References

[1] Dilley J., Crawford D.: Mass Dependence of Energy Loss in Collisions of Icy Spheres: An Experimental Study. *J Geophys Res* **101(E4)**:9267-9270, 1996.

[2] Uenishi K., Yano R., Yamagami K., Takahashi T., Akakabe K., Suzuki K.: Fundamental Experimental Study on the Dynamics of Collision and Fracture of Ice Materials. *Proceedings of the Materials and Mechanics Conference*, GS31, 2 pages, The Japan Society of Mechanical Engineers, Tokyo, Japan, 2013.

[3] Uenishi K., Yano R., Yoshida T., Yamagami K., Suzuki, K.: Inelastic Collisions between Icy Bodies: Dependence on Impact Velocity and Its Fluctuations. *Proceedings of the Japan Geoscience Union Meeting 2013*, PPS21-P20, The Japan Geoscience Union, Tokyo, Japan, 2013.

SHEAR STRESS PEAK RADIATED AHEAD OF RAPIDLY ACCELERATING FRICTIONAL RUPTURE

Ilya Svetlizky[1a)], Daniel Pino Muñoz[2], Mathilde Radiguet[2], David S. Kammer[1], Jean-François Molinari[2] & Jay Fineberg[1]

[1] *The Racah Institute of Physics, The Hebrew University of Jerusalem, Jerusalem, Israel*

[2] *Materials Science and Engineering Institute, Ecole Polytechnique Fédérale de Lausanne, Switzerland*

Summary We study rapidly accelerating rupture fronts at the onset of frictional motion by performing high-temporal-resolution measurements of both the real contact area and the strain fields surrounding the propagating rupture tip. We observe large-amplitude and localized shear stress peaks that precede rupture fronts and propagate at the shear-wave speed. These localized stress waves are initiated during the rapid rupture acceleration phase and are capable of nucleating a secondary supershear rupture. The amplitude of these localized waves roughly scales with the dynamic stress drop and does not decrease as long as the rupture front driving it continues to propagate. These experimental results are qualitatively described by a self-similar analytical solution of a suddenly expanding shear crack. Quantitative agreement with experiment is provided by realistic finite element simulations that describe both their amplitude growth and spatial scaling. Our results demonstrate the extensive applicability of brittle fracture theory to fundamental understanding of friction.

INTRODUCTION

The onset of motion along a frictional interface entails rupture front propagation. These rupture fronts have long been considered to have much in common with propagating cracks [1-4]. Recent friction experiments [6] have shown that the stresses and material motion surrounding the tip of a propagating rupture are indeed quantitatively described by the linear elastic fracture mechanics (LEFM) solutions for shear cracks.

Previous analytical work [3, 4] by employing self-similarity has shown that non-steady processes such as rapid rupture velocity variations result in the generation of stress-wave radiation. These solutions, under shear loading (Mode II), predict a localized shear stress peak that propagates ahead of the rupture tip at the shear wave velocity. Radiated shear stress peaks have, for decades, drawn special attention, as they are thought to be an important vehicle for the nucleation of supershear ruptures, a class of ruptures that propagate beyond the shear wave speed, C_S. These ruptures surpass the Rayleigh wave speed, C_R, the classical "speed limit" for rapid singular cracks [1, 2, 5]. Despite their importance, experimental studies of radiated stress-waves have been very limited. Here we present direct measurements of the stress fields surrounding the tips of rapidly propagating ruptures and show how a shear stress peak is formed. Supplementing experiments with finite-element calculations, we provide a detailed description of both the scaling and space-time structure of this phenomena [7].

EXPERIMENTAL OBSERVATIONS

Two poly(methylmethacrylate) blocks are pressed together by an external normal force, (2-6 MPa nominal pressure). Shear force is applied quasistatically until the transition from stick to slip occurs. The complete 2D strain tensor, ε_{ij}, is measured at 19 locations along and $\sim 3.5mm$ above the frictional interface separating the blocks. Each strain component is measured at rates of 1,000,000 samples/sec. Concurrent high spatial resolution measurements of the real area of contact, *A(x,t)* (x being the coordinate along the quasi-1D frictional interface), are obtained at 580,000 frames/sec by means of direct optical imaging of *A(x,t)* along the entire $200mm \times 5.5mm$ frictional interface.

The onset of frictional motion is marked by propagating crack-like rupture fronts that leave in their wake significantly reduced *A(x,t)* [6]. A typical example of a rupture front, asymptotically accelerating to rupture velocities, $C_f \to C_R (\sim 1237 m/s)$, is presented in Fig. 1A (top). The location of the rupture tip is defined as the point where a sharp reduction of *A(x,t)* occurs (orange to blue boundaries in Fig. 1 A(top)).

Fig. 1A (bottom) presents temporal measurements of shear strain variations, $\Delta\varepsilon_{xy}$, at two spatially separated locations along the frictional interface. It is evident that prominent peaks in the shear strain component precede the rupture tip arrival. Analysis of peak arrival times (e.g. Fig. 1A(top)) reveals that they propagate at $C_S (\sim 1345 m/s)$ as they progressively distance themselves from the rupture tips that created them. Furthermore, the measurements of *A(x,t)* reveal the sudden nucleation ($x \approx 155mm$) of a secondary supershear rupture front (propagating at $C_f > C_S$). The synchronized measurements of ε_{xy} and $A(x,t)$ provide direct evidence that the supershear rupture was triggered by the arrival of the shear stress peak. This type of transition is not uncommon.

Experiments [6] have shown that the strain components surrounding the tip of a propagating frictional ruptures, are well-described by the universal singular form describing propagating shear cracks. When $C_f \to C_R$, however, the singular form fails to adequately describe shear ($\Delta\varepsilon_{xy}$) measurements ahead of the rupture tip (i.e. when $t - t_{tip} < 0$), as demonstrated in Fig. 1B (black line). To gain intuition for the explicit form of this radiation, we turn to a self-similar analytic solution that describes

[a)] Corresponding author. Email: ilya.svetlizky@mail.huji.ac.il

bilaterally expanding ruptures that initiate with zero initial length and propagate at a constant velocity ($C_f < C_R$) under uniform remote shear stress. The solution to the problem describes a singular ($\Delta\sigma_{ij} \sim 1/\sqrt{r}$) propagating crack tip that is preceded by a sharp and relatively localized shear stress peak.

Figure 1B shows that the self-similar solution of an expanding shear rupture, can describe ***all*** of the measured strain components rather well. In particular, this solution can capture both the initial shear loading, ε_{xy}^0, as well as the propagating shear stress peak, ε_{xy}^S, far before the rupture tip arrival. This demonstrates the importance of the non-singular contributions to strains at finite distances from the rupture front tip and highlights the underlying physical picture; rapid rupture front acceleration (mimicked by infinite acceleration in the self-similar problem) results in radiation in the form of a localized shear stress peak propagating at C_S.

What determines the shear stress peak amplitude? Fig. 1C indicates that the dynamic shear drop, $\varepsilon_{xy}^0 - \varepsilon_{xy}^r$, significantly affects the overall amplitude of the shear peak, $\varepsilon_{xy}^S - \varepsilon_{xy}^0$. To make quantitative comparisons with the experiments, we performed 2D finite-element calculations in which the plane-stress hypothesis, block dimensions, their elastic moduli and fracture energy correspond to the experimental system. The shear peak amplitude, as was originally shown in [2], grows with the propagation distance. The amplitude of the shear peak is indeed consistent with the experiments. Shear peak growth effect, however, is difficult to distinguish from experimental uncertainties.

While ruptures along natural faults are generally considered to be complex, we would expect, under certain simplified conditions, to see evidence of the shear stress peak followed by the characteristic signature of the singularity at the rupture tip, as the rupture passes by the measurement point. If so, measurements at small angles relative to the fault could provide hitherto inaccessible information about both propagating earthquakes and their acceleration phase.

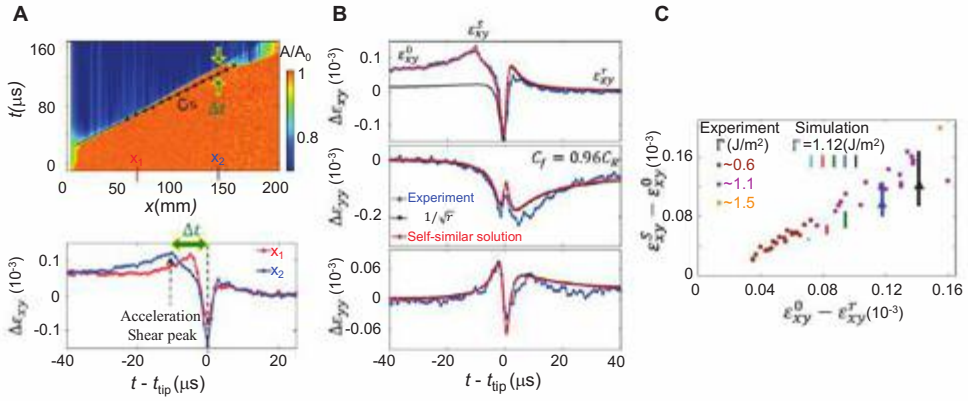

Fig. 1. **Prominent shear stress peaks due to accelerating frictional rupture fronts. *(*A, top)** Real contact area, *A(x,t)*, evolution (normalized at nucleation time, t=0), along the quasi-1D interface due to a rupture front that nucleated at $x \sim 0$, rapidly accelerated to $\sim C_R$ and transitioned to supershear at $x \approx 155$mm. **(bottom)** Shear strain variations, relative to the rupture tip arrival time, t_{tip}, at the two locations, x_1(red) and x_2(blue) denoted above, show prominent amplitude shear strain peaks preceding the rupture tip arrival. Successive measurements (black points in upper panel) reveal that these peaks propagate at C_S, and (in this case) trigger supershear rupture. **(B)** Comparison of $\Delta\varepsilon_{ij}$ measured at $y = 3.5$mm, $x = x_2$ (blue) during a rupture event in **(A)** with both the singular LEFM predictions and the self-similar solution. The singular term of the LEFM solution is plotted in black ($C_f = 0.9C_R, \Gamma = 0.6\,J/m^2$). While it captures $\Delta\varepsilon_{xx}$ and $\Delta\varepsilon_{yy}$ well, the singular term fails to describe $\Delta\varepsilon_{xy}$ for $t - t_{tip} < 0$. Red - The corresponding self-similar solution ($C_f = 0.96C_R, l = 100mm$) entirely captures all measured strain components including the initial shear strain, ε_{xy}^0, and the shear stress peak far before the rupture tip arrival. **(C) Scaling of the propagating shear stress peak.** Experiments indicate that the shear peak amplitude, $\varepsilon_{xy}^S - \varepsilon_{xy}^0$ roughly scales with the dynamic shear drop, $\varepsilon_{xy}^0 - \varepsilon_{xy}^r$. Each solid point corresponds to a single experimental event. Γ varies (see legend) with the normal load. Lines corresponding to the numerical growth of shear strain peak amplitude in x are superimposed. The spread of the measurements is wholly consistent with the growth.

References

[1] Burridge R., Admissible speeds for plane-strain self-similar shear cracks with friction but lacking cohesion. Geophys J R Astron Soc 35(4):439–455, 1973.

[2] Andrews D.J, Rupture velocity of plane strain shear cracks. J Geophys Res 81(32):5679–5687, 1976.

[3] Madariaga R., High-frequency radiation from crack (stress drop) models of earthquake faulting. Geophys J Int 51(3):625–651, 1977.

[4] Dunham E.M., Conditions governing the occurrence of supershear ruptures under slip-weakening friction. J Geophys Res 112(B7):B07302, 2007.

[5] Xia K, Rosakis A.J, Kanamori H., Laboratory earthquakes: The sub-Rayleigh-to supershear rupture transition. Science 303(5665):1859–1861, 2004.

[6] Svetlizky, I., Fineberg J., Classical shear cracks drive the onset of dry frictional motion. Nature 509(7499):205–208, 2014.

[7] Svetlizky, I., Muñoz, D.P, Radiguet, M., Kammer, D.S, Molinari, J.-F. & Fineberg. J., Properties of the shear stress peak radiated ahead of rapidly accelerating rupture fronts that mediate frictional slip , PNAS Early Edition , 2016.

NEAR-FIELD EQUATION FOR QUANTITATIVE EVALUATION OF FLUCTUATIONS

Terumi Touhei *[1]
[1]*Department of Civil Engineering, Tokyo University of Science, Japan*

Summary Quantitative evaluation of fluctuations of Lamé constants in an elastic half-space is dealt in this paper. A near-field equation developed by Fata and Guzina[1] is modified via the Lippmann-Schwinger equation so that it expresses the relationship between the fluctuation of the wavefield and scattered waves. Since the near-field equation uses Green's functions from the probing points as the scattered wavefields, evaluation of the fluctuation becomes also possible by means of the Green's function from the probing points. As a result, an algorithm for the evaluation of the fluctuations is free from the limitation of the finite number of grid points of the observation surface, that was used to obtain the near-field operator. Several numerical calculations are carried out to examine the accuracy of the present method.

INTRODUCTION

A linear sampling method presented by Colton and Kirsch[2] is for the reconstruction of the supports of the scattering object without the information of the type of the boundary conditions. Fata and Guzina extended the linear sampling method to the problem of elastodynamics in a half-space by introducing the near-field equation[1]. In this paper, we use the near-field equation not only to reconstruct the supports of the scattering object but also to reconstruct the quantitative evaluation of the fluctuations of Lamé constants in an elastic half-space.

FORMULATION FOR THE METHOD

Figure 1 shows the concept of the scattering problem of an elastic half-space including fluctuations. There are source and observation surfaces at the free surface of the wavefield denoted by Γ_1 and Γ_2, respectively. Distributed loads are applied to the source surface to cause the incident wave toward the fluctuations. The scattered waves are observed at the observation surface. The near-field operator is constructed from the information of distributed loads and observed scattered waves. The near-field equation for the scattering problem is expressed as

$$\Big(F_{ij}\tau_j\Big)(x) = g_{ij}(x,z)d_j, \quad (x \in \Gamma_2) \tag{1}$$

where F_{ij} is the near-field operator, τ_j is the distributed load at the source surface, g_{ij} is the Green's function for a homogeneous elastic half-space, z is the probing point and d_j is the force vector. Note that the subscript index denotes the components of the coordinate system for that the summation convention is applied. The near-field equation seeks the solution of the distributed load τ_j so that the scattered waves from the fluctuations at Γ_2 become equal to the Green's function from the probing point. We use the Lippmann-Schwinger equation for an elastic half space(eg. [3][4]). Then, the left side of the near-field equation can be modified into the following:

$$\Big(M_{ij}q_j\Big)(x) = g_{ij}(x,z)d_j, \quad (x \in \Gamma_F) \tag{2}$$

where q_j is the states vector describing the fluctuations of the wavefield[3], M_{ij} is the operator mapping from the fluctuation of the wavefield into the scattered wave field and Γ_F is the whole of the free surface. The construction of the operator M_{ij} is possible via the Lippmann-Schwinger equation as well as τ_j as the solution of the near-field equation. Note that the observation area in Eq. (2) is extended from Γ_2 to Γ_F due to the uniqueness of the scattered wavefield[1]. In this sense, Eq. (2) is free from the limitation of the number of the grid points set at the observation surface. We expect that the reconstructed results should be accurate in the area close to the probing points.

NUMERICAL EXAMPLES

The target model for the analysis is shown in Figure 2, in that two box-shaped fluctuations are both embedded at a depth of 5 km, and they are in the form of cubes with a side length of 3 km. The source and observation surface are discretized by grid points just above the fluctuations. For the background structure of the wavefield, the velocities of the S and P waves are set at 1 km/s and 2 km/s, respectively, and the mass density is 2 g/cm^3. The fluctuations are expressed by the deviation of the Lamé constants from the back ground structure of the wave field:

$$\tilde{\lambda} = 0.1\mathrm{GPa}, \quad \tilde{\mu} = 0.1\mathrm{GPa} \tag{3}$$

*Corresponding author. Email: touhei@rs.noda.tus.ac.jp

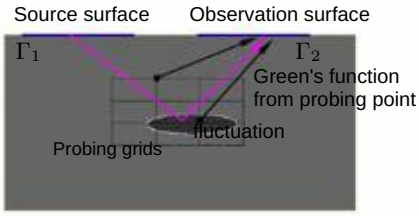

Figure 1: Concept of the scattered wave field

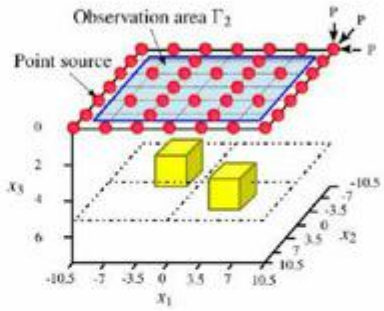

Figure 2: Target model

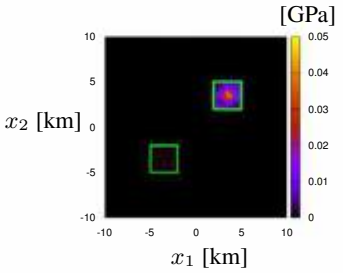

(a) Probing point (3.5,3.5,4)

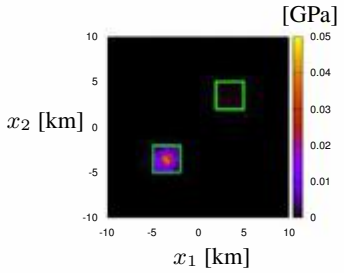

(b) probing point (-3.5,-3.5,4)

Figure 3: Reconstruction of the fluctuation of μ

where λ and μ are the fluctuations of the Lamé constants of λ and μ, respectively.

Figures 3 (a) and (b) shows the reconstruction of μ in the horizontal plane at the depth of 4 km. The boxed areas (green lines) show the locations of the fluctuations. Figures 3 (a) (b) are the solution of Eq. (2) due to different probing points. For simplicity, the Born approximation is employed to construct the operator M_{ij} in Eq. (2). In addition, the Tikhonov regularization method is also employed to solve Eq. (2), where the regularization parameter was 1×10^{-5}. The reconstructed fluctuations are 0.05 GPa in the areas close to the probing points. The amplitude is the 50% of the target model.

CONCLUSIONS

A possibility of the near-field equation is discussed for the quantitative evaluation of the fluctuations wavefield. The near-field equation is modified so that the equation describe the relationship between the fluctuation of the wavefield and the scattered waves that is expressed by the Green's function from the probing points. As a results, mathematical formulation itself is free from using the observed scattered waves at the limited observation points. The reconstructed results were expected to provide accurate results in the area close to the probing points. The numerical results showed that 50% of the fluctuation were reconstructed realized close to the probing points. Improvements of the accuracy is the task for the future. For example, without the Born approximation, the construction of M_{ij} in Eq. (2) is not very difficult. Effects of the Born approximation will be further investigated.

References

[1] Fata, S.N. and Guzina. B.B.: A linear sampling method for the near-field inverse problems in elastodyamics. Inverse Problems 20, pp. 713-736, 2004.

[2] Colton, D. and Kirsch, A.: A simple method for solving inverse scattering problems in the resonance region. Inverse problems 12, pp. 383-393, 1996.

[3] Touhei, T, Hinago, T. and Fukushiro,Y.:Inverse scattering analysis of an elastic half-space by means of the fast volume integral equation method,. Enginnering analysis with boundary elements 44, pp. 130-142, 2014.

[4] Touhei, T., Fukushiro, Y. and Tanaka, T.: A linear sampling method for detecting fluctuations of the wavefield in an elastic half space. International journal of solids and structures, 72, pp. 26-37, 2015.

RUPTURE DYNAMICS ALONG BIMATERIAL INTERFACES: A LENGTH SCALE FOR THE SHEAR-NORMAL STRESS COUPLING?

Jean-Pierre Vilotte[1], Antonio Scala[1,2] & Gaetano Festa[2]
[1]*Istitut de Physique du Globe de Paris, Paris, France*
[2]*Department of Physics, University of Naples Federico II, Naples, Italy*

Summary Faults often separate materials with different elastic properties. Understanding dynamic rupture along bi-material interfaces is therefore a challenging issue for earthquake source dynamics. Numerical simulations of in-plane rupture dynamics along a frictional bi-material interface were performed using the non-smooth Spectral Element Method (SEM) to investigate the coupling between shear strength and normal stress perturbations during non-stationary rupture propagation. In particular, we analyse numerically slip-weakening friction regularization, in which the shear strength evolves continuously with time in response to an abrupt change of normal traction, both during the acceleration and the asymptotic stationary phases of the rupture. This leads to a re-formulation of this regularisation and to propose an extension in terms of a non-local regularization model with a dynamic length scale that is shown to scale as the cohesive zone.

INTRODUCTION

Faults often separate materials with different elastic properties. This is even more evident for subduction zones where oceanic plate subducts below an over riding continental plate down to the continental mantle.

Several analytical studies in the case of steady-state rupture propagation between different materials, starting with the pioneering work by Weertman (1980), showed a break of symmetry that leads to an ill-posed problem for a wide-range of elastic material contrasts with classical friction law. Laboratory experiments (Prakash & Clifton, 1993) revealed a not instantaneous response of shear strength in response to an abrupt perturbation of the normal stress. Based on these experimental results, a experimental-based regularization law was proposed originally proposed by Cochard and Rice (2000) and Ranjith and Rice (2001) and further analysed numerically by Rubin and Ampuero (2007).

INVESTIGATION OF THE REGULARIZATION

The Prakash-Clifton regularization introduces a time delay between the normal stress perturbation and the frictional shear strength response: the effective normal stress σ_{eff}, used in the friction law is forced to smoothly vary as an effect of normal stress variations. This delay can be written as:

$$\dot{\sigma}_{eff}(\mathbf{x},t)=\left[\alpha\frac{1}{t_{dyn}(\mathbf{x},t)}+(1-\alpha)\frac{1}{t^*}\right]\left(\sigma_n(\mathbf{x},t)-\sigma_{eff}(\mathbf{x},t)\right)\qquad t_{dyn}(\mathbf{x},t)=\frac{\delta l}{|\delta v(\mathbf{x},t)|} \tag{1}$$

where δl and $|\delta v|(\boldsymbol{x},t)$ represent a characteristic slip and the local slip rate respectively, whereas t^* is a characteristic time scale. The delay depends on two time scales: the former ($\alpha = 1$) is a dynamic time scale that varies accordingly to slip rate, the latter ($\alpha = 0$) is a constant time scale. This model is able to regularize the problem both analytically and numerically, providing numerical solutions independent of grid size. We investigate here numerically the physical meaning of both terms in (1) and their effects on the numerical rupture dynamics, and the numerical convergence, through a parametric study.

For the dynamic time scale ($\alpha=1$), varying δl in a range between 1% and 100% of D_c, the critical slip weakening distance, we found that as δl decreases, finer mesh discretization is required grid convergence. Similar results are achieved for constant time scale ($\alpha=0$) as t^* decreases. For dynamic time scale, there exists a critical value δl^* below which the perturbations of σ_{eff} - and thus the dynamics of models – do not depend on the regularization (Fig. 1a). For this critical δl^*, the normal stress relaxation occurs for a slip smaller than the critical slip distance Dc.

We also propose a new regularization based on a non local criterion, with the introduction of a critical dynamic length scale proportional to the actual size of the cohesive zone PZ_{length} :

a) Corresponding author. Email: **vilotte@ipgp.fr**

$$\sigma_{eff} = \frac{1}{t^*}\left(\sigma_n - \sigma_{eff}\right) \qquad t^* = \frac{\beta PZ_{length}(t)}{V_{asymptotic}} \tag{2}$$

where the dynamic time scale is defined as the ratio between process zone length and the asymptotic rupture speed $V_{asymptotic}$, for $0 < \beta < 1$. This regularization is shown to provide similar results as the previous dynamic scale regularization, suggesting a critical length L^* below which the regularization no longer affects the dynamics. This dynamic length scale is controlled and proportional to the process zone.

This length scale can be analyzed within the framework of singular fracture mechanics in the context of interfacial crack in relation with the near crack-tip oscillatory behavior (Williams, 1959). This oscillatory singularity induces complex Stress Intensity Factors (SIFs) requiring the definition of a nontrivial length scale.

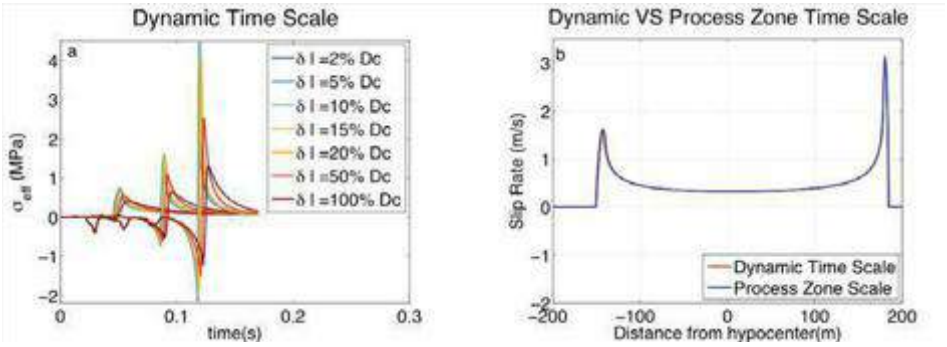

Figure 1: For a dynamic time scale during all acceleration phase the solution are convergent for $\delta l \leq 10\% Dc$. The three groups of curves represent σ_{eff} at different points at different distances from hypocenter (a). The regularizations based on dynamic slip rate time scale and process zone scale provide the same results in terms of kinematic parameter along the fault (b)

CONCLUSIONS

Dynamic simulation of rupture propagation along bimaterial interfaces requires a frictional regularization with a dynamic time scale. This time scale may be defined as the ratio between the critical slip weakening distance and the slip rate. Other regularization can also be obtained by introducing a dynamic time scale based on the ratio between the actual size of the cohesive zone and the asymptotic rupture speed. We argue that a physical length scale governs the shear and normal stress coupling for rupture propagating along interfaces between dissimilar materials.

References

[1] Cochard A. and Rice J.: Fault rupture between dissimilar materials: Ill-posedness, regularization, and slip-pulse response, J. Geophys. Res. **105**: 25,891-25,907,2000

[2] Prakash V., Clifton R.J.: Time resolved dynamic friction measurements in pressure-shear. In: Ramesh, K.T. (Ed.), Experimental Techniques in the Dynamics of Deformable Solids, AMD-vol. 165. ASME, New York, 1959 33-48, 1993.

[3] Ranjith K. and Rice J.R.: Slip dynamics at an interface between dissimilar materials, J. Mech. Phys. Sol. **49**: 341-361, 2001

[4] Rubin A.M. and Ampuero J.-P.: Aftershock asymmetry on a bimaterial interface. *J. Geophys. Res.* **112(B5)**:B05307, 2007

[5] Weertman J.: Unstable slippage across a fault that separates elastic media of different elastic constants. *J. Geophys. Res.* **85**:1445-1461, 1980.

[6] Williams M. L.: The Stress Around a Fault or Crack in Dissimilar Media. Bull. Of Seism. Soc. of Am., **49**(2):199-203, 1959

ON THE EFFECTS OF PLASTICITY IN HYDRAULIC FRACTURES

Jason R. York *[1], John T. Foster[1], and Mukul M. Sharma[1]
[1]*Department of Petroleum Engineering, The University of Texas at Austin, Austin, Texas*

Summary A yield surface composed of multiple yield functions, including tension cut-off and cap hardening modes, is proposed and implemented in a peridynamic framework. The model is incorporated in a hydraulic fracture simulator, allowing the influence of inelasticity in hydraulic fracturing to be investigated and compared to experimental observation.

INTRODUCTION

It is not uncommon for classical geophysical models to assume a linear elastic state throughout the duration of a highly deforming, or fracture inducing simulation. This assumption may be conditionally supported by laboratory experiments, if in-situ conditions are neglected. However, under geologic confinement, in-situ conditions may be great enough to produce non-brittle response in geomaterials, resulting in inelastic behavior due to pore collapse and micro-crack coalescence. The numerical complexities required for such modeling is compounded by the limitations of classical local theories in incorporating discontinuities, such as those found in fractured media. In response to such limitations, a new formulation of continuum mechanics, known as peridynamics, was introduced by Silling[1, 2]. This work expands on the description of non-local, ordinary peridynamic inelastic behavior described by Mitchell[3], and Lammi[4], where a peridynamic constitutive model was related to the classical Drucker-Prager plasticity model. A cap model is proposed, expanding on the current pressure dependent yield model to include the hardening effects associated with inelastic dilatation. The model is compared to classical compaction experiments, and further applied to in-situ hydraulic fracture applications, where confinement results in inelastic behavior, resulting in enhanced modeling of additional yield regimes.

APPLICATION TO HYDRAULIC FRACTURE

In the effort to create new technology to enhance our ability to retrieve usable hydrocarbons, the technique of hydraulic fracturing has shown to be extremely beneficial. This involves pumping fluids at high pressures to induce and propagate fractures near the wellbore to stimulate production in otherwise low permeability reservoirs. In order to better understand the physical processes involved, several models have been proposed with varying assumptions and applicability. Under the description of classical continuum mechanics, discontinuities such as fractures introduce a singularity at the fracture tip where stresses become infinite. This unrealistic behavior is explained by the effects of inelasticity, where permanent deformation is occurring. Inelasticity introduces blunting at the crack tip, making the resulting stresses finite. However, incorporating such effects is numerically challenging, as the equations may be highly non-linear and require additional numeric solvers. Due to the complexities of these models, including strong fluid-solid coupling, it is often assumed that the mechanical behavior will adhere to classical linear-elastic fracture mechanics. This assumption is adequate when inelastic regions are relatively small, but even so, special conditions must be imposed at the fracture tips. As hydraulic fracturing models continue to advance, it is becoming evident that the resulting fractures or fracture networks are much more complicated than a single planar fracture, as is often modeled. This should be kept in mind when deciding the influence of inelastic behavior. It has been observed that hydraulic fracturing models using the linear-elastic theorem may underestimate the net-pressures required to propagate fractures [5]. This is especially true for the case of ductile soft or unconsolidated reservoirs, where plasticity has demonstrated the ability to more accurately describe observed field and laboratory values of fracture geometry and the net-pressure required to propagate fractures.

FORMULATION OF YIELD FUNCTIONS

The proposed model is composed of three yield surfaces, which may depend on the deviatoric force state, $\underline{t}^d$, the peridynamic pressure, p, and a hardening parameter, p_c. These yield surfaces, displayed in fig: 1, include a Drucker-Prager related failure surface $F_1(\underline{t}^d, p)$, elliptical cap $F_2(\underline{t}^d, p, p_c)$, and tension cutoff $F_3(p)$.

Here, a set of allowable scalar force states, $\mathcal{N}$, within the set of all scalar force states, $\mathcal{S}$, is defined by yield surface functions, F_i, that define the yield surface.

$$\mathcal{N} = \{\underline{t} \in \mathcal{S} | F_i \leq 0\} \; for \; i = 1, 2, 3 \tag{1}$$

*Corresponding author. Email: jryork12@gmail.com

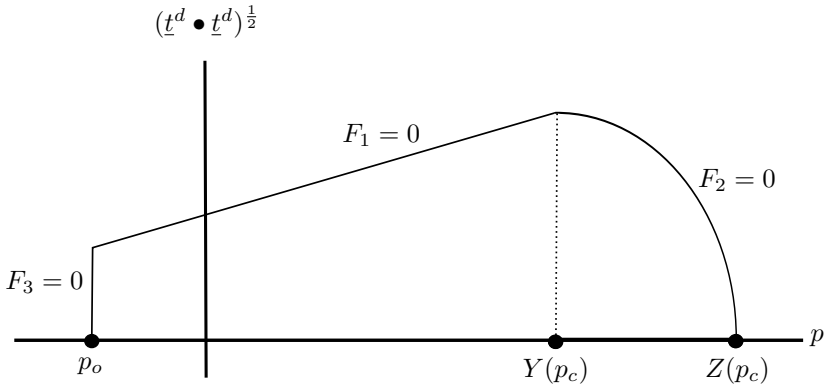

Figure 1: Yield Surface Diagram

The proposed elliptical cap F_2 is defined as :

$$F_2(\underline{t}^d, p, p_c) = F_{cap}(\underline{t}^d, p, p_c) \nearrow (\beta p + t_o), \ for \ p_c \leq p \leq Z(p_c) \tag{2}$$

where

$$F_{cap}(\underline{t}^d, p, p_c) = \sqrt{(\underline{t}^d \bullet \underline{t}^d) + \left(\frac{\beta}{R}\right)^2 [p \nearrow Y(p_c)]^2} \tag{3}$$

In the above, β is an internal friction constant described in [4], t_o is a material strength parameter, R is a material parameter describing the cap, and $Y(p_c)$ is defined as:

$$Y(p_c) = \left\{ \begin{array}{ll} p_c & \text{if } p_c > 0 \\ 0 & \text{if } p_c \leq 0 \end{array} \right\} \tag{4}$$

References

[1] Silling SA. Reformulation of elasticity theory for discontinuities and long-range forces. *Journal of the Mechanics and Physics of Solids*, **48**: 175-209 (2000)

[2] Silling SA, Epton M, Weckner O, Xu J, Askari E. Peridynamic states and constitutive modeling. *Journal of Elasticity*, **88**: 151-184 (2007)

[3] Mitchell J. A nonlocal, ordinary, state-based plasticity model for peridynamics. *Sandia Report* (2011) [SAND2011-3166]

[4] Lammi C., Vogler T. A nonlocal peridynamic plasticity model for the dynamic flow and fracture of concrete. *Sandia Report* (2014) [SAND2014-18257]

[5] Papanastasiou P. The influence of plasticity in hydraulic fracturing. International Journal of Fracture, **84**: 61-79. (1997)

DRIVING MECHANISMS OF DEEP GEODYNAMIC PROCESSES

Abay Baimukhametov*[1], Anatoliy Egorov[1], Kapal Koksalov[1], Nikolay Martynov[1], Murat Baimukhametov[1], Amanzhol Tanirbergenov[1]
[1]Institute of mechanics and machine sciences, Almaty, Kazakhstan

Summary Deep geodynamics is determined by the spatial movement of the Earth: rotation around its own axis and orbital revolution around the Sun in the Newtonian gravitational field interactions Moon, the Sun and the planets of the Solar System. These interactions are the external forces of cosmic origin. The forces of inertia rotation of the Earth, along with the forces of interaction between the inner layers and temperature gradients, apply to internal body forces. Taking into account forces operating to the Earth driving mechanisms of deep geodynamic processes are constructed.

INTRODUCTION

In Kazakhstan, many problems in the mechanics of the Earth in its unified interpretation set by academician Zh.S.Erzhanov and solved by his pupils [1-6]. In researches of deep geodynamics to the fore a problem with the study of the structure and the processes occurring in the boundary between the mantle and the core layer [7]. The mechanism of interaction between the internal and external layers of the Earth is based on the dynamics of the Earth's axial rotation. Influences of endogenous processes apply to all external covers of the Earth. Geodynamo generates the Earth's outer core magnetic field covers the entire planet. Uneven rotation of the inner solid core, caused by external factors, manifested in the relief and seismicity of the Earth. The greatest influence on the Earth has a moon. The gravitational effect of the sun is also one of the reasons for the solid tides, although on a smaller scale than the moon.

LAYERED VISCOELASTIC MECHANICS OF THE EARTH

Layered viscoelastic mechanics of the Earth where the source of its dynamic development, the force of inertia of the internal asynchronous rotation and viscous forces from the spherical Couette flow in the liquid layers is constructed. These forces determine the nature of the internal geodynamic pressure and tangential tensions. It was found that depending on the difference between the angular velocities of the inner covers Earth can be under full compression or expansion.

BIFURCATION VIBRATIONS DILATED MODEL OF THE EARTH

The dynamic buckling vibrations dilated model of the Earth, rotating in a force field due to the moon and the sun were investigated. The main subcritical stress-strain state of the model of the Earth was found. Determined the disturbance associated with fluctuations in the bifurcation model of the Earth. Were derived the boundary conditions for the stability of oscillation. Were abstracted the frequency of bifurcation oscillations dilated model of the Earth. Was found a measure of the dynamic susceptibility, depending on the frequency of the bifurcation of oscillations and the observed frequency of free oscillations, which provides resonance phenomenon.

MECHANISM OF LOCAL CHANGES LITHOSPHERE THICKNESS

The mechanism of local changes of thickness of a lithosphere as a result of instability of deformation of an ellipsoidal lithosphere cover of the Earth under the influence of the internal pressure and volume forces of inertia of rotation was founded (Fig.1). Stability of deformation was investigated by a Leybenzon-Ishlinsky method. The main stress and strain state is considered in the same form the boundaries of the body, and in view of the disturbed elements turns the borders of the body in the process of transition to a related form of equilibrium. Was determined the asymmetric form of disturbances that lead to loss of stability of an ellipsoid of revolution. There is an exponential growth of perturbations of components in time, accompanied by vibration changes.

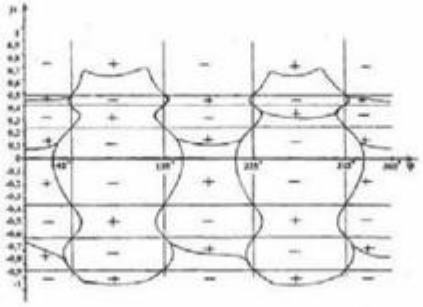

Fig. 1. Lines of the maximum thinning

*Corresponding author. Email: abayab@mail.ru

DYNAMICS OF EARTH'S INNER CORE

The dynamics of the Earth's inner core, taking into account the forces of viscous resistance of the outer core and its own gravitational force was examined. Studied the oscillatory motion of the inner core on a small time interval in its own gravitational field. Investigated the damping of the amplitude of the vibration motion of the inner core to the large time interval in its own gravitational field (Fig.2). The conclusion was that the core has the property of eccentricity. The motion of the inner core of the Earth in case of registration of the geomagnetic field was investigated. Was concluded about the smallness of the magnetic field effect on the overall picture of the inner core. Investigated the oscillatory motion of the inner core of the Earth in a Newtonian field of external center of attraction. Founded influence the mechanical properties of the core and the outer center of attraction in its oscillatory mode. As an example, consider the gravity field of the Moon and the Sun's gravity field.



Fig. 2. Fluctuations of the inner core on time intervals of two periods and 120 days

MECHANICS DEEP SALT DIAPIRISM

Based on the model Rayleigh-Taylor instability in the Boussinesq approximation with an exponential dependence of viscosity on temperature is developed and justified a numerical model of the formation of the salt diapirs at great depths the Earth's interior. Then conducted numerical simulation allowed us to estimate the basic parameters, patterns and characteristics of the nonlinear stage of the formation of the deep salt diapirism. The carried-out then numerical modeling allowed to estimating key parameters, regularities and features of a nonlinear stage of process of formation of a deep salt diapirism (Fig.3). Was suggested method of estimating the possible areas of oil and gas traps. It has been shown that hydrocarbon reservoirs are attached to areas of high temperature gradients.



Fig. 3. Spatial profiles of a deep salt diapirism in various time points

CONCLUSION

Described driving mechanisms complement a wide class of models of the motion of matter in the subsoil of the Earth, the mechanism of the dynamic interaction of the components of the Earth in close connection with the evolution of the Earth's interior tasks during the period of formation and development of Earth.

References

[1] Erzhanov Zh.S., Kalybaev A.A., Baimukhametov A.A., Korzhymbaev T.T.: Motion and stability of shared Earth. Almaty, Kazakhstan 1986.

[2] Baimukhametov A.A.: Mechanics of geooscillations. Almaty, Kazakhstan 2003.

[3] Egorov A.K., Baimukhametov A.A., Baimukhametov M.A.: Analysis of bifurcation frequencies in the Earth's dilatation model. Fundamental and applied questions of mining sciences 1(1): 98-104, 2014.

[4] Koksalov K.K., Baimukhametov A.A.: Lithospheric thinnings and the thickenings caused by instability of deformation under the influence of internal pressure and forces of inertia of rotation. World Applied Sciences Journal 27(12): 1643-1648, 2013.

[5] Baimukhametov A.A., Martynov N.I., Tanirbergenov A.G.: Thermo gradient model of formation of oil and gas traps at salt diapirizm. Proceeding of the 23d ICTAM. Beijng, China 2012.

[6] Baimukhametov A.A., Martynov N.I., Tanirbergenov A.G.: Mechanics of deep salt diapirism. Collection of papers of the XI All-Russian Congress on basic problems of theoretical and applied mechanics: 298-300, 2015.

[7] Sorokhtin O.G., Chilingar G.V., Sorokhtin N.O.: Theory of development of Earth. Moscow, Russia 2010.

MOVEMENTS OF EARTH'S SURFACE IN A SOURCE ZONES OF LITHOSPHERE BY SATELLITE DATA

Zhumabek Zhantayev[1], Alexandr Kim[2], Alena Ivanchukova[2], Venera Junisbekova[2a)], Arman Turgumbaev[2]
[1]*JSC "National Center of Space Research and Technology", Almaty, Kazakhstan*
[2]*LLP Institute of Ionosphere, Almaty, Kazakhstan*

Summary The experimental study of the modern movements of the Earth's surface was developed and based on the processing and analysis of satellite GPS data from international center SOPAC. The slow crustal movements of the Northern Tien Shan in tectonic faults was investigated using the methods of satellite radar interferometry and GPS data processing [1-2]. Initial data for Almaty city, located in a high seismic activity, was selected from ENVISAT ASAR archive. Satellite data from 2003 to 2010 totaled 90 images for the area of 100x100 km, covering the city area. A result was performed with StaMPS software package. The study of slow tectonic motions on Nothern Tien Shan region based on GPS data processing and analysis using GAMIT/GLOBK software package. Maps of the velocity distribution in tectonic faults of the Northern Tien Shan for 2003-2014 in the reference system related to the Eurasian continent.

Seismicity of the mountain regions and surrounding flatlands of Kazakhstan is caused by their accessory to the difficult Eurasian continent in the geodynamic relation within which orogenesis is a consequence of interaction of large lithospheric plates. The Northern Tien Shan region characterizes with the greatest activity for the last 125 years where there were strongest earthquakes. Urbanized agglomeration Almaty with a dense population is located in this seismic active area [3]. All these listed factors define a relevance of this research.

Data of satellite measurements are actively used in study of the Earth's surface movements at the present stage. Intensity of tectonic Earth's movements usually are measured by millimeters a year and to distinguish them from other processes happening both on the Earth's surface and in subsoil, it is possible only applying various tool methods and taking high-precision long measurements. The modern movements come to light by complex application of various methods, including geological, geomorphological, geophysical, geochemical, astronomical, geodetic.

For definition slow earths movements of the Northern Tien Shan in tectonic breaks zones there were used methods of a spaceborne radar interferometry and processing of GPS data. The method of a satellite interferometry is based on the effect of an interference of electromagnetic waves and mathematical processing of coherent amplitude-phase measurements of several images on the same site on the Earth's surface. For interferometric processing of Almaty city input data was chosen images from the satellite ENVISAT ASAR.

Processing of GPS data was carried out by the GAMIT/GLOBK software. For comparison parameters of modern movements of the Earth's surface region were calculated in two reference systems, rather Eurasian continent and the Earth's center. For each GPS point of a network graph of annual temporary displacements were analyzed on each of three components in the directions the South-North (SN), the West-East (WE), up-down (UP) with removal from the subsequent calculations of abnormal deviations of the technogenic nature.

The studied region includes 30 stations of the International Ground Station (IGS) Network and 10 GPS stations of a local network. Maps of the velocity field of movement of the Earth's surface of the Northern Tien Shan for 2000-2014 were processed in a geocentric reference system concerning the Earth's center of gravity. Concerning the Earth's center the prevailing horizontal movement of the region is the movement in the direction the East North East at values of the velocity of 1-6 mm/year for northern the SN components and 21-28 mm/year for east WE. In the vertical movement was established the steady raising of the western part of the territory with a velocity of 1.5-3.0 mm/year and lowering east with velocity of 1.5-2.0 mm/year. The vertical displacement velocities of the Northern Tien Shan territory by GPS data don't conflict with modern concepts of seismotectonic zoning and confirmed by the latest figures zoning epi-platformal orogens on motion mode. Sign-variable sites of vertical velocities coincide with areas of uplift and subsidence (foothill and intermountain hollows) of various temporary duration and reflect the modern active geodynamic movements of the territory.

As a result of the processing of the Persistent Scatterers method the map of vertical movements of the Earth's surface was received for the period from 2003-2010 according to SAR imaging on the territory of Almaty city. The resultant product of processing of the PS method belongs to measurement of linear shifts and gives output values of height of separate reflectors (points) [4]. The values of vertical movements of the Earth's surface calculated on the PS method are defined with millimeter accuracy.

The preliminary results received by data processing of SAR imaging on the territory of Almaty city showed that the most part of the settling reflectors are located in foothill areas and surrounding territories. The map of vertical displacements of the Earth's surface of Almaty city for 2003-2010 years according to satellite radar imagery is shown in figure 1.

[a)] Corresponding author. Email: venerbolat@gmail.com.

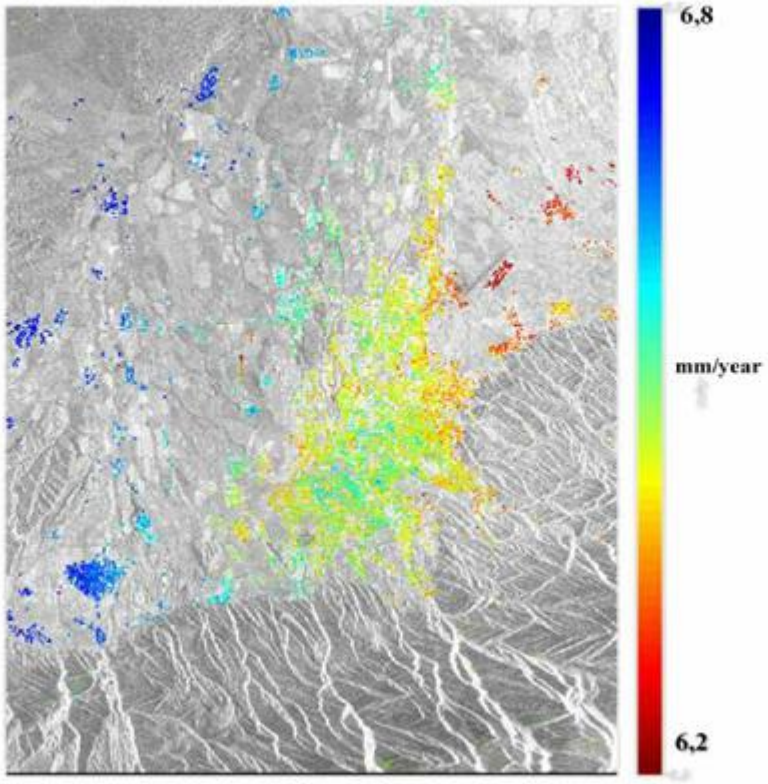

Figure 1 – The map of vertical displacements of the Earth's surface of Almaty city for 2003-2010

CONCLUSIONS

The analysis of spatio-temporal distribution of velocities and displacements of the Earth's surface of the Northern Tien Shan from 2000 to 2014 was carried out by results of GPS monitoring on stationary points. The created maps reflect the general trend of the direction of the movement of the Earth's surface in the region and confirm structurally tectonic constructions according to geologic-geophysical data. The vertical movements of the earth surface in the region of Almaty were studied based on radar images from satellite ENVISAT ASAR. Based on these maps of vertical displacements of the Earth's surface by satellite radar interferometry were noted intensive vertical movements in fault zones of the southern part of the considered Almaty region.

References

[1] Zubovich A.V., Trapeznikov J.A., Bragin V.D., Mosiyenko O.I., Shchelochkov G.G., A.K. Rybin, Batalev V.Y.: Deformation field, deep crustal structure and the spatial distribution of the seismicity of the Tien Shan. Geology and Geophysics, vol.42, № 2, 200, pp. 1634-1640.

[2] Zubovich A.V., X.-q. Wang, Y.G. Scherba, G.G. Schelochkov, R. Reilinger, C. Reigber, O.I. Mosienko, P. Molnar, W. Michajljow, V.I. Makarov, J. Li, S.I. Kuzikov, T.A. Herring, M.W. Hamburger, B.H. Hager, Y.-m. Dang, V.D. Bragin and R.T. Beisenbaev:GPS velocity field for the Tien Shan and surrounding regions. Tectonics, Vol. 29, 2010, doi:10.1029/2010TC002772.

[3] Timush A.V.: Seismotectonics of a lithosphere of Kazakhstan. Scientific publication. Almaty, 2011, pp.5-7.

[4] Hooper, H. Zebker, P. Segall, and B. Kampes: "A new method for measuring deformation on volcanoes and other non-urban areas using InSAR persistent scatterers". Geophysical Research Letters, vol. 31, December 2004.

A CLOSED-FORM SOLUTION FOR THE ELASTOPLASTIC ANALYSIS OF CIRCULAR OPENINGS IN ROCK MASS OBEYING THE GENERALIZED HOEK-BROWN FAILURE CRITERION

Shailendra Sharan[a)]
Bharti School of Engineering, Laurentian University, Sudbury, Ontario, Canada

Summary In this paper, a closed-form solution is proposed for the axisymmetric elastoplastic plane strain analysis of displacements around circular openings in rock mass governed by the generalized Hoek-Brown failure criterion. Both associated and non-associated plasticity are considered. The solution is obtained by linearizing the non-linear failure criterion piecewise using the least-squares regression. The existing closed-form solution is based on a simplifying assumption that may result in significant errors. Other analytical solutions require the numerical solution of a differential equation. By comparing the results obtained by using the proposed solution with those obtained by using a numerical method for several cases, it is shown that the proposed solution produces reasonably accurate results even if a bilinear or trilinear approximation is considered and any desired level of accuracy may be achieved by using multilinear approximations.

INTRODUCTION

For many types of rock, particularly for a jointed rock mass, the conventionally used Mohr-Coulomb failure criterion may not be suitable [1]. For such rock masses, the recently proposed generalized Hoek-Brown [2] failure criterion is more appropriate. This failure criterion is expressed as follows:

$$\sigma_1 = \sigma_3 + \sigma_{ci}\left(m_b \frac{\sigma_3}{\sigma_{ci}} + s\right)^a \tag{1}$$

where σ_1 and σ_3 are the major and minor principal stresses at failure, σ_{ci} is the uniaxial compressive strength of the intact rock material, and m_b, s and a are material constants which depend upon the Geological Strength Index of the rock mass and the degree of disturbance to which the rock mass has been subjected by blast damage and stress relaxation.

For the preliminary analysis and design of underground openings encountered in engineering projects such as tunnelling, mining, hydroelectric power generation, disposal of nuclear wastes and underground storage, a closed-form solution is preferred. If the material non-linearity and plasticity have to be considered, such solutions are generally feasible for simplified axisymmetric problems only. For this reason, it is generally assumed that the rock mass is homogeneous, isotropic and extending to infinity, the circular opening is 'deep' and a plane strain situation is valid.

Based on these assumptions, analytical solutions for stresses and displacements around circular openings in elastoplastic and elastic-brittle-plastic rock masses governed by the generalized Hoek-Brown failure criterion were presented in [3-4]. These solutions require numerical methods for the solutions of a nonlinear equation to obtain stresses and a differential equation to compute displacements. To circumvent this, approximate closed-form solutions were proposed for stresses in [5] and for displacements in [4]. The solution for displacements was based on the simplifying assumption that the elastic strain parts in the plastic zone are given by the elastic solutions for the plastic annulus [6]. As a result of this approximation, the error in displacements could become significantly large [4] for some cases of dilating rock masses.

The objective of this paper is to propose an accurate closed-form solution for the axisymmetric elastoplastic analysis of displacements around circular openings in rock mass governed by the generalized Hoek-Brown failure criterion considering both associated and non-associated plasticity.

THE PROPOSED ANALYSIS

To derive the proposed solution for displacements in the plastic zone, the existing solutions [4-5] for stresses at the elastic-plastic interface were used. The nonlinear generalized Hoek-Brown failure criterion was then linearized piecewise within the existing range of the minor principal stress. For the ith linearization segment, the failure criterion may be written as

$$\sigma_1 = M_i \sigma_3 + C_i \tag{2}$$

where M_i and C_i are linearization parameters that may be expressed in terms of the equivalent cohesion and the angle of internal friction of the rock mass for Mohr-Coulomb failure criterion. The linearization was done by using the least-squares regression. Explicit expressions for M_i and C_i were thus obtained by solving the following systems of linear equations:

[a)] Corresponding author. Email: sharan@laurentian.ca.

$$2M_i\left(\sigma_{3_i}^3 - \sigma_{3_{i-1}}^3\right) + 3C_i\left(\sigma_{3_i}^2 - \sigma_{3_{i-1}}^2\right) = 6\int_{\sigma_{3_{i-1}}}^{\sigma_{3_i}} \sigma_3 f(\sigma_3) d\sigma_3 \quad (3a)$$

$$M_i\left(\sigma_{3_i}^2 - \sigma_{3_{i-1}}^2\right) + 2C_i\left(\sigma_{3_i} - \sigma_{3_{i-1}}\right) = 2\int_{\sigma_{3_{i-1}}}^{\sigma_{3_i}} f(\sigma_3)\, d\sigma_3 \quad (3b)$$

where $\sigma_{3_{i-1}}$ and σ_{3_i} are the minimum and maximum principal stresses in the ith linearization segment and $f(\sigma_3) = \sigma_1$ is given by Equation (1). The integrations in the above equations are carried out analytically.

The corresponding plastic potential function Q_i for the ith linearization segment was assumed to be linear and given by

$$Q_i = \sigma_1 - N_i\sigma_3 \quad (4)$$

where N_i represents the dilatancy of the rock mass expressed in terms of the angle of dilation. Special cases of $N_i = M_i$ and $N_i = 1$ for all segments correspond to the associated plasticity and a non-dilating rock mass, respectively.

An existing closed-form solution [7] for the piecewise-linear Mohr-Coulomb failure criterion was extended and then applied to the present problem. The solution for displacements was then obtained in the form of a closed-form finite series. Solutions for bilinear and trilinear approximations were then obtained as special cases.

NUMERICAL VALIDATION

In order to validate the solution thus obtained, several example cases were analysed by varying the mechanical properties of rock mass, in situ stresses and the support pressure. Convergence tests were performed by increasing the number of linearization segments. Results thus obtained were compared with 'exact' solutions computed by solving the differential equation numerically.

The proposed closed-form solution was found to produce reasonably accurate results even if only a bilinear or trilinear approximation was used and a high level of accuracy could be achieved by considering multilinear approximations.

CONCLUSION

An accurate closed-form solution was proposed and validated for the axisymmetric elastoplastic plane strain analysis of displacements around circular openings in rock mass governed by the generalized Hoek-Brown failure criterion considering associated and non-associated plasticity. Practically accurate results were obtained by using a bilinear or trilinear approximation of the failure criterion and any desired level of accuracy could be achieved by using multilinear approximations.

References

[1] Hoek E., Brown E.T.: Empirical Strength Criterion for Rock Masses. ASCE *J. Geotech Eng* **106**:1013-1036, 1980.

[2] Hoek E., Carranza-Torres C., Corkum B.: Hoek-Brown Failure Criterion – 2002 Edition. North American Rock Mechanics Symposium. Toronto, Canada 267-273, 2002.

[3] Carranza-Torres C.: Elasto-plastic Solution of Tunnel Problems using the Generalized form of the Hoek-Brown Failure Criterion. *Int J. Rock Mech Min Sci* **41**:480-481, 2004.

[4] Sharan S.K.: Analytical Solutions for Stresses and Displacements around a Circular Opening in a Generalized Hoek-Brown Rock. *Int J. Rock Mech Min Sci* **45**:78-85, 2008.

[5] Sofianos A.I., Nomikos P.P.: Equivalent Mohr-Coulomb and Generalized Hoek-Brown Strength Parameters for Supported Axisymmetric Tunnels in Plastic or Brittle Rock. *Int J. Rock Mech Min Sci* **43**:683-704, 2006.

[6] Sharan S.K.: Exact and Approximate Solutions for Displacements in Elastic-brittle-plastic Hoek-Brown Rock. . *Int J. Rock Mech Min Sci* **42**: 542-549, 2005.

[7] Kennedy T.C., Lindberg H.E.: Tunnel Closure for Nonlinear Mohr-Coulomb Functions. ASCE *J. Eng Mech* **104**:1313-1326, 1978.

ANALYSIS ON THE STRENGH OF ROCK MASS BASED ON FRACTURE FRACTAL EVOLUTION

Guangming Yu [1a)], Gang Li[1,2], Guoyan Wang [1] & Yongjun Qin [3]
[1] School of Civil Engineering, Qingdao Technological University, Qingdao, Shandong Province, China
[2] Institute of Architectural Engineering, Qingdao Agricultural University, Qingdao , Shandong Province, China
[3] College of Architecture Engineering, Xinjiang University, Urumqi, Xinjiang Province, China

Summary There are a large number of cracks in rock mass of the mine and tunnel, which affect the strength of the rock mass, and then affect the stability of mine and tunnel engineering. With the fractal theory and statistical fracture mechanics method, the statistical strength of rock mass under the rock mass fracture evolution is studied. The relationship between the rock mass strength and fractal dimension is established, and the corresponding relation diagram is drawn. Analysis results show that the fractal dimension can be used as a parameter of rock mass damage state, and the strength of rock mass decreases with the increase of fractal dimension.

INTRODUCTION

The rock mass is different from other materials because of the random distribution characteristics of the fractures, and it is difficult to describe the irregularity by the traditional Euclidean geometry. On the basis of the former work, we improve the way to analyze the statistical strength of rock mass. With the similar material model test and fractal geometry theory, we give out its fractal evolution law. Based on different crack types, the relevant rules of the fractal dimension and the strength of rock are explored, which provide a way to study the mechanical characteristics of the fractured rock mass by using the nonlinear mathematical method. The study is useful for the analysis of the distribution of the rock mass cracks in the underground engineering, and it can provide theoretical basis for practical engineering.

FAILURE MODE AND CONDITION OF FRACTURED ROCK MASS

By the analysis of the strength of fractured rock mass, we find the failure mechanism of the crack in rock mass. When the crack size is much smaller than the size of rock mass and the lithology of rock mass is hard and brittle, the crack damage can induce cracks and weaken strength of the rock mass, which can be analyzed by statistical fracture mechanics. Some experts and scholars in the previous analysis were only considered a single crack influence, this paper uses two types of crack analysis and consider the existence of multiple crack interaction.

Type Ⅰ *Failure criterion*
With the help of fracture mechanics and the corresponding mathematical transformation:

$$K_I = \frac{\sigma}{\alpha}\sqrt{\pi a}\sqrt{\frac{2b}{\pi a}\tan\frac{\pi a}{2b}} \qquad (1)$$

In the above equation, $\sqrt{\frac{2b}{\pi a}\tan\frac{\pi a}{2b}}$ is a correction factor. It indicates the effect of other cracks on K_I.

Type Ⅱ *Failure criterion*

$$K_{II} = \frac{\tau}{\alpha}\sqrt{\pi a}\sqrt{\frac{2b}{\pi a}\tan\frac{\pi a}{2b}} = \frac{\sigma_1-\sigma_2}{2\alpha}\sin 2\theta\sqrt{2b\tan\frac{\pi a}{2b}} \qquad (2)$$

RELATIONSHIP BETWEEN AVERAGE STRENGTH AND FRACTAL DIMENSION

The probability of fracture failure can be obtained through the Weibull hypothesis of the defect distribution and the weakest link of the fault events: $P_{f(\sigma)} = 1 - [1 - F(\sigma)]^N \approx 1 - exp\,[-NF(\sigma)]$ (3)

The distribution function of the crack size is: $F(\alpha) = 1 - (\frac{\alpha}{\alpha_0})^{-D}$ (4)

Type Ⅰ *Crack analysis:* Combine Eq.(1)(3)(4): $P_{f(\sigma)} = 1 - exp\left\{-N\left[\frac{\pi}{2b\alpha_0}tan^{-1}\frac{(\alpha K_{1C})^2}{2b\sigma^2}\right]^{-D}\right\}$ (5)

[a)]Corresponding author. Email: yu-guangming@263.net.

Take the average intensity of rock mass as Mathematical expectation of strength:

$$\sigma_c = \int_0^{\infty} exp\left\{-N\left[\frac{\pi}{2ba_0}tan^{-1}\frac{(\alpha\kappa_{1c})^2}{2b\sigma^2}\right]^{-D}\right\}d\sigma \quad (6)$$

Type Ⅱ Crack analysis: According to the weakest link of the fracture event:

$$\bar{\sigma} = \int_0^1 \sigma\, dP_f = \int_0^{\infty}(1-P_f)\,d\sigma = \int_0^{\infty}\exp\left[-N\int_0^{\pi} g(\theta)\,d\theta\int_{a_c}^{\infty} f(a)da\right]d\sigma \quad (7)$$

Inserting Eq.(2) into (3), and consider the distribution of cracks. So:

$$\bar{\sigma} = \int_0^{\infty} exp\left\{-\frac{N}{\sqrt{2\pi}W}\left[\frac{\pi a_0}{2btan^{-1}\dfrac{2(\alpha K_{IIC})^2}{\sigma^2 b(1-\gamma)^2 sin^2 2\theta}}\right]^D \int_0^{\pi} exp\left[-\frac{(\theta-\bar{\theta})^2}{2W^2}\right]d\theta\right\}d\sigma \quad (8)$$

Through numerical analysis, the relationship curves are obtained (*Fig.1*). From the Figure 1, type I and type II all showed that the strength of rock mass decreases sharply with the increase of fractal dimension, tends to be stable value, and the fractal dimension value can be used to describe the strength of rock mass.

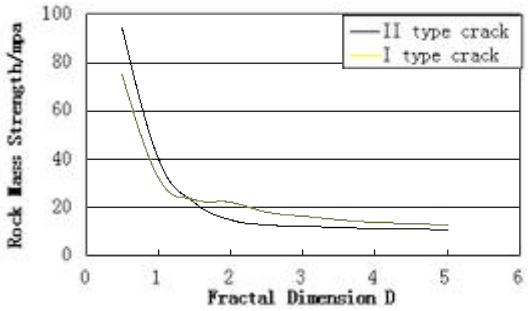

Fig.1 The curve of mining fractured rock mass strength and the fractal dimension value

CONCLUSIONS

The failure criterion of type I and type II crack was analyzed by using Westergaurd method. The fractured rock mass strength caused by type I crack and type II crack is analyzed, the relationship of rock mass strength and fractal dimension is established. The analysis results show that the fractal dimension can be used as the parameters of rock mass damage state, the strength of rock mass decreases with the increase of fractal dimension, and the strength of rock mass can be estimated by the fractal dimension of fracture evolution.Through the analysis of the average strength of fractured rock mass under different types of crack failure mode, the relationship between rock mass strength and fractal dimension is obtained by means of numerical analysis. The analysis results show that the strength of fractured rock mass is related to the fractal dimension of fracture distribution, and the fractal dimension can be used as the parameters of rock mass damage state, and the strength of rock mass decreases with the increase of fractal dimension, the strength of rock mass can be estimated by the fractal dimension of fracture evolution, and the distribution of micro cracks and cracks is introduced into. the micro mechanical model.

Acknowledgements: The project's supported by Qingdao Technological University (Cooperative Innovation Center of Engineering Construction and Safety in Shandong Blue Economic Zone)and National Natural Science Foundation of China(No.51374135, 51179080).

References

[1] Xie, H.P.: Introduction of fractal rock mechanics. *M*. Beijing, Science Press, 1996.

[2] Yi, S.M., Zhao, W.Q.: The Fractal characteristics of rock fracture of in dam foundation of the Three Gorges project under uniaxial compression. *J*. Chinese Journal of rock mechanics and engineering, 1999,18 (05): 512-515.

[3] Chang J., Xu J., Mutch Y.: A general mixed-mode brittle fracture criterion for cracked materials. *J*. Engineering Fracture Mechanics.2006(9): 1249-1263.

[4] Gao, F., Zhong, W.P., Li, L.Y., Xie, H.P.: Fractal and statistical analysis of strength of jointed rocks. *J*. Chinese Journal of rock mechanics and engineering, 2004 (21): 3608-3612.

[5] Xie, H.P., Gao, F.: Fractal characteristic of damage evolution of rock materials. *J*.. Chinese Journal of rock mechanics and engineering, 1991 (01): 74-82.

SM07 - Impact Mechanics and Wave Propagation

TS.SM07-1.01	Chen, Wayne - High-speed damage visualization and xrd in materials under impact (INVITED)	2190
TS.SM07-1.02	Thevamaran, Ramathasan - Dynamic Behaviour of Single Crystalline Silver Microcubes	2192
TS.SM07-1.03	Kettenbeil, Christian - Experimental investigation of the dynamic behavior of metaconcrete	2194
TS.SM07-1.04	Kanel, Gennady - Appearance of dislocations multiplication in the dynamics of elastic-plastic waves in solids	2196
TS.SM07-1.05	Schwab, Martin - Modelling Laminated Fabric Composites under Impact Loads	2198
TS.SM07-1.06	Matthes, Melissa - Hypervelocity impact of Ti6Al4V alloy materials	2200
TS.SM07-2.01	Morozov, Nikita - The Lavrentiev-Ishlinsky problem of transverse vibration of rods (INVITED)	2202
TS.SM07-2.02	Gambarotta, Luigi - Wave Propagation in Lattice Metamaterials with Viscoelastic Inertial Resonators	2204
TS.SM07-2.03	Metrikine, Andrei - Transition radiation in continua excited by a moving load	2206
TS.SM07-2.04	Pal, Raj Kumar - Effect of large deformation pre-loads on linear wave propagation in hexagonal lattices	2208
TS.SM07-2.05	Wang, Xiaodong - Modelling and Simulation of Elastic Waves in Periodic Media Using Pseudo-Incident Wave Method	2210
TS.SM07-2.06	Seisson, Gabriel - POREQST extension to shock-release hysteresis of graphite	2212
TS.SM07-3.01	Nesterenko, Vitali F. - Strongly nonlinear waves generated by impact in weakly and strongly dissipative sonic vacuum (INVITED)	2214
TS.SM07-3.02	Salupere, Andrus - Solitons and solitonic structures: What is visible and what is hidden	2216
TS.SM07-3.03	Samsonov, Alexander - Bulk Strain Solitons in Lengthy Solids: From Phenomenon to a Work Tool	2218
TS.SM07-3.04	Chen, Zhen - Staggered MD and MPM for Multiscale Simulation of Impact Responses	2220
TS.SM07-3.05	Wang, Lifeng - Harnessing structural hierarchy to design lightweight phononic crystals	2222
TS.SM07-3.06	Van Gemmeren, Valentin - Energy focusing using the dispersion of flexural waves	2224
TS.SM07-4.01	Zaretsky, Eugene - The Influence of Temperature and Crystal Structure on High Strain Rate Behavior of Metals (INVITED)	2226
TS.SM07-4.02	Czarnota, Christophe - Shock wave structures in porous media accounting for micro-inertia effects	2228
TS.SM07-4.03	Zhou, Tingting - Void collapse and hot spot formation in shocked HMX: A large-scale molecular dynamics study	2230
TS.SM07-4.04	Thomson, Stuart - Violent elastic-plastic wave interactions	2232
TS.SM07-4.05	Trainiti, Giuseppe - Broken time-reversal symmetry in beams in longitudinal motion	2234
TS.SM07-5.01	Engelbrecht, Jüri - Interaction of deformation waves with internal structures in solids	2236
TS.SM07-5.02	Thorin, Anders - Nonsmooth modal analysis of piecewise-linear impact systems	2238
TS.SM07-5.03	Grinberg, Itay - Multi-site discrete breathers in finite vibro-impact chain	2240

TS.SM07-5.04	Urman, David - Nonlinear modes of vibration of vibro-impact duffing oscillators	2242
TS.SM07-5.05	Singh, Harmeet - Pick-up, impact and peeling	2244
TS.SM07-5.06	Fehr, Joerg - Acceleration of car crash simulaions	2246
PO.SM07-1.01.264	Abdul-Latif, Akrum - New concept of passive energy dissipating system based on plastic buckling	2248
PO.SM07-1.02.265	Cherniaev, Aleksandr - Hypervelocity Impact Damage in Composite Materials Fabricated by Filament Winding	2250
PO.SM07-1.03.266	Danishevskyy, Vladyslav - Propagation of elastic waves in cyllindrically structured cancellous bones	2252
PO.SM07-1.04.267	Fadodun, Odunayo - A new time fractional wave propagation in a solid cylinder	2253
PO.SM07-1.05.268	Fan, Tao - Dynamic crushing properties of functionally graded honeycombs with defects	2255
PO.SM07-1.06.269	Franco Navarro, Pedro - Shock waves scaling in Al/W laminates excited by impact	2257
PO.SM07-1.07.270	Furukawa, Akira - BEM for 3-D wave scattering in general anisotropic fluid-saturated porous media	2259
PO.SM07-1.08.271	Hanagud, Sathya - Mixture and density functional theories for shock induced reactions	2261
PO.SM07-1.09.272	Kim, Alexandr - Non-stationary processes in nidal zone at sudden appearance of break	2263
PO.SM07-1.10.273	Komijani, Mohammad - An enriched finite element method for wave propagation analysis in discontinuous domain	2265
PO.SM07-1.11.274	Li, Hongliang - Interaction of cavities, inclusions and a crack near semi-cylindrical gap	2267
PO.SM07-1.12.275	Lou, Jianfeng - A numerical method based on thermo-mechanical coupled material model for simulating Steven test	2269
PO.SM07-1.13.276	Murashkin, Evgenii - Compatibility Conditions in Micropolar Thermoelasticity	2271
PO.SM07-1.14.277	Qiao, Chuan - Energy absorption of a novel self-locked tube system	2273
PO.SM07-1.15.278	Rai, Nirmal Kumar - Sensitivity analysis of energetic materials using an Eulerian solver SCIMITAR3D	2275
PO.SM07-1.16.279	Shi, Yulin - Semismooth Newton solver for periodically-forced solutions to a unilateral contact formulation	2277
PO.SM07-1.17.280	Vaz-Romero Santero, Alvaro - On the interplay between material flaws and dynamic necking	2279
PO.SM07-1.18.281	Wang, Yi-Ze - Longitudinal wave localization in phononic crystals with negative capacitance	2281
PO.SM07-1.19.282	Yu, Huangchao - The coupled dynamic behavior of layered piezoelectric structures.	2283

HIGH-SPEED DAMAGE VISUALIZATION AND XRD IN MATERIALS UNDER IMPACT

Weinong W. Chen[1a)], Matt Hudspeth[1], Ben Claus[1], Niranjan Parab[1], Kamel Fezzaa[2] & Tao Sun[2]
[1]Schools of Aero/Astro & Mat'ls Engr., Purdue University, West Lafayette, Indiana, USA
[2]Advanced Photon Source, Argonne National Laboratory, Argonne, Illinois, USA

Summary Post-peak damage and failure of materials under impact loading is a critical aspect in impact energy dissipation, but challenging to experimentally characterize, especially in opaque materials. We recently integrated Kolsky compression/tension bars with high-speed x-ray phase contract imaging (PCI) and simultaneous x-ray diffraction (XRD) capabilities to visualize the material impact damage at different length scales in real time. The effectiveness of the novel union between these powerful techniques is demonstrated by a series of dynamic experiments on a variety of material systems, including particle interaction in granular materials, fiber-matrix debonding in cruciform specimens, ligament-bone junction damage, and microstructural evolutions in an aluminum and a shape-memory alloy.

PROBLEM DEFINITION

In impact applications, materials are desired to be used to withstand the impact load and to dissipate the impact energy effectively. The total energy absorbed by the material is the proportional to the area under the stress-strain curve under dynamic loading. Thus, the post-peak behaviour of the materials contributes significantly to the energy dissipation. It is desired to understand the damage initiation and propagation in the materials, in addition to the stress-strain curves to understand the damage and failure mechanisms and the associated amounts of energy dissipation. However, the damage initiation and propagation are not visible in most materials that are opaque to optical high-speed cameras. Therefore, non-optical based high-speed imaging methods are in demand.

EXPERIMENTAL SETUP

To visualize the dynamic microstructure evolution process, both before and after peak load, inside opaque materials in real time, we recently integrated a stress-wave loading technique, namely Kolsky compression and tension bars, with synchrotron x-ray high-speed imaging and x-ray diffraction methods. In this new experimental method, the illumination source of high-speed imaging in stress-wave loading dynamic experiments is replaced by a strong x-ray source for high-speed x-ray imaging. To ensure proper contrast at the interfaces among material phases, phase contrast imaging (PCI) technique is adopted. With the x-ray illuminating the specimen, high-speed x-ray diffraction (XRD) is a by-product. Both the x-rays from the direct PCI and diffraction pass scintillators that convert the images from x-ray to visible lights to be recorded by conventional high-speed cameras. Figure 1 shows a schematic of the experimental setup with simultaneous high-speed x-ray PCI and XRD during a Kolsky bar experiment.

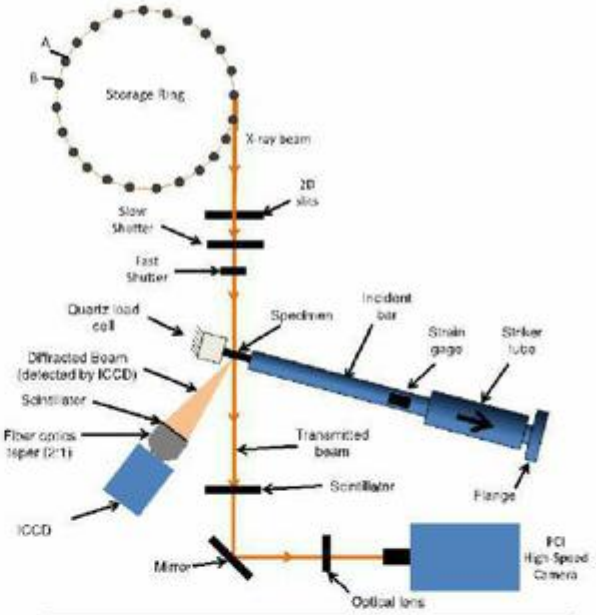

Figure 1. A schematic of the integrated Kolsky bar with high-speed x-ray PCI and XRD.

EXPERIMENTAL RESULTS

To evaluate the capabilities of this new experimental method, dynamic experiments have conducted on a variety of material at Beamline 32 ID-B of the Advanced Photon Source (APS) at Argonne National Laboratory in US. High-speed damage and failure processes have examined in material systems include brittle particles under compression, glass under cutting, fibers under tension, glass fiber and epoxy interface dynamic debonding, ligament and bone interface tensile failure, and metallic samples under tension. Here we present two examples. Figure 2 shows the dynamic tensile damage and failure process of ligament getting pulled off from the bone it was attached to. In each of the images, the nearly vertical line dividing a darker area (the bone) on the right and a lighter region (the ligament) is the interface in between. The dynamic tensile load is applied horizontally. The tensile damage in the ligament is clearly recognized with the corresponding loading history displayed below the x-ray images. Figure 3 is the composition of a series of x-ray diffraction images that were taken from a shape memory alloy under dynamic tension. The changes in the diffraction patterns are clearly visible as the specimen is deformed under tensile loading, which induces phase transformation in the specimen. After the

a) Corresponding author. Email: wchen@purdue.edu.

specimen fails under tensile loading, the diffraction pattern become similar to these recorded before the dynamic loading, indicating a reverse transformation in the specimen.

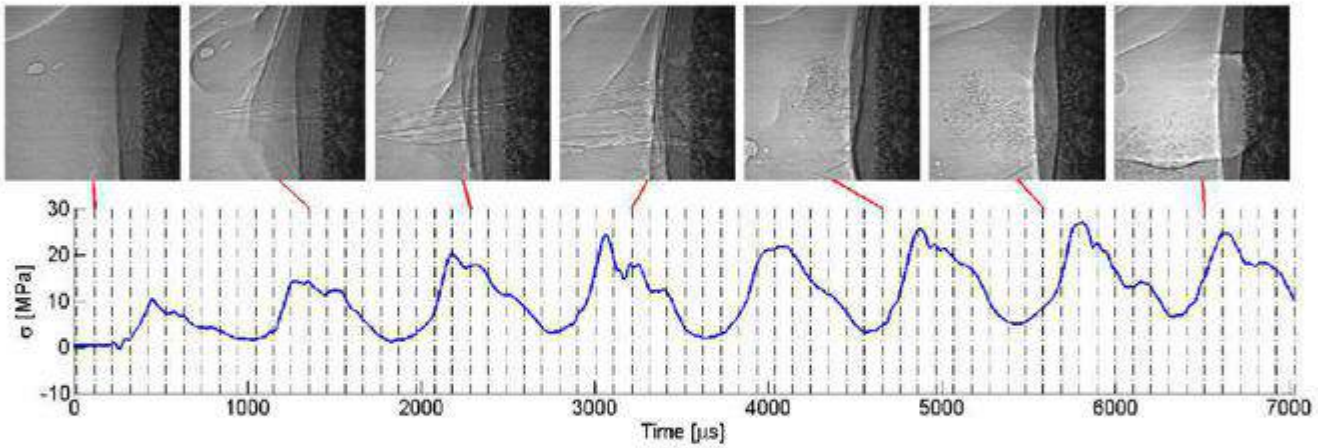

Figure 2. High-speed x-ray PCI images of dynamic damage in a ligament with corresponding loading history.

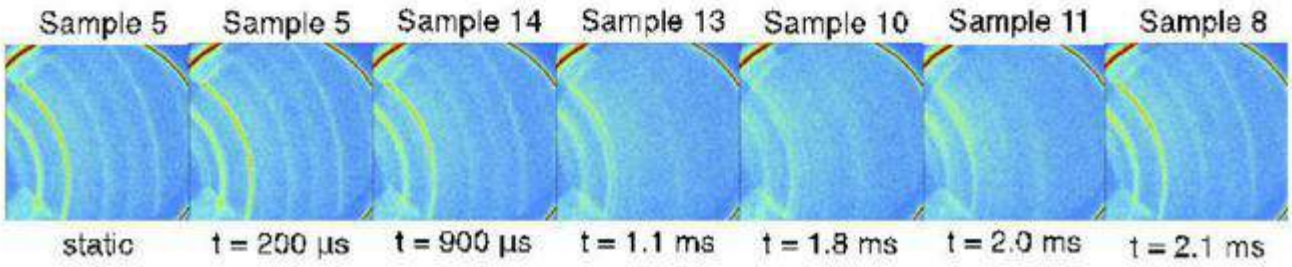

Figure 3. High-speed x-ray diffraction history in a shape memory alloy under dynamic tension.

CONCLUSIONS

The integration of Kolsky bars with high-speed x-ray phase contrast imaging and x-ray diffraction enables a new angle in impact experiments. Real-time visualization of damage processes in most materials becomes feasible. High-speed x-ray diffraction further enables the high-speed measurement of elastic crystal straining and material phase transformation. Two examples of the application of this new experimental method are presented in this paper to illustrate the feasibility and capability of the technique. Experimental results on other material systems under stress-wave loading will be presented at the conference.

References

[1] Chen W. *et al.*: In Situ Damage Assessment using Synchrotron X-ray in Materials Loaded by a Hopkinson Bar. *Philosophical Transactions A*, **372**: 20130191, 2014.

[2] Hudspeth M.C. *et al.*: Investigation of Material Deformation Mechanisms During High-Rate Loading via Simultaneous X-ray Diffraction and Phase Contrast Imaging. *Journal of Synchrotron Radiation*, **22**: 49-58, 2015.

[3] Levine S.: Dynamic Debonding between a Glass Fiber and its Matrix. *MS Thesis*, Purdue University AAE School, West Lafayette, 2016.

[4] Zbib M.B. et al.: New Pulverization Parameter Derived from Indentation and Dynamic Compression of Brittle Microspheres. *Powder Technology*, **283**: 57-65, 2015.

DYNAMIC BEHAVIOUR OF SINGLE CRYSTALLINE SILVER MICROCUBES

Ramathasan Thevamaran[1,a)], Olawale Lawal[1], Sadegh Yazdi[1], Seog-Jin Jeon[2], & Edwin L. Thomas[1,a)]
[1]*Department of Materials Science and NanoEngineering, Rice University, Houston, Texas, USA.*
[2]*Department of Polymer Science and Engineering, University of Massachusetts, Amherst, Massachusetts, USA*

Summary We present the high-velocity impact response of nanoscale face centred cubic metals, using defect-free single crystalline silver microcubes as model materials. A laser induced projectile impact test (LIPIT) apparatus accelerates the microcubes as projectiles at velocities between 300 and 1000 ms^{-1}, and the microcubes directly impact a rigid target along different crystal symmetry directions. We use scanning electron microscopy (SEM) and transmission electron microscopy (TEM) techniques to characterize the dynamic deformation mechanisms. We explore the deformation textures resulting from different impact directions, and aim to develop a fundamental understanding of how the crystal structure of single crystalline nanoscale metals evolves due to extreme strain-gradient and strain-rate.

INTRODUCTION

High-velocity impacts and shock compression of matter occur in various circumstances including, automobile and aircraft crashes, collision of space debris and micrometeorites with spacecrafts, particle impacts on turbines, and armour penetrations. A fundamental understanding of material behaviour in extreme environments—of high pressure, temperature, strain, and strain-rate—is crucial to develop materials for protective shields and functional engineering components. Recent advances in nanoscale mechanical characterization techniques have enabled us to investigate the intrinsic material properties at small-scales and discover the novel scaling laws that emerge at these scales—for example, the strengthening effects with decreasing crystallite sizes [1]. However, most of the studies on nanoscale metals so far has been limited to quasistatic loading rates ([2,3] and references therein) due to the difficulties in conducting fast timescale experiments. Generating shockwaves using lasers has recently been used [4,5] to probe into material responses at small lengthscales and fast timescales. In this study, we use a laser induced projectile impact testing technique to study the high velocity impact response of face centred cubic metals, using single crystalline silver microcubes as model materials.

MATERIAL AND METHODS

Material. We synthesized the single crystalline silver micro/nanocubes through a moderate control of oxygen in the reaction environment in a seed-growth process [6]. This bottom-up synthesis process results in mono-dispersed, nearly defect-free, single crystalline silver micro/nanocubes in large quantities. By controlling the reaction duration, we were able to synthesize silver micro/nanocubes over a broad size range from 100 nm to 2.5 μm (size is defined along the face-diagonal). Detailed descriptions of the synthesis technique and the sample's morphological characterizations can be found in [6]. The 2 μm sized silver microcubes (Fig.1(a)) are used in this study to investigate the effects of impact direction and velocity on the resultant deformation mechanisms.

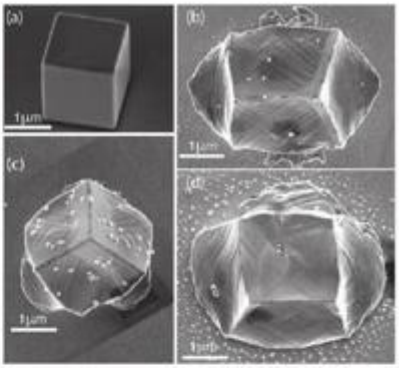

Fig.1: SEM images of a **(a)** pristine, **(b)** [100] impacted, **(c)** [110] impacted, and **(d)** [111] impacted single crystalline silver microcubes.

Mechanical Testing. The LIPIT setup built in our laboratory [7] allows selective launching of a projectile at controlled velocities between 300 ms^{-1} to 1000 ms^{-1}, and measurement of its in-flight velocity. It consists of four main components: (i) an Nd: YAG pulse laser (λ=1064 nm) and optical components for to launch the projectile by laser ablation, (ii) launch pad—a glass substrate that is coated first with a 50 nm gold film and then a 20 μm polydimethylsiloxane (PDMS) layer, in which the gold layer absorbs laser energy and vaporizes causing the PDMS to rapidly expand and launch the projectile at velocities proportional to the laser energy, (iii) rigid target—a silicon substrate coated with 100 nm gold film, and (iv) *in-situ* imaging of projectile in-flight by a CCD camera with microscopic lens that is illuminated by three coherent pulses at 32.5 ns intervals from another Nd: YAG laser (λ=532 nm). The setup is also equipped with another CCD camera with microscopic lens and LED illumination to visualize and align the projectile to the focal point of the ablation laser on the launch pad. The silver microcube samples preserved in ethanol are drop-cast on top of the PDMS layer and air-dried on the launch pad before LIPIT.

Post-impact Characterizations. We perform high resolution SEM analysis of the impacted samples in a FEI Helios NanoLab 660 DualBeam system. We also prepare thin lamella in the Helios NanoLab system for subsequent TEM study. The TEM-lamella is prepared by first, coating the sample with platinum to prevent damage from focused ion beam (FIB) milling; then, cutting trenches and performing *in-situ* lift-out and attachment to a TEM half-grid; finally, thinning down of the sample to below 100 nm using low current FIB milling. It is then analysed in FEI Titan Themis[3] Scanning/Transmission Electron Microscope (S/TEM). We perform both selective area diffraction (SAD) analysis in TEM-mode and convergent beam electron diffraction (CBED) analysis in STEM-mode to investigate the nanoscale deformation mechanisms.

[a)] Corresponding author. Emails**:** thevamaranr@rice.edu and elt@rice.edu

RESULTS AND DISCUSSIONS

The impacted silver microcubes exhibit impact-direction-sensitive deformation characteristics. As shown in Fig.1 (b-c), the samples impacted at ~400 ms^{-1} appropriately along [100], [110], and [111] crystallographic directions exhibit $\{111\}\langle 110\rangle$ slip systems that are governed by Schmid's law, which states that the critically resolved shear stress is equal to the stress applied on the material multiplied by the Schmid's factor—the multiplication of the cosines of the angles, the loading direction makes with glide plane, and the glide direction. The slip system with the highest Schmid's factor is the first one to get activated, and as it can be seen in Fig.1 (b-c), dislocation avalanches exit the crystal leaving surface steps on the faces of deformed cube. Moreover, impacts along different crystallographic directions result in unique deformation symmetries (Fig.1 (b-c)). The direct impact at very high strain-rates (>10^8 s^{-1}) also causes extreme strains on the impacted side, generating plastic flow of material, while the top free-surface experiences minimal strains. Large strains in the impacted side of the sample are also evident from the wrinkle-like deformation contours that are visible on the FIB cross-section (indicated by arrows on Fig.2(b)). The high nominal strain gradient resulted from impact suggests extreme changes in the crystallographic structure of the material.

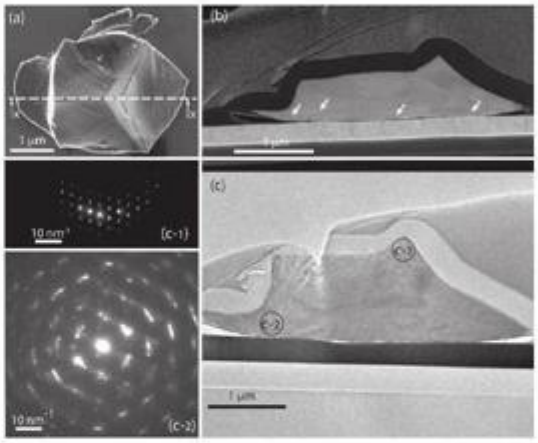

Fig.2: TEM and SAD patterns of a thin section of an impacted silver microcube. **(a)** An SEM image of the sample indicating the direction of TEM-section, **(b)** FIB cross-section of the sample as seen at 52^0 tilt in SEM, and **(c)** the bright-field TEM image of the sample with regions **(c-1)** and **(c-2)** showing the SAD patterns obtained at the locations indicated on (c).

The SAD analysis clearly shows the effects the impact had on the initial defect-free single crystalline structure of silver microcubes. The top corner of the sample that appears undeformed in SEM image (Fig.2 (a)), and indicated as (c-1) on Fig.2, displays a single crystalline diffraction pattern (Fig.2(c-1)). In contrast, the highly deformed region on the impacted side, indicated as (c-2) on Fig.2, shows a diffraction pattern (Fig.2(c-2)) that almost resembles that of a nanocrystalline material. Such drastic changes in the crystallographic structure have not been found previously in quasistatic compression or shock compression of single crystalline materials. We believe that the extreme strain-rates and the nearly adiabatic compression in an extremely short timescale (~10 ns), and the subsequent rapid cooling of the small volume of sample may have resulted in dynamic recrystallization, leading to a nanocrystalline structure within the highly deformed region of the sample. The role of strain gradient is also evident from these diffraction patterns. Furthermore, the compression wave generated during impact, and its successive multiple reflections as tensile waves off the free-surfaces of the small sample, has generated a significant amount of dislocations throughout the crystal. Such dislocations were observable on the dark-field TEM images, even in the regions that remain single crystalline.

CONCLUSIONS

We have shown the role of crystal symmetry on the high strain-rate deformation symmetries of single crystalline face centred cubic metals, using silver microcubes as a model material. The extreme strain gradients and the high strain-rates caused during the direct impact in LIPIT results in creation of a nanoscale crystallographic structure. Further studies are in progress to understand the deformation mechanisms that are employed by the crystal in undergoing plastic deformation and large shape changes, and their sensitivity to the strain-rate. Our studies also suggest pathways to making stronger nanocrystalline metals with gradient-nanostructure that provides more ductility, which will alleviate catastrophic brittle failure observed in nanocrystalline metals [8].

Acknowledgements

We acknowledge Dr. Siddartha Pathak (University of Nevada, Reno) and Dr. Nathan Mara (Los Alamos National Laboratories) for conducting quasistatic compression studies on our samples, and Mr. Matthew Janish, Dr. Katherine Jungjohann and Dr. William Mook (Sandia National Laboratories) for the initial TEM studies, which provided improved understanding for this work.

References

[1] Greer J.R., Oliver W.C., Nix W.D.: Size dependence of mechanical properties of gold at the micron scale in the absence of strain gradients. Acta Mater 53:1821–30, 2005.
[2] Greer J.R., De Hosson J.T.M.: Plasticity in small-sized metallic systems: Intrinsic versus extrinsic size effect. Prog Mater Sci 56:654–724, 2011.
[3] Greer J.R., Jang D., Gu X.W.: Exploring Deformation Mechanisms in Nanostructured Materials. JOM 64:1241–52, 2012.
[4] Youssef G., Crum R., Prikhodko S.V., et al.: The influence of laser-induced nanosecond rise-time stress waves on the microstructure and surface chemical activity of single crystal Cu nanopillars. J Appl Phys 113:84309, 2013.
[5] Colorado H.A., Navarro A., Prikhodko S.V., et al.: Ultrahigh strain-rate bending of copper nanopillars with laser-generated shock waves. J Appl Phys 114:233510, 2013.
[6] Jeon S-J., Lee J-H., Thomas E.L.: Polyol synthesis of silver nanocubes via moderate control of the reaction atmosphere. J Colloid Interface Sci 435:105–11, 2014.
[7] Lee J-H., Loya P.E., Lou J., et al.: Dynamic mechanical behavior of multilayer graphene via supersonic projectile penetration. Science 346:1092–6, 2014.
[8] Lu K.: Making strong nanomaterials ductile with gradients. Science 345:1455–6, 2014.

EXPERIMENTAL INVESTIGATION OF THE DYNAMIC BEHAVIOR OF METACONCRETE

Christian Kettenbeil[1], Guruswami Ravichandran[1]
[1]*Graduate Aerospace Laboratories, California Institute of Technology, Pasadena, California, US*

ABSTRACT

This study investigates the dynamic material behavior of a new type of concrete called Metaconcrete. Instead of sand, stone and gravel, the concrete mortar is filled with spherical lead aggregates that are encapsulated by a soft coating. This locally resonant metamaterial exhibits bandgaps that lead to the attenuation of applied stress waves at the inclusion's eigenfrequencies. Plate-impact experiments are being conducted to prove the viability of the underlying physical concepts for the attenuation of elastic waves. To reduce the effects of porosity and inhomogeneity, the mortar material is substituted by an epoxy matrix. Strain gauges on the specimen surface are used to evaluate the performance of the Metaconcrete microstructure. Initial conditions were varied with respect to impact velocities (18 m/s - 100 m/s) and flyer plate thickness (0.8 mm – 25.4 mm). The elastic waves were attenuated by 43% - 72%, showing the potential of Metaconcrete in the dynamic loading regime.

EXPERIMENTAL PROCEDURE

Specimen Design

Previous numerical investigations of Metaconcrete [1], showed that the Young's modulus of the soft coating should be one order of magnitude lower than the modulus of the matrix phase. This stiffness ratio was found to be a good compromise between impeding oscillations and transferring energy to the resonant aggregates. Since the mortar was substituted by an epoxy, a softer inclusion coating made from Polyurethane was selected. The specimen design is shown in Figure I.

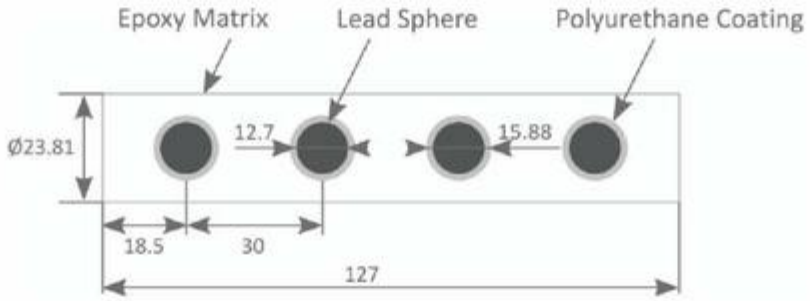

Figure I. Dimensions and composition of Metaconcrete specimen

The stiffness and geometry of the soft coating was tailored such that the resonance frequency of the heavy cores falls well within the frequency content of the applied stress waves. For frequencies above resonance ($f > f_{res}$), a negative effective mass is obtained due to the out of phase motion of the heavy aggregates, which results in favorable wave attenuation properties. The resonance frequency f_{res} can be approximated by a one dimensional, analytical framework that considers the Young's modulus E_c and the thickness t of the soft coating as well as the radius R_l and density ρ_l of the lead aggregates [2]. A frequency range of 10 – 14 kHz is obtained for the studied Metaconcrete microstructure, depending on the value of E_c, which is different for tensile and compressive loading.

Experimental Setup

In order to create stress waves containing frequency content that is representative of impact events, the Plate-Impact technique was employed. An Al 7075 flyer plate (thickness 0.8 - 25.4 mm) is accelerated in a 25.4 mm diameter gas gun to impact the Metaconcrete specimen. The flyer plate is attached to a low density foam sabot to guarantee a planar impact. Propagating stress waves are measured using three strain gauges that are applied to the specimen surface centered between two inclusions. A Phantom v310 high-speed camera (78,000 frames per second) was used to measure the projectile velocity, confirm a planar impact and observe fracture patterns during the experiment. Additonal experiments were carried out to extract frequency information from the oscillating heavy cores. For this purpose, the high-speed camera was used to record images of a speckle pattern that was applied to the lead spheres before the coating process. Digital image correlation (DIC) is employed to measure displacements using a 49x49 pixel correlation window. Complicating refraction effects due to the non-planar geometry of both the inclusions and the specimen mean that only a small area, close to the aggregate's center, can be used for correlation. However, this information is sufficient for the extraction of the sphere's rigid-body motion and its associated eigenfrequencies.

[a] Corresponding author. Email: ravi@caltech.edu

RESULTS AND DISCUSSION

Figure II shows the strain gauge readings for the impact of a 2.3 mm thick aluminum flyer plate. As a reference, an identical experiment was conducted on a homogeneous epoxy specimen. Even though the impact velocity for the Metaconcrete specimen was 10% higher (48.8 m/s vs. 44.6 m/s), a reduction of 63% in maximum strain, compared to the epoxy specimen, was obtained after the 3rd inclusion.

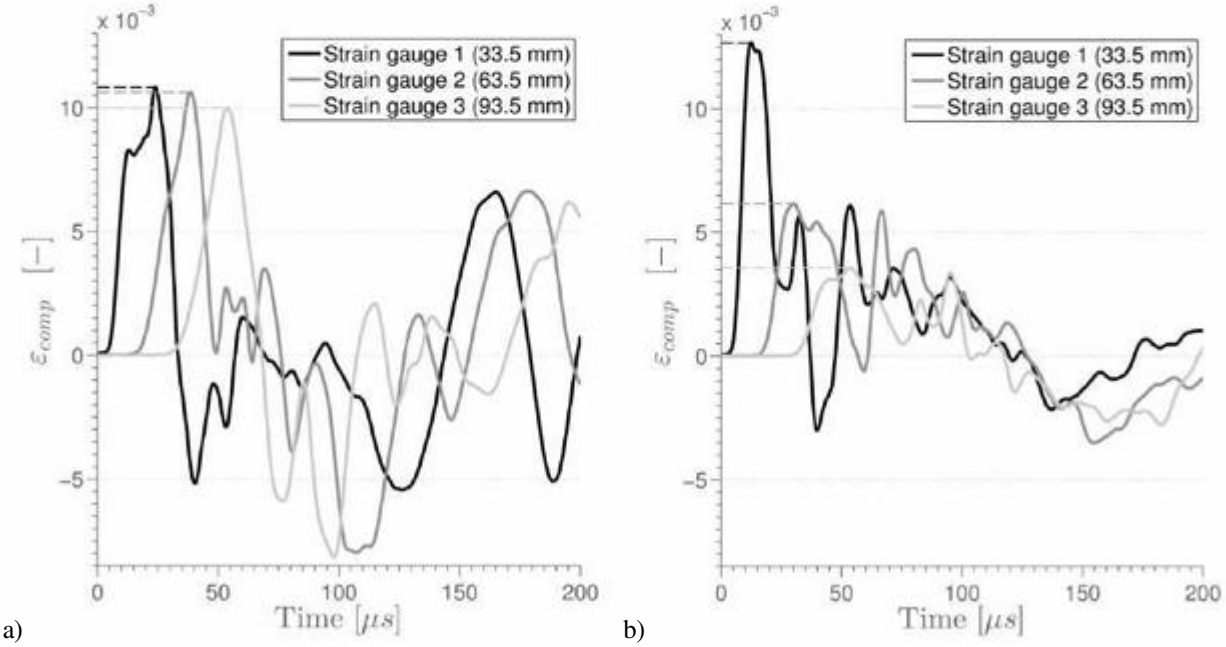

Figure II. Comparison of the (a) Epoxy and (b) Metaconcrete specimen strain attenuation under plate impact with a 2.3 mm thick Al-flyer plate at 44.6 m/s and 48.8 m/s, respectively.

Additional experiments with equal impact energies have been carried out to study the effect of the flyer plate thickness. The thickest, tested flyer (25.4mm) only reduced the maximum, longitudinal strain in the specimen by 43% compared to a homogeneous epoxy specimen. In contrast, the thinnest flyer reached an attenuation of 72%. Since the frequency content should not depend strongly on the flyer thickness, the results suggest that a longer stress wave duration has a negative impact on the Metaconcrete performance.

Experiments with higher impact velocities (100 m/s) lead to fracture processes in the specimen. Nevertheless, a reduction in the maximum, longitudinal strain of 49% could be observed. This result is of great importance considering possible applications in impact shielding using a mortar matrix, which is prone to brittle fracture.

Based on the results of the DIC measurements, distinct oscillatory modes could be identified. The frequency of the first mode (11.15 kHz) falls well within the range given by the analytical approximation (10-14 kHz). This shows that the energy absorption mechanisms are well understood and can be characterized using simple, analytical models. Thus, Metaconcrete microstructures can be tuned to be effective in a given frequency range.

CONCLUSION

The work presented here proves the viability of locally resonant metamaterials for structural applications involving stress wave loading. It has been shown that an appropriately structured Metaconcrete can attenuate the maximum strain experienced by the matrix material by more than 70% after only three oscillating inclusions. This favorable material behavior persists in the presence of fracture, which encourages the use of this microstructure for brittle materials such as concrete mortar.

References

[1] Mitchell J., Pandolfi A. and Ortiz M.: Metaconcrete: designed aggregates to enhance dynamic performance. *J. of the Mechanics and Physics of Solids,* **65**:69-81, 2014.

[2] Milton G. W. and Willis J. R.: On modifications of Newton's second law and linear continuum elastodynamics. *Proceedings of the Royal Society of London A: Mathematical*, *Physical and Engineering Sciences*, **463**:855-880, 2007.

APPEARANCE OF DISLOCATIONS MULTIPLICATION IN THE DYNAMICS OF ELASTIC-PLASTIC WAVES IN SOLIDS

G.I. Kanel[1a)], S.V. Razorenov[2], G.V. Garkushin[2]
[1]*Joint Institute for High Temperatures of RAS, Moscow, 125412 Russia*
[2]*Institute of Problems of Chemical Physics of RAS, Chernogolovka, 142432, Russia*

Summary Information about resistance of materials to inelastic deformation at strain rates more than 10^4 s^{-1} is obtained by means of analysis of an evolution of plane shock waves in studied materials. In the course of such study, we observed some features of profiles of elastic-plastic waves which were not expected and are not described by existing theories. The presentation will summarize these exotic effects with the goal to stimulate development of a theory of wave dynamics in relaxing media.

INTRODUCTION

The necessity for the prediction of the response of materials to intense dynamic loads requires the development of corresponding models and constitutive relationships which could be used for calculating the resistance to inelastic deformation and fracture over wide ranges of the load durations, strain rates, strains and temperatures. With this goal we have recently started [1] a systematic study of the resistance to high-rate deformation of different metals under the conditions of shock-wave loading at various temperatures. The measurements are based on the analysis of decay of elastic precursor waves and on the measurements of the rise times of plastic shock waves.

EXPERIMENTAL OBSERVATIONS

Figure 1 presents the examples of measured free-surface velocity histories of "as-rolled" and annealed titanium plates of two different thicknesses. All the recorded velocity histories contain a distinct elastic precursor wave followed by a plastic shock wave. The shock compression of "as-rolled" titanium occurs monotonically and the parameters at the elastic precursor wave remain almost unchanged as the wave propagates. The annealing decreased the density of dislocations in the material. Because of that, higher dislocation speeds and correspondingly higher stresses are required to provide high strain rates. As a result, the recorded HEL value turns out to be higher for the annealed material in spite of its lower hardness. The following plastic deformation is accompanied by multiplication of dislocations that causes the stress relaxation and forming of a spike in the frontal part of the elastic precursor wave. The compression rate in plastic shock wave is practically the same for both materials that probably means the same density of mobile dislocations at this stage of the compression.

Figure 2 presents plastic strain rates as functions of the shear stress in accordance with the decay rate of the elastic precursor wave. Over the range of the wave propagation distances from 0.25 mm to 4 mm in the annealed material the plastic strain rate in the elastic precursor wave varies with the shear stress as $\dot{\gamma} = 2.5 \cdot 10^6 (\tau/\tau_0)^{4.8}$ s^{-1} (where τ_0 = 1 GPa). For the "as-rolled" material the dependence is much stronger. Fig. 2 also shows the estimated shear stresses and plastic strain rates in the plastic shock waves**.** The comparison of the data shows that, at the same level of the shear stress the rate

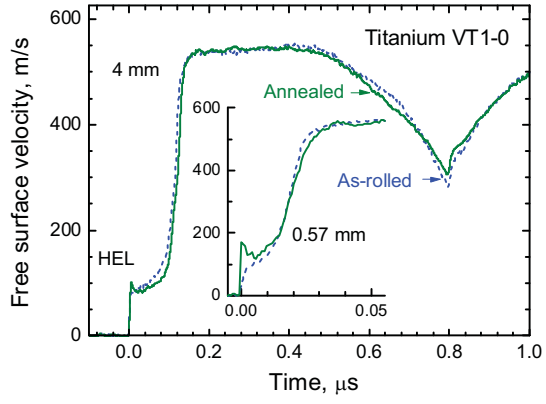

Figure 1. The free surface velocity histories of "as-rolled" and annealed titanium plates 4 mm and 0.57 mm thick. Data for "as-rolled" samples are shown by the dashed lines; the solid lines present the data for the annealed samples.

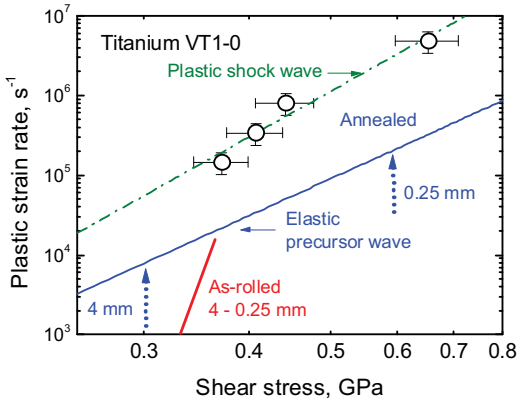

Figure 2. The dependences of plastic strain rates on the shear stress in the elastic precursor wave for annealed and "as-rolled" titanium VT1-0. The circles present the data for middle of plastic shock waves of varying intensity.

of plastic deformation at the middle of the plastic shock wave is more than by an order of magnitude higher than the initial plastic strain rate at the wave's foot. Such acceleration of the plastic deformation seems to be a result of an intense multiplication of the mobile dislocations.

Figure 3 shows the front parts of the free surface velocity histories of 2-mm copper plates impacted at different temperatures [2]. The data show sudden increase of the HEL and the change of the shape of the elastic precursor wave above 1100 K. The transformation of the shape of elastic precursor wave is accompanied by a sharp decrease of the rise time of the elastic shock front. The front of the elastic compression wave is the place where the processes dislocations generation and multiplication may start. The increase of the material's viscosity with temperature leads to the increase of the stress behind the elastic shock and, respectively, to the decrease of its rise time. Finally, the duration of the front rise becomes a limitation for dislocation multiplication. As result, the multiplication process shifts to the space behind elastic shock and causes the stress relaxation.

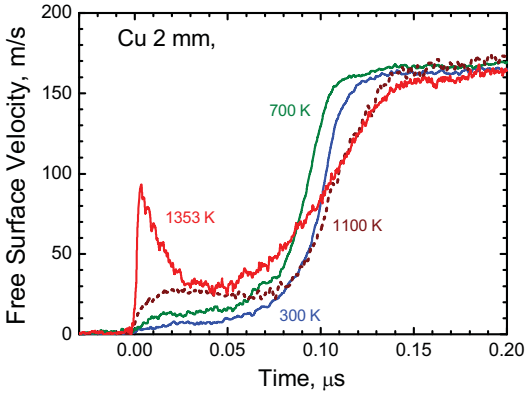

Figure 3. Front parts of the free surface velocity histories of 2-mm copper samples impacted at different temperatures (indicated by numbers at waveforms).

Figure 4 shows results of experiments [3] with shock, ramp and ramp-shock loading of annealed vanadium samples of two different thicknesses. The peak stress was approximately the same in these experiments. The increase of the rise time of the ramp part accelerates the precursor decay. In the case of the replacing of the shock part of the loading pulse by extension of the ramp compression the effect is even larger. Figure 5 illustrates decay of the elastic precursor wave in vanadium at different dynamic loading. The coincidence of the decays of the wave parameters in the minimum points means that the material arrives at this point with the same density of mobile dislocations in spite of different loading paths. The set of obtained data shows that the current values of HEL and plastic strain rate are not so much determined by the local rate of compression as by the result of the elastic precursor decay. In other words, parameters of decaying elastic-plastic wave are not so much controlled by the local response of the material as by the accumulation of the stress relaxation effects during the preceding wave propagation.

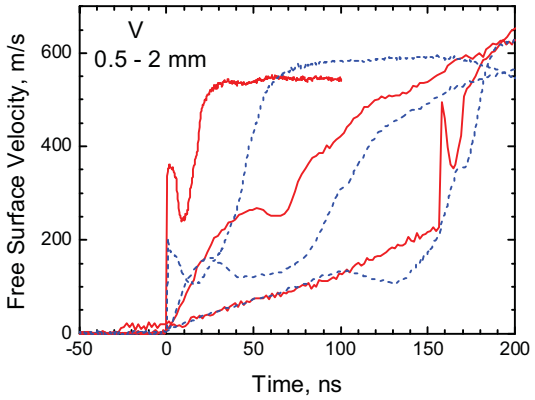

Figure 4. Comparison of the free surface velocity histories of the shock, ramp and ramp-shock loaded vanadium samples of 0.5 and 2 mm thickness.

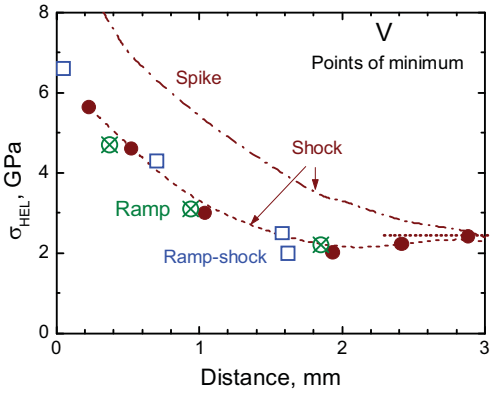

Figure 5. Decay of the elastic precursor wave at the shock, ramp and ramp-shock loading of annealed vanadium samples. The points correspond to the stress minimum between the elastic and plastic waves.

Acknowledgement

Financial support from the Russian Science Foundation via Grant No 14-12-01127 is gratefully acknowledged.

References

[1] Kanel G. I. Influence of relaxation processes on the wave dynamics of shock compression of solids. *Mechanics of Solids*, **49**(6):605-615, 2014.

[2] Zaretsky E. B. and Kanel G. I. Response of copper to shock-wave loading at temperatures up to the melting point. *J. Appl. Phys.* **114**:083511, 2013.

[3] Kanel G. I., Razorenov S. V., Garkushin G. V., Savinykh A. S., and Zaretsky E. B. Stress relaxation in vanadium under shock and shockless dynamic compression. *J. Appl. Phys*. **118**:045901, 2015.

MODELLING LAMINATED FABRIC COMPOSITES UNDER IMPACT LOADS

Martin Schwab*[1] and Heinz E. Pettermann[1]
[1]*Institute of Lightweight Design and Structural Biomechanics, Vienna University of Technology, Vienna, Austria*

Summary A multiscale modelling approach for predicting impact damage in fabric reinforced laminated composites is presented. Thereby, the fabric topology of a multi-layered laminate is modelled at the level of individual tows for a sub-domain, which is embedded in a region with a homogenised representation of the laminate. This way, inherent effects arising from the fabric topology are accounted for. As an example, numerical simulations of a laminated plate in a drop tower impact test setup are conducted. The modelling approach is verified against experimental data, where very close agreement between the predictions and the experiments is found. The predicted energy absorption is compared to predictions of an equivalent ply-level model with a homogenised representation of the fabric plies, where significant differences in the energy contributions of individual mechanisms are observed. Furthermore, the effect of different weaving styles on the energy absorption of the laminate is investigated.

INTRODUCTION

Laminated fabric composites are widely used within the aerospace and automotive industries, as their high stiffness to weight and strength to weight ratios are key features in lightweight applications. Impact on laminated composites represents a complex, highly dynamic event involving nonlinear material behaviour. Various damage and failure mechanisms, i.e. fibre rupture, matrix cracking, delamination or plasticity-like effects, occur during impact. Each of these mechanisms contributes to the overall impact response and their interaction results in penetration or even perforation of the laminate, depending on the actual impact scenario. Experimental testing of the impact behaviour of laminated composites is very time consuming and expensive and, in most cases, only information on the overall impact behaviour is gained. Hence, predictive tools such as simulations by means of the Finite Element Method (FEM) are needed for an efficient and detailed assessment of the characteristics of laminated fabric composites subjected to impact loads.

The present paper presents a multiscale embedding approach (MEA) based on [1, 2] for simulating impact on multi-layered laminated fabric composites, where the fabric topology is discretised at the level of individual tows. This way, inherent effects arising from the fabric topology, such as fluctuations in the stress and strain fields, are accounted for. In order to assess their influence on the impact response of the laminate, a ply-level based modelling approach with homogenised representation of the fabric plies, cf. [3], is utilised for comparison. As an application example, numerical simulations of a laminated plate consisting of eight carbon fabric reinforced plies in a drop tower impact test setup are conducted. The numerical simulations are realised using the explicit FEM code Abaqus/Explicit v6.14 (Dassault Systemes Simulia Corp., Providence, RI, USA).

MODELLING APPROACH

A fabric reinforced laminate exhibits a complex topology. Each layer of such a laminate consists of interwoven resin impregnated bundles of fibres (i.e. tows) and unreinforced resin zones (i.e. matrix pockets). The present approach utilises a shell element based modelling strategy to model the fabric topology at the tow-level, cf. [1]. In order to maintain reasonable computational efficiency, a multiscale modelling technique is utilised, cf. [2]. Thereby, the fabric topology is considered within a sub-domain in the proximity of the impact zone, where a nonlinear material response is expected. This detailed sub-domain is embedded in a region with a homogenised representation of the laminate.

Within the detailed sub-domain the fabric topology is discretised assuming typical geometrical idealisations, i.e. a perfectly periodic weaving pattern, a piecewise linear tow undulation path and a rectangular tow cross-section which is uniform along

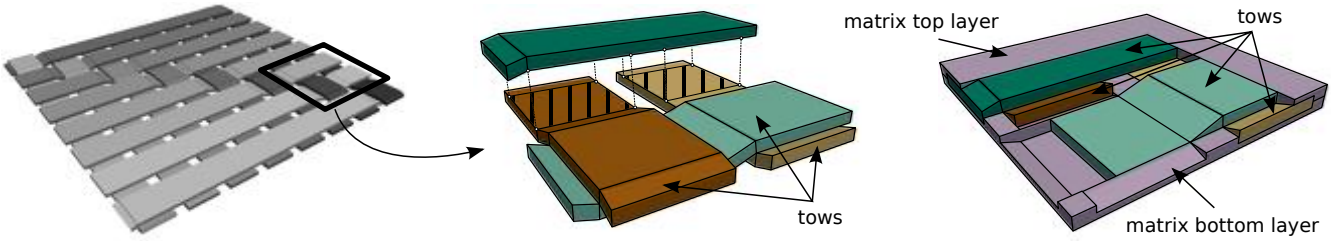

Figure 1: Schematic of a section of an eight harness satin fabric as modelled by the present approach [2].

*Corresponding author. Email: mschwab@ilsb.tuwien.ac.at



Figure 2: Comparison of the failure pattern predicted by the MEA-model (left) and the experimentally observed one (middle) at the back face of the laminated plate [2]. Effect of the fabric topology on the energy absorption of the laminate (right).

the undulation path, cf. Fig. 1. Considering a single ply, each tow, as well as the matrix pockets are modelled by individual layers of shell elements. As these individual shell layers within a ply are not connected directly, appropriate couplings are introduced. A multi-layered laminate is modelled by stacking such plies with cohesive zone elements (CZEs) between the surfaces of adjacent plies. The constitutive behaviour of the tows is modelled by an energy based continuum damage mechanics (CDM) approach which also accounts for plastic deformation due to shear loads. This material model is available as a built-in VUMAT in Abaqus/Explicit v6.14. The matrix pockets are modelled as isotropic elasto-plastic with isotropic strain hardening. Damage and failure within the matrix pockets is accounted for by a ductile damage approach. The CZEs at the interfaces between adjacent plies feature a traction-separation based constitutive law accounting for mixed-mode delamination conditions. The surrounding (embedding) domain is considered as homogeneous orthotropic material and modelled using a single layer of shell elements with layered section definition and linear elastic material behaviour. The elastic properties of the plies within the embedding domain are identical to the homogenised properties of the plies within the sub-domain. The edges at the transition between the two domains are coupled according to shell kinematics. A detailed description of this modelling approach is presented in [2].

The differences of the present modelling strategy to typical ply-level based discretisations are evaluated by comparison to a stacked shell modelling approach, cf. [3], where each ply of a laminate is considered as homogeneous material and discretised by an individual layer of shell elements with CZEs in-between. This ply-level model features a CDM approach for modelling damage and failure within the plies and accounts for plastic deformations due to shear. Delamination is modelled by the CZEs in combination with a traction-separation based constitutive law.

APPLICATION EXAMPLE

As an application example, numerical simulations of a rectangular laminated composite plate with quasi-isotropic layup in a drop tower impact test setup are conducted. The laminate consists of eight carbon fabric plies and is impacted by a spherical rigid body with an energy of 400J. The MEA modelling approach is verified by comparing the simulation results of a laminate with eight harness satin reinforcement to results from equivalent experiments. The spatial distribution of intra- and inter-ply damage, as well as the amount of absorbed energy by the laminate are found to be in very close agreement, cf. Fig. 2 (left and middle). Comparing the MEA-model and the equivalent ply-level model, a slight difference in the total amount of energy absorbed by the laminate is observed, cf. Fig. 2 (right). Considering the energy contributions of individual mechanisms, however, significant differences between these models are found. The capabilities of the MEA-model are demonstrated by investigating the effect of three different weaving styles (plain, 2/2 twil, eight harness satin) on the impact behaviour and, in particular, the energy absorption of the laminate. It is observed that the laminate with the most undulated reinforcement shows the highest amount of absorbed energy, cf. Fig. 2 (right).

References

[1] Gager J, Pettermann HE: Numerical homogenization of textile composites based on shell element discretization. Compos Sci Tech 2012;72(7):806-12.

[2] Schwab M, Todt M, Pettermann HE: A multiscale approach for modelling impact on woven composites under consideration of the fabric topology. Compos A: Appl 2016. submitted

[3] Schwab M, Todt M, Wolfahrt M, Pettermann HE: Failure mechanism based modelling of impact on fabric reinforced composite laminates based on shell elements. Compos Sci Technol 2016. submitted

XXIV ICTAM, 21-26 August 2016, Montreal, Canada
DOE/NV/25946--2718

HYPERVELOCITY IMPACT OF TI6AL4V ALLOY MATERIALS

Melissa Matthes[1], Brendan O'Toole[1(a)], Mohamed Trabia [1], Cameron Hawkins[2], Thomas Graves[3], Robert Hixson[3], Edward Daykin[2], Zach Fussell[2], Austin Daykin[2], Michael Heika[2], Shawoon Roy[1], Richard Jennings[1], Eric Bodenchak[1], & Matthew Boswell[1]

[1]Department of Mechanical Engineering, University of Nevada, Las Vegas, Las Vegas, Nevada;
[2]National Security Technologies, LLC, North Las Vegas;
[3]National Security Technologies, LLC, New Mexico Operations, Los Alamos Office

This article presents a study of dynamic failure events in forged, layered, and additive manufactured (AM) titanium alloy subject to hypervelocity impact. Experiments were conducted using a two stage light-gas gun, 0.22-caliber Lexan projectiles, and different types of titanium target plates. A four-channel Photonic Doppler Velocimetry (PDV) system was used to study the free surface velocities to provide an understanding of the different failure mechanisms in these materials. The experimental measurements were used to validate computational simulations, which describe the behavior of these materials under shock. It was determined that AM, forged titanium, and multi-layered stacks produce similar velocity profiles during the early stage of impact, with the AM targets exhibiting spall at lower velocities and the multi-layered stacks exhibiting vibrations between plates. Simulations of solid and layered forged materials provide a good match to experimental data.

INTRODUCTION

The Electron Beam Additive Manufacturing process is currently being used in industry and a quasi-static analysis showed only a 3%-5% reduction in mechanical properties compared to a forged titanium counterpart. The different microstructural morphology influences the damage and fracture behavior of the AM parts, potentially making it more brittle-like and causing early onset of damage [1]. This study compares damage mechanisms between forged and AM target plates under impact conditions. The complex microstructure of the AM materials is difficult to model computationally. Layered target plates made from forged titanium were also studied to provide an intermediate level of complexity for validating simulations.

Impact experiments were designed to produce large deformations on the back surface of targets without allowing full penetration of the projectile. Time domain velocity profiles measured on the rear surface can be used to infer shock propagation information during impact. Deformation geometry and velocity profiles were used to validate LS-Dyna computational simulations.

EXPERIMENTAL METHODS

A series of hypervelocity impact experiments were conducted with a two-stage light gas gun, which uses a powder breech to fire a plastic piston into a pump tube filled with hydrogen. The gas is compressed as the piston moves through the pump tube and a petal valve that separates the pressurized gas for the launch tube ruptures, causing the projectile to accelerate down the launch tube and into the experimental tank [2]. The projectile is a Lexan cylinder with a 5.6 mm diameter and 8.61 mm length. Impact velocities ranged from 4.8 to 6.9 km/s. Target configurations included a) solid forged titanium alloy, Ti6Al4V, 12.7 mm thick, b) two layers of forged titanium alloy, with 6.35 mm layer thickness, c) four layers of forged titanium alloy with 3.175 mm layer thickness, and d) three variations of EBAM titanium alloy with 12.7 mm thickness. A four-channel laser interferometry system, Photon Doppler Velocimetry (PDV), was used to record the basic dynamic failure mechanisms in these complex structures. PDV is a heterodyne interferometer that gathers velocity data constructed by measuring displacement using optical fiber probes [3].

COMPUTATIONAL METHODS

Computational simulations of the solid and layered forged targets being impacted by a 0.22-caliber Lexan projectile were performed using a Smooth Particle Hydrodynamics (SPH) code in LS-DYNA. Johnson-Cook material models with Mie-Grüneisen equation of state (EOS) were utilized [4]. Two dimensional axisymmetric models were created for projectiles and targets and no boundary constraints were applied. Particle spacing for these models was 0.1 mm. This modelling approach was verified for homogeneous materials in previous studies [2 & 5].

RESULTS AND DISCUSSION

Differences in deformation and failure of six types of titanium were documented for three different impact velocities. The AM, forged titanium, and multi-layered stacks produced similar velocity profiles during the early stage of impact, with the AM targets exhibiting spall at lower velocities and the multi-layered stacks exhibiting vibrations between plates. Figure 1(a) compares target back surface velocity profiles for six target configurations. The forged computational model compared

[a)] Brendan O'Toole. Email: Brendan.otoole@unlv.edu.

with experimental data is shown in Figure 1(b). Figure 2 shows the experimental results of the multi-layered target plates compared with the computational model. The multi-layer simulations still require some validation, however the simulations are able to capture the basic damage of the plates. The EBAM targets are extremely challenging to model because of the microstructure, porosity, and quasi-static property differences and have not been included in this work.

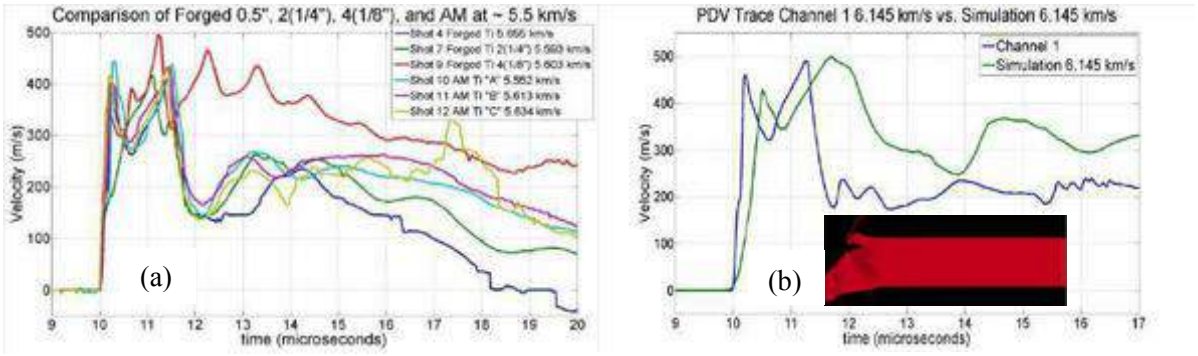

Figure 1. Velocity traces: (a) PDV data forged, layered, and AM material and (b) Experimental vs. simulation for forged titanium

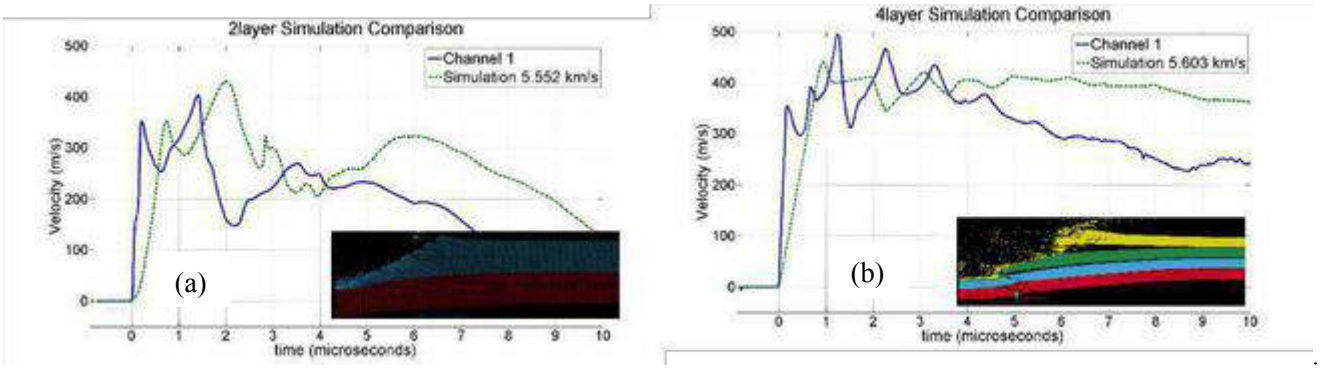

Figure 2. Experimental vs. simulation velocity traces: (a) two layers of forged titanium and (b) four-layers of forged titanium

CONCLUSIONS

The 4-channel PDV experiments were successfully completed to explore the dynamic behavior of forged titanium, stacked forged titanium, and AM titanium target plates. Differences in deformation and failure of six different types of titanium were documented for three different impact velocities. The AM material shows more damage than the forged plate for similar impact velocities and observations from these experiments indicate that the penetration velocity would be lower for the AM targets. Computational models were developed to simulate projectile-target interaction for the forged and multi-layered titanium plates. Reasonable agreement was found with experimental data. Additional microstructural geometry details and material property variations are needed in order to develop models for the AM titanium.

REFERENCES

[1] Steve Needler, "F-35 Direct Manufacturing: Material Qualification Results", AeroMat Conference and Exposition 2012, presentation (WDJ1.1), Charlotte, North Carolina, June 18 – 21 2012. https://asm.confex.com/asm/aero12/webprogram/Paper30786.html.

[2] S. Roy, et al., "Study of Hypervelocity Projectile Impact on Thick Metal Plates", Shock and Vibration, vol. 2016, Article ID 4313480.

[3] O.T. Strand, et al., Compact system for high-speed velocimetry using heterodyne techniques. Rev Sci Instrum 2006;77:083108:1–9. doi:10.1063/1.2336749.

[4] X. Wang and J. Shi. "Validation of Johnson-Cook Plasticity and Damage Model Using Impact Experiment." Int J Impact Engineering, 2013, 67-75.

[5] B. O'Toole, et al., "Modeling Plastic Deformation of Steel Plates in Hypervelocity Impact Experiments", Procedia Engineering 103 (2015) pp 458 - 465.

This manuscript has been authored by National Security Technologies, LLC, under Contract No. DE AC52-06NA25946 with the U.S. Department of Energy and supported by the Site-Directed Research and Development Program. The United States Government retains and the publisher, by accepting the article for publication, acknowledges that the United States Government retains a non-exclusive, paid-up, irrevocable, world-wide license to publish or reproduce the published form of this manuscript, or allow others to do so, for United States Government purposes. The U.S. Department of Energy will provide public access to these results of federally sponsored research in accordance with the DOE Public Access Plan (http://energy.gov/downloads/doe-public-access-plan).

THE LAVRENTIEV-ISHLINSKY PROBLEM OF TRANSVERSE VIBRATION OF RODS

Alexander Belyaev [1, 2], Nikita Morozov [1, 2a)], Peter Tovstik [1], & Tatyana Tovstik [2]
[1] *St. Petersburg State University, St. Petersburg, Russia*
[2] *Institute for Problems in Mechanical Engineering, St. Petersburg, Russia*

Summary The problem of the stability of a direct rod loaded by longitudinal impact force is considered. Lavrentiev and Ishlinski studied the simplified variant supposing that the external load expanded instantly and discovered some new effects. The given investigation presents the complicated variant with impact loading having wave character expansion. Application of the Bubnov-Galerkin approach results in a system of ordinary differential equations with periodic coefficients, which is reduced to Mathieu equations. The instability zones for different set of parameters are studied, which gives some unexpected results. In particular some specific characteristics of initial period of vibration process are investigated.

The problem of the axial compression of rods has a rich history. It begins with the works by Euler [1] who addressed two static limiting problems: (i) in the linear approximation the critical load and the possible buckling modes were found out and (ii) in the framework of nonlinear approach the various buckling modes of the rod were determined. This statement is referred now to as the Euler elastica.

The presentation is concerned with study of dynamics of rod which is subjected to a suddenly applied constant longitudinal load. This is a celebrated problem that was first stated by Michail Lavrentiev and Alexander Ishlinsky in 1949. The paper by Lavrentiev and Ishlinsky [2] dealt with the case in which the compressive load was much higher than the Euler force. It was found that the maximum growth rate of amplitude of the transverse deflection corresponds to a higher buckling mode rather than to the proper buckling mode provided that the inertia force of transverse motion is considered. The further studies [3-11] took into account both the inertia forces of transverse motion of the rod and propagation of the longitudinal waves. The short-term impact on the rod generating parametric resonance in the linear approximation was considered in [6-8]. In the framework of the nonlinear approach these resonances produce beats accompanied by exchange of energy between the axial and transverse vibration, cf. [9] In the case of long-term axial load application the evolution of the shape of elastic line from the harmonic shape by Lavrentiev-Ishlinsky-with a large number of half-waves to a stable Euler elastics was traced in [10]. The possibility of buckling under a load whose magnitude is smaller than the critical Euler load was reported in [11].

A linear statement of the problem is assumed and both axial and bending vibrations are considered. The result is a system of linear differential equations for the bending vibration with the coefficients which are periodic functions of time. The appearance of the time-dependent periodic coefficients is due to the fact and the axial vibration affects the bending vibrations. Application of the Galerkin procedure leads to an infinite system of coupled ordinary linear differential equations with time-dependent periodic coefficients. This system of coupled equations can be reduced a system of infinite uncoupled equations by determining the principle terms. It leads to a system of Mathieu equations. Each Mathieu equation is known to have a number of instability regions, among which the main instability regions being more dangerous. These regions are studied in detail.

A special analysis is carried out with the intent to determine the sets of rod parameters resulting in instability under the axial load of the magnitude less than the first Euler critical force. It is shown that it is possible if one takes into account the combinational parametric resonances. In particular, on a specific example we demonstrate that a flatter instability occurs under the jump axial load with the magnitude of 95% of the first Euler critical force.

A special attention is paid to dynamics of rod subjected to a suddenly applied constant longitudinal load at the initial stage of motion in the linear approximation. Under the initial stage we understand the double time path of the longitudinal wave along of the rod length. At any fixed time instant the compressed part of the rod is considered and its static stability is proved. As a result the time instant of the buckling is determined and its value turns out to depend on the length of this part. The growth of a given initial curvature coinciding with the shape of possible buckling is investigated at the initial stage of motion. The deflection was found to increase proportionally to the square of time as time progresses. However the previous studies were not sufficient to answer the question as to how large can be the transverse deflection at the initial stage of motion. The problem is reported to be solved in the linear approximation, and for this reason the ratio of additional deflection of buckling to the amplitude of the initial deflection is taken as a measure of instability. Two variants of the boundary conditions are considered and the solution is constructed in the form of a Fourier series in terms of the eigenfunctions.

Acknowledgement. Financial support by Russian Foundation for Basic Research, grants 01-05903-a and the joint Russia-Taiwan project, as well as the Program by the Mechanics Division of Russian Academy of Sciences is acknowledged.

[a)] Corresponding author. Email: morozov@nm1016.spb.edu.

References

[1] Euler L.: Method of determining curved lines possessing the properties of maximum or minimum or solution to isoperimetric problem in the broadest sense. Gostekhizdat, Moscow, 1934. (in Russian)

[2] Lavrentiev M.A., Ishlinsky A.Yu.: Dynamic forms of loss of stability of elastic systems. Dokl. Phys. **64**:779-782, 1949. (in Russian)

[3] Bolotin V.V.: Transverse displacement and critical velocities. Publishers of Academy of USSR Sciences, vol.1 1951, vol. 2 1953. (in Russian)

[4] Lindberg H.E.: Impact buckling of a thin bar. J. Appl. Mech. **32**:315-322, 1965.

[5] Hutchinson J.W., Budiansky B.: Dynamic buckling estimates. AIAA J. **4**:525-530, 1966.

[6] Morozov N.F., Tovstik P.E.: Dynamics of rod under axial impact. Vestn. St. Petersburg University, Series 1. **2**:105-111, 2009. (in Russian)

[7] Belyaev A.K., Il'in D.N., Morozov N.F.: Dynamic approach to the problem by Lavrentiev and Ishlinsky. Mech. Sol. **5**:28-33, 2013.

[8] Morozov N.F., Tovstik P.E.: Transverse vibrations of rod caused by axial impact. Dokl. Phys. **452**:37-41, 2013. (in Russian)

[9] Morozov N.F., Tovstik P.E., Tovstik T.P.: Statics and dynamics of rod under axial loading. Vestnik South-Ural University, Series Mathematical Modeling and Programming. **7**:76-89, 2014. (in Russian)

[10] Morozov N.F., Tovstik P.E., Tovstik T.P.: Once again on the problem by Lavrentiev and Ishlinsky. Dokl. Phys. **455**:412-415, 2014. (in Russian)

[11] Morozov N.F., Tovstik P.E.: On dynamic loss of stability of rod under a load lower than Euler force. Dokl. Phys. **453**:282-285, 2013. (in Russian)

WAVE PROPAGATION IN LATTICE METAMATERIALS WITH VISCOELASTIC INERTIAL RESONATORS

Andrea Bacigalupo[1] & Luigi Gambarotta[2a)]
[1]School for Advanced Studies IMT, Lucca, Italy
[2]Department of Civil, Chemical and Environmental Engineering, University of Genoa, Genoa, Italy

Summary The present paper is focused on the acoustic behavior of periodic beam-lattices metamaterials containing local viscoelastic resonators and deals with two different aims. A first issue concerns the assessment of the influence of the dynamic and viscoelastic properties of the resonators on the acoustic behaviour of the metamaterials. A further issue concerns the formulation of a high-frequency homogenization technique in micropolar generalized continua equivalent to the discrete model. The validity limits of the micropolar model with respect to the complex spectrum are assessed by comparing the dispersion curves of the model in the irreducible Brillouin domain with those obtained by the discrete model.

INTRODUCTION

It is well known that the propagation of elastic waves may be strongly affected by periodic arrangement of scatterers in the material microstructure. This has spurred many researches on new materials such as phononic crystals and metamaterials for the control of dispersive waves [1,2]. In fact, the periodicity of the material microstructure may lead to destructive interferences inducing attenuation of the amplitude of the travelling waves for some bands of frequencies called acoustic wave spectral gap or band gaps. In this respect, the complex band structure associated to damped Bloch wave in periodic materials is analysed in [3], a high-frequency homogenization in micropolar generalized continua for chiral metamaterials have been proposed in [4] and optimal design of auxetic hexachiral metameterials are investigated in [5].

In present paper a simplified model of periodic beam-lattice metamaterials containing local viscoelastic resonators has been formulated to obtain a better understanding of the influence of the dynamic characteristics of the local resonators on the acoustic behaviour. The beam-lattice models are made up of a periodic array of rigid heavy rings, each one connected to the others through elastic slender massless ligaments and containing an internal resonator made of a rigid disk in a soft viscoelastic annulus. The band structure and the occurrence of low frequency band-gaps are analysed through a discrete model. For both the quadrilateral and the triangular beam-lattice, the complex Floquet-Bloch spectrum is determined and six complex modes are identified. Its real part and its imaginary part characterize the attenuation and propagation modes of dispersive waves, respectively. The influence of the dynamic characteristics of the resonator on those modes is analyzed together with some properties of the band structure. By approximating the ring displacements of the discrete model as a continuum field and through an application of the generalized macro-homogeneity condition, a generalized micropolar equivalent continuum has been derived, together with the overall equation of motion and the constitutive equation given in closed form. The validity limits of the dispersion functions provided by the micropolar model are assessed by a comparison with those obtained by the discrete model.

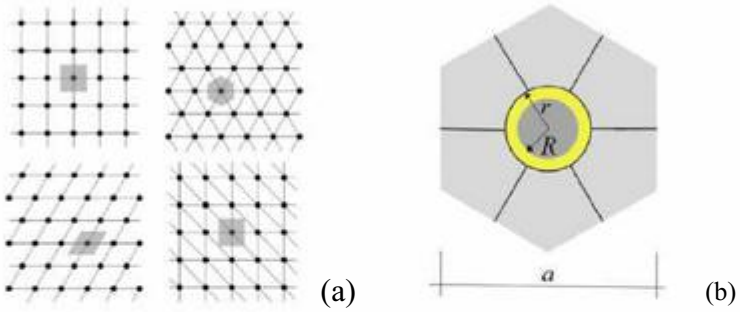

Figure 1: (a) beam-lattices metamaterials and periodic cells; (b) inertial resonator.

DISCRETE AND CONTINUUM MODELS

Let us consider the 2-D quadrilateral and triangular beam-lattices metamaterials characterized by periodic cells shown in Figure 1(a). Each cell is made up of a ring with mean radius r and n (=4,6) slender ligaments of length l, section width w and unit thickness, rigidly connected to the rings. A heavy disk with external radius R shown in Figure 1(b) (in dark grey), is located inside the ring through a soft viscoelastic annulus (in yellow). This inclusion plays the role of low-frequency

a) Corresponding author. Email: luigi.gambarotta@unige.it.

resonator. The Young modulus of the ligaments is denoted by E_s, while the translational and the rotatory inertia of the rings are M_1 and J_1, respectively. The soft viscoelastic coating inside the resonator is characterized by the relaxation functions $k_d\ t$ and $k_\theta\ t$. The translational and rotatory inertia mass density of the internal resonator are M_2 and J_2, respectively. The motion of the rigid ring is denoted by the displacement vector $\mathbf{u}$ and the rotation ϕ, respectively, while the motion of the internal resonator is denoted by the displacement vector $\mathbf{v}$ and the rotation θ.

The equation of motion of the reference cell are written as a system of six integral-ordinary differential equations taking the form

$$E_s\left(\frac{w}{l}\right)\sum_{i=1}^{n}\left\{\left[\ \mathbf{d}_i\quad\mathbf{d}_i+\left(\ \right)^2\ \mathbf{t}_i\quad\mathbf{t}_i\ \right]\mathbf{u}_i\quad\mathbf{u}\right)-\frac{1}{2}\left(\ \right)^2\mathbf{t}_i\left(\ +\ _i\right)\Bigg\}+\int_{-\infty}^{t}k_d\ t-\tau\right)\frac{d}{d\tau}\left(\mathbf{v}\quad\mathbf{u}\right)d\tau-\ _1\ddot{\mathbf{u}}\quad\mathbf{0}, \tag{1}$$

$$E_s\left(\frac{w}{l}\right)^3\sum_{i=1}^{n}\left\{\frac{a}{2}\mathbf{t}_i\quad\mathbf{u}_i\quad\mathbf{u}\right)-\frac{a^2}{4}\left(\ +\ _i\right)+\frac{l^2}{12}\left(\phi_i-\phi\right)\Bigg\}+\int_{-\infty}^{t}k_\theta\ t-\tau\right)\frac{d}{d\tau}\left(\theta-\phi\right)d\tau-\ _1\ddot{\phi}=0, \tag{2}$$

$$\int_{-\infty}^{t}k_d\ t-\tau\right)\frac{d}{d\tau}\left(\mathbf{v}\quad\mathbf{u}\right)d\tau+\ _2\ddot{\mathbf{v}}\quad\mathbf{0}, \tag{3}$$

$$\int_{-\infty}^{t}k_\theta\ t-\tau\ \frac{d}{d\tau}\left(\theta-\phi\right)d\tau+\ _2\ddot{\theta}=0, \tag{4}$$

where the unit vector $\mathbf{d}_i$ represents the i-th ligament orientation, $\mathbf{t}_i\quad\mathbf{e}_3\quad\mathbf{d}_i$ is the unit vector normal to $\mathbf{d}_i$ and $\mathbf{u}_i$, ϕ_i are the displacement and the rotation of the adjacent i-th ring, respectively.

Applying the Laplace transform $\left(\mathcal{L}\bullet=\int_{-\infty}^{+\infty}\bullet\ e\ dt\right)$ to the equation of motion (1)-(4) and imposing the Floquet-Bloch conditions in the Laplace space ($\mathcal{L}\left(\mathbf{u}_i\right)-\mathcal{L}\left(\mathbf{u}\right)\quad\mathbf{u}\left[e^{i\mathbf{k}\ \mathbf{x}_i}-1\right]$, $\mathcal{L}\ \phi_i\ \pm\mathcal{L}\ \phi\ =\phi\left[e^{i\mathbf{k}\ \mathbf{x}_i}\pm1\right]$ with $\mathbf{x}_i$ the vector position of the centre of *i*-th ring and $\mathbf{u}$, ϕ the displacement and rotation in Bloch-Laplace space) the generalized Christoffel equation is obtained in terms of the complex angular frequency s and wave vector $\mathbf{k}$. The Floquet-Bloch spectrum $s\ \mathbf{k}$ is obtained by solving the transcendental characteristic equations associated to the generalized Christoffel equation, from which six dispersive branches are obtained in the irreducible Brillouin zone. The real part $\mathrm{Re}\left[s\left(\mathbf{k}\right)\right]$ and the imaginary part $\mathrm{Im}\left[s\ \mathbf{k}\ \right]$ of the complex angular frequency characterize the attenuation and propagation modes of dispersive waves, respectively.

It is observed that the equation of motion in the Laplace space obtained by replacing the Laplace transform of the viscoelastic terms $k_d*\left(\cdot\quad\cdot\right)$ and $k_\theta\quad\cdot\quad\dot{\phi}\right)$ (where $*$ is denoted the convolution product) with their first order Taylor polynomials $\mathcal{L}\left(k_d\ t\quad s\mathcal{L}\left(\mathbf{v}\quad\mathbf{u}\right)\approx\left(k_d^0+\ ^1_d+\quad\right)\mathcal{L}\left(\mathbf{v}\quad\mathbf{u}\right)$ and $\mathcal{L}\left(\ _\theta(\ )\quad\mathcal{L}\left(\theta-\phi\right)\approx\left(\hat{k}_\theta^0+\ ^1_\theta+\quad\right)\mathcal{L}\left(\theta-\phi\right)$ is equivalent to that obtained by a discrete model with classical viscous damped [2, 3].

An approximation to the description of motion of the discrete model is obtained by introducing continuous fields of displacement and rotation to describe the generalized displacement of rings and resonators. The displacement vector and the rotation of the ring of the *i*-th neighbouring cell may be approximated through a second-order Taylor expansion in terms of: i) the first and second macro-displacement gradient $\mathbf{H}=\nabla\mathbf{u}$ and $\nabla\mathbf{H}$; ii) the curvature $\chi=\nabla\phi$ and the gradient of the curvature $\nabla\chi$. Substituting the second-order Taylor expansion of the generalized displacement of the *i*-th ring in the Laplace transform of the equation of motion of the discrete model (1)-(4), the macroscopic equation of motion of a generalized micropolar continuum is obtained. Finally, the overall mechanical properties of the beam-lattice metamaterials are analytically obtained in terms of the geometric and mechanical properties to the micro-scale.

References

[1] Pennec Y., Vasseur J.O., Djafari-Rouhani B., Dobrzyński L., Deymier P.A., Two-dimensional phononic crystals: Examples and applications, Surface Science Reports, 65, 229–291, 2010.

[2] Hussein M.I., Leamy M.J., Ruzzene M.: Dynamics of Phononic Materials and Structures: Historical Origins, Recent Progress and Future Outlook, *Appl. Mech. Rev.,* **66**, 040802-1-37, 2014.

[3] Hussein M.I., Theory of Damped Bloch Waves in Elastic Media, *Phys. Rev. B*, **80**, p. 212301, 2009.

[4] Bacigalupo A., Gambarotta L., Simplified modelling of chiral lattice materials with local resonators, Int. J. Solids and Structures, in press, 2016.

[5] Bacigalupo A., Lepidi M., Gnecco G., Gambarotta L., Optimal design of auxetic hexachiral metamaterials with local resonators, *Smart Materials and Structures*, in press, 2016.

TRANSITION RADIATION IN CONTINUA EXCITED BY A MOVING LOAD

Karel N. van Dalen*[1] and Andrei V. Metrikine[1]
[1]*Department of Structural Engineering, Delft University of Technology, Delft, The Netherlands*

Summary Transition radiation is emitted when a perturbation moves along a straight line at constant velocity in or near an inhomogeneous medium. Transition radiation of elastic waves is emitted, for example, by train wheels due to track inhomogeneities. Such radiation was analyzed using several 1-D and 2-D elastic systems, but few fundamental studies focus on elastic continua. In this study, we consider a continuum consisting of two elastic layers coupled at a vertical interface. Both layers are in plane strain, have a rigid bottom, and are subject to a load that moves along the upper surface and crosses the layer interface; the upper surface is either stress free or connected to a thin flexible plate. Using semi-analytical solutions, we study the characteristics of the excited free wave fields. Results show peculiar angular distributions of the associated energy flux, which strongly depend on the load velocity and the contrast in material parameters.

INTRODUCTION

Transition radiation is emitted when a perturbation source, which does not possess an inherent frequency, moves along a straight line at a constant velocity in an inhomogeneous medium or near such a medium. This phenomenon was described for the first time by [1], who analyzed radiation of electromagnetic waves by a charged particle crossing the boundary between an ideal conductor and a vacuum. In these early studies concerned with transition radiation, it has already been explained that this phenomenon is universal from the physical point of view, meaning that it occurs irrespective of the physical nature of the source (e.g., it can be an electric charge, an acoustic monopole, or a mechanical load).

Transition radiation of elastic waves is emitted, for example, by a train running on a railway track. The wheels of the train excite elastic waves in the railway due to track inhomogeneities such as sleepers, non-uniform subsoil and bridge supports. A review of the early studies on transition radiation of elastic waves in 1-D and 2-D elastic systems (i.e., strings, beams, membranes and plates) can be found in [2]. Recently, the problem of a beam resting on an inhomogeneous Winkler foundation again attracted attention due to the introduction of some new solution methods [e.g., 3]. Furthermore, non-linear springs were incorporated aiming at a more realistic description of the railway track substructure [4]. Transition radiation was also studied using 3-D finite-element or combined boundary-element and finite-element models for evaluating the effect of specific measures to mitigate amplified responses in railways [e.g., 7]. Finally, transition radiation was explicitly addressed – apart from possibly giving rise to vehicle instability and passenger discomfort – as one of the causes of track degradation due to the associated amplification of stresses and strains [e.g., 4].

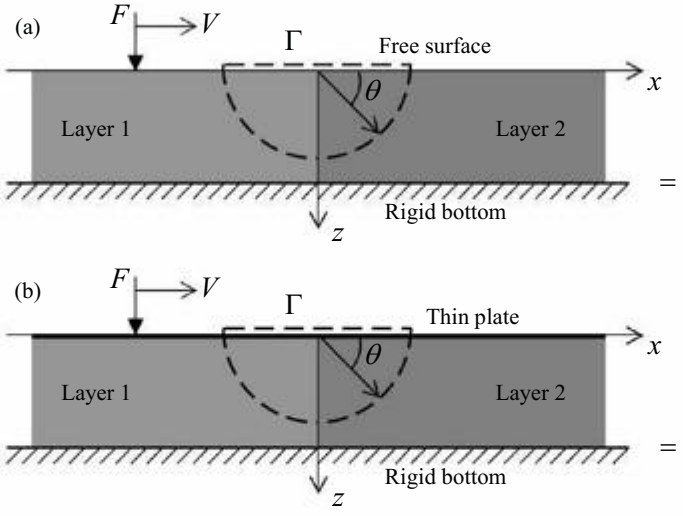

Figure 1: A surface line load F moving over the interface of two semi-infinite homogeneous isotropic elastic layers at constant velocity V. The layers are in plane strain. In the first model (a), the layers have a free surface, while there is a thin flexible plate mounted on top in the second model (b). Γ is the surface through which the energy flux is considered (see Fig. 2).

*Corresponding author. Email: k.n.vandalen@tudelft.nl

Transition radiation of waves in an elastic continuum was first theoretically described in [5]. Two elastic half-planes were considered under the action of a constant, uniformly moving load that crosses the interface between the half-planes along the path normal to this interface. Though the chosen model has no direct practical application, the study provided physical insight into the mechanism of transition radiation in an elastic continuum. Compressional and shear waves as well as interface waves (i.e., Stoneley waves) can be excited, while the energy radiation spectra of the former show peculiar directivities, which is due to the coupling of the radiated waves at the interface. In another paper, the phenomenon of transition radiation was analyzed in a more realistic continuum model consisting of two elastic layers that are coupled at a vertical interface [6]. Both layers in this model have a free surface and are fixed to a rigid bottom, while the load is assumed to move along the free surface and cross the layer interface (Fig. 1(a)). The most important difference compared to the above-discussed continuum model is the presence of the free surface, which allows for the existence of surface waves. A semi-analytical solution was obtained by expanding the transitional wave field in each layer (i.e., free fields) into a set of propagating and evanescent guided modes. The free fields are coupled at the vertical interface, and the interface conditions were used to determine the modal coefficients.

In the current study, we show that the model introduced in [6] can be extended by mounting a thin flexible plate on top of the layers, as shown in Fig. 1(b). In fact, this modifies one of the boundary conditions (at $z = 0$) and consequently the properties of the guided modes, which are now modes of the combined system. However, the solution method is generic and can still be applied. The semi-analytcial solution is used to study the characteristics of the free fields. In particular, the influence of the plate on the directivity of the energy radiation spectra is analyzed.

PRELIMINARY RESULTS

We here give some initial results for the model shown in Fig. 1(a), similar as those presented in [6]. In particular, Fig. 2 shows the free-field contribution to the energy flux through the circular part of the surface Γ, as introduced in Fig. 1(a). Clearly, the energy flux associated with the free fields has a peculiar angle dependence, and it is extreme in specific directions. We can verify that the free-field contribution is extreme along the free surface, along the layer interface or into the medium, depending on the contrast in material parameters and the load velocity. Furthermore, the free field can become powerful for a large contrast and may even dominate the total energy flux for high load velocities, which confirms earlier findings.

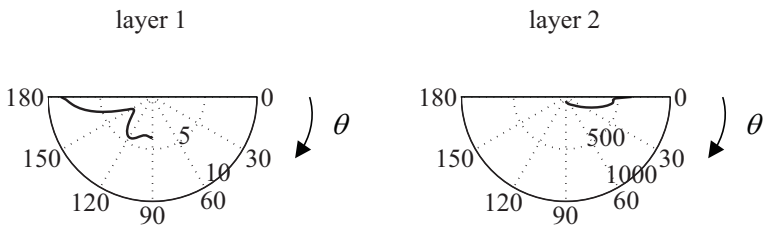

Figure 2: Free-field contribution to the total energy flux [J·s/m] through the circular part of Γ (Fig. 1(a)) versus θ (in degrees).

References

[1] Ginzburg V. L., Frank I. M.: Radiation arising from a uniformly moving electron as the electron crosses from one medium into another. J. Exp. Theor. Phys. 16:15–30, 1946.

[2] Vesnitskii A. I., Metrikin A. V.: Transition radiation in mechanics. Phys. Usp. 39:983–1007, 1996.

[3] Dimitrovová Z.: A general procedure for the dynamic analysis of finite and infinite beams on piece-wise homogeneous foundation under moving loads. J. Sound Vib. 329:2635–2653, 2010.

[4] Varandas J. N., Hölscher P., Silva M. A. G.: Settlement of ballasted track under traffic loading: Application to transition zones. Proc. Inst. Mech. Eng. Part F, J. Rail Rapid Transit 228:242–259, 2014.

[5] van Dalen K. N., Metrikine A. V.: Transition radiation of elastic waves at the interface of two elastic half-planes. J. Sound Vib. 310:702–717, 2008.

[6] van Dalen K. N., Tsouvalas A., Metrikine A. V., Hoving J. S.: Transition radiation excited by a surface load that moves over the interface of two elastic layers. Int. J. Solids Struct. 73-74:99–112, 2015.

[7] Galvín P., Romero A., Domínguez J.: Fully three-dimensional analysis of high-speed traintracksoil-structure dynamic interaction. J. Sound Vib. 329:5147–5163, 2010.

EFFECT OF LARGE DEFORMATION PRE-LOADS ON LINEAR WAVE PROPAGATION IN HEXAGONAL LATTICES

Raj Kumar Pal*[1], Julian Rimoli[1,2], and Massimo Ruzzene[1,2]

[1]*Daniel Guggenhiem School of Aerospace Engineering, Georgia Institute of Technology, Atlanta, Georgia, USA*
[2]*George W. Woodruff School of Mechanical Engineering, Georgia Institute of Technology, Atlanta, Georgia, USA*

Summary We study linear wave propagation in nonlinear hexagonal lattices capable of undergoing large deformations, under different levels of pre-load. The lattices are composed of a set of masses connected by linear axial and angular springs, with the nonlinearity arising solely from geometric effects. By applying different levels of pre-load, the small amplitude linear wave propagation response can be varied from isotropic to highly directional. Analytical expressions for the stiffness of a unit cell in the deformed configuration are used to analyze the dispersion surfaces under different levels of pre-load. Numerical simulations on finite lattices demonstrate the validity of our unit cell dispersion analysis predictions and illustrate the wave steering potential of our lattice.

THEORETICAL BACKGROUND AND NUMERICAL METHODOLOGY

We focus on lattices undergoing large deformations which have been a subject of recent interest in developing tunable metamaterials [1], smart morphing structures [2], deployable shells and structures [3], etc. We study the effect of pre-load on wave propagation as a hexagonal lattice deforms and evolves to the topologically equivalent re-entrant configuration.

The lattices are a collection of nodes and edges with point masses located at the nodes, while the edges are massless. The masses interact via two types of springs in the lattice: each edge acts as a linear axial spring, which resists change in its length, while an angular spring between any two adjacent edges sharing a node resists the change in angle between the two edges. The axial and angular springs' stiffness are respectively, denoted as k_a and k_t and the undeformed length of an edge is L. The angular stiffness k_t is normalized and a non-dimensional lattice parameter η is defined as $\eta = k_t/k_a L^2$. The lattice is located in the xy-plane and its degrees of freedom are the nodal coordinates, i.e., location of the point mass at each node. The equation of motion of a mass at node i, subjected to an external force $\mathbf{f}_i$ is $\ddot{\mathbf{x}}_i + \partial P/\partial \mathbf{x}_i = \mathbf{f}_i$.

We study small amplitude wave propagation under various deformed configurations of the lattice. The deformed configuration is first obtained by solving the equations of motion quasi-statically under prescribed boundary conditions using a Newton-Raphson procedure. Then the equations of motion are linearized about this deformed configuration and wave propagation is studied using the linearized system. By using superposition principle and Bloch-analysis on the linearized equations of a single unit cell, the dynamic behavior of an infinite lattice are characterized.

LINEAR WAVE PROPAGATION IN INFINITE LATTICES: DISPERSION ANALYSIS

We study linear wave propagation in lattices which have been pre-loaded by applying uniform uniaxial tension or compression along the y-direction. The level of pre-load is quantified using the strain β. We examine the dispersion surfaces associated with the first P-mode. The dispersion contours are plotted in the wavenumber (μ_x, μ_y) plane. Figure 1(a) illustrates the dispersion contours for the lattice at a strain $\beta = 0.33$. The constant frequency contours are circular, which indicates

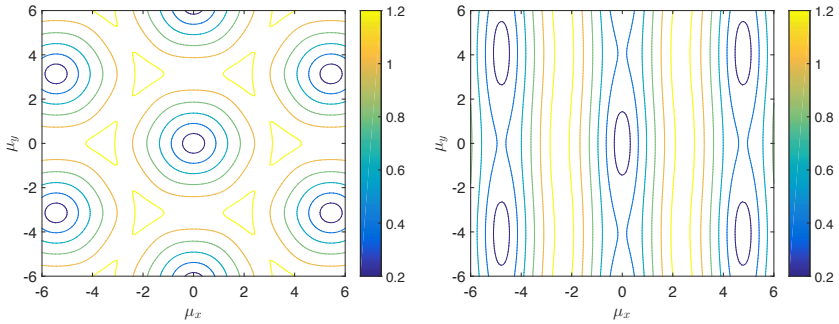

Figure 1: Dispersion surface contours for the $\eta = 6 \times 10^{-3}$ lattice at strain levels: (a) $\beta = 0.33$ and (b) $\beta = -0.1$. Colorbar denotes frequency ω.

*Corresponding author. Email: raj.pal@aerospace.gatech.edu

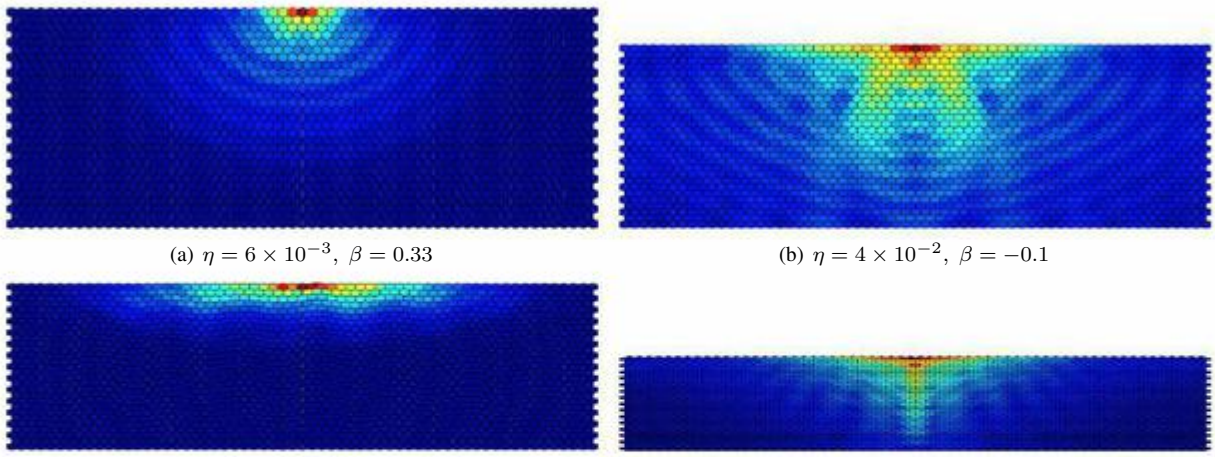

(a) $\eta = 6 \times 10^{-3},\ \beta = 0.33$ (b) $\eta = 4 \times 10^{-2},\ \beta = -0.1$

(c) $\eta = 6 \times 10^{-3},\ \beta = -0.1$ (d) $\eta = 4 \times 10^{-2},\ \beta = -0.48$

Figure 2: Contours of displacement amplitude for $\eta = 6 \times 10^{-3}$ lattice: (a) $\beta = 0.2$, (c) $\beta = -0.1$. For $\eta = 4 \times 10^{-2}$ lattice: (b) $\beta = -0.1$ and (d) $\beta = -0.48$. The behavior changes significantly in both cases with increasing pre-strain.

that the wave propagation for this corresponding mode is isotropic. Figure 1(b) displays the dispersion contours at a strain level $\beta = -0.1$. In contrast to the earlier case, the behavior is anisotropic, with most of the wave propagation along the x-direction. Furthermore, the contours associated with high frequencies are parallel to the $y-$axis. This feature indicates the existence of directional wave motion at these frequencies.

NUMERICAL SIMULATIONS ON FINITE LATTICE

We now demonstrate the behavior of finite lattices of 60×30 unit cells subjected to external dynamic loading. A constant static force is applied on the boundary nodes of the pre-strained lattice to maintain the lattice in equilibrium in the deformed configuration. The dynamic force amplitude is sufficiently small so that the effects of nonlinearity are negligible.

Strain induced Isotropic-to-boundary wave transition

We consider a lattice with non-dimensional torsional stiffness $\eta = 6 \times 10^{-3}$ under two levels of pre-strain: $\beta = 0.2$ (Fig. 2(a)) and $\beta = -0.1$ (Fig. 2(c)). The response of the leading wave is observed to be close to isotropic for a pre-strain $\beta = 0.2$. In contrast, in the $\beta = -0.1$ case, the wave propagation is confined to the boundary, along the $\pm x$ directions. The behavior in both cases is consistent with the dispersion surfaces observed in Fig. 1. Thus the wave propagation in the lattice can be altered over a wide range from isotropic to only propagation along the boundaries by varying the amount of pre-strain.

Re-entrant lattice: Strain induced wave-focusing

We next consider a lattice with high $\eta = 4 \times 10^{-2}$ under two levels of pre-strain: $\beta = -0.1$ (Fig. 2(b)) and $\beta = -0.48$ (Fig. 2(d)) in which the lattices are in hexagonal and re-entrant configuration, respectively. At low strains, the waves are focused along the $x = \pm y$ directions, while at high strains, they are focused along the y-axis and these waves correspond to the first S-mode. Thus the level of pre-strain has a significant effect on the direction of wave propagation in a lattice.

CONCLUSIONS

The paper presents the analysis of small amplitude linear wave propagation in hexagonal lattices under various pre-load conditions. Dispersion analysis on a unit cell and numerical simulations on finite lattices are presented to illustrate the effect of pre-strain on the dynamic properties of the lattices. Our work also demonstrates the highly tunable nature of these lattices by varying the level of pre-load and it has applications for wave steering.

References

[1] Hussein M. I., Leamy M. J., Ruzzene M. Dynamics of photonic materials and structures: Historical origins, recent progress and future outlook. Appl. Mech. Rev., 2014.

[2] Schaeffer M., Ruzzene M. Wave propagation in reconfigurable magneto-elastic kagome lattice structures. J. Appl. Phys., 2015.

[3] Schioler T., Pellegrino S. Space frames with multiple stable configurations. AIAA Jour., 2007.

MODELLING AND SIMULATION OF ELASTIC WAVES IN PERIODIC MEDIA USING PSEUDO-INCIDENT WAVE METHOD

Xiaodong Wang *, Chen Wang, and Zhengwei Li
Department of Mechanical Engineering, University of Alberta, Edmonton, Alberta, Canada

Summary The multiple interaction of inhomogeneities in periodic elastic media subjected to inplane harmonic elastic waves is studied using a pseudo-incident wave (PsIW) method, which combines the analytical solutions of single inhomogeneities with a numerical assembling process to accurately determine local stress field caused by large number of inhomogeneities. Illustrative examples under different loading and geometric conditions are presented to evaluate elastic wave propagation in such complicated media. The current method can also be potentially used to study periodic elastic metamaterial systems.

INTRODUCTION

Elastic waves in inhomogeneous materials are receiving more and more attention because of their importance in advanced structural applications, such as damage tolerance design against dynamic failure, the non-destructive evaluation, and the potential filter and resonator applications associated with structural periodicity. For these applications, both local and global responses play important roles and reliable modelling tools are needed to accurately evaluate the wave propagation. Because of the complicated interaction involved, these problems are very difficult to deal with analytically, or numerically. To overcome the difficulties, Pseudo-incident wave method has been used to study the dynamic interaction between inhomogeneities in composite media [1], which provides a convenient way to handle multiple interaction by combining analytical and numerical treatments. Recent application of this method to antiplane dynamic interaction problems in composite media showed very promising results [2]. In the current study Pseudo-incident wave method will be applied to the interaction between multiple circular inhomogeneities subjected to inplane elastic waves. As examples of application, the elastic wave interaction between inhomogeneities with specific geometries will be simulated to evaluate the behaviour of waves in such media.

FORMULATION OF THE PROBLEM

The problem envisaged is the plane strain multiple interactions between inhomogeneities distributed in an elastic matrix, subjected to harmonic inplane elastic waves. Without loss of generality each inhomogeneity in the medium can be considered to be a single one subjected to a pseudo incident wave, which consists of the original incident wave and unknown scattered waves from other inhomogeneities. As a result, the analytical solution of the single inhomogeneity problem can be obtained and used as a building block for the interaction problem, which will then be assembled based on the relation between inhomogeneities to model interaction.

The fundamental solution of a single inhomogeneity problem

The displacements of an inhomogeneity and the matrix are controlled by two displacement potentials, which satisfy the Helmholtz equation, or wave equation. The general solution of displacement potentials can be expressed as

$$\phi = \sum_{n=-\infty}^{\infty} \left[J_n\left(kr\right) B_n e^{in\theta} + H_n^{(1)}\left(kr\right) A_n e^{in\theta} \right] , \tag{1}$$

where J_n and $H_n^{(1)}$ are Bessel and Hankel functions of the first kind, k is the corresponding wave number and A_n and B_n are unknown constants to be determined from the boundary/interface conditions, with r and θ being the local polar coordinates measured from the center of the inhomogeneity. $k = k_L$ or k_T, $k_L = \omega/c_L$ and $k_T = \omega/c_T$ are the wave numbers, with c_L and c_T being the longitudinal and shear wave speeds, respectively.

Modelling multiple interaction using pseudo-incident wave method

When multiple inhomogeneities are included and the system is subjected to an incident wave w_0, the concept of pseudo-incident waves can be used to find the relation between different inhomogeneities [1], based on the continuity condition along the interface. Using the analytical solutions of single inhomogeneities and considering the relation between inhomogeneities, a set of linear equations for the expansion coefficients given in Eq. (1) can be obtained as

$$\begin{bmatrix} [I]_1 & -[Q]_1[M]_{12} & \cdots & -[Q]_1[M]_{1N} \\ -[Q]_2[M]_{21} & [I]_2 & \cdots & -[Q]_2[M]_{2N} \\ \cdots & \cdots & \cdots & \cdots \\ -[Q]_N[M]_{N1} & -[Q]_N[M]_{N2} & \cdots & [I]_N \end{bmatrix} \begin{bmatrix} \{A^{(1)}\} \\ \{A^{(2)}\} \\ \cdots \\ \{A^{(N)}\} \end{bmatrix} = \begin{bmatrix} [Q]_1\{w_0^{(1)}\} \\ [Q]_2\{w_0^{(2)}\} \\ \cdots \\ [Q]_N\{w_0^{(N)}\} \end{bmatrix} \tag{2}$$

*Corresponding author. Email: xiaodong.wang@ualberta.ca; This research was supported by the Natural Sciences and Engineering Research Council of Canada (NSERC).

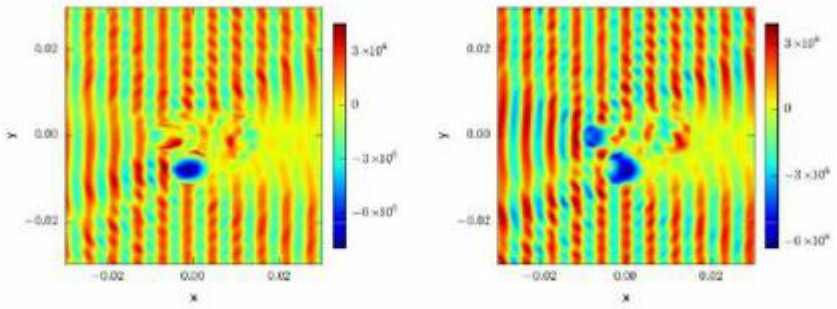

Figure 1: Stress field σ_x: real and imaginary parts

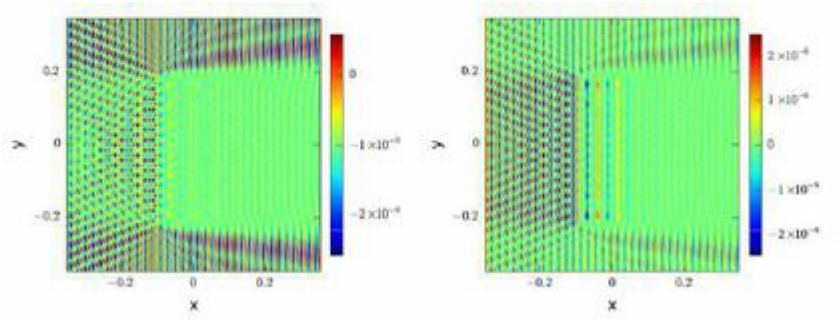

Figure 2: Stress field σ_{xy}: real and imaginary parts

where the vectors $w_0^{(k)}$ represent the original incident wave at the interface of kth inhomogeneity, and the matrices $[I]$ are the identity matrices, matrices $[Q]$ are from single inhomogeneity solutions, and matrices $[M]$ relate to the geometry of interacting inhomogeneities. The expansion coefficients can then be determined by solving these equations, from which the displacement and the stress of the wave field in the matrix and in the inhomogeneity can be calculated directly.

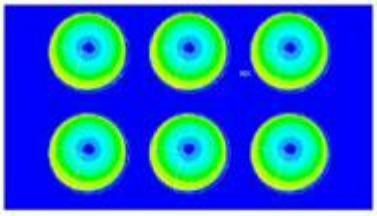

Figure 3: A two-dimensional metamaterial system with local rotation

RESULTS AND DISCUSSION

Considered first is a soft matrix (rubber) and three hard inhomogeneities (aluminum, steel and lead), subjected to a horitontal P wave. The computed real and imaginary parts of stress component σ_x is shown in Fig. 1, from which multiple interaction is clearly seen. Fig. 2 shows the shear stress field when a horizontal shear wave passes a matrix with 90 inhomogeneities. At the frequency considered, most of the wave has been blocked by the inhomogeneities, showing a stop band effect. This phenomenon is also observed in other geometries. The current method can also be used in more complicated interacting problems, for example, composites of metamaterials, which usually show abnormal properties such as negative apparent mass. Since Pseudo-incident wave method can be used to easily assemble different inhomogeneities, the method can be extended to handle such a new material system. Fig. 3 shows the displacement of a metamaterial system with local rotation, which is suitable for the application of PsIW method.

References

[1] Wang X. D. and Meguid S. A.: Diffraction of SH wave by interacting matrix crack and an inhomogeneity. Journal of Applied Mechanics, 64(3): 568575, 1997.

[2] Wang C. and Wang X. D.: Modelling and simulation of wave scattering of multiple inhomogeneities in composite media. Composite Part B, in press, 2016.

POREQST EXTENSION TO SHOCK-RELEASE HYSTERESIS OF GRAPHITE

Gabriel Seisson *[1], Benjamin Jodar[2], David Hébert[2], Isabelle Bertron[2], Michel Boustie[3], and Laurent Berthe[4]

[1]*CEA DIF, Bruyères-le-Châtel, 91297 Arpajon Cedex, France*
[2]*CEA CESTA, 15 avenue des Sablières CS60001, 33116 Le Barp Cedex, France*
[3]*Institut P' UPR3346, 1 avenue Clément Ader, 86961 Futuroscope Cedex, France*
[4]*Laboratoire PIMM UPR8006, 151 boulevard de l'Hôpital, 75013 Paris, France*

Summary Because of its thermal and shock-wave attenuation properties, porous graphite is widely used in the aerospace industry. No residual compaction of this material after compression-release cycles has been experimentally observed that contradicts the usual numerical dynamic porous models such as POREQST. We suggest to enhance the latter taking into account this phenomenon. The new model H-POREQST was tested for simulating plate impact experiments at moderate pressure onto porous graphite. It proved to be in far better agreement with experimental data than the original model.

INTRODUCTION

EDM3 is a commercial grade of porous graphite similar to those used in C/C composites. It revealed no residual compaction after static compression (Fig. 1), a behavior also expected after a shock-release loading. Thus, there is a need of a numerical model able to reproduce this mechanism. POREQST [1] has been chosen for being enhanced since investigations on this model have already been conducted [2, 3, 4, 5] to shape a first set of parameters for EDM3.

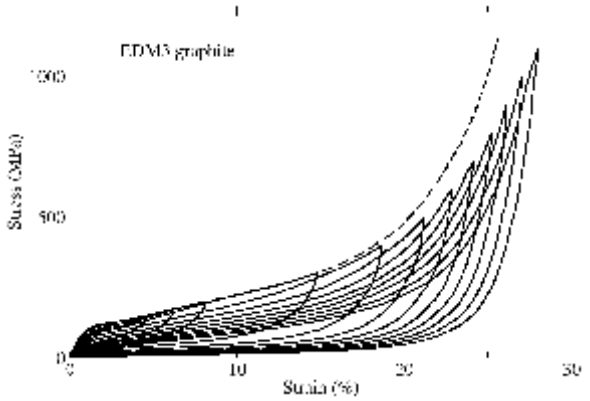

Figure 1: Quasi-static uni-axial strain tests onto EDM3 adapted from [2], an isotropic porous grade of graphite sintered by the company POCO (see www.poco.com). Dashed: simple confined compression test. Solid: cycled confined compression-release test showing no residual compaction. The initial density ρ_0 is 1754 kg/m^3 corresponding to a porosity of 22 %.

MODEL DESCRIPTION

Fig. 2(a) presents an overview (in the zero internal energy plane) of the POREQST model [1] that supplies constitutive relations for porous materials under dynamic loading. Static experimental data (e.g. elastic moduli, compaction curve, etc.) can be used as input parameters. Dense material is described by its own EOS and a pore re-opening curve defined via the parameter σ_l is included. Without failure model, tension leads to low and inconsistent densities (dashed arrow). Thus, when the pressure in a Lagrangian cell is located on the pore re-opening curve, pressure and stresses are annealed and the tension strength is withdrawn setting σ_l to zero. The residual compaction predicted by POREQST after compression does not seem realistic regarding EDM3. We suggest an enhancement named H-POREQST (Fig. 2(b)): a linear hysteresis curve is introduced and defined by the parameter σ_h. Hence, pressure relaxation follows successively the intermediate and the hysteresis curves.

APPLICATION

An experiment have been performed consisting in a 2-mm copper plate impacting at 330 m/s a 3-mm plate of EDM3. The rear surface velocity of the latter was recorded and is displayed in Fig. 3(a) (circles) along with computation results. All the parameters were the same for the two models (except σ_h that does not exist in POREQST). H-POREQST clearly improves the first velocity peak, the pull-back is quite well reproduced as well as the spall velocity. It confirms that hysteresis behavior also occurs in the dynamic regime. It is well understood thanks to Fig. 3(b) that schematizes the P-u diagram of the target. The target undergoes a compression following a path made of the initial elastic surface (1) and the compaction curve (2) up to a maximum pressure (3). The shock break-out on the rear surface involves a pressure decrease (4) depending on the model. It results in a maximum velocity higher for H-POREQST (V_h instead of V_o).

*Corresponding author. Email: gabriel.seisson@cea.fr

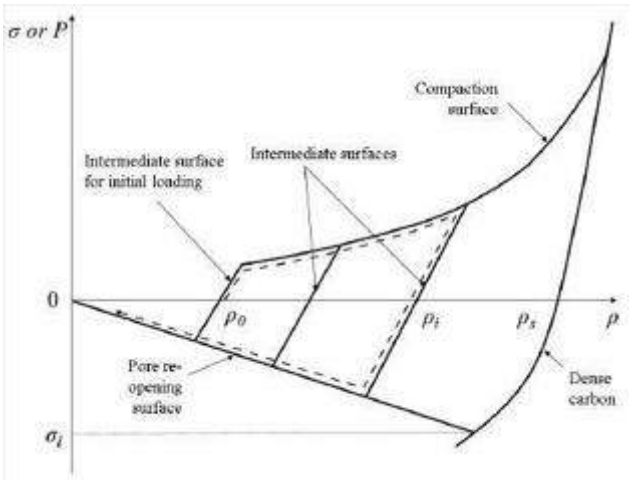

(a) Original POREQST model [1].

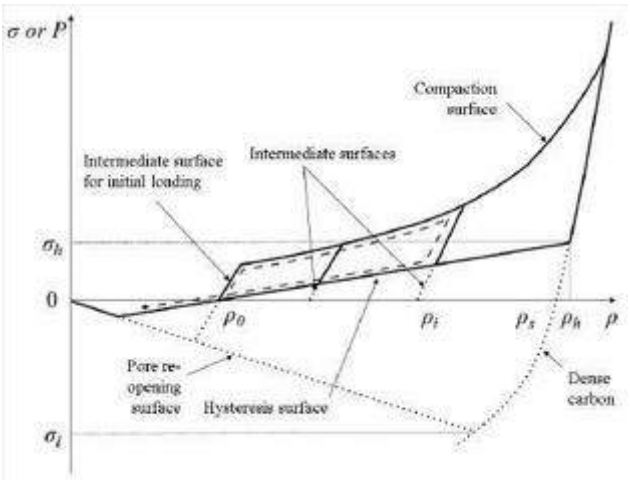

(b) New H-POREQST model.

Figure 2: POREQST vs H-POREQST. Dashed arrows: typical compression-tension paths (without damage). σ is the stress, P the pressure and ρ the density.

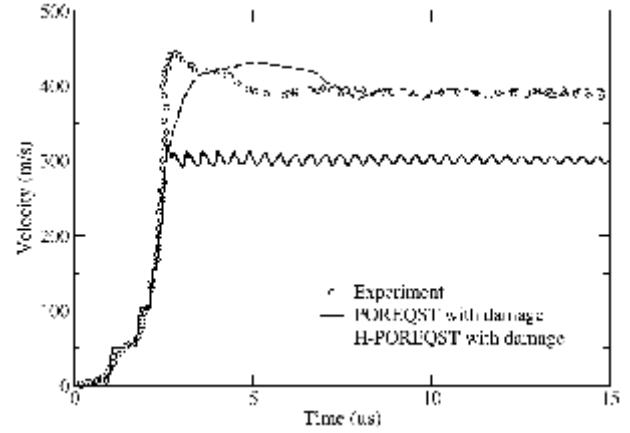

(a) Free surface velocity of the EDM3 target. Experiment vs 1D planar simulations with Hésione, a Lagrangian hydrocode from CEA.

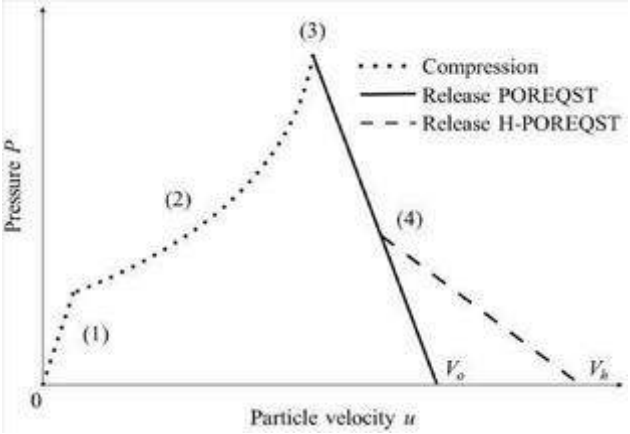

(b) Schematic and theoretical P-u diagram of the experiment. Comparison between POREQST and H-POREQST.

Figure 3: Comparison between POREQST and H-POREQST for a plate impact experiment on EDM3 with spallation.

CONCLUSION

We enhanced the POREQST model in order to reproduce the assumed density recovery of a porous graphite after a shock-release cycle. Therefore, we introduced a new constitutive curve beside the original ones defined through a single parameter. It was tested for a 1D impact experiment on a commercial graphite and clearly improved the target free surface velocity. It thereby confirmed the existence of the hysteresis behavior under shock-release loading.

References

[1] Seaman L. et al.: Computational representation of constitutive relations for porous materials. SRI Tech. Report DNA-3412F, 1974.

[2] Seisson G. et al.: Experimental and theoretical study of the damaging of graphite under dynamic loading - Application to hypervelocity impacts. Ph.D. thesis of the ISAE-ENSMA Poitiers, 2014.

[3] Seisson G. et al.: Dynamic cratering of graphite: Experimental results and simulations. Int. J. Imp. Eng. 63, p.18-28, 2014.

[4] Seisson G. et al.: Modeling of laser-driven water-confined shocks into porous graphite. J. Phys. Conf. Ser. 500:11, 2014.

[5] Hébert D. et al.: Plate impact experiments and simulation on porous graphite. J. Phys. Conf. Ser. 500:18, 2014.

STRONGLY NONLINEAR WAVES GENERATED BY IMPACT IN WEAKLY AND STRONGLY DISSIPATIVE SONIC VACUUM

Vitali F. Nesterenko[1,2a)], S. Y. Wang[2] & Yichao Xu[1]
[1]*Depart. of Mechanical and Aerospace Engineering, University of California, San Diego, La Jolla, California, USA*
[2]*Materials Science and Engineering Program, University of California, San Diego, La Jolla, California, USA*

Summary The discrete system of particles with strongly nonlinear interacting forces (no linear part is present) can be described as sonic vacuum because long wave sound speed is equal zero. Plate impact on this system results in unique wave dynamics. In the nondissipative case it is governed by strong nonlinearity and dispersion resulting in the solitary wave trains, number of solitary waves in the train depending on the ratio of striker mass and mass of particles. Dissipation can dramatically change this behaviour. This paper presents results of numerical and experimental research related to the nature of pulses generated by impact in nondissipative, weakly and strongly dissipative sonic vacua. Weak dissipation results in decreasing of amplitude of emerging solitary waves or in the oscillatory shock like stress wave. Strong dissipation results in single bell shape waves or in the monotonous shock like stress waves. The effective viscosity is introduced to separate these regimes.

INTRODUCTION

Granular beds composed from iron shots effectively mitigate contact explosion being supportive media in explosive chambers. The simplest model of this media – one dimensional chains of elastic particles (e.g., steel beads) interacting by Hertz law exhibit nonclassical strongly nonlinear wave dynamics. For example, it supports new type of solitary waves, shock waves and periodic waves. In case of zero precompression these chains are characterized as "sonic vacuum" [1,2].

Important feature of this weakly dissipative system is fast transformation of incoming pulse into the train of solitary waves due to the strong nonlinearity of Hertzian contact interaction and dispersive behavior caused by the chain periodicity.

There is no direct way to find the parameters of separated solitary waves in the train far away from the impact end based on conservation laws. This presentation will explore the limits of the analytical approach to calculate the parameters of solitary wave train generated by striker based on two conservation laws using imaginary scenario [2] and explore a role of dissipation on the wave response of strongly nonlinear discrete systems.

IMPACT ON NONDISIPATIVE CHAINS

Numerical calculations and experiments were conducted to explore dynamic response of two strongly nonlinear discrete chains composed from steel spheres and steel cylinders [3] and from steel cylinders and Nitrile O-rings [4]. Fig. 1 represents result of impact by striker on the chain of steel spheres and cylinders with similar masses m_s. From Fig. 1 it is clear that initial pulse excited by striker with mass significantly larger than mass of particles in nondissipative chain is split into train of solitary waves. Striker impact with smaller masses resulted in faster decrease of the amplitudes of solitary wave in the train. When striker mass was equal or less than mass of particles only single solitary wave was generated.

Parameters of these solitary waves in far field can be found analytically based on imaginary scenario of striker impact with mass equal mass of solitary wave similar to [5]. Conservation of linear momentum and energy in the sequential impacts of the striker with the imaginary mass in rest with effective mass m_{eff}=1.3m (the striker mass $m_{st} > m_{eff}$) results in the following equation for linear momentum P_n of the n-th solitary wave generated by the n-th impact of the striker:

$$P_n = \frac{2P_0(B-1)^{n-1}}{(B+1)^n}, \tag{1}$$

where P_0 is the initial linear momentum of the striker, $B = m_{st}/m_{eff} > 1$, and number n corresponds to the n-th solitary wave.

In case if striker mass is smaller than effective mass of solitary wave ($B = m_{st}/m_{eff} < 1$) then in the proposed scenario only one impact event happened with the chain and linear momentum of generated single solitary wave P is

$$P = \frac{2P_0}{(B+1)}. \tag{2}$$

The multiple impacts of striker and the mass equal to m_{eff} transfer all initial linear momentum and energy of striker into the chain generating infinite number of solitary waves with decreasing amplitude without recoil of the striker if $B > 1$.

Comparison of analytical approach with numerical calculations for different masses of striker m_{st} ($0.1m_s$, $0.5m_s$, $2m_s$, $4.8m_s$, $18.8m_s$) demonstrated reasonable agreement of results for the parameters of the leading solitary waves with accuracy 12% or better, less accurate agreement (16%) was obtained for striker mass 48 m_s.

Striker's behavior changes when its mass is close to $1.4m_s$: rebound of the striker from sonic vacuum at mass less than $1.4m_s$ or gradual decrease of its velocity to zero at larger mass. This critical mass of striker is close to the effective mass of

a) Corresponding author. Email: vnesterenko@eng.ucsd.edu

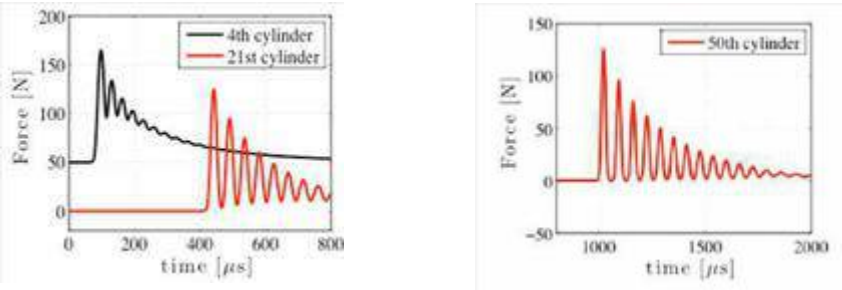

(a) (b)

Figure 1. Waves generated by striker impact (m_{st} =18.8m_s) on nondissipative steel spheres/steel cylinders chain: (a) forces inside 4th and 21st cylinders; (b)- and inside 120th cylinder. The curves are offset for visual clarity, zero time is arbitrary.

solitary wave supporting proposed scenario resulting in Eqs. 1-2. It reflects the striker interaction with collective of particles near impacted end. This striker's behavior is important when it is necessary to avoid its rebound.

IMPACT ON DISSIPATIVE CHAINS

Experimental profiles of forces in 4th and 21st cylinders are presented in the Fig. 2(a). It is clear that dissipation in experiments in the system of steel spheres and cylinders can be characterized as weak dissipation because experimental profiles are oscillatory as in nondissipative numerical calculations (Fig. 1(a)).

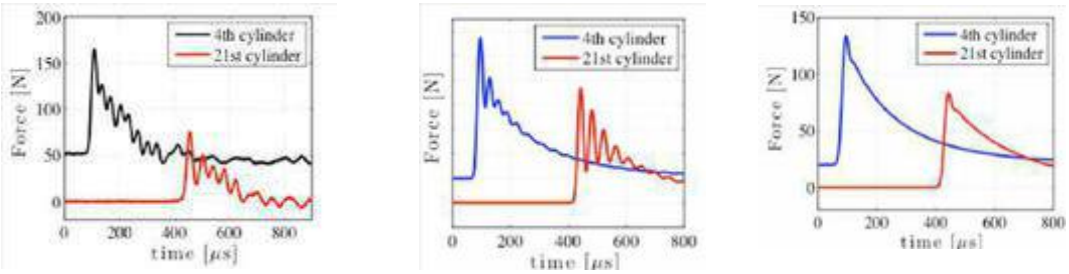

(a) (b) (c)

Figure 2. Experimental and numerical results in chains of steel cylinders and steel spheres: (a) experimental profiles, (b) numerical calculations with effective damping coefficient 6 kg/s, and (c) 40 kg/s. Impact by striker with m_{st} =18.8m_s.

It is clear that dissipation can dramatically change the nature of propagating wave from the train of solitary waves to oscillatory wave profile or to monotonous triangular pulse. The transition to the latter strongly dissipative regime was observed at critical viscosity coefficient equal about ½ of critical viscosity corresponding to the transition from oscillatory to monotonous stationary shock wave [6]. Strongly dissipative behavior was observed experimentally and modeled using effective viscosity in the discrete, strongly nonlinear sonic vacuum composed from steel cylinders and Nitrile O-rings.

CONCLUSIONS

The simplified imaginary scenario for striker interaction with sonic vacuum provided a reasonable estimation for the amplitude of the leading solitary wave in nondissipative chain and change of striker behavior depending on its mass. The critical value of viscosity preventing splitting of the initial pulse into oscillatory shock wave was found in numerical calculations. Behavior of weakly and strongly dissipative granular chains will be presented based on experiments and numerical calculations.

References

[1] Nesterenko V.F.: Dynamics of Heterogeneous Materials, Chapter 1, Springer-Verlag, New York, 2001.

[2] Nesterenko V.F: Strongly nonlinear discrete metamaterials: origin of new wave dynamics. *Physics Procedia*, **70**, 815-818, 2015.

[3] Wang S.Y., Nesterenko V. F.: Attenuation of short strongly nonlinear stress pulses in dissipative granular chains. *Phys. Rev. E*, **91**, 062211, 2015.

[4] Xu Y., Nesterenko V.F: Attenuation of short stress pulses in strongly nonlinear dissipative metamaterial. *Journal of Applied Phys*. **117**, 114303, 2015.

[5] Tichler A.M., Gomez L.R., Upadhyaya N., Campman, X., Nesterenko V.F., Vitelli V.:Transmission and reflection of strongly nonlinear solitary waves at granular interfaces, *Phys. Rev. Letters*, **111**, 048001, 2013.

[6] Herbold E.B., Nesterenko V.F.: Shock Wave Structure in a Strongly Nonlinear Lattice with Viscous Dissipation. *Phys. Rev. E*, **75**, 021304, 2007.

SOLITONS AND SOLITONIC STRUCTURES – WHAT IS VISIBLE AND WHAT IS HIDDEN

Andrus Salupere *[1]

[1]*Institute of Cybernetics at Tallinn University of Technology, Estonia*
[2]*Department of Mechanics, Tallinn University of Technology, Estonia*

Summary Wave propagation in nonlinear dispersive media is studied in the present paper. It is well known that if there exist a certain balance between nonlinear and dispersive properties of the media solitary waves, solitons, and solitonic structures can emerge. We analyze results of numerical experiments carried out for different model equations and demonstrate how to detect hidden solitons in emerged solitonic structures.

INTRODUCTION

Solitons were discovered by John Scott Russell in the middle of the 19th century in natural and physical experiments. However, the soliton theory was extensively elaborated only in the second half of the 20th century after the celebrated paper by Norman Zabusky and Martin Kruskal [1]. Classical soliton theory says that solitons must be related to integrable systems and to infinite number of conservation laws. In the framework of this theory different analytical methods are worked out, analytical solutions to solitonic equations are found, properties of solitons are determined etc [2]. The inverse scattering method should be pointed out here as one of the most known analytical method in soliton theory [3]. Unfortunately analytical methods work only under very strict assumptions of the classical theory of solitons. As a rule, in natural experiments one does not have infinite number of conservative laws. Notwithstanding this fact, solitary waves that have soliton like behavior have been frequently observed in nature as well as in many physical experiments (including experiments by John Scott Russell). Corresponding equations that describe wave propagation in such natural systems are nonintegrable as well and therefore besides analytical methods various numerical techniques are applied in order to detect solitonic behavior of nonlinear waves.

In the present study we do not care about the integrability and define **soliton** as a solitary wave that propagates at constant speed and shape and interacts elastically with other solitons (i.e., they (almost) restore their shape and speed after the interaction). Such a definition is widely used by many authors, e.g. Drazin [2], and corresponds to wave tank experiments by John Scott Russell as well as to numerical experiments by Zabusky and Kruskal. In addition, we define **solitonic structure** as two or more nonlinear waves that behave like solitons.

STATEMENT OF THE PORBLEM AND NUMERICAL METHOD

We are interested in wave propagation in nonlinear dispersive systems. For that reason several model equations have been solved numerically. Very often these equations can be considered as Boussinesq type or Korteweg–de Vries type wave equations. The first type is known as two wave equation and the second as one wave equation or evolution equation. For initial conditions harmonic, cnoidal and localized waves have been applied. The main goal of numerical experiments have been to study formation and propagation of various wave-structures and to elucidate when the behavior of the wave-structure has solitonic character and therefore can be called solitonic structures. In the present paper we demonstrate that some components of solitonic structures can be considered as hidden solitons.

For numerical integration Discrete Fourier Transform (DFT) based pseudospectral method (PsM) is applied. Due to the usage of the DFT boundary conditions are periodic.

HIDDEN SOLITON CONCEPT

If to analyze the behavior of solitonic structures, one can demonstrate that in many cases beside clearly visible solitons, which interact with each other, there exist also solitons that either emerge in wave-profiles for a short time intervals (due to the phase-shifted trajectories) or can be detected only by their influence to other solitons, i.e., by specific changes in amplitude curves and in soliton trajectories. These are called hidden solitons [4].

Hidden soliton concept can be introduced as follows: (i) hidden solitons can emerge from periodic initial excitations and they have the same physical background as visible solitons; (ii) hidden solitons can be detected in wave profiles for a short-time interval only when several soliton interactions have taken place and the reference state is fluctuating; (iii) hidden solitons cause changes, specific to soliton-type interaction, in amplitudes and trajectories of other solitons interacting with them.

*Corresponding author. Email: salupere@ioc.ee

NUMERICAL RESULTS AND DISCUSSION

As an example we consider here an equation, which describes propagation of axisymmetric deformation waves in circular cylindrical rods of compressible hyperelastic material:

$$u_\tau + \sigma_1 u u_\xi + \sigma_2 u_{\xi\xi\tau} + \sigma_3(2u_\xi u_{\xi\xi} + u u_{\xi\xi\xi}) = 0. \tag{1}$$

Here u is a quantity measuring the radial deformation, dimensionless independent variables ξ and τ correspond to the moving frame, parameters σ_1, σ_2 and σ_3 are related to the material constants and the initial stretch of the rod, and the last bracketed term represents the coupling effect of the material nonlinearity and the geometric size of the rod. The model equation is derived by Hui-Hui Dai, see [5] for details. Equation (1) is solved numerically under harmonic initial conditions. Numerical

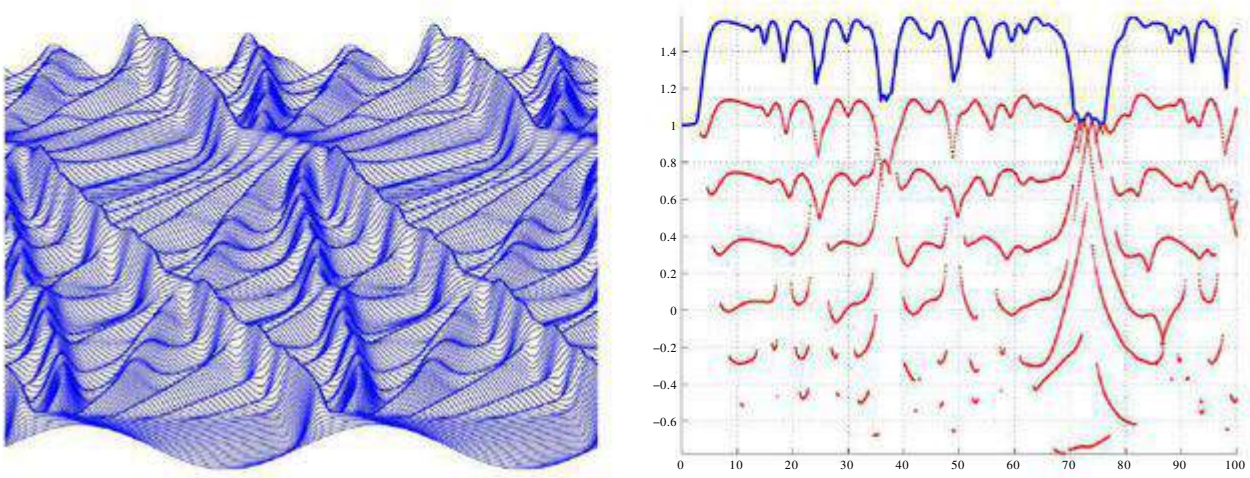

Figure 1: Formation of a solitonic structure from initial harmonic wave. The left panel presents time-slice plot over two space periods and the right panel amplitude curves (wave-profile maxima) against time variable τ.

results for $\sigma_1 = -0.3051$, $\sigma_2 = -0.0022$ and $\sigma_3 = -0.003$ are presented in Fig. 1. Similarly to the KdV equation a train of solitons forms from initial sine wave in the present case. However, in case of the KdV the higher the soliton the faster it moves to the left, but here the highest solitons are moving to the right. The time-slice plot as well as the amplitude curves demonstrate that train of seven solitons forms near $\tau = 10$. According to our definitions these seven are called visible solitons and the behavior of their amplitudes and trajectories can be easily traces in $u - \tau$ and $\xi - \tau$ planes respectively (trajectories are not presented here). Rigorous analysis of these curves demonstrates that one more soliton must take part in the interaction process. It causes phase-shifts in trajectories and minima in amplitude curves of visible solitons. According to introduced definitions, this one is called hidden soliton. One can detect the hidden soliton in wave profiles for very short time intervals only, e.g. near $\tau = 35$, $\tau = 50$, and $\tau = 100$ (see the right panel in Fig.1).

We have carried out numerous numerical experiments with different model equations, which have demonstrated that in case of periodic initial waves (e.g. harmonic or cnoidal waves) hidden solitons can be often detected in solitonic structures. Detailed description of the procedure for detection of hidden solitons and more examples that demonstrate the existence of hidden solitons will be given during the presentation.

Acknowledgment

The research was supported by the Estonian Research Council (IUT3324).

References

[1] Zabusky N.J., Kruskal M.D.: Interaction of solitons in a collisionless plasma and the recurrence of initial states. Phys. Rev. Lett., 15, 240–243, 1965.

[2] Drazin P.G., Johnson R.S.: Solitons: an Introduction. Cambridge University Press, 1989.

[3] Ablowitz M., Clarkson P.: Solitons, Nonlinear Evolution Equations and Inverse Scattering Cambridge University Press, 1991.

[4] Salupere A.: The pseudospectral method and discrete spectral analysis. In E. Quak and T. Soomere (eds), Applied Wave Mathematics, Springer, Berlin, 301-334, 2009.

[5] Dai H.-H., Huo Y.: Solitary shock waves and other travelling waves in a general compressible hyperelastic rod, Proc. R. Soc. Lond. A 456 (1994), 331–363, 2000.

BULK STRAIN SOLITONS IN LENGTHY SOLIDS: FROM PHENOMENON TO A WORK TOOL

A.M. Samsonov[1,a)], I.V. Semenova[1)]
[1] *The Ioffe Physical Technical Institute, St. Petersburg, 194021 Russia*

Summary The problems of nonlinear elastic bulk strain wave generation and observation in bars, plates and shells are considered. We derived the governing equations, and have shown in both theory and experiments how the bulk solitary waves can be used in applications to macro- and nanocomposites, impact mechanics, non-destructive testing, the 3d order elastic moduli estimation.

THEORETICAL BACKGROUND

Dynamical behaviour of lengthy and nonlinearly elastic structures is of remarkable interest for physics and engineering, and the bulk solitary strain waves in nonlinearly elastic basic structural elements – rods, plates, shells - with variable geometrical and physical parameters are widely studied now in both theory and physical experiments. We consider the nonlinear elastic bulk long wave generation and observation in lengthy basic elements to demonstrate how the strain solitons can be found as the mathematical solution, observed in genuine physical experiments and, eventually, how it can be used in problems of non-destructive evaluation. Recently the studies of nonlinear guided long strain waves in lengthy elements were encouraged due to the remarkably low attenuation of the waves proven in physical experiments, [1]. Moreover, the structural bulk elements used now in various technologies are quite often made of laminated composite materials and are subject to delamination, which detection is not simple.

To derive the governing nonlinear wave equations we use the Hamilton principle, defining the action functional S as an integral over time t and volume of a wave guide Q of the specific density of the Lagrange function per unit volume, $L(U, V, W; x, r, \phi; t)$, which is equal to difference between specific kinetic (K) and potential (P) energy densities. The displacements (U,V,F) are defined in (x,r,ϕ) coordinates, and torsion is neglected for simplicity ($F=0$) in absence of external forces applied to a waveguide. The nonlinearity influence on the waveguide elasticity is dual: via the finite deformation tensor **C** components (the so-called geometrical nonlinearity) and via the tensor **C** invariants, in which the potential energy P should be expanded, say, according to the Murnaghan model (physical nonlinearity). Both types of nonlinearity are to be taken into account simultaneously, and nonlinearity is balanced by spatial dispersion provided due to non-infinitesimal transversal size of a waveguide. The Hamilton principle leads to two coupled Euler-Lagrange equations for two displacement components (U,V). For bulk longitudinal waves in rods and plates we reduced the problem to the only equation for U, the so called Doubly Dispersive Equation (DDE) for a new variable $u=U_x$ in the form

$$u_{tt} - W^2 u_{xx} = (\beta u^2 + a u_{xx} + b u_{tt})_{xx}$$

and obtained its solitary wave solution $u=A\ cosh^{-2}\ (x-Wt)$, among others, while for nonlinear bulk waves in shells the problem required further analysis and was not solved until recently [2]. For example, for bulk nonlinear wave in a cylindrical shell we found similar solitary wave solution, too, and proved that the sign of the soliton amplitude A should correspond to the sign of an integrative non-linearity coefficient β, namely, if $\beta< 0$, then $A < 0$ and only a compression solitary wave may exist, while $\beta > 0$ corresponds to $A > 0$, i.e., to a tensile solitary wave. The solitary wave velocity W is proven to be bounded also: $1 < 1/(1-\nu^2) < (W/c)^2 < 1/[(1-2\nu)(1+\nu)]$, where ν is the Poisson ratio of solids, i.e., the bulk soliton velocity in a tube is always greater than the linear sound velocity and is limited from above.

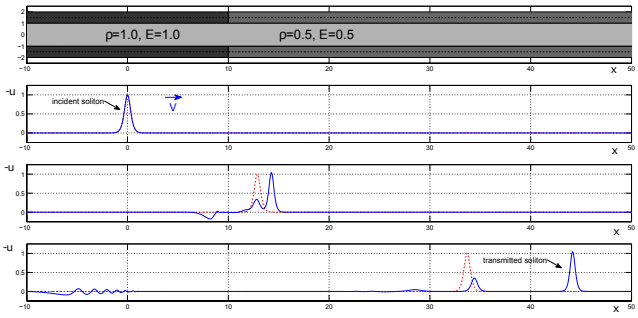

Fig.1

The nonlinear wave solutions were rigorously studied in detail [2,3], that provided a proper background for physical experiments and numerical simulations of complex problems. Numerical approach required a new version of conservative finite difference scheme and led to the detailed description of the solitary wave behaviour in dependence of elasticity and geometry variations [4], see, e.g., Fig.1, where an initial bulk soliton in a shell at $x=10$ propagates into another nonlinearly elastic material with the same linear wave velocity, generating the secondary soliton and a reflected wave package.

[a)] Corresponding author. Email: samsonov@math.ioffe.ru

BULK STRAIN SOLITONS IN REAL PHYSICAL EXPERIMENTS

Without genuine physical experiments the studies of bulk strain solitons would be incomplete. We started with experiments, using nonlinearly elastic optically transparent lengthy polymer wave guides for generation and observation of bulk strain solitons. The experimental schematic is presented in Fig.2. The experimental approach is based on the pulse laser generation and subsequent optical holography recording of the waves under study. The strain soliton is formed in the uniform rod from an initial shock wave generated in water nearby its input cross section via laser evaporation of the metallic foil. The rod (10 mm in diameter, 50 mm long) provides optimal conditions for the soliton formation and ensures that it is really the bulk soliton entering the solids under study This rod is to be bonded to each wave guide under study, e.g., bar, plate, thin walled shell, the two-layered bar etc, all made of PS, PC or PMMA, and some of them with layers containing nanoinclusions.

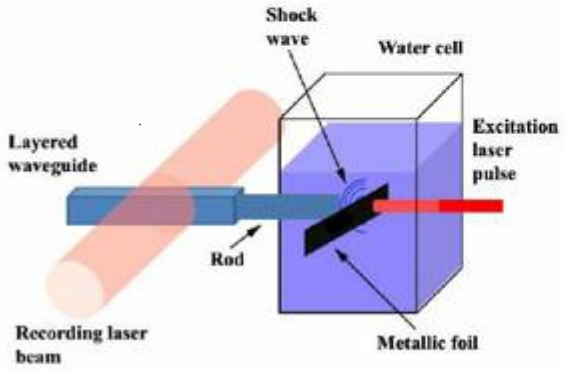

Fig.2

The interferogram processing includes measurements of fringe shifts, calculations of bulk wave parameters, amplitude and length. Various defects in interference fringes, discontinuities in particular, complicate or even preclude automatic fringe tracking and interferogram processing by means of available algorithms. We process holographic interferograms in finite width fringes using an algorithm developed for reconstruction of off-axis digital holograms [5]. This algorithm was applied for processing of interferograms of strain soliton evolution in various wave guides. In Fig.3. we present a typical picture containing holographic interferograms (a), (b) and corresponding phase distributions (c), (d) for the strain soliton moving from left to the right in a bar with bonded layers made of PS and PMMA at the distance 20-70 mm

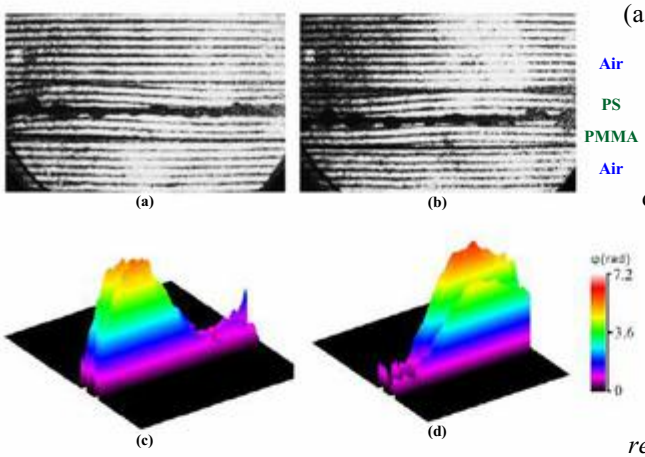

Fig.3

(a,c) and 70-120 mm (b,d) from the layered part input. The soliton parameters can be directly obtained from the fringe shifts on interferograms or from the reconstructed arrays of phase shift values, using direct and simple formuli, [1-4]. The wave patterns representing strain soliton behaviour in bonded and delaminated waveguides with layers made of different materials are substantially different. In delaminated layers solitons propagate independently exhibiting wave parameters, specific for each material.

CONCLUSIONS

Bulk strain solitons in solids, unlike any linear bulk wave, can propagate over lengthy wave guides *without remarkable decay,* their parameters depend on the material parameters, and waves carry various information about impurities, inclusions and elasticity of material to holographic recording. Comparison of behavior of strain solitons in three different wave guides made of the same material provides another instrument to study material properties of solids, e.g., the 3d order elasticity moduli. To sum up, we have shown that bulk solitary waves can be used in applications to nanocomposites and impact mechanics, non-destructive evaluation, the 3d order elastic moduli estimation etc.

This study was supported by the Russian Scientific Fund grant no. 14-12-00342.

References

[1] A. M. Samsonov, G. V. Dreiden, I. V. Semenova. *Proc IMechE, vol.222, Part C: J. Mech Engng Sci.,* 1975-1980 (2008).
[2] G.V. Dreiden, A.M. Samsonov, I.V. Semenova , A.G. Shvartz. *Appl Physics Lett.,* 105, 211906 (2014); doi: 10.1063/1.4902899
[3] A. M. Samsonov, G. V. Dreiden, I. V. Semenova, A. G. Shvartz, *AIP – CP*, 1684, 1–16; doi: 10.1063/1.4934283, (2015)
[4] A. Shvartz, A. Samsonov, G. Dreiden and I. Semenova. *AIP-CP*, vol. **1685**, 070014.
[5] A.V. Belashov, N.V. Petrov, I.V. Semenova. Technical Physics Letters,, vol. **41**, no. 7, 713–716. (2015)

STAGGERED MD AND MPM FOR MULTISCALE SIMULATION OF IMPACT RESPONSES

Zhen Chen[1,2a)], Yu-Chen Su[1], Jun Tao[2,1] and Shan Jiang[3]
[1]*Department of Civil & Environmental Engineering, University of Missouri, Columbia, Missouri, USA*
[2]*Faculty of Vehicle Engineering and Mechanics, Dalian University of Technology, Dalian, China*
[3]*Department of Chemistry, University of Missouri, Columbia, Missouri, USA*

Summary A particle-based multiscale simulation procedure is being developed to simulate composite structural responses and multiphase (solid, fluid and gas) interactions under extreme loading conditions, in which molecular dynamics (MD) at nano scale is linked to dissipative particle dynamics (DPD) at meso scale via a hierarchical approach while the DPD is combined with the material point method (MPM) at micro scale within a concurrent framework. Since the DPD forcing functions are not well-developed for metals, it is proposed that a staggered MD and MPM procedure be designed for concurrent simulation of impact responses between metal specimens. In the conference, preliminary results will be presented to demonstrate the proposed procedure, and future research tasks will be discussed on the multiscale and multiphase interactions involving failure evolution.

INTRODUCTION

To better simulate multi-phase interactions involving failure evolution without invoking master/slave nodes, the material point method (MPM, **http://en.wikipedia.org/wiki/Material_Point_Method**) has evolved for more than twenty years since the original MPM was published in 1994 [1]. The MPM is an extension from computational fluid dynamics to computational solid dynamics. The essential idea of the MPM is to take advantage of both the Eulerian and Lagrangian methods while avoiding the shortcomings of each. As can be found from the open literature, significant efforts have been made by the international research community over the last twenty years to advance the MPM for promoting simulation-based engineering science (SBES). Recently, a particle-based multiscale simulation procedure is being developed to simulate structural responses and multiphase interactions under extreme loading conditions, in which molecular dynamics (MD) at nano scale is linked to dissipative particle dynamics (DPD) at meso scale via a hierarchical approach while the DPD is combined with the MPM at micro scale within a concurrent framework [2 and 3, among others]. As illustrated in Fig. 1, the continuum body in the MPM region is discretized into a set of material points with different levels of resolution. The constitutive law governing the continuum element represented by a specific material point is evaluated at the material point position, which generates the internal force vector to be mapped to the background grid nodes based on the distance between the material point and corresponding grid nodes. There is no cutoff radius for the internal force vector. On the other hand, the continuum body in the DPD region is discretized into a set of DPD particles. Although a uniform background grid is used in Fig. 1 for the illustration convenience, the number of DPD particles inside a specific cell could be much more than that of material points in the corresponding cell. Each DPD particle represents a given number of molecules via a hierarchical coarse-graining process that smears out the thermal fluctuations as inherent in MD simulation. The discrete forcing functions in both MD and DPD have different values of cutoff radius, with the DPD cutoff radius being at least one-order larger than the MD one. To provide a seamless bridge between the MPM and DPD regions for concurrent simulation, the interface MPM particles inside the intermediate region and within the cutoff radius of any DPD particle are treated as the DPD particles when any DPD particle finds its discrete forcing function based on the cutoff radius. However, the internal force vector of an interface MPM particle is mapped only to the corresponding grid nodes without being affected by any cutoff radius.

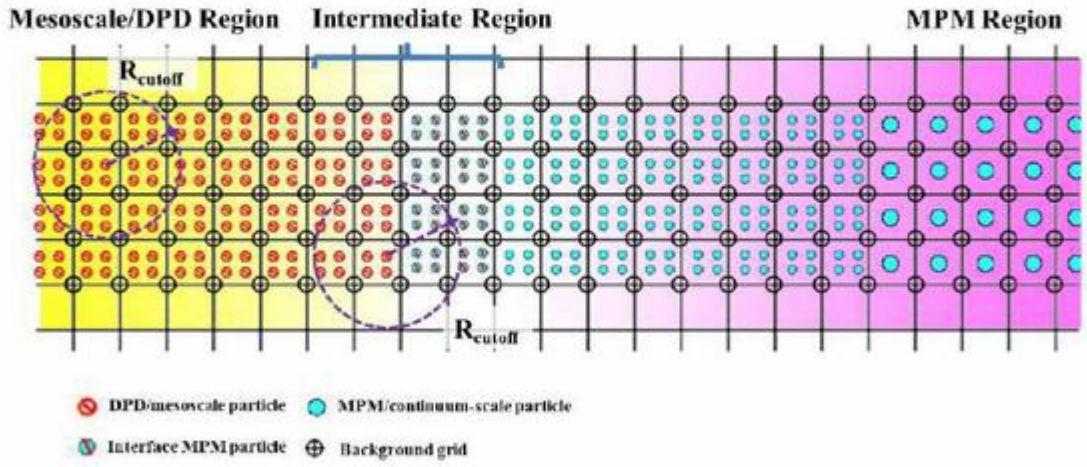

Figure 1. Illustration of multiscale simulation scheme [3].

[a)]Corresponding author. Email:chenzh@missouri.edu.

PROPOSED PROCEDURE

Although only DPD particles are shown in Fig. 1, the multiscale simulation scheme should also be applicable to the cases where MD, DPD and MPM particles concurrently occur in the single computational domain if the thermal fluctuation in MD simulations could be appropriately handled. In addition, it has been found that the MPM mapping and remapping procedure could effectively coarse-grain the DPD simulation details, as shown by Fig. 2(a) for the DPD-only simulation of a copper target subjected to impact loading, and by Fig. 2(b) for the corresponding DPD-MPM simulation (in which the DPD forcing functions are mapped onto the background grid nodes to solve the governing equations on the grid nodes). Since the mapping functions are linear, the detailed dislocation pattern could be smeared out. The dislocation pattern could be further coarse-grained with the increase of cell size, but the stress-strain relation of any DPD particle would converge with the decrease of cell size and finally approach to that produced by the DPD-only simulation [2]. It should be noted that the coarse-graining process in both spatial and temporal domains could be achieved at the same time because the time step of the explicit time integration for the MPM depends on the cell spacing instead of particle spacing. Hence, a robust concurrent procedure could be designed based on the recent findings [2, 3] for multiscale simulations of impact responses if the size effects [4] are considered.

To deal with the thermal fluctuation in MD for the concurrent simulation with MD, DPD and MPM in a single computational domain, a staggered MD and MPM procedure is proposed in this study in which the MD simulation box is chosen along the MPM background grid cell boundary so that the interfacial treatment as illustrated in Fig. 1 could be easily employed. In each MPM time step (much larger than a typical MD time step), the MD relaxation is performed inside the simulation box while DPD or MPM particles (for which there is no thermal fluctuation) outside the box will contribute to the nodal forces based on their discrete forcing functions or constitutive models, respectively. As a result, the molecular details could be observed if required. In the end of the MD relaxation process, the discrete forcing function of each molecule is mapped onto corresponding grid nodes for the concurrent simulation, and the updated nodal velocities are then mapped back to corresponding molecules to update their positions in the same way as for the DPD or MPM particles. The smoothed molecular dynamics method improved by alternating with molecular dynamics (AltSMD) [5] might be combined with the staggered MD and MPM procedure to speed up the MD part, although the AltSMD need be further developed for impact and wave propagation problems. The impact problem investigated with MD simulations [4] will be considered to demonstrate the proposed procedure. Since the target corners play an important role in the size-dependent impact responses, the corners and impacted surface will be simulated with MD while the other parts of the target will be handled via MPM in order to better understand the size effects on multiscale impact responses involving failure evolution.

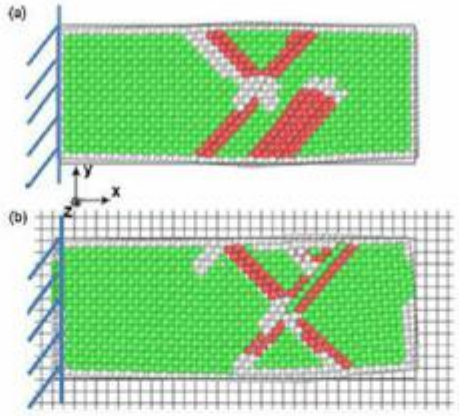

Figure 2. Coarse-graining of the MPM mapping and remapping procedure for a copper target under impact loading [2].

References

[1] Sulsky D., Chen Z., Schreyer H.L.: A Particle Method for History-Dependent Materials. *Computer Methods in Applied Mechanics and Engineering* ***118,*** 179-196, 1994.

[2] Chen Z., Jiang S., Gan Y., Liu H., Sewell T.D.: A Particle-Based Multiscale Simulation Procedure within the Material Point Method Framework. *Computational Particle Mechanics* ***1****, 147-158*, 2014.

[3] Jiang S., Chen Z., Sewell T.D., Gan Y.: Multiscale Simulation of the Responses of Discrete Nanostructures to Extreme Loading Conditions Based on the Material Point Method. *Computer Methods in Applied Mechanics and Engineering* ***297***, 219-238, 2015.

[4] Chen Z., Jiang S., Gan Y., Oloriegbe, S.Y., Sewell, T.D., Thompson, D.L.: Size Effects on the Impact Response of Copper Nanobeams. *Journal of Applied Physics* ***111***, 113512, 2012.

[5] He N., Liu Y., Zhang X.: An Improved Smoothed Molecular Dynamics Method by Alternating with Molecular Dynamics. *Computer Methods in Applied Mechanics and Engineering* ***296***, 273-294, 2015.

HARNESSING STRUCTURAL HIERARCHY TO DESIGN LIGHTWEIGHT PHONONIC CRYSTALS

Yanyu Chen [1] and Lifeng Wang[1],
[1]*Department of Mechanical Engineering, State University of New York at Stony Brook, Stony Brook, New York 11794, USA*

Summary We numerically investigate the elastic wave propagation in hierarchical honeycombs that are constructed by replacing the cell walls of regular honeycombs with hexagonal, kagome, and triangular substructures, respectively. We show that the hierarchically architected honeycombs can exhibit broad and multiple phononic band gaps, which result from the multiple scatterings in the hierarchical architectures. Our analysis reveals that the existence of these prominent wave attenuation features strongly depend on two geometric parameters, hierarchical length ratio and number of substructures away from the central axis. Furthermore, the introduction of structural hierarchy also endows the hierarchical honeycombs with enhanced stiffness. We predict that the proposed hierarchical honeycombs can realize unique combinations of the prominent wave attenuation capability and enhanced specific stiffness, thereby providing opportunities to design lightweight phononic crystals.

INTRODUCTION

In recent years, phononic crystals have gained increasing research interests because their rationally designed periodic architectures and constituent materials enable them to modify phononic dispersion relations, thereby providing avenues to tailor group velocities and hence the flow of vibrational energy. When the structural periodicities of phononic crystals are comparable to the wavelengths of propagating waves, multiple scatterings arise at the interfaces between constituent materials. This mechanism gives rise to complete wave band gaps: frequency ranges where incident mechanical waves are not allowed to propagate. This prominent property leads to a variety of potential applications, including wave filtering,[1-3] waveguiding,[4-7] and energy harvesting.[8-10] However, the inherent architectures and constituent materials, if not designed properly, could not generate desired phononic band gaps and even lead to undesired mechanical instability.

Recently, it has been explored the possibilities to manipulate wave propagation by harnessing multiscale characteristic of hierarchical architectures.[3,11-14] These rationally designed hierarchical architectures can give rise to multiple and broadband phononic band gaps as well as low frequency band gaps. Moreover, the designed hierarchical architectures also enable the coexisting of multiband wave filtering and waveguiding in an ultrawide frequency range.[14] Aside from these prominent phononic properties, outstanding mechanical properties such as strength, stiffness, and fracture toughness can be simultaneously achieved. Meanwhile, there have been great efforts to develop tunable phononic band gaps through intriguing the structural instability thereby changing the lattice symmetries of phononic crystals.[15]

Despite these considerable efforts, challenges still remain. For example, to achieve the desired wave attenuation, soft materials using thermally coupled dissipation mechanism are often employed in engineering practice. In this regard, the wave attenuation capability strongly depends on the thickness of the materials, thus posing a great challenge to design lightweight materials with strong wave attenuation ability. Further, conventional phononic crystals with periodic architectures can only provide limited frequency band gaps since the Bragg scattering mechanism requires that the wavelength must be comparable to the given structural periodicity. Lightweight phononic crystals with broadband and multiband wave attenuation ability remain unrealized. Here we choose honeycomb lattices with hexagonal, kagome, and triangular substructures as our model system to address the above challenges.

RESULTS

Figure 1 (a) shows a typical regular honeycomb lattice material. By replacing the cell walls with hexagonal substructures, we obtain the hierarchical honeycombs (Figure 1(b)). Here we define two geometric parameters, hierarchical length ratio and the number of hexagonal substructures away from the central axis, N, to uniquely describe the shape of the hierarchical honeycombs. Subsequently, hierarchical honeycombs with kagome and triangular substructures are designed by connecting the midpoints and vertices of the hexagonal substructures, respectively (Fig.1(c)-(d)). Note that the thicknesses of cell walls in the designed hierarchical honeycombs are determined based on relative density equivalence between regular honeycombs and hierarchical honeycombs.

Figure 2 shows the phonon dispersion relation of regular and hierarchical honeycombs. For the regular honeycomb, we only observe one narrow band gap. By contrast, the introduction of structural hierarchy in the regular honeycombs leads to much broader band gaps (Fig.2 (b)-(d)). Since the only difference between the regular honeycombs and the hierarchical honeycomb is the structural hierarchy, we therefore conclude that structural hierarchy can be considered as an effective approach to achieve broad and multiple band gaps.

We also simulate the mechanical responses of regular and hierarchical honeycombs. We note that hierarchical honeycombs with hexagonal substructures have comparable yet slightly lower stiffness than that of regular honeycomb. Remarkably, hierarchical honeycombs with kagome and triangular substructures show improved stiffness.

[a)] Corresponding author and presenting author. Email: lifeng.wang@stonybrook.edu.

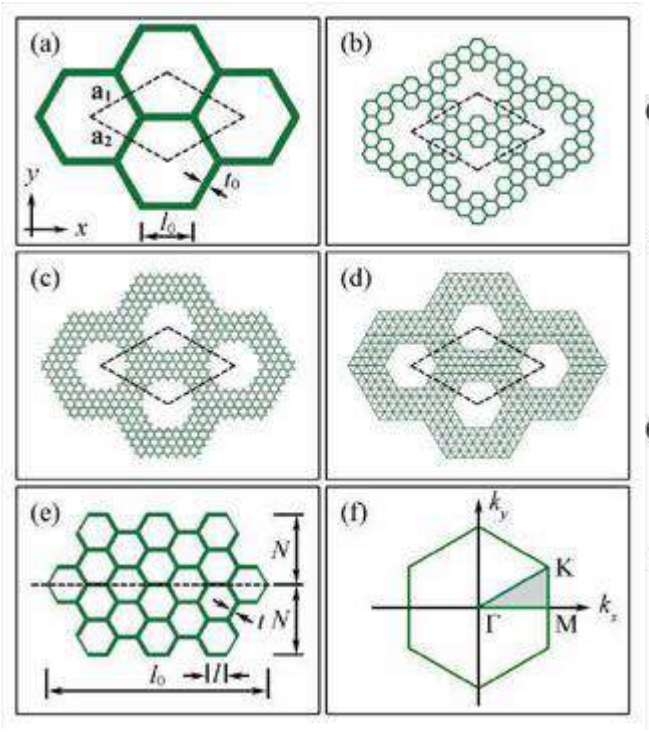

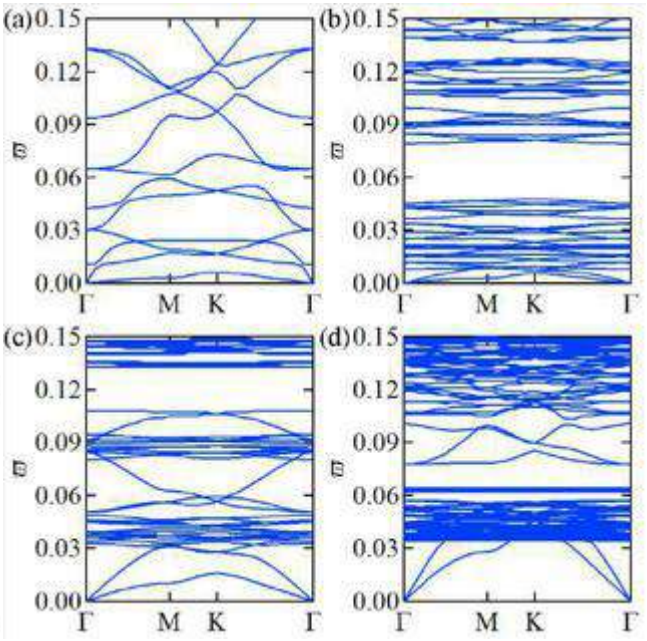

Figure 1(Left). (a) Regular honeycomb. l_0 and t_0 are the length and thickness of cell walls. (b)-(d) honeycomb with hexagonal, kagome, and triangular substructure, respectively. (e) a schematic of cell wall with hexagonal substructure, where l and t are the length and thickness of cell walls in hexagonal, kagome, and triangular substructure. N is the number of substructures away from the central axis of the cell wall. (f) The associated first Brillouin zone.

Figure 2(Right). Phonon dispersion relations of regular and hierarchical honeycombs. (a) Regular honeycomb; (b)-(d) hierarchical honeycomb with hexagonal substructure, kagome substructure, and triangular substructure, respectively.

CONCLUSIONS

In summary, we have investigated the wave attenuation capability of hierarchical honeycombs with hexagonal, kagome, and triangular substructures. We show that broad and multiple band gaps can be achieved by introducing structural hierarchy in regular honeycombs, provided that the hierarchical length ratio and number of substructures are rationally designed. Remarkably, hierarchical honeycombs with kagome and triangular substructures exhibit improved specific stiffness as compared to that of regular honeycombs. Here we propose a new structural concept for designing phononic crystals, that is, the introduction of structural hierarchy in regular honeycombs. It should be emphasized that the achieved outstanding wave attenuation capability and enhanced mechanical property are solely dictated by the structural hierarchy, and thus are material independent. The findings presented here will provide new opportunities to design lightweight phononic crystals for applications including underwater wave mitigation in submarines and other structural vibration mitigation in automobiles and aircrafts.

References

[1] J. S. Jensen, Journal of Sound and Vibration 266, 1053 (2003).
[2] Y. Pennec, B. Djafari-Rouhani, J. Vasseur, A. Khelif, and P. Deymier, Physical Review E 69, 046608 (2004).
[3] P. Zhang and A. C. To, Applied physics letters 102, 121910 (2013).
[4] A. Khelif, A. Choujaa, S. Benchabane, B. Djafari-Rouhani, and V. Laude, Applied Physics Letters 84, 4400 (2004).
[5] J. Vasseur, P. Deymier, B. Djafari-Rouhani, Y. Pennec, and A. Hladky-Hennion, Physical Review B 77, 085415 (2008).
[6] A. Khelif, A. Choujaa, B. Djafari-Rouhani, M. Wilm, S. Ballandras, and V. Laude, physical Review B 68, 214301 (2003).
[7] F.-L. Hsiao, A. Khelif, H. Moubchir, A. Choujaa, C.-C. Chen, and V. Laude, Physical Review E 76, 056601 (2007).
[8] S. Gonella, A. C. To, and W. K. Liu, Journal of the Mechanics and Physics of Solids 57, 621 (2009).
[9] H. Lv, X. Tian, M. Y. Wang, and D. Li, Applied Physics Letters 102, 034103 (2013).
[10] L.-Y. Wu, L.-W. Chen, and C.-M. Liu, Applied Physics Letters 95, 013506 (2009).
[11] R. C. Norris, J. S. Hamel, and P. Nadeau, Journal of Applied Physics 103, 104908 (2008).
[12] N.-K. Kuo and G. Piazza, Applied Physics Letters 99, 163501 (2011).
[13] L. Xiao-Jian and F. You-Hua, Chinese Physics B 22, 036101 (2013).
[14] Y. Chen and L. Wang, Extreme Mechanics Letters 5, 18 (2015).
[15] J.-H. Jang, C. Y. Koh, K. Bertoldi, M. C. Boyce, and E. L. Thomas, Nano letters 9, 2113 (2009).

ENERGY FOCUSING USING THE DISPERSION OF FLEXURAL WAVES

Valentin van Gemmeren*[1], Robert Ernst[1], Stefan Künzli[1], Martin Veidt[2], and Jürg Dual[1]
[1]*Institute for Mechanical Systems, Swiss Federal Institute of Technology Zurich, Zurich, Switzerland*
[2]*School of Mechanical and Mining Engineering, University of Queensland, Brisbane, Australia*

Summary The phase velocity of flexural waves depends strongly on their frequency, which leads to the distortion of traveling broadband pulses. This effect is used to focus strain energy at a particular location in a wave guide. Bending waves are excited at one end of a glass beam and focus to a sharp peak at another location of the beam. The excitation is determined from a time reversed spectral element simulation. The focusing of the bending waves in the glass beam is measured using a Laser Doppler vibrometer. Strong focusing was observed.

INTRODUCTION AND THEORY

Introduction

Flexural waves in plates and beams show a strong dispersive behaviour [1]. This means that the phase velocity depends on the frequency content of the wave package. Accordingly a broadband pulse is distorted as it propagates in a wave guide. This effect has been exploited in previous work to locate defects in tubes with many circumferential measurements [2], as well as in beams [3, 4] and plates [5] with a one point displacement measurement: The elastic waves originating from the defect (e.g. acoustic emissions) are detected at one point of the structure. Subsequently their propagation path is retraced in a time reversal simulation, where the distorted wave pulse refocuses at the location of the defect, which can thus be identified.

In this work the dispersive behaviour of flexural waves is used in a similar manner to focus strain energy in a glass beam: One end of the beam is excited in such a way, that the propagating waves focus at a certain location of the beam and form a sharp peak. Hence energy can be pumped into the beam over a longer amount of time and the effect of the transducer can be amplified with the ultimate objective to induce enough strain energy to break the beam at the focal point of the guided waves.

Theory

In a first step the excitation signal for the transducer has to be determined: Therefore the propagation of a sharp pulse (here the second derivative of the Gauss curve was used) in the glass beam is simulated using spectral elements as proposed by Doyle [6] and several reflections at the ends of the beam are taken into account. The simulated displacement at the left end of the beam is time-reversed and adjusted according to the transfer function of the transducer to obtain the excitation signal (see figure 1).

In a second step this signal is applied to the transducer, which is mounted to the left end of the beam. It induces a series of dispersed guided waves, which focus - after several reflections - at the desired location of the beam.

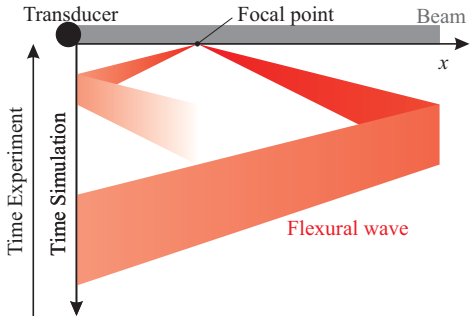

Figure 1: The time reversal of the simulated flexural wave packages leads to a refocusing of the pulse in the experiment.

EXPERIMENTS AND RESULTS

Experimental setup

The experimental setup consists of a circular Duran® glass tube (outer diameter of 5 , inner diameter of 3. , length of 1 0), which serves as wave guide and is supported on two foam cushions. To one end of the tube a magnetic sphere is glued with the polarisation pointing in radial direction. Thus a bending moment can be induced by applying a magnetic field in axial direction. The deflection of the glass beam is measured with a Laser Doppler vibrometer. It is mounted on a positioning stage, so that measurements at multiple locations of the beam can be carried out in subsequent experiments.

Measuring procedure

With the Laser Doppler vibrometer the deflection of the glass beam can only be measured at one point at a time. However it is mandatory to measure the deflection all along the beam, as to be able to see the full dispersive behaviour of the flexural waves. Hence a series of subsequent experiments is carried out, where several measurements are taken and averaged for a set of positions on the glass beam. Putting all those measurements together one obtains a time-space diagram, in which the paths of all wave packages can be retraced.

*Corresponding author. Email: vangemmeren@imes.mavt.ethz.ch

Results

A first series of experiments was carried out with the glass tube and the transducer design described beforehand. The resulting time-space diagram is shown in figure 2. As can be seen a total of 4 pulses are sent from the left side ($x = 0$ mm) into the beam, with the earliest pulse undergoing 3 reflections before focusing on the desired location at $x = 600$ mm together with the subsequent pulses. Because of the dispersive behaviour of the flexural waves, the pulses disperse again after having focused on one spot. The maximum observed stress was 5.8 MPa. The stress was deduced from the deflection measurement using Timoshenko beam theory.

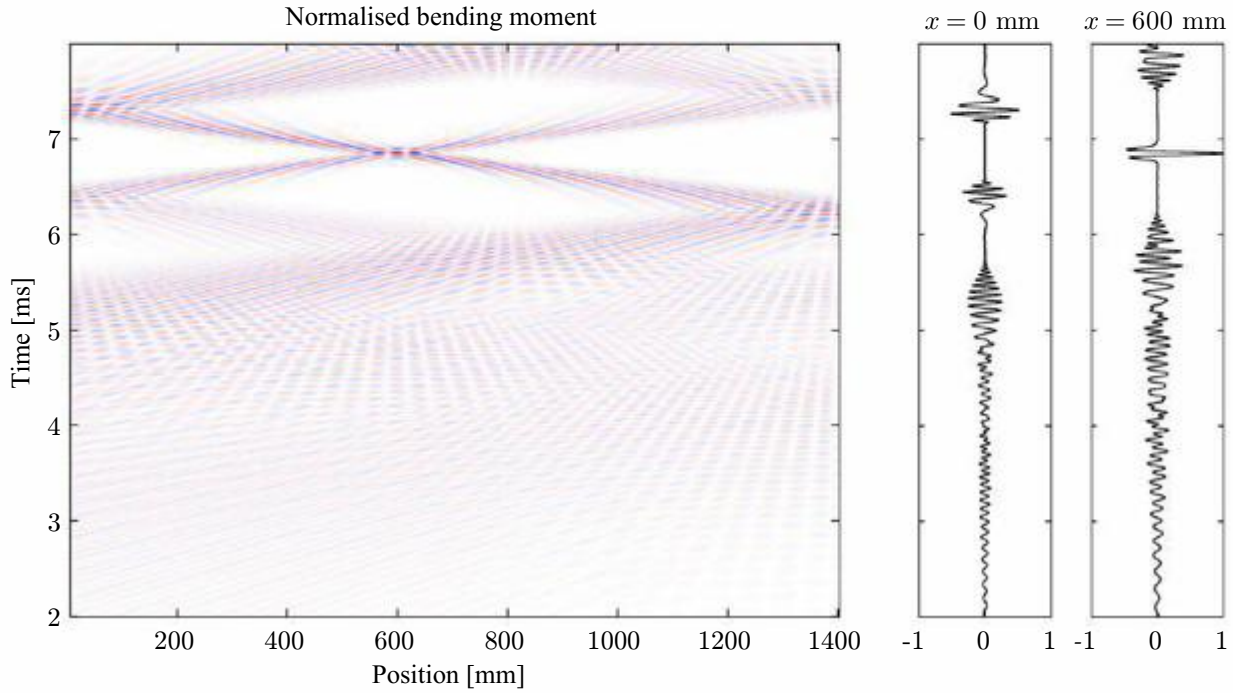

Figure 2: Time-space diagram showing the focusing of the bending waves at the position $x = 600$ mm for $t = 6.85$ ms. The bending waves are excited at the position $x = 0$ mm. The earliest wave package is reflected three times before reaching the focal point. The time histories of the normalised bending moment at the positions $x = 0$ mm (excitation) and $x = 600$ mm (focal point) are shown on the right hand side to illustrate the amplification of the transducer input. The bending moment is derived from the deflection measurement.

CONCLUSION AND OUTLOOK

It has been shown that energy can be focused at one spot of a wave guide, by exploiting the dispersive behaviour of flexural waves, thus amplifying the transducer input. In a first step the defocussing of a flexural wave pulse in a beam was simulated using spectral elements. The resulting deflection was set as excitation boundary condition in an experiment, where several wave packages were refocused and superimposed at one location, thus inducing an estimated stress peak of 5.8 MPa. It is envisaged that with a more sophisticated transducer design breaking of the glass beam by dispersive wave focusing will be possible.

References

[1] Graff K. F.: Wave Motion in Elastic Solids. Dover Publications, 1975.

[2] Leutenegger T., Dual, J.: Non-destructive testing of tubes using a time reverse numerical simulation (TRNS) method. Ultrasonsics 41(10):811-822, 2004.

[3] Ernst R., Dual J.: Acoustic emission localization in beams based on time reversed dispersion. Ultrasonics 54(6):1522-1533, 2014.

[4] Ernst R., Dual J.: Quantitative guided wave testing by applying the time reversal principle on dispersive waves in beams. Wave Motion 58:259-280, 2015.

[5] Ernst R., Zwimpfer F., Dual J.: One sensor acoustic emission localization in plates. Ultrasonics 64:139-150, 2016.

[6] Doyle J. F.: Wave Propagation in Structures. Springer, 1989.

THE INFLUENCE OF TEMPERATURE AND CRYSTAL STRUCTURE ON HIGH STRAIN RATE BEHAVIOR OF METALS

Eugene Zaretsky[a]
Department of Mechanical Engineering, Ben Gurion University, Be'er Sheva, Israel

Summary The paper presents results of planar impact experiments conducted at ambient and elevated temperatures with the samples of pure metals. The results show that the shock wave experiments deepen our understanding of high-strain-rate behavior of solids and provide quantitative information for microscopic modelling of the behavior.

Shock wave experiments provide a valuable insight into microscopic phenomena accompanying the high strain rate loading of solids. In particular, measuring the decay of the elastic precursor wave amplitude σ_{el} with propagation distance h at different temperatures enables us to relate the precursor amplitude with the plastic strain rate $\dot{\gamma}$ at the initial stages of plastic deformation and with the density ρ_m of mobile dislocations responsible of the material's inelastic response [1-3]. Our recent studies of precursor decay in five BCC metals revealed the character of precursor decay unobserved previously [4, 5]. In the studied FCC metals the amplitude of strongly decaying precursor always follows a single dependence $\sigma_{el} = s_0 h^{-\alpha}$ with $\alpha \approx 0.35 \div 0.7$, Fig. 1(a, b) [1-3]. In BCC metals after 0.5 to 1 mm precursor traverse a similar, a strong one, dependence $\sigma_{el}(h)$ is substituted by much weaker one with the exponent $\alpha \approx 0.1$, Fig. 1(c, d).

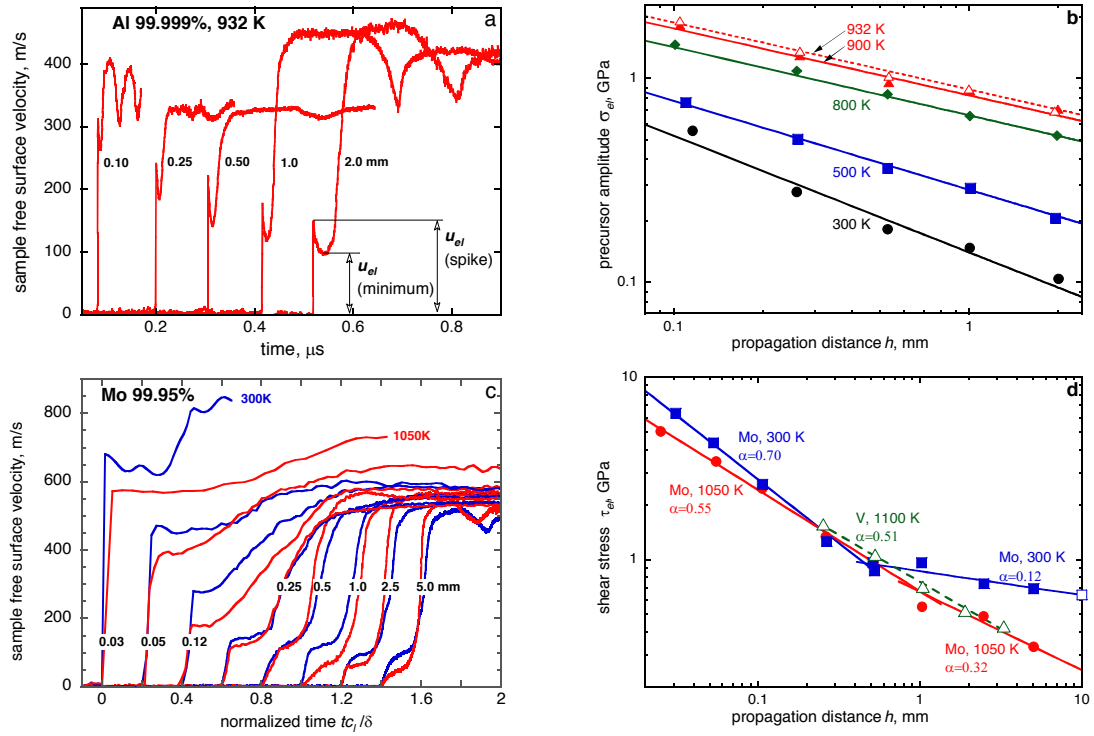

Figure 1. Sample free surface velocity histories recorded with typical FCC (Al, a) and BCC (Mo, c) metals and variations of precursor amplitude in Al (b) and Mo and V (d) with propagation distance. The t_{el} corresponding to 10-mm propagation distance (open square, d) is taken from [6].

The change of the decay regime in BCC metals is associated with the change of the character of the dislocation motion accompanying the decrease of the shear stress τ_{el} at the precursor top. At high strain rate $\dot{\gamma}$ (high τ_{el}, small propagation distance h) the motion of dislocations is a glide over the summits of the Peierls relief (over-barrier glide) accompanied by interaction of the dislocation core with the lattice phonons (phonon drag, PD, [7]).At lower strain rates (smaller τ_{el}, larger h) the motion of the dislocations is controlled by generation and motion of the dislocation double-kinks which are thermally activated (TA) [8]. At small propagation distances the high rate of deformation limits the time available for waiting of appearance of a proper thermal fluctuation while the shear stress is high enough for continuous motion of the dislocation over the potential barriers without a hold-up in the valleys of the potential relief. At this regime an average dislocation velocity is proportional to the acting shear stress, $v = \tau b/B$, where b is the dislocation Burgers vector, and B is the

[a] Corresponding author. Email: zheka@bgu.ac.il.

dislocation drag coefficient [7]. At lesser strain rates the waiting time becomes sufficient for thermally activated generation of the double-kinks and for further widening of the kink bounded dislocation segment.

The transition from PD to TA regime takes place in a close vicinity of the material's Peierls stress (the height of the Peierls relief). This transition is accompanied by the change of the dependence of dislocation velocity on the shear stress. In the TA regime the dependence is $v = v_0(\tau/\tau_0)^n$ [8], where $n = H_k/4kT$, H_k is the kink activation energy, and v_0 and τ_0 are constants [9]. In TA regimes the value of n varies between 2 and 20 [8]. Note that PD regime corresponds to n =1. Since the exponent n decreases with temperature it is not impossible that at sufficiently high, $T \approx H_k/k$, temperature the value of n will approach to unit, At this temperature the thermal fluctuations are large enough to make the duration of stay of the dislocation line at the potential valley negligibly small with respect of that above the potential summits. Respectively, the two, PD and TA, dislocation glide regimes, and, as well, the rates of the precursor decay governed by the two mechanisms should become indistinguishable as in the case of precursor decay in vanadium preheated up to 1100 K, Fig. 1d.

In the course of the studies of elastic precursor decay in BCC metals we found that in the case of Mo, Nb, and Fe in which the PD-TA transition takes place at the propagation distances of about 0.5 mm it is possible to capture the power α for both the regimes with reasonable accuracy. For all the three metals the α_{PD} decreases while α_{TA} increases with temperature and should become equal at normalized temperatures $\theta^* = T^*/T_m$ ~0.55÷0.65. Assuming that at T^* n = 1 (and keeping in mind a relatively large uncertainty of linear extrapolation of α for determination of T^*) gives for the three metals at room temperature: $n_{Nb} = 6.1\pm1$, $n_{Mo} = 5.5\pm1$, and $n_{Fe} = 4.1\pm1$. These figures are in a reasonable agreement with the values of n obtained by etch pit technique at room temperature: $n_{Nb} = 6.7$ [10], $n_{Mo} = 5.45$ [11], and $n_{Fe} = 2.89$ [9]÷5 [12].

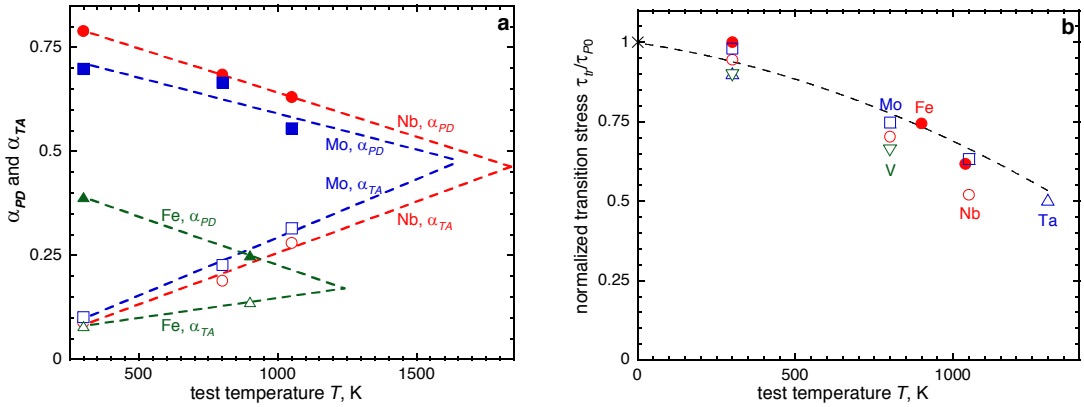

Figure 2. Temperature variations of α_{PD} and α_{TA} (a) and of normalized transition stress τ_{tr}/τ_{P0} (b) of five BCC metals.

Closeness of the measured values of the shear stress τ_{tr} corresponding to the change of decay regime to the zero-Kelvin Peierls stress τ_{P0} of the studied metals (Fig. 2b) confirms the role of the PD-TA transition in this change. Moreover, the temperature variations of τ_{tr}/τ_{P0} for all five metals follow a single curve and virtually coincide with the temperature dependence of the stress at which thermally-activated and phonon-dragged dislocation velocities found by method of Molecular Dynamics [13] become equal.

The presented results confirm the importance of the shock wave studies of different solids for better understanding of the microscopic mechanisms responsible of their constitutive behavior.

References

[1] Zaretsky E. B. and Kanel G. I.: *Journ. Appl. Phys.*: 110: 073502 (2011)
[2] Zaretsky E. B. and Kanel G. I.: *Journ. Appl. Phys.*: 112: 073504 (2012).
[3] Zaretsky E. B. and Kanel G. I.: *Journ. Appl. Phys.*: 114: 083511 (2013).
[4] Zaretsky E. B. and Kanel G. I.: *Journ. Appl. Phys.*: 115: 243502 (2014).
[5] Zaretsky E. B. and Kanel G. I.: *Journ. Appl. Phys.*: 117: 195901 (2015).
[6] Millett J. C. F., Cotton M., Bourne N. K.: *Journ. Appl. Phys.*: 115: 073506 (2014)..
[7] Brailsford A.D.: *Journ. Appl. Phys.*: 43: 1380 (1972).
[8] Seeger A.: *Phil. Mag.*: 1:651 (1956).
[9] Turner A.P.L.: *PhD Thesis*, California Institute of Technology, Pasadena, California, 1969
[10] Guberman H. D.: *Acta Met.*: 16: 713 (1968).
[11] Prekel H. L., Conrad H.: *Acta Met.*: 15: 955 (1967).
[12] Stein D.F.: *Acta Met.*: 14:99 (1967)
[13] Barton N. R., Bernier., J. V., Becker R., et al.: *Journ. Appl. Phys.*: 109: 073501 (2011).

SHOCK WAVE STRUCTURES IN POROUS MEDIA ACCOUNTING FOR MICRO-INERTIA EFFECTS

Christophe Czarnota*[1], Alain Molinari[1], and Sébastien Mercier[1]

[1]*Laboratoire d'Etude des Microstructures et de Mécanique des Matériaux, LEM3 - UMR CNRS 7239, Université de Lorraine, Metz, France*

Summary The present work deals with steady shock waves propagation in porous media containing a homogeneous population of voids. The matrix material is representative of some aluminium, assumed here non linear elastic viscoplastic, but the analysis is general and could be applied to any porous metallic materials. The process is assumed quasiisentropic; the effect of the temperature is disregarded, so that our approach is valid for shocks of moderate stress amplitudes. Quasi-static compression curves (no rate effect) are used to describe the constitutive response of the porous medium under various stress levels. The Rayleigh line defines the shock path. Our results show that micro-inertia effects bring an important contribution to the shock wave structure.

INTRODUCTION

The response of porous materials under shock wave is analyzed in the present work. This field of research is of particular interest in numerous domains. It may concern the dynamic compaction of powders, development of blast mitigation strategies, collision processes in the solar system...Few research contributions combine the role of the initial porosity, the balance between viscous and micro-inertia effects during shock propagation [1]. Both effects bring a rate dependency that tends to delay the void evolution. The present work provides a better understanding of how micro-inertia is controlling the compaction process. Micro-inertia effects reveal that void radius appears as a key factor controlling the shock wave structure.

KINEMATIC AND CONSTITUTIVE EQUATIONS

Kinematic

Consider a porous medium, of initial porosity f_0, containing a homogeneous population of voids of initial radius a_0. It is considered that a representative volume element (RVE) can be represented by a hollow sphere. The current porosity is f. The matrix material, assumed plastically incompressible, of initial density ρ_0, has a non linear elastic/viscoplastic behavior.
The porous medium is subjected to plate impact experiment generating a propagating shock wave in the $\mathbf{e_1}$ direction. Beyond a certain propagation distance, the wave becomes steady. A Lagrangian formalism is adopted. For these planar shock waves, uniaxial strain prevails, and the macroscopic deformation gradient tensor has the form:

$$\mathbf{F} = \lambda_1 \mathbf{e}_1 \otimes \mathbf{e}_1 + \mathbf{e}_2 \otimes \mathbf{e}_2 + \mathbf{e}_3 \otimes \mathbf{e}_3 \tag{1}$$

where λ_1 is the longitudinal stretch. It is next assumed that changes in porosity are only related to the plastic deformation of the matrix. The plastic part of the deformation gradient tensor is thus given by:

$$\mathbf{F}^{\mathrm{p}} = \lambda_1^{\mathrm{p}} \mathbf{e}_1 \otimes \mathbf{e}_1 + \left[\left(\frac{1-f_0}{1-f} \right)^{1/2} \left(\lambda_1^{\mathrm{p}} \right)^{-1/2} \right] (\mathbf{e}_2 \otimes \mathbf{e}_2 + \mathbf{e}_3 \otimes \mathbf{e}_3) \tag{2}$$

Constitutive behavior of the porous solids

By definition, the Cauchy stress tensor $\mathbf{\Sigma}$ is related to the 1st Piola-Kirchhoff stress tensor $\mathbf{T}$ by $\mathbf{T} = \mathbf{\Sigma} \det(\mathbf{F}) \mathbf{F}^{-\mathbf{T}}$:

$$\mathbf{\Sigma} = T_1 \mathbf{e}_1 \otimes \mathbf{e}_1 + \frac{T_2}{\lambda_1} \mathbf{e}_2 \otimes \mathbf{e}_2 + \frac{T_2}{\lambda_1} \mathbf{e}_3 \otimes \mathbf{e}_3 \tag{3}$$

where T_1 (resp. T_2) is the component of the Piola-Kirchhoff stress tensor in the wave propagation direction (resp. transverse direction). Based on previous works [2, 3] which have demonstrated the role of micro-inertia during dynamic processes, the macroscopic Cauchy stress tensor $\mathbf{\Sigma}$ is the sum of a micro-inertia independent part $\mathbf{\Sigma}^{\star}$ and a micro-inertia dependent part $\mathbf{\Sigma}^{\mathrm{dyn}}$. Under shock loading, we also assume that micro-inertia acts only on the spherical part of the stress tensor. So the Cauchy mean stress $\Sigma_{\mathrm{m}} = \mathrm{tr}(\mathbf{\Sigma})/3$ (tr denotes the trace operator) is given by:

$$\Sigma_{\mathrm{m}} = \Sigma_{\mathrm{m}}^{\star} + \frac{\rho a_0^2}{3} \left(\frac{1-f_0}{f_0} \right)^{2/3} \left[\frac{f^{-1/3}-1}{(1-f)^{5/3}} \ddot{f} + \frac{-\frac{1}{6} f^{-4/3} + 2 f^{-1/3} - \frac{11}{6}}{(1-f)^{8/3}} \dot{f}^2 \right] \tag{4}$$

*Corresponding author. Email: christophe.czarnota@univ-lorraine.fr

The micro-inertia contribution in Eq.(4) corresponds to the theory of Carroll and Holt [4]. The micro-inertia independent part $\mathbf{\Sigma}^\star$ is obtained from a GTN potential combined to an overstress formulation describing the viscoplatic response of the matrix material. The elastic response of the porous medium and the matrix viscous behavior are based on Clifton [5] modeling (see also [6]). The work [6] is dedicated to dense materials, and has been extended here to include the effect of porosity.

SHOCK STRUCTURE AND SHOCK WIDTH - RESULTS

For a steady shock wave, an observer may follow the wave propagation from a moving coordinate system $\xi = X - Ct$, with C standing for the Lagrangian velocity of the plastic shock. Within this moving frame, the shock path is defined by the relationship:

$$T_1^- - T_1^+ = \rho_0 C^2 \left(1 - f_0\right)\left(\lambda_1^- - \lambda_1^+\right) \tag{5}$$

Eq.(5) defines the Rayleigh line. T_1^-, negative in compression, is the prescribed shock amplitude (corresponding stretch λ_1^-). T_1^+, also negative, is defined by adopting the chord criterion (the chord is tangent to the quasi-static curve at one of its end points, see Fig. 1), and is associated to the stretch λ_1^+. States (+) and (-) are thus identified here from isothermal quasi-static curves, following Clifton's assumption that the deformation process is quasiisentropic [5], at least for moderate shock amplitudes.

The porous material is representative of a 6061-T6 aluminium, see [5, 6]. Figure 1a shows quasi-static responses of porous aluminium for various initial porosities. The efficiency of porous solids as shock absorber is clearly displayed. As f_0 is increased, the dissipated energy is increased. Some results are presented in Figure 1b by considering a porous material with $f_0 = 0.03$ and various initial void radii. Different shock amplitudes are also tested. Figure 1b shows the evolution of the shock width $w_e = -\frac{C}{\max\left(D_{\text{eq}}^p\right)} \ln\left[\frac{\lambda_1^{p-}}{\lambda_1^{p+}}\left(\frac{1-f^-}{1-f^+}\right)^{1/3}\right]$ as a function of the shock amplitude $-T_1^-$. D_{eq}^p is the equivalent macroscopic plastic strain rate. It is shown that w_e is increased as a_0 is larger. In addition, at a given void radius, a saturation of w_e value is observed for very large shock amplitude $-T_1^-$. These results allow for optimizing the microstructure of porous metals to enhance blast mitigation.

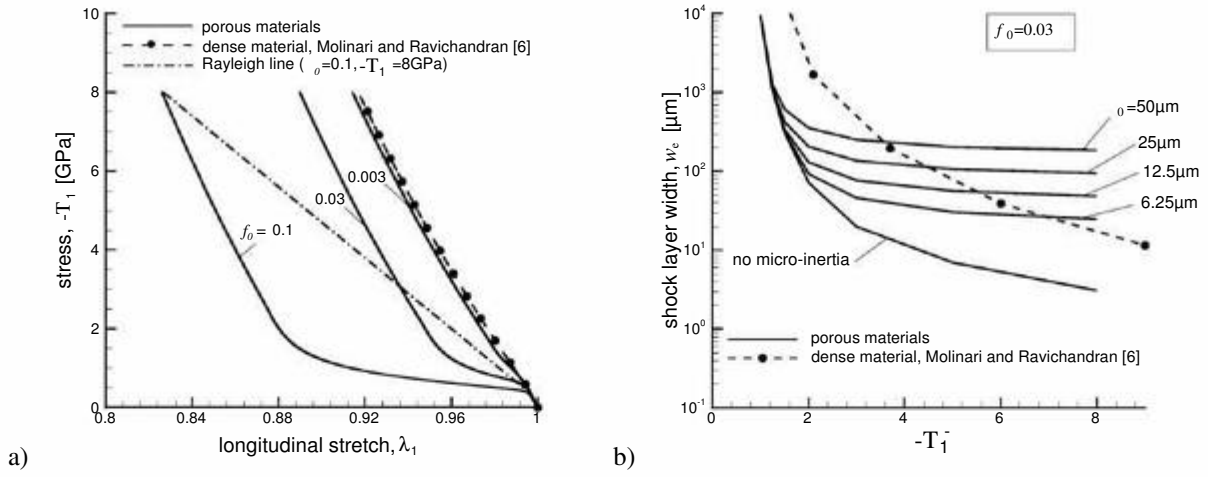

Figure 1: a- Quasi-static compression curves for dense and porous aluminium. The Rayleigh line is also added for f_0=0.1, $-T_1^-$=8GPa. -b) Shock width w_e vs shock stress $-T_1^-$ for various initial void radii a_0.

References

[1] Nesterenko V.F.: Dynamics of Heterogeneous Materials, Springer-Verlag, New York, 2001.

[2] Molinari A., Mercier, S.: Micromechanical modelling of porous materials under dynamic loading. J. Mech. Phys. Solids 49, 1497–1516, 2001.

[3] Czarnota C., Jacques N., Mercier S., Molinari, A.: Modelling of dynamic ductile fracture and application to the simulation of plate impact tests on tantalum. J. Mech. Phys. Solids 56, 1624–1650, 2008.

[4] Carroll, M. M., Holt, A. C.: Static and dynamic pore collapse relations for ductile porous materials. J. Appl. Phys. 43 (4), 1626–1636, 1972.

[5] Clifton R. J.: On the analysis of elastic/visco-plastic waves of finite uniaxial strain. In: Burke, J. J., Weiss, V. (Eds.), Shock Waves and the Mechanical Properties of Solids. Syracuse University Press, pp. 73–116, 1970.

[6] Molinari A., Ravichandran G.: Fundamental structure of steady plastic shock waves in metals. J. Appl. Phys. 95, 1718 – 1732, 2004.

VOID COLLAPSE AND HOT SPOT FORMATION IN SHOCKED HMX: A LARGE-SCALE MOLECULAR DYNAMICS STUDY

Tingting Zhou[a], Huajie Song, Jianfeng Lou & Tao Hong
Institute of Applied Physics and Computational Mathematics, Beijing, China

Summary It has been suggested that crystal property such as internal defect and surface morphology plays key roles in the shock-induced hot spot formation and initiation of detonation in energetic materials. We herein present a large-scale reactive molecular dynamics simulation of shock initiation of HMX single crystal with void defect to investigate the void collapse and hot spot formation at the atomistic level. Results show that shocked-induced jetting composed of the upstream HMX molecules travels across the void and collides with the downstream void surface, leading to void collapse, greatly local temperature increase and hot spot formation, and subsequent chemical reaction initiation. The effects of void size as well as geometry and shock strength on the dynamical process are also probed.

INTRODUCTION

Apart from chemical components, it has been experimentally suggested that the crystal property including grain size and distribution, crystal internal defect, and crystal surface morphology has great influence on the mechanical strength, sensitivity, and stability of energetic materials (EMs).[1-3] Particularly, it plays important roles in shock-induced hot spot formation and initiation of detonation, thus affect the shock sensitivity of EMs. However, current experiment techniques are unable to resolve the interior of shocked samples on the length scale of nanometer and time scale of picosecond, making it impossible to directly measure or observe the hot spot formation, dissociation or formation of chemical bonds, or energy release. The results from continuum hydrodynamic shock simulations are strongly dependent on material models such as strength, viscosity, reaction kinetics, none of which is calibrated on the involved length scale and time scale.

Molecular dynamics (MD) simulation, which is capable of providing atomistic-level understanding, allows another way to explore the role of crystal property on the responses of shocked EMs. Employing a reactive force field, the mutual coupling of chemical reactions with mechanical deformations can be examined in a consistent manner. Recently, several studies using reactive MD simulation have been reported pertaining to defect induced hot spot formation and reaction initiation, shedding some light on these issues.[4-6] In this work, we perform a large-scale reactive MD simulation of a realistic model of HMX single crystal with nanometer-scale void to explore the void collapse, hot spot formation, and chemical reaction initiation subjected to shock loading. The effects of void size as well as geometry and shock strength on the dynamical process are also examined.

COMPUTATIONAL DETAILS

The ReaxFF reactive force field as implemented in the Large-scale Atomic/Molecular Massively Parallel Simulator (LAMMPS) software package was used to model the shock dynamical process. The particular version of the force field used here was developed for nitramines, including RDX, PETN, TATB, and nitromethane.[7] We first validated the accuracy of the ReaxFF for HMX by comparing the equation of state under hydrostatic compression, the chemical reaction mechanisms, and the Us-Up relation under shock to other theoretical and experimental results. Then, the simulation system was prepared as follows. The structure of HMX starting from a unit cell with experimental structure is optimized using isothermal-isobaric MD simulation at ambient conditions, leading to equilibrium structure very close to experimental result. The optimized structure was then expanded to large supercell, and a spherical void with various diameters ranging from 4 to 10 nm was introduced by removing molecules whose centers of mass are within the radius of the void. We also introduced a cylindrical void with the diameter of 8 nm to examine the influence of void geometry. After introducing the void, the crystal was relaxed for 5 ps at a temperature of 300 K. Subsequently, periodic boundary conditions were removed to create a free surface in the *x*-*z* plane, and again the system was relaxed for 4 ps. The dimensions of the system with an 8 nm spherical void are $27.58 \times 55.86 \times 26.21$ nm^3 and contains 3.5 million atoms. A planar shock wave was initiated at the bottom (010) surface by driving it against a rigid and reflective wall. Various particle velocities from 0.5 to 3 km/s were simulated to explore the effect of shock strength on the dynamical process.

RESULTS AND DISCUSSIONS

For particle velocity Up = 1 km/s and void radius R = 4 nm, shock wave propagates into the crystal and reaches the upstream void surface at 2 ps, after which the upstream molecules begin to travel across the void and form a jet with an increasing velocity. The maximum velocity rises to 2 km/s after 4ps, and then decreases quickly due to the collision with the downstream void surface, resulting in the closure of the void. This collision leads to the energy transformation from kinetic energy to thermal energy, contributing to dramatic temperature increase and hot spot formation in the localized region.

[a] Corresponding author. Email: zhou_tingting@iapcm.ac.cn.

Fig. 1 presents the spatial distribution of temperature in the shocked HMX crystal as a function of time. The temperature is calculated by grouping atoms into small cubic bins based on their position, and the temperature of each bin is calculated as the average kinetic energy of each atomic degree of freedom after subtracting the streaming velocity of all the atoms in the bin. Temperature of the hot spot increases very quickly after the collision between the upstream molecules and the downstream ones and approaches to the maximum value of 2000 K at 5 ps, and it drops quickly to 1750 K during the next 0.5ps because of molecular relaxation. After that, the hot spot temperature decreases gradually due to heat diffusion from the inner to the outside, leading to the temperature increment of outside region.

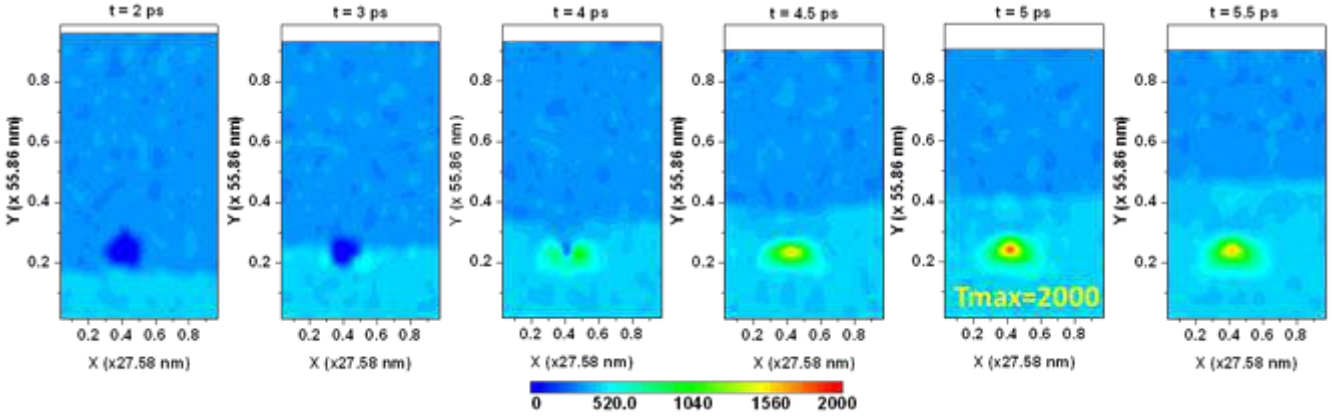

Fig. 1 spatial distribution of temperature in the shocked HMX crystal as a function of time for R = 4 nm and Up = 1 km/s

The high temperature of the localized hot spot benefits the chemical reaction initiation. It is found that the N-NO2 bond dissociation generating NO2 plays the leading role in the initial reaction mechanism, although other products like NO3, HONO, O2, and C3H6N2 are observed. The onset of N-NO2 bond breaking begins at 4.7 ps, at which the void has collapsed and the temperature of the hot spot is high enough. The position of NO2 is the center of the hot spot, validating that it is the high temperature in the hot spot that promotes chemical reaction. The bulk temperature after shock compression is only about 500 K, which is too low to ignite HMX crystal.

With the increase of void size, the velocity of HMX molecules traveling across the void gets higher, leading to stronger impact with the downstream molecules. Thus higher hot spot temperature and larger hot spot area are formed, which result in more dramatic chemical reactions. These phenomena are also observed with velocity increment, and the enhancing effect is much more evident compared to that of the void size. Spherical void generates a hot spot that is more intense than that of the cylindrical void of the same size due to the larger impact area. Although the temperature is lower for the cylindrical geometry, the dynamical process leads to hot spot formation are qualitatively consistent with that occurring in the spherical configuration.

CONCLUSIONS

Million-atom reactive molecular dynamics simulations of shock initiation of HMX crystal containing a void with various sizes were performed. The dynamical process leading to hot spot formation includes shock induced jetting of the upstream molecules, void collapse, and collision between the upstream molecules and the downstream. The collision greatly enhances the hot spot temperature and thus chemical reaction initiation. With the increase of void size or shock strength, the enhancement gets more obvious, leading to higher hot spot temperature and more violent chemical reactions. The dynamics process is similar for the spherical void and the cylindrical void, although the latter leads to less intense hot spot.

References

[1] Walley S. M., Field J. E., Greenaway M. W.: Crystal sensitivities of energetic materials, *Mater. Sci. Technol*, 22: 402–413, 2006.

[2] Stoltz C. A., Mason B. P., Hooper J.: Neutron scattering study of internal void structure in RDX. *J. Appl. Phys*., 107: 103527–1–6, 2010.

[3] Bellitto V. J., Melnik M. I.: Surface defects and their role in the shock sensitivity of cyclotrimethylene-trinitramine. *Applied Surface Science*, 256: 3478–3481, 2010.

[4] Herring S. D., Germann T. C., Jensen N. G.: Effects of void size, and arrangement on deflagration and detonation sensitivity of a reactive empirical bond order high explosive. *Phys. Rev. B*, 82: 214108–1–12, 2010.

[5] Nomura K, Kalia R K, Nakano A, Vashishta P: Reactive nanojets: nanostructure-enhanced chemical reactions in a defected energetic crystal. *Appl. Phys. Lett*., 91: 183109–1–3, 2007.

[6] Shan T. R., Wixom R, Thompson A. P.: Micron-scale Reactive Atomistic Simulation of Void Collapse and Hot spot Growth in Pentaerythritol Tetranitrate. Proceeding of 15th International Detonation Symposium, San Francisco, CA, USA, Jul. 13–18, 2014, p962–969.

[7] Liu L. C., Liu Y., Zybin S. V., Sun H., Goddard III W. A.: ReaxFF-lg: Correction of the ReaxFF Reactive Force Field for London Dispersion, with Applications to the Equations of State for Energetic Materials. *J. Phys. Chem. A*, 115: 11016–11022, 2011.

VIOLENT ELASTIC-PLASTIC WAVE INTERACTIONS

Stuart Thomson*[1], Hilary Ockendon[1], John Ockendon[1], and Peter Howell[1]

[1]*Mathematical Institute, University of Oxford, Andrew Wiles Building, Oxford OX2 6GG, UK*

Summary In isentropic compression experiments, millimetre thick metal samples are subjected to pressures on the order of $10 - 10^2$ GPa, while the yield strength of the material can be as low as 10^{-1} GPa. In such regimes the metal can be treated as a barotropic compressible fluid in which the strength, measured by the ratio of the yield stress to the applied stress, is negligible to lowest order. We present a new model of elastoplasticity which incorporates the effects of strength as a small perturbation to the leading order model based on barotropic flow. We then consider the elastic/plastic waves that propagate through the metal sample and the consequences of their interactions on obtaining equation of state information for the highly plasticised metal.

INTRODUCTION

To simulate the mechanical response of a metal undergoing violent elastic-plastic deformation, one must provide accurate equation of state (EoS) information for the material under study. In recent times, so-called isentropic compression experiments (ICEs) have become a standard method by which to extract equation of state information experimentally. A schematic of a typical experiment is shown in Fig. 1. Using a magnetic pressure drive, a ramped compression wave is made to propagate through the target material, and then detected at the rear face of the sample using velocity interferometry (VISAR) [1]. The results from a typical experiment are shown in Fig. 2. Existing analyses to determine the EoS of the material under study from this data have so far neglected the effects of shear strength, instead treating the metal as an inviscid compressible fluid [2, 3]. We present here a mathematical model which takes into account both the compressibility of the material and the small but measurable effects of elastic strength.

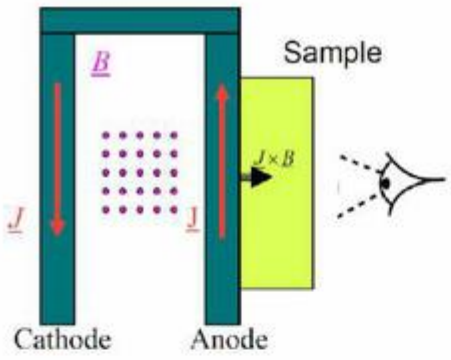

Figure 1: Schematic of a ramped isentropic compression experiment.

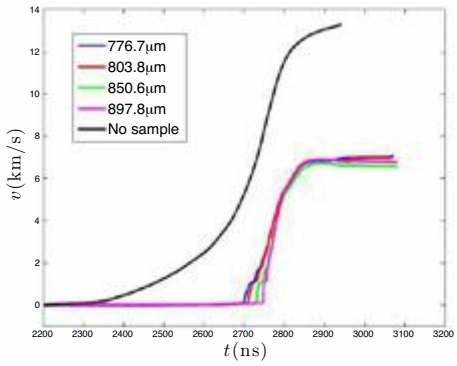

Figure 2: Boundary velocimetry data obtained from the 3 MBar compression of lead.

MATHEMATICAL MODEL

We focus our attention on one-dimensional, uniaxial strain where the specific volume ν, the velocity u and the deviatoric strain ε are all functions of the Lagrangian variable X and time t. A uniformly valid model which captures the essential phenomena of violent elastic-plastic deformation consists of the following three nonlinear, hyperbolic PDEs, namely

$$\frac{\partial \nu}{\partial t} - \frac{\partial u}{\partial X} = 0 \qquad \text{(conservation of mass)}, \tag{1}$$

$$\frac{\partial u}{\partial t} + \frac{\partial}{\partial X}\left(p_s(\nu) - \frac{2\delta G}{3\nu}\varepsilon\right) = 0 \qquad \text{(conservation of momentum)}, \tag{2}$$

$$\delta\tau\left(\frac{2}{3\nu}\frac{\partial \nu}{\partial t} - \delta\frac{\partial \varepsilon}{\partial t}\right) = h(\varepsilon) = \begin{cases} 0, & \text{if } \varepsilon > -1 \\ \varepsilon + 1, & \text{if } \varepsilon \leq -1 \end{cases} \qquad \text{(flow rule)}. \tag{3}$$

*Corresponding author. Email: thomson@maths.ox.ac.uk

The non-dimensional parameters in our model are: the relaxation time τ for the stress to relax back to the yield surface; and the ratio $\delta \ll 1$ of the yield stress to the applied stress. In the limit $\delta = 0$, the model reduces to the equations of barotropic flow with EoS $p_s(\nu)$. However, in regions where the strain is $O(\delta)$, the deviatoric and isotropic contributions to the strain balance, and hence we expect elastic effects to be noticeable near the tails of propagating waves.

Numerical solutions

We simulate the response of a metal sample whose face at $X = 0$ is displaced by an imposed velocity $U_0(t)$. The rear face of the target is stress-free. The appropriate initial and boundary conditions are therefore

$$\nu(X,0) = 1, \qquad u(X,0) = 0, \qquad \varepsilon(X,0) = 0, \qquad u(0,t) = U_0(t) = 1 \nearrow {}^{-t}, \qquad p_s(\nu) \nearrow \frac{2\delta G}{3\nu}\,\varepsilon\Big|_{X=1} = 0. \tag{4}$$

For comparison with the leading order barotropic flow model we use the ideal gas EoS: $p_s(\nu) = \nu^{-\gamma}/\gamma$.

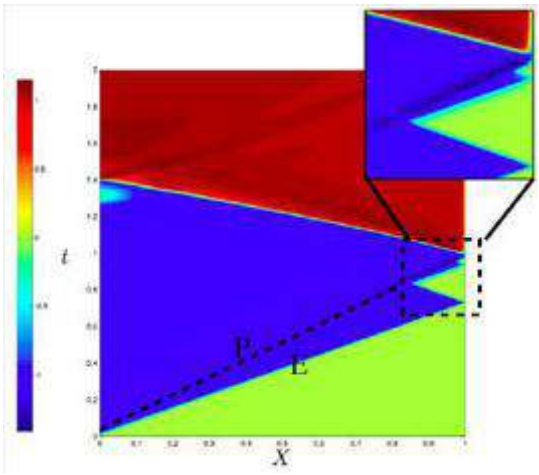

Figure 3: Numerical solution of the model (1)–(4) for the deviatoric strain ε, with $\delta = 0.01$, $\tau = 10$, $G = 2$ and $\gamma = 5/3$.

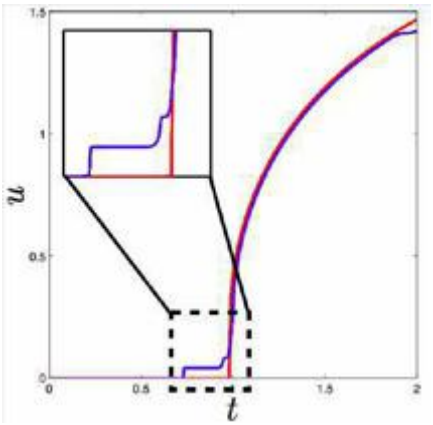

Figure 4: Free-surface velocity $u(1,t)$. Blue: our model (1)–(3); red: barotropic flow.

Figure 3 shows an X–t plot for the deviatoric strain ε. Initially an elastic wave, labelled E, propagates ahead of a much larger plastic wave, labelled P. When the elastic wave reaches the free surface $X = 1$, it reflects back toward the plastic wave. During the interaction of the two waves (see the inset), part of the elastic wave is transmitted through the plastic wave, while part is reflected back toward the free surface. The elastic wave thus reverberates back and forth until the eventual arrival of the much larger plastic wave at the free surface. The velocity $u(1,t)$ measured at the rear face of the target material is plotted in Figure 4, and compared with the corresponding results for barotropic flow (i.e. $\delta = 0$). A small elastic precursor arrives ahead of the large plastic wave, and the reverberation leads to a staircase-like feature, with the velocity increasing through a series of small steps. These significant features cannot be explained or resolved by barotropic flow alone.

CONCLUSIONS

We presented a mathematical model of elastoplasticity in the regime where the applied stress greatly exceeds the yield stress, and used the model to analyse the interactions of elastic and plastic waves during the violent deformation of a metal sample. We showed that key information is lost when elastic strength is neglected. It is the subject of current work to understand the structure of the interactions described here mathematically and hence develop a more accurate method to derive EoS approximations from real-life velocimetry data.

References

[1] Rothman, S. D. et al.: Measurement of the principal isentropes of lead and lead-antimony alloy to 400kBar by quasi-isentropic compression. J. Phys. D, 2005

[2] Ockendon H., Ockendon J.R., Platt J.D.: Determining the equation of state of highly plasticised metals from boundary velocimetry: Part 1. J. Eng. Math. Springer, 2010.

[3] Hinch E.J.: Determining the equation of state of highly plasticised metals from boundary velocimetry: Part 2. J. Eng. Math. Springer, 2010.

BROKEN TIME-REVERSAL SYMMETRY IN BEAMS IN LONGITUDINAL MOTION

Giuseppe Trainiti*[1] and Massimo Ruzzene[1,2]

[1]*Daniel Guggenheim School of Aerospace Engineering, Georgia Institute of Technology, 270 Ferst Dr, Atlanta, GA 30332, USA*

[2]*George W. Woodruff School of Mechanical Engineering, Georgia Institute of Technology, 801 Ferst Dr, Atlanta, GA 30332, USA*

Summary This work investigates the class of problems in which the material properties of the structures, *i.e.* the Young's modulus E and density ρ, are periodic functions of space and time. This periodic variation of the medium's characteristics in space and time challenges the notion of reciprocity of wave motion, leading to unidirectional wave propagation. Broken time-reversal symmetry is analytically investigated in beams in longitudinal motion and results presented in the form of band diagrams. Numerical simulations verify the theoretical predictions. This study suggests a rigorous approach to study a new class of active periodic metamaterials with superior tunability features, with applications in vibration and noise control.

MOTIVATION OF THE WORK

Metamaterials are structured media with exceptional wave propagation properties and applications in optics, acoustics and mechanics, to name a few [1]. Several recent studies focused on enhancing the performance of such materials by endowing them with tunable properties, for instance by inducing a structural reconfiguration through mechanical loading [2], in which a modification of the spatial symmetry of the structure leads to dramatic changes in its wave propagation behavior. A further step can be taken and a deeper control over the structure's properties achieved by conveniently modulating the properties of the structure not only in space, but also in time. As a result of that, the structure displays ranges of frequency for which wave propagation is allowed in one direction only. Recent studies envision the possibility of exploiting unidirectional properties to obtain backscattering-immune devices [4]. In the present study, we present a rigorous approach to study this new class of metamaterials.

THEORETICAL BACKGROUND

We consider the case of propagation of longitudinal waves in beams in which the Young's modulus E and density ρ are functions of space and time, therefore the following expression for the equation of motion of the beam has to be considered:

$$\frac{\partial}{\partial x}\left[E(x,t)\frac{\partial u(x,t)}{\partial x}\right] = \frac{\partial}{\partial t}\left[\rho(x,t)\frac{\partial u(x,t)}{\partial t}\right] \tag{1}$$

We also assume that E and ρ are periodic functions of space and time, thus they write $E(x,t) = E(x+\lambda_m, t+T_m)$ and $\rho(x,t) = \rho(x+\lambda_m, t+T_m)$, with λ_m and T_m spatial and time periods, respectively. We refer to this periodic variation of the material properties as modulation. Periodicity allows us to express $E(x,t)$ and $\rho(x,t)$ in the form of the following Fourier series:

$$E(x,t) = \sum_{p=-\infty}^{+\infty} \hat{E}_p e^{ip(\omega_m t - \kappa_m x)} \qquad \rho(x,t) = \sum_{p=-\infty}^{+\infty} \hat{\rho}_p e^{ip(\omega_m t - \kappa_m x)} \tag{2}$$

in which ω_m and κ_m are the frequency and the wavenumber of the material properties modulation, respectively. Assuming that a periodic solution of Eq.1 exists, it can be written in the form of the following Fourier series:

$$u(x,t) = e^{i(\omega t - \kappa x)} \sum_{n=-\infty}^{+\infty} \hat{u}_n e^{in(\omega_m t - \kappa_m x)} \tag{3}$$

By substituting Eq. 3 and Eq. 2 into Eq. 1 and by exploiting orthogonality, we obtain a quadratic eigenvalue problem (QEP) to be solved for the frequency ω:

$$\left[\omega^2 \hat{\mathbf{L}}_2 + \omega \hat{\mathbf{L}}_1 + \hat{\mathbf{L}}_0\right)\hat{\mathbf{u}} = \mathbf{0} \tag{4}$$

in which the coefficient matrices $\hat{\mathbf{L}}_r$, with $r = 0, 1, 2$, depend on the wavenumber κ and the coefficients $\hat{E}_p$ and $\hat{\rho}_p$. The solution of the QEP gives the dispersion relation $\omega = \omega(\kappa)$ for the structure, useful in any wave propagation problem and that can be represented in the form of band diagrams [3].

*Corresponding author. Email: giuseppe.trainiti@aerospace.gatech.edu

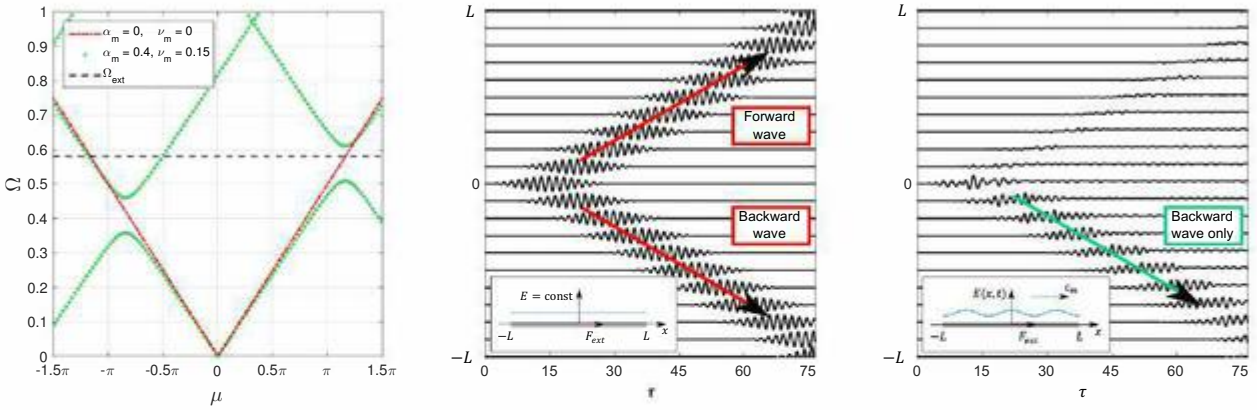

(a) (b) (c)

Figure 1: Band diagrams for non-modulated beam (red dash-dot line) and modulated beam (green dot line) (a) and the relative transiet responses to narrow-band excitation centered at Ω_{ext} for non-modulated (b) and modulated beam (c). In the latter case, due to modulation of the Young's modulus, only the backward wave propagates, therefore one way propagation is realized.

RESULTS

We discuss the results for the simple case in which $E(x,t) = E_0 + E_m \cos(\omega_m t - \kappa_m x)$ and $\rho(x,t) = \rho_0$, with $c_0 = \sqrt{\frac{E_0}{\rho_0}}$ wave velocity in the non-modulated medium and $c_m = \frac{\omega_m}{\kappa_m}$ modulation velocity. We define the dimensionless frequency, wavenumber and time as $\Omega = \frac{\omega \lambda_m}{2\pi c_0}$, $\mu = \kappa \lambda_m$ and $\tau = \frac{t c_0}{\lambda_m}$, respectively. Furthermore, we introduce the dimensionless modulation speed $\nu_m = \frac{c_m}{c_0}$ and the dimensionless modulation amplitude $\alpha_m = \frac{E_m}{E_0}$. As shown in Fig. 1a, when no modulation is applied, *i.e.* $\alpha_m = 0$ and $\nu_m = 0$, the beam's dispersion relation writes $\Omega = \pm \frac{\mu}{2\pi}$ and it is represented in the band diagram as two straight lines that are symmetric with respect to the frequency axis Ω, which means that backward-propagating waves and forward-propagating waves have the same behavior, thus mechanical reciprocity holds. On the contrary, Fig. 1a shows that, if modulation is applied with $\alpha_m = 0.4$ and $\nu_m = 0.15$, the dispersion relation obtained by solving Eq. 4 produces a band diagram with different band gaps for forward-propagating waves and backward-propagating waves, therefore mechanical reciprocity is violated. Indeed, the modulated beam allows forward-propagating waves only for $\Omega \in [0.36, 0.46]$ and backward-propagating waves only for $\Omega \in [0.51, 0.61]$. In order to verify our predictions, we use the commercial finite element software COMSOL Multiphysics to compute the transient response to narrow-band excitation of longitudinal waves in non-modulated and modulated beams of length $2L$. In both cases, the excitation is imposed at the middle of the fixed-fixed beam and a narrow-band signal centered at $\Omega_{ext} = 0.58$ is used. Results are presented in the form of waterfall plots in Fig. 1b and Fig. 1c for non-modulated and modulated beam, respectively. As expected, both backward waves and forward waves propagate in the non-modulated beam, as shown in Fig. 1b. Conversely, backward-propagating waves only are allowed in the considered frequency range if modulation is applied, as shown in Fig. 1c, thus one way propagation of elastic waves is realized in the beam.

CONCLUSIONS

We suggest a fully analytical approach to investigate a new and promising class of metamaterials, which are able to violate the principle of mechanical reciprocity and induce unidirectional propagation.

References

[1] Hussein M. I., Leamy M. J., Ruzzene M.: Dynamics of Phononic Materials and Structures: Historical Origins, Recent Progress, and Future Outlook. Appl. Mech. Rev 66(4), 040802, 2014.

[2] Bertoldi K., Boyce M. C.: Mechanically triggered transformations of phononic band gaps in periodic elastomeric structures. Phys. Rev. B 77, 052105, 2008.

[3] Brillouin L.: Wave propagation in periodic structures: electric filters and crystal lattices. Dover Publications, 1953.

[4] Swinteck N., Matsuo S., Runge K., Vasseur J. O., Lucas P., Deymier P. A.: Bulk elastic waves with unidirectional backscattering-immune topological states in a time-dependent superlattice, J. Appl. Phys. 118, 063103, 2015

INTERACTION OF DEFORMATION WAVES WITH INTERNAL STRUCTURES IN SOLIDS

uri Engelbrecht*[1], Arkadi Berezovski[1], Tanel Peets[1], and Kert Tamm[1]

[1]Centre for Nonlinear Studies, Institute of Cybernetics at Tallinn University of Technology, Estonia

Summary Wave propagation in solids is strongly influenced by accompanying physical effects. The existence of the microstructure (internal structure) of solids leads to dispersive and/or diffraction effects. Two cases must be distinguished: (i) disordered and (ii) regular microstructures. In the first case one-scale and two-scale models are analysed and it is shown that the dispersion together with nonlinearities may cause the emergence of solitary waves. The existence of the negative group velocity is demonstrated in the two-scale model. A typical regular microstructure is an embedded grating made of a different material. The diffraction pattern emerging after a wave passes through a grating is analysed assuming that the matrix and the grating both are elastic. The possible energy localization in such a process is demonstrated.

MICROSTRUCTURE MODELS

Basic concepts

There is a growing interest to microstructured materials in contemporary engineering. The main reason for the wide usage of such materials is related to possible enhancing the properties of materials under complicated loading conditions and to possible design of materials using the emerging physical effects. Here the attention is paid to modelling of wave motion in microstructured materials. In principle, the microstructures might be irregularly distributed (functionally graded materials, alloys, crystallites, etc) or regularly localized (isolated inclusions, gratings, composites). In the first case the dispersive effects are of importance, in the second case the diffraction is the leading process. Figure 1 shows these cases schematically.

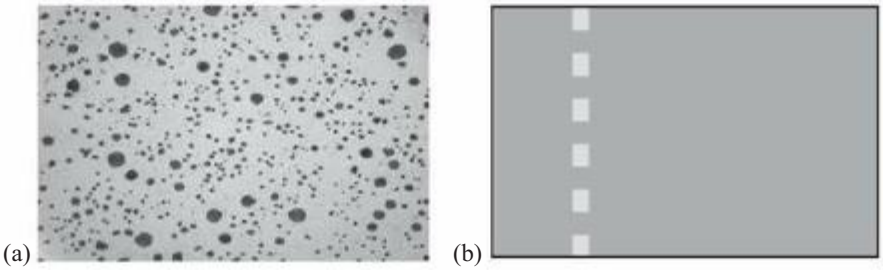

Figure 1: (a) Disordered microstructure, (b) Diffraction grating.

The influence of the disordered microstructure on wave propagation in solids is modelled best if (i) microinertia is taken into account, and (ii) the corresponding dispersion relation includes both acoustic (in-phase) and optical (out-of-phase) branches. In the case of regular internal structure, the wave field can be simulated accurately by solving the elastodynamic equations for the matrix and the scatterers respectively.

Disordered microstructure(s)

The mathematical models for wave motion are derived using the concept of dual internal variables which describes the embedded microstructure(s) as internal fields [1]. A typical one-scale 1D wave equation is the following:

$$u_{tt} = c_1^2 u_{xx} + A\left(u_{tt} - c_2^2 u_{xx}\right)_{xx} + B\left(u_{tt} - c_3^2 u_{xx}\right)_{tt}, \tag{1}$$

with material parameters A and B and velocities c_1, c_2 and c_3. Here the role of dispersion is reflected by higher order derivatives. This basic model can be generalized to describe nonlinear effects and the two-scale situation (a scale within scale). The respective characteristics of waves are analysed including the deriving of governing nondimensional parameters [2]. The two-scale model demonstrates also the existence of the negative group velocity due to the pre-resonant situation of internal modes of close frequencies. The conditions for existence of the negative group velocity are derived [3]. A possibility for the emergence of the negative group velocity exists also for waves in the wool felt. The similar modelling ideas are also implemented for deriving the governing wave equations of biomembranes. In this case the nonlinearities are expressed in terms of displacements rather than in deformations like in solids. This difference affects also the emergence of solitary waves.

*Corresponding author. Email: je@ioc.ee

Localized microstructure(s)

The main attention is focused to analysing the influence of properties of gratings on wave motion. In optics, the gratings are considered as rigid, in case of solid mechanics both the matrix and the grating are elastic. In the latter case, wave motion is studied numerically in the plain strain setting. Standard 2-D wave equation is solved by means of a finite volume numerical scheme. The interaction of waves after passing through a periodically ordered elastic grating leads to a self-imaging Talbot effect for the wave length equal or close to the grating size [4]. The effect of energy localization is observed at the vicinity of the grating (see Figure 2).

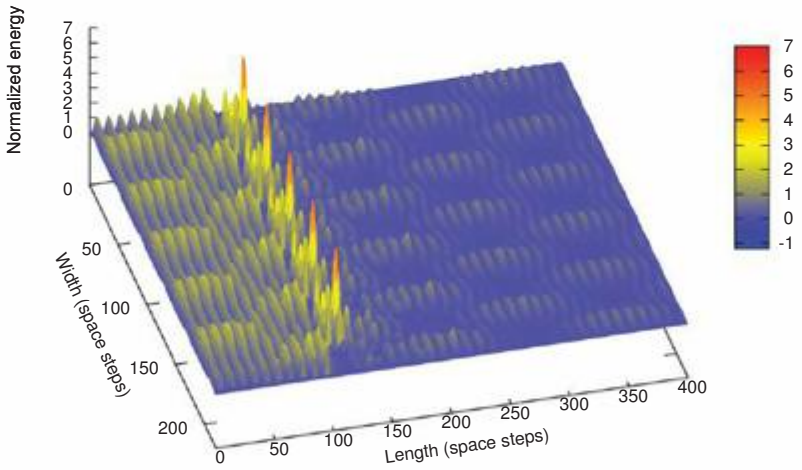

Figure 2: Energy localization in the vicinity of an elastic grating

The optical, acoustic and elastic diffraction processes are compared and differences explained. The observed difference between acoustic and elastic cases is unavoidable and should be taken into account in the topological optimization of composites for the controlling of elastic waves.

CONCLUSIONS

The mechanisms of interaction of waves with the microstructures (internal structure) in solids are analysed. The coupling of the macro- and microstructure leads to changes in velocities and wave profiles. The influence of the disordered microstructure leads to strong dispersive effects including the possible negative group velocity. Such modelling opens vistas for dispersion engineering of materials with specific properties. Numerical simulations of the elastic wave diffraction on elastic gratings show both similarities and differences with the case of a rigid grating where waves are not transmitted through inclusions. The localized microstructure may cause energy localization in emerging wave fields.

Acknowledgements. This research was supported by the European Union through the European Regional Development Fund and the Estonian Research Council (PUT 434).

References

[1] Engelbrecht J., Berezovski A.: Internal structures and internal variables in solids. J. Mech. Materials and Structures 10:983-996, 2012.

[2] Berezovski A., Engelbrecht J., Salupere A., Tamm K., Peets T., Berezovski M.: Dispersive waves in microstructured solids. Int. J. Solids and Structures 50:1981-1990, 2013.

[3] Peets T., Kartofelev D., Tamm K., Engelbrecht J.: Waves in microstructured solids and negative group velocity. EPL, 103:16001, 2013.

[4] Berezovski A., Engelbrecht J., Berezovski M.: Pattern formation of elastic waves and energy localization due to elastic grating. Int. J. Mech. Sci. 101-102:137-144, 2015.

NONSMOOTH MODAL ANALYSIS OF PIECEWISE-LINEAR IMPACT SYSTEMS

Anders Thorin*[1], Pierre Delezoide , and Mathias Legrand[1]
[1]*Department of Mechanical Engineering, McGill University, Montreal, Quebec, Canada*

Summary Periodic solutions of autonomous and conservative second-order dynamical systems of finite dimension n undergoing a single unilateral contact condition are investigated in continuous time. The unilateral constraint is complemented with a purely elastic impact law conserving total energy. The dynamics is linear away from impacts. It is proven that the phase-space is primarily populated by one-dimensional continua of periodic solutions, generating an invariant manifold which can be understood as a *nonsmooth mode of vibration* in the context of vibration analysis. Additionally, it is shown that nonsmooth modes of vibration can be calculated by solving only $k-1$ equations where k is the number of impacts per period. Results are illustrated on a mass-spring chain whose last mass undergoes a contact condition with an obstacle.

MOTIVATION

Nonlinear modal analysis consists in calculating, in the phase space, two-dimensional manifolds which are continuous families of periodic trajectories [1]. When dealing with nonsmooth systems, *i.e.* systems subjected to impact and friction [2], the induced discontinuities are usually regularized [3]. The novelty of the proposed work here is to incorporate the discontinuities in the formulation to exhibit continuous families of periodic nonsmooth trajectories, thus leading to *nonsmooth modal analysis*. The results hold for all autonomous linear dynamical systems subjected to a single contact condition modeled through a unilateral linear sceleronomic constraint complemented with a perfectly elastic impact law.

FORMULATION

The vector of generalized coordinates $\mathbf{x}$ is an element of $\mathbb{R}^n$ where n is the number of dofs of the system. During free flights, that is away from impacts, the dynamics is governed by $\mathbf{M}\ddot{\mathbf{x}}+\mathbf{K}\mathbf{x}=\mathbf{0}$ where $\mathbf{M}$ and $\mathbf{K}$ are the mass and stiffness matrices. Introducing $\overline{\mathbf{x}}=[\mathbf{x}^\top,\dot{\mathbf{x}}^\top]^\top$, this differential equation can be reformulated in the first-order form as $\dot{\overline{\mathbf{x}}}=\mathbf{A}\overline{\mathbf{x}}$ hence if no impact occurs in time interval $[t,t']$, $\overline{\mathbf{x}}(t)=\mathbf{S}(t-t')\overline{\mathbf{x}}(t')$ with $\mathbf{S}(t)=\exp(t\mathbf{A})$. The signed contact distance (gap function) is $g(\mathbf{x})=\mathbf{w}^\top\mathbf{x}+g_0$. It is shown that the impact law, written in terms of normal contact velocities $\gamma^+=-\gamma^-$, reads in terms of as $\overline{\mathbf{x}}^+=\mathbf{N}\overline{\mathbf{x}}^-$ where $\mathbf{N}=\mathbf{M}^{-1/2}(\mathbf{I}-2\mathbf{r}\mathbf{r}^\top)\mathbf{M}^{1/2}$ and $\mathbf{r}$ is the unit vector given by $\mathbf{r}^\top=[\mathbf{0}_{1,n},\mathbf{M}^{1/2}\mathbf{w}(\mathbf{w}^\top\mathbf{M}^{-1}\mathbf{w})^{-1/2}]^\top\in\mathbb{R}^{2n}$. We introduce the times of impact $t_0,\dots,t_k$ with the convention $t_0=0$ and period $T=t_k$ so that k is the number of impacts per period (ipp). The dynamics is a succession of free flights of duration t_i-t_{i-1} and impacts at t_i, $i\in[\![1,k]\!]$, so for $t\in[t_{i-1},t_i)$:

$$\overline{\mathbf{x}}(t)=\mathbf{S}(t-t_i)\mathbf{N}\mathbf{S}(t_i-t_{i-1})\mathbf{N}\dots\mathbf{N}\mathbf{S}(t-t_0)\overline{\mathbf{x}}(t_0). \tag{1}$$

This expression shows that there exists a linear mapping from a vector of initial conditions to the current state at t. Let u be the endomorphism of matrix $\overline{\mathbf{N}\mathbf{S}}(t_k-t_{k-1})\overline{\mathbf{N}}\dots\overline{\mathbf{N}\mathbf{S}}(t_1-t_0)$ in the canonical basis of $\mathbb{R}^{2n}$. The problem of finding periodic solutions of the dynamics with impact times $t_1,\dots,t_k$ is formulated in three necessary conditions (NC) to be satisfied by $\overline{\mathbf{x}}_0$: Given $T\in\mathbb{R}^*$ and $k\in\mathbb{N}^*$, find $\overline{\mathbf{x}}_0\in\mathbb{R}^{2n}$ and $t_1,\dots,t_k$ such that:

$$\begin{cases} u(\overline{\mathbf{x}}_0)=\overline{\mathbf{x}}_0 & \text{NC1} \quad (2a)\\ \overline{\mathbf{x}} \text{ determined by } \overline{\mathbf{x}}_0 \text{ using (1) is such that:} & \\ \forall i\in[\![1,k]\!],\ \overline{g}(\overline{\mathbf{x}}(t_i))=0 & \text{NC2} \quad (2b)\\ \forall t\in[0,T],\ \overline{g}(\overline{\mathbf{x}}(t))\geq 0 & \text{NC3} \quad (2c)\end{cases}$$

with $\overline{g}(\overline{\mathbf{x}}):=g(\mathbf{x})$. Eq. (2a) enforces periodicity through a sequence of free flights over (t_{i-1},t_i) punctuated by perfectly elastic impacts at t_i, $i\in[\![1,k]\!]$. Eq. (2b) guarantees that the impact law only applies when the separating gap is closed. Ineq. (2c) is necessary to ensure that the unilateral contact condition is not violated during the free flights.

MATHEMATICAL RESULTS

We can show that there is an isomorphism φ between the invariant (maximal) subspace of u and the kernel of a known skew-symmetric matrix $\mathbf{\Pi}$ of size $k\times k$ and function of the impact times. This implies that NC1 is satisfied if and only if there exists a $\boldsymbol{\lambda}\in\mathbb{R}^k$ such that $\mathbf{\Pi}(t_1,\dots,t_k)\boldsymbol{\lambda}=\mathbf{0}$, and then $\overline{\mathbf{x}}_0$ can be retrieved using $\overline{\mathbf{x}}_0=\varphi(\boldsymbol{\lambda})$. We also know that NC2 is satisfied by $\overline{\mathbf{x}}$ if and only if $\mathbf{\Sigma}(t_1,\dots,t_k)\varphi(\overline{\mathbf{x}}_0)=-g_0\mathbf{j}$ where $\mathbf{\Sigma}$ is a symmetric $k\times k$ matrix and $\mathbf{j}=[1,\dots,1]^\top\in\mathbb{R}^k$.

*Corresponding author. Email: anders.thorin@mcgill.ca

The expressions of $\mathbf{\Pi}$, $\mathbf{\Sigma}$ and φ are known explicitly but are not provided here; they depend only on $\mathbf{M}$, $\mathbf{K}$, g and $t_1, \ldots, t_k$. Satisfying NC1 and NC2 reduces to finding $t_1, \ldots, t_k$ and $\boldsymbol{\lambda}$ such that $\mathbf{\Pi}\boldsymbol{\lambda} = \mathbf{0}$ and $\mathbf{\Sigma}\boldsymbol{\lambda} = -g_0\mathbf{j}$. Then, $\mathbf{\Sigma}$ is generically invertible so it suffices to find $t_1, \ldots, t_k$ such that $\mathbf{\Pi}\mathbf{\Sigma}^{-1}\mathbf{j} = \mathbf{0}$, and then recover $\bar{\mathbf{x}}_0 = \varphi(-g_0\mathbf{\Sigma}^{-1}\mathbf{j})$. The non-generic cases exhibit very specific properties which are not described here. If $\bar{\mathbf{x}}_0$ satisfies NC1 and NC2, it is a solution iff it satisfies NC3. This last condition has to be tested numerically.

It is then proved that if $\bar{\mathbf{x}}_0$ is a solution for $g_0 \neq 0$ then, generically, it lies on a two-dimensional manifold of the phase space. As opposed to smooth nonlinear modes, here the manifolds feature discontinuities, corresponding to the discontinuities at impact times. The positions and velocities as a function of time emanating from the initial conditions $\bar{\mathbf{x}}_0$ can then be calculated. The results are summarized in Fig. 1.

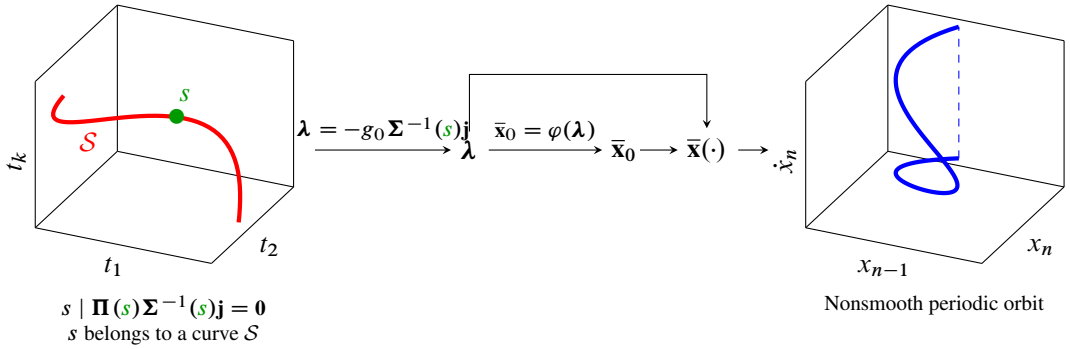

Figure 1: Summary of the mathematical results in the generic case with $g_0 \neq 0$. When $s = (t_1, \ldots, t_k)$ travels along the red curve $\mathcal{S}$, the periodic solution describes a nonsmooth mode with k impacts per period.

APPLICATION TO A MECHANICAL SYSTEM

The mathematical developments prove the existence of nonsmooth modes yet also give a constructive way of calculating them by solving $k-1$ equations ($\mathbf{\Pi}\mathbf{\Sigma}^{-1}\mathbf{j} = \mathbf{0}$) independently of the number of dofs. Results are illustrated on a simple spring-mass chain whose free mass is subjected to an elastic Newton impact law, see Fig. 2. A nonsmooth mode with 7-ipp

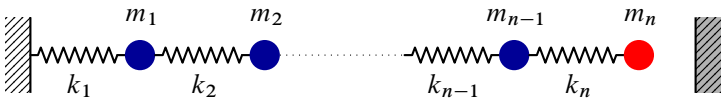

Figure 2: Simple spring-mass chain whose free mass is subjected to impacts.

was calculated following the methodology of Fig. 1 for this system with $n = 5$. The position of the last mass is represented for two initial conditions on the nonsmooth mode in Fig. 3, illustrating the possibilities given by the derivations.

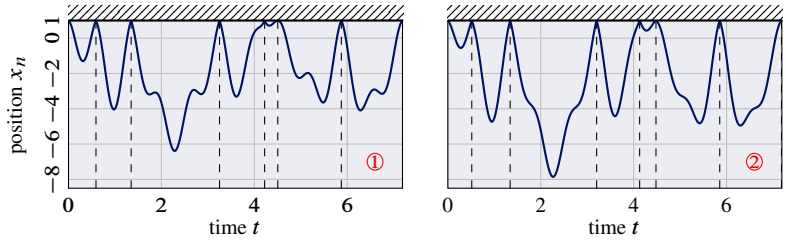

Figure 3: Two periodic trajectories with 7 ipp belonging to the same nonsmooth mode represented in $(\dot{x}_n, t)$. Dashed lines correspond to impact times.

References

[1] Shaw, S.W. and Pierre, C.: Non-linear normal modes and invariant manifolds. Journal of Sound and Vibration, 150:170–179, 1991.

[2] Acary, V. and Brogliato, B.: Numerical methods for nonsmooth dynamical systems: applications in mechanics and electronics. Springer, vol. 35, 2008.

[3] Chen, S.-L. and Shaw, S.W.: Normal modes for piecewise linear vibratory systems. Journal of Nonlinear Dynamics, 10:135–164, 1996.

MULTI-SITE DISCRETE BREATHERS IN FINITE VIBRO-IMPACT CHAIN

Itay Grinberg*[1] and Oleg V. Gendelman[1]

[1]*Faculty of Mechanical Engineering, Technion – Israel Institute of Technology, Haifa, Israel*

Summary Exact solution of a discrete breather with multiple localization sites is derived for both conservative and forced-damped vibro-impact chain of finite size. The finite dimension of the chain also allows accurate stability analysis via Floquet theory without approximations. Two mechanisms of stability loss are revealed and numerically verified. Additionally, effects of chain length and localization sites proximity is being investigated.

Localization in physical systems has been of increasing interest in recent years. Localization can be caused by some defect in otherwise homogeneous media. However, a more interesting case is when it appears in disordered or purely homogeneous nonlinear media. This work focuses on the discrete breather (DB) – exponentially localized phenomenon appearing in nonlinear lattices – sometimes referred to as Intrinsic Localized Modes (ILM) or Discrete Solitons.

The investigated system consists of a finite chain of linear oscillators. In addition to the linear coupling, each mass is subjected to an on-site interaction – a linear spring and a pair of barriers inducing vibro-impact located at $u_n = \pm 1$ t where u_n is the displacement of the nth mass.

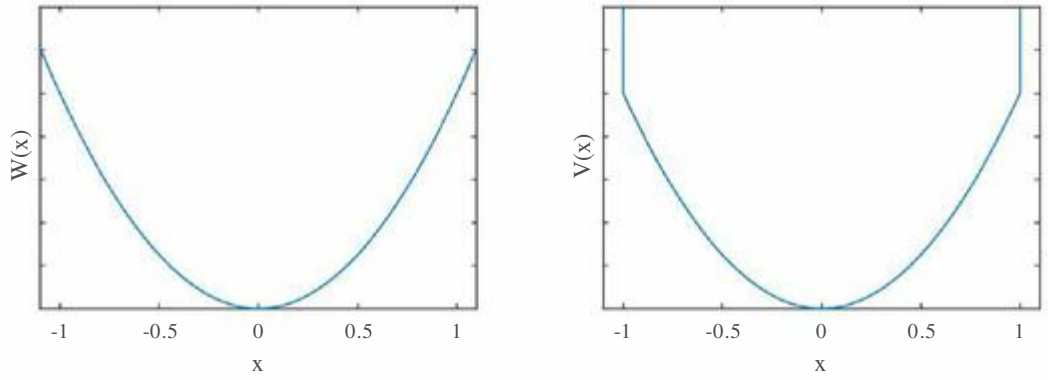

Figure 1: Coupling (left) and on-site (right) potentials

The Hamiltonian of the can now be extracted:The Hamiltonian of the systems for $(N+1)$ masses is as follows:

$$H = \sum_{n=0}^{N} \left(\frac{1}{2} p_n^2 + V(u_n) \right) + \sum_{n=0}^{N-1} W(u_n - u_{n+1}) + W(u_N - u_0) \tag{1}$$

$$V(x) = \begin{cases} \frac{\gamma_1}{2} x^2 & |x| < 1 \\ \text{Impact} & |x| = 1 \end{cases} \tag{2}$$

$$W(x) = \frac{\gamma_2}{2} x^2 \tag{3}$$

where $p_n = \dot{u}_n$ is the momentum, γ_1 and γ_2 are the on-site and coupling stiffness respectively and $V(x)$ and $W(x)$ are the on-site and coupling potentials respectively. The impact condition is $u_n(t_b) = \pm 1$, and the impact law is given by $\dot{u}_n(t_b+) = -e u_n(t_b-)$ where e is the coefficient of restitution.

Based on works by Gendelman and Manevich[1, 2] an exact solution of a symmetric DB is obtained for both conservative model, and more importantly, forced-damped model by means of Fourier series. Due to the complexity of the solution, the localization is only verified numerically. However, One can clearly see the exponential localization around the DB sites when $N \to \infty$.

*Corresponding author. Email: GrinbergItay@gmail.com or gitay@technion.ac.il

Additionally, the zone of existence is determined and it's stability is examined via Floquet multipliers[3], i.e. eigenvalues of the Monodromy matrix that is described explicitly for an approximate finite system, hence the Fluquet multipliers are not extracted numerically from the mapping as is usually the case but are derived directly from the Monodromy matrix. It is important to note that since both models are VI models, producing the Monodromy matrix is not a simple task and must be done separating the linear regime from the instance of the impact where one must use a saltation matrix [4].

The obtained solution is characterised by a strongly localized frame enveloping the synchronously oscillating masses. The frame is presented in fig. 2 for two set of parameters of the Hamiltonian model.

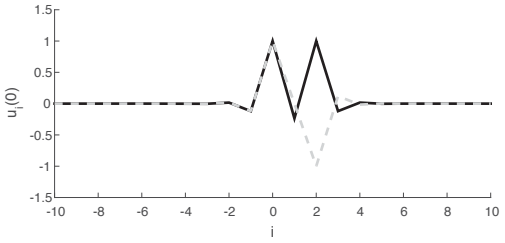

Figure 2: Comparison of the displacement amplitude of the masses between in-phase (black) and anti-phase (dashed gray) 2-site DB. Negative indices denotes the ith mass in the chain where $i = N + 1 + (\text{negative index})$ to better represent the periodic boundary condition.

The stability analysis reveals two mechanisms for loss of stability as seen in the stability map in fig. 3. The first is the Hopf bifurcation corresponding to some spatial modes of the linear chain and possibly related to resonance frequencies. The second is the pitchfork bifurcation which appears to be of localized nature and corresponds to breaking of the DB's symmetry as demonstrated in fig. 4.

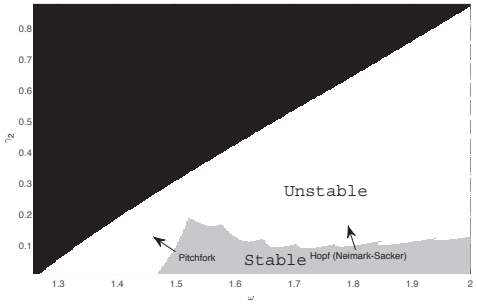

Figure 3: Stability map for a 2-site Forced DB with sites at 0 and 1 for $N = 20$, $\gamma_1 = 0.1$, $e = 0.9$ and $A = 1.5$.

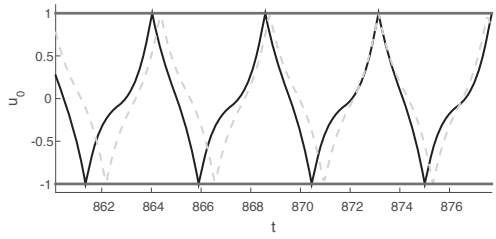

Figure 4: Analytic prediction (dashed gray) and numerical approximation (black) of the displacement of an impacting mass for $N = 20$ and $\gamma_2 = 0.07$ with a 2-site forced DB after breaking of the symmetry.

References

[1] O. V. Gendelman and L. I. Manevitch: Discrete breathers in vibroimpact chains: Analytic solutions. Phys. Rev. E, 78:026609, Aug 2008.

[2] O. V. Gendelman: Exact solutions for discrete breathers in a forced-damped chain. Phys. Rev. E, 87:062911, Jun 2013.

[3] Ali H Nayfeh and Balakumar Balachandran: Applied nonlinear dynamics, Wiley.com, 2008.

[4] Mats H Fredriksson and Arne B Nordmark: On normal form calculations in impact oscillators. Proceedings of the Royal Society of London, Series A: Mathematical, Physical and Engineering Sciences, 456(1994):315329, 2000.

NONLINEAR MODES OF VIBRATION OF VIBRO-IMPACT DUFFING OSCILLATORS

David Urman* and Mathias Legrand
Department of Mechanical Engineering, McGill University, Montreal, Quebec, Canada

Summary The objective of this research is to develop numerical methods for finding periodic solutions to autonomous conservative vibro-impact Duffing oscillators. The investigated model consists of serially connected masses the last of which collides a rigid wall. The connecting stiffness are quadratic functions of the displacements. Dedicated Ritz methods and continuation algorithms are developed in order to find families of admissible natural vibratory responses commonly named *nonlinear modes of vibration*.

MOTIVATIONS

Vibration analysis is critical for many common mechanical systems: jet engines, bridges, pistons, and acoustic resonators are some examples of systems for which the study of vibration is crucial [1]. Within a linear framework, one way to understand the behaviour of such oscillatory systems is by exploring their natural frequencies of oscillation in the vicinity of an equilibrium state. Such behaviour is called autonomous vibration and its analysis aids in predicting more complex behaviours of the investigated system. The analysis becomes much more challenging when the investigated mechanical system features smooth as well as nonsmooth nonlinearities: two typical examples are cubic nonlinearities capturing large displacements and impacts reflecting unilaterally constrained dynamics. Such a system, reduced to 2-degree-of-freedom (dof) vibro-impact Duffing oscillator, is numerically investigated in the light of vibration modal analysis.

MODELLING AND GOVERNING EQUATIONS

The system of interest, depicted in Fig. 1, consists of two nonlinear cubic springs serially connecting two masses the last of which impacts a rigid non-moving wall. Unilateral contact is mathematically expressed as a Signorini complementarity condition.

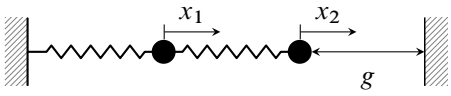

Figure 1: 2-dof vibro-impact Duffing oscillator: stiffnesses are nonlinear functions of x_1 and x_2, see Equation (1a).

For discrete systems, an additional impact law has to be incorporated in the formulation for well-posedness purposes [6]. In this work, the well-known Newton impact law with the restitution coefficient $e = 1$ is considered [3, 4]. One-impact-per-period solutions only are targeted and the complementarity conditions are advantageously replaced by a simple numerical test on the admissibility of the found solution [5, 7]. This simplified formulation tracks a subset of all possible admissible solutions. Periodic solutions with one impact per period are assumed to exist but the period T is unknown. Without loss of generality, the assumed impact occurs at $t = 0$ and the governing equations read:

- Free-flight $\forall t \in]0\,;T[$:

$$\begin{bmatrix} m_1 & 0 \\ 0 & m_2 \end{bmatrix} \begin{pmatrix} \ddot{x}_1 \\ \ddot{x}_2 \end{pmatrix} + \begin{bmatrix} k_1 + k_2 & -k_2 \\ -k_2 & k_2 \end{bmatrix} \begin{pmatrix} x_1 \\ x_2 \end{pmatrix} + \varepsilon \begin{pmatrix} (x_1 - x_2)^3 \\ (x_2 - x_1)^3 \end{pmatrix} = \begin{pmatrix} 0 \\ 0 \end{pmatrix} \tag{1a}$$

- Continuity and impact condition

$$x_i(0) = x_i(T), \quad i = 1, 2 \tag{1b}$$

$$x_2(0^+) = g \quad \text{and} \quad \dot{x}_2(0^+) = -\dot{x}_2(T^-) \tag{1c}$$

SOLUTION METHODS

When $\varepsilon = 0$, closed-form solutions to system (1) exist [5]. When the cubic springs are effective, the construction of an approximation relying on the Ritz method is implemented. Ritz methods are designed to approximate the solution using a set of known functions [1] which satisfy the boundary conditions of the formulation. In this research, the Ritz functions are defined in the time-domain and should comply with the continuity and impact conditions (1b) and (1c). The two following families

$$\phi_i(t) = \cos(i\omega(T/2 - t)) \quad \text{and} \quad \psi_i(t) = \cos(2\pi i t/T), \quad i = 1, 2, \ldots \tag{2}$$

*Corresponding author: david.urman@mail.mcgill.ca

to approximate the displacement of the impacting mass and non-impacting mass, respectively. In Equation (2), ω is the frequency of the motion when impact is ignored: this is an unknown of the formulation and is introduced to generate a discontinuity $\dot{x}_2(0^+) = -\dot{x}_2(T^-)$ in a straightforward manner. The period of the unknown displacement (x_1, x_2) solution to (1) is T and not $2\pi/\omega$. The approximate solution is then inserted into (1a) and a Galerkin Projection [1] is performed on the family ψ_i (solely) to find the participation of the Ritz functions in the solution. As such, the formulation has always more one unknown than the number of available equations: this can be understood as a *generalized* eigenvalue problem where the period and the displacement have to be found. The solution set is intricate and organized as multiple co-existing one-parameter families of periodic orbits, some of which can be tracked through continuation strategies starting from the linear solutions.

RESULTS

Solutions were obtained for a 2-dof system but the proposed method extends to larger systems at the cost of an increased computational effort. It was concluded, from numerous tests, that the developed Ritz method converges when a sufficient number of Ritz functions is incorporated into the formulation. The admissibility of the found solution has to be continuously checked as unexpected grazing trajectories might arise when the energy of the motion increases.

The effects of the impact is indicated in Fig. 2 [left] by the first change of slope in the Frequency-energy plot. The well-known stiffening effect induced by the cubic springs is observed when ε is increased. Other branches were also found

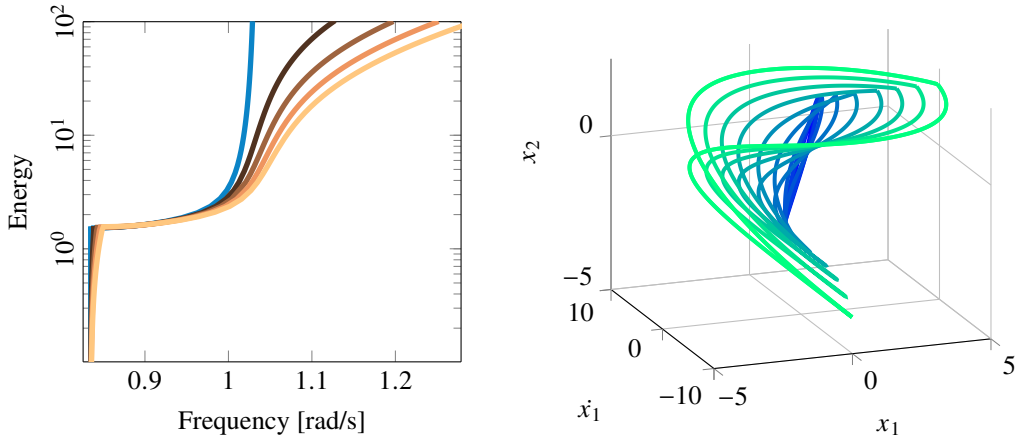

Figure 2: Left: Frequency-Energy plot of the first nonlinear vibration mode in the vicinity of the first natural frequency ω_1 with $\varepsilon = 0$ [blue curve, linear oscillator with impact] and $\varepsilon \in [0.0\,;0.2]$ [brown curves from dark to bright]. Parameters $m_1 = m_2 = k_2 = 1$, $k_1 = 3$, and $g = 2$. Right: Invariant manifold for $\varepsilon = 0.2$

in the neighbourhoods of the subharmonics of the system's natural frequencies. Further work is currently undertaken on the theoretical aspects of the existence of such manifolds. It should be noted that the internal resonances expected in the Duffing oscillator (with no impact) will generate unexplored difficulties when impact is introduced. Finally, finding solutions with multiple impacts per period is a direct extension to this work, yet much more challenging.

References

[1] Paidoussis, M.P. (1994) *Notes for Mechanics of Systems: MECH 305-419.* McGill University, Department of Mechanical Engineering.

[2] Strogatz, S. (1994). *Nonlinear Dynamics and Chaos: With applications to physics, biology, chemistry, and engineering*. Persus Books Publishing.

[3] Babitsky, V. (1998). *Theory of vibro-impact systems and applications*. Springer.

[4] Sofonea, M., and Matei, A. (2012). *Mathematical models in contact mechanics*. Cambridge University Press.

[5] Legrand, M. Junca, and S. Sokly, H. (2015) *Nonsmooth modal analysis of a N-degree-of-freedom system undergoing a purely elastic impact law*, (submitted)

[6] Acary, V. and Brogliato, B. (2008) *Numerical Methods for Nonsmooth Dynamics*. Springer.

[7] Kim, W.-J. and Perkins N.C. (2003) *Harmonic balance/Galerkin method for non-smooth dynamic systems*. Journal of Sound and Vibration **261**(2):213:224.

PICK-UP, IMPACT AND PEELING

Harmeet Singh[1] and James Hanna*[2]

[1,2]*Engineering Mechanics Program, Department of Biomedical Engineering and Mechanics, Virginia Tech, U.S.A.*

Summary We consider a class of problems involving a one-dimensional, inextensible body with a propagating discontinuity (shock) associated with partial contact with a rigid obstacle providing steric, frictional, or adhesive forces. This class includes the pick-up and impact of an axially flowing string or cable, and the peeling of an adhesive tape. The dynamics are derived by applying an action principle to a non-material volume. The resulting boundary conditions provide momentum and energy jump conditions at the shock. These are combined with kinematic conditions on velocities and accelerations to obtain families of steady-state solutions parameterized by the shock velocity and momentum and energy sources.

In our presentation, we will apply these findings to specific cases, compare with other results in the literature on chain fountains, falling folded chains, and impulsively loaded cables, and examine the dynamics of the shock when steady-state solutions are perturbed.

Point discontinuities propagating in one dimensional flexible media, such as chains and strings, are ubiquitous in nature. Physical examples of such moving discontinuities (shocks) are, lift off points of chains being picked up from a rigid surface, points of contact of impacting chains, and peeling fronts of adhesive tapes. Figures 1 and 2 show two counterintuitive behaviors involving contact discontinuities.



Figure 1: Snapshots from an experiment where two identical chains were dropped simultaneously. The chain on the right was impeded by a table, and accelerated faster than the freely falling chain on the left (video by Rick Warner).



Figure 2: A chain fountain. One end of a heap of chain is dropped from a parking garage roof, causing part of the chain to rise up in the air. The pick up point of the bucket is a shock that enables the formation of the fountain [1].

For a flexible inextensible string, parametrized by the arc length s and containing a moving discontinuity at $s = s_0(t)$, the following action is minimized to obtain the dynamics [2],

$$A = \int dt \int^{s_0(t)} ds\, \mathcal{L}\,, \tag{1}$$

where $2\mathcal{L} = \mu \partial_t \mathbf{X} \cdot \partial_t \mathbf{X} - \sigma(\partial_s \mathbf{X} \cdot \partial_s \mathbf{X} - 1)$, μ is the mass density, and σ is a Lagrange multiplier enforcing inextensibility of the string. Assuming that the string does not break, a velocity compatibility condition, $[\![\partial_t \mathbf{X} + \partial_t s_0 \partial_s \mathbf{X}]\!] = 0$, must hold at the shock, where $[\![Q]\!] \equiv Q^+ - Q^-$. The superscripts '+' and '−' represent field quantities on either side of the shock. A spatial variation of (1) yields the bulk term $\mu \partial_t^2 \mathbf{X} - \partial_s(\sigma \partial_s \mathbf{X}) = 0$, and the boundary condition

$$\mathbf{P} + [\![\sigma \partial_s \mathbf{X} + \mu \partial_t s_0 \partial_t \mathbf{X}]\!] = 0\,, \tag{2}$$

where $\mathbf{P}$ is the force injection (per unit area) at the shock, usually arising from the contact of the string with an external obstacle. Similarly, the time variation of (1) leads to the jump condition

$$E + [\![\sigma \partial_s \mathbf{X} \cdot \partial_t \mathbf{X} + \tfrac{1}{2} \mu \partial_t s_0 \partial_t \mathbf{X} \cdot \partial_t \mathbf{X}]\!] = 0\,. \tag{3}$$

The power injection (per unit area) is defined as the quantity $E = E - \frac{1}{2}\mathbf{P} \cdot \{\partial_t \mathbf{X}\}$, where $\{Q\} \equiv Q^+ + Q^-$. A negative value of E would imply dissipation. This particular definition of the power injection renders the energy equation Galilean invariant. Using the velocity compatibility, the energy jump can also be written as,

$$E = \tfrac{1}{4} \partial_t s_0 [\![\sigma]\!] [\![\partial_s \mathbf{X}]\!] \cdot [\![\partial_s \mathbf{X}]\!]\,. \tag{4}$$

*Corresponding author. Email: hannaj@vt.edu

The force and power injections are not entirely arbitrary. Using the velocity compatibility along with (2), it can be shown that the power and force jumps are related by the following expression,

$$E\{\partial_s \mathbf{X}\} \cdot \{\partial_s \mathbf{X}\} = -\tfrac{1}{2}\partial_t s_0 \mathbf{P} \cdot \{\partial_s \mathbf{X}\}[\![\partial_s \mathbf{X}]\!] \cdot [\![\partial_s \mathbf{X}]\!] \,. \tag{5}$$

The formalism developed above may be applied to pick-up, impact, peeling, and other problems. Solutions for the pick-up problem are presented here. As shown in Figure 3, a piece of string in contact with a surface and moving with axial velocity T_1 is connected by a discontinuity to a free piece of string moving with axial velocity T_2 and a translational velocity V.

Using the velocity compatibility condition at the shock, the magnitude of the lateral velocity can be related to the axial flows as $V = T_2 - T_1$.

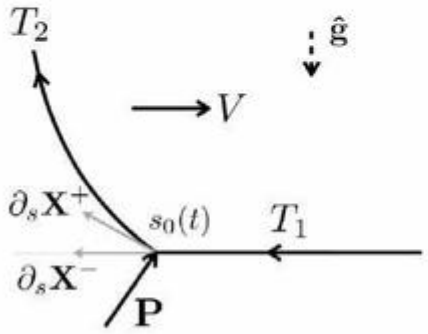

Figure 3: A string being picked up from a frictionless solid surface with a lateral velocity $\mathbf{V}$. The axial velocities of the two parts separated by the shock at $s = s_0(t)$ are given by T_1 and T_2. The direction of gravity is given by the unit vector $\mathbf{g}$.

The steady state solutions for the shock velocity and stresses in the vicinity of the shock are given by the following relations,

$$\partial_t s_0(t) = -T_2 \,, \tag{6}$$

$$\sigma^- = \mu T_2^2 - \frac{\mathbf{P} \cdot [\![\partial_s \mathbf{X}]\!]}{[\![\partial_s \mathbf{X}]\!] \cdot [\![\partial_s \mathbf{X}]\!]} + \frac{2E}{T_2 [\![\partial_s \mathbf{X}]\!] \cdot [\![\partial_s \mathbf{X}]\!]} \,, \tag{7}$$

$$\sigma^+ = \mu T_2^2 - \frac{\mathbf{P} \cdot [\![\partial_s \mathbf{X}]\!]}{[\![\partial_s \mathbf{X}]\!] \cdot [\![\partial_s \mathbf{X}]\!]} - \frac{2E}{T_2 [\![\partial_s \mathbf{X}]\!] \cdot [\![\partial_s \mathbf{X}]\!]} \,. \tag{8}$$

These solutions have been obtained with the aid of (2), (4) and the velocity compatibility only. The bulk equations have not been invoked yet. The velocity $\mathbf{V}$, if not parallel to the string on the table, would affect the shock velocity. Quantities like $\mathbf{P}$ and E would be affected indirectly through the shock velocity. Equation (4) shows that zero power injection (dissipation) must imply continuity of stress σ across the shock, if the tangents are discontinuous. In the absence of gravity, the bulk solution of part 2 of the string enforces $\sigma^+ = \mu T_2^2$. For no power injection (dissipation), the continuity of stresses implies $\sigma^- = \mu T_2^2$, which in turn would lead to $\mathbf{P} = 0$ from the momentum balance equation given by $\mathbf{P} = -[\![(\sigma - \mu T_2^2)\partial_s \mathbf{X}]\!]$.

In the presence of a gravity force $\mu g \mathbf{g}$, the bulk solution for the picked up part yields,

$$\sigma^+ = \mu \left(T_2^2 + g \frac{\sqrt{a^2 s_0^2 + 1}}{a} \right) , \tag{9}$$

where a is a negative constant. In view of (9) above, and the momentum balance across the shock, it can be concluded that a nonzero reaction force is now required to sustain the kink. Using (5), it can also be shown that if the only source of a reaction force is a frictionless surface, i.e. $\mathbf{P} \cdot \partial_s \mathbf{X}^- = 0$, a discontinuity in the tangents across the point of partial contact cannot exist.

Solutions for the impact problem can be obtained by reversing the signs of the axial flows T_1 and T_2. To describe the peeling of an adhesive tape, an additional term in the form of adhesion energy per unit length is incorporated into the Lagrangian. The kinematics remain the same as those of the pick-up problem with no axial velocity on the contacting portion of string, $T_1 = 0$.

ACKNOWLEDGMENT

This work is supported by the National Science Foundation under grant CMMI-1462501.

References

[1] J. Miller. Self siphoning bead ball-chain - from a parking garage roof. www.youtube.com/watch?v= ZhJFCSIzR8.

[2] J. A. Hanna. Jump conditions for strings and sheets from an action principle. *International Journal of Solids and Structures*, 62:239–247, 2015.

ACCELERATION OF CAR CRASH SIMULATIONS

Jörg Fehr*[1] and Dennis Grunert[1]

[1]*Institute of Engineering and Computational Mechanics, University of Stuttgart, Germany*

Summary The automotive industry is in need of fast crash test simulations. Instead of using faster hardware, a modern approach consists of reducing the system size of the underlying equations while retaining important system properties and controlling the approximation error. Linear variants of this so-called model order reduction are well explored and therefore used as much as possible. In a car crash scenario, some parts of the automobile exhibit large deformations, whereas others experience mostly small vibrations. We therefore identify linear behaving parts of the model and separate/reduce them with modern, improved Component Mode Synthesis approaches. The interface plays a crucial role in the speedup, hence an interface reduction is also required. The application to a kart model delivers promising results. Additionally, a workflow is developed, which can be adopted to a full car model consisting of more than one million degrees of freedom.

MOTIVATION

Unlike several decades ago, hardware crash tests are now commonly substituted by simulations in the development phase of a new car. Usually, thousands of simulations are run for only one car to ensure its crash safety over all stages of the development. Combined with detailed finite element (FE) models, this leads to a high demand of computing power and long response time for the design engineer. For shorter response times, the automotive industry currently uses huge computer clusters, which are costly and harmful to the environment. These problems can alternatively be solved by applying model order reduction (MOR) to the underlying system, i.e., substituting it by a smaller system with preferably low approximation error.

In structural mechanics, linear model order reduction is applied for a long time and well understood. Small reduction errors and large acceleration of the simulation can be achieved with, e.g., modal reduction, Krylov methods or techniques based on the singular value decomposition or Gramian matrices. While this is true for mechanical systems with small deformations, it is certainly not the case in a crash test simulation with large deformations, nonlinear material behavior and complex contact scenarios leading to nonlinear differential equations. Unfortunately, nonlinear reduction techniques are not yet as mature and can be found rarely in industrial applications. Therefore, goals are the improvement of nonlinear reduction techniques in the field of crash test simulations and the application of linear, mature methods whenever possible.

IMPLEMENTATION

Several ideas presented below are developed and implemented to accelerate car crash simulations. The 2001 Ford Taurus model [4] of the National Crash Analysis Center and a simplified model of a racing kart serve as examples.

Identification of Nonlinear Parts

Instead of using nonlinear MOR for the complete car model, it is beneficial to separate it in parts which can be considered to behave linear and parts considered to behave nonlinear. Linear respectively nonlinear methods can then be applied accordingly, cf. [3]. It is also possible to not reduce the nonlinear part at all to ensure correctness of the simulation. Since our workflow should be easily applicable in the industry, we use the widely-used FE program LS-DYNA to simulate the crash. Unfortunately, it is not only feature-rich but closed-source, therefore, the underlying, nonlinear differential equations are not visible to the user. Thus, only heuristic identification remains. In [1], clustering algorithms are used to identify similar behaving parts of the car within a set of simulation runs. This approach is adopted to our use case and improved after some problems are identified. Exemplarily, a cluster crossmember of a frontal crashed Ford Taurus is depicted in Fig. 1. The green area behaves ”probably linear” whereas the rest of the crossmember in red behaves ”probably nonlinear”.

Model Order Reduction with Interface Reduction

Once the model is separated in two parts as described above, the substructuring needs to be represented in the equations of motion to allow an isolated treatment of each subbody. Since several decades, the Component Mode Synthesis (CMS) with the Craig-Bampton method as its well-known special case is the default substructuring approach. CMS assumes a partition of the degrees of freedom (DOFs) in boundary and internal DOFs and uses so-called component modes as ansatz functions for the model order reduction. Craig-Bampton, for example, uses a combination of fixed-interface eigenmodes, i.e., the solutions to the eigenproblem of the internal dynamics (the system restricted to only the internal DOFs) and static condensation modes, which are resulting from deformations on only one boundary DOF each.

*Corresponding author. Email: joerg.fehr@itm.uni-stuttgart.de

An improvement of the Craig-Bampton method called CMS-Gram consists in replacing the fixed-interface modes by ansatz functions resulting from input-output based reduction schemes like the Proper Orthogonal Decomposition, Krylov methods or Balanced Truncation. Though this leads to an improvement in the convergence rate of the approximation error, it still does not suffice due to the high number of interface nodes since each interface DOF leads to one static condensation mode. The interface can then be reduced by a spectral decomposition, i.e., taking only the most significant modes into account or by taking dominant deformation patters after an initial analysis of the model. All these methods are implemented in our in-house reduction program Morembs[1].

There are a vast selection of nonlinear MOR methods available, including POD-DEIM and its variants, hyperreduction with GNAT and local basis, Energy-Conserving Sampling and Weighting (ECSW), Trajectory Piecewise Linear (TPWL), etc. So far, we gained experience with the first two methods in other projects. Unfortunately, they are not directly applicable to LS-DYNA models since they need access to the underlying differential equation and sometimes even to the solver. In order to overcome this problem, a co-simulation of the reduced model with a user-defined function in LS-DYNA is one possible solution.

Results and Outlook

CMS-Gram enhanced with interface reduction is applied to a simplified kart model in [3] for a frontal crash scenario against a rigid pole. The model is simple enough to choose the separation manually according to plastic deformation after a few unreduced simulations, though an automatic detection is possible, too. The complete workflow consisting of the preparation of LS-DYNA input files for unreduced and reduced simulations, model reduction with CMS-Gram, interface reduction, exchanging binary files with LS-DYNA and error analysis is implemented in the Matlab version of Morembs.

An initial frequency domain analysis shows that the type of interface reduction dominates the reduction error. All methods, however, lead to small errors while resulting in a small system size with the exception of Craig-Bampton. Therefore, the interface reduced models are used in the nonlinear car crash simulation yielding to a reduced system which is still consistent with the original one. In Fig. 2, the deformed model and maximum plastic strain of the reduced, nonlinear kart model is depicted. The deformation behavior and maximum plastic strain is very similar to the original system. While it was expected that the Craig-Bampton method leads to a small time step and thus long simulation time, the computational effort of the other reduction methods also doesn't improve as expected from other projects.

One area of improvement is obviously the exploitation of the theoretically possible speedup, which is not yet achieved in combination with LS-DYNA. In order to scale the workflow to the full car model, there also needs to be some improvement in the code. Currently, the nonlinear behaving part is not reduced with LS-DYNA. Therefore, nonlinear reduction schemes can be used with a restriction to those which can be implemented for proprietary simulation software used in the industry.

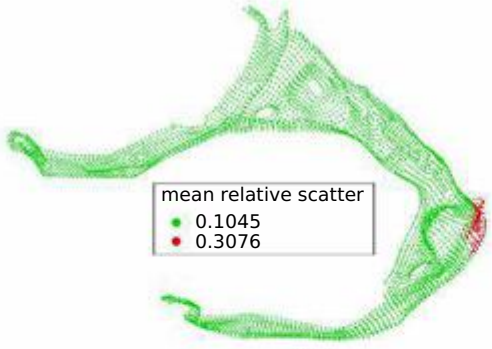

Figure 1: Crossmember clustered in "probably linear" (green) and "probably nonlinear" (red) parts.

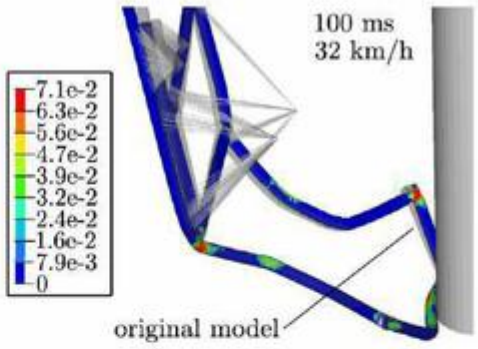

Figure 2: Deformed kart frame after crash against a pole with highlighted plastic strain.

References

[1] B. Bohn, J. Garcke, R. Iza-Teran, A. Paprotny, B. Peherstorfer, U. Schepsmeier, and C.-A. Thole. Analysis of car crash simulation data with nonlinear machine learning methods. *Procedia Computer Science*, 18:621–630, 2013.

[2] J. Fehr and D. Grunert. Model reduction and clustering techniques for crash simulations. *Proceedings in Applied Mathematics and Mechanics*, 15(1):125–126, 2015.

[3] J. Fehr, P. Holzwarth, and P. Eberhard. Interface and model reduction for efficient simulations of nonlinear vehicle crash models. Submitted to Mathematical and Computer Modelling of Dynamical Systems, 2015.

[4] D. Marzougui, R. R. Samaha, C. Cui, and C.-D. S. Kan. Extended validation of the finite element model for the 2001 ford taurus passenger sedan. Technical Report NCAC 2012-W-004, The National Crash Analysis Center, The George Washington University, 45085 University Drive, Ashburn, VA 20147 USA, July 2012.

[1] `http://www.itm.uni-stuttgart.de/research/model_reduction/MOREMBS_en.php`

NEW CONCEPT OF PASSIVE ENERGY DISSIPATING SYSTEM BASED ON PLASTIC BUCKLING

A. Abdul–Latif•, A. Ahmed-Ali, R. Baleh, D. Razafindramary
Laboratoire Quartz, Supméca, 3, rue Fernand Hainaut - 93407 St Ouen Cedex – France

Summary Thin steel tubes are characterized by a case-hardened surface of 15% of tubes outer surface for a certain depth with different geometrical shapes via carbonitriding process. The patented idea [1] aims to enhance the resistance of the tubes against external loadings. Different shapes of the treated surface are proposed: 4 different ring-shape configurations (2, 3, 4 and 5 rings), a shape with 3 uniformly distributed vertical strips parallel to the axis of the tube and three helically treated cases with tilt angles of 30°, 45° and 60°. These tubes are tested via a dynamic drop mass bench of a maximum impact velocity of 9.5 m/s showing their behavior during dynamic plastic buckling. The obtained results reveal that the 4-ring case provides the best energy absorption enhancement of 65% compared to non-treated tube.

INTRODUCTION

In different transport vehicles, the thin-walled tubular structures are widely used as a passive safety concept (energy dissipating device). Different studies reveal that the crushing process remains sensitive to several key parameters like magnitude, type and method of application of loads, strain rates, deformation or displacement patterns and material properties [e.g., 2-5]. Dynamic axial crushing of tube is an effective shock absorber device and is generally dependent on the strain rate [2,3]. The plastic buckled tubes can dissipate a large amount of energy due to the bending and stretching strains combination and its progress along the buckled tube which guarantees the participation of material in the absorption of energy. The limit of the performance of axially crushed tubes can be enhanced using an innovated idea [1]. This is based on the generation of local heterogeneities dictated by the two steel phases (hard and soft phase), where, hard phases generated by carbonitriding heat treated surface of 15% of tubes outer surface with different shapes.

EXPERIMENTAL PROGRAM

This study uses the new concept [1]. Enhancement of the energy absorption capacity of tubes is considered through different treated surface shapes under dynamic loading regime. Tubes of 40mm diameter, 1mm thickness and 140 mm length are employed. The opportunity is therefore to give a careful choice in controlling the geometrical parameters (the shape and the depth of the treated zone) via carbonitriding heat treatment for a depth of 0.4 mm. The different defined shapes are: 4 different ring-shape configurations (2, 3, 4 and 5 rings noted respectively 2H, 3H, 4H and 5H), a configuration with three uniformly distributed vertical strips parallel to the axis of the tube (noted 3V) and three helically treated cases with tilt angles of 30°, 45° and 60° (designated respectively He30°, He45° and He60°) (Fig. 1). Tests are conducted under initial impact velocity of about 9.5 m/s.

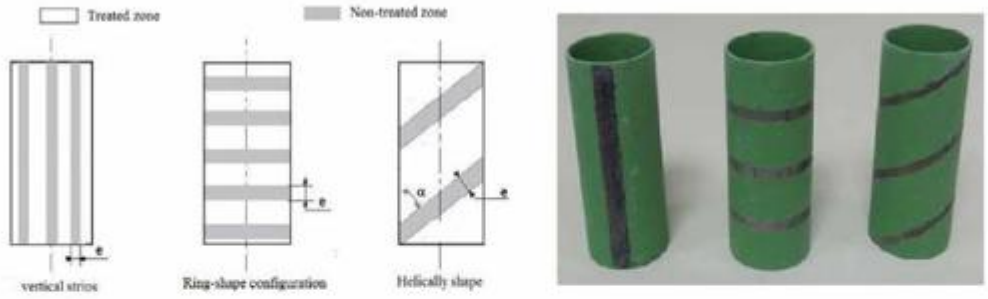

(a) (b)

Fig. 1: (a) Scheme of the proposed configurations, (b) View of 3V, 3H and He45° configurations before heat treatment

EXPERIMENTAL RESULTS AND DISCUSSION

The typical example of load-deflection curve under dynamic loading situation is given in Fig. 2a for the 3H shape. In fact, this curve is characterized by a noticeable peak collapse load appeared during the first plastic flow phase. Beyond this peak load, the curve is defined by a load decrease and then a series of peaks with an evolutionary character (oscillatory nature) about a mean post-buckling load, the peaks and troughs being directly related to the formation of buckles and folding at various buckling levels. A typical example of axisymmetric deformation mode is given in Fig. 3b. It is well-

• Corresponding author aabdul@iu2t.univ-paris8.fr (A. Abdul-Latif)

known that the dynamic velocity decreases naturally and progressively during crushing process to join roughly the quasi-static state (Fig. 2b). For this reason and to give a maximum of objectivity to determine the mean collapse load for each case, a value of axial deflections of 40 mm is chosen. The influence of the heat-treated zone shapes on the mean crushing load (F_{av}) is presented in Fig. 3a. Actually, the shape effect on F_{av} under dynamic loading regime is pointed out. The enhancement in F_{av} is determined with respect the as-received tube (As-R). Under dynamic load, the increase in the F_{av} is: 65% for 4H against 47%, 45%, 43%, 35%, 32%, 29% and 25% for He60°, He30°, He45°, 3H, 3V, 5H, 2H cases, respectively. One can conclude that the recorded mean collapse loads provide a remarkable energy absorption enhancement. Furthermore, results under quasi-static loading are considered to study the sensitivity of tube material to strain rate. Figure 3a shows the sensitivity of tubes to the strain rate as well. For example, in the He45° case, the sensitivity is quantified by a value of 23%.

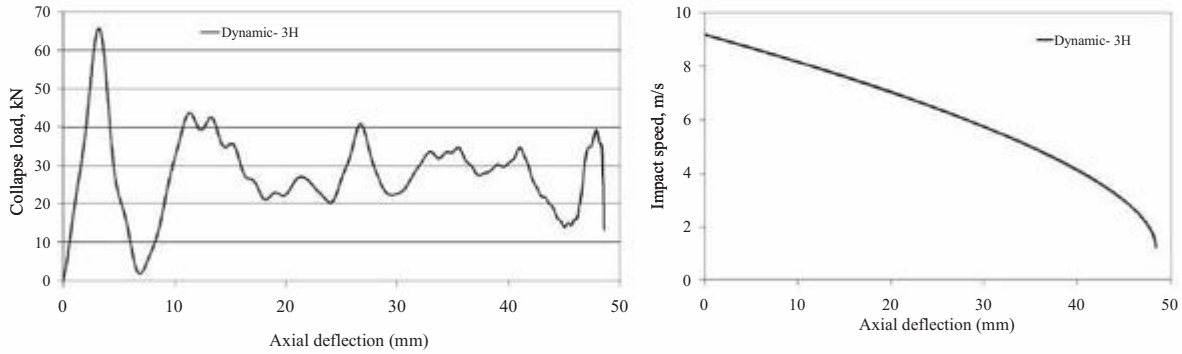

(a) (b)

Fig. 2: (a) Example of typical evolution of dynamic collapse load versus deflection (b) impact speed evolution during crushing process

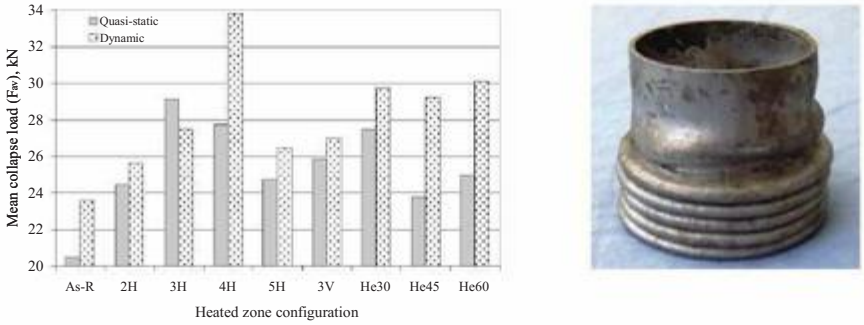

(a) (b)

Fig. 3 : (a) Histograms showing effect of the different heat treated shapes on F_{av} for an axial deflection of δ=40 mm; (b) deformation mode of axisymmetric type in the case of 4H

CONCLUSIONS

The enhancement in the energy absorption of the used devices, notably in the case of 4-ring is confirmed and it is higher than 65% for dynamic loading compared to the non-treated tube. Whatever the shape of the treated zone, the recorded results show a noticeable sensitivity of the tube to the strain rate range.

References

[1] Abdul-Latif, A. : Système d'absorption d'énergie à organe en composite métallique déformable plastiquement, *INPI* No. BT 890/1400843, France 2015

[2] Jones, N.: Several Phenomena in Structural Impact and Structural Crashworthiness, *European J. of Mechanics A/Solids*, 22, pp. 693-707, 2003

[3] Karagiozova, D., and Jones, N.: On Dynamic Buckling Phenomena in Axially Loaded Elastic-Plastic Cylindrical Shells, *Int. J. Non-Linear Mechanics*, 37, pp. 1223-1238, 2002

[4] Abdul-Latif, A., R. Baleh and Aboura, Z.: Some improvements on the energy absorbed in axial plastic collapse of Hollow cylinders, *Int. J. Solids and Structures*, 43, 1543-1560, 2006

[5] Menouer A., Baleh R., Djebbar A. and Abdul-Latif A.: New generation of energy dissipating systems based on biaxial buckling, *J. Thin-Walled Structures*, 85, pp. 456-465, 2014

HYPERVELOCITY IMPACT DAMAGE IN COMPOSITE MATERIALS FABRICATED BY FILAMENT WINDING

Aleksandr Cherniaev[1], Igor Telichev [1]
[1]*Department of Mechanical Engineering, University of Manitoba, Winnipeg, Manitoba, Canada*

Summary This paper investigates the behavior of composite materials fabricated by filament winding when subjected to hypervelocity impacts (HVI) by orbital debris. Conducted experiments allowed obtaining the evidence of significant dependence of the HVI damage in the filament-wound composites from the following parameters: impactor energy, pre-loading and degree of interweaving of filament bands. Findings of the study may be useful for the design of spacecraft components fabricated by filament winding, e.g. composite overwrapped pressure vessels.

INTRODUCTION

Composite materials are being extensively used in space applications, including carbon fiber composite overwrapped pressure vessels (COPVs). These vessels are essential to spacecraft propulsion and attitude control systems, life support applications, etc. Common manufacturing technique for COPVs is filament winding, which is characterized by mesoscale inhomogeneity of the fabricated material in addition to microscopic inhomogeneity inherent to all types of composites [1]. The former feature results from multiple interweaving of filament bands forming a filament-wound composite part.

As parts of spacecraft systems, COPVs are exposed to orbital debris (OD) environment and, therefore, may be subjected to hypervelocity impacts (HVI) by orbital debris particles. The behavior of composites under HVI has been studied experimentally and numerically by many researchers, e.g. [2 - 4]. However, most of the reported work was confined to the class of standard laminated composites, whereas no attention has been paid to the *filament-wound materials*.

Preliminary numerical studies conducted by *Cherniaev* and *Telichev* [5] indicated that HVI damage of filament-wound materials may significantly depend on the degree (or "density") of interweaving of the elementary filament bands. The degree of interweaving, in turn, is a manufacturing parameter; and its value may vary in a relatively wide range due to the flexibility of filament winding equipment. An example of winds with different degrees of interweaving is given in Fig.1.

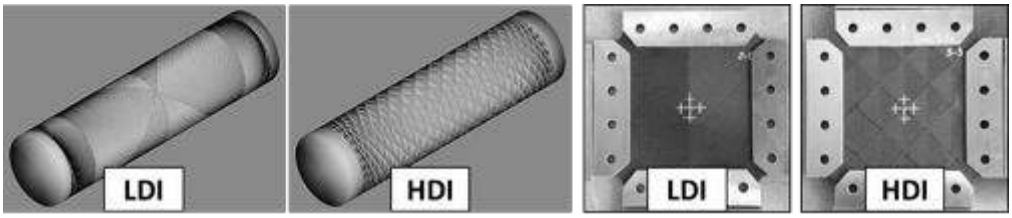

Figure 1 – Helical winds with different densities of interweaving of filament bands (left) and test specimens fabricated from them (right): LDI - "low" density; HDI - "high" density of interweaving

This paper presents results of *experimental studies* that assess the effect of the following parameters on HVI damage of filament-wound composite: 1) impactor energy (in terms of projectile diameter); 2) pre-loading; and 3) degree of interweaving («low» vs. «high», see Fig. 1).

EXPERIMENTAL STUDIES

Experimental model is an experimental representation of attributes of a real physical system that is being studied. The experimental model employed in this study represents the following constituents of the physical system:

- *Environment*: all tests were conducted in a vacuum chamber in order to represent conditions encountered in space. However, some pressure (~30 Torr of nitrogen) was retained to assist in sabot separation during HVI tests.
- *Orbital debris*: orbital debris was represented by aluminum spheres of two different diameters, namely 3.175 mm and 4.763 mm with a nominal speed of 7.0 km/s. Aluminum projectiles represent the medium-density class prevailing in the space debris population.
- *Composite pressure vessel*:

a) The front wall of a pressure vessel was represented by 3 mm-thick composite panels manufactured via filament winding (see Fig. 1).

b) Wall stresses created in a COPV by inflation pressure were represented via pre-loading of the composite panels. In order to simplify the pre-loading apparatus, control and interpretation of measurements, the loading of the composite panels was uniaxial, as compared to biaxial stress state generated by inflation pressure in a shell of a real COPV.

[a)] Corresponding author. Email: Aleksandr.Cherniaev@umanitoba.ca.

• *External OD shielding*: pressure vessels pertain to the critical spacecraft systems of highest vulnerability to orbital debris impacts, and therefore typically have to be protected from highly probable impacts of submillimeter debris. The presence of such protection was modeled by placing a 0.8 mm aluminum bumper at a standoff of 23 mm from the composite panels.

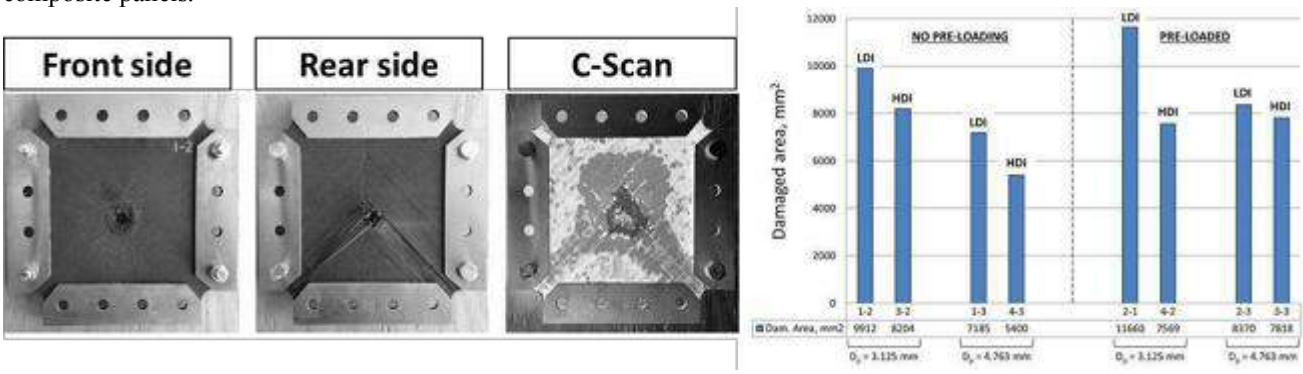

Figure 2 – Exemplary HVI damage of the composite specimen (left) and the total damaged areas of the specimens (right)

In total, 8 composite specimens (4 LDI and 4 HDI) were tested at different impact/pre-loading conditions. Inspection of the visible and subsurface damage of the specimens revealed the following *qualitative* features:

1. Visible damage on the *front side* in all cases was represented by the entry crater only.
2. Peeling of the significant amount of material was observed on the *rear surface* of all LDI specimens. HDI specimens revealed almost no rear surface material peeling at all or very limited amount of it.
3. Both photographs and obtained C-scan images reveal qualitatively different damage patterns for LDI and HDI specimens.

The following *quantitative* observations were made:

1. In all cases, damage zone area in the HDI specimens is smaller as compared with the LDI specimens. The difference varies from 7 to 35%, depending on impact conditions.
2. In most cases, pre-loading leads to formation of a larger damage zone. This is especially the case for LDI specimens, where damage zone area drastically increases (~15%, almost independent on impactor's energy) with the introduction of pre-loading. Primarily, it is associated with an increase of subsurface delamination area, whereas visible surface damage remains almost the same for both pre-loaded and not pre-loaded LDI specimens. This trend remains for the HDI specimens impacted with the higher energy (dp = 4.763 mm), where damage zone area demonstrates ~30% increase with application of pre-loading. However, in this case its growth is associated with both delamination and increase of the surface damage. On the contrary, HDI specimens impacted with the lower energy (dp = 3.125 mm) did not reveal noticeable sensitivity to pre-loading.
3. In most of the cases, impacts of smaller projectiles result in larger delamination area. This can be explained by different energy absorption mechanisms dominating at different impact conditions. With smaller projectiles (dp = 3.125 mm), system «aluminum bumper – composite specimen» is close to its ballistic limit. The dominating energy absorption mechanism in this case is delamination. On the contrary, with larger projectile dominating energy absorption mechanism is fiber breakage (larger energy of impact and, in general, larger individual fragments of the projectile).
4. The size of the perforated holes does not show dependence on the filament-winding pattern (although some fluctuations exist). This result is expectable as properties of all panels are almost identical in the through-the-thickness direction.

CONCLUSIONS

Hypervelocity impact damage of a filament-wound composite is significantly dependent on filament winding pattern used in its fabrication. Patterns with higher degree of interweaving of filament bands demonstrated the ability to better impede propagation of HVI-induced damage, even in the presence of pre-loading. Pre-loading by itself may result in significant increase of the area affected by impact damage. On the contrary, an increase of impactor energy may be a reason for the change of the dominating energy absorption mechanism in the composite panel and result in a reduction of the area damaged by the impact.

References

[1] Peters, S.T.: Composite filament winding. ASM International, Materials Park (2011).

[2] Yew C.H., Rodney BK. A study of damage in composite panels produced by hypervelocity impact. Int J Impact Eng 1987; 5:729-38.

[3] Tennyson RC, Lamontagne C. Hypervelocity impact damage to composites. Compos A 2000; 31(1): 785-94.

[4] Wicklein M, Ryan S, White DM, Clegg RA. Hypervelocity impact on CFRP: testing, material modelling, and numerical simulation. Int J Impact Eng2008; 35(1):1861-1869.

[5] Cherniaev A, Telichev I. Numerical simulation of impact damage induced by orbital debris on shielded wall of composite overwrapped pressure vessel. Appl Compos Mat 2014; 21(6):861-884.

PROPAGATION OF ELASTIC WAVES IN CYLINDRICALLY STRUCTURED CANCELLOUS BONES

Vladyslav Danishevskyy[1a)], Julius Kaplunov[1] & Graham Rogerson[1]
[1]*School of Computing and Mathematics, Keele University, UK*

Summary A new theoretical approach to describe the propagation of elastic waves in fluid-saturated porous bones is proposed. We use the asymptotic homogenisation method and the Floquet-Bloch theory. As an illustrative example, anti-plane shear waves in a cylindrically structured cancellous bone are considered. The effects of damping and scattering are predicted and numerical results are given.

The problem of wave propagation in bone tissues has a great practical importance, in particular, for the development of ultrasound techniques for a non-invasive diagnosis of osteoporosis. Measuring velocities and attenuation of acoustic waves at different frequencies can provide us with additional information about the microstructure and to allow prediction of the density and the porosity of the bone tissue. Generally, frequency-dependent dynamic properties of the bone may be considered as a kind of "identification portrait", which is unique for every sample. The larger is the explored frequency range, the more accurate is the "portrait" that can be compiled. This should give a possibility to detect even very small variations of the internal bone texture.

To date, many studies of acoustic waves in porous media were based on a continuum theory developed by Biot. Biot's approach had a significant impact on the dynamics of porous media and allowed to receive important results in many practical applications (for a comprehensive review of the subject we refer to de Boer [1]). Despite this, it cannot be considered as a rigorous fundamental theory. Biot's models include a number of phenomenological parameters, which for real materials remain unknown and are expected to be determined in a purely experimental way.

Another limitation is that Biot's theory does not take into account the internal length scale of a heterogeneous medium. Thus, it can be applicable only if the wavelength is considerably larger than the typical size of the microstructure. However, for frequencies of about 1MHz (which are commonly used in experiments) the length of acoustic waves approaches the diameter of pores in the bone tissue [2]. Therefore, the scattering of the wave field by the microstructure may become significant.

We propose a new theoretical approach to model the propagation of elastic waves in fluid-saturated porous bones. Our approach is based on the homogenisation method [3] (for a long-wave limit) and on the Floquet-Bloch theory [4] (for a short-wave case). As an illustrative example, propagation of anti-plane shear waves through a cylindrically structured cancellous bone is studied. The skeleton component is considered to be purely elastic and the pores are filled by a viscous marrow. The obtained solutions predict both the effect of damping (caused by the viscosity of the marrow) and the effect of dispersion (caused by the wave scattering at the microstructure). The numerical results for the dispersion curves, wave speeds, and attenuation coefficients are evaluated.

A significant peculiarity of Biot's theory is that it describes the appearance of two types of longitudinal waves (so called fast and slow waves). The fast wave corresponds to an in-phase movement of the solid and the fluid component, while the slow wave corresponds to an out-of-phase movement of the components. The slow wave can never be observed in homogeneous media and its appearance in real materials was questioned many times. To our knowledge, Hosokawi and Otani [5] were the first who provided a solid experimental confirmation of the existence of the slow wave. In the present paper, we propose a theoretical justification of the slow wave using the Floquet-Bloch approach and considering different types of the local solutions (periodic and anti-periodic) within the unit cell.

The developed approach can be extended to analyse different types of elastic waves in various porous media.

ACKNOWLEDGEMENT

This work has received funding from the European Union's Horizon 2020 research and innovation programme under Marie Sklodowska-Curie grant agreement no. 655177.

References

[1] de Boer R.: Theory of Porous Media. Highlights in Historical Development and Current State. Springer, Berlin, Heidelberg, 2005.

[2] Steeb H.: Ultrasound propagation in cancellous bone. Arch. Appl. Mech. 80:489-502, 2010.

[3] Danishevskyy V.V., Kaplunov J.D., Rogerson G.A.: Anti-plane shear waves in a fibre-reinforced composite with a non-linear imperfect interface. Int. J. Non-Linear Mech. 76:223-232, 2015.

[4] Andrianov I.V., Bolshakov V.I., Danishevskyy V.V., Weichert D.: Higher-order asymptotic homogenization and wave propagation in periodic composite materials. Proc. R. Soc. A 464:1181-1201, 2008.

[5] Hosokawa A., Otani T.: Ultrasonic wave propagation in bovine cancellous bone. J. Acoust. Soc. Am. 101:1-5, 1997.

[a)] Corresponding author. Email: v.danishevskyy@keele.ac.uk

A NEW TIME FRACTIONAL WAVE PROPAGATION IN A SOLID CYLINDER

Odunayo O. Fadodun[1], Olawanle P. Layeni & Adegbola P. Akinola
Department of Mathematics, Obafemi Awolowo University, Ile-Ife, Nigeria

Summary This study considers radial vibration of transversely-isotropic solid cylinders with a view to model the mechanical diffusive waves propagating in the bodies. The effect of finite deformation is investigated. The problem is described by state equation of motion taking into account the Khalil et al. fractional order derivatives. The obtained time fractional wave equation and its solution generalize some results in literature. It is shown that waves in finite deformation exhibit some additional term even in the absence of time fractional operator. Furthermore, the obtained results degenerate to the classical waves in solid cylinders. Finally, this study reinforces the view that factional derivative helps to apprehend processes in-between diffusion and wave propagation.

INTRODUCTION

It is known that waves attenuate in material which exhibits power-law frequency variation; and any time some hereditary mechanisms of power-law type are present in wave phenomena, the appearance of fractional derivatives in time is inevitable. Consequently, a time fractional wave equation governs the propagation of mechanical diffusive waves in bodies which exhibit power-law frequency-dependent attenuation. In fact, there are many works in literature in which the integer order differential equations, modelling classical processes such as relaxation, oscillation, diffusion, and wave propagation have been generalized to fractional-order differential equation. In the context of small deformation, Mainardi modelled a time fractional diffusion-wave equation by replacing the second-order time derivative with a fractional derivative of order β, $0<\beta\le 2$. In his work, he used Reimann-Liouvile fractional derivatives. The obtained solution reduces to classical wave and diffusion equations when $\beta=1,2$ respectively [1]. The obligation to adopt finite deformation approach in problems of solid mechanics is imposed by the fact that small deformation theory is a gross approximation of the process modelled [2]. In this paper, we consider radial vibration of a solid cylinder undergoing finite deformation. A conformable fractional derivative introduced by Khalil et al. is employed with a view to model the time fractional waves propagation in solid cylinder. The cylinder is transversely-isotropic in structured, designed with the aid of homogenized theory. It is made of a semi-linear material of John's type.

GEOMETRY OF DEFORMATION AND CONSTITUTIVE LAW

We consider the radial deformation of a transversely-isotropic cylinder $\Omega\in\Re^3$ of radius a from the reference configuration Ω_0 into the current configuration Ω. The position vectors of points of the cylinder in $(\Omega_0(\vec{r}))$ and $(\Omega(\vec{R}))$ are given respectively as:

$$\vec{r}=r\vec{e}_r+z\vec{k}\,,\qquad \vec{R}=R(r,t)e_R+z\vec{k}\,, \tag{1}$$

where $\vec{e}_r,\vec{e}_\theta,\vec{k}$ are the orthogonal covariant basis vector associated with the cylindrical coordinates (r,θ,z) in $\Omega_0(\vec{r})$ and $\vec{e}_R,\vec{e}_\phi,\vec{k}$ are the corresponding local basis vectors associated with the cylindrical coordinates (R,ϕ,z) in $\Omega(\vec{R})$. The geometry of deformation $\nabla\vec{R}$ is the gradient tensor of the position vector $\vec{R}$ in $\Omega(\vec{R})$ taking in $\Omega_0(\vec{r})$:

$$\nabla\vec{R}=\frac{\partial R(r,t)}{\partial r}\vec{e}_r\vec{e}_R+\frac{R(r,t)}{r}\vec{e}_\theta\vec{e}_\phi+\vec{k}\vec{k}\,. \tag{2}$$

Now, decomposing the geometry of deformation $\nabla\vec{R}$ into product of stretch symmetric tensor $\widetilde{U}$ and orthogonal rotation tensor $\widetilde{O}^D$, the energy function in the case of isotropic and transversely-isotropic for a semi-linear material of John's type is

$$W=\mu I_1(\widetilde{U}-\widetilde{E})^2+\frac{1}{2}\lambda I_1(\widetilde{U}-\widetilde{E});\ W=\lambda_2 I_1(\widetilde{U}-\widetilde{E})^2+\frac{1}{2}\lambda_1 I_1(\widetilde{U}-\widetilde{E})+\lambda_0\vec{c}\cdot\widetilde{U}^2\cdot\vec{c} \tag{3}$$

where $I_1(\widetilde{U}-\widetilde{E})=\widetilde{E}\cdot\cdot(\widetilde{U}-\widetilde{E})$ is the first invariant of the tensor $(\widetilde{U}-\widetilde{E})$, $\widetilde{E}$ is the unit tensor, and $\vec{c}$ is the unit vector characterizing the direction of anisotropy. λ,μ are the Lame constants, and $\lambda_2,\lambda_1,\lambda_0$ are the effective material characteristics that result from applying homogenization theory to composite/heterogeneous media that in turn has reduced to a transversely-isotropic one. Invoking the hypothesis of hyperelasticity of Cauchy-Truesdell [3], we take the

Corresponding author. Email: ofadodun@oauife.edu.ng

Frechect derivative of the energy function (3) with respect to the geometry of deformation $\nabla\vec{R}$ and obtain the constitutive law, Piola-Kirchhoff stress tensor $\widetilde{T}$ to which it is energy conjugate:

$$\widetilde{T} = \widetilde{T}(\vec{R}) = \frac{\partial W}{\partial \nabla \vec{R}} = 2\lambda_2 \nabla\vec{R} + (\lambda_1 I_1(\widetilde{U} - \widetilde{E}) - 2\lambda_2)\widetilde{O}^D + \lambda_0 \vec{c}\vec{c} \cdot \nabla\vec{R}. \tag{4}$$

TIME FRACTIONAL WAVE EQUATION AND ITS SOLUTION

In order to model the time fractional wave propagation in solid cylinders, we reflect the constitutive law (4) and the geometry of deformation (2) in the generalized motion equation

$$\nabla \cdot \widetilde{T} + \vec{f} = \rho \frac{\partial^\alpha}{\partial t^\alpha} \vec{R}(r,t), \qquad 1 < \alpha \le 2, \tag{5}$$

subject to the boundary condition $\vec{R}(r,t) = \vec{0}$ at $r = a$, and the initial conditions $\vec{R}(r,0) = \frac{\partial}{\partial t}\vec{R}(r,0) = \vec{0}$

The resulting time fractional wave equation is

$$c_1^2 \frac{\partial}{\partial r}\left(\frac{1}{r}\frac{\partial}{\partial r}(rR(r,t))\right) + \kappa \frac{R(r,t)}{r^2} = t^{2-\alpha} \frac{\partial^2 R(r,t)}{\partial t^2}, \tag{6}$$

$$R(a,t) = 0, \quad R(r,0) = 0, \quad \frac{\partial}{\partial t} R(r,0) = 0. \tag{7}$$

where c_1 is the speed of the wave, $c_1^2 = \frac{2\lambda_2 + \lambda_1 + 2\lambda_0}{\rho}$, $\kappa = \frac{2\lambda_0 - \lambda_1}{\rho}$, and $\alpha \in (1,2]$ is the order of the derivative. It is observed that for $1 < \alpha < 2$, equation (6) describes the mechanical diffusive waves. Further, the extra term $\kappa \frac{R(r,t)}{r^2}$ on the L.H.S of (6) constitutes finite deformation effect; and when $\alpha = 2$, $\lambda_0 = \frac{1}{2}\lambda_1$ the time fractional wave equation (6) degenerates to the classical wave equation in solid cylinders.

$$c_1^2 \frac{\partial}{\partial r}\left(\frac{1}{r}\frac{\partial}{\partial r}(rR(r,t))\right) = \frac{\partial^2 R(r,t)}{\partial t^2}. \tag{8}$$

The solution of wave equation (6) together with the conditions (7) is

$$R(r,t) = J_m\left(\frac{\chi_n}{a} r\right)\left\{\sqrt{t} J_{\frac{1}{\alpha}}\left(\frac{2c_1\chi_n t^{\frac{1}{2}\alpha}}{a\alpha}\right) + \sqrt{t} Y_{\frac{1}{\alpha}}\left(\frac{2c_1\chi_n t^{\frac{1}{2}\alpha}}{a\alpha}\right)\right\}, \qquad 1 < \alpha \le 2 \tag{9}$$

where $m = \sqrt{\frac{2(\lambda_2 + \lambda_1)}{2\lambda_2 + \lambda_1 + 2\lambda_0}}$, a is the radius of the cylinder, and χ_n is the nth positive zero of $J_m(r)$.

CONCLUSIONS

We derived a time fractional wave equation which governs the propagation of mechanical diffusive waves in bodies exhibiting power-law frequency variation. The obtained equation and its solution generalized some results in literature. When $\alpha = 2$ and the effective material characteristics $\lambda_0 = \frac{1}{2}\lambda_1$, the obtained result degenerates to the classical waves in solid cylinders.

References

[1] Mainardi F.: The Time Fractional Diffusion-Wave Equation. *Radiophysics and Quantum Electronics*, **38**:13-24, 1995.

[2] Aknola A.P.: An Energy Function for Transversely-Isotropic Elastic Material and Ponyting Effec,. Korean J. Comput. 6, 639-649, 1999 .

[3] Truesdell C.: The Element of Continum Mechanics, Springer, Berlin, 1966.

D NAMIC CRUSHING PROPERTIES OF FUNCTIONALL GRADED HONE COMBS WITH DEFECTS

Tao Fan[1a)]

[1]*Department of Engineering Mechanics, College of Aerospace and Civil Engineering, Harbin Engineering University, Harbin ,150001, China*

Summary Due to the superior properties on energy absorption, noise reduction, heat insulation, flame retardant and electromagnetic shielding, honeycomb materials and structures are extensively applied to architecture, aerospace, biological engineering, packaging engineering, electrical technique. In this paper, the in-plane impact characteristics of functionally graded honeycombs are studied with the consideration of defects. The influences of the defect location on the dynamic crushing characteristics of the honeycombs are discussed. Based on a given relative density, the dynamic deformation modes and energy absorption of the honeycombs with different density gradients are investigated. The results show that the energy absorption abilities for the honeycombs with the negative density gradient are much stronger than those with the positive ones. This paper is helpful for the design and analysis of the mechanical characteristics of the honeycomb materials and structures.

INTRODUCTION

In recent years, with the characteristics of light weight, good shock absorption capability and ease of fabrication, the honeycomb structures have shown various potential applications such as aerospace, architecture, electrical techniques and biological engineering [1, 2]. Therefore, both the theoretical and exponential works are carried out. Moreover, due to the processing technique, it is rather difficult to avoid the defects in manufactured honeycombs. During the past several years, the effects of defects on the mechanical property in honeycomb structures have been received a lot of attention.

In the other hand, functionally graded materials (FGM) have brought a new revolution in aerospace, nuclear, biological engineering and many other fields. Recently, the concept of the FGM design has been applied to honeycomb structures. However, as a new scientific topic, researches on honeycomb structures with functionally graded properties are rather limited. In the present paper, with the functionally graded properties, the in-plane dynamic crushing of the triangular honeycombs with defects is investigated.

ANAL SIS MODEL

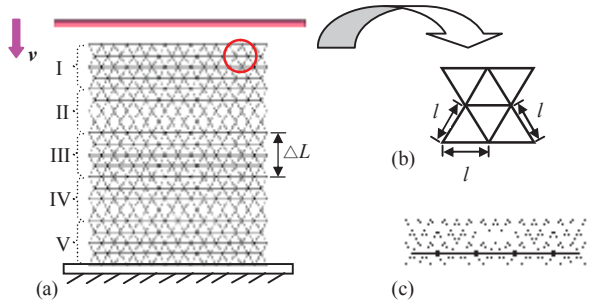

Fig.1. Analytical model: (a) the honeycomb structure with the impact plate, (b) the unit cell and (c) the location of defects consisting of missing consecutive cell walls in every region (I to V).

As shown in Fig.1(a), the two-dimensional honeycomb structure is composed of equilateral triangular cells. The bottom of the honeycomb model is fixed and the top side is impacted by a rigid plate with the velocity of 80m/s. The material constants used in the calculation are the Young's modulus E = 69 GPa, yielding stress σ_s=76MPa, the mass density ρ =2700 kg/m^3 and the Poisson ratio ν = 0.3. The relative density of honeycombs is given as

$$\frac{\rho^*}{\rho_s} = C_1 \frac{t}{l}(1 - D_1 \frac{t}{l}) \quad , \tag{1}$$

where ρ^* and ρ_s are the densities of honeycomb structures and the materials.

The side length of the unit cell is l=4.5mm. The thickness of cell walls t = 0.5mm for homogeneous honeycombs but is a variable for functional graded honeycomb models on the basis of the same relative density. The density gradient γ is

$$\gamma = \frac{\rho_i - \rho_{i+1}}{\Delta L} \quad , \tag{2}$$

where ρ_i is the relative density of ith region shown in Fig. 1(a), ΔL is the height of every region. It should be noted that the positive density gradient γ means the thicknesses of the cell walls decrease along the impact direction and the negative density gradient γ denotes the thicknesses of the cell walls increase along that direction.

a) Corresponding author. Email: fantao@hrbeu.edu.cn

NUMERICAL RESULTS AND DISCUSSIONS

Def r n es f f nc n r e ne c s efec s

Defects are introduced by missing some consecutive cell walls. In Fig.1(a), the honeycomb structures are divided into 5 equal regions along the impact direction. The thicknesses of cell walls in the same region are constant but follow the relation shown in Eq.(2) in different regions, which denotes the functional graded characteristics of the honeycomb systems. In order to study the influence of defects on the deformation modes and energy absorption ability of honeycomb structures, the defects are located in different graded parts, which are shown in Fig.1(c).

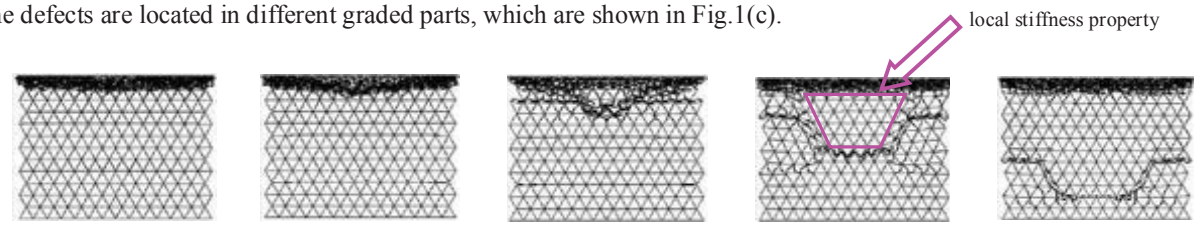

Fig.2. Deformation modes for different defective locations in the honeycomb structures with $\gamma = -0.01$ corresponding to the defects in region I to V at 40 % crushing.

In Figs.2(a)-(e) show that all of the first deformation bands for five cases occur from the impact sides. Then the second deformation bands with isosceles-trapezoid-shape appear and develop illustrated in Fig.2(c). For defects in region IV and V, the most important feature is that the second deformation bands with the upper half X-shape can be observed and the lower side of the deformation bands are along the defects. Moreover, as shown in Fig.2(d), the cells in the upper half X-shape behave nearly non-deformation. However the cells out of the area deform. This phenomenon is called local stiffness property. Compared with the perfect honeycombs, the defect position plays an important role on the deformation modes.

Ener s r n f f nc n r e ne c s efec s

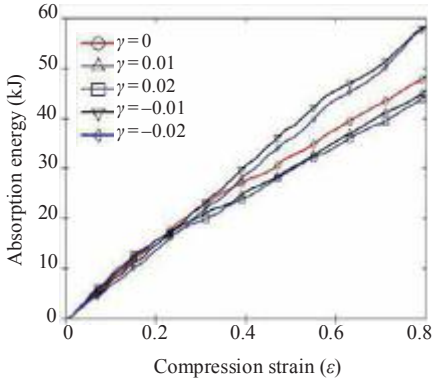

Fig.3. Energy absorption ability of honeycombs with different density gradients for defects in region III.

Fig.3 displays that the density gradient affects the energy absorption obviously. The energy absorption is almost the same when the compression strain is smaller than 23.5% (i.e. $\varepsilon < 0.235$). However, with the compression strain increasing, the energy absorption becomes distinct for different density gradients. For higher compression strains (i.e. $\varepsilon > 0.235$) of honeycomb structures, the energy absorption abilities for $\gamma < 0$ are much stronger than those for $\gamma > 0$. It can be observed that the ability of energy absorption for the homogeneous structure always rank in the middle in the whole crushing process.

CONCLUSIONS

In this work, the in-plane impact properties of functional graded honeycombs with defects are studied. Both effects of the defect location and density gradient on the dynamic crushing characteristics are discussed. This paper could be useful for the optimum design of the inhomogeneous honeycomb structures.

References

[1] Gibson, L.J., Ashby, M.F., 1997. Cellular Solids: Structure and Properties, 2nd ed. Cambridge University Press, Cambridge.

[2] Fleck, N.A., Deshpande, V.S., Ashby, M.F., 2010. Micro-architectured materials: past, present and future. Proceedings of the Royal Society A 466, 2495–2516.

SHOCK WAVES SCALING IN Al/W LAMINATES EXCITED BY IMPACT

Pedro Franco Navarro[1], David J. Benson[2] & Vitali F. Nesterenko [1,3a)]
[1]*Depart. of Mechanical and Aerospace Engineering, University of California, San Diego, La Jolla, California, USA*
[2] *Department of Structural Engineering, University of California, San Diego, La Jolla, California, USA*
[3] *Materials Science and Engineering Program, University of California, San Diego, La Jolla, California, USA*

Summary Quasistationary shock waves generated by plate impact in Al/W laminate with different mesostructure were investigated using numerical simulations. Different time/space scales have been identified in the relations to the establishment of a quasistationary shock wave and its structure: distances travelled from impacted end to reach a quasistationary profile, and scales of leading front width, and width of the stationary shock wave. It is shown that the mentioned spatial/time scales are related to the mesostructured, nonlinear and dissipative parameters of components. The approach based on Korteweg-de-Vries equation allows approximation of the amplitude and the width of the leading front.

INTRODUCTION

In homogeneous materials, the width of the shock is determined by the dissipation and nonlinear behaviour of the material [1-3]. The fourth power law, which relates maximum strain rate and stress behind the shock in the form $\dot{\epsilon} = \alpha\sigma^4$, was proposed in [1]. Based on experiments for laminate materials a different equation was proposed ($\dot{\epsilon} = \alpha\sigma^2$) [4].

In materials with various mesostructures incoming disturbances with different durations and amplitudes can generate waves of different nature. Short incoming pulses in Al/W laminates result in attenuating solitary like waves or their trains [5,6]. Here, we focus on the response of Al/W laminate to long incoming impulse created by impact of Al plate with the thickness much larger than the cell size of the laminate. This impact results in an oscillatory shock profile.

Traditional approach for homogenous materials assumes a steady state behind the stationary shock [7-8]. We demonstrate that at sufficiently wide impactor, a quasiequilibrium state behind the shock can be achieved only after relatively long propagation distance, and a Hugoniot approach can predict the state of the loaded material behind the shock.

Main space/time scales were identified in the numerical calculations: propagation distance when shock excited by external disturbance becomes stationary (it has achieved steady amplitude, oscillating profile and final state); shock front width determined by the time difference corresponding to 0.1 of maximum stress amplitude and time when plastic deformation is replaced by slowly decaying elastic reverberations (quasiequilibrium state); and leading front width determined by time difference between points with 0.1 and 0.9 of maximum stress amplitude. The latter time difference determines the maximum strain rate in the stationary shock.

NUMERICAL SIMULATIONS AND RESULTS

One dimensional numerical simulations were conducted using LS-DYNA, geometry and material data can be found in [5]. The simulations correctly reproduce the dissipative properties of each material which play an important role in shock formation. Wave structures in laminates with 0.5+0.5 mm, 1+1 mm and 2+2 mm Al/W layers generated by the impact of Al plates with thickness 80 and 800 mm and velocity 2800 m/s were investigated.

Fig. 1 illustrates the example of the establishment of the stationary leading front (Fig. 1(a)), shock front (Fig. 1(b)), and quasiequilibrium state behind shock with slowly attenuating elastic oscillations and saturated plastic strain (Fig. 1(c)) in 2+2 Al/W laminate impacted by 800 mm Al plate. The final state can be described by Hugoniot approach yielding a final stress of 43.2 GPa, compared to the average stress of 43.42 GPa in our numerical calculations. A steady shock wave was also established under the same impact conditions in the laminate with a refined cell sizes (0.5+0.5 and 1+1 mm).

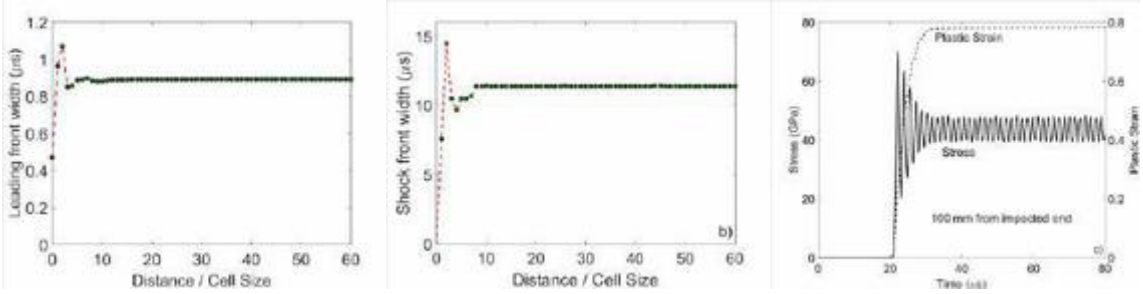

FIGURE 1. Characteristic time scales related to the stationary shock profile in 2+2 laminate impacted by 800 mm Al plate.

A quasiequilibrium state behind shock wave in the 2+2 laminate is not reached in the wave generated by impact of 80 mm Al plate, though the leading front was already established (Fig. 2(a)). This state was reached behind shock wave in the refined laminates (0.5+0.5 and 1+1 mm Al/W laminates) under the same conditions of impact.

[a)] Corresponding author. Email: vnesterenko@eng.ucsd.edu

The characteristic space scales for the investigated 2+2 laminate are the following: distance to establish a stationary leading front width is 8 cells, distance to establish stationary shock wave is 25 cells as shown in Fig. 2(b).

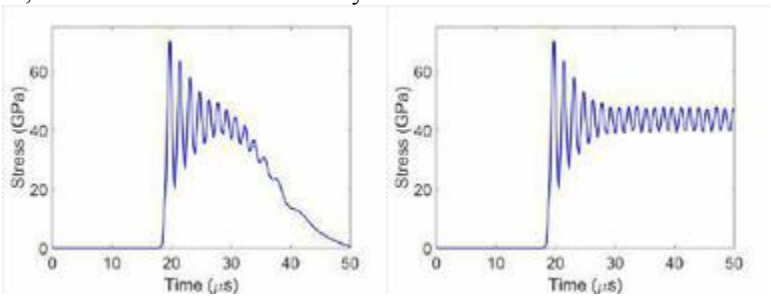

FIGURE 2. Nonstationary shock wave structure generated by impact of 80 mm Al plate (a) and stationary shock wave excited by impact 800 mm Al plate (b) in 2+2 Al/W laminate. Both waves are shown after propagation of the distance 100 mm (25 cells) from the impacted end.

It is clear that practically identical leading parts of the shock wave were formed at the distance 100 mm (25 cells) independently of establishments of the steady state behind shock wave.

Approximation of the leading front of the stationary shock wave

It was demonstrated in [5,6] that the KdV solitary wave provides a satisfactory description of the localized waves in the Al/W laminate. The KdV equation with added dissipative term has a stationary shock like solution which is monotonous (strongly dissipative case) or oscillatory with the leading front closely approximated by the shape of solitary wave (weakly dissipative case) [9,10]. We found that shock like waves in Al/W laminates are weakly dissipative in the investigated case of impact. Thus it is natural to explore if the leading part of the oscillatory shock wave in the Al/W laminate can be described by the shape of solitary wave with appropriate materials properties. We found that it was indeed the case. Thus the following equation can be used for the width of the leading front of the shock wave with the maximum strain ξ_m,

$$\Delta = \frac{1.55 d K_{eq}^{\frac{1}{2}}}{(2\alpha_{eq}\xi_m)^{\frac{1}{2}}} \qquad (1)$$

d is the cell thickness, and the constants K_{eq}, α_{eq} represent the linear and nonlinear behaviour of the laminate components can be found in [5]. This equation can be used to calculate the maximum strain rate in the shock. We would like to emphasize that though dissipation is necessary to establish a stationary shock wave structure with the steady state behind, the leading front is mostly determined by the balance of dispersive and nonlinear properties of the laminate.

CONCLUSIONS

Main time and space scales related to stationary shock wave formation in Al/W laminates have been identified. The KdV solitary solution can be used to approximate the shape and leading front width of the shock wave relating these parameters to the sound speeds of components and their nonlinear properties and geometry. The sound speeds, nonlinear properties of components and their thicknesses determine the maximum strain rate in the investigated shock waves in Al/W laminates. It is natural to expect that similar scaling will be observed for other weakly dissipative laminates at high amplitude of shock.

References

[1] Swegle, J. W., and Grady, D. E., *Journal of applied physics* 58.2 (1985): 692-701.
[2] Grady, D. E., *Journal of Applied Physics*, 107(1):013506-013506, 2010.
[3] Grady, D. E., *Journal of Applied Physics* 117.16 (2015): 165905.
[4] Zhuang, S., Ravichandran G., and Grady, D. E.. *Journal of the Mechanics and Physics of Solids*, 51(2):245-265, 2003.
[5] Franco Navarro, P., D. J. Benson, and V. F. Nesterenko. *Physical Review E* 92.6 (2015): 062917.
[6] Franco Navarro, P., D. J. Benson, and V. F. Nesterenko. *Bulletin of the American Physical Society* 60 (2015).
[7] Kinslow, Ray, ed. High-velocity impact phenomena. Elsevier, 2012.
[8] McQueen, R. G., S. P. Marsh, and J. N. Fritz., *Journal of Geophysical Research* 72.20 (1967): 4999-5036.
[9] Sagdeev, R. Z. *Soviet Physics-Technical Physics* 6.10 (1962): 867.
[10] Karpman, V. I. *Non-Linear Waves in Dispersive Media: International Series of Monographs in Natural Philosophy*. Vol. 71. Elsevier, 2013.

BEM FOR 3-D WAVE SCATTERING IN GENERAL ANISOTROPIC FLUID-SATURATED POROUS MEDIA

Akira Furukawa * [1], Takahiro Saitoh [2], and Sohichi Hirose[1]
[1]*Department of Mechanical and Environmental Informatics, Tokyo Institute of Technology, Japan*
[2]*Division of Civil and Environmental Engineering Science, Gunma University, Japan*

Summary This paper presents a boundary element method for 3-D wave scattering in general anisotropic fluid-saturated porous media. Biot's model is used for describing dynamic effects in the porous media. The presented method is a frequency-domain one and wave scattering by a cavity is solved. Scattered wave fields of displacement and fluid pressure are obtained and waves generated by the mode conversion are confirmed near the cavity.

INTRODUCTION

Rocks under the ground include pores and aligned cracks which are saturated with fluid (e.g. groundwater and oil). These materials can be considered and modeled as a fluid-saturated porous medium in numerical simulations. Wave analysis for the porous media has been aggressively studied in the fields of seismology and geophysical exploration. These studies provide importance of consideration of three wave properties in the porous media, i.e., anisotropy, dispersion, and dissipation. This study develops a boundary element method for wave analysis in general anisotropic fluid-saturated porous media. A mechanical model presented by Biot[1] is used for describing dynamic effects of the porous media. The following sections present boundary element formulation, numerical example, and conclusions. Throughout this paper, the summation convention is valid for the repeated indices. In addition, the subscripts written by small and capital letters take the values from 1 to 3 and from 1 to 4, respectively.

BOUNDARY ELEMENT METHOD APPLIED TO BIOT'S MODEL

Biot's model

Biot's model is a mechanical model for describing dynamic behavior of general anisotropic fluid-saturated porous media. This model is defined as a two-phase model which consists of solid skeleton and pore fluid. With σ_{ij} and p denoting total stress components of the porous media and fluid pressure respectively, the constitutive equations are given as follows:

$$\sigma_{ij} = A_{ijkl}u_{k,l} + \alpha_{ij}Mw_{k,k},\ p = -\alpha_{kl}Mu_{k,l} - Mw_{k,k} \tag{1}$$

where u_i and w_i are displacement of solid skeleton and flow of the fluid relative to the solid in the unit section, respectively. M and α_{ij} represent Biot's elastic modulus and effective-stress coefficients for general anisotropy, respectively. Moreover, $(\ )_{,i} = \partial/\partial x_i$ and $A_{ijkl} = C_{ijkl} + \alpha_{ij}\alpha_{kl}M$ where C_{ijkl} is the elastic tensor of solid skeleton. Dynamic behavior of the Biot's model is expressed by the following equations of motion:

$$\sigma_{ij,j} + \rho b_i = \rho\ddot{u}_i + \rho_f\ddot{w}_i,\ p_{,i} + \rho_f c_i = -\rho_f\ddot{u}_i - m_{ij}\ddot{w}_j - \eta r_{ij}\dot{w}_j \tag{2}$$

where ρ_f and ρ denote densities of pore fluid and the porous media, respectively. The density ρ is given as $\rho = (1-\beta)\rho_s + \beta\rho_f$ where β and ρ_s are porosity and density of solid skeleton, respectively. b_i and c_i are body force components of the porous media and pore fluid, and $\dot{(\ )} = \partial/\partial t$. m_{ij} denotes mass matrix determined by geometry of pores. η is fluid viscosity, and r_{ij} represents the flow resistivity matrix.

Properties of waves in general anisotropic fluid-saturated porous media are as follows: (1) Four body waves are generated in porous media, i.e., a quasi-fast compressional wave (qP1), a quasi-slow compressional wave (qP2), and two quasi-shear waves (qS1 and qS2). (2) Phase velocity and attenuation of the waves depend on not only propagation direction but also frequency.

Boundary integral equations in frequency-domain

This section presents a frequency-domain boundary element method applied to Biot's model. Boundary integral equations for wave scattering as shown in Fig.1 are expressed as follows:

$$C(\mathbf{x})\tilde{q}_I(\mathbf{x},\omega) = \tilde{q}_I^{\mathrm{in}}(\mathbf{x},\omega) + \int_S \tilde{U}_{IK}(\mathbf{x},\mathbf{y},\omega)\tilde{s}_K(\mathbf{y},\omega)dS(\mathbf{y}) - \int_S \tilde{W}_{IK}(\mathbf{x},\mathbf{y},\omega)\tilde{q}_K(\mathbf{y},\omega)dS(\mathbf{y}),\ \mathbf{x}\in V_1 \tag{3}$$

*Corresponding author. Email: furukawa.a.aa@m.titech.ac.jp

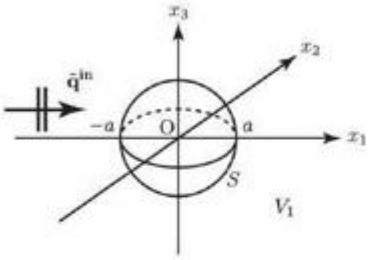

Figure 1: Wave scattering by a spherical cavity in 3-D porous domain.

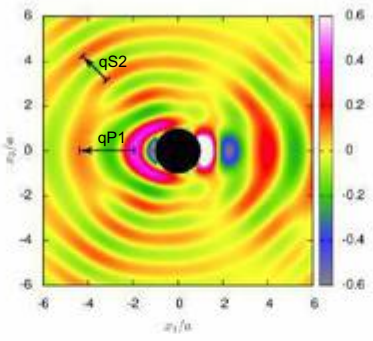

Figure 2: Scattered waves near the cavity. (Real part of displacement component $u_1/|\mathbf{u}^{\mathrm{in}}|$)

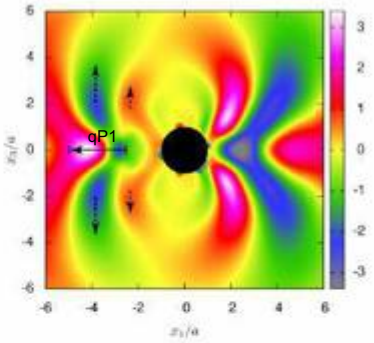

Figure 3: Scattered waves near the cavity. (Real part of fluid pressure $a\tilde{}\ (\mu^*|\mathbf{u}^{\mathrm{in}}|)$)

where $\mathbf{x}$ and $\mathbf{y}$ represent observation and source points, respectively, and ω denotes an angular frequency. $C(\mathbf{x})$ is a free term. $U_{IK}(\mathbf{x},\mathbf{y},\omega)$ and $W_{IK}(\mathbf{x},\mathbf{y},\omega)$ denote fundamental solutions and their double layer kernels which can be derived in a manner similar to the 2-D problem[2]. The boundary values q_I and s_I are given as $q_I = \{\{u_i\}^{\mathrm{T}},\ \tilde{}\}^{\mathrm{T}}$ and $q_I = \{\{t_i\}^{\mathrm{T}},\ \tilde{}_n\}^{\mathrm{T}}$, respectively. Note that $\tilde{}$) appeared in these functions shows the Fourier transform of the corresponding time-domain quantities. t_i and p_n denote the traction component and the fluid flow through the unit section on the boundary S. In addition, the notation $\{\ \}^{\mathrm{T}}$ denotes the transpose of vector.

Introducing spatial discretization with constant shape function provides the following discretized boundary integral equations:

$$\frac{1}{2}q_{M;I} = \tilde{q}^{\mathrm{in}}_{M;I} + \sum_{N=1}^{N_e}\left[A_{MN;IK}s_{N;K} - B_{MN;IK}q_{N;K}\right],\ M = 1,2,\cdots,N_e \tag{4}$$

where N_e is the number of boundary element. The influence functions $A_{MN;IK}$ and $B_{MN;IK}$ are expressed as follows:

$$A_{MN;IK} = \int_{S^N} U_{IK}(\mathbf{x}^M,\mathbf{y},\omega)dS(\mathbf{y}),\quad \tilde{}_{MN;IK} = \int_{S^N} W_{IK}(\mathbf{x}^M,\mathbf{y},\omega)dS(\mathbf{y}) \tag{5}$$

where $\mathbf{x}^M$ denotes the center point of the boundary element S^M. Prescribing appropriate boundary conditions for Eq.(4) and solving the resulting equations, the unknown boundary values are obtained.

NUMERICAL RESULTS

As a numerical example using our proposed method, wave scattering by a cavity as shown in Fig.1 is solved. Infinite sandstone domain V_1 whose pores are saturated with brine[3] is considered, and the boundary conditions on the surface of the spherical cavity are given as $s_I = 0$. The radius of the cavity is $a = 25$ m, and the cavity is discretized into 1,334 boundary elements. The incident wave $\mathbf{q}^{\mathrm{in}}$ is the plane qP1 wave propagating in the positive x_1-direction. The frequency of the incident wave is $f = 100$ Hz. Figure 2 and 3 show scattered wave fields in terms of the displacement component $\tilde{}_1/|\mathbf{u}^{\mathrm{in}}|$ and the fluid pressure $a\tilde{}\ (\mu^*|\mathbf{u}^{\mathrm{in}}|)$ where $\mu^* = C_{1212}$, respectively. From these results, the scattered qP1 wave propagates in the negative x_1-direction and the scattered qS2 wave is generated by the mode conversion.

CONCLUSIONS

This paper presents a boundary element method for wave scattering in anisotropic fluid-saturated porous media. The formulation is based on Biot's theory, and boundary integral equation is formulated in frequency-domain. Collocation method is used for spatial discretization. Wave scattering by a spherical cavity is solved using our proposed method, and the scattered qP1 and qS2 waves, which are generated by incident qP1 wave, are confirmed near the cavity.

References

[1] Biot M. A.: Mechanics of deformation and acoustic propagation in porous media, J. Appl. Phys., 33:1482-1498, 1962.
[2] Furukawa A., Saitoh T., Hirose S.: A boundary element method for wave scattering in fluid- saturated porous rocks, BEM/MRM, 38:185-195, 2015.
[3] Carcione J. M.: Wave propagation in anisotropic saturated porous media: Plane-wave theory and numerical simulation, J. Acoust. Soc. Am., 99:2655-2666, 1996.

MIXTURE AND DENSITY FUNCTIONAL THEORIES FOR SHOCK- INDUCED REACTIONS

S. Hanagud [1], V. Narayanan[1], and R. Zaharieva[2]
1. Georgia Institute of Technology, Atlanta, Georgia, U.S.A
2. Bulgarian Academy of Science Acad. Georgy Bonchev Str. B1.1 Sofia, Bulgaria

Summary: Past two decades have seen a significant amount of interest in understanding the mechanics of binary functional reactive materials, their constitutive relations, effect of impact of shock waves and their exothermic reactions. In this paper, the formulation of constitutive relations, propagation shock waves and shock induced chemical reactions are studied in the frameworks of non-equilibrium thermodynamics and mixture theory. Numerical results include shock induced reactions in binary material combinations of aluminum-nickel; and aluminum and iron oxide. The modeling included selection of internal variables and thermodynamic fluxes. Because the mixture theory was in the framework of continuum framework and there were only limited number of experimental results, determination of material reaction constants are discussed in the framework of quantum mechanics based density functional theory.

INTRODUCTION

Usually motivation for selection of aerospace structural materials is to realize required strength characteristics and favorable strength to weight ratios. The term strength implies resistance to loads experienced during the service life of the structure, including resistance to fatigue loads, corrosion and other extreme conditions. Thus, basically the structural materials are single function materials that resist loads experienced during the service life of the structure. However, it is desirable to select materials that are capable of offering more than one basic function of strength. Very often, the second function is the capability to provide functions of sensing and actuation. In this paper, the second function is different. The second function is the energetic characteristics. Thus, the choice of dual functions of the material are the structural characteristics and energetic characteristics. These materials are also known by other names such as the reactive material structures or dual functional structural energetic materials [1-3]. Specifically the selected reactive materials include mixtures of selected metals and metal oxides that are also known as thermite mixtures, reacting intermetallic combinations and oxidizing materials. There are several techniques that are available to synthesize these structural energetic materials or reactive material structures and new synthesis techniques for high density, high strength and large release of exothermic energy are open research areas .This paper is addressed is to the characterization of multi-functional structural-energetic materials or reactive structural materials and their shock induced or thermally induced reaction capabilities. Because the subject of studies of the characterization of these materials and nonlinear shock or thermally induced chemical reactions of the two solids that comprise these reactive materials, from first principles (or quantum molecular dynamics approaches), is a relatively new field of study it is necessary to identify parallel fields of the ab initio or ab initio-molecular dynamics studies and mixture theory based continuum mechanics. The specific approach in this paper is as follows.

PROBLEM FORMULATION

The governing system of PDE's is formulated in the framework of irreversible thermodynamics and a mixture theory in which the N components of the mixture are homogeneously distributed through the continuum. Transition state based chemical reaction models are introduced and incorporated, along with the mixture constitutive models, with the conservation equations to calculate and thus simulate the nonlinear shock induced chemical reactions. The energy that should be supplied to reach the transition state has been theoretically modeled by considering both the pore collapse mechanism and plastic flow behind the shock.

SOLUTION TECHNIQUE

The system of conservation equations, constitutive equations, and chemical reaction equations are integrated numerically under one dimensional strain conditions. , by using a numerical method that is known as the MUSCL scheme that can accommodate nonlinear system of equations with shock waves. This is the first application of the numerical scheme to study shock induced chemical reactions in binary energetic materials. The choice of the MUSCL scheme was to reduce computationally induced oscillations. Numerical results are for Fe-Al and Ni-Al

Corresponding author Email: hanagud@ae.gatech.edu

The results indicate that as the porosity and plastic flow increase, the temperature in the mixture also increases leading to the transition state. The relaxation times associated with the pore collapse and chemical reactions are modeled as functions of the state of the system.

NEED FOR AB INITIO METHODS & DENSITY FUNCTIONAL THEORY

The theoretical model, in the continuum state, requires parameters that should be determined experimentally. The experimental studies have many challenges in measurement techniques and nano instrumentation. Thus, the required constants are not available. An alternate approach to determine these parameters, through density functional theory based approaches are used in this paper. Also the ab initio method for calculating chemical reactions are based on the thermally induced reactions because shock propagation with density functional theory is not well understood
Some Results:

1. Shock induced chemical reaction with new products and exothermic reaction:

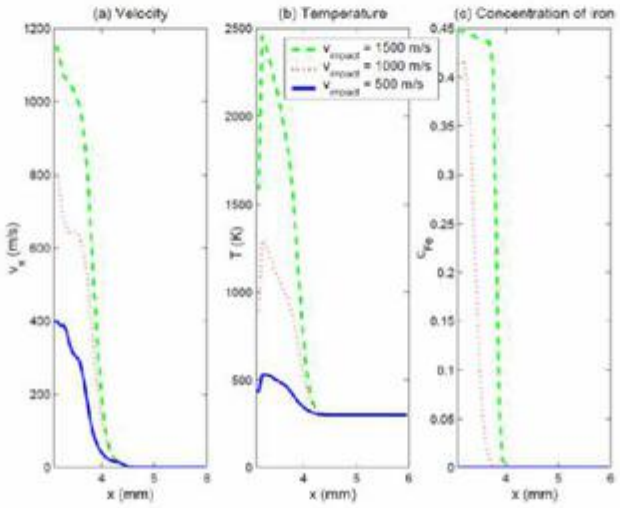

2. Ab Initio Calculation of Thermally Induced Chemical Reaction

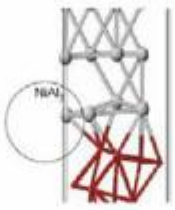

CONCLUSIONS

This is only the beginning of the exploration of the mixture theory and density functional theories to study mechanics of binary functional reactive materials. The studies can be significantly extended to enhance and enrich the mechanics community,

References:

1. S. Hanagud Final Report, AFOSR, 2008, 2.. D. Redding and S. Hanagud, J. Appl. Phys. 2009; 3 R. Zaharieva and S. Hanagud, IJSET, 3, No.9, 1167-69, 2014

NON-STATIONARY PROCESSES IN NIDAL ZONE AT SUDDEN APPEARANCE OF BREAK

Alexandr Kim[1a)]
[1]*JSC "National Center of Space Research and Technology", Almaty, Kazakhstan*

Summary An initial boundary problem of non-stationary processes in the tense environment at sudden appearance of a semi-infinite break with a viscous contact of banks that simulates the process of earthquake's occurrence was considered and analytically solved. It was revealed that behind the front of seismic waves in the perturbed zone there is an inversion of acceleration, and the arrangement of the inversion zones is connected with the break's orientation. It was found that the contact interaction of the break shores has a significant impact on intensity of acceleration in the environment and the size of seismic wave's impact. It was found that in the presence of viscous interaction between the shores of the break at the time of its occurrence, a partial discharge stress happens, as opposed to a complete reset of stress on the break, banks of which do not interact.

Introduction

Currently, theoretical and experimental results that significantly advanced the solution of the problem on creating a system of earthquake prediction have been achieved. The most significant of them are the phenomena in the ionosphere and geomagnetic field that accompany earthquakes and precede them and that were found by both terrestrial and satellite studies. Over the epicenters of strong earthquakes, the bursts of magnetic and electric field components of low-frequency noise emissions several hours before the main seismic impact were recorded by the satellite data. Changes in electrical and magnetic field components of low-frequency radiation, which are recorded on the satellite board at intersection of the projection of his route over the deep faults of the lithosphere, have been detected. These emissions are caused by features of non-stationary processes in the focal areas of the earth's crust.

Statement of the initial boundary problem

In the elastic isotropic pre-stressed space with uniformly distributed shear tension $\tau_{yz} = q$ at the moment of $t = 0$ time, there is an instantaneous break of the continuity of the environment along the half-plane $y = 0,\ x < 0$, when contact conditions change immediately on the break. Assume that on the break for $t > 0$ viscous contact conditions suddenly appear when the stress depends on the speed of mutual movement of break's shores. In the context of longitudinal shear the vector of the tension $\boldsymbol{p} = (p_x, p_y, p_z)$, which is valid for $t > 0$ in the axis z direction on the upper side of the cut $y = 0,\ x < 0$ with the normal $\boldsymbol{n} = (0, -1, 0)$, has a non-zero component, which we define as in linear relationship, when the tension inhibiting the movement effects on the upper edge

$$p_z = -\eta \frac{\partial a}{\partial t}, \quad a = w(x, +0, t) - w(x, -0, t) = [w(x, y, t)]_{y=0} \tag{1}$$

where η – coefficient of viscous friction of the contact; a – the value of the mutual displacements of the break; x, y – Lagrangian Cartesian coordinates; t – time. p_z component of the stress vector is connected with components of the stress tensor by the formula $p_z = n_x \cdot \tau_{xz} + n_y \cdot \tau_{yz} + n_z \cdot \tau_{zz}$, где $n_x = 0,\ n_y = -1,\ n_z = 0$. Therefore, for $t > 0$ at the break $y = 0,\ x < 0$, $\tau_{yz} = \eta \frac{\partial a}{\partial t}$ condition is performed that specifies the conditions of viscous contact shores. The nonzero component of the displacement vector satisfies the wave equation:

$$\rho \frac{\partial^2 w}{\partial t^2} = \frac{\partial \tau_{xz}}{\partial x} + \frac{\partial \tau_{yz}}{\partial y} \tag{2}$$

where ρ - density of the environment, $\mu -$ shear modulus.

The initial conditions in a tense environment at $t \le 0$ for $y > 0$ $y < 0$ have the form:

$$\tau_{xz} = \mu \frac{\partial w}{\partial x} = 0, \quad \tau_{yz} = \mu \frac{\partial w}{\partial y} = q, \quad w = \frac{qy}{\mu}, \qquad \frac{\partial w}{\partial t} = 0, \qquad y > 0 \qquad y < 0, \ t \le 0 \tag{3}$$

Conditions at infinity have the form:

$$\tau_{xz} \to 0, \quad \tau_{yz} \to q, \qquad r = \sqrt{x^2 + y^2} \to \infty, \quad -\infty < t < \infty \tag{4}$$

Terms on line $y = 0$.

At $y = 0, x < 0$ at the break of continuity of the tense environment there are given instantly changing contact conditions at $t = 0$:

a) Corresponding author. Email: **kim.as@mail.ru.**

$$\tau_{\hat{}\,z} \hat{}\ q, \qquad t < 0$$
$$\tau_{\hat{}\,z} \hat{}\ \eta \frac{\partial a}{\partial t}, \qquad t > 0 \quad , y \hat{}\ 0, x < 0 \tag{5}$$
$$a \hat{}\ 0, \qquad t \hat{}\ 0 \quad)$$

In continuation of the gap medium under consideration maintains the continuity of the state and condition of movement continuity

$$a \hat{}\ 0, \qquad y \hat{}\ 0, \ x \geq 0, \ \infty < t < \infty \tag{$\hat{}$}$$

It was assumed that at the axis origin, when $t \leq 0$, the movements are equal zero, and the energy of elastic deformation caused by τ_{xz} and $\tau_{\hat{}\,z}$ stress is finite in any limited volume.

Analytical solution of the initial boundary problem

The task can be regarded as marginal for the cases of instant break along the strip width L, when the time $t < L/b$, where b – is the speed of transverse waves. The oddness of the function $w(x, y, t)$ for y is sufficient to consider the half-space $y > 0$. With the help of superposition

$$w \hat{}\ w^0 + w^d; \ \ w^0 \hat{}\ \frac{qy}{\mu}; \ \ \eta \hat{}\ \frac{\mu\hat{\eta}}{b}; \ \ t \hat{}\ \frac{L\hat{t}}{b}; \ \ (x, y, w^d) \hat{}\ L(\hat{x}, \hat{y}, \hat{w}); \ \ q \hat{}\ \mu\hat{q}$$

the problem under consideration is given to the boundary, the solution of which in dimensionless form is received by the method of Wiener-Hopf (later the index "cover" for dimensionless quantities is omitted) as

$$\frac{\partial^2 w(r,\theta,t)}{\partial t^2} \hat{}\ \frac{1}{\pi}\frac{q}{1+2\eta}\frac{H(t-r)}{\sqrt{t^2-r^2}} Re\{tg\zeta_0 e^{-g(\zeta_{\hat{}})}\} + \frac{q}{1+2\eta}\delta(t-r \qquad \theta)\, H \hat{}\theta - \frac{\pi}{2}) \tag{7}$$

$$g(\zeta_0) \hat{}\ \frac{1}{\pi}\int_{\pi/2}^{\zeta_{\hat{}}} \frac{1}{\nu + cos\zeta}\left[\eta\zeta - \frac{1}{2}arccos(-\nu) \qquad \zeta\right] d\zeta - \frac{1}{\pi}\int_{\frac{\pi}{2}}^{\zeta_{\hat{}}} \frac{1}{\nu - cos\zeta}\left[\eta\zeta - \frac{1}{2}arccos\nu \qquad \zeta\right] d\zeta \tag{8}$$

$$\zeta_0 \hat{}\ \theta + i\xi_0, \ \ \xi_0 \hat{}\ \frac{t + \sqrt{t^2 - r^2}}{r}, \ \ i \hat{}\ \sqrt{-1}, \ \ \nu \hat{}\ \sqrt{1 - 4\eta^2}, \ \ d \hat{}\ \sqrt{4\eta^2 - 1}, \ \ \nu \hat{}\ -id, \ \ H(\xi) \hat{}\ \begin{cases} 1, & \xi > 0 \\ \frac{1}{2}, & \xi \hat{}\ 0 \\ 0, & \xi < 0 \end{cases}$$

$$\delta(\xi) - \qquad , \ h \hat{}\ (d + 2\eta); \ \ 0 < r < \infty, \ \ 0 < \theta < \pi, \ \ 0 < t < \infty, \ \ 0 < \eta < \infty.$$

When $\eta > 1/2$ it is more convenient to use the following equivalent form of writing the function $g(\zeta_0)$

$$g(\zeta_0) \hat{}\ \frac{1}{\pi}\int_{\pi/2}^{\zeta_{\hat{}}} \frac{1}{id + cos\zeta}\left[\eta\zeta - \frac{\pi}{4}\, sin\,\zeta - \frac{ih}{2} \qquad \zeta\right] d\zeta - \frac{1}{\pi}\int_{\frac{\pi}{2}}^{\zeta_{\hat{}}} \frac{1}{id - cos\zeta}\left[\eta\zeta - \frac{\pi}{4}\, sin\,\zeta + \frac{ih}{2} \qquad \zeta\right] d\zeta \tag{9}$$

Basic results got on the basis of analytical decision

Analytical formulas for speed, acceleration and moving of environment are obtained; the numerical analysis and computer visualization of the process of seismic waves' propagation is conducted; the intensity of the wave radiation, depending on the orientation of the break and viscid interaction of its banks, is studied; non-stationary processes on the break are explored. The task solution is generalized in case of transversely isotropic environment with the break in isotropy plane and in case of viscoelastic break with the damping element of Voigt - Kelvin.

CONCLUSIONS

New possibilities of computer modeling, numerical-analytical calculations and visualization that appeared at present time make the analytical formulas, which describe non-stationary processes and previously presented a difficulty for application and analysis of geodynamic processes in the earth's crust during periods of seismic activity, relevant nowadays.

AN ENRICHED FINITE ELEMENT METHOD FOR WAVE PROPAGATION ANALYSIS IN DISCONTINUOUS DOMAIN

Mohammad Komijani[1] and Robert Gracie *[2]

[1,2]*Department of Civil and Environmental Engineering, University of Waterloo, Waterloo, Ontario, Canada*

Summary In this paper a numerical method has been developed in the context of Generalized Finite Element (GFEM) method to analyse the wave propagation analysis in cracked media. The method combines the advantage of partition of unity finite element with phantom node method to investigate the problem of mechanical wave propagation in cracked domains. The Phantom Node Methodology has been implemented to specify the cracks (discontinuities) in the domain. Also, GFEM has been considered to eliminate the spurious oscillation that appear in regular FEM analysis of transient wave propagations due to numerical dispersion and Gibb's phenomenon.

INTRODUCTION

Finite element analysis has been considered as an effective tool in investigation of boundary value problems in mechanics. However, consideration of the piecewise polynomials to interpolate the unknown objective functions through the element has been found to be inappropriate in the problems in which there are sudden and abrupt variations in the objective functions. For instance, In the case of transient wave propagation using regular finite element may result in spurious oscillations that appear due to numerical dispersion resulting from the Gibb's phenomenon [1]. These non-physical oscillations may impair the results including the wave velocity as the wave travels far distance in the domain. To address this problem a noticeable amount of research has been conducted in the framework of the spectral method, the spectral element method, and spectral finite element method. The spectral method approaches are very likely to provide numerical solutions that are very close to the actual solutions since they use harmonic functions as basis functions that indeed appear in the analytical solutions of waves. Recently, some research works have been performed to include the concept of spectral method in the context of finite elements by using harmonic enriched basis functions. Ham and Bathe [1] developed a new finite element method using trigonometric enrichment functions to investigate the problem of wave propagation in general 3D case of continuous domain. In this paper it has been shown that the spurious oscillations can be significantly suppressed by using a combination of harmonic functions as enrichment basis functions.

In [2] a new representation of the local partition of unity finite element has been developed by Song et.al to model a discontinuity in a domain. In this work, cracks are treated by adding phantom nodes to the original real nodes that already exist in a mesh. In this essence the distribution of the unknown functions within a cracked element is represented by superposing two completely regular elements with real and phantom nodes.

To the best of the authors's knowledge no work has been reported on treating the numerical dispersion that can appear in the analysis of wave propagation. To overcome this gap in the literature, in this work, a new computational implementation has been developed on the basis of partition of unity FEM to assess the problem of wave propagation in cracked domains based on a combination between the GFEM models that have been developed based on including harmonic basis functions for wave propagation analysis and phantom node method to include the effect of discontinuity.

MATHEMATICAL FORMULATION

The weak form of the two-dimensional motion equation is considered as the governing relation of the problem.

The interpolation of the displacement field within the continuous elements are represented in the context of GFEM as [1]

$$\begin{aligned} u(x,y,t) = \sum_{\alpha} \psi_{\alpha} \Big(u_{(\alpha,0,0)} + \sum_{k_x=1}^{n} [cos(\frac{2\pi k_x x}{\Lambda_x}) u^{C}_{(\alpha,k_x,0)} + sin(\frac{2\pi k_x x}{\Lambda_x}) u^{S}_{(\alpha,k_x,0)}] + \\ \sum_{k_y=1}^{m} [cos(\frac{2\pi k_y y}{\Lambda_y}) u^{C}_{(\alpha,0,k_y)} + sin(\frac{2\pi k_y y}{\Lambda_y}) u^{S}_{(\alpha,0,k_y)}] + \\ \sum_{k_x=1}^{n} \sum_{k_y=1}^{m} [cos(\frac{2\pi k_x x}{\Lambda_x} + \frac{2\pi k_y y}{\Lambda_y}) u^{C+}_{(\alpha,k_x,k_y)} + sin(\frac{2\pi k_x x}{\Lambda_x} + \frac{2\pi k_y y}{\Lambda_y}) u^{S+}_{(\alpha,k_x,k_y)} + \\ cos(\frac{2\pi k_x x}{\Lambda_x} - \frac{2\pi k_y y}{\Lambda_y}) u^{C-}_{(\alpha,k_x,k_y)} + sin(\frac{2\pi k_x x}{\Lambda_x} - \frac{2\pi k_y y}{\Lambda_y}) u^{S-}_{(\alpha,k_x,k_y)}] \Big) \end{aligned} \tag{1}$$

*Corresponding author. Email: rgracie@uwaterloo.ca

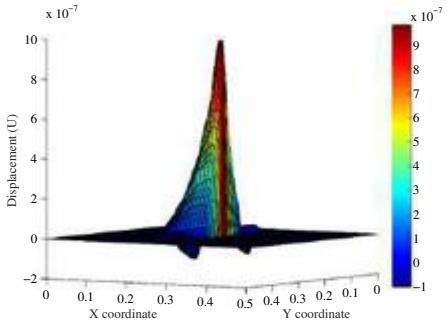

Fig. 1: Wave pattern obtained by regular FEM.

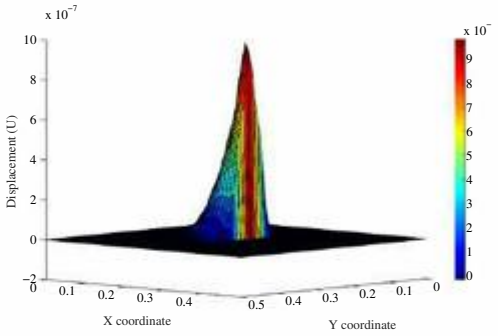

Fig. 2: Wave pattern obtained by GFEM.

where ψ_α represents the regular FE shape function and α is the local element node number, and n and m are the cutoff numbers for enrichment functions in x and y directions, respectively, and Λ_x and Λ_y are wavelengths.
As stated before, the Phantom Node Method is used to model a crack in the domain. In this approach, the discontinuous element is replaced by two continuous elements with real and phantom nodes [2]. The signed distance function $f(x, y)$ is used to define the surface of discontinuity such that $f(X) = 0$ specifies the discontinuous surface.

Taking advantage of both GFEM and Phantom Node Method, the displacement field for cracked element can be represented as:

$$u(x,y,t) = \sum_{I\in S_1}\sum_{J,K\in\gamma} u^1_{(I,J,K)}(t)N_{(I,J,K)}(x,y)H(-f(x,y)) + \sum_{I\in S_2}\sum_{J,K\in\gamma} u^2_{(I,J,K)}(t)N_{(I,J,K)}(x,y)H(f(x,y)) \qquad (2)$$

S_1 and S_2 are sets of original and phantom nodes for superposed elements one and two, respectively, and γ is the set of regular and enriched degrees of freedom as shown in Eq. (1), and $N_{(I,J,K)}$ represents the associated shape functions. H(x) is the Heaviside function.

RESULTS AND DISCUSSION

Figures 1 and 2 depict the wave propagation pattern in a 0.5 $\times$ 0.5 m domain containing a vertical crack of length 0.3 m based on regular FEM and GFEM, respectively. In this example a suddenly applied point force $P = 100KN$ in X direction is imposed at the centre of the plate. As seen, regular finite element analysis results in spurious oscillations that can affect the accuracy of the solution. However, in the case of GFEM the mentioned non-physical oscillations are suppressed by including the harmonic basis functions as enrichments. As expected, wave does not propagate across the crack faces.

CONCLUSIONS

Combining Generalized FEM and Phantom Node Method, a new computational implementation is developed in this work to treat the numerical dispersion in the problem of wave propagation in elastic cracked domains.

References

[1] Ham S., Bathe K.J.: A finite element enriched for wave propagation problems. Computers and Structures 94-95:1-12, 2012.

[2] Song J.H., Areias P.M.A., and Belytschko T.: A method for dynamic crack and shear band propagation with phantom nodes. International Journal for Numerical Methods in Engineering 67-95:868-893, 2006.

INTERACTION OF CAVITIES, INCLUSIONS AND A CRACK NEAR SEMI-CYLINDRICAL GAP

Hongliang Li[1a)], Yu Wang[1]
[1]*Department of Engineering Mechanics, College of Aerospace and Civil Engineering, Harbin Engineering University, Harbin ,150001, China*

Summary In natural medium, engineering composite materials, earthquake engineering, it can be found that there are some gaps at the edge of the matrix, and shallow-buried cavity or inclusion structure near the gaps. When the matrix is impacted by dynamic load, defects could be found around the cavities and inclusions. In this paper, Green's function method and crack division method are used to investigate the problem of dynamic stress concentration of multiple cavities, inclusions and a linear crack near semi-cylindrical gap for incident SH wave. The expressions of the displacement and stress are given, and an example is provided to show the effect of cavities, inclusions and crack on the dynamic stress concentration.

INTRODUCTION

In natural medium, engineering composite materials, earthquake engineering, it can be found that there are some gaps at the edge of the matrix, and shallow-buried cavity or inclusion structure near the gaps. When the matrix is impacted by dynamic load, scattering field will be produced because of the cavity or the inclusion, and it could cause dynamic stress concentration at the edge of the cavity or inclusion. When the structure is overloaded or the load is changed regularly, cracks emerge and spread near the cavities. Dynamic stress concentration could greatly decrease the bearing capacity of the matrix, and reduce the service life of the matrix.

In this paper, the method of Green's function is used to investigate the problem of dynamic stress concentration of multiple cylindrical cavities, inclusions and a linear crack near semi-cylindrical gap for incident SH wave[1]. Multi-polar coordinate system is used too.

MODEL AND GREEN'S FUNCTION

The model is shown as Fig.1, elastic semi-space containing a gap, multiple cylindrical cavities, inclusions and a linear crack. The governing equation of W can be written as

$$\frac{\partial^2 W}{\partial\ \partial^{-}}+\frac{1}{4}k^2W=0 \tag{1}$$

The Green's function used in this paper is regarded as the displacement response to the elastic semi-space containing a gap, multiple cylindrical cavities and inclusions impacted by anti-plane harmonic linear source force at any point. The boundary conditions can be expressed as below:

$$\tau_{rz}=0(where\ |z|=R_0)\ ,\ \tau_{\theta z}=0(where\ \theta=0\ and\ \theta=\pi)\ ,\ \tau_{\theta z}=\delta(\ -\ _G)\ (\ =\ _G)\ ,$$
$$\tau_{rz}=0(where\ \ |z-c_j|=R_j\ \ j=1,2,...,N)\ ,W=W^{\ sm}\ \ (|z-C_k|=\ '_k\ \ =1,2,...,M)\ ,\ \ \tau_{rz}=\tau_{rz}^{sm}\ \ (|z-C_k|=R'_k\ \ k=1,2,...,M) \tag{2}$$

The wave displacement due to the line source load $\delta(\ -\ _G)$ and the scattering wave can be written as:

$$G^{\ i}=\frac{i}{4\mu}[H_0^{(1)}\ k|z-z_G|)+H_0^{(1)}\ k|z-\bar{z}_G|)] \tag{3}$$

$$G^{\ is}=\sum_{j=1}^{N}\sum_{n=-\infty}^{\infty}A_n^j\ H_n^{(1)}\ k|z-c_j|)(\frac{-\ _j}{-\ _j})^n+H_n^{(1)}\ k|z-\bar{c}_j|)(\frac{z-\bar{c}_j}{-\ _j})^{-n}]+\sum_{k=1}^{M}\sum_{n=-\infty}^{\infty}B_n^k\ H_n^{(}\ k|z-C_k|)(\frac{z-C_k}{|z-C_k|})^n+H_n^{(1)}\ k|z-\bar{C}_k|)(\frac{z-\bar{C}_k}{|z-\bar{C}_k|})^{-n}] \tag{4}$$

where A_n^j, B_n^k are unknown coefficients. c_j represents the center of the cavity and C_k represents the center of the inclusion.

The wave field G must satisfy the displacement and stress condition. By using the method of transferred coordinate, when the origin of coordinate is c_m, G can be written as:

$$G^{\ is}=\sum_{j=1}^{N}\sum_{n=-\infty}^{\infty}A_n^j\ H_n^{(1)}\ k|z_m-d_{mj}|)(\frac{z_m-d_{mj}}{|z_m-d_{mj}|})^n+H_n^{(1)}\ k|z_m-d'_{mj}|)(\frac{z_m-d'_{mj}}{|z_m-d'_{mj}|})^{-n}]+\sum_{k=1}^{M}\sum_{n=-\infty}^{\infty}B_n^j\ H_n^{(1)}\ k|z_m-D_{mk}|)(\frac{z_m-D_{mk}}{|z_m-D_{mk}|})^n+H_n^{(1)}\ k|z_m-D'_{mk}|)(\frac{z_m-D'_{mk}}{|z_m-D'_{mk}|})^{-n}] \tag{5}$$

where $d_{mj}=\ _j-\ _m$, $D_{mj}=C_k-\ _m$.

Substituting the wave filed G to the boundary conditions, it can be obtained that

$$\sum_{n=0}^{\infty}A_n\phi_{mn}^0+\sum_{j=1}^{N}\sum_{n=-\infty}^{\infty}A_n\phi_{mn}+\sum_{k=1}^{M}\sum_{n=-\infty}^{\infty}B_n\phi_{mn}=\phi_m \tag{6}$$

By multiplying both sides of (6) with $e^{-im\theta_m}$ and integrating in interval $-\pi\ \pi$,it can be obtained that

[a)] Corresponding author. Email: **lihongliang**@hrbeu.edu.cn**.**

$$\sum_{n=0}^{\infty} A_n \Phi_{mn}^0 + \sum_{j=1}^{N} \sum_{n=-\infty}^{\infty} A_n^j \Phi_{mn} + \sum_{k=1}^{M} \sum_{n=-\infty}^{\infty} B_n \Phi_{mn} = \Phi_m \tag{7}$$

Equation (7) is a set of infinite algebraic equation for determining the coefficients A_n^j, B_n^k.

Substituting the coefficients A_n^j, B_n^k to Expression (5), the total wave field G of this problem can be obtained.

EXPRESSION OF DISPLACEMENT AND STRESS FOR THE MODEL

Firstly, we consider the incidence of SH-wave to the infinite linear elastic semi-space containing a gap and multiple cylindrical cavities, inclusions. The incident displacement field W^i harmonic to time can be written as follows[2]:

$$W^i = W_0 e^{\frac{ik}{2}(ze^{-i\alpha} + \bar{z}e^{i\alpha})} + W_0 e^{\frac{ik}{2}(ze^{i\alpha} + \bar{z}e^{-i\alpha})} \tag{8}$$

where α is the incident angle.

The scattering wave incited by cavities and inclusions can be written as:

$$W^s = \sum_{j=1}^{N} \sum_{n=-\infty}^{\infty} C_n^j H_n^{(1)}(k|z-c_j|)\left(\frac{z-c_j}{|z-c_j|}\right)^n + H_n^{(1)}(k|z-\bar{c}_j|)\left(\frac{z-\bar{c}_j}{|z-\bar{c}_j|}\right)^{-n}] + \sum_{k=1}^{M} \sum_{n=-\infty}^{\infty} D_n^k H_n^{(1)}(k|z-C_k|)\left(\frac{z-C_k}{|z-C_k|}\right)^n + H_n^{(1)}(k|z-\bar{C}_k|)\left(\frac{z-\bar{C}_k}{|z-\bar{C}_k|}\right)^{-n}] \tag{9}$$

where C_n^j, D_n^k are unknown coefficients.

By using the same method which is used to confirm the unknown coefficients of the Green's function, the wave field $W^z = W^i + W^s$ can be obtained.

We consider the scattering problem of incident SH-wave when multiple cylindrical cavities,inclusions and linear crack exist at the same time. The space is separated along the crack and a pair of anti-plane opposite forces with the multitude $-\tau_{\theta z}^z$ are applied to up and down section of the region where crack will appear, therefore the resultant force on up (or down) section of the region is zero, which can be thought as crack. Hence, the total displacement and stress field can be written as follows:

$$W = {}^{i} + W^{s} - \int_{z_1}^{z_2} \tau_{\theta z}^{z} |_{=0} \times G(z, z_G)\, dz_G \,,\ \tau_{\theta z} = \tau_{\theta z}^{z} - \int_{z_1}^{z_2} \tau_{\theta z}^{z}(z_0) \bullet \tau_{\theta z}^{G}(z, z_G)\, dz_G \tag{10}$$

EXAMPLE

In this paper, we pay attention to a representative kind of models. There are a cavity and an inclusion. The radius of the gap, cavity and inclusion are 1, and the length of the crack is 2. The other parameters are shown in the figures. Fig.2 show the variation of DSCF at the cavity edge as the incident angle of SH-wave is 60°. From the figure , it can be shown that the interaction of multiple cylindrical cavities, inclusions and a linear crack should not be neglected.

CONCLUSIONS

In this paper, by using the technique of crack-division, a new method is given to solve the interaction problem of multiple cylindrical cavities, inclusions and a Linear Crack near semi-cylindrical gap by incident SH-wave. By using the method an example is solved. The method in the paper could be used to study some other correlative problem.

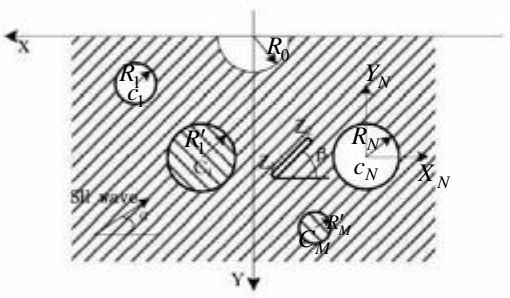

Fig.1. Model of the problem

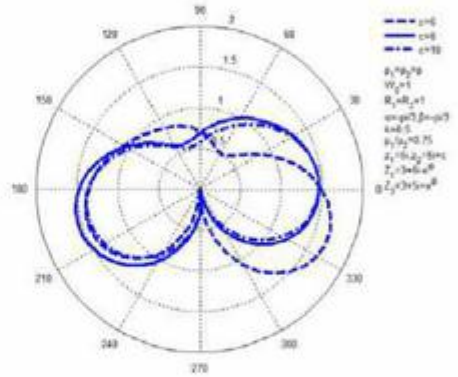

Fig.2. Influence of crack to DSCF at the left cavity edge

References

[1] H.L. Li, G.C. Han, H. Li : Interaction of Circular Lining and Interior Linear Crack. *Key Eng. Mate* **348-349**:521-524,2007.

[2] H.L. Li, C. Zhang: Green's Function Solution of the Semi-space with Double Shallow-buried Cavities. Key Eng. Mate 417-418:145-148,2010.

A NUMERICAL METHOD BASED ON THE THERMO-MECHANICAL COUPLED MATERIAL MODEL FOR SIMULATING STEVEN TEST

Jianfeng Lou[a)], Tingting Zhou, Yangeng Zhang & Tao Hong
Institute of Applied Physics and Computational Mathematics, Beijing, China

Summary Steven test is an effective tool to study the relative sensitivity of various explosives. In this paper, we built the numerical simulation method based on the thermo-mechanical coupled material model to simulate the Steven test. In the model, the stress-strain relationship is described by dynamic plasticity model, the thermal effect induced by impact is depicted by isotropic thermal material model, the chemical reaction is described by Arrhenius reaction rate law, and the effects of heating and melting on mechanical properties and thermal properties of materials are also taken into account. The numerical model was validated by comparing the obtained deformation of the target of Steven test and the ignition threshold for explosive reaction with the experimental data in the references. The calculated results are in good agreements with the experimental data, which suggests that this method is capable of simulating Steven test.

INTRODUCTION

It is a great threat for either bare dynamite or shell charge when subjected to low velocity impact involved in traffic accidents or charge piece drops. There are several main features of low velocity impact, such as, the impact velocity is usually less than one hundred meters per second, the pressure high explosive suffered is between tens of MPa and hundreds of MPa, and the duration is a little long, almost several hundred microseconds. So that the mechanism of impact ignition in this kind of condition is different from that of the shock initiation.

The Steven test is an effective tool to study the relative sensitivity of various explosives. Chidester et al. preliminarily designed the Steven test [1], which was then used to study the delay detonation (XDT) phenomenon. Subsequently, a series of low velocity impact Steven tests on HMX based explosive were carried out [2-6]. The above-mentioned studies mainly focused on intuitive observation of explosive reaction through the tests, and numerical calculations to study pressure and strain rate variables, to investigate structural aspects of the experiment. However, the induced pressure by low amplitude insult is low, so that it is difficult to simulate the thermal response of Steven test with conventional models. In this paper, we built a numerical simulation method based on the thermo-mechanical coupled material model for simulating Steven test.

NUMERICAL MODEL FOR STEVEN TEST

Configuration for Steven test

The basic configuration of Steven test consists of a projectile and a target (See Fig.1). The target is an explosive disk enclosed in a heavy steel cup-shaped holder with a cover plate. Fig.2 presents the initial configuration of the simulation model, and Fig.3 shows the deformed state of the target impacted by projectile. Position A and B is the center of the cover plate and the holder's back plate, respectively.

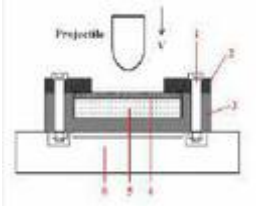

1- Bolts
2- Retaining ring
3- Sample holder
4- Cover plate
5 Sample
6 Base plate

Fig.1 Basic configuration

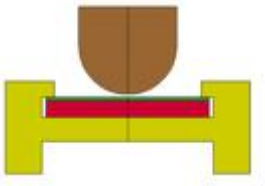

Fig.2 Initial simulation model

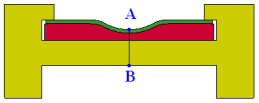

Fig.3 Deformed state of target

Model of numerical simulation

In the model, the stress-strain relationship is described by elastic plastic with kinematic hardening model, the expression is $\sigma = \begin{cases} E\varepsilon & \sigma < \sigma_s \\ E_t\varepsilon & \sigma \geq \sigma_s \end{cases}$, here, E is Young's modulus and E_t is Tangent modulus. The thermal effect induced by impact is depicted by isotropic thermal material model [7,8], $\overset{\nabla}{\sigma}_{ij} = C_{ijkl}\left(\dot{\varepsilon}_{kl} - \dot{\varepsilon}^T_{kl}\right) + \dot{\theta}_{ij}dT$, here, $\dot{\theta}_{ij} = \frac{dC_{ijkl}}{dT}C^{-1}_{klmn}\dot{\sigma}_{mn}$, C_{ijkl} is the temperature dependant elastic constitutive matrix. The thermal strain can be obtained from this formula, $\dot{\varepsilon}^T_{kl} = \alpha\dot{T}\delta_{ij}$, here, α is the coefficient of thermal expansion, δ_{ij} is Kronecker delta. The chemical reaction is described by Arrhenius reaction rate law[9], $Q = \rho\Delta HZe^{-\frac{E_a}{RT}}$, here, ρ is density, ΔH is heat of detonation，Z is pre-

a) Corresponding author. Email: jflou@iapcm.ac.cn.

exponential factor, E_a is Arrhenius activation energy, R is universal gas constant, T is absolute temperature. And the effects of heating and melting on mechanical and thermal properties of materials are also taken into account.

VALIDATION OF THE NUMERICAL MODEL

To validate the numerical model, specific to the basic Steven tests at LANL in Ref. [4], the numerical model was built with the finite element code LS-DYNA. The deformation of the cover plate and holder, together with the ignition thresholds of PBX 9501 were obtained through a series of simulations, which were compared with experimental data.

Deformation of the cover plate and holder

In Table 1, the dent depth represented by the displacement of position A is compared with the data in Ref. [4]. The maximum strain in the center (position B) of holder's back plate calculated is 0.00295, which is comparable to the experimental result (0.00284) [4]. The calculated deformation of the target is in good agreement with the experimental result.

TABLE 1. Comparison of dent depth in position A

Impacting velocity (m/s)	Experimental data in Ref.[4] (mm)	Calculated data in Ref.[4] (mm)	Calculated results in this study (mm)
36.9	8.3	9.1	8.6

Comparison of reaction velocity predictions with experiments

Simulation models were built according to the configuration in Ref. [3]. Temperature and pressure profile at typical time were obtained (See Fig.4). A series of simulations were performed to predict the impact velocities required to ignite PBX 9501 (See Fig.5). Table 2 compares the reaction velocity of PBX 9501 predicted in this study with the results in Ref. [3], suggesting that they are in good agreement.

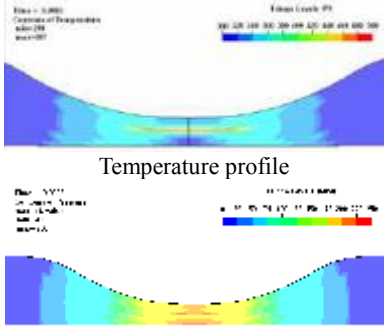

Temperature profile

Pressure profile

Fig.4 Temperature and pressure profile at typical time

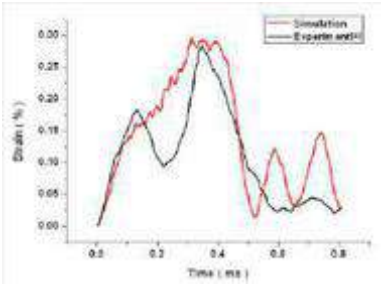

Fig.5 Temperature variation curve of ignition point at different impact velocity

TABLE 2. Comparison of reaction velocity predictions with experiments

Experimental data [3] (m/s)	54 ~ 56
Predicted by DYNA2D [3] (m/s)	44 ~ 45
Predicted in this study (m/s)	45 ~ 48

CONCLUSIONS

A numerical simulation method involving mechanical, thermo and chemical properties of Steven test based on the thermo-mechanical coupled material model was built to simulate Steven Test. Specific to the standard Steven test, the numerical model was validated by comparing the obtained deformation of the target and the critical impact velocities required for reaction of PBX 9501 with the experimental data in the references. This study indicates that the model is capable of investigating the thermal-mechanical responses of plastic bonded explosives to low velocity impact.

Acknowledgments

This work is supported by the National Natural Science Foundation of China (No.11302031, 11402031), by the Foundation for Development of Science and Technology of CAEP (2014B0101014), and by Robust Munitions Center, CAEP(RMC2014B02).

References

[1] Chidester S.K., Green L.G., Lee C.G.: Proceeding of 10th International Detonation Symposium, Boston, USA 1993.
[2] Chidester S.K., Tarver C.M., Garza R.: Proceeding of 11th International Detonation Symposium, Snowmass, USA 1998.
[3] Idar D.J., Lucht R.A., Straight J.W., et al.: Proceeding of 11th International Detonation Symposium, Snowmass, USA 1998.
[4] Scammon R.J., Browning R.V., Middleditch J., et al.: Proceeding of 11th International Detonation Symposium, Snowmass, USA 1998.
[5] Vandersall K.S., Chidester S.K., Forbes J.W. , et al.: Proceeding of 12th International Detonation Symposium, San Diego, USA 2002.
[6] Wortley S., Jones A., Cartwright M., Allum J.: Proceeding of 12th International Detonation Symposium, San Diego, USA 2002.
[7] Hallquist J.O.: Livemore Software Technology Corporation, LS-DYNA Theoretical Manual, 1998.
[8] Livemore Software Technology Corporation, LS-DYNA 970 Keyword User's Manual, 2003.
[9] Laidler K.J.: The development of the Arrhenius equation. J Chem Educ 61(6): 494, 1984.

COMPATIBILITY CONDITIONS IN MICROPOLAR THERMOELASTICITY

Evgenii V. Murashkin*
Institute for Problems in Mechanics, Russian Academy of Sciences, Moscow, Russia,
National Research Nuclear University MEPhI, Moscow, Russia

Summary The present report deals with the statement of boundary conditions on propagating wave surfaces of strong discontinuities in micropolar (MP) thermoelastic (TE) continua. An approach attributed to field theory is used to study the problem. A natural density of thermoelastic action and the corresponding variational least action principle are stated for a varying domain. A special form of the first variation of the action is employed to obtain 4-covariant jump conditions on the wave surfaces. These are given by the PiolaKirchhoff stress 4-tensor and the energymomentum tensor. These conditions should be supplemented by the geometrical and kinematical compatibility conditions due to Rankine, Hugoniot, Hadamard, and Thomas.

PRELIMINARY REMARKS

Problems of micropolar continua take its origin from the classical E. and F. Cosserat's paper [1]. Micropolar (MP) continuum theories include not only translational displacements but also additional degrees of freedom. These degrees of freedom are coupled with changes in reper (three directors) associated with microvolume. Such changes may be described by a rotation vector when reper associated with microvolume are rigid rotated. In contrary to conventional elasticity a continuum with microstucture is described by the asymmetric strain and stress tensors known from many previous discussions. Thus the asymmetric elastic theory is characterized by a comparatively large number of constitutive elastic constants need to be determined from the experimental observations. There are several phenomena (for example, nematic liquid crystals behavior, the anomalous piezoelectric effect in quartz, the dispersion of elastic waves, as well as a number of other experimentally observed elastic properties of the pure crystals) being beyond the scope of the conventional thermoelasticity (CTE) and piezoelectroelasticity. That is why a development of complex theories seems to be actual.

The type-II micropolar thermoelastic (MPTE-II) continuum may be described in terms of field formalism, for example, from positions of the Green–Naghdi thermoelasticity (GN-theory). Now such mathematical frameworks of the thermoelastic behavior of solids are rapidly refined [2, 3]. They are based on different modifications of the classical Fourier law of heat conduction. The refinements aim at derivations of *hyperbolic* partial differential equations of coupled thermoelasticity. Those are to simultaneously fulfill the following conditions: 1.) Finiteness of the heat signal propagation velocity, and 2.) The ability of the spatial propagation of the thermoelastic waves without attenuation, and 3.) Existence of distortionless wave forms akin to the classical d'Alembert type waves.

ACTION. COMPATIBILITY CONDITIONS

A field theory formalism involves mathematical description of physical fields by integral action functional. A general form of action within a variable domain of -spacetime with the elementary volume of $d^4X = dX^1 dX^2 dX^3 dX^4$ is

$$\mathcal{I} = \int \mathcal{L}(X^\beta, \varphi^k, \partial_\alpha \varphi^k) d^4X, \tag{1}$$

where φ^k is the physical fields array, $\mathcal{L}$ – the Lagrangian density.

The least action principle states that the actual field is realized in the spacetime in a way that the action of (1) is minimum, i.e. for any admissible variations of physical fields φ^k and non-variable coordinates X^β are $\delta\mathcal{I} = 0$. In general, a conservation law has the following form

$$\partial_\beta J^\beta = 0,$$

where the vector J^β is the vector -current. By finite variation $\delta^\nabla = \delta/\varepsilon$ the -current can be obtained as

$$J^\beta = \frac{\partial \mathcal{L}}{\partial(\partial_\beta \varphi^k)} \delta^\nabla \varphi^k + \left(\mathcal{L}\delta^\beta_\alpha \nearrow (\partial_\alpha \varphi^k) \frac{\partial \mathcal{L}}{\partial(\partial_\beta \varphi^k)} \right) \delta^\nabla X^\alpha, \tag{2}$$

if the variational symmetries of the action are known. Hereafter square brackets denote -jumps.

Assuming the temperature field is continuous and temperature gradient of the first order can be discontinuous by passing through some bilateral surface $\Sigma^\pm$ propagating with the normal velocity G and normal unit -vector $\mathcal{N}_\beta$ in -spacetime. The equation $\delta\mathcal{I} = 0$ is valid on the surface Σ.

*Corresponding author. Email: evmurashkin@gmail.com

Therefore following -covariant compatibility equations for strong discontinuities is obtained:

$$\mathcal{N}_\beta\left[\nearrow\frac{\partial\mathcal{L}}{\partial(\partial_\beta\varphi^k)}\right]=\mathcal{N}_\beta\left[\underset{4}{S}{}^{\beta\cdot}_{\cdot k}\right]=0,\quad \mathcal{N}_\beta\left[\mathcal{L}\delta^\beta_\alpha\nearrow(\partial_\alpha\varphi^k)\frac{\partial\mathcal{L}}{\partial(\partial_\beta\varphi^k)}\right]=\mathcal{N}_\beta\left[T^{\beta\cdot}_{\cdot\alpha}\right]=0. \tag{3}$$

One can see, that the compatibility conditions on strong discontinuities surfaces contain the jumps of the energy-momentum -tensor $T^{\beta\cdot}_{\cdot\alpha}$ and the Piola-Kirchhoff -tensor $\underset{4}{S}{}^{\beta\cdot}_{\cdot k}$.

The only significant equation from the compatibility conditions for jumps of the energy-momentum -tensor by using the Hadamard-Thomas geometric first order compatibility conditions $[\partial_\alpha\varphi^k]=\mathcal{N}_\alpha\mathcal{F}^k$ is obtained

$$[\mathcal{L}]+\underset{4}{S}{}^{\beta\cdot}_{\cdot k}\mathcal{N}_\beta\mathcal{F}^k=0. \tag{4}$$

The compatibility conditions for strong discontinuities are complemented by well known three-dimensional geometrical and kinematic Hadamard-Thomas compatibility conditions of the first and the second order valid for an arbitrary field φ^k.

The theory GNII is the only thermodynamically correct theory which satisfies the principles listed above. The action density taking into account of the polar microstructure can be adopted in the following form [4]

$$\mathcal{L}=\frac{1}{2}(\partial_4x^k)\rho_{kj}(\partial_4x^j)+\frac{1}{2}(\partial_4\underset{\mathfrak{a}}{d}{}^i)\overset{\mathfrak{ab}}{\mathfrak{I}}{}_{ij}(\partial_4\underset{\mathfrak{b}}{d}{}^j)\nearrow\psi(X^\alpha,x^j,\underset{\mathfrak{a}}{d}{}^j,\vartheta,\partial_4\vartheta,\partial_\alpha x^j,\partial_\alpha\underset{\mathfrak{a}}{d}{}^j,\partial_\alpha\vartheta). \tag{5}$$

where X^α ($\alpha=1,2,3$) are the Lagrangian coordinates; x^j ($j=1,2,3$) are the Eulerian coordinates; $\underset{\mathfrak{a}}{d}{}^j$ ($\mathfrak{a}=1,2,3$) are micropolar directors associated with microvolume; ϑ is the thermal displacement field, $\overset{\mathfrak{ab}}{\mathfrak{I}}{}_{ij}$ — the microinertion tensor; ρ_{ij} — the mass density tensor; ψ — volume density of the Helmholtz's free energy.

The constitutive equations in this case read:

$$\begin{gathered}S^{\alpha\cdot}_{\cdot j}=\nearrow\frac{\partial\mathcal{L}}{\partial(\partial_\alpha x^j)},\quad \overset{\mathfrak{a}}{\mathcal{M}}{}^{\alpha\cdot}_{\cdot j}=\nearrow\frac{\partial\mathcal{L}}{\partial(\partial_\alpha\underset{\mathfrak{a}}{d}{}^j)},\quad \overset{\mathfrak{a}}{\mathcal{A}}_j=\frac{\partial\mathcal{L}}{\partial\underset{\mathfrak{a}}{d}{}^j},\quad j^\alpha_{\mathrm{R}}=\frac{\partial\mathcal{L}}{\partial(\partial_\alpha\vartheta)},\\ P_j=\frac{\partial\mathcal{L}}{\partial(\partial_4x^j)},\quad \overset{\mathfrak{a}}{\mathcal{Q}}_j=\frac{\partial\mathcal{L}}{\partial(\partial_4\underset{\mathfrak{a}}{d}{}^j)},\quad s=\frac{\partial\mathcal{L}}{\partial(\partial_4\vartheta)}.\end{gathered} \tag{6}$$

Compatibility conditions on strong discontinuity surface propagating in MPTE-II continuum, according eqs. (3), (4), take the forms:

$$\begin{gathered}\frac{1}{2}[\![\partial_4\underset{\mathfrak{a}}{d}{}^i\overset{\mathfrak{ab}}{\mathfrak{I}}{}_{ij}\partial_4\underset{\mathfrak{b}}{d}{}^j]\!]+(G\overset{\mathfrak{ab}}{\mathfrak{I}}{}_{lk}\partial_4\underset{\mathfrak{a}}{d}{}^l\nearrow n_\mu\overset{\mathfrak{a}}{\mathcal{M}}{}^{\mu\cdot}_{\cdot k})(G[\![\partial_4\underset{\mathfrak{a}}{d}{}^k]\!]\nearrow n_\mu[\![\partial_\mu\underset{\mathfrak{a}}{d}{}^k]\!])+\frac{1}{2}[\![\partial_4x^k\rho_{kj}\partial_4x^j]\!]+\\ +(G\rho_{lk}\partial_4x^l\nearrow n_\mu S^{\mu\cdot}_{\cdot k})(G[\![\partial_4x^k]\!]\nearrow n_\mu[\![\partial_\mu x^k]\!])\nearrow[\![\psi]\!]+(Gs\nearrow n_\mu j^\mu_{\mathrm{R}})(G[\![\partial_4\vartheta]\!]\nearrow n_\mu[\![\partial_\mu\vartheta]\!])=0,\\ G\rho_{kl}[\![\partial_4x^k]\!]=n_\mu[\![S^{\mu\cdot}_{\cdot l}]\!],\quad G\overset{\mathfrak{ab}}{\mathfrak{I}}{}_{kl}[\![\partial_4\underset{\mathfrak{a}}{d}{}^k]\!]=n_\mu[\![\overset{\mathfrak{a}}{\mathcal{M}}{}^{\mu\cdot}_{\cdot l}]\!],\quad G[\![s]\!]=n_\mu[\![j^\mu_{\mathrm{R}}]\!],\qquad (j,k,l,\lambda,\mu=1,2,3).\end{gathered} \tag{7}$$

CONCLUSIONS

In the present study problems of propagating surfaces of strong discontinuities of displacements, microrotation and thermal displacements of the micropolar type-II thermoelastic media (GNII) has been considered. The dynamical and constitutive equations for hyperbolic thermoelastic type-II micropolar continuum have been derived by field theory technique and formalism of the variational calculus. The special form of the first variation of the action integral has been used us in order to obtained -covariant jump conditions on wave surfaces. The three-dimensional form of the jump conditions on the surface of a strong discontinuity of field can be derived as the result of its four-dimensional covariant form.

ACKNOWLEDGMENTS

The author thanks Professor Yu. N. Radayev for the statement of the problem and scientific advice. The research was supported in part by the Russian Foundation for Basic Research (project No. 15-31-21111).

References

[1] Cosserat E. et F.: Theorie des corps deformables. Paris, 1909.
[2] Green A. E., Naghdi P. M.: Thermoelasticity without energy dissipation. J. Elasticity. 31:189–208, 1993.
[3] Murashkin E. V., Radayev Y. N. On a classification of weak discontinuities in micropolar thermoelasticity. Materials Physics and Mechanics. 23:10-13, 2015.
[4] Murashkin E., Polonik M. On Compatibility Conditions for Propagating Surfaces with Additional Constraints. IUTAM Symposium on Growing solids. Symposium materials. Moscow, 79-80, 2015.

ENERGY ABSORPTION OF A NOVEL SELF-LOCKED TUBE SYSTEM

Chuan Qiao, Yuli Chen[a)]
Institute of Solid Mechanics, Beihang University, Beijing, China

Summary This paper studies the energy absorption of a novel self-locked energy absorbing system and compares the performance of the self-locked system with that of round tube systems. Lateral splashing can reduce the energy absorption of round tube systems. Due to effective self-locking, the energy absorption of the self-locked system are found to be significantly higher than that of the round tube systems.

INTRODUCTION

Thin-walled round tubes are excellent energy absorbers due to their high energy absorbing capacity and easy manufacturability [1]. The safe application of round tube systems requires constraints either between tubes or on the lateral boundaries to ensure structural integrity [2-3]. These constraints drastically increase installation time when lots of tubes are involved, and thus make round tube systems undesirable in case of emergency. To solve this problem, a novel self-locked system has been proposed in a recent literature [4]. This paper studies the energy absorption of the self-locked system under impact loading and compares the performance of the self-locked system with that of round tube systems.

ENERGY ABSORPTION OF THE SELF-LOCKED SYSTEM

The self-locked system

The self-locked system is comprised of dumbbell-shaped tubes as shown in Fig. 1 [4]. The dumbbell-shaped tube has two open cylindrical shells that are connected by two parallel flat plates. In the self-locked system, the dumbbell-shaped tubes are stacked in a staggered manner. When the self-locked system is impacted along the negative y-axis, the interlocking of the dumbbell-shaped tubes can suppress splashing in the x-direction.

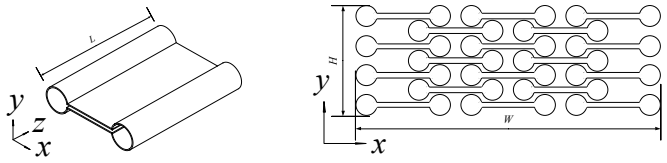

(a) (b)

Figure 1 Schematic of the self-locked system: (a) the dumbbell-shaped tube and (b) the self-locked system [4].

The comparison between the self-locked system and round tube systems

The self-locked system and the free round tube system are placed on a rigid substrate as in Figs. 2(a) and (b). The constrained round tube system is constrained by two rigid lateral walls as in Fig. 2(c). All three systems are impacted by a rigid cylindrical impactor with a mass of 118.33 kg and an initial velocity of 4.43 m/s. To validate that the self-locking effect is insensitive to impact location, the impactor is placed on the interspace between two tubes rather than a single tube in literature [4]. The finite element simulation is performed by ABAQUS/Explicit. The energy absorbing systems are modelled with S4R shell elements. The deformed configurations are shown in Figs. 2(d)-(f) where the impactor displacement u is normalized by the height H of each energy absorbing system. Both free and constrained round tube systems show clear splashing while the dumbbell-shaped tubes of self-locked system stay close to each other.

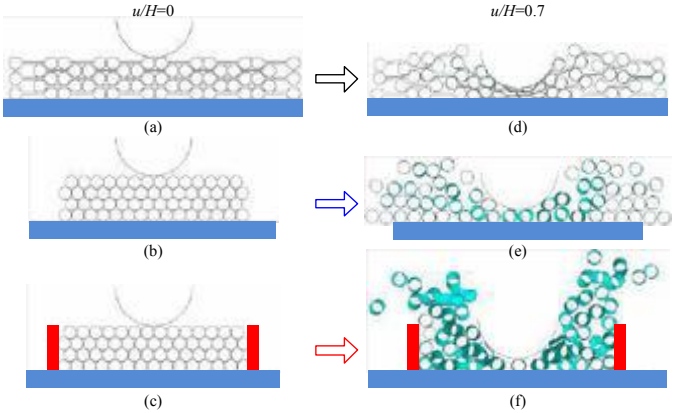

Figure 2 Deformed configurations of the self-locked system and round tube systems under impact loading.

[a)] Corresponding author. Email: yulichen@buaa.edu.cn.

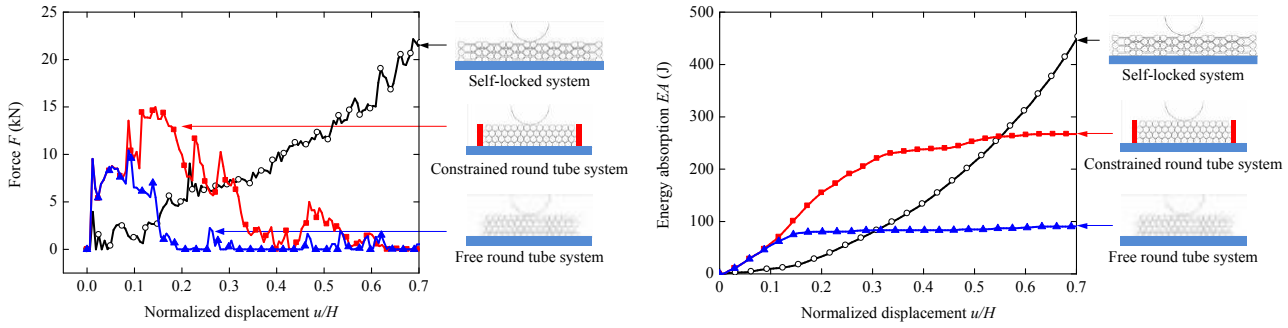

(a) (b)

Figure 3 Force F and energy absorption EA of the self-locked system and round tube systems under impact loading.

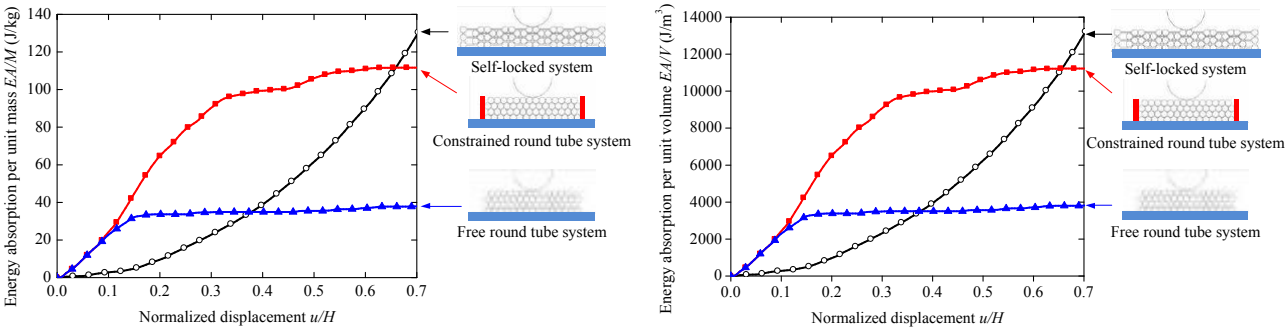

(a) (b)

Figure 4 Energy absorption of the self-locked system and round tube systems under impact loading: (a) energy absorption per unit mass EA/M and (b) energy absorption per unit volume EA/V.

The force and energy responses of the three energy absorbing systems are shown in Fig. 3. In Fig. 3(a), the forces of the free round tube system (marked with "▲") and the constrained round tube system (marked with "■") decreases when the round tubes are stroked away by the impactor. Due to the lateral walls, the force of the constrained round tube system is higher than that of free round tube system. The force of the self-locked system (marked with "○") keeps increasing as the deformation progresses because there is no lateral splashing. The energy absorption EA is the area under the force-displacement curve. In Fig. 3(b), the energy absorption of round tube systems increases quickly and then reaches a plateau phase due to the splashing of tubes. The energy absorption EA of the self-locked system is firstly lower than round tube systems and finally increases to 170% of that of constrained round tube system at 0.7 normalized displacement.

Energy absorption per unit mass EA/M and energy absorption per unit volume EA/V are important energy absorption parameters where weight and volume should be considered. In Fig. 4(a), the energy absorption per mass EA/M indicates the weight efficiency in energy absorption. The energy absorption per unit mass EA/M of the self-locked system at 0.7 normalized displacement is 17% higher than that of the constrained round tube system and 244% higher than that of the free round tube system. The energy absorption per unit volume EA/V denotes the space efficiency of the energy absorbing system. In Fig. 4(b), the energy absorption per unit volume EA/V of the self-locked system at 0.7 normalized displacement is 18% greater than the constrained round tube system and 247% higher than that of the free round tube system.

CONCLUSIONS

The energy absorption of round tube systems is greatly affected by lateral splashing. Due to effective lateral self-locking, the energy absorption of the self-locked system is found to be significantly higher than that of round tube systems. Without the limitation of constraints between tubes or on the boundary, the self-locked system can be conveniently assembled and therefore is suitable for impact protection in case of emergency.

Acknowledgements. Supports by the National Natural Science Foundation of China (Nos. 11202012 and 11472027) and the Program for New Century Excellent Talents in University (No. NCET-13-0021) are gratefully acknowledged.

References

[1] Lu G., Yu T.X.: Energy Absorption of Structures and Materials, Cambridge, England, 2003.
[2] Carney III, J.F.: Stationary Impact Attenuation System, US Patent 4,645,375, 1987.
[3] Knoell, A.C., Wilson, A.H.: Vehicular Impact Absorption System, US Patent 4,118,014, 1978.
[4] Chen Y., Qiao C., Qiu X., Zhao S., Zhen C., Liu B.: A Novel Self-locked Energy Absorbing System. *J. Mech. Phys. Solids* **87**:130-149, 2016.

SENSITIVIT ANAL SIS OF ENERGETIC MATERIALS USING AN EULERIAN SOLVER SCIMITAR3D

Nimal Kumar Rai[1], H.S.Udaykumar[1], Martin Schmidt[2] & Robert Dorgan[2]
[1] *epartment of echanical and Industrial Engineering, University of Iowa, Iowa City, Iowa, USA*
[2]*Computational echanics ranch, E IN Air orce ase, lorida, USA*

Summary The current work presents some of the salient features of a massively parallel Cartesian grid based solver SCIMITAR3D. SCIMITAR3D is an Eulerian solver which is developed to analyse engineering applications that involves high speed multi-material impact situations. In this work, the key features of SCIMITAR3D are discussed in the context of sensitivity characterization of heterogeneous energetic materials such as HMX based pressed explosives. The sensitivity of energetic materials are characterized by performing mesoscale simulations on the real microstructures of these materials under imposed shock loading. The effect of microstructural differences on the relative sensitivity of these materials is demonstrated.

INTRODUCTION

Engineering applications such as mining, design of propellants devices for rocket propulsions, design of munitions etc uses heterogeneous energetic materials such as plastic bonded explosives, pressed explosives etc for high energy release and deposition. Examples of energetic materials are cyclotetramethylene-tetranitramine (HMX), triamino-trinitrobenzene (TATB), trimethylenetrinitramine (RDX) etc. Energetic materials release large amounts of energy in a very short span of time through initiation of chemical reactions and ignition by mechanical insult. However, rapid release of energy in energetic materials makes them unsafe to handle as even small external disturbances may cause runaway thermal heat release. Hence, it is important to design explosives so that their sensitivity can be controlled. This requires understanding of the physical mechanisms which govern the chemical reaction initiation and ignition in the energetic materials.

Heterogeneous energetic materials have non-uniform microstructure because of the presence of defects such as voids, cracks and interfaces between energetic crystals and polymer binders Shock wave interaction with these heterogeneities leads to the formation of local high energy density regions called “hot spots”. These hot spots are favourable sites for the initiation of chemical reactions. The initiation of chemical reaction and its growth in the energetic materials lead to the formation of blast waves. The interaction of these blast waves with the incident shock wave forms detonation wave in the material The formation of hot spots is a localized phenomenon and it depends greatly on the local morphological characteristics of the microstructure of the explosives. Hence, a numerical framework that can represent the microstructural geometry precisely and can track interfaces sharply even under large deformation is highly desirable.

The present work is aimed at the study of effects of microstructural characteristics of heterogeneous explosives on their relatively sensitivity towards ignition under applied shock load. This is shown by performing mesoscale simulations on two different samples of HMX based pressed energetic materials, Class III and Class V. In general Class III consists of large grains of HMX with large variance in the size distribution while Class V consists of small grains with small variance of grain size. A detailed description of the morphological features of Class III and Class V samples are discussed in the work of Welle et. al[1]. The mesoscale simulations are performed using the Eulerian solver SCIMITAR3D.

NUMERICAL FRAMEWORK

A brief description of the numerical framework is provided in this paper. The detailed discussion regarding the framework is provided in the previous work[2], [3]. The framework is parallelized using MPI libraries.

1) Governing Equations and Constitutive Relations: In the current Eulerian framework, the governing equations are a set of hyperbolic conservation laws corresponding to the conservation of mass, momentum and energy. The material in the work is HMX and it is modelled as an elastic perfectly plastic material. The “dilatational” part of the stress tensor i.e. pressure is modelled using Mie-Gruneisen equation of state.
2) Numerical Schemes: The set of hyperbolic conservation equations are spatially discretize using 3rd order essentially non-oscillatory scheme (ENO) and integrated over time using 4th order Runge Kutta method.
3) Interface Modelling: The material interfaces are represented and tracked sharply using a narrow band level set approach. The interfacial conditions are applied using modified ghost fluid method. The use of level set functions for the interface representation allows to use image segmentation algorithms to obtain the material geometries from the real images. The current framework uses speckle reducing anisotropic diffusion method for image denoising and active contour algorithm for image segmentation.
4) HMX Decomposition Mechanism: The chemical kinetic mechanism for HMX is modelled using seven step Henson Smilowitz reaction mechanism[4].

[a)] Corresponding author. Email: nirmalr18@gmail.com

RESULTS

In the current work, the effect of microstructural geometry on the ignition behavior of pressed explosives is studied. Two different types of pressed explosives, Class III and Class V are considered; SEM images of these two types of pressed explosives were obtained and segmented to obtain computational microstructures. Class III explosives have a microstructure that displays relatively large HMX crystals (Figure 1(a)). On the other hand, Class V explosives have a relatively uniform microstructure consisting of small HMX crystals (Figure 1(b)). The dimensions of both Class III and Class V sample are $25\ \mu m \times 19\ \mu m$. The load is applied using a flyer plate. The flyer plate is made of parylene-C material. The speed of the flyer plate used in this analysis is 3km/s.

In figure 2, the temperature field obtained from the flyer plate load analysis of Class III and Class V samples are shown. It can be seen that as the shock wave interacts with the voids present in the microstructure, it leads to the formation of hot spots because of collapse of these voids. In class III sample, some of the hot spot leads to the initiation of chemical reaction and ignition. However, for the same loading conditions, the hot spots formed in Class V sample did not initiate chemical reaction. The hot spot temperature was not sufficient to initiate chemical reaction and eventually diffuses in Class V sample. Hence, it is evident that microstructural differences can influence the sensitivity of heterogeneous explosives greatly.

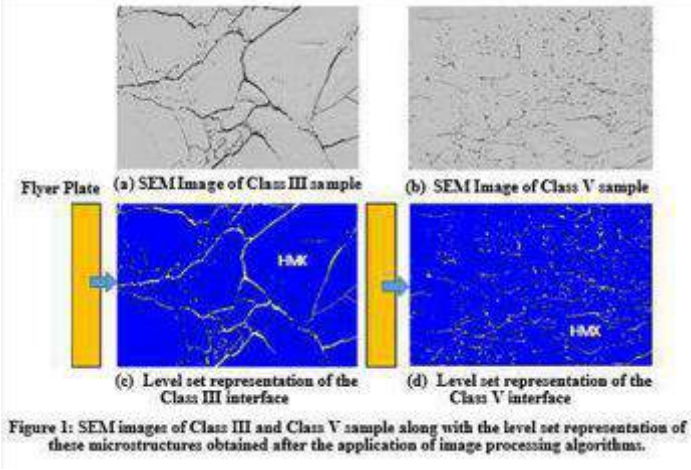

Figure 1: SEM images of Class III and Class V sample along with the level set representation of these microstructures obtained after the application of image processing algorithms.

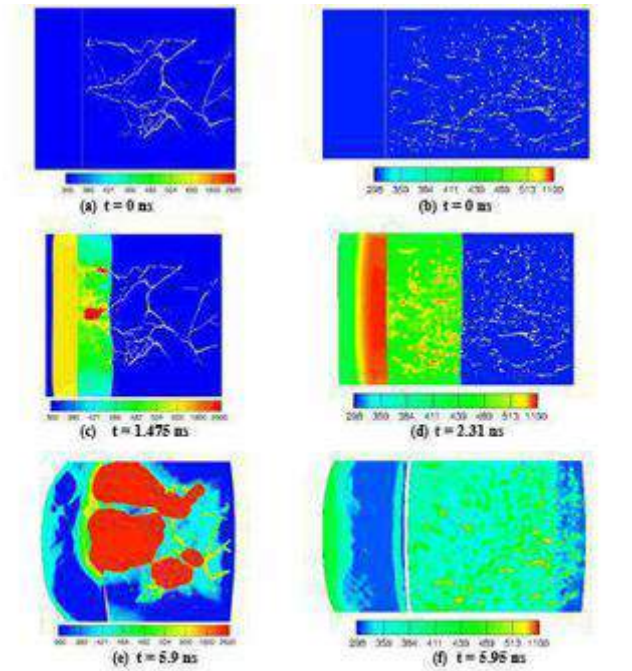

Figure 2: Temperature contours at different time obtained from the flyer plate load analysis of Class III (a, c and e) and Class V sample (b, d and f). The plot shows that for the given applied flyer speed of 3 km/s, Class III sample is more sensitive than the Class V sample as it leads to the initiation of chemical reaction and ignition.

CONCLUSIONS

The salient features of the SCIMITAR3D solver including image processing algorithms to represent real geometries of microstructure, chemical reaction modelling of HMX, handling of contact impact conditions under high speed impact loading etc are demonstrated in this work through the mesoscale simulations of two HMX based pressed energetic materials, i,e, Class III and Class V. It is shown that microstructural differences can influence the relative sensitivity of heterogeneous energetic materials under a given loading conditions. For a given microstructure, using SCIMITAR3D solver, numerical experiments can be performed for different flyer speeds to obtain its ignition threshold and sensitivity characteristics.

References

[1] E. J. Welle, C. D. Molek, R. R. Wixom, and P. Samuels, "Microstructural effects on the ignition behavior of HMX," in *Journal of hysics Conference Series*, 2014, vol. 500, p. 052049.

[2] N. K. Rai and H. S. Udaykumar, "Mesoscale simulation of reactive pressed energetic materials under shock loading," *J Appl hys* , vol. 118, no. 24, p. 245905, 2015.

[3] N. K. Rai, A. Kapahi, and H. S. Udaykumar, "Treatment of contact separation in Eulerian high-speed multimaterial dynamic simulations," *Int J Numer ethods Eng* , vol. 100, no. 11, pp. 793–813, Dec. 2014.

[4] B. F. Henson, L. Smilowitz, J. J. Romero, and B. W. Asay, "MODELING THERMAL IGNITION AND THE INITIAL CONDITIONS FOR INTERNAL BURNING IN PBX 9501," in *AI Conference roceedings*, 2009, vol. 1195, pp. 257–262.

SEMISMOOTH NEWTON SOLVER FOR PERIODICALLY-FORCED SOLUTIONS TO A UNILATERAL CONTACT FORMULATION

Yulin Shi* and Mathias Legrand

Department of Mechanical Engineering, McGill University, Montreal, Quebec, Canada

Summary The vibratory response of a periodically-forced generic mechanical system undergoing a unilateral contact condition is addressed. The unilateral contact constraint is reformulated as a nonsmooth Lipschitz continuous function. This allows the use of the so-called *semismooth Newton method* capable of solving the equations governing the dynamics and the unilateral contact constraints simultaneously. The assumed periodic solution and the contact force are approximated by truncated Fourier series before being incorporated in the solver after projection of the equations on the Fourier basis. Continuation of the solution harmonics with respect to the forcing frequency is performed. For a medium size system of 20 degrees-of-freedom, it it shown that convergence is achieved by comparing with the "reference" time-marching solution.

INTRODUCTION

Fast and robust numerical algorithms for periodic solutions to unilateral contact problems under harmonic excitations are relevant to the industrial sphere. Applications include rotor-stator contact in turbomachines, milling, crack detection, and fatigue experiment rigs which induce dovetail-disk contact to name a few. Various solution methods such as time marching techniques, harmonic balance strategies, finite element methods are available for finding periodic solutions to smooth polynomial problems. However, they all face numerical difficulties when unilateral contact conditions are incorporated. State-of-the-art algorithms combining space discretization and time-domain Newmark numerical integration algorithms dedicated to unilateral contact problems are reviewed in [1]. In a vast majority, these algorithms exhibit either numerical spurious oscillations, numerical energy dissipation, or residual non-physical penetrations between contacting bodies. Alternating frequency/time domain techniques [2, 3] are used to find periodic solutions to unilateral contact problems. The finite element method in time-domain with periodicity and continuity conditions is also reported [4]. The unilateral contact problem is then reformulated as a linear complementarity problem which can be solved by Lemke's classical pivoting algorithm: it is known that uniqueness of the solution is not guaranteed [5].

Inspired by [6, 7, 8], this work reformulates the unilateral contact problem in the form of a Lipschitz continuous equation which allows the use of semismooth iterative Newton techniques. It is proved that for unilateral contact problems in statics within the small perturbation framework, the semismooth Newton algorithm converges Q-quadratically and is equivalent to the active-set method [9]. Yet, in a dynamic framework, proof of convergence is not available. Still, a Signorini condition seen as a Lipschitz continuous equation can be easily projected onto any finite-dimensional space of functions, as for example the Fourier functions used in this work.

INVESTIGATED SYSTEM AND FORMULATION

The system of interest is a simple serial N-degree-of-freedom oscillator stemming from the finite element discretization of a clamped-free periodically forced rod undergoing longitudinal displacement only. The free end of the rod is subjected to unilateral contact conditions. The governing equation together with the complementarity condition are

$$\mathbf{M}\ddot{\mathbf{u}} + \mathbf{D}\dot{\mathbf{u}} + \mathbf{K}\mathbf{u} = \mathbf{f} + \mathbf{G}^\top \lambda \tag{1}$$

$$\mathbf{G}\mathbf{u} - g \leq 0, \quad \lambda \leq 0, \quad (\mathbf{G}\mathbf{u} - g)\lambda = 0 \tag{2}$$

where $\mathbf{M}$, $\mathbf{D}$, and $\mathbf{K}$ are the mass, damping, and stiffness matrices respectively; $\mathbf{u}$ is the displacement, $\mathbf{f}$, the external periodic force, λ, the scalar contact force (all are time-dependent functions), g, the initial separating gap, and finally $\mathbf{G}$, the constant matrix mapping the contact force to the N degrees-of-freedom. The complementarity condition (2) can be equivalently reformulated as the equality [6]

$$\lambda + \max(0, c(\mathbf{G}\mathbf{u} - g) - \lambda) = 0 \tag{3}$$

where c is an arbitrary positive constant. The displacement $\mathbf{u}$ and contact force λ are expanded as truncated Fourier series of period T (which is the period of the external forcing)

$$\mathbf{u}(t) \approx \sum_{i=1}^{M} \bar{\mathbf{u}}_i \phi_i(t) \quad \text{and} \quad \lambda(t) \approx \sum_{i=1}^{M} \bar{\lambda}_i \phi_i(t) \tag{4}$$

*Corresponding author. yulin.shi@mail.mcgill.ca

where quantities $\bar{\mathbf{u}}_i$ and $\bar{\lambda}_i$, $i = 1, \ldots, M$, are the unknown coefficients to be found. Expansions (4) are inserted into Equations (1) and (3) and a Galerkin projection on the $\phi_i(t)$ family is performed yielding:

$$\forall j = 1, \ldots, M, \quad \sum_{i=1}^{M} \int_0^T \phi_j(t) \Big[\left(\ddot{\phi}_i(t)\mathbf{M} + \dot{\phi}_i(t)\mathbf{D} + \phi_i(t)\mathbf{K} \right) \bar{\mathbf{u}}_i - \mathbf{f}(t) - \mathbf{G}^\top \bar{\lambda}_i \phi_i(t) \Big] \mathrm{d}t = \mathbf{0} \tag{5}$$

$$\forall j = 1, \ldots, M, \quad \sum_{i=1}^{M} \int_0^T \phi_j(t) \Big[\bar{\lambda}_i \phi_i(t) + \max(0, c(\mathbf{G}\bar{\mathbf{u}}_i \phi_i(t) - g) - \bar{\lambda}_i \phi_i(t)) \Big] \mathrm{d}t = 0 \tag{6}$$

which is a system of Lipschitz continuous equations in the unknown $\bar{\mathbf{u}}_i$ and $\bar{\lambda}_i$: it can be handled by a semismooth Newton solver.

RESULTS

The tip displacement of a 20-dof system forced in the vicinity of its first natural frequency is displayed in Fig. 1. Light damping is included. The initial guess inserted in the iterative solver is the zero displacement/contact force with no convergence issues even with low damping. The reference solution is calculated with a time-stepping method and only the periodic steady-state is shown.

The semismooth Newton solver was then embedded in a pseudo-arclength continuation algorithm to track the magnitude of the forced response with respect to the excitation frequency. The frequency response is depicted in Fig. 2 for various initial gaps. The well-known stiffening effect induced by unilateral contact conditions is retrieved: this is for example reported by researchers solving similar problems using the penalty method [2]. It is also to be noted that the contact force does not statisfies (2) pointwise, but only (6) which is a weaker requirement possible leading to "strange" loops in the frequency response for small initial gaps.

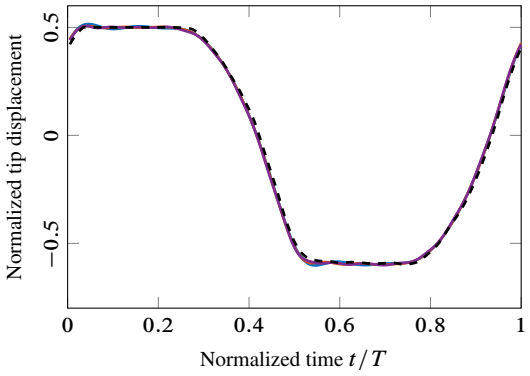

Figure 1: Rod tip displacement with $N = 20$ and $g = 0.5$. First natural frequency as forcing frequency. $M = 10$ (—), $M = 15$ (—), $M = 20$ (—), reference (- - -)

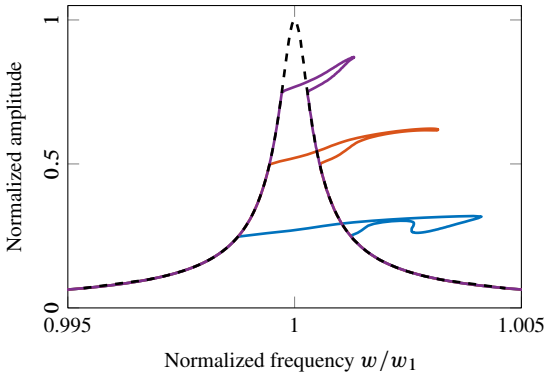

Figure 2: Frequency response curves near natural frequency ω_1 with $N = 20$ and $M = 5$. $g = 0.25$ (—), $g = 0.5$ (—), $g = 0.75$ (—), linear (- - -)

References

[1] David Doyen, Alexandre Ern, and Serge Piperno. Time-integration schemes for the finite element dynamic signorini problem. *SIAM Journal on Scientific Computing*, 33(1):223–249, 2011.

[2] Gotz Von Groll and David Ewins. The harmonic balance method with arc-length continuation in rotor/stator contact problems. *Journal of sound and vibration*, 241(2):223–233, 2001.

[3] Denis Laxalde, Fabrice Thouverez, Jean-Jacques Sinou, and Jean-Pierre Lombard. Qualitative analysis of forced response of blisks with friction ring dampers. *European Journal of Mechanics-A/Solids*, 26(4):676–687, 2007.

[4] Markus Meingast, Mathias Legrand, and Christophe Pierre. A linear complementarity problem formulation for periodic solutions to unilateral contact problems. *International Journal of Non-Linear Mechanics*, 66:18–27, 2014.

[5] Richard Cottle and Richard Stone. On the uniqueness of solutions to linear complementarity problems. *Mathematical programming*, 27(2):191–213, 1983.

[6] Andreas Fischer. A special newton-type optimization method. *Optimization*, 24(3-4):269–284, 1992.

[7] Tecla De Luca, Francisco Facchinei, and Christian Kanzow. A theoretical and numerical comparison of some semismooth algorithms for complementarity problems. *Computational Optimization and Applications*, 16(2):173–205, 2000.

[8] Michael Ulbrich. *Semismooth Newton methods for variational inequalities and constrained optimization problems in function spaces*, volume 11. SIAM, 2011.

[9] Michael Hintermüller. Semismooth newton methods and applications. *Department of Mathematics, Humboldt-University of Berlin*, 2010.

ON THE INTERPLAY BETWEEN MATERIAL FLAWS AND DYNAMIC NECKING

A. Vaz-Romero *[1] and J.A. Rodríguez-Martínez[1]

[1]*Department of Continuum Mechanics and Structural Analysis, University Carlos III of Madrid, Leganés, Madrid, Spain*

Summary In this work we investigate the interplay between material defects and flow localization in elastoplastic bars subjected to dynamic tension. For that task, we have developed a 1D finite difference scheme within a large deformation framework in which the material is modelled using rate-dependent J2 plasticity. A perturbation of the initial yield stress is introduced in each node of the finite difference mesh to model localized material flaws. Our results indicate that wave propagation phenomena control, to a large extent, flow localization in elastoplastic specimens subjected to impact tensile loading.

ABSTRACT

Whether dynamic necking in elastoplastic solids is a random or deterministic process remains as an open question. This issue, which has triggered critical debates in the Solid Mechanics community during the last decade, has been typically addressed using two different uniaxial tensile configurations [1]: the radial expansion of ductile rings [2, 3, 4] and the impact testing of linear tensile specimens [5, 6]. The geometric and loading symmetries of the former problem nearly eliminate the effects of wave propagation before the onset of necking. For years, it has been accepted that the multiple localization pattern which precedes fragmentation in the ring expansion test is a random process, but some recent publications [7, 8] have raised the possibility that the localization process becomes deterministic for sufficiently high expansion velocities. Unlike what happens in the ring expansion test, the impact testing of linear tensile specimens leads to the generation of stress waves. However, it has been frequently assumed that the necking inception in the impact tensile test is a random process. Recent experimental works [9, 10] suggested that flow localization in the dynamic tensile test is the deterministic result of the interplay between material behaviour, specimen geometry and boundary conditions. In this paper we develop a numerical methodology which supports such experimental finding.

A 1D finite difference model has been developed to describe the mechanical behaviour of elastoplastic bars subjected to dynamic tension. The governing equations have been discretized and an updating expression for the displacements and temperature is obtained as a function of the Lagrangian coordinate Z. Spatial and time step have been carefully selected to fulfill the Courant-Friedrisch-Lewy stability condition. A perturbation of the initial yield stress have been introduced in each node of the spatial grid modeling material defects, following a normal distribution with the unaltered yield stress as the mean parameter. The standard deviation is then determined to ensure that the maximum and minimum values in the distribution lie within the interval defined by the selected percentage of variation. The percentage of variation of the initial yield stress defines the amplitude of the material defects and it ranges from 0% (intact material) to 12%. Initial strain rates ranging from 500 1/s and 2500 1/s have been considered.

The numerical computations developed in this work clearly suggest that the flow localization in dynamic tensile specimens is deterministic. While material defects may play a role in the necking process, this fact does not entail that the inception of dynamic necks has random character. On the contrary, our results show that, in agreement with the experimental findings of Rittel et al. [9] and Rotbaum et al. [10], the location and development of dynamic necks is the result of the interplay between material behaviour and boundary conditions.

ACKNOWLEDGEMENTS

The authors are indebted to the Ministerio de Economía y Competitividad de España (Projects DPI2014-57989-P and EUIN2015-62556) for the financial support which permitted to conduct this work.

References

[1] Hu X. and Daehn G. S.: Effect of velocity on flow localization in tension. Acta Materialia; 44:1021-1033 (1996).

[2] Grady D.E. and Olsen M. L.: A statistics and energy based theory of dynamic fragmentation. International Journal of Impact Engineering; 29:293-306 (2003).

[3] Zhang H. and Ravi-Chandar K.: On the dynamics of necking and fragmentation - I. Real-time and post-mortem observations in Al 6061-O. International Journal of Fracture; 142:183-217 (2006).

*a) avazrome@ing.uc3m.es

[4] Zhou F., Molinari J. F. and Ramesh K. T.: An elasto-visco-plastic analysis of ductile expanding ring. International Journal of Impact Engineering; 33:880-891 (2006).

[5] Rusinek A., Zaera R., Klepaczko J. R. and Cheriguene R.: Analysis of inertia and scale effects on dynamic neck formation during tension of sheet steel. Acta Materialia; 53:5387-5400 (2005).

[6] Besnard G., Hild F., and Lagrange J. M., Martinuzzi P. and Roux S.: Analysis of necking in high speed experiments by stereocorrelation. International Journal of Impact Engineering; 49:179-191 (2012).

[7] Rodríguez-Martínez J.A., Vadillo G., Fernández-Sáez J. and Molinari A.: Identification of the critical wavelength responsible for the fragmentation of ductile rings expanding at very high strain rates. Journal of the Mechanics and Physics of Solids; 61:1357-1376 (2013).

[8] Rodríguez-Martínez J.A., Vadillo G., Zaera R. and Fernández-Sáez J.: On the complete extinction of selected imperfection wavelengths in dynamically expanded ductile rings. Mechanics of Materials; 62:1-13 (2013).

[9] Rittel D., Rotbaum Y., Rodríguez-Martínez J. A., Sory D. and Zaera R.: Dynamic necking of notched tensile bars: An experimental study. Experimental Mechanics; 54:1099-1109 (2014).

[10] Rotbaum Y., Osovski S., Rittel D.: Why does necking ignore notches in dynamic tension?. Journal of the Mechanics and Physics of Solids; 78:173-185 (2015).

LONGITUDINAL WAVE LOCALIZATION IN PHONONIC CRYSTALS WITH NEGATIVE CAPACITANCE

Yi-Ze Wang[1a)] &Yue-Sheng Wang[1]
[1]*Institute of Engineering Mechanics, Beijing Jiaotong University, Beijing* 100044*, China*

*Summary*A new kind of phononic crystals consisting of elastic rod by piezoelectric shunt with negative capacitance is presented. By the continuity conditions at the interface between different unit cells, the transfer matrix is derived. Based on the Lyapunov exponent of elastic waves in periodic structures and the algorithm presented by Wolf, the localization factor is presented. Numerical calculations are performed for the both the ordered periodic structures and random disorder of the negative capacitance. Results show the influences of the negative capacitance on the stop band properties and localization characteristics of longitudinal elastic waves. It provides a method to tune the band gap properties and control the propagation of elastic waves by the electric circuit method which is different from the traditional mechanical ones.

INTRODUCTION

Phononic crystals are periodic composite structures and have frequency stop band in which the elastic waves cannot propagate freely. Then, phononic crystals can provide a new way to tune elastic wave propagation and some engineering applications can be achieved, such as vibration and acoustic filter, noise isolation technology, etc. Among the interesting features of phononic crystals, the property of stop band is an important issue. As a result, a lot of investigations have been reported on the methods of changing the stop bands [1-4]. Previous changing ways are mainly focused on the mechanical methods, such as material parameters, structural arrangements, etc. But these methods are not easy to perform in the practical engineering applications and people tune their attention to the electrical or even active control ways which can be applied conveniently. It is well known that the piezoelectric shunt technology can be used to reduce the vibration of mechanical systems. As a typical component of the piezoelectric shunt, the negative capacitance has shown its interesting application [3-5]. Moreover, because of the mismatch of exerted control components during the practical engineering, electrical disorder can appear which result in the localization of elastic waves in periodic systems. This work discusses the elastic waves in phononic crystals rods consisting of piezoelectric shunt with the negative capacitance. Both the band gap properties for ordered systems and wave localization characteristics for randomly disordered periodic structures with the negative capacitance are presented.

MODEL DESCRIPTION

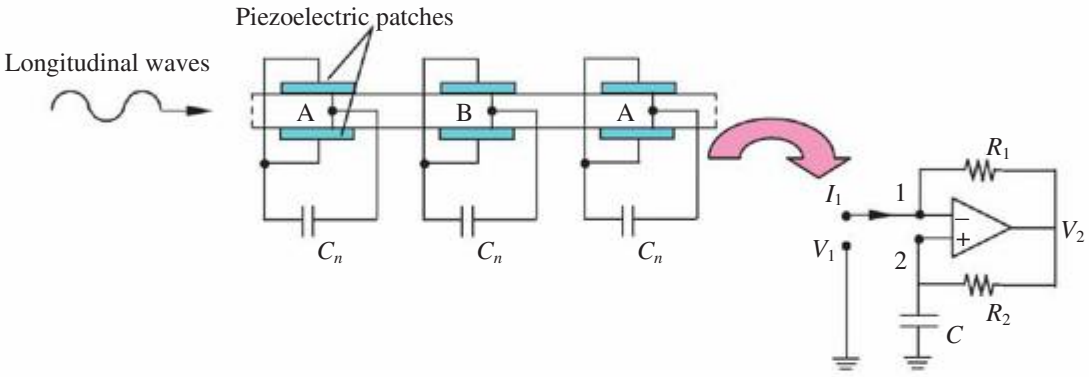

Fig. 1. Longitudinal waves in periodic rods consisting of piezoelectric shunt with negative capacitance.

As shown in Fig.1, the longitudinal elastic waves in phononic crystals are studied which are composed by piezoelectric shunt with negative capacitance. The length, width and thickness of the piezoelectric patch are $a_P = 0.02$m, $l_p = 0.02$m and $h_p = 0.0005$m. The material constants of the piezoelectricity are the piezoelectric compliance $s_{11} = 1.65\times10^{-11}$ m^3/N, mechanical and electrical coupling constant $d_{31} = -2.74\times10^{-10}$ C/m^2, dielectric constant $\in_{33} = 3.01\times10^{-9}$ F/m, mass density $\rho_P = 7500$ kg/m^3. Then, the inherent capacitance of the piezoelectric patch (C_p) can be calculated. Moreover material parameters of the elastic rod are the elastic modulus E_E=4.35×10^9 Pa, mass density $\rho_E = 1180$ kg/m^3 and length $a_E = 0.06$m.

[a)]Corresponding author. Email:wangyz@bjtu.edu.cn.

NUMERICAL RESULTS

Based on the discussion about the Lyapunov exponent and localization factor in Refs.[1, 2], the both the transfer matrix and localization factor can be derived, in which the localization factor being zero means the pass band. The relation between the localization factor and the normalized wave number are shown in Figs.2(a) and 2(b) for the ordered periodic structures and randomly disordered systems with the negative capacitance changing, respectively. The coefficient of variance (δ) denotes the randomly disordered degree of the periodic system, in which $\delta = 0$ means the ordered structure and $\delta \neq 0$ denotes the randomly disordered case. In Fig.2(a), different values of the negative capacitance are applied to present the control properties of elastic wave band gaps. The negative capacitances used are C_n= 0, 0.5 and 0.7C_p for the ordered periodic structure and the length ratio of different parts are 1:1. The regions corresponding to the location factor being zero are the pass bands and the other parts in which location factor is not zero mean the stop bands. It can be observed that if the wave number is small, such effect is not obvious. But the stop band characteristics can be changed significantly by the negative capacitance for larger normalized wave numbers. The pass band in which the elastic waves can propagate freely perhaps becomes the stop band with the negative capacitances changing. With the increasing of the negative capacitance, the number of the stop band becomes smaller.

Moreover, the relation between the localization factor and normalized wave number for the randomly disordered periodic system is shown in Fig.2(b). The negative capacitance is assumed to be a uniformly distributed random variable with a mean value $\overline{C}_p$ and coefficient of variance δ. We can see that for the disordered periodic structures, the pass band regions corresponding to the complete periodic structure vanish and the localization of elastic waves appears.

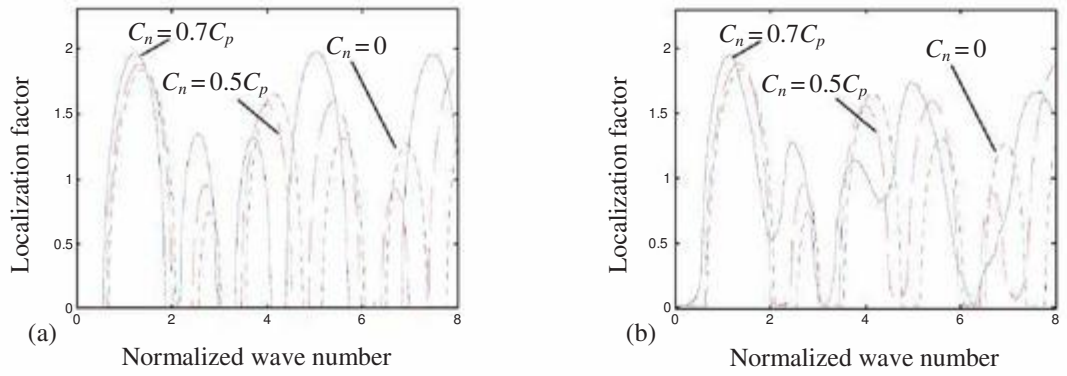

Fig. 2. Relation between the localization factor and normalized wave number for: (a) order periodic structures ($\delta = 0$) and (b) randomly disordered system with the negative capacitance changing ($\delta = 0.1$).

ACKNOWLEDGMENT

Support by the National Natural Science Foundation of China under Grant no. 11532001 is greatly appreciated. Y.Z. Wang also acknowledges the support by the National Natural Science Foundation of China (No. 11372090)

References

[1] Li F.M., Wang Y.S.. Study on wave localization in disordered periodic layered piezoelectric composite structures. *International Journal of Solids and Structures* **42**: 6457-6474, 2005.

[2] Wang Y.Z., Li F.M., Kishimoto K., Wang Y.S., Huang W.H.. Wave localization in randomly disordered periodic piezoelectric rods with initial stress. *Acta Mechanica Solida Sinica* **21**: 529-535, 2008.

[3] Chen S.B., Wen J.H., Yu D.L., Wang G., Wen X.S.. Band gap control of phononic beam with negative capacitance piezoelectric shunt. *Chinese Physics B* **20**: 014301, 2011.

[4] Chen Y.Y., Huang G.L., Sun C.T.. Band gap control in an active elastic metamaterial with negative capacitance piezoelectric shunting. *ASME Journal of Vibration and Acoustics* **136**: 061008, 2014.

[5] Manzoni S., Moschini S., Redaelli M., Vanali M.. Vibration attenuation by means of piezoelectric transducer shunted to synthetic negative capacitance. *Journal of Sound and Vibration* **331**: 4644-4657, 2012.

THE COUPLED DYNAMIC BEHAVIOUR OF LAYERED PIEZOELECTRIC STRUCTURES

Huangchao Yu[a] and Xiaodong Wang
Department of Mechanical Engineering, University of Alberta, Edmonton, Alberta, Canada, T6G 2G8

Summary This article presents a theoretical model of the coupled dynamic behaviour of a layered piezoelectric structure under in-plane harmonic loads with the transverse inertia and debonding of the piezoelectric layer considered. The dynamic behaviour is studied to evaluate the dynamic load transfer from the substrate to the surface-bonded layer. The dynamic strain ratio and wave field under different loading frequencies and material combinations are obtained by using the Fourier transform and solving the appropriate singular integral equations using Chebyshev polynomials. This model is validated by comparing with the corresponding FEM results. The interfacial debonding has a significant influence on the wave propagation in the structure, and its effects on surface stress are studied, which can be used to detect the debonding position under proper frequencies.

INTRODUATION

Much attention has been paid to the development of techniques of generating and collecting diagnostic elastic wave signals to realize continuous monitoring of structural integrity. Solid substrates with thin piezoelectric layers are typical structures to achieve this goal, and one of the fundamental issues is to evaluate their coupled dynamic behaviour and wave propagation. Huang et al.[1] studied the dynamic behaviour of layered piezoelectric structures with debonding under antiplane mechanical loads. Of particular interest to the current study is the in-plane wave propagation in a piezoelectric thin-sheet bonded to structures with both the axial deformation and the transverse inertia considered. The coupled dynamic behaviour in the structure with and without debonding under a longitudinal harmonic loading will be studied to evaluate the dynamic load transfer from the substrate to the surface-bonded layer.

METHOD AND MODELLING

The piezoelectric layered structure is shown in Fig. 1, which consists of a homogeneous and isotropic elastic substrate and a thin piezoelectric sheet with uniform thickness h. The coupled dynamic behaviour of the structure under a harmonic in-plane load of frequency ω is investigated. The piezoelectric layer can be modelled as an electro-elastic thin film subjected to a distributed axial force τ/h and a transverse normal force σ. The substrate is subjected to a harmonic incident wave and interfacial surface stresses, as shown in Fig. 1(a). The incident wave will be reflected and the surface stresses will generate a dynamic field in the substrate. Therefore, the wave field inside the substrate can be expressed by superimposing the wave field in Fig.1(b) and (c), which can be solved by conducting elastodynamic analysis[2]. If the piezoelectric layer is perfectly bonded to the substrate, the displacement should be continuous at the upper surface of the substrate and the lower surface of the sensing layer. By substituting the solutions of the layer and the substrate into the boundary conditions and applying Fourier transform, the displacement and stress fields along the piezoelectric layer can be determined.

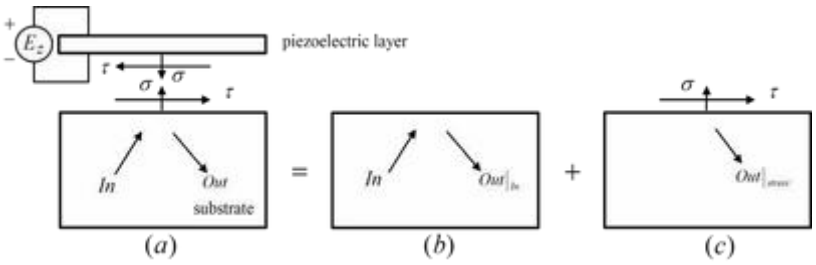

Figure 1. The piezoelectric layered structure and wave propagation in the substrate

When a debonding of length c occurs, the displacement field will be discontinuous along the interface between the layer and the substrate. The displacement discontinuity can be expressed by two dislocation density functions. After substituting the wave solutions without debonding into these two functions, and performing the appropriate asymptotic analysis, the crack surface boundary conditions can be reorganized as two singular integral equations, whose solutions include the well-known square root singularity and can be expressed as Chebyshev polynomials. If Chebyshev polynomials are truncated to the Nth term and these singular integral equations are satisfied at N collocation points along the crack surface given by $y_l = c\cos[(l-1)\pi/(N-1)],\ l=1,2,\cdots,N,$ then, the problem reduces to the solution of the following linear algebraic equations:

$$\begin{cases}\sum_{j=1}^{N} c_j[-\frac{1-\nu}{\mu}f_j^{(1)}(y_l)+\frac{1}{\mu}f_j^{(2)}(y_l)-\frac{i}{\mu\rho h\omega^2}f_j^{(3)}(y_l)]+\sum_{j=1}^{N} d_j[\frac{1-2\nu}{2\mu}f_j^{(4)}(y_l)+\frac{1}{\mu}f_j^{(5)}(y_l)]=k_1^2[m_{12}(k_1)u_z^l(y_l)-m_{22}(k_1)u_y^l(y_l)]\\ \sum_{j=1}^{N} c_j[-\frac{1-2\nu}{2\mu}f_j^{(4)}(y_l)-if_j^{(6)}(y_l)]+\sum_{j=1}^{N} d_j[\frac{1-\nu}{\mu}f_j^{(1)}(y_l)-f_j^{(7)}(y_l)]=k_1^2[m_{21}(k_1)u_y^l(y_l)-m_{11}(k_1)u_z^l(y_l)]\end{cases}$$

where $f_j^{(1)}=\dfrac{\sin[\frac{j(l-1)}{N-1}\pi]}{\sin(\frac{l-1}{N-1}\pi)}$, $f_j^{(3)}(y_l)=\dfrac{\cos[\frac{j(l-1)}{N-1}\pi]}{c\sin(\frac{l-1}{N-1}\pi)}+\dfrac{\cos(\frac{l-1}{N-1}\pi)\cos[\frac{j(l-1)}{N-1}\pi]}{c^2[\sin(\frac{l-1}{N-1}\pi)]^{3/2}}$, $f_j^{(4)}=\dfrac{\cos[\frac{j(l-1)}{N-1}\pi]}{\sin(\frac{l-1}{N-1}\pi)}$,

[a] Corresponding author. Email: huangcha@ualberta.ca

$$f_j^{(2)} = (-1)^n c\int_0^\infty (\frac{\alpha s k_T^2}{\Delta} - \nu + 1)p(y_l)ds,\quad f_j^{(5)} = (-1)^n c\int_0^\infty [\frac{s^2(2\alpha\beta - 2s^2 + k_T^2)}{\Delta} - \frac{1-2\nu}{2}]q(y_l)ds,\quad f_j^{(6)} = (-1)^n c\int_0^\infty [sm_{21}(s) + \frac{i(1-2\nu)}{2\mu}]q(y_l)ds,$$

$$f_j^{(7)} = (-1)^n c\int_0^\infty [sm_{11}(s) - \frac{1-\nu}{\mu}]p(y_l)ds,\quad p(y_l) = J_j(sc)\begin{cases}(-1)\sin(sy_l) & j=2n\\ \cos(sy_l) & j=2n+1\end{cases},\quad q(y_l) = J_j(sc)\begin{cases}\cos(sy_l) & j=2n\\ \sin(sy_l) & j=2n+1\end{cases},$$

$$m_{11}(s) = \frac{1}{E_p h(s^2 - \omega^2/c_p^2)} - \frac{k_T^2\beta}{\mu\Delta},\quad m_{12}(s) = -\frac{is}{\mu\Delta}(2s^2 - k_T^2 - 2\alpha\beta),\quad m_{21}(s) = -m_{12}(s),\quad m_{22}(s) = -\frac{\alpha k_T^2}{\mu\Delta} - \frac{1}{\rho h\omega^2},$$

$$k_I = \omega\sin\theta_I / c_L,\quad c_p = \sqrt{E_p/\rho},\quad k_L = \omega/c_L,\quad k_T = \omega/c_T,\quad \Delta = (2s^2 - k_T^2)^2 - 4s^2\alpha\beta,\quad \alpha = \sqrt{s^2 - k_L^2},\quad \beta = \sqrt{s^2 - k_T^2},$$

$$E_p = E + e^2/\lambda,\quad E = c_{11} - c_{13}^2/c_{33},\quad e = e_{13} - e_{33}c_{13}/c_{33},\quad \lambda = \lambda_{33} + e_{33}^2/c_{33},$$

with ρ, c_{ij}, e_{ij}, λ_{ij} being the density, the stiffness parameters, the piezoelectric constants and the dielectric constants of the piezoelectric layer, and μ, ν, c_L, c_T the shear modulus, the Poisson's ratio, the longitudinal velocity and the transverse velocity of the substrate, respectively. The solution of c_j and d_j can be determined from these linear algebraic equations, and then all displacement, strain and stress wave field components in the layer and substrate can be obtained.

RESULTS AND DISCUSSION

Wave propagation in PZT4-Aluminum layered structure is studied. The analysis will focus on the dynamic load transfer from the substrate to the surface-bonded layer under different geometric, loading and bonding conditions. In order to validate the current model, the finite element method (FEM) has been used. Fig. 2 (a) shows the magnitude of the normal stress along the interface for an incident longitudinal displacement wave with amplitude of 0.002 and angle of 30° using the current model, in comparison with the corresponding FEM results. Very good agreement is observed.

The dynamic strain ratio represents the percentage of deformation transferred from the host medium to the sensor. It is an index of the sensing characteristics of the piezoelectric layer. Specific examples are given in both perfect-bonding and imperfect-bonding cases. Fig. 2(b) shows the amplitude of the dynamic strain ratio with different material combinations under different loading frequencies without debonding. The strain ratio will increase gradually with the decrease of the loading frequency and the increase of the material combination, which is defined as the ratio of the Young's modulus of the substrate and that of the piezoelectric layer. Therefore, in order to gain a good dynamic strain ratio, high levels of loading frequency should be avoided and the stiffness of layers should not exceed that of the substrate too much. In imperfect bonding case, the dynamic strain ratio is dependent on the location along the interface. As shown in Fig. 2(c), the loading frequency has significant effects upon the load transfer. At the crack tip position, the stress concentration can be clearly observed. As expected, the measured surface stresses or voltage is very sensitive to the debonding position. In order to get clear deformation signals of the structure, interface debonding should be avoided.

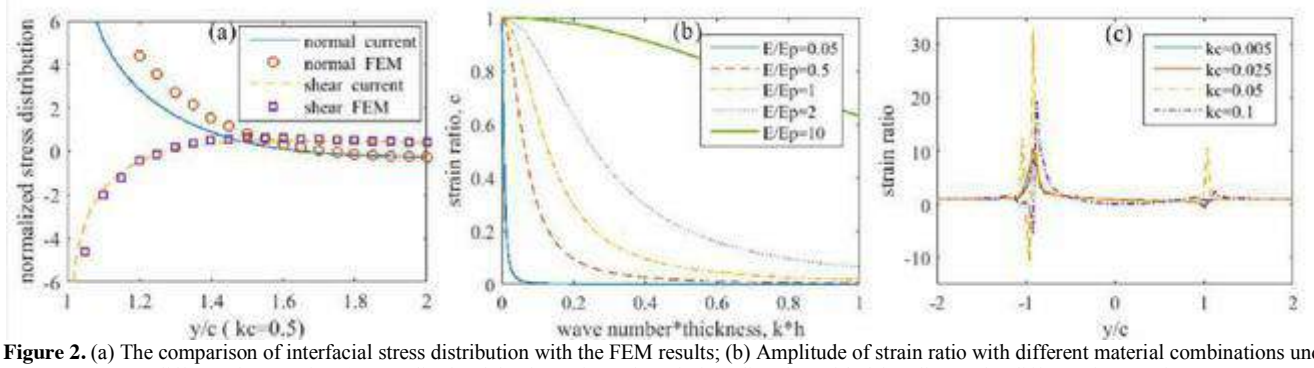

Figure 2. (a) The comparison of interfacial stress distribution with the FEM results; (b) Amplitude of strain ratio with different material combinations under different frequencies; (c) Amplitude of the dynamic strain ratio in y direction with debonding under different frequencies

CONCLUSIONS

The in-plane dynamic behaviour of the layered piezoelectric structure is studied to evaluate the dynamic load transfer from the substrate to the layer under different loading frequencies and material combinations. In order to gain a good dynamic strain ratio, high levels of loading frequency should be avoided and the stiffness of layers should not exceed that of the substrate too much. In the case with debonding, the interfacial crack has a significant influence on the load transfer. The stress concentration at the crack tips may cause abnormal surface deformation or voltage, which can be used to detect the debonding position under proper frequencies. Then the sensing layer can be changed or repaired timely to retrieve clear deformation signals.

References

[1] G. L. Huang and X. D. Wang, "On the dynamic behaviour of interfacial cracks between a piezoelectric layer and an elastic substrate," *Int. J. Fract.*, vol. 141, no. 1, pp. 63–73, 2006.

[2] J. D. Achenbach, *Wave propagation in elastic solids*. North-Holland Pub. Co., 1973.

SM08 - Multi-component Materials and Composites

TS.SM08-1.01	Ponte Castañeda, Pedro - Fully optimized variational estimates for the macroscopic response of nonlinear composites (INVITED)	2288
TS.SM08-1.02	Lopez-Pamies, Oscar - Nonlinear Electroelastic Deformations of Dielectric Elastomer Composites	2290
TS.SM08-1.03	Brenner, Renald - Approximate plastic yield criterion and hardening of porous single crystals	2292
TS.SM08-1.04	Mattei, Ornella - Bounds on the response of viscoelastic composites in the time domain	2294
TS.SM08-1.05	Doghri, Issam - Finite strain viscoelastic-viscoplastic modeling of polymers and application to composites	2296
TS.SM08-1.06	Voropaieff, Jean-Pierre - Modeling and identification of the constitutive behaviour of MRE's.	2298
TS.SM08-2.01	Brassart, Laurence - Homogenization-based constitutive modelling for diffusion problems (INVITED)	2300
TS.SM08-2.02	Bornert, Michel - Experimental investigation of grain boundary sliding in polycrystalline halite	2302
TS.SM08-2.03	Madra, Anna - A macroscale model of short fiber composite based on x-ray microtomography	2304
TS.SM08-2.04	Kubair, Dhirendra - Statistically augmented boundary conditions for statistically equivalent RVEs	2306
TS.SM08-2.05	Vandepitte, Dirk - Modelling variability in composite fibre reinforcement geometry data	2308
TS.SM08-2.06	Cho, Hansohl - Morphological Micromechanics of Copolymeric Elastomers	2310
TS.SM08-3.01	White, Scott - Self-healing of impact damage in woven composites (INVITED)	2312
TS.SM08-3.02	Ochoa, Ozden - An experimental and computational study on a NiTi/polyimide Matrix composite interface	2314
TS.SM08-3.03	Wu, Jiangtao - Active composites by multi-material 3d printing	2316
TS.SM08-3.04	Li, Tiantian - Design of co-continuous composite materials using 3d printing technique	2318
TS.SM08-3.05	Sottos, Nancy - Effects of microstructural variations on transverse crack initiation in composites	2320
TS.SM08-3.06	Daniel, Isaac - Yield criteria for matrix and composite materials under static and dynamic loading	2322
TS.SM08-4.01	Boechler, Nicholas - Dynamics of microscale granular crystals (INVITED)	2324
TS.SM08-4.02	Bonnet, Guy - Dynamic behaviour with metamaterial properties in elastic composites	2326
TS.SM08-4.03	Tsai, Peiying - Embedded nanoparticle arrangements on permittivity of elastomeric composites	2328
TS.SM08-4.04	Bodkhe, Samapda - Effect of nanoparticle addition on the mechanical and piezoelctric properties of 3D printed PVDF	2330
TS.SM08-4.05	Ray, Tyler - Field-Assisted 3D-Printing of Aligned Composites	2332
TS.SM08-4.06	Hohe, Jörg - Modelling of material uncertainties in long fibre reinforced thermoplastics	2334
TS.SM08-5.01	Jensen, Henrik - Steady State Kink Band Broadening in Layered Materials	2336

TS.SM08-5.02	Mallika Arachchige, Nuwan Dewapriya - Modelling adhesion of defective graphene interfaces	2338
TS.SM08-5.03	Mirkhalaf, Mohammad - Carving 3D architectures to transform the mechanics and performance of materials	2340
TS.SM08-5.04	Manzhirov, Alexander - Fundamentals of surface growth of solids in nature and technology	2342
PO.SM08-1.01.133	Abderrafai, Yahya - Design and 3D printing of polymer/ceramic composite structures	2344
PO.SM08-1.02.134	Abedi, Mehrnoosh - Damping of laminated plates: boundary condition and lamination sequence effects	2346
PO.SM08-1.03.135	Arif, Abul-Fazal - Thermal conductivity estimation of nanocomposites with randomly distributed inclusions	2348
PO.SM08-1.04.136	Barboura, Salma - Analytical Inclusion Green Operators in Transversally Isotropic Media	2350
PO.SM08-1.05.137	Chaudhry, Salman - High strain rate response of carbon nanotubes based elasotmer composites	2352
PO.SM08-1.06.138	Constantin, Nicolae - Impact Force Hystory Patterns on Sandwiches Versus Post-impact Behaviour	2354
PO.SM08-1.07.139	Fazili, Amin - Vibration of doubly tapered laminated composite beams by hierarchical FEM	2356
PO.SM08-1.08.140	Gao, Yuanwen - Electromechnical Behaviors of Multi-filament Twisted Superconducting Strand	2358
PO.SM08-1.09.141	Kaabi, Abderrahmen - Effect of ATH particle size on properties of vinyl ester matrix composites	2360
PO.SM08-1.10.142	Karamian-Surville, Philippe - Morphological parameters impact on the properties of 3D composite materials	2362
PO.SM08-1.11.143	Maruta, Tomohiro - Study on Fatigu Characteristics of Honeycomb Sandwich Panels	2364
PO.SM08-1.12.144	Mejak, George - Extreme elastic anisotropy of composites with periodic structure	2366
PO.SM08-1.13.145	Monetto, Ilaria - RVE size estimates for elastic matrices with spherically multi-layer inclusions	2368
PO.SM08-1.14.146	Ouadday, Rim - Effect of ATH concentration on properties of vinylester/ATH composite	2370
PO.SM08-1.15.147	Rahbar, Nima - Analytical studies on lamellar-structured composites made by freeze-casting	2372
PO.SM08-1.16.148	Serpilli, Michele - Magneto-electro-thermo-elastic interface models: an asymptotic approach	2374
PO.SM08-1.17.149	Ustrzycka, Aneta - Assessment of the strength of nanocomposites based on interface bonding analysis	2376
PO.SM08-1.18.150	Xiong, Jian - Mechanical behaviors of carbon fiber composite three dimensional latttice grid structures	2378
PO.SM08-1.19.151	Xu, Chao - Three-dimensional direct-write printing of metallic microstructures	2380
PO.SM08-1.20.152	Zhang, Qiancheng - Vibration and damping characteristics of sandwich beam with fiber felt core	2382
PO.SM08-1.21.153	Zhang, Zhijia - Free vibration analysis of sandwich beams with foam-corrugated core	2384

PO.SM08-1.22.154 Zhu, Hanxing - Composites with enhanced conductivity and Young's modulus and desired Poisson's ratio 2386

FULLY OPTIMIZED VARIATIONAL ESTIMATES FOR THE MACROSCOPIC RESPONSE AND FIELD STATISTICS OF NONLINEAR COMPOSITES

P. Ponte Castañeda*[1]

[1]*Department of Mechanical Engineering and Applied Mechanics, University of Pennsylvania, Philadelphia, Pennsylvania, USA*

Summary A variational method is proposed to estimate the macroscopic constitutive response of composite materials with nonlinear properties. The method derives from a stationary variational principle for the macroscopic potential in terms of the corresponding potential of a linear comparison composite (LCC) whose properties are the trial fields in the variational principle. The resulting estimates for the macroscopic response are guaranteed to be exact to second-order in the heterogeneity contrast, and to satisfy known bounds. In addition, the new method allows full optimization with respect to the properties of the LCC, leading to estimates that are fully stationary and exhibit no duality gaps. Consequently, the macroscopic response and field statistics of the nonlinear composite can be estimated directly from the suitably optimized linear comparison composite, without the need for difficult-to-compute correction terms. The method is applied to a porous viscoplastic material, and the results are compared with earlier estimates.

INTRODUCTION

Macroscopic samples of metals and minerals usually appear in the form of aggregates of large numbers of one, or more types of single crystal grains, and other inhomogeneities, such as voids and cracks, which are distributed with random positions and orientations in the sample. For this reason, it is of scientific and technological value to characterize the *effective* or *average* response of such macroscopic material samples from the properties of their constituents and known statistical information about their distribution, or microstructure. In addition, it is often of interest to also be able to extract information about the statistics of the stress and strain fields in the constituents of these composite materials. These problems—which are difficult in general—become especially challenging when the physical mechanisms of deformation are nonlinear, as in metals-forming operations, or polar ice flows. The objective of this work is to develop homogenization techniques to characterize the macroscopic response and field statistics in viscoplastic composites and polycrystals.

The simplest and perhaps most commonly used homogenization procedure in plasticity is the uniform strain-rate bound of Taylor [10]. Other commonly used approximations include the 'incremental' self-consistent approximation of Hill [2]. Improved bounds of the Hashin-Shtrikman type [1] for nonlinear composites were first developed by Talbot and Willis [9], making use of a nonlinear generalization of the Hashin-Shtrikman variational principles [11]. More general bounds and estimates were provided by Ponte Castañeda [3] by means of the 'variational linear comparison' method. This method makes use of a 'linear comparison composite' (LCC), whose properties are determined as trial fields in a suitably designed variational principle, leading to a 'secant' linearization of the constitutive response of the nonlinear phases, evaluated at the *second moments* of the stresses in the phases of the LCC [6]. In particular, 'variational linear comparison' self-consistent estimates have been proposed by Ponte Castañeda [3] for viscoplastic composites, and were later shown to improve on the earlier 'incremental' self-consistent estimates [2], especially for large heterogeneity contrasts and small rate-sensitivity exponents. It should also be mentioned that Suquet [7] proposed an alternative method for power-law materials, by making use of Hölder's inequality.

More accurate estimates for the macroscopic response of viscoplastic composites were given by Ponte Castañeda [5] by means of the 'second-order' homogenization method [4]. The 'second-order' method makes use of more general LCCs incorporating suitably selected eigenstrains, leading to an improved 'generalized secant' approximation for the nonlinear constitutive relations and ensuring that the resulting estimates are exact to second-order in the heterogeneity contrast, and thus in agreement with exact perturbation expansions [8]. In spite of the improved accuracy of the 'second-order' homogenization estimates [5] relative to the earlier 'variational' estimates [3], these estimates have certain undesirable features, arising from the lack of optimality of the eigenstrains, which hamper their efficient application in practice. These include the facts that the macroscopic constitutive relation and fields statistics cannot be obtained directly from the LCC, and the existence of a 'duality gap' (i.e., when the estimates resulting from the primary and complementary variational statements are different)—strongly suggesting the possibility of further improvements in the accuracy of its predictions. In this work, we propose a new variational method, where the properties of the constituent phases of the LCC are generated by a consistent optimization procedure. This leads to 'full stationarity' for the resulting estimates, which are still exact to second-order in the contrast, but have all the advantages of the earlier 'variational' estimates in that the macroscopic constitutive relation and fields statistics of the nonlinear composite can be conveniently expressed in the terms of the corresponding quantities for the suitably optimized LCC.

*Corresponding author. Email: ponte@upenn.edu

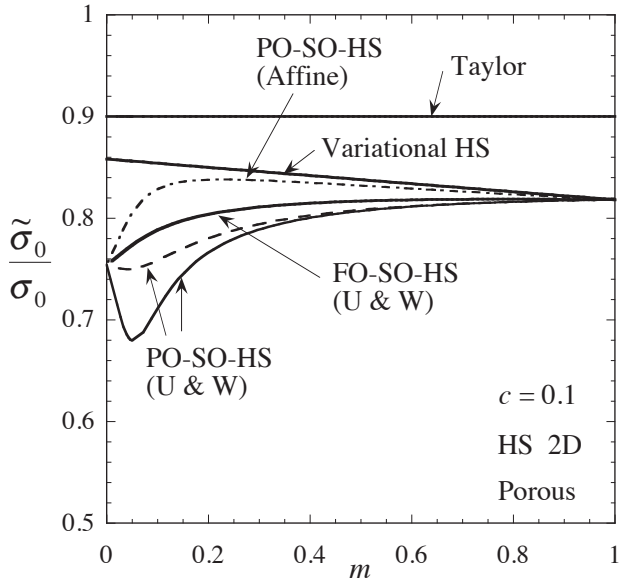

Figure 1: Predictions by the fully optimized second-order (FO-SO) method for the effective flow stress $\tilde{\sigma}_0$, normalized by the flow stress of the matrix σ_0, for porous power-law materials, as a function of the strain-rate sensitivity m, for a given porosity ($c = 0.1$). Comparisons are given with the Taylor and Variational Hashin-Shtrikman bound, as well as with earlier partially optimized second-order (PO-SO) estimates (refer to text for details).

APPLICATION TO POROUS VISCOPLASTIC MATERIAL

For the purpose of illustrating the capabilities of the new homogenization method, we provide here results for power-law materials weakened by aligned cylindrical voids in such a way that the overall symmetry of the composite is transversely isotropic. For further simplicity, we also consider plane strain conditions and purely deviatoric loading, so that the macroscopic response of the porous viscoplastic material can be described in terms of the effective flow stress $\tilde{\sigma}_0$, normalized by the flow stress of the matrix σ_0, as a function of the porosity c and the strain-rate sensitivity m. Thus, Fig. 1 shows the new fully optimized second-order (FO-SO) estimate, as a function of m, for a fixed porosity $c = 10\%$. The results are compared with the Taylor [10] and Variational Hashin-Shtrikman [3] upper bounds, as well as with the earlier partially optimized second-order (PO-SO) estimates [5]. In this connection, it is noted that all the second-order estimates have also made use of the Hashin-Shtrikman estimates for the effective properties of the LCC, and for this reason they agree with the HS bound in the limit of linear behavior ($m = 1$). However, for other values of the strain-rate sensitivity ($0 < m < 1$), the new results (FO-SO) can be seen to lie below the Taylor and HS bounds, and to be different from the earlier PO-SO estimates. In fact, as a consequence of the full optimality of the new SO method, the estimates obtained from the primal (W), dual (U) and directly from the LCC (affine) are precisely identical. On the other hand, the earlier second-order method [4], for which the properties of the LCC are only partially optimized, provides 3 generally distinct estimates, depending on the version (U, W, or affine). In this regard, it is interesting to remark that the FO-SO and PO-SO estimates also agree in the ideally plastic limit ($m = 0$), for which the PO-SO estimates were already known to agree. In conclusion, it can be seen that the new FO-SO estimates provide a significant improvement over the earlier PO-SO estimates. Further results for the corresponding fully optimized field statistics will also be obtained and discussed.

References

[1] Hashin Z, Shtrikman S. 1963 A variational approach to the theory of the elastic behaviour of multiphase materials. *J. Mech. Phys. Solids* 11, 127–140.

[2] Hill R. 1965 Continuum micro mechanics of elasto-plastic polycrystals. *J. Mech. Phys. Solids* 13, 89–101.

[3] Ponte Castañeda P. 1991 The effective mechanical properties of nonlinear isotropic composites. *J. Mech. Phys. Solids* 39, 45 – 71.

[4] Ponte Castañeda P. 2002 Second-order homogenization estimates for nonlinear composites incorporating field fluctuations: I.– Theory. *J. Mech. Phys. Solids* 50, 737 – 757.

[5] Ponte Castañeda, P. 2002 Second-order homogenization estimates for nonlinear composites incorporating field fluctuations: II.– applications. *J. Mech. Phys. Solids*, 50(4):759 – 782.

[6] Ponte Castañeda P, Suquet P. 1998 Nonlinear Composites. *Adv. Appl. Mech.* 34, 171–302.

[7] Suquet, P, 1993. Overall potentials and extremal surfaces of power law or ideally plastic materials. *J. Mech. Phys. Solids* 41, 981–1002.

[8] Suquet P, Ponte Castañeda P. 1993 Small-contrast perturbation expansions for the effective properties of nonlinear composites. *C. R. Acad. Sci. Paris II*, 317, 1515–1522.

[9] Talbot DRS, Willis JR. 1985 Variational principles for inhomogeneous nonlinear media. *IMA J. Appl. Math.* 35, 39–54.

[10] Taylor GI. 1938 Plastic strains in metals. *J. Inst. Metals* 62, 307–324.

[11] Willis JR. 1983 The overall response of composite materials. *J. Appl. Mech.* 50, 1202–1209.

NONLINEAR ELECTROELASTIC DEFORMATIONS OF DIELECTRIC ELASTOMER COMPOSITES

Oscar Lopez-Pamies* and Victor Lefèvre
Department of Civil and Environmental Engineering, University of Illinois, Urbana–Champaign, IL 61801, USA

Summary In this talk, we will present homogenization solutions for the macroscopic elastic dielectric response — under finite deformations and finite electric fields — of dielectric elastomer composites with two-phase isotropic particulate microstructures. Specifically, solutions will be presented for three classes of microstructures: i) an isotropic iterative microstructure wherein the particles are infinitely polydisperse in size and non-spherical in shape, ii) an isotropic distribution of polydisperse spherical particles of a finite number of different sizes, and iii) an isotropic distribution of monodisperse spherical particles. The solution for the iterative microstructure, which corresponds to the viscosity solution of a Hamilton-Jacobi equation in five "space" variables, is constructed by means of a novel high-order WENO finite-difference scheme. The solutions for the microstructures with spherical particles are constructed by means of hybrid finite elements.

Aimed at gaining physical insight into the extreme enhancement in electrostrictive properties displayed by emerging dielectric elastomer composites, various cases wherein the dielectric elastomer is non-Gaussian and the filler particles are nonlinear elastic dielectrics that exhibit polarization saturation will be discussed in detail. Contrary to an initial conjecture in the literature, it will be shown (*inter alia*) that the isotropic addition of a small volume fraction of stiff high-permittivity particles to dielectric elastomers does *not* lead to the extreme electrostriction enhancements observed in experiments. It will be posited that such extreme enhancements are the intricate manifestation of interphasial phenomena.

INTRODUCTION

Since the turn of the millennium, dielectric elastomer composites — specifically, dielectric elastomers filled with high-permittivity or (semi-)conducting particles — have received increasing attention by the materials research community because of their potential to outperform unfilled dielectric elastomers for employment in emerging technologies. At present, however, the microscopic mechanisms responsible for the superior electromechanical properties of this type of electroactive composite materials remain unresolved. In the literature, there are two mechanisms that have been identified as possibly dominant: i) the nonlinear elastic dielectric nature of elastomers which heightens the role of the fluctuations of the electric field in the presence of filler particles [1, 2] and ii) the presence of high-dielectric interphases and/or interphasial free charges surrounding the filler particles [3].

The objective of this work is to investigate the first of the two mechanisms stated above in the context of nonlinear electroelastic deformations. That is, we view dielectric elastomer composites as two-phase particulate composites — comprising a continuous dielectric elastomer matrix filled by a statistically uniform distribution of firmly bonded inclusions — and study their homogenized (macroscopic or overall) elastic dielectric response when subjected to finite deformations and finite electric fields. In light of the fact that the majority of existing experimental evidence pertains to dielectric elastomers filled with particles of roughly spherical shape that are distributed randomly without a biased direction, we focus our attention on dielectric elastomer composites with isotropic microstructures.

THE PROBLEM

The general problem to be addressed is that of determining the macroscopic elastic dielectric response of a dielectric elastomer, filled with an isotropic distribution of particles firmly bonded across interfaces, that is subjected to arbitrarily large deformations and electric fields. The sizes of the particles are taken to be much smaller than the macroscopic size. The constitutive behaviors of the dielectric elastomer and filler particles are characterized by isotropic incompressible free-energy functions $W_{\rm m}$ and $W_{\rm p}$ of the deformation gradient $\mathbf{F}$ and Lagrangian electric field $\mathbf{E}$ so that the Lagrangian pointwise constitutive relation for the composite is formally given by

$$\mathbf{S} = \frac{\partial W}{\partial \mathbf{F}}(\mathbf{X},\mathbf{F},\mathbf{E}) \nearrow p\mathbf{F}^{-T} \quad \text{n} \quad \mathbf{D} = \nearrow \frac{\partial W}{\partial \mathbf{E}}(\mathbf{X},\mathbf{F},\mathbf{E}) \quad \text{w} \qquad W(\mathbf{X},\mathbf{F},\mathbf{E}) = [1 \nearrow \theta(\mathbf{X})]W_{\rm m}(\mathbf{F},\mathbf{E}) + \theta(\mathbf{X})W_{\rm p}(\mathbf{F},\mathbf{E}) \tag{1}$$

Here, $\mathbf{S}$ and $\mathbf{D}$ denote the first Piola-Kirchhoff stress tensor and Lagrangian electric displacement field, p stands for the arbitrary pressure associated with the incompressibility constraint $\mathbf{F} = 1$, while θ is the indicator function of the spatial regions occupied collectively by the particles, taking the value of 1 if the position vector $\mathbf{X}$ lies in a particle and zero otherwise.

The dielectric elastomer composite is considered to occupy a domain Ω, with boundary $\partial\Omega$, in its undeformed stress-free polarization-free configuration. The macroscopic response of the material is defined as the relation between the averages of the first Piola-Kirchhoff stress $\mathbf{S}$ and the deformation gradient $\mathbf{F}$ over the volume Ω under affine displacement and electric potential boundary conditions: $\mathbf{x} = \overline{\mathbf{F}}\mathbf{X}$ and $\Phi = \nearrow \overline{\mathbf{E}} \cdot \mathbf{X}$ on $\partial\Omega$, where the second-order tensor $\overline{\mathbf{F}}$ and vector $\overline{\mathbf{E}}$ are prescribed quantities. In this case, it follows from the divergence theorem that $|\Omega|^{-1} \int_\Omega \mathbf{F}(\mathbf{X}) \ \mathbf{X} = \overline{\mathbf{F}}$ and $|\Omega|^{-1} \int_\Omega \mathbf{E}(\mathbf{X}) \ \mathbf{X} = \overline{\mathbf{E}}$, and

*Corresponding author. Email: pamies@illinois.edu

hence the derivation of the macroscopic response reduces to finding the average stress $\overline{\mathbf{S}} \doteq |\Omega|^{-1}\int_\Omega \mathbf{S}(\mathbf{X})\mathrm{d}\mathbf{X}$ and average electric displacement $\overline{\mathbf{D}} \doteq |\Omega|^{-1}\int_\Omega \mathbf{D}(\mathbf{X})\mathrm{d}\mathbf{X}$ for given $\overline{\mathbf{F}}$ and $\overline{\mathbf{E}}$. The result reads formally as [4]

$$\overline{\mathbf{S}} = \frac{\partial \overline{W}}{\partial \overline{\mathbf{F}}}\left(\overline{\mathbf{F}},\overline{\mathbf{E}},c\right) - \overline{p}\,\overline{\mathbf{F}}^{-T} \quad \text{and} \quad \overline{\mathbf{D}} = -\frac{\partial \overline{W}}{\partial \overline{\mathbf{E}}}\left(\overline{\mathbf{F}},\overline{\mathbf{E}},c\right) \quad \text{with} \quad \overline{W}\left(\overline{\mathbf{F}},\overline{\mathbf{E}},c\right) = \min_{\mathbf{F}\in\mathcal{K}}\max_{\mathbf{E}\in\mathcal{E}} |\Omega|^{-1}\int_\Omega W\left(\mathbf{X},\mathbf{F},\mathbf{E}\right)\mathrm{d}\mathbf{X}. \tag{2}$$

In these last expressions, $\overline{W}$ corresponds physically to the total electroelastic free energy (per unit undeformed volume) of the composite, $c = \int_\Omega \theta(\mathbf{X})\mathrm{d}\mathbf{X}$ is the initial volume fraction or concentration of particles, and $\mathcal{K}$, $\mathcal{E}$ denote sufficiently large sets of admissible deformation gradients $\mathbf{F}$ and curl-free electric fields $\mathbf{E}$ consistent with the applied affine boundary conditions.

RESULTS

By means of a combination of iterative techniques, Lopez-Pamies [4] constructed an exact solution for the variational problem $(2)_3$ for a fairly general (anisotropic) class of two-phase particulate microstructures wherein the particles are infinitely polydisperse in size. When specialized to isotropic distributions of filler particles and to matrix and filler particle behaviors characterized by the isotropic incompressible free energies W_{m} and W_{p}, his result for the finite branch (i.e., for isochoric deformations when $\det\overline{\mathbf{F}} = 1$) of the effective free-energy function $\overline{W}$ can be written as $\overline{W}(\overline{I}_1,\overline{I}_2,\overline{I}_4^E,\overline{I}_5^E,\overline{I}_6^E,c) = \overline{U}(\overline{I}_1,\overline{I}_2,\overline{I}_4^E,\overline{I}_5^E,\overline{I}_6^E,c) - W_{\mathrm{m}}(\overline{\mathbf{F}},\overline{\mathbf{E}})$, where $\overline{I}_1 = \overline{\mathbf{F}}\cdot\overline{\mathbf{F}}$, $\overline{I}_2 = \overline{\mathbf{F}}^{-T}\cdot\overline{\mathbf{F}}^{-T}$, $\overline{I}_4^E = \overline{\mathbf{E}}\cdot\overline{\mathbf{E}}$, $\overline{I}_5^E = \overline{\mathbf{F}}^{-T}\overline{\mathbf{E}}\cdot\overline{\mathbf{F}}^{-T}\overline{\mathbf{E}}$, $\overline{I}_6^E = \overline{\mathbf{F}}^{-1}\overline{\mathbf{F}}^{-T}\overline{\mathbf{E}}\cdot\overline{\mathbf{F}}^{-1}\overline{\mathbf{F}}^{-T}\overline{\mathbf{E}}$ and $\overline{U}$ corresponds to the viscosity solution of a Hamilton-Jacobi equation in the five "space" variables $\overline{I}_1,\overline{I}_2,\overline{I}_4^E,\overline{I}_5^E,\overline{I}_6^E$ and the "time" variable c. In this talk, we will present solutions for this effective free energy that are computed by means of a novel high-order WENO finite-difference scheme.

Complimentary to the above analytical approach, we will also present finite-element (FE) homogenization solutions for the macroscopic elastic dielectric response of isotropic dielectric elastomer composites wherein the filler particles are spherical in shape. These are viewed as infinite periodic media where their defining repeated unit cells contain a large but finite number of particles that are randomly distributed so as to approximate their isotropy; see Fig. 1(a) for an example. The independent variables in the conforming hybrid FE formulation that we adopt are taken as the deformation field, a pressure field, and the electric potential, which allow for the analysis of the locally incompressible behaviors of interest in this work. The nonlinear algebraic equations that result from the FE discretization are solved by means of an arc-length method in order to be able to carry calculations passed the electromechanical limit loads inherent to nonlinear electroelastostatics.

By way of an example, Fig. 1(b) shows results for the macroscopic response of an ideal elastic dielectric matrix (with initial shear modulus μ and initial permittivity ε) filled with a concentration $c = 0.05$ of stiff high-dielectric particles under loading conditions of uniaxial electrostriction: $\overline{\mathbf{S}} = \mathbf{0}$ and $\overline{\mathbf{E}} = (0,0,\overline{E})$, which result in a macroscopic deformation gradient and electric displacement of the form $\overline{\mathbf{F}} = \mathrm{diag}(\overline{\lambda}^{-1/2},\overline{\lambda}^{-1/2},\overline{\lambda})$ and $\overline{\mathbf{D}} = (0,0,\overline{D})$.

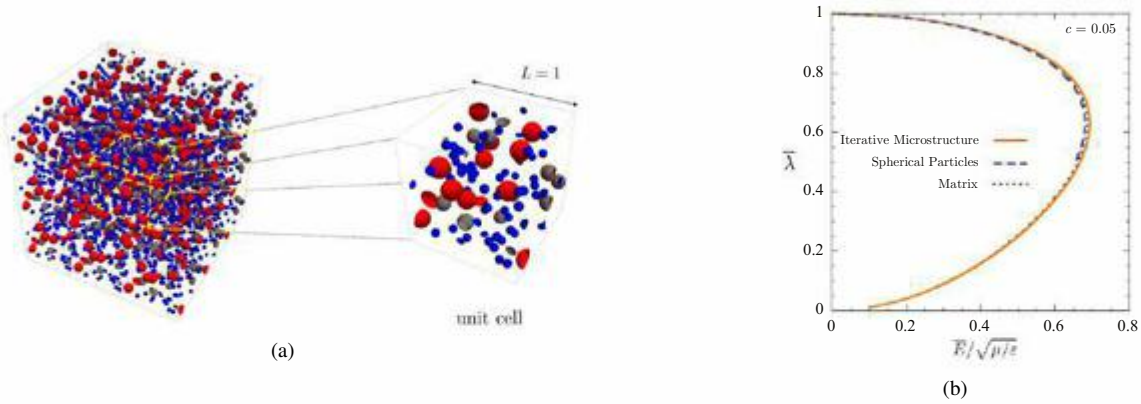

(a) (b)

Fig. 1: (a) Sample microstructure made out of the periodic repetition of a cubic unit cell with randomly distributed spherical particles of three different sizes (shown in blue, gray, and red, in order of increasing size). (b) Electrostriction stretch $\overline{\lambda}$ as a function of the applied electric field $\overline{E}$ for an ideal elastic dielectric matrix isotropically filled with a concentration $c = 0.05$ of stiff high-dielectric particles. Results are shown for the iterative microstructure of Lopez-Pamies [4] and for a distribution of monodisperse spherical particles. The response of the unfilled matrix is also shown for comparison purposes.

References

[1] Li J.Y.: Exchange coupling in P(VDF-TrFE) copolymer based all-organic composites with giant electrostriction. Phys. Rev. Lett. 90:217601, 2003.

[2] Tian L., Tevet-Deree L., deBotton G., Bhattacharya K.: Dielectric elastomer composites. J. Mech. Phys. Solids 60: 181–198, 2012.

[3] Lopez-Pamies O., Goudarzi T., Meddeb A.B., Ounaies Z.: Extreme enhancement and reduction of the dielectric response of polymer nanoparticulate composites via interphasial charges. Appl. Phys. Lett. 104:24290, 2014.

[4] Lopez-Pamies O.: Elastic dielectric composites: Theory and application to particle-filled ideal dielectrics. J. Mech. Phys. Solids 64:61–82, 2014.

APPROXIMATE PLASTIC YIELD CRITERION AND HARDENING OF POROUS SINGLE CRYSTALS

Joseph Paux, Renald Brenner *, and Djimedo Kondo

Sorbonne Universités, UPMC Univ Paris 06, CNRS, UMR 7190, Institut Jean le Rond d'Alembert, F-75005, Paris, France

Summary This study is devoted to the description of the plastic behaviour of porous single crystals in the context of rate-independent dislocation mediated plasticity. Such heterogeneous materials belong to the class of two-phase nonlinear composites with anisotropic local constitutive law. By making use of a regularized form of the Schmid law, an approximate plastic yield criterion is proposed in the context of limit-analysis. It has been assessed by comparison with unit-cell computations results. The model is then extended to hardenable crystals by performing a limit-analysis on a plastically deformed crystalline hollow sphere. The plastic strain field, and thus the local resistance of the material (i.e plastic yield surface), is assumed fixed. Comparisons are shown for the overall behaviour and porosity evolution with finite element unit-cell computations, from the literature, for body-centred cubic single crystals.

CONTEXT AND OBJECTIVES

As compared to the studies on polycrystals, relatively few works exist on the constitutive response of plastic single crystals containing voids. However, the importance of the crystalline anisotropy to describe the stress state surrouding intragranular voids has been clearly evidenced experimentally and numerically [1, 2]. The consideration of this anisotropy is thus important for the understanding of the ductile failure of monocrystalline materials or, more generally, polycrystalline materials with intragranular porosity. This calls for a constitutive model of the plastic response of voided crystals. To tackle this problem, two main approaches can be envisaged: nonlinear homogenization techniques for statistically homogeneous microstructures or limit-analysis for a specific elementary volume (typically a single hollow sphere).

Following works extending the well-known Gurson model to materials with anisotropic plastic criterion (see, for instance, [3]), a limit-analysis based yield criterion is first proposed. Then, the issue of the hardening description is considered in an approximate manner. The influence of the hardening is approximately accounted for using a procedure inspired from the one proposed in [4]. It is extended to the case of crystalline plasticity with a hardening law described at the slip system scale. It takes into account the spatially non-uniform evolution of the local strength domain and the spherical void growth. Results for the initial yield surface, the overall stress-strain response and the porosity evolution are presented.

PLASTIC YIELD CRITERION FOR HARDENABLE POROUS SINGLE CRYSTALS

To derive the yield criterion of porous single crystals, a single hollow sphere is considered. Its solid part is made of a single crystal, with arbitrary crystalline structure, which presents K plastic slip systems. Classically, plastic slip occurs on a slip system k when the resolved shear stress τ_k reaches a threshold value τ_k^c.Its local plastic strength domain C is classically described by the (multi-criterion) Schmid law

$$C = \{\boldsymbol{\sigma} \text{ such that } f_k(\boldsymbol{\sigma}) = \boldsymbol{\mu}_k : \boldsymbol{\sigma} \nearrow \tau_k^c \leq 0,\ \forall k = 1, \ldots, K\},\ \tau_k = \boldsymbol{\mu}_k : \boldsymbol{\sigma}, \tag{1}$$

with $\boldsymbol{\mu}_k$ the Schmid tensor of slip system k and $\boldsymbol{\sigma}$ the local Cauchy stress tensor. By adopting a regularized form of the Schmid law, an approximate plastic yield function is derived for the porous single crystal in the context of limit-analysis. Its general form is

$$\left(\sum_{k=1}^{K}\left(\frac{\boldsymbol{\mu}_k : \boldsymbol{\Sigma}}{\widetilde{\tau}_k^c(\mathbf{E})}\right)^n\right)^{2/n} + 2\,q f(E_m) \qquad (\kappa(\mathbf{E})\,\Sigma_m) \nearrow 1 \nearrow (q f(E_m))^2 = 0. \tag{2}$$

with $\boldsymbol{\Sigma}$ and $\mathbf{E}$ the overall stress and strain tensors, Σ_m and E_m the mean macroscopic stress and strain, f the porosity, $n \geq 2$ the regularization parameter of the Schmid law and $q > 1$ a fitting parameter. This criterion has been first proposed in the context of non-hardening crystals with cubic crystalline symmetry [5]. For this class of crystals, this criterion reduces, in the case of a quadratic regularization ($n = 2$), to the Besson and Benzerga criterion [3]. Following Leblond *et al.* [4], the hardening is described by distinct functions for the deviatoric and hydrostatic parts of the criterion, namely the effective critical shear stresses $\widetilde{\tau}_k^c(\mathbf{E})$ and the parameter $\kappa(\mathbf{E})$. They are obtained by determining the macroscopic strength domain of a hollow sphere which has been previously subjected to an overall strain $\mathbf{E}$. The corresponding plastic strain field within the sphere is given by the integration of an approximate strain rate field represented by a uniform deviatoric part and an incompressible radial expansion. Explicit expressions for $\widetilde{\tau}_k^c(\mathbf{E})$ and $\kappa(\mathbf{E})$ are obtained. They require the numerical evaluation of few volume integrals over the sphere. The plastic response of the porous material is finally obtained by considering an associated flow rule.

*Corresponding author. Email: renald.brenner@upmc.fr

RESULTS

Instantaneous response

FCC crystals under axisymmetrical loading have been considered, that is $\mathbf{\Sigma} = \Sigma_1(\mathbf{e}_1 \otimes \mathbf{e}_1 + \eta(\mathbf{e}_2 \otimes \mathbf{e}_2 + \mathbf{e}_3 \otimes \mathbf{e}_3))$. Figure 1a reports comparisons for $[100]$ crystalline orientation with FE results [6]. The prediction of our criterion for all crystalline orientations is shown in Figure 1b. Besides, our model agrees well with recent nonlinear homogenization results [7].

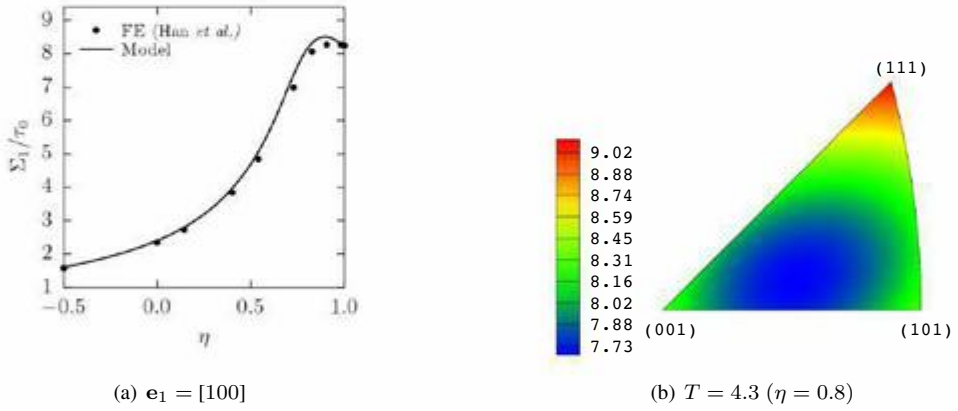

(a) $\mathbf{e}_1 = [100]$ (b) $T = 4.3$ ($\eta = 0.8$)

Figure 1: Plastic yield stress for porous FCC crystals under axisymmetrical loading: evolution with (a) the triaxiality and (b) the crystalline orientation ($f = 0.01$).

Hardening and porosity evolution

Our analytical model has been assessed by comparisons with FE results on the plastic response of BCC crystals with a nonlinear evolution of the critical shear stresses (i.e saturating hardening law) [2] (Figure 2).

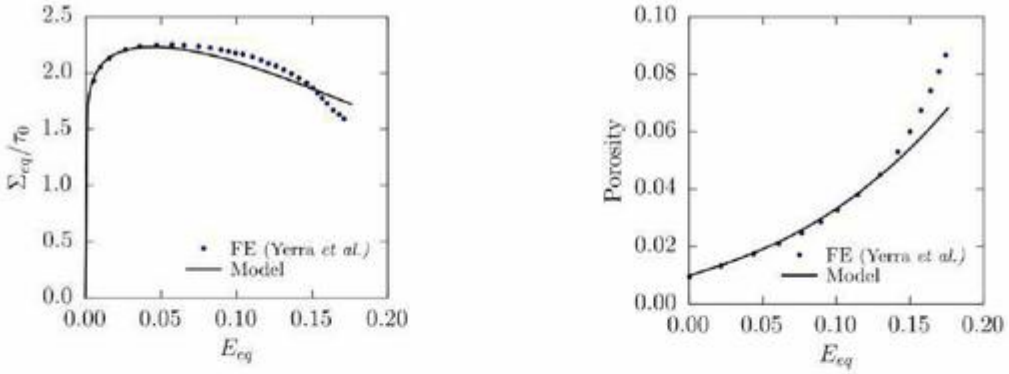

(a) (b)

Figure 2: Overall behaviour and porosity evolution for BCC porous crystal with [100] orientation for a triaxiality $T = 3$

References

[1] Kysar J. W., Gan Y. X., Mendez-Arzuza G.: Cylindrical void in a rigid-ideally plastic single crystal. Part I: Anisotropic slip line theory solution for face-centered cubic crystals. Int. J. Plast., 21:1481-1520, 2005.

[2] Yerra S., Tekoglu C., Scheyvaerts F., Delannay L., van Houtte P., T. Pardoen.: Void growth and coalescence in single crystals. Int. J. Solids Struct., 47:1016-1029, 2010.

[3] Benzerga A. A. and Besson J.: Plastic potentials for anisotropic porous solids. Eur. J. Mech. A/Solids, 20:397-434, 2001.

[4] Leblond J.-B., Perrin G., Devaux J.: An improved Gurson-type model for hardenable ductile metals. Eur. J. Mech. A/Solids 14:499-527, 1995.

[5] Paux J., Morin L., Brenner R., Kondo D.: An approximate yield criterion for porous single crystals. Eur. J. Mech. A/Solids 51:1-10, 2015.

[6] Han X., Besson J., Forest S., Tanguy B., Bugat S.: A yield function for single crystals containing voids. Int. J. Solids Struct., 50:2115-2131, 2013.

[7] Mbiakop A., Constantinescu A., Danas A.: An analytical model for porous single crystals with ellipsoidal voids. J. Mech. Phys. Solids, 84:436-467, 2015.

BOUNDS ON THE RESPONSE OF VISCOELASTIC COMPOSITES IN THE TIME DOMAIN

Ornella Mattei*[1] and Graeme W. Milton[1]

[1]*Department of Mathematics, University of Utah, Salt Lake City, Utah, USA*

Summary In order to derive bounds on the strain and stress response of a two-component composite material with viscoelastic phases, we revisit the so-called analytic method [1], first conceived for problems involving cyclic loadings in the frequency domain. The novelty of the present investigation lies in the application of such a method to derive bounds in the time domain for the antiplane viscoelasticity case. In particular, different sets of bounds are derived on the basis of the available information about the composite, such as the knowledge of the volume fractions or the transverse isotropy of the composite. In the examples studied, the results turn out to be very accurate estimates: if sufficient information about the composite is available, the bounds can be quite tight over the entire range of time, allowing one to predict the transient behavior of the composite.

OVERVIEW OF THE PROBLEM

In this investigation we propose a new approach to derive bounds on the response of a two-component viscoelastic composite under antiplane loadings in the time domain. The starting point is represented by the so-called analytic method, first proposed by Bergman [1] to bound effective conductivities when the component conductivities are real, and later extended to bound the complex effective tensor of a two-component dielectric composite in the frequency domain (see, for instance, Milton [3, 4], and Bergman [2]). The rigorous proof of the method was proposed by Golden and Papanicolaou [5]. To the best of our knowledge, the method until now has been applied only in the frequency domain, for cyclic external actions at a certain frequency. This work may be the first to extend the field of applicability of the analytic method to problems defined in the time domain with non-cyclic external actions.

The core of the analytic method is based on the fact that, by virtue of the analyticity property of the effective tensor of the viscoelastic composite in the Laplace transform domain, $\boldsymbol{\mathcal{L}}^h(p)$ (p is the Laplace transform parameter), with respect to the moduli of the components, i.e., the shear moduli $\mu_1(p)$ and $\mu_2(p)$ (we suppose both phases are isotropic), one can write the complex effective tensor as the sum of poles, s_i, $i = 0, 1, ..., m$, weighted by positive semi-definite matrix valued residues, $\mathbf{B}_i$, $i = 0, 1, ..., m$, as follows

$$\boldsymbol{\mathcal{L}}^h(p) = \mu_2(p) \left(\mathbf{I} \nearrow \sum_{i=0}^{m} \frac{\mathbf{B}_i}{s(p) \nearrow s_i} \right)$$

where $\mathbf{I}$ is the unit tensor and

$$s(p) = \frac{\mu_2(p)}{\mu_2(p) \nearrow \mu_1(p)}$$

Consequently, the response of the material in the time domain turns out to depend only on the position of the poles and on the value of the associated residues, which are the variational parameters of the problem. In particular, with reference to the stress response, the averaged stress field $\overline{\boldsymbol{\sigma}}(t)$ in the time domain is given by

$$\overline{\boldsymbol{\sigma}}(t) = \mu_2(0)\overline{\boldsymbol{\epsilon}}(t) + \dot{\mu}_2(t) \star \overline{\boldsymbol{\epsilon}}(t) \nearrow \sum_{i=0}^{m} \mathbf{B}_i \, \mathscr{L}^{-1} \left[\frac{p \, \mu_2(p)}{s(p) \nearrow s_i} \right] (t) \star \overline{\boldsymbol{\epsilon}}(t) \tag{1}$$

where $\overline{\boldsymbol{\epsilon}}(t)$ is the averaged strain field, the symbol $\star$ denotes the convolution product, the dot symbol represents the time derivative, and $\mathscr{L}^{-1}$ is the inverse of the Laplace transform.

The aim is to find the combinations of poles and residues which provide the maximum (or minimum) response of the composite for each moment of time. The optimization of the response of the material is performed in two steps. First, all the available information about the composite, such as the knowledge of the volume fraction of the constituents or of the value of the response of the material at a certain moment of time, is translated into (linear) constraints on the poles and residues. For instance, if the volume fractions f_1 and $f_2 = 1 \nearrow f_1$ of the phases are known, then the following constraints hold:

$$\sum_{i=0}^{m} \mathbf{B}_i = f_1 \mathbf{I} \qquad\qquad \left(\sum_{i=0}^{m} \mathbf{B}_i s_i \right) = f_1 \, f_2$$

Then, the response of the material being linear in the residues (see equation (1)) allows one to apply the theory of linear programming to limit the number of non zero residues, so that the problem is reduced to a new one with a relatively small number of non zero residues. Finally, the optimization over the positions of the poles is performed numerically for two specific cases: when the stress response has to be bounded, we consider a composite made of an elastic phase and a phase with a behavior described by the Maxwell model, whereas when we bound the strain response, we consider a composite made of an elastic phase and a phase modeled by the Kelvin-Voigt model. It is clear that the method is not limited to these particular models, but they are studied as, then, part of the calculations can be done analytically rather than numerically.

*Corresponding author. Email: o.mattei@unibs.it

NUMERICAL RESULTS

The estimates given by the numerical results prove to be increasingly accurate the more information about the composite is incorporated. In particular, when information such as the volume fraction of the components or the value of the response at a specific time is considered, the bounds are quite tight over the entire range of time, thus allowing one to predict the transient behavior of the composite. Most noticeably, when combinations of information are considered, such as the knowledge of the volume fractions and the eventual transverse isotropy of the composite, the bounds are extremely tight at certain specific times, suggesting the possibility of measuring the response of such times and, by using the bounds in an inverse fashion, almost exactly determining the volume fraction of the components of the composite.

As an example, let us consider the determination of bounds on one of the components of the averaged stress field, say $\overline{\sigma}_{12}(t)$, for each moment of time. In Figs. 1 and 2 we show the bounds obtained by considering various situations: the bounds become tighter and tighter as more information about the composite structure is included.

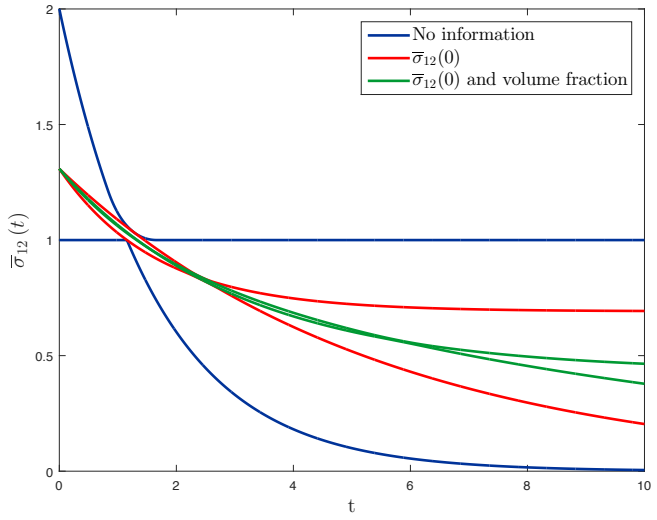

Figure 1: Comparison between the lower and upper bounds on $\overline{\sigma}_{12}(t)$ in the following three cases: no information about the composite is given; the value of $\overline{\sigma}_{12}(t)$ at $t = 0$ is prescribed; and the value of $\overline{\sigma}_{12}(t)$ at $t = 0$ and the volume fractions are known ($f_1 = 0.$).

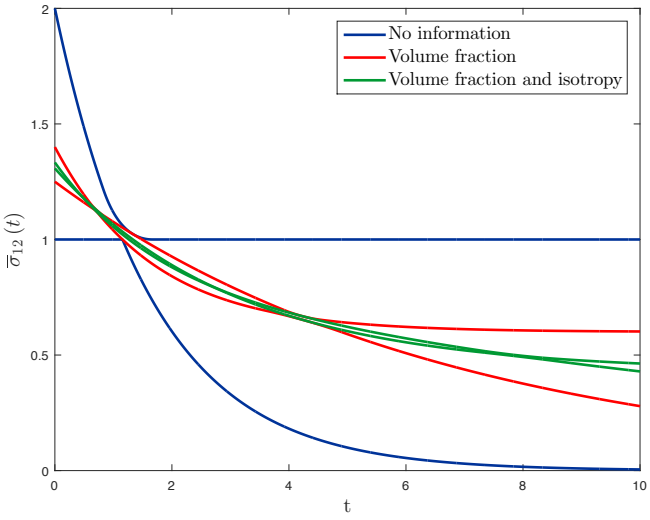

Figure 2: Comparison between the lower and upper bounds on $\overline{\sigma}_{12}(t)$ in the following three cases: no information about the composite is given; the volume fraction of the components is known ($f_1 = 0.$); and the composite is isotropic with given volume fractions.

It is worth noting that the bounds thus derived are always optimal, that is, they are always achieved by some particular microstructure (the so-called laminates of laminates), except in the case when the isotropy condition is applied.

References

[1] Bergman D.J.: The dielectric constant of a composite material - A problem in classical physics. Phys. Rep., C(43):377407, 1978.

[2] Bergman D.J.: Exactly solvable microscopic geometries and rigorous bounds for the complex dielectric constant of a two-component composite material. Phys. Rev. Lett., 44:12851287, 1980.

[3] Milton G.W.: Bounds on the complex permittivity of a two-component composite material. J. Appl. Phys., 52(8):52865293, 1981.

[4] Milton G.W.: Bounds on the transport and optical properties of a two-component composite material. J. Appl. Phys, 52(8):52945304, 1981.

[5] Golden K., Papanicolaou, G.: Bounds for effective parameters of heterogeneous media by analytic continuation. Comm. Math. Phys., 90(4):473491, 1983.

FINITE STRAIN THERMODYNAMICALLY-BASED VISCOELASTIC-VISCOPLASTIC MODELING OF POLYMERS AND APPLICATION TO COMPOSITES

Issam Doghri[1], Muralidhar Gudimetla[1]
[1]*iMMC/MEMA, Université catholique de Louvain, Louvain-la-Neuve, Belgium*

Summary A finite strain thermodynamically-based constitutive model coupling viscoelasticity (VE) and viscoplasticity (VP) is proposed for neat polymers. One version is suitable for Epoxy resins and another for thermoplastic polymers. A multiplicative decomposition of the total deformation gradient into VE and VP parts is assumed. Constitutive equations satisfying Clausius-Duhem's non-negative dissipation condition are derived. Unit cell finite element simulations for continuous fiber reinforced composites with a VE-VP Epoxy matrix are carried out. Numerical simulations are presented and discussed for both neat polymers and composites.

INTRODUCTION

Epoxy resin based fiber-reinforced composites are used in fields such as aerospace and automotive due to their structural efficiency and light weight. Accurate prediction of failure in such structures is of utmost importance. Usually the damage in fiber-reinforced composites appears in the form of cracks in matrix material, fiber-matrix debonding, fiber-breakage and delamination. In order to predict the initiation and/or propagation of damage in fiber-reinforced composite structures, it is quite essential to understand the thermo-mechanical behavior of matrix material i.e, the epoxy resin.
From the experimental data reported for untoughened epoxy resin Epon 862 in Poulain et al.[1] and Morelle [2], it is evident that these resin system exhibits rate-, temperature- and pressure- dependent yielding. The present work is aimed at developing a thermodynamically based finite strain constitutive model for epoxy resin systems which can represent the thermo-mechanical behavior at complex loading conditions. This constitutive model is suitable for implementation into multi-scale modeling of fiber-reinforced composites in order to predict the softening/degradation of the ply response.

CONSTITUTIVE MODELING

Most constitutive models for polymers are either viscoelastic (VE) or elasto-viscoplastic (EVP). In finite strain EVP, most models assume an additive decomposition of the rate of deformation tensor into elastic and inelastic parts ($\boldsymbol{d} = \boldsymbol{d}^{\mathrm{e}} + \boldsymbol{d}^{\mathrm{p}}$), and a hypoelastic relation between an objective Kirchhoff or Cauchy stress rate (e.g., Jaumann, Green-Naghdi-Mc Innis, etc.) and $\boldsymbol{d}^{\mathrm{e}}$. However, this is suitable for metals where elastic strains are small, but not for polymers. In addition, polymers usually exhibit viscous effects at all ranges of deformations.
Based on the previous observations, we propose a constitutive model for polymers which possesses the following features. It is a coupled viscoelastic-viscoplastic (VE-VP) model, which can be seen as a generalization to finite strains of the infinitesimal strain models of Miled et al. [3] and Krairi and Doghri [4]. It is based on a multiplicative decomposition of the deformation gradient into VE and VP parts ($\boldsymbol{F} = \boldsymbol{F}^{\mathrm{ve}}.\boldsymbol{F}^{\mathrm{vp}}$). Contrary to many other models, the present one is thermodynamically-based, and the starting point is the satisfaction of the Clausius-Duhem inequality which requires the dissipation to be non-negative. The Helmholtz free energy functional has an integral form similar to the one proposed by Christensen [5] for finite strain pure VE. In one version of the model, we use the VE Green-Lagrange (G-L) strain instead of Christensen's total G-L strain. The symmetric second Piola-Kirchhoff ($\boldsymbol{S}$) is then found to be a Boltzmann-type integral of the history of VE G-L strains. General Prony series are considered for the time-dependent VE moduli. As for the VP response, remarkably it is found that significant portions of the finite strain elasto-plasticity formulation proposed by Vladimirov el al. [6] applies to our case. The yield function, VP potential and viscosity function depend on a stress tensor $\boldsymbol{Y} = \boldsymbol{C}.\boldsymbol{S}$, defined with respect to the reference configuration, where $\boldsymbol{C}$ is the right Cauchy-Green (C-G) strain ($\boldsymbol{C} = \boldsymbol{F}^{\mathrm{T}}.\boldsymbol{F}$). All three functions depend on deviatoric as well as hydrostatic stresses. The VP flow rule takes a simple form in terms of the rate of $\boldsymbol{C}^{\mathrm{vp}}$, the right VP C-G strain.
There are two versions of the model. One is suitable for Epoxy –a thermoset polymer- where strongly nonlinear finite strain response is observed in compression-dominated deformation mode, while much smaller strains are reached in tension. A wealth of experimental data for Epoxy was recently obtained by Morelle [2]. Another version of the model is suitable for thermoplastic polymers and extends the VE-VP-damage model of Krairi et al. [4] to finite strains and pressure-dependent yield function, VP potential and viscosity function. Computationally, a fully implicit time integration algorithm was developed and implemented. The results of numerical simulations are presented and discussed.

Fiber-reinforced polymer matrix composites

A current application concerns Epoxy resins reinforced with continuous Carbon fibers. The Epoxy material obeys the finite strain VE-VP model described above. The continuous Carbon fibers are elastic and transversely isotropic.

[a] Corresponding author. Email: ictam2016papers@legendconferences.com.

Heterogeneous unit cells under periodic conditions are generated, meshed and simulated numerically with the finite element (FE) method. Simulation results are presented and discussed. Future work (not expected to be ready for the conference) involves the development of a homogenized anisotropic finite strain VE-VP constitutive model for the composite material.

References

[1] Poulain, X., Benzerga, A.A, Goldberg, R.K.: Finite-strain elasto-viscoplastic behavior of an epoxy resin : Experiments and modeling in the glassy regime, Int. Journal of Plasticity 62 (2014), 138-161.

[2] Morelle, X., Ph.D. thesis in Engineering sciences, Université catholique de Louvain, Belgium, 2015.

[3] Miled, B., Doghri, I., Delannay, L.: Coupled viscoelastic-viscoplastic modeling of homogeneous and isotropic polymers: numerical algorithm and analytical solutions, *Computer Methods in Applied Mechanics and Engineering*, **200**, 3381-3394, 2011.

[4] Krairi, A., Doghri, I.: A thermodynamically-based constitutive model for thermoplastic polymers coupling viscoelasticity, viscoplasticity and ductile damage, *International Journal of Plasticity*, **60**, 163-181, 2014.

[5] Christensen, R.M.: *Theory of viscoelasticity*, Academic Press.

[6] Vladimirov, I.N., Pietryga, M.P., Reese, S.: Anisotropic finite elastoplasticity with nonlinear kinematic and isotropic hardening and application to sheet metal forming, *International Journal of Plasticity*, 26, 659-687, 2010.

MODELING AND IDENTIFICATION OF THE CONSTITUTIVE BEHAVIOUR OF MRE's

Jean-Pierre Voropaieff [1], Laurence Bodelot[1], Kostas Danas[1], and Nicolas Triantafyllidis [*1,2]
[1] *Solid Mechanics Laboratory, Ecole Polytechnique, 91128 Palaiseau Cedex, France*
[2]*Aerospace & Mechanical Engineering Department, University of Michigan, Ann Arbor, MI 48109-2140, USA*

Summary In this paper, we study a class of active materials named magneto-rheological elastomers (MREs) with a main focus on their coupled magneto-mechanical response up to large strains and high magnetic fields. With the purpose of achieving a coupled characterization for the efficient design of MRE-based devices, this work encompasses the constitutive modeling of MREs. Based on the general theoretical framework for transversely isotropic magneto-elastic continua proposed by Kankanala and Triantafyllidis [1], we develop the coupled magneto-mechanical constitutive laws for both isotropic and anisotropic MREs in order to identify the corresponding constitutive model's material parameters. The actual experimental characterization of MREs conducted thanks to a specially designed specimen and novel experimental setup allowing tensile tests up to large strains and under high magnetic fields is presented in Pössinger [3]. The experimental data thus obtained provide the constitutive models for the isotropic and anisotropic MREs needed as input for subsequent numerical simulations.

MOTIVATIONS AND APPLICATIONS

Magneto-rheological elastomers (MREs) are smart materials composed of an elastomeric matrix filled with magnetic particles. The viscoelastic characteristics of the matrix combined with the magnetic properties of the particles allow these flexible composites to deform in response to a relatively low externally applied magnetic field. The rapid response, the high level of deformations and the possibility to control these deformations by adjusting the field make these materials of special interest in modern engineering. Yet, the characterization of the magneto-mechanical properties for finite strains and high magnetic fields is still far from being optimal, thus limiting the efficient design of MRE-based devices.

THEORETICAL CHARACTERIZATION

In what follows, we present general constitutive laws for the coupled magneto-mechanical response. For a detailed derivation of the governing equations, the reader is referred to the work of Danas, Kankanala and Triantafyllidis ([1] and [2]). Of interest here is the determination of the specific free energy ψ that best fits the MRE experiments. Using the general theory of transversely isotropic functions, one obtains that the general form of the specific Helmholtz free energy is given by

$$\rho_0\psi = W(I_1, I_2, I_3, I_4, I_5, I_6, I_7, I_8, I_9, I_{10}) \tag{1}$$

where I_i are ten independent invariants. Each of those invariants depend on **F** the deformation gradient, **m** the magnetization vector and the unit vector **N** which defines the initial orientation of the particle chains. Based on the work of Kankanala and Triantafyllidis [1], we get the following expressions for the Cauchy stress $\boldsymbol{\sigma}$ and the Eulerian h-field field **h** if we consider an incompressible material

$$\boldsymbol{\sigma} = \boldsymbol{\sigma}^T = \rho\frac{\partial\psi}{\partial\mathbf{F}}\cdot\mathbf{F}^T + \mathbf{hb} + (p \nearrow \mu_0(\mathbf{h}\cdot\mathbf{m} + \frac{1}{2}\mathbf{h}\cdot\mathbf{h}))\mathbf{I}, \qquad \mu_0\mathbf{h} = \rho\frac{\partial\psi}{\partial\mathbf{m}}, \tag{2}$$

where ρ is the current material density and **b** is the Eulerian magnetic field. The Lagrange multiplier p denotes the internal pressure (required by the incompressibility constraint $det\mathbf{F} = 1$). Based on those expressions, the energy function W is identified by use of experimental results (the experimental procedure is discussed in the following sections).

FABRICATION OF SAMPLES

In the perspective of obtaining a material in which magneto-mechanical coupling is optimal (i.e. largest deformation produced by the smallest magnetic field) for a possible application in tactile MRE interface, the selected matrix material is a very soft silicone elastomer. The filler phase is made of spherical iron particles with a median diameter of $3.5\,\mu$. Those particles are magnetically "soft", meaning that they do not retain magnetization once the magnetic field is turned off.

During the fabrication process, the magnetic particles of micron size are added to the uncured elastomer constituents and the obtained compound is thoroughly mixed and degassed, before curing is conducted in a mold of the desired shape. Moreover, the presence or the absence of a magnetic field during curing gives the possibility to produce either transversely isotropic (due to the formation of chain-like particle structures) or isotropic samples, respectively.

*Corresponding co-author. Email: nick@lms.polytechnique.fr

When characterizing MREs, a uniform field distribution (both mechanical and magnetic) within the sample should be achieved since field gradients can lead to additional deformation of the material on top of the original magneto-rheological effect. Even if the externally applied field $\mathbf{b}_0$ is assumed to be perfectly uniform, the shape of the magnetized MRE sample can create field gradients within the specimen. Magneto-static field equations and the corresponding boundary conditions suggest that the magnetization **m** as well as the total magnetic field **b** are uniform within the body only for ellipsoids of revolution. As a result, in order to find a compromise between the homogeneity of mechanical and magnetic quantities, the samples used are composed of a cylindrical gage area made of MRE and terminated at both ends by an ellipsoidal cap fixed to non-magnetic heads (see Figure 1(b)).

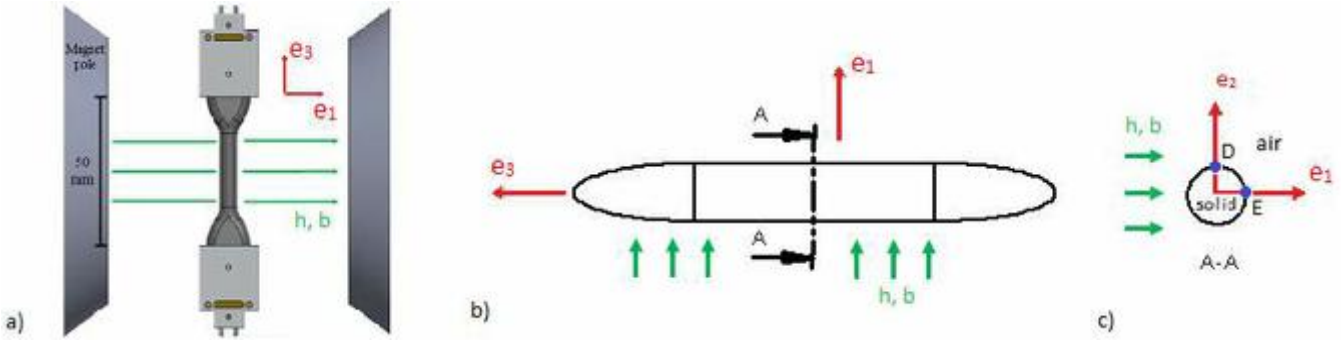

Figure 1: (a): Sample mounted on the uniaxial tension setup which is integrated into a magnetic field
(b and c): Cylindrical gage area terminated at both ends by an ellipsoidal cap (heads are not represented). The sample is subjected to an externally applied magnetic field along direction $\mathbf{e}_1$.

EXPERIMENTS

To obtain the macroscopic behavior of different MRE samples under coupled magneto-mechanical loading, we use a uniaxial tension setup integrated into a magnetic field (see Figure 1(a)). First, we perform a uniaxial tension test up to large deformations with no magnetic fields to get the purely mechanical parameters. Then, to determine the rest of the coefficients, a purely magnetic test is conducted in which the sample is subjected to an externally applied magnetic fied (up to 0.8T) but no mechanical loads. Finally, to check the predictability of our model, we carry out a coupled magneto-mechanical test.

Mechanical strains in the gage area of the sample are measured via non-contact video extensometry and the force exerted on the sample during loading is measured by two single-point load cells. In situ magnetic field measurements are carried out with two transversal Hall probes. One probe (named probe h) comes behind the sample at its center (postion E, see Figure 1(c)) and the second probe (named probe m) comes on the side of the sample (postion D, see Figure 1(c)). Since the samples for the magnetic measurements have a nearly ellipsoidal MRE body, the **h**-field, the magnetization **m** and the total magnetic field **b**, are all assumed to be uniform within the material. This assumption is accurate at relatives moderate strains (eg. in the order of 10% which is the case in this study) but is expected to become less accurate at larger strains since in that case the shape diverges from an ellipsoid.

Due to the continuity of the tangential component of **h**, the Hall probe h placed at the back of the sample gives access to the total field $\mu_0\mathbf{h}$ $[T]$ inside the material since the contribution of the magnetization **m** vanishes at that point. Due to the continuity of the normal component of **b**, the total magnetic field **b** $[T]$ inside the sample - now including the contribution of the total **h**-field (measured at the back) plus the contribution of the magnetization **m** - is measured by the lateral Hall probe m, which then gives access to the magnetization **m** inside the sample.

However, since the sensitive elements of the Hall probes cannot be placed exactly at the sample/air discontinuity interface due to geometrical limitations, we need to correct the measurement's systematic error due to the probe position. Expressions for the evolution of the magnetic field along direction $\mathbf{e}_1$ and $\mathbf{e}_2$ covering the discontinuity interface sample/air (see Figure 1(c)) are found analytically and checked experimentally.

References

[1] Kankanala, Triantafyllidis : On finitely strained magnetorheological elastomers. Journal of the Mechanics and Physics of Solids, 52:2869-2908, 2004.

[2] Danas, Kankanala, Triantafyllidis: Experiments and modeling of iron-particle-filled magnetorheological elastomers. Journal of the Mechanics and Physics of Solids, 60:120-138, 2012.

[3] Pössinger: Experimental characterization, modeling and simulation of magneto-rheological elastomers. PhD thesis, Ecole Polytechnique, France, 2015.

HOMOGENIZATION-BASED CONSTITUTIVE MODELLING FOR DIFFUSION PROBLEMS

Laurence Brassart *[1] and Laurent Stainier[2]
[1]*Department of Materials Science and Engineering, Monash University, Clayton, Victoria, Australia*
[2]*Institut de Recherche en Génie Civil et Mécanique (GeM, UMR 6183 CNRS), École Centrale de Nantes, France*

Summary This work investigates the effective thermodynamic and transport properties of inhomogeneous media in which one mobile species can diffuse. These properties are important for a variety of applications, including energy-storage materials and soft materials, where they further couple with the mechanical properties. Here we develop a first-order homogenization framework according to which the effective chemical behaviour can be obtained based on an analysis on a RVE of the microstructure. Based on a Hill-Mandel macro-homogeneity condition, expressions for the effective concentration rates and fluxes (conjugated respectively to the macroscopic chemical potential and its gradient) are derived. The framework is used to identify and calibrate non-classical, homogenized constitutive relations. In particular, we show that the commonly adopted assumption of local chemical equilibrium generally does not hold at the macroscopic scale.

A number of problems in materials science involve the transport of mobile species in materials, e.g. hydrogen diffusion in alloys, lithium diffusion in battery electrodes, solvent transport in polymer networks and gels, to name only a few. The diffusion medium is often heterogeneous, comprising phases, pores and interfaces with distinct thermodynamic (chemical capacity) and transport (mobility coefficients) properties. Micromechanics-based effective chemo-mechanical theories are highly desirable to describe the behaviour of such materials at a macroscopic scale. This preliminary work focuses on chemical properties only, with the long-term objective of modelling chemo-mechanical couplings.

We formulate effective constitutive relations within the framework of the thermodynamics of irreversible processes. The thermodynamic state of a material point at the macroscopic scale is described by an effective concentration, c, and possibly a set of internal variables collectively denoted by $\boldsymbol{\alpha}$. In the absence of chemical reaction, the effective concentration obeys the balance equation $\dot{c} + \boldsymbol{\nabla} \cdot \boldsymbol{j} = 0$. We can then postulate the existence of an effective free energy density function $W(c, \boldsymbol{\alpha})$. The following fundamental thermodynamic inequality holds (free energy imbalance):

$$\mathcal{D} = \mu \dot{c} \nearrow \dot{W} \nearrow \boldsymbol{j} \cdot \boldsymbol{\nabla} \mu = \left(\mu \nearrow \frac{\partial W}{\partial c} \right) \dot{c} \nearrow \boldsymbol{j} \cdot \boldsymbol{\nabla} \mu \nearrow \frac{\partial W}{\partial \boldsymbol{\alpha}} \bullet \dot{\boldsymbol{\alpha}} \geq 0. \tag{1}$$

Note that we do not a priori assume local chemical equilibrium. Rather, the chemical potential μ is treated as a primary variable quantifying the energy supply due to macroscopic transport of species. In practice, it must be computed such that the species conservation equation is satisfied. The inequality (1) must be satisfied by kinetic models for species insertion, species transport and evolution of internal variables:

$$\dot{c} = \mathcal{F}(\mu, \boldsymbol{\nabla} \mu, \boldsymbol{\alpha}), \ \boldsymbol{j} = \mathcal{G}(\mu, \boldsymbol{\nabla} \mu, \boldsymbol{\alpha}), \ \dot{\boldsymbol{\alpha}} = \mathcal{H}(\mu, \boldsymbol{\nabla} \mu, \boldsymbol{\alpha}) \tag{2}$$

We aim to investigate the mathematical structure of the effective free energy function and kinetic models that emerge from an analysis at the microscale. To this end, we developed a first-order homogenization framework for the diffusion problem (Figure 1). A Representative Volume Element (RVE) is attached to each macroscopic point and subjected to linear chemical potential boundary conditions. Energy conservation requires that $W = \langle W_m(\boldsymbol{y}, c) \rangle$, where the subscript m denotes microfields, $\boldsymbol{y}$ is the microscale position vector, and $\langle \cdot \rangle$ represents a volume average over the RVE. We further postulate a Hill-Mandel chemical macrohomogeneity condition, from which the macroscopic concentration rate and flux are related to their microscopic counterparts:

$$\dot{c} = \langle \dot{c}_m \rangle, \quad \boldsymbol{j} = \langle \boldsymbol{j}_m \rangle \nearrow \langle \dot{c}_m (\boldsymbol{y} \nearrow \boldsymbol{y}_0) \rangle. \tag{3}$$

Relation (3) shows that the macroscopic flux is not given by the volume average of the microscopic flux, as classically obtained under a local steady-state assumption [1]. Rather, the macroscopic flux and rate of species insertion are both affected by the "chemical inertia" of the RVE, which in general depends on the RVE size. In general, they will both depend on μ, $\boldsymbol{\nabla} \mu$ as well as on the microscopic field of concentration, requiring effective constitutive relations of the general form (2).

We narrow down our analysis to the case of two-phase composites consisting of one continuous matrix phase of high diffusivity containing inclusions of much lower diffusivity: $D_{mat} \gg D_{icl}$. One can distinguish two limiting regimes of the heterogeneous diffusion process. For a sufficiently large sample size, $(L/a)^2 \gg D_{mat}/D_{icl} \gg 1$, the overall relaxation of the system is limited by macroscopic transport of species over long distances though the fast percolating matrix phase, while the RVE analysis can be conducted under the steady-state assumption. In the other limit of small sample size, $1 \ll (L/a)^2 \ll D_{mat}/D_{icl}$, the concentration evolution is limited by diffusion within the inclusion phase, while the chemical potential has

*Corresponding author. Email: laurence.brassart@monash.edu

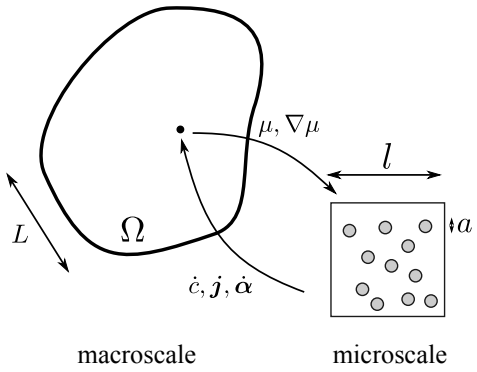

Figure 1: Scale transition for the transient diffusion problem

reached macroscopic steady-state. Transition between these regimes can be captured by a simple model without internal variable. The kinetic model of insertion if of the Kelvin-Voigt type [2]:

$$\frac{\dot{c}}{c_0} = \frac{1}{\tau}\left(\frac{\mu}{kT} \nearrow \frac{1}{kT}\frac{dW}{dc}\right), \tag{4}$$

where τ is a characteristic relaxation time associated with diffusion within the inclusion phase and depends on the inclusion size. Macroscopic transport is described by the classical diffusion model:

$$\boldsymbol{j} = \nearrow \mathcal{C} M \boldsymbol{\nabla}\mu \equiv \nearrow \mathcal{D}\boldsymbol{\nabla} c. \tag{5}$$

Effective kinetic coefficients are calibrated based on RVE simulations. We illustrate this simple model in the 1D problem of a thin plate immersed in an bath where the chemical potential of the diffusing species is fixed. The initial concentration in the plate is c_0, and the chemical potential $\bar{\mu}$ in the bath drives species to migrate within the plate until the concentration is uniform, with $c(x) = c_{eq}$. The relaxation time shows a transition between a length-independent, insertion-limited regime and a diffusion-limited, Fickian regime at larger sizes (Figure 2(a)). The transition takes place at a characteristic length $\Lambda = \sqrt{D\tau}$. For a thick plate, one recovers a classical Fickian behaviour (Figure 2(b)). In contrast, when the plate thickness becomes comparable to or lower than the intrinsic length, the effective transport becomes anomalous due to micro-diffusion. These preliminary results suggest that the commonly adopted assumption of local chemical equilibrium generally does not hold at the macroscopic scale. Kinetic models for species insertion can be exploited for formulating non-classical chemo-mechanical theories [2].

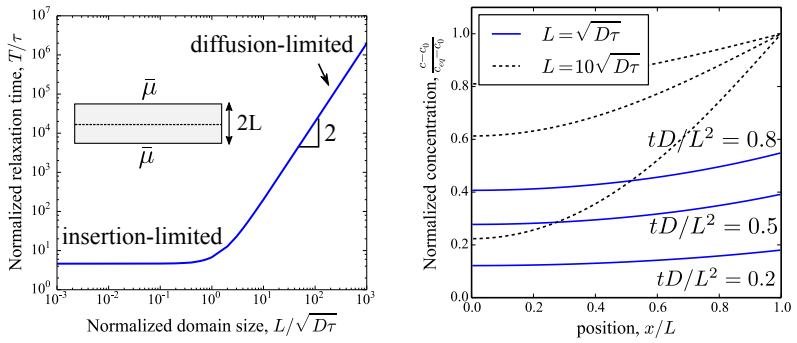

(a) (b)

Figure 2: 1D diffusion solution accounting for insertion kinetics due to micro-transport. a) Relaxation times as a function of the plate thickness. b) Concentration profiles for two values of the plate thickness at different simulation times.

References

[1] Torquato S.: Random heterogeneous media. Springer, 2002.

[2] Brassart L., Suo Z.: Reactive flow in solids. J. Mech. Phys. Solids 61:61-77, 2013.

EXPERIMENTAL INVESTIGATION OF GRAIN BOUNDARY SLIDING IN POLYCRYSTALLINE HALITE

Michel Bornert*[1], Ababacar Gaye[1], Matthieu Bourcier[2], Alexandre Dimanov[2], Jean Raphanel[2], Eva Héripré[2], and Andrew King[3]

[1]*Laboratoire Navier, CNRS UMR8205, IFSTTAR, ENPC, Université Paris-Est, Marne-la-Vallée, France*

[2]*LMS, CNRS UMR7649, École polytechnique, Université Paris-Saclay, Palaiseau, France*

[3]*Psiché beamline, Synchrotron Soleil, Gif-sur-Yvette, France*

Summary Deformation mechanisms of synthetic halite are investigated at the scale of its polycrystalline microstructure. Both crystal slip plasticity, associated with several slip systems with contrasted critical resolved shear stresses, and grain boundary sliding are observed during in situ compression tests inside the chamber of a scanning electron microscope (SEM). Specific digital image correlation tools provide access to a quantification of the relative contribution of both mechanims to the overall strain of the sample and show that grain boundary sliding is present from the beginning of plasticity, establishing that plastic deformation of such a rock is not possible without simultaneous damage. These surface measurements are complemented with full 3D investigations based on computed X-rays absorption tomography and digital volume correlation, performed on samples that are also investigated in the SEM. Obtained data provide a way to compare the statistics of local fields in the bulk of samples and near free surfaces.

INTRODUCTION

Polycrystalline materials exhibit complex behaviors when they deform in their plastic regime, as a consequence of their various active physical deformation mechanism at grain scale and the heterogeneity associated with local lattice orientation which varies from grain to grain, and possibly also inside grains. Better insight on the physics of such materials can be obtained from full-field strain measurements at microscale over sets of interacting grains inside a sample submitted to various loading conditions. Many studies have been reported in this line during the last decades [1] and highlight strong strain heterogeneities at local scale. Such an experimental methodology is applied in the present study on halite, which is a rock forming mineral with industrial applications, such as deep underground storage of hydrocarbons, or more recently, of compressed air in the context of temporary storage of "green energy". In addition to exhibiting several slip systems with temperature-dependent critical resolved shear stresses as in many polycrystalline metals, halite deforms also by means of an additional deformation mechanism which is grain boundary sliding, as qualitatively evidenced in a former study [2] based on compression tests inside a scanning electron microscope (SEM) and processing of the recorded images by means of digital image correlation (DIC). The co-existence of both mechanisms makes halite also an interesting material from an academic point of view. Indeed, the dodecaedric "easy" slip systems [3] generate only a 2-dimensional set of strains at grain scale, so that additional deformation mechanisms are necessary to accommodate arbitrary overall strains. These can be either additional harder crystalline slip systems (octaedric or cubic), or the above mentioned interfacial mechanism. The prediction of the relative contribution of such mechanisms would be a challenging question for multiscale theoretical models of the mechanical behavior of such polycrystals. This question addresses also more practical issues: indeed grain boundary sliding is associated with local damage, for instance in the form of pore growth at triple junctions of grains, as observed in [2], which has consequences on both the mechanical resistance of the material and its permeability. The present work aims at extending the former study in two ways. First, specific image processing routines have been developed to accurately quantify the relative contribution of crystal slip plasticity and grain boundary sliding to the overall deformation of halite. These procedures have been applied to SEM images of halite submitted to compression at room temperature and 350 degrees. Second, these purely surface investigations have been complemented with full 3D investigations based on synchrotron absorption X-rays computed tomography (XRCT) imaging, performed on the new Psiché beamline of Synchrotron Soleil (France), and digital volume correlation (DVC). More specifically, strain fields in the bulk have been characterized together with strain fields at the free surface of the same sample at the same level of overall strain, so that the influence of the free boundary conditions of the local deformation at grain scale can be investigated.

QUANTIFICATION OF RELATIVE CONTRIBUTION OF CSP AND GBS

Synthetic halite samples have been obtained by hot pressing high purity NaCl powder under various thermomechanical conditions to control grain size and reduce residual porosity. The $5 \times 5 \times 10$ mm samples considered for the SEM analysis exhibit rather large equiaxed grains, with a typical size ranging from 250 to 500 μm. DIC routines requires a local contrast at a scale much smaller than grain size, which was provided by the dewetting of a thin gold film sputtered over the mechanically

*Corresponding author. Email: michel.bornert@enpc.fr

polished observation surface of the sample. This generates micron-sized beads stuck to the surface of the sample providing an excellent contrast in SEM imaging. Samples are uniaxially compressed in the chamber of a SEM (FEI Quanta 600) at various load levels. At each step, high definition images with various magnifications are recorded in secondary electron mode. A first test has been performed at room temperature, and a second at 350°C by means of an adapted micro-oven surrounding the sample and in which an observation hole is machined.

An adapted DIC algorithms has been developed to quantify separately the components of the average deformation gradient inside grains and the displacement discontinuities at the grain boundaries [4]. It is based on masking techniques which ensure that the image contrast used to quantify the kinematics of a grain is strictly located inside the considered grain, and appropriate contour integrals to separate the overall gradient into its bulk and interfacial contributions. The analysis shows that GBS has only a limited contribution to overall strain, but also that this contribution is present from the very beginning of plasticity. At room temperature strain due to GBS is proportional to overall strain and represents about 2.5% for the axial component, and 6% for the transverse one. The larger contribution to the transverse strain is associated with the opening of longitudinal interfaces. At high temperature, GBS is also present from the beginning but evolves nonlinearly with load: its contribution decreases at larger load levels. This is likely to be associated with the activation of a second family of slip systems which makes GBS less necessary for the accommodation of strain incompatibilities induced by the activation of the first family of slip systems.

COMBINED 2D AND 3D LOCAL STRAIN FIELD MEASUREMENTS

In order to apply DVC techniques to the XRCT images of such materials an appropriate contrast is required at grain scale, which is not naturally present in single phase polycrystalline materials. That's why a specific material has been manufactured, also with HIP techniques, in which small copper particules, a few micrometers in diameter, have been embedded. These markers are located inside grains and at grain boundaries; appropriate thermomechanical processing allowed to obtain grains up to a grain size of about 50 μm to 250 μm. Samples with a typical size of $\times$ $\times$ mm have been fully imaged at four compression levels (0.5% to 4% total residual strain) with a voxel size of 3.04μm. Tests had to be performed ex-situ because intense X-rays tend to harden halite which becomes then brittle under uniaxial compression. A thermal treatment has been applied to the sample after each CT scan, in order to restore ductility. Uniaxial tests have been monitored with macroscopic optical digital image correlation tools. In addition to these 3D observations at small scale, high definition SEM surface measurements over about 2×2 mm regions of interest, have been performed at each step of deformation, using 9 high-definition images with a pixel size of 240nm. Surface DIC routines could be applied thanks to the dewetting of a pure copper thin layer which generates an appropriate contrast. DVC routines could also be applied to the 3D XRCT images but at the price of specific developments to deal with the sparse contrast provided by the copper particules. The spatial resolution of the 3D strain mapping was thus about 10 times coarser than the 2D one, but comparisons are nevertheless possible. Both techniques highlight the complex localisation patterns of the strain field at grain scale, with in particular long range features which spread over several grains. The spatial resolution of the 3D technique is however too coarse to directly link these features to inter- or intra- granular mechanisms. A preliminary statistical comparison of the strain at intermediate scale is however possible between near surface areas and areas in the bulk of the samples. In addition, qualitative signs of damage are also found in the bulk of the samples: they appear as longitudinal cracks located at grain interfaces parallel to the compression axis. A first quantification of their contribution to overall deformation is provided by the spherical part of the measured strain, and confirms the presence of these mechanisms in the first deformation steps. More detailed 2D/3D comparisons are currently underway and should be available at the time of the conference.

Aknowledgments

The presented study was funded by the ANR project "MicroNaSel" under grant number ANR-10-BLAN-935. The SEM used for in situ compression tests has been acquired with the financial support of Région Île de France (SESAME 2004 Program). Soleil beam time has been allocated under proposal number 20140313.

References

[1] Héripré, E., Dexet, M., Crépin, J., Gélébart, L., Roos, A. Bornert, M. and Caldemaison, D. Coupling between experimental measurements and polycrystal finite element calculations for micromechanical study of metallic materials, International Journal of Plasticity, Vol. 23(9)1512-1539, 2007

[2] Bourcier, M., Bornert, M., Dimanov, A., Héripré, E., and Raphanel, J. L. Multiscale experimental investigation of crystal plasticity and grain boundary sliding in synthetic halite using digital image correlation, Journal of Geophysical Research, Solid Earth, 118(2), 511-526, 2013

[3] Carter, N., and Heard, H. Temperature and rate dependent deformation of halite. American Journal of Science, 269, 193?249. 1970

[4] A. Gaye, Analyse multiéchelle des mécanismes de déformation du sel gemme par mesures de champs surfaciques et volumiques, PhD manuscript, Université Paris-Est, 2015

A MACROSCALE MODEL OF SHORT FIBER COMPOSITE BASED ON X-RAY MICROTOMOGRAPHY

Anna Madra*[1,2], Alain Rassineux[1], François Trochu[2], and Piotr Breitkopf[1]
[1]*Laboratoire Roberval, UMR 7337 UTC-CNRS, Université de Technologie de Compiègne, Compiègne, France*
[2]*Chair on Composites of High Performance (CCHP), Mechanical Engineering Department, Center of Research on Polymers and Composites (CREPEC), École Polytechnique de Montréal, Montréal, Québec, Canada*

Summary We propose a consistent approach for the generation of macroscale models of short fiber composites. We extract geometrical features and distribution gradients of the fibers from X-ray microtomography. Based on this data, we generate new continuous, voxel or mesh fiber geometry by Diffuse Approximation with volume conservation. Newly generated fibers are distributed in an arbitrary 3D domain. Such domain may contain inclusions in the vicinity of which, fibers position and orient themselves depending on the chemical nature of the inclusion. The observed fiber distribution gradients help to identify these fiber behaviors and distribute geometry in the new 3D domain. The method enables to extrapolate geometrical representations of microscale geometry of composite materials obtained with X-ray microtomography to provide accurate 3D mesh for macro scale numerical simulations.

INTRODUCTION

The modeling of material behavior requires a deep understanding of the microstructure which is especially important for highly heterogeneous composite materials. Such insight is has been nowadays allowed by the full-field methods like X-ray microtomography. The main disadvantage is the limited size of the analyzed specimens, which prohibits their application for macro scale computations of manufactured parts. Recent works [1, 3, 4] that approach the generation of the geometry of random heterogeneous materials . Their limitations are either lack of accurate material parameters or unrealistic, even orientation. Our goal is to provide a method which encompasses several steps of reconstruction, from X-ray microtomography study of the microstructure to macro scale model, intended for computational purposes, e.g. homogenization.

METHODOLOGY

X-ray microtomography

The first step is an X-ray microtomography study of the material, in our case a composite of thermoset polymer matrix reinforced with short flax fiber. 3D scans of the material are processed with Fast Random Forest algorithm to segment them into a fiber, impurity, polymer and air phases. The segmented images of the fiber phase are then examined using a previously developed approach based on expectation-minimization clustering algorithm. This treatment provides probability distributions of geometrical features of different classes of the reinforcement such as fiber diameter, length, orientation, volume, surface and their local variations. A further study of the segmented microtomographic scans is performed with level set algorithms which provide the gradient information on the fiber volume fraction and orientation in the vicinity of different inclusions that are stored as voxel maps.

Individual fiber reconstruction

We use the probability distributions obtained from X-ray tomography for diameter and length and local orientation variations. Depending on the fiber volume fraction intended for the microstructure, the volume fraction of different reinforcement classes is calculated which is followed by the estimation of the amount of objects present in the model as well as their properties, e.g. to prohibit generation of fibers larger than the computational domain. The single fiber geometry is reconstructed by Bezier curve of the centerline considering point-wise local orientations. Then, a series of ellipses with varying diameters is placed on the centerline. The ensemble is used to reconstruct the fiber surface as NURBS continuous model (Fig. 1).

3D fiber distribution

Based on the gradient maps for fibers and the arbitrary matrix domain of the composite containing inclusions, a fiber distribution and orientation is calculated and described with level set functions. Such description is used to distribute fiber geometries accordingly in the 3D space. The intersections that may result from this operation are mitigated by exclusion zones defined after placement of each fiber. This also ensures that the fiber volume fraction is conserved.

*Corresponding author. Email: anna.madra@utc.fr



Figure 1: Three types of individual fiber geometry resulting from the presented approach



Figure 2: Example of a microstructure model with different types of inclusions

Finite Element mesh

The resulting model consists of NURBS curves thus, its application for numerical simulations is limited due to high computational requirements and numerous artifacts. For this reason, two different representations are proposed. The first is a voxel representation that is interesting for comparative studies with original microstructure obtained with full-field imaging methods. The second is an optimized Finite Element (FE) mesh of the fiber surface and volume. This representation is produced by treating the continuous model with Diffuse Approximation method [2]. The resulting mesh (Fig. 1) conserves the volume of the material fraction at the same time having sufficient quality required for finite element simulations.

RESULTS

The X-ray microtomography study has identified four different classes of the reinforcement, namely dust, particle, whisker and short fiber and three classes of inclusions: voids, air bubbles, and inorganic impurities. The generated microstructures included 3 types of inclusions to compare different fiber behavior (Fig. 2).

CONCLUSIONS

The X-ray microtomography has provided an insight in the topology of the reinforcement through identification of additional classes of the reinforcement (dust, whiskers). Also, fiber clustering near the surface of the specimen has been observed which indicates fiber flotation during manufacture. The generated microstructures have similar fiber topology and distribution gradients to the ones seen in the microtomographic scans that were not used to create the model. Further works will include adding more constraints during reconstruction, like for example periodicity necessary for homogenization. Another project is the implementation of the method on graphic processors (GPU) for improved performance.

References

[1] Abdin, Y., Lomov, S. V, Jain, A, Lenthe, G. H. Van, Verpoest, I.: Composites : Part A Geometrical characterization and micro-structural modeling of short steel fiber composites. Composites Part A 67:171–180, 2014.

[2] Rassineux, A. , Breitkopf, P., Villon, P. Simultaneous surface and tetrahedron mesh adaptation using mesh-free techniques. Int. J. Numer. Meth. Eng. 57(3):371-389, 2003.

[3] Sliseris, J., Yan, L., Kasal, B. Numerical modelling of flax short fibre reinforced and flax fibre fabric reinforced polymer composites. Composites Part B 89:e29–e30, 2015.

[4] Sonon, B., Francois, B., Massart, T. J. An advanced approach for the generation of complex cellular material representative volume elements using distance fields and level sets. Comput. Mech. 56(2):221–242, 2015.

STATISTICALLY AUGMENTED BOUNDARY CONDITIONS FOR STATISTICALLY EQUIVALENT RVEs

Dhirendra V. Kubair * [1] and Somnath Ghosh[1]

[1] *Center of Excellence in Integrated Materials Modeling, Civil Engineering Department, Johns Hopkins University, USA*

Summary Statistically equivalent representative volume elements (SERVEs) are used to obtain homogenized constitutive responses of composite microstructures with non-periodic (random) dispersion of heterogeneities. SERVEs are subjected to affine transformation based displacement, constant-traction or periodic boundary conditions ignoring the influence of the exterior microstructure, thus, leading to very large SERVE sizes. Novel statistically augmented boundary conditions (SABCs) derived in this paper accounts for the interaction between heterogeneities in the SERVE and exterior domain through the incorporation of microstructural statistics via the one-point and two-point correlation functions S_1 and S_2, respectively. The converged size of the SERVE is significantly smaller with the SABCs in comparison with the conventional boundary conditions.

INTRODUCTION

Numerical homogenization of multiphase composites constitutes an important step in the integrated computational materials engineering (ICME) design. Simplistic forms of homogenization assume that composites are made of periodic repetition of unit-cell representative volume elements (RVEs). Real composite microstructures comprise of arbitrarily dispersed reinforcement phases. The arbitrariness in the shape, size and spatial distribution of the reinforcing phases (particles or fibers) alter the effective response of the composites. Suitable tailoring of the microstructure leads to efficient designs of the composite systems. Definition of the RVE in the case of arbitrarily dispersed composite media requires elaborate numerical simulations. Two of the most popular methodologies are the statistically equivalent representative volume elements (SERVEs) (Swaminathan et al., 2006) and the statistical volume elements (SVEs). Both these approaches simulate smaller volumes (compared to the microstructural volume element (MVE) that consists of 1000s of fibers) of the arbitrarily dispersed composite using numerical techniques (finite element being widely popular). The classical definition of SERVEs or SVEs consider only the simulated volume and ignore the influence of fibers exterior to the simulated domain. Classically SERVEs or SVEs are subjected to boundary conditions such as the affine transform (constant strain), periodic or constant stress boundary conditions and completely ignore the microstructural details exterior to the selected RVEs. The classical boundary conditions leads to large converged RVE sizes to obtain effective properties. In the present work, novel boundary conditions that account for the microstructural details of the exterior are derived using the statistically informed Green's functions (SIGF) approach that results in the statistically augmented boundary conditions (SABCs), which are prescribed on the SERVEs. SERVEs subjected to SABCs leads to smaller converged SERVE sizes that are computationally more efficient compared to classical boundary conditions. Brief description of the SIGF and SABCs are provided in the next section. In Section 3, the efficacy of the SABCs is illustrated for arbitrarily dispersed unidirectional fiber composite system and is compared with the SVEs.

STATISTICALLY AUGMENTED BOUNDARY CONDITIONS

Fiber interactions play an important role in evaluating effective properties of arbitrarily dispersed composites. Various statistical descriptors are used to characterize the fiber dispersions, namely, local-volume-fraction distribution, nearest neighbor distribution and n-point correlation functions (Ghosh et al., 1997). In the present study, the affine transform boundary conditions are augmented with the perturbation displacements that account for the interactions of the fibers exterior to the SERVE using the two-point correlation functions. The two-point correlation function is defined as

$$S_2\left(r,\theta\right) = \int\limits_{\Omega} \iota\left(x_i\right) \iota\left(x_i + re^{\theta\sqrt{-1}}\right) d\Omega, \tag{1}$$

where Ω is the volume of the microstructural volume element (MVE), $\iota\left(x_i\right) = 1 \forall x_i \in \Omega^F$ is the indicator function and Ω^F is the volume of a given individual fiber.

The affine transformation based displacements are given by $u_i^A = \epsilon_{ij}^0 \left(x_j \nearrow x_j^C\right)$, with ϵ_{ij}^0 being the applied constant strain and x_j^C is the centroid of the SERVE (or SVE). A pair of interacting exterior-interior fibers are illustrated in Figure 1. The perturbation displacements u_i^* are dependent on the distance and orientation of the fibers with each other and the observation point o. The distances (d_{12}, d_{1o} and d_{2o}) are arbitrary (or random) in real composites and can be represented by the two-point

*Corresponding author. Email: dv.kubair@gmail.com

correlation function of the composite microstructure using the law of the unconscious statistician (LOTUS). The Green's function solution to the interaction of the fibers is obtained in terms of the eigen-strains ϵ^{Λ}_{kl} in the fibers as

$$\int_{\Omega^F} \left[\mathbb{I}^M_{ijpq} \nearrow C^F_{ijpq}\iota\left(x_m\right)\right)^{-1} C^M_{pqkl}\iota\left(x_m\right) \nearrow (S_{ijkl}\iota\left(x_m\right) + G_{ijkl}\left(x_p\right)\left(1 \nearrow \iota\left(x_m\right)\right)) \Big] \epsilon^{\Lambda}_{kl} d\Omega = \epsilon^0_{ij}. \tag{2}$$

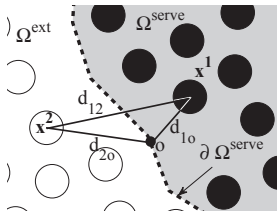

Figure 1: Two interacting fibers

In the above equation C^F_{ijkl}, C^M_{ijkl} are the elasticity tensors of the fiber and matrix. S_{ijkl} and $G_{ijkl}\left(x_p\right)$ are the interior and exterior Eshelby tensors of the interacting fibers. The eigen-strains can be written in a compact form as $\epsilon^{\Lambda}_{ij} = A_{ijkl}\left(x_p\right)\epsilon^0_{kl}$, where A_{ijkl} corresponds to transfer function that maps the applied strain to the eigen-strain in the fibers. The perturbation displacements are related to the applied constant strains ϵ^0_{ij} as given by

$$u^*_i = \left[\int_{\Omega \setminus \Omega^F} L_{imn}\left(x_p\right) A_{mnkl}\left(x_p\right) S_2\left(r,\theta\right) d\Omega \right] \epsilon^0_{kl}, \tag{3}$$

where the L_{imn} is the tensor that maps the eigen-strains to the perturbation displacements u^*_i. The SABCs are obtained by augmenting the affine transform displacements as $u^{SABC}_i = u^A_i + u^*_i$.

EFFICACY OF THE STATISTICALLY AUGMENTED BOUNDARY CONDITIONS

The efficacy of the SABCs are illustrated by the convergence study of the SERVEs. The SERVEs are subjected to classical (affine transform and periodic boundary conditions) as well as the SABCs. The homogenized (volumetric average) stiffness is used as the measure of convergence. The size of the SERVE (L) (and the number of fibers N_F) is systematically increased and the homogenized responses obtained by detailed three dimensional finite element simulations. The moduli ratios of the fiber and matrix was chosen to be $E_F/E_M = 25$. The SERVEs were subjected to a constant strain of $\epsilon^0_{11} = 1$ and the dominant normalized homogenized stiffness $\bar{C}_{1111}/E^M$ is shown (Figure 2) as a function of the SERVE size L. The homogenized stiffness converges for large SERVE sizes $L > 100\mu m$ when subjected to conventional affine transform and periodic boundary conditions, while the converged SERVE size is around $L = 35\mu m$ when subjected to SABCs illustrating the efficacy of the SABCs.

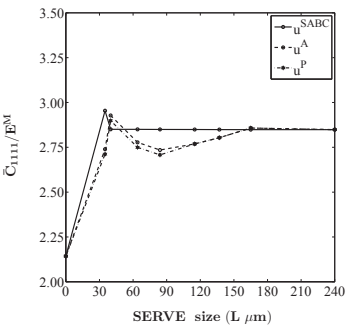

Figure 2: Variation of the normalized homogenized stiffness tensor $\bar{C}_{1111}/E^M$ as a function of the SERVE size.

CONCLUSIONS

Conventional definition of SERVEs accounts only for the volume of the composite simulated. The exterior domain is assumed to be comprised of a constant strain-energy-density medium, and hence predicts large SERVE sizes. Novel SIGF based SABCs that account for the interactions of the fibers via the two-point correlation function are derived and prescribed on the SERVEs. The converged size of SERVEs subjected to SABCs are significantly smaller than the ones obtained from either the classical affine transform or periodic boundary conditions. The present work clearly illustrates the necessity and importance of including the description of the exterior microstructural morphology in the definition of the SERVEs.

References

[1] Swaminathan, S., Ghosh, S., Pagano, N.: Statistically equivalent representative volume elements for unidirectional composite microstructures: Part I-Without damage. Jour. Comp. Mat. 40 (7), 583604, 2006.

[2] Ghosh, S., Nowak, Z., Lee, K.: Quantitative characterization and modeling of composite microstructures by voronoi cells. Acta Mat. 45 (6), 22152234, 1997.

[3] Kubair, D., Ghosh, S.: Statistically augmented boundary conditions for statistically equivalent representative volume elements. Under review. 2016.

MODELLING VARIABILITY IN COMPOSITE FIBRE REINFORCEMENT GEOMETRY DATA

Andy Vanaerschot[1], Stepan Vladimirovich Lomov[2], David Moens[1] & Dirk Vandepitte[1a)]
[1]*Department of Mechanical Engineering, KU Leuven, Leuven, Belgium*
[2]*Department of Materials Engineering, KU Leuven, Leuven, Belgium*

Summary Non-determinism requires much attention in the certification procedure of complicated structural components. Composite materials are gaining much interest because of their high performance, especially for transportation applications. However, the multitude of design, material and process parameters add to the complexity of the analysis, and procedures for certification and quality assurance are demanding. Uncertainty and scatter on critical material parameters need to be quantified in close relation to the application and also to the production process which is used, with a particular focus on the geometrical characteristics of the fibre reinforcement architecture. This paper proposes a procedure to experimentally identify the statistical characteristics on physical realisations of the material and to subsequently generate a population of virtual samples which possesses the same statistical characteristics as the real components. Virtual models allow for a much wider and cheaper analysis of product performance and they replace the expensive campaign with repeated physical experiments.

NON-DETERMINISM IN STRUCTURAL ANALYSIS

The performance of modern computer hardware is ever increasing. In the application of structural analysis of complicated systems, the analyst develops highly advanced models which closely represent physical reality in a wide range of load cases. Nominal models are used to optimise the performance and to improve efficiency. In parallel, awareness is growing that product quality can only be guaranteed when off-nominal behaviour is also taken into account.

Oberkampf et al. [1] have developed a comprehensive nomenclature to describe the nature of non-determinism as it occurs in design and verification procedures in modern engineering reality when developing advanced structures. In the assumption that the model and the numerical procedures which are used are correct, non-determinism is considered on model parameters only. They distinguish between on the one hand epistemic uncertainty, also simply called uncertainty, when knowledge is insufficient or information is incomplete, and on the other hand aleatory uncertainty, also called variability, when system characteristics vary from one realisation to another one or from one condition of utilisation to another. Intermediate categories may also apply. Different numerical formalisms are proposed to handle both categories [2]. Conditions of epistemic uncertainty with insufficient information require a non-probabilistic approach, either using interval arithmetic or with fuzzy analysis. Conditions of aleatory uncertainty occur when scatter on model parameters over different realisations is well quantified, in all aspects, including correlation between different model parameters, and in such case probabilistic analysis is viable. Probabilistic approaches are obviously preferred as they allow for statistical interpretation of the result, such as probability of failure. It is observed however that many engineering practitioners, both in the scientific community and in industry, consciously or unconsciously adopt a probabilistic procedure although probability density functions (pdf) are not fully validated and complemented with subjective data, such as assumptions on the nature of the pdfs, on the magnitude of the coefficients of variation or on cross-correlations between different model parameters. Results are then unreliable.

VARIABILITY IN FIBRE REINFORCED COMPOSITE MATERIALS AND MODEL GENERATION

Composite materials have at least two constituents, with some kind of fibre reinforcement embedded in a matrix. The number of model parameters which is required to represent such a system is large, with material data, process characteristics, reinforcement morphology and tow path geometry as the dominant features, and many variations in each category, depending on the fibre/matrix/process system which is considered. Schuëller et al. [3] call upon material scientists to establish a validated data base for a realistic representation of such a complex, multi-parameter system. In this paper, the authors develop a general 3 step approach (see Fig.1) to quantify variability on geometrical tow parameters (x, y and z co-ordinates of tow centroid position, tow area, tow aspect ratio and orientation), based on experiments with extensive data analysis. The first step is the collection of experimental data and the subsequent statistical analysis. Two length scales are considered, one on the level of the representative volume element using μCT and the other on the scale of multiple unit cells. The former set gives precise positional and cross-sectional data on the meso-level. Average trends, standard deviation and correlation lengths are identified. The second step is the stochastic multi-scale modelling, including the definition of systematic and handling trends from the experimental data, the generation of zero-mean deviations correlated along and between neighbouring tow paths. Cross-correlations are taken into account, a cross-correlated series expansion is used, based on a Karhunen-Loève decomposition, as proposed by Vorechovskỳ [4]. In the third and final step, WiseTex models are generated. WiseTex [5] is a pre-processor for the generation of virtual 3D models of a wide range of textile composite architectures. The pre-processor prepares for the generation of finite element models for the mechanical analysis of composite structures. The statistics of the virtual models which are generated match all statistical characteristics of the hardware samples, both in short range and in long range.

[a)] Corresponding author. Email: dirk.vandepitte@kuleuven.be

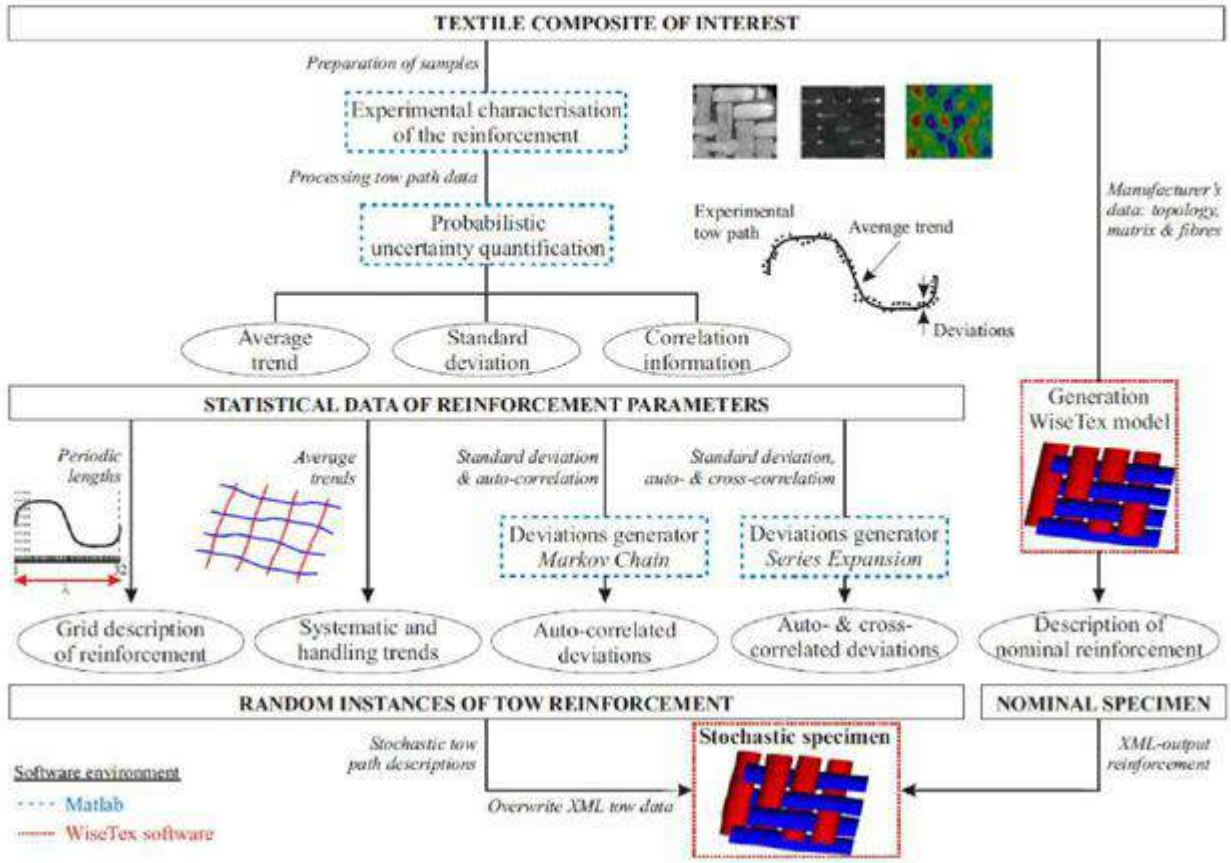

Figure 1: the proposed procedure: (1) data acquisition, (2) statistical data analysis and (3) generation of virtual models

Application to a carbon fibre reinforced composite material

The procedure is applied to a carbon fibre reinforcement system with a complicated architecture. Figure 2 shows the μCT image of the cross-section (left) and a WiseTex model of one of the samples which is generated (right). Statistics of the full set of the generated samples match the statistics of the experimental data set.

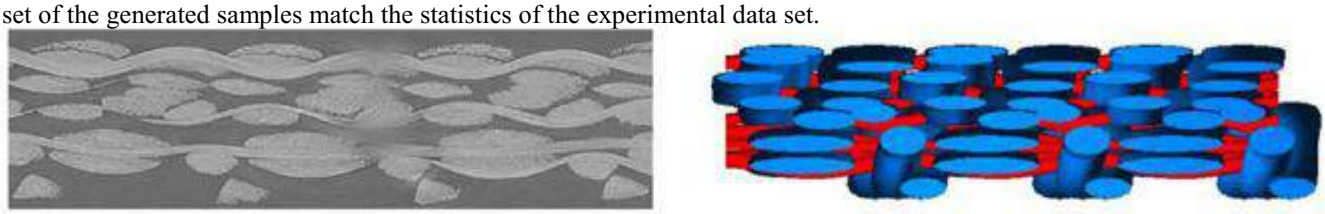

Figure 2: cross-section of the carbon fibre reinforced material in warp direction: μCT scan (left) and virtual sample (right)

CONCLUSIONS

This paper presents a global strategy to develop a set of virtual material samples with all statistical characteristics matching the experimental data set. The virtual data set may be used to build material and finite element models, enabling full statistical interpretation of the structural analysis.

Authors gratefully acknowledge the financial support of FWO-Vlaanderen, IWT-Vlaanderen and KU Leuven Research Fund.

References

[1] Oberkampf W., DeLand S., Rutherford B., Diegert K., Alvin K., A new methodology for the estimation of total uncertainty in computational simulation, *Proceedings of the 40th AIAA/ASME/ASCE/AHS/ASC Structures, Structural Dynamics and Materials Conference*, AIAA-99-1612:3061-3083, 1999

[2] Moens D., Vandepitte D.: A survey of non-probabilistic uncertainty treatment in finite element analysis, *Computer Methods in Applied Mechanics and Engineering*, **194** (14–16):1527–1555, 2005

[3] Charmpis D.C., Schuëller G.I., Pellissetti M.F., The need for linking micromechanics of materials with stochastic finite elements: a challenge for materials science, *Computational Materials Science*, **41**(1):27-37, 2007

[4] M. Vorechovský, D. Novák, Correlation control in small-sample Monte Carlo type simulations 1: A simulated annealing approach, *Probabilistic Engineering Mechanics*, **24**(3):452-462, 2009

[5] http://www.mtm.kuleuven.be/Onderzoek/Composites/software/wisetex, 2015

MORPHOLOGICAL MICROMECHANICS OF COPOLYMERIC ELASTOMERS

Hansohl Cho[1], Gregory C. Rutledge[1] & Mary C. Boyce[2]
[1]*Department of Chemical Engineering, Massachusetts Institute of Technology, Cambridge, MA, USA*
[2]*The Fu Foundation School of Engineering and Applied Sciences, Columbia University, New York, NY, USA*

Summary: This work studies the morphological micromechanics of copolymeric elastomers comprising two dissimilar domains. New three-dimensional representative volume elements (RVE) are proposed to mimic more realistic morphological microstructures based on the Voronoi tessellation. We examined the micromechanical behaviours of bi-continuous and dispersed-particle morphologies derived from the Voronoi tessellation for specified volume fractions (v_{hard}: 36% and 49%) of hard and soft domains. The random yet bi-continuous morphology was found to show better the inelastic stress-strain features of copolymeric elastomers under large deformation than the dispersed morphology, in which the hard aggregates are more likely to be isolated. The micromechanical results also show the topological connectivity in the two domains plays a critical role in the resilient yet dissipative mechanical behaviours extensively reported in this class of phase-separated elastomeric materials.

INTRODUCTION

Copolymeric elastomers are versatile materials for a myriad of engineering and biological applications due to their remarkable mechanical features under large straining.[1] The design of thermodynamically incompatible segmental microstructures is often used to create phase-separated morphologies comprising hard and soft domains. The two-phase nature results in a remarkable combination of both glassy and rubbery polymeric features including substantial hysteresis and shape recovery as well as rate-dependent hyperelastic-viscoplasticity.[1,2] In addition to the intrinsic properties of constituent polymers, the geometric features of the phase-separated microstructures critically influence the macroscopic mechanical behaviours. In this work, we investigate the morphological micromechanics of new RVEs in which the two domains are described by hyperelastic-viscoplasticity (hard) and hyperelastic (soft) constitutive laws. A random yet bi-continuous RVE is first presented using the Voronoi tessellations of space using random spatial points, as well as its dispersed counterpart, for a specified volume fraction. The stress-strain behaviours are then examined under finite straining in micromechanical models of the two RVEs, in which a three-dimensional periodic boundary condition was imposed to compute macroscopic responses of the RVEs.

RESULTS AND DISCUSSION

Figure 1a shows a transmission electron microscopy (TEM) image of an exemplar material (a thermoplastic polyurethane: TPU) in which the volume fraction of hard domain was ~ 49%. As shown in the TEM image, the hard domain (brighter regions) was found to be highly continuous within the soft matrix (darker regions). At relatively high volume fractions of hard component, the microstructures in this class of copolymeric materials are more likely to have interpenetrating and bi-continuous morphologies in which the constituent domains are connected. To mimic the highly bi-continuous microstructures, a new representative volume element (RVE) was proposed, for specified volume fractions of hard and soft domains, as follows. First we drew a pre-determined number of spatially random points within the unit cell. Then we performed a standard Voronoi tessellation about these spatial points. **Figure 1b** schematically presents the Voronoi tessellated space for 5 random points under three-dimensional periodic boundary condition. In this rendering, the cylindrical rods represent edges of the tessellated polyhedral cells while the grey particles represent the original, randomly chosen points. The Voronoi tessellation provided information on the neighbour list for each of polyhedral cells. Then the neighbouring points were connected to the centre point of the given polyhedral cell via cylindrical rods if equal radii, chosen to meet the specified volume fraction of hard domains. Furthermore, when conducting the Voronoi-tessellation, we constructed 26 images of the central unitcell to assure the three-dimensional periodicity of the RVEs. **Figure 1c** shows a bi-continuous RVE, having a hard fraction of 49%. The dispersed RVE was constructed simply by locating spherical domains at the centre points upon which the tessellated polyhedral cells were based, as shown in **Figure 1d**. Again, 26 images of the central unitcell were constructed and the RVE was taken from the supercell (3 by 3 by 3) to assure the three-dimensional periodicity. In this RVE, it should be noted that the particles were allowed to overlap each other to form dispersed aggregates within the unitcell. As shown in **Figure 1d**, some of the hard particles were slightly overlapped.

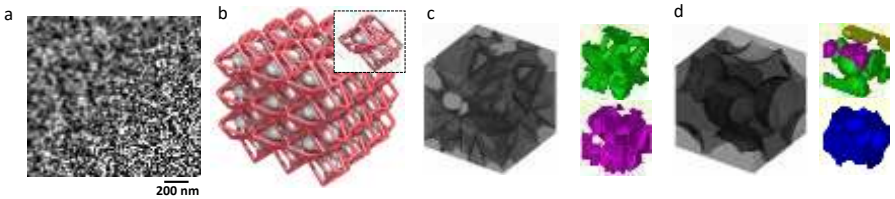

Figure 1 Representative microstructure in a TPU with v_{hard}: 49%. (a) TEM image (bright: hard, dark: soft); (b) Voronoi-tessellated super cell (3by3by3); the Voronoi-tessellated unit cell (5 random points) is shown in the inset; (c) Bi-continuous RVE; (d) Dispersed RVE; the RVEs are presented together with its hard and soft domains; v_{hard}: 49% in both RVEs

We then performed a micromechanical analysis of the RVEs in which a hyperelastic-viscoplastic model and a hyperelastic model were used for the constitutive laws of hard and soft domains, respectively. The representative constitutive responses of two domains under compression are shown schematically in the inset of *Figure 2a*. The RVEs were subjected to a macroscopic simple compression under periodic boundary conditions.[3] *Figure 2a* shows representative volume-averaged stress-strain responses of the two RVEs (v_{hard}: 36% and 49%) at a macroscopic strain rate of 0.01 /s. The stress responses in the bi-continuous RVEs were found to be much greater than those in the dispersed RVEs for the both cases since the hard ligament network deformed significantly at all macroscopic strains. However, in the dispersed RVEs, the macroscopic deformation was carried throughout the soft matrices, especially at small strains. Substantial deformation was localized within the hard aggregates only at large strains, which resulted in a stress upturn. Moreover, the yield-like stress-rollover was more clearly evident in the bi-continuous RVEs in both cases of 36% and 49%. As evidenced in *Figure 2b* and *Figure 2c* on the contours of inelastic strain rate, the inelastic flow was more evenly developed throughout the rod-like hard ligament network within the bi-continuous RVE while it was observed only at the interfaces between the hard aggregates, where severe deformation was localized. The stress-strain behaviours were further examined under cyclic deformation conditions. *Figure 2d* shows the simulated stress-strain curves of the two RVEs (v_{hard}: 36%) under a loading-unloading cycle up to a macroscopic strain of 0.6 at a strain rate of 0.01 /s. Under cyclic deformation, hysteresis in the bi-continuous RVE was much greater than that found in the dispersed RVE. In particular, much greater energy was dissipated, accompanied by greater residual deformation upon unloading within the bi-continuous RVE. The fully-developed inelastic deformation in the hard ligament network was mainly responsible for the highly dissipative stress-strain behaviours in the bi-continuous RVE; moreover, it still exhibited remarkable resilience as evidenced by the shape recovery upon unloading, which has been reported extensively in this class of copolymeric elastomers at this particular range of volume fractions.[1, 2] However, the dispersed RVE exhibited more "rubber-like" behaviours involving relatively small hysteresis with much greater shape recovery upon unloading.

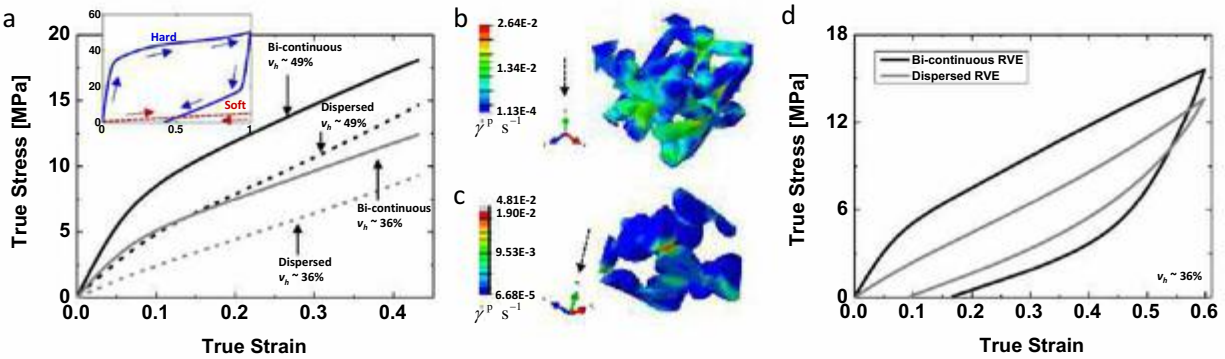

Figure 2 Micromechanical modeling result of bi-continuous and dispersed RVEs. (a) Representative stress-strain behaviors of RVEs (v_{hard}: 36% and 49%; the inset shows the stress-strain curves of hard and soft component); (b) Contours of inelastic strain rate (within the intermolecular mechanism; here only the hard domain was shown) in RVEs (v_{hard}: 36%) at a macroscopic true strain of 0.15 (the dashed arrows represent the loading directions); (c) Representative stress-strain behaviors of RVEs upon loading and unloading (v_{hard}: 36%)

CONCLUSION

In this work, we investigated the microstructural deformation mechanisms of a copolymeric elastomer under finite straining by using a micromechanical analysis. A fully three-dimensional RVE was proposed to mimic realistic microstructural morphologies often found in this class of materials. The micromechanically-simulated stress-strain curves in the bi-continuous RVEs exhibited highly nonlinear elastic-plastic behaviours accompanied by substantial hysteresis and shape recovery upon unloading. The topological connectivity was found to influence critically the highly dissipative yet resilient mechanical behaviours of the materials, over and above the intrinsic properties and the volume fractions of dissimilar domains. We suggest that the proposed three-dimensional random RVEs can provide a better representation for a sound understanding of the macro- and microscopic deformation mechanisms of other phase-separated polymeric materials and cellular materials having complicated morphological microstructures across a wide range of length-scales.

Acknowledgment
Authors gratefully acknowledge financial support from BASF.

References
[1] Hepburn, C. Polyurethane elastomers. Springer Science & Business Media, 2012.
[2] Yi, J., Boyce, M. C., Lee, G. F., & Balizer, E. Large deformation rate-dependent stress–strain behavior of polyurea and polyurethanes. Polymer, 47(1), 319-329, 2006
[3] Danielsson, M., Parks, D. M., & Boyce, M. C. Three-dimensional micromechanical modelling of voided polymeric materials. Journal of the Mechanics and Physics of Solids, 50(2), 351-379, 2002

SELF-HEALING OF IMPACT DAMAGE IN WOVEN COMPOSITES

Scott White[1,2a], Kevin Hart[2] & Nancy Sottos[1,3]
[1]*Beckman Institute, University of Illinois at Urbana-Champaign, USA*
[2]*Department of Aerospace Engineering, University of Illinois at Urbana-Champaign, USA*
[3]*Department of Materials Science, University of Illinois at Urbana-Champaign, USA*

Summary Self-healing of impact damage in glass/epoxy composites is demonstrated using a vascular delivery network. Transverse (out-of-plane) impact was carried out on vascular composite beams and flexural strength post-impact was measured. Self-healing resulted in ca. 50% recovery of flexural strength and over 80% recovery of flexural modulus at 15 J impact energy.

INTRODUCION

Despite excellent performance-to-weight characteristics, composites are susceptible to damage from out-of-plane impact events which introduce damage in the form of transverse shear cracks, matrix tensile cracks, interply delamination, fiber pull-out, fiber rupture, and penetration (Figure 1). Impact-induced damage is often difficult to detect as it may occur at low impact energies and often leaves no visible sign of damage on the material surface. As a result, internal impact-induced damage frequently goes undetected and severely compromises the mechanical integrity of the composite. In order to combat flaw sensitivity, biologically inspired self-healing concepts have been utilized for autonomous, non-invasive material repair.

Pioneered in 2001 [1], self-healing materials have the ability to heal damage autonomously when and where it occurs through damage-triggered release of reactive components. Self-healing materials can be broadly classified into three separate classes based on the method used to sequester healing agents: capsule-based, vascular, and intrinsic systems [2]. Capsule-based self-healing materials sequester the healing agent in microcapsules that are dispersed throughout the host material. Damage triggers the release of agents once the capsules are ruptured and their delivery to the damage region facilitates chemical reactions that repair the damage. Vascular self-healing materials house the agents in microchannel networks that perfuse the host material. Similar to capsule-based systems, as the vasculature is damaged, the contents spill into the damage region, reacting and ultimately healing the damage. Finally, intrinsic self-healing materials do not sequester healing agents, but instead possess a latent self-healing function of the host material that is usually triggered by an external energy source (e.g. heat, UV light).

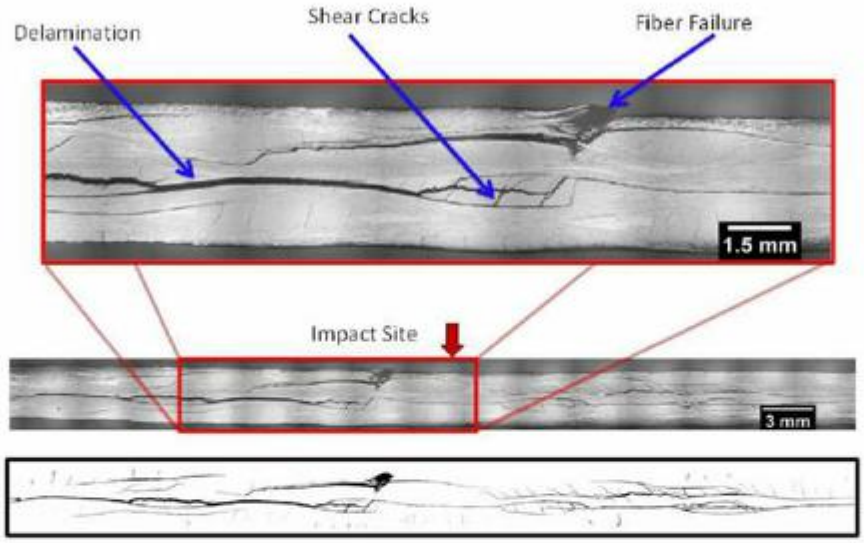

Figure 1. Cross-sectional optical image and binary conversion of a damaged glass/epoxy composite after an out-of-plane impact event. Delamination damage, shear cracks and fiber failure are visible.

MATERIALS AND METHODS

Vascular self-healing composites were fabricated from 2D glass fiber woven textiles infused with an epoxy resin matrix. Vascular networks were created by VaSC processing [3] of sacrificial fibers that were woven into the textile preform prior to processing. Epoxy infiltration was accomplished by vacuum assisted resin transfer molding in a convection oven at 70 °C to reduce the viscosity of the resin during infiltration. Immediately following infiltration, the sample was heated to 121 °C

[a] Corresponding author. Email: swhite@illinois.edu

at 3 °C / min and held for 8 h to facilitate curing. Following cure, the composite was de-molded and cut into 110 mm x 20 mm x ~3 mm beam specimens. The beam samples were then placed into a vacuum oven at 200 °C for 24 h to achieve evacuation of the sacrificial fibers. Finally, microchannels were sequentially flushed with dichloromethane, de-ionized water, and air to ensure clear fluid pathways.

Impact testing of beam specimens was conducted on an Instron 8250 drop-weight Charpy tower. Samples were clamped in a fixed-fixed configuration with a span of 40 mm and impacted across the width using a cylindrical impact tup (25.4 mm radius of curvature). The total mass of the impactor apparatus was 3.41 kg. Drop heights of 299 mm or 448 mm were used to deliver 10 J or 15 J of impact energy, respectively. After the initial impact event, healing agents were delivered to the specimen via a syringe pump coupled to an air-assisted reagent delivery system. The healing agent used is an epoxy resin and hardener with precedence in self-healing literature [4]. Delivery of reagents was held constant at 18.8 µL / min and 10 µL / min, respectively, for the resin and hardener.

HEALING PERFORMANCE

Post-impact flexural strength as a function of impact energy for vascularized control and self-healing samples is provided in Figure 2a. Strength recovery at 10 J and 15 J of impact energy was 36.9% and 46.9%, respectively. Incomplete recovery of strength is attributed to incomplete damage volume filling, which was confirmed by cross-sectional imaging. Damage filling is more complete for 15 J of impact energy, likely the result of more complete damage connectivity. Since healing agent distribution emanates from a microchannel network, the damage must intersect that network in order to be filled. A cross-section of an impacted and healed beam specimen is shown in Figure 2b. Regions of unhealed and healed delaminations are visible supporting the hypothesis of incomplete damage filling (and connectivity) after the healing protocols.

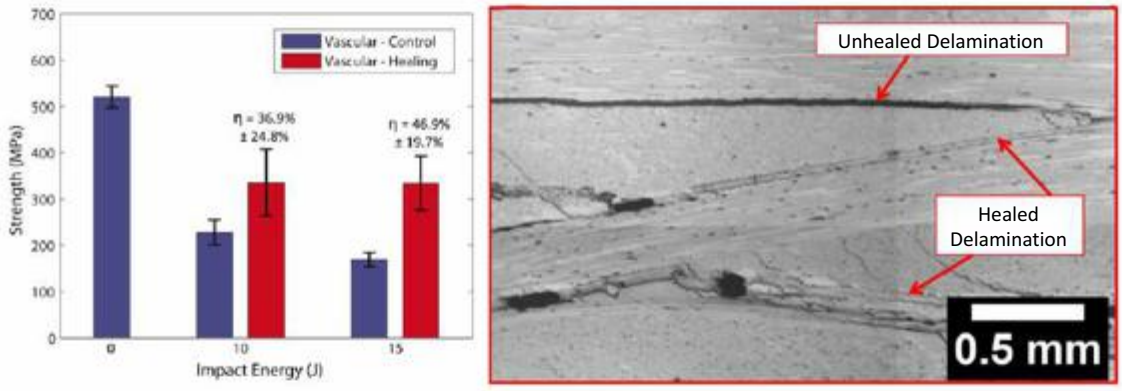

(a) (b)

Figure 2. Self-healing of impact damage in vascular composites. (a) Recovery of flexural strength after impact. (b) Optical cross-sectional image of specimen after self-healing with healed delaminations indicated.

CONCLUSIONS

The healing of impact-induced damage in composite beam specimens was achieved using a vascular healing agent delivery scheme. Up to 47% recovery of post-impact strength and up to 83% recovery of stiffness was demonstrated. Incomplete recovery is attributed to incomplete damage volume filling resulting from lack of damage connectivity after impact. The presence of healed material in the crack plane was verified using cross-sectional imaging and confocal Raman spectroscopy.

References

[1] S. R. White, N. R. Sottos, P. H. Geubelle, J. S. Moore, M. R. Kessler, S. R. Sriram, E. N. Brown, and S. Viswanathan, "Autonomic healing of polymer composites," *Nature*, vol. 409, no. 6822, pp. 794–797, Feb. 2001.

[2] B. J. Blaiszik, S. L. B. Kramer, S. C. Olugebefola, J. S. Moore, N. R. Sottos, and S. R. White, "Self-Healing Polymers and Composites," *Annual Review of Materials Research*, vol. 40, no. 1, pp. 179–211, Jun. 2010.

[3] A. P. Esser-Kahn, P. R. Thakre, H. Dong, J. F. Patrick, V. K. Vlasko-Vlasov, N. R. Sottos, J. S. Moore, and S. R. White, "Three-Dimensional Microvascular Fiber-Reinforced Composites," *Advanced Materials*, vol. 23, no. 32, pp. 3654–3658, Aug. 2011.

[4] K. S. Toohey, C. J. Hansen, J. A. Lewis, S. R. White, and N. R. Sottos, "Delivery of Two-Part Self-Healing Chemistry via Microvascular Networks," *Advanced Functional Materials*, vol. 19, no. 9, pp. 1399–1405, May 2009.

AN EXPERIMENTAL AND COMPUTATIONAL STUDY ON A HIGH TEMPERATURE NiTi/POLYIMIDE MATRIX COMPOSITE INTERFACE

Hieu Truong[1a)], Ozden Ochoa[1], Dimitris Lagoudas[2], John Connell[3] & Frank Palmieri[3]
[1]*Mechanical Engineering Department, Texas A&M University, College Station, Texas, USA*
[2]*Aerospace Engineering Department, Texas A&M University, College Station, Texas, USA*
[3]*Advanced Materials & Processing Branch, NASA Langley Research Center, Hampton, Virginia, USA*

Abstract For the first time, shape memory alloys (SMA) were successfully co-cured in a polyimide matrix composite to create high temperature, smart, hybrid composite laminates. In the work presented herein, the nickel-rich nickel titanium (NiTi) foil was used as the SMA constituent. A combination of laser ablation and amide acid sol-gel surface treatment performed on the NiTi foil created robust adhesion between the foil and the polyimide matrix. The mode-I fracture toughness of the hybrid SMA-composite interface was investigated via the double cantilever beam (DCB) test with in-situ digital image correlation (DIC) measurements. The dominant mode of failure revealed after the DCB tests was cohesive. Phase transformation in the NiTi foil was observed during the isothermal DCB tests at 25°C. Finite element analyses of the hybrid DCB specimen indicated that the NiTi foil underwent stress-induced phase transformation in the vicinity of the crack tip prior to and during crack propagation.

INTRODUCTION

Hybrid high temperature composite materials are excellent candidates as lightweight structural materials for supersonic and hypersonic vehicles. Recently, the integration of SMA actuators into polymer matrix composite (PMC) laminates has attracted significant interest as a means to create smart and morphing aerospace components. The active attribute of hybrid SMA-PMC composites is inherent in the thermo-mechanically induced phase transformation of the SMA constituent. The effectiveness of load transfer between the SMA actuators and the composites dictates functionality of the hybrid structures. This load transfer effectiveness depends on the ability of the interface between the SMA and the PMC to propagate energy. It has been reported that hybrid SMA-PMC structures have been created by adhesively joining the components [1]. However, in these adhesive joints, there are two distinct interfaces (SMA-adhesive and adhesive-PMC) and therefore require a unique adhesive that can form robust interfaces with the two distinct materials to assure the optimal structural integrity of the hybrid composite. In this study, the SMA was surface-treated by laser ablation followed by treatment with a custom synthesized sol-gel formulation, and the hybrid composites were co-cured. Thus, the SMA-PMC hybrid interface was created without using an adhesive. That is, adhesion was achieved directly between the treated SMA surface and the polymer matrix of the PMC upon curing. Fabrication and investigations on hybrid, co-cured interfaces between Al, Ti, NiTi and epoxy-based matrices were previously performed by Truong *et al*. [2-4]. This paper details our approach to develop high temperature, smart material systems using a custom designed robust interface to fabricate NiTi foil/polyimide matrix hybrid composites. The results of this experimental and computational investigation are presented herein.

APPROACHES

Experimental Approach

The hybrid composite laminate was fabricated with a single layer of Ti-50.8at%Ni foil (127 μm thick) sandwiched between four layers of composite pre-preg on each side. The pre-preg used in this study was 8-harness satin weave T650 carbon fabric/AFR-PE-4 matrix (cured T_g = 392 °C). Two layers of 50-μm thick Kapton film were used to create the pre-crack for fracture toughness tests. Prior to placing the NiTi foil in the panel layup, the foil was heat treated at 500 °C for 1 hour followed by aging at 400 °C for 45 min, and water quenching to activate the shape memory effects. In addition, a combination of laser ablation [5] and amide acid sol-gel surface treatment technique [6] was performed on both sides of the NiTi foil surfaces to create strong adhesion through covalent bond formation with the polyimide matrix. No adhesive was used at the NiTi-PMC interface. The composite laminate was cured in a Wabash hot-press under a 12-hour curing cycle at temperature and pressure up to 371°C and 1.4 MPa, respectively. The quasi-static double cantilever beam (DCB) tests with in-situ DIC measurements were performed at room and elevated temperatures. Each DCB specimen was tested by displacement-controlled loading to an opening displacement of 25 mm then unloaded to zero displacement. Other characterizations of the hybrid laminates and NiTi foil included differential scanning calorimetry (DSC), thermal-mechanical analysis (TMA) and dynamic mechanical analysis (DMA) as well as optical microscopy (OM) and scanning electron microscopy/energy dispersive spectroscopy (SEM/EDS) on the cross-sections and fracture surfaces of the tested DCB specimens.

Computational Approach

Two-dimensional finite element analyses (FEA) of the DCB specimen were carried out using the commercial FEA software ABAQUS to study the mode-I delamination behavior of the hybrid interface. The virtual crack closure technique (VCCT) with B-K mixed mode fracture criterion was used to model crack propagation at the NiTi-PMC interface. Linear incompatible plane strain elements (CPE4I) were used together with the built-in nonlinear geometric option in ABAQUS activated. Transversely isotropic linear elastic material properties were used for the PMC while the NiTi foil's nonlinear isotropic material properties were modelled using a user material subroutine (UMAT) defining the SMA behaviors based on the constitutive relations developed by Lagoudas *et al*. [7].

[a)] Corresponding author. Email: hieutruong@tamu.edu

PRELIMINARY RESULTS AND DISCUSSION

The micro-roughness pattern created by laser ablation on the NiTi foil surface is shown in Figure 1(a). Figure 1(b) shows the fracture surfaces at the hybrid interface after a DCB test at 25 ^{o}C. It was observed that the dominant mode of failure was cohesive. The crack first started adjacent to the NiTi surface (adhesive failure) then migrated into the PMC region (cohesive failure) and remained there until the test completion. This suggests a strong hybrid NiTi-PMC interface was achieved in this work. The critical mode-I fracture toughness of this interface is 685±7 J/m^2. DSC measurements showed that after undergoing laser ablation treatment and curing cycle, the NiTi foil still exhibited SMA behavior, and at 25 ^{o}C, the material was fully in the austenitic phase. The DCB test results indicated phase transformation occured in the NiTi foil during the test. This was evidenced by the residual opening displacement at no load after the test as illustrated in the load-displacement plot in Figure 1(c) as well as the actual specimen shown in Figure 2(b) where the gap between the two arms is ~1 mm. The FEA results illustrated in Figure 2(a) revealed that the residual displacement was 1.016 mm.

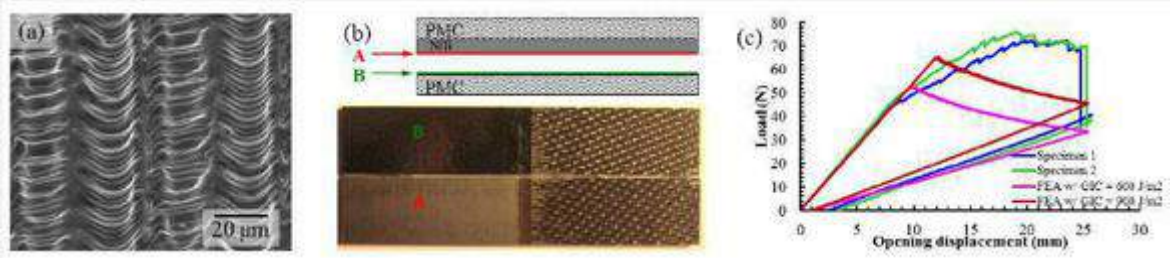

Figure 1. (a) Laser ablated NiTi surface (b) Fracture surfaces (c) Load-displacement curves from DCB tests at 25 ^{o}C and FEA

It can be seen from Figure 2(b) that stress-induced phase transformation occured in the NiTi foil in the vicinity of the crack tip. Note that before loading, the foil was completely in the austenitic phase (0% martensitic vol. fraction). Before crack growth from the pre-crack, the martensitic volume fraction in the foil reached 15.8% at the crack tip. As the crack propagated, the region containing martensitic phase in the NiTi foil grew accordingly with a martensitic vol. fraction of approximately 8%.

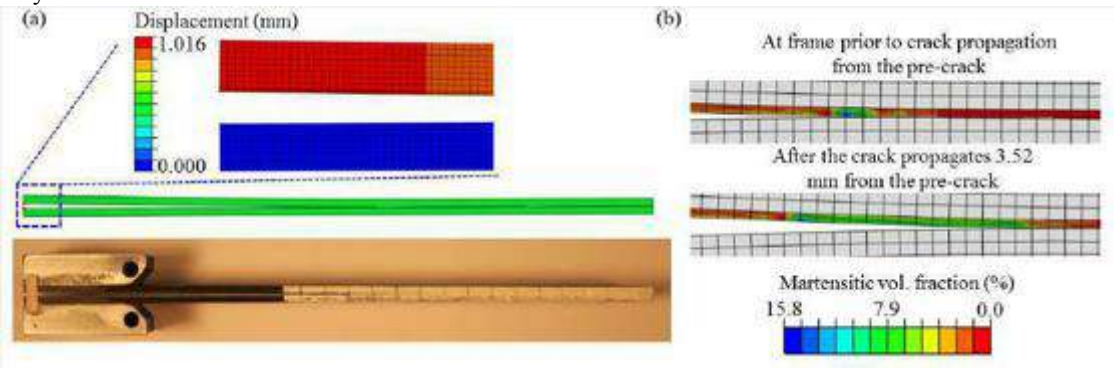

Figure 2. (a) Residual displacement in the DCB after unloading (b) Martensitic volume fraction in the NiTi foil near the crack tip

CONCLUSIONS

NiTi foil was successfully joined to a polyimide matrix composite laminate by co-curing. Robust adhesion between the NiTi foil and composite was achieved by performing a combination of laser ablation and amide acid sol-gel treatment on the NiTi surfaces. The mode-I fracture toughness of the hybrid interface was investigated by the DCB tests as well as FE analyses. It was observed both experimentally and computationally that the NiTi foil underwent a phase transformation during the DCB tests at 25 ^{o}C. Current analyses using DIC measurements and FEA are carried out to investigate the effects of SMA phase transformation as well as interfacial architecture (topography created by laser ablation on the NiTi foil and woven fabric reinforcements) on the strain energy release rates upon crack propagation.

ACKNOWLEDGEMENT

The authors acknowledge the financial support of the NASA Space Technology Research Fellowship Grant No. NNX14AM41H. The fabrication, characterization, and fracture testing of the composites were performed at NASA Langley Research Center, Hampton, VA.

References

[1] Zimmerman T. et al.: Adhesive Bonding of Hybrid Actuated Shape Memory Alloy-Composite Structures. SAMPE Fall 2010, Utah, USA, 2010.
[2] Truong H.T.X. et al.: Fracture Toughness of Fiber Metal Laminates: CNT Modified Ti-PMC Interface. *J. Comp Mat* **48**(**22**):2697-2710, 2014.
[3] Truong H.T.X. et al.: An Investigation on Hybrid Interface Using On-line Monitoring Experiment and FEA. ICCM20, Copenhagen, Denmark 2015.
[4] Truong H.T.X. et al.: Experimental and Computational Investigations of Hybrid Interfaces in Hybrid Composite Laminates. ASC30, Michigan, USA 2015.
[5] Palmieri F.L. et al.: Laser Ablative Surface Treatment for Enhanced Bonding of Ti-6Al-4V Alloy. *ACS App Materials & Interfaces* **5**(**4**):1254-1261, 2013.
[6] Park C. et al.: Polyimide-Silica Hybrids Using Novel Phenylethynyl Imide Silanes as Coupling Agents for Surface-Treated Alloy. *Int J. Adhesion & Adhesives* **20**:457-465, 2000.
[7] Lagoudas D.C. et al.: Constitutive Model for Polycrystalline SMA with Smooth Transformation Surfaces. *Int J. Plast* **32-33**:155-183, 2012.

ACTIVE COMPOSITES BY MULTI-MATERIAL 3D PRINTING

Jiangtao Wu[1], Chao Yuan[2], Zhen Ding [3], Tiejun Wang[2], Martin L. Dunn[3], H. Jerry Qi[1a)]

[1]*The School of Mechanical Engineering, Georgia Institute of Technology, Atlanta, GA 30332, USA*
[2]*Department of Engineering Mechanics, Xi'an Jiaotong University, Xi'an 710049,China*
[3]*Digital Manufacturing and Design Centre, Singapore University of Technology and Design, Singapore*

Abstract In this paper, we design and 3D print active shape memory polymer (SMP) composites which can show multi-shape memory effect when stimulated by heat. This is achieved by carefully allocating two groups of fibers made of different digital shape memory polymers that have different thermomechanical properties into different locations within the composite. After programming, these fibers recover their shapes at different temperature, leading multiple shape change. By tuning the prescribed strain, programming temperatures, and spatial distributions of these fibers, we can control the shape changing behavior of the printed structure. A theoretical model is also applied to predict the deformation behavior of the sample during recovery procedure. The printed active composites (PAC) are then used to create self-folding and self-opening structures.

INTRODUCTION

Active structures that are able to change the shape when subject to external stimuli such as temperature, light, electricity, have great potentials in the packaging, aerospace exploring and bio-medical application [1][2]. Recent researches which employ 3D printing to fabricate active structures have added new dimension to 3D printing, which is termed as 4D printing [3][4]. The SMP fibers were embedded in the elastomeric matrix by 3D printing to create active structures, which was able to fix a temporary shape and recover to the permanent shape when subject to heat. The multiple material 3D printing technologies enable us to print multiple SMPs in one structure simultaneously, which provides a convenient method to introduce more than one glass transitions points. By taking advantage of this advance, we can create structures with multi-shape memory effects if carefully designed. In this paper, we apply 3D printing to design and create multi-shape memory composites by printing different digital SMP fibers in a rubbery matrix. After being programmed with simple thermal-mechanical training, the printed material is able to form multiple temporary shapes and recover to the flat permanent shape. To understand the shape memory behavior of the PACs, a theoretical thermomechanical model is established to investigate the shape variation during the shape recovery procedure. The influence of the strain on the initial and maximum curvature of the PACs is determined by experiments and theoretical modeling. Using the design methods and theoretical prediction, we can design and fabricate several self-folding and opening structures by 3D printing.

RESULTS AND DISCUSSION

The shape memory behavior of the PAC strips.

The composites consist of three materials with different glass transition temperatures (T_gs). All the samples are fabricated using the multi-material 3D printer (Objet260 Connex, Stratasys Inc). Fig. 1a shows the design of a two-layer composite. The matrix is TangoBlack+, which has the lowest T_g (~2℃). Two families of digital SMP fibers with different T_gs (fiber 1: DM8530, T_g~58℃; fiber 2: DM9895, T_g~40℃,) are embedded in the two layers, respectively, with prescribed volume fractions as shown in Fig. 1b. The common thermomechanical programming steps for shape memory effects are used. We first stretch the composite strip at an elevated programming temperature T_H=70℃, to a prescribed strain (ε_0=10%), and then cool it to the low temperature 0℃ (T_L, which is Lower than T_gs of both fiber materials) while maintaining the strain ε_0. The applied strain is then released, which fixes the composite in the first temporary shape as shown in Fig. 1(b).

Upon heating, the strip gains the ability to deform due to the temperature dependent viscoelastic properties of the matrix and fibers; the amount of deformation depends on the thermomechanical properties of the fibers and the matrix, the programming strain and the ambient temperature. When we heat the sample to a temperature higher than the T_g of the matrix but lower than that of the fibers, the sample is able to change to a second temporary shape. Due to the long stress relaxation time of the fibers at low temperatures, we are able to obtain a series of temporary shapes with different bending curvatures if we increase the temperature in a staggered manner. Fig. 1(b) shows the experimental results of the shape of the sample in three different temperatures (15℃, 30℃，60℃). The sequence of transformations of the 3D printed SMP composites indicates that we can achieve multiple shape memory effects using convenient 3D printing technology with a single simple programming process. Unlike conventional SME in polymers where the shape change is simply from one to another; here, a simple stretch can create multiple shape changes.

Theoretical model for the multi-shape memory behaviors.

In order to better understand the deformation behavior of the SMP composites, a theoretical model is developed that

a) Corresponding author. Email: qih@me.gatech.edu.

can be used to design SMP composites. In this model, the bending behavior of the composite strip is described using classical laminate theory, and a multi-branch model is used to describe the viscoelastic mechanical behavior of the matrix and fibers. Since the recovery speed is relatively fast, the heat transfer problem is considered to capture the non-uniform temperature distribution in the sample during the heating process. Fig. 1g shows the comparison of the experimental and theoretical predictions of the initial and maximum curvatures of the PAC sample with different prescribed strains during the heating process. We can see that the model can predict the shape memory behavior well.

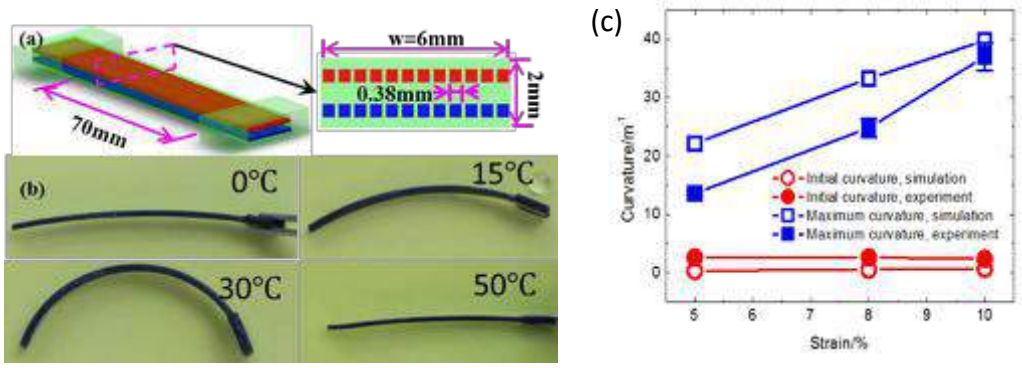

Figure 1 Multi-shape memory effects of a PAC strip. (a) The design of the sample (b) Shapes of the sample at different temperature. (c) The comparison of the experimental and theoretical predictions of the initial and maximum curvatures of the sample when different prescribed strains are applied.

Application of the PACs: self-folding and self-opening structure.

As described above, by tuning the prescribed strain, the bending of the SMP composites can be controlled. We design and fabricate self-folding and opening structure that exploits this phenomenon based on our understanding. Here we show one example: a smart hook (Fig. 2). In this design, two 3D printed composites strips are connected at the ends. The structure was stretched by10%, cooled to 0℃ and relaxed under 0℃ water. The programmed flat sample can be used as a hook move a small box from one container to another. The sample was first put into hot water with temperature of 30℃ (Fig 2b-c). After 38s, the sample becomes a curved hook. Using this hook, we can lift up a small basket from water (Fig. 2d). To move the box into another container, we increase the temperature of the sample to be higher than the T_gs of the fibers (Fig. 2e-f). From the simple design, we can see the great potential of using the 3D PACs in creating smart structures.

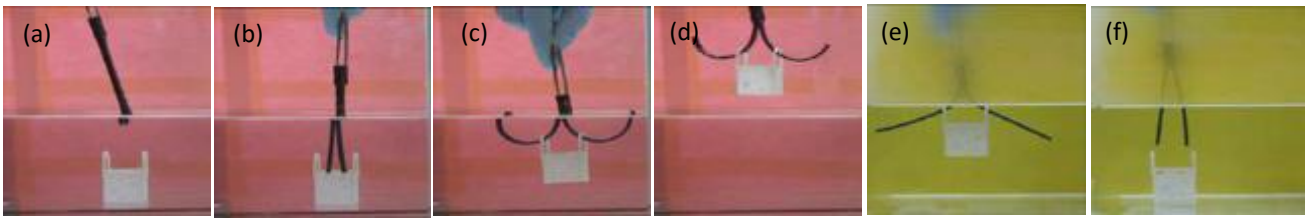

Figure 2 Self-folding and self-opening structures: smart hook.

CONCLUSIONS

3D printing is applied to design and create multi-shape memory composites. After being programmed by simple thermal-mechanical training, the PACs are able to show multi-shape memory effects when stimulated by the external heating. To understand the multi-shape memory behaviour of the PACs, a theoretical thermo-mechanical model is established to investigate the curvature evolution during the shape recovery process. The influence of the programming strains on the initial and maximum curvature of the PACs is studied by experiments and theoretical analysis. Using the design methods and theoretical prediction, we show the great potential of PACs in self-folding and opening structures applications.

Reference

[1] Leng, J., Lan, X., Liu, Y. & Du, *Progress in Materials Science* **56**, 1077(2011).
[2] Childers, E. P., Wang, M. O., Becker, M. L., Fisher, J. P. & Dean, D. MRS Bulletin 40, 119-126, (2015).
[3] Ge, Q., Qi, H. J. & Dunn, M. L. Applied Physics Letters 103, 131901 (2013).
[4] Ge, Q., Dunn, C. K., Qi, H. J. & Dunn, M. L. Smart Materials and Structures 23, 094007 (2014).

DESIGN OF CO-CONTINUOUS COMPOSITE MATERIALS USING 3D PRINTING TECHNIQUE

Tiantian Li[1] and Lifeng Wang [1]
[1]*Department of Mechanical Engineering, State University of New York at Stony Brook, Stony Brook, New York, USA*

Summary Co-continuous polymer composite materials are designed and fabricated using 3d printing technique. Compression and 3 point bending tests are performed to achieve stiffness, strength and energy absorption abilities. The experimental results will be compared to the simulation results and to validate and improve the design of structures. The co-continuity of the structures contains cracking and spreads of the plastic deformation leading to enhancements of energy dissipation, which also provides damage tolerance of the co-continuous composites.

INTRODUCTION

Interpenetrating phase composites (IPCs), also known as co-continuous composites, have been proposed to improve the dispersion and to increase the volume fraction of reinforcing phases [1, 2]. Natural and synthetic co-continuous composites, comprised of hard and soft materials, can provide excellent effective properties including stiffness, strength, impact resistance, toughness, and energy dissipation [3, 4]. In this research, we propose to develop high-performance co-continuous polymer composite materials through an integrated approach combining design, fabrication, analysis and testing aspects to better understand structure-property-function relationships for achieving desired mechanical properties.

EXPERIMENTATION

Three types of co-continuous truss structures with simple cubic (SC), body-centered cubic (BCC), and face-centered cubic (FCC) Bravais lattices were designed and fabricated with an Objet Connex500 3D multi-material printer (Objet260 Connex, USA). VeroWhite, an acrylic-based photo-polymer, was used for the truss phase structures, and TangoPlus, a rubber-like flexible material was used for the inverse phase structures. For each set of designs, the volume fraction of truss phase were held as 20%, 30%, 40% and 50%. The 50%/50% composites consists of 4x4x4 unit cells for compression testing and 4x4x24 unit cells for flexure testing. Three samples of each design were tested and average values were determined and presented for the analysis.

Compression tests and three point bending tests were performed using a MTS mechanical tester for force displacement measurements in conjunction with a video camera. All experiments were quasi-static with a constant strain rate of 0.05 mm/s for compression tests and 0.1 mm/s for three point bending tests. Three samples of each design were tested, and average values were determined and presented for this analysis.

We also investigate the elastic-plastic mechanical response of these composites using finite element analysis (FEA) of micromechanical models of representative volume elements (RVEs) for each microstructure with 50% volume fraction of each phase.

RESULTS

The experimental and simulated stress-strain curve of the three co-continues composites for compression testing are shown in Fig. 1(a). Typically, three regimes in the course of deformation are clearly observed in the stress-strain curve of the composites: (i) initial linear elastic region; (ii) plastic collapse plateau region, so called transition zone; and (iii) densification region. The computed stress-strain curve predicts the typical three regions well, which is in agreement with the experimental data. The simulated stresses are higher than the corresponding experimental values most likely due to the fidelity of the 3D print process. Although Objet260 has a stated resolution of ~30 μm, the accuracy can still affect the volume fraction and distribution of each phase. Also layer to layer structures may induce the sliding process during the uniaxial compression which may reduce the Young's modulus and yield stress as shown in BCC and FCC composites. The nominal stress-strain curves show the repeatability up to 40% compression strain of BCC and FCC composites while less than 10% compression strain of SC composites. Fig. 1(b) shows the comparison of the von Mises stress of the co-continuous composites and the experimental images. Cracking is observed to occur in the interior of a glassy polymer region rather than at an interface between phases at large strains (26% of BCC). However, these cracks do not reduce the stress level. Because the co-continuity of the structure constrains the cracking and enables these composites to provide energy absorption to larger strains before catastrophic failure in BCC and FCC composites. For FCC composite, cracking is not observed, instead a global shear failure occurs. Thus for this composite, strain hardening curves are smooth. The SC structure possesses an axially oriented columnar glassy region which supports load in direct compression deformation giving the stiffer stronger behaviour as compared to the FCC structure which carriers the <100> loading primarily through bending/shear deformation of the constituents. Similar to experimental results, simulation results indicate that deformation

[a)] Corresponding author. Email: lifeng.wang@stonybrook.edu.

of glassy polymer in the SC, BCC and FCC structure was restricted by the presence of rubbery elastomer phase. The elastomer also acted as a barrier to crack propagation, forcing the crack to keep growing within the glassy polymer. These results suggest good ability to tailor the microstructures to achieve different failure mechanisms to enhance energy dissipation under large deformation.

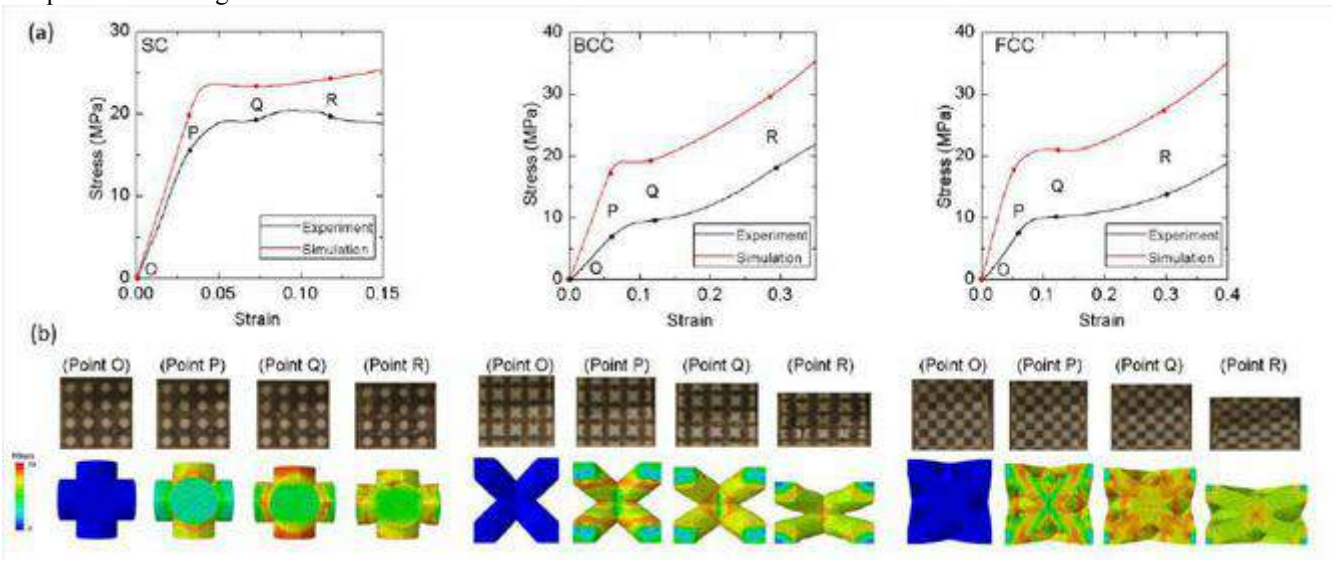

Fig. 1 (a)Simulated and experimental stress-strain curves upon uniaxial compression with SC, BCC, FCC composites; (b) Comparison of experimental images and computed von Mises stress of three co-continuous composites (only glassy polymer is shown) during uniaxial compression in the FE model. Points O, P, Q and R denote each position in the stress-strain curve (marked in (a)) .

Fig. 2 indicates the flexure properties of three samples. It can be seen that the SC composites exhibit higher flexural stiffness as well as maximum allowable loading compared to BCC and FCC composites. On the other hand, the FCC composites exhibit higher resilience compared to SC and BCC composites with approximately 100% more maximum deflection. This will contribute to the total energy absorption of FCC samples. Furthermore, BCC composites show both weak flexure stress and flexure strain properties. Simulation results fit very well with experimental results. The comparison of von Mises stress of three samples show that FCC structures exhibit more dispersed localized stress concentration while SC and FCC structures exhibit localized stress concentration at the point where fracture are observed.

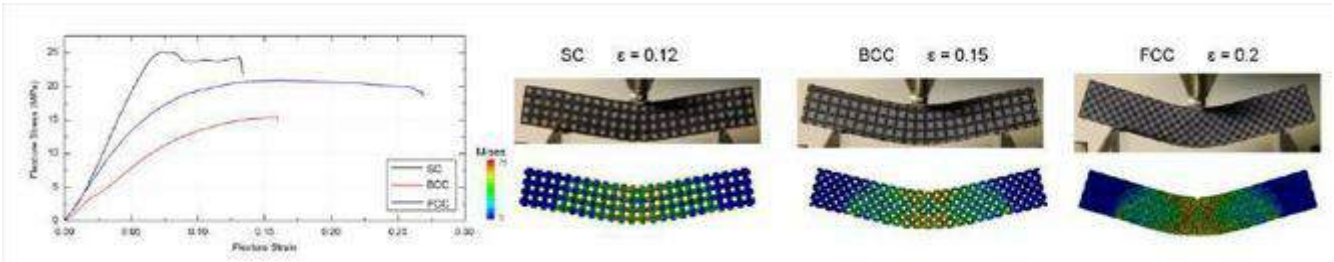

Fig. 2 Experimental flexure stress-strain curves upon three point bending tests with SC, BCC, FCC composites. Comparison of experiment and simulation (only glassy polymer is shown).

CONCLUSIONS

In the current work, the compression and bending tests revealed that our co-continuous structures exhibit large energy dissipation while maintaining sufficient stiffness and possess considerable potential specifically for energy absorption applications. This could be largely due to the co-continuity of the structures by containing cracking and by spreading of the plastic deformation, which also provides damage tolerance of the co-continuous composites.

References

[1] Clarke, D. R.: Interpenetrating phase composites. *J. Am. Ceram. Soc.* **75**, 739-759, 1992.

[2] Poniznik, Z., Salit, V., Basista, M. & Gross, D.: Effective elastic properties of interpenetrating phase composites. *Comput. Mater. Sci.* **44**, 813-820, 2008.

[3] Melcher, R., Travitzky, N., Zollfrank, C. & Greil, P.: 3D printing of Al_2O_3/CuO interpenetrating phase composites. *J. Mater. Sci.* **46**, 1203-1210, 2011..

[4] Wang, L.F., Lau, J., Thomas, E.L. & Boyce, M.C.: Co-continuous composite materials for stiffness, strength and energy dissipation. *Advanced Materials* **23**, 1524-1529, 2011.

EFFECTS OF MICROSTRUCTURAL VARIATIONS ON TRANSVERSE CRACK INITIATION IN COMPOSITES

C. Montgomery[1], M. Rossol[1,2], S. Zacek[3], P.H. Geubelle[3], D. Nepal[4], N.R. Sottos[1,2a]
[1]*Department of Materials Science, University of Illinois at Urbana-Champaign, USA*
[2]*Beckman Institute for Advanced Science and Technology, University of Illinois at Urbana-Champaign, USA*
[3]*Department of Aerospace Engineering, University of Illinois at Urbana-Champaign, USA*
[4]*Air Force Research Lab (AFRL), Wright Patterson Air Force Base, Dayton OH, USA*

Summary We present a multiscale experimental and computational investigation of the effects of interphase and microstructural variations on the initiation and density of transverse cracks in carbon fiber reinforced composites. Interface and matrix properties are systematically varied by fabricating composites with a range of surface treated carbon fibers under different processing conditions. Fiber/matrix interface strength is characterized through single fiber microbond experiments. Spatial variation in interphase chemical composition is measured using a new atomic force microscope based infrared spectroscopy (AFM-IR) technique. Composites are tested in transverse tension and the initiation and density of cracks correlated with changes in interface/interphase properties. Results from experiments are used to calibrate and compare to predictions from an interface-enriched finite element model.

INTRODUCTION

Characterization of the failure process in fiber-reinforced polymeric composites is complex and spans multiple length scales. Thermal and mechanical fatigue loading initiate failure of the fiber-matrix interface and cause significant matrix microcracking. This micron and submicron level damage reduces stiffness and weakens resistance to environmental exposure, facilitating larger scale delamination's and crack growth. Damage at the level of the fiber-matrix interface also plays a key role in the fracture response of the composite. The progressive debonding and pull-out of fibers in the bridging zone behind the crack front provide a major source of energy dissipation and toughening to the composite.

The formation of transverse matrix cracks in cross-ply polymer matrix composites leads to reduced stiffness, diminished elastic properties, and the potential for reduced strength and damage tolerance. Although a widely studied problem, improved understanding of the variables controlling transverse crack initiation is still needed for accurate modeling of this damage mode. In this study, digital image correlation is used to measure full field strains in a model cross-ply laminate system. These strain fields are correlated with the fiber/matrix interface properties, stochastic variations in the microstructure, and the residual stresses induced during processing. The experimental results are used to calibrate an interface-enriched finite element model (IGFEM) being developed in collaboration with this work.

INTERPHASE CHARACTERIZATION

We first characterized interface strength and interphase gradients for systematic variations in carbon fiber surface treatments and epoxy matrix cure conditions. An atomic force microscope based infrared spectroscopy (AFM-IR) technique, shown schematically in Fig. 1a, was used to detect chemical gradients in carbon fiber (AS4) reinforced epoxy (diglycidyl ether of Bisphenol-A, butanedioldiglycidyl ether, 2,2'-Dimethyl-4,4'methylenebis(cyclohexylamine)) systems. AFM-IR can measure the full IR spectra at localized points, or map the absorption of a single wavenumber over an area with 100 nm resolution. AFM-IR spectra of the bulk matrix material were in good agreement with spectra collected by traditional FTIR, particularly in the high wavenumber range above 2500/cm. Aromatic, aliphatic, hydroxyl, and ether groups are independently mapped in parallel with AFM topography. Significant contrast differences in the aromatic and aliphatic responses occurred in a region less than 1 micron from the fiber's surface. The influence of fiber surface treatments on interphase formation was also investigated by sampling multiple fiber types: untreated, oxidized, and epoxy-compatible sized. Fibers are characterized by measuring the elemental compositions at their surface using x-ray photoelectron spectroscopy (XPS). The interfacial shear strengths of these composite systems are measured using the single fiber microbond test [1]. The influence of the interphase region on interfacial shear strength, residual stress development and local matrix toughness is discussed in the context of interface failure.

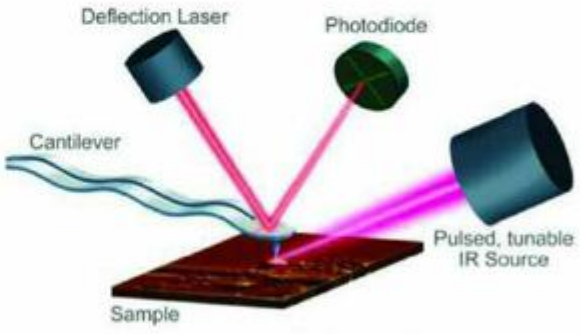

Figure 1. Schematic diagram of nano-IR2 components and representative spectra (image taken from Anasys Intruments).

[a)] Corresponding author. Email: n-sottos@illinois.edu

TRANSVERSE CRACK INTIATION AND EVOLUTION

Micromechanical and laminate level characterization was carried out on carbon fiber /epoxy composites fabricated from the identical constituent materials used in fiber/matrix interface investigation. Hence composite laminates with systematic variations in fiber surface treatment (interface strength) and matrix cure state (residual stress) were investigated.

We have developed a unique experimental capability to measure full field strains at the microscale in composites [2,3]. Fluorescent nanoparticles were fabricated and used as a speckle pattern for digital image correlation (DIC). Composite specimens are tested in a custom load frame under a fluorescent microscope. Figure 2 contains a plot of full field strain measured under transverse loading of a carbon fiber composite. Significant strain concentrations occur in resin rich regions of the microstructure. Here, we investigate the effect of carbon fiber interfacial surface treatment and matrix cure state on localized transverse strain fields and crack initiation. The full field data generated for the different types composites also provide a means for validation of multiscale numerical models.

In addition to microscale characterization of strain fields, we carried out macroscale transverse loading of composite laminates to calculate the effects of fiber surface treatments and matrix cure states on crack initiation, crack density and spacing of cracks in these laminates. Acoustic emission was used to determine crack initiation and crack density was characterized by optical imaging. Changes in elastic modulus were also measured as a function of crack damage evolution. The data generated provided macrolevel validation of the simulations of transverse damage.

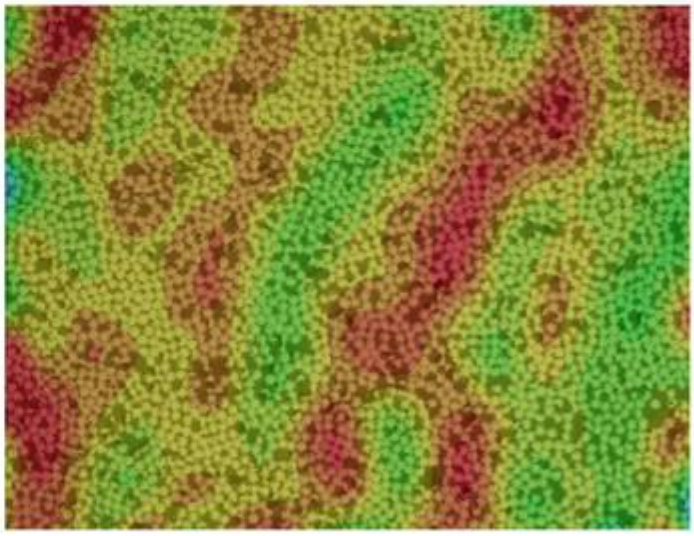

Figure 2. Localized, full field strain contours of a carbon fiber/epoxy matrix composite under transverse loading. Strain contour plot at ε_{xx} = 0.31% and σ = 158 MPa overlaid on optical image of composite specimen [4].

CONCLUSIONS

A multiscale experimental and computational investigation was carried out to elucidate the effects of interphase and microstructural variations on the initiation and density of transverse cracks in carbon fiber reinforced composites. Composites were fabricated with varying interface properities under different processing conditions. Single fiber level microbond experiments revealed significant changes in interfacial shear strength for different fiber surface treatments and cure conditions. Spatial variation in interphase chemical composition was characterized by atomic force microscope based infrared spectroscopy (AFM-IR) technique. Microscale level strain measurements revealed significant changes in strain distribution with variations occur in interface properties and microstructure. Composite level tests showed that the initiation and density of transvers cracks also correlated with changes in interphase properties and processing conditions. The experimental results were used to calibrate and compare to predictions from an interface-enriched finite element model.

References

[1] Jones, A.R., Blaiszik, B.J., White, S.R. and Sottos, N.R., *Composites Science and Technology*, **79**, 1-7 (2013). DOI: 10.1016/j.compscitech.2013.02.007

[2] Berfield, T.A., Patel, J.K., Shimmin, R.G., Braun, P.V., Lambros, J. and Sottos, N.R., *Small,* **2** (5), 631-635 (2006).

[3] Berfield, T.A., Patel, J.K., Shimmin, R.G., Braun, P.V., Lambros, J. and Sottos, N.R., *Experimental Mechanics,* 47, 51-62 (2007).

[4] Wilhelmsen, A.N., Characterization of Local Strain Fields in Cross-ply Composites under Transverse Loading, MS Thesis, Department of Aerospace Engineering, University of Illinois (2015).

YIELD CRITERIA FOR MATRIX AND COMPOSITE MATERIALS UNDER STATIC AND DYNAMIC LOADING

Isaac M. Daniel[1a], Joseph D. Schaefer[2] and Brian T. Werner[3]
[1]Northwestern University, Evanston, IL 60208, USA
[2]The Boeing Company, St. Louis, MO 63166, USA
[3]Sandia National Laboratory, Livermore, CA 94550, USA

Summary. A quasi-brittle polymer material used as matrix in composites was characterized under various states of stress at various strain rates. It was shown that characteristic properties, such as the yield stress, vary linearly with the logarithm of strain rate. Furthermore, it was observed that the onset of yielding under any state of stress is governed by the tensile yield stress or yield strain. The onset of yielding in a composite lamina was also characterized under multi-axial states of stress and varying strain rates. It was shown that yielding can be described by criteria entirely analogous to the Northwestern failure criteria. Yield stresses varied linearly with the logarithm of strain rate. Thus, a master yield envelope was obtained for the lamina for varying strain rates and states of stress. Excellent agreement was shown with experimental results.

INTRODUCTION

A new failure theory was introduced recently, the NU-Daniel theory. It was shown how this theory can be applied to predict failure of composite materials under multi-axial loading at various strain rates [1-3]. The significance of this work is that it provides an accelerated process for screening and adoption of new materials and understanding the behavior of composite structures under multi-axial static and dynamic loads.

In the case of multidirectional laminates it is important to determine the in-situ state of stress in every lamina and follow damage progression starting with first-ply yielding (FPY), first-ply failure initiation (FPFI), first-ply failure saturation, or characteristic damage state (CDS) and ultimate laminate failure (ULF). The yield analysis described in this work provides a conservative lower bound for design. It then leads to understanding the failure progression up to ultimate laminate failure (ULF).

PROCEDURES AND RESULTS

Yield criterion for polymeric matrix

A quasi-brittle polymer material used as matrix in composites was characterized under tension, compression, shear and combinations of shear and normal tensile or compressive stress. Testing was performed over a wide range of strain rates, ranging from quasi-static to dynamic [4]. Stress-strain curves were obtained for all loading conditions. It was shown that characteristic properties, such as the yield point, vary linearly with the logarithm of strain rate. Furthermore, it was observed that the onset of yielding under any state of stress is governed by the tensile yield stress or yield strain (Fig. 1). This led to the proposal of a simple one property yield criterion which may be independent, or at least not sensitive, to strain rate [5].

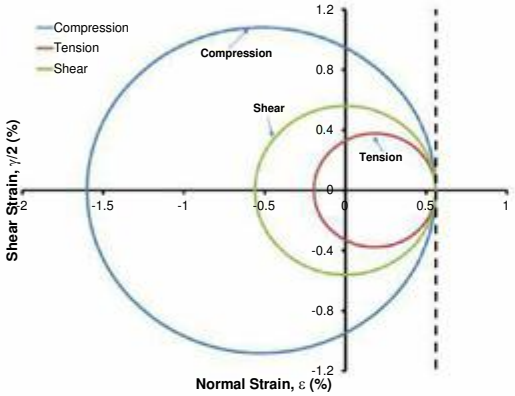

Fig. 1. Mohr circles of strain transformation for a polymeric matrix under uniaxial tension, compression and shear

Yield criteria for composite lamina

The onset of yielding in a composite lamina was also characterized under multi- axial states of stress and varying strain rates. It was shown that the onset of yielding can be described by criteria entirely analogous to the Northwestern failure criteria. Yield stresses varied linearly with the logarithm of strain rate. Thus, a master yield envelope was obtained for the lamina for varying strain rates and states of stress. Excellent agreement was shown with experimental results (Fig. 2)

[a)] Corresponding author. Email: imdaniel@northwestern.edu

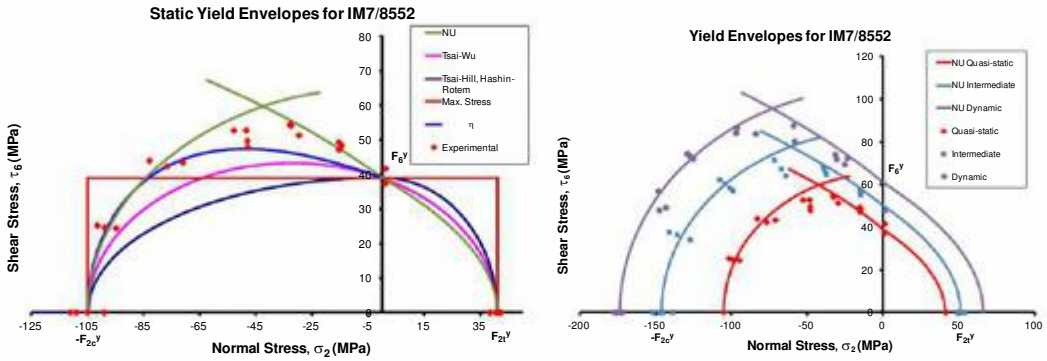

Fig. 2. Comparison of classical and NU yield envelopes with experimental results for IM7/8552 composite under quasi-static and higher strain rates

Yielding behaviour of angle-ply laminates

The yield analysis of the lamina was applied to angle-ply laminates under similar loading conditions. Processing residual stresses were calculated and included in the determination of in-situ lamina stresses. Yield stresses and yield envelopes were determined for the laminates and yield envelopes were obtained. Again, taking advantage of linear variation of yield stresses with the logarithm of strain rate, leads to the collapse of the various yield envelopes into one master yield envelope. All yield envelopes were in very good agreement with experimental results (Fig. 3).

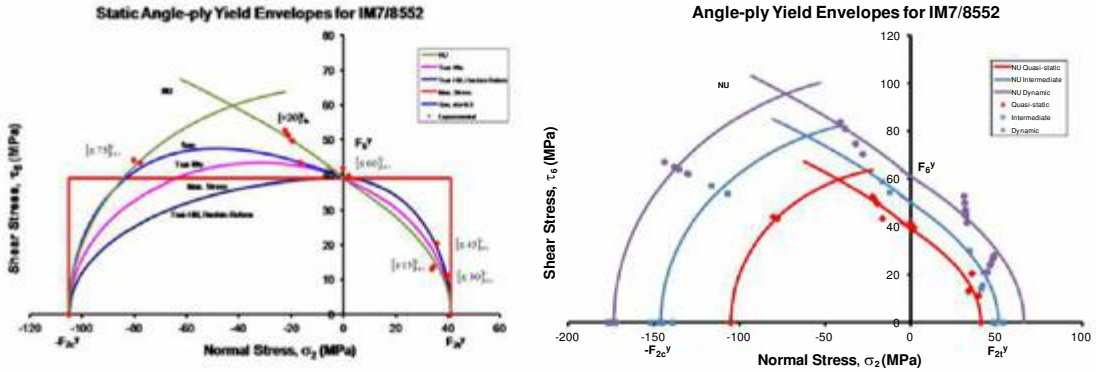

Fig. 3. Angle-ply yield envelopes and experimental results under quasi-static and high strain rate loading

CONCLUSION

The research described above is based on an interactive experimental/analytical approach yielding easily implemented design tools for composite structures. Steps are described for a systematic approach for analysis of progressive failure in structural composite laminates, starting from matrix yielding, to lamina yielding, followed by first-ply-yielding in a laminate, first-ply failure initiation, lamina failure saturation up to ultimate laminate failure. The research offers a unique and expedient path for screening, evaluation and adoption of new candidate materials obviating the need for lengthy and expensive test protocols. Results of this research serve as an indispensable input for numerical programs.

References

[1] Daniel I.M., Luo J.-J., Schubel P. M., Werner B. T.: Interfiber/interlaminar Failure of Composites Under Multi-Axial States Of Stress. *Composites Science and Technology;* **69**(6): 764-771, 2009.

[2] Daniel I. M., Werner B. T., Fenner J. S.: Strain-Rate-Dependent Failure Criteria for Composites. *Composites Science and Technology;* **71**(3): 357-364, 2011.

[3] Schaefer J. D., Werner B. T. Daniel I. M.: Strain-Rate-Dependent Failure of a Toughened Matrix Composite. *Experimental Mechanics;* **54**(6), 1111-1120, 2014.

[5] Werner B. T., Daniel I. M.: Characterization and Modeling of Polymeric Matrix under Multi-Axial Static and Dynamic Loading. *Composites Science and Technology;* 102, 113-119, 2014.

[6] Werner B. T., Daniel I. M.: Yield Criterion for Polymeric Matrix under Static and Dynamic Loading. *Proc. of SEM XIV International Congress and Exposition on Experimental and Applied Mechanics,* 2014.

DYNAMICS OF MICROSCALE GRANULAR CRYSTALS

Nicholas Boechler *[1]
[1]*Department of Mechanical Engineering, University of Washington, Seattle, WA, USA*

Summary The contact-based dynamics of ordered and reduced-dimensional arrays of microspheres, or "microscale granular crystals," are investigated. Mono- and multilayer microscale granular crystals are fabricated on substrates using self-assembly fabrication methods, and their dynamics are characterized using laser ultrasonic techniques. The observed dynamics are compared with analytical and computational models. As part of these studies, we have made several recent findings. We revealed interparticle-contact-mediated dynamics of microsphere monolayers that occur within the sagittal plane, including an out-of-plane mode of the monolayer and two transverse-rotational modes. We characterized the variation of the out-of-plane contact resonance with microsphere radius and oscillation amplitude. Finally, we studied plane and surface wave propagation in multilayer microscale granular crystals. These studies will lead to a better understanding of microscale contact dynamics and to a new class of microstructured materials for stress wave tailoring that can be assembled en-masse via self-assembly fabrication techniques.

Granular materials are a complex mechanical system known to yield rich acoustic phenomena [1]. Such phenomena results from granular media's often heterogeneous structure and the nonlinear contact mechanics between its constituent particles. Within this scope, ordered and reduced-dimensional arrays of elastic spherical particles in contact have proven to be systems of considerable interest [1, 2, 3]. These simplified systems, often referred to as "granular crystals," provide an avenue for gaining a broader understanding of granular media dynamics and can be configured as nonlinear phononic crystals or metamaterials for stress wave manipulation and acoustic signal processing applications [2]. While granular crystals have hitherto been typically constructed from macroscale particles [3], the acoustics of microscale granular crystals is a recently emerging field [4, 5, 6, 7]. The study of microscale granular crystals involves physical phenomena that are unique from their macroscale counterparts. For instance, van der Waals adhesion can be neglected when describing the contact mechanics between macroscale particles, but plays a major role in the contact mechanics of microscale particles.

The microscale granular crystals utilized in our experiments are fabricated using self-assembly techniques. Particle materials include silica and polystyrene, and particle diameters range from 300 nm to 4 μm. Two-dimensional crystals, as shown in Fig. 1, are fabricated using two techniques: a "wedge-cell" convective self-assembly technique, and a modified Langmuir-Blodgett technique where the microspheres are assembled at an air-water interface and transferred to a substrate. To fabricate three-dimensional structures, we utilize a vertical deposition convective self-assembly technique.

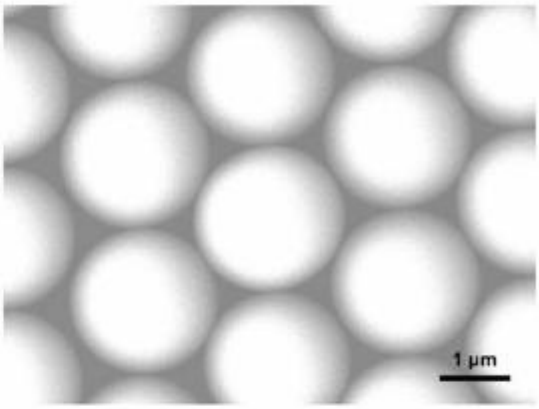

Figure 1: Scanning electron microscope image of a two-dimensional microscale granular crystal on a substrate.

The acoustic response of the microscale granular crystals are characterized using several complementary laser ultrasonic techniques. In each case, acoustic waves are generated by rapid thermoelastic expansion of metal transducer film on a substrate caused by the absorption of nanosecond "pump" laser pulses. The microscale granular crystal is adhered to the transducer film such that the crystal and substrate are excited dynamically. Several types of excitation are utilized, including line sources and large diameter (compared to the microsphere diameter) pump spot excitations that have spatially-periodic or gaussian amplitude profiles. To measure the resulting dynamics of the microscale granular crystals, we leverage several optical characterization approaches or that utilize interferometric, diffractive, and deflection mechanisms. Each approach provides unique information regarding the crystal's acoustic response.

Our initial studies focused on the dynamics of a two-dimensional microscale granular crystal on a substrate. For a two-dimensional microscale granular crystal on an substrate, three modes of vibration are predicted having motion in the sagittal plane, including including one having out-of-plane motion of the spheres, and two with combined rotational and in-plane translational motion [6]. For spheres of ~ 1 μm diameter, these modes are expected to have resonance frequencies ranging from tens to hundreds of megahertz. In our experiments, we observed each of these three modes by studying the resonant attenuation of broadband surface acoustic waves (SAWs) propagating in the substrate [7]. The broadband SAWs were generated using a line source located outside of the granular crystal. The SAW wavepacket crosses into the granular crystal at a flat interface created using a micro contact printing technique. The propagating SAWs are measured using a photo-deflection

*Corresponding author. Email: boechler@uw.edu

technique. By calculating the two-dimensional Fourier transform magnitudes of the spatiotemporal data corresponding to the SAWs propagating in the region with the monolayer, the dispersion curves were visualized. In the dispersion curves, the middle, and most strongly coupled, resonance, which corresponds to the out-of-plane mode, showed a clear avoided crossing with the Rayleigh surface acoustic wave branch. The other two resonances, corresponding to rotational-translational modes, appeared as attenuation zones along the Rayleigh branch. The nature of each mode was further confirmed by the utilization of a large pump spot excitation with interferometric detection, which is predominantly sensitive to the out-of-plane motion of the monolayer. We also coated the granular crystal with varying thicknesses of aluminum, which stiffens the interparticle contact and selectively shifts the frequency of the rotational-translational modes as was predicted by our models [6]. Following these experiments, the dependence of the out-of-plane contact resonance on amplitude and particle size was also studied, and compared with predictions utilizing elastic and elasto-plastic contact models.

The acoustic response of ordered and disordered multilayer microscale granular crystals were also studied. The multilayer microscale granular crystals studied ranged from two to ~ 50 layers thick. For crystals that are a few layers thick, surface waves were generated and measured using laser induced transient grating spectroscopy and compared with analytical models describing surface waves in a layered half space. For thicker samples, the effect of static compression and pump amplitude on plane wave propagation in the microgranular medium was explored utilizing large pump spot generation and inteferometric detection. The measurements were compared with effective medium models accounting for effects due to particle contact nonlinearity.

These experiments open the door for the study of ordered and reduced-dimensional microscale granular systems. In contrast to their macroscale counterparts, microscale granular crystals offer similar potential as dynamically adaptive material systems, but have smaller overall system scales, can be fabricated in rapidly and in large quantities utilizing self-assembly techniques, and may enable multifunctional material system concepts with acousto-optic or acousto-plasmonic functionalities. The experiments presented in these works represent a novel method for characterizing the contact dynamics of microscale particle networks. These studies provide new information regarding microscale particle contact mechanics and network formation, and will lead to an improved understanding of wave propagation in microscale granular media. Applications of these findings may include areas such as shock mitigation, energetic materials, seismic exploration, powder processing, and acoustic signal processing and sensing.

The author acknowledges the collaborators on these projects: J. Eliason, A. Kumar, N. Fang, T. Gan, A. Maznev, K. Nelson, N. Vogel, V. Gusev, A. Khanolkar, M. Hiraiwa, S. Wallen, and M. Abi Ghanem. The author also acknowledges support from the National Science Foundation (grant no. CMMI-1333858), the Army Research Office (grant no. W911NF-15-1-0030), and the University of Washington Royalty Research Fund.

References

[1] V. Nesterenko, *Dynamics of Heterogeneous Materials* (Springer, New York, NY, 2001).

[2] G. Theocharis, N. Boechler, and C. Daraio, Nonlinear Periodic Phononic Structures and Granular Crystals, Acoustic Metamaterials and Phononic Crystals, (Springer, Heidelberg, 2013), pp. 217-251.

[3] M. A. Porter, P. G. Kevrekidis, and C. Daraio, Granular crystals: Nonlinear dynamics meets materials engineering, Physics Today 68, 44 (2015).

[4] N. Boechler, J. K. Eliason, A. Kumar, A. A. Maznev, K. A. Nelson, and N. Fang, Interaction of a Contact Resonance of Microspheres with Surface Acoustic Waves, Phys. Rev. Lett. 111, 036103 (2013).

[5] A. Khanolkar, S. Wallen, M. Abi Ghanem, J. Jenks, N. Vogel, and N. Boechler, A self-assembled metamaterial for Lamb waves, Applied Physics Letters, 107, 071903 (2015)

[6] S. P. Wallen, A. A. Maznev, and N. Boechler, Dynamics of a monolayer of microspheres on an elastic substrate, Phys. Rev. B. 92, 174303 (2015).

[7] M. Hiraiwa, M. Abi Ghanem, S. P. Wallen, A. Khanolkar, A. A. Maznev, and N. Boechler, Complex contact-based dynamics of microsphere monolayers revealed by resonant attenuation of surface acoustic waves, arXiv:1510.05975 (2015).

DYNAMIC BEHAVIOUR WITH MATEMATERIAL PROPERTIES IN ELASTIC COMPOSITES

Guy Bonnet*[1] and Vincent Monchiet[2]

[1,2]*Université Paris-Est, Laboratoire Modélisation et Simulation Multi-Echelle,MSME UMR 8208 CNRS, 5 Boulevard Descartes, 77454 Marne la Vallée Cedex, France*

Summary Double scale asymptotic expansion provides the dynamic constitutive equations of a composite containing homogeneous inner inclusions. Under specific conditions, this behaviour exhibits a frequency dependent specific mass that can become negative for some frequency ranges, i.e. the composite is a metamaterial. The paper presents the exact computation of the frequency dependent specific mass for composites containing inner spherical inclusions, after solving the dynamic localization problem.

INTRODUCTION

A significant amount of research has been devoted recently to metamaterials, first in the field of electromagnetism and more recently in the field of acoustics. One of the main features of metamaterials is the occurence of a frequency varying specific mass that becomes negative within some frequency ranges. Such a feature was early predicted by using homogenization methods based on multiple scale expansions[1, 2] in the case of elastic composites containing homogeneous inclusions. From a practically point of view, the negative specific mass can be obtained by solving a localization problem. We present the solution of this problem for spherical inclusions, including the resonance frequencies and the participation factors of the different modes.

ASYMPTOTIC EXPANSION RESULTS

One considers an elastic matrix(m)-inclusions(i) composite. This composite is characterized by the elasticity tensors $\mathbf{a}_{(k)}$, with $k = m, i$ and specific masses $\rho_{(k)}$ ot the constituents and submitted to a harmonic excitation at radial frequency ω . The size l of the inclusions is assumed to be small compared with the size of the domain containing the solid composite. In addition, it is assumed that there is no diffraction of waves by inclusions, i.e. the wavelength Λ within the matrix related to radial frequency ω is large compared with l. As a consequence, a natural scaling parameter is the ratio $\epsilon = \frac{l}{\Lambda}$. If the inclusions are soft enough, resonance can occur within the inclusions, i.e. "inner resonance" appears. Finally, it has been shown [1, 3] that such an inner resonance occurs under the following conditions:

$$\begin{array}{rcl} \frac{\rho_{(i)}}{\rho_{(m)}} & = & O(1) \\ \frac{||\mathbf{a}_{(i)}||}{||\mathbf{a}_{(m)}||} & = & O(\epsilon^2) \end{array} \tag{1}$$

Under these conditions it has been shown that one can consider each inclusion as being submitted to the inertial acceleration $\boldsymbol{\gamma}_{(m)} = -\omega^2 \mathbf{u}_{(m)}$ of the matrix in the neighborhood of that inclusion. Then, the composite exhibits a tensorial frequency dependent dynamic specific mass given by:

$$\boldsymbol{\rho}_{eff}(\omega) =< \rho > \mathbf{i} + \rho_{(i)} \mathbf{h}(\omega) \tag{2}$$

where tensor $\mathbf{h}(\omega)$ is a function of ω depending on the eigenfrequencies ω^p and eigenmodes $\mathbf{v}^p$ that are solutions within the inclusion of

$$div(\mathbf{a}_{(i)} : \boldsymbol{\epsilon}(\mathbf{v}^p) + \rho_{(i)} (\omega^p)^2 \mathbf{v}^p = 0 \tag{3}$$

with $\mathbf{v}^p = 0$ on the boundary of the inclusion (fixed boundary.

The eigenmodes of interest are those that are excited for a direction of $\boldsymbol{\gamma}_{(m)}$ along a given unit vector $\mathbf{e}_z$. Having obtained these eigenmodes, tensor $\mathbf{h}$ is isotropic (for spherical inclusions) with $\mathbf{h} = h\mathbf{i}$ where

$$h = c_i \Sigma_{p=1}^{\infty} \frac{(< \mathbf{v}^p > .\mathbf{e}_z)^2}{< ||\mathbf{v}^p||^2 >} . \frac{1}{(\frac{\omega^p}{\omega})^2 - 1} = c_i \Sigma_{p=1}^{\infty} K^p . \frac{1}{(\frac{\omega^p}{\omega})^2 - 1} \tag{4}$$

$< f >$ represents the volume average of f over the inclusion, c_i is the volume concentration of inclusions and K^p the participation factor related to mode p. This function and therefore the dynamic specific mass tends to $-\infty$ for ω just above each eigenfrequency ω^p. As a consequence, the overall specific mass becomes also negative in some frequency range.

*Corresponding author. Email: guy.bonnet@univ-paris-est.fr

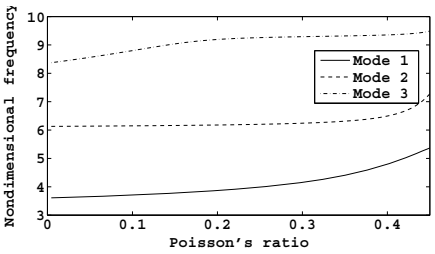

(a) Nondimensional resonance frequencies $\omega^* = \omega a/c_s$ of the first three modes

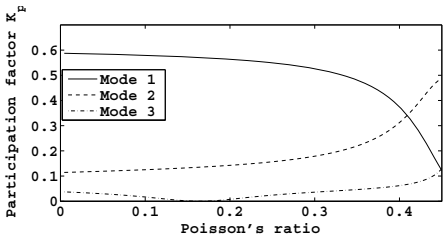

(b) Participation factors K^p of the first three modes

Figure 1: Resonance frequencies and participation factors for composites containing soft spherical inclusions of radius a

EIGENMODES OF A SPHERICAL INCLUSION

Classical works provide the eigenmodes of a sphere free at its boundary [7, 8]. The case of fixed boundary is less frequently seen but was studied early by Debye[6]. Some eigenfrequencies for the fixed boundary were obtained also by Schafbuch et al.[5]. The eigenmodes are obtained from the classical solution of the dynamic displacement field in spherical coordinates [7] using separated variables , that can be expressed by using spherical bessel functions j_n and associated Legendre functions P_n^m. An important part of our work has been to select the eigenfrequencies of interest for the homogenization problem. Indeed, taking into account the axial symmetry of the problem related to a given direction of matrix acceleration $\boldsymbol{\gamma}_{(m)}$ and due to the fact that the integral over the sphere of many of the separated solutions is null, the only case to consider corresponds to $m = 0, n = 1$. Then, the solution of the boundary problem within the sphere (omitting p index) is given using spherical coordinates by:

$$\begin{array}{rcl} v_r & = & \frac{A}{r}[U_1(\alpha r) + q.U_3(\beta r)]cos\theta \\ v_\theta = & = & -\frac{A}{r}[V_1(\alpha r) + q.V_3(\beta r)]sin\theta \end{array} \tag{5}$$

where U_1, U_3, V_1, V_3 are expressed using spherical Bessel functions j_1 and j_2, A and q being constants. α and β are the wavenumbers $\alpha = \omega/c_p, \beta = \omega/c_s$ where c_p and c_s are velocities of P-waves and S-waves. The eigenfrequencies are obtained by writing the boundary condition of null displacement at the boundary $r = a$ of the sphere, leading to the equation for the nondimensional eigenfrequencies:

$$[j_1(q\omega^*) - q\omega^* j_2(q\omega^*)][2j_1(\omega^*) - \omega^* j_2(\omega^*)] - 2j_1(\omega^*)j_1(q\omega^*) = 0 \tag{6}$$

where $q = c_s/c_p$ and $\omega^* = \omega a/c_s$. The expressions of v_r and v_θ are obtained by introducing the eigenfrequencies within equations (5), that allows us to compute the averages in (4) and therefore the participation factors K_p. Figure 1a displays the eigenfrequencies as functions of the Poisson's ratio and figure 1b displays the related participation factors. The figure shows that the resonance frequencies increase with the Poisson's ratio, as for the case of composites containing composite inclusions [4]. The participation factor of the first mode is predominant at lowest values of Poisson's ratio ν, but its contribution decreases with the Poisson's ratio, becoming inferior to the one of the second mode near $\nu = 0.5$. The higher modes, not shown here, have all participation factors lower than 0.1.

CONCLUSIONS

A dynamic behaviour of metamaterial type is obtained for composites containing soft spherical inclusions, using asymtotic expansion to characterize the scaling of physical poperties leading to such a behaviour. An explicit expression of the dynamic effective specific mass has been obtained for the case of spherical inclusions, including only the eigenfrequencies that contribute to the specific mass.

References

[1] Auriault J.L., Bonnet G.: Dynamique des composites lastiques priodiques. Arch. Mech. 37(4-5):269-284, 1985.
[2] Auriault J.L.: Acoustics of heterogeneous media: macroscopic behavior by homogenization. Curr. Topics Acoust. Res. 1:63-90, 1994.
[3] Auriault J.L.,Boutin C.: Long wavelength inner-resonance cut-off frequencies in elastic composite materials. Int. J. Solids Struct. 49:3269-3281, 2012.
[4] Bonnet G., Monchiet V.: Low frequency locally resonant metamaterials containing composite inclusions. J. Acoust. Soc. Am. 137(6):3263-3271, 2015.
[5] Schafbuch P.J., Rizzo F.J., Thompson R.B.: Eigenfrequencies of an elastic sphere with fixed boundary conditions. J. Appl. Mech. 59:458-459, 1992.
[6] Debye P.: Zur Theorie der Spezifischen Wärmen. Ann. der Phys. 39:789:839, 1912.
[7] Eringen A.C., Suhubi E.S., Elastodynamics,Vol.II. Acad.press. New York, USA, 1975.
[8] Love A.E.H., A treatise on the mathematical theory of elasticity. Dover, New York, USA, 1944.

EMBEDDED NANOPARTICLE ARRANGEMENTS ON PERMITTIVITY OF ELASTOMERIC COMPOSITES

Peiying J. Tsai[1], Suchitra Nayak[1], Suvojit Ghosh[2], and Ishwar K. Puri [*1,2]

[1]*Department of Mechanical Engineering, McMaster University, Hamilton, Ontario, Canada*
[2]*Department of Engineering Physics, McMaster University, Hamilton, Ontario, Canada*

Summary Elastomers are used as the dielectric layer in capacitors. Their electric capacitance depends on the configuration of parallel conductive plates and the permittivity of the dielectric material. The properties of composite materials can be altered by varying their filler structures. We examine the influence of chain-like structures introduced into polydimethylsiloxane-iron particle dielectric composites on its permittivity using numerical approaches. Parameters studied include the filler volume fraction, clearance between the chain ends and the conductive plates, spacing between adjacent chains, inter-particle spacing within each chain, and radius of the filler particles. The permittivity increases with volume fraction and inter-chain spacing but decreases as particle size increases. The introduction of chains into polydimethylsiloxane(PDMS) increases the permittivity up to ≈ 1.8 times that of composite with randomly distributed particles, but the particle must be connected for this enhancement. This result is useful for further development of the electrical applications of elastomeric composites.

INTRODUCTION

Rubber-like materials, such as silicone rubber, are good electrical insulators and serve as the dielectric medium in capacitors due to their low cost, light weight, and excellent hydrophobicity. Adding conductive filler particles into the elastomer improves the electric properties such as the effective permittivity of the composite. Based on conventional theory, the effective properties of a composite depends only on the volume fractions of the respective individual constituents and their properties. The geometry of the filler constituent also influences these effective properties [1]. An embedded geometry can be created by applying an external field on a liquid polymer that is infused with suspended particles, e.g., a magnetic field with the magnetic nanoparticles (MNPs) contained in a ferrofluid [2]. After the polymer is cured, the nanoparticle distribution is locked in place and the external field can be removed. A common geometry created using MNPs is chain-like structure. The influence of embedded chain structures on the electric permittivity of an elastomeric composite is not well understood, whereas it could be beneficial for the development of electronic applications such as 3D circuit boards [3], flexible electronics [4], 3D printed sensors [5], data storage [6] and optics [7] etc.

METHODS

A DC electric capacitor with dielectric PDMS and iron particle composite was modeled at steady state using COMSOL Multiphysics® 5.1 to investigate the effect of particle organization on the permittivity of the composite. The capacitor was constructed using two parallel plates containing a particulate filled elastomer as the dielectric medium that had embedded linear chains of spherical particles, as shown in Fig. 1. The investigation considered the influence of (1) inter-particle distance h_1, (2) inter-chain distance h_2, (3) clearance between the upper plate and the chain end h_3, (4) particle radius r, and (5) filler volume fraction ψ.

The effective relative permittivity of this dielectric composite was obtained from the capacitance of the parallel plate capacitor using the relation,

$$C = \frac{\varepsilon_0 \varepsilon A}{d}\,, \tag{1}$$

where C denotes the capacitance, ε_0 the absolute permittivity of free space, ε the relative permittivity of the dielectric medium, A the surface area of single plate, and d the distance between the two parallel plates of the capacitor. The permittivity of PDMS is 2.69 and of iron is assumed to be 2.8×10^5, which approaches an inordinately large value compared to 2.69 for an ideal metal [8]. A, d, and the applied voltage across the plates were kept constant as 314 μm^2, 7 μm, and 1 μV, respectively. Once the overall capacitance is obtained from the simulation, the effective relative permittivity of the composite can be determined.

In order to study the effect of the embedded chain structure, a permittivity index is introduced as

$$\text{Permittivity Index} = \frac{\varepsilon}{\varepsilon_{random}}\,, \tag{2}$$

that rationalizes the effect on the permittivity of the composite with chain structure (ε) by normalizing it to the permittivity of the same composite with randomly distributed filler particles (ε_{random}). Various procedures were performed to verify this model approach.

*Corresponding author. Email: ikpuri@mcmaster.ca

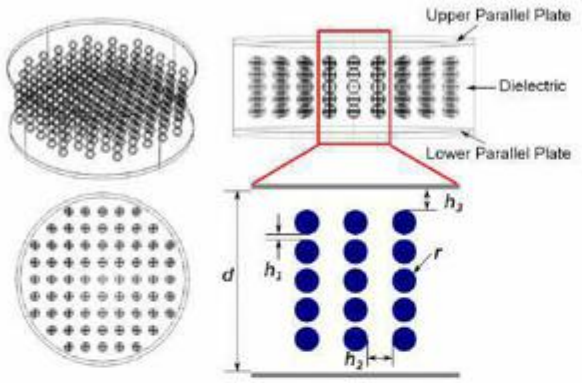

Figure 1: Demonstrations of the simulation model and the schematic of the chain-like structure. d is the constant distance between the two plates. The parameters studied are h_1 inter-particle spacing, h_2 inter-chain spacing, h_3 clearance between the top plate and the chain end, and r the radius of the particle.

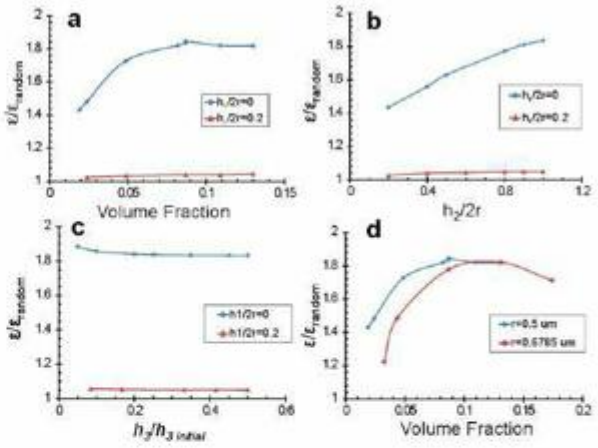

Figure 2: The permittivity index $\varepsilon/\varepsilon_{random}$ influenced by (a) inter-particle spacing $h_1/2r$, (b) inter-chain spacing $h_2/2r$, (c) chain end clearance $h_3/h_{3\text{initial}}$, and (d) particle size r. (a) and (d) are functions of ψ while (b) and (c) are at $\psi = 0.87$

RESULTS AND DISCUSSIONS

By organizing the filler particles into chain structures, the effective permittivity of the composite material is enhanced. The permittivity increases with increasing filler volume fraction and reaches saturation when the volume fractions are above 0.09 (Fig. 2a and d). Increasing the inter-chain spacing h_2 also increases the permittivity (Fig. 2b). When linear chains are placed off center, the change in the clearance h_3 does not have a strong influence on the permittivity (Fig. 2c). When the composite contains chains composed of smaller particles, its permittivity is higher than with bigger particles when the volume fraction is less than 0.1. For larger volume fractions, the difference between use of smaller and larger particles is negligible (Fig. 2d). Permittivity is enhanced when particles become connected, i.e., $h_1/2r = 0$ and it drops rapidly with increasing inter-particle spacing h_1.

The permittivity enhancement can be explained by observing how electric field lines reorient and concentrate around the linear chains of the conductive filler particles. The reorientation and concentration of electric field lines induces a more organized and stronger polarization within the dielectric composite that has an organized chain structure than one with randomly distributed particles. The higher polarization leads to a larger decrease in the electric field in between the plates and a higher charge accumulation at the parallel plates of the capacitor. Since a higher charge results in a higher capacitance for a constant voltage, the higher effective relative permittivity of the composite is achieved by maintaining other parameters in Eq. 1 the same.

Admittedly, our results are based on assumptions and generalizations made in the simulations, such as constant particle sizes, the absence of entangled and branched chains rather than the ideal linear chains we have considered, a steady electrostatic condition, temporally stable composite properties, and absence of fatigue and hysteresis. Despite these assumptions, our findings provide a conceptual trend for designing materials with improved electric permittivities by simply organizing the particles into chain-like structures with (1) connected conductive particles, (2) large inter-chain spacing, and (3) smaller size particles.

References

[1] Fragouli D., Das A., Innocenti C., et al.: Polymeric Films with Electric and Magnetic Anisotropy Due to Magnetically Assembled Functional Nano fibers. ACS Applied Materials & Interfaces, 6(6), 45354541, 2014.

[2] Ghosh S., Puri I. K.: Soft polymer magnetic nanocomposites: microstructure patterning by magnetophoretic transport and self-assembly. Soft Matter, 9, 2024, 2013.

[3] Juskey F. J., Suppelsa A. B., Dorinski D. W.: Method of forming a three-dimensional printed circuit assembly. US Patent 5,264,061, 1993.

[4] Siegel A. C., Phillips S. T., Dickey M. D., et al.: Foldable printed circuit boards on paper substrates. Advanced Functional Materials, 20(1), 2835, 2010.

[5] Frutiger A., Muth J. T., Vogt D. M., et al.: Capacitive Soft Strain Sensors via Multicore-Shell Fiber Printing. Advanced Materials, 27(15), 24402446, 2015.

[6] Sun Z. Z., Lopez A., Schliemann J.: Zero-field magnetization reversal of two-body Stoner particles with dipolar interaction. Journal of Applied Physics, 109(10), 104303, 2011.

[7] Ge J., He L., Hu Y., et al.: Magnetically induced colloidal assembly into field-responsive photonic structures. Nanoscale, 3(1), 177183, 2011.

[8] Klimchitskaya G. L., Mohideen U., Mostepanenko V. M.: The Casimir force between real materials: Experiment and theory. Reviews of Modern Physics, 81(4), 18271885, 2009.

EFFECT OF NANOPARTICLE ADDITION ON THE MECHANICAL AND PIEZOELCTRIC PROPERTIES OF 3D PRINTED PVDF

Sampada Bodkhe, Frederick P Gosselin & Daniel Therriault[a)]
Laboratory of Multiscale mechanics, Department of Mechanical Engineering,
Centre for Applied Research on Polymers and Composites (CREPEC)
Ecole Polytechnique de Montreal, C.P. 6079, succ. Centre-Ville, Montreal, Quebec, Canada

Summary The effect of filler addition on the mechanical and piezoelectric properties of polyvinylidene fluoride (PVDF) is studied for two reinforcements, namely, multi-walled carbon nanotubes (MWCNTs) and barium titanate ($BaTiO_3$) nanoparticles. Addition of $BaTiO_3$ nanoparticles and MWCNTs to PVDF resulted in reduction of Young's modulus by approximately 60 and 75%, respectively. $BaTiO_3$ nanoparticles increased elongation at break by about five times that of PVDF and generated about 3.5 mV of output.

INTRODUCTION

Polyvinylidene fluoride (PVDF) is a well-known piezoelectric polymer used in actuation, sensing and energy harvesting applications. Being a polymer, PVDF possesses the characteristics of low density, flexibility and printability in contrast to the conventional highly piezoelectric ceramic materials like lead zirconium titanate (PZT) and barium titanate ($BaTiO_3$). The piezoelectric coefficient (d_{33}) of PVDF is 33 $pC.N^{-1}$ [1], which is much lower than that of PZT, 360 $pC.N^{-1}$ [2], and $BaTiO_3$, 260 $pC.N^{-1}$ [3]. The addition of multi-walled carbon nanotubes (MWCNTs; 0.03 wt.%) has shown to increase the piezoelectric coefficient of PVDF to 57.6 $pC.N^{-1}$ [4]. But the addition of fillers can have an adverse effect on the flexibility and printability of PVDF. The effect of nanoparticle addition on printability was studied in our previous work using solvent-cast 3D printing technique [5]. PVDF/$BaTiO_3$ nanocomposites were more printable than PVDF/MWCNT nanocomposites due to the inhomogeneous mixing of the nanotubes leading to considerable nozzle clogging during printing. Here, the effect of addition of MWCNTs and $BaTiO_3$ nanoparticles on the mechanical and piezoelectric properties of PVDF is investigated.

MATERIALS AND METHODS

PVDF (Sigma Aldrich) was mixed with 1 wt.% $BaTiO_3$ nanoparticles (Nanostructured & Amorphous Materials Inc.) and MWCNTs (Nanocyl^{TM}) by ultrasonication to prepare nanocomposites according to the process described in [6]. PVDF and its nanocomposite solutions (further referred to as 'inks') were poured into 3 mL syringe barrels to enable printing. The syringe barrels were placed into a dispensing system (HP-7X, EFD) to apply a precise pressure for extruding the inks. A robotic head (I&J2200-4, I&J Fisnar Inc.), controlled by a commercial software (JR Points for Dispensing, Janome Sewing Machine) enabled the deposition of the inks on a moving platform. Films were printed with the inks at an extrusion pressure of 1000 kPa using a 100 μm nozzle and robotic speed of 20 $mm.s^{-1}$.

Tensile tests were carried out on an MTS Insight testing machine according to ASTM D882 standard. Five samples for each type of film (width = 6 mm; gauge length = 50 mm; avg. thickness = 120 μm), were tested at a grip separation rate of 500 mm/min using a 1000 N load cell.

To form the film sensors, silver (3 cm × 3 cm) was first hand painted near one edge of rectangular acrylic beams (32 cm × 3 cm) to form the bottom electrode. The inks were 3D printed on top of the electrode with the same parameters as used for tensile tests. After complete evaporation of the solvent, another layer of silver was painted on nanocomposite layers to form the top electrode. For piezoelectric tests, the beam was mounted on an electromagnetic shaker (Model# K2007E01, The Mode Shop Inc.). The strain generated by the harmonic excitations from the shaker to the beam caused the PVDF sensor to alternatively stretch and compress in the in-plane direction, producing charges along the thickness. The charges were amplified and converted into voltages by a charge amplifier (Piezo Film Lab Amplifier, Measurement specialities). The voltage generated by PVDF based sensors was compared with that of a commercial force sensor (288D01 SN 2960, PCB Piezotronics).

RESULTS AND DISCUSSION

The stress-strain curves in Figure 1a show decreased tensile strengths in the nanocomposite films. Addition of the nanoparticles also lowered the Young's modulus of PVDF from 237 MPa to 63 MPa in PVDF/MWCNT and to 95 MPa in PVDF/$BaTiO_3$. MWCNTs did not have any considerable effect on the elongation properties whereas the incorporation of $BaTiO_3$ nanoparticles exhibited an increase in elongation by over 5 times that of neat PVDF films.

[a)] Corresponding author. Email: Daniel.therriault@polymtl.ca.

The decreased moduli and strength, and the increased elongation in the nanocomposites might be attributed to the porous nature of the films. SEM images (insets in Figure 1a) show increased porosity in case of the nanocomposite films; PVDF/MWCNT possesses highest porosity (~10%, areal) supporting the decrease in modulus. The increased elongation at break along with the decreased modulus in PVDF/$BaTiO_3$ films is an added advantage in sensing applications as the films will have larger deformation at the same load, thereby, increasing the sensitivity and thus, the output voltage as compared to the PVDF/MWCNT films.

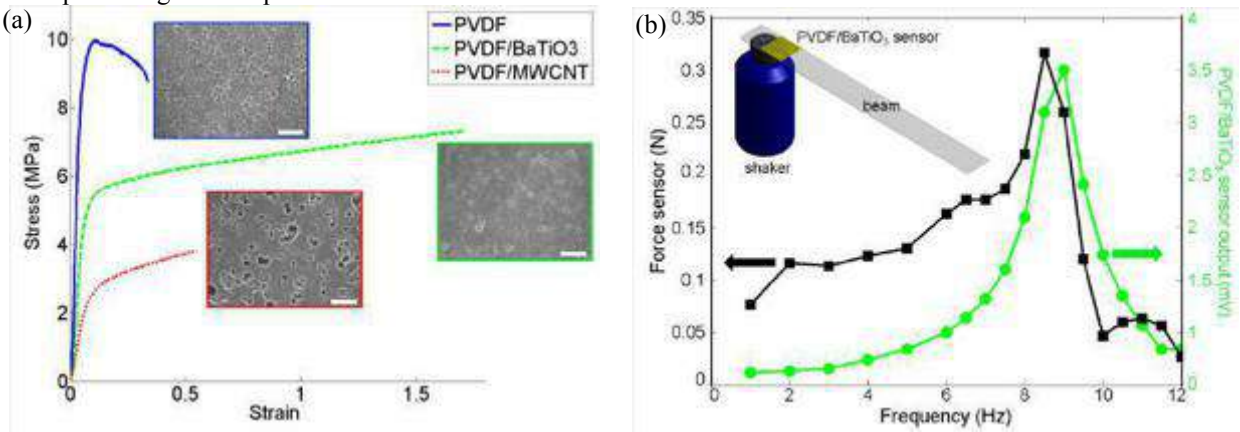

Figure 1: (a) Stress-strain curves obtained from the tensile tests of PVDF, PVDF/$BaTiO_3$ and PVDF/MWCNT films. Insets show SEM images of the films corresponding to each curve (Scale bar: 10 μm). (b) PVDF/$BaTiO_3$ and commercial force sensor output as a function of frequency. Inset shows the schematic of the test setup where the sensor is printed on the upper surface of the beam near the clamped extremity.

The beams with the printed sensors were excited sinusoidally between 1-12 Hz using the electromagnetic shaker. The maximum response of the sensors was obtained close to the theoretical natural frequency of the beam (8.4 Hz). Amongst the three sensors, the one with 1 wt.% $BaTiO_3$ nanoparticles (voltage output shown in Figure 1b) produced higher voltages, which is coherent with the results from the mechanical tests. The highest voltage generated by PVDF/$BaTiO_3$ sensor was about 3.5 mV; this corresponded to a transverse force of 0.34 N as detected by the commercial force sensor placed at the tip of the shaker. Higher voltage generation in case of PVDF/$BaTiO_3$ sensors is attributed to the high piezoelectric coefficients in $BaTiO_3$ as compared to MWCNTs and the increased flexibility as seen from the tensile tests. The effect of multiple loading cycles on the flexibility should further be studied.

CONCLUSIONS

PVDF/$BaTiO_3$ films exhibited over five times more elongation than neat PVDF and led to the generation of measurable voltages. Although the PVDF sensors fabricated in this work produced measurable voltages, they are significantly lower than those of the piezoelectric ceramics and the sensor is not very sensitive away from the resonance frequency. Future studies with higher $BaTiO_3$ nanoparticle contents could be pursued to attain higher piezoelectric properties and facilitate the sensing measurements.

ACKNOWLEDGEMENTS

The authors thank Isabelle Nowlan and Benedict Besner (Dept. of Mechanical Engg.) for their assistance and Lab. of Vibration and Acoustics for providing the electromagnetic shaker and data acquisition system.

References

[1] Piezo Film Sensors Technical Manual, 1999, Measurement Specialties, Inc: Norristown, PA
[2] Greeshma, T.: PVDF Phase Formation and Its Influence on Electrical and Structural Properties of PZT-PVDF Composites. *Ferroelectr Lett Sect***40**:41-55,2013.
[3] Simon-Seveyrat, L.: Re-investigation of synthesis of $BaTiO_3$ by conventional solid-state reaction and oxalate coprecipitation route for piezoelectric applications. *Ceram Int***33**:35-40,2007.
[4] Pu, J.: Piezoelectric actuation of direct-write electrospun fibers. *Sens Actuators, A***164**:131-136,2010.
[5] Guo, S.Z.: Solvent cast three-dimensional printing of multifunctional microsystems. *Small9*:4118-4122,2013.
[6] Bodkhe, S.:Three-dimensional printing of polyvinylidene fluoride nanocomposites. *20th International Conference on Composite Materials*. Copenhagen, Denmark 2015.

[a] Corresponding author. Email: Daniel.therriault@polymtl.ca.

FIELD-ASSISTED 3D-PRINTING OF ALIGNED COMPOSITES

Tyler Ray[1a], Rachel Collino,[1] Leanne Friedrich, [1] James Cornell [1] & Matthew Begley [1]
[1]*Materials Department, University of California, Santa Barbara, Santa Barbara, California, United States of America*

Summary: The deposition of multi-phase materials with microstructural control enables the integration of microstructure and structural features, which creates new pathways towards optimizing component performance. Here, we demonstrate that acoustic microfluidic print nozzles are an effective pathway to control SiC whisker orientation and packing density in printed composites. In addition to the ability to tune microstructure along a single print line, the overall concentration of reinforcements can be increased by selectively isolating a stream of focused fibers, enabling the deposition of material with higher fiber volume fractions than the initial ink composition. We show that even modest volume fractions of acoustically-focused and concentrated SiC fibers can produce printed composites with unprecedented control over microstructural ordering that exhibit strengths rivaling polymer-matrix composites with higher volume fractions of stiffer fibers.

The ability to control fiber alignment at high volume fractions would create new opportunities to print ultra-strong composite materials with engineered anisotropic properties (mechanical, electrical, thermal, and optical). A promising approach for achieving top-down control over microstructure is to combine field-assisted assembly with direct deposition. While electrostatic or electromagnetic fields are suitable for a narrow range of ink compositions and particle types, acoustic fields are broadly applicable to a wide class of colloids, spanning a broad range of composition, particle shape, and size We demonstrate acoustic-field-assisted deposition of two-phase aligned composites, such as SiC fibers in epoxy, using microfluidic print nozzles coupled to inexpensive piezoelectric actuators. Mechanical characterization of printed materials with varying microstructures show that significant gains in strength with even modest additions of SiC fibers in epoxy as a result of unprecedented control of the printed microstructure.

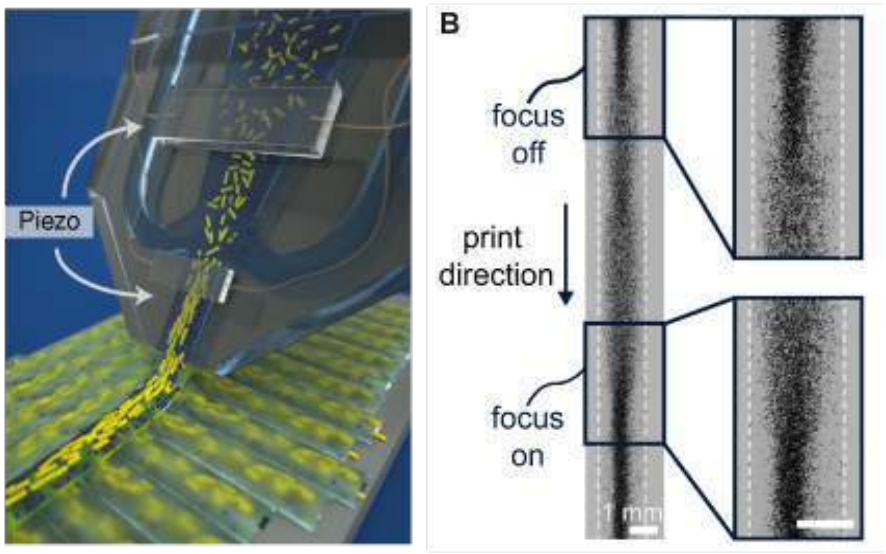

Figure 1: (A) Conceptual illustration of acoustic print nozzle. Piezoelectric actuation generates acoustic forces that align fibers during printing. Multiple piezos in series enable enhancement of fiber volume fraction of the printed via removal of flash. (B) Printed line with continuously varied microstructure. The focusing frequency is tuned to induce focusing of SiC fibers in epoxy; when the frequency is tuned away from resonance ("focus off"), the fibers spread to the width of the deposited line.

The two-stage acoustic nozzle schematic shown in Figure 1 illustrates the alignment of fibers in a viscoelastic matrix, which results from an applied acoustic force generated by piezoelectric elements mounted above the nozzle pathway. These nozzles are microfabricated in silicon (150 μm deep) with a bonded glass capping layer according to the procedures in Ref. [1], with piezoelectrics bonded to the nozzle to generate standing waves in the channel.

Critically, acoustic focusing enables control of the microstructure of the deposited line "on the fly" by modulating acoustic excitation parameters, as demonstrated in Figure 1B for SiC fibers in epoxy. In this case, when the excitation frequency is tuned to induce focusing ("focus on"), fibers collapse to the center of the print line. The focusing transition occurs quickly enough to tune the microstructure from densely packed to distributed fibers within approximately one filament width. When the excitation frequency is changed ("focus off"), fibers spread nearly uniformly throughout the print line. The transition between focused and de-focused microstructures, and vice versa, is approximately symmetric; this transition is influenced by the shape of the focus zone in the *(x,z)*-plane and the flow speed in the channel.

Figure 2A is a schematic of the single-channel nozzle geometry; in all cases, the print nozzle is stationary and the print substrate moves relative to the printhead. The effect of excitation voltage on microstructure is shown in Figure 2B for 0 and 23 V (peak-to-peak). For the control condition (0 V), no fiber focusing is apparent, and cross-sectional imaging reveals a

[a)] Corresponding author. Email: Tyler.Ray@icloud.com

distribution of fiber orientations; as the voltage is increased, deposited fibers focus to a smaller cross-section within the printed line.

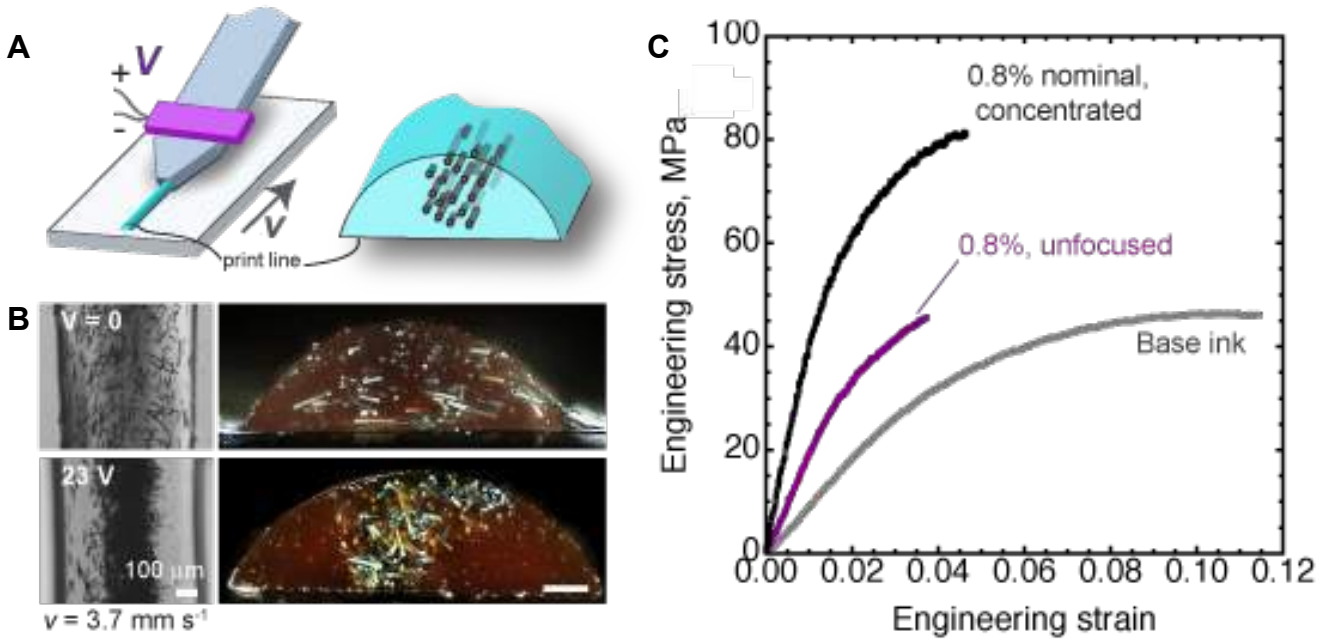

Figure 2: (A) Schematic of a microfluidic print nozzle with a coupled piezoelectric actuator driven at a peak-to-peak voltage (V), with deposition speed controlled by the substrate velocity (v). Print line microstructures for a constant deposition speed of 3.7 mm s^{-1} and increasing excitation voltage from 0 to 23 V in plan view (left) and cross-section (right). (B) Mechanical characterization of SiC/epoxy inks for tensile tests of the base ink material (epoxy, no fibers) as well as inks with 0.8 vol% SiC fibers for unfocused and focused conditions.

Figure 2C shows representative tensile test results for base ink (with no fibers) and inks with varying SiC fiber distribution (focused *vs.* unfocused). The base ink exhibits significant ductility and moderate strength and Young's modulus. The addition of 0.8 vol% SiC increases both strength and modulus and decreases ductility. The tensile test results in Figure 2C indicate that the printed microstructure has significant effects on the modulus and strength of printed parts. The different microstructures (focused *vs.* unfocused) exhibit different moduli for the same fiber loading, with only the latter approaching values estimated from an upper-bound rule-of-mixtures calculation[2]. A possible explanation for the lower moduli of focused samples is a difference in stress transfer from fibers to the matrix (*vs.* that in unfocused samples with distributed fibers), as suggested by the shear-lag model of Halpin and Tsai[3] for short-fiber composites. In the focused condition, it is likely that aggregated fibers are close enough to preclude load transfer across the entire fiber surface: in essence, the surface-area-to-volume-ratio decreases for a focused “band” of closely arranged fibers, leading to lower composite modulus values for a given fiber volume fraction. Consequently, this enables new printing modalities such as the ability to modulate the stiffness locally in a printed part by temporally varying excitation to manufacture functionally graded materials or custom lattice structures. In terms of overall stiffness and tensile strength, these results are highly promising, as even the small volume percentage of SiC fibers used in the present work have significant effect on measured Young's modulus and the strength of concentrated samples rivals that of epoxy composites with higher volume fractions of stiffer carbon fibers[4].

Although the focus is on acoustic print nozzles, the approach is scalable upwards in terms of fiber size, in that acoustic focusing forces increase with the volume of the fibers in solution. Our approach is also highly parallelizable in the sense that multiple print nozzles of the scale presented here can be utilized simultaneously. As a relatively material agnostic technique for microstructural control, acoustic-focusing-assisted additive manufacturing greatly expands the library of printable multiphase inks and is thus highly complementary to existing and emerging 3D-printing technologies.

References

[1] Collino, R. R., Ray, T.R., Fleming, R. C., Cornell, J. D., Compton, B. G., Begley, M. R. Deposition of Ordered Two-Phase Materials using Microfluidic Print Nozzles with Acoustic Focusing. *Extreme Mech Lett* **5**: 37-46, 2015.

[2] Chawla, K.: Composite Materials: Science and Engineering. New York, USA 2012.

[3] Halpin, J. C., Tsia, S. W. Effects of Environmental Factors on Composite Materials, AFML-TR-67-423, 1969.

[4] Compton, B. G., Lewis, J. A. 3D-Printing of Lightweight Cellular Composites. *Adv Mater* **26**:5930-5935, 2014.

MODELLING OF MATERIAL UNCERTAINTIES IN LONG FIBRE REINFORCED THERMOPLASTICS

Jörg Hohe[*1], Hanna Paul[2], and Carla Beckmann[1]
[1] *Fraunhofer-Institut für Werkstoffmechanik IWM, Freiburg, Germany*
[2] *Fraunhofer-Institut für Kurzzeitdynamik, Ernst-Mach-Institut, EMI, Freiburg, Germany*

Summary The present contribution is concerned with an investigation into the material uncertainties in long fibre reinforced thermoplastic materials (LFT) with disordered microstructure. In a preliminary experimental investigation, the local strains on standard size specimens are determined using an optical grey-scale correlation system. Based on the results, the probability distributions for the effective elasticity parameters are determined. For the consideration of the material uncertainties in structural analyses, a probabilistic elasticity model is proposed, treating the local fibre volume fraction as well as the parameters controlling the fibre orientation variability as random variables. In a validation of the numerical predictions against the experimental observations, the model proves to be accurate and numerically efficient.

INTRODUCTION

Long fibre reinforced thermoplastic materials (LFT) are a fairly new class of composite materials, which are suitable especially for industrial scale production of composite structures. They have the advantage that they can easily be processed to rather complex shapes at reasonable expenses using standard processes for polymeric materials like injection and compression moulding (Henning et al. [3]). Due to their increased fibre length of up to 50 mm, they outperform classical short fibre reinforced polymeric materials. Their main disadvantage is their disordered, process and position dependent microstructure, leading to a distinct uncertainty in the local material response (Bednarcyk et al. [2], Hohe et al. [4]). The uncertainty in the material response makes a accurate prediction of the response of LFT structures difficult and in many cases – due to the necessity of large safety margins – prevents the full exploitation of their lightweight potential. The present study is concerned with the development of a probabilistic elasticity model for LFT materials in order to enable a simple, comprehensive probabilistic analysis of LFT structures.

EXPERIMENTAL INVESTIGATION

For assessment of the material uncertainty, an experimental investigation is performed, using a glass fibre reinforced polyamide 6.6 matrix composite (PA6.6GF40), manufactured in a compression moulding process as a model material. The material is characterised in quasi-static tensile experiments on specimens taken from the flow range apart from the strand inlay position of a plane PA6.6GF40 plate, considering both, the direction longitudinal and perpendicular to the flow direction (Figure 1(a)). During the experiments, the local strains on the specimen surfaces within the loading direction and transversal to the loading direction were determined by means of an optical greyscale correlation system (Figure 1(b)). The results are evaluated in a stochastic manner (Figure 1(c)). Assuming that, for equilibrium reasons, the local stresses in the specimen gauge section do not vary significantly, local stress strain characteristics can be determined from the results.

PROBABILISTIC ELASTICITY MODEL AND VALIDATION

To make the uncertainties in the material response accessible for a stochastic finite element analysis on the macroscopic level, a probabilistic material model is proposed. The model is defined in three steps. On the first stage, the single fibre problem is considered (Figure 2), for which the effective properties can be estimated by the classical rules of mixture.

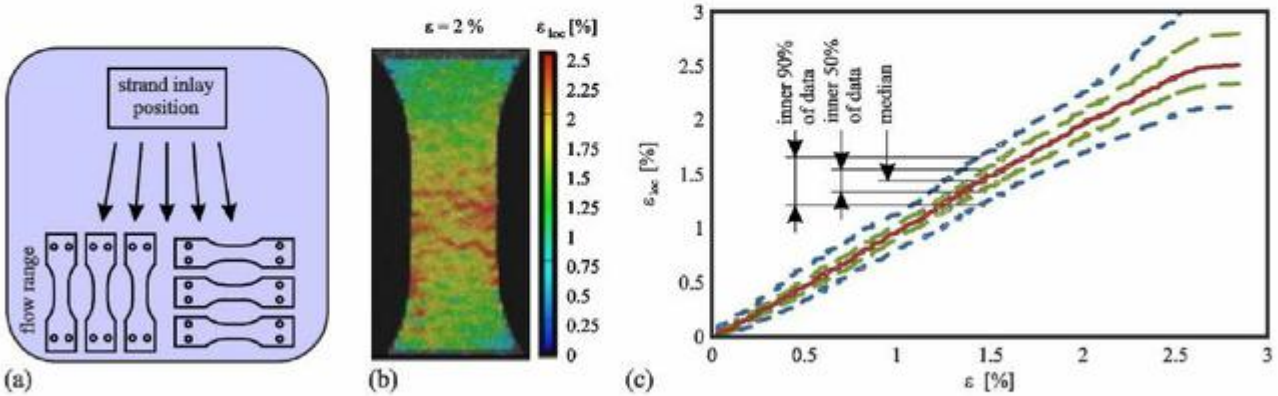

Figure 1: Probabilistic material characterization: (a) specimen extraction, (b) local strains, (c) local strain envelopes.

* Corresponding author. Email: joerg.hohe@iwm.fraunhofer.de.

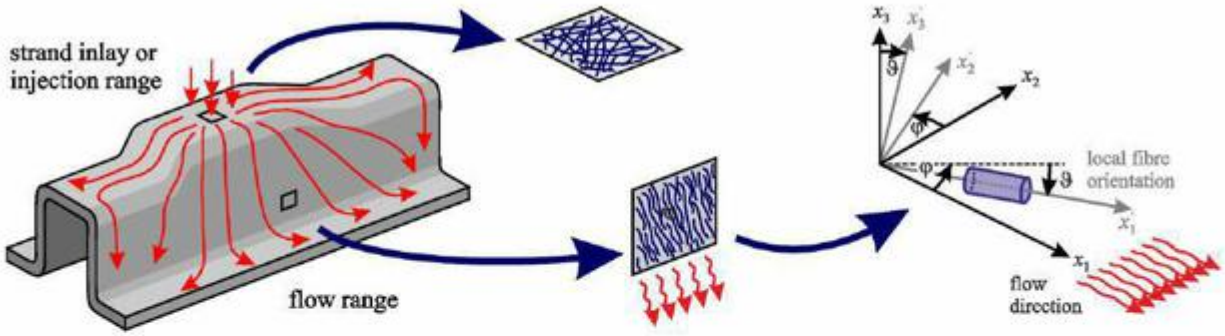

Figure 2: Probabilistic material model.

Subsequently, the effective elasticity tensor is transformed into the global system. The transition to the multi fibre problem is made via an ensemble average of all possible fibre orientations, taking their probability into account. On the third stage, a probabilistic enhancement is performed by assuming the local fibre volume fraction ρ_f as well as the parameters controlling the variability of the fibre orientation angles with respect to the flow direction (Figure 1(a)) as stochastic variables, each provided with an appropriate probability distribution (Hohe et al. [4]).

For validation of the model, the Young's moduli for the flow range of the material longitudinal and perpendicular to the flow direction are considered. The results for the probability distributions $F(E_i)$ are presented in Figure 3 where subfigure (a) is related to the experimental results whereas subfigure (b) contains the numerical predictions. As expected, the Young's modulus within the fibre direction is larger than its counterpart perpendicular to this direction due to the larger amount of fibres oriented towards the flow direction (Figure 3(a)). In both cases, a significant uncertainty of the results is obtained. An increasing size of the grid for determination leads to decreasing scatter band widths. Figure 3(b) contains the results of a parameter study, where the expectation value of the fibre volume fraction is varied from 18.3% to 28.3% at a constant standard deviation of 5%. An increase in the mean fibre volume fraction especially affects the Young's modulus in the flow direction whereas less distinct effects are observed perpendicular to the flow direction and for the direction transverse to the plate. For a mean fibre volume fraction of 23.3%, coinciding with a weight volume fraction of 40%, the experimentally determined probability distributions and their numerical predictions are found in a rather good agreement.

CONCLUSION

The present contribution is concerned with the uncertainties in the effective material response of long fibre reinforced materials with disordered, process dependent microstructure. Based on a preliminary experimental investigation, revealing distinct scatter in the local stress strain response of a PA6.6GF40 compression moulded composite, a probabilistic material model is proposed. In a validation and parameter studies, the model proves to be both, accurate and numerically efficient. The model can easily be extended in order to cover further uncertainties such as uncertainties in the constituent material.

References

[1] Beckmann, C., Hohe, J.: Mech. Mat. 78: 22-43, 2014.
[2] Bednarcyk, B., Aboudi, J., Arnold, S.M.: Compos. B 66: 97-108, 2014.
[3] Henning, F., Ernst, H., Brüssel, R., Geiger O., Krause W.: Reinf. Plastics 49: 24-33, 2005.
[4] Hohe, J., Beckmann, C., Paul, H.: Mat. Des. 66, 390-399, 2015.

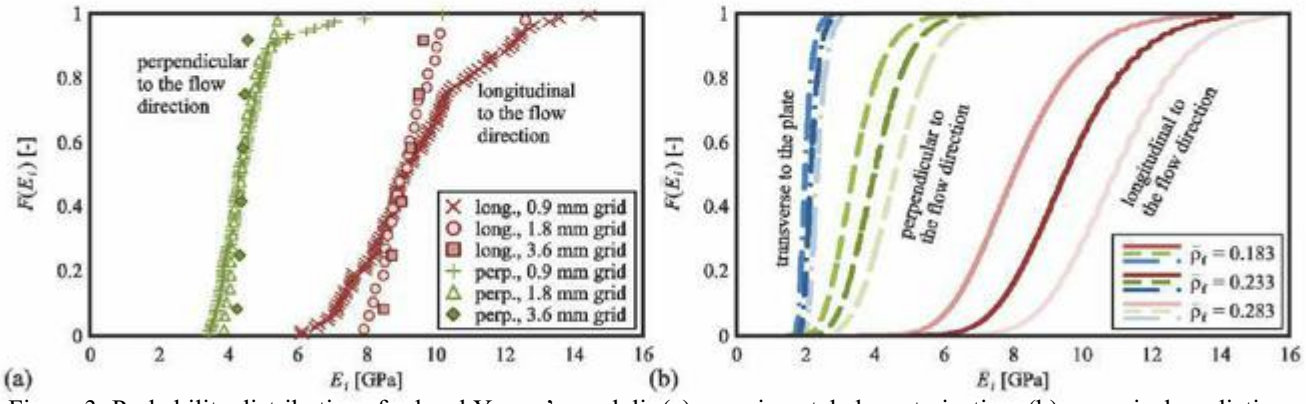

Figure 3: Probability distributions for local Young's moduli: (a) experimental characterization, (b) numerical prediction.

STEADY STATE KINK BAND BROADENING IN LAYERED MATERIALS

Jens Lycke Wind & Henrik Myhre Jensen[1]
Department of Engineering, Aarhus University, Aarhus, Denmark

Summary Theoretical predictions of steady state kink band broadening in compressed layered materials are compared to numerical calculations using the finite element method. Numerical predictions of infinite kink band formation and evolution follow a scheme in which a thin slice of material with individually discretized fiber and matrix layers are subject to periodic boundary conditions.

KINK BAND FORMATION

Composites loaded by compression along the fibers are prone to fail by the development of so-called kink bands. These are bands of material where the fibers inside the band have rotated relative to the fibers outside the band. The failure mechanism is critical in the sense that the load carrying capacity of the material is in most cases lost at that stage. Kink band formation as a failure mechanism is observed in unidirectional fibers as well as in multi layered composites with different layups inside the individual layers. For structural components loaded in bending, it is this failure mode which should be used as a design load since the critical stress in compression is considerably lower than the critical load in tension in absolute values. The critical stress for kink band formation is known to be sensitive to structural imperfections such as misalignments of the fibers relative to the load direction, and to non-linear material behavior of the matrix material due to plastic deformation. This makes theoretical investigations as well as finite element predictions of kink band formation challenging as they must involve large deformations allowing for non-linear behavior of the constituents as deformations evolve. A sketch of the infinite kink band geometry is shown in Fig. 1(a).

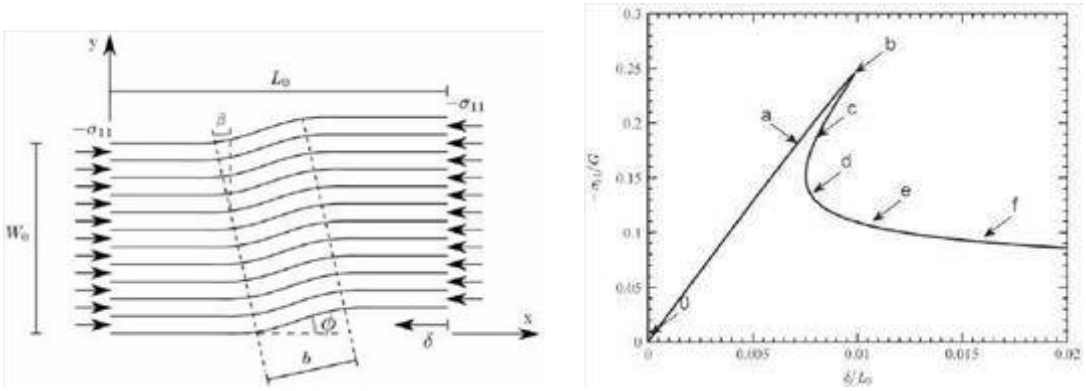

(a) (b)

Figure 1. Schematic illustration of kink band geometry (a), and a typical normalized stress, $-\sigma_{11}/G$, *vs*. normalized end shortening, δ/L_0, response (b). Kink band inclination, β, fiber rotation, ϕ, and band width, b, is indicated.

A typical, corresponding stress *vs*. end shortening response is shown in Fig. 1(b) where the kink band is initiated at stage (b) following an almost linear pre-bifurcation response (a). The deformations localize from stage (b) via stages (c) and (d) to stage (e) in Fig. 1(b). This involves a snap back behavior in the stress *vs*. shortening response. After stage (e) in Fig. 1(b), the deformations inside the kink band stabilize, and upon further loading, a steady state is achieved in which the kink band starts to broaden, *i.e*. the band width, b, increases at constant applied external stress, $-\sigma_{11}$, which in the figure above is normalized by the elastic shear modulus, G, of the composite. The later stages of deformation from stage (e) to (f) and beyond in Fig. 1(b) is referred to as the kink band broadening regime and is the focus of the present work.

KINK BAND BROADENING

Strain localization in the form of kink bands in uni-directional composites loaded by compression in the fiber direction may, as previously stated, for sufficiently ductile constituents be followed by a response in which the matrix material inside the kink band undergoes stiffening. This state is in the literature referred to as the lock-up condition, and when this occurs it restricts further deformation inside the band. Instead, upon external loading, overall deformation takes place by broadening of the kink band at fixed external load or stress. The phenomenon of kink band broadening was described initially in [1] based on experimental observations in a carbon/PEEK fiber/matrix system. Only few theoretical analyses of kink band

[1] Corresponding author. Email: hmj@eng.au.dk

broadening exist *e.g.* [2] and [3]. The lock-up conditions necessary for determining the steady state broadening response was in [2] taken as the condition $\phi(=(2\beta$ formulated initially by experimental observations in geological materials. The condition $\phi(=(2\beta$ corresponds to a zero volumetric straining condition. In [3], an energetic approach to determine the lock-up condition was taken by equating the work done by external loading on the overall deformations to the internal work done by stresses on strains in the kink band at steady state propagation. The analysis was based on the constitutive model for composite materials developed in [4-5]. Good agreement between the lock-up conditions in [2] and [3] was achieved.

Computational models for studying kink band formation include individually discretized fiber and matrix models *e.g.* [6] and [7]. Such models have been successful in capturing kink band initiation and the response immediately after but they have not been effective in capturing the steady state broadening response. The present work is devoted to a study of efficient numerical modelling of kink band broadening using individually discretized fiber and matrix layers in combination with the finite element method.

Calculations are performed for a thin slice of alternating fiber and matrix layers with periodic boundary conditions prescribed to model an infinite kink band. One of the difficulties with the individually discretized fiber and matrix models is the wide-spread influence observed of the boundary conditions on the kink band formation and propagation. In Fig. 2(a), results are shown for the predicted stress *vs.* end shortening response demonstrating that a steady state has been reached where the stress is constant.

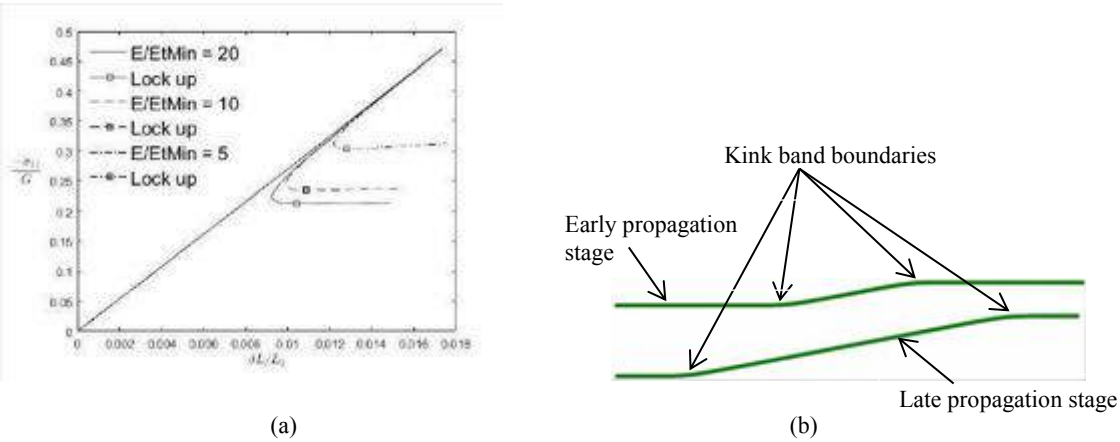

Figure. 2. Load *vs.* end shortening response (a), and (b) two stages of deformation of a thin slice of alternating fiber/matrix layers showing broadening of the kink band. A minimum value, Et,min , for the tangent modulus of the matrix material has been included.

In Fig. 2(b), two stages of deformation in the composite are shown during steady state broadening of the kink band. The top slice is at an early stage of propagation and the bottom slice at a late stage, where it is seen that the deformation inside the kink band between the kink band boundaries remains constant and the overall deformation takes place by broadening of the kink band, *i.e.* with reference to Fig. 1(a), b increases between the two stages. This takes place at a constant overall stress applied to the composite material.

CONCLUSIONS

Finite element calculations of kink band broadening using periodic boundary conditions for a thin slice of alternating fiber and matrix layers are presented. Comparison with previous results for the broadening stress and the state of deformation inside the kink bands show good agreement.

References

[1] Moran, P.M., Liu, X.H., Shih, C.F.: Kink Band Formation and Band Broadening in Fiber Composites under Compressive Loading. *Acta Mater*. **43**: 2943-2958, 1995.

[2] Budiansky, B., Fleck, N.A., Amazigo, J.C.: On Kink-Band Propagation in Fiber Composites. *J. Mech. Phys. Solids*. **46**: 1637-1653, 1998.

[3] Jensen, H.M.: Analysis of Compressive Failure of Layered Materials by Kink Band Broadening. *Int. J. Solids Structures*.,**36**: 3427-3441, 1999.

[4] Christoffersen, J. & Jensen, H.M. Kink Band Analysis Accounting for the Microstructure of Fiber Reinforced Materials. *Mech. Mat*. **24**:305-315, 1996.

[5] Jensen, H.M. & Christoffersen, J.: Kink Band Formation in Fiber Reinforced Materials. *J. Mech. Phys. Solids*. **45**:1121-1136, 1997.

[6] Kyriakides, S., Arseculeratne, P., Perry, E.J., Liechti, K.M., On the Compressive Failure of Fiber Reinforced Composites, *Int. J. Solids Structures* **32**:689–738, 1995.

[7] Wind, J.L., Steffensen, S., Jensen, H.M. Comparison of a Composite Model and an Individually Fiber and Matrix Discretized Model for Kink Band Formation. *Int. J. Non-Linear Mech*. **67**: 319-325, 2014.

MODELLING ADHESION OF DEFECTIVE GRAPHENE INTERFACES

Dewapriya, M. A. N[1a)] & Rajapakse, R. K. N. D.[1]
[1]*School of Engineering Science, Simon Fraser University, Burnaby, British Columbia, Canada*

Summary We develop a homogenous spring model to characterize the influence of surface defects on the adhesion properties of graphene interfaces. The modeled correlation between cohesive energy and interfacial separation of graphene silicon-dioxide interface is compared with molecular dynamics simulations, and the results are in good agreement.

The exceptional electromechanical properties of graphene have facilitated the development of the next generation of nanodevices. These state-of-the-art nanodevices, such as sensors and transistors, have profound impacts in numerous engineering disciplines, ranging from biomedicine to aerospace [1]. Recent experiments show that graphene could also be used as an ultra-strong reinforcement for composite materials [2]. Using graphene as reinforcement provides an excellent opportunity to transfer the superior electromechanical properties of graphene, across multiple length scales, up to the macroscopic level. In both graphene-based nanodevices and composite materials, graphene is in contact with adjoining materials, creating mechanically weak interfaces between graphene and the other materials. On the other hand, during the fabrication of graphene-based systems, defects such as surface impurities are unavoidable. These defects could highly deteriorate the mechanical properties of graphene [3-6], which will ultimately influence the performance of graphene-based systems. Therefore, understanding the effects of defects on the mechanical properties of both graphene and graphene interfaces is critically important in designing reliable graphene-based systems.

In this paper, we develop a homogenous spring model to characterize the influence of surface defects (e.g., vacancies, adatoms) on the adhesion properties of graphene interfaces. Discrete nature of this interface model allow us to investigate the influence of point defects such as vacancies and adatoms, which breaks the continuity of the interface; therefore, the continuum-based models (e.g., [7-9]) cannot be employed. We use the adhesion properties of graphene-silicon-dioxide (SiO_2) interface, which is one of the most widely studied interfaces [9,10], obtained using molecular dynamics (MD) simulations to validate the proposed model.

We modelled the interfacial adhesion of graphene-SiO_2 system using Lennard-Jones (LJ) potential, and the adhesion between carbon atoms of graphene and the SiO_2 substrate is represented by nonlinear springs. Fig. 1(a) graphically demonstrates the graphene-SiO_2 system, and Fig. 1(b) shows the proposed spring model characterizing the interaction between graphene and SiO_2 substrate. One end of the springs are attached to carbon atoms of graphene and the other ends are connected to the substrate, which is assumed infinitely rigid considering the magnitude of van der Waals force and the stiffness of SiO_2 and other typical substrate materials. During the delamination process, graphene sheet is assumed to be conforming completely to a flat SiO_2 substrate. The separation distance between graphene and SiO_2 substrate is l, and the dimensions of the SiO_2 substrate are considered infinitely large. Energy stored in a nonlinear spring, $U(l)$, can be expressed in terms of the van der Waals energy between a carbon atom and the SiO_2 substrate as

$$U(l) = \sum_j \left[4\pi\rho_j \varepsilon_{cj} \sigma_{cj}^3 \left(\frac{\sigma_{cj}^9}{45 l^9} - \frac{\sigma_{cj}^3}{6 l^3} \right) \right], \tag{1}$$

where, ε_{cj} and σ_{cj} are LJ constants, and the subscript j represents substrate atoms, which are silicon and oxygen in SiO_2; ρ_j is the atomic density of the atom type j. More detail on the development of the spring model is given in [11].

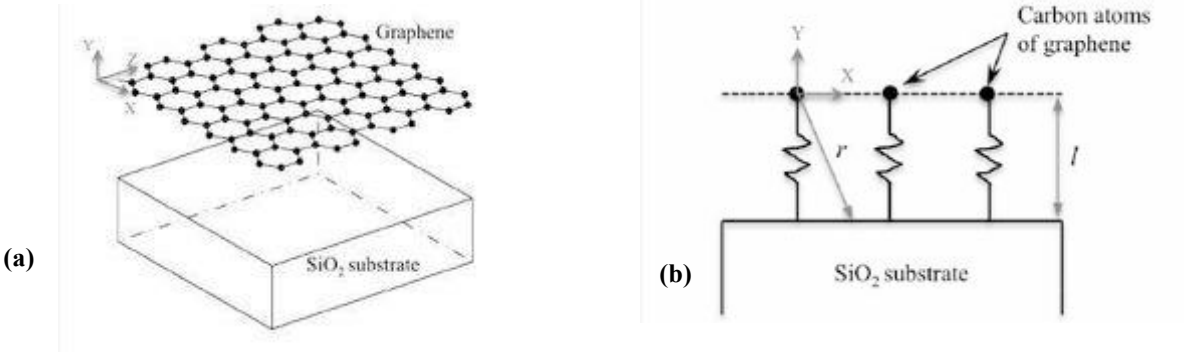

Fig. 1 (a) Three-dimensional view of the graphene-SiO_2 system. (b) The proposed spring model characterizing interfacial adhesion between graphene and SiO_2 substrate.

[a)] Corresponding author. Email: mandewapriya@sfu.ca.

Figure 2(a) shows the theoretical model characterizing the interfacial adhesion of a defective graphene-SiO_2 interface. The hydrogen adatom is assumed to be on the side of SiO_2 substrate, inducing a higher influence on the adhesive properties. l_1 is the out-of-plane deformation of the carbon atom attached to an adatom, and the distance between the plane of graphene and the hydrogen adatom is l_2. Using MD simulations, we found the values of l_1 and l_2 are 0.5 Å and 1.58 Å, respectively. Moreover, these values are independent of the interfacial separation l and the concentration of adatoms. The spring S_d in Fig. 2(a) models a carbon atom with an adatom, and this spring has an energy contribution from the adatom as well. Therefore, energy stored in the spring (U_d) can be expressed as

$$U_d(l) = 4\pi \sum_j \left[\rho_j \varepsilon_{cj} \sigma_{cj}^3 \left(\frac{\sigma_{cj}^9}{45(l-l_1)^9} - \frac{\sigma_{cj}^3}{6(l-l_1)^3} \right) + \rho_j \varepsilon_{hj} \sigma_{hj}^3 \left(\frac{\sigma_{hj}^9}{45(l-l_2)^9} - \frac{\sigma_{hj}^3}{6(l-l_2)^3} \right) \right]. \quad (2)$$

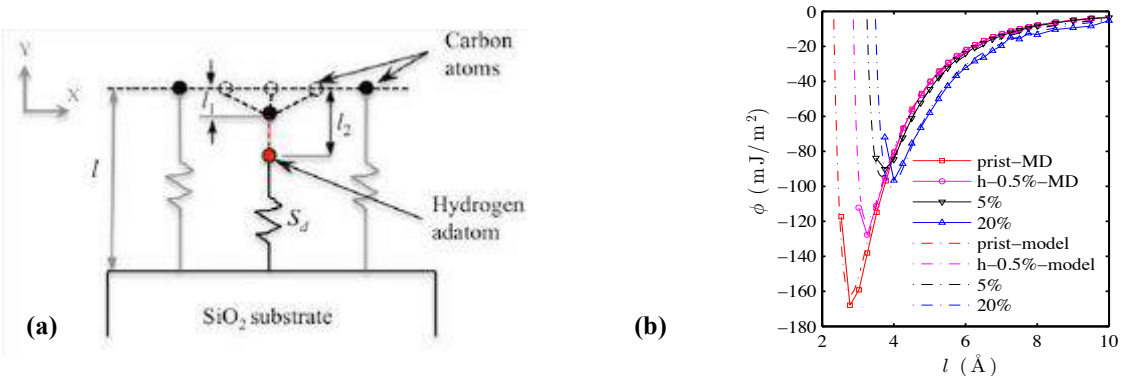

Fig. 2 (a) The spring model characterizing graphene-SiO_2 interface with hydrogen adatoms. (b) Comparison of the proposed model with MD simulations.

Figure 2(b) compares the MD simulation results with the developed homogenous spring model. MD simulation results show that as the hydrogen adatom concentration increases, initially the equilibrium cohesive energy of graphene-SiO_2 system (i.e. $|\phi_{max}|$) rapidly decreases. However, after a certain concentration of hydrogen adatoms (~10%), the cohesive energy starts to increase again; whereas, the equilibrium separation continually increases with the adatom concentration. The proposed spring model captures these variations of cohesive energy accurately, and the model is accurate even at a concentration of 20%. According to the model, equilibrium cohesive energy of a pristine interface is 162.8 mJ/m^2, which is in between the experimentally measured values: 96 mJ/m^2 [12] and 450 mJ/m^2 [13]. The model is a computationally efficient tool to analyze the interfacial properties of advanced graphene-based systems, and the model can also be parameterized to investigate the properties of any material interface at the atomic scale.

Acknowledgement: This research was financially supported by Natural Sciences and Engineering Research Council (NSERC) of Canada.

References

[1] Novoselov K.S., Fal'ko V.I., Colombo L., Gellert P.R., Schwab M.G. & Kim K.: A roadmap for graphene. *Nature* **490**:192-200, 2012.

[2] Lahiri D., Hec F., Thiesse M., Durygind A., Zhang C., Agarwal A.: Nanotribological behavior of graphene nanoplatelet reinforced ultra high molecular weight polyethylene composites. *Tribology International*. **70**:165-169, 2014.

[3] Zandiatashbar A., Lee G.H., An S.J., et al.: Effect of defects on the intrinsic strength and stiffness of graphene. *Nat Communica.* **5**:3186, 2014.

[4] Dewapriya M.A.N. and Rajapakse R.K.N.D.: Molecular dynamics simulations and continuum modeling of temperature and strain rate dependent fracture strength of graphene with vacancy defects. *J. Appl. Mech.* **81**:081010, 2014.

[5] Dewapriya M.A.N., Rajapakse R.K.N.D. and Phani A.S.: Atomistic and continuum modelling of temperature-dependent fracture of graphene. *Int. J. Fract.* **187**:199-212, 2014.

[6] Dewapriya M.A.N., Rajapakse R.K.N.D. and Nigam N.: Influence of hydrogen functionalization on the fracture strength of graphene and the interfacial properties of graphene-polymer nanocomposite. *Carbon* **93**:830-842, 2015.

[7] Zhang Z. and Li T.: Determining graphene adhesion via substrate-regulated morphology of graphene. *J. Appl. Phys.* **110**(8), 2011.

[8] Jiang L.Y., Huang Y., Jiang H., Ravichandran G., Gao H., Hwang K.C., et al. A cohesive law for carbon nanotube/polymer interfaces based on the van der Waals force. *J. Mech. Phys. Solids* **54**:2436-2452, 2006.

[9] Gao W. and Huang R.: Effect of surface roughness on adhesion of graphene membranes. *J. Phys. D-Applied Physics* **44**:45, 2011.

[10] Gao W., Xiao P.H., Henkelman G., Liechti K.M. and Huang R.: Interfacial adhesion between graphene and silicon dioxide by density functional theory with van der Waals corrections. *J. Phys. D-Applied Physics* **47**:25, 2014.

[11] Dewapriya M.A.N. and Rajapakse R.K.N.D.: Development of a homogenous nonlinear spring model characterizing the interfacial adhesion properties of graphene with surface defects, submitted.

[12] Ishigami M., Chen J.H., Cullen W.G., Fuhrer M.S. & Williams E.D.: Atomic structure of graphene on SiO_2. *Nano Letters* **7**:1643-1648, 2007.

[13] Koenig S.P., Boddeti N.G., Dunn M.L. & Bunch J.S.: Ultrastrong adhesion of graphene membranes. *Nature Nanotechnology* **6**:543-546, 2011.

CARVING 3D ARCHITECTURES TO TRANSFORM THE MECHANICS AND PERFORMANCE OF MATERIALS

Mohammad Mirkhalaf, Jeremy Tanguay and Francois Barthelat [a)]
Department of Mechanical Engineering, McGill University, Montreal, Quebec, Canada

Summary: Combining high strength, hardness and high toughness remains a tremendous challenge in materials engineering. In particular hard materials like ceramics tend to be brittle, while more ductile and tough materials like metals are not as hard. In this work we increase the toughness of glass panels by carving architectures within the material using three-dimensional laser engraving. Glass is relatively stiff and hard but it has no microstructure, no inelastic deformation mechanism, low toughness and poor resistance to impacts. Here we demonstrate how introducing a controlled architecture in glass completely changes the way this material deforms and fails. In particular these new architectured glass panels can absorb two to four times more impact energy compared to plain glass. Architectured glass panels also display non-linear deformation and progressive damage and failure. Micro-architecture, bio-inspiration and top-down fabrication strategies can offer new pathways to completely transform the mechanics and performance of materials and structures.

INTRODUCTION

Despite large efforts in material development and mechanics, there are still combinations of mechanical properties which remain inaccessible to engineering materials. For example achieving materials which are simultaneously hard and tough is highly desirable for many applications, yet these properties remain mutually exclusive in engineering materials [1]. Recently, materials with sophisticated three-dimensional architectures have emerged in an attempt to fill these gaps. Architectured materials introduce specific structural features at a length scale which is intermediate between their microstructure and the size of the component. Because the length scale associated with this architecture is larger than traditional microstructures, higher level of morphological control can be achieved using existing fabrication technologies. This high morphological control results in a tight control over the deformation and fracture mechanisms [2]. In dense architectured materials, stiff building blocks are assembled in larger structures, and the interfaces between the blocks are weak so they can generate a wealth of non-linear deformation mechanisms and crack deflection, which echo the concepts found in natural materials. In topologically interlocked materials (TIMs) the blocks have specific shapes which interlock to form architectured materials with combined strength and toughness under transverse static and impact loading. These materials also display quasi-ductile behavior, localized damage, and re-manufacturability [3].

FABRICATION OF ARCHITECTURED GLASS PANELS

In this work we present a new fabrication technique based on a top-down strategy and where weak interfaces are carved within a hard but brittle material. We used glass as a base material, and three dimensional laser engraving to generate weak interfaces within the bulk of the material. We generated topologically interlocked interfaces using a three-dimensional laser engraver (Model Vitrolux, Vitro Laser Solutions UG, Minden, Germany) equipped with a pulsed UV laser (355 nm, 0.5W cw pumped, 4 kHz repetition rate, 4-5 ns pulse duration). The laser engraver focused a nano-second ultraviolet laser beam into the glass panel, generating micro-defects at the successive focal points (Fig. 1a). Arrays of these defects generated weak interfaces which could control and channel deformation and failure mechanisms [4]. The interfaces defined three-dimensional blocks of glass shown on Fig. 1b. Two of the sides are tilted inward and the other two outward by the same angle θ, called interlocking angle. The architectured panel is composed of several of these blocks, arranged in order to form a dense, interlocked structure (Fig. 1c). Using this strategy, the deformation mechanisms of a panel made of stiff but brittle blocks was augmented by sliding at the interfaces between the blocks.

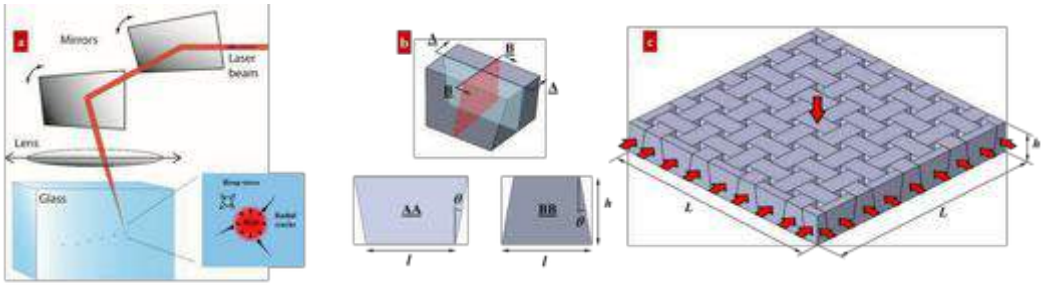

Fig. 1: Fabrication of architectured glass panel: (a) A nanosecond pulsed laser focused beam creates micro-defects at its focal point. Arrays of these defects define the weak interfaces between the individual blocks; (b) The geometry of the individual building blocks is obtained from truncating a tetrahedron; (c) The 7×7 simply supported architectured panel developed in this study. The panel is placed in a frame that generates the confinement required for interlocking.

[a)] Corresponding author. Email: francois.barthelat@mcgill.ca

MECHANICAL PERFORMANCE

We assessed the performance of the glass panels at high deformation rates by impacting them with a 67.3g, 25 mm diameter steel ball. The glass panels were positioned so the ball impacted the panel in the center (Fig. 2a). The protocol to assess impact resistance was as follows: the steel ball was first released from a small height (80mm) onto the panel. If the panel survived this first strike, the height was increased and the test was repeated until the sample failed. The failure of plain glass panels was typical to a brittle material: sudden and catastrophic, with multiple cracks emanating from the indentation site and extending to the edges of the panel (Fig. 2b). The nature of the failure mode indicates a flexural failure, which is representative of the type of failure for larger glass panels. In contrast, the architectured glass panels failed by the sliding of the building blocks on one another and out of the panel. Failure was also confined to only a few blocks, the rest of the panel remaining intact (Fig. 2b). Fig. 2c summarizes the results of the impact tests. The energy required to break the plain glass panels was 330±30 mJ (N= 3). The energy required to fail the architectured glass was significantly higher than for plain glass, because of the frictional energy dissipation at the interface. We also measured the deflection of individual blocks upon the onset of damage for the architectured panel. The results shown on Fig. 2d show significant residual deflections reaching about 800 microns and resulting from the sliding of the blocks on one another. Many blocks showed this residual deflection, defining a "zone of influence" which extended to the entire panel. Some blocks also appeared to have been pushed upwards during the impact. This result confirms that in impact situation the frictional sliding of the blocks is a prominent deformation and dissipative mechanism in the architectured panels. We also tested samples where the interfaces of the architectured glass panels were infiltrated with an ionomer (Surlyn 9320, Dupont, ON, CA). The inomer generated another dissipative mechanism through viscoplastic deformation, improving the impact resistance of the panel even further. Impact resistance was four times higher than that of the plain glass, and ~2.5 times higher than that of the non-infiltrated architectured glass (Fig. 2c).

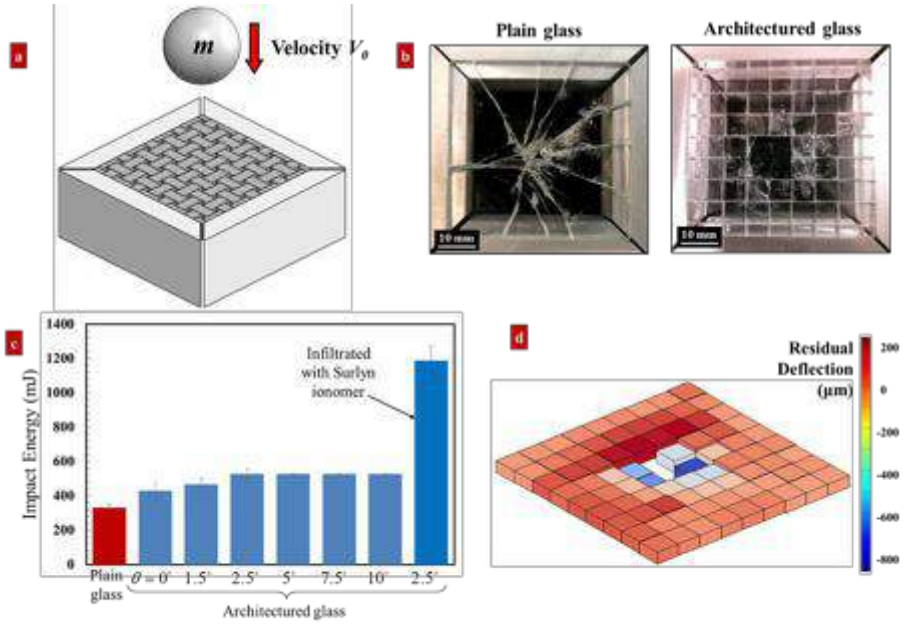

Fig. 2: (a) Ball impact setup; (b) Typical post mortem samples for plain and architectured glass panels; (c) Impact energy required to break the panels; (d) Collective deflection of individual blocks measured at the onset of damage.

CONCLUSIONS

Combining hardness, strength, toughness and impact resistance remains a tremendous challenge in engineering materials. Generating architectures in materials may provide new pathways to achieving these properties simultaneously. Here we apply these concepts on glass panels, using a top-down fabrication approach where interfaces are carved within the material using three-dimensional laser engraving. Glass is an amorphous material with no microstructure and no toughening mechanisms, and as a result it has no inelastic deformation capabilities when subjected to tensile or flexural loads at ambient temperatures. This work demonstrates how the introduction of a controlled architecture at a length scale which is intermediate between the molecular scale and the scale of the component completely transforms the way glass deforms and fractures. In in this case, while plain glass panel failed in a brittle fashion, catastrophically and with extensive damage, the architectural glass panels failed progressively and "graciously", with damage only confined to only a few blocks.

References

[1] Ritchie RO. The conflicts between strength and toughness. Nature Materials 2011;10:817-22.
[2] Barthelat F. Architectured materials in engineering and biology: fabrication, structure, mechanics and performance. To appear in International Materials Reviews 2016.
[3] Khandelwal S, Siegmund T, Cipra RJ, Bolton JS. Transverse loading of cellular topologically interlocked materials. International Journal of Solids and Structures 2012;49:2394-403.
[4] Mirkhalaf M, Dastjerdi AK, Barthelat F. Overcoming the brittleness of glass through bio-inspiration and micro-architecture. Nature communications 2014;5:3166.

FUNDAMENTALS OF SURFACE GROWTH OF SOLIDS IN NATURE AND TECHNOLOGY

Alexander V. Manzhirov[1a)] & Narinder K. Gupta[2]
[1]Department for Modeling in Solid Mechanics, Institute for Problems in Mechanics of the Russian Academy of Sciences, Moscow, Russia; Department of Applied Mathematics, Bauman Moscow State Technical University, Moscow, Russia; Department of Higher Mathematics, National Research Nuclear University MEPhI, Moscow, Russia; Department of Higher Mathematics, Moscow Technological University, Moscow, Russia
[2]Department of Applied Mechanics, Indian Institute of Technology, Delhi New Delhi, India

Summary The fundamentals of the mathematical theory of surface growth are under consideration. We focus on the surface growth when deposition of a new material occurs at the boundary of a growing solid. The constitutive equations and boundary conditions for growing solids are presented. Non-classical boundary value problems are formulated. Methods for solving these problems are proposed. They are illustrated by solutions of several model problems that demonstrate the unique mechanical behavior of growing solids.

INTRODUCTION

A vast majority of objects around us arise from some growth processes. Many natural phenomena such as growth of biological tissues, glaciers, blocks of sedimentary and volcanic rocks, and space objects may serve as examples. Similar processes determine specific features of many industrial processes which include crystal growth, laser deposition, melt solidification, electrolytic formation, pyrolytic deposition, polymerization and concreting technologies. There are two main ways of continuous growth in technology and nature known to researchers. They are volumetric and surface growth processes. Let us consider the latter case with a reference to the monographs [1, 2] where fundamental results concerning volumetric growth have been presented.

GENERAL CONCEPTS

Recent research has shown that solids formed by growth processes differ in their properties essentially from solids in the traditional view. Moreover, the classical approaches of solid mechanics to modeling the growing solids behavior fail. They should be replaced by new ideas and methods of modern mechanics, mathematics, physics, and engineering sciences.
An approach proposed deals with the construction of adequate model of surface growth processes of solids (see also [3-13]). This approach is based on the following statements:

- ❖ We simulate the surface growth of a solid by moving of its boundary due to the influx of new material to the surface of this solid.
- ❖ We obtain specific boundary conditions on the moving boundary (growth surface) as the result of an additional contact interaction problem between 3D solid and 2D surface which depends on particular features of the growing process.
- ❖ We state the compatibility of the rate of deformation tensor (or rate of stretching tensor) for a growing solid while its strain tensor is incompatible as a rule.

The last statement leads to the case in which it is absolutely natural to choose the rate of stress tensor, the rate of deformation tensor, and the vector of velocity as the basic variables of the governing system of equations for description of the surface growth process.
In general, boundary value problem for a growing solid contains three dependent controlled groups of values: the surface and bulk loadings, the tension of new adhering surfaces, and the velocity of influx of adhering surfaces.

SURFACE GROWTH OF A SOLID

If the velocity of the boundary particles of a growing solid is substantially small as compared with the velocity of influx of new particles and the surface of growth is closed then the boundary value problem can be written in the form

$$\nabla\cdot\mathbf{S}=\mathbf{0},\quad \mathbf{D}=\frac{1}{2}\left[\nabla\mathbf{v}+(\nabla\mathbf{v})^{*}\right],\quad \mathbf{S}=\mathrm{G}\left[2\mathbf{D}+(\mathrm{K}-1)\mathrm{I}_1(\mathbf{D})\mathbf{I}\right],$$

$$\mathbf{n}\cdot\mathbf{S}\big|_{\partial\Omega_1}=\mathbf{g},\quad \mathbf{v}\big|_{\partial\Omega_2}=\mathbf{v}_0,\quad \mathbf{n}\cdot\mathbf{S}\big|_{\partial\Omega(\mathrm{t})}=\mathrm{p}\,\mathbf{n},$$

$$\mathbf{S}=\frac{\partial\mathbf{T}}{\partial\mathrm{t}},\quad \mathbf{g}=\frac{\partial\mathbf{f}}{\partial\mathrm{t}},\quad \mathbf{v}_0=\frac{\partial\mathbf{u}_0}{\partial\mathrm{t}},\quad \mathrm{p}=-\mathrm{s}_\mathrm{n}\left(\mathscr{T}_\mathrm{S}:\mathscr{L}_\mathrm{S}\right),\quad \mathrm{s}_\mathrm{n}=\mathbf{v}\cdot\mathbf{n},$$

a) Corresponding author. Email: manzh@inbox.ru.

where $\mathbf{T}$ is the stress tensor, $\mathbf{D}$ is the rate of deformation tensor, $\mathbf{u}$ is the displacement, G and K are the elastic moduli, I_1 is the first invariant of a tensor, $\mathbf{I}$ is the unit tensor, $\mathbf{n}$ is the unit vector normal to the surface of the solid, $\mathbf{f}$ is the surface force, $\partial\Omega_1$ and $\partial\Omega_2$ are the fixed domains of the solid surface, $\partial\Omega(t)$ is the growth surface, $\mathscr{T}_S$ is the 2D tensor of tension of adhered surface, $\mathscr{L}_S$ is the 2D tensor of adhered surface curvature, surface force on the growth surface as well as bulk force supposed to be zeros.

One can easily see that the boundary value problem obtained have the same form as the classiacal boundary value problem of elasticity and we can use all known analytical and numerical methods for the solution of this problem.

In order to obtain the values of stresses and displacement one should use the formulas as follows (we denote by τ^* the time of adhesion of the surface to the growing solid and assume that growth surface is always free of surface load)

$$\mathbf{T} = \mathbf{T}(\tau^*) + \int_{\tau^*}^{t} \mathbf{S} d\tau, \quad \mathbf{T}(\tau^*) = \mathscr{T}_S + (\mathbf{n}\cdot\mathbf{0})\,\mathbf{n}\otimes\mathbf{n}, \quad \mathbf{u} = \mathbf{u}(\tau^*) + \int_{\tau^*}^{t} \mathbf{v} d\tau .$$

In the equations above we chose the case of small deformations only for definiteness. In the case of finite deformation one should simply change the linear Hook's law by nonlinear constitutive relations.

This approach can be developed for the case of viscoelastic and aging materials using methods of [13–18]. The solution of the problem of the accretion of a viscoelastic ageing solid can be obtained by the solution of the mathematically identical problems with a parameter, which have the same form as the boundary value problem of the classical theory of elasticity. Then the true stresses and displacements in the growing solid can be reconstructed using derived formulas.

CONCLUSIONS

Thus, using the presented approach for mechanical research of growing solids from elastic and viscoelastic materials one can determine the strength and the shape of final solids and products. Moreover, on the basis of this mechanical analysis one can work out effective recommendations for improving the growth processes observed in nature and technology.

ACKNOWLEDGEMENT

This work was financially supported by the Russian Science Foundation under the Project No. 14-19-01280.

References

[1] Maugin G. A.: Material Inhomogeneities in Elasticity. Chapman and Hall, London, 1993.

[2] Epstein M.: The Geometrical Language of Continuum Mechanics. Cambridge University Press, Cambridge, New York, 2014.

[3] Manzhirov A. V.: Mechanics of growing solids: New track in mechanical engineering. *Proceedings of ASME 2014 International Mechanical Engineering Congress & Exposition, IMECE2014, November 14–20*, 10 p. Montreal, Canada, 2014.

[4] Manzhirov A. V , Gupta N. K., Indeitsev D. A. (Eds): Topical Problems in Solid and Fluid Mechanics. Elite Publishing, New Delhi, 2011.

[5] Gupta N. K., Manzhirov A. V., Velmurugan R. (Eds): Topical Problems in Theoretical and Applied Mechanics. Elite Publishing House, New Delhi, 2013.

[6] Manzhirov A. V, Lychev S. A.: The mathematical theory of growing solids: Finite deformations. *Doklady Physics* **57**(4): 160–163, 2012.

[7] Lychev S. A., Manzhirov A. V.: The mathematical theory of growing bodies. Finite deformations. *J. Appl. Math. Mech.* **77**(4): 421–432, 2013.

[8] Lychev S. A., Manzhirov A. V.: Reference configurations of growing bodies. *Mech. Solids* **48**(5): 553–560, 2013.

[9] Manzhirov A. V: Mechanics of growing solids and phase transitions. *Key Engineering Materials* **535–536**: 89–93, 2013.

[10] Manzhirov A. V, Lychev S. A., Gupta N. K.: Nonlinear models of growing solids. *Proc. Indian Natl Sci. Acad.* **79**(4): 529–545, 2013.

[11] Manzhirov A. V, Lychev S. A.: Mathematical modeling of additive manufacturing technologies. *Lecture Notes in Engineering and Computer Science: World Congress on Engineering*, pp. 1404–1409, 2014.

[12] Manzhirov A., Gupta N.: Fundamentals of continuous growth processes in technology and nature. *IUTAM Symposium on Growing solids. Symposium Materials*, pp. 73–76. Moscow, IPMech RAS, 2015.

[13] Manzhirov A. V., Lychev S. A.: An approach to modeling of additive manufacturing technologies. *Transactions on Engineering Technologies: World Congress on Engineering 2014*, pp. 99–115. Springer, Netherlands, 2015.

[14] Lychev S. A., Manzhirov A. V., Bychkov P. S.: Discrete and continuous growth of deformable cylinder. *Transactions on Engineering Technologies: World Congress on Engineering 2014*, pp. 239-254. Springer, Netherlands, 2015.

[15] Manzhirov A. V.: The general non-inertial initial-boundary value problem for a viscoelastic ageing solid with piecewise-continuous accretion. *Journal of Applied Mathematics and Mechanics* **59**(5): 805–816, 1995.

[16] Manzhirov A. V.: Mechanical design of viscoelastic parts fabricated using additive manufacturing technologies. *Lecture Notes in Engineering and Computer Science: Proceedings of the World Congress on Engineering 2015, 1-3 July, 2015, London, U.K.*, pp. 710–714. IAENG, London, 2015.

[17] Manzhirov A. V, Parshin D. A.: Arch Structure Erection by an Additive Manufacturing Technology under the Action of the Gravity Force, Mech. Solids **50** (5): 559-570 (2015).

[18] Manzhirov A. V, Parshin D. A.: The influence of the erection mode on the stress state of a viscoelastic arch structure which is built up using an additive manufacturing technology under the action of the gravity force. Mech. of Solids **50**(6), (2015).

DESIGN AND 3D PRINTING OF POLYMER/CERAMIC COMPOSITE STRUCTURES

Yahya Abderrafai[1], Francois Barthelat[2] & Daniel Therriault[1a]
[1]*Department of Mechanical Engineering, Ecole Polytechnique de Montreal, Montreal, Quebec, Canada*
[2]*Department of Mechanical Engineering, McGill University, Montreal, Quebec, Canada*

Summary. We use the ultraviolet-assisted direct-write (UV-DW) process to print halloysite nanotube-reinforced polyurethane. The aim of this study is to investigate the challenges imposed by nanocomposite inks and complex shapes and propose necessary adjustments to adapt the existing printing protocol to highly mineralized polymer nanocomposite for high stiffness. Surface treatment of the nanoparticles and mixing strategy were studied. This paper demonstrates a method to coalesce polymers with ceramics in order to produce mineralized materials with highly tailored properties as well as a 71% increase in Young's Modulus.

INTRODUCTION

Alignment and multi-layered organization of reinforcements inside a soft polymeric matrix provide two promising approaches to tailor in-plance properties properties in composite materials and enable interesting functional characteristics. An example of a great functional material is the *Polypterus Senegalus* fish scale [1]. The *ganoid* scale of this "living fossil" fish possesses a rare multi-layered organization, with varying ratios of hard mineral crystals inside a soft polymer. On the outer layer, the mineral crystals have a high aspect ratio and are oriented towards the surface explaining its high stiffness. This optimized reinforcement organization yields a protective shell for the fish without scarifying its swimming mobility. Mimicking this material microstructures can be beneficial for various applications such as personal protection equipment and dental implants. The microstructures observed in the scale could be fabricated with extrusion-based 3D printing: (1) the micro-extrusion of the reinforced ink allows a shear-induced alignment of the reinforcements [2] leading to improved properties in the printing direction, and (2) the characteristics in the stacking direction is controlled by varying the matrix-to-reinforcement ratio of individual layers. The objective of this work is to adapt the ultraviolet-assisted direct-write (UV-DW) technique [3] to a polymer/mineral composite blend for enabling unique mechanical properties.

MATERIALS AND METHODS

Materials

The matrix and reinforcements employed in our study are a UV-curable photopolymer: polyurethane (NEA 123 HGA, Norland Products) and halloysite nanotubes (HNT) (Halloysite nanoclay, Sigma Aldrich) of 30-70 nm diameter and 1-3 μm length, respectively.

HNT Surface Treatment

HNTs were dispersed in Toluene (Toluene, Alfa Aesar) and 2 mL/g Silane coupling agent GOPTS (3-Glycidoxypropyltrimethoxysilane, Alfa Aesar) was added for the surface treatment of the HNTs [4]. The solution is stirred for 4 h at 120 °C. The solution was then filtered and rinsed with ethanol, before drying for 24 h at 80 °C.

Photopolymer Blends

Multiple batches of the nanocomposite with different reinforcement concentrations were prepared. 10, 20, 30 wt. % of GOPTS-coupled HNTs were manually stirred into the photopolymer resin and 1g of ethanol. Five sessions of ball milling were undertaken; each session consisted of a 1 min milling time followed by a 15 min cool-down period. The mixed batches were then degassed in a vacuum chamber and poured into 3 mL syringes for printing. A syringe with neat (0% HNT) polyurethane was also prepared as a benchmark material.

Nanocomposite Printing

UV-DW of the nanocomposites consists of the dispensing the resin at the desired locations (programmed by a CAD software) and then curing the material exiting the nozzle by UV exposure [3]. A precise positioning robot (I&J2200, I&J Fisnar Inc.) combined to a pneumatic dispenser (HP7-X, EFD) are utilized for the micro-extrusion. As soon as the photopolymer is extruded from the syringe, UV light directed through optic fibers cures the nanocomposites in order to create a solid filament which will form layer-by-layer a three-dimensional (3D) structure [3].

Fiber tensile tests

Nanocomposite fibers were printed on a glass substrate with a 250 μm nozzle, and post-cured at 80 °C for 4 h. Tensile tests were performed on a MTS Insight machine with a 1kN load cell (MTS 569327-02) in accordance with the ASTM D3822 standard.

[a)] Corresponding author. Email: daniel.therriault@polymtl.ca

RESULT AND DISCUSSION

The different nanocomposite inks manufactured presented agglomerates and inconsistency during the preliminary mixing steps. Limiting these issues required the utilization of the ball milling method instead of ultrasonication or manual mixing. However since the photopolymer used can also cure with heat, the ball milling sessions were designed to be short and combined with long cool down phases to avoid excessive heating.

Each nanocomposite type exhibited a different viscosity and polymerisation behaviour which highly influenced the 3D printing parameters. Thus, the printing parameters for different nanocomposites were calibrated by printing straight filaments through a 250-µm nozzle on a glass substrate and by adjusting mainly the extrusion pressure and robot velocity. In addition at 20 wt.% of HNTs, needle clogging was recurrent with the unmodified HNTs due to the presence of important agglomerates. Surface treatment of the HNTs was investigated in order to reduce the presence of agglomerates and facilitate the extrusion of higher HNT concentrations. The printing of nanocomposites with up to 30 wt.% of treated HNTs was achieved and the extruded material was observed to keep its filament shape.

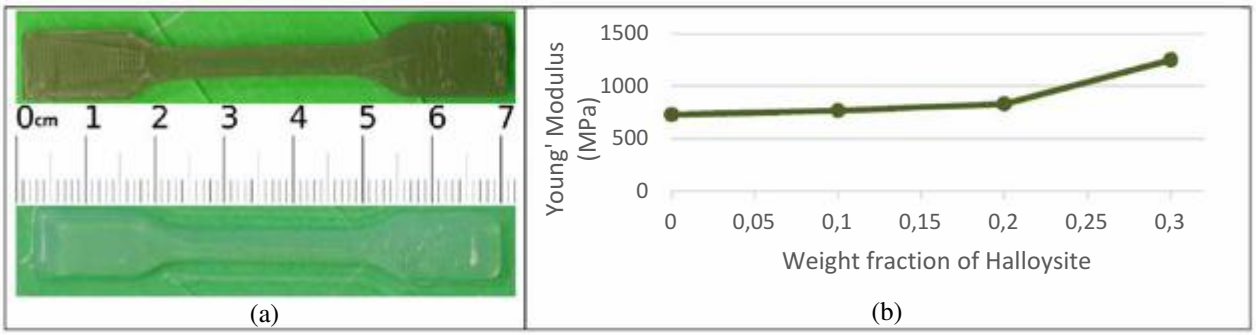

Figure 1: (a) Printed dog-bone specimens made of neat polymer (bottom) and 20 wt.% nanocomposites (top). (b) Tensile properties of nanocomposite fibers.

Dogbone (Figure 1(a)) has been chosen as a geometry to test the UV-DW as a mean to print complex parts with high number of points. The geometry was drawn in a CAD software (Catia V5, Dassault systems) and a commercial FDM 3D printing software (Simplify3D, Simplify3D) was acquired and used to generate a code in a 3D printer machine language based on the geometry. A Python script is then used to modify the code into a format understandable to the robot.

Fibers specimens of the composites were tested in lieu of standard dogbone specimens because of the presence of voids in the latter that could potentially skew the results. Figure 1(b) shows the augmentation of Young's modulus in with regards to the weight fraction of Halloysite. The improvement on Young's modulus attained a 71% increase for a weight fraction of 30%.

CONCLUSIONS

The printing procedure of polymers with the UV-DW method was adapted for highly mineralized nanocomposites. Polyurethane reinforced with up to 30 wt.% surface-treated HNTs was printed with a high rate of success. Future work will involve the mechanical characterisation of the different nanocomposites to assess not only the properties of this new and promising printable materials but also the quality of the print (e.g., porosity analysis, anisotropic properties). Additionally, the printing self-supporting structures will be investigated in order to produce more complex structures.

References

[1] Bruet B. J.F.: Materials design principles of ancient fish armour, *Nat. Mat.* **7**:748-756, 2008.

[2] Compton B. G.: 3D printing of Lightweight Cellular composite. *Adv, Mat.* **26**:5930-5935, 2014.

[3] Lebel L. L.: UV-Assisted Direct-Write Fabrication of Carbon nanotubes/polymer nanocomposite microcoils, *Adv. Mat.* **22**:592-596, 2010.

[4] Jiang J.: Simultaneous reinforcement and toughening of Polyurethane composites with carbon nanotubes/Halloysite nanotubes hybrides. *Composites Sc. Tech., 91:98*-103, 2014.

[a)] Corresponding author. Email: daniel.therriault@polymtl.ca

DAMPING OF LAMINATED PLATES: BOUNDARY CONDITION AND LAMINATION SEQUENCE EFFECTS

Mehrnoosh Abedi[a], Ramin Sedaghati & Mehdi Hojjati
Department of Mechanical Engineering, Concordia University, Montreal, Quebec, Canada

Summary The present study is aimed at determination of an optimal fiber orientation for the maximum modal structural damping of laminates based on in-plane viscoelastic properties obtained for a highly directional out-of-autoclave carbon/epoxy system using the dynamic mechanical analysis. The validation of material loss factors is also provided by conducting experimental modal analysis on unidirectional beam components with preferential ply angles subjected to an impulse excitation. Three different lamination sequences under the combination of clamped and free boundary conditions are taken into account. Under each boundary condition, the effect of fiber orientation on variation of modal loss factor and frequency associated with the first mode of flexural vibration is also studied.

Keywords Fiber-reinforced composite, Modal damping, Boundary conditions, Lamination sequence.

INTRODUCTION

Owing to their polymer-based matrix, fiber-reinforced materials exhibit more damping capacity compared with isotropic or metallic materials. Moreover, damping in fiber-reinforced laminates can be altered due to its dependency on the lamination arrangement, boundary condition, geometrical aspect ratio, and dissipation properties at lamina level. Thus, besides the strength, damping can also be tailored to a desired value in composite laminated materials. The analytical study of damping in composite materials can be basically addressed using micromechanical and macromechanical models. Macromechanical models such as the viscoelastic damping and the modal strain energy are popular and widely used as they can be easily utilized to investigate the effects of the lamination parameters on damping properties of composites. Using the viscoelastic damping model, the dissipative response of a system can be effectively predicted in which the dissipative parameters are defined through the concept of the complex-value moduli, established by Hashin [1]. The modal loss factor of a structure as a measure of structural damping may then predicted by the ratio of the imaginary part to real part of the squared complex eigenfrequencies obtained from the numerical modelling. A higher degree of correlation between experimental and theoretical modal responses of these models directly depends on the input elastic and viscoelastic material properties in the numerical model. In the view of experimental studies on composite materials, considerable direct and indirect methods have been applied for determination of viscoelastic characteristics along material coordinates. As for characterization of damping coefficients, unidirectional beams are mostly analyzed under forced flexural vibrations excited by a coil/electromagnet drive transducer fixed to the midpoint of a free-free beam [2, 3] or an impulse excitation of a flat cantilever beam [4, 5]. In the present work, the variation trend of structural damping property of laminated plates has been further investigated in order to define the impact of plate layup and its mode shapes under various boundary conditions.

MATERIAL CHARACTERIZATION AND VALIDATION

In order to estimate structural damping parameters of a composite system, determination of dissipation parameters varying with direction at each layer or material level plays a key role. In the current study, the dynamic mechanical analysis (DMA) is initially utilized to experimentally evaluate viscoelastic material properties of an out-of-autoclave prepreg system (referred as Cycom 5320-1) by the proper selection of the DMA three-point bending configuration yielding accurate DMA data for high-modulus fiber-reinforced materials. Table 1 lists the results for in-plane loss factors and flexural storage moduli obtained from unidirectional beam coupons with fiber angles of 0°, 90° and 45, while the nominal ply thickness is 0.135 mm.

Table 1. Storage moduli and loss factors from DMA testing on 12-ply samples undergoing 3-point bending mode.

Property	**Storage Modulus (GPa)**			**Loss Factor (%)**		
Value	E_{LL}= 143.90	E_{TT}= 9.475	G_{LT}= 5.613	η_{LL}= 0.2574	η_{TT}= 1.0274	η_{LT}= 1.7640

The measured storage moduli and loss factors are then used as input parameters in the developed finite element (FE) model to predict the linear modal vibration response behaviour of composite structures. Subsequently, modal vibration tests on various laminated composite beams have been conducted experimentally to validate the simulated modal parameters and thus indirectly the measured material characteristics using the DMA test. Table 2 compares the theoretical and experimental modal results for clamped beams of 20 mm × 200 mm undergoing flexural mode in response to an impulse excitation.

RESULTS AND DISCUSSIONS

The nature of the layup is investigated for three different symmetric lamination sequences, namely unidirectional, cross-ply, and angle-ply. Referring to the clamped and free edges as C and F, the boundary conditions CFFF, CCCC, CCFF, and CFCF are also taken into account. The physical meaning of fiber orientation is defined with respect to the first uppermost layer as the reference ply. It is inferred that the fiber angle of plies is kept alternately at 90° and -2θ with respect to that of the reference ply in the direction toward the mid-surface, in the case of cross- and angle-ply laminates, respectively. The ply angle is defined with respect to the *x*-axis of the coordinate system. The ply angle is also varied from -90° to 90° with an interval of

[a] Corresponding author. Email: mehrnoosh.abedi@concordia.ca.

5°. It is noted that all graphs showing the variation of modal loss factor are symmetric with respect to the vertical axis when the angle is changed from 0° to either -90° or +90°, except the plots for CCFF boundary condition. The modal parameters presented here are predictions obtained from the FE model based on the properties taken from the DMA testing.

Table 2. Fundamental modal damping parameter for unidirectional beams of 20 mm × 200 mm obtained experimentally.

Fiber Orientation	**0°**		**30°**		**45°**		**60°**		**90°**	
	FE[a]	EXP[b]	FE	EXP	FE	EXP	FE	EXP	FE	EXP
Frequency (Hz)	63.89	62.98	27.79	27.61	20.81	20.33	17.62	17.54	15.92	15.79
Loss factor (%)	0.251	-----	1.452	-----	1.431	-----	1.268	-----	1.001	-----
Damping factor (%)	0.126	0.133	0.726	0.723	0.716	0.715	0.634	0.642	0.500	0.582

[a] Finite element; [b] Experiment.

The maximum loss factor and its corresponding frequency along with the highest frequency under each boundary condition are reported in Table 3 in terms of the lamination sequence and the optimal fiber orientation for plate components of 120 mm × 120 mm. The results illustrate that the maximum loss factor over the given range of fiber orientation is achieved when the respective fundamental frequency is minimum. As a result, the maximum fundamental frequency and the optimal loss factor are not obtained at the same fiber orientation. Therefore, an increase in damping occurs at the expense of a decrease in frequency. To better realize this, the variation in fundamental loss factors of three given stacking sequences with respect to fiber orientation under different boundary conditions is also presented in Fig. 1.

Table 3. Maximum loss factors (%) and frequencies (Hz) of 12-ply square laminates under hybrid clamped and free boundary conditions.

Parameter	**CFFF**		**CCCC**		**CCFF** $-90° \le \theta \le 0°$		**CCFF** $0° \le \theta \le 90°$		**CFCF**	
Max. loss factor	Angle-ply (±70°)	1.140	UD (±45°)	0.580	UD (-30° & -60°)	1.041	UD (45°)	0.635	UD (±70°)	1.118
Frequency @ Max. loss factor		49.66		994.30		129.80		212.60		315.40
Max. frequency	Angle-ply & UD (0°)	176.97	Cross-ply (0° & 90°)	1194.67	Cross- & Angle-ply (-45°)	224.70	Cross- & Angle-ply (45°)	239.00	Angle-ply & UD (0°)	1114.31

For all boundary conditions except CFFF, the unidirectional configuration yield the maximum fundamental modal loss factor. It is also noticed that the angle-ply configuration under CFFF boundary condition nearly follows the trend of results of the unidirectional configuration in the case of CFCF boundary condition, offering the same optimum fiber angle. Furthermore, CCCC boundary condition leads to a relatively lower maximum loss factor due to more constrained edges, which, in turn, results in a higher bending stiffness and thus frequency. Comparing the modal loss factor of the unidirectional square plate under CFFF boundary condition with that of the beam component with the aspect ratio of 10 (see Table 2), the influence of geometry on shifting the optimum angle from 70° to 30° can also be inferred.

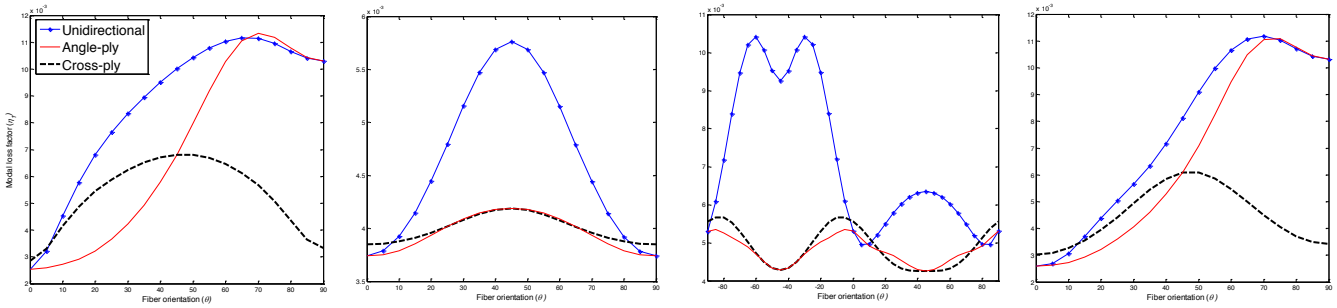

CFFF CCCC CCFF CFCF

Fig.1 Variation of fundamental loss factor with fiber orientation for laminates with maximum loss factor under combination of clamped and free boundary conditions.

References

[1] Hashin, Z., *Complex moduli of viscoelastic composites—II. Fiber reinforced materials*. International Journal of Solids and Structures, 1970. **6**(6): p. 797-807.

[2] Adams, R.D. and D. Bacon, *The dynamic properties of unidirectional fibre reinforced composites in flexure and torsion*. Journal of Composite Materials, 1973. **7**(1): p. 53-67.

[3] Adams, R. and D. Bacon, *Measurement of the flexural damping capacity and dynamic Young's modulus of metals and reinforced plastics*. Journal of Physics D: Applied Physics, 1973. **6**(1): p. 27.

[4] Berthelot, J.-M. and Y. Sefrani, *Damping analysis of unidirectional glass and Kevlar fibre composites*. Composites science and technology, 2004. **64**(9): p. 1261-1278.

[5] Suarez, S., R. Gibson, and L. Deobald, *Random and impulse techniques for measurement of damping in composite materials*. Experimental Techniques, 1984. **8**(10): p. 19-24.

THERMAL CONDUCTIVITY ESTIMATION OF NANOCOMPOSITES WITH RANDOMLY DISTRIBUTED INCLUSIONS

M. U. Siddiqui and Abul Fazal M. Arif[1a)]
[1]*Mechanical Engineering Department, King Fahd University of Petroleum & Minerals, Dhahran, Saudi Arabia.*

Summary In this paper, the formulation of two-scale homogenization methodology is presented. The formulated effective medium theory approach can be used to model nanocomposites with multiple randomly oriented or aligned inclusions that are non-homogeneously dispersed in the matrix. The applications of the formulated effective medium theory are demonstrated using previously published experimental and numerical results for several particulate nanocomposites.

INTRODUCTION

The problem of estimation of the effective thermal conductivity of composite materials has been widely studied. Early works in the area were done by Maxwell[1] and Lord Rayleigh[2] who studied the thermal conductivities of composites with low concentrations of inclusions. Expressions for the effective thermal conductivity of composites with dilute concentrations of inclusions of different shapes have been presented by Nan et al[3]. A modified effective medium theory for nanocomposites was presented by Minnich and Chen[4] for spherical inclusions and was extended by Ordonez-Miranda et al.[5] for spheroidal inclusions. The current work shows the formulation of a two-scale homogenization methodology which can be used to determine the effective thermal conductivity of particulate nanocomposites. The proposed methodology overcomes several shortcomings in the effective medium theory approaches reported in literature. These include capabilities to include effect of multiple nanometer-sized inclusions, effect of oriented (randomly or at any angle relative to heat flow direction) spheroidal inclusions and the effect of non-uniformly dispersed inclusions.

GENERALIZED EFFECTIVE MEDIUM THEORY

The formulation of the generalized effective medium theory is presented in this section. First, the effect of multiple nanometer-sized inclusions on the thermal conductivity is derived. Second, the effective medium theory formulation for multiple inclusions is presented. Lastly, a two-scale approach to handle non-uniformly dispersed inclusions is presented.
The effect of multiple nanometer-sized inclusions oriented in any random direction on the thermal conductivities of the matrix and inclusions can be calculated by extending the approach of Minnich and Chen[4]. According to their approach, the addition of the nanometer-sized particles modifies the thermal conductivities of the matrix and the inclusions. The modified thermal conductivities are calculated by first calculating the effective mean free path of the energy carriers (phonons or electrons) in the matrix or the inclusions using Matthiessen's rule. This results in the following modified matrix and inclusion thermal conductivities.

$$K_x^{mat} = \frac{K_{x,bulk}^{mat}}{1+\Lambda_{x,\mathrm{bulk}}^{mat}\left(\varphi_1 + r_{V2}\varphi_2 + \ldots + r_{VN}\varphi_2\right)\sigma_{\perp 1}} \quad (1)$$

$$K_x^{inc.i} = \frac{K_{x,bulk}^{inc.i}}{1+\Lambda_{x,bulk}^{inc.i}/\Lambda_{coll}^{inc.i}} \quad (2)$$

$$c_{12}^{inc.i} = \begin{cases} \dfrac{8a_1^{inc.i}}{3\pi\varepsilon}\dfrac{\left(1+\varepsilon^2\right)K_{ellip}\left(-\varepsilon^2\right)-\left(1-\varepsilon^2\right)E_{ellip}\left(-\varepsilon^2\right)}{\varepsilon\sqrt{1+\varepsilon^2}+\operatorname{arcsinh}\left(\varepsilon\right)}, & \text{for } p<1 \\ \dfrac{8a_1^{inc.i}}{3\pi\left(i\varepsilon\right)}\dfrac{\left(1-\varepsilon^2\right)K_{ellip}\left(\varepsilon^2\right)-\left(1+\varepsilon^2\right)E_{ellip}\left(\varepsilon^2\right)}{\left(i\varepsilon\right)\sqrt{1-\varepsilon^2}+\operatorname{arcsinh}\left(i\varepsilon\right)}, & \text{for } p\geq 1 \end{cases} \quad (3)$$

$$\Lambda_{coll}^{inc.i} = \begin{cases} \min\left(\dfrac{c_{12}^{inc.i}}{\sin\theta^{inc.i}}, c_{33}^{inc.i}\right), & \text{for } p\geq 1 \\ \min\left(\dfrac{c_{33}^{inc.i}}{\cos\theta^{inc.i}}, c_{12}^{inc.i}\right), & \text{for } p<1 \end{cases} \quad (4)$$

where x can be p or e for phonons or electrons respectively, $r_{Vi} = V_1/V_2$, V_i and φ_i are the volume and volume fraction of a single particle of inclusion type i, $\sigma_{\perp 1} = A_{\perp 1}/V_1$ and $\Lambda_{x,\mathrm{bulk}}^{y}$ is the bulk mean free path of the energy carriers, p is the inclusion aspect ratio, ε is the eccentricity, K_{ellip} and E_{ellip} are elliptic integrals of first and second kind.
A generalization of Nan et al.'s EMT[3] to multiple inclusions can be derived by considering the background of the Nan et al.'s derivation[6].The effective thermal conductivity of the composite can then be calculated using eq. (5) where the definition of individual terms in the equations is same as in Nan et al.[3]. A major drawback of the effective medium theory approach is its inability to handle non-uniform dispersion of inclusions. In the current work, a two-scale approach is proposed that combines the EMT approach at the lower scale with computational homogenization[7,8] at the upper scale to introduce the effect of non-uniform dispersion of inclusions in the matrix on the effective thermal conductivity of the composite. The application of the method

a) Corresponding author. Email: afmarif@kfupm.edu.sa

requires a quantitative knowledge of inclusion distribution in the matrix. This could a statistical parameter like standard deviation of inclusion volume fraction that can be used to develop an RVE for computational homogenization.

$$K_{eff,11} = K_{eff,22} = K_m \frac{2 + \sum_{i=1}^{N} \varphi_i \left[\beta_{11}^i \left(1 - L_{11}^i\right)\left(1 + \left\langle \cos^2\theta \right\rangle^i\right) + \beta_{33}^i \left(1 - L_{33}^i\right)\left(1 - \left\langle \cos^2\theta \right\rangle^i\right)\right]}{2 - \sum_{i=1}^{N} \varphi_i \left[\beta_{11}^i L_{11}^i \left(1 + \left\langle \cos^2\theta \right\rangle^i\right) + \beta_{33}^i L_{33}^i \left\langle 1 - \cos^2\theta \right\rangle^i\right]}$$

$$K_{eff,33} = K_m \frac{1 + \sum_{i=1}^{N} \varphi_i \left[\beta_{11}^i \left(1 - L_{11}^i\right)\left(1 - \left\langle \cos^2\theta \right\rangle^i\right) + \beta_{33}^i \left(1 - L_{33}^i\right)\left(\left\langle \cos^2\theta \right\rangle^i\right)\right]}{1 - \sum_{i=1}^{N} \varphi_i \left[\beta_{11}^i L_{11}^i \left(1 - \left\langle \cos^2\theta \right\rangle^i\right) + \beta_{33}^i L_{33}^i \left\langle \cos^2\theta \right\rangle^i\right]} \tag{5}$$

APPLICATIONS OF THE TWO-SCALE APPROACH

In this section, the methodology formulated above is applied to Germanium-Silicon nanocomposites. The generalized EMT formulated in the current work can be applied to Ge-Si composites for cases already studied in literature i.e. spherical inclusions and aligned spheroidal inclusions as well as for cases not reported previously e.g. randomly oriented spheroidal inclusions and non-uniformly distributed Si inclusions. Figure 1 shows the effect of inclusion size, aspect ratio and dispersion non-uniformity on the estimated effective thermal conductivities of Ge-Si composite.

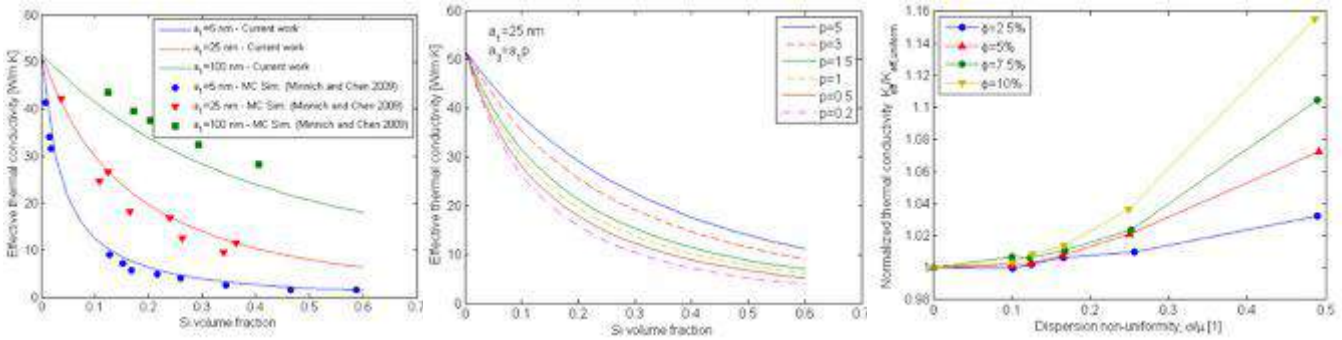

(a) inclusion size effect (b) aspect ratio effect (c) dispersion non-uniformity effect

Figure 1. Thermal conductivity of Ge-Si effective thermal conductivity

CONCLUSIONS

In this paper, a two-scale homogenization methodology is presented for the estimation of the effective thermal conductivity of particulate nanocomposites. The formulated EMT has the capability to incorporate the effects of size, shape, orientation and non-uniform dispersion of multiple inclusions on the estimated thermal conductivity.

Acknowledgement

The authors acknowledge the support provided by KACST) through the project 12-NAN2374-04 as part of NSTIP.

References

[1] J. Maxwell, *A Treatise on Electricity and Magnetism*, 2nd ed. (Oxford University Press, 1904).
[2] Lord Rayleigh, Philos. Mag. Ser. 5 **34**, 481 (1892).
[3] C.-W. Nan, R. Birringer, D.R. Clarke, and H. Gleiter, J. Appl. Phys. **81**, 6692 (1997).
[4] A. Minnich and G. Chen, Appl. Phys. Lett. **91**, 4 (2007).
[5] J. Ordonez-Miranda, R. Yang, and J.J. Alvarado-Gil, Appl. Phys. Lett. **98**, 2009 (2011).
[6] C.-W. Nan, Prog. Mater. Sci. **37**, 1 (1993).
[7] A. El Moumen, T. Kanit, A. Imad, and H. El Minor, Comput. Mater. Sci. **97**, 148 (2015).
[8] T. Wu, İ. Temizer, and P. Wriggers, Cem. Concr. Compos. **35**, 59 (2013).

ANALYTICAL INCLUSION GREEN OPERATORS IN TRANSVERSALLY ISOTROPIC MEDIA

Salma Barboura[a] & Patrick Franciosi[b]
[a]*Université Paris13, Sorbonne Paris Cité, LSPM CNRS, Villetaneuse, France*
[b]*LSPM, CNRS UPR3407, Université Paris 13, Sorbonne Paris Cité, Villetaneuse, France*

Summary We present a simple analytical solution, based on the Radon transform and its inversion formula, for the local and mean Green operator of long or flat (not only ellipsoidal) inclusions with general orientation in any medium with transversally isotropic (TI) and possibly coupled properties. This "Radon method", already applied to various situations, allows quick checking of operator variations with inclusion aspect ratio and orientation with regard to various matrix TI anisotropy and of related effective properties of composites.

INTRODUCTION

Estimates of effective properties of various composite structures from homogenization frameworks are based on the knowledge of the so-called Green (G) operators, or of the Eshelby (E) tensors for inclusions or phase arrangement symmetries. The here reported analytical solution, based on the Radon transform and its inversion formula, provides the (mean when not uniform) G operator in various cases of inclusions in transversally isotropic (TI) reference matrices. As exemplified for spheroids, it allows quick checking of inclusion orientation, aspect ratio and matrix anisotropy variations.

THE MEAN GREEN OPERATOR FORM USING THE RADON TRANSFORM METHOD

By the Radon method [1-3], the mean Green (G) operator over a 3D inclusion V of *any* shape $\overline{\boldsymbol{t}^V} = \mathrm{v}^{-1}\int_V \boldsymbol{t}^V(\mathbf{r})\,\mathrm{d}\mathbf{r}$ (say, the average over all points **r** in V of the integral over V of the modified G operator $\boldsymbol{t}^V(\mathbf{r})$ [1]) in an infinite medium with (static, linear) properties of *general* anisotropy, can be written, with $\omega = (\theta,\phi)$, $\mathrm{d}\omega = \sin\theta\,\mathrm{d}\theta\,\mathrm{d}\phi$ and Ω the unit sphere:

$$\overline{\boldsymbol{t}^V} = \int_\Omega \mathbf{t}^{\mathrm{P}}(\omega)\,\overline{\psi_{\mathrm{V}}}(\omega)\,\mathrm{d}\omega \quad ; \quad \overline{\psi_{\mathrm{V}}}(\omega) = \mathrm{v}^{-1}\int_{\mathrm{v}} \psi_{\mathrm{V}}(\omega,\mathbf{r})\,\mathrm{d}\mathbf{r} \quad ; \quad \psi_{\mathrm{V}}(\omega,\mathbf{r}) = -\frac{1}{8\pi^2}\frac{\partial^2 \mathrm{s}_{\mathrm{V}}(\mathrm{z},\omega)}{\partial \mathrm{z}^2(\omega)} = \frac{-\mathrm{s}_{\mathrm{V}}''(\mathrm{z},\omega)}{8\pi^2} \qquad (1a),$$

$$\overline{\psi_{\mathrm{V}}}(\omega) = -\frac{1}{8\pi^2 \mathrm{v}}\int_{\mathrm{D_V^-}(\omega)}^{\mathrm{D_V^+}(\omega)} \mathrm{s}_{\mathrm{V}}''(\mathrm{z},\omega)\,\mathrm{s}_{\mathrm{V}}(\mathrm{z},\omega)\,\mathrm{dz} = \frac{-1}{8\pi^2 \mathrm{v}}\left(\mathrm{s}_{\mathrm{V}}(z,\omega)\mathrm{s}_{\mathrm{V}}'(z,\omega)\Big|_{\mathrm{D_V^-}(\omega)}^{\mathrm{D_V^+}(\omega)} - \int_{\mathrm{D_V^-}(\omega)}^{\mathrm{D_V^+}(\omega)} (\mathrm{s}_{\mathrm{V}}'(\mathrm{z},\omega))^2\,\mathrm{dz}\right) \qquad (1b).$$

In $\psi_{\mathrm{V}}(\omega,\mathbf{r})$ and in $\overline{\psi_{\mathrm{V}}}(\omega)$, the $\mathrm{s}_{\mathrm{V}}(\mathrm{z},\omega)$ function is the section area of V by the plane of $z = \boldsymbol{\omega}.\mathbf{r}$ equation, passing through **r** and of **ω** normal. $\left(\mathrm{D_V^-}(\omega), \mathrm{D_V^+}(\omega)\right)$ is the inclusion breadth in direction ω. The second z-derivatives $\mathrm{s}_{\mathrm{V}}''(\mathrm{z},\omega$ are constant for ellipsoids and yield uniform shape function and G operator [1-3]. The elementary operators $\mathbf{t}^{\mathrm{P}}(\omega)$ are the Green operators of infinitely flat spheroids, or of laminate layers, normal to the direction **ω**. They only depend on the matrix properties of concern. Using the generalized elasticity notation [3,4], they read:

$$\mathrm{t}^{\mathrm{p}}_{\mathrm{qIJp}}(\omega) = \mathrm{t}^{\mathrm{p}}_{\mathrm{qIJp}}(\theta,\phi) = \left((M^{-1})_{\mathrm{IJ}}(\omega)\,\omega_{\mathrm{q}}\,\omega_{\mathrm{p}}\right)_{(Iq),(Jp)} \qquad ; \qquad M_{IJ} = C_{pIJq}\omega_p\omega_q \qquad (2).$$

In Eq. 2, $\boldsymbol{C}$ is the generalized stiffness moduli tensor, and M has dimension 5x5 for magneto-electro-elastic (MEE) coupling. The first step to obtaining the G operator is to calculate all the $\mathrm{s}_{\mathrm{V}}''(\mathrm{z},\omega)$ derivatives for the shape of concern.

In isotropic media (not allowing property coupling) all the elementary operators are equivalent up to a rotation and all the G operator terms reduce to combinations of trigonometric functions of the form $\sin^{2r}\theta\cos^{2s}\theta\sin^{2u}\phi\cos^{2v}\phi$ [1,2]. In TI media, with the ϕ integral running in the medium symmetry plane $x_1 - x_2$, all the elementary operators take the form of one or a sum of rational fractions of polynoms in $\cos^2\theta$ (θ being counted from the medium x_3 TI symmetry axis) which all are of degree 4 at the most in the case of MEE coupling [3] (Thermal coupling enters as for thermal-elasticity [5]). All of them can be decomposed into several terms of the unique form $p/(\cos^2\theta - q)$, where q is one of the (real or complex) root of the denominator of the polynomial fraction and p a coefficient [3]. Up to now, off-axes oriented inclusions in TI media have no (or no simple) analytical G operator forms, except for laminates what is a trivial result from the Radon method [3].

[1] $\boldsymbol{t}^V(\mathbf{r}) = \int_V \boldsymbol{\Gamma}(\mathbf{r}-\mathbf{r}')\,\mathrm{d}\mathbf{r}'$, $\Gamma_{\mathrm{ijpq}}(\mathbf{r}-\mathbf{r}') = -\partial^2/\partial x_p \partial x_q\left(\mathrm{G_{ij}}(\mathbf{r}-\mathbf{r}')\right)$, $\mathbf{G}(\mathbf{r}-\mathbf{r}')$ is the Green function of the medium, $\mathbf{r} = (x_1, x_2, x_3)$.

[a] Corresponding author. Email: salma.barboura@univ-paris13.fr.

RESULTS AND CONCLUSION

According to the Radon method, the (ellipsoidal or not) inclusion shapes in a TI medium can be ranged into 3 groups: (i) integrals over ϕ and over θ((in $\overline{\boldsymbol{t}^V}$ are independent, (ii) θ is a simple function of ϕ(such that a single ϕ integral remains, and (iii) ϕ and θ integrals in $\overline{\boldsymbol{t}^V}$ remain coupled. Case (i) includes axial (from flat to long) spheroids and other axially symmetric shapes as finite cylinders or half-spheres, case (ii) includes (possibly elliptic) fibres of general orientation and case (iii) contains the ellipsoid of general position with the particular spheroidal type from axial to transverse direction. Cases (i) and (ii) are fully analytical. In case (iii) the last integral may need computational assistance. For ellipsoids, the double (θ,ϕ) integrals to be performed formally read, with the $F^{(u,v)}(\phi)$ being the same trigonometric ϕ-functions as in fully isotropic media [1,2]:

$$I_q\Big|_V^{(u,v)} = \int_{\phi=0}^{2\phi}\left(\int_{x=-1}^{1}\frac{1}{x^2-q}\psi_V^{\mathrm{Ell}}(x,\phi)\,\mathrm{d}x\right)F^{(u,v)}(\phi)d\phi \qquad (3).$$

For spheroids with general (θ°,ϕ°) orientation in the medium, for each ϕ value, the θ elementary integral reads [3]:

$$I_q^{\omega^\circ(\phi)}\Big|_\zeta = \frac{1}{2}\int_{-1}^{1}\frac{\zeta}{x^2-q}\left(1+(\zeta^2-1)\left(\sin\theta^\circ\sqrt{1-x^2}\,\cos(\phi-\phi^\circ)+\cos\theta^\circ x\right)^2\right)^{-3/2}dx\,,\quad x=\cos\theta \qquad (4).$$

The Figures 1 and 2 exemplify spheroid G operators $\boldsymbol{t}$ (normalized by the matrix shear modulus μ) at different θ angle from the TI medium symmetry axis, varying the aspect ratios ζ from flat 10^{-2} to long 10^{2} spheroids and for two opposite matrix (elastic) property anisotropies, with $C=C_{iiii}$, $\mu=C_{1212}$ and $C^*=C_{1122}=C-2\mu$, i=1,2 in the x1x2 symmetry plane.

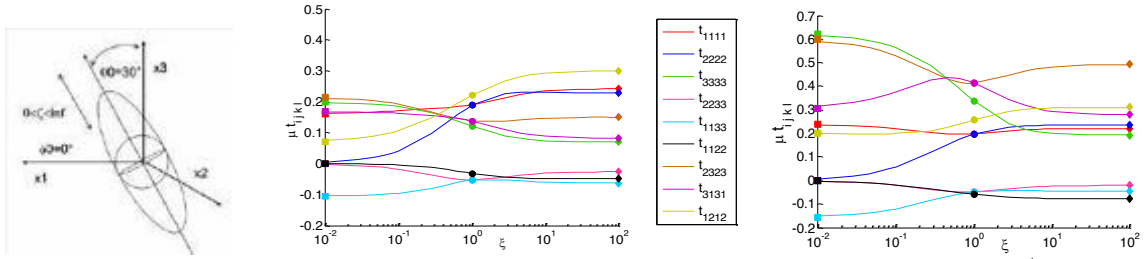

Figure 1: spheroid G operator at ϕ°=0 and θ°=30° from the TI matrix symmetry axis for cases of (left) μL=2μ, CL=2C and CL=2(C-2μ) and (right) μL=μ/2, CL=C/2 and CL*=(C-2μ)/2*

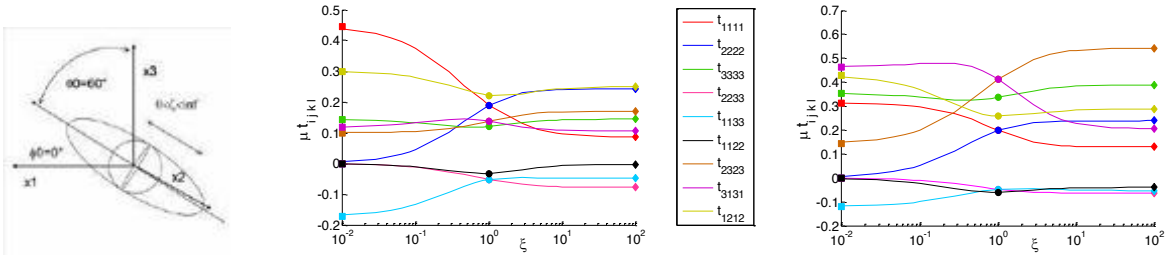

Figure 2: spheroid G operator at ϕ°=0 and θ°=60° from the TI matrix symmetry axis for cases of (left) μL=2μ, CL=2C and CL=2(C-2μ) and (right) μL=μ/2, CL=C/2 and CL*=(C-2μ)/2*

The dots on Figures 1 and 2 represent the G operator terms for the laminates, sphere and infinite cylindrical fibres, with fully explicated analytical solutions given in [3], together with the one for infinite elliptical fibres. Analytical solutions are also at hand for the (mean) G operator of finite long or flat cylinders [2] and of some other shapes to be presented soon. The Radon method solution allows an easy check of how optimizing (possibly coupled) properties of composite structures from modulating the medium TI anisotropy together with the shape and orientation of the inclusions.

References

[1] Franciosi P., Lormand G.: Using the Radon Transform to solve inclusion problems in elasticity. *Int. J. Solids and Structures*, **41**, 585-606, 2004.

[2] Franciosi P., Barboura S., Charles Y.: Analytical mean Green operators / Eshelby tensors for patterns of coaxial finite long or flat cylinders in isotropic matrices. *Int. J. Solids and Structures*, **66**, 1-19, 2015.

[3] Franciosi P.: Transversally isotropic Magneto-Electro-Elastic composites with co-(dis)continuous phases. *Int. J. Solids and Structures*, **50**, 1013-1031, 2013.

[4] Barnett D.M., Lothe J.: Dislocations and line charges in anisotropic piezoelectric insulators. *Phys. Stat. Solidi B*, **67**, 105-111, 1975.

[5] Levin V.M.: Thermal expansion coefficients for heterogeneous materials. *Mekhanika Tverdogo Tela* 2, 88–94 (English translation: *Mechanics of Solids* 11, 58–61) 1967.

HIGH STRAIN RATE RESPONSE OF CARBON NANOTUBES BASED ELASOTMER COMPOSITES

Salman Chaudhry [1], Aleksander Czekanski[2]
[1]*Earth and Space Science Engineering, York University, Toronto, Ontario, Canada*
[2]*Department of Mechanical Engineering, Lassonde School of Engineering, Toronto, Ontario, Canada*

Summary The article investigates the response of nanoparticle reinforced elastomer composites under dynamic impact. The preparation, characterization and testing methodology of polydimethylsiloxane based elastomers reinforced with multi walled carbon nanotubes is discussed in detail. Under quasi-static condition the presence of CNT network resulted in an enhanced stiffness. When subjected to high strain rates of compressive loading the presence of CNTs influenced the stress – strain curve characteristics (e.g. transition point from strain hardening to softening region) while greatly improving the energy storing capabilities. To test under high rates of strain, some necessary modification were also made to the dynamic testing apparatus (Kolsky bar/Split Hopkinson bar).

INTRODUCTION

Elastomers are rubberlike material exhibiting characteristics of viscoelastic nature, low elastic modulus, high strain at failure and weak inter-molecular interactions. Quite recently considerable attention has been devoted to develop multi-dimensional composite system through introducing a nano-filler network. Some typical reinforcing fillers includes cubic and spheroidal fillers (calcium carbonate, silica, carbon black), fiber fillers (glass, aramid fibers) and nanofillers (carbon nanotubes, nanoclays, nanosilica) [1]. Depending on their structural and geometric characteristics, nano-fillers network interacts with the polymers matrix differently resulting in enhanced mechanical and electrical properties of the resulting composite system. The use of Carbon nanotubes to fabricate elastomer based composites has gained importance due to their high Young's modulus, superior electrical and thermal conductivity and large aspect ratio. These elastomeric nanocomposites, however, require preparation procedure that are different than most polymer-based nanocomposites since their performance greatly depend on the rate of dispersion, and degree of alignment.

It is quite evident and well established that CNTs (when incorporated into elastomer network), results in improvement in stiffness over large strain deformation. However, under moderate to high strain rates, response of elastomers can vary from being purely rubber like to glassy behaviour [2]. Investigations on the performance of these reinforcement when subjected to high strain rates are still lacking. The main objective of the research is to characterise the effect of CNT filler loading on the stiffing of the elastomeric composite under quasi-static and dynamic impact conditions. The typical setup required to study the response of materials under impact is the Split Hopkinson bar/Kolsky bar. However, to test low impedance, and low strength material some modifications are required to it.

EXPERIMENTAL

Fabrication

For the matrix network polydimethylsiloxane (PDMS) base (DOW SYLGARD 184) was used in 10:1 ratio with HR-C catalyst. First the PDMS base was extensively mixed with multi walled carbon nanotube MWCNT (NC7000) having an average diameter and length of 9.5 nm and 1.5 μm respectively. To achieve better dispersion of CNTs the solution was sonicated for 30 mins. After the addition of catalyst, the CNT/PDMS solution was further mixed in a paste mixer and degassed in a vacuum chamber. Before it was ready to be cured at 150 ^{o}C for 15 mins, the resulting paste was poured into mold and vacuum bagged to ensure the removal of tiny air bubbles that may have been captured during the transfer to the mold. To characterize the stiffing effect due to the presence of filler network, the CNT were added in varying weight percent (% wt) with the elastomer base.

Testing

Uniaxial tension tests were carried in a MTS-43 electromechanical load frame using a dumbbell specimen with a thickness of 3.3 mm and width 5.5 mm at a loading rate of 0.1 mm/s^{-1}. For the dynamic impact test, a modified Kolsky bar was developed suitable to test low impedance soft materials like rubbers. In a Kolsky bar a cylindrical sample is a sandwiched between an incident and transmission wave. Dynamic loading is produced in the form of elastic wave when the incident bar is impacted using a striker of same diameter. This is called the incident wave, upon reaching the bar specimen interface some of this wave is reflected back while the rest is transmitted through the specimen to the transmission bar. The incident, reflected and transmitted waves are recorded through strain gauges, to compute the response of the specimen. To avoid interfacial frictional and inertial effect which may results in a noise, the specimen geometry was optimized to be 8.5 mm diameter and 2mm thickness. The trapezoidal incident wave was also shaped through pulse shaping technique into a smoother pulse with an elongated rise time to avoid the effects of axial and radial inertia. The geometry of pulse shaper (annealed C11000) was optimized to be cylindrical with diameter of 3.5 mm and thickness of 1.6 mm. The dimension of the incident and hollow

[a)] Corresponding author. Email: alex.czekanski@lassonde.yorku.ca
4700 Keele Street, York University, Toronto, Ontario
Canada, M3J 1P3

transmission bars were 20mm in diameter and length of 2m and 1.8 m respectively. The complete operational details of the testing apparatus can be found in [3] and [4].

RESULTS AND DISCUSSION

Figure 1 (a) illustrates the response for quasi static uniaxial tension of samples with varying concentration of CNT filler. Under the quasi-static loading the stress – strain response of PDMS as well as reinforced composites exhibits behavior typical of elastomers; a linear elastic response under low strain followed by a slightly non-linear behavior. Increasing the CNT loading in the elastomer network results in enhanced stiffening. However, increasing the amount CNT also effects the max level of strain attained in the sample. This effect can be attributed to the existence of CNT agglomerates at higher weight percentages, which are not well dispersed. These bundles of CNTs acts as stress concentrators contributing to the origin of cracks.

Figure 1(b) shows that under constant strain rate (2500 s^{-1}), increasing the amount of CNT filler from 0 wt% to 2.0 wt%, not only enhances the level of endured stresses but also accumulates much larger strain. The stress increases linearly with the strain in the initial loading. After the yield point, the curve exhibits regions of strain hardening followed by strain softening region. This transition is also influenced by the amount of CNT nano-reinforcement present in the PDMS matrix. At a constant rate of loading the energy absorption is improved by ~ 33 % in samples containing 2 wt % of CNT as compared to the neat ones.

It can be seen from Figure 1(c) that the mechanical response of composites under uniaxial compression exhibits great strain rate dependent characteristics. In comparison to the quasi-static testing, the high strain rate results show higher stress values at comparable strain.

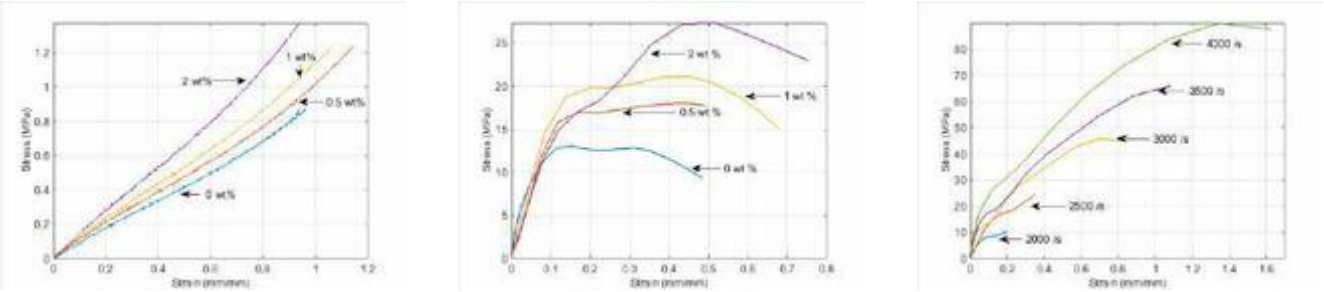

(a) (b) (c)

Figure (1): (a) uniaxial tension under quasi-static conditions for PDMS samples with varying CNT loading. (b) Uniaxial compression results for the samples at a constant strain rate of 2500 s^{-1} (c) Response of 2 wt% CNT reinforced PDMS samples under varying strain rate from 2000 s^{-1} to 4300 s^{-1}.

CONCLUSION

In this study, the quasi-static and high strain response of CNT based PDMS composites has been investigated. To test under impact conditions, a modified Kolsky bar apparatus was developed. The addition of CNT as nano-reinforcements have shown to enhance stiffening and energy absorption characteristics of the material. In the high strain rate regime, more prominent effect is seen on the maximum level of stress (enhanced by 120 %) and strain attained. The presence of CNT's influence strain related hardening and softening regions. Interestingly, the response of the composite also exhibited a strong strain rate dependency on the shock absorbing capability – an increase by 43 times from 2000 s^{-1} 4300 s^{-1}

References

[1] Ing Kong and Robert Shanks, "Thermoplastic Elastomers," in *Thermoplastic Elastomers*, ISBN:978-953-51-0346-2, 2012.

[2] Sai S. Sarva, Stephanie Deschanel, Mary C. Boyce and Weinong Chen, "Stress-Strain Behaviou of a Polyurea and a Polyurethans from Low to High Strain Rates," *Polymer,* vol. 48, pp. 2208-2213, 2007.

[3] M.S. Chaudhry, R. Carrick and A. Czekanski, "Design of Kosky Bar to Characterize The Dynamic Response of Elastomers Under High Strain Rate," in *CANCAM*, London Canada, 2015.

[4] M.S. Chaudhry, R.Carrick and A.Czekanski, "Finite Element Modelling anf Validation of a Modififed Kolsky Bar Developed for High Strain Rate Testing of Elastomers.," in *ASME-IMECE*, Texas, Houston, 2015.

IMPACT FORCE HISTORY PATTERNS ON SANDWICHES VERSUS POST-IMPACT BEHAVIOUR

Nicolae Constantin[a)], Marin Sandu, Mircea Găvan & Constantin Valentin Epuran
Department of Strength of Materials, The University "Politehnica" of Bucharest, Bucharest, Romania

Summary The paper presents results obtained during low velocity impact tests made on sandwich materials aimed to be used for the manufacturing of various structural parts of a small integrated renewable energy unit. The shape of the recorded impact force history curves have been first analysed in each case, in order to get prime information about the possible damage produced in the material. The impact tests have been followed by mechanical tests, which offered quantitative information about the residual strength of the material, as valuable data concerning the damage tolerance of the materials. The whole scenario has to be put in place especially for new or improved materials which are intended to be used, creating a strong background for designers and very useful in exploitation, for achieving high in-service structural reliability. The research effort is underway, with results promising good mechanical performance of the proposed materials.

INTRODUCTION

Small integrated renewable energy units are the answer for affordable and flexible energy sources in the case of isolated, completely off-grid buildings or complementary solutions for buildings with access to energy utility providers. Integration means presence of various green energy sources, like a wind turbine sided by photovoltaic and thermal solar panels and energy storage devices, like water tanks and batteries. In this way, good flexibility in providing energy the year round is secured, with corresponding high degree of energetic autonomy. All that components are mounted on a supporting tower, the whole structure involving a wide range of materials. Sandwich type composites offer the highest versatility in terms of optimum design, letting room for adequate solutions from both structural and cost points of view. It is the reason for which that class of composites has been chosen for manufacturing some main parts of the turbine runner and the tower platforms.

Most composites are very sensible to low velocity impact events which, unlike high velocity ones, may produce damages in the material on areas considerably larger than the zone of direct contact with the impactor. The small renewable energy units are running not only various weather conditions, but also in the vicinity of buildings and trees. Consequently, low velocity impact due to hail, tree branches, roof tiles or mishandled tools can affect the structural integrity of the materials. The damage induced by impact can be detected tracking irregularities on the impact force history curves [1]. Such a test can be seen as a reference meant to evaluate the propensity to failure and coupled with post-impact testing, measuring the residual strength and/or stiffness, it can give valuable information about the damage tolerance for various materials. The impact test and the post-impact test are standardised in two reference documents for layered fibre reinforced plastics (FRPs) [2][3]. In the paper, the experimental procedures are adapted for sandwich materials, the most important point being the replacement of compression after impact test (CAI) with bending after impact test (BAI), idea presented already in [4].



Fig. 1. Modified Charpy hammer.

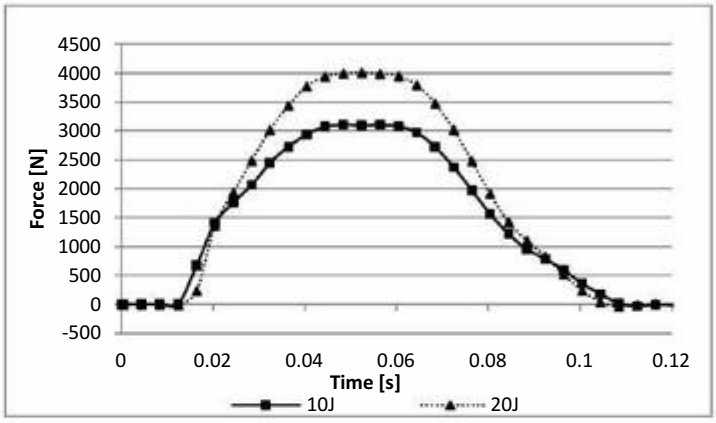

Fig. 2. Impact force history curves for sandwiches with coremat core.

DESCRIPTION OF THE EXPERIMENTAL WORK

The impact tests were performed on an adapted impact hammer, commonly used for Charpy and Izod impact tests. Adding a force transducer, complementary instrumentation and an adequate rig for mounting the samples (Fig. 1) makes this installation very affordable for tests performed at low and medium energy levels. Various samples have been used, in order to assess different materials and comply with adequate standards. The sandwich materials had skins made from layered glass fibre reinforced plastics (GFRP), with coremat®, honeycomb and polyurethane foam cores. Dimensions for the

[a)] Corresponding author. Email: nicolae.constantin@upb.ro.

first type were 100 x 350 mm, while for the others 100 x 450 mm. In this way, the minimum dimension complied with that imposed by [3], while the other dimensions complied with [5], as the low velocity tests and subsequent 3-point BAI tests for getting residual mechanical performance in bending followed the pending standards. Relevant results are presented below.

The regularity of the impact force history curves obtained under 10J and 20J energies for the sandwiches with coremat core (Fig. 2) quite naturally implied quasi-unchanged strength after BAI tests, in line with results found for most FRPs.

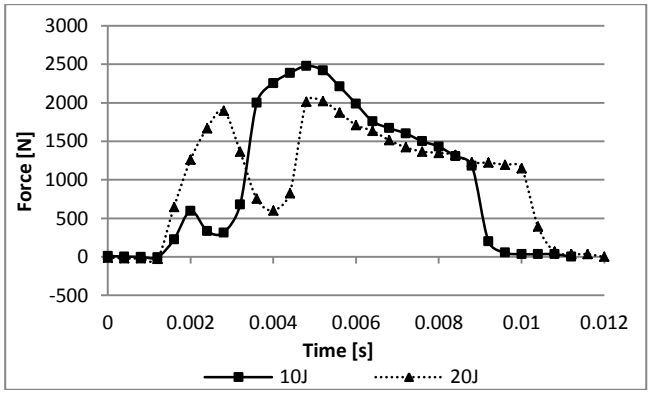

Fig. 3. Impact force history curves for honeycomb-sandwiches.

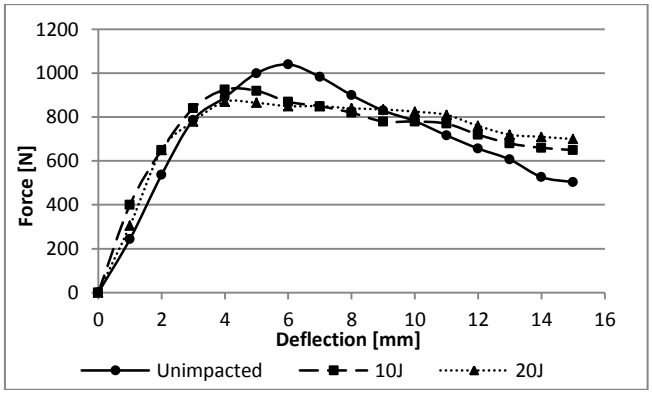

Fig. 4. Bending behaviour of sandwiches with honeycomb core.

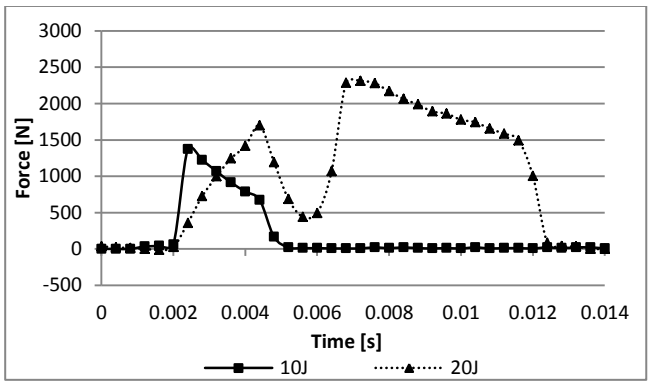

Fig. 5. Impact force history curves for sandwiches with foam core.

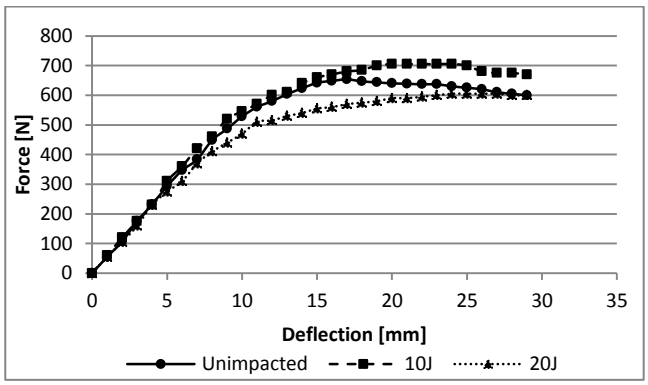

Fig. 6. Bending behaviour of sandwiches with foam core.

One can expect that the very deformed shapes of the impact force history curves obtained for sandwiches with honeycomb core (Fig. 3) mean a very consistent diminishing of the residual strength. Instead, it was observed a modest one (Fig. 4), even for the samples where a quasi-penetration of the impacted upper skin took place under 20J energy impact.

The impact force history curves obtained for sandwiches with foam core show a stunning difference between those recorded for the 10J and the 20J energy impact (Fig. 5). The short, low amplitude first ones prove even a beneficial effect on the bending strength, while the irregular, extended second ones witness a slight lowering of that strength (Fig. 6).

CONCLUSIONS

The link between impact force history curves obtained for thick sandwiches is less informative than those obtained for FRPs and thin, compact sandwiches. For relevant data about the post-impact behaviour, CAI and BAI tests have to be made.

Acknowledgment. The research work was performed under project 258/2014, financed by the Romanian Ministry of Education and Scientific Research, through its dedicated body (MEN-UEFISCDI), in the "Partnership in priority domains - PN II" programme.

References

[1] Herup E. J. & Palazotto A. N.: Low-velocity impact damage initiation in graphite/epoxy/nomex honeycomb-sandwich plates. *Composite Sci Tech 57*:1581-1598, 1997.

[2] ASTM D 7136 – Standard test method for measuring the damage resistance of a fiber reinforced polymer matrix composite to a drop impact event, *Annual Book of ASTM standards*: 430-445, 2005.

[3] ASTM D 7136 – Standard test method for compressive residual strength properties of damaged polymer matrix composite plates. *Annual Book of ASTM standards*: 446-463, 2005.

[4] Constantin N., Găvan M. Sorohan Ş. Borîtu A. & Tănase D.: Impact and post-impact behaviour of layered composites. Proc. 5th EWSHM: 578-583, 2010.

[5] ASTM C 393: Standard Test Method for Flexural Properties of Sandwich Constructions, ASTM International, West Conshohocken, PA, 2011.

VIBRATION OF DOUBLY TAPERED LAMINATED COMPOSITE BEAMS BY HIERARCHICAL FEM

Amin Fazili [1a)] & Rajamohan Ganesan[1]
[1]*Department of Mechanical and Industrial Engineering, Concordia University, Montreal, Quebec, Canada*

Summary Free vibration response of symmetric linear-thickness-and-width-tapered laminated composite beams is studied. For this purpose, a hierarchical finite element formulation is developed based on trigonometric hierarchical functions. Comparison of the hierarchical finite element solution with the Rayleigh-Ritz and a higher-order finite element solution is performed. A parametric study is conducted on the internally-tapered composite beams to investigate the effects of boundary conditions, width-ratio, thickness-tapering angle, and damping on the free vibration response.

INTRODUCTION AND FORMULATION

Tapered laminated composite beams provide stiffness-tailoring and mass-tailoring design capabilities. They are increasingly and widely being used in engineering applications including aircraft wings, helicopter yokes and wind turbine blades. The composite beam that is being analyzed in the present study has a large length-to-thickness ratio as shown in Figure 1, and therefore by applying the cylindrical bending theory and considering classical laminate theory, one can get the equation of motion in variational form as:

$$\int_0^L b(x)\,D_{11}(x)\left(\frac{\mathrm{d}^2w}{\mathrm{d}x^2}\right)\left(\frac{d^2\delta w}{\mathrm{d}x^2}\right)dx-\int_0^L b(x)N_x\left(\frac{\mathrm{d}w}{\mathrm{d}x}\right)\left(\frac{\mathrm{d}\delta w}{\mathrm{d}x}\right)dx-\omega^2\int_0^L\int_{-H/2}^{H/2}\rho\,b(x)\,w\delta w dx dz=0 \tag{1}$$

in which L is the length of the tapered beam, $b(x)$ is the width of the beam, N_x is the compressive axial force (if present), and $D_{11}(x)$ is the coefficient of bending stiffness of the laminated composite beam [1] which can be calculated as:

$$D_{11}(x)=\sum_{k=1}^{n}\left[t_k z_k^2-\frac{{t_k}^3}{12}\right]\left(\overline{Q}_{11}\right)_k \tag{2}$$

where t_k denotes the thickness of kth ply and $\left(\overline{Q}_{11}\right)_k$ denotes the transformed reduced stiffness coefficient of the kth ply[2].

It is also assumed that the deflection in (transverse) z-direction is: $w(x,t)=W(x)e^{i\omega t}$. Using the Hierarchical Finite Element Method (HFEM), considering two nodes per element and two physical degrees of freedom per node, that are, transverse deflection and rotation (Figure 1), first a third-order polynomial is used as the basis for the expression of deflection to satisfy the boundary conditions as:

$$W(x)=c_1+c_2x+c_3x^2+c_4x^3 \tag{3}$$

The displacement function is then modified by adding trigonometric or polynomial functions at the end of the equation[3]. In this study, the trigonometric hierarchical functions are used as:

$$W(x)=c_1+c_2x+c_3x^2+c_4x^3+\sum_{i=1}^{N}c_{i+4}\sin\frac{i\pi x}{l_e},\quad i=1,2,3,\ldots \tag{4}$$

in which l_e is the length of the element and N is the number of hierarchical terms.

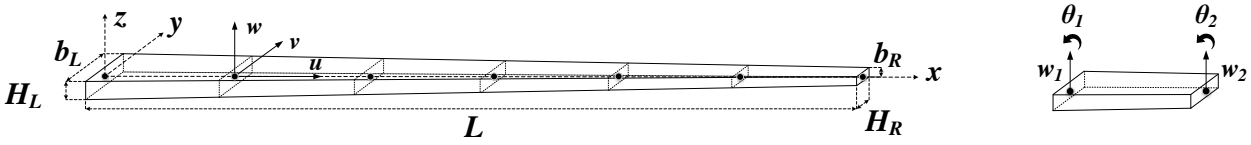

Figure 1 Global and local co-ordinates (left), and nodal displacements and rotations (right)

After determining and incorporating the corresponding shape functions, the element stiffness $[k]$ and mass $[m]$ matrices are defined for each element as:

$$[k]=\int_0^{l_e}b(x)\left[D_{11}(x)[N^M]^T[N^M]-N_x[N^d]^T[N^d]\right]dx \tag{5}$$

$$[m]=\int_0^{L}b(x)\left(\rho_pH_p+\rho_rH_r\right)[N^w]^T[N^w]dx \tag{6}$$

In which $[N^w]$is the shape function matrix and $[N^d]$ and $[N^M]$ are the first and second derivatives of $[N^w]$, respectively.

After assembly of global stiffness [K] and mass [M] matrices of the beam, the equation of motion transforms into:

$$\left[[K]-\omega^2[M]\right]\{u\}=0 \tag{7}$$

In which {u} is the matrix of nodal displacements and rotations in global coordinate system. The above equation is an eigenvalue problem and can be solved to determine the natural frequencies of the beam.

[a)] Corresponding author. Email: a_faz@encs.concordia.ca

NUMERICAL RESULTS AND DISCUSSION

A thickness- and width-tapered composite beam made of NCT-301 graphite-epoxy prepreg, and with $[0/90]_{9S}$ laminate configuration is considered. Different boundary conditions are considered as shown in Figure 2. The taper configuration considered is shown in Figure 3. A program is written using MATLAB to calculate the natural frequencies. In each step of the parametric study, one variable is considered while all other variables remain constant. As an example, free vibration response in terms of first natural frequency is determined and plotted against the width-ratio and length of the tapered section (or equivalently corresponding taper angle) for different boundary conditions, in Figure 4.

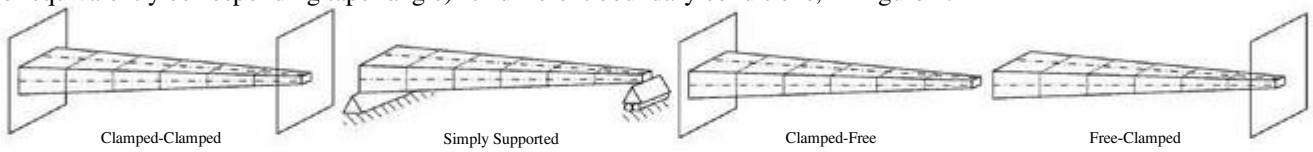

Figure 2 Boundary Conditions

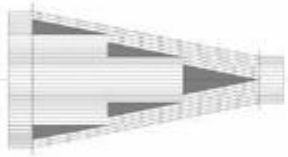

Figure 3 Taper Configuration D

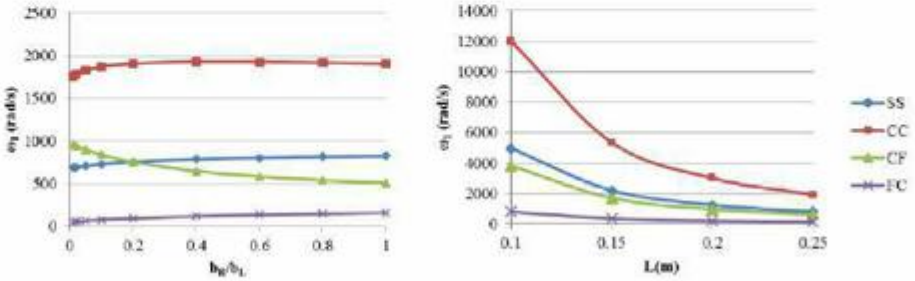

Figure 4 Effect of the width-ratio (left) and taper angle (right) on the fundamental natural frequency

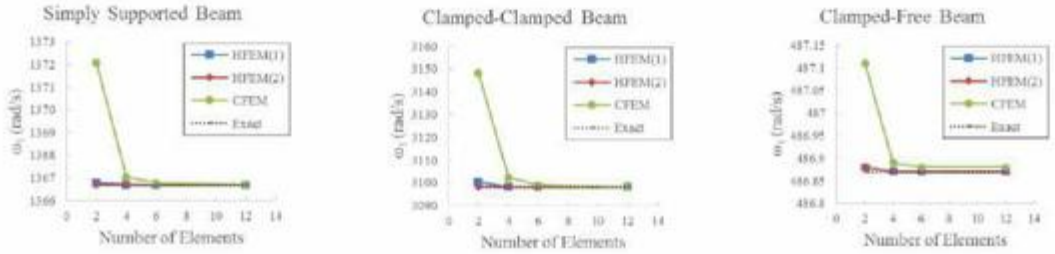

Figure 5 The comparison between results obtained using CFEM and HFEM

CONCLUSIONS

HFEM provides a better accuracy than Conventional FEM with less number of elements that will significantly reduce the time required for the computations and the stress/strain discontinuities across nodes. In addition, there is no significant difference between the results when the second hierarchical term is added, as it is shown in Figure 5. Moreover, a comparison with the results obtained using R-R (Rayleigh-Ritz method) [4] and a HOFEM (Higher-Order Finite Element Method) [5] is also shown in this figure. HFEM provides accurate results within 0.2% of difference from the above-mentioned methods, which is very acceptable. The order of magnitude of natural frequencies for different boundary conditions corresponds to the order: Clamped-Clamped (CC), Simply-Supported (SS), Clamped-Free (CF) and Free-Clamped (FC). By decreasing the length of the tapered beam (or equivalently increasing the thickness-taper angle), the natural frequencies increase dramatically. By increasing the width-ratio, the natural frequencies increase for SS, CC and FC boundary conditions but they decrease for the CF boundary condition because by increasing the width-ratio, the additional material on the free side of the beam results in the corresponding changes in the stiffness and mass of the beam and consequently, decrease in natural frequencies. Addition of damping results in reduction of the natural frequencies. The amount of reduction highly depends on the damping ratio (ξ).

References

[1] J.-M. Bertholet, Composite materials : mechanical behavior and structural analysis. New York: Springer, 1999.

[2] R. Ganesan and A. Zabihollah, "Vibration analysis of tapered composite beams using a higher-order finite element. Part I: Formulation," Composite Structures, vol. 77, pp. 306-318, 2007.

[3] J. N. Reddy, Mechanics of Laminated Composite Plates: Theory and Analysis: CRC Press, Inc., 1997.

[4] V. K. Badagi, "Dynamic response of width- and thickness-tapered composite beams using Rayleigh- Ritz method and modal testing," M.A.Sc. Thesis, Concordia University, 2012.

[5] P. Salajegheh, "Vibrations of Thickness-and-width Tapered Laminated Composite Beams with Rigid and Elastic Supports," M.A.Sc. Thesis, Concordia University, 2013.

ELECTROMECHNICAL BEHAVIORS OF MULTI-FILAMENT TWISTED SUPERCONDUCTING STRAND

Yuanwen Gao[1] &Xu Wang[1]
[1]*College of civil engineering and Mechanics, Lanzhou University, Lanzhou, China*

Summary The mechanical behaviours and electric properties of multi-filament twisted superconducting (SC) strands are investigated based on a 3D FEM model with consideration of damage of filament, the initial thermal residual stress, etc. The distribution of the damage of the filaments and its evolution and the movement of the neutral axis caused by it are studied and displayed in detail. Besides, the normalized critical current of SC strands under bending load is also calculated based on the invariant temperature and field strain functions. The non-negligible influences of the pitch length of the filaments on both the mechanical behaviors and the normalized critical current are discussed.

A MULTI-FILAMENT TWISTED FEM MODEL FOR SUPERCONDUCTING STRAND

As the basic structure generating the magnetic confinement for the fusion plasma in the International Thermonuclear Experimental Reactor (ITER), the strand works under strong magnetic field (12 T) and low temperature (4 K). Due to the current carried herein and the change of the temperature, the strand is always subjected to the bending (Lorentz force) and axial (thermal expansion) deformation, which will lead to the degradation of the superconductivity.

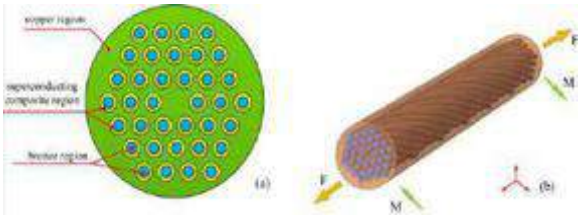

Fig.1 3D FEM model of multi-filament twisted strand

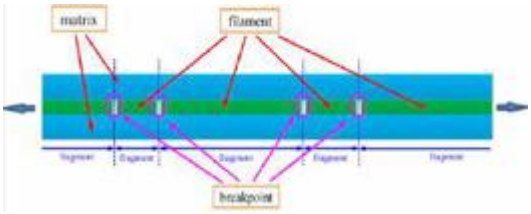

Fig.2 the RVE of superconducting filament bundle

In this study, a 3D multi-filament twisted FEM model is developed according to the real structure of the LMI strand, as shown in Fig.1. Some important factors, such as the initial thermal residual stress, the breakages of superconducting filament and twist pitch are taken into account. During the drawing and heat treatment of the superconducting strand, there exists a strong thermal residual stress system due to different thermal expansion properties of materials. We calculate this thermal residual stress system by the models of Mitchell [1] and Boso [2], and apply the results into the Multi-filament twist model. Due to the brittleness of superconducting filament, there will occur many breakages in superconducting filaments. For considering the influence damage of SC filament on the electromechanical behavior of SC strand, with the assumption that the deformation of a filament does not affect by other nearby filaments' stress state, we choose the representative volume element (RVE) as a concentric cylinder with a single filament in the matrix, as shown in Fig. 2. The radiuses of this filament and the RVE are determined according to their volume fraction and the number of the filaments in a bundle. Since the damage of the filament and its evolution are almost random, hence, we consider the distribution of the break points to be of a Weibull form. According to the model of Curtin and Zhou[3], the effective constitutive relation of this RVE can be obtained. So a 3D FEM model of SC strand is built, which can be used to calculate the electromechanical behaviors of strand.

MECHANICAL BEHAVIORS OF SUPERCONDUCTING STRAND

Figure 3a displays the computed transverse load-deflection curve of the strand and the comparison with the experiment and Nijhuis' model [4]. In this figure, the experimental data shows a nonlinear characteristics, which is not reflected in Nijhuis' model. While, the computed results for our model shows the nonlinear characteristics prominently, and more close to the experiment. The calculated axial stress-strain characteristics of the strand with every factor taken into consideration and the comparison with the experiment is also shown in Fig. 3b. From this figure we can see that the thermal residual stress in the strand has a significant impact on the tensile behavior of the strand, and when the strain is large, the influence of the damage of the filaments is obviously. From the comparisons with these two experiments in axial tension and bending respectively we can see that our model has good accuracy in the prediction of the mechanical behavior of the SC strand. In addition, in order to describe the fracture situation in the strand, a scalar variable $d = 1 - E_{unload} / E_{initial}$ is employed, the evolution of the damage of the filaments in the strand in the whole loading process is also calculated and discussed.

[a] Corresponding author. Email: ywgao@lzu.edu.cn

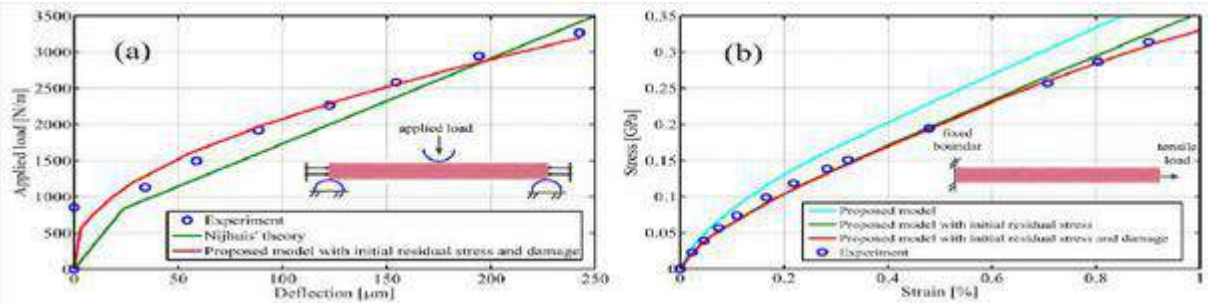

Fig.3 Comparison of the bending behaviors (a) and axial stress-strain characteristics (b) with experimental data

CALCULATION OF THE CRITICAL CURRENT OF SC STRAND

Due to the strong strain sensitivity of the superconducting material Nb_3Sn, the superconductivity of the strand is closely related with the mechanical properties of the strand. According to the scaling law [5], the critical current density of the filament depends on the magnetic field B , temperature T and strain ε . Our proposed model has the ability to predict the three-dimensional deformation of the materials in the strand, which can be used to calculate the critical current density of the strand with combining of the scaling law of critical current. The critical current of strand varies with the strain or bending moments for different pitch length are shown in Fig.4, The predicted results of critical current have a good agreement with the experimental data. The influence of the current transfer length, the pitch length of filaments, the movement of the neutral axis and the damage and its evolution of the filaments, are also investigated and discussed in this work, respectively.

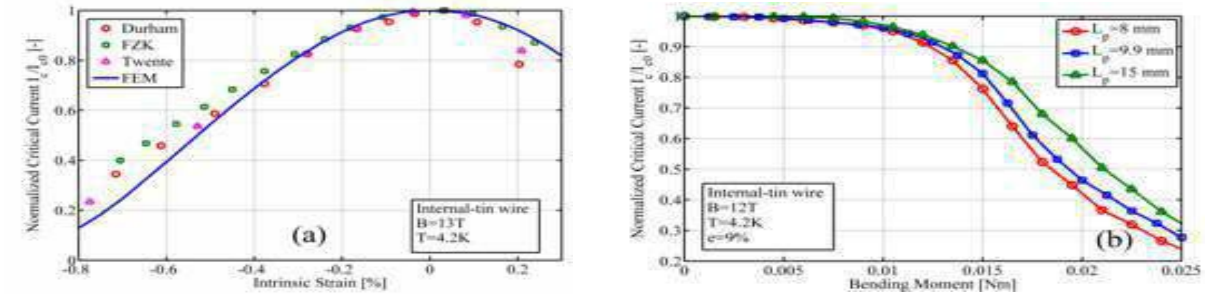

Fig.4 Comparison of the normalized critical current versus strain (a) and bending moments for different pitch length (b)

CONCLUSIONS

A 3D FEM model with the consideration of the helical structures of the filaments, the thermal residual stress in the strand and the damage of the filaments is proposed to investigate the electromechanical behavior of the multifilament twisted composite SC strand. The factors affecting the mechanical behavior of the strand are analyzed in detail. Comparison the simulations of tension and bending cases, it can be seen that in the bending case, different from the tension, the influence of the thermal residual stress is quite small and could be neglected, and the effect of the fracture of the filaments on the moment-angle characteristics of the strand is more significant. The critical current of the strand under axial and bending loads are calculated with the invariant temperature and field strain functions. Based on the results calculated by the proposed model, the results indicate that the damage and current transfer length in the strand have significant effects on the critical current. The calculated critical currents under tensile and bending load with every factor taken into consideration agree well with the experiments.

References

[1] Mitchell, N. : Finite element simulations of elasto-plastic processes in Nb_3Sn strands. *Cryogenics, 45*(7), 501-515, 2005

[2] Boso, D. P. : A simple and effective approach for thermo-mechanical modelling of composite superconducting wires. *Supercond Sci Technol, 26*(4), 045006,2013

[3] Curtin, W. A., & Zhou, S. J.: Influence of processing damage on performance of fiber-reinforced composites. *J Mech Phy Solids, 43*(3), 343-363, 1995

[4] Nijhuis, et al., : Spatial periodic bending and critical current of bronze and PIT Nb_3Sn strands in a steel tube. *IEEE Transactions on Applied Superconductivity, 17*(2), 2680-2683, 2007

[5] Taylor, D. M. J., Hampshire, D. P.: The scaling law for the strain dependence of the critical current density in Nb_3Sn superconducting wires. *Supercond Sci Technol, 18*(12), S241-S252.05, 2005

EFFECT OF ALUMIN TRIHYDRATE PARTICLE SIZE ON PHYSICAL AND MECHANICAL PROPERTIES OF VINYL ESTER MATRIX COMPOSITE

Rim Ouadday, Abderrahmen Kaabi, Rachid Boukhili & Aurelian Vadean
Department of Mechanical Engineering, Ecole Polytechnique de Montréal, Montréal, Canada,

Summary Alumina trihydrate (ATH) fillers are commonly used flame retardant for polymer composites because of its high performance in fire and its low cost. It is available in different particle sizes. This study aims to investigate the size effect of ATH particles on the properties of vinylester matrix composites. Five particle sizes of ATH fillers were used: 2, 4, 6, 8 and 12μm. The ATH fraction was maintained constant at 20% weight. This investigation reports the effect of alumina hydrate particle size on mixture viscosity, shrinkage, exotherm peak, gel time and the composite flexural properties were studied and discussed in this work.

INTRODUCTION

Using of fillers to improve or/and to modify the properties of polymer matrix composite is in full expansion. Alumina trihydrate (ATH) fillers are used for their flame retardant performance in serval sectors, as such army, aircraft and automotive [1, 2]. A lot of studies have been published about this subject [3-6]. While few studies were interested on their effect on mechanical proprieties of finished product (composite) and physical properties during manufacturing step (mixture). This work aims to understand the size effect of ATH fillers on thermal and rheology of mixtures with vinyl ester resin (VE). This study also addresses the issue of the mechanical properties of VE-ATH composites in bending.

EXPERIMENTAL METHOD

Five sizes of ATH particles (2, 4, 6, 8 and 12 μm) are designated for study the effect on physical, thermal and mechanical properties of the vinyl ester resin. ATH particles are gradually added to vinyl ester resin by mixing. The filler fraction presents 20% of total weight. The polymerization was realized in open casting mold at room temperature. Brookfield® viscometer, DV2T Model, was used for measure viscosity of mixtures. Furthermore, the temperature was recorded during polymerization by thermocouple which was fixed at the middle-thickness of the sample for determine gel-time and exotherm peak. The cured samples were tested in bending, in according to ASTM D790.

RESULTS AND DISCUSSION

The effect of ATH filler size on mixture viscosity is illustrated by figure 1. The measured viscosity of vinyl ester resin without ATH filler is 780 cPs, not shown in this figure. When 20% wt ATH is added to vinyl ester resin, the dynamic viscosity increases from 35 to 100%. This increase is distinctly pronounced for 2 and 4 μm particle sizes. The mixtures with ATH particle size is higher than 6 μm have almost similar viscosity which remains significantly higher than that of pure resin. The filler size affects greatly the viscosity and consequently the expended energy for mixture flow, especially the smaller sizes.

Figure 2-a shows temperature-time graphs during the polymerization of mixtures for various particle sizes. This graphs reveals that the filler particle size has an effect on the maximum temperature and time to the occurrence of this peak. Size is smaller, temperature-time curve moves up and right. i.e. the exothermic peak and the gel time increase together when the particle size increases, figure 2-b. This can be explained by the difference in specific area size. For the same weight, the small size particles have a larger specific area than larger size ones. Composites including a high specific area with the fillers have a higher heat exchange, which reduces its peak temperature during polymerization.
Figure 3 shows the effect of ATH particle size on calculated volume shrinkage of mixtures form measured linear shrinkage. The mixtures with smaller particle sizes have a lower volume shrinkage than those with higher particle size of fillers. For example the volume shrinkage jumps from 3.4% to 4.2% when 12 μm particles replace 2 μm particles. At most, the incorporation of ATH fillers in vinyl ester resin reduces its volume shrinkage, which is close to 5.7%.

The ATH incorporated vinyl ester composites were tested in three point bending. The effect of varying ATH size on ultimate flexural strength, flexural modulus and maximum strain is shown respectively by graph a, b and c of figure 4. Although the results are not perfectly conclusive, filler particle size seems does not significantly affect the modulus but its higher values can slightly increased the maximum strain and ultimate strength.

[a)] Corresponding author. Email: rim.ouadday@polymtl.ca.

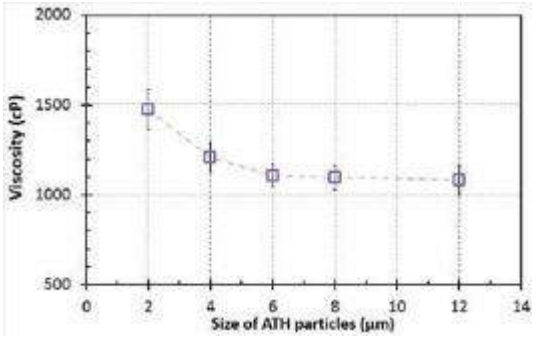

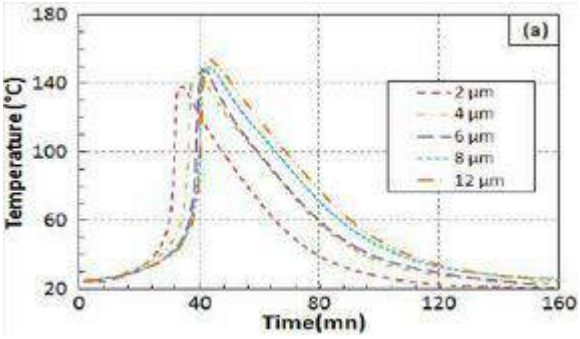

Fig.1: Effect of the ATH particle size on dynamic viscosity of vinyl ester mixture (wt: 20%)

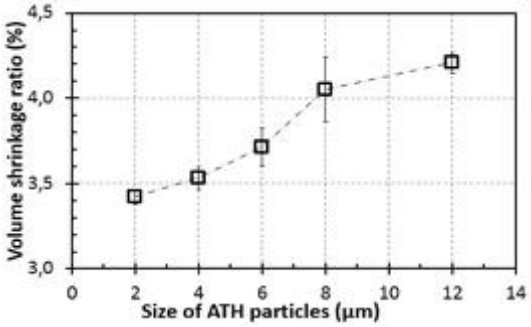

Fig.3: Effect of the ATH particle size on volume shrinkage of vinyl ester mixture (wt: 20%)

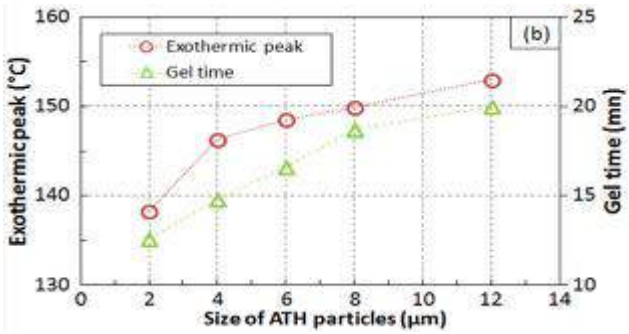

Fig.2: Effect of the ATH particle size on exotherm peak and gel time of vinyl ester mixture (wt: 20%)

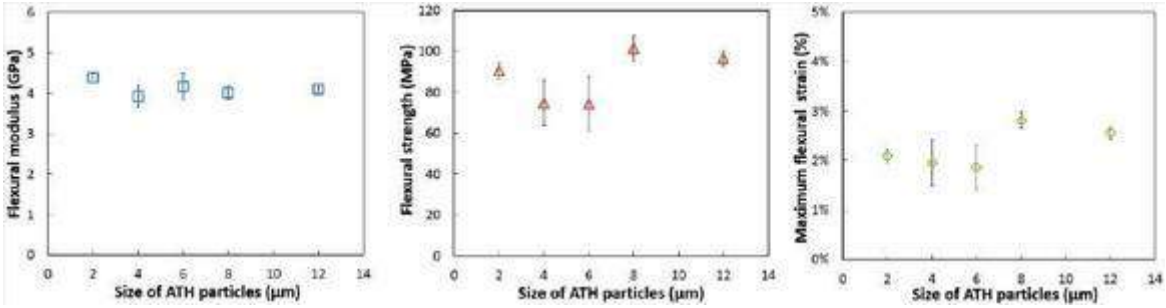

Fig.4: Effect of the ATH particle size on flexural modulus, ultimate strength and maximum strain of vinyl ester composites (20%wt)

CONCLUSIONS

This experimental study showed that the size of incorporated ATH fillers affect at different levels the physical and mechanical properties of vinyl ester resin. Increasing the size of ATH fillers reduces the mixture viscosity and the volume shrinkage, retards the polymerization reaction and grows the exothermic temperature. In bending, the modulus was not significantly changed, but the ultimate strength and the maximum strain are lightly varied in the same direction of filler size changing.

References

[1] H. S. Katz and J. Mileski, *Handbook of fillers for plastics*: Springer Science & Business Media, 1987.

[2] R. Rothon, *Particulate-filled polymer composites*: iSmithers Rapra Publishing, 2003.

[3] S. Zhang and A. R. Horrocks, "A review of flame retardant polypropylene fibres," *Progress in Polymer Science*, vol. 28, pp. 1517-1538, 2003.

[4] T. Tanaka, G. Montanari, and R. Mulhaupt, "Polymer nanocomposites as dielectrics and electrical insulation-perspectives for processing technologies, material characterization and future applications," *Dielectrics and Electrical Insulation, IEEE Transactions on*, vol. 11, pp. 763-784, 2004.

[5] I. Ramírez, E. Cherney, and S. Jarayam, "Silicone rubber and EPDM micro composites filled with silica and ATH," in *Electrical Insulation and Dielectric Phenomena (CEIDP), 2011 Annual Report Conference on*, 2011, pp. 20-23.

[6] D. O. Yener, O. Guiselin, and R. Bauer, "Applications of shaped nano alumina hydrate as barrier property enhancer in polymers," ed: Google Patents, 2013.

MORPHOLOGICAL PARAMETERS IMPACT ON THE PROPERTIES OF 3D COMPOSITE MATERIALS

Philippe Karamian-Surville[1], Vladimir Salnikov *[2], Sophie Lemaitre[1], and Daniel Choi[1]

[1]*Normandie Univ, France; UNICAEN, LMNO, F-14032 Caen, France ; CNRS, UMR 6139, F-14032,France*
[2]*University of Luxembourg, Mathematics Research Unit 6, rue Richard Coudenhove-Kalergi, L-1359 Luxembourg*

Summary The forecast of thermal and mechanical behavior for reinforced composites is a key issue for those studying these materials from numerical simulations. The effective thermal and mechanical properties are obtained from the microscale information. The periodic Lippmann-Schwinger equation is solved to obtain effective thermal conductivity tensor and the effective stiffness tensor. For electrical properties a novel approach based on connectivity graph analysisis is used. The representative volume elements (RVEs) are generated with a mixture of spherical, ellipsoidal and cylindrical inclusions, by the Random Sequential Adsorption scheme or the time driven Molecular Dynamics. This paper focuses on generating the RVEs and the study of their effective thermal, electrical and mechanical behavior of 3D representative volume elements (RVEs) of multiphased composite materials constituted by a matrix and inclusions randomly distributed with periodic boundaries. Various geometries of inclusions based on corrugated shapes, excavated and/or by removed pieces of inclusions are also considered.

RVE GEMERATION

In composite homogenization, the RVE generation including inclusions is a key stage and a real challenge especially with periodic boundary conditions. The generation scheme must be robust, reliable, fast and able to reach high volume fraction of inclusions. The RVE consists of a random mixture in 3D of inclusions which are spherical, ellipsoidal and cylindrical without intersection in a first state, and in a second state with variations on inclusions shapes. There are many works with ellipsoidal or spherical inclusions ([1], [2]) but the case with cylinders presents geometric difficulties that we have resolved and detailed in [3]. However, another key point is how to generate samples randomly. There are two families of generation algorithm: Random Sequential Adsorption (RSA) and Molecular Dynamics (MD). RSA is based on sequential addition of inclusion until there is no intersection with any other inclusion already inserted. This method generates RVEs with about 30% volume fraction and aspect ratio up to 18. For higher volume fraction and for high aspect ratio, this method can stuck and one prefers the second method based on molecular dynamics. MD consists in generating all inclusions and after moving them to the desired configuration using a time-driven version. This method allows the generation up to $50\% - 60\%$. For more details, the two algorithms are given in [4]. Our calculations have been made with both methods due to the choice of the morphology parameters. To illustrate the type of RVE used, we present two examples with a mixture of non intersecting spherical and cylindrical, spherical and ellipsoidal inclusions (Fig. 1 (a) and (b)). Concerning the inclusions with shape variations ([5]), we consider corrugated inclusions, or, we remove some pieces of inclusions (see the Fig. 1 (c) and (d)) after generating spheres and cylinders at the pixelization (or voxelization) step. For these RVEs, we have created inclusions with distorted shapes to compare their behaviour with the non distorted ones.

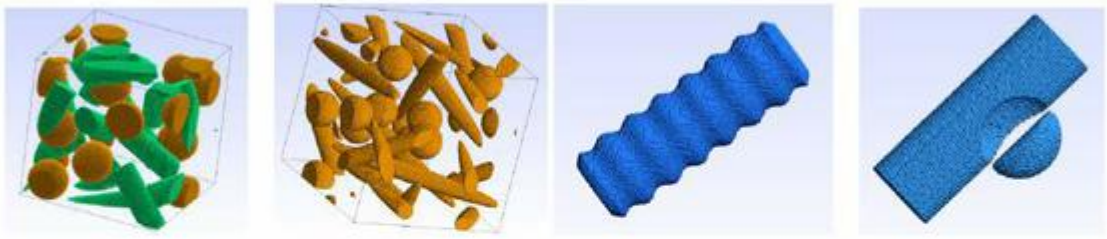

(a) Spheres and cylinders (b) Spheres and ellipsoids (c) First variation: corrugation (d) Second variation: broken piece

Figure 1: Tow examples of RVE and two types of variations studied

HOMOGENIZATION PROCESS

The global approach we focus on, is called 'stochastic homogenization'. In this approach, the classical deterministic homogenization techniques and procedures are used to compute the macroscopic parameters of a composite starting from its

*Philippe Karamian-Surville. philippe.karamian@unicaen.fr

microscopic properties. The stochastic part is due to averaging over some series of samples, and the fact that these samples fit into the concept of RVE (Representative Volume Element) in order to reduce the variance effect.

The homogenization procedure is chosen depending on the property we are interested in. For the mechanical and thermal behavior a scheme based on Fast Fourier Transform ([6], [7],[8])works perfectly well. For electrical properties we suggest a novel approach based on connectivity graph analysis. In all the three cases we compare the approaches with standard Finite Elements techniques. In some cases it is also possible to combine several approaches in order to optimize computational costs, for instance using the domain decomposition methods.

INFLUENCE OF PARAMENTERS

A statistical study has been conducted to determine the influence of morphological parameters. We describe the trends for λ_{app} versus the parameter studied. First, spherical inclusions (Fig. 2) and next cylindrical inclusions are considered. Fig. 2(a) exhibits the boxplots for each number of inclusion for the case $f_{sp} = f_{cyl} = 0.15$ and $contrast = 20\ \ 8$. The higher the number of inclusions is and less the repartition of λ_{app} seems increasing. We can also note that from 20 (20 cylinders and 20 spheres), the range of λ_{app} seems to be stable. Thus for the further computations, a number of 20 inclusions is considered.

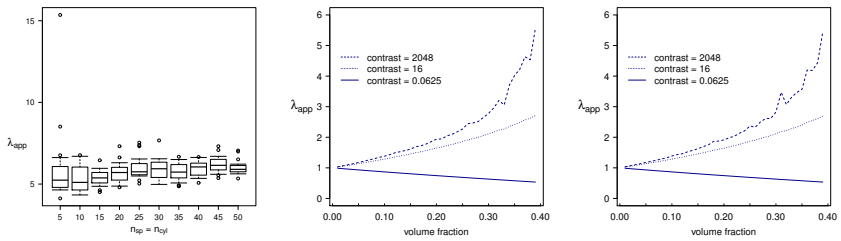

(a) $n_{sp} = n_{cyl}$ (b) $n_{sp} = 15$ (c) $n_{sp} = 2$

Figure 2: Dependence of thermal conductivity of a composite versus volume fraction of spherical inclusions, $n_{sp} = 15, 20$.

Fig. 2(b) and Fig. 2(c) also show that the trends are similar for 15, 20 spheres. λ_{app} increases non linearly for contrasts greater than 1 and decreases for contrasts smaller than 1. These effects are more pronounced for contrast greater than 1. Same conclusions more enhanced with adding the effect of the aspect ratio are observed. Similar phenomenon had been noticed for the mechanical properties in [3].

CONCLUSIONS

A wide range of RVE with numerous parameters (volume fraction of spheres or cylinders, number of spheres or cylinders, morphology of cylinders with their aspect ratio, the irregularities as the shape with corrugations or cuts of inclusions) is provided. For each generated RVE the mechanical, thermal and electrical behaviour for several values of contrast had been computed. An interesting database for inverse problems and statistical point of view is now available.

References

[1] J. Segurado, J. Llorca, A numerical approximation to the elastic properties of sphere-reinforced composites, Journal of the Mechanics and Physics of Solids, 50 (2002) 2107-2121

[2] E. Ghossein, M. Lévesque, A fully automated numerical tool for a comprehensive validation of homogenization models and its application to spherical particles reinforced composites, International Journal of Solids and Structures 49, (2012) 1387-1398

[3] V. Salnikov, S. Lemaitre, D. Choi, Ph. Karamian-Surville Measure of combined effects of morphological parameters of inclusions within composite materials via stochastic homogenization to determine effective mechanical properties, Composite Structures Volume 129 pp 122-131, October 2015

[4] V. Salnikov, D. Choi, Ph. Karamian-Surville On efficient and reliable stochastic generation of RVEs for analysis of composites within the framework of homogenization, Computational Mechanics, Volume 55, Issue 1, 2015.

[5] S. Lemaitre, V. Salnikov, D. Choi, P. Karamian Approche par la dynamique moléculaire pour la conception de VER 3D et variations autour de la pixellisation, accepted for publication in the proceedings of the CSMA 2015

[6] D.J. Eyre, G.W. Milton A fast numerical scheme for computing the response of composites using grid refinement, Journal of Physique III 1999; 6; 41-47

[7] H. Moulinec and P. Suquet, A fast numerical method for computing the linear and non linear properties of composites, C.R Acad. Sc. Paris II 318 (1994) 1417-1423

[8] J.C. Michel, H. Moulinec, P. Suquet A computational scheme for linar and non-linear composites with arbitrary phase contrast , Int. J. Numer. Meth. Engng. 2001; 52:139-160(DOI: 10.1002/nme.275)

STUDY ON FATIGUE CHARACTERISTICS OF HONEYCOMB SANDWICH PANELS

Tomohiro Maruta[1], Jianmei He[1]
[1]*Kogakuin University, Mechanical Engineering, 1-24-2, Nishi-shinjuku, Shinjuku-ku, Tokyo, Japan*

SUMMARY

Light-weight and high-strength honeycomb sandwich panels having aluminum honeycomb cores and CFRP (Carbon Fiber Reinforced Plastics) laminate faces are usually bonded by using two-liquid type epoxy resin-based adhesives with room-temperature curing to minimize thermal residual stresses. The purpose of this study is to establish experimental method for fatigue characteristics evaluation of such light-weight and high-strength honeycomb sandwich panels' bond structures. Bending fatigue experiments using the cantilever beam specimens of honeycomb sandwich panels under different bending deflections were carried out with improved experimental fixtures and the results are reported in this study.

INTRODUCTION

Light weight and high rigidity performances are very important in structural designs, especially remarkable for large structural designs satellite frame or radiators for space utilizations. Honeycomb sandwich panels [1] boned with light-weight honeycomb cores and high stiffness & strength FRP laminate faces are desired and becoming to be more and more used in many fields such as automobiles, ships, architect, and aerospace areas as shown in Fig.1.

Durability of adhesive bonded structures between honeycomb cores and FRP faces are very important for honeycomb sandwich panel constructions, while it is difficult to be evaluated successfully because of the preliminary fractures occurred at the honeycomb cores near the fixture with thick honeycomb sandwich panels [2],[3]. The purpose of this study is to establish the appropriate experimental method for fatigue characteristics evaluation of such light-weight and high-strength honeycomb sandwich panels' bond structures.



Fig.1 Sample applications of honeycomb sandwich panels

HONEYCOMB SANDWICH PANELS INTRODUCED FOR EXPERIMENTAL INVESTIGATIONS

In this study, honeycomb sandwich panel specimens constructed from commercial CFRP laminate and aluminium honeycomb cores are bonded using two-liquid type epoxy adhesive for bending fatigue experiments as shown in Fig.2. 1.0mm thick CFRP laminates and aluminium honeycomb cores with 30.0mm height, 0.001inch foil thickness and 1/4inch cell size are introduced for the panel specimens. The specimen shape and size are also shown in Fig.3.

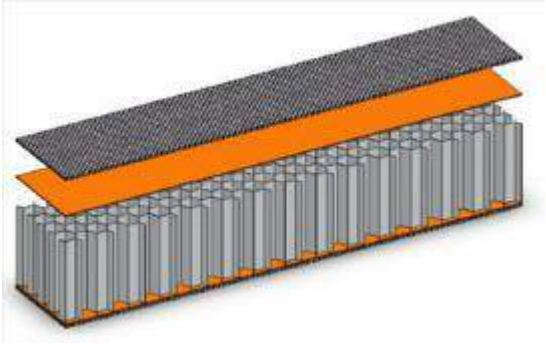

Fig.2 Honeycomb sandwich panel specimen for bending fatigue experiments

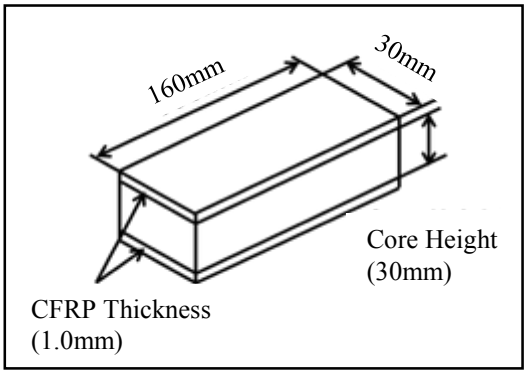

Fig.3 Size of panel specimen

[a] Corresponding author. Email: am15059@ns.kogakuin.ac.jp

CANTILEVER BEAM FATIGUE TESTS OF HONEYCOMB SANDWICH PANELS

Bending fatigue tests of the cantilever beam with 1.0mm, 2.0mm and 3.0mm deflections are carried out for the honeycomb sandwich panel specimen with 10^6 cyclic numbers. The testing instrument and specimen configurations are basically along the ASTM D 671-63 T standard (Standard Test Method for Flexural Fatigue of Plastics by Constant-Amplitude-of-Force) and shown in Fig.4 and Fig.5. Because this test machine configuration is originally used to evaluate the bending fatigue properties of thin plates, special testing fixtures are designed for the thick honeycomb sandwich panel's application. Strain gauges are used to monitor the panel face's strain responding near the fixture and linear gauge is introduced to figure out the zero bending deflection position of the specimens.

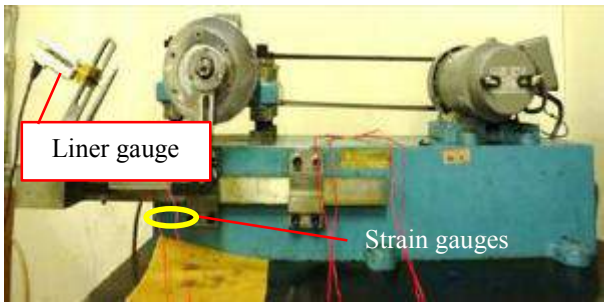

Fig.4 Bending fatigue test configurations

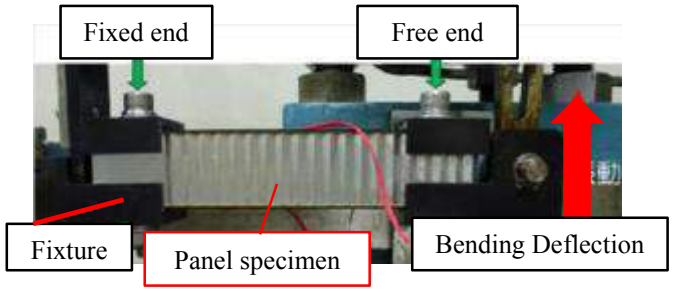

Fig.5 Cantilever beam's bending

In this study, improvement on specimen preparations and fixture are carried out to solve the problems occurred in our past investigations. Holes are created on the panel specimens for bolt fixations and this perhaps the main reason of causing the preliminary fractures of honeycomb cores near the fixture. To solve this problem, it is considered necessary to make holes gradually with a plurality of cutting drills to mitigate damage to the specimen in drilling as hole-drilling technique improvement. Another problem is that the bending deflection loadings are not applied along the center line of panel's height because of the fixture configurations and then stress concentrations on one side of the panel becomes more severe and cause the preliminary buckling or breaking of honeycomb cores [4]. New fixtures and spacers are introduced to improve this problem. The large strain data obtained from the fatigue testing are manipulated using DIAdem2011 software and Fig.6 shows the sample strain date from the bending fatigue test of honeycomb sandwich panel. Horizontal axis represents the number of loading cycle and vertical axis represents the strains obtained from the strain gauges.

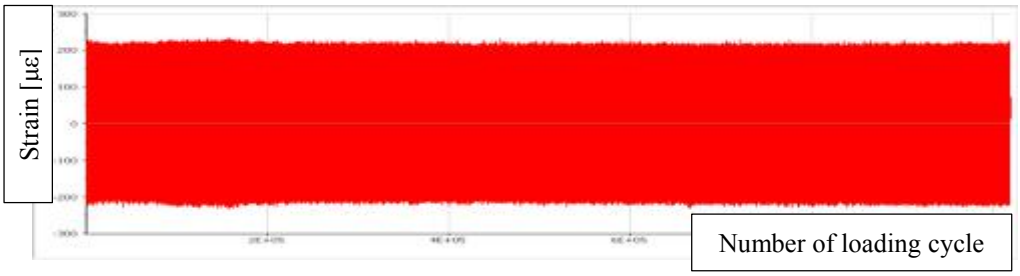

Fig.6 Sample bending fatigue test result（1.0bending deflection）

CONCLUSIONS

Based on the improved fixtures and specimen preparation, strain data obtained from the bending fatigue experiments show that the bending deflection loading are almost applied on the centre line and the fractures at honeycomb cores near fixture are become very small. Because small fractures on honeycomb cores near the fixture end are still observed, fixation method of honeycomb sandwich panels using bolts have to be instead to avoid the hole-drilling on specimens and then further improvements on the experimental configurations are needed to be done in future study.

References

[1] Sentanzairyougizyutukyoukai ed.,: Hanikamukouzouzairyou No Ouyou－(Application of Honeycomb Structure Materials－). CMC, 2002

[2] Nihonzairyougakkai ed.,: Sentanzairyousiri-zu Hakai To Zairyou – (Tip Materials Series Destruction and Materials-). Shoukabou

[3] Kokubo Kunio , Gotou Yoshiki , Mori Takao , Tateno Masayoshi eds,.: zairyourikigaku-(Strength of Materials-). Maruzen Co. Ltd

[4] T. Mitsui and J. He, Experimental Investigation on Fatigue Performance of Light-weight Honeycomb Sandwich Panels, The 5th TSME International Conference on Mechanical Engineering, AMM019, 2014/12

EXTREME ELASTIC ANISOTROPY OF COMPOSITES WITH PERIODIC STRUCTURE

George Mejak *[1]

[1]*Faculty of Mathematics and Physics, University of Ljubljana, Ljubljana, Slovenia*

Summary Extreme elastic anisotropy of composites with periodic microstructure is studied. After reviewing anisotropy measures attention is paid to the computation of the effective elastic properties. Two method are considered, the asymptotic homogenization and the averaging approach based on the equivalent inclusion method. Pro and cons of the methods are underlined. Numerical results are given for the glass epoxy composites with spherical or cubical inclusions. It is found that the anisotropy of cubic structures with a spherical inclusion monotonically increases with the volume fraction. For cubic structures with a cubic inclusion the maximal anisotropy is computed at intermediate values.

INTRODUCTION

Composites with periodic microstructure are intrinsically anisotropic. Usually they are tailored by structural strength, weight or thermal requirements with little attention paid to their elastic anisotropicity. However, anisotropy is of great importance in many applications such as dislocation dynamics, phase transformation, wave propagation and geophysical science to name but a few. The anisotropy depends upon the constituents of the composite, their geometric arrangements within the unit cell and their volume fractions. To focus presentation, only two phase composites with a centered single spherical or cuboidal heterogeneity within the cuboidal unit cell is considered in the paper. In particular, variation of the anisotropy with respect to the volume fraction is studied in details.

ANISOTROPIC MEASURES

In the literature several measures of the elastic anisotropy are known, such as universal elastic anisotropy index A_{U}, Ledbetter-Migliori anisotropy index A_* or the Zener anisotropy index A, [1]. For composites the indices A_{U} and A are determined on the basis of the effective/homogenized elasticity tensor. On the other hand, A_* is given as the square of the ratio of the maximal over minimal shear sound wave velocities among all propagation directions. However, within the long wave length approximation it can be also determined using the effective elasticity tensor. For the cubic symmetry $A_{\mathrm{U}} = \frac{6}{5}\left(\sqrt{A_*}\nearrow 1/\sqrt{A_*}\right)^2 = \frac{6}{5}\left(\sqrt{A}\nearrow 1/\sqrt{A}\right)^2$ and therefore all three anisotropy measures, although of different magnitude, are simultaneously extremal as the functions of the volume fraction f. Since $A_{\mathrm{U}} \geq 0$ and A_{U} is zero for the isotropic material, extremum of interest is the maximum. Assuming that the matrix phase is isotropic, it follows that $A_{\mathrm{U}}(f = 0) = 0$ and thus the maximum is either attained at the maximal volume fraction f_{max} or at some intermediate value, with the latter case of particular interest. For the simple cubic microstructure with an isotropic cuboidal inclusion the intermediate case always occurs as $A_{\mathrm{U}}(f_{max}) = 0$.

DETERMINATION OF THE ELASTICITY TENSOR OF THE COMPOSITE

Since the material has a periodic microstructure its effective elasticity tensor can be determined either using the asymptotic homogenization method or the averaging approach based on the equivalent inclusion method. Each one has its own merits and shortcomings; the former one can handle quite general inclusion shapes and all elastic symmetries while the latter is restricted only to some simple shapes. However, the first one is computationally more involved, to find the effective tensor a system of partial differential equations must be solved and this can be done only numerically. On the other hand, the equivalent inclusion method, with some further approximation on the nature of the inclusion eigenstrain, allows determination of the effective tensor in a symbolic form. Mastering both approaches, the plan is obvious. The symbolic computation is used to qualitatively assess variation of the anisotropy with respect to the volume fraction while the numerical solution is used to validate the result and further improve its accuracy.

Asymptotic homogenization

It is well known [2] that the effective tensor is given by $C^{\mathrm{eff}}_{ijkh} = \langle C_{ijkh}\rangle \nearrow \left\langle C_{ijlm}e_{lm}(\underline{\chi}_{kh})\right\rangle$ where $\underline{\chi}_{kh}$ are solutions of the auxiliary boundary value problems(BVP) with periodic boundary conditions. These are solved using the finite element method(FEM). Since anisotropy is the key issue, the FEM mesh must fully respect the symmetry of the problem. For problems with the cubic symmetry this is accomplished by rewriting the problem as the BVP with Dirichlet boundary conditions on

*Corresponding author. Email: george.mejak@fmf.uni-lj.si

the first octant of the unit cell. To retain the cubic symmetry, the octant is discretizied in such a way that the mesh has a three fold symmetry around the body diagonal of the octant. To the best author's knowledge this is a novel approach. Using the symmetric FEM mesh determination of the effective elasticity tensor readily follows. The mesh obviously depends upon the volume fraction f. However, by the very nature of the FEM dicretization this dependence is not globally continuous and thus the variation of the anisotropy can be studied only locally. Of course, a global picture can be obtained by tabulating the anisotropy index for different values of f or, alternatively, more efficiently by the approximation based on the equivalent inclusion method.

Equivalent inclusion method

Determination of the effective elasticity tensor by the equivalent inclusion method(EIM) is possible only for inclusions with a known closed form of the Eshelby tensor. A crucial step in using EIM is how to determine the equivalent eigenstrain. In the paper the approach from [3] is used and further generalized to quadratic eigenstrains and the Fourier approximation of the Eshelby tensor of a cuboidal inclusion. It was found that in the case of spherical inclusions quadratic eigenstrains give much better results than the radial approximation. On the other hand, a piecewise constant eigenstrain approximation is preferable in the case of cuboidal inclusions.

RESULTS

Here we present results for the glass epoxy composite with $E_{\mathrm{i}} = 3$GPa, $\nu_{\mathrm{i}} = 0.35$ and $E_{\mathrm{m}} = \ 0$GPa, $\nu_{\mathrm{i}} = 0.2$ for the matrix and inclusion phase, respectively. First we compare simple cubic, body centered and face centered cubic structures with spherical inclusions. It was found that for all three structures A_{U} is monotonically increasing with a maximal value at the close-packing fraction f_{max}. The estimated maximal values of A_{U} for SC, BCC and FCC structures are $0.\ , 0.15$ and 0.25. The values are only approximate because the EIM for spherical inclusions with quadratic eigenstrains is reliably only up to 90% of f_{max}. Also, at f_{max} FEM mesh is essentially singular.

Next we consider a simple cubic structure with a cubic inclusion. Comparing FEM and EIM results it was surprisingly found that the EIM with a constant eigenstrain gives qualitatively correct results for all values of f and that the relative error is more pronounced for small and medium values of f than for large values, see Fig. 1. The comparison is further improved with a piecewise constant eigenstrain approximation. With the maximal A_{U} are closely associated extreme Poisson's ratios. Although, extreme Poisson's ratios are significantly different from the Poisson's ratios of the phases, it was found that composites with periodic cubic inclusions are never auxetics unless the phases are already auxetics. We note also that the maximal A_{U} is much smaller for composites with a stiff matrix and soft inclusion.

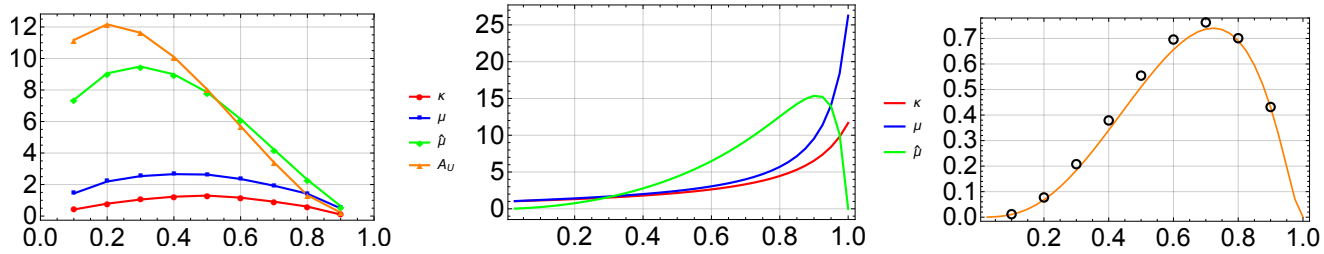

Figure 1: Relative error in % of the EIM approximation with 64 piecewise constant eigenstrains, effective bulk and shear moduli and A_{U} with respect to f. In the rightmost figure comparison between FEM and EIM for A_{U} is given.

CONCLUSIONS

It is shown that the asymptotic homogenization and the averaging method based on the EIM give the same effective elastic properties. Using a simple eigenstrain approximation effective elastic properties can be determined by symbolic computation and this enables a quick consideration of a variety of potential interesting material configurations. Once a promising configuration is found, asymptotic FEM computation is called upon to refine accuracy of the results. This approach is exemplified by determination of the extreme elastic anisotropy of composites.

References

[1] Ranganathan S.I., Ostoja-Starzewski M.: Universal Elastic Anisotropy Index, Phys. Rev. Lett. 101, 055504, 2008.

[2] Cioranescu D., Donato P.: An Introduction to Homogenization, Oxford UP, 1999.

[3] Mejak G.: Variational formulation of the equivalent eigenstrain method with an application to a problem with radial eigenstrains. Int. J. Solids Struct. 51: 1601-1616, 2014.

RVE SIZE ESTIMATES FOR ELASTIC MATRICES WITH SPHERICALLY MULTI-LAYER INCLUSIONS

Ilaria Monetto[1]
[1]*Department of Civil, Chemical and Environmental Engineering, University of Genoa, Genoa, Italy*

Summary A micromechanics-based nonlocal constitutive equation for a matrix containing a random distribution of homogeneous solid spheres is employed to analyze the case of spherically multi-layer inhomogeneous inclusions. The analysis builds on and generalizes previous papers focused on two-phase composites. In particular, it is shown how the task of the derivation of elastic properties for the inclusion phase can be make reasonable by replacing inhomogeneous inclusions with homogeneous spheres having equivalent elastic moduli. The constitutive equation is then used to explore nonlocal effects of layer distribution in the inclusions on the response of the composite material and derive quantitative estimates of the minimum RVE size over which a nonlocal correction to the standard local model is needed to provide a sensible description of the constitutive response of the material.

INTRODUCTION

Within the mathematical modeling of the mechanical behavior of elastic composites, classical approaches usually treat the material as being macroscopically homogeneous with constant overall properties and develop constitutive equations relating suitable averages of microscopic stress and strain fields over a Representative Volume Element (RVE). As well known, the accuracy of the related local constitutive equations depends on how large RVE, compared to the characteristic microstructural length of the material, is. A more comprehensive knowledge of nonlocal effects due to microstructure on the constitutive response of the composite requires a comparison with a nonlocal constitutive law.

NONLOCAL MODELING OF TWO-PHASE ELASTIC COMPOSITES

The formulation of nonlocal modeling of interest here was that first developed by Drugan and Willis [1] and then generalized by Monetto and Drugan [2-3]. Employing a generalization of the Hashin-Shtrikman variational formulation, these authors developed a micromechanics-based nonlocal constitutive equation relating the ensemble averages of stress and strain for random linear elastic composite materials. With reference to two-phase composites under the assumptions of statistical uniformity and ergodicity, a nonlocal constitutive equation was derived in closed form for an isotropic homogeneous matrix containing isotropic homogeneous inclusions and presenting macroscopically an either isotropic or transversely-isotropic behavior. The microstructure was described statistically by using up through two-point correlation functions. Nonlocal terms up through the second gradient of ensemble-averaged strain were included. In particular, completely explicit results were obtained for non-overlapping identical spheres [1-2] and spheroids with fixed or random orientation [2-3].

The final constitutive equation has the form:

$$\langle \boldsymbol{\sigma} \rangle(\mathbf{x}) = \mathbf{L}^{(0)} \langle \mathbf{e} \rangle(\mathbf{x}) + \mathbf{L}^{(1)}_{mn} \frac{\partial^2 \langle \mathbf{e} \rangle(\mathbf{x})}{\partial x_m \partial x_n} \tag{1}$$

where angle brackets denote ensemble average; $\boldsymbol{\sigma}$ and $\mathbf{e}$ are the stress and infinitesimal strain tensors; $\mathbf{x}$ is the position vector; $\mathbf{L}^{(0)}$ is the local fourth-order tensor of effective elastic moduli and $\mathbf{L}^{(1)}$ is a sixth-order tensor of nonlocal correction to the standard constant-effective-modulus constitutive model. The detailed forms of $\mathbf{L}^{(0)}$ and $\mathbf{L}^{(1)}$ can be found in the references just cited. Here, it is of interest to recall only that their components depend on the elastic properties of the two (matrix and inclusions) phases and on the volume concentration, shape and size of the inclusions.

The main goal of the present paper is to show how to employ this nonlocal constitutive equation to model the response of multi-phase composites treated as a wider class of two-phase composites containing inhomogeneous inclusions and analyze the nonlocal effects of such specific internal microstructure on the effective properties of the composite.

MODEL OF IMPENETRABLE INHOMOGENEOUS INCLUSIONS

The model of impenetrable inclusions considered here consists of nonoverlapping identical spheres with a homogeneous core surrounded by firmly bonded concentric spherical shells of different homogeneous material. These can correspond to multi-phase inclusions made up of two or more different materials, as well as homogeneous inclusions with a sufficiently thick coating surrounding them at the interface with the matrix.

In order to employ previous explicit definitions of local and nonlocal tensors, inhomogeneous spheres are replaced by equivalent homogeneous ones. The shear and bulk moduli of such equivalent spheres are then evaluated as suitable averages of bulk and shear moduli of all inclusion phases using thicknesses of the shells as weighting.

[a] Corresponding author. Email: ilaria.monetto@unige.it.

RESULTS AND CONCLUSIONS

As a generalization of previous results, the micromechanics-based nonlocal constitutive equation derived for two-phase composites in [1-3] is employed to analyze matrices containing a random distribution of spherically multi-layer inclusions. It is shown how the task of the derivation of elastic properties for the inclusion phase can be make reasonable by replacing spherically multi-layer inclusions with homogeneous ones having equivalent elastic moduli.

The constitutive model described is then employed to derive quantitative estimates of the characteristic internal length of the random composite under consideration, defined as the minimum RVE size over which a nonlocal correction to the standard local model is needed to provide a sensible description of the constitutive response of the material. In order to do this, ensemble-averaged strain fields sinusoidally-varying with position are considered and the wavelengths of the variation at which the nonlocal correction to the local term in Eq. (1) is not negligible are determined.

These estimates permit one to draw interesting conclusions about the effects of layer distribution in the inclusions on the nonlocal response of the composite material.

As an example, thin hollow inclusions show longer-range nonlocal effects than thick hollow inclusions. Furthermore, the minimum RVE size of coated solid spheres is smaller for thin coating than for thick coating.

References

[1] Drugan W.J., Willis J.R.: A micromechanics-based nonlocal constitutive equation and estimates of representative volume element size for elastic composites. *J. Mech Phys Solids* **44**:497-524, 1996.

[2] Monetto I., Drugan W.J.: A micromechanics - based nonlocal constitutive equation for elastic composites containing randomly-oriented spheroidal heterogeneities. *J. Mech Phys Solids* **52**:359-393, 2004.

[3] Monetto I., Drugan W.J.: A micromechanics - based nonlocal constitutive equation for elastic composites containing aligned spheroidal heterogeneities. *J. Mech Phys Solids* **57**:1578-1595, 2009.

EFFECT OF ATH CONCENTRATION ON PHYSICAL AND MECHANICAL PROPERTIES OF VINYLESTER/ALUMIN TRIHYDRATE COMPOSITE

Rim Ouadday, Abderrahmen Kaabi, Rachid Boukhili & Aurelian Vadean
Department of Mechanical Engineering, Ecole Polytechnique de Montréal, Montréal, Canada,

Summary: Aluminum trihydrate (ATH) is mostly incorporated into polymer composite to make the flame retardant. Improving the flame retardant properties of these composites have been studied and published in the literature, but ATH effect on the mechanical strength, thermal and physical properties have not been thoroughly addressed. This investigation reports the effect of alumina thrihydrate (ATH) particles on the physical and mechanical properties of ATH filled vinyl ester casting. The bending properties, viscosity, shrinkage, exothermic peak and gel-time were explored and discussed.

INTRODUCTION

Casting made of thermoset resins (Epoxy, unsaturated Polyester, vinylester, etc.) are used as core materials for sandwich structures were high compressive properties of the core are required as for applications in civil, electric and marine engineering [1, 2]. For some applications requiring thick cores, the cure of large amount of thermoset resins lead to unacceptable exothermic temperature peaks. Non-organic fillers are added to the casting formulation to control the peak temperature and shrinkage properties as well as other physical and mechanical properties [3, 4]. Among the numerous available inorganic fillers, aluminum trihydrate (ATH) is a well-known low cost flame retarder and smoke suppressor and these aspects are well documented in the open literature [5-7]. However, the effect of ATH on the mechanical, thermal and physical properties in thermoset plastics has received less attention. This investigation reports the effect of alumina thrihydrate (ATH) particles on the physical and mechanical properties of ATH filled vinyl ester casting.

EXPERIMENTAL METHOD

- **Preparing samples**

To understand the effect of ATH concentration on the physical, thermal and mechanical properties of vinyl ester resin, five composites with different ATH fractions were prepared (10, 20, 30, 40 and 50% of total weight). The polymerization occurs in open casting mold at room temperature. The size of ATH fillers is 2 µm.

- **Physical, thermal and mechanical tests**

Viscosity: the viscosity of pure vinyl ester resin and that of ATH incorporated composite was measured during the polymerization, by Brookfield® viscometer, Model DV2T. This property is an important factor for manufacturing technique.

Exothermal: The time-temperature evolution was recorded during polymerization in mid-thickness of the sample, using thermocouples (K).

Three point bending flexural test: The samples were manufactured by specific mold adapted for bending test, in according to ASTM D790, and afterwards cut to the desired thickness.

RESULTS AND DISCUSSION

Figure 1 shows the effect of ATH fraction on viscosity of vinyl ester. The mixture viscosity is solely influenced by ATH fraction. When the ATH fraction increases from 10 to 50%, the viscosity jumps from 1.2 times higher to 47 times higher than that of vinylester (≈ 780 cPs). The relationship between filler fraction and viscosity is non-linear.

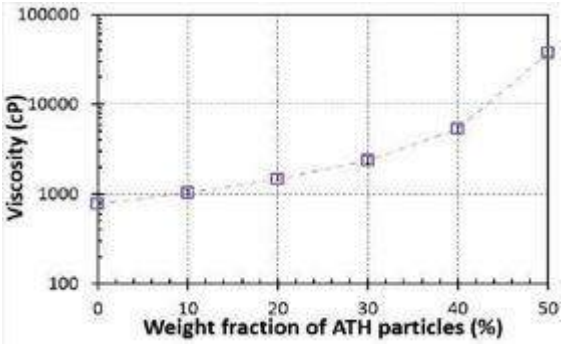

Fig.1: Effect of ATH weight fraction on dynamic viscosity of vinyl ester mixture

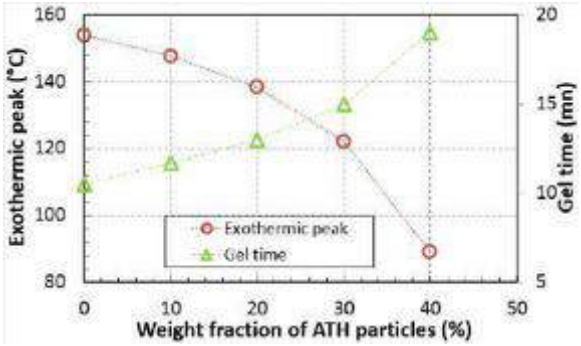

Fig.2: Effect of ATH weight fraction on Gel-time and Exothermic peak of vinyl ester

[a] Corresponding author. Email: rim.ouadday@polymtl.ca.

The Figure 2.a reveals that ATH fraction changes two parameters at least: the temperature at exothermic-peak and gel-time. Indeed, when ATH fraction increases, the reaction is delayed and the exotherm-peak temperature decreases. This effect is mainly due to the decreasing of resin quantity in sample, and secondly by the thermal effect of fillers which act as local micro-heat sink. Consequently ATH particles restrict the speed of polymerization reaction progress.

Vinyl ester has a volume shrink close to 5.7%. Figure 3 shows the effect of ATH particles on volume shrinkage ratio of vinyl ester resin. When filler concentration increases from 10 to 50%, the volume shrinkage falls from 4.1% to 0.75%. This effect can be explained by two reasons: the first is related to the decreasing of temperature gradient during polymerization and the second is explained by the lower coefficient of thermal expansion (CTE) of ATH.
The VE/ATH composites present a brittle behavior, which is characterized by rupture without any noticeable prior change in the rate of elongation, figure 4. However, the ATH particles contribute on improvement of rigidity of the material. Figure 5 shows the effect of ATH fraction on flexural properties of ATH-VE composites. When the ATH fraction increases, flexural modulus increases, but the ultimate flexural strength and maximum strain decline.

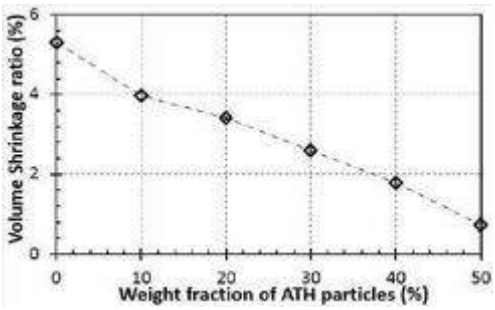

Fig.3: Effect of ATH weight fraction on volume shrinkage ration of Vinyl ester composites

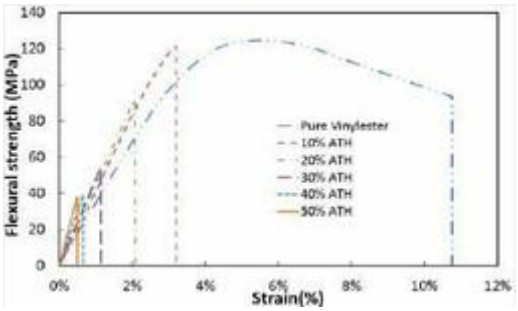

Fig.4: Effect of ATH weight fraction on flexural behaviors of Vinyl ester composites

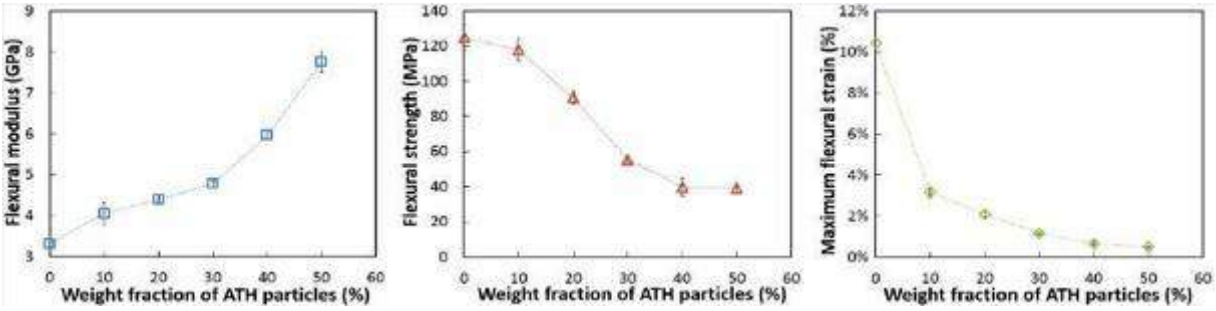

Fig.5: Effect of ATH weight fraction on flexural modulus, ultimate strength and maximum strain

CONCLUSION

According to all the results of this experimental study, ATH fillers affect the mechanical and physical properties of vinyl ester matrix composites. ATH increases viscosity, retards polymerization reaction, and decreases exothermic temperature. Furthermore, ultimate bending strength and the maximum flexural strain decrease when ATH concentration increases. While the flexural modulus increases proportionally to the ATH concentration. This research has shown that if the incorporation of ATH fillers improves composite flame performance, as demonstrated in the literature, this is can be associate to significant processability difficulties and substantial mechanical performance modifications.

References

[1] J. K. Pandey, K. R. Reddy, A. P. Kumar, and R. Singh, "An overview on the degradability of polymer nanocomposites," *Polymer degradation and stability*, vol. 88, pp. 234-250, 2005.

[2] R. Rothon, *Particulate-filled polymer composites*: iSmithers Rapra Publishing, 2003.

[3] H. S. Katz and J. Mileski, *Handbook of fillers for plastics*: Springer Science & Business Media, 1987.

[4] N. Gupta, B. S. Brar, and E. Woldesenbet, "Effect of filler addition on the compressive and impact properties of glass fibre reinforced epoxy," *Bulletin of Materials Science*, vol. 24, pp. 219-223, 2001.

[5] S. Zhang and A. R. Horrocks, "A review of flame retardant polypropylene fibres," *Progress in Polymer Science*, vol. 28, pp. 1517-1538, 2003.

[6] I. Ramírez, E. Cherney, and S. Jarayam, "Silicone rubber and EPDM micro composites filled with silica and ATH," in *Electrical Insulation and Dielectric Phenomena (CEIDP), 2011 Annual Report Conference on*, 2011, pp. 20-23.

[7] D. O. Yener, O. Guiselin, and R. Bauer, "Applications of shaped nano alumina hydrate as barrier property enhancer in polymers," ed: Google Patents, 2013.

ANALYTICAL STUDIES ON LAMELLAR-STRUCTURED COMPOSITES MADE BY FREEZE-CASTING

Sina Askarinejad[1] and Nima Rahbar *[2]

[1]*Department of Mechanical Engineering, Worcester Polytechnic Institute, Worcester, MA*
[2]*Department of Civil and Environmental Engineering, Worcester Polytechnic Institute, Worcester, MA*

Summary Previous studies on mechanical performance of natural multilayered materials such as nacre show that their outstanding properties are direct results of the nanoscale features and the optimized arrangement of the elements. One of the most effective methods to fabricate multilayered composites inspired by nacre, is "freeze casting". The lamellar-structured samples made by this method show interesting behavior. In this study first alumina/PDMS and Alumina/PU composites were made and tested and then analytical solutions for effective properties of lamellar-structured composites were developed. Analytical verification of all suggested deformation and toughening mechanisms is explored. The experimental results are in an excellent agreement with the analytical model. Detailed relationships are presented to identify future directions for material development.

INTRODUCTION

Optimized structure and properties of natural composites make them a strong source of inspiration. Many researchers studied the relation between structure and mechanical performance of natural composites such as nacre [1, 2] and bamboo [3] as well as other artificial structural composites [4, 5]. Nacre is a natural composite made of 95 % brittle aragonite platelets [6] and only 5 % biological macromolecules which has an important effect on nacre's fracture resistance [7]. Many studies show the important role of organic matrix in mechanical response of nacre, hence there is a great need to investigate more mechanics-based details [8], [9]. Shuchun and Yueguang (2007) [10] used shear-lag model to study the interdependence of the overall elastic modulus and number of hierarchical levels in bone-like materials. There are other analytical approaches to study the structure of nacre [11]. There are different experimental approach to make structural materials similar to nacre [12]. Among them, freeze casting is one of the most efficient methods to make macroscale samples with micro and nano structure.

MATERIALS AND METHODS

Freeze-casting which is templating of porous ceramic scaffolds by the solidification of a solvent, was used in this study. Lamellar alumina scaffolds were prepared by freeze-casting water-based suspensions. PDMS and PU was infiltrated into the sintered porous structure. In order to discuss the effective properties of the multilayered composite, the balance of forces for the components of its unit-cell following by period boundary condition should be applied. Hence, the shear-lag theory employed on a simplified 2D unit-cell was taken into consideration.
considering the layers with even numbers as the stiff layers and $P_{I,\infty}$ is the far field or steady state tensile stresses in each layer when there are no shear stress boundary conditions; in other words, the tensile forces in the layers under constant axial stress far away from any end or from any discontinuities or breaks in any layers.The idealized composite geometry is shown in Fig. 2. The wallpaper symmetry group is pmm, with two bricks per unit cell, which are separated by one brick height vertically, and shifted by s horizontally. It assumed that the components deform only in the x-direction (the arrangement of the bricks in the through-thickness direction does not factor into the response).

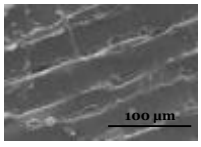

Figure 1: SEM image of lamellar-structured composite after PDMS infiltration.

The equation for part 1 is as following. The same approach can be used to write the equation for all four parts.

$$u_1{}'' = \frac{G_m}{E_b.h.b}(u_1 \nearrow u_2) \nearrow\!\!\rightarrow 0 < x < s \tag{1}$$

Using these boundary conditions the displacement of the different parts of model, u_1, u_2, u_3 and u_4 can be calculated.

*Corresponding author. Email: nrahbar@wpi.edu

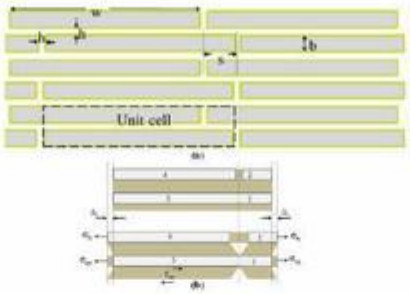

Figure 2: (a) Schematic of idealized super-cell structure (b) Unit-cell structure assumed to apply the shear-lag theory.

RESULTS AND DISCUSSION

From the equations above, the effective properties of the composite can be obtained. First of all the elastic modulus of the samples can be calculated as:

$$E_c = \frac{wE_b[(\frac{1}{2}sinh(Bs) + a(cosh(Bs)+1))sinh(B(s-w)) - asinh(Bs)(1+cosh(B(s-w))]}{[(1+aw)(cosh(Bs)+1)]sinh(B(s-w)) - sinh(Bs)[(1+aw)(1+cosh(B(s-w)) - \frac{w}{2}B]} \quad while \quad B = 2\sqrt{\frac{G_m}{E_b.h.b}} \quad \& \quad a = \frac{E_m}{E_b.t} \tag{2}$$

CONCLUSIONS

This study presented a mechanics based model for exploring the mechanical properties of nacre and multilayered materials. Stiffness, strength and inelastic deformation of the suggested model agree well with the experimental data. The experimental results show that there is an optimum structure for an specific combination of ceramic and polymer and the analytical studies can help us to find this optimum structure for the materials combination.

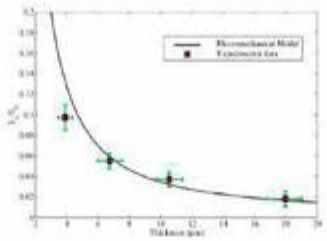

Figure 3: Effect of ceramic lamellae thickness on the elastic modulus of the samples.

References

[1] Rosso M, (2006) Ceramic and metal matrix composites: Routes and properties. J. Mater. Process. Technol. 175(1), 364-375.

[2] Askarinejad, S., & Rahbar, N. (2015). Toughening mechanisms in bioinspired multilayered materials. J.Royal Soc. Interface, 12(102), 20140855.

[3] Askarinejad, S., Kotowski, P., Shalchy, F., & Rahbar, N. (2015). Effects of humidity on shear behavior of bamboo. Theo. App. Mech Let., 5(6), 236-243.

[4] Askarinejad, S., Rahbar, N., Sabelkin, V., Mall, S. (2015). Mechanical behavior of a notched oxide/oxide ceramic matrix composite in combustion environment: experiments and simulations. Composite Structures, 127, 77-86.

[5] Dimas LS, Buehler MJ. 2012. Influence of geometry on mechanical properties of bio-inspired silica-based hierarchical materials. BB, 7(3), 036024.

[6] Ji, B., & Gao, H. (2004). Mechanical properties of nanostructure of biological materials. J. Mech. and Phys. Solids, 52(9), 1963-1990.

[7] Jackson AP, Vincent JFV, Turner RM. 1989 A physical model of nacre. Compos. Sci. Technol. 36(3), 255-266.

[8] Menig, R., Meyers, M. H., Meyers, M. A. Vecchio, K. S. (2000). Quasi-static and dynamic mechanical response of Haliotis rufescens shells. Acta Mater. 48(9), 2383-2398.

[9] Song, F., Soh, A. K., & Bai, Y. L. (2003). Structural and mechanical properties of the organic matrix layers of nacre. Biomaterials, 24(20), 3623-3631.

[10] Shuchun, Z., Yueguang, W. (2007). Effective elastic modulus of bone-like hierarchical materials. Acta Mechanica Solida Sinica, 20(3), 198-205.

[11] Begley, M. R., Philips, N. R., Compton, B. G., Wilbrink, D. V., Ritchie, R. O., & Utz, M. (2012). Micromechanical models to guide the development of synthetic brick and mortarcomposites. Journal of the Mechanics and Physics of Solids, 60(8), 1545-1560.

[12] Launey, M. E., Munch, E., Alsem, D. H., Saiz, E., Tomsia, A. P., & Ritchie, R. O. (2010). A novel biomimetic approach to the design of high-performance ceramicmetal composites. Journal of the Royal Society Interface, 7(46), 741-753.

MAGNETO-ELECTRO-THERMO-ELASTIC INTERFACE MODELS: AN ASYMPTOTIC APPROACH

Michele Serpilli*
Department of Civil and Building Engineering, and Architecture, Polytechnic University of Marche, Ancona, Italy

Summary We study the quasi-static behavior of a magneto-electro-thermo-elastic assembly constituted by a thin magneto-electro-thermo-elastic plate-like layer inserted between two generic magneto-electro-thermo-elastic bodies by means of an asymptotic analysis. After defining a small dimensionless parameter ε, which will tend to zero, we characterize two different limit models and their associated limit problems, the so-called weak and strong magneto-electro-thermo-elastic interface models, respectively. Moreover, we identify the non classical magneto-electro-thermo-elastic transmission conditions at the interface between the two three-dimensional bodies.

Smart multi-functional materials have been used over the past few decades in several applications in all fields of aeronautical, mechanical and civil engineering. For what concerns with smart multi-functional structures, the strain state is constantly under control by means of sensors and actuators, usually made of piezoelectric and/or piezomagnetic materials, integrated within the structure. The promising application of piezoelectric and piezomagnetic composites makes it imperative to develop new methods and analysis tools for better understanding mechanisms and behaviors of such structures which are subjected to mechanical, electric, magnetic and thermal interactions. The mechanical coupling of piezoelectric and piezomagnetic components in such structures gives rise to the so-called magnetoelectric effect, which is not present in the individual components, as well as pyroelectricity and pyromagnetism. In particular, these last two effects may be relevant for what concerns energy harvesting. Piezoelectric/piezomagnetic materials may be applied onto a host structure to change its shape and to enhance its mechanical properties with different configurations: for instance, a piezoelectric/ piezomagnetic transducer can be embedded into the structure to be controlled or it can be glued on it. Moreover, the same actuators are often obtained by alternating different thin layers of material with highly contrasted magneto-electro-thermo-elastic properties. This generates different types of complex multimaterial assemblies, in which each phase interacts with the others.

The asymptotic methods have been successfully applied to obtain a mathematical justification of thin structure models in the field of elasticity and piezoelectricity (see, e.g., [3, 6, 2]): this has stimulated the research toward a rational simplification of the modeling of complex structures obtained joining elements of different dimensions and/or materials of highly contrasted properties. A thin interphase represents one of the most peculiar bonded joint between two media. The treatment of the thin interphase as a separate phase by a standard finite element analysis is too expensive from a computational point of view and the presence of strong contrasts in the geometry and mechanical properties causes numerical instabilities. The asymptotic analysis allows to replace the original problem by a set of problems in which the thin interphase is substituted by a two-dimensional surface, i.e., a so-called imperfect interface, between the two three-dimensional bodies with non classical transmission conditions (see [1, 4, 5] within the theory of elasticity and piezoelectricity).

The goal of the present work is to study the behavior (considering the quasi-static assumptions for the Maxwell's equations) of a magneto-electro-thermo-elastic assembly constituted by a thin magneto-electro-thermo-elastic layer surrounded by two generic magneto-electro-thermo-elastic bodies by means of an asymptotic analysis. By defining a small real parameter ε, associated with the thickness ($h^\varepsilon = \varepsilon h$) and the magneto-electro-thermo-elastic properties of the middle layer, we perform an asymptotic analysis. We consider two particular cases by varying the magneto-electro-thermo-elastic stiffnesses ratios between the middle layer $\Omega^{m,\varepsilon} = \omega \times (-\varepsilon h, \varepsilon h)$ and the adherents $\Omega^{\pm,\varepsilon}$: namely, the *weak* magneto-electro-thermo-elastic interface model, for which we scaled the electromechanical coefficients of the intermediate domain with ε, and the *strong* magneto-electro-thermo-elastic interface model, for which we choose $\frac{1}{\varepsilon}$ as scaling. We also identify the non classical magneto-electro-thermo-elastic transmission conditions at the interface and the expressions of the stresses, electric displacements, magnetic induction and heat flow inside the interlayer.

The magneto-electro-thermo-elastic state is determined by the quadruplet $\mathcal{U}^\varepsilon := (\mathbf{u}^\varepsilon, \varphi^\varepsilon, \zeta^\varepsilon, \theta^\varepsilon)$, constituted by the displacement field, the electric potential, the magnetic potential and the temperature, respectively. Given a certain state $\mathcal{U}^\varepsilon$, for all test functions $\mathcal{V}^\varepsilon = (\mathbf{v}^\varepsilon, \psi^\varepsilon, \xi^\varepsilon, \eta^\varepsilon)$ and for any fixed $t \in (0, T)$ we introduce the following bilinear form (see [2]):

$$\begin{aligned} A^\varepsilon(\mathcal{U}^\varepsilon(t), \mathcal{V}^\varepsilon) := {} & \rho^\varepsilon(\ddot{\mathbf{u}}^\varepsilon, \mathbf{v}^\varepsilon) + c(\eta^\varepsilon, \dot{\mathbf{u}}^\varepsilon) + c_v(\dot{\theta}^\varepsilon, \eta^\varepsilon) - d(\eta^\varepsilon, \dot{\varphi}^\varepsilon) - e(\eta^\varepsilon, \dot{\zeta}^\varepsilon) + a_u(\mathbf{u}^\varepsilon, \mathbf{v}^\varepsilon) + b(\varphi^\varepsilon, \mathbf{v}^\varepsilon) - b(\psi^\varepsilon, \mathbf{u}^\varepsilon) + \\ & + f(\zeta^\varepsilon, \mathbf{v}^\varepsilon) - f(\xi^\varepsilon, \mathbf{u}^\varepsilon) - c(\theta^\varepsilon, \mathbf{v}^\varepsilon) + a_\varphi(\varphi^\varepsilon, \psi^\varepsilon) + a_\zeta(\zeta^\varepsilon, \xi^\varepsilon) + g(\zeta^\varepsilon, \psi^\varepsilon) + g(\varphi^\varepsilon, \xi^\varepsilon) + \\ & - d(\theta^\varepsilon, \psi^\varepsilon) - e(\theta^\varepsilon, \xi^\varepsilon) + a_\theta(\theta^\varepsilon, \eta^\varepsilon), \end{aligned}$$

*Corresponding author. Email: m.serpilli@univpm.it

where $(\cdot,\cdot)$ is the scalar product in $L^2(\Omega^\varepsilon)$, $\dot{v} := \partial_t v$ denotes the time derivative and the bilinear forms are defined as follows:

$$a_u(\mathbf{u}^\varepsilon,\mathbf{v}^\varepsilon) := \int_{\Omega^\varepsilon} C_{ijk\ell} e^\varepsilon_{k\ell}(\mathbf{u}^\varepsilon) e^\varepsilon_{ij}(\mathbf{v}^\varepsilon) dx^\varepsilon, \quad a_\varphi(\varphi^\varepsilon,\psi^\varepsilon) := \int_{\Omega^\varepsilon} X_{ij}\partial^\varepsilon_j\varphi^\varepsilon\partial^\varepsilon_i\psi^\varepsilon dx^\varepsilon, \quad a_\zeta(\zeta^\varepsilon,\xi^\varepsilon) := \int_{\Omega^\varepsilon} M_{ij}\partial^\varepsilon_j\zeta^\varepsilon\partial^\varepsilon_i\xi^\varepsilon dx^\varepsilon,$$

$$a_\theta(\theta^\varepsilon,\eta^\varepsilon) := \frac{1}{T_0}\int_{\Omega^\varepsilon} K_{ij}\partial^\varepsilon_j\theta^\varepsilon\partial^\varepsilon_i\eta^\varepsilon dx^\varepsilon, \quad b(\psi^\varepsilon,\mathbf{u}^\varepsilon) := \int_{\Omega^\varepsilon} P_{kij}\partial^\varepsilon_k\psi^\varepsilon e^\varepsilon_{ij}(\mathbf{u}^\varepsilon) dx^\varepsilon, \quad c(\eta^\varepsilon,\mathbf{u}^\varepsilon) := \int_{\Omega^\varepsilon} \eta^\varepsilon\beta_{ij}e^\varepsilon_{ij}(\mathbf{u}^\varepsilon) dx^\varepsilon,$$

$$d(\eta^\varepsilon,\varphi^\varepsilon) := \int_{\Omega^\varepsilon} \eta^\varepsilon p_k\partial^\varepsilon_k\varphi^\varepsilon dx^\varepsilon, \quad e(\eta^\varepsilon,\zeta^\varepsilon) := \int_{\Omega^\varepsilon} \eta^\varepsilon m_k\partial^\varepsilon_k\zeta^\varepsilon dx^\varepsilon, \quad f(\xi^\varepsilon,\mathbf{u}^\varepsilon) := \int_{\Omega^\varepsilon} R_{kij}\partial^\varepsilon_k\xi^\varepsilon e^\varepsilon_{ij}(\mathbf{u}^\varepsilon) dx^\varepsilon,$$

$$g(\zeta^\varepsilon,\psi^\varepsilon) := \int_{\Omega^\varepsilon} \alpha_{ij}\partial^\varepsilon_j\zeta^\varepsilon\partial^\varepsilon_i\psi^\varepsilon dx^\varepsilon.$$

Let $V(\Omega^\varepsilon) := \left\{v^\varepsilon \in H^1(\Omega^\varepsilon);\ \ v^\varepsilon = 0 \text{ on } \Gamma_0^\varepsilon\right\}$, $\Omega^\varepsilon := \Omega^{+,\varepsilon}\cup\Omega^{m,\varepsilon}\cup\Omega^{-,\varepsilon}$, the weak formulation of the problem takes the following form

$$\begin{cases} \text{Find } \mathcal{U}^\varepsilon(t) \in [V(\Omega^\varepsilon)]^3\times V(\Omega^\varepsilon)\times V(\Omega^\varepsilon)\times V(\Omega^\varepsilon),\ t\in(0,T), \text{ such that} \\ A^{+,\varepsilon}(\mathcal{U}^\varepsilon(t),\mathcal{V}^\varepsilon) + A^{-,\varepsilon}(\mathcal{U}^\varepsilon(t),\mathcal{V}^\varepsilon) + A^{m,\varepsilon}(\mathcal{U}^\varepsilon(t),\mathcal{V}^\varepsilon) = L^\varepsilon(\mathcal{V}^\varepsilon), \end{cases} \tag{1}$$

for all $\mathcal{V}^\varepsilon \in [V(\Omega^\varepsilon)]^3\times V(\Omega^\varepsilon)\times V(\Omega^\varepsilon)\times V(\Omega^\varepsilon)$, where $L^\varepsilon(\cdot)$ denotes the work of the external loads applied in $\Omega^{\pm,\varepsilon}$. In order to study the asymptotic behavior of the solution of problem (1) when ε tends to zero, we use the approach by [3] and develop the solution as a series of powers of ε, namely $\mathcal{U}(\varepsilon) := \mathcal{U}^0 + \varepsilon\mathcal{U}^1 + \varepsilon^2\mathcal{U}^2 + \ldots$. By choosing the two different scalings for the magneto-electro-thermo-elastic interlayer moduli, we derive the following interface limit problems (see, e.g., [5]).

The weak magneto-electro-thermo-elastic interface model

Let us define the functional space $W(\Omega) := \{v\in L^2(\Omega);\ v^\pm \in H^1(\Omega^\pm),\ v = 0 \text{ on } \Gamma_0\}$, the variational formulation of the weak magneto-electro-thermo-elastic interface model reads as follows:

$$\begin{cases} \text{Find } \mathcal{U}^0(t) \in [W(\Omega)]^3\times W(\Omega)\times W(\Omega)\times W(\Omega),\ t\in(0,T) \text{ such that} \\ A^-(\mathcal{U}^0(t),\mathcal{V}) + A^+(\mathcal{U}^0(t),\mathcal{V}) + \mathcal{A}^m(\mathcal{U}^0(t),\mathcal{V}) = L(\mathcal{V}), \end{cases}$$

for all $\mathcal{V} = (\mathbf{v},\psi,\xi,\eta) \in [W(\Omega)]^3\times W(\Omega)\times W(\Omega)\times W(\Omega)$ where

$$\mathcal{A}^m(\mathcal{U}^0,\mathcal{V}) := \frac{1}{2h}\int_\omega \Big\{\left(C^m_{i3j3}[\![u^0_j]\!] + P^m_{3i3}[\![\varphi^0]\!] + R^m_{3i3}[\![\zeta^0]\!]\right)[\![v_i]\!] + \left(-P^m_{3i3}[\![u^0_i]\!] + X^m_{33}[\![\varphi^0]\!] + \alpha^m_{33}[\![\zeta^0]\!]\right)[\![\psi]\!] +$$
$$+ \left(-R^m_{3i3}[\![u^0_i]\!] + \alpha^m_{33}[\![\varphi^0]\!] + M^m_{33}[\![\zeta^0]\!]\right)[\![\xi]\!] + K^m_{33}[\![\theta^0]\!][\![\eta]\!]\Big\}\, d\tilde{x}, \quad \text{with } [\![f]\!] := f^+ - f^-,$$

is associated with a limit surface energy depending on the jump of the displacement field $[\![\mathbf{u}^0]\!]$, electric potential $[\![\varphi^0]\!]$, magnetic potential $[\![\zeta^0]\!]$ and temperature $[\![\theta^0]\!]$, evaluated at the interface ω. This transmission problem can be considered as a multiphysical generalization of the results obtained in [4, 5].

The strong magneto-electro-thermo-elastic interface model

Let us define the functional space $X(\tilde{\Omega}) := \{v\in H^1(\tilde{\Omega});\ v|_\omega \in H^1(\omega),\ v = 0 \text{ on } \Gamma_0\}$, $\tilde{\Omega} := \Omega^+\cup\omega\cup\Omega^-$, the variational formulation of the strong magneto-electro-thermo-elastic interface model takes the following form:

$$\begin{cases} \text{Find } \mathcal{U}^0(t) \in [X(\tilde{\Omega})]^3\times X(\tilde{\Omega})\times X(\tilde{\Omega})\times X(\tilde{\Omega})\, t\in(0,T), \text{ such that} \\ A^-(\mathcal{U}^0(t),\mathcal{V}) + A^+(\mathcal{U}^0(t),\mathcal{V}) + \mathcal{B}^m(\mathcal{U}^0(t),\mathcal{V}) = L(\mathcal{V}), \end{cases}$$

for all $\mathcal{V} \in [X(\tilde{\Omega})]^3\times X(\tilde{\Omega})\times X(\tilde{\Omega})\times X(\tilde{\Omega})$, where

$$\mathcal{B}^m(\mathcal{U}^0,\mathcal{V}) := 2h\int_\omega \left\{\tilde{\sigma}_{\alpha j}\partial_\alpha v_j - \tilde{D}_\alpha\partial_\alpha\psi - \tilde{B}_\alpha\partial_\alpha\xi + \dot{\tilde{\mathcal{S}}}\eta - \tilde{q}_\alpha\partial_\alpha\eta\right\} d\tilde{x},$$

represents the two-dimensional bilinear form defined on the interface ω, associated with a magneto-electro-thermo-elastic membrane energy. Moreover, $\tilde{\sigma}_{\alpha j} := \tilde{C}^m_{i\beta j\alpha}\partial_\beta u^0_i + \tilde{P}^m_{\beta\alpha j}\partial_\beta\varphi^0 + \tilde{R}^m_{\beta\alpha j}\partial_\beta\zeta^0 - \tilde{\beta}^m_{\alpha j}\theta^0$, $\tilde{D}_\alpha := \tilde{P}^m_{\beta\alpha i}\partial_\beta u^0_i - \tilde{X}^m_{\alpha\beta}\partial_\beta\varphi^0 - \tilde{\alpha}^m_{\alpha\beta}\partial_\beta\zeta^0 + \tilde{p}^m_\alpha\theta^0$, $\tilde{B}_\alpha := \tilde{R}^m_{\beta\alpha i}\partial_\beta u^0_i - \tilde{\alpha}^m_{\alpha\beta}\partial_\beta\varphi^0 - \tilde{M}^m_{\alpha\beta}\partial_\beta\zeta^0 + \tilde{m}^m_\alpha\theta^0$, $\tilde{\mathcal{S}} := \tilde{\beta}^m_{\beta i}\partial_\beta u^0_i - \tilde{p}^m_\beta\partial_\beta\varphi^0 - \tilde{m}^m_\beta\partial_\beta\zeta^0 + \tilde{c}^m_v\theta^0$ and $\tilde{q}_\alpha := -\tilde{K}^m_{\alpha\beta}\partial_\beta\theta^0$ represent, respectively, the reduced stress vector, electric displacement, magnetic induction, thermodynamic entropy and heat flow of the interface. By taking into account all the possible multiphysical interactions, we manage to generalize the results obtained in [1, 5].

References

[1] Bessoud A.-L., Krasucki F., Michaille G.: Multi-materials with strong interface: variational modelings, Asympt. Anal. 1: 1-19, 2009.

[2] Bonaldi, F., Geymonat, G., Krasucki, F., Serpilli, M.: An asymptotic plate model for magneto-electro-thermo-elastic sensors and actuators, Math. Mech. Solids, DOI: 10.1177/1081286515612885, 2015

[3] Ciarlet P.G.: Mathematical Elasticity, vol. II: Theory of Plates, North-Holland, Amsterdam, 1997.

[4] Geymonat G., Krasucki F., Lenci S.: Mathematical analysis of a bonded joint with a soft thin adhesive, Math. Mech. Solids 4: 201-225, 1999.

[5] Serpilli M.: Mathematical Modeling of Weak and Strong Piezoelectric Interfaces, J. Elasticity 121: 235-254, 2015.

[6] Weller T., Licht C.: Asymptotic modeling of thin piezoelectric plates, Ann. Solid Struct. Mech. 1: 173-188, 2010.

ASSESSMENT OF THE STRENGTH OF NANOCOMPOSITES BASED ON INTERFACE BONDING ANALYSIS

R.B. Pęcherski[1a], K. Nalepka[2], P. Nalepka[3], K. Sztwiertnia[4], S. Kret[5], A. Ustrzycka[1]
[1]*Institute of Fundamental Technological Research, Polish Academy of Sciences, Warsaw, Poland*
[2]*AGH University of Science and Technology, Krakow, Poland*
[3]*Agriculture University in Krakow, Krakow, Poland*
[4]*Institute of Metallurgy and Materials Science, Polish Academy of Sciences, Krakow, Poland*
[5]*Institute of Physics, Polish Academy of Sciences, Warsaw, Poland*

Summary Recent investigations reveal that interface bonding strength is dependent on the relative orientation of crystallites of the both phases [2]. The experimental, theoretical and computational investigations confirm this observation in the case of Cu/α-Al_2O_3 system, [3], [4]. It is shown that the statistical distribution of the values of interface strength for different relative orientations of bonded phases should be included in the phenomenological model of the damage initiation in nanocomposites. The novelty of the presented study is the combination of different experimental techniques: HRTEM, EBSD and molecular dynamics simulations with phenomenological theory of damage development in nanocomposites due to debonding at the interphase boundary [5], [6], [7]. A class of new models with the yield condition determined by one of quadric surfaces, in particular paraboloid or ellipsoid one is considered and the comparison with popular Gurson approach is discussed, [8].

INTRODUCTION

In recent studies on modern materials the information from sophisticated observation techniques and molecular simulations at different levels flows across scales into the decision process of modelling and design, which enables rational tailoring of materials [1]. The concept of workflow integration rather than multiscale integration is applied in the presented paper.

The experimental studies show that the geometry of interphase boundaries and in particular the relative orientation of crystallites of the both phase is one of the crucial factors determining the toughness of metal/ceramic composites [2]. The experimental, theoretical and computational investigations presented in [3], [4] confirm this observation in the case of Cu/α-Al_2O_3 system. Until now there is lack of a model adequately tuned to include the dependence of the strength of the interface bonding on the phase orientation . It is also known observation that the size of the ceramic inclusion embedded in metal matrix decides about the mode of fracture initiation in the composite. If the inclusion is of nanosize diameter the far-field stresses produce the particle/matrix debonding, while in the case of larger particles cracks in ceramic inclusion are developing, [5].

The aim of the paper is identification of the structure, strain, bonding strength and the fracture process at the bimaterial interface. The particular value of the final result consists in using the series of experimental data from complementary investigation methods: EBSD and HRTEM. The first of them provides the information statistically valid and the other one enables detailed local characterization. The experimental data are supplemented by the results of molecular dynamics (MD) computations and a theoretical analysis. The discussed complex characterization of the bimaterial interface is performed on the example of Cu/α-Al_2O_3 boundary. As a result the mechanism of bonding is revealed and a new phenomenological model is proposed that enables introducing the statistical distribution of the bonding strength into the prediction of nanocomposite material toughness.

PHYSICAL MOTIVATION

EBSD examination: orientation relationships at interphase boundaries

Corundum nano-particles (red) embedded in a copper matrix (green) were investigated with the use of Electron Back Scattered Diffraction technique (EBSD), [3], [4], Fig. A. Picture B demonstrates an example of EBSD results showing the interphase boundaries: basic orientation relationship (red) and new ones with improved bonding strength (green and yellow).

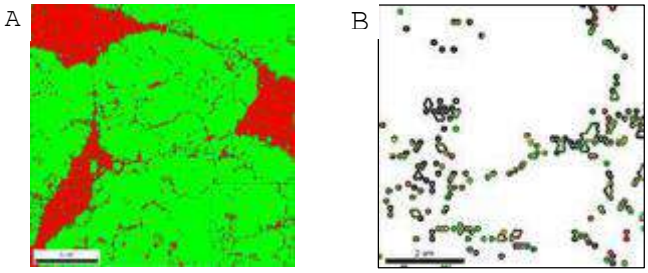

HRTEM studies: microstructure observations and modelling

The set of orientation relationships uncovered by EBSD method in composites manufactured by the powder metallurgy is observed also in the Cu/α-Al_2O_3 heterostructures obtained by Pulsed Laser Deposition (PLD). It leads to the conclusion that the revealed misorientations are typical for the copper/ corundum interphase boundary regardless of a synthesis way. The interface with the basic orientation relationship was studied with the use of HRTEM technique. The obtained images are used to three-dimensional reconstruction of the junction microstructure by MD simulations [5]. The results show that strong

[a)]rpecher@ippt.pan,pl

bonding between copper and α-Al_2O_3 induces structural changes in the (111) Cu layer nearest the substrate and leads to formation of the system of partially dissociated dislocations in the next layer. In consequence, the Cu/α-Al_2O_3 interface becomes the semicoherent system. The lattice matching regions of the individual Cu layers are significantly lowered, which results in strong deformations along the closed packed planes (see the pictures below). The interfaces with the improved strength (see images from EBSD investigation) exhibit more intense structural changes which reach much deeper into the metal layer [4].

Distribution of elastic strain energy density in the copper section with the thickness 8 Å, [6].

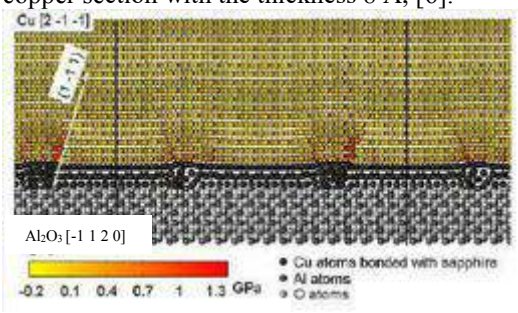

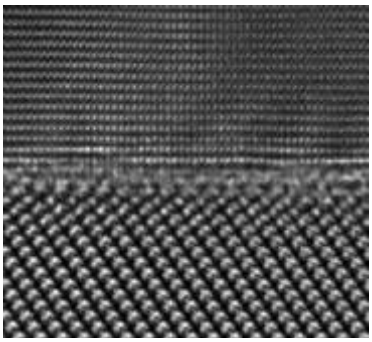

HRTEM image of the Cu/α-Al_2O_3 interface, [6].

An example of the MD simulation of the stacking faults areas. The Cu atoms (yellow) limited by partial dislocations (red) within the planes (1 -1 1), (-1 1 1) and (1 1 -1). The position of atoms belonging to the first Cu layer (grey scale), [7].

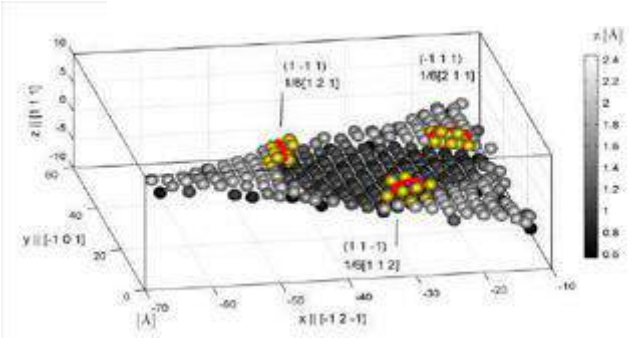

MAIN RESULTS AND CONCLUSION

The presented discussion reveals the necessity of accounting for the statistical distribution of the values of interface strength for different relative orientations of bonded phases into the phenomenological model of nanocomposites subjected to damage initiation due to debonding. An energy-based approach resulting in the new model of damaged nanocomposites with the yield condition determined by one of quadric surfaces, in particular paraboloid or ellipsoid one is considered, [8]. Also the comparison with the popular Gurson criterion is discussed. The novelty of the presented multidisciplinary study is the combination of different experimental techniques: HRTEM and EBSD in relation with the results of MD computations with phenomenological theory of damage development in nanocomposites due to ceramic particles debonding.

REFERENCES

[1] G. Goldbeck, Foreword, in: Industrial Applications of Molecular Simulations, M. Meunier (ed.), CRC Press, Taylor & Francis Group, Boca Raton, 2012.

[2] A.R.S. Gautam, J.M. Howe, A method to predict the orientation relationship, interface planes and morphology between a crystalline precipitate and matrix. Part I Approach, Phil. Mag. **91,** 3203-3227, 2011

[3] K. Nalepka, K. Sztwiertnia, P. Nalepka, R.B. Pęcherski, The strength analysis of Cu/α-Al_2O_3 interfaces as a key for rational composite design, Archives Metallurgy and Materials, **60**, 1953-1956, 2015.

[4] K. Nalepka, K. Sztwiertnia, P. Nalepka, Preferred orientation relationships at the Cu/α-Al_2O_3 interface: Identification and theoretical explanation, Acta Materialia, **104**, 156-165, 2016.

[5] Ken Gall, M.F. Horstemyer, Mark Van Schilfgaarde, M.I. Baskes, Atomistic simulations on the tensile debonding of an aluminium-silicon interface, Journal of the Mechanics and Physics of Solids, **48**, 2183-2212, 2000.

[6] K. Nalepka, J. Hoffman, S. Kret, P. Nalepka, Z. Szymański, Laser-deposited Cu/α-Al_2O_3 nanocomposite: experiment and modelling, Appl. Phys. A**.** Materials Science & Processing**, 117**, 169-173, 2014.

[7] P. Nalepka, Identification of deformation fields in the copper/corundum interface, PhD thesis (doctoral supervisor: R.B. Pęcherski).

[8] Pęcherski R.B., Nalepka K., Frąś T., Nowak M., Inelastic flow and failure of metallic solids. Material effort: study across scales, in: Constitutive Relations under Impact Loadings. Experiments, Theoretical and Numerical Aspects, Springer, CISM, Udine, T. Łodygowski, A. Rusinek (Eds.), 552, pp.245-285, 2014.

MECHANICAL BEHAVIORS OF CARBON FIBER COMPOSITE THREE DIMENSIONAL LATTICE GRID STRUCTURES

Jian Xiong[1] & Ying Gao [1]
[1]*Center for Composite Materials and Structures, Harbin Institute of Technology, Harbin 150080, P.R.China*

Summary Mechanical properties and failure modes of carbon fiber composite Egg and pyramidal grids cores were studied in present paper. Interlocking method has been developed for both kinds of three dimensional grids. The out of plane compression, in-plane compression and three point bending responses of the both panels were tested until failure. Crushing mode and energy absorption in quasi-static uniform compression have been investigated. Euler or core shear macro-buckling, face wrinkling, face inter-cell buckling and face sheet crushing were considered and theoretical relationships for predicting the failure load associated with each mode were presented under in plane compression. Face wrinkling and core debonding have been investigated under three point bending. Failure mechanism maps were constructed to predict the failure of composite sandwich panels with pyramidal and egg grid cores subjected to in plane compression and bending.

DESIGN AND FABRICATION

A method for fabricating carbon fiber composite egg and pyramidal grid cores has been developed in this section. First, carbon fiber composite laminates with $0^o/90^o$ were made by T700/epoxy prepreg of thickness 0.15 mm (T700/epoxy composite, Beijing Institute of Aeronautical Materials, China). Two pieces of grid plates were cutted by electronic engraving machine (Harbin Weijifen Organic Glass Products Co., Ltd.), and then these plates are assembled together basing on interlocking method as shown in the left side of Figure 1(a) and (b). Each plate interlocked with other plate only from the long caulking groove in order to form egg lattice cores and each plate interlocked with other plates including both long and short caulking grooves to form pyramidal lattice cores. The fabricated egg and pyramidal grid cores are sketched in the right side of Figure 1 (a) and (b), respectively. Finally, two face sheets will be bonded on the top and bottom of the grid core to form a sandwich panel.

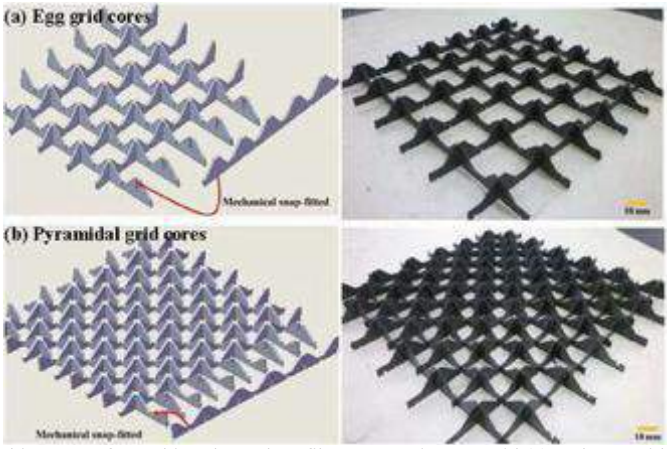

Figure 1 Interlocking route for making the carbon fiber composite egg grid (a) and pyramidal grid cores (b)

OUT OF PLANE COMPRESSION

Out of plane compression tests were performed to study the compressive stiffness and strength in the out of plane direction. Pyramidal and Egg grid cores with two different relative densities were studied in this section. According to the displacement curves, there are two peak strengths for each curve. The curves of pyramidal grid cores are similar with that of egg grid cores. Delamination and fracturing were found near the top end of girds cores and these failures will run through all the grid cores with the increasing of compressive load. At the same time, fracturing was discovered near the slots of grids cores due to initial defect. The compression curves reveal long deformation plateaus, suggesting that both egg and pyramidal grid sandwich panels may potentially be good energy-absorbing materials. The energy per unit mass of both egg and pyramidal grid cores have been calculated in order to be compared with square honeycombs. Compared to the referenced panels with square honeycombs cores made by carbon fiber composites [1-2], the present three dimensional grid sandwich structures have superior specific energy absorbing ability than that of other square honeycombs under low densities between 101 Kg/m^3 and 10^2 Kg/m3. The reason is that at the same low densities, present grid structures will occur crushing not Euler buckling failure but square honeycombs are very easy to be failed with Euler buckling. Thus, the present

[a)] Corresponding author. Email: xiongjian0309@126.com.

method provides a novel fabrication and prototyping method for carbon fiber composite grids cores with through inner space, and can be can be used to make ultra-light structures with good energy absorption.

IN PLANE COMPRESSION

We will develop the full range of analytical predications for the failure modes of both 3-D grids cores sandwich column made by carbon fiber reinforced composite. Four different failure modes of sandwich panels with 3-D grid cores under axial compression were considered: i) Euler or core shear macro-buckling, ii) face wrinkling, iii) Face intra-cell buckling, and iv) face crushing including face delamination and plastic micro-buckling. Failure mechanism maps will be constructed with four competing failure modes, Face sheets with three different layers stacking will be investigated and the relationship between the failure mechanism maps and material mechanical properties will be discussed. In this section, we provide predictive failure maps for carbon fiber reinforced composite egg and pyramidal grids core sandwich panels basing on above analytical parameters. The stacking sequence of the face sheets and the topologies of grids core can have significant effect on the overall behaviour and failure of composite sandwich panels. Results of sandwich columns failure in compression expressed in terms of maps facilitate visualization during the design stage. In constructing such a map, it is assumed that the operative failure mode is the one associated with the lowest critical load. In our previous paper [3], we point out that the choice of material properties for the parent material significantly influences the locations of the boundaries between failure modes for carbon fiber composite sandwich columns. Failure mechanism maps are constructed based on different laminate stack sequences and core configurations. This reminds us that the highest weight efficient sandwich structure can be obtained by changing the laminate stack sequence and truss core configuration. Three different specimens have been designed for egg and pyramidal grid cores, respectively. Almost all the failure modes mentioned above have been found in our tests and several different models can be investigated for the same specimen.

THREE POINT BENDING

Under three point bending, possible failure modes of a carbon fiber sandwich panel are: (i) face sheet crushing or wrinkling, (ii) face sheet intra-cell buckling, (iii) core member crushing (including grid core's delamination or fracture) or buckling and (iv) debonding between face sheet and grid cores. The collapse of the panel is generally dictated by one of the competing mechanisms that depend on the geometry of the panel and the mechanical properties of the face and core materials. Three different stacking sequence and two kinds of three dimensional grid cores have been considered in order to draw the failure mechanism map under three point bending. Face wrinkling, Face crushing, core member crushing and core debonding have been investigated in our maps. The stacking sequence and thickness of the face sheets can have significant effect on the overall behaviour and failure of composite sandwich panels. We performed three point bending tests on sandwich panel specimens with different geometries. Both pyramidal and egg grid structures with two different thickness of face sheet have been investigated. For the deviation between analytical calculation and experiment, The first reason is that the shear deflection was restricted by the end and the second reason is that the shear deformation of facesheet was not considered in the analytical models. The adhesion strength between the three dimensional grid cores and face sheet appeared to be the limiting factor in several cases, debonding is always the last and also dominate failure modes. All beams almost failed by the predicted dominate mode, some failure modes can occur at the same time due to the complex of composite three dimensional grid cores.

CONCLUSIONS

Carbon fiber composite sandwich panels with egg and pyramidal grid cores have been designed and manufactured by interlocking method. Out of plane compression, in plane compression and three point bending tests were carried out to study the mechanical behaviors of the grids and sandwich panels. Analytical models and failure maps have been conducted in order to predict the mechanical response and failure modes of all the specimens. Core buckling and crushing have been found under out of plane compression, energy absorptions have been concluded for each specimens. Macro shear Euler buckling, face wrinkling and face crushing have been investigated under in plane compression. Face wrinkling and debonding have been indicated under three point bending. In general, the measured peak loads obtained in the experiments showed good agreement with the analytical predictions. The data could provide insight into the design of optimized or near-optimized sandwich panels. Three dimensional grid cores with interconnected void spaces appear most promising as candidates for the cores in sandwich structures intended for lightweight and multifunctional application.

References

[1] Russell B.P., Deshpande V.S., Wadley H.N.G: Quasistatic deformation and failure modes of composite square honeycomb. *J. Mech Mater Struct* 3:1315–1340, 1999.

[2] Fan H.L., Meng F.H., Yang W: Sandwich panels with Kagome lattice cores reinforced by carbon fibers. Compos Struct 81: 533-539, 2007.

[3] Xiong J., Ma L., Pan S.D., Wu L.Z., Papadopoulos J., Vaziri A: Shear and bending performance of carbon fiber composite sandwich panels with pyramidal truss cores. Acta Mater 60: 1455-1466, 2012.

THREE-DIMENSIONAL DIRECT-WRITE PRINTING OF METALLIC MICROSTRUCTURES

Chao Xu[1], Arslane Bouchemit[2], Mathieu Boudreau[2], Gilles L'Espérance[2], Louis Laberge Lebel[3] & Daniel Therriault[1 a)]

[1]*Laboratory for Multiscale Mechanics (LM2), École Polytechnique de Montréal, Montréal, Québec, Canada*

[2]*Centre de Caractérisation Microscopique des Matériaux, (CM)[2], École Polytechnique de Montréal, Montréal, Québec, Canada*

[3]*Department of Mechanical Engineering, École Polytechnique de Montréal, Montréal, Québec, Canada*

Summary Three-dimensional (3D) printing is referred to create objects by adding material layer-by-layer rather than traditionally removing material from a part. In this study, we developed a method to fabricate metal 3D microstructures consisting of 3D printing at room temperature and two following processes: sintering and copper infiltration. 3D structures such as scaffolds and planetary gears with the filament diameter of 250 μm are printed using a steel micro powders/polylatic acid (PLA) composite at a printing speed of 10 mm/s. The ink concentration is up to 98.28 wt%. Filament porosity of sintered samples is 1.7% ± 0.2%. After sintering, copper is infiltrated into the sintered sample to obtain steel and copper alloy 3D structures.

INTRODUCTION

Direct-write (DW) is an extrusion based three-dimensional (3D) printing method, which has been used for several years in various fields such as micro fabrication [1], tissue engineering [2] and electronics [3]. Lewis et al. [4] developed a direct-write printing method to print TiH_2/polymer composite 2D sheet at room temperature and fold them into 3D structures. Then the samples were annealed to remove the polymer and obtain Ti or TiO_2 microstructures by employing different atmospheres. In this study, we achieved to print 3D structures with steel/PLA composite at room temperature, sinter printed samples to remove PLA and use copper to infiltrate sintered samples to fill the pores created during the sintering process.

METHODS

Figure 1 shows a schematic representing the process used. A multilayer scaffold is fabricated by solvent-cast direct write [5] (a 3D printing method using polymer composite solved in volatile solvent as the ink) at room temperature (Figure 1a) and following processes are carried on this scaffold (Figure 1b). First, polylactic acid (PLA 4032D, Nature works, LLC) is dissolved in dichloromethane (DCM, VWR, LLC) and the solution is rested for 48 hours. Then the steel micro powders (~20μm) are mixed with the solution in the mixer (8000M Mixer/Mill, SPEX SamplePrep) for 5 minutes to obtain the metallic ink. Secondly, the metallic ink is poured into a syringe (PN7012074, Nordson, EFD) under the fume hood. A steel/PLA composite 3D scaffold is printed with the metallic ink at room temperature. Third, the printed scaffold is heated in a tube furnace to burn the PLA and sinter the micro powders. The temperature increases from room temperature to 300℃ at a rate of 60℃/h for the degradation of PLA. Then the temperature is raised from 300℃ to 1165℃ at a rate of 600℃/h and held at 1165℃ for 2h to sinter the steel micro powders. A porous steel scaffold was obtained after sintering. Finally, the sintered scaffold is heated in the furnace with a piece of copper on the top of it. The temperature goes form room temperature to 1120℃ at a rate of 600℃/h and held at 1120℃ for 0.5h. The copper is melted and infiltrates the porous scaffold by capillary force and gravity.

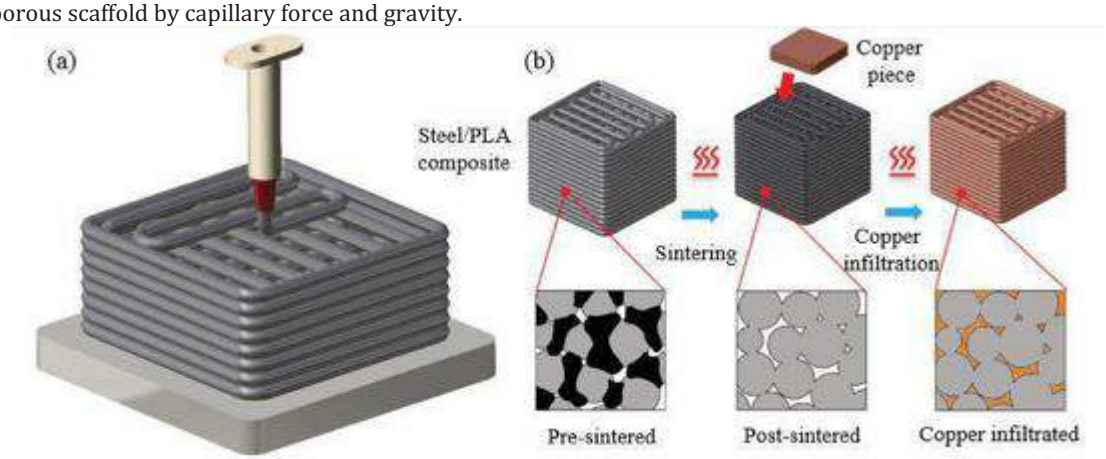

Figure 1. Schematic of a fabrication method of metal and hybrid 3D microstructures combined by (a) Solvent-cast direct write and (b) sintering and copper infiltration

a) Corresponding author. Email: Daniel.Therriault@polymtl.ca.

RESULTS & DISCUSSION

Figure 2a shows the printing process of a tensile test sample with 95 wt% steel/PLA ink and 250μm diameter tapered nozzle at a printing speed of 10 mm/s. The ink of 98.28 wt% steel/PLA can be printed. While the surface quality of the sample is not as good as that made of 95 wt% steel/PLA ink. Various 3D microstructures such as tensile test samples and 20-layers scaffolds were 3D printed at room temperature (Figure 2b). Figure 2c shows an optical image of pre-sintered, post-sintered and copper infiltrated 20-layers scaffolds. Figure d, e and f show SEM images of these samples respectively. In the pre-sintered scaffold, the steel micro powders are covered and bounded by PLA. It is a relatively weak connection. While in the post-sintered scaffold, the PLA is removed and the steel micro powders are sintered together. The sintered scaffold becomes conductive and the mechanical properties are improved. However, there are pores inside the filament of the sintered scaffold. The porosity of the filament of the scaffold made of 95 wt% steel/PLA ink is down to 1.7% ± 0.2%. In the copper infiltrated scaffold, the pores are filled by melted copper. It improves the electrical conductivity and the mechanical properties of the scaffold.

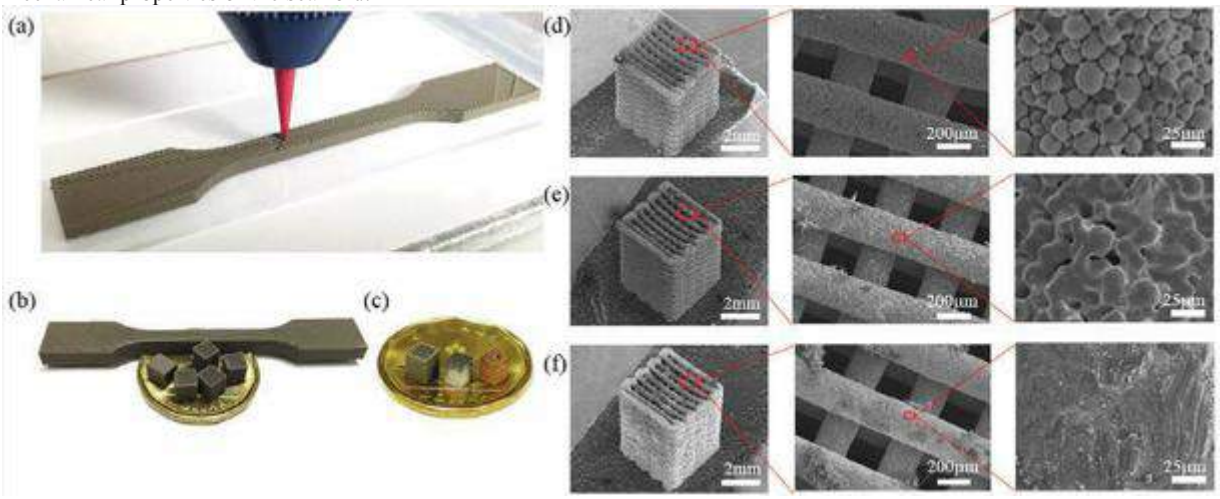

Figure 2. Optical and SEM images of microstructures printed with 95 wt% steel/PLA ink and 250μm diameter tapered nozzle, printing speed at 10 mm/s (a) printing process of a tensile test sample, (b) pre-sintered samples, (c) 20-layers scaffolds of (d) pre-sintered, (e) post-sintered and (f) copper infiltrated and their close-up views

The samples are printed at room temperature, which requires only simple setups. The ink concentration used in this method is up to 98.28 wt%, which ensures low porosity of the sintered samples. The filaments of the samples printed by this method align well and the shape of the samples does not deform after sintering and copper infiltration. However, there are some current limitations in this method. First, oxidation is observed on the sintered and copper infiltrated samples. The nitrogen will be replaced by a mixture of argon and hydrogen as the protective atmosphere to solve this problem. Secondly, the resolution is relatively low. It would be improved by using finer metal powders.

CONCLUSION

We developed a direct-write 3D printing method to print metal microstructures combining with solvent cast direct write at room temperature and following processes: sintering and copper infiltration. Many 3D microstructures such as scaffolds, tensile test samples and planetary gears were fabricated by this method. 3D microstructures made of pure metal without pores were obtained by following sintering and copper infiltration. The future work will be mechanical and electrical characterizations of the sintered and copper infiltrated samples, printing more complex geometry samples and achieving faster printing speed.

References

[1] Therriault, Daniel, Scott R. White, and Jennifer A. Lewis. "Chaotic mixing in three-dimensional microvascular networks fabricated by direct-write assembly." *Nature materials* 2.4 (2003): 265-271.

[2] Ho, Chee Meng Benjamin, Sum Huan Ng, and Yong-Jin Yoon. "A review on 3D printed bioimplants." *International Journal of Precision Engineering and Manufacturing* 16.5 (2015): 1035-1046.

[3] Kim, Min-Saeng, et al. "Direct metal printing of 3D electrical circuit using rapid prototyping." *International Journal of Precision Engineering and Manufacturing* 10.5 (2009): 147-150.

[4] Ahn, Bok Yeop, et al. "Printed origami structures." *Advanced Materials* 22.20 (2010): 2251-2254.

[5] Guo, Shuang-Zhuang, et al. "Solvent-Cast Three-Dimensional Printing of Multifunctional Microsystems." *Small* 9.24 (2013): 4118-4122.

VIBRATION AND DAMPING CHARACTERISTICS OF SANDWICH BEAM WITH FIBER FELT CORE

Qiancheng Zhang[1,2a)], Bin Han[1,3], Zhijia Zhang[1,2], Feng Jin[1,2a)], Tian Jian Lu[1,2]
[1]*MOE Key Laboratory for Multifunctional Materials and Structures, Xi'an Jiaotong University, Xi'an 710049, PR China*
[2]*State Key Laboratory for Mechanical Structure Strength and Vibration, Xi'an Jiaotong University, Xi'an 710049, PR China*
[3]*School of Mechanical Engineering Xi'an Jiaotong University, Xi'an 710049, PR China*

Summary The vibration and damping characteristics of sandwich structure with two porosity of fiber felt core were investigated in this paper. Based on the cantilever sandwich beam, modal testing and analysis of those sandwich structures and their corresponding steel beam with equal mass were carried out. The results show that the natural frequency and damping ratio are higher than those of the steel beam.With the increases of core porosity, each order natural frequency is reduced. Furthermore, with the increase of porosity, the second order and third order damping ratio are reduced.

INTRODUCTION

Due to the low density and good mechanical properties, ultra-light porous fiber felt core sandwich structures are widely used in aerospace, mechanical and special engineering field. As a kind excellent structural and functional composite material, mechanical properties of fiber felt core sandwich structures such as tension and compression has been widely studied [1, 2]. While little concerne about their vibration performance. Vibration and damping characteristics of sandwich structure should also be the focus in the design process. In this paper, the free vibration and damping characteristics of fiber felt core sandwich beam were investigated. As a comparison, the modal experiment of sandwich structures with different porosity core and the corresponding steel beam with equal mass were carried out for the case of clamped-free boundary conditions.

EXPERIMENTS

Fiber felt core sandwich beams are composed of 304 stainless steel panels and fiber felt core. Two different porosity sandwich beams as shown in Fig. 1 and their corresponding steel beam with equal mass were designed. The porosity of fiber felt cores are 75% and 90%, with their corresponding panel thickness of 1.5mm, and 1mm, respectively. Modal vibration tests were performed on sandwich beams under clamped-free boundary condition. Experimental equipment includes the PCB impact hammer, B&K Type 4366 accelerometers, a BK3560D Signal generator, an electromagnetic vibration machine and BK3560D modal analysis system. The scheme adopted in this experiment is: first step is white noise excitation to determine the first three order natural frequencies of the sandwich beam; then frequency sweeping method is used to adjust the frequency resolution to 0.125. Only the average values of three tests were reported in the present study.



(a) (b)

Fig. 1. Fiber felt core sandwich beam with the porosity of (a) 75% and (b) 90%.

RESULTS AND DISCUSSIONS

The acceleration admittance diagrams of sandwich beams and their corresponding steel beam with equal mass are presented in Fig. 2. The first two order natural frequencies of the sandwich structure are larger than those of the corresponding steel beam with equal mass. But the third order natural frequency of fiber felt core sandwich beam with the porosity of 90% is slightly lower than that of their corresponding steel beam with equal mass. It implies that the porosity of the fiber felt core will affect the natural frequency of the sandwich structure. In order to get the natural frequency and the damping ratio of the sandwich structure more accurately, frequency sweeping method is employed. According to the half power point method, the $1/\sqrt{2}$ time peak value of acceleration admittance of two frequency points, ω_L and ω_H, are

[a)] Corresponding author. zqc111999@mail.xjtu.edu.cn; jinzhao@mail.xjtu.edu.cn.

found to obtain the damping ratio. The damping ratio is obtained by: $\zeta=(\omega_H-\omega_L)/2\omega$, where ω is the frequency of peak value point of acceleration admittance.

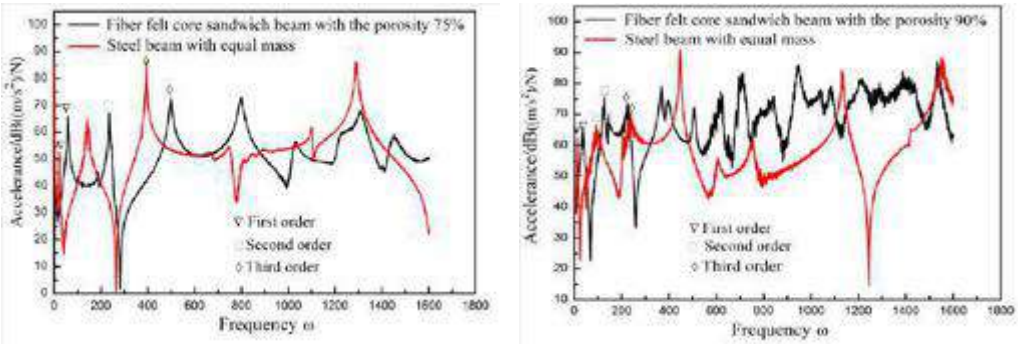

(a) (b)

Fig. 2. The Acceleration admittance diagram of sandwich beam and the corresponding steel beam with equal mass with the porosity of (a) 75% and (b) 90%

Table 1 The natural frequency and damping ratio of sandwich beam and the corresponding steel beam with equal mass.

Order	75% fiber felt core		Equal mass steel beam		90% fiber felt core		Equal mass steel beam	
	Frequency (HZ)	The damping ratio	Frequency (HZ)	The damping ratio	Frequency (HZ)	The damping ratio	Frequency (HZ)	The damping ratio
First	60	0.0061	21.2	0.021	35	0.0168	12.75	0.0100
Second	232.8	0.0097	140.3	0.0023	121.5	0.0040	82.875	0.0003
Third	493	0.0104	394	0.0007	227.7	0.0052	233	0.0002

The natural frequency and damping ratio of sandwich beams and their corresponding steel beam with equal mass are given in Table 1. The measured first order damping ratio of the steel beam with the same mass as that of the sandwich beam with core porosity of 75% is 0.021, which exists large errors. According to the literature [3], damping proportion of steel structure usually is about 0.0001-0.002. However, the damping characteristic of the fiber felt core sandwich structure is better than that of their corresponding steel beam with equal mass. By comparing the two groups of experiments, the porosity of core influences greatly the natural frequency and damping ratio of sandwich beam. It can be found that the natural frequency of each order will be reduced with the increasing of core porosity.

It is mainly because that the porosity of the fiber felt is inversely proportional to its density, which implies that the strength of the low density material will decrease. Therefore, the flexural rigidity of the sandwich structure with high porosity is low and the natural frequency decreases. By comparing the second and third order damping ratio, the damping ratio is reduced as the porosity increases. It is attributed that lower porosity of metal fibre corresponds to larger mass with denser micro fibers in unit volume. For the vibration of the sandwich beam, the relative displacement among the metal wires occurs and the friction resistance will increase. As a result, the damping characteristics are better.

CONCLUSIONS

The free vibration and damping characteristics of sandwich structure with fiber felt core were investigated based on the cantilever sandwich beam. The first three order natural frequencies and damping ratio are obtained by modal tests. It can be found the natural frequency and damping ratio of the sandwich structures with fiber felt core are better than those of the corresponding steel beam with equal mass. The natural frequency and the damping ratio of each order would be reduced with the increasing of core porosity.

References

[1] Evans A G, Hutchinson J W, Ashby M F. Multifunctionality of cellular metal systems [J]. Progress in Materials Science, 1998, 43(3): 171-221.

[2] Jichao Q, Zhengping X, Huiping T, et al. Review on Mechanical Properties of Porous Fiber Metals[J]. RARE METAL MATERIALS AND ENGINEERING, 2009, 38: 267-270.

[3] Depei Dai. Engineering application of damping technology [M]. Science press. 1991.

FREE VIBRATION ANALYSIS OF SANDWICH BEAMS WITH FOAM-CORRUGATED CORE

Zhijia Zhang[1,2], Bin Han[1,3], Weiwei Hui[1,2], Qiancheng Zhang[1,2a)], Feng Jin[1,2a)]
[1]*MOE Key Laboratory for Multifunctional Materials and Structures,*
Xi'an Jiaotong University, Xi'an 710049, PR China
[2]*State Key Laboratory for Mechanical Structure Strength and Vibration,*
Xi'an Jiaotong University, Xi'an 710049, PR China
[3]*School of Mechanical Engineering*
Xi'an Jiaotong University, Xi'an 710049, PR China

Summray The vibration performance of foam-filled corrugated sandwich beam was investigated in this paper. Based upon a micromechanics-based model, the effective elastic constants of foam-filled corrugations are derived by the homogenization method. It is used to predict the natural frequencies and vibration modes of the sandwich beam. In order to validate the equivalent model, model testing under clamped-free boundary conditions was carried out. The results using a homogenization method show good agreement with experimental tests.

INTRODUCTION

Hybrid-cores are constructed to enhance mechanical properties of sandwich structures. Such hybrid sandwich cores include pin-reinforced foams, foam-filled lattices. Among the hybrid lattice cores, metallic corrugations filled with polymer foams have attracted special attention on account of their relatively low manufacturing cost and good structural performance. As for the vibration of sandwich structures, it is important to predict the natural frequencies for design purposes. The analytic methods are tedious for sandwich structure. Finite element method (FEM) can be used for vibration analysis of complicated structures. But in order to accurately simulate porous material, it will cost high expense for the calculations, especially when the complicated problem needs greater accuracy. Generally, the equivalent model can be used to simplify the model. For the previous investigations, Liu et al [1, 2] derived the effective stiffness matrix of empty corrugated core. Han et al [3] obtained the equivalent elastic constants of foam reinforced corrugated core. In this paper, based on the equivalent model presented by Han, the model was simplified by ignoring the coupling of corrugated members and foam filling. Based on the above, the vibration performance of foam-filled corrugated sandwich beam was investigated for the case of clamped-free boundary conditions. In order to validate the equivalent model, the experimental tests were carried out.

THEORETICAL ANALYSIS

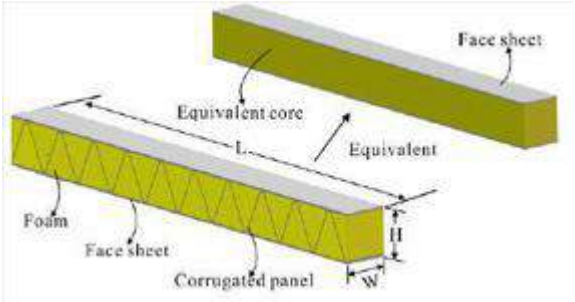

Fig. 1. Equivalent diagram of foam-filled corrugated sandwich beam.

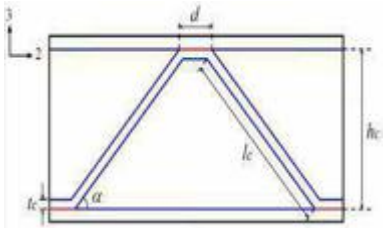

Fig. 2. Geometric parameters of hybrid core.

The foam-corrugation hybrid cores are treated as homogeneous orthotropic materials through principals of force equilibrium and energy equivalence as shown in Fig. 1. The face sheet and the corrugated members are made of 304 stainless steel, with the material properties of $E_s = 210\,\text{GP}$, $\rho_s = 7900\,\text{kg/m}^3$ and $\lambda_s = 0.3$. For Polymer foam Rohacell is $E_f = 70\,\text{MPa}$, $\lambda_f = 0.3$ and $\rho_f = 52\,\text{kg/m}^3$. Geometric parameters of sandwich core as indicated in Fig. 2 are: corrugated plate length $l_c = 44\,\text{mm}$, corrugation angle $\theta = 65^o$, width of corrugation platform $d = 4\,\text{mm}$, core height $h_c = 40\,\text{mm}$, the corrugated member thickness $t_c = 0.3\,\text{mm}$, and the face sheet thickness $t_f = 0.4\,\text{mm}$. The relative density of the hybrid core is $\rho_c = \nu_s + \rho_f(1-\nu_s)$, in which $\nu_s = 2\text{t}_f / l_c \cos 2\theta$ is the volume fraction of the core occupied by corrugation.

Estimation of the elastic stiffness of the core based on simple strength of materials formulas is informative as to the role of the foam. The contribution of coupling effect derived from foam filling on the deformation of corrugated members is little, and has been neglected. Only the contributions of stretching and bending deformation mechanisms for the corrugated

a) Corresponding author. zqc111999@mail.xjtu.edu.cn; jinzhao@mail.xjtu.edu.cn.

members and foam filling are considered in the elastic stiffness. The elastic stiffness of foam-corrugated hybrid core is given as:

$$C_{11}^H = \frac{\lambda E_s}{(1-\nu_s^2)} + \frac{(1-\lambda)E_f}{(1-\nu_f^2)}\ ; \quad C_{12}^H = \frac{\lambda \nu E_s}{(1-\nu_s^2)}\cos^2\theta + \frac{(1-\lambda)\nu_f E_f}{(1-\nu_f^2)}\ ; \quad C_{13}^H = \frac{\lambda \nu E_s}{(1-\nu_s^2)}\sin^2\theta + \frac{(1-\lambda)\nu_f E_f}{(1-\nu_f^2)}\ ;$$

$$C_{22}^H = \frac{E_s}{(1-\nu_s^2)}\left(\frac{t}{l}\right)\frac{\cos^3\theta}{\sin\theta} + \frac{E_s}{(1-\nu_s^2)}\left(\frac{t_c}{l_c}\right)^3 \sin\theta\cos\theta + (1-\lambda)C_{11}^f\ ; \quad C_{33}^H = \frac{E_s}{(1-\nu_s^2)}\left(\frac{t_c}{l_c}\right)\frac{\sin^3\theta}{\cos\theta} + \frac{E_s}{(1-\nu_s^2)}\left(\frac{t_c}{l_c}\right)^3 \sin\theta\cos\theta + (1-\lambda)C_{11}^f\ ;$$

$$C_{23}^H = \frac{E_s}{(1-\nu_x^2)}\left(\frac{t_c}{l_c}\right)\sin\theta\cos\theta - \frac{E_s}{(1-\nu_s^2)}\left(\frac{t_c}{l_c}\right)^3 \sin\theta\cos\theta + (1-\lambda)C_{12}^f\ ; C_{44}^H = \frac{E_s}{(1-\nu_s^2)}\left(\frac{t_c}{l_c}\right)\sin\theta\cos\theta + \frac{1}{4}\frac{E_s}{(1-\nu_s^2)}\left(\frac{t_c}{l_c}\right)^3\left(\frac{\sin^3\theta}{\cos\theta} + \frac{\cos^3\theta}{\sin\theta} - 2\sin\theta\cos\theta\right) + (1-\lambda)C_{66}^f\ ;$$

$$C_{55}^H = \lambda G_s \sin^2\theta + (1-\lambda)G_f\ ; \quad C_{66}^H = C_{55}^H\ .$$

EXPERIMENTS AND SIMULATIONS

Modal vibration tests were performed on sandwich beams for the case of calmed-free boundary condition. Experimental equipment includes the PCB impact hammer, B&K Type 8206-002 accelerometers, a charge amplifier, clamping system and LMS-Test-Lab modal analysis system. The experiment was carried out by mufti-point excitation and single point measurement. Only the averages of the measured results were reported in the present study. The equivalent mode was created by ABAQUS. The three-dimensional elements were employed for both the face sheets and the core of equivalent model. A mesh convergence study was carried out. A linear perturbation analysis step was created, and frequency extraction procedure was carried out with the lances solver.

VALIDATION AND DISCUSSION

The first three mode shapes and natural frequencies of sandwich beams have been obtained by numerical calculation and experiments, which are shown in Fig. 2. Good agreements between the results derived from equivalent model and experiments are obtained. The first and third shapes are the bending mode, while the second shape is a lateral mode. The discrepancy is less than 5% for first natural frequency of both methods, and less than 10% for the third frequency.

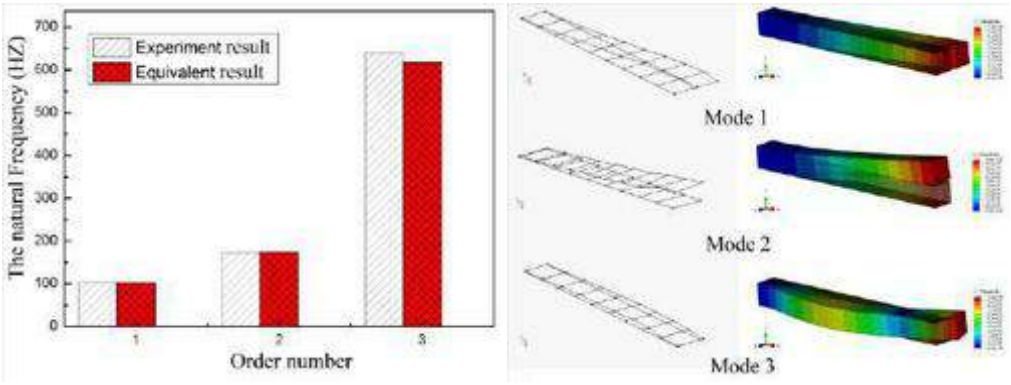

(a) (b)

Fig. 2. (a) The first three natural frequencies; (b) The first three vibration modes.

CONCLUSIONS

It has been shown from the comparison of the results from equivalent and experimental methods that equivalent models are well suited for calculating the frequencies and vibration modals of different sandwich beams with foam-filled corrugated cores. The results of the equivalent model presented in present study are obtained with good accuracy. The equivalent model is an efficient approach for the reduction of the cost and the time in the vibration analysis. Present study could give a hint for the researchers in the design and practical applications of the foam-filled sandwich structures.

References

[1] Liu T, Deng Z C, Lu T J. Structural modeling of sandwich structures with lightweight cellular cores[J]. Acta Mechanica Sinica, 2007,23(5):545-559.

[2] Liu T, Deng Z C, Lu T J. Minimum weights of pressurized hollow sandwich cylinders with ultralight cellular cores[J]. International journal of solids and structures, 2007,44(10):3231-3266.

[3] Han B, Qin K K, Yu B, et al. Design optimization of foam-reinforced corrugated sandwich beams [J]. Composite Structures, 2015, 130: 51-62.

COMPOSITES WITH ENHANCED CONDUCTIVITY AND YOUNG'S MODULUS AND DESIRED POISSON'S RATIO

Hanxing Zhu*
School of Engineering, Cardiff University, Cardiff CF24 3AA, UK

Summary We have designed two types of composites with size from macro- down to micro- and nano-scale. One type of the composites has an isotropic conductivity almost the same as the maximum possible upper limit, and the other type has an isotropic conductivity much greater than the conventional isotropic composites. The designed two types of composites can have an almost isotropic Young's modulus significantly greater than the Voigt limit and a Poisson's ratio at a desired value, e.g. positive, negative or 0. The designed composites have wide applications in many different structures from space aircrafts, land vehicles/buildings to underwater submarines.

GEOMETRICAL STRUCTURE OF THE COMPOSITES

We have designed two types of composites [1, 2], which are made of two different isotropic constituent materials, filler A and matrix B. The Young's moduli of the two constituent materials are assumed to be E_A and E_B, the Poisson ratios to be v_A and v_B, and the conductivities to be μ_A and μ_B, respectively. In the type-I composites, material A is assumed to have the geometrical structure of a perfect regular closed-cell foam with a large number of identical cubic cells of edge length L and square cell walls of uniform thickness t; material B is assumed to be identical cubes of edge length L-t, which are located at each of the cell centers of material A. Fig. 1(a) shows the representative volume element (RVE) of the type-I composites. In the type-II composites, material A is assumed to have the geometrical structure of a perfect regular open-cell foam with a large number of identical cubic cells which have uniform edges of length L and square cross-section of side t; material B is the matrix which fills the space of material A. The representative volume element (RVE) of the type-II composites is shown in Fig. 1(b).

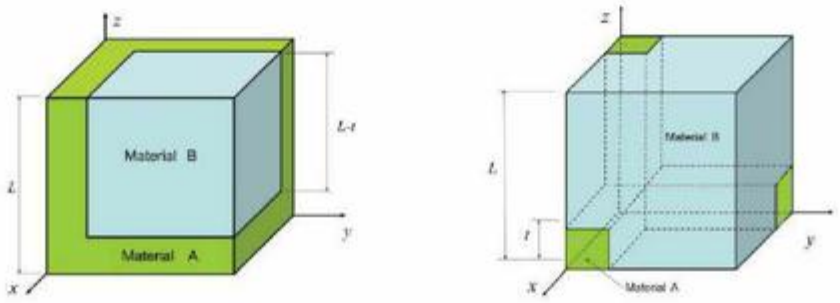

(a) Type-I (b) Type-II

Fig. 1. Cubic periodic representative volume elements (RVEs) of the two types of composite materials.

ELASTIC PROPERTIES OF THE COMPOSITES

1. Enhanced Young's modulus

As the two types of composites have cubic symmetry, they have only three independent elastic constants [3] and are almost isotropic. When $E_A = 2E_B$ and $v_A =$ $_B$, the relationship between the Young's modulus of the composites and the volume fraction of material A is shown in Fig. 2(a), where Young's modulus is normalized by the Voigt limit. The Hashin—Shtrikman's upper and lower bounds, and the Reuss limit are also included for comparison. As can be seen in Fig. 2(a), when the effects of the Poisson ratios are absent (i.e. $v_A =$ $_B$), the type-I composites are in general stiffer than

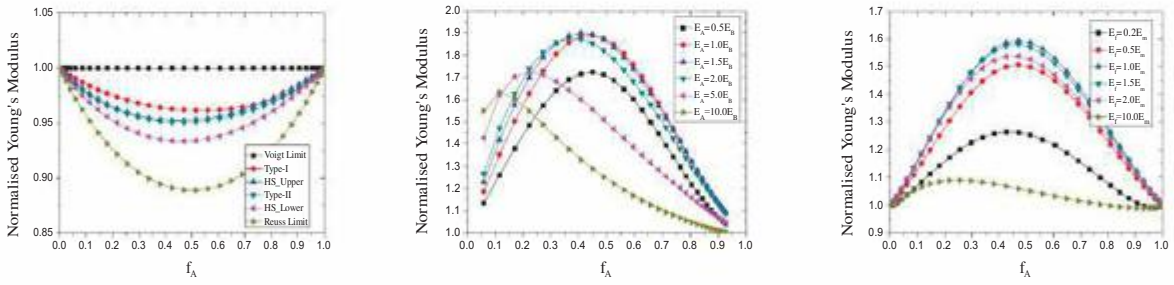

(a) (b) (c)

Fig. 2. Relationship between the Young's modulus of the composites and the volume fraction of material A.

* Email: zhuh3@cf.ac.uk

the Hashin-Shtrikman's upper limit, and the stiffness of the type-II composites is very close to the Hashin-Shtrikman's upper limit and much greater than their lower limit. As the Hashin-Shtrikman's upper limit is generally recognized as an unexceedable upper limit for isotropic composites when the effects of the Poisson's ratios are absent, the results in Fig. 2(a) clearly demonstrate that the designed structures of the two types of composites can significantly enhance the stiffness of composites [1, 2]. For isotropic solid materials, the value of the Poisson's ratio is in the range between 0.5 and -1.0. When $\nu_A = 0.45$ and $\nu_B = -0.8$, the relationships between the effective Young's modulus of the two types of the designed composites and the volume fraction of materials A are shown in Figures 2(b) and 2(c), where the Young's modulus is normalized by the Voigt limit. As can be seen, for different combinations between the Young's moduli of materials A and B, the normalized Young's moduli of the composites are much larger than 1.0, and hence much larger than the Voigt limit [1, 2].

2. Desired Poisson's ratio

When $\nu_A = 0.45$ and $\nu_B = -0.8$, the relationships between the effective Poisson's ratio of the two types of the designed composites and the volume fraction of materials A are shown in Figures 2(b) and 2(c). As can be clearly seen, the Poisson's ratio of the composites could be designed to have a desired value, e.g. positive, negative or 0 [1, 2].

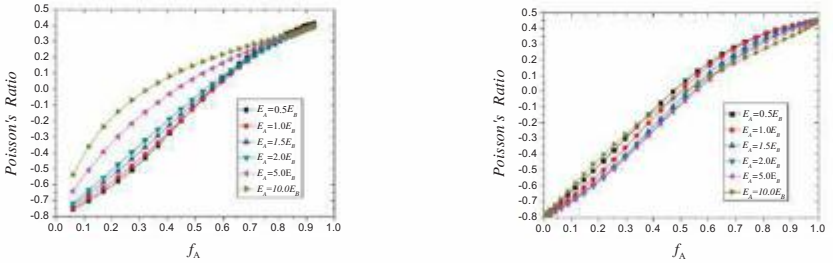

(a) Type-I (b) Type-II

Fig. 3. Relationship between the Poisson's ratio of the composites and the volume fraction of material A.

CONDUCTIVITIES OF THE COMPOSITES

When $\mu_A = 10\mu_B$, the relationship between the normalised effective conductivity of the two types of composites and the volume fraction of material A is presented in Fig. 4, where the Voigt limit, the Hashin-Shtrikman's upper and lower limits and the Reuss limit are included for comparison. The Hashin-Shtrikman's upper limit is generally recognized as an unexceedable upper limit for the conductivity of isotropic composites. As can be seen, the structure of the type-I composites can maximize the isotropic conductivity and the type-II composites have an isotropic conductivity very close to the Hashin-Shtrikman's upper limit and much greater than their lower limit [4].

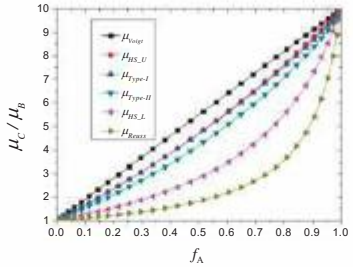

Fig. 4. Comparison between the conductivities of the two types of composites and the well known limits.

CONCLUSIONS

The designed two types of composites have not only enhanced stiffness and conductivity, but also a desired value of Poisson's ratio. The size of the designed composites can be at macro- down to micro- and nano-scale. They have very important applications in many different structures from space aircrafts, land vehicles/buildings to underwater submarines.

REFERENCES

[1] Zhu H.X., Fan T.X. and Zhang D.: Composite Materials with enhanced dimensionless Young's modulus and desired Poisson's ratio, *Nature Scientific Reports*, **5**: 14103, 2015. http://www.nature.com/articles/srep14103

[2] Zhu H.X., Fan T.X., Xu C.H. and Zhang D.: Nano-structure composited with enhanced Young's modulus and desired Poisson's ratio, *submitted for publication.*

[3] Zhu H.X., Knott J.F. and Mills N.J.: Analysis of the elastic properties of open-cell foams with tetrakaidecahedral cells, *J. Mech. Phys. Solids*, **45**: 319-343, 1997.

[4] Zhu H.X., Fan T.X. and Zhang D.: Composite materials with enhanced conductivities, *Adv. Eng. Mater.*, to appear, 2016.

SM09 - Phase and Chemical Transformations and Thermomechanical Phenomena

TS.SM09-1.01	Guduru, Pradeep - The influence of elastic strain on catalytic activity (INVITED)	2390
TS.SM09-1.02	Belyaev, Alexander - An approach to modeling the effect of hydrogen on stress-strain material law	2392
TS.SM09-1.03	Di Leo, Claudio - Chemo-mechanics theory for amorphous Silicon electrodes	2394
TS.SM09-1.04	Freidin, Alexander - Chemical affinity tensor and kinetics of stress-assisted chemical reaction front	2396
TS.SM09-1.05	Song, Jizhou - Purification of single-walled carbon nanotubes based on thermocapillary flow	2398
TS.SM09-2.01	Elliott, Ryan - Reversible temperature- and stress-induced martensitic transitions in crystals	2400
TS.SM09-2.02	Biggs, Daniel - Periodic and propagating instabilities in superelastic NiTi wire twists	2402
TS.SM09-2.03	Charkaluk, Eric - Full-field based thermomechanical determination of elastoplastic parameters in polycrystals	2404
TS.SM09-2.04	Xia, Minglu - Jump phenomena of thermomechanical responses for nonlinear vibration with NITI	2406
TS.SM09-2.05	Le, Khanh Chau - Dislocation mechanism of microstructural changes in ductile single crystals	2408
TS.SM09-3.01	Levitas, Valery - Phase field approach to phase transformations, twinning, dislocations, and their interaction (INVITED)	2410
TS.SM09-3.02	Silling, Stewart - The thermodynamic form of peridynamics with application to phase transformations	2412
TS.SM09-3.03	Ahluwalia, Rajeev - Phase field modeling of martensitic transformations in nanocrystalline materials	2414
TS.SM09-3.04	Jiang, Dongjie - Modelling of axial buckling and recovery of pseudoelastic NiTi tubes	2416
TS.SM09-3.05	Song, Zilong - An analytical model for phase transitions of an SMA wire under uniaxial tension	2418
TS.SM09-3.06	Wheeler, Robert - Actuator lifetime predictions for Ni60Ti40 shape memory alloy plate actuators	2420
TS.SM09-4.01	Sun, Qingping - Enhance fatigue resistance of NiTi by grain size gradient (INVITED)	2422
TS.SM09-4.02	Constantinescu, Andrei - Two scale analysis of the fatigue of shape memory alloys	2424
TS.SM09-4.03	Daly, Samantha - The effect of microstructure on phase transformation in shape memory alloys	2426
TS.SM09-4.04	Favier, Denis - Uniform or localized pure bending deformation of superelastic NiTi thin wires	2428
TS.SM09-4.05	Lepage, William - Thermomechanical Characterization of Shape Memory Alloy Mode I Fracture Behavior	2430
TS.SM09-4.06	Phillips, Francis - Fracture of Ni60Ti40 shape memory alloy notched plates under cooling	2432
TS.SM09-5.01	Qu, Jianmin - Interface-reaction controlled diffusion in binary solids (INVITED)	2434

TS.SM09-5.02	Guo, Shu - An integrated temporal multi-scale multi-physics model with damage in multifunctional materials	2436
TS.SM09-5.03	Panchenko, Artem - Analysis of Mie-Gruneisen equation of state for two-dimensional crystal lattices	2438
TS.SM09-5.04	Babenkov, Mikhail - Unsteady heat conduction processes in a harmonic crystal with a substrate potential	2440
TS.SM09-5.05	Akbarzadeh, Hamid - Multiscale Modeling of Thermal Wave: From Non-local Continuum to Molecular Dynamics	2442
TS.SM09-5.06	Issa, Sally - Influence of martensitic phase transformation on crack propagation in austenitic steel	2444
PO.SM09-1.01.284	Demmouche, Younes - Martensite and temperature effect on the mechanical behavior of a TRIP stainless steel	2446
PO.SM09-1.02.285	Du, Haiyang - Shape recovery properties of shape memory polymer tube under torsion deformation	2448
PO.SM09-1.03.286	Tsvetkov, Denis - Energy distribution in one-dimensional crystal	2450
PO.SM09-1.04.287	Yin, Bingbing - Finite element simulation of TGO growth stress in TBC system considering large deformation	2452
PO.SM09-1.05.288	Zemskov, Andrei - General algorithm of solution of 2-dimension problems of mechano-diffusion	2454
PO.SM09-1.06.289	Zhao, Xian Feng - The attractive force and repulsive force of a HTS/PM system under field cooling condition	2456

THE INFLUENCE OF ELASTIC STRAIN ON CATALYTIC ACTIVITY

Kai Yan[1], A.Khorshedi[1], T.A.Maark[1], A.Peterson[1] & P.R.Guduru[1]
[1]*School of Engineering, Brown University, Providence, Rhode Island, USA*

Summary Understanding the role of elastic strain in modifying catalytic reaction rates is crucial for catalyst design, but experimentally, this effect is often coupled with a ligand effect. To isolate the strain effect, we have successfully investigated the influence of externally applied elastic strain on catalytic activity of metal films towards the hydrogen evolution reaction (HER). We show that elastic strain tunes the catalytic activity in a controlled and predictable way. Both theory and experiment show strain controls reactivity in a controlled manner consistent with the qualitative predictions of the HER volcano plot and the d-band theory: Ni and Pt's activity were accelerated by compression, while Cu's activity was accelerated by tension. By isolating the elastic strain effect from the ligand effect, this study provides a greater insight into the role of elastic strain in controlling electrocatalytic activity.

The role of elastic strain in tuning catalytic reaction rates has evolved rapidly in the last decade and has initiated a significant re-evaluation of catalyst design. Specifically, researchers have examined the role of misfit strain arising when a catalytically-active metal overlayer is epitaxially deposited on another metal substrate or when a shell metal is deposited around a core metal to form a core/shell nanoparticle.[1] In general, the misfit strain changes the width of the d-band through changes to the d-orbital interactions that are quite sensitive to interatomic spacing r, scaling as r^{-5}.[1b, 2] Changes in the d-band width modify reactivity of the strained surface by shifting the mean d-band energy (the "d-band center") relative to the Fermi energy, which influences the bonding and anti-bonding states of adsorbates and reactants on the metal surface.[3] Early experimental evidence of strain effects on phenomena related to catalysis was reported by Gsell *et al*.[4] who demonstrated that O adsorption on Ru could be enhanced under tensile strain. Strasser *et al*. studied PtCu@Cu core@shell system formed by de-alloying Pt-Cu nanoparticles,[5] and attributed increases in catalytic activity for oxygen reduction reaction (ORR) to the elastic strain in the de-alloyed shell. Recently, Deng *et al*.[6] studied the influence of elastic strain in 111-textured thin films of Au and Pt on polyimide on its electrocatalytic activity for HER. More recently, Yang *et al*.[7] demonstrated a similar effect on a Pd-based metallic glass catalyst film under both tensile and compressive strains, which have opposite effect on catalytic activity towards ORR.

Here we report a systematic study of the effect of externally applied elastic strain on catalytic activity of pure metal films towards HER. Production of H_2 from water splitting is one of the most well-studied electrocatalytic reactions.[18] HER, which is the half-cell reaction responsible for the evolution of H_2, it is ideally suited for studying the effect of elastic strain as it is well established that the binding energy of H_2 --- expressed as the free-energy change of hydrogen adsorption (ΔG_H) --- is the primary predictor of the effectiveness of an electrocatalyst for HER, with an ideal catalyst having ΔG_H of 0 eV. Catalytic activity of various metals for HER is often represented by a volcano plot, which shows activity versus ΔG_H. On such a plot, the peak of the volcano (maximum activity) occurs at ΔG_H of 0 eV. The activity decreases to the left of volcano peak due to stronger H binding ($\Delta G_H < 0$), the activity decreases to the right of the peak as well where H binding is weaker ($\Delta G_H > 0$).[20] According to the d-band model, compressive strains generally weaken the binding strength of adsorbates whereas tensile strains enhance it.[14, 21] Hence, we should expect compressive strain to weaken the H binding energy on metals to the left of the volcano peak, moving them towards the peak and thus enhancing their activity towards HER; tensile strain should decrease activity. However, strain is expected to have the opposite qualitative effect on metals to the right of the volcano peak, i.e., compressive strains should move those metals further from the volcano peak and decrease the HER activity; while tensile strains should increase activity. In this investigation, we choose three metals that span the volcano plot: Ni (left of the peak), Pt (near the peak) and Cu (right of the peak), which provide a representative set to investigate the effect of elastic strain and the predictions of the d-band model. The metal films are subjected to externally applied compressive and tensile loading while they are participating in HER. Simultaneously, we performed density functional theory (DFT) calculations on Pt, Ni, and Cu(111) surfaces under various loading conditions to more precisely quantify the theoretical predictions, and further interpret the experimental measurements in terms of changes in the H binding energy.

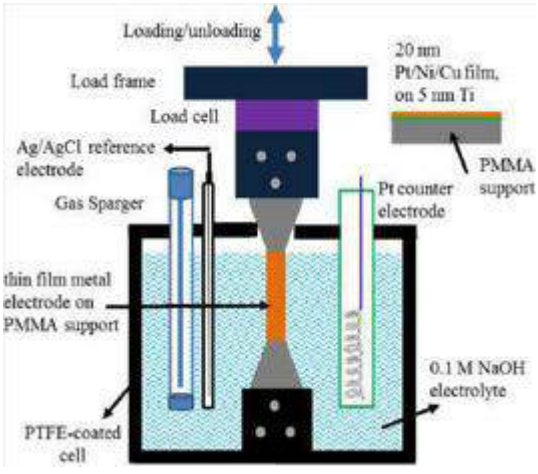

Figure 1. Experimental setup to subject thin metal films to elastic straining by applying compressive or tensile loading on the PMMA substrates in a universal mechanical tensing machine.

[a] Corresponding author. Email: Pradeep_guduru@brown.edu.

Thin films of the three metals under consideration (Pt, Ni and Cu) were synthesized by sputtering on PMMA (polymethylmethaacrylate) substrates. Elastic strains were applied on the films by subjecting the PMMA substrates to tensile and compressive loading. An electrochemical cell was designed to be integrated with a universal mechanical testing machine as shown in Figure 1. The activity of the films for HER was studied at each load value through cyclic voltammetry (CV) in 0.1 M NaOH electrolyte by monitoring the changes in the potential at specified values of HER current. The samples were held at each constant strain while CV scans were collected. Experimental measurements of the CV shift for all three metals, i.e., Pt, Ni and Cu are shown in Figures 2a-c; note that compressive and tensile strains were taken as negative and positive respectively. Moreover, the shift of the CV to the right (i.e. reduction in overpotential or increase in activity) was taken as positive and that to the left (increase in overpotential or lower activity) is taken as negative. Figure 2 reveals a number of important features: (i) The CV shift was approximately linear with applied elastic strain for all three metals in the experimentally accessed strain range. The magnitude of the slope of the linear relation was in the range of 10 mV per 1% strain for all three metals. (ii) Compressive strain increased the HER activity of Pt and Ni and decreased that of Cu. This is a striking observation and is in good agreement with the theoretical predictions also shown in the figure, discussed further below. (iii) These results cleanly separate the strain effect from the ligand effect, thus establishing the magnitude of the former, which can provide a useful guideline for design of nanostructured catalysts.

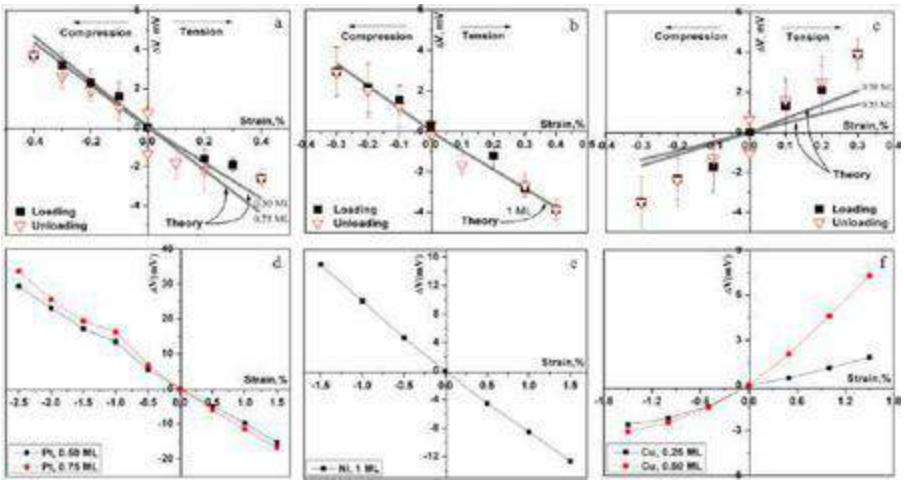

Figure 2. CV-curve-shifts relative to the zero strain level as a function of applied elastic strain for (a) Pt, (b) Ni and (c) Cu. Positive potential shift denotes reduction in overpotential and vice versa. Note the qualitative difference between Cu and the other two metals; compressive strain increases catalytic activity for Pt and Ni whereas the effect is opposite for Cu, which is on the other side of the volcano peak. The solid lines (gray color) on the experimental data represent the computational results from the bottom row of figures. Bottom row shows the potential shifts obtained computationally for (d) Pt(111), (e) Ni(111), and (f) Cu(111) surfaces at different hydrogen coverages as a function of in-plane predominantly uniaxial strain. The plots shown are average responses for straining along perpendicular in-plane directions. Note that the computationally accessible range of strain values is much larger than what was experimentally accessible.

We carried out density functional theory (DFT) calculations of the hydrogen binding energy on fcc(111) surfaces for the same metals under the application of in-plane uniaxial loading in the range of ±1.5%. The computational results within the experimental loading range were superposed on the experimental data in Figures 2a-c as gray solid lines. Despite the simplicity of the computational model, the agreement with the experimental data is remarkably good in all three cases. In particular the computations also capture the reversal in the strain effect on HER activity of Cu compared to that of Pt and Ni. This also suggests that the peak of the volcano plot is correctly placed to the right of Pt; that is, Pt binds H slightly too strongly.

In summary, we experimentally demonstrate that externally applied elastic strain can influence the HER activity of Pt, Ni and Cu thin films catalysts in a predictable way, consistent with the predictions of the d-band model on the hydrogen binding energy and with the hydrogen-evolution volcano. By separating the strain effect from the ligand effect, we demonstrate that the effect of strain on metals on opposite sides of the volcano peak is reversed, i.e., compressive strain increases the catalytic activity of metals to the left of the volcano peak and reduces that of the metals to the right. Tensile strain has the opposite effect. The experimental observations match theoretical calculations qualitatively and quantitatively. The combined experimental and computational study presented here shows the power of separating the strain and ligand effects and offers new insights into the design of catalysts not only for HER, but also other electrocatalytic reactions of interest.

References

[1] a) M. Mavrikakis, B. Hammer, J. K. Nørskov, *Phys. Rev. Lett.* 81: 2819-2822, 1998; b) J. R. Kitchin, J. K. Nørskov, M. A. Barteau, J. G. Chen, *Phys. Rev. Lett. 93:* 156801, 2004;

[2] a) B. Hammer, et al. *Phys. Rev. Lett.76:* 2141-2144, 1996; b) A. Ruban et al. *J. Mol. Catal. A* 115: 421-429, 1997; c) B. Hammer, et al. 343:211-220, 1995.

[3] L. A. Kibler et al. *Angew. Chem. Int. Ed. 44:* 2080-2084, 2005.

[4] M. Gsell et al. *Science* 280: 717-720, 1998.

[5] P. Strasser et al. *Nature Chem.2:* 454-460, 2010.

[6] Q. Deng et al. *J. Catal.* 309: 351-361, 2014.

[7] Y. Y. Yang, et al. *Phys. Chem. Chem. Phys.* 17: 1746-1754, 2015.

AN APPROACH TO MODELING THE EFFECT OF HYDROGEN ON STRESS-STRAIN MATERIAL LAW

Alexander Belyaev [1a)], Vladimir Polyanskiy [1]
[1]*Mechanics and Control Dept., Peter-the-Great St. Petersburg Polytechnic University, St. Petersburg, Russia*

Summary A general approach to modeling the effect of hydrogen on stress-strain state of materials is addressed. A two-continua model is constructed which allows one to describe the kinetics of hydrogen in metals. The developed rheological model is appropriate for estimation of the hydrogen transition from mobile to bounded state depending on the stress-state relation and description of the localization of the connected hydrogen that results in the material fracture. A novel approach to modeling the solids with account for the influence of hydrogen on the properties of free surface on monocrystals at various scales is suggested.

One of the most challenging problems of the material science is the influence of hydrogen on the mechanical properties of materials. This influence itself is a good example of crucial importance of small parameter in mechanics since the mean mass concentration of 0.4-0.8 ppm (part per million) causes hydrogen embrittlement in aluminum alloys. The hydrogen embrittlement is a source of many technical catastrophes and for this reason its nature is carefully investigated, e.g. [1]. Nowadays the structural design is not possible without precise strength computation. However the hydrogen considerably affects the strength of metals, that is, modeling of the hydrogen influence is a subject of permanent interest.

Several approaches will be discussed in the presentation. They are: (i) account of the influence of hydrogen on origination and motion of dislocations, (ii) account of the influence of hydrogen on the crack development, (iii) account of the internal pressure of hydrogen in metals and (iv) some physical approaches. Origination and motion of dislocations as well as the hydrogen-enhanced localized plasticity (HELP) [2] in the vicinity of the crack tips leads to the local plasticity because of the high concentration of dislocations. However the calculations in [3] demonstrated that this model demonstrates some considerable change in the strain-stress law only under the concentration about 9000 ppm which is not extremely high concentration for the majority of metals and not feasible for the real engineering structures. Another model which is analogous to the HELP is the De-cohesion model (hydrogen enhanced decohesion model, HEDE for short), cf. [4]. The difference between them is that the HEDE model takes into account that the energy of appearance of the free surfaces of fracture reduces with increase of the local hydrogen concentration. The HELP approach requires a great computational costs for solving any practical problems, cf. [5]. For this reason the only solution is utilizing a continual model of dislocation growth however this substitution turns out to be not adequate and the authors suggest to make use of the criterion of growth of submicrocrack, i.e. they reduce all the hydrogen problems to the modeling of the crack developing and reduction of the crack resistance.

The adequate modeling of the behaviour of structures affected by hydrogen requires a special approach which is capable for account for influence of small concentration of hydrogen on the mechanical characteristics of materials. We suggest a two-component continuum for modelling the hydrogen effects. However it is necessary to understand that the natural hydrogen exists in both diffuse and bound forms in any material. An important role is played by the binding energy of hydrogen in material. It is known that, inside the materials, hydrogen is found in traps with different binding energies. In steels the total hydrogen content is 0.1-6 n.cm3/100g, while it is only hydrogen with a low binding energy that affects the strength, i.e. diffusively mobile hydrogen. In aluminum alloys the entire hydrogen diluted in the metal has a low binding energy – about 0.2-0.8 eV. The concentrations that are critical for the mechanical strength of weakly bound hydrogen in steels and aluminum alloys are similar – they are decimal ppm fractions. In aluminium alloys it includes the entire diluted hydrogen, while in steels it amounts to 5-10% of the total amount of diluted hydrogen. However the hydrogen with low binding energy tends to zones of tensile stresses (Gorsky's effect [6]). Accumulation of hydrogen in the destruction zone occurs both by the input from outside and by redistribution of natural hydrogen inside the material. The hydrogen with low binding energy is diffuse however its interaction with material is very weak. The hydrogen with high binding energy interacts with material very intensively resulting in degradation of the mechanical material properties because of this interaction.

The scheme of constructing the new rheological model is as follows. Two states of the hydrogen are assumed, namely a diffuse (mobile) one and a bounded (settled) one. For each state the equations for the mass balance are formulated and the equation governing the exchange between these states is derived, too. These equations are reformulated in terms of concentrations of the both states of the natural hydrogen in materials. It allows one to describe the process of redistribution of the diffuse and bounded hydrogen inside the material. The equation of dynamics for the structural materials is used to derive the the rheological model of the material containing hydrogen. The model is assumed to consist of two continua. The first continuum is a solid and plays a part of a carrying structure. The second one describes the behavior of hydrogen inside the first continuum and is considered as an ideal gas. The equation of dynamics is written down for each continuum and the interaction between them is modeled by a source term depending upon the velocities of each component.

[a)] Corresponding author. Email: vice.ipme@gmail.com

For the sake of simplicity the presentation is limited to the one-dimensional case since it allows one to catch the main idea of construction of the rheological model for material with low hydrogen concentration. In one-dimensional case a virgin lattice can be schematically depicted as a 1D spring. The weakening of the internuclear bonds caused by "landing" of the hydrogen particles can produce the chain formations of new internuclear bonds as the serial connections of elastic bonds of the basic lattice and the introduced elastic bonds of new elements which are the hydrogen particles. Obviously, such a consideration is reasonable for the case of low hydrogen concentration. The overall elastic modulus of the resulting lattice with hydrogen can be much lower than the elastic modulus of the virgin material and strongly depends on concentration of the bound hydrogen. In turn, the latter is determined by the diffusion of the mobile hydrogen however the distribution of the mobile hydrogen depends upon the stress distribution in the structure under consideration. In 1D case, the overall system of equations counts 14 equations and some dependences are strongly nonlinear. In particular, the state equation for the hydrogen pressure is temperature-dependent since we apply the equation for the ideal gas occupying the clear space (voids) in porous medium. This system can be linearised since the problem has some natural small parameters such as low hydrogen concentrations. It allows us to introduce the factors of sorption and desorption of the hydrogen and solve a few problems. The result is some closed form expressions for the hydrogen concentration in the material. The obtained results were compared with the experimental data in [20,21] the maximal tensile stress versus the concentration of the diffuse mobile hydrogen in AISI 4135 steel and demonstrated a good match.

As a summary we can say that a rheological model is constructed which allows one to describe the kinetics of hydrogen in metals, and in particular to estimate the hydrogen transition from mobile into bounded state depending on the stress-state relation and to describe the localization of the connected hydrogen resulting in the material fracture. This distribution affects the stress-strain material law, too. We suggest a novel approach to modeling the solids with account for the influence of hydrogen on the properties of free surface on monocrystals at various scales. Application of the two-component model to describing the multiscale materials allows obtaining the adequate results which describe the influence on properties of these structures. In particular, the suggested approach is also applicable at the nanoscale. For example, in contrast to the homogeneous materials, the nanocrystal materials in the presence of hydrogen demonstrate stabilization of their properties since the hydrogen decreases the surface energy of crystals in material and prevent their increasing up to the microsize.

Acknowledgement. The research is carried out under the financial support by Russian Science Foundation, grant 15-19-00091.

References

[1] R. J. Bourcierf, D. A. Koss Hydrogen Embrittlement of Titanium Sheet Under Multiaxial States of Stress, Acta metall. V. 32, No. 11, pp. 2091-2099, 1984

[2] H.K. Birnbaum, P. Sofronis, Hydrogen-enhanced localized plasticity—a mechanism for hydrogen-related fracture, Mat. Sci. and Eng.: A, V. 176, I. 1–2, 31 1994, pp. 191-202

[3] P. Sofronis, Y. Liang, N. Aravas, Hydrogen induced shear localization of the plastic flow in metals and alloys, European J. of Mech. - A/Solids, V. 20, I. 6, 2001, Pages 857-872

[4] A.G. Varias, A.R. Massih, Simulation of hydrogen embrittlement in zirconium alloys under stress and temperature gradients, J. of Nuclear Mat., V. 279, I. 2–3, 2000, p. 273-285

[5] A.V. Ignatenko, I.K. Pokhodnya, A.P. Paltsevich, V.S. Sinyuk, Dislocation Model of Hydrogen-Enhanced Localizing of Plasticity in Metals With BCC Latttice, The Paton Weld J., I. 3, 2012, p. 15-19

[6] Gorsky W.S."Theorie des elastichen Nachwirkung in ungeordneten Mischkristallen (elastische Narchwirkung zweiter Art)", Phys. Zeitschrift der Sowjetunion, 8, p. 457–471, (1935)

[7] E. Lunarska, Z. Wokulski, Effect of hydrogen charging on stress-strain curves for iron whiskers, Acta Metallurgica, V. 30, I. 12, 1982, p. 2173-2179

[8] Yihong Nie, Yuuji Kimura, Tadanobu Inoue, Fuxing Yin, Eiji Akiyama, Kaneaki Tsuzaki, Hydrogen Embrittlement of a 1500-MPa Tensile Strength Level Steel with an Ultrafine Elongated Grain, Metallurgical and Materials Trans. A V. 43 N. 5, 2012 p. 1670-1687

CHEMO-MECHANICS THEORY FOR AMORPHOUS SILICON ELECTRODES

Claudio V. Di Leo *[1], Elisha Rejovitzky[2], and Lallit Anand[2]
[1]*School of Aerospace Engineering, Georgia Institute of Technology, Atlanta, United States*
[2]*Department of Mechanical Engineering, Massachusetts Institute of Technology, Cambridge, United States*

Summary In this work, we formulated, numerically implemented, and calibrated a fully-coupled diffusion-deformation model for amorphous Silicon (a-Si) anodes. Importantly, the model, and accompanying computational implementation, are capable of reproducing both the mechanical and electrochemical experimentally measured response of these anodes. We applied our calibrated simulation capability to modeling cycling of hollow a-Si nanotubes, and showed that our simulations results, without parameter adjustment, are in good agreement with the experimentally-measured voltage vs. state-of-charge (SOC) at various charging rates. Further, using our theory and simulations, we identified and quantified two major effects of plasticity on the electrochemical performance of a-Si anodes:

INTRODUCTION

Amorphous Silicon (a-Si) is an attractive material for Li-Ion batteries due to its ≈ 10 fold increase in gravimetric capacity over current generation graphite anodes. To mitigate deleterious effects associated with the outward expansion of the a-Si as it is lithiated, researchers have developed complex anodes, such as hollow Si/SiO_2 double-walled nano tubes [1], which effectively restrict the outward expansion of the a-Si as it is being lithiated. Much has been done in the field of modeling a-Si anodes recently (cf. [2] and references therein); however, few models and simulation tools have been built (and validated) which can capture the mechanical and electrochemical response of complex anodes. This work satisfies this need by formualting, calibrating, and validating a theory and numerical capability for modeling a-Si anodes.

SUMMARY OF THE THEORY

We employ a multiplicative decomposition of the form

$$\mathbf{F} = \mathbf{F}^e\mathbf{F}^p\mathbf{F}^s, \quad \text{with} \quad \mathbf{F}^s = (J^s)^{1/3}\mathbf{1}, \quad \text{and} \quad J^s = 1 + \Omega(c_{\text{R}} - c_{\text{R}0}). \tag{1}$$

Here, $\mathbf{F}^e$, $\mathbf{F}^p$, and $\mathbf{F}^s$ denote the elastic, plastic, and swelling distortions respectively. The swelling distortion $\mathbf{F}^s$ is taken to be spherical and to depend on the lithium concentration as shown, where Ω is the partial molar volume of Li in the body, c_{R} is the molar concentration of Lithium in the reference body, and $c_{\text{R}0}$ the initial concentration.

The Cauchy stress $\mathbf{T}$, is given by the elastc Mandel stress $\mathbf{M}^e$ through

$$\mathbf{T} = J^{e-1}\mathbf{R}^e\mathbf{M}^e\mathbf{R}^{e\top}, \quad \text{and} \quad \mathbf{M}^e = 2G\mathbf{E}^e + (K - (2/3)G)\,(\text{tr}\mathbf{E}^e)\mathbf{1} \tag{2}$$

where $\mathbf{E}^e$ is an elastic logarithmic strain measure, and G and K are concentration dependent elastic moduli. The plastic distortion $\mathbf{F}^p$ evolves according to

$$\mathbf{F}^p = \frac{3}{2}\epsilon^p\frac{\mathbf{M}^e_0}{\sigma}, \quad \text{with} \quad \epsilon^p = \begin{cases} 0 & \text{if} \quad \sigma \le Y\ c) \\ \epsilon_0\left(\dfrac{\sigma - Y\ c)}{Y\ c)}\right)^m & \text{if} \quad \sigma > Y\ c) \end{cases} \tag{3}$$

Here, $\epsilon^p \ge 0$ is the equivalent tensile plastic strain, σ is the equivalent tensile stress, and $\mathbf{M}^e_0$ is the deviator of $\mathbf{M}^e$. Further, in (3), $Y\ c)$ is a *concentration-dependent yield strength*, ϵ_0 is a reference tensile plastic strain rate, and m is a measure of the strain-rate sensitivity of the material. To model the experimentally-observed concentration-dependent change in the yield strength of a-Si we adopt the following specific form for $\hat{Y}(^-)$,

$$\hat{Y}(^-) = Y_{\text{sat}} + (Y_0 - Y_{\text{sat}})\exp(-c/c_*), \tag{4}$$

with $\{Y_0, Y_{\text{sat}}, {}^-{}_*\}$ three positive-valued material parameters which must be determined, and c a normalized concentration.

The diffusion of Li is governed by the local balance of species concentration through

$$c_{\text{R}} = -J\text{Div}\mathbf{j}, \quad \text{with} \quad \mathbf{j} = -m\text{grad}\mu, \quad m = \frac{D_0}{R\vartheta}c(1 - {}^-), \quad \text{and} \quad \mu = \mu^0 + R\vartheta\log\left(\gamma\frac{c}{1-c}\right) - \Omega\frac{1}{3}\text{tr}\mathbf{M}^e \tag{5}$$

Here, $\mathbf{j}$ is the spatial flux of Li, m is the mobility which is concentration dependent and given by the diffusivity D_0, and μ is the chemical potential, where γ is a concentration dependent activity (cf. [2]).

Finally, in a simulation we wish to prescribe a constant current I at a point and measure the corresponding Voltage V in order to compare to galvanostatic (constant current) experiments from the literature. To achieve this we use symmetric Butler-Volmer kinetics which yields that the voltage may be compute from (see [3] for details)

*Corresponding author. Email: cvdileo@gatech.edu

$$V = V_0 - \text{———} + 2\text{—} \qquad \left(-\text{- - -}\right), \quad \text{with} \quad I_0 = \quad {}_0 \quad - c\ c) \quad . \tag{6}$$

Here, μ^{surface}

additional material parameter, a reaction constant k_0 which must be experimentally determined as is done next.

CALIBRATION OF THE MATERIAL PARAMETERS

In order to determine these parameters we have simulated the experimental results of Pharr an co-authors [4]. They performed galvanostatic cycling experiments on thin a-Si films while simultaneously measuring the voltage-charge behavior, and the film stress vs. charge behavior. The film stress was measured using a substrate curvature technique. The figure on the right compares our simula-

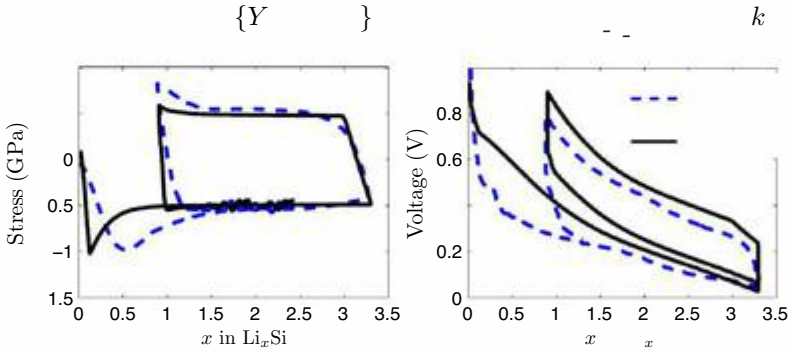

both as functions of the stoichiometric amount x in Li$_x$Si. The final list of material parameters used can be found in [3].

MODELING HOLLOW DOUBLE-WALLED A-SI NANOTUBE ANODES

In order to mitigate the deleterious effects associated with the outward expansion of a-Si as it is being Lithiated, various research groups have proposed the use of novel a-Si anode designs which restrict the deformation of the anode. One such design, experimentally realized by [1], involves fabricating hollow a-Si nanotubes whose outside has been oxidized, see Fig (a) below.

nanotube.

We have applied our *fully calibrated theory* to modeling these hollow double-walled nanotubes. On the Figure to the right, (b) shows contours of normalized concentration c and equivalent plastic strain ϵ^p after three

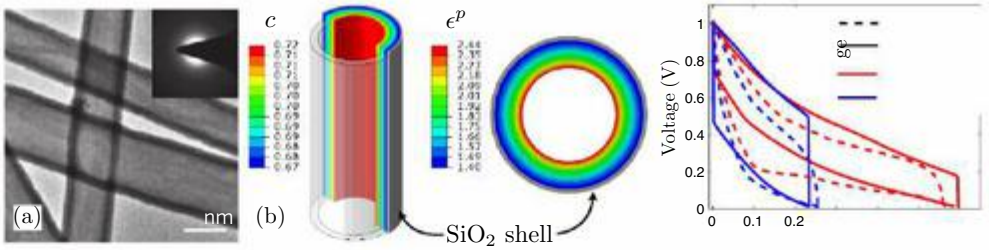

adjustment,

parameters in the theory have been calibrated to results from experiments reported in the literature. We have applied our fully-calibrated numerical simulation capability to model galvanostatic charging of hollow a-Si nanotubes whose walls have been oxidized to prevent outward expansion. We have shown that the results from out numerical simulations are in good agreement with the experimentally-measured electrochemical behavior. Finally we used our simulation tool to investigate the role of plasticity on the electrochemical performance of this anode.

References

[1] Wu, H., Chan, G., Choi, J.W., Yao, Y., McDowell, M.T., Lee, S.W., Jackson, A., Yang, Y., Hu, L., Cui, Y., 2012. Nat. Nanotechnol. 7 (5), 310?315.

[2] Bucci, G., Nadimpalli, S.P., Sethuraman, V.A., Bower, A.F., Guduru, P.R., 2014. J. Mech. Phys. Solids 62, 276?294.

[3] Di Leo, C.V., Rejovitzky, E., Anand, L., 2015. Int. J. Solids Struct. 67-68, 283-296

[4] Pharr, M., Suo, Z., Vlassak, J.J., 2014. J. Power Sour. 270, 569-575.

CHEMICAL AFFINITY TENSOR AND KINETICS OF STRESS-ASSISTED CHEMICAL REACTION FRONT

Alexander B. Freidin*[1,2,3], Elena N. Vilchevskaya[1,2], Leah L. Sharipova[1], Igor K. Korolev[1], Sergey P. Aleschenko[1], and Svetlana E. Petrenko[1,2]

[1]*Institute for Problems in Mechanical Engineering of Russian Academy of Sciences, St. Petersburg, Russia*

[2]*Peter the Great St. Petersburg Polytechnic University, St. Petersburg, Russia*

[3]*St. Petersburg State University, St. Petersburg, Russia*

Summary We develop an approach to studying the influence of stresses and strains on the kinetics of chemical reaction fronts based on the chemical affinity tensor. After the derivation of the expression of the chemical affinity tensor we formulate a kinetic equation for the chemical reaction front propagation in a form of the dependence of the reaction front velocity on the normal component of the chemical affinity tensor. We describe a locking effect – blocking the reaction by mechanical stresses, and construct the forbidden regions formed by strains or stresses at which the chemical reaction cannot go. Finally we present a number of analytical and numerical solutions of boundary-value problems for solids with propagating chemical reaction fronts.

INTRODUCTION

Oxidation processes in silicon microscale parts of MEMS and in nanowires, lithiation of silicon in lithium ion batteries, chemical transformations of particles in composites are among important examples of stress-assist chemical reactions (see, e.g., [1, 2, 3]) The influence of external and internal stresses on the reaction front kinetics was examined by many researches, and a number of models have been developed. To take into account stress effects, these models proposed stress-dependent oxidation parameters such as oxidant diffusivity and oxide viscosity, a reaction rate parameter (see references in our recent papers [4, 5]). Another type of models starts from the statement that the velocity of the reaction front may be controlled rather by the reaction rate than by the diffusivity and suggests to consider stress-dependent scalar chemical potential [6, 7, 8, 9].

Our approach takes into account the fact that the reaction takes place at oriented surface elements and depends on the orientation of the surface element with respect to stresses. The approach is based on a concept of the chemical affinity tensor allowing for a natural and thermodynamically sound way to take into account the effect of a stress-strain state on the kinetics of the reaction front. Note that in the second part of the XX century it was realized that the chemical potential was to be a tensor in the case of solid phases. It was shown that the chemical potential tensor was determined by the Eshelby energy-momentum tensor (see [10] and reference therein). The tensorial nature of the chemical potential also have been discussed later in [11].

The expression of the chemical affinity tensor was derived at first for the case of nonlinear elastic solid constituents and then in [12] for a system "diffusive constituent – solid of arbitrary rheology" in the case of finite strains (see also [13, 4]). Solutions of various boundary value problems for the case of linear-elastic solids were obtained [4, 5]. In the present paper we discuss the notion of the forbidden region formed by strains or stresses at which the reaction cannot go and describe a locking effect – blocking the reaction by strains or stresses. We also give examples of analytical and numerical solving boundary value problems for elastic and inelastic solids with propagating reaction fronts.

CHEMICAL AFFINITY TENSOR AND REACTION FRONT KINETICS

We consider a chemical reaction between solid and gaseous constituents $n_-B_- + n_*B_* \to n_+B_+$ where B_-, B_* and B_+ are the chemical formulae of an initial solid constituent, a gasous constituent and a transformed solid constituent, $n_\pm$ and n_* are stoichiometric coefficients. The reaction is localized at the reaction front and sustained by the diffusion of the gaseous constituent. It can be derived that the the energy dissipation per unit area of the propagating reaction front takes the form

$$D_g = \omega_N \left(A_{NN} + \hat{q}^g\right) \geq 0, \qquad \hat{q} = (1-\alpha)\, q_\Gamma \, \frac{n_+ M_+}{\hat{\rho}_+}$$

where ω_N is the reaction rate at the surface element with the normal $\mathbf{N}$, q_Γ is the heat release due to the reaction, $\hat{\rho}_+$ is the surface source of the constituent B_+, parameter $0 < \alpha < 1$ characterizes an additional energy barrier, $A_{NN} = \mathbf{N} \cdot \mathbf{A} \cdot \mathbf{N}$ is the normal component of the chemical affinity tensor

$$\mathbf{A} = n_- M_- \mathbf{M}_- + n_* M_* \mu_* \mathbf{I} - n_+ M_+ \mathbf{M}_+ + \{\text{dynamical terms}\},$$

$\mathbf{M}_-$ and $\mathbf{M}_+$ are the chemical potential tensors of the solid constituents, μ_* is the chemical potential of the gas constituent. To find $\mathbf{M}_\pm$ and μ_* one has to find stresses and strains at the reaction front and to solve the diffusion problem.

*Corresponding author. Email: alexander.freidin@gmail.com

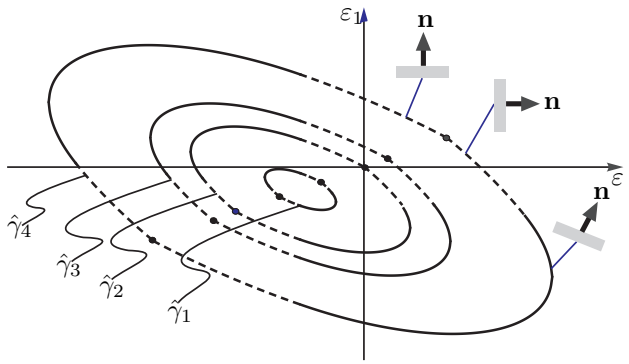

Figure 1: The cross-sections of the forbidden regions by the plane $\varepsilon_2 = \varepsilon_3 \equiv \varepsilon$ at various $\hat{\gamma}$: $\hat{\gamma}_1^* > \hat{\gamma}_2^* > \hat{\gamma}_3^* > \hat{\gamma}_4^*$

Substituting A_{NN} instead of the scalar chemical affinity A into the classical formula we obtain that the reaction rate and the normal component of the reaction front velocity W are given by the formulas

$$\omega_N = k_* c \left\{ 1 - \exp\left(-\frac{A_{NN}}{RT} \right) \right\}, \quad W = \frac{n_+ M_+}{\rho_+} k_* c \left\{ 1 - \exp\left(-\frac{A_{NN}}{RT} \right) \right\}.$$

where k_* is the kinetic constant, c is the molar concentration of the gaseous constituent.

FORBIDDEN REGIONS

The inequality $\max\limits_N A_{NN} < 0$ restricts stresses and strains which form forbidden regions in stress or strain space. The parameter $\hat{\gamma}$ in Fig. 1 depends on chemical energies (do not depend on stresses). The reaction cannot go inside the domains. Dashed and solids segments correspond to different directions of the reaction front propagation with maximal velocity.

CONCLUSION

The chemical affinity tensor may by an effective tool for studying coupled problems of mechanochemistry.

ACKNOWLEDGMENT

This work was supported by RFBR (Grant 16-01-00815).

References

[1] Buttner, C.C., Zacharias, M.: Retarded oxidation of Si nanowires. *Appllied Phys. Lett.* **89**: 263106, 2006.
[2] Muhlstein, C., Ritchie, R.: High-cycle fatigue of micron-scale polycrystalline silicon films: fracture mechanics analyses of the role of the silica/silicon interface. *Int. J. Fracture* **119/120**: 449–4745, 2003.
[3] Sethuramana, V.A., Michael J. Chonb, M.J., Shimshakb, M., Srinivasana, V., Guduru, P.R.: In situ measurements of stress evolution in silicon thin films during electrochemical lithiation and delithiation. *J. Power Sources* **195**: 50625066, 2010.
[4] Freidin, A.B., Vilchevskaya, E.N., Korolev, I.K.: Stress-assist chemical reactions front propagation in deformable solids. *Int. J. Engineering Science* **83**: 57-75, 2014.
[5] Freidin, A., Morozov, N., Petrenko, S., Vilchevskaya, E.: Chemical reactions in spherically symmetric problems of mechanochemistry. *Acta Mech.* **227**(1): 43-56, 2016.
[6] Loeffel, K., Anand, L.: A chemo-thermo-mechanically coupled theory for elasticviscoplastic deformation, diffusion, and volumetric swelling due to a chemical reaction. *Int. J. Plasticity* **27**: 1409–1431, 2011.
[7] Levitas, V.I., Attariani, H.: Anisotropic compositional expansion and chemical potential for amorphous lithiated silicon under stress tensor. *Sci. Rep.* **3**: 1615, 2013.
[8] Jia, Z, Li, T.: Stress-modulated driving force for lithiation reaction in hollow nano-anodes. *Journal of Power Sources* **275**: 866–876, 2015.
[9] Cui, Z., FengGao, F., Qu, J.: A finite deformation stress-dependent chemical potential and its applications to lithium ion batteries. *J. Mechanics and Physics of Solids* **60**: 1280-1295, 2012
[10] Grinfeld, M.A., Thermodynamic methods in the theory of heterogeneous systems. Longman, New York, 1991.
[11] Rusanov, A. I.: Surface thermodynamics revisited. *Surface Science Reports* **58**: 111-239, 2005.
[12] Freidin, A.: Chemical affinity tensor and stress-assist chemical reactions front propagation in solids. *ASME 2013 International Mechanical Engineering Congress and Exposition, San Diego, California, USA*. V. 9: Paper No. IMECE2013–64957, V009T10A102, 2013.
[13] Freidin, A.: On a chemical affinity tensor for chemical reactions in deformable solids. *Mechanics of Solids* **50**(3): 260–285, 2015.

PURIFICATION OF SINGLE-WALLED CARBON NANOTUBES BASED ON THERMOCAPILLARY FLOW

Jizhou Song[1, a)]
[1]*Department of Engineering Mechanics, Zhejiang University, Hangzhou, China*

Summary Single-walled carbon nanotubes (SWNTs) grow as mixture of both metallic and semiconducting tubes and this heterogeneity frustrates their practical use in high performance electronics. We will discuss the recently developed purification techniques based on nanoscale thermocapillary flow of thin film, which enables complete elimination of metallic SWNTs from as-grown arrays. We then studied the thermocapillary flow to purify SWNTs analytically and established a simple scaling law for the evolution of thin film thickness. It is found that the normalized thickness profile only depends on the normalized power density. The results may serve as useful design guidelines for process optimization.

1. INTRODUCTION

Single-walled carbon nanotubes (SWNTs) represent one of the most promising candidates for next generation semiconductor devices due to their superior electrical properties. As-synthesized SWNTs, however, contain a mixture of both metallic and semiconducting tubes (m-SWNTs and s-SWNTs), which frustrates their use in high performance devices. Recently developed approaches based on nanoscale thermocapillary flows enable complete elimination of m-SWNTs with the ability to meet the most demanding purity requirements [1-3]. Figure 1(a) shows a schematic illustration of the process for purifying SWNTs, beginning with the growth of perfectly aligned SWNT arrays on a quartz substrate followed by the deposition of an ultrathin (~20nm) film on the top. The injection of current induces Joule heating only in m-SWNTs, which drives local flows in the thin film to open trenches around the m-SWNTs, thereby exposing them for complete removal by reactive ion etching. Removing the thin film completes the process to yield arrays of only s-SWNTs. As shown in Fig. 1(b), the trenches gradually widen and deepen as the time increases.

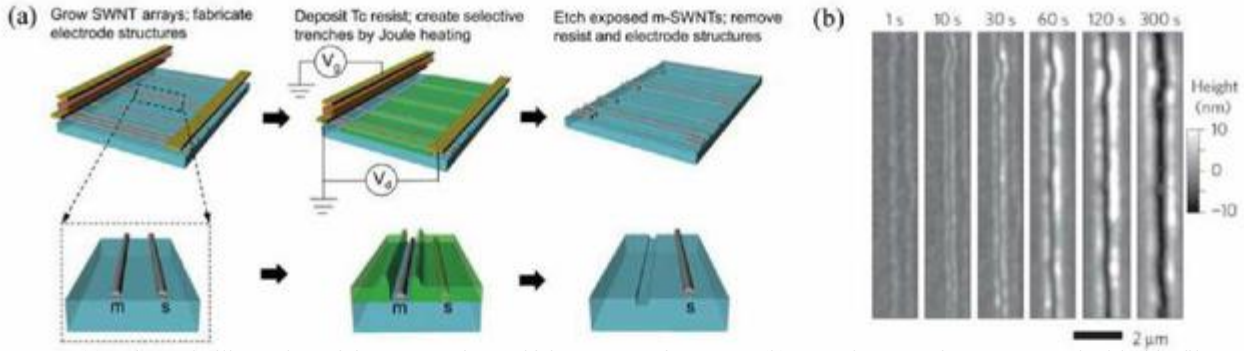

FIGURE 1. (a) Schematic illustration of the process for purifying arrays of SWNTs. (b) AFM images of SWNT coated with thin film after Joule heating for 1, 10, 30, 60, 120 and 300s. (Reprinted with permission from Ref. (1))

One critical issue in thermocapillary enabled purification lies in the control the parameters (e.g., time and power) to obtain narrow trenches, to prevent the exposure of surrounding s-SWNTs. The objective here is to establish a scaling law for the trenches and obtain the critical condition to form a full trench.

2. THERMOMECHANICAL MODELING AND RESULTS DISCUSSIONS

The thermocapillary flow can be approximated as unidirectional since the SWNT length is much larger than its diameter. The assumption of the thin film to be a Newton liquid yields the evolution of the film thickness *h(x,t)* as [4,5]

$$\frac{\partial h}{\partial t}+\frac{\partial}{\partial x}\left[\frac{\tau h^2}{2\mu}+\frac{h^3}{3\mu}\frac{\partial}{\partial x}\left(\gamma\frac{\partial h^2}{\partial x^2}\right)\right]=0, \tag{1}$$

with boundary conditions $h(\pm\infty, \ = \ _f$ and $\partial^2 \ /\partial \ ^2(\pm\infty \ t)=0$ (zero pressure), and initial condition $h \ x \ t = \ )=h_f$. Here, x is the coordinate along the direction normal to the SWNT axis, γ is the surface tension, which usually depends linearly on the surface temperature rise i.e., $\gamma=\gamma_0-\gamma_1\Delta T_{surface} \ x$, where γ_0 is the surface tension at T_∞ and γ_1 is the temperature coefficient of surface tension, $\tau=\partial\gamma/\partial \ \cdot\partial \ /\partial$ is the thermocapillary stress, and μ is the film viscosity at T_∞.

A steady-state analysis for heat conduction can be performed to obtain the temperature distribution resulting from a m-SWNT with power dissipation per unit length Q_0 embedded in a thin film with thickness h_f on a quartz substrate. The surface temperature rise of film is given by [5]

a) Corresponding author. Email: jzsong@zju.edu.cn.

$$\Delta T_{surface}\ x\ = \frac{Q_0}{\pi k_s}\int_0^{L/2}\ \eta\int_0^{\infty} J_0\left(\xi\sqrt{x^2+\eta^2}\right)\Big/\left[\cosh\left(\xi h_f\right)+k_f\sinh\left(\xi h_f\right)\Big/k_s\right]\mathrm{d}\xi\,, \tag{2}$$

where k_f and k_s are thermal conductivities of film and substrate, respectively, J_0 is the 0th-order Bessel function of the first kind. By introducing the non-dimensional terms $\overline{\Delta T_{surface}} = \gamma_1 \Delta T_{surface}/\gamma_0$, $\bar{\ } = \ /\ $, $\bar{\ } = \ /\ _f$, $\bar{t} = \gamma_0 t\ \left(\mu h_f\right)$, $\bar{\ } = \ /\ _f$, $\bar{\ } = \ \gamma\ /\left(k_s\gamma_0\right)$, $\bar{k} = k\ /k_s$, $\bar{\xi} = \xi h$ and $\bar{\eta} = \eta/h_f$, Eqs. (1) and (2) then become

$$\frac{\partial \bar{h}}{\partial \bar{t}} + \frac{\partial}{\partial \bar{x}}\left\{-\frac{\bar{h}^2}{2}\frac{\overline{\Delta\ _{surface}}}{d\bar{x}} + \frac{\bar{h}^3}{3}\frac{\partial}{\partial \bar{x}}\left[\left(1-\overline{\Delta T_{surface}}\right)\frac{\partial^2 \bar{h}}{\partial \bar{x}^2}\right]\right\} = 0\,,\quad \overline{\Delta T_{surface}}\ \bar{x}\ = \frac{\bar{Q}}{\pi}\int_0^{L/2} d\bar{\eta}\int_0^{\infty}\frac{J_0\left(\bar{\xi}\sqrt{\bar{x}^2+\bar{\eta}^2}\right)}{\cosh\ \bar{\xi}\ +\bar{k}\sinh\ \bar{\xi}}\mathrm{d}\bar{\xi}\,, \tag{3}$$

which yields a simple scaling law for the film thickness

$$\bar{\ } = \ /\ _f = \bar{h}\ \bar{x} = \bar{t}\ \bar{L}\ \bar{k}\ \bar{Q}\ \approx \bar{h}\ \bar{x}\ \bar{t}\ \bar{Q}\Big)\,, \tag{4}$$

with the approximation holding for $L >> h_f$ and $k_s >> k_f$.

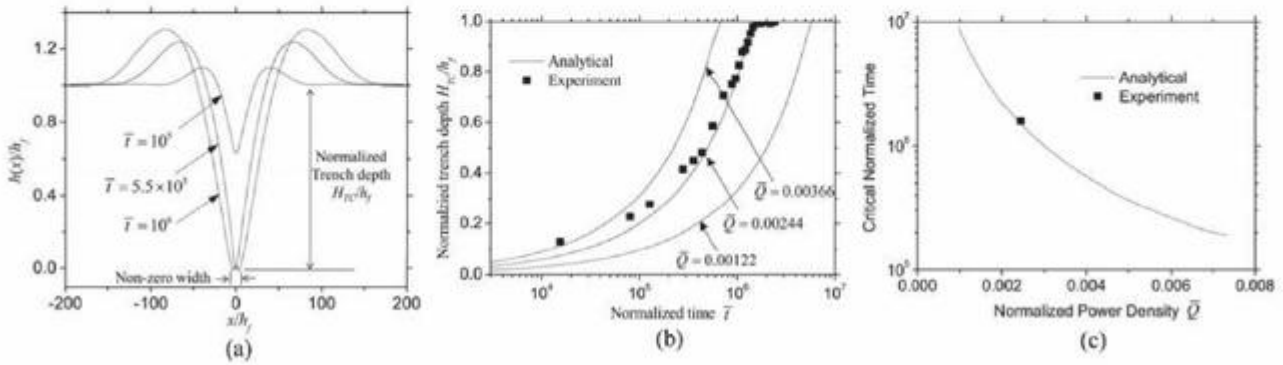

FIGURE 2. (a) Evolution of the trench profile from the scaling law. (b) The normalized trench depth versus the normalized time. (c) The critical normalized time versus the normalized power density. (Reprinted with permission from Ref. (5))

Figure 2(a) shows the evolution of the trench profile from the simple scaling law in Eq. (4) at $\bar{Q} = 0.0041$. As the time increases, the trench widens and deepens. At a critical normalized time of 5.5×10^5, a full trench forms (i.e., $H_{TC}/h_f = 1$). As the time further increases, the surrounding s-SWNTs may be exposed due to the formation of a non-zero width at the trench bottom. Figure 2(b) shows the normalized trench depth versus the normalized time $\bar{t}$ at different normalized power densities $\bar{Q}$. The normalized trench depth increases as the normalized power density increases since a larger normalized power density yields a larger thermocapillary stress τ which could accelerate the formation of trenches. Although there are some deviations at a smaller normalized time, the scaling law gives a good prediction for the critical normalized time $\bar{t}_{cr}$ at which a full trench forms (i.e., $H_{TC}/h_f = 1$). Figure 2(c) shows the critical normalized time as the function of the normalized power density. The critical normalized time decreases as the normalized power density increases. It should be noted that we assumed the viscosity to be a constant in the above analysis and this is true since the temperature increase is only a few degrees for the power density on the order of ~10W/m in experiments. For large power density, we must account for the temperature dependent viscosity [6].

3. CONCLUSIONS

An analytical model for the thermocapillary flow in the purification process of SWNTs is developed, which yields a simple scaling law for the thickness profile. The normalized thickness during thermocapillary motion as well as the crtical time to form a full trench only depends on the normalized power density. These results may serve as design guidelines to determine the optimal condition in the purification process.

References

[1] Jin SH, Dunham SN, Song J et al., Using nanoscale thermocapillary flows to create arrays of purely semiconducting single-walled carbon nanotubes. Nature Nanotechnology 8: 347-355, 2013.

[2] Du F, Felts JR, Xie X et al., Laser-induced nanoscale thermocapillary flow for purification of aligned arrays of single-walled carbon nanotubes. ACS Nano 8: 12641-12649, 2014.

[3] Xie X, Jin SH, Wahab MA et al., Microwave purification of large-area horizontally aligned arrays of single-walled carbon nanotubes. Nature Communications 5:5332, 2014.

[4] Darhuber AA, Davis JM and Troian SM. Thermocapillary actuation of liquid flow on chemically patterned surfaces. Physics of Fluids 15: 1295-1304, 2003.

[5] Song J, Lu C, Jin SH et al., Purification of single-walled carbon nanotubes based on thermocapillary flow. Journal of Applied Mechanics 82:071010, 2015.

[6] Jin SH, Song J, Chung HU et al., Fundamental effects in nanoscale thermocapillary flow. Journal of Applied Physics 115:054315, 2014

REVERSIBLE TEMPERATURE- AND STRESS-INDUCED MARTENSITIC TRANSITIONS IN CRYSTALS

Ryan S. Elliott *[1], Nicolas Triantafyllidis[2], and John A. Shaw[3]

[1]*Department of Aerospace Engineering and Mechanics, University of Minnesota, Minneapolis, MN USA 55455*
[2]*Laboratorie de Mechanique des Solides (CNRS UMR 7649), Ecole Polytechnique, Route de Saclay, France*
[3]*Department of Aerospace Engineering, University of Michigan, Ann Arbor, MI USA 48109*

Summary Temperature-dependent atomic potentials and path-following and bifurcation techniques are used to solve the nonlinear equilibrium equations for a perfect, infinite, periodic bi-atomic crystal to find temperature- and stress-induced martensitic phase transformations. A uniaxial Biot stress lowers the symmetry of the problem and leads to a large number of stable equilibrium paths. To determine which ones are possible *reversible* martensitic transformations, we use the (kinematic) concept of the *maximal Ericksen–Pitteri neighborhood* (max EPN) to select those equilibrium paths with lattice deformations that are closest, with respect to lattice-invariant shear, to the austenite phase and thus capable of a reversible transformation. For our chosen parameters only one stable structure (distorted αIrV) is found within the max EPN of the austenite in an appropriate stress window. The energy density of the corresponding configurations shows features of temperature- and stress-induced phase transformations between the higher symmetry austenite and lower symmetry martensite phases.

METHODS AND RESULTS

A modeling approach, based on temperature-dependent atomic potentials and path-following and bifurcation techniques, has been introduced by the authors (*Elliott et al.*, 2002, 2006b,a, 2011), to study the temperature- and stress-induced martensitic phase transformations in perfect, equi-atomic binary B2 crystals. This approach is motivated by (1) its simplicity and (2) the limitation of electronic structure density functional theory (DFT) simulations to zero Kelvin.

In *Elliott et al.* (2006a) a bifurcation diagram of the model's temperature-dependent, stress-free behavior is constructed. The high symmetry B2 cubic austenite structure's equilibrium path is found to transition from stable to unstable as the temperature decreases past a critical value, at which several bifurcated equilibrium paths emerge. Upon continuation, one of these paths becomes stable for lower temperatures, where the B2 phase is unstable at the same temperature. Furthermore, this path corresponds to the orthorhombic B19 crystal structure, which is a SMA martensite phase found in equi-atomic binary crystals.

The paths obtained by solving the equilibrium equations for the special case of zero stress (i.e., by using the dimensionless temperature θ as the load parameter with $\Sigma = 0$) are plotted as the largest principal stretch, λ_{max}, versus dimensionless temperature θ in Fig. 1a. Bifurcation and limit points are depicted respectively by open and filled circles. Stable equilibrium path segments are depicted by solid lines while unstable segments of these paths are depicted by broken lines. A magnified view of the many bifurcated equilibrium paths emerging from the principal branch is shown in the inset of Fig. 1a. Several crystal structures are found for the bifurcated equilibrium paths: one tetragonal ($L1_0$), two orthorhombic (B19 and αIrV), and one monoclinic (P2/m). Of the four structures discovered, only the αIrV, B19, and $L1_0$ equilibrium branches have stable portions. The stable αIrV phase appears in the higher temperature range (approximately $0. \leq \theta \leq 1.1$), while the B19 and $L1_0$ are stable at lower temperatures (approximatively $\theta \leq 0.$ and $\theta \leq 0.\,5$, respectively). As expected the B2 austenite phase is stable for high temperatures and unstable for low temperatures. Also, it is interesting to note that $L1_0$ and B19 are common SMA martensite structures (*Bhattacharya*, 2003), and the αIrV structure has previously been observed (although not mentioned by name) in the numerical computations of *Ding et al.* (2006).

In *Elliott et al.* (2011), the imposition of a uniaxial stress (of magnitude Σ) on the cubic B2 austenite crystal lowers the symmetry of the system, thus leading to a dramatic increase in the number of critical points found along the principal B2 path. This, in turn, results in a multitude of secondary paths bifurcating from the principal one with a large set of critical points found along each secondary path, and so on. Using continuation methods to follow all bifurcated equilibrium branches (the current investigation accounts for all branches up through the quartenary paths within a large window in temperature and stress space), hundreds of paths are identified. Consequently, one needs to determine which of these numerous equilibrium solutions are plausible reversible martensitic transformations. By investigating the stability of each branch, using the phonon and Cauchy–Born (CB) stability criteria discussed in *Elliott et al.* (2006b), one can eliminate most of the equilibrium paths as unstable. The final task is to determine which of the remaining stable equilibrium path segments, still relatively numerous, are possible reversible martensitic transformations. This selection relies on the *maximal Ericksen–Pitteri neighborhood* (max EPN) concept, a kinematic concept which selects those equilibrium solutions with lattice deformations which are *closest* to the reference austenite phase and thus likely to result in a reversible transformation.

The calculations produced the principal B2 path, 18 secondary bifurcated paths, 135 tertiary paths and 114 quartenary paths. From these, 22 stable segments, with respect to both the CB and phonon criteria, are found. The stable segments of the dimensionless stress Σ/C_{11} versus conjugate stretch λ curves, each labeled by its symmetry group, are shown in Fig. 1b. For the paths that include zero stress, their names and corresponding crystal structures are also shown.

*Corresponding author. Email: relliott@umn.edu

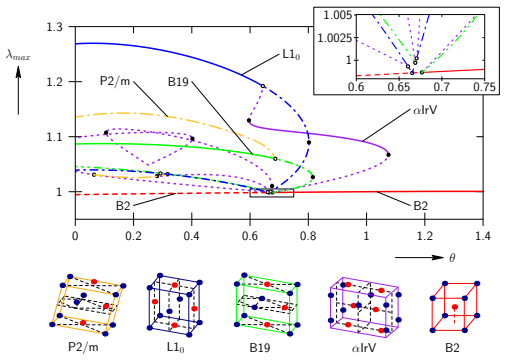

(a) Largest principal stretch $\lambda_{\max}$, with respect to the reference configuration, versus dimensionless temperature θ for the stress-free bifurcated equilibrium paths connected to the B2 austenite phase and their crystal structures. The stable portion of each path is depicted by a solid line.

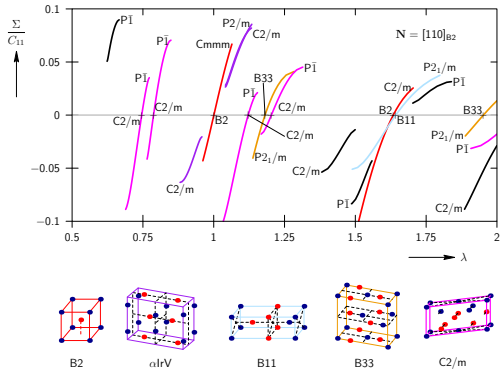

(b) Dimensionless stress versus conjugate stretch graph for all the stable equilibrium paths under $[110]_{\mathrm{B2}}$ Biot loading, each labeled by its symmetry group. For the paths going through zero stress, their names and corresponding crystal structures are also depicted.

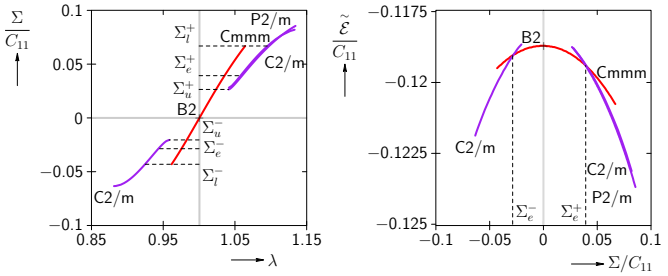

(c) Dimensionless stress versus conjugate stretch graphs for the martensite paths in (left) and corresponding dimensionless energy density versus dimensionless stress shown in (right) for $[110]_{\mathrm{B2}}$ uniaxial Biot loading at $\theta = 1.2$.

Figure 1: (a) Temperature-induced; (b) Stress-induced; (c) Reversible stress-induced martensitic transformations.

It turns out that only one stable structure, a distorted αIrV crystal structure, is a reversible martensitic transformation candidate within the max EPN of the austenite principal path in an appropriate stress window. Investigation of the energy density of the corresponding paths shows evidence of a transformation between the higher symmetry austenite and lower symmetry martensite phases and the existence of a hysteretic stress–strain loop under isothermal load–unload conditions.

The model is successful in its qualitative prediction of both stress- and temperature-induced transformations with transformation strains in the correct range (2–5%) for typical SMAs. Better results for the perfect crystal model could likely be obtained by generalizing the interatomic potential to include explicit bond-angle dependencies; however, care must be taken to avoid overfitting the interatomic potential (leading to accurate predictions for fitted properties, but wildly erroneous predictions for other properties). Despite these successes, the perfect crystal model over-predicts the critical stresses as well as the Clausious–Clapeyron slope when compared to experimental values measured from real polycrystalline samples. However, we believe that more sophisticated multiscale models (incorporating the effects of non-stoichiometric alloying, defects, precipitates, and grain boundaries) are required to obtain quantitative agreement with this type of experimental data.

ACKNOWLEDGMENTS

This work was supported by NSF grant—CMS 0409084—to the University of Michigan, by the NSF CAREER grant—CMMI-0746628—to the University of Minnesota, and by The University of Minnesota Supercomputing Institute.

References

K. Bhattacharya. *Microstructure of Martensite: Why it forms and how it gives rise to the shape-memory effect*. Oxford University Press, first edition, 2003.

X. Ding, T. Suzuki, X. Ren, J. Sun, and K. Otsuka. Precursors to stress-induced martensitic transformations and associated superelasticity: Molecular dynamics simulations and an analytical theory. *Phys. Rev. B*, 74(10), 2006. doi:10.1103/PhysRevB.74.104111.

R. S. Elliott, J. A. Shaw, and N. Triantafyllidis. Stability of thermally-induced martensitic transformations in bi-atomic crystals. *J Mech Phys Solids*, 50(11):2463–2493, 2002. doi:10.1016/S0022-5096(02)00012-1.

R. S. Elliott, J. A. Shaw, and N. Triantafyllidis. Stability of crystalline solids—II: Application to temperature-induced martensitic phase transformations in bi-atomic crystals. *J Mech Phys Solids*, 54(1):193–232, 2006a. doi:10.1016/j.jmps.2005.07.008.

R. S. Elliott, N. Triantafyllidis, and J. A. Shaw. Stability of crystalline solids—I: Continuum and atomic-lattice considerations. *J Mech Phys Solids*, 54(1):161–192, 2006b. doi:10.1016/j.jmps.2005.07.009.

R. S. Elliott, N. Triantafyllidis, and J. A. Shaw. Reversible stress-induced martensitic phase transformations in a bi-atomic crystal. *J Mech Phys Solids*, 59(2):216–236, 2011. doi:10.1016/j.jmps.2010.10.011.

PERIODIC AND PROPAGATING INSTABILITIES IN SUPERELASTIC NITI WIRE TWISTS

Daniel Biggs[1] and John Shaw *[1]

[1]*Aerospace Engineering, University of Michigan, Ann Arbor, Michigan, USA*

Summary Shape memory alloy cables made from stranded NiTi wires are a relatively new adaptive structure that has only recently been explored. While straight SMA wires typically have a single nucleating front that propagates along the length of the wire, SMA cables have a varied propagation behavior from wire-like to a more spatially diffuse transformation. Experiments on 1x3 twists with varying twist helix angles were performed to establish the role of helix angle on the superelastic response of the material. The strain and temperature fields were also captured using stereo digital image correlation and thermography to record the propagation behavior. Finite element analysis simulations of the twists with a material model calibrated from straight wire data were shown to accurately predict the experimental data. The larger helix angle twists were shown to have increased stiction and relative motion between the wires leading to more wear.

INTRODUCTION

Shape memory alloys (SMA) are a subset of adaptive materials that are well known for two characteristic thermomechanical responses, namely superelasticity and the shape memory effect. These characteristics arise from a crystallographic reorientation from a solid-to-solid phase transition between a high symmetry cubic austenite phase (A) to a low symmetry monoclinic martensite phase (M). Superelasticity is characterized by an apparent plastic plateau region in the loading path of an isothermal stress-strain curve, around 6% strain, that upon unloading can be completely recovered. This is made possible by a stress-induced transformation from A to M on loading, then back to A on unloading. The shape memory effect starts with material that is fully M and is deformed to retain an apparent permanent plastic deformation, but upon heating to A fully recovers the deformation. Both effects have been well studied, albeit not fully understood, for straight wire.

SMA cables are a novel SMA structure that exhibit benefits of conventional stranded wire rope (increased failure tolerance and bending flexibility) and the adaptive properties of SMA wires. These unique properties as well as a relatively high specific damping capacity make SMA cables attractive, for example, for seismic isolation and dampening systems of buildings and bridges. This example application requires scaling up traditional SMA structural elements, which has been a longstanding issue. Scaling up an SMA wire to the size of a bar typically degrades the adaptive properties and greatly increases the manufacturing cost. This issue, however, is conveniently addressed by conventional wire stranding techniques that provide an opportunity to scale up SMA elements for the intended large civil applications.

One unanticipated feature of superelastic SMA cables' mechanical response is their varying localized strain propagation behavior. Reedlunn et al. reported a wire-like propagating front in a 7x7 SMA cable, but a diffuse propagation in a 1x27 SMA cable [1]. The presented work focuses on superelastic NiTi 1x3 twists with various helix angles, which were chosen as a simple structure to study the varying propagating behaviors witnessed in SMA cables. Experimental data collected with stereo digital image correlation to capture the propagating behavior was combined with finite element numerical simulations to find the role of helix angle for the 1x3 twists.

SETUP

The 1x3 twist specimen, as the name implies, are three NiTi wires (1mm diameter) twisted together then heat treated to remove residual stresses and set the twisted shape as the permanent set. Straight wire which underwent the same processing including final heat treatment was also acquired. Specimen of four different helix angles (angle of wire with respect to axial direction) of 0°, 10°, 17°, and 21° were included in the study (with 0° corresponding to a single straight wire). The study consisted of characterization experiments which utilized stereo digital image correlation (DIC) and thermography, and Abaqus software for finite element analysis (FEA) simulations. The experimental setup had a MTS hydraulic load frame, a load cell and torque cell, two CCD cameras for stereo DIC, LED light panels to provide adequate lighting for the DIC images, and an IR camera for thermography. The setup gripped the specimen in clamped-clamped condition to prevent any rotation and the specimen was loaded in displacement control at prescribed loading rates. The wire twists were then modeled in Abaqus FEA using a full 3D mesh of quadratic continuum elements. General contact was prescribed between the wires with a friction coefficient of $\mu = 0.$. The stress-induced phase transformation was simulated using a J2 plasticity model, which was calibrated to a trilinear plasticity curve using the straight wire experimental data. This proved to work well because the wire twists' deformation is dominated by axial and bending deformation, with little shear. The simulations only modeled the loading portion of the transformation, as no back-stress is imposed to promote a reverse transformation.

*Corresponding author. Email: jashaw@umich.edu

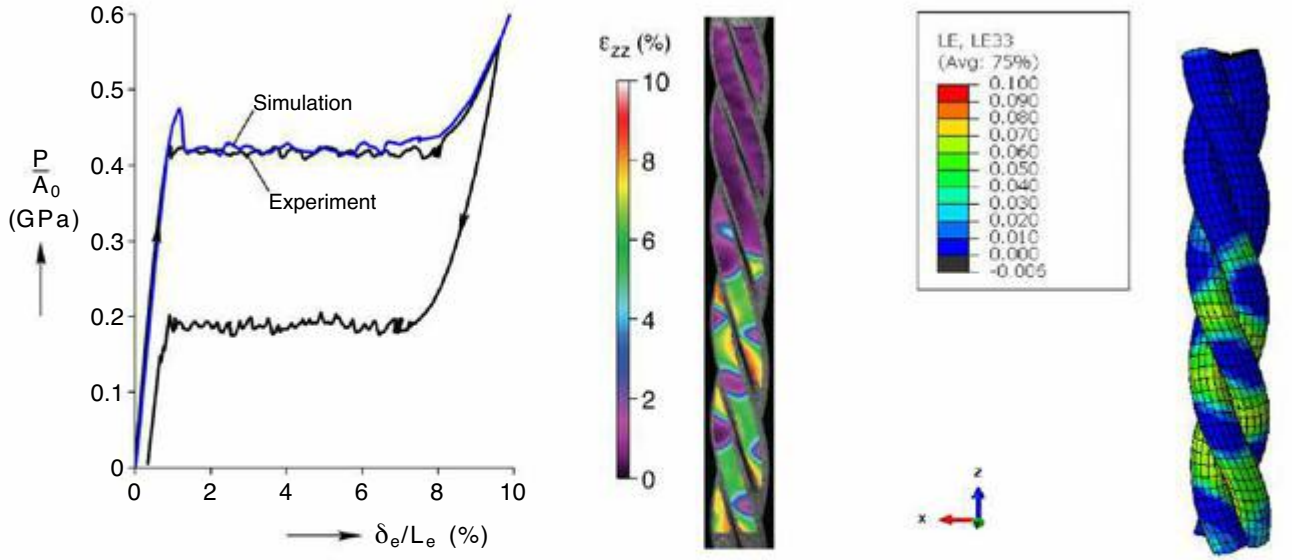

(a) Mechanical responses.

(b) DIC snapshot of Lagrangian strain (axial component).

(c) FEM snapshot of true strain (axial component).

Figure 1: Tensile data for 1x3 twist with 21° helix angle.

RESULTS

The propagation behavior of the 10° twist was observed to have a single propagating front that progressed from one end of the specimen towards the other, similar to the behavior of a straight wire. The 21° twist had a unique propagation behavior, where the transforming region helically propagated along the specimen leaving behind pockets of untransformed material. The measured normalized force-displacement curve is shown in Figure 1a, and a snapshot of the the DIC strain field in the axial direction, is in Figure 1b. The transformation plateau region is an up and down wavelike behavior, which was absent in the straight wire and 10° twist data. These dips were observed to correspond to nucleating bands as seen in the DIC.

The mechanical response simulated via Abaqus FEA (blue curve in Figure 1a) shows remarkable agreement with the experimentally measured response. The simulation captures the divots in the loading transformation plateau as well as the plateau length and plateau stress accurately. The strain field can be seen in Figure 1c, and is shown to capture the helically propagating nucleation bands as well as the untransformed pockets of material. This simulation was a true predictor of the material response because the material model was calibrated using a straight wire specimen and not a twist.

The simulations also gleamed insight into the essential role of friction in the propagating behavior of the different twists. It was found that friction had little impact on the 10° twist, but noticeable impact on the 21° twist's transformation plateau characteristics as well as the strain field. Upon further investigation, it was observed that the propagating bands and untransformed pockets of material were the result of stiction between the three wires. Scanning electron microscopy confirmed that there was additional wear between the wires of the 21° twist compared to the 10° twist.

CONCLUSIONS

This work experimentally characterized NiTi 1x3 wire twists which showed that the larger helix angle twists had periodic, propagating bands of localized transformation (apparent by high strain regions), but the smaller helix angle twists which had a single propagating front (similar to straight wire). These different propagation behaviors influenced how the latent heat was released spatially, and thus affected the loading rate sensitivity and shakedown/fatigue behavior of the twists. Simulations utilizing FEA provided accurate predictions of the measured data, which showed that superelastic SMA cable behavior could be modeled with only prior knowledge of the straight wire material behavior. Analysis showed that a larger helix angle impacted the propagation behavior by increasing the frictional force and amount of relative sliding between the wires.

References

[1] Benjamin Reedlunn, Samantha Daly, John Shaw, Superelastic shape memory alloy cables: Part I and II – Isothermal tension experiments, International Journal of Solids and Structures, Volume 50, Issues 20–21, 1 October 2013

FULL-FIELD BASED THERMOMECHANICAL DETERMINATION OF ELASTOPLASTIC PARAMETERS AT MACRO- AND MICROSCALE IN POLYCRYSTALS

Eric Charkaluk *[1], Rian Seghir[2], and Pierre Baudoin[3]
[1]*Laboratoire de Mecanique de Lille, UMR 8107, Ecole Centrale de Lille, France*
[2]*Department of Engineering Sciences, University of Southampton, United Kingdom*
[2]*Laboratoire de Mecanique des Solides, UMR 7649, Ecole Polytechnique, France*

Summary In this work, thermomechanical couplings during plastic deformation are studied in order to improve elastoplastic models. These analyses are conducted at the macro- and microscale of a A316L stainless steel polycrystal and are based on full-field measurements through a simultaneous visible and infrared wavelength coupled experimental approach. The obtained data enables (i) to determine the CRSS in grains and (ii) to establish energy balance. Based on these data, numerical simulations based on macroscopic elastoplastic models as well as crystal-based plasticity are conducted. The obtained results show (i) the interest of such thermomechanical data on parameters estimation and (ii) the high heterogeneity of the Taylor-Quinney ratio at the grain scale. Therefore, these results demonstrate the great interest of establishing experimental energy balance at different scales in order to propose thermodynamically admissible constitutive models.

INTRODUCTION

Polycrystalline metallic materials are made of an aggregate of grains more or less well oriented, with respect to the loading axis, for plastic gliding. Under mechanical loading, this leads to a heterogeneous deformation at the microstructure scale. This heterogeneity takes place inside the grains due to plastic slip activated on different slip systems and it conducts also to elastic residual stress fields between grains due to the strain incompatibilities from grain to grain. In terms of energy balance, this heterogeneity conducts to different contributions: a thermal dissipation caused by plastic irreversibilities, a stored energy associated to the plastic hardening and an elastic stored energy due to the intergranular residual stress field [1]. Homogenized approaches exhibit these different contributions [2] but experimental estimations of these later ones are very difficult. This work aims at using thermomechanical full-fields, including experimental energy balance, in order to estimate elastoplastic parameters at different scales in polycrystals [4].

EXPERIMENTAL AND NUMERICAL ASPECTS

In this work, some experimental and numerical works are presented in order to estimate the different stored energy contributions in polycrystals during the plastic deformation. Some original experimental works enabling the simultaneous determination of thermal and strain fields, in the same area, at this scale have already been realized in house on a A316L stainless steel [3]. Two complementary ways have been followed: some numerical treatments in order to access to experimental dissipations and the development of a consistent constitutive model. Both aspects are presented in this communication and a dialogue between microstructural texture coming from EBSD analysis, local deformation mechanism and thermal localization phenomenon is introduced.

The treatment of the full-field measurements is done with respects to the polycrystalline texture of the material. Under different assumptions, strain and thermal fields are obtained grain to grain [4]. The local disorientation, the different grain sizes and the crystallographic orientations are the main aspects, which have an influence on the strain localization process at the grain scale. The analysis of the local temperature evolutions is a key important feature of this coupled analysis as it enables, for example, the determination of the critical resolved shear stress from grain to grain. The numerical implementation in a FE code of a fully coupled crystalline plasticity constitutive model has been realized and is the other main part of this work [5]. It enables to compare the local kinematic and thermal distributions during monotonic tests and to study the heterogeneity of the stored energy at grain scale.

RESULTS

Then, with these experimenal and numerical coupled approaches, some energy balances are conducted at the global scale but also grain to grain.

At a global scale, some comparison are realized between the experimental estimations realized in this work with macroscopic results coming from literature [6]. It is shown that the hardening and residual elastic stored energy contributions are highly depending on the grain size. Estimations and evolutions of these different parts are shown on figure 1. These energy balances are then compared to the prediction of elastoplastic non linear phenomenological models. Moreover, experimental temperature data at the grain scale (see figure 2(d)) allows the identification of the Critical Resolved Shear Stress of such A316L stainless-steel. Then, this parameter associated to data coming from literature are used in coupled thermomechanical

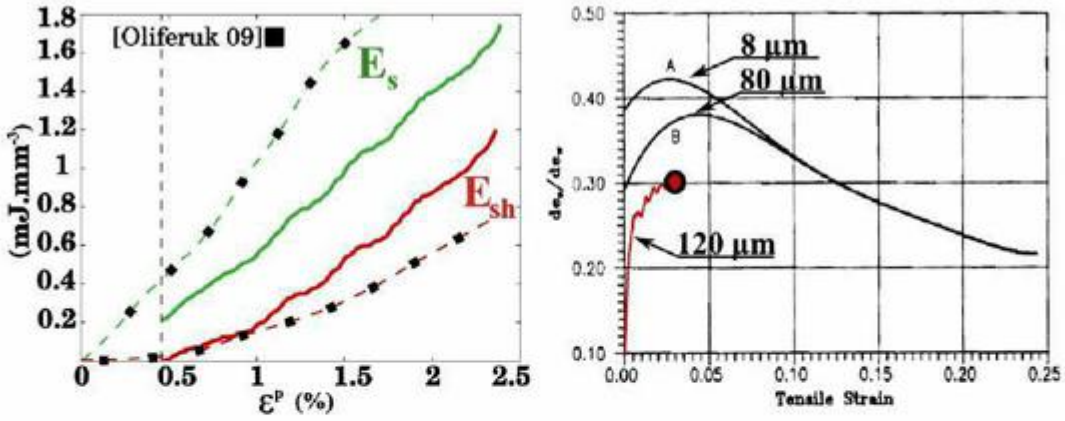

Figure 1: Evolution of hardening (Esh) and residual (Es) stored energies during the deformation and comparison with Oliferuk's work [6]

crystal based thermoplastic simulations. Numerical results at grain size show some large plastic dissipation heterogeneities at this scale, associated to the slip activity. Then, the Taylor-Quinney (TQ) ratio evolution and distribution can be estimated at the grain scale (see figure 2(a)) and associated to the experimental observed slip activity. Such analysis show that the TQ ratio differs from one system to an other one. This work gives then new information in order to propose thermodynamically admissible macroscopic or crystal based plasticity models.

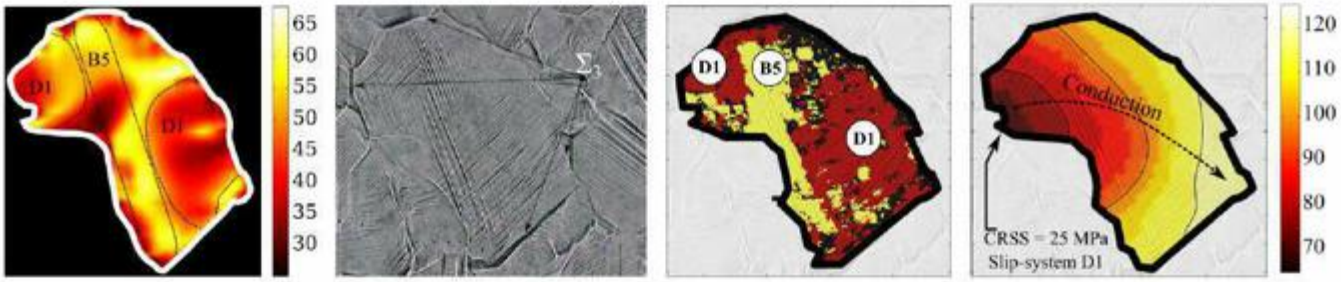

Figure 2: (a) numerical Taylor-Quinney ratio in a grain, (b) slip bands (micrography after test), (c) detected activated slip systems and (d) thermal detection of CRSS as a function of the nominal stress

References

[1] N. Aravas, K-S. Kim and F-A. Leckie, On the calculations of the stored energy of cold work. *J. Engng. Mat. Tech.* 112:465-470, 1990.

[2] P. Suquet, Elements of homogenization for inelastic solid mechanics, in: E. Sanchez-Palencia and A. Zaoui, eds., *Homogenization techniques for composite media*, Springer-Verlag, Wien, New York, CISM Courses and Lectures no. 105, pp. 193-278, 1987.

[3] L. Bodelot, L. Sabatier, E. Charkaluk, and P. Dufrénoy. Experimental set up for fully coupled kinematic and thermal measurements at the microstructure scale of an AISI 316L steel. *Mat. Sci. Eng. A* 501:52-60, 2009.

[4] E. Charkaluk, R. Seghir, L. Bodelot, J-F. Witz and P. Dufrénoy. Microplasticity in polycrystals: a thermomechanical experimental perspective. *Exp. Mech.* 55(4):741-752, 2015.

[5] R. Seghir, L. Bodelot, E. Charkaluk and P. Dufrénoy. Numerical and experimental estimation of thermo- mechanical fields heterogeneity at the grain scale of 316L stainless steel. *Comp. Mat. Sci.* 53(1) :464-473, 2012.

[6] W. Oliferuk and J. Man. Stress-strain curve and stored energy during uniaxial deformation of polycrystals. *Eur. J. Mech./A* 28:268-272, 2009.

JUMP PHENOMENA OF THERMOMECHANICAL RESPONSES FOR NONLINEAR VIBRATION WITH NITI

Minglu Xia[a] & Qingping Sun
Department of Mechanical and Aerospace Engineering, Hong Kong University of Science and Technology, Clear Water Bay, Kowloon, Hong Kong, China

Summary Jump phenomena of rotational angle and temperature for a nonlinear torsional vibration system with phase transformable NiTi wire are investigated in the frequency, amplitude and time domains. At fixed excitation amplitude, jump phenomena of thermomechanical responses are identified on the FRC by monotonically changing the excitation frequency. Similarly, by sweeping the excitation amplitude with small intervals, jump phenomena are captured in the amplitude domain. Under critical external excitations, spontaneous jumping process from the lower branch to the alternative upper branch is identified by experiments in the time domain. It's shown that the jump phenomena are directly affected by the external excitation and disturbance. External excitation changes the magnitude of thermomechanical responses and further determines the nonlinearity and damping capacity of the dynamic system. Accumulation of internal and external disturbance triggers the jump phenomena in the time domain, revealing the nonlinear dynamic instabilities of the system with NiTi SMA.

INTRODUCTION AND BACKGROUND

Originating from the first-order martensitic phase transition, NiTi has large recoverable strain and damping capacity. Therefore it has been gradually used in automotive industry, civil and aerospace engineering. However, there are two major challenges in the applications of the smart material. The first challenge is the strong coupling effects between the stress-strain relation and temperature oscillation in the stress-induced cyclic phase transition via two intrinsic internal heat sources (latent heat and hysteresis heat) [1]. The mechanical aspect and thermal aspect of the material should always be considered in parallel. The second problem is the nonlinear instabilities (e.g., jump phenomena) of the thermomechanical responses in the mechanical system due to the softening nonlinear hysteretic constitutive relation of NiTi SMA. A lack of direct experimental exploration of the jump phenomenon endangers the entire system [2] and prevents further applications of the material. In this context, this paper performs an experimental investigation on the jump phenomena of thermomechanical responses in the frequency, amplitude and time domains for a nonlinear torsional vibration system with NiTi wire.

METHODOLOGY AND RESULT

A polycrystalline superelastic NiTi wire is used as the softening nonlinear spring in a typical torsional vibration system. Before the experiments, the NiTi wire was trained by two-way cyclic torsion to remove the cyclic plasticity and then characterized by pure torsion at different rotational angles and frequencies. An electrical rotational stepping motor provides an external sinusoidal angular excitation. Synchronized measurements of rotational angle ($\Delta\theta$) and temperature oscillation (ΔT) of the NiTi wire are realized with rotary motion sensor and infrared camera respectively.

For each of the five selected excitation amplitudes (A), independent torsional vibration tests were performed at different frequencies (f) following ascending and descending frequency orders with a small interval (Δf=0.005 Hz) to search for the jump-up and jump-down. As A increases, $\Delta\theta$ and ΔT grow larger and FRCs gradually evolve from linear to softening nonlinear, bending to the left. Finally simultaneous jump-up of $\Delta\theta$ and ΔT following ascending frequency order and jump-down following descending order are observed on the FRCs. When further increasing A, the jump frequency gap and jump magnitudes of thermomechanical responses consistently grow larger and the jump phenomena become more significant.

Similarly, to capture the jumps in the amplitude domain, A slowly changes according to ascending and descending amplitude orders with a small interval (ΔA=0.1°) under five different f. ARCs do not have a peak response in the middle and both $\Delta\theta$ and ΔT monotonically increase with A. As f increases, lower branch of ARC consistently drifts up and upper branch drifts down. At f=0.52 Hz, simultaneous jump-up of $\Delta\theta$ and ΔT following ascending amplitude order and jump-down following descending order are observed on the ARCs. The jump-up amplitude is different from jump-down amplitude, thus forming a meta-stable multi-valued region. With further increased f, the entire ARCs are on the upper branch without jumps.

To explore how jump phenomena happen, we'll have to go to the time domain where the jumps may exist in a single experiment under some critical excitations. It's seen that evolutions of θ and T are completely different from the ordinary cases. After the initial transient state, the system responses go into meta-stable state I, where the oscillations are similar to the lower branch. So far θ and T show no difference from normal cases and there are no sign of the jump phenomena. However, after about 110s, a new transient state spontaneously comes into being, during which the dynamic responses smoothly but quickly switch from small magnitude oscillation to large magnitude oscillation. Meanwhile, θ and T experience phase inversion and this is another key characteristic of the jump phenomena. In the following meta-stable state II, characteristics of the thermomechanical responses are close to the steady state on the upper branch. In this way, the thermomechanical responses spontaneously jump up from the lower branch of solution to the alternative upper branch.

[a] Corresponding author. Email: mxiaaa@connect.ust.hk.

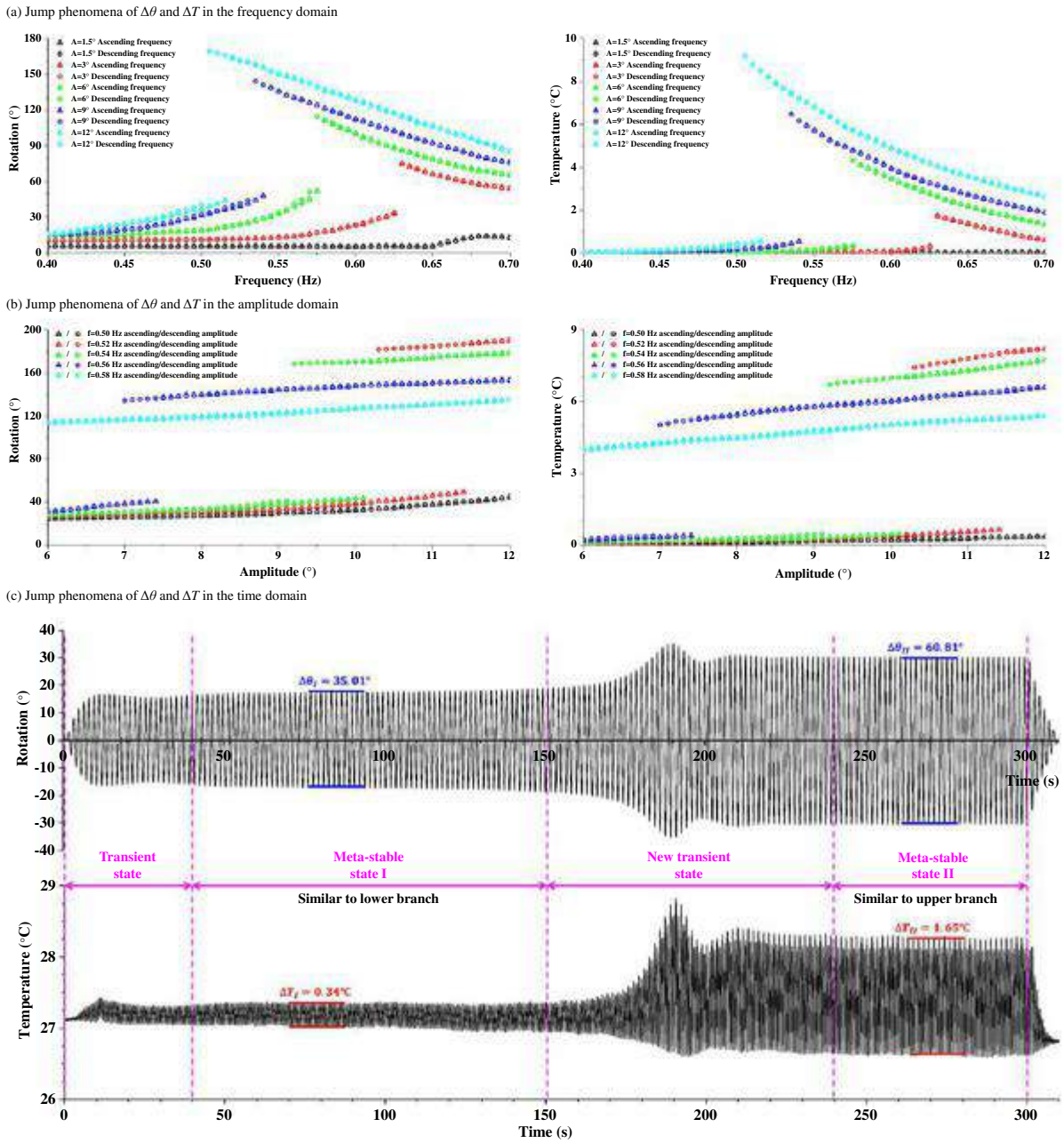

Figure 1. Jump phenomena of thermomechanical responses in the (a) frequency, (b) amplitude and (c) time domain.

SUMMARY AND CONCLUSION

This paper investigates the jump phenomena of rotational angle and temperature in the frequency, amplitude and time domains for a NiTi wire in a nonlinear torsional vibration system. Simultaneous jumps of mechanical and thermal responses are captured in multiple domains. It's shown that the jump phenomena are directly associated with the external excitation and disturbance. The effects of excitation (both amplitude and frequency) and disturbance (both internal and external) on such jump phenomena of thermomechanical responses are further explored. At critical external excitations, jump phenomena occur spontaneously without any external interference. At excitations within the meta-stable region in the frequency or amplitude domain, an external disturbance with proper direction and magnitude can help overcome the stability barrier and trigger the jump phenomena. Nonlinear dynamic instabilities of a mechanical system with phase transformable NiTi component are identified.

References

[1] Shaw J. A., Kyriakides S.: Thermomechanical aspects of NiTi. *J. Mech. Phys. Solids* **43**:1243-1281, 1995.

[2] De Silva C. W.: Vibration: Fundamentals and Practice. United States of America 2006.

DISLOCATION MECHANISM OF MICROSTRUCTURAL CHANGES IN DUCTILE SINGLE CRYSTALS

Christina Günther[1], Michael Koster[1], Khanh Chau Le *[1], and Binh Duong Nguyen[1]
[1]*Lehrstuhl für Mechanik-Materialtheorie, Ruhr-Universität Bochum, Bochum, Germany*

Summary The present paper considers two problems: i) martensitic phase transition involving dislocations, ii) formation of grain boundaries during severe plastic deformations. Both problems turn out to be non-convex variational problems of energy minimization that will be solved within the continuum dislocation theory (CDT).

INTRODUCTION

Structural changes in metals and alloys may occur due to the coordinated and collective movement of groups of atoms. The typical example of such change is the martensitic phase transition in carbon steels or in shape memory alloys like NiTi or Cu-Zn-Al. Mechanical models of metals and alloys allowing for martensitic phase transition have been proposed in various papers and are now widely used. However, there are many other types of structural changes in metals and alloys due to the collective movement of defects like dislocations or vacancies: formation of grain and subgrain boundaries during severe plastic deformation, recrystalization, deformation twinning, polygonization, texturing, to name just a few. The structural changes of metals and alloys at microlevel may influence the macroscopic properties of these materials directly, as the Taylor and Hall-Petch relations show. As a consequence, new materials with exceptionally high strength could be created in this way. Therefore, the following question, interesting from the theoretical and important from the practical point of view, arises: what kind of theory can we develop to explain and predict such microstructural changes as well as the accompanying macroscopic responses of the materials? Unfortunately, so far there is no comprehensive answer to this question except for some particular cases. However, one thing is for sure: since the plastic slip as the product of collective movement of a huge number of dislocations and grain boundaries are the active participants in this structural rearrangement, any physically meaningful theory of formation and evolution of microstructure should capture their behavior in a proper way.

One of the main guiding principles in seeking an appropriate theory of formation of microstructure in metals and alloys has first been proposed in form of the so-called LEDS-hypothesis: the dislocation structures in the final state of deformation minimize the energy of crystals. However, it is still difficult to develop the theory of formation of dislocation structures based on this principle alone. The crucial step in this direction has been done in crystal plasticity by introducing a new ingredient to the energy minimization, namely the non-convexity of the energy. But crystal plasticity, as a phenomenological theory, operates with plastic slips while ignoring their source: dislocations. To achieve an agreement with experiments it has to introduce several phenomenological concepts like back stress or hardening as internal variables obeying additional constitutive equations which would otherwise be derivable as natural consequences of a more general continuum dislocation theory. The aim of this paper is to show that dislocations causing the plastic slip give rise to the required non-convexity of the energy and guarantee the structural rearrangement of material under certain conditions.

MARTENSITIC PHASE TRANSITION

In the first part of this talk we consider a model combining the reversible transformation strain with the dislocation based plastic slip within the framework of nonlinear continuum dislocation theory which is laid down recently in [3]. Since there are still several issues in nonlinear CDT, we work out first these issues in kinematics and thermodynamics of continuously distributed dislocations to fix our framework. Then we will propose the simple model of martensitic phase transition involving dislocations. As the physical idea stands at the focus of this paper rather than the proposition of the theory in its full generality, we restrict ourselves here to the most simple situation of single crystal strip deforming under a plane strain constrained shear. We admit only one slip system with the slip direction parallel to the strip axis. The variational problem of minimizing the relaxed energy functional which incorporates the transformation strain among all admissible plastic slip is studied in details [4]. We show that the energy minimizing sequence must have piecewise constant plastic slip such that its average value

*Corresponding author. Email: ictam2016papers@legendconferences.com

vanishes. The phase interfaces are incoherent and can be presented as the arrays of dislocations. The finer microstructure is possible if obstacles are present in this material. The stress-strain curve must show some load-drop at the onset of phase transition and the elastic behavior of the second phase when the phase transition is finished followed by perfectly plastic behavior afterwards. The work hardening behavior is also possible if the side boundaries of the strip are clamped forcing the dislocations to pile up near these boundaries.

FORMATION OF GRAIN BOUNDARIES

In the second part of this talk we want to extend the above nonlinear continuum dislocation theory to the case of crystals containing newly formed grain boundaries. Regarding grain boundaries as surfaces of weak discontinuity in placement but strong discontinuity in plastic slip, we include the energy of such boundaries into the energy functional of the crystal and study the variational problem of minimizing the energy of crystal containing dislocations and grain boundaries [2]. We derive from this variational problem the whole set of equilibrium equations, boundary conditions, and jump conditions at the grain boundaries. It turns out that the grain boundaries will stay in equilibrium if and only if the thermodynamic driving force, including also the curvature of the jump surface, vanishes. This explains why the microstructure obtained in the final state of deformation must be lamellar [1]. Second, we apply the developed theory to two plane strain problems for single crystal deforming in single slip under the condition of simple shear or uniaxial compression. Due to the non-convexity of the energy in certain ranges of the overall shear or stretch, the construction of the lamellae with piecewise constant plastic and elastic deformation leads to the energy minimizing sequences as the solutions of these non-convex variational problems. In case of plate under uniaxial compression the uniform states are not rank-one connected, so dislocations and grain boundaries should adapt to the elastic strains chosen from the homogeneous states in a smart way to satisfy the compatibility condition and, at the same time, to minimize the energy. It turns out that the whole set of jump conditions is needed to determine the orientation of grains (which are misoriented with respect to the slip direction), the plastic slips, and the elastic rotations.

References

[1] Koster, M., Le, K.C., 2015. Formation of grains and dislocation structure of geometrically necessary boundaries. Mater. Sci. Eng. A 643, 12-16.

[2] Koster, M., Le, K.C., Nguyen, B.D., 2015. Formation of grain boundaries in ductile single crystals at finite plastic deformations. Int. J. Plasticity 69, 134-151.

[3] Le, K.C., Günther, C., 2014. Nonlinear continuum dislocation theory revisited. Int. J. Plasticity 53, 164–178.

[4] Le, K. C., Günther, C., 2015. Martensitic phase transition involving dislocations. J. Mech. Phys. Solids 79, 67-79.

PHASE FIELD APPROACH TO PHASE TRANSFORMATIONS, TWINNIG, DISLOCATIONS, AND THEIR INTERACTION

Valery I. Levitas[a]
Department of Aerospace Engineering, Mechanical Engineering, and Material Science and Engineering, Iowa State University, Ames, IA, USA

Summary Phase field approach to multivariant martensitic phase transformations, transformation between martensitic variants (twinning), dislocations, and their interaction is developed at large strains. Various important requirements to the thermodynamic potential are formulated and satisfied. Phase transformation, twinning, and dislocation nucleation criteria are obtained from the thermodynamic lattice instability conditions under 3D stress state. Kinematics of interaction between phase transformations (twinning) and dislocations takes into account inheritance of dislocations during direct and reverse transformations. A number of important problems are solved using finite element method, and various experimental phenomena are reproduced and interpreted.

THEORY

Interaction between martensitic phase transformations (PTs), twinning, and dislocational plasticity is one of the most fundamental, important, and complex problems in the theory of PTs, with numerous applications in physics, material science, geophysics, and material technologies. Dislocations drastically alter PT thermodynamics, microstructure, kinetics of nucleation and growth, transformation hysteresis and irreversibility. Here, we present our recent developments on the phase field approach (PFA) to each of these processes separately and their interaction.

Multivariant martensitic phase transformations and twinning

Large-strain PFA for multivariant martensitic phase transformations and twinning was formulated in [1,2]. It includes explicit expression for the Helmholtz free energy as functions of the order parameters, each for corresponding martensitic variants, and gradient of the order parameters in the reference state. The transformation deformation gradient is also an explicit function of the order parameters. These functions satisfy important formulated requirements related to thermodynamic equilibrium and instability conditions and the possibility to correctly introduce all known material properties of each phase. Biaxial interface stresses with the magnitude equal to the nonequilibrium interface energy are introduced in [3,4] for small and in [5] for large strains. This required resolving the long-term outstanding problem on the definition of the position of the Gibbs dividing surface and nonequilibrium interface energy [4,5]. Even for small strains, introducing interface stresses requires implementation of some geometrically nonlinear features; in particular, gradient energy depends on the gradient of the order parameters in the actual (deformed) configuration. Since in most cases martensitic variants are in a twin relationship, the theory of multivariant martensitic PTs automatically includes twinning in the martensite. However, in contrast to austenite-martensite PT, variant-variant transformations in [1-5] and all previous theories were described by simultaneous change of two order parameters; there is no analytical solution for a propagating interface, which does not allow one to calibrate parameters of the model and introduce interface stresses. This problem was resolved by introducing spherical order parameters [6] or a penalizing term that allows one to control or avoid the third phase at the interface between two other phases [7,8]. It is also shown in [9] that, in order to introduce anisotropic interface energy and stresses without contradiction, without violation of the angular momentum balance and principle of material objectivity, the gradient energy should be an isotropic function of the gradient of the order parameters in the actual configuration and depend on the normal to the interface in terms of the gradient of the order parameters in the reference configuration.

Phase fields approach to dislocations. A thermodynamically consistent, large strain PFA to dislocation nucleation and evolution is developed in [10,11]. The relationship between the rates of the plastic deformation gradient and the order parameters is consistent with crystal plasticity. Thermodynamic and stability conditions for homogeneous states are formulated and satisfied by the proper choice of the Helmholtz free energy and the order parameter dependence on the Burgers vector. They allow us to reproduce desired lattice instability conditions and a stress - order parameter curve, as well as to obtain a stress-independent equilibrium Burgers vector and to avoid artificial dissipation during elastic deformation. A crystalline energy coefficient for dislocations is defined as a periodic step-wise function of the coordinate along the normal to the slip plane, which provides an energy barrier normal to the slip plane and determines the desired mesh-independent height of the dislocation bands independent of the slip system orientation. Gradient energy contains an additional term, which excludes the localization of a dislocation within a height smaller than the prescribed height, but it does not produce artificial interface energy. Numerical examples and parameter identification methods are presented in [10,12].

Interaction between phase transformations and dislocations. PFA for coupled multivariant martensitic PTs, including cyclic PTs, variant-variant transformations, and dislocation evolution is developed at large strains [13,14]. One of our key points is in the justification of the multiplicative decomposition of the deformation gradient into elastic,

[a] Corresponding author. Email: vlevitas@iastate.edu.

transformational, and plastic parts. The plastic part includes four mechanisms: dislocation motion in martensite along slip systems of martensite and slip systems of austenite inherited during PT, and dislocation motion in austenite along slip systems of austenite and slip systems of martensite inherited during reverse PT. The plastic part of the velocity gradient for all of these mechanisms is defined in the crystal lattice of the austenite utilizing just slip systems of austenite and inherited slip systems of martensite and just two corresponding types of order parameters. Thermodynamic treatment resulted in the determination of the driving forces for change of the order parameters for PTs and dislocations. Ginzburg-Landau equations for dislocations include variation of properties during PTs, which in turn produces additional contributions from dislocations to the Ginzburg-Landau equations for PTs.

NUMERICAL RESULTS AND PHENOMENA

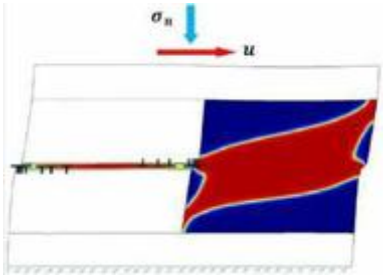

Fig. 1. Stationary solution for dislocations and high pressure phase (red) in a bicrystal under normal stress and shear [15].

Various problems on PTs, twinning, dislocations, and their interaction have been solved using FEM [2,6-8,10,12,13,15]. In particular, complex nanostructures with bending and splitting martensitic twin tips and twin crossing are obtained, which is in quantitative agreement with known experiments [6,7]. Reduction by an order of magnitude of the PT pressure due to applied plastic shear observed in experiments is explained in our simulations (Fig. 1) [15]. Strong dependence of the critical thermodynamic force to initiate propagation of the semi-coherent phase interface on the ratio of the interface width to the Burgers vector is predicted [13,16]. Propagation and arrest of martensitic plate by dislocations generated during plate growth is reproduced, which is in agreement with experiments on plate-lath martensite morphological transition [13,16]. Generally, dislocations play a dual role in PTs: (a) they promote PT by creating strong nucleation sites (stress concentrators) and relaxing elastic stresses, but (b) they suppress PT by relaxing the same stress concentrators and producing athermal resistance to the interface motion.

CONCLUSIONS

PFA to the interaction between PTs and dislocations at large strains is presented, which includes: (a) justified multiplicative kinematic decomposition of the deformation gradient into elastic, transformational, and plastic contributions; (b) inheritance of dislocations during direct and reverse PT; (c) dependence of all material parameters for dislocations on the order parameters for PT. A number of important problems is solved using FEM and various experimental phenomena are reproduced and interpreted.

References

[1] Levitas V.I.: Phase-field theory for martensitic phase transformations at large strains**.** *Int. J. Plast.* **49**: 85-118, 2013.

[2] Levin V. A., Levitas V. I., Zingerman K.M., Freiman E.I.: Phase-field simulation of stress-induced martensitic phase transformations at large strains**.** *Int. J. Solids Structures*, **50:** 2914-2928, 2013.

[3] Levitas V.I.: Thermodynamically consistent phase field approach to phase transformations with interface stresses**.** *Acta Materialia*, **61**, 4305-4319, 2013.

[4] Levitas V.I.: Unambiguous Gibbs dividing surface for nonequilibrium finite-width interface: Static equivalence approach. *Phys. Rev. B*, **89:** 094107, 2014.

[5] Levitas V.I.: Phase field approach to martensitic phase transformations with large strains and interface stresses. *J. Mech. Physics Solids*, **70:** 154-189, 2014.

[6] Levitas V.I., Roy A.M., Preston D. L.: Multiple twinning and variant-variant transformations in martensite: Phase-field approach. *Phys. Rev. B*, **88**: 054113, 2013.

[7] Levitas V.I. and Roy A.M.: Multiphase phase field theory for temperature- and stress-induced phase transformations. *Phys. Rev. B*, **91**: 174109, 2015.

[8] Levitas V.I. and Roy A.M.: Multiphase phase field theory for temperature-induced phase transformations: formulation and application to interfacial phases. *Acta Materialia*, **105:** 244-257, 2016.

[9] Levitas V.I. and Warren J. A.: Thermodynamically consistent phase field theory of phase transformations with anisotropic interface energies and stresses. *Physical Review B*, **92:** 144106, 2015.

[10] Levitas V.I. and Javanbakht M.: Advanced phase field approach to dislocation evolution. Phys. Rev. B, **86:** 140101(R), 2012.

[11] Levitas V.I. and Javanbakht M.: Thermodynamically consistent phase field approach to dislocation evolution at small and large strains. *J. Mech. Physics Solids*, **82:** 345-366, 2015.

[12] Javanbakht M. and Levitas V.I.: Phase field approach to dislocation evolution at large strains: Computational aspects. *Int. J. Solids Structures*, DOI: 10.1016/j.ijsolstr.2015.10.021, 19 pp., 2016.

[13] Levitas V.I. and Javanbakht M.: Phase field approach to interaction of phase transformation and dislocation evolution. *Appl. Phys. Let.*, **102:** 251904, 2013.

[14] Levitas V.I. and Javanbakht M.: Interaction between phase transformations and dislocations at the nanoscale. Part 1. General phase field approach. *J. Mech. Physics Solids*, **82:** 287-319, 2015.

[15] Levitas V.I. and Javanbakht M.: Phase transformations in nanograin materials under high pressure and plastic shear: nanoscale mechanisms. *Nanoscale*, **6**: 162 – 166, 2014.

[16] Javanbakht M. and Levitas V.I.: Interaction between phase transformations and dislocations at the nanoscale. Part 2. Phase field simulation examples. *J. Mech. Physics Solids*, **82:** 164-185, 2015.

THE THERMODYNAMIC FORM OF PERIDYNAMICS WITH APPLICATION TO PHASE TRANSFORMATIONS

Stewart A. Silling
Multiscale Science Department, Sandia National Laboratories[1], Albuquerque, New Mexico, USA

Summary The peridynamic theory is a nonlocal generalization of the standard theory of solid mechanics that was developed primarily to model crack growth and long-range internal forces. Thermodynamics can be incorporated into the peridynamic framework in a way that is fully consistent with the mechanics. Nonlocal statements of the first and second laws of thermodynamics have been developed, along with nonlocal equations for heat transport and the diffusion of chemical species. Restrictions on material response can be derived from the second law. A nonlocal dissipative material model that takes advantage of the unique features of peridynamic material models can be applied within a moving phase boundary. The resulting motion of an elastic body with a nonconvex potential energy function selects, in effect, a kinetic relation for phase boundary motion without the need for a supplemental equation that is traditionally needed to prescribe the phase boundary velocity.

The needs of contemporary technology, particularly at the nanoscale, motivate the extension of the traditional theory of solid mechanics to enable the modeling, within the basic equations, of long-range internal and surface forces and the growth of defects. The peridynamic theory of solid mechanics [1] was proposed as step toward achieving this goal. The peridynamic equation of motion explicitly includes long-range forces between material points within a continuous body:

$$\rho\ddot{y}(x,t) = \int_{\mathcal{H}_x} f(q,x,t)dV_x + b(x,t) \tag{1}$$

where ρ is the density, x is the position vector in the reference configuration, y is the motion, and b is the body force density field. f is a force density that represents the interaction in the *bond* from any x to a nearby material particle q. $\mathcal{H}_x$ is a neighborhood of x whose radius is called the *horizon*, denoted by δ. The horizon is a cut-off distance in the reference configuration for force interactions. The bond force density f is determined by the deformation of $\mathcal{H}_x$ through the material model. Because, unlike the PDEs of the standard theory, equation (1) can be applied directly on discontinuities, the peridynamic mechanical theory has become a standard technique for the modeling of brittle fracture computationally. The general form of f can be expressed as the vector sum of partial bond force vectors arising from the material model applied at x and q separately:

$$f(q,x,t) = T[x,t]\langle q-x\rangle - T[q,t]\langle x-q\rangle \tag{2}$$

Recently, a thermodynamic version of the peridynamic continuum theory was proposed [2]. The thermodynamic theory uses nonlocal forms of the first and second laws that are fully consistent with the mechanics. By partitioning each bond force into contributions from the two endpoints of the bond, the first law expression unambiguously assigns the appropriate rate of work on x and q:

$$\dot{\varepsilon}(x,t) = \int_{\mathcal{H}_x} (T[x,t]\langle q-x\rangle)\cdot\big(\dot{y}(q,t)-\dot{y}(x,t)\big)dV_x + r(x,t), \tag{3a}$$

$$\dot{\varepsilon}(q,t) = \int_{\mathcal{H}_q} (T[q,t]\langle x-q\rangle)\cdot\big(\dot{y}(x,t)-\dot{y}(q,t)\big)dV_x + r(q,t) \tag{3b}$$

where ε is the internal energy density field and r includes the energy source rate and heat transport. It can be shown [2] that the resulting internal energy is additive. This apparently resolves a long-standing question about whether or not it is possible to define an additive notion of internal energy density in the presence of long-range forces [3].

Material models can be expressed in terms of a free energy function ψ with the following dependencies:

$$\psi(x,t) = \hat{\psi}\big(y(\mathcal{H}_x,t),\theta(x,t)\big) \tag{4}$$

where the notation $y(\mathcal{H}_x,t)$ means the deformation of the entire neighborhood of x, and θ is the temperature. The second law expression

[1] Sandia National Laboratories is a multi-program laboratory operated by Sandia Corporation, a wholly owned subsidiary of Lockheed Martin Corporation, for the U.S. Department of Energy's National Nuclear Security Administration under contract DE-AC0494AL85000.

Email: sasilli@sandia.gov

$$\dot{\eta} \geq \theta r \tag{5}$$

together with a Coleman-Noll argument yields a dissipation inequality and restrictions on the material model.

Nonlocal diffusion of heat can be modeled with evolution equations that are analogous to the mechanical equation of motion [4,5]. The simplest approach is to treat each bond as a conduction pathway within which the rate of energy transport depends on the temperature difference between the endpoints. This is a special case of a more general transport equation in which the conduction in a bond can depend additionally on the temperature differences along the other bonds in the neighborhood. Nonlocal fluid transport in porous and fractured media has been modeled using a peridynamic diffusion model [6]. The need for such a nonlocal flow model (sometimes called *anomalous diffusion*) arises from the presence of fractures of different lengths and conductivities in a porous solid.

A fully coupled thermomechanical model, in which temperature evolution and mechanical deformation depend on each other through the thermodynamic form of the material model in equation (4), is described in [7]. Chemical reactions can also be included by extending the thermodynamic material description and adding appropriate kinetics [8].

The application of the peridynamic mechanical model to martensitic phase boundary motion was investigated by Dayal and Bhattacharya [9] for an elastic material model in which the free energy is a nonconvex function of bond elongation. These authors demonstrated the spatial structure of the phase boundary, which has finite thickness due to the nonlocality of the model, as well as the kinetics of phase boundary motion in response to changes in loading at the boundary. In general, the system seeks out global minimizers of potential energy in equilibrium. A moving phase boundary in the elastic peridynamic continuum releases stress waves because there is no dissipation in the elastic material model.

Recent work by the author adds a novel dissipative term to the nonconvex material model. This term applies a rate-dependent form of the *bond-pair* type of peridynamic material model [2]:

$$T[x,t]\langle\xi\rangle = T^e[x,t]\langle\xi\rangle + \alpha\big(\dot{y}(x+\xi,t) - 2\dot{y}(x,t) + \dot{y}(x-\xi,t)\big) \tag{6}$$

where T^e is the elastic (nonconvex) material response, ξ is the bond vector, and α is a constant. The rate of dissipation at a point depends on a nonlocal approximation to the second spatial derivative of displacement. This dissipative term consumes energy in the interior of a quasi-statically moving phase boundary. When the stress differs from the Maxwell stress in a quasi-static motion, that is, when the system is metastable, the rate of energy dissipation determines the velocity of the phase boundary. This effectively determines a kinetic relation for phase boundary motion. This apparent capability of the peridynamic model to uniquely predict a phase boundary velocity as a function of the stress avoids the need for a supplemental kinetic relation, as is needed in the classical theory [10].

References

[1] Silling S.A.: Reformulation of Elasticity Theory for Discontinuities and Long-Range Forces *J. Mech. Physics Solids* **48**:175-209, 2000.

[2] Silling S.A., Lehoucq R.B.: Peridynamic Theory of Solid Mechanics, *Adv. Appl. Mech.* **44**:73-166, 2010.

[3] Gurtin M.E., Williams W.O.: On the First Law of Thermodynamics, *Arch. Rat. Mech. Analysis*. **42**:77-92, 1971.

[4] Duangpanya M., Bobaru F.: A Peridynamic Formulation for Transient Heat Conduction in Bodies with Evolving Discontinuities, *J. Comp. Physics* **231**: 2764-2785, 2012.

[5] Oterkus S., Madenci E., Agwai A.: Peridynamic Thermal Diffusion, *J. Comp. Physics* **265**: 71-96, 2014.

[6] Katiyar A., Foster J.T., Ouchi H., Sharma M.M.: A Peridynamic Formulation of Pressure Driven Convective Fluid Transport in Porous Media, *J. Comp. Physics* **261**: 209-229, 2014.

[7] Oterkus S., Madenci E., Agwai A.: Fully Coupled Peridynamic Thermomechanics, *J. Mech. Physics Solids* **64**:1-23, 2014.

[8] Chen Z., Bobaru F.: Peridynamic Modeling of Pitting Corrosion Damage, *J. Mech. Physics Solids* **78**:352-381, 2015.

[9] Dayal K., Bhattacharya K.: Kinetics of Phase Transformations in the Peridynamic Formulation of Continuum Mechanics, *J. Mech. Physics Solids* **54**:1811-1842, 2006.

[10] Abeyaratne R., Knowles J.K.: Kinetic Relations and the Propagation of Phase Boundaries in Solids, *Arch. Rat. Mech. Analysis*. **114**:119-154, 1991.

PHASE FIELD MODELING OF MARTENSITIC TRANSFORMATIONS IN NANOCRYSTALLINE MATERIALS

Rajeev Ahluwalia, Siu Sin Quek & David T. Wu
Institute of High Performance Computing, Singapore

Summary We have studied stress induced martensitic transformations in nanocrystalline materials using a Ginzburg Landau/phase field approach. We incorporate the effect of grain boundary energy in our simulations and show that if the grain boundary energy of the martensite phase is larger than that of austenite, a local suppression of the transformation can occur at the grain boundaries. For small grain sizes, this leads to an overall suppression of the transformation, which also reflects in the stress-strain curve. In accordance with experimental observations, a reduction of hysteresis associated with the superelastic stress strain curves is also observed.

The subject of martensitic transformation in nanocrystalline materials has received recent attention [1-2]. It has been demonstrated that below a certain grain size, the temperature induced transformation can be completely suppressed. For the stress induced transformation, it is found that the hysteresis loops associated with the superelastic deformation exhibit reduced hysteresis (area enclosed by the stress-strain curve) as the grain size decreases. To understand this behaviour, we have used a phase field approach to study martensitic transformation in nanocrystalline materials undergoing martensitic transformations. A phase field model for martensitic transformation in polycrystal is extended to incorporate the effect of grain boundaries [3], which are expected to play a significant role in nanocrystalline materials. The grain boundary contributions are modelled by an energy barrier at the grain boundaries. The strength of this barrier can be related to the difference between the grain boundary energies of martensite and austenite. Our simulations of temperature induced transformations show that when the grain boundary energy of austenite and martensite are same, no significant grain size effects are observed for the transformation as well as the stress strain response. However, if the grain boundary energy of the martensite phase is larger than that of the austenite phase, the transformation is suppressed at the grain boundaries (Fig 1). This suppression also influences the behaviour within the grains, which is clear from Fig 1 where we observe that for smallest grain size, no martensite is observed.

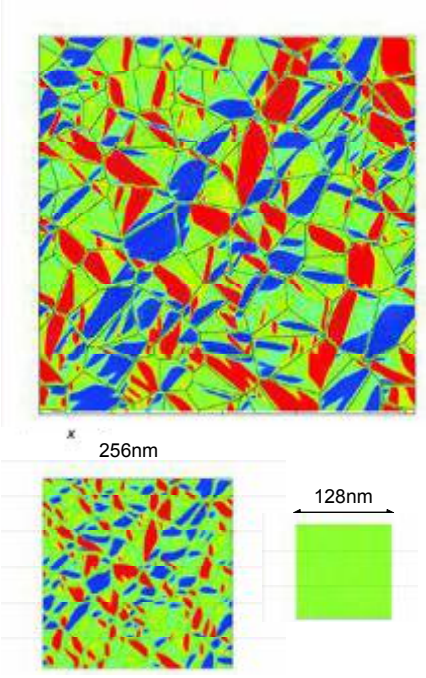

Fig 1: Martensite domain patterns at different grain sizes for temperature induced transformation. Red and blue correspond to martensite variants and green referes to the austenite.

For stress induced martensitic transformations, suppression of transformation leads to “slimming” of the hysteresis loops, which leads to a reduced hysteresis at small grain sizes. The simulated stress strain curves for three different grain sizes are

[a] Corresponding author. Email: ictam2016papers@legendconferences.com.

shown in Fig. 1(A) where we clearly see that area enclosed by the curves decreases as grain size is decreased. Fig 1(B) and Fig 1(C) show the martensite patterns at the maximum applied strain. It is clear that for small grain sizes, the over all transformed fraction is less and the martensite domain pattern is also quite different form the larger grain size case.

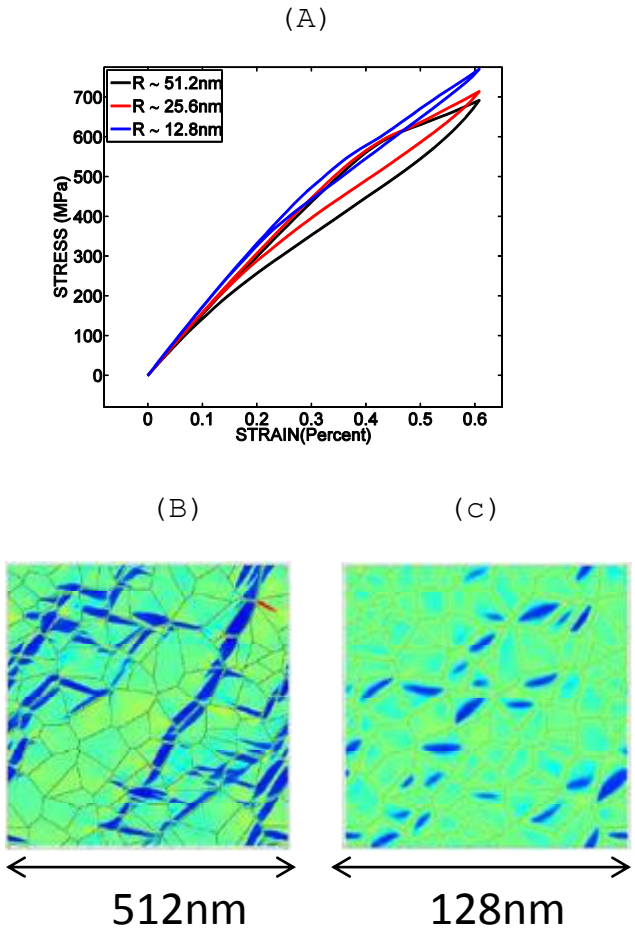

Fig 2: (A) shows the stress strain curves at three grain sizes. (B) depicts martensite domain patterns at different grain sizes for strrain induced martensite at maximum applied strain. Red and blue correspond to martensite variants and green referes to the austenite.

Our simulations have provided insights into the nature of martensitic transformations in nanocrystalline alloys. We are further studying the role play grain size distributions (such as bimodal). These results will be presented at the meeting.

References

[1] Waitz T, Tsuchiya TK, Antretter T,and Fischer FB., *MRS Bulletin* **34**:814, 2009.

[2] Ahadi A and Sun QP.,.: Appl. Phy. Lett **103**, 021902, 2013.

[3] Ahluwalia R, Quek SS and Wu DT., J. Appl. Phys **117**, 244305, 2015

MODELLING OF AXIAL BUCKLING AND RECOVERY OF PSEUDOELASTIC NITI TUBES

Dongjie Jiang[1], Chad M. Landis[1] & Stelios Kyriakides[1]
[1]*Research Center for Mechanics of Solids, Structures & Materials, University of Texas at Austin, Austin, Texas, USA*

Summary The axial buckling of pseudoelastic NiTi tubes is studied through a combination of experiment and analysis. On reaching the martensite transformation stress the tube buckles first into an axisymmetric mode and subsequently locally collapses developing a non-axisymmetric mode with three circumferential waves. Under displacement control, collapse leads to progressive development of additional mode-3 lobes. On unloading, the material transforms back to austenite, deformation is recovered, and the buckling lobes are erased. A finite element model coupled with a custom constitutive model is used to successfully simulate the experiment. The constitutive model uses kinematic hardening to simulate the stress nonlinearity associated with the reversible phase transformation, and incorporates the tension/compression asymmetry exhibited by the material used.

INTRODUCTION

Pseudoelasticity is the property of a shape memory alloy like NiTi to be deformed to strain levels of a few percent and recover on unloading, characteristics endowed by the associated solid-state phase transformations. This work examines the effects of this behavior on the axial buckling of a 6.35 mm diameter NiTi tube (D/t = 23.6). On reaching the compressive transformation stress, the initially austenitic phase (A) begins to transform to martensite (M), in the process tracing a relatively softer response. Because of this material nonlinearity, the tube buckles first into an axisymmetric wrinkling mode that initially grows stably, but at some point yields to an unstable non-axisymmetric mode with three circumferential waves. This mode localizes first into a single lobe and subsequently to a second one and potentially more. On unloading, the material transforms back to A resulting in recovery of deformation, erasure of the buckles, and a nearly closed hysteresis [1]. In the present work, the buckling and recovery are simulated using a finite element model described in [1] coupled to a nonlinear kinematic hardening model capable of capturing the nonlinearities associated with the reversible phase transformations. The constitutive model is calibrated to measured tensile and compressive uniaxial responses of the NiTi tubes used [2]. It incorporates the recorded tension/compression asymmetry and allows for permanent deformations that can occur when the transformed M yields as outlined below.

ANALYSIS

In the present model (ASY) the strain rate is decomposed into elastic, transformation, and plastic components $\varepsilon_{ij} = \varepsilon^{e}_{ij} + \varepsilon^{t}_{ij} + \varepsilon^{p}_{ij}$. The elastic component has elastic constants (E, ν). A transformation surface $\Phi^{t} = 3(s_{ij} - s^{B}_{ij})(s_{ij} - s^{B}_{ij})/2 - \sigma_o^2 = 0$ is established with the corresponding strain rate $\dot{\varepsilon}^{t}_{ij} = \Lambda^{t}(s_{ij} - s^{B}_{ij})$ being normal to it and the back stress defined as $\sigma^{B}_{ij} = \partial\psi^{t}/\partial\varepsilon^{t}_{ij}$. Tension-compression asymmetry is introduced through the back stress potential $\psi^{t}(\bar{\varepsilon})$ where $\bar{\varepsilon} = J^{e}_{2} f(J^{e}_{3}/J^{e}_{2})$. The function $f(x) = \cos\{\arccos[1 - a(x^3 + 1)]/3\}$ with $a = 0.99225$ scales the equivalent transformation strain and hence the back stress with the same factor but in inverse manners producing the tensile and compressive responses shown in Fig. 1 that are close to the measured values. Beyond a stress level the transformed material yields. The plastic strain obeys a flow rule $\dot{\varepsilon}^{p}_{ij} = \Lambda^{p} s_{ij}$ and a yield function $\Phi^{p} = 3 s_{ij} s_{ij}/2 - \sigma_y^2$.

The constitutive model in implemented as a UMAT in ABAQUS and is attached to the finite element model of the tube (see [1]). An initial imperfection $w/t = [\omega_o \cos\frac{\pi x}{\lambda} + \omega_3 \cos\frac{\pi x}{2\lambda}\cos 3\theta]\exp(-\beta(x/L)^4)$ is assigned to the mesh to help trigger buckling. The model tube is compressed between two rigid plates and contact between the plates and the tube is assumed to be "hard" with friction. The compression is performed by prescribing the axial displacement of one plate while the other is fixed. The results of the case whose predictions are closest to the experiment is presented in the next section.

RESULTS

The calculated axial stress-shortening ($\sigma - \delta/L$) response (ASY) is shown in Fig. 2 together with the corresponding experimental one. Fig. 3 shows a set of deformed configurations corresponding to the numbered bullets on the response. Initially the tube is compressed elastically until the onset of martensitic transformation, following which the stress enters a plateau. By point ⑥ the non-axisymmetric mode is excited and the model starts to collapse. Deformation has localized into one lobe with three circumferential waves (image⑦). Locally transformation is completed and collapse is arrested as the material enters the

[a] Corresponding author. Email: skk@mail.utexas.edu

second stiff branch (M-phase elastic modulus). Collapse continues by the development of a second lobe as shown in images ⑧ and ⑨. Upon unloading from ⑩ the deformation is recovered and the buckling lobes are progressively erased following the reverse order. Overall, the calculated response follows reasonably closely the experimental one and the predicted buckling/recovery deformation history closely resembles that observed in the experiment (see Fig. 3 of [1]).

Included in Fig. 2 is the $\sigma - \delta / L$ response calculated with the same FE model using a simpler version of the constitutive model outlined above (SYM). SYM is calibrated strictly on the compressive response, in other words the tension/compression asymmetry is neglected. The buckling and recovery are also reproduced but the loading part of the response traces a much higher stress level than in the experiment after the mode-3 buckling initiates. This has the effect of also raising the unloading response and the significant under-prediction of energy dissipation during the loading-unloading cycle. Furthermore, this stiffer material required significantly larger imperfection amplitudes to achieve this level of performance. This comparison demonstrates that, although in this problem the primary loading is compression, the tension-compression asymmetry plays an important role in predicting this structural buckling behaviour as some tension develops in the buckling lobes.

The present family of models do not capture the unstable behavior exhibited under primarily tensile stress states. This material characteristic is bound to play a role in the behavior of NiTi structures like the present example. Inclusion of this behavior is guiding ongoing extensions of this modelling framework.

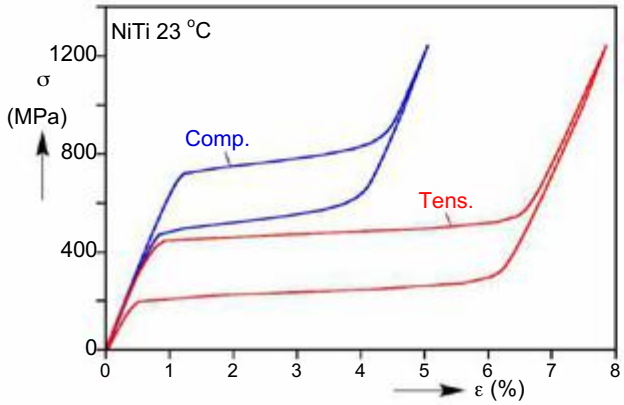

Fig. 1 Tensile and compressive stress-strain responses of NiTi exhibiting the measured asymmetry.

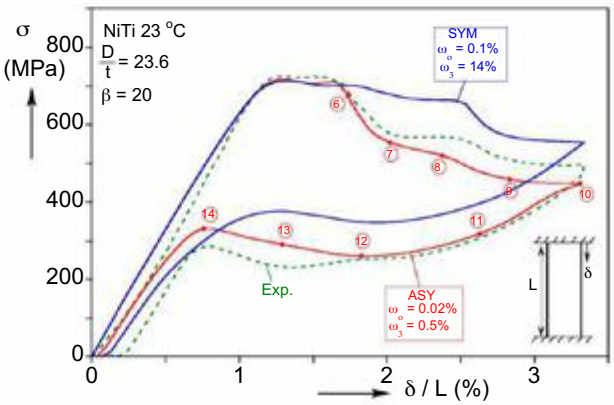

Fig. 2 Calculated tube compressive responses using two constitutive models and the measured response.

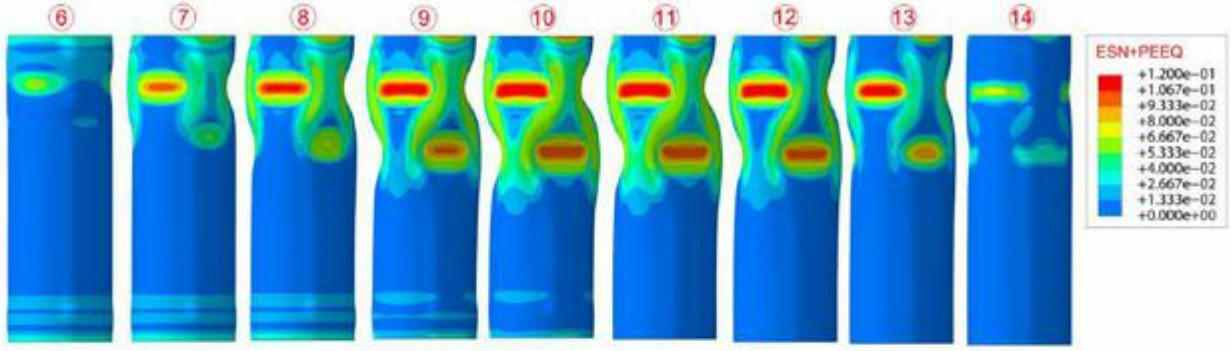

Fig. 3 Sequence of deformed configurations with superimposed strain contours showing the buckling and recovery predicted using the ASY constitutive model

Acknowledgement

The authors acknowledge with thanks the financial support received for this work from the National Science Foundation under grant no. CMMI-12000465.

References

[1] Jiang D., Bechle N.J., Landis C.M., Kyriakides S.: Buckling and recovery of NiTi tubes under axial compression. *Int'l J. Solids Struct.* **80**:52-63, 2016.

[2] Jiang D., Landis C.M., Kyriakides S.: Buckling and recovery of NiTi tubes under axial compression. Part II: Analysis with More Comprehensive Constitutive Modelling. *Int'l J. Solids Struct.* (in preparation)

[3] Bechle N.J., Kyriakides S.: Localization in NiTi tubes under bending. *Int'l J. Solids Struct.* **51**:967-980, 2014.

AN ANALYTICAL MODEL FOR PHASE TRANSITIONS OF AN SMA WIRE UNDER UNIAXIAL TENSION

Zilong Song* [1] and Hui-Hui Dai[1]

[1]*Department of Mathematics, City University of Hong Kong, Kowloon Tong, Hong Kong*

Summary This paper considers isothermal stress-induced phase transitions of shape memory alloys (SMAs) based on a two-variant constitutive model. Specifically, inhomogeneous deformations of a slender circular cylinder under uniform axial stress are investigated analytically. By utilizing two small parameters, the complex three-dimensional (3-D) mechanical system is reduced to a 1-D coupled system of two strains for each of three phase regions. Then, for given load parameter, inhomogeneous deformations with two and three regions are constructed, and many analytical period-k solutions are found for the first time. For displacement-controlled process, the transition from homogeneous states to localized inhomogeneous ones is identified, capturing the possible instabilities at nucleation. The analytical results reveal that phase transition starts from a small band rather than a point. This work can also shed light on the difficulties of direct numerical simulations.

INTRODUCTION

Shape memory alloys (SMAs) such as Ni-Ti have been employed for numerous real-world applications in various industries. Many experiments on SMA wires under tension show that the stress-induced phase transitions exhibit Lüders-like behavior, i.e, they are realized by nucleation of martensite band and subsequent propagation of transformation front [1]. At nucleation, initial homogeneous deformation will be replaced by localized inhomogeneous deformations.

Various models have been proposed to study such inhomogeneous deformations, including phenomenological models [2], phase field models (e.g. Levitas, Lee & Preston 2010) and strain gradient models (e.g. Chang, Shaw & Iadicola 2006). The original 3-D problem can be considered a free boundary problem, where the location and shape of interfaces are not known beforehand. To the authors' knowledge, analytical results for such a complicated problem are rare and how the material and geometric parameters influence the transition process is unclear. Based on [2], this work will examine analytically the inhomogeneous deformations of an SMA wire with finite length, subjected to uniaxial tension in a 3-D setting. Analytical solutions with two or three phase regions will be constructed, with explicit dependence on material and geometric parameters. The transition process and the associated instabilities will be clarified. Also, this work can potentially provide certain guidance for direct numerical simulations.

THE CONSTITUTIVE MODEL AND GOVERNING SYSTEM

A two-variant constitutive model

For phase transitions of SMAs, we adopt a two-variant constitutive model [2], which is based on two scalar functions, Helmholtz free energy Φ and rate of mechanical dissipation ξ. Let the volume fraction of martensite phase be α ($0 \le \alpha \le 1$), and the natural configuration of martensite phase be $\mathbf{G} = \mathrm{diag}[1-s_1, 1-s_1, 1+s_2]$. Then, Φ is adopted as

$$\Phi(\mathbf{F},\alpha) = |\mathbf{G}_\alpha|[(1-\alpha)\Phi_1(\mathbf{F}_\alpha)+\alpha\Phi_2(\mathbf{F}_\alpha)]+B\alpha(1-\alpha)+[(1-\alpha)\phi_1+\alpha\phi_2], \quad \mathbf{G}_\alpha = (1-\alpha)\mathbf{I}+\alpha\mathbf{G}, \quad \mathbf{F}_\alpha = \mathbf{F}\mathbf{G}_\alpha^{-1}, \tag{1}$$

where $\mathbf{F}$ is the deformation gradient, Φ_1, Φ_2 and ϕ_1, ϕ_2 are strain energy functions and thermal free energies of austenite and martensite phases, and B is the interfacial constant. And for ξ, we adopt a rate-independent form

$$\xi = A^+(\alpha)|\dot\alpha| := (k^+\alpha + Y^+)|\dot\alpha|, \quad \text{if} \quad \dot\alpha \ge 0; \quad \xi = A^-(\alpha)|\dot\alpha| := [k^-(1-\alpha)+Y^-]|\dot\alpha|, \quad \text{if} \quad \dot\alpha \le 0, \tag{2}$$

where $k^\pm, Y^\pm$ are dissipative constants. Whenever phase transition happens, the evolution of α is determined by $-\partial\Phi/\partial\alpha = \pm A^\pm(\alpha)$ for loading and unloading processes.

The mechanical system

Now, we consider a slender SMA circular cylinder with radius a and length L subjected to a uniform axial stress γ. It is assumed that $a/L \ll 1$, and we set $L = 1$ in the following. The reference and deformed positions are denoted by coordinates (R, Θ, Z) and (r, θ, z), then the concerned deformation is of the form

$$r(R,Z) = R + V(R,Z), \quad \theta = \Theta, \quad z(R,Z) = Z + W(R,Z), \quad 0 \le R \le a, \quad 0 \le Z \le 1. \tag{3}$$

Accordingly, $\mathbf{F}$ can be easily obtained, and subsequently the nominal stress $\mathbf{\Sigma}$ is determined by the formula $\mathbf{\Sigma} = \partial\Phi/\partial\mathbf{F}$. The mechanical system is given by

$$\mathrm{Div}\mathbf{\Sigma} = \mathbf{0}, \quad \Sigma_{Rr}(a,Z) = \Sigma_{Rz}(a,Z) = 0, \quad \Sigma_{Zz}(R,Z)|_{Z=0,1} = \gamma, \quad \Sigma_{Zr}(R,Z)|_{Z=0,1} = 0, \tag{4}$$

which will be coupled with the evolution of α in the previous section.

*Corresponding author. Email: buctsongzilong@163.com

The reduced system

Two kinds of small parameters arise in the present system. First, the strains are small, thus we keep only leading terms, or equivalently, we set Φ_1, Φ_2 to be the elastic energies of linear isotropic materials. And for simplicity, we assume $\Phi_1 = \Phi_2$. Second, it follows from the geometry that a is small, and so is the radial variable R. Thus, we expand the displacements in the form $V(R,Z) = R\sum_{k=0}^{\infty} V_k(Z)R^{2k}/2(1+k), W(R,Z) = \sum_{k=0}^{\infty} W_k(Z)R^{2k}$. By the technique in [3], the recursive formulas for coefficients $\mathbf{u}_k := [W_k', V_k]^T$ can be deduced from the field equation $(4)_1$ together with evolution of α, and the conditions in $(4)_2$ furnish the governing equations for $\mathbf{u}_0$. By keeping up to $O(a^2)$ terms, we get a final vector equation $\mathbf{u}_0'' + \mathbf{A}\mathbf{u}_0 = \mathbf{f}$ for each of three regions: austenite region (AR), martensite region (MR) and phase transition region (PTR, $0 < \alpha < 1$). Proper boundary conditions for $\mathbf{u}_0$ at $Z = 0, 1$ can be deduced from $(4)_{3,4}$ with consistent order $O(a^2)$. Note that the coupling of axial and radial strains, and hence the high-dimensional effect, is kept in the reduced system.

INHOMOGENEOUS SOLUTIONS AND THE TRANSITION PROCESS

Inhomogeneous solutions with given load parameter γ

The general solutions in each phase region can be readily obtained from the preceding linear equation of $\mathbf{u}_0$, e.g. in PTR

$$\mathbf{u}_0(Z) = \mathbf{u}_{0p} + C_1\mathbf{q}_1 e^{d_3 Z} + C_2\mathbf{q}_1 e^{-d_3 Z} + C_3\mathbf{q}_2\cos(d_4 Z) + C_4\mathbf{q}_2\sin(d_4 Z), \tag{5}$$

where $\mathbf{u}_{0p}$ is the particular solution, C_i are integrating constants, and $\pm d_3, \pm d_4 i$ and $\mathbf{q}_1, \mathbf{q}_2$ are eigenvalues and eigenvectors.

Experiments show that phase transition often takes place in the middle part of the wire. Suppose it starts exactly in the middle, then the symmetric conditions for the two strains are adopted: $W_0''(0.5) = 0, V_0'(0.5) = 0$. First, we analyze two-region solutions composed of AR and PTR, with a planar interface in between. Given γ, the general solutions contain eight undetermined integrating constants, and the location of interface Z_0 is also unknown. The unknown constants can be determined by four conditions at $Z = 0, 0.5$ and five connection conditions at Z_0 derived from the continuity of $\mathbf{F}$ and α. Analytically, other constants can be expressed by Z_0, which has period-k solutions of the form $Z_0^{(k)} = 0.5 - (\arctan d_5 + k\pi)/d_4$, $(k = 1, 2..)$. By a similar procedure, one can obtain inhomogeneous solutions with three regions AR, PTR and MR, and analytical period-k solutions are found for γ near Maxwell stress. There are also other connecting solutions, when the interface interacts with the middle surface (or boundary), see [3] for more details and for the nonsymmetric case.

Analysis on displacement-controlled process

In this section, we analyze the stress-elongation curves, as shown in many experiments. Based on the preceding (period-1) solutions, Figure 1(a) shows the curves near nucleation for a relatively small $a = 0.01$. There are three solutions for each fixed elongation in a small interval $[\Delta_1, \Delta_2]$, and by minimum energy criteria, the solution will jump from homogeneous state to an inhomogeneous one at $\Delta = \Delta_1$ and soon goes along a stress plateau (Maxwell stress) with three-region solutions, as in Figure 1(b). The complete loading curve is shown in Figure 1(c), as observed in experiments. The transition process does depend on the parameters, e.g. for $a = 0.03$ the transition will be smooth and stable without such a jump.

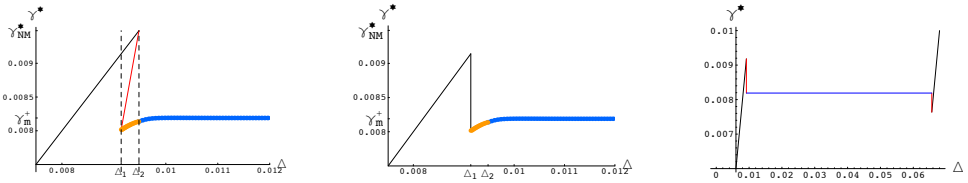

(a) for all period-1 solutions (b) real curve near nucleation (c) complete loading curve

Figure 1: The stress-elongation curves with $a = 0.01$, $\gamma^* = \gamma/E$ and $E = 4 * 10^4$MPa, see [3] for other material parameters.

CONCLUSIONS

In this paper, inhomogeneous deformations of an SMA wire with finite length are investigated analytically, and the transition process is identified. Phase transition starts from a finite band rather than a point, since the transition region in inhomogeneous deformations is always of finite width. This work can also shed light on the difficulties in direct numerical simulations (e.g. mesh sensitivity and convergence difficulty), since multiple solutions exist for certain fixed elongation near nucleation.

References

[1] Tse K.K.K., Sun Q.P.: Some Deformation Features of Polycrystalline Superelastic NiTi Shape Memory Alloy Thin Strips and Wires Under Tension. Key Eng. Mater., 177: 455-460, 2000.

[2] Rajagopal K.R., Srinivasa A.R.: On the Thermomechanics of Shape Memory Wires. ZAMP 50(3):459-96, 1999.

[3] Song, Z.: Analytic Studies on Martensitic Transformations of a Ni-Ti Shape Memory Alloy Wire Under Uniaxial Tension. PhD Thesis, CityU, 2013.

ACTUATOR LIFETIME PREDICTIONS FOR $NI_{60}TI_{40}$ SHAPE MEMORY ALLOY PLATE ACTUATORS

Robert Wheeler[1A], Cade Ottmers[1], Brett Hewling[1], & Dimitris Lagoudas [1,2]
[1]*Department of Aerospace Engineering, Texas A&M University, College Station, TX, United States*
[2]*Department of Materials Science and Engineering, Texas A&M University, College Station, TX, United States*

Abstract: Shape memory alloys (SMAs), due to their ability to repeatedly recover substantial deformations under applied mechanical loading, have the potential to impact the aerospace, automotive, biomedical, and energy industries as weight and volume saving replacements for conventional actuators. While numerous applications of SMA actuators have been flight tested and can be found in industrial applications, these actuators are generally limited to non-critical components, are not widely implemented and frequently one-off designs, and are generally overdesigned due to a lack of understanding of the effect of the loading path on the fatigue life and the lack of an accurate method of predicting actuator lifetimes. Previous efforts have been effective at predicting actuator lifetimes for isobaric dogbone test specimens. This study builds off of previous work and investigates the actuation fatigue response of plate actuators with various stress concentrations.

INTRODUCTION

Shape Memory Alloys (SMAs) are metals which possess the ability to sustain large amounts of deformation and recover a designed geometry when heated above a critical temperature. SMAs recover these strains, induced by mechanical or thermal loading, by transforming from martensite to austenite. This phenomenon is referred to as the Shape Memory Effect (SME) and recovered strains range between 2% and 10%, depending on the material and processing. The fact that this SME is highly repeatable, coupled with their high actuation energy density, makes SMAs viable actuators for many engineering applications, such as morphing aerostructures, deployable space structures, and light-weight/small volume replacements for conventional actuators. For most actuator applications, the SMA is loaded mechanically (either axially or torsionally) and then heated in order to recover strain in the direction of the loading [1].

Currently, the lack of standard testing methods which accurately characterize and model thermomechanical fatigue in SMA actuators frequently limits their use to non-structural/non-critical components or results in actuators being severely overdesigned. Recent studies [2-4] have demonstrated the predictive capabilities of work-based modelling for determining actuator lifetimes; however, previous work on SMA actuation fatigue has primarily been focused on dogbone or wire actuators. In order to further current modelling efforts and develop design tools for SMA actuators, fatigue specimens with more complex geometries must be studied. In the following work, a previously developed damage model [2], which utilizes a function of the actuation work as a fatigue indication parameter, is calibrated with actuation fatigue data from isobaric, dogbone tests and implemented to predict failure of plate actuators with simulated rivet holes at various locations (centered in the plate actuator and at the edge).

EXPERIMENTAL METHODS

Actuation fatigue testing of nickel-rich ($Ni_{60}Ti_{40}$) specimens was performed on custom thermomechanical fatigue frames. Thermomechanical fatigue was achieved through subjecting the actuators to a mechanical load, which was applied via a constant weight, while thermal cycling was conducted via resistive heating and convective cooling; the test frame can be seen in Figure 1a. Three actuator specimen geometries were considered: dogbones[B], plates with centered holes (Figure 1b), and notched plates[C] (Figures 1b and 1c).

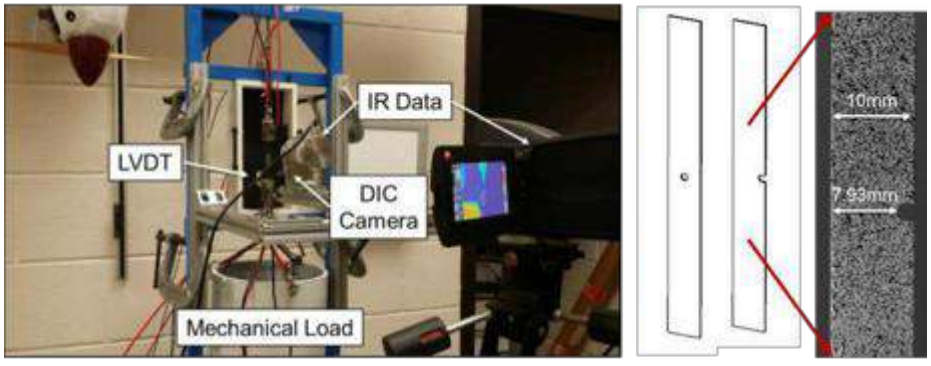

Figure 1: a) Thermomechanical fatigue frame b) Plate actuators c) Speckled notched plate actuator

High-resolution images were captured at a rate of 10hz throughout the initial 25 cycles while cyclic images (one at fully martensite and one at fully austenite) were captured during the remaining cycles. Digital image correlation (DIC) was utilized in order to determine localized transformation strains at critical points on the plate actuators, while the average values were taken from the dogbone experiments through the use of an extensometer (LVDT). Further discussion of the experimental methods can be found in previous work [3].

All specimens were cut via electro-discharge machining (EDM) and painted with a high emissivity thermal paint. Speckle patterns were then applied to the plate actuators with a high contrast paint with comparable thermal emissivity to allow for thermography studies during the tests to ensure consistent thermal cycling. The speckle pattern can be seen in Figure 1c on a notched plate. All actuators were subjected to a constant mechanical load, which was calculated based on the

[A)] Corresponding author. Email: robw11@tamu.edu
[B)] Dogbone geometry: 42.5mm gage length, 2.6mm width, 1mm thickness
[C)] Plate geometries: 100mm length, 10mm width, 1mm hole radius, 1.07mm notch (notched plates)

initial geometry of each actuator. The dogbone actuators were subjected to loads ranging between 125 and 300MPa while the plate actuator loads were selected such that the initial stress at the stress concentration was approximately 400MPa.

RESULTS

In order to calibrate the damage model proposed in [2] and implemented in [3], isobaric actuation fatigue tests were conducted at five different stress levels between 125MPa and 300MPa. An example fatigue response of a dogbone actuator can be seen in Figure 2. Throughout the fatigue life, the actuation strain remains nearly constant at approximately 1.5%.

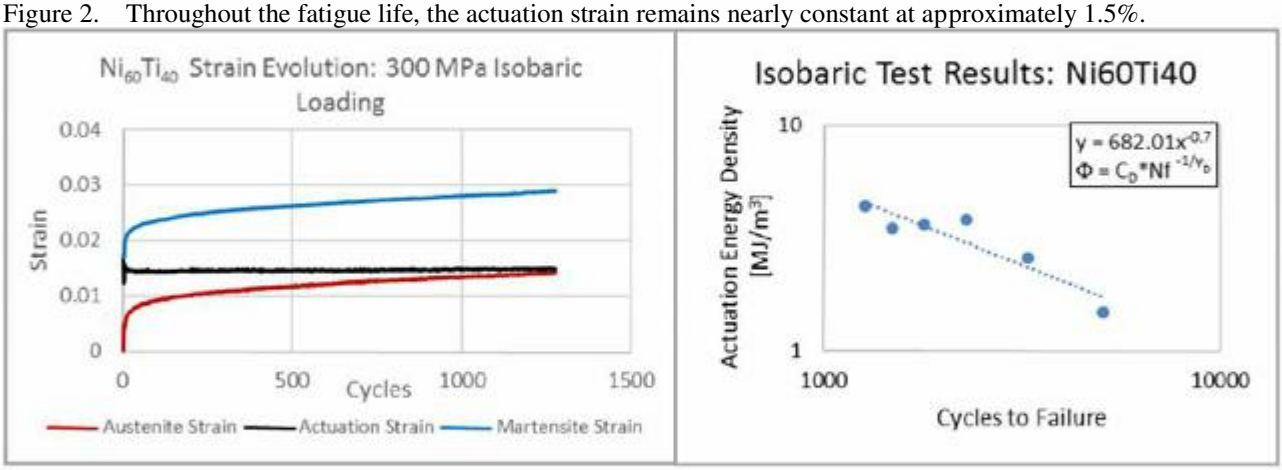

Figure 2: a) Actuation fatigue response of dogbone actuation under 300MPa load b) Actuation energy density vs. cycles to failure for all isobaric tests

Additionally, the evolution of the martensitic and austenitic strains is illustrated in Figure 2a, as they continuously increase throughout the fatigue life as transformation induced plasticity (TRIP) is developed. It should also be noted that, after the first 100 cycles, the rate of TRIP development is nearly constant, as the fatigue response has stabilized.

The summary of the calibration tests can be seen in Figure 2b. Both the fitting parameters for the damage function (C_D and γ_D) are found through the correlation shown in Figure 2b. Once the damage model was calibrated, the thermomechanical response of the plate actuators was simulated in Abaqus in order to determine the transformation strain at the notch. These values were then utilized by the damage model to make the fatigue life predictions listed in Table 1. A comparison between an Abaqus simulation and DIC measurement can be seen in Figure 3.

Table 1: Fatigue Life Predictions

Specimen	***Actuation Strain at Stress Concentration***	***Predicted Actuation Strain***	***Experimental Cycles to Failure***	***Predicted Cycles to Failure***	***Actuation Energy Density [MJ/m^3]***
Centered 1	1.34%	1.43%	973	936	5.28
Centered 2	1.52%	1.43%	872	936	6.08
Notched 1	0.98%	0.98%	1523	1590	3.92
Notched 2	0.96%	0.98%	1573	1590	3.84

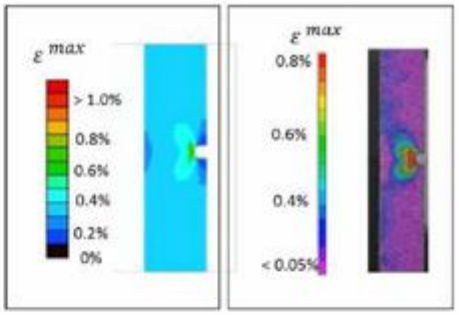

Figure 3: Comparison of actuation strain (principle or max) between Abaqus simulation and DIC measurements for a notched plate actuator (Notched 1).

CONCLUSIONS

For both plate actuator geometries, the transformation can be seen to initiate at the stress concentration in both the DIC results and simulations, as expected. Additionally, the predicted actuation strain (obtained from Abaqus simulations) agrees very well with experimentally observed actuation strains at the stress concentration, as does the experimental cycles to failure with the predicted cycles to failure, as shown in Table 1. From these results, it is clear that the actuation work represents a promising fatigue indication parameter and that the fatigue life prediction method utilized herein merits further development. Future work on this project will entail incorporation of the TRIP into the simulations (in order to account for changing actuator geometry) as well as the study of additional geometries and thermomechanical loading paths.

References

[1] D.J. Hartl and D.C. Lagoudas. Aerospace applications of shape memory alloys. *Proceedings of the Institution of Mechanical Engineers, Part G: Journal of Aerospace Engineering*, 221(4):535-552, 2007.

[2] D.J. Hartl, et al. "Three-dimensional constitutive model considering transformation-induced damage and resulting fatigue failure in shape memory alloys" SPIE Smart Structures and Materials+ Nondestructive Evaluation and Health Monitoring. International Society for Optics and Photonics, 2014.

[3] Wheeler, Robert W., et al. "Modeling of thermo-mechanical fatigue and damage in shape memory alloy axial actuators." SPIE Smart Structures and Materials+ Nondestructive Evaluation and Health Monitoring. International Society for Optics and Photonics, 2015.

[4] Calhoun, C, et al. Actuation fatigue life prediction of shape memory alloys under the constant-stress loading condition. *Scripta Materialia, Vol. 95,* 58-61, 2015

ENHANCE FATIGUE RESISTANCE OF NITI BY GRAIN SIZE GRADIENT

Qingping SUN[1 a)], Jian LU[2], Minglu XIA[1], Parham KARBIRIFAR[1] & Kuo ZHANG[1]
[1]*Department of Mechanical and Aerospace Engineering, Hong Kong University of Science and Technology, Kowloon, Hong Kong, China*
[2]*Department of Mechanical and Biomedical Engineering, City University of Hong Kong, Kowloon, Hong Kong, China*

Summary Recent research shows that NiTi with GS=10nm can significantly suppress the crack nucleation and enhance the fatigue life but at the expenses of reduced ductility and crack growth resistance. In this paper, surface mechanical attrition treatment (SMAT) is used to create a nanocrystallined Grain-Size-Gradient (GSG) surface layer with smooth GS distribution to enhance fatigue life of NiTi. The key idea is to suppress the surface crack nucleation and growth by the Hall-Petch strengthening and the high residual compressive stress, both due to the severe plastic deformation of the GSG layer. Fatigue experiment under cyclic tension is performed and the intrinsic and extrinsic fatigue and toughening mechanisms and their GSG dependence is discussed. The importance of hybridizing the size dependent material properties and developing the next generation fatigue resistant NiTi alloy by grain size engineering is demonstrated.

EFFECTS OF GRAIN SIZE ON THERMOMECHANICAL PROPERTIES OF NITI

Grain size (GS) is one of the key microstructural factors of NiTi SMA and significant GS dependence in strength, damping capacity, latent heat and temperature dependence of stress have been discovered. In particular, nanocrystallined NiTi with GS=10nm can significantly suppress the crack nucleation and enhance the fatigue life but at the expenses of reduced ductility and crack growth resistance [1-4] (see Fig. 1). One possible way to solve this dilemma is to use novel fabrication and microstructure design methods to hybridize the properties at different length scales so as to achieve an overall optimization of fatigue life together with other functions of NiTi SMA devices.

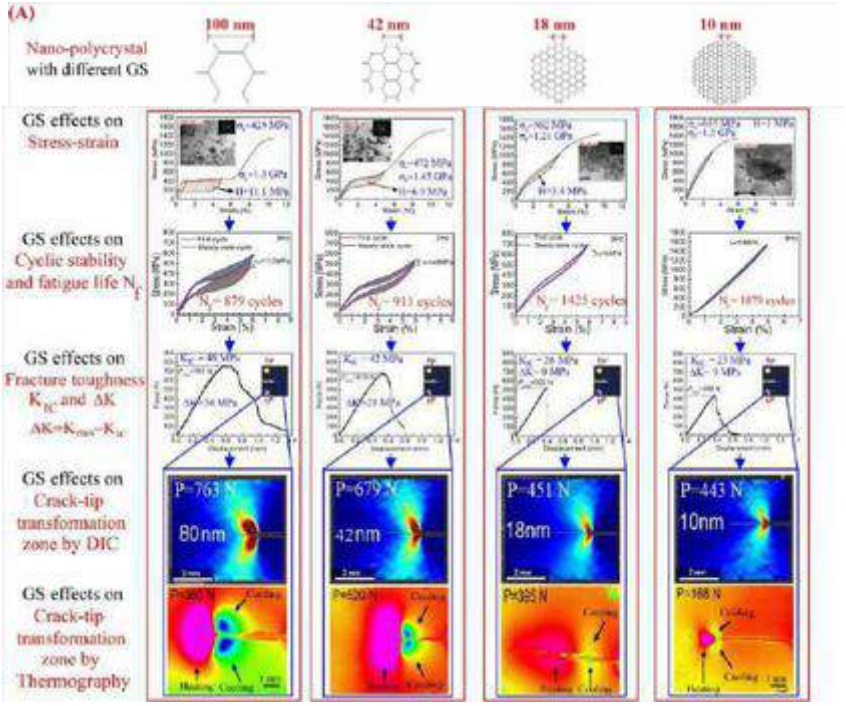

Fig. 1 Grain-Size (GS) dependent thermomechanical properties of nc NiTi: stress-strain responses, cyclic stability and fatigue life, fracture toughness and crack growth resistance, phase transition zone size.

ENHANCE FATIGUE RESISTANCE OF NITI BY GRAIN SIZE GRADIENT

In this paper, surface mechanical attrition treatment (SMAT) is used to create a nanocrystallined Grain-Size-Gradient (GSG) surface layer with smooth GS distribution to enhance fatigue life of NiTi. The key idea is to suppress the surface crack nucleation and growth by the Hall-Petch strengthening and the high residual compressive stress, both due to the severe plastic deformation of the GSG layer (Fig. 2). Fatigue experiment under cyclic tension is performed and the intrinsic and extrinsic fatigue and toughening mechanisms and their GSG dependence is discussed. The importance of hybridizing the size dependent material properties and developing the next generation fatigue resistant NiTi alloy by grain size engineering is demonstrated.

[a)] Corresponding author. Email: ictam2016papers@legendconferences.com.

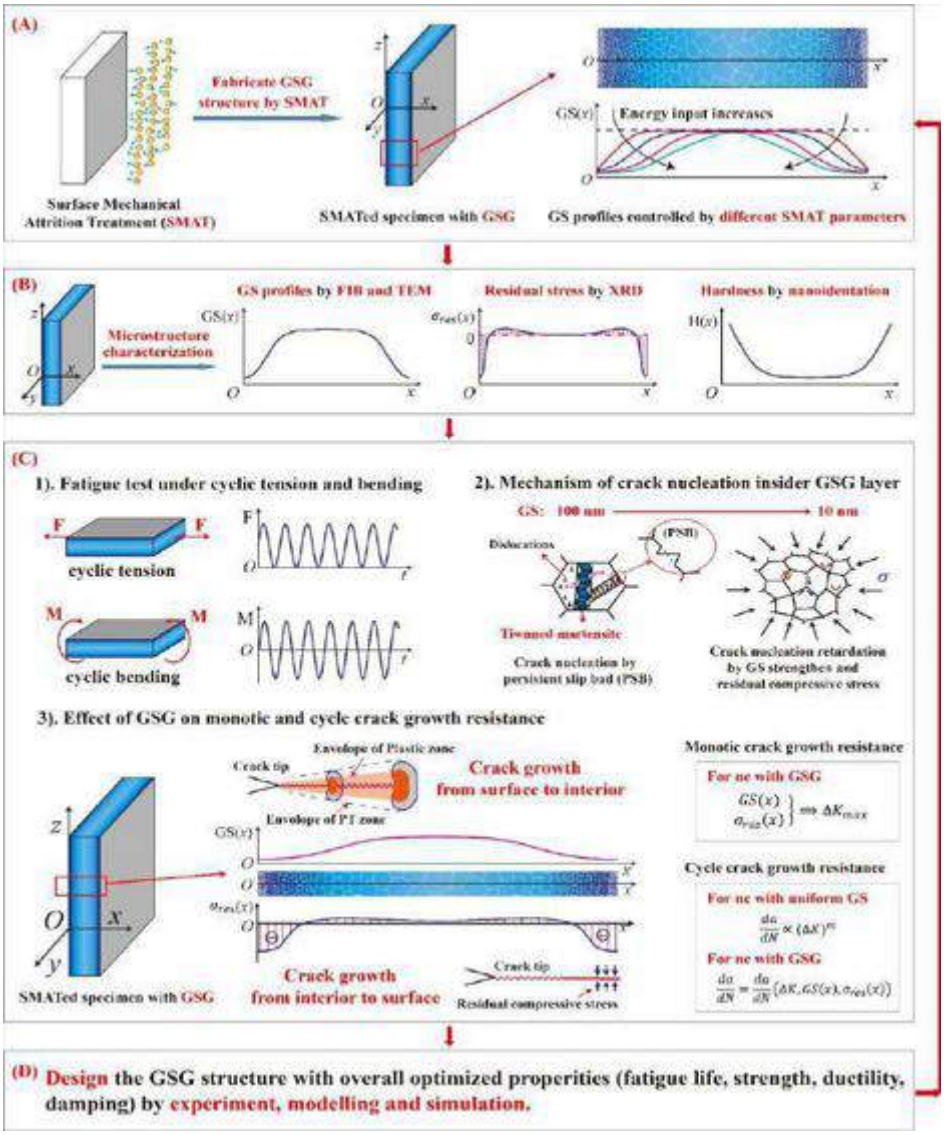

Fig. 2 (**A**) nc NiTi plate with controlled GSG profile by SMAT; (**B**) Microstructure characterization of the GSG; (**C**) Fatigue life and mechanisms of crack nucleation and toughening of GSG structure; (**D**) Overall optimized performance of GSG structure by experiment, modelling and design.

CONCLUSIONS

Nanocrystallined Grain-Size-Gradient (GSG) surface layer has been obtained by SMAT method to enhance fatigue life of NiTi SMA. The key idea of the method is to suppress the surface crack nucleation and growth by the Hall-Petch strengthening and the high residual compressive stress, both due to the severe plastic deformation of the GSG layer. Fabrication parameters of the GSG structure and the resulting intrinsic and extrinsic mechanisms of fatigue crack nucleation and crack growth resistance are identified. The dual benefits of strengthening and toughening which are usually exclusive to each other for most metals have been obtained in superelastic NiTi plates by SMAT method. The intrinsic and extrinsic fatigue and toughening mechanisms and their GSG dependence are revealed, which demonstrated the importance of hybridizing the size dependent material properties and developing the next generation fatigue resistant NiTi alloy by grain size engineering.

References

[1] A. Aslan and Q. P. Sun, *Applied Physics Letters* 103, 021902 (2013).
[2] Sun Q. P., A. Ahadi, Li M. P. and Chen M. X, *Science China Technological Sciences*, 2014, 57: 671–679.
[3] A. Ahadi and Sun Q. P., *Acta Materialia*, 76 (2014) 186–197.
[4] A. Ahadi and Sun Q. P., *Acta Materialia*, 90 (2015) 272–281.
[5] Ahadi A. and Q. P. Sun, Scripta Materialia 113 (2016) 171–175.

A TWO SCALES ANALYSIS OF THE FATIGUE OF SHAPE MEMORY ALLOYS

A. Constantinescu *[1], F. Auricchio[2], C. Menna[3], and G. Scalet[1,2]
[1]*Laboratoire de Mécanique des Solides - CNRS UMR 7649, École Polytechnique, 91128 Palaiseau cedex, France*
[2]*Dipartimento di Ingegneria Civile e Architettura, Università di Pavia, 27100 Pavia, Italy*
[3]*Dipartimento di Strutture per l'Ingegneria e l'Architettura, Università di Napoli 'Federico II', 80125 Napoli, Italy*

Summary Shape memory alloys (SMAs) are employed in innovative applications experiencing millions of cycles during their lifetime. The existing failure criteria are purely phenomenological based on macroscopic experimental results and ignore their complex microstructure. The proposed paper presents a two-scale fatigue criterion based on the elastic shakedown of the austenitic and martensitic grains of the Dang Van - Papadopoulos class. The underlying assumptions and predictions are discussed on a series of novel experiments and compared with results from literature.

INTRODUCTION

Shape memory alloys (SMAs) possess unique properties, known as shape memory effect and pseudoelasticity. These properties result from reversible diffusionless solid-solid transformations (known as martensitic transformations) between a relatively ordered parent phase, called austenite (A), and a less ordered product phase, called martensite (M). Their peculiar properties are successfully exploited in many fields, ranging from structural engineering, to robotics or biomedical industry. In particular, a wide segment is covered by SMA actuation systems, innovative devices for the control of civil structures and self-expandable vascular stents.

The rather complex micromechanical behavior of SMAs also induces unusual fracture and fatigue responses when compared with standard polycrystalline metallic alloys. It has already been discussed, in several papers, that classical fatigue criteria cannot be directly applied due to the uncertain role of the phase transformation under cyclically varying deformations and the stress and/or thermally-induced microstructural evolution of the different phases. Transformations between austenitic and martensitic phases, moving martensite interfaces, and accumulation of dislocations are believed to play an important role in the fatigue lifetime of SMAs.

The novelty of the present predictive fatigue failure methodology for cyclic loading of SMAs is based on a shakedown analysis performed at different scales of the materials [2, 3, 4]. The results rely on recent mathematical and theoretical advancements on shakedown theorems [5] and constitutive models for SMAs [1]. The proposed fatigue criterion (i) predicts high cycle fatigue crack initiation; (ii) is based on a multiscale analysis taking into account the complexity of the phase transformation between austenite and martensite and (iii) preserves the multiaxial character of the phenomena.

The papers presents (a) the fatigue criterion based a thermodynamical consistent framework using shakedown concepts and (b) the analysis of novel fatigue results of the research group and from literature [6, 7]. The experimental results of the group permit to evaluate the micromechanical assumptions of the theoretical deduction from evolution of macroscopic strain and the local distribution of phases in the microstructure. The experimental are completed with results from literature to asses the lifetime prediction capability of the proposed criterion.

THEORY

Assuming a small strain regime, the initial configuration of the local SMA material state is described by the total strain $\boldsymbol{\epsilon}$, the temperature θ, and an internal variable $\boldsymbol{\alpha}$. The variable α represents the inelastic strain and can include the description of several physical phenomena characterizing SMA behavior, ranging from permanent plasticity and phase transformations, up to void generation and fracture. A series of constitutive models, as for example [1], can be cast in the framework of standard generalized materials. As such we have a direct estimation of the shakedown state under cyclic loading, due to the recent results by Peigney [5].

The proposed fatigue criterion aims to predict the onset on infinite lifetime for polycrystalline SMAs. It starts from the experimental observation that, in high cycle fatigue, only few grains of the material undergo inelastic strains, whilst most of the material remains elastic. Furthermore, the elastic cycles described at the scale of the structure or of the crystalline grains of the polycrystal can be characterized by using the shakedown concepts [5]. Moreover the idea of a weak, inelastic element embedded in an elastic matrix represented by two springs was initially proposed by Orowan in 1939 and it is a key element in the development of the Dang Van-Papadopuolos fatigue criteria [4].

Starting from this observation a proposed *Dang Van (DV) fatigue criterion for SMAs* can be defined as:

*Corresponding author. Email: constant@lms.polytechnique.fr

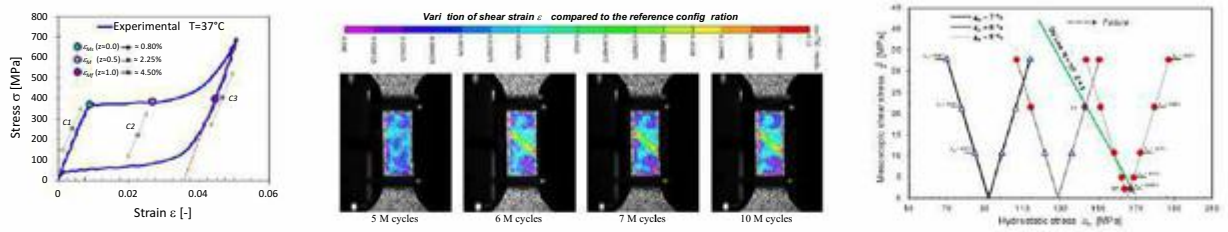

(a) (c)

Figure 1: High cycle experimental data on SMAs: (a) position of applied cycles compared with the constitutive law in the stress-strain space (b) evolution of the shear strain map during cycling at $x \times 10^6$ cycles and (c) a typical Dang Van fatigue diagram resulting from available experimental data from literature[6, 7].

Dang Van (DV) fatigue criterion for SMAs. *A structure subjected to cyclic loading has an infinite lifetime expressed as an elastic shakedown state at both macroscopic and mesoscopic scale, if and only if:*

$$\max_{t>t_0}\{\tau(\mathbf{x},t) + a\ \alpha\ \mathbf{x}\quad \sigma\quad \mathbf{x},t)\} \leq b(\alpha(\mathbf{x})) \tag{1}$$

for all points $\mathbf{x}$ *of the structure. If the condition* (1) *is not respected in a point, fatigue crack will initiate and the structure will have a finite lifetime.*

Here, τ and σ_h are expressed in terms of the instantaneous position of stress with respect to the smallest hypersphere encompassing the stress path for large times and represent a norm of the deviatoric and hydrostatic part respectively.

EXPERIMENTS AND RESULTS

The group has performed a series of high cycle fatigue experiments on plain and notched dog-bone specimens of commercial Nitinol offered by the courtesy of `www.memry.com`. The specimens have been submitted to cyclic tensile loading on stress-strain path as presented in Figure 1(a) in a temperature controlled environment. The strain field on the complete surface of the specimens has been recorded at different moments of the lifetime using digital image correlation reported in Figure 1(b). The plain specimens run out without failure at $\approx 10^7$ cycles. Notched specimens present a stress concentration and recorded lifetimes have been much smaller and will not be discussed in the abstract for brevity. At the grain scale, further observations will analyze using SEM the evolution of the microstructure, i.e. phase change, in the failure region and the evolution of the local strain fields as displayed in Figure 1(b). The lifetime can now be analyzed using the proposed Dang Van-type fatigue criterion as depicted in Figure 1(c). This diagram here shows that the proposed criterion is also capable to distinguish correctly failure in data coming from literature [6, 7].

CONCLUSIONS AND PERSPECTIVES

This paper has investigated the elastic shakedown behavior of SMA materials and has presented the extension of the DV high cycle fatigue criterion to SMAs and opens a novel way to analyze the onset of damage for materials involving phase change. The analysis also open a realm of new questions ranging from additional insight into microscopic deformation and damage mechanisms at the phase boundaries to innovative methods for the fast identification of fatigue limits, such as infrared thermography measurements.

References

[1] Auricchio, F., Reali, A., Stefanelli, U., 2009 A macroscopic 1D model for shape memory alloys including asymmetric behaviors and transformation-dependent elastic properties. Comput. Methods in Appl. Mech. Eng. 198, 1631–1637.

[2] Bertolino, G., Constantinescu, A., Ferjani, M., Treiber, P., 2007. A multiscale approach of fatigue and shakedown for notched structures. Theoretical and Applied Fracture Mechanics 48 (2), 140–151.

[3] Constantinescu, A., Dang Van, K., Charkaluk, E., 2003. A unified approach for high and low cycle fatigue based on shakedown concepts. Fatigue Fract. Eng. Mater. Struct. 26, 561–568.

[4] Dang Van, K., 1999. High-cycle metal fatigue in the context of mechanical design. In: Van, K., Papadopoulos, I. (Eds.), CISM Courses and Lectures no 392. Springer-Verlag, pp. 57–88.

[5] Peigney, M., 2014. On shakedown of shape memory alloys structures. Annals of Solid and Structural Mechanics 6 (1-2), 17–28.

[6] Pelton, A., 2011. Nitinol Fatigue: A Review of Microstructures and Mechanisms. J. Mater. Eng. Perform. 20 (4-5), 613–617.

[7] Robertson, S., Pelton, A., Ritchie, R., 2012. Mechanical fatigue and fracture of Nitinol. Int. Mater. Rev. 57 (1), 1–37.

THE EFFECT OF MICROSTRUCTURE ON PHASE TRANSFORMATION IN SUPERELASTIC SHAPE MEMORY ALLOYS

Michael Kimiecik[1], J. Wayne Jones[1], Sam Daly[2,a]
[1]*Department of Materials Science and Engineering, The University of Michigan, MI, USA*
[2]*Department of Mechanical Engineering, The University of California at Santa Barbara, CA, USA*

An experimental study to determine the effect of microstructure on phase transformation in the superelastic shape memory alloy Nickel Titanium (Nitinol) was conducted. Full-field, sub-grain-size microscale strain measurements were made *in situ* during cycling using distortion-corrected Digital Image Correlation combined with Scanning Electron Microscopy. The effect of parameters including grain size and orientation was investigated. It was found that similarly oriented grains do not necessarily transform similarly, in contrast to a common assumption in mean-field theories. Specifically, grains with similar orientation (as determined by the misorientation of the grain and specimen axes) showed variation in both the mean strain of the grain as well as the range (heterogeneity) of strain across the grain, as determined from surface measurements. Additionally, neither grain size nor degree of misorientation (of common crystal axes from the loading axis) affected the mean strain and strain range.

INTRODUCTION AND BACKGROUND

Nickel-Titanium (NiTi) alloys belong to a class of materials commonly referred to as shape memory alloys (SMAs). The defining characteristic of SMAs is the ability to recover strains as large as 10% through a solid-to-solid, diffusionless phase transformation. In the case of NiTi, this transformation takes place between a high symmetry cubic (B2) austenite and one or more monoclinic (B19′) martensite variants. While the crystallography and thermomechanical properties of this transformation are well understood for single crystals, the mechanisms of transformation are unclear in polycrystalline SMAs. Mean-field and phenomenological models of phase transformation use properties derived from observing single crystal behavior and assumptions about the similarity and completeness of martensite transformation in grains of similar orientation to predict macroscopic stress-strain curves of polycrystalline SMAs. While these predictions are reasonable approximations of averaged macroscopic behavior under simple loading conditions, their underlying assumptions have not been validated and may not be widely applicable. The aim of this work was to examine current assumptions about the effect of microstructure on transformation, for example that grain orientation is sufficient to predict the magnitude of martensite transformation strain and that grains transform fully.

EXPERIMENTAL AND ANALYTICAL APPROACHES

The use of scanning electron microscopy paired with digital image correlation (SEM-DIC) to measure full-field surface displacements was chosen because it provided the necessary high-resolution, high accuracy data across a large field of view relative to the microstructure to extract a statistically significant analysis of surface deformation behavior. Full-field displacements were calculated by DIC, which operates by tracking image subsets between reference and deformed image pairs. Subsets are matched between images by minimizing a cross-correlation coefficient, which often requires the application of a high contrast, uniformly distributed pattern to the sample surface. Full-field strains from each image were subsequently aligned with the underlying microstructural data for analysis.

Superelastic SE508 NiTi sheet was obtained from Nitinol Devices and Components. Dogbone-shaped specimens were cut using electro-discharge machining, with the tensile loading axes parallel to the sheet rolling direction. Specimens were held at 625°C for 10 minutes and annealed at 450°C for 10 minutes to produce an equiaxed microstructure with an typical grain diameter of 5 μm. A rolling texture of $\{1\bar{1}1\}[110]$ was largely preserved, albeit slightly weakened, through this recrystallization treatment. Samples were manually ground to a thickness of approximately 300 μm and polished to a mirror surface, with a final step of vibratory polishing in colloidal silica. Platinum markers were deposited to delineate a nominally 100μm × 100μm imaging area and to later align crystallographic and strain data sets. Electron backscatter diffraction (EBSD) was used to map grain boundary locations and orientations of individual austenite grains. Samples were patterned for micro deformation tracking using a self-assembly of gold nanoparticles secured to the sample surface by a silane monolayer [2]. Patterned

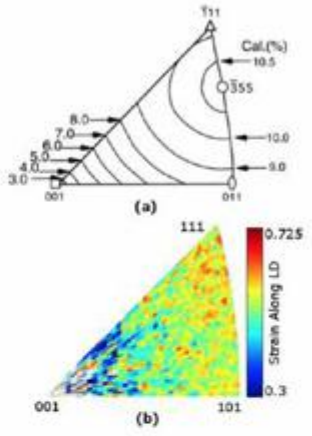

Figure 1(a) Inverse pole figure (IPF) map of accommodated strain from martensite transformation based on loading direction of single crystals from [1]; and (b) polycrystalline SEM-DIC data from these experiments. The overall trends of low strains along {100} directions and highest strains along {111} directions remain intact. However, the measured polycrystalline strain shows ~3% less strain over much of the IPF space.

[a] Corresponding author. Email: samdaly@umich.edu.

specimens were tested in-SEM under uniaxial tension at room temperature using a microtensile heating-straining stage, through one complete transformation cycle—from austenite to 'fully transformed' martensite and back to austenite. 'Fully transformed' martensite was defined by the complete propagation of localized bands of martensite and the corresponding completion of the stress plateau in the macroscopic stress-strain curve. However, note that 'fully transformed' martensite is not actually fully transformed, as residual areas of low strain, locked-in austenite remain. Micrographs of the patterned surface were captured *in situ* throughout the loading cycle using a Tescan Mira 3 FEG SEM. Initial correlation was performed using commercial software (Vic3D, Correlated Solutions Inc.) to obtain raw displacement data that was corrected for image distortions using custom MATLAB scripts described in [3,4].

RESULTS AND DISCUSSION

Models based on the phenomenological theory of martensite formation base their macroscopic stress-strain predictions on the assumption that grains with the same orientation, including those related by crystallographic symmetry, produce the same transformation strain in a polycrystalline material. However, in this work it was found that neither grain orientation nor grain size significantly affected either the mean strain or the strain range of individual grains. While averaging single crystal properties across a field of view containing approximately 5000 grains produced roughly correct trends in the macroscopic strains (Figure 1), predicting transformation from single crystal properties did not produce the correct mean strains inside of each grain and did not capture the wide range of strain that they can encompass.

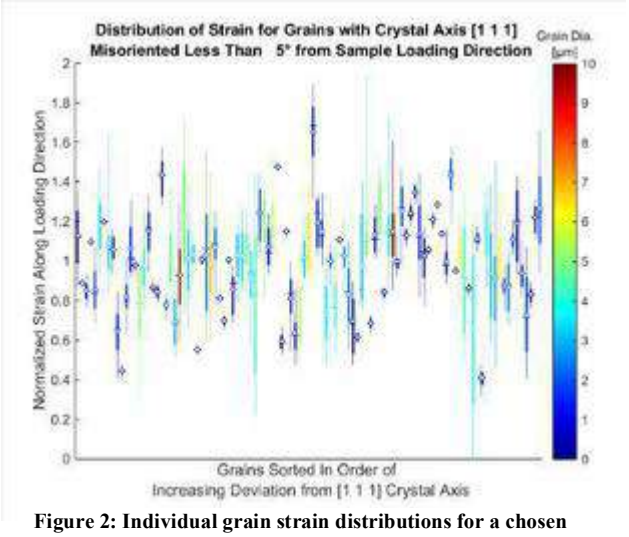

Figure 2: Individual grain strain distributions for a chosen orientation. To facilitate comparison between different orientations, all strain values were normalized to the predicted transformation strain of twinned martensite.

Using two metrics — mean strain and strain spread — measured in each grain, it was determined that grains of similar orientation did not transform similarly. The chosen metrics were confirmed to correspond with mean transformation volume fraction and transformation heterogeneity for maps of local transformation strain of a small test group of similarly oriented grains. The sampled population was then expanded to include all those grains with small deviations from low-index orientations. In both populations, no causal link between orientation and extent of martensitic transformation was detected. To examine transformation strain and heterogeneity with respect to crystallographic orientation, the full-field strain data at the microstructural length scale was segmented into grain-by-grain strain distributions. An example is shown in Figure 2, where each bar represents the experimentally-measured surface strain values over an individual grain. The middle 50% of the strain data is denoted as the thick bar, the 95th percentile bounds are denoted by thin bars, the median of each distribution is marked by a crossbar, and the open circles mark the mean strain of each grain. The grains were sorted along the x-axis by the misorientation between the [hkl] crystal axis and the sample loading axis. Each grain was color coded by grain size, showing there is no apparent effect of size on strain distribution. This analysis was performed for grains with favorable orientations for transformation, including hte {111} {355} and to a lesser extent the {110} families of the parent austenite phase. Nor was it the case that favorably oriented grains exhibited a higher degree of homogeneity. Tracking the strain spread across all orientations and grain sizes indicated that the heterogeneity did not strongly depend on either orientation or grain size. Despite some trends in mean strain existing across the inverse pole figure, the mean strain spread for the same orientations yielded a uniform distribution. Unlike mean strain, the strain range (degree of transformation heterogeneity) did not have a significant dependence on grain size. The strain range (degree of transformation heterogeneity) of individual grains also did not depend on the grain size. The findings of this experimental work are in contrast to the assumption in several mean-field theories that similarly oriented grains transform similarly, and in contrast to the assumption that a single preferred variant nucleates and subsumes the entire grain.

Acknowledgement: This work was supported by the U.S. Department of Energy, Office of Science, Basic Energy Sciences, under Award #DE-SC0003996.

References

[1] Miyazaki S, Kimura S, Takei F, Miura T, Otsuka K, Suzuki Y. *Scr Metall* **17**:1057–62, 1983
[2] Kammers A, Daly S. *Exp Mech* **53:**1333–41, 2013
[3] Sutton M, Li N, Joy D, Reynolds A, Li X. *Exp Mech* **47**:775–787, 2007.
[4] Kammers A, Daly S. *Exp Mech* **53**:1743–1761, 2013.

UNIFORM OR LOCALIZED PURE BENDING DEFORMATION OF SUPERELASTIC NiTi THIN WIRES

Gabriel Antherieu[1,2], Nathanael Connesson[1,2], Pierre Mozer[3], Yohan Payan[1,2], and Denis Favier [*1,2]
[1]*Université Grenoble Alpes, TIMC IMAG, F-38000 Grenoble, France*
[2]*CNRS, TIMC IMAG, F-38000 Grenoble, France*
[3]*Pitié-Salpétrière Hospital, AP-HP, Academic Department of Urology, Paris, France*

Summary Most medical applications involving superelastic Ni-Ti shape memory alloys are based on thin wires or tubes. If the tensile behavior of such specimens has been extensively described in the literature, only few studies deal with their mechanical behavior under pure bending and compressive load [1]. In this paper, Ni-Ti wire behaviors were experimentally investigated using pure bending and uni-axial tensile experiments. Uniform or localized behaviors were observed depending on the thermo-mechanical treatment of the wire. Theoretical bending model was proposed. For nonlocalized tests, it allowed to analyze tension-compression asymmetry. Tension and compression constitutive equations were proposed to model localization in bending.

INTRODUCTION

This paper aims at identifying the influence of thermo-mechanical treatment on Ni-Ti thin wires behavior under tensile, compressive and pure bending load. Uni-axial tensile and pure bending tests were performed on Ti 50.8%atNi wires of diameter 0.5 mm supplied by Fort Wayne Metals in their cold worked conditions. Three different thermomechanical treatments were realized $200\,^o$C for 30 min, $250\,^o$C for 30 min and $500\,^o$C for 60 min.

TENSION AND PURE BENDING EXPERIMENTS

Uni-axial tensile tests were performed in nearly isothermal conditions using a Gabo EPLEXOR 500N machine. Tensile nominal stress strain curves are plotted in Fig. 1, (a). A localization phenomenon has been observed for the $500\,^o$C wire.

Pure bending experiments were performed using a home-made device [2]. Curvatures were estimated using pictures taken during the test and synchronized with the bending moment measurement. Global curvature was estimated by fitting an arc of circle on the deformed wire of length 10 mm. Bending moment-global curvature curves are plotted in Fig. 1, (b).

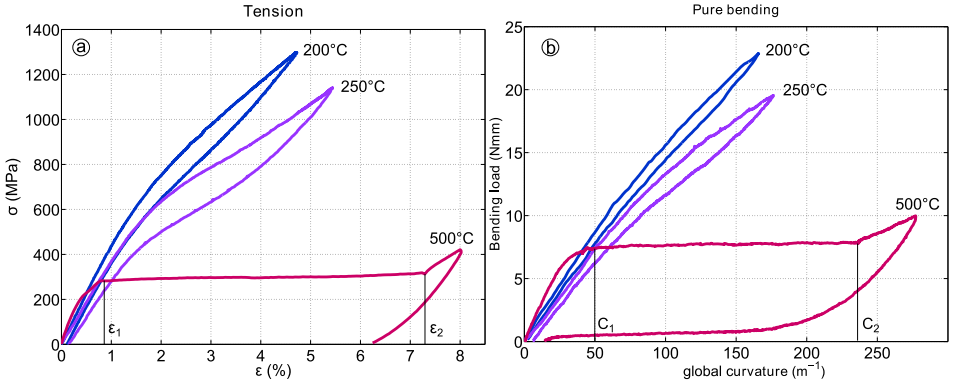

Figure 1: Experimental thin NiTi wire behaviors: (a) under tensile stress, (b) under pure bending load.

The local curvatures of the samples along their curvilinear abscissa s were also identified during the pure bending experiments. For the $200\,^o$C (not shown here) and $250\,^o$C wires, the local curvature remained uniform along the sample during the whole experiment (Fig. 2, (a)). In contrast, local curvature along the $500\,^o$C wire was found to be highly non-uniform, suggesting localization occurred during the test (Fig. 2, (b)).

MODELLING

A bending model was proposed assuming Navier-Bernoullis hypothesis, i.e. that a plane section of the wire normal to its longitudinal axis prior to loading remains plane and normal to the deformed neutral axis after the loading. Using Digital Image Correlation measurement, this hypothesis has been experimentally verified for wires [3]. This model allows to estimate

*Corresponding author. Email: denis.favier@imag.fr

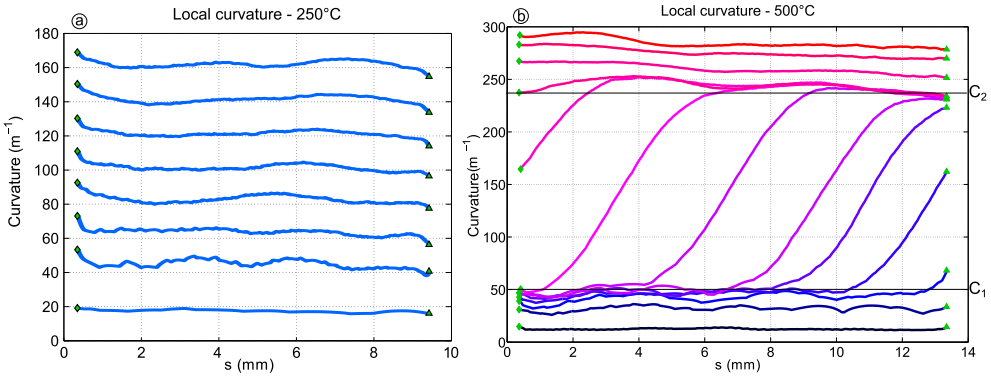

Figure 2: Local curvature during pure bending test along initial curvilinear abscissa s: (a) thin NiTi wire treated at $250\,^o$C, (b) thin NiTi wire treated at $500\,^o$C, a localization phenomena can be noticed.

the moment as function of the curvature and the position of the neutral fiber as function of the constitutive equations in tension and compression.

For wires treated at $200\,^o$C and $250\,^o$C, axial strain (resp. local curvature) is uniform during tension tests (resp. bending tests). Tension and bending results were combined to determine wires compressive behavior during the first loading. The obtained compression stress-strain curves are plotted in Fig. 3, (a). Asymmetric tension-compression behavior is well observed [4].

For the wire treated at $500\,^o$C, using the compressive constitutive equation represented Fig. 3, (b), green full line, and the experimental tensile curve as the constitutive equation in tension, the model predicts the curve presented Fig. 3, (b) black dashed line. This result is inconsistent with a localization phenomenon in bending. If the curve shown Fig. 3, (b) red full line, is adopted as the constitutive equation in tension [5], the predicted bending behavior (Fig. 3, (c) black full line) is compatible with the localization experimentally observed (Fig. 2, (b)).

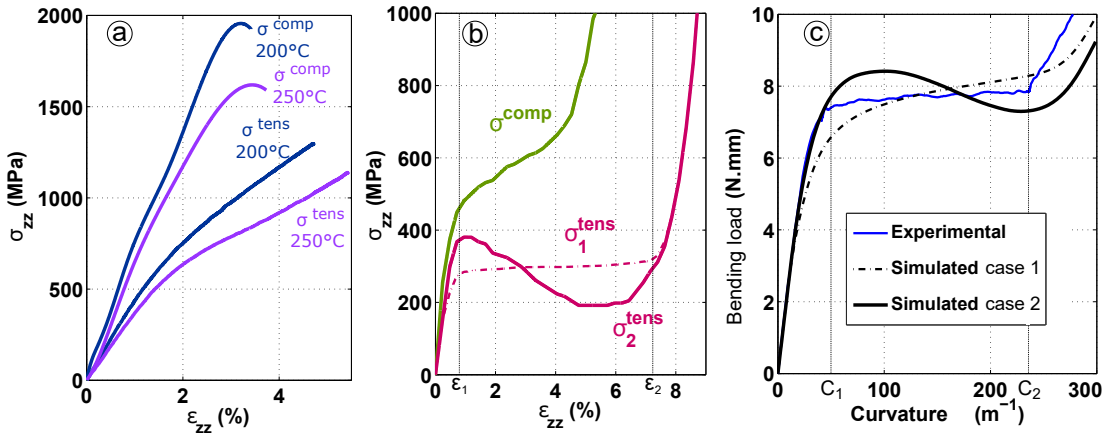

Figure 3: Result of the modelisation: (a) for wires $200\,^o$C and $250\,^o$C, (b) for wire $500\,^o$C, (c) corresponding bending moment for wire $500\,^o$C.

References

[1] NJ Bechle and S Kyriakides. Localization in NiTi tubes under bending. *International Journal of Solids and Structures*, 51(5):967–980, mar 2014.

[2] G. Antherieu, N. Connesson, D. Favier, P. Mozer, and Y. Payan. Principle and Experimental Validation of a new Apparatus Allowing Large Deformation in Pure Bending: Application to thin Wire. *Experimental Mechanics*, 2015.

[3] Ryan Watkins. *Thermomechanical Characterization and Modeling of Superelastic Shape Memory Alloy Beams and Frames by*. PhD thesis, University of Michigan, 2015.

[4] L Orgéas and D Favier. Stress-induced martensitic transformation of a NiTi alloy in isothermal shear, tension and compression. *Acta Materialia*, 46(15):5579–5591, 1998.

[5] Julian F. Hallai and Stelios Kyriakides. Underlying material response for L??ders-like instabilities. *International Journal of Plasticity*, 47:1–12, 2013.

THERMOMECHANICAL CHARACTERIZATION OF SHAPE MEMORY ALLOY MODE I FRACTURE BEHAVIOR

William LePage *[1], John Shaw[3], and Samantha Daly[1,2]

[1]*Department of Mechanical Engineering, University of Michigan, Ann Arbor, Michigan*
[2]*Department of Materials Science and Engineering, University of Michigan, Ann Arbor, Michigan*
[3]*Department of Aerospace Engineering, University of Michigan, Ann Arbor, Michigan*

Summary This work presents a combination of full-field surface displacement and temperature measurements through the use of stereo digital image correlation (3-D DIC) and infrared thermography to characterize the thermomechanical behavior of NiTi SMA during quasistatic mode I fracture. Previous experimental works have characterized the mode I fracture behavior of NiTi shape memory alloy (SMA) using a variety of techniques, but little experimental work has connected the thermal and mechanical responses of SMA during fracture.

BACKGROUND

Although the first prominent commercial SMA application was a shape memory NiTi shrink-to-fit coupler for the F-14 jet [1], the majority of SMA applications to date have been superelastic NiTi biomedical devices. These NiTi devices have sub-millimeter feature length-scales and are used in applications where fatigue is the driving failure mechanism. However, an increasing number of NiTi applications such as SMA actuators have geometries that can sustain stable crack growth [2]. As SMA devices grow in size and extend into additional critical applications, fracture becomes increasingly relevant.

Since SMA behavior has strong coupling between thermal and mechanical responses, this work uses synchronous measurements of surface displacements and temperatures to characterize SMA fracture. Existing works have applied various experimental techniques to quantify the fracture behavior of NiTi SMA, including one-dimensional load-displacement responses for stress intensity factor measurements [35], in-situ XRD for detection of stress-induced martensite around the crack tip in the through-thickness of a specimen [5], infrared thermography for the detection of both stress-induced and reverse-transforming martensite [6], and digital image correlation [7]. Fracture energy measurements across the range of transformation temperatures for SMAs are necessary for validating recent SMA fracture models with temperature dependence [8,9].

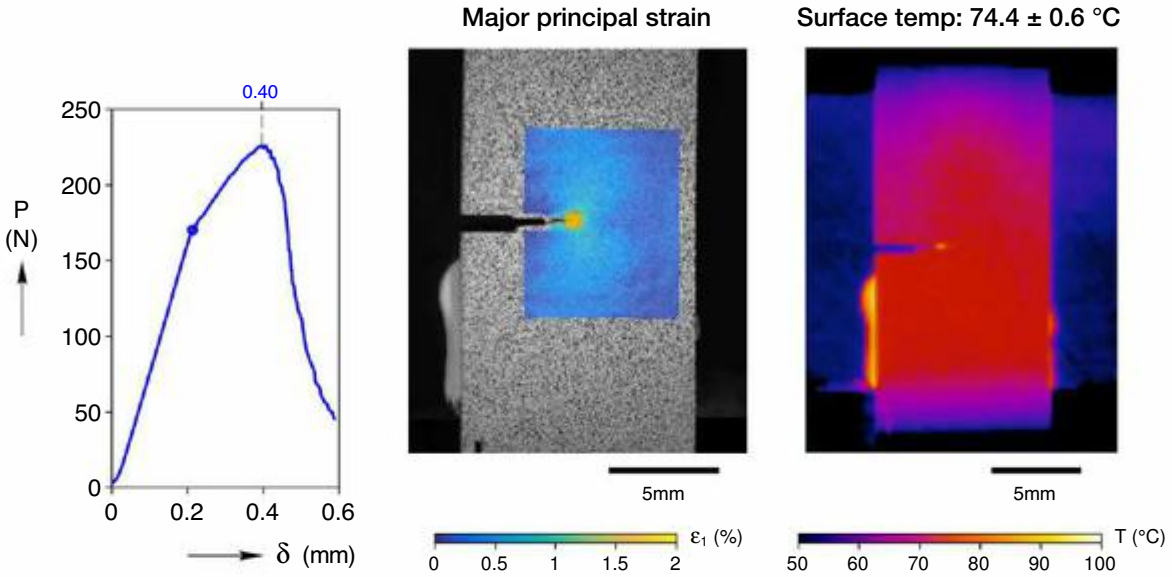

Figure 1: During the fracture process, the load (P) and grip displacement (δ) measurements (left) are synchronized with surface displacements and strains from 3-D DIC (center) and with surface temperatures from IR thermography (right).

*Corresponding author. Email: wlepage@umich.edu

METHODS

Mode I fracture samples were produced from superelastic and shape memory SMA with as-received NiTi sheets from Johnson Matthey (superelastic P/N 83813, lot 014226; shape memory P/N 83429, lot 016022). The samples were cut with wire electro-discharge machining into ASTM E647 single-edge notch fracture specimens with a pin-to-pin spacing of 25.9 mm. The samples were mechanically polished and surface speckle patterns were airbrush painted onto the samples using an Iwata CM-B airbrush and Golden high flow acrylic black and white paints. The samples were fatigue pre-cracked in a test frame with a load cell that measured load P. During fatigue pre-cracking and subsequent fracture, surface displacements were measured with 3-D DIC using GRAS-50S5M CCD cameras, and surface temperatures were measured with infrared (IR) thermography using a FLIR SC5600 IR camera.

Fatigue pre-cracks were initiated in the samples using a maximum applied stress intensity factor that remained below a threshold value that was informed by the maximum recovered strains surrounding the crack tip. The light sources and the camera lenses used polarizing filters placed orthogonally with one another to increase contrast and attenuate glare from the samples, for enhanced DIC accuracy and precision [10].

After fatigue pre-cracking, the samples were loaded in monotonic displacement control for crack propagation. Sample temperature was increased from room temperature with a custom conduction heater on the non-imaged side of the sample. Surface strains were computed from DIC surface displacements (Fig. 1). Crack tip location is inferred from the distinct pattern of the principal strain angle contour. In a similar approach to a recent finite element analysis [8], crack tip energy release rates were computed from surface displacements and strains with the J- and I-integrals. Although the multi-axial response of superelastic NiTi is still an active area of study, the multi-axial stress-strain response was approximated by a transformation-criterion approach in the cases when phase transformation was thermodynamically attainable.

References

[1] G. B. Kauffman and I. Mayo, The Story of Nitinol: The Serendipitous Discovery of the Memory Metal and Its Applications, Chem. Educ., vol. 2, no. 2, pp. 121, 1997.

[2] T. Baxevanis and D. C. Lagoudas, Fracture Mechanics of Shape Memory Alloys: Review and Perspectives, pp. 138, 2015.

[3] S. W. Robertson, a. Mehta, a. R. Pelton, and R. O. Ritchie, Evolution of crack-tip transformation zones in superelastic Nitinol subjected to in situ fatigue: A fracture mechanics and synchrotron X-ray microdiffraction analysis, Acta Mater., vol. 55, no. 18, pp. 61986207, Oct. 2007.

[4] R. Vaidyanathan, D. C. Dunand, and U. Ramamurty, Fatigue crack-growth in shape-memory NiTi and NiTi TiC composites, vol. 289, pp. 208216, 2000.

[5] S. Gollerthan, M. L. Young, a. Baruj, J. Frenzel, W. W. Schmahl, and G. Eggeler, Fracture mechanics and microstructure in NiTi shape memory alloys, Acta Mater., vol. 57, no. 4, pp. 10151025, Feb. 2009.

[6] S. Gollerthan, M. L. Young, K. Neuking, U. Ramamurty, and G. Eggeler, Direct physical evidence for the back-transformation of stress-induced martensite in the vicinity of cracks in pseudoelastic NiTi shape memory alloys, Acta Mater., vol. 57, no. 19, pp. 58925897, Nov. 2009.

[7] S. Daly, A. Miller, G. Ravichandran, and K. Bhattacharya, An experimental investigation of crack initiation in thin sheets of nitinol, Acta Mater., vol. 55, no. 18, pp. 63226330, Oct. 2007.

[8] T. Baxevanis, C. M. Landis, and D.C. Lagoudas, On the Fracture Toughness of Pseudoelastic Shape Memory Alloys, J. Appl. Mech., vol. 81, no. 4, p. 041005, Sep. 2013.

[9] T. Baxevanis, A.F. Parrinello, and D.C. Lagoudas, On the driving force for crack growth during thermal actuation of shape memory alloys, Journal of the Mechanics and Physics of Solids, 2015.

[10] W. LePage, S. Daly, and J.A. Shaw, Cross polarization for improved digital image correlation, Experimental Mechanics, accepted, 2016.

FRACTURE OF $NI_{60}TI_{40}$ SHAPE MEMORY ALLOY NOTCHED PLATES UNDER COOLING

Francis Phillips[1], Robert Wheeler[1], Theocharis Baxevanis[1] & Dimitris Lagoudas [1,2,a]
[1]*Department of Aerospace Engineering, Texas A&M University, College Station, TX, United States*
[2]*Department of Materials Science and Engineering, Texas A&M University, College Station, TX, United States*

Abstract As shape memory alloys become more commonly used for structural applications, there is a need to better understand the failure behaviour of these materials. Notched plates of $Ni_{60}Ti_{40}$ were subjected to tensile loads until fracture while in pure austenite, pure martensite, and during phase transformation from austenite to martensite. Through experimental observations, it was determined that this material exhibits a high-speed, brittle fracture and that the ultimate tensile stress of the material while undergoing phase transformation is lower than the pure phase.

INTRODUCTION

Shape Memory Alloys (SMAs) are metallic materials which are able to recover large amounts of seemingly plastic deformation through a thermo-mechanically driven phase transformation. The phase transformation is accomplished through a reversible diffusionless solid to solid transformation from an austenite phase to a martensite phase and vice-versa [1]. The phase transformation can provide a large actuation stress or strain for a relatively small volume when compared to conventional actuators [2-4].

The ability to recover deformation has driven much interest in these materials. Current SMA applications are mainly in the biomedical field where the loads experienced are generally small, hence limiting the amount of fracture data currently available in the literature. However, in order to utilize SMAs in the additional industries and in new applications, a more thorough understanding of the fracture properties of SMAs is needed.

There are multiple shapes and configurations in which SMAs must be tested in order to validate their ability to perform properly in these new industries. One such shape is in the form of a plate. Furthermore, in many existing structural applications, plates are often bound together through the use of rivets. The use of a rivet further implies that the plate must therefore have a hole or notch through it in order to allow the rivet to be inserted. It is well known that such features generally cause a stress concentration in the area surrounding the feature in the plate. Specifically for SMAs, it has been found that inclusion of notches on specimens can cause failure at stress levels as low as 60% of the pure phase ultimate tensile stress [5]. Therefore, this paper will focus on analysing the fracture of an SMA plate in which a notch has been introduced.

MATERIALS AND METHODS

All experiments were performed on $Ni_{60}Ti_{40}$ material in sheet form. A sample was used to obtain the transformation temperatures using Differential Scanning Calorimetery (DSC). Experimental samples were formed into 100 mm (length) by 10 mm (width) by 0.5 mm (thick) samples using Electron Discharge Machining (EDM). The machined plates were then coated with a thin layer of speckle pattern in order to allow collection of localized strain information through Digital Image Correlation (DIC). See Figure 1.a for a sample specimen with speckle pattern.

The specimens where loaded into a MTS Insight load frame with an attached thermal chamber. The maximum capacity of the load frame is 30 kN. Based on the DSC results gathered, specimens were loaded until failure at temperatures below the martensite finish (M_f) temperature and above the martensite desist (M_d) temperature in order to obtain a baseline for the ultimate tensile stress of these notched SMA plates under pure phase conditions. After determining the ultimate tensile stress of the pure phase, another specimen was loaded above M_d to 80% of the ultimate tensile stress of the pure phase and cooled until fracture.

Analysis of the results was performed through a combination of visual techniques. DIC frames were collected using an Edmond Optics camera connected to uEye cockpit software. High speed video was also collected with a Photron SA1 high speed video camera running at 54,000 frames per second. The DIC and high speed images were then processed through Vic2D software in order to determine the local strain fields. In order to obtain a closer examination of the fracture surface, failed specimens were examined under scanning electron microscopy (SEM). The SEM analysis were conducted on a Tescan Vega 3 SEM under high vacuum operation.

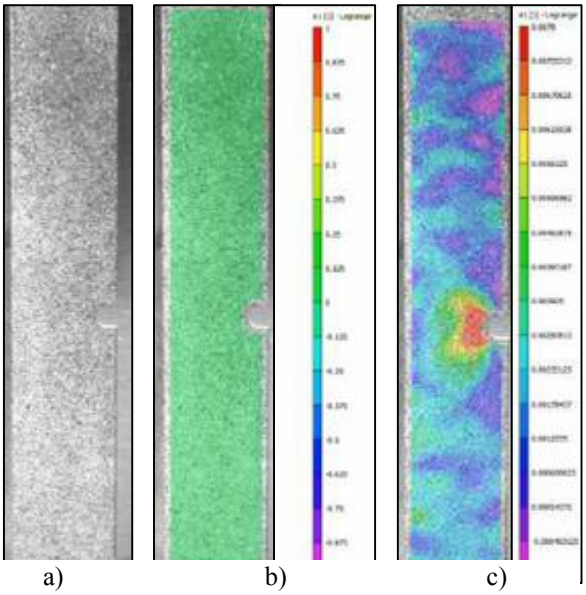

Figure 1: $Ni_{60}Ti_{40}$ plate used for fracture upon cooling experiment. a) Speckle Pattern for DIC; b) Strain at beginning; c) Strain prior to failure

[a] Corresponding author. Email: lagoudas@tamu.edu

RESULTS

For the material provided, the DIC results indicate a martensite finish temperature, M_f, of 25 °C and austenite finish temperature, A_f, of 70 °C. Therefore, the M_d temperature was calculated to be approximately 100 °C. Utilizing these values, the ultimate tensile stress of martensite and austenite were determined at room temperature (~23.4 °C) and 150 °C, respectively. The ultimate tensile stress for both pure phases was determined to be 460 MPa. Therefore, the fracture under cooling experiment was ran at a stress of 375 MPa. Figure 1.b shows the initial zero strain field of the fracture under cooling experiment as collected through DIC. The localized strain fields as measured through DIC indicate that the largest strain at any given temperature and stress condition occurs at the notch and tends to propagate out in "butterfly wing" type of bands. The localized DIC strain field immediately prior to failure is shown in Figure 1.c, more clearly illustrating the butterfly wing behaviour of the localized strain field. The fracture under cooling occurred at 46.4 °C, as shown in the strain v temperature plot shown in Figure 2.

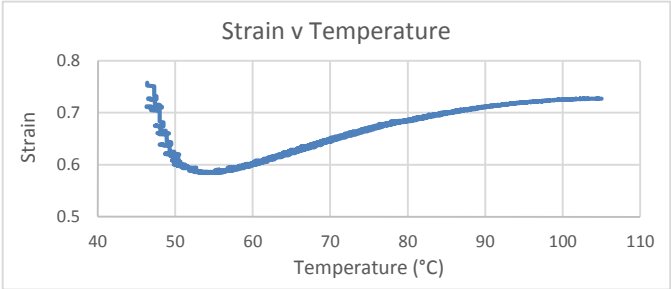

Figure 2: Strain v temperature plot for specimen which failed during phase transformation

In order to gain a better understanding of the fracture properties, the fracture surface was further examined through SEM. Figure 3 shows the fracture surface of the fracture under cooling specimen near the notch as well as at the opposite edge. These SEM images show very little dimpling on the surface, indicating a very brittle fracture. The SEM results indicating a brittle fracture correlate well with the high-speed camera results. Through frame by frame analysis of the fracture of the pure phase and fracture under cooling experiments, it is found that the crack propagated through the entire cross section of the specimens within 2 frames while recording at 54,000 frames per second. The frames during fracture for the fracture under cooling specimen are shown in Figure 4. Although the actual fracture speed could not be determined, the high speed frames indicate that the fracture propagated through the specimens at more than 216 m/s regardless of the phase of the material.

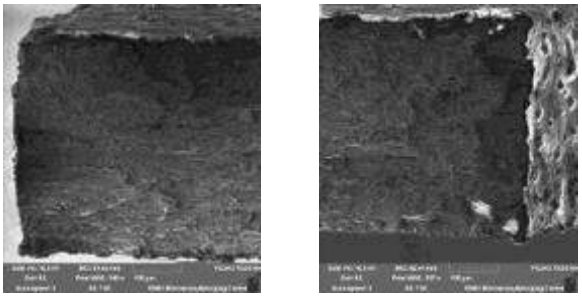

a. b.

Figure 3: SEM image of fracture surface a) edge away from notch; b) notch edge.

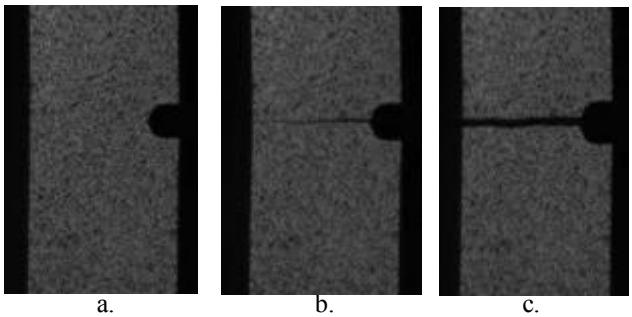

a. b. c.

Figure 4: High speed camera frames for failure during cooling. a) frame before fracture; b) frame during fracture; c) frame after fracture

CONCLUSIONS

The fracture of notched plates of $Ni_{60}Ti_{40}$ was analysed through DIC and SEM observation in order to gain understanding into the fracture properties of SMAs undergoing actuation through thermal cycling. The results indicate a very high speed and brittle fracture at a stress level below the ultimate tensile stress of the pure phase of this alloy. Therefore, in designing any actuator, it is important to account for the lower ultimate tensile stress while the SMA is undergoing actuation, especially given the high speed and highly brittle nature of the fracture.

References

[1] P.K. Kumar and D.C. Lagoudas. Introduction to Shape Memory Alloys. In D.C. Lagoudas, editor, *Shape Memory Alloys: Modeling and Engineering Applications*, chapter 1, pages 1{51. Springer New York, New York, NY, 1 edition, 2008.
[2] D.J. Hartl and D.C. Lagoudas. Aerospace applications of shape memory alloys. *Proceedings of the Institution of Mechanical Engineers, Part G: Journal of Aerospace Engineering*, 221(4):535-552, 2007.
[3] M. Sreekumar, T. Nagarajan, M. Singaperumal, M. Zoppi, and R. Mol_no. Critical review of current trends in shape memory alloy actuators for intelligent robots. *Industrial Robot: An International Journal*, 34(4):285-294, 2007.
[4] A. Nespoli, S. Besseghini, S. Pittaccio, E. Villa, and S. Viscuso. The high potential of shape memory alloys in developing miniature mechanical devices: A review on shape memory alloy mini-actuators. *Sensors and Actuators A: Physical*, 158(1):149-160, 2010.
[5] T. Baxevanis and D.C. Lagoudas. Fracture mechanics of shape memory alloys: review and perspectives. *International Journal of Fracture*, 191 (1-2):191-213, 2015.

INTERFACE-REACTION CONTROLLED DIFFUSION IN BINARY SOLIDS WITH APPLICATIONS TO LITHIATION OF SILICON IN LITHIUM ION BATTERIES

Zhiwei Cui[1], Feng Gao[2] and Jianmin Qu[3a)]
[1]*Vehicle Optimization Group, General Motors, Warren, MI, 48093, USA*
[2]*Well Construction Group, Weatherford International, Houston, TX 77041, USA*
[3]*Department of Mechanical Engineering, Tufts University, Medford, MA 02155, USA*

Summary Solid state diffusion in a binary system, such as lithiation into crystalline silicon, often involves two symbiotic processes, namely, interfacial chemical reaction and bulk diffusion. In this paper, we develop a mathematical framework to investigate the interaction between bulk diffusion and interfacial chemical reaction in binary systems. As an example, the model is used to study the lithiation of a spherical silicon particle. It is found that a dimensionless parameter β plays a significant role in determining the kinetics of the lithiation process. This parameter, analogous to the Biot number in heat transfer, represents the ratio of the rate of interfacial chemical reaction and the rate of bulk diffusion. Smaller β means slower interfacial reaction, which would result in higher and more uniform concentration of lithium in the lithiated region.

PROBLEM STATEMENT

Recently, silicon (Si) has attracted significant attention because of its potential as a high capacity anode material in lithium (Li) ion batteries. Extensive effort has been invested in the last decade to understand the lithiation process. Earlier studies in this area modeled lithiation as a diffusion-controlled process, from which Li distribution can be computed [1, 2]. However, recent experimental observations show that there is a sharp interface between lithiated and unlithiated phases, indicating that the lithiation process may be controlled by interfacial chemical reaction [3-10].

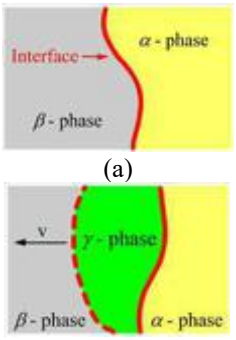

Fig. 1. Schematic of the (a) initial configuration and (b) current configuration.

To develop a chemo-mechanics model to simulate the formation of such sharp interface, we consider a solid phase called the $\alpha-\text{phase}$ consisting of species A, and another solid phase called the $\beta-\text{phase}$ consisting of species B. Let the two phases be in intimate contact initially, see Fig. 1a. Assume that under certain driving forces (e.g., chemical affinity or externally applied voltage), species A starts to react with species B to form a new phase called the $\gamma-\text{phase}$, which consists of species $\text{P}=\text{A}_{x_0}\text{B}$, i.e.,

$$x_0\text{A}+\text{B}\rightarrow\text{A}_{x_0}\text{B}\quad . \tag{1}$$

As time progresses, species A diffuses through the $\gamma-\text{phase}$ towards the $\beta-\text{phase}$, and reacts continuously with species B at the $\beta-\gamma$ interface. This sustained reaction produces more species P and drives the interface move further into the $\beta-\text{phase}$, see Fig. 1b. For simplicity, we assume that the $\beta-\text{phase}$ is impervious to species A, and, as the interface moves, species B is fully converted into the $\gamma-\text{phase}$ at the $\beta-\gamma$ interface via the interfacial chemical reaction (1). Our main interest is to find the shape and velocity of the $\beta-\gamma$ interface, and the concentration of species A in the $\gamma-\text{phase}$.

INTERFACIAL CHEMICAL REACTION

In addition to the well-known equations of deformation kinematics, mechanical equilibrium, and species diffusion, we need to derive the equation that governs the interfacial chemical reaction. To this end, let the $\beta-\gamma$ interface be described by $\mathbf{X}=\mathbf{X}_s$, and R_s denote the moles of the product A_{x_0}B produced per current unit area per unit time at the interface, or rate of production (in moles) of the product $\text{P}=\text{A}_{x_0}\text{B}$ per current unit area. Then, R_s can be written as [11,12]

$$R_s=k_f\left(\hat{\rho}_\text{A}-\frac{x_0}{J_\gamma V_m^B}\right)^p\left(\hat{\rho}_\text{B}\right)^q-k_b\left(\hat{\rho}_\text{P}\right)^r\quad\text{for}\quad\mathbf{X}=\mathbf{X}_s\,, \tag{2}$$

where k_f and k_b are, respectively, the rate constants for the forward and backward reactions described by (1), and $p+q$ and r are the orders of the forward and backward interfacial chemical reactions, respectively. These parameters are material properties and are usually determined experimentally [13]. All the molar concentrations in (2) are evaluated at the $\beta-\gamma$ interface. Since they may not be continuous across the interface, we assume that $\hat{\rho}_\text{B}$ is evaluated at the $\beta-\text{phase}$ side, while $\hat{\rho}_\text{A}$ and $\hat{\rho}_\text{P}$ are evaluated at the $\gamma-\text{phase}$ side of the $\beta-\gamma$ interface.

a) Corresponding author. Email: jianmin.qu@tufts.edu

Next, by the conservation of mass, the following continuity conditions at the $\beta-\gamma$ interface can be established,

$$\mathbf{JN} = -x_0 R_S \quad , \quad V_N = -V_m^B R_S \quad \text{, for} \quad \mathbf{X} = \mathbf{X}_s \,, \tag{3}$$

where V_N is the speed of the $\beta-\gamma$ interface in its normal direction. To fully determine the interface, we assume that, without loss of generality, the $\beta-\gamma$ interface is described by $f(\mathbf{X}_s,t)=0$, where $f(\mathbf{X}_s,t)$ is a smooth function of $\mathbf{X}_s$ and t. It can be shown [14] that $f(\mathbf{X}_s,t)$ must satisfy the following partial differential equation

$$\frac{\partial f(\mathbf{X}_s,t)}{\partial t} - V_m^B R_S \frac{\Delta f(\mathbf{X}_s,t)}{\left|\nabla f(\mathbf{X}_s,t)\right|} = 0 \quad . \tag{4}$$

LITHIATION OF A SPHERICAL SILICON PARTICLE

As an example to illustrate the use of the above formulation, we consider the lithiation of a spherical crystal silicon (Si) particle with initial radius R_0. A Lagrangian spherical coordinate system is set up so that the origin of the Si particle is located at $R=0$ at the initial time $t=0$. This Si particle is immersed in a liquid electrolyte that contains sufficient lithium ions Li^+. Under the driving force of an electrical current, Li ions in the electrolyte enter into the Si particle at its surface $R=R_0$ through a complex electrochemistry process. Upon entering into the Si particle, Li^+ are reduced into Li. The Li atoms then diffuse the center of the Si particle to form the Li_xSi alloy which is typically amorphous.

RESULTS AND DISCUSSIONS

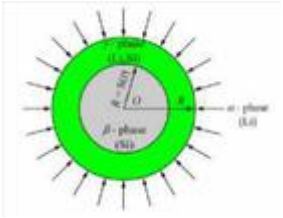

Fig. 2 Schematic of the reaction at a moving boundary during lithiation into a Si pristine particle.

A dimensional analysis leads to a dimensionless parameter $\beta = k_f^e V_m^{\mathrm{B}} R_0 / D_0$, where k_f^e is the forward chemical reaction rate at the $\beta-\gamma$ interface and D_0 is the rate of diffusion of Li in the $\gamma-\text{phase}$. It is seen that β is a measure of the relative rates between the chemical reaction at the Si-Li_xSi interface and the diffusion of Li in the Li_xSi. This dimensionless parameter is analogous to the well-known Biot number in heat transfer, so we will call β the chemo-mechanics Biot number. Our numerical results show that smaller β means slower interfacial reaction, which would result in higher concentration of lithium in the lithiated region. On the other hand, large β means faster interfacial reaction. In the limit of $\beta\to\infty$, the current solution reduces to that of [2] where the interfacial chemical reaction rate is assumed infinite. Our solution shows that the unlithiated and lithiated regions are separated by a sharp interface, resulting in a core-shell structure consistent with experimental observations. This sharp interface moves towards the particle center as lithiation progresses. The interface velocity predicted by our model is comparable to the existing experimental measurements. Furthermore, we found that, for a given β, the lithiation process is always controlled by the interfacial chemical reaction initially, until sufficient silicon has been lithiated so that the diffusion distance for lithium reaches a threshold value, beyond which bulk diffusion becomes the slower process and controls the overall lithiation kinetics. Further, our numerical results show that the entire lithiation process is controlled by interfacial chemical reaction for Si particles with radius less than 150nm. This suggests a strategy to relax the tensile hoop stress on the surface quickly by doping Si with other elements to increase the rate of interfacial chemical reaction.

References

[1] Bower, A.F., P.R. Guduru, and V.A. Sethuraman, *J. Mechanics and Physics of Solids*, 2011. **59**: p. 804-828.
[2] Cui, Z.W., F. Gao, and J.M. Qu, *J. Mechaics and Physics of Solids*, 2012. **60**(7): p. 1280-1295.
[3] Cui, L.F., R. Ruffo, C.K. Chan, H.L. Peng, and Y. Cui, *Nano Letters*, 2009. **9**(1): p. 491-495.
[4] Liu, X.H. and J.Y. Huang, *Energy & Environmental Science*, 2011. **4**(10): p. 3844-3860.
[5] Yang, H., S. Huang, X. Huang, F.F. Fan, W.T. Liang, X.H. Liu, L.Q. Chen, J.Y. Huang, J. Li, T. Zhu, and S.L. Zhang, *Nano Letters*, 2012. **12**(4): p. 1953-1958.
[6] Lee, S.W., M.T. McDowell, J.W. Choi, and Y. Cui, *Nano Letters*, 2011. **11**(7): p. 3034-3039.
[7] Lee, S.W., M.T. McDowell, L.A. Berla, W.D. Nix, and Y. Cui, *Proc. National Academy of Sciences*, 2012. **109**(11): p. 4080-4085.
[8] Chan, C.K., H.L. Peng, G. Liu, K. McIlwrath, X.F. Zhang, R.A. Huggins, and Y. Cui, *Nature Nanotechnology*, 2008. **3**(1): p. 31-35.
[9] Chon, M.J., V.A. Sethuraman, A. McCormick, V. Srinivasan, and P.R. Guduru, *Physical Review Letters*, 2011. **107**(4).
[10] Liu, X.H., L. Zhong, S. Huang, S.X. Mao, T. Zhu, and J.Y. Huang, *ACS Nano*, 2012. **6**(2): p. 1522-1531.
[11] Yang, F.Q., Journal of Applied Physics, 2010. **107**(10): p. 103516.
[12] Zhou, H.G., J.M. Qu, and M. Cherkaoui, *Mechanics of Materials*, 2010. **42**(1): p. 63-71.
[13] Chandrasekaran, R., A. Magasinski, G. Yushin, and T.F. Fuller, *J. Electrochemical Society*, 2010. **157**(10): p. A1139-A1151.
[14] Katardjiev, I.V., G. Carter, M.J. Nobes, S. Berg, and H.O. Blom, *J. Vacuum Science & Technology*, 1994. **12**(1): p. 61-68.

AN INTEGRATED TEMPORAL MULTI-SCALE MULTI-PHYSICS MODEL WITH DAMAGE IN MULTIFUNCTIONAL MATERIALS

Shu Guo[1], Reza Yaghmaie[1], and Somnath Ghosh *[2]
[1]*Graduate Research Assistant, Department of Civil Engineering, Johns Hopkins University*
[2]*M. G. Callas Professor, Departments of Civil and Mechanical Engineering, Johns Hopkins University*

Summary To simulate multi-physics phenomena that occur in multi-functional devices such as load bearing antennae and piezoelectric induced damage detectors, a model is developed to couple transient electromagnetic (EM) and dynamic mechanical fields in a finite deformation setting with damage evolution features. To achieve a versatile coupling scheme between fields, the problems are solved in a staggered way using a time-domain finite element (FE) method by a high performance parallel program. A constitutive model of a piezoelectric material is implemented with a phenomenological damage model to simulate piezoelectric damage sensors undergoing dynamic finite deformation. Moreover, A multi-time scaling method is implemented to overcome the computational infeasibility posed by analyzing the rapidly varying EM quantities while accounting for the effects of the slow evolution of the mechanical displacement field in deformable antenna applications.

INTRODUCTION

In recent times, there has been a significant interest in multi-functional structures governed by multi-physics principles such as mechanical and EM relations. Some examples of these structures may be components of small unmanned airborne vehicles (UAVs), active skins of aircraft, or meta-materials for optical and communication systems. There is a need for robust, coupled multi-physics computational models and codes supporting meaningful design of multi-functional structures and devices. In the present work, a generalized framework is developed for coupling transient EM and dynamic mechanical fields to predict the evolution of the EM field in a vibrating substrate and to simulate the piezoelectric effect during finite deformation. To couple the EM field and dynamic mechanical field effectively in the time domain, a wavelet transformation based multi-time scaling method, WATMUS, is implemented to avoid single time scale integration. Rigorous adaptivity and sensitivity study of WATMUS is carried out. Some application examples are presented to validate WATMUS.

FORMULATIONS FOR THE TRANSIENT ELECTROMAGNETIC PROBLEM IN A FINITE DEFORMATION DYNAMICAL SETTING

The weak forms of the coupled transient EM equations are formulated in the reference configuration. It is derived from the Lagrangian density of the EM problem in the reference configuration with a penalty term to weakly enforce the gauge condition,

$$\mathcal{L} = \frac{\varepsilon J}{2} C_{JK}^{-1} \tilde{E}_J \tilde{E}_K - \frac{J^{-1}}{2\mu} (C_{LM} B_L B_M) + J_N A_N - Q\Phi + \frac{1}{p} (A_{P,P})^2 \tag{1}$$

where ε is permittivity, μ is permeability. J is the Jacobian, $C_{IJ}(= \frac{\partial x_k}{\partial X_I} \frac{\partial x_k}{\partial X_J})$ is the right Cauchy-Green deformation tensor. The term $\frac{1}{p}$ is the penalty coefficient. The scalar potential Φ and vector potential A_I are the independent variables constituting the Galilean transformation of the electric field $\tilde{E} = -\Phi_{,I} - \dot{A}_I + \varepsilon_{IJK} \frac{\partial X_J}{\partial t} \varepsilon_{KMN} A_{N,M}$ and the magnetic field $B_I = \varepsilon_{IJK} A_{K,J}$. Q is the charge density, and J_N is the conducting current density. Enforcing the variation of the Lagrangian density with respect to Φ and $\mathbf{A}$ to be zero yields the weak forms of the EM field. The detailed derivation can be found in [1].

The constitutive relation of the hyperelastic material for finite strains is assumed to be neo-Hookean combining with the piezoelectric effect. The electric enthalpy density in the reference configuration is expressed as

$$H = \Psi - \left[\frac{\varepsilon J}{2} C_{JK}^{-1} E_J E_K + E_P H_{PMN} E_{MN} \right] \tag{2}$$

where $\Psi(\mathbf{C})$ is the Helmholtz free energy function, $E_I = -\Phi_{,I}$ is the electric field neglecting the magnetic effect in piezoelectric problems. E_{MN} is the Green strain. The isotropic damage process is implemented by introducing a scalar damage parameter D to $\Psi(\mathbf{C}, D)$. The second Piola-Kirchhoff stress $S_{MN} = \frac{\partial H}{\partial E_{MN}}$ and electric displacement field $D_I = \frac{\partial H}{\partial E_I}$ are obtained accordingly.

Numerical implementation is conducted for the coupled problem using a staggered approach, where the dynamic displacement field is solved first followed by the solution of the EM problem. A fully coupled multi-physics code is developed in

*Corresponding author. Email: sghosh20@jhu.edu

three dimensions employing the PETSc library for parallelization. The code is validated by comparing with both analytical cases and numerical examples in existing commercial software. The robust platform covers many features that can be applied to simulations for numerous EM problems in deforming media. For instance, the coupling effect in deformable antennae requires solving the complete set of Maxwell's equations (both pertaining to the electric and magnetic fields), but the coupling from the EM field back to the mechanical field is not necessary since the Lorentz force is negligible. For piezoelectric damage detectors, the constitutive relationship requires that the piezoelectric effect and phenomenological damage model be incorporated. The full coupling between electric and mechanical fields is employed without considering the magnetic field.

WAVELET TRANSFORMATION BASED MULTI-TIME SCALING METHOD (WATMUS)

To couple two disparate fields which have large differences in frequencies, conventional single time scale integration progressing in the time scale of the higher frequency field causes computational infeasibility while attempting to address issues related to the lower frequency field. A wavelet transformation based multi-time scaling method, WATMUS [2] is implemented to overcome this issue. The response function is resolved in two time scales, viz. (i) a slowly varying response in terms of the wavelet coefficients identified with the cycle scale N, and (ii) a rapidly oscillating response within each cycle corresponding to the EM field fine time scale τ. The projected wavelet coefficients only depend on the cycle number N and are independent of the τ-scale as follows,

$$y(\mathbf{x},t) = y(\mathbf{x},N,\tau) = \sum_{k=1}^{n} c_k(\mathbf{x},N)\psi_k(\tau) \quad \forall \quad \tau \in [NT,(N+1)T] \tag{3}$$

where $c_k(\mathbf{x},N)$ are the cycle-scale coefficients of the fine-scale orthogonal basis functions $\psi_k(\tau)$. An efficient choice of ΔN, the allowed jump of the EM field cycle within the integration interval of the mechanical cycle, accelerates the simulation significantly. The accuracy and convergence are studied in [2].

SIMULATION RESULTS AND DISCUSSION

A piezoelectric damage detector is proposed based on the capacity of the numerical tool. The geometry and boundary conditions are shown in Fig. 1a. The material incorporates the piezoelectric effect and phenomenological damage model. An alternating voltage is applied at the top and bottom surfaces (z-faces) with the frequency $\omega = 2\pi\ Hz$, which is the same as the external load. Two conditions, one with the damage model and the other one without the damage model, are simulated to analyze how the electric responses vary with respect to the damage evolution in the piezoelectric substrate. Since the piezoelectric effect generates a load which is much smaller than the external load, the difference between two observed displacements is very limited. However, there is a significant difference in the electric displacement fields as in Fig. 1b.

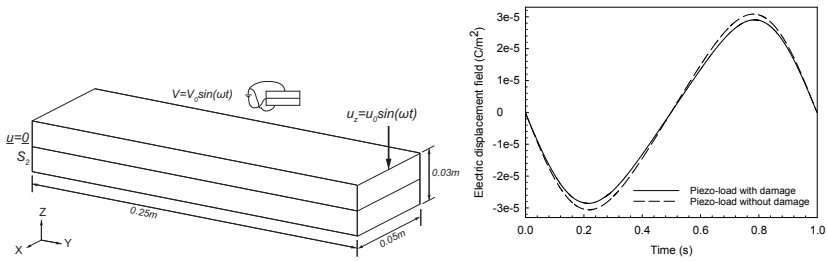

(a) (b)

Figure 1: A vibrating piezoelectric material substrate with an external load: (a) Schematic model; (b) Plot of electric displacement field d_z with time.

References

[1] S. Guo and S. Ghosh. A finite element model for coupled 3d transient electromagnetic and structural dynamics problems. Comput. Mech., 2014.

[2] R. Yaghmaie, S. Guo, and S. Ghosh. Wavelet transformation induced multi-time scaling (WATMUS) model for coupled transient electro-magnetic and structural dynamics finite element analysis, Comput. Meth. Appl. Mech. Eng., accepted.

ANALYSIS OF MIE–GRUNEISEN EQUATION OF STATE FOR TWO-DIMENSIONAL CRYSTAL LATTICES

Artem Panchenko*[1,2] and Anton Krivtsov[1,2]

[1]*Department of Theoretical Mechanics, Peter the Great St. Petersburg Polytechnic University, St. Petersburg, Russia*

[2]*Laboratory of Discrete models in Mechanics, Institute for Problems in Mechanical Engineering, St. Petersburg, Russia*

Summary For triangular crystal lattice we derive tensor form of Gruneisen coefficient in terms of the deformation temperature tensor. Molecular dynamics simulations for different strain state are performed. The ratio of deformation temperature tensor eigenvalues does not dependent on pair potential but is primarily determined by the shear strain. The results are used to determine Mie–Gruneisen equation of state for different types of interaction potential and crystal structures.

Recent advance in nanotechnology has lead to the necessity of determining mechanical properties of solids with microstructure in a wide range of temperatures and mechanical loads. Basing on analytically derived Mie–Gruneisen equations of state for crystalline solids [1], we can broaden the class of problems allowing analytical solutions without molecular dynamics simulation. Generally, methods of statistical mechanics [2] are applied to predict thermodynamic properties from microscopic properties of a material. V. Kuzkin and A. Krivtsov have obtained equation of state for chain [3] and close-packed crystal lattices [1] with pair interactions in the form of (1). The expression (1) is a generalization of the Mie–Gruneisen equation for the thermal part of Cauchy stress tensor $\widetilde{\boldsymbol{\tau}}$, Gruneisen function $\boldsymbol{\Gamma}(V)$, that is a tensor, and the thermal part of the internal energy of the system $\widetilde{U}$.

$$\widetilde{\boldsymbol{\tau}} = \nearrow\frac{1}{V}\boldsymbol{\Gamma}(V)\widetilde{U}. \tag{1}$$

Internal energy $\widetilde{U}$ is calculated as a sum of the kinetic $\widetilde{E}_{kin}$ and the potential $\widetilde{E}_p$ energies; zero potential energy corresponds to the stationary state, and motion is divided into "fast" (oscillatory$\widetilde{\ }$) and "slow" (cold$\widehat{\ }$) parts.

Vector $\mathbf{A}_k$ connecting the reference particle with particle k can be also represented as:

$$\mathbf{A}_k = \widehat{\mathbf{A}}_k + \widetilde{\mathbf{A}}_k, \tag{2}$$

where $\widehat{\mathbf{A}}_k$ and $\widetilde{\mathbf{A}}_k$:

$$\widehat{\mathbf{A}}_k = \langle \mathbf{A}_k \rangle, \widetilde{\mathbf{A}}_k = \mathbf{A}_k \nearrow \widehat{\mathbf{A}}_k. \tag{3}$$

Following [1], let us expand the expressions for the thermal parts of stress tensor and internal energy in series with respect to $\widetilde{\mathbf{A}}_k$. We leave only first non-zero terms after averaging and make nearest neighbor interaction assumption:

$$\boldsymbol{\Gamma} = \nearrow\frac{1}{2}\frac{\sum_k \left(\widehat{A}_k^2\widehat{\Pi}_k''' + \Theta\widehat{A}_k\widehat{\Pi}_k'' \nearrow \Theta\widehat{\Pi}_k'\right)\widehat{\mathbf{A}}_k\widehat{\mathbf{A}}_k}{\sum_k \widehat{A}_k\widehat{\Pi}_k'' + \Theta\widehat{\Pi}_k'}, \tag{4}$$

where Π is pair potential, $\Theta = \dfrac{\langle\widetilde{\mathbf{A}}_k\widetilde{\mathbf{A}}_k\rangle_{yy}}{\langle\widetilde{\mathbf{A}}_k\widetilde{\mathbf{A}}_k\rangle_{xx}}$.

In order to calculate the tensor Gruneisen coefficient $\boldsymbol{\Gamma}$, we need to determine Θ, which is the ratio of the "deformation temperature" tensor $\langle\widetilde{\mathbf{A}}_k\widetilde{\mathbf{A}}_k\rangle$ components. These components have a clear physical meaning: square of thermal deformation of $\mathbf{A}_k$ along its initial direction (x-axis) $\langle\widetilde{\mathbf{A}}_k\widetilde{\mathbf{A}}_k\rangle_{xx}/a^2$ and in orthogonal direction (y-axis) $\langle\widetilde{\mathbf{A}}_k\widetilde{\mathbf{A}}_k\rangle_{yy}/a^2$. The special case ($\Theta = 1$) of the resulting formula (4) was obtained in [1], expression for trace of the $\boldsymbol{\Gamma}$ tensor was obtained by Stacey [4] by another method.

Further investigation is carried out by means of molecular dynamics (MD) simulation. We construct a square sample with a triangular lattice, periodic boundary conditions are used. The interaction between the particles is described by Morse potential:

$$\Pi(A_k) = D\left[e^{2\alpha(1-A_k/a)} \nearrow 2e^{\alpha(1-A_k/a)}\right], \tag{5}$$

where D is the depth of the potential well, α is responsible for the well width, and a is the equilibrium bond distance. Initially the particles have random velocity with normal distribution so that the average kinetic energy of the particle is about five orders of magnitude smaller than the depth of the potential well D, and center of mass of the system remains fixed. The

*Corresponding author. Email: artemqt@yandex.ru

system evolution is described by the solution of the Cauchy problem for the set of ordinary differential equations for the particles using the Verlet algorithm [7].

For relaxed triangular lattice and small temperatures we get that $\Theta = 1.435 \pm 0.016$ and tensors $\mathbf{\Gamma}$, $\widetilde{\boldsymbol{\tau}}$ are isotropic. Θ does not depend in fact on potential parameters or the number of interacting particles. The mean value of Θ depends monotonically on temperature, and increases by approximately 5% at melting temperature. Correction to Gruneisen coefficient with respect to previously assumed $\mathbf{\Gamma}|_{\Theta=1}$ [1] is equal to 2.5%, but the differences in $\widetilde{\boldsymbol{\tau}}$ and $\widetilde{U}$ are 20% and 22% respectively.

Fig. 1 shows an influence of volumetric deformation (*a*) and distortion (*b*) on the coefficient Θ. Hydrostatic compression of the sample leads to nonlinear growth of Θ up to 25% for 80% strain. At tension Θ decreases until $\Pi'' = 0$, i.e. the bonds are broken. We can see significant changes of Θ at distortion, and maximum is observed, though not shown, on the boundary of the stability domain [5, 6].

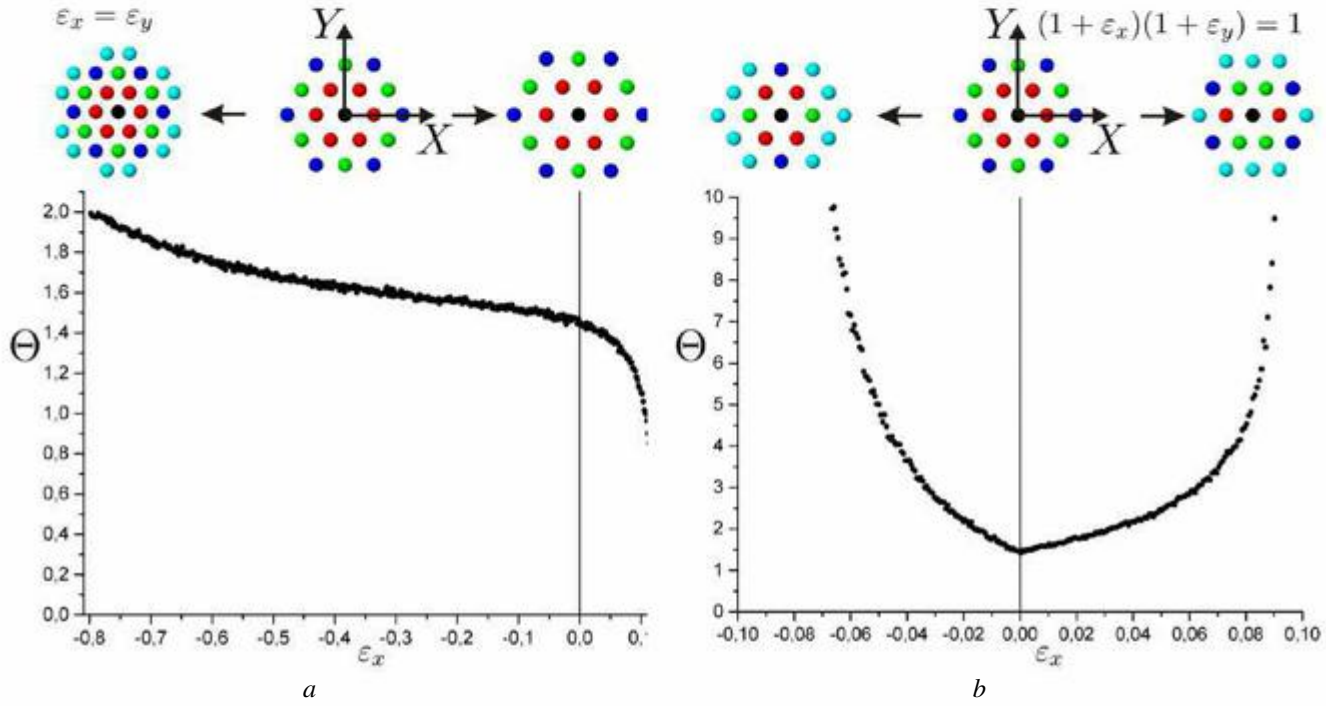

a *b*

Figure 1: Equation of strain path is specified above graphs with deformed lattice relative to stress-free (central) configuration. *a*) Θ dependence for volumetric straining path, *b*) Θ dependence for constant volume straining path.

In this work, we obtain the expression for the Gruneisen coefficient $\mathbf{\Gamma}$ in terms of the tensor of the deformation temperature. Tensor $\langle \mathbf{A}_k \mathbf{A}_k \rangle$ is not an isotropic, and the ratio of its eigenvalues Θ, corresponding to deformation along the bond and perpendicular to them. The value of Θ depends only on crystal structure but not on the system size or the type of the pair potential and weakly depends on temperature, for stress-free triangular lattice $\Theta = 1.435 \pm 0.016$. On the other hand, there is an essential dependence of Θ on the deformed state, and the main contribution provided by the shear strain. The obtained results are applied to obtain the equation of state for discrete systems.

References

[1] Krivtsov A.M., Kuzkin V.A.: Derivation of Equations of State for Ideal Crystals of Simple Structure. Mech. Solids 46(3):387-399, 2011.

[2] Hoover Wm.G.: Computational Statistical Mechanics. Studies in Modern Thermodynamics. Elsevier Science, Amsterdam, 1991.

[3] Kuzkin V.A., Krivtsov A.M.: Nonlinear Positive/Negative Thermal Expansion and Equations of State of a Chain with Longitudinal and Transverse Vibrations. Physica Status Solidi B 252(7):1664-1670, 2015.

[4] Irvine R.D., Stacey F.D.: Pressure Dependence of the Thermal Gruneisen Parameter, with Application to the Earth's Lower Mantle and Outer Core. Phys. Earth Planet 11(2):157-165, 1975.

[5] Podolskaya E.A., Krivtsov A.M., Panchenko A.Yu., Tkachev P.V.: Stability of Ideal Infinite Two-Dimensional Crystal Lattice. Doklady Akademii Nauk 442(6):755-758, 2012.

[6] Podolskaya E.A., Panchenko A.Yu., Freidin A.B., Krivtsov A.M.: Loss of Ellipticity and Structural Transformations in Planar Simple Crystal Lattices. Acta Mechanica 227(1):185-201, 2016.

[7] Verlet, L.: Computer "Experiments" on Classical Fluids. I. Thermodynamical Properties of Lennard-Jones Molecules. Phys. Rev. 159:98-103, 1967.

UNSTEADY HEAT CONDUCTION PROCESSES IN A HARMONIC CRYSTAL WITH A SUBSTRATE POTENTIAL

Mikhail B. Babenkov*[1,2], Anton M. Krivtsov [1,2], and Denis V. Tsvetkov [1,2]
[1]*Peter the Great Saint Petersburg Polytechnic University, St. Petersburg, Russia*
[2]*Institute for Problems in Mechanical Engineering RAS, St. Petersburg, Russia*

Summary An analytical model of high frequency oscillations of the kinetic and potential energies in a one-dimensional harmonic crystal with a substrate potential is obtained by introducing the nonlocal energies [1]. A generalization of the kinetic temperature (nonlocal temperature) is adopted to derive a closed equation determining the heat propagation processes in the harmonic crystal with a substrate potential.

EQUATIONS OF MOTION

Non-Fourier heat conduction processes in ideal crystal structures have been intensively studied in the recent decades. The literature is surveyed in the review papers [2, 3]. In this work we consider a one-dimensional crystal in the form of a chain of identical particles with mass m that are connected by linear springs with each other and with a fixed base, described by the following equations of motion:

$$\ddot{u}_n = \omega_0^2\big(u_{n-1} - (2+\epsilon)\,u_n + u_{n+1}\big), \qquad \epsilon = C_1/C_0, \qquad \omega_0 = \sqrt{C_0/m} \tag{1}$$

where u_n is the displacement of the n-th particle, m is the particle mass, C_0 is the stiffness of the interparticle bond, C_1 is the stiffness of the bond between a particle and the fixed base, and dots denote partial time derivatives. The crystal is infinite: the index n is an arbitrary integer.

The initial conditions [1, 4] are

$$u_n|_{t=0} = 0 \qquad \dot{u}_n|_{t=0} = \sigma(x)\varrho_n, \tag{2}$$

where ϱ_n are independent random values with zero expectation and unit variance; $\sigma^2(x)$ is variance of the initial velocities, which is a slowly varying function of the spatial coordinate $x = na$, where a is the lattice constant. These initial conditions correspond to an instantaneous temperature perturbation, which can be induced in crystals, for example, by an ultrashort laser pulse.

High frequency energy oscillations

The dynamic transition of the kinetic energy into the potential energy of the bonds deformation is accompanied by high frequency oscillatory process with decreasing amplitude [5]. Similar oscillations can appear in solids during fast transient processes, for example, under the impact of a short laser impulse. In order to derive the equations describing such energy oscillations, we introduce the following nonlocal energies [1, 4]:

$$K_n = \frac{1}{2}m\langle \dot{u}_s \dot{u}_{s+n}\rangle, \quad \mathit{\Pi}_n = \frac{1}{2}C_0\langle \varepsilon_s \varepsilon_{s+n}\rangle + \frac{1}{2}C_1\langle u_s u_{s+n}\rangle, \tag{3}$$

where K_n is nonlocal kinetic energy, $\mathit{\Pi}_n$ is nonlocal potential energy, operator $\langle \dot{u}_s \dot{u}_{s+n}\rangle$ gives the covariance of the particles' velocities with the indexes difference of n, $\varepsilon_s = u_s - u_{s-1}$ is the deformation of the bonds. Formulae (3) at $n = 0$ give the conventional energies.

Differentiation of the nonlocal energies with the use of dynamic equations (1) allows us to derive the following equation for the nonlocal Lagrangian L_n:

$$\ddot{L}_n = 4\omega_0^2\big(L_{n-1} - (2+\epsilon)\,L_n + L_{n+1}\big), \qquad L_n = K_n - \mathit{\Pi}_n \tag{4}$$

which coincides in form with the dynamic equation of chain (1) and differs only by the value of the coefficient on the right side. Assuming that the initial velocities of various particles are independent and the initial displacements are absent, the initial conditions for (4) can be written as [1]:

$$L_n|_{t=0} = E\delta_n, \qquad \dot{L}_n|_{t=0} = 0, \tag{5}$$

*Email: mikhail.babenkov@gmail.com

where E is the full initial energy of the crystal, $\delta_n = 1$ for $n = 0$ and $\delta_n = 0$ for $n \neq 0$. The solution of the problem (4)–(5) at $n = 0$ gives the conventional Lagrangian for the dynamical system (1) in the form:

$$L = E\left(J_0\left(2\sqrt{4+\epsilon}\,\omega_0 t\right) - 2\sqrt{\epsilon}\,\omega_0 \int_0^t J_0\left(2\sqrt{4+\epsilon}\,\omega_0(t-\tau)\right) J_1\left(2\sqrt{\epsilon}\,\omega_0\tau\right) d\tau\right) \tag{6}$$

Due to the complexity of this expression, two limiting cases are considered. The following asymptotic representation shows the behaviour of (6) at the low values of ϵ (so-called "soft substrate" case, if $\epsilon \ll 1$):

$$L \simeq E\left(J_0\left(2\sqrt{4+\epsilon}\,\omega_0 t\right) - \frac{1}{2}\sqrt{\epsilon} J_1\left(2\sqrt{\epsilon}\,\omega_0 t\right)\right) \tag{7}$$

Otherwise, if the value of ϵ is sufficiently high, then (6) can be approximated as ("rigid substrate" case, $\epsilon \gg 1$):

$$L \simeq E J_0\Big(\left(\sqrt{4+\epsilon} - \sqrt{\epsilon}\right)\omega_0 t\Big) \cos\Big(\left(\sqrt{4+\epsilon} + \sqrt{\epsilon}\right)\omega_0 t\Big) \tag{8}$$

Considering the nonlocal energy conservation law [5], one can obtain dependencies of the kinetic and potential energies on time:

$$K(t) = E\,\frac{1+L(t)}{2}, \qquad \Pi(t) = E\,\frac{1-L(t)}{2}$$

NONLOCAL TEMPERATURE

We adopt an approach based on the covariance analysis [6, 4] for the velocities to obtain a closed equation system determining unsteady thermal processes. The nonlocal temperature $\theta_n(x)$ is introduced as [1, 4]:

$$k_B(-1)^n\,\theta_n(x) = m\langle \dot{u}_i \dot{u}_j\rangle, \tag{9}$$

where k_B is the Boltzmann constant, $n = j - i$ is the covariance index, $x = \frac{i+j}{2}a$ is the spatial coordinate, a is the lattice constant. If $n = 0$ then $i = j$ and quantity θ_n coincides with the kinetic temperature T: $\theta_0(x,t) = T(x,t) = \frac{m}{k_B}\langle \dot{u}_i^2\rangle$, where $i = x/a$. The use of the correlation analysis [1, 4] and the long wavelength approximation allows one to obtain a differential-difference equation for θ_n:

$$\left(\theta_{n+1} + (2+\epsilon)\theta_n + \theta_{n-1}\right)^{\cdot\cdot} = -\frac{1}{4}c^2\left(\theta_{n+2} - 2\theta_n + \theta_{n-2}\right)'', \tag{10}$$

where primes denote partial coordinate derivatives. The initial conditions for equation (10) corresponding to original initial conditions (2) are given by [1]:

$$\theta_n|_{t=0} = T_0(x)\delta_n \qquad \dot{\theta}_n|_{t=0} = 0, \tag{11}$$

where $T_0(x) = \frac{1}{2k_B} m\sigma^2(x)$ is the initial temperature distribution; Problem (10)–(11) can be solved by the means of discrete-time Fourier transform [4], which allows to formulate the initial value problem for the kinetic temperature $T(x,t)$ in a simple form:

$$\ddot{T} + \frac{1}{t}\dot{T} = c_*^2 T'', \qquad T|_{t=0} = T_0(x), \qquad \dot{T}|_{t=0} = 0, \tag{12}$$

where $c_* = c\left(\sqrt{\epsilon+4} - \sqrt{\epsilon}\right)/2$ is the velocity of a heat wave propagating in a harmonic crystal with a substrate potential, $c = \omega_0 a$ is the sound velocity in a simple harmonic crystal.

References

[1] Krivtsov A.M. On Unsteady Heat Conduction in a Harmonic Crystal. arXiv preprint arXiv:1509.02506, 2015.

[2] F. Bonetto, J. L. Lebowitz, and L. Rey-Bellet: Fouriers law: a challenge to theorists, in Mathematical Physics 2000, edited by A. Fokas et al. (Imperial College Press, London, 2000), p. 128150.

[3] S. Lepri, R. Livi, and A. Politi: Thermal conduction in classical low-dimensional lattices, Phys. Rep. **377**, 180 (2003).

[4] Krivtsov A.M. Heat transfer in infinite harmonic one-dimensional crystals. Doklady Physics 2015 (Vol. 60, No. 9, pp. 407-411).

[5] Krivtsov A.M. Energy oscillations in a one-dimensional crystal. Doklady Physics 2014 (Vol. 59, No. 9, pp. 427-430).

[6] Z. Rieder, J. L. Lebowitz, and E. Lieb: Properties of a harmonic crystal in a stationary nonequilibrium state, J. Math. Phys. **8**, 10731078 (1967).

MULTISCALE MODELING OF THERMAL WAVE: FROM NON-LOCAL CONTINUUM TO MOLECULAR DYNAMICS

A.H.Akbarzadeh[1a)], Y.Cui[3] & Z.T.Chen[3]
[1]*Department of Bioresource Engineering, McGill University, Ste-Anne-de-Bellevue, Island of Montreal, QC, H9X 3V9, Canada*
[2]*Department of Mechanical Engineering, McGill University, Montreal, QC, H3A 0C3, Canada*
[3]*Department of Mechanical Engineering, University of Alberta, Edmonton, AB, T6G 2G8, Canada*

Summary It is renowned that Fourier's law of heat conduction violates the relativity theory, admits an instantaneous thermal response, and assumes a quasi-equilibrium thermodynamic condition. Heat transport is a non-equilibrium phenomenon with a finite thermal wave speed for applications involving very low temperature, extremely high temperature gradient, and ballistic heat transfer. To accommodate effects of thermomass and size-dependency of thermophysical properties on micro/nanoscale heat transport and to remove the theoretical singularity of temperature at thermal wavefront, a nonlocal fractional-order three-phase-lag heat conduction is first introduced. To affirm the existence of thermal wave, a molecular dynamics simulation is implemented for the heat transfer of a nanoscale beam and temperature distribution is tracked. Correlating thermal responses in continuum and atomistic scales gives an insight into the effect of length scale, fractional order, and phase-lags on the multiscale heat transport and is of practical importance for microelectromechanical systems, photothermal techniques, and laser assisted manufacturing.

Introduction

The empirical Fourier's law of heat conduction assumes a linear relation between heat flux $(\vec{q})$ and temperature gradient $T)$ via thermal conductivity (k) as: $\vec{q} = -k\nabla T$. Although Fourier's law is well established for a broad range of practical applications, it results in parabolic heat conduction with an infinite speed for the conductive heat transport which contradicts the relativity theory [1, 2]. In reality, the applicability of Fourier's law for ultra-small, spatial and temporal, application has been controversial. Experiments have reported the violation of nano/microscale heat conduction from the Fourier's law. To reconcile this contradiction, Cattaneo and Vernotte (C-V) [1] presented the first non-Fourier heat conduction theory via the introduction of relaxation time. Although C-V model leads to a hyperbolic heat conduction equation and detects the experimentally proven thermal wave, the model lacks a physical basis, violates thermodynamics law, and can not accurately describe experimental data. The culprits of C-V model are the inconsistency with the second-law of thermodynamics and overlooking microstructural effects on the heat transport process. To consider the non-equilibrium thermodynamics of ultrafast heat transport and the micro-macro interaction of heat carriers, two-step phenomenological models were derived by Qiu and Tien [3] from the Boltzmann transport equation. The model is appropriate for femtosecond laser irradiation since it considers three mechanisms of laser energy absorption by electrons, the transport of energy by electrons, and heating of the lattice by electron–lattice interactions. For ultrafast heating process, Tzou [4] presented dual-phase-lag (DPL) heat conduction, accounting for microscale temporal and spatial effects of heat transport via phase-lags of heat flux (τ_q) and temperature gradient (τ_T). A three-phase-lag (TPL) heat conduction theory was later proposed by Choudhuri [5] to encompass all previous theories for non-Fourier heat conduction. Introducing the phase-lag of thermal displacement (τ_v), in addition to τ_q and τ_T, provided a rigorous heat conduction model to better predict thermal responses. The hyperbolic models of non-Fourier heat conduction suffer from the singularity of temperature at thermal wavefront. The fractional calculus for differentiation and integration of arbitrary order can be effective to remove the singularity and to modify the existing formulation for physical processes in chemistry, biology, electronics, wave propagation, and chaos/fractals. For example, a fractional derivative of the phase-lag heat conduction has been introduced [6].

All the aforementioned non-Fourier heat conduction models were based on the local/classical continuum approach. To accommodate the effect of thermomass, the distinctive mass of heat, of dielectric lattices in the heat conduction, Tzou [7] has included the nonlocal (NL) behavior of heat transport in space in addition to the thermal lagging, in time. However, this NL C-V model still predict an unrealistic discontinuous temperature distribution around the thermal wavefront. As a result, in this investigation we first propose a novel nonlocal fractional three-phase-lag (NL FTPL) heat conduction to detect thermal wave propagation; then, we implement a molecular dynamics (MD) simulation to approve the validity of the continuum model.

NON-LOCAL CONTINUUM HEAT CONDUCTION

Herein, we introduce NL FTPL heat conduction for multiple length scales. The model takes into account the size-dependency of thermophysical properties, sub/super diffusion of heat transport, and phonon-electron interaction in ultrafast heat transport. The constitutive equation of is:

$$\vec{q}\left(\vec{t}+\bar{\lambda}_q, t+\tau_q\right) = -\left[k^T I^{\alpha_F - 1}\ \ T(\vec{t}, t+\tau_T) + k^{*T} I^{\alpha_F - 1}\ \ v(\vec{t}, t+\tau_v)\right] \quad 0 \le \alpha_F \le 2 \tag{1}$$

a) Corresponding author. Email: hamid.akbarzadeh@mcgill.ca.

Where $\overrightarrow{\lambda_q}$, $\overrightarrow{\lambda_T}$, and $\overrightarrow{\lambda_v}$ are correlating nonlocal lengths of heat flux, temperature gradient, and thermal displacement gradient; α_F is the order of time-fraction, and I^{α_F} is the Riemann–Liouville fractional integral. The heat conduction equation for NL FTPL can be obtained by eliminating the heat flux between Eq. (1) and energy equation [1].

MOLECULAR DYNAMICS SIMULATION OF HEAT TRANSPORT

To identify the characteristics of thermal wave in nano/micro scales, MD simulation is used to capture thermal wave propagation in atomistic level during the ultrafast heat transport. The atomistic interaction for heat conduction simulation is the classical embedded atom model (EAM) potential. The total potential energy of a chosen atom is given as

$$E_i = F_\alpha\left(\sum_{i\neq j}\rho_\beta\,(r_{ij})\right) + \frac{1}{2}\sum_{i\neq j}\emptyset_{\alpha\beta}(r_{ij}) \tag{2}$$

where r_{ij} is the distance between atoms i and j, ρ_β is the contribution of the electron charge density, F_α is the embedding function, and $\emptyset_{\alpha\beta}$ is a pair-wise potential function between atoms. While the first term in the right hand side of Eq. (1) contribute to the interaction among an atom in a specific position and its surrounding electrons, the second term is associated with the interaction between atoms. The temperature calculated by MD is associated with the total kinetic energy as

$$\sum_i \frac{m_i}{2}\left(\frac{dq_i}{dt}\right)^2 = \frac{M}{2}kT \tag{3}$$

The Large-scale Atomic/Molecular Massively Parallel Simulator (LAMMPS) has been used, in this work, for MD simulation.

NUMERICAL RESULTS AND DISCUSSION

In this section, we consider the heat conduction in an isotropic, homogenous, one-dimensional nanobeam subjected to a sudden temperature rise on its left side. Temperature distribution are predicted by both NL FTPL model and MD simulation. For brevity, two representative results of NL FTPL are given in Fig. 1. Figure 1a presents the effect of fractional order α_F on temperature distribution at no-dimensional time $\beta = 1$. As seen in Fig. 1a, α_F is an alternative for removing the singularity of thermal wave. Figure 1b shows the effect of non-dimensional TPL parameter C_K and correlation length L on thermal behavior. As shown in Fig. 1b, temperature is increased by an increase in either C_K or L. It is found that the correlation length L does not alter the thermal wave speed of NL FTPL, opposed to those given in [7] for NL C-V model.

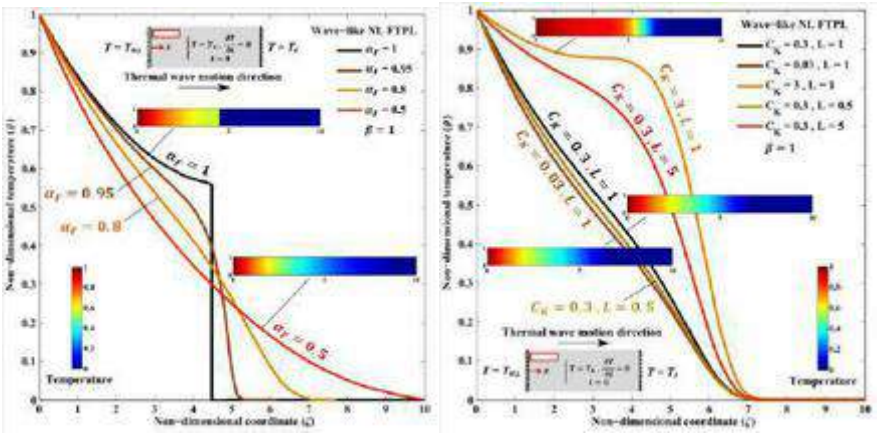

(a) (b)

Fig. 1 Thermal wave propagation: (a) effect of α_F, (b) effect of C_K and L.

References

[1] Akbarzadeh A.H., Chen Z.T..: Heat conduction in one-dimensional functionally graded media based on the dual-phase-lag theory. *Proc IMechE Part C: J. Mechanical Engineering Science* **227**(4): 744–759, 2012.

[2] Wang M., Yang N., Guo Z.Y.: Non-Fourier heat conductions in nanomaterials. *J. Appl. Phys.* **110**: 064310, 2011.

[3] Qiu T.Q., Tien C.L., Heat transfer mechanisms during short-pulse laser heating of metals, *J. Heat Transfer* **115**: 835–841, 1993.

[4] Tzou D.Y., A unified field approach for heat conduction from macro-to microscales, *J. Heat Transfer* **117** (1): 8–16, 1995.

[5] Choudhuri S.K.R., On a thermoelastic three-phase-lag model, *J. Therm. Stresses* **30** (3): 231–238, 2007.

[6] Ezzat M.A., El Karamany A.S., Fayik M.A., Fractional order theory in thermoelastic solid with three-phase lag heat transfer, *Arch. Appl. Mech.* **82**: 557–572, 2012.

[7] Tzou D, Guo Z.Y., Nonlocal behavior in thermal lagging, *Int. J. Therm. Sci.* **49**:1133-7, 2010.

INFLUENCE OF MARTENSITIC PHASE TRANSFORMATION ON CRACK PROPAGATION IN AUSTENITIC STEEL

Sally Issa*, Mathias Wallin, Håkan Hallberg, Alexander Lundberg, and Sara Eliasson
Division of Solid Mechanics, Lund University, Lund, Sweden

Summary In this work, the influence of martensitic phase transformation on crack propagation is investigated. A continuum model, developed for austenitic steel, that accounts for phase transformation is combined with a cohesive zone model. Simulations have been performed at different ambient temperatures and using different formulations of the cohesive zone model.

BACKGROUND

Austenitic steel is commonly used due to its corrosion resistance and many applications are found at cryogenic temperatures. As a consequence, fracture toughness at low temperatures is an important property. Since martensitic phase transformation affects crack propagation, the interaction between plasticity, phase transformation and crack propagation is investigated in the present work.

Martensitic phase transformation is associated with a 3% volume increase which will introduce plasticity in the weaker parent phase although the load level is below the yield stress [1]. If the material that increases in volume is surrounded by untransformed material, compressive stresses will be generated, which can be expected to reduce the driving force for crack propagation.

In this work, the crack propagation is modeled using a cohesive zone model. The cohesive zone is used to model the propagation of the crack with a constitutive behavior described by a traction-separation law. A traction-separation law influenced by the amount of transformed martensite at the crack tip, similar to the approach used for hydrogen embrittlement in [2], is proposed.

Martensitic phase transformation - Constitutive model

A phenomenological model of martensitic phase transformation, previously established in [3], is used in this work. The constitutive model is based on finite strain plasticity and includes austenite to martensite phase transformation. A yield potential and a transformation potential is used to model the interaction between plasticity and phase transformation. The model is based on a multiplicative split of the deformation gradient, $\boldsymbol{F}$, into an elastic and an irreversible part according to

$$\boldsymbol{F} = \boldsymbol{F}^e \boldsymbol{F}^{ir} \tag{1}$$

where $\boldsymbol{F}^e$ and $\boldsymbol{F}^{ir}$ are the elastic and irreversible deformation gradient, respectively. The yield function is of the von Mises-type

$$f(\boldsymbol{\tau}, z, \kappa) = \sigma_{eff}(\boldsymbol{\tau}) - \sigma_{y0}(z) - R(\kappa) \leq 0 \tag{2}$$

where $\boldsymbol{\tau}$ is the Kirchhoff stress tensor, $\sigma_{eff}(\boldsymbol{\tau})$ is the effective von Mises stress defined as $\sigma_{eff} = \sqrt{3J_2}$ and $J_2 = \frac{1}{2}\text{tr}(\boldsymbol{\tau}^{dev}\boldsymbol{\tau}^{dev})$. The thermodynamic force used to describe the hardening behavior of the material is choosen to be $R(\kappa) = H\kappa$, where H is the hardening modulus, and κ is the internal variable associated with the hardening. The homogenized static initial yield stress, $\sigma_{y0}(z)$, is assumed to depend on the volume fraction of martensite z. Non-associated plasticity is used with the convex potential function $g(\boldsymbol{\tau}, z, \kappa)$ governing the plastic evolution

$$g(\boldsymbol{\tau}, z, \kappa) = f(\boldsymbol{\tau}, z, \kappa) + \frac{1}{2}\frac{R^2(\kappa)}{R_\infty} \tag{3}$$

where the parameter R_∞ defines the saturation of the hardening.

The phase transformation will occur when the mechanical driving force reaches a transformation threshold. In accordance with [3], the transformation potential is chosen as

$$h = \bar{F}(\boldsymbol{\tau}) - F_{trans}(z) \leq 0 \tag{4}$$

where $\bar{F}$ is the mechanical driving force and where the threshold for the phase transformation is denoted F_{trans}.

*Corresponding author. Email: sally.issa@solid.lth.se

Cohesive zone model

With the traction vector denoted by $\boldsymbol{t}$, a traction-separation law that accounts for the volume fraction of martensite at the crack-tip is proposed as

$$\boldsymbol{t} = \boldsymbol{t}(\delta, z) \tag{5}$$

where δ is the relative normal displacement between the crack surfaces. With increasing separation, the traction reaches a maximum, $\boldsymbol{t}_{max}$, then starts to decrease until a complete decohesion of the crack faces is reached. Several constitutive traction-separation laws are considered in this work where the peak traction is modeled to depend on the volume fraction of martensite, z. In Fig. 1a, a schematic illustration of the traction-separation law is shown.

RESULTS

The presentation will include numerical examples where the constitutive model and the cohesive zone model are implemented as user routines in ABAQUS, run at different temperatures and using different traction-separation laws. The simulations have been carried out with a mode I displacement field applied on a disc-shaped body. One example is presented in Fig. 1b. The simulations are performed at 213 K and the results are compared with a simulation where phase transformation is not taken into consideration. It can be seen in Fig. 1b that the martensitic phase transformation slows down the propagation of the crack.

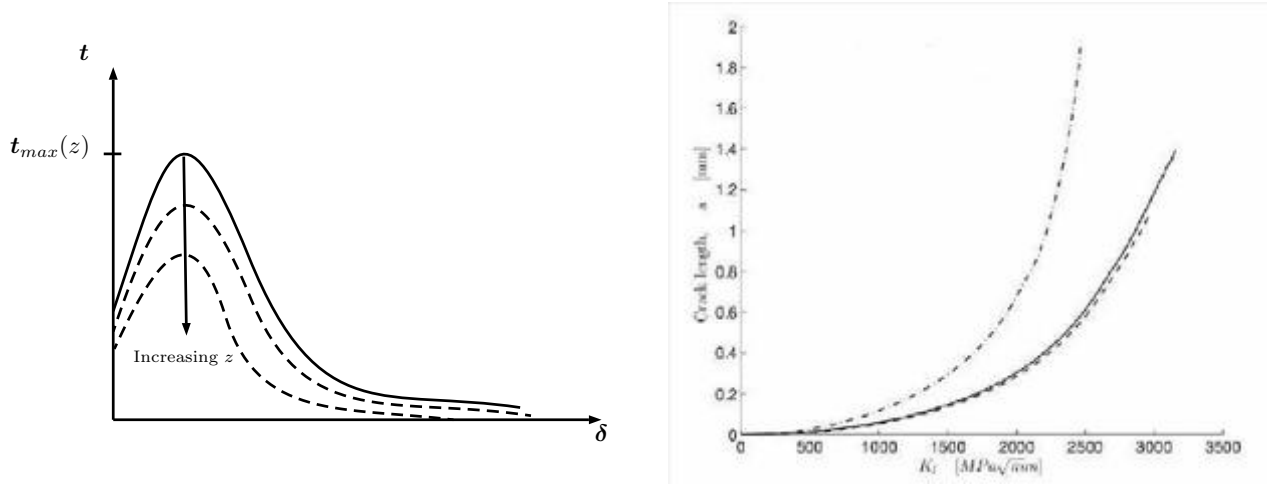

Figure 1: (a) Schematic illustration of the traction-separation law for different fractions of martensite. (b) The crack propagation as function of the stress intensity factor K_I. (–) Traction-separation law with influence of z, (- -) traction-separation law without influence of z and (-.-) no phase transformation is taken into consideration.

CONCLUSIONS

Numerical simulations of phase transformation have been performed using a cohesive zone model to investigate the effects of martensite formation on crack propagation. It was found that phase transformation at lower temperatures prevents the crack from propagating due to the local increase in volume that creates compressive stresses in the region around the crack tip.

References

[1] Greenwood G.W., Johnson R.H.: The deformation of metals under small stresses during phase transformation. Proceedings of the Royal Society, 283 A: 403-422, 1965.

[2] Olden V., Thaulow C., Johnsen R., Ostby E.: Cohesive zone modeling of hydrogen-induced stress cracking in 25% Cr duplex stainless steel. Scripta Materialia: 615-618, 2007.

[3] Hallberg H., Håkansson P., Ristinmaa M.: A constitutive model for the formation of martensite in austenitic steels under large strain plasticity. I. J. Plasticity: 1213-1239, 2007.

MARTENSITE AND TEMPERATURE EFFECT ON THE MECHANICAL BEHAVIOR OF A TRIP STAINLESS STEEL

Younes Demmouche[1], Guillaume Helbert[2], Luc Saint-Sulpice[2], Nicolas Laurain[3], Oussama Yousfi[3], Shabnam Arbab Chirani[2], Sylvain Calloch[1]

1ENSTA-Bretagne, Institut de Recherche Dupuy de Lôme, FRE3744 IRDL, Brest, France

[2] ENIB, Institut de Recherche Dupuy de Lôme, FRE3744 IRDL, Brest, France

[3]GTT (GAZTRANSPORT & TECHNIGAZ) SA, Saint-Rémy-Lès-Chevreuse, France

Summary

Austenitic stainless steels are largely used in liquefied natural gas (LNG) industry due to their mechanical properties such as ductility and resistance to corrosion. Transformation-induced-plasticity (TRIP) steels exhibit complex material behavior, because of martensitic transformation during plastic deformation. This study aims to modeling the mechanical behavior for such TRIP materials using a two kinematic and isotropic hardening model taking into account the evolution of the martensitic transformation rate during mechanical loading. This model was developed on austenitic stainless steels material and could be extended to describe different TRIP materials behavior. This model was then implemented in FE software abaqus/explicit in order to describe mechanical properties and martensitic transformation evolution during isothermal mechanical process. Simulation of forming process with FE abaqus/explicit was carried out and compared to experimental data. It was concluded that the numerical results show a good agreement with experimental ones in terms of mechanical properties and martensitic transformation rate.

TENSILE TESTS

1.2 mm thickness temper-rolled stainless steel sheets provided by Gaz transport & Technigaz (GTT) are used for this study. Isothermal tensile tests were carried out at different temperatures using an electro-mechanical Zwick Z050 machine equipped with a high deformation extensometer (TC-EX MACRO) to measure the strain evolution during tests. The temperature control is provided by a thermal chamber equipped with two thermocouples and temperature regular. In-situ electric resistance technique was used to measure the volume fraction of martensite. This method was validated on several materials such as AISI-301 stainless steel and shape memory alloys. The principle of the method is described in [2]. Strain rate controlled tensile tests were carried out at: 25°C, 0°C, -30°C and -60°C.

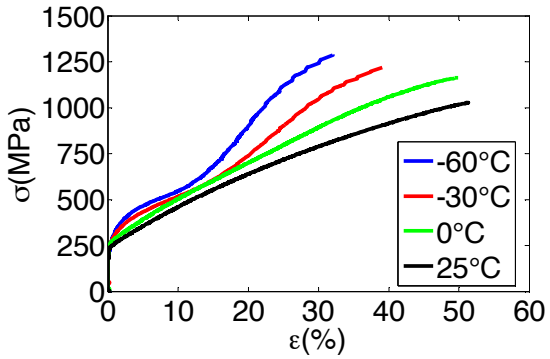

Figure 1: stress-strain curves at different temperatures

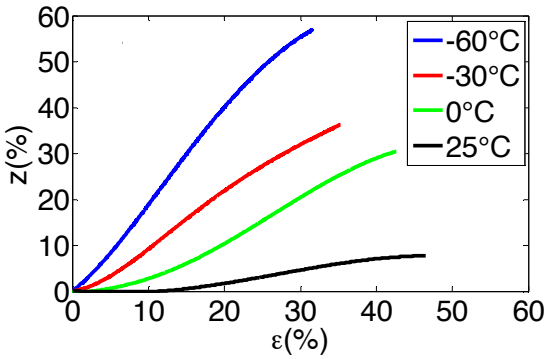

Figure 2: volume fraction of martensite function of strain at different temperatures

Figure 1 shows mechanical behaviour of the material at different temperatures. It can be noted that a second hardening appears after a plastic strain threshold witch depends on the temperature. This second hardening is related to the martensite transformation effect. No significant change of yield stress is observed. Figure 2 shows the evolution of the volume fraction of martensite depending on the plastic strain and temperature. The martensite transformation is accentuated with decreasing the temperature.

[a)] Corresponding author. Email: ictam2016papers@legendconferences.com.

MODELLING

Given the context of this study, a 3D macrosopic model was choosen to describe the mechanical behavior of the 304L stainless steel [3]. Different transformation kinetics were proposed to describe the evolution of the volume fraction of martensite depending on plastic strain. The Ludwigson and Burger model [1] is used to gain more information about the deformation induced martensitic transformation.

The volume fraction of martensite *(Z)* with respect to the cumulative plastic strain *(p)* is given by the equation 1.

$$1. \quad Z(p,T) = \varphi(T).[1 + \frac{p^{-b}}{A(T)}]^{-1}$$

Where $\varphi(T)$ is the saturation value of the volume fraction of martensite at a given temperature T. *A(T)* is the transformation kinetics term and *(b)* is a parameter of the material.

To describe the mechanical behavior, a two kinematic hardening model is proposed. The Kinematic hardening can be written as:

$$X = X_1 + X_2$$

X_1 is the kinematic hardening corresponding to the austenitic phase and X_2 the part of the kinematic hardening taking into account the martensitic transformation effect. X_1 and X_2 are given by Armstrong-Frederick model and written respectively in equations 2 and 3.

$$2. \quad \dot{X_1} = \frac{2}{3} C_1 \dot{\varepsilon_p} - \gamma_1 X_1 \dot{p}$$

$$3. \quad \dot{X_2} = \frac{2}{3} C_2(z) \dot{\varepsilon_p} - \gamma_2 X_2 \dot{p}$$

With $C_2(z) = C_{2z} * Z(p,T)$ is a function of volume fraction of martensite *Z*.
The isotropic hardening *(R)* takes the form given by the equation 4:

$$4. \quad \dot{R} = b(Q - R)\dot{p}$$

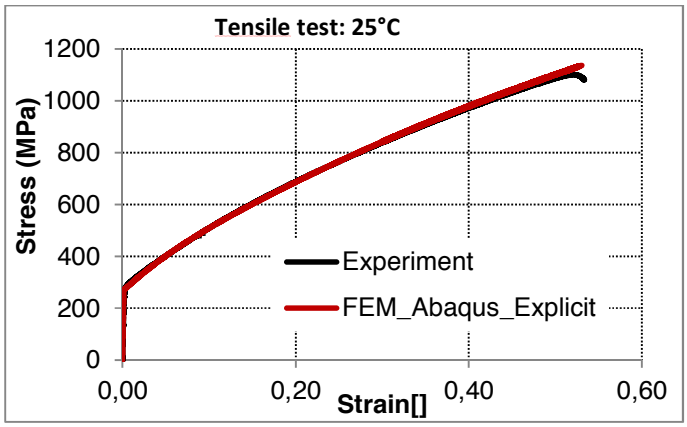

Figure 4 : comparison FEM model/experiment result

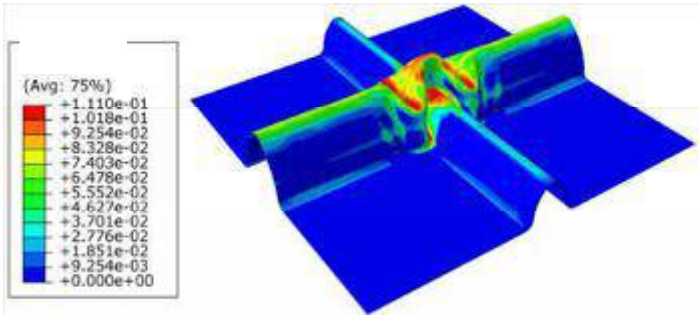

Figure 3: Vol.fract of martensite after forming process

CONCLUSIONS

A 3D macroscopic model is proposed to describe the mechanical behaviour of TRIP 304L stainless steel taking into account the martensite transformation induced by plastic strain at different temperatures. The set of the model parameters was identified at different temperatures from load-unload tensile tests. The FEM model results are compared to the experimental ones and implemented in abaqus explicit to simulate corrugations knots forming.

References

[1] A.A. Lebedev, V.V. Kosarchuk. Influence of phase transformations on the mechanical properties of austenitic stainless steels. *International Journal of Plasticity*, 16:749-767, 2000.

[2] Luc Saint-Sulpice, Mohamed Lakrit, Shabnam Arbab Chirani, Sylvain Calloch. Variation in electric resistivity in metastable alloys during thermomechanical loading: Effects of temperature, elasticity, plasticity and phase transformation . *Mechanics of Materials*, 71(0):1- 9, 2014.

[3] Jens SCHOLZ. Experimental analysis and modelling of the mechanical behaviour of an unstable austenitic stainless steel. 2002.

SHAPE RECOVERY PROPERTIES OF SHAPE MEMORY POLYMER TUBE UNDER TORSION DEFORMATION

Haiyang Du[1], Zhao Wei[1], Liwu Liu[1 a)], Yanju Liu[1], Jinsong Leng[2]
[1]*Department of Astronautic Science and Mechanics, Harbin Institute of Technology, Harbin, Heilongjiang, China*
[2]*Centre for Composite Materials and Structures, Harbin Institute of Technology, Harbin, Heilongjiang, China*

Summary As a kind of stimulus-responsive materials, shape memory polymers (SMP) has attracted more and more researchers and the application fields for SMPs have covered widely ranges from aerospace to biomedicine engineering, due to the unique advantages of high shape deformation and recovery ability, good biocompatible and biodegradation, low cost, etc. In the paper, a kind of SMP tubes under torsion deformation are designed firstly; after that, the finite element method (FEM) is applied to simulate the shape memory process of SMP tube under torsion deformation, the shape recovery process is demonstrated, the shape recovery properties are characterized to show the good shape fixity and shape recovery ability. The results from FEM can provide some guide for fabrication and deformation of SMP tube.

PREVIOUS WORK

As a kind of stimulus-responsive materials, shape memory polymer (SMP) can keep one temporary shape and recovery the original shape under some external stimulus, such as temperature, light, solution, and so on [1-3]. SMPs are attracting more and more researchers to take part in the theory and experimental investigation since 1990 [1], due to the advantages of high shape deformation and recovery ability, good biocompatible and biodegradation, low cost, etc [1-3]. However, the low stiffness and strength hinder the development of SMP, so various shape memory polymers composites (SMPCs) reinforced with carbon black, carbon fiber and carbon nanopaper are developed to increase the mechanical properties, at the same time, the actuation methods have been developed by electricity and magnetic fields [1].

A classical thermomechanical cycle for SMP can be shown in Fig. 1. Firstly, the original shape of SMP is fabricated; then, heating the sample and applying force to deform the original shape into a temporary shape (U shape); after that, keeping the temporary shape and cooling the temperature until room temperature, the shape is kept and strain energy is stored; then, the removing the external force, the temporary shape is kept (pre-deformed shape); finally, reheating the sample above glass transition temperature and the stored strain is released, the temporary shape nearly recovers the original shape.

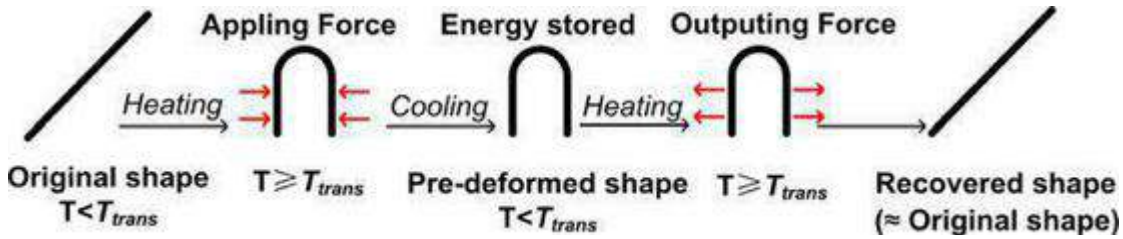

Fig. 1 A classical thermomechanical cycle of SMP [1]

Theory

In our work, the general Maxwell model and WLF equation are applied to simulate the thermomechanical behaviours of SMP tubes under large torsion deformation, in which the general Maxwell model is used to characterize the stress relaxation under some special temperature, the WLF equation is used to shift the stress relaxation under different temperature, the general Maxwell model can be shown as follows:

$$E(t) = E0 + \sum_{1}^{n} E_i * \exp(-t/\tau_i)$$

Where E, $E0$, E_i denote the effective elastic modules, equalization elastic modules and every relaxation modulus in Maxwell model, responsively; i is the number of Maxwell model.

The WLF can be shown as follows:

$$\lg a_T = \frac{-C_1(T - T_g)}{C_2 + (T - T_g)}$$

Where a_T, C_1, C_2, T, T_g denote the shift factor, two shift parameters, temperature, and reference temperature, responsively.

a) Corresponding author. Email: liuliwu_006@163.com.

STRUCTURE DESIGN AND FINITE ELEMENT SIMULATION

A kind of SMP tube before and after torsion deformation are demonstrated Fig. 2. The tube is thickness 2mm, length 120mm and torsion 90° under outer torsion moment. The temporary shape can be got by heating, deforming, cooling and removing force. The shape will recover the original straight tube after reheating above glass transition temperature. The finite element method is carried out by software ABAQUS to simulate the deform and recover of the SMP tube, the general Maxwell model with WLF equation are implanted into the software and used to characterize the material properties under different temperature, the finite element simulation results for shape memory process under 5°C/min are shown in Fig. 3.

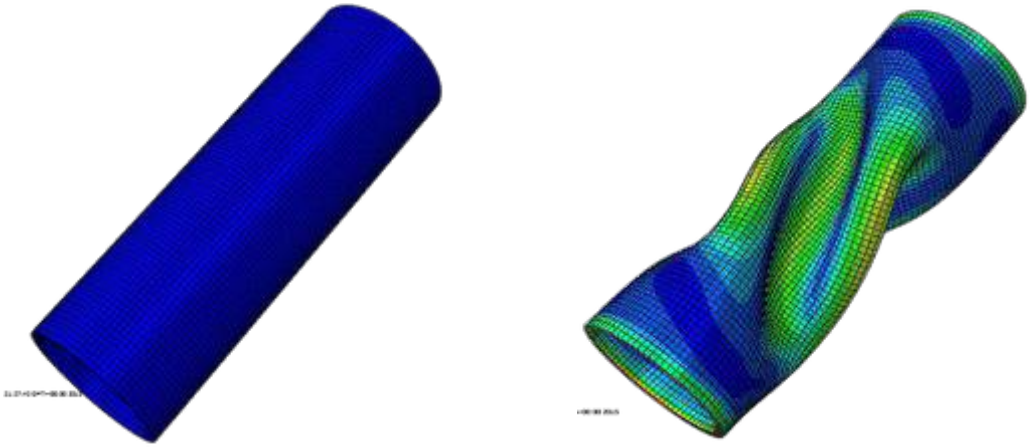

Fig. 2 The shape of SMP tube before and after torsion deformation.

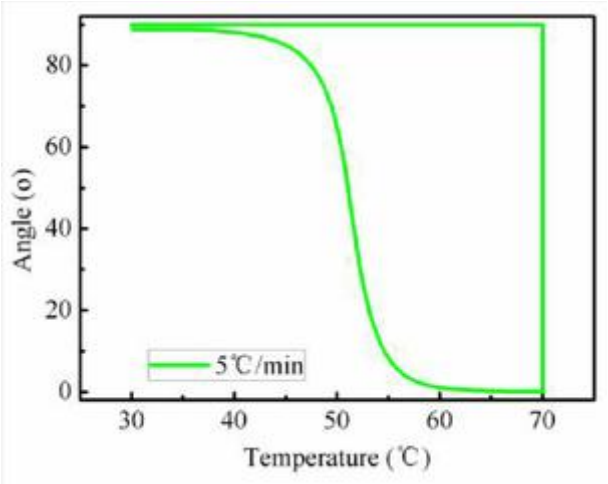

Fig. 3 Finite element simulation results for SMP tube under torsion deformation

CONCLUSIONS

In this paper, a kind of SMP tube under torsion deformation is designed and analysed by ABAQUS software, the shape memory process is shown to characterized the good shape fixity and shape recovery ability, these results can provide some guide for future experimental design.

References

[1] Leng JS, Lan X, Liu YJ, and Du SY. Shape memory polymers and their composites: Stimulus methods and applications, Progress in Materials Science, 2011, 56(7): 1077-1135.

[2] Meng H, and Li GQ. A review of stimuli-responsive shape memory polymer composites, Polymer, 2013, 54(9): 2199-2221.

[3] Sun L, Huang WM, Ding Z, Zhao Y, Wang CC, Purnawali H, and Tang C. Stimulus-responsive shape memory materials: A review, Materials and Design, 2012, 33: 577-640.

ENERGY DISTRIBUTION IN ONE-DIMENSIONAL CRYSTAL

Denis V. Tsvetkov*[1,2] and Anton M. Krivtsov[1,2]
[1]*Peter the Great Saint Petersburg Polytechnic University*
[2]*Institute for Problems in Mechanical Engineering, Russian Academy of Sciences*

Summary Reversible transfer between mechanical and thermal energy is considered for α-Fermi-Pasta-Ulam (FPU) crystal. Numeric study for long enough periods of time demonstrate numerous transitions between mechanical and thermal degrees of freedom. Influence of initial velocity fluctuations on the energy transfer process is analyzed.

INTRODUCTION

Nowadays, one of the most rapidly developing areas of modern mechanics is the mechanics of nanostructures [1, 2, 3]. Thanks to nanotechnologies it is possible to obtain almost ideal, defectfree materials. Therefore, prediction of the properties and behavior of this materials is a topical problem. Understanding of heat transfer at microlevel is significant to obtain link between microscopic and macroscopic description of solids [4, 5]. Development of computer technology allows to simulate large enough pieces of material, and to investigate their behavior on the required time interval.

The important close topic is Zermelo's Paradox, resulting from the Poincare recurrence theorem [6, 7], which can be effectively studied using finite one-dimensional crystals. We study the celebrated α-Fermi-Pasta-Ulam (FPU) system [8, 9], for which some questions still remain open.

In this regard, in this paper we consider the process of converting the mechanical energy of a nonlinear one-dimensional crystal into heat and back over time. We also study the times much greater then the system return time.

PROBLEM DEFINITION

A chain of identical particles of mass m, connected by the same nonlinear springs with stiffness C is considered.

The dynamic equations have the form: $\ddot{u}_k = \omega_0^2(u_{k-1} \nearrow 2u_k + u_{k+1})(1 + u_{k+1} \nearrow u_{k-1}), \quad \omega_0 \stackrel{\text{def}}{=} \sqrt{\frac{C}{m}}$, where u_k — displacement of kth particle; k — index that is arbitrary integer. The boundary conditions are periodical: $u_{k+N} = u_k$, where $N \gg 1$ — number of independent particles. Two cases are considered: deterministic and stochastic problem.

DETERMINISTIC PROBLEM

Initial conditions

Initial displacement is zero. Initial velocity in the crystal is defined as follows: $v(x)|_{t=0} = A \quad \text{n}\left(\frac{\pi x}{L}\right)$, where A — amplitude, L — crystal length, $x \in [0, L]$.

The crystal shape determining method

For small time velocity distribution along the length of the crystal clearly has a sinus form. However, over the time the chain distribution loses its shape and motion of particles indistinguishable from the heat. This happens due to the nonlinear interaction between the particles. However, over the time the chain takes the form of a sine again but curved by thermal motion. To determine how the chain shape is close to a sine more accurately, we calculate the parameter E^* — ratio of the total mechanical energy E to the total initial mechanical energy E_0.$E^* \in [0, 1]$. The larger the parameter E^*, the greater the crystal shape is similar to a sine.

Analysis of the solution of the problem for a long period of time

Time in this section is measured in the number of oscillations of the sinus. According to the graph $T(t)$ (Fig. 1a) you can see that after some time system returns to a state close to the original. This means that the velocity distribution regains the sine shape. It also shows that the system does not return to the initial state perfectly, but with some deviations. Fig. 1b shows the same graph, but for a longer period of time. It is seen that the peak height isn't constantly decreasing, but varying according to a certain law.

STOCHASTIC PROBLEM

Initial conditions

Initial displacement in the crystal is zero. Initial velocity is defined as follows (Fig. 2a): $v(x)|_{t=0} = A\sqrt{2} \quad \text{n}\left(\frac{\pi x}{L}\right) + \sqrt{3\sigma}\rho)$, where A — amplitude, L — crystal length, $x \in [0, L]$, σ — dispersion, ρ — random variable, $\rho \in [\nearrow 1, 1]$.

*Corresponding author. Email: dvtsvetkov@ya.ru

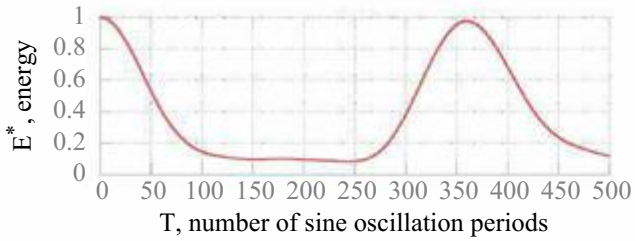

a) For small T

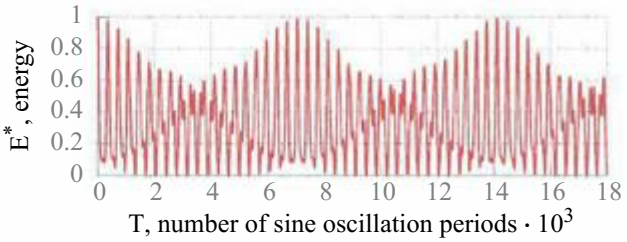

b) For big T

Figure 1: Results

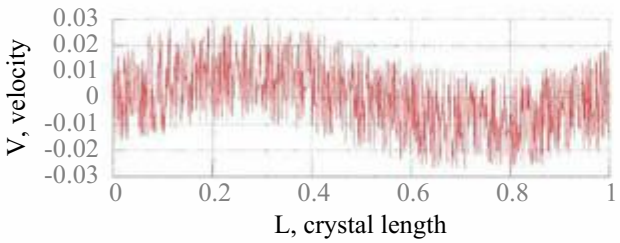

a) Initial conditions

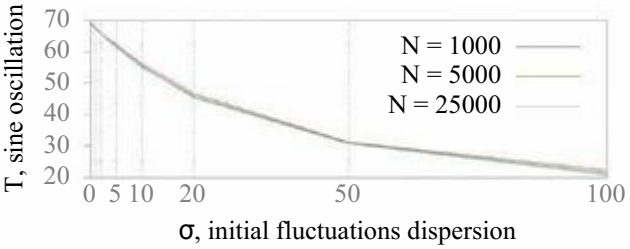

b) Results

Figure 2: Stochastic problem

Results

Time T_α, for which the function $E^*(T)$ falls below a certain value α, depending on the initial fluctuations dispersion σ, was determined. $\alpha = 0.1$, so we get the time value, for which 90% of the mechanical energy is converted into heat. Amplitude $A = 0.01 \cdot \sqrt{2} \approx 0.0141$.

Three cases are calculated for the following amount of particles: $N = 1000$, $N = 5000$ and $N = 25000$ giving almost the same results. In each case, the time T_α calculated for the variance $\sigma = 0; 1; 2; 5; 10; 20; 50; 100$. The results are shown in Fig. 2b. This graph shows that the addition of thermal energy to mechanical at the initial time leads to the fact that the mechanical energy converting into thermal energy becomes faster. It is also seen that the decay rate function $E^*(T)$ for the initial dispersion of the investigated fluctuation range is practically independent from the number of particles.

CONCLUSIONS

The problem of converting of the mechanical energy into thermal energy and back over the time in one-dimensional non-linear crystal is studied. If the crystal is short enough, after some time part of the thermal energy converts back into mechanical energy. The longer is the crystal, the longer one needs to wait for the reverse transformation of the energy and the less thermal energy goes back into mechanical energy. Time to reverse energy transformation is inversely proportional to the amplitude of the velocity fluctuations. The addition of thermal energy to mechanical at the initial time leads to the fact that the mechanical energy converts into thermal energy faster. By adding thermal energy 100 times greater than mechanical energy, the transformation rate of the mechanical energy into thermal energy increases by about 3.5 times. For the investigated range of the particles in the crystal (1000–25000), the rate of the mechanical energy conversion into thermal energy is practically independent from the particle number in the crystal.

References

[1] Goldstein R.V., Morozov N.F.: Mechanics of deformation and fracture of nanomaterials and nanotechnology. Physical mesomechanics. 2007. vol. 10. 5. pp.1730.

[2] Krivtsov A.M., Morozov N.F.: About mechanical properties of nanoscale objects. Solid state physics. 44, 2158-2163, 2002.

[3] Krivtsov A.M.: Heat transfer in infinite harmonic one-dimensional crystals. Doklady Physics 60, 407–411, 2015.

[4] Hoover W.G., Hoover C.G.: Simulation and control of chaotic nonequilibrium systems. Advanced Series in Nonlinear Dynamics: Vol. 27, World Scientific, 2015.

[5] Charlotte M., Truskinovsky L.: J. Mech. and Phys. of Solids 60, 1508, 2012.

[6] Katok A.B., Hasselblatt B.: Introduction to the modern theory of dynamical systems, Factorial, 1999. p. 768.

[7] Arnold V.I.: Mathematical methods of classical mechanics. Ed. 5th stereotype, Editorial URSS, 2003. - p. 62.

[8] Fermi E., Pasta J., Ulam S.: Studies of Nonlinear Problems. Los Alamos report LA-1940, published later in Collected Papers of Enrico Fermi, E. Segre (Ed.), University of Chicago Press, 1965.

[9] Onoratoa M., Vozellaa L., Promentb D., Lvovc Y.V.: Route to thermalization in the α-Fermi-Pasta-Ulam system, Proceedings of the National Academy of Sciences, 2015.

FINITE ELEMENT SIMULATION OF TGO GROWTH STRESS IN TBC SYSTEM CONSIDERING LARGE DEFORMATION

B. B. Yin[1,2], Y. C. Zhou[1,2 a)], L. Yang[1,2 a)] & Q. Shen[1,2]
[1]*Key Laboratory of Low Dimensional Materials & Application Technology (Ministry of Education), Xiangtan University, Xiangtan, Hunan 411105, China*
[2]*School of Materials Science and Engineering, Xiangtan University, Xiangtan, Hunan 411105, China*

Summary In this work, stress distributions and TGO growth in thermal barrier coatings (TBCs) are simulated simultaneously by finite element method considering large deformation. TGO growth is based on the diffusion-reaction equations. TGO profiles and thickness obtained by FEM are in good agreement with the experimental observations reported in the literature. Thereafter, a simple cylinder theory model based on large deformation theory is developed to explain the stress fields simulated through FEM. In the model, TGO growth is described by growth deformation gradient, and then the total deformation gradient is decomposed into elastic deformation gradient and growth deformation gradient. The results obtained by theory model validate the finite element method for TGO growth stress simulation. So it is an effective approach to calculate stress distributions and TGO thickness simultaneously which are important for predicting the failure positions and lifetime of TBCs.

INTRODUCTION

Thermal barrier coatings (TBCs) are widely used to reduce the service temperature and prolong the lifetime of high temperature components in turbine engines[1]. Failure of a TBC system often occurs either by debonding at the TGO/BC interface, or the TC/TGO interface. As emphasized by Evans et al.[1], growth of the TGO layer was directly responsible for all the intrinsic failure mechanisms of TBCs. The stresses in the TBCs play an important role on TBCs failure. Understanding these stresses is crucial to any model of durability. There are two main sources of stresses: one from the thermal expansion misfit upon cooling and the other from TGO growth. The stresses originating from the difference between the coefficients of thermal expansion of the TBCs layers had been studied extensively over the past decade. The analytical models, numerical simulations and experimental methods were developed for thermal misfit stresses analysis, and the results were accepted by many researchers.

The growth stresses, due to its complicated oxidation process, were still not understood completely. Evans et al.[1] applied a sphere model to obtain the elastic solution of the local stress field around undulating TGO. Sun et al.[2] proposed a sphere model to analytically predict the stress evolution due to TGO isothermal growth in a TBC system. Finite element models are able to reflect more realistic geometry, and they also present valuable calculations for local stress evolution. Ranjbar-fa et al.[3] modeled the TGO growth by swelling of the elements in the TGO layer. Busso et al. proposed a coupled constitutive framework to describe the oxidation processes of TBCs, and implemented it into the finite element code to study the stress distribution in TBCs[4].

Generally, the true mean volumetric strain is about 0.122 according to the Pilling and Bedworth ratio(PBR). However, most of previous works were studied based on small deformation. As emphasized by Loeffel et al.[5], the local large deformation is generated in TBCs during TGO growth. In his paper, a chemo-thermo-mechanically coupled theory for chemical reaction was developed considering large deformation. Then, the author numerically studies the TGO growth and decohesion of TC/TGO based on the coupled theory[6]. Moreover, it is still a challenge to faithfully simulate TGO growth and accurately predict the associated stress evolution using finite element method. In this paper, we develop a finite element method to simulate the growth stress and TGO thickness considering the large deformation.

RESULTS AND DISCUSSION

As shown in Fig. 1., after 50 and 100 h high temperature exposure, uneven TGO forms at the rough TGO/bond coat interface. With increasing of the exposure time, uneven growth of TGO becomes visible and uneven locations increase at the top coat/bond coat interface. It can be seen that, with the increase of exposure time, the TGO thickness increases. The TGO thickness at peak and valley locations is different, which is observed in many experiments[7-9]. The thickness of the TGO at peak and valley locations is 12 μm and 7.2 μm after 1000 h as shown in Fig.2.

[a)] Corresponding author. Email: Zhouyc@xtu.edu.cn, Lyang@xtu.edu.cn

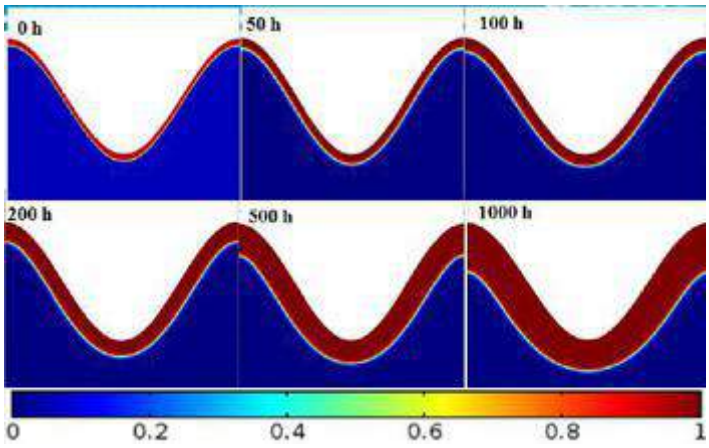

Fig. 1. TGO morphology evolution with oxidation time

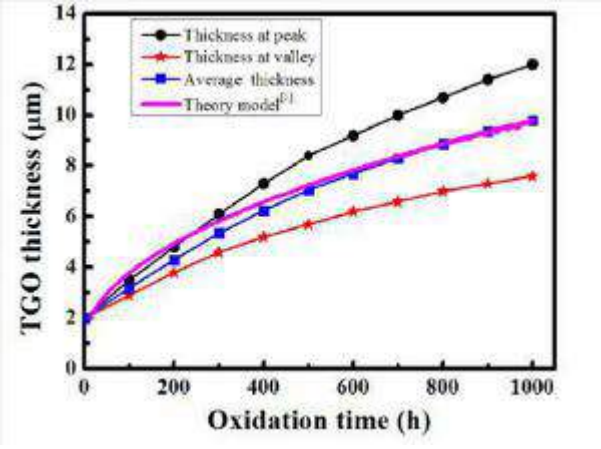

Fig. 2. TGO thickness evolution with oxidation time

The stress distribution in TBCs due to the continuous TGO growth are shown in Fig. 3 and Fig. 4. In Fig. 3, we find the tensile stresses at the valley of TC layer rises from 100 to 350 MPa with the time increasing, and the tensile stress region increases and extends from the valley to the middle of the waves.However , the maximum tensile stress in TGO and BC is obtained at the peak of TGO/BC interface as shown in Fig. 4. Cracks may occur at the TBC/TGO interface or the TGO/BC interface.

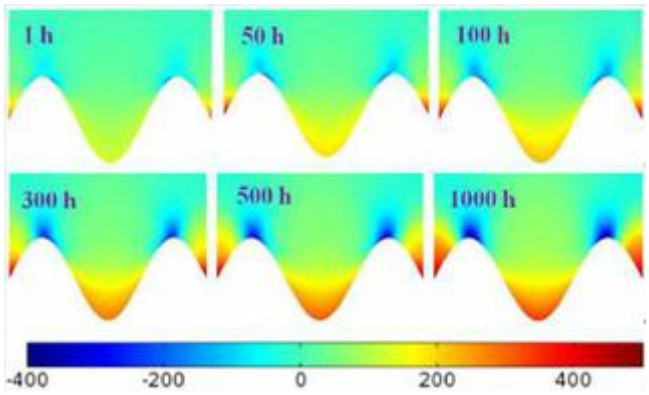

Fig. 3. The stresses distribution in TC at different oxidation time

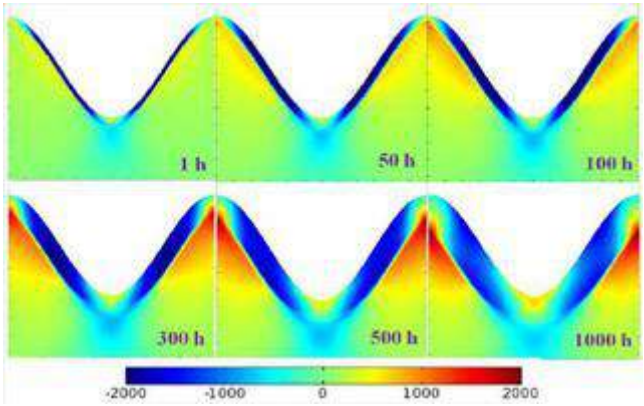

Fig. 4. The stresses distribution in TGO and BC at different oxidation time

CONCLUSIONS

In this work, a 2D finite element method for TGO growth stress considering the large deformation in TGO was presented based on diffusion–reaction equations. The main results can be summarized as follows: (1) Uneven growth of TGO becomes visible at the top coat/bond coat interface with the oxidation times, which is observed in many experiments. (2)The maximum tensile stress in TGO and BC is obtained at the peak of TGO/BC interface, which is always the failure position of TBCs.

References

[1] A.G. Evans, D.R. Clarke, C.G. Levi, J. Eur. Ceram. Soc., 28 (2008) 1405-1419.
[2] Y. Sun, J. Li, W. Zhang, T.J. Wang, Surf. Coat. Technol., 216 (2013) 237-250.
[3] M. Ranjbar-Far, J. Absi, G. Mariaux, F. Dubois, Materials & Design, 31 (2010) 772-781.
[4] E.P. Busso, J. Lin, S. Sakurai, Acta Mater., 49 (2001) 1529-1536.
[5] K. Loeffel, L. Anand, Int. J. Plast., 27 (2011) 1409-1431.
[6] K. Al-Athel, K. Loeffel, H. Liu, L. Anand, Surf. Coat. Technol., 222 (2013) 68-78.
[7] K. Ma, J.M. Schoenung, Surf. Coat. Technol., 205 (2011) 5178-5185.
[8] O. Trunova, T. Beck, R. Herzog, R.W. Steinbrech, L. Singheiser, Surf. Coat. Technol., 202 (2008) 5027-5032.
[9] C. Che, G.Q. Wu, H.Y. Qi, Z. Huang, X.G. Yang, Surf. Coat. Technol., 203 (2009) 3088-3091.

GENERAL ALGORITHM OF SOLUTION OF 2-DIMENSION PROBLEMS OF MECHANO-DIFFUSION

Andrei Zemskov[1], Dmitry Tarlakovskii[2]
[1]*Moscow Aviation Institute (National Research University), Department of Control systems, computer science and power plants, Moscow, Russia*
[2]*Institute of Mechanics Lomonosov Moscow State University, Laboratory of dynamic tests, Moscow, Russia*

Summary. The present study proposes an approach towards solving two-dimension initial boundary value problem of elastic diffusion based on relations connecting the right sides of boundary conditions of various types. With two initial boundary value problems at hand, whereas the solution of one of them is known, the solution of another one will depend on the solution of the first one with a system of type I Volterra integral equations. They are solved with quadrature formulas.

INTRODUCTION

Solving nonstationary problems in continuum mechanics including those in elastic diffusion presents lots of mathematical challenges. Depending on certain types of boundary conditions solution of such problems can be found using Fourier trigonometric series [1,2].

In order to develop the solution of initial boundary value problem with random boundary it is proposed to build relations among boundary conditions of different types [3]. In this case it will be sufficient to solve one (benchmark) problem while all other problems will be reduced to it by the relations given below. The proposed method is shown in an example of two dimensional non-stationary problems in elastic diffusion for an orthotropic layer.

Problem description

Let there be given a two-dimensional initial boundary value problem hereinafter referred to as "the original problem":

$$\mathbf{L}(\mathbf{u}) = 0,\ \mathbf{u} = \{u_1(x_1, x_2, t), u_2(x_1, x_2, t)\},\ (x_1, x_2) \in D = \Re \times [0, l],\quad t > 0, \tag{1.1}$$

$$\mathbf{M}_1(\mathbf{u})\big|_{x_2=0} = \mathbf{f}_1(x_1, t),\ \mathbf{M}_2(\mathbf{u})\big|_{x_2=l} = \mathbf{f}_2(x_1, t). \tag{1.2}$$

where $\mathbf{L}$, $\mathbf{M}_1$ and $\mathbf{M}_2$ are linear matrix differential operators; t is time, $\mathbf{f}_1$ and $\mathbf{f}_2$ are vector functions of the right sides of boundary conditions (2).

Simultaneously, a benchmark original boundary value problem is being considered where the required function satisfies equation (1.1) and boundary conditions

$$\mathbf{N}_1(\mathbf{u})\big|_{x_2=0} = \mathbf{g}_1(x_1, t),\ \mathbf{N}_2(\mathbf{u})\big|_{x_2=l} = \mathbf{g}_2(x_1, t) \tag{1.3}$$

where $\mathbf{N}_1$ and $\mathbf{N}_2$ are linear matrix differential operators; $\mathbf{g}_1$ and $\mathbf{g}_2$ are vector functions of the right sides of boundary conditions (1.3).

The solution of the problems (1.1), (1.3) will be presented as follows:

$$\mathbf{u} = \int_0^t \mathbf{G}_1(x_1, x_2, t, \tau) * \mathbf{g}_1(x_1, \tau) d\tau + \int_0^t \mathbf{G}_2(x_1, x_2, t, \tau) * \mathbf{g}_2(x_1, \tau) d\tau \tag{1.4}$$

Here $\mathbf{G}_1$ and $\mathbf{G}_2$ are Green's functions of problem (1.1), (1.3); the asterisk $*$ means x_1 variable convolution.

Assuming that functions $\mathbf{G}_1$ and $\mathbf{G}_2$ are known, and claiming that $\mathbf{g}_1$ and $\mathbf{g}_2$ satisfy the conditions (1.2), we arrive at a system of integral equations with regards to $\mathbf{g}_1$ and $\mathbf{g}_2$:

$$\int_0^t \mathbf{M}_k[\mathbf{G}_1(x_1, x_2, t, \tau)] * \mathbf{g}_1(x_1, \tau) d\tau + \int_0^t \mathbf{M}_k[\mathbf{G}_2(x_1, x_2, t, \tau)] * \mathbf{g}_2(x_1, \tau) d\tau = \mathbf{f}_k,\ k = 1,\ x_2 = 0;\quad k = 2,\ x_2 = l. \tag{1.5}$$

Substituting the solution of this system to (1.4) gives the solution of the original problem.

DEMONSTRATION OF ALGORITHM

As an example, let there be a two-dimensional problem of elastic diffusion for a layer bounded by surfaces $x_3 = 0$ and $x_3 = L$ ($Ox_1x_2x_3$ is a rectangular Cartesian coordinate system). Physical and mechanical processes in the medium are described by the equations [1,2,4]:

[a] Corresponding author. Email: azemskov1975@mail.ru.

$$C_{ijkl}\frac{\partial^2 u_k}{\partial x_j \partial x_l}=\frac{\partial^2 u_i}{\partial \tau^2}+\alpha_{ij}\frac{\partial \eta}{\partial x_j},\quad D_{ij}\frac{\partial^2 \eta}{\partial x_i \partial x_j}=\frac{\partial \eta}{\partial \tau}+\Lambda_{ijkl}\frac{\partial^3 u_k}{\partial x_i \partial x_j \partial x_l}, \tag{2.1}$$

$$\sigma_{12}\big|_{x_2=0,1}=f_{1q}^1(x_1,\tau),\ u_2\big|_{x_2=0,1}=f_{2q}^1(x_1,\tau),\ \eta\big|_{x_2=0,1}=f_{3q}^1(x_1,\tau),\quad q=1,\ x_2=0;\quad q=2,\ x_2=1; \tag{2.2}$$

$$u_i\big|_{\tau=0}=\frac{\partial u_i}{\partial \tau}\bigg|_{\tau=0}=\eta\big|_{\tau=0}=0 \tag{2.3}$$

Here the following dimensionless values are used (they are primed where the tracings are identical, hereafter primes are omitted):

$$x_i'=\frac{x_i}{L},\ u_i'=\frac{u_i}{L},\ \tau=\frac{Ct}{L},\ C^2=\frac{C_{2222}}{\rho},\ \eta'=\frac{\eta}{n_0},\ C_{ijkl}'=\frac{C_{ijkl}}{\rho C^2},\ \alpha_{ij}'=\frac{n_0\alpha_{ij}}{\rho C^2},$$

$$D_{ij}'=\frac{D_{ij}}{CL},\ \Lambda_{ijkl}'=\frac{\Lambda_{ijkl}}{n_0 CL},\ f_{1q}'^1=\frac{f_{1q}^1}{C_{1212}},\ f_{2q}'^1=\frac{f_{2q}^1}{L},\ f_{3q}'^1=\frac{f_{3q}^1}{n_0 C D_{22}}\quad (q=1,2).$$

where the repeating Latin indices mean summation from 1 to 2; t is time; $u_i(x_1,x_2)$ means coordinates of displacement vector; T_0 is absolute ambient temperature; $\eta=n-n_0$ is volume concentrations increment of substance n as compared with the initial concentration n_0; C_{ijkl} are elastic constants tensor components; σ_{ij} are stress tensor components; ρ - medium density; α_{ij} - tensor components describing volume change due to diffusion; D_{ij} are self-diffusion coefficients; $\Lambda_{ijkl}=n_0 D_{ij}\alpha_{kl}/RT_0$; R is universal gas constant.

As a benchmark problem, let there be a problem with the following boundary conditions:

$$\sigma_{12}\big|_{x_2=0,1}=f_{1q}^2(x_1,\tau),\quad u_2\big|_{x_2=0,1}=f_{2q}^2(x_1,\tau),\quad J_2\big|_{x_2=0,1}=f_{3q}^2(x_1,\tau),\quad q=1,\ x_2=0;\quad q=2,\ x_2=1. \tag{2.4}$$

Here J_2 is a component of the vector of diffusion flow.

The solution for problem (2.1), (2.3), (2.4) can be found in works [1,2] and in an integral form is as follows (asterisks mean convolution of time and axis x_1):

$$u_i=\sum_{m=1}^{3}G_{im}**\left[f_{m1}^2+(-1)^i f_{m2}^2\right],\quad \eta=\sum_{m=1}^{3}G_{3m}**\left(f_{m1}^2-f_{m2}^2\right) \tag{2.5}$$

Here $G_{im}=u_i,\ G_{3m}=\eta$ $\left(m=\overline{1,3},\ i=1,2.\right)$ are Green functions of the problem (2.1), (2.3), (2.4). The system (1.5) takes the form:

$$\begin{aligned}&G_{33}^F(\omega,0,\tau)*f_{31}^{2F}(\omega,\tau)-G_{33}^F(\omega,1,\tau)*f_{32}^{2F}(\omega,\tau)=\varphi_1^F(\omega,\tau),\\ &G_{33}^F(\omega,1,\tau)*f_{31}^{2F}(\omega,\tau)-G_{33}^F(\omega,0,\tau)*f_{32}^{2F}(\omega,\tau)=\varphi_2^F(\omega,\tau),\end{aligned} \tag{2.6}$$

where « F » means Fourier transform, ω, parameter of Fourier transformation,

$$\varphi_1^F(\omega,\tau)=f_{31}^{1F}(\omega,\tau)-\sum_{k=1}^{2}\left[G_{3k}^F(\omega,0,\tau)*f_{k1}^{2F}(\omega,\tau)-G_{3k}^F(\omega,1,\tau)*f_{k2}^{2F}(\omega,\tau)\right]$$

$$\varphi_2^F(\omega,\tau)=f_{32}^{1F}(\omega,\tau)-\sum_{k=1}^{2}\left[G_{3k}^F(\omega,1,\tau)*f_{k1}^{2F}(\omega,\tau)-G_{3k}^F(\omega,0,\tau)*f_{k2}^{2F}(\omega,\tau)\right]$$

The system (2.6) will be solved numerically with quadrature formulas. The convolutions (2.5) are found also numerically.

CONCLUSIONS

The algorithm developed will allow solving initial boundary value problems easily enough with random boundary conditions. To make the algorithm work one solved problem of the corresponding type would be suffice.

This work was done with financial support of the Russian Foundation for Basic Research (project 14-08-01161).

References

[1] Zemskov A.V., Tarlakovskii D.V.: *Uchenye Zapiski Kazanskogo Universiteta. Seriya Fiziko-Matematicheskie Nauki*, **157**(4), 2015.

[2] Zemskov A.V., Tarlakovskii D.V.: *Journal of Applied Mechanics and Technical Physics*, **56**(6), 2015.

[3] Zemskov A.V., Tarlakovskiy D.V.: *Materials Physics and Mechanics*, **23**(1), 2015.

[4] Tarlakovskii D.V., Vestyak V.A., Zemskov A.V. *Encyclopedia of Thermal Stresses* (Springer, Dordrecht, Heidelberg, New York, London), 2014.

THE ATTRACTIVE FORCE AND REPULSIVE FORCE OF A HTS/PM SYSTEM UNDER FIELD COOLING CONDITION

Xian-Feng Zhao[1a)], Yuan Liu[1]
[1]*School of Civil Engineering, Lanzhou Jiaotong University, Lanzhou, Gansu, China*

Summary Based on Ampère circulation theorem and Kim critical model, the attractive force and the repulsive one in a superconducting levitation system are investigated under field cooling condition. The simulation result fits to the experiment ones very well. The penetration profiles of shielding currents and magnetic field in HTS are employed to explain the internal mechanism of the dependence of levitation force on the critical current density constant. These results are very interesting to physical research and helpful for the practical designing and applications.

INTRODUCTION

Recently research on superconducting levitation and its extensive application has been developed, especially in superconducting bearings and high-Tc superconducting levitation maglev [1]. To estimate these systems quality, levitation force is considered as one of the main characteristics. Most of them pay their attention to zero field cooling (ZFC) state [2]. Only a few works were done in field cooling (FC) state, i.e. the HTS is cooled initially under liquid nitrogen temperature as the PM is approach to the HTS. In this paper we will present an approach to levitation force under field cooling consideration based on Ampère circulation theorem and Kim critical state model. A realistic system will be discussed.

FUNDAMENTAL EQUATIONS

We will consider a coaxial superconducting levitation system composed of a PM and a non-ideal type-II HTS. As shown in fig.1, the HTS is fixed and the PM can move upon the HTS. The center of top surface of HTS is considered as the origin of cylindrical coordinates. For this configuration, the vector potential of the PM has only one component along the direction, which can be derived by integrating the vector potential of a circular current loop with radius along the thickness, i.e.

$$A_\phi(\rho,\mathrm{z})=\sum_i \frac{\mu_0 I}{4\pi}\int_0^{2\pi}\frac{R_{PM}\cos(\varphi')}{[R_{PM}^2+\rho^2-2R_{PM}\rho\cos(\varphi')+(z-z_{PM,i})^2]^{1/2}}d\varphi' \qquad (1)$$

where I denotes the equivalent current density and μ_0 is magnetic permeability in air. Then the radial and perpendicular components of magnetic induction of the PM could be given from the partial derivative of the vector potential.

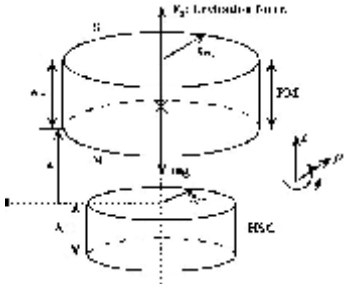

Fig.1 Sketch of a HTS-PM superconducting levitation system.

When the PM moves up or down over the HTS, shielding currents will be formed in HTS so as to compensate the variation of the internal field. The levitation force comes from the interaction of the magnetic field produced by PM and shielding currents. Here we assume that superconducting shielding currents are described by the Kim critical model [3]. In this model the shielding currents is considered to be related to magnetic field in HTS:

$$J_c(|\boldsymbol{B}_i|)=\frac{J_{c0}B_0}{B_0+|\boldsymbol{B}_i|} \qquad (2)$$

where J_c is critical current density in HTS, J_{c0} denotes a constant about J_c, and B_0 is a parameter on magnetic field, $\boldsymbol{B}_i$ is the internal magnetic induction in HTS.

In the process of increasing the external field or decreasing it, the layer of shielding currents extends inwards with time until another reversal value of the external field is reached. At this point the inward progress of the previous superconducting shielding current layer is terminated and a new inward-extending current layer is formed. The previously induced layers of persisting superconducting shielding currents stay still and represent the past history of the temporal variations of the external field. Thus it can be concluded that, at any instant of time, there exists several layers of persisting superconducting shielding currents. These currents have opposite directions in adjacent layers. We can get the levitation force based on Lorentz formula

$$\boldsymbol{F}_z=\int_V \boldsymbol{J}_c\times\boldsymbol{B}_i dV \qquad (3)$$

where V denotes the volume filled by shielding currents, which can be calculated by considering the sandwich structure of the HTS.

For a HTS, the internal magnetic field and the critical currents are subjected to Ampère circulation law $\nabla\times\boldsymbol{B}=\mu_0\boldsymbol{J}_c$.

[a)] Corresponding author. Email: zhaoxf@mail.lzjtu.cn

Because of axi-symmetry of the system, the shielding currents within the HTS have only on component along the ϕ direction. In this case, we can get an equation about penetration depth of superconducting shielding currents as follows:

$$B_{i0}^2(\rho_P)+2B_0B_{i0}(\rho_P)+sign(\boldsymbol{J}_c)2\mu_0B_0J_{c0}(R_{SC}-\rho_P)(1-N)-\left(2B_0B_{R_{SC}}-B_{R_{SC}}^2\right)=0 \qquad (4)$$

where ρ_P is penetration depth of superconducting shielding currents. Since the initial value of B_{i0} is dependent on ρ_P, the Eq. (4) is an implicative function on ρ_P. The Newton-Raphson method is employed to solve the equation.

RESULTS AND DISCUSSIONS

In a case study, the radius and the thickness of the HTS are set as R_{HTS}=9mm and H_{HTS}=10mm respectively. The one of the PM are R_{PM}=12.5mm and H_{PM}=22.5mm. The critical current density constant J_{c0} is $1.0\times10^7 A/m^2$. In calculation the HTS is divided into n_h layers along the thickness and n_ρ circles along the radius. For enough decision they are chosen as $n_h=200$ and $n_\rho=650$. Initially, the HTS is cooled by liquid nitrogen after the PM is placed at a certain gap (0.5mm). The maximum attractive force can be achieved during the ascending procedure and the maximum repulsive force will be gained when the gap is 0.1mm at the followed descending procedure.

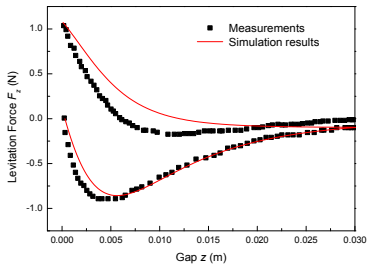

Fig.2 The magnetic levitation force under field cooling condition

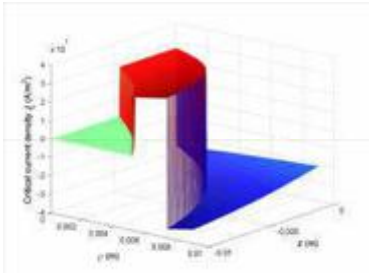

Fig.3 Shielding currents distribution when the movement is terminated

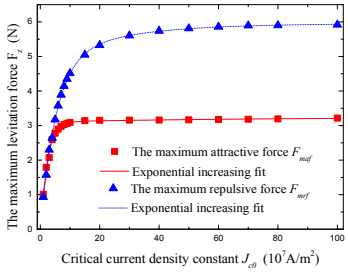

Fig.4 The dependence of levitation force to the critical current density constant

The magnetic levitation force under field cooling condition is presented as shown in fig.2. The simulation result is consistent to the experiment ones very well. The main consideration is due to the frozen magnetic field in HTS. The penetration depth in HTS is confirmed to their effectiveness to the simulation. There are two layers of shielding currents in the HTS when the PM falls down as shown in fig.3. The induced currents with minus direction always penetrate into the HTS from the edge to the interior and wipe out the previous plus shielding currents. The penetration depth of minus shielding currents decreases with the decreasing of the gaps and the one of plus shielding currents doesn't change.

The effect of levitation force on critical current density is demonstrated by calculating the levitation force for different J_{c0}. The results are shown in fig4. The maximum repulsive force and the maximum attractive one are shown as solid triangles and squares respectively. We can find that they saturate for larger J_{c0}. The results show an exponential increasing function. We can get the limits of $F_{z,\max}^{mrf}(J_{c0})$ and $F_{z,\max}^{maf}(J_{c0})$ are 5.8N and 3.2N respectively. A ratio of these limits can be given by $\kappa=\lim_{J_{c0}\to\infty}F_{z,\max}^{mrf}(J_{c0})\Big/\lim_{J_{c0}\to\infty}F_{z,\max}^{maf}(J_{c0})=1.8$. The limit ratio can help us to get the maximum attractive force based on some information on the maximum repulsive force given in experiments easily.

CONCLUSIONS

In this paper an approach to levitation force under field cooling consideration is presented, based on Ampère circulation theorem and Kim critical state model. The hysteresis characteristic is obtained with magnetic history of HTS. The dependence of the repulsive force and attractive one on critical current density constant are investigated with the penetration process of shielding currents. The results could be expected to direct the application of superconducting levitation systems.

References

[1] Zhou Y. H., Zhao X. F.: Dynamical analysis to the levitated systems of high temperature superconductors with hysteresis. *Physica C442*:55-62, 2006.

[2] Zhao X. F., Zhou Y. H.: Dependence of equilibrium height of a magnet on initial magnetization process in a high T_c superconducting levitation system. *Applied Electromagnetics and Mechanics* 33(1,2):519-525, 2010.

[3] Kim Y.B., Hempstead C.F. and Strand A.R.: Resistive states of hard superconductors. *Rev. Modern Phys.* 36:43-49, 1964.

SM10 - Sizescale Effects in Materials

TS.SM10-1.01	Geers, Marc - On the role and modelling of internal boundaries in size effects for metals (INVITED)	2460
TS.SM10-1.02	Mesarovic, Sinisa - Size-dependent Energy of Elastic-plastic Crystals	2462
TS.SM10-1.03	Svendsen, Bob - Strongly versus weakly non-local dislocation transport and pile-up	2464
TS.SM10-1.04	Du, Chaowei - The role of sub-structure boundaries on lath martensite plasticity	2466
TS.SM10-1.05	Hochrainer, Thomas - Small scale plasticity simulated with continuum dislocation dynamics	2468
TS.SM10-1.06	Zhuang, Zhuo - Discrete dislocation-based crystal plasticity at micron-nano scales	2470
TS.SM10-2.01	Voyiadjis, George - Large scale atomistic simulation of size effects during nanoindentation	2472
TS.SM10-2.02	Lu, Guoxing - Investigation into the behaviour of the graded cellular foam under impact	2474
TS.SM10-2.03	Piccolroaz, Andrea - Dispersion and localization in flexural waves supported by Rayleigh beam structures	2476
TS.SM10-2.04	Legarth, Brian - Plastic size-effects on a mode I loaded crack	2478
TS.SM10-2.05	Martínez-Pañeda, Emilio - Strain gradient plasticity beyond micron-scale applications: Fracture and damage modelization	2480
TS.SM10-2.06	Gerberich, William - Enhanced fracture toughness in silicon at small scale	2482
TS.SM10-3.01	Massart, Thierry J. - Ultra-High Ductility of TRIP-Assisted Seels Modelled by Gradient Plasticity (INVITED)	2484
TS.SM10-3.02	Asgharzadeh, Mohammadali - Continuum analysis of precipitation hardening using SGP theory	2486
TS.SM10-3.03	Stupkiewicz, Stanislaw - Phase-field study of size effects in martensitic microstructures	2488
TS.SM10-3.04	Niordson, Christian - Finite strain gradient plasticity with application to micron scale void growth	2490
TS.SM10-3.05	Ling, Chao - Modelling size effects on void growth and coalescence in single crystals	2492
TS.SM10-3.06	Nielsen, Kim Lau - Size Effects in Void Coalescence	2494
TS.SM10-4.01	Bardella, Lorenzo - Implicit finite element algorithms for higher-order gradient plasticity theory (INVITED)	2496
TS.SM10-4.02	Altenbach, Holm - An Energy-Based Formulation of Equivalent Inhomogeneity for Interphase Models	2498
TS.SM10-4.03	Reddy, Daya - Some features of dissipative theories of strain-gradient plasticity	2500
TS.SM10-4.04	Juul, Kristian - Steady-state numerical modeling of size effects in wire drawing	2502
TS.SM10-4.05	Lebensohn, Ricardo - Spectral non-local crystal plasticity modelling of size effects in polycrystals	2504
TS.SM10-4.06	Puri, Saurabh - Modeling of size effects in plasticity using field dislocation mechanics	2506
TS.SM10-5.01	Mayeur, Jason - A study of two approaches to higher-order single crystal plasticity (INVITED)	2508
TS.SM10-5.02	Petryk, Henryk - A minimal gradient-enhancement of crystal plasticity theory	2510
TS.SM10-5.03	Yalcinkaya, Tuncay - Microstructure evolution in plasticity	2512

TS.SM10-5.04	Wei, Yujie - Mechanical properties and deformation mechanisms in materials with gradient twin structures	2514
TS.SM10-5.05	Guo, Ya-Fang - Investigation on the size effect of twinning in HCP single crystals	2516
TS.SM10-5.06	Zhu, Linli - Modeling the mechanical properties of FCC polycrystalline metals with hierarchical twins	2518
TS.SM10-6.01	Husser, Edgar - The mechanical behavior of gold-polymer nanocomposites: A numerical study	2520
TS.SM10-6.02	Ponga, Mauricio - Understanding Prismatic Dislocation Loops in Mg by means of large-scale ab-initio simulations	2522
TS.SM10-6.03	Klusemann, Benjamin - Study of Intrinsic and Extrinsic Size Effects on Shear Bands in Metallic Glasses	2524
TS.SM10-6.04	Linder, Christian - A micromechanical model for strain-induced crystallization in rubber	2526
TS.SM10-6.05	Kordolemis, Alexis - Axially loaded pretwisted nonlinear thin plates: A strain gradient analogy	2528
TS.SM10-6.06	Barrioz, Pierre-Olivier - Experimental assessment of nanovoids growth	2530
PO.SM10-1.01.291	Bae, Suwon - Molecular dynamics investigation of single chain polymer nanoparticles	2532
PO.SM10-1.02.292	Bormann, Franz - Numerical model for dislocation transmission across a phase boundary	2534
PO.SM10-1.03.293	Liang, Lihong - Size Effect of Mechanical Behavior of Coating Systems	2536
PO.SM10-1.04.294	Liu, Mingchao - Surface effect on the adsorption-induced deformation of ordered porous material	2538
PO.SM10-1.05.295	Ma, Hansong - Influence of nanoinclusion's size-dependence on composite with micropolar matrix	2540
PO.SM10-1.06.296	Ma, Yanhui - Size-dependent and tunable mechanical properties of stochastic fibrous structres	2542
PO.SM10-1.07.297	Mohammed Ameen, Maqsood - Higher-order asymptotic homogenization of periodic materials at low scale separations	2544
PO.SM10-1.08.298	Peng, Xiang-Long - Modeling surface penetration by dislocation pileup model with image effect	2546
PO.SM10-1.09.299	Pouriayevali, Habib - A study of grain and grain-boundaries based on a gradient crystal-plasticity model	2548
PO.SM10-1.10.300	Sargsyan, Samvel - Geometrically nonlinear theory of micropolar elastic thin plates and shells	2550
PO.SM10-1.11.301	Sigaeva, Taisiya - Effect of the surface on hyperelastic properties of materials at smaller scales	2552
PO.SM10-1.12.302	Solyaev, Yury - Surface effects in the pure bending problem in the theory of elastic materials with voids	2554
PO.SM10-1.13.303	Verma, Deepti - Sizescale Effects in Bending Flexibility of Phosphorene and its 2D Allotropes	2556

ON THE ROLE AND MODELLING OF INTERNAL BOUNDARIES IN SIZE EFFECTS FOR METALS

Marc Geers,* Varvara Kouznetsova, and Ron Peerlings

Department of Mechanical Engineering, Eindhoven University of Technology, The Netherlands

Summary This paper focuses on the role of grain and phase boundaries in restricting dislocation motion, giving rise to size effects. Some essential features of a thermodynamically consistent model for a grain boundary are presented, which accounts for the grain boundary energy and defect structure and evolution. The role of a phase boundary is investigated with a dislocation transport driven crystal plasticity model, revealing the explicit role of the plastic phase contrast and phase boundary resistance. Interesting size effects are thereby recovered. Size effects can also be eliminated or inhibited by other microstructural mechanisms. Two cases are addressed to illustrate this. The first case reveals the role of dislocation climb and its effectiveness in dissolving dislocation pile-ups. The second case concerns a very thin austenitic phase in martensite, whereby the particular structure of the phase and its interface give rise to preferential sliding mechanisms that circumvent the common dislocation driven size effects.

INTRODUCTION

Size effects are a key ingredient to control and improve the mechanical behaviour of metallic microstructures and miniaturized components. The analysis of size effects in metals has received continuous attention in the past two decades, both experimentally and numerically. Size effects can be categorized according to the underlying mechanisms or origins:

- statistical size effects: these result from the local variations of the actual number of grains in miniaturized specimens (typically 'small is weak')
- first-order size-effects: related to the influence of the ratio between microstructural size (e.g. grain size) and the characteristic specimen/component dimensions, e.g. inducing texture effects.
- second-order size effects: typically induced by lattice curvature in metals or dislocation pile-ups, modelled by a strain gradient (crystal) plasticity approach (typically 'small is strong')

Some size effects are the intrinsic result of specimen fabrication (processing-induced). Exploiting size effects implies to substructure materials in order to retrieve ultra-fine phases in a microstructure, typically accompanied by many internal boundaries. This contribution on size effects focuses on the role and modelling of internal boundaries on the one hand, and on mechanisms that tend to eliminate or circumvent size effects triggered by internal boundaries.

SIZE EFFECTS THROUGH INTERNAL BOUNDARIES

Grain boundaries

The first classical example of an internal boundary is the grain boundary. Grain boundaries typically constrain dislocation motion and may induce pile-ups that are largely responsible for the observed Hall-Petch effect. A multiscale grain boundary plasticity framework is briefly presented, which is an extension of a dislocation based gradient enhanced crystal plasticity framework [1]. Driven by the need for a physically based continuum scale description of the grain boundary energy required in continuum modelling frameworks, a multiscale approach is proposed that leads to a continuum representation of the initial grain boundary structure defect content and energy, based on the output of atomistic simulations. A continuum model is developed that incorporates the description of the defect redistribution along the grain boundary into the grain boundary plasticity model. The effect of these mechanisms on the mechanical response will be demonstrated.

Phase boundaries

Phase boundaries reveal a large contrast in (plastic) properties and are therefore more effective in impeding or restricting dislocation motion. Here, the effect of a phase boundary will be demonstrated through a dislocation transport based crystal plasticity model [2]. The influence of the drag resistance in the different phases is addressed in particular. The interface properties of the phase boundary are varied, ranging from a transparent boundary to an impenetrable barrier for dislocations. A qualitative analysis is performed to study the effect of interface, material and geometrical parameters on the overall response of a two-phase laminate. The continuum dislocation transport model reveals a composite behaviour that cannot be captured by classical averaging methods. Interesting size effects emerge due to the dislocation transport.

*Corresponding author. Email: mg@tue.nl

MICROMECHANICAL MECHANISMS AGAINST SIZE EFFECTS

Interfacial mechanisms triggering size effects may be neutralized by other microstructural mechanisms. Two cases are examined in more detail. The first case extends a strain gradient crystal plasticity model with vacancy diffusion assisted climb. The second case focuses on a particular interface in high-strength steels, where very thin austenite films exist within laths of martensite.

Dislocation climb coupled to vacancy diffusion

To investigate the role of dislocation climb on size effects, a fully coupled glide-climb crystal plasticity model is used [3]. Dislocation climb is thereby controlled by the diffusion of vacancies. The governing strain gradient crystal plasticity model is extended, whereby the climbing dislocations are incorporated in the governing transport equations. The kinematics of the extended model accounts for the contribution of climb in the crystallographic split of the plastic strain rate tensor. Using this extended formulation, it is shown that dislocation climb is a efficient mechanism to gradually dissolve pile-ups, thereby having a significant influence on the resulting size effects.

Austenitic thin films in martensite

Martensite is generally known as a hard and brittle phase. However, ductile deformation of martensite is also often reported in the literature. One of the possible explanations is the presence of thin films of retained austenite in the martensitic laths. Whereas this constitutes a very thin phase, along with phase boundaries, the net effect is opposite to what might be expected from the classical size effect reasoning. It is shown that the crystallographic orientation relationship between both phases on the one hand, and the particular atomic interfacial structure on the other hand, both favour plastic deformation (sliding) parallel to the phase boundary [4]. As a result thereof, deformation localizes around these thin films, giving rise to large apparent deformations in the embracing martensitic phase without size effect strengthening.

CONCLUSIONS

This paper adresses the strengthening role of internal boundaries, constituting a major contribution to size effects in metals. It is shown that besides dislocation pile-ups, other mechanisms may be essential. For grain boundaries, the defect absorption and redistribution matters. For phase boundaries, phase contrast in dislocation transport alone already contributes to size effects. Moreover, dislocation-pile ups can be dissolved through climb at higher temperatures or circumvented by other particular micromechanisms. This analysis effectively illustrates that predicting size effects in metals quantitatively remains a major challenge.

References

[1] van Beers P.R.M., Kouznetsova V.G., Geers M.G.D.: Defect redistribution within a continuum grain boundary plasticity model. J. Mech. Phys. Solids 83:243-262, 2015.

[2] Dogge M.M.W., Peerlings R.H.J., Geers M.G.D.: Interface modeling in continuum dislocation transport. Mechanics of Materials. 88:30-43, 2015.

[3] Geers M.G.D., Cottura M., Appolaire B., Busso E.P., Forest S., Villani A.: Coupled glide-climb diffusion-enhanced crystal plasticity. J. Mech. Phys. Solids. 70:136-153, 2014.

[4] Maresca F., Kouznetsova V.G., Geers M.G.D.: Subgrain lath martensite mechanics: a numerical-experimental analysis. J. Mech. Phys. Solids. 73:69-83, 2014.

SIZE-DEPENDENT ENERGY OF ELASTIC-PLASTIC CRYSTALS

Sinisa Dj, Mesarovic[1a)], Samuel Forest[2] & Jovo P. Jaric[3]
[1]*School of Mechanical and Materials Engineering, Washington State University, Pullman, WA, USA*
[2]*Centre des Matériaux, Mines ParisTech/CNRS, Evry, France*
[3]*Faculty of Mathematics, University of Belgrade, Serbia*

Summary. We consider two questions relevant for the development of a meso-scale, size-dependent plasticity: (1) Can the phenomenological expression for size-dependent energy, as quadratic form of Nye's dislocation density tensor, be justified from the point of view of dislocation mechanics and under what conditions? (2) How can physical or phenomenological expressions for size-dependent energy be computed from dislocation mechanics in the general case of elastically anisotropic crystal? While the analysis based on symmetries implies the negative answer to the first question, the coarsening method developed in response to the second question, introduces additional symmetries, so that the equivalence between the phenomenological and the physical expressions is possible, but only if the multiplicity of characteristic lengths associated with different slip systems, is sacrificed. We discuss the consequences of such assumption.

INTRODUCTION

Following numerous observations of size effects in plasticity of metals, equally numerous phenomenological theories have appeared in the last two decades, e.g., [1]. The size-dependent portion of internal energy is typically a function of Nye's dislocation density tensor. Since this portion of energy has its roots in elastic interactions of dislocations, the quadratic form leading to a linear constitutive law is appropriate:

$$\tfrac{1}{2}\mathbf{A}:\mathbf{M}:\mathbf{A}=\tfrac{1}{2}A_{ji}M_{ijkl}A_{lk}\,. \tag{1}$$

Symmetries of tensors analogous to **M** have been analyzed [2]. For materials with isotropic, cubic and hexagonal symmetries, the tensor **M** has 3, 4 and 8 independent constants, respectively.

PHYSICAL THEORIES AND LENGTH SCALES

The analysis of a 2D random field of dislocations based on the self-consistent method [3] yields a single characteristic length – the average spacing of dislocations. Upon linearizing and generalizing to 3D, the size-dependent portion of the total energy takes the form:

$$\tfrac{1}{2}\{\rho b\}^T[K]\{\rho b\}=\tfrac{1}{2}\sum_{I=1}^{N_T}\sum_{J=1}^{N_T}(\rho b)^I K^{IJ}(\rho b)^J\,. \tag{2}$$

Analysis of an ordered field of periodically stacked pile-ups against an obstacle [4] requires that each slip system carries a characteristic length, ℓ^α, interpreted as the average spacing of discrete slip planes for that slip system. These are associated with slip planes, rather than with slip systems, so that, for *fcc* crystals, *at any material point*, there will be only 4 characteristic lengths, each covering 3 slip systems. The triad $(\mathbf{s}^\alpha,\mathbf{m}^\alpha,\mathbf{t}^\alpha)$ forms the local orthonormal basis for the slip system. The slip field $\gamma^\alpha(\mathbf{x})$ is associated with each slip system. The in-plane components of its gradient define the partial (i.e., for that slip system) densities of edge $(\perp)$ and screw $(\odot)$ dislocations:

$$\mathbf{g}^\alpha=g^\alpha_\odot\mathbf{t}^\alpha+g^\alpha_\perp\mathbf{s}^\alpha\,. \tag{3}$$

with $g^\alpha_\odot=\mathbf{t}^\alpha\cdot\nabla\gamma^\alpha$ and $g^\alpha_\perp=\mathbf{s}^\alpha\cdot\nabla\gamma^\alpha$. The energy analogous to (2) is the sum of quadratic forms for each slip system:

$$\tfrac{1}{2}\sum_{\alpha=1}^{N_s}\sum_{\beta=1}^{N_s}\mathbf{g}^\alpha\cdot\mathbf{D}^{\alpha\beta}\cdot\mathbf{g}^\beta;\qquad \mathbf{D}^{\alpha\beta}=\ell^\alpha\ell^\beta\left[d^{\alpha\beta}_{\perp\perp}\mathbf{s}^\alpha\mathbf{s}^\beta+d^{\alpha\beta}_{\perp\odot}\mathbf{s}^\alpha\mathbf{t}^\beta+d^{\alpha\beta}_{\odot\perp}\mathbf{t}^\alpha\mathbf{s}^\beta+d^{\alpha\beta}_{\odot\odot}\mathbf{t}^\alpha\mathbf{t}^\beta\right]. \tag{4}$$

The physical interpretation of (2, 4) is the *coarsening error* in interaction energy of dislocations, i.e., the difference in energy computed from discrete dislocations as line defect, and the energy computed from the kinematically equivalent, smooth Nye's fields. The interaction energy of dislocations *represented as continuous densities* is included in the simple (size-independent) elastic-plastic continuum as the strain energy associated with incompatible elastic strains [5, 6]. This energy error is localized to the region of the size comparable to the characteristic length.

SYMMETRY ANALYSIS

In trying to reconcile (2, 4) with (1), it is convenient to use a somewhat different formulation of (1): $\mathbf{A}^T:\bar{\mathbf{M}}:\mathbf{A}$, where the components of $\bar{\mathbf{M}}$ are obtained by simply switching the first two indices of **M**. Then:

[a)] Corresponding author. Email: mesarovic@mme.wsu.edu

$$\mathbf{D}^{\alpha\beta} = -\mathbf{m}^{\alpha} \times (\mathbf{s}^{\alpha} \cdot \bar{\mathbf{M}} \cdot \mathbf{s}^{\beta}) \times \mathbf{m}^{\beta}; \quad \alpha, \beta = 1, ..., N_S . \tag{5}$$

Thus, there are $2N_S(N_S+1)$ scalar conditions, which are to be satisfied by no more than 45 independent components $\mathbf{M}$. For *fcc* crystals with 12 slip systems, the number of scalar conditions is 312. Should the multiplicity of length scales be discarded (either for physical reasons or for mathematical convenience), there would be a reduction in the number of independent material constants. Moreover, the screw components in systems are indistinguishable. An analysis, analogous to the one leading to (46), can be applied to the other definition of the size-dependent energy (3), yielding

$$K^{IJ} = (\boldsymbol{\xi}\mathbf{s})^{I} : \bar{\mathbf{M}} : (\mathbf{s}\boldsymbol{\xi})^{J}; \quad I, J = 1, ..., N_T . \tag{6}$$

With symmetric [K] and $\mathbf{M}$, the maximum number of independent conditions is $N_T(N_T+1)/2$ (171 for *fcc*). The reduction in the number of independent scalar conditions, from (5) to (6) is accompanied by the loss of multiplicity of characteristic lengths.

To determine the number of independent parameters $d_{XY}^{\alpha\beta}$ $(X, Y = \perp, \odot)$ in (4), and thus (with a single length scale) the number of independent conditions (5, 6), we consider symmetries in the slip system geometry, in particular mirror reflections. Such analysis yields the following conclusions: The $\{111\}/<\bar{1}10>$ family of *fcc* slip systems requires 13 independent constants, while in *bcc* crystals, the two most common slip families $\{110\}/<\bar{1}11>$ and $\{211\}/<\bar{1}11>$, taken separately, each require 22 independent constants.

COARSENING METHOD

The coarsening method, first used in [4], then generalized in [7], is based on the expression for interaction energy of the two types of dislocations [5]:

$$E^{\alpha\beta} = \frac{1}{2}\int_V dV^{\alpha} \int_V dV^{\beta} \frac{(\rho b)^{\alpha}(\rho b)^{\beta}}{R} (\mathbf{s}^{\alpha}\boldsymbol{\xi}^{\alpha}) : \mathbf{L} : (\boldsymbol{\xi}^{\beta}\mathbf{s}^{\beta}); \; R = |\mathbf{R}|, \; \mathbf{R} = \mathbf{x}^{\beta} - \mathbf{x}^{\alpha}; \; \mathbf{r} = \mathbf{R}/R; \; \mathbf{L} = \mathbf{L}(\mathbf{r}), \tag{7}$$

Let S_0 be the surface of the unit sphere. Then, the coarsening method used in [7] results in:

$$\bar{\mathbf{M}}^{\alpha\beta} \sim \ell^{\alpha}\ell^{\beta}\mathbf{m}; \quad \mathbf{m} = \int_{S_0} dS\mathbf{L}(\mathbf{r}) \; . \tag{8}$$

Thus, a unique tensor $\bar{\mathbf{M}}$ does exist in the general case. However, if the characteristic lengths are assumed equal, $\ell^{\alpha} = \ell$ for all α, the expression (8) provides a recipe for computing $\bar{\mathbf{M}}$ (or $\mathbf{M}$). For example, for the isotropic system, thus derived tensor $\mathbf{M}$ will have 2 independent constants, one less than required by symmetry. Similar results are obtained for crystals with cubic symmetry. In general, the tensor $\bar{\mathbf{M}}$ satisfies the index *reversal* symmetry $\bar{M}_{ijkl} = \bar{M}_{lkji}$ for any symmetry group. While isotropic and cubic symmetry groups include this symmetry, other symmetry groups do not.

DISCUSSION

The physical interpretation of the characteristic length of a slip system is the average spacing between the stacked pile-ups of dislocations, which evolves with plastic deformation. For a well-annealed crystal, the initial characteristic length is determined by the average spacing between the Frank-Read sources. In the later stages, the characteristic length is the cross-slip distance. If the second slip system is activated at later stages of deformation, the two characteristic lengths will be very different. In small volumes where interfaces dominate, the dissipative dislocation-interface reactions (penetration, dissociation, relaxation) are critical for determining the macroscopic behavior of materials. Computation of energy is the essential first step in determining the dissipation mechanism at the boundary. Comparison between discrete dislocation dynamics and the continuum model [8], indicate that the characteristic length has little or no effect on the initial yield, but its effect on hardening is significant.

References

[1] Gurtin, M.E. 2002 *J. Mech. Phys. Solids* **50**, 5–32.
[2] Zheng, Q.S. & Spencer, A.J.M. 1993 *Int. J. Eng. Sci.* **31**(4), 617–635.
[3] Groma, I., Gyorgyi, G. & Kocsis, B. 2006 Debye screening of dislocations. *Phys. Rev. Lett.* **96**, 165503.
[4] Mesarovic, S.Dj, Baskaran, R. & Panchenko, A. 2010 *J. Mech. Phys. Solids* **58** (3), 311-29.
[5] Mesarovic, S.Dj. 2005 *Int. J. Plasticity* **21**, 1855–1889.
[6] Yassar, R.S., Mesarovic, S.Dj. & Field, D.P. 2007 *Int. J. Plasticity* **23**, 1901-1917.
[7] Mesarovic, S.Dj., Forest, S. & Jaric, J.P. 2015 *Proc. R. Soc. A* **471**, 20140868
[8] Mesarovic, S.Dj. & Baskaran, R. 2011 *Proc. 3rd Int. Conf. on Heterogeneous Material Mechanics* (ICHMM-2011) May 22-26, 2011, Shanghai.

STRONGLY VERSUS WEAKLY NON-LOCAL DISLOCATION TRANSPORT AND PILE-UP

Jaber Rezaei Mianroodi *[1], Ron Peerlings[2], and Bob Svendsen[1,3]
[1]*Material Mechanics, RWTH Aachen University, Aachen, Germany*
[2]*Mechanics of Materials Group, Eindhoven University of Technology, Eindhoven, The Netherlands*
[3]*Microstructure Physics and Alloy Design, Max-Planck-Institut fur Eisenforschung GmbH, Düsseldorf, Germany*

Summary The purpose of this work is the continuum modeling of transport and pile-up of infinite discrete dislocation walls driven by non-local interaction and external loading. The underlying model for dislocation wall interaction is based on the non-singular Peierls-Nabarro (PN) model [e.g., 4, Chapter 8]. The influence of strongly non-local (SNL; long-range) interaction, and its approximation as weakly non-local (WNL; short-range), are studied in the context of wall pile-up at a boundary. The boundary is modeled via a spatially dependent dislocation mobility. The pile-up behavior predicted by the current SNL-based continuous wall distribution modeling is consistent with that predicted by discrete wall distribution modeling [e.g., 1, 6]. Both deviate substantially from the pile-up behavior predicted by WNL-based continuous wall distribution modeling [e.g., 2, Chapter 2]. As such, it is essential to account for the intrinsic SNL character of the interaction between same-sign dislocations "close" to the boundary. Gradient-based WNL "approximation" of this interaction is not justified.

BASIC RELATIONS

Consider a family of infinite, straight edge dislocation lines in an isotropic linear elastic medium with constant shear modulus G and Poisson's ratio ν. Let the lines be oriented parallel to z with Burgers vector of length b in the x direction. Assume the lines glide only and remain in their glide planes. The glide plane of each line is then parallel to the (x,z) plane, and the glide plane normal is parallel to y. Assume that the dislocations arrangement in the y direction perpendicular to the glide planes takes the form of straight walls with uniform spacing h between adjacent dislocations in each wall. Consequently, each wall itself represents an h-periodic discrete distribution of lines. Given no climb, each such wall is maintained at all times. Since the distribution is then h-periodic in y, we can (without loss of generality) focus attention on a single glide plane, for example at $y=0$, and the only remaining spatial dependence is in x. Let $\rho(x,t)$ represent the number of mobile walls per unit length at (x,t). Then $1/\rho$ represents the wall spacing in x direction. The initial value $\rho(x,0)=\rho_0(x)$ is assumed to be known and the total number of dislocations, i.e. the integral of ρ over the one-dimensional region under consideration, is constant. Under the influence of external loading and interaction, the walls flow (glide) in x direction, resulting in a change in their number per unit length along x. The transport relation takes the form $\partial\rho/\partial t+\partial\Phi/\partial x=0$ in terms of the dislocation flux $\Phi(x,t)=\rho(x,t)\,v(x,t)$ depending on the wall (line) velocity $v(x,t)$. A positive flux implies that the (positive) walls flow in the $+x$ direction. Restricting attention to quasi-static conditions and overdamped motion, $v(x,t)=m(x)\,b\,\{\tau+\sigma(x,t)\}$ holds via Peach-Koehler in terms of the wall (line) mobility $m(x)$, Burgers vector magnitude b, and the shear stress field $\tau+\sigma(x,t)$ on the glide plane $y=0$. In the current work, this depends on the constant applied external shear stress τ and the contribution $\sigma(x,t)$ resulting from wall interaction. In view of the inherently long-range character of dislocation interaction, the basic model relations are completed by the strongly non-local (SNL) form $\sigma(x,t)=\sigma_{\rm w}*\rho\,(x,t)$ for $\sigma(x,t)$ as the convolution of the stress field $\sigma_{\rm w}(x)$ of a single dislocation wall with $\rho(x,t)$. In what follows, all stresses are scaled by $G/(1\nearrow\nu)$, all lengths by b, and the t-dependence of fields is suppressed for notational brevity.

Given the assumption of uniform spacing h of wall dislocations, the relation

$$\sigma_{\rm w}^{\rm PN}(x)=\frac{1}{2\pi}\,\frac{x}{x^2+c^2}\nearrow\frac{x}{\pi h^2}\,\Re\,\psi^{(1)}(\zeta_{h,c}(x))\nearrow\frac{c}{\pi h^2}\,\Im\,\psi^{(1)}(\zeta_{h,c}(x)) \tag{1}$$

[5] holds for the (equilibrium) xy component of the (non-dimensional) stress field for a wall consisting of Peierls-Nabarro (PN) edge dislocations located at $y=0$. Here, $\Re\,\psi^{(1)}$ represents the real, and $\Im\,\psi^{(1)}$ the imaginary, part of the first-order polygamma function $\psi^{(1)}(z)$. As well, $\zeta_{h,c}(x):=1+c/h+\imath x/h$, $\imath=\sqrt{\nearrow 1}$, and $c:=d/2(1\nearrow\nu)$ in terms of the glide-plane spacing d. The weakly non-local (WNL) approximation is based as usual on the Taylor series expansion of $\rho(x\nearrow\xi)$ in $\sigma(x)=\sigma_{\rm w}*\rho\,(x)$ about $\rho(x)$ assuming $|\xi|\ll 1$, yielding $\sigma_{\rm WNL}^{\rm PN}=\nearrow 1/2\,(c+1/3\,h)\,\partial\rho/\partial x$ represents the lowest-order WNL approximation to $\sigma_{\rm SNL}^{\rm PN}$. In case of SNL model, the convolution is calculated with the help of the fast Fourier transform (FFT). The time integration of the transport relation is based on first order forward finite difference (FD) approximation while upwind FD is employed for discretizing the space.

*Corresponding author. Email: jaber.rezaeimianroodi@rwth-aachen.de

EXAMPLE RESULTS

The SNL and WNL models are compared here in the context of dislocation pile-up. The results are shown in Figure 1 for different mobility functions in the form of $m(x;a,p) := \mathrm{n}\ (2ap)/\quad (2ax) + \quad (2ap)$ with p the position of the center of the boundary region, and $1/a$ its effective width. As expected, the dislocation "penetration depth" increases, and the maximum pile-up density $\rho_{\max}$ decreases, as the boundary width $1/a$ increases. As seen in Figure 1 (left), away from the boundary, the PN-WNL density profile for the sharpest boundary (blue curve, $ah = 200$) agrees with Volterra (V)-based WNL results of [2, §2.4.2] (dashed line). Analogous results for the PN-SNL case are shown in Figure 1 (right). In contrast to the WNL case, $\rho(x)$ is non-linear next to the boundary and in the tail region, and linear in between. Note that the PN (blue

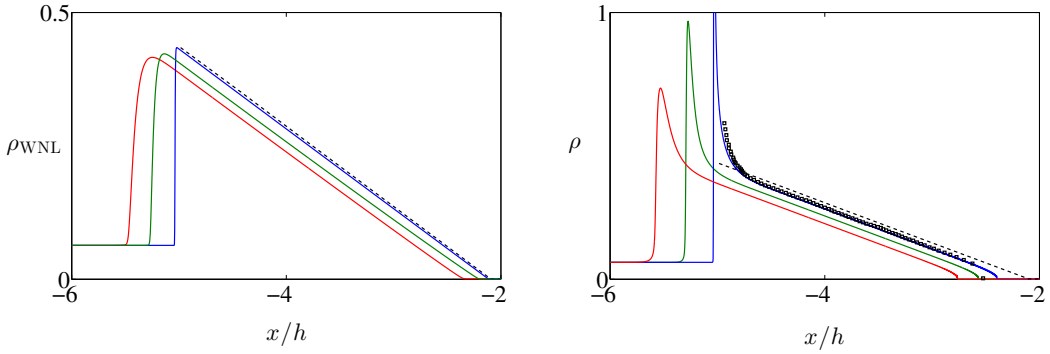

Figure 1: Pile-up distribution resulting from wall transport driven by the external stress $\tau = \nearrow 1/\ 0$ [2, §2.4.2] and wall interaction based on $\sigma^{\mathrm{PN}}_{\mathrm{WNL}}$ (left) and $\sigma^{\mathrm{PN}}_{\mathrm{SNL}}$ (right) for $m(x) = f(x;a,p = 5h)$ with $ah = 10$ (red), $ah = 20$ (green), $ah = 200$ (blue). Shown for comparision is the result (dashed line) of [2, §2.4.2] based on $\sigma^{\mathrm{V}}_{\mathrm{WNL}}$ assuming an impenetrable boundary ($a = \infty$) and the pile-up distribution in *discrete* ensembles of Volterra-based walls [e.g., 1, 6] (hollow squares). Material parameter values chosen are for aluminum.

curve) and continuous Volterra results (dashed curve) for $\rho(x)$ in Figure 1 (right) converge for a spacing of $1/\rho \geqslant 2$ (this compares with $d = \sqrt{2}/\sqrt{3}$). This agrees with a corresponding convergence of the Volterra- and PN-based stress profiles. More results and comparison between WNL and SNL models including the effects of the initial distribution, free surface and the corresponding pile-up stress fields will be shown in the presentation.

CONCLUSIONS

A model for transport and strongly non-local interaction of infinite discrete dislocations walls has been developed in this work based on the Peierls-Nabarro (PN) dislocation model [e.g., 4, Chapter 8]. The pile-up distribution predicted by the current PN-SNL-based continuous distribution modeling agrees both qualitatively and quantitatively quite well with that predicted by Volterra-based discrete distribution modeling [e.g., 1, 6]. In particular, this is true for the non-linear distribution next to the wall and in the tail of $\rho(x)$. Between these two regimes in the linear part of the distribution, the WNL-based results agree well with the corresponding SNL-based ones. The deviation of WNL- and SNL-based results near the boundary and in the tail could be related for example to the breakdown of shielding or screening effects [e.g., 3] in these regions. As such, it is important to account for the SNL nature of the interaction near the boundary.

References

[1] de Geus, T., Peerlings, R. H. J., Hirschberger, C., 2013. An analysis of the pile-up of infinite periodic walls of edge dislocations. Mechanical Research Communications 54, 7–13.

[2] Dogge, M. M. W., 2014. Mechanics of phase boundaries in multi-phase steels. Ph.D. thesis, TU Eindhoven.

[3] Groma, I., Györgyi, G., Kocsis, B., 2006. Debye screening of dislocations. Physical Review Letters 96, 165503.

[4] Hirth, J. P., Lothe, J., 1982. Theory of Dislocations, 2nd Edition. Wiley, New York.

[5] Mianroodi, J. R., Peerlings, R., Svendsen, B., 2015. Strongly non-local modeling of dislocation transport and pile-up. Philosophical Magazine (submitted).

[6] Roy, A., Peerlings, R. H. J., Geers, M. G. D., Kasyanyuk, Y., 2008. Continuum modeling of dislocation interactions: why discreteness matters? Materials Science and Engineering A 486, 653–661.

THE ROLE OF SUB-STRUCTURE BOUNDARIES ON LATH MARTENSITE PLASTICITY

Chaowei Du[1], Johan Hoefnagels, Rene Vaes & Marc Geers
Department of Mechanical Engineering, Eindhoven University of Technology, Eindhoven, The Netherlands

Summary Well-defined uniaxial micro-tensile tests were performed on lath martensite with two configurations. In the first configuration, boundaries are parallel to loading direction. Boundaries play a role of strengthening by hampering crystallographic slip and it was found that the effect of sub-block boundary is only slightly lower than that of block boundaries. The difference between them is that sub-block boundary cannot capture the fracture surface while block boundary is capable of stopping fractures. In the second configuration, samples have tilted boundaries to the loading direction. Sliding of the substructures occurs at all types of boundaries, e.g. block, sub-block and lath boundaries at relatively lower stresses. Thus the boundaries does not only strengthen the materials, but also mitigate the plastic deformation. In addition, sliding mechanism is in competition with crystallographic slip to carry overall plastic deformation.

Introduction

Lath martensite, the most typical morphology of martensite, has high industrial relevance being the prime constituent that elevates the strength in many high strength steels. One prior austenite grain, after austenite-to-martensite phase transformation, shows hierarchical substructure that one austenite grain forms 4 martensite packets, each of which are composed of blocks. The blocks are then further divided into sub-blocks which are composed of laths. Thus a large amount of sub-structure boundaries exist inside lath martensite, playing an important yet not completely understood role in mechanical behavior. In this study we use well-defined micro-tensile test to understand the role of block boundaries and sub-block boundaries with samples having different oriented boundary to the loading direction.

Experimental methods

The whole testing procedure involves the following steps: (i) wedge shape fabrication from a lath martensite sheet by grinding/polishing/electro-chemical etching, (ii) careful selection of the specimen location based on large-area EBSD maps. (iii) careful focused ion beam (FIB) milling of the micro-tensile specimens with a constant cross-section along the length direction (Fig.1 (a)), (iv) detailed top- and bottom-side Electron backscatter diffraction (EBSD) analysis of each specimen (Figs. 2), (v) uniaxial tensile tests with highly accurate specimen alignment and force- and displacement measurement (Fig. 1(b,c)) under (vi) *in-situ* optical microscopy enabling microscopic slip trace analysis. A detailed description of sample preparation and testing can be found in [1]. Two groups of specimens are tested, one with their boundaries roughly aligned parallel and one tilted to the loading direction, to reveal the different roles of the boundaries.

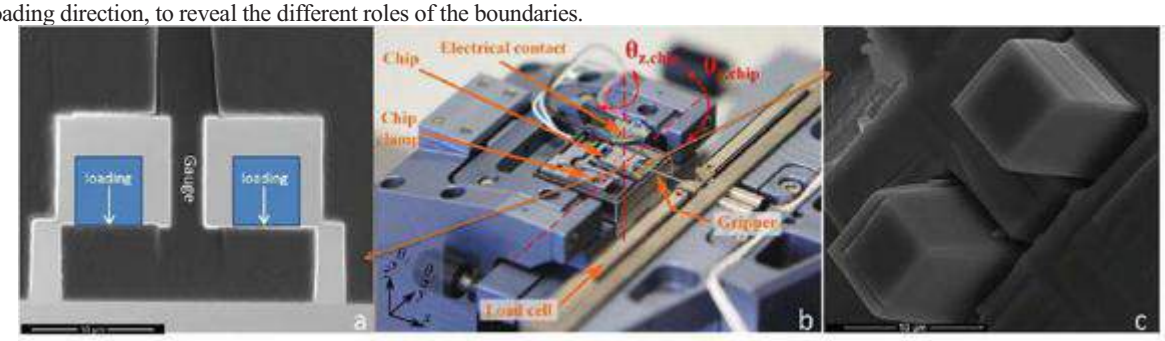

Fig.1. (a) Top-view image of a uniaxial-tension specimen with a gauge size of 9×3×2.5 μm^3. The two schematic squares indicate the top view of the two teeth of loading gripper shown in (c), which is used to apply well-aligned tensile loading. (b) The home-built nano-force tensile stage, with highly precise specimen alignment, force and displacement measurement [2]. The starting points of arrows which point to (a) and (b) are the positions of the micro tensile specimens and the gripper respectively. (c) The 'two-teeth' gripper to load the specimens.

Results

Group 1: Samples with sub-structure boundaries parallel to loading[3]

This group can be divided into two sub-groups. The first sub-group(Fig.2a$_{1\text{-}4}$) of specimens have block boundaries and the second one is only with sub-block boundaries (single block specimens) (Fig.2$_{1\text{-}4}$). For multi-block specimens, it is observed that the fracture surfaces join at the block boundary (Fig.2a$_{1\text{-}3}$). Specimens get stronger with increasing number of block boundaries. In contrast, the fracture surface is straight in single block specimens even though the fracture surface crosses sub-block boundaries(Fig.2b$_{1\text{-}3}$). The observed slip traces match the slip system with the highest Schmid factor. Similar to block boundary, sub-block boundaries clearly strengthen the material. A Hall-Petch type relationship was found between $\tau_{critical}$ and number of both block and sub-block boundaries, with the strengthening of sub-block boundaries only slightly less effective as that of block boundaries.

[1] Corresponding author. Email: c.du@tue.nl.

Group 2: Samples with sub-structure boundaries tilted to loading[4]

A series of micro-tensile specimens with boundaries tilted to the loading directions are tilted. Fig.2c shows one sample with tilted boundaries. Obvious steps can be exactly at boundaries (Fig.2c_{1-3}), indicated by the arrows. In other samples not shown here, it is found that sliding can occur at all type of boundaries, e.g. lath boundary, sub-block boundary and block boundary. In this configuration, the plastic behaviour of lath martensite is completely different from the scenario in group 1 in which crystallographic slip needs to cross the boundaries.

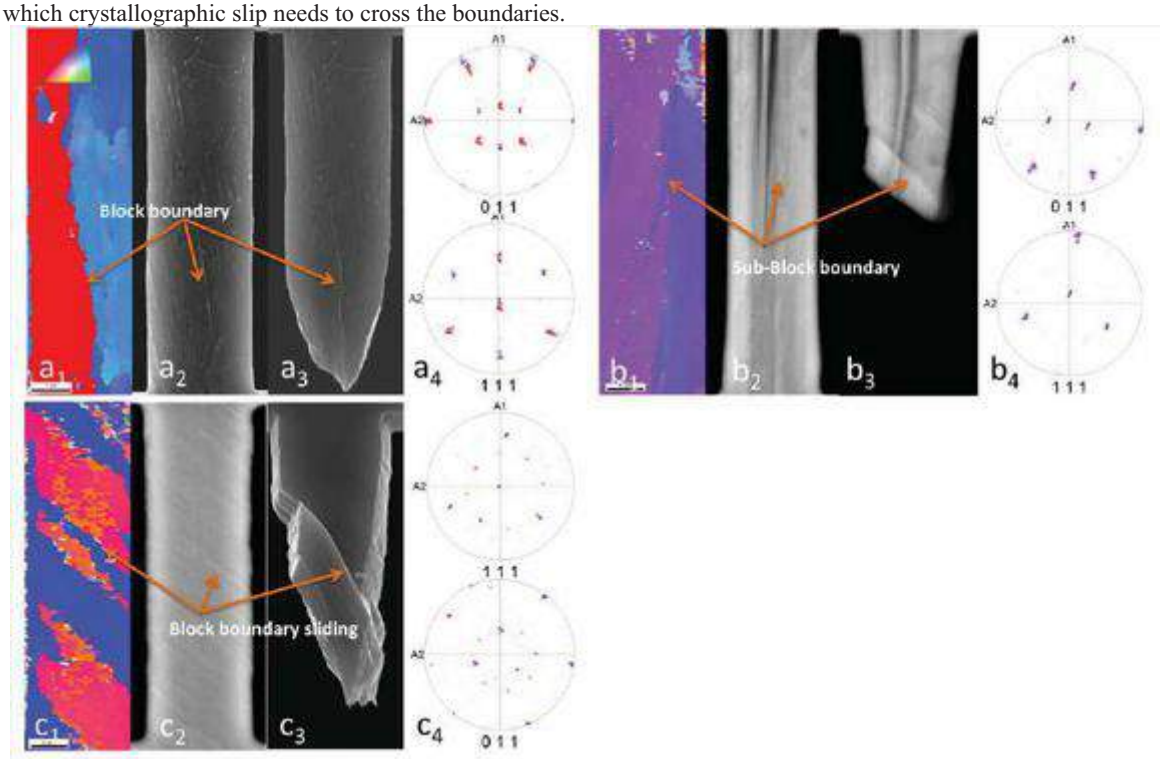

Fig. 2(left). Inverse pole figure map(1), scanning electron microscope image before (2) and after(3) deformation, together with {110} and {111} pole figures (4) of gauge parts of three micro-tensile specimens with different boundary configurations：a, sample with a single block boundary in the middle, which shows that block boundary is able to capture fracture surface; b, single block sample with a sub-block boundary in the middle, which demonstrates that sub-block boundary cannot stop fracture propagation, leading to a straight fracture surface. The pole figure shows that it is a single block sample; and c, sample with tilted block boundary to the loading direction, showing clear boundary sliding at a block boundary. The length of the samples is 9um.

Conclusion

Uniaxial micro-tensile testing was conducted to investigate the role of block and sub-block boundaries of lath martensite. In configuration that the boundaries is parallel to the loading direction, crystallographic slip has to cross the boundaries, thus both block and sub-block boundaries strengthen the material although the effect of the latter is slightly weaker. The difference between these two boundaries is that the fracture surface can cross sub-block boundary but not the block boundary. When the boundaries are tilted to the loading direction, sliding of the substructures can occur at all types of investigated boundaries, e.g. block, sub-block and lath boundaries at relatively lower stresses. Thus the boundaries does not only strengthen the materials, but also mitigate the plastic deformation.

References

[1] C. Du, J.P.M. Hoefnagels, L.J. Bergers, M.G.D. Geers, submitted for publication (2016).

[2] L.J. Bergers, J.P.M. Hoefnagels, M.G.D. Geers, J. Phys. D: Appl. Phys., 47 (2014).

[3] C. Du, J.P.M. Hoefnagels, Rene Vaes , M.G.D. Geers, submitted for publication (2016).

[4] C. Du, J.P.M. Hoefnagels, Rene Vaes , M.G.D. Geers, submitted for publication (2016).

SMALL SCALE PLASTICITY SIMULATED WITH CONTINUUM DISLOCATION DYNAMICS

Alireza Ebrahimi[1,2] , Thomas Hochrainer[1,2a)]
[1]*BIME, Universtiy of Bremen, Bremen, Germany*
[2]*MAPEX Center for Materials and Processes, University of Bremen, Bremen, Germany*

Summary In small scale plasticity, size-effects have been observed in nearly every miniaturized materials test. In the current contribution we present crystal plasticity finite element simulations of several small scale tests, employing the so-called continuum dislocation dynamics as constitutive law. The resulting materials response and local dislocation evolution are compared to according experiments and discrete dislocation simulations from the literature. We demonstrate that crystal plasticity laws based on continuum dislocation dynamics are able to predict various kinds of size-effects, whether they relate to strain gradients (micro-bending), dislocation line-tension (thin film bending) or dislocation starvation (micro compression).

INTRODUCTION

When characteristic dimensions of classical materials tests reach the scale of several micro-meters and smaller, many classical materials parameters in plasticity, as yield stress and hardening modulus, turn out to be dependent on the absolute size of the sample. Such size-effects have been observed, e.g., in micro-bending, micro-compression, thin film deformation and nano-indentation tests. The origin of size-effects is always connected to the microscopic processes underlying crystal plasticity, which is the existence and motion of dislocations. The size-effect in micro-bending is usually associated with so-called geometrically necessary dislocations (GNDs), i.e., plastic strain gradients [1]. For very thin films with passivated surfaces, dislocation line tension effects may dominate initial yielding [2]. In micro-compression tests, dislocation source limitation and dislocation starvation lead to unorthodox phenomena including mechanical annealing [3]. Crystal plasticity laws capable of predicting these kinds of size effects necessarily require strain gradient dependent constitutive laws, a measure of dislocation curvature to indicate line tension effects and flux equations for all dislocations (not only GNDs). Such dislocation density based theories have recently been introduced as so-called continuum dislocation dynamics [4, 5].

Continuum dislocation dynamics (CDD)

Continuum dislocation dynamics provides flux-type evolution equations of dislocation variables which capture the kinematics of moving curved dislocations. The simple-most CDD theory is based on three internal variables per slip system, which are the total dislocation density ρ, the dislocation density (or GND) vector $\boldsymbol{\rho}$, and the dislocation curvature density q. A slip system is characterized by the slip plane normal $\boldsymbol{n}$ and the Burgers vector $\boldsymbol{b}$, or likewise the normalized slip direction $\boldsymbol{m}$ $\boldsymbol{b}/b$, where $b=|\boldsymbol{b}|$. A constitutive law for CDD specifies the dependency of the average dislocation velocity v on the current stress and dislocation state. Orowan's law then yields the plastic shear rate on the slip system as $\dot{\gamma}=\rho v b$, and the `plastic velocity gradient' derives as $\boldsymbol{L}^{\mathrm{p}}=\dot{\gamma}\boldsymbol{m}$ $\boldsymbol{n}$. The evolution of the dislocation state is given by flux type evolution equations for the density variables [5]. All evolution equations are determined by the average dislocation velocity. A thermodynamically consistent average dislocation velocity was recently derived [6], assuming that a free energy density $\Psi(\boldsymbol{\sigma}\ \rho\ \boldsymbol{\rho}\ q)$ of the system may be formulated in terms of stress $\boldsymbol{\sigma}$ and the density variables (compare [7]). The velocity is thermodynamically consistent if it is proportional to the net shear stress $\tau_{\mathrm{net}}=\ +\ _{\mathrm{g}}-\tau_{\mathrm{lt}}-\tau_{\mathrm{b}}+\tau_{\mathrm{qg}}+\tau_{\mathrm{qb}}$, where τ is the resolved shear stress on the slip system, while τ_{g} τ τ τ_{qg}, and τ_{qb} are mesoscopic shear stress contributions deriving from variational derivatives of the free energy. In the current contribution we neglect the last two stress contributions τ_{qg} and τ_{qb}. The other three shear stress contributions are the density gradient stress $\tau_{\mathrm{g}}=(b\rho)^{-1}\nabla\ \ \nabla\ \partial_{\rho}\Psi)$, the back stress $\tau_{\mathrm{b}}=b^{-1}\nabla\cdot(\boldsymbol{n}\times\partial_{\boldsymbol{\rho}}\Psi)$, and the line tension stress $\tau_{\mathrm{lt}}=q\ b\rho)^{-1}\partial_{\rho}\Psi$. For a free energy functional with a $\rho\log\rho$ type dependency on the density and a quadratic dependency on the dislocation density vector $\boldsymbol{\rho}$, as suggested by recent work of Zaiser [7], the gradient stress contains a first order strain gradient, while the back stress contains a second order strain gradient. CDD therefore naturally accounts for size effects due to strain gradients and dislocation curvature, as well as due to dislocation fluxes.

RESULTS

We implemented the above mentioned CDD theory as a crystal plasticity law in Abaqus® using the crystal plasticity framework DAMASK [8]. In the talk we present simulations of micro-bending, thin-film bending and micro-compression simulations using CDD as constitutive law and compare them to experiments and discrete dislocation simulations.

In this abstract we exemplarily show results from a simulation of a four-point bending test on a single-crystal micro-beam of dimension $40\,\mu\mathrm{m}\times 4\,\mu\mathrm{m}\times 4\,\mu\mathrm{m}$. The beam is supposed to be a face centered cubic crystal, where the {100} faces are aligned with the

a) Corresponding author. Email: hochrain@uni-bremen.de.

beam surfaces. Only the $(1\,\bar{1}\,\bar{1})[01\,\bar{1}]$ glide system is taken to be active. We initially prescribe constant total dislocation density $\rho_0 = 10^{12}\,\mathrm{m}^{-2}$, GND vector $\boldsymbol{\rho}_0 = 0$, and curvature density $q_0 = 0$. The boundary conditions are such that dislocations may leave the crystal at the surfaces.

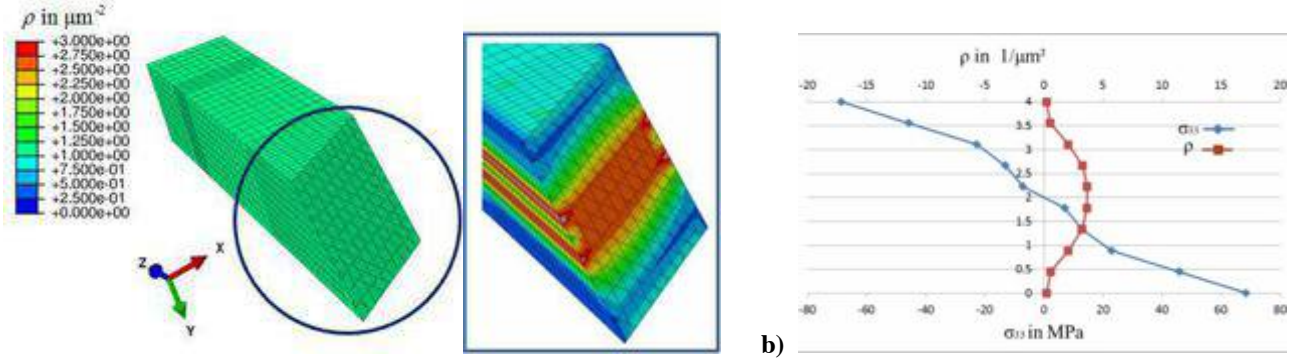

Figure 1. a) The total dislocation density in the central region of a micro-beam, left: initial density, right: final density (time step 210). b) Line plot of normal stress in longitudinal direction and total dislocation density along a vertical line in the center of the beam at time step 400.

In Figure 1a) we provide contour plots of the dislocation density in a beam cut in the centre along the slip plane in the initial state and after 210 time steps. The density distribution in the deformed state illustrates how the dislocations pile up around the neutral plane while density is lost at the free surfaces. In Figure 2b) we provide line plots of the longitudinal normal stress and the dislocation density along a vertical line in the centre of the beam after 400 time steps. The stress displays a mitigation of the stress gradient in the central region, where the dislocation density is high.

DISCUSSION

The dislocation density distribution and the normal stresses depicted in Figure 1 qualitatively reflect what has been observed in discrete dislocation simulations of micro bending by Motz [9]; which is an accumulation of dislocation density around the neutral plane of the beam, where concurrently the stress gradient and normal stress are low. In the current simulations the stresses are not as low as expected in the centre, because the single slip system may not produce a general plastic deformation. Unique to the employed CDD model is the loss of dislocations at the boundaries. Due to this, the simulation correctly predicts low dislocation density close to the top and bottom surface of the beam, where plastic shear is maximal (cf. [10]) and a high density towards the centre of the beam, where plastic slip is small. We note that this contradicts expectations from classical strain hardening, while it conforms to the results from discrete dislocation simulations [9].

CONCLUSIONS

The dislocation flux based CDD constitutive law is able to reflect salient features of small scale plasticity in accordance with discrete dislocation simulations. A thorough study of CDD predictions of size effects and micro-structure evolution in small scale plasticity is currently under way.

References

[1] Ashby, M.F..: The deformation of plastically non-homogeneous materials. *Philos. Mag.* **21**(170): 399-424, 1970.

[2] Arzt. E.: Size effects in materials due to microstructural and dimensional constraints: a comparative review. *Acta. Mater.* **46**(16):5611-5626, 1998.

[3] Shan, Z. W. et al.: Mechanical annealing and source-limited deformation in submicrometre-diameter Ni crystals. *Nature Mater.* **7**: 115–119, 2007.

[4] Hochrainer T, et al..: Continuum dislocation dynamics: towards a physical theory of plasticity. *J. Mech. Phys. Solids* **63**: 167-178, 2014.

[5] Hochrainer T.: Multipole expansion of continuum dislocation dynamics in terms of alignment tensors. *Philos. Mag.* **95**(12): 1321-1367, 2015.

[6] Hochrainer T.: Thermodynamically consistent continuum dislocation dynamics. *J. Mech. Phys. Solids* **88**: 12-21, 2016.

[7] Zaiser, M.: Local density approximation for the energy functional of three-dimensional dislocation systems. *Phys. Rev. B* **92:** 174120, 2015

[8] Roters, F. et al..: DAMASK: the Düsseldorf Advanced MAterial Simulation Kit for studying crystal plasticity using an FE based or a spectral numerical solver: *Procedia IUTAM 3*: 3-10, 2012.

[9] Motz, C., Dunstan, D.J.: Observation of the critical thickness phenomenon in dislocation dynamics simulation of microbeam bending. *Acta. Mater.* **60**:1603-1609, 2012

[10] Ebrahimi, A., Hochrainer, T.: Three-dimensional continuum dislocation dynamics simulations of dislocation structure evolution in bending of a micro-beam, *MRS Advances*, accepted for publication

DISCRETE DISLOCATION-BASED CRYSTAL PLASTICITY AT MICRON-NANO SCALES

Zhuo Zhuang, Zhanli Liu, Yinan Cui
AML. School of Aerospace Engineering, Tsinghua University, Beijing 100084, China

Summary Crystal plasticity at micron-nano scales involves many new interesting issues. The atypical plastic behavior at submicron scales cannot be effectively investigated by either traditional crystal plastic theory or large-scale molecule dynamics simulation. Accordingly, a discrete-continuous crystal plastic model is developed, which is coupling the discrete dislocation dynamics with finite element method. Three kinds of plastic deformation mechanisms for the single crystal pillar at submicron scale are investigated: (1) Single arm dislocation source controlled plastic flow; (2) Confined plasticity in coated micropillars; (3) Dislocation starvation under low amplitude cyclic loading. The predicted critical conditions of dislocation starvation agree well with the experimental data.

DISCRETE-CONTINUOUS CRYSTAL PLASTIC MODEL

Crystal plasticity at micron-nano scales involves many new interesting issues. Some results are obtained for uniaxial compression experiments conducted on FCC single crystal micro-pillars, e.g. size effect and strain burst, etc. [1]. In these experiments, the surfaces are transmissible and loading gradients are absent. Therefore, the strain gradient theory could not well explain these new mechanical behaviors. This in turn has led to several hypotheses based on intuitive insights, classical theory and dislocation plasticity in order to study the size effect at submicron scale. In the model proposed [2], mobile dislocations may escape from the free surface leading to the state of dislocation starved whereby an increase in the applied stress is necessary to nucleate or activate new dislocation sources. By performing in-situ TEM [3], the dislocation motion affected the material properties is observed. However, the atypical plastic behavior at submicron scales cannot be effectively investigated by either traditional crystal plastic theory or large-scale molecule dynamics simulation. Accordingly, a three dimensional discrete-continuous crystal plastic model (DCM) is developed, which is coupling the discrete dislocation dynamics (DDD) with finite element method (FEM), as shown in Fig.1 [4].

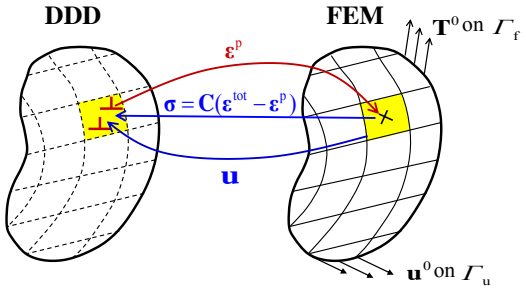

Fig. 1 Discrete-continuous crystal plastic model

THREE KINDS OF PLASTIC DEFORMATIN MECHANISMS

Three kinds of plastic deformation mechanisms for the single crystal pillar at submicron scale are investigated. (1) Single arm dislocation source (SAS) controlled plastic flow. It is found that strain hardening is virtually absent due to continuous operation of stable SAS and weak dislocation interactions. When the dislocation density finally reaches stable value, a ratio between the stable SAS length and pillar diameter obeys a constant value, as shown in Fig. 2 and Fig. 3.

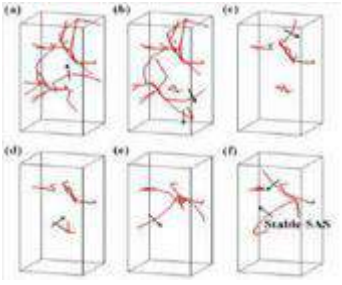

Fig. 2 Single arm dislocation source nucleation and escape

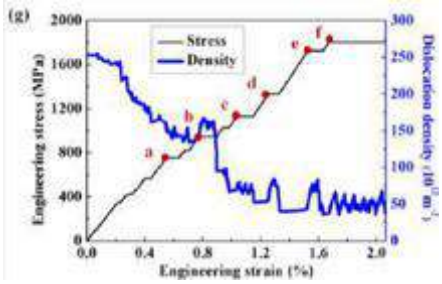

Fig. 3 Evolution of stress and dislocation density

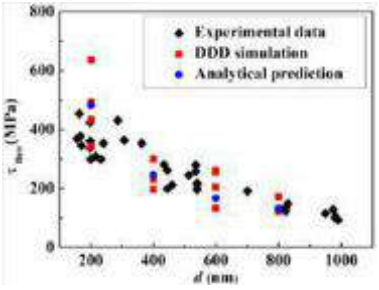

Fig. 4 Theory and computation results compare with experiment data

[a] Corresponding author. Email: zhuangz@tsinghua.edu.cn.

A theoretical model is developed to predict DDD simulation results and experimental data, as given in Fig. 4 [5]. (2) Confined plasticity in coated micropillars. Based on the simulation results and stochastic distribution of SAS, a theoretical model is established to predict the upper and lower bounds of stress-strain curve in the coated micropillars [6]. (3) Dislocation starvation under low amplitude cyclic loading. This work argued that the dislocation junctions can be gradually destroyed during cyclic deformation, even when the cyclic peak stress is much lower than that required to break them under monotonic stress. The cumulative irreversible slip is found to be the key factor of leading to junction destruction and promoting dislocation starvation under low amplitude cyclic loadings. Based on this mechanism, a proposed theoretical model successfully reproduces dislocation annihilation behavior observed experimentally for small pillar and dislocation accumulation behavior for large pillar [7]. The predicted critical conditions of dislocation starvation agree well with the experimental data.

References

[1] Uchic M.D., Dimiduk D.M., Florando J.N., Nix W.D.: Sample dimensions influence strength and crystal plasticity. *Science*, 305, 986-989, 2004

[2] Greer J.R., Oliver W.C., Nix W.D.: Size dependence of mechanical properties of gold at the micron scale in the absence of strain gradients. *Acta Mater*, 53, 1821-1830, 2005

[3] Shan Z.W., Mishra R.K., SAS. ASIF, et al.: Mechanical annealing and source-limited deformation in submicrometre-diameter Ni crystals. *Nat Mater*, 7, 115-119, 2008

[4] Liu Z.L., Liu X.M., Zhuang Z., You X.C.: A multi-scale computational model of crystal plasticity at submicron-to-nanometer scales. *Int. J. Plasticity*, 25, 1436-1455, 2009

[5] Cui Y.N., Lin P., Liu Z.L., Zhuang Z.: Theoretical and numerical investigations of single arm dislocation source controlled plastic flow in FCC micropillars. *Int. J. Plasticity*, 55, 279-292, 2014

[6] Cui Y.N., Liu Z.L., Zhuang Z., Theoretical and numerical investigations on confined plasticity in coated pillars at microscale. *J. Mech. Phys. Solids*, 76, 127-143, 2015

[7] Wang Z.J., Li Q.J., Cui Y.N., Liu Z.L., Ma E., Li J., Sun J., Zhuang Z., Dao M., Shan Z.W., Suresh S.. Cyclic deformation leads to defect healing and strengthening of small-volume metal single crystals. *PNAS*, 10/14/1518200112, 2015

LARGE SCALE ATOMISTIC SIMULATION OF SIZE EFFECTS DURING NANOINDENTATION

George Z. Voyiadjis[1a)], Mohammadreza Yaghoobi[2]
[1] Computational Solid Mechanics Laboratory, Department of Civil and Environmental Engineering, Louisiana State University, Baton Rouge, LA 70803, United States

Summary Size effects in a Ni single crystal thin film during nanoindentation experiment are studied using large scale atomistic simulation. The main focus of this paper is to evaluate the presented size effects theories of nanoindentation experiment using atomistic simulation. The hardness obtained directly from MD simulation is compared with the one which is determined using the dislocation density and theoretical models. Next, sources of size effects in nanoscale thin films are studied. A Ni single crystal thin film is indented using a conical indenter with a spherical tip. The final step is to investigate the size effects sources using the microstructural information obtained from MD simulation. The results show that the initial governing mechanism of size effects is source exhaustion. Increasing the indentation depth, the total dislocation length also increases which activates the forest hardening model and Taylor hardening model can successfully capture the size effects at higher indentation depths.

SIMULATION DETAILS AND METHODOLOGY

To model the size effect in thin films during nanoindentation, a Ni thin film with the dimensions of 1200 Å, 1200 Å, and 600 Å along $[1\,\bar{1}\,0]$, $[1\,1\,\bar{2}]$, and $[1\,1\,1]$ directions is generated and simulated using the classical molecular dynamics (MD). The total number of atoms in the samples is 79,473,309. Two different indenter shapes of cylindrical and conical are incorporated. To integrate Newton's equations of motion, the velocity Verlet algorithm with a time step of 2 fs is incorporated [1]. The parallel MD code LAMMPS is used [2]. All simulations are performed using NPT ensemble [2]. The nickel embedded-atom method (EAM) potential developed by Mishin et al. [3,4] is incorporated to simulate the atomic interaction of Ni-Ni. The contact area A is precisely evaluated incorporating the atoms which are directly in contact with the indenter at each step [5]. The Crystal Analysis Tool developed by Stukowski and his co-workers [6-9] is incorporated to visualize the dislocations. In order to study the sources of size effects, the indenter geometry is a conical indenter with an angle of $\theta = 60^{\circ}$ and a spherical tip with the radius of R=10 nm to study the sources of size effects at smaller length scales [10].

RESULTS AND DISCUSSIONS

The applicability of Taylor hardening model at smaller length scale is studied. The Taylor hardening model can be described as follows

$$H = {}^{-} + 3\sqrt{3}\alpha\mu b\sqrt{\rho} \qquad (2)$$

where ρ is the dislocation density and H is the hardness. In the current work, the plastic zone is defined as a hemisphere. The radius of hemisphere is $R_{\mathrm{pz}} = f a_c$ in which f is a constant. Fig. 1 compares the hardness obtained from the microstructural information including the dislocation density and Taylor hardening model with the hardness obtained by the indentation force divided by the contact area and compared to the one obtained directly from MD simulation, which is the indentation force divided by the contact area $H = \ / \ .$

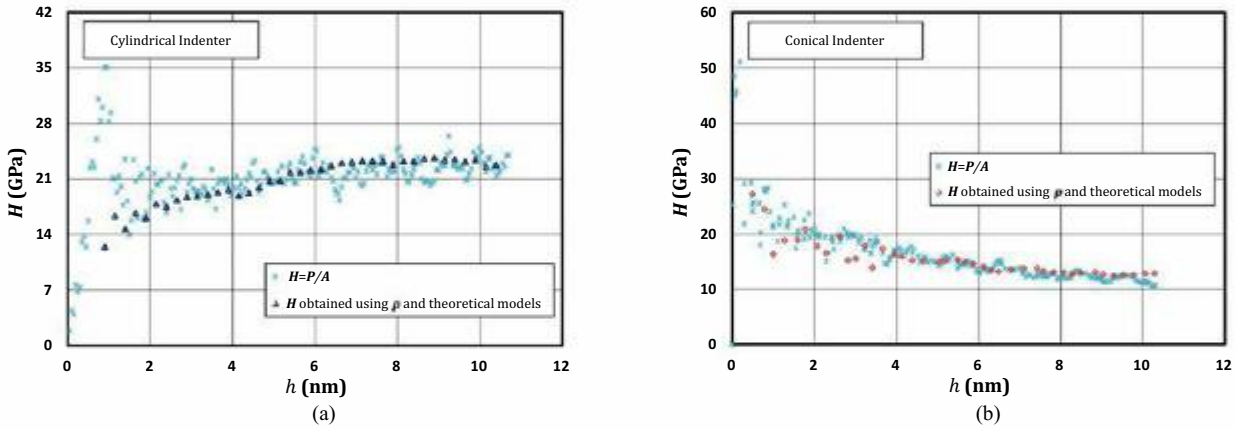

(a) (b)

Fig. 1. Comparison of hardness directly obtained from MD simulation with the one obtained using dislocation density and theoretical models in samples indented by the (a) cylindrical indenter (b) conical indenter.

The results show that the Taylor hardening model can capture the size effects at higher indentation depth. However, at lower indentation depth, the agreement is not good. In order to study the mechanisms which are controlling the size effects at lower indentation depth, the results of indentation using the conical indenter with the spherical tip should be studied. Fig.

[a)] voyiadjis@eng.lsu.edu (George Z. Voyiadjis).

2 shows the variation of dislocation density versus the indentation depth for the plastic zone of different sizes. The results indicate that as the indentation depth increases, the dislocation density firstly increases and then become nearly constant for different values of f. Fig. 3 shows the variation of mean contact pressure ($p_m = \ / \ $), which is equivalent to the hardness H in the plastic region, versus the indentation depth. It shows that the hardness initially decreases and then becomes nearly constant. Based on the Taylor hardening model, since the dislocation density initially increases as the indentation depth increases (Fig. 2), the hardness should also increase. However, Fig. 3 shows that as the indentation depth increases, the hardness initially decreases. In other words, the results show that the forest hardening model cannot capture the size effect in the case of the low indentation depths. However, increasing the dislocation density, the forest hardening mechanism is also activated. As the dislocation density becomes a nearly constant value, the hardness also becomes nearly constant according to the Taylor hardening model. The results confirm the data presented in Fig. 1 and show that the forest hardening mechanism is not the governing mechanism of size effects at lower indentation depths. In order to unravel the controlling mechanism of size effects at lower indentation depths, one should note that the resulting mobile dislocation density is insufficient at this region. Hence, the applied stress should be increased to sustain the plastic deformation and source exhaustion hardening is the governing mechanism of size effects. By increasing the indentation depth, the dislocation length and density increases as well, which provides more dislocation sources. Also, the source lengths increase which reduces the critical resolved shear stress. Consequently, the applied stress required to sustain flow during nanoindentation decreases, i.e. hardness decreases as indentation depth increases. At higher indentation depths, the dislocation density and length are large enough in a way that the forest hardening is also activated.

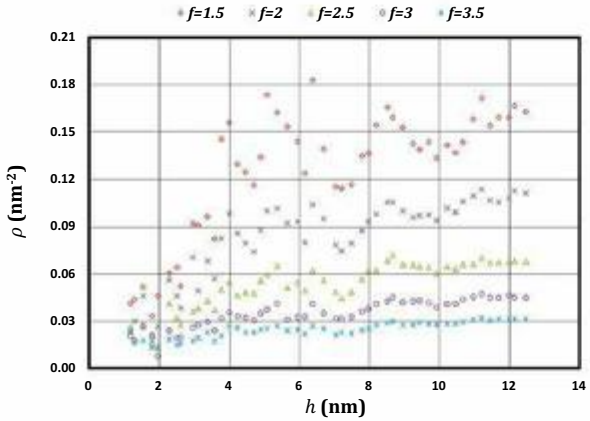

Fig. 2. Dislocation density obtained from MD simulation for different values of f (factor for radius of plastic zone) during nanoindentation.

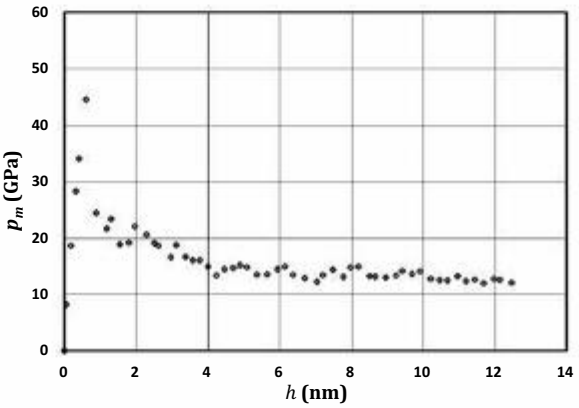

Fig. 3. Variation of mean contact pressure p_m as a function of indentation depth h.

CONCLUSIONS

The current work studies the governing mechanisms of size effects during nanoindentation using the large scale atomistic simulation. The hardness is predicted from the atomistic information and theoretical models and compared to the hardness obtained from nanoindentation simulation. The results show that the initial governing mechanism of size effects is source exhaustion. Increasing the indentation depth, the total dislocation content also increases which activates the forest hardening model. Taylor hardening model can successfully capture the size effects at higher indentation depths.

References

[1] M. Yaghoobi, G.Z. Voyiadjis, Comput. Mater. Sci. 95 (2014) 626–636.
[2] S. Plimpton, J. Comput. Phys. 117 (1995) 1–19.
[3] Y. Mishin, D. Farkas, M.J. Mehl, D.A. Papaconstantopoulos, Phys. Rev. B 59 (1999) 3393–3407.
[4] C.A. Becker, F. Tavazza, Z.T. Trautt, R.A. Buarque de Macedo, Curr. Opin. Solid State Mater. Sci. 17 (2013) 277–283. **http://www.ctcms.nist.gov/potentials**
[5] G.Z. Voyiadjis and M. Yaghoobi, Mater. Sci. Eng. A 634 (2015) 20–31.
[6] A. Stukowski, Model. Simul. Mater. Sci. Eng. 20 (2012) 045021.
[7] A. Stukowski, K. Albe, Model. Simul. Mater. Sci. Eng. 18 (2010) 085001.
[8] A. Stukowski, V.V. Bulatov, A. Arsenlis, Model. Simul. Mater. Sci. Eng. 20 (2012) 085007.
[9] A. Stukowski, JOM 66 (2014) 399-407.
[10] M. Yaghoobi, G.Z. Voyiadjis, Comput. Mater. Sci. 111 (2016) 64-73.

INVESTIGATION INTO THE BEHAVIOUR OF THE GRADED CELLULAR FOAM UNDER IMPACT

Changjian Shen[1], Guoxing Lu[1a)] & Tongxi Yu[2]
[1]*Faculty of Science, Engineering and Technology, Swinburne University of Technology, Hawthorn, Australia*
[2]*Department of Mechanical and Aerospace Engineering, Hong Kong University of Science and Technology, Clear Water Bay, Kowloon, Hong Kong*

Summary Recent studies by the authors for the behaviour of the graded cellular foam are summarized in this presentation. Finite element (FE) simulations employing a honeycomb structure were presented first to investigate the in-plane impact modes. Subsequently, a simple one-dimensional analytical work was proposed based on the rigid-perfect plastic-locking (R-PP-L) material model. Gradient in yielding strength was introduced to a one-dimensional cellular rod. A more-realistic case, in which a gradient in the cellular density was later introduced. Two compaction zones, known as double shock mode, were identified. An impact experiment was designed to test specimens (ALPORAS closed-foam aluminium foam) with graded cross-sections along the impact direction. Comparisons are made between the experimental and theoretical results, which shows a fairly good agreement.

Introduction

Due to their excellent properties, including low weight, high stiffness and strength and heat insulation, cellular materials are widely used in engineering applications [1-3], especially in the aerospace and defence industries, as energy absorption devices. Introducing a gradient in material parameters into the cellular material will significantly influence the behaviour of the cellular material under impact loadings. Current paper summarizes our research progress on the investigation into the influence of the gradient on the behaviour of the graded cellular material under impact conditions, including the deformation mode, underlying mechanism, energy absorption capacity and the transmitted force on the protected structure. Finite element simulation, analytical study and experimental investigation are involved in this research [4-8].

Finite element work on the honeycomb structure with stress gradient

As a first step, honeycomb composing of regular two dimensional cells is modelled using Finite Element software (ABAQUS/EXPILCIT). The yielding stress of the parent material linearly increases or decreases along the loading direction, thus introducing a gradient in the quasi-static plateau stress, shown in Fig. 1. Constant velocities are applied to the impact plate. Deformation modes are identified from the observation of the deformation process. Empirical equations for critical velocities, at which the deformation mode transmits, are summarized in terms of the cell thickness, yielding stress and the gradient.

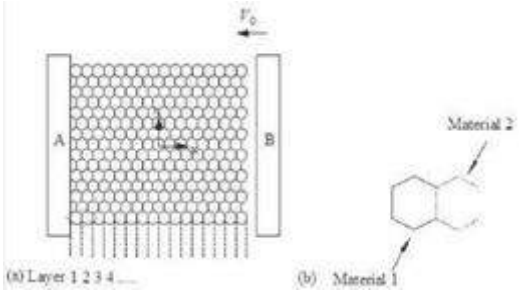

Fig.1 FE model and the material distribution. (a) Finite element model composed by 16 hexagonal cells in X1 direction and 15 cells in X2 direction; (b) Within a cell, five edges have the same material property while the left one is assigned with different yielding stress. Plate A is fixed and Plate B is the impinging plate.

Analytical work on the one-dimensional graded cellular rod

With the deformation modes observed from the FE work, an analytical model was proposed to illustrate the two compactions zones, which were called double shock (DS) mode. For simplification, rigid-perfect plastic-locking (R-PP-L) material model and stress gradient were employed to implement the analysis. Fig. 2 shows a typical DS mode in the graded cellular rod. Crushing occurs initially from both the distal and impinged end. In this DS mode, a forward shock and a backward shock propagate simultaneously before they finally meet, if the input energy is sufficiently large. V_1 is the velocity of the impinging mass and V_2 is the velocity of the undeformed zone between the two shock fronts. By using the conservation of momentum and mass and geometry relationships, the governing equations of motion could be derived in terms of the gradient and intrinsic properties of the cellular foam, e.g. density, yielding stress, etc. Consequently, this approach was adopted for a more realistic case, in which the density of the foam varies along the loading direction. The two basic deformation modes also exist in the case of density gradient. Finite element simulations using a continuous crushable

[a)] Corresponding author. Email: glu@swin.edu.au.

foam model shows a similar trend to that of the analytical study, but considerable difference is found at the densification stage, due to the simplification of the rigid-perfectly plastic-locking material model.

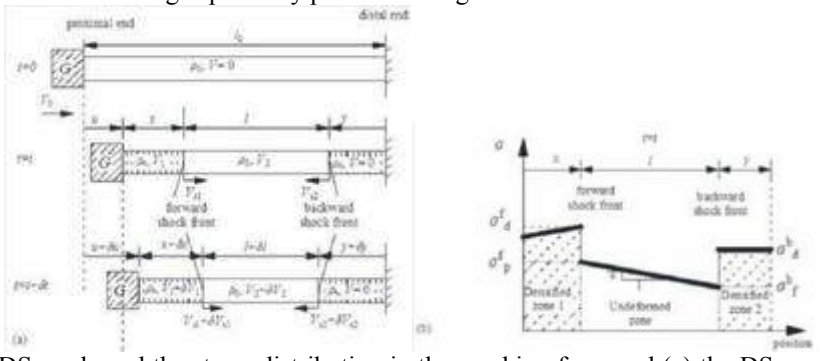

Fig.2 Schematic of the DS mode and the stress distribution in the crushing foam rod (a) the DS mode in the graded cellular rod impinged by a rigid mass (negative gradient, double shock fronts); (b) corresponding stress distribution in the graded cellular rod at instant t.

Experimental work on the graded cellular block with varying cross-section

Finally, an experimental study is conducted by using a gas gun, impinging a rigid mass onto a stationary aluminium foam block with a gradient in its cross-section. A high speed camera was placed to capture the crushing process of the foam specimen. Figure 15 shows a typical double shock mode. The force and velocity histories are plotted in Figure 3a and the corresponding deformation profiles are shown in Figure 3b. To give better predictions from the analytical result, the R-PP-L material model was replaced with the real stress-strain curve, in which the stress-strain curve were described with a power-law hardening material model so that the densification strain is related to the impact velocity. Comparisons were made between the improved analytical model and experiments shows good agreement. Similar approaches have been employed in recent research work [9-11].

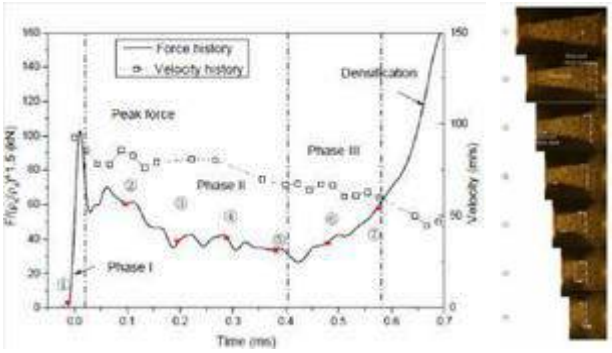

Fig.3 Force and velocity histories and deformation profiles at 7 instant. (a) Force and velocity histories of the tapered specimen; (b) The corresponding deformation process. The impact velocity is 88 m/s, the relative density is 10.8% and the time interval is 0.133 ms.

References

[1] Gibson, L.J., Ashby, M.F., 1997. Cellular solids : structure and properties, 2nd ed. Cambridge University Press, Cambridge ; New York.

[2] Tan, P.J., Reid, S.R., Harrigan, J.J., Zou, Z., Li, S., 2005a. Dynamic compressive strength properties of aluminium foams. Part I - experimental data and observations. J Mech Phys Solids53, 2174-2205.

[3] Tan, P.J., Reid, S.R., Harrigan, J.J., Zou, Z., Li, S., 2005b. Dynamic compressive strength properties of aluminium foams. Part II - 'shock' theory and comparison with experimental data and numerical models. J Mech Phys Solids 53, 2206-2230.

[4] Shen, C.J., Lu, G., Yu, T.X., 2013. Dynamic behavior of graded honeycombs - A finite element study. Compos Struct 98, 282-293.

[5] Shen, C.J., Yu, T.X., Lu, G., 2013. Double shock mode in graded cellular rod under impact. Int J Solids Struct 50, 217-233..

[6] Shen, C.J., Lu, G., Yu, T.X., 2014. Investigation into the behavior of a graded cellular rod under impact. Int J Impact Eng 74, 92-106

[7] Shen, C.J., Lu, G., Yu, T.X., Ruan, D., 2015. Dynamic response of a cellular block with varying cross-section. Int J Impact Eng.

[8] Shen, C.J., Lu, G., Ruan, D., Yu, T.X., Propagation of the Compaction Waves in a Cellular Block with Varying Cross-Section Accepted by Int J Solids Struct

[9] Karagiozova, D., and Alves. M. 2015. Propagation of compaction waves in cellular materials with continuously varying density. Int J Solids Struct 71, 323-337.

[10] Barnes, A. T., Ravi-Chandar, K, Kyriakides, S., Gaitanaros, S.. 2014. Dynamic crushing of aluminum foams: part I – experiments. Int. J. Solids Struct., 51, 1631–1645

[11] Barnes, A. T., Ravi-Chandar, K, Kyriakides, S., Gaitanaros, S.. 2014. Dynamic crushing of aluminum foams: part II – analysis. Int. J. Solids Struct., 51, 1646–1661

DISPERSION, LOCALIZATION AND DEGENERACIES IN FLEXURAL WAVES SUPPORTED BY RAYLEIGH BEAM STRUCTURES

Andrea Piccolroaz * [1] and Alexander Movchan[2]
[1]*Dipartimento di Ingegneria Meccanica e Strutturale, Università di Trento, Trento, Italy*
[2]*Department of Mathematical Sciences, University of Liverpool, Liverpool, UK*

Summary The paper presents novel analysis of Floquet-Bloch flexural waves in a periodic lattice-like structure consisting of flexural beam ligaments. A special feature of this structure is in the presence of the rotational inertia, which is commonly neglected in conventional models of the Euler-Bernoulli type. The dispersion properties of the Rayleigh beam structure with rotational inertia include degeneracies linked to Dirac cones on the dispersion diagrams as well as directional anisotropy and special refraction properties. Steering of Dirac cones is described for rectangular flexural structures with a rotational inertia. The paper also brings a comparative analysis between dynamic models of couple-stress elastic materials and structured Rayleigh beams on a Winkler foundation. Although physical phenomena have different physical origins, the underlying equations appear to be similar, and hence mathematical models have a lot in common.

INTRODUCTION

Dispersion of Floquet-Bloch waves in periodic flexural systems is a topic of high importance, that attracts attention of experts across a wide range of fields. The papers [1, 2] have presented an asymptotic approach to derivation of the model and analysis of Floquet-Bloch waves in pre-stressed periodic layers on an elastic half-space, as well as control of band gaps on the dispersion diagram by applying a prestress to the elastic system.

In the recent paper [3], a comparative analysis was presented for Floquet-Bloch waves in structured Rayleigh and Euler beams subjected to prestress and the action from an elastic foundation. There was also a formal connection made to formulations of the constrained Cosserat approach in antiplane elasticity, or a couple stress analysis. In particular, it has been demonstrated in [3] that the waves in Rayleigh beams become non-dispersive at high frequencies, whereas the low-frequency for both Rayleigh and Euler beams are similar. Effects of prestress discussed in [3] have been presented in close form analytical form, which was also followed by description of defects based on dynamic Green's functions. Of course, one-dimensional studies [3] did not allow for the dynamic anisotropy, and it is highly important to study anisotropy in the dynamic response of the Euler and Rayleigh two-dimensional flexural systems.

The purpose of the present study is to address the challenge of analytical description of a dynamically anisotropic response of doubly periodic structures of beams in the cases of Euler-Bernoulli beams and the Rayleigh beams. Specifically we are looking for the frequency regimes where the difference between the Rayleigh beams and the Euler-Bernoulli beams becomes significant, and we identify regimes for which the Rayleigh beams systems exhibit negative refraction if analysed as a cluster subjected to an incident wave.

Dispersion surfaces and the isofrequency contours (or slowness contours) contain significant information about standing wave regimes, band gaps and dynamic anisotropy. We construct and give a comparative analysis the dispersion surfaces for both Rayleigh beams as well as the Euler-Bernoulli beams. Special interest is deserved by the so-called Dirac points representing multiple roots of the dispersion equation, where the dispersion surfaces may become non-smooth.

SLOWNESS CONTOURS AND DYNAMIC ANISOTROPY

The slowness contours (also referred often as isofrequency contours) are used to describe the dynamic anisotropy of the structured medium. A nice exposition of this approach for vector problems of elasticity in periodic lattices is presented in the paper [4]. The case we study involves a scalar fourth-order problem, and we focus on analysis of dispersion surfaces (in particular, of Dirac cones) in addition to the slowness contours. As shown in Fig. 1 presented for a square lattice, the slowness contours have a shape (squares with rounded corners) which indicates preferential directions along the coordinate axes both for the Rayleigh and the Euler-Bernoulli beams, used as constituents of the lattice.

In terms of effective dynamic response for low frequency, the square lattice of flexural beams (both the Euler-Bernoulli and the Rayleigh) gives an anisotropic response in contrast to the membrane problem, where the square lattice of harmonic springs would respond isotropically for the low frequencies, and hence the dispersion surface for such a structured membrane would be a cone with the circular cross-section. This difference between flexural plates and elastic membranes is expected. However, there are additional unexpected features of flexural Bloch waves, which are rather counter-intuitive.

As demonstrated in the earlier paper [3], the main difference between the periodic Euler-Bernoulli beam and the Rayleigh beam occurs at higher frequencies. This difference in a two-dimensional periodic configuration is clearly shown in Fig. 1,

*Corresponding author. Email: roaz@ing.unitn.it

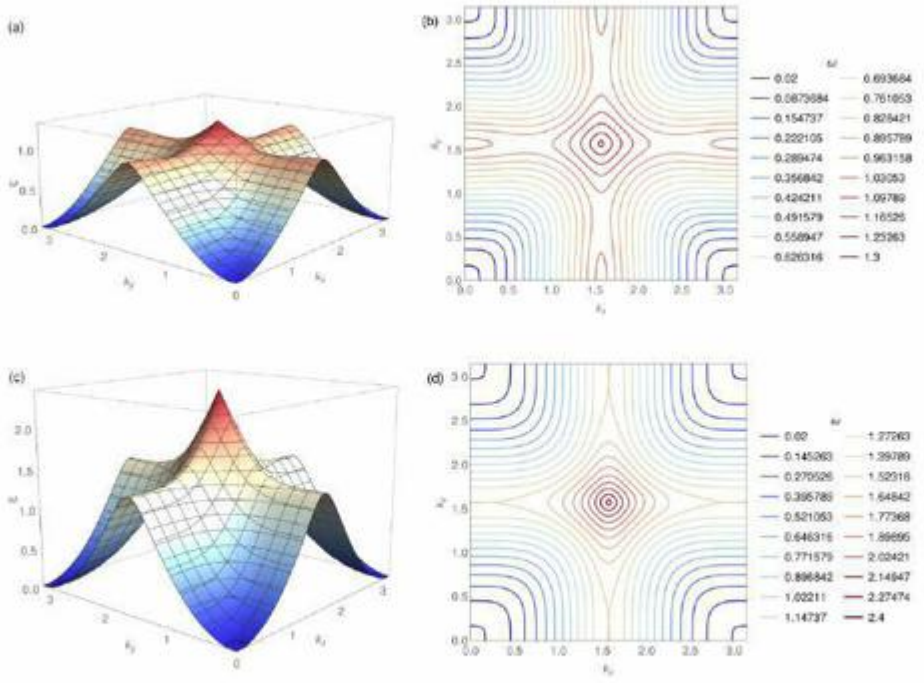

Figure 1: Low-frequency dispersion surface (a) and slowness contours (b) for a lattice made of Rayleigh beam ligaments. Low-frequency dispersion surface (c) and slowness contours (d) for a lattice made of Euler-Bernoulli beam ligaments.

where the slowness contours for the Rayleigh beam and the Euler-Bernoulli beam are non-convex (Fig. 1b) and convex (Fig. 1d), respectively.

The latter observation has a special significance in applications linked to transmission problems and structured interfaces, which are "built" of the square lattice of beam-like elastic ligaments. Namely, the non-convex slowness contours for the lattice consisting of Rayleigh beams imply the effect of the negative refraction. Hence, compared to the classical Euler-Bernoulli beams, the square lattice of the Rayleigh beams gives both a strong anisotropy and a negative refraction.

CONCLUSIONS

The paper has addressed an important class of problems that arise for flexural Bloch waves in elastic systems with rotational inertia and prestress. This has been done for so-called Rayleigh beams and structured Rayleigh beams. We have also highlighted a direct analogy with the models of couple-stress materials; although physical origins of the two problems are different, the mathematical underlay is identical and hence the mathematical study of the dynamic response of structured Rayleigh beams also brings a valuable insight into the study of shear waves in Cosserat type composites.

References

[1] Bigoni, D., Gei, M., Movchan, A.B.: Dynamics of a prestressed stiff layer on an elastic half space: filtering and band gap characteristics of periodic structural models derived from long-wave asymptotics. J. Mech. Phys. Solids 56:2494-2520, 2008

[2] Gei, M., Movchan, A.B., Bigoni, D.: Band-gap shift and defect-induced annihilation in prestressed elastic structures. J. Appl. Phys. 105:063507, 2009.

[3] Piccolroaz, A., Movchan, A.B.: Dispersion and localization in structured Rayleigh beams. Int. J. Solids Struct. 51:4452-4461, 2014.

[4] Srikantha Phani, A. ,Woodhouse, J., Fleck, N. A.: Wave propagation in two-dimensional periodic lattices, J. Acoust. Soc. Am. 119:19952005, 2006.

Acknowledgements. AP would like to acknowledge financial support from the European Union's Seventh Framework Programme FP7/2007-2013/ under REA grant agreement number PCIG13-GA-2013-618375-MeMic. AM gratefully acknowledges financial support from the European Union's Seventh Framework Programme FP7/2007-2013/ under REA grant agreement number PITN-GA-2013-606878-CERMAT2.

PLASTIC SIZE-EFFECTS ON A MODE I LOADED CRACK

Brian Nyvang Legarth*[1] and Christian F. Niordson[2]

[1,2]*Department of Mechanical Engineering, Solid Mechanics, Technical University of Denmark, Kgs. Lyngby, Denmark*

Summary Crack growth is investigated numerically using the strain-gradient plasticity theory of Gudmundson[1] in a plane small-strain visco-plastic formulation as adopted by Legarth and Niordson[2]. The J-integral[4] is evaluated along several paths showing that it is path independent up to the very near region of the cohesive crack tip, and the size of this region scales with the material length parameter of the gradient model in addition to the size of the fracture process zone. The distributions of the effective plastic strain and stress are also shown for both conventional and gradient enhanced cases. At the same amount of crack growth is the plastic strain level higher for the gradient enhanced case due to contribution from the gradients.

PROBLEM DESCRIPTION

Size-effects have been observed experimentally in various different applications, such as torsion, bending and thin films. The trend is that "smaller is stronger". Such effects cannot be captured by conventional theories as no material length scale exists in conventional models. For this reason, phenomenological strain-gradient plasticity approaches have been proposed by introducing the gradients of the strain tension with a corresponding set of material length scale parameters.

Here, crack growth in an elasto-viscoplastic material is studied numerically using the strain-gradient enriched plasticity theory of Gudmundson[1]. In this theory strain-gradient effects are accounted for by an enhanced measure of the effective plastic strain, E^p. Hence, denoting the rate (the time derivative) by a superposed dot, $\dot{(\,)}$, the rate of the non-conventional plastic strain is

$$\dot{E}^{p^2} = \dot{\epsilon}^{p^2} + \sum_{I=1}^{3} (L_d^{(I)})^2 \dot{\epsilon}_{ij,k}^{(I)} \dot{\epsilon}_{ij,k}^{(I)} \quad ; \quad \dot{\epsilon}^{p^2} = \frac{2}{3} \dot{\epsilon}_{ij}^{p} \dot{\epsilon}_{ij}^{p} \tag{1}$$

Here, $L_d^{(I)}$ are three material length scale parameters and the gradient, $\epsilon_{ij,k}^p$, of the plastic strain tensor, ϵ_{ij}^p, is decomposed into three orthogonal tensors, $\epsilon_{ij,k}^p = \sum_{I=1}^{3} \epsilon_{ij,k}^{(I)}$, according to Smyshlyaev and Fleck[3]. The subscript 'd' refers to dissipative. Exploiting symmetry, Fig. 1 shows the discretisized domain analyzed by the finite element method.

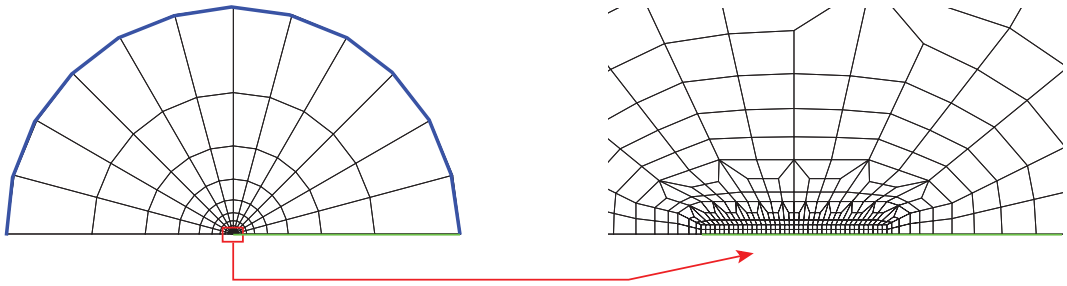

Figure 1: The finite element mesh used. At the tip of the shape crack is the mesh highly refined and uniform.

Assuming small scale yielding the boundary conditions are prescribed remotely according to the elastic mode I solution. Thus, at the outer edge (blue in Fig. 1) displacements are prescribed as

$$\begin{aligned} \dot{u}_1(r,\theta) &= \tfrac{1+\nu}{4\pi E}\sqrt{2\pi r}\left[(2\kappa-1)\cos\left(\tfrac{\theta}{2}\right) - \cos\left(\tfrac{3\theta}{2}\right)\right]\dot{K}_I \\ \dot{u}_2(r,\theta) &= \tfrac{1+\nu}{4\pi E}\sqrt{2\pi r}\left[(2\kappa+1)\sin\left(\tfrac{\theta}{2}\right) - \sin\left(\tfrac{3\theta}{2}\right)\right]\dot{K}_I \end{aligned} \tag{2}$$

where $\dot{K}_I$ is the rate of the stress intensity factor. Along the green line a standard cohesive law is imposed, such that crack growth only occurs along this green line.

*Corresponding author. Email: bnl@mek.dtu.dk

NUMERICAL RESULTS

The J-integral is defined as[4]

$$J = \int_{\Gamma} [W dx_2 - T_i u_{i,1} \, ds] \tag{3}$$

where W is the strain energy and Γ is some path from the lower crack surface to the upper crack surface and ds is along this path. For plane strain is $J = J_{app} = \frac{1-\nu^2}{E} K_I^2$, where K_I is the applied load. Fig. 2 shows the J-value evaluated at several paths near the crack tip and good agreement with the prescribed K_I-values is found.

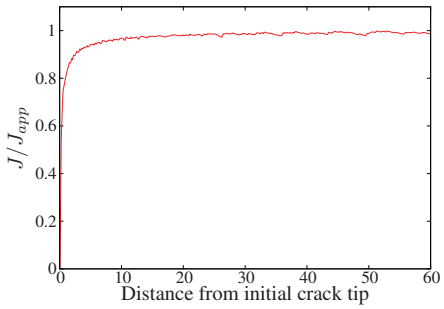

Figure 2: Normalized value of the J-integral when evaluated along several contours a different distances from the crack tip.

Fig. 3 shows contours of the effective plastic strain and stress after failure of the first cohesive element for conventional and gradient enhanced theory. It is seen from the color-bar that the gradient effects intensify the plastic strains (compare a) to b)). Fig. 3(c) shows the effective stress work conjugated to E^p, which also intensifies near the crack tip due to strain gradients.

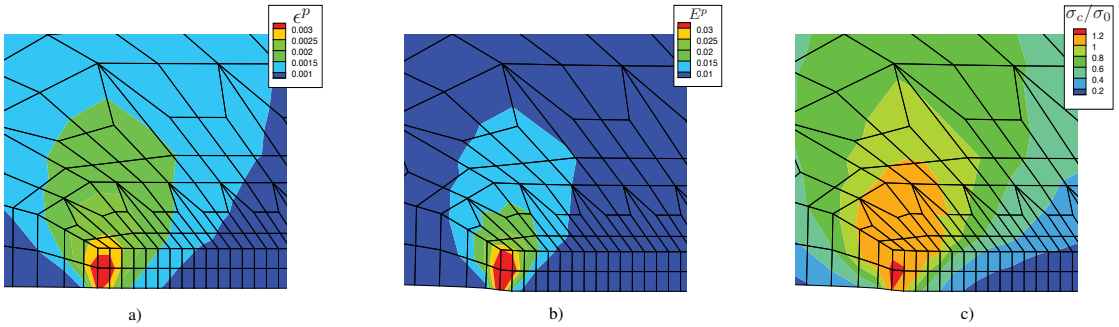

Figure 3: Effective plastic strain and stress contours near the crack tip after failure of the first cohesive element. a) Conventional theory, $L_d^{(I)} = 0$ with $\epsilon^p = E^p$. b)+c) Gradient enhanced theory, $L_d^{(1)} = L_d^{(2)} = L_d^{(3)} = 0.001 R_p$. b) The enhanced effective plastic strain, E^p and c) Effective stress work conjugated to E^p.

CONCLUSIONS

When the material length scale parameter is introduced, the effective plastic strain is found to be larger compared to the conventional case for the same amount of crack growth. This influences the resistance to crack growth. It is expected that, as the material length scale parameter increases, plasticity is suppressed and crack growth initiates at a load level determined solely by the elastic constants of the material and the fracture energy described through the cohesive zone. Resistance curves will be presented for different values of the involved material length scale parameters and compared to predictions by conventional plasticity. As the material length scale parameters increase, plasticity is suppressed and crack growth is predicted at load levels approaching the elastic limit described by the elastic constants of the material and the fracture energy in the cohesive zone.

ACKNOWLEDGMENT

Prof. Viggo Tvergaard is acknowledged for useful discussions and for providing the routine used for generating the mesh.

References

[1] Gudmundson P.: A unified treatment of strain gradient plasticity. Journal of the Mechanics and Physics of Solids 52(6):1379-1406, 2004.

[2] Legarth B. N., Niordson, C. F.: Debonding failure and size effects in micro reinforced composites International Journal of Plasticity 26: 149-165, 2010.

[3] Smyshlyaev, V. P., Fleck, N. A.: The role of strain gradients in the grain size effect for polycrystals Journal of the Mechanics and Physics of Solids 44: 465-495, 1996

[4] Rice, J. R.: A Path Independent Integral and the Approximate Analysis of Strain Concentration by Notches and Cracks, Journal of Applied Mechanics 35, 379-386, 1968.

STRAIN GRADIENT PLASTICITY BEYOND MICRON-SCALE APPLICATIONS: FRACTURE AND DAMAGE MODELIZATION

Emilio Martínez-Pañeda[1a], Christian F. Niordson[2], Vikram S. Deshpande[3] & Norman A. Fleck[3]

[1]*Department of Construction and Manufacturing Engineering, University of Oviedo, Gijón, Spain*
[2]*Department of Mechanical Engineering, Technical University of Denmark, Kgs. Lyngby, Denmark*
[3]*Department of Engineering, University of Cambridge, Cambridge, United Kingdom*

Summary In this work a general framework for damage and fracture assessment accounting for the role of geometrically necessary dislocations (GNDs) is provided. Crack tip fields are characterized, within both infinitesimal and finite deformation theories, by means of different strain gradient plasticity (SGP) formulations and their finite element implementation. Moreover, the impact of SGP theories on fracture and damage problems is further assessed by modelling several scenarios of particular interest: hydrogen diffusion towards the fracture process zone, environmentally assisted cracking, crack growth initiation and subsequent resistance and probabilistic-based cleavage fracture assessment. Results show a strong influence of GNDs, revealing the need to incorporate its influence in continuum models in order to adequately characterize behaviour at the small scales involved in crack tip deformation.

INTRODUCTION

Experiments have consistently shown that metallic materials display strong size effects at the micron and sub-micron scales, with smaller being harder. As a result, a significant body of research has been devoted to model this size-scale dependent plastic phenomena (see [1] and references therein). At the continuum level, phenomenological strain gradient plasticity (SGP) formulations have been employed to extend plasticity theory to small scales. Grounded on the physical notion of geometrically necessary dislocations (GNDs, associated with non-uniform plastic deformation), SGP theories relate the plastic work to both strains and strain gradients, introducing a length scale in the constitutive equations.

While the modelization of size effects in metal plasticity was motivated at first by growing interest in micro-technology, the use of SGP formulations has been extended to a wide range of applications where GNDs are expected to play a major role. Particularly, gradient-enhanced modelling of fracture and damage appears imperative (independently of the size of the specimen) as the plastic zone adjacent to the crack tip is – generally – physically small and contains strong spatial gradients of deformation. Several authors have shown that GNDs close to the crack tip promote local strain hardening, leading to a much higher stress level as compared with classical plasticity predictions (see, e.g., [2]). However, SGP theories have not been comprehensively embraced in damage and fracture predictions for several reasons. Most importantly, the majority of studies highlighting the influence of gradient plasticity in crack tip fields have been conducted within the infinitesimal deformation theory and consequently the role of GNDs in the large strains blunting dominated zone must be examined.

STRAIN GRADIENT PLASTICITY: MATERIAL MODELS AND NUMERICAL FRAMEWORK

Three different SGP formulations are employed with the aim of covering a wide range of classes of gradient plasticity theories. Thus, Gao et al. [3] mechanism-based model, Fleck and Hutchinson [4] phenomenological higher order theory and a Gudmundson's type formulation (incorporating dissipative and energetic terms) [5,6] are employed. A special finite element framework is used in all cases; particularly, Fleck-Hutchinson theory is implemented through a monolithic approach, where – in addition to the nodal displacement increments – the nodal effective plastic strain increments appear directly as unknowns [7]. A staggered solution procedure is employed for the formulation corresponding to the most recent class of SGP theories, where dissipative and energetic length scales are constitutively involved [5], following the two minimum principles developed by Fleck and Willis [6].

After the corresponding sensitivity study, a very refined mesh is employed in all the boundary value problems examined in order to accurately capture the influence of strain gradients in the vicinity of the crack. The majority of case studies addressed require a further development of the numerical framework, so as to incorporate a cohesive zone model [8], a mixed Ritz-finite element method [9] or a mass diffusion scheme (through an extended version of Fick's law), among other features.

RESULTS

When incorporating large strains and rotations, gradient-enhanced results reveal several remarkable features (see Fig. 1). Namely: (i) crack tip stresses are substantially elevated compared to classical plasticity predictions, (ii) the distance over which this stress elevation occurs may span several tens of micro-meters, embracing the critical distance of many damage mechanisms, (iii) while conventional plasticity predicts a peak in the stress distribution at a distance from the crack of

[a)] Corresponding author. Email: mail@empaneda.com.

approximately 2 times the blunting radius, SGP stresses are highest at the tip, with no evidence of a maximum, (iv) unlike classical plasticity, the gradient-enhanced stress level depends on the applied load K_I and (v) results are impacted by both the specific SGP formulation employed and the value(s) of the material length scale(s).

As the stress distribution of finite strain length-independent plasticity provides the basis for the majority of damage models, results reveal that GNDs may significantly impact a wide range of applications. Particularly, this work shows that SGP theories: play a fundamental role in hydrogen transport ahead of the crack, predicting high levels of lattice hydrogen concentration near the tip; reduce the parameter dependence of environmentally assisted cracking models, enhancing quantitative predictions; profoundly influence toughness estimations, enabling higher peak cohesive stresses to be overcome; and re-calibrate Weibull parameters, predicting an increased probability of fracture relative to that based on conventional plasticity.

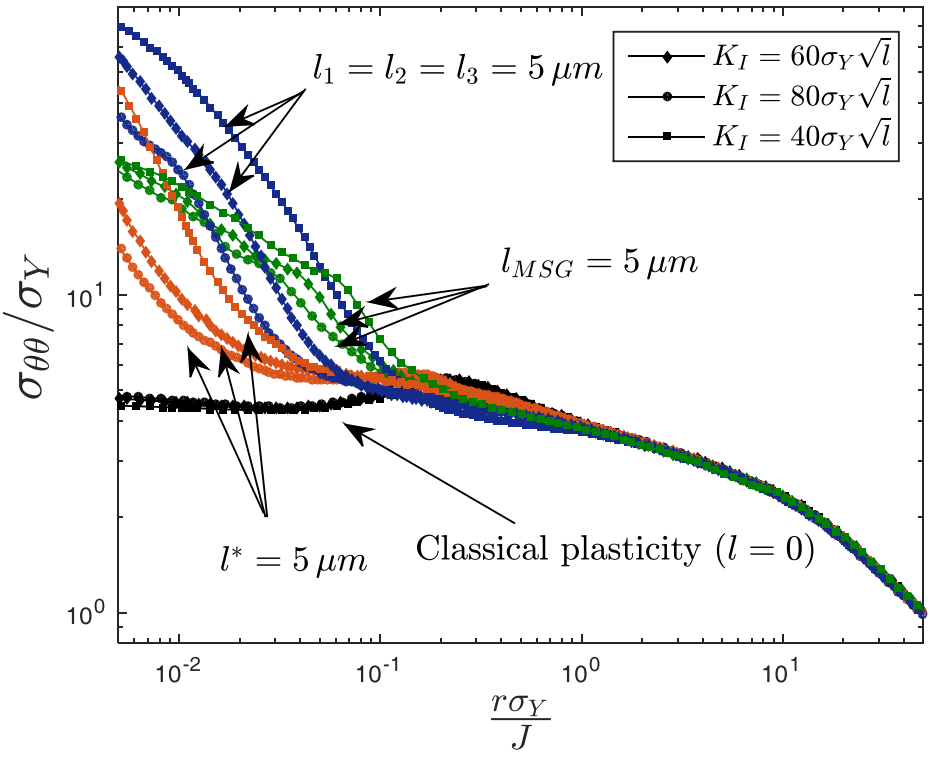

Fig. 1. Double logarithm plot of the normalized opening stress distribution ahead of the crack tip ($\theta = 0°$) for classical plasticity and both mechanism-based and phenomenological SGP approaches. The distance to the crack tip is normalized by the external load $r\sigma_Y/J$. Material properties: $\sigma_Y = 0.2\%E$, $\nu = 0.3$ and $N = 0.2$. Finite deformation theory

CONCLUSIONS

First and foremost, results reveal the need to incorporate the influence of geometrically necessary dislocations in the continuum modelization of several fracture and damage phenomena. Moreover, by employing a strain gradient plasticity framework, insight is gained into the small scale mechanisms involved in the aforementioned phenomena.

References

[1] Niordson, C.F., Hutchinson, J.W.: *Int. J. Numer. Methods Eng.* **56**: 961-975, 2003.
[2] Martínez-Pañeda, E., Betegón, C.: *Int. J. Solids Struct.* **59**: 208-215, 2015.
[3] Gao, H., Huang, Y., Nix, W.D., Hutchinson, J.W.: *J. Mech. Phys. Solids* **47**: 1239-1263, 1999.
[4] Fleck, N.A., Hutchinson, J.W.: *J. Mech. Phys. Solids* **49**: 2245-2271, 2001.
[5] Gudmundson, P.: *J. Mech. Phys. Solids* **52**: 1379-1406, 2004.
[6] Fleck, N.A., Willis, J.R.: *J. Mech. Phys. Solids* **57**: 1045-1057, 2009.
[7] Martínez-Pañeda, E., Niordson, C.: *Int. J. Plast.* (in press)
[8] Xu, X.-P., Needleman, A.: *Modelling Simul. Mater. Sci. Eng.* **1**: 111-132, 1993.
[9] Tvergaard, V.: *J. Mech. Phys. Solids* **24**: 291-304, 1976.

ENHANCED FRACTURE TOUGHNESS IN SILICON AT SMALL SCALE

Eric Hintsala[1,3a)], Roberto Ballarini[2] & William Gerberich[3]
[1]*Hysitron Inc., Eden Prairie, MN, USA*
[2]*Department of Civil Engineering, University of Houston, Houston, Texas, USA*
[3]*Department of Materials Science and Chemical Engineering, University of Minnesota, Minneapolis, MN, USA*

Summary: Based on crack initiation loads for *in-situ* SEM micro-scale bend tests of single crystal silicon at temperatures from 298 to 873 K, there appears to be a minimum fracture toughness at a temperature intermediate from room temperature and the DBT which occurs at 900-950 K for bulk silicon. This may correspond to an activation volume transition in the vicinity of 600 K, which appears to be on the order of 4 x 10^{-29} m^3. This, together with measured yield strengths between 4 and 8 GPa for 100 to 1000 nm length scale nanoindentation and nanopillars would predict a decrease in fracture toughness upon heating from room temperature before the activation volume transition increases the activation energy for fracture.

MAIN TEXT

As a model for brittle materials, single crystal silicon at small scales has several advantages, namely:

- Initially defect-free crystals or ones with known point and line defect densities are easily obtainable for evaluation;
- Many variables which affect plasticity, such as dopants, are known and characterized to some degree;
- A large database of theoretical modelling efforts is available, including atomistic potentials for both classical and density functional theory;
- Both *in-situ* TEM, with sub-nm resolution allowing generation and observation of crystalline defects in real-time, and *in-situ* SEM, with higher load and better temperature control up to 1100 K are available;
- Measurements of fundamental mechanical parameters with which to verify atomistic simulations are at hand.

Considering these advantages together with the known size effects leading to smaller being tougher and stronger, many rich studies will be available within the next decade. These will be part of the pathway for verifying atomistic and multi-scale models as they improve their ability to predict real-time experimental behaviour. While much of this is still in the exploratory stages, there is little question that this will produce fertile research problems for theorists and experimentalists in tandem.

One such problem is the brittle-to-ductile transition (BDT) of single crystal silicon as a function of temperature. St. John [1] first quantified this transition to be on the order of 900 – 950 K. We and others [2] now have the ability to address that temperature regime as a function of length scale. An interesting phenomena results when examining literature data for the micron and sub-micron scales. It is found that a transition in the activation volume associated with dislocation nucleation and/or dislocation mobility may occur in the vicinity of about 600K for such small scales which would be either 0.7 b^3 or 3 b^3 depending on whether full or partial dislocations are controlling. At the same time, at the 1 μm scale, it appears that the yield strength increases by 75 percent over this same temperature range [3], see Figure 1. This clearly will reduce the stress-dependant activation energy and allow either a decrease in dislocation nucleation or an increase in dislocation velocities. Either way, one might anticipate an increase in fracture toughness near room temperature compared to slightly elevated temperatures. For the small scale regime then, there should be a fracture resistance minimum in the vicinity of 600K as the activation volume is nearly constant for 298 to 600K.

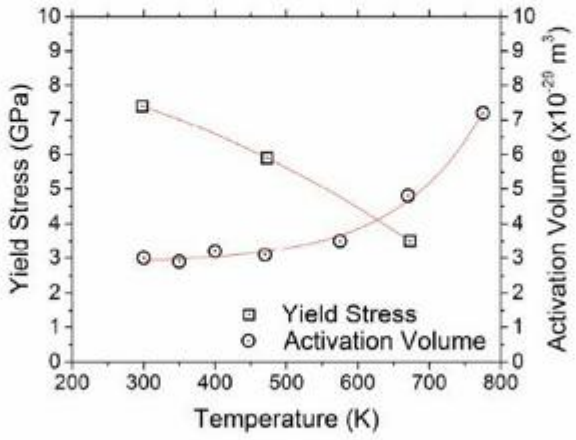

Figure 1: Activation volumes involving partial dislocations at very high stress and low temperatures in nanopillars and confined pressure experiments and yield stress for the same nanopillars; from [3,5,6].

a) Corresponding author. Email: ehintsala@hysitron.com

This has been partially verified based on crack initiation loads, Figure 2a, from *in-situ* SEM bend testing of pre-notched, 1μm thick single crystal silicon beams. An SEM micrograph of a representative beam as fabricated by focused ion beam (FIB) is shown in Figure 2b. These were tested in displacement control using a Hysitron PI-87 PicoIndenter equipped with a ~500nm radius of curvature wedge probe, operating inside an FEI Versa FIB/SEM. Temperature was varied from 298 to 873 K using independent feedback-controlled sample and probe heaters. The crack initiation load in Figure 2a can be seen to decrease from 298 to 423K, then increase over 150 K intervals up to 873K, where the silicon beam shows a dramatic change to ductile behaviour. The total range of crack initiation loads represented is a 400μN change based solely on temperature variation. Due to the constraint configuration of the focused-ion beam fabrication system, finite element analysis (FEA) is required to convert these load-displacement curves to fracture toughness and strain energy release rate values, a work currently in progress. However, the scaling in the load for crack initiation should represent the fracture toughness trend as all tested specimens were fabricated to possess the same nominal geometry and crystalline orientation.

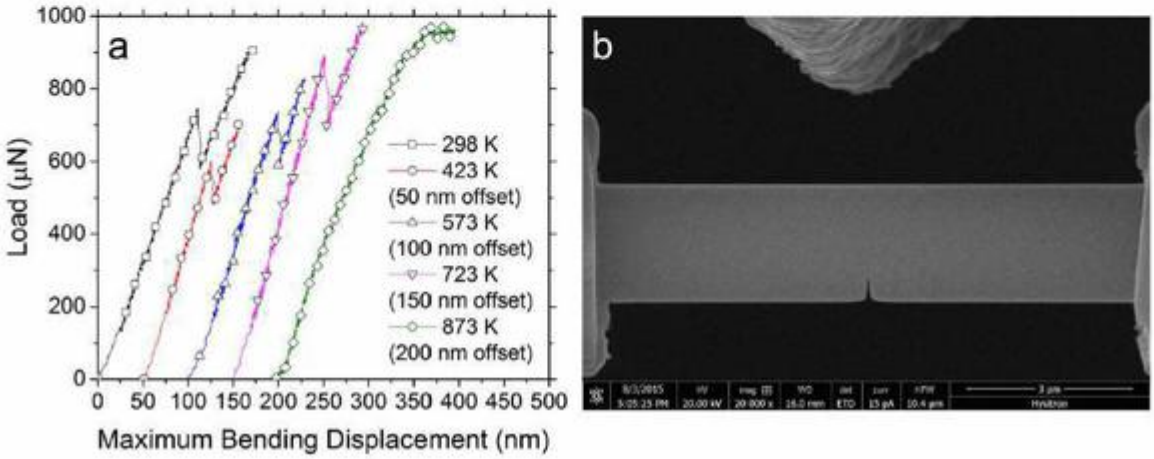

Figure 2: a) Load – maximum bending deflection curves for 5 example Si bending beams up to crack initiation tested at temperatures from 298 to 873 K; b) SEM micrograph of an example pre-notched Si bending beam, showing the double clamped end constraints and the probe at the top of the frame.

As a general trend for small scale silicon, we anticipate an increase in toughness compared to the bulk. One previous result on a 156 nm thick beam has shown a factor of 3.6 increase in work per unit fracture area (G_{IC}) over the accepted room temperature value for bulk silicon [4] after appropriate conversion from load to applied stress intensity as determined by FEA. Beyond scale and temperature effects, doping should also influence the temperature dependence of the activation volume and yield stress [5,6], opening additional avenues for study.

CONCLUSIONS

Our view is that a new field of endeavour made possible by *in-situ* studies in both scanning and transmission electron microscopes will enable new insight into the detailed microstructural factors for improved fracture resistance. This should result in fracture mechanism maps with unprecedented accuracy that could include elemental and microstructural variation at the nm scales. With such detail, verification of various types of atomistic potentials and multi-scale models would proceed more rapidly.

References

[1] St. John C.: The Brittle-to-Ductile Transition in Pre-Cleaved Silicon Single Crystals. *Phil. Mag.* **32**: 1193-1212, 1975.

[2] Hirsch P. B., Roberts S. G., Samuels J.: The Brittle-Ductile Transition in Silicon. II. Interpretation. *Proc. Roy. Soc. London, A* **421**: 25-53, 1989.

[3] Rabier J., Montagne A., Wheeler J. M., Demenet J. L., Michler J., Ghisleni, R.: Silicon Micropillars: High Stress Plasticity. *Phys. Stat. Sol. (c)* **10**:11-15, 2013.

[4] Hintsala E., Ballarini R., Gerberich W. W.: Future Nanomechanical Approaches to Brittleness Transitions. *Submitted to U. S. National Committee on Theoretical and Applied Mechanics*

[5] George A., Champier G.: Velocities of screw and 60° dislocations in n-and p-type silicon. *Phys. Stat. Sol. (a)* **53**: 529, 1979.

[6] Rabier J., Veyssiere P., Demenet, J.: Plastic Deformation of Silicon at Low Temperature and the Influence of Doping. *J. De Physique* **44**: 243-253, 1983.

ULTRA-HIGH DUCTILITY OF TRIP-ASSISTED STEELS MODELLED BY GRADIENT PLASTICITY

Mahdi K. Hatami [1], Thomas Pardoen[2], Gauthier Lacroix [2], Peter Z. Berke [1], Pascal J. Jacques [2], Thierry J. Massart [1a)]
[1]*BATir Department, Université libre de Bruxelles (ULB), Brussels, Belgium*
[2]*Institute of Mechanics, Materials and Civil Engineering, Université catholique de Louvain, Louvain-La-Neuve, Belgium*

Summary TRansformation Induced Plasticity (TRIP) is an attractive route to increase the strain hardening capacity of steels containing a fraction of metastable austenite, leading to higher strength and uniform elongation. In spite of performances reached in the past decades, microstructure optimization is complex due to the interplay of coupled effects on the transformation kinetics and work hardening (phase stability, size of austenite grains, temperature and loading path). An averaging scheme is developed for predicting the response of TRIP-aided multiphase steels using strain gradient plasticity. The model parameters, based on transformation kinetics, are identified based on experimental results at different temperatures. Classical plasticity cannot capture the TRIP effect on the mechanical response, while strain gradient plasticity predicts the variation of strain hardening with deformation and temperature, paving the way towards microstructure optimization.

INTRODUCTION

Over the last decades, the demand for steels with enhanced hardening capacity, led to the manufacturing of various TRIP (TRansformation Induced Plasticity) assisted multiphase steels [1]. Transformation induced plasticity is an efficient strategy to obtain superior strength/ductility balance, by raising the strain hardening capacity through the continuous transformation along deformation of a fraction of metastable austenite retained thanks to specific metallurgical treatments. By varying the composition and processing route, the volume fraction, stability, size and initial strength of retained austenite can be controlled, leading to different transformation kinetics and plastic behavior [1]. The size-dependent response in TRIP steels was considered in [2], showing that strain gradient plasticity (SGP) effects associated to the phase transformation can have a first order effect, as the transformation occurs in regions in the range of 1μm. This model revealed strong effects related to plastic strain gradients on the TRIP mechanism. However, unit cells representing only one grain were considered, preventing a qualitative reproduction of experimentally observed trends. Here, this approach is extended to allow direct comparison with experimental data. This requires addressing representative volume elements rich enough to encompass a large number of austenite grains transforming at different levels of deformation.

HOMOGENIZATION PROCEDURE

The behaviour of each phase is described by the Fleck-Hutchinson gradient plasticity theory [3], in which the effective plastic strain is generalized, incorporating plastic strain gradients within a term that accounts for geometrically necessary dislocations (GNDs). A 2D plane stress element is used, with higher-order boundary conditions on the plastic strain field, applied at the boundary of the appearing martensitic phase, with a vanishing plastic flow upon transformation.

A simplified 2D unit cell, containing a circular austenitic inclusion within a ferritic matrix, is used, see Fig. 1. Upon loading, the austenitic inclusion partially transforms into a martensitic phase. The phases volume fractions are based on experimental data [4]. The unit cell is embedded in a surrounding medium to iso-strain or iso-stress transformation conditions. The mechanical influence of the transformation on the unit cell average behavior is examined, assuming that the final volume fraction of the martensitic phase appears at once with evolving material properties. This is achieved in three stages: (i) the material is subjected to the loading conditions until a specific average unit cell strain level, (ii) the material properties of the elliptical zone are updated gradually from the austenite to the martensite properties, with the external loading temporarily stopped and with a transformation eigenstrain imposed to the appearing martensitic phase, (iii) the mechanical loading is resumed after the transformation.

In order to capture the global response of the TRIP steel corresponding to experimentally observed heterogeneous transformation kinetics, one should account for the fact that a variant of austenite transforms fast and not progressively, but that different austenite grains transform at different deformation levels. An averaging procedure is used in which the overall material is represented by several unit cells, assuming that each can be simulated independently. The experimental transformation kinetics is exploited to identify the distribution of macroscopic strain levels at which the transformation initiates. The transformation kinetics is therefore discretized, providing a set of macroscopic strain levels at which transformations start. For a given kinetics, a set of unit cells thus predicts the local behavior for different starts of transformation. After computing individual unit cell responses corresponding to different transformation initiation strains (Fig.1), they are recombined by means of a weighted sum to evaluate the global material behavior. An equal weighting factor is imposed here on each unit cell. As a result of the use of a finite number of unit cells, the global material response exhibits an oscillatory pattern as depicted in Fig. 1 that requires subsequent smoothing.

[a)] Corresponding author. Email: thmassar@ulb.ac.be

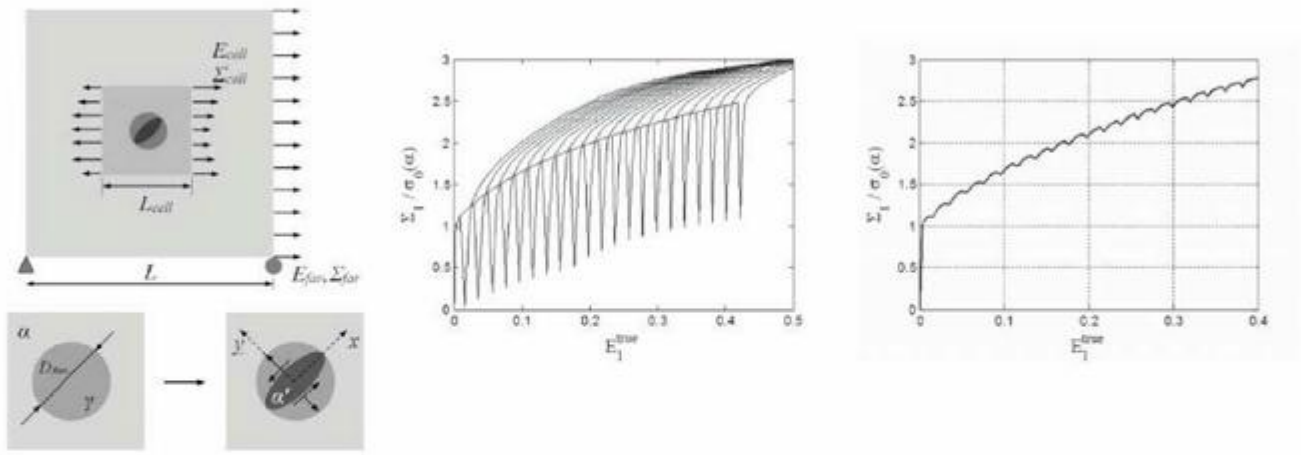

Fig. 1. (left) unit cell and embedded cell to model transformation without average stress or strain control, (center) set of unit cell responses with increasing strains at transformation according to experimental kinetics, (right) resulting average stress-strain response.

SIMULATION OF ISOTHERMAL TENSILE DEFORMATION TESTS

Using parameters reported in [4], the model allows semi-qualitatively reproducing experimentally observed results. Hardening laws are adjusted to reproduce the results corresponding to an isothermal tensile test at 80°C, as shown in Figure 2 for material parameters in the range used in [5]. The internal length is selected as the one allowing the best agreement with experimental results at this temperature. Using this set of parameters, corresponding to a SGP intrinsic length scale l_*/D_{aust} = 0.75, the drop of ductility observed for faster kinetics observed at lower temperatures can be captured by the SGP model. The classical plasticity model, on the contrary, cannot capture any significant drop in the strain at necking, see Fig 2. A similar qualitative agreement can also be shown for non-isothermal tensile conditions with more complex kinetics.

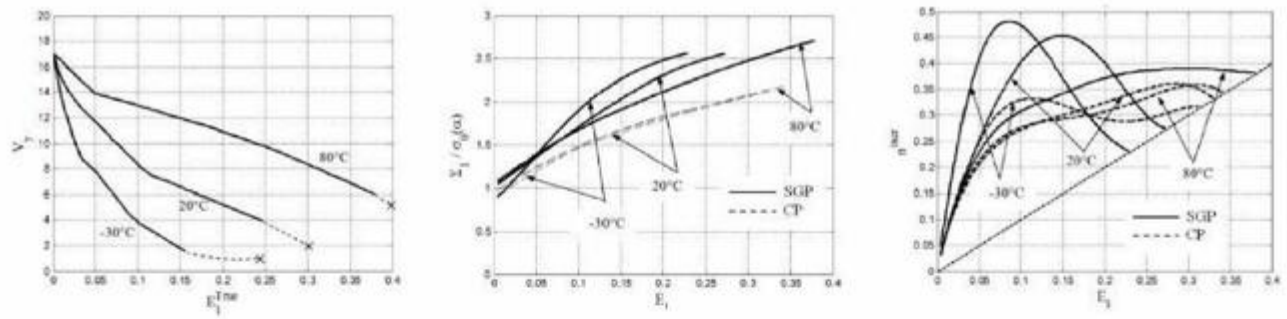

Fig. 2. (left) Experimental transformation kinetics (evolution of austenite volume fraction during straining) for isothermal tests [4], (center) Stress-strain response for Strain Gradient (SGP) and Classical (CP) Plasticity, (right) Considere plot for necking detection.

CONCLUSIONS

A comparison of the size dependent results with the trends obtained with a classical plasticity shows that a size dependent framework is a key feature in order to capture the effect of the transformation kinetics on the overall material behavior of TRIP assisted steels. Based on experimentally identified material parameters, the computational results agree well with the experiments in terms of the prediction of the ductility as a function of the transformation kinetics. Future works will focus on the means to generate refined microstructures, and on the practical generation of microstructures exhibiting tailored transformation kinetics towards optimized ductility of TRIP assisted steels.

References

[1] Jacques P.J.: Transformation-induced plasticity for high strength formable steels. *Curr. Op. Solid State Mat. Sci* **8(3)**:259-265, 2004.

[2] Mazzoni L. et al.: Strain gradient plasticity analysis of transformation induced plasticity in multiphase steels. Int. J. Sol. Struct **45(20)**:5397-5418, 2008.

[3] Fleck N. A., Hutchinson J.W: A reformulation of strain gradient plasticity. J. Mech. Phys. Sol. **49(10)**:2245-2271, 2001.

[4] Lacroix G. et al.: The fracture toughness of TRIP-assisted multiphase steels. Acta Mat. **56(15)**:3900-3913, 2008.

[5] Delannay L. et al.: Modelling of the plastic flow of trip-aided multiphase steel based on an incremental mean-field approach. Int. J. Sol. Struct, **45(6)**:1825-1843, 2008.

CONTINUUM ANALYSIS OF PRECIPITATION HARDENING USING SGP THEORY

Mohammad-Ali Asgharzadeh[1], Jonas Faleskog[1a)] & Carl Dahlberg[1]
[1]*Department of Solid Mechanics, Royal Institute of Technology, Stockholm, Sweden*

Summary A comprehensive study of precipitation hardening has been carried out by use of the strain gradient plasticity theory. Different parameters governing the behavior of the material in the presence of particles have been studied, which showed that two key parameters dominate the outcome of the analyses. These are the particle spacing and interface strength. The results show that the hardening increases when there is a more dense distribution of particles, and it also increases by making the particles more incoherent.

INTRODUCTION

The presence of heterogeneous deformation on the micro scale introduces size scale effects in the material. Precipitation hardening is one of the underlying sources of micro scale heterogeneity, which strongly depends on the particle size and inter-particle spacing. Strain Gradient Plasticity (SGP), justified by dislocation theory, assumes that hardening is caused by the accumulation of dislocations, which correlates with the gradient of plastic strain [1]. A comprehensive parametric study of different distributions of particles within a matrix has been carried out in this work by use of the SGP theory. The model results have been applied to predict precipitation hardening effects in some metals reinforced with incoherent particles, and compared to experimental data.

PROBLEM DEFINITION AND MODELING

Considering a periodic distribution of spherical particles in a matrix with hexagonal cells, the model which is used in FE-calculations has been approximated by a cylindrical cell enclosing the spherical particle (Fig. 1). If only uniaxial or biaxial loadings are considered, the combination of geometry and loading compose an axisymmetric problem. The constitutive behavior for the matrix is supposed to be governed by a SGP theory, the particle is supposed to behave totally elastic, and there is an energetic interface layer between particle and the matrix to mimic the particle-dislocation interactions [2]. For more general loadings, a 3D analysis has been carried out to capture the cutting mechanism. In the 3D analysis, the effects of both size and spatial distribution of particles have also been studied.

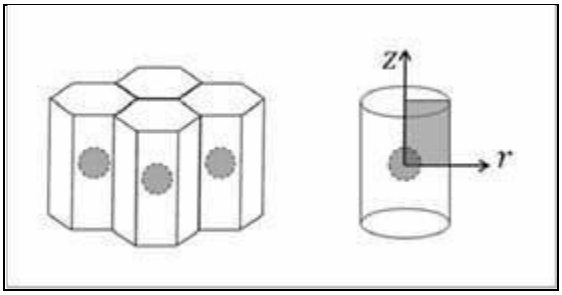

Figure 1-The schematic of the model

RESULTS AND CONCLUSION

The two key parameters controlling the behavior of this model are the intrinsic material length scale (l) and the resistance against plastic straining at the interface (η). There are also other parameters that have been studied using this model, namely the volume fraction of the particles, hardening of the matrix, and the stiffness mismatch between the matrix and the particles. The results have been verified by comparison with experimental data.

By using the aforementioned model, the results show the ability to capture the essence of the strengthening mechanism associated with a distribution of particles. In addition to that, the interface model captures the behavior of the incoherent particle-matrix interface. As results suggest (Fig. 2), the hardening increases by decreasing the particle spacing (which is represented by the non-dimensional quantity $2R/l$) and also making the interface stronger (which means a lower value of η). This leads to an increase in the 0.2%-offset yield stress (Fig. 2).

As described above, the characteristics of the model have been studied based on a default matrix material with ideal plastic behavior. The parameters of the model, however, could be manipulated in order to be applicable to different material

[a)] Corresponding author. Email: faleskog@kth.se.

systems. This was done for aluminum, magnesium and copper reinforced with incoherent particles, and the outcome of the model predictions agreed fairly well with available experimental data from the literature.

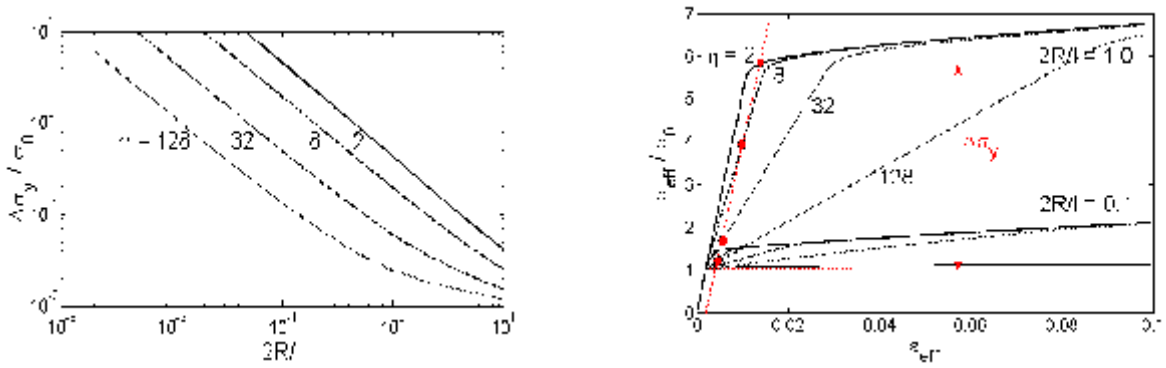

Figure 2-(Left) The increase in the 0.2%-offset yield stress according to the particle hardening. (Right) Hardening curves showing the effects of particle-matrix interaction and inter-particle spacing.

References

[1] Fleck N.A. et al.: Strain gradient plasticity: Theory and experiment. *Acta Metallurgica Et Materialia* **42**:475-487, 1994.

[2] Dahlberg C.F.O., Faleskog J.: Strain gradient plasticity analysis of the influence of grain size and distribution on the yield strength in polycrystals. *European Journal of Mechanics, A/Solids* **44**:1-16, 2014.

PHASE-FIELD STUDY OF SIZE EFFECTS IN MARTENSITIC MICROSTRUCTURES

Karel Tůma[1], Stanisław Stupkiewicz [*1], and Henryk Petryk[1]

[1]*Institute of Fundamental Technological Research (IPPT), Polish Academy of Sciences, Warsaw, Poland*

Summary Formation of martensitic microstructures is usually explained by energy minimization, while the competition between the bulk and interfacial energy contributions provides a natural intrinsic length scale and makes the microstructures size-dependent. In this work, size-dependent microstructures in CuAlNi shape memory alloy have been computed using a phase-field method, and the corresponding predictions have been compared to the results of sharp-interface modelling. Both approaches account for interfacial energy effects, though in a different manner. In the computations, a finite-strain phase-field model recently developed by the authors has been used. The model involves several new ingredients, including a volume-preserving logarithmic mixing rule, hierarchical order parameters and bound constraints enforced on order parameters.

INTRODUCTION

Martensitic phase transformation in shape memory alloys (SMA) is responsible for their unusual behaviour associated with pseudoelasticity, shape recovery, and related effects. Martensitic transformation proceeds by formation of microstructure, and martensitic microstructures have been extensively studied over last decades [1]. While formation of microstructure is usually explained by energy minimization, the competition between the bulk and interfacial energy contributions provides a natural intrinsic length scale and makes the microstructures size-dependent. The related size effects are studied in this work using a recently developed finite-strain phase-field model [2] as well as using the sharp-interface approach [3, 4], and consistency of the two approaches is illustrated by numerical examples.

FINITE-STRAIN PHASE FIELD MODEL OF MARTENTSITIC TRANSFORMATION

A finite-strain model has been developed for phase-field modelling of twinning and martensitic transformation in shape memory alloys [2]. The model is set in the energy minimization framework so that the constitutive equations are fully defined by specifying the free energy function and the dissipation potential. The free energy involves the bulk and the interfacial energy contributions, the latter describing the energy of diffuse interfaces, which is typical for phase-field approaches [5].

Compared to other finite-strain phase-field models for twinning [6, 7], the present model uses another mixing rule within diffuse interfaces which can be directly generalized to multiple variants or phases with volume changes treated in a consistent manner. Specifically, the transformation part of the deformation gradient is obtained by averaging the logarithmic transformation strains of individual phases rather than by mixing the transformation stretches, cf. [8]. Furthermore, the inequality constraints are here directly imposed on order parameters interpreted as volume fractions so that the physically motivated bounds are not violated. In the numerical implementation, the augmented Lagrangian method is used for that purpose [9].

Modelling of microstructures that involve austenite and twinned martensite requires further extension of the model. Two order-parameters are introduced to adequately describe the three involved constituents: the austenite and two variants of martensite. The order parameters are arranged hierarchically so that one parameter differentiates between austenite and martensite while the second one differentiates between the two variants of martensite. As a result, two types of interfaces (austenite-martensite and martensite-martensite) are described in a natural manner. The bulk free energy and the dissipation potential are generalized accordingly.

ANALYSIS OF AUSTENITE–TWINNED MARTENSITE MICROSTRUCTURES

The finite-strain phase-field model has been implemented in a finite element code and applied to study size effects in a CuAlNi shape memory alloy undergoing the cubic-to-orthorhombic transformation. In particular, several realistic microstructures have been computed by solving a generalized 2D boundary value problem in a plane orthogonal to both the twinning and habit planes. This class of 2D problems has been examined earlier using the sharp-interface approach [3].

The interface between austenite and twinned martensite has been studied for four crystallographically distinct microstructures (denoted by M1 to M4, cf. [3]), see Fig. 1. A periodic unit cell corresponding to one twin spacing has been simulated, and each microstructure has been replicated in Fig. 1 for better visualization. Larger green areas denote austenite while blue and red areas correspond to the two variants of martensite. Local incompatibility of transformation strains is accommodated by elastic strains in a transition layer along the austenite–martensite interface. The corresponding elastic-strain energy is interpreted at a higher scale as the interfacial energy $\gamma^{\mathrm{e}}_{\mathrm{am}}$, and the energy factor $\mathrm{y}^{\mathrm{e}}_{\mathrm{am}} = \gamma^{\mathrm{e}}_{\mathrm{am}}/h_{\mathrm{tw}}$, where h_{tw} denotes the

*Corresponding author. Email: sstupkie@ippt.pan.pl

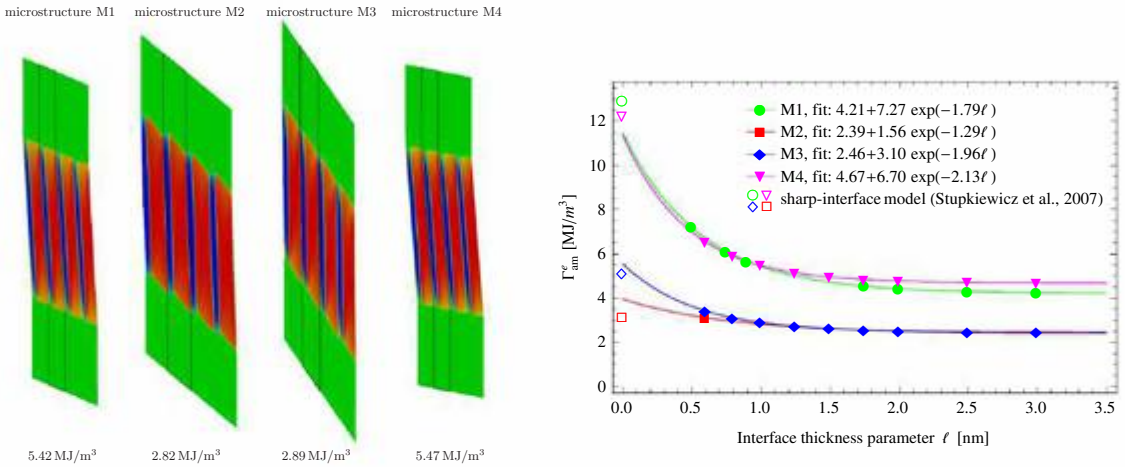

Figure 1: Austenite–twinned martensite interface in CuAlNi: morphology of the transition layer for four crystallographically distinct microstructures (left) and the dependence of elastic micro-strain energy factor $\Gamma^{\mathrm{e}}_{\mathrm{am}}$ on interface thickness parameter ℓ (right).

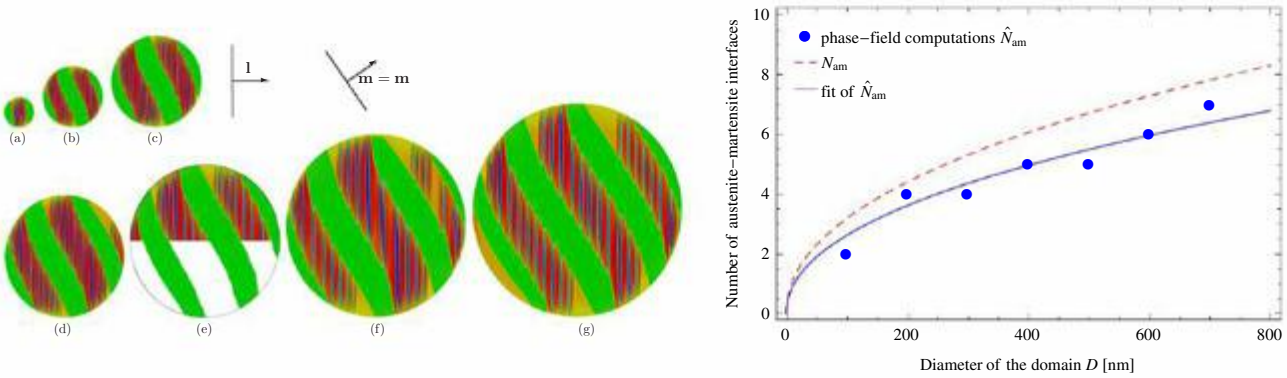

Figure 2: Rank-two austenite–twinned martensite laminates formed within a cylindrical grain of the diameter varying between 100 and 700 nm (left). The number of austenite–martensite interfaces predicted by the phase-field model (dots) and by a sharp-interface model (dashed line), the latter following the approach developed in [4] (right).

twin spacing, is also reported for each microstructure. The dependence of the energy factor $\Gamma^{\mathrm{e}}_{\mathrm{am}}$ on the phase-field interface thickness parameter ℓ is also shown in Fig. 1. In the sharp-interface limit, the phase-field results are consistent with the sharp-interface predictions [3].

Formation of a rank-two laminated microstructure within a cylindrical grain is reported in Fig. 2. It can be seen that characteristic dimensions of the microstructure depend on the grain size. Predicted size-dependent spacing of martensite plates, characterized by the number of austenite–martensite interfaces, has been compared to a sharp interface model [4], and again consistent results have been obtained.

References

[1] Bhattacharya K.: Microstructure of martensite: why it forms and how it gives rise to the shape-memory effect. Oxford University Press, Oxford, 2003.

[2] Tůma K., Stupkiewicz S., Petryk, H.: Size effects in martensitic microstructures: finite-strain phase field model versus sharp-interface approach, 2016 (submitted for publication).

[3] Stupkiewicz S., Maciejewski G., Petryk H.: Low-energy morphology of the interface layer between austenite and twinned martensite. Acta Mater. 55: 6292–6306, 2007.

[4] Petryk H., Stupkiewicz S., Maciejewski G.: Interfacial energy and dissipation in martensitic phase transformations. Part II: Size effects in pseudoelasticity. J. Mech. Phys. Solids 58: 373–389, 2010.

[5] Steinbach I.: Phase-field model for microstructure evolution at the mesoscopic scale. Annu. Rev. Mater. Res. 43: 89–107, 2013.

[6] Clayton J., Knap J.: A phase field model of deformation twinning: Nonlinear theory and numerical simulations. Physica D 240: 841–858, 2011.

[7] Hildebrand F., Miehe C.: A phase field model for the formation and evolution of martensitic laminate microstructure at finite strains. Phil. Mag. 92: 4250–4290, 2012.

[8] Levitas V.I.: Phase-field theory for martensitic phase transformations at large strains. Int. J. Plast. 49: 85–118, 2013.

[9] Stupkiewicz S., Petryk H.: A robust model of pseudoelasticity in shape memory alloys. Int. J. Num. Meth. Engng. 93: 747–769, 2013.

FINITE STRAIN GRADIENT PLASTICITY WITH APPLICATION TO MICRON SCALE VOID GROWTH

Christian F. Niordson*[1] and Viggo Tvergaard[1]

[1]*Department of Mechanical Engineering, Solid Mechanics, Technical University of Denmark, Kgs. Lyngby, Denmark*

Summary A finite strain generalization of the thermodynamically consistent strain gradient plasticity (SGP) theory by Gudmundson [1] is proposed. The SGP theory, as originally formulated, employs both dissipative and energetic strain gradient effects, and it is shown that a finite strain generalization is readily developed when ignoring energetic gradient effects. An updated Lagrangian finite element method is formulated, and matters of the finite strain implementation turn out to be mainly those associated with generalizing conventional plasticity theory. The framework developed is applied to ductile void growth on the micron scale. Quantitative predictions show that the growth rate for micron size voids is suppressed compared to that predicted by conventional plasticity.

PROBLEM DESCRIPTION

Micron scale experiments show that increased hardening and yield resistance follow from the presence of large plastic strain gradients. Such non-trivial size effects can not be captured by conventional plasticity, and the field of strain gradient plasticity have been developed due to the need for quantitative predictions of material response on the micron scale. The strain gradient plasticity theory by Gudmundson [1] can be based on the principle of virtual work for the body occupying the volume V bounded by the surface S

$$\int_V \left[\sigma_{ij}\delta\epsilon_{ij} + (q_{ij} - \sigma'_{ij})\delta\epsilon^p_{ij} + \tau_{ijk}\delta\epsilon^p_{ij,k}\right] dV = \int_S [T_i\delta u_i + t_{ij}\delta\epsilon^p_{ij}]dS \tag{1}$$

where σ_{ij} and $\delta\epsilon_{ij}$ are the stress tensor and the variation of the total strain tensor, respectively. The micro stress q_{ij} is the work conjugate to the plastic strain tensor ϵ^p_{ij}, and σ'_{ij} is the stress deviator. The higher order stress, τ_{ijk} is work conjugate to the plastic strain gradient $\epsilon^p_{ij,k}$. The right hand side includes the traction vector, T_i, the virtual displacement vector δu_i in addition to the higher order traction vector t_{ij} and the variation of plastic strain. The latter term introduces non-standard boundary conditions, relevant to many micron scale applications, on plastic strain or its work conjugate.

Constitutive equations are based on the notion of a gradient enhanced effective plastic strain measure describing dissipation due to plastic strain as well as the plastic strain gradient

$$\dot{E}^{p^2} = \frac{2}{3}\dot{\epsilon}^p_{ij}\dot{\epsilon}^p_{ij} + L_D^2\dot{\epsilon}^p_{ij,k}\dot{\epsilon}^p_{ij,k} \tag{2}$$

where L_D is a constitutive dissipative length scale. Further constitutive input to the theory is the uniaxial stress-strain behavior specified by the dependence of the effective stress on plastic strain and plastic strain rate: $\sigma_c[E^p, \dot{E}^p]$. Based on this, a dissipation potential is defined as

$$\Phi[E^p, \dot{E}^p] = \int_0^{\dot{E}^p} \sigma_c[E^p, \dot{E}'^p]d\dot{E}'^p \tag{3}$$

and the dissipative constitutive equations may be derived as

$$q_{ij} = \frac{2}{3}\frac{\sigma_C}{\dot{E}^P}\dot{\epsilon}^p_{ij} \quad \text{and} \quad \tau_{ijk} = L_D^2\frac{\sigma_C}{\dot{E}^P}\dot{\epsilon}^p_{ij,k} \tag{4}$$

As the above constitutive equations deliver the micro stress q_{ij} and the higher order stress τ_{ijk} directly from the plastic strain rate field, the minimization of the following functional, as proposed by [2] (here expressed in the absence of energetic strain gradient effects) may be used even in a finite strain context to deliver a solution in higher order stress equilibrium:

$$H[\dot{\epsilon}^p_{ij}] = \int_V \left(\Phi[E^p, \dot{E}^p]\dot{\epsilon}^p_{ij,k} - \sigma'_{ij}\dot{\epsilon}^p_{ij}\right) dV - \int_S t_{ij}\dot{\epsilon}^p_{ij}dS \tag{5}$$

Employing an updated Lagrangian formulation, the iterative finite element procedure ($l = 1, 2, 3...$) (treated in the context of linear kinematics in [3]) may be expressed as

$$\begin{aligned}&\int_V \begin{pmatrix}\sigma_c[\dot{E}^p, E^p] \\ \dot{E}^p\end{pmatrix}_{(l-1)} \left(\frac{2}{3}M^{(n)}_{ij}M^{(m)}_{ij} + L_D^2 M^{(n)}_{ij,k}M^{(m)}_{ij,k}\right) dV \cdot \dot{\epsilon}^{p(m)}_{(l)} \\ &= \int_V \left(\sigma'_{ij}M^{(n)}_{ij}\right) dV + \int_S t_{ij}M^{(n)}_{ij}dS\end{aligned} \tag{6}$$

*Corresponding author. Email: cn@mek.dtu.dk

where $\dot{\epsilon}^p_{ij} = \sum_{n=1}^{N} M^{(n)}_{ij} \dot{\epsilon}^{p(n)}$ expresses the relation between the plastic strain rate field, the N shape functions $M^{(n)}_{ij}$ and the nodal variables, $\dot{\epsilon}^{p(n)}$.

When the plastic strain rate field has been determined from 6, conventional methods for the velocity field may be used as described by McMeeking and Rice [4].

NUMERICAL RESULTS

Plane strain void growth of a cylindrical void of initial radius R_0 is analyzed, and results are presented below. A standard visco-plastic power-law is employed by $\dot{E}^P = \dot{\epsilon}_0(\sigma_c/\sigma_y)^{1/m}$, where $\dot{\epsilon}_0$, m and σ_y denote the reference strain rate, the visco-plastic exponent and the yield stress of the material, respectively. The material parameters employed are $\sigma_y/E = 0.004$, $\nu = 0.3$, $\dot{\epsilon}_0 = 0.005\text{s}^{-1}$. For simplicity the material is assumed to be non hardening, but it is easily extended to account for hardening. Growth of a single void subjected to a biaxial loading $\sigma_{22} = \rho\sigma_{11}$ is treated in the results below. Fig. 1 shows results for the the development of void volume normalized by initial void volume for different length parameters $L_D/R_0 = 0.0,\ 0.5, 1, 0$. The results show that as the void size decreases (L_D/R_0 increases), the curves shift to the right indicating that higher levels and load and deformation are needed to drive void growth. Hence, void growth is suppressed in the micron scale. Fig. 1a shows results for equi biaxial tension ($\rho = 1.00$) with different values of the visco-plastic exponent. As the far field strain rate is prescribed as the reference strain rate for the material, a large effect of m is observed, with the size-effect being even more distinct for increasing rate sensitivities. In Fig. 1b results are shown for $m = 0.01$, and for different values of the load ratio, ρ. The results show that although void growth is delayed for smaller values of ρ, a strong size effect is present for all load ratios.

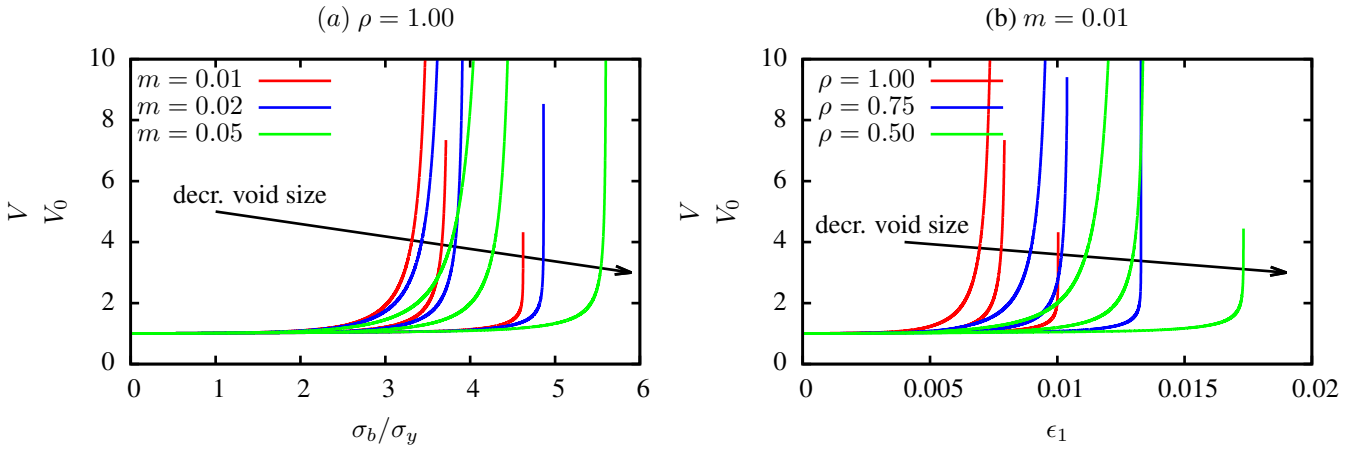

Figure 1: Relative void volume growth curves for three different values of the material length parameter $L_D/R_0 = 0.0,\ 0.5,\ 1.0$. (a) Results are shown for equi biaxial tension ($\rho = 1.00$) as a function of normalized applied equi-biaxial stress for three different values of the visco-plastic exponent, $m = 0.01,\ 0.02,\ 0.05$. (b) Results are shown for $m = 0.01$ as a function of applied strain for three values of the applied load ratio, $\rho = 0.50,\ 0.75,\ 1.00$.

CONCLUSIONS

A thermodynamically consistent finite strain SGP theory is proposed. The theory is based on the higher order SGP theory by Gudmundson [1]. It is shown that for dissipative gradient effects, the minimum principles laid out by Fleck and Willis [2] can readily be employed as a basis for the finite strain extension. A finite element implementation in an updated Lagrangian framework is proposed. The problem of void growth is analyzed, and predictions for how void growth in the micron scale is suppressed are shown.

ACKNOWLEDGMENT

C. F. Niordson gratefully acknowledges financial support from the Danish Council for Independent Research under the research career program Sapere Aude in the project "Higher Order Theories in Solid Mechanics".

References

[1] Gudmundson P.: A unified treatment of strain gradient plasticity. Journal of the Mechanics and Physics of Solids 52, 1379-1406, 2004.

[2] Fleck, N. A., Willis, J. R.: A mathematical basis for strain-gradient plasticity theory. Part II: Tensorial plastic multiplier. Journal of the Mechanics and Physics of Solids 57, 1045-1057, 2009.

[3] Niordson, C. F., Hutchinson, J. W. Basic strain gradient plasticity theories with application to constrained film deformation. Journal of Mechanics of Materials and Structures 6, 395-416, 2011.

[4] McMeeking R., Rice, J. R.: Finite-element formulations for problems of large elastic-plastic deformation. International Journal of Solids and Structures 11, 601-616, 1975.

MODELLING SIZE EFFECTS ON VOID GROWTH AND COALESCENCE IN SINGLE CRYSTALS

Chao Ling *[1,2], Benoît Tanguy[1], Samuel Forest[2], Jacques Besson[2], Felix Latourte[3], and Elodie Bosso[3]

[1]*CEA Saclay, Université de Paris-Saclay, DEN, Laboratoire de Comportement Mécanique des Matériaux Irradiés, 91191 Gif-sur-Yvette cedex, France*

[2]*MINES ParisTech, PSL Research University, MAT - Centre des matériaux, CNRS UMR 7633, BP 87 91003 Evry, France*

[3]*EDF R&D, MMC, Site des Renardières, F-77818 Moret-sur-Loing cedex, France*

Summary In this work, a single crystal strain gradient plasticity model is derived at finite strains. The gradient enhancement is based on a scalar strain measure of plastic slip of single crystals. It is implemented in the finite element code Zset and then used to investigate size effects on void growth and coalescence in single crystals. 3D unit cell finite element simulations are performed and the results are compared with those obtained with classical single crystal plasticity model.

CONTEXTS

In nuclear reactors, irradiation leads to formation of various defects in their components. Especially in the core internals made of austenitic stainless steels, intragranular voids can be created, which may induce macroscopic swelling at high irradiation levels. When the material is subjected to mechanical loading, the formed voids play a role in the process of ductile fracture, which is generally known as a result of void nucleation, growth and coalescence. At initial stage of fracture, voids are much smaller than the grain size so that one can consider the voids as embedded in an infinitely large single crystal matrix under homogeneous loading. In this work, size effects on void growth and coalescence in single crystals are investigated.

Size-dependent behaviours have been widely observed in metallic materials, such as size-dependent strength of micro-specimens, the Hall-Petch effect, etc. As classical continuum theories cannot predict such size effects, many authors developed non-local models (see [1] and references therein). These enriched models suppose that the stress state of a material point depends on the state of a finite neighbourhood or on strain gradient variables.

MODEL DESCRIPTION

A single crystal strain gradient plasticity model is proposed at finite strains. The strain gradient enhancement is based on a scalar strain measure of plastic slip (cf. [2]). One additional degree of freedom γ_χ is introduced. The set of degrees of freedom (DOF) and that of their Lagrangian gradients are therefore defined as

$$\text{DOF} = \{\underline{\boldsymbol{u}}\,, \gamma_\chi\} \;\text{ and }\; \text{GRAD} = \left\{ \underset{\sim}{\boldsymbol{F}} = \underset{\sim}{\mathbf{1}} + \frac{\partial \underline{\boldsymbol{u}}}{\partial \underline{\boldsymbol{X}}},\; \underline{\boldsymbol{K}} = \frac{\partial \gamma_\chi}{\partial \underline{\boldsymbol{X}}} \right\}. \tag{1}$$

As a result, an additional balance equation and boundary condition are derived for the crystalline body V:

$$\mathrm{v}\, \underline{\boldsymbol{m}} \nearrow s = 0,\ \forall \underline{\boldsymbol{x}} \in V \;\text{ and }\; m = \underline{\boldsymbol{m}}\,.\underline{\boldsymbol{n}}\,,\ \forall \underline{\boldsymbol{x}} \in \partial V, \tag{2}$$

where s and $\underline{\boldsymbol{m}}$ are the generalised stresses respectively work conjugate to the microdeformation γ_χ and the eulerian gradient of the microdeformation $\underline{\boldsymbol{k}} = \dfrac{\partial \gamma_\chi}{\partial \underline{\boldsymbol{x}}}$, m is the surface double force density and $\underline{\boldsymbol{n}}$ is the unit normal vector to the surface.

The deformation gradient $\underset{\sim}{\boldsymbol{F}}$ is multiplicatively decomposed into elastic and plastic parts $\underset{\sim}{\boldsymbol{F}} = \underset{\sim}{\boldsymbol{F}}^e.\underset{\sim}{\boldsymbol{F}}^p$. The elastic strain is defined as

$$\underset{\sim}{\boldsymbol{E}}^e = \frac{1}{2}(\underset{\sim}{\boldsymbol{F}}^{eT}.\underset{\sim}{\boldsymbol{F}}^e \nearrow \underset{\sim}{\mathbf{1}}), \tag{3}$$

and the plastic strain rate is

$$\dot{\underset{\sim}{\boldsymbol{F}}}^p \underset{\sim}{\boldsymbol{F}}^{p-1} = \sum_s \dot{\gamma}^s \underset{\sim}{\boldsymbol{N}}^s, \tag{4}$$

with plastic slip rate $\dot{\gamma}^s$ and the Schmid tensor $\underset{\sim}{\boldsymbol{N}}^s = \underline{\boldsymbol{l}}^{\,s} \otimes \underline{\boldsymbol{n}}^{\,s}$ for the slip system s, where $\underline{\boldsymbol{l}}^{\,s}$ is the slip direction vector and the normal to the slip plan $\underline{\boldsymbol{n}}^{\,s}$. Inspired from the form of the residual dissipation, the plastic slip rate $\dot{\gamma}^s$ is assumed to be

$$\dot{\gamma}^s = \left\langle \frac{|\tau^s| \nearrow (\tau_c^s \nearrow J_e s)}{K} \right\rangle^n \operatorname{sign}(\tau^s)\,. \tag{5}$$

*Corresponding author. Email: chao.ling@mines-paristech.fr

The microdeformation γ_χ is related to the total cumulative slip $\gamma_{\text{cum}} = \sum_s |\gamma^s|$ via the relative cumulative slip e

$$e(\underline{\boldsymbol{X}}, t) = \gamma_{\text{cum}} - \gamma_\chi. \tag{6}$$

e measures the departure of the microdeformation γ_χ from the total cumulative slip, which will be associated with a cost in the free energy potential.

It is assumed that the free energy potential ψ takes the following quadratic form:

$$\rho\psi = \frac{1}{2}\frac{\rho}{\rho_i}\underset{\sim}{\boldsymbol{E}}^e : \underset{\approx}{\boldsymbol{\Lambda}} : \underset{\sim}{\boldsymbol{E}}^e + \frac{1}{2}H_\chi e^2 + \frac{1}{2}A\underline{\boldsymbol{k}}.\underline{\boldsymbol{k}}, \tag{7}$$

with the density ρ at the current configuration, the density ρ_i at the the intermediate configuration, fourth-order elasticity tensor $\underset{\approx}{\boldsymbol{\Lambda}}$, two additional moduli parameters: H_χ (unit MPa) and A (unit MPa.mm^2). As a result, one has

$$\underline{\boldsymbol{m}} = A\underline{\boldsymbol{k}} \quad \text{and} \quad s = H_\chi e = H_\chi(\gamma_{\text{cum}} - \gamma_\chi). \tag{8}$$

Considering the balance equation, it follows

$$s = \operatorname{div}\underline{\boldsymbol{m}} = A\operatorname{div}\operatorname{grad}\gamma_\chi = A\Delta_x\gamma_\chi, \tag{9}$$

which introduces the gradient effect in eq. (5).

The free energy potential can also be taken of the alternative form:

$$\rho\psi = \frac{1}{2}\frac{\rho}{\rho_i}\underset{\sim}{\boldsymbol{E}}^e : \underset{\approx}{\boldsymbol{\Lambda}} : \underset{\sim}{\boldsymbol{E}}^e + \frac{1}{2}H_\chi e^2 + \frac{1}{2}\frac{\rho}{\rho_0}A\underline{\boldsymbol{K}}.\underline{\boldsymbol{K}} \tag{10}$$

with the density ρ_0 at the reference configuration, which leads to a linear relation in the reference configuration:

$$\underline{\boldsymbol{M}} = A\underline{\boldsymbol{K}} \quad \text{and} \quad s = A\operatorname{div}\left(\frac{\rho}{\rho_0}\underset{\sim}{\boldsymbol{B}}.\operatorname{grad}\gamma_\chi\right). \tag{11}$$

SIZE-DEPENDENT VOID GROWTH

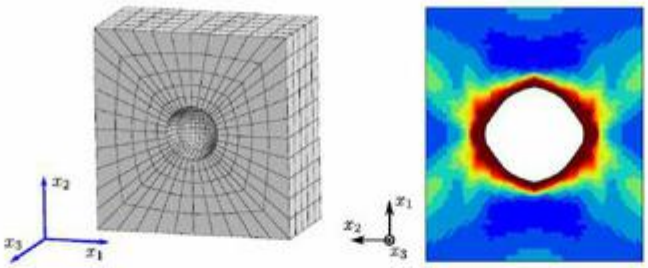

(a) (b)

Figure 1: (a) 3D finite element mesh of voided unit cell. Only half of the mesh is shown. (b) Field of total cumulative slip, obtained by the local single crystal plasticity model, in the middle x_1-x_2 cross section of the unit cell for the [100]-[010]-[001] orientation at stress triaxiality $T = 3$.

The proposed model is used to investigate the size-dependent void growth by 3D finite element unit cell simulations (see fig. 1a). Void growth in a single crystal matrix under triaxial loading is simulated with different internal length scales. The evolution of void volume fraction, the overall stress-strain response, and the local plastic strain fields are compared to those obtained by classical single crystal plasticity. Fig. 1b gives an example of unit cell simulation with classical single crystal plasticity. Results of our simulations will also be discussed regarding dislocation dynamics and molecular dynamics studies dedicated to void growth in the literature, e.g., [3].

References

[1] Aslan, O., Cordero, N. M., Gaubert, A., Forest, S.: Micromorphic approach to single crystal plasticity and damage. Int. J. of Eng. Sci., 49:1311-1325, 2011.

[2] Wulfinghoff S., Böhlke T.: Equivalent plastic strain gradient enhancement of single crystal plasticity: theory and numerics. Proc. of the Royal Society A, 468:2682-2703, 2012.

[3] Hussein, M., Borg, U., Niordson, C., Deshpande, V.: Plasticity size effects in voided crystals. J. of Mech. and Phy. of Solids, 56:114-131, 2008.

SIZE EFFECTS IN VOID COALESCENCE

Kim Lau Nielsen *[1]
[1]*Department of Mechanical Engineering, Solid Mechanics, Technical University of Denmark, DK-2800 Kgs. Lyngby, Denmark*

Summary The importance of the strain gradients that evolves at the onset of void coalescence at micron-scale is demonstrated through a detailed numerical study. Here, a 3D numerical framework is exploited to grain a parametric understanding of the influence of void size and void spacing, and a direct comparison to a recent extension of the coalescence criterion by Thomason is presented. Taking into account the intrinsic length scales inherited by the ductile failure process shows a clear increase in the level of the average volume stress, perpendicular to the plane of localization, at which void coalescence occurs. Oblate voids are particularly affected by the evolving strain gradients. The increase in stress level predicted in a gradient enhanced matrix material are, however, yet to be properly addressed in existing continuum models as both the Thomason criterion, as-well as the Gurson modeling framework, rest on conventional plasticity theory.

INTRODUCTION

The governing mechanics in ductile failure have been subject to intensive studies through decades of research (Tvergaard, 1990; Benzerga and Leblond, 2010), and it has been established that ductile failure generally progress by void nucleation and growth to coalescence at the micron-level. However, existing state-of-the-art micro-mechanics based damage models do not include the experimentally observed intrinsic length scales related to the void size, but instead only account for the void volume fraction (Gurson, 1977) - occasionally in combination with the void shape or a non-local measure of porosity (Gologanu et al., 1997). However, materials that plastically deform by dislocations movement are known to display size effects by elevated stress levels and restricted plastic flow. The general trend in metals is that *smaller is stronger*. Recent research has proven size effects to be important to problems where deformation varies significantly in the micrometer range - the range where the void coalescence process unfolds. Thus, the intrinsic length scale will inevitably influence the ductile failure process.

The present work focuses at the onset of coalescence by adopting the model set-up from Tekoğlu et al. (2012), but here includes a gradient enriched matrix material. The aim is to bring out the effect of the strain gradients that evolves during the interaction between voids at the micron level, and to highlight their implications on existing coalescence models. E.g. a direct comparison to a recent extension of the coalescence criterion by Thomason (1990) (see Eq. 1) is presented. To facilitate this comparison, only void coalescence modes located near the x_1x_3-plane are of interest (see Fig. 1a). The Thomason criterion reads:

$$\frac{\sum_{22}^{c}}{\sigma_0} = (1-\eta\chi^2)\left[\alpha^{Th}\left(\frac{1-\chi}{W\chi}\right)+\beta^{Th}\frac{1}{\sqrt{\chi}}\right] \tag{1}$$

where σ_0 is the conventional yield stress, W is the void aspect ratio, χ the relative void spacing, $\eta=\pi/4$ for a cubic unit cell, and $\alpha^{Th}=0.0819W-0.0373$, $\beta^{Th}=0.0036W^5-0.003W^4-0.1694W^3+0.8499W^2-1.6743W+2.5022$, respectively.

MODELING FRAMEWORK

A full 3D numerical modeling framework based on the Fleck and Willis (2009) strain gradient theory has been purpose build for the study presented. The incremental procedure for this model formulation consists of two successive steps in which "Step 1" determines the plastic strain rate field based on the known stress/strain conditions in the current state, whereas "Step 2" subsequently determines the corresponding incremental displacement solution (see Nielsen and Niordson, 2014, for details). To analyze the onset of void coalescence a small strain/deflection set-up is adopted, and the considered unit cell model is shown in Fig. 1a. The cell consists of a rectangular block of matrix material that surrounds a spheroidal void with aspect ratio, $W=R_2/R_1$ (and $R_1=R_3$), and a relative void spacing of $\chi=R_1/L_1$. Here, R_i and L_i are the void radii in the three directions and the dimensions of the unit cell, respectively. The boundary and loading conditions on the unit cell are adopted from Tekoğlu et al. (2012) such that the average volume stress components: $\sum_{11}$, $\sum_{22}$, $\sum_{33}$, and $\sum_{12}$ can be controlled through the prescribed macroscopic straining; $E_{ii}=U_i/(2L_i)$ and $E_{12}=U_t/(2L_2)$, where U_i are the normal displacements at the unit cell boundaries and U_t is the shear displacement. In this preliminary study, however, the shear displacement remains zero. All FE calculations are preformed with 20-node 3D elements using reduced Gauss integration ($2\times2\times2$) for the displacement field, whereas 8-node 3D elements with corresponding Gauss integration are used for the plastic strain rate field.

As the study concentrate on the onset of void coalescence a limit-load type analysis is in focus and, hence, an attempt is made to mimic an incompressible material by employing a Poisson ratio of $\nu=0.49$, together with a perfectly plastic response of the matrix material. Thus, upon loading plastic flow will localize and the material response reach a limit load at which the critical volume stress perpendicular to the x_1x_3-plane (the $\sum_{22}^{c}$) is extracted.

*Corresponding author. Email: kin@mek.dtu.dk

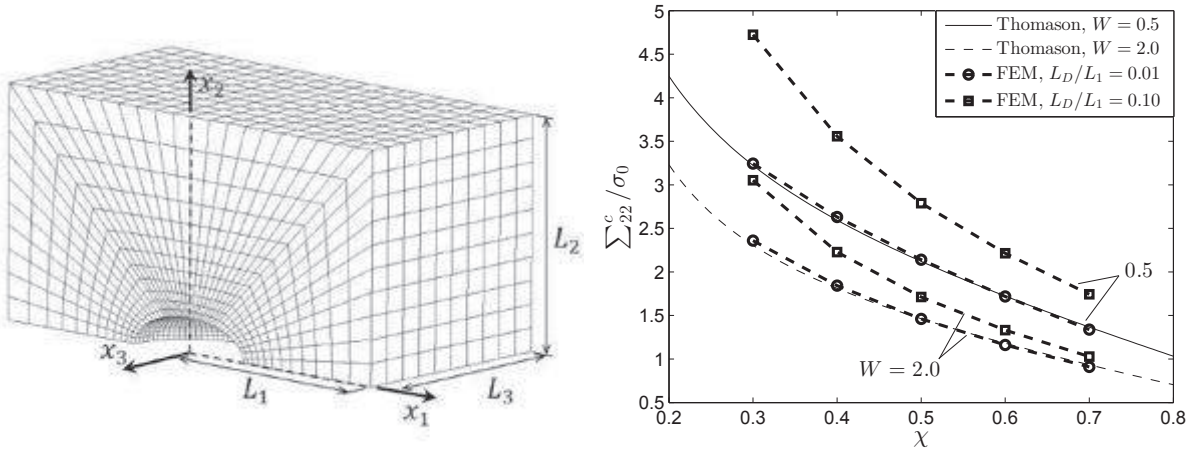

(a) (b)

Figure 1: a) Unit cell model displaying a typical mesh ($W = 0.5$), b) Evolution of $\sum_{22}^{c}$ with the relative void spacing, χ, including results with/without influence of strain gradients ($L_D = 0$ is the conventional limit and reflects J2 flow theory).

RESULTS

The predicted critical volume stress (the $\sum_{22}^{c}$), at which void coalescence takes place, is displayed in Fig. 1b. Here, shown for various void spacings, χ, and two void aspect ratios that correspond to prolate ($W = 2$) and oblate ($W = 0.5$) voids, respectively. First and foremost, a comparison to the Thomason criterion from Eq. (1) reveals accurate predictions in the conventional limit ($L_D/L_1 = 0.01$). But, the strengthening behavior from the plastic strain gradients at micron-scale lift the stress level at which void coalescence occurs - particularly at low relative void spacing. Moreover, it is noticed that oblate voids seem more sensitive to gradient effects as the stress level has increased the most for $W = 0.5$.

CONCLUSION

The present study of the intrinsic length scale effects, related to void coalescence, displays an increased level of the critical stress at which localization of plastic flow occurs between micro-voids. The effect originates from the strengthening behavior predicted for gradient enhanced materials, and one might want to think its implications into a stress based coalescence criterion such as that of Thomason. To fully exploit the findings of the present study, however, new development to the Gurson modeling framework is required. As it sits, this classical micro-mechanics based damage model omits any gradient effects and, hence, cannot accurately represent the stresses over the multiple scales involved in the ductile failure process.

ACKNOWLEDGEMENT

The work is financially supported by the VILLUM FOUNDATION Young Investigator Programme in the project ”A New Phenomenon Yet to be Resolved in ductile PLATE tearing”, grant VKR023451.

References

[1] Benzerga, A., Leblond, J.-B. : Ductile fracture by void growth to coalescence, Advances in Applied Mechanics 44:169305, 2010.
[2] Fleck, N., Willis, J.R. : A mathematical basis for strain-gradient plasticity. Part II: Tensorial plastic multiplier, J. Mech. Phys. Solids, 57:10451057, 2009.
[3] Gologanu, M., Leblond, J.-B., Perrin, G. and Devaux, J. : Recent extensions of Gursons model for porous ductile metals, In: Suquet, ed., Continuum Micromechanics, CISM Courses and Lecture 377 Continuum Micromechanics, Springer-Verlag, Berlin, 61130, 1997.
[4] Gurson, A.: Continuum theory of ductile rupture by void nucleation and growth - i. yield criteria and flow rules for porous ductile media, J. Eng. Mater. Technol., 9:215, 1977.
[5] Nielsen, K.L, Niordson, C.F., : A numerical basis for strain-gradient plasticity theory: Rate-independent and rate-dependent formulations, J. Mech. Phys. Solids, 63:113-127, 2014.
[6] Tekoğlu, C., Leblond, J.-B., Pardoen, T.: A criterion for the onset of void coalescence under combined tension and shear. J. Mech. Phys. Solids, 60:1363-1381, 2012.
[7] Thomason, P.F. : Ductile Fracture of Metals, 1st ed. Pergamon Press, Oxford, England, 1990.
[8] Tvergaard, V. : Material failure by void growth to coalescence, Advances in Applied Mechanics, 27:83151, 1990.

IMPLICIT FINITE ELEMENT ALGORITHMS FOR HIGHER-ORDER GRADIENT PLASTICITY THEORY

Andrea Panteghini[1] and Lorenzo Bardella *[1]
[1]*Department of Civil, Environmental, Architectural Engineering and Mathematics, University of Brescia, Italy*

Summary We propose an implicit time integration Finite Element (FE) algorithm for Gradient Plasticity (GP) theory, involving both energetic and dissipative higher-order contributions. We consider both phenomenological and crystal GP, in which the free energy includes the so-called defect energy, a function of Nye's dislocation density tensor. By considering many benchmarks (simple shear of a constrained strip, torsion of thin wires, bending of thin foils, micro-indentation), we show that the conceptually most straightforward FE implementation, in which the displacements and the relevant plastic components are employed as nodal degrees of freedom, leads to a very efficient FE algorithm if a proper regularisation of the viscoplastic potential is adopted, the latter in general involving dissipative higher-order terms. The proposed viscoplastic constitutive law can also accurately represent rate-independent behaviour, without losing computational efficiency.

INTRODUCTION

This investigation is concerned with the modelling of the size-dependent mechanical behaviour of metallic micro-devices undergoing inhomogeneous plastic flow (see, e.g., [1, 2, 3, 4]). In particular, we focus on work-conjugate, higher-order GP theories (see, e.g., [5, 6, 7, 8, 9, 10]), extending both *phenomenological* and *crystal* plasticity theories. About phenomenological GP theories, we distinguish between Strain Gradient Plasticity (SGP) and Distortion Gradient Plasticity (DGP), depending on whether the contribution of the plastic spin is neglected (see, e.g., [7]) or not (see [8, 11, 12] and references therein).

The development of the GP theories here concerned has long been hampered by difficulties in efficiently and accurately solving relevant boundary value problems. In fact, the partial differential equations governing higher-order GP have been known to be difficult to solve for two- and three-dimensional boundary value problems by using standard implicit FE integration algorithms (see, e.g., [13]). To address this issue, some investigators have developed non-standard FE codes. Among them, we mention a few noticeable examples. Niordson and co-authors (e.g., [14, 15]) have successfully developed explicit FE codes for various higher-order SGP theories. Forest and co-workers have instead proposed a micromorphic approach (see, e.g., [16, 17] and references therein), consisting of a penalty method applied to GP. We propose implicit time integration FE algorithms for work-conjugate GP theories involving energetic and dissipative higher-order contributions. A common feature of all the GP theories here considered is the free energy term called the defect energy [6], written in terms of Nye's dislocation density tensor $\boldsymbol{\alpha}$, defined as $\boldsymbol{\alpha} = \mathrm{curl}\boldsymbol{\gamma}$, with $\boldsymbol{\gamma}$ denoting the plastic distortion. We will show that the conceptually most straightforward FE implementation, in which displacements and either plastic distortion components or plastic slips are employed as nodal degrees of freedom, leads to a very efficient FE algorithm if a proper regularisation of the viscoplastic potential is adopted. It will be also shown that the proposed viscoplastic constitutive law can accurately reproduce rate-independent material behaviour for an appropriate choice of a rate-sensitivity material parameter, without losing computational efficiency.

THE VISCOPLASTIC POTENTIAL REGULARISATION

To present our proposal, here we restrict our attention to Gurtin [8] DGP theory (see also [11], adopting the same notation employed here). In this theory, whose governing equations are provided in [8, 11], the dissipative stresses depend on the following effective plastic flow rate, $\dot{E}^p$, and effective flow resistance, Σ:

$$\dot{E}^p = \sqrt{\frac{2}{3}|\dot{\boldsymbol{\varepsilon}}^p|^2 + \chi|\dot{\boldsymbol{\vartheta}}^p|^2 + \frac{2}{3}L^2|\nabla\dot{\boldsymbol{\varepsilon}}^p|^2}\,, \quad \Sigma = \sqrt{\frac{3}{2}|\boldsymbol{\rho}|^2 + \frac{1}{\chi}|\boldsymbol{\omega}|^2 + \frac{3}{2L^2}|\boldsymbol{T}|^2} \tag{1}$$

in which $\dot{\boldsymbol{\varepsilon}}^p = \mathrm{sym}\dot{\boldsymbol{\gamma}}$ is the plastic strain rate (work conjugate to the stress $\boldsymbol{\rho}$), $\dot{\boldsymbol{\vartheta}}^p = \mathrm{skw}\dot{\boldsymbol{\gamma}}$ is the plastic spin (work conjugate to the stress $\boldsymbol{\omega}$), $\boldsymbol{T}$ is a third-order stress work-conjugate to $\nabla\dot{\boldsymbol{\varepsilon}}^p$, L is a dissipative material length parameter, and χ is the material parameter governing the dissipation due to $\dot{\boldsymbol{\vartheta}}^p$. $\dot{E}^p$ and Σ are work conjugate under the following stress prescription:

$$\boldsymbol{\rho} = \frac{2}{3}\frac{\Sigma}{\dot{E}^p}\dot{\boldsymbol{\varepsilon}}^p\,, \quad \boldsymbol{\omega} = \chi\frac{\Sigma}{\dot{E}^p}\dot{\boldsymbol{\vartheta}}^p\,, \quad \boldsymbol{T} = \frac{2}{3}L^2\frac{\Sigma}{\dot{E}^p}\nabla\dot{\boldsymbol{\varepsilon}}^p \tag{2}$$

satisfying the 2nd Law independently of the adopted constitutive law for $\Sigma(\dot{E}^p, E^p)$. This type of constitutive assumption, in which the *rates* of some appropriate measures of plastic deformation are conjugate to *finite* stress measures, characterises the so-called *non-incremental* theories [18]. Viscoplasticity, given by the dependence of Σ on $\dot{E}^p$, allows plasticity to develop at

*Corresponding author. Email: lorenzo.bardella@ing.unibs.it

any stress level, in an amount dependent on the material rate-sensitivity. Within this framework, one avoids the implementation of any yield criterion or special treatment of the internal surfaces between elastic and plastic domains, the latter being an important issue to be addressed in rate-independent formulations (see, e.g., [15]). Although we employ a viscoplasticity framework, thus retaining its well-known computational advantages, in the following we propose a law $\Sigma(\dot{E}^p, E^p)$ allowing the use of very small rate-sensitivity. More specifically, we will demonstrate that the proposed law for $\Sigma(\dot{E}^p, E^p)$ leads to results that are substantially rate-independent, without losing computational efficiency. A convenient form of $\Sigma(\dot{E}^p, E^p)$, very often adopted in literature, assumes $\Sigma(\dot{E}^p, E^p) = \sigma_Y(E^p)V(\dot{E}^p)$ in which $\sigma_Y(E^p)$ includes the isotropic hardening law. In this contribution, the choice of $V(\dot{E}^p)$ is a key point, as it plays a crucial role in obtaining a very efficient kinematics-based FE algorithm. In literature, the most exploited form of $V(\dot{E}^p)$ is the power-law $V(\dot{E}^p) \propto (\dot{E}^p)^n$, which has many convenient features [19]. However, numerically, a plain power-law may turn out in lack of convergence if the increment in plastic flow is not large enough, for small rate-sensitivity exponent n. In particular, in plasticity applications $n \in (0, 1)$, so that the derivative of $V(\dot{E}^p)$ with respect to $\dot{\boldsymbol{\gamma}}$, necessary to compute the tangent stiffness, is unbounded for $\dot{E}^p \to 0$, resulting in an ill-conditioned FE system to solve. To overcome this difficulty, here we propose:

$$V(\dot{E}^p) = \begin{cases} \dot{E}^p & \text{if } \dfrac{\dot{E}^p}{\dot{\varepsilon}_0} \leq 1 \\ 2\dot{\varepsilon}_0 & \\ 1 - \dfrac{1}{2}\dfrac{\dot{\varepsilon}_0}{\dot{E}^p} & \text{if } \dfrac{\dot{E}^p}{\dot{\varepsilon}_0} > 1 \end{cases} \tag{3}$$

in which $\dot{\varepsilon}_0 > 0$ is a material parameter and the rate-independent limit is attained for $\dot{\varepsilon}_0 \to 0$. Function (3) is a suitably smooth regularisation of a unit-step function and admits a convex potential. Such a function comes from a well-known approximation of the modulus function, whose robustness was proven in the Sixties in the context of Mathematical Statistics [20]. Note that choice (3) of $V(\dot{E}^p)$ was already adopted in [12], in an even richer form involving one more parameter. However, in [12] attention was restricted to the one-dimensional description of the torsion problem, in which the displacement field is assumed pointwise, so that the balance equations in weak form are solved for $\dot{\boldsymbol{\gamma}}$ only.

CONCLUSIONS

In this contribution we will demonstrate the computational efficiency of the viscoplastic function (3) for general purpose FE implementation of GP, with emphasis on very small rate-sensitivity, to accurately model material rate-independence. To this purpose, we will plug the viscoplastic function (3) both in the above mentioned Gurtin [8] DGP and in the crystal GP developed in [21] to model the latent hardening size effect predicted by discrete dislocation dynamics simulations.

References

[1] Ashby M.F.: The deformation of plastically non-homogeneous materials. Philos Mag 21:399-424, 1970.
[2] Fleck N.A., Muller G.M., Ashby M.F., Hutchinson J.W.: Strain gradient plasticity: theory and experiments. Acta Metall Mater 42:475-487, 1994.
[3] Nix W.D., Gao H.: Indentation size effects in crystalline materials: A law for strain gradient plasticity. J Mech Phys Solids 46:411-425, 1998.
[4] Stölken J.S., Evans A.G.: A microbend test method for measuring the plasticity length scale. Acta Mater 46:5109-5115, 1998.
[5] Fleck N.A., Hutchinson J.W.: Strain gradient plasticity. Adv Appl Mech 33:295-361, 1997.
[6] Gurtin M.E.: A gradient theory of single-crystal viscoplasticity that accounts for geometrically necessary dislocations. J Mech Phys Solids 50:5-32, 2002.
[7] Gudmundson P.: A unified treatment of strain gradient plasticity. J Mech Phys Solids 52:1379-1406, 2004.
[8] Gurtin M.E.: A gradient theory of small-deformation isotropic plasticity that accounts for the Burgers vector and for dissipation due to plastic spin. J Mech Phys Solids 52:2545-2568, 2004.
[9] Bardella L.: A deformation theory of strain gradient crystal plasticity that accounts for geometrically necessary dislocations. J Mech Phys Solids 54:128-160, 2006.
[10] Kuroda M., Tvergaard V.: On the formulations of higher-order strain gradient crystal plasticity models. J Mech Phys Solids 56:1591-1608, 2008.
[11] Bardella L.: Size effects in phenomenological strain gradient plasticity constitutively involving the plastic spin. Int J Eng Sci 48:550-568, 2010.
[12] Bardella L., Panteghini A.: Modelling the torsion of thin metal wires by distortion gradient plasticity. J Mech Phys Solids 78:467-492, 2015.
[13] Lele S.P., Anand L.: A small-deformation strain-gradient theory for isotropic viscoplastic materials. Philos Mag 88:3655-3689, 2008.
[14] Niordson C.F., Legarth B.N.: Strain gradient effects on cyclic plasticity. J Mech Phys Solids 58:542-557, 2010.
[15] Nielsen K.L., Niordson C.F.: A numerical basis for strain-gradient plasticity theory: Rate-independent and rate-dependent formulations. J Mech Phys Solids 63:113-127, 2014.
[16] Mazière M., Forest S.: Strain gradient plasticity modeling and finite element simulation of Lüders band formation and propagation. Continuum Mech Therm 27:83-104, 2015.
[17] Chang H.-J., Cordero N.M., Déprés C., Fivel M., Forest S.: Micromorphic crystal plasticity versus discrete dislocation dynamics analysis of multilayer pile-up hardening in a narrow channel. Arch Appl Mech 86:21-38, 2016.
[18] Fleck N.A., Hutchinson J.W., Willis J.R.: Strain gradient plasticity under non-proportional loading. Proc. R. Soc. London A 470:20140267, 2014.
[19] Needleman A.: Material rate dependence and mesh sensitivity in localization problems. Comput Method Appl M 67:69-85, 1988.
[20] Huber P.J.: Robust Estimation of a Location Parameter. Ann Math Statist 35:73-101, 1964.
[21] Bardella L., Segurado J., Panteghini A., Llorca J.: Latent hardening size effect in small-scale plasticity. Modelling Simul Mater Sci Eng 21:055009, 2013.

ENERGY-BASED FORMULATION OF EQUIVALENT INHOMOGENEITY FOR INTERPHASE MODELS

Lidiia Nazarenko[1], Henryk Stolarski[2] & Holm Altenbach [1a)]
[1]*Institute of Mechanics, Otto von Guericke University Magdeburg, Magdeburg, Germany*
[2]*Department of Civil, Environmental and Geo- Engineering, University of Minnesota, Minneapolis, USA*

Summary A new concept of equivalent inhomogeneity is proposed to analyze the effective properties of composites with interphases using techniques devised for problems without interphases. The basic idea is to replace the inhomogeneity and the surrounding it interphase by a single equivalent inhomogeneity, combining properties of both, which is then perfectly boned to the matrix. The definition of the equivalent inhomogeneity proposed in this work is based on Hill's energy equivalence principle. It is more general than definitions proposed in the past in that, conceptually and practically, it allows considering inhomogeneities of various shapes and various models of interphases. This is illustrated considering spherical inhomogeneity with two models of interphases, Gurtin-Murdoch material surface model and spring layer model. Comparisons with the best available solutions are made and other possible applications are discussed.

GENERAL FORMULATION OF THE PROBLEM

The main idea of the Energy Equivalent Inhomogeneity (EEI) consists in using the energy approach to replace the system consisting of the original inhomogeneity and surrounding interphase of thickness h by a single uniform inhomogeneity. Various types of interphases may be considered, but both the interphase and the inhomogeneity are assumed elastic with their own distinct properties.

To find the properties of the EEI it is assumed that the displacements at the matrix/interphase boundary result from an arbitrary constant strain $\boldsymbol{\varepsilon}_{eq}$. At equilibrium these displacements cause the attendant strain fields (or displacement jumps) within the original inhomogeneity and the interphase, both of which depend on $\boldsymbol{\varepsilon}_{eq}$. The strain energy associated with the equilibrium state of such system, being the sum of the energies of the original inhomogeneity and its interphase, is then a quadratic function of $\boldsymbol{\varepsilon}_{eq}$. Given that the interphase is typically thin and that the matrix/interphase displacements correspond to a constant $\boldsymbol{\varepsilon}_{eq}$, it is plausible to assume that the strain field within the original inhomogeneity will be nearly uniform $\boldsymbol{\varepsilon} \neq \boldsymbol{\varepsilon}_{eq}$. it is assumed that the original spherical inhomogeneity undergoes rigid body motion, described by a constant small strain tensor . Consequently, the mathematical expression of energy equivalence takes the form [1]:

$$E = \frac{1}{2} V_{eq} \boldsymbol{\varepsilon}_{eq} : \mathbf{C}_{eq} : \boldsymbol{\varepsilon}_{eq} = E_{\mathrm{i}}\left(\boldsymbol{\varepsilon}_{eq}, \boldsymbol{\varepsilon}(\boldsymbol{\varepsilon}_{eq})\right) + \frac{1}{2}\int_{V_1} \boldsymbol{\varepsilon}(\boldsymbol{\varepsilon}_{eq}) : \mathbf{C}_1 : \boldsymbol{\varepsilon}(\boldsymbol{\varepsilon}_{eq})\, dV_1 , \tag{1}$$

where V_{eq} is the sum of the volumes of the original inhomogeneity V_1 and of the interphase V_{i}, E_{i} is the strain energy of the interphase, $\mathbf{C}_1$ and $\mathbf{C}_{eq}$ are the constitutive tensors of the original inhomogeneity and of the equivalent inhomogeneity (to be determined), respectively. E_{i} depends on the specific model of the interphase employed and various possibilities are possible in this regard. In each of those possibilities E_{i} is described by a quadratic form on the set $\{\boldsymbol{\varepsilon}, \boldsymbol{\varepsilon}_{eq}\}$. Minimization of the energy described by Eq. (1) with respect to $\boldsymbol{\varepsilon}$ yields a relation of the type

$$\boldsymbol{\varepsilon} = \mathbf{T} : \boldsymbol{\varepsilon}_{eq} . \tag{2}$$

Gurtin-Murdoch surface model

The model is based on the assumption that the interphase is infinitesimally thin, coherent (i.e., displacements are continuous), and develops its own surface stresses $\boldsymbol{\sigma}_S$. Consequently, the interphase conditions take the following form

$$[\![\mathbf{u}]\!]_{S_{\mathrm{i}}} = \mathbf{0}, \qquad [\![\boldsymbol{\sigma}]\!]_{S_{\mathrm{i}}} \cdot \mathbf{n} + \mathrm{div}_{S_{\mathrm{i}}} \boldsymbol{\sigma}_S = \mathbf{0}, \tag{3}$$

where $\mathbf{u}$ is the displacement vector, $\boldsymbol{\sigma}$ is the stress tensor in the bulk material and $\mathbf{n}$ is unit vector normal to interphase; $[\![\bullet]\!]$ indicates the jump of field quantities across the surface while $\mathrm{div}_{S_{\mathrm{i}}}$ represents the surface divergence. The material surface constitutive equation is described by the following equation

$$\boldsymbol{\sigma}_S = \tau_0 \overset{2}{\mathbf{I}}_S + 2\left(\mu_S - \tau_0\right)\boldsymbol{\varepsilon}_S + \left(\lambda_S + \tau_0\right)\mathrm{tr}\,\boldsymbol{\varepsilon}_S \overset{2}{\mathbf{I}}_S + \tau_0 \nabla_S \mathbf{u} . \tag{4}$$

in which $\boldsymbol{\varepsilon}_S$ is the surface strain tensor, $\overset{2}{\mathbf{I}}_S$ represents the identity tensor in the plane tangent to the surface, τ_0 is the magnitude of the deformation-independent (residual) surface stress, λ_S, μ_S are surface Lamé parameters, while $\nabla_S \mathbf{u}$ denotes the surface gradient of the interface displacement field.

[a)] Corresponding author. Email: holm.altenbach@ovgu.de.

To find the properties of the energy-equivalent inhomogeneity Eq. (1) is evaluated. Under the specific assumptions of the model one has $\boldsymbol{\varepsilon}_1 = \boldsymbol{\varepsilon}_{eq}$. This leads to the following expression describing the energy equivalence, [1]:

$$E = \frac{1}{2} V_1 (\boldsymbol{\varepsilon}_{eq} : \mathbf{C}_{eq} : \boldsymbol{\varepsilon}_{eq}) = \frac{1}{2} V_1 (\boldsymbol{\varepsilon}_{eq} : \mathbf{C}_1 : \boldsymbol{\varepsilon}_{eq}) + E_i \,, \tag{5}$$

where V_1 is the volume of the inhomogeneity and

$$E_i = \frac{1}{2} \oint_S \left[2(\mu_S - \tau_0) \boldsymbol{\varepsilon}_S : \boldsymbol{\varepsilon}_S + (\lambda_S + \tau_0) \, \mathrm{tr}(\boldsymbol{\varepsilon}_S)^2 + \tau_0 \nabla_S \mathbf{u} : \nabla_S \mathbf{u} \right] dS \,. \tag{6}$$

Spring layer model of interphase

In all past discussions of spring layer that model its thickness was assumed to be negligible and, consequently, it was also assumed that the interphase tractions remain continuous while displacements suffer a jump. In this work the spring layer thickness is small but finite. As a result its mathematical description is

$$[\![\boldsymbol{\sigma} dS]\!]_S \cdot \mathbf{n} = \left[\boldsymbol{\sigma}_2 dS_2 - \boldsymbol{\sigma}_1 dS_1 \right] \cdot \mathbf{n} = \mathbf{0} \,, \qquad \mathbf{K} \cdot [\![\mathbf{u}]\!]_S = \boldsymbol{\sigma}_1 \cdot \mathbf{n} \,, \tag{7}$$

where the superscripts 1 and 2 indicate that the appropriate quantities are evaluated on the inhomogeneity or the matrix side of the spring layer. $\mathbf{K} = K_n \mathbf{n} \otimes \mathbf{n} + K_s \mathbf{s} \otimes \mathbf{s} + K_t \mathbf{t} \otimes \mathbf{t}$ is a second-order tensor which contains the spring layer stiffness parameters K_n and K_t in normal and tangential directions, respectively, while $\mathbf{s}$ and $\mathbf{t}$ represent two orthogonal unit vectors in the plane tangent to the interface. For soft, isotropic and elastic interphase K_n and K_t are $K_n = (\lambda_i + 2\mu_i)/h$, $K_t = \mu_i / h$. The surface elements dS_1 and dS_2 in Eq. $(7)_1$ are assumed to be related to the inhomogeneity side of the layer, the area dS_2 – to the matrix side. In this case the general formula of energy equivalence given in Eq. (1) takes form [2]:

$$E = \frac{1}{2} V_2 (\boldsymbol{\varepsilon}_{eq} : \mathbf{C}_{eq} : \boldsymbol{\varepsilon}_{eq}) = \frac{1}{2} V_1 (\boldsymbol{\varepsilon} : \mathbf{C}_1 : \boldsymbol{\varepsilon}) + E_i \,, \quad \text{where} \quad E_i = \oint_{S_1} \frac{1}{2} \left\{ K_n \left| \Delta \mathbf{u}_n \right|^2 + K_t \left| \Delta \mathbf{u}_t \right|^2 \right\} dS \,, \tag{8}$$

with $\Delta \mathbf{u}_n$ and $\Delta \mathbf{u}_t$ denoting normal and tangential displacement jumps which are dependent on $\boldsymbol{\varepsilon}$ present in Eq. (1). To determine the stiffness tensor of the equivalent inhomogeneity the energy of the inhomogeneity/spring-layer system is first minimized with respect to $\boldsymbol{\varepsilon}$ to relate those tensors to $\boldsymbol{\varepsilon}_{eq}$ (cf. Eq. (2)). The energy at the minimum is assumed to be the energy of the equivalent inhomogeneity from which its properties result.

NUMERICAL RESULTS

The effective bulk and shear moduli, evaluated for various models of interphases (Gurtin-Murdoch surface model – (a) and (b); spring layer model – (c)) on the basis of the method of conditional moments [3] in combination with EEI approach are presented in Fig.1 and are in a good agreement with numerical results available in the literature [2].

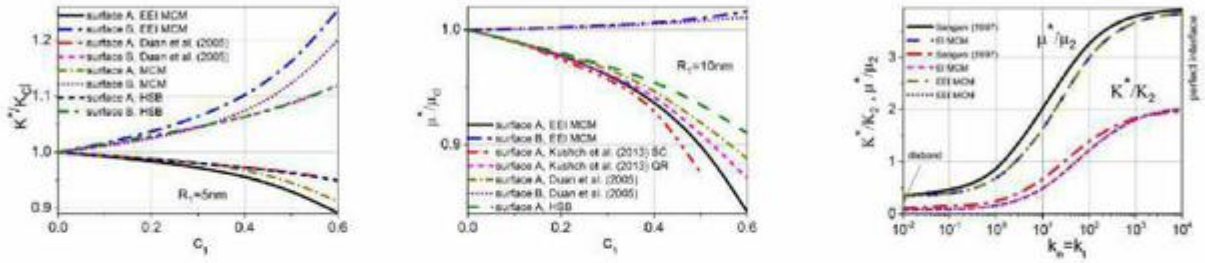

a) b) c)

Fig. 1: Dependence: the normalized bulk modulus K^* / K_{cl} (a) and shear modulus μ^* / μ_{cl} (b) on the void volume fraction c_1 for the radius of a spherical nanocavity $R_1 = 10$ (nm) and normalized bulk K^* / K_2 and shear μ^* / μ_2 moduli (c) for a material with rigid inhomogeneities on tangential and normal bond parameters $k_t = R_1 K_t$ and $k_n = R_1 K_n$ if $k_n = k_t$.

References

[1] Nazarenko L., Bargmann S., Stolarski H.: Energy-equivalent inhomogeneity approach to analysis of effective properties of nano-materials with stochastic structure. *Int. J. Solids Struct.* **59**:183-197, 2015.

[2] Nazarenko L., Stolarski H.: Energy-based definition of equivalent inhomogeneity for various interphase models and analysis of effective properties of particulate composites. *Compos. Part B*, [Under Review].

[3] Nazarenko L., Khoroshun, L., Müller, W.H., Wille, R.: Effective thermoelastic properties of discrete-fiber reinforced materials with transversally-isotropic components. *Cont. Mech. Thermodyn.* **20**:429-458, 2009.

SOME FEATURES OF DISSIPATIVE THEORIES OF STRAIN-GRADIENT PLASTICITY

Daya Reddy *[1], Andrew McBride[2], Francois Ebobisse[3], Carsten Carstensen[4], and Paul Steinmann[1]

[1]*Department of Mathematics & Applied Mathematics, University of Cape Town, Rondebosch, South Africa*
[2]*School of Engineering, University of Glasgow, Glasgow, United Kingdom*
[3]*Department of Mathematics & Applied Mathematics, University of Cape Town, Rondebosch, South Africa*
[4]*Centre for Scientific Computing, Humboldt University Berlin, Berlin, Germany*
[5]*Chair of Applied Mechanics, University of Erlangen-Nuremberg, Germany*

Summary A critical investigation is carried out of a strain-gradient plasticity theory. The theory is dissipative in nature, in the sense that the plastic strain-gradient terms and associated length scale enter through the flow relation, rather than through the free energy. It is shown that the yield condition and flow relation take a global form, in contrast to conventional theories in which these are posed locally, that is, pointwise in the domain. Recent studies of particular examples of non-proportional loading have highlighted interesting and novel features of dissipative strain-gradient theories. These features, such as a delayed resumption of plastic loading following non-proportional increments in loading, are explored further computationally, and the behaviour thus obtained is studied with a view to relating it to the specific features of the flow relation in the dissipative theory.

INTRODUCTION

Strain-gradient theories of plasticity were first proposed some three decades ago, with a view to extending conventional theories of plasticity in such a way as to capture length-dependent effects, which are important at the mesoscale. Among the various strain-gradient theories now in existence, a popular class relates to those in which stress terms conjugate to the plastic strain and its gradient are introduced, for example through a virtual power principle, and which furthermore are thermodynamically consistent. Gradient theories can be energetic in nature, in the sense that they incorporate gradient terms in the specification of the free energy. Alternatively or in addition, they can be dissipative, in that the gradient terms appear in the flow relation. In the latter case the flow relation follows directly from a reduced dissipation inequality that involves the plastic strain and its gradient, with the conjugate stress quantities.

In this presentation the model of strain-gradient plasticity proposed in [1], and further developed for the rate-independent case in [2], is adopted as the model for further investigation. In this model there are various features of the dissipative formulation that distinguish it quite markedly from the classical problem. For example, the yield function and flow relation are posed locally in terms of the conjugate stress quantities rather than the Cauchy stress. This begs the question as to how yield is determined, given that these conjugate quantities are indeterminate in the elastic region. It has been shown [2] that it is necessary for the flow relation to be posed in weak or global form in order that it might be expressed in terms of the Cauchy stress.

Further unusual features of the dissipative formulation are discussed in [3]. These authors explore the differences between dissipative and energetic models by studying simple examples of non-proportional loading. They investigate in detail one-dimensional problems with non-proportional loading effected through the imposition of passivation of the surfaces of the bodies after these have developed plastic behaviour. A key feature of the behaviour following passivation in the plastic range is the existence of an elastic gap: that is, a phase of elastic behaviour, with a delayed resumption of plastic loading.

CURRENT WORK

The aim of this contribution is to explore further theoretically and computationally the features of the dissipative model of strain-gradient plasticity, in this way complementing the study in [3] and developing a better understanding of the mathematical and mechanical aspects of the model.

Theoretical studies of the flow relation

By exploiting the formulation of the flow relation in terms of a dissipation function, we show how the conjugate stresses may be eliminated through a global approach, so that the relation may be expressed in terms of the Cauchy stress. This in turn allows yield to be determined in the usual way, albeit in terms of a global rather than local criterion. We focus on a dissipation function D of the form $D(\dot{E}^p) = \sigma_0 \dot{E}^p$ in which σ_0 is a measure of initial yield stress, $\dot{E}^p = \sqrt{|\dot{\varepsilon}^p|^2 + \ell^2 |\nabla \dot{\varepsilon}^p|^2}$ is a generalized plastic strain rate, and ℓ is a length scale. It is shown that the process for determining yield based on the global dissipation $\mathcal{D} = \int_\Omega D(\dot{E}^p)\, dx$ is complex, and as far as the authors can determine, not amenable to closed-form solution. Progress is however made by examining instead a spatially discrete version of the global flow relation, of the form that arises

*Corresponding author. Email: daya.reddy@uct.ac.za

for example in the use of finite element approximations. The discrete form of $\mathcal{D}$ is shown to depend on a quadratic function of the discrete stresses. This differs however from the yield function that is obtained simply by generalizing the classical von Mises yield condition, and emphasizes the global nature of the flow relation for the dissipative problem.

Numerical studies

A series of numerical examples is studied with a view to exploring some of the features that emerge from the theoretical investigation. One of the problems studied is that of a rod in tension, and with two possible boundary conditions on the plastic strain: either microhard, in which the plastic strain is prescribed, or microfree, in which flux of the plastic strain gradient is prescribed. Passivation of the boundary in the plastic range – essentially, changing the boundary condition to microhard – leads to an initial elastic response and elastic gap, of the kind observed in [3]. The presence of two curves, for the two boundary conditions, helps to identify the elastic gap as a means by which to move from one yield surface, corresponding to one boundary condition, to another, corresponding to the other boundary condition.

A second example is that of a plate loaded biaxially, with similarly alternative boundary conditions. These and other numerical examples shed light on the behaviour peculiar to the dissipative formulation, and allow the differences between this and the energetic formulation of the strain-gradient theory to be better understood.

References

[1] Gurtin M. E. and Anand L.:A Theory of Strain-Gradient Plasticity for Isotropic, Plastically Irrotational Materials. Part I: Small Deformations. J. Mech. Phys. Solids 53:1624-1649, 2005.

[2] Reddy B. D.: The Role of Dissipation and Defect Energy in Variational Formulations of Problems in Strain-Gradient Plasticity. Cont. Mech. Thermodyn. 23:527-549, 2011.

[3] Fleck N. A., Hutchinson J. W. and Willis J. R.: Strain Gradient Plasticity Under Non-Proportional Loading. Proc. R. Soc. A 470, DOI: 10.1098/rspa, 2014.0267, 2014.

STEADY-STATE NUMERICAL MODELING OF SIZE EFFECTS IN WIRE DRAWING

Kristian J. Juul *[1], Kim L. Nielsen[1], and Christian F. Niordson[1]
[1]*Department of Mechanical Engineering, Solid Mechanics, Technical University of Denmark, DK-2800 Kgs. Lyngby, Denmark*

Summary Wire drawing processes at micron scale receive increased interest as micro wires are increasingly required in micro electrical components. At the micron scale, size effects become important and have to be taken into consideration. The goal is to optimize the semi-cone angle of the tool in terms of drawing force. The present study employs a steady-state modelling technique that omits the transient regime, thus creating a basis for comprehensive parameter studies. The steady-state procedure is based on the streamline integration method presented by Dean and Hutchinson [1]. This approach allows elastic-plastic loading/unloading to be taken into account and it is readily implemented into an existing finite element program. The numerical model deals with a time dependent material model that includes strain gradient effects according, to Fleck and Willis theory [2]. The analysis indicates that size effects reduce the optimal semi-cone angle of the tool with up to 40%.

FRAMEWORK

The wire drawing process is used in manufacturing at all scales, ranging from several centimetres to a few microns, and the growing production of micro components has increased the demand for micro wires (diameter $\sim 10\mu$m). Micro wires are typically applied in semiconductors and electrical winding coils. At this scale, so-called size effect are inevitable in the production and therefore requires attention. The size effects are explained by the effect of geometrically necessary dislocations which follows from the development of large strain gradients. It is well established that size effects appear as either increased hardening or strengthening at the micron scale.

A numerical investigations of wire drawing at the micron scale in steady-state can be found in Byon et. al. [3]. Their work however, is based on rigid plasticity, where residual stresses and the associated material behaviour is neglected. The steady-state model employed in the current study readily accounts for these effects and is based on the early work of Dean and Hutchinson [1] for crack growth problems. The objective of the present study is to present a method which lends itself nicely for numerical implementation and is capable of handling elastic unloading and size effects within a steady-state framework. The model developed will be exploited to quantify the effect of strain gradients related to the wire drawing process. Similar studies concerning rolling has recently been conducted by Nielsen [4].

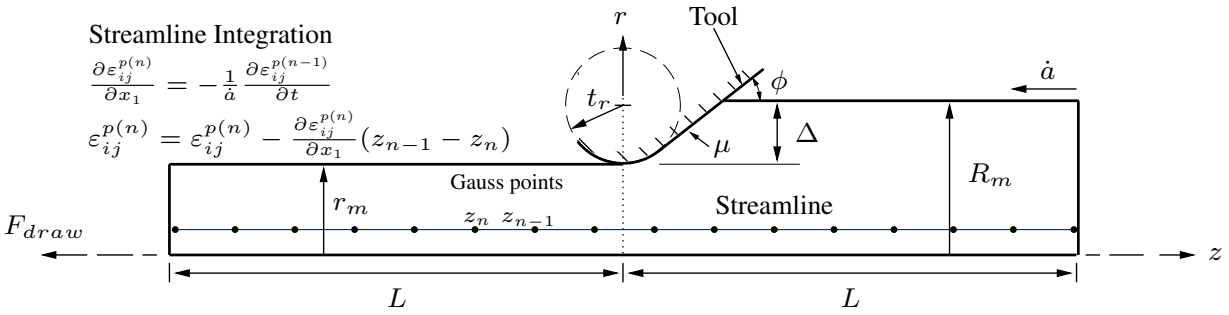

Figure 1: Parametrization of the wire drawing process in the adopted steady-state framework with axisymmetry around z. Throughout the study, $R_m/(2L) = 1/10$ and the finite element mesh employed consists of square elements with side length $L^{(e)}/R_m = 20$.

The framework for the numerical analysis is based on a finite element elastic-viscoplastic steady-state model, accounting for strain gradient effects. The model is formulated in 2D, under the assumptions of axisymmetry where the tensor notation should be interpreted as components 1,2,3 being the radial (r), axial (z) and angular (θ) direction, respectively.

To accommodate the size effect in the mirco wire drawing process, an accurate numerical model is required to represent material behaviour over the range of length scales involved. Several numerical models capable of handling size effects have been developed over the years and, in the current study, the higher order elastic-viscoplastic material model presented by Fleck and Willis [2] is adopted. For a first approximation, Coulomb friction and small strains are accepted.

In the steady-state framework, the domain remain fixed relative to the tool while the material moves through the domain whereby the field quantities become stationary to an observer located at the tool. Thus, stationarity simplifies the numerical task of modelling effects such as the contact with the tool. Based on the definition of the steady-state, time derived quantities $\dot{f}$ in the constitutive model can be related to a spatial derivative through the velocity $\dot{a}$ along a streamline (illustrated in Fig. 1), according to $\dot{f} = \not{\dot{a}} \partial f/\partial z$. Thus, any incremental quantity at a given material point can be evaluated by integrating along a streamline in the direction of the material movement, starting upstream of the tool and ending at the point of interest. The point of interest will then contain the history of all upstream points.

*Corresponding author. Email: krjoju@mek.dtu.dk

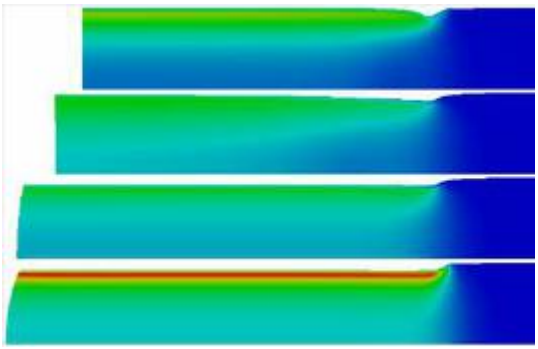

(a) Effective plastic strain in the wire through the iteration stages of the steady-state procedure ($L_D/H = 0$). Deformations are amplified by a factor of 10.

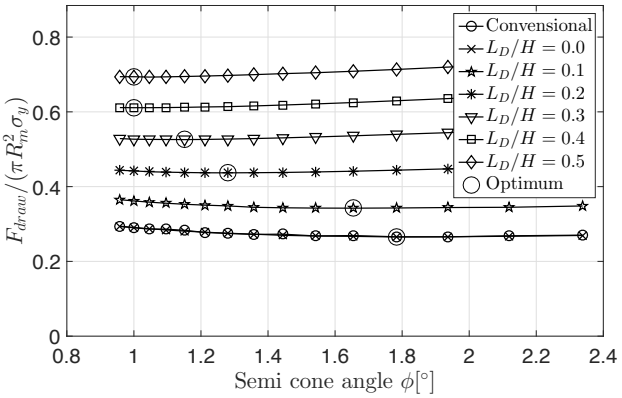

(b) Drawing force F_{draw} vs. semi-cone angle ϕ.

Figure 2: Wire drawing for conventional and strain gradient models with $\Delta/R_m = 0.01$, $\mu = 0.1$, $N = 0.2$, $m = 0.02$, $\sigma_y/E = 0.001$, $\dot{\varepsilon}_0 = 0.001$, $\dot{a} = \alpha R_m \dot{\varepsilon}_0$ (with $\alpha = 500$), and $t_r/R_m = 0.25$. The energetic length parameter $L_E = 0$.

RESULTS

The iterative process of determining the steady-state is illustrated in Fig. 2a. Four steps in the iteration is presented (start, two intermediate and final), where the first step corresponds to the tool being pressed into the material. In the following steps, the history dependence, obtained through streamline integration, will ensure that the material downstream hold the load history of the tool contact. In the last step, the converged solution is obtained. A small elastic spring back is observed as a result of the residual stresses accounted for in the model. Fig. 2b presents an example of the effect from strain gradients in terms of drawing force as a function of the semi-cone angle, ϕ, for various dissipative length parameter L_D. For $L_D \to 0$, the model reduces to a conventional J2 flow theory model neglecting size effects, which is also confirmed in Fig. 2b by a direct comparison. An increase in L_D is found to lower the optimal semi-cone angle. In general, an increasing gradient effect lead to increasing drawing force as a result of the strain gradient hardening effect. In Fig. 2b, the optimum points are marked with circles. When observing optimum points across length parameters, the sensitivity to gradient effects are seen to be significant for small L_d/H, while the tool angle seems to converge to a constant value for large L_D/H.

CONCLUDING REMARKS

The steady-state procedure presented by Dean and Hutchinson [1] offers a simple way to include history dependent elastic-plastic behaviour, thus allowing elastic unloading and residual stresses/strains to be accounted for (key in cold working processes). Combined with the gradient enhanced elastic-viscoplastic material model by Fleck and Willis [2] a model for comprehensive parameter studies of size effects in the wire drawing process has been established as an example.

The study demonstrates how strain gradients decrease the optimal semi-cone angle with up to approximately 0% as a result of the additional micron scale hardening.

ACKNOWLEDGEMENT

The work is financially supported by The Danish Council for Independent Research in the project "New Advances in Steady-State Engineering Techniques", grant DFF-4184-00122.

References

[1] Dean R.H., Hutchinson J.W.: Quasi-Static Steady Crack Growth in Small-Scale Yielding, Fracture Mechanics: Twelfth Conference, ASTM STP700, American Society for Testing and Materials, pp. 383-405, 1980.

[2] Fleck N.A., Willis J.R.: A mathematical basis for strain-gradient plasticity theory. Part II: Tensorial plastic multiplier, Mech. Phys. Solids, 57, pp. 1141-1057, 2009.

[3] Byon S.M., Moon C.H., Lee Y.: Strain gradient plasticity based finite element analysis of ultra-fine wire drawing, J. Mech. science & technology, 23, pp. 3374-3384, 2009.

[4] Nielsen K. L.: Rolling induced size effects in elastic-viscoplastic sheet metals, Euro. J. Mech., 53, pp. 259-267, 2015

SPECTRAL NON-LOCAL CRYSTAL PLASTICITY MODELLING OF SIZE EFFECTS IN POLYCRYSTALS

Ricardo A. Lebensohn[1a)] & Alan Needleman[2]
[1] Materials Science and Technology Division, Los Alamos National Laboratory, MS G755, Los Alamos, NM 87845, USA
[2] Department of Materials Science and Engineering, Texas A&M University, College Station, TX 77843, USA

Summary The numerical implementation of a non-local polycrystal plasticity theory using the FFT-based formulation of Moulinec and Suquet [1] is presented. Gurtin's [2] non-local formulation has been incorporated in the elasto-viscoplastic (EVP-FFT) algorithm of Lebensohn et al. [3]. Numerical procedures for the accurate estimation of higher order derivatives of micromechanical fields, required for feedback into single crystal constitutive relations, are identified and applied. A simple case of a periodic laminate made of two fcc crystals is first used to assess the soundness and numerical stability of the proposed algorithm. Different behaviors at grain boundaries are explored, and the one consistent with the micro-clamped condition gives the most pronounced size effect. The new formulation is applied to the case of 3-D fcc polycrystals, illustrating the possibilities offered by the proposed scheme to accurately solve large problems in reasonable computing times.

INTRODUCTION

Since the main mechanism of metal plasticity is dislocation slip, and dislocations are characterized by a length scale given by the Burgers vector, size dependence naturally emerges. Plastic strain gradients give rise to dislocation structures, termed geometrically necessary dislocations (GNDs) that induce a size effect at the micro-scale. We have developed a computational capability for predicting the size dependence of the mechanical response of polycrystals based on a phenomenological size-dependent crystal plasticity theory. In particular, our calculations are based on the theory introduced by Gurtin [2], which accounts for size dependence arising from plastic strain gradients and, as a consequence, involves slip gradients and higher order boundary conditions. These complicate crystal plasticity (CP) finite element (FE) calculations, which have been generally restricted to single crystal two-dimensional problems.

In recent years, a highly efficient alternative to CPFE for the numerical treatment of plasticity of heterogeneous media using fast Fourier transforms (FFT) has been proposed and applied to a suite of problems involving the determination of micromechanical fields and effective response in polycrystalline materials. This spectral formulation, originally developed by Suquet and co-workers (e.g. [1]) as an efficient method to compute the micromechanical response of periodic heterogeneous materials, including the possible use of direct input from microstructural images, has been adapted to polycrystals deforming in the elasto-viscoplastic regime [3].

MODEL

The local EVP-FFT method for 3-D polycrystals has been extended to account for size dependence arising from slip gradients. The salient aspects of the non-local plasticity theory [2] and the casting of the latter into the EVP-FFT algorithm [3], including the computation of a back-stress field that in the non-local theory affects the constitutive behaviour at the single crystal level is given in Ref. [4]. The resulting formulation is applied here to the case of a simple bicrystal laminate configuration in order to demonstrate the numerical stability of the method. Further, it was also applied to study the influence of various model parameters and interface conditions on the prediction of size dependence (see [5] for details). We also report here cases of 3-D polycrystals, considering two types of boundary conditions at grain boundaries: (i) one corresponding to allowing slip to freely pass through the boundary and (ii) one completely blocking slip.

RESULTS

The proposed FFT-based non-local polycrystal plasticity numerical implementation is illustrated by applications to: 1) bicrystals, by means of which we demonstrate the numerical stability of the proposed scheme. We have also conducted parametric studies [4], highlighting the influence of different numerical and constitutive parameters on the predictions of the non-local model, and 2) 3-D polycrystals, which allows us to exemplify the robustness and efficiency of the present numerical scheme to solve large 3-D problems.

The bicrystal configuration adopted here to assess the proposed formulation consists of a periodic unit cell made of two fcc single crystal laminates of the same volume fraction. The crystals are infinitely extended along the y- and z-directions and separated by straight interfaces normal to the x-direction. The axes of both crystals are aligned with sample axes. Heterogeneity is introduced in the plastic properties by specifying two different initial values of the flow strength. Both crystals have the same isotropic elastic properties. A uniaxial stress state along x is prescribed. The symmetry of the loading

a) Corresponding author. Email: lebenso@lanl.gov

with respect to the crystals' orientation determines that 8 out 12 (111)<110> slip systems are equally activated. The laminate geometry determines that some strain components and the complementary stress components are uniform throughout the unit cell. Moreover, the local plasticity theory predicts that the 8 active slip fields are uniform within each crystal, with the amplitude of the jump across the interface being determined by the contrast in flow strength C. This implies that the non-local theory should predict a progressive build-up of back-stress fields near the interface. Figure 1 shows the influence of the material length-scale. All cases correspond to a contrast C=2 in plastic properties. Figures 1a and 1b show a zoom near the interface of the back-stress and slip fields, respectively, for different values of the ratio of grain size to material length d/l. The non-local theory predicts the formation of a boundary layer region in which the slip fields smoothly vary between the two different uniform values in the bulk of each laminate, and back-stress peaks on both sides of the interface, showing a smooth decay to zero as the distance from the interface increases. Specifically concerning the effect of the material length-scale, the back-stress and the thickness of the boundary layer increase as d/l decreases, that is when the material length-scale becomes comparable with the grain size, in which case the size effect becomes stronger.

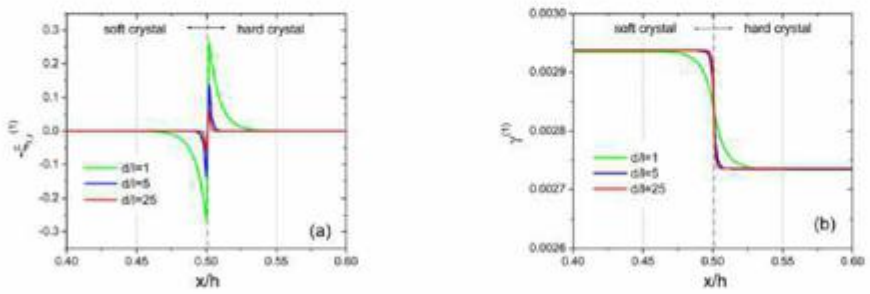

Figure 1: Influence of the material length-scale. Zoom near the interface of: (a) back-stress and (b) slip fields, for active slip system #1 after 1% strain, for different d/l ratios.

Figure 2 shows results of the non-local theory for micro-free and micro-clamped interfaces for 3-D polycrystals made of fcc grains generated by Voronoi tessellation. In the micro-free case, grains in which the back-stress associated with a given slip system has high positive or negative values are those where the slip on that system is favored, and their immediate neighbors. In terms of macroscopic response, a very mild effective stress increase is obtained using the non-local formulation with micro-free interfaces, compared with the local theory [4]. In the micro-clamped case, the back-stress is concentrated at grain boundaries with peak values that are more than one order of magnitude higher than in the micro-free case. The slip fields are more heterogeneous, adopting relatively high values in the bulk of some well oriented grains that tend to vanish in the proximities of grain boundaries. The effective stress-strain curves predicted by the local formulation and the non-local theory for different d/l ratios under micro-clamped conditions confirms that the size effect on the effective stress-strain response for this boundary condition at grain boundaries (GB) is significant.

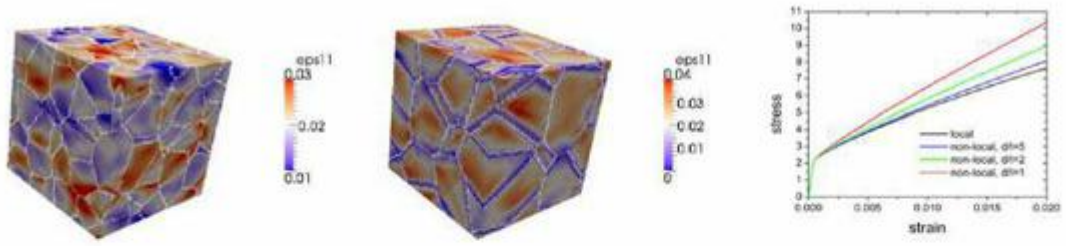

(a) (b) (c)

Figure 2: Predicted strain field (d/l=1) for: a) micro-free, b) micro-clamped GB conditions. c) Stress strain response for different d/l ratios, for micro-clamped GB conditions.

CONCLUSIONS

A non-local polycrystal plasticity theory has been numerically implemented using a FFT-based formulation. Numerical procedures for the accurate estimation of higher order derivatives of micromechanical fields were identified and different behaviors at grain boundaries were explored. Further details of the formulation and additional results can be found in Ref. [4].

References

[1] Moulinec, H., Suquet, P.: Numerical method for computing the overall response of nonlinear composites with complex microstructure. *Comput. Methods in Appl. Mech. Eng.* **157**, 69, 1998.

[2] Gurtin, M.E.: A gradient theory of single-crystal viscoplasticity that accounts for geometrically necessary dislocations. *J. Mech. Phys. Solids* **50**, 5, 2002.

[3] Lebensohn, R.A. Kanjarla, A., Eisenlohr, P.: An elasto-viscoplastic formulation based on fast Fourier transforms for the prediction of micromechanical fields in polycrystalline materials. *Int. J. Plasticity* **32-33**, 59, 2012.

[4] Lebensohn, R.A., Needleman, A.: Numerical implementation of non-local polycrystal plasticity using Fast Fourier Transforms. *J. Mech. Phys. Solids*, in press.

MODELING OF SIZE EFFECTS IN PLASTICITY USING FIELD DISLOCATION MECHANICS

Saurabh Puri[1a)], Amit Acharya[2]
[1]*Dassault Systemes Simulia Corp, Johnston, RI, USA*
[2]*Department of Civil and Environmental Engineering, Carnegie Mellon University, Pittsburgh, PA, USA*

Summary In this talk, the effect of sample size on the mechanical response of micron-sized crystals will be analysed using a mesoscopic model of field dislocation mechanics. The computational experiments performed using this field model show that the spatial distribution of statistical dislocation sources and polar dislocations, and dislocation accumulation along the grain boundaries and passivation layers, are responsible for these experimentally observed size effects. Continuum representation of the microscopic features, such as operation of dislocation sources and interaction of grain boundaries with dislocations, will also be discussed in this talk.

INTRODUCTION

It is observed in an array of experiments that plastic response of micron-sized crystalline solids depends on the size of the specimen (e.g. Uchic et al., 2004; Xiang and Vlasaak, 2006). Smaller specimens show a stiffer mechanical response and a significantly stronger Bauschinger effect in comparison to the large-sized specimens. The classical continuum plasticity approach cannot model these size effects due to the absence an explicit representation of dislocations. A mesoscopic field model of dislocation mechanics (MFDM), developed by (Acharya and Roy, 2006), can simulate permanent deformation at the mesoscale. The evolution equation for mesoscale dislocation density imposes a jump condition across a material interface. This jump condition allows modeling of interaction of dislocations with interfaces (Acharya, 2007).

A study of the effect of sample size on the mechanical response of single crystals and multicrystalline thin films using MFDM will be presented in this talk. The equations of MFDM are briefly discussed in the next section, followed by a description of crucial results. The paper ends with some concluding remarks.

THEORY

A fine scale field model of dislocation mechanics (FDM) combines the conventional plasticity framework and the theory of continuously distributed defects (Kroner 1981; Mura 1963) by specifying the rate of change of plastic distortion as (Acharya, 2001),

$$\dot{\boldsymbol{U}}_{\boldsymbol{p}} = \boldsymbol{\alpha} \times \boldsymbol{V} \tag{1}$$

where $\boldsymbol{\alpha}$ is the polar dislocation density tensor field and $\boldsymbol{V}$ represents the velocity of polar dislocations. $\boldsymbol{U}_{\boldsymbol{p}}$ is decomposed uniquely into compatible and incompatible parts as (Acharya and Roy, 2006),

$$\boldsymbol{U}_{\boldsymbol{p}} = grad\boldsymbol{z} - \boldsymbol{\chi} \tag{2}$$

where the gradient of the vector field $\boldsymbol{z}$ represents the compatible part of $\boldsymbol{U}_{\boldsymbol{p}}$ and $\boldsymbol{\chi}$ represents the incompatible part of $\boldsymbol{U}_{\boldsymbol{p}}$. $\boldsymbol{\chi}$ cannot be written as a non-trivial gradient and is given by,

$$curl\,\boldsymbol{\chi} = \boldsymbol{\alpha},\ div\,\boldsymbol{\chi} = \boldsymbol{0},\ \boldsymbol{\chi n} = \boldsymbol{0} \text{ on } \partial B \tag{3}$$

where $\boldsymbol{n}$ is the unit normal on the boundary ∂B of the body. The field $\boldsymbol{z}$ obeys the relation,

$$div(grad\,\dot{\boldsymbol{z}}) = div\dot{\boldsymbol{U}}_{\boldsymbol{p}} \tag{4}$$

The highly nonlinear transport of polar dislocation density is characterized by a partial differential equation based on the conservation of Burgers vector:

$$\dot{\boldsymbol{\alpha}} = -curl\dot{\boldsymbol{U}}_{\boldsymbol{p}} \tag{5}$$

The stress tensor and polar dislocation velocity need to be specified constitutively. FDM has been shown to predict the stress field of a single dislocation using linear elasticity (Roy and Acharya, 2005) as well as model the evolution of single dislocation and dislocation walls using non-convex energy (Das et. al, 2013, Zhang et al. 2015). An elementary space-time averaging of the equations of this fine scale model results in the mesoscopic field dislocation mechanics model (Acharya and Roy (2006)). On averaging, all of the above equations have the same form except the equation for the rate of plastic distortion. The average rate of plastic distortion is calculated as follows:

$$\dot{\bar{\boldsymbol{U}}}_{\boldsymbol{p}} = \overline{\boldsymbol{\alpha} \times \boldsymbol{V}} = \bar{\boldsymbol{\alpha}} \times \bar{\boldsymbol{V}} + \boldsymbol{L}_{\boldsymbol{p}} \tag{6}$$

where bar represents the averaged quantity. $\boldsymbol{L}_{\boldsymbol{p}}$ **r**epresents that part of the total slip strain rate which is not represented by the slipping produced by the averaged polar dislocation density. Thus, MFDM incorporates the plastic slip due to the long range interactions of polar dislocations as well as the short range interactions of statistical dislocations. In the MFDM model, the stress tensor, mean signed velocity of dislocation segments, and $\boldsymbol{L}_{\boldsymbol{p}}$ need to be specified constitutively based on the non-

[a)] Corresponding author. Email: **saurabhpuri2005@gmail.com**

negativity of plastic work. Linear elasticity is used in the problems that will be presented in this talk. MFDM is implemented using the finite element method, as described in Roy and Acharya (2006) and Puri et al. (2009).

RESULTS

Size effect in single crystals (Puri et al., 2009)

MFDM was used to model the experimentally observed size effects in unconstrained single crystals (Uchic et al. (2004)). For problems mentioned in this subsection, $\boldsymbol{L_p}$ is based on the *J2* plasticity model. Two different cases were considered. In the first case, cubical samples with a predefined spatial distribution of statistical dislocation sources were considered and in the second case, an initial predefined distribution of polar dislocation density was considered. It was deduced from these numerical experiments that the discrete description of sources and physical length scales in dislocation velocity cause size effect in unconstrained single crystals. Also, the mechanical response of these specimens changed significantly on changing the spatial distribution of statistical dislocation sources.

Size effect in multicrystalline thin films (Puri et al., 2011)

The effect of film thickness, grain orientation, grain boundary constraints to plastic flow, and surface passivation on the mechanical response of multicrystalline thin films was studied using MFDM. $\boldsymbol{L_p}$ was specified using the crystal plasticity model with a nonlinear kinematic hardening law based on the Armstrong-Frederick (1966) form. The back stress was assumed to be a function of polar dislocation density tensor. The jump condition, imposed by the evolution equation for polar dislocation density, was used to model different plastic flow conditions through a grain boundary. It was found that dislocation accumulation along the constraints, such as grain boundaries and passivation layers, is responsible for the strong size and Bauschinger effect in thin films undergoing subsequent cycles of loading and unloading.

CONCLUSIONS

MFDM successfully modeled the size effects in mechanical response of crystalline solids, caused by discrete microstructures, such as a network of polar dislocations, distribution of statistical dislocation sources, and grain boundaries. The novel feature is that the effect and evolution of these microstructures can be reliably modeled using this continuum approach at physically reasonable strain rates.

References

[1] Acharya A.: A model of crystal plasticity based on the theory of continuously distributed dislocations. *Journal of the Mechanics and Physics of Solids* **49**: 761- 785, 2001.

[2] Acharya A.: Jump condition for GND evolution as a constraint on slip transmission at grain boundaries. *Philosophical Magazine* **87**: 1349-1359, 2007.

[3] Acharya A., Roy A.: Size effects and idealized dislocation microstructure at small scales: Predictions of a Phenonmenological model of Mesoscopic Field Dislocation Mechanics: Part I. *Journal of the Mechanics and Physics of Solids* **54**: 1687- 1710, 2006.

[4] Armstrong P.J., Frederick C.O.: A mathematical representation of the multiaxial Bauschinger effect. *Technical Report C. E. G. B.*, Report RD/B/N731, Berkeley Nuclear Laboratories, 1966.

[5] Das A., Acharya A., Zimmer J., Matthies K.: Can equations of equilibrium predict all physical equilibria? A case study from Field Dislocation Mechanics. *Mathematics and Mechanics of Solids* **18**: 801-820, 2013.

[6] Kroner E.: Continuum theory of defects. *In: Balian, R., et al. (Ed.), Physics of Defects, North-Holland Publishing Company, Amsterdam*: 217–315, 1981.

[7] Mura T.: Continuous distribution of moving dislocations. *Philosophical Magazine* **89**: 843–857, 1963.

[8] Puri S., Das A., Acharya A.: Mechanical response of multicrystalline thin films in mesoscale field dislocation mechanics. *Journal of the Mechanics and Physics of Solids* **59**: 2400-2417, 2011.

[9] Puri S., Roy A., Acharya A., Dimiduk D.M.: Modeling dislocation sources and size effects at initial yield in continuum plasticity. *Journal of Mechanics of Materials and Structures* **4**: 1603-1618, 2009.

[10] Roy A., Acharya A.: Finite element approximation of field dislocation Mechanics. *Journal of the Mechanics and Physics of Solids* **53**: 143-170, 2005.

[11] Roy A., Acharya A.: Size effects and idealized dislocation microstructure at small scales: Predictions of a Phenonmenological model of Mesoscopic Field Dislocation Mechanics: Part II. *Journal of the Mechanics and Physics of Solids* **54**: 1711- 1743, 2006.

[12] Uchic M. D., Dimiduk D. M., Florando J. N., Nix W. D.: Sample dimensions influence strength and crystal plasticity. *Science* **305**: 986-989, 2004.

[13] Xiang Y., Vlassak J. J.: Bauschinger and size effects in thin-film plasticity. *Acta Materialia* **54**: 5449-5460, 2006.

[14] Zhang X., Acharya A., Walkington N. J., Bielak J.: A single theory for some quasi-static, supersonic, atomic, and tectonic scale applications of dislocations. *Journal of the Mechanics and Physics of Solids* **84:** 145-195, 2015.

[a)] Corresponding author. Email: **saurabhpuri2005@gmail.com**

A STUDY OF TWO APPROACHES TO HIGHER-ORDER SINGLE CRYSTAL PLASTICITY

Jason Mayeur[1] and David McDowell *[2]

[1]*Theoretical Division, Los Alamos National Laboratory, Los Alamos, New Mexico, USA*
[2]*Woodruff School of Mechanical Engineering, Georgia Institute of Technology, Atlanta, Georgia, USA*
[2]*Georgia Tech Institute for Materials, Atlanta, Georgia, USA*

Summary In the following, we examine the theoretical structure and numerical predictions of micropolar and Gurtin type models of higher-order single crystal plasticity. The models are discussed within a continuum thermodynamic setting, which facilitates identification of equivalent terms and their roles in the respective models. Finite element simulations are used to elucidate the various scale-dependent strengthening mechanisms and their effect of material response. Our analysis shows that the two theories contain many analogous features and qualitatively predict the same trends in mechanical behavior, in spite of substantially different points of departure. This is significant since the micropolar theory affords a simpler numerical implementation that is less computationally expensive.

INTRODUCTION

Generalized single crystal plasticity theories can be separated into two distinct classes: i) low-order theories and ii) higher-order theories, which are differentiated, in part, by the order of the governing differential equations. Higher-order theories are further subdivided into work conjugate and non-work conjugate theories [1], with the distinction that work conjugate theories feature higher-order stress measures (hyperstresses) and nonstandard expressions of deformation power. Higher-order theories have recently gained favor amongst researchers since they admit boundary conditions on slip or alternative supplementary kinematic variables that are necessary for modeling certain classes of problems. In the following, we examine both Gurtin type and micropolar theories of single crystal plasticity. A key aspect of work conjugate higher-order theories is the separation of gradient strengthening effects into energetic and dissipative contributions. Energetic gradient effects reflect scale-dependent behavior that emerges from the free energy dependence on nonlocal variables, whereas dissipative gradient effects contribute to size-dependent dissipation. It has been argued that both energetic and dissipative gradient behavior must be accounted for in order to capture trends exhibited for certain sets of experimental data. Gurtin's [2] model has been adopted and advanced by many researchers, therefore, it is beneficial to understand how alternative nonlocal theories relate to it. We have been working with one such alternative, micropolar single crystal plasticity [3], that built upon earlier work of Forest and collaborators [4]. Despite appreciable foundational differences, the micropolar model was demonstrated to predict many of the same trends in scale-dependent behavior as exhibited by Gurtin type theories. Significantly, both models have also established that they can capture certain aspects of two-dimensional discrete dislocation dynamics simulations [5, 6]. Motivated by these results and the fact that the micropolar theory offers a simpler and less computationally expensive numerical implementation, we explore the relationship between the two frameworks.

MODEL SUMMARY AND METHODS

The essential distinction between the micropolar and Gurtin type theories is that the additional power conjugate kinematic variables in the former are introduced via a microrotation field, whereas the slip system shears are used in the latter. Some consequences of choosing the slip system shears, i.e. inelastic variables, as the additional micro degrees-of-freedom (dof) are: (1) an alternative thermodynamic approach in which energetic-dissipative decompositions are proposed for the thermodynamic tensions rather than proposing elastic-plastic decompositions for the thermodynamic displacements associated with the newly introduced micro dofs, (2) the admissibility of Dirichlet boundary conditions on slip fields, and (3) a more computationally expensive formulation since the number of global dofs scales with the number of slip systems considered. Due to these foundational differences, we have carried both theoretical and finite element (FE) analysis to study the relationships between the seemingly disparate approaches generalized single crystal plasticity. To do so, we cast the governing equations of the respective theories within a thermodynamic setting to facilitate the identification of equivalent terms and to ensure that the proposed constitutive equations are thermodynamically consistent. Attendant FE simulations are used to demonstrate the qualitative agreement of several aspects of predicted scale-dependent material behavior. The simulation results also highlight model differences that become apparent when dissipative gradient behavior is considered, which is directly related to underlying structural differences of the governing equations.

*Corresponding author. Email: jmayeur@lanl.gov

RESULTS AND DISCUSSION

Theoretical comparison of the Gurtin type and micropolar models reveals marked similarities between the frameworks and also some important differences. Both models were developed to describe the scale-dependent mechanical response due to the presence of geometrically necessary dislocations (GNDs). Significantly, the models contain back stresses that are proportional to GND density and/or lattice torsion-curvature gradients and arise from the higher-order balance laws. By presenting the models within a thermodynamic setting, we were able to establish numerous model equivalences with respect to the kinematics, kinetics, and dissipative constitutive relations. Comparison of simulation results demonstrates that the two models predict the same qualitative scale-dependent trends in material behavior when isotropic and energetic gradient strengthening components are isolated, an example of which is shown in Figure 1. Figure 1 shows the cumulative slip contours for a two-dimensional particle reinforced composite material predicted by both models. However, when dissipative gradient effects are active, the models give noticeably different responses, which ultimately can be traced back to the choice of micro dofs within each theory. In the Gurtin type theory, dissipative gradient strengthening can be isolated in the sense that it can be active even in the absence of energetic gradient strengthening. This scenario is precluded in the micropolar theory where it is possible to have energetic gradient strengthening without dissipative gradient effects, but not vice versa. This result is illustrated by comparing the microforce balance from Gurtin's theory to the inverted flow rule from the micropolar theory, both of which have been augmented by specific constitutive equations:

$$\tau^{\alpha} + \tilde{g}_0 \ell_{en}^2 \nabla \cdot \left[\left(\nabla \gamma^{\alpha} \cdot \mathbf{s}^{\alpha} \right) \mathbf{s}^{\alpha} \right] + L_d^2 \nabla \cdot \left[\tilde{g}^{\alpha} \left(\frac{d^{\alpha}}{d_0} \right)^{\frac{1}{m}} \frac{\left(\nabla \dot{\gamma}^{\alpha} \cdot \mathbf{s}^{\alpha} \right) \mathbf{s}^{\alpha}}{d^{\alpha}} \right] \nearrow \tilde{g}^{\alpha} \left(\frac{d^{\alpha}}{d_0} \right)^{\frac{1}{m}} \frac{\dot{\gamma}^{\alpha}}{d^{\alpha}} = 0 \tag{1}$$

$$\tau^{\alpha} + \mu \ell_e^2 \mathbf{t}^{\alpha} \cdot \left(\prod \cdot \bar{\boldsymbol{\kappa}}^{\mathrm{T}} \right) \nearrow \frac{\mu \ell_e^2}{L_p} \mathbf{t}^{\alpha} \cdot \left(\nabla \cdot \sum_{\beta} \varphi_{\perp}^{\beta} \mathbf{s}^{\beta} \otimes \mathbf{t}^{\beta} \right) \nearrow g^{\alpha} \left(\frac{\dot{\lambda}^{\alpha}}{\dot{\lambda}_0} \right)^{\frac{1}{m}} \frac{\dot{\gamma}^{\alpha}}{\dot{\lambda}^{\alpha}} = 0 \tag{2}$$

Note that the energetic and dissipative length scales appear isolated in separate terms in Eq. (1), whereas the third term in the inverted micropolar flow rule (Eq. (2)) contains both the elastic and plastic length scales. Therefore, both energetic and dissipative gradient effects are eliminated when $\ell_e = 0$; however, specifying a large value for L_p suppresses the dissipative gradient term irrespective of the value of ℓ_e. Another, perhaps more subtle, difference revealed by Eqs. (1) and (2) is that the dissipative gradient term in the microforce balance is a function of slip rate gradients, while it is a function of total plastic curvature in the inverted micropolar flow rule. These differences and their impact on predicted size-dependent behavior of polycrystalline ensembles will be explored in future work.

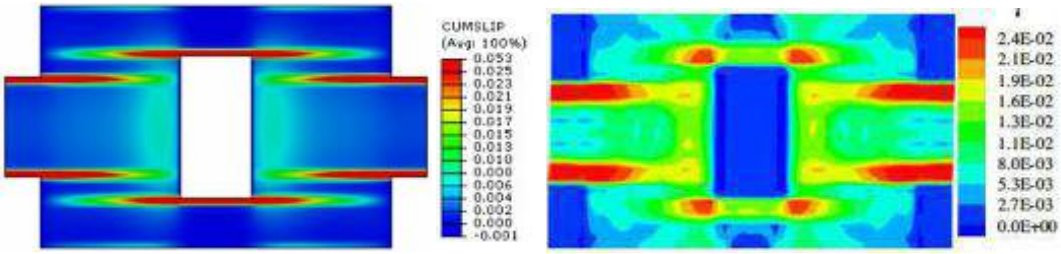

(a) (b)

Figure 1: Contours of cumulative slip at y = 0.006 (a) micropolar model and (b) Gurtin type model [5] ($H = C$).

References

[1] Kuroda M., Tvergaard V.: A finite deformation theory of higher-order gradient crystal plasticity. J. Mech Phys Solids 56:2573-2584, 2008.

[2] Gurtin, M. E.: A gradient theory of single-crystal viscoplasticity that accounts for geometrically necessary dislocations. J. Mech Phys Solids 1:5-32, 2002.

[3] Mayeur J. R., McDowell D. L., Bammann D. J.: Dislocation-based micropolar single crystal plasticity: Comparison of multi- and single criterion theories. J. Mech Phys Solids 59: 398-422, 2011.

[4] Forest S., Barbe F., Cailletaud G.: Cosserat modelling of size effects in the mechanical behaviour of polycrystals and multi-phase materials. Int J. Solids Struct 46: 7105-7126, 2000.

[5] Bittencourt E., Needleman A., Gurtin M. E., van der Giessen E.: A comparison of nonlocal continuum and discrete dislocation plasticity predictions. J. Mech Phys Solids 2: 281-310, 2003.

[6] Mayeur J. R., McDowell D. L.: An evaluation of higher-order single crystal strength models for constrained thin films subjected to simple shear. J. Mech Phys Solids 61: 1935-1954, 2013.

A MINIMAL GRADIENT-ENHANCEMENT OF CRYSTAL PLASTICITY THEORY

Henryk Petryk*[1] and Stanislaw Stupkiewicz[1]

[1]*Institute of Fundamental Technological Research (IPPT), Polish Academy of Sciences, Warsaw, Poland*

Summary A minimal gradient-enhancement of the continuum multislip theory of crystal plasticity for incorporating size effects is proposed. The concept of the tensorial density of geometrically necessary dislocations generated by in-plane slip gradients is combined with the classical Taylor formula for a flow stress. The derived internal length scale is expressed through standard parameters so that no extra assumption is needed to define a characteristic length. It is shown that this internal length scale is related to the mean free path of dislocations and hence possesses physical interpretation which is frequently missing in other gradient-plasticity models. While the resulting gradient-enhancement is extremely simple and involves no adjustable length-scale parameter, its verification by 3D finite element simulations of spherical indentation in a Cu single crystal shows good agreement with the experimentally observable size effect.

INTRODUCTION

The classical continuum theory of single crystals deformed plastically by multislip at finite strain [1] involves no internal length scale. To incorporate size effects, a number of strain-gradient theories of crystal plasticity have been proposed that use different sets of basic assumptions and exhibit different degrees of complexity, cf. [2, 3, 4]. The number of related 3D examples calculated with the use of a full set of slip systems is rather limited, which indicates the current need for developing a simple and verifiable gradient-enhanced crystal plasticity model. The following question is examined here: how to include the effect of the slip-rate gradients in a possibly simple way such that the internal length scale possess a physical meaning.

THE MAIN CONCEPT

We begin with the well-known observation [2] that the total dislocation density as an internal state variable is affected by slip-rate gradients that induce geometrically necessary dislocations (GNDs). Instead of analyzing GNDs separately for different slip systems and dislocation types as in more complex theories, the main concept here for monotonic deformation is as follows: while a fully general hardening moduli matrix $(h_{\alpha\beta})$ is taken from the classical theory, the gradient-enhancement is restricted to isotropic hardening part only. As the outcome, the following compact formula has been derived:

$$\dot\tau_\alpha^c = \sum_\beta h_{\alpha\beta}\dot\gamma_\beta + \theta\ell\dot\chi\,.$$

Here, τ_α^c is the current critical value of the resolved shear stress τ_α and $\dot\gamma_\alpha \geq 0$ is the slip-rate on the α-th slip system, so that without the last term we have the classical hardening law. In the gradient-sensitive last term of the derived form, ℓ is an internal length scale, θ an isotropic hardening modulus, and $\dot\chi$ the 'effective' plastic strain gradient rate defined by

$$\dot\chi = |\sum_\alpha (\mathbf{m}_\alpha \times \bar{\mathbf{F}}^{p\,\mathrm{T}}\,\nabla\dot\gamma_\alpha)\otimes\mathbf{s}_\alpha|\,,$$

where $\mathbf{m}_\alpha\otimes\mathbf{s}_\alpha$ denotes the α-th slip system dyad, $\mathbf{F}^p$ the plastic deformation gradient, and ∇ a reference gradient.

In particular, if the classical Taylor formula $\tau = a\mu b\sqrt{\rho}$ is adopted for an isotropic part τ of τ_α^c then the factor standing at $\dot\chi$ above takes the specific form

$$\theta\ell = \frac{a^2\mu^2 b}{2\tau}\,,$$

where the coefficient a, elastic shear modulus μ and Burgers vector modulus b are known constants for a given material. The gradient enhancement of any size-independent hardening rule $\dot\tau_\alpha^c = \sum_\beta h_{\alpha\beta}\dot\gamma_\beta$ by the term $\theta\ell\dot\chi$ is thus obtained in a definite way, with no length-scale parameter left free for describing the effects of slip-rate gradients represented by $\dot\chi$.

This minimal gradient-enhancement of crystal plasticity, as briefly outlined above, has not been found in the literature.

We have also shown that ℓ above is related to the mean free path of dislocations in a manner dependent on the dynamic recovery (annihilation) term in the equation for the net storage of dislocations [5] other than GNDs, and reduces to the dislocation mean free path in the special case when the annihilation term is disregarded. Hence, the present internal length scale ℓ possesses physical interpretation which is frequently missing in other gradient-plasticity models.

3D EXAMPLE: FINITE ELEMENT SIMULATION OF SPHERICAL INDENTATION

The gradient-enhanced crystal plasticity model has been implemented in a displacement-based finite element (FE) code. Incremental constitutive equations have been obtained by applying the implicit backward-Euler time integration scheme.

*Corresponding author. Email: hpetryk@ippt.pan.pl

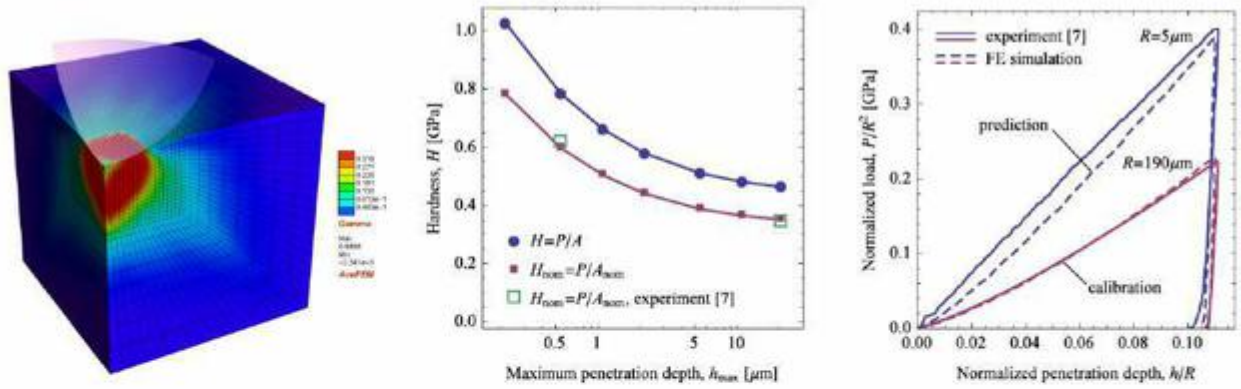

Figure 1: FE simulation of spherical indentation of (001)-oriented Cu single crystal: accumulated total plastic slip (left), dependence of hardness on the maximum penetration depth at fixed ratio $h_{\max}/R = 0.11$ (middle), and normalized size-dependent load–penetration depth curves (right).

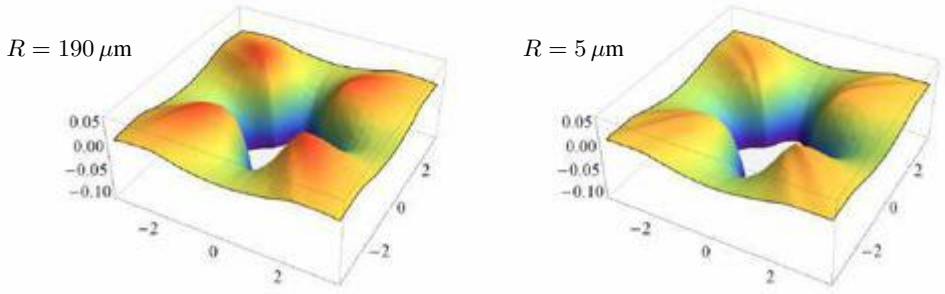

Figure 2: Predicted size-dependent normalized residual impressions: $R = 190\,\mu$m (left), $R = 5\,\mu$m (right).

The nonlinear FE equations are solved using the Newton method simultaneously with respect to all global unknowns, i.e. displacements, slip increments, as well as Lagrange multipliers for contact and symmetry constraints. The computations are carried out using *AceFEM*, a flexible FE code that is integrated with *AceGen*, an automatic code generation system [6].

Spherical indentation of a (001)-oriented Cu single crystal has been simulated for different values of indenter radius R. By exploiting the related symmetry, the actual computational domain is reduced to one quarter of the problem (Fig. 1, left). It is found that hardness as the ratio of penetration force P to contact area (nominal $A_{\rm nom}$ or actual A) increases with decreasing penetration depth h at fixed ratio $h/R = 0.11$ (Fig. 1, middle). The related effect on residual pile-up/sink-in topography is illustrated in Fig. 2. Comparison of calculated and experimental hardness and load–penetration depth curves (Fig. 1, experimental data after [7]) shows that the present model predicts the size effect quite satisfactorily, which is remarkable in view of no possibility of adjusting the internal length scale ℓ responsible for the size effect.

CONCLUSION

The proposed minimal gradient-enhancement of crystal plasticity theory leads to a good prediction of the experimentally observed size-effect in spherical indentation, in spite of the absence of any adjustable length-scale parameter in the model.

Acknowledgement. This work has been partially supported by the National Science Center (NCN) in Poland through Grant No. 2014/13/B/ST8/04286.

References

[1] Hill R., Rice J.R.: Constitutive analysis of elastic-plastic crystals at arbitrary strain. J. Mech. Phys. Solids 20:401-413, 1972.
[2] Nix W.D., Gao H.: Indentation size effects in crystalline materials: a law for strain gradient plasticity. J. Mech. Phys. Solids 35:300-314, 1998.
[3] Gurtin, M.E.: A finite-deformation, gradient theory of single-crystal plasticity with free energy dependent on the accumulation of geometrically necessary dislocations. Int. J. Plasticity 26:1073-1096, 2010.
[4] Miehe C., Mauthe S., Hildebrand F.: Variational gradient plasticity at finite strains. Part III: Local-global updates and regularization techniques in multiplicative plasticity for single crystals. Comput. Meth. Appl. Mech. Eng. 268:735-762, 2014.
[5] Kocks U.F., Mecking H.: Physics and phenomenology of strain hardening: the FCC case. Progress Mater. Sci. 48:171-273, 2003.
[6] Korelc J.: Multi-language and multi-environment generation of nonlinear finite element codes. Engineering with Computers, 18:312–327, 2002.
[7] Kucharski S., Stupkiewicz S., Petryk H.: Surface pile-up patterns in indentation testing of Cu single crystals. Exp. Mech. 54:957-969, 2014.

MICROSTRUCTURE EVOLUTION IN PLASTICITY

Tuncay Yalçinkaya*[1]

[1]*Department of Aerospace Engineering, Middle East Technical University, Ankara, Turkey*

Summary Deformation of polycrystalline metallic materials induces intrinsic formation and evolution of various types of microstructures at different length scales due to different underlying physical mechanisms affecting the plasticity, damage and fracture behavior. At nano-micro scale metals under irradiation develop certain zones free from irradiation and localization occurs in these areas as so-called clear bands affecting the ductility and the failure of the material. At meso scale dislocations form various dislocation cell structures induced by the deformation. At grain level polycrystalline materials develop stress and strain localization around the grain boundaries which could lead to inter-granular cracking e.g. through stress corrosion cracking. These are some examples to illustrate the influence of the microstructure on the global behavior of materials. In this context, the current work addresses different microstructure formation examples, focusing especially on the inter-granular deformation localization, through a strain gradient crystal plasticity framework and links it to different failure mechanisms.

THE MODEL

The employed crystal plasticity framework is developed in [1] as a non-convex model for deformation patterning modelling in single crystals. In this paper the convex counter-part of the model is also employed to model the inter-granular microstructure evolution in metallic materials (see (1)). The model is based on the additive decomposition of the strain into elastic and plastic components and the plastic slip field evolution is governed by

$$\dot{\gamma}^\alpha = \dot{\gamma}_0^\alpha \left(|\tau^\alpha + \nabla \cdot \xi^\alpha| / s^\alpha\right)^{\frac{1}{m}} \operatorname{sign}(\tau^\alpha + \nabla \cdot \xi^\alpha) \tag{1}$$

where $\tau^\alpha = \sigma : \mathbf{P}^\alpha$ is the resolved Schmid stress on the slip systems with $\mathbf{P}^\alpha = \frac{1}{2}(\mathbf{s}^\alpha \otimes \mathbf{n}^\alpha + \mathbf{n}^\alpha \otimes \mathbf{s}^\alpha)$, the symmetrized Schmid tensor, where $\mathbf{s}^\alpha$ and $\mathbf{n}^\alpha$ are the unit slip direction vector and unit normal vector on slip system α, respectively and ξ^α is the microstress vector $\xi^\alpha = \partial\psi_{\nabla\gamma}/\partial\nabla\gamma^\alpha = A\nabla\gamma^\alpha$ bringing the plastic slip gradients into the plasticity formulation. A is a scalar quantity, which includes an internal length scale parameter, and in this work it is defined as $A = ER^2/(16(1-\nu^2))$ as used in [2] where R is a typical length scale for dislocation interactions. In these types of models the internal length scale could be related to different microstructural features and the value would vary, e.g. [4] relates it to dislocation spacing, and [5] to grain size. In the following example we relate R to a certain percentage of the grain size to study its influence. (1) is considered as one of the governing equations together with linear momentum balance which are weighted, integrated and linearized in the finite element context and implemented as a coupled user element subroutine in ABAQUS software.

EXAMPLE

The current example concerns the inter-granular localization and its macroscopic size-effect in polycrystalline materials. Different geometries of polycrystalline aggregates containing 14, 110 or 212 grains are considered through Voronoi tessellation [3] Fig. 1. For each aggregate three different average grain sizes are used: D_{avg}=50, 100 and 150 μm. This compares well with the average grain sizes of AISI 304 stainless steels (1 to 47 μm, [6]) and AISI 316L (13 to 107 μm [7]).

Displacement loads are applied to the left and right edges in the global -X direction (left edge) and the global +X direction (right edge), resulting in macroscopic $< \epsilon_{11} >$=10 %. The symbol $\langle\rangle$ represents the Macaulay bracket, indicating a

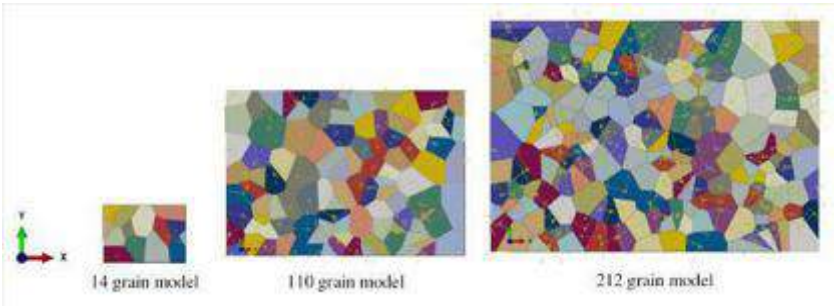

Figure 1: 14, 110 and 212 grain models. Grain orientations are given by local coordinate systems.

*Corresponding author. Email: yalcinka@metu.edu.tr

macroscopically averaged value. Rigid body movement is prevented by fixing the bottom left and bottom right nodes of the model in global Y direction. Material parameters are taken directly from the literature [1] and are used to demonstrate the strain gradient effects in the polycrstalline aggregates. The results of the heterogeneous local stress and strain distributions are presented in Fig. 2.

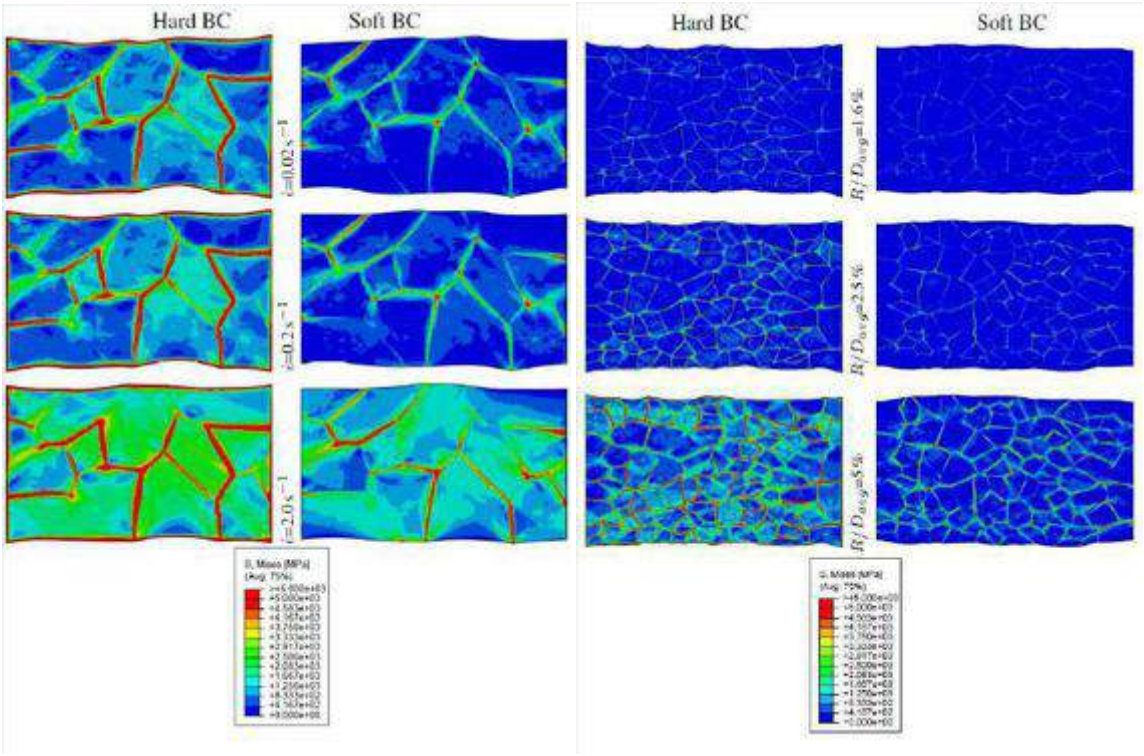

Figure 2: The effect of strain rates on the stress fields in a 14 grain aggregate with R/D_{avg}=5 % (on the left). The effect of different R/D_{avg} ratios on the stress fields in a 110 grain aggregrate with $\dot{\epsilon}$=0.02 s^{-1} (on the right).

CONCLUSIONS

In this paper a strain gradient crystal plasticity approach is applied for inter-granular deformation localization in polycrystalline materials. The presented results illustrate the influence of the deformation rate, boundary conditions and the grain size on the heterogeneous microscopic plastic deformation distribution. Macroscopic constitutive response and the intra-granular localization aspects through a non-convex potential term will be further discussed.

ACKNOWLEDGMENTS

T. Yalçinkaya gratefully acknowledges the support by the Scientific and Technological Research Council of Turkey (TÜBİTAK) under the 3001 Programme (Grant No. 215M381). The contributions of Dr. Izzet Ozdemir and Dr. Igor Simonovski in the numerical simulations are acknowledged as well.

References

[1] Yalçinkaya, T., Brekelmans, W., and Geers, M.: Non-convex rate dependent strain gradient crystal plasticity and deformation patterning. Int J. Solids Struct. 49:2625-2636, 2012.
[2] Bayley, C., Brekelmans, W., and Geers, M.: A comparison of dislocation induced back stress formulations in strain gradient crystal plasticity. Int J. Solids Struct. 43:7268-7286, 2006.
[3] Aurenhammer, F.: Voronoi Diagrams - A Survey of a Fundamental Geometric Data Structure. ACM Computing Surveys 23:345–405, 1991.
[4] Nix, W. D., and Gao, H.: Indentation size effects in crystalline materials: a law for strain gradient plasticity. J. Mech. Phys. Solids 46:411-425, 1998.
[5] Voyiadjis, G. Z., Abu Al-Rub, R. K.: Gradient plasticity theory with a variable length scale parameter. Int J. Solids Struct. 42:3998-4029, 2005.
[6] Di Schino, A., Kenny, J.: Grain size dependence of the fatigue behaviour of a ultrafine-grained AISI 304 stainless steel. Matter. Lett. 57:3182-3185, 2003.
[7] Feaugas, X., and Haddou, H.: Grain-size effects on tensile behavior of nickel and aisi 316l stainless steel. Metall. Mater. Trans. A 34:23292340, 2003.

XXIV ICTAM, 21-26 August 2016, Montreal, Canada

MECHANICAL PROPERTIES AND DEFORMATION MECHANISMS IN MATERIALS WITH GRADIENT TWIN STRUCTURES

Yujie Wei[1a)], Zhiwei Ma[1], Yongqiang Li[1], Lianchun Zhu[1], Yao Liu[1], Xianqi Lei[1], Gang Wang[2], Yanxin Wu[3], Zhenli Mi[3], Jiabin Liu[4], Hongtao Wang[4], Huajian Gao[5]

[1]LNM, Institute of Mechanics, Chinese Academy of Sciences, Beijing 100190, P.R. China

[2]Laboratory for Microstructures, Shanghai University, Shanghai 200444, P.R. China

[3]National Engineering Research Center for Advanced Rolling Technology, University of Science and Technology Beijing, Beijing 100083, P.R. China

[4]Institute of Applied Mechanics, Zhejiang University, Hangzhou, Zhejiang, 310027, China

[5]School of Engineering, Brown University, Providence, RI 02912, USA

Summary In this of discussion, we present experimental observation on how gradient twins could enhance the strength of a twin-induced plasticity steel while retaining its tensile ductility. The mechanisms accounting for the exceptional mechanical properties were investigated at the microscopic level. The switch of twinning systems at the grain level during different deformation stages and the subsequent formation of hierarchical nanotwinned structure are responsible for the strengthening and toughening of the material. In addition, we show how gradient microstructure in 304 austenitic steel enhances its fatigue performance.

INTRODUCTION

The outmost surface of engineering materials typically faces the most severe risk of damage. When such boundary conditions are given, employment of graded structures is desired to enhance the safety of the structure in an economic way. Mechanically, adopted gradient structures typically involves change in Young's modulus or strength, and are beneficial to crack shielding, reducing stress concentration, retarding shear localization, etc. In this talk, we cover the mechanical properties of materials when gradient structure is introduced. We will show how gradient twin could enhance the strength of TWIP steel while retain its ductility. In addition, the gradient structure could dramatically enhance the fatigue life of daily used steel.

EVADING THE STRENGTH-DUCTILITY TRADE-OFF IN TWIP STEEL

After applying torsion to cylindrical TWIP steel samples to generate a gradient nanotwinned structure along the radial direction, we find that the yielding strength of the material can be doubled at no reduction in ductility. It is shown that this evasion of strength-ductility trade-off is due to the formation of a gradient hierarchical nanotwined structure during pre-torsion and subsequent tensile deformation. A series of finite element simulations based on crystal plasticity are performed to understand why the gradient structure can cause strengthening and ductility retention, and how sequential torsion and tension lead to the observed hierarchical nanotwinned structure through activation of different twinning systems.

ENHANCES FATIGUE RESISTANCE OF STEELS WITH STRENGTH GRADIENT

We further show that by introducing a gradient microstructure into 304 austenitic steel, the fatigue life of the material could be substantially enhanced. Pre-notched samples with negative strength gradients in front of the notch's tip endure many more fatigue cycles than do samples with positive strength gradients during the crack initiation stage, and samples with either type of gradient perform better than do gradient-free samples with the same average yield strength. However, as a crack grows, samples with positive strength gradients exhibit better resistance to fatigue crack propagation than do samples with negative gradients or no gradient. This study demonstrates a simple and promising strategy for using gradient structures to enhance the fatigue resistance of materials and complements related studies of strength and ductility.

CONCLUSIONS

~~Graded materials are widely used~~ in engineering applications to provide, e.g., better resistance to thermomechanical loads in aero- and astronautical structures. Various ceramic and metallic alloys have been engineered to include spatial variations in material properties to provide improved performance with low weight and cost. Our study suggests that hardness or strength gradients could not only enhance the strength-ductility combination in some materials, but also improve the fatigue resistances of materials and calls for further studies to promote both fundamental understanding and practical applications of graded materials and structures.

References

[1] Fang, T. H., Li, W. L., Tao, N. R. & Lu, K.: Revealing extraordinary intrinsic tensile plasticity in gradient nano-grained copper. *Science* **331**,1587–1590, 2011.

[2] Lu, K.: Making strong nanomaterials ductile with gradients. *Science* **345**, 1455-1456, 2014.

[3] Wei, Y. J., Li, Y. Q., Zhu, L. C., Liu, Y., Lei, X. Q., Wang, G., Wu, Y. X., Mi, Z. L., Liu, J. B., Wang, H. T. & Gao, H. J.: Evading the strength-ductility trade-off dilemma in steel through gradient hierarchical nanotwins, *Nature Communications* **5**:3580, 2014.

[4] Ma, Z., Liu, J., Wang, G., Wang, H., Wei, Y., Gao, H.: Strength gradient enhances fatigue resistance of steels. *Sci. Reports*, in submission, 2015.

INVESTIGATIO ON THE SIZE EFF CT OF T INNING IN HCP S NGLE C YSTALS

Ya-Fang Guo[1a)], Shu ng Xu[1] , Xiao-Zhi Tang[1] & Qun Zu[1]
[1] *epartment o Mechanics, Beijing Jiaotong University, Beijing, hina*

Summary inning is generally consider d to be the p imary deformation mechanism for hexag nal close-pac ed (hcp) met ls due to their limited slip systems. Recent microcompression experiments point to strong size ef ects indicatin that pyrami al slips can do inate in deformation under compression. In this work, olecular dynamics simulations are applied to investig te the deformation mechanis s of magnesium and titani m single cry tals under compression at he nanoscale. It is found t at pyramidal slip dominate the comp ession defor ation, which is consis ent with e perimental bservations on microcompression. We als present anal sis on the twinnability of a ideal hcp si gle crystal at the nanoscale. A criterion or deformation twinning is derived by considering the elastic lattice-rotation strain. his analysis gives an inter retation of size effects in def rmation twin ing, at the sa e time it provides an explanation for the so-called stren th differential effect.

I TRODUCT ON

Because he number o slip systems is limited, deformation twinning plays significant role in the pla tic deformation of hexagonal close-packe (hcp) metals and alloys. In recent ye rs, microcompression exp riments on hcp metals have revealed intriguing aspects of twinning echanism, namely, a pronounced size effect on deformation in co pression. From in situ nano compression measurements in hcp tita ium, it was found for si gle crystal samples belo 1 μm in si e, deformation winning was entirely replaced by dislocation plasticity. At the same time, micropillar compression results or pure magnesium single-cr stal showed o twinning i samples fro approximately 2 to 10 μ in diameter, and pyrami al slips were r ported to dominate the plasticity.Alth ugh the size regime where the defor ation twinning vanished in magnesium is larger than that observ d in titaniu , the trend of transition in the defor ation mode from twinni g dominated to dislocation dominated is similar.

In the pr sent work, molecular dyna ics simulations are applied to investigate the deformation mechanis s of magnesi m and titanium ingle crystals under compression at the n noscale. A new criterion b sed on analy is of the elas ic strain caused by lattice-rot tion to describe the twinnability of a hcp crystal material is also presented.

M LECULAR DYNAMIC SIMULAT ONS

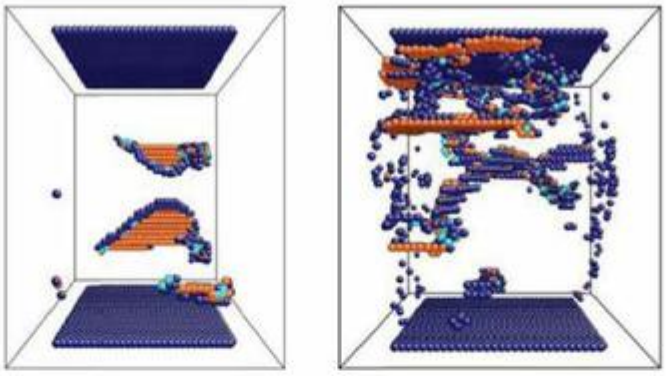

Fig.1. D formation of t e magnesium quare nanopill r under c-axis compression at different strains. (a) ε =-0.081;(b) ε =-0.2

3-D MD simulations of magnesium and titanium anopillars u der c-axis compression are applied. Tw perfect single-crystal nano illar models, cylindrical and square in c oss section, are studied, with the diameter and side-length 15 nm a d 10nm, respe tively, and a length-to-dia eter ratio of 2:1. At the beginning, the model was fully relaxed for 20 000 steps (120 picoseconds). After the relaxation process, the ompressive strain were performed at th strain rate of 1×10^{9}/s. T simulations re carried ou until the maximal strain reached about 30% while t e temperature is controlle at 10K by t Nosé-Hoove thermostat. Fig.1 show the atomic configurations of magnesium square nanopillar under different compressive strains. In Fi . 1(a), we see the first slip nucleates at t e free surface initially an then travels across the pillar on the pyramidal plane. T e slip plane an be identified clearly as the $\{10\bar{1}1\}$ plane. It is w rth noting that the nucleated dislocations re partial dislocations, onl leading partials and stacking faults can be found when the strain is below 0.1. A a larger strain s shown in F g. 1(b), it can be identified that the deformation is largely homogen ous along th long axis, with a slight asymmetric in-pla e shearing. It is consistent ell with recent microcom ression tests. Besides, detail investigations

a) Correspondi g author. Ema l: yfguo@bjtu.edu.cn.

at other stra n levels also reveal that o compression twins are observed, the nucleation and multiplication of <c+ pyramidal slip and basal sl p accommod te the defor ation along t e c-axis.

The com ression deformation behaviours of titani m with c/a-r tio of 1.588 re also investigated. At the strain of 0.0 4, the initial sli can be identified as the $\{\bar{2}\}$ slip. At the strain of 0.087, the as mmetric in-plane shearing caused by ba al slip is also o served, and point defects a e left in the pillar after the nucleated dislocations escaped. The resu ts are similar to those of magnesium, nam ly, no twins could be obs rved under c-axis compression, and <c a> slip alon the pyrami al planes is main mechanism of plastic def rmation. Mo eover, another EAM potential is applied in these 3-D D simulations of both magnesium and tit nium single crystals, and similar results are obtained showing no compression tw ns.

CALC LATION OF LATTICE ROTATIO STRAIN

When deformation twinning occurs, a region o the crystal is transformed by the external loading into its mirror counterpart. rystal rotati n occurs wit no volume hange after t inning, while the twinne region is sy metrical to t original matrix about the t in plane. D e to the small size and the single orient tion of the single crystal, the elastic str in caused by lattice rotation cannot be cancelled out by ther deforma ion. Under this condition, e think that he elastic str in energy may lay a more i portant role n the twinnability of metals at the nanoscale.

We establish the sche e of a twin structure as shown in Fig. 1. The representative unit in the untwined crystal (t elementary cell of the periodic lattice st ucture) will transfers to unit N after the lattice rotation due to twin ing. Therefo e, the lattice strain along the - or y- direction due to the lattice rotati n can be calculated varied with the misorientation an le α. For the hc magnesium, we select the representative unit *M* as t e elementary cell of the periodic structure in the $\{\bar{1}2\,\bar{1}0\}$ plane. The side lengths of nit *M* are *c* nd $\sqrt{3}a$, respectively, parallel and perpendicular to the *c*-axis direc ion. Because of the c/a-ratio of 1.623, unit *M* is a rectangle, rather than a square, with $L_x = 1.732a$ and $L = 1.623a$ (t e ratio of side lengths is enlarged in this scheme to d splay clearly the rectangu ar structure). The misorientation angle for the $\{10\,\bar{1}2\}$ twin and the $\{10\,\bar{1}1\}$ twin are 86.3° and 56°, respectively. Under *c*-axis loadi g, the lattice strains alon the *c*-axis re obtained as $\varepsilon_c = 0.0626$ f r the $\{10\,\bar{1}2\}$ twin and $\varepsilon_c = 0.0396$ for the $\{10\,\bar{1}1\}$ in, both are positive. Whe a compression is applied al ng the *c*-axis, the lattice elongation alo g the *c*-axis irection cou teracts again t the effect o twinning, thus making twin ing more difficult. Theref re, both the $\{10\,\bar{1}1\}$ twin nd the $\{10\,\bar{1}2\}$ twin are n t preferred to occur under *c*-axis compression.

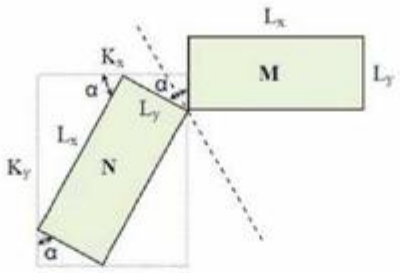

Fig.2. Scheme of a twin structure. The repre entative unit is in the origi al matrix and *N* in the twinned region. α is the misorientation angle.

AC NOWLEDGMENT

Support b the National Natural Science Foundation of China (Gr nt no. 11372032) is greatly ppreciated.

References

[1] Yu Q., Sha Z.W., Li J., Hua g X., Xiao L., Sun J., Ma E.: Stron crystal size effect on deformation twinning. *Nature* **463**: 335-338, 2010.

[2] Lilleodden E.: Microcompression study of Mg (0 0 0 1) single cr stal. *Scripta Mat r.* **62**: 532-535, 2 10.

[3] Byer C.M., Li B., Cao B., Ra esh K.T.: Microcompression of si gle-crystal magn sium. *Scripta Mater.* **62**: 536-539, 2010.

[4] Guo Y.F., ang X.Z., Wang Y.S., Wang Z.D.,Yip S.: Compression Deformation echanisms at the Nanoscale in Magnesium Single rystal. *Acta Met ll. Sin. (Engl. ett.)* **26**: 75-84, 2 13.

[5] Guo Y.F., u S.,Tang X.Z., ang Y.S., Yip S.: Twinnability of cp metals at the anoscale. *Journa of Applied Physi s* **115**: 224902, 2 14.

MODELING THE MECHANICAL PROPERTIES OF FCC POLYCRYSTALLINE METALS WITH HIERARCHICAL TWINS

Linli Zhu[1, a)] , Shaoxing Qu[1], Xiang Guo[2] &Jian Lu[3, a)]
[1]*Department of Engineering Mechanics and Key Laboratory of Soft Machines and Smart Devices of Zhejiang Province, Zhejiang University, Hangzhou 310027, Zhejiang Province, China*
[2]*School of Mechanical Engineering, Tianjin University, Tianjin 300072, China*
[3]*Department of Mechanical and Biomedical Engineering, City University of Hong Kong, Hong Kong, China*

Summary Experiments demonstrated that the polycrystalline face-centered cubic (fcc) metals with hierarchical twins performed the higher yield strength with keeping a good elongation. In this work, the extended-dislocation density-based plastic model for constitutive description of nanotwinned fcc metals is applied to simulate the twin spacing and grain size-dependent mechanical properties such as the yield strength and ductility in hierarchically nanotwinned fcc metals. A analytical model on nucleating the deformation twins is also addressed to predict the critical twin spacing in the lowest twin lamellae for generating the subordinate twins. The numerical results show that the global flow stresses are sensitive to the twin spacings in different levels and the grain size. The existence of the hierarchical nanotwins gives rise to the significant enhancement in the strength, and the predicted failure strain decreases with decreasing the twin spacing. The size-dependent critical twin spacing for generating subordinate twins is also studied in details.

INTRODUCTION

The simultaneously high strength and good ductility in nanostructured metallic material is expected in applications of metals and alloys in modern technologies. This expectation can be realized through various approaches, for example mixing the various sizes of microstructures in nanostructured materials [1] and generating internal boundaries in polycrystalline metals [2]. Nanotwinned metals have been proved to possess a good combination of strength and ductility[3]and considered to be suitable for the applications where both factors are important. Such metals derive their reinforced mechanical performance from the intrinsic properties of twin lamellae, which includes the inner twin boundaries acting as the obstacles to move the dislocations and the increasing twinning partials benefit to the pronounced strain hardening.

Through the surface mechanical attrition treatment (SMAT) or equal-channel angular processing (ECAP), the primary and secondary nanoscale twin lamellae have been observed in the ultrafine/nanocrystalline [4], and the secondary and tertiary nanotwins also have been monitored in TWIP steels[5,6]. These hierarchical nanotwins are beneficial to enhancing simultaneously the strength and ductility in the fcc polycrystalline metals. Motivated by these observations, a theoretical model to predict the relationship between the hierarchical twins and the mechanical properties is needed. In the present work, the mechanism-based generalized strain gradient plasticity model of nanotwinned metals is extended for the case of the hierarchically nanotwinned polycrystalline fcc metals in order to study the twin spacing and grain size dependence of the yield strength and tensile elongation in these hierarchical nanostructures.

A SETUP OF THEORETICAL MODEL

The twin boundaries are often regarded as the additional blocks for the dislocations movement. Due to the appearance of hierarchical twin lamellae in nanotwinned fcc metals [5,6], the volume fraction of twin boundaries will increase dramatically. Due to a plenty of dislocations accumulated along these boundaries, the dislocation pileup zones (DPZ) of twin boundaries and grain boundaries are introduced in the nanotwinned polycrystalline fcc metals. Since there exists significant strain gradient in the DPZs, the mechanism-based strain gradient plasticity theory[7] is adopted here to simulate the constitutive relation of the polycrystalline fcc metal with hierarchical nanotwins. Here, the Taylor-type flow stress is presented in the elastoplastic constitutive model, expressed as[8]

$$\sigma_{flow} = M\alpha\mu b\sqrt{\rho_I + \rho_{GB} + \sum_i^N \rho_{TB}^i}\,, \tag{1}$$

where ρ_I is the dislocation density in the interior crystal, ρ_{GB} and ρ_{TB}^i are the ones in the GBDPZ and the dislocation densities in the TBDPZs in *i*th layer of twin lamellae. *N* is the order of hierarchical twin lamellae. M , α , μ and b are the Taylor modulus, the empirical constant, the shear modulus and the Burger constant, respectively. Since the onset of fracture in materials often originates from the nucleation of dislocations. In describing cracks associated with dislocations, the opening crack can be represented by a continuous array of dislocations [9]. When the crack grows, more dislocations will be nucleated at the front of the crack. Based on this point of view, the stress-based failure criterion is proposed to evaluate the uniform elongation of the hierarchically nanotwinned metal as follows

$$\tau_{flow}^L \geq \tau_{crit}\,. \tag{2}$$

[a)] Corresponding author. Email: **llzhu@zju.edu.cn and jianlu@cityu.edu.hk**

Here, the local shear flow stress τ_{flow}^{L} in the lowest twin lamellae is given as $\tau_{flow}^{L} = \alpha\mu b\sqrt{\rho_I +_L \rho_{TB}}$, in which ${}_L\rho_{TB}$ is the local dislocation density related to the twin boundaries. The critical applied shear stress τ_{crit} to generate a dislocation has been identified completely by Asaro and Rice [10].

For the sake of nucleating a deformation twin, the twinning partial needs to prevail over the trailing partial, leading to that the critical twinning stress must be less than the stress to move the trailing partial, namely $\tau_{twin} < \tau_{trail}$. In the hierarchically nanotwinned metal, the local flow stress must be greater than the critical twinning stress to generate the subordinate twin lamellae by deformation twinning, $\tau_{flow}^{L} > \tau_{twin}$. As a result, one can identify the lower bound and upper bound of twin spacing for nucleating the deformation twins by

$$\tau_{twin} < \tau_{flow}^{L} < \tau_{trail} \tag{3}$$

NUMERICAL RESULS AND CONCLUSIONS

Fig. 1(a) shows the flow stress as the function of secondary twin spacing with different tertiary twin lamellae. It is noticeable from the figure that with decreasing twin spacing, the flow stress decreases first and then increases to reach the maximum point, after that decreases again. In Fig. 1(b), we show the curves of the failure strain as the function of the secondary twin spacing with different size of primary twin lamellae. The failure strains for the primary twin spacing of 50 nm and 100 nm are approximately proportional to the secondary twin spacing. For the small size of primary twin spacing, the variation in the failure strain becomes nonlinear with the size of secondary twin lamellae when it is greater than 80 nm. Experimental observation of the tensile ductility in hierarchically nanotwinned stainless steels has shown that the ductility of the materials decrease with the twin spacing of the secondary twin lamellae decreasing [6]. The present theoretical prediction for the failure behavior based on the proposed criterion is consistent with this experimental observation. We plot the critical size of the secondary twin spacing as the function of the primary twin spacing in Fig. 1 (c). It can be found that the critical twin spacing increases significantly as the primary twin spacing increases in the range of the size below 100 nm. When the size of primary twin lamellae is greater than several hundreds nanometers, the variation of the critical twin spacing with the primary twin spacing becomes smoothly.

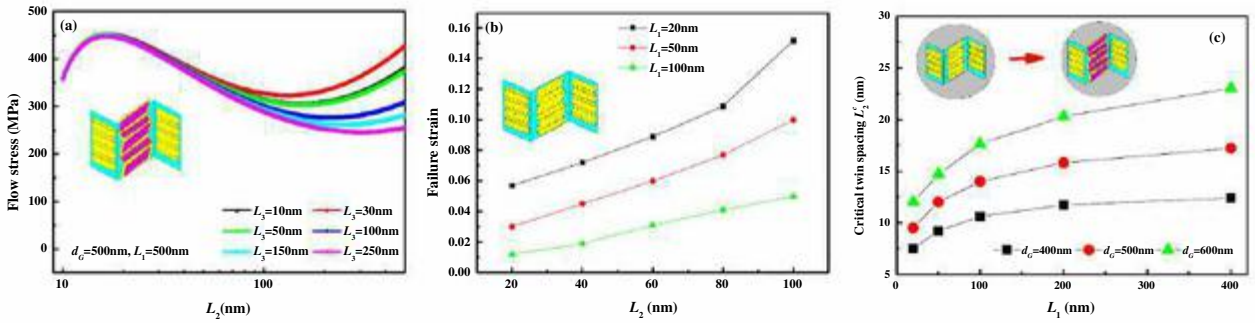

Fig.1 The flow stress(a), failure strain(b) and critical twin spacing (c) varied with the twin spacing

ACKNOWLEDGEMENT

The authors gratefully acknowledge the support under the grants nos. 11472243, 11302189, 11321202, 11102128 and 11372214, 20130101120175, 2015CB856800, and GRF/CityU519110, the Croucher Fundation CityU9500006.

References

[1] Y. M. Wang, M.W. Chen, F. H .Zhou and E. Ma, Nature 419: 912, 2002.
[2] K. Lu, L. Lu and S. Suresh, Science 324: 349, 2009.
[3] L. Lu, X. Chen, X. Huang and K. Lu, Science 323: 607, 2009.
[4] N. R. Tao, K. Lu, Scr. Mater. 60: 1039, 2009.
[5] Y. J. Wei, et al., Nat. Comm. 5: 3580, 2014.
[6] H. N. Kou, J. Lu, Y. Li, Adv. Mater. 26: 5518, 2014.
[7] Y. Huang, S. Qu, K. C. Hwang, M. Li and H. Gao, Int. J. Plasticity 20: 753, 2004.
[8] L. L. Zhu, S. X. Qu, X. Guo, J. Lu, J. Mech. Phys. Solid. 76: 162, 2015.
[9] H. Gao, Y. Huang, P. Gumbsch and A. J. Rosakis, J. Mech. Phys. Solids 47: 1941,1999.
[10] R. J. Asaro and J. R. Rice, J. Mech. Phys. Solids 25: 309, 1977.

THE MECHANICAL BEHAVIOR OF GOLD-POLYMER NANOCOMPOSITES: A NUMERICAL STUDY

Edgar Husser[1], Celal Soyarslan[2], and Swantje Bargmann*[1,2]

[1]*Institute of Materials Research, Materials Mechanics, Helmholtz-Zentrum Geesthacht, Geesthacht, Germany*
[2]*Institute of Continuum Mechanics and Material Mechanics, Hamburg University of Technology, Germany*

Summary Inhomogeneities in plastic shear affect the work hardening of small-scaled plastic crystals by causing storage of geometrically necessary dislocations (GNDs). One widely observed phenomenon is the yield stress drop after reversal loading, termed as mechanical Bauschinger effect. This effect is attributed to internal back stresses which arise due to accumulated GNDs in the material. The focus of this contribution is to present an explicit modeling approach for the Bauschinger effect by accounting additionally for reverse GND interactions. This effect is found to be very pronounced in gold-polymer nanocomposites. For that reason, cyclic shearing of gold single crystals of two characteristic sample sizes has been performed in the three-dimensional framework. As a demonstrative example, a single slip crystal set-up is considered where the reverse direction is explicitly incorporated.

INTRODUCTION

Non-local, continuum-based crystal plasticity models are well suited for numerical studies of the mechanics of crystals at small scales. For instance, former studies have shown that localized plasticity as commonly observed in microcompression experiments can be very well reproduced by strain gradient models, cf. [1], where in general, the coupling between GND densities and plastic strain gradients introduces a size dependence within the constitutive model. With respect to microbending tests, non-idealized boundary conditions other than microfree or microhard allow to account for a more realistic interplay between dislocations and surfaces leading to more pronounced size effects, see [2, 3]. A numerical example is presented to demonstrate the effect of reverse GND interactions on the mechanical response of a single crystal under cyclic loading.

DUAL-MIXED CRYSTAL PLASTICITY FRAMEWORK

In this work, the strain gradient crystal plasticity model is based on the large deformation theory, i.e., the deformation gradient $\boldsymbol{F} = \boldsymbol{F}_{\mathrm{E}} \cdot \boldsymbol{F}_{\mathrm{P}}$ is split multiplicatively into an elastic $\boldsymbol{F}_{\mathrm{E}}$ and a plastic part $\boldsymbol{F}_{\mathrm{P}}$. In turn, this leads to the definition of the (intermediate or elastic) right Cauchy-Green strain tensor $\boldsymbol{C}_{\mathrm{E}} = \boldsymbol{F}_{\mathrm{E}}^{\mathrm{T}} \cdot \boldsymbol{F}_{\mathrm{E}}$. Following a thermodynamically consistent formulation, all constitutive relations have their origin in the postulated free energy density $\psi_{\mathrm{i}}(\boldsymbol{C}_{\mathrm{E}}, \boldsymbol{\gamma}, \nabla_{\mathrm{i}}\boldsymbol{\gamma})$, where $\boldsymbol{\gamma}$ is a set of $\alpha \nearrow$slip systems and $\nabla_{\mathrm{i}}\boldsymbol{\gamma}$ represent their gradients with respect to the intermediate configuration as is henceforth denoted by the index $_{\mathrm{i}}$. Moreover, an additive decomposition of the free energy is assumed into elastic $\psi_{\mathrm{i}}^{\mathrm{e}}$, local hardening $\psi_{\mathrm{i}}^{\mathrm{l}}$, and gradient hardening $\psi_{\mathrm{i}}^{\mathrm{g}}$ (non-local) contribution, i.e.,

$$\psi_{\mathrm{i}}(\boldsymbol{C}_{\mathrm{E}}, \boldsymbol{\gamma}, \nabla_{\mathrm{i}}\boldsymbol{\gamma}) = \psi_{\mathrm{i}}^{\mathrm{e}}(\boldsymbol{C}_{\mathrm{E}}) + \psi_{\mathrm{i}}^{\mathrm{l}}(\boldsymbol{\gamma}) + \psi_{\mathrm{i}}^{\mathrm{g}}(\nabla_{\mathrm{i}}\boldsymbol{\gamma}). \tag{1}$$

From the concept of work-conjugated variables, one can find the following constitutive relations: the second Piola-Kirchhoff (PK) stress $\boldsymbol{S}_{\mathrm{E}} = 2\partial\psi/\partial\boldsymbol{C}_{\mathrm{E}}$ and the first PK stress $\boldsymbol{P} = \boldsymbol{F}_{\mathrm{E}} \cdot \boldsymbol{S}_{\mathrm{E}} \cdot \boldsymbol{F}_{\mathrm{P}}^{-\mathrm{T}}$; the local microstress $\kappa_{\alpha}^{\mathrm{l}} = \partial\psi/\partial\gamma_{\alpha}$; the non-local (vectorial) microstress $\boldsymbol{\kappa}_{\alpha}^{\mathrm{g}} = \partial\psi/\partial\nabla_{\mathrm{i}}\gamma_{\alpha}$. The latter results in the non-local back stress $\kappa_{\alpha}^{\mathrm{b}} = \mathrm{Div}_{\mathrm{i}}(\boldsymbol{\kappa}_{\alpha}^{\mathrm{g}})$ and extents the flow function to read: $\phi_{\alpha} = \tau_{\alpha} \nearrow \kappa_{\alpha}^{\mathrm{l}} + \kappa_{\alpha}^{\mathrm{b}} \nearrow Y_{\alpha}$ where Y_{α} denotes the critical resolved shear stress of the slip system and $\tau_{\alpha} = \boldsymbol{s}_{\alpha} \cdot \boldsymbol{S}_{\mathrm{E}} \cdot \boldsymbol{C}_{\mathrm{E}} \cdot \boldsymbol{n}_{\alpha}$ is the resolved shear stress. As usual, each slip system α is determined by an orthonormal system of vectors comprising slip direction $\boldsymbol{s}_{\alpha}$, transverse direction $\boldsymbol{n}_{\alpha}$, and slip plane normal $\boldsymbol{n}_{\alpha}$. Finally, the flow rule reads

$$\dot{\gamma}_{\alpha} = \dot{\gamma}_0 \left[\frac{< \phi_{\alpha} >}{C_0}\right]^m, \tag{2}$$

with material parameters $\dot{\gamma}_0$, C_0, and m. Eq. (2) represents a local and slip system-based field relation which is coupled with globally defined GND densities $g_{\mathrm{i}\alpha}$ via back stresses $\kappa_{\alpha}^{\mathrm{b}}$. GND densities are taken to evolve in the form

$$\dot{g}_{\mathrm{i}\alpha} = \sum_{\beta} f\,(\boldsymbol{n}_{\alpha} \cdot \boldsymbol{n}_{\beta})\, g_{\mathrm{i}\beta}\,[\boldsymbol{s}_{\alpha} \cdot \boldsymbol{s}_{\beta}]\,\dot{\gamma}_{\alpha} + \sum_{\beta} g_{\mathrm{i}\beta}\,[\boldsymbol{n}_{\alpha} \cdot \boldsymbol{s}_{\beta}]\,\dot{\gamma}_{\alpha} \nearrow \frac{1}{b} \nabla_{\mathrm{i}}\dot{\gamma}_{\alpha} \cdot \boldsymbol{s}_{\alpha}. \tag{3}$$

While the last term is a well-known measure for edge-type GND densities, i.e., the projected slip gradient per closest-packed interatomic spacing (Burgers vector magnitude), the other two terms account for contributions of interfering GNDs. In this

*Corresponding author. Email: swantje.bargmann@tu-harburg.de

respect, the step function $f(\boldsymbol{n}_\alpha \cdot \boldsymbol{n}_\beta) \in [0,1]$ in the first term on the right-hand side allows for interaction contribution of coplanar systems such that $f = 1$ only for $\boldsymbol{n}_\alpha \cdot \boldsymbol{n}_\beta = 1$, otherwise $f = 0$. In contrast to this, the second term on the right-hand side is limited to interaction contributions from noncoplanar systems as a result of the dot product $\boldsymbol{n}_\alpha \cdot \boldsymbol{s}_\beta$. In the end, the highly non-linear coupled field problem - global/global: balance of linear momentum $\mathrm{Div}_{\mathrm{i}}(\boldsymbol{S}_{\mathrm{E}} \cdot \boldsymbol{C}_{\mathrm{E}}) = 0$ and Eq. (3); global/local or dual-mixed Eq. (3) and Eq. (2) - is solved in terms of the dual-mixed finite-element method.

CYCLIC SHEAR LOADING OF GOLD SINGLE CRYSTALS

In the hereby presented numerical example of a cyclically sheared single crystal (with respect to the $X_1 - X_3$ plane), the slip system configuration is limited to single slip aligned in X_1-direction. The reverse direction is considered explicitly in the formulation. Consequently, the second term in Eq. (3) vanishes. All material parameters are identical to the one used for the gold phase within the follow-up study of nanocomposites, cf. [4]. Three loading cycles have been applied, each up to a macroscopic shear strain of $\gamma = 0.05$. Fig. 1 shows the resulting stress-strain curves in terms of the Piola-Kirchhoff shear stress component P_{13} for a cube with edge length a) $L_0 = 10$ µm and b) $L_0 = 1$ µm. As can be seen in case of the large crystal, hardening is mostly due to the locally evolving microstress $\kappa^{\mathrm{l}}_\alpha$ and, hence, the impact of non-local effects as well as GND interactions is small. A completely different mechanical response is obtained for the smaller crystal. In addition to the expected size-dependent increase in hardening leading to highly localized plasticity (see contour plots of plastic slip), the impact of the back stress $\kappa^{\mathrm{b}}_\alpha$ can be clearly seen in terms of a yield stress drop upon load direction change, accompanied by a cyclically increasing work hardening rate. Due to locally accumulating GNDs, the polarity of the stress field is coinciding with the externally applied load sign after each load reversal. The resulting Bauschinger effect is even more pronounced when GND interactions between both slip directions are explicitly considered. In this case, GND fields of opposite sign affect each other directly via the interaction term - and not just because of the stress field development.

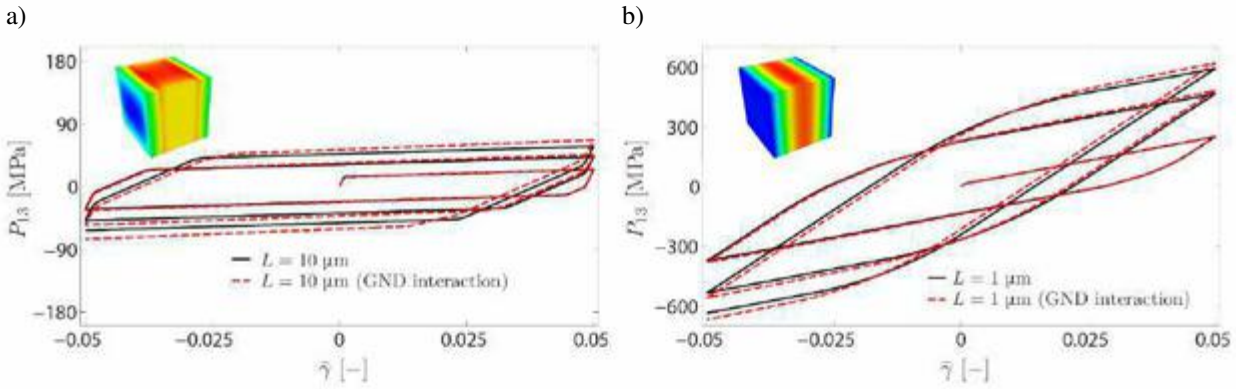

Figure 1: Stress-strain response of crystal with a) $L_0 = 10$ µm and b) $L_0 = 1$ µm edge length after cyclic shear loading.

CONCLUSIONS

The proposed strain gradient crystal plasticity model is highly qualified for numerical studies of single crystals at the submicron regime where size-dependent phenomena affect the mechanical response of the material. One current application is referred to gold-polymer nanocomposites where the metal phase equals a network of small-scaled ligaments [4].

Acknowledgments

We gratefully acknowledge financial support from the German Research Foundation (DFG) via SFB 986 "M^3".

References

[1] E. Husser, E. Lilleodden, S. Bargmann: Computational modeling of intrinsically induced strain gradients during compression of c-axis-oriented magnesium single crystal. Acta Mater, 71:206-219, 2014.

[2] E. Husser, S. Bargmann: The role of geometrically necessary dislocations in cantilever beam bending experiments of copper single crystal. Submitted, 2015.

[3] M. Ekh, S. Bargmann, M. Grymer: Influence of grain boundary conditions on modeling of size-dependence in polycrystals. In: Acta Mech, 218(1-2):103-113, 2011.

[4] S. Bargmann, C. Soyarslan, E. Husser, N. Konchakova: Materials based design of structures: computational modeling of the mechanical behavior of gold-polymer nanocomposites. Mechanics of Materials, 2015, doi:10.1016/j.mechmat.2015.11.008.

UNDERSTANDING PRISMATIC DISLOCATION LOOPS IN MG BY MEANS OF LARGE SCALE *AB-INITIO* SIMULATIONS

Mauricio Ponga, *[1], Kaushik Bhattacharya[2], and Michael Ortiz[2]

[1]*Department of Mechanical Engineering, The University of British Columbia, Vancouver, BC, Canada.*
[2]*Division of Engineering and Applied Science, California Institute of Technology, Pasadena, CA, USA.*

Summary Partial dislocation loops of different sizes have been studied with the novel Coarse-Graining Density Functional Theory method (CG-DFT). The CG-DFT method uses a combination of a linear scaling technique in addition to a coarse-grained description achieving a sublinear scaling with respect to the number of electrons in the system. This ability allows us to study Partial Dislocation Loops (PDLs) in Magnesium (Mg) including the true and long range elastic effect with quantum mechanics. The binding energy of loops of different size were measured for cell sizes including approximately 100,000 atoms. Our simulations reveal that vacancies tend to collapse in cluster of vacancies leading to the formation of nanovoids and ultimately to PDLs.

INTRODUCTION

Density Functional Theory (DFT) [1, 2] have been played a significant role in accurately predicting many aspects of materials behavior over the last two decades. DFT reduces the many-body Schrodinger equation of interacting electrons into an equivalent problem of non-interacting electrons in an effective mean field that is governed by electron-density greatly reducing the complexity of the original problem [2]. A major drawback, however, is that the complexity of DFT equations scale to the cube with the number of electrons in the system making the calculation of large samples prohibitively expensive [3, 4, 5, 6]. To tackle this challenge, a number of linear scaling algorithms have been developed exploring different properties of the density matrix, spectral quadratures, etc. [7, 8, 9]. However, in the study of crystalline defects, an extra challenge is encountered since the concentration of defects is as low as part per million atoms or less and linear scaling does not suffice this issue.

In this work, we apply a coarse-graining approach for the DFT of Ponga *et al*. [10]. The CG-DFT method is based on a linear scaling method and a spatial reduction of the computational domain through judicious kinematic constrains. The spatial discretization is taken to be dense near defects, but coarse in the vast regions of asymptotic decay. This adaptive mesh discretization greatly reduces the size of the problem with little loss of accuracy leading to a sublinear scaling.

The CG-DFT approach is implemented in our computational platform, MacroDFT, that has been validated with different test problems involving defects in Mg-HCP [10]. In this work we seek to understand the mechanisms that create such PDLs and their associated biding energy including the long range elastic field of the defect.

METHODOLOGY AND RESULTS

In this work we have applied the CG-DFT method developed by Ponga *et al*. [10]. The CG-DFT is based on the Linear Scaling Gauss Quadrature Method [11] and a coarse-grained approach similar to the one proposed by Gavini *et al*. [12]. The main advantage of CG-DFT is that the calculation of the electronic quantities and energies can be achieved at a sublinear scaling cost $\mathcal{O}(N^p)$, where N is the number of electrons in the system and $p < 1$. This properties allows the simulation of computational cells with large number of atoms.

We have implemented and studied the LSSGQ method with Hexagonal-Closed-Packed Magnesium. We use a real space Bulk-derived Local Pseudopotential (BLPS) [13] and the Local Density Approximation (LDA) for the exchange and correlation functional [14]. The SCF iteration is accelerated using the Broyden multisecant method combined with mixing, as proposed by Fang and Saad [15]. The energy-convergence tolerance is set to 10^{-5} eV. The equilibrium configurations of the nuclei are obtained by energy-minimization using a non-linear conjugate gradient [16] based on the Hellman-Feynman forces. The force-convergence tolerance is set to 10^{-3} eV/Å per atom. These values are consistent with those used in other finite

Table 1: Binding energy for PDLs of different sizes after relaxation. In all cases, the number of atoms in the simulation is approximately 100,000.

	Sim1	Sim2	Sim3
Cluster Size [Atoms]	7	19	38
Binding energy [eV]	0.51	1.51	2.04

*Corresponding author. Email: mponga@mech.ubc.ca

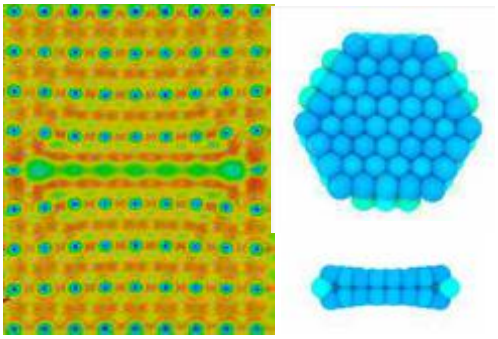

Figure 1: PDLs after energy relaxation. a) Electron density neat the defect, b) top view of the atoms that create the PDL and c) cut along the $[2110]$ plane.

difference methods [3] and plane wave methods. The implementation is parallelized using a domain decomposition technique and the Message Passing Interface (MPI) library in combination with threads using OpenMP.

The minimum energy configuration for the bulk crystal is found at $a = 3.109$ Å and $c/a = 1.626$, and these are consistent with values previously obtained with other *ab-initio* calculations with other pseudopotentials [13] (e. g. $a = 3.11$ Å and $c/a = 1.624$). Then, a cluster of vacancies of variable size is located at the center of a computational cell. The computational cell is terminated by enforcing bulk conditions on all fields at the boundary of the cell. The overall length of the computational domain is $36a_0 \times 36a_0 \times 36c_0$ containing 93,312 atoms. The values of the binding energy after energy minimization are reported on Table 1.

CONCLUSIONS

In this work we have studied the binding energy of prismatic dislocation loops in Magnesium by using the Coarse-Grained Density Functional Theory method. Our analysis includes the true long range elastic effect of dislocations and reveals that vacancies are more like it to aggregate and collapse in a nanosized voids. This conclusion is based on the fact that the binding energy of PDLs increases with the loop size. Therefore, larger cluster of vacancies are more energetically favorable than single isolated vacancies. This result is important in many applications, including dynamic failure driven by nucleation, growth and coalescence of nanovoids.

References

[1] P. Hohenberg and W. Kohn. Inhomogeneous electron gas. *Physical Review*, 136:B864–B871, 1964.

[2] W. Kohn and L. J. Sham. Self-consistent equations including exchange and correlation effects. *Physical Review*, 140:A1133–A1138, 1965.

[3] James R. Chelikowsky, N. Troullier, and Y. Saad. Finite-difference-pseudopotential method: Electronic structure calculations without a basis. *Physical Review Letters*, 72:1240–1243, 1994.

[4] G. Kresse and J. Furthmüller. Efficient iterative schemes for ab initio total-energy calculations using a plane-wave basis set. *Physical Review B*, 54:11169–11186, 1996.

[5] J. E. Pask, B. M. Klein, C. Y. Fong, and P. A. Sterne. Real-space local polynomial basis for solid-state electronic-structure calculations: A finite-element approach. *Physical Review B*, 59:12352–12358, 1999.

[6] S. Ismail-Beigi and T.A. Arias. New algebraic formulation of density functional calculation. *Computer Physics Communications*, 128:1–45, 2000.

[7] G. Galli and M. Parrinello. Large scale electronic structure calculations. *Physical Review Letters*, 69:3547–3550, 1992.

[8] F. Mauri, G. Galli, and R. Car. Orbital formulation for electronic-structure calculations with linear system-size scaling. *Physical Review B*, 47:9973–9976, 1993.

[9] S. Goedecker. Linear scaling electronic structure methods. *Reviews of Modern Physics*, 71:1085–1123, 1999.

[10] M. Ponga, K. Bhattacharya, and M. Ortiz. A sublinear-scaling approach for the density functional theory study of crystalline defects. *submitted to Journal of the Mechanics and Physics of Solids*, 2016.

[11] P. Suryanarayana, K. Bhattacharya, and M. Ortiz. Coarse-graining Kohn-Sham density functional theory. *Journal of the Mechanics and Physics of Solids*, 61:38–60, 2013.

[12] V. Gavini, K. Bhattacharya, and M. Ortiz. Quasi-continuum orbital-free density-functional theory: A route to multi-million atom non-periodic dft calculation. *Journal of the Mechanics and Physics of Solids*, 55:697–718, 2007.

[13] C. Huang and E. A. Carter. Transferable local pseudopotentials for magnesium, aluminum and silicon. *Physical Chemistry Chemical Physics*, 10:7109–7120, 2008.

[14] J. P. Perdew and Y. Wang. Accurate and simple analytic representation of the electron-gas correlation energy. *Phys. Rev. B*, 45:13244–13249, Jun 1992.

[15] H. Fang and Y. Saad. Two classes of multisecant methods for nonlinear acceleration. *Numerical Linear Algebra with Applications*, 16:197–221, 2009.

[16] W. T. Vetterling, W. H. Press, B. P. Flannery, and S. A. Teukolsky. *Numerical Recipes Example Book C++*. Cambridge University Press, 2002.

STUDY OF INTRINSIC AND EXTRINSIC SIZE EFFECTS ON SHEAR BANDS IN METALLIC GLASSES

Benjamin Klusemann *[1,2], Celal Soyarslan[3], and Swantje Bargmann[2,3]

[1]*Institute of Product and Process Innovation, Leuphana University of Lüneburg, Lüneburg, Germany*
[2]*Institute of Materials Research, Helmholtz-Zentrum Geesthacht, Geesthacht, Germany*
[3]*Institute of Continuum and Material Mechanics, Hamburg University of Technology, Hamburg, Germany*

Summary In the present contribution intrinsic and extrinsic size effects on the shear band propagation behavior in metallic glasses are studied. To this end, a thermodynamically consistent finite strain viscoplasticity model is formulated. The strongly coupled and highly non-linear system of field equations consisting of deformation, free volume and plastic strain field, is implemented into the finite element method, resulting in a non-local model formulation. The results show that the proposed continuum plasticity model is well suited to predict stable or delayed shear localization process with decreasing sample size. With an underlying microstructure, the material behavior in metallic glasses can be significantly influenced, as demonstrated numerically in this contribution on the basis of porous structures.

INTRODUCTION

Despite their superb mechanical property combinations [1], their significantly flawed ductility at room temperature bounds application of metallic glasses with homogeneous structure [2]. Various strategies to remedy this lack of ductility include pre-deformation, synthesizing composite materials reinforced with a secondary crystalline phase or introduction of soft glass-glass interfaces or pores. All these seemingly different strategies aim at proliferation of shear bands through *extrinsic* stress concentrators instead of a single catastrophic one. It is also known that reducing the sample size in the sub-micron range, experimental observations indicate that the shear localization process is delayed or even suppressed [3], i.e., *smaller is stronger*. Mathematical modeling allows clarification of the interplay between *intrinsic* and *extrinsic* length scales by allowing try outs which are mostly not accessible to experiments, see, e.g., [4, 5, 6] for numerical notch and defect sensitivity investigations. In this work we elaborate further in this direction and report on our recent findings which demonstrate the influence and use of *intrinsic* and *extrinsic* size effects in the amorphous metals making use of a gradient dependent continuum plasticity [7, 8] and various specimen size and geometries and loading scenarios.

MODEL FORMULATION

The material model is formulated in the framework of continuum thermodynamics and rate variational methods. The metallic glass consists of atoms of different sizes. This leads to a free volume ξ inside the material which determines the inelastic deformation. The free volume generation $\dot{\xi} = \zeta\,\dot{\gamma} + \dot{\xi}_{\mathrm{m}}$ is either induced by plastic shearing (i.e., plastic strain γ) or other mechanisms (i.e., diffusion, hydrostatic pressure or structural relaxation) which are accounted for by ξ_m. ζ denotes the free-volume creation factor which accounts for the tension-compression asymmetry, characteristic for metallic glasses. In [9] it is demonstrated that a von Mises-type plastic yield criterion and flow rule most accurately describes the plastic yield and flow behavior of metallic glasses. As shown elsewhere [8], application of rate variational methods leads to the flow rule the evolution equation for the free-volume generation as

$$\dot{\xi}_{\mathrm{m}} = \left[v_m \tfrac{s_{\xi 1}}{s_{\xi 3}}\right] \quad \mathrm{v}(\nabla\xi) \nearrow \tfrac{v_m}{s_{\xi 3}} \left[\bar{p} + s_{\xi 2}\,[\xi \nearrow \xi_{\mathrm{T}}]\right], \quad \dot{\gamma} = \dot{\gamma}_0 \left[\tfrac{f^p}{c}\right]^{1/a}, \tag{1}$$

where $f^p := \bar{\tau} \nearrow \zeta \left[\bar{p} + s_{\xi 2}\,[\xi \nearrow \xi_{\mathrm{T}}]\right] + \zeta\, s_{\xi 1} \quad \mathrm{v}(\nabla\xi)$. $s_{\xi 2}$ is a material constant representing the defect-free energy coefficient, ξ_{T} denotes the fully annealed free volume, $s_{\xi 1}$ the gradient free energy coefficient where its value depends on the material lengthscale l, $\dot{\gamma}_0$ the reference strain (shearing) rate, a the strain-rate sensitivity parameter of the material, c the intrinsic resistance, v_m a frequency-like term and $s_{\xi 3}$ a material constant representing the resistance to free-volume generation due to mechanisms other than plastic shearing. Also $\bar{p} = \nearrow \tfrac{1}{3} \quad (\boldsymbol{M})$ is the hydrostatic pressure and $\bar{\tau} := \sqrt{\tfrac{1}{2}}| \quad \mathrm{v}(\boldsymbol{M})|$ the equivalent shear stress in terms of the Mandel stress tensor $\boldsymbol{M}$. Following [7], the model is completed by the evolution equation for the cohesion $\dot{c} = c\,\frac{k\,\dot{\varepsilon}}{\cosh\left(\frac{\cdot}{f_\star}\right)}$ with the initial resistance $c(0) = c_0$, the dimensionless fitting constant k and the characteristic frequency $f_\star$. This strongly coupled and highly nonlinear system of equations is solved by different numerical implementation schemes including implicit and explicit gradient computations leading to similar numerical results.

*Corresponding author. Email: benjamin.klusemann@leuphana.de

RESULTS

The numerical examples in the following illustrate the shear localization process in submicron metallic glasses and porous heterostructures at room temperature. The first example is an investigation on a rectangular specimen loaded in compression. The shear band is triggered by a local imperfection placed near the center. The stress-strain behavior as well as the spatial distribution of the free volume for different samples sizes is shown in Figure 1a. The numerical results show that the shear localization process is delayed or even suppressed with decreasing sample size. These results indicate that the failure mode changes from fragmentation (catastrophic failure) for large bulk metallic glasses to shear fracture which is in agreement with experimental observations [10].

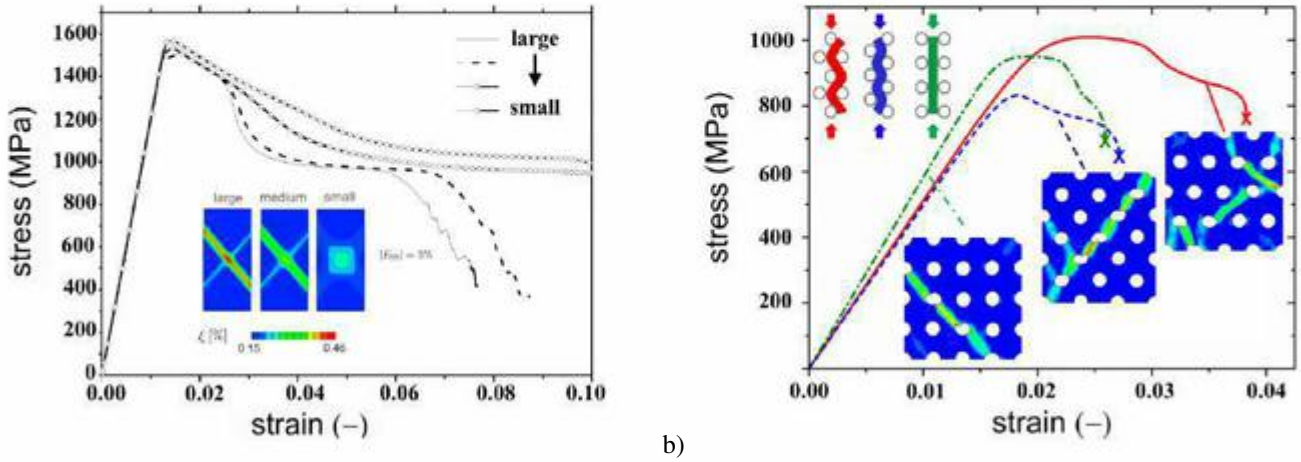

a) b)

Figure 1: a) Stress-strain responses and spatial distributions of free volume at 3% strain for different specimen sizes (20 nm - 1 μm) illustrating the delay in shear localization and fracture process due to the sample size effect. b) Influence of pore configuration on the mechanical behavior of metallic glass samples of same size [11]. Enhanced mechanical properties (larger plastic deformation) are achieved for AB stacking configuration with specific lateral pore spacing distance (red curve). The shear band distribution is based on the free volume illustrated for the different microstructures.

Additionally, the effect of an underlying microstructure by introducing randomly or regularly distributed pores is displayed in Figure 1b. The results highlight the importance of the microstructure, here in particular the pore configuration. An appropriate arrangement of the pores and spacing ratio to internal lengthscale, intrinsic size effects can be used to enhance the material properties. The results indicate that shear localization is interrupted by the pore configuration with AB stacking configuration with specific lateral pore spacing distance.

It is clearly demonstrated that the proposed model captures the different size effects in metallic glasses. In contrast to bulk metallic glasses, where a catastrophic localization process is observed, a decreasing sample size as well as a specific microstructure stabilize, delay and even suppress shear localization process. This insight can be used for the design of such samples for certain applications. Additional results, including a variation of the overall porosity, diameter to spacing ratio of the pores, the influence of crystalline nanoprecipitates rather than pores and comparison to experimental observations will be presented and discussed during the conference.

References

[1] Ashby M.F., Greer, A.L.: Metallic glasses as structural materials. Scrip Mater 54:321326, 2006.
[2] Trexler M. M., Thadhani N. N.: Mechanical properties of bulk metallic glasses. Prog Mater Sci 55:759839, 2010.
[3] Chen D. Z., Jang D., Guan K. M., An Q., Goddard III W. A., Greer J. R.: Nanometallic Glasses: Size Reduction Brings Ductility, Surface State Drives Its Extent. Nano Lett 13(9):44624468, 2013.
[4] Singh I., Narasimhan R.: Notch sensitivity in nanoscale metallic glass specimens: Insights from continuum simulations. J Mech Phys Solids 86:5369, 2016.
[5] Sarac B., Klusemann B., Xiao T., Bargmann S.: Materials by design: An experimental and computational investigation on the microanatomy arrangement of porous metallic glasses. Acta Mater 77:411422, 2014.
[6] Sopu D., Soyarslan C., Sarac B., Bargmann S., Stoica M., Eckert J.: Structure-property relationships in nanoporous metallic glasses. Acta Materialia, Accepted for publication.
[7] Thamburaja P.: Length scale effects on the shear localization process in metallic glasses: A theoretical and computational study. J Mech Phys Solids 59:15521575, 2011.
[8] Bargmann S., Xiao T., Klusemann, B.: Computational modeling of sub-micron sized metallic glasses. Philos Mag 94:1-19, 2014.
[9] Thamburaja P., Klusemann B., Adibi S., Bargmann S.: The plastic yield and flow behavior in metallic glasses. Appl Phys Lett 106:051903, 2015.
[10] Wu F., Zheng W., Wu S., Zhang Z., Shen J.: Shear stability of metallic glasses. Int J Plasticity 27:560 575, 2011.
[11] Partially reprinted from [5], with permission from Elsevier.

A micromechanical model for strain-induced crystallization in rubber

Christian Linder* and Reza Rastak
Civil and Environmental Engineering, Stanford University, 473 Via Ortega, Stanford, CA 94305, USA

Summary A micromechanical model for strain-induced crystallization in rubber-like materials is proposed. Combining the evolution of the crystallization of a single polymer chain with the maximal advance path based homogenization method, we are able to predict this complex process. The crystallization of the material leads to an anisotropic mechanical response, which our model is able to capture. The representative numerical simulation results are in good quantitative agreement to experimental data for both, uniaxial extension and three-dimensional multiaxial simulations of strain induced crystallization around a cracked region.

INTRODUCTION

Many polymeric materials such as natural and synthetic rubbers, polyethylene, polyethylene terephthalate (PET), polylactide (PLA) are subject to polymer crystallization under certain conditions. It can be observed in both vulcanized and unvulcanized polymers well above the glass transition temperature. What is essential for this phenomenon is the chemical composition of the material which must enable the crystallization in principle. Segments of the macromolecules have to possess a mutually conforming atomistic structure so that they can arrange themselves into a regular crystalline order. Crystallization occurs in materials which are essentially solids (crosslinked elastomers) or at least display solid-like stiff behavior in short and moderate time limits (uncrosslinked plastics). This transition turns an amorphous solid into a partially crystalline solid and is accompanied by volume change, being a first-order change. Unlike conventional crystallization this transition is not rapid and does not cause any phase separation. In fact amorphous and crystalline fractions coexist and the ratio between them changes gradually. The thermodynamics of this process is governed by the latent heat of fusion and the entropic free energy change in the amorphous fraction. The relation between these two factors indicates whether the crystallization is thermodynamically admissible. Accordingly the crystallization can be triggered through influencing this relation either by thermal action (decreasing the temperature) or by mechanical action (stretching the material). The latter is the key to strain-induced crystallization (SIC) of polymers, to be considered in this work. In particular, we propose a micromechanical motivated model mimicking the physical phenomena of SIC at the microscopic scale and incorporate it into the macroscopic response of polymeric materials through the development of a proper homogenization technique. Numerical simulation results are presented including uniaxial tension tests and complex 3D simulation of SIC around a cracked region.

THEORY

The application of macroscopic strain to a polymer induces certain deformation of its network microstructure. Chains get aligned with the directions of tension and attain stretch values which can reach magnitudes of several hundred percent. In this highly stretched state chains display the tendency to form oriented crystallites of certain morphology. To describe the crystallinity at the microscopic scale, we define the chain crystallinity fraction as the ratio of the semi-crystalline chains to the totally amorphous chains in a specific orientation. Its evolution is constituted based on the physical principles of crystallization thermodynamics and molecular kinetics of polymers [1], also adopted in recent computational works [2, 3]. This results in micromechanical models with physically grounded material parameters.

The orientation and stretch of polymer chains play an essential role in the overall phenomenon of SIC. To correctly evolve the crystallinity at the microscopic scale, the macroscopic deformation of the polymer will be connected to the microscopic deformation through the recently developed maximal advance path homogenization framework [4]. This model assigns different amounts of stretch in different orientations so that the evolving crystallinity can predict the resulting anisotropic response of the material undergoing SIC. The model takes into account the network functionality as well as stretch variation over the orientations using the kinematic tensorial constraint

$$\langle \boldsymbol{\lambda} \otimes \boldsymbol{\lambda}_0 \rangle \;=\; \frac{1}{|S_0|} \int_{S_0} \boldsymbol{\lambda}(\boldsymbol{\lambda}_0) \otimes \boldsymbol{\lambda}_0 \, |d\boldsymbol{\lambda}_0| = \; \tfrac{1}{3}\, \bar{\boldsymbol{F}} \tag{1}$$

where $\bar{\boldsymbol{F}}$ is the isochoric portion of the deformation gradient and $\boldsymbol{\lambda}_0$ and $\boldsymbol{\lambda}$ represent the normalized unstretched and stretched end-to-end vectors of the chains, respectively. The averaging symbol $\langle \cdot \rangle$ in (1) is computed through an integration of the integrant over all possible orientations of the unit sphere S_0.

We will explore two methods of how to obtain the resulting crystallinity distribution over that orientation space S_0. One approach is to use the amount of crystallinity fraction at all the numerical integration points of S_0. While this method is

*Corresponding author. Email: linder@stanford.edu

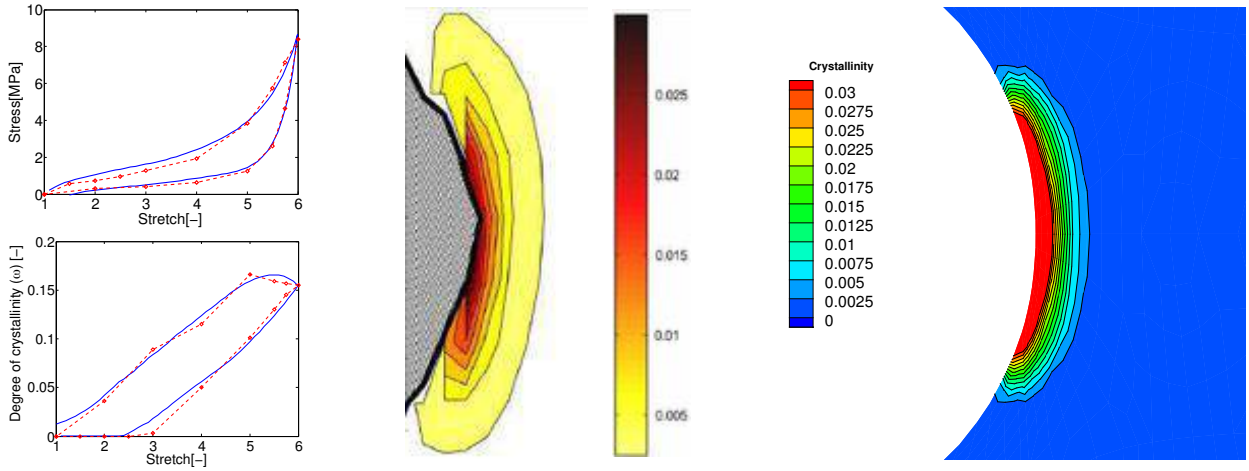

Figure 1: Stress (top left) and crystallinity (bottom left) response of natural rubber during uniaxial loading and unloading. The numerical results (solid lines) are compared with experimental results (dashed lines) taken from [5]. Experimental [7] and numerical results of the distribution of the degree of crystallinity around a Mode I crack tip are shown in the center and on the right, respectively.

straightforward to implement, it does not provide a smooth representation of the crystallinity distribution. Alternatively, a smooth function of the crystallinity distribution will be proposed. At each step, the rate of change of the parameters describing that smooth distribution is obtained by computing the rate of change of the crystallinity of chains in different orientations through a least-square minimization. Unlike the former method, the latter contains considerably less number of history variables, is able to perform adaptive refinement of the integration scheme, and provides a smooth evolution of crystallinity over the sphere.

RESULTS

We will use uniaxial experimental results of SIC to calibrate the parameters of our model. Figure 1 shows the stress-stretch response of natural rubber (top left) as well as its crystallinity evolution (bottom left) and compares those with experiments of [5]. The simulation assumes a viscoelastic response [6] in addition to the SIC constitutive model in order to capture the large hysteresis of the stress curve. To examine multiaxial loading conditions and the effect of SIC on fatigue properties of rubber, simulations are performed on a cracked specimen and the response of the material close to the crack tip is studied and compared with experimental results provided in [7] (see right of Figure 1). In the future the micromechanical SIC model will be used to examine the toughening of rubber also during the process of crack propagation [8, 9, 10].

References

[1] Flory, P. J.: Thermodynamics of crystallization in high polymers. I. Crystallization induced by stretching. The Journal of Chemical Physics, 15(6):397, 1947.

[2] Kroon, M.: A constitutive model for strain-crystallising rubber-like materials. Mechanics of Materials, 42(9):873-885, 2010.

[3] Mistry, S. J., Govindjee, S: A micro-mechanically based continuum model for strain-induced crystallization in natural rubber. International Journal of Solids and Structures, 51(2):530-539, 2014.

[4] Tkachuk M., Linder C.: The maximal advance path constraint for the homogenization of materials with random network microstructure. Philosophical Magazine, 92(22):2779-2808, 2012.

[5] Toki, S., Sics, I., Ran, S., Liu, L., Hsiao, B.S.: Molecular orientation and structural development in vulcanized polyisoprene rubbers during uniaxial deformation by in situ synchrotron X-ray diffraction. Polymer, 44(19):6003-6011, 2003.

[6] Linder, C., Tkachuk, M., Miehe, C.: A micromechanically motivated diffusion-based transient network model and its incorporation into finite rubber viscoelasticity. Journal of the Mechanics and Physics of Solids, 59(10):2134-2156, 2011.

[7] Rublon, P., Huneau, B., Verron, E., Saintier, N., Beurrot, S., Leygue, A., Mocuta, C., Thiaudière, D., Berghezan, D.: Multiaxial deformation and strain-induced crystallization around a fatigue crack in natural rubber. Engineering Fracture Mechanics, 123:59-69, 2014.

[8] Linder, C., Zhang, C.: A marching cubes based failure surface propagation concept for three-dimensional finite elements with non-planar embedded strong discontinuities of higher order kinematics. International Journal for Numerical Methods in Engineering, 96:339-372, 2013.

[9] Linder, C., Zhang, C.: Three-dimensional finite elements with embedded strong discontinuities to model failure in electromechanical coupled materials. Computer Methods in Applied Mechanics and Engineering, 273:143-160, 2014.

[10] Raina, A., Linder, C.: A micromechanical model with strong discontinuities for failure in nonwovens at finite deformation. International Journal of Solids and Structures, 75-76:247-259, 2015.

AXIALLY LOADED PRETWISTED NONLINEAR THIN PLATES: A STRAIN GRADIENT ANALOGY

Alexis Kordolemis *[1] and Paul M. Weaver[1]
[1]*ACCIS, Department of Aerospace Engineering, University of Bristol, Bristol, United Kingdom*

Summary In the present work a pre-twisted thin plate subjected to axial loading is analysed. The analysis is conducted within the framework of linear elasticity assuming that the plate undergoes large deformations associated with small strains, i.e. the generalised Hookes law is utilised. The problem is attacked under different conceptual perspectives. First, a classical structural theory is employed where the effect of warping of the non-circular cross section of the plate is introduced. Adopting an energy variational statement the governing partial differential equation is explicitly derived. Secondly, the problem is formulated in terms of second gradient elasticity theory involving only one material length parameter , in addition to the two classical Lame constants. It is shown, by the analogy, that the material length parameter can be expressed on physical ground through the geometrical aspects of the plate and the loading providing a thorough insight of the role of micro-structure.

INTRODUCTION

The theory of thin plates has been used in the analysis of many high end technological applications in a range spanning the micro-scale (e.g. electromechanical nano-films) to the macro-scale (e.g. air-foil blades, propellers). Many practical problems regarding thin plates are solved primarily through the assumption of Kirchhoff-Love hypothesis provided that the stresses normal to the neutral mid-plane are negligible compared to the stresses in the plane of the plate and the strains vary linearly through the plate thickness. Numerous research efforts have been devoted to the loading and the imposed boundary conditions as well as proposed solution methods depending on the problem at hand. Most of the time, in order for practical problems to be solved various approximate methods have been used. i.e. finite element method, asymptotic analysis, etc.[1],[2],[3],[4]. Satisfactory agreement between experimental findings and theoretical formulations prove that this hypothesis works well in real engineering problems.

CLASSICAL STRUCTURAL ANALYSIS

In the present work an initially twisted thin plate subjected to axial loading is discussed. We assume that the deflection w of the plate's mid-surface is of the same order of magnitude as of the thickness, h, and the in-plane displacements, namely u, v, in the x, y direction respectively, are infinitesimal. Furthermore, in the non-linear strain-displacement relationship only the non-linear terms that depend on the mid-surface deflection are retained. Under these assumptions the von Karman theory for thin plates is employed.The plate's material is assumed to be isotropic and linear elastic, i.e. the stress-strain relationship will be provided through the generalised Hooke's law.

The initial twist is assumed to vary linearly along the x-axis along which the axial load is applied and the cross section of the thin plate experiences an additional displacement along this direction. Within this context, the von-Karman's strain-displacement relationships are modified, by including the warping terms, in order to account for the non-uniform twist (restrained warping) of the plate's cross section. It should be pointed out that in the initial twist a restriction is placed in such a way that thin shallow shell theory is applicable.

The problem is formulated in terms of a variational statement through the expression of the energy density function of the pre-twisted thin plate and the work done by the external forces where the body forces prescribed per unit area of the mid-plane and the bi-moment related to the warping distortion of the cross section are included apart the boundary terms. Minimising the potential energy of the plate four coupled governing equilibrium equations emerge with respect to the primary unknowns, namely, the displacements and the warping displacement, along with the boundary condition expressions. Through some lengthy but straightforward manipulations, the equations are decoupled and an explicit expression in terms of only the deflection w is derived. To the authors' knowledge, such an analytical expression describing the thin shallow shell mechanical response only in terms of the deflection of the mid-surface does not exist in the literature and is presented here for the first time. The analytical expression presented here refers to quasi-static loading conditions but it can be applicable to stability and buckling analysis of thin shallow shells as well as in dynamic problems including the inertia terms.

*Corresponding author. Email: alexis.kordolemis@bristol.ac.uk

LINEAR ELASTIC STRAIN GRADIENT ANALYSIS

It is well known that when the dimensions of a structure become comparable to the size of its material micro-structure, size effects are observed. Typical examples are thin plates and in general composite materials which are reinforced with particles or fibers. Classical continuum mechanics theory, and hence classical linear elasticity theory, are inadequate to describe the mechanical behaviour of such materials due to the lack of length scale parameters. In that essence, resort should be sought to enhanced continuum theories where the role of the micro-structure is involved with the macro-structure through intrinsic parameters entering the constitutive equations or the equations of motion of the considered elastic continuum. To put it simply, generalised continuum theories come to play when the macroscopic mechanical behaviour becomes dependent on the component size, i.e. the underlying micro-structure plays a dominant role.

In the simplest generalized continuum theories era two main schools of thought were established. The first school adopts the idea that the material's underlying micro-structure can be better addressed by inserting additional degrees of freedom within the continuum. The first attempt in this direction was made by the Cosserat brothers[5] in the beginning of the past century establishing the backbone of the so called higher order generalized theories[6]. The second school of thought adopts another approach to interpret the effects of the underlying micro-structure, having as a basis the gradient of strain taken into account into the strain energy density function. Various versions of these theories were established in the literature and the key difference among them is related to the high order gradients taken under consideration each time. The more general case is the multipolar theory where all the higher gradient of the strain taken into account[7]. First strain gradient and second strain gradient theories are simplified versions of this category.

In the present work,the gradient elastic theory of form II due to Mindlin[8] is employed which has been used in many practical engineering problems[9]. In this case, apart from the two classical Lame constants, only one material length parameter enters the constitutive equations which is related to the volumetric strain energy function of the material. This approach constitutes a simplified version of the original Mindlin's general theory of elasticity with micro-structure which involves five material constants. Taking as a departure point the equilibrium and compatibility equations of a thin shallow shell under axial loading the governing equation of equilibrium of gradient elastic shallow thin shell is explicitly derived. To the authors' knowledge, the analytical expression presented here, describing the response of a gradient elastic thin shallow shell in terms only of the mid-surface deflection w is not available in the literature and it is presented here for the first time.

CONCLUSIONS

In the present study, the problem of an initially twisted thin plate under axial loading is addressed. The problem is tackled through two conceptually different methods and in both cases explicit expressions were derived. A direct analogy emerges between the two approaches which enables the internal material parameter correlated to the underlying micro-structure to be related through macroscopic geometrical aspects of the cross section of the pre-twisted plate, firmly placing the derivation on physical grounds. Such kind of analogies can constitute a direct and thorough response to the main criticism of generalised continuum theories that the intrinsic material parameters are physically meaningless in practical engineering problems.

References

[1] Ramamurti V.,Kielb R.: Natural frequencies of twisted rotating plates. Journal of Sound and Vibration 97:429-449,1984.

[2] Qatu M.S.,Leissa A.W.: Vibration studies for laminated composite twisted cantilever plates.International Journal of Mechanical Sciences 33:927-940,1991.

[3] Walker K.P. :Vibrations of cambered helicoidal fan blades. Journal of Sound and Vibration 59:35-57,1978.

[4] Timoshenko S, Woinowsky-Krieger S.:Theory of plates and Shells, McGraw-Hill Book Company, New York, 1959.

[5] Cosserat E.,Cosserat F.: Theories des Corps Deformables. Hermann et Fils, 1909.

[6] Eringen C.A.: Nonlinear theory of continuous media.McGraw Hill, New York,1962.

[7] Green A.E., Rivlin R.S.:Simple force and stress multipoles. Archive for Rational Mechanics and Analysis 16:325-353,1964.

[8] Mindlin R.D.:Micro-structure in linear elasticity. Archive for Rational Mechanics and Analysis 16:51-78,1964.

[9] Papargyri-Beskou S.,Beskos D.E.:Stability analysis of gradient elastic circular cylindrical thin shells. International Journal of Engineering Science 47:1379-1385,2009.

EXPERIMENTAL ASSESSMENT OF NANOVOIDS GROWTH

Pierre-Olivier Barrioz *[1], Jérémy Hure[1], and Benoît Tanguy[1]
[1]*CEA Université Paris-Saclay, DEN, Service d'Études des Matériaux Irradiés, 91191 Gif-sur-Yvette cedex, France*

Summary The growth of nanovoids in crystalline metallic material is assessed experimentally as a function of the applied macroscopic plastic strain, stress triaxiality and crystal orientation. Nanovoids - of diameter ranging from 20 to 80nm - are generated by performing heavy-ion irradiation on austenitic steel, leading to a model material constituted of a well-defined nanovoids distribution. Pre- and post-straining Transmission Electron Microscope (TEM) observations allow to quantify the growth and the evolution of aspect ratio as a function of plastic strain. Size and crystal orientation effects are evaluated. Experiments are compared to the results of crystal plasticity finite element simulations.

BACKGROUND

Numerous theoretical and numerical studies have been conducted to assess the growth of nanovoids under mechanical loading [1], showing size effects (the lower the size of the void, the lower the growth rate), crystal orientation effects (growth rate depending on the crystallographic orientation) and describing dislocation mechanisms involved as a function of the applied macroscopic stress. However, very limited experimental data are available in literature, and only for high strain rates / high applied stress. Thus the aim of this study is to assess experimentally nanovoid growth in the low stress regime, as a function of applied strain, stress triaxiality and crystal orientation.

EXPERIMENTAL INVESTIGATIONS

Nanovoids are usually observed in metallic materials under irradiation in nuclear power plant. These voids come from interactions between high energy particles and atoms of the material, that generate point defects ultimately leading to nanosized defects [2]. Irradiation is therefore used here to generate well-defined distributions of nanovoids, creating a model nanoporous material. Ion-irradiation was performed at the JANNuS facility [3] on austenitic steel (316L), leading to spherical nanovoids - of diameter ranging from 20 to 80nm - in high density (Fig. 1), observed with Transmission Electron Microscope (TEM). As void growth under mechanical loading is very sensitive to stress triaxiality [4], tensile and biaxial tensile samples were used in this study. Post to irradiation, specimens were strained up to different levels of macroscopic plastic strain. Quantification of the evolutions of void size and aspect ratio as a function of plastic strain and crystal orientation, for different stress triaxiality, was done using TEM observations (Fig. 2).

RESULTS AND DISCUSSION

Nanovoid deformation under mechanical loading is shown to be sensitive to crystal orientation, as predicted by numerical and theoretical predictions: for some orientations, the void aspect ratio stays close to unity, while very elongated voids have been observed for other orientations (Fig. 2). The evolution of void size and aspect ratio as a function of plastic strain is studied as a function of applied strain, for some crystal orientations. Results are finally compared to predictions of finite elements simulations using crystal plasticity constitutive equations.

*Corresponding author. Email: pierre-olivier.barrioz@cea.fr

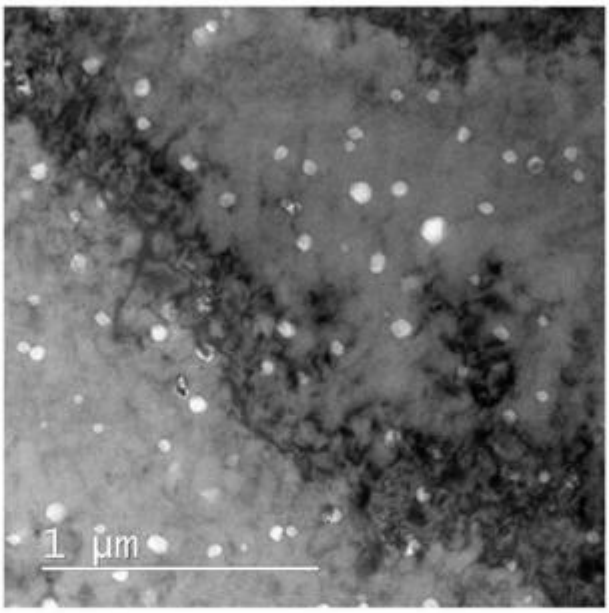

Figure 1: Spherical nanovoids observed by Transmission Electron Microscope (TEM) after ion-irradiation in austenitic steel

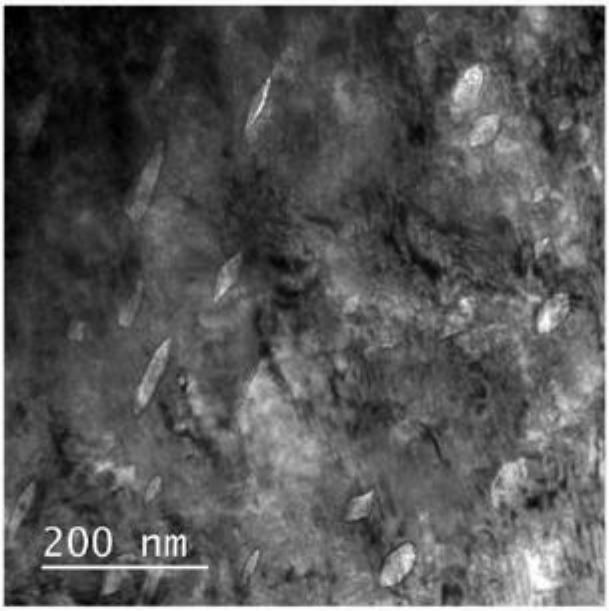

Figure 2: Nanovoids observed by Transmission Electron Microscope (TEM) in ion-irradiated austenitic steel after straining to 30%

References

[1] Chang H-J, Segurado J, de la Fuente R, Pabón B M, Llorca J, Modelling Simul. Mater. Sci. Eng. 21, 2013.

[2] Zinkle S J , Was G S : Materials challenges in nuclear energy, Acta Mat. 61:735-758, 2013.

[3] Beck L, Serruys Y, Miro S, Trocellier P, Bordas E, Leprêtre F, Brimbal D, Loussouarn T, Martin H, Vaubaillon S, Pellegrino S, Bachiller-Perea D: Ion irradiation and radiation effect characterization at the JANNUS-Saclay triple beam facility, J. Mater. Res. 30:1183-1194, 2015

[4] Segurado J, Llorca J : An analysis of the size effect on void growth in single crystals using discrete dislocation dynamics, Acta Mat. 57:1427-1436, 2009.

MOLECULAR DYNAMICS INVESTIGATION OF SINGLE CHAIN POLYMER NANOPARTICLES

Suwon Bae[1] and Meredith Silberstein *[2]
[1, 2]*Department of Mechanical and Aerospace Engineering, Cornell University, Ithaca, NY, USA*

Summary Single chain polymer nanoparticles (SCPN) have potential as building blocks for a new class of polymers. Here, a molecular dynamics approach is utilized to investigate the mechanical properties of individual SCPN as a function of cross-link density. A polyethylene-like polymer is used as the representative SCPN. It is shown that the cross-linked particles have a stiffer response to compressive loading than have the linear ones. Adding cross-links does not directly increase bond-stretching and total potential energy of the cross-linked particle. The cross-links do constrain the particle to remain relatively stable and respond to compression with increased angle, dihedral and non-bonded energy.

INTRODUCTION

Polymer properties can be controlled independently of monomer chemistry by choice of underlying architecture. In this sense, single chain polymer nanoparticle (SCPN) assemblies are an emerging paradigm for tailoring polymer properties. Here we investigate the individual SCPN mechanical properties as a first step towards designing SCPN assembly-based polymers. Specifically, we use molecular dynamics (MD) simulations to investigate a polyethylene (PE)-like SCPN as a function of molecular weight and cross-link density.

METHODS

The structures of the SCPN are based on a linear PE chain 500 monomers long. The PE is explicitly represented with atomic interactions captured by the Dreiding potential. The initial structure was generated using Amorphous Cell in Materials Studio. A parallel MD code, LAMMPS, was used. Simulations were conducted under NVT dynamics with a Nosé-Hoover thermostat used for the temperature control. The velocity-Verlet time stepping scheme was adopted with a time step of 0.1 fs. The chain was collapsed into a particle by introducing an artificial atom at the center of mass that exerts an attractive force onto each atom of the polymer chain. The collapsed chain was then annealed with the artificial atom removed. The total momentum and the total angular momentum were set to be zero in order to cancel both translation and rotation of the chain. The cross-linked PE particles were constructed from the fully equilibrated MD model for linear PE particles. Cross-links were created between each pair of two active atoms within a preassigned distance range. This cross-linking was carried out sequentially with cross-link assignments alternating with equilibration steps until the desired percentage of cross-links was reached.

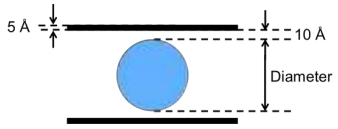

Figure 1: Schematic of MD simulation of SCPN compression.

The prepared PE particles were then compressed by two rigid flat plates displaced toward each other at a constant speed. The compression tests were implemented in LAMMPS. Rigid flat plates of thickness 5 Å were placed above and below the prepared particle with a gap of 10 Å as shown Figure 1. Repulsive forces were assigned between the plates and particle by a non-bonded potential. The mechanical response for each particle type is averaged from five different initial configurations. Force was calculated from the virial stress tensor as a function of relative wall distance. Relative wall distance is defined as z_{plate}/R_z where z_{plate} is the distance over the plate moves and R_z is the initial radius of the particle along the compressive axis. Radius of gyration and energy components were also observed.

RESULTS AND DISCUSSION

SCPN with four different degrees of cross-linking were prepared: linear particles and cross-linked particles with 5%, 10%, and 15% of cross-links. For instance, equilibrated MD models for 0% and 15% cross-linked SCPN are shown in Figure 2. The cross-linked particles have a greater radius of gyration and higher potential energy than have the linear ones. However, the degree of cross-linking made negligible difference in the radius of gyration and the total potential energy.

The responses of the SCPN to compressive loading are shown in Figure 3(a). It is observed that force responses are relatively linear and have minimal difference among until a relative wall distance of 0.4. Beyond this wall distance, the responses exhibit non-linearity and dependence on the cross-link density. The higher the degree of cross-linking, the stiffer the response to compressive loading. The radii of gyration vary with compression. While the linear particles have the smallest

*Corresponding author. Email: ms2682@cornell.edu

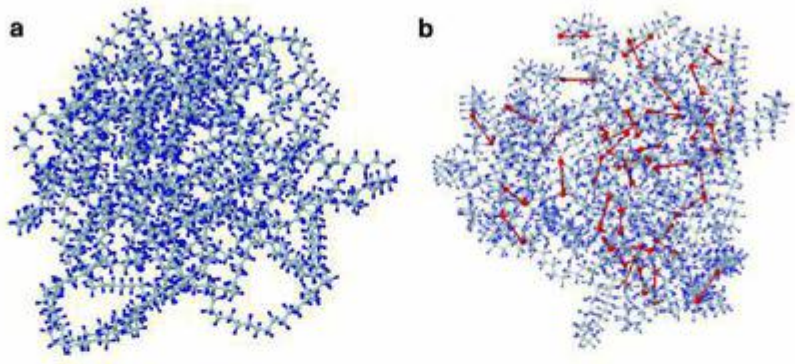

Figure 2: Equilibrated congiuration of (a) linear SCPN and (b) cross-linked SCPN (15% cross-links) before compression. Light blue beads and blue ones are representative of hydrogen and carbon atoms, respectively. Red beads are cross-linked sites.

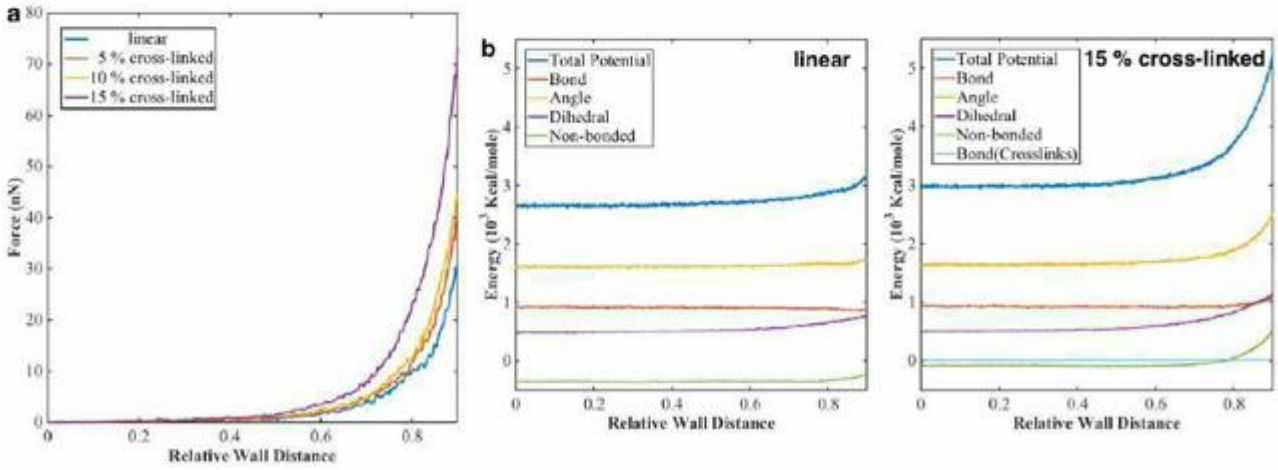

Figure 3: Results of SCPN compression. (a) Force response versus relative wall distance. (b) Energy components versus relative wall distance.

value for the initial radius of gyration, it increases the most per applied strain. The highest degree of cross-linking exhibits the smallest increase in the radius of gyration per applied strain. The evolutions of each component of the total potential energy of the linear and 15 % cross-linked particles during compression are shown Figure 3(b). The angle, dihedral and non-bonded components of the cross-linked particles increase more with the increasing relative wall distance than the corresponding energies from the linear particle.

CONCLUSION

The SCPN with the highest degree of cross-linking show the smallest increase in radius of gyration during compression, implying that the cross-links add stability and strength to the SCPN. The increased stiffness of the cross-linked SCPN at large strain relative to the linear SCPN is due to angle, dihedral, and non-bonded energy contributions. Although the direct contribution of cross-links to the bond-stretching energy and to the total potential energy is negligible even during deformation the cross-links do confine the polymer chain to induce a stiffer response.

References

[1] Mayo, S., Olafson, B., Goddard, W.: DREIDING: a generic force field for molecular simulations. J. Phys. Chem. 94:8897-8909, 1990.

[2] Plimpton, S.: Fast Parallel Algorithms for Short-Range Molecular Dynamics. J. Comput. Phys. 117:1-19, 1995.

[3] Materials Studio: Accelrys, Inc.

[4] Jmol: an open-source Java viewer for chemical structures in 3D. http://www.jmol.org/

[5] Zhao, J., Nagao S., Odegard, G., Zhang Z., Kristiansen H., He, J.: Size-dependent mechanical behavior of nanoscale polymer particles through coarse-grained molecular dynamics simulation. Nanoscale Research Lett. 8:541, 2013

NUMERICAL MODEL FOR DISLOCATION TRANSMISSION ACROSS PHASE BOUNDARIES

Franz Bormann[1], Ron Peerlings[1], and Marc Geers[1]
[1]*Department of Mechanical Engineering, Eindhoven University of Technology, Eindhoven, The Netherlands*

Summary A 2D FEM approach for studying dislocation-phase boundary interaction is proposed. By adopting the classical Peierls-Nabarro model as a glide plane model, a natural interplay between dislocations, external boundaries and phase boundary is provided. Thereby the local dislocation induced stress field in the vicinity of the phase boundary can be fully captured. Modelling dislocation dipoles (loops) in a finite-sized grain introduces a grain-size dependency. With this model the effect of dislocations piling up against a phase boundary and dislocation transmission are studied for a glide plane perpendicular to a fully coherent and non-damaging interface.

INTRODUCTION

Interface decohesion due to dislocation activity in polycrystalline microstructures is a complex processes that is not fully understood yet. For a better insight into the underlying mechanisms numerical approaches are necessary in order to resolve the small scale phenomena of dislocation-phase boundary interaction. Existing studies are based on atomistic simulations [1] or Discrete Dislocation Dynamics (DDD) [2]. However, both approaches involve shortcomings such as limited spatial and temporal scales (atomistics) or complicated numerical treatments of dislocations-phase boundary interactions (DDD).

METHODOLOGY

In the present research we propose a 2D FEM-approach, in which the aforementioned shortcomings of atomistic simulations and DDD are overcome. Embedded in a finite elastic medium lies a glide plane represented by a periodic shear traction-disregistry (F-Δ) law in accordance with the Peierls-Nabarro model [3]:

$$F(\Delta) = \frac{\mu b}{2\pi d} \; \mathrm{n}\left(\frac{2\pi\Delta}{b}\right) \; , \tag{1}$$

with the shear modulus μ, the Burgers vector b and the interplanar spacing d – see Figure 1. A cohesive zone along the phase boundary enables the simulation of interface crack nucleation due to dislocation induced stress concentrations. With such a model, a natural interplay between dislocations, external boundary conditions and phase boundary is provided. It is furthermore possible to break down the complexity of the problem into the investigation of the single influences of specific parameters such as elastic parameters of the crystal and those of the glide plane and phase boundary.

In the present study we limit ourselves to a glide plane perpendicular to a fully coherent interface between two phases, A and B, and neglect the effect of decohesion. By adopting point-symmetry on the left-hand side of the model (cf. Figure 1), dislocation dipoles are included. With this model it is possible to investigate the dislocation transmission across the fully coherent interface as a function the material properties and grain size.

Considering dual phase materials where a dislocation moves towards a phase of higher shear modulus, a natural resistance against dislocation transmission is present. This resistance is both material dependent and size dependent. The material dependency is related to the phase contrast and leads to an increase of: 1) the dislocation induced repulsive shear stresses in phase B and 2) the resistance against dislocation motion according to the original Peierls-Nabarro model. The size dependency arises from the dislocation dipole self-stresses that strongly depend on the width of the dipole and thus on the size of grain A, L_A. An increase in self-stresses with decreasing L_A becomes apparent and this in turn leads to a higher external stress required for transmission of the dislocations to the harder phase B.

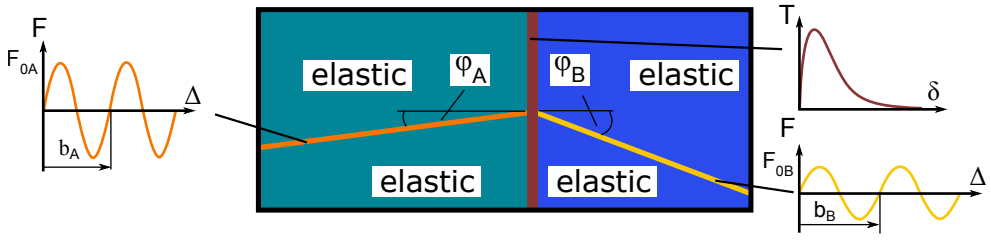

Figure 1: Peierls-Nabarro FEM Model for dislocation interaction with a phase boundary.

RESULTS

By applying simple shear boundary conditions and pre-multiplying the glide plane stress according to Eq. (1) with a factor C for phase B, the influence of the Peierls-Nabarro model alone on transmission of a single dislocation is studied. Figure 2 shows this for a pre-factor $C = 2$ and a grain size $L_A = 800b$ with a close-up view of the dislocation position and its induced normal stress σ_{xx} for different shear strains γ.

After nucleation at $\gamma = 0.2 \cdot 10^{-2}$ the dislocation moves towards the interface and gets stuck. Only after increasing the shear strain to $\gamma = 5.1 \cdot 10^{-2}$ the dislocation is transmitted to the second phase. It is noteworthy that in the course of the transmission the normal stress σ_{xx} increases from a characteristic value in phase A ($\approx 25.$) to a higher characteristic value in a phase B (≈ 3 .). This is an important finding for later considerations on interface failure and shows the necessity of a high resolution for capturing the local stress field.

By allowing multiple dislocations to nucleate, a pileup can form as shown in figure 3. Instead of artificially amplifying the Peierls-Nabarro model, the shear modulus of phase B is now enhanced with $\mu_B = 1.5\mu_A$. Like in the case of single dislocation transmission, the grain size equals $L_A = 800b$. The close-up view of the dislocation induced normal stress σ_{xx} displays the state right after dislocation transmission for a mean shear strain of $\overline{\gamma} = 1.5 \cdot 10^{-2}$.

As stated before, a decreasing grain size L_A leads to elevated self-stresses. Thus, the shear strain at dislocation transmission measured in both investigations increases accordingly.

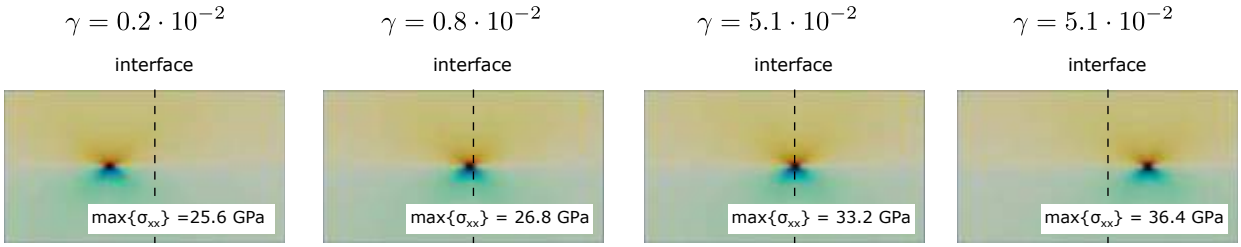

Figure 2: Process of dislocation transmission to a harder phase for a single dislocation. Close-up snapshots of the dislocation position and its induced normal stress at different shear strains γ.

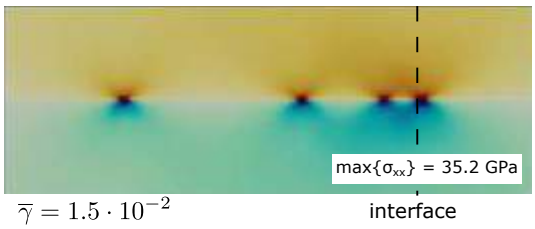

Figure 3: Dislocation pileup against a harder phase right after dislocation transmission. Close-up view of the dislocation positions and the induced normal stress.

CONCLUSIONS

A model for a natural interplay between dislocations, external boundary conditions and phase boundary as a function the material properties and grain size was presented. With this model the effects of dislocation transmission and dislocations piling up inside a dual-phase material with a glide plane perpendicular to a fully coherent interface was shown. By extending the current model with cohesive zones it is possible to investigate the competition between interface decohesion and dislocation transmission for different material properties and grain sizes.

References

[1] Cui C., Beom H.: Molecular statics simulations of intergranular fracture along S11 tilt grain boundaries in copper bicrystals. J. Mater. Sci. 49:8355-8364, 2014.

[2] Cleveringa H., Van der Giessen E., Needleman A.: A discrete dislocation analysis of mode I crack growth. J. Mech. Phys. Solids 48:1133-1157, 2000.

[3] Hirth J.P., Lothe J.: Theory of dislocations. Wiley, New York, 1982.

SIZE EFFECT OF MECHANICAL BEHAVIOR OF COATING SYSTEMS

Lihong Liang[1a)], Haiyan, Liu[1], Yueguang Wei [1]
[1]*LNM, Institute of Mechanics, Chinese Academy of Sciences, Beijing, China*

Abstract The mechanical behaviour of coating systems with different thickness coatings were studied under in situ 3-point and 4-ponit bending experiments, and crack evolution was observed with load-displacement curves. Fracture and damage characteristics of the coating systems were analyzed, and a catastrophic damage model was introduced. The result indicates that fracture mode and damage propagation depend on the size of the coatings and loading condition, the interface fracture and shear failure dominate the thick coating systems under 3-ponit bending, and the multiple transverse cracks emergence and tensile failure dominate the thin coating systems under 3-ponit bending and both coating samples under 4-ponit bending. Furthermore, the damage of the thick coating systems is faster than that of the thin coating systems both under 3-ponit bending and 4-ponit bending, and the damage of both systems obeys the same power law behaviour with power exponent of 0.5 as the corresponding controlling variable increases.

INTRODUCTION

The ceramic coatings are widely used in mechanical engineering, chemical engineering, aerospace, marine, etc. due to their good properties such as thermal protect, anti-corrosion, and oxidation-resistance. For example, ceramic coatings of several hundreds of microns are often sprayed or deposited on the alloy substrates for thermal protection of the blades of the aerospace engine [1]. However, ceramic coatings are brittle and easy fractured due to the interface mismatch between the coatings and the substrates under thermal and mechanical loading, once the coatings fracture or spall from the substrates, the alloy substrates will failure at high temperature environment. Therefore, the study on the fracture and damage of the coating systems attract great attention.

Fracture and damage of coating systems were studied by many researchers [2-3], but size effect was few attended, which is important not only in optimizing the coatings and enhancing mechanical properties of the coating/substrate systems, but also in scientific understanding of size effect in materials. In this paper, thin and thick coating samples were prepared to study thickness effect of coating systems under 3-point and 4-point bending loading. The size-dependent fracture characteristics and size-independent damage scaling law were respectively revealed.

EXPERIMENTAL METHOD

The thin coating and thick coating samples with coating thickness of 100-300 μm and 350-500 μm, respectively, were prepared, and the coatings were sprayed on the same alloy substrates [4]. The samples were placed in the sample room of the scanning electron microscope, and were applied 3-point bending and 4-ponit bending loading by the designed jigs and the mechanical testing apparatus. The load was applied on the surface of the substrates, and the crack map in the side face can be obtained real time with the load-displacement curves. The 3-point sample size is 15 mm ×3 mm ×1.5 mm, and the span is 10 mm. The 4-point sample size is 30 mm ×3 mm ×1.5 mm, and the inner and outer spans are 8 mm and 24 mm, respectively. The loading rate is 0.1 mm/min.

EXPERIMENTAL RESULTS

The transverse cracks in the coating, vertical to the interface between the coating and the substrate experience initial, propagation and saturation steps as the load increases, and the multiple transverse cracks occurs simultaneously as the load is close to the peak value for the thin coating samples under 3-point and 4-ponit bending and also for the thick coating samples under 4-point bending as shown in Fig. 1(a). The interface crack occurs and propagates besides one transverse crack in the coating for the thick coating samples under 3-point bending as shown in Fig. 1(b). The transverse crack density of the thin coatings is larger than that of the thick coatings under 4-point bending. Therefore, the fracture modes and characteristics depend on the size of the coatings under the same loading condition.

DISCUSSIONS

According to the two-layer composite beam theory, the tensile and the shear stress of the coating in the interface can be calculated based on the elastic modulus and the load of the transition point in the load-displacement curve corresponding to the multiple transverse cracks through the substrate or the interface fracture, etc. The result indicates that the tensile stress is larger than the strength of the coatings, thus the transverse crack occurs in the coatings. The shear stress is smaller for the thin coatings, and the shear stress is larger than the interface strength for the thick coatings under 3-point bending, thus interface crack occurs for the thick coatings under 3-point bending. Therefore, the interface shear failure dominates the thick

[a)] Corresponding author. Email: lianglh@lnm.imech.ac.cn

coatings under 3-point bending, and the tensile failure dominates the thin coatings under 3-point bending and both coatings under 4-point bending.

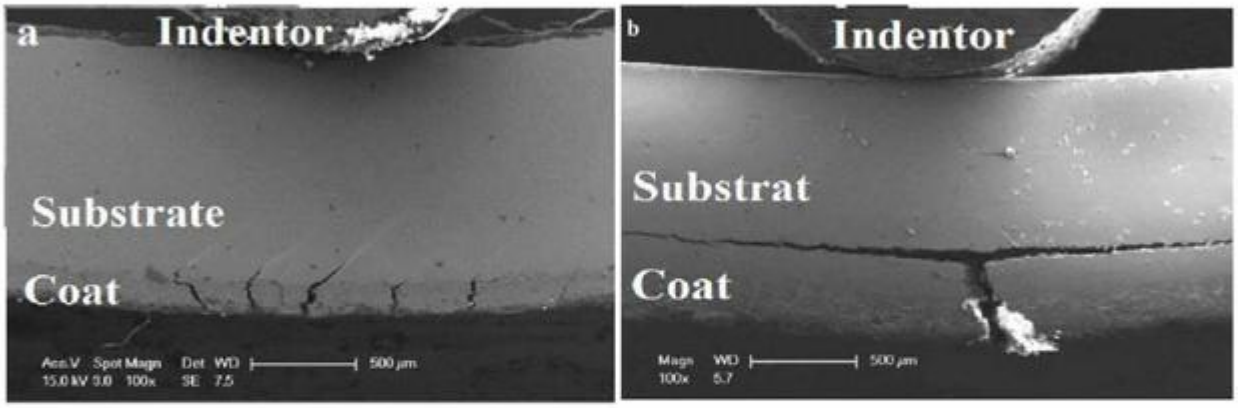

Fig. 1. The fracture map of (a) thin coating of 186 μm thickness; (b) thick coating of 487 μm under three-point bending.

The transverse crack or the interface crack length was measured to be as the damage variable for the tensile failure or the shear failure dominated coatings, respectively, and the crack evolution was observed with increased tensile or shear stress as the controlling variable. The experimental results show that the damage increases with increasing stress, reaches to be complete at the failure point. According to the brittle catastrophic damage model [5], the damage rate tends to be infinite at the failure point, a similar model on the controlling stress, as the Taylor's expansion of the damage variable, was proposed to describe the damage evolution in the coating systems. The results show that the model can explain the experimental phenomena well, the damage obeys the power law relation of the stress with the power exponent of 0.5 for all kinds of coating systems here, and the damage rate shows the power law singularity at the critical value. Furthermore, the damage coefficient can be obtained by the initial and the failure damage and the corresponding controlling stress. Comparison of the thin and thick coating systems both under 3-ponit and 4-ponit bending shows that the damage coefficient is smaller for the thin coatings, and thus the damage is slower for the thin coatings. The thin coating systems may be a good mechanical design if the thermal protect application is satisfied firstly.

CONCLUSIONS

The size effect of the coating systems was studied by a series of thickness coatings under in situ 3-point and 4-point bending tests. The crack modes and evolution were observed and measured as the damage variable with increasing loading or the controlling stress. The study indicates that the fracture characteristics depend on the size of the coatings, but the damage for all kinds of coating systems obeys the same power law relation, and the power exponent is size independent.

Acknowledgements

This work was supported by the National Basic Research Programs of China (No. 2012CB937500), and the NSFC grants of China (Nos. 11372318, 11023001, 11432014, and 91216108).

References

[1] Evans A. G., Mumm D. R., Hutchinson J. W., Meier G. H., Pettit F. S.: Mechanism controlling the durability of thermal barrier coatings. Prog. Mater. Sci. **46**: 505-553, 2001.

[2] Renusch D., Schütze, M.: Measuring and modeling the TBC damage kinetics by using acoustic emission analysis. Surf. Coat. Technol. **202:** 740–744, 2007.

[3] Chen Z. B., Wang Z. G., Zhu S. J.: Tensile fracture behavior of thermal barrier coatings on superalloy. Surf. Coat. Technol. 205: 3931–3938, 2011.

[4] Liang L. H., Wei H., Li X. N., Wei Y. G.: Size-dependent interface adhesive energy and interface strength of nanostructured systems. Surf. Coat. Technol. **236:** 525-530, 2013.

[5] Hao S. W., Rong F. , Lu M. F., Wang H. Y., Xia M. F., Ke F. J., Bai Y. L.: Power-law singularity as a possible catastrophe warning observed in rock experiments, Int. J. Rock Mech. Mining Sci. **60:** 253-262, 2013.

SURFACE EFFECT ON THE ADSORPTION-INDUCED DEFORMATION OF ORDERED POROUS MATERIAL

Mingchao Liu[1], Yixiang Gan[2], Jian Wu[1] & Changqing Chen[1a)]
[1]*Department of Engineering Mechanics, CNMM & AML, Tsinghua University, Beijing, China*
[2]*School of Civil Engineering, The University of Sydney, Sydney, NSW, Australia*

Summary Adsorption-induced deformation of the ordered porous material is an important physical phenomenon with a wide range of applications, which can be characterized by the pore-load modulus and affected by the surface effect when the pore size reduce to nanoscale. By introducing the surface elastic constants, closed-form solutions of the pore-load modulus are obtained, which turn out to be a function of the porosity, the material properties of the matrix, and the geometrical arrangement of pores. Furthermore, it also depends on the pore size and surface elastic constant when the surface effect cannot be ignored.

INTRODUCTION

Ordered porous materials have attracted increasing attention in recent years due to their unique optical, electrical, and catalytic properties [1]. Gas or fluid adsorption in the porous solid with ordered channel-like independent pores is an interesting topic and it also has a wide range of applications in the fields of geology, biology, chemistry, etc [2]. In the process of adsorption or desorption of gas or fluid, as a consequence of the physical and chemical interactions between the guest molecules and the solid pore walls, the porous solids will contract or expand. This phenomenon is known as adsorption-induced deformation and can be characterized by the pore-load modulus [3].

There are several theoretical models proposed to describe the relationship between the pore-load modulus and the geometric and material parameters of the matrix [4]. However, up to now, the influence of surface effect has not yet been investigated. In this paper, a theoretical framework with surface effect on the adsorption-induced deformation of ordered nanoporous material is developed, the effect of surface energy is demonstrated by introducing the surface elastic constants. When the surface effect is negligible, the theoretical model will reduce to classical solution without size effect. The predictions of our analytical model show good agreement with the FEM results.

THEORETICAL ANALYSIS

Since surface possesses a large fraction in nanoporous material, the influence of surface energy becomes important in its mechanical performance and should be taken into account [5]. For a linear isotropic surface without residual surface tension, the surface stress is given by $\sigma^s_{\alpha\beta} = 2\mu_s\varepsilon^s_{\alpha\beta} + \lambda_s\varepsilon_{rr}\delta_{\alpha\beta}$, where μ_s and λ_s are the surface Lame constants, which can be determined through atomic simulations or experiments.

For the typical ordered nanoporous material like MCM-41 of SBA-15, as shown in Fig. 1 (a), all exhibiting cylindrical pores are arranged on a well ordered two-dimensional (2D) hexagonal lattice. Gor *et al.* [4] pointed out that the dilatational strain in the plate with many pores can be approximated to the engineering strain of the unit cell of pressurized cylinder, with the outer diameter equaling half of the pore spacing. However, it should be noted that each cylinder will be affected by the neighboring cylinders. For nanoporous material with hexagonal lattice, there are six pores near the central unit cell. (See Fig. 1(b)). Hence, the outer boundary of the cylinder cannot be considered as free surface.

Let us consider a single pressurized thick-wall cylinder with inner radius *a* and outer radius *b*, subjecting the inner and outer pressure p_i and p_o under plane-strain condition, as shown in Fig. 1(c). According to the classical theory of elasticity [6], and combining the surface effect on the boundary condition at inner surface, the size-dependent stress and displacement components are obtained. The engineering strain of a single cylinder pore can be calculated as $\varepsilon_e = u(b)/b$. Thus, the pore-load modulus of the nanoporous material can be easily got by the definition $M_{pl} = p_i/\varepsilon_e$ as

$$M_{pl} = \frac{E\{[1+(1+v)k]-[1-(1+v)(1-2v)k]\varphi\}}{(1+v)\{(1-2v)[1-\alpha(1+(1+v)k)]-[\alpha(1-(1+v)(1-2v)k)\varphi-1]\}\varphi} \tag{1}$$

where *E* and *v* are the Young's modulus and Poisson ratio of the solid matrix respectively, and φ is the porosity of the porous material. α is a geometrical factor depend on the arrangement of pores, for porous material with hexagonal lattice, $\alpha = 1/3$, and $\alpha = 1/2$ for square lattice. $k = (2\mu_s + \lambda_s \,/\, Ea)$ is a dimensionless parameter describing the surface effect. For the plane stress condition, only the parameters *E* and *v* need to be replaced by $E/(1-v^2)$ and $v/(1-v)$.

It can be found that the surface effect parameter *k* plays an important role on the pore-load modulus of nanoporous material. For the porous material with given mechanical properties, *k* is increasing with the decreasing of the pore radius, and indicating the surface effect more obvious. As a limited case, when the pore radius is larger enough that *k* approaches zero, Eq. (1) will reduce to the classical solution without surface effect as

$$M_{pl} = \frac{E(1-\varphi)}{(1+v)[(1-2v)(1-\alpha)-(\alpha\varphi-1)]\varphi} \tag{2}$$

a) Corresponding author. Email: chencq@tsinghua.edu.cn.

RESULTS AND DISCUSSION

In order to validate the proposed theoretical model of the pore-load modulus, the FEM simulations are performed to calculate to the adsorption-induced deformation of the ordered porous material with hexagonal and square lattice. Science the surface effect is not easy to achieve in the FEM model, we just focus on the degraded model without surface effect in this case. Numerical experiment shows that the used model size is sufficient to show the homogenized responses of porous materials. Moreover, mesh sensitivity study has been conducted to ensure the numerical convergence of the models.

The FEM predicted porosity-dependent pore-load modulus of the porous material, which are normalized by the Young's modulus of the solid matrix, are shown in Fig. 2 for the plane strain and plane stress condition as upper and down triangular symbols, respectively. The corresponding theoretical predictions given by Eq. (2) with different elastic parameters are included as solid lines for the purpose of comparison. For both the hexagonal and square lattice cases, one can find that our theoretical model can predict the FEM results on a quantitative basis.

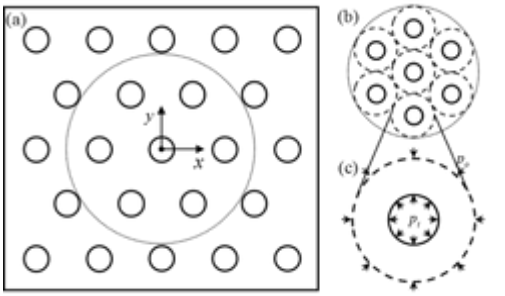

Figure 1. Schematic of a 2D ordered porous material and the unit cell of hollow cylinder.

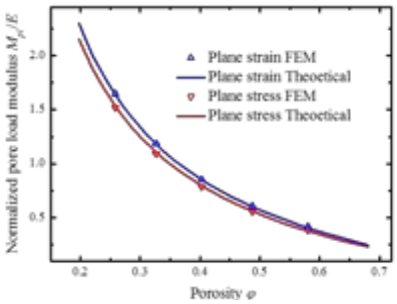

Figure 2. Comparison of FEM simulation and theoretical predictions of M_{pl}.

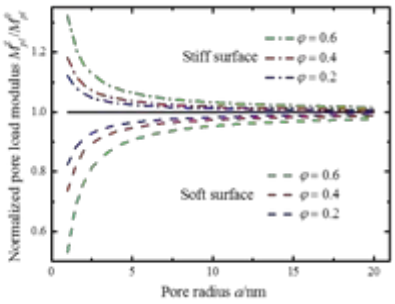

Figure 3. Predictions for the size-dependent pore-load modulus.

In order to further investigate the size-dependent effect of the pore-load modulus, the nanoporous material with different pore radius are considered. Atomistic calculations indicate that a solid surface can be either elastically softer or stiffer than their bulk counterparts. Thus, two typical sets of surface elastic constants for isotropic surfaces of aluminium are used [7]. $\mu_s = -6.22\,\mathrm{N/m}, \lambda_s = 3.49\,\mathrm{N/m}$ for surface [100], called as the "soft" surface, and $\mu_s = -0.38\,\mathrm{N/m}, \lambda_s = 6.48\,\mathrm{N/m}$ for surface [111], called as the "stiff" surface.

The normalized pore -load modulus for the two sets of surface properties as functions of the pore radius given by Eq. (1) are plotted in Fig. 3. Where the dashed and dotted lines denote the two sets of surfaces, respectively, and three samples with different porosities, from 0.2 to 0.6, are contained showing with different colour. It can be found that the surface effect cause the pore-load modulus to reduce (increase) with decreasing pore size for the soft (stiff) surface. Evidently, for both the two surfaces, the surface effect on the pore-load modulus becomes more and more significant as the pore radius decreases less than 10 nm. Moreover, the surface effect is more prominent for a nanoporous sample with a bigger porosity.

CONCLUDING REMARKS

In conclusion, this work has studied the influence of surface energy on the adsorption-induced deformation of the ordered nanoporous material. An analytical solution for the pore-load modulus with surface effect is derived based on the micromechanical model of a pressurized thick-wall cylinder unit cell, and the surface elastic constants are adopted to describe the influence of surface energy. The proposed theoretical model are validated by comparing with FEM simulations for the limited case without surface effect and show great agreement. It also reveals that the surface energy plays an important role on the elastic response for nanoporous material, and the pore-load modulus shows significant size-dependent characteristics. The present study is helpful for measuring the mechanical properties of nanoporous materials and for designing nanoporous material based sensor and actuator in various applications.

References

[1] Lu G. Q., Zhao X. S.: Nanoporous Materials - Science and Engineering. London, United Kingdom 2004.

[2] Rasaiah J. C., Garde S., Hummer G.: Water in nonpolar confinement: From nanotubes to proteins and beyond. *Annu. Rev. Phys. Chem.* **59**: 713-740, 2008.

[3] Prass J., Muter D., Fratzl P., Paris O.: Capillarity-driven deformation of ordered nanoporous silica. *Appl. Phys. Lett.* 95: 083121, 2009.

[4] Gor G. Y., Bertinetti L., Bernstein N., Hofmann T., Fratzl P., Huber P.: Elastic response of mesoporous silicon to capillary pressures in the pores. *Appl. Phys. Lett.* 106: 261901, 2015.

[5] Sharma P., Ganti S., Bhate N.: Effect of surfaces on the size-dependent elastic state of nano-inhomogeneities. *Appl. Phys. Lett.* 82: 535, 2003.

[6] Timoshenko S., Goodier J.: Theory of Elasticity, 3rd Ed. New York, United States 1970.

[7] Miller R. E., Shenoy V. B.: Size-dependent elastic properties of nanosized structural elements. *Nanotech.* 11: 139, 2000.

INFLUENCE OF NANOINCLUSION'S SIZE-DEPENDENCE ON COMPOSITE WITH MICROPOLAR MATRIX

Hansong Ma[1a)], Lihong Liang[1] & Yueguang Wei[1]
[1]*LNM, Institute of Mechanics, Chinese Academy of Science, Beijing, China*

Summary The material parameters of nanomaterials are different from those of bulk ones, such as elastic modulus, thermal conductivity etc., which are known as the intrinsic size-dependence effects. In this paper, the intrinsic size effect of Young's modulus is introduced into nanocomposite to study its influence on the effective elastic moduli of composite, especially the composite with micropolar matrix. It is shown that the intrinsic size-dependence of nanoinclusion can lead to the size-dependence of the effective elastic moduli of composite. Especially for the micropolar composite, the variations of the effective muduli of composite with the inclusion's size from nanometre to micrometre will be displayed completely.

INTRODUCTION

Nanomaterials, such as nanoparticles, nanowires, nanotubes, have excellent mechanical, electronic and other properties, which bring potential and broad application fields of aerospace, electronics, medical and so forth, so that have attracted wide attentions. Many researchers have reported that nanomaterials display the different properties from the corresponding bulk materials, such as the high elastic modulus, the low thermal conductivity, and so on. One of the important applications of nanomaterials is to be used as reinforcement for high-performance composite. Therefore, to understand the influence of these peculiar properties of nanoparticle on the overall properties of composite is very important.

In this paper, we shall introduce the nanoinclusion's size-dependence effect into micromechanical models of composite to predict the size-dependent effective elastic modulus of composite, especially the composite with micropolar matrix.

MODELS

Based on the the inherent lattice strain and the binding energy change of nanocrystals compared with the bulk crystals, Liang et al. [1] established an analytical model about the size-dependent elastic modulus of nanocrystalline metals. In the model, the bond length and bond energy of nanocrystalline lattice are size-dependent, which indicate that it is a kind of intrinsic property, and there is no free parameter in the obtained formula. The predictions of the model for Cu, Ag, Si thin films, nanoparticles, and TiO2 nanoparticles are in agreement with the computational simulations, the continuum mechanics calculations, and the experimental results.

This intrinsic size-dependent property of nanoparticle derived by Liang[1] will be introduced into composite micromechanical models to predict the size-dependent effective elastic modulus of composite, especially the composite with micropolar matrix in the paper.

Micromechanics was successfully used to predict the effective elastic modulus of composite, such as Mori-Tanaka method[2], self-consistent method and so on. However these micromechanical models based on classical continuum theory fail to predict the size effect well-observed for metal matrix composite. Based on the micropolar theory, which is one of high order theories, Liu & Hu and Ma and Hu [4] extended the classical Mori-Tanaka model to micropolar theory and proposed a high order micromechanical model to describe the size effect of composite. Since both sizes of inclusion and microstructure of matrix are with the similar order, the matrix of composite was described by micropolar theory in the model. Both the inclusion and the overall composite were still classical materials. An analytical formula was derived for the effective elastic modulus of composite and it can describe the size effect of composite caused by the microstructure of matrix only.

In this paper, the influence of size-dependent inclusion derived from Liang[1] will be introduced into the expressions of effective elastic moduli derived from the classical Mori-Tanaka model[2] and the Micropolar Mori-Tanaka model[3].

RESULTS

The composite composed of Al matrix and TiO_2 nanoparticles is taken into account. The figure 1 shows the variation of the effective moduli of the composite with the size of inclusion. It is shown that the size-dependent property of nanoinclusion can lead to the composite's size effect whether the classical model or the micropolar model. But for classical composite, the size effect almost disappears at the size of inclusion 40nm and then the classical result is recovered. For micropolar composite, the size effect can be revealed with the size of inclusion from nanometer to micrometer and then the classical result is recovered.

[a)] Corresponding author. Email: mahs@lnm.imech.ac.cn

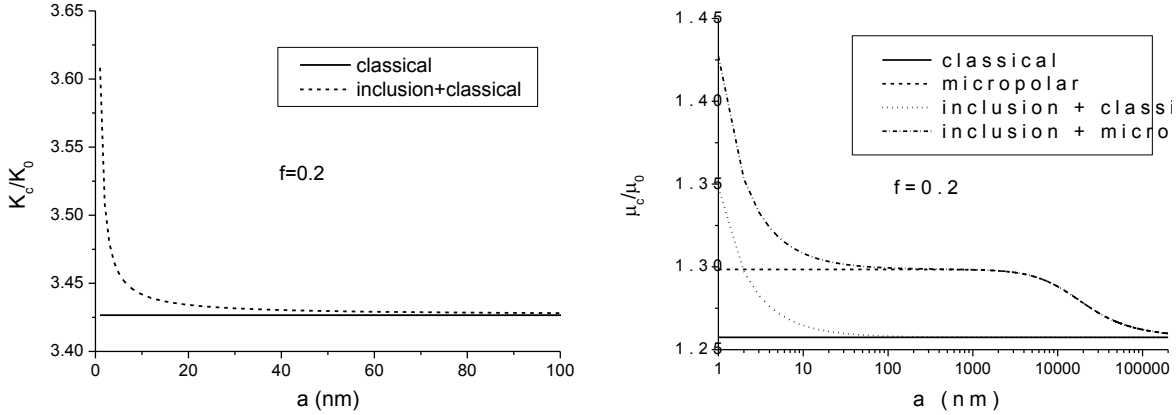

(a) volume moduli (b) shear moduli

Fig 1. Effective elastic moduli of composite

CONCLUSIONS

In the presentation, we have studied the influence of the intrinsic size-dependence of nanoinclusion on the effective elastic moduli of composite. The results have shown that the intrinsic size-dependence of nanoinclusion can lead to the size effect of the overall composite, and when the size of inclusion is large enough, the classical results are recovered.

References

[1] Lihong Liang, Hansong Ma, Yueguang Wei: Size-dependent Elastic Modulus and Vibration Frequency of Nanocrystals. *Journal of Nanomatrerials* 2011:670857, 2011.

[2] Mori T, Tanaka K.: Average stress in matrix and average elastic energy of materials with misfitting inclusions, *Acta Metall. Mater*., 21: 571~574, 1973.

[3] Liu, X.N., Hu, G.K: A continuum micromechanical theory of overall plasticity for particulate composites including particle size effect. *Int. J. Plasticity* 21: 777-799, 2005.

[4] Ma, H.S., Hu, G.K.: Influence of fiber's shape and size on overall elastoplastic property for micropolar composites, *International Journal of Solids and Structures* ,43: 3025~3043, 2006.

SIZE-DEPENDENT AND TUNABLE MECHANICAL PROPERTIES OF MICRO-AND NANO-SIZED STOCHASTIC FIBROUS STRUCTRES

Yanhui Ma[1], Hanxing Zhu[1*], Bo Su[2]
[1]*Engineering School, Cardiff University, Cardiff, UK*
[2]*School of Oral and Dental Sciences, University of Bristol, Bristol, UK*

Abstract Filamentous networks can be widely found in biomaterials at the micro- and nano-scales. Some conventional theories may not apply to the materials with dimension at the micro- or nano-scale. The effects of strain gradient at the micro-meter scale and the effects of surface elasticity and initial stresses/strains at the nano-scale are incorporated into the deformation mechanisms in the analysis of stochastic fibrous structures. A random beam network model with cross-linkers has been developed to describe the fibrous networks whose relative density can be controlled to different values by adjusting the concentration of cross-linkers. The size-dependent effects on the relationships between the relative density and the elastic constants of micro- and nano-sized fibrous structures are investigated.

INTRODUCTION

Fibrous materials are another type of porous materials with low density and high stiffness and strength, which promise for a wide range of engineering applications. Fibrous structure can be widely found in biomaterials at the micro- and nano-scales. For instance, a typical extra-cellular matrix (ECM) is composed of structural protein nanofibres such as collagen with a diameter of the order of microns [1]. Increasing evidence has shown that the mechanical stiffness of ECM plays an important role in regulating cellular behaviours, including adhesion, proliferation and differentiation of mesenchymal stem cells (MSCs) [2]. Cytoskeleton (CSK) is a network of filamentous proteins within a cell's cytoplasm, composing of filamentous actin (F-actin), microtubules and intermediate filaments with diameters of the order of nanometers [3]. The mechanical stiffness of intracellular material, to a great extent, is governed by the cytoskeleton. In industrial engineering, micro- and nano-structured fibrous materials can be used in micro-electro-mechanical systems (MEMS) and nano-electro-mechanical systems (NEMS) devices, which are of great interest to scientists and engineers. The understanding of the mechanical properties of macro-sized porous materials has well been established. However, when the dimensions of fibrous structures are reduced to the micro- or nano-scale, the stiffness or rigidity is much different from that of their macro-sized counterparts.

It is crucial to incorporate the strain gradient effects at the micro-meter scale, and the surface elasticity and initial stress effects at the nano-meter scale into the deformation mechanism of fibrous materials. To the best of our knowledge, the size dependent mechanical behaviour of fibrous materials has not been reported. The objective of this paper is to investigate the effects of relative density on the size-dependent mechanical properties of micro- and nano-sized fibrous structures.

SIZE-DEPENDENT EFFECTS AT MICRO-SCALE

At the micro scale, the strain gradient has a dominant effect on the mechanical behaviour of the stochastic fibrous materials. l_m/d is used to describe the gradient strain effects in the micro-scale [4, 5], where the l_m is the intrinsic material length at the micrometer scale (which can be experimentally measured and is usually in the range between submicron and microns, and different for different materials), d is the diameter of the circular cross-section of the fibres. We have conducted the simulations for different values of l_m/d ($l_m/d = 0, 0.2, 0.5, 1.0$) to investigate the size-dependent effects on the elastic properties of the stochastic fibrous materials at the micro scale. It should be noted that when l_m/d is 0, in which the diameter of the fibres is much larger than the intrinsic material length scale l_m, the size-dependent effect vanishes and the elastic constants reduce to those of their conventional counterparts. The three-dimensional random beam model with cross-linkers developed to describe the stochastic fibrous networks is given in Fig1. The simulation results suggest that the smaller is the diameter of the fibres, the larger are the dimensionless Young's moduli of the fibrous materials; and that the larger is the relative density of the fibrous materials, the larger are the dimensionless Young's moduli, as shown in Fig2.

SIZE-DEPENDENT EFFECTS AT NANO-SCALE

It has been found that at the nanometer scale, the surface elasticity and the initial strain (stress) can significantly affect the mechanical behaviours [4-6]. l_n/d is used to describe the surface elasticity effects at the nanoscale, where the l_n is the material intrinsic length at the nanometer scale, which can be expressed by $l_n = S/E_s$ (where S is the surface elasticity modulus) and may vary over a range from 0.01nm to 0.1nm[6] for different materials. ε_0^L is the initial strain in the length direction of the fibres, whose amplitude can be controlled to vary by an applied electric potential [7]. We have conducted the simulations using finite element software for different values of l_n/d ($l_n/d = 0, 0.2, 0.5, 1.0$) and ε_0^L ($\varepsilon_0^L = -0.06, -0.03, 0, 0.03, 0.06$) to separately investigate the surface elasticity effects and the initial strain effects on the elastic properties of the stochastic fibrous materials at the nanometer scale. Note that when $l_n/d = 0$ and $\varepsilon_0^L = 0$, the size-

* Corresponding author. Email: ZhuH3@cardiff.ac.uk

dependent effects at the nanoscale vanish and the elastic constants reduce to those of their conventional counterparts. The simulation results suggest that for nano-sized fibrous structures, the smaller the size, the larger the Young's modulus as shown in Fig3. Moreover, the non-dimensional Young's modulus can be controlled to vary by adjusting the amplitude of an applied initial strain as shown in Fig4.

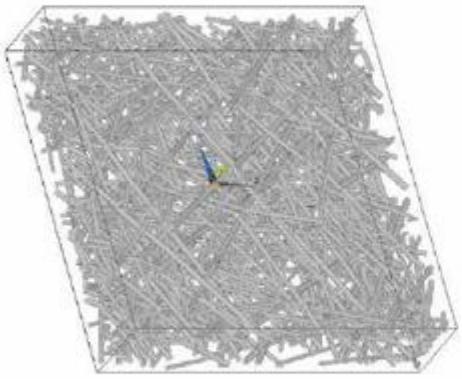

Fig1. Three-dimensional random beam model with cross-linking.

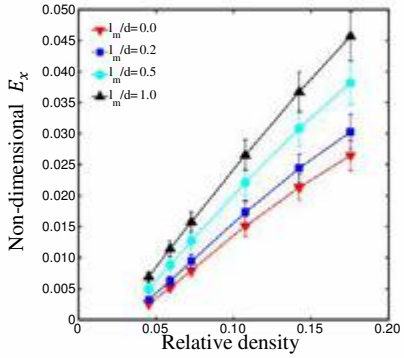

Fig2. Size-dependent effect on the relationship between the non-dimensional Young's modulus in the x direction and the relative density of stochastic fibrous materials at micro-meter scale.

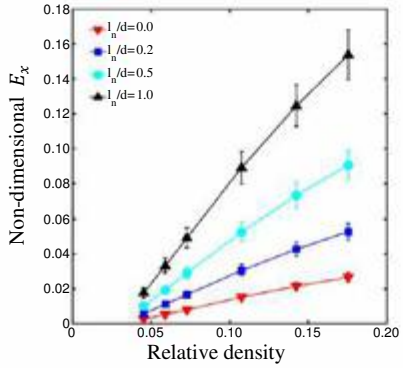

Fig3. Size-dependent effect on the relationship between the non-dimensional Young's modulus in the x direction and the relative density of stochastic fibrous materials at nano-meter scale.

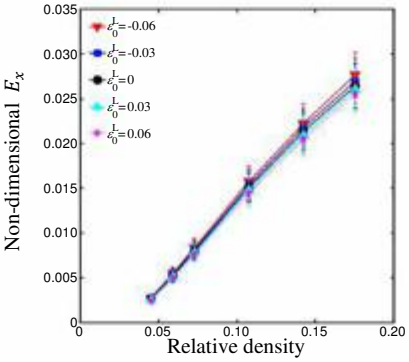

Fig4. Non-dimensional Young's modulus E_x v.s. the relative density of nano-sized stochastic fibrous networks with the presence of the effects of initial strains/stresses.

CONCLUSIONS

The elastic properties of filamentous networks are size-dependent at the micro- and nano- scales. By incorporating the strain gradient effects at the micro-scale and the effects of surface elasticity and initial strains at the nano-meter scale into the deformation mechanisms, the size-dependent mechanical properties are investigated for the micro- and nano-sized fibrous structures, which could give a good reference for the scientists in tissue engineering and serve as a guide in the design of MEMS and NEMS.

References

[1] Pedersen, J.A., and Swartz, M. A.: Mechanobiology in the third dimension. Annals of biomedical engineering 33.11 : 1469-1490, 2005

[2] Discher, D. E., Janmey, P. and Wang, Y.L.: Tissue cells feel and respond to the stiffness of their substrate. Science 310.5751 : 1139-1143, 2005

[3] Fuchs, E. and Cleveland, D. W.: A structural scaffolding of intermediate filaments in health and disease. Science 279.5350: 514-519,1998

[4] Zhu, H.X.: Size-dependent elastic properties of micro- and nano-honeycombs, J. Mech. Phys. Solids, *58*: 696-709, 2010.

[5] Zhu, H.X. and Wang Z.B.: Size-dependent and tunable elastic and geometric properties of hierarchical nano-porous materials, Science of Advanced Materials, *5*: 677-686, 2013.

[6] Miller, R. E. and Shenoy, V. B.: Size-dependent elastic properties of nanosized structural elements. Nanotechnology 11.3 : 139, 2000

[7] Zhu, H.X.: The effects of surface and initial stresses on the bending stiffness of nanowires. Nanotechnology 19.40: 405703, 2008

HIGHER-ORDER ASYMPTOTIC HOMOGENIZATION OF PERIODIC MATERIALS AT LOW SCALE SEPARATION

Maqsood Ameen,* Ron Peerlings, and Marc Geers
Department of Mechanical Engineering, Eindhoven University of Technology, Eindhoven, The Netherlands

Summary In this work, we investigate the limits of classical homogenization theories pertaining to homogenization of periodic composite materials at low scale separations and demonstrate the effectiveness of higher-order periodic homogenization in alleviating this limitation. Classical homogenization techniques are very effective for materials with large scale separation between the scale of the heterogeneity and the macro-scale dimension, but inaccurate at low scale separations. Literature suggests that asymptotic homogenization is capable of pushing the limit to smaller scale separation by taking on board higher-order terms of the asymptotic expansion. We show that the classical homogenization deviates from the actual solution for scale ratios below 10. Beyond this limit, the higher-order asymptotic homogenization solution still gives a very good approximation which becomes better as more higher-order terms are included. This results in a size-dependent macroscopic model, which indeed allows one to push the limitations of homogenization in the direction of less scale separation.

INTRODUCTION

All matter is heterogeneous at some scale, but frequently it is convenient to treat it as homogeneous. Some of the well-known examples are metal alloys, concrete, porous structures and fibrous composites. The distinct features of their microstructures respond quite differently to mechanical loading and hence their deformation is heterogeneously distributed at the fine scale. It is the combination of the different microstructural features which governs the overall response of the material to the loading.

Homogenization is a mathematical technique for studying partial differential equations with rapidly oscillating coefficients, which are typical of the equations that govern the physics of heterogeneous materials. An important aspect in the analysis of multiphase materials is to deduce their effective behavior (e.g. mechanical stiffness, thermal expansion properties, etc.) from the corresponding single-phase behaviors and the geometrical arrangement of the phases. This concept of rendering "homogeneous" a heterogeneous material is what we call homogenization.

Conventional homogenization methods are based on *a separation of scales*, given by: $l << L$, where l is the size of the heterogeneity and L represents the macroscopic length scale. However, if the microstructural size is of the same order as the macroscopic length scale, then most of the classical homogenization schemes break down. Literature [1-4] suggests that the asymptotic homogenization method is capable of pushing the limit to smaller scale separation, by generating a hierarchy of problems which can be solved sequentially to generate a solution that asymptotically converges to the exact (homogenized) solution.

Problem Description

A qualitative and quantitative assessment of the scale separation limits of the classical and the higher order periodic homogenization methods is performed on two-dimensional elastic two-phase composites, consisting of stiff circular inclusions in a soft matrix material, subjected to anti-plane shear by means of a periodic body force. This anti-plane shear problem can be described by the following partial differential equation:

$$\frac{\partial}{\partial x_1}\Big(G\frac{\partial u_3}{\partial x_1}\Big)+\frac{\partial}{\partial x_2}\Big(G\frac{\partial u_3}{\partial x_2}\Big)+F=0 \tag{1}$$

where $u_3 = u(x_1, x_2)$ is the resulting out-of-plane displacement, G is the Shear Moduli distribution function and F is a bisinusoidal bodyforce given by $F = F_0 \quad \mathrm{n}\left(\frac{2\pi x_1}{L}\right) \quad \mathrm{n}\left(\frac{2\pi x_2}{L}\right)$.

The period of the material's microstructure is *l* and that of the body force is *L*, and the ratio *L/l* hence characterises the scale separation. The homogenized properties are defined not for a specific microstructural configuration with respect to a period of the body force, but by taking an ensemble average for a family of all possible microstructures.

Methodology

On the one hand, reference solutions are created using direct numerical simulation of a family of microstructural configurations for a range of scale ratios. On the other hand, asymptotic homogenization is used to obtain homogenized properties for zeroth order and higher orders. Predictions made using these homogenized properties are then compared against the reference solutions. Fig.1 shows a schematic of the outline of the solution methodology.

*Corresponding author. Email: m.ameen@tue.nl

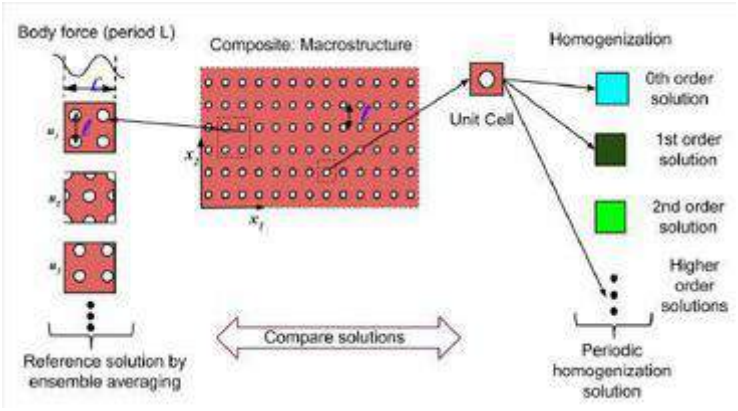

Figure 1: Schematic of the problem: Comparison of periodic homogenization solution with reference solution created by full-scale simulation for various scale ratios

RESULTS

Fig.2 shows the average peak displacement, normalized by that predicted by the classically homogenized solution, as a function of the scale ratio L/l. Shown are the reference solution, the classical homogenization solution and higher order solutions, for a phase contrast of 20. The zeroth order classical homogenization solution is independent of the scale ratio and hence is a straight line as shown in the plot. For scale ratios $L/l > 10$, the reference solution converges to this constant value, but at low scale separations it deviates from it significantly. The higher order periodic homogenization solutions closely match with the reference solution even for low scale ratios. The second order solution starts to deviate from the reference solution at $(L/l) = \ .5$, while the fourth order solution can still give a good approximation for even lower scale ratios.

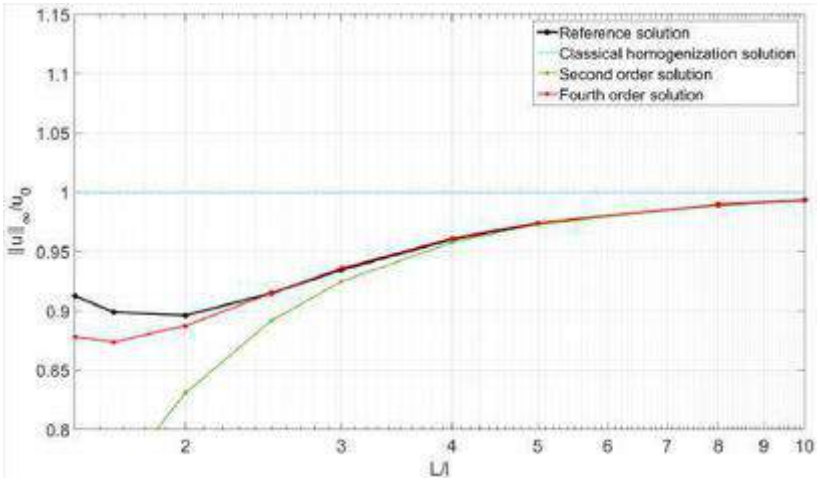

Figure 2: Scale separation plot: Norm of the displacement solution vs. scale separation, for various cases

CONCLUSIONS

We show that the zeroth order classical homogenization deviates from the actual solution for scale ratios *L/l* below 10. Beyond this limit, higher-order asymptotic homogenization solution gives a very good approximation. The approximation in the low scale separation regime becomes better as more higher-order terms are included. This shows that the higher-order theory indeed allows one to push the limitations of homogenization in the direction of less scale separation.

References

[1] Smyshlyaev V. P., Cherednichenko K. D.: Strain gradient effects in periodic heterogeneous media. JMPS 48:1325-1357, 2000.
[2] Boutin C.: Microstructural effects in elastic composites. IJSS 33: 1023-1051, 1996.
[3] Drugan W., Willis J.: A micromechanics-based estimates of RVE size for elastic composites. JMPS 44:497-524, 1996.
[4] Peerlings R. H. J., Fleck .N. A.: Computational evaluation of strain gradient elasticity constants. IJMCE 2, 2004.

MODELING SURFACE PENETRATION BY DISLOCATION PILEUP MODEL WITH IMAGE EFFECT

Xiang-Long Peng[1], Gan-Yun Huang[1a)]
[1]*Department of Mechanics, School of Mechanical Engineering, Tianjin University, Tianjin, PR China*

Summary In the present short paper, a continuum dislocation pileup model considering image effect (IE) is developed to study the onset of dislocation penetration at surface in thin films. It is found that due to IE, more dislocations accumulate at the surface and their absorption by surface become easier. Moreover, the critical load for penetration exhibits a "smaller is stronger" type size effect but different from the classical Hall-Petch relation. The present results may cast some light on constructing higher-order strain gradient crystal plasticity theories with IE.

INTRODUCTION

The requirement to capture the size-dependent plastic behaviours in small scaled crystalline materials has triggered the construction of numerous strain gradient crystal plasticity theories, among which the higher-order theories [1] are of particular interest due to their capability to consider dislocation-surface/interface interactions via the microscopic boundary conditions. In the higher-order theories, the important concept of back stress induced by geometrically necessary dislocations interactions has been usually derived from the stress field of a dislocation in an infinite medium, and the boundary condition adopted implies surfaces as barriers to dislocations. However, both discrete dislocation dynamics simulations [2] and experiments [3] have demonstrated the significant effects of image effect (IE) and the penetrable surfaces. To address such effects, as a preliminary study, the onset of dislocation penetration at surface of a thin film is modeled by a continuum dislocation pileup model with IE taken into account.

MODEL DESCRIPTION, RESULTS AND DISCUSSION

Let us consider a pileup of edge dislocations on a slip plane in a single crystalline thin film bonded to a similar semi-infinite elastic substrate. The uniformly applied resolved shear stress is τ_o, see the inset in Fig. 1. At the continuum level, distribution of the dislocations may be characterized by a density function $n(t)$ denoting the number of dislocations per unit length [4]. Based on the elastic field of a dislocation in a half-plane and by considering the force balance on the dislocations, the following singular integral equation that determines $n(t)$ can be obtained as,

$$\tau_0 b-\frac{\mu b^2}{2\pi(1-\nu)}\left[\int_{-L/2}^{L/2}\frac{n(s)}{s-t}ds-\int_{-L/2}^{L/2}f^{im}(t,s,h,\theta)n(s)ds\right]=0,\quad -\frac{L}{2}\le t\le\frac{L}{2} \tag{1}$$

where μ, ν and b are the shear modulus, the Poisson's ratio and the magnitude of the Burgers vector respectively, and $f^{im}(t,s,h,\theta)$ resulting from the surface IE reads

$$\begin{aligned} f^{im}(t,s,h,\theta)=&[(\tilde{x}+\tilde{h})^2+\tilde{y}^2]^{-2}[(s_\theta^3-s_\theta c_\theta^2)(\tilde{x}+\tilde{h})^3+(c_\theta^3-5c_\theta s_\theta^2)\tilde{y}(\tilde{x}+\tilde{h})^2+(-s_\theta^3+5s_\theta c_\theta^2)\tilde{y}^2(\tilde{x}+\tilde{h})\\ &+(-c_\theta^3+c_\theta s_\theta^2)\tilde{y}^3]+2\tilde{h}[(\tilde{x}+\tilde{h})^2+\tilde{y}^2]^{-3}\{(s_\theta^3+3s_\theta c_\theta^2)(\tilde{x}+\tilde{h})^4\\ &+(s_\theta^3+s_\theta c_\theta^2)[-2\tilde{h}(\tilde{x}+\tilde{h})^3-6\tilde{y}^2(\tilde{x}+\tilde{h})^2+6\tilde{h}\tilde{y}^2(\tilde{x}+\tilde{h})]+(-6c_\theta^3-2c_\theta s_\theta^2)\tilde{y}(\tilde{x}+\tilde{h})^3\\ &+(c_\theta^3+c_\theta s_\theta^2)[6\tilde{h}\tilde{y}(\tilde{x}+\tilde{h})^2-2\tilde{h}\tilde{y}^3]+(2c_\theta^3+6c_\theta s_\theta^2)\tilde{y}^3(\tilde{x}+\tilde{h})+(s_\theta^3-s_\theta c_\theta^2)\tilde{y}^4\} \end{aligned} \tag{2}$$

which is obtained based on the stress field of an edge dislocation in semi-infinite space derived by Head [5]. And $s_\theta=\sin\theta$, $c_\theta=\cos\theta$, $L=(h-2d)/s_\theta$, $\tilde{h}=d+(L/2-t)s_\theta$, $\tilde{x}=d+(L/2-t)s_\theta$, $\tilde{y}=(t-s)c_\theta$, where θ is the inclined angle between the slip plane and the surface, h is the film thickness, L is the pileup length, and $d=2b$ is assumed to be the small distance between the two leading dislocations and the surface or the interface to avoid the singularity on their stress field. For the dislocation sources activated in grain interior as considered herein, equal numbers of positive and negative dislocations are generated, which gives an additional condition to ensure the uniqueness of the solution

$$\int_{-L/2}^{L/2}n(s)ds=0 \tag{3}$$

Eq. (1) along with the condition (3) is similar to that for the problem of a shear crack and can be readily solved numerically by Erdogan and Gupta method [6], and the details are omitted here for brevity. If one takes $f^{im}(t,s,h,\theta)=0$ in Eq. (1), the problem is reduced to that of a dislocation pileup in an infinite medium [4]. For $\theta=\pi/3$, $h=2\mu$m and $b=0.25$nm, the dislocation density distribution $n(t)$ has been calculated and plotted in Fig.1. For the purpose of comparison, the distribution for the pileup in an infinite medium is also presented in the figure. It can be found that due to the attraction by the surface, the dislocation density close to the surface is much higher than that in an infinite medium. It is consistent with

a) Corresponding author. Email: gyhuang@tju.edu.cn.

the recent findings by El-Naaman et al. [7] who pointed out that the usual higher-order theories involving in back stress without IE predicts dislocation distributions more uniform than those observed experimentally. In addition, the density is singular at $t=\pm L/2$, which is again similar to the crack problem. Consequently by analogy with energy release rate in the crack problem, one may define a thermodynamic force as [8]

$$F(\tau_0)=\lim_{t\to L/2} A(t-L/2)n^2(t) \tag{4}$$

with $A=-\pi\mu b^2/[4(1-\nu)]$, which is indeed the driving force for the dislocation pileup to move towards the surface. Naturally one may expect that if the driving force is large enough, the surface will be penetrated by dislocations. Thus, it is reasonable to assume that surface penetration occurs when the following condition is satisfied,

$$F(\tau_0)=b\tau_{ss} \tag{5}$$

where τ_{ss} the surface resistance for penetration is assumed to be a constant here . The condition is similar to some classical pileup models for yielding in grain interior [4]. Through Eqs. (4) and (5), the critical applied resolved shear stress for surface penetration τ_y is readily obtained. As shown in Fig. 2 where the normalized τ_y as a function of $h^{-1/2}$ for different values of θ is displayed, it is obviously not proportional to $h^{-1/2}$, which is different from the Hall-Petch size effect, i.e., τ_y depends on $h^{-1/2}$ linearly as would be predicted when no IE is present. In fact, the attractive image forces make surface penetration easier. It is also seen that different values of θ induce different pileup length L and hence influence τ_y significantly.

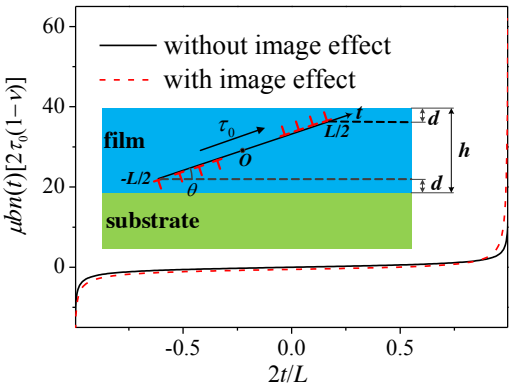

Fig. 1. Dislocation density distribution within the pileup

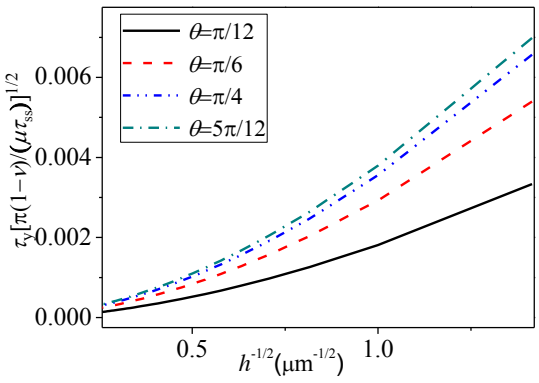

Fig. 2. Normalized τ_y versus $h^{-1/2}$ for different θ

CONCLUSIONS

In conclusion, the surface penetration of thin films by a continuum dislocation pileup model with account of IE is studied. It is found that IE has dramatic influence on the dislocation density distribution and the critical load for surface penetration and hence should be decently involved into the higher-order strain gradient crystal plasticity. Noteworthy is that in present preliminary model, possible effect of dislocation sources, elastic interaction between dislocation pileups on different slip planes and non-uniform applied stress are not considered and will be left for the future study.

The work is supported by the Nature Science Foundation of China under Grant No. 11572216 and the National Key Basic Research Scheme of China under Grant No. 2012CB937500.

References

[1] Kuroda M., Tvergaard V.: On the formulations of higher-order strain gradient crystal plasticity models. *J. Mech. Phys. Solids* **56**:1591-1608, 2008.

[2] Yasin H., Zbib H. M., Khaleel M. A.Z.: Size and boundary effects in discrete dislocation dynamics: coupling with continuum finite element. *Mater. Sci. Eng. A* **309-310**: 294-299, 2001.

[3] Oh S. H., Legros M., Kiener D., Dehm G.: In situ observation of dislocation nucleation and escape in a submicrometre aluminium single crystal. *Nature Mater.* **8**: 95-100, 2009.

[4] Hirth J. P., Lothe J.: Theory of dislocations. New York, United States of American 1982.

[5] Head A. K.: Edge dislocations in inhomogeneous media. *Proc. Phys. Soc. London, Sect.* B **66** : 793-801, 1953.

[6] Erdogan F., Gupta G. D.: On the numerical solution of singular integral equations. *Q. Appl. Math.*: 525-534, 1972.

[7] El-Naaman S. A., Nielsen K. L., Niordson C. F.: On modeling micro-structural evolution using a higher order strain gradient continuum theory. *Int. J. Plast.***76**: 285-298, 2016.

[8] Eshebly J. D., Bilbly B. A.: Fracture::an advanced treatise, vol. I, Microscopic and macroscopic fundamentals. New York, United States of American 1968.

A STUDY OF GRAIN AND GRAIN-BOUNDARIES BASED ON A GRADIENT CRYSTAL-PLASTICITY MODEL

Habib Pouriayevali[1a)], Bai-Xiang Xu[1]
[1] *Mechanics of Functional Materials Division, Institute of Material Science, Technische Universitat Darmstadt, Petersenstrasse 32, D-64287 Germany,*

Summary In this study, a well-defined finite-deformation gradient crystal-plasticity model which has been proposed by Gurtin [1] is employed and represented with respect to the reference configuration to study size-dependent hardening behavior of a single crystal. A recoverable defect-energy which incorporates geometrically necessary dislocation (GND) density is introduced. The constitutive model is implemented in the finite-element software ABAQUS via a user-defined subroutine (UEL). The primary aim of the current study is an understanding of effect of energetic and dissipative gradient-strengthenings as well as self- and latent-hardening in stress-strain response of a single crystal. Rate and size-dependent responses along with Bauschinger-like behavior under a cyclic simple-shear loading are investigated. Moreover, plastic flows in predefined slip systems and accumulation of GNDs are distinctly observed. This constitutive model is further developed for multicrystals. Penetration of dislocations through soft boundaries and accumulation of GNDs at hard boundaries are also investigated.

RESULTS

In order to observe the effect of scale variation in the directional plastic flows and accumulation of GNDs, a simple-shear loading is applied to three different single crystals defined by crystal sizes $D = 0.5\,\mu m$, $1\,\mu m$ and $2\,\mu m$. Fig. 1 compares numerical results. Based on the results depicted in Fig. 1-rows (a, b), it can be concluded that an increase in the crystal size results in a larger magnitude of plastic flows as well as a more expansion of plastic flows towards the boundary. Smaller crystals show a higher aggregation of plastic flows towards the center of crystals. Results presented in Fig. 1-row (c) indicate the greatest magnitude of GND density (dislocations pile-up) in an area close to the hard-boundary. It can also be concluded that a decrease in the crystal size yields an increase in accumulation of GNDs towards the boundary. Smaller crystals undergoing a more expansive accumulation of GNDs are subjected to a larger value of gradient strengthening, thus the phenomenon 'smaller is stronger' is easily validated here

CONCLUSIONS

The numerical results reveal that energetic and dissipative gradient-strengthenings yield respectively the kinematic-hardening behavior and yield-strengthening response. It is also concluded that dissipative and energetic length-scales act differently; the former affects the onset of plastic flow, and the latter results in a change of post-yield strain-hardening response. Moreover, self- and latent-hardening are evolved via an effective flow-rate which is a function of accumulation rates of SSDs and GNDs and represents a measure of formation of short-range interactions between SSDs and GNDs. These interactions turn to impede dislocation movements and yield isotropic-hardening responses which are induced via self- and latent-hardening. In addition, rate-dependent stress-strain response of single crystal is simply observed here, and the phenomenon 'smaller is stronger' is easily validated for different crystal sizes.

ACKNOWLEDGMENT

The support rendered by the German Research Foundation (DFG) for research grant SFB 666 is cordially acknowledged.

[a)] Corresponding author. E-mail address: pouriayevali@mfm.tu-darmstadt.de

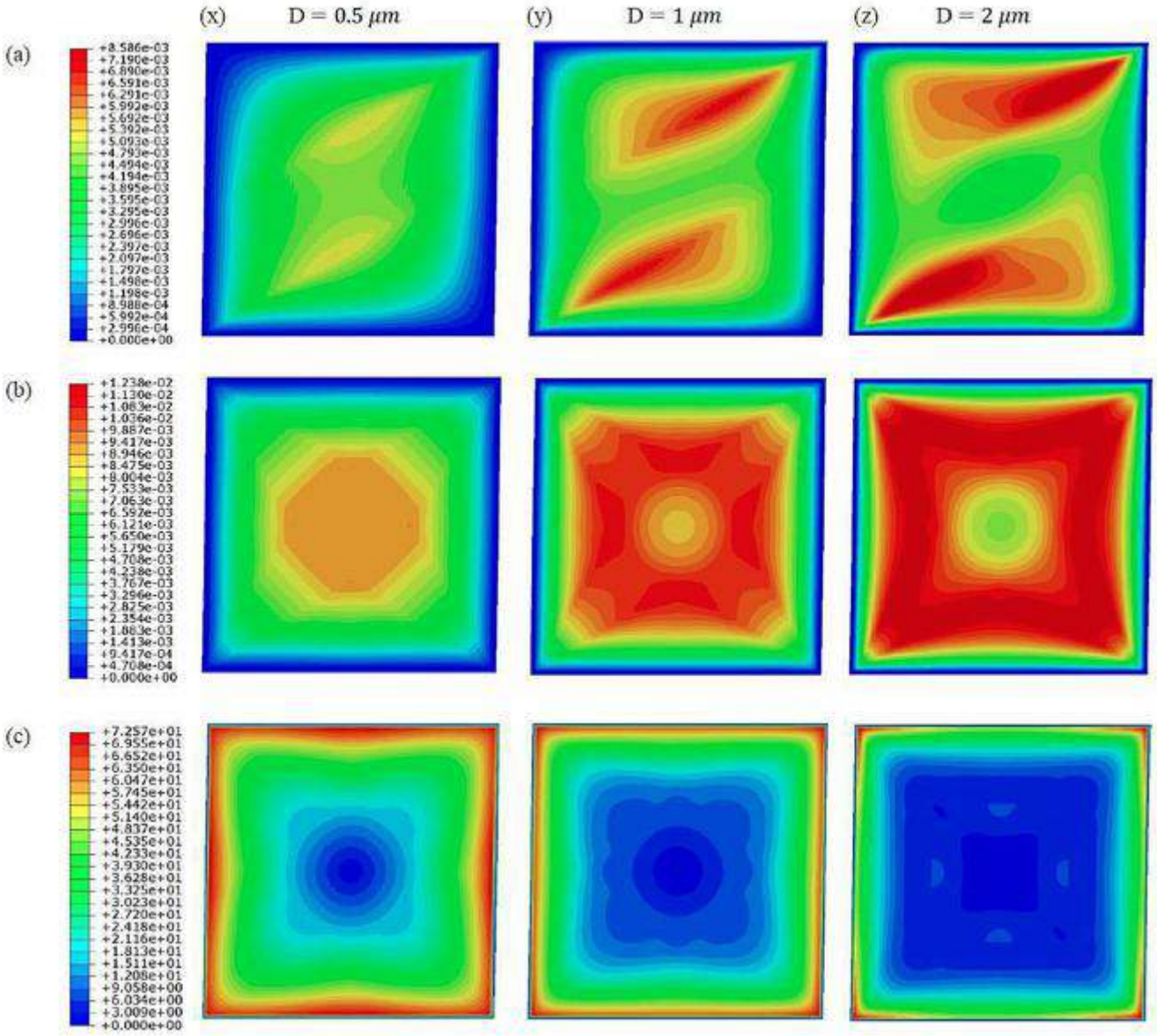

Fig. 1. Numerical results corresponding to 1.6 % shear strain are presented. Columns (x, y, z) represent results obtained for crystal size $D = 0.5\mu m$, $1\mu m$ and $2\mu m$, respectively. Row (a) Contours of directional plastic flow based on a predefined slip system. Row (b) contour of a combination of plastic flows. Row (c) contour of accumulation of dislocation densities.

References

[1] Gurtin, M. E. (2008). "A finite-deformation, gradient theory of single-crystal plasticity with free energy dependent on densities of geometrically necessary dislocations." International Journal of Plasticity 24(4): 702-725.

GEOMETRICALLY NONLINEAR THEORY OF STATICS AND DYNAMICS OF MICROPOLAR ELASTIC THIN PLATES AND SLOPING SHELLS

Samvel Sargsyan[1]

[1]*Department of Physics and Mathematics, Gyumri State Pedagogical Institute, Gyumri, Armenia*

Summary General geometrically nonlinear theory of statics and dynamics of single and multilayered micropolar elastic thin plates and sloping shells is introduced in this paper. Variation approach is developed for the constructed theory and specific problems of statics, stability and vibration for rectangular and circular plates and sloping shells are studied, specific properties of micropolar material are revealed.

In papers [1-3] general applied linear theory of micropolar elastic thin plates and shells is constructed on the basis of hypotheses method, that adequately reflect asymptotic properties of behavior of the solutions of three-dimensional boundary-value problems in the relevant thin domains.

Presently, the construction of general applied theory of geometrically nonlinear (flexible) micropolar elastic thin plates and sloping shells is one of the actual and fundamentally significant problems. It should be noted that the theory of micropolar flexible plates and shells is less or, rather, not investigated at all.

The present paper is concerned with the theoretical basis and methods of calculation of strength, stability and vibrations of micropolar elastic flexible plates and sloping shells.

During the construction of geometrically nonlinear theory of micropolar elastic thin sloping shells (plates) the kinematic and static hypotheses of works [1-3] will be applied in combination with basic Marguerre assumptions (1938) (Föppl– von Kármán (1907 , 1910) -in the case of the plate) [4], which underlie the basis of deformation of flexible sloping shells (plates).

On the basis of mathematically accepted kinematic hypotheses, it is assumed that the displacement and free rotation of the points of a three-dimensional thin sloping shell (plate) are linear functions along shell's thickness as follows [1-3]:

$$U_i = u_1(x_1, x_2) + z\psi_i(x_1, x_2), \quad i = 1,2, \quad U_3 = w(x_1, x_2), \tag{1}$$

$$\omega_i = (\Omega_1(x_1, x_2), \quad i = 1,2, \quad \omega_3 = (\Omega_3(x_1, x_2) + z\iota(x_1, x_2). \tag{2}$$

Here, U_i и U_3 are the components of the displacement vector; ω_i and ω_3 are the components of the free rotation; u_i are tangential displacements of the points of the plate middle plane, w is the deflection of the plate, and Ω_i ,Ω_3 are the free rotations of the points of the middle surface around the relevant axes; ψ_i are angles of complete rotation around axis x_i of the element, which is normal to the median surface (axis $x_i, i = 1,2,$ are located in the middle surface and are directed along the lines of curvature); ι is the intensity of rotation of points of three dimensional shell around the axis z (the axis z is perpendicular to the middle surface). It should be mentioned that as the formula (1) for the displacement expresses Tymoshenko's kinematic hypothesis in the classical case, the kinematic hypotheses (1), (2) are called Tymoshenko's generalized hypotheses in the case of micropolar shells (plates).

On the basis of the kinematic hypotheses (1), (2), the components of tensors of deformation and bending-torsion for the sloping shells (plates) will be defined by the following expressions:

$$\gamma_{ii} = (\Gamma_{ii}(x_1, x_2) + zK_{ii}(x_1, x_2), \quad \gamma_{ij} = (\Gamma_{ij}(x_1, x_2) + zK_{ij}(x_1, x_2), \quad \gamma_{i3} = (\Gamma_{i3}(x_1, x_2),$$

$$\gamma_{3i} = (\Gamma_{3i}(x_1, x_2), \quad \chi_{ii} = k_{ii}(x_1, x_2), \quad \chi_{ij} = k_{ij}(x_1, x_2), \quad \chi_{33} = (\iota(x_1, x_2), \tag{3}$$

where

$$K_{ii} = \frac{\partial \psi_i}{\partial x_i}, \quad K_{ij} = \frac{\partial \psi_j}{\partial x_i} - ((-1)^j \iota, \quad \Gamma_{i3} = \frac{\partial w}{\partial x_i} + (-1)^j \Omega_{j3i}, \quad \Gamma_{3i} = \psi_i - (-1)^j \Omega_j,$$

$$k_{ii} = \frac{\partial \Omega_i}{\partial x_i}, \quad k_{331} = (\iota(x_1, x_2), \quad k_{ij} = \frac{\partial \Omega_j}{\partial x_i}, \quad k_{i3} = \frac{\partial \Omega_3}{\partial x_i}, \quad l_{i3} = \frac{\partial \iota}{\partial x_i}, \quad i,j = 1,2. \tag{4}$$

In case of large deflections, deformations $\Gamma_{ii}(x_1, x_2)$ and shears of the middle surface $\Gamma_{ij}(x_1, x_2)$ will be determined on the basis of Marguerre assumptions (1938) (Föppl–von Kármán (1907, 1910) -for flexible sloping shells (plates)):

$$\Gamma_{ii} = \frac{\partial u_i}{\partial x_i} - k_i w + \frac{1}{2}\left(\frac{\partial w}{\partial x_i}\right)^2, \quad \Gamma_{ij} = \frac{\partial u_j}{\partial x_i} - (-1)^j \Omega_3 + \frac{1}{2}\frac{\partial w}{\partial x_i}\frac{\partial w}{\partial x_j}, \quad i,j = 1,2, \tag{5}$$

where k_i , $i = 1,2,$ are initial curvatures of lines $x_i, i = 1,2$ ($k_i = 0, \ i = 1,2,$ in case of the plate).

On the basis of static hypotheses [1-3] and Hooke's law for micropolar isotropic materials force and moment stresses, averaged along the thickness of the sloping shell (plate) forces, moments and hypermoments and further physical relations of elasticity for micropolar flexible sloping shell (plate) are determined. Differential equations of equilibrium and the

a) Corresponding author. Email: s_sargsyan@yahoo.com

natural boundary conditions are obtained on the basis of the application of Lagrange variation equations (geometrically nonlinear variant for micropolar medium with the account of the above mentioned assumptions).

As a result of these studies, general applied theory of micropolar isotropic elastic flexible sloping shells and plates is constructed. The constructed theory is generalized: 1) for the dynamic case, 2)for thermal stresses, 3) single- and multilayer micropolar elastic orthotropic sloping shells and plates.

On the basis of the constructed theory of micropolar elastic flexible sloping shells and plates the problems of implementation of algorithms of variation methods are discussed for solving boundary value problems of statics, stability, vibrations and the clapping effect (for sloping shells) of rectangular and circular plates, sloping cylindrical, conical and spherical shells. On the basis of the developed programs detailed analysis on the significance of the micropolar material is carried out, the efficiency in terms of strength, stiffness, stability of such materials and the perspectives of obtainance and further application of such material for structural elements in the micro and nano instrumentations are established.

CONCLUSIONS

Mathematical modelling of micropolar thin paltes and shells is one of the actual problems in the field of nanomaterials. In the present paper hypotheses of construction of general linear theory of micropolar plates and shells [1-3] with the approach of Föppl–von Kármán and Marguerr of geometrically nonlinear deformation of thin-walled constructions are combined and as a result, general geometrically nonlinear theory of micropolar elastic single and multilayered thin plates and sloping shells is constructed. Variation methods are developed for the solution of problems of statics, stability and vibrations of nonlinear micropolar elastic thin plates and sloping shells of different form. Numerical results are studied and the characteristic features of micropolar materials are analyzed in comparison to the classical materials.

References

[1] Sargsyan S. H.: General Theory of Micropolar Elastic Thin Shells. *Journal of Physical Mezomechanics*..**15, 1-2**:69-79, 2012.

[2] Sargsyan S. H.: Mathematical Model of Micropolar Elastic Thin Plates and Their Strength and Stiffness Characteristics. *Journal of Applied Mechanics and Technical Physics*. **53, 2**: 275-282. 2012.

[3] Sargsyan S. H.: The General Dynamic Theory of Micropolar Elastic Thin Shells. *Doklady Physics*. **56,1:**39-42. 2011.

[4] Grigolyuk E.I., Mamay V.I.: Nonlinear Deformation of Thin Walled Constructions. Moscow, 1997.

EFFECT OF THE SURFACE ON HYPERELASTIC PROPERTIES OF MATERIALS AT SMALLER SCALES

Taisiya Sigaeva and Aleksander Czekanski *
Department of Mechanical Engineering, Lassonde School of Engineering, York University, Toronto, Canada

Summary In this work, well-known continuum models in the framework of hyperelasticity are generalized for certain applications where the scale of the problem decreases to nano-level. At this length scale, the surface and residual surface stresses have a critical effect on the overall deformation of the bulk material. The proposed models employ the Gurtin-Murdoch theory to represent the surface effect as a residually prestressed thin hyperelastic film of separate elasticity, perfectly bonded to the bulk. Obtained results demonstrate remarkable changes in the effective mechanical properties of materials at smaller scales that are not captured by classical theories.

INTRODUCTION

Nanostructured materials and nanodevices have demonstrated unusual mechanical, thermo-mechanical, electrical, optical and magnetic properties, that have opened new horizons for applications in engineering and biology. Particularly, researchers working in the emerging area of nanomechanics have found that at the nano-scale the bounding surface significantly influences the overall deformation of the bulk and should be taken into account in continuum models.

Gurtin, Murdoch and co-workers first proposed a continuum-based theory (the so-called "Gurtin-Murdoch model") to account for surface energies, stresses and tension [1]. The Gurtin-Murdoch model is mathematically equivalent to the assumption of a surface coated by or reinforced with a thin, stiff solid film with different elastic properties. As a result, even in the absence of external loading, residual stresses occur in the area of bonding [2]. Both surface and residual surface stresses have a pronounced effect on the material properties at smaller scales and cannot be ignored.

During the past decade there has been increasing research into the role of surface mechanics in small deformations of linearly elastic solids. However, linear elastic theories are not applicable to many of today's elastomeric applications. It is relevant to consider surface effects since elastomers are being increasingly utilized in nanodevices, and nanostructured polymers is an active research area. To fill this void in the literature we employ the theory of hyperelasticity in conjunction with surface mechanics to generalize some well-known continuum models for applications at smaller scales and demonstrate the pronounced effect of the surface on such effective properties as extensional stiffness, torsional and bending rigidity.

METHODOLOGY

We consider the equilibrium of a deformable solid occupying a region Ω and made of a homogeneous, initially isotropic and incompressible hyperelastic material. Part of the surface $\partial\Omega^s$ of this body is coated with a thin reinforcing film representing the surface effect. This film is made of a homogeneous, isotropic hyperelastic material with elastic constants different from those of the bulk. The rest of the boundary is denoted by $\partial\Omega^b$, so that $\partial\Omega = \partial\Omega^b \cup \partial\Omega^s$.

Physical creation of the solid and thin film as well as their bonding can generate residual stresses in the undeformed configuration. To account for this we introduce "fictitious stress-free" or "natural" configurations and employ the multiplicative decomposition rule for deformation gradients. For instance, let us assume that the thin reinforcing film from its natural configurations (Fig. 1a) is decomposed to the reference configuration with the help of the deformation gradient F_0^s so that there exist a stress field before any forces are applied (Fig. 1c). When subjected to external loadings, the deformation gradient F^s is used to map the coating from reference configuration to the current configuration (Fig. 1d). Therefore, it can be concluded that the surface hyperelastic strain energy density is a function of $F^s \cdot F_0^s$, i.e. $\mathcal{U} = \mathcal{U}(F^s \cdot F_0^s)$. Similarly, we can deduce that the strain energy of the bulk is given by $\mathcal{W} = \mathcal{W}(F \cdot F_0)$, where F and F_0 are the corresponding deformation gradients for the bulk (Figs. 1b-1d).

To establish constitutive law for the bulk we use an incompressible Neo-Hookean material model which is the simplest hyperelastic model. To accurately model the material behavior of the thin reinforcing film representing the surface effect we use two approaches. In the first approach, we simply use the existing surface hyperelastic strain energy density and constitutive equations that reduce to classical linear elastic Gurtin-Murdoch relations (e.g. [3]). In the second approach, which is physically-motivated, we assume that the surface strain energy can be decoupled into the part that does not change the area of the surface and the part that does, i.e. $\mathcal{U} = \mathcal{U}_{constA}(\bar{F}^s) + \mathcal{U}_{varA}(J^s)$ with $J^s = \det F^s$, $\bar{F}^s = (J^s)^{-1/2} F^s$, $\det \bar{F}^s = 1$.

*Corresponding author. Email: alex.czekanski@lassonde.yorku.ca

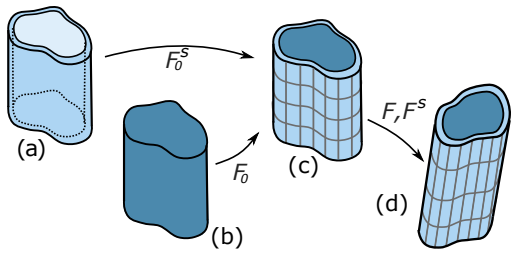

Figure 1

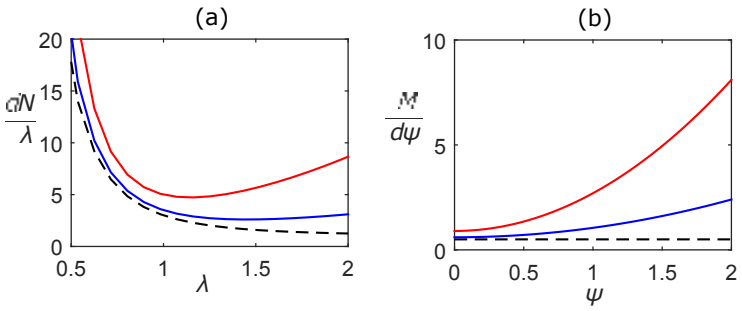

Figure2

Figure 1. Configurations of the model: fictitious stress-free configuration for the thin film representing the surface effect (a) and bulk (b); common reference configuration (c) and current configuration (d) for the solid and its coating.
Figure 2. Influence of the surface effect on values of effective axial stiffness plotted versus axial stretch λ (a) and on values of torsional rigidity plotted versus total angle of twist ψ (b) for a combined tension and torsion of a circular cylinder. Here black dashed line represent the response of the cylinder with no surface effect , blue line - with slight surface effect, red line - with strong surface effect.

Finally, to couple deformations of the solid and thin film, we introduce the following boundary value problem for which addition of the surface effect gives a rise to a nonstandard boundary condition on $\partial\Omega^s$:

$$\begin{aligned} \nabla \cdot \sigma &= 0 \quad in\ \Omega, \\ \sigma \cdot n &= t_1 \quad on\ \partial\Omega^b, \\ \sigma \cdot n - \nabla^s \cdot \sigma^s &= t_2 \quad on\ \partial\Omega^s. \end{aligned}$$

Here σ and σ^s represent, respectively, the Cauchy bulk and surface stresses; ∇ and ∇^s are the usual (3D) and tangential differential (2D) nabla operators. Normal to the surface is given by n; and t_1, t_2 are the prescribed tractions.

The surface effect, described by the model introduced above, can significantly changes the mechanical response of the bodies to applied deformations. A relevant example of the contribution of the surface effect for finite deformations is given in [3], where an axially extended rod is considered. The results obtained demonstrate how the addition of a prestressed reinforcing film will impact the extensional stiffness of the cylinder. We further explore the influence of the surface and residual surface stresses on the mechanical response in the following well-known continuum mechanics problems.

Combined tension and torsion of a circular cylinder

The problem of a solid circular cylinder under combined torsion and axial extension is of great theoretical and practical importance and has many interesting nonlinear effects such as variation of torsional rigidity with angle of twist and the Poynting effect. All these effects can be demonstrated in our comparative study. Assume that a cylinder with length l and the surface effect on the lateral side is extended/compressed to a length λl by force N and twisted to a total angle of ψ by moment M. Fig. 2 shows the case with no residual surface stresses, where effective axial stiffness $\frac{dN}{d\lambda}|_{\ \psi}$ and torsional rigidity $\frac{dM}{d\psi}|_{\ \lambda}$ of the cylinder increase with increasing contribution of the surface effect. Moreover, the axial stiffness monotonically decreases with the extension ratio λ, while addition of the surface effect causes nonmonotonical behavior where the trend reverses so the stiffness increases after some value of λ is achieved (Fig. 2a).

Class of bending problems

In this example we introduce the surface effect and residual surface stresses into all representatives of bending families, i.e. bending of a rectangular block into a sector of cylinder, straightening of a cylindrical sector and bending of one cylindrical sector into another. Since all these models have their own unique features, the main objective of this example is to investigate the methodology of implementing the surface effect. Also it will give us a representative idea of how the bending rigidity of the body is changing when the surface effect is taken into account.

References

[1] Gurtin, M. E., Murdoch, A.: A continuum theory of elastic material surfaces. Arch. Ration. Mech. An. 57:291-323, 1975.
[2] Huang Z., Wang J.: A theory of hyperelasticity of multi-phase media with surface/interface energy effect. Acta Mech. 182: 195-210, 2006.
[3] Altenbach H., Eremeyev V. A., Morozov N. F.: On the influence of residual surface stresses on the properties of structures at the nanoscale. In: Altenbach H., Morozov N. F. (eds.): Surface Effects in Solid Mechanics, Adv. Struct. Mater., Vol. 30., Berlin, Springer, 21-32, 2013.

SURFACE EFFECTS IN THE PURE BENDING PROBLEM IN THE THEOR OF ELASTIC MATERIALS WITH VOIDS

Yury Solyaev[a)], Alexander Volkov & Sergey Lurie
Institute of Applied echanics AS, oscow, ussia

Summary We consider the pure bending problem in the theory of linear elastic materials with voids using modified type of boundary conditions. First, it is shown that micro-dilatation theory is a special case of the general theory of media with conserved dislocations. Variational statement of the last one provides a specific and more common type of boundary conditions due to presence of surface stresses. It is known that pure bending solution in the micro-dilatation theory contains the nonzero values of transverse normal stresses in the beam, which do not appear in the classical linear elasticity. We prove that it could be found the solutions without transversal stresses, due to special values of surface parameters in the considered model. Additionally it is shown the possibility of the effective elastic properties introduction in the problem of pure bending, which depends on the thickness of a beam and surface parameter.

INTRODUCTION

Classical formulation of the theory of linear elastic materials with voids [1] contains additional kinematic parameter - the change of the volume fraction: $\varphi \quad \Lambda - \Lambda_0$, $\Lambda = \quad _{matri} / \quad$. It could be shown that the modified statement of the linear elasticity with voids and surface effects is following from the theory of media with conserved dislocations [2] in the case of non-zero value of free dilatation. Using Cowin's notation we could find the Lagrangian of the modified theory in the following form:

$$= \overline{A} - \iiint U \; d \quad - \oiint U \; d$$

$$2U \quad = 2\theta \quad + 2\mu\varepsilon_i \, \varepsilon_i + 2\beta\varphi\theta + \xi\varphi^2 + \alpha\varphi \quad \varphi$$

$$2U \quad = \xi \; \varphi^2$$

Here $\overline{A}$ is a work of external forces, U - bulk strain energy density, U - surface strain energy density. $\varepsilon_i = (u_i \quad + u \quad _i)/2$ - classical strain, $\theta \quad \varepsilon$ - dilatation, α - void-diffusion constant, β - micro-dilatation coupling modulus, ξ - voids «stiffness» [3]. Surface modulus ξ is an additional parameter of the model. Constitutive equations could be derived in the following form:

$$\sigma_i = \partial U_v / \partial \varepsilon_i = \lambda\theta\delta_i + 2\mu\varepsilon_i + \beta\varphi\delta_i, \; h_i = \partial U_v / \partial \varphi_{,i} = \alpha\varphi_{,i}$$

$$g = \partial U_v / \partial \quad = -\xi\varphi - \beta\theta, \quad g \quad = \partial U \quad / \partial \quad = \xi \; \varphi$$

PURE BENDING OF A BEAM

Cowin and Nunziato used semi-inverse method to solve the problem of a pure bending [2]. They used polynomials to approximate displacements. Boundary conditions had the following form:

$$x_1 \quad 0, \quad : \; 2 \int_{-h}^{h} {}_1\sigma_{33} d \; _1 = - \quad , \quad x_2 = \pm w : \; 2 \int_{-h}^{h} {}_1\sigma_{22} d \; _1 = 0$$

Here *h, b* and are the beam thickness, width and length, consequently (Figure 1).

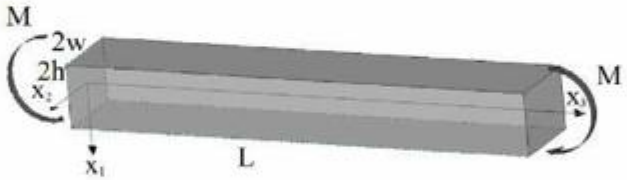

Figure 1. Pure bending of a beam.

The change of the volume fraction was derived from the equation:

$$\varphi_{,11} - \frac{1}{l_0^2}\varphi = \frac{\beta}{\alpha}\frac{(1 \quad 2\nu)}{(1 \quad \nu)}(C_1 + C_2 \quad _1$$

[a)] Corresponding author. Email: yos@iam.ras.ru

Here $1/l_0^2 = (\xi - \beta/\alpha$ and $= \beta / E$).

In the original work [1] there was the Neumann type of boundary conditions $\varphi\ h = \varphi\ -h =$, but, using suggested model with surface effects we have the Robin type: $\varphi\ h + \xi\ \varphi\ h = \varphi\ -h - \xi\ \varphi\ -h =$.

After some calculations we could find the representation for stresses:

$$\sigma_{22} = \frac{-J}{I - J)}\left\{ {}_1 - \frac{l_0}{}\left(\frac{1}{0} - A\frac{\sinh\left(\frac{1}{l_0}\right)}{\cosh\left(-\right)} \right)\right\},\ \sigma_{33} = \frac{-}{I - J}\left\{ -J\ {}_1 - \frac{l_0 J}{S}\left(\frac{1}{l_0} - A\frac{\sinh\left(\frac{1}{l_0}\right)}{\cosh\left(-\right)} \right)\right\}$$

Here $J = {}^2\frac{1-\nu}{1+\nu}S = \frac{l_0 E}{\alpha + \nu}$, $S = -A\frac{l_0^3}{h^3}\left(\frac{h}{l_0} - \tanh[\frac{h}{l_0}]\right)$ and $A = \frac{(1+h\frac{\xi}{\alpha})\cosh\left(-\right)}{\cosh\left(-\right) + \frac{\xi}{\alpha} l_0 \sinh\left(-\right)}$ is a new parameter in this solution which depends on the surface modulus.

Now let us compare the displacements in the voids elasticity solution [1] and in the classical solution for the equivalent beam, described by some effective elastic constants E_{eff} and ν_{eff} . We can write:

$$u_2^{class} = \frac{\nu_{eff}}{E\ I}\ {}_{1\ 2} = u_2^{voids} = \frac{}{EI(1-J)}\left(\nu - \frac{J}{2} + \nu\right)\ {}_{1\ 2},$$

$$u_3^{class} = -\frac{}{E\ I}\ {}_{1\ 3} = u_3^{voids} = -\frac{}{EI(1-J)}\left(1 - \frac{J}{2} + \nu\right)\ {}_{1\ 3}.$$

Therefore, we could find the effective properties in the following form:

$$E_{eff} = E\frac{1-J}{-J + \nu},\ \nu_{eff} = \frac{\nu - J + \nu}{-J + \nu}$$

It could be shown that these values of the effective properties allow us to satisfy the equality of deflections of the surfaces of classical beam and beam with voids. However, the internal distribution of displacements, strains and stress in the volume of porous and classical beams are different. Note that the shear modulus of the equivalent beam is constant: ${}_{eff} = E_{eff}/(2(1+{}_{eff})) = E + \nu =$.

The representations of the effective elastic constants of the equivalent classical beam depend on the non-classical modules $\alpha\ \beta\ \xi\ \xi$ and beam thickness. Thus, it can be concluded that the experimentally measured deflections and the flexural modulus of porous beams may have the non-classical dependence on the samples thickness in the pure bending tests. But it is easy to show, that if $\xi = -\alpha/h$, then the free dilatations distribution through the thickness of the beam is linear, transversal normal stresses σ_{22} vanishes and size effects also vanish. Thus, the classical Saint-Venant hypotheses are valid [4] in this case.

CONCLUSIONS

In this paper, we show that, using modified boundary conditions we could eliminate the transversal normal stress σ_{22} in the pure bending solution in the theory of linear elastic materials with voids. Due to effective properties introduction we could check out the presence of scale effects and identify the additional volume and surface parameters of the model in the bending flexural tests.

References

[1] Cowin, S. C., Nunziato J. W.: Linear Elastic Materials with Voids, *J Elast* **3**:125-147, 1983.

[2] Lurie S. A., Kalamkarov A. L.: General Theory of Continuous Media with Conserved Dislocations. *Int J Sol Struct* :7468-7485, 2007.

[3] Ramezani H., Steeb H., Jeong J.: Analytical and Numerical Studies on Penalized Micro-Dilatation (PMD) Theory: Macro-micro Link Concept. *Eur J ech A Sol*, **3** :130-148, 2012.

[4] Dell'Isola F., Batra, R. C.: Saint-Venant's Problem for Porous Linear Elastic Materials. *J of Elast*, :73–81, 1997.

SIZESCALE EFFECTS IN BENDING FLEXIBILITY OF PHOSPHORENE AND ITS 2D ALLOTROPES

Deepti Verma*[1] and Traian Dumitrică[2]

[1]*Department of Chemical Engineering and Materials Science, University of Minnesota, USA*
[2]*Department of Mechanical Engineering, University of Minnesota, USA*

Summary α-Phosphorene, a newly discovered two-dimensional (2D) derivative of Black Phosphorus [1], has an inherent band gap with a high current on/off ratio. We study bending flexibility of α-phosphorene and its 2D allotropes by modeling them as large diameter phosphorene nanotubes (PNTs). We use objective boundary conditions (OBC) [2, 3] coupled with a density functional tight binding model (DFTB) that facilitates drastic reductions in the number of atoms in the simulations of PNTs of arbitrary chirality. We further combine the results of our bending strain calculations with an orthotropic thin shell model to develop equivalent continuum structure (ECS) for phosphorene and its allotropes.

INTRODUCTION

The 2D α-phosphorene has attracted great attention due to its exceptionally highly anisotropic mechanical and electronic properties. A direct band-gap of 2eV, a high-charge carrier mobility tunable by bending and in-plane strains along with highly anisotropic elastic stiffness hold significant importance in making highly exotic strain engineered devices [4]. Interestingly, there are two more 2D allotropes of α-phosphorene which are also potential candidates for new generation electronic devices. We study the origin of bending rigidity with a novel technique of Objective Structures. Combining simulation results of bending and inplane strain we develop an equivalent continuum structure for α-phosphorene and its allotropes. We also propose an elastic constants and thickness for phosphorene allotropes and observe the size scale effects that show up due to single layer bending. The information of thickness can be used to predict bending and wrinkling deformations of phosphorene.

METHOD

In this work, we explore the bending rigidity of α-phosphorene and its 2D allotropes by modeling bent α-phosphorene as large diameter nanotubes [5] using objective boundary conditions (OBCs) [2, 3]. The OBCs are given by

$$\mathbf{X}_\xi = \mathbf{R}_\theta{}^\eta \mathbf{R}_\phi{}^\xi \mathbf{X}_0 + \xi \mathbf{T},\ \xi \in \mathbb{Z},\ \eta = 0, ..., n \nearrow 1, n \in \mathbb{Z}. \tag{1}$$

In the above equation, the helical symmetry is defined by a rotation of angle ϕ about $\hat{\mathbf{z}}$ axis is described by matrix $\mathbf{R}_\phi$ coupled with a translation of $\mathbf{T} = T\hat{\mathbf{z}}$. Similarly, the rotation symmetry is described by the matrix $\mathbf{R}_\theta$. There is are 4 atoms located as motif at position $\mathbf{X}_0$ in the $\eta = \xi = 0$ simulation cell. The OBCs is currently the only way to simulate an infinite long chiral α-phosphorene nanotube and it is impossible to achieve this with current periodic boundary conditions at most.

RESULTS AND DISCUSSION

The obtained ideal rolled-up geometry of phosphorene as nanotube is relaxed and in our simulations we find a negligible expansion of about $10^{-5}\%$ in nanotube radius. This shows that the large nanotubes behave as an ideal rolled-up phosphorene plate. Similarly, we find that the axial and torsional deviations are negligible for large-diameter PNT structures. This corroborates that these nanotubes closely correspond to phosphorene sheet under pure bending. Also, the plot of strain energy (with respect to flat phosphorene) varies quadratically as a function of curvature for nanotubes (of a particular chirality). This is used to obtain bending stiffness D. From our inplane strain simulations we notice that α-phosphorene is highly anisotropic and in particular orthotropic, which is a manifestation of orthotropic unit cell structure of phosphorene. Now using orthotropic plate model and fitting inplane stiffnesses for α-phosphorene from 2D and bending stiffness from bent structures (large-diameter α-PNTs) for a range of chiralities we derive the equivalent continuum thickness for α-phosphorene. The information of knowing correct thickness is helpful because it can be used to predict bending and wrinkling deformations, without further need of atomistic calculations.

Interestingly, the sizescale effects show up in phosphorene bending. The bending stiffness D has a dependence other than inplane stiffness and thickness squared. Due to this the thickness obtained by comparing bending and inplane stiffness depends on chirality of nanotube or the direction of bending of phosphorene. This result is unusual in the sense that there is no single value for thickness h (as well as Young's and shear modulii) to describe inplane stretching using equivalent continuum structure. But bending in a particular direction is describable by an equivalent continuum structure with a particular thickness. We also derived an equation for thickness of α-phosphorene depending on bending direction.

*Corresponding author. Email: verma083@umn.edu.

With the discovery of α-phosphorene its other 2D allotropes were also predicted to exist. We also repeated the same calculations on 2D allotropes of α-phosphorene i.e. β- and γ-phosphorene (shown in the figure). These are, respectively, isotropic and orthotropic phases with respect to mechanical stiffnesses. γ-phosphorene shows chiral dependence on thickness where as thickness is a constant for β-phosphorene.

CONCLUSIONS

Using DFTB with OBCs we use large-diameter nanotubes to study bending deformation of phosphorene and its allotropes. We also develop ECS by de-convoluting the thickness, and young's and shear moduli from bending stiffness and inplane stiffnesses.

References

[1] Li et al., "Black phosphorus field-effect transistors," Nature Nanotechnology, 9, 372?377, 2014.

[2] R. D. James, "Objective structures," Journal of Mechanics and Physics of Solids, 54, 2354-2390, 2006.

[3] T. Dumitrica, R. D. James, "Objective molecular dynamics," Journal of the Mechanics and Physics of Solids, 55 (10), 2206-2236, 2007.

[4] Liu et al., "phosphorene: An Unexplored 2D Semiconductor with a High Hole Mobility," ACS Nano, 8 (4), 4033?4041, 2014.

[5] I Nikiforov, E Dontsova, R. D. James, T. Dumitrică, "Tight-binding theory of graphene bending," Physical Review B 89 (15), 155437, 2014.

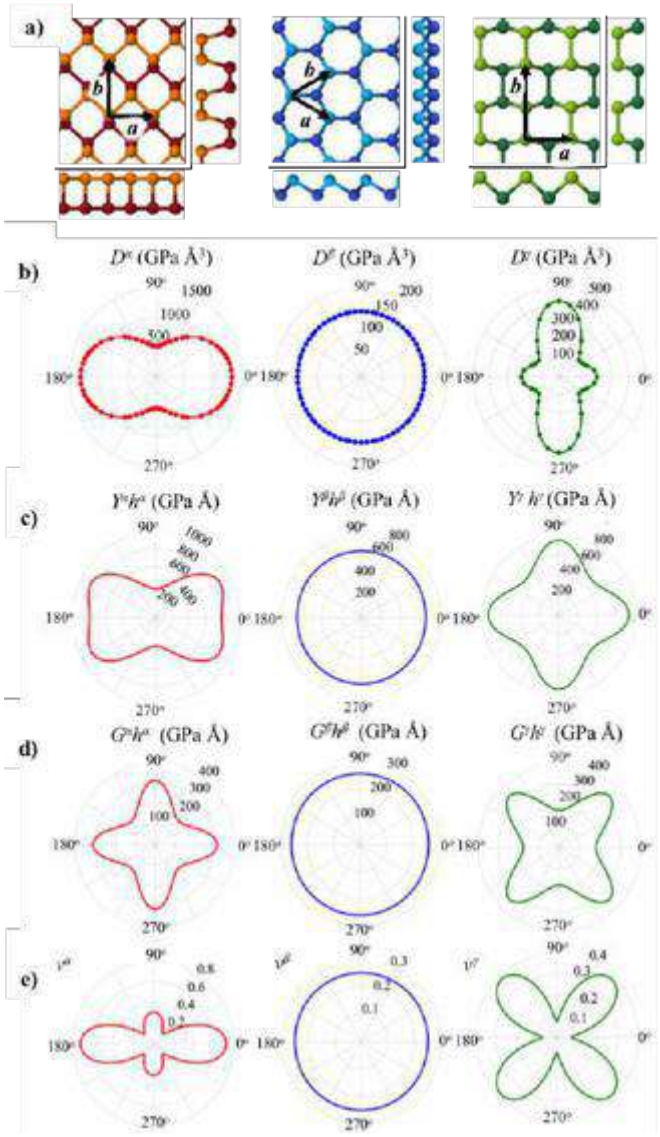

Figure 1: a) Top, side views, and lattice vectors of α-phosphorene (left) β-phosphorene (center) and γ-phosphorene (right). b) Bending moduli of phosphorene as a function of direction. Data points are the DFTB calculations. c) Surface Young's, d) shear moduli, and e) Poisson's ratios of phosphorene as a function of direction.

SM11 - Multibody and Vehicle Dynamics

TS.SM11-1.01	Bruls, Olivier - Modelling of multibody systems in the local frame (INVITED)	2559
TS.SM11-1.02	Avedisov, Sergei - Analysis of vehicle handling for front wheel drive and rear wheel drive vehicles	2561
TS.SM11-1.03	Berbyuk, Viktor - Global sensitivity analysis and multiobjective optimization of bogie suspension	2563
TS.SM11-1.04	Eberhard, Peter - Coupling of Mechanical and Optical Methods for Simulations and Measurements	2565
TS.SM11-1.05	Zhao, Xiaonan - Nonlinear rotor motion: Influence of thrust bearings on subsynchronous oscilations	2567
TS.SM11-2.01	Ellermann, Katrin - Parameter estimation in vehicle dynamics: Train, track and fault monitoring (INVITED)	2569
TS.SM11-2.02	Liu, Jiapeng - The evaluation of steering performance of drilling assemblies based on multibody dynamics approach	2571
TS.SM11-2.03	Meijaard, Jacob - A modified generalized strain formulation for flexible multibody system modelling	2573
TS.SM11-2.04	Orosz, Gabor - Analysis of Heterogeneous Connected Vehicles via Modal Perturbation Method	2575
TS.SM11-2.05	Schiehlen, Werner - From IUTAM Symposia to the International Association of Vehicle System Dynamics	2577
TS.SM11-3.01	Seifried, Robert - A Servo-constraint Framework for Control of Various Types of Underactuated Multibody Systems	2579
TS.SM11-3.02	Steiner, Wolfgang - The discrete adjoint method in multibody dynamics	2581
TS.SM11-3.03	Tian, Qiang - Nonlinear dynamics of flexible multibody systems with uncertain interval parameters	2583
TS.SM11-3.04	Tromme, Emmanuel - Optimal design of flexible mechanisms using a generalized equivalent static load method	2585
TS.SM11-3.05	Jarzębowska, Elżbieta - An underwater inertia-based propelled vehicle dynamics and performance	2587
PO.SM11-1.01.156	Foster, John - A variationally consistent approach to constrained motion	2589
PO.SM11-1.02.157	Kita, Eisuke - Simulation of a vehicle separated from vehicule platoon	2591
PO.SM11-1.03.158	Lu, Daixing - Solver Coupling with Algebraic Constraints: An Index-2 Co-Simulation Approach	2593
PO.SM11-1.04.159	Luo, Kai - Parametric study on flexible multibody dynamics via model reduction	2595
PO.SM11-1.07.162	Spinello, Davide - Peristaltic wave locomotion with a millipede inspired mechanism	2597
PO.SM11-1.08.163	Yong, Jiawang - Design and validation of an electric booster brake system with hardware-in-the-loop simulation	2599
PO.SM11-1.09.164	Zhou, Wei - Deformable-rigid switch in computational simulation of bus rollover test	2601

MODELLING OF MULTIBODY SYSTEMS IN THE LOCAL FRAME

Olivier Brüls [*1] and Valentin Sonneville[1]

[1]*Department of Aerospace and Mechanical Engineering (LTAS), University of Liège, Belgium*

Summary A local frame finite element approach is proposed to describe the kinematics of a flexible multibody system, derive the equations of motion and solve them numerically. It is argued that this approach leads to reduced geometric nonlinearities and improved computational efficiency.

KINEMATICS IN THE LOCAL FRAME

Let us consider a body whose configuration in space is represented by the position field $\mathbf{x}_p(t, \mathbf{X}_p)$, where t is the time, $\mathbf{x}_p \in \mathbb{R}^3$ represents the position of the material point p in the current configuration with respect to an inertial frame and $\mathbf{X}_p \in \mathbb{R}^3$ is the position of the same material point in the reference configuration. In multibody dynamics, some kinematic assumptions on the position field are often introduced:

- under the rigid body assumption, $\mathbf{x}_p(t, \mathbf{X}_p) = \mathbf{x}(t) + \mathbf{R}(t)\mathbf{X}_p$, where $\mathbf{x}(t) \in \mathbb{R}^3$ is the position of a reference point on the body, $\mathbf{R}(t) \in SO(3)$ is a rotation matrix and $SO(3)$ is the finite rotation group,
- under the Timoshenko elastic beam assumption, $\mathbf{x}_p(t, \alpha_1, \beta_2, \beta_3) = \mathbf{x}(t, \alpha_1) + \mathbf{R}(t, \alpha_1)(\beta_2\mathbf{E}_2(\alpha_1) + \beta_3\mathbf{E}_3(\alpha_1))$, where α_1 is the curvilinear coordinate of the centerline, $\mathbf{x}(t, \alpha_1)$ represents the position of the centerline, $\mathbf{R}(t, \alpha_1)$ is the cross section orientation, and the vectors $\mathbf{E}_2(\alpha_1)$ and $\mathbf{E}_3(\alpha_1)$ span the cross section in the reference configuration,
- under the Reissner-Mindlin elastic shell assumption, $\mathbf{x}_p(t, \alpha_1, \alpha_2, \beta_3) = \mathbf{x}(t, \alpha_1, \alpha_2) + \mathbf{R}(t, \alpha_1, \alpha_2)\beta_3\mathbf{E}_3(\alpha_1, \alpha_2)$, where α_1, α_2 are the coordinates of the mid-surface, $\mathbf{x}(t, \alpha_1, \alpha_2)$ is the position of the mid-surface, $\mathbf{R}(t, \alpha_1, \alpha_2)$ defines the orientation of the normal director and $\mathbf{E}_3(\alpha_1, \alpha_2)$ is the normal director in the reference configuration.

In these three cases, the configuration is fully represented by a translation field $\mathbf{x}(t, \boldsymbol{\alpha})$ and a rotation field $\mathbf{R}(t, \boldsymbol{\alpha})$, where $\boldsymbol{\alpha}$ belongs to $\emptyset$, $\mathbb{R}$ or $\mathbb{R}^2$, depending on the specific kinematic assumption. At a given time and for a given value of $\boldsymbol{\alpha}$, the *local frame of reference* is defined with respect to the inertial frame by the reference point $\mathbf{x}(t, \boldsymbol{\alpha})$ and the rotation matrix $\mathbf{R}(t, \boldsymbol{\alpha})$.

A representation of the velocity field is then needed to derive the equations of motion. A reference frame has to be selected for that purpose. Let us define the velocity variables $\mathbf{u}(t, \boldsymbol{\alpha})$, $\mathbf{U}(t, \boldsymbol{\alpha})$, $\boldsymbol{\omega}(t, \boldsymbol{\alpha})$ and $\boldsymbol{\Omega}(t, \boldsymbol{\alpha})$ such that

$$\dot{\mathbf{x}} = \mathbf{u}, \quad \dot{\mathbf{x}} = \mathbf{R}\mathbf{U}, \quad \dot{\mathbf{R}} = \widetilde{\boldsymbol{\omega}}\mathbf{R}, \quad \dot{\mathbf{R}} = \mathbf{R}\widetilde{\boldsymbol{\Omega}} \tag{1}$$

with the tilde operator such that the components satisfy $(\widetilde{\boldsymbol{\Omega}})_{ij} = \not{\epsilon}_{ijk}(\boldsymbol{\Omega})_k$. Clearly, $\mathbf{u}$ is the inertial frame linear velocity, $\mathbf{U}$ is the local frame linear velocity, $\boldsymbol{\omega}$ is the inertial frame angular velocity, and $\boldsymbol{\Omega}$ is the local frame angular velocity. In the literature, the inertial frame representation $\mathbf{u}, \boldsymbol{\omega}$ and the mixed representation $\mathbf{u}, \boldsymbol{\Omega}$ are frequently used. In the present work, we propose to select the *local frame representation* $\mathbf{U}, \boldsymbol{\Omega}$.

For convenience, let us introduce the representation of the position field in terms of a $\times$ matrix $\mathbf{H}(t, \boldsymbol{\alpha})$, which belongs to the special Euclidean group $SE(3)$, and the representation of the velocity field in terms of a $\times 1$ velocity vector $\mathbf{v}(t, \boldsymbol{\alpha})$ such that

$$\mathbf{H}(t, \boldsymbol{\alpha}) = \begin{bmatrix} \mathbf{R}(t, \boldsymbol{\alpha}) & \mathbf{x}(t, \boldsymbol{\alpha}) \\ \mathbf{0}_{1\times 3} & 1 \end{bmatrix}, \ \mathbf{v}(t, \boldsymbol{\alpha}) = \begin{bmatrix} \mathbf{U}(t, \boldsymbol{\alpha}) \\ \boldsymbol{\Omega}(t, \boldsymbol{\alpha}) \end{bmatrix}, \ \dot{\mathbf{H}} = \mathbf{H}\widetilde{\mathbf{v}}, \ \widetilde{\mathbf{v}} = \begin{bmatrix} \widetilde{\boldsymbol{\Omega}} & \mathbf{U} \\ \mathbf{0}_{1\times 3} & 0 \end{bmatrix} \tag{2}$$

The vector $\mathbf{v}$ is actually a screw representation of the velocities. In a similar manner, virtual displacements $\delta\mathbf{H} = \mathbf{H}\widetilde{\delta\mathbf{h}}$ and spatial gradients $\partial\mathbf{H}/\partial\alpha_i = \mathbf{H}\widetilde{\mathbf{f}}_i$ can be represented by $\times 1$ vectors $\delta\mathbf{h}$ and $\mathbf{f}_i$ whose components are defined in the local frame.

DYNAMICS IN THE LOCAL FRAME

In the local frame formalism, the kinetic energy can be expressed as a functional of the velocity field $\mathbf{v}(t, \boldsymbol{\alpha})$ only and the internal strain energy can be expressed as a functional of the spatial gradients $\mathbf{f}_i(t, \boldsymbol{\alpha})$ only. This means that the position and orientation of the local frame do not explicitly appear in the expression of these energies, but only their time or spatial derivatives. This intrinsically guarantees that these expressions do not depend on the choice of the position and orientation of the inertial frame, i.e., they are frame invariant.

*Corresponding author. Email: o.bruls@ulg.ac.be

Following the finite element approach, a spatial semi-discretization is performed leading to a description of the configuration in terms of a variable $\mathbf{H}_{AN}$ which collects the nodal variables of nodes A to N

$$\mathbf{H}_{AN} = (\mathbf{H}_A, \ldots, \mathbf{H}_N) \tag{3}$$

In each deformable finite element, the shape functions can be obtained by a nonlinear interpolation of $\times$ matrices on $SE(3)$, see [3]. In this case, the spatial gradient of the interpolation field expressed in the local frame only depends on the *relative* displacements within the element $\mathbf{H}_{AN}^{rel} = (\mathbf{H}_I^{-1}\mathbf{H}_A, \ldots, \mathbf{H}_I^{-1}\mathbf{H}_N)$, where I is an arbitrary node of the element. Also, the interpolation of velocities only depends on $\mathbf{H}_{AN}^{rel}$ and on the nodal velocities $\mathbf{v}_{AN} = (\mathbf{v}_A, \ldots, \mathbf{v}_N)$. The consequence is that the strain energy only depends on $\mathbf{H}_{AN}^{rel}$ and the kinetic energy only depends on $\mathbf{v}_{AN}$ and $\mathbf{H}_{AN}^{rel}$.

Based on the energies and on the kinematic constraints which are used for example to model kinematic joints between bodies, the equations of motion are then derived in the local frame using the Hamilton principle [2]

$$\begin{aligned} \mathbf{M}(\mathbf{H}_{AN}^{rel})\dot{\mathbf{v}}_{AN} \nearrow\!\widehat{\mathbf{v}}_{AN}^T\mathbf{M}(\mathbf{H}_{AN}^{rel})\mathbf{v}_{AN} + \mathbf{g}^{int}(\mathbf{H}_{AN}^{rel}) + \mathbf{B}^T(\mathbf{H}_{AN}^{rel})\boldsymbol{\lambda} &= \mathbf{g}^{ext}(\mathbf{H}_{AN}, t) && (4)\\ \boldsymbol{\Phi}(\mathbf{H}_{AN}^{rel}) &= \mathbf{0} && (5) \end{aligned}$$

where $\widehat{\bullet}$ is a linear operator which maps a vector to a matrix, and we have the internal forces $\mathbf{g}^{int}$, the external forces $\mathbf{g}^{ext}$, the kinematic constraints $\boldsymbol{\Phi}$, the matrix of constraint gradients $\mathbf{B}$ and the Lagrange multipliers $\boldsymbol{\lambda}$.

One observes that the terms on the left-hand-side of Eqs. (4-5), i.e., the inertia forces, the internal forces, the constraint forces and the kinematic constraints, depend on the configuration only through the relative displacements within the element. In a beam or shell finite element, the amplitude of the relative displacements decreases with the size of the element. Therefore, a mesh refinement leads to a reduction in the geometric nonlinearities within each element, even though the complete system undergoes finite amplitude motions.

IMPLICIT TIME INTEGRATION IN THE LOCAL FRAME

The equations of motion can be solved using a Lie group implicit time integration method [1]. This scheme requires the solution of the linearized dynamics at each Newton iteration of each time step. If one disregards the contribution of the external forces, the linearized equations of motion about a configuation $\mathbf{H}_{AN}^{rel,*}, \mathbf{v}^*, \dot{\mathbf{v}}^*, \boldsymbol{\lambda}^*$ are written as

$$\begin{aligned} \mathbf{r}^* + \mathbf{M}(\mathbf{H}_{AN}^{rel,*})\Delta\dot{\mathbf{v}}_{AN} + \mathbf{C}_t(\mathbf{H}_{AN}^{rel,*}, \mathbf{v}^*)\Delta\mathbf{v} + \mathbf{K}_t(\mathbf{H}_{AN}^{rel,*}, \mathbf{v}^*, \dot{\mathbf{v}}^*)\Delta\mathbf{h}_{AN}^{rel} + \mathbf{B}^T(\mathbf{H}_{AN}^{rel,*})\Delta\boldsymbol{\lambda} &= \mathbf{0} && (6)\\ \boldsymbol{\Phi}^* + \mathbf{B}(\mathbf{H}_{AN}^{rel,*})\Delta\mathbf{h}_{AN}^{rel} &= \mathbf{0} && (7) \end{aligned}$$

where $\mathbf{r}^*$ and $\boldsymbol{\Phi}^*$ are the residuals at the linearization point, $\mathbf{C}_t$ is the tangent damping matrix and $\mathbf{K}_t$ is the tangent stiffness matrix. If the relative displacements within each element are small enough and if the dependency of these matrices with respect to the velocities and accelerations is neglected, the linearized form simply becomes

$$\begin{aligned} \mathbf{r}^* + \mathbf{M}^0\Delta\dot{\mathbf{v}}_{AN} + \mathbf{C}_t^0\Delta\mathbf{v} + \mathbf{K}_t^0\Delta\mathbf{h}_{AN}^{rel} + (\mathbf{B}^0)^T\Delta\boldsymbol{\lambda} &= \mathbf{0} && (8)\\ \boldsymbol{\Phi}^* + \mathbf{B}^0\Delta\mathbf{h}_{AN}^{rel} &= \mathbf{0} && (9) \end{aligned}$$

where the matrices $\mathbf{M}^0$, $\mathbf{C}_t^0$, $\mathbf{K}_t^0$ and $\mathbf{B}^0$ are evaluated at the initial time and remain constant during the motion. In this special case, an implicit nonlinear analysis with finite amplitude motions can be completely performed without any update of the linearized model used in the Newton iterations. In this way, the cost of the re-evaluation and re-factorization of the tangent matrices is avoided, leading to significant reduction in the CPU cost of the simulation.

In the general case, Eqs. (8-9) are only an approximation. However, this approximation often captures many dominant terms of the linearized system and can be exploited to build efficient numerical algorithms.

CONCLUSION

The local frame approach limits the importance of the geometric nonlinearities in multibody dynamics models. Even if the system undergoes large amplitude motions, the energies, forces and tangent operators are only sensitive to the *relative* motion within each finite element. This property can be exploited to reduce the computational cost of the numerical methods.

References

[1] Brüls O., Cardona A., Arnold M.: Lie group generalized-α time integration of constrained flexible multibody systems. Mech. Mach. Theory, 48:121–137, 2012.

[2] Sonneville V., Brüls O.: A formulation on the special Euclidean group for dynamic analysis of multibody systems. J. Comput. Nonlinear Dyn., 9:041002, 2014.

[3] Sonneville V., Cardona A., Brüls O.: Geometrically exact beam finite element formulated on the special Euclidean group SE(3). Comput. Methods Appl. Mech. Eng., 268:451–474, 2014.

ANALYSIS OF VEHICLE HANDLING FOR FRONT WHEEL DRIVE AND REAR WHEEL DRIVE VEHICLES

Sergei S. Avedisov *, Chaozhe R. He, Wubing B. Qin, and Gábor Orosz

Department of Mechanical Engineering, University of Michigan, Ann Arbor, MI, 48105, USA

Summary Steady state handling characteristics of rear wheel drive (RWD) and front wheel drive (FWD) vehicles are compared. Each configuration is modeled by a bicycle model equipped with a brush tire model, and the nonlinear dynamics are derived through the Appelian framework. The steady state solutions of the nonlinear equations are investigated via numerical continuation for understeer and oversteer scenarios. The results are summarized using bifurcation diagrams for several different steering angles.

INTRODUCTION

As shown in [2, 3], numerical bifurcation analysis can be used to characterize vehicle handling. One may obtain the global picture of the various steady states while varying parameters including states with high lateral acceleration that cannot be obtained by traditional analysis [1]. In prior works, due to geometrical simplifications, no distinction was made between rear wheel drive (RWD) and front wheel drive (FWD) vehicles. In this paper we use the Appelian framework to derive the nonlinear dynamics of bicycle models for automotive steering considering rear wheel drive (RWD) and front wheel drive (FWD) configurations. We show that these two configurations yield different dynamical equations, and analyze the steady state motions for understeer and oversteer scenarios and different steering angles. This analysis can lay the foundation for the design of future vehicle control systems tailored to the drive type of the vehicle.

DERIVATION OF VEHICLE DYNAMICS

Figure 1(a) shows the bicycle model for automotive steering. The bicycle model is composed of the body of length ℓ, mass m and mass moment of inertia J_c with two massless wheels. The center of mass is located at distance d in front of the rear axle. The tires are modeled using the brush tire model with a parabolic pressure distribution.

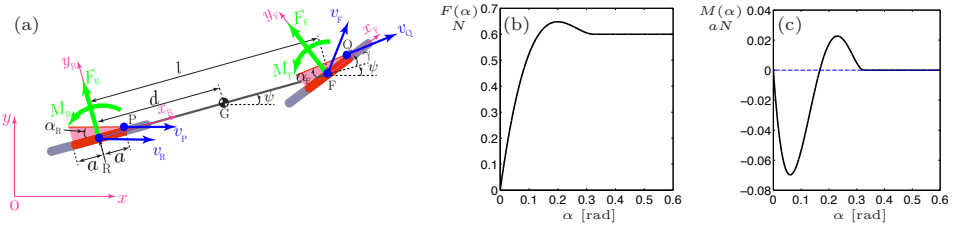

Figure 1: (a): Bicycle model with the steering angle γ, generalized coordinates x, y and ψ, and the geometrical parameters ℓ and d. (b): Lateral tire force F (scaled by the normal force N) as a function of the slip angle α. (c): Aligning moment M (scaled by aN) as a function of the slip angle α.

The motion of the bicycle is described by the position of the center of mass (x,y) and the heading angle ψ. Using the constraint that the rear wheel (front wheel) is rolling with a constant velocity v_0 in the RWD (FWD) model and assuming quasi-steady lateral tire deformations, we can obtain the equations for the lateral velocity $\sigma_1 = \not{\sin}(\phi)\dot{x} + \cos(\phi)\dot{y}$ and yaw rate $\sigma_2 = \dot{\phi}$ though the Appellian framweork. The handling dynamics of the RWD bicycle model are given by

$$\begin{bmatrix} m & 0 \\ 0 & J_c \end{bmatrix} \begin{bmatrix} \dot{\sigma}_1 \\ \dot{\sigma}_2 \end{bmatrix} = \begin{bmatrix} \not{m} v_0 \sigma_2 \\ 0 \end{bmatrix} + \begin{bmatrix} F_R + F_F \cos(\gamma) \\ \not{d}\, F_R + (\ell \not{d}) F_F \cos(\gamma) + M_R + M_F \end{bmatrix}, \tag{1}$$

where the forces $F_R = F(\alpha_R)$ and $F_F = F(\alpha_F)$ are shown in Figure 1 (b) as the function of the slip angle α. Similarly, the moments $M_R = M(\alpha_R)$ and $M_F = M(\alpha_F)$ are depicted in Figure 1 (c). The slip angles for the RWD dynamics are given by

$$\tan(\alpha_R) = \frac{\not{\sigma}_1 + (d \not{a})\sigma_2}{v_0}, \qquad \tan(\alpha_F) = \frac{v_0 \sin(\gamma) \not{(}\sigma_1 + (\ell \not{d})\sigma_2)\cos(\gamma) \not{a}(\sigma_2 + \dot{\gamma})}{v_0 \cos(\gamma) + (\sigma_1 + (\ell \not{d})\sigma_2)\sin(\gamma)}. \tag{2}$$

Similarly, the handling dynamics of the FWD bicycle model are given by

$$\begin{bmatrix} \frac{m}{\cos^2(\gamma)} & m(\ell \not{d})\tan^2(\gamma) \\ m(\ell \not{d})\tan^2(\gamma) & J_c + m(\ell \not{d})^2 \tan^2(\gamma) \end{bmatrix} \begin{bmatrix} \dot{\sigma}_1 \\ \dot{\sigma}_2 \end{bmatrix} = \begin{bmatrix} \not{m} \frac{\tan(\gamma)}{\cos^2(\gamma)} (\sigma_1 + \sigma_2(\ell \not{d}) \not{v}_0 \sin(\gamma)) \dot{\gamma} \not{m} \frac{v_0 \sigma_2}{\cos(\gamma)} + m(\ell \not{d}) \tan(\gamma) \sigma_2^2 \\ \not{m}(\ell \not{d}) \frac{\tan(\gamma)}{\cos^2(\gamma)} (\sigma_1 + \sigma_2(\ell \not{d}) \not{v}_0 \sin(\gamma)) \dot{\gamma} \not{m}(\ell \not{d}) \tan(\gamma) \sigma_1 \sigma_2 \end{bmatrix} \tag{3}$$

$$+ \begin{bmatrix} F_R + \frac{1}{\cos(\gamma)} F_F \\ \not{d}\, F_R + \frac{(\ell \not{d})}{\cos(\gamma)} F_F + M_R + M_F \end{bmatrix}.$$

The forces and moments are still given by Figure 1 (b) and (c), respectively, while the slip angles become

$$\tan(\alpha_R) = \frac{(\nearrow\sigma_1 + (d \nearrow a)\sigma_2)\cos(\gamma)}{v_0 \nearrow\sigma_1 \sin(\gamma) \nearrow(\ell \nearrow d)\sigma_2 \sin(\gamma)}, \qquad \tan(\alpha_F) = \frac{v_0 \sin(\gamma) \nearrow\sigma_1 \nearrow(\ell \nearrow d)\sigma_2 \nearrow a(\sigma_2 + \dot{\gamma})\cos(\gamma)}{v_0 \cos(\gamma)}. \tag{4}$$

In traditional steady state handling analysis the simplifications $a \approx 0$, $\gamma, \alpha_R, \alpha_F \ll \frac{\pi}{2}$, $F(\alpha) \approx 2ka^2\alpha$, $M(\alpha) \approx 0$ are used yielding the steady states

$$\sigma_1^* = \frac{2k_R a^2 \ell\gamma}{2k_R a^2 \ell d \nearrow mv_0^2(\ell \nearrow d)} \frac{\ell}{v_0} + K_{us}\frac{v_0}{g}, \qquad \sigma_2^* = \frac{\gamma}{\frac{\ell}{v_0} + K_{us}\frac{v_0}{g}}, \qquad K_{us} = \frac{mg}{2\ell}\left(\frac{d}{k_F a^2} \nearrow \frac{\ell \nearrow d}{k_R a^2}\right), \tag{5}$$

for the lateral velocity and yaw rate both for RWD and FWD. Here K_{us} represents the understeer coefficient, and for $K_{us} > 0\,(K_{us} < 0)$ the vehicle understeers (oversteers) according to the SAE convention.

COMPARISON OF STEADY STATE CORNERING FOR FWD AND RWD CONFIGURATIONS

In this section we compare the steady state solutions of (1,2) and (3,4) for SAE understeer ($K_{us} > 0$) and SAE oversteer ($K_{us} < 0$) scenarios for different steering angles. Figure 2 shows the stable and unstable steady state solutions as solid green and dashed red curves, respectively, as well as the traditional (SAE) steady state cornering solutions (5), as gray curves while varying the speed v_0 for different values of the steering angle γ. The equilibrium value of σ_1 is denoted by σ_1^*.

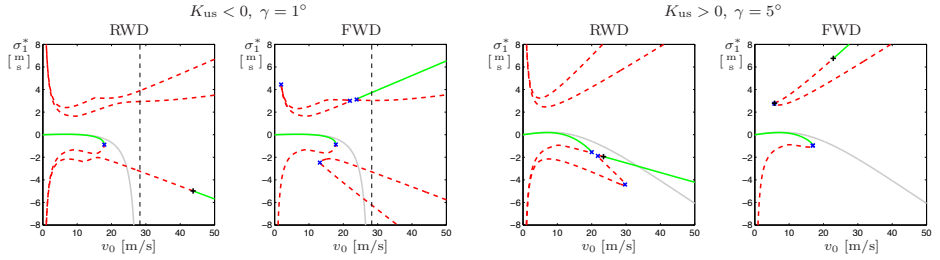

Figure 2: Bifurcation diagrams for the RWD/FWD vehicle models for various K_{us} and γ values. The left two figures denote the SAE oversteer configuration ($K_{us} < 0$), while the right two figures denote an SAE understeer configuration ($K_{us} > 0$). The solid gray line represents the SAE cornering solution. Stable solutions of (1,2) and (3,4) are marked by solid green curves, while unstable solutions are marked by dashed red curves. The blue crosses denote fold and pitchfork bifurcations, while the black pluses denote Hopf bifurcations. In the oversteer configuration the vertical black dashed line represents the value of v_0 when the vehicle loses stability in the simplified case (5).

For $K_{us} < 0$, $\gamma = 1°$ the low-speed stable solution loses stability via fold bifurcation for both FWD and RWD configurations below the critical speed predicted by the SAE solution. At high speed the RWD dynamics yield a stable solution corresponding to negative σ_1 born via Hopf bifurcation, whereas the FWD dynamics yield a stable solution corresponding to positive σ_1 born via fold bifurcation.

For $K_{us} > 0$, $\gamma = 5°$ the low-speed stable solution also loses stability via fold bifurcation for both RWD and FWD configurations, where the SAE solution does not show a critical speed at all. Stable solutions at high speed arise via Hopf bifurcations for both RWD and FWD configurations. In the RWD case these stable solutions correspond to negativeσ_1 and in the FWD case they correspond to positive σ_1.

In general we observe that the stable solutions arising at high speeds are characterized by negative σ_1 in RWD dynamics and by positive σ_1 in FWD dynamics. Hence the RWD vehicle tends to oversteer at high speeds, whereas the FWD vehicle tends to understeer at high speeds. This confirms with common notions about the handling characteristics of FWD and RWD cars in extreme scenarios [4]. This demonstrates the predictive power of the models developed in this paper.

References

[1] Gillespie T. D.: Fundamentals of Vehicle Dynamics. Society of Automotive Engineers. 1992.

[2] Ono E., Hosoe S., Tuan H. D., Doi S.: Bifurcation in vehicle dynamics and robust front wheel steering control. IEEE Transactions on Control System Technology: 6(3), 412-420, 1998.

[3] Rossa F. D., Mastinu G., Piccardi C.: Bifurcation analysis of an automobile model negotiating a curve. Vehicle Systems Dynamics: International Journal of Vehicle Mechanics and Mobility: 50(10), 1539-1562, 2012.

[4] Heisler H.: Advanced Vehicle Technology. Society of Automotive Engineers International. 2002.

GLOBAL SENSITIVITY ANALYSIS AND MULTIOBJECTIVE OPTIMIZATION OF BOGIE SUSPENSION

Seyed Milad Mousavi Bideleh & Viktor Berbyuk[a)]
Department of Applied Mechanics, Chalmers University of Technology, Gothenburg, Sweden

Summary Multiobjective optimization of nonlinear multibody systems with many degrees of freedom is a burdensome computational challenge. A feasible practical methodology for global sensitivity analysis (GSA) of multibody systems with respect to design parameters is proposed based on the multiplicative dimensional reduction method. The computational efficiency of optimization is significantly improved by restricting the input design parameters only to those identified by the GSA. The methodology is applied for GSA of a railway vehicle dynamics with respect to the bogie suspension characteristics. Several multiobjective optimization problems are then formulated and solved for a railway vehicle model with 50 degrees of freedom using genetic algorithm. The results obtained yield practical information regarding the optimized bogie suspension properties which improve the dynamics behavior of the vehicle from various perspectives. The proposed algorithm can be used in design optimization of nonlinear multibody systems with different applications.

INTRODUCTION

Bogie primary and secondary suspension stiffness and damping components can affect railway vehicle dynamics behavior from different perspectives such as safety, ride comfort, and wheel/rail contact wear. The bogie suspension components might have conflicting effects on the system dynamics. Furthermore, vehicle's speed, track irregularities, and radius of curvature of the track can also affect the vehicle's dynamics. Therefore, to satisfy various design requirements it is necessary to formulate and solve multiobjective optimization problems for railway vehicles modeled as multibody systems.

Multiobjective optimization problem of a nonlinear multibody system with many degrees of freedom (DOFs) is an elaborate task which requires high computational efforts. Number of input design parameters is one of the most critical issues which can significantly affect the computational burden of the optimization. Sensitivity analysis makes it possible to recognize those design parameters that most affect the system dynamics response and attenuate the number of inputs for optimization. Here, an efficient method for the GSA of multibody systems is proposed. The methodology is then applied for the GSA and optimization of a railway vehicle dynamics with respect to suspension stiffness and damping components.

GLOBAL SENSITIVITY ANALISYS

The Monte Carlo simulation is one of the most common methods for GSA. But the main drawback is heavy computational effort which makes it unfeasible to be applied to complex multibody systems. Analysis of variance decomposition or high dimensional model representation (HDMR) decomposes the response function of a high dimensional system into a combination of a set of low dimensional systems and dramatically reduces the computational and sampling efforts. Zhang and Pandey [1] proposed a multiplicative form of the dimensional reduction method (M-DRM) for GSA. The main advantages of using such an approximation are simplicity, high accuracy, computational efficiency, and closed-form representation for the global sensitivity indices. Based on the HDMR and M-DRM concepts the closed-form formulation of the global sensitivity index of an objective function with respect to the ith design parameter x_i is introduced as:

$$S_i^{\mathrm{T}} \approx \frac{1-\alpha_i^2/\beta_i}{1-\left(\prod_{k=1}^{n}\alpha_k^2/\beta_k\right)} \tag{1}$$

where S_i^{T} is the total sensitivity index. Variables α_k and β_k are calculated using the Gaussian quadrature integration method, see, e.g. [2]. It has been shown that these indices are as accurate as those obtained from the Monte Carlo simulation but with a dramatically less computational effort. Here, this methodology is employed to evaluate the sensitivity of different objective functions such as ride comfort ($S_{\Gamma_{\mathrm{C}}}^{\mathrm{T}}$), wear ($S_{\Gamma_{\mathrm{W}}}^{\mathrm{T}}$), and three safety criteria namely track shift force ($S_{\Gamma_{\mathrm{TS}}}^{\mathrm{T}}$), risk of derailment ($S_{\Gamma_{\mathrm{RD}}}^{\mathrm{T}}$), and running stability ($S_{\Gamma_{\mathrm{St}}}^{\mathrm{T}}$) of a one-car railway vehicle with respect to the 14 bogie suspension components listed in Table 1.

Table 1: Design parameters for sensitivity analysis.

No	1	2	3	4	5	6	7	8	9	10	11	12	13	14
Parameter	k_x^{p}	c_x^{p}	k_y^{p}	c_y^{p}	k_z^{p}	c_z^{p}	k_x^{s}	c_x^{s}	k_y^{s}	c_y^{s}	k_z^{s}	c_z^{s}	k^{AR}	k^{TR}

Here, k and c denote stiffness and damping values, respectively. The subscripts x, y, z indicate the longitudinal, lateral, and vertical directions, respectively. The superscripts p, s, AR, and TR denote primary, secondary, anti-roll bar, and traction rod

[a)] Corresponding author. Email: viktor.berbyuk@chalmers.se

components, respectively. The simulations are carried out and analyzed for a vehicle running at maximum admissible speed on a curved track with very small radius of curvature R=300 m.

MULTIOBJECTIVE OPTIMIZATION

The GSA results shown in Fig. 1(a) are obtained with merely 168 simulations and include informative data regarding the design optimization of bogie suspension components. As an example, to reduce contact wear and improve ride comfort only parameters number 1, 3, 7, 8, and 11 can be considered as the design parameters in the multiobjective optimization problem. Therefore, the fourteen initial variables are reduced to five. This significantly improves the computational efficiency of the optimization. The wear/comfort Pareto optimization can be formulated as follows: for a given vehicle model, prescribed structural parameters, feasible initial states, and a set of operational scenarios it is required to determine the optimized vector of the design parameters ($\mathbf{d}^*$) such that the variational equation $\boldsymbol{\Gamma}(\mathbf{d}^*) = \min_{\mathbf{d}\in\Omega} \boldsymbol{\Gamma}(\mathbf{d})$ is satisfied subject to the following constraints: $\Gamma_{TS}(\mathbf{d}^*) \le \Gamma_{TS}^{max}$, $\Gamma_{St}(\mathbf{d}^*) \le \Gamma_{St}^{max}$, $\Gamma_{RD}(\mathbf{d}^*) \le \Gamma_{RD}^{max}$. Here, $\boldsymbol{\Gamma} = [\Gamma_W \quad \Gamma_C]^T$ is the vector of objective functions and Ω is the domain of the input design variables ($\mathbf{d}$). Limits Γ_{TS}^{max}, Γ_{St}^{max} and Γ_{RD}^{max} are the maximum admissible values of the track shift force, stability and risk of derailment considered as thresholds to the optimization problem.

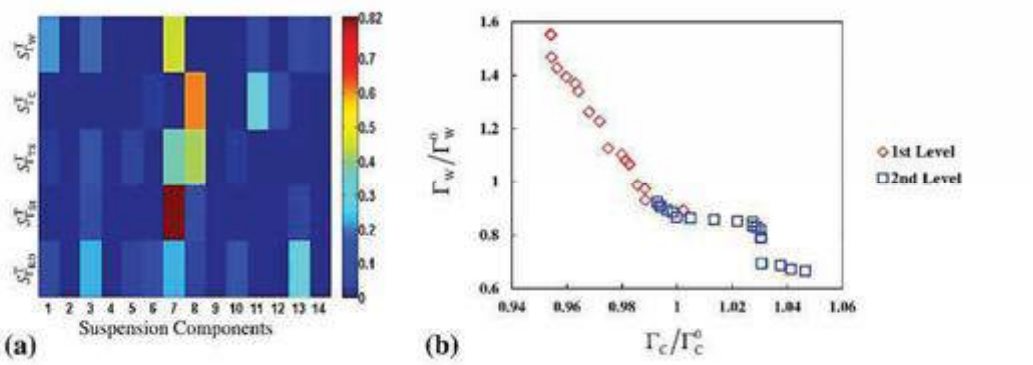

Figure 1: a) GSA results of a one-car railway vehicle with 50 DOFs with respect to the suspension components; b) Normalized wear/comfort Pareto front.

To further improve the computational efficiency the five design parameters recognized by the GSA are classified into two sets (first set with 3 and second set with 2 design parameters) and the wear/comfort Pareto optimization is accordingly carried out in two levels. The formulated problem is solved using a genetic algorithm (GA) based routine integrated in a MATLAB/SIMPACK co-simulation interface. The normalized wear/comfort Pareto front achieved by the first and second optimization levels are compared in Fig. 1(b). The results proved that it is possible to reduce contact wear and improve ride comfort for the considered railway vehicle model while a satisfactory safety level is guaranteed.

CONCLUSIONS

This study showed the feasibility and efficiency of the proposed M-DRM based method for the GSA of multidimensional nonlinear multibody systems which provided the results in a computationally efficient framework. The proposed methodology has been used for the GSA of a one-car railway vehicle dynamics behavior with respect to the bogie suspension components and revealed remarkable practical results which significantly reduced the number of input design parameters for optimization. The analysis of the GSA and Pareto optimization results showed that it is possible to solve optimization problem of a railway vehicle with realistic structural parameters and track irregularities in a computationally efficient manner and reduce wear and improve comfort while a satisfactory safety level is guaranteed. The proposed methodology can be used in the GSA and design optimization with different applications.

ACKNOWLEDGMENTS

The Ekman family foundation which is cordially appreciated for the financial support of this research.

References

[1] Zhang, X., Pandey, M.D.: An effective approximation for variance-based global sensitivity analysis, *Reliab. Eng. Syst. Saf.*, **121**: pp. 167-174, 2014.
[2] Mousavi Bideleh S.M., Berbyuk V.: Global sensitivity analysis of bogie dynamics with respect to suspension components. *Multibody System Dynamics,* 2016, http://dx.doi.org/10.1007/s11044-015-9497-0

Coupling of Mechanical and Optical Methods for Simulations and Measurements

Peter Eberhard* and Johannes Störkle

Institute of Engineering and Computational Mechanics, University of Stuttgart, Stuttgart, Germany

Summary In order to investigate and analyse the dynamical-optical behavior of high precision optical systems like lithographic objectives and astronomical telescopes with low computational cost, integrated modeling methods and strategies are proposed. During an astronomical observation, even small mechanical vibrations can be sufficient to produce aberrated images. The mechanical behavior of such optical systems can be described by a combination of rigid body motion and small deformations. This leads to the utilization of elastic multibody approaches and model order reduction methods in combination with techniques from optical simulations. As a result, the exposed image influenced by mechanical excitations and structural deformations can be simulated and assessed.

INTRODUCTION

High precision optical systems are very sensitive with respect to mechanical influences. In order to investigate and analyse the dynamical-optical behavior of high precision optics, integrated modeling strategies and methods are proposed, see also [1], [2] and [3]. For deriving a simplified mechanical model for time simulations with low computational cost, the method of elastic multibody systems (EMBS) in combination with model order reduction methods is used. Mechanical and optical simulation models are derived and implemented according to the workflow shown in Figure 1. In order to clarify these methods, mirror and lens applications are chosen as academic examples. Ground-based telescopes are highly resoluting optical systems consisting of precise mirrors. They are accurately mounted and they are very sensitive with respect to vibrations. During the observation time, small mechanical vibrations can be sufficient to produce inacceptably aberrated images. Even the adaptive optical unit or other motion systems can unintentionally excite the whole construction. Similar effects can happen at wafer scanning systems which use lithography objectives to project structures in a reticle onto wafers. Thereby, lens deformations and related stresses also influence the optical behavior during the exposure time [4].

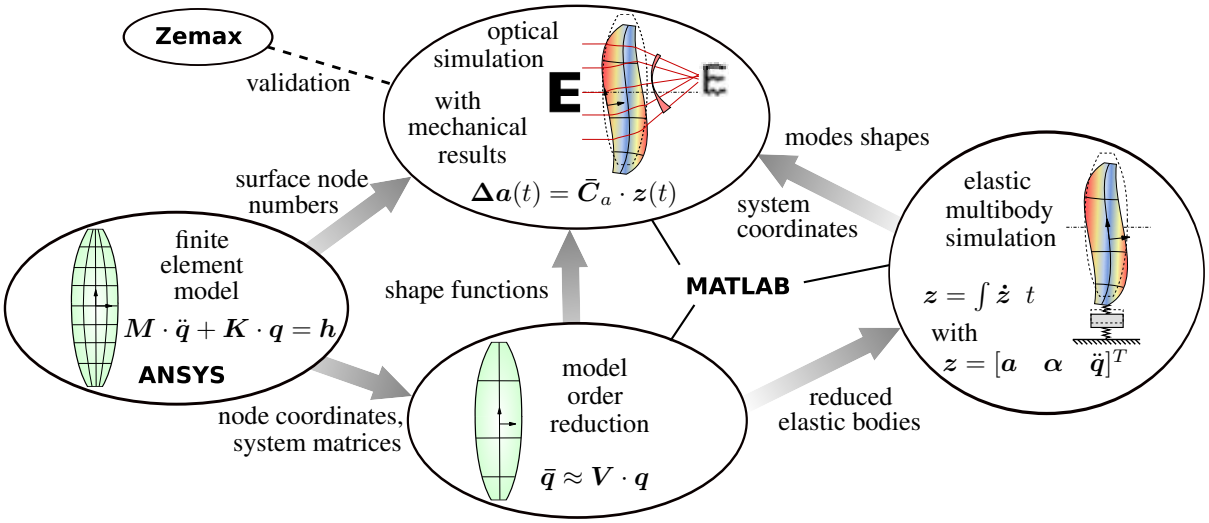

Figure 1: Basic procedure for describing dynamical-optical simulations.

MECHANICAL MODEL

The mechanical model is based on EMBS with the floating frame of reference. In contrast to a detailed and large global model based on the finite element method, a reduced and modular EMBS leads to low computational effort for simulations in the time domain. Furthermore, the system can be analysed and assembled step by step and it is able to include only the relevant dynamical behaviour due to appropriate model order reduction methods. For a single elastic body in an EMBS, the structure of the equations of motion read

$$\left[\begin{array}{cc|c} m\boldsymbol{I} & m\tilde{\boldsymbol{c}}^T(\boldsymbol{q}) & \boldsymbol{C}_t^T \\ m\tilde{\boldsymbol{c}}(\boldsymbol{q}) & \boldsymbol{J}(\boldsymbol{q}) & \boldsymbol{C}_r^T \\ \hline \boldsymbol{C}_t & \boldsymbol{C}_r & \bar{\boldsymbol{M}}_e \end{array}\right] \cdot \begin{bmatrix} \boldsymbol{a} \\ \boldsymbol{\alpha} \\ \ddot{\boldsymbol{q}} \end{bmatrix} + \begin{bmatrix} \boldsymbol{0} \\ \boldsymbol{0} \\ \bar{\boldsymbol{D}}_e \cdot \dot{\boldsymbol{q}} + \bar{\boldsymbol{K}}_e \cdot \boldsymbol{q} \end{bmatrix} + \boldsymbol{h}_\omega = \boldsymbol{f}_a + \boldsymbol{f}_r, \tag{1}$$

*Corresponding author. Email: peter.eberhard@itm.uni-stuttgart.de

whereby the reduced equations of motion describing the deformation of the elastic body are embedded and the rigid body dynamics are included according to [5]. These equations can describe the mechanical system behaviour and the consideration of the optical behaviour is discussed in the following.

OPTICAL MODEL

For sequential ray tracing through several lenses and mirrors during the optical simulation, a continuous description of the mechanically deformed surfaces is required. Thereby, the line of sight (LOS) describes the displacement of the center of intensity and the wavefront aberrations fitted by Zernike polynomials characterise the blurring and image quality [6]. In order to take also wave optical effects during an image simulation into account, Fourier optical methods are utilized. Furthermore, the relationship between a kinematic degree of freedom given by the generalized coordinates $\boldsymbol{q}$ and the relative aberrations $\Delta\boldsymbol{a}$ containing the LOS and the Zernike coefficients c_j can be expressed by the kinematic-optical sensitivities. They can be collected in the matrix $\boldsymbol{C}_a$. This corresponds to the relations

$$\Delta\boldsymbol{a} = [\underbrace{\Delta x_{\mathrm{los}} \quad \Delta y_{\mathrm{los}}}_{\Delta\boldsymbol{a}_{\mathrm{los}}} \quad \underbrace{c_1 \quad c_2 \quad \dots \quad c_j \quad \dots \quad c_k}_{\Delta\boldsymbol{a}_{\mathrm{wfa}}}]^T = \boldsymbol{C}_a \cdot \boldsymbol{q} \approx \underbrace{\boldsymbol{C}_a \cdot \boldsymbol{V}}_{\underline{a}} \cdot \boldsymbol{q}. \tag{2}$$

The so-called matrix of optical mode shapes $\boldsymbol{C}_a$ is derived in combination with the projection matrix $\boldsymbol{V}$ of the model order reduction and can be obtained by means of ray tracing analyses during a static mode shape deformation.

Figure 2 illustrates results of an exemplary dynamical-optical simulation. On the left, a snapshot of a deformed mirror structure is visualized in an exaggerated manner. On the right, the time-accumulated irradiance is depicted, which delivers the exposed image of a regarded object.

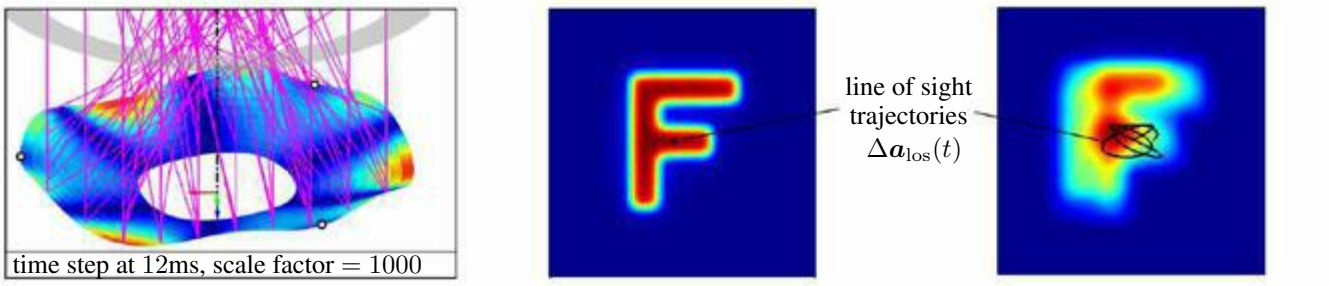

(a) ray tracing simulation (b) neglecting mechanical vibrations (c) considering mechanical vibrations

Figure 2: Results of the dynamical-optical simulation.

INVESTIGATIONS AND CONCLUSIONS

The influence of different model order reduction methods will be presented and analysed for an exemplary integrated model. It is based on an annular lightweight mirror with a parabolic shape made of aluminum. Here, the influence of the model order reduction methods is analysed and the mechanical-optical transfer behaviors of different wavefront aberrations are investigated. It is shown, that the mechanical-optical sensitivities depend on the frequency of excitation. Moreover, it is investigated, whether the sensitivities can be used during the model order reduction in order to describe the overall behavior with an optimized model. Finally, the performance of different simulation strategies is assessed and the application limits are identified.

References

[1] Andersen, T. and Enmark, A.: *Integrated Modeling of Telescopes*, Astrophysics and Space Science Library, Springer, New York, 2011.

[2] Wengert, N.: *Gekoppelte dynamisch-optische Simulation von Hochleistungsobjektiven (in German, submitted for publication)*, Dissertation, Schriften aus dem Institut für Technische und Numerische Mechanik der Universität Stuttgart, Shaker Verlag, Aachen, 2015.

[3] Störkle, J., Wengert, N., and Eberhard, P.: "Strategies for the dynamical-optical simulation of high-performance optics (submitted for publication)," in *Proceedings of the Integrated Modeling of Complex Optomechanical Systems II*, SPIE Digital Library, 2015.

[4] Wengert, N., Nefzi, M., Eberhard, P., and Geuppert, B.: "Dynamics in lithographic projection objectives," *Multibody System Dynamics* **30**(2), 233–245, 2013.

[5] Schwertassek, R. and Wallrapp, O.: *Dynamik flexibler Mehrkörpersysteme (in German)*, Vieweg, Braunschweig, 1999.

[6] Gross, H., Singer, W., and Totzeck, M., Eds.: *Handbook of Optical Systems, Systems Image Formation*, Wiley-VCH Verlag, Weinheim, 2005.

NONLINEAR ROTOR MOTION: INFLUENCE OF THRUST BEARINGS ON SUBSYNCHRONOUS OSCILATIONS

Xiaonan Zhao[1a)], Ioannis Chatzisavvas[1], Panagiotis Koutsovasilis[2] & Bernhard Schweizer[1]
[1]*Institute of Applied Dynamics, Technical University Darmstadt, Darmstadt, Germany*
[2]*Rotordynamics & Preventive Acoustics, Global Engineering Core Science, BorgWarner Turbo Systems Engineering GmbH, Kirchheimbolanden, Germany*

Summary A nonlinear automotive turbocharger rotor/bearing system is considered, and this work is focused on the influence of the thrust bearing on the nonlinear, self-excited rotor vibrations. To investigate dynamically loaded thrust bearings, run-up simulations based on a fully-coupled model are performed. Of special interest is the effect of the elastic deformation of the thrust bearing.

INTRODUCTION

Thrust bearings are important components in rotor systems. The type of the thrust bearing used in a rotor system is chosen according to the specific application. An overview on bearings of different geometries and a comparison of their advantages and disadvantages can be found in Refs. [1–4]. In this work, high-speed turbocharger rotors are considered, which are usually equipped with taper-flat thrust bearings. An experimental study on such bearings in Ref. [5] provided the comprehensive understanding of their hydrodynamic behaviour.

In order to design and dimension such bearings, precise information on the dynamic axial loads is needed. Therefore, simulation models are required to predict accurately the exerted axial forces under transient operation conditions. The dynamic oil pressure and temperature in hydrodynamic thrust bearings can be described by Reynolds equation for fluid films. Under high axial loads, the elastic deformation of the thrust bearing should also be taken into account for a better prediction of the oil pressure and load capacity. For this purpose, a fully-coupled approach is used to calculate the load in the thrust bearing of dynamically loaded rotor systems. The rotor (described with a multibody model) is simulated simultaneously with the transient Reynolds equation (solved by a global Galerkin approach) and the partial differential equation, which represents the elastic deformation of the bearing pad (solved by a finite element approach).

MODEL DESCRIPTION

Multibody model of the rotor/bearing system

A sketch of the turbocharger rotor investigated here is depicted in Figure 1a. The rotor consists of a compressor wheel, a turbine wheel and an elastic shaft. The rotor is radially supported by two full-floating ring bearings (Figure 1b), while a hydrodynamic taper-flat thrust bearing (Figure 1c) is used in the axial direction. The system is excited by two imbalance masses attached at the wheels.

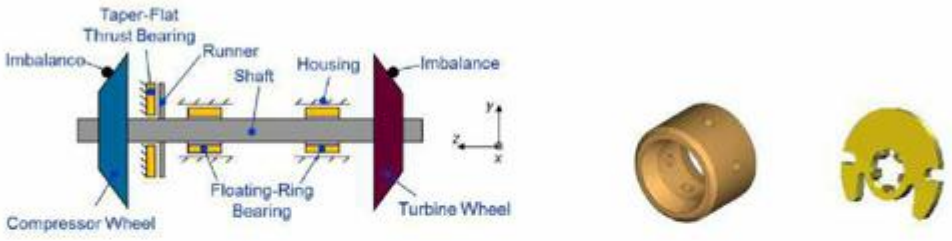

(a) (b) (c)

Figure 1: (a) Sketch of turbocharger rotor/bearing system; (b) CAD model of a floating-ring bearing; (c) CAD model of a taper-flat thrust bearing

This system is modelled as a flexible multibody system, which reads in the stabilized index-2 formulation:

$$\dot{\boldsymbol{q}} = \mathbf{K}(\boldsymbol{q})\boldsymbol{p} - \boldsymbol{G}^T(t,\boldsymbol{q})\boldsymbol{\mu}\,, \quad \boldsymbol{M}(\boldsymbol{q})\dot{\boldsymbol{p}} = \boldsymbol{f}_e(t,\boldsymbol{q},\boldsymbol{p}) - \boldsymbol{G}^T(t,\boldsymbol{q})\boldsymbol{\lambda}$$
$$\mathbf{0} = \boldsymbol{g}(t,\boldsymbol{q})\,, \quad \mathbf{0} = \boldsymbol{G}^T(t,\boldsymbol{q})\boldsymbol{p} + \frac{\partial \boldsymbol{g}(t,\boldsymbol{q})}{\partial t}$$

It is described by υ generalized coordinates, which are collected in the position vector $\boldsymbol{q} = (q_1, \dots, q_\upsilon)^T \in \mathbb{R}^\upsilon$. The vector $\boldsymbol{p} = (p_1, \dots, p_\upsilon)^T \in \mathbb{R}^\upsilon$ contains the generalized velocities, which are related to the generalized coordinates $\boldsymbol{q}$ by the

[a)] Corresponding author. Email: zhao@ad.tu-darmstadt.de.

kinematical differential equations $\dot{\boldsymbol{q}} = \mathbf{K}(\boldsymbol{q})\boldsymbol{p}$. The mass matrix $\boldsymbol{M}(\boldsymbol{q}) \in \mathbb{R}^{\upsilon \times \upsilon}$ is assumed to be symmetric and positive definite. The externally applied forces and torques are arranged in the vector $\boldsymbol{f_e}(t, \boldsymbol{q}, \boldsymbol{p})$. The system is constrained by n_c rheonomic algebraic constraint equations $g_i(t, \boldsymbol{q}) = 0 \text{//} (i = 1, \dots, \upsilon_c)$, which are arranged in the constraint vector $\boldsymbol{g} \in \mathbb{R}^{\upsilon_c}$. The corresponding constraint forces and toques are defined by $\boldsymbol{G}^T(t, \boldsymbol{q})\boldsymbol{\lambda}$ with the matrix $\boldsymbol{G} = \frac{\partial \boldsymbol{g}}{\partial \boldsymbol{q}} \in \mathbb{R}^{\upsilon_c \times \upsilon}$ and the vector $\boldsymbol{\lambda} = (\lambda_1, \dots, \lambda_{\upsilon_c})^T \in \mathbb{R}^{\upsilon_c}$ collecting the Lagrange multipliers.

Thrust bearing model

The pressure generation p in the thrust bearing is mathematically described by Reynolds fluid film equation [1-4]:

$$\frac{\partial}{\partial r}\left(r h^3 \frac{\partial p}{\partial r}\right) + \frac{1}{r}\frac{\partial}{\partial \theta}\left(h^3 \frac{\partial p}{\partial \theta}\right) = 6\mu\omega r \frac{\partial h}{\partial \theta} + 12\mu r \frac{\partial h}{\partial t}$$

where r and θ are the radial and circumferential coordinates, h the oil-film thickness, μ the viscosity of the oil, ω the rotational speed of the rotor and t the time.

The temperature in the oil film is computed with an appropriate energy equation, see Ref. [1]. The information of the elastic deformation due to the oil pressure can be acquired from a 3D-linear-elastic structural model, which is integrated into the multibody model using a model reduction approach.

SIMULATION RESULTS

Run-up simulations are performed with the fully-coupled model. A spectrum of a run-up simulation is shown in Figure 2a. The system response is highly non-linear and exhibits different self-excited vibration effects. A detailed description of the nonlinear effects can be found in Ref. [6], for instance. The elastic deformation of the thrust bearing is depicted in Figure 2b.

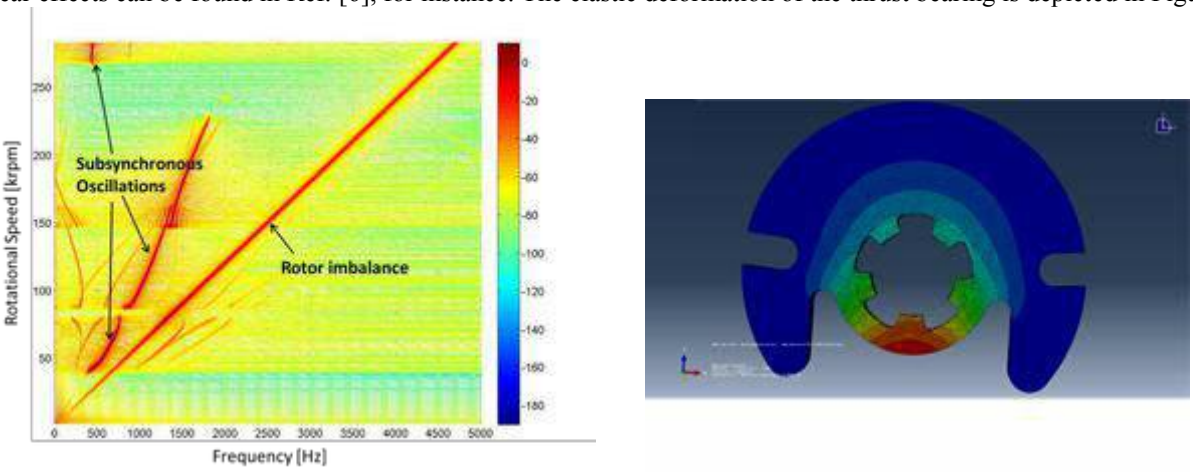

(a) (b)

Figure 2: (a) Spectrum of a run-up simulation; (b) elastic deformation of the taper-flat thrust bearing

CONCLUSION

An analysis of a coupled model has been conducted to find out the dynamic behaviour and transient bearing loads of an automotive turbocharger. The rotor system shows a highly nonlinear behaviour including different bifurcations, self-excited vibrations and jump phenomena. For that reason, a quasi-static approach, which is often used to dimension bearings, is not applicable for the considered turbocharger model, and a detailed fully-coupled model is necessary to predict the nonlinear interaction phenomena correctly.

References

[1] O. Pinkus, B. Sternlicht, Theory of hydrodynamic lubrication, McGraw-Hill, 1961.

[2] A. Z. Szeri, Fluid film lubrication, Cambridge University Press, 2010.

[3] Y. Hori, Hydrodynamic lubrication, Springer Tokyo, 2006.

[4] M. M. Khonsari, E. R. Booser, Applied tribology: Bearing design and lubrication, John Wiley & Sons, 2008

[5] Y. Henry, J. Bouyer, M. Fillon, An experimental hydrodynamic thrust bearing device and its application to the study of a tapered-land thrust bearing, Journal of Tribology 136 (2) (2014) 021703–021703.

[6] B. Schweizer, M. Sievert, Nonlinear oscillations of automotive turbocharger turbines, Journal of Sound and Vibration 321 (35) (2009) 955 – 975.

PARAMETER ESTIMATION IN VEHICLE DYNAMICS: TRAIN, TRACK AND FAULT MONITORING

Katrin Ellermann*[1] and Mathias Jesussek[2]
[1]*Institute of Mechanics, Graz University of Technology, Graz, Austria*
[2]*Magna Powertrain, Lannach, Austria*

Summary This paper presents examples for the use of Kalman filtering techniques: Parameters which influence the dynamics of a train are identified from acceleration data. The algorithm identifies critical changes in spring and damper characteristics. Random influences due to the naturally occurring track irregularities are included.

INTRODUCTION

Railway vehicles are susceptible to different types of damage: Wheels, springs, dampers and various other structural components are important for a safe operation of the vehicle. A good maintenance of the vehicles is therefore important for safety reasons. As monitoring during operation is currently not possible for some components, the most critical components are sometimes replaced based on operation time, even if the component might be fully functional. This work is focused on techniques to check the system's health during operation. Several authors have presented approaches of using state-estimation techniques in vehicle dynamics – and in some cases they have used them also for parameter estimation or fault detection, see e. g. [1, 2, 3, 4]. A possible way of doing this is based on acceleration data measured at different points on the vehicle's body. The motion of these reference points is caused by the interaction of the different components of the vehicle.

DYNAMIC MODEL

The vehicle's dynamics is described as a multibody system. The excitation is random due to the interaction of the wheel with an uneven rail. The parameters, like spring- and damper-characteristics, masses and moments of inertia influence the nonlinear dynamics of the vehicle. Multiple nonlinear components are included in the train model, which serves as an example for the described techniques. Often, the exact values of the parameters are unknown and might even change over time.

The dynamic model of the vehicle under consideration is shown in Figure 1: It consists of a car body, two bogies, four wheelsets and two motors. Several suspension elements are included in the model (solid lines in the close-up), these elements are connected to the different bodies (circles).

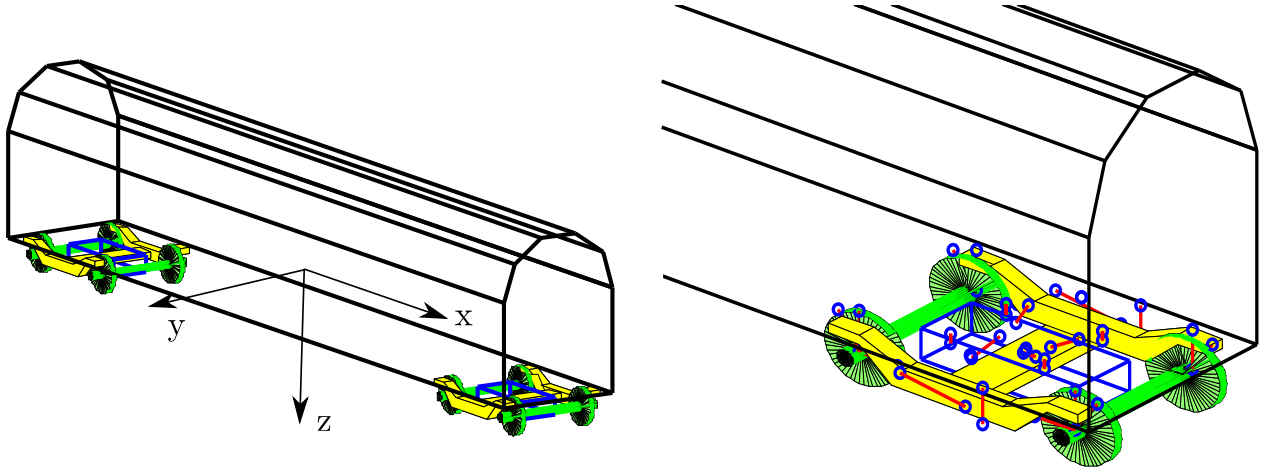

Figure 1: Components of the train model

Car body, bogie and motor dynamics can be characterized by six degrees of freedom each. Prescribing constant speed, the wheelset dynamics is considered as two dimensional and characterized by lateral y^w and yaw motion ψ^w.

*Corresponding author. Email: ellermann@tugraz.at

Using Newton-Euler equations, and transforming the equations of motion into state-space form, we obtain a system of equations in the form

$$\begin{aligned}\dot{\mathbf{x}}_s &= \mathbf{A}_s\mathbf{x}_s + \mathbf{B}_s\mathbf{x}_r \\ \mathbf{y}_s &= \mathbf{C}_s\mathbf{x}_s + \mathbf{D}_s\mathbf{v}\end{aligned}$$

where $\mathbf{A}_s$ is the state matrix, $\mathbf{B}_s$ is the process noise matrix resulting from the track, $\mathbf{C}_s$ is the output matrix and $\mathbf{D}_s$ is the measurement noise matrix.

A common approach for the description of the random track irregularities is based on power spectral densities: A general form of these spectra is given in ERRI B176 [5] and based on the coefficients in the polynomial description of these spectra, the track irregularities are described by a set of form filters as

$$\begin{aligned}\dot{\mathbf{x}}_{\text{ffi}} &= \mathbf{A}_{\text{ffi}}\mathbf{x}_{\text{ffi}} + \mathbf{B}_{\text{ffi}}\mathbf{w}_{\text{ffi}} \\ \mathbf{y}_{\text{ffi}} &= \mathbf{C}_{\text{ffi}}\mathbf{x}_{\text{ffi}} \quad .\end{aligned}$$

Combining the equation of the train and the track in one set of equations gives

$$\begin{aligned}\dot{\mathbf{x}} &= \mathbf{A}\mathbf{x} + \mathbf{B}\mathbf{w} \\ \mathbf{y} &= \mathbf{C}\mathbf{x} + \mathbf{D}\mathbf{v} \quad .\end{aligned} \tag{1}$$

with

$$\mathbf{A} = \begin{bmatrix}\mathbf{A}_s & \mathbf{B}_s\mathbf{C}_{\text{ffi}} \\ 0 & \mathbf{A}_{\text{ffi}}\end{bmatrix},\ \mathbf{B} = \begin{bmatrix}0 \\ \mathbf{B}_{\text{ffi}}\end{bmatrix},\ \mathbf{C} = \begin{bmatrix}\mathbf{C}_s & 0\end{bmatrix},\ \mathbf{x} = \begin{bmatrix}\mathbf{x}_s \\ \mathbf{x}_{\text{ffi}}\end{bmatrix}.$$

EVALUATION

The general form of a multibody system as described before is then used in state estimation – but sets with slightly different parameter values are considered in the estimation process. The estimation of the system's state is obtained from an optimal and robust filter. Thus, state-space data is generated, which is then compared with the reference system, i. e. the motion data from the train under consideration. The procedure is a fault detection and identification (FDI) process. Linear and nonlinear residual generators are applied for the detection and isolation of faults in the system. The parameter set with the best fit for the state-space data of the real system is considered as the closest fit for the system description. This parameter set gives information about critical changes in the components of the train but it also holds information about the wheel-rail interaction.

The analysis of selected test cases shows that for the given system it is possible to detect a failure of the suspension system from the system's dynamic response and different possible sources for the changes in the dynamical behavior are presented.

References

[1] Li, P.; Goodall, R.; Weston, P.; Ling, C. S.; Goodman, C.; Roberts, C.: Estimation of railway vehicle suspension parameters for condition monitoring, Control Engineering Practice 15 (1), p. 43–55, 2007.

[2] Li, P.; Goodall, R.: Model-based Condition Monitoring for Railway vehicle Systems, Control, University of Bath, 2004.

[3] Hayashi, Y.; Tsunashima, H.; Marumo, Y.: Fault Detection of Railwas Vehicles Using Multiple Model Approach, SICE-ICASE, p. 2812–2817, 2006.

[4] Thite, A.,N.; Banvidi, S.; Ibicek, T.; Bennett, L.: Suspension parameter estimation in the frequency domain using a matrix inversion approach, Vehicle System Dynamics 50(7), p. 1121-1135, 2012.

[5] ERRI B176/3, Benchmark problem – Results and assessment", B176/DT290, Utrecht 1993.

THE EVALUATION OF STEERING PERFORMANCE OF DRILLING ASSEMBLIES BASED ON MULTIBODY DYNAMICS APPROACH

Jiapeng Liu[1a)], Zaibin Cheng[2], Yingjie Lu[1] & Gexue Ren[1]
[1] *Department of Engineering Mechanics, Tsinghua University, Beijing, People's Republic of China*
[2]*CNOOC Research Institute, Beijing, People's Republic of China*

Summary The multibody dynamics approach is introduced to simulate the whole drilling process of the directional drilling system combined with bit-rock interaction principle, which results the new born wellpath while drilling. The drilled wellpath trajectory of the simulation results can be used to evaluate the steering performance of a specific drilling assembly clearly and intuitively as a reference for directional driller.

INTRODUCTION

Directional drilling is widely used to reach a reservoir which is inaccessible with normal vertical drilling. The wellpath control is very important to reach the target zone of the reservoir. However, the wellpath is difficult to predict before drilling and influenced by many factors such as bottom hole assembly configuration (position, gauge and quantity of the stabilizers, length and diameter of the drill collars), drilling parameters (weight on bit, rotation speed), formation anisotropy. Therefore, a multibody model of drilling system is built to predict the wellpath and experimental results are compared with simulation results to validate the effectiveness of the multibody model of drilling assembly.

MULTIBODY MODEL OF DRILLING SYSTEM

As illustrated in Fig. 1(a), the drilling system consists of two subsystems: the surface driving system and the downhole drillstring system. The surface driving system includes drawworks which is used to raise or lower the drillstring through the drill line. Topdrive is used to rotate the whole drillstem clockwise under the commands from the control room. Drillpipe and bottomhole assembly (BHA), which steers the wellbore trajectory are included in the downhole drillstring system. The drill pipes connect the surface system to the downhole drillstring and transmit the torque from the surface to the BHA. The main parts of the the BHA consist of drill collars, measurement while drilling (MWD), stabilizers, and drill bit. Drill collars are used to provide sufficient weight on bit (WOB) for efficient drilling and control the control the wellbore trajectory combined with stablizer (Fig. 1(b)). MWD measures real-time inclination, azimuth of the wellbore and transmit these measurements to the surface control room through the mud pulses. When the drillstring is dropped and rotated, the drill bit scraps the rock. Hence the new wellbore is born and extends.

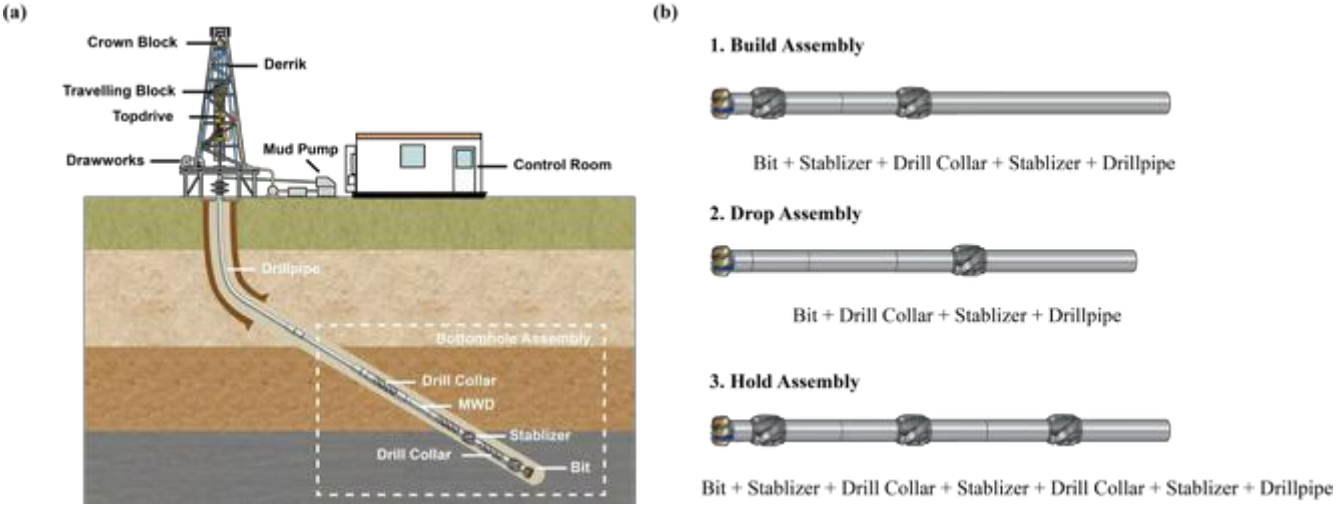

Fig. 1 (a). Schematic of drilling system (b). Different configurations of BHA assembly

The drilling system is built under the frame of multibody dynamics. The bit, stabilizer, drawworks, topdrive are modelled with rigid bodies. The drillpipe, drill collar, MWD are simulated with flexible Timoshenko beam.[1] The threaded connection between neighbouring drill components is formulated with fixed joints. Contact force between the drillstring and the wellbore is specially modelled by force element through contact points which are used to identify whether there is contact between them or not. Bit-rock interaction principle is used to connect the WOB and rate of penetration (ROP) to drill a new wellpath resulting a dynamic boundary for the drilling system.[2]

[a)] Corresponding author. Email: liujp13@mails.tsinghua.edu.cn

SIMULATION RESULTS AND EXPERIMENT VALIDATION

INSIDES (In Silico Dynamical Experiment Simulator) developed by Tsinghua University under the frame of multibody dynamics is used to simulate the drilling system of COSL (China Oilfield Services Limited) in XinJiang, China. As is shown in Fig. 2, simulation wellpath and experimental wellpath from the measure depth of 2693m to 2721m are compared. And we can find that the simulation result fits well with the experimental result. The difference between them is no more than 0.5m. In addition to that, the influence of outer diameter of drill collars is shown in Fig. 3. We can see that drilling assembly which has smaller outer diameter drill collars will have larger build (better steering performance), which is in accordance with field tests.

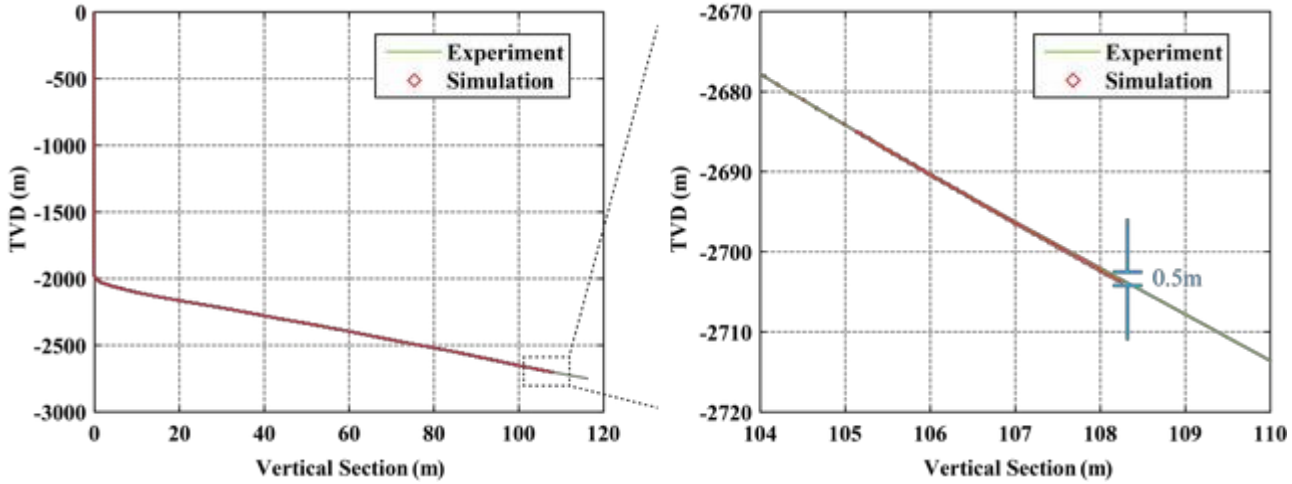

Fig. 2 The comparison between Simulation result and experiment result

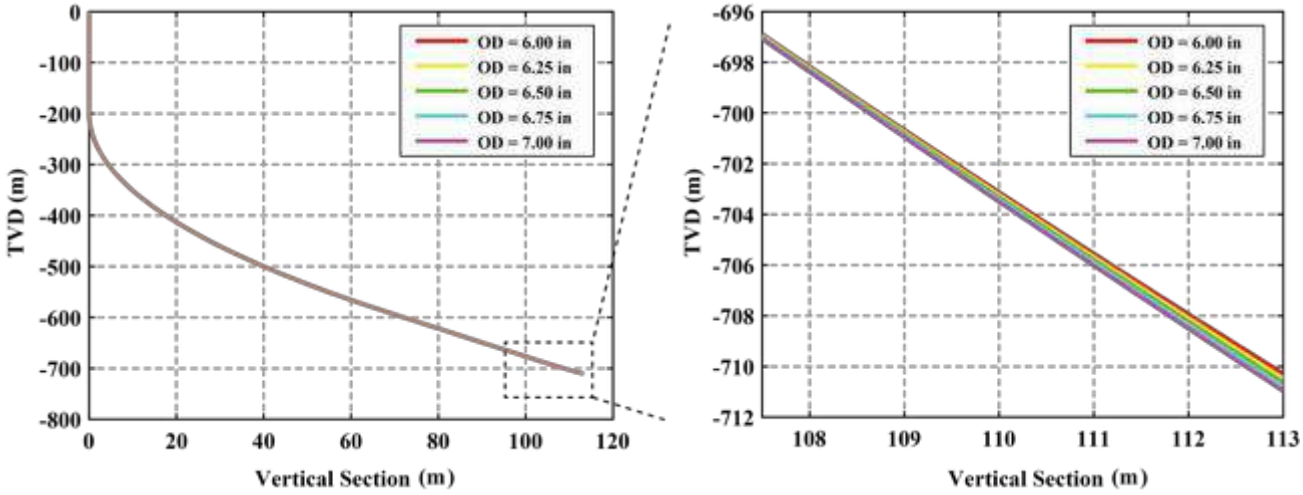

Fig. 3 The simulation result of different outer diameter (OD) of drill collars

CONCLUSIONS

The multibody dynamics approach can be used to simulate the whole drilling process of the directional drilling system and evaluate the steering performance of a specific drilling assembly clearly and intuitively as a reference for directional driller on the basis of drilled wellbore trajectory.

ACKNOWLEDGEMENT

This work was supported by the National High-tech R&D Program (863 Program) in the 12th Five-year plan funded by the Ministry of Science and Technology of the People's Republic of China (No. 2013AA092401)

References

[1] Cheng Z, Jiang W, Ren G, et al. A Multibody Dynamical Model for Full Hole Drillstring Dynamics[J]. Applied Mechanics and Materials, 2013, 378

[2] Wang N Y, Cheng Z B, Lu Y J, et al. A multibody dynamics model of contact between the drillstring and the wellbore and the rock penetration process[J]. Advances in Mechanical Engineering, 2015, 7(5)

A MODIFIED GENERALIZED STRAIN FORMULATION FOR FLEXIBLE MULTIBODY SYSTEM MODELLING

J. P. Meijaard [*1]

[1] *Olton Engineering Consultancy, Enschede, The Netherlands*

Summary A modification of a multibody formulation making use of generalized strains is proposed in which the generalized strains are defined by implicit constraint functions. This modification yields a greater freedom in defining these strains so they can more closely fit the actual behaviour of deformable finite elements. Modified planar and spatial beam elements are presented. Examples involving large deflections of beams are presented to show the improved performance of the modified elements.

OUTLINE OF THE PROCEDURE

A finite element formulation for modelling flexible multibody systems was initiated by van der Werff and Jonker [1, 2] and further developed to the present day. This formulation makes use of generalized strains and geometric transfer functions. For each element, generalized strains, $\boldsymbol{\varepsilon}^e$, are defined as explicit functions of the nodal coordinates, $\boldsymbol{x}^e$,

$$\boldsymbol{\varepsilon}^e = \boldsymbol{\mathcal{D}}^e(\boldsymbol{x}^e), \tag{1}$$

where the deformation functions are denoted by $\boldsymbol{\mathcal{D}}^e$. The number of independent generalized strains for an element is equal to the number of independent nodal coordinates minus the number of degrees of freedom of the element as a rigid body.

It is proposed to make the formulation more general by the use of implicit relations between the generalized strains and the nodal coordinates, which can be expressed as constraint equations,

$$\boldsymbol{\mathcal{C}}^e(\boldsymbol{\varepsilon}^e, \boldsymbol{x}^e) = \boldsymbol{0}, \tag{2}$$

where the form of Eq. (1) is a special case with $\boldsymbol{\mathcal{C}}^e = \boldsymbol{\mathcal{D}}^e(\boldsymbol{x}^e) - \boldsymbol{\varepsilon}^e$. An advantage of this modification is the greater generality and freedom of choosing the generalized strains, so they can be described by simpler expressions or they can more closely match physical strain distributions. Also the number of generalized strains for a type of element can be reduced if some modes of deformation are suppressed or increased if additional internal modes of deformation need to be described in order to obtain a higher accuracy or to describe superelements [3]. Disadvantages are the possibly higher complexity of the constraints and the increased size of some system matrices.

The formulation of the procedure to derive the equations of motions is largely analogous to the original procedure. Dependent coordinates and generalized strains can be chosen, so that their number is equal to the number of constraints in Eq. (2), and the other free coordinates and generalized strains are degrees of freedom. Geometric transfer functions that give the coordinates and the generalized strains as functions of the degrees of freedom, and also their derivatives, can be calculated. A difference from the original formulation is that Lagrangian multipliers dual to the constraints can be introduced, besides the generalized stresses $\boldsymbol{\sigma}^e$ dual to $\boldsymbol{\varepsilon}^e$, which still have a clear physical meaning in most cases.

SOME FINITE ELEMENTS

Flexible beams are statically determinate structures, that is, no compatibility equations exist between the six beam deformations, and therefore an assumed strain approach to formulate finite beam elements can be easily applied. For the planar beam element, a constant axial strain and a linearly varying curvature can be assumed. The differential equations for the elastic line can be integrated from one nodal point to the other to obtain three constraint equations of the form (2). The integration can be done exactly or approximately. As the derivatives are easy to calculate, a Taylor series approximation is used here. Transverse shear can be included with or without introducing additional generalized strains. For a higher accuracy, additional assumed strains for the axial strain of the central line and the curvature can be introduced.

For spatial systems, the rotations of nodal points are described by Euler parameters. The constraint for the Euler parameters can be described by an equation of the form (2) without the need to introduce a generalized strain with a dual generalized stress with an ambiguous physical meaning.

A spatial beam element can be modelled in a way similar to the planar beam element, where the curvatures in the two bending directions are linearly interpolated and the specific torsion angle as well as the axial strain are constant. A more accurate element can be obtained by interpolation the specific torsion angle by a linear or a quadratic function, which allows in addition the description of constrained warping for thin-walled beams.

The mass distribution needed for the derivation of the equations of motion can be described by an independent interpolation; as no spatial derivatives are needed, a lower order of accuracy can be used. The existing description [4] is still satisfactory for the basic planar and spatial beam elements.

*Corresponding author. Email: J.P.Meijaard@olton.nl

ILLUSTRATIVE EXAMPLES

Some example systems that have been analysed before are used to illustrate the performance of the presented beam elements. A planar cantilever beam with a transverse tip load undergoing large deflections is used as a first example. For the static deflection, a quartic rate of convergence is obtained, which contrasts with the original formulation of the beam element, which has a quadratic rate of convergence [5]. Even a higher rate of convergence is obtained if a higher order interpolation of the strains is used.

As a second example, a spatial curved beam bent in a circular arc of 45 degrees, clamped at one end and loaded by a tip force perpendicular to its plane, is considered. It is shown that the initial shape of the beam can be described exactly in a straightforward manner. In this case, the rate of convergence is quadratic, as for the original beam element, but the error constant is smaller. The order of convergence can be increased to quartic by choosing a linearly varying specific torsion angle. In all cases, fewer elements are needed to obtain an accurate solution.

As a dynamic example, a planar falling flexible beam is simulated. The flexural rigidity of the beam can be made very small and large deflections of the beam may occur, especially near the tip of the beam. The simulation does not break down for this case, as does a simulation with the original beam element, although the solution may become inaccurate near the tip of the beam.

CONCLUSIONS

The proposed modification of the definition of generalized strains for modelling multibody dynamic systems is shown to be feasible and to lead to a versatility that can be used to obtain sufficiently accurate solutions with fewer elements. This advantage countervails the disadvantage of a more complicated formulation.

References

[1] van der Werff K.: Kinematic and Dynamic Analysis of Mechanisms, a Finite Element Approach. PhD Thesis, Delft University Press, Delft, 1977.

[2] van der Werff K., Jonker J.B.: Dynamics of Flexible Mechanisms. In Haug E.J. (ed.): Computer Aided Analysis and Optimization of Mechanical System Dynamics. Berlin: Springer-Verlag, 381-400, 1984.

[3] Boer S.E., Aarts R.G.K.M., Meijaard J.P., Brouwer D.M. Jonker J.B.: A Nonlinear Two-Node Superelement With Deformable-Interface Surfaces for Use in Flexible Multibody Systems. Multibody Syst Dyn 34:53-79, 2015.

[4] Meijaard J.P.: Validation of Flexible Beam Elements in Dynamics Programs. Nonlinear Dyn 9:21-36, 1996.

[5] Jonker J.B., Meijaard J.P.: A Geometrically Non-Linear Formulation of a Three-Dimensional Beam Element for Solving Large Deflection Multibody System Problems. Int J Non-Linear Mech 53:63-74, 2013.

ANALYSIS OF HETEROGENEOUS CONNECTED VEHICLES VIA MODAL PERTURBATION METHOD

Gábor Orosz *[1] and Sergei S. Avedisov[1]

[1]*Department of Mechanical Engineering, University of Michigan, Ann Arbor, MI, USA*

Summary The dynamics of connected vehicle networks with long-range connections are investigated. The stability of uniform traffic flow is examined using a modal perturbation analysis that is tailored for high dimensional systems with near-symmetric network structure. The modes of the network are approximated about the modes of the corresponding symmetric network. This approach allows one to obtain modal dynamics and assess the impacts of long range communication on the stability of traffic flow of connected vehicle systems.

INTRODUCTION

Using wireless vehicle to vehicle (V2V) communication, connected vehicles may act upon information obtained from multiple other vehicles ahead, including those beyond line of sight. The connected cruise control (CCC) algorithm considered here not only implements information from the vehicle directly ahead [2], but also uses relative velocity with respect to vehicles located further downstream. This can significantly increase highway lane capacity compared to human driven traffic, where each vehicle only uses information from its immediate predecessor [1]. In early implementation of connected vehicle systems such CCC vehicles will be mixed with human-driven vehicles. Thus, the applied control strategy shall have a high level of modularity and shall exploit all available V2V information from transmitting vehicles ahead. To be able to evalueate the performance of such networks requires a method that can account for heterogeneity over the network without being computationally demanding. Here we use perturbation theory to incorporate long-range connections and decompose the network dynamics into oscillatory modes. Then we analyze the stability of each mode, where dynamics are described by a small number of equations. This allows us to quantify the benefits and drawbacks of ad-hoc wireless communication on the traffic flow.

NETWORK-BASED MODAL PERTURBATION ANALYSIS

We consider N vehicles traveling on a single-lane ring road, so that the i-th car follows the $i+1$-st car and the position of its front bumper is denoted by s_i while its velocity is v_i. The motion of the i-th vehicle is described by

$$\begin{aligned} \dot{s}_i &= v_i, \\ \dot{v}_i &= \alpha \prod\!\!\!\!\!\!\diagup \big(s_{i+1} \diagup\!\!\!\!\!\!\diagup s_i \diagup\!\!\!\!\!\!\diagup \ell\big) \diagup\!\!\!\!\!\!\diagup v_i\big) + \beta \left(v_{i+1} \diagup\!\!\!\!\!\!\diagup v_i\right) + \sum_{\sigma=2}^{\sigma_{\max}} \beta_{i\sigma} (v_{i+\sigma} \diagup\!\!\!\!\!\!\diagup v_i), \end{aligned} \tag{1}$$

where α and β are the control gains for the headway $h_i = s_{i+1} \diagup\!\!\!\!\!\!\diagup s_i \diagup\!\!\!\!\!\!\diagup \ell$ and relative velocity $v_{i+1} \diagup\!\!\!\!\!\!\diagup v_i$, and $V(h)$ is the optimal velocity function which gives the desired velocity for each vehicle as a function of headway [2]. The relative velocity feedback using the velocity of vehicle $i+\sigma$ has gain $\beta_{i\sigma} \neq 0$ if vehicle $i+\sigma$ transmits its information to vehicle i. The uniform flow pseudo-equilibrium is given by $s_i = v^* t + s_i^0$ such that $s_{i+1}^0 \diagup\!\!\!\!\!\!\diagup s_i^0 = h_i \equiv h^*$ and $v_i \equiv v^* = V(h^*)$ for $i = 1,\ldots,N$. Linearizing the dynamics of the resulting connected vehicle network in the vicinity of uniform flow we obtain

$$\dot{\hat{\mathbf{y}}} = \Big(\hat{\mathbf{J}}_0 + \sum_{i_1=1}^{N} \sum_{\sigma_1=0}^{\sigma_{\max}} \hat{\mathbf{J}}_{\mathrm{p}}(i,\sigma)\beta_{i\sigma}\Big)\hat{\mathbf{y}}, \tag{2}$$

where $\hat{\mathbf{y}} = [\mathbf{y}_1^{\mathrm{T}},\ldots,\mathbf{y}_N^{\mathrm{T}}]$ with $\mathbf{y}_i = [\widetilde{s_i}, \widetilde{v_i}]^{\mathrm{T}}$ represent the deviations about the uniform flow. The matrix $\hat{\mathbf{J}}_0$ contains the terms arising from the nearest-neighbor headway and relative velocity feedback, whereas the matrices $\hat{\mathbf{J}}_{\mathrm{p}}(i_1,\sigma_1)$ represent the long-range communication.

When no long-range links are present ($\beta_{i\sigma} = 0$ for all i and σ), the block-circulant structure of $\hat{\mathbf{J}}_0$ allows us to perform a modal coordinate transformation $\hat{\mathbf{y}} = \hat{\mathbf{T}}_0 \hat{\mathbf{z}}$, where the matrix $\hat{\mathbf{T}}_0$ represents a discrete Fourier transformation [3]. In the new modal coordinates $\hat{\mathbf{z}} = [\mathbf{z}_1^{\mathrm{T}},\ldots,\mathbf{z}_N^{\mathrm{T}}]^{\mathrm{T}}$ the dynamics of the system are given by $\dot{\hat{\mathbf{z}}} = \hat{\mathbf{D}}_0 \hat{\mathbf{z}}$, where $\hat{\mathbf{D}}_0$ is block diagonal, meaning that the dynamics of the modes are decoupled, i.e., $\dot{\hat{\mathbf{z}}}_k = [\hat{\mathbf{D}}_0]_k \hat{\mathbf{z}}_k$ for $k = 1,\ldots,N$. These modal coordinates describe traveling waves along the road, and the stability of all modes guarantees the stability of the uniform flow.

*Corresponding author. Email: orosz@umich.edu

To determine the effects of the long-range links, we approximate the modal dynamics of the system using Taylor expansions around the symmetric network with respect to $\beta_{i\sigma}$:

$$[\hat{\mathbf{D}}]_k = [\hat{\mathbf{D}}_0]_k + \sum_{i_1=1}^{N}\sum_{\sigma_1=2}^{\sigma_{\max}} [\hat{\mathbf{D}}_1^{(1)}]_k \beta_{i_1\sigma_1} + \frac{1}{2}\sum_{i_1,i_2=1}^{N}\sum_{\sigma_1,\sigma_2=2}^{\sigma_{\max}} [\hat{\mathbf{D}}_2^{(1,2)}]_k \beta_{i_1\sigma_1}\beta_{i_2\sigma_2} + \frac{1}{6}\sum_{i_1,i_2,i_3=1}^{N}\sum_{\sigma_1,\sigma_2,\sigma_3=2}^{\sigma_{\max}} [\hat{\mathbf{D}}_3^{(1,2,3)}]_k \beta_{i_1\sigma_1}\beta_{i_2\sigma_2}\beta_{i_3\sigma_3} + \dots \tag{3}$$

where $[\hat{\mathbf{D}}]_k$ represents the dynamics of mode k. To perform this expansion we must determine a transformation matrix $\hat{\mathbf{T}}$ as an expansion about $\hat{\mathbf{T}}_0$, that block diagonalizes $\hat{\mathbf{J}}$ to some order in $\beta_{i\sigma}$. The expansion can be performed up to arbitrary order and the circulant structure of $\hat{\mathbf{J}}_0$ allows one to reduce the complexity of equations for arbitrarily large numbers of vehicles and arbitrary communication structure. The obtained modal approximations (3) can then be used to characterize the effects of the long-range links on the stability of the uniform flow.

RESULTS

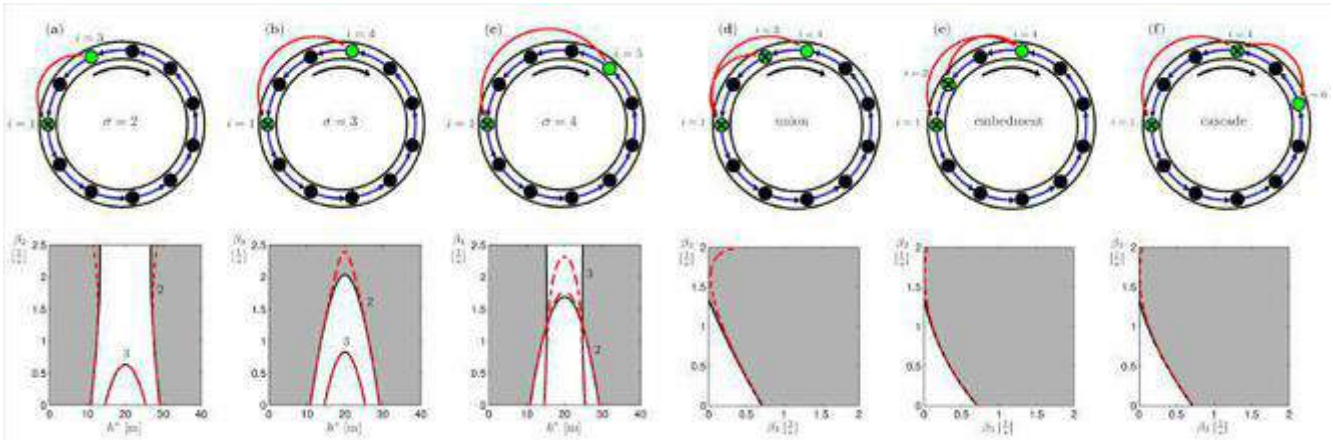

Figure 1: (a-c) Top: Connected vehicle system with $N = 11$ and V2V links of length $\sigma = 2,3,4$. Bottom: Stability charts in the (h^*, β_σ)-plane with $\alpha = 1$ and $\beta = 0.3$. (d-f) Top: Connected vehicle system with $N = 11$ and V2V links of length $\sigma = 2$ and $\sigma = 3$ in union, embedment, and cascade configurations. Bottom: Stability charts in the (β_3, β_2)-plane for $h^* = 20$, $\alpha = 1$, $\beta = 0.6$. Note, that we used the simplified notation $\beta_{i\sigma} = \beta_\sigma$. Black solid curves are stability boundaries of modes 2 and 3, red dashed curves are boundaries obtained using (3) expanded up to third order in $\beta_{i\sigma}$. In the gray shaded region the uniform flow is stable, in the white region the uniform flow is unstable.

Using the developed methodology we first examine the effect of adding a long-range communication link of given length. Figure 1 (a-c) shows stability charts for an 11-car network with extra links of lengths 2, 3, and 4. Indeed, the stability improves with increasing the corresponding β_σ. Longer links are more effective for stabilizing modes with lower mode numbers, while shorter links are more effective for stabilizing modes with higher mode numbers.

The modal perturbation approach can also be used to examine the effects of multiple V2V links. Figure 1(d-f) shows stability charts for 3 different configurations of an 11-car system with one V2V link of length 2 and one V2V link of length 3. The stability boundaries in the three cases are slightly different, namely for the embedment and cascade configurations the boundaries are convex, meaning that combining the V2V links in these configurations is beneficial for stability.

References

[1] Shladover S., Su D., Lu X.: Impacts of cooperative adaptive cruise control on freeway traffic flow. Transportation Research Board: 2324, 63-70, 2012.

[2] Avedisov S.S., Orosz G.: Nonlinear network modes in cyclic systems with applications to connected vehicles. Journal of Nonlinear Science: 25(4), 1015-1049, 2015.

[3] Olson B.J., Shaw S.W., Shi C., Pierre C., Parker R.G.: Circulant matrices and their application to vibration analysis. Applied Mechanics Reviews: 66(4), 040803, 2014.

FROM IUTAM SYMPOSIA TO THE INTERNATIONAL ASSOCIATION OF VEHICLE SYSTEM DYNAMICS

Werner Schiehlen
Institute of Engineering and Computational Mechanics, University of Stuttgart, Stuttgart, Germany

Summary The Union is engaged in the scientific work in all branches of theoretical and applied mechanics, one of them is vehicle dynamics. International organizations occupied in closely related fields are admitted by IUTAM as affiliated organizations. In this paper it is shown how IUTAM served as protagonist for IAVSD to be established as a worldwide association. Road vehicle suspensions, e.g., are a topic of general interest to IUTAM and of high priority to IAVSD.

EARLY DEVELOPMENTS

The First International Conference on Vehicle Mechanics was held May 16 – 19, 1968 at Wayne State University, Detroit, Michigan, USA, under the chairmanship of Herbert K. Sachs who served as editor of the Proceedings [1], too. The 2nd International Conference on Vehicle Mechanics took place September 6 – 9, 1971 at Paris VI University, France, followed by the 3rd meeting renamed as International Conference on Vehicle System Dynamics (VSD), August 12 – 15, 1974 at Virginia Polytechnic Institute and State Univerisity, Blacksburg, USA. The Proceedings [2] and [3] were also published by Swets & Zeitlinger, Amsterdam, The Netherlands. In addition, due to the great importance of the topic a journal [4] was established.

IUTAM SYMPOSIA

Encouraged by IUTAM President Warner Koiter in 1972 the Division for Mechanics of the Dutch Royal Institute of Engineeers applied for the sponsorship of a IUTAM Symposium on Dynamics of Vehicles on Roads and Railway Tracks. At the General Assembly of IUTAM held 1972 in Moscow, Russia, it was decided to accept the Dutch application and to hold 1975 the IUTAM Symposium at Delft University of Technology in Delft, The Netherlands under the chairmanship of Hans Pacejka. This 1st IUTAM Symposium was also announced as the 4th Conference on Vehicle System Dynamics. The Symposium dealt with the dynamics of vehicle-road and vehicle-rail systems. The scope of the subjects has been restricted mainly to those problems where the contact forces, acting between vehicle and road or guiding system, are of primary importance. Attention was given to the presentation of new methods and techniques which are useful in tackling vehide dynamics problems like lateral dynamics, stability and control analysis, vehicle ride on rigid and elastic supports [5].

In 1977 the 5th VSD – 2nd IUTAM Symposium on Dynamics of Vehicles on Roads and Railway Tracks was held September 19 – 23, 1977 in Vienna, Austria under the chairmanship of Alfred Slibar and Helmut Springer [6]. Due to the high competition for IUTAM Symposia sponsorship, the Union had decided to decline further applications on a regular basis from the vehicle dynamics community. Therefore, an International Association for Vehicle System Dynamics (IAVSD) has been formed by decision of the Scientific Committee of the 5th VSD – 2nd IUTAM Symposium in Vienna, Austria on September 20, 1977. On September 22, 1977 the first Board of the Association was formed, consisting of five officers and six trustees.

The main objectives of the Association include the promotion of the development of the Science of Vehicle Dynamics, a discipline that is based upon the theory of motion of ground based vehicle systems, and to encourage engineering applications of this field of science. These objectives fit so perfectly to objectives of IUTAM that IAVSD was immediately admitted as Affiliated Organization [7].

The objectives of IAVSD are based on theoretical mechanics, and they are characterized by the common application to road and rail vehicles. This is visualized in its logo.



The rolling motion of ground vehicles requires sophisticated method from the theory of contact mechanics, and the fundamental principles of steel wheels on steel tracks are similar to those of rubber wheels on concrete tracks. These are the challenges of vehicle system dynamics and the mystery of its success.

Corresponding author. Email: schiehlen@itm.uni-stuttgart.de

IAVSD SYMPOSIA

Starting with the 6th IAVSD Symposium held in Berlin, Germany, September 3 – 7, 1979, the series of biennial symposia at selected locations around the world has been set up. The accompanying symposium proceedings have contributed greatly to a better understanding of problems related to ground vehicle system dynamics. The latest 24th IAVSD Symposium took place in Graz, Austria, August 17 – 24, 2015 and was again a great success. The forthcoming 25th IAVSD Symposium will be held in Rockhampton, Australia. Then, IAVSD has visited all continents of the world.

A big event for IAVSD was the selection of its proposal for a Minisymposium on the topic "Vehicle System Dynamics" by the IUTAM Congress Committee to be included in the 20th International Congress of Theoretical and Applied Mechanics (ICTAM200) held in Chicago, Illinois, USA, August 28 to September1, 2000. The Minisymposium comprised one sectional lecture and four introductory lectures all published in the ICTAM 2000 Proceedings [8]:

Adaptive Nonlinear and Learning Techniques for Control of Vehicle Ride Dynamics by T.J. Gordon,
Software Tools: From Multibody System Analysis to Vehicle System Dynamics
by W. Kortuem, W. Schiehlen, M. Arnold,
Rail Vehicle Dynamics for the 21st Century by R.J. Anderson, J.A. Elkins, B.V. Birkle,
Fundamentals of the Lateral Dynamics of Road Vehicles by R.S. Sharp,
A Mechatronic Approach to Advanced Vehicle Control Design by M. Abe, K. Hedrick.

Additonal selected papers of the Minisymposium were published [9], too.

EXAMPLE ROAD VEHICLE SUSPENSIONS

Vehicle ride dynamics is for IUTAM and IAVSD of scientific interest due to the complexity of modelling and the advanced solution methodologies. An early paper [10] from the 2nd IUTAM Symposium deals with the computational modelling of a semi-trailing arm suspension using the multibody dynamics software and sinusoidal road roughness resulting in frequency responses for ride comfort and ride safety. A recent paper [11] from the 24th IAVSD Symposium considers new premium cars with controllable adaptive shock absorbers allowing the driver to change the characteristics of the car during driving. Electronically adjustable dampers are available, e.g., from ThyssenKrupp Bilstein and applied by BMW as electronic damper control (EDC). Then, there remain three uncertain parameters, damping *dA*, tire stiffness and body mass, and fuzzy arithmetic techniques are required as an advanced solution methodology like the software package FAMOUS. The result is shown in the conflict diagram of standard deviations for comfort over safety due to random road roughness.

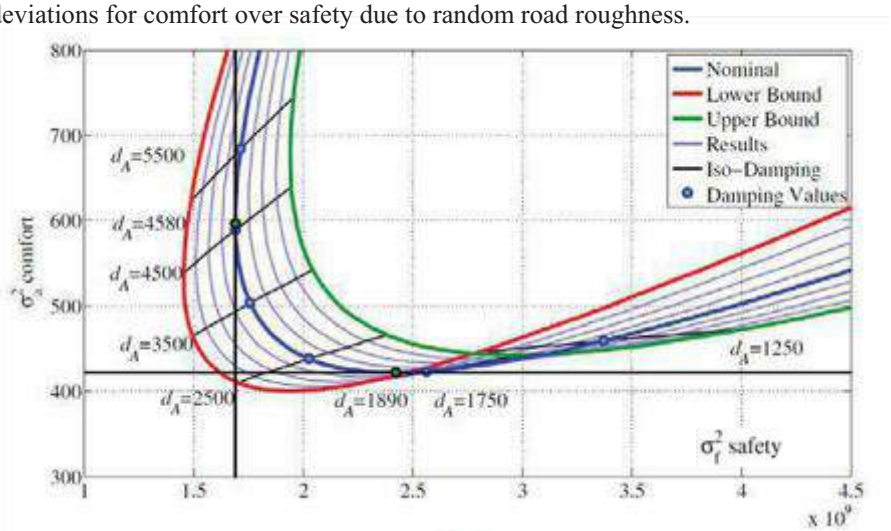

References

[1] Sachs H.K.: Proceedings of the First International Conference on Vehicle Mechanics. Amsterdam, The Netherlands 1969.

[2] Rapin P., Sachs H.K.: Proceedings of the Second International Conference on Vehicle Mechanics. Amsterdam, The Netherlands 1973.

[3] Sachs H.K.: Proceedings of the Third International Conference on Vehicle Mechanics. Amsterdam, The Netherlands 1975.

[4] *Vehicle System Dynamics*, www.tandfonline.com/vsd

[5] Pacjeka H.: The Dynamics of Vehicles on Roads and Railway Tracks. Proceedings of IUTAM Symposium Delft 1975. Amsterdam 1976.

[6] Slibar A., Springer, H.: The Dynamics of Vehicles. Proceedings of IUTAM Symposium Vienna, Austria 1977. Amsterdam 1978.

[7] www.iavsd.org

[8] Aref H., Phillips J.W.: Mechanics for a New Millenium. Proceedings of the 20th ICTAM 2000. Dordrecht, The Netherlands 2001.

[9] Lugner P., Hedrick, K.: ICTAM 2000. Lisse, The Netherlands, 2001.

[10] Schiehlen W.: Dynamical Analysis of Suspension Systems. In [6]: 40-48, 1978.

[11] Schiehlen, W.; Hanss, M.; Iroz, I.: Robust Design of Road Vehicle Suspensions using Fuzzy Logic. In Bernasch, J.; Rosenberger, M. (Eds.): Proceedings 24th IAVSD Symposium, paper 3.3, pdf, 10 pp. Graz: Virtual Vehicle, 2015.

A SERVO-CONSTRAINT FRAMEWORK FOR CONTROL OF VARIOUS TYPES OF UNDERACTUATED MULTIBODY SYSTEMS

Robert Seifried*[1], Merlin Morlock[1], and Svenja Otto[1]
[1]*Institute of Mechanics and Ocean Engineering, Hamburg University of Technology, Germany*

Summary The control of underactuated multibody systems is often a challenging task since less control inputs than degrees of freedom are available. A systematic approach for feedforward control design of underactuated multibody systems is the use of servo-constraints for model inversion. For various systems the dynamics of the obtained inverse model can be very different. Therefore different numerical solution approaches are required. The obtained feedforward control can then be combined with feedback control. The presented framework is verified experimentally using two underactuated multibody systems with very different structural properties, namely an overhead crane and a flexible parallel manipulator. Questions concerning practical implementation and real-time capability are addressed.

INTRODUCTION

Underactuated multibody systems have less control inputs than generalized coordinates. Typical examples of underactuated multibody systems are manipulators with passive joints, cranes, cable robots, and flexible multibody systems. One challenging control task for multibody systems is end-effector trajectory tracking. Thereby the system output is an end-effector point which should follow a trajectory predefined in time and space, e.g. the tool center point of a manipulator or the load of a crane. In order to obtain a good performance in end-effector trajectory tracking a two design-degree of freedom control structure is often used, combining feedforward control with additional feedback control action. Both parts can be designed largely independent from each other. In trajectory tracking of multibody systems the major control action is due to the feedforward control, while the feedback control has only to account for small disturbances and uncertainties. The feedforward control is given by the inverse model of the multibody system. Due to the underactuation, classical approaches known from fully actuated systems, such as inverse kinematics and inverse dynamics, cannot be applied here. A very appealing and efficient feedforward control design approach for underactuated multibody systems is the use of so-called servo-constraints, which can be seen as generalization of classical geometric constraints [1, 2]. In contrast to methods from nonlinear control theory [3], this does not require burdensome symbolic computations and allows a systematic treatment of different systems.

SERVO-CONSTRAINTS FOR MODEL INVERSION

The basic idea of servo-constraints is the enforcement of output trajectory tracking by introducing constraint equations, yielding a set of differential-algebraic equations (DAEs),

$$\boldsymbol{M}(\boldsymbol{q})\ddot{\boldsymbol{q}} + \boldsymbol{f}(\boldsymbol{q},\dot{\boldsymbol{q}}) = \boldsymbol{C}^T(\boldsymbol{q})\boldsymbol{\lambda} + \boldsymbol{B}(\boldsymbol{q})\boldsymbol{u}, \tag{1}$$

$$\boldsymbol{c}_g(\boldsymbol{q}) = \boldsymbol{0}, \tag{2}$$

$$\boldsymbol{c}(\boldsymbol{q}) = \boldsymbol{h}(\boldsymbol{q}) \nearrow \boldsymbol{y}_d = \boldsymbol{0}. \tag{3}$$

Thereby, Eq. (1) represents the equation of motion of a multibody system, with generalized coordinates $\boldsymbol{q}$, mass matrix $\boldsymbol{M}$, generalized forces $\boldsymbol{f}$, input matrix $\boldsymbol{B}$ and control inputs $\boldsymbol{u}$. Equation (2) arises if additional geometric constraint are present, e.g. due to kinematics loops. Then, in the equation of motion (1) the Lagrangian multipliers $\boldsymbol{\lambda}$ are introduced, with $\boldsymbol{C} = \frac{\partial \boldsymbol{c}_g(\boldsymbol{q})}{\partial \boldsymbol{q}}$. These are the reaction forces due to the geometric constraint given by $\boldsymbol{c}_g$. This case also occurs, if the system's kinematics are described using cartesian coordinates instead of generalized coordinates. Finally, Eq. (3) represents the servo-constraints, which should be enforced by the control. Thereby $\boldsymbol{h}(\boldsymbol{q})$ is the system output and $\boldsymbol{y}_d$ is the desired output trajectory. Equations (1)-(2) represent the forward dynamics. Adding Eq. (3) yields the inverse model. The numerical solution of this inverse model provides the control inputs $\boldsymbol{u}_d$ which are necessary to reproduce the desired output trajectory $\boldsymbol{y}_d$. In addition, the inverse model provides the trajectories of all generalized coordinates $\boldsymbol{q}_d$, which are necessary for feedback control design.

Comparing the forward dynamics model with geometric constraints (given by Eq. (1)-(2)) with the inverse model (given by Eq. (1)-(3)) shows firstly some structural similarities. In both cases a constraint equation on position level is introduced. However, in the case of geometric constraints, the constraints are enforced by the Lagrangian multipliers $\boldsymbol{\lambda}$ which are collocated with the geometric constraint. Then, the matrix $\boldsymbol{P} = \boldsymbol{C}\boldsymbol{M}^{-1}\boldsymbol{C}^T$ is non-singular and thus the resulting DAE of the forward dynamics has differentiation index 3. In contrast, in the case of servo-constraints, the constraints are enforced by the control inputs $\boldsymbol{u}$, which are mostly not collocated with the servo-constraints. For systems in minmal coordinates it is $\boldsymbol{P} = \boldsymbol{H}\boldsymbol{M}^{-1}\boldsymbol{B}$ with $\boldsymbol{H} = \frac{\partial \boldsymbol{h}(\boldsymbol{q})}{\partial \boldsymbol{q}}$, which corresponds to the decoupling matrix in nonlinear control theory [2]. If additional

*Corresponding author. Email: robert.seifried@tuhh.de

constraint equations $\boldsymbol{c}_g$ are present, they can be treated as special case of servo-constraints. Due to the non-collocation, servo-constraint problems can show much more complex properties, which have to be understood in order to obtain a meaningful numerical solution for the inverse model. Different cases can occur for underactuated multibody systems:

Case 1: The matrix $\boldsymbol{P}$ is non-singular, and therefore the DAE has also differentiation index 3. In this case the inverse model is also a dynamic model. In reference to nonlinear control theory this dynamics is called internal dynamics [3]. Due to the non-collocation the internal dynamics might be stable or unstable. In the case of stable internal dynamics, the inverse model can be computed by forward time integration of the DAE (1)-(3). Examples of such systems are flexible manipulators, where the system output is not the end-effector point but the joint angles collocated with the drives.

Case 2: As in case 1 the matrix $\boldsymbol{P}$ is non-singular, however the internal dynamics is unstable. Then, forward time integration of the DAE (1)-(3) would yield unbounded control inputs $\boldsymbol{u}_d$, and is therefore not feasible. Alternatively one might compute a bounded solution for the DAE (1)-(3) from a two-sided boundary value problem [2]. The boundary values are the unstable and stable manifold of the internal dynamics at starting-point and end-point, respectively. While the obtained control input remains bounded, it is non-causal, i.e. some small control action before the start of the trajectory tracking is necessary. Examples of such systems are flexible manipulators, where the system output is the end-effector point.

Case 3: The matrix $\boldsymbol{P}$ is singular, and it can be shown that then the DAE has index larger 3. The remaining internal dynamics might be again stable or unstable. Examples are manipulators with so-called joint elasticity with added damping, i.e. elasticity and damping in the drive train between the motors and the manipulators' links.

Case 4: Differentially flat systems can be inverted purely by algebraic manipulations and using a finite number of differentiations of the desired output trajectory $\boldsymbol{y}_d$. In this case the matrix $\boldsymbol{P}$ is singular, i.e. the DAE has again index larger 3. However, the inverse model does not contain any dynamics. Therefore, the system (1)-(3) can be solved efficiently with very simple implicit integrators, such as Euler-backwards integration. Examples of such differentially flat systems are cranes.

APPLICATION EXAMPLES AND EXPERIMENTAL VALIDATION

Two underactuated multibody systems are considered to demonstrate the control design framework using servo-constraints for different cases. The first system is a parallel manipulator with flexible links, see Fig. 1 left. The manipulator consists of two carts moving on linear axes which are actuated by linear servo-drives [4]. On top of each cart one elastic link is mounted with a revolute joint which are connected to each other via a third revolute joint in the middle of the longer arm. This is a system which represents either case 1 or 2, where internal dynamics remains in the inverse model. If the tip of the longer arm is used as system output the internal dynamics is unstable, representing case 2. If a slightly different system output is used, the internal dynamics can become stable and case 1 occurs. The second example is an overhead crane such as used for containers, see Fig. 1 right. The system consists of a crane cart which is actuated along a linear axis. On this cart 4 motors are mounted, each of them actuating the length of one crane cable. If the load is the system output, the underactuated system represents case 4. The system is differentially flat and the inverse model does not contain any dynamics. Experimental results for both systems are presented, showing the efficiency and accuracy of the presented framework. Also aspects of implantation, real time capability of the inverse model, and possible additional feedback control are discussed.

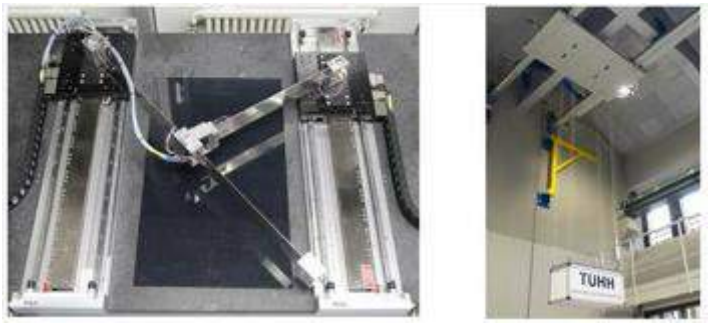

Figure 1: Considered underactuated multibody systems: parallel flexible manipulator (left) and overhead crane (right).

References

[1] Blajer W., Kołodziejczyk K.: A Geometric Approach to Solving Problems of Control Constrains: Theory and a DAE Framework. Multibody System Dynamics, 11(4): 343-364, 2004.

[2] Seifried R.: Dynamics of Underactuated Multibody Systems. Springer, Berlin, 2014.

[3] Isidori A.: Nonlinear Control Systems. Springer, London, 1995.

[4] Burkhardt M., Seifried R., Eberhard P.: Experimental Studies of Control Concepts for a Parallel Manipulator with Flexible Links. Journal of Mechanical Science and Technology, 29(7):2685-2691, 2015.

THE DISCRETE ADJOINT METHOD IN MULTIBODY DYNAMICS

Wolfgang Steiner*[1], Karin Nachbagauer[1], and Thomas Lauss[1]

[1] *Faculty of Engineering and Environmental Sciences, University of Applied Sciences Upper Austria, Wels, Austria*

Summary A problem arising frequently in multibody dynamics is to determine unknown input signals such that an objective function is minimized. The adjoint method is the most efficient way to compute the gradient of any objective function by solving a system of "adjoint" differential algebraic equations backwards in time. The key idea of this method can also be applied directly to the time-discrete multibody system resulting in a set of adjoint difference equations, which yield the gradient of the discretized objective function. In this paper we present the discrete adjoint equations associated to the equations of motion of a multibody system, which are discretized by any implicit one-step integration method and describe how the obtained gradients can be transformed for varying time discretizations.

We consider multibody systems with redundant generalized coordinates $\mathbf{q} \in \mathbb{R}^{N_q}$ in the descriptor form

$$\mathbf{M}(\mathbf{q})\ddot{\mathbf{q}} + \mathbf{C}_\mathbf{q}^\mathsf{T}\boldsymbol{\lambda} = \mathbf{Q}(\mathbf{q}, \dot{\mathbf{q}}, \mathbf{u}, t), \quad \mathbf{C}(\mathbf{q}) = \mathbf{0} \tag{1}$$

where $\mathbf{M}$ denotes the mass matrix, $\mathbf{C}_\mathbf{q} = \partial\mathbf{C}/\partial\mathbf{q}$ the constraint Jacobian, $\boldsymbol{\lambda} \in \mathbb{R}^{N_\lambda}$ the vector of Lagrange multipliers and $\mathbf{Q}$ the vector of generalized forces. Moreover, $\mathbf{u} \in \mathbb{R}^{N_u}$ is a vector of time dependent input signals which should be determined such that an objective function of the form $J(\mathbf{u}) = \int_{t_0}^{t_1} \phi(\mathbf{q}, \dot{\mathbf{q}}, t)\, dt$ is minimized. The adjoint method serves as the most efficient way to compute the gradient of J, see [3] or [1]. It determines its first variation from the solution of linear adjoint equations with time variant coefficients resulting from the solution of Eqs. (1). There are two strategies for this purpose, the equations of motion of the multibody system and adjoint equations may either be separately discretized from their representations as differential-algebraic equations, or, alternatively, the equations of motion of the multibody system may be discretized first, while the discrete adjoint equations are derived directly from the discrete multibody system equations.

DISCRETE ADJOINT GRADIENT COMPUTATION

To solve the system equations (1) a proper numerical integration scheme must be applied, which computes positions, velocities, accelerations and the Lagrange multipliers at a time instant t_i. Denoting the state vector $\mathbf{x}^\mathsf{T} = (\mathbf{q}, \dot{\mathbf{q}}, \ddot{\mathbf{q}}, \boldsymbol{\lambda})$ and the inputs $\mathbf{u}$ at time t_i as $\mathbf{x}_i$ and $\mathbf{u}_i$, an implicit one-step method and an initial condition have the general form

$$\mathbf{F}(\mathbf{x}_i, \mathbf{x}_{i-1}, \mathbf{u}_i, \mathbf{u}_{i-1}, t_i, t_{i-1}) = \mathbf{0}, \ i = 1 \dots n \quad \text{and} \quad \mathbf{G}(\mathbf{x}_0, \mathbf{u}_0, t_0) = \mathbf{0} \tag{2}$$

For example, the HHT-algorithm [2] is given by the function

$$\mathbf{F}(\mathbf{x}_i, \mathbf{x}_{i-1}, \mathbf{u}_i, \mathbf{u}_{i-1}, t_i, t_{i-1}) = \begin{pmatrix} (\mathbf{M}\ddot{\mathbf{q}})_i + (1+\alpha)\left(\mathbf{C}_\mathbf{q}^\mathsf{T}\boldsymbol{\lambda} - \mathbf{Q}\right)_i - \alpha\left(\mathbf{C}_\mathbf{q}^\mathsf{T}\boldsymbol{\lambda} - \mathbf{Q}\right)_{i-1} \\ \mathbf{q}_i - \mathbf{q}_{i-1} - h\dot{\mathbf{q}}_{i-1} - \frac{1}{2}h^2[(1-2\beta)\ddot{\mathbf{q}}_{i-1} + 2\beta\ddot{\mathbf{q}}_i] \\ \dot{\mathbf{q}}_i - \dot{\mathbf{q}}_{i-1} - h[(1-\gamma)\ddot{\mathbf{q}}_{i-1} + \gamma\ddot{\mathbf{q}}_i] \\ \mathbf{C}(\mathbf{q}_i) \end{pmatrix} \tag{3}$$

where $h = t_i - t_{i-1}$ is the timestep size and α, β, γ are parameters. For a given control sequence $\mathbf{u}_0 \dots \mathbf{u}_n$ Eq. (2) defines the sequence of state vectors $\mathbf{x}_0 \dots \mathbf{x}_n$ at given time steps $t_0 \dots t_n$. (The function $\mathbf{G}$ defines initial postions, velocities, accelerations and Lagrange multipliers at t_0.) The goal is to determine the gradient of the discretized objective function

$$\hat{J} = \sum_{i=0}^{n} \eta_i \phi(\mathbf{x}_i, t_i) = \sum_{i=0}^{n} \eta_i \phi(\mathbf{x}_i, t_i) + \mathbf{y}_0^\mathsf{T}\mathbf{G}(\mathbf{x}_0, \mathbf{u}_0, t_0) + \sum_{i=1}^{n} \mathbf{y}_i^\mathsf{T}\mathbf{F}(\mathbf{x}_i, \mathbf{x}_{i-1}, \mathbf{u}_i, \mathbf{u}_{i-1}, t_i, t_{i-1}) \tag{4}$$

with respect to $\mathbf{u}_i$. Here, η_i are proper weighting factors which are used to approximate an integral in the continous objective function. Moreover, we have also added the terms $\mathbf{y}_0^\mathsf{T}\mathbf{G}(\mathbf{x}_0, \mathbf{u}_0, t_0)$ and $\mathbf{y}_i^\mathsf{T}\mathbf{F}(\mathbf{x}_i, \mathbf{x}_{i-1}, \mathbf{u}_i, \mathbf{u}_{i-1}, t_i, t_{i-1})$ to $\hat{J}$, which are zero for any choice of the *adjoint state vectors* $\mathbf{y}_0 \dots \mathbf{y}_n$ because Eqs. (2) must hold. Consider now a control sequence $\mathbf{u}_0 \dots \mathbf{u}_n$ for which the states $\mathbf{x}_0 \dots \mathbf{x}_n$ have been computed by solving Eqs. (2) and $\hat{J}$ has been evaluated by inserting into Eq. (4). We ask, what happens to $\hat{J}$ if the controls are slightly changed by $\delta\mathbf{u}_i$. For that purpose, we introduce the Jacobian matrices

$$\mathbf{A}_0 := \frac{\partial\mathbf{G}}{\partial\mathbf{x}_0}, \quad \mathbf{B}_0 := \frac{\partial\mathbf{G}}{\partial\mathbf{u}_0} \quad \text{and for } i = 1 \dots n\text{:} \quad \mathbf{A}_i := \frac{\partial\mathbf{F}}{\partial\mathbf{x}_i}, \quad \mathbf{A}'_i := \frac{\partial\mathbf{F}}{\partial\mathbf{x}_{i-1}}, \quad \mathbf{B}_i := \frac{\partial\mathbf{F}}{\partial\mathbf{u}_i}, \quad \mathbf{B}'_i := \frac{\partial\mathbf{F}}{\partial\mathbf{u}_{i-1}}$$

*Corresponding author. Email: wolfgang.steiner@fh-wels.at

Moreover, we set $\phi_{\mathbf{x},i} := \partial\phi/\partial\mathbf{x}_i$. With these notations the first variation of the objective function (4) is given by

$$\begin{aligned}\delta\hat{J} &= \sum_{i=0}^{n} \eta_i \phi_{\mathbf{x},i}^{\mathsf{T}}\,\delta\mathbf{x}_i + \mathbf{y}_0^{\mathsf{T}}\left(\mathbf{A}_0\,\delta\mathbf{x}_0 + \mathbf{B}_0\,\delta\mathbf{u}_0\right) + \sum_{i=1}^{n} \mathbf{y}_i^{\mathsf{T}}\left(\mathbf{A}_i\,\delta\mathbf{x}_i + \mathbf{A}'_i\,\delta\mathbf{x}_{i-1} + \mathbf{B}_i\,\delta\mathbf{u}_i + \mathbf{B}'_i\,\delta\mathbf{u}_{i-1}\right) \\ &= \sum_{i=0}^{n-1}\left\{\left(\eta_i\phi_{\mathbf{x},i}^{\mathsf{T}} + \mathbf{y}_i^{\mathsf{T}}\mathbf{A}_i + \mathbf{y}_{i+1}^{\mathsf{T}}\mathbf{A}'_{i+1}\right)\delta\mathbf{x}_i + \left(\mathbf{y}_i^{\mathsf{T}}\mathbf{B}_i + \mathbf{y}_{i+1}^{\mathsf{T}}\mathbf{B}'_{i+1}\right)\delta\mathbf{u}_i\right\} + \left(\eta_n\phi_{\mathbf{x},n}^{\mathsf{T}} + \mathbf{y}_n^{\mathsf{T}}\mathbf{A}_n\right)\delta\mathbf{x}_n + \mathbf{y}_n^{\mathsf{T}}\mathbf{B}_n\delta\mathbf{u}_n\end{aligned} \tag{5}$$

If we now define $\mathbf{y}_0 \ldots \mathbf{y}_n$ by the equations

$$\eta_i\phi_{\mathbf{x},i}^{\mathsf{T}} + \mathbf{y}_i^{\mathsf{T}}\mathbf{A}_i + \mathbf{y}_{i+1}^{\mathsf{T}}\mathbf{A}'_{i+1} = \mathbf{0},\ i = 0\ldots n \nearrow 1, \quad \text{and} \quad \eta_n\phi_{\mathbf{x},n}^{\mathsf{T}} + \mathbf{y}_n^{\mathsf{T}}\mathbf{A}_n = \mathbf{0} \tag{6}$$

the first variation of $\hat{J}$ reduces to $\delta\hat{J} = \sum_{i=0}^{n-1}\left(\mathbf{y}_i^{\mathsf{T}}\mathbf{B}_i + \mathbf{y}_{i+1}^{\mathsf{T}}\mathbf{B}'_{i+1}\right)\delta\mathbf{u}_i + \mathbf{y}_n^{\mathsf{T}}\mathbf{B}_n\delta\mathbf{u}_n$ since the terms with $\delta\mathbf{x}_i$ cancel out. Considering $\hat{J}$ ultimately as a function of $\mathbf{u}_0 \ldots \mathbf{u}_n$ this formula yields the gradients

$$\frac{\partial\hat{J}}{\partial\mathbf{u}_i} = \mathbf{B}_i^{\mathsf{T}}\mathbf{y}_i + \left(\mathbf{B}'_{i+1}\right)^{\mathsf{T}}\mathbf{y}_{i+1},\ i = 0\ldots n \nearrow 1, \quad \text{and} \quad \frac{\partial\hat{J}}{\partial\mathbf{u}_n} = \mathbf{B}_n^{\mathsf{T}}\mathbf{y}_n \tag{7}$$

For that purpose, the adjoint variables must be computed from Eqs. (6). Notice that theses equations are linear and can be solved recursively by starting with the last one to obtain $\mathbf{y}_n$ and then computing $\mathbf{y}_{n-1}, \mathbf{y}_{n-2}, \ldots \mathbf{y}_0$.

OPTIMIZATION AND VARYING DISCRETIZATIONS OF THE OBJECTIVE FUNCTION

The gradient given by Eq. (7) can be used to find a minimum of the objective function $\hat{J}(\mathbf{u}_0 \ldots \mathbf{u}_n)$. In the simplest case, one can update a guessed control sequence $\mathbf{u}_0 \ldots \mathbf{u}_n$ in the direction of the negative gradient by setting $\mathbf{u}_i \to \mathbf{u}_i \nearrow \kappa\partial\hat{J}/\partial\mathbf{u}_i$, where κ is a parameter which can be found, for example, by means of a line search method, such that $\hat{J}$ becomes as small as possible with the updated control sequence. By repeating this process we will approach a local minimum of $\hat{J}$ after a number of iterations. An alternative optimization strategy is to look for a solution of the equations $\partial\hat{J}/\partial\mathbf{u}_i = 0$. For example, the well-known BFGS-method [1] can be applied for that purpose, which estimates the Hessian matrix of $\hat{J}$ from the gradients of succesive iterations. However, in both cases one has to take care about the fact that the time discretization $t_0 \ldots t_n$ used for Eq. (2) may change during the optimization process, in particular, if the numerical error is controlled. Hence, we need a way how to associate the gradients for different discretizations of a continous objective function J. Let $\hat{J}(\mathbf{u}_0 \ldots \mathbf{u}_n)$ be a discretization of J, and let $\partial\hat{J}/\partial\mathbf{u}_i$ be its gradient computed with the discrete adjoint method. Moreover, suppose that $\hat{J}'(\mathbf{u}'_0 \ldots \mathbf{u}'_{n'})$ is a different discretization of J. Then the gradient $\partial\hat{J}'/\partial\mathbf{u}'_i$ can be determined as follows.

The first variation of a continous objective function $J(\mathbf{u}(t))$ is a linear functional with the form $\delta J = \int_{t_0}^{t_1} H_{\mathbf{u}}(t)\,\delta\mathbf{u}(t)\,dt$. Herein, $H_{\mathbf{u}}$ is the derivative of the Hamiltonian function with respect to the controls, which is associated to any optimal control problem, e. g. see [3]. Hence, δJ can be approximated by

$$\delta J \approx \sum_{i=1}^{n} \eta_i H_{\mathbf{u}}(t_i)\delta\mathbf{u}(t_i) \approx \sum_{i=1}^{n} \frac{\partial\hat{J}}{\partial\mathbf{u}_i}\delta\mathbf{u}_i \quad \text{and by} \quad \delta J \approx \sum_{i=1}^{n'} \eta'_i H_{\mathbf{u}}(t'_i)\delta\mathbf{u}(t'_i) \approx \sum_{i=1}^{n'} \frac{\partial\hat{J}'}{\partial\mathbf{u}'_i}\delta\mathbf{u}'_i \tag{8}$$

Since $\delta\mathbf{u}(t_i) = \delta\mathbf{u}_i$ and $\delta\mathbf{u}(t'_i) = \delta\mathbf{u}'_i$ we recognize that $\partial\hat{J}/\partial\mathbf{u}_i = \eta_i H_{\mathbf{u}}(t_i)$ and $\partial\hat{J}'/\partial\mathbf{u}'_i = \eta'_i H_{\mathbf{u}}(t'_i)$. Thus, the values of the continous function $H_{\mathbf{u}}(t)$ at $t_0, t_1, t_2, \ldots$ are given by $H_{\mathbf{u}}(t_i) = \eta_i^{-1}\partial\hat{J}/\partial\mathbf{u}_i$. They can be used to interpolate the values of $H_{\mathbf{u}}(t)$ at the time step t'_i and to compute $\partial\hat{J}'/\partial\mathbf{u}'_i = \eta'_i H_{\mathbf{u}}(t'_i)$.

CONCLUSIONS

We presented the discrete adjoint method for a general implicit one-step solver of the equations of motion of a multibody system in descriptor form. The are two advantages of this approach compared with the continous adjoint method: 1. No seperate solver is required for the continous adjoint equations. 2. Using the discrete adjoint method, e. g. in combination with the HHT-algorithm, the objective function may also depend on the accelerations. In the continous case, accelerations are not contained in the state vector, but have to be expressed by the equations of motion, which lead to very complex Jacobians.

References

[1] Nachbagauer K., Oberpeilsteiner S., Sherif K., Steiner W.: The use of the adjoint method for solving typical optimization problems in multibody dynamics. Journal of Computational and Nonlinear Dynamics, vol. 10, p. 061011, April 2015.

[2] Negrut D., Rampalli R., Ottarsson G., Sajdak A.: On an implementation of the Hilber-Hughes-Taylor method in the context of index 3 differential-algebraic equations of multibody dynamics. Journal of computational and nonlinear dynamics, vol. 2, no. 1, pp. 7385, 2007.

[3] Steiner W., Reichl S.: The Optimal Control Approach to Dynamical Inverse Problems. J. Dyn. Sys., Meas., Control, Volume 134, Issue 2, March 2012.

NONLINEAR DYNAMICS OF FLEXIBLE MULTIBODY SYSTEMS WITH UNCERTAIN INTERVAL PARAMETERS

Qiang Tian[a], Zhe Wang & Haiyan Hu
School of Aerospace Engineering, Beijing Institute of Technology, Beijing, China

Summary The dynamics of flexible multibody systems with interval parameters is initially studied. The flexible multibody systems with rigid and flexible bodies are described by using a unified mesh of the absolute nodal coordinate formulation (ANCF). A non-intrusive computation methodology is proposed to efficiently solve the governing Interval Differential Algebraic Equations (IDAEs). Firstly, the Interval Differential Algebraic Equations (IDAEs) are directly transformed into the nonlinear interval algebraic equations by using the generalized-alpha algorithm. Then, the Chebyshev surrogate models for these nonlinear interval algebraic equations are established by using the Chebyshev tensor product (CTP) sampling method and Chebyshev collocation method (CCM). To circumvent the interval explosion problem and maintain computation efficiency, the scanning method is used to determine the upper and lower bounds of the deducted surrogate models. Finally, two numerical examples are studied to check the efficiency and effectiveness of the proposed methodology.

INTRODUCTION

The multibody systems inevitably contain uncertain parameters, such as the uncertain material density, uncertain Young's modulus, uncertain geometrical parameters, and uncertain excitation amplitudes. For example, the dynamics of the multibody systems with joint clearance has been extensively studied by Flores et al. [1] and Tian et al. [2]. However, the clearance sizes for all their simulated models are deterministic parameters. In fact, due to wearing problems, manufacture and assembly errors these clearance sizes cannot be accurately measured. Therefore, the dynamic analysis of multibody systems without taking these uncertainties into account cannot accurately reveal these systems true dynamic behaviors.

The Monte Carlo simulation is one of the most widely used methods to study the uncertain problems. However, it is well known that the Monte Carlo simulation is very inefficient. The non-statistic methods are more efficient and have a broader scope of application. Sandu et al. [3] used the polynomial chaos (PC) methods to simulate a rigid planar single pendulum mathematically described by a set of Differential-Algebraic Equations (DAEs) with index-3. However, for the PC methods the probability density functions of all the system random parameters are required, which is very difficult to obtain. For practical multibody systems, it is usually easier to get the bounds of the uncertain parameters than to obtain the probability density functions of uncertain parameters. The interval method is one of the non-probabilistic methods and mainly used to study the problems with uncertain, but bounded parameters. However, there are very few studies focused the dynamics of flexible multibody systems with many uncertain interval parameters. The main reasons are the wrapping effect inherited from the interval operations [4] and inefficiency of the solution algorithms for Interval DAEs (IDAEs). Based on the work by Wu et al. [5], the authors [6] proposed a Chebyshev tensor product (CTP) sampling method and a Chebyshev collocation method (CCM) to study the dynamics of rigid-flexible multibody systems with many uncertain interval parameters. The lower and upper bounds of dynamic responses are determined by scanning the Chebyshev surrogate model not the IDAEs. In this work, the efficiency of the algorithms previously proposed are further improved, and the dynamics of multibody system with interval clearance size is also initially studied.

DESCRIPTION OF FLEXIBLE MULTIBODY SYSTEMS VIA ANCF

In this study, the rigid-flexible multibody system is meshed by using a unified mesh of the Absolute Nodal Coordinate Formulation (ANCF). That is, the flexible parts are meshed by using the finite elements of the ANCF, while the rigid parts are described via the ANCF Reference Nodes (ANCF-RNs). The ANCF was originally proposed by Shabana [7] to accurately model the flexible multibody system subject to both large overall motions and large deformations. Many finite elements of the ANCF have been proposed and used to mesh the flexible parts of various flexible multibody systems. It has also been demonstrated that by using the ANCF-RN many complex constraint conditions can be simplified.

COMPUTATION METHODOLOGY FOR SOLVING THE IDAES

Under the framework of ANCF, the flexible multibody systems with uncertain interval parameters can be mathematically described by a set of IDAEs with index-3, as

$$\begin{cases} \mathbf{M}(\boldsymbol{\mu},\boldsymbol{\xi})\ddot{\mathbf{q}}(\boldsymbol{\mu},\boldsymbol{\xi}) + \mathbf{F}(\mathbf{q}(\boldsymbol{\mu},\boldsymbol{\xi})) + \boldsymbol{\Phi}_{\mathbf{q}}^{\mathrm{T}}(\mathbf{q}(\boldsymbol{\mu},\boldsymbol{\xi}),t)\boldsymbol{\lambda}(\boldsymbol{\mu},\boldsymbol{\xi}) = \mathbf{Q}\left(\mathbf{q}(\boldsymbol{\mu},\boldsymbol{\xi}),\dot{\mathbf{q}}(\boldsymbol{\mu},\boldsymbol{\xi})\right) \\ \boldsymbol{\Phi}(\mathbf{q}(\boldsymbol{\mu},\boldsymbol{\xi}),t) = \mathbf{0} \end{cases} \tag{1}$$

By using the definition of interval array and according to the generalized-alpha algorithm, the solution of Eq. (1) can be obtained by solving the nonlinear algebraic equations,

[a] Corresponding author. Email: tianqiang_hust@aliyun.com.

$$\begin{bmatrix} \mathbf{M}(\tilde{\xi},\zeta)\ddot{\mathbf{q}}^{(n+1)}(\tilde{\xi},\zeta)+\mathbf{F}\left(\mathbf{q}^{(n+1)}(\tilde{\xi},\zeta)\right)+\mathbf{\Phi}_{\mathbf{q}}^{\mathrm{T}}\boldsymbol{\lambda}^{(n+1)}(\tilde{\xi},\zeta)-\mathbf{Q}^{(n+1)}(\tilde{\xi},\zeta) \\ \mathbf{\Phi}(\mathbf{q}^{(n+1)}(\tilde{\xi},\zeta),t^{(n+1)}) \end{bmatrix}=\mathbf{0} \tag{2}$$

Once, the solution of Eq. (2) is obtained, the interval response can be further calculated by

$$\begin{cases} [\hat{V}_i]=[\min(\tilde{V}_i(\tilde{\xi},\zeta)),\max(\tilde{V}_i(\tilde{\xi},\zeta))],\ (i=1,2,...,k) \\ \tilde{\mathbf{V}}(\tilde{\xi},\zeta)=[\tilde{V}_1(\tilde{\xi},\zeta),\tilde{V}_2(\tilde{\xi},\zeta),...,\tilde{V}_k(\tilde{\xi},\zeta)]^{\mathrm{T}}=[\mathbf{q}(\tilde{\xi},\zeta)^{\mathrm{T}},\boldsymbol{\lambda}(\tilde{\xi},\zeta)^{\mathrm{T}}]^{\mathrm{T}} \end{cases} \tag{3}$$

By using the CTP sampling method the sampling value in Eq. (2) of the interval parameters can be obtained. The computation processes are also parallelized by using OpenMP directives.

NUMERICAL EXAMPLES

Figure 1 shows the initial configuration of a six-arm flexible robot. Let all the six-arm lengths contain the uncertainty of 10% of their nominal values. Figure 2 gives the *Y*-displacement interval bounds of the robot end-effector. According to the computational time for solving the deterministic DAEs once, the estimated total computational time for solving the scanned IDAEs would be 1850 days. While the computational time for solving the scanned CCM surrogate model is just 9796.97 seconds. Figure 3 shows a planar slider-crank system with revolute clearance joint. The size of joint clearance is regarded as an uncertain interval parameter, and is set as [0.3 0.6] mm. Figure 4 depicts the slider acceleration interval responses.

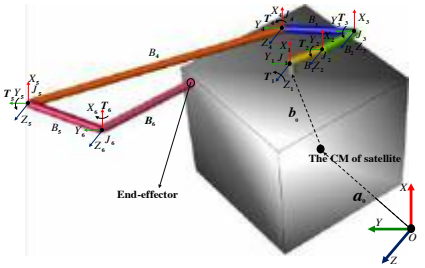

Fig. 1 Space six-arm flexible manipulator

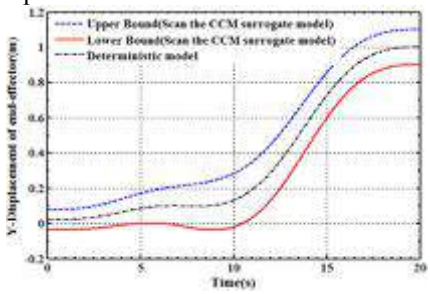

Fig. 2 The robot end-effector displacements

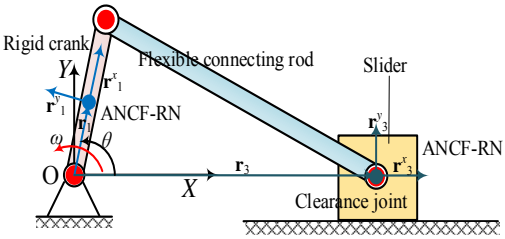

Fig. 3 Slider-crank system with revolute clearance joint

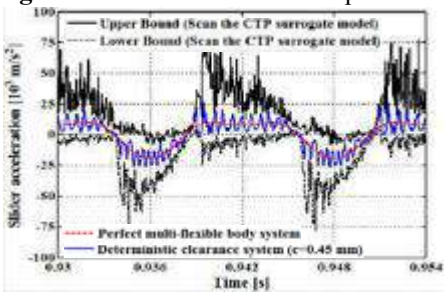

Fig. 4 Slider interval accelerations

CONCLUSIONS

An efficient non-intrusive computation methodology is proposed to study the dynamics of the complex flexible multibody systems with many uncertain interval parameters. The computation methodology is initially used to study dynamics of systems with joint clearance. Many new dynamics behaviours are observed. More results will be presented at the conference.

References

[1] Flores P., Ambrósio J., Claro J. C. P., Lankarani, H. M.: Kiematics and dynamics of multibody systems with imperfect joints: models and case studies. Lecture Notes in Applied and Computational Mechanics.34, Springer, Berlin, Heidelberg, New York 2008.

[2] Tian Q., Zhang Y. Q., Chen L. P., Flores P.: Dynamics of spatial flexible multibody systems with clearance and lubricated spherical joints. *Computers and Structures* **87**: 913-929, 2009.

[3] Sandu C., Sandu A., Ahmadian M.: Modeling multibody systems with uncertainties. part II: numerical applications. *Multibody System Dynamics* **15**: 241-262, 2006.

[4] Alefeld G.: Interval analysis: theory and applications. *Journal of Computational and Applied Mathematics* **121**: 421-464, 2000.

[5] Wu J. L., Luo Z., Zhang Y. Q., Zhang N., Chen L. P.: Interval uncertain method for multibody mechanical systems using Chebyshev inclusion functions. *International Journal for Numerical Methods in Engineering* **95**: 608-630, 2013.

[6] Wang Z., Tian Q., Haiyan Hu.: Dynamics of spatial rigid–flexible multibody systems with uncertain interval parameters. *Nonlinear Dynamics* 2015. DOI: 10.1007/s11071-015-2504-4.

[7] Shabana A.A.: An absolute nodal coordinates formulation for the large rotation and deformation analysis of flexible bodies. Technical Report. No. MBS96-1-UIC, University of Illinois at Chicago 1996.

OPTIMAL DESIGN OF FLEXIBLE MECHANISMS USING A GENERALIZED EQUIVALENT STATIC LOAD METHOD

Emmanuel Tromme*[1], Valentin Sonneville[2], James K. Guest[1], Olivier Brüls[2], and Pierre Duysinx[2]
[1]*Department of Civil Engineering, Johns Hopkins University, Baltimore, MD, USA*
[2]*Aerospace and Mechanical Engineering Department, University of Liège, Liège, Belgium*

Summary The equivalent static load (ESL) method is a powerful approach to solve dynamic response structural optimization problems. The method transforms the dynamic response optimization into a static response optimization under multiple load cases. The ESLs are defined based on the transient analysis response whereupon all the standard techniques of static response optimization can be used. In the last decade, the ESL method has been applied to perform structural optimization of flexible components of mechanical systems modeled as multibody systems. This method considers the optimization of isolated components during the static response optimization. The present research proposes a generalized ESL method accounting for the entire system during the static response optimization, which enables to formulate the constraints with respect to the mechanism and not restricted to the individual components. The proposed method relies on a Lie group formalism which has appealing properties to derive efficiently the ESL. Examples validate the method.

TWO APPROACHES FOR THE OPTIMAL DESIGN OF FLEXIBLE MECHANISMS

Nowadays, two approaches can be identified to perform the structural optimization of mechanical system components. The first one, namely the fully coupled approach, incorporates the time response coming directly from the MBS analysis into the optimization problem. Hence, this approach leads to a dynamic response optimization problem. The computational cost to solve this problem may be high as it requires the computation of the sensitivities of the displacements, velocities and accelerations. Further, the treatment of time-dependent constraints is an essential problem as it drastically affects the convergence of the optimization process. However, this approach is totally general and can accommodate all types of constraints. In order to reduce the computational cost, a lot of research has been conducted to remove the time dependency out of the problem. An important breakthrough has been made by Kang, Park and Arora [3] who proposed a rational method to define Equivalent Static Loads (ESL) to optimize flexible mechanisms. This method leads to the second approach, namely the weakly coupled approach, wherein an ESL is evaluated for each time step and for each component to design, producing the same displacement field as the one generated by the dynamic load at the considered time step. These ESLs are fixed during the static response optimization process whereupon cycles between the MBS analysis and the optimization process are required to account for the design variable change over the ESLs. Nonetheless, even if the method is general, it has been developed for MBS based on the floating frame of reference formalism. This formalism separates the elastic coordinates from those describing the gross motion of the rigid bodies. The traditional ESL method [3] relies on this property which enables to define the ESLs for each optimized component by simply isolating some parts of the equations of motion. Indeed, this formalism computes the component deformation with respect to its material (body-attached) frame whereupon the ESL definition is unambiguous.

NONLINEAR FINITE ELEMENT FORMULATION

In the present work, a nonlinear finite element approach formulated on a particular Lie group is considered. The nonlinear finite element approach aims at accounting for the full flexibility of the different components in an integrated manner and enables the analysis of mechanism deformation undergoing large and fast joint motions. Moreover, this approach is well-suited to solve advanced optimization problems such as topology optimization problems, which renders it appealing to design optimal flexible mechanisms.

The Lie group theory offers several advantages for the finite element analysis of systems with large rotation variables [4]. Firstly, the equations of motion are derived and solved directly on the nonlinear manifold, without an explicit parameterization of the rotation variables, which leads to important simplifications in the formulations and algorithms. Secondly, displacements and rotations are represented as increments with respect to the previous configuration, and those increments can be expressed in the material frame. Therefore, global geometric nonlinearities are automatically filtered from the relationship between incremental displacements and elastic forces, which strongly reduces the fluctuations of the iteration matrix during the simulation [1]. Taking profit of these properties, the ESLs can be evaluated efficiently. It turns out that they can be defined as the internal forces of each component since these latter are defined in the nodal local frame [5]. This contrasts with a classical nonlinear finite element formulation [2] wherein a post-processing step must be added to define the ESLs.

Hence, during the static response optimization problem, for each time step n, the deflection of body b, $\Delta\mathbf{n}^b$, resulting from the ESL, $\mathbf{g}^b_{n,eq}$, is computed as,

$$\mathbf{K}^b_t(\mathbf{p})\,\Delta\mathbf{n}^b = \mathbf{g}^b_{n,eq}, \tag{1}$$

where $\mathbf{K}^b_t(\mathbf{p})$ is the tangent stiffness matrix of body b, depending on the design parameter vector $\mathbf{p}$ but not on the time step n.

*Corresponding author. Email: etromme@jhu.edu

LIMITATION

A severe limitation of the ESL method concerns the static response optimization that is performed on decoupled components. As observed in Eq. 1, the superscript b indicates that the equation is related to a lone component. Ergo, the optimization problem must be formulated in such a way that each component has its own set of constraints. Imposing multicomponent-based constraints, e.g. a global behavior constraint, is thus difficult since the components are optimized independently.

GENERALIZATION OF THE TRADITIONAL ESL METHOD

The proposed method removes this limitation by generalizing the traditional ESL method to account for the entire system during the static response optimization problem so that multicomponent-based constraints can be considered. In order to compute the deflection of the system, $\Delta\mathbf{n}$, resulting from the global ESL, $\mathbf{g}_{n,eq}$, Eq. 1 must be extended to account for kinematic joints between components. Resorting to the equations of motion of the mechanism and linearizing them around the deformed configuration at time step n, the deflection of the system is obtained by solving iteratively the following equation,

$$\begin{bmatrix} \mathbf{K}_t & \mathbf{B}_n^T \\ \mathbf{B}_n & \mathbf{0} \end{bmatrix} \begin{bmatrix} \Delta\mathbf{n} \\ \Delta\boldsymbol{\lambda} \end{bmatrix} = \begin{bmatrix} \mathbf{g}_{n,eq} \\ \Delta\boldsymbol{\Phi} \end{bmatrix}, \tag{2}$$

where $\mathbf{B}_n$ is the gradient matrix of the kinematic constraints $\boldsymbol{\Phi}$, which are used, e.g., to model kinematic joints. The Lagrangian multiplier vector $\boldsymbol{\lambda}$ results from the Lagrange multiplier method to incorporate kinematic constraints.

This generalization is performed efficiently within the Lie group formalism since the system flexibility is accounted in an integrated way and the tangent stiffness matrix, which is defined in the local nodal frames, can be considered as independent of n. The additional cost to solve the nonlinear equation is rather limited since the update at each iteration is limited to the matrix $\mathbf{B}_n$, which accounts for the modification of the component relative displacement.

The proposed generalization has been validated on classical benchmarks, such as the structural optimization of a 2-dof robot (Fig. 1(a)) and a 4-bar mechanism (Fig. 1(b)). The results are in agreement with the fully coupled method which is considered as the reference method.

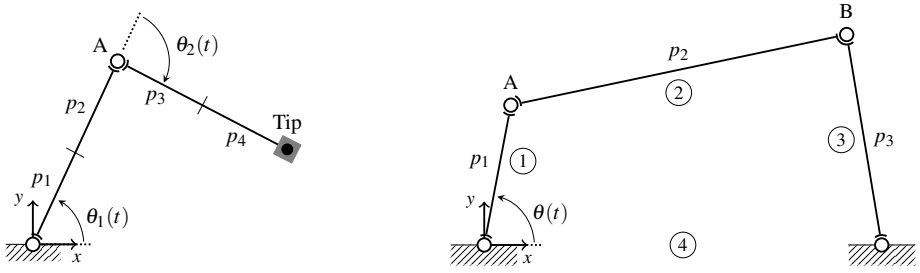

(a) 2-dof robot

(b) 4-bar mechanism

Figure 1: Kinematic models.

CONCLUSIONS

The proposed method supersedes the traditional ESL method by considering the entire system during the static response optimization and removing the implicit assumption of optimizing decoupled components. The use of the Lie group formalism enables this generalization at a low extra-cost since the cost to solve the nonlinear problem is limited to the update of the kinematic constraint gradient matrix. This approach seems promising to solve industrial applications.

The first author acknowledges support provided by the Whiting School of Engineering at the Johns Hopkins University.

References

[1] O. Brüls, M. Arnold, and A. Cardona. Two Lie group formulations for dynamic multibody systems with large rotations. In *Proceedings of the IDETC/MSNDC Conference*, Washington D.C., USA, 2011.

[2] M. Géradin and A. Cardona. *Flexible Multibody Dynamics: A Finite Element Approach*. John Wiley & Sons, New York, 2001.

[3] B.S. Kang, G.J. Park, and J.S. Arora. Optimization of flexible multibody dynamic systems using the equivalent static load method. *AIAA Journal*, 43(4):846–852, 2005.

[4] V. Sonneville and O. Brüls. A formulation on the special Euclidean group for dynamic analysis of multibody systems. *Journal of Computational and Nonlinear Dynamics*, 9(4), 2014.

[5] E. Tromme, V. Sonneville, O. Brüls, and P. Duysinx. On the equivalent static load method for flexible multibody systems described with a nonlinear finite element formalism. *International Journal for Numerical Methods in Engineering*, 2015, *submitted*.

AN UNDERWATER INERTIA-BASED PROPELLED VEHICLE DYNAMICS AND PERFORMANCE

Elżbieta Jarzębowska[a)]
Institute of Aerospace Engineering and Applied Mechanics, Warsaw University of Technology, Warsaw, Poland

Summary The paper addresses dynamics of variable mass or configuration mechanical systems subjected to holonomic or nonholonomic constraints, which are imposed due to systems desired performance, tracking specified motions or control needs. It presents an analytical dynamics modeling framework whose novelty is that nonholonomic constraints can be merged into variable mass system dynamics and final motion equations are free of the constraint reaction forces so they can be used directly to control design. Many engineering systems change their mass or configuration when they move, e.g. inertia-based propelled underwater vehicles or mobile robots and manipulators transporting loads. An underwater inertia-based propelled vehicle model dynamics and performance illustrate the theoretical development presented in the paper. The paper contribution is two folded. It presents a unified approach to constrained variable mass or configuration systems modeling and introduces analytical dynamics methods to nonlinear control for solving engineering problems.

INTRODUCTION

The paper addresses dynamics of variable mass or configuration mechanical systems, which can be additionally subjected to holonomic or nonholonomic constraints. The constraints on these systems are due to their desired performance, tracking pre-specified motions or are control constraints. There is quite a lot of engineering systems whose mass or configuration change when they move or change of mass is their way of propulsion. The examples of significant engineering importance are underwater vehicles which are often inertia–based propelled, ground mobile robots and manipulators, whose mass or configuration change due to carrying loads, or excavating machines or others transporting various materials. They work and deliver services so they are controlled systems with specified performance, see e.g. [1].

The beginning of the theory of variable mass systems is attributed to Mieszczerskii [2]. The Second World War and years after it brought new results oriented to military and space exploration applications. The beginning of analytical mechanics of variable mass systems is dated when Lagrange equations were derived for them [3]. Research on variable mass systems is intensive and latest results with references to other works can be found in [4]. There, holonomic systems with mass being mostly a time function are considered.

There are no, to the best of the author knowledge, a unified approach to generation of variable mass systems motion equations, when they are constrained by holonomic and nonholonomic constraints. Additionally, the equations should be applicable for a model-based controller design. A good example of a variable mass and configuration system is an underwater vehicle which is inertia–based propelled in both pure mechanical and hybrid case, when additional batteries are added to facilitate or speed up its maneuvers. The vehicle changes its mass due to the change of amount of water in its tanks and its inertia changes due to an extra mass, which may move inside the vehicle to support maneuvers such as turning, pitching and yawing. Underwater vehicles serve many purposes, e.g. sea bottom exploration, military purposes, or elimination of pollutions from sea waters. Variety of mission related control goals, written in constraint equation forms, may be formulated for them, e.g. monitoring tasks, motion along pre-specified trajectories or with pre-defined velocity changes. Underwater vehicles are thus constrained variable mass and configuration systems, which need to be controlled.

The paper presents a unified dynamics modeling framework which enables generating equations of motion for constrained variable mass and configuration systems. The novelty of the framework is that variable mass systems may be subjected to holonomic or nonholonomic constraints, which may be material, control based or task based, provided they can be presented in the form of algebraic or differential equations.

The paper contribution is two folded. It presents a unified modeling method for constrained variable mass and configuration systems and introduces the latest analytical dynamics methods to nonlinear control.

An example of underwater glider dynamics and performance illustrates the theoretic analytical modeling method.

VARIABLE MASS AND CONFIGURATION SYSTEM DYNAMICS

Assumptions for derivation of motion equations for variable mass systems are that the mass change undergoes the Mieszczerskii mass change scheme [1], mass may be a function of time, positions and velocities, and a system may be subjected to holonomic or nonholonomic constraints.

The unified constrained dynamics for variable mass systems yields the following equations of motion specified in generalized coordinates q for $q \in R^n$

$$\frac{d}{dt}\left(\frac{\partial T}{\partial \dot{q}_\mu}\right) - \frac{\partial T}{\partial q_\mu} - Q_\mu - P_\mu + \sum_{\beta=1}^{b}\left[\frac{d}{dt}\left(\frac{\partial T}{\partial \dot{q}_\beta}\right) - \frac{\partial T}{\partial q_\beta} - Q_\beta - P_\beta\right]\frac{\partial g_\beta^{(1)}}{\partial \dot{q}_\mu} = 0 . \qquad \mu=b+1,\ldots,n \qquad (1)$$

[a)] Corresponding author email: elajarz@meil.pw.edu.pl

where: T is the system kinetic energy, Q_σ are generalized forces that act upon a system, σ=1,...,n, mass $m_i = m_i(t,q,\dot{q})$. The constraint equations are presented in the form

$$\dot{q}_\beta = g_\beta^{(1)}(t,q_1,....,q_n,\dot{q}_{k+1},....,\dot{q}_n) \tag{2}$$

with the partition of the generalized velocity vector as $\dot{q} = (\dot{q}_\beta,\dot{q}_\mu)$, $\dot{q}_\beta \in R^k, \dot{q}_\mu \in R^{n-k}$.

P_σ are generalized forces due to the mass change and

$$P_\sigma = \sum_{i=1}^{N}\left[\left(\Phi_i + \frac{dm_i}{dt}v_i\right)\frac{\partial r_i}{\partial q_\sigma} - \frac{v_i^2}{2}\frac{\partial m_i}{\partial q_\sigma} + \frac{d}{dt}\left(\frac{v_i^2}{2}\frac{\partial m_i}{\partial \dot{q}_\sigma}\right)\right] \quad \text{or} \quad P_\sigma = \iiint_V\left[\left(\Phi + \frac{d\rho}{dt}v\right)\frac{\partial r}{\partial q_\sigma} - \frac{v^2}{2}\frac{\partial \rho}{\partial q_\sigma} + \frac{d}{dt}\left(\frac{v^2}{2}\frac{\partial \rho}{\partial \dot{q}_\sigma}\right)\right]dV,$$

with $\Phi_i = \frac{dm_i}{dt}c_i$ being a reactive force, $c_i = u_i - v_i$ are relative velocity vectors of mass *dm* joining *i-th* particle of a system. Both u_i and v_i have to be presented in generalized coordinates.

Equations (1) admit the following properties:

- They are free of constraint reaction forces so they can be directly transformed into a dynamic control model by adding control forces at their right hand sides.
- Constraint equations, both position and kinematic material and task-based, can be merged into (1).
- Their form is the same as for constant mass systems so they can be used when a system configuration changes only.
- They reduce to Maggi equations for first order nonholonomic systems when mass is constant [5].

DYNAMICS AND PERFORMANCE OF AN INERTIA-BASED PROPELLED UNDERWATER VEHICLE

The underwater glider inertia-based propelled and equipped with two water tanks located at the front and back of the vehicle. The longitudinal plane is a symmetry plane for the glider with the water tanks. The motion equations for the glider are derived based upon (1) in its body frame. The constraints (2) are put upon the glider velocity components.

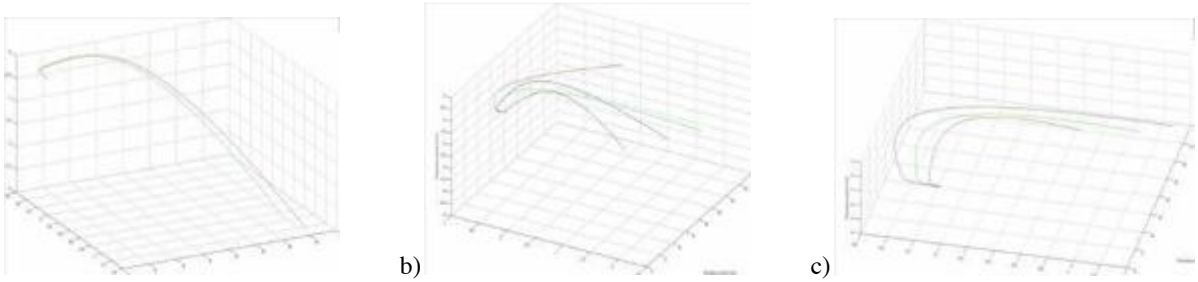

a) b) c)

Figures below present the following: a) change of the vehicle vertical motion when the water in the water tanks is gradually reduced to half, b) the influence of the pre-specified velocity for the vehicle range of motion, c) turn of the vehicle with different forward velocities and the same vertical one.

References

[1] Antonelli G.: Underwater Robots, Heidelberg, Springer, 2014.

[2] Mieszczerskii I. V.: Motion equations of a variable mass particle in a general case - Works on mechanics of variable mass bodies, Gostiechisdat, (in Russian), Moscow, 1949.

[3] Kosmodemianskii A. A.: Lectures in Mechanics of Bodies with Variable Mass, Uczionnye zapiski M.G.U.. vol. 154, Mechanics, 1951.

[4] Cveticanin L.: Dynamics of Bodies with Time-Variable Mass, Heidelberg, Springer, 2016.

[5] Jarzębowska E.: Model-Based Tracking Control of Nonlinear Systems, Taylor & Francis, Boca Raton, 2012.

A VARIATIONALLY CONSISTENT APPROACH TO CONSTRAINED MOTION

John T. Foster *[1]

[1]*Departments of Petroleum Engineering and Aerospace and Engineering Mechanics, , The University of Texas at Austin, Austin, TX*

Summary A variationally consistent approach to constrained rigid-body motion is presented that extends DAlemberts principle in a way that has a form similar to Kane's equations. The method results in minimal equations of motion for both holonomic and nonholonomic systems without *a priori* consideration of preferential coordinates.

INTRODUCTION

Deriving equations-of-motion for rigid-bodies subject to constraints has a rich research history dating the work of Lagrange. For holonomic constraints, the classical approach is to utilize Lagrange's equations augmented with undetermined (Lagrange) multipliers. In the more problematic case of nonholonomic constraints, several principles have been proposed and debated, notably a general principle for nonlinear, nonholonomic constraints attributed to Appell by Ray [1]. Both of these methods involve casting the problem with excess degrees-of-freedom in the form of Lagrange multipliers that are later eliminated in the solution process.

Udwadia and Kalaba [2] provided a new perspective on constrained motion through the use of the Moore-Penrose psuedo-inverse to generate a matrix that proportionally weights unconstrained accelerations to come into compliance with the constraints of the system. They make the clever analogy that the abstract proportionality matrix is Nature's feedback controller, limiting unconstrained accelerations. The resulting equations derived via their technique are minimal with respect to the generalized coordinates without *a priori* selection or use of "felicitous" coordinates. However, their approach, based on generalized inverse operations, is quite mathematical in nature and the mechanistic interpretation is somewhat fuzzy. Additionally, their method requires that the constraints are linear with respect to the generalized accelerations. In a brief and apparently overlooked interpretation of Udwadia and Kalaba's method, Barhorst [3] provided a variational principal that is shown to be equivalent to the abstract proportionality matrix approach for the case considered, but is provided from a physical perspective that extends from D'Albembert's principle. The equations that Barhorst presented can be utilized to efficiently generate equations of motion for rigid-bodies with either holonomic or nonholonomic constraints. They are also formulated in a vector-based approach familiar to engineers and have a form that makes computer implementation straightforward. As it has been ignored in subsequent literature on the subject, the utility of these equations seems to not be apparent. This may be because Barhorst's primary goal in his Brief Note was to provide an alternative view on the results of Udwadia and Kalaba, he presented the fundamental variational principle without derivation (and only for the linear motion of particles), and left an important component in a generic form, i.e. the explicit form of the constraint-coupling matrix is not given. Additionally, no examples for how to use these equations have ever appeared in literature. The purpose of this paper is to complete the variational principle presented by Barhorst and provide an example for the application of the principle for a nonholonomic system.

BARHORST'S METHOD FOR GENERATING UNCONSTRAINED EQUATIONS OF MOTION

A variational principle that can be used to generate equations-of-motion subject to holonomic or nonholonomic constraints is (presented without derivation for brevity)

$$\begin{aligned} 0 = &\sum_i (\mathbf{F}^i \nearrow \mathbf{I}^i) \cdot \left(\frac{\partial \dot{\mathbf{x}}^i}{\partial \dot{q}_n} + \frac{\partial \dot{\mathbf{x}}^i}{\partial \dot{q}_m} \frac{\partial \dot{q}_m(\dot{q}_n)}{\partial \dot{q}_n} \right) \delta \dot{q}_n + \\ &\sum_i (\mathbf{T}^i \nearrow \mathbf{J}^i) \cdot \left(\frac{\partial \boldsymbol{\omega}^i}{\partial \dot{q}_n} + \frac{\partial \boldsymbol{\omega}^i}{\partial \dot{q}_m} \frac{\partial \dot{q}_m(\dot{q}_n)}{\partial \dot{q}_n} \right) \delta \dot{q}_n. \end{aligned} \tag{1}$$

for $\dot{q}_n$ independent generalized speeds, and $\dot{q}_m$ dependent generalized speeds, who's dependence is specified by $k = 1, 2, \ldots, m$ constraint equations of the form

$$C_k(q_j, \dot{q}_j) = 0 \qquad j = 1, 2, \ldots, n+m.$$

$\mathbf{F}^i$ and $\mathbf{I}^i$ are the internal and D'Alembert interial force vectors of the body i in the inertial reference frame, respectively. $\dot{\mathbf{x}}^i = \dot{\mathbf{x}}^i(q_j, \dot{q}_j, t)$ is the translational velocity. $\boldsymbol{\omega}^i = \boldsymbol{\omega}^i(q_j, \dot{q}_j, t)$ is the angular velocity of the body i in the inertial reference frame, $\mathbf{T}$ are external torques, $\mathbf{J}$ are rotational inertia vectors. This variational principle will be utilized in to generate equations-of-motion for arbirary $\delta \dot{q}_n$ on a nonholonomic example in the sequel.

*Corresponding author. Email: jfoster@austin.utexas.edu

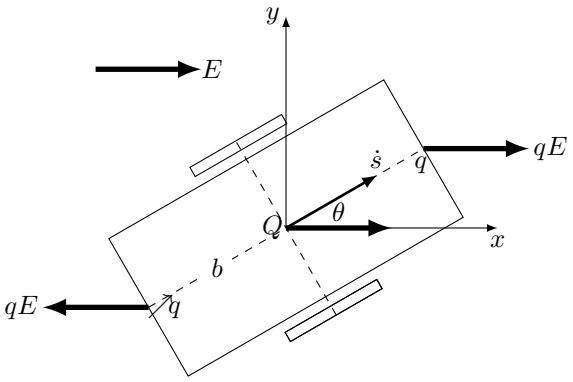

Figure 1: Two-wheeled cart driven by electrostatic forces. The wheels turn independently.

A NONHOLONOMIC EXAMPLE

A physical setting for a true nonholonomic problem that incorporates both external forces and torques is given in [4]. Consider the cart shown in fig. 1 which has distributed electric charges on it and is subject to an external electric field E in the x direction. The cart is a rectangular block of mass $\widetilde{M}$ and moment-of-inertia, I. It has massless wheels that can turn independently allowing it to move along any smooth path. The wheels do not slip, so that motion is always perpendicular to the axle. The motion of the cart is the distance traveled along the path s in the direction θ relative to x. The forward speed of the cart is $\dot{s}$. The cart has a charge Q at its center and charges q and $\nearrow q$ at the front and rear a distance b from its center, respectively. Clearly, the velocity of the cart in the x, y plane is constrained to the following conditions

$$C_1 = \dot{x} \nearrow \dot{s} \quad \theta = 0, \qquad C_2 = \dot{y} \nearrow \dot{s} \quad \mathrm{n}\,\theta = 0. \tag{2}$$

Now utilizing the approach presented in the previous section for which no modification is needed for the nonholonomic system. First we choose $\dot{x}$ and $\dot{y}$ to be the dependent speeds, i.e. $\dot{x} = \dot{s} \quad \theta$ and $\dot{y} = \dot{s} \quad \mathrm{n}\,\theta$. Exercising the projection equations, without giving any consideration to preferential or felicitous coordinates, the first term of (1) for arbitrary $\delta\dot{q}_n$ and the fundamental lemma of the calculus of variations is

$$0 = (\mathbf{F} \nearrow \mathbf{I}) \cdot \left(\frac{\partial \dot{\mathbf{x}}}{\partial \dot{s}} + \frac{\partial \dot{\mathbf{x}}}{\partial \dot{x}} \frac{\partial \dot{x}}{\partial \dot{s}} + \frac{\partial \dot{\mathbf{x}}}{\partial \dot{y}} \frac{\partial \dot{y}}{\partial \dot{s}} \right) = (\mathbf{F} \nearrow \mathbf{I}) \cdot \left(\frac{\partial \dot{\mathbf{x}}}{\partial \dot{s}} + \quad \theta \frac{\partial \dot{\mathbf{x}}}{\partial \dot{x}} + \quad \mathrm{n}\,\theta \frac{\partial \dot{\mathbf{x}}}{\partial \dot{y}} \right). \tag{3}$$

Substituting in the vectors

$$\mathbf{F} = EQ\,\hat{\mathbf{i}}, \qquad \mathbf{I} = \widetilde{M}(\ddot{x}\,\hat{\mathbf{i}} + \ddot{y}\,\hat{\mathbf{j}}), \qquad \dot{\mathbf{x}} = \dot{x}\,\hat{\mathbf{i}} + \dot{y}\,\hat{\mathbf{j}},$$

and evaluating

$$0 = \widetilde{M}\ddot{s} \nearrow EQ \quad \theta, \tag{4a}$$

where the time-differentiated form of (2) is used to eliminate $\ddot{x}$ and $\ddot{y}$. The second equation of motion can be derived via the second term (1) for arbitrary $\delta\dot{q}_n$ in a similar fashion resulting in

$$I\ddot{\theta} + 2bEq \quad \mathrm{n}\,\theta = 0. \tag{4b}$$

(4) can be verified correctly using Lagrange's equations with multipliers. Again, the advantage of the approach shown here are that the introduction of multipliers is completely unnecessary.

References

[1] John R Ray. Nonholonomic constraints and Gauss's principle of least constraint. *American Journal of Physics*, 40(1):179–183, 1972.

[2] Firdaus E Udwadia and Robert E Kalaba. A new perspective on constrained motion. *Proceedings: Mathematical and Physical Sciences*, pages 407–410, 1992.

[3] Alan A Barhorst. An alternative derivation of some new perspectives on constrained motion. *Journal of applied mechanics*, 62(1):243–245, 1995.

[4] Ian R Gatland. Nonholonomic constraints: A test case. *American journal of physics*, 72(7):941–942, 2004.

SIMULATION OF A VEHICLE SEPARATED FROM VEHICULE PLATOON

Eisuke Kita[1,2,a)], Hiroto Takaue[1], Mi-ichiro Yamada[1] & Hiroki Sakamoto[1]
[1]Graduate School of Information Science, Nagoya University, Nagoya, Japan
[2]Graduate School of System Informatics, Kobe University, Kobe, Japan

Summary When four vehicles move in the platoon, one vehicle separates from the platoon. The velocity control model of the vehicles is presented in this study. The model is defined by means of the multi-leader type Helly model. The model parameters are determined by minimizing the objective function defined as the summation of delay time, overshoot, deviation and so on. The model is applied for the simulation of the traffic flow in four vehicles platoon. The results show that the model can control the velocity of the vehicles adequately.

INTRODUCTION

Vehicle platoon attracts the attention for enhancing the traffic capacity safely and overcoming traffic congestion. The vehicle platoon allows many vehicles to move in the very short vehicle distance and accelerate or brake simultaneously. Since it is difficult for human beings to control vehicles safely in the very short vehicle distance, electric and mechanical control system is necessary. In this study, the vehicle platoon of four vehicles is considered and then, one vehicle separates from the platoon. The model for controlling the vehicle velocity is formulated from the vehicle following model. The model parameters are determined by solving the optimization problem. The objective function is defined as the weighted sum of the variables. The parameters are applied for controlling the velocity of the vehicles in the platoon and a vehicle separating from the platoon.

CONTROL MODEL

Velocity Control Model

The velocity control model is formulated by Helly model [1]. The model to control velocity according to the information from the nearest forehand and the leader vehicles is given as follows.

$$\ddot{x_n}(t+\Delta t) = \alpha\big(\dot{x}_{n-1}(t) - \dot{x}_n(t)\big) + \beta\big(x_{n-1}(t) - x_n(t) - D_n(t)\big) + \gamma(\dot{x}_0(t) - \dot{x}_n(t)) \quad (1)$$

The variable $x_n(t)$, $x_{n-1}(t)$ and $x_0(t)$ denotes the positions of the vehicle n, the nearest forehand vehicle of the vehicle n and the lead vehicle of the platoon respectively. The parameter α, β and γ denote the sensitivities (model parameters). The function $D_n(t)$ gives the desired vehicle distance, which is given as follows [2].

$$D_n(t) = 0.3049\dot{x}(t) + 0.0029\{\dot{x}_n(t)\}^2 \quad (2)$$

Parameter Design

The optimization problem is defined as follows.

$$\text{minimize } J \qquad \alpha, \beta, \gamma \in [0,1], \quad (3)$$
$$\text{Subject to } [\Delta x_{n-1}(t)], [\dot{x}_0(t)] \quad (4)$$

The objective function is given as follows.

$$J = \omega_1 T_d + \omega_2 O_s + \omega_3 E_{lim} + \omega_4 D \quad (5)$$

The variable T_d, O_s, E_{lim} and D denote the delay time, overshoot, steady-state deviation and the value of the integral of the difference between the desired and the measured vehicle distances, respectively. The variable $\omega_1, \omega_2, \omega_3$ and ω_4 denote the weight parameters.

SIMULATION RESULT

Traffic flow simulation is performed when one vehicle separates from the platoon of four vehicles (Fig.1). The positions of four vehicles in the platoon are shown in Figure 2. The graph is plotted with the time as the horizontal axis and the vehicle position as the vertical axis, respectively. At the time of 12.5 second, the 1st follower vehicle separates from the platoon. After that, the 2nd and 3rd follower vehicles accelerate and reach the forehand vehicles.

a) Corresponding author. Email: kita@is.nagoya-u.ac.jp.

CONCLUSIONS

The velocity control model of the vehicles in the platoon was presented in this study. The model was defined by means of the multi-leader type Helly model. The model parameters were determined by solving the optimization problem. The model was applied for the simulation of the traffic flow in four vehicles platoon. One vehicle separates from the platoon successfully and then, the vehicles following to the separating vehicle accelerate the leader vehicle adequately.

Acknowledgement

This work was supported by JSPS KAKENHI Grant Number 15K05760.

References

[1] W. Helly, Simulation of Bottlenecks in Single Lane Traffic Flow, Theory of Traffic Flow Symposium, pp.207-238, 1961.

[2] T. Tamaki, S. Yasue and E. Kita, Traffic Flow Simulation Using Cellular Automata, Proceedings of Civil and Structural Engineering Computing, pp.163-164, 2003.

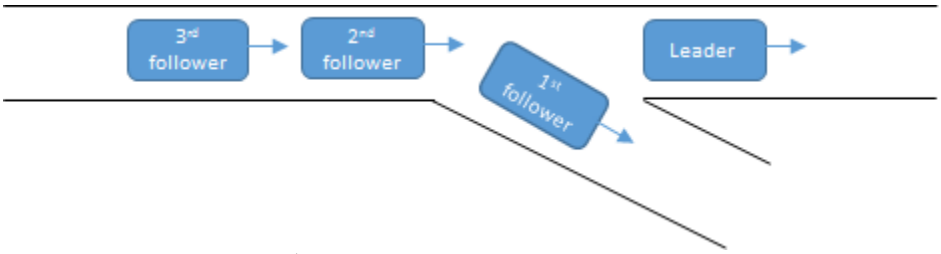

Figure 1: 1st follower vehicle separated from the platoon

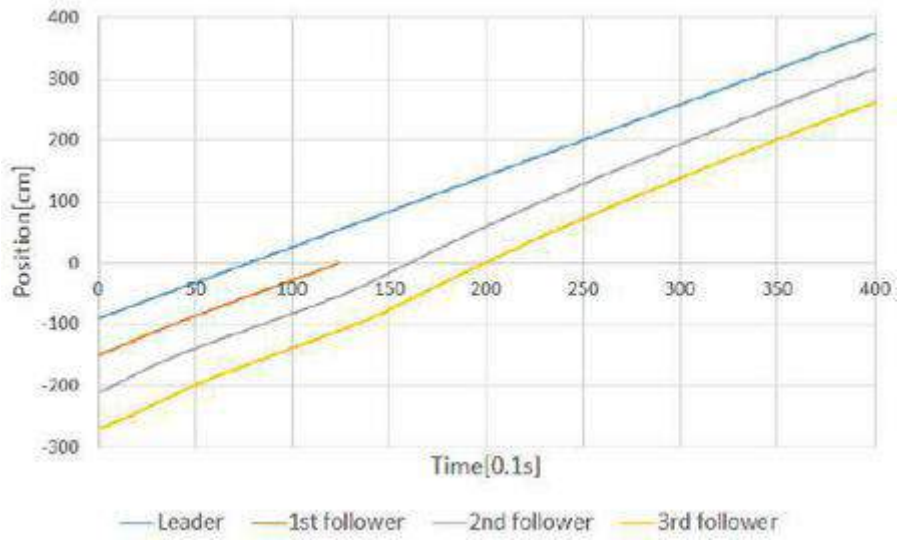

Figure 2: Positions of vehicles in platoon.

SOLVER COUPLING WITH ALGEBRAIC CONSTRAINTS: AN INDEX-2 CO-SIMULATION APPROACH

Daixing Lu[1a)], Pu Li[1] & Bernhard Schweizer[1]
[1]*Institute of Applied Dynamics, Technical University of Darmstadt, Darmstadt, Germany*

Summary A co-simulation method on index-2 level is presented and analyzed with respect to numerical stability and convergence behavior. Therefore, two arbitrary mechanical subsystems are considered, which are coupled by algebraic constraint equations (i.e. by rigid joints). In this work, we act on the assumption that each subsystem has its own solver, which integrates independently from the other subsystem solver. A weak coupling approach is used for coupling the two subsystem solvers. The coupling method analyzed here is based on the well-known stabilized index-2 formulation for multibody systems (GGL-formulation). The presented coupling technique is semi-implicit and based on a predictor/corrector approach.

CO-SIMULATION TECHNIUQUE

Starting with the pioneer work of Ref. [4] on multirate methods for the simulation of subsystems with different time scales by using different time steps in each subsystem, a large number of methods for solver coupling have been developed and applied in many different fields of application. Solver coupling and co-simulation methods have been successfully used in the field of vehicle and engine dynamics, for solving fluid/structure interaction problems and for analyzing multidisciplinary problems including coupled electromechanical problems [2][5][8][11]. An important field for co-simulation methods is represented by coupled multibody/finite-element problems. Coupled multibody/finite-element models have for instance been used in Ref. [1] to simulate pantograph-catenary interaction problems. For the combined simulation of multibody and hydraulic systems, co-simulation approaches have been applied in Ref. [7]. Solver coupling incorporating smoothed particle hydrodynamics and discrete particle models in connection with multibody dynamics has for instance been used in Ref. [10]. On the one hand, co-simulation methods are frequently applied for solving multidisciplinary problems. On the other hand, solver coupling is also used in monodisciplinary applications for parallelizing the solution process.

Concerning the physical coupling of the subsystems, one has generally to distinguish between solver coupling with algebraic constraints and solver coupling based on constitute laws. Coupling two mechanical subsystems for instance can be accomplished either by physical force/torque laws (i.e. by applied forces/torques) [1][2][5] or by algebraic constraint equations (i.e. by reaction forces/torques) [6][9]. In the current work, we only consider constraint coupling. As for numerical time integration methods, one can distinguish between explicit, implicit and semi-implicit solver coupling methods.

The coupling technique investigated here uses the equations of motion in the stabilized index-2 formulation according to Ref. [3]. The key idea of this formulation is to use the constraint equations on position and on velocity level simultaneously. Incorporation of the constraint equations on velocity level is accomplished by defining additional Lagrange multipliers. With the additional multipliers a projection term can be introduced in the kinematical differential equations so that the constraint equations on velocity level can be fulfilled together with the constraint equations on position level.

NUMERICAL ANALYSIS

Application of the stabilized index-2 co-simulation approach for coupling 2 arbitrary multibody subsystems by algebraic constraints is in detail described in Ref. [9]. As an example, we consider the classical planar four-bar linkage depicted in Figure 5. This system consists of three rigid links and four ideal revolute joints. To decompose the overall system into two subsystems, link 2 is split into two parts (m_{21} and m_{22}). The first subsystem contains link 1 ($m_1 = 1\,\mathrm{kg}$, $J_1 = 1/12\,\mathrm{kg}\,m^2$, $l_1 = 1\,\mathrm{m}$) and the left part of link 2 ($m_{21} = 1\,\mathrm{kg}$, $J_{21} = 1/12\,\mathrm{kg}\,m^2$, $l_{21} = 1\,\mathrm{m}$). The second subsystem is represented by the right part of link 2 ($m_{22} = 1\,\mathrm{kg}$, $J_{22} = 1/12\,\mathrm{kg}\,m^2$, $l_{22} = 1\,\mathrm{m}$) and by link 3 ($m_3 = 2\,\mathrm{kg}$, $J_3 = 2/3\,\mathrm{kg}\,m^2$, $l_3 = 2\,\mathrm{m}$). The two subsystems are coupled by a fixed joint as shown in the figure. The system is driven by the torque $M_z(t) = 0.5 \cdot t\,\mathrm{Nm}$, which is applied at the center of mass of link 1. Gravity acts in negative y-direction ($g = 9.81\,\mathrm{m/s^2}$). As initial conditions, $\varphi_{1,0} = \frac{\pi}{4}\,\mathrm{rad}$ and $\dot{\varphi}_{1,0} = 0\,\mathrm{rad/s}$ have been chosen. Simulation results are collected in Figure 1, where the displacement $x_{21}(t)$ of the center of mass S_{21} is shown. The figure also depicts the coupling equation $g_{ca_x}(t) = (x_{21} + 0.5 \cdot l_{21} \cdot \cos\varphi_{21}) - (x_{22} - 0.5 \cdot l_{22} \cdot \cos\varphi_{22}) = 0$ for the fixed joint in x-direction. The co-simulation has been carried out with different macro-step sizes, namely $H = 1E-3$, $H = 5E-4$ and $H = 1E-4$.

[a)] Corresponding author. Email: lu@ad.tu-darmstadt.de.

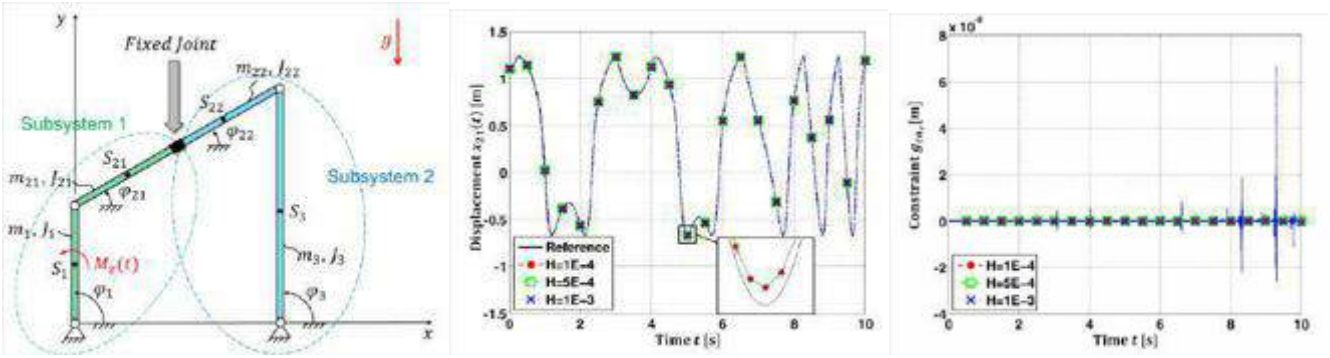

Figure 1. Planar four-bar linkage: interpretation as two double pendulums coupled by a fixed joint; simulation results for the four-bar linkage for different macro-step sizes: displacements $x_{21}(t)$, constraint equations $g_{ca_x}(t)$.

CONCLUSIONS

The semi-implicit co-simulation technique investigated here shows stable and convergent simulation results for the case that the coupling variables are remained constant during the macro-step. The presented method is tailored for solver coupling with algebraic constraints and uses a formulation on index-2 level without numerical drift. Since explicit methods often fail in connection with constraint coupling, the investigated method may represent an efficient and robust technique to handle solver coupling with algebraic constraints. A direct comparison with explicit coupling schemes shows the improved stability of the semi-implicit method. The proposed method requires no detailed subsystem information, since the Jacobian matrices have small dimensions and can simply be calculated numerically by finite differences. The presented co-simulation approach shows good numerical stability properties. Stable simulations can be achieved in a wide parameter range and also for the case that the subsystems have very different mechanical properties. The global errors of the position and velocity variables converge with $\mathcal{O}(H^2)$; the corresponding locals errors converge with $\mathcal{O}(H^3)$.

References

[1] J. Ambrósio, J. Pombo, F. Rauter, M. Pereira. A Memory Based Communication in the Co-simulation of Multibody and Finite Element Codes for Pantograph-Catenary Interaction Simulation. In C. Bottasso (Ed.) Multibody Dynamics: Computational Methods and Applications. pp. 231-252, Springer, 2009.

[2] M. Datar, I. Stanciulescu, D. Negrut. A co-simulation environment for high-fidelity virtual prototyping of vehicle systems. International Journal of Vehicle Systems Modelling and Testing, Vol. 7, pp. 54-72, 2012.

[3] C.W. Gear, G.K. Gupta, B.J. Leimkuhler. Automatic integration of the Euler-Lagrange equations with constraints. J. Comp. Appl. Math., 12&13:77-90, 1985.

[4] C.W. Gear, D.R.Wells. Multirate linear multistep methods. BIT 24, pp. 484-502, 1984.

[5] F. Gonzalez, M. Angel Naya, A. Luaces, M. Gonzalez. On the effect of multirate co-simulation techniques in the efficiency and accuracy of multibody system dynamics. Multibody System Dynamics, Vol. 25, Issue 4, pp. 461-483, 2011.

[6] B. Gu, H.H. Asada. Co-simulation of algebraically coupled dynamic subsystems without disclosure of proprietary subsystem models. Journal of Dynamic Systems, Measurement and Control, Vol. 126, pp. 1-13, 2004, DOI: 10.1115/1.1648307.

[7] M. Naya, J. Cuadrado, D. Dopico, U. Lugris. An efficient unified method for the combined simulation of multibody and hydraulic dynamics: comparison with simplified and co-integration approaches. Archive of Mechanical Engineering, vol. 58, pp. 223-243, 2011.

[8] D. Negrut, D. Melanz, H. Mazhar, D. Lamb, P. Jayakumar, M. Letherwood. Investigating through simulation the mobility of light tracked vehicles operating on discrete granular terrain. SAE Int. JPasseng. Cars - Mech. Syst. 6:369-381, DOI: 10.4271/2013-01-1191, 2013.

[9] B. Schweizer, D. Lu. Stabilized index-2 co-simulation approach for solver coupling with algebraic constraints. Multibody System Dynamics, DOI: 10.1007/s11044-014-9422-y, 2014.

[10] F. Spreng, P. Eberhard, F. Fleissner. An approach for the coupled simulation of machining processes using multibody system and smoothed particle hydrodynamics algorithms. Theoretical and Applied Mechanics Letters, Vol. 3, Issue 1, pp. 013005, 2013.

[11] T. Solcia, P. Masarati. Efficient Multirate Simulation of Complex Multibody Systems Based on Free Software. In ASME 2011 International Design Engineering Technical Conferences and Computers and Information in Engineering Conference, pp. 29-39, Washington, DC, USA, 2011.

PARAMETRIC STUDY ON FLEXIBLE MULTIBODY DYNAMICS VIA MODEL REDUCTION

Kai Luo, Cheng Liu [a] & Haiyan Hu
School of Aerospace Engineering, Beijing Institute of Technology, Beijing, China

Summary The paper presents an approach of reduced-order model (ROM) for parameterized flexible multibody systems described by the Absolute Nodal Coordinate Formulation (ANCF). The finite elements of ANCF is capable of describing nonlinear dynamics of flexible multibody systems with coupled overall motions and large deformations. In a neighborhood of specified parameters, the sampling ROMs are obtained offline by projecting the system dynamic equations onto the subspace of the reduced-order bases (ROBs) using the Proper Orthogonal Decomposition (POD) and Galerkin methods. Then the remaining ROMs with uncertain sets of parameters in the neighborhood can be computed for online simulation via a manifold interpolation approach so that the dimension of a parametric multibody system is significantly reduced. The accuracy and efficiency of the proposed approach is validated through a case study of a free-falling double-pendulum system composed of two flexible beams with uncertain parameters, such as Young's modulus, beam length and gravitational acceleration.

INTRODUCTION

The large-scale flexible multibody systems subject to overall motions and large deformations can be modeled by the nonlinear finite elements of Absolute Nodal Coordinate Formulation (ANCF) [1-3], which however requires high computational cost. Model reduction methods provide remarkable potentials for efficient simulations of flexible multibody dynamics by properly approximating the system. The POD (Proper Orthogonal Decomposition) method [4], one of the most popular model reduction methods, gives the optimal reduced linear representation of the original model in the sense of the average squared distance from the statistical viewpoint. Generally, the model reduction is performed using a Galerkin or Petrov-Galerkin projection. The obtained low-dimensional reduced-order model (ROM) is expected to be applied to the problems of flexible multibody systems, such as design optimization, control system design, uncertainty quantification, stability analysis, real-time simulations etc. Most of the applications mentioned above involve changes of parameters, say, material parameters, geometry parameters, input forces and other physical parameters. Therefore, the present study focuses on model reduction for parametric flexible multibody systems. The POD-based ROM can reproduce accurately the nonlinear dynamics of the full-order system whereas it lacks robustness when varying the values of parameters. Thus, a method of interpolation on manifold for the reduced-order bases (ROBs) [5] can be used to obtain a new ROM with respect to an unknown set of parameters in the neighborhood of several pre-computed sampling points. After that, an efficient online simulation can be performed by using the new ROM combined with a hyper reduction technique [6].

MODEL REDUCTION AND MANIFOLD INTERPOLATION

Solution scheme for parametric flexible multibody systems

The parametric flexible multibody systems in this study are modeled by using the finite elements of ANCF, of which the generalized coordinates contain the global position coordinates and the position gradient coordinates. Consequently, the derived dynamic equations of the system have a constant mass matrix and show no centrifugal and Coriolis forces explicitly. Therefore, the key issue of the present study is to solve efficiently the Differential Algebraic Equations (DAEs) associated with numerous sets of unknown parameters by using model reduction. The total process can be divided into two phases, including the offline one and the online one. The sampling ROBs and ROMs with respect to several sets of specified parameters are computed offline by using the POD scheme and Galerkin projection. And the ROBs and ROMs associated with the desired parameters for online simulation can be subsequently obtained with the manifold interpolation method.

Model reduction using POD and Galerkin projection

The POD scheme is performed to compute the ROBs by extracting the solution snapshots (the time series of generalized coordinate increments) from the full-order model of high-fidelity. Then the truncated ROBs are carefully chosen according to the dominant oriented energy of the snapshot data. Afterwards, the ROM is obtained based on the Galerkin projection of the full-order model onto the subspace of the ROBs. In the offline stage of a parametric problem, the above reduction operation needs to be repeated for several times to derive ROBs and ROMs associated with specified parameters.

ROM adapting via interpolation on manifolds with respect to parameter changes

With the pre-computed sets of ROBs, a new set of ROBs with respect to arbitrary parameters in the neighborhood of the sampling ones can be obtained via interpolation. However, direct interpolation of the ROBs cannot guarantee the orthogonality of the constructed ones, which may lead to the breakdown of simulation. Since the ROBs belong to the Grassmann manifold, a manifold interpolation approach [5] can be applied. First, the sampling ROBs are mapped onto a tangent space to the manifold so as to release the orthogonality constraint. Subsequently, the mapped data is interpolated in

[a] Corresponding author. Email: liucheng_bit@aliyun.com

this space using a preferable univariate or multivariate approximation method. Finally, the interpolated result is mapped back to the original manifold to derive the desired ROBs, and the ROBs is further applied to construction of a new ROM for online simulation.

CASE STUDY

Free falling of a double pendulum of two beams with uncertain parameters

This case study presents the effectiveness of the proposed method by simulating the dynamics of a flexible double-pendulum system with changes of parameters, including Young's modulus, beam length and gravitational acceleration. Figure 1 shows the initial configuration of the double pendulum composed of two beams with square cross-sections. There involve there uncertain parameters, namely, Young's modulus of the two beams $E \in [1.0e9\ \text{Pa}, 1.0e10\ \text{Pa}]$, the length of Beam 2 $L_2 \in [0.4\ \text{m}, 0.6\ \text{m}]$ and the gravitational acceleration $g \in [g_{\text{earth}}/6, g_{\text{earth}}]$ where $g_{\text{earth}}=9.81\ \text{m/s}^2$. Other related geometry sizes and the connected relationship between ground and Beam1 and between the two beams are also shown in Fig. 1. The material density and Poisson's ratio are set to be 1610 kg/m^3 and 0, respectively. Figure 2 a, b and c shows the time history of Y-displacement of the tip point C for different models corresponding to the desired parameters E, L_2 and g, respectively. It can be indicated that the dynamics responses computed by the interpolated ROM are in good consistency with those of the full-order model and the directly computed ROM based on POD.

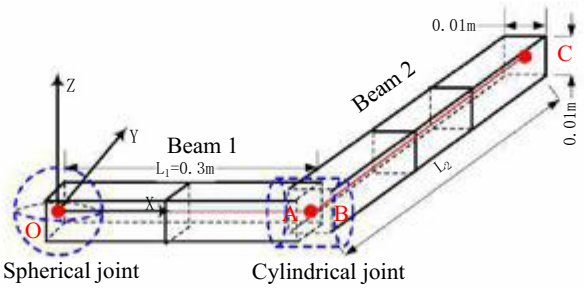

Figure 1 Initial configuration of a double pendulum

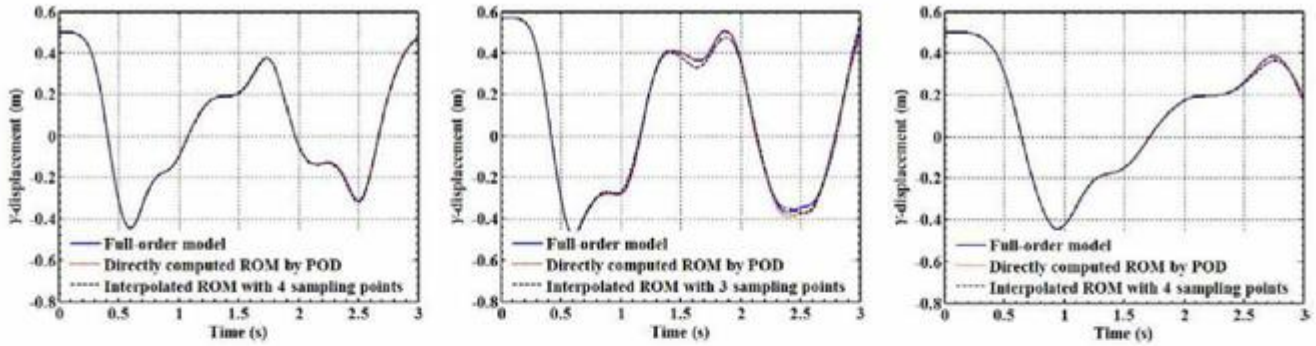

a. E=3.5e9 Pa, L_2=0.5 m, $g=g_{\text{earth}}$ b. E=1.0e9 Pa, L_2=0.57 m, $g=g_{\text{earth}}$ c. E=1.0e9 Pa, L_2=0.5 m, $g=2g_{\text{earth}}/5$

Figure 2 Time history of Y-displacement of tip C with respect to different uncertain parameters

References

[1] Liu C., Tian Q., Hu H. Y.: New Spatial Curved Beam and Shell Elements of Gradient Deficient Absolute Nodal Coordinate Formulation, *Nonlinear Dynamics*, **70**: 1903–1918, 2012.

[2] Liu C., Tian Q., Yan D., Hu H. Y.: Dynamic Analysis of Membrane Systems Undergoing Overall Motions, Large Deformations and Wrinkles via Thin Shell Elements of ANCF, *Computer Methods in Applied Mechanics and Engineering*, **258**(1): 81–95, 2013.

[3] Liu C., Tian Q., Hu H. Y.: Dynamics of a Large Scale Rigid-Flexible Multibody System with Composite Laminated Plates, *Multibody System Dynamics*, **26**:283–305, 2011.

[4] Kerschen G., Golinval J. C., Vakakis A. F., Bergman L. A.: The Method of Proper Orthogonal Decomposition for Dynamical Characterization and Order Reduction of Mechanical Systems: An Overview, *Nonlinear Dynamics*, **41**(1-3): 147–169, 2005.

[5] Amsallem D., Farhat C.: An interpolation method for adapting reduced-order models and application to aeroelasticity, *AIAA Journal*, **46**(7): 1803–1813, 2008.

[6] Farhat C., Avery P., Chapman T., Cortial J.: Dimensional reduction of nonlinear finite element dynamic models with finite rotations and energy-based mesh sampling and weighting for computational efficiency, *International Journal for Numerical Methods in Engineering*, **98**(9): 625–662, 2014.

PERISTALTIC WAVE LOCOMOTION WITH A MILLIPEDE INSPIRED MECHANISM

Javad S. Fattahi[1] and Davide Spinello*[2]

[2]*Department of Mechanical Engineering, University of Ottawa, Ottawa, Ontario, Canada*
[1]*SUNLAB, University of Ottawa, Ottawa, Ontario, Canada*

Summary We propose the model of a flexible mechanism that adapts to unstructured terrains. The locomotion mechanics is inspired by the one of multi-legged organisms such as millipedes and millipedes, whose efficiency in exploring unstructured environments is due to high redundancy and robustness of their locomotion system based on multiple contacts with the terrain. Leg to ground contact kinematics can be modeled as a peristaltic displacement wave [1], with periodic contact that provides redundancy and robustness for locomotion. The body of the mechanism is modeled as a Timoshenko beam, whose kinematics captures the basic morphology of millipedes and centipedes bodies. With respect to our work in [2] we propose a different locomotion model that is based on the mechanics of legged peristaltic locomotion [3]. A Lagrangian approach is used to derive the governing equations of the system that couple locomotion and shape morphing, that are illustrated by simulation results.

RELATED WORK

An important part of current robotic research has been and is inspired by features characterizing animal organisms, due to their inherent robustness and adaptability to uncertainties in the interaction with unstructured environments [4]. In order to achieve robustness and system adaptability with respect to different environments, mobile multibody robots have been developed from classical manipulators by considering rigid body chains interacting with the environment in a variety of modes. In the framework of flexible members, several researches have recently proposed finite dimensional (with large number of degrees of freedom) and distributed systems capable of high deformability and large displacement of the end effector [5].

DESCRIPTION OF THE MODEL AND RESULTS

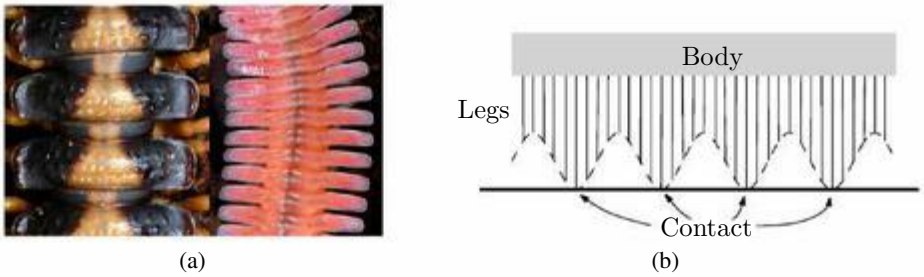

(a) (b)

Figure 1: (a) Details of the dorsal structure of selected millipedes. (By Animalparty (Own work) [CC-BY-SA-3.0 (`http://creativecommons.org/licenses/by-sa/3.0`)], via Wikimedia Commons; (b) schematic snapshot of the profile of the legs' extremities.

Millipedes have a slender body comprised of an exoskeleton which can be schematized as a chain of coaxial rings with two legs each, which possesses an internal cartilaginous spine with spinal elements connected by three degrees of freedom joints, see Fig. 1(a). The locomotion can be characterized by two mechanisms, namely the spinal locomotion and the concertina locomotion, and it is schematized by the two stages kinematics illustrated in Fig. 1(b), comprised of a stage in which the leg is in contact with the ground to create the thrust associated to friction, and a recovery stage in which the leg is not in contact. In the works [3, 1] the overall pattern has been identified as analogous to a peristaltic wave, that typically propagate in the bodies of warm-like organisms. This mechanism is inherently redundant and robust as many contact points with the ground ensure persistent thrust for forward locomotion, and allows shape morphing with respect to nonzero curvature of the substrate, with filtering of local asperities through the coupling between the legs and the body. Fig. 1(b) schematically shows a snapshot of the profile of the legs' extremities; by considering a continuous distribution of legs, we approximate the contact profile by the traveling wave

$$r \sin\left(\frac{2\pi N}{\ell}x + ct\right),\ x \in [0, \ell],$$

*Corresponding author. Email: dspinell@uottawa.ca

where r is the length of the limbs (assumed to be the same), c is the speed of propagation, x is the abscissa along the body of length ℓ, and the integer N represents the number of legs in contact with the substrate at a given time t. Note that the sign of the time term in the traveling wave profile is chosen so that contact points travel left to right with respect to the body oriented as in Fig. 1(b).

To describe the motion of the system we consider the composition of a rigid body placement with a small deformation about the rigid body configuration. The rigid body placement is described by the change of coordinates $\mathbf{x}(\mathbf{X},t) = \mathbf{d}(t) + \mathbf{R}(\theta(t))\,(\mathbf{X} \nearrow \delta\ell\mathbf{E}_1)$ that maps $\mathbf{X}$ from the reference configuration to $\mathbf{x}$ in the current rigid body configuration. The rigid change of coordinates is as usual composed of a rigid body displacement $\mathbf{d}$ with respect to the origin of a fixed reference frame, and by the action of the rotation tensor $\mathbf{R}(\theta)$. The small deformation about the rigid body placement is described by a map $\boldsymbol{\chi}$ that takes points $\mathbf{x}$ and maps them to the point $\boldsymbol{\chi}(\mathbf{x},t)$ in the current deformed configuration as $\boldsymbol{\chi}(\mathbf{x},t) = \mathbf{x} + \mathbf{U}(\mathbf{x},t)$, where $\mathbf{U}$ is a small deformation, that consistently with the the linearized planar Timoshenko beam theory is given by $\mathbf{U}(\mathbf{x},t) = (u(x_1,t) \nearrow X_2\psi(x_1,t))\mathbf{e}_1 + w(x_1,t)\mathbf{e}_2$, where $\mathbf{e}_i$ are rotated orthonormal basis vectors (floating reference frame) that are used to describe the rigid body placement, and u, ψ and w are respectively the axial displacement, the rotation of the cross section, and the traversal displacement all with respect to the rigid body placement. The velocity of a point $\boldsymbol{\chi}$ in $\mathcal{P}$ is obtained as its material time derivative, that is therefore given by

$$\dot{\boldsymbol{\chi}} = \dot{\mathbf{d}} + \dot{\theta}\mathbf{W}(\mathbf{x} \nearrow \mathbf{d}) + \dot{\mathbf{U}} \tag{1}$$

where $\dot{\theta}\mathbf{W}$ is the skew-symmetric tensor $\dot{\mathbf{R}}\mathbf{R}^{\mathsf{T}}$. The system is driven by the peristaltic wave pattern on the legs described above, which is either constitutively related to a distributed action on the body, in which case the action is equivalent to an external force, or it is geometrically related to kinematic descriptors in (1), in which case it acts as a prescribed kinematic term. The evolution equations are then obtained by by minimizing the action functional, and the corresponding weak form of the system of governing partial differential equations is reduced to a system of ordinary differential equations by projecting the spatial parts of the deformation fields along the Timoshenko beam basis functions [2].

Simulation results in Fig. 2 are obtained by setting a nondimensional peristaltic wave propagation speed $c = 0.1$, and by letting the system track a profile composed as the sequence of parabolic and straight portions, with non-smooth curvature transition between the two parts. Figure 2(a) shows eight snapshots of the system, with the state across the point with change of curvature occurring around time 100 . The zoom of this snapshot is shown in Fig. 2(b). Results illustrate how the system driven by legs' peristaltic locomotion patterns result in path tracking and shape morphing, and it delineates a theoretical and simulation framework to design a class of autonomous mobile robotic devices.

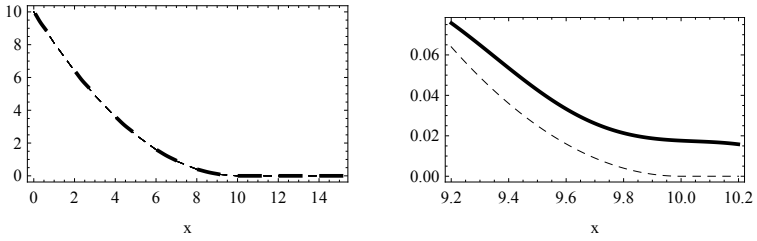

(a) (b)

Figure 2: (a) Snapshots of the system tracking a profile (terrain) and shape morphing while driven by a peristaltic wave; and (b) zoom of the snapshot at the critical point corresponding to non-smooth change of curvature of the terrain.

References

[1] Shigeru Kuroda, Itsuki Kunita, Yoshimi Tanaka, Akio Ishiguro, Ryo Kobayashi, and Toshiyuki Nakagaki. Common mechanics of mode switching in locomotion of limbless and legged animals. *Journal of The Royal Society Interface*, 11(95):20140205, 2014.

[2] J. Fattahi and D. Spinello. Path Following and Shape Morphing With a Continuous Slender Mechanism. *ASME Journal Dynamic Systems, Measurements, Control*, 2015.

[3] Yoshimi Tanaka, Kentaro Ito, Toshiyuki Nakagaki, and Ryo Kobayashi. Mechanics of peristaltic locomotion and role of anchoring. *Journal of The Royal Society Interface*, 9(67):222–233, 2011.

[4] M. Sitti, A. Menciassi, A. Jan Ijspeert, K. H. Low, and S. Kim. Survey and Introduction to the Focused Section on Bio-Inspired Mechatronics. *IEEE/ASME Transactions on Mechatronics*, 18(2):409–418, Apr 2013.

[5] Frédéric Boyer, Shaukat Ali, and Mathieu Porez. Macrocontinuous dynamics for hyperredundant robots: Application to kinematic locomotion bioinspired by elongated body animals. *Robotics, IEEE Transactions on*, 28(2):303–317, 2012.

DESIGN AND VALIDATION OF AN ELECTRIC BOOSTER BRAKE SYSTEM with HARDWARE-IN-THE-LOOP SIMULATION

Jiawang Yong[1], Nenggen Ding[1] & Yuping He[2a)]
[1]*School of Transportation Science and Engineering, Beihang University, Beijing, China*
[2]*Department of Automotive, Mechanical and Manufacturing Engineering, University of Ontario Institute of Technology, Oshawa, Canada*

Summary This paper presents an electric booster brake system, consisting of a motor and a rotational-to-linear motion mechanism which may replace the traditional vacuum booster. The system meets all the relevant requirements of electric vehicles and active safety technologies, such as brake booster without vacuum pump, coordination with regenerative braking, active brake function, etc. A sliding mode controller is proposed to implement the brake booster function using Lyapunov function approach to ensure the algorithm robustness. A number of simulations are conducted using a hardware-in-the-loop test rig. The simulation results show that the proposed controller leads to fast generation of booster brake forces, and provides a comfortable brake pedal feeling.

INTRODUCTION

Nowadays, most road vehicles still use conventional brake systems based on vacuum boosters. However, there exist two distinct disadvantages of the conventional brake systems: (1) it requires an engine to drive the vacuum booster, and motors and vacuum pumps will be needed for electric vehicles to provide vacuum source, thereby causing the brake system bulky and expensive; and (2) friction brakes will produce braking forces as long as the driver presses the brake pedal, and it makes the conventional brake systems not able to coordinate with regenerative braking.

To meet the two requirements for a non-vacuum system and to coordinate regenerative braking [1], an electric booster brake system (E-booster) is developed in this research; a vacuum booster is replaced with a motor, and the motor can be easily controlled to generate different brake pedal feeling depending on respective driver expectation. The E-booster can realize different working modes under different conditions, such as brake booster mode and regenerative braking mode. Shown in Figure 1 is the block diagram of the E-booster actuator, the motor is used to drive the actuator by using a ball-screw to amplify the output torque, and the ball-screw converts rotational motion into linear motion, thereby forcing the master cylinder piston into reciprocating motion to regulate hydraulic pressure.

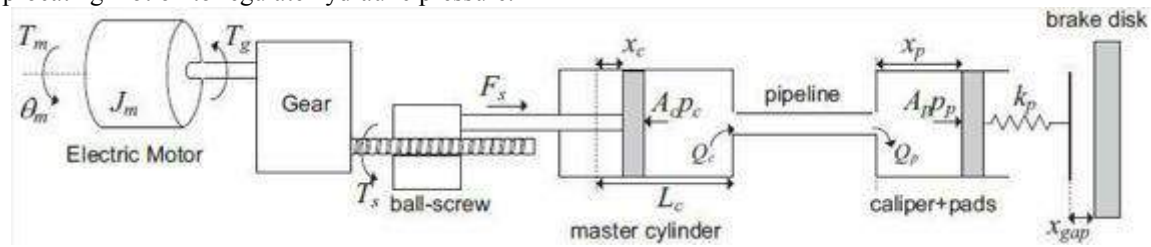

Figure 1. Block diagram of the E-booster actuator

BRAKE BOOSTER CONTROLLER DESIGN

The goal of the brake booster controller is to generate proper brake booster force in order to assist the driver to stop the vehicle, and also provide comfortable pedal feeling. A sliding mode controller is proposed in this paper to control the ball-nut tracking with the push rod. As shown in Figure 1, the torque balance equation of the E-booster actuator can be expressed as follows [2]

$$T_{\mathrm{m}} = J_m\ddot{\theta}_m + B_m\dot{\theta}_m + g(t) \tag{1}$$

where $g(t)$ represents the sum torque caused by the master cylinder pressure and system friction, J_m the inertia of the motor, B_m the coefficient of the motor.

The sliding surface σ in a domain D is defined by

$$\sigma = (\dot{x}_n - \dot{x}_p) + c(x_n - x_p) \tag{2}$$

where $x_n = k_m\theta_m$ represents the ball-nut stroke, it is determined by the rotor angle of the motor, $x_p = k_p\theta_p$ represents the push rod stroke, which is determined by the brake pedal angle, c represents a positive constant, θ_m and θ_p can be measured by the pedal angle and motor angle sensors respectively, and:

$$D = \{|\sigma| < \varepsilon\} - \{0\} \tag{3}$$

where ε is a positive constant. The Lyapunov function is defined as follows

$$V = \frac{1}{2}J_m\sigma^2 \tag{4}$$

[a)]Corresponding author. Email:yuping.he@uoit.ca.

Differentiating Equation (4) with respect to time, and using Equation (1),

$$V^{'} = \sigma\left(k_m\left(T_m - B_m\dot{\theta}_m - g(t)\right) - J_m k_p\ddot{\theta}_p + J_m c(k_m\dot{\theta}_m - k_p\dot{\theta}_p)\right) \tag{5}$$

In the domain D , we assumed that σ satisfies the following inequality

$$|\Delta(t,\theta_m,\theta_p)| \le \delta$$

where

$$\Delta(t,\theta_m,\theta_p) = -B_m\dot{\theta}_m - g(t) - \frac{J_m k_p}{k_m}\ddot{\theta}_p + J_m c(\dot{\theta}_m - \frac{k_p}{k_m}\dot{\theta}_p) \tag{6}$$

and δ is a known positive constant, substituting Equation (6) into Equation (5), yields

$$V^{'} = k_m\sigma\left(T_m + \Delta(t,\theta_m,\theta_p)\right) \tag{7}$$

Let

$$T_m = -K\,\mathrm{sgn}(\sigma) \quad (K > \delta)$$

After some manipulations, Equation (7) becomes

$$V^{'} = k_m\sigma\left(-K\,\mathrm{sgn}(\sigma) + \Delta t(\theta_m,\theta_p,I)\right) = -k_m K|\sigma| + k_m\Delta t(\theta_m,\theta_p,I) \le -k_m(K-\delta)|\sigma| < 0 \tag{8}$$

From Equation (4) and Equation (8), yields

$$2\sqrt{V}\Big|_{V(\sigma(0))}^{V(\sigma(t))} \le -k_m(K-\delta)\sqrt{\frac{2}{J_m}}t$$

$$|\sigma(t)| \le |\sigma(0)| - \frac{k_m(K-\delta)}{J_m}t$$

Thus, σ will reach the sliding surface $\sigma = 0$ in a finite time, and the controller is stable according to Equation (8).

SIMULATION RESULTS

Shown in Figures 2 and 3 are the hardware-in-the-loop simulation results using the brake booster controller. Figure 2 presents the time history of master cylinder pressure, ball-nut stroke, and pedal force. The brake pedal force is significantly decreased by using the brake booster function of the E-booster prototype, and the pedal feeling is comfortable due to the smooth and continuous pedal force curve. Figure 3 presents the time history of σ , push rod stroke, ball-nut stroke, push rod velocity, and ballnut velocity. At the beginning, there exists a gap between the push rod and the ball nut, thus, $\sigma > 0$; however, it is quickly reduced to zero after the brake pedal is applied, the stroke and velocity of the ball-nut follow the stroke and velocity of the push rod well, respectively. The experimental results verify the robustness of the brake booster algorithm.

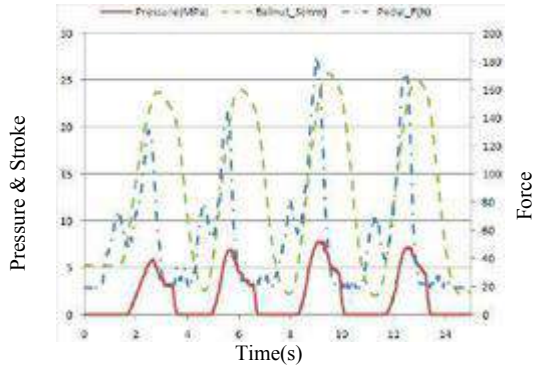

Figure 2. Ball nut stroke, pedal force and pressure

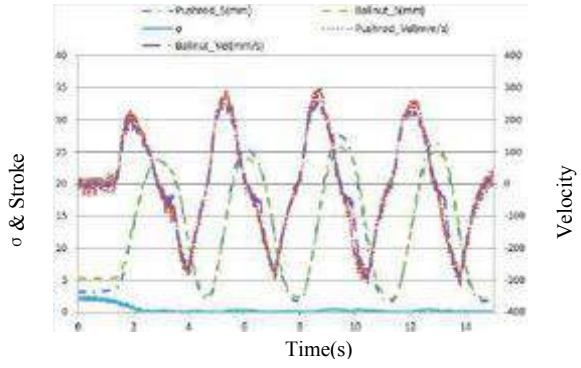

Figure 3. σ , stroke and velocity

CONCLUSIONS AND FUTURE DEVELOPMENTS

An electric booster brake system is developed with the replacement of the traditional vacuum booster by a motor, and a sliding mode brake booster controller is also proposed using Lyapunov function to ensure controller robustness. The simulation results show that the E-booster can realize the brake booster function, and the proposed algorithm generates booster brake forces fast, and forces the ball-nut to track the push rod well to ensure comfortable brake pedal feeling. The future work will focus on the coordination with regenerative braking by using the E-booster.

References

[1] Yukio Ohtani, et al.: Development of an Electrically-Driven Intelligent Brake Unit, SAE Technical Paper: 2011-01-0572.

[2] Jiawang Yong, et al.: Hardware-in-the-loop Simulation for an Integrated Braking System, SAE Technical Paper: 2015-01-1582.

DEFORMABLE-RIGID SWITCH IN COMPUTATIONAL SIMULATION OF BUS ROLLOVER TEST

Wei Zhou[1 a)], Anton Kuznetcov[1], Igor Telichev[1] & Christine Wu[1]
[1]*Mechanical Engineering, University of Manitoba, Winnipeg, Manitoba, Canada*

Summary This paper presents the application of deformable-rigid (D2R) switch technique in the computational analysis of a bus rollover test, in accordance with ECE R66 regulation. Using an explicit nonlinear dynamic finite element code LS-Dyna, a bus bay section model for rollover is prepared. All parts are switched to be rigid and merged with a master part in the free falling process. To tune the model with the real test, the flow chart and key parameters are given. The result proves the validity of D2R in the rollover analysis, and the mass and inertia are kept unchanged. The D2R switch makes the run of the detailed model applicable by reducing computation cost, thus making it valuable for design analysis and evaluation.

Introduction

The Regulation No.66 of Economic Commission for Europe (ECE R66) is enforced to guarantee the passenger safety in ground vehicle rollover accident. Residual space is the main concern due to the requirement to be not penetrated by any structures or components in the rollover accident to ensure the passenger safety. In the latest version of the ECE R66 Regulation (v.2006) [1], a computer simulation of rollover test of complete vehicle is accepted as a method equivalent to the physical testing of complete vehicle and body sections.

In the ECE R66 test, the vehicle is placed on a slowly tilting platform, and it starts to fall off at its equilibrium position when its centre of gravity reaches the highest position. To consider the 3D motion [2], the free falling process is necessary to be included in the simulation. The vehicle behaves as a rigid body before contact with the ditch surface, and starts to deform under impact. Usually, on account of the model complexity and limited computation resources, the deformable-rigid (D2R) switch technique, provided in LS-Dyna, is necessarily used to reduce the computation time cost.

Using the D2R switch in the vehicle model, key parameters and the flow chart of simulation are given and discussed in the paper in order to tune the model according to the real test data. It is also shown to be applicable and promising for the evaluation of the structural integrity and design improvement of a complete full-scale vehicle model using the D2R switch.

Deformable-rigid (D2R) switch and finite element model

D2R switch

Shown in ***Fig.1***, the model needs to be switched from the "deformable" to the "rigid" state at the beginning (Position A), and get a reverse switch back to the original state before the hitting of ground (Position B). This round-way switch can be implemented in LS-Dyna using the keyword *DEFORMABLE_TO_RIGID_AUTOMATIC. The activation of the switch can be controlled by the time [3].

It's recommended to switch all parts in the model to avoid error in mass calculation [4]. A master rigid body is suggested to be specified for the D2R switch. It is chosen as one of initial rigid bodies in the model. During the switch, all deformable bodies are merged with the master rigid body. The choice of master rigid body can be arbitrary, whereas it needs to avoid the one with special boundary conditions. Rigid bodies initially existing in the model should be excluded from the switch list [4], otherwise they will also be merged with the master. This merge is irreversible, and it leads to inaccuracy of model.

The potential energy variation during the free falling process is the key factor for the rollover analysis. Thus, the mass and inertia of the model must be kept unchanged by the D2R switch, which can be verified in results [4].

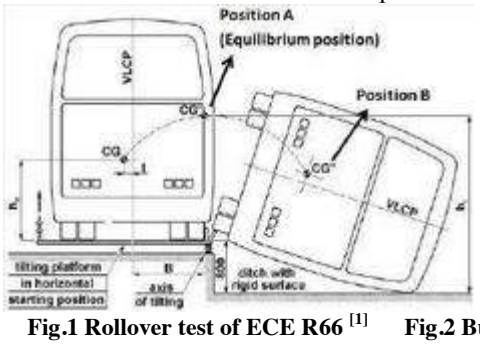

Fig.1 Rollover test of ECE R66 [1]

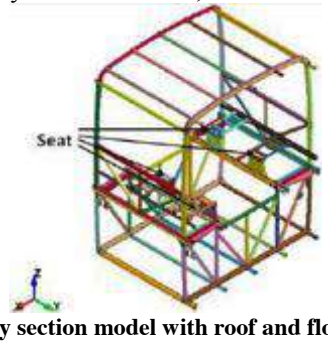

Fig.2 Bus bay section model with roof and floor hidden

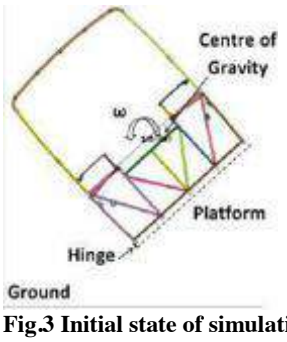

Fig.3 Initial state of simulation

FE model

Fig. 2 illustrates a model of the bay section built to simulate the rollover test for the typical bus. The total mass of the unloaded bay section (without passengers) is 1811 kg. The model contains approximately 187,000 shell elements, using

a) Corresponding author. Email: zhouw346@myumanitoba.ca.

four-node Belytschko-Tsay formulation with 5 integration points through the thickness. The material model includes materials of type 24 (024 PIECEWISE_LINEAR_PLASTICITY) and type 20 (020 RIGID). Contact and constrain cards are used for the inter-connection of both deformable and rigid parts. Welding is modelled using the tied contact between parts with type 24 shell elements as welds.

The simulation starts with the equilibrium position shown in ***Fig.3***. The initial rotation velocity is set to a negligible value. The gravity is applied as the external loading. A rotary hinge is built where the lower frame touches the platform shoulder. The lower half of hinge is fixed in space while the upper half is connected with the frame. Thus, the hinge here replaces the contact definition. The failure of hinge is activated when the bay section leaves the platform.

The contact of the bay section and ground is implemented as *RIGIDWALL_PLANAR, also shown in ***Fig.3***.

The simulation was performed for 4.5s of event using MPP LS-Dyna on the supercomputing facility ***GREX, Westgrid*** (Compute Canada) with 12 cores. The simulation time was 12.3 hours. The rigid state of D2R lasts for 2.48s. It's found that the simulation during this D2R rigid state is about 3.4 times faster than the rest of simulation.

Key parameters and simulation process

In order to tune the model with the available rollover test data (video providing deformation history), the key parameters are identified and shown in ***Fig.4*** along with the flow chart of simulation. It is summarized below.

Firstly, set "Initial rotational velocity", then do initial run and record "Hitting time", which is expected to be equivalent to the test data; set "D2R switch time" smaller than "Hitting time" but very close to it, and "Contact birth time" to be equal to "D2R switch time"; Secondly, set a proper "Time step" during D2R switch to get an accepted mass increase due to mass scaling; Finally, set "Hinge failure time" obtained from the test video as the time when the bay section leaves the platform.

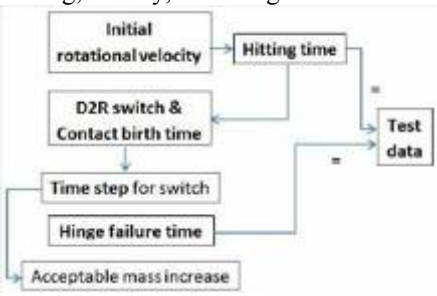

Fig.4 Key parameters and tuning process

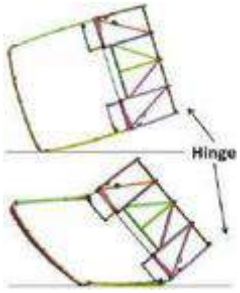

Fig.5 Moments of hitting ground and maximum deformation

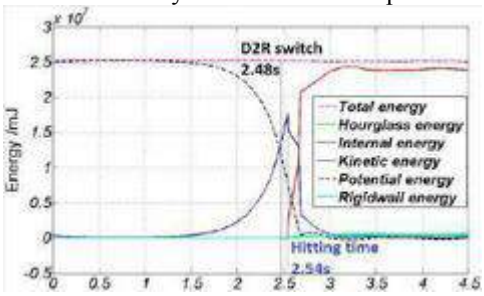

Fig.6 Energy curve

Results and discussion

The results of simulation when the bay section hits the ground and when the deformation of structure is maximal are presented in ***Fig.5***. It's shown that the side frame is severely bent at seats' connection.

The energy curve is shown in ***Fig.6***. At 2.54s, the bay section hits the ground, thus kinetic energy reaches the peak and internal energy starts to increase rapidly. The total energy is kept conserved before and after the rollover, thus the validity of the model is proved.

From the obtained result one may conclude that as the kinetic energy and resultant velocity is continuous, the model mass is kept correct during the D2R switch. By choosing different master rigid bodies, it's shown that the potential energy curves are the same. Then it proves that the D2R switch doesn't change the inertia.

Conclusion

The D2R is an efficient technique in LS-Dyna for the vehicle rollover analysis which reduces the computation cost of simulation treating the model as rigid in the free falling process. Also, it's necessary to avoid wrong internal energy developed by gravity in free falling. Application of D2R in a complete vehicle model will be useful for design improvement evaluation to meet the regulation requirement. Extracted loading will be beneficial to the refinement of bus components.

References

[1] JASIC, ECE. "Regulation No. 66 01-Strength of Superstructure." Economic Commission for Europe (2006): 1-49.

[2] Rogov, P. S., et al. "Comparative Estimation Between Computer Simulation Results of the Bus Body Section Rollover and Experimental Data." Acta Technica Jaurinensis 7.3 (2014): 258-266.

[3] LSTC, LS-DYNA. "Keyword user's manual volume I." LS-DYNA Dev (2013).

[4] Zhu, Ling. "Development of guidelines for deformable and rigid switch in LS-Dyna simulation." Mechanical (and Materials) Engineering--Dissertations, Theses, and Student Research (2009): 3.

SM12 - Nanostructures and MEMS

TS.SM12-1.01	Bertoldi, Katia - Architected materials: Performance through bistability (INVITED)	2605
TS.SM12-1.02	Xu, Baoxing - Mechanics of evaporation-driven folding of graphene sheets	2607
TS.SM12-1.03	Chen, Xue - Asymmetric bifurcation of FGM microbeam actuated by thermo-electrical loadings	2609
TS.SM12-1.04	Comi, Claudia - Pull-in and nonlinear dynamic behavior of torsional microresonators	2611
TS.SM12-1.05	Elhebeary, Mohamed - Mechanical Characterization of Materials At Micro/Nanoscale Under Bending	2613
TS.SM12-1.06	Endo, Daichi - Utilization of Self-Excited Oscillation for Mass Sensing in Liquid	2615
TS.SM12-2.01	Gao, Huajian - Recoverable plasticity in penta-twinned metallic nanowires (INVITED)	2617
TS.SM12-2.02	Farokhi, Hamed - Nonlinear behaviour of carbon nanotube-based resonators	2619
TS.SM12-2.03	Guo, Jian-Gang - Theoretical studies on adsorption and diffusion of Li-ion on graphene surface	2621
TS.SM12-2.04	Guo, Wanlin - Mechanical-electric-magnetic coupling and energy conversion in two-dimensional materials	2623
TS.SM12-2.05	Gupta, Ankit - Multi scale modeling of mechanical behaviour of 2D single wall carbon nanotube network	2624
TS.SM12-2.06	Ke, Changhong - Nanomechanical characterization of boron nitride and carbon nanotubes polymer interfaces	2626
TS.SM12-3.01	Misseroni, Diego - Serpentine motion through a frictionless channel (INVITED)	2628
TS.SM12-3.02	Lei, Xiao-Wen - Complex energy landscapes of carbon nanotubes with defects	2630
TS.SM12-3.03	Lengiewicz, Jakub - Two-Domain Model of Volumetric Actuators	2632
TS.SM12-3.04	Li, Teng - Anomalous scaling law of mechanical properties of cellulose nanopaper	2634
TS.SM12-3.05	Liechti, Kenneth - Graphene interactions by displacement-controlled nanoindentation	2636
TS.SM12-4.01	Zhu, Yong - Giant Anelasticity and Energy Dissipation in Single-Crystalline Nanowires (INVITED)	2638
TS.SM12-4.02	Linne, Marissa - Examination of interactions between deformation mechanisms in fcc thin films using SEM-DIC	2640
TS.SM12-4.03	Mirzazadeh, Ramin - On-chip testing device for the micromechanical characterization of polysilicon films	2642
TS.SM12-4.04	Pan, Fei - Stiffness threshold of randomly distributed carbon nanotube networks	2644
TS.SM12-4.05	Richter, Gunther - Growth and mechanical properties of metal nanowhiskers	2646
TS.SM12-5.01	Ardito, Raffaele - Multiphysics analysis and design of an air-coupled pzt-based pmut	2648
TS.SM12-5.02	Tolladay, Mat - Predicting piezoelectric effects in atomistic finite element simulations	2650
TS.SM12-5.03	Vairo, Giuseppe - A 3-layered non-linear homogenization approach for nanoporous materials	2652
TS.SM12-5.04	Alneamy, Ayman - Electrostatic versus Electromagnetic Micromirror Actuation	2654
TS.SM12-5.05	Zhang, Jiaxi - Development of a Robust Coupled Atomistic-continiuum Model for Crack Progagation	2656

PO.SM12-1.01.166	Chen, Cheng - Effects of lateral strain and corner geometry on self-rolling of nanomembranes	2658
PO.SM12-1.02.167	Damasceno, Daniela - Mechanical behavior of graphene sheet using atomic-scale finite element method	2660
PO.SM12-1.03.168	Effa, David - Analysis of thermal noise in frequency-modulated gyroscopes	2662
PO.SM12-1.04.169	Gilchrist, Michael - Polymer injection molding of micro/nano structured devices	2664
PO.SM12-1.05.170	Guz, Igor - Effect of a special reinforcement on the nanocomposite properties	2666
PO.SM12-1.06.171	Kang, Wonmo - Study of the electromechanical behavior of metals using a microdevice method	2668
PO.SM12-1.07.172	Wang, Binglei - Size-dependent nonlinear behavior for electrostatic actuated NEMS with Casimir force	2670
PO.SM12-1.08.173	Wang, Chaoying - Effects of dislocation on the performance of Si anode in Na and Mg-ion batteries	2672
PO.SM12-1.09.174	Wu, Bingjie - Effect of an applied force on ripple formation of free graphene ribbons	2674

ARCHITECTED MATERIALS: PERFORMANCE THROUGH BISTABILITY

Katia Bertoldi[1], Jordan Raney[1], Sicong Shan[1], Sung Hoon Kang[2], Jennifer Lewis[1], Neel Nadkarni[3], Chiara Daraio[4], Dennis Kochmann[3]

[1]*School of Engineering and Applied Sciences, Harvard University, Cambridge, United States*
[2]*Department of Mechanical Engineering, John Hopkins University, Baltimore, United States*
[3]*Graduate Aerospace Laboratories, California Institute of Technology, Pasadena, United States*
[4]*Department of Mechanical and Process Engineering, ETH Zurich, Zurich, Switzerland*

Summary Although the study of the effect of shape and geometry on the mechanical response of solid objects has a long history, the surge of modern techniques to fabricate structures of complex form paired with our ability to simulate and better understand their response has created new opportunities for the design of architected materials with novel functionalities (also referred to as metamaterials). In this talk I will show that by carefully designing the meso-structure, novel effective behavior at the macroscale can be achieved.

In recent years we have witnessed the emergence of materials in which the meso-scale structure has a prominent role and whose mechanical behavior is governed by structure rather than chemistry. Here, I will focus on the mechanical properties of a specific class of such architected materials: highly non-linear periodic and elastic structures comprising bistable elements.

Harnessing snap-through instability to design reusable energy absorbing materials

Energy absorbing materials are widely deployed for personnel protection, crash mitigation in automobiles and aircrafts, and protective packaging of delicate components. Many strategies have been investigated to create materials that efficiently dissipate mechanical energy, including plastic deformation in metals, fragmentation in ceramics, and rate-dependent viscous processes. However, in all of these systems there are challenges associated with either reusability or rate dependency. Most recently, mechanical metamaterials have been fabricated in novel geometries to realize recoverable energy-absorbing behavior in elastic systems, suggesting novel strategies for mechanical dissipation of energy.

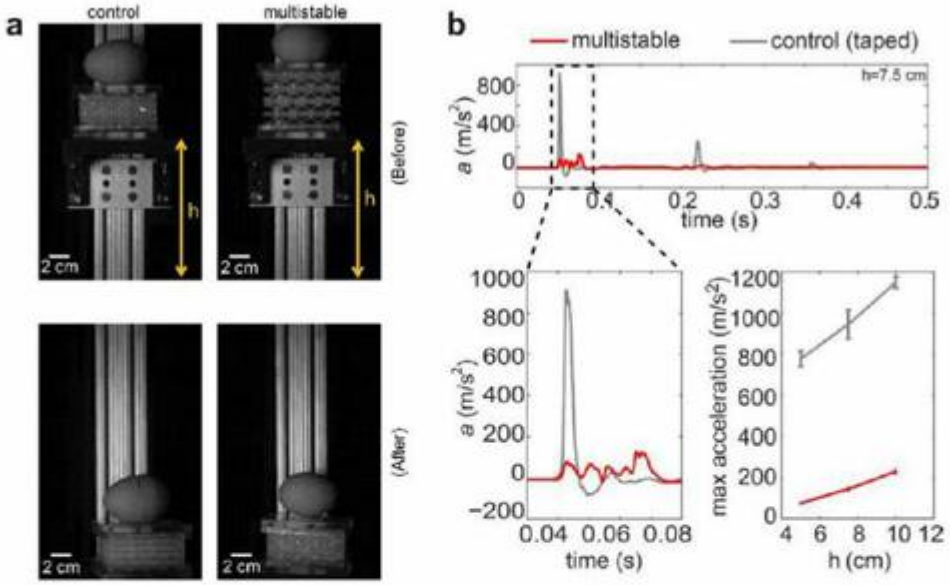

Figure 1: (a) Drop of multistable and control samples (consisting of the same structures but taped to make all beams intentionally collapsed prior to the drop test) with raw eggs attached to their top from h = 12.5 cm. The eggs attached to the multistable structures survive, while those on the control samples break upon impact. (b) Acceleration–time curve for a multistable structure and the corresponding control sample dropped from h = 7.5 cm

We recently reported a new class of architected materials in which the energy inserted into a system during loading is trapped in the form of elastic deformation of a large number of bistable elastic beams [1]. Our design is motivated by the

[a] Corresponding author. Email: bertoldi@seas.harvard.edu

observation that, in contrast to an elastic beam that buckles under axial compression, but fully recovers its initial shape when unloaded, a bistable beam snaps between two different stable configurations and retain its deformed shape after unloading. Therefore, such a bistable beam is capable of locking in most of the energy inserted into the system during loading and can be used as an energy absorbing element.

We first combined experiments and simulations to systematically investigate the effects of the beam geometry on its mechanical response and then demonstrated that bistable elastic beams can be arranged to form energy-trapping materials (Fig. 1). Our strategy offers several advantages; it can be applied to structures with various length scales (from micro to macro) and provides a simple modular design scheme, so that the mechanical response can be tuned by controlling geometric parameters guided by a ``phase diagram''. Moreover, the loading process is fully reversible, allowing the structures to be consistently reused many times, with the energy absorption unaffected by loading rate or history.

Harnessing snap-through instability to achieve stable propagation of mechanical signals in soft media

Soft structures with rationally designed architectures capable of large, nonlinear deformation present opportunities for the design of unprecedented, highly-tunable devices and machines. However, the highly-dissipative nature of soft materials has inherently limited the way in which such systems can be used. We recently investigated an architected soft system comprised of elastomeric, bistable beam elements connected by elastomeric linear springs. The dissipative nature of the polymer readily damps linear waves, preventing propagation of any mechanical signal beyond a short distance, as expected. However, the unique architecture of the system enables propagation of stable, nonlinear solitary transition waves with constant velocity and pulse geometry over arbitrary distances. Since the high damping of the material removes all other linear, small amplitude excitations, the desired pulse propagates with high fidelity and controllability. This phenomena can be used for control signals as we demonstrate through the design of soft diodes and soft mechanical logic gates.

References

[1] Shan S, Kang SH, Raney J, Wang P, Fang L, Candido F, Lewis J, Bertoldi K. Multistable Architected Materials for Trapping Elastic Strain Energy. Advanced Materials. 2015;27(29):4296

MECHANICS OF EVAPORATION-DRIVEN FOLDING OF GRAPHENE SHEETS

Qingchang Liu & Baoxing Xu [a)]
Department of Mechanical and Aerospace Engineering, University of Virginia,
Charlottesville, VA 22904, USA

Summary We propose a mechanics theory of folding two-dimensional (2D) graphene sheets from rapid evaporation of its liquid suspension. Using an energy criterion that contains the competition among bending energy of graphene sheets, surface energy of graphene sheets and liquid and their interfacial energy, and binding energy of folded graphene sheets, we are able to quantitatively correlate folded three-dimensional (3D) graphene structures with both geometric size and surface wettability of 2D graphene sheets. Theoretical predictions of folded 3D graphene structures agree well with parallel molecular dynamics simulations. Our theory is of immediate interest to the study of crumping/folding original 2D structures to 3D shapes through evaporation of a liquid suspension.

INTRODUCTION

Crumpling or folding two-dimensional (2D) structures such as graphene sheets into three-dimensional (3D) structures has been considered a facile route to scale up them to macroscopic level. The formed crumpled structures can inherit the merits of 2D structures such as superhigh specific surface area, extreme electrical conductivity and ultrahigh toughness by resisting aggregation of planar graphene sheets when they are packed up to macroscopic scale, and attracts tremendous attention for wide applications from supercapacitors to energy absorbers. In comparison with 3D graphene patterns that are often achieved through mechanical buckling deformation in a substrate [1], the recent developed liquid-assisted folding of graphene sheets from evaporation of its liquid suspension provides a novel manufacturing technique due to easy delivery of folded structures. For example, crumpled balls of graphene are observed in experiment through rapid evaporation of an aerosol dispersion of micrometer-sized graphene oxide sheets [2-4]. When the solvent solution or concentration of graphene oxide sheets changes, 3D porous graphene oxide structures can also form spontaneously through evaporation of the liquid phase [5]. The crumpling mechanism of graphene sheets are expected to be led by the competition of interfacial energy and elastic bending energy of graphene sheet, with the former promoting and later resisting folding of structures. Herein, we will present the first theory for quantitatively describing the folding process of 2D graphene sheets from evaporation of liquid. By considering the competition of solid-liquid interfacial energy, liquid/solid surface energy, binding energy and elastic bending energy of graphene sheets in water liquid, we construct an energy criterion that takes into account both geometric size and surface wettability of graphene and can be used to identify the folded pattern and stability of 3D graphene structures. Extensive molecular dynamics (MD) simulations are also performed in parallel to examine the folding process and show good consistence with theoretical predictions.

ENERGY ANALYSIS AND THEORY MODEL

Consider a mixture of a single flexible graphene sheet and water liquid (Figure 1a), depending on surface wettability of the graphene, it either wraps the water droplet with one side in contact with water and the other exposed to the air, or is wrapped up by water droplet with both sides in contact with water at equilibrium. The wrapping state can be determined by classic Young's equation via a contact angle of water droplet sitting on a graphene surface θ_c. At $\theta_c < 90^\circ$, the surface of graphene sheet is hydrophilic, and it will be wrapped by the water droplet, and at $\theta_c > 90^\circ$, the surface of graphene is hydrophobic and it stays outside the water droplet. Given the volume of water droplet, V, the radius of water droplet, $r_w^e=(3V^e/4V)^{1/3}$, can be obtained by approximately simplifying to a spherical ball at equilibrium, where the superscript e represents equilibrium state without evaporation of water. Along with formation of the water droplet ball due to minimization of surface energy, the graphene sheet will deform and the deformation is dominated by energy, E:

$$E = E_{surface} + E_{interface} + E_{bending} + E_{binding} \quad (1)$$

where $E_{surface}$ includes surface energy of both water droplet and graphene, $E_{interface}$ is the water-graphene interfacial energy, $E_{bending}$ is the elastic bending energy of the graphene sheet, and $E_{binding}$ is the binding energy of the graphene sheet that overlaps together if happens. Once the evaporation of water liquid occurs, the equilibrium of water-graphene interactions will break. If the profiles of graphene sheet at equilibrium (i.e. Figure 1 patterns I, II, III, IV) will continue to deform, the energy E will decrease, otherwise they will recover, where if the recovery happens, we consider the evaporation will not fold the graphene sheet. Therefore, an energy variation, ΔE, can be employed to determine the evaporation-driven folding of the graphene sheets after equilibrium, that is,

$$\Delta E = E - E^e \quad (2)$$

[a)] Corresponding author. Email: bx4c@virginia.edu

Obviously, if $\Delta E > 0$, evaporation of water liquid will not fold the graphene sheet, and if $\Delta E < 0$, the energy E will decrease, favorable to further folding graphene sheet. Though analysis, ΔE can be obtained. For example, for pattern I, we have:

$$\Delta E = \frac{1}{8\pi^3} L^3 + \frac{(2h+w)}{4\pi^2} L^2 + \left(\frac{h^2+wh-2r_w^2}{2\pi} - \frac{E_0}{4\pi^2\gamma_w} \right) L + \frac{Bw}{2\gamma_w} / \quad (3)$$

where L and w is graphene length and width, respectively. B is the bending stiffness of the graphene sheet and γ_w is the surface tension of water molecules. By solving Eq.3, the critical graphene sheet $L_c = 9.8 nm$ that corresponds to $\Delta E = 0$ can be obtained. Beyond the L_c, $\Delta E < 0$ and pattern I will continue to deform with the evaporation of water molecules. Similar procedures as Eq. 3, Equations can be constructed for patterns II, III and IV and the corresponding critical length of graphene sheets for self-folding can be determined.

To predict the size of final folding patterns and geometric features, we will continue to employ the energy criterion. For example, for the patterns I, assume it is composed of an overlapped part with length l_o and interlayer distance of t and bended graphene with a partial circle of radius r_g, with a small increment Δl_o, we can have:

$$\Delta E = -2\Delta l_o w\gamma_g + B\pi w \left(\frac{2\pi}{L-2(l_o+\Delta l_o)} - \frac{2\pi}{L-2l_o} \right) - \Delta l_o w\gamma_{binding} \quad (4)$$

The stable folded pattern with the overlapped length l_o can be estimated by $\Delta E = 0$. Figure 1b shows the overlap length l_o obtained from theoretical estimations. Comparison with MD results shows good agreement for all unfolding and folding patterns, validating the robustness of theoretical models.

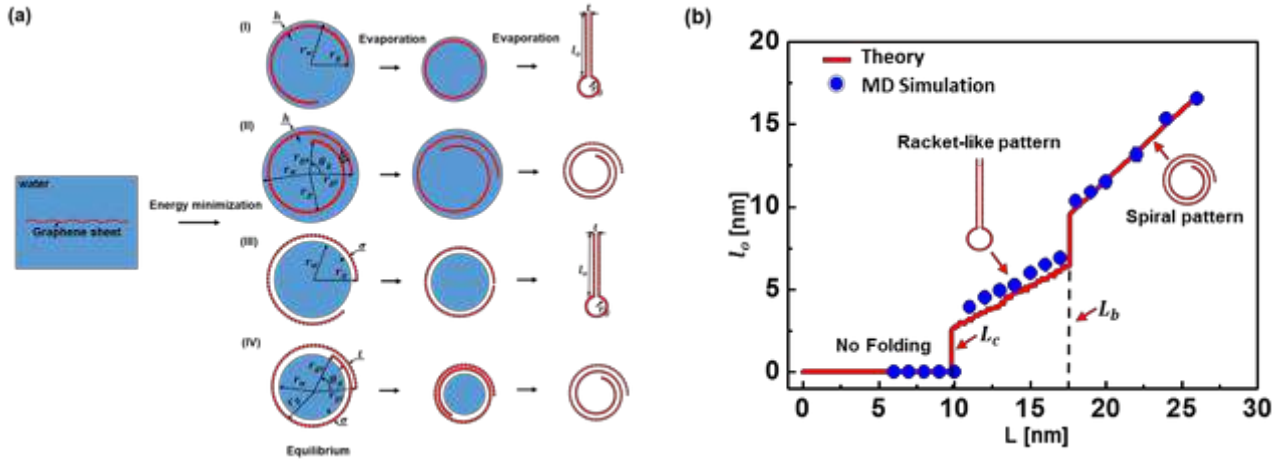

Figure 1: (a) Mixture of a single graphene sheet with water liquid and stable patterns of formed graphene sheet accommodated with water droplet in equilibrium. (I) and (III) represents an open circle pattern, and (II) and (IV) represents a spiral pattern. The wrapping state of water droplet with graphene sheet depends on the surface wettability of graphene, patterns I and II correspond to a hydrophilic surface of graphene, and pattern III and IV correspond to a hydrophobic surface of graphene. **(b)** Comparison of theoretical prediction and MD simulation of the overlap length l_o in the ultimate stable folded patterns for different lengths of graphene sheets L in water liquid.

CONCLUSIONS

We have investigated the folding of graphene sheet in a liquid environment from evaporation of liquid phase and developed an energy criterion that drives the folding process by considering the competition of surface, interfacial, bending and binding energies. Two folding patterns of racket-like and spiral profiles that depends on the geometric shape and surface wettability of graphene sheet are found. The extensive MD simulations have verified the competition of energy and agrees well with theoretical analysis.

References

[1] Zang J., Ryu S., Pugno N., Wang Q., Tu Q., Buehler M.J., and Zhao X.: *Nat. Mater.* 12: 321-325, 2013.

[2] Ma X., Zachariah M.R., and Zangmeister C.D.: *Nano Lett.* 12:486-489, 2012.

[3] Chen Y., Guo F., Jachak A., Kim S.P., Datta D., Liu J., Kulaots I., Vaslet C., Jang H.D., Huang J., Kane A., Shenoy V.B., Hurt R.H.: *Nano Lett.* 12:1996-2002, 2012

[4] Luo J., Jang H.D., Sun T., Xiao L., He Z., Katsoulidis A.P., Kanatzidis M.G., Gibson J.M., and Huang J.: *ACS Nano* 5: 8943-8949, 2011.

[5] Lee S. H., Kim H. W., Hwang J. O., Lee W. J., Kwon J., Bielawski C. W., Ruoff R. S., and Kim S. O. : *Angew. Chem. Int.* Ed. 49: 10084-10088, 2010.

ASYMMETRIC BIFURCATION OF FGM MICROBEAM ACTUATED BY THERMO-ELECTRICAL LOADINGS

Xue Chen [1] & Shaker A. Meguid [1a)]
[1]*Department of Mechanical and Industrial Engineering, University of Toronto, Toronto, Ontario, Canada.*

Summary This paper investigates the symmetric snap-through buckling and asymmetric bifurcation behaviours of an initially curved functionally graded material microbeam subject to the electrostatic force and uniform/non-uniform temperature field. The beam model is developed in the framework of Euler-Bernoulli beam theory, accounting for the through-thickness power law variation of the beam material and the physical neutral plane. Based on the Galerkin decomposition method, the beam model is simplified as a two-degree-of-freedom reduced-order model, from which the necessary snap-through and symmetry breaking criteria are derived. The work results reveal the significant effects of the power law index on the snap-through and symmetry breaking criteria. They also reveal that the non-uniform temperature field can actuate the functionally graded material microbeam and induce the snap-through and asymmetric bifurcation behaviours.

INTRODUCTION

The bistable Micro-Electro-Mechanical Systems based on initially curved microbeams have drawn considerable attention from the research community due to their various potential applications such as optical switches, micro-valves, and non-volatile memories. The initially curved beam (arch) under transverse forces may exhibit two main instabilities: symmetric snap-through buckling and asymmetric bifurcation. Studies on snap-through and asymmetric bifurcation of homogeneous microbeams have been largely reported in the literature [e.g., 1−4]. In this paper, we extend our earlier work [4] to study the snap-through and asymmetric bifurcation of the initially curved functionally graded material (FGM) microbeam under thermo-electrical loadings.

MODEL FORMULATION

The studied FGM microbeam system is shown in Fig. 1(a). By using Euler-Bernoulli beam theory and taking the first two buckling modes in Galerkin decomposition method, we obtain the two-degree-of-freedom reduced-order model as:

$$\gamma \quad + {}_{t1}\Delta \quad + \left(b_{11} - \gamma\, n\, s^2 q^2 - \Delta \quad {}_{11}\right) q_1 + \gamma\, n\, s\ \ s\ \ q\, q^2 - b_{11} q_0 = -\beta_v I\ \ q\ \ q \tag{1a}$$

$$\gamma\, n\, s^2 q^3 + {}_{t2}\,\Delta T\ n + \left(b_{22} - \gamma\, n\, s\ \ s\ \ q^2 - P\,\Delta T\ n\, s \quad q_2 + \gamma\, n\, s\ \ s\ \ q^2 q = -\beta_v I_2\ q_1\ q \right. \tag{1b}$$

where q_0 is the dimensionless initial arch rise, q_1 is the dimensionless midpoint deflection, and q_2 is the generalized coordinate of the second buckling mode; γ is stretching parameter, P is thermal axial force, I_{t1} and I_{t2} represent the transverse force from thermal moment, and β_v is voltage parameter; I_1 and I_2 are integrals depending on q_1 and q_2, b_{11}, b_{22}, s_{11}, and s_{22} are constants; ΔT is temperature variation, and n (≥ 0) is a power law index determining the variation of beam material (see Fig. 1(b)). Detailed derivations of Eq. (1), and expressions and values of the parameters can be found in [5].

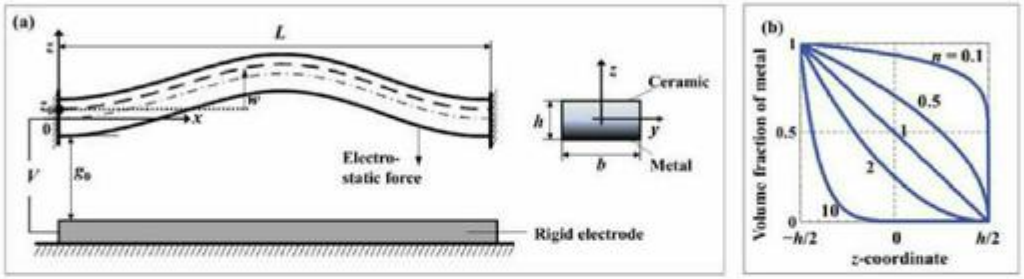

Fig. 1. (a) Initially curved functionally graded material microbeam under distributed electrostatic force (direction indicated by arrow). (b) Variation of volume fraction of metal along beam thickness at different levels of power law index n.

FGM MICROBEAM ACTUATED BY ELECTRICAL LOADING

Considering an FGM microbeam under a uniform temperature increase and using Eq. (1), we show the effects of power law index n on the snap-through and asymmetric bifurcation behaviours in Figs. 2(a) and (b). We also derive the analytical expressions of necessary criteria for the existence of snap-through and asymmetric bifurcation, and plot them in Figs. 2(c) and (d). The power law index influences the temperature-induced axial force, which in turn influences the instability behaviours and the corresponding criteria.

[a)] Corresponding author. Email: meguid@mie.utoronto.ca.

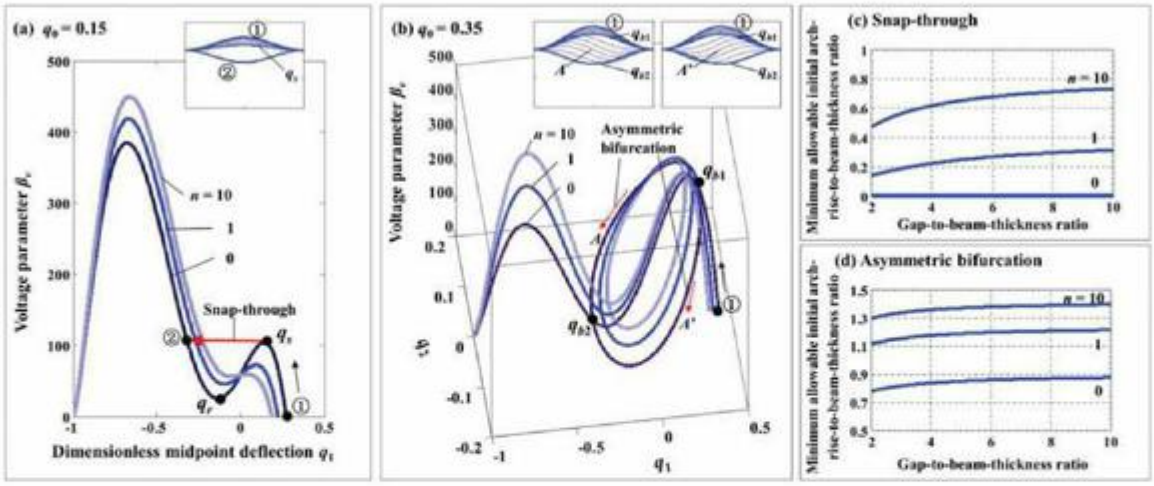

Fig. 2. (a), (b) Bifurcation diagram of FGM microbeam actuated by electrical loading. (c), (d) Minimum allowable ratio between the initial arch rise and the beam thickness for the existence of snap-through and asymmetric bifurcation.

FGM MICROBEAM ACTUATED BY THERMAL LOADING

By generating a uniform heat source in the beam and applying a temperature change to the beam ends, we can also actuate the FGM microbeam, and induce snap-through and asymmetric bifurcation behaviours as shown in Fig. 3.

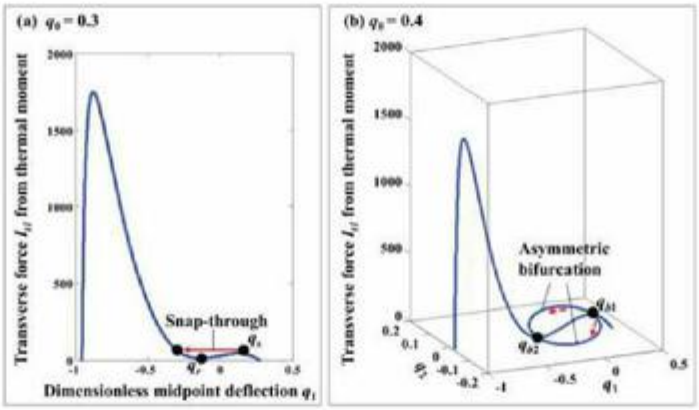

Fig. 3. Bifurcation diagram of FGM microbeam actuated by thermal loading.

CONCLUSIONS

This paper is concerned with a unified study on snap-through and asymmetric bifurcation of an initially curved functionally graded material (FGM) microbeam under thermo-electrical loadings. The two-constituent material variation through the beam thickness is taken into account using a power law model. The governing equations, which consider the physical neutral plane, are developed and solved by the Galerkin decomposition method. Our results, which are based on the two-degree-of-freedom reduced-order model, show that the power law index plays a significant role in the snap-through and symmetry breaking criteria. Our results also show that the FGM microbeam can be actuated by the non-uniform temperature field.

References

[1] Krylov S., Ilic B. R., Schreiber D., Seretensky S., Craighead H.: The pull-in behavior of electrostatically actuated bistable microstructures. *J Micromech Microeng* **18**:055026, 2008.

[2] Das K., Batra R. C.: Pull-in and snap-through instabilities in transient deformations of microelectromechanical systems. *J Micromech Microeng* **19**:035008, 2009.

[3] Medina L., Gilat R., Krylov S.: Symmetry breaking in an initially curved micro beam loaded by a distributed electrostatic force. *Int J Solids Struct* **49**:1864–1876, 2012.

[4] Chen X., Meguid S. A.: Snap-through buckling of initially curved microbeam subject to an electrostatic force. *Proc R Soc A* **471**:20150072, 2015.

[5] Chen X., Meguid S. A.: Asymmetric bifurcation of thermally and electrically actuated FGM microbeam. *Proc R Soc A*, 2016 (accepted, to appear).

PULL-IN AND NONLINEAR DYNAMIC BEHAVIOR OF TORSIONAL MICRORESONATORS

Claudia Comi *[1], Alberto Corigliano[1], Valentina Zega[1], and Sarah Zerbini[2]
[1]*Civil and Environmental Engineering, Politecnico di Milano, Milan, Italy*
[2]*AMS group, STMicroelectronics, 2010 Cornaredo, Milan, Italy.*

Summary Torsional microresonators find application in a number of microdevices, including gyroscopes and resonant accelerometers [1], magnetometers, mass detection devices and micro-mirrors. The study of torsional resonators, also in the nonlinear regime, is therefore needed in order to properly design and test such devices. Here a static characterization of the resonator is shown together with a study of the non-linear dynamic behavior. Two analytical approximations (III and V order) of the dynamic frequency response of the torsional resonators are compared to the numerical solution of the full dynamic model and a limit domain is found in the bias voltage - actuation voltage plane.

TORSIONAL RESONATOR AND STATIC PULL-IN

Figure 1a shows the top SEM image of the silicon torsional microresonator here studied. A mass is connected to the substrate by two torsional springs which allow for its out-of-plane rotation θ (counterclockwise positive). During the dynamic functioning, the torsional resonator is kept in resonant oscillation according to its torsional natural mode by the driving electrode located below it on the substrate with an initial gap g_0, while one further independent electrode placed on the substrate allows for motional current detection (see Fig. 1b).

For the electrostatic characterization, the mass of the resonator, together with the sensing electrode, are grounded while the driving electrode is swept with a constant incremental voltage V_P until pull-in occurs. The experimental results in terms of capacitance variation versus polarization voltage V_P are shown in Fig. 1c by dots: they are in very good agreement with the analitical prediction (continuos line). The static pull-in voltage turns out to be 20.5 V.

NON-LINEAR DYNAMIC BEHAVIOR OF TORSIONAL RESONATOR

In the real device operation condition, the mass is polarized at $V = V_P$ and a varying actuation voltage v_a is applied to the driving electrode. Starting from the one-degree-of-freedom approximation presented in [3], here a numerical solution of the full nonlinear dynamic model is shown together with two different analytical solutions, valid under the hypothesis $V_P >> |v_a|$ and $\theta << 1$ rad: the 'III order approximation' usually used for describing this kind of devices [4] and the more accurate 'V order approximation'. While the three solutions behave in the same way in the linear regime, in Fig. 2a it is shown how the 'III order approximation' is not accurate to describe the non-linear dynamic behavior of this resonator even in the range of small θ. Moreover, when the hypothesis $V_P >> |v_a|$ is no more valid, both the III and V order approximations are not suitable to give the real behavior as shown in Fig. 2b.

Finally, in order to fully characterize the dynamic behavior of the resonator under study, a limit domain in the $V_P - |v_a|$ plane has been numerically obtained (see Fig. 3a). For values of the actuation and polarization potentials below the black

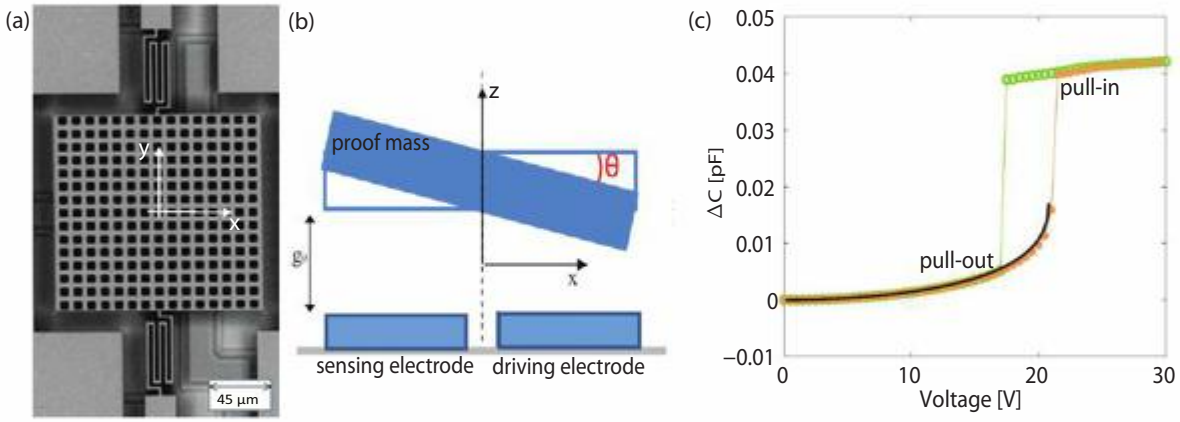

Figure 1: (a) SEM image of the torsional resonator fabricated through the Thelma© surface micromachining process of STMicroelectronics [2]; (b) schematic side view of the torsional resonator; (c) capacitance variation for different bias voltages: experimental measurements for increasing and decreasing voltage (dots) and theoretical prediction (black curve).

*Corresponding author. Email: claudia.comi@polimi.it

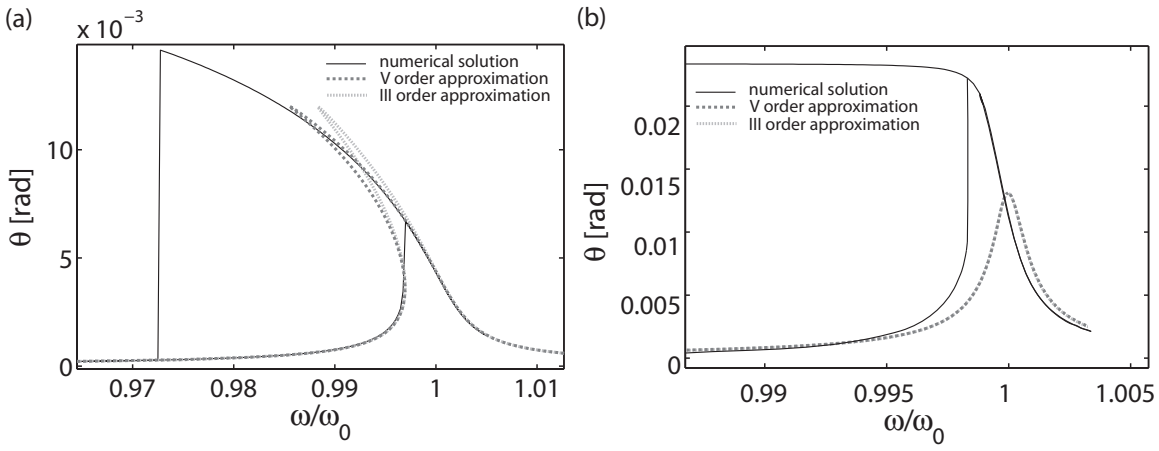

Figure 2: Frequency response of the torsional resonator of Fig. 1 for different actuation conditions: analytical III and V order approximations are shown together with the numerical curve. (a) V_P =7 V and $|v_a| = 61$ mV; (b) $V_P = 0.5$ V and $|v_a| = 1$ V.

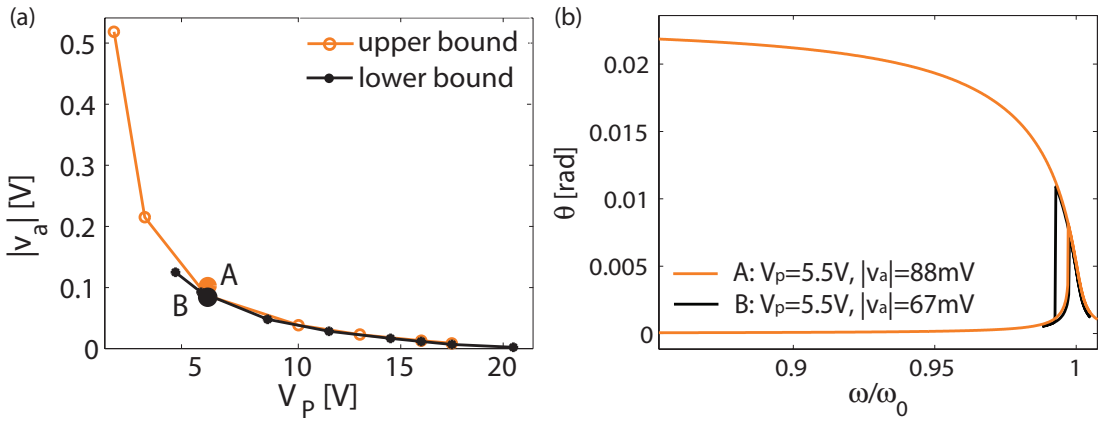

Figure 3: (a) Limit domain of the torsional resonator shown in Fig. 1; (b) frequency responses of the torsional resonator under the actuation conditions A and B shown in Fig. 3a by dots.

curve, the numerical frequency response of the resonator shows the 'common' hysteretical non-linear behavior with two jumps between the two stable branches (see the black curve in Fig. 3b and in Fig. 2a), while for combinations of V_P and $|v_a|$ above the orange curve, a different non-linear behavior is obtained (see the orange curve in Fig. 3b and the black curve in Fig. 2b): the resonant curve for decreasing frequencies reaches, without any hysteretical phenomena, an asymptotic value of $\theta = 0.023$ rad which is the maximum rotation physically allowed to the resonator.

CONCLUSIONS

A static characterization of the torsional resonator is here presented and a good agreement between theoretical prediction and experimental data is found. As for the non-linear dynamic behavior, the limits of the commonly used analytical 'III order approximation' are underlined. A new more accurate analitical V order approximation is here obtained and compared with the numerical solution. Finally, the limit domain that can guide both the design and the operation phases is presented.

References

[1] Comi C., Corigliano A., Ghisi A. and Zerbini S.: A resonant micro accelerometer based on electrostatic stiffness variation. Meccanica 48:1893-1900, 2013.

[2] Corigliano A., Masi B. D., Frangi A., Comi C., Villa A. and Marchi M.: Mechanical characterization of polysilicon through on chip tensile tests. J. Microelectromech. Syst. 13:200-219, 2004.

[3] Caspani A., Comi C., Corigliano A. ,Langfelder G. ,Zega V. and Zerbini S.: Dynamic Non-Linear Behaviour of Torsional Resonators in MEMS. J. of Micromech. and Microeng. 24:1-9, 2014.

[4] Nayfeh A. H. and Mook D. T.: Nonlinear Oscillations. Wiley Classics Library Edition Published, 1995.

MECHANICAL CHARACTERIZATION OF MATERIALS AT MICO/NANOSCALE UNDER BENDING

Mohamed Elhebeary[1] & Taher Saif [1a)]
[1]*Mechanical Science and Engineering Department, University of Illinois Urbana-Champaign, Illinois, USA*

Summary This paper presents a new method for testing materials at the micro/nanoscale under bending in-*situ* in SEM and TEM. The method consists of a straining stage with built-in force and displacement sensors. The sample is co-fabricated with the stage to eliminate any misalignment error. The method is applied to test the strength of silicon micro-beams under bending. The study reveals significant strengthening of silicon compared to that under uniform tension. This strengthening is contributed by stress localization near the surface of the beams close to the anchors, and the stress gradient from the surface to the neutral axis. Stress localization reduces the incidence of flaws that typically trigger premature fracture in the uniformly loaded samples, i.e., uniaxial tension. Most MEMS supporting beams are subjected to bending during operation. Their design landscape can be broadened by exploiting the effective strengthening of materials under bending – a paradigm that remains untapped to date.

BACKGROUND

Most of the reported bending tests were carried out using AFM [1,2] or nanoindenteation[3,4]. However, there are several uncertainties in the directionality and the location of the applied load [5,6]. In addition handling and misalignment errors are unavoidable [7]. In the current design the sample is co-fabricated with the stage to avoid these shortcomings. The chip-based stage, actuated by a piezoactuator, applies bending moments on micro/nanoscale beam specimens. The new stage minimizes uniaxial state of stress in the specimen, but maximizes bending stress over a small volume such that high stresses can be reached within a small volume on the specimen without a premature failure by fracture.

DESCRIPTION OF THE NEW TESTING TECHNIQUE

Analytical and finite element (FE) models are developed to predict the behavior of the novel stage. The analytical model accounts for the geometric non-linearity of the sample, but assumes simplified boundary conditions. The numerical model, employing a FE package, tests the validity of the analytical model. Figure 1 shows a 3D schematic of the new design. One end of the stage is held fixed during the test, while the other is displaced along the loading direction using a pin fitted through the hole and connected to a piezoactuator (Fig. 1.a). A bending sample with a rectangular cross section is placed transverse to the straining direction (Fig. 1.c). The long two parallel soft beams (S) serve the function of the horizontal spring of the schematic (Fig. 2.b). During straining, they allow the end of the bending sample to approach each other with minimal resistance, thus minimizing the tension on the sample. Due to the double beam design, they prevent rotation of the sample beam at the anchor, mimicking the zero slope boundary condition. The $P=P(\delta_y)$ relation from both the models match (Fig 2), implying that the analytical model can be used to optimize the stage design.

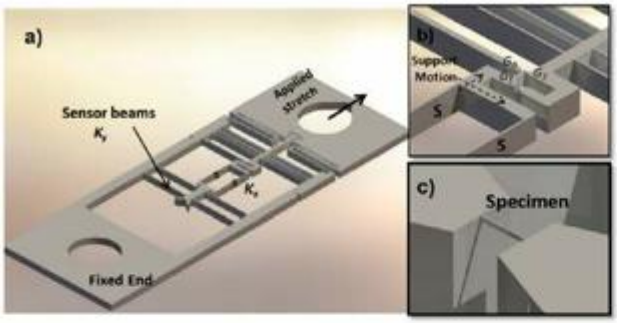

Figure 1 a) 3D schematic of the proposed stage with b) a close-up near the bending specimen and c) the specimen.

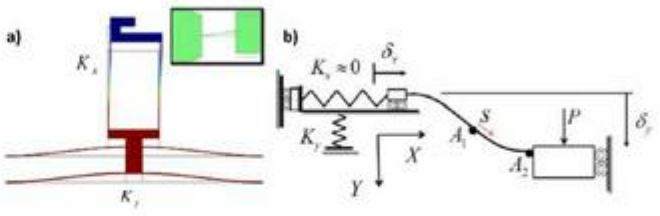

Figure 2 a) FE model of the stage , and b) 2D schematic of the stage during loading

EXPERIMENTAL RESULTS AND CONCLUSIONS

A 3D printed stage was fabricated to illustrate the capabilities of the new design (Fig.3a). The elastic modulus of PA2200 was measured (E=637.8MPa) which matches the results from uni-axial tension tests on the same specimen. Guided by the theory, the bending stage is fabricated according to the process (Fig.4). Figure 5 shows the 200μm thick chip and the co-

[a)] Corresponding author. Email: saif@illinois.edu

fabricated specimen and sensor gauges. The chip is stretched by applying voltage to the piezoactuator inside scanning electron microscope (SEM) to bend the SCS specimen (32x39x2.5μm^3) until fracture (Fig.5d,e). The load-deflection relation during loading and unloading is linear and reversible implying elastic response (Fig.6). The elastic modulus of silicon along <110> is found to be 169.9±5.8 GPa, in good agreement with literature [8,9]. Bending stress measured at the anchors of the specimen reached 4.15 GPa before failure, about three times higher than the failure stress of silicon under uniaxial tension [9].

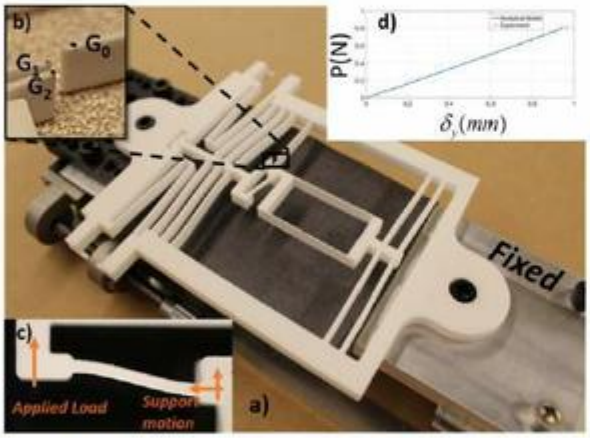

Figure 3 a) 3D printed stage (PA2200) during testing, b) and c) are close-up views of the gauges of the stage and the sample, and d) force-deflection relation of the sample during loading

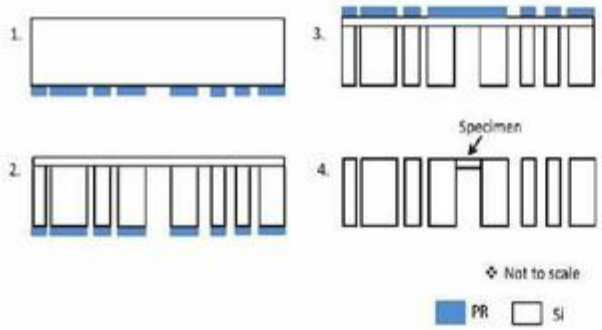

Figure 4 Fabrication process flow 1) patterning the backside, 2) DRIE etching, 3) Patterning the top side, and finally 4) DRIE etching the top side.

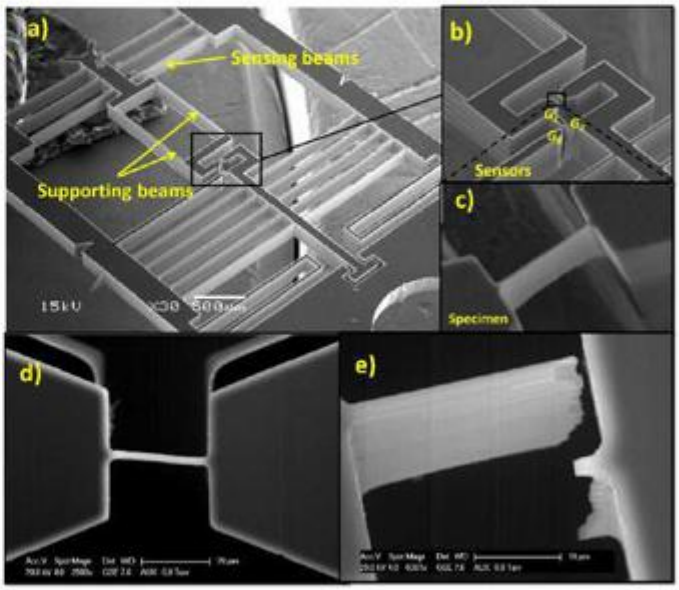

Figure 5 a) SEM image of the stage with a zoom-in view on the b) sensors area (applied load, P=K_y , is the change in distance between G_0- G_1 , and $_y$ is the change in distance between G_1- G_2), and c) specimen, d) deformed beam during testing, and e) specimen after failure

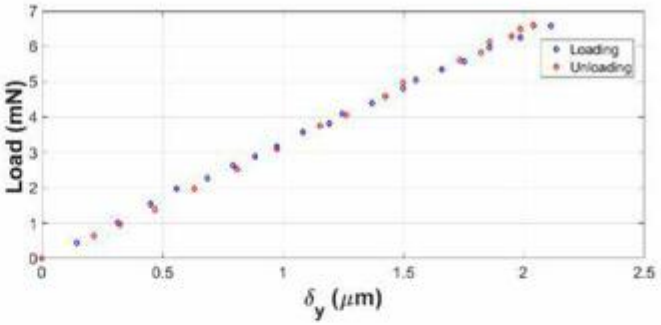

Figure 6 Force-deflection relation during loading and unloading of the specimen

References

[1]Y. Kim, K. Son, and I. Choi, Adv. Funct. Mater. 279 (2011).
[2]S. Hoffmann, I. Utke, B. Moser, J. Michler, S.H. Christiansen, V. Schmidt, S. Senz, P. Werner, U. Gösele, and C. Ballif, Nano Lett. **6**, 622 (2006).
[3]J.N. Florando and W.D. Nix, J. Mech. Phys. Solids **53**, 619 (2005).
[4]T. Weihs, S. Hong, J.C. Bravman, and W.D. Nix, J. Mater. Res. **94305**, (1988).
[5]Y. Sohn, J. Park, G. Yoon, and J. Song, WIREs Comput Mol Sci **2**, 817 (2010).
[6] M. Gordon, T. Baron, F. Dhalluin, P. Gentile, and P. Ferret, Nano Lett. 2 (2009).
[7] D.-M. Tang, C.-L. Ren, M.-S. Wang, X. Wei, N. Kawamoto, C. Liu, Y. Bando, M. Mitome, N. Fukata, and D. Golberg, Nano Lett. **12**, 1898 (2012).
[8]T. Tsuchiya, M. Hirata, and N. Chiba, J. MICROELECTROMECHANICAL Syst. **14**, 1178 (2005).
[9]T. Yi, L. Li, and C. Kim, Sensors Actuators A Phys. 172 (2000).

UTILIZATION OF SELF-EXCITED OSCILLATION FOR MASS SENSING IN LIQUID

Daichi Endo[1], Hiroshi Yabuno*[1], Yasuyuki Yamamoto[2], and Sohei Matsumoto[2]

[1]*Graduate School of Systems and Information Engineering, University of Tsukuba, Tsukuba, Ibaraki, Japan*
[2]*National Institute of Advanced Industrial Science and Technology(AIST), Tsukuba, Ibaraki, Japan*

Summary The ultrasensitive mass detection in viscosity regime is investigated which is based on the relative change of the amplitude ratio in using self-excited coupled microcantilevers, depending on the mass to be measured. The velocity feedback to produce self-excited oscillation to the microcantilevers compensates the influence of the viscous damping effect in measurement environment and enables the detection of a very small mass with nano-gram order in the viscosity regime. It is expected by the proposed method to perform high-accuracy quantitative measurements of biological samples such as human cells and DNA in liquid environments, where they are active. In this presentation, we will show the design of coupled microcantilevers and the measurement result for the mass in liquid.

INTRODUCTION

Recently, high-performance sensors using a microcantilever have been developed for a variety of purpose including measurements of substances such as pH in solution[1] and surface sensing by atomic force microscope[2]. In particular, the studies of ultrasensitive mass sensor using cantilever have been investigated widely[3], and it is known that the method based on the eigenstate shift in coupled cantilevers has much more accuracy compared with based on the eigenvalue (frequency) shift[4]. In conventional methods, the eigenstate has been identified from the magnitude ratio of the resonance peak of the frequency response curve in the coupled cantilevers under the external excitation[4]. However, this method is not suitable to the mass sensing in viscous environments because the peak of the frequency response curve does not exactly reflect the eigenstate due to the viscosity. Moreover, in much higher-viscosity environments where the resonance peak itself does not exist in the frequency response curves. In order to overcome a such difficulty, we have proposed a novel method by using self-excited oscillation[5]. The method directly determines the eigenstate without the frequency response curve. The mass detecting experiment was performed using the coupled microcantilevers in air. The validity of our proposed method was investigated in our research[5, 6]. In this study, we report the detection of the very small mass using self-excited coupled microcantilevers in liquid. The accuracy of experimental results is quantitatively discussed.

DESIGN OF COUPLED MICROCANTILEVERS

Figure 1(a) is the picture of the coupled microcantilevers with the mass to be measured. The cantilevers are fabricated by etching from an SOI wafer and the dimensions of each cantilever are $500\ \mu\mathrm{m}\times100\ \mu\mathrm{m}\times10\ \mu\mathrm{m}$. The area surrounded by a black dashed line in Fig. 1 (a) corresponds to the overhang for the coupling and its dimensions are $150\ \mu\mathrm{m}\times100\ \mu\mathrm{m}$. The mass to be measured are build by using the 3D laser lithography system (nanoscribe.:Photonic Professional GT) on the tip of the cantilever 2 and their constructions are an arch-shape as frangible. Their mass are 2.48 ng calculated from the density of the photoresist(=1.190 g/cm^3) and the volume of the structure.

Figure 1(b) is a discretized analytical model, where x_1 and x_2 correspond the displacements of cantilevers, 1 and 2, relative to the lateral excitation Δx of the supporting point of the coupled cantilevers, respectively.

As in our previous study[5], the first eigenstate of the coupled microcantilevers is expressed as follows:

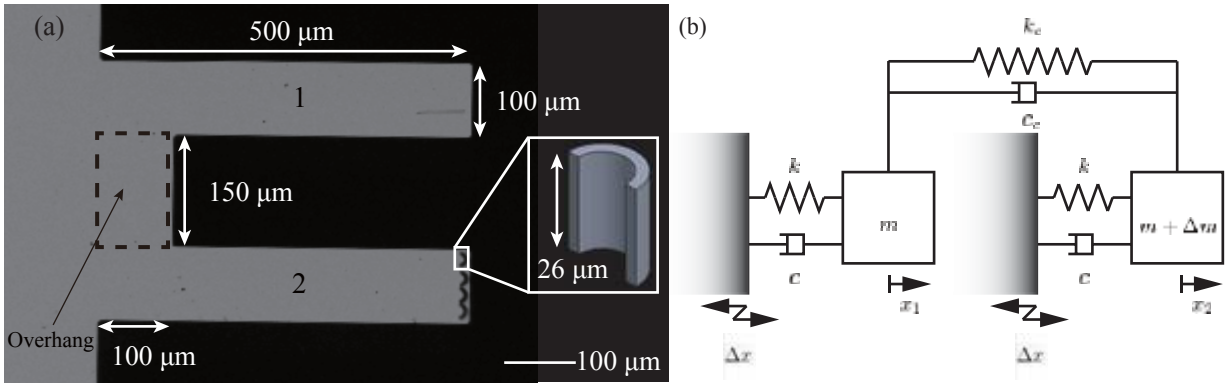

Figure 1: (a) Picture of the coupled microcantilevers with the mass to be measured. (b) Discretized analytical model.

*Corresponding author. Email: yabuno@esys.tsukuba.ac.jp

$$\boldsymbol{p_1} = \begin{bmatrix} 1 \\ 1 \Big/ \left\{ \sqrt{(1+\delta) + \frac{\delta^2}{4\kappa^2}(1+\kappa^2)} - \frac{\delta}{2\kappa}(1+\kappa) \right\} \end{bmatrix} \simeq \begin{bmatrix} 1 \\ 1/\left(1 - \frac{\delta}{2\kappa}\right) \end{bmatrix}, \tag{1}$$

where $\kappa = k_c/k$ and $\delta = \Delta m/m$ are the dimensionless coupling stiffness and dimensionless added mass ratio, respectively. When the sample to be measured is not attached, i.e., $\delta = 0$, the amplitude ratio of cantilevers 1 and 2 is 1:1 from Eq. (1), and when the sample is attached on the tip of the cantilever 2, the amplitude ratio deviates from 1:1 and the magnitude of the amplitude of the cantilever 2 increases in accordance with Eq. (1). Even if the mass to be measured is very small, by making the the dimensionless coupling stiffness κ weak, we can obtain the deviation of the amplitude ratio from 1:1 largely and realize the small mass detection with high-sensitivity.

MEASUREMENT RESULTS IN VISCOUS REGIME

We have conducted the mass measuring experiment using coupled microcantilevers shown in Fig. 1(a). In the experiment, cantilevers are fixed to an acrylic case filled with water and vibrated by a piezoelectric actuator sticked on the bottom of the acrylic case. The vibrations of cantilevers are measured by laser Doppler vibrometers (Polytec.:MSA-500 Micro System Analyzer). In order to induce self-excited oscillation in the coupled cantilevers, the signal of the displacement of cantilever 1 integrated by an analog circuit is input to the piezoelectric actuator. As a result, we can generate self-excited oscillation to the coupled microcantilevers in accordance with the previously proposed feedback rule[5].

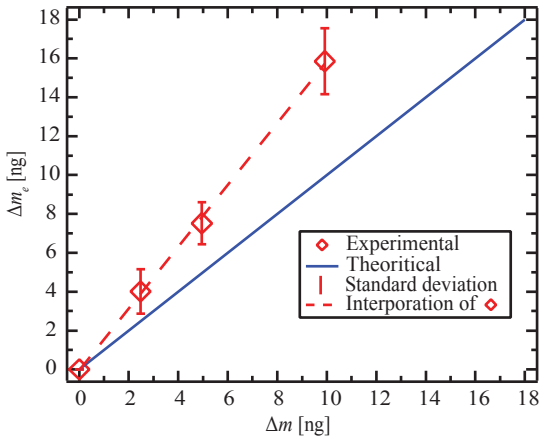

Figure 2: Measurement results for structures to be measured in liquid.

Figure 2 shows measurement results for the mass to be measured in liquid. The ordinate and abscissa indicate the experimentally determined mass values of the structure to be measured (Δm_e) and their nominal values calculated from the density and the volume of structures (Δm), respectively. The plots $\diamond$ are mass values obtained from the eigenstates shift under self-excited oscillation in the experiment. When the plots $\diamond$ fall on the straight line of gradient 1, the experimentally determined mass values are in complete agreement with the nominal values. As can be seen from Fig. 2, the plots $\diamond$ deviate from the straight line, however, the plots $\diamond$ are changing linearly, so that we can realize the quantitatively mass sensing by using the interpolation of the experimental data as a calibration line.

CONCLUSIONS

In this study, we have achieved the measurement of a mass with the order of nanogram in liquid by self-excited oscillation using the coupled microcantilevers. By fabricating the smaller coupled microcantilevers and optimizing the coupling stiffness of overhang between two cantilevers, we expect that the sensitivity could be in picogram range or less. In near future works, we perform high-accuracy quantitative measurements of biological samples such as human cells and DNA in liquid environments, where they are active. Furthermore, it is expected by the method to measure the reaction process of biological samples.

This work was partially supported by a Grant-in-Aid for Scientific Research C (Grant No. 25420195) from Japan Society for the Promotion of Science (JSPS) and Mitsutoyo Association for Science and Technology (MAST).

References

[1] R. Bashir, J. Z. Hilt, O. Elibol, A. Gupta, and N. A. Peppas, Appl. Phys Lett., 81: 3091, 2002
[2] H. Yabuno, H. Kaneko, M. Kuroda, and T. Kobayashi, Nonlinear Dyn., 54: 137, 2008
[3] B. Ilic, D. Czaplewski, M. Zalalutdinov, H. G. Craighead, P. Neuzil, C. Campagnolo, and C. Batt, J. Vac. Sci. Technol. B, 19: 2825, 2001
[4] M. Spletzer, A. Raman, A. Q. Wu, X. Xu, and R. Reifenberger, Appl. Phys. Lett., 88: 254102, 2006.
[5] H. Yabuno, Y. Seo, and M. Kuroda, Appl. Phys. Lett., 103: 063104, 2013.
[6] D. Endo, H. Yabuno, K. Higashino, Y. Yamamoto, and S. Matsumoto, Appl. Phys. Lett., 106: 223105, 2015.

RECOVERABLE PLASTICITY IN PENTA-TWINNED METALLIC NANOWIRES

Qingquan Qin,[1*] Sheng Yin,[2*] Guangming Cheng,[1] Xiaoyan Li,[3] Tzu-Hsuan Chang,[1] Gunther Richter,[4] Yong Zhu,[1#] and Huajian Gao[2#]

[1]*Department of Mechanical and Aerospace Engineering, North Carolina State University, Raleigh, NC 27695, USA,*
[2]*School of Engineering, Brown University, Providence, RI 02912, USA,*
[3]*Centre of Advanced Mechanics and Materials, Applied Mechanics Laboratory, Department of Engineering Mechanics, Tsinghua University, Beijing 100084, People's Republic of China,*
[4]*Max Planck Institute for Intelligent Systems, Heisenbergstrasse 3, D-70589 Stuttgart, Germany*

Abstract There has been relatively little study on time-dependent mechanical properties of nanowires, in spite of their utmost importance for the design, fabrication and operation of nanoscale devices. Here we report a dislocation-mediated, fully recoverable, plastic behavior in penta-twinned silver nanowires. In-situ tensile experiments inside scanning and transmission electron microscopes show that penta-twinned silver nanowires undergo stress relaxation upon loading and complete plastic strain recovery upon unloading, while the same experiments on single-crystalline silver nanowires do not exhibit such a behaviour. Molecular dynamics simulations reveal that the observed behaviour in penta-twinned nanowires originates from the surface nucleation, propagation and retraction of partial dislocations. More specifically, vacancies reduce dislocation nucleation barrier, facilitating stress relaxation, while the twin boundaries and their intrinsic stress field promote retraction of partial dislocations, resulting in full strain recovery.

Introduction

One-dimensional (1D) nanostructures are widely regarded as among the most important building blocks for a broad range of applications including nanoelectronics, optoelectronics, energy harvesting and storage, and nano electromechanical devices. In the case of metallic nanowires (NWs), dislocation nucleation from free surfaces has been identified as a dominant deformation mechanism, in contrast to the forest dislocation dynamics in bulk materials. Here we report an unusual time-dependent deformation behaviour in penta-twinned Ag NWs, with stress relaxation upon loading and complete strain recovery upon unloading (*1*).

In-situ tensile testing of Ag NWs

We performed *in-situ* tensile experiments inside scanning and transmission electron microscope (SEM/TEM) using a microelectromechanical system (MEMS)-based testing system (*2*). First, stress relaxation experiments were conducted by loading the thermal actuator to a given displacement and, while the actuator displacement was held constant, the specimen relaxed as a function of time. Since the experiment was not under true displacement control, the load on the specimen decreased and the specimen elongation increased at the same time. Subsequently, complete strain recovery was observed after unloading when turning off the thermal actuator. Fig. 1a shows the stress–strain response during a typical tensile test of a penta-twinned Ag NW in four steps: loading, relaxation, unloading and recovery. During the relaxation step, the stress decreased with time while the strain increased. Fig. 1b shows the strain and stress as functions of time at three stress levels. Upon unloading, the strain in the NW completely recovers in about the same amount of time as the relaxation.

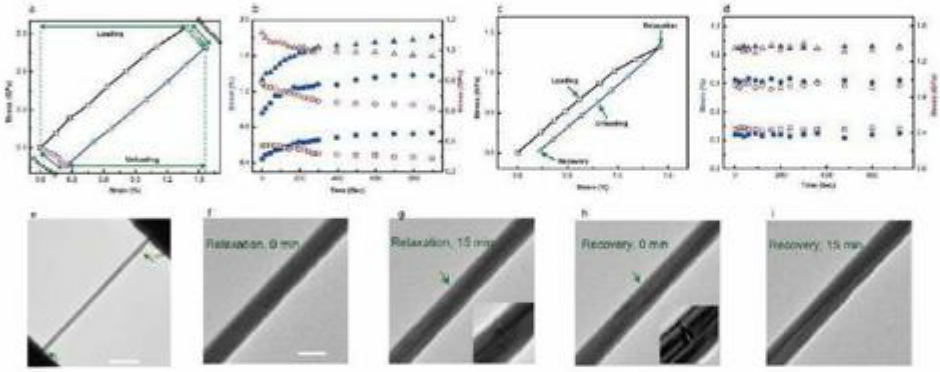

Figure 1 | *In situ* measurements of stress and strain evolution in Ag NWs.

In-situ TEM tensile testing indicated that the stress relaxation and strain recovery in the penta-twinned Ag NW are accompanied by nucleation and annihilation of dislocations, respectively, as shown in Fig. 1(f-i). Before the relaxation step (Fig. 1f), there were no dislocations in the NW as the strain increased to 1.6 %. At the relaxation step, a dislocation network appeared in < 5 min. The dislocations were terminated at the TBs (Fig. 1g). During the unloading step, the applied load gradually decreased to zero but the dislocations remained (Fig. 1h). In the recovery step, the dislocation network gradually retracted and suddenly disappeared after ~8 min (Fig. 1i). After 15 min, the NW was totally recovered. Overall the same relaxation and recovery behaviours were observed in all five penta-twinned Ag NWs with different diameters (48 to 121 nm). The same experiments were conducted for five single-crystalline Ag NWs with diameters of 70 to 152 nm at similar stress levels for the penta-twinned Ag NWs, but neither stress relaxation nor recovery of plastic strain were observed in any of them as shown in Fig.1(c-d).

MD simulations of stress relaxation and strain recovery

To reveal the underlying mechanisms behind the observed relaxation and recovery behaviours of penta-twinned Ag NWs, we performed a series of molecular dynamic (MD) simulations. We introduced a population of vacancies with concentration from 0% to 2% in the simulated samples. To investigate stress relaxation behaviors, we first stretched the simulated samples to a strain of 1.8%, and then monitored stress relaxation while the applied strain was held fixed. With 1% vacancies introduced in the penta-twinned NWs, the stress gradually decreased from an initial stress of 1.15 GPa by about 200 MPa in 2 ns, as illustrated in Fig. 2a. The insets in Fig. 2a capture a sequence of partial dislocation nucleation events in the TB-separated nanograins. The partial dislocation nucleation events exhibit a one-to-one correspondence with discrete stress drops in the stress relaxation profile shown in Fig. 2a, indicating that the stress relaxation is a direct consequence of dislocation nucleation in the penta-twinned nanostructure.

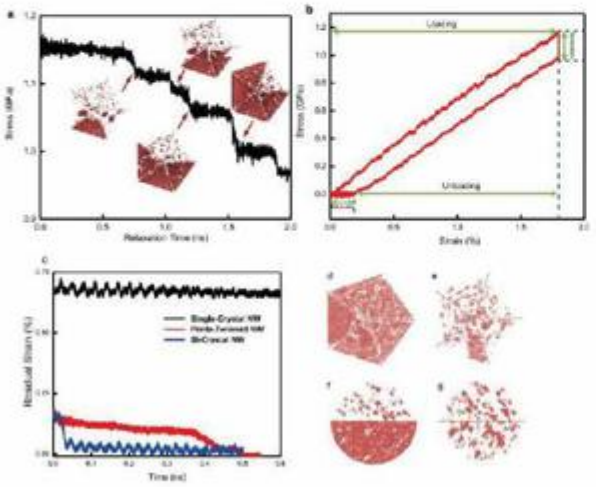

Figure 2 | Recoverable plasticity and associated dislocation activities.

Similar to experiments, after stress relaxation the simulated samples were subsequently unloaded to a stress-free state. When the applied stress came down to zero, there was still a 0.21 % of strain remaining in the sample, as shown in Fig. 2b. Continuing relaxation of the sample under zero stress resulted in complete recovery of the residue strain after 0.3 ns (see Fig. 2c). This behavior is very similar to the experimental observations. Figure 2d and 2e illustrate two snapshots of the deformed sample during relaxation and recovery, respectively. During stress relaxation, partial dislocation loops were found to nucleate spontaneously from aggregated vacancy clusters near free surface and then expand through the grain interiors separated by the five TBs. Each discrete dislocation nucleation event leads to a visible stress drop in our simulation. During subsequent strain recovery after unloading, partial dislocation loops were seen to retract from the five-fold TBs under zero applied stress, resulting in complete strain recovery. It is known that there exists a repulsive force between TB and curved dislocation loop. When the external stress is removed, the repulsive force from the TBs appears to induce reverse motion of dislocations by pushing the non-inserted segments as well as extracting the inserted segments from the TBs back toward where the dislocations were nucleated.

To further demonstrate the unique role of TBs in the recovery behaviour of NWs, we performed two additional simulations for a single-crystalline NW and a bi-crystalline NW with a single TB in the middle – a mono-twinned NW. We observed nearly full plastic strain recovery in the mono-twinned NW, but not in the single-crystalline NW. In the mono-twinned NW, the TB effectively blocks the motion of leading partials, preventing them from escaping out of the sample (see Fig. 2f-g), allowing them to retract back from the TB under the residual internal stress field upon unloading, leading to plastic strain recovery. In contrast, in the single-crystalline NW, dislocations nucleated travelled across the NW and eventually escaped out of the sample, leaving a permanent surface step. Besides the twinned NW, we have also investigated bi-crystalline NWs with different types of regular GBs (such as low-angle/high-angle tilt GBs and mixed GB). It is found that the tilt and tilt-twist mixed GBs either failed to block the dislocation or trapped the dislocation, resulting in no strain recovery.

In summary, we have discovered an unusual dislocation-based stress relaxation and strain recovery behaviour in penta-twinned Ag NWs via *in-situ* SEM/TEM tensile testing, TEM microstructural characterizations and large-scale MD simulations. This behaviour consists of two facets: stress relaxation under an applied strain and complete plastic strain recovery upon unloading. Our studies indicate that stress relaxation originates from the nucleation of leading partial dislocations assisted by vacancy diffusion, while the complete strain recovery is due to the reverse motion of partial dislocations driven by the repulsive force from the TBs and the intrinsic stress field due to the five-fold twin. The simulations demonstrate that the TBs play a crucial role in the observed phenomenon: TBs are effective obstacles for dislocations and produce a repulsive force to drive the reverse motion of dislocations during unloading. In contrast to previous studies in nanocrystalline metals due to a cooperation of dislocation- and GB- mediated processes (*3*); the present study demonstrates a new type of stress relaxation and full plastic strain recovery induced by TB-dislocation interactions. Our study opens up a promising prospect of designing one-dimensional nanostructures with time-dependent strain recovery capabilities.

References

1. Q. Qin *et al.*, Recoverable plasticity in penta-twinned metallic nanowires governed by dislocation nucleation and retraction. *Nature communications* **6**, (2015).
2. Y. Zhu, H. D. Espinosa, An electromechanical material testing system for in situ electron microscopy and applications. *PNAS* **102**, 14503-14508 (2005).
3. X. Y. Li, Y. J. Wei, W. Yang, H. J. Gao, Competing grain-boundary- and dislocation-mediated mechanisms in plastic strain recovery in nanocrystalline aluminum. *PNAS* **106**, 16108-16113 (2009).

NONLINEAR BEHAVIOUR OF CARBON NANOTUBE-BASED RESONATORS

Hamed Farokhi*[1], Michael P. Païdoussis[1], and Arun K. Misra[1]
[1]*Department of Mechanical Engineering, McGill University, Montreal, QC, Canada*

Summary In the present study, a new size-dependent nonlinear model is developed for analyzing the behaviour of carbon nanotube-based resonators. Molecular dynamics simulation is then performed in order to parametrize and validate the size-dependent continuum model at the nano scale. The equations of motion are discretized by means of the Galerkin technique and solved employing the pseudo-arclength continuation technique. A new universal pull-in formula is also developed for predicting the voltage corresponding to the static pull-in.

INTRODUCTION

Recent technological advances have facilitated the development of nanoelectromechanical systems (NEMS). NEMS devices operate at significantly high frequencies with very low power consumption. Carbon nanotubes (CNTs) [1] can be used as suitable candidates for nanomechanical resonator due to their light mass and high stiffness. The investigations on the static and dynamic characteristics of CNT-based resonators are based on either continuum or molecular models. There are a few studies utilizing molecular dynamics (MD) simulations to predict the behaviour of carbon nanotube resonators, for instance, by Yoon et al. [6]and Kang and Kwon [2]. Reviewing the continuum-based studies, Sapmaz et al. [5] performed a theoretical investigation on the nano-electro-mechanical effects in a doubly clamped suspended CNT. Poot et al. [4] studied the bending mode vibration in suspended CNTs. These investigations were continued by Ouakad and Younis [3] who examined the nonlinear dynamics of electrically actuated CNT resonators under DC and AC electric loads.

In the present study, for the first time, the fully nonlinear coupled longitudinal-transverse equations of motion of a CNT-based resonator are derived employing the modified couple stress theory. The equations of motion are expanded while keeping the nonlinear terms up to fifth order, and then discretizd using the Galerkin technique. A molecular model is also constructed so as to obtain Young's modulus of the CNT and validate the continuum model. The validated size-dependent continuum model is then employed in order to examine the nonlinear behaviour of the CNT-based resonator.

MODEL DEVELOPMENT

Consider a doubly clamped CNT-based resonator, consisting of a single-walled CNT of length L, cross-sectional area A, second moment of area I, radius R, thickness h, and Young's modulus E, positioned at a distance b from the gate underneath. x and z denote the axial and transverse coordinates; $u(x,t)$ and $w(x,t)$ represent the longitudinal and transverse displacements, respectively. For such a system, the fully nonlinear equations of motion can be obtained as

$$\rho A\frac{\partial^2 u}{\partial t^2}-EA\frac{\partial}{\partial x}\left(\varepsilon_0\cos\psi\right)-EI\frac{\partial}{\partial x}\left(\frac{\partial\kappa}{\partial x}\frac{\sin\psi}{1+\varepsilon_0}\right)-\frac{1}{4}\mu Il^2\frac{\partial}{\partial x}\left(\frac{\sin^2\psi}{1+\varepsilon_0}\frac{\partial^4\cos\psi}{\partial x^4}\right) \tag{1}$$
$$-\frac{1}{4}\mu Al^2\frac{\partial}{\partial x}\left[\frac{\sin\psi\cos\psi}{1+\varepsilon_0}\frac{\partial^2}{\partial x^2}\left(\sin\psi+\frac{\partial w}{\partial x}\right)-\frac{\sin^2\psi}{1+\varepsilon_0}\frac{\partial^2\cos\psi}{\partial x^2}\right]+P\frac{\partial\cos\psi}{\partial x}+c_u\frac{\partial u}{\partial t}=0,$$

$$\rho A\frac{\partial^2 w}{\partial t^2}-EA\frac{\partial}{\partial x}\left(\varepsilon_0\sin\psi\right)+EI\frac{\partial}{\partial x}\left(\frac{\partial\kappa}{\partial x}\frac{\cos\psi}{1+\varepsilon_0}\right)+\frac{1}{4}\mu Il^2\frac{\partial}{\partial x}\left(\frac{\sin\psi\cos\psi}{1+\varepsilon_0}\frac{\partial^4\cos\psi}{\partial x^4}\right)+P\frac{\partial\sin\psi}{\partial x}+c_w\frac{\partial w}{\partial t} \tag{2}$$
$$+\frac{1}{4}\mu Al^2\frac{\partial}{\partial x}\left[\left(1+\frac{\cos^2\psi}{1+\varepsilon_0}\right)\frac{\partial^2}{\partial x^2}\left(\sin\psi+\frac{\partial w}{\partial x}\right)-\frac{\sin\psi\cos\psi}{1+\varepsilon_0}\frac{\partial^2\cos\psi}{\partial x^2}\right]$$
$$-\frac{\pi\epsilon\left(V_{\rm DC}+V_{\rm AC}\cos\left(\omega t\right)\right)^2}{\sqrt{\left(b-w\right)\left(2R+b-w\right)}\left[\cosh^{-1}\left(1+\frac{b-w}{R}\right)\right]^2}=0,$$

where ε_0 and κ are the strain and curvature of the centreline, respectively, and ψ is the angle of the centreline with the x axis; μ is the shear modulus, and P is the axial load; c_u and c_w are damping coefficients; $V_{\rm DC}$ and $V_{\rm AC}$ are the DC and AC voltages, respectively.

Expanding Eqs. (1) and (2) and keeping nonlinear terms up to fifth-order and discretizing the resultant equations, employing the Galerkin technique, yields a set of nonlinear ordinary differential equations. This set is solved numerically employing the pseudo-arclength continuation technique.

*Corresponding author. Email: hamed.farokhi@mail.mcgill.ca

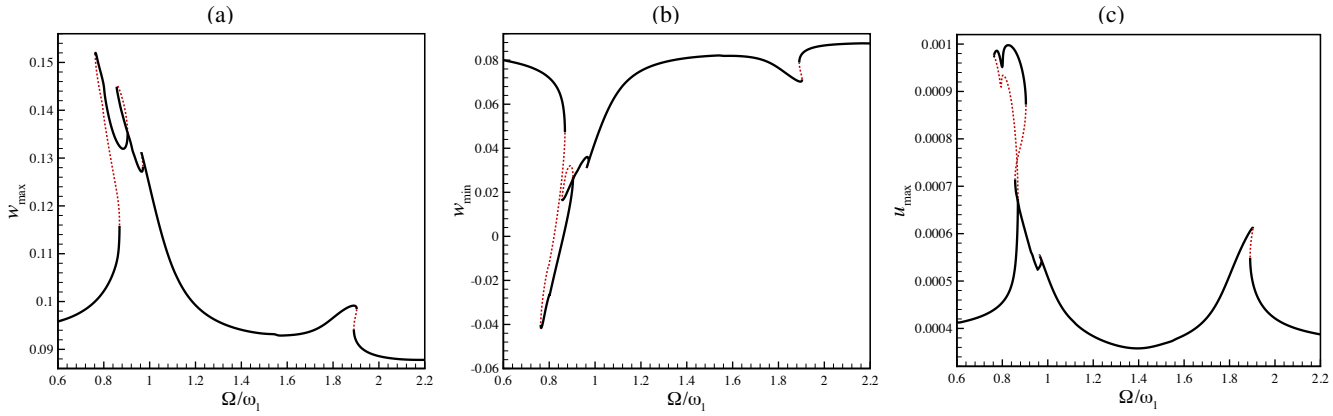

Figure 1: AC frequency-amplitude curves of the system with $V_{DC} = 2.0$ and $V_{AC} = 0.16$: (a, b) the maximum and minimum amplitudes of the transverse motion at $x = 0.5$, respectively; (c) the maximum amplitude of the longitudinal motion at $x = 0.75$. Solid and dashed lines represent the stable and unstable solutions, respectively.

RESULTS

Employing molecular dynamics simulations, Young's modulus of CNT is predicted to be 905 GPa. The numerical results are then obtained for a CNT-based resonator with $L = 3000$ nm, $R = 1.0$ nm, and $b = 300$ nm, employing the continuum model; $l = 0$ and $P = 0$. Figure 1 shows the AC frequency-amplitude curves of the system when $V_{DC} = 2.0$ and $V_{AC} = 0.16$. The figure shows that the system displays a complicated resonant response with many bifurcation points as well as softening and hardening behaviours. Comparing sub-figures (a) and (b) shows that the system oscillation around the deflected configuration is not symmetric. It is worth noting that, when varying the excitation frequency, a secondary resonant region appears in the vicinity of $\Omega/\omega_1 = 1.9$, with only hardening-type behaviour.

UNIVERSAL PULL-IN FORMULA

Developing a universal pull-in formula for CNT-based resonators allows for fast estimation of the pull-in voltage. The following analytical-empirical formula is suggested for estimating the pull-in voltage (with less than 5% error) for a *clamped-clamped* CNT-based resonator with $1000 \leq L \leq 5000$ nm, $1 \leq R \leq 5$ nm, and $0.06 \leq b/L \leq 0.18$:

$$V_{\text{pull-in}} = \sqrt{\left[(EAb^4)\,/\,(2\pi\epsilon L^4)\right]\left[76.36\,(b/R)^{0.213} - 91.66\right]}. \tag{3}$$

CONCLUSIONS

The nonlinear behaviour of a CNT-based resonator has been examined numerically. Molecular dynamics simulation is performed to obtain Young's modulus of the CNT. The nonlinear resonant response of the system is examined showing complicated response and different bifurcation points, even for small actuation voltages. A universal pull-in formula is also developed for predicting the pull-in voltage in clamped-clamped CNT-based resonators.

REFERENCES

References

[1] S. Arghavan and A. V. Singh. On the vibrations of single-walled carbon nanotubes. *Journal of Sound and Vibration*, 330(13):3102–3122, 2011.

[2] J. W. Kang and O. K. Kwon. A molecular dynamics simulation study on resonance frequencies comparison of tunable carbon-nanotube resonators. *Applied Surface Science*, 258(6):2014–2016, 2012.

[3] H. M. Ouakad and M. I. Younis. Nonlinear dynamics of electrically actuated carbon nanotube resonators. *Journal of Computational and Nonlinear Dynamics*, 5(1):011009–011009, 2009.

[4] M. Poot, B. Witkamp, M. A. Otte, and H. S. J. van der Zant. Modelling suspended carbon nanotube resonators. *physica status solidi (b)*, 244(11):4252–4256, 2007.

[5] S. Sapmaz, Y. M. Blanter, L. Gurevich, and H. S. J. van der Zant. Carbon nanotubes as nanoelectromechanical systems. *Physical Review B*, 67(23):235414, 2003.

[6] J. W. Yoon and H. J. Hwang. Molecular dynamics modeling and simulations of a single-walled carbon-nanotube-resonator encapsulating a finite nanoparticle. *Computational Materials Science*, 50(9):2741–2744, 2011.

THEOR TICAL S UDIES O ADSORPTION AN DIFFUSION OF LI-ION ON RAPHEN SURFAC

Yan-Zi Yu[1], Jian-Gang Guo [a)] & Li-Jun hou[2]
[1] *chool of Me hanical Engineering, Tianjin University, Tianjin, hina*
[2] *Depa tment of Me hanical En ineering, Ti njin University of Technology and Ed cation, Tian in, China*

Summary Theoretical investi ations on adso ption and diffusion of Li-ion on graphene surface are made based on an analytical model. The equilibrium position, binding nergy and ads rption stability are discussed. The path-depe dence and periodic characteri tics of interaction energy and tangential forces are analyzed for diffusing of Li ion on graphene surface. In addition, the influence of size, e ge and defects of graphene on th diffusion of Li-ion is investig ted.

I TRODUCTION

In recent decade, grap ene has been paid much attention as an ideal candid te for the de elopment of high-sensitivity sensors [1], drug delivery ystem (DDS) [2], and rechargeable lithi m-ion graph ne battery [3] and so on. However, there is still a com on unsolved major scie tific question for these applications. It's to develop an anal tical model to quantitativel describe the adsorption and diffusion f atom/ion o graphene surface, which can be further applied to t e interaction b tween nano- articles or at mic force mi roscopy (AF) and graph ne surface.

ANALYTICAL ODEL

A monolayer graphen is assumed to be perfect, flat and infi ite at atomic scale (as sh wn in Fig. 1(a)). Due to its periodic hon ycomb lattic structure, th total interaction potential ($\boldsymbol{r}$) of adsorption atom/ion and graphene is also periodic. Then, the pe iodic nature f the total interaction pote tial $u(\boldsymbol{r})$ can e expressed as Fourier series [4]. It is assumed that the interaction potential betw en the adso ption atom/i n and carbo atom in the graphene can be expressed by 6-12 -J potential. Th n the interaction potential etween atom/ion and grap ene surface can be derived as [5]:

$$u\ r \quad \varepsilon\frac{2\pi}{A}q\left(\frac{2\sigma}{5z^{10}}-\frac{\sigma^6}{z^4}\right)-\varepsilon\frac{2\pi}{A}\left[\frac{\sigma^{12}}{}\left(\frac{g}{z}\right)^5 \quad {}_5\ gz\ -\ \sigma^6\left(\frac{}{z}\right)^2 K_2\ gz\ \right]\left[2\cos\left(\frac{2\pi y}{\sqrt{3}a}\right)\mathrm{c}\ \mathrm{s}\left(\frac{2\pi x}{a}\right)+\mathrm{co}\ \left(\frac{4\pi y}{\sqrt{3}a}\right)\right] \tag{1}$$

If following imensionless variables ar introduced $A^*=A\ a^2\ z^*\ \ z\ a\ g^*=ga,\sigma^*=\sigma\ a\ x^*\ \ x\ a\ y^*=\ \ \ u^*=\ /\varepsilon$, then the dimensionless form o total energy can be obtai ed. Further ore, let $\mathbf{F}^*=-\nabla u^*\ \mathbf{r}$, an then the no mal and late al interaction forces between the atom/ion and graphene can be obtain d in the Cart sian coordin te system [5].

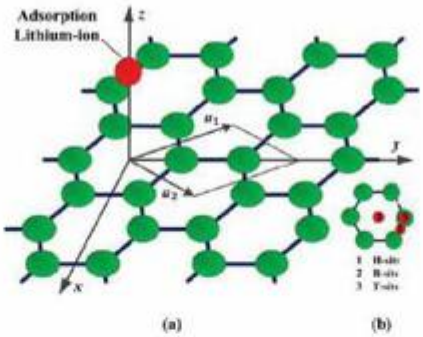

Figure 1. Schematics of the graphene wh re (a) the rhombus connecting the centers of four adjacent h xagonal is selected as a two-dimensional primitive unit cell, (b) hexagon with three particular adsorption sites: hollow (on top of a hexagon, H-), top (on top of a C-C bond, T-), and bridge (on top of a carbon atom, -) [5].

RESUL S AND DIS USSIONS

The equ tion (1) defi es the interaction potenti l between a single atom/ion and grap ene surface. Obviously, i 's dependent on the position f the adsorption atom/ion n graphene and the param ters of L-J potential. In thi work, Li-ion is selected as the adsorption ion to study t e interaction characteristics. At first, th equilibrium height and binding energy of Li-ion on thr e particular ositions, including hollow (on top of a hexagon, H-), top (on top of a C-C bond, T-), and bridge

[a)] Correspondi g author. Email: guojg@tju.e u.cn

(on top of a arbon atom, -) sites (as s own in Fig. 1(b)) are calculated. We found that H-site is the most s able adsorption site, and T-si e is the most unstable.

The initi l adsorption site is assume to be H-site, and a Li-ion is assumed to migrate alon different directions, such as 0º, 15º, 30º, 0º angles from the x-axis. The interacti n potential and tangential force betwee the Li-ion and graphene or different diffusion directions are shown in the Fig. . It can be s en from these figures that the interacti n potential and tangential fo ce are path-d pendent for ifferent diffusion directions. Simultaneously, it can b found along the same lattice orientation, such as 0º and 60º angles, the variations of interaction potential and t ngential forc are the same [5].

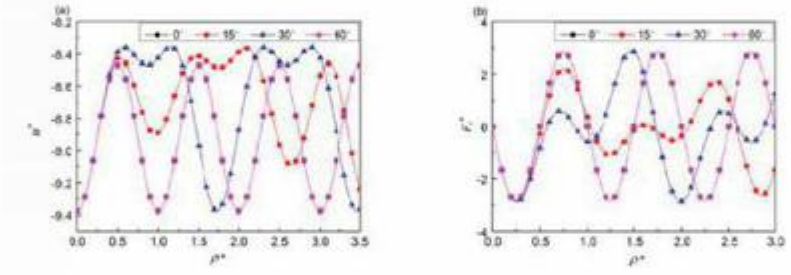

Figure 2. The variations of (a) interaction pote tial, and (b) int raction force b tween a Li-ion and graphene f r different diff sion directions, 0º, 15º, 30º, 60º angles from the x-axis [5].

The geometric sizes an edges of graphene have influence on th adsorption a d diffusion of an atom/ion on the graphene surface [6]. ive kinds of monolayer gr phene sheets with different geometric sizes (n=1, 7, 19, 37 and 61, where n is the number of h xagonal carb n rings, as s own in Figure 3(a), n=37 is given only) are constructed to analyz the interaction between the dsorbing Li-i n and graphene. When a Li-ion diffuses long the x di ections on th surface of the graphene with different geo etric sizes, the variations of interaction potential can be illustrated in the Figure 3(b). Obvious size and edge effects can be seen. In addition, the influence of vacanc defects in graphene (as sh wn in Figure (a)) is considered to study the diffusion of i-ion. The int raction potential of Li-ion igrating across defective area has apparent variations, and a hexago al ring defect h s a greater effect than a single-atom vacancy defect. When the vacancy defect is big enough, Li-ion can migr te through the g aphene form acancy defec ive area to an ther side.

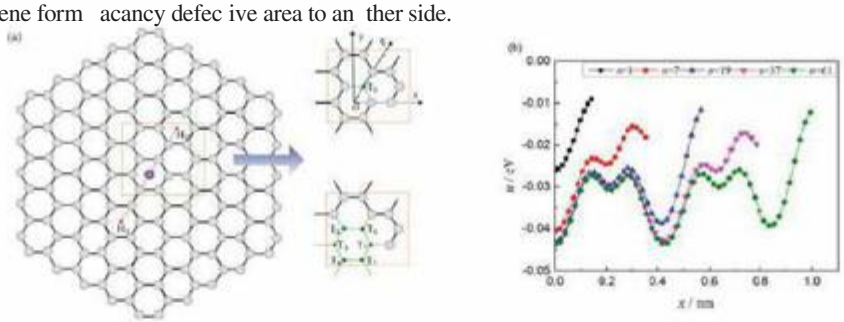

Figure 3. Sche atics of (a) the graphene with he size n=37, a d two kind of vacancy defects, (b) the variatio s of interaction potential between the i-ion and mon layer graphene with different g ometric sizes along the x-direction [6].

ONCLUSIONS

Theoretic l analyses of equilibrium eight, adsorption stability and diffusion for a single Li-ion on grap ene surface re presented based on an analytical model, a d the mechanism of adsorption and diffusion are revealed. The results in this paper re advantageous to improve the efficiency of drug delivery based on gra hene, high-performance rechargeable lithium-ion batteries, and lithium storage in carb n materials, and which can be further applied to manuf cture more advanced techn logy equipm nt to enhance th energy trans er efficiency.

References

[1] Huang L, ang Z P, Zhang J K, Pu J L, Lin Y J, Xu S H, She L, Chen Q and Shi W Z 2014 F lly printed, rapid-response sensors based on chemically modified graphene for detecting NO_2 at room t mperature ACS Appl. Mater. Inter. **6** 7426-7433.

[2] Park K 201 Controlled drug delivery systems: Past forward and future back J Control Release **190** -8.

[3] Buldum A nd Tetiker G 2013 First-principles tudy of graphene lithium structures for battery applications J. Appl. Phys. **113** 154312.

[4] Steel W A 1973 The physical interaction of gases with crystallin solide I. Gas-solid energies and pr perties of isolate adsorbed atoms Surf. Sci. **36** 317-352.

[5] Yu Y Z, G o J G, Kang Y L 015 An analytical model for adsor tion and diffusion of atoms/ions on graphene surface, J. Nanomat., **2015** 382474.

[6] Yu Y Z, Guo J G, Zhou L J 2016 Theoretical investigation on the adsorption and diffusion of lithium-ion on and between graphene layers with size nd defect effects, Adsorpt. Sci. T chnol., **34** In pre s.

MECHANICAL-ELECTRIC-MAGNETIC COUPLING AND ENERGY CONVERSION IN TWO-DIMENSIONAL MATERIALS

Wanlin Guo [a)]

State Key Laboratory of Mechanics and Control for Mechanical Structures and Key Laboratory of Intelligent Nano Materials and Devices of Ministry of Education, Nanjing University of Aeronautics and Astronautics. Yudao Street, 29, Nanjing, 210016, China,

Summary Nanoscale materials and devices are distinctly different in both properties and functions from their macroscopic counterparts. Having a deep insight into these peculiar properties and functions are crucial to realizing innovative nanotechnology. In two-dimentianl materials, the energy dissipation, structure-dependent dynamic characters and the coupling between external fields and intrinsic local fields are essential issues for developing nanoelectromechanical systems and high-efficient energy conversion technology.

It is widely known that when the spatial scale goes down from macroscale to nanoscale, temporal scale will reduce to nano to femtosecond. It is more important that the related energy scale of an externally applied field will drop for eighteen orders from joule (1 Newton times 1 meter) to attojoule (1 nanoNewton times 1 nanometer = 6.42 eV), falling into the energy scale of the local fields of matter which consist of electronic structures, charge, molecular orbital and spin states. Therefore, at nanoscale, matters will show distinctly different performances from their bulk materials mainly due to the strong coupling between the local fields of matter and external applied fields. Such nanoscale multifield couplings can turn very common materials such as carbon, even insulating boron nitride, into functional nanomaterials with fantastic properties we expected for nanoelectronics, spintronics as well as high efficient energy conversion devices.

It will also be demonstrated by our recent findings that exceptional functional properties in the intrinsically insulating h-BN nanostructures (Nano Lett. 10, 5049, 2010; 13, 3232, 2013; JACS 133, 14831, 2011, Small 2015) and exotic properties of transition metal dichalcogenide (ACS Nano 7, 7126-7131, 2013; Phys. Rev. Lett. 112, 205502, 2014).

Recently we also found that an induced 'waving electronic potential' can be observed in graphene as it is dipped - 'waved' - in and out of seawater1. We also found that drawing a droplet of ionic solutions over the surface of graphene can induce "drawing electric potential" in the graphene2. The potentials are found to be raised by the moving boundary of the electric double layer formed at the interface of the droplet and graphene surface, or the solid-air-liquid boundary of a graphene sheet across a liquid surface. The findings extend centuries' old theories of electrokinetic effects and help understand the behaviour of carbon nanomaterials in liquids, which has been subject to conflicting reports for over a decade. The novel effects have been used to demonstrate energy harvest from dropping droplets, sensing the handwriting on graphene and stimulating a sciatic nerve of a frog. The waving potential, which is proportional to both the speed and the size of the graphene, can also be scaled up by connecting in series or parallel for possible applications in self-powered functional sensors such as tsunami monitors to wave energy harvest, monitors and remote ocean devices.

It is more interesting that the coupling promising us to break the 10 nanometer limitation of energy beam fabrication down to subnanometre scale3,4. Such extraordinary mechanical-electric-magnetic coupling effects in nano systems open up new vistas in functional nanodevices compatible with the concurrent technology for efficient energy conversion, self-powering flexible devices and novel functional systems.

References:

[1] Jun Yin, Zhuhua Zhang, Xuemei Li, Jin Yu, Jianxin Zhou, Yaqing Chen & Wanlin Guo*, Waving potential in graphene. Nature Communications 5, 3582 (2014).
[2] Jun Yin, Xuemei Li, Jin Yu, Zhuhua Zhang, Jianxin Zhou & Wanlin Guo*, Generating electricity by moving a droplet of ionic liquid along graphene. Nature Nanotechnology 9 (5), 378-383 (2014).
[3] Xiaofei Liu, Tao Xu, Xing Wu, Zhuhua Zhang, Jin Yu, Hao Qiu, Jinhua Hong, Chuanhong Jin, Jixue Li, Xinran Wang, Litao Sun*, Wanlin Guo*, Top-down fabrication of sub-nanometre semiconducting nanoribbons derived from molybdenum disulfide sheets, Nature Communications 4, 1776 (2013).
[4] Wanlin Guo*, Xiaofei Liu, 2D materials: Metallic when narrow. Nature Nanotech. 9, 413 (2014).

[a)] Corresponding author. Email: wlguo@nuaa.edu.cn.

MULTI SCALE MODELING OF MECHANICAL BEHAVIOUR OF 2D SINGLE WALL CARBON NANOTUBE NETWORK

Ankit Gupta[1] & Elizabeth Holm[1a)]
[1]*Department of Materials Science and Engineering, Carnegie Mellon University, Pittsburgh, USA*

Abstract Single Wall Carbon Nanotube (SWCNT) aerogels form 3D nanotube networks that are held together via van der Waals interactions at the nodes. These aerogels show an initial elastic deformation up to a compressive strain of 9%. However this observation is contradicted by the fact that the VDW interaction between two nanotubes is strongest when they are parallel to each other. Therefore, a fundamental understanding of mechanical properties of nanotube aerogels and their relationship with the node properties is required. In this work we propose a model for studying the mechanical behavior of a SWCNT random network using a multi scale modeling approach. Van der Waals interaction at the nodes between two nanotubes is modeled using Molecular Dynamics (MD). Results obtained from the atomistic simulation are fed into a Finite Element Model (FEM) to study the mechanical behavior of the random network of nanotubes at continuum scale.

INTRODUCTION

Single Wall Carbon Nanotube (SWCNT) aerogels are highly porous, isotropic structures with random filamentous networks of nanotubes cross-linked at nodes via VDW interactions as shown in figure 1a.[1,2] Figure 1b shows a schematic stress-strain curve for SWCNT based aerogels under compression.[2] This curve shows three characteristic regimes: a linear elastic regime (strain < 9%), a plateau regime (9% < strain < 60%) and a densification regime (strain > 60%). It is speculated that the initial linear elasticity may be caused by bending of nanotubes[2] or rotation of nanotubes about the nodes between nanotubes.[4] The plateau region can be associated with the collapse of cells due to elastic buckling of the nanotubes[2] and/or breaking of nodes.[2] In the densification regime, when opposing cell walls touch each other, deformation is due to the compression of nanotubes, giving rise to a sharp increase in stress.[3]

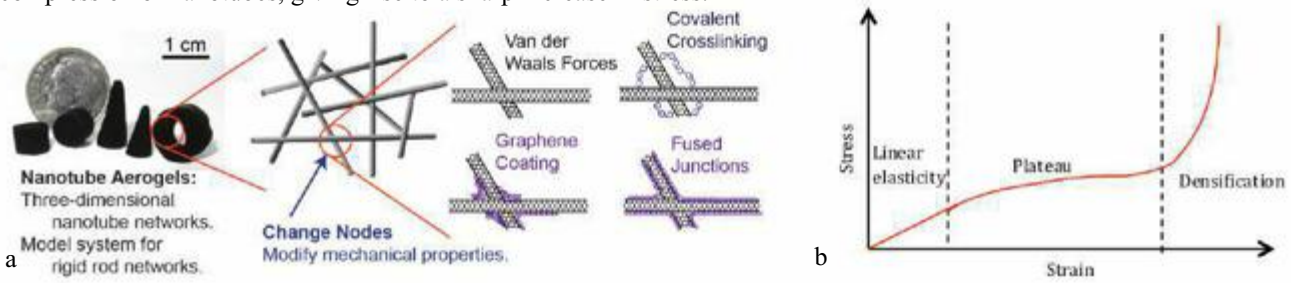

Figure 1: a) Free standing aerogels with tailorable node properties.[2] b) Stress-strain curve of an aerogel.

The fact that aerogel networks with unmodified (Van der Waals) node properties show some amount of elasticity without the presence of any restorative force at the nodes is intriguing. In this paper we try to explain this fact by studying the non-linear behavior of a SWCNT random network using a multi scale modeling approach. Our model in this study is confined to a two dimensional network.

a

$$\sigma_y = \frac{F_{y1} + F_{y2}}{2L}$$

$$E_n = \frac{\sigma_y}{\varepsilon}$$

b

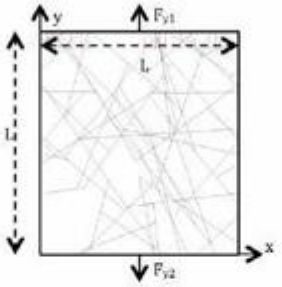

c



Figure 2: a) Calculation of stress and elastic modulus of the SWCNT network. b) The random network of SWCNTs used in the FEM calculations. c) The atomic configuration for MD simulations.

METHOD

A random network is generated by sequentially placing nanotubes at random in a periodic unit cell until the desired network density is reached. A node is formed wherever two nanotubes intersect. Dangling ends and isolated nanotube clusters are removed prior to FE analysis. In FEM, carbon nanotubes are modeled as Euler-Bernoulli beam elements with three degrees of freedom at each node (two translation and one rotation). A node between two carbon nanotubes is modeled as a combination of three 2D uncoupled springs. Two of them resist translation in the x and y directions, and the third is a torsional spring that resists rotation along z-direction. The network is subjected to cyclic boundary conditions.[5] A compressive strain ε is applied in y direction. The solution is obtained using ANSYS Mechanical APDL software. The resulting forces in the y-direction on the nodes located at the top and bottom boundary of the network are stored and the data is used to calculate the elastic modulus E_n of the network as shown in figures 2a and 2b. VDW interactions between

a) Corresponding author. Email: eaholm@andrew.cmu.edu

nanotubes are modeled via MD simulations using the Lennard-Jones potential and the configuration shown in figure 2c.[6] In the first simulation, the angle between nanotubes γ is varied, while in the second simulation the sliding of one nanotube against the other is studied. The variation of the total energy of the system is plotted in both cases.

RESULTS & DISCUSSION

Figures 3a and 3b show the variation of energy curve obtained from the two MD simulations. For the first case, the energy of system is minimum when γ is zero; thus, the parallel configuration of the nanotubes is most stable. The second derivative of this curve gives stiffness of the torsional spring that is used in the FEM. A pre-strain term equal to the value of stiffness times the angle between two nanotubes is added at each node in the FEM in order to account for the torque that acts to bring nanotubes in equilibrium configuration. Similarly, the second derivative of the energy curve in the second case gives the stiffness of springs that resist translational motion in x and y directions. Force resulting from compression and stretching of these springs can be obtained from the first derivative. The maximum value of this force is taken as the fracture strength of the nodes between nanotubes.

a b

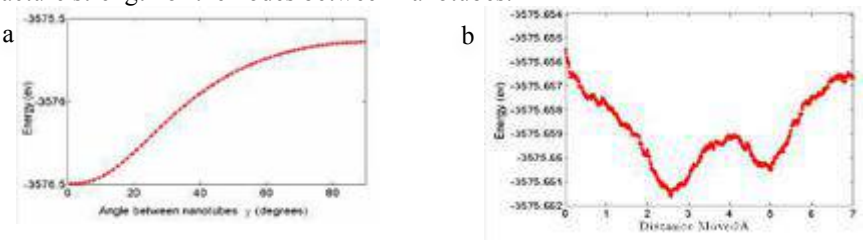

Figure 3: a) Variation of energy with respect to γ b) Variation of energy in case of sliding

Figure 4a shows the variation of elastic modulus of the network E_n with respect to stiffness of the torsional spring, K_z. For small values of K_z, E_n varies linearly and becomes constant at a value that is comparable to the bending stiffness of the nanotube. This means that for weak nodes, deformation of the network is governed by the rotation of nanotubes about nodes, while for stronger nodes, bending of nanotube dictates the overall deformation. Figure 4b shows the stress-strain curve for the network when both fracture of nodes between nanotubes and pre-strain term is taken into account. The curve shows an initial linear elastic regime. The response starts deviating from linear elasticity when a significant number of nodes have broken (shown in red). Eventually the network fails at around 10% strain when there are not enough nodes left to form a connected network. Note that even though a pre-strain term is added, that accounts for irreversible nature of VDW interactions; the stress-strain response is still very similar to the case of no pre-strain (shown in blue). This is because VDW interactions are very weak in nature.

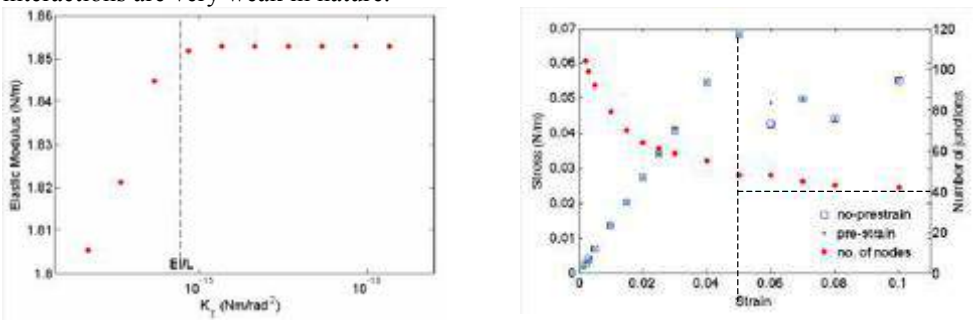

a b

Figure 4: a) Variation of elastic modulus of the SWCNT network with torsional spring stiffness, K_z. b) Stress-strain curve of the network.

CONCLUSIONS

In this work, a multi scale modeling method to study mechanical behavior of SWCNT network is established. MD simulations provided insight into VDW interactions of nanotubes at atomistic scale simultaneously providing a measure of resistance offered against sliding and rotation of nanotubes at nodes. FEM results show that in linear regime deformation of network is governed by rotation of nanotubes about nodes since value of K_z obtained from MD simulation is very small. These results also suggest that nanotubes networks can be elastic in initial linear regime as observed experimentally.[2,7] This is attributed to the very weak nature of VDW interactions The linear elastic regime is followed by a nonlinear stress-strain curve when a significant number of nodes in the network have ruptured.

References

[1] M. B. Bryning, D. E. Milkie, M. F. Islam, L. A. Hough, J. M. Kikkawa, and A. G. Yodh, *Advanced Materials,* vol. 19, pp. 661-664, 2007.

[2] K. H. Kim, Y. Oh, and M. F. Islam, *Advanced Functional Materials,* vol. 23, pp. 377-383, 2013.

[3] L. J. Gibson and M. F. Ashby, *Cellular Solids, Strucutre and properties*. New York: Pergamon, 1997.

[4] K. H. Kim, Y. Oh, and M. F. Islam, *Nat Nano,* vol. 7, pp. 562-566, 09//print 2012.

[5] S. Heyden, "A network model applied to cellulose fibre materials," Division of Structural Mechanics, LUND UNIVERSITY, Sweden, 1996.

[6] S. Plimpton, "Fast Parallel Algorithms for Short-Range Molecular Dynamics, " J Comp Phys, vol. 117, pp. 1-19, 1995.

[7] E.K.Hobbie, D.O.Simien, J.A.Fagan, J.Y.Huh, J.Y.Chung, S.D.Hudson*, et al.*, *Phys. Rev. Lett,* vol. 104, p. 125505, 2010.

NANOMECHANICAL CHARACTERIZATION OF BORON NITRIDE AND CARBON NANOTUBES POLYMER INTERFACES

Xiaoming Chen[1] and Changhong Ke[1,2a)]
[1]*Department of Mechanical Engineering, State University of New York at Binghamton, Binghamton, New York, USA*
[2]*Materials Science and Engineering Program, State University of New York at Binghamton, Binghamton, New York, USA*

Summary The mechanical strengths of the interfaces formed by individual boron nitride and carbon nanotubes with epoxy resins and poly(methyl methacrylate) (PMMA) are characterized by *in situ* electron microscopy nanomechanical single-tube pull-out techniques. The nanomechanical measurements reveal the shear lag effect for the load transfer on the tested nanotube-polymer interfaces. Boron nitride nanotubes are found to be capable of forming stronger binding interfaces with polymers than comparable carbon nanotubes. Both boron nitride and carbon nanotubes bind more strongly with epoxy than PMMA. The research findings help to better understand the load transfer on the tube-polymer interface and the tube's reinforcing mechanism, and ultimately contribute to the optimal design and performance of nanotube-reinforced polymer nanocomposites.

INTRODUCTION

The unique light-weight and high-strength characteristics of fiber-reinforced polymer nanocomposites are attractive for a number of structural applications ranging from bodies of aerospace shuttles and aircraft to automobile and sports equipment components. Carbon and boron nitride nanotubes (CNTs and BNNTs) are two types of light and strong one-dimensional fibers and hold great promise as reinforcing additives for polymer nanocomposites. However, the mechanical performance of nanotube-reinforced polymers remains far from reaching the anticipated level. Understanding the interfacial stress transfer and ultimately having a good command of the nanotube-polymer interface are one of the key scientific challenges to be tackled. This is because the realization of the reinforcing effect of the high-strength additive nanotubes relies on an adequate load transfer on the tube-polymer interface. To date, a vast majority of the studies on nanotube-reinforced polymers were performed at the macroscopic level and yielded merely bulk material properties, from which the interfacial strength properties can only be evaluated qualitatively and indirectly. Direct and quantitative measurements of the interfacial strength between individual nanotubes and polymers by using microscopic-level single-tube pull-out techniques remain quite limited (for CNTs) or unexplored (for BNNTs). In this paper, we present and discuss the experimental characterization of the mechanical strengths of CNT and BNNT polymer interfaces by using *in situ* electron microscopy nanomechanical testing techniques.

EXPERIMENTAL AND METHODS

The nanotube polymer interface strength was characterized by using an *in situ* electron microscopy nanomechanical single-tube pull-out technique [1], as illustrated in Figure 1. In this testing scheme, the nanotube-polymer interface is engineered inside a sandwiched polymer-tube-polymer thin-film composite. A protruding tube is stretched by an incrementally displaced atomic force microscopy (AFM) cantilever until the embedded tube segment is pulled out of the polymer matrix. The CNTs and BNNTs employed in this study are synthesized using chemical vapor deposition and high-temperature pressure methods, respectively, and their diameters are found to be polydispersed and mostly within the ranges of 2-4.2 nm and 1.9-3.9 nm, respectively [2, 3]. Epoxy resin (Epon 828) and PMMA are the two types of polymer matrices employed in this study.

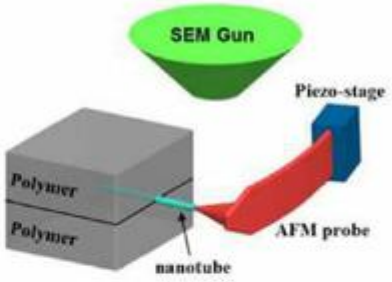

Figure 1 3D illustration of our *in situ* nanomechanical single-tube pull-out measurement inside a scanning electron microscope.

The nanomechanical single-tube pull-out tests were performed inside an FEI Nanolab 600 scanning electron microscope (SEM). Pre-calibrated AFM probes with spring constants within the range of 0.04-0.09 N/m were employed as the force sensors. The AFM sensor was mounted to a 3D piezo stage that possesses 1 nm displacement resolution in the X-Y-Z axes. Electron beam induced deposition of Pt was utilized to weld the free end of the protruding tube to the tip of the AFM sensor.

RESULTS AND DISCUSSION

Figure 2(a) shows one representative single-tube pull-out measurement on a CNT-epoxy interface [2]. Figure 2(b) shows the dependences of the measured pull-out load on the embedded tube length for the four types of interfaces formed by CNTs and BNNTs with epoxy and PMMA [1-3]. For all four types of interfaces, the pull-out load first increases with the embedded

a) Corresponding author. Email: cke@binghamton.edu

length, and then reaches a plateau, which is a clear sign of the shear lag effect for the load transfer on the nanotube-polymer interfaces. The interfacial shear strengths of BNNT-polymer interfaces are found to be higher than those of the comparable CNT-polymer interfaces. The maximum interfacial shear strengths of BNNT-epoxy and BNNT-PMMA interfaces reach about 323 and 219 MPa [3], respectively, compared with about 270 MPa for CNT-epoxy interfaces [2] and about 163 MPa for CNT-PMMA interfaces [1]. The superior load transfer capacity of BNNT-polymer interfaces is ascribed to both the strong van der Waals interactions and Coulomb interactions on BNNT-polymer interfaces. Our studies also reveal that both BNNTs and CNTs bind more strongly with epoxy than PMMA. The findings of the extraordinary mechanical strength of BNNT-polymer interfaces suggest that BNNTs are excellent reinforcing nanofiller materials for light-weight and high-strength polymer nanocomposites. This study demonstrates that our *in situ* nanomechanical single-tube experimental technique can be used to characterize the unique nanomechanical signatures of the interfaces formed by nanotubes with a variety of polymer matrices, thus enabling a convincing quantification and comparison of the interfacial strength across different nanotube-polymer material systems.

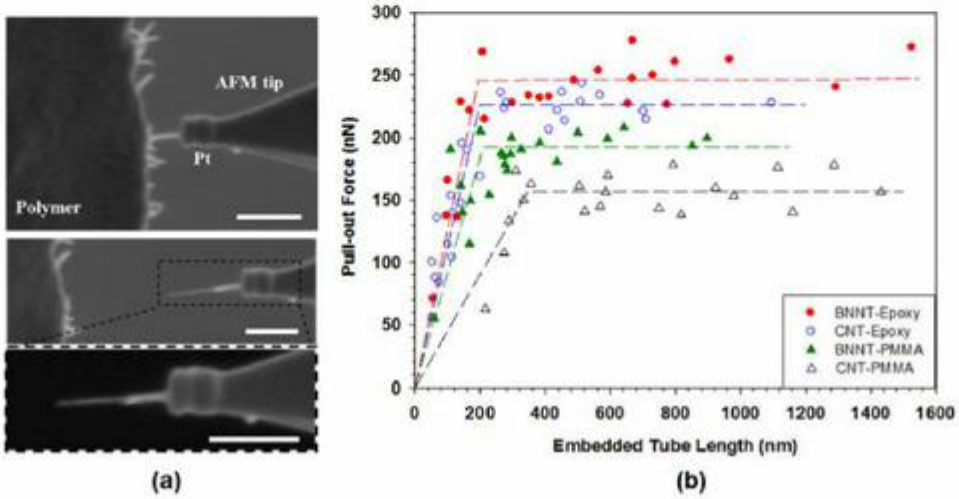

Figure 2 (a) Selected SEM snapshots of one representative single-tube pull-out test on a CNT-epoxy composite: (*top*) before and (*bottom*) after pull-out. All scale bars represent 500 nm. (b) The measured dependence of the pull-out load on the embedded tube length for the four types of interfaces formed by CNTs and BNNTs with epoxy and PMMA. The dots represent the experimental data. The dashed lines represent the respective linear fitting curves to the data sets whose tube embedded lengths are below or above the critical embedded length.

CONCLUSIONS

In this paper, we report the experimental measurements on the mechanical strengths of CNT and BNNT polymer interfaces using *in situ* electron microscopy nanomechanical single-tube pull-out techniques. Our nanomechanical measurements reveal that BNNTs can form stronger binding interfaces with polymers than comparable CNTs, and their binding strengths with epoxy are higher than those with PMMA. The research findings contribute to a better understanding of the load transfer on the tube-polymer interface and the tube's reinforcing mechanism, and ultimately the optimal design and performance of nanotube-reinforced polymer nanocomposites.

References

[1] Chen X.-M., Zheng M., Park C., Ke C.-H.: Direct Measurements of the Mechanical Strength of Carbon Nanotube-Poly(methyl methacrylate) Interfaces, *Small* **9**:3345–3351, 2013.

[2] Chen X.-M., Zhang L.-Y., Zheng M., Park C., Wang X.-Q., Ke C.-H.: Quantitative Nanomechanical Characterization of the van der Waals Interfaces between Carbon Nanotubes and Epoxy, *Carbon* **82**:214-228, 2015.

[3] Chen X.-M., Zhang L.-Y., Park C., Fay C.C., Wang X.-Q., Ke C.-H.: Mechanical Strength of Boron Nitride Nanotube-Polymer Interfaces, *Appl. Phys. Letts.* **107**:253105, 2015.

SERPENTINE MOTION THROUGH A FRICTIONLESS CHANNEL

Diego Misseroni[1], Davide Bigoni[1], Francesco Dal Corso[1], Nicola M. Pugno[1],
Alexander B. Movchan[2] and Natalia V. Movchan[2]
[1]DICAM, University of Trento, Trento, Italy
[2]Department of Mathematical Sciences, University of Liverpool, UK

Summary Serpentine (or undulatory) motion within a smooth channel is theoretically investigated and fully validated by systematic experiments. The experiments are performed on an elastic rod, straight in its unloaded configuration, constrained within a rigid and frictionless curved channel. A proof-of-concept model for a channel is designed and realized, with the shape of an Euler spiral, in which friction is reduced to a negligible amount by using roller bearings.

INTRODUCTION

Gray was the pioneer in the study of snake propulsion and he identified four mechanisms for snake locomotion: serpentine motion, concertina movement, side-winding, and rectilinear propulsion, see [1,2,3]. The principal mechanical concept underlying serpentine locomotion was explained by Gray [1,2,3] in terms of a release of elastic energy generated through muscular contraction. His model, based on a chain of rigid pieces connected to each other with rotational springs, explains the counterintuitive phenomenon where locomotion can occur in the absence of friction. This is also in agreement with the experimental observation that serpentine motion ceases when a snake is confined to a straight or circular channel.

More recently, Bigoni and his co-workers [4, 5, 6] have discovered the relation between configurational forces (or Eshelby-like forces) and the mechanism of motion through a release of elastic energy. In [7] they have shown how longitudinal propulsion can be achieved in a perfectly frictionless and smooth channel by applying a torque at the end of the structure.

The presentation focuses on the theoretical derivation and the experimental proof of serpentine (or undulatory) motion, the first type of the four mechanisms for of snake locomotion. We consider an elastic rod, straight in its undeformed configuration, and constrained within a rigid and frictionless curved channel as shown in Fig. 1.

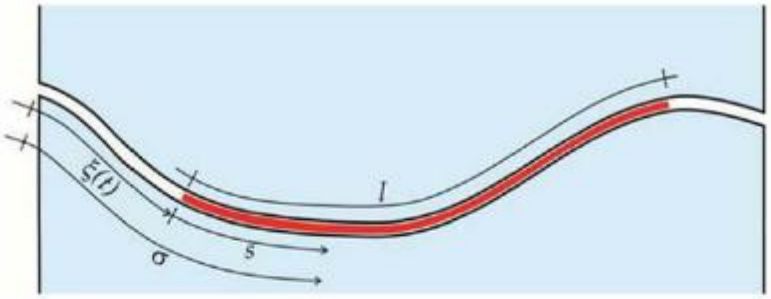

Fig.1: An extensible elastic rod (rectilinear in its undeformed configuration) of length l within a smooth curvilinear channel. Its configuration is defined by the evolution in time of the curvilinear coordinate $\xi(t)$.

The propulsive force is generated through a release of elastic energy stored within the elastic rod and is strictly connected to the development of Eshelby-like (or configurational) forces. The propulsive force is derived through different approaches: (a) energetic formulation, (b) integration of the equations of motion, complemented by a 'micromechanical' derivation of the channel reactions acting on the elastic rod (Fig. 2) and providing the Eshelby-like forces.

[a)] Corresponding author. Email: diego.misseroni@unitn.it

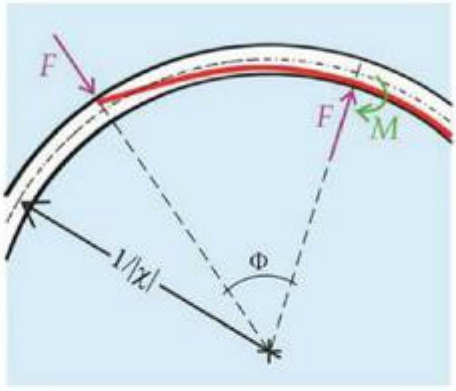

Fig 2: Micromechanics of an elastic rod inside a frictionless rigid channel that shows the reactions developing at the contact points

Finally, a frictionless channel with the shape of a clothoid spiral was designed and realized. The friction between the rigid channel and the elastic rod was reduced by employing modified roller bearings. The experiments, performed on elastic rods with uniform and variable bending stiffness, fully confirm the theoretical predictions.

CONCLUSIONS

The serpentine (or undulatory) motion within a frictionless channel was theoretically investigated by using both variational calculus and micromechanics. The analytical results are substantiated through experiments using purpose designed and built apparatus.

ACKNOWLEDGEMENT

The authors gratefully acknowledge financial support from the ERC Advanced Grant "Instabilities and nonlocal multiscale modelling of materials" FP7-PEOPLE-IDEAS-ERC-2013-AdG (2014-2019).

References

[1] Gray, J. The mechanism of locomotion in snakes. *J. Exp. Biol*. **23**, 101–120, 1946.

[2] Gray, J. How animals move. *Cambridge University Press*, 1953.

[3] Gray, J. and Lissmann H.W. The kinetics of locomotion of the grass-snake. *J. Exp. Biol*. **26**, 354–367, 1950.

[4] Bigoni, D., Bosi, F., Dal Corso, F. and Misseroni, D. Eshelby-like forces acting on elastic structures: theoretical and experimental proof. *Mech. Materials* **80**, 368374, 2015.

[5] Bigoni, D, Bosi, F., Dal Corso, F. and Misseroni, D. (2014) Instability of a penetrating blade. *J. Mech. Phys. Solids* **64**, 411–425, 2014.

[6] Bosi, F., Dal Corso, F., Misseroni, D. and Bigoni, D. (2014) An Elastica Arm Scale. *Proc. R. Soc*. A, **470**, 20140232, 2014**.**

[7] Bigoni, D., Dal Corso, F., Misseroni, D. and Bosi, F. (2014) Torsional locomotion*. Proc. R. Soc. A*, **470**, 20140599, 2014.

COMPLEX ENERGY LANDSCAPES OF CARBON NANOTUBES WITH DEFECTS

Xiao-Wen Lei[1,2] and Akihiro Nakatani *[1]

[1]*Department of Adaptive Machine Systems, Osaka University, Suita, Osaka, Japan*
[2]*Department of Mechanical Engineering, University of Fukui, Fukui, Japan*

Summary Defects in carbon nanotubes influence their properties. In this research, the energy landscape is calculated for a variety of distributions of Stone–Wales defects and pentagon-heptagon (5-7) defects using a model based on the dislocation theory. The equilibrium configurations are solved using the conjugate gradient method, and the saddle point on the minimum energy path between two equilibrium configurations is calculated using the nudged elastic band method. Many equilibrium configurations related to the lattice trapping of the 5-7 defects are obtained. The configurations are stable, because the Peierls-Nabarro barrier of the movement of these defects are relatively large. The total energy depends not only on the mean value of relative displacement but also on the complexity of the configurations of the defects. Evolution of the defects is organized based on the graph theory. The results provide fundamental information to discuss the stability of thermal activation of defects.

ANALYSIS MODEL OF CNTS WITH STONE–WALES DEFECTS

Carbon nanotubes (CNTs) have extraordinary mechanical properties and distinctive applications [1]. Generally, their properties can be affected by defects such as Stone–Wales (SW) and pentagon-heptagon (5-7) defects. SW defects can be separated into pairs of 5-7 defects [2]. Plastic deformation due to slip of the 5-7 defect pair and pseudoclimb has been reported theoretically [3]. In this study, we use a theoretical formulation in terms of the relative displacement on the slip-plane [4] and the relationship between energy and the configuration of the 5-7 defects. Figures 1 (a) and (b) show schematics of cross–section of a perfect (11,0) CNT and a CNT with SW defect, respectively. The relative slip in the cross–section can be expressed by the relative displacement of atomic sites denoted as $(-5, -4, \cdots, 4, 5)$. Open and solid circles indicate the position of the upper and lower atoms, respectively.

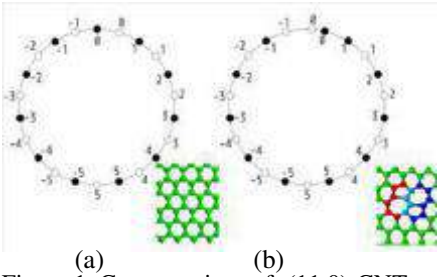

(a) (b)

Figure 1: Cross-section of (11,0)-CNT: (a) Perfect lattice, (b) with Stone-Wales defect

Table 1: Constants and valuables

$\gamma(u)$	Generalized stacking fault energy (γ – surface)
u_l	$= u(s_l)/a$; Nondimensional relative displacement
a	Lattice constant
d	$= a/\sqrt{12}$; Lattice spacing between slip planes
Δ	A parameter ($0.15 \sim 0.19$, depending on radius of CNT)
b_0^s	$= \mu(1+\nu)a$; A parameter of stiffness
b_0^r	$= \mu(1+\nu)a/\{8\sqrt{3}(1+3\nu)\}$; A parameter of stiffness
μ, ν	Elastic constants
f_{ext}	An external force

EQUILIBRIUM CONFIGURATIONS AND MINIMUM ENERGY PATH

According to the theoretical formulation by Wang et al.[4], the total energy E_{total} is described as the sum of Peierls-Nabarro potential, E_γ, elastic interaction, E_Ω, interaction between neighboring sites, E_b and potential of external force, E_f as shown in the following equations. Each term is described using the relative displacement, u_l $(l = 1, n)$. For (11,0)-CNT, sites $l = 1, 2, \cdots, 6, \cdots, 11$ correspond to $-5, -4, \cdots, 0, \cdots, 5$, respectively.

$$E_{\text{total}}(\boldsymbol{u}) = E_\gamma + E_\Omega + E_b (+E_f), \quad \text{where} \quad \boldsymbol{u} = (u_1, u_2, \cdots, u_n), \tag{1}$$

$$E_\gamma \left(= \oint \gamma(u(s)) ds \right) = \sum_{l=1}^{n} \frac{a}{2} \frac{\mu a^2}{4\pi^2 d} \Big(1 - \cos(4\pi u_l) \Big) \Big(1 + \Delta \sin^2(2\pi u_l) \Big), \tag{2}$$

$$E_\Omega = \sum_{l=1}^{n} \sum_{j=1}^{n} \frac{1}{2a} \Omega_{lj} (a u_j)(a u_l), \quad \text{where} \quad \Omega_{lj} = \frac{b_0^s}{n} \left[\cot\left((l-j) + \frac{1}{2} \right) \frac{\pi}{n} - \cot\left((l-j) - \frac{1}{2} \right) \frac{\pi}{n} \right], \tag{3}$$

$$E_b = \sum_{l=1}^{n} \frac{1}{2} b_0^r a^2 (u_l - u_{[l-1]})^2, \quad \text{where} \quad (u_{[l]} = u_{\text{MOD}(n+l-1,n)+1}), \qquad E_f = -\sum_{l=1}^{n} f_{\text{ext}} \frac{a}{2} u_l \tag{4}$$

The parameters are shown in Table 1. The static equilibrium configurations are obtained to solve $\partial E_{\text{total}} / \partial \boldsymbol{u} = \boldsymbol{0}$ using the conjugate gradient method. Then, the nudged elastic band method (NEB) [5] is used to determine the minimum energy path (MEP) between two equilibrium states.

*Corresponding author. Email: nakatani@ams.eng.osaka-u.ac.jp

RESULTS AND DISCUSSION

Figure 2(a) shows the distribution of relative displacement for equilibrium configurations obtained using the conjugate gradient method and the saddle points obtained using the NEB method. The distribution of atomic displacement is highly localized at the core region of the 5-7 defects. Figure 2(b) shows a set of energy as functions of the average slip $\bar{u} = \frac{1}{n}\sum_{l=1}^{n} u_l$; E_{total}(black), E_γ(red), E_Ω(yellow), E_b(blue). It is found that the physical meaning of configuration 'sol.2' is the unstable equilibrium point (saddle point) between perfect lattice and SW defect. Figure 2(c) shows the configurational force (Peach-Koehler force), which is defined as the derivative of the total energy with respect to average relative displacement, of the 5-7 defects. The overall character of the profile of the curve agrees with the prediction according to the dislocation theory, but the curve oscillates locally. Many equilibrium configurations exists due to the lattice trapping of 5-7 defects. These configurations are stable, because the Peierls-Nabarro barrier between them are relatively large. Figure 3 shows the graph of transition, annihilation, and movement of defects in CNTs. The schematic illustrations of configurations are located on an energy-relative displacement plane, and the processes of structural change are shown with the activation energy and released energy. One 5-7 defect pair in SW defect can be separated from another with energy consumption, and the SW defect is annihilated with significantly reduced energy to attain stability.

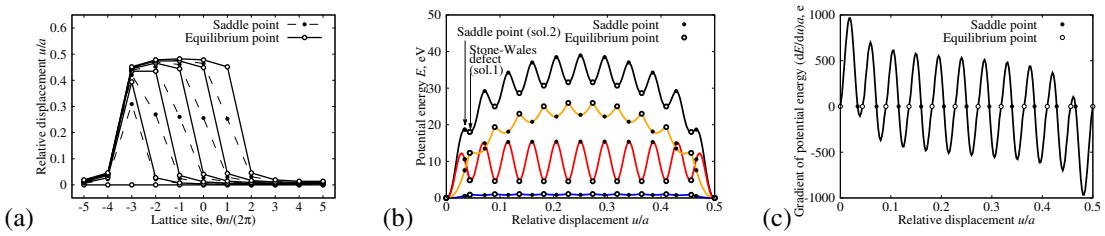

Figure 2: Configuration and energy landscape: (a) Relative displacement, (b) energy landscape, and (c) configurational force

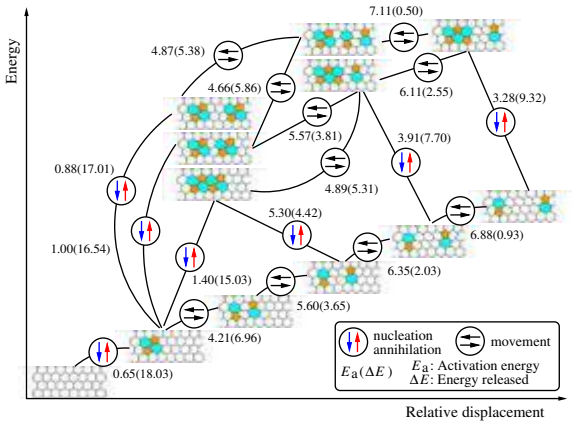

Figure 3: A schematic illustration of energy graph for CNTs with different transition and annihilation defects

CONCLUSIONS

The equilibrium configurations of defects in CNTs and their related MEP have been determined using a lattice defect theory, and then transition processes of the structural changes of defects have been discussed from the graph theory point of view. The quantitative results provide fundamental information of complex energy landscape to discuss the stability of thermal activation of defects.

Acknowledgement: This work was supported by MEXT/JSPS KAKENHI Grant Numbers 26870348, 23109010, 25286100.

References

[1] Lei X. W., Natsuki T., Shi J. X., Ni Q. Q.: An atomic-resolution nanomechanical mass sensor based on circular monolayer graphene sheet: Theoretical analysis of vibrational properties. J. Appl. Phys. 113:154313(6 pages), 2013.

[2] Lei X. W., Nakatani A.: A continuum mechanics analysis of lattice defects in carbon nanotube. ESMC, Spain 2015.

[3] Ding F., Jiao K., Wu M., Yakobson B. I.: Pseudoclimb and dislocation dynamics in superplastic nanotubes. Phys. Rev. Lett. 98:075503(4 pages),2007.

[4] Wang, S. W., Yao, Y., Zhang, H. L., Wang, R.: StoneWales defect as a dipole of dislocation and anti-dislocation. Phys. Lett. A, 375:4109-4112, 2011.

[5] Zarkevich N. A., Johnson D. D.: Nudged-elastic band method with two climbing images: Finding transition states in complex energy landscapes, J. Chem. Phys. 142:024106(5 pages), 2015.

TWO-DOMAIN MODEL OF VOLUMETRIC ACTUATORS

Jakub Lengiewicz*, Michał Kursa, and Paweł Hołobut
Institute of Fundamental Technological Research, Polish Academy of Sciences, Warsaw, Poland

Summary In the present work we propose a framework for modeling *volumetric actuators* – a special class of mechanical systems that can transform the parallel work of micro-actuators, distributed throughout an actuator's volume, into a macroscopic force that scales with this volume. The proposed model takes into account the expected finite deformation of actuators and the coupling between the deformation and micro-actuation, which can strongly influence an actuator's behavior. Finite element implementation details are presented, together with numerical examples and results.

VOLUMETRIC ACTUATORS

Volumetric actuators are a specific class of mechanical systems. Their output forces are produced by micro-actuators distributed over their volumes and working in parallel. This is in contrast to other actuators, examples of which are hydraulic and pneumatic cylinders, whose forces often result from surface interactions and are proportional to their cross-sectional areas. The advantage of well-designed volumetric actuators is that their maximum output forces are proportional to the number of micro-actuators in their interior, and so to their volumes.

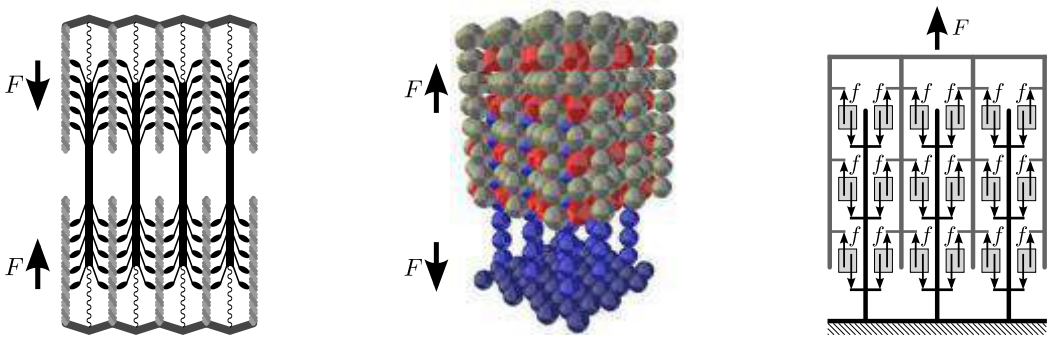

Figure 1: Volumetric actuators. Left: schematic of a sarcomere—a subunit of animal muscles. Center: DEM model of a modular-robotic collective actuator, built of spherical units. Right: principle of operation of a volumetric actuator.

An example of such systems is the sarcomere [1], which is ubiquitous as a fundamental active subunit of animal muscles. Similar artificial systems are also being considered, e.g., as an application of the MEMS and NEMS technology. In Fig. 1(left), a schematic of the sacromere is presented, with heads of myosin molecules (black) working as micro-actuators, pulling adjacent actin filaments (gray), and producing an overall contracting force. Quite similarly, an artificially designed modular-robotic structure works as a two-directional actuator [2, 3], see Fig. 1(center). Here, the spherical micro-robots form two separate, strongly bonded frames (blue and gray) that are pushed/pulled against each other by active (red) modules.

Finally, Fig. 1(right) shows the general principle of operation of a (linear-motion) volumetric actuator. The actuator is composed of two interdigitated solid structures (black and gray in the figure), with micro-actuators (gray rectangles) distributed between them throughout the volume. Each micro-actuator pushes (or pulls) the two structures in opposite directions, exerting a micro-force f. The micro-forces sum over the volume, yielding the total force F produced by the actuator.

TWO-DOMAIN MODEL

In the proposed two-domain model, two inter-penetrating domains Ω_1 and Ω_2, see Fig. 2, move against each other along some permitted directions (isolines $\Psi_i = \text{const}$). Actuators can, in general, undergo finite deformations that can affect their properties, and vice-versa. Neglecting body forces, the weak form for two interacting actuator parts can be written as

$$G(\boldsymbol{\varphi}, \delta\boldsymbol{\varphi}) = G_1(\boldsymbol{\varphi}, \delta\boldsymbol{\varphi}_1) + G_2(\boldsymbol{\varphi}, \delta\boldsymbol{\varphi}_2) + G_c(\boldsymbol{\varphi}, \delta\boldsymbol{\varphi}) = 0, \tag{1}$$

where $\delta\boldsymbol{\varphi} = \{\delta\boldsymbol{\varphi}_1, \delta\boldsymbol{\varphi}_2\}$ are the variations vanishing on y_i^u,

$$G_i(\boldsymbol{\varphi}, \delta\boldsymbol{\varphi}_i) = \int_{\Omega_i} \frac{W_i}{\boldsymbol{F}_i} \cdot \nabla\delta\boldsymbol{\varphi}_i dV_i \nearrow \int_{\Gamma_i^t} \boldsymbol{T}_i^* \cdot \delta\boldsymbol{\varphi}_i dS_i, \;\; i \in \{1, 2\} \tag{2}$$

*Corresponding author. Email: jleng@ippt.pan.pl

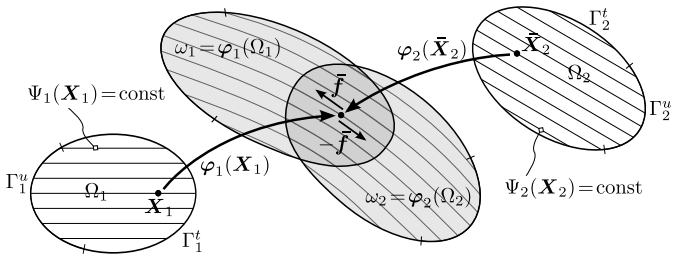

Figure 2: Continuum mechanics model.

are the weak forms derived form (hyper)elastic potentials W_i, with deformation gradients $\boldsymbol{F}_i = \nabla\boldsymbol{\varphi}_i$, and

$$G_c(\boldsymbol{\varphi}, \delta\boldsymbol{\varphi}) = \int_{\bar{\Omega}_1} \left[\rho \prod\nolimits_1(\boldsymbol{X}_1) \nearrow \Psi_2(\bar{\boldsymbol{X}}_2)) \, \frac{\partial \Psi_2}{\partial \bar{\boldsymbol{X}}_2} \left(\nabla\bar{\boldsymbol{\varphi}}_2\right)^{-1} + \bar{f} \frac{\boldsymbol{F}_1 \nabla\bar{\Psi}_1}{\|\boldsymbol{F}_1 \nabla\bar{\Psi}_1\|} \right] \cdot (\delta\boldsymbol{\varphi}_1 \nearrow \delta\boldsymbol{\varphi}_2) \, dV_1 \tag{3}$$

is the contact part of the weak form (1), in which $\bar{\boldsymbol{X}}_2$ is a point of Ω_2 such that $\bar{\boldsymbol{\varphi}}_2 = \boldsymbol{\varphi}_2(\bar{\boldsymbol{X}}_2)$ coincides with the point $\boldsymbol{\varphi}_1(\boldsymbol{X}_1)$, $\bar{\Omega}_1 = \boldsymbol{\varphi}_1^{-1}(\omega_1 \cap \omega_2)$, and $\bar{\Psi}_1$ is a scalar field complementary to Ψ_1 in the sense that $\nabla\bar{\Psi}_1$ are parallel to the isolines of Ψ_1. The first term in (3) is the enforcement of the condition that corresponding isolines of Ψ_1 and Ψ_2 must coincide, and the second term imposes actuation of the intensity $\bar{f}$ in the direction tangent to a deformed isoline $\nabla\bar{\Psi}_1$.

The above formulation has strong analogies to earlier works on formulations for contact problems [4], and it is particularly suitable for the finite element method implementation. In the present work, the necessary FE procedures have been derived using the symbolic system *AceGen*, and the subsequent FE calculations are performed in the *AceFEM* environment [5].

EXEMPLARY 2D FEM RESULTS

As an example, a two-dimensional contracting actuator is analyzed, as depicted in Fig. 3. Two constituent parts of the actuator are 20×10 mm^2 rectangles, clamped at opposite sides, with the initial 5 mm overlap. A plain-strain hyperelastic material model for both parts is applied, with the Young's modulus $E = 1$ MPa and Poisson's ratio $\nu = 0$. .



Figure 3: Exemplary FEM results. Left: initial mesh ($\bar{f} = 0$). Right: deformed mesh ($\bar{f} = 0.03\,[\text{N}/\quad^3]$).

In Fig. 4, the expected non-uniform deformation is presented, with horizontally-aligned stress gradients in the contact zone, which is characteristic of volumetric actuators.

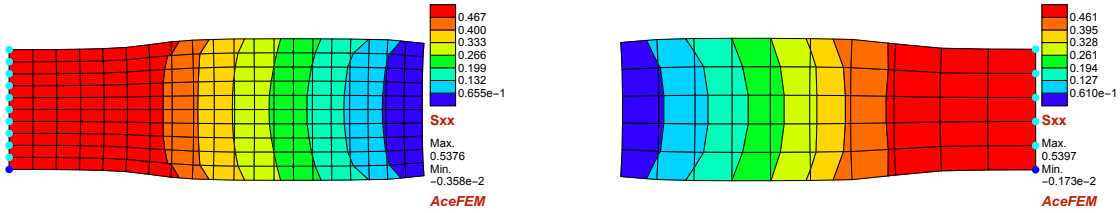

Figure 4: S_{xx} stress field in the deformed configuration for the left and right part of the actuator ($\bar{f} = 0.03\,[\text{N}/\quad^3]$).

Acknowledgement This work was partially supported by the project "Micromechanics of Programmable Matter" (contract no. 2011/03/D/ST8/04089 with the National Science Centre in Poland).

References

[1] McNeill Alexander R.: Principles of Animal Locomotion. Princeton, United States, 2006.

[2] Hołobut P., Kursa M., Lengiewicz J.: Efficient modular-robotic structures to increase the force-to-weight ratio of scalable collective actuators. Proc. 2015 IEEE/RSJ Int. Conf. on Intelligent Robots and Systems (IROS), Hamburg, Germany:3302–3307, 2015.

[3] Lengiewicz J., Kursa M., Hołobut P.: Modular-robotic structures for scalable collective actuation. Robotica, doi:10.1017/S026357471500082X, 2015.

[4] Lengiewicz J., Korelc J., Stupkiewicz S.: Automation of finite element formulations for large deformation contact problems. Int. J. Numer. Meth. Engng 85:1252–1279, 2011.

[5] Korelc J.: AceGen and AceFEM user manuals. Available at http://www.fgg.uni-lj.si/Symech/, 2009.

ANOMALOUS SCALING LAW OF MECHANICAL PROPERTIES OF CELLULOSE NANOPAPER: DEFEATING THE CONFLICT BETWEEN STRENGTH AND TOUGHNESS

Shuze Zhu,[1,#] Zheng Jia,[1,#] Hongli Zhu,[2,#] Sepideh Parvinian,[2] Yuanyuan Li,[2] Oeyvind Vaaland,[2] Liangbing Hu,[2] Teng Li[1,a]

[1] *Department of Mechanical Engineering, University of Maryland, College Park, MD 20742*

[2] *Department of Materials Science and Engineering, University of Maryland, College Park, MD 20742*

[#] *These authors contributed equally to this work.*

Summary A long-standing challenge in material design is to overcome the conflict between strength and toughness, as they are generally mutually exclusive. To address this challenge, we rationally design cellulose-based nanopaper and investigate the dependence of their mechanical properties on constituent cellulose fiber size. Surprisingly, we find that both the strength and toughness of the nanopaper increase simultaneously (40 and 130 times, respectively) as the average diameter of constituent cellulose fibers decreases from 27 micrometers to 11 nanometers, suggesting the promising potential toward an anomalous but highly desirable scaling law: The smaller, the stronger AND the tougher. There are abundant opportunities to utilize the fundamental bottom-up strategy to design a novel class of functional materials that are both strong and tough.

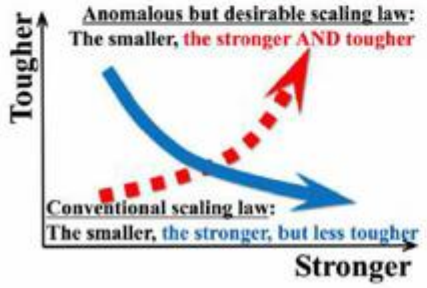

Fig. 1. An anomalous but desirable scaling law of mechanical properties requires defeating the conventional conflict of strength vs. toughness.

The mechanical properties of materials are inherently tied to the material structure, ranging from atomic structure to grains, fibrils, and layers. There have been tremendous efforts in recent years to develop materials with higher strength, by using smaller scale material structures (down to nms). For example, by decreasing the grain size of crystalline metals (thus more grain boundaries), dislocation motions (thus plasticity) are more restricted, leading to a higher strength. On the other hand, such treatments also minimize the possible mechanisms (e.g., crack-tip blunting) to relieve local high stress, resulting in lower toughness. The atomic scale origins of high strength of a material, e.g., strong directional bonding and limited dislocation mobility, are also essentially the roots for brittleness and low toughness of the material. In short, *the well-recognized scaling law of "The smaller, the stronger" comes with a price of sacrificing toughness* (Fig. 1).

Despite the consensus on mutual exclusiveness of strength and toughness, a significant gap exists between engineering practice and scientific considerations. So far, there exists only rather limited success in attaining both strength and toughness, which often involve material-specific, complicated or expensive synthesis processes and thus are hardly applicable to other materials. A general and feasible mechanism to address the conflict between strength and toughness still remains elusive.

To gain insight toward a generally applicable solution to the challenge of attaining both strength and toughness, we investigate the mechanical properties of cellulose-fiber-based paper, with constituent building block size ranging from 10s mm down to 10 nm, from which we unveil a highly desirable but hard-to-achieve scaling law of mechanical properties of cellulose-based nanopaper that is anomalous to conventional understanding: both the strength and toughness of the nanopaper increase simultaneously (40 and 130 times, respectively) as the size of the constituent cellulose building blocks decreases (from a diameter of 27 μm to 10 nm). These stimulating results suggest the promising potential toward a new and highly desirable scaling law: the smaller, the stronger AND the tougher.

Cellulose is the most abundant biopolymer on earth and has long been used as the sustainable building block for paper. Wood fibers are the main natural source of cellulose and have an intrinsically hierarchical structure (Fig. 2a). A 20~50 μm thick wood fiber comprises thousands of nanofibrillated cellulose (NFC, 5-50 nm in diameter), each of which can be disintegrated into finer



Fig. 2. (a) Hierarchical structure of wood biomass and the characteristic of cellulose fibrils. Note the rich inter-chain hydrogen bonds between neighboring cellulose molecular chains. (b) Single cellulose chain repeat unit. Note the six hydroxyl groups (red solid circles) in each repeat unit.

[a)] Corresponding author. Email: lit@umd.edu

elementary fibrils consisting of cellulose molecular chains.

Cellulose molecule is a linear chain of ringed glucose molecules, with a repeat unit (Fig. 2b) comprising two anhydroglucose rings ($C_6H_{10}O_5$) linked through C-O-C covalent bond. Rich hydroxyl groups in cellulose molecule (six in each repeat unit) enable facile formation of hydrogen bonds, both intra-chain and inter-chain.

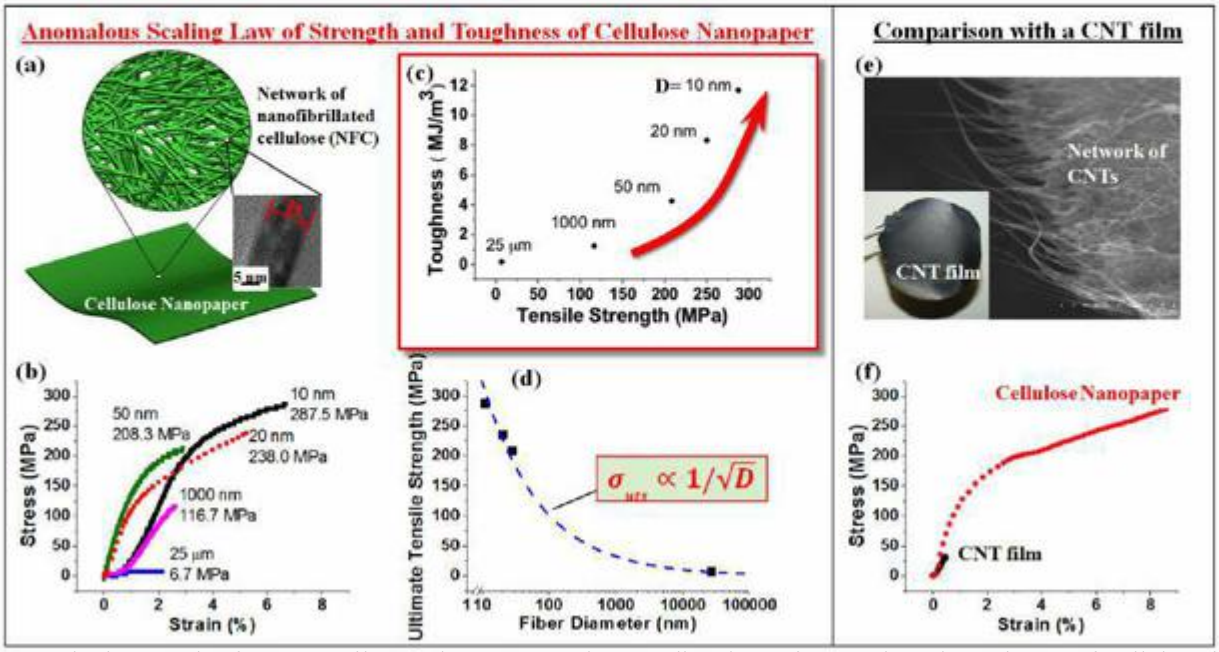

Fig. 4. Intriguing results from our pilot study: an anomalous scaling law of strength and toughness of cellulose-based nanopaper. (a) Schematic of cellulose nanopaper, made of a network of NFC. Inset shows HR-TEM image of a ~10nm NFC. (b) Stress-strain curves of cellulose paper made of NFC of various diameters. As the NFC diameter decreases, both tensile strength and ductility of the cellulose paper increases, leading to an anomalous scaling law shown in (c): The smaller, the stronger AND the tougher. (d) Further reveals that the tensile strength scales inversely with the square root of NFC diameter. (e) Optical (inset) and SEM images of a CNT film made of network of CNTs. (f) Lack of inter-CNT hydrogen bonds, the CNT film is shown to have a much lower tensile strength, and toughness than the cellulose nanopaper, although the constituent CNTs and NFCs have similar diameter (~10nm).

Motivated by the unique molecular feature and attractive mechanical properties of cellulose, we rationally designed highly transparent, mechanically strong nanopaper and investigate the dependence of mechanical properties of nanopaper on constituent NFC size. Surprisingly, we revealed the simultaneous and significant increase of both the tensile strength and toughness of nanopaper as the constituent NFC diameter decreases, a highly desirable but hard-to-achieve scaling law in advanced materials design (Fig. 4a-d). To further shed insight on the anomalous scaling law of strength and toughness of the cellulose nanopaper, we also fabricated CNT films of comparable thickness that are made of network of CNTs with diameter similar with NFC fibers (Fig. 4e). It turns out that the strength and toughness of cellulose nanopaper are also much higher (9 and 195 times, respectively) than those of the CNT films (Fig. 4f).

The above results suggest the following mechanistic understanding on the exceptional mechanical properties and anomalous scaling law of cellulose nanopaper: while the increase in tensile strength of cellulose nanopaper is attributed to reduced intrinsic defect size as the constituent NFC size decreases (the smaller, the stronger); the simultaneous increase in toughness essentially results from the significant increase of hydrogen bonding among NFC fibers as their diameter decreases (and thus their surface area increases).

CONCLUSIONS

We conducted a first-of-its-kind pilot study on the mechanical properties of cellulose-fiber-based paper, with constituent building block size ranging from 10s mm down to 10 nm, from which we reveal a fundamental bottom-up strategy to achieve both high strength and toughness that is generally applicable for a wide range of other material building blocks.

References

[1] H. Zhu, S. Zhu, Z. Jia, S. Parvinian, Y. Li, O. Vaaland, L. Hu, T. Li, Anomalous scaling law of strength and toughness of cellulose nanopaper, ***Proceedings of the National Academy of Sciences of the United States of America (PNAS)***, 112(29), 8971-8976 (2015).

GRAPHENE INTERACTIONS BY DISPLACEMENT-CONTROLLED NANOINDENTATION

Ji Won Suk[1], Seung Ryul Na[2], Rodney S. Ruoff[3] and Kenneth M. Liechti[2a]
[1]School of Mechanical Engineering, Sungkyunkwan University, Suwon, 440-746, Republic of Korea
[2] Research Center for the Mechanics of Solids, Structures and Materials
Department of Aerospace Engineering and Engineering Mechanics
The University of Texas at Austin
Austin, Texas 78712
[3]Institute of Basic Sciences Center for Multidimensional Carbon Materials & Department of Chemistry and School of Materials Science and Engineering
Ulsan National Institute of Science and Technology, Ulsan 689-798, Republic of Korea

Summary In this paper, we examine the adhesive interactions between a diamond indenter and mono-, bi- and trilayer graphene on silicon oxide. Nanoindentation experiments were also conducted on bare silicon oxide and highly ordered pyrolytic graphite (HOPG) as controls. Force profiles obtained under displacement control revealed the complete adhesive interactions during approach and withdrawal. The strength, range and energy of the underlying interactions between the tip and the contact surface in addition to those between graphene and silicon were extracted by an inverse, numerical analysis at the continuum level. There was evidence of both Van der Waals and capillary forces and graphene did appear to screen interactions between the probe and silicon oxide.

INTRODUCTION

The wet-transfer of graphene grown by chemical vapor deposition has been the standard procedure for transferring graphene to any substrate. However, the nature of the interactions between large area graphene and target substrates under these conditions is relatively unknown. The adhesion energy associated with interactions between graphene and silicon has been measured by particle intercalation and blister tests [1-3]. While the energy levels are commensurate with van der Waals interactions, recent wedge tests coupled with interferometry have revealed that the strength and range of the interactions were respectively much smaller and larger than those typically associated with van der Waals forces [4]. The objective of the work presented here is to examine such interactions over smaller spatial domains by nano indentation, supported by continuum analysis, in order to extract traction-separation relation parameters based on force profiles.

EXPERIMENTS and ANALYSIS

Graphene was grown on copper foil using chemical vapor deposition. A thin layer of PMMA was spin coated on the graphene as a reinforcing layer for the wet transfer process, which consisted of etching away the copper foil, transferring the graphene to a silicon chip and then removing the PMMA with solvent and heating to 400°C in a hydrogen/argon atmosphere. The process was repeated for bi- and trilayer graphene. Bare silicon oxide surfaces were cleaned with piranha solution just prior to indentation and fresh HOPG surfaces were prepared by exfoliation. The contact surface of the specimen was indented under displacement control in a Hysitron Triboindenter with a corner cube indenter. This provided force profiles that were able to detect the adhesive interactions between the probe and the graphene during approach and retraction (Fig. 1). There was adhesive hysteresis in the force profiles from samples consisting of bare silicon oxide, mono-, bi- and trilayer graphene on silicon oxide and graphite. There was also evidence of partial separation between monolayer graphene and silicon.

The configuration was analyzed numerically using ABAQUS with interactions between the probe and contact surface being accounted for by traction-separation relations that differed for approach and retraction (Fig. 2a). The procedure that was adopted to determine the traction-separation relations that provided the best fit to the measured force profiles was as follows: For approach, in all cases, the measured force profiles were subtracted from the Hertz force profile. Since this is the zero interaction

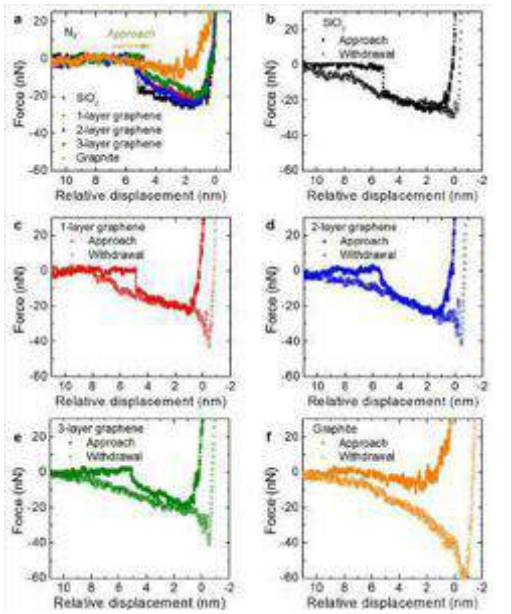

Fig. 1: Force profiles a) comparison of all samples, b) bare silicon oxide, c) monolayer, d) bilayer and e) trilayer graphene and f) graphite.

[a)] Corresponding author. Email: kml@mail.utexas.edu

case, any difference was taken to be due to the interactions between the contact pairs. The traction-separation relations that provided the best fit to this difference in force profiles were determined iteratively. For withdrawal, different mechanisms had to be accounted for: a) for silicon oxide, capillary effects were dominant and were modeled by a constant traction (10 MPa) over the interaction range (10 nm); b) for single layer graphene, delamination between the graphene and silicon oxide and capillary interactions between graphene and the diamond tip were considered; c) for graphite, the initial part of the traction-separation relation for interactions between the tip and graphite during withdrawal was obtained using the same fitting process that was used for approach (comparison with Hertz force profile) until capillary interactions became dominant. It is possible that there may also have been interlayer delamination in the graphite, but this was beyond the scope of the present study. The interaction between graphene and silicon oxide was also accounted for with an adhesion energy of 420 mJ/m^2, a strength of 100 MPa and a range of 9.6 nm. The energy level was obtained from previous wedge tests [4], but the strength of the interaction had to be much higher and the range lower than previously determined in order to make sure that complete separation did not occur along the graphene/silicon interface, as this mechanism was never observed.

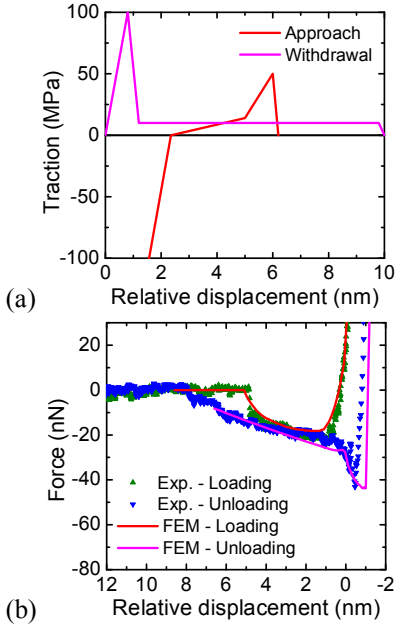

Fig. 2: a) traction-separation relations for interactions between diamond and graphene for approach and withdrawal, (b) comparison of measured and fitted force profiles.

RESULTS

The traction-separation relations for diamond/graphene interactions (Fig. 2a) serve as a template for all other cases. The initial snap due to water bridge formation when the tip was 6 nm from the surface. The peak tensile traction σ_0^a was 50 MPa. It was necessary to include a repulsive interaction σ_r of -200 MPa and an equilibrium spacing of 2.35 nm in order to capture the rising portion of the force profile. The initial withdrawal was captured with a peak tensile interaction σ_0^w of 100 MPa between the diamond and graphene, followed by a constant traction of 10 MPa for 10 nm to represent the thinning of the water bridge. Similar features but with differing magnitudes were extracted for the other cases as noted in Table 1. It can be seen that, for approach, the interaction between diamond and HOPG was the weakest, but conditions encountered during contact made it much stronger

CONCLUSIONS

In summary, the displacement-controlled nano indentation experiment, with ultralow-noise force measurements, allowed the complete nonlinear adhesive interactions between a diamond indenter and mono-, bi- and trilayer graphene on silicon oxide to be observed. As the number of graphene layers was increased, there was a transition in the adhesive interactions between the tip and the surfaces that ranged from that of bare silicon oxide to that of graphite. Nonetheless it appears that even monolayer graphene is able to screen interactions between the probe and silicon oxide.

Approach	**σ_r (GPa)**	**z_0 (nm)**	**σ^a_0 (MPa)**	**δ_c (nm)**
Diamond-SiO_2	-200	1.2	70	5.3
Diamond-Graphene1	-200	2.35	50	6
Diamond-HOPG	-0.5	2.30	4.2	5.6
Initial Withdrawal		**σ^w_0 (MPa)**	**δ_c (nm)**	
Diamond-Graphene1		100	0.8	
Diamond-HOPG		230	0.8	

Table 1. Parameters for traction-separation relations of interactions during approach and withdrawal. In all cases the second portion of withdrawal was captured by constant traction of 10 MPa for 10 nm to represent the thinning of the water bridge.

References

1. Zong, Z., et al., *Direct measurement of graphene adhesion on silicon surface by intercalation of nanoparticles.* Journal of Applied Physics, 2010. **107**(2): p. 026104.
2. Cao, Z., et al., *A blister test for interfacial adhesion of large-scale transferred graphene.* Carbon, 2014. **69**: p. 390-400.
3. Koenig, S.P., et al., *Ultrastrong adhesion of graphene membranes.* Nature Nanotechnology 2011. **6**: p. 543-546.
4. Na, S.R., et al., *Ultra long-range interactions between large area graphene and silicon.* ACS Nano, 2014. **8**(11): p. 11234-11242.

GIANT ANELASTICITY AND ENERGY DISSIPATION IN SINGLE-CRYSTALLINE NANOWIRES

Guangming Cheng[1†], Chunyang Miao[2,4†], Qingquan Qin[1], Jing Li[3], Feng Xu[1], Hamed Haftbaradaran[2], Elizabeth C. Dickey[3], Huajian Gao[2a)] and Yong Zhu[1,3a)]

[1]*Department of Mechanical & Aerospace Engineering, North Carolina State University, Raleigh, NC, USA*

[2]*School of Engineering, Brown University, Providence, RI, USA*

[3]*Department of Materials Science and Engineering, North Carolina State University, Raleigh, NC, USA*

[4]*Institute of Nano Science, Nanjing University of Aeronautics and Astronautics, Nanjing, P.R. China*

Abstract Anelastic materials exhibit gradual full recovery of deformation once a load is removed. At macroscopic scale, however, anelaticity is usually very small or negligible. Here we show that single-crystalline ZnO can exhibit anelastic behaviour that is up to four orders of magnitude larger than the largest anelasticity observed in bulk materials, with a time-scale in the order of minutes. In-situ SEM tests of individual NWs showed that, upon removal of the bending load and instantaneous recovery of the elastic strain, a substantial portion of the total strain gradually recovers with time. We attribute the observed large anelasticity to stress-gradient-induced migration of point defects, as supported by electron energy loss spectroscopy (EELS) measurements, analytical modeling and also by the fact that no anelastic behaviour could be observed under tension. Finally, we show that ZnO NWs exhibit a high damping merit index, suggesting NWs with point defects are promising for damping applications.

Introduction

NWs exhibit a host of novel properties that are being exploited for many applications including energy harvesting and storage, flexible/stretchable electronics, sensing, and nanoelectromechanical systems. So far a vast majority of research on mechanical properties of NWs has been focused on size-dependent elastic modulus and strength [1], with very few studies on time-dependent responses. This work reports an unexpected phenomenon of large anelastic relaxation and energy dissipation in single-crystalline NWs under bending [1].

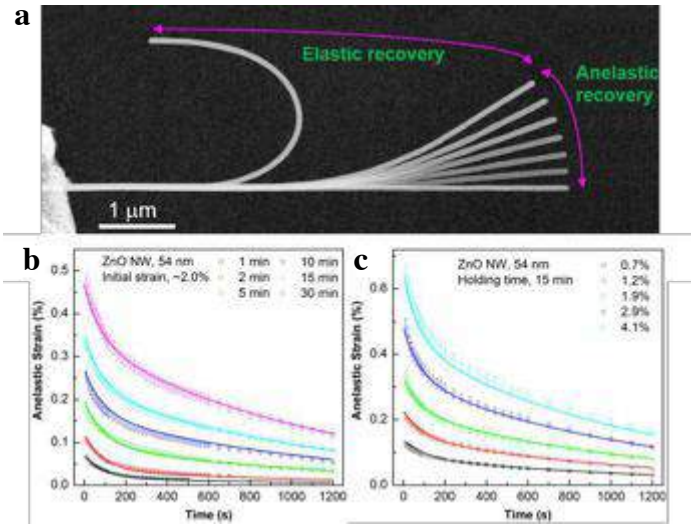

Figure 1 Recovery and damping behaviors of a ZnO NW. (a) series of images showing the elastic and anelastic recovery. (b) Anelastic strain as a function of recovery time for six different durations of holding time. The NW diameter was 54 nm and the initial bending strain was 1.94%. (c) Anelastic strain as a function of recovery time for five different initial bending strains. The holding time was 15 minutes in all five cases. Solid lines in both (a) and (b) represent the fitting data from finite element analysis. Error bars for strain measurement in (b) and (c) were ~5.4%.

In-situ bending test of ZnO NWs

The bending tests were performed at the room temperature using a microelectromechanical system (MEMS) based nanomechanical testing stage inside an SEM [2,3]. After the NW was held at a bent configuration for certain time (holding time), the MEMS actuator was retracted and the shape of the NW was monitored in real time (Fig. 1). It can be seen that a large portion of the bending strain recovered instantaneously while the rest recovered gradually with time, as shown in Fig. 1a.

Fig. 1b shows the evolution of the anelastic strain of a ZnO NW (54 nm in diameter) for an initial (total) bending strain of 1.94% with six different durations of holding time. Here the initial or total strain is the sum of anelastic strain and elastic strain, right before the load is removed. It can be seen that the recovery of the anelastic strain depends on the holding time – the shorter the holding time, the faster the recovery. Fig. 1c shows the evolution of the anelastic strain for a holding time of 15 minutes under five different initial strains. Larger initial strain led to larger anelastic strain. The anelastic strain almost fully recovered with time (e.g., Supplementary Fig. 1b, with holding time of 15 minutes and recovery time up to 40 minutes). The anelastic strain was as large as 0.64% (in the case of 4.1% total strain). A theoretical model was developed to understand the relationship between the diffusion of point defects and the measured anelastic behaviour [2]. Finite element simulations were performed to simulate the bending and relaxation processes under the same conditions as in the experiments. A number of defect types with corresponding diffusivities and initial concentrations were considered. The

a) Corresponding author. Email: yzhu7@ncsu.edu

evolution of the anelastic strain was calculated as functions of the initial strain and holding time, and compared to the experimental results (Fig. 1).

To corroborate the conclusion that the anelastic behaviour results from diffusion of point defects, further investigation on the defect structures in ZnO NWs was performed. Transmission electron microscopy (TEM) investigations shows that ZnO NWs are uniform in diameter and there is no extended structural defects (e.g., stacking faults or dislocations) in them. Aberration-corrected STEM/EELS was employed to investigate the stoichiometry of ZnO NWs under bending. Diffusion of point defects across the diameter would lead to a difference in stoichiometry at the two sides of a bent NW (named as inner side and outer side in the following). Here, an individual ZnO NW protruding from a TEM grid was bent into a loop. Five positions with different bending strains were chosen along the axial direction (Fig. 2a, b). The quantitative EELS results showed that the atomic percentage of oxygen (i.e., stoichiometry) is different at the inner and outer sides; the outer side is always richer in oxygen than the inner side. By contrast, for un-deformed (straight) regions the inner side and outer side have nearly the same stoichiometry, as expected. The same phenomenon was observed in three additional NWs in a similar bending geometry. The differences in oxygen atomic percentage between inner and outer sides for the selected points are shown in Fig. 2c. The largest difference in oxygen atomic percentage is at Position #3, ~4.2 at.%, which corresponds to the largest total bending strain, ~2.9%. Fig. 2d shows a nearly linear relationship between the difference in oxygen concentration and the bending strain as well as the anelastic strain (following Fig. 2b). The EELS results suggested that during relaxation, more oxygen vacancies diffuse from the tensile (outer) to the compressive (inner) side than zinc interstitials in the opposite direction, leading to higher oxygen percentage in the outer side.

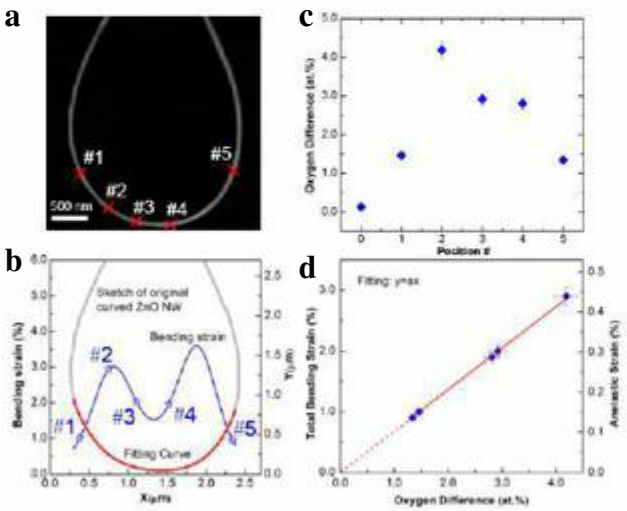

Figure 2 (a) HAADF-STEM image showing a bent NW for EELS analysis. (b) Bending strain as a function of positions in the bent ZnO NW. (c) EELS analysis showing the difference in oxygen concentration between outer and inner sides of the bent ZnO NW at different positions. Position #0 was taken from a straight part with zero bending strain. Error bars are from the variation in stoichiometry (~0.5 at.%). (d) Linear relationship between the difference in oxygen concentration (between outer and inner sides) and the total bending strain and the anelastic strain.

In summary, we have reported large anelastic behaviour in single-crystalline NWs governed by stress-gradient-induced migration of point defects. The observed anelasticity was attributed to a type of nonlinear Gorsky relaxation that involves the diffusion of two types of point defects under an inhomogeneous stress field. The large anelasticity in ZnO NWs resulted in high mechanical damping with the merit index of 1.13. The large magnitude of the anelasticity is attributed to the high strain applied to the NWs, while the small diffusion distance, enormous stress gradient and large diffusivity result in the short relaxation (recovery) time scale. The large diffusivity in NWs is due to the surface-mediated bulk diffusion and reduced activation energy under ultrahigh stress. The present study also suggests a useful experimental approach to study transport and equilibrium properties of point defects at the nanoscale. Since point defects have been reported to exist in many nanostructures [4], the reported anelasticity is expected to have broad impacts in nanotechnology. With the rapid progress in large-scale synthesis of NWs, our study suggests that crystalline NWs with point defects could serve as highly efficient damping materials for a broad range of applications in aerospace, automotive, energy and biomedical industries.

References

[1] Zhu Y. In-situ Nanomechanical Testing of Crystalline Nanowires in Electron Microscopes, JOM 68 (1), 84-93 (2016).

[2] Cheng G., Miao C., Qin Q., Li J., Xu F., H. Haftbaradaran, Dickey E.C., Gao H. & Zhu Y. Large Anelasticity and Energy Dissipation in Single-Crystalline Nanowires Nat. Nanotechnol. 10, 687-691 (2015).

[3] Zhu, Y. & Espinosa, H. D. An electromechanical material testing system for in situ electron microscopy and applications. Proc. Natl. Acad. Sci. U. S. A. 102, 14503–14508 (2005).

[4] Perea, D. E. et al. Direct measurement of dopant distribution in an individual vapour-liquid-solid nanowire. Nat. Nanotechnol. 4, 315–319 (2009).

EXAMINATION OF INTERACTIONS BETWEEN DEFORMATION MECHANISMS IN FCC THIN FILMS USING SEM-DIC

Marissa Linne[1], Samantha Daly[2a]
[1]*Dept. of Materials Science and Engineering, University of Michigan, Ann Arbor, MI, USA*
[2]*Dept of Mechanical Engineering, University of Michigan, Ann Arbor, MI, USA*

Summary This presentation will discuss an on-going experimental investigation of the interaction between dislocation glide and grain boundary sliding (GBS) in columnar Al thin films under tensile loading. Due to the oligocrystalline microstructure of the specimen, these mechanisms can be characterized without sub-surface ambiguity. In this investigation, tensile strain was applied in-SEM to Al films with thicknesses of hundreds of nanometers, using a custom thermal actuator MEMS device, and full-field surface displacements were measured using a high-resolution combination of scanning electron microscopy and digital image correlation. Novel methods for microscale pattern deposition and SEM spatial and temporal distortion corrections were utilized for high accuracy results. Analysis of the resulting full-field, high resolution data linking deformation behavior and underlying texture provided insight into the interaction between GBS and dislocation-based deformation mechanisms in Al thin films.

INTRODUCTION

This research is aimed towards understanding the relationship between deformation mechanisms, particularly grain boundary sliding (GBS) and dislocation glide, in polycrystalline columnar thin films. It is hypothesized that a synergistic relationship exists between these mechanisms, and that the nature of this relationship will vary from bulk material due to the magnified effects of free surfaces. These claims are supported by (a) the fact that increasing shear stress on a grain boundary (GB) simultaneously enables GBS and decreases the energy barrier for slip transmission through the boundary; and (b) there is evidence that the in-grain dislocations, commonly observed in bulk materials, exist in very low densities in films with thicknesses on the order of 100 nm [1,2]. Current research and modeling of crystal plasticity largely treats deformation mechanisms as separate events. Thus, the relationships between them -- whether collaborative or competitive, simultaneous or sequential -- remain unclear and supported by limited experimental data. These ambiguities lead to inaccuracies in material modeling, and consequently a failure to optimize material design. This paper and talk discusses experimental investigations aimed towards improving predictions of damage-inducing stress localization, and ultimately towards improving the capability to develop small-scale materials with greater resistance to failure.

EXPERIMENTAL METHODS

A unique experimental approach is taken that accounts for the inhomogeneities in polycrystalline materials, unlike methods that employ either property values that are bulk averages or micro- and nanoscale analyses (e.g. nanoindentation) that only sample very small fractions of the specimen. My experimental approach addresses these shortcomings by capturing a full-field strain analysis of polycrystalline thin film deformation using SEM-enabled digital image correlation (termed here as SEM-DIC)[3-5] combined with spatial/temporal distortion corrections and chemically functionalized nanoparticle deposition for unprecedented resolution and accuracy. DIC is a technique by which surface strains are determined by comparing digital images captured during the deformation process. By tracking the movement of identifiable surface features, full–field strains can be calculated. This approach is used to map strains in columnar free-standing thin films under tensile load, applied via MEMS-based actuation. In order to generate a comprehensive strain map, Au nanoparticles are self-assembled on a chemically functionalized sample to create a random, high contrast, traceable pattern. GBs are located by pre-test electron forescattered diffraction (EFSD) [6-8] grain orientation maps. SEM micrographs of the same area (identified using FIB-applied platinum markers) are captured in-situ during tensile loading, and used to create strain maps via SEM-DIC. Since the accuracy of the SEM image is of critical importance for calculating strains, temporal and spatial distortions that occur in the micrographs are corrected using a proven MATLAB code created by this research group[4].

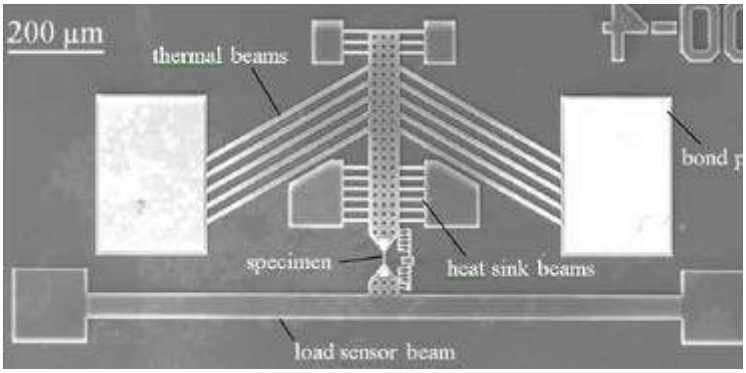

Fig.1 Electrothermal MEMS actuator used to strain the thin film specimen; chevron thermal beam are oriented so they expand and push the center shuttle forward when joule heated, straining the attached specimen

[a)] Corresponding author. Email: samdaly@umich.edu.

Aluminum (Al) is used as the model test material for two primary reasons. First, it is commonly used numerous applications microelectronics to lightweight structural alloys. Second, Al has a face centered cubic (fcc) crystal structure, and therefore only 12 slip systems, making it ideal for examination of GB sliding and dislocation slip. The thickness of the columnar films will be on the order of 100 nm, with <111> fiber texture and variable grain sizes. The specimens will be co-fabricated with a MEMS actuator similar to that described in [9]. The actuator-sample system, seen in Fig.1, was chosen because (a) it is capable of high-resolution stress application, necessary for testing nanostructured samples; and (b) precise sample alignment is accomplished by using a single photolithography mask for the device-sample unit. Fabrication of the sample-device unit was performed at the Lurie Nanofabrication Facility at the University of Michigan.

RESULTS AND DISCUSSION

The acquired SEM-DIC strain fields are expected to provide insight into relationships between deformation mechanisms and microstructural neighborhoods in the film. As demonstrated by past work, both GBS and dislocation glide are active at room temperature, but grain size of the film, magnitude of GB misorientation and dislocation source concentration will determine the dominant mechanism. Prior studies have shown that GB sliding becomes more significant with decreasing grain size, while dislocation glide behavior becomes more significant with increasing grain size (Hall-Petch behavior) and low angle boundary misorientation [10-13]. A related trend is expected to be observed by testing specimen with various average grain sizes, achieved by varying deposition and annealing temperatures during fabrication. Computational work indicates that a transitional nanoscale grain size range likely exists, between the GB slide and dislocation glide dominated regimes [10]. However, the significant decrease in dislocation density, commonly observed in fcc thin films [1,2], may cause a shift in the bulk transitional grain size (~10 nm). Results of this work will provide experimental insight into this transitional regime, and how it is affected by low dislocation concentration. Observed interaction between these two deformation mechanisms will be compared to computational studies.

Understanding polycrystalline deformation in nanostructures is significant for numerous applications, yet present knowledge of the subject is limited. The next step to take in advancing this knowledge is to examine deformation mechanisms as interrelated systems, rather than individual occurrences. This innovative and comprehensive experimental approach moves beyond bulk property averages and assumptions of homogeneity to address the complexities of polycrystalline thin film microstructure. Outcomes from this research will contribute to the advancement of nanotechnology and integrated circuits as well as a more sophisticated understanding of plastic deformation.

References

[1] Haque, M.A., Saif, M.T.A.: In situ tensile testing of nanoscale freestanding thin films inside a transmission electron microscope. *J Mater Res* **20**: 1769, 2005.

[2] Espinosa, H.D., Porok, B.C., Peng, B. plasticity size effects in free-standing submicron polycrystalline fcc films subjected to pure tension. *J Mech Phys Solids* **52**:667, 2004.

[3] Sutton, M.A., Li, N., Garcia, D., Cornille, N., Orteu, J.J. McNeill, S.R., Schreier, H.W., Li., X. *Meas Sci Technol* **17**: 2613, 2006.

[4] Kammers, A., Daly, S. Self-assembled nanoparticle surface patterning for improved digital image correlation in a scanning electron microscope. *Exp Mech* **53**:1333, 2013.

[5] Kammers, A. Daly, S. Digital image correlation under scanning electron microscopy: methodology and validation. Exp Mech **52**:1743, 2011.

[6] Keller, R.R., Geiss, R.H. Transmission EBSD from 10 nm domains in a scanning electron microscope. J Microscopy **245**: 245, 2012.

[7] Brodusch, N., Demers, H., Trudeau, M., Gauvin, R. Acquisition parameters optimization of a transmission electron forward scatter diffraction system in a cold-field emission scanning electron microscope for nanomaterials characterization. Scanning **35**:375, 2013.

[8] Trimby, P.W., Cao, Y., Chen, Z., Han, S., Hemker, K.J., Lian, J., Liao, X., Rottmann, P., Samudrala, S., Sun, J., Wang, J.T., Wheeler, J., Cairney, J. M. Characterizing deformed ultrafine-grained and nanocrystalline materials using transmission Kikuchi diffraction in a scanning electron microscope. Acta Mater **62**: 69, 2014.

[9] Yilmaz, M., Kysar, J.W. Monolithic integration of nanoscale tensile specimens and MEMS structures. Nanotechnology **24**: 165502, 2013.

[10] Van Swygenhoven, H., Spaczer, M., Caro, A., Farkas, D. Competing plastic deformation mechanisms in nanophase metals. *Phys Rev B* **60**: 22, 1999.

[11] Zheng, Y.G., Zhang, H.W., Chen, Z., Lu, C., Mai., Y.W. Roles of grain boundary and dislocations at different deformation stages of nanocrystalline copper under tension. Phys Lett A **373**: 570, 2009.

[12] Zhu, B., Asaro, R.J., Krysl, P., Bailey, R. Transition of deformation mechanisms and its connection to grain size distribution in nanocrystalline metals. Acta Mater **53**: 4825, 2005.

[13] Vo, N.Q., Averback, R.S., Bellon, P., Odunuga, S., Caro, A. Quantitative description of plastic deformation in nanocrystalline Cu: dislocation glide versus grain boundary sliding. Phys Rev B **77**:134108, 2008.

ON-CHIP TESTING DEVICE FOR THE MICROMECHANICAL CHARACTERIZATION OF POLYSILICON FILMS

Ramin Mirzazadeh[a], Aldo Ghisi & Stefano Mariani
Politecnico di Milano, Department of Civil and Environmental Engineering, Milano, Italy

Summary Due to an increasing miniaturization demand, the characteristic size of moving parts of MEMS devices may become comparable to the material length-scale, i.e. to the average grain size in case of polysilicon films. This can lead to a deviation of the response of the device from the expected one, or to an increased scattering due to stochastic features of the film morphology. In this work, an on-chip test is exploited to assess the effects of film morphology on the overall mechanical response of thin, slender specimens. Different electrostatic actuation/sensing configurations have been designed, to also distinguish the said mechanical effects from those due to overetch. To explain the observed scattering in the MEMS output, two coupled electro-mechanical models of the system have been developed: an analytical reduced-order one, and a numerical one to fully account for the heterogeneity of the film.

INTRODUCTION: THE ON-CHIP TESTING DEVICE

On-chip testing might be a viable tool to characterize the structural films of MEMS (micro electro-mechanical systems) at the micromechanical level. The sensitivity of the device response to the investigated properties should be as higher as possible, avoiding instability phenomena like pull-in [1]. When the properties of the moving structure are somehow different from those of the substrate upon which the film is (epitaxially) grown, the effects of residual stresses should be also kept to a minimum.

In compliance with the above reported requirements, a device has been designed for on-chip testing of polysilicon films, see Fig. 1: the tested specimen is a thin beam, whose in-plane width is $2\,\mu$m. The beam is connected on one side to a massive anchor, and on the other side to a proof mass, denoted as rotor in Fig. 1. The beam can be subjected to different loadings, thanks to the two sets of stators around the plate: the lateral stator mainly induces a translation of the rotor, and so a coupled shear/bending deformation of the beam; the (electrically connected) anti-symmetric top and bottom stators cause instead an in-plane rotation of the rotor, and so a pure bending of the beam. Both the mentioned stators can also sense the motion of the rotor, through the change of the capacitance between the two electrodes. The size of rotor and stators and the initial gap between them have been designed to allow electrostatic sensing/actuation with a rather standard laboratory equipment, delaying considerably the pull-in instability.

Table 1. Geometric dimensions of the device.

Parameter	value
beam length (l)	$2, 3, 4, 5, 10, 20\,\mu$m
in-plane beam width (w)	$2\,\mu$m
out-of-plane beam thickness (t)	$22\,\mu$m
initial gap between rotor and stators (g_o)	$2\,\mu$m

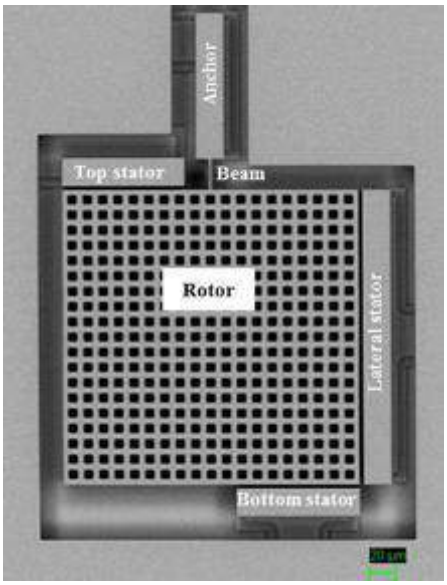

Figure 1. SEM picture of the on-chip test device featuring a $20\,\mu$m-long beam.

The dimensions of the device are reported in Table 1; due to its small size, within each single die several devices have been fabricated with a varying length l of the beam. The varying in-plane slenderness of the beam l/w, and the two types of sensing/actuation have been devised to distinguish the effects of: i) polysilicon morphology, ii) stress intensification close to reentrant corners, and iii) overetch linked to the fabrication process. As the average grain size of the tested polysilicon is

[a] Corresponding author. Email: ramin.mirzazadeh@polimi.it

around 1 μm, the very small ratio between the beam width and the said grain size has allowed to enhance the scattering in the mechanical response of the device due to the polycrystalline morphology.

To induce a quasi-static loading, the voltage has been varied smoothly and slowly in time during each test. Results are reported in Fig. 2 for the exemplary case of the 20 μm-long beam, in terms of capacitance change vs applied voltage when top and bottom stators are used for both actuation and sensing; experimental data are compared in the two graphs with the outcomes of analytical and finite element models, described in what follows. The classical nonlinear response is shown, see e.g. [1], with a tendency to pull-in around 40 V. An interesting scattering in the response of the 15 tested samples can be also observed, proving the sensitivity of the output to defects or micromechanical features of the polysilicon film [2,3].

MODELING

To provide a micromechanical interpretation of the experimental results, a reduced-order analytical model has been first set by exploiting the equilibrium between electrostatic and elastic forces. Due to its slenderness, the sample has been modelled according to Euler-Bernoulli beam bending theory, and the electric fringe fields have been neglected. Next, a coupled electro-mechanical model has been developed in the commercial finite element code ANSYS-APDL. In this latter case, polysilicon has been modelled in a Monte Carlo analysis with a random morphology, obtained with two-dimensional Voronoi tessellations featuring a stochastic orientation of the crystal lattice of all the grains. To also bound the mentioned spreading of the experimental curves, two solutions have been computed with the two models, with silicon being assumed as a single-crystalline orthotropic material with the direction featuring its maximum or minimum value of the Young's modulus, in the crystal plane (100) [4], aligned with the longitudinal beam direction. The results of the two models are compared with the experimental data in Fig. 2.

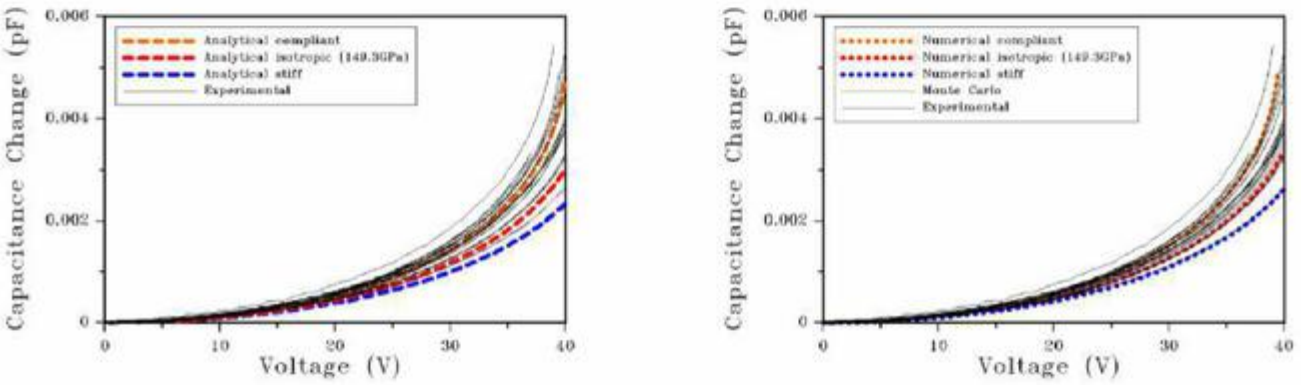

Figure 2. Comparison of the experimentally measured sample response in the case $l = 20$ μm, with (a) analytical and (b) numerical results.

DISCUSSION AND CONCLUSIONS

As reported in Fig. 2a, the analytical model somehow overestimates (as expected) the system stiffness, and therefore predicts a capacitance change under the applied voltage lower than the experimental output. The numerical model, see Fig. 2b, yields instead more accurate bounds, as it can catch the real deformation field in the beam, especially close to the anchor and the connection with the plate. The scattering in the results of the Monte Carlo analysis due to the random morphology of polysilicon only, obviously leads to a better estimation of the real beam response in comparison with the homogeneous cases.

Although the model results have provided much insight into the coupled electro-mechanical response of the system, out-of-bounds experimental trends can be always found and must be properly understood. Since polysilicon morphology is not the only source of uncertainties at the microscale, further effects due to imperfections and to a non-homogenous overetch of the film, as a result of the fabrication process, will be considered next. To help distinguish these effects, further measurements and simulations using all the other sensing/actuation configurations will be accordingly carried out.

References

[1] Younis M.: MEMS Linear and Nonlinear Statics and Dynamics. Springer Science+Business Media, 2011.

[2] Corigliano A., De Masi B., Frangi A., Comi C., Villa A., Marchi M.: Mechanical Characterization of Polysilicon Through On-Chip Tensile Tests. *J Microelectromech Syst* **13**: 200-219, 2004.

[3] Mariani S., Martini R., Ghisi A., Corigliano A., Beghi M.: Overall elastic properties of polysilicon films: a statistical investigation of the effects of polycrystal morphology. *Int J Multiscale Com* **9**: 327-346, 2011.

[4] Hopcroft M. A., Nix W. D., Kenny T. W.: What is the Young's Modulus of Silicon? *J Microelectromech Syst* **19**: 229-238 2010.

STIFFNESS THRESHOLD OF RANDOMLY DISTRIBUTED CARBON NANOTUBE NETWORKS

Fei Pan[1], Yuli Chen[1,2a)]

[1] *Institute of Solid Mechanics, Beihang University (BUAA), Beijing, China*

[2] *State Key Laboratory for Strength and Vibration of Mechanical Structures, Xi'an Jiaotong University, Xi'an, China*

Abstract The properties of carbon nanotube (CNT) networks (CNTNs) may change suddenly with the variation of network density, such as the onset of conductivity at the electrical percolation threshold. In this paper, the stiffness of CNTNs is studied and especially the existence of stiffness threshold is revealed. Two stiffness thresholds, which are critical densities to judge whether or not the network can carry load and whether or not it can carry load effectively respectively, are found by theoretical analysis as well as numerical simulation, and are predicted by simple invariants. The two thresholds divide the stiffness behaviour into three stages: zero stiffness, bending dominated and stretching dominated stages, which can be described by a piecewise function of network density and the CNT aspect ratio. This work provides a theoretical foundation for the design optimization and property prediction of CNTNs.

Keywords: threshold; mechanical properties; stiffness; carbon nanotube

INTRODUCTION

Carbon nanotube (CNT) is well known for its remarkable electrical and mechanical properties. To utilize these micro-scale superior properties in macro-scale structural and functional materials, CNT network (CNTN), with low density and high porosity, is considered as an effective structure form, thus has wide applications and draws many attentions. Studies show that with increasing network density of CNTNs, there may be sudden changes in the properties, such as the sudden change in electrical conductivity at the electrical percolation threshold [1]. Besides, some sudden changes in mechanical properties are observed experimentally and numerically in CNT composites and some other similar materials. Therefore, it is reasonable to infer that increasing CNT density in CNTNs may lead to sudden change in their mechanical properties. The aims of this paper are to reveal the stiffness threshold mechanism for randomly distributed CNTNs, and to establish the relation between topology and stiffness of CNTNs, which may be readily used to guide the design optimization and strength analysis in practical applications.

THE STIFFNESS THRESHOLD AND THE BENDING-STRETCHING TRANSITIONAL THRESHOLD

Qualitative investigation on the stiffness thresholds

CNTN is conductive only when the conductive path is formed. The lowest CNT density to form the conductive path is the electrical percolation threshold. Similarly, the load-transfer path must be constructed for CNTN to carry load, and the corresponding critical CNT density is defined as stiffness threshold, which is a criterion to judge whether or not the network is capable of carrying load. Moreover, when CNTNs can carry load, the deformation modes of CNTs have significant influence on the efficiency of load transfer. For CNTs, axial stretching can transfer load more efficiently than bending, and thus leads to higher stiffness. Hence there is a critical point at which the dominated deformation mode of CNTs changes from bending to stretching. The corresponding CNT density is defined as the bending-stretching transitional threshold, which is criterion to measure whether or not most of the CNTs in network are utilized effectively to carry load.

Theoretical analysis on the stiffness thresholds

To predict the thresholds and explain their underlying mechanisms, the load-transfer analysis as well as geometric probability analysis is employed. The stiffness threshold is considered to be determined by the statical determinacy of CNTs, which is dependent on their topological relation, as shown in Fig.1, and is estimated quantitatively by the stabilization fraction [2] of network. The bending-stretching transitional threshold is supposed to be influenced by the CNT intersection type in CNTN, as shown in Fig.2, and is evaluated by the defect fraction [2] of network.

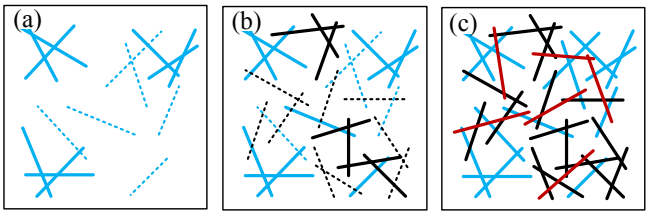

Fig. 1 The stabilization processes of CNTs in CNTN

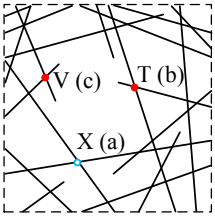

Fig. 2 Three typical intersections in CNTN

[a)] Corresponding author. Email: yulichen@buaa.edu.cn.

Two stiffness thresholds, i.e. stiffness threshold $\hat{\rho}_{\text{th}}^{\text{E1}}$ and bending-stretching transitional threshold $\hat{\rho}_{\text{th}}^{\text{E2}}$ are found and validated to divide the stiffness behaviour into three stages: zero stiffness, bending dominated and stretching dominated stages [2]. Both the two thresholds are larger than the electrical percolation threshold $\hat{\rho}_{\text{th}}^{\text{e}}$. Therefore, CNTNs present 4 different types of behaviours with increasing network density $\hat{\rho}$, as illustrated in Fig. 3: (1) neither electrical conductive nor able to carry load; (2) electrical conductive but unable to carry load; (3) electrical conductive and able to carry load by bending dominated deformation; and (4) electrical conductive and able to carry load by stretching dominated deformation.

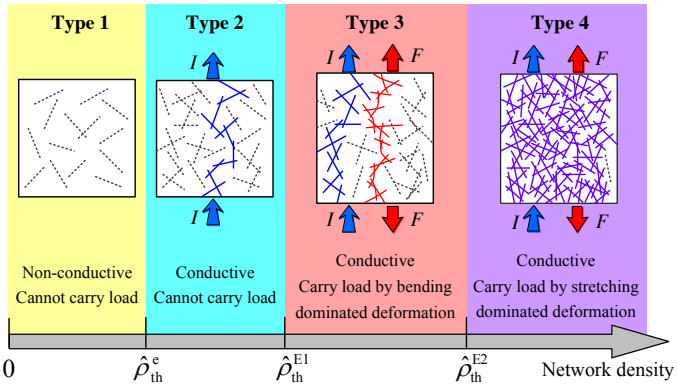

Fig. 3 Overall views on the four types of electrical and mechanical properties of CNTNs, with three critical values: electrical percolation threshold $\hat{\rho}_{\text{th}}^{\text{e}}$, stiffness threshold $\hat{\rho}_{\text{th}}^{\text{E1}}$, and the bending-stretching transitional threshold $\hat{\rho}_{\text{th}}^{\text{E2}}$.

According to the theoretical analysis and the numerical simulation, the average intersection number on each CNT $\bar{N}_{\text{int}}$ is revealed as the only dominant factor for the electrical percolation and the stiffness thresholds, it is approximately 3.7 and 5.2 for $\hat{\rho}_{\text{th}}^{\text{e}}$ and $\hat{\rho}_{\text{th}}^{\text{E1}}$ of 2D networks respectively. For 3D networks, they are 1.4 and 4.4 respectively. Moreover, $\bar{N}_{\text{int}}$ also affects the bending-stretching transitional threshold, combined with the CNT aspect ratio. The average intersection number divided by the fourth root of CNT aspect ratio $\bar{N}_{\text{int}}\lambda_{\text{CNT}}^{-1/4}$ is found to be an invariant at $\hat{\rho}_{\text{th}}^{\text{E2}}$, which is 6.7 and 6.3 for 2D and 3D networks, respectively.

STIFFNESS PREDICTION BASED ON THE THRESHOLDS

Based on the two thresholds, a simple piecewise expression is proposed to describe the normalized elastic modulus of CNTNs $\hat{E}$, and is expressed as

$$\hat{E}=\begin{cases} 0 & 0<\hat{\rho}\le\hat{\rho}_{\text{th}}^{\text{E1}} \\ k_{\text{E}}\left(\hat{\rho}-\hat{\rho}_{\text{th}}^{\text{E1}}\right)^2\Big/\left[2\left(\hat{\rho}_{\text{th}}^{\text{E2}}-\hat{\rho}_{\text{th}}^{\text{E1}}\right)\right] & \hat{\rho}_{\text{th}}^{\text{E1}}<\hat{\rho}<\hat{\rho}_{\text{th}}^{\text{E2}} \\ k_{\text{E}}\left[\hat{\rho}-\left(\hat{\rho}_{\text{th}}^{\text{E1}}+\hat{\rho}_{\text{th}}^{\text{E2}}\right)\Big/2\right] & \hat{\rho}\ge\hat{\rho}_{\text{th}}^{\text{E2}} \end{cases}, \tag{1}$$

where k_{E} is the linear slope of the stretching dominated stage, and is taken as $\pi/12$ and 1/6 for 2D and 3D networks, respectively.

CONCLUSION

This paper studies the sudden change in stiffness of the CNTNs and especially reveals the existence of stiffness threshold. Simple formulas to predict the stiffness and stiffness thresholds are established, and will provide great convenience for the optimum design and property prediction of CNTNs.

Acknowledgments Supports by the National Natural Science Foundation of China (Nos. 11202012 and 11472027) and the Program for New Century Excellent Talents in University (No. NCET-13-0021) are gratefully acknowledged.

References

[1] Chen Y, Pan F, Wang S, Liu B, Zhang J: Theoretical estimation on the percolation threshold for polymer matrix composites with hybrid fillers. *Compos Struct*. **124**:292-9, 2015.

[2] Chen Y, Pan F, Guo Z, Liu B, Zhang J: Stiffness threshold of randomly distributed carbon nanotube networks. *J Mech Phys Solids*. **84**:395-423, 2015.

GROWTH AND MECHANICAL PROPERIES OF METAL NANOWHISKERS

Gunther Richter[1,a], Wenting Huang[1], Zeliha Kara-Yagmur[1], & Semanur Baylan[1]
[1]*Max Planck Institute for Intelligent Systems, Stuttgart, Germany*

Summary Single-crystalline, defect and flaw free nanowhiskers were grown by physical vapour deposition under ultra-high vacuum conditions. The investigated microstructure of the nanowhiskers is unique, no dislocations or grain boundaries were detected. The shape of the prismatic body can be explained by a classical Wulff theorem. The mechanical properties of the nanowhiskers were investigated by tensile and bending set-ups. For both set of experiments mechanical strength close to the predicted theoretical values were found. The onset of plasticity is determined by the nucleation and propagation of Shockley partial dislocations. Advanced nanostructures based on said nanowhiskers are also reported and their behaviour under mechanical loading is presented.

INTRODUCTION

Physical properties of materials changes if the dimension of the investigated devices decrease. This is especially true if one of the dimensions falls below a certain threshold; often this critical size is found to be in the order of ~100 nm, but depends strongly on the physical property which is investigated in a particular experiment. One reason for the size effects is the changing ratio of bulk volume to surfaces, it is moot weather the surfaces are free (crystal)-surfaces or internal interfaces. Also the influence of other defects, as dislocations or vacancies increases with decreasing dimensions. Since nanostructures are anticipated to be the building blocks for future nanodevices in several research areas as nanorobotics, biomedicine or sensor technology, knowledge on fabrication, handling and corresponding properties of zero- (e.g. nanoparticles), one- (e.g. nanowires) and two- (e.g. ultra-thin films) dimensional nanostructures has to be gathered. Quantitative results can be received by usage of structures with tailored microstructure. In the past our group concentrated in growing thin films physical vapour deposition (PVD) and recently conceived a method to fabricate one-dimensional metal crystals with the same methods.

NANOWHISKER GROWTH

One-dimensional nanostructures attracted in the past years a high interest due to their properties. Ceramics, semiconductor and carbon materials are easily synthesized as in nanowire shape with typical diameters of several dozen nanometers and length-diameter ratios of 1000:1. However, only the metals as one of the oldest were difficult to fabricate in similar geometries. From the start of the last century up to the 1950ies microscopic and macroscopic whiskers were synthesized by metal halide reduction [1], the original fabrication process was already published in a mining book from 1574 by Lazarus Ercker. The fundamental principles of these processes were the evaporation of a metal salt, the reduction of said salt in the vapour phase and the condensation of the elemental metal atoms on a usable substrate.

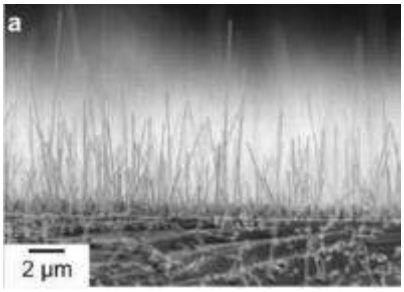

Figure 1: SEM micrographs of Cu nanowires grown on Si (111) substrate surfaces. The deposition rate was 0.05 nm/s; the growth temperature 680°C.

We modified this ancient recipe to be accommodated in ultra-high vacuum PVD systems and grow perfect defect and flaw free nanostructures with diameters of several ten nanometers, attached on substrates. Metals with face centred (Cu, Ag, Au, Pd), body centred (Fe), and hexagonal (Co) crystal structure were synthesized successfully as one-dimensional nanowhiskers (NWs) with the new technique. Suitable substrates are, for most metals, Si crystals, or Mo and W wires covered with 30 nm C by magnetron sputtering. The metals are deposited at high substrate temperatures (~60% T_M) and low deposition rates (0.05 nm/s). Figure 1 show a typical scanning electron microscopy image for Cu grown on Si(111) substrates.

NANOWHISKER PROPERTIES

Microstructure

Scanning and Transmission Electron Microscopy (SEM and TEM) analysis on the NW microstructure for fcc NWs yielded the following results: (i) The NWs are freestanding and prismatic with no taper along the NW axis; (ii) the surface facets are the low energy surface planes of the corresponding metals, typical four {111} and two {100} planes; (iii) the

[a)] Corresponding author. Email: richter@is.mpg.de

cross-section is close to the predicted Wulff shape; (iv) the NWs axis is parallel to the <110> crystal direction; (v) the NWs are perfect single-crystals, no flaws, dislocations nor grain boundaries are typically observed in the bulk of the NWs.

Physical properties

The investigations of the physical properties of the NWs focused on the mechanical strength and the onset of the plastic deformation. Mechanical test were performed on the grown elemental NWs [2-5]. Independent of testing method, either bending or tensile test, the NWs performed remarkably well. Due to the perfect crystal structure, the NWs exhibit tensile and bending strengths close to the predicted theoretical strength [6]. Post mortem and in-situ TEM revealed that the deformation is carried by partial dislocation nucleation and propagation, therefore by formation of stacking faults. Nucleation of further partial dislocations on adjunct planes leads consequently to twin formation. The twin boundary is a perfect $\Sigma 3\{111\}<110>$ symmetrical tilt grain boundary.

Correlating with the low defect density in the NWs is the low conductivity. No size effect is observed but a constant conductivity, again, close to the theoretical limits. Also, the magnetic domain structure was studied by electron holography. Only one single domain is present in ferromagnetic metallic nanowhiskers.

Stress evolution in bilayer NWs

Because the NWs are freestanding, one sided coatings can be easily achieved by depositing a second material without rotation of the specimens. Applying rotation would yield core-shell structures. Mismatches in lattice parameters and growth stresses lead to bending of the nanostructure. Annealing could lead (i) to stress relaxation or (ii) change in bending due to the difference in thermal expansion coefficients. Figure 2 depicts such a case where a Cu NW was covered on one side with a polycrystalline Ni layer. Due to annealing to 600°C, first the growth stress is relaxed and then secondly with cooling the NW bends slightly to the opposite direction because of the differences in thermal expansion.

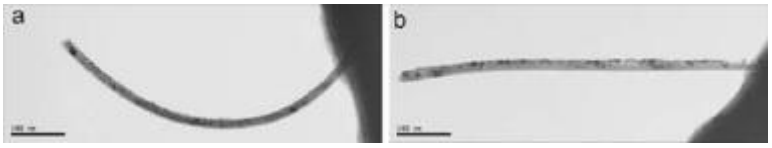

Figure 2: TEM micrograph of Ni/Cu nanowire. a) due to the lattice mismatch the structure is bend towards the Ni layer. b) increasing of the temperature leads to straightening and cooling to slight reverse bending.

CONCLUSIONS

Concluding we will present a brief summary on the growth of single-crystalline, defect and flaw free NWs and then explore (i) the consequences of the perfect microstructure on mechanical properties and (ii) the possibilities to use the uniqueness in crystal quality to fabricate novel new nanostructures. Core-shell structures, layered NWs, bamboo-structures and nanotubes were grown and the most recent results will be presented and discussed.

References

[1] Hardy H.K.: The filamentary growth of metals. *Progress in Metal Physics* **6**: 45-73, 1956.

[2] Schopf, C., Schamel, M., Strunk, H. P., Richter, G.: Cyclic cantilever bending of copper nanowhiskers. *Adv. Eng. Mat.* **14**: 975-980, 2012.

[3] Sedlmayr, A., Bitzek, E., Gianola, D. S., Richter, G., Mönig, R., Kraft, O.: Existence of two twinning-mediated plastic deformation modes in Au nanowhiskers. *Acta Mat.* **60**: 3985-3993, 2012.

[4] Roos, B., Kapelle, B., Richter, G., Volkert, C. A.: Surface dislocation nucleation controlled deformation of Au nanowires. *Appl. Phys. Lett.* **105**: 201908, 2014

[5] Qin, Q., Yin, S., Cheng, G., Li, X., Chang, T.-H., Richter, G., Zhu, Y., Gao, H.: Recoverable plasticity in penta-twinned metallic nanowires governed by dislocation nucleation and retraction. *Nature Comm.* **6**: 5983, 2015.

[6] Chen, L. Y., He, M.-r., Shin, J., Richter, G., Gianola, D. S.: Measuring surface dislocation nucleation in defect-scarce nanostructures. *Nature Mat.* **14**: 707-713, 2015.

MULTIPHYSICS ANALYSIS AND DESIGN OF AN AIR-COUPLED PZT-BASED PMUT

Raffaele Ardito[1a)], Alberto Corigliano[1], Luca D'Alessandro[1], Carlo Prelini[2] & Francesco Procopio[2]
[1]*Department of Civil and Environmental Engineering, Politecnico di Milano, Milan, Italy*
[2]*Analog, MEMS and Sensor Group, ST Microelectronics, Cornaredo (MI), Italy*

Summary The paper deals with simulation issues that can be raised during the design process of a piezoelectric micromachined ultrasound transducer (PMUT). The presence of multiple interactions between electric, mechanical and acoustic fields is accounted for by a multiphysics computational model, which is adopted in order to carry out parametric analyses and design-of-experiments with the main objective of optimizing the device performances. The complexity of the model is increased by the possible presence of large deformation, which are treated in the framework of geometric non-linear analysis.

INTRODUCTION

Piezoelectric Micromachined Ultrasound Transducers (PMUTs [1]) are widely used for many practical purposes. Medical acoustic imaging is a primary field of application, related to the propagation and reflection of acoustic waves in human tissues; hydrophones exploit the in-water propagation of ultrasonic pulses; rangefinders are related to in-air wave propagation, with by far lower frequency than those required for water-coupled devices; fingerprint recognition can greatly benefit from the peculiar features of PMUTs; further applications are represented by non-destructive testing, velocity sensing and object recognition. In many cases, a large array of PMUTs is adopted, in order to increase the spatial resolution [2]. In this paper, focus is on an air-coupled PMUT, whose vibration frequency should be around a few hundred kHz. The active material is represented by lead zirconate titanate (PZT), which in the past has been avoided for such applications, in spite of its good figures of merit, because of technological issues related to the integration of PZT thin films in MEMS [3]. In recent years, much progress has been made in improving PZT thin films and their properties [4], so that PZT can now be effectively adopted in MEMS. A suitable computational model of the air-coupled, PZT-based PMUT can be profitably used to carry out parametric analyses and design-of-experiments, with the main purpose of increasing the device's performances.

MODELLING ISSUES

The paper is related to modelling issues of an air-coupled PMUT, which can be schematically described as a suspended membrane (of circular shape) with active material stacked on its top surface (see Figure 1). The design of such a device calls for accurate, fast and reliable simulation techniques. The model should be able to capture the multiple interactions between the electric, mechanical and acoustic fields. The ultrasound transducers are plate-like structures, which can be modelled by means of a modified CLT model, with the introduction of piezoelectric effects [5]. The latter has been simplified by neglecting the "direct effect", namely the creation of electric current due to mechanical deformation. The "indirect effect" is represented by a planar strain, induced by the current flowing in the vertical direction: such an applied strain yields the vertical deflection of the plate. The aforementioned simplification is correct in the actuation phase only, whereas the sensing of the echoes requires the conversion of the mechanical deformation into an electrical signal. The model has been completed by the acoustic coupling with the surrounding medium, to provide a numerical estimate of the emission efficiency, and has been implemented in the context of the Finite Element Method, with shell-like elements for the laminate structure and solid elements for the acoustic fields. A suitable structural-acoustic interface has been introduced, to correlate the pressure and the velocity in the mechanical and the acoustic domains.

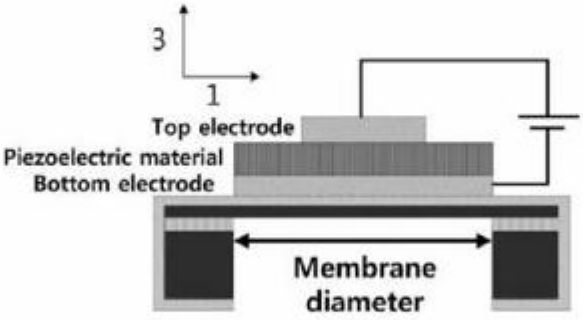

Figure 1. Cross-section schematic view of a MEMS ultrasound transducer: the structural suspended diaphragm is a poly-silicon layer; the active layer is located on the upper surface, with top and bottom electrodes.

[a)] Corresponding author. Email: raffaele.ardito@polimi.it.

Moreover, it was necessary to account for some non-linearity, given by the presence of residual stresses, whose presence has been evidenced in previous works [6]. A geometric non-linear analysis has been devised, so that the stiffness variation due to residual stress is suitably accounted for. It was also mandatory to consider that the initial shape of the membrane is no longer flat, since the residual stresses are not evenly distributed on the various layers that constitute the cross-section. The initial configuration was represented by a curved surface, whose shape should be computed at the beginning of the analysis. Such a behaviour has an important impact on the dynamical response of the device. The proposed model has been developed in order to cope with that effect, which has been somewhat overlooked in previous works.

RESULTS

The proposed model has been used to explore the capabilities of PZT-based PMUT and to carry out some parametric analyses. The laminate cross-section, whose detailed view is not reported here for the sake of brevity, contained the structural polysilicon layer, the electrodes and the PZT layer in different configurations: (i) a central disc of PZT with lower radius with respect to the structural membrane; (ii) an annular ring of PZT, which started from the outer clamped-in edge of the structural layer. Some of the results of parametric analyses are reported in Figure 2, with reference to configuration (i). Two geometric parameters are considered: the radius of the structural membrane and the coverage ratio of the PZT layer. It is possible to notice that the diaphragm's stroke (which is connected to the emission efficiency) attains a maximum value at a certain PZT ratio around 72% and is steadily increasing along with the membrane's radius. On the other hand, it is necessary to consider the variation of the first vibration eigen-frequency f_0, which is related to the operation conditions of the PMUT. A trade-off situation is envisaged, which should be carefully considered in the design procedure.



Figure 2. Parametric analyses with respect to the radius of the structural membrane and the coverage ratio of the PZT upper disc.

CONCLUSIONS

A non-linear multiphysics model has been developed in order to provide a suitable simulation tool for air-coupled, PZT-based micromachined ultrasound transducers. The model is able to capture the phenomena, which occur in the real operation of the device and which have been in some cases disregarded. The execution of the analyses is fast enough to be used in parametric studies, which represent an important point in the design procedure. The obtained results highlight some interesting features of the device's behaviour.

References

[1] Muralt P., Baborowsky J.; Micromachined Ultrasonic Transducers and Acoustic Sensors Based on Piezoelectric Thin Films. *J. Electroceramics* **12**:101-108, 2004.

[2] Lu Y., Heidari A., Horsley D.A.: A High Fill-Factor Annular Array of High Frequency Piezoelectric Micromachined Ultrasonic Transducers. *J. Microelectromech. Syst.* **24**:904-913, 2015.

[3] Griffin B.A., Williams M.D., Coffman C.S., Sheplak M.: Aluminum Nitride Ultrasonic Air-Coupled Actuator. *J. Microelectromech. Syst.* **20**:476-486, 2011.

[4] Lab4MEMS, FET-ENIAC Project, web site http://www.lab4mems.upb.ro

[5] Webber K.G., Hopkinson D.P., Lynch C.S.: Application of a Classical Lamination Theory Model to the Design of Piezoelectric Composite Actuators. *J. Intell. Mat. Syst. and Struct.* **17**:29-34, 2006.

[6] Sammoura F., Smyth K., Kim S.-G., Lin L.: An Accurate Equivalent Circuit for the Clamped Circular Multiple-Electrode PMUT with Residual Stress. *IEEE International Ultrasonics Symposium, IUS* 275-278, 2013

PREDICTING PIEZOELECTRIC EFFECTS IN ATOMISTIC FINITE ELEMENT SIMULATIONS

Mat Tolladay[1], Fabrizio Scarpa[1], Dmitry Ivanov[1], and Neil Allan[2]

[1]*ACCIS, Department of Aerospace Engineering, Bristol University, Bristol, UK*
[2]*Centre for Computational Chemistry, School of Chemistry, Bristol University, Bristol, UK*

Summary As our ability to build ever smaller machines develops so does the need for simulation techniques that can accurately capture the behaviour of these nanocomponents. To empower designers, new simulation methods must be developed to allow for easy and fast iterations of designs. To this end we have sought to incorporate piezoelectric modelling within an atomistic finite element model of boron nitride nanotubes. The ability to capture these effects allows for the design of nano scale electromechanical devices. We built and tested the model by using it to calculate the piezoelectric tensor coefficients for armchair boron nitride nanotubes, subjected to an axial torsional loading and compared our values to those generated using density functional theory that are available in the literature.

INTRODUCTION

Interest in nanotubes and their potential applications has been growing ever since their initial prediction over two decades ago. Different materials have been investigated as potential candidates for nanotube formation starting with the most well known, carbon, but other materials such as carbon nitrides, boron nitrides, sulphides, selenides, halides and transition metal oxides have been investigated [1]. Concurrently, there has been development of micro, meso and nano scale machines looking to provide new technological capabilities in many different research fields. Components of these miniature machines are an obvious application for nanotubes, however new methods for accurately modelling these structures are required. The standard methods for macro scale modelling rely on the assumptions of continuum mechanics, where as at smaller scales the molecular structure of the materials becomes apparent leading to unacceptable inaccuracies. Although computational chemistry has produced tools for modelling molecular structures they normally require significant computational resources when attempting to model large systems of atoms. One method that attempts to provide molecular modelling capabilities while allowing for rapid computation is to model the molecular structure as a space frame structure (as can be seen in figure 1a) by using force constants developed for molecular mechanics software to provide the effective beam (Euler-Bernoulli or Timoshenko) properties [2]. These "atomistic" finite element models have been investigated for over a decade by multiple authors, examining different nano materials and using different finite element beam formulations [3, 4, 5].

We want to expand this technique by providing a method for calculating properties other than the mechanical ones that have been investigated previously. The focus of this work was on developing a novel method for calculating the piezoelectric response of nanotubes. Boron nitride nanotubes have been shown to have piezoelectric properties which have been investigated, mostly computationally, providing us with a means for testing the validity of our method.

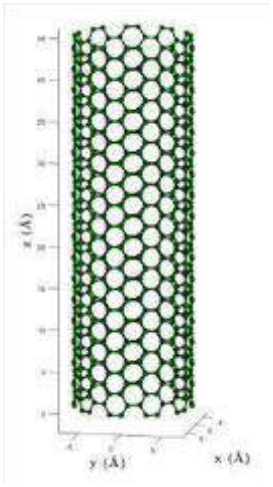

(a) The finite element model of a nanotube showing beam elements as black lines and the nodes as green circles.

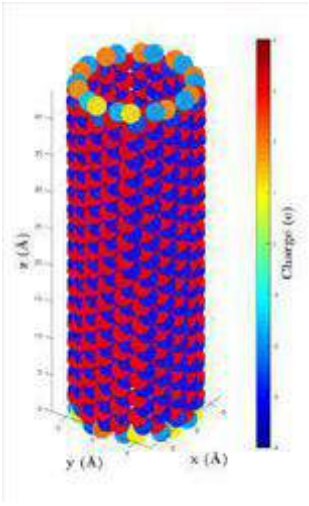

(b) The charges of the atoms of the boron nitride nanotube as calculated using QEq.

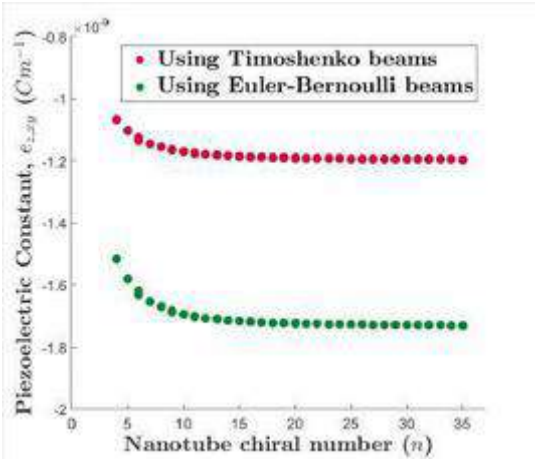

(c) The results of our simulations showing a similar trend in the piezoelectric coefficient as the nanotube chiral number (an analogue for the tube radius) is increased.

Figure 1

THE METHOD

Piezoelectric phenomena are generated by the creation of atomic dipoles in a material which are at least somewhat aligned. In the case of boron nitride nanotubes the atomic dipoles are caused by distortions of the nanotube lattice that result in breaking of the threefold symmetry of the lattice. This symmetry breaking leads to dipole creation whereby the electron distribution of the atoms loses symmetry resulting in a dipole moment of the atom.

A simple method for understanding this behaviour is to consider a polarisability of the atom, a constant which describes the ratio of the dipole moment of the atom generated by an external applied field and the strength of the applied field. Using atomic polarisability we can calculate the dipole moment of an atom due to an applied field, for our purposes it was thus necessary to find a suitable method for calculating the electric field at the atom sites of our deformed nanotube lattice.

The method we used was one developed for use with molecular mechanics simulations called charge equilibration (QEq). This method uses physical properties of the atoms, the ionisation energies and electron affinities, and the atom positions as the initial inputs for a method to approximate the charge distribution within a molecule (an example of which can be seen in figure 1b). Using this method we were able to generate charges for the atoms in the deformed nanotube and then use these charges and the position data for the atoms to calculate the electric field at the atom sites. With the field calculated we could then apply the polarisability to find the dipole moments of the atoms.

TESTING THE METHOD

To determine the accuracy of the method we chose to generate the piezoelectric coupling tensor coefficients of a variety of different sized armchair boron nitride nanotubes under an axial shear load (for results see figure 1c). By varying the degree of the shear stress in the tube due we could calculate the dipole moment per unit area (dipole density) of the tube for each applied shear stress. We were then able to find the gradient of the dipole density as a function of shear stress using finite differences. This gradient is the tensor coefficient for the piezoelectric coupling tensor.

Table 1: Results from our model and other authors work.

Authors	Method	$e_{z,xy}$ (Cm^{-1})
Current work	Atomistic FE with QEq	$\nearrow 1. \times 10^{-9}$
Sai & Mele [6]	DFT/Berry's phase	$\nearrow 3.3 \times 10^{-10}$
	DFT/Ab initio	$\nearrow 2.0 \times 10^{-10}$
Naumov et al [7]	DFT	$\nearrow 3.5 \times 10^{-10}$

Our results show reasonable agreement with calculations for the tensor values based on DFT calculations (see table 1) but further refinement of the method is required. Future work will seek to address this by examining other piezoelectric nanotubes, such as zinc oxide, so that suitable corrections can be introduced to the relevant physical constants.

CONCLUSIONS

We developed and tested a method for the simulating piezoelectric response of boron nitride nanotubes. The method provides us with an approximation of the piezoelectric properties of the nanotubes but will be refined through future work. We have shown the method has potential to be used for simulating nanostructures and therefore has the potential to be used as a tool for designing nano scale machines that utilise piezoelectric effects that are present in certain materials.

References

[1] V V Pokropivnyi. Non-carbon nanotubes (review). II. types and structure. *Powder metallurgy and metal ceramics*, 40(422):582–594, 2001.

[2] Chunyu Li and Tsu-Wei Chou. A structural mechanics approach for the analysis of carbon nanotubes. *International Journal of Solids and Structures*, 40(10):2487–2499, may 2003.

[3] K. I. Tserpes and P. Papanikos. Finite element modeling of single-walled carbon nanotubes. *Composites Part B: Engineering*, 36(5):468–477, 2005.

[4] F Scarpa, S Adhikari, and A Srikantha Phani. Effective elastic mechanical properties of single layer graphene sheets. *Nanotechnology*, 20(6):065709, 2009.

[5] M Meo and M Rossi. Prediction of Youngs modulus of single wall carbon nanotubes by molecular-mechanics based finite element modelling. *Composites Science and Technology*, 66(11-12):1597–1605, 2006.

[6] Na Sai and E. J. Mele. Microscopic theory for nanotube piezoelectricity. *Physical Review B*, 68(24):241405, dec 2003.

[7] Ivan Naumov, Alexander M. Bratkovsky, and V. Ranjan. Unusual Flexoelectric Effect in Two-Dimensional Noncentrosymmetric sp^{2}-Bonded Crystals. *Physical Review Letters*, 102(21):217601, 2009.

A 3-LAYERED NON-LINEAR HOMOGENIZATION APPROACH FOR NANOPOROUS MATERIALS

Giuseppe Vairo*[1], Stella Brach[1,2], Luc Dormieux[3], and Djimedo Kondo[2]

[1]*Department of Civil Engineering and Computer Science, University of Rome "Tor Vergata", Rome, Italy*
[2]*Institut D'Alembert, UMR 7190 CNRS, University Pierre and Marie Curie, Paris, France*
[3]*UR Navier, Ecole des Ponts ParisTech, Champs-sur-Marne, France*

Summary In this paper, the strength properties of a ductile nanoporous material are investigated by means of a non-linear homogenization approach based on the modified secant method. The material is described as a rigid ideal-plastic solid matrix, obeying to a von Mises strength criterion, and containing isotropically- distributed spherical nanovoids. Aiming to properly account for local strain-rate heterogeneities, a 3-layered model is adopted. A novel closed-form macroscopic strength criterion is established, and successfully compared with available numerical data, resulting in an effective enhancement of previous-established theoretical predictions.

The development of materials characterised by a nanosized microstructure has recently given rise to a growing research interest, involving experimental tests, numerical simulations and theoretical models, aiming to investigate the influence of nano-inclusions or nanopores on the overall material response. An important class of nanostructured materials consists in nanoporous media, characterised by reduced mass density, high surface-to-volume ratio, good levels of strength and generally exhibiting a ductile behaviour. From a mechanical point of view, one of the most important aspect concerns the influence, for a fixed porosity value, of the size of voids on the macroscopic material strength properties. In the framework of a continuum approach, such a void-size effect has been generally addressed by adopting coherent-imperfect interface laws to describe cavity surfaces. Early works involving void-size effects have been focused on the effective elastic properties of nanoporous materials. In contrast, few attention has been paid so far to the influence of the size of voids on the material plastic behaviour. In the framework of non-linear homogenization (NLH) methods, mention is made to the very recent model [2] (denoted in the following as DK), consisting in a generalization of the well-established strength criterion [5] for classical porous materials to nanoporous ones. However, the DK strength model strongly overrates available numerical evidence [4, 6], mainly for high stress-traxiality levels. In this light and in the framework of NLH-based techniques, present paper (see [1]) aims to establish a consistent and accurate strength criterion for nanoporous materials properly accounting for void-size effects and able to recover available benchmarking evidence.

Let Ω be a material representative volume element (RVE), whose exterior boundary is $\partial\Omega$. Let the RVE be comprised of a rigid ideal-plastic solid matrix Ω^{s}, obeying to a von Mises strength criterion with support function π^{s}, and isotropically-distributed spherical cavities of radius a. The RVE is assumed to undergo homogeneous strain-rate boundary conditions, prescribed in terms of the constant tensor $\mathbf{D}$. Denoting as $\boldsymbol{\sigma}$, $\mathbf{d}$, and $\mathbf{v}$ the microscopic stress, strain-rate and velocity fields, respectively, the following boundary-value problem, involving equilibrium, compatibility and plastically-admissibility conditions, is introduced.

Problem $\mathcal{P}$ *For a given* $\mathbf{D}$*, find* $\left\{\boldsymbol{\sigma}(\mathbf{z}), \mathbf{d}(\mathbf{z}), \mathbf{v}(\mathbf{z})\right\}$ *s.t.*

$$\mathrm{v}\,\boldsymbol{\sigma} = \mathbf{0} \qquad \text{in } \Omega \tag{1a}$$

$$\mathbf{d} = (\nabla\mathbf{v}) \qquad \text{in } \Omega \tag{1b}$$

$$\boldsymbol{\sigma} = \frac{\partial\pi(\mathbf{z},\mathbf{d}(\mathbf{z}))}{\partial\mathbf{d}} \qquad \text{in } \Omega \tag{1c}$$

$$\mathbf{v} = \mathbf{D}\cdot\mathbf{z} \qquad \text{in } \partial\Omega \tag{1d}$$

where vector $\mathbf{z}$ *identifies the position of a point in* Ω*, and* π *is equal to* π^s *in* Ω^s *and zero otherwise.*

By considering the local support function π as the potential of a fictitious viscous material, equation (1c) can be thought as representative of a fictitious non-linear behaviour described by the constitutive relationship

$$\boldsymbol{\sigma}(\mathbf{z}) = \begin{cases} \mathcal{C}\left[\mathbf{z}\right]\mathbf{d}(\mathbf{z})\big) : \mathbf{d}(\mathbf{z}) & \text{if} \quad \mathbf{z}\in\Omega^{\mathrm{s}} \\ \mathbf{0} & \text{if} \quad \mathbf{z}\in\Omega\setminus\Omega^{\mathrm{s}} \end{cases} \tag{2}$$

where the the fourth-order secant stiffness tensor $\mathcal{C}$ is isotropic, with volumetric (namely, k) and shear (μ) secant muduli equal to:

$$k\to+\infty, \qquad \mu(\mathbf{z},\mathbf{d}(\mathbf{z})) = \frac{\hat{\sigma}(\mathbf{z})}{2\sqrt{3}}\frac{1}{\sqrt{J_2^{\mathrm{d}}(\mathbf{d}(\mathbf{z}))}} \tag{3}$$

*Corresponding author. Email: vairo@ing.uniroma2.it

σ and $J_2^{\mathrm{d}} = \mathbf{d}_{\mathrm{d}} : \mathbf{d}_{\mathrm{d}}/2$ (with $\mathbf{d}_{\mathrm{d}}$ the deviatoric part of $\mathbf{d}$) being the von Mises strength (possibly varying in space) and the deviatoric second strain-rate invariant , respectively. Accordingly, Problem $\mathcal{P}$ can be considered as associated to a fictitious incompressible material, whose constitutive law (2) is representative of a non-linear (owing to the dependency of $\boldsymbol{\mathcal{C}}$ on the strain rate $\mathbf{d}$ by means of J_2^{d}) and pointwise homogeneous (due to the space dependency of σ and $\mathbf{d}$) response.

In order to obtain an analytical solution, a simplified version of Problem $\mathcal{P}$ is introduced, by describing $\boldsymbol{\mathcal{C}}$ as a piecewise-constant (in space) tensor. With reference to the n-layered model [3], the sub-domain partition $\Omega = \cup_{\alpha=1}^{n+1}\Omega_\alpha$ with $n = 3$ shown in Fig. 1a is considered, consisting in 3-layered composite spheres, confocal to nanovoids and embedded into the solid matrix. Each composite sphere comprises the void region, an imperfect-coherent interface (allowing for void-size effects) and an interface-to-matrix transition zone. In each subregion Ω_α, both the von Mises parameter and the second strain-rate invariant are assumed to be constant in space, namely $\sigma(\mathbf{z}) = \hat{\sigma}_\alpha$ and $J_2^{\mathrm{d}}(\mathbf{d}(\mathbf{z})) = J_{2\alpha}^{\mathrm{d}}$. Thereby, the non-linear problem underlying the determination of strength properties for nanoporous materials is reduced to a non-linear viscous one defined on a fictitious piecewise homogenenous medium. Due to previous assumptions, Eq. (2) simplifies as follows:

$$\boldsymbol{\sigma}(\mathbf{z}) = \begin{cases} \boldsymbol{\mathcal{C}}_\alpha : \mathbf{d}(\mathbf{z}) & \text{if} \quad \mathbf{z} \in \Omega_\alpha \quad \text{with } \alpha \in \{2, \dots, 4\} \\ \mathbf{0} & \text{if} \quad \mathbf{z} \in \Omega_1 \end{cases} \tag{4}$$

where $\boldsymbol{\mathcal{C}}_\alpha$ is defined in terms of secant moduli (3), with $\mu = \mu_\alpha$ and $\mu_\alpha = \hat{\sigma}_\alpha/(2\sqrt{3J_{2\alpha}^{\mathrm{d}}})$.

By solving via a perturbative procedure Problem $\mathcal{P}$ with Eq. (4) in place of (1c), and by means of NLH-based techniques [7], a novel analytical closed-form strength criterion (denoted as BDKV [1], herein not reported for brevity) is derived. A suitable value for the volume fraction of the composite spheres is determined, aiming to optimize the criterion performance at pure hydrostatic stress states. As a consistency indication and as special cases, BDKV criterion recovers previously-established NLH-based analytical strength estimates both accounting [2] or not [5] for void-size effects. Results obtained via BDKV highlight that a suitable description of void-size effects can be experienced, resulting in an increase of the predicted strength features as the void length decreases, especially for high triaxiality levels (Fig.1b). Furthermore, comparisons with respect to both theoretical predictions [2] and finite-element-based calculations [4, 6] show consistency and accuracy of the proposed formulation, resulting in a significant improvement of the benchmarking NLH-based model DK [2] (Fig.1b).

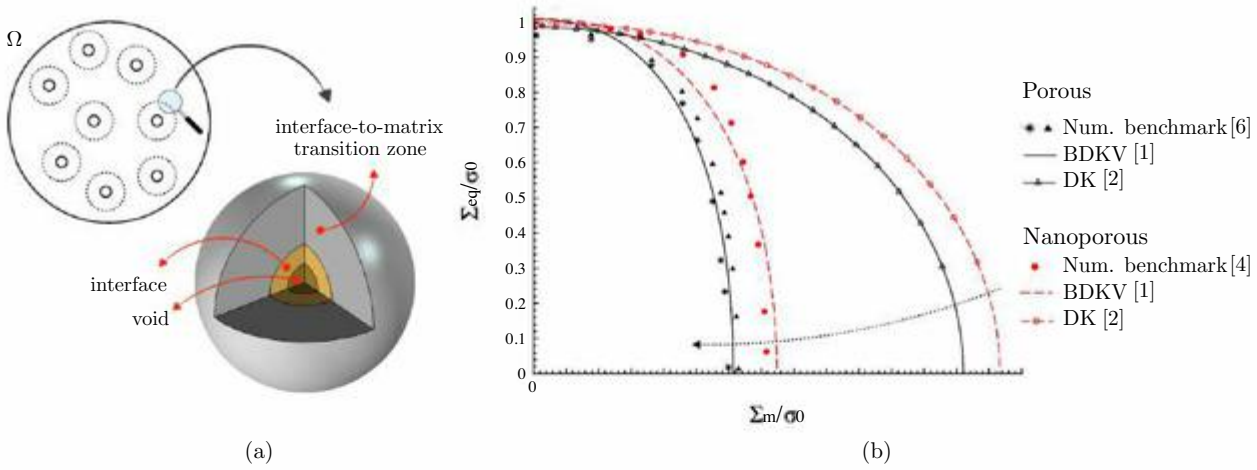

Figure 1: (a) 3-layered partition. (b) Strength profiles in the plane of macroscopic stresses (Σ_{m}, $_{\mathrm{eq}}$ $_{0}$ parameter of Ω^{s}

References

[1] Brach S., Dormieux L., Kondo D., Vairo G.: Strength properties of nanoporous materials: a 3-layered based non-linear homogenization approach with interface effects. Submitted, 2015.

[2] Dormieux L., Kondo D.: Non linear homogenization approach of strength of nanoporous materials with interface effects. Int J Eng Sci 71:102-110, 2013.

[3] Herve E., Zaoui A.: n-Layered inclusion-based micromechanical modelling. Int J Eng Sci 31:1-10, 1993.

[4] Morin L., Kondo D., Leblond J.-B.: Numerical assessment, implementation and application of an extended Gurson model accounting for void size effects. Eur J Mech A-Solid 51:183-192, 2015.

[5] Ponte Castañeda P.: The effective mechanical properties of nonlinear isotropic composites. J Mech Phys Solids 39:45-71, 1991.

[6] Trillat M., Pastor J.: Limit analysis and Gursons model. Eur J Mech A-Solid 24:800-819, 2005.

[7] Suquet P.: Overall properties of nonlinear composites: a modified secant moduli theory and its link with Ponte Castañeda's non linear variational procedure. C R Acad Sci Ser B 11:563-571, 1995.

ELECTROSTATIC VERSUS ELECTROMAGNETIC MICROMIRROR ACTUATION

A. M. Alneamy *[1], M. Khater[2], S. Park[1], E. M. Abdel-Rahman[1], and G. R. Heppler[1]

[1]*Systems Design Engineering, University of Waterloo, Waterloo, Ontario, Canada*
[2]*Mechanical Engineering, KFUPM, Dahran, Saudi Arabia*

Summary This paper compares the performance of electrostatically actuated and electromagnetically actuated micromirrors. The static and dynamic characterization of both types of micromirrors is carried out. We find that micromirrors actuated electromagnetically via a Lorentz force can realize much larger (20 times more) torsion angles than electrostatically actuated micromirrors for the same mirror structure.

INTRODUCTION

Micro-Electro-Mechanical Systems (MEMS) are widely used microfabricated sensors and actuators. Torsional MEMS actuators, such as torsional micromirrors, are an important MEMS application extensively used in digital projection displays and optical switches. MEMS are actuated electrostatically, electromagnetically and electrothermally. Electrostatic actuation is quite efficient, however, it is limited by the pull-in instability [1]. Electrostatic micromirrors use fixed electrodes to rotate a mirror plate around a suspension axis. Zhang [2], found that the mirror torsion angle is highly dependent on the size and position of the electrodes. In addition, the electrostatic force used to rotate the mirror also produces a downward (piston) motion bringing the mirror closer to the electrode leading to early pull-in.

Electromagnetic MEMS actuators based on the Lorantz force have also been used in many applications because they provide a large stroke [1]. Cho et al. [3], fabricated an electromagnetically actuated micromirror that can rotate around the x and y axes and deflect along the z axis. They found that, utilizing z axis actuation is useful in aligning the light path between the source and micromirror which results a good coupling among optical components. In this paper, micromirrors that utilize electrostatic and electromagnetic actuation have been statically and dynamically evaluated and compared to investigate the relative merits of the two actuation methods.

ACTUATOR MODEL

We investigate a micromirror, Fig. 1, consisting of two parallel cantilever beams supporting a reflective microplate and two identical left and right electrodes placed below it. The micromirror is made of polysilicon with dimensions show in Figure 1. The equations of motion of the microplate deflection w and torsion ϕ under electrostatic actuation are given by:

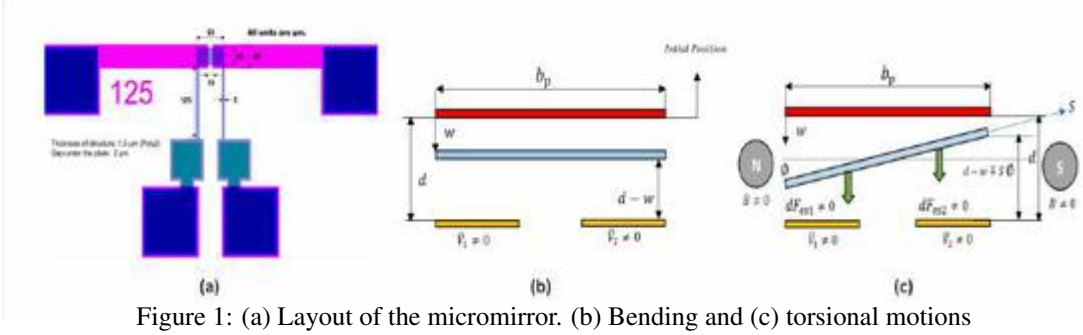

Figure 1: (a) Layout of the micromirror. (b) Bending and (c) torsional motions

$$m_{eq}\ddot{w} + (c_{vb} + c_s)\dot{w} + k_{eq}w = F_{es1} + F_{es2} \qquad (1)$$

$$J_t\ddot{\phi} + c_{vt}\,\dot{\phi} + k_t\phi = T_{es_1} + T_{es_2} \qquad (2)$$

where F_{es1} , F_{es2} , T_{es1}, and T_{es2} are the electrostatic forces and torques applied by the left and right electrodes on the microplate, respectively, c_{vb} and c_{vt} are the viscous damping in bending and torsion, and c_s is the squeeze film damping. Moeover, the microplate is actuated electromagnetically to enhance the torsional angle, and the equation of motion is given by:

$$J_t\ddot{\phi} + c_{vt}\dot{\phi} + k_t\phi = T_{em} \qquad (3)$$

where T_{em} is the electromagnetic torque due to the interaction of the current passing in the loop made of the support beams and microplate and an external magnetic field due to the permanent magnets marked by N and S in Fig. 1(c).

RESULTS

Figure 2(a) shows the variation of the static torsional angle as the DC voltage of the left electrode only is increased obtained from numerically solving Eqs. (1) and (2) and an FEM of the micromirror. The maximum torsion angle under electrostatic forces was $0.0\ ^\circ$ at 13.5 V. Beyond that point, the edge of the micromirror comes in contact with the substrate.

Solving Eq. (3) numerically for the torsion angle under electromagnetic actuation with a current I = 3.3 mA and variable magnetic field density B, we achieved a maximum torsion angle of 1° at 1.4 T, Fig. 2(b). Due to the linear relationship between the magnetic field B and Lorentz force, a linear relationship is seen in Fig. 2(b) between B and ϕ.

*Corresponding author. Email: aalneamy@uwaterloo.ca

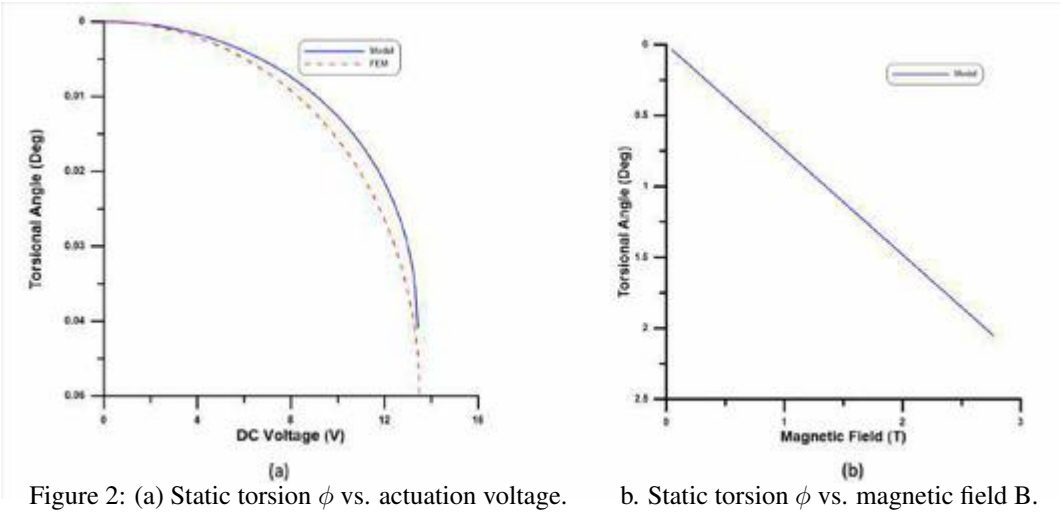

Figure 2: (a) Static torsion ϕ vs. actuation voltage. b. Static torsion ϕ vs. magnetic field B.

The dynamic response of the micromirror under harmonic electromagnetic excitation was also found by integrating Eq. (3) numerically and compared to experimental results. The micromirror was actuated by a current I = 3.3 mA and an external magnetic field B = 64 mT. The FFT of the mirror edge displacement and velocity measured using a laser vibrometer is compared in Fig. 3 to the FFT of the numerically predicted motions at the natural frequency of the micromirror torsional motions $\omega_n = 182\,\text{kHz}$. Good agreement is seen between the numerical and experimental results.

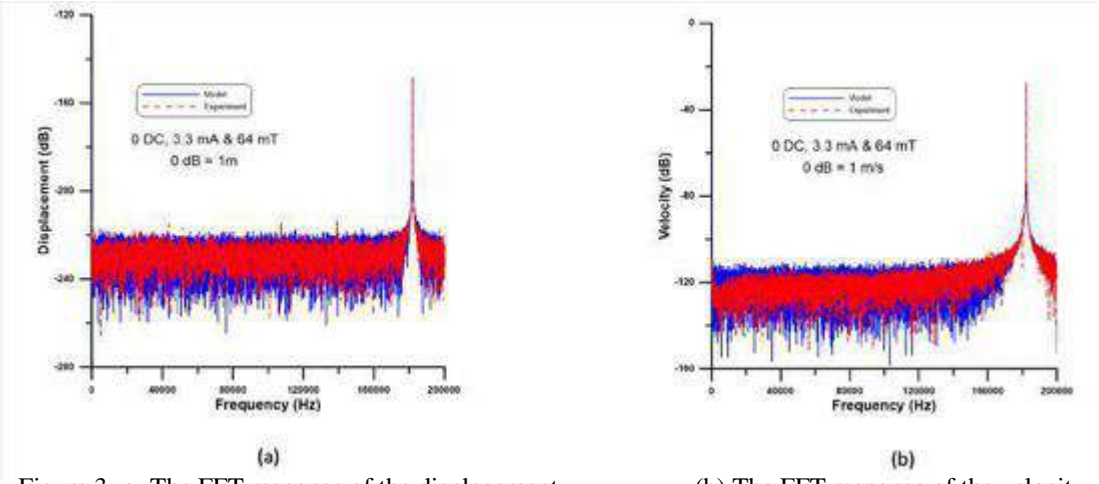

Figure 3: a. The FFT response of the displacement. (b) The FFT response of the velocity

CONCLUSIONS

We compared numerically and experimentally electrostatic and electromagnetic micromirrors. The results show that electromagnetic excitation is more efficient than electrostatic actuation. Specifically, the maximum torsion angle obtained under electromagnetic actuation is 1° which is more than 20 times the maximum angle obtained under electrostatic actuation $0.0\ ^\circ$. The underlying reason is under electrostatic actuation the micromirror moves towards the bottom electrode as it rotates in torsion. This piston motion reduces the space available for the mirror torsional motion. On the other hand, electromagnetic actuation does not induce piston motions leaving the space between the mirror and the substrate for use by torsional motions only. Moreover, we validated the dynamic model of the electromagnetically actuated micromirror by comparing its results to experimental measurements at resonance.

Acknowledgment: The first author would like to acknowledge the support of Jazan University, Saudi Arabia.

References

[1] Younis M. I.: MEMS Linear and Nonlinear Statics and Dynamics. Springer, 2011.

[2] Zhang X. M.: A study of the static characteristics of a torsional micromirror.Sensors and Actuators, 2001.

[3] Cho. J. et al.: A low-voltage three-axis electromagnetically actuated micromirror for fine alignment among optical devices. Journal of Micromechanics and Microengineering, 2009.

DEVELOPMENT OF A ROBUST COUPLED ATOMISTIC-CONTINIUUM MODEL FOR CRACK PROGAGATION IN CRYSTALLINE MATERIAL

Jiaxi Zhang[1], Subhendu Chakraborty[2], and Somnath Ghosh*[3]

[1]*Graduate Research Assistant,Departments of Civil Engineering, Johns Hopkins University*
[2]*Graduate Research Assistant,Departments of Mechanical Engineering, Johns Hopkins University*
[2] *M. G. Callas Professor, Departments of Civil and Mechanical Engineering, Johns Hopkins University*

Summary A robust finite temperature force-based atomistic-continuum model is developed incorporated with non-linearity of atomic potential considered. The model is implemented using LAMMPS and parallel FEM codes making it scalable for 3D problems to investigate the crack propagation in crystalline material focused on the critical stress state and energy release rate. Furthermore, we compare the results of coupled model with pure MD simulation to investigate the size dependence and demonstrate the necessity of using coupled model.

INTRODUCTION

Modeling deformation processes of materials at nano-scale help us understands the fundamentals of material behavior. While molecular dynamics(MD) simulations has been widely used for atomistic level studies, the spacial and temporal scale limitation causes many issues such as unphysical boundary conditions, extremely large strain rate. For spacial scale specifically, many efforts have been made to develop different kinds of coupled atomistic-continuum methods to save computational cost and increase simulation domain size. In this work, we present a coupled framework focused on following features: 1. Non-linearity of the atomic interaction considered; 2. Finite temperature in atomistic domain; 3. Efficient parallel implementation to solve large 3D problem. It is shown that in nickel the non-linearity plays very important role in reducing the error of coupling model, similar trend is expected to be seen in other metallic materials. The coupled model is then used to investigate the crack propagation in single crystal nickel with center crack embedded. Bi-axial loading is applied to suppress dislocation at beginning. For both coupled model and pure atomistic model, stress distribution, the strain energy release rate and critical stress are analyzed. Analysis shows that if given same whole domain size, the coupled model gives similar results as pure atomistic model while saving significant computational cost. And size-reduced MD model underestimates the energy release rate of crack propagation process.

ROBUST COUPLED ATOMISTIC-CONTINUUM MODEL

The whole simulation domain is subdivided into three domain, atomistic domain Ω_A, continuum domain Ω_C and interface domain Ω_I. Ω_A is governed by atomic interactions using LAMMPS and Ω_C is governed by nonlinear elastic constitutive relation using FEM respectively. Continuum and atomistic representation coexist in Ω_I, where the compatibility and force equilibrium conditions are applied. The compatibility is achieved by enforcing the position of the node being the time average of all nearby atoms surrounded:

$$u_k^c = \left\langle \sum_i (w_i u_i^a) \right\rangle \tag{1}$$

where u_k^c is the displacement of node k, u_i^a is the displacement of one neighbor atom i, w_i denotes the weight function, taken as $1/n_k$ with n_k being all neighbor atoms of node k, and $\langle\cdot\rangle$ denotes the time average.

The force equilibrium is achieved by applying the external force on atoms based on the reaction force at the node.

$$f_k^c = \sum_i (w_i f_i^{ext}) \tag{2}$$

where f_k^c is the reaction force of node k since it is given displacement boundary condition, u_i^a is the external force on atom i. We use an iterative process to find equilibrium configuration when all interface node stops moving.

We apply Langevin dynamics and damping at atomistic system inside interface domain to keep canonical ensemble and have unwanted elastic waves with large wave length damped. More details of the coupled model and implementation can be found in [1].

*Corresponding author. Email: sghosh20@jhu.edu

NON-LINEAR ELASTIC CONSTITUTIVE RELATION

It is known that for most atomic iterations, the elastic strain energy can be approximated by quadratic form only near the equilibrium position. At nanoscale, due to the locally defect-free feature the crystalline material can withhold several percent strain before crack or dislocation nucleation. Therefore non-linear elastic behavior can not be ignored for these highly deformed nano-scale samples.

For simplicity, a third order constitutive relation is used to consider non-linear effect. With proper calibration, a defect free sample under 5% uniform bi-axial deformation shows the difference of considering non-linear effect in figure 1.

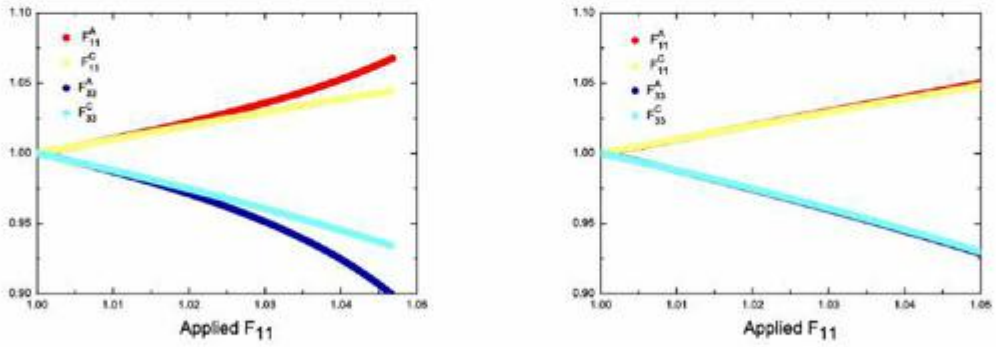

(a) (b)

Figure 1: Comparing of average deformation gradient at interface of atomistic and continuum: (a) linear elasticity (b) non-linear elasticity .

RESULT

The stress distribution of single crystal nickel with center crack applied with biaxial loading and energy release rate measured is shown in figure 2. The stress distribution demonstrates the effectiveness of coupling give a consistent stress contour from two domains. And the energy release rate plot shows that using larger domain granted by coupled model gives more accurate value of energy release rate.

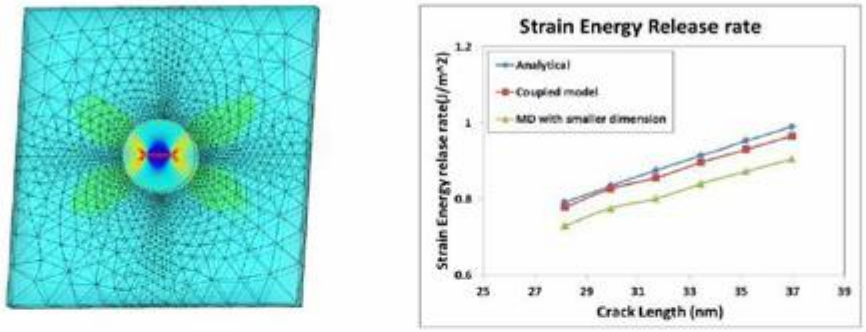

(a) (b)

Figure 2: (a)σ_{22} distribution under bi-axial loading, (b)energy release rate measured by coupled model and smaller pure atomistic sample

References

[1] Zhang J. Chakraborty S., Ghosh S.: Development of a robust coupled atomistic-continuum model for crack propagation in crystalline material. To be submitted.

EFFECTS OF LATERAL STRAIN AND CORNER GEOMETRY ON SELF-ROLLING OF NANOMEMBRANES

Cheng Chen and Jun Song[a)]
Department of Mining and Materials Engineering, McGill University

Summary The present study, for the first time, systematically examined the role of lateral (thermal/lattice) mismatch strain on the self-rolling of nanomembranes. Employing (finite-element modeling) FEM simulations and analytical method, the root cause for the considerable discrepancy between theoretically predicted and experimentally measured curvatures is quantitatively clarified, and the significance of lateral strain to longitudinal/lateral rollup competition is demonstrated. A novel design strategy based on *corner geometry engineering* has been proposed to enhance the yield of unidirectional rollup, validated by FEM simulations.

BACKGROUND / STATE OF THE ART

The broad applications of self-rolling nanomembranes in nano-elecromechanical/micro-electromechanical systems (NEMS/MEMS) have driven extensive research efforts, aiming to control the size and shape of the rollup structure[1,2]. To achieve this objective, accurate knowledge of the mechanics underlying the rollup process is of vital importance. Nonetheless, despite many theoretical studies[3-5], considerable discrepancies (e.g., in rollup curvature) between model predictions and experimental measurements exist. Various possibilities have been proposed to explain the discrepancy, including nonlinear strain effect[6], surface tension and reconstruction[7]. Nonetheless, inconsistency exists and quantitative assessement remains absent. Furthermore, one important component missing in previous modeling studies is the considerable of lateral (thermal/lattice) mismatch strain and competition of roll-up direction.

DESCRIPTION OF METHOD/MODEL

Based on Ritz minimization techniques and Von-Karman formula[8], we proposed one analytical model for bidirectional rolling up of nanomembranes. In this model the contributions of both the longitudinal and tansverse mismatch strains to the rolloing curvature are considered. Quasi-static and dynamic FEM simulations have been performed on a bilayer nanomembrane model system, illustrated in Fig. 1a. The 4-node doubly curved thin/thick shell element with reduced integration (S4R) was used. The variation of mismatch strain was achieve by assigning different thermal expansion coefficients to materials and varying temperature.

RESULTS AND DISCUSSION

The FEM simulated evolution of the rollup diameter of curvature (D) as a function of the longitudinal mismatch strain ε_0 is presented in Fig. 1b, in comparision to the model prediction for unidirectional rollup, under different degree of lateral straining (represented by the parameter η that is defined as $\varepsilon_1/\varepsilon_0$ with ε_1 being the lateral strain), showing great agreement. The vertical blue dash line and the star symbol in Fig. 1b respectively correspond to the particular case of GaAs/InGaAs and the D value reported in a previous experiment [9,10], indicating the significant influence of lateral strain on rollup curvature. The competition between longitude and lateral rollups is also demonstrated. We show that this competition can be effectively modulated through the strategy of *corner geometry engineering*, as illustrated in Figs.2. Our findings provide valuable insights towards the controllable fabrication of rollup structures for NEMS/MEMS applications.

[a)] Corresponding author. Email: jun.song2@mcgill.ca

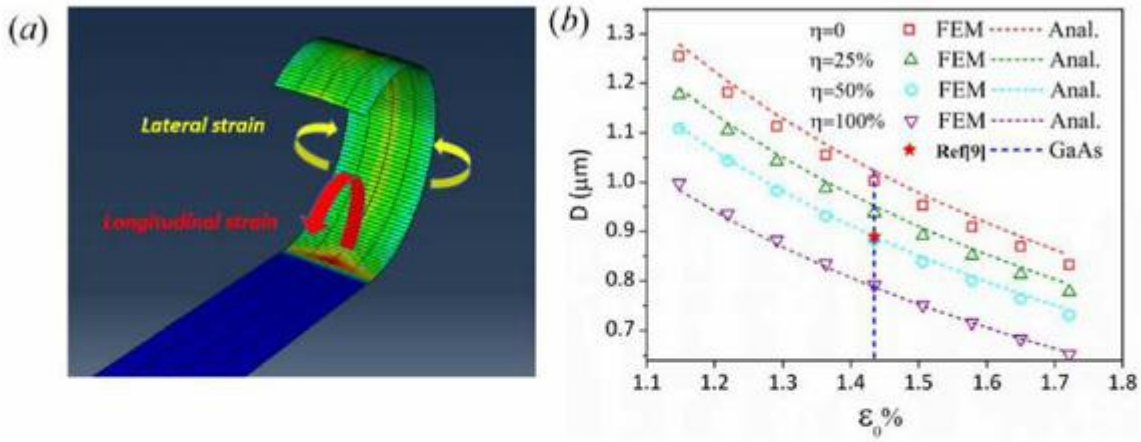

Fig.1 (a) Schematic illustration of a nanomembrane model in the FEM simulation. (b) The FEM simulated (open symbols) and model predicted (dashed lines) rolling diameter D as a function of the longitudinal mismatch strain ε_0 under different degrees of lateral (indicated by the parameter η). The verticle blue dash line corresponds to the particular case of GaAs/InxGaAs (i.e., ε_0=1.43 and the solid star symbol indicates the D value reported in the study by Chun et al [9].

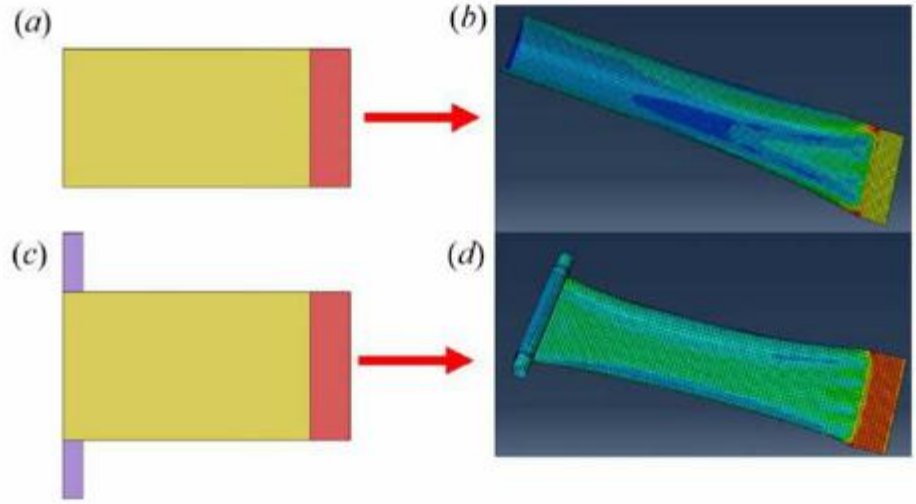

Fig. 2 FEM simulation results for rectangular nanomembranes (a) with and (c) without coner attachments (purple segaments), showing (b) long-edge rolling and (d) short-edge rolling respectively. The red segaments indicate the clamped regions in rectangular nanomembranes, while the rest of the nanomembrane is unconstrained.

References

[1] I. S. Chun, A. Challa, B. Derickson, K. J. Hsia, and X. L. Li, Nano Letters **10,** 3927 (2010).
[2] B. A. Korgel, Science **309,** 1683 (2005).
[3] Y. Y. Hu and W. M. Huang, Journal of Applied Physics **96,** 4154 (2004).
[4] G. P. Nikishkov, Journal of Applied Physics **94,** 5333 (2003).
[5] Y. C. Tsui and T. W. Clyne, Thin Solid Films **306,** 23 (1997).
[6] M. Grundmann, Applied Physics Letters **83,** 2444 (2003).
[7] J. Zang, M. H. Huang, and F. Liu, Physical Review Letters **98** (2007).
[8] S. Vidoli, International Journal of Solids and Structures **50,** 1241 (2013).
[9] I. S. Chun, V. B. Verma, V. C. Elarde, S. W. Kim, J. M. Zuo, J. J. Coleman, and X. Li, Journal of Crystal Growth **310,** 2353 (2008).
[10] X. L. Li, Journal of Physics D-Applied Physics **41** (2008).

MECHANICAL BEHAVIOR OF GRAPHENE SHEET USING ATOMIC-SCALE FINITE ELEMENT METHOD

Daniela Damasceno[1a)], Euclides Mesquita [1)], Nimal Rajapakse [2)] & Renato Pavanello[1)]
[1]*Faculty of Mechanical Engineering, Unicamp, Campinas, SP, Brazil*
[2]*Department of Civil & Environmental Engineering, Carleton University, Ottawa, Canada*

Summary In this work we continue to further develop the atomic-scale finite element method (AFEM) [1,3,4], to study the mechanical behavior of pristine graphene sheets as well as those with vacancy defects. In the present AFEM implementation, the stiffness matrices were obtained from a second-generation reactive empirical bond order (REBO) potential energy expression for hydrocarbons, as given by [2]. The force-strain relationships for a pristine graphene sheet and a sheet with crack are obtained from AFEM and Molecular Dynamics (MD) simulations in order to compare the accuracy and efficiency of AFEM. We also define the basic atomic elements on the edges and close to a row of vacancies, and compare the total energy of the atomic elements from AFEM and MD, in order to study the influence of nanoscale cracks and boundary conditions on the strength of graphene. The current formulation with modified atomic finite elements show good stability and convergence.

ATOMIC SCALE FINITE ELEMENT MODELING

AFEM, as proposed by Liu *et al*., is formulated by finding a state of minimum total energy E_{tot} of the system under analysis with respect to the vector describing the position of the atoms, $\underline{x}$.

$$\frac{dE_{tot}}{d\underline{x}} = 0 \tag{1}$$

The total energy of the system is given by:

$$E_{tot} = \sum_{<}^{N} U_{ij}\ \ x_j - \ _i\big) - \sum_{i=1}^{N} F_i \cdot x_i \tag{2}$$

In equation (2), U_{ij} denotes the internal energy stored within the atomic bonds. In this work, the "second generation" empirical potential of Brenner *et al* [2] is used to describe the interaction between the atoms:

$$U_{ij} = f\ \ r\ \ \ V_{ij}^{R} + b\,V^{A}\big) \tag{3}$$

where r_{ij} is the distance between the atoms *i* and *j*; b_{ij} is the bond order term; V_{ij}^{R} and V_{ij}^{A} are the repulsive and attractive term. The term F_i, in Equation (2), is the external force acting on the ith atom.

Considering Taylor expansion of the total energy E_{tot} around the equilibrium point and substituting it into Equation (1), the AFEM equations are given by:

$$\underline{K}\ \ \underline{u}\ \ \underline{u} = \underline{P} \tag{4}$$

with the stiffness matrix $\underline{K}\,(\underline{u})$ and the non-equilibrium load vector $\underline{P}$, respectively, given by:

$$\underline{K}\ \ \underline{u}\ \ = \ \ \frac{d^2\ U_{tot}}{d\ \underline{x}\ d\ \underline{x}}\bigg|_{\underline{\ } = \underline{\ }_0} \tag{5}$$

$$\underline{P}\ =\ \underline{F}_i\ -\ \frac{d\ U_{tot}}{d\ \underline{x}}\bigg|_{\underline{x} = \underline{x}^0} \tag{6}$$

IMPLEMENTATION STRATEGY AND NUMERICAL RESULTS

With AFEM it is possible to simulate the mechanical behaviour of nanomaterials such as a graphene sheet. Fig.1(a) shows the complete atomic element (10 atoms). The central atom, number 1, interacts with the first and second set of neighbours. The total energy of this element determined through the REBO potential [2] is U_{el}= -7.8073 eV/Å, at zero strain. Fig. 1(b) shows a finite graphene sheet mesh. The physical domain to be analyzed lays within the red hatched box. The atoms in red are considered to be outside the physical mesh, which means that their potential energy should not be included in the energy of the whole system. On the edges of the physical domain the basic atomic element will have to be modified to account for the atoms and connections that are missing, or outside the analyzed physical domain, as can be seen in Fig. 1(c). The central atom of this edge element is indicated by a black circle in Fig. 1(c). The atoms in blue represent the complete atomic element. Notice that some

[a)] Corresponding author. Email: daniela@fem.unicamp.br.

atoms are not in the physical domain. The modified element that must be considered for this edge is represented by a thicker black line. The total energy for this edge atomic element is $U_{el\text{-}edge}$= - 5.2864 eV/Å. A similar procedure must be applied to all kinds of edge-elements.

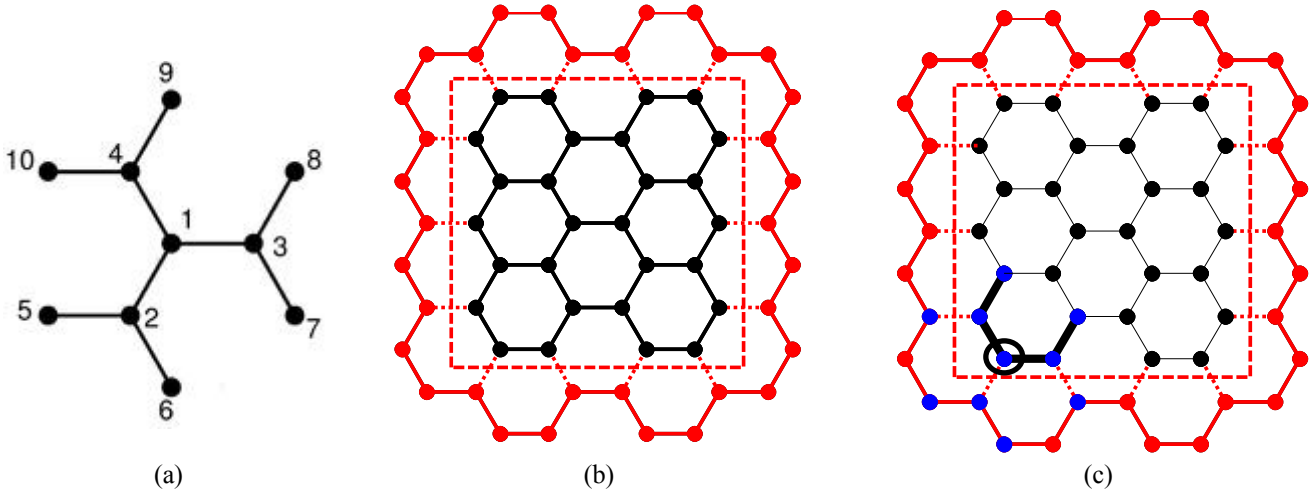

(a) (b) (c)

Figure 1: (a) complete atomic element; (b) graphene sheet; (c) a modified edge atomic element

Fig. 2(a) shows a graphene sheet with a missing atom, intended to simulate a defect. Atom vacancies also require the basic element to be modified. In our previous work using only the basic element in Figure 1 (a), we noted substantial convergence and stability issues with defects as well as edges [3,4]. The atoms in blue shows the modified basic atomic element because of the vacancy defect. The total energy for this atomic element is $U_{el\text{-}mod}$= -4.9821 eV/Å, at zero strain. Applying the described concepts, the force-strain curve from AFEM implementation is compared in Fig. 2(b) to the results obtained using the molecular dynamics (MD) code LAMMPS. In the MD simulations, the same Brenner potential at 1 K and non-periodic boundary conditions were used.

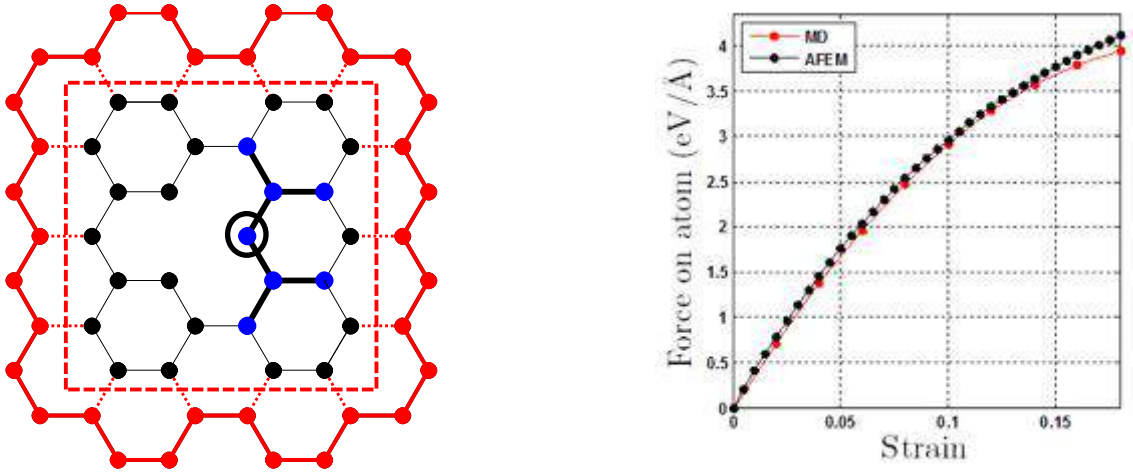

(a) (b)

Figure 2: (a) Graphene sheet with vacancy defect; (b) force-strain relationship from AFEM and MD

CONCLUSIONS

The "second generation" empirical potential of Brenner *et al* was implemented to calculate the total energy for the complete atomic element, and for different arrangement of atomic elements, taking into account edge and vacancy effects. AFEM and MD results show good agreement with the use of modified basic atomic finite elements compared to our previous studies that showed stability and convergence problems with the basic AFEM.

References

[1] Liu, B., Huang, Y., Jiang, H., Qu, S., and Hwang, K. C. Comput. Methods Appl. Mech, 2004.
[2] Brenner D.W., Shenderova O.A., Harrison J.A., Stuart S.J., Ni B. and Sinnott S.B. J. Phys, 2002.
[3] Damasceno, D., Dewapriya, M.A.N., Rajapakse, R.K.N.D. and Mesquita, E., ASCE-EMI, Hong Kong, 2015.
[4] Damasceno, D., Dewapriya, M.A.N., Mesquita, E., and Rajapakse, R.K.N.D., PACAM, Argentina, 2015.

ANALYSIS OF THERMAL NOISE IN FREQUENCY-MODULATED GYROSCOPES

David Effa[1], Eihab Abdel-Rahman[2] and Mustafa Yavuz[3]
[1, 3] Mechanical and Mechatronics, University of Waterloo, Waterloo, Ontario, Canada
[2] Systems Design Engineering, University of Waterloo, Waterloo, Ontario, Canada

Summary Thermal noise in microgyroscope arise due to molecular agitation inside beam springs, suspended mass and the surrounding environment. It is one of the fundamental limits to the precision of micro-electro mechanical system (MEMS). Previously research has been done on thermal noise for amplitude modulated microgyroscope. This paper presents analysis of thermal noise for frequency modulation microgyroscope. The microgyroscope is comprised of a cantilever beam with a proof mass at its free end coupled electrostatically with two fixed electrodes. The microgyroscope undergoes coupled flexural vibrations in two orthogonal directions when subjected to base rotation around the beam's longitudinal axis. The rotation rate is measured by detecting the shift in the natural frequencies of two closely spaced global vibration modes. We investigate the effect of thermal noise on the natural frequency of the microgyroscope. We analyzed analytical expressions for the effect of thermal noise on the frequency modulation microgyroscope and compare the output signals due to both the rotation rate and thermal noise.

INTRODUCTION

The MEMS microgyroscope offers key advantages over conventional inertial sensing technologies, including compact design and low cost [1]. Microgyroscopes measure angular displacement or speed in a wide range of applications including consumer electronics, navigation, and control of aerial systems and ground vehicles [2]. Most microgyroscopes operate as amplitude modulation systems, where the mechanical sense-mode response is excited by the input angular velocity, which is modulated by the drive-mode vibration caused by the Coriolis Effect [3]. This paper presents the effect of thermal noise on frequency modulated (FM) microgyroscope. The FM method implements a resonant sensing technique, which directly measures the angular rate by detecting the difference between the natural frequencies shift of the two closely spaced vibration modes.

Noise generated by temperature fluctuation occurs in any mechanical system. Commonly in large-scale sensors, this kind of noise is usually neglected. However, as a device is reduced in size, these thermal noises or vibrations become significant for MEMS scale sensors [1]. Generally, microgyroscope are limited by a number of noise sources including electrical noise and systematic errors, and thermal noise. However, for such small mechanical structures and low values of displacement in the sensing direction, thermal noise mainly considered as the theoretical sensitivity limiting factor. Mechanical thermal noise occurs due to vibrations of atoms in the materials from which a device is made and the environment in which the device operates.

ANGULAR RATE DETECTION BASED ON FREQUENCY MODULATION

The microgyroscope presented here operates based on the resonant sensing principle. In FM microgyroscope, the shift in natural frequency of the system is measure when it is subjected to a variation in a given physical quantity. In this case, a high-Q cantilever vibrating on resonance serves as the frequency-determining component of the angular input. Angular rotation perpendicular to the sense and driver direction cause instantaneous changes in the oscillator frequencies which are detected by a frequency modulated methods. This technique is highly sensitive and has the potential to address a large dynamic range [4]. The MEMS gyroscope described here, include a suspended mass, which is excited in the direction perpendicular to the substrate (z-axis). The cantilever is kept oscillating at its resonant frequency by applying positive feedback through the oscillator control amplifier. This amplifier is equipped with an automatic gain control (AGC) circuit which maintains the vibration amplitude at a constant level. When the system applied with angular rate along the x-axis, it generates periodic vibrations in an orthogonal sense direction (y-axis) due to the Coriolis Effect, Figure 1. The angular rate is then measured by analysing the shift in the natural frequencies of the sense and drive modes.

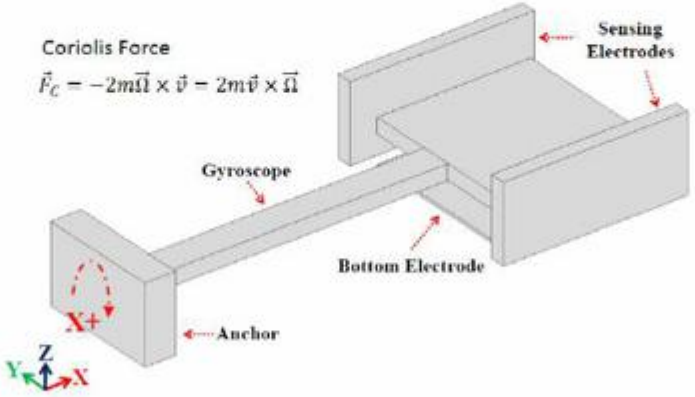

Figure 1. A 3D model of the Microgyroscope.

*Corresponding author. Email: deffa@uwaterloo.ca

THERMAL NOISE IN FREQUENCY-MODULATED GYROSCOPES

The equipartition theorem states that energy is shared equally amongst all energetically accessible degrees of freedom. Hence, it relates the temperature of a system with its average energies in the cantilever motion described by [5]

$$\frac{1}{2}m\omega_o\langle y_{th}^2\rangle = \frac{1}{2}k_BT \tag{1}$$

where $\langle y_{th}^2\rangle$ is the mean-square displacement of the end of the cantilever beam due to thermal excitation. The spectral noise density ($N_{th}(f)$) and mean-square displacement are related by [5]

$$\langle y_{th}^2\rangle = \frac{1}{2\pi}\int_0^\infty N_{th}(f)df \tag{2}$$

and spectral noise density can be further described by

$$N_{th}(f) = |G(f)|^2\Psi_{th}(f) \tag{3}$$

where $|G(\omega)|^2$ is the response function of the cantilever (damped harmonic oscillator) given by

$$|G(f)|^2 = \frac{1/m^2}{(f_0^2 - f^2)^2 + (f_0 f/Q)^2} \tag{4}$$

and $\Psi_{th}(f)$is the thermal white noise drive given by

$$\Psi_{th}(f) = 4mf_0k_BT/Q \tag{5}$$

If we ignore noise components with a modulation frequency on the order of the oscillator linewidth and less, we may write an approximate expression for the spectral noise density N^{th} in each sideband in terms of the modulation frequency as follows:

$$N_{th}(f_m) = K_BT/mf_oQf_{mod}{}^2 \tag{6}$$

The phase noise energy is given by $N_{op}(f_m) = kN_{th}(f_m)/2)$ and in the case where it is necessary to calculate the effective frequency deviation over some finite baseband bandwidth say $(f_{n1} - f_{n2})$ then [6]:

$$(\delta f)^2 = \int_{f_{n1}}^{f_{n2}} \left(\frac{2N_{op}(f_m)}{E_c} f_m{}^2 df_m\right) \tag{7}$$

where δf is the mean-square frequency modulation due to this noise source C, is the oscillator energy (carrier power) given by $E_c = k_l y_{osc}^2$) over the bandwidth of measurement. Integrating Eq. (7) over the bandwidth of measurement, the minimum detectable frequency shift of a cantilever beam oscillator incorporated in a self-oscillating system with positive feedback has been estimated.

$$\delta f = \sqrt{\frac{f_0k_BTB}{kQ\langle y_{osc}^2\rangle}} \tag{8}$$

CONCLUSIONS

In conclusion, analytical expressions for the effect of thermal noise on the FM microgyroscope has been presented. We found a general expression for thermal frequency noise as a function of measurement bandwidth and a cantilever microgyroscope oscillation. The frequency modulated detection system offers an alternative to conventional amplitude modulated which allows increased sensitivity through increased cantilever Q and eliminate the trade-off between the gain-bandwidth and dynamic range. By taking advantage of this increased sensitivity, the frequency modulated technique allows the measurement of much weaker angular rate, opening new applications of MEMS gyroscope.

References

[1]. James J. Allen "Micro Electro Mechanical System Design" Taylor & Francis Group, LLC, 2005
[2]. Gyro Technology 1997, Stuttgart, Germany, 16–17 September 1997, paper 3.
[3]. T.B. Gabrielson, Mechanical–thermal noise in micromachined acoustic and vibration sensors, IEEE Transactions on Electron Devices 40 (5) (1993) 903–909.
[4]. H. Sorg (Ed.), Proceedings of Symposium Gyro Technology 1997, Stuttgart, Germany, 16–17 September 1997.
[5]. C V Heer Statistical Mechanics, Kinetic Theory, and Stochastic Proc& e; (Academic, New York, 1972).
[6]. W . P . Robins, Phase Noise in Signal Sources, IEE Telecommunications Series 9, edited by J. E. Flood and C. J. Hughes (Peregrinus, London, 1982).

POLYMER INJECTION MOLDING OF MICRO/NANO STRUCTURED DEVICES FOR DISPOSABLE POINT-OF-CARE DIAGNOSTIC APPLICATIONS

Michael D. Gilchrist[1] & Nan Zhang[2]
1: Mechanical & Materials Engineering, University College Dublin, Belfield, Dublin 4, Ireland
2: Centre of MicroNano Manufacturing Technology (MNMT), Tianjin University, China

Summary Tooling is critical in replicating multi-scale patterns for mass production of polymer microfluidic devices using the microinjection molding process. The present work compares the fabrication of various micro/nano structured tool inserts using stainless steel, nickel and Bulk Metallic Glasses (BMGs). Tool performance is evaluated in terms of surface roughness, hardness and tool life. Compared to stainless steel, nickel and BMGs are capable of integrating length scales from 10^0 to 10^{-8} m and are good candidates to rapidly produce polymer microfluidic chip components in mass manufacturing quantities.

INTRODUCTION

Developments in microsystems technology show there is an increasing requirement to integrate multi-scale functionality on progressively smaller platforms. Typically, microfluidic devices for DNA/protein separation and single DNA molecular manipulation exhibit a series of micro-scale channels with integrated sub-micron and nanometre scale features. Producing such components and systems requires integrating manufacturing processes across the length scales from 10^{-2} to 10^{-7} m. Most of these devices are fabricated using silicon or glass so as to take advantage of well-developed patterning technologies. Developing future applications and markets for microfluidic technologies, such as point-of-care diagnostics, and public health and environmental monitoring, will require large volumes of inexpensive products. This requires using mass production methods. For a variety of reasons, polymers are gradually replacing silicon and glass for the fabrication of microfluidic devices. Injection molding is a most cost-effective method to mass produce polymer micro-components and is increasingly important in manufacturing microsystems. Bulk metallic glasses (BMGs) can be machined or thermoplastically-formed with sub-micron precision while still retaining often-desirable metallic properties such as high compressive strength. These novel materials thus have enormous potential for use as multi-scale tools for high-volume manufacturing of polymeric MEMS and information storage devices.

TOOL MANUFACTURING

Figure 1 compares the simplest manufacturing process chains that we have used [1] to produce mold insert tools from Stavax stainless steel, Nickel and BMG. In die-sinking EDM, the microfluidic pattern was first milled on a graphite/copper electrode; a thermal erosion process then takes place between the tool and workpiece under a controlled electric spark, which has the effect of eroding the workpiece to form a replica of the electrode on a stainless workpiece (Fig. 1(a)). This process offers force free machining independently from the mechanical properties of the processed material and allows batch production of micro dies and molds for injection molding and hot embossing. We have also used two processes to fabricate Ni tool inserts, namely, using a micro milled Al master (Figure 1(b)) or a Si master (not shown) with a wide range of features varying in size from tens to hundreds of microns. Finally, we fabricated a BMG tool from a ternary BMG (composition $Zr_{47}Cu_{45}Al_8$) and used an FEI Quanta 3D FEG Dual Beam FIB to machine sub-micron and nano scale features, as shown in Figure 1(c).

DEMONSTRATOR DEVICE

Based on the separation principle using electrophoresis [2], a demonstration chip was designed, as shown in Figure 15. The mixed sizes of DNA molecules are injected into the top two square chambers (Figure 2). Once the voltage is applied to DNA, the charged DNA molecules move to the other end chamber. The chip contains multi scale features including sub micron pillar arrays. The presentation will describe the manufacturing of this component and will discuss high volume processing issues.

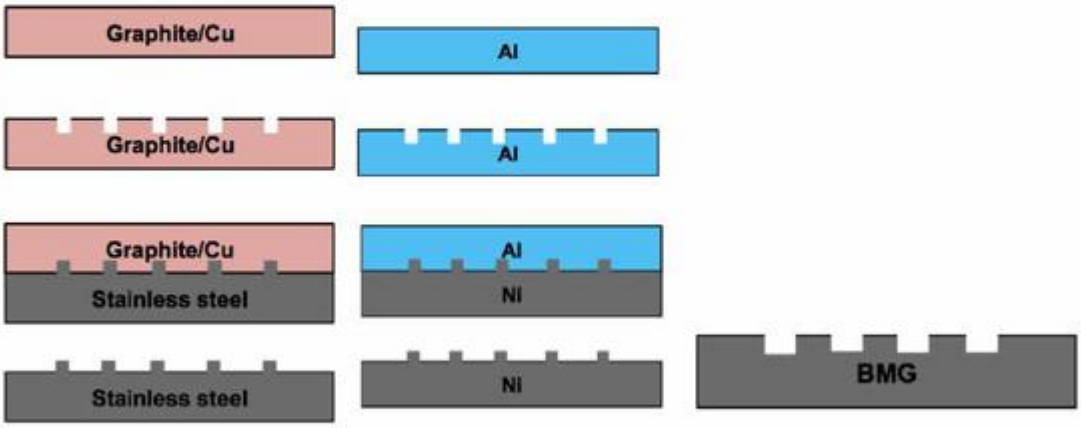

Figure 1. Process chains for manufacturing tool inserts. (a) Micromilling of graphite/copper electrode and die-sinking EDM of stainless steel; (b) machining of an aluminium master with trenches using micromilling and the subsequent creation of a Ni insert tool with inverted trench patterns by electroforming and dissolving of Al; (c) direct Focussed Ion Beam milling on a BMG workpiece.

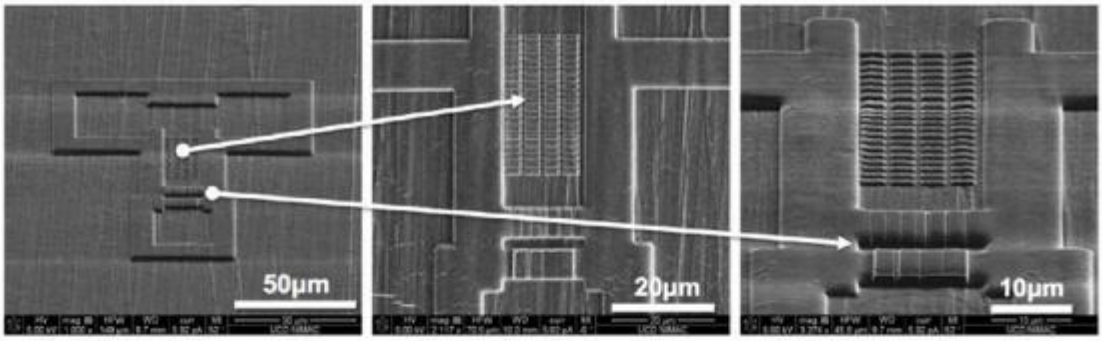

Figure 2. Demonstrator nanofluidic design (polymer component) manufactured in HDPE via injection molding using BMG insert tool.

CONCLUSIONS

A prototype BMG injection molding tool capable of producing centimeter long polymeric components, with sub-micron surface features has been used to manufacture a nanofluidic component. This offers significant potential for commoditizing next generation diagnostic devices.

References

1. Zhang N, Srivastava A, Kirwan B, Byrne R, Fang F, Browne DJ, Gilchrist MD, *J. Micromech. Microengng*. **25** 095005, 2015.
2. Baba M, Sano T, Iguchi N, Iida K, Sakamoto T, Kawaura H, *Appl. Phys. Lett.,* **83** 1468-70, 2003.

EFFECT OF A SPECIAL REINFORCEMENT ON THE NANOCOMPOSITE PROPERTIES

Igor Guz[a)]
Centre for Micro- and Nanomechanics, School of Engineering, University of Aberdeen, Scotland, UK

Summary A multi-component model for predicting the mechanical properties of nanocomposites reinforced with whiskers and nanocomposites reinforced with bristled nanowires is presented. The mathematical formulation of the model is based on using the Muskhelishvili complex potentials for each domain occupied by a separate component. As an example, the effective elastic constants are computed for a generic fibrous composite with three different densities of bristles growing on the core reinforcing fibres.

INTRODUCTION

A new brush-like nano-composition was reported in [1]: the CdTe nanowires coated with SiO_2 nanowires, nearly parallel bristles growing perpendicular to the surface. The structure "CdTe nanowire - SiO_2 nanowires" consists of three components: CdTe wire forms the solid core, which is jointed continuously with coating from SiO_2 nanowires in the form of some solid shell, and then the shell is coated periodically by bristled and smooth zones. Bristled nanowires can be used for the ultimate purpose of fabricating composite materials with improved fibre-matrix adhesion and hence the increased shear strength. In order to study the effective properties of the entire composite and the effect of reinforcement with bristled nanowires on the overall performance of the material, a four-component model is required.

DERIVING THE EXPLICIT EXPRESSIONS FOR EFFECTIVE CONSTANTS

This work follows the general methodology presented in [2-4]. The model assumes that fibres are arranged in the matrix periodically as a quadratic or hexagonal lattice. Then the representative volume element (unit cell) consists of the matrix and a coated fibre, Fig. 1. At that, the coating itself has several sub-components, which is a new feature of the model: the coated fibre consists of three different parts: a solid core, a solid coating (homogeneous shell), and a "bristled coating" (composite shell). The fourth component in the model is the matrix. A segment of the model representing the core fibre with solid coating and bristles attached to the solid coating is shown in Fig. 2. Subsequently, the following notations are used: (1) for the fibre core, (2) for the fibre solid coating, (3) for the fibre bristled coating and (4) for the matrix.

Three out of four components are homogeneous materials, e.g., EPON828 epoxy matrix, SiO_2 solid coating and CdTe solid fibre core, with known properties. However, the bristled coating is itself a composite consisting of, e.g., the EPON828 matrix reinforced by SiO_2 nanowires. The effective properties of this component must be evaluated separately beforehand, for instance, by using the classical Voigt and Reuss bounds [5]. For this purpose, we would need to know the diameter and the length of bristles, and their number per unit surface area of nanowires. Also, in order to use the known formulas of the rule of mixture, we assume here that all the bristles are parallel to each other, i.e. that the properties of the bristled coating (3), Fig. 1, do not change with the radius, since the length of SiO_2 nanowires used for reinforcement is rather small.

The mathematical formulation of the model is based on considering the four simple states of plane elastic equilibrium of the unit cell (a square with the side l_{unit}, Fig. 3) - i.e. longitudinal tension, transverse tension, longitudinal shear and transverse shear - and using the Muskhelishvili complex potentials [6] for each domain occupied by a separate component. The model yields explicit formulas for five effective elastic constants. The possible case of imperfect adhesion between the fibre core and the matrix can be taken into account by considering one of the four components, i.e. the coating layer, with the appropriately reduced properties.

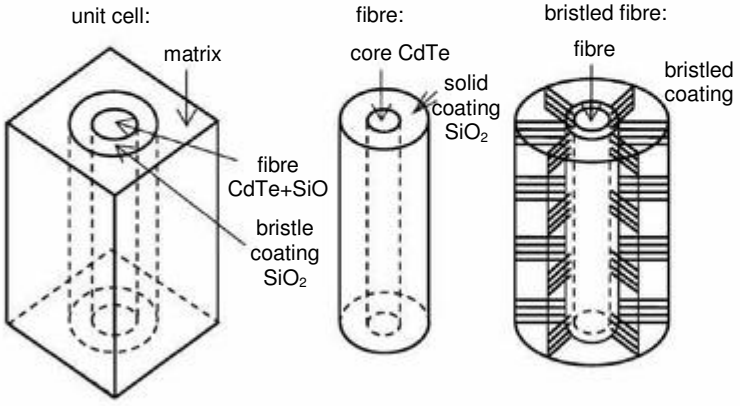

Figure 1.

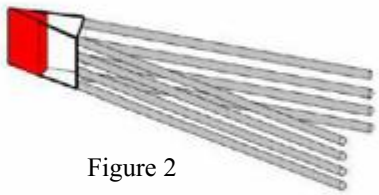

Figure 2

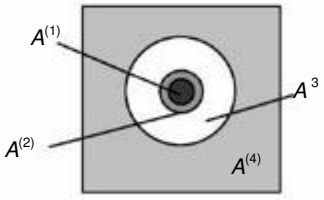

Figure 3.

[a)] Corresponding author. Email: i.guz@abdn.ac.uk.

The cornerstone of the analytical procedure is the representation of the Muskhelishvili potentials by: a harmonic complex function, which is regular in the domain of fibre core (circle $A^{(1)}$ in Fig. 3); a function in the form of Laurent series, which is regular in the domain of fibre solid coating (ring $A^{(2)}$ in Fig. 3); a function in the form of Laurent series, which is regular in the domain of fibre bristle coating (ring $A^{(3)}$ in Fig. 3):

$$\varphi_{(1)}(z)=\sum_{k=0}^{\infty}a_{2k}^{(1)}\frac{z^{2k+1}}{2k+1},\qquad \varphi_{(2)}(z)=\sum_{k=-\infty}^{\infty}a_{2k}^{(2)}z^{2k+1},\qquad \varphi_{(3)}(z)=\sum_{k=-\infty}^{\infty}a_{2k}^{(3)}z^{2k+1},$$

and a doubly-periodic function constructed utilising the Weierstrass functions in the domain of the matrix ($A^{(4)}$ in Fig. 3):

$$\varphi_{(4)}(z)=a_0^{(4)}z-\lambda^2a_2^{(4)}\left(\frac{1}{z}-\sum_{n=1}^{\infty}\alpha_{n,0}\frac{z^{2n+1}}{2n+1}\right)+\sum_{k=}^{\infty}\sum_{n}^{\infty}a_{2k+2}^{(4)}\lambda^{2k+2}\alpha_{n,k}\frac{z^{2n+1}}{2n+1}-\sum_{k=1}^{\infty}\frac{a_{2k+2}^{(4)}\lambda^{2k+2}}{(2k+1)z^{2k+1}},$$

where $\alpha_{n,k}$ are the constants used in the theory of Weierstrass functions; $\lambda = 2r_{(3)}/l_{unit}$; $a_{2k}^{(1)}$, $a_{2k}^{(2)}$, $a_{2k}^{(3)}$, $a_{2k}^{(4)}$ are the yet unknown coefficients in the series; z is a complex co-ordinate in the transverse cross section, and i is imaginary unit. Then the averaged stresses and strains for each of the domains are calculated using the contour integrals [4] and substituted into the three boundary conditions of perfect bonding between the components on the domain interfaces, Fig. 3. This procedure results in the following expression for the effective longitudinal shear modulus of entire four-component composition, G^*:

$$G^*=G_{12}^*=[G_{(4)}c^{(4)}+2c^{(3)}+c^{(4)}G_{(4)}G_{(3)}^{-1}+4c^{(2)}\left(1+G_{(3)}G_{(2)}^{-1}\right)^{-1}+8c^{(1)}\left(1+G_{(3)}G_{(2)}^{-1}\right)^{-1}\left(1+G_{(2)}G_{(1)}^{-1}\right)^{-1}]\left[c^{(4)}+(2-c^{(4)})G_{(4)}G_{(3)}^{-1}\right]^{-1}$$

where $c^{(1)}$, $c^{(2)}$, $c^{(3)}$ and $c^{(4)}$ are the volume fractions of the fibre core, the fibre solid coating, the fibre bristled coating and the matrix, respectively. The above equation yields the well-known formulas for two-component and three-component models [7] as the particular cases, see [3,4]. The latter will follow from the above if the volume fraction of bristled coating $c^{(3)} = 0$ and the shear moduli of bristled, $G_{(3)}$, and solid, $G_{(2)}$, coatings are the same; the former will follow if, additionally, the volume fraction of solid coating $c^{(2)} = 0$ and the shear moduli of solid coating, $G_{(2)}$, and fibre core, $G_{(1)}$, are the same.

Similarly, the explicit expressions for other effective constants for the entire four-component composition are deduced. The developed method can be also extended to the case of multiple fibre coatings, which is useful for studying the mechanical response of other nano-scale structures, e.g., multi-walled nanotubes. In this case we will have a (N+3)-component model for fibre core (1), the fibre solid coating (2) (which is simulated by a thick shell), the matrix (4), and the bristled coating (3) consisting of N thin sub-coatings [4].

RESULTS AND DISCUSSION

To illustrate the proposed method, a generic nanocomposite with three different densities of bristles growing on the core reinforcing fibres was considered. The values of all five effective elastic constants representing the transversely-isotropic material response were computed. The results for composites reinforced by the bristled nanowires show that the properties in longitudinal direction are the most sensitive to the density of bristles. The increase in the number of bristles per unit surface of the fibres gives a very strong rise to the value of Young's modulus. However, the shear modulus, which is the driving parameter for the strength estimation of the entire composite, is less sensitive to this factor [3]. The difference between the values of shear modulus for the considered cases of sparse, medium, and dense density of bristles is less than 3%. In the same time, the presence of bristled fibres itself – either with dense, medium, or sparse density of bristles – gives the significant increase in the shear modulus in composites if compared with the case without bristles. In the considered examples, the increase in the shear modulus from 1.4 times in the case of sparse reinforcement to 2 times in the case of dense reinforcement was achieved (depending on the volume fraction of the matrix) [4]. As a next step, after gathering the necessary experimental data, the effective properties for various practical nanocomposites can be computed using the proposed four-component model.

The suggested approach is the first step towards modelling bristled nanowires and their application. Even a four-component model is an idealisation of the complex internal structure of the considered materials. However, it can provide us with important insight into some basic relationships between the properties of constituents and the overall performance of such materials.

References

[1] Wang Y., Tang Z.Y., Liang X.R., Liz-Marzan L.M., Kotov N.A.: SiO_2-coated CdTe nanowires: Bristled nano centipedes. *Nano Letters*, 4(2):225-231, 2004.

[2] Guz I.A., Rodger A.A., Guz A.N., Rushchitsky J.J.: Predicting the properties of micro and nanocomposites: From the microwhiskers to bristled nano-centipedes. *The Philosophical Transactions of the Royal Society A*, 366(1871):1827–1833, 2008.

[3] Guz I.A., Guz A.N., Rushchitsky J.J.: Modelling properties of micro- and nanocomposites with brush-like reinforcement. *Materialwissenschaft und Werkstofftechnik*, 40(3):154-160, 2009.

[4] Guz I.A., Rushchitsky J.J., Guz A.N.: Effect of a special reinforcement on the elastic properties of micro- and nanocomposites with polymer matrix. *The Aeronautical Journal,* 117(1196):1019-1036, 2013.

[5] Kelly A., Zweben, C. (eds.): Comprehensive Composite Materials, vols. 1-6. Amsterdam, Elsevier Science, 2000.

[6] Muskhelishvili N.I.: Some Basic Problems of the Mathematical Theory of Elasticity. Noordhoff, Leiden, 1953.

[7] Nemat-Nasser S., Hori M.: Micromechanics: Overall Properties of Heterogeneous Materials. Amsterdam: North-Holland, 1999.

STUDY OF THE ELECTROMECHANICAL BEHAVIOR OF METALS USING A MICRODEVICE METHOD

Wonmo Kang[1], Iyoel Beniam[2] & Siddiq M. Qidwai[3a)]
[1]*Materials, Corrosion and Environmental Technologies Division, Leidos Corporation, Arlington, Virginia, USA*
[2]*Materials and Systems Branch, US Naval Research Laboratory, Washington, District of Columbia, USA*
[3]*Multifunctional Materials Branch, US Naval Resear h Laboratory, Washington, District of Columbia, USA*

Summary The passage of low-density electric current (10's-100's of A/mm^2) through metals to improve their formability is becoming an accepted practice in the manufacturing industry. In this study, we seek to determine if, as suggested, the formability is simply due to Joule heating or an entirely new class of deformation mechanism, such as electrically induced plasticity. We have developed a micro-device testing method that allows *in situ* observation of electromechanical behavior in metals in transmission electron microscopes. The advantage of this method is that due to the nanoscale size of the specimen high current densities are achieved without appreciable increase in temperature, which removes the Joule heating aspect. We have used this method to study the *in situ* behavior of single crystal copper (SCC) under nominal strain and current density of up to 5000 A/mm^2. The results show that at least for SCC electric current does not affect dislocation behavior.

INTRODUCTION

In recent years, researchers have shown many interesting and advantageous effects of the concurrent application of low-density electric current (10^1-10^2 A/mm^2) on the formability of metals that can be utilized to markedly improve material processing techniques involving bulk or localized deformations. Complete elimination of springback, reductions in flow stresses of up to one order of magnitude, and enhancements in strains-to-failure by up to eight times have been demonstrated for various pure metals and alloys under uniaxial loading conditions (e.g., [1,2]). Two hypotheses have been proposed for the enhanced behavior: 1) the Joule heating effect, and 2) the electroplasticity effect (e.g., electron interaction with dislocations). Historically, both of these hypotheses originated in response to experiments conducted in the 1970s and 80s, in which high-amperage, short-duration (mostly alternating) current pulses (~10^3-10^8 A/mm^2; <10^{-5} s) were applied to mechanically deforming metals [3]. However, interpretation of material responses observed in those experiments has proven difficult due to the dynamic, transient effects of the coupled thermal, electrical and mechanical fields [4]. It is also suggested here that the overreliance on bulk scale observations to date (e.g., [3,4]) has been a detriment in understanding the nature of the electrically assisted deformation of metals (EADM). To address these limitations in conventional approaches, we have developed a micro-device testing method that utilizes the unique advantages of micro/nanotechnology in *in situ* investigation of coupled material behavior [5]. Using this *in situ* capability, we have directly investigated electron-dislocation interplay in single crystal copper (SCC) with a focus on electroplasticity without the Joule heating effect. In the ensuing text, we describe the micro-device testing method followed by results and discussion, and conclusions.

MICRO-DEVICE TESTING METHOD

The microdevice has three main components: an electrically insulated (SiO_2-coated) Si frame, a dog-bone shaped specimen, and silver wires (Figure 1a). The frame is designed to prevent mechanical loading of the specimen during handling/operations and to fit onto a commercial electromechanical TEM holder. The silver wires are connected on one end to the electrical feedthrough from the TEM holder and on the other to the sample, which itself is attached to the frame with an Ag epoxy. The microdevice is fixed on one end and the other can be pulled in nominal displacement control. This particular device offers multiple advantages: 1) *in situ* electromechanical TEM capability, 2) ability to achieve high (~10^3 A/mm^2) current density owing to the submicron-size specimen cross-section, 3) uniform electrical current and nominal stress, up to the small strain limit, in contrast to traditional TEM specimens, and 4) effective thermal management.

The first feature provides an opportunity to directly observe the movement of dislocations due to electric current, if any. The second allows minimal power and safety management because the input electric current requirement goes down to mA range. The third feature is critical in simplifying the analysis of the operative deformation mechanisms, and the last feature is invaluable because it is obtained through the removal of any significant Joule heating despite the vacuumed environment, which permits independent observation of the electron-dislocation interaction. This is directly the result of the fact that for a given electric current density, the current and power scale by the square and cube of the characteristic length of the specimen. And, since the characteristic length of the specimen is in microns, as will be shown next, the power generated due to Joule heating is negligible. In fact, analytical and numerical simulations show that for a pure copper sample with the gauge length of 10 μm and cross-section of 100 nm X 10 μm, only 5 mA of current produces 5000 A/mm^2 of current density with a corresponding power of 8.33 μW that results in a maximum temperature increase of <1 °C in the sample.

For brevity, details of the fabrication of the Si frame, assembly of the microdevice, and procedure for the *in situ* electromechanical experiments in the FEI Tecnai G2 TEM are withheld here, and instead some information is only given for the intricate sample preparation. Foils of single crystal copper (SCC) of 50 μm are spin-coated with photoresist layers. Then

[a)] Corresponding author. Email: siddiq.qidwai@nrl.navy.mil.

laser patterning is done with a solid-state, frequency tripled $Nd:YVO_4$ pulsed laser (355 nm, 10 W, repetition rate of 50 kHz, and ~90 nsec pulse width) to co-fabricate the specimen frame (5 mm x 1.5 mm) and the dog-bone shaped specimens (20-40 μm in width) from the foil. Liquid ferric chloride etching is subsequently applied to clear the potentially damaged surfaces. The specimen frame with the specimen is then assembled with other components of the micro-device after which the nanoscale gauge section (10 μm length, 100 nm x 10 μm cross-section) is obtained with focused ion beam milling (FEI Nova 600) (Figure 1b-c). Lastly, the specimen frames are cut by either laser or mini-scissors, as seen in Figure 1a.

RESULTS AND DISCUSSION

To experimentally confirm the absence of significant Joule heating the thermal drift of the specimen was quantified first. Matlab-based image correlation algorithms were used to analyze images at different current densities. With a current of 500 A/mm^2 and without current, comparable drifts of 18.45 nm/min and 15.0 nm/min, respectively, were measured. Additionally, no change in the microstructure of the SCC specimen was found. To observe electron-dislocation interaction, the following *in situ* procedure was adopted. First, tensile strain was applied incrementally using the TEM holder to the point that dislocations under observation started mobilizing. One or, if possible, several of such dislocations were held in the field of view at that strain, and a specific electric current density is concurrently allowed to pass through the specimen continuously. In the next step, the electric current is shut off and the smallest incremental strain is applied again. TEM images were taken at every step a minute after the application of mechanical or electrical loading to achieve steady state. This experimental procedure was carried out a few times on two different specimens and showed no effect of electric current on dislocation motion. For example, in one such case, a dislocation loop formed at a given mechanical strain but the application of 500 A/mm^2 current density showed no movement in that dislocation. However, the smallest possible strain increment by the controller applied after that yielded a movement. This behavior was consistent up to 5 kA/mm^2 current density, as shown in Figure 1d-e.

While these results show no electron-dislocation interaction in SCC, they do not disprove its potential existence in other metals, such as titanium [1] and duplex steel alloys, with much larger set of slip systems and diverse dislocation dynamics mechanisms compared to the face-centered cubic system of SCC. A near-term study is planned along these lines in which polycrystalline samples of progressively complex material systems will be investigated.

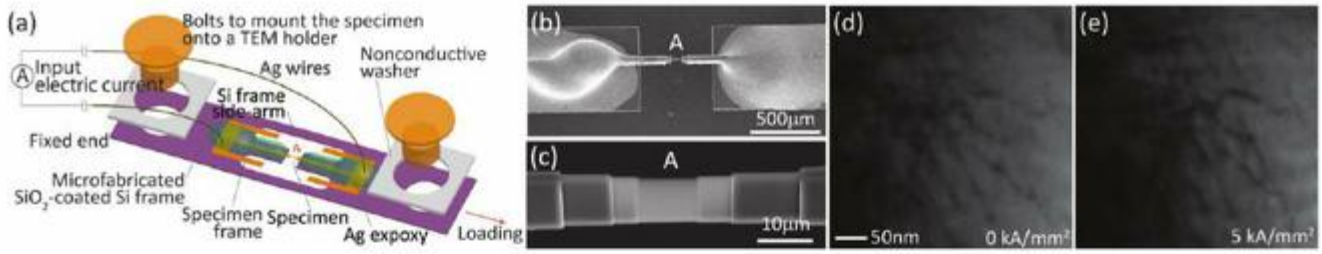

Figure 1: The novel method for *in situ* electromechanical testing of metals: (a) a schematic of the micro-device with major component detailsl; (b)-(c) close-up view of the sample (A) showing the intricate design and size; and (d)-(e) dislocations w/o (d) and w/ (e) application of current in a mechanically strained state without any changes in their location.

CONCLUSIONS

In the course of this study, we have been able to develop a micro-device method for the *in situ* characterization of submicron-micron scale specimens under concurrent electromechanical loading, which has not been done before in attempts to understand EADM. It provides a great opportunity to test the hypothesis of electroplasticity because the observations can be made in the absence of Joule heating at the very scale at which electron-dislocation interactions are expected. Any changes observed from the pure mechanical behavior have to be induced by electric current only. This absence of heating remains effective for very large current densities (at least until 5 kA/mm^2). Additionally, the uniform cross-section of the specimen also ensures that the interpretation of results remains a simpler prospect. The utility of the micro-device method is demonstrated through the investigation of EADM in pure SCC, and while the effect has not been observed the roadmap for further studies on other material systems has been streamlined.

References

[1] Ross C.D., et al.: Effect of DC on the Formability of Ti-6AL-4V. *J Eng Mater Technol* **131(3)**: 0310041-03100411, 2009.

[2] Siopis M.S., Kinsey B.L.: Experimental Investigation of Grain and Specimen Size Effects during Electrical-Assisted Forming. *J Manuf Sci Eng* **132(2)**: 0210041-0210047, 2010.

[3] Okazaki K., Kagawa M, Conrad H.: A Study of the Electroplastic Effect in Metals. *Scr Metall* **12(11)**: 1063-1068, 1978.

[4] Gallo F., et al.: Strain evolution in metal conductors subjected to short-duration current pulses. *IEEE Trans Magn* **43(1)**: 338-342, 2007.

[5] Espinosa H.D., Bernal R.A., Filleter T.: In situ TEM electromechanical testing of nanowires and nanotubes, *Small*, **8(21)**, 3233-3252, 2012.

SIZE-DEPENDENT NONLINEAR BEHAVIOR FOR ELECTROSTATIC ACTUATED NEMS WITH CASIMIR FORCE

Binglei Wang[1a)], Long Zhang[1] & Shenjie Zhou[2]
[1]*School of Civil Engineering, Shandong University, Jinan, China*
[2]*School of Mechanical Engineering, Shandong University, Jinan, China*

Summary A size-dependent model for the electrostatically actuated Nano-Electro-Mechanical Systems (NEMS) is presented with Casimir force. Based on strain gradient elasticity theory and Hamilton principle, the governing equation and boundary conditions are derived. The numerical solution is obtained with help of Generalized differential quadrature method and pesudo-arclength algorithm. The results reveal that the pull-in voltage of system is reduced by Casimir force, So it is important for design to make a study of the effect of Casimir force on NEMS.

1. Introduction

With the development of science and technology, the structure of the micro/nano scale is widely used in physics, chemistry, biology and other fields due to its small volume, low power consumption advantages. However, micro/nano structure different from the traditional mechanical structure. So far, a large number of experimental studies have found that when the characteristic size of structure size is enough small, it's mechanical properties will change, that is size effect phenomena.

A typical electrostatically actuated NEMS includes two parts: a fixed electrode and a conductive deformable electrode (figure 1). An applied voltage between the two electrodes. When the voltage increases beyond a critical value, the movable electrode becomes unstable and collapses onto the fixed electrode, which is called the pull-in instability phenomenon.

The strain gradient elasticity theory[1] is proposed to predict the size-dependent phenomena. has been applied to study the linear and nonlinear Euler beam, linear and nonlinear Timoshenko beam and Reddy-Levinson beam, and is also employed to investigate the size-dependent pull-in phenomena in MEMS[2].

In quantum field theory, the Casimir effect is physical forces arising from a quantized field. So the Casimir force should be considered with the decrease in device dimensions from the micro to nanoscale[3,4]. For nanoscale structures in NEMS which will be studied in the present paper, the nonlinearities and Casimir force together with strain gradient terms are considered simultaneously here.

2. Theoretical formulations

Consider a straight beam subjected to voltage V between the two electrode plates, as shown in Fig. 1.

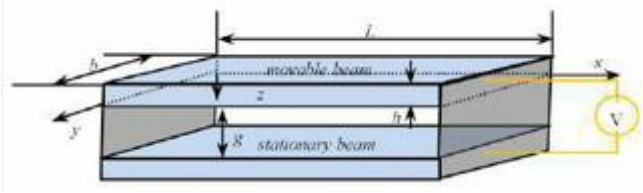

Figure 1 Schematic of a fixed-fixed NEMS

The Casimir effect energy between the two electrodes is

$$F_c = \frac{\hbar c \pi^2 b}{240(\mathrm{g}-w)^4} \tag{1}$$

where Planck's constant $\hbar$ =1.055×10-34 $J \cdot S$.

$$F_e = \frac{\bar{\varepsilon} b V^2}{2(\mathrm{g}-w)^2}\left(1+\frac{2}{\pi}\frac{g-w}{b}\right) \tag{2}$$

in which, $\bar{\varepsilon} = 8.854\times10^{-12} C^2 N^{-1} m^{-2}$ is the dielectric constant of the gap medium.

Based on the Bernoulli-Euler beam assumption, the governing equation, with strain gradient incorporated, is expressed by [2]

$$\begin{aligned} &-D_2\frac{\partial^6 w}{\partial x^6}+D_1\frac{\partial^4 w}{\partial x^4}+\rho bh\frac{\partial^2 w}{\partial t^2}-\left[\frac{EA}{2l}\int_0^l\left(\frac{\partial w}{\partial x}\right)^2 dx+N_0\right]\frac{\partial^2 w}{\partial x^2}=F_e+F_c \\ &D_1 = EI+2\mu Al_0^2+\frac{8}{15}\mu Al_1^2+\mu Al_2^2 \\ &D_2 = 2\mu Il_0^2+\frac{4}{5}\mu Il_1^2 \end{aligned} \tag{3}$$

in which, x is the position along the beam length, w is bending displacement. *A* and *I* are the area and moment of inertia of the cross section. N_0 is is positive or negative depending on either a tensile or compressive axial applied load or residual force. *E* is

a)Corresponding author. Email:bwang@sdu.edu.cn

Young's modulus. μ is shear modulus, l_0, l_1 and l_2 are the independent material length scale parameters (MLSPs) associated with the dilatation gradients, deviatoric stretch gradients, and symmetric rotation gradients, respectively.

The both ends clamped boundary conditions are as follows,

$$w = 0, \quad \frac{\partial w}{\partial x} = 0, \quad \frac{\partial^3 w}{\partial x^3} = 0 \qquad for \ x = 0, L \tag{4}$$

in which, the first and second equstions are the classical boundary conditions and the last is the non-classical boundary conditions.

The static problem of a electrostatically actuated micro beam can be solved numerically with help of Generalized differential quadrature method[5] and pesudo-arclength algorithm.

3. Numerical Results and Discussion

Studying the Casimir force effect on micro-electromechanical system for clamped-clamped beam. The geometrical and material properties of the system are L=400μm, b=100μm, h=1μm, d=0.2μm, E=151Gpa and Poisson's ratio v=0.3. We assume that all material length scale parameters are the same, i.e. l_0=l_1=l_2=l. Here l=0.1μm, residual stress is zero. The numerical results is shown in figure 2, where red line represents the result without considering Casimir force effect, and purple line represents the result considering Casimir force effect. The figure shows that Casimir force not only reduces pull-in voltage V_{pl}, but also reduces pull-in displacement w_{pl} significantly from p1 to p_2. To study the size effect induced by strain gradient, the beam with parameters L/k=2000nm, b/k=500nm, h/k=15nm, d/k=$10nm$, E=151Gpa, v=0.3 are studied, where k is size scale as defined above. The MLSP is taken to be Cl=0.1μm. The results predicted by the present model are also compared with classical model as shown in figure 3. the pull-in voltage increases firstly and then decreases sharply to zero with size scale k decreasing when Casimir force is considered.

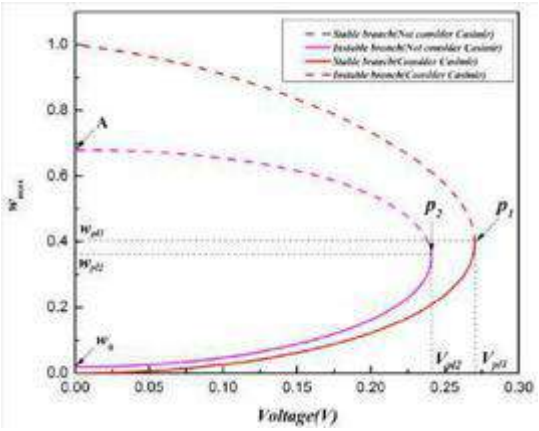

Figure 2 Effect of Casimir force on the pull-in voltage

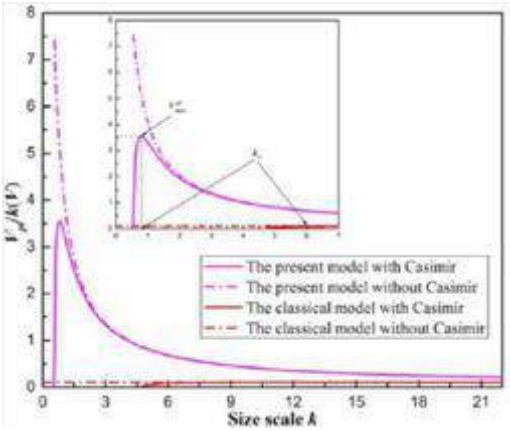

Figure 3 The effect of size scale (k) on the normalized pull-in voltage (V_p/k)

4. Conclusions

By considering Casimir force, a size-dependent model for electrostatically actuated nanobeam device is established based on the strain gradient elasticity theory and Hamilton principle. The governing equation together with boundary conditions is solved numerically with GDQ method. The results show that Casimir force can reduce the external applied voltage.

References

[1] Lam D. C. C., Yang F., Chong A. C. M.: Experiments and theory in strain gradient elasticity, *J, Journal of the Mechanics and Physics of Solids*, 51(8): 1477-1508, 2003.

[2] Wang B.L., Zhou S.J., Zhao J.F.: Size-dependent pull-in instability of electrostatically actuated microbeam-based MEMS, *J, Journal of Micromechanics and Microengineering* 21, 2011.

[3] Liang B., Zhang L., Wang B.: A variational size-dependent model for electrostatically actuated NEMS incorporating nonlinearities and Casimir force, *J, Physica E: Low-dimensional Systems and Nanostructures*, 71, 21-30, 2015.

[4] Lin W. H., Zhao Y. P.: Nonlinear behavior for nanoscale electrostatic actuators with Casimir force. *J. Chaos Solitons & Fractals* 23(5): 1777-1785, 2005.

[5] Shu C., Richards B. E.: Parallel simulation of incompressible viscous flows by generalized differential quadrature, *J, Computing Systems in Engineering*, 3(1-4): 271-281, 1992.

EFFECTS OF DISLOCATION ON THE PERFORMANCE OF SI ANODE IN NA AND MG-ION BATTERIES

Chaoying Wang[1a)] , Hecheng Li[1], Chenliang Li[1], Guoxun Wu[1] & Lijun Yang[2]
[1] *College of Aerospace and Civil Engineering, Harbin Engineering University, Harbin 150001, P. R. China*
[2] *Key Laboratory of Mesoscopic Chemistry of MOE, School of Chemistry and Chemical Engineering, Nanjing University, Nanjing 210093, P. R. China*

Summary While the perfect Si can't be used to store Na and Mg interstitials in Na-ion batteries (NIBs) and Mg-ion batteries (MIBs), the defects of 30° partial dislocation caused by the mismatch strain may improve the performance of Si anode according to the multi-scale simulation results. It is found that deformation can provide more stable sites to accommodate impurities and enhance the binding strengths. Moreover, it is thermodynamically and kinetically favorable for Na and Mg concentrating in the defect areas. On the other side, those defects may restrict the diffusion of interstitials and turn into limiting factors of charge/discharge rate of NIBs and MIBs.

INTRODUCTION

In recent years, rechargeable metal-ion batteries are receiving greater interest since their convenience and wide application [1]. Batteries based on Na and Mg ions are currently attracting increasing attention as alternatives to LIBs [1]. Using conversion chemistry to form alloys is the general method to store a large number of ions. One of the representative examples is Si, which has high theoretical Mg (Mg_2Si) and Na (NaSi) capacity [2]. To promote the application of Si anode, many works have been presented about the interaction of Na [3] and Mg [4] with perfect Si crystal. Unfortunately, recent investigations indicate that Si anode is unsuitable for the storage of Na and Mg ions [5] since the binding strength is not sufficient [3,4]. However, all the previous literatures do not consider defects, such as dislocations, which may potentially change distribution and diffusion of dopants [6-9]. With the insertion of Li, Na and Mg interstitials, Si anode experiences a large volume expansion [4]. If the corresponding stress exceeds the yield value, Si anode will undergo plastic deformation companied by the nucleation and motion of dislocations [10]. Those dislocations have the records of trapping impurities (As, Al, P and Li) in their cores [6-9]. The 30° partial are chosen in this work to comprehensively investigate the effects of defects on the performance of Si anode.

COMPUTIONAL METHODS AND MODELS

We use the multi-scale simulation method for coupling quantum mechanical (QM) and molecular mechanical (MM) methods in the investigations. As shown in Fig. 1a, the DFT method is used to accurately study the interaction of inserted dopants with QM region. The force field method is used to deal with the rest areas (MM region). More details of the multi-scale simulation method can be found in Ref. 11. An infinite system with 30° partial dislocation dipoles is calculated by the application of periodic boundary conditions (PBCs). The whole model is oriented along the [111], [11-2] and [1-10] directions with the size of 9.51, 16.14 and 2.33 nm, respectively. All the Si atoms in the MM region are calculated by the Stillinger-Weber (SW) potential [12]. The calculations of QM region are performed by using the program package of SIESTA [13]. More details of the parameters and validity tests can be found in our previous literature [6].

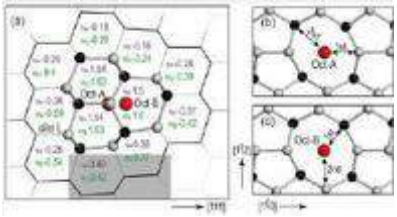

Fig. 1. (a) The binding energy differences (eV) with respect to tetrahedral (T_d) site in the 30° partial dislocation core and surrounding areas. The microstructures and nearest neighbors of (b) Oct-A and (c) Oct-B.

RESULTS AND DISCUSSION

The stable positions, binding energies and migration barriers of Na and Mg in perfect Si are calculated by using the SW potential. It is found that Na and Mg prefer to stay at the tetrahedral (T_d) site with the binding energies of -0.82 eV and -1.01 eV, respectively. The negative signs indicate that the binding of Na and Mg with Si are insufficient. From the T_d site, Na and Mg periodically move along the route of T_d-Hex-T_d. The migration barrier of Na is 1.04 eV and Mg is 1.02 eV.

As shown in Fig. 1, the calculated stable positions in the dislocation core are denoted Oct-A and Oct-B, respectively. The binding energy of Na (Mg) at Oct-A is 0.72 (0.622) eV, which is 1.54 (1.63) eV larger than the T_d site. At Oct-B site,

[a)] Corresponding author. Email: chaoyingwang.hit@163.com.

the binding energy of Na (Mg) is 0.684 (0.6) eV, which is 1.5 (1.6) eV larger than the T_d site. Those energy differences may be caused by the fact that the deformation of dislocation may provides more space than perfect Si to accommodate the compressed interstitials. More important, 30° partial dislocation can change the negative binding energy to positive. As a result, Si anode is suitable for the storage of Na and Mg impurities. This may shed light on the design and application of Si anode in NIBs and MIBs.

The binding energy differences of Na and Mg with respect to T_d site are shown in Fig. 1a. Those differences present how strong the outside regions of dislocation enhance (positive) or weaken (negative) the binding of Na and Mg with host Si atoms. Because the energy differences of Oct-A and site L are almost the biggest, we studied the diffusion properties of Na and Mg among those two sites, which are shown in Fig. 2. It can be seen that it is thermodynamically favorable for them to diffuse into the 30° partial dislocation core but not to diffuse out. Since the barriers of Na and Mg diffusion into the dislocation core (site L→Oct-A) are 0.18 eV and 0.17 eV less than the results of perfect Si crystal, it is kinetically favorable for them to diffuse into the dislocation core. Finally, Na and Mg interstitials may concentrate in the dislocation core.

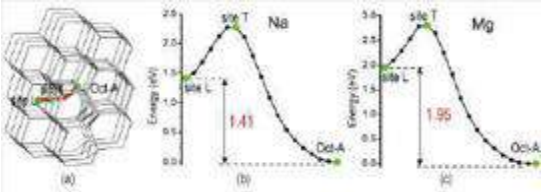

Fig. 2. (a) The schematic view of Na and Mg diffusion among 30° partial dislocation core (Oct-A) and surrounding area (site L). (b) and (c) are the corresponding lowest energy path of Na and Mg, respectively.

The diffusions of Na and Mg in 30° partial dislocation core are mainly dominated by the motion among Oct-B sites with barriers of 2.73 eV and 2.81 eV, respectively. The corresponding schematic trajectories and lowest energy curves in one period are presented in Fig. 3. Those energies are 1.69 eV and 1.79 eV larger than the defect-free Si. In other words, the presence of the 30° partial may retard the motion of dopants and become a limiting factor of charge/discharge rate of NIBs and MIBs.

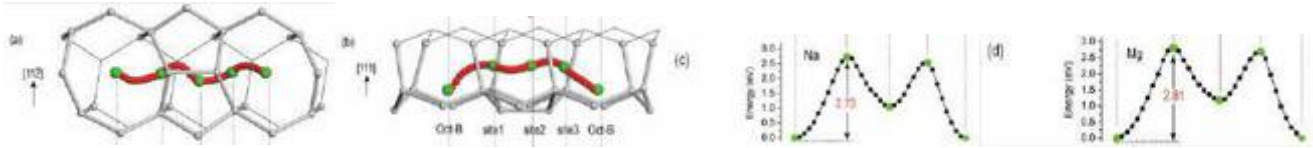

Fig. 3. (a)-(b) The schematic view of interstitials diffusion along the 30° partial dislocation core from Oct-B, and the corresponding lowest energy pathway of (c) Na and (d) Mg in one period.

CONCLUSIONS

The multi-scale simulation method is used to study the effects of 30° partial dislocation on the performance of Si anode in NIBs and MIBs. Because of the deformation of 30° partial dislocation, Si anode is suitable for the storage of Na and Mg impurities. In addition, Na and Mg interstitials may tend to concentrate in these defects areas. However, the presence of 30° partial dislocation may lead to low rate capability of NIBs and MIBs.

References

[1] Ellis B.L., *et al*.: A multifunctional 3.5 V iron-based phosphate cathode for rechargeable batteries. *Nat*. *Mater* **6**:749-753, 2007.

[2] Tran T.T., Obrovac M.N.: Alloy Negative Electrodes for High Energy Density Metal-Ion Cells. *J*. *Electrochem*. *Soc* **158**:A1411-A1416, 2011.

[3] Malyi O.I., Tan T.L., Manzhos S.: A comparative computational study of structures, diffusion, and dopant interactions between Li and Na insertion into Si. *Appl*. *Phys*. *Express* **6**:027301, 2013.

[4] Malyi O.I., Tan T.L., Manzhos S.: In search of high performance anode materials for Mg batteries: computational studies of Mg in Ge, Si, and Sn, *J*. *Power Sources* **233**: 341-345, 2013.

[5] Kim Y., *et al*.: An amorphous red phosphorus/carbon composite as a promising anode material for sodium ion batteries. *Adv*. *Mater* **25**: 3045-3049, 2013.

[6] Wang C.Y., *et al*.: Multi-scale simulation of lithium diffusion in the presence of a 30° partial dislocation and stacking fault in Si. *J*. *Appl*. *Phys* **115**: 043532, 2014.

[7] Wang C.Y., *et al*.: Atomic simulation of the dynamic properties for a double period structure with 90° partial dislocation in Si. *J*. *Appl*. *Phys* **116**: 213504, 2014.

[8] Antonelli A., et al.: Interaction of As impurities with 30° partial dislocations in Si: An ab initio investigation. *J*. *Appl*. *Phys* **91**:5892-5895, 2002.

[9] Legros M., Dehm G., Arzt E., Balk T.J.: Observation of giant diffusivity along dislocation cores. *Science* **319**:1646-1649, 2008.

[10] Liu Q.F., Shen S.P.: On the large-strain plasticity of silicon nanowires: Effects of axial orientation and surface. *Int*. *J*. *Plast*. **38**:146-158, 2012.

[11] Choly N., *et al*.: Multiscale simulations in simple metals: A density-functional-based methodology. *Phys*. *Rev*. *B* **71**:094101, 2005.

[12] Stillinger F.H., Weber T.A.: Computer simulation of local order in condensed phases of silicon. *Phys*. *Rev*. *B* **31**: 5262-5271, 1985.

[13] Soler J.M., *et al*.: The SIESTA method for ab initio order–N materials simulation. *J*. *Phys*.*: Condens*. *Matter* **14**: 2745-2779, 2002.

EFFECT OF AN APPLIED FORCE ON RIPPLE FORMATION OF FREE GRAPHENE RIBBONS

Bingjie Wu[1a)], C Q Ru[1]
[1]*Department of Mechanical Engineering, University of Alberta, Edmonton, Alberta T6G 2G8, Canada*

Abstract One phenomenological expression for self-rippling energy is used to study the effect of an applied force on ripple formation of otherwise free-standing graphene ribbons. The two coefficients of the used expression depend on specific mechanism of self-rippling and can be determined based on observed wavelength and amplitude of ripple mode. Thus the obtained model is challenged by detailed comparison of its predictions with some known data available in literature. The present model predicts that the rippling can be controlled or even suppressed with an applied tensile force, or collapsed into narrow wrinkles (of deformed wavelengths down to around 2 nm) under an applied compressive force. In particular, the estimated minimum tensile strain to eliminate rippling is about 0.06-0.26%, in remarkable agreement with known data (0.25%-0.4%).

INTRODUCTION

Intrinsic rippling has been observed in free-standing single-layer graphene sheets [1] and has aroused researchers' enormous interest. Such self-rippling is characterized by out-of-plane deflection which causes stable periodic ripple mode. Since rippling have a profound impact on electronic, chemical and mechanic properties of graphene sheets, it is of great interest to understand the intrinsic driving force for self-rippling and to develop simple theoretical models for rippling-related mechanical phenomena. Motivated by the role of van der Waals attractive force in rippling-related phenomena [2], an approximate model was proposed in a previous work [3] for the rippling energy of free graphene ribbons. However, a technical difficulty associated with the simplified rippling energy expression derived in [3] is that the derived expression cannot be written as a desired smooth integral form of the deflection and its derivatives, which limits its applicability to other rippling-related mechanical phenomena. Here, instead, a phenomenological integral expression proposed in [3] is employed to study the effect of an applied force on ripple formation of free graphene ribbons, whose two undetermined coefficients can be estimated by the observed wavelength and amplitude of associated ripple mode.

THE PROPOSED MODEL AND DETERMINATION OF ITS TWO COEFFICIENTS

For a free-standing graphene ribbon treated as an elastic beam, with the proposed expression of rippling energy, the total potential energy can be written into a desired elegant integral form as

$$U_L(A,m)=\frac{EI}{2}\int_0^L (w_{xx})^2[1+(w_x)^2]dx-\mu\int_0^L (w_x)^2(1-4\gamma w^2)dx, \tag{1}$$

where L is the length of the graphene ribbons, EI is the bending rigidity of the ribbon, μ and γ are two undetermined positive parameters, w is the deflection of graphene ribbon. For a periodic ripple mode $w(x)=A\sin(mx)$, where A is the amplitude and m is the wavenumber, the total potential energy (per unit length) of the graphene ribbon is

$$U(A,m)=\frac{EI}{2}A^2m^4(1+\frac{1}{4}A^2m^2)-\mu A^2m^2(1-\gamma A^2). \tag{2}$$

the minimization conditions of (2) give

$$\begin{cases}\mu=\dfrac{EI}{2}(3+A^2m^2)m^2,\\ \gamma=\dfrac{1}{A^2}\dfrac{1+\frac{1}{4}A^2m^2}{3+A^2m^2},\end{cases} \tag{3}$$

where $EI=b\times 1$ eV is the bending rigidity of graphene ribbon of width *b*. Thus, the parameter pair μ,γ for a graphene ribbon of width b can be determined based on known experimental data of the wavelength and amplitude of observed ripple mode from (3). Using the known experimental data [1, 4-6] on wavelength (5-10 nm) and amplitude (0.5-1 nm) of ripple modes of free-standing monolayer graphene at room temperature, the estimated ranges of the two coefficients γ and μ by (3) are

[a)] Contact person. Email: bingjie3@ualberta.ca

$$\begin{cases} \dfrac{\mu}{b} \approx 0.107 \sim 0.427 (Jm^{-2}), \\ \gamma \approx 3.3\times10^{17} \sim 1.3\times10^{18} (m^{-2}), \end{cases} \tag{4}$$

THE EFFECT OF AN APPLIED FORCE ON RIPPLE FORMATION

With the model with the above-listed two determined coefficients, it is of great interest to challenge the model by detailed comparison of its predictions to some known data. For this purpose, let us study the effect of an applied force on ripple formation. For a periodic rippling mode $w(x) = A\sin(mx)$ and with the rippling energy, the total potential energy (per unit length) of a single-layer graphene ribbon subjected to a constant axial force T is

$$U_{total}(A,m) = \frac{EI}{2} A^2 m^4 (1 + \frac{1}{4} A^2 m^2) + \frac{T}{2} A^2 m^2 \times (1 + \frac{3}{16} A^2 m^2) - \mu A^2 m^2 (1 - \gamma A^2). \tag{5}$$

Using the minimization condition of (5) with respect to both A^2 and m^2, the effect of an applied force (Tb/μ) on the deformed wavelength (which is the wavelength observed in experiments) given by $\lambda' = (1+\varepsilon)\lambda$, where λ is the wavelength in the undeformed configuration and ε is the effective contraction of graphene ribbon) and the associated amplitude-wavelength ratio of the ripple mode is shown in Fig.1 for a graphene nanoribbon of width b with a chosen typical parameter pair $\mu/b = 0.427(Jm^{-1}), \gamma = 1.3\times10^{18}(m^{-2})$.

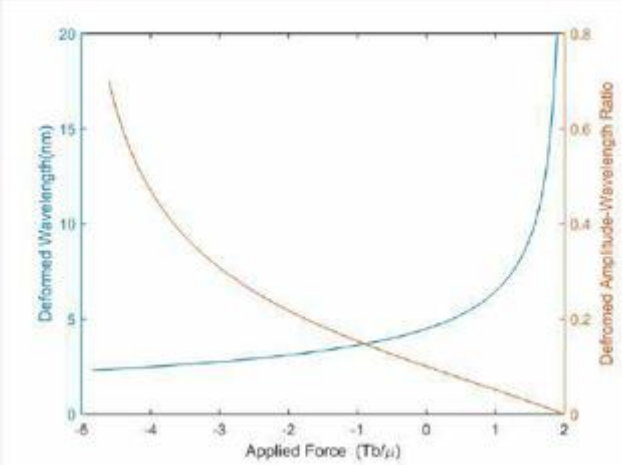

Fig.1 The effect of an applied force (Tb/μ) on "deformed wavelength" and "deformed amplitude-wavelength ratio"

It is concluded from Fig.1 that

1. With an applied tensile force, ripples can be controlled or even fully suppressed. This conclusion is consistent with relative references, such as [7].
2. The minimum tensile strain to eliminate rippling is about 0.06-0.26%, in remarkable agreement with known data (0.25%-0.4%) [8].
3. Under sufficient compressive stress, ripples would be collapsed into narrow standing wrinkles (of minimum wavelengths around 2 nm) with relatively large amplitude-to-wavelength ratio. This is consistent with known references, such as [2, 9].

References

[1] J. C. Meyer, A. K. Geim, M. I. Katsnelson, K. S. Novoselov, T. J. Booth, and S. Roth, "The structure of suspended graphene sheets," Nature 446, 60 (2007).

[2] W. Zhu, T. Low, V. Perebeinos, A. A. Bol, Y. Zhu, H. Yan, J. Tersoff, and P. Avouris, "Structure and electronic transport in graphene wrinkles," Nano Lett. 12, 3431 (2012).

[3] C.Q. Ru, "Ripple formation of free graphene ribbons driven by self-attractive forces," Appl Phys Lett, 103, 043104(2013).

[4] U. Bangert, M. H. Gass, A. L. Bleloch, R. R. Nair, and A. K. Geim, "Manifestation of ripples in free-standing graphene in lattice images obtained in an aberration-corrected scanning transmission electron microscope," Phys. Status Solidi A 206, 1117 (2009)

[5] R. Zan, C. Muryn, U. Bangert, P. Mattocks, P. Wincott, D. Vaughan, X. Li, L. Colombo, R. S. Ruoff, B. Hamilton, and K.S. Novoselov, "Scanning tunnelling microscopy of suspended graphene," Nanoscale 4, 3065 (2012).

[6] R. Breitwieser, Y. C. Hu, Y. C. Chao, R. J. Li, Y. R. Tzeng, L. J. Li, S. C. Liou, K. C. Lin, C. W. Chen, W. W. Pai, "Flipping nanoscale ripples of free-standing graphene using a scanning tunneling microscope tip," Carbon, 77 ,236(2014).

[7] C. H. Lui, L. Liu, K. F. Mak, G. W. Flynn, and T. F. Heinz, "Ultraflat graphene,"Nature. 462, 339 (2009).

[8] R. Roldán, A. Fasolino, K. V. Zakharchenko, and M. I. Katsnelson, "Suppression of anharmonicities in crystalline membranes by external strain," Phys. Rev. B 83, 17 (2011)

[9] K. K. Bai, Y. Zhou, H. Zheng, L. Meng, H. Peng, Z. Liu, J.-C. Nie, and L. He, Creating one-dimensional nanoscale periodic ripples in a continuous mosaic graphene monolayer, Phys. Rev. Lett. 113, 086102 (2014).

SM13 - Plasticity, Viscoplasticity and Creep

TS.SM13-1.01	Danas, Kostas - An analytical model for porous single crystals with ellipsoidal voids (INVITED)	2678
TS.SM13-1.02	Ahmed, Benallal - An extension of the gurson model involving lode angle	2680
TS.SM13-1.03	Balint, Daniel - Rate sensitivity in discrete dislocation plasticity	2682
TS.SM13-1.04	Bassani, John - Continuum model and simulations for microstructural evolution in deformation processes	2684
TS.SM13-1.05	Bedzra, Rex - Modelling fiber reinforced composites exhibiting elastoplastic deformation	2686
TS.SM13-1.06	Brach, Stella - Strength properties of nanoporous materials: A molecular dynamics approach	2688
TS.SM13-2.01	Dolzmann, Georg - Analytical and numerical tools for relaxation in crystal plasticity (INVITED)	2690
TS.SM13-2.02	Cazacu, Oana - Role of the matrix plastic flow on the mechanical response of porous solids	2692
TS.SM13-2.03	Corona, Edmundo - Ductile Failure of Shear-Dominated "Hat" Specimens	2694
TS.SM13-2.04	Hoc, Thierry - Fem crystal plasticity law based on dislocation dynamics ultrasonic shot peening	2696
TS.SM13-2.05	Joshi, Shailendra - Unraveling texture, triaxiality and anisotropy effects in hcp polycrystals	2698
TS.SM13-2.06	Kondo, Djimedo - Ductile porous materials with a Mohr-Coulomb matrix: Theory and numerical bounds	2700
TS.SM13-3.01	Hütter, Markus - Stress-Tensor Expression in Two-Temperature Models for the Aging and Yielding of Glasses (INVITED)	2702
TS.SM13-3.02	Le Graverend, Jean-Briac - 3D directional coarsening in single crystal superalloys for multiaxial applications	2704
TS.SM13-3.03	Li, Jianjun - A theoretical model revealing strong strain hardening in gradient nano-grained materials	2706
TS.SM13-3.04	Sauzay, Maxime - Internal stresses in deformation-induced microstructures	2708
TS.SM13-3.05	Scales, Martin - Ductile Failure of an Aluminum Alloy Under Moderate to Low Triaxialities	2710
TS.SM13-4.01	Leblond, Jean-Baptiste - Toward a general description of transformation plasticity in metals and alloys (INVITED)	2712
TS.SM13-4.02	Skoczeń, Błażej - Constitutive model of serrated yielding at extremely low temperatures including radiation damage	2714
TS.SM13-4.03	Tabin, Jakub - Strain localization during discontinuous plastic flow at extremely low temperatures	2716
TS.SM13-4.04	Tang, Xiaozhi - Thermally Activated Mechanisms in the Dislocation Plasticity at Variant Strain Rates	2718
TS.SM13-4.05	Idiart, Martin - Bounds for the plastic strength of polycrystalline voided solids	2720
TS.SM13-5.01	Tzavaras, Athanasios - Localization emerging from competition of rate dependence and Hadamard instability	2722
TS.SM13-5.02	Yu, Long - A Self-consistent Model for Nano-metallic-multilayers with He Bubbles	2724
TS.SM13-5.03	Xiao, Xiazi - Prediction of mechanical behaviors of radiated Fe-Cr alloys by plasticity theory	2726

TS.SM13-5.04	Mak, Eleanor - Inertial Effects on a Thermomechanical Dislocation Dynamics Model for Plastic Deformation	2728
TS.SM13-5.05	Madi, Yazid - Modeling the 3D plastic anisotropy of magnesium AZ31B alloy	2730
PO.SM13-1.01.176	Abedini, Armin - Constitutive response of a rare-earth magnesium alloy sheet in monotonic and cyclic loadings	2732
PO.SM13-1.02.177	Borokinni, Adebowale - A theory of strain gradient-divergence plasticity	2734
PO.SM13-1.04.179	Burns, Timothy - Estimation of shear stress in machining using the temperature distribution on the tool face	2736
PO.SM13-1.05.180	Faucheux, Pierre - Modeling of shot peen-forming operations using eigenstrains	2738
PO.SM13-1.06.181	Guo, Xiang - Dependence of strength and ductility of coarse-grained metals on the nanotwin volume fraction	2740
PO.SM13-1.07.182	Hanoglu, Umut - Simulation of hot shape rolling by using plastic material response	2742
PO.SM13-1.08.183	Li, Zhen - A Novel Material Model for the Large-Scale Simulation of Temperature Dependent Inelasticity	2744
PO.SM13-1.09.184	Lomakin, Evgeny - Plastic deformation of materials with stress state dependent properties	2746
PO.SM13-1.10.185	Minton, Jeremy - A slab model for ring rolling	2748
PO.SM13-1.11.186	Nakatani, Akihiro - Analysis of criterion for kink banding in layered solids	2750
PO.SM13-1.12.187	Petersmann, Manuel - A mean-field model for trip - algorithms and parameter identification	2752
PO.SM13-1.13.188	Scherzinger, William - Yield surface effects on stability and failure	2754
PO.SM13-1.14.189	Soare, Monica - Microstructural effects in nickel-based alloys damage during plastic loading	2756
PO.SM13-1.15.190	Song, Weidong - A crystal plasticity modeling for plane strain deformation of pure magnesium	2758
PO.SM13-1.16.191	Szymczak, Tadeusz - An Influence of Cyclic Loading on Stress Component Reduction in the Transversal Direction	2760
PO.SM13-1.17.192	Teltayev, Bagdat - Experimental research of creep, recovery and fracture processes of asphalt concrete under tension	2762

AN ANALYTICAL MODEL FOR POROUS SINGLE CRYSTALS WITH ELLIPSOIDAL VOIDS

Armel Mbiakop[1], Andrei Constantinescu[1], and Kostas Danas*[1]
[1]*LMS, CNRS, Ecole Polytechnique, University of Paris-Saclay, Palaiseau, France*

Summary A rate-(in)dependent constitutive model for porous single crystals with arbitrary crystal anisotropy (e.g., FCC, BCC, HCP etc) containing general ellipsoidal voids is developed. The proposed model, denoted as modified variational model (MVAR), is based on the nonlinear variational homogenization method. Periodic multi-void finite element simulations are used in order to validate the MVAR for a large number of parameters including cubic (FCC, BCC) and hexagonal (HCP) crystal anisotropy, various creep exponents, several stress triaxialities, various void shapes and orientations and porosities. The MVAR model is in good agreement with the FE results for all cases considered in the rate-dependent context. A simple way of calibrating the MVAR is also depicted in the rate-independent context so that an excellent agreement with the FE simulation results is obtained. In this last case, this proposed model can be thought as a generalization of the Gurson model in porous single crystals.

INTRODUCTION

The constitutive response of metallic alloys is strongly affected by voids originating in the manufacturing process, that have an important effect on the lifetime as well as deformability of materials. Indeed, the growth of initially present processing induced voids in a nickel based single crystal superalloy as well as in standard polycrystals played a significant role in limiting creep life, as recently shown by experimental observations [1] at high enough temperatures on tensile specimens.

Even so, there have been only a handful of models for porous single crystals which deal with special void geometries, loading conditions and slip system orientations. Such studies involve the study of cylindrical voids with circular cross-section in a rigid-ideally plastic face-centered cubic (FCC) single crystals or that of spherical voids and general loading conditions [2, 3]. While each one of these studies has its own significant contribution to the understanding of the effective response of porous single crystals none of them is general enough in the sense of arbitrary void shapes and orientations and general loading conditions.

In this regard, in the present study we develop a three-dimensional model that is able to deal with arbitrary crystal anisotropy, arbitrary ellipsoidal void shapes at any given orientation and general loading conditions [5]. The proposed model is based on appropriate extension of a former work of the authors [4] in two-dimensional porous single crystals.

THEORY

In this section, we define first the constitutive response of the matrix phase which follows a classical crystal viscoplastic law and then we summarize the homogenized model for the porous single crystal.

Constitutive response of the matrix

Let us consider now a reference single crystal which undergoes viscoplastic deformation on a set of K preferred crystallographic slip systems. At this stage, for simplicity in the homogenization procedure elasticity effects are neglected. These systems are characterized by the second-order Schmid tensors $\boldsymbol{\mu}^{(s)}$ $(\forall s = 1, ..., K)$ and the the Schmid law given by

$$\boldsymbol{\mu}^{(s)} = \frac{1}{2}\left(\mathbf{m}^{(s)} \otimes \mathbf{s}^{(s)} + \mathbf{s}^{(s)} \otimes \mathbf{m}^{(s)}\right), \qquad \tau^{(s)} = \boldsymbol{\sigma} \cdot \boldsymbol{\mu}^{(s)}. \tag{1}$$

with $\mathbf{m}^{(s)}$ and $\mathbf{s}^{(s)}$ denoting the unit vectors normal to the slip plane and along the slip direction in the sth system, respectively, while $\boldsymbol{\sigma}$ is the applied stress and $\tau^{(s)}$ is the resolved shear stress acting on the sth slip system. The constitutive behavior of the matrix phase is then characterized by the viscoplastic stress potential U such that

$$U(\boldsymbol{\sigma}) = \sum_{s=1}^{K} \frac{\dot{\gamma}_0^{(s)} \tau_0^{(s)}}{n+1} \left(\frac{\left|\tau^{(s)}\right|}{\tau_0^{(s)}}\right)^{n+1}. \tag{2}$$

Obviously, in this last expression, U is a homogeneous function of degree $n+1$ in the stress $\boldsymbol{\sigma}$, K is the total number of active slip systems, $n \geq 1$, $\dot{\gamma}_0^{(s)}$ and $\tau_0^{(s)}$ denote the creep exponent, the reference slip-rate and the reference flow stress (also denoted as critical resolved shear stress CRSS) of the sth slip system, respectively. In addition, let us notice that the limiting values of the exponent, $n = 1$ and $n \to \infty$ correspond to linear viscoelasticicty and rate-independent perfect plasticity, respectively.

*Corresponding author. Email: kdanas@lms.polytechnique.fr

Homogenized model for porous single crystal

The MVAR effective stress potential of a porous single crystal is given by

$$\widetilde{U}_{mvar}\left(\overline{\boldsymbol{\sigma}};s_\alpha\right)=(1-f)^{-n}\sum_{s=1}^{K}\frac{\gamma_0^{(s)}\left(\tau_0^{(s)}\right)^{-n}}{n+1}\left(\overline{\boldsymbol{\sigma}}\cdot\widehat{\mathbf{S}}^{(s)}\cdot\overline{\boldsymbol{\sigma}}\right)^{(n+1)/2}, \tag{3}$$

where

$$\widehat{\mathbf{S}}^{(s)}=\boldsymbol{\mu}^{(s)}\otimes\boldsymbol{\mu}^{(s)}+\frac{f}{K}\left[\widehat{\mathbf{Q}}^{-1}(\boldsymbol{\mu}^{(s)},w_1,w_2,\mathbf{n}^{(i)})-\sum_{r=1}^{K}\boldsymbol{\mu}^{(r)}\otimes\boldsymbol{\mu}^{(r)}\right]. \tag{4}$$

where f is the porosity, $\widehat{\mathbf{Q}}$ is a fourth-order microstructural tensor [5] and is related to the well known Eshelby tensor serving to bring the dependence of the model upon the void shape (aspect ratios w_1 and w_2) and orientation vectors ($\mathbf{n}^{(i)}$, $i=1,2,3$).

RESULTS

Figure 1 shows cross-sections of the effective gauge surfaces in the $\overline{\Sigma}_m-\overline{\Sigma}_{eq}$ plane for (a) FCC, (b) BCC and (c) HCP porous single crystals. Various creep exponents $n=(1,2,5,10)$ are considered while the porosity is set to $f=1\%$. In the context of this figure, we observe a very good agreement between the MVAR predictions and the FE results for the entire range of creep exponents n. In any case, the maximum error is found to be in the order of $\sim 5\%$. For $f=1\%$, in Fig. 1a, and relatively high triaxialities, the $n=1$ curve crosses the rest of the curves leading to a stiffer response at large stress triaxialities X_Σ but this is not the case in the case of a BCC crystal in Fig. 1b. In turn, in the context of HCP porous crystals (Fig. 1c), we find, rather surprisingly, that the MVAR estimate leads to a fully incompressible response in the case C_1 (3 slip systems), irrespective of the value of porosity, void shape or orientation used, as shown in Fig. 1c. The explanation of such a response can be attributed to virtual "rigid" directions in the composite thus leading to pressure-independent response. To investigate this further, we consider the cases of HCP singles crystal with pyramidal Π_2 (C_2) and combination of basal, prismatic and pyramidal Π_2 active slip systems (C_3). In these cases where more slip systems are activated, the MVAR predictions lead gradually to more compressible responses. In other words, in Fig. 1c, one observes that the HCP crystal C_3, with 12 slip systems is more compressible than the HCP crystal C_2, with 6 slip systems. These predictions are fully confirmed by corresponding FE calculations.

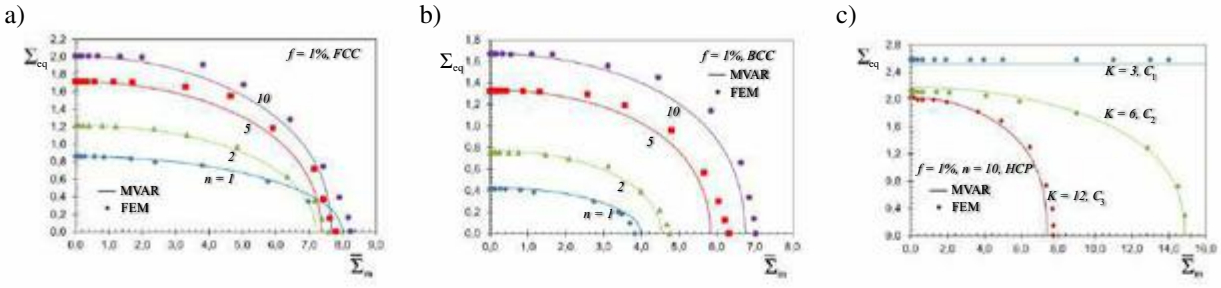

Figure 1: Gauge surfaces in the $\overline{\Sigma}_m-\overline{\Sigma}_{eq}$ plane in the case of a porous (a) FCC, (b) BCC and (c) HCP single crystal comprising spherical voids for range of creep exponent n. Comparison between the MVAR model and the FE results for a porosity $f=1\%$. In (c) different number of active slip systems are considered.

References

[1] A. Srivastava, S. Gopagoni, A. Needleman, V. Seetharaman, A. Staroselsky, and R. Banerjee: Effect of specimen thickness on the creep response of a ni-based single-crystal superalloy. Acta Materialia, 60:5697–5711, 2012.

[2] X. Han, J. Besson, S. Forest, B. Tanguy, and S. Bugat: A yield function for single crystals containing voids. International Journal of Solids and Structures, 50:2115–2131, 2013.

[3] J. Paux, L. Morin, R. Brenner, and D. Kondo: An approximate yield criterion for porous single crystals (in press). Eur. J. Mech. A/Solids, 51: 1–10, 2015.

[4] A. Mbiakop, A. Constantinescu, and K. Danas: A model for porous single crystals with cylindrical voids of elliptical cross-section. Int. J. Solids Struct., 64-65: 100–119, 2015a.

[5] A. Mbiakop, A. Constantinescu, and K. Danas: A model for porous single crystals with cylindrical voids of elliptical cross-section. J. Mech. Physics Solids, 84:436–467, 2015b.

AN EXTENSION OF THE GURSON MODEL INVOLVING LODE ANGLE

Ahmed Benallal

LMT-Cachan, ENS cachan/CNRS/Université Paris-Saclay, Cachan, France

Summary A parametric representation of the effective yield surface for a voided material with yielding of the matrix governed by both the effective stress and the third stress invariant is formulated here in the framework of the Gurson approach to ductile fracture.

INTRODUCTION

While earlier micromechanical analyses suggests ductile fracture to be dependent on stress triaxiality [1, 2, 3], experimental evidence also shows effects of Lode angle (see e.g. Barsoum and Fakeslog [4]. In a recent paper [5] we assessed the effects of the third stress invariant in the yielding of ductile porous solids in the framework of the Gurson approach with the yielding behavior of the matrixwith von Mises yielding criterion.The present study goes along the same lines and its objective is the consistant introduction of the Lode angle in the framework of the Gurson approach when the yielding behaviour of the matrix is dependent on both the effective stress and the third stress invariant.

CONSTITUTIVE RELATIONS FOR POROUS SOLIDS INVOLVING THE LODE ANGLE

We use the following notations. σ and $\dot{\epsilon}$ denote the microscopic stress and strain rate in the matrix while the macroscopic stress and strain rate are called respectively Σ and $\dot{\mathbf{E}}$. The invariants of the microscopic stress tensor are the hydrostatic stress σ_m, the von Mises equivalent stress σ_{eq} and the stress Lode angle ω respectively defined by $\sigma_m = \frac{1}{3}\sigma_{ii}, \sigma_{eq} = \sqrt{\frac{3}{2}s_{ij}s_{ij}}$ and $\omega = \frac{1}{3}$ $\left(\frac{27}{2}\frac{\det \mathbf{s}}{\sigma_{eq}^3}\right)$ where $\mathbf{s}$ is the stress deviator and repeated summation is used. The invariants for the macroscopic stress are defined exactly in the same way and denoted Σ, Σ_{eq} and Θ. We also use the invariants of the microscopic strain rate tensor $\dot{\epsilon}$ defined similarly by $\dot{\epsilon}_m = \frac{1}{3}\dot{\epsilon}_{ii}$, $\dot{\epsilon}_{eq} = \sqrt{\frac{2}{3}\dot{\epsilon} : \dot{\epsilon}}$, $\zeta = \frac{1}{3}$ $\left(\frac{4\det \dot{\epsilon}}{\dot{\epsilon}_{eq}^3}\right)$ and those of the macroscopic strain rate $\dot{\mathbf{E}}$ denoted $\dot{E}_m$, $\dot{E}_{eq}$ and η.

The constitutive behavior of the matrix of the porous solid is considered as incompressible, isotropic, rigid-plastic and the plastic flow obeys to normality. The yielding of the matrix is described by a yield function f positive and homogeneous of degree one in the stress in the form $f(\boldsymbol{\sigma}) = \sigma_{eq}g(\omega)$. Function $g(\omega)$ describes possible effects of the third invariant of stress on yielding. The yield surface defined by $\sigma_{eq}g(\omega) \nearrow \sigma_0 \leq 0$ is assumed convexe and smooth, thus satisfying in particular $g'(0) = g'(\frac{\pi}{3}) = 0$.

The dissipation function, denoted π, is defined by $\pi(\dot{\epsilon}) = \sigma : \dot{\epsilon}$. Owing to convexity of the yield function f and normality, the function $\pi(\dot{\epsilon})$ is obtained for every $\dot{\epsilon}$ by usual procedures and found to be $\pi(\dot{\epsilon}) = \frac{\sigma_0\dot{\epsilon}_{eq}}{\sqrt{g^2(\omega(\zeta))+(g'(\omega(\zeta)))^2}} = \sigma_0\dot{\epsilon}_{eq}G(\zeta)$. The function π is only dependent on the Lode angle of the strain rate ζ.

With the Gurson 's cell [3], a hollow sphere cell with external radius b and a void with radius a, and porosity $f = \frac{a^3}{b^3}$, one uses a spherical coordinate spherical system (r, θ, ϕ) and the variable change $\lambda = \frac{b^3}{r^3}$. The trial field used by Rice and Tracey [2] and Gurson [3] is given by $\dot{\epsilon} = \dot{\mathbf{E}}' + \lambda\dot{E}_m e^D$ with $e^D = \mathbf{1} \nearrow 3\, e_r \otimes e_r$ where e_r is the unit vector in the radial direction and $\mathbf{1}$ the second order unit tensor. Defining the quantities

$$\delta = \frac{1}{8}\left(\nearrow 2\sqrt{3}\ \ \mathrm{n}(2\eta)\quad (2\theta)\ \ \mathrm{n}^2(\phi) + \quad (2\eta)(3\quad (2\phi) + 1) + \ \right) \tag{1}$$

$$\mu = \frac{1}{4}\left(2\sqrt{3}\ \ \mathrm{n}(\eta)\quad (2\theta)\ \ \mathrm{n}^2(\phi) + 3\quad (\eta)\quad (2\phi) + \quad (\eta)\right) \tag{2}$$

together with the strain rate triaxiality ratio $H = \frac{\dot{E}_m}{\dot{E}_{eq}}$, the effective strain rate and the Lode angle are respectively given by $\dot{\epsilon}_{eq} = \dot{E}_{eq}\sqrt{1 \nearrow\ \mu\lambda H + \ H^2\lambda^2}$ and $3\zeta = \frac{\cos 3\eta + 6(1-2\delta)\lambda H + 12\mu\lambda^2H^2 - 8\lambda^3H^3}{(1-4\mu\lambda H + 4H^2\lambda^2)^{\frac{3}{2}}}$.

Parametric representation of the yield criterion

Computing the macroscopic dissipation by $\Pi(\dot{\mathbf{E}}) = \frac{1}{V}\int_V \pi(\dot{\epsilon})\ V$ with V the volume of the porous material and using the general results for porous plasticity given in [5], the following parametric representation of the effective yield criterion is obtained with $\mathrm{d}\Omega = \ \mathrm{n}\varphi\ \theta\ \varphi$

$$\frac{\Sigma_m}{\sigma_0} = \frac{1}{6\pi}\int_1^{\frac{1}{f}}\int_\Omega \frac{G(\zeta)[2\lambda H-\mu]}{\sqrt{1-4\mu\lambda H+4H^2\lambda^2}}\frac{\mathrm{d}\lambda\mathrm{d}\Omega}{\lambda} +$$
$$\frac{1}{6\pi}\int_1^{\frac{1}{f}}\int_\Omega \frac{1}{\sin 3\zeta}\frac{g'(\omega(\zeta))G(\zeta)}{g((\zeta))}\left[\frac{1-2\delta+4\lambda H\mu-4\lambda^2H^2}{1-4\mu\lambda H+4H^2\lambda^2} \nearrow \frac{(\cos 3\eta+6(1-2\delta)\lambda H+12\mu\lambda^2H^2-8\lambda^3H^3)(2\lambda H-\mu)}{(1-4\mu\lambda H+4H^2\lambda^2)^2}\right]\frac{\mathrm{d}\lambda\mathrm{d}\Omega}{\lambda} \quad (3)$$

$$\Sigma_{eq} = U^2+V^2, \qquad 3\Theta = \frac{U\left(U^2 \nearrow 3V^2\right) \quad 3\eta \nearrow V\left(V^2 \nearrow 3U^2\right) \quad \mathrm{n}\,3\eta}{\left(U^2+V^2\right)^{3/2}} \quad (4)$$

$$U = \frac{\partial\Pi}{\partial\dot{E}_{eq}} = \frac{\sigma_0}{4\pi}\int_1^{\frac{1}{f}}\int_\Omega \frac{G(\zeta)[1-2\mu\lambda H]}{\sqrt{1-4\mu\lambda H+4H^2\lambda^2}}\frac{\mathrm{d}\lambda\mathrm{d}\Omega}{\lambda^2} +$$
$$\frac{\sigma_0}{4\pi}\int_1^{\frac{1}{f}}\int_\Omega \frac{1}{\sin 3\zeta}\frac{g'(\omega(\zeta))G(\zeta)}{g(\omega(\zeta))}\left[\frac{\cos 3\eta-4H\lambda(1-2\delta)+4\mu\lambda^2H^2}{1-4\mu\lambda H+4H^2\lambda^2} \nearrow \frac{(\cos 3\eta+6(1-2\delta)\lambda H+12\mu\lambda^2H^2-8\lambda^3H^3)(1-2\lambda H\mu)}{(1-4\mu\lambda H+4H^2\lambda^2)^2}\right]\frac{\mathrm{d}\lambda\mathrm{d}\Omega}{\lambda^2} \quad (5)$$

$$V = \frac{1}{\dot{E}_{eq}}\frac{\partial\Pi}{\partial\eta} = \frac{\sigma_0 H}{2\pi}\int_1^{\frac{1}{f}}\int_\Omega \frac{G(\zeta)\left[-\frac{\partial\mu}{\partial\eta}\right]}{\sqrt{1-4\mu\lambda H+4H^2\lambda^2}}\frac{\mathrm{d}\lambda\mathrm{d}\Omega}{\lambda} +$$
$$\frac{\sigma_0}{4\pi}\int_1^{\frac{1}{f}}\int_\Omega \frac{1}{\sin 3\zeta}\frac{g'(\omega(\zeta))}{g(\omega(\zeta))}G(\zeta)\left[\frac{-\sin 3\eta-4H\lambda(\frac{\partial\delta}{\partial\eta})+4H^2\lambda^2(\frac{\partial\mu}{\partial\eta})}{1-4\mu\lambda H+4H^2\lambda^2} + \frac{2H\lambda(\cos 3\eta+6(1-2\delta)\lambda H+12\mu\lambda^2H^2-8\lambda^3H^3)\frac{\partial\mu}{\partial\eta}}{(1-4\mu\lambda H+4H^2\lambda^2)^2}\right]\frac{\mathrm{d}\lambda\mathrm{d}\Omega}{\lambda^2} \quad (6)$$

In the absence of Lode angle effects in the yield behaviour of the matrix and after integration with respect to λ, the results obtained in [5] are recovered. The parametric representation given above allows for some explicite results.

For purely hydrostatic loadings $H \to \pm\infty$, the macroscopic stress is also purely hydrostatic. One finds that $\frac{\Sigma_m}{\sigma_0} \to \frac{\frac{2}{3}\ln f}{g(0)}$ when $H \to \nearrow\infty$ while $\frac{\Sigma_m}{\sigma_0} \to \frac{-\frac{2}{3}\ln f}{g(\frac{\pi}{3})}$ if $H \to +\infty$. This result is also directly obtained if one analyses the hollow sphere considered here on its own, subjected to macroscopic hydrostatic stress Σ_m. Notice here how the Gurson result is changed and especially the fact that positive mean stresses are affected by $g(\frac{\pi}{3})$ while negative mean stresses are affected by $g(0)$.

When $H \to 0$, it is easily checked that expression of the macroscopic yield surface is $\Sigma_{eq}g(\Theta) = (1 \nearrow f)\sigma_0$. which is up to the size reduction factor $1 \nearrow f$ exactly the equation of the yield surface of the matrix. The situation is similar as in the Gurson model and actually holds for any matrix yield surface.

With some approximations, it is felt that a full explicite expression can be obtained under more general situations. This will be discussed in the future.

References

[1] McClintock, F.A.: A criterion of ductile fracture by the growth of holes. Journal of Applied Mechanics, 35, 363-371, 1968.

[2] Rice, J.R., Tracey, D.M.:On the ductile enlargement of voids in triaxial stress fields. J. Mech. Phys. Solids 17, 201-217, 1969.

[3] Gurson, A.L.: Continuum Theory of ductile rupture by void nucleation and growth Part I. Yield criteria and flow rules for porous ductilemedia. J. Engrg. Mat. Tech. 99, 215, 1977.

[4] Barsoum, I., Faleskog, J.: Rupture in combined tension and shear: Experiments. Int. J. Solids Structures 44, 1768-1786, 2007.

[5] Benallal, A., Desmorat, R. and Fournage, M.: An assessment of the roles of the third invariant of stress in the Gurson approach for ductile fracture. European J. of Mech./A Solids, Vol.47,400-414, 2014.

RATE SENSITIVITY IN DISCRETE DISLOCATION PLASTICITY

Zebang Zheng[1], Daniel Balint[2a)] & Fionn Dunne[1, 2]
[1]*Department of Materials, Imperial College London, London, United Kingdom*
[2] *Department of Mechanical Engineering, Imperial College London, London, United Kingdom*

ABSTRACT

The origin of the rate-sensitive behaviour of plasticity over strain rate regimes from 10^{-5} to $10^{5}\mathrm{s}^{-1}$ has been assessed with reference to three key mechanisms: dislocation nucleation, time of flight (dislocation mobility) and thermally activated escape of pinned dislocations. A new mechanistic formalism for incorporating thermally activated dislocation escape into discrete dislocation plasticity (DDP) modelling techniques is presented. It is shown that nucleation and dislocation mobility produce rate-sensitive behaviour for strain rates in the range 10^{2} to $10^{5}\mathrm{s}^{-1}$, but cannot do so for significantly lower strain rates, for which thermally-activated dislocation escape becomes the predominant rate-controlling mechanism. At low strain rates, the strong experimentally observed rate-sensitive behaviour of Ti alloys, manifested as stress relaxation and creep, is shown to be captured well by the new thermal activation DDP model.

INTRODUCTION

The rate sensitivity of the plastic deformation of alloys has long been of scientific interest and technological relevance. Rate sensitivity is strongly material dependent and much work has been done in order to understand its mechanistic basis. Its manifestation is often through the observed progressive increase in flow stress from low strain rates $(\dot{\varepsilon} < 10^{3}\mathrm{s}^{-1})$ to high strain rates $(\dot{\varepsilon} \geq 10^{3}\mathrm{s}^{-1})$ in a positively rate sensitive material. It is argued that the plastic deformation is moderated by thermal activation events at low strain rates while being controlled primarily by viscous drag at high rates. Discrete dislocation plasticity is a modelling technique in which slip on defined active crystallographic systems is represented through explicit representation and motion of discrete dislocations. In the classical two-dimensional DDP model, there are two parameters associated with time scale: first, the dislocation source nucleation time t_{nuc} describes the operation of the Frank-Read source from a trapped dislocation segment to a full, glissile loop, and second, the ratio of viscous drag coefficient and shear modulus B/G characterises the time scale of a dislocation moving within an obstacle-free crystal matrix. A systematic study of rate sensitivity in DDP revealed that quasi-static DDP is able to predict the rate sensitivity in the high strain rate regime of $\dot{\varepsilon} \geq 10^{3}\mathrm{s}^{-1}$. Beyond $\dot{\varepsilon} = 10^{3}\mathrm{s}^{-1}$, plasticity is controlled primarily by viscous dissipation, and the constitutive rules used in classical DDP models give rise to the rate dependence of the material. When obstacles are present, rate sensitivity is affected by the strength assigned to obstacles since, ordinarily, there is no explicit time associated with obstacle escape, i.e. the leading dislocation is released from an obstacle immediately after the resolved shear stress exceeds a critical strength, so that classical DDP cannot account for the rate sensitivity in the low strain rate regime. In this paper, we address the roles of dislocation nucleation and time of flight or mobility, and present a new formalism for incorporating thermally activated dislocation escape in numerical DDP techniques. We utilise a systematic methodology by considering single crystal stress relaxation in order to study the mechanistic contributions to observed rate-sensitive behaviour over the strain rate regime 10^{-5} to $10^{5}\mathrm{s}^{-1}$.

RESULTS AND DISCUSSIONS

The motion of dislocations can be hindered by several types of obstacle such as forest dislocations, solute atoms and small precipitates, etc. In the DDP formulation presented here, obstacles are modelled as points on the slip planes and may be assigned a time t_{obs}, which is a thermal activation-related, stress-related variable describing the required time for pinned dislocations to escape obstacles. We consider a dislocation line gliding along its slip plane that becomes pinned by a group of obstacles. The dislocation experiences a thermal activation event under the applied stress τ enabling it to attempt to overcome the energy barrier and escape the obstacles. The frequency of successful jumps Γ to escape obstacles considering only forward activation was first introduced by Gibbs and subsequently utilised by Dunne, considering both forward and backward activation events. The value of t_{obs} can be derived based on the local thermal activation event which may be expressed as the inverse of the successful jump frequency, i.e. $t_{obs} = 1/\Gamma$.

In order to investigate the rate sensitivity dependence arising from nucleation, mobility and thermal activation systematically, these three processes are analysed independently using a consistent methodology: a single HCP crystal undergoing prismatic slip is considered, under conditions of stress relaxation with uniaxial loading. The crystal is first stretched plastically followed by a period of strain hold at the maximum strain, and the resulting stress relaxation during the hold period is examined for each mechanism in turn to quantify the resulting rate sensitivity.

[a)] Corresponding author. Email: d.balint@imperial.ac.uk.

As shown in Fig.1a, both the analytical solutions and DDP simulations reveal that the rate sensitivity manifested as stress relaxation resulting from both dislocation nucleation and mobility diminishes to insignificant levels for strain rates lower than $10^3 s^{-1}$. At higher strain rates greater than $10^5 s^{-1}$, there is found to be a contribution to rate sensitivity from both dislocation nucleation and mobility mechanisms, and the effect from nucleation is found to be stronger at lower strain rates than that for mobility. On the other hand, as shown in Fig.1b, at low strain rates the rate sensitivity is predominated by the thermal activation process and the rate-sensitive range is affected by the activation energy. It is seen that increasing activation energy appropriately leads to a higher energy barrier and as a consequence, a larger obstacle escape time constant. The rate-sensitive range of strain rate shifts to higher strain rate for lower activation energy, since in this case, pinned dislocations more easily overcome the energy barrier required to escape obstacles. Hence the average dislocation velocity is higher which leads to a higher rate-sensitive range.

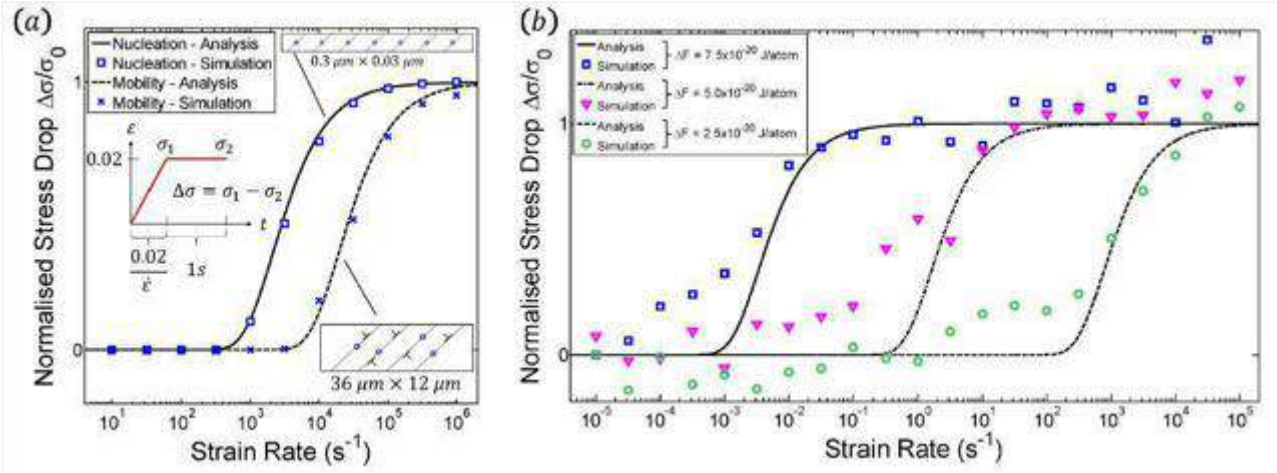

Fig.1. Relative contributions of (a) nucleation time, mobility of dislocations and (b) thermally activated dislocation escape on controlling stress relaxation and its time response from DDP simulations (symbols) and analytical results (lines).

CONCLUSIONS

The rate sensitivity of 2D discrete dislocation plasticity has been studied systematically, and is argued to originate from three independent mechanisms which are, respectively, dislocation nucleation, time of flight (the dislocation mobility) and finally, thermally-activated dislocation escape from pinning obstacles. The thermal activation of escape has been addressed in this paper and a formalism presented for its incorporation within numerical DDP modelling techniques. The regimes of strain rate from 10^{-5} to $10^5 s^{-1}$ over which each of the three mechanisms operates and predominates has been examined. It has been shown that at high strain rate ($\dot{\varepsilon} \geq 10^3 s^{-1}$), the rate sensitivity is largely controlled by the dislocation nucleation process and the free flight (mobility) of dislocations. At low strain rate ($\dot{\varepsilon} < 10^3 s^{-1}$), there is little or no rate sensitivity originating from either the nucleation process nor the dislocation mobility, and it is argued that the predominant mechanistic basis for observed rate sensitivity originates from thermally activated processes which assist dislocations pinned at obstacles to escape.

References

[1] E. Van der Giessen, A. Needleman. Discrete dislocation plasticity: a simple planar model, Modelling and Simulation in Materials Science and Engineering 3 (1995) 689.

[2] P.K. Agnihotri, E. Van der Giessen. On the rate sensitivity in discrete dislocation plasticity, Mechanics of Materials (2015).

[3] F.P.E. Dunne, D. Rugg, A. Walker. Lengthscale-dependent, elastically anisotropic, physically-based hcp crystal plasticity: Application to cold-dwell fatigue in Ti alloys, International Journal of Plasticity 23 (2007) 1061-1083.

[4] G.B. Gibbs. Thermodynamic analysis of dislocation glide controlled by dispersed local obstacles, Materials Science and Engineering 4 (1969) 313-328.

CONTINUUM MODEL AND SIMULATIONS FOR MICROSTRUCTURAL EVOLUTION IN DEFORMATION PROCESSES

John L. Bassani[1a)]

[1] *Mechanical Engineering and Applied Mechanics, University of Pennsylvania, Philadelphia, PA, USA*

Summary A model is developed for a class of anisotropic elastic-plastic solids in which the orthotropic triad that characterizes the symmetry of the microstructure evolves with deformation. Constitutive equations for microstructural spin are based upon an exact relationship between that spin, the material spin, and the plastic rate of stretching that has been derived using representation theory for tensor-valued functions. Simulations of necking, shear banding, and buckling display significant effects of microstructural evolution on strain localization. Recent work on microstructure evolution in complex fluids also will be discussed.

Introduction

Processes involving large-strain, deformation of metallic alloys, metal-matrix composites, polymers, or polymer matrix composites, as well as many mechanisms of ductile failure, typically involve significant changes in microstructure and the corresponding evolution of ansiotropic macroscopic properties. In particular, limits to formability that are critical to many important manufacturing technologies as well as processing of materials depend strongly on the evolution of microstructure. Nevertheless, relatively simple and analytically-tractable continuum models that account for microstructural evolution and can be readily employed in computer-aided design, in process control, and in failure analyses are lacking.

Over the last 40 years or so, there has been substantial progress in modeling large-strain plastic deformation[1,2] ranging from phenomenological engineering plasticity theories to more elaborate micromechanical models. Modeling capabilities for fixed microstructures (with an array of available yield functions and associated flow rules) are well in hand[3]. Nevertheless, accurate models at a comparable level of phenomenology that account for microstructural changes with the concomitant evolution of (local) anisotropy are essentially non-existent. Micromechanically-based models have been developed, but they typically involve levels of complexity that are not practical for engineering design and analysis.

Two prominent applications among many where simulation-based design has tremendous potential are in the stamping of metallic sheet materials and deformation processing of polymers. The forming of complex shapes typically involves large inelastic deformations and the evolution of microstructure. Micromechanically-based models for texture evolution in polycrystals have steadily developed, with pioneering work coming from the Los Alamos group lead by U. F. Kocks[4] and building on the rigorous computational procedures of Asaro and Needleman[5] and others. In addition to the simpler Taylor model and finite element simulations with individual grains discretized, Tome and Ponte Castaneda and co-workers[6] have been developing non-linear homogenization techniques which greatly improve on Taylor models for grain-level fields while being less computationally intensive than the full finite element calculations. Several general observations follow: i) those approaches are generally much more computationally intensive than any engineering plasticity model, including those with anisotropic behaviors; ii) constitutive assumptions that enter those models, e.g. at the single crystal level, are necessarily idealizations of real behaviors; and, in any event, iii) those models are generally far too complex to be used by designers.

The framework for microstructural evolution developed here, which is at the same level of complexity and phenomenology as the widely-used flow rules for plastic strains, circumvents those issues and can be readily fit to experiments and micromechanical simulations. A finite element implementation also has been developed. Several problems involving strain localization are considered, including necking, neck propagation, shear banding, and buckling. In each of those problems, microstructural evolution is shown to have a strong effect.

The Model and a Simulation of Sheet Necking

The evolution of microstructure, e.g. polycrystalline texture, void or particle distributions, or molecular orientation, is known to affect anisotropic macroscopic response. For example, initially random (isotropic) textures evolve through large strain processes to impart continuously-varying preferred orientations. As a result, wire drawing leads to transversely isotropic properties and sheet rolling leads to orthotropic properties. As a polycrystalline sample is deformed into a complex shape or as damage progresses, texture continues to evolve and inevitably will be non-uniform throughout the part. For deformation-induced anisotropy, it is plausible to assume that the local anisotropy possesses three mutually orthogonal symmetry planes at each material point, which we call persistent orthotropic symmetry. The principle axes of anisotropy are, therefore, orthotropic unit vectors, denoted $\hat{\mathbf{e}}_i$, $i = 1,3$, that characterize the effective symmetries of the microstructure and rotate (locally) as the material deforms. Rotation of the symmetry axes is determined by the *microstructural spin,* which is an anti-symmetric tensor that is taken to be the difference between the material and plastic spins. To fully characterize microstructural evolution, constitutive relations are required for both the plastic parts of the rate of stretching and the spin.

[a)] Corresponding author. Email: bassani@seas.upenn.edu.

In the setting of finite elastic-plastic deformations, the standard multiplicative decomposition $\mathbf{F} = \mathbf{F}^{\mathrm{e}}\mathbf{F}^{\mathrm{p}}$ is adopted. The velocity gradient, $\mathbf{L} = \dot{\mathbf{F}}\mathbf{F}^{-1}$ is partitioned into elastic and plastic parts $\mathbf{L} = \mathbf{L}^{\mathrm{e}} + \mathbf{L}^{\mathrm{p}}$, and each further partitioned into symmetric and asymmetric parts. Since the microstructural vectors are assumed to remain orthonormal at every stage of deformation (i.e., in the current configuration), their evolution can be expressed in rate form in terms of the anti-symmetric tensor ω that governs the spin of the microstructure:

$$\dot{\mathbf{e}}_i = \omega \mathbf{e}_i, \quad i = 1,2,3 \quad , \qquad \text{where} \qquad \omega = \mathbf{W}^{\mathrm{e}} = \left(\dot{\mathbf{F}}\mathbf{F}^{-1} \right)_{\mathrm{a}} = \mathbf{W} - \mathbf{W}^{\mathrm{p}}, \tag{1}$$

and $\mathbf{W}$ $\mathbf{W}^{\mathrm{e}}$ and $\mathbf{W}^{\mathrm{p}}$ are the asymmetric parts of the material, elastic and plastic velocity gradients. Therefore, to evolve the microstructure, a constitutive relation for the plastic spin, $\mathbf{W}^{\mathrm{p}}$, is required. Using representation theory, Pan and Bassani[7] have shown that $\mathbf{W}_{\mathrm{I}}^{\mathrm{p}}$ is directly related to the shear components of $\mathbf{D}_{\mathrm{I}}^{\mathrm{p}}$, where the subscript I denotes tensors pulled-back to the so-called intermediate configuration. With respect to the bases $\hat{\mathbf{e}}_{oi}$ which define the material symmetry:

$$\hat{W}^{\mathrm{p}}_{\mathrm{I}12} = \eta_3 \hat{D}^{\mathrm{p}}_{\mathrm{I}12}, \quad \hat{W}^{\mathrm{p}}_{\mathrm{I}13} = \eta_2 \hat{D}^{\mathrm{p}}_{\mathrm{I}13}, \quad \hat{W}^{\mathrm{p}}_{\mathrm{I}23} = \eta_1 \hat{D}^{\mathrm{p}}_{\mathrm{I}23}, \tag{2}$$

where η_i are scalar-valued functions depending on well-defined invariants of stress and the microstructural (2nd order) tensors, and the overstrike ^ denotes components with respect to the orthotropic bases $\hat{\mathbf{e}}_{oi}$. The key relations (2), which imply *persistent orthotropic material symmetry*, are exact and reflect the non-coaxiality in the intermediate configuration of the plastic part of the rate of stretching and the orthonormal director vectors.

As noted above, microstructural evolution generally has a significant effect on strain localization. One example is the formation of a shear band in sheet material whose texture evolves with deformation. The three scalar functions η_i in (2) are fit to experimental data for microstructural evolution in a textured steel sheet taken from the literature[7]. We have implemented the model as a user material model in ABAQUS. One fully three-dimensional simulation is depicted in Fig. 1. The effects of microstructural evolution, as summarized in the figure caption, are very large.

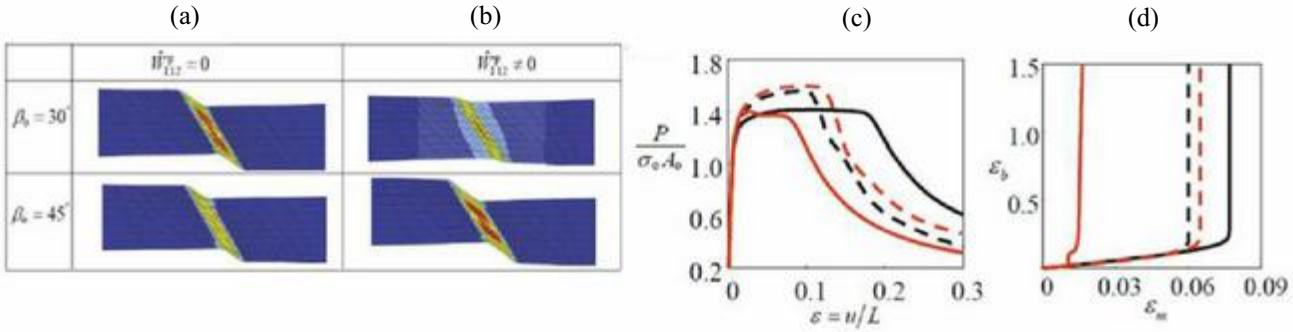

Fig. 1. Finite element simulation of localized sheet necking in uniaxial loading. Graphics are plastic strain distributions: (a) with zero plastic spin corresponding to dashed curves in (c) and (d); (b) with the microstructural evolution model fit to data for a sheet steel corresponding to solid curves in (c) and (d). Two initial orientations β_o of the tensile axis relative to the initial principle axis of anisotropy (e.g., the sheet rolling direction) are considered: $\beta_o = 30^o$ (black curves) and $\beta_o = 45^o$(red curves). Microstructural evolution, which is accounted for with plastic spin, significantly affects the forming limit: the maximum loads in (c) are reduced; the forming limit in (d) increases by 30% for $\beta_o = 30^o$ and decreases by a factor of 4 for $\beta_o = 45^o$, which is a huge affect.

CONCLUSIONS

The framework for microstructural evolution described in this brief note is at the same level of complexity and phenomenology as the widely-used flow rules for plastic strains and can be readily fit to experiments and micromechanical simulations. Through analyses and simulations, we have demonstrated significant effects of microstructural evolution on various large elastic-plastic deformation processes including necking, shear banding, and buckling.

References

[1] Nemat-Nasser, Sia, Plasticity: A Treatise on Finite Deformation of Heterogeneous Inelastic Materials. Cambridge University Press, 2004.
[2] Asaro, Robert J., Lubarda, Vlado A., *Mechanics of Solids and Materials.* Cambridge University Press, 2006.
[3] Banabic, Dorel, Barlat, Frédéric, Cazacu, Oana, Kuwabara, Toshihiko, *Int. J. Mater. Form.* 3, 165-189, 2010.
[4] Beaudoin, A.J., Dawson, P.R., Mathur, K.K., Kocks, U.F., Korzekwa, D.A., *Comput Methods Appl. Mech. Engrg*. 117, 49-70, 1994.
[5] Asaro, R.J., Needleman, A., *Acta Metall.* 33, 923-953, 1985.
[6] Lebensohn, R. A., Tomé, C. N. Ponte Castañeda, P., *Philosophical Magazine.* 87, 4287-4322, 2007.
[7] Bassani, J. L. and Pan, H.. Comptes Rendus Mecanique 340, 369-377, 2012.

MODELLING FIBER REINFORCED COMPOSITES EXHIBITING ELASTOPLASTIC DEFORMATION

Rex Bedzra [*1,2], Jaan-W. Simon[1], and Stefanie Reese[1]
[1]*Institute of Applied Mechanics, RWTH Aachen University, Mies-van-der-Rohe-Straße 1, 52074 Aachen, Germany*
[2]*AICES, RWTH Aachen University, Schinkelstraße 2, 52062 Aachen, Germany*

Summary In this paper, a nonlinear constitutive model accounting for anisotropic plasticity using the concept of structural tensors and formulated in the framework of multi-surface plasticity is proposed. To determine the parameters of the constitutive model and to further validate the model, a finite element model of a plain weave repeating unit cell (RUC) is set-up. The model is fitted and compared to volume averaged stress-strain response generated from the RUC.

MATERIAL MODEL

Plastic anisotropy is described using the method of structural tensors as developed by [1]. A second order structural tensor is defined as $\mathbf{M}_i = \mathbf{N}_i \otimes \mathbf{N}_i (i = 1,2,3)$ where $\mathbf{N}_i (i = 1,2,3)$ are unit vectors pointing in priveleged directions of the material. Additionally, the unit vectors $\mathbf{N}_i$ are orthogonal to each other.

In general, orthotropic materials can be characterized by three symmetry planes, described by the structural tensors $\mathbf{M}_i (i = 1,2,3)$. To this end, two yield functions are defined

$$\Phi_i = \sqrt{\boldsymbol{\sigma} \cdot (\boldsymbol{\mathcal{A}}_i[\boldsymbol{\sigma}])} \nearrow (\sigma_{yi} \nearrow R_i), \quad \boldsymbol{\mathcal{A}}_i = a_i (\mathbf{M}_i \otimes \mathbf{M}_i) \quad i = 1,2 \tag{1}$$

such that they account for yielding in $\mathbf{N}_1$ and $\mathbf{N}_2$ directions respectively. Furthermore, a third yield function to account for yielding in $\mathbf{N}_3$ direction and shear yielding is defined as:

$$\begin{aligned} \Phi_3 &= \sqrt{\boldsymbol{\sigma} \cdot (\boldsymbol{\mathcal{A}}_3[\boldsymbol{\sigma}])} \nearrow (\sigma_{y3} \nearrow R_3) \\ \boldsymbol{\mathcal{A}}_3 &= a_3 (\mathbf{M}_3 \otimes \mathbf{M}_3) + a_4 (\boldsymbol{\mathcal{I}} \nearrow (\mathbf{M}_1 \otimes \mathbf{M}_1 + \mathbf{M}_2 \otimes \mathbf{M}_2 + \mathbf{M}_3 \otimes \mathbf{M}_3)) + a_5 \left[\!\!\left[\boldsymbol{\mathcal{D}}^1 \nearrow (\mathbf{M}_1 \otimes \mathbf{M}_1)\right]\!\!\right] \\ &\quad + a_6 \left[\!\!\left[\boldsymbol{\mathcal{D}}^2 \nearrow (\mathbf{M}_2 \otimes \mathbf{M}_2)\right]\!\!\right] \end{aligned} \tag{2}$$

where the fourth-order tensors $\boldsymbol{\mathcal{D}}^1$ and $\boldsymbol{\mathcal{D}}^2$ are given by $\mathcal{D}^{\alpha}_{ijkl} = \frac{1}{2}\left(M^{\alpha}_{ik}\delta_{jl} + M^{\alpha}_{jl}\delta_{ik} + M^{\alpha}_{il}\delta_{jk} + M^{\alpha}_{jk}\delta_{il}\right), \alpha = 1,2$ and $\boldsymbol{\mathcal{I}}$ is the fourth-order identity tensor. The prefactors $a_i (i = 1,2,3)$ are related to the uniaxial yield stresses $\bar{\sigma}_{11}$, $\bar{\sigma}_{22}$ and $\bar{\sigma}_{33}$ in the three orthogonal directions, whereas the coefficients $a_i (i = \ , 5, \ )$ are related to the shear yield stresses $\bar{\sigma}_{12}$, $\bar{\sigma}_{13}$ and $\bar{\sigma}_{23}$. The final form of the constitutive equations of the model is summarized below:

- Stress tensor $\quad \boldsymbol{\sigma} = \dfrac{\partial \psi_e}{\partial \boldsymbol{\varepsilon}} (E_1, E_2, E_3, G_1, G_2, G_3, \nu_{12}, \nu_{13}, \nu_{23})$
- Yield functions $\quad \Phi_i = \sqrt{\boldsymbol{\sigma} \cdot (\boldsymbol{\mathcal{A}}_i[\boldsymbol{\sigma}])} \nearrow (\sigma_{yi} \nearrow R_i), \quad i = 1,2,3$
- Evolution equations $\quad \dot{\boldsymbol{\varepsilon}}_p = \sum_{i=1}^{3} \dot{\lambda}_i \dfrac{\mathcal{A}[\boldsymbol{\sigma}]}{\sqrt{\boldsymbol{\sigma} \cdot (\mathcal{A}[\boldsymbol{\sigma}])}}, \quad \dot{\kappa} = \sum_{i=1}^{3} \dot{\lambda}_i$
- Discrete Kuhn-Tucker conditions $\quad \dot{\lambda}_i \geqslant 0, \quad \Phi_i \leqslant 0, \quad \dot{\lambda}_i \Phi_i = 0 \qquad i = 1,2,3$

The linearized version of the strain energy function ψ_e proposed for modelling biaxial composite materials in [2] and Voce's exponential hardening function $R_i = \nearrow Q_i (1 \nearrow e^{-\beta_i \kappa})$ are here chosen for all numerical considerations. For the numerical aspect and the implementation of multi-surface plasticity, the reader is referred to [3].

MESO MODEL

To determine the material parameters of the constitutive model and for verification, an idealized geometry of the internal architecture of a plain weave repeating unit cell (RUC) is generated with a length of $3.8mm$ and a thickness of $0. \ mm$, see Figure 1. Furthermore, the RUC is assumed to be part of a much larger material specimen, therefore periodic boundary conditions are applied through equation constraints in the ABAQUS/standard software package. The tows and the matrix are modelled as General Electric 218CS (GE218CS) continuous tungsten wire and cold worked oxygen free high conductivity copper (OFHC) material respectively, with actual experimental data obtained from [4]. A standard von-Mises yield function with isotropic hardening is here adopted. The material parameters obtained after fitting are given in Table 1.

*Corresponding author. Email: rex.bedzra@rwth-aachen.de

Material	E [MPa]	ν	Q_0 [MPa]	β
Tungsten	677887.67	0.28	987.2	52.6
Copper	135248.74	0.34	148.1	2994

Table 1: Tow and matrix material constants

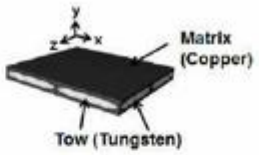

Figure 1: Meshed RUC

RESULTS AND DISCUSSIONS

First, the parameters of the constitutive model are identified by subjecting the RUC to σ_{11}, σ_{22}, σ_{33} uniaxial tensile stress as well as τ_{12} and τ_{23} shear loading. Based on the obtained stress-strain response, the engineering constants, the yield stresses and the constants of the three exponential hardening functions are determined after fitting the constitutive model, see Table 2. The fit is performed such that $\sigma_{33} - \varepsilon_{33}$ matches best as it is impossible to match all four flow curves with Q_3 and β_3, see Figure 2.

E_1 [MPa]	E_3 [MPa]	G_{12} [MPa]	G_{13} [MPa]	ν_{12}	ν_{13}	ν_{23}
513,665.83	414,945.00	386,167.50	284,167.50	0.274	0.313	0.437
σ_{11} [MPa]	σ_{22} [MPa]	σ_{33} [MPa]	σ_{12} [MPa]	σ_{23} [MPa]	σ_{13} [MPa]	
1097.71	1097.71	1014.14	463.126	249.255	249.255	
Q_1[MPa]	Q_2[MPa]	Q_3[MPa]	β_1	β_2	β_3	
745.00	745.00	794.50	49.86	49.86	53.09	

Table 2: Constants of the constitutive model

For verification, the RUC is subjected to a bidirectional tensile test. From Figure 3, both models agree very well. Also the yield stress for uniaxial tension in comparison with biaxial tension appears to be the same. This implies that the yield functions Φ_1, Φ_2 and Φ_3 form a cuboid in stress space and are independent of each other. For this reason the yield stress for uniaxial tension, bidirectional tension as well as tension and compression will result in the same value.

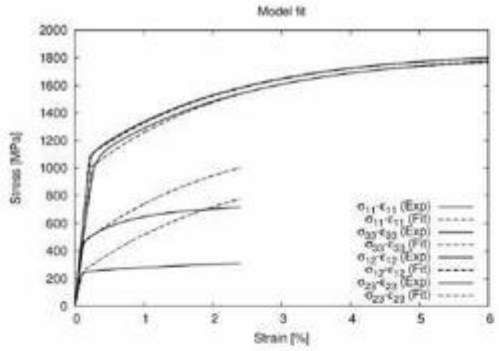

Figure 2: A fit of the constitutive model to the RUC response

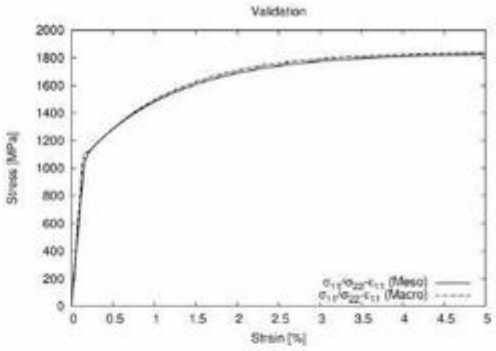

Figure 3: Comparison between meso- and macro-model

CONCLUSION

To properly describe plastic anisotropy, it is important that the yield functions responsible for the projection of the normal components of the Cauchy stress tensor in privileged directions of the material are dependent on all three normal stresses.

References

[1] Spencer A.J.M.: Theory of invariants. Continuum Physics, vol. 1. Academic Press, New York: 239-353, 1971.

[2] Reese S., Raible T., Wriggers P.: Finite element modelling of orthotropic material behaviour in pneumatic membranes. Int. J. Sol. Struct. 38:95259544, 2001.

[3] Simo J.C., Hughes T.J.R.: Computational inelasticity. Springer-Verlag, New York, 1998.

[4] Sanfeliz J.G.: Elastic-plastic finite element analyses of a unidirectional, 9 vol % tungsten fiber reinforced copper matrix composite. Nasa Tech. Memo. 106304, 1993.

STRENGTH PROPERTIES OF NANOPOROUS MATERIALS: A MOLECULAR DYNAMICS APPROACH

Stella Brach [*1,2], Luc Dormieux[3], Djimedo Kondo[2], and Giuseppe Vairo[1]
[1]*Department of Civil Engineering and Computer Science, University of Rome "Tor Vergata", Rome, Italy*
[2]*Institut D'Alembert, UMR 7190 CNRS, University Pierre and Marie Curie, Paris, France*
[3]*UR Navier, Ecole des Ponts ParisTech, Champs-sur-Marne, France*

Summary Strength properties of an aluminium single crystal containing a spherical nanovoid are investigated by means of a Molecular Dynamics (MD) approach, in the case of a fixed porosity level and for different values of the void size. Elasto-plastic mechanical response, under triaxial strain-based conditions and including axisymmetric and shear states, are numerically investigated, and allows to identify the corresponding limit stress states. The dependence of the macroscopic strength properties on all the three stress invariants is quantified. Void-size effects are clearly shown. In detail, it is observed that reducing the void radius induces a strengthening of the sample. Furthermore, the occurrence and the amount of void-size effects strongly depend on the Lode angle, resulting in a shape transition of both meridian and deviatoric strength surfaces when the void radius is varied.

Since the recent arising of advanced nano-technologies, as well as of innovative engineering design approaches, nanoporous materials have been extensively studied in the last two decades, leading to a considerable worldwide research interest in both industrial and academic domains. In fact, owing to their excellent rigidity and strength properties, nanoporous materials open towards groundbreaking applications in several technical fields, involving ultra-high performance devices and challenging multifunctional uses. In order to fulfil to these promising applications, one of the most fundamental aspect consists in characterising and predicting the strength properties of these materials, as dependent on the size of voids.

Due to the lack of an exhaustive experimental characterization, numerical methods addressing Molecular Dynamics can be considered as an effective alternative to provide benchmarking evidence (see for instance [4, 5]). As a matter of fact, MD-based simulations account for material arrangement at the atomistic level, automatically furnishing helpful insights on nanoscale effects. Nevertheless, current MD simulations are generally limited to the analysis of particular admissible stress states only (computed under uniaxial, volumetric or shear conditions), without considering more complete multiaxial scenarios, and thereby not allowing for more comprehensive insights. In this sense, the central purpose of the present paper is to investigate strength properties of nanoporous materials under multiaxial loadings via a MD-based approach (see [1]).

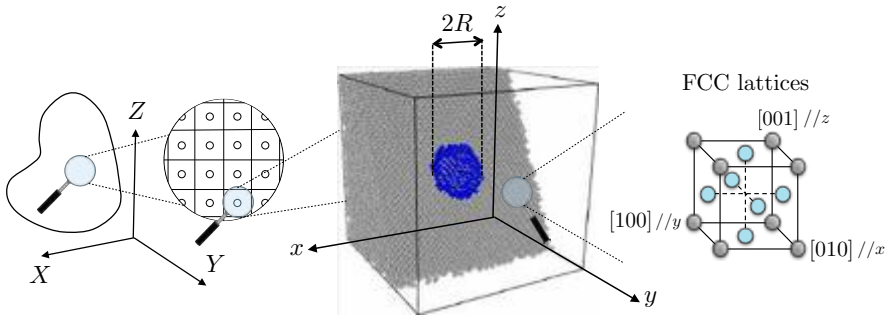

Figure 1: Synoptic scheme of proposed Molecular Dynamics model.

Let a material neighbourhood of a nanoporous medium be considered (Fig. 1), characterized by a periodic nanostructure along the global Cartesian directions X, Y and Z. The representative cell consists in a nano-single crystal of aluminium (i.e., FCC lattices), embedding a spherical void of radius R. The simulation domain, undergoing to periodic boundary conditions, is subjected to triaxial strain-based expansion ($\mathrm{TXE_D}$) and compression ($\mathrm{TXC_D}$), as well as to shear strain conditions ($\mathrm{SHR_D}$). For each case, different triaxiality levels have been considered, describing deformation paths ranging from pure deviatoric states to pure hydrostatic ones. Denoting as $\boldsymbol{\Sigma}$ the computed macroscopic stress tensor (with $\boldsymbol{\Sigma}_\mathrm{d}$ its deviatoric part) the Haigh-Westergaard invariants $\zeta = \quad \boldsymbol{\Sigma}/\sqrt{3}$, $r = (\boldsymbol{\Sigma}_\mathrm{d} : \boldsymbol{\Sigma}_\mathrm{d})^{1/2}$, $\quad 3\theta_\Sigma = (3\sqrt{\quad}\quad \boldsymbol{\Sigma}_\mathrm{d})/(\boldsymbol{\Sigma}_\mathrm{d} : \boldsymbol{\Sigma}_\mathrm{d})^{3/2}$ are adopted for giving a three-dimensional description of the strength states. For a fixed porosity value ($p = 1\%$), strength properties of nanoporous samples have been investigated by varying the void radius from $0.5\ \ 1$ nm to $2.9\quad$ nm.

The strength properties of bulk (i.e., $p = 0$) and nanoporous ($p = 1\%$) samples are depicted in Fig. 2 in the meridian (ζ, r) (Figs. 2a and 2c) and in the deviatoric $\zeta = \text{const}$ (Figs. 2b and 2d) planes. As main aspects, performed computations show: (i) a clear influence of all the three stress invariants on strength properties; (ii) a complex relationship between the applied

*Corresponding author. Email: brach@ing.uniroma2.it

strain states and the obtained stress ones; (iii) significant void-size effects. With reference to Figs. 2a and 2b, the strength domain of the bulk sample is characterised by a significant pressure-dependence and a clear influence of the stress Lode angle, resulting in triangular-shaped cross sections in the deviatoric plane. In the case of nanoporous domains, meridian and deviatoric strength surfaces in Figs. 2c and 2d are shown to be significantly affected by void-size effects, mainly resulting in the improvement of the strength properties when void radius reduces. The occurrence and the amount of such a strengthening effect strongly depend on the value of the stress Lode angle. In detail, referring to Fig. 2d for a fixed hydrostatic stress level ζ, the highest (respectively, lowest) influence is observed in the case of a triaxial expansion (resp., compression). As a result, a shape transition occurs in the deviatoric profiles, passing from a multi-sided polygonal shape to a triangular-like one, when the void size reduces. For the herein-adopted porosity level, the dependence of strength properties on the void radius has been shown to practically disappear when void size assumes values greater than 2.7 nm.

Accordingly, present numerical results can be considered as an useful contribution to provide comparative benchmarks for validating and calibrating theoretical strength criteria for nanoporous materials. In detail, proposed computations clearly indicate some criticisms in available continuum mechanics-based strength models (e.g., [2, 3]), suggesting the need to derived novel and more comprehensive theoretical formulations.

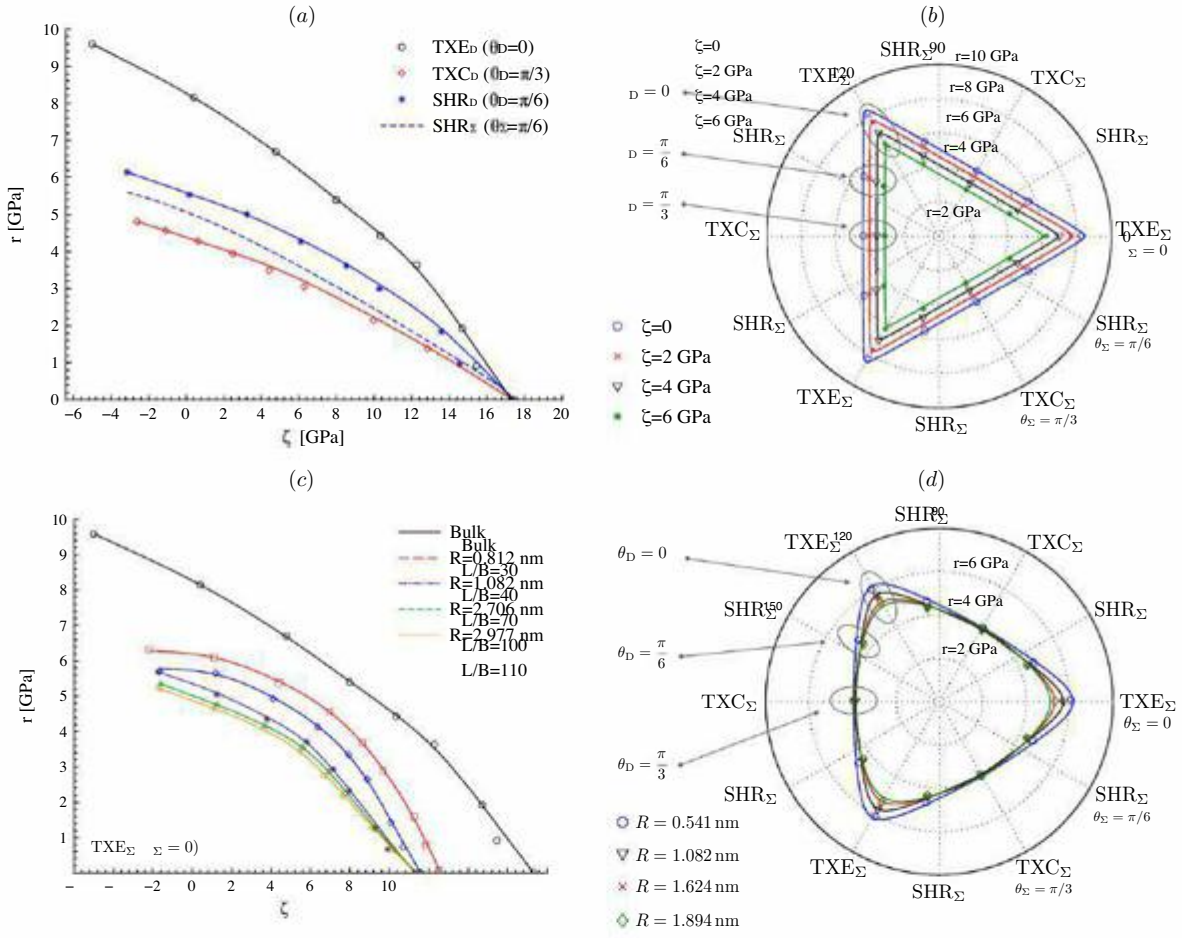

Figure 2: Relevant results for: (a) and (b) bulk samples; (c) and (d) nanoporous samples.

References

[1] Brach S., Dormieux L., Kondo D., Vairo G.: Void-size effects on strength properties of nanoporous materials: An insight via a Molecular Dynamics approach. Submitted, 2015.

[3] Dormieux L., Kondo D.: Non linear homogenization approach of strength of nanoporous materials with interface effects. Int J Eng Sci 71:102-110, 2013.

[4] Mi C., Buttry D.A., Sharma P., Kouris D.A.: Atomistic insights into dislocation-based mechanisms of void growth and coalescence. J Mech Phys Solids 59:1858-1871, 2011.

[5] Traiviratana S., Bringa E.M., Benson D.J., Meyers M.A.: Void growth in metals: Atomistic calculations. Acta Mater 56: 3874-3886, 2008.

ANALYTICAL AND NUMERICAL TOOLS FOR RELAXATION IN CRYSTAL PLASTICITY

Sergio Conti[1] and Georg Dolzmann [*2]

[1]*Institut für Angewandte Mathematik, Universität Bonn, Germany*
[2]*Fakultät für Mathematik, Universität Regensburg, Germany*

Summary Results concerning the relaxation of variational models in crystal plasticity will be presented. These results include complete analytical formulas for the relaxation of special model energies in simplified geometries and two dimensions and a proposed concept for a fully discrete numerical algorithm that can be used to compute the relaxation for a given deformation gradient or to compute this relaxation for many gradients at the same time and during a finite element calculation.

RELAXATION

The starting point of our discussion is the time discrete model for the evolution in the framework of crystal plasticity which was in particular advocated in [3, 11, 13]. We use the multiplicative decomposition of the deformation gradient in the spirit of [9, 10], i.e., $F = F_e F_p$ where $F = Du$ denotes the deformation gradient, F_e the elastic and F_p the plastic part of the deformation gradient. This plastic part encodes the deformation obtained from one or several simple shear deformations in a prescribed number of slip systems, see [14] for a justification of the continuum framework. If we represent the simple shear in one of the finitely many slip systems as $F_p = I + \gamma_i s_i \otimes m_i$ then the model energy can be written as

$$W(F) = \begin{cases} \tau\gamma + \kappa\gamma^2 & \text{if } F = R(I + \gamma s_i \otimes m_i), R \in SO(n),\, \gamma \in \mathbb{R},\, i \in \{1, \dots, N\}\,, \\ \infty & \text{otherwise}\,, \end{cases}$$

where τ is the critical shear stress and κ the strain hardening modulus. It is well-known that the resulting energy density does not have the right convexity properties in order to allow an application of the direct method in the calculus of variations and therefore one passes to the relaxed energy

$$W^{\mathrm{qc}}(F) = \inf_{\phi \in W_0^{1,\infty}((0,1)^n;\mathbb{R}^n)} \int_{(0,1)^n} W(F + \nabla\phi) dx\,, \tag{1}$$

see [8, 12] a detailed discussion of all the technical aspects of relaxation and the fundamental role of relaxation in modern mathematical theories for materials and [4] for first results towards relaxation with the constraint of incompressibility.

It turns out to be an extremely hard problem to find closed analytical formulas for the relaxation given by the foregoing formula. In a two-dimensional model situation with two orthogonal slip systems this was studied in [7] and just recently the case of three slip systems has been analyzed in [5].

In view of these analytical difficulties, it is mandatory to develop numerical schemes. If a part of the analytical relaxation can be carried out, then one may use semi-discrete approaches in the sense of [1, 2]. However, if the situation is too complex, then a fully discrete scheme might be the only solution. We will present one approach in this direction of a scheme that computes laminates of higher orders at all Gauss points in a finite element simulation. Finally outstanding open questions will be discussed.

References

[1] Bartels, S., Carstensen, C., Hackl, K., Hoppe, U.: Effective relaxation for microstructure simulations: algorithms and applications. Comput. Methods Appl. Mech. Engrg. 193:5143-5175, 2004.

[2] Carstensen, C., Conti, S., Orlando, A.: Mixed analytical-numerical relaxation in finite single-slip crystal plasticity. Cont. Mech. Thermod. 20:275–301, 2008.

[3] Carstensen C., Hackl K., Mielke A.: Non-convex potentials and microstructures in finite-strain plasticity. R. Soc. Lond. Proc. Ser. A Math. Phys. Eng. Sci. 458:299-317, 2002).

[4] Conti, S., Dolzmann, G.: On the theory of relaxation in nonlinear elasticity with constraints on the determinant. Arch. Ration. Mech. Anal. 217:413-437, 2015.

[5] Conti, S., Dolzmann, G.: Relaxation in crystal plasticity with three active slip systems. Cont. Mech. Thermodynamics (in print).

[6] Conti, S., Dolzmann, G., Kreisbeck, C.: Asymptotic behavior of crystal plasticity with one slip system in the limit of rigid elasticity. SIAM J. Math. Anal. 43:2337-2353, 2011.

[7] Conti, S., Dolzmann, G., Kreisbeck, C.: Relaxation of a model in finite plasticity with two slip systems. Math. Models Methods Appl. Sci. 23:2111-2128, 2013.

[*]Corresponding author. Email: Georg.Dolzmann@ur.de

[8] Dacorogna, B.: Direct methods in the calculus of variations. Springer 2007.
[9] Kröner, E.: Allgemeine Kontinuumstheorie der Versetzungen und Eigenspannungen. Arch. Rational Mech. Anal. 4:273-334, 1960.
[10] Lee, E.H.: Elastic-plastic deformation at finite strains. Journal of Applied Mechanics 36:1-5, 1969.
[11] Miehe, C. Schotte, J. Lambrecht M.: Homogeneization of inelastic solid materials at finite strains based on incremental minimization principles. application to the texture analysis of polycrystals. J. Mech. Phys. Solids 50:2123-2167, 2002.
[12] Müller, S.: Variational models for microstructure and phase transitions. In *Calculus of variations and geometric evolution problems* Springer 1999.
[13] Ortiz, M. Repetto, E. A.: Nonconvex energy minimization and dislocation structures in ductile single crystals. J. Mech. Phys. Solids 47:397-462, 1999.
[14] Reina, C., Conti, S.: Kinematic description of crystal plasticity in the finite kinematic framework: a micromechanical understanding of $F = F^e F^p$. J. Mech. Phys. Solids 67:40-61, 2014.

ROLE OF THE MATRIX PLASTIC FLOW ON THE MECHANICAL RESPONSE OF POROUS SOLIDS

Oana Cazacu[1a)], Benoit Revil-Baudard[1] & Nitin Chandola[1]
[1]*Department of Mechanical &Aerospace Engineering, University of Florida/REEF, Shalimar, Fl, U.S.A*

Summary It is shown that the mechanical response of porous metallic materials is strongly influenced by the particularities of the plastic flow of the matrix. This is demonstrated by comparing the dilatational response of porous solids for which the matrix is described by Tresca, von Mises, and Cazacu et al. [1] yield criterion, respectively. The analytical plastic potentials of the respective porous solids are developed using rigorous limit analysis theorems and upscaling techniques. If the matrix plastic response is governed by Tresca's yield criterion, the rate of void growth or collapse is much faster than in a porous von Mises solid. However, if the plastic flow of the matrix is described by an odd function that accounts for both slip and twinning at single crystal level, the yield locus of the porous solid does not display any symmetry, with dramatic consequences in terms of the rate of void evolution, and ductility.

In this study a kinematic homogenization approach is used to study how the particularities of the plastic flow of the matrix affect the effective response both in terms of yielding and void evolution. Specifically, analytical plastic potentials are developed for porous solids for which the plastic behavior of the matrix is described by von Mises yield criterion, and by criteria depending on both invariants of the stress deviator, namely Tresca and Cazacu et al. [1] criterion. In each case, the porous solid is supposed to contain randomly distributed spherical voids. The limit-analysis is conducted for both tensile and compressive loadings, the imposed local velocity being compatible with uniform macroscopic strain rate boundary conditions. If the plastic behavior of the matrix is governed by the von Mises criterion, the plastic dissipation is

$$\pi\ \mathbf{d}^{\text{Mises}} = \sigma_T \sqrt{2\ \left(d_I^2 + d_{II}^2 + d_{III}^2\right)/3} = \sigma_T \sqrt{4\ D_m^2 \left(b/r\right)^6 + 4D_{11}'^2 + 2D_{11}' D_m \left(b/r\right)^3 \left(1+3\cos 2\theta\right)}\ , \tag{1}$$

while in the case when the matrix obeys Tresca's criterion, the local plastic dissipation is

$$\pi\ \mathbf{d}^{\text{Tresca}} = \sigma_T \left(|d_I| + |d_{II}| + |d_{III}|\right)/2, \tag{2}$$

where d_I, d_{II}, d_{III} are the principal values of the local strain **d**, **D** is the imposed macroscopic strain rate tensor, which is supposed to be constant and axisymmetric; **D'** its deviator, D_m its mean, while σ_T is the uniaxial yield in tension of the matrix, and r and θ are spherical coordinates. Because Tresca's yield criterion depends on both invariants of the local stress deviator, the corresponding plastic dissipation depends on both the sign and ordering of the principal values of **d** (see Eq. (2)) Thus, unlike the case when plastic flow is governed by the von Mises criterion, the expression of the local plastic dissipation in terms of the invariants of the imposed strain rate tensor **D** is not unique. For example, if $D_m \geq$ and $D_{11}' \geq$:

$$\pi\ \mathbf{d}^{\text{Tresca}} = \sigma_T \left[\begin{array}{l} (1/2)\sqrt{D_m^2 \left(b/r\right)^6 + D_{11}'^2 + 2D_{11}' D_m \left(b/r\right)^3} + \\ (3/2)\sqrt{D_m^2 \left(b/r\right)^6 + 2D_{11}' D_m \left(b/r\right)^3 \cos\ 2\theta\ + D_{11}'^2} \end{array}\right] \tag{3}$$

(for all possible expressions of the local plastic dissipation see Cazacu et al. [2]). Comparison between Eq.(1) and Eq.(3) shows the strong differences between the plastic dissipation associated with Mises and Tresca criterion, respectively. Note that in the literature (e.g. [3]) it is usually assumed that coupling between shear and mean stress effects, i.e. the "cross-term" $D_{11}' D_m$ can be neglected. However, this assumption amounts to erasing the specificities of the plastic flow of the matrix, since this leads to: $\pi\ \mathbf{d}^{\text{Mises}} = \pi\ \mathbf{d}^{\text{Tresca}} \cong \sigma_T \sqrt{4\ D_m^2\ \ b\ \ r)^6 + 4D'^2}$, and the resulting effective yield criterion for the porous solid being the same, i.e. that of Gurson [3]. However, the plastic potential of either the porous Tresca or porous Mises solid can be calculated analytically without making such an assumption (see [2], [4]), leading to new insights concerning ductile damage. Specifically, if the plastic behavior of the matrix is governed by either the Von Mises or Tresca criterion, the overall yield surface ought to be centro-symmetric. For triaxialities T different from 0 or ±∞, there are very specific combined effects of the mean stress, σ_m and third-invariant J_3 on yielding, the yield point characterized by $J_3 \geq 0$ and a given triaxiality T being symmetric, with respect to the axis $\sigma_m = 0$, to the yield point characterized by $J_3 \leq 0$ and (-T). The two criteria coincide only for purely deviatoric or purely hydrostatic loadings. The centro-symmetry of the respective yield loci has dramatic influence on the void evolution, which depends on the sign of J_3 as well as on the sign of the triaxiality, T. Fig.1 show the predicted void growth and void collapse in terms of the effective macroscopic equivalent strain, E_e for axisymmetric loadings at fixed triaxiality, T=2 corresponding to $J_3 \leq 0$. Note that the rate of void evolution is much faster in a

a) Corresponding author. Email: cazacu@reef.ufl.edu.

porous solid with Tresca matrix than in a porous solid with von Mises matrix. Furthermore, Gurson's [3] predicts the slowest void growth (half of that predicted by Tresca's).

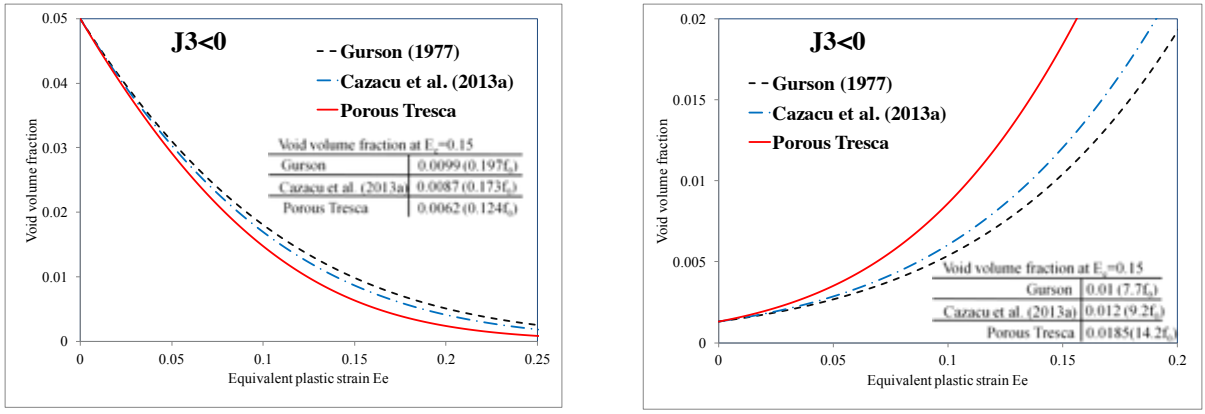

(a) (b)

Figure 1: Evolution of the void volume fraction: comparison between the predictions of Gurson's [3] and Cazacu et al [4] criteria for porous solids with von Mises matrix and that of Cazacu et al [2] criterion for a porous solid with Tresca matrix for triaxiality T = 2.

Cazacu et al [1] proposed an yield criterion that accounts for the specific plastic deformation mechanisms as single crystal level through a parameter k. If plastic deformation is due to slip obeying Schmid law, k=0 and the criterion reduces to von Mises criterion whereas if plastic deformation is due to both slip and twinning, k is non-zero, and the yield criterion accounts for tension-compression asymmetry. In the latter case, the yield locus of the respective porous solid lacks any symmetry, and there is a strong effect of J_3 for all triaxialities.

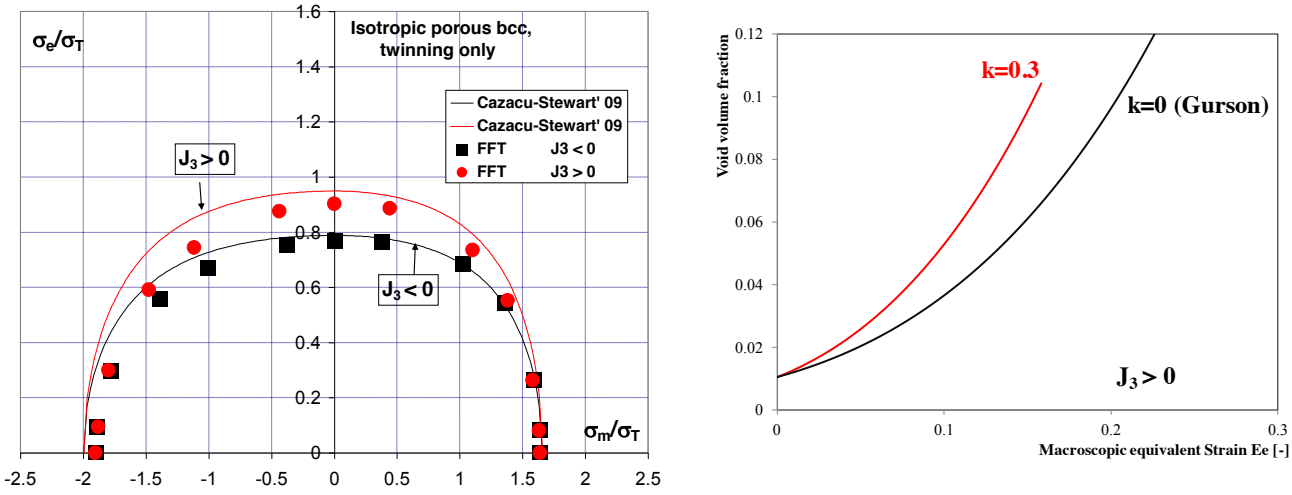

(a) (b)

Figure 2: (a) Comparison between gauge surfaces from FFT full-field simulations (symbols) and Cazacu and Stewart's [5] yield surface (k=0.3), for loadings with $J_3 > 0$ and $J_3 < 0$; (b) Effect of k on void growth: comparison between predictions according to [5]and Gurson [3] for T = 2.

These unusual features have been confirmed by full-field calculations (Fig. 2(a)) and lead to specific effects in terms of void evolution (see Fig. 2(b)).

References

[1] Cazacu,O., Plunkett, B., Barlat, F.. *Int.. J. .Plasticitcity*, **22,** 1171-1194, 2006.

[2] Cazacu, O., Revil-Baudard, B., Chandola N., Kondo, D, *Int. J. Solids. Struct.*, **51**, 861-874, 2014.

[3] Gurson, A. L. *J. Engng. Matl.* Tech. Trans. ASME, Series H, **99**, 2-15, 1977.

[4] Cazacu, O., Revil-Baudard, B., Lebensohn, R. A., Garajeu, M., *J. Appl. Mech.*, **80** , 064501-03, 2013.

[5] Cazacu, O., Stewart, J.B., *J. Mech .Phys .Solids*, **57**, 325-341, 2009.

DUCTILE FAILURE OF SHEAR-DOMINATED "HAT" SPECIMENS

Edmundo Corona *[1]

[1]*Solid Mechanics, Sandia National Laboratories, Albuquerque, New Mexico, USA*

Summary This work addresses the response and ductile failure of an A286 steel "hat" specimen that develops high shear deformations when loaded in compression. After significant plastic flow, the load-deflection response of the specimen exhibits a maximum followed by a gradual decrease in the load culminating in catastrophic failure. Finite element models with calibrated elastic-plastic response and a Johnson-Cook failure model failed to predict the load maximum. Introducing lower ductility to a small percentage of the elements caused material failure to nucleate and induce the load maximum in the simulations. As observed in the experiments, relatively little material damage was needed to produce the load maximum.

INTRODUCTION

Many penetration and puncture problems are influenced by the ductile failure of metals under high states of shear. Numerical simulations of such problems require implementation and calibration of appropriate plasticity models and ductile failure criteria that can replicate the response of the material. In order to accomplish this, it is essential to also experimentally measure the actual material response. In this work careful material experiments conducted on A286 steel followed by numerical modeling of the response and failure of shear-dominated "hat" specimens were considered. An expanded presentation of the experimental work is given in [1].

The experimental set-up and a close-up picture of the shear specimen are shown in Fig. 1. The specimen is 1.25 in. (3.2 cm) tall and has a width of 0.395 in. (1.0 cm). It was compressed quasi-statically in displacement control between two platens as shown, thus symmetrically inducing high shear deformation at two locations, which will be referred as "ligaments". Both the compressive load P and the distance between the two platens Δ were recorded during the tests. The typical load-deflection response of the specimen is labeled "Test" in Fig. 2, with Δ normalized by the ligament height $H = 0.125$ in. (3.2 mm). The repeatability of this response was verified through 15 test repetitions.

The specimen response was characterized by a load maximum, followed by a slow decrease in load with further displacement until catastrophic failure occurred. Figure 3 shows that two cracks growing through the high-shear ligament, starting at the two extremes, were responsible for the decrease in load. The length of these cracks grew steadily until a critical point was reached where the two joined through the complete thickness of the specimen resulting in catastrophic failure.

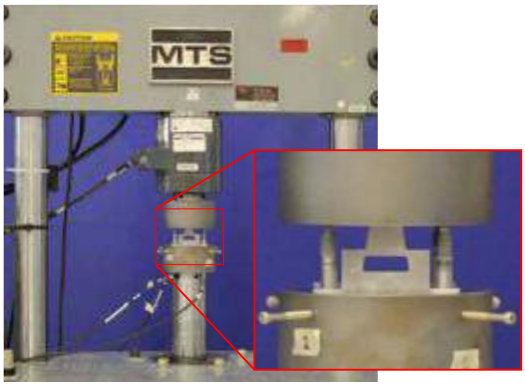

Figure 1: Photographs of experimental set-up and a specimen.

MATERIAL CHARACTERIZATION AND FINITE ELEMENT MODELING

A separate set of tests were conducted on uniaxial tension specimens of circular cross-section cut from the parent plate at three in-plane orientations 45 degrees apart. The tests indicated that the yield stress of the material in shear was approximately 5% lower than would be expected from isotropic yield. This was accounted for in the numerical simulations by using Hill's yield criteria in a classical elastic-plastic model with isotropic hardening. A series of tests on axisymmetric notched specimens

*Corresponding author. Email: ecorona@sandia.gov

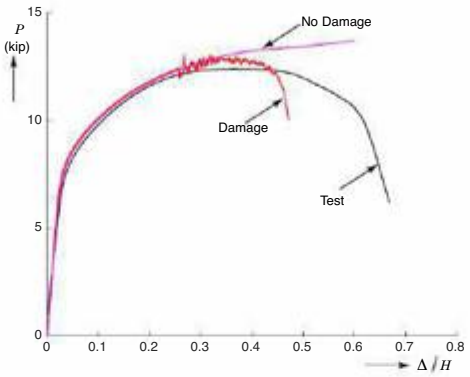

Figure 2: Comparison of experimental and numerically generated load-deflection responses.



Figure 3: Micrograph showing cracks growing through one high shear ligament.

subjected to tension were also conducted to fit a Johnson-Cook failure criterion. The test data exhibited the expected increase in ductility with decreasing triaxiality.

A doubly-symmetric finite element model of the specimen was constructed using hexahedral continuum elements. Mesh convergence of the load-deflection response was verified, suggesting that elements with sides in the range of 0.002 in. (0.05 mm) were needed in the vicinity of the high-shear ligaments. Material failure was simulated via immediate element deletion upon satisfying the Johnson-Cook criterion.

NUMERICAL RESULTS

The results obtained when the model described above was used are shown in Fig. 2 with the label “No Damage”. Up until the point where the calculations were stopped, the Johnson-Cook failure criterion had not yet been satisfied at any location in the specimen. Note that the model does not produce the load maximum observed in the experiments and is unsatisfactory. Based on experimental observations that inclusions in the metal were breaking and generating mini-cracks, the model was modified to include a small percentage of elements with lower ductility to seed material damage at relatively low strains. The Johnson-Cook criterion was not modified in the rest of the elements. The predicted results when 5% of the elements were given lower ductility are shown by the curve labeled “Damage”. It can be seen that this model produced a load maximum, although the subsequent load decrease occurred much faster indicating that the crack growth is not predicted accurately. The nucleation of damage in the simulations, however, occurred at the same locations observed experimentally. As in the experiments, the model showed that only a small amount of damage is required to induce a load maximum. Although work remains, a possible material damage mechanism has been implemented in simulations that produced results that were closer to experimental observations.

References

[1] Corona, E., Deibler, L.A., Reedlunn, B., Ingraham, M.D. and Williams, S.: An Experimental Study of Shear-Dominated Failure in the 2013 Sandia Fracture Challenge Specimen. Sandia Report SAND2015-2850. Albuquerque, NM, 2015

FEM CRYSTAL PLASTICITY LAW BASED ON DISLOCATION DYNAMICS: ULTRASONIC SHOT PEENING.

Thomas Rousseau[1,2] , Cecile Nouguier[1] , Philippe Gilles[1] & Thierry Hoc[1],
[1]*LTDS UMR 5513 CNRS Ecole Centrale de Lyon, 36 av guy de Collonges, 69134 Ecully Cedex, France.*
[2] *AREVA NP, Tour AREVA, 1 place Jean Millier, 92084 Paris La Défense Cedex, France, France.*

Summary Ultrasonic shot peening is a cold surface treatment used to extend the fatigue life of metallic components. a long time process generated a strong plastic deformation, which could lead to a surface nanostructuration. Finite element crystal plasticity allows describing both modification microstructure and residual stress computation. In the present study, numerical simulation of ball impact was performed using a crystal plasticity based dislocation dynamics code.

MANUSCRIPT

Ultrasonic Shot Peening (USP) is a cold surface treatment derived from Conventional Shot Peening (CSP). These processes are used to improve the fatigue life of metallic components. Indeed, Roland et al. [1] performed traction-compression fatigue tests on peened and non-peened stainless steel samples and showed fatigue life improvement due to shot peening. The same type of experiment was performed by Tian et al. [2] but with nickel-based alloy samples. Lu and Lu [3] showed that thousands of impacts induced hardening on a treated surface, while Ortiz et al. [4] focused on microstructure modification and Xing and Lu [5] on residual compressive stress. Moreover, Lu, K. and Lu, J. [6] observed that a long time process generated a strong plastic deformation, which could lead to a surface nanostructuration.

The experimental study of ultrasonic shot peening showed that the number of impacts increased with the number of beads while the mean value of impact depths decreased. Discrete Element Method (DEM) analysis was consistent with experimental surface analysis regarding the number of impacts and predicted a decrease in the mean value of impact velocities with an increasing number of beads. Then, impact effects on the material were analyzed using explicit finite element simulations. The impact depth, absolute maximal compressive stress and its corresponding depth were obtained regardless of the initial impact conditions identified by DEM analysis.

Moreover, combined DEM-FEM analysis showed that the mean value of impact depths decreased with increasing number of beads. This result, consistent with surface analysis, appeared to be linked to the decrease in impact velocities. Furthermore, the present analysis allowed for differentiating both configurations in terms of residual stress to determine the effect of the process according to the number of beads.

Then combined analysis was a reliable tool for predicting residual stress induced by USP. Furthermore, USP is also used for microstructure change at the surface, leading to nanostructuration. Thus, the introduction of a mechanical behavior based on crystal plasticity would complete the understanding of process effects by analyzing microstructure change under impacts.

As noted by Cottrell in 1953, work hardening is the most challenging problem in dislocation theory. Progress in multiscale modeling, now provides means for incorporating more physics into current strain hardening models. Substantial progress has been achieved regarding the connection between mesoscale studies and the continuum framework. Codes for crystal plasticity appeared some years ago. Recent codes for the polycrystal treat the local nature and number of active slip systems inside the grains, as well as their evolution. The current trend is, then, to develop dislocation-based constitutive formulations at the scale of slip systems. Such models involve, however, extensive parameter fitting and are, paradoxically, totally unable to treat the complex behavior of single crystals.

The objective of the present work is to show that the predictive ability of crystal plasticity code can be considerably improved by making use of the available information arising from theory, and dislocations dynamics simulations. For this purpose, a dislocation-based constitutive formulation for strain hardening in face-centered cubic crystals will be presented [7,8]. This multiscale approach is based on the storage-recovery framework expanded at the scale of slip systems. A parameter-free formulation is established for the critical stress and the storage rate, taking advantage of recent results yielded by dislocation dynamics simulations. The storage rate of dislocations in the presence of forest obstacles is modeled for the first time at the level of dislocation intersections and reactions.

[a)] Corresponding author. Email: Thierry.hoc@ec-lyon.fr

The mean free path per slip system is found to be inversely proportional to the critical stress. It also depends on the number of active slip systems, which leads to an orientation dependence of stage II strain hardening in agreement with experimental data. The total storage rate is obtained by including three additional contributions, notably that of the self-interaction, which leads to a model for stage I hardening.

In a first step, results obtained by implementing such a constitutive framework in the crystal plasticity code ANAIS for the single crystal are shown. In a second time, integration of grain boundary effect in such behavior law based on actual distance and back stress effect will be presented. And finally, a comparison between experimental and numerical results obtained on an ultrasonic shot peening test will be analyzed. A Typical result is given on figure 1. In particular, the number of balls on the residual stress induced by USP will be studied.

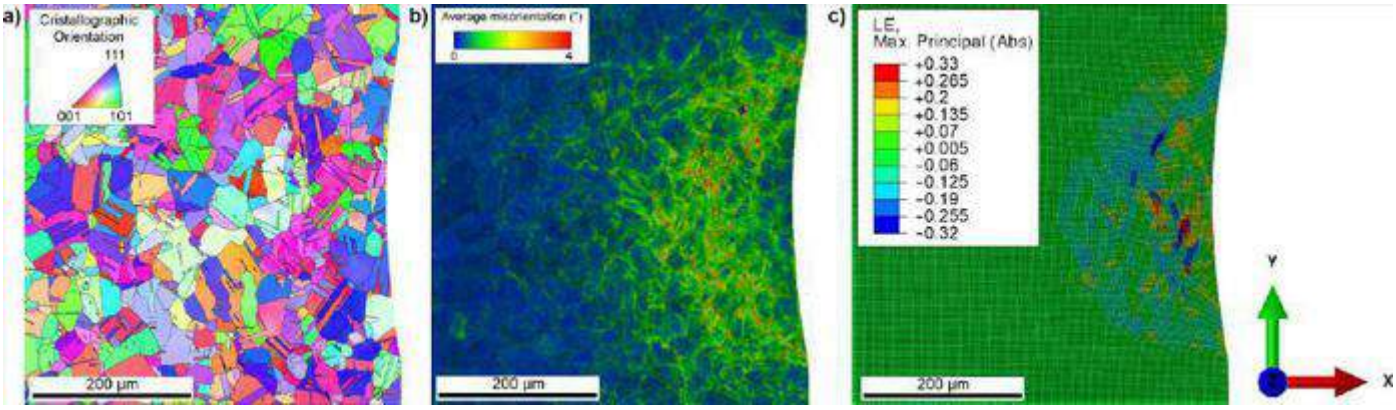

Figure 1: EBSD mapping of disorientation and strain map calculated by crystal plasticity approach for one impact obtained after ultrasonic shot peening test

Keywords: Crystal Plasticity, Finite element, Ultrasonic shot peening

Acknowledgement: The authors sincerely acknowledge the SONATS company for its technical support.

References

[1] Roland, T., Retraint, D., Lu, K., Lu, J., 2006. Fatigue life improvement through surface nanostructuring of stainless steel by means of surface mechanical attrition treatment. Scr. Mater. 54, 1949–1954.

[2] Tian, J., Villegas, J., Yuan, W., Fielden, D., Shaw, L., Liaw, P., Klarstrom, D., 2007. A study of the effect of nanostructured surface layers on the fatigue behaviors of a C-2000 superalloy. Mater. Sci. Eng: A 468–470, 164–170.

[3] Lu, K., Lu, J., 1999. Surface nanocrystallization (SNC) of metallic materials-presentation of the concept behind a new approach. J. Mater. Sci. Technol. 15, 193–197.

[4] Ortiz, A., Tian, J., Villegas, J., Shaw, L., Liaw, P., 2008. Interrogation of the microstructure and residual stress of a nickel-base alloy subjected to surface severe plastic deformation. Acta Mater. 56, 413–426.

[5] Xing, Y., Lu, J., 2004. An experimental study of residual stress induced by ultrasonicshot peening. J. Mater. Process. Technol. 152, 56–61.

[6] Lu, K., Lu, J., 2004. Nanostructured surface layer on metallic materials induced by surface mechanical attrition treatment. Mater. Sci. Eng: A 375–377, 38–45.

[7] Devincre B., Hoc T., Kubin L., Dislocation mean free paths and strain hardening of crystals, SCIENCE, 320, p 1745-1748, 2008.

[8] Madec R. Kubin L. Devincre B. Hoc T. and Rodney D., The role of collinear interaction in dislocation-induced hardening, SCIENCE, 301, 1879, 1882, 2003.

UNRAVELING TEXTURE, TRIAXIALITY AND ANISOTROPY EFFECTS IN HCP POLYCRYSTALS

Shailendra P. Joshi *[1], Balaji Selvarajou[2], and A. Amine Benzerga[3]

[1]*Department of Mechanical Engineering, National University of Singapore, Singapore*
[2]*Department of Mechanical Engineering, National University of Singapore, Singapore*
[3]*Department of Aerospace Engineering and Department of Materials Science and Engineering, Texas A& M University, College Station, Texas, USA*

Summary We discuss the complex interactions arising from inherent plastic anisotropy, texture and stress triaxiality in Mg polycrystals using crystal plasticity modeling and simulation. The micromechanics of deformation originating from initial textural variations are mapped and their influence on the deformed textures for increasing triaxiality is resolved. We discuss the implications of the distribution and evolution of the deformation modes at increasing amounts of triaxiality on failure. The results demonstrate the role of the inherent plastic anisotropy at the single crystal level on the macroscopic deformation anisotropy, limit loads and strain localization.

INTRODUCTION

Magnesium (Mg) and Mg alloys are exemplary candidate materials that find use in applications ranging from automotive to biomedical sectors. However, the complex intrinsic plastic anisotropy at the single crystal level and strong texture effects often relate to damage intolerance in Mg alloys limiting their acceptance as a preferred structural material. This is further exacerbated under complex loading conditions, which influence their micromechanics and macroscopic responses in a complicated manner. Recent experimental studies indicate that stress triaxiality, defined as $\mathsf{T} = \sigma_h/\sigma_e$ where σ_h is the mean hydrostatic stress and σ_e is the von Mises equivalent stress, significantly affects the failure characteristics of Mg alloys [1, 2]. Developing a sound understanding of the coupling between the intrinsic plastic anisotropy, texture and stress triaxiality is imperative in order to enable designing lightweight micro and macrostructures using Mg alloys. In particular, it is critical to understand the role of deformation mechanisms in textural evolution and its implications on the failure processes with varying triaxiality conditions, which is not well understood. Motivated by these outstanding issues, we investigate the micromechanics of polycrystalline Mg subjected to triaxial stress states using a three dimensional HCP crystal plasticity modeling framework [3]. Observations from 3D finite element simulations of smooth and notched round bar specimens subjected to tensile loading are compared with the experimental results reported in Ref. [1].

MODEL DESCRIPTION

In the polycrystal FE model, we define each grain comprising multiple finite element as an Euler angle set $\{E\} = \{\phi_1, \phi, \phi_2\}$ using the Bunge rotation scheme to obtain the actual orientation of the grain in the polycrystalline ensemble. In the present work, ϕ_1 causes rotation of $[10\bar{1}0]$ in the plane of the sheet, ϕ causes rotation of $[0001]$ away from the sheet normal direction and ϕ_2 results in rotation of $[10\bar{1}0]$ out of the plane of the sheet. We assume a normal distribution for each of the three angles in $\{E\}$ with their mean values equal to zero and standard deviations $\{\Delta E\} = \{\Delta\phi_1, \Delta\phi, \Delta\phi_2\}$, respectively. In the following, we present some illustrative results from our simulations for different microstructural fabrics that mimic rolled sheet textures. In addition to smooth round bar geometry, two notched round bar geometries are considered - RN10 and RN2 (see Ref. [1] for appropriate definitions of RNα) where RN2 has higher notch acuity than RN10.

RESULTS AND DISCUSSION

Macroscopic responses: Figure 1a shows the normalized load (F/A_0) at a fixed applied strain for the smooth, RN10 and RN2 specimens for different $\{\Delta E\} = \{\Delta\phi_1, \Delta\phi, 0\}$ combinations. In smooth specimens, for a given in-plane texture ($\Delta\phi_1$) the weakening of out-of-plane texture (higher $\Delta\phi$) shows in a non-monotonic load behavior. In notched specimens the trend appears monotonic with a weaker out-of-plane texture resulting in weaker load carrying capacity.

An interesting observation shown in Fig. 1b is that, smooth specimens exhibit strain localization in the form of a shear band. While this aspect was reported by Kondori and Benzerga [1] it is rather unusual given the bar geometry. Our analysis shows that this uncommon behavior results from unequal distribution of slip on prismatic systems. Moreover, the critical strain to localization depends on the textural strength exhibiting a non-monotonic trend as a function of $\Delta\phi_1$.

*Corresponding author. Email: shailendra@nus.edu.sg

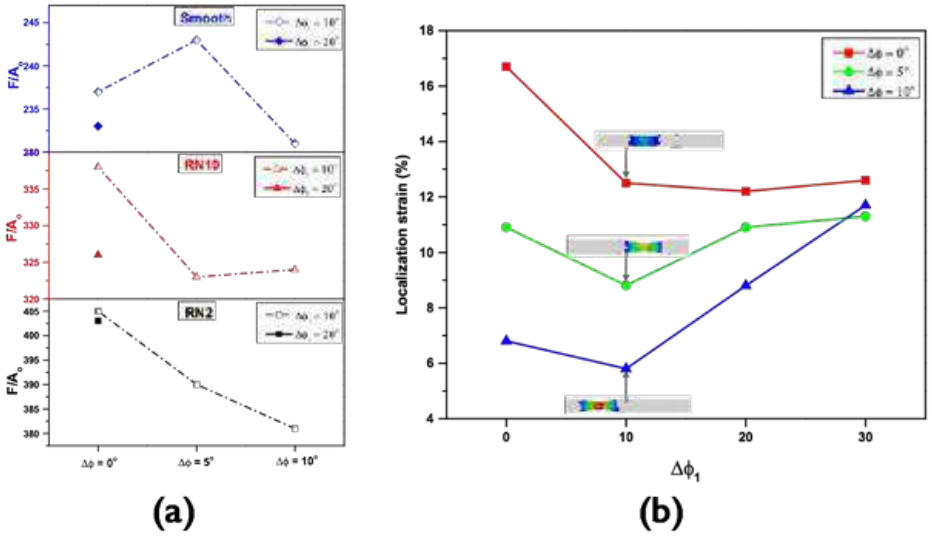

Figure 1 Macroscopic characteristics of Mg polycrystalline specimens under different stress triaxiality conditions. Panel (a) shows normalized load (MPa) and Panel (b) shows critical strain for initiation of shear localization for different $\{\Delta E\}$ cases

.

Micromechanical characteristics: While the detailed micromechanical characteristics will be discussed during the presentation, here we briefly mention the role of deformation mechanisms. The most active slip modes are prismatic $\langle a \rangle$ (prism slip) along the sheet transverse (T) direction and pyramidal $\langle c + a \rangle$ slip (P2 slip) along the sheet normal (thickness, S) direction, which are systematically affected by the initial textural variations. Notched specimens show relatively higher P2 slip activity compared to prism slip whereas the reverse is true in the smooth specimens (for the same initial texture). Further, they also exhibit increasing propensity to extension twinning (ET), shown in Fig. 2. In comparison, ET activity is much smaller in smooth specimens and becomes more negligible for initially sharper textures (i.e. low $\Delta\phi_1$ and $\Delta\phi$.

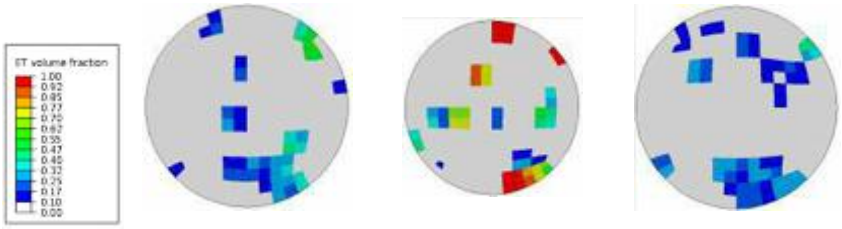

(a) $h_L = +\ .25$ **(b)** $h_L =$ **(c)** $h_L = -\ .25$

Figure 2 Distribution of ET along the normalized notch height (h_L in RN10 specimen with $\{\Delta E\} = \{10^\circ, 0^\circ, 0^\circ\}$ at a fixed strain $\varepsilon_A = 0.2$.

CONCLUSIONS

Textural variations and inherent plastic anisotropy couple with triaxiality to produce rich mechanical characteristics of Mg microstructures. Detailed investigations reveal that the modulation of deformation mechanisms at the microscopic scale affect the macroscopic deformation anisotropy, which could in turn affect failure characteristics in a non trivial manner. Such numerical investigations are expected to provide insight into designing stronger and tougher Mg microstructures.

References

[1] Kondori, B and Benzerga, A: Effect of stress triaxiality on the flow and fracture of Mg alloy AZ31. Metall Mater Trans A 45.3292–3307, 2014

[2] Kaushik, V, Narasimhan, R and Mishra, R: Experimental study of fracture behavior of magnesium single crystals. Mater Sci Eng A 590. 174–185. 2014.

[3] Zhang, J and Joshi, SP: Phenomenological crystal plasticity modeling and detailed micromechanical investigations of pure magnesium. J Mech Phys Solids 60. 945–972. 2012

DUCTILE POROUS MATERIALS WITH A MOHR-COULOMB MATRIX: THEORY AND NUMERICAL BOUNDS

Djimedo Kondo *[1], Kokou Anoukou[1], Franck Pastor[2], and Joseph Pastor[3]

[1]*Institut D'Alembert, UMR 7190 CNRS, Sorbonne Universite (UPMC), Paris, France*
[2]*Athenee royal Victor-Horta, rue de la Rhetorique, 16, Bruxelles, Belgium*
[3]*Laboratoire LOCIE, UMR 5271 CNRS, universite de Savoie, 73376 Le Bourget du Lac, France*

Summary We investigate the specific effects of Mohr-Coulomb matrix on the strength of ductile porous materials. To this end, we first perform a theoretical study based on a careful kinematics limit analysis. Then, we develop an advanced numerical procedure which delivers for the strength properties both static (lower) and kinematic (upper) bounds. The latter are used to assess and validate the theoretical model.

Following Gurson [4], consider a hollow sphere model, but here with a rigid perfectly plastic Mohr-Coulomb matrix, subjected to axisymmetric uniform strain rate boundary conditions. A specific aspect of the Mohr-Coulomb yield function is its dependency on all the three stress invariants (the equivalent stress σ_e, the mean stress σ_m and the Lode angle $\theta_{\scriptscriptstyle L}$):

$$\mathcal{F}(\boldsymbol{\sigma}) = \sigma_e + \frac{\sin(\phi)}{\zeta(\theta_{\scriptscriptstyle L})}\left(\sigma_m - \frac{c}{\tan(\phi)}\right) = 0 \tag{1}$$

with

$$\zeta(\theta_{\scriptscriptstyle L}) = \frac{1}{\sqrt{3}}\cos(\theta_{\scriptscriptstyle L}) - \frac{1}{3}\sin(\phi)\sin(\theta_{\scriptscriptstyle L})$$

Note that the case of a Drucker-Prager matrix, already studied by [3], corresponds to a criterion depending only on the first two invariants. Moreover, for an internal friction angle $\phi = 0$, the Mohr-Coulomb yield function reduces to the Tresca one.

Taking advantage of an appropriate family of three-parameter trial velocity fields accounting for the specific plastic deformation mechanisms, we first provide a solution of the constrained minimization problem required for the determination of the macroscopic dissipation function. The macroscopic strength criterion is then obtained by means of a Lagrangian method combined with Karush-Kuhn-Tucker conditions. Owing to the above mentioned specificities of the Mohr-Coulomb matrix (plastic compressibility, sensitivity to third stress invariant), a careful analysis and discussion of the plastic admissibility condition (which involves the knowledge of the sign of the principal strain rates) is required.

The proposed procedure leads to a parametric closed-form expression of the macroscopic strength criterion (see [1]). The later explicitly shows a dependency on the three macroscopic stress invariants. In the special case of a friction angle equal to zero, the established criterion reduced to recently available results for porous Tresca materials [2]. For completeness, the macroscopic plastic flow rule and the voids evolution law are fully detailed.

For validation purpose, an advanced numerical Limit Analysis of a hollow sphere having a Mohr-Coulomb matrix is carried out. The static and kinematic limit analysis approaches are recalled for the numerical purposes. Then, we present the hollow sphere model, together with its axisymmetric FEM discretization. After an adaptation of a previous static code, an original mixed (but fully kinematic) approach dedicated to the axisymmetric problem has been elaborated with a specific quadratic velocity field associated to the triangular finite element. Despite the less good conditioning inherent to the axisymmetric modeling, the final conic mixed code appears very efficient, allowing to take into account numerical meshes highly refined. After a first validation in the case of spherical cavities and isotropic loadings, for which the exact solution is known, numerical lower and upper bounds bounds of the macroscopic strength are provided for axisymmetric loading states. The numerical data are used to assess and fully validate the theoretical results. Effects of the the friction angle and that of the porosity are illustrated.

In detail, considering axisymetric loadings ($\Sigma_x = \Sigma_y$), let us introduce the generalized loading vector in a Cartesian coordinates system (with orthonormal basis $(\underline{e}_x, \underline{e}_y, \underline{e}_z)$): $\Sigma_m = \frac{1}{3}(2\Sigma_x + \Sigma_z)$, $\Sigma_{gps} = \Sigma_x - \Sigma_z$.
Figure 1 illustrates effects of the porosity, while in Figure 2 are displayed the effects of material friction angle. The results are normalized by the matrix cohesion c. In general, a significant improvement of the numerical results is obtained, comparatively to that presented in [5].

*Corresponding author. Email: djimedo.kondo@upmc.fr

Moreover, a very remarkable agreement is obtained between theory and the present numerical bounds [6]. A marked effect of porosity is noted, in particular in compression zone. Significant asymmetries of the obtained surfaces are also observed, more particularly when the friction angle increases and the porosity is fixed: in particular, the tension and the compression hydrostatic points are reduced and increased respectively with an increase of ϕ). Note that the particular asymmetry of the obtained strength surfaces is a signature of the dependency of the macroscopic criterion on all three stress invariants (and notably the third one).

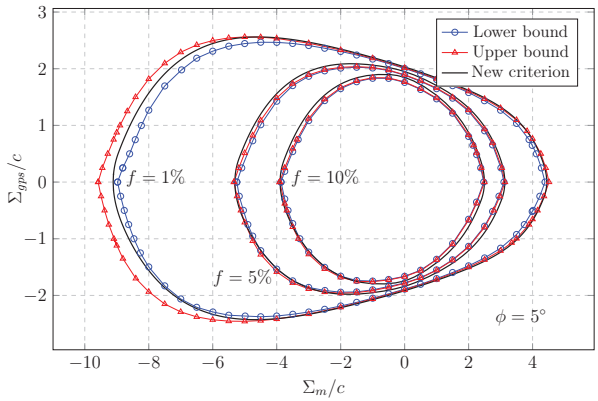

Figure 1: Porous Mohr-Coulomb material: comparison of the predictions by the proposed strength criterion with the numerical bounds for a friction angle $\phi = 5$ degrees and different values of porosity: $f = 0.01$ and $f = 0.10$.

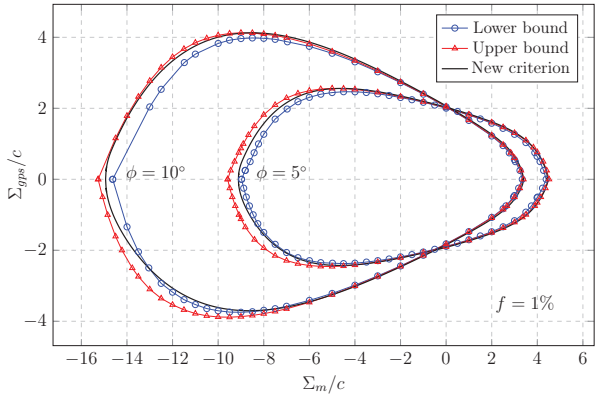

Figure 2: Porous Mohr-Coulomb materials: comparison of the predictions by the proposed strength criterion with the numerical bounds for a porosity: $f = 0.01$ and different values of friction angle $\phi = 5$ degrees, $\phi = 10$ degrees and $\phi = 25$ degrees.

References

[1] Anoukou K., Pastor F., Dufrenoy P., Kondo D.: Limit analysis and homogenization of porous materials with Mohr-Coulomb matrix. Part I: theoretical formulation. J. Mech. Phys. Solids, *Accepted*, 2016.

[2] Cazacu, O., Revil-Baudard, B., Chandola, N., Kondo, D., 2014. New analytical criterion for porous solids with tresca matrix under axisymmetric loadings. Int. J. Solids Struct. 51, 861874.

[3] Guo T., Faleskog J., Shih C.: Continuum modeling of a porous solid with pressure-sensitive dilatant matrix. J. Mech. Phys. Solids 56, 21882212, 2008.

[4] Gurson A.L.: Continuum theory of ductile rupture by void nucleation and growth: Part I. - Yield criterion and flow rules for porous ductile media. J Eng Mater Tech, 99:2-15, 1977.

[5] Pastor, J., Thor, P., Pastor, F.: Limit analysis and numerical modeling of spherically porous solids with Coulomb and Drucker-Prager matrices. Journal of Computational and Applied Mathematics 234:21622174, 2010.

[6] Pastor F., Anoukou K., Pastor J., Kondo D.: Limit analysis and homogenization of porous materials with Mohr-Coulomb matrix. Part II: Numerical bounds and assessment of the theoretical model. *Under revision*, 2016.

STRESS-TENSOR EXPRESSION IN TWO-TEMPERATURE MODELS FOR THE AGING AND YIELDING OF GLASSES

Misha Semkiv[1,2] & Markus Hütter[1a)]
[1]*Mechanical Engineering, Polymer Technology, Eindhoven University of Technology, Eindhoven, The Netherlands*
[2]*Dutch Polymer Institute (DPI), Eindhoven, The Netherlands*

Summary This paper is concerned with modeling the influence of physical aging on the yield- and postyield-behavior of glassy materials. To that end, the concept of two distinct subsystems (kinetic and configurational) is combined with elasto-viscoplasticity. Using nonequilibrium thermodynamics, it is shown that the stress tensor is in general not simply related to the derivative of the thermodynamic potential with respect to deformation, but that there can be non-potential contributions (akin to hypoelasticity) that vanish as the system tends to thermal equilibrium.

MODELING THE YIELDING-RESPONSE OF AGING GLASSES

The yielding of glassy systems, e.g. glassy polymers, is strongly affected by the ongoing physical aging of the material. The aging process roots in the fact that microstructural changes occur on different time scales: There are both frequent (and small) changes to the microstructure around local-equilibrium states, as well as much more rare (and more drastic) microstructural changes due to transitions from one local minimum across an energy barrier to another local minimum. The latter dynamics is observed as aging. To account for this discrepancy in time-scales and for the aging dynamics, one has advocated using two subsystems (called 'kinetic' or 'vibrational, and 'configurational') that equilibrate at significantly different rates. To that end, a so-called fictive / effective / configurational temperature has been employed [1-3], in addition to the regular (kinetic) temperature. To describe the effect of aging on the yielding response of glasses, continuum approaches to elasto-viscoplasticity (e.g. [4]) have been combined with the two-subsystem concept, e.g. see [2, 3].

IDENTIFICATION OF THE CONSTITUTIVE RELATION FOR THE STRESS TENSOR

In this contribution, the General Equation for the Non-Equilibrium Reversible-Irreversible Coupling (GENERIC) [5-7] is used to study in detail the thermodynamic restrictions on such two-subsystem elasto-viscoplasticity formulations [8]. Specifically, we concentrate on the proper identification of the constitutive relation for the stress tensor. It is shown that the Hamiltonian structure of the reversible dynamics in GENERIC, particularly the Jacobi identity, imposes severe constraints on that constitutive relation. However, within these constraints, there is room for stress tensor contributions that cannot be expressed in terms of the derivative of the thermodymamic potential with respect to deformation, but rather there are non-potential contributions allowed (akin to hypoelasticity). The origin of these additional contributions can be explained as follows: The constitutive relation for the stress tensor is tightly linked with the reversible dynamics of all dynamic system variables, including the two variables that describe the kinetic and configurational subsystems. If these two subsystems are coupled with each other in a non-trivial way during reversible dynamics, this automatically gives rise to additional contributions to the stress tensor.

It can be shown that these additional stress tensor contributions vanish as the system approaches thermal equilibrium. However, since much of the mechanical experiments on glasses are performed while aging is still ongoing, careful re-examination of experimental results may help to determine the non-potential stress contributions. In this contribution, these additional non-potential stress-tensor contributions are compared with latest modelling efforts in the literature on glassy materials [2, 3], and their significance is discussed in the light of processes of the underlying microstructure. Finally, this contribution closes with a comparison to complex fluids modelling [7, 9], where the non-trivial coupling of microstructural variables also gives rise to additional stress tensor contributions.

CONCLUSIONS

It has been demonstrated that, in two-temperature models for the aging and yielding of glasses, the stress tensor in general can contain contributions that are not related to the derivative of the thermodynamic potential with respect to deformation. These non-potential contributions have an effect on how experimental results can be described by such two-temperature models. This, in turn, carries potential for improving the current modelling of stress-relaxation in aging glassy systems.

Acknowledgment
This research forms part of the research program of the Dutch Polymer Institute (DPI), project no. EU-FP-001 COMPNANOCOMP.

[a)] Corresponding author. Email: M.Huetter@tue.nl.

References

[1] Tool A. Q.: Relaxation of Stresses in Annealing Glass. *J. Res. Natl. Bur. Stand.(US)* **34**:199-211, 1945.

[2] Kamrin K., Bouchbinder E.: Two-Temperature Continuum Thermomechanics of Deforming Amorphous Solids. *J. Mech. Phys. Solids* **73**:269-288, 2014.

[3] Xiao R., Nguyen T. D.: An Effective Temperature Theory for the Nonequilibrium Behavior of Amorphous Polymers. *J. Mech. Phys. Solids* **82**:62-81, 2015.

[4] Hütter M., Tervoort T. A.: Thermodynamic Considerations on Nonisothermal Finite Anisotropic Elastoviscoplasticity. *J. Non-Newtonian Fluid Mech.* **152**:53-65, 2008.

[5] Grmela M., Öttinger H. C.: Dynamics and Thermodynamics of Complex Fluids. I. Development of a General Formalism. *Phys. Rev. E* **56**:6620-6632, 1997.

[6] Öttinger H. C., Grmela M.: Dynamics and Thermodynamics of Complex Fluids. II. Illustrations of a General Formalism. *Phys. Rev. E* **56**:6633-6655, 1997.

[7] Öttinger H. C.: Beyond Equilibrium Thermodynamics. Wiley, Hobroken, 2005.

[8] Semkiv M., Hütter M.: Modeling Aging and Mechanical Rejuvenation of Amorphous Solids. *J. Non-Equil. Thermodyn.*, accepted, 2016.

[9] Öttinger H. C.: Modeling Complex Fluids with a Tensor and a Scalar as Structural Variables. *Rev. Mex. Fís.* **48**(Supl 1):220-229, 2002.

3D DIRECTIONAL COARSENING IN SINGLE CRYSTAL SUPERALLOYS FOR MULTIAXIAL APPLICATIONS

Jean-Briac le Graverend[1]
[1]*Department of Aerospace Engineering, Texas A&M University, College Station, Texas 77843, USA*

Summary Turbine blades are used in the hottest part of the aero-engines and are made of Ni-based single-crystal superalloys chosen for their exceptional mechanical performances at high temperatures. However, at high temperature/low stress conditions, Ni-based single crystal superalloys are subjected to a directional coarsening of the strengthening γ' phase, known as γ' rafting. This microstructural evolution influences the mechanical behavior and the damage. When subjected to multiaxial state of stresses, the microstructure is highly convoluted and has to be modeled in order to improve the mechanical response and lifetime prediction. A 3D formulation of the γ' directional coarsening is therefore expressed and compared with a high-temperature creep test performed on a bi-notched specimen developing multiaxial stress/strain fields. The 3D microstructural model is providing good performances and can be then used for improving the mechanical and lifetime prediction of turbine blades experiencing multiaxial state of stresses due to their complex geometry.

INTRODUCTION

The development and exploitation of gas-turbine blades casted from nickel-base superalloys in single crystal form has been one of the most successful industrial and commercial ventures relating to advanced structural materials over the last twenty years. These limiting components are used in the hot section of the engine and are therefore subjected to high-temperature creep deformations during in-service operations. This extreme thermo-mechanical environment leads to phase transformations as well as stress and microstructure gradients which dramatically alter mechanical properties. Indeed, a directional coarsening, known as γ'-rafting (see **Figure 1**), is observed in single-crystal superalloys for temperatures above 800 °C and sufficiently high applied stresses [**1**, **2**]. This phenomenon corresponds to a change in the γ'-phase aspect from a cuboidal to a platelet shape and is correlated to the sign of the misfit [**3**, **4**], the crystallographic orientation [**4**, **5**], and the amount of plastic deformation [**6**].

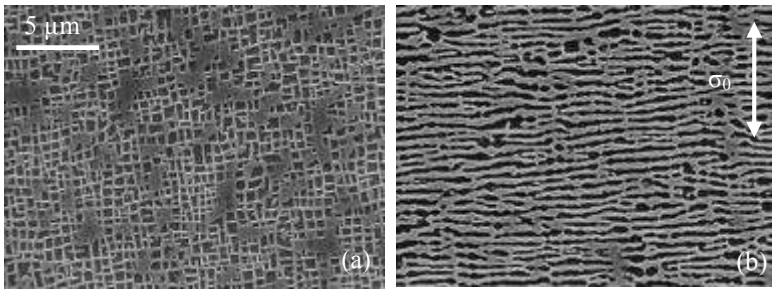

Figure 1: MC2 γ/γ' microstructural evolution during a multi-interrupted creep-fatigue test at 1050 °C/160 MPa: (a) at the beginning of the experiment (cuboidal γ' morphology) and (n) after 2.41 h (secondary creep stage – rafted γ' morphology). Note that the γ' phase appears in dark.

The orientation of the γ' rafts is dependent on the principal stresses [**7**]. Thus, multiaxial loading due to the intricate geometry of the turbine blades and the mechanical gradient generated by the cooling channels is highly disturbing the microstructure which modifies the local mechanical response. It is therefore essential to determine properly the evolution of the γ channel thickness in 3D in order to improve the predictability of models dealing with multiaxial state of stresses.

MODEL PRESENTATION

The 3D directional coarsening model is based on a work previously done by the author who developed a microstructure-sensitive model in a crystal plasticity framework [**8**]. This model is able to predict the mechanical response and the lifetime of specimens subjected to thermo-mechanical loading. The strain rate formulation of the γ'-phase evolution is taken into account the dissolution/precipitation of γ' precipitates during non-isothermal loading ($f_{thermic}$) , as developed in [**9**, **10**] and validated by synchrotron radiation [**11**], the homothetic growth due to high temperature conditions which leads to a spheroidization of the γ' precipitates ($f_{homothetic}$) , and the directional coarsening due to dislocation motions inside the γ channels ($f_{mechanic}$) . The final expression of the γ' thickness may be summarized by the following equation:

$$w = w_0 f_{thermic} \times (1 + f_{mechanic} + f_{homothetic}) \qquad \textbf{Eq. 1}$$

γ' rafts are perpendicular to the maximum principal stress, as shown by Cormier *et al*. [**7**] nearby pores. Therefore, the principal plastic strains are used since principal stresses and principal strains occur in the same directions and Matan *et al*. have shown that a creep strain threshold is necessary to be overcome so that the γ' rafting process become significant and can proceed [**12**]. So, the former expression for $f_{mechanic}$ based on the accumulated plastic strain is modified as follow:

[a] Corresponding author. Email: jblgpublications@gmail.com

$$f_{mechanic} = \frac{f_{diffusion}\sqrt[3]{\nu}}{1+\sinh^{-1}(\xi\nu_0)} \rightarrow \underline{f}_{mechanic} = \frac{f_{diffusion}\sqrt[3]{\underline{\varepsilon}_p^p}}{1+\sinh^{-1}(\xi\nu_0)} \qquad \textbf{Eq. 2}$$

In this equation, ν is the accumulated viscoplastic strain, ξ is a strain rate dependent function, ν_0 is a temperature dependent material parameter, $f_{diffusion}$ is a function taken into account the fact that the γ' microstructural evolution is a temperature-dependent phenomenon, and $\underline{\varepsilon}_p^p$ is the principal plastic strain vector.

NUMERICAL RESULTS

A <001>-oriented specimen was designed to generate a non-uniform and multiaxial complex mechanical field by the presence of two asymmetrical notches (see
Figure 2). Thus, the γ/γ' microstructure should evolve according to the local mechanical field of this sample which was tested under non-isothermal conditions with a reference level at 1050 °C/F = 410 N. An overheating of 20 s at 1200 °C under load was performed after 24 h of creep to obtain the influence of the plastic strain on the kinetics of both dissolution/precipitation and γ' rafting development. After the overheating, the specimen was crept for 30 more minutes at 1050 °C.

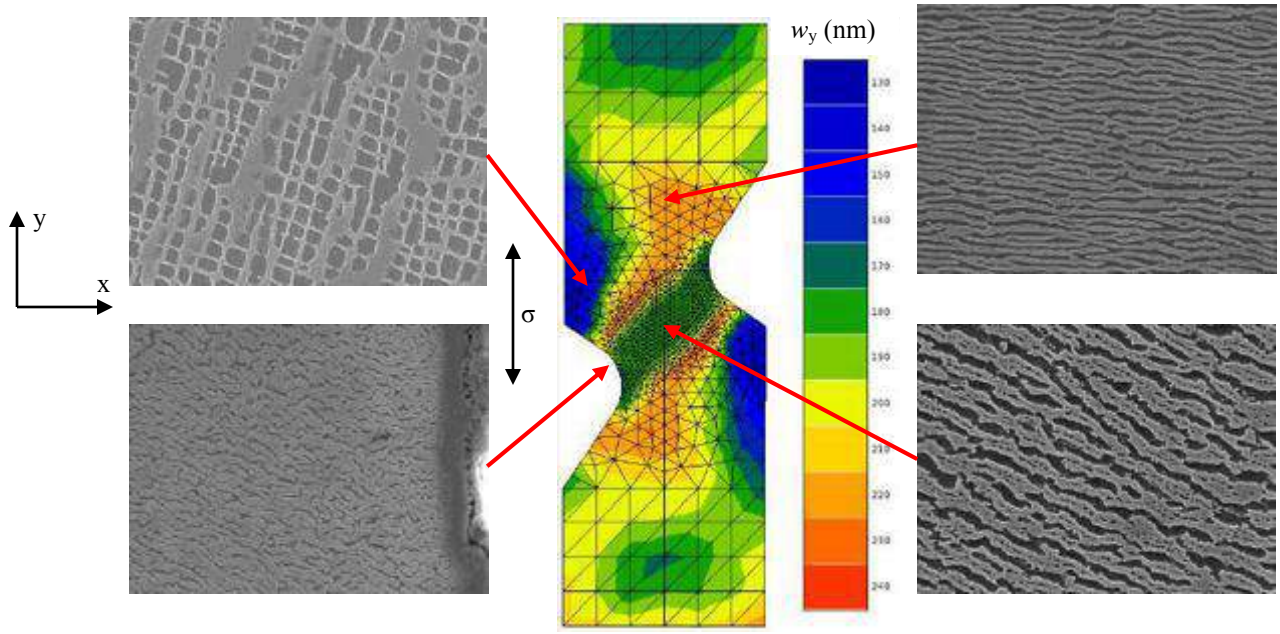

Figure 2: Microstructural observations of the γ' rafted microstructure at the end of the test by scanning electron microscopy and compared with the microstructural state predicted by the FE simulation for the y direction.

As observed in **Figure 2**, the 3D coarsening model gives a good result in terms of microstructural prediction. Indeed, the model is well predicting where the non-rafted microstructure is located (top-left microstructure) and where the γ' thickness is reduced due to the precipitation of fine γ' precipitates within the γ channels (bottom-right microstructure).

CONCLUSIONS

The model performance was tested comparing finite element simulations and experimental results on a bi-notched specimen generating strong multiaxial strain/stress fields. A rather good agreement of the microstructure model's predictions with the observation was obtained. The new 3D directional coarsening model is then able to tackle complex geometries and loads at high temperatures.

References

[**1**] Tien J. et al., Metall. & Mater. Trans. B 2 (1971) 215. [**2**] Pollock T. M. et al., Acta Metall. Mater. 42 (1994) 1859. [**3**] Pineau A., Acta Metall. 24 (1976) 559. [**4**] Kamaraj M. et al., Scripta Mater. 38 (1998) 589. [**5**] Tian S. G. et al., J. Alloy Compd. 563 (2013) 135. [**6**] Matan N. et al., Acta Mater. 47 (1999) 1549. [**7**] Cormier J. et al., Mat. Sci. Eng. A 501 (2009) 61. [**8**] le Graverend J.-B. et al., Int. J. Plast. 59 (2014) 55. [**9**] Cormier J. et al., Mater. Sci. & Eng. A 527 (2010) 6300. [**10**] Ghighi J. et al., Tech. Mech. 32 (2012) 205. [**11**] le Graverend J.-B. et al., Metall. & Mater. Trans. A 43 (2012) 3946. [**12**] Matan N. et al., Acta Mater. 47 (1999) 2031.

A THEORETICAL MODEL REVEALING STRONG STRAIN HARDENING IN GRADIENT NANO-GRAINED MATERIALS

Jianjun Li[1,2,a)], Shaohua Chen[3], Xiaolei Wu[3] & A.K. Soh[4]
[1]*Department of Engineering Mechanics, Northwestern Polytechnical University, Xi'an, Shaanxi, P. R. China*
[2]*Department of Microstructure and Alloy Design, Max-Planck-Institut für Eisenforschung GMBH, Germany*
[3]*State Key Laboratory of Nonlinear Mechanics, Institute of Mechanics, Chinese Academy of Sciences, P. R. China*
[4]*School of Engineering, Monash University Malaysia, Bandar Sunway, Salangor, Malaysia*

Summary Gradient nano-grained (GNG) materials possess both high strength and high ductility. Recent experiments attributed the outstanding synergetic properties to the extra hardening induced by the grain size gradient (GSG) structure. Here we developed a theoretical model to reveal the underlying correlation between the strong extra strain hardening achieved in the nano-grained layers of the gradient structure and the non-uniform deformation of the lateral surface observed in experiments. The proposed model led to the establishment of a simple physical law that can be expressed as $H^* = A^*$, where H^* and A^* are two dimensionless parameters. The former represents the extra strain hardening, while the latter characterizes the non-uniform deformation of the lateral surface. The values of these two parameters can be obtained through the experimental data, which undoubtedly validated the proposed physical law.

INTRODUCTION

Nano-grained metals and alloys are usually strong but brittle. However, one of our co-authors Wu et al. [1] observed a strong strain hardening behavior (Fig. 1) in the nano-grained layers of the GSG region in a GNG interstitial free (IF) steel sample, up to a tensile engineering strain of 0.25. They attributed the extra strain hardening to the non-uniform deformation in the lateral surface (Fig. 2). However, the critical issue of how the non-uniform lateral surface deformation induces the extra hardening has yet to be addressed [2]. Therefore, in the present study a theoretical model will be developed to quantitatively correlate the non-uniform deformation in the lateral surface of the GNG sample with the extra strain hardening achieved in the GSG layer based on the experimental observations made by Wu et al. [1] and the concept of geometrically necessary dislocations (GNDs) [3, 4].

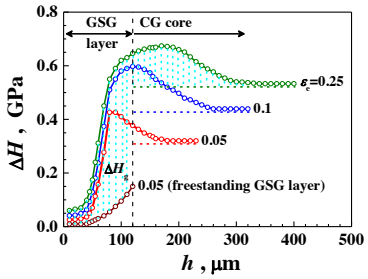

Figure 1. Variation of hardness increment ΔH (defined as the difference between the hardness along the thickness dimension of the sample "*after*" and "*before*" a tensile test) of GNG IF steel samples subjected to various tensile strains with respect to the depth h [1]. The short dashed lines represent the extra hardening (i.e., ΔH_g) achieved in the GSG structure resulting from the non-uniform deformation in the lateral surface for $\varepsilon_e = 0.25$.

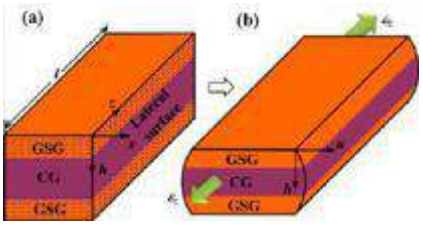

Figure 2. Schematic diagram of a GNG sample subjected to a uniform tensile strain ε_z : (a) before tensioning and (b) after tensioning before occurrence of necking. The GNG sample consists of two GSG surface layers sandwiching a CG core.

MODEL DESCRIPTION

a) Corresponding author. Email: jianjunli.mech@hotmail.com; j.li@mpie.de.

It has been widely accepted by researchers that non-uniform deformation is usually accommodated by GNDs [3, 4]. In this section, we will develop a physical model to correlate the non-uniform deformation in the lateral surface with the extra strain hardening (ΔH_g in Fig. 1) achieved in the GSG layer of the GNG sample based on the concept of GNDs. Fig. 3(a) presents a schematic diagram of the GNDs induced by the non-uniform deformation near the lateral surface of the GSG layer. A unit layer of thickness Δh is selected for analysis. The value of Δh is assumed to be small enough such that the deformed lateral surface can be approximated as a straight plane, that is, 'AB' can be viewed as a straight line. It is assumed that the GNDs are spaced equally along the sample depth h near the deformed lateral surface in the unit layer. The density of GNDs is then derived as: $\rho_{GSG} = a\Big/\left[b\left(\Delta h\right)^2\right]$, where b is the magnitude of Burger's vector of GNDs. By using Taylor's relation and Von Mises flow rule, we obtained a physical law that can be expressed as in a simple form as: $H^* = A^*$, where $H^* = \Delta H_g\left(2H - \Delta H_g\right)\Big/\mu^2$ (μ is shear modulus) and $A^* = a\Big/a^*$ (a^* is a constant) are two dimensionless parameters, which represent the extra strain hardening achieved in the GSG region and the non-uniform lateral surface deformation, respectively.

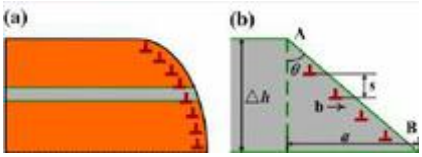

Figure 3. The GNDs in a GNG sample subjected to uniaxial tension. (a) GNDs near the deformed lateral surface in the GSG region; (b) GNDs in a unit layer (grey area in (a)).

RESULTS AND DISCUSSIONS

Fig. 4 presents the variation of two dimensionless parameters derived from the proposed model, i.e., H^* and A^*, with respect to the sample depth h for a GNG IF steel sample at $\varepsilon_e = 0.25$ in the GSG region. The results show that the values of both parameters first increase to a maximum value and then decrease, and they are comparable in magnitude. The value of A^* at $\Delta h = 0.314$ μm is in good agreement with that of H^* at large h, i.e., $h \in (80,120\ \mu\text{m})$, and they approximately approach an equal maximum value at the same sample depth h. The significant quantitative difference between the two parameters at small h is due to the significant influence of noise in the measured height profile data, because a small noise in lateral displacement data could generate a significant error in calculating its slope, i.e., the value of parameter a. As a result, the two parameters are deemed in agreement with each other, thus validating the proposed physical law.

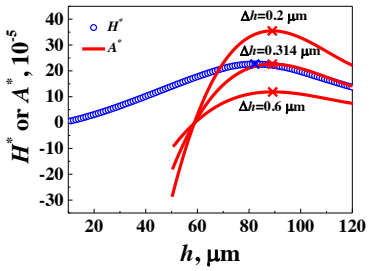

Figure 4. Comparison of two sample depth dependent dimensionless parameters, i.e., H^* and A^*.

CONCLUSIONS

A physical law has been derived to correlate the strong extra strain hardening (H^*) achieved in a grain size gradient structure with the non-uniform deformation (A^*) in the lateral surface of a GNG material based on the existing experimental observations and the concept of GNDs.

References

[1] X. Wu, P. Jiang, L. Chen, F. Yuan, Y.T. Zhu, Proc. Natl. Acad. Sci. U. S. A., 111 (2014) 7197-7201.
[2] K. Lu, Science, 345 (2014) 1455-1456.
[3] W.D. Nix, H.J. Gao, J Mech Phys Solids, 46 (1998) 411-425.
[4] M. Ashby, Philos Mag., 21 (1970) 399-424.

INTERNAL STRESSES IN DEFORMATION-INDUCED MICROSTRUCTURES

Maxime Sauzay[a] & Laurent Dupuy
CEA-Saclay, DEN-DMN-SRMA, bâtiment 455, 91191 Gif-sur-Yvette cedex, France

Summary Crystal FE computations are carried out to evaluate back and forward stresses in deformation-induced microstructures made of soft channels and hard walls. The computed mean phase values and profiles are close to the measured ones, showing that PSB and cell backstresses amount to 10-20% of the remote stresses whereas vein/channel ones are negligible. The plasticity behaviour in walls is taken into account based on DD computation results. Consequences in terms of maximum stable dipole height, crystal kinematic hardening and similitude laws are finally discussed.

INTRODUCTION

The amplitude of the internal stresses generated by dislocation microstructures such as persistent slip bands (Fig. 1 a), cells and veins / channels [1] has been the subject of many controversies. Based on dislocation measurement by TEM, some authors claim that their amplitude may reach one-half of the remote stress in dislocation poor channels of PSBs and several times the remote stress in the neigbouring dislocation rich walls [2]. X ray diffraction measurements lead to mean soft phase internal stresses of about 20% of the remote stress in both PSBs and cells produced by tensile deformation [3]. Some of these measurements based on the asymmetrical broadening of line profiles have been recently validated, at least qualitatively by using submicrometer spatial resolution [4]. On the contrary, other authors notice that the dipole height histograms are similar in walls and channels, which makes them think that internal stresses are in fact negligible [5,6]. More recently, CEBD measurements [6] have shown that the local stresses do not differ much in the veins and channels [4].
The composite model proposed by Mughrabi [1] explains the origin of internal stresses induced by the incompatible plastic deformations in soft and hard phases. Nevertheless, the accurate modelling of the internal stresses produced by the various deformation-induced dislocation microstructures is still missing. The deduced close-form expressions of internal stresses may allow the improvement of the simulation of crystal tensile hardening and the Bauschinger effect. Such physically-based modelling is still lacking whereas hardening laws due to dislocation-dislocation interactions have been proposed recently [7].

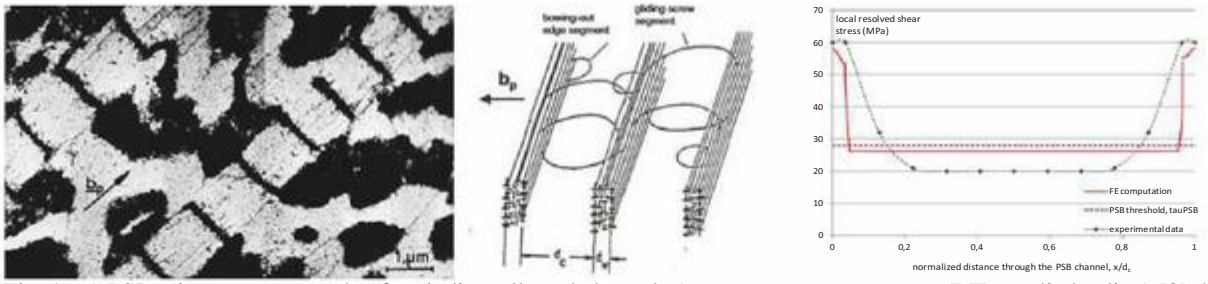

Fig. 1 : a) PSB microstructure made of periodic walls and channels (copper, room temperature (RT), cyclic loading) [8]; b) sketch of the PSB microstructure and c) computed & measured profiles of the resolved shear stress through wall and channel in PSBs, copper, RT. (experimental data: [6] after [2]). The left & right wall sides correspond respectively to $x/d_c=0$ & $x/d_c=1$.

COMPUTATION OF INTERNAL STRESSES

Crystal finite element (FE) computations are carried out using numerous meshes of PSBs (Fig. 1 a) embedded in an elastic matrix. Cubic elasticity and crystal plasticity laws are used together with the FE software, Cast3M. The values of PSB thickness, channel & wall widths have been measured by TEM at various temperatures in nickel and copper and reported in literature. In a first approach, walls are assumed to behave elastically in qualitative agreement with in-situ TEM observations [9] and theoretical evaluations of the wall critical shear stresses induced by their high densities of dipolar loops [5,10]. Therefore, on the worst, an overestimation of the internal stresses is expected. On the contrary, channels deform plastically. It has been checked that the specific values of the channel shear stress and hardening slope affect negligibly back and forward stresses. Additional FE computations are carried out in order to evaluate internal stresses in cells and veins / channels critical. Finally, discrete dislocation dynamics computations [11] are carried out accounting for PSB walls made of dipolar loops using measured densities [5]. The mean phase stresses and stress profiles computed by both approaches are compared together. The wall plasticity laws walls are deduced from DDD & incorporated in the previous FE computations for the sake of comparison.

RESULTS

[a] Corresponding author. Email: maxime.sauzay@cea.fr

As assuming elastic walls, the computed mean channel backstresses in copper and nickel PSBs range between 10 and 20% of the remote stress whatever the temperature. Their contribution to the remote stress decreases with temperature increasing. Because the average internal stress is equal to zero and the wall volume fraction is generally low (Fig. 1 a), the mean wall forward stresses are much higher and reach about two times the remote stresses (Figs. 1 c & 2 c). At room temperature, the backstresses reach 10-15% of the remote stress whereas the forward stresses around 125%. The computed mean phase values agree well with the values measured in PSBs [1,3,6]. The difference between predicted and computed stresses is within the measurement accuracy. Moreover, the predicted resolved shear stress profiles through walls and channels are rather close to the ones measured by TEM observations (Figs. 1 c & 2 a). But they differ somewhat close to the walls. It should be noticed that mean internal stresses should be equal to zero, which holds for the computed profiles, but not for the measured ones. The stress evaluation close to walls may be biased by small loop radius measurement & crude tension line coefficient values.
In the case of cells widely observed during either high amplitude cyclic loading or tensile straining, the backstresses computed in the soft phase are definitively not negligible with respect to the remote stress. They reach about 20% of the flow stress whatever the metal, crystal orientation and plastic strain magnitude. The predicted and measured values differ generally by less than the measurement accuracy [3]. The microstructure configuration of veins/channels is finally investigated. The predicted values are generally low and almost negligible. These results agree once more with the values measured by CEBD [6] and X-ray diffraction [3]. Therefore, the computed mean soft phase internal stresses can reach 20% of the flow stress in PSBs and cells, but are negligible in looser microstructures such as the vein / channel one. Such discrepancies may be explained by the differences between the PSBs and cells geometries on one side and the veins/channels geometry on the other side. In the first case, the plastic deformation of the soft phase is clearly hindered by the hardly deformable walls, whereas in the second case, the soft matrix contains hard phase inclusions, which configuration is more deformable than the first one.
The evaluations of PSB wall forward stresses allow an improvement in the prediction of the maximum stable edge dipole in PSB walls whatever the metal and temperature (Fig. 2 b), using the classical formula reported in [5]. This explains the huge discrepancy between measured heights and the ones computed as using the remote stress, often reported in literature [5,6].
Interestingly, the computed channel backstresses obey similitude laws with respect to channel thickness as the remote stress does [1]. Finally, for PSBs and cells, close-form expressions are deduced from the numerous FE computation results allowing the proposal of constitutive laws. Nevertheless, the prediction of deformation-induced microstructure characteristic lengths depending on material, temperature and loading conditions is still missing for closing the whole set of equations.

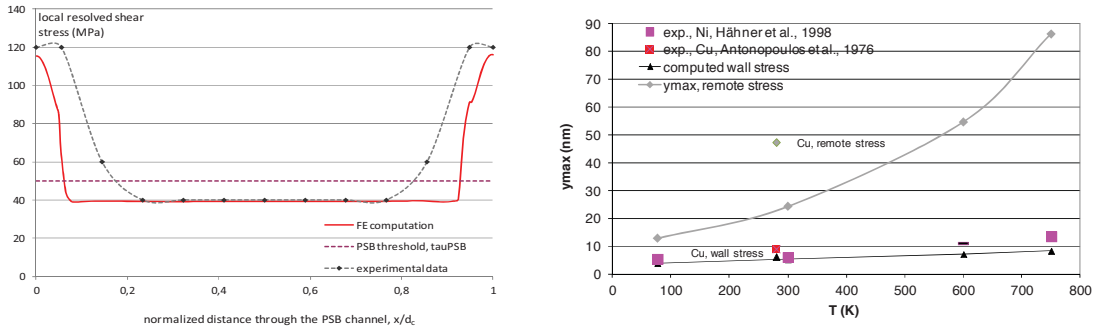

Fig. 2: a) same plots as in Fig. 1 c but for Ni at RT (experimental data [3]); b) computed and measured maximum dipole heights in copper and nickel PSB walls [12,5]. Either the remote shear stress or the wall shear stress (including forward stress) is used in the computation of the maximum stable dipole height.

References

[1] Sauzay M, Kubin L.P. *Prog. Mat. Sci.* **56**:725-784, 2011.
[2] Mughrabi H. *Acta Metall*. **31**:1367–79, 1983.
[3] Hecker M., Thiele E., Holste C. *Z. Metall*. **88**:321–328, 1997.
[4] Levine L.E., Larson B.C., Yang W., Kassner M.E., Tischler J.Z., Delos-Reyes M.A., Fields R.J., Liu W. *Nature Materials*, **5**:619-622, 2006.
[5] Hähner P., Tippelt B., Holste. *Acta. Mater*. **46**:5073-5084, 1998.
[6] Kassner M.E., Geantil P., Levine L.E. *Int. J. Plast*. **45**:44-60, 2013.
[7] Kubin L.P., Hoc Th., Devincre. *Acta Mater.* **57**:2567–2575, 2009.
[8] Mughrabi H., Ackermann F., Herz K. In: Fong JT, editor. *Fatigue mechanisms (ASTM-STP 675)*. Philadelphia (PA): ASTM 69–105, 1979.
[9] Tabata, T., Fujita, H., Hiraoka, M.-A., Onishi K. *Phil. Mag. A* **47**:841–857, 1983.
[10] Sauzay M. *Int. J. Plast*. **24**:727–745, 2008.
[11] Shi X.J., Dupuy L., Devincre B., Terentyev D., Vincent L. *J. Nucl. Mat.* **460**:37-43, 2015.
[12] Antonopoulos J.G., Brown L.M., Winter A.T. *Philos. Mag.* **34**:549–63, 1976.

DUCTILE FAILURE OF AN ALUMINUM ALLOY UNDER MODERATE TO LOW TRIAXIALITIES

Martin Scales[1a)], Nicholas Tardif[2], Kelin Chen[1], & Stelios Kyriakides[1]
[1]*Research Center for Mechanics of Solids, Structures & Materials, University of Texas at Austin, Austin, Texas, USA*
[2]*Université de Lyon, CNRS, INSA-LYON, LaMCoS, Villeurbanne Cedex, France*

Summary Custom Al-6061-T6 tubular specimens with a 1 mm thick test section are loaded to failure under radial paths of shear and tension. Deformations are measured with 3D digital image correlation. The thin-walled test section and use of DIC allow the stress and local deformations to be established from experimental measurements alone. The stress and deformation within the test section are uniform until a load maximum is reached, beyond which deformation localizes into a circumferential band with width the order of the wall thickness. A series of experiments show that the strain at failure monotonically increases as the triaxiality decreases, in contrast to previously-reported results for this alloy. The strains at failure are also significantly larger than previously-reported values. Numerical simulations demonstrate that the deformation, including localization, can be reproduced reasonably accurately to large strains with suitably-calibrated plasticity models.

BACKGROUND

Recent work on ductile failure under shear-dominant stress states has challenged the long-accepted premise that the strain at failure monotonically decreases with increasing triaxiality. Advancement in the field is challenged by the fact that ductile failure is preceded by large, highly localized deformations which are difficult to monitor and introduce an unknown stress state. We present results from experiments on tubular specimens loaded to failure under radial paths of shear and tension. A thinner test section machined into the specimens has nearly uniform stress and deformation up to the onset of localization, and provides minimum constraint to its development. 3D digital image correlation (DIC) is used to monitor the localized deformation up to rupture. The results differ significantly from other recent findings, and highlight the role that localization plays in accurately establishing a material's strain at failure.

EXPERIMENTAL

Setup and Procedure

Our specimens are machined out of commercially available 51 mm diameter Al-6061-T6 tubes. Each specimen is 230 mm long and has a uniform test section at mid-length that is 10.2 mm long and 0.965 mm thick. The ends of the tubes are gripped leaving approximately 12.7 mm lengths on either side of the test section unconstrained. The specimens are loaded to failure under radial paths of axial and shear stress in an axial/torsional biaxial testing machine. Loading is accomplished by prescribing a rotation (or displacement) and using the corresponding torque (force) as the command signal for the force (torque) – see [1,2]. 3D DIC is used to monitor surface strains across the full test section. This setup allows the stress and local deformations to be established directly from the experimental measurements.

A Typical Experiment

A radial stress experiment in which the nominal axial and shear stress are equal is outlined here. The specimen was loaded in rotation control. Figure 1 shows the nominal shear stress ($\mathcal{T}$) plotted against the relative rotation (ϕ) between the edges of the test section. The response follows the expected path with a linearly elastic region followed by mild hardening. The stress reaches a maximum (^) of 168 MPa at a rotation of about 7 deg. Beyond the limit load deformation localizes in a circumferential zone with a height that is of the order of the wall thickness (t_o). The test section rotates an additional 2.5 deg. with the stress decreasing. The rate at which the stress decreases accelerates just before failure, which is accompanied by a sudden load drop. The axial stress-elongation response follows a similar trajectory, with a normalized elongation (δ/L_g) of 0.035 at the limit load and 0.044 at failure.

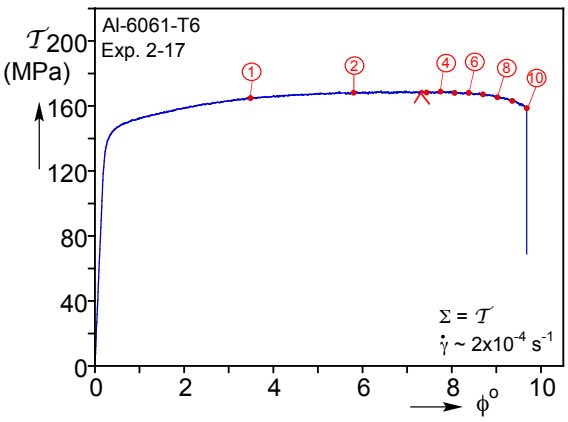

Fig. 1 Nominal shear stress-rotation response

The deformation of the test section and accompanying localization is qualitatively demonstrated in Fig. 2 with an image of the test section and the strains computed by the DIC system superimposed on the surface in the final image prior to failure. The relative rotation between the top and bottom of the test section is seen through the misalignment of the yellow triangles, which were initially aligned, and by the distortion of the originally-rectangular analyzed zone.

[a)] Corresponding author. Email: filipp@utexas.edu.

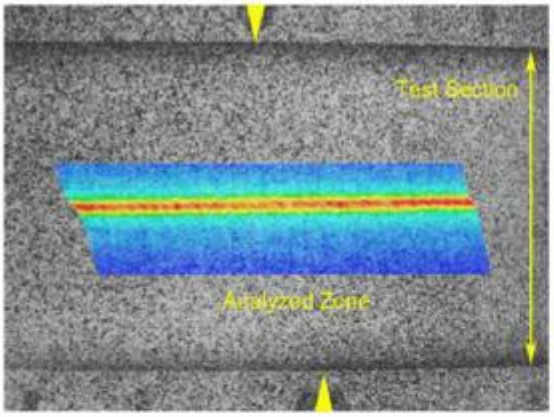

Fig. 2 Deformed specimen test section

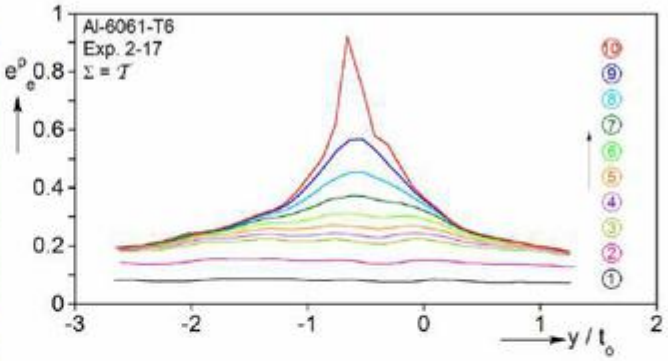

Fig. 3 Strain profiles across localization zone.

A quantitative visualization of the deformation and severity of localization is shown in Fig. 3, where profiles of equivalent plastic strain across the height of the analyzed zone are plotted. Profile numbers correspond to the 10 stations marked on the response in Fig. 1. Profiles ① and ②, corresponding to stations preceding the limit load, show that the strain is essentially uniform across the analyzed zone. In ③, just after the limit load, the profile bends upward indicating that localization has commenced. At stations ⑤ through ⑧ the strain grows in an increasingly narrower zone. At station ⑨, just before failure, the strain has grown significantly within a span of about $1.5t_o$ and reaches a maximum of 0.57. In the last station recorded, ⑩, the strain has increased further but intensifies over a central span of just one wall thickness, reaching a peak of 0.921. Collectively the results demonstrate the very high strain gradients that develop prior to rupture.

Summary of Failure Strains

A set of experiments with varied stress ratios was conducted to span triaxialities from 0.072 to 0.57. In Fig. 4, the maximum equivalent plastic strain in the last DIC image recorded prior to failure (DIC Max) is plotted against the corresponding triaxiality. Also shown are the failure locii for this material of Johnson-Cook and Beese et al. [3]. The present failure strains monotonically increase with decreasing triaxiality and are nearly three-times higher than those previously reported. These results demonstrate the importance of an experimental setup that permits localized deformation to develop free of constraints, coupled with a diagnostic method capable of capturing the high gradients that develop. This combination enabled measurements of stress and strain at failure directly from the experiments and without resort to numerical analysis and constitutive models.

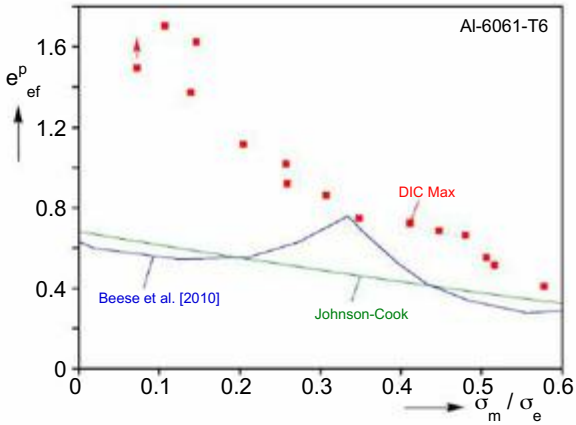

Fig. 4 Measured failure strains vs. triaxiality.

ANALYSIS

Results from numerical simulations of the experiments demonstrate that the deformation, including localization, can be reproduced quite accurately to large strains by suitably-calibrated plasticity models that include the prevalent anisotropy (e.g., [4]).

Acknowledgement

Financial support received for this work from the ssupport of this work from Ford Motor Company and Sandia National Laboratories is acknowledged with thanks.

References

[1] Haltom, S.S., Kyriakides, S., Ravi-Chandar, K.: Ductile Failure Under Combined Shear and Tension. *Int. J. Solids Stru.* **50**:1507-1522, 2013.

[2] Scales, M., Tardif, N., Kyriakides, S.: Ductile Failure of Aluminum Alloy Tubes Under Combined Torsion and Tension. *Int. J. Solids Stru.* (in preparation)

[3] Beese, A.M., Luo, M., Li, Y., Bai, Y., Wierzbicki, T.: Partially Coupled Anisotropic Fracture Model for Aluminum Sheets. *Eng. Fract. Mech.* **77**:1128–1152, 2010.

[4] Barlat, F., Aretz, H., Yoon, J.W., Karabin, M.E., Brem, J.C., Dick, R.E.: Linear Transformation-Based Anisotropic Yield Functions. *Int. J. Plast.* **21**,1009–1039, 2005.

TOWARD A GENERAL DESCRIPTION OF TRANSFORMATION PLASTICITY IN METALS AND ALLOYS

Jean-Baptiste Leblond[1a)], Gilles Perrin[2]
[1]*UPMC Univ Paris 06, CNRS, UMR 7190, Institut Jean Le Rond d'Alembert, Tour 65-55, 4 place Jussieu, 75252 Paris Cedex 05, France*
[2]*AREVA, Tour Areva, 1 place Jean Millier, 92084 Paris La Défense Cedex, France*

Summary An innovative approach to the modelling of transformation plasticity in metals and alloys is undertaken, considering the sole Greenwood-Johnson mechanism wherein the phenomenon is attributed to microplasticity in the weaker mother phase, arising from differences of specific volume between the two phases. This approach is based on combination of analytical calculations, micromechanical numerical simulations and experiments. This paper is devoted to the analytical part. A model of growth of an ellipsoidal core of daughter phase in an ellipsoidal volume of mother phase, in the absence or presence of some external stress, is developed. The case of a prolate, spheroidal core is envisaged in a first step. The results evidence the influence of the core shape upon the overall deformation of the cell obtained after its complete transformation, in the absence or presence of some external stress.

PRESENTATION OF CONTEXT

The wording *transformation plasticity* has been coined to designate the anomalous plastic behaviour of metals and alloys during solid-solid phase transformations, especially during cooling. It is commonly observed that during such transformations, plastic flow occurs without any threshold, that is for any level of applied stress, no matter how small; the rate of plastic strain is not arbitrary but governed by the rate of transformation from the mother- to the daughter-phase, and increases with the stress applied. Accurate modelling of this phenomenon is of paramount importance for numerical simulations of welding, quenching and more generally all thermomechanical processes involving solid-solid phase changes, in order to correctly predict residual stresses and distortions.

Transformation plasticity is commonly attributed to two distinct mechanisms proposed some years ago by Greenwood-Johnson [1] and Magee [2] respectively. In Greenwood and Johnson's interpretation, transformation plasticity arises from standard (dislocation-induced) plasticity at the microscopic scale, occurring in the weaker, mother phase even in the absence of external stress, because of the difference of specific volume between the two phases which generates internal stresses. In Magee's interpretation, transformation plasticity is not due to ordinary plasticity but to the (elastic-like) "transformation strain" accompanying the transformation, which is "oriented" by the external stress applied. In practice, the Greenwood-Johnson mechanism seems in most cases to account for most of the effect observed, the sole exception being the case of shape memory alloys in which the specific volumes of the phases are almost identical so that this mechanism is absent.

Theoretical models of transformation plasticity have been developed, generally considering the sole mechanism of Greenwood and Johnson since it seems to be the only one amenable to some theoretical treatment through homogenization. The most classical one is that of Leblond et al. [3]. This model is based on consideration of a spherical cell of mother phase subjected to some external stress, in which a spherical core of daughter phase gradually grows. It yields an expression of the rate of the overall plastic strain (the "transformation plastic strain rate") during the transformation, involving the external stress and the rate of transformation. This expression does not involve any adjustable parameter, but only the yield stress of the mother phase and the difference of specific volume between the phases. It has repeatedly been found to satisfactorily reproduce the results of dilatometry experiments under small applied stresses, and used many times in numerical simulations of thermomechanical processes.

One drawback of this model, however, lies in the overall isotropy of the (spherical) model geometry considered. This isotropy implies that in the absence of external stress, the microscopic plastic strain in the mother phase must average out to zero, because the average value must be a multiple of the unit tensor, and its trace is necessarily zero; that is, the overall strain after complete transformation of the volume must only reflect the difference of specific volume between the phases, in the absence of any macroscopic expression of plasticity. Unfortunately this is often observed not to be true in actual experiments, the overall strain after complete transformation being clearly influenced by plasticity: for instance, the specimen often does not recover its original dimensions at the end of a full thermal cycle, clearly indicating the presence of irreversible effects. The current explanation of such features lies in the overall morphological anisotropy of the transformation: for various reasons, the growing cores of daughter phase are closer to ellipsoids with specific principal directions than to spheres, so that the average value of the microscopic plastic strain in the mother phase has no reason to be a multiple of the unit tensor and consequently does not vanish, even in the absence of external stress.

[a)] Corresponding author. Email: jbl@lmm.jussieu.fr.

PURPOSE OF THE WORK

With the accurate prediction of residual stresses and distortions in mind, it is therefore important to develop an extended model of transformation plasticity in metals and alloys, based on consideration of the sole mechanism of Greenwood and Johnson like that of Leblond [3], but incorporating effects of possible morphologic anisotropy. A research programme has just been launched for this purpose.

OUTLINE OF RESEARCH PROGRAMME

The programme will involve three aspects:

1) Analytical calculations extending that of Leblond [3] through consideration of growth of an ellipsoidal core of daughter phase within an ellipsoidal volume of mother phase, instead of a spherical core within a spherical volume. Two types of calculations are planned, in the absence and presence of some external stress.
2) Micromechanical numerical simulations of the growth of cores of daughter phase within a matrix of mother phase, aimed at confirming or improving the analytical calculations. Two types of simulations are planned: elementary ones, performed by the finite element method, involving the growth of an ellipsoidal core of daughter phase within an ellipsoidal volume of mother phase, just like in the analytical calculations; and more complex simulations, using Moulinec and Suquet's [4] FFT-based numerical homogenization scheme, involving multiple cores of daughter phase more or less randomly dispersed within a large volume of mother phase.
3) Experiments of free (unconstrained) dilatometry or dilatometry under various applied stresses, aimed at measuring the overall strain during and at the end of transformations, and simultaneously examining morphologic anisotropies (as characterized by the final shape and orientation of the grains of daughter phase).

ANALYTICAL CALCULATION OF THE GROWTH OF A PROLATE SPHEROIDAL CORE OF DAUGHTER PHASE WITHIN A PROLATE SPHEROIDAL VOLUME OF MOTHER PHASE

The talk is devoted to the presentation of the first analytical calculations performed, which consider the growth of a prolate spheroidal core of daughter phase within a confocal prolate spheroidal volume of mother phase. Two distinct calculations, in the absence and presence of an external stress, are presented. These calculations make a heavy use of (axisymmetric) spheroidal coordinates (λ, β, ϕ) for which the iso-λ surfaces are confocal spheroids while the iso-β surfaces are orthogonal hyperboloids, plus a trial incompressible velocity field expressed in these coordinates, approximately describing the velocity field in the surrounding shell of mother phase resulting from the transformation-induced expansion of the spheroidal core of daughter phase. This field was discovered by Gologanu et al. [5] and successfully used by these authors to study void growth and ductile rupture in porous metals containing prolate spheroidal cavities, so it is hoped to also be a good approximate field for the phase growth problem.

The main results of these calculations are two-fold:

1) In the absence of external stress, the overall strain after complete transformation has a nonzero deviatoric component due to plasticity: the expansion of the cell, instead of being one third of the difference of specific volume between the phases in all directions of space, is less than this value in the direction of the axis of rotational symmetry of the spheroids, and more in the two orthogonal directions.
2) In the presence of some external stress, the transformation plastic strain (that is, the difference between the plastic strains obtained without and with the external stress) is slightly less than for growth of a spherical core within a spherical matrix.

Both of these theoretical predictions seem to be in qualitative agreement with the results of some old but high-quality experiments of Desalos [6].

References

[1] Greenwood G.W., Johnson R.H.: The Deformation of Metals under Small Stresses during Phase Transformations. *Proc. Roy. Soc. London* **A 283**:403-422, 1965.

[2] Magee C.L.: Transformation Kinetics, Microplasticity and Ageing of Martensite in Fe-31Ni, PhD Thesis, Carnegie-Mellon University, Pittsburgh, 1966.

[3] Leblond J.B., Devaux J., Devaux J.C.: Mathematical Modelling of Transformation Plasticity in Steels – I: Case of Ideal-Plastic Phases. *Int. J. Plast.* **5**:551-572, 1989.

[4] Moulinec H., Suquet P.: A Numerical Method for Computing the Overall Response of Nonlinear Composites with Complex Microstructures. *Comput. Meth. Appl. Mech. Engng*. **157**:69-94, 1998.

[5] Gologanu M., Leblond J.B., Devaux J.: Approximate Models for Ductile Metals Containing Non-Spherical Voids - Case of Axisymmetric Prolate Ellipsoidal Cavities. J. Mech. Phys. Solids **41**:1723-1754, 1993.

[6] Desalos Y.: Comportement Dilatométrique et Mécanique de l'Austénite Métastable d'un Acier A533, IRSID Report #95349401, 1981.

CONSTITUTIVE MODEL OF SERRATED YIELDING AT EXTREMELY LOW TEMPERATURES INCLUDING MECHANICAL AND RADIATION DAMAGE

Błażej Skoczeń[1], Jan Bielski[1]
[1] *Institute of Applied Mechanics, Cracow University of Technology, Poland*

Summary The paper describes the constitutive model of discontinuous plastic flow (DPF, serrated yielding), that occurs at extremely low temperatures. A physically-based constitutive description of material behaviour, including damage evolution of mechanical and radiation origin, has been developed. The stress serrations are evaluated on the basis of changes in dislocations density, instead of a phenomenological unobservable function of state parameters. The mechanical damage description is based on the Lemaitre-Chaboche approach, whereas, the post-irradiation damage evolution is based on the Rice and Tracey evolution law for the size of clusters of micro-voids.

DISCONTINUOUS PLASTIC FLOW (DPF)

The problem of constitutive modelling of material, that exhibits instability at extremely low temperatures, was examined by the authors in Ref. [4] and Ref. [5], for uniaxial and multiaxial cases, respectively. Also, some conference presentations addressed the problem, e.g. Ref. [1], [2]. The phenomenon is met during monotonic tension of a sample at extremely low temperatures (for instance in liquid helium at 4.2K). First, elastic deformation is followed by regular plastic flow. However, after some plastic strain threshold is exceeded, the yielding becomes discontinuous (serrated). At the macroscopic scale one observes repeated sudden drops of stress value, while strain increases monotonically (Fig. 1a). After each drop of stress, short relaxation process goes on (stress value decreases asymptotically), and then elastic reloading follows until an updated yield surface is reached. The macro scale effect is physically explained at the micro level, by postulating thermo-mechanical nature of the observed instability. Namely, the density of dislocations (ρ) increases significantly due to the evolution of lattice barriers (Lomer-Cotrell locks), which block their motion. After critical interaction of L-C barriers density (B) and shear stress (τ_e) at the head of dislocation pile-up, the barriers are broken and spontaneous motion of dislocations happens. Such a collective effect triggered by avalanche-like crossing of Lomer-Cottrell locks by edge dislocation pile-ups manifests itself in the form of macroscopic slip (sudden increase of the permanent plastic strain) and temperature increase (due to plastic power dissipation). It is observed that the slip takes place at a fixed value of total strain. Since the plastic part of strain increases jump-like, the elastic one decreases by the same value, and hence the drop of stress is observed. Together with the plastic strain, the mechanical damage evolves in the material. For initially irradiated material, the mechanically induced damage is combined with the radiation-induced counterpart.

NEW FEATURES OF CONSTITUTIVE MODEL

Stress serrations

The way the drop-of-stress value is calculated, is the key point of any constitutive model that includes the DPF phenomenon. Here, new approach, based on micro scale, is proposed. The relation between the after-serration stress (σ) in the lattice and the after-serration density of dislocations (ρ_0) is defined as:

$$\sigma = M\left(\tau_0 + G\alpha b\sqrt{\rho_0}\right) \tag{1}$$

whereas, just before serration the stress value (σ^p) stays on the yield surface and is related to dislocation density by:

$$\sigma^p = M\left(\tau_0 + G\alpha b\sqrt{\rho}\right) \tag{2}$$

where M is the Taylor factor, τ_0 stands for the shear stress of internal friction, G is the shear modulus, α is the coefficient of dislocations interaction, b denotes length of the Burgers vector. Hence, the plastic strain serration increment is expressed as:

$$\Delta\varepsilon_p^{serr} = MG\alpha b / E\left(\sqrt{\rho} - \sqrt{\rho_0}\right) \tag{3}$$

depending on the density of dislocations before and after the drop of stress (Fig. 1b). The evolution law for the density of dislocations prior to serration, including creation and annihilation terms, is given in Ref. [3, 4, 5]. It is assumed that after-serration density of dislocations is not kept at initial level ($\rho_0{}^0$), but evolves during the loading process and depends on the current plastic strain and density of dislocations prior to serration:

$$\rho_0 = \left(\frac{0.00031}{\varepsilon_p{}^{1.5}} + 0.2\right)\rho \tag{4}$$

Also, the value of B does not entirely vanish after a particular serration. After-serration values of these parameters are 'foot prints' of the repeated process of accumulation, followed by failure of the barriers.

[a] Corresponding author. Email: **Blazej.Skoczen@pk.edu.pl**

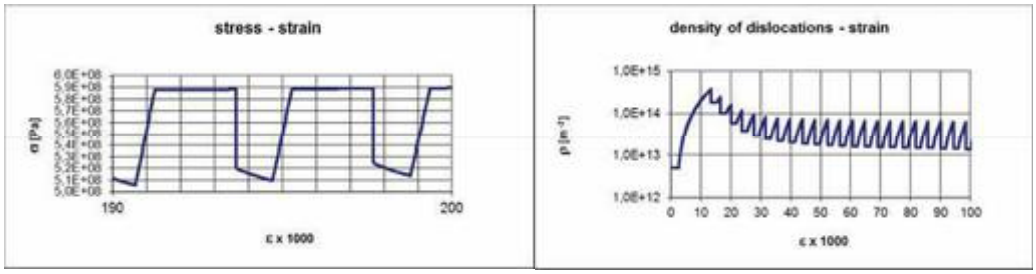

Figure 1: a) Four stages of plastic flow: continuous hardening, serration, relaxation, elastic reloading back to hardening curve; b) Density of dislocations in the course of serrated yielding

Mechanical damage

Within the framework of continuum damage mechanics, the mechanically induced damage is ruled by the plastic strain and is described by a parameter D_{m}, following the Lemaitre-Chaboche kinetics:

$$\Delta D_{\mathrm{m}} = \left(\frac{\sigma^2}{(1-D)^2 2ES_0}\right)^{s_0} \Delta\varepsilon_p \quad \text{for } \varepsilon_{\mathrm{p}} > \varepsilon_{\mathrm{pD}} \tag{5}$$

Post-irradiation damage

The evolution of post-irradiation damage parameter (D_{ir}) is also ruled by the plastic strains [6]:

$$\Delta D_{\mathrm{ir}} = q_{\mathrm{A}}\pi r^2\left(exp\left(2A\varepsilon_{\mathrm{p}}\right) - 1\right)\Delta\varepsilon_{\mathrm{p}} \tag{6}$$

where q_{A} stands for surface density of clusters of voids caused by radiation and depends on the irradiation dose; r is the mean cluster radius and evolves according to the Rice and Tracey law: $\Delta r = r\left(exp\left(A\varepsilon_{\mathrm{p}}\right) - 1\right)$. It is postulated that the increments of the mechanically induced damage parameter and the post-irradiation damage parameter are added to obtain increment of total damage parameter $\Delta D = \Delta D_{\mathrm{m}} + \Delta D_{\mathrm{ir}}$. The macroscopic emanation of damage evolution consists in degradation of the elasticity modulus (unloading and reloading modulus) from initial Young's modulus to a current effective one (Fig. 2) $E_{\mathrm{ef}} = E(1 - D)$.

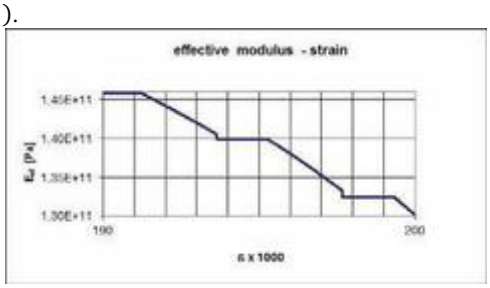

Figure 2. Change of the effective modulus in the course of serrated yielding due to mechanically induced damage.

CONCLUSIONS

A new approach is proposed for evaluation of drop of stress during serrated yielding. The physically based formulation is based on the density of dislocations met in the material just before and just after serration. These values are likely to be estimated in experiments. The foot prints of repeated serrations are included by the assumption of evolution of the initial density of dislocations, which, after serration, is not restored to a virgin material value. Also, the after-serration density of the LC locks is reduced to non-zero value. The constitutive model is supplemented with damage evolution, including the mechanically induced as well as the post-irradiation damage.

References

[1] Bielski, J., Skoczeń, B., Multiscale constitutive model of discontinuous plastic flow (DPF) at cryogenic temperatures, 3rd Int. Conf. on Material Modelling incorporating the 13th European Mechanics of Materials Conf., Book of abstracts, Dłużewski, P., Jurczak, G., Young, T.D., Eds, IPPT PAN, 55, 2013.

[2] Bielski, J., Skoczeń, B., Modified constitutive model of discontinuous plastic flow in intermetallic composites, PCM-CMM-2015 – 3rd Polish Congress of Mechanics & 21st Computer Methods in Mechanics September 8th –11th 2015, Gdansk, Poland

[3] Bouquerel, J., Verbeken, K., De Cooman, B.C., Microstructure-based model for the static mechanical behaviour of multiphase steels, Acta Materialia 54, 1443–1456, 2006

[4] Skoczeń, B., Bielski, J., Sgobba, S., Marcinek, D., Constitutive model of discontinuous plastic flow at cryogenic temperatures, International Journal of Plasticity, 26 (12), pp. 1659-1679, 2010.

[5] Skoczeń, B., Bielski, J., Tabin, J., Multiaxial constitutive model of discontinuous plastic flow at cryogenic temperatures, Int. J. of Plast. 55, 198-218, 2014.

[6] Skoczeń, B., Ustrzycka, A., Kinetics of evolution of radiation induced micro-damage in ductile materials subjected to time-dependent stresses, Applied Mechanics and Materials, 2015, (Vol. 784, pp. 43-50). Trans Tech Publications.

STRAIN LOCALIZATION DURING DISCONTINUOUS PLASTIC FLOW AT EXTREMELY LOW TEMPERATURES

Jakub Tabin [a] & Błażej Skoczeń
Institute of Applied Mechanics, Cracow University of Technology, Cracow, Poland

Summary The phenomenon of strain localization in the course of discontinuous plastic flow (DPF) at extremely low temperatures is investigated. DPF is observed mainly in fcc metals and alloys strained in cryogenic conditions, practically down to absolute zero. Recent experiments indicate strong strain localization in the form of shear bands propagating along the sample. The Dirac-like temperature response is measured by thermometers located within the gauge length of the sample. Spatio-temporal correlation indicates smooth shear band propagation, as long as the process of phase transformation remains on hold. The model of temperature distribution represented by Green-like solution of heat diffusion equation describes the strain localization effect.

DPF VERSUS PLC

The phenomenon of strain localization in the course of discontinuous plastic flow (DPF, serrated yielding) at extremely low temperatures has not been addressed in the literature. On the other hand, a significant effort has been focused on the mechanism of shear bands initiation and propagation during the so-called PLC (Portevin-Le Chatelier) effect, observed in certain materials at room temperature. The reason for such a dramatic lack of information on the behaviour of materials at extremely low temperatures is related to testing conditions. The experiments are carried out inside a double-wall cryostat, which is not transparent and usually tightly equipped with necessary instruments. Thus, there is practically no possibility to scan the surface of the sample by means of such instruments like thermographic camera, in order to detect possible effects of strain localization. In order to do so, specific deduction methods have to be used, which has been explained in the present paper.

MOTION OF SLIP BANDS DURING DPF

Thermodynamic conditions of DPF are strictly linked to the so-called thermodynamic instability, related to vanishing specific heat when the temperature approaches absolute zero. Macroscopic character of DPF is reflected by stress oscillations as a function of strain (time) and generation of plastic power partially converted to heat during each serration. The relevant stress-strain and temperature-strain curves are shown in Fig. 1.

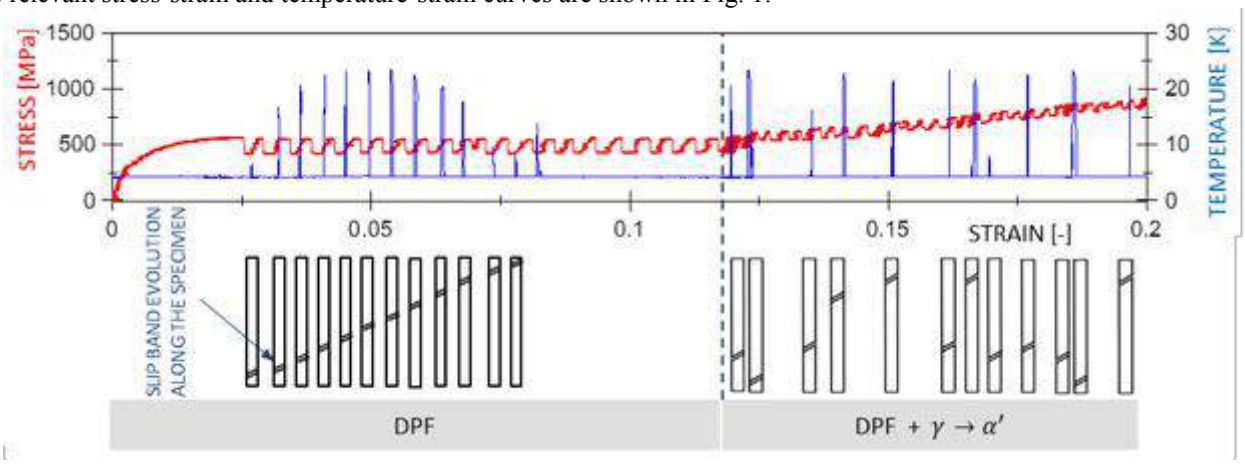

Figure 1 Tensile test results: the stress-strain curve (red) and temperature-strain curve (blue) for 304 stainless steel at liquid He temperature (4.2 K). Visualization of slip band evolution along the specimen.

It is worth pointing out, that during tensile tests of stainless steel (304, 304L, 316, 316LN) the plastic strain induced $\gamma \rightarrow \alpha'$ phase transformation [1] is also observed. This fcc-bcc phase transformation is represented by hardening effect, well visible in the stress-strain curve. The stress-strain and the temperature-strain characteristics (Fig. 1) indicate the nature of slip band propagation during cryogenic tensile test performed on 304 stainless steel. Analyzing the results, it is worth focusing on temperature spikes distribution in the range without phase transformation (no hardening). The envelope of the temperature-strain curve (spikes) may suggest the nature of slip band evolution during tensile test at liquid He. Temperature distribution in this range has regular form (comb-like profile), which occurs when the slip band freely propagates from one extremity of the specimen to the other. On the other hand, distribution of temperature spikes in the hardening range is random, which reflects irregular and constrained motion of the slip bands (Fig. 1).

[a] Corresponding author. Email: kubatabin@mech.pk.edu.pl.

MULTISCALE THERMO-MECHANICAL CONSTITUTIVE MODEL OF DPF

Such experimental evidence of strain localization process must be taken into account in the constitutive model of DPF by locating the representative volume element (RVE) inside the slip band. DPF consists in massive failure of lattice barriers associated with increase of the resolved shear stress at the heads of dislocations pile-ups, until the stresses reach the level of cohesive strength of the material [2,3]. The kinetics of DPF is expressed by:

$$\dot{B} = F_{\mathrm{LC}}^{+}\left(\rho, T, \underline{\underline{\sigma}}\right)\dot{p}H\left(p - p_{\mathrm{LC}}\right)$$

Where $\dot{B}$ denotes rate of the number of barriers per unit surface, F_{LC}^{+} is function of dislocations density ρ, temperature T and stress σ, whereas, p_{LC} represents the threshold above which the lattice barriers massively develop and $H(..)$ denotes the Heaviside function.

The plastically active process, including plastic slip accompanied by abrupt drop of stress, takes place inside the slip band and the plastic work is partially converted to heat. For what concerns the thermodynamic aspect of slip band propagation, the amount of heat generated in the course of loading can be approximately estimated by means of simple energy balance. It leads to evaluation of temperature increase (spike), resulting from low temperature thermodynamic instability (Fig. 2a). The experimental results indicate that the response of thermometer (size of spike) depends on the place where the slip band occurs (Fig. 2b).

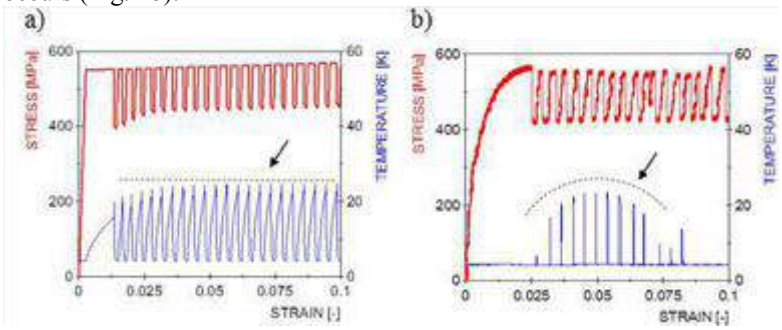

Figure 2 Comparison of a) numerical and b) experimental stress-strain (red) and temperature-strain (blue) curves corresponding to DPF (304 stainless steel).

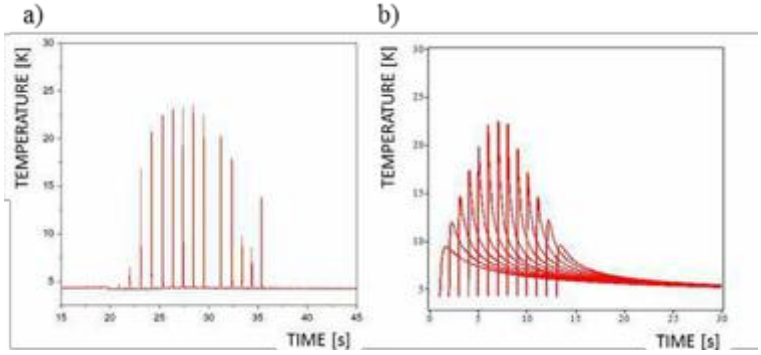

Figure 3 Time response of thermometer during tensile test of 304 stainless steel at liquid He temperature, a) experimental results, b) numerical results.

The thermo-mechanical process leading to temperature oscillations can be more precisely described by means of heat diffusion analysis, including temperature response at a distance from the heat source. Temperature profile (spikes) obtained as a result of heat diffusion analysis (involving thermodynamic parameters and variables depending on temperature) turns out very similar to what is measured during the experiment (Fig. 3) .

However, as soon as the phase transformation process takes place, the motion of slip bands is hindered by formation of the secondary phase inclusions. For this reason, the temperature spikes occurring during the phase transformation are randomly redistributed (Fig. 1). Most probably, the free path of a slip band is limited to the average distance between the secondary phase inclusions and the initiation of slip band has random character. This part of the process, seen from the point of view of temperature measurements, has disordered character.

CONCLUSIONS

Physically based multiscale constitutive model of DPF has been substantially improved by adding correct description of slip band propagation and related thermo-mechanical effects. An explanation of DPF coupling with the fcc-bcc phase transformation process at extremely low temperatures is underway.

References

[1] Ortwein, R., Skoczeń, B., Tock, J.Ph., 2014, Micromechanics based constitutive modeling of martensitic transformation in metastable materials subjected to torsion at cryogenic temperatures. International Journal of Plasticity, 59,152-179.

[2] Skoczen, B., Bielski, J., Marcinek, D., Sgobba, S., 2010. Constitutive model of discontinuous plastic flow at cryogenic temperatures. International Journal of Plasticity 55, 198–218.

[3] Skoczen, B., Bielski, J., Tabin, J., 2014. Multiaxial constitutive model of discontinuous plastic flow at cryogenic temperatures. International Journal of Plasticity 26, 12, 1659-1679.

THERMALLY ACTIVATED MECHANISMS IN THE DISLOCATION PLASTICITY AT VARIANT STRAIN RATES

Xiaozhi Tang[1], Yafang Guo[1a)], Lixin Sun[2], Sidney Yip[2], & Bilge Yildiz[2b)]
[1]*Institute of Engineering Mechanics, Beijing Jiaotong University, Beijing, China*
[2]*Department of Nuclear Science and Engineering, Massachusetts Institute of Technology, Cambridge, MA, USA*

Summary We aim to investigate the interaction between an edge dislocation and a self-interstitial-atom cluster in body-centered-cubic Fe. In our simulations, dislocation climb mechanism is introduced into the deformation process at low strain rates, and a newly discovered defect attached to the dislocation line pins down the dislocation incompletely at high strain rates. The difference on thermally activated mechanisms during the dynamic response of plastic deformation induces the variation of critical resolved shear stress, which reflects the lattice resistance of dislocation gliding. In this study we see the coupling of strain rate and thermal activation governs nonequilibrium reaction mechanisms in the defect evolutions.

INTRODUCTION

In the plasticity of most pure metal and some alloys, the coupled displacive-diffusional mechanism dominates deformation at low strain rates and high temperature [1]. In irradiated metals, both athermal glide of dislocation and thermal activation of point defect diffusion are responsible for the kinetic process of plastic flow. Point defect clusters act as obstacles to moving dislocations, leading to hardening when self-diffusion rate are not significant. While the absorption of point defect creates individual jogs, a unit process through which dislocation climb occurs [2]. Unfortunately, dislocation climb is almost impossibly obtained from conventional molecular dynamics, which is incapable of offering atomic-scale details in the low strain-rate regime due to the time scale limitations [3].

In 2013, a newly developed atomistic approach [4] based on transition state theory (TST) [5] and the concept of a strain-dependent effective activation barrier was proved to be useful in revealing the deformation mechanism over strain rates from 10^{-7} s-1 to 10^{7} s-1. We chose edge dislocations for the sensitivity of its low intrinsic lattice resistance to strain rates would be more interesting, and the climb mechanism of edge dislocations is what we mostly concern about.

RESULTS AND DISCUSSION

First, we searched the transition states by ABC method without any external load applied, to find out possible diffusion processes between the SIA cluster and the edge dislocation. The reaction pathway varies according to the relative position of the two defects, and obviously to the local strain environment also. There are two transition states before the SIA cluster is totally absorbed by the edge dislocation. In the first transition state, the SIA cluster finds itself a new position which is closer to the dislocation by a migration towards it, and in the second transition state, the SIA cluster attaches to the dislocation in a configuration we call C3 here. By NEB method, the diffusion barriers associated to these states are determined. The transition state of the cluster migration needs activation energy as high as 0.54 eV, for it reveals cross-core diffusion in which SIAs behave like solute atoms. From compress strain field to tensile strain field, lattice resistance is significant and complicated even though the SIA cluster generally has a high mobility in the bulk. More importantly, the energy barrier from C3 configuration to a jog pair of the dislocation is found out to be 0.48 eV in the compressive-strain-field case and 0.58 in the other. Such high barriers indicate that the SIA cluster which composes of two dumbbells is not easily absorbed by an edge dislocation.

The recently developed atomistic approach named ABC-T method is applied for constructing a mechanism map in the phase space of strain rate. To present the dynamic response of the system, the stress-strain curves at strain rates of 10^{-2} s^{-1} and 10^{5} s^{-1} are plotted and separately colored into green and blue in Fig. 1. When the SIA cluster is placed in the compressive strain field, at strain rate of 10^{-2} s^{-1}, jog pair forms almost immediately when the system begin to deform, with activation energy of 0.41 eV. The jogged dislocation glides at a stress of 100 MPa which is actually the lattice resistance brought by periodically spaced jog pairs with intervals of 8 nm, the length of simulation cell along dislocation line. At strain rate of 10^{5} s^{-1}, the SIA cluster is attached to the dislocation in C3 configuration when the dislocation moves to a new position where two defects are only 4 angstroms away from each other. The difficulty of C3 configuration diffuse to jog pair declared by the high energy barrier we found by NEB method introduces quite strong "quasi-pinning" effect at this high strain rate. The "quasi-pinning" effect we named here refers to the phenomenon that, it needs nearly 160 MPa to drag C3 configuration along with the dislocation to move together. This phenomenon implies a low mobility of C3 configuration, and meantime an intimate bond between C3 configuration and the dislocation. Due to this "quasi-pinning" effect, the dislocation line would be bowed between the C3 configurations such as Fig. 2 shows, since PBC is applied along $[11\bar{2}]$ direction.

[a)] Corresponding author. Email: yfguo@bjtu.edu.cn. [b)] Corresponding author. Email: byildiz@mit.edu.

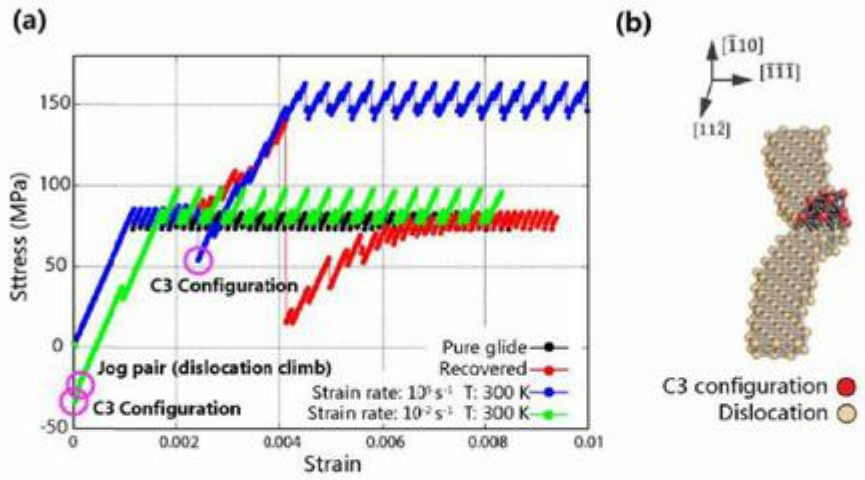

Fig. 1 (a) T e dynamic response of the s stem under different strain rates when the cluster is loca ed in the com ressive stress fiel . (b) The atomic configurati n of the dislo ation line reflects the "quasi-pinning effect" brought by he C3 nfiguration.

CO CLUSIONS

The strain rate effect is re lected by the RSS variation of dislocation liding. The in rease of the st ess needed for overcome the intrinsic lattice resistance s induced by j g pair formed at strain rate of 10^{-2} s-1, and lso by the def ct attached to dislocation line which cou d not be absorbed at strain rate of 10^{5} s-1. This defect we ame C3 confi uration here r presents the difficulty of the thermally ctivated mec anisms leadin to dislocatio climb, and causes "quasi-pinning" effect that raises th CRSS to almost the doubles of Peierls-Nabarro stres . The C3 configuration has lower mobility than the dislocation but sti l could be carried away by the dislocati n. Similar mechanism has been observed ia in-situ TE in BCC Ti alloy in previous research. The defect evolutions in the dynamic response of a pure sh aring plastic eformation revealed in this work extend the time-scale of atomistic si ulation. It co ld be seen that the coupling of strain rate and thermal activation govern nonequilibrium reaction mechanisms in the defect evo ution we foun here.

References

[1] S. Sarkar, J. Li, W.T. Cox, E. itzek, T.J. Lenos y, Y. Wang. Finding activation path ay of coupled di placive-diffusional defect processes in atomistics: Dislocation climb in fcc copper, Phys Rev B 86 (2012) 014115.
[2] F.D. Fischer, J. Svoboda. Che ically and mecha ically driven creep due to generation and annihilation of vacancies with non-ideal sources a d sinks, Int J Plasticity 27 (2011) 1384-1390.
[3] A. Kushima, J. Eapen, J. Li, S. Yip, T. Zhu. Time scale bridging i atomistic simulation of slow dyna ics: viscous relax tion and defect activation, Eur. Phys. J. B 82 (2011) 271-293.
[4] F. Yue, Y.N. Osetskiy, S. Yip, . Yildiz. Mappin strain rate dependence of dislocatio -defect interactions by atomistic sim lations, Proc Natl Acad Sci 110 (2013) 17756-177 1.
[5] G.H. Vineya d. Frequency fact rs and isotope effects in solid state ra e processes, J Phys Chem Solids 3 (1957) 121-127.

BOUNDS FOR THE PLASTIC STRENGTH OF POLYCRYSTALLINE VOIDED SOLIDS

Martín I. Idiart*[1,2] and Juan E. Ramos Nervi[1,3]
[1]*Departamento de Aeronáutica, Facultad de Ingeniería, Universidad Nacional de La Plata, Avda. 1 esq. 47 S/N, La Plata B1900TAG, Argentina*
[2]*Consejo Nacional de Investigaciones Científicas y Técnicas (CONICET), CCT La Plata, Calle 8 N° 1467, La Plata B1904CMC, Argentina*
[3]*Nucleoeléctrica Argentina S.A., Arribeños 3619, Ciudad Autónoma de Buenos Aires C1429BKQ, Argentina*

Summary The elastoplastic response of polycrystalline voided solids is idealized here as rigid-perfectly plastic. Bounds on the macroscopic plastic strength for prescribed microstructural statistics and single-crystal strength are computed be means of a linear-comparison homogenization technique. Hashin-Shtrikman and Self-Consistent results in the form of yield surfaces are reported for cubic and hexagonal polycrystals with isotropic texture and varying degrees of crystal anisotropy. Improvements over earlier linear-comparison bounds of up to forty per cent are found at high stress triaxialities. In the case of deficient crystals, the Self-Consistent results assert that voided aggregates of crystals with four independent systems can accommodate arbitrary deformations, those with three independent systems can dilate but not distort, and those with less than three independent systems cannot deform at all. We report the sharpest bounds available to date for all classes of material systems considered.

INTRODUCTION

Plastic growth of microcavities in polycrystalline ductile solids can be significantly influenced by the crystallographic and morphological textures of the aggregate [1]. Theoretical analysis of this process requires micromechanical models that relate the macroscopic stress state with the microscopic plastic deformation in polycrystalline voided systems. A fairly simple approach to the problem consists in idealizing the mechanical response of the individual grains as elastically rigid and plastically non-hardening, and employing homogenization techniques to bound the macroscopic plastic strength of the polycrystal in terms of the single-crystal strength and the statistics of the morphology and orientation distributions of the grains and voids.

It is already known that the first-order bounds of Taylor and Reuss become futile in the presence of a vacuous phase —the Reuss bound predicts vanishing strength, while the Taylor bound predicts infinite strength under purely hydrostatic loadings. Sharper bounds incorporating higher-order statistics were derived by deBotton & Ponte Castañeda [2] making use of the idea of a linear-comparison medium that is optimally selected via a suitably designed variational principle. This allows the use of any linear homogenization approach to generate corresponding results for nonlinear polycrystals. Idiart & Ponte Castañeda [3] later showed that these bounds make implicit use of a relaxation in the variational scheme which weakens the resulting bounds. Eliminating this relaxation leads to sharper bounds at the expense of increasing the computational complexity. In this work we evaluate the impact of the relaxation in the context of cubic and hexagonal systems with varying degrees of crystal symmetry and porosity.

RESULTS

Figure 1 reports results for polycrystalline solids with hexagonal crystal symmetry with ratio $c/a = 1.59$. Single crystals are assumed to deform plastically on three sets of slip systems: three basal systems $\{0001\}\langle 1120\rangle$, three prismatic systems $\{1010\}\langle 1120\rangle$, and twelve first-order pyramidal-$\langle c+a\rangle$ systems $\{1011\}\langle 1123\rangle$. Two hundred crystal orientations were prescribed according to a Sobol sequence in order to generate textures as close as possible to isotropy —see [4]. Relaxed (double-primed) and non-relaxed (unprimed) bounds were generated by means of the Hashin-Shtrikman (HS) and Self-Consistent (SC) approaches to homogenize the linear-comparison medium. The bounds are seen to produce smooth, closed and convex surfaces that are enclosed by the Taylor surface, as they should, and the relaxation is seen to have a notorious detrimental impact on these surfaces, especially at large stress triaxialities. Indeed, the overall impact of the relaxation as measured by the norms of the "elastic" domains is $\sim 21\%$, but the impact on the shear strength is $\sim\ 1\%$ while on the hydrostatic strength is $\sim 40\%$. Similar results —not shown— have been obtained for cubic polycrystals. More striking, however, is the fact that the non-relaxed HS bounds are sharper than the relaxed SC" bounds above a certain stress triaxiality, a feature never observed in the context of fully dense systems. Recall that the Hashin-Shtrikman approach provides bounds for the entire class of polycrystals with prescribed one- and two-point statistics, which includes the subclass of polycrystals that realize the Self-Consistent scheme. Thus, the non-relaxed HS results constitute rigorous upper bounds for all other results, including the relaxed SC" results. This is an indication that the loss resulting from the relaxation depends more crucially on material parameters such as heterogeneity contrast than on the number of slip systems of the constituent crystals. It is recalled that linear-comparison

*Corresponding author. Email: martin.idiart@ing.unlp.edu.ar

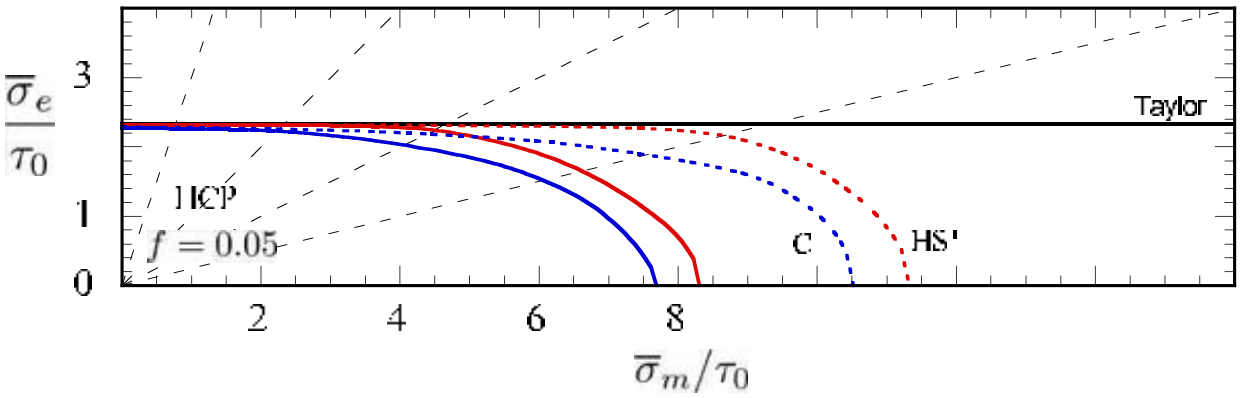

Figure 1: Bounds on the yield surface of isotropic hexagonal polycrystals with porosity $f = 0.05$, subjected to axisymmetric loadings. Relaxed (double-primed) and non-relaxed (unprimed) bounds of the Hashin-Shtrikman (HS) and Self-Consistent (SC) type. Dashed lines indicate directions of constant stress triaxialities $X_\sigma = 1/3, 1, 2, 4$.

techniques like the ones considered in this work are known to give fairly accurate predictions for voided systems under low to moderate stress triaxialities but unrealistically strong predictions under high triaxialities —see [4]. While the significant improvements found in this work are not expected to render the predictions for high triaxialities realistic, they are expected to enlarge the range of stress triaxialities for which the predictions are accurate.

Further calculations as a function of crystal anisotropy show that the shear and hydrostatic strengths of voided polycrystals behave like $\sigma_e^c \sim M^{\gamma_e}$ and $\sigma_m^c \sim M^{\gamma_m}$ as $M \to \infty$, where M is the relevant slip contrast. The exponents depend on the bounding method and the number J of linearly independent slip systems of the single crystals left in the limit. When J is less than five, the crystals become deficient. In this case, the Taylor bound predicts $\gamma_e = 1$ and γ_m is undefined, while for the Hashin-Shtrikman bounds predict $\gamma_e = \gamma_c = 1$ independently of crystal symmetry. By contrast, the exponents γ_e and γ_c displayed by the Self-Consistent bounds are different and do depend on crystal symmetry. From the numerical results generated for various cubic and hexagonal systems it was inferred that $\gamma_e = (4 - J)/2$ and $\gamma_m = (4 - J)(3 - J)/2$. The expression for γ_e is the same as that previously inferred in [5] for the shear plastic strength of fully dense polycrystals. According to these laws, there can be voided aggregates of deficient crystals that can still accommodate arbitrary macroscopic deformations. However, *spherical* deformations cannot be accommodated by polycrystals with less than *three* independent systems, while *deviatoric* deformations cannot be accommodated by polycrystals with less than *four* independent systems. In other words, the Self-Consistent results assert that voided aggregates of crystals with four independent systems can accommodate arbitrary deformations, aggregates of crystals with three independent systems can dilate but not distort, and aggregates of crystals with two independent systems cannot deform at all.

References

[1] Millet, J.C.F., Whiteman, G., Bourne, N.K., Gray III, G.T.: The role of anisotropy in the response of the titanium alloy Ti-6Al-4V to shock loading. J. App. Phys. 104:073531, 2008.

[2] deBotton, G., Ponte Castañeda, P.: Variational estimates for the creep behavior of polycrystals. Proc. R. Soc. Lond. A 448:121–142, 1995.

[3] Idiart, M.I., Ponte Castañeda, P.: Variational principles and bounds for nonlinear composites with anisotropic phases. I. General results. Proc R Soc Lond A 463:907-924, 2007.

[4] Lebensohn, R.A., Idiart, M.I., Ponte Castañeda, P., Vincent, P.-G.: Dilatational viscoplasticity of polycrystalline solids with intergranular cavities. Phil. Mag. 91:3038-3067, 2011.

[5] Nebozhyn, M.V., Gilormini, P., Ponte Castañeda, P.: Variational self-consistent estimates for cubic viscoplastic polycrystals: the effects of grain anisotropy and shape. J. Mech. Phys. Solids 49:313–340, 2001.

Localization out of the competition of rate dependence and Hadamard instability

Theodoros Katsaounis[1,2], Min-Gi Lee[1], and Athanasios E. Tzavaras [*1,2]
[1]*Computer, Electrical, Mathematical Sciences & Engineering Division, King Abdullah University of Science and Technology (KAUST), Thuwal, Saudi Arabia*
[2]*Institute of Applied and Computational Mathematics, FORTH, Heraklion, Greece*

Summary Materials deformed under high strain rates can exhibit failure through formation of shear bands. Shear band formation is often associated with Hadamard instability and strain localization into an emerging coherent structure. We assess the contributions of various effects leading to localization in the simplest model for which the stress exhibits strain softening and strain rate sensitivity. A linearized analysis indicates that the combined effect leads to Turing instability. Then we consider the nonlinear problem and introduce a set of self-similar variables. A class of special solutions is obtained which pinpoints the emergence of a coherent localized structure and the formation of a shear band. This solution is associated to a heteroclinic orbit of a certain dynamical system. The orbit is constructed numerically and yields almost explicit shear localizing solutions.

A SIMPLE PARADIGM FOR LOCALIZATION

Shear bands are narrow regions of intense shear observed during the plastic deformation at high strain rates; they form one of the most striking instances of material instability and have been analyzed extensively *e.g.* [8, 2, 1, 4, 6]. From early studies [7] it was recognized that Hadamard instability due to strain softening response plays a key role to the onset of instability. At the same time, once instability sets in, higher-order effects like rate dependence or strain-gradients get triggered and affect the response. The objective of this paper is to analyze the competition between Hadamard instability (caused by strain-softening inelastic response) and strain-rate dependence. We consider the model

$$v_t = \left(\frac{v_x^n}{\gamma}\right)_x, \quad \gamma_t = v_x\,, \tag{1}$$

which describes a shearing deformation with v the velocity in the shear direction and γ the (plastic) strain. Here, elastic effects are ignored and the strain is the total plastic strain, n measures the effect of strain-rate sensitivity. Note that for $n = 0$ the system (1) reduces to the system of elasticity with stress-strain response $\tau = \tau(\gamma) = \frac{1}{\gamma}$ in the unstable regime. This system is elliptic in the t-direction and exhibits Hadamard instability. Despite this fact, for $n \geq 0$, (1) admits the class of universal solutions

$$v_s(x) = x, \quad \gamma_s(t) = t + \gamma_0\,, \quad \sigma_s(t) = \frac{1}{t+\gamma_0}. \tag{2}$$

describing uniform shearing with the parameter γ_0 measuring the initial strain. The objective of this work is to analyze the competition between Hadamard instability and strain-rate dependence, and in particular to describe the stability or instability of the uniform shearing solutions both at (a) the linearized as well as (b) the nonlinear level. It is well known that Hadamard instability is connected to the catastrophic growth of oscillations. One issue to address is how rate dependence kills the oscillations and produces a concentration of strain, as observed in experimental studies of shear bands.

The model (1) is among the simplest where this competition can be analyzed. As (2) is a time dependent solution it generally will lead to non-autonomous systems. An exception is for the response $\tau(\gamma) = \frac{1}{\gamma}$ which offers the great simplification that it leads to autonomous sytems and is thus selected here. Exploiting this fact, through a transformation into relative variables, the problem of studying the stability properties of (2) is transformed into the study of the stability properties of the equilibrium $(1, 1, 1)$ for the nonlinear system

$$V_\tau = \Sigma_x = \left(\frac{(V_x)^n}{\mathrm{y}}\right)_x, \quad \mathrm{y}_\tau = V_x \nearrow \mathrm{y}\,. \tag{3}$$

System (3) describes relative perturbations, for instance $\Sigma = \sigma/\sigma_s(t)$, and thus offers the right yardstick to judge stability of the time dependent solution (2), in the spirit of [4].

LINEARIZED STABILITY ANALYSIS

First, we perform a linearized stability for the equilibrium $(1, 1, 1)$ for the system (3). The linearized analysis gives the following result: (a) For $n = 0$, as expected, all modes grow exponentially fast and indicate catastrophic growth and Hadamard instability. (b) For $0 < n < 1$, the modes still grow and are unstable but at a tame growth rate. In fact, in this regime the behavior is that of *Turing instability*. (c) For $n > 1$ strain-rate dependence is strong and stabilizes the motion.

*Corresponding author. Email: athanasios.tzavaras@kaust.edu.sa

THE NONLINEAR PROBLEM

In the second part we study in detail the nonlinear system (3). Motivated by scaling properties of the system we look for a self-similar solution of the form

$$V(x,\tau) = e^{\lambda \frac{n}{2-n}\tau}\,\bar{V}(\xi)\,, \quad \mathrm{y}(x,\tau) = e^{\lambda \frac{n}{2-n}\tau}\,\bar{\mathrm{y}}(\xi)\,, \quad \Sigma(x,\tau) = e^{\lambda\left(1+\frac{n}{2-n}\right)\tau}\,\bar{\Sigma}(\xi) \quad \text{where } \xi = xe^{\lambda\tau}, \tag{4}$$

where $\lambda > 0$ is a parameter. One can easily check, that if such solutions exist, then they will localize as time proceeds. Their existence is based on constructing a solution for the nonlinear system of singular ordinary differential equations

$$\lambda\left(\frac{n}{2-n}\bar{V} + \xi\bar{V}_\xi\right) = \bar{\Sigma}_\xi\,, \quad \lambda\left(\frac{2}{2-n}\bar{\mathrm{y}} + \xi\bar{\mathrm{y}}_\xi\right) = \bar{V}_\xi - \bar{\mathrm{y}}\,, \quad \bar{\Sigma} = \frac{\bar{V}_\xi^{\,n}}{\bar{\mathrm{y}}}\,, \tag{5}$$

that determines the profile $(\bar{V}, \bar{\mathrm{y}}, \bar{\Sigma})$. Such singular systems may (or may not) have solutions and this is determined by a case-by-case analysis. In the present case, one can remarkably de-singularize the problem and transform it to an autonomous system of three first-order differential equations. One then shows by a combination of dynamical systems techniques and numerical computation that the system has a one-parameter family of heteroclinic connections. Of these, a special one corresponds to a smooth heteroclinic connection for the nonlinear system (5) that in turn gives rise to a coherent localizing structure. The heteroclinic orbit is represented by the red dotted line if Figure (a), while the variables depicting the velocity v and the strain-rate $u = v_x$ are depicted in Figures (b) and (c), respectively. The rigorous analysis validates the heuristic asymptotic results

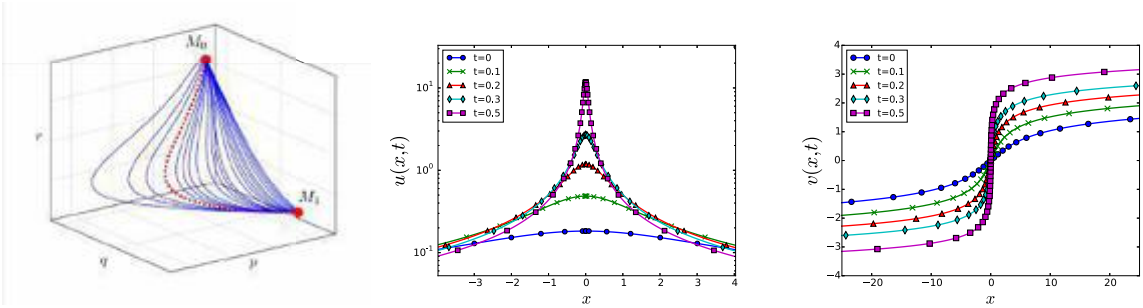

(a) The heteroclinic orbit (red dotted line) (b) Localizing strain rate (c) Localizing velocity profile

Figure 1: (a) the heteroclinic orbit; (b) and (c) the emerging structure

in [3] that the onset of localization can be predicted by an asymptotic analysis in the style of the Chapman-Enskog expansion of the kinetic theory.

CONCLUSIONS

The instability occuring in rate-dependent localization resembles (at the linearized level) the so-called Turing instability familiar from problems of morphogenesis [5]. The combined effect of Hadamard instability and rate dependence can suppress, at the nonlinear level, the oscillations and result into a single run-up of concentration that appears like the shear bands observed in experiments.

References

[1] Clifton R.J., Duffy J., Hartley K.A., Shawki T.G.: On critical conditions for shear band formation at high strain rates. Scripta Met, 18:443-448, 1984.
[2] Hutchinson J.W., Neale K.W.: Influence of strain-rate sensitivity on necking under uniaxial tension. Acta Met, 25:839-846, 1977.
[3] Katsaounis Th., Tzavaras A.E.: Effective equations for localization and shear band formation. SIAM J App Math, 69:1618-1643, 2009.
[4] Molinari A., Clifton R.J.: Shear band formation in thermal viscoplastic materials. Mech Materials, 8:13-43, 1989.
[5] Turing A.M,: The chemical basis of morphogenesis. Phil Trans R Soc Lon B, 237:37-72, 1952.
[6] Wright T.W., Walter J.W.: On stress collapse in adiabatic shear bands. J Mech Phys Solids, 35:701-720, 1987.
[7] Wu F.H., Freund L.B.: Deformation trapping due to thermoplastic instability in one-dimensional wave propagation. J Mech Phys Sol, 35:701-720, 1987.
[8] Zener C., Hollomon J.H., Effect of train rate upon plastic flow of steel. J Appl Phys, 15:22-32, 1944.

A SELF-CONSISTENT MODEL FOR NANO-METALLIC-MULTILAYERS WITH HE BUBBLES

Long Yu[1], Xiazi Xiao[1], Lirong Chen[1], Haijian Chu[2], Huiling Duan[1a)]
[1] *State Key Laboratory for Turbulence and Complex Systems, Department of Mechanics and Engineering Science, College of Engineering, Peking University, Beijing, P. R. China*
[2]*Department of Mechanics and Shanghai Institute of Applied Mathematics and Mechanics, Shanghai University, Shanghai, P. R. China*

Summary Nano-metallic-multilayers (NMMs) are one of the irradiation-tolerant materials due to the high ratio of interfaces that can act as effective sinks for irradiation-induced defects, like helium (He) bubbles. The mechanical behaviours of NMMs can be both affected by the interface and He bubbles, which are closely related to the layer thickness. In this paper, the macroscopic mechanical behaviours of Cu/Nb multilayer with He bubbles are explored by crystal plasticity model (CPM) coupled with the elastic-viscoplastic self-consistent (EVPSC) method. At the microscopic grain level, the dislocation forest hardening, layer thickness-dependent He bubble hardening and interface hardening are considered in the CPM for different types of individual grains (Cu and Nb). Next, the mechanical behaviors of the composite grain (equivalent inclusion) are obtained by the Mori-Tanaka method. At the macroscopic level, the self-consistent scheme is adopted to predict the macroscopic mechanical behavior of NMMs.

INTRODUCTION

Helium can be produced in nuclear materials by nuclear transmutation, and He atoms usually exist in the form of nanometric bubbles or clusters due to their low solubility. The presence of nanometric He bubbles in metals has a significant influence on their plastic behaviors, especially the synergistic effects of He and other existing radiation-induced defects. To help design He-tolerant materials and predict the life time of components in nuclear reactors, many studies have been performed, including the corresponding research on NMMs[1,2]. It is found that multilayers have not only high strength, but also excellent irradiation tolerance. The interface of NMMs is effective sinks for radiation-induced point defects, He atoms, etc. Hence, multilayer systems may be applied in nuclear fusion reactors in the future. However, up to now, there are few theoretical models proposed to study their mechanical properties with He irradiation effect. Therefore, in this work, we build a theoretical framework to simulate the elastic-viscoplastic deformation behaviors of NMMs with He irradiation effect by using the CPM coupled with EVPSC.

THEORETICAL MODEL

Elastic-viscoplastic self-consistent scheme with composite grains

In order to predict the macroscopic mechanical behavior of He irradiated NMMs systems which are made of various kinds of individual grains in each layer, a representative volume element (RVE) occupying a region V is chosen from the multilayer system, as shown in Fig.1(a). The RVE, occupying both the regions of layer A and layer B, and the interface between them, contains N inclusions with interface, and every inclusion is called a composite grain. The property of each composite grain is decided by the behaviours of individual grains in layer A and B, their volume fractions and the interface between them. Then, the composite grain is embedded in the effective medium, and the macroscopic elastic-viscoplasitc behavior of NMMs can be obtained by the EVPSC method[3-5].

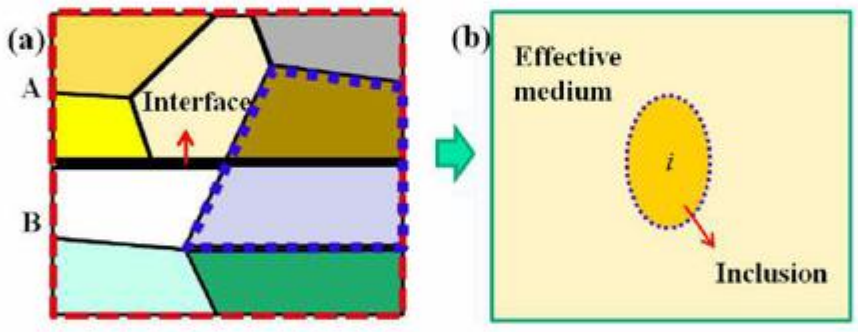

Fig. 1 Schematic view of the elastic-viscoplastic self-consistent method for NMMs. (a) An RVE with N inclusions (made of the grains from layer A and B, and the interface between). (b) A representative individual inclusion embedded in an infinite homogenous effective medium.

a) Corresponding author. Email: hlduan@pku.edu.cn

The mechanical behaviour of inclusion can be obtained by using Mori-Tanaka approximation, i.e.,

$$\mathrm{B}_i^{\mathrm{AB}} = \left[f_i^{\mathrm{A}}\mathrm{B}_i^{\mathrm{B}} + f_i^{\mathrm{B}}\mathrm{B}_i^{\mathrm{A}}\colon \mathrm{A}_i^{\mathrm{AB,vp}}\right]\colon\left[f_i^{\mathrm{A}}\mathbf{I}^{(4)} + f_i^{\mathrm{A}}\mathbf{I}^{(4)}\colon \mathrm{A}_i^{\mathrm{AB,vp}}\right]^{-1}$$

where $\mathrm{A}_i^{\mathrm{AB,vp}}$ is the viscoplastic concentration tensor linking the viscoplastic deformation of grain A ($\mathrm{B}_i^{\mathrm{B}}$) and grain B ($\mathrm{B}_i^{\mathrm{B}}$), f_i^{A} and f_i^{B} denote the volume fraction of the grain A and grain B in the i-th inclusion, respectively. The local mechanical behavior of different inclusions is related to the macroscopic behaviour, which can be derived from the secant self-consistent scheme:

$$\dot{\boldsymbol{\varepsilon}}_i^{\mathrm{AB}} = \mathrm{A}_i^{\mathbf{c}^{\mathrm{e}}}\colon\left[\dot{\mathbf{E}} - \dot{\mathbf{E}}^{\mathrm{vp}} + \left(\mathbf{I}^{(4)} - \mathbf{S}^{\mathrm{E}}\right)\colon \mathrm{A}_i^{\mathbf{B}^{\mathrm{e}}}\colon\dot{\mathbf{E}}^{\mathrm{vp}} + \mathbf{S}^{\mathrm{E}}\colon\mathbf{S}^{\mathrm{e}}\colon \mathrm{C}_i^{\mathrm{AB}}\colon\dot{\boldsymbol{\varepsilon}}_i^{\mathrm{AB,VP}}\right]$$

$$\dot{\boldsymbol{\sigma}}_i^{\mathrm{AB}} = \mathrm{C}_i^{\mathrm{AB}}\colon\mathrm{A}_i^{\mathbf{c}^{\mathrm{e}}}\colon\left[\left(\dot{\mathbf{E}} - \dot{\mathbf{E}}^{\mathrm{vp}}\right) + \left(\mathbf{S}^{\mathrm{E}} - \mathbf{I}^{(4)}\right)\colon\dot{\boldsymbol{\varepsilon}}_i^{\mathrm{AB,VP}} - \mathrm{A}_i^{\mathbf{B}^{\mathrm{e}}}\colon\dot{\mathbf{E}}^{\mathrm{vp}}\right]$$

where $\mathbf{S}^{\mathrm{E}}$ is the well-known Eshelby tensor. The macroscopic strain rate $\dot{\mathbf{E}}$ and stress rate $\dot{\boldsymbol{\Sigma}}$ of heterogeneous materials can be expressed as

$$\dot{\mathbf{E}} = \sum_{i=1}^{N} f_i\,\dot{\boldsymbol{\varepsilon}}_i^{\mathrm{AB}} \qquad \text{and} \qquad \dot{\boldsymbol{\Sigma}} = \sum_{i=1}^{N} f_i\,\dot{\boldsymbol{\sigma}}_i^{\mathrm{AB}}$$

where f_i is the volume fraction of the i–th inclusion.

Constitutive equations for single crystal

Based on the classical crystal plasticity, the viscoplastic deformation can be expressed by

$$\dot{\boldsymbol{\varepsilon}}^{\mathrm{vp}} = \sum_{\alpha=1}^{N_s}\mathbf{R}^{\alpha}\dot{\gamma}^{\alpha}$$

where $\mathbf{R}^{\alpha}$ and N_s respectively denote the Schmid tensor and the number of slip system ($N_s = 24$ for BCC and $N_s = 12$ for FCC). $\dot{\gamma}^{\alpha}$ is the strain rate of slip system α, it can be expressed as

$$\dot{\gamma}^{\alpha} = \dot{\gamma}_0\left(\frac{|\tau^{\alpha}|}{\tau_c^{\alpha}}\right)^{/}\ \mathrm{sign}(\tau^{\alpha})$$

where τ^{α} is the resolved shear stress, and τ_c^{α} is the critical resolved shear stress which includes intrinsic lattice friction τ_0, the dislocation forest hardening τ_d^{α}, the interface hardening τ_{inter}, and the He bubble hardening τ_{He}. Therefore, the CRSS can be expressed as

$$\tau_c^{\alpha} = \tau_0 + \tau_d^{\alpha} + \tau_{inter} + \tau_{He}$$

RESULTS

We present a micromechanical theory framework to study the size-dependent mechanical behaviors of NMMs with/without He ion implantation effect. According to the result we obtained by comparing the numerical results with corresponding experimental data, it can be found that: (1) the numerical results match well with the experimental data[2,6]. (2) The dislocation forest hardening plays a significant role for NMMs, and the strain hardening coefficient (SHC) is almost zero after yielding. (3) The contribution of He bubble hardening reduces with the decrease of layer thickness. (4) The mechanisms of interface hardening and dislocation forest hardening dominate in the case of thin layer, and the He bubble hardening becomes a dominant one when the layer becomes thicker.

References

[1] Li N., Nastasi M., Misra A.: Defect Structure and Hardening Mechanisms in High Does Helium Ion Implanted Cu and Cu/Nb Multilayer Thin Film. *International Journal of Plasticity*. 32-33:1-16,2012.

[2] Li N., Mara N.A., Wang Y.Q., Nastasi M., Misra A.: Compressive Flow Behavior of Cu Films and Cu/Nb Multilayers Containing Nanometer-Scale Helium Bubble. *Scripta Materialia*. 64:974-977,2011.

[3] Xiao X.Z., Song D.K., Chu H.J., Xue J.M., Duan H.L.: Mechanical Properties for Irradiated Face-Centred Cubic Nanocrystalline Metals. *Proceedings of the Royal Society A*. 471, 20140832,2015.

[4] Xiao X.Z., Song D.K., Xue J.M., Chu H.J., Duan H.L.: A self-consistent plasticity theory for modeling the thermo-mechanical properties of irradiated FCC metallic polycrystals. *Journal of the Mechanics and Physics of Solids*. 78,1-16,2015.

[5] Capolungo L., Benkassem S., Cherkaoui M., Qu J.: Self-consistent transition with imperfect interfaces: Application to nanocrystalline materials. *Acta Materialia*. 56,1546-1554,2008.

[6] Misra A., Hirth J.P., Hoagland R.G.: Length-Scale-Dependent Deformation Mechanisms in Incoherent Metallic Multilayered Composites. *Acta Materialia*. 53,4817-4824,2005.

PREDICTION OF MECHANICAL BEHAVIORS OF RADIATED FE-CR ALLOYS BY PLASTICITY THEORY

Xiazi Xiao[1,2,4], Dmitry Terentyev[3],Huiling Duan[1,2a)]&Jianmin Qu[4]
[1]*State Key Laboratory for Turbulence and Complex System, Department of Mechanics and Engineering Science, College of Engineering, Peking University, Beijing, P.R. China*
[2]*CAPT, HEDPS and IFSA Collaborative Innovation Center of MoE, Peking University, Beijing, P.R. China*
[3]*Structural Material Group, Institute of Nuclear Materials Science, SCK-CEN, Mol, Belgium*
[4]*Departmentl of Mechanical Engineering, Tufts University, Medford, MA, USA*

Summary The mechanical behavior of non-irradiated and neutron irradiated Fe-Cr alloys is studied by means of a self-consistent plasticity theory, which accounts for the radiation-induced defects at the grain level by using an elastic-viscoplastic self-consistent method as the scale transition to obtain polycrystalline responses. Attention is paid to two types of radiation-induced defects: interstitial dislocation loops and solute rich clusters, which are the main sources of hardening in Fe-Cr alloys at medium irradiation doses. Both the hardening mechanisms and microstructure evolutions are investigated by a crystal plasticity model by using recently available experimental data on microstructures, and by implementing hardening rules on the basis of atomistic data. Dislocation loops are treated as strong thermally activated obstacles and solute rich clusters as weak precipitates that can break under shear. Good agreement with experimental data is achieved for both the yield stress and strain hardening of non-irradiated and irradiated Fe-Cr alloys.

INTRODUCTION

Irradiation-induced hardening and premature fracture are major concerns for the intermediate-temperature application of high Cr ferritic/martensitic steels as structural materials in nuclear reactors below 300~350 ^{0}C. The microstructural changes at the sub-nanometre scale in irradiated Fe-Cr alloys have been studied extensively by several complementary experimental techniques, such as positron annihilation and small angle spectroscopy as well as atom probe tomography (APT) techniques. In the range of low to moderate irradiation doses (0.1 ~ 1 dpa), several types of irradiation-induced defects have been identified, namely, (i) DLs of size up to ten nm (see e.g. Ref. [1]), (ii) α' clusters (Cr rich precipitates) of size not exceeding several nanometres, (iii) sub-nanometre vacancy clusters containing several point defects, and (iv) SRCs (NiSiPCr-enriched clusters) containing Mn, Ni, P, Si and Cr of a few nanometres. Based on the previously established experimental data and theoretical knowledge on the role that DLs and Cr solid solutions play on the plastic flow, we extend in this paper the crystal plasticity method [2] (CPM), already developed for pure Fe, to study the plastic deformation of Fe-Cr alloys under neutron irradiation. Despite extensive studies, it is still not clear how the SRCs affect the material behavior. To this end, we will attempt two scenarios representing the limiting cases:(a) assuming that SRCs are small DLs that are decorated by solutes, and therefore can be treated as $a_0/2<111>$DLs enabling their instantaneous absorption, and (b) assuming that SRCs originate from the vacancy-solute drag and clustering, so that solute gathering is enhanced by the presence of vacancies. In this case, according to our previous studies on Fe-Ni-Cu alloys, the SRCs should be treated as weak precipitates whose shear strength smoothly decreases with the amount of plastic deformation as a result of multiple shearing events.

CONSTITUTIVE EQUATIONS

Single crystal model

According to the standard power law, the plastic shearing rate $\dot{\gamma}^{\alpha}$ is expressed as:

$$\dot{\gamma}^{\alpha} = \dot{\gamma}_0 \left(\frac{\tau^{\alpha}}{\tau^{\alpha}_{\mathrm{CRSS}}}\right)^{\frac{1}{\mathrm{m}}} \mathrm{sign}(\tau^{\alpha}), \tag{1}$$

where τ^{α} and $\dot{\gamma}_0$ denote the resolved shear stress (RSS) and a reference shearing rate and m is the strain rate sensitivity. The critical resolved shear stress (CRSS) $\tau^{\alpha}_{\mathrm{CRSS}}$ consists of the contributions of the irradiation-induced DLs ($\tau^{\alpha}_{\mathrm{l}}$), SRCs ($\tau^{\alpha}_{\mathrm{c}}$), Cr solutes ($\tau_{\mathrm{s}}$), lattice friction ($\tau_{\mathrm{f}}$), network dislocation ($\tau^{\alpha}_{\mathrm{n}}$) and grain boundaries ($\tau_{\mathrm{GB}}$), i.e.,

$$\tau^{\alpha}_{\mathrm{CRSS}} = \tau^{\alpha}_{\mathrm{l}} + \tau^{\alpha}_{\mathrm{c}} + \tau_{\mathrm{s}} + \tau_{\mathrm{f}} + \tau^{\alpha}_{\mathrm{n}} + \tau_{\mathrm{GB}}. \tag{2}$$

Self-consistent model for polycrystals

The elastic-viscoplastic self-consistent (EVPSC) method is applied to obtain the macroscopic behavior of irradiated polycrystals, which effectively accounts for the mutual interaction of individual grains and their orientations [3]. The local mechanical behavior of different grains is related to the macroscopic behavior through the strain rate concentration relation, which can be derived from the secant self-consistent scheme:

[a)]Corresponding author. Email:hlduan@pku.edu.cn.

$$\dot{\varepsilon}_i = A_i^{c^e} : \left[\left(\dot{E} - \dot{E}^{vp}\right) + A_i^{B^e} : \dot{E}^{vp} + S^E : S^e : \left(C_i : \dot{\varepsilon}_i^{vp} - C^e : A_i^{B^e} : \dot{E}^{vp}\right)\right] \quad (3)$$

$$\dot{\sigma}_i = C_i : A_i^{C^e} : [S^e : \dot{\Sigma} + (S^E - I_4) : \left(\dot{\varepsilon}_i^{vp} - A_i^{B^e} : \dot{E}^{vp}\right)] \quad (4)$$

where $\mathbf{S^E}$ is the well-known Eshelby tensor. The macroscopic strain rate $\dot{E}$ and stress rate $\dot{\Sigma}$ of heterogeneous materials can be expressed as

$$\dot{E} = \sum_{i=1}^{N} f_i \dot{\varepsilon}_i \text{ and } \dot{\Sigma} = \sum_{i=1}^{N} f_i \dot{\sigma}_i \quad (5)$$

where f_i is the volume fraction of the i-th grain.$\dot{\varepsilon}_i$ and $\dot{\sigma}_i$denote the average rates of strain and stress in the i-th grain, respectively.

RESULTS

For the irradiated Fe-Cr alloys, both the yield stress and flow stress would be affected by the presence of radiation-induced defects. As shown in Fig. 1(a), the yield stress increases from 230 MPa up to 420 MPa for the Fe-9Cr alloy irradiated up to 0.6 dpa and tested at 573 K. Meanwhile, the strain hardening rate decreases for the irradiated samples. These results correspond to the model where the SRCs are treated as weak precipitates under shear. The presence of SRCs with high density significantly increases the level of flow stress, and therefore assists the stress activated absorption of DLs. The detailed analysis of different hardening contributions to the yield stress measured after irradiation to 0.6 dpa at 573 K is given in Fig. 1(b).

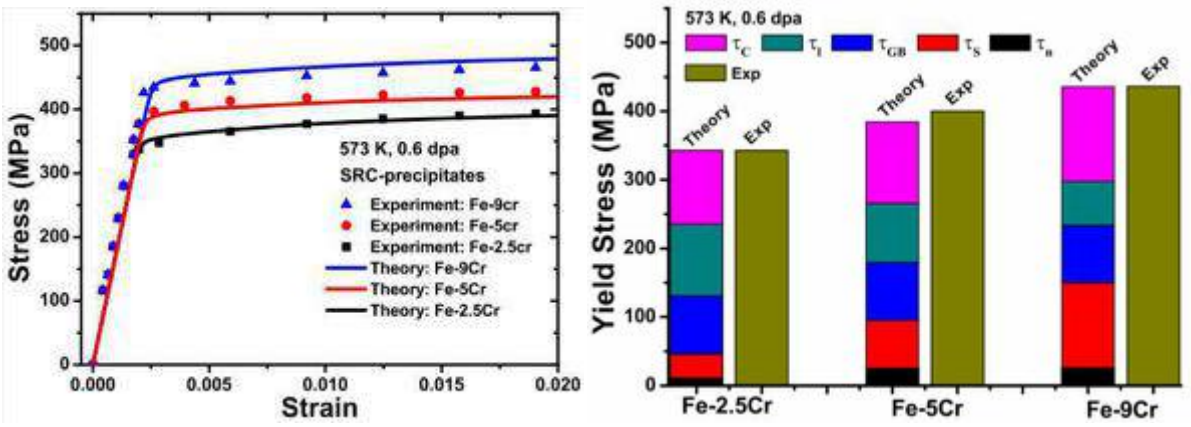

Figure 1. (a) Left: stress-strain curves of irradiated Fe-Cr alloys at 573 K and 0.6dpa. Solid lines are theoretical results and solid points are experimental data. The SRCs are treated as weak precipitates under shear. (b) Right: the contribution of different hardening mechanisms to the yield stress compared with experimental data for irradiated Fe-Cr alloys at 0.6 dpa and 573 K.

CONCLUSIONS

In this work, we proposed a theoretical model for the thermo-mechanical plastic response of Fe-Cr alloys accounting for the neutron irradiation induced defects at elevated temperatures. A CPM accounting for irradiation-induced defects (DLs and SRCs), Cr solid solution and grain boundary strengthening is developed to describe the stress-strain responses at the grain level. The EVPSC method is then used to obtain the macroscopic behavior of polycrystalline Fe-Cr alloys. Finally, the model is parameterized using existing experimental data. The numerical results based on the proposed model indicate that (1) In the non-irradiated Fe-Cr alloys, the yield stress increases almost linearly with the Cr content, and the solid solution hardening dominates at the elevated temperatures, (2) In the Fe-Cr alloys irradiated up to 0.6 dpa, TEM-visible DLs and nanometric SRCs provide major contributions to the net flow stress, (3) The analysis of the evolution of DLs and SRCs in conjunction with the plastic deformation suggests that the best agreement with the experimental data is achieved if the SRCs are treated as weak obstacles under shear.

References

[1] Matijasevic M., Almazouzi.: Effect of Cr on the mechanical properties and microstructure of Fe-Cr model alloys after n-irradiation. *J. Nucl. Mater* 377:147-154, 2008

[2] Xiao X. Z., Song D. K., Xue J. M., Chu H. J., Duan H. L.: A size-dependent tensorial plasticity model for FCC single crystal with irradiation. *Int. J. Plast* 65:152-167.

[3] Xiao X. Z., Song D. K., Xue J. M., Chu H. J., Duan H. L.: A self-consistent plasticity theory for modelling the thermo-mechanical properties of irradiated FCC metallic polycrystals. *J. Mech. Phys. Solids* 78:1-16.

INERTIAL EFFECTS ON A THERMOMECHANICAL DISLOCATION DYNAMICS MODEL FOR PLASTIC DEFORMATION

Eleanor Mak[1], Oxana Skiba[2] & Robert Gracie [3a)]
[1,2,3]*Department of Civil and Environmental Engineering, University of Waterloo, Waterloo, Ontario, Canada*

Summary High strain rate plastic deformation results in significant temperature rise due to the rapid rate of heat generation by dislocation motion. Dislocation dynamics (DD) models have historically been purely mechanical and quasi-static. The neglect of thermomechanical effects is a significant source of error in predicting stress loading behaviour observed in high strain rate DD simulations. A two-dimensional, fully-coupled thermomechanical DD model based on the eXtended Finite Element Method (XFEM-DD) was recently developed to address thermomechanical effects by capturing heat generation of dislocation motion. Simulations using this model have qualitatively demonstrated the increased significance of thermal effects and temperature rise with increased strain rates, as well as increased accuracy in capturing stress-strain behaviour. The XFEM-DD will be refined through the inclusion of previously neglected inertial effects and the impact on the accuracy of load behaviour will be determined.

BACKGROUND

Plastic deformation of crystalline solids is attributed to the mechanisms of dislocations (crystallographic defects) at the atomic level [1]. Significant temperature rise is caused by the rapid rate of heat generation by dislocation motion as a result of high strain rate plastic deformations [2]. Dislocation dynamics (DD) models have been widely used as a framework to investigate plastic phenomena [3]. However, DD models have historically neglected thermal effects which has been found to be a significant source of error [2, 4]. Consequently, a two-dimensional, fully coupled thermomechanical dislocation dynamics model based on the eXtended Finite Element Method (XFEM-DD) was recently developed as a first step in addressing thermomechanical effects by considering dislocations as individual moving heat sources [2].

METHODOLOGY

The governing equations which form the basis of the existing XFEM-DD [2] have been augmented with inertial terms.

Consider a domain Ω which contains n_d dislocations and is bounded by Γ. For dislocation α, the active part of the glide plane (i.e., where slip has occurred) is denoted as Γ_d^α.

The differential equations governing the coupled model are the equilibrium equation and the heat equation:

$$\nabla \cdot \boldsymbol{\sigma} + \rho \mathbf{f} = \rho \ddot{\mathbf{u}} \tag{1}$$

$$C_p \rho \dot{\boldsymbol{\theta}} + \nabla \cdot \mathbf{q} = S \tag{2}$$

where $\boldsymbol{\sigma}$ is the Cauchy stress tensor, $\mathbf{f}$ is the body force, $\ddot{\mathbf{u}}$ is the acceleration, $\mathbf{q}$ is the heat flux density, $\boldsymbol{\theta}$ is the absolute temperature change from a stress-free reference temperature Ω_0 at the point $\mathbf{x} \in \Omega$ at time t, S is the body heat source, and $\dot{\boldsymbol{\theta}}$ is the material time derivative of $\boldsymbol{\theta}$. Material properties of the body including mass density, specific heat capacity, and coefficient of thermal conductivity are denoted as ρ, C_p, and k, respectively.

XFEM

The approximation for the temperature field uses the standard finite element approximation. For local displacement, the application of XFEM uses enrichments to reflect discontinuities created by edge dislocations in addition to the standard displacement approximation [2]. A dislocation is described by the location of its core, the orientation of its glide plane, and by its Burgers vector. Enrichments are locally applied only to nodes of elements intersected by the active part of the glide plane. We can then denote $\mathcal{S}$ and $\mathcal{S}^\alpha$ as the set of all nodes and the set of nodes with supports cut by Γ_d^α, respectively. Accordingly, the local displacement approximation for a domain with n_d edge dislocations with Burgers vectors $\mathbf{b}^\alpha$ per [2] is

$$\mathbf{u}^h(\mathbf{x},\mathrm{t}) = \underbrace{\sum_{I \in \mathcal{S}} N_I^u(\mathbf{x}) \mathbf{d}_I(\mathbf{x},t)}_{\text{standard interpolation}} + \underbrace{\sum_{\alpha=1}^{n_d} \mathbf{b}^\alpha \sum_{J \in \mathcal{S}} N_J^u(\mathbf{x}) \left[H\left(f^\alpha(\mathbf{x})\right) - H\left(f^\alpha(\mathbf{x}_J)\right) \right]}_{\text{enriched interpolation}} \tag{3}$$

[a)] Corresponding author. Email: rgracie@uwaterloo.ca

where N_I^u are the standard FEM shape functions, $\mathbf{d}_I$ are the nodal degrees of freedom, $\mathbf{x}_J$ are the coordinates of node J, H is the Heaviside step function, and f^α is the signed distance to Γ_d^α.

It is important to note that a unique feature of the XFEM-DD is that heat generation within the domain is captured by considering the motion of individual dislocations as moving heat sources [2]. The heat generated by each moving dislocation α at time t is calculated through the rate of work done by the Peach-Koehler force on the dislocation [2]:

$$s_\alpha(t) = \beta[\mathbf{F}^\alpha(t) \cdot \mathbf{v}^\alpha(t)] \tag{4}$$

where $\mathbf{F}^\alpha$ is the Peach-Koehler force on dislocation α, $\mathbf{v}^\alpha$ is the velocity of dislocation α, and β is a coefficient which represents the fraction of work converted to heat.

Thus, the body heat source term in Equation (2) which represents the heat generated by the motion of all dislocations in the domain is

$$S(\mathbf{x}, t) = \sum_{\alpha=1}^{n_d} s_\alpha(t)\delta(\mathbf{x} - \mathbf{x}_\alpha) \tag{5}$$

where $\mathbf{x}_\alpha$ is the position of dislocation α, and s_α is the heat generated by the motion of dislocation α at time t.

RESULTS

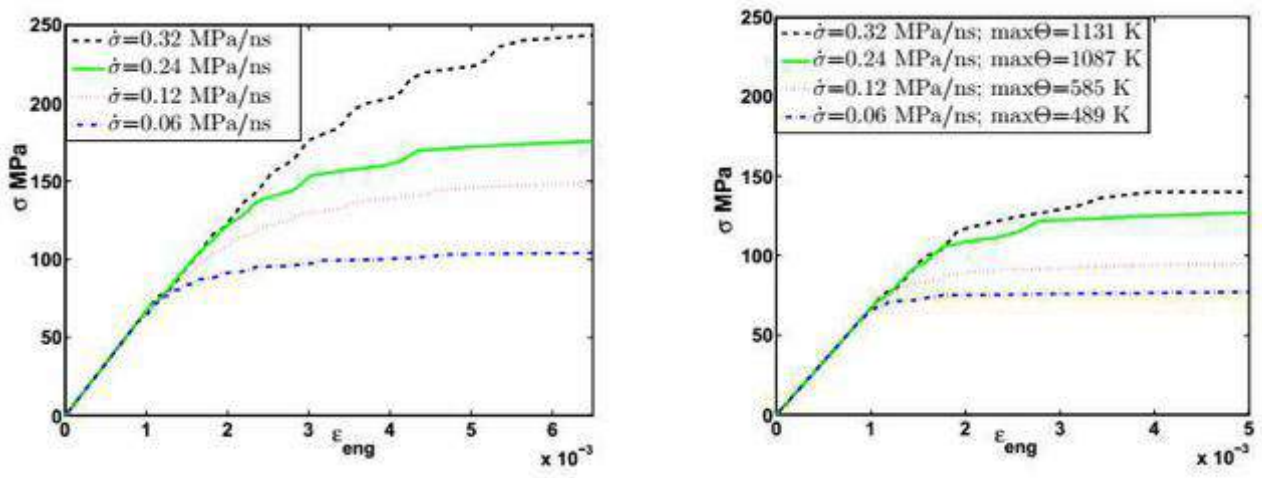

Figure 1. Stress-strain behavior at different loading rates without (left) and with (right) thermomechanical coupling [2]

The refined XFEM-DD model will consider inertial effects through augmentation of the governing equations described in the last section. Using this model, stress-strain behaviour of the coupled model will be compared to uncoupled results. Simulations using the existing XFEM-DD have been able to qualitatively capture the increased importance of thermal effects and impact of temperature rise, in particular, softened stress-strain behaviour (see Figure 1) [2]. Accordingly, the relationship between temperature rise and increased strain rate of the refined model will be investigated. Finally, the cost-benefit between accuracy and computational costs will be assessed with respect to the existing and refined XFEM-DD model.

References

[1] Weertman, J., & Weertman, J. R. (1966). Elementary dislocation theory.

[2] Skiba, O. (2015). Multiphysical dislocation dynamics models for high strain rate plastic deformation (Doctoral dissertation, University of Waterloo).

[3] Ghoniem, N. A. M., Tong, S. H., & Sun, L. Z. (2000). Parametric dislocation dynamics: a thermodynamics-based approach to investigations of mesoscopic plastic deformation. Physical Review B, 61(2), 913.

[4] Langer, J. S., Bouchbinder, E., & Lookman, T. (2010). Thermodynamic theory of dislocation-mediated plasticity. Acta Materialia, 58(10), 3718-3732.

MODELING THE 3D PLASTIC ANISOTROPY OF MAGNESIUM AZ31B ALLOY

Yazid Madi *[1,2], Amine Benzerga[3], and Jacques Besson[1]
[1]*MINES ParisTech, PSL Research University, MAT - Centre des matriaux, CNRS UMR 7633, Evry, France*
[2]*EPF-Ecole d'Ingénieur-e-s, Sceaux, France*
[3]*Department of Aerospace Engineering, Texas A&M University, College Station, USA*

Summary In this paper, the quasi-static plastic deformation of a hot-rolled magnesium AZ31B thick plate is investigated at room temperature in both tension and compression. A macroscopic two-surface model is used to describe the complex anisotropic behavior of this material. The model accounts for plastic anisotropy as well as yielding asymmetry due to twinning. The primary deformation mechanisms, glide by dislocation motion and twinning, are treated separately. A comprehensive database is used for model identification, which includes specimens along the plate principal directions and off-axes specimens along diagonal orientations in principal planes. Flow stresses and strain anisotropy (*R-value*) coefficients are included in the identification procedure. The parameter optimization strategy is presented. It is shown that the model captures the anisotropic behavior of the material.

MATERIAL AND TESTING

The material used is from a 32mm-thick, hot-rolled AZ31B plate provided by Magnesium Elektron company in the H24 condition (strain hardened and partially annealed) [1]. The plate rolling direction is referred to as L, the long transverse direction as T and the short transverse or through-thickness direction as S. Specimens are tested in tension and compression at a strain rate of 10^{-3} s^{-1} for loading along principal directions (L, T and S) and along all diagonal orientations within principal planes (LT, LS and TS) (Fig. 1-a). Uniaxial compression tests are obtained from a previous study [2] with the experimental procedure described in [1]. These were supplemented with new uniaxial tension tests. All tests were carried out at room temperature on a servo-hydraulic testing machine under displacement control. A mechanical extensometer was used to measure axial strains and in addition, each test was paused at regular strain intervals to measure the lateral diameters using a caliper.

CONSTITUTIVE MODEL

The constitutive model proposed in [3] was used to describe the material elastoplastic behavior. Two plastic yield surfaces are introduced so as to account for both glide and twinning mechanisms. Each surface describes plastic anisotropy using the linear transformation method proposed in in Barlat et al. [4] (symmetric yield surface for glide) and Cazacu et al. [5] (non-symmetric yield surface for twinning). The total inelastic strain tensor results from the additive contribution of glide $\underline{\varepsilon}_g$ and of twinning $\underline{\varepsilon}_t$.

Plastic deformation due to glide

The model is based on the definition of an effective stress σ_g function of the stress tensor $\underline{\sigma}$:

$$\sigma_g = \left(\frac{1}{2} \prod_g^2 \nearrow S_g^3|^{a_g} + |S_g^3 \nearrow S_g^1|^{a_g} + |S_g^1 \nearrow S_g^2|^{a_g} \right)^{1/a_g} \tag{1}$$

where S_g^1, S_g^2 and S_g^3 are the eigenvalues of a modified stress deviator $\underline{s}_g$ defined as: $\underline{s}_g = \underline{\underline{L}}_g : \underline{\sigma}$ where $\underline{\underline{L}}_g$ is a fourth order tensor which introduces 6 parameters to describe the anisotropic distorsion of the yield surface along the axes of orthography [4]. The yield surface is expressed as:

$$\Phi_g = \sigma_g \nearrow R_g(p_g, p_t) \tag{2}$$

where $R_g(p_g, p_t)$ corresponds to the flow stress expressed as a function of the cumulated plastic strain due to glide p_g and twinning p_t. $R_g(p_g, p_t)$ is expressed as:

$$R_g(p_g, p_t) = R_g^0 + Q_g^1 \left(1 \nearrow e^{-b_g^1 p_g} \right) + Q_g^2 \left(1 \nearrow e^{-b_g^2 p_g} \right) + H_g p_t \tag{3}$$

Parameter R_g^0 is set to the yield stress in transverse direction (T). Plastic flow associated to dislocation glide is then obtained assuming normality as:

$$\dot{\underline{\varepsilon}}_g = \dot{p}_g \frac{\partial \sigma_g}{\partial \underline{\sigma}} \tag{4}$$

with: $\sigma_g \dot{p}_g = \dot{\underline{\varepsilon}}_g : \underline{\sigma}$. This equation provides an implicit definition of the cumulated plastic strain p_g.

*Corresponding author. Email: yazid.madi@mines-paristech.fr

Plastic deformation due to twinning

The yield surface for twinning is based on the definition of an effective stress σ_t function of the stress tensor:

$$\sigma_t = \left(\frac{1}{2} \left(\left(|S_t^1| - kS_t^1 \right)^{a_t} + \left(|S_t^2| - kS_t^2 \right)^{a_t} + \left(|S_t^3| - kS_t^3 \right)^{a_t} \right) \right)^{1/a_t} \tag{5}$$

where S_t^1, S_t^2 and S_t^3 are the eigenvalues of a modified stress tensor $\underline{s}_t$ defined as: $\underline{s}_t = \underline{\underline{L}}_t : \underline{\underline{J}} : \underline{\sigma}$ where $\underline{\underline{J}}$ is the fourth order tensor that relates a second order tensor to its deviator. $\underline{\underline{L}}_t$ describes anisotropy and introduces 9 material parameters [5]. k describes the strength differential effect ($-1 < k < 1$). The yield surface is finally expressed as:

$$\Phi_t = \sigma_t - R_t(p_t) \tag{6}$$

where $R_t(p_t)$ corresponds to the flow stress expressed as a function of the cumulated plastic strain due to twinning p_t. $R(p_t)$ is expressed as:

$$R_t(p_t) = R_t^0 + Q_t^1 \left(e^{b_t^1 p_t} - 1 \right) + Q_t^2 \left(1 - e^{-b_t^2 p_t} \right) + H_t p_t \tag{7}$$

Parameter R_t^0 is set to the yield stress in the transverse direction (T). As for gliding, the flow rule is obtained applying the normality rule as: $\underline{\varepsilon}_t = \dot{p}_t \dfrac{\partial \sigma_t}{\partial \underline{\sigma}}$. The cumulated plastic stran p_t is obtained by: $\underline{\varepsilon}_g : \underline{\sigma} = \dot{p}_t \sigma_t$

IDENTIFICATION AND RESULTS

The identification of the various material parameters was performed following an iterative procedure similar to one presented in [3]. Flow stresses and strain anisotropy (*R-value* coefficient) are taken into account in the identification. From the comparison between simulations and experiments of illustrative directions presented in Fig. 1, it is shown that the model can capture very well the material complex behavior. A relatively good agreement is obtained both in terms of plastic flow stresses and strain anisotropy.

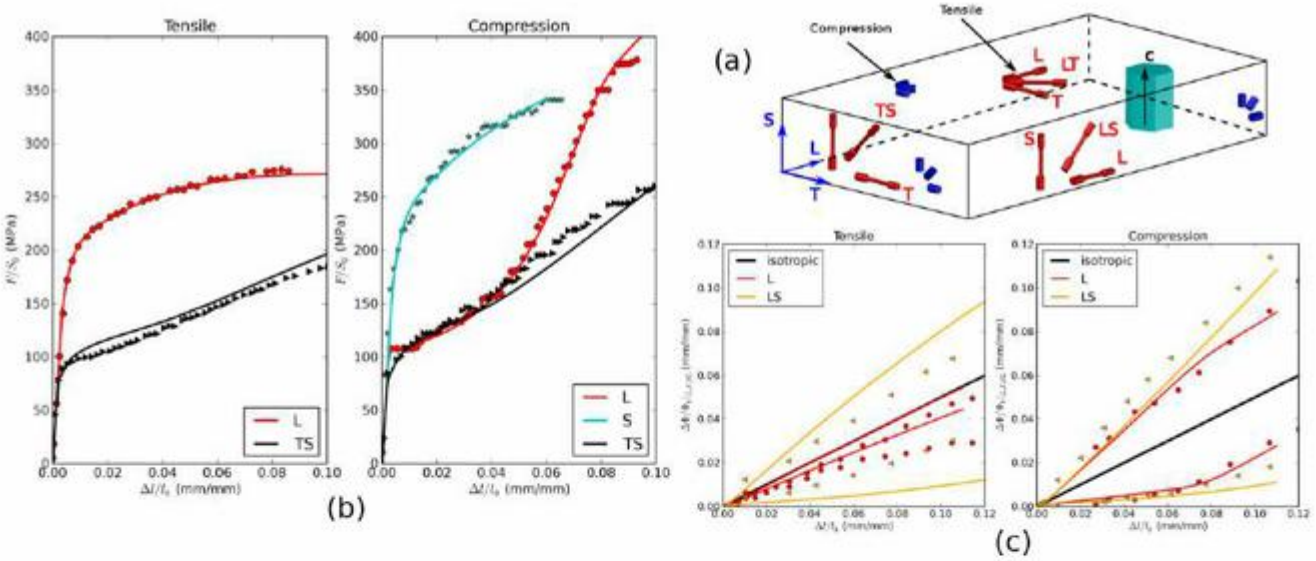

Figure 1: Results from experiments (symbols) versus simulations (lines). (a) Orientation of the specimens extracted from a hot-rolled magnesium AZ31B thick plate. (b) Engineering stress, F/S_0, versus axial strain, $\Delta l/l_0$. (c) Radial contraction, $\Delta\Phi/\Phi_0$, versus axial strain, $\Delta l/l_0$.

References

[1] Kondori, B. and Benzerga, A., Effect of stress triaxiality on the flow and fracture of mg alloy az31, Met. and Mater. Trans. A 45A (2014) 3292–3307.

[2] Kondori, B., Ductile fracture of magnesium alloys: characterization and modeling, Ph.D. thesis, Texas A&M University (2015).

[3] Steglich, D. and Tian, X. and Besson, J., Mechanism-based modelling of plastic deformation in magnesium alloys, Eur. J. Mech.A/Solids 55 (2016) 289–303.

[4] Barlat, F. and Lege, D.J. and Brem, J.C., A six–component yield function for anisotropic materials, Int. J. Plasticity 7 (1991) 693–712.

[5] Cazacu, O. and Plunkett, B. and Barlat, F., Orthotropic yield criterion for hexagonal closed packed metals, Int. J. Plasticity 22 (2006) 1171–1194.

CONSTITUTIVE RESPONSE OF A RARE-EARTH MAGNESIUM ALLOY SHEET IN MONOTONIC AND CYCLIC LOADINGS

Armin Abedini [1a], Cliff Butcher [1], Michael Worswick [1] & Timothy Skszek [2]
[1]*Department of Mechanical and Mechatronics Engineering, University of Waterloo, Waterloo, Ontario, Canada*
[2]*Magna International, Troy, Michigan, USA*

Summary Experimental tests under different proportional loading conditions were performed to investigate the constitutive behaviour of a rare-earth magnesium alloy (ZEK100) rolled sheet at room temperature, under quasi-static conditions. An anisotropic yield function for HCP materials with yield asymmetry, CPB06, was calibrated from monotonic experimental data. To evaluate the performance of the yield criterion, non-proportional experiments were performed with an emphasis on the cyclic shear test. It was observed that although slip and twinning mechanisms govern the response of the magnesium alloy under proportional loadings, reversed loadings can activate the de-twinning mechanism as well leading to a substantial Bauschinger effect.

INTRODUCTION

Magnesium alloys have the potential for significant weight reduction and improved fuel economy in the automotive industry due to their low density and high specific ultimate tensile strength compared to conventional steel and aluminium alloys. However, the implementation of magnesium alloys as wrought products is currently limited because of their low ductility at room temperature due to a limited number of available deformation mechanisms in their HCP crystal structure. The dominant slip systems of magnesium alloys at room temperature are basal slip followed by prismatic and pyramidal slips with higher critical resolved shear stress (CRSS). Twinning can also provide an independent deformation mechanism [1]. Under cyclic loading with strain path changes, a de-twinning mechanism can also appear [2]. In general, magnesium alloys in the form of rolled sheets or extrusions exhibit severe anisotropy and tension-compression asymmetry [3].

The objective of the present work was to investigate the room temperature constitutive behaviour of a rare-earth magnesium alloy sheet, ZEK100, under quasi-static strain rates undergoing monotonic and cyclic loadings. The material was subjected to a variety of monotonic and proportional loading conditions including uniaxial tension, equal-biaxial tension, shear, plane-strain tension and uniaxial compression. Furthermore, the behaviour of the material under cyclic shear condition was investigated. Studying the behaviour of the material under both monotonic and cyclic deformation can shed light into the type of deformation mechanisms accommodating plastic deformations and provide insight into utilizing suitable constitutive modelling approaches for predicting the response of materials.

PROCEDURE, RESULTS AND DISCUSSION

A rare-earth rolled magnesium sheet, ZEK100 (O-temper), with a nominal thickness of 1.55 mm was used in the present study (1.3%wt. Zn, 0.2%wt. Nd, 0.25%wt. Zr and 0.01%wt. Mn). The monotonic experiments performed on the ZEK100 were selected to cover a wide range of stress states to reveal the anisotropic behaviour of the material. Using the results of experimental tests, the CPB06ex2 yield criterion [4] was calibrated for one plastic work level (corresponding to the equivalent plastic strain of 0.01 for the uniaxial tension test in the rolling direction). The severely anisotropic behaviour of the material is apparent from inspection of the yield surface in Figure 1 with a clear asymmetry between the tension region (first quadrant) and compression region (third quadrant). This can be explained by deformation being slip-dominated in tensile loading while yielding in compression is mostly governed by the twinning mechanism which activates at lower stresses [3]. Abedini et al. [5] has demonstrated the significant evolution of the ZEK100 yield surface with deformation as the shape of the yield surface and level of tension-compression asymmetry changes during deformation. At larger strain levels, the yield stress in compression eventually becomes larger than in tension.

Fully-reversed cyclic shear tests were performed on the ZEK100 to complete a full cycle and half with a cumulative shear strain of approximately15%. The cyclic shear response of the material is plotted in Figures 2 for the shear test loaded in the diagonal direction of the sheet with the principal stress components in the rolling and transverse directions. It can be seen from Figure 2 that the shear response of the ZEK100 in reversed conditions shows a lower value of yield stress indicating a Bauschinger phenomenon that is attributed to the de-twinning mechanisms. This can be explained with the fact that the twin nucleation stress is higher than the stress needed for de-twinning for which no nucleation is needed [2]. Furthermore, it can be seen from Figure 2 that the second and third yielding regions demonstrate a more gradual yielding compared with the abrupt initial yielding transition. It has been reported that twinning mechanisms result in a sharp yielding behaviour while de-twinning is characterized by gradual yielding [2] indicating again that a de-twinning mechanism is active in reverse shear conditions.

[a)] Corresponding author. Email: aabedini@uwaterloo.ca

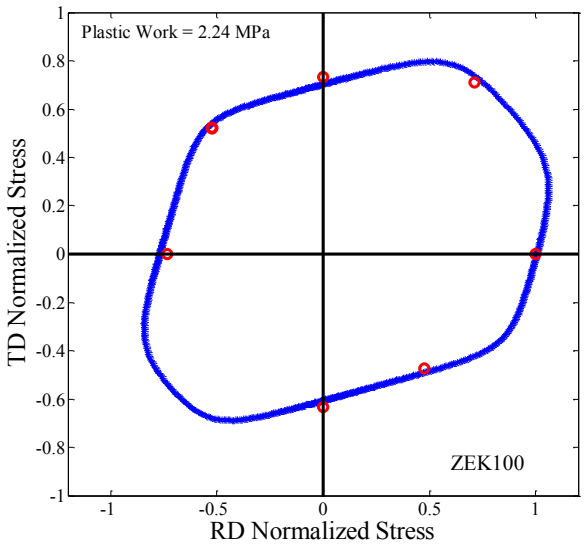

Fig 1: CPB06ex2 yield locus at plastic work level of 2.24 MPa (equivalent plastic strain of 0.01). Circles show the experimental results.

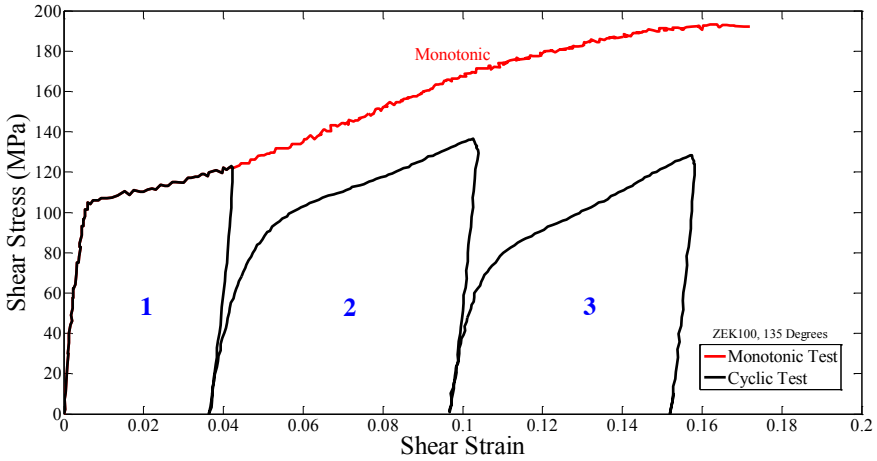

Fig 2: Absolute shear stress vs. absolute cumulative shear strain response for the ZEK100 in cyclic condition. The shear response in monotonic condition is also plotted for comparison [6]. The vertical axis represents the absolute shear stress. The first region of loading is labelled as "1" while the reversed loading is labelled as "2". Finally the last region "3" is in the same direction as the initial loading.

CONCLUSIONS

Monotonic and cyclic tests were performed on a rare-earth magnesium alloy sheet (ZEK100). It was shown that the monotonic response of the ZEK100 is highly anisotropic with tension-compression asymmetry due to the activation of slip and twinning mechanisms in tension and compression, respectively. The shear response of the material in reversed loadings exhibited the Bauschinger effect indicative of activation of the de-twinning mechanism. Constitutive modelling of the response of the material in monotonic and cyclic conditions will be considered in future contributions.

References

[1] Lou X. Y., Li M., Boger R. K., Agnew S. R., Wagoner R. H.: Hardening Evolution of AZ31B Mg Sheet. *Int. J. Plasticity*. **23**:44-86, 2007.

[2] Qiao H., Agnew S. R., Wu P. D.: Modeling Twinning and Detwinning Behavior of Mg Alloy ZK60A during Monotonic and Cyclic Loading. *Int. J. Plasticity*. **65**:61-84, 2015.

[3] Kurukuri S., Worswick M. J., Bardelcik A., Mishra R. K., Carter J. T.: Constitutive Behavior of Commercial Grade ZEK100 Magnesium Alloy Sheet over a Wide Range of Strain Rates. *Metall. Mater. Trans. A* **45 (8)**:3321-3337, 2014.

[4] Plunkett B., Cazacu O., Barlat F.: Orthotropic Yield Criteria for Description of the Anisotropy in Tension and Compression of Sheet Metals. *Int. J. Plasticity*. **54(16)**:4159-4169, 2008.

[5] Abedini A., Butcher C., Worswick M. J., Williams B., Skszek T., Kuwabara T.: Anisotropic Constitutive Response of a Rare-earth Magnesium Alloy Sheet: Characterization of Yield Locus Evolution. *NUMIFORM Conference*, Troy, France, 2016.

[6] Abedini A., Butcher C., Anderson D., Worswick,M. J., Skszek T.: Fracture Characterization of Automotive Alloys in Shear Loading. *SAE Int. J. Mater. Manf.* **8(3)**: 2015.

A THEORY OF STRAIN GRADIENT-DIVERGENCE PLASTICITY

Adegbola P. Akinola[1], Adebowale S. Borokinni[2] & Olawanle P. Layeni[1]
[1]*Department of Mathematics, Obafemi Awolowo University, Ile-Ife, Osun, Nigeria*
[2]*Distance Learning Institute, University of Lagos, Akoka, Lagos, Nigeria*

Summary This work develops a gradient-divergence theory of small deformation viscoplasticity based on a set of microstresses; the second law of thermodynamics and; a constitutive theory accounting for the divergence of the plastic strain. Using the principle of virtual power, a microforce balance is obtained. Restricted by the local free energy imbalance, the constitutive relations together with microforce balance are shown to constitute a nonlocal flow rule which is a nonlinear partial differential equation in the plastic strain tensor. Thus the flow rule is shown to generalize the Gurtin-Anand model in [3].

INTRODUCTION

The study of strain gradient plasticity has been motivated due to inability of the classical plasticity to model material behaviour at infinitesimal length scales. However, existing strain gradient theories such as that of [1] and [3] do not account for dependence on the divergence of the plastic strain and the effect of an internal microforce. Hence, the need of a plasticity theory which addresses these situations. This work is aimed at obtaining the flow rule of a strain gradient theory that accounts for the divergence of the plastic strain wherein each microstress is assumed to be additively decomposed into energetic and dissipative part, thus extending the work in [3].

BASIC KINEMATICS

Let $\boldsymbol{u}(\boldsymbol{x},t)$ be the displacement vector of a point $\boldsymbol{x}$ in a body B undergoing small deformation. The displacement gradient $\nabla\boldsymbol{u}$ is assumed to be additively decomposed as

$$\nabla\boldsymbol{u} = \boldsymbol{H^e} + \boldsymbol{E^p}, \;\; tr\, \boldsymbol{E^p} = 0 \tag{1}$$

$\boldsymbol{H^e}$ accounts for stretching and rotation of material and $\boldsymbol{E^p}$ is known as the plastic strain that accounts for irreversible restructuring of material. The basic kinematic variables for this work are $\boldsymbol{H^e}$, $\boldsymbol{E^p}$ and $\boldsymbol{u}$. To account for some specific defects in material structure, plastic strain gradient $\nabla\boldsymbol{E^p}$, divergence of plastic strain $div\, \boldsymbol{E^p}$, and Burgers tensor $\nabla \times \boldsymbol{E^p}$ would be incorporated into power expenditure expression so as to obtain a microforce balance for a body undergoing plastic deformation. Each of these kinematic terms or variables would be conjugate to some microstresses. These microstresses would be related to each other through the microforce balance. It should be recalled that the kinematic terms $\nabla \times \boldsymbol{E^p}$ and $div\, \boldsymbol{E^p}$ can be expressed in terms of the plastic strain gradient $\nabla\boldsymbol{E^p}$. Clearly by definition

$$(\nabla \times \boldsymbol{E^p})_{ij} = \epsilon_{ipq} E^p_{jq,p} \tag{2}$$

$$(div\, \boldsymbol{E^p})_i = E^p_{ik,k} = \delta_{kr} E^p_{ik,r}. \tag{3}$$

Therefore in formulating the microforce balance, the conjugate of these kinematics terms must be put into consideration. Since the Burgers tensor $\nabla \times \boldsymbol{E^p}$ can be written in terms of the plastic strain gradient, we shall assume that the free energy includes dependence on the Burgers tensors in a way that the plastic strain gradient is dropped. It should also be noted that the plastic strain gradient $\nabla\boldsymbol{E^p}$ can be written in terms of the Burgers tensor $\nabla \times \boldsymbol{E^p}$ given in component form as

$$E^p_{ij,k} = E^p_{ik,j} - \epsilon_{sjk} G_{si}, \tag{4}$$

where $G_{si} = (\nabla \times \boldsymbol{E^p})_{si}$. Thus in obtaining the microforce balance, we would assume that the conjugate microstress of the plastic strain gradient contains a microstress conjugate to the Burgers tensor which can be written in terms of the plastic strain gradient written in (2).

FORCE BALANCES

It would be assumed that: an internal microforce $\boldsymbol{\chi}$ is work-conjugate to $div\, \boldsymbol{E^p}$; a macrostress $\boldsymbol{T}$ is work-conjugate to $\boldsymbol{H^e}$; a microstress $\boldsymbol{T^p}$ is work-conjugate to $\boldsymbol{E^p}$ and; a polar microstress $\mathbb{K}^p$ is work-conjugate to $\nabla\boldsymbol{E^p}$. The internal power expenditure over an arbitrary region P of B takes the form

$$W_{int} = \int_P \left(\boldsymbol{T}\colon \dot{\boldsymbol{E}}^{\boldsymbol{e}} + \boldsymbol{T^p}\colon \dot{\boldsymbol{E}}^{\boldsymbol{p}} + \boldsymbol{\chi} \cdot div\, \dot{\boldsymbol{E}}^{\boldsymbol{p}} + \mathbb{K}^{\boldsymbol{p}} \vdots \nabla\dot{\boldsymbol{E}}^{\boldsymbol{p}}\right) dV \tag{5}$$

and the external power expenditure due to the body force $\boldsymbol{b}$ on P, macrotraction $\boldsymbol{t}$ and microtraction $\boldsymbol{K}$ on ∂P is given by

$$W_{ext} = \int_{\boldsymbol{P}} \boldsymbol{b} \cdot \dot{\boldsymbol{u}}\, dV + \int_{\partial P} \left(\boldsymbol{t} \cdot \dot{\boldsymbol{u}} + \boldsymbol{K}\colon \dot{\boldsymbol{E}}^{p}\right) dA. \tag{6}$$

Let $\vartheta = (\boldsymbol{\delta\dot{u}}, \boldsymbol{\delta\dot{H}}^{e}, \delta\dot{\boldsymbol{E}}^{p})$ be a list of virtual velocities. The principle of virtual power states that

Corresponding author. Email: **aborokini@unilag.edu.ng**

$$W_{int}(P,\vartheta) = W_{ext}(P,\vartheta). \tag{7}$$

This principle allows us to obtain the macroforce balance given by

$$div\,\boldsymbol{T} + \boldsymbol{b} = \boldsymbol{0}, \tag{8}$$

with the traction condition given as

$$\boldsymbol{Tn} = \boldsymbol{t}. \tag{9}$$

This macroforce is obtained by choosing $\delta\dot{\boldsymbol{E}}^{\boldsymbol{p}} = \boldsymbol{0}$. Using the same principle of virtual power (where we choose $\delta\dot{\boldsymbol{u}} = \boldsymbol{o}$ and apply the divergence theorem) we obtain the microforce balance

$$\boldsymbol{T}_o = \boldsymbol{T^p} - sym_o(\nabla\boldsymbol{\chi}) - div\,\mathbb{K}^p, \tag{10}$$

with microtraction condition

$$\boldsymbol{K} = sym_o(\boldsymbol{\chi}\otimes\boldsymbol{n}) + \mathbb{K}^p\boldsymbol{n}. \tag{11}$$

$\boldsymbol{T}_o$ is the deviatoric part of the macrostress $\boldsymbol{T}$, $sym_o(\nabla\boldsymbol{\chi})$ is called the symmetric deviatoric part of the gradient of the microforce $\boldsymbol{\chi}$. The tensor product $\boldsymbol{\chi}\otimes\boldsymbol{n}$ is a dyad.

CONSTITUTIVE RELATIONS AND FLOW RULE

Following the work in [2] we assume that each microstress say $\boldsymbol{\Pi}$ is additively decomposed as

$$\boldsymbol{\Pi} = \boldsymbol{\Pi}_{en} + \boldsymbol{\Pi}_{dis}, \tag{12}$$

where $\boldsymbol{\Pi}_{en}$ and $\boldsymbol{\Pi}_{dis}$ are the energetic and dissipative parts of $\boldsymbol{\Pi}$ respectively. The free energy imbalance for this plastic process is obtained as (following the second law of thermodynamics)

$$\dot{\psi} - \boldsymbol{T}\!:\dot{\boldsymbol{E}}^{\boldsymbol{p}} - \boldsymbol{\chi}\cdot div\,\dot{\boldsymbol{E}}^{p} - \boldsymbol{T^p}\!:\dot{\boldsymbol{E}}^{\boldsymbol{p}} - \mathbb{K}^{\boldsymbol{p}} \vdots \nabla\dot{\boldsymbol{E}}^{\boldsymbol{p}} \le 0, \tag{13}$$

where ψ is called the Helmholtz free energy, taking the form

$$\psi = \psi(\boldsymbol{E^e}, \boldsymbol{E^p}, div\,\boldsymbol{E^p}, \nabla\times\boldsymbol{E^p}). \tag{14}$$

Consistent with the free energy imbalance and the formulation in [2], we define and deduce

$$\boldsymbol{T} = \frac{\partial\psi}{\partial\boldsymbol{E^e}},\quad \boldsymbol{T^p} = \frac{\partial\psi}{\partial\boldsymbol{E^p}},\quad \boldsymbol{\chi_{en}} = \frac{\partial\psi}{\partial div\,\boldsymbol{E^p}},\qquad \text{and } \left(\mathbb{K}^{\mathrm{p}}_{en}\right)_{jqp} = (sym_o\,\mathbb{P})_{jqp}, \tag{15}$$

where $(\mathbb{P})_{jqp} = \frac{\partial\psi}{\partial G_{ij}}\epsilon_{ipq}$ and $G_{ij} = \epsilon_{irs}E^p_{js,r}$. The free energy is obtained in quadratic form as

$$\psi = \frac{1}{2}\kappa|tr\,\boldsymbol{E}^e|^2 + \mu|\boldsymbol{E}^{\boldsymbol{e}}_o|^2 + \frac{1}{2}\mu|\boldsymbol{E^p}|^2 + \frac{1}{2}\mu Q^2|div\,\boldsymbol{E^p}|^2 + \frac{1}{2}\mu L^2|\nabla\times\boldsymbol{E^p}|^2, \tag{16}$$

where Q and L are called energetic length scales associated with $div\,\boldsymbol{E^p}$ and $\nabla\times\boldsymbol{E^p}$ respectively. The dissipative microstresses based on the von Mises yield criterion are given in terms of their corresponding power conjugate as follows

$$\boldsymbol{\chi}_{dis} = q^2S_o\left(\frac{d^p}{d_o}\right)^m\frac{div\,\dot{\boldsymbol{E}}^{\boldsymbol{p}}}{d^p},\quad \boldsymbol{T^p_{dis}} = S_o\left(\frac{d^p}{d_o}\right)^m\frac{\dot{\boldsymbol{E}}^{\boldsymbol{p}}}{d^p},\quad \mathbb{K}^{\boldsymbol{p}}_{dis} = l^2S_o\left(\frac{d^p}{d_o}\right)^m\frac{\nabla\,\dot{\boldsymbol{E}}^{\boldsymbol{p}}}{d^p}. \tag{17}$$

S_o is the initial yield strength, d_o is the initial flow rate, m is the rate sensitivity parameter and d^p is the effective flow rate defined by

$$d^p = \sqrt{\left|\dot{}^{\,p}\right|^2 + q^2\left|div\,\dot{\boldsymbol{E}}^2\right|^2 + l^2\left|\nabla\dot{\boldsymbol{E}}^p\right|^2}, \tag{18}$$

where q and l are called dissipative length scales associated with $div\,\boldsymbol{E^p}$ and $\nabla\boldsymbol{E^p}$ respectively. Substitute (15) and (17) in (10), we obtain the consequent flow rule of viscoplasticity

$$\begin{aligned}&\boldsymbol{T}_o + \mu(L^2\Delta\boldsymbol{E^p} + (Q^2 - L^2)sym_o(\nabla div\,\boldsymbol{E^p}) - \boldsymbol{E^p})\\ &= S_o\left(\frac{d^p}{d_o}\right)^m\frac{\dot{\boldsymbol{E}}^{\boldsymbol{p}}}{d^p} - q^2S_o\left(sym_o\left(\nabla\left[\left(\frac{d^p}{d_o}\right)^m\frac{div\,\dot{\boldsymbol{E}}^{\boldsymbol{p}}}{d^p}\right]\right)\right) - l^2S_o\,div\left[\left(\frac{d^p}{d_o}\right)^m\frac{\nabla\,\dot{\boldsymbol{E}}^{\boldsymbol{p}}}{d^p}\right].\end{aligned} \tag{19}$$

CONCLUSIONS

Thus relation (19) constitutes a more generalized form of the Gurtin-Anand model. It reduces to the Gurtin-Anand plastic flow rule [3] in either cases: $Q = 0$, the free energy is independent of the plastic strain and $q = 0$ or; $Q^2sym_o(\nabla\,div\,\boldsymbol{E^p}) - \boldsymbol{E^p} = \boldsymbol{0}$ and $q = 0$.

References

[1] Gudmundson P.: A unified treatment of strain gradient plasticity. *J. Mech. Phys. Solids 52: 1379-1406*, 2004.

[2] Gurtin M. E.: On a framework for small-deformation visco-plasticity: free-energy, microforces, strain gradient *Int. J. Plast. 9: 47-90*, 2003.

[3] Gurtin M. E, Anand L.: A theory of strain gradient plasticity for istropic, plastically irrotational materials. Part I: Small deformations. *J. Mech. Phys. Solids 53: 1624-1649*, 2005.

ESTIMATION OF SHEAR STRESS IN MACHINING USING THE TEMPERATURE DISTRIBUTION ON THE TOOL FACE

Timothy J. Burns[1] & Bert W. Rust[1]
[1]Applied and Computational Mathematics Division, NIST, Gaithersburg, Maryland, USA

Summary Given an experimentally determined discrete set of steady-state temperature measurements along the region of contact of the work material with the rake face of the tool, an inverse method is used to obtain an estimate of the shear stress in the work material near the tool-material interface.

INTRODUCTION

Despite many years of study, the determination of accurate constitutive response models for the flow stress in materials for finite-element simulations of high-speed machining operations remains a difficult unsolved problem. Most attempts to model the material response using experimental data have been based on direct methods that fit compression test data of small samples of the material of interest to a given highly nonlinear constitutive response model. The main problem with this approach has been that the conditions under which compression tests can be performed are not nearly as extreme as the actual conditions that are present in a typical high-speed machining operation [1], so that a machining process simulation using the nonlinear material response model necessarily requires huge extrapolations in order to simulate the cutting conditions.

One area of machining research in which significant progress has been made in the past few years has been on the measurement of the 2D temperature distribution on the chip–tool interface, using infrared thermography. In particular, Menon and Madhavan [2] have reported high accuracy temperature measurements during high-speed machining of a titanium alloy, using single wavelength thermography with an instrumented transparent tool. For their experimental cutting conditions, they have obtained a 1D temperature distribution as a function of distance along the rake face of the tool, along an internal cross section of the chip–tool interface, with an estimated combined standard uncertainty of less than 1%.

OUTLINE OF RESULTS

Motivated by this work, we have been investigating a new approach to the problem of estimating flow stress in machining, that is based on an inverse method. By finding an asymptotic solution of a convection-diffusion problem that models the flux of heat into the chip and the tool during a cutting experiment, the temperature distribution along the tool face can be shown to satisfy Abel's equation, a Volterra integral equation of the first kind with a weakly singular kernel, convolved with the flow stress [3]. Inversion of this Abel transform provides an estimate of the distribution of flow stress in the chip material near the tool-chip interface.

Because the temperature data are experimentally determined, estimation of the flow stress by inversion of the Abel transform under these circumstances is an ill-posed problem. In this talk, we will show that the Truncated Singular Components Method (TSCM) of Rust [4],[5], which has been successfully used to find approximate numerical solutions of Fredholm integral equations of the first kind with noisy data, can also be applied to find approximate numerical solutions of the Abel equation, and thus an estimate of the flow stress in the work material can be obtained.

CONCLUSIONS

We have applied our method to three sets of temperature data on the tool-chip interface that were obtained in a series of orthogonal cutting experiments on AISI 1045 steel by Davies, et al. [6]. In these tests, the cutting speed was held fixed at 3.7 m/s, and the temperature distribution along the rake face of the tool was determined for three different uncut chip thicknesses h_1; the temperature results are plotted on the figure below (left). The corresponding estimates of the shear flow stress τ_f using our method, without correcting for the heat flow into the tool, are also plotted in the figure (right).

[a] Corresponding author. Email: burns@nist.gov.

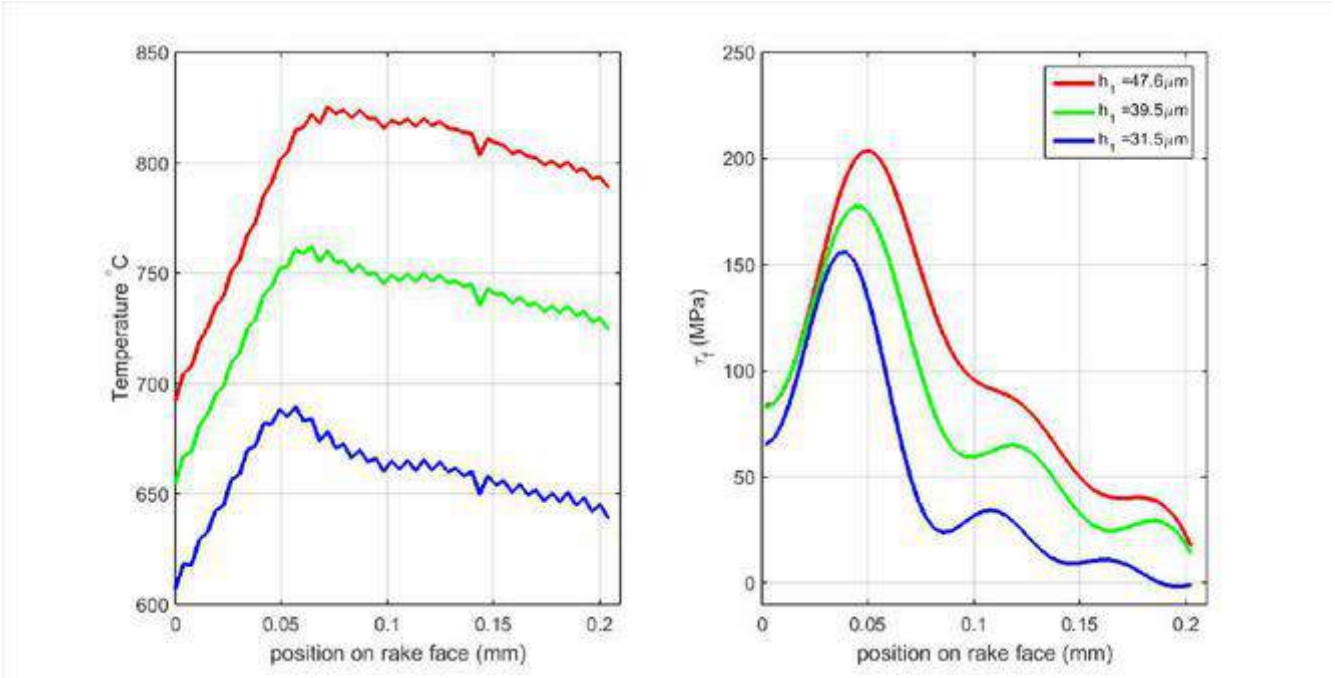

References

[1] S. P. Mates, R. L. Rhorer, E. P. Whitenton, T. J. Burns, and D. Basak, A Pulse-Heated Kolsky Bar Technique for Measuring Flow Stress of Metals Subjected to High Loading and Heating Rates, Experimental Mechanics 48 (2008), 799–807.
[2] T. Menon and V. Madhavan, Infrared Thermography of the Chip-Tool Interface through Transparent Cutting Tools, Proceedings of the North American Manufacturing Research Institution/SME, Ann Arbor, MI, June 2014.
[3] T. J. Burns, S. P. Mates, R. L. Rhorer, E. P. Whitenton, and D. Basak, Inverse Method for Estimating Shear Stress in Machining. J. Mechanics and Physics of Solids 86 (2016), 220–236.
[4] B. W. Rust, Truncating the Singular Value Decomposition for Ill-Posed Problems, NIST IR 6131, July 1998.
[5] B. W. Rust and D. P. O'Leary, Residual Periodograms for Choosing Regularization Parameters for Ill-Posed Problems, Inverse Problems 24 (2008), 034005 (30 pages). DOI:10.1088/0266-5611/24/3/034005.
[6] M. A. Davies, H. Yoon, T. L. Schmitz, T. J. Burns, and M. D. Kennedy, Calibrated Thermal Microscopy of the Tool–Chip Interface in Machining, Machining Science and Technology 7 (2003), 167–190.

MODELING OF SHOT PEEN-FORMING OPERATIONS USING EIGENSTRAINS

Pierre Faucheux[1], Martin Lévesque[1a)] & Frédérick P. Gosselin [1]
[1]Laboratory for Multiscale Mechanics, École Polytechnique de Montréal, Montréal, Québec, Canada

Summary Shot peen forming is a cold work process that consists in impacting a thin metallic part with small shots at high velocities so that the plastic deformations of the material close to the surface generates a significant distortion of the whole structure. In this work, we use the concept of eigenstrains (/stress-free deformations) to predict the result of conventional peen forming treatments when applied to large aluminium sheets. A set of validation experiments consisting in uniformly shot peened rectangular aluminium panels is presented and compared to simulations outcomes. The results are in qualitative agreement only but nevertheless represents progress in comparison with existing procedures.

BACKGROUND

Shot peening is a mechanical surface treatment that consists in the controlled bombardment of the surface of a metallic part with hard shots at high velocities. Under the effect of impacts, the surface of the part is plastically deformed over a depth of several tenth of a millimetres for typical applications. The incompatibility of deformations between the upper layer and the core of the part, unaltered by the treatment, has two consequences: (i) the introduction of a compressive residual stress field near the surface beneficial for fatigue applications and (ii) a distortion of the structure that is all the more important when its flexural rigidity is low (peen forming).

Peen forming has been extensively used by the aerospace industry over the past fifty years as a viable and economical way to shape wing skins and fuselage panels. Nevertheless, in spite of several contributions from the peening community, numerical tools developed so far either require significant calibration, hence lacking flexibility, or do not have the ability to make quantitative predictions. As a result, the determination of appropriate process parameters for each new part to be formed relies on the 'know how' of a few experts and often implies costly trial an error adjustments. More problematic perhaps, the full potential of the process, that is the whole range of achievable deformed shapes, is under exploited.

Our work aims at addressing this issue by developing a procedure able to simulate the full industrial process – including the peen forming of pre-stressed parts – with a degree of accuracy high enough for use during preliminary design phases. Here, some progress made on the simulation of conventional peen forming are presented.

MODELING APPROACH

Only treatments with a high density of impacts are considered so that the state of the matter after peening can be considered the same over the whole part.

For a given target material and treatment couple, the post-peening state is characterized by the distribution of plastic strains $\underline{\underline{\varepsilon}}^{pl}$ as a function of depth only. The latter is obtained either experimentally or numerically. Here, plastic strains are seen as eigenstrains [1], i.e. a generic source of anelastic deformation installed in the structure, the physical cause of which is of no importance as long as we are only interested in the deformed shape of the part.

Following a procedure similar to the one used in Ref. [2], the eigenstrain profile is inputted in a finite element model of the whole part by thermal analogy: the part is discretized using multi-layer shell elements and 'virtual' thermal expansion coefficients $\underline{\underline{\alpha}}$ are defined in each ply so that $\underline{\underline{\varepsilon}}^{pl}(z_i) = \underline{\underline{\alpha}}_i \Delta T$ in the ith ply. The model is then subjected to a unit increment of temperature ΔT leading to the deformed shape. In the event of identical in plane components for the eigenstrain profile (perfectly isotropic material or lack of experimental data), small amplitude random noise is superimposed to the thermal expansion coefficients in order to trigger geometrical instabilities likely to occur when panels of regular geometry are uniformly peened (See *fig.1.b-c*).

RESULTS

A preliminary validation of the procedure has been conducted on flat 1m x 1m aluminium 2024-T351 panels of uniform thicknesses (5, 10 and 15mm). These panels were subjected to three different peen forming treatments representative of industrial conditions. During peening, the parts were free to deform and the orientation of the shots feed was kept perpendicular to the initial surface. Plastic strain profiles have been determined both from impact simulations and experimentally extracted from X-Ray diffraction measurements using the inverse procedure described in [3].

The simulations (*fig.1.d*) are in qualitative agreement with experimental data. The procedure also proved to be able to capture a transition in the deformed shape of the panels from a spherical to a cylindrical one as the thickness is decreased for a given treatment.

[a)] Corresponding author. Email: martin.levesque@polymtl.ca

DISCUSSION

The initial objective of quantitative predictions has not been achieved yet. Several avenues for improvement have been identified, namely, a better characterization of the eigenstrains fields and the correction of a flow in our peening setup. A second experimental campaign is on the way at the time of writing. Significant progress in comparison with existing procedures has nevertheless been made with regard to the simulation of the process. The idea of working with eigenstrains – well established in other domains like welding and laser peening – that was so far overlooked by the shot peening community enables to:

(i) Estimate the deformed shape of large parts in a single computational step: since the plastic strain field is not altered by the springback of the structure as long as the transformation remains elastic, the introduction of the appropriate eigenstrain field yields the expected result provided a potential path dependency is taken into account.

(ii) Ease the simulation of complex treatments:
   (a) Partition of the finite element model to take into account different (or the absence of) treatments in some areas is straightforward.
   (b) Eigenstrains fully characterize the post peening state ([4]) and are mostly independent of the geometry of the part ([5]). It is therefore conceivable to establish databases of such profiles that could be used to simulate most peening operations from scratch through a procedure similar to the one presented here.

ACKNOWLEDGEMENTS

Funding from Airbus Operations Ltd. is gratefully acknowledged

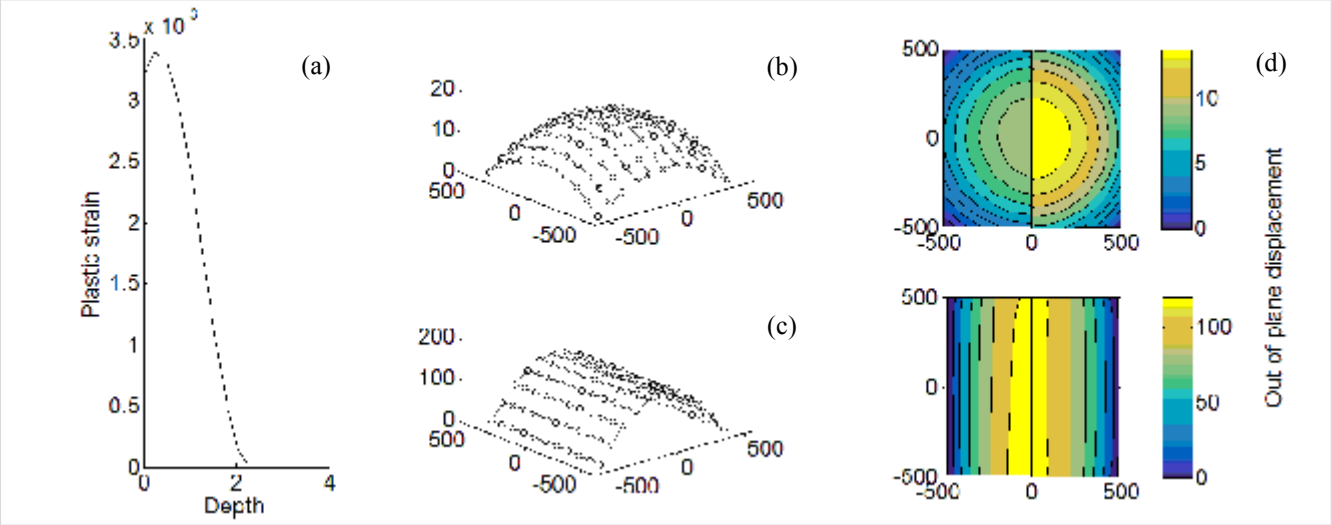

Figure 1 – (a) Eigenstrain profile corresponding to a reference treatment extracted from residual stress XRD measurements using the inverse procedure described in [3] – Deformed shape of a 15mm (b) and 5mm (c) thick AA2024-T51 panel subjected to the reference treatment – (d) Comparison of experimental (left) and numerical (right) out of plane displacements for the two panels. The eigenstrain profile from fig1.a has been used for the simulations – All dimensions are in mm

References

[1] Mura T., Micromechanics of defects in solids, 2nd edition, Martinus Nijhoff publishers, Dordrecht, Netherland

[2] Hu Y., Grandhi R.V., Efficient numerical prediction of residual stress and deformation for large-scale laser shock processing using the eigenstrain methodology, Surface and Coatings Technology, 2012, vol. 206, n 5, p.1137-1148

[3] Korsunsky A.M., On the modelling of residual stresses due to surface peening using eigenstrain distributions, Jrnl. Of Str. Anal. For Eng. Design, 2005, vol. 40, n 8, p.817-824

[4] Renaud P., Modélisation numérique de grenaillage de pièces initialement cémentées ou carbonitrurées, 2001, PhD. Thesis, Ecole Nationale Supérieure des Arts et Métiers, Paris, France

[5] Zhang S.Y, Venter A. et al., High-energy synchrotron X-ray analysis of residual plastic strains induced in shot peened steel plates, Jrnl. Of Str. Anal. For Eng. Design, 2008, vol. 43, n 4, p.229-241

DEPENDENCE OF STRENGTH AND DUCTILITY OF COARSE-GRAINED METALS ON THE NANOTWIN VOLUME FRACTION

X. Guo[1a)], Q.D. Ouyang[1], G.J. Weng[2], L.L. Zhu[3] & J. Lu[4]
[1] *School of Mechanical Engineering, Tianjin University, Tianjin, China*
[2] *Department of Mechanical and Aerospace Engineering, Rutgers University, New Brunswick, NJ, USA*
[3] *Department of Engineering Mechanics, School of Aeronautics and Astronautics, Zhejiang University, Hangzhou, Zhejiang, China*
[4] *Department of Mechanical and Biomedical Engineering, City University of Hong Kong, Hong Kong*

Abstract Coarse-grained (CG) metals strengthened by nanotwinned (NT) regions have both high strength and good ductility. Here, numerical simulations based on the strain gradient plasticity model and the Johnson–Cook failure criterion are carried out to investigate effects of shape and volume fraction of the NT regions on the strength and ductility of CG metals. Our results indicate that they have significant effects on both properties and that the shape effects also change with the volume fraction.

INTRODUCTION

Dynamic plastic deformation followed by recovery annealing can fabricate coarse-grained (CG) metals strengthened by nanotwined (NT) regions with both high strength and good ductility [1,2]. Experimental observations have in general contributed to the understanding of NT metals [3-7], but as the exact NT region shape and volume fraction are difficult to reproduce, a complete understanding is still missing. This computational work seeks to provide this missing information.

METHOD

We generate three idealized tensile specimen (300×60 μm^2 in Fig. 1) with the green CG matrix and the red NT regions. The volume fraction of the NT regions, *f*, is almost the same in these three microstructures. Microstructures A, AR, and AR-45 have the array-arranged uniform NT regions. We change *f* from 7% to 38.5%.

A NT region contains ultrafine grains and a grain has a few to more than a hundred twin lamellas [6]. The dislocation-pileup-zones (DPZ) near twin boundaries (TBs) and grain boundaries (GBs) have significant strain gradients so that a constitutive relation based on the strain gradient plasticity was derived [8]. Taylor's model [9] suggests that the flow stress can be expressed as $\sigma_{\text{flow}} = M\alpha\mu b\sqrt{\rho_{\text{I}} + \rho_{\text{TB}} + \rho_{\text{GB}}}$, where ρ_{I} denotes the dislocation density in the grain interior of a unit cell, ρ_{TB} denotes that in the TBDPZ, and ρ_{GB} that in GBDPZ. ρ_{TB} is derived as a function of twin spacing (4 nm in this paper) [8]. ρ_{GB} can be related to the local strain gradient in the GBDPZ. Intragrain dislocation-mediated interaction dominates the plastic deformation of the ultrafine grains and ρ_{I} obeys Kocks and Mecking's model [10]. The plastic strain rate is proportional to the deviatoric stress and the equivalent plastic strain rate is determined by $\dot{\varepsilon}_{\text{e}}^{\text{p}} = \dot{\varepsilon}_{\text{e}}[\frac{\sigma_{\text{e}}}{\sigma_{\text{flow}}}]^{m_0}$ where $\dot{\varepsilon}_{\text{e}}$ is the equivalent strain rate, σ_{e} the von Mises stress, and m_0 the strain-rate sensitivity exponent [11]. The Johnson–Cook plasticity model [12] is used to describe constitutive behaviors at high strain rate, i.e., $\sigma_{\text{e}} = \left[A + B(\varepsilon_{\text{e}}^{\text{p}})^n\right]\left[1 + C\ln\left(\frac{\dot{\varepsilon}_{\text{e}}^{\text{p}}}{\dot{\varepsilon}_0}\right)\right]\left[1 - \left(\frac{T - T_{\text{r}}}{T_{\text{m}} - T_{\text{r}}}\right)^m\right]$, where *A, B, C*, *m*, and *n* are parameters, $\varepsilon_{\text{e}}^{\text{p}}$ is the equivalent plastic strain, $\dot{\varepsilon}_0$ the reference strain rate, T the temperature, T_{r} the room temperature, and T_{m} the melting temperature. The Johnson–Cook failure criterion [13] is employed to relate the damage parameter *D* to the plastic strain increment $\text{d}\varepsilon_{\text{e}}^{\text{p}}$, i.e., $D = \int \frac{1}{\varepsilon_{\text{f}}} \text{d}\varepsilon_{\text{e}}^{\text{p}}$, where ε_{f} is the failure strain.

RESULTS AND DISCUSSION

NT regions have higher yield stress and lower failure strain so that failure of the material is always initiated by interfacial debonding between two phases. We have computed the engineering stress–strain curves at different *f*. It is found that, as *f* increases, the ductility decreases monotonically, while the nominal strength continues to increase, in a good agreement with experimental reports [2]. Fig. 2 shows the true stress–strain curves for microstructure A with different *f*. It is seen that, as *f* increases, the peak true stress decreases first and then increases. The other microstructures also exhibit the same trend. It shows that the resistance of the material to deformation becomes weaker and then stronger as *f* increases. This finding is new in two-phase materials.

We have also calculated the engineering stress–strain relations for all microstructures. As *f* increases, the strength increases and scatters, while ductility decreases monotonically and gets closer. Therefore, the effect of microstructure is

[a)] Corresponding author. Email: xiangguo@tju.edu.cn.

weakened on ductility while enhanced on strength. In terms of strength, as *f* increases, mic ostructure AR is stronger than the others so that it has better strengthening effect at high volume fraction, as illustrated in Fig. 3. In terms of ductility, microstructure AR is the best when *f*=7 . In other cases, microstructure AR-45 is the most d ctile, as shown in Table 1, and thus it has better toughening effect at high volume fraction. We have also analyzed the intrinsic mechanisms from the standpoint of microcrack initiation sites and microcrack propagation paths.

CONCLUSIONS

We have found that in the CG metals strengthened by NT regions, as the nanotwin volu e fraction increases, the shape effect of NT regions on the ductility g adually decreases but its effect on strength becomes stronger. Also, in most cases, microstructure AR-45 has been found t have the best ductility. This study has shed significant insights into the dependence of the strength and ductility of CG met ls over a wide range of shape and volume fraction of T regions.

ACKNOWLEDGMENTS

Guo and Zhu acknowledge the support from National Natural Science Foundation of China (Project nos. 11102128, 11372214, 11302189, and 11472243). Weng thanks the support of NSF Mechanics of Materials and Structures Program under CMMI-1162431. Lu acknowledges the National Key Basic Research Program of hina (Grant 2012CB932203), GRF/CityU519110, and the Croucher Foundation CityU9500006.

References

[1] Xiao G.H., Tao N.R., Lu K.: Strength-ductili y combination of nanostructured Cu-Zn alloy with nanotwin bundles. *Scr. Mater.* **65**:119-122, 2011.

[2] Yan F.K., Liu G.Z., Tao N.R., Lu K.: Strength and ductility of 316L austenitic stainless steel strengthened b nano-scale twin bundles. *Acta Mater.* **60**:1059-1071, 2012.

[3] Dao M., Lu L., Asaro R., Hosson J.D., Ma E.: Toward a quantitative understanding of mechanical behavior of nanocrystalline metals. *Acta Mater.* **55**:4041-4065, 2007.

[4] Jerusalem A., Dao M., Suresh S., Radovitz y R.: Three-dimensional model of strength and ductility of polyc ystalline copper containing nanoscale twins. *Acta Mater.* **56**:4647-4657, 2008.

[5] Shan Z.W., Lu L., Minor A.M., Stach E.A., ao S.X.: In-situ TEM observation on deformation of Cu nano-twi s. *JOM* **60**(9):71-74, 2008.

[6] Lu L., Chen X., Huang X., Lu K.: Revealing the Maximum Strength in Nanotwinned Copper. *Science* **323**:607-610, 2009.

[7] Singh A., Tang L., Dao M., Lu L., Sures S.: Fracture toughness and fatigue crack growth characteristics of nanotwinned copper. *Acta Mater.* **59**:2437–2446, 2011.

[8] Zhu L.L., Ruan H.H., Li X.Y., Dao M., Gao H.J., Lu J.: Modeling grain size dependent optimal twin spacing f r achieving ultimate high strength and related high ductility. *Acta Mater.* **59**:5544-5557, 2011.

[9] Gao H., Huang Y., Nix W.D., Hutchinson J. .: Mechanism-based strain gradient plasticity – I. Theory. *J. Mech. Phys. Solids* **47**:1239-1263, 1999.

[10] Kocks U.F., Mecking H.: The physics and henomenology of strain hardening. *Prog. Mater. Sci.* **48**:171-273, 003.

[11] Huang Y., Qu S., Hwang K.C., Li M., Gao H.J.: A conventional theory of mechanism-based strain gradient plasticity. *Int. J. Plast.* **20**:753-782, 2004.

[12] Johnson G.R., Cook W.H.: A constituti e model and data for metals subjected to large strains, high strain rates and high temperatures. In: Proceedings of the 7th International Symposium on Ballistics, The Hague, The Netherlands, 1983.

[13] Johnson G.R., Cook W.H.: Fracture chara teristics of three metals subjected to various strains, strain rates, t mperatures and pressures. *Eng. Fract. Mech.* **21**:31-48, 1985.

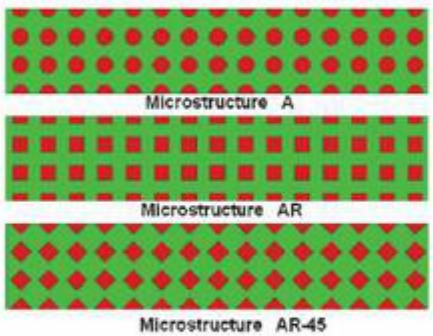

Fig. 1. Three idealized microstructures.

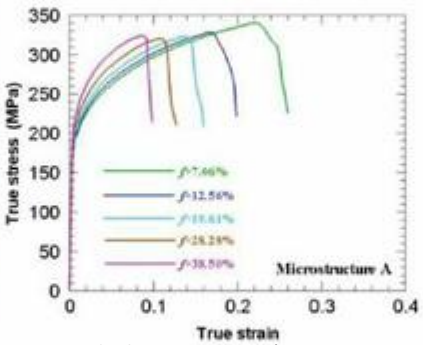

Fig. 2. True stress-strain curves.

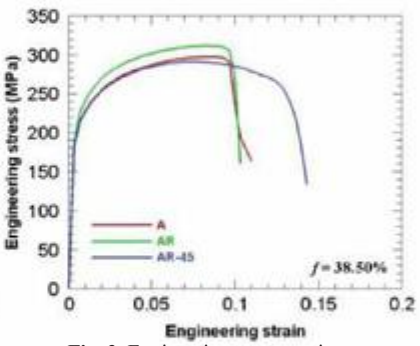

Fig. 3. Engineering stress-strain curves.

Table 1 Ductility comparison.

f	7%	12.6%	19.6%	28.3%	38.5%
	AR>AR-45>A	AR-45>AR>A	AR-45>AR>A	AR-45>A>AR	AR-45>AR>A

SIMULATION OF HOT SHAPE ROLLING BY USING PLASTIC MATERIAL RESPONSE

Umut Hanoglu[1a] & Božidar Šarler[1,2]
[1]*Laboratory for Simulation of Materials and Processes, Institute of Metals and Technology, Ljubljana, Slovenia*
[2]*Laboratory for Multiphase Processes, University of Nova Gorica, Nova Gorica, Slovenia*

Abstract In this work, a numerical simulation of hot shape rolling is done by using a novel Local Radial Basis Function Collocation Method (LRBFCM). This meshless method requires no integration or any mesh generation (polygonisation). The simulation is based on strong form mechanical and thermal models. Overall, this 3D rolling process is reduced to 2D slices, used as computational domains, aligned towards the rolling direction. On each slice the deformation and temperature fields are calculated by assuming that there is no strain or heat flow in the rolling direction. By this approach large deformations can be calculated through a series of small deformation increments on each slice. Ideal plastic material model is considered in the calculations. A computer application based on C# is developed to analyze and visualize the results of this method. Simulation of continuous steel rolling mill is considered as demonstration of the approach.

INTRODUCTION

Computational solid mechanics has always been an important task for researchers. There are numerous cases to perform and many different methods to solve the complex system of equations, each with its own advantages and disadvantages. The rolling simulation is an example of a very complex 3D problem. However, it is also critical to simulate the deformation steps due to better understanding and control of the system. The main aim of the simulation is to make correlation between input process variables and numerical results over the workpiece in terms of displacement, strain, stress and temperature. Recently meshless numerical methods [1] gained an important role for being a substantial alternative to the classical numerical methods, such as Finite Element method (FEM) [2]. Meshless methods is a numerical technique that uses collocation nodes over the domain and boundary. An outstanding choice to solve fluid flow and solid mechanics problems is the Local Radial Basis Function Collocation Method (LRBFCM). This method was first used to solve the diffusion problems in [3] and elasticity problems in [4]. Moreover, this method is successfully applied to solve fluid mechanics [5] and solid mechanics [6-8] problems. In this paper, simulation of hot shape rolling is performed by using LRBFCM.

PHYSICAL MODEL

The rolling simulation system is analysed over 2D slices aligned towards the rolling direction which is also called traveling of a slice. Each slice has time depended position, area and velocity. The rolling simulation is capable of running over a complete rolling schedule which consists of up to 10 rolling stands and each with specific groove geometry. One slice is calculated at a time and continued by the next one until it reaches end of the rolling schedule. First it is checked if there is a contact with the groove of not, if so both mechanical and thermal modes are run. If there is no contact, only the thermal model is run.

Thermal model

The governing equation of the thermal model over a 2D slice is

$$\rho c_p \frac{\partial T}{\partial t} = \nabla \cdot (\ \nabla\ ) + \dot{Q},$$

with $\rho, c_p\ T\ t\ k\ \dot{Q}$ standing for density, specific heat, temperature, time, thermal conductivity and heat generation rate due to deformation, respectively. The boundary condition applied on the boundaries of slice is Robin type in point $\mathbf{p}$

$$-k \frac{\partial T(\mathbf{p},t)}{\partial \mathbf{n}_\Gamma} = \left[\ (\mathbf{p},t) - T_\Gamma^R(\mathbf{p},t)\right]; \mathbf{p} \in \Gamma,$$

at slice boundaries Γ, with h standing for the heat transfer coefficient, T_Γ^R standing for the reference temperature.

Mechanical Model

In the mechanical model, the displacement filed is calculated from the governing equation

$$\mathbf{L}^T\boldsymbol{\sigma} + \mathbf{b}\quad \mathbf{0},$$

where $\mathbf{L}$ is the derivative operator, $\boldsymbol{\sigma}$ is the vector of stresses, and $\mathbf{b}$ is the body force vector, considered $\mathbf{b}\quad \mathbf{0}$. Using different stress-strain relations depending on either elastic or plastic material model, stresses can be related to displacements using plastic stiffness matrix $\mathbf{C}$ which includes effective stress $\bar{\sigma}$ and effective strain $\bar{\varepsilon}$ relation. Later the system of nonlinear equations are solved by direct iteration.

[a)] Corresponding author. Email: umut.hanoglu@imt.si.

$$\mathbf{C} = \frac{2}{3}\frac{\bar{\sigma}}{\bar{\varepsilon}}\begin{bmatrix} 2 & 1 & 0 \\ 1 & 2 & 0 \\ 0 & 0 & 1/2 \end{bmatrix}$$

Essential and natural boundary conditions are used on the boundaries

$$\mathbf{u} = \bar{\mathbf{u}},$$

$$\mathbf{n}^{\mathrm{T}}\boldsymbol{\sigma} = \bar{\boldsymbol{\tau}},$$

respectively, where $\mathbf{u}$ is the displacement vector, $\bar{\mathbf{u}}$ is the prescribed displacement vector, $\mathbf{n}$ is the unit normal vector and $\bar{\boldsymbol{\tau}}$ is the prescribed traction vector.

SOLUTION PROCEDURE

Thermo-mechanical rolling simulation starts with creating a uniform node arrangement over the initial computational domain or slice. The solution procedure is based on overlapping 8 noded ($N_\omega = 8$) local influence domains. A function and its derivatives can be approximated for a node position using its neighbouring points in a local influence domain. Radial basis Functions (RBF), $\psi_n(\mathbf{p}) = \sqrt{(p_x - p_{xn})^2 + (p_y - p_{yn})^2 + c^2}$, c is set to 32 and first order polynomial functions ($N_p = 3$), $\psi_{n+1}(\mathbf{p}) = 1$, $\psi_{n+2}(\mathbf{p}) = p_x - x_{\text{mean}}$, $\psi_{n+2}(\mathbf{p}) = p_y - y_{\text{mean}}$, are used as approximation functions which are multiplied with collocation functions. The details of the calculation of the collocation constants and solution procedure are explained in [8].

NUMERICAL EXAMPLE

A computer application with user friendly interface has been created to see the results for each slice during the rolling simulation. The results can be seen over a specific slice in terms of temperature, displacement, strain and stress fields.

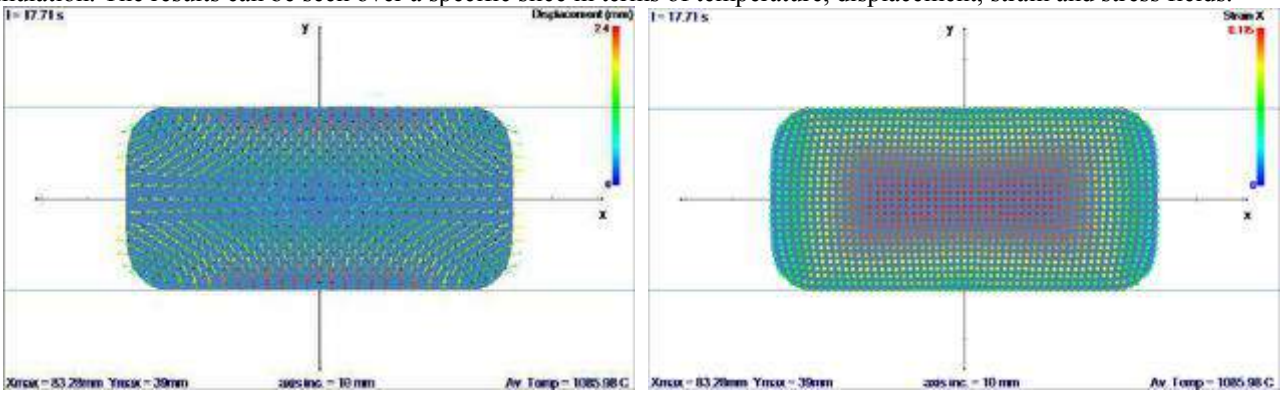

Figure 1: A rolling schedule which consists of 6 rolling stands, when the initial size of the billet is 105 X 60 mm is simulated. The figures of displacement vector field on the left and strain vector component (ε_{xx}) filed on the right are shown for the last contacting slice under the last roll.

CONCLUSIONS

In this paper, numerical simulation of hot shape rolling of steel is described based on LRBFCM. The solution procedure is a carried out by straight forward meshless method based on RBFs. In the calculations, the slice method is used to reduce the 3D system to 2D. Thermal and mechanical models are described with their corresponding boundary conditions. An example of the simulation results is shown. This paper differs from [7] by inclusion of the ideal plastic deformation.

References

[1] Li H., Mulay S.S.:Meshless Methods and their Numerical Properties. Cornwall, Great Britain 2013.

[2] Glowacki M.: The mathematical modelling of thermo-mechanical processing of steel during multi-pas shape rolling. *J. Mater Process Tech* **168**:336-343, 2005.

[3] Šarler B., Vertnik V.: Meshfree local radial basis function collocation method for diffusion problems. *Comput Math Appl* **51**:1269-1282, 2006.

[4] Tolstykh A.I., Shirobokov D.A.: On using radial basis functions in a "finite difference mode". *Comp Mech* **33**:68-79, 2003.

[5] Šarler B., Vertnik V.: Simulation of continuous casting of steel by a meshfree technique. *Int J. Cast Metal Res* **22**:311-313, 2009.

[6] Mavrič B., Šarler B.: Local radial basis function collocation method for linear thermoelasticity in two dimensions. *Int J. Numer Method H* **25**:1488-1510, 2015.

[7] Hanoglu U., Islam S., Šarler B.: Thermo-mechanical analysis of hot shape rolling of steel by a meshless method. *Procedia Eng* **10**:3173-3178, 2011.

[8] Hanoglu U.: Simulation of hot shape rolling of steel by a meshless method. PhD Thesis, University of Nova Gorica, Nova Gorica, 2015.

A NOVEL MATERIAL MODEL FOR THE LARGE-SCALE SIMULATION OF TEMPERATURE DEPENDENT INELASTICITY

Zhen Li[1], Max O. Bloomfield[1], and Assad A. Oberai *[1]
[1]*Scientific Computation Research Center, Department of Mechanical Aerospace and Nuclear Engineering, Rensselaer Polytechnic Institute, Troy, New York, 12180 United States of America*

Summary Solder is a fundamental material used to connect chip to chip carrier. The reliability of electronic packaging is limited by the ability of the chip/chip carrier interconnects (solder balls) to withstand thermo-mechanical strain. The primary cause for this strain is thermal mismatch in properties among the constituent materials. In this study, a novel material model for simulating the mechanical response of the solder balls during the packaging process is developed. The model includes Norton creep, J_2 plasticity and thermo-elasticity within a finite strain framework. A finite element based numerical method, together with a return-mapping algorithm, is developed from the constitutive equations. The numerical routine is implemented into the multi-physics code `ALBANY` for simulating large-scale solder ball problems on high performance computers.

INTRODUCTION AND MOTIVATION

Electronic products serve an essential role in our daily lives. During the use of an electronic device information is electronically transmitted between integrated circuits (ICs) . Physically, ICs are small dies made of silicon or other semiconducting materials that are interconnected by several levels of electronic packaging. The first level of electronic packaging is mounting ICs on a chip carrier, which protects the die from the environment and makes the device easy to handle [1]. This is the focus of our work.

Flip chip packaging is a method used in the first-level packaging for interconnecting semiconductor devices, such as IC chips, to external circuitry [2]. One critical stage in this method is the cooling stage. The composite device that consists of chip, solder balls and chip carrier undergoes such a cooling stage after the solder balls are melted with hot air reflow. The cooling stage raises some concerns about the reliability of solder balls. There is often a mismatch of coefficient of thermal expansion (CTE) between the chip, the chip carrier material, and the solder balls, resulting in a stress across the solder balls [3]. This stress may eventually lead to fatigue failures. The failure of a single solder joint could compromise the functionality of an entire device.

The mechanical response of the solder ball material is often inelastic, with a rate-independent component (J_2 plasticity) and a rate-dependent component (creep). When modeling the creep response of metals, there are two common choices: Anand's creep model and the Norton creep model. Anand's model is popular, however, it has many parameters which makes it difficult to calibrate and employ in practice. Norton's model is simpler with fewer parameters. However, to our knowledge a finite deformation counterpart of this model that works in concert with rate-independent elasticity has not been developed. This forms the major thrust of our effort.

MATHEMATICAL FORMULATION

The equation of equilibrium for a material undergoing slow, quasi-static deformation is given by

$$\mathrm{v}\mathbf{P} + \rho_0 \mathbf{B} = \mathbf{0}, \quad \mathrm{n}\,\mathcal{B} \tag{1}$$

where $\rho_0 : \mathcal{B} \to \mathbb{R}$ is the reference density and $\mathbf{B}$ is the body force. $\mathbf{P}$ is the $1st$ Piola-Kirchhoff stress tensor, has the following relationship with Cauchy stress tensor $\boldsymbol{\sigma}$,

$$\mathbf{P} = J\boldsymbol{\sigma}\mathbf{F}^{-\mathbf{T}}. \tag{2}$$

Here $\mathbf{F}$ is the deformation gradient and $J = \quad \mathbf{F}$ is the determinate. $\boldsymbol{\tau} := J\boldsymbol{\sigma}$ is the Kirchhoff stress tensor.

We employ a multiplicative split of the deformation into an elastic and an inelastic part. The stress depends on the elastic component through a standard compressible, Neo-Hookean relation. The evolution of the inelastic part is governed by an associative flow rule. The flow rule contains two inelastic strain rates: plastic and creep. The J_2 plastic part is driven by a Von-Mises yield condition, and a strain hardening law.

The creep-rate is governed by a Norton creep model, which can be expressed as,

$$\gamma_{cr} = A \;\; \mathrm{xp}\left[\nearrow\!\frac{Q}{R} \cdot \frac{1}{T(t)}\right] \|\mathbf{s}\|^{c_1} \tag{3}$$

where γ_{cr} is creep strain rate, A is a relaxation parameter of the material, Q is an activation energy, R is the gas constant, T is the absolute temperature at time t, $\mathbf{s}$ is a measure of stress and c_1 is a stress exponent.

*Corresponding author. Email: oberaa@rpi.edu

NUMERICAL ALGORITHM

We apply the finite element to solve the equations of equilibrium. The Galerkin method then yields,

$$\boldsymbol{F}^{int}(\boldsymbol{\sigma}_n) - \boldsymbol{F}^{ext}(t_n) = \mathbf{0}, \quad n = 0, 1, 2, \cdots, N. \tag{4}$$

$\boldsymbol{F}^{int}$ is the global internal force vector, which is a function of $\boldsymbol{\sigma}_n$, $\boldsymbol{F}^{ext}$ is the global external force vector and is a function of t_n. Equation (4) holds for all time discrete time instances, t_n.

We solve the non-linear system (4) with Newton's method in `ALBANY`. To evaluate the left hand side, we develop a return-mapping algorithm, $\mathcal{F}$, that given $\{\boldsymbol{\sigma}_n, \mathbf{F}^i_n, \mathbf{F}_n, \alpha_n\}$, together with the nodal displacement information $\mathbf{d}_{n+1}$ and constitutive equations, yields $\{\boldsymbol{\sigma}_{n+1}, \mathbf{F}^i_{n+1}, \mathbf{F}_{n+1}, \alpha_{n+1}\}$. That is

$$\boldsymbol{\sigma}_{n+1} = \mathcal{F}(\mathbf{d}_{n+1}). \tag{5}$$

Using this algorithm (5) in (4), we arrive at a set of non-linear equations for the nodal displacements $\mathbf{d}_{n+1}$. We employ the Newton's method to solve this equation, and within this we evaluate the Jacobian by applying automatic differentiation.

We implement the above numerical algorithms within `ALBANY` and verify our model. The numerical results from our model compare well with analytical solutions when we perform uni-axial tension tests on a cube, with both infinitesimal and finite strains.

APPLICATIONS

We have performed simulations of solder ball problems using the model developed in the previous sections. We consider small and large-scale simulations, with more than billion degrees of freedom. In the figures below we show a simulation result from a 3×3 solder ball array with 8.2 million finite elements.

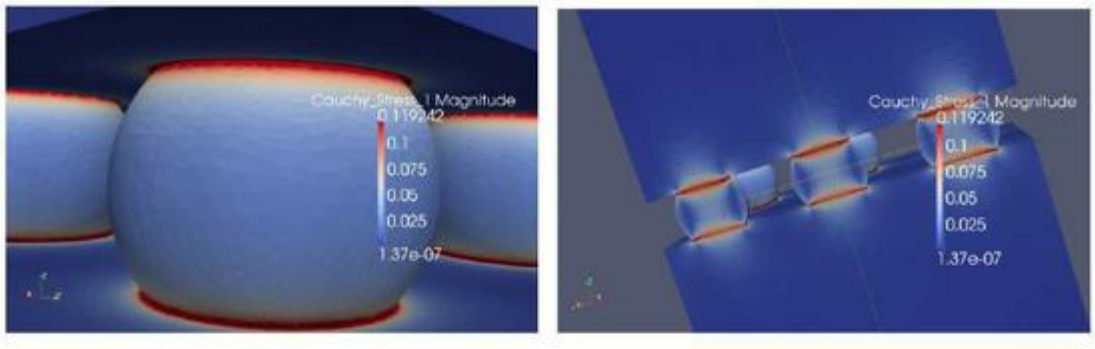

Figure 1: Stress distribution for a 3×3 solder ball array as it relaxes.

References

[1] E. A. Stout V.:Characterization of Electronic Packaging Using Moire Interferomertry. Master Thesis of Science in Theoretical and Applied Mechanics, University of Illinois at Urbana-Champaign , 1997.

[2] R. Wanyne Johnson.:Flip Chip Assembly and Underfilling. Chapter 19, preprint.

[3] P. Elenius, L. Levine.:Comparing Flip-Chip and Wire-Bond Interconnection Technologies. Chip Scale Review, July/August, 2000.

PLASTIC DEFORMATION OF MATERIALS WITH STRESS STATE DEPENDENT PROPERTIES

Evgeny Lomakin[1a)], Ivan Ovchinnikov[2]
[1]*Center of Experimental Mechanics, Perm National Research Polytechnic University, Perm, Russia*
[2]*Department of Mechanics and Mathematics, Lomonosov Moscow State University, Moscow, Russia*

Summary The results of experimental studies of irreversible deformation of heterogeneous materials that contain micro-cracks, pores, inclusions, and other structural heterogeneities are analysed. The dependencies of deformation properties of the materials on loading conditions are examined and common mechanisms and some features of their behaviour are specified. The constitutive relations for elastoplastic materials, which properties are susceptible to the stress state types are proposed. The features of irreversible bulk deformation are studied and the conditions for unique solution of boundary value problem are formulated. The applicability of proposed constitutive relations is demonstrated on the solution of plane stress crack problem for materials under consideration.

MECHANICAL PROPERTIES OF HETEROGENEOUS METERIALS

For heterogeneous materials there is no single curve of the dependence between von Mises equivalent stress and equivalent strain. The equivalent stress-strain curves depend on loading conditions [1]. These effects are revealed in structural graphite materials, rocks, concrete, refractory ceramics, cast iron, some composite materials and others. The stress state type can be defined by the parameter $\xi = \sigma/\sigma_0$, where $\sigma = \frac{1}{3}\sigma_{ii}$ is the hydrostatic component of the stresses and σ_0 is von Mises equivalent stress, $\sigma_0 = \sqrt{\frac{3}{2}S_{ij}S_{ij}}$, $S_{ij} = \sigma_{ij} - \sigma\delta_{ij}$. This parameter determines on the average the ratio of normal stresses to shear stresses in solids and it is named stress triaxiality. The mechanical properties of media under consideration can be illustrated by experimental data for rocks. Diagrams of the dependence between effective stress σ_0 [MPa] and effective strain $\varepsilon_0 = \sqrt{\frac{2}{3}e_{ij}e_{ij}}$, where $e_{ij} = \varepsilon_{ij} - \frac{1}{3}\varepsilon\delta_{ij}$, $\varepsilon = \varepsilon_{ii}$ is bulk strain, obtained under proportional loading of cylindrical specimens of white marble are shown in Fig. 1. The experiments were carried out under axial compression and lateral pressure with different ratios of axial stress to lateral pressure. Curve 1 corresponds to uniaxial compression, $\xi = -0.333$, and curves 2–7 correspond to the following values of parameter ξ: −0.407 (2), −0.464 (3), −0.55 (4), −0.63 (5), −0.79 (6), −1.39 (7). The samples of white marble had the density 2.71 g/cm3 and the porosity 0.92%. The relation between the hydrostatic component of stresses and bulk strain for the same types of proportional loading are shown in Fig. 2. Instead of a single curve there is a set of curves $\sigma_0 \sim \varepsilon_0$. It means that the shear and bulk properties of this material are interrelated. From Fig. 2 one can see that under conditions of compressive stresses, the dilatation of a material is possible, so that the hydrostatic stress and the bulk strain may have different signs, although under the uniform triaxial compression, the material exhibits a linear dependence of the bulk strain on the hydrostatic stress.

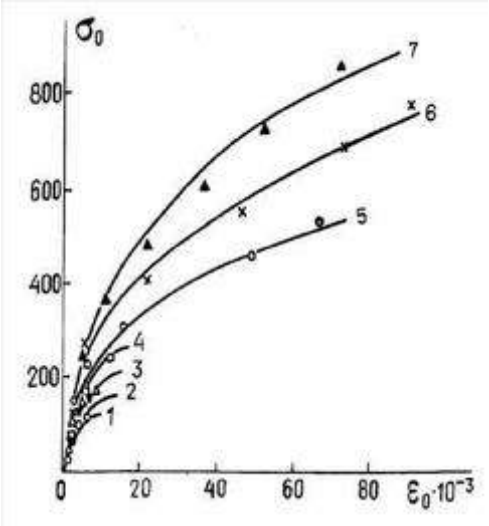

Fig. 1: Equivalent stress-strain curves for white marble under different conditions of proportional loading.

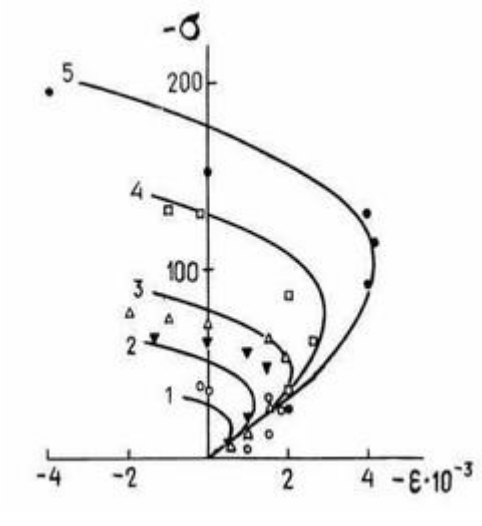

Fig. 2: Relations between hydrostatic component of stresses and bulk strain for white marble.

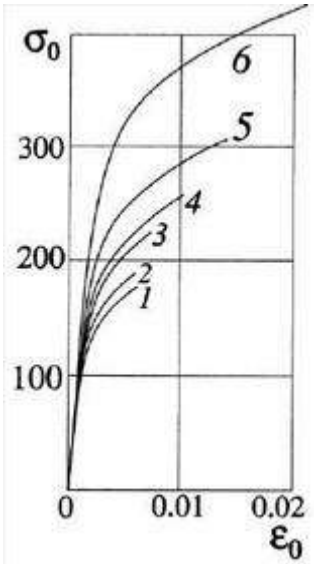

Fig. 3: Equivalent stress-strain curves for cast iron

a) Corresponding author. Email: lomakin@mech.math.msu.su

Similar equivalent stress – strain curves can be obtained for the cast iron SCh 15-32. Curves 1 and 6 correspond to the uniaxial tension ($\xi = 0.333$) and the uniaxial compression ($\xi = -0.333$), curve 3 corresponds to the simple shear ($\xi = 0$), and curves 2, 4, and 5 correspond to the proportional loading with the values of parameter ξ equal to 0.232, 0.064, and 0.126, respectively. These diagrams are essentially nonlinear. The volume residual change can exceed 0.6%, which is commensurable with the shear strains.

CONSTITUTIVE RELATIONS

The constitutive equations for the media under consideration can be formulated on the base of the deformation theory of plasticity using the complementary potential energy function, that can be represented in the form $\Phi = \frac{1}{2}(A + B\xi^2)\sigma_0^2 + [1 + \kappa(\xi)]g(\sigma_0)$. For the power law function $g_0(\sigma_0) = k\sigma_0^n/n$ the generalized stress-strain relations are

$$\varepsilon_{ij} = \frac{3}{2}[A + \lambda(\xi)k\sigma_0^{n-2}]S_{ij} + \frac{1}{3}[B + \Lambda(\xi)k\sigma_0^{n-2}]\sigma\delta_{ij},$$
$$\lambda(\xi) = 1 + \kappa(\xi) - \kappa'(\xi)\xi/n, \;\; \Lambda(\xi) = \kappa'(\xi)/(\xi n \;).$$

The equivalent bulk strain and bulk strain are determined by the equations

$$\varepsilon_0 = [A + \lambda(\xi)k\sigma_0^{n-2}]\sigma_0, \;\; \varepsilon = [B + \Lambda(\xi)k\sigma_0^{n-2}]\sigma.$$

The bulk strain and the equivalent strain are interrelated, and this relationship depends on the type of stress state in a medium. A quite satisfactory correspondence between theoretical stress - strain curves shown in Fig. 1 and Fig. 2 by solid lines and experimental values of stresses and strains marked by points corresponding to different types of loading is observed. The approximations for material functions are suggested. The conditions for the uniqueness of solution of boundary value problem are the following:

$$A + [(n-1)\lambda(\xi) - \xi\lambda'(\xi)]k\sigma_0^{n-2} > 0,$$
$$B + [\Lambda(\xi) + \xi\Lambda'(\xi)]k\sigma_0^{n-2} - \frac{[\lambda'(\xi)k\sigma_0^{n-2}]^2}{A + [(n-1)\lambda(\xi) - \xi\lambda'(\xi)]k\sigma_0^{n-2}} > 0,$$
$$\frac{1}{2}(A + B\xi^2)\sigma_0^2 + [\lambda(\xi) + \xi^2\Lambda(\xi)]k\sigma_0^n/n > 0.$$

The crack problem under remote tensile stress normal to the crack plane is considered to study the influence of features of material's behavior on stress and strain fields near a crack tip and conditions for crack growth.

CONCLUSIONS

On the base of analysis of results of experimental studies of different heterogeneous materials, the constitutive relations are proposed to describe the stress state susceptibility of materials properties, materials dilatation and other features of materials behaviour. Quite satisfactory correspondence between experimental data and theoretical dependencies is demonstrated. For specific material functions, the distributions of stresses, strains, and displacements near the crack tip are studied. The conditions of the crack growth initiation are determined with the use of the invariant integral. It is shown that the amplitude of singularity for the material with stress-state dependent properties is substantially lower than the corresponding value obtained for the incompressible material.

Acknowledgements The work was carried out in the Perm National Research Polytechnic University with support of the Government of Russian Federation (The Decree № 220 on April 9, 2010) under the Contract № 14.B25.310006, on June 24, 2013 and Russian Foundation for Basic Research, grants 14-01-00199, 14-01-92002.

References

[1] Lomakin E.V. Constitutive models of mechanical behavior of media with stress state dependent properties. In: Altenbach H., Maugin G.A., Erofeev V. (ed) Mechanics of generalized continua, Advanced Structured Materials, 7:339-350. Heidelberg: Springer, 2011.

A SLAB MODEL FOR RING ROLLING

Jeremy Minton * [1], Chris Cawthorn [2], and Ed Brambley[3]

[1]*Phd Candidate, DAMTP, Cambridge University, Cambridge, United Kingdom*
[2]*Research Associate, DAMTP, Cambridge University, Cambridge, United Kingdom*
[3]*Royal Society University Research Fellow, DAMTP, Cambridge University, Cambridge, United Kingdom*

Summary A slab model with non-vertically aligned contact points is coupled with an elastic model of a split ring to model ring rolling. The slab model uses rigid plasticity and Coulomb friction. The workpiece is assumed to be at yield on the rolls and locally has circular free surfaces otherwise. The choice of four contact points and two neutral points are used to satisfy force and geometry end conditions within the roll bite. A variable thickness and variable curvature beam model approximate the split ring. End conditions for both models must be compatible, producing a coupling between the two models. Additionally, to time step through the process, the plastic deformation within the roll gap must be estimated and tracked to update the unstressed thickness and curvature of the outer model. Comparisons will be made to finite element simulations for a range of parameters and several methods of curvature prediction.

INTRODUCTION

Ring rolling is a common forming process to produce metal rings. The thickness of forged ring blanks are reduced while the circumference is increased by passing the workpiece between two rolls with a separation less than the current thickness to incrementally thin the workpiece. Analytical models remain of interest as short evaluation are required in closed loop control.

Slab ring rolling models have previously been presented [3, 2], however, none include the behaviour of the elastic ring or properly treat the positioning of the contact points. Recent slab sheet rolling models have been developed to make curvature predictions of the workpiece [4, 1] which is necessary for predicting the deformation of the outer ring.

MODEL FORMULATION

During ring rolling, plastic deformation predominantly occurs within the roll bite, indicated by the shaded region in Figure 1. By assuming it is limited to this region, the process can be considered in two parts: the 'inner' problem of plastic deformation between the roll bites and the 'outer' problem of the elastic ring. The inner and outer models are coupled by matching forces and geometry at the entrance and exit to the roll bite.

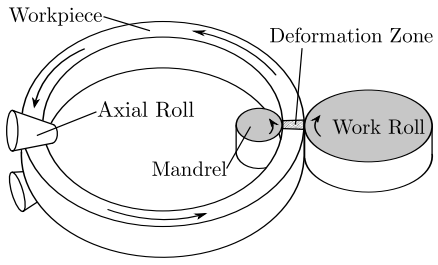

Figure 1: Illustration of the ring rolling process.

Roll Bite Formulation

The roll bite model is formulated similar to that in [4]. The rolls are considered rigid, the workpiece perfectly plastic and transverse material flow is neglected. Roll-workpiece interactions are modelled with a Coulomb friction model,

$$\tau = \frac{v \nearrow U}{|v \nearrow U|}\mu p, \tag{1}$$

where τ is the shear, p is the roll pressure, μ is the friction coefficient, v is the workpiece velocity on the boundary and U is the roll velocity. A force balance of each vertical element provides conditions to determine ordinary differential equations for the mean through thickness shear, $\bar{\tau}$; horizontal (in the x direction of Figure 2) stress on the top roll surface, σ_{top}; and horizontal stress on the bottom roll surface, σ_{bot}. To close these equations through thickness variation in horizontal stress is assumed to be linear and the workpiece is assumed to be at yield when in contact with roll surfaces,

$$(\sigma_x \nearrow \sigma_y)^2 + (\mu\sigma_y)^2 = k^2 \tag{2}$$

where k is the yield stress in shear. The force balances can then be solved for

$$\frac{d\sigma_{\mathrm{bot}}}{dx}\frac{(h_{\mathrm{top}} \nearrow h_{\mathrm{bot}})^2}{} = \frac{F_{v,top} + F_{v,bot}}{2} \nearrow F_{\mathrm{h,top}}\left(h_{\mathrm{top}} + \frac{h'_{\mathrm{top}}}{2}\right) + F_{\mathrm{h,bot}}\left(h_{\mathrm{bot}} + \frac{h'_{\mathrm{bot}}}{2}\right)$$
$$+ \frac{\sigma_{\mathrm{bot}}}{} \prod h_{\mathrm{top}}h'_{\mathrm{top}} \nearrow h_{\mathrm{top}}h'_{\mathrm{bot}} \nearrow h'_{\mathrm{top}}h_{\mathrm{bot}} \nearrow 2h_{\mathrm{bot}}h'_{\mathrm{bot}}) + \frac{\sigma_{\mathrm{top}}}{} \prod 2h_{\mathrm{top}}h'_{\mathrm{top}} + h_{\mathrm{top}}h'_{\mathrm{bot}} + h'_{\mathrm{top}}h_{\mathrm{bot}} \nearrow\ h_{\mathrm{bot}}h'_{\mathrm{bot}})$$
$$\nearrow \frac{1}{(h_{\mathrm{top}} \nearrow h_{\mathrm{bot}})} \prod 2h^2_{\mathrm{top}} \nearrow h_{\mathrm{top}}h_{\mathrm{bot}} \nearrow h^2_{\mathrm{bot}}) \left(F_{\mathrm{h,top}} + F_{\mathrm{h,bot}} + \frac{\sigma_{\mathrm{top}} + \sigma_{\mathrm{bot}}}{2} \prod h_{\mathrm{top}} \nearrow h'_{\mathrm{bot}})\right)$$

*Corresponding author. Email: jeremyminton@damtp.cam.ac.uk

$$\frac{d\sigma_{\rm top}}{dx} = \frac{2}{h_{\rm top} - h_{\rm bot}} \left(F_{\rm h,top} + F_{\rm h,bot} + \frac{\sigma_{\rm top} + \sigma_{\rm bot}}{2} \left(h_{\rm top} h'_{\rm bot} \right) \right) + \frac{d\sigma_{\rm bot}}{dx}$$

$$\frac{d\bar{\tau}}{dx} = \frac{1}{h_{\rm top} - h_{\rm bot}} \left(\bar{\tau} \left(h_{\rm top} h'_{\rm bot} \right) + F_{v,top} + F_{v,bot} \right).$$

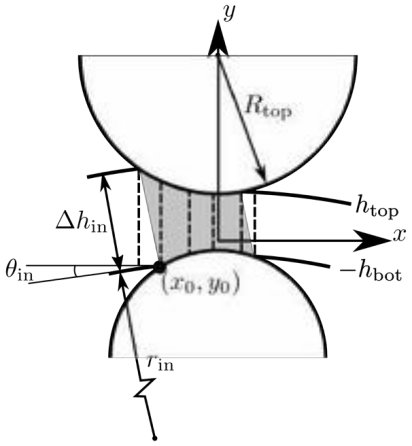

Figure 2: Illustration of the roll bite geometry.

where primes indicate differentiation in x and $F_{\rm h/v,top/bot}$ is the horizontal/vertical force acting on the top/bottom boundary.

The key development from [4] is to allow the inlet and outlet contact points to vary. This requires assumed geometry of the free surfaces of the workpiece to close the force balances in these regions. The geometry is detailed in Figure 2, It also requires six points, where the friction conditions change, to be determined: inlet contact, neutral point and outlet contact on the top and bottom rolls.

The surface velocity ratio at the neutral points must equal the roll speed ratio,

$$\frac{U_{\rm top}}{U_{\rm bot}} = \frac{v(x_{\rm N,top})}{v(x_{\rm N,bot})}.$$

where $v(x) = v_{\rm in} \Delta h_{\rm in} / \Delta h(x)$. This condition can be used to solve one neutral point from the other.

Given the bottom contact point of either end, the top contact point can be determined using geometry. Assuming both the top free surface of the workpiece and the rolls are circular, as depicted in Figure 2, the boundary equations are

$$\left(x - x_0 - r_{\rm in} \sin\left(\theta_{\rm in}\right)\right)^2 + \left(y - y_0 + r_{\rm in} \cos\left(\theta_{\rm in}\right)\right)^2 = r_{\rm in}^2$$
$$x^2 + \left(R_{\rm top} + g_{\rm top} - y\right)^2 = R_{\rm top}^2.$$

where $g_{\rm top}$ is the clearance between the defined axis and the bottom of the top roll. Eliminating y between these equations produces a quadratic equation for the top contact point.

The remaining three points are then determined to satisfy both inlet and outlet conditions on the mean shear, $\bar{\tau}$; top horizontal stress, $\sigma_{\rm top}$; and bottom horizontal stress, $\sigma_{\rm bot}$.

Ring Formulation

A curved elastic beam model with variable thickness and curvature is used to model the workpiece outside the roll gap as a split ring. The extent to which the split is separated determines the relative angles, curvature and forcing at the ends of the ring. These values define the geometry and end conditions of the inner problem so are iteratively solved between both models to find values that satisfy both.

This formulation requires a known, unstressed thickness and curvature profile. As the process starts with a workpiece of known geometry this requirement is initially satisfied but subsequent plastic deformations must be tracked as the processes continues in a time stepping manner. As plastic deformation only occurs in the roll bite, predictions of the plastic roll reduction and curvature change from the roll bite model are sufficient. Several approximations of curvature prediction have been proposed in literature [4, 1] and these are compared within this framework.

CONCLUSIONS AND FURTHER WORK

We have extended a slab model to allow the position of the contact points to be determined. This accommodates more arbitrary end conditions to be coupled to a curved beam model to describe the outer ring of the workpiece. To step forward in time, as the workpiece is reduced, curvature and thickness predictions are required and must be tracked around the workpiece. This will be implemented and comparisons will be made to finite element simulations for a range of parameters. Several existing curvature predictions from slab models will be compared in this application.

References

[1] F. Farhatnia and M. Salimi. Effect of entry bending moment on exit curvature in asymmetrical rolling. *International Journal of Engineering, Science and Technology*, 3(4):147–163, 2011.

[2] A. Parvizi, K. Abrinia, and M. Hamedi. An Analytical Approach to Ring Rolling Using Modified Slab Analysis. *Advanced Materials Research*, 383-390(9):4634–4641, 2011.

[3] A. Parvizi, K. Abrinia, and M. Salimi. Slab Analysis of Ring Rolling Assuming Constant Shear Friction. *Journal of Materials Engineering and Performance*, 20(9):1505–1511, 2011.

[4] M. Salimi and F. Sassani. Modified slab analysis of asymmetrical plate rolling. *International Journal of Mechanical Sciences*, 44:1999–2023, 2002.

ANALYSIS OF CRITERION FOR KINK BANDING IN LAYERED SOLIDS

Akihiro Nakatani*[1] and Xiao-Wen Lei[1,2]

[1]*Department of Adaptive Machine Systems, Osaka University, Suita, Osaka, Japan*
[2]*Department of Mechanical Engineering, University of Fukui, Fukui, Japan*

Summary The deformation mechanism of kink bands in a layered solid with a single-slip system is studied. The computational analysis from our previous work, which used a spring–mass model is developed to discuss the criterion for the kink banding. An idealized model from a viewpoint of the kinematic condition of compatibility formulated for the development of a ridge-shaped kink structure(RSKS) is used to explain the results. A theoretical consideration based on the Maxwell stability criterion for the simple idealized model predicts the dependency of the intensity of interlayer interaction.

INTRODUCTION

Nucleation of kink deformation under a compressive force in the direction parallel to the layers can be regarded as a type of instability phenomenon[1,2]; the deformation mechanism is closely related to the geometrical nonlinearity of the layered solid. In our previous works, the kinematic condition of compatibility is formulated for the development of a ridge-shaped kink structure(RSKS) [3], and computational analysis of kink deformation is carried out using a practical model of layered ceramics to study the effects of inter-layer slip and delamination[4]. In this study the deformation mechanism is discussed from the viewpoint of the instability theory based on the Maxwell stability criterion[5].

MODEL AND METHOD OF COMPRESSION TEST

Computational simulation of kink deformation

A specimen of layered solid is compressed parallel to its layers as shown in Figure 1 . The force field of particles system is given by total energy Φ that consists of contribution of the distance of neighboring particles in the same layer, $\Phi_{\rm bond}$, contribution of the angle of neighboring bonds, $\Phi_{\rm angle}$, and nonlinear interaction of different layers, $\Phi_{\rm interlayer}$. Table 1 shows parameters to study the effects of both intrinsic character of material (the inter-layer strength R and the stiffness of in-layer bending, C_θ) and external conditions (the velocity of constraint particle, $v_{\rm bc}$ and the stiffness of elastic support, k).

Theoretical prediction of stress–strain relationship

An ideal model of kink deformation is studied for the theoretical prediction of mechanical properties as shown in Figure 2. We use the variables l, h, α, u, α^*, $\gamma^{(1)}$, γ^*, ω^* and their associated formulations from Ref. [3]. Under the ideal plasticity assumption that the resolved shear stress $\tau^* = \sigma \sin(2\alpha^*)\cos(2\alpha^*)$ in a RSKS is a constant critical resolved shear stress (CRSS), τ_0, during the development of kink deformation, the nominal compressive stress σ and the nominal strain $\varepsilon = u/l$ are expressed by α^*. The stress σ is evaluated by:

$$\sigma = E\varepsilon \quad \text{(pre-kinking)}, \quad \text{and} \quad \sigma = E(\varepsilon - \varepsilon_{\rm p}) \quad \text{(kinking and post-kinking)} \tag{1}$$

where E denotes Young's modulus. The plastic strain is $\varepsilon_{\rm p} = (h/l)\gamma^{(1)} = (h/l)[\tan(2\alpha^*) - 2\tan\alpha^*]$.

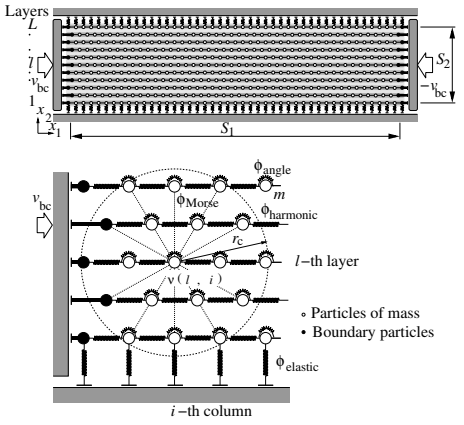

Figure 1: Spring–mass model(see Ref. [4])

Table 1: Analysis conditions(see Ref. [4])

Case	R	$v_{\rm bc}/v_0$	$k/C_{\rm pair}$
Case 1	1.0	1.0	10^{-4}
Case 2	1.0	2.0	10^{-4}
Case 3	0.3	1.0	10^{-4}
Case 4	0.3	2.0	10^{-4}
Case 5	0.1	1.0	10^{-4}
Case 6	0.1	2.0	10^{-4}
Case 3s	0.3	1.0	10^{-3}
Case 5s	0.1	1.0	10^{-3}

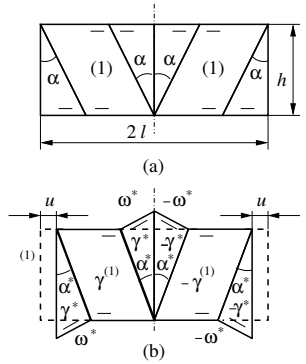

Figure 2: A simple model of RSKS under uniaxial compressive loading: (a) initial shape, and (b) deformed shape (See, Ref. [3])

*Corresponding author. Email: nakatani@ams.eng.osaka-u.ac.jp

RESULTS AND DISCUSSION

Figure 3 shows structures for Case 3s. The gradation in the figure corresponds to the amount of rotation ω^* from $-60°$(blue) to $60°$ (red). The kink bands develop with lattice rotation. Figure 4 shows the force–displacement diagrams. All curves are composed of three stages: Stage 1) the force increases roughly in proportion to the displacement (pre-kinking), Stage 2) the force drops rapidly (kinking), Stage 3) the force continues to stay low, then increases gradually with increasing displacement (kinking and post-kinking). The transition from Stage 1 to Stage3 can be regarded as a instability, and the value of the critical force for kinking primarily depends on the intensity of interlayer interaction, R, from a rough evaluation.

Figure 5 shows the force–displacement diagram predicted by Eq.(1) under a simplified condition. Here, h/l is set to 1/4, and the three curves correspond to the case of a CRSS for interlayer slip, $\tau_0/E = 0.04$, 0.012, and 0.004, assuming τ_0 is related to R. The force as a function of displacement is multivalued, and there is a range in which three of its values are associated with a displacement. The shape of function is similar to the curve obtained for other microstructures[6].

The computational results cannot show the multivalue nature of the function, but simply show sudden drops of the force. This phenomenon can be explained by the concept of the Maxwell stability criterion[5] (the Maxwell construction). That is, during kinking, the released strain energy assists further deformation. Applying the Maxwell stability criterion to the curves of Figure 5 gives us a good explanation of the dependence on R seen in Figure 4.

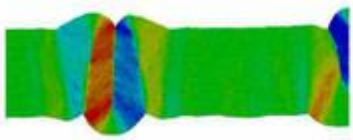

(a) $\varepsilon = 0.0920$

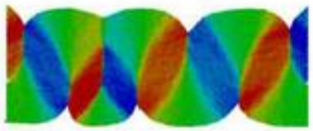

(b) $\varepsilon = 0.2024$

Figure 3: Structures of specimen (Case 3s)

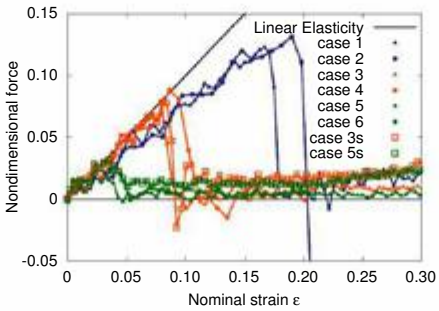

Figure 4: Force–displacement diagram (computational results)

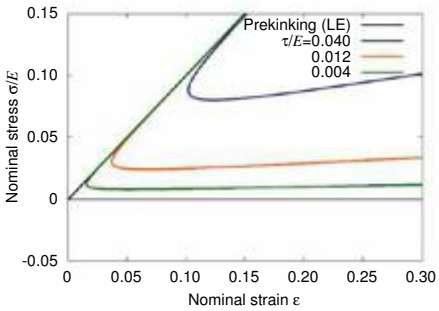

Figure 5: Force–displacement diagram (theoretical prediction)

CONCLUDING REMARKS

We discussed the deformation mechanism of kink bands in a layered solid with a single-slip system. The criterion of the kinking obtained through a computational approach was clarified by a theoretical consideration using a simple idealized model based on the Maxwell stability criterion under the kinematic condition of compatibility.

Acknowledgements

This work was supported by MEXT/JSPS KAKENHI Grant Numbers 23109010, 25286100, 26870348.

References

[1] Bigoni D.: Nonlinear Solid Mechanics Bifurcation Theory and Material Instability. Cambridge University Press, 2012.

[2] Bažant Z. P., Gedolin L.: Stability of Structures Elastic, Inelastic, Fracture and Damage Theories. World Scientific, 2010.

[3] Lei X. W., Nakatani A.: A Deformation Mechanism for Ridge-Shaped Kink Structure in Layered Solids. Trans ASME J. Appl Mech 82:071016 (6 pages), 2015.

[4] Lei X. W., Nakatani A.: Analysis of Kink Deformation and Delamination Behavior in Layered Ceramics. J. Eur Ceram Soc, (in press).

[5] Maxwell J. C.: On the Dynamical Evidence of the Molecular Constitution of Bodies. Nature 11:357-358, 1875.

[6] Hunt G. W., Peletier M. A., Wadee M. A.: The Maxwell Stability Criterion in Pseudo-Energy Models of Kink Banding. J. Struct Geol 22:669-681, 2000.

A MEAN-FIELD MODEL FOR TRIP - ALGORITHMS AND PARAMETER IDENTIFICATION

Manuel Petersmann[1,2], Georges Cailletaud[2], Thomas Antretter[1], and Ulrich Ehlenbröcker[3]
[1]*Montanuniversitaet Leoben, Institute of Mechanics, Franz-Josef Straße 18 8700 Leoben, Austria*
[2]*MINES ParisTech, PSL Research University, MAT - Centre des Matériaux, CNRS UMR 7633, BP 87 91003 Évry, France*
[3]*Chair of Engineering Mechanics, University of Paderborn, Warburger Straße 100, 33100 Paderborn, Germany*

Summary Recently a meso-macro mean-field model formulated in the framework of viscoplasticity, including backstress effects, has been proposed to depict the effects of transformation induced plasticity (TRIP) in Maraging steels for non-proportional loadings [1]. This model has now been implemented in an implicit return-mapping formalism in the finite element code Zebulon. The implementaion is discussed and the stability of the solution as a function of the time step is compared to an explicit solution. Performance tests for fully implicit and mixed implicit-explicit solutions are carried out on larger structures. Local divergence issues, arising from the application of the Newton-Raphson scheme and the strong coupling between the phase fraction and evolution equations are discussed. As a next step a micro-scale model incorporating realistic transformation strains for lath martensite and crystal plasticity is developed, for the calibration of the macroscopic transformation yield function as well as stress and temperature dependent kinetics.

For constitutive models capturing dissipative mechanisms, stress update algorithms are always required. In the strain-driven process within a finite element model, the goal of such update algorithms is the computation of the state variables at time t^{n+1} by means of the internal variables at time t^n and the current strain tensor. An overview of stress update algorithms can be found in [2] and in the references cited therein. Here it is pointed out that recently, so-called variational constitutive updates, which were long known but rarely implemented, are increasingly gaining momentum [3]. Here we follow the nowadays, most frequently applied implementation scheme, i.e. the so-called return-mapping or projection scheme. Within this scheme, evolution equations and the flow rule are discretized by a backward Euler time integration and the unknowns such as the plastic strain increment are computed by solving a system of nonlinear equations, with a standard Newton-Raphson iteration. In our model, formulated in a small strain formalism at the macro-scale, the interaction of plasticity and TRIP is taken into account via a coupling of backstresses, supported experimentally by a certain percentage of recoverable TRIP strain upon load reversal. Evidently, these backstress effects become an issue for non-proportional loading paths, i.e. whenever the local stress state varies with time. The additional strain rate originating from TRIP is frequently described by a flow rule in analogy to classical plasticity [4, 5]. The anisotropy of the transformation strain is reflected in the macroscopic transformation-yield function. Basic ideas on its formulation on the RVE level in analogy to plasticity can be found in [6]. For instance tension-compression asymmetry is achieved with a third invariant. The resulting orientation meanfield tensor $\boldsymbol{\varepsilon}^o$, which is purely deviatoric, gives an average value of crystallographic orientation strains arising in the martensitic phase pursuant to specifically activated martensitic variants. The variant interaction is taken into account on the mesolevel by introducing an orientation back stress tensor. For the coupling between martensitic transformation and accompanied plastic deformation, the β-rule [7] has been adopted only for the deviatoric strain parts, meaning that in the austenitic phase plastic deformation and in the martensitic phase orientation strains and plasticity are taken into account. The volumetric strains are treated with a linear scale transition rule. Thereby, the Greenwood–Johnson and Magee effect are dealt with separately on the mesolevel. The modified β-rule also couples the meanfield orientation tensor, with plasticity of both phases on the mesoscale directly. Therefore, i) each newly growing martensitic domain arises with the meanfield value of those variants preferred due to the actual phase stress field and ii) further internal variables and evolution equations for orientation induced plasticity can be omitted. While the direction of microstructure evolution can be described by thermodynamics it is the strong influence of thermodynamic non-equilibrium mechanisms that entails the large variety and complexity of microstructures. Maybe the most challenging part of models like this is to quantitatively describe the phase-fraction kinetics depending on the interplay between stress, strain and temperature rates, by finding relations of reasonable parameters for internal transformation driving and dragging forces. Note that this can no longer be done on a macroscopic level where only phase-averaged quantities appear, therefore we develop a model on the microscale within one grain taking into account the highly anisotropic transformation strains and rate independent crystal plasticity. The model should help to determine suitable parameters for yield functions such as that of our model [1]. In maraging steels, martensite appears in the form of laths in a hierarchical manner, which is a general feature of quenched steels with a low or negligible carbon content, such as plain low-carbon steels, low-carbon and low-alloy steels, and interstitial free (IF) steels [8]. Particularly, laths having the same densest planes ($\{111\}$) form a block, blocks form a packet, where each packet contains exactly 6 variants, and packets partition the grains [9]. Many models merely use the Bain strains as strain input. However, the Bain orientation relationship does not exist. Therefore, it is not appropriate for calculating transformation texture [10]. A complete crystallographic set of habit-plane shape strains calculated from the phenomenological crystallographic-theory of martensite transformations including: The habit plane, the

shape deformation and the orientation relationship (and implicitly the lattice-invariant deformation normally calculated with a double shear formalism [11].) For the non-thermoelastically grown martensite considered here, the midrib of the lens like plates (plane of initial, unconstrained growth) can be seen as the habit-plane [12]. The evolution the martensitic variants is modelled within a visocplastic framework. Let λ^i be the volume fraction of the i-th variant, then the evolution of each martensite variant fraction is given by (see [13]):

$$\dot{\lambda}^i = \frac{1}{\nu_{tr}} \langle \mathbf{\Phi}^i_{tr} \rangle \prod \boldsymbol{H}_s[\lambda^0, \lambda^i]\big)^{n_{tr}} \quad i > 0 \qquad \text{with} \quad \mathbf{\Phi}^i_{tr} = \prod^0 \nearrow \Lambda^i\big) \nearrow f_c \quad \text{and} \quad \boldsymbol{H}_s[\lambda^0, \lambda^i] = (\lambda^0)^{s_1} (\lambda^i)^{s_2} \tag{1}$$

where $\mathbf{\Phi}^i_{tr}$ is a overstress function ensuring that variants only start to form out of the austite if the difference between the free enthalpies of austenite and martensite exceeds an energetic barrier f_c [13]. The general formalism for multiple transforming variants can be found in [14]. At the same time rate-independent single-crystal plasticity for a face-centered cubic lattice is considered to quantify the plastic deformations in the untransformed austenite.

References

[1] M. Fischlschweiger, C. Cailletaud, and Antretter T. A mean-field model for transformation induced plasticity including backstress effects for non-proportional loadings. *International journal of plasticity*, pages 53–71, 2012.

[2] J.C. Simo and T.J.R. Hughes. *Computational Inelasticity*. Interdisciplinary Applied Mathematics. Springer New York, 2006.

[3] N. Bleier J. Mosler. Efficient variational constitutive updates by means of a novel parameterization of the flow rule. *International Journal for Numerical Methods in Engineering*.

[4] J.B. Leblond. Mathematical modelling of transformation plasticity in steels ii: coupling with strain hardening phenomena. *International journal of plasticity*, 5(6):573–591, 1989.

[5] J.B. Leblond, J Devaux, and JC Devaux. Mathematical modelling of transformation plasticity in steels i: case of ideal-plastic phases. *International journal of plasticity*, 5(6):551–572, 1989.

[6] R. Mahnken, A. Schneidt, and T. Antretter. Macro modelling and homogenization for transformation induced plasticity of a low-alloy steel. *International Journal of Plasticity*, 25(2):183–204, 2009.

[7] G. Cailletaud. *Une approche micromécanique phénoménologique du comportement inélastique des métaux*. PhD thesis, Université Paris 6.

[8] S. Morito, X. Huang, T. Furuhara, T. Maki, and N. Hansen. The morphology and crystallography of lath martensite in alloy steels. *Acta Materialia*, 54:5323–5331, 2006.

[9] L. Qi, A.G. Khachaturyan, and J.W. Morris Jr. The microstructure of dislocated martensitic steel: Theory. *Acta Materialia*, 76(0):23 – 39, 2014.

[10] H. Abreu H. K. D. H. Bhadeshia, S. Kundu. *Microstructure and Texture in Steels*. Springer, 2009.

[11] P. M. Kelly. Crystallography of lath martensite in steels. *Materials Transactions*, 33(3):235–242, 1992.

[12] E. Hornbogen and H. Warlimont. *Metalle*, volume 5. Springer-Verlag Berlin Heidelberg, 2006.

[13] R. Mahnken and S. Wilmanns. A projected newton algorithm for simulation of multi-variant textured polycrystalline shape memory alloys. *Computational Materials Science*, 50(9):2535–2548, 2011.

[14] K. Hackl and R. Heinen. A micromechanical model for pretextured polycrystalline shape-memory alloys including elastic anisotropy. *Continuum Mechanics and Thermodynamics*, 19(8):499–510, 2008.

YIELD SURFACE EFFECTS ON STABLITY AND FAILURE

William M. Scherzinger *
Solid Mechanics, Sandia National Laboratories, Albuquerque, New Mexico, USA

Summary This work looks at the effects of yield surface description on the stability and failure of metal structures. We consider a number of different yield surface descriptions, both isotropic and anisotropic, that are available for modeling material behavior. These yield descriptions can all reproduce the same nominal stress-strain response for a limited set of load paths. However, for more general load paths the models can give significantly different results that can have a large effect on stability and failure. Results are shown for the internal pressurization of a cylinder and the differences in the predictions are quantified.

INTRODUCTION

Stability and failure in structures is an important field of study that provides solutions to many practical problems in solid mechanics. The boundary value problems require careful consideration of the geometry, the boundary conditions, and the material description. In metal structures the material is usually described with an elastic-plastic constitutive model, which can account for many effects observed in plastic deformation. Crystal plasticity models can account for many microstructural effects, but these models are often too fine scaled for production modeling and simulation. In this work we limit the study to rate independent continuum plasticity models.

When using a continuum plasticity model, the hardening behavior is important and much attention is focused on it. Equally important, but less well understood, is the effect of the yield surface description. For classical continuum metal plasticity models that assume associated flow the yield surface provides a definition for the elastic region of stress space along with the direction of plastic flow when the stress state is on the yield surface. Often the direction of plastic flow is overlooked even though it can have the greatest effect on the results of a simulation. For comparisons we consider a number of models that employ different yield surface descriptions that describe isotropic and anisotropic material behavior. We consider the yield surfaces due to Tresca, von Mises, Hosford [1], Hill [2], Barlat, et. al. [3], and Karafillis and Boyce [4].

As an example boundary value problem we examine the internal pressurization of an aluminum cylinder. The analysis results show significant sensitivity to the form of the yield surface and insight into how assumptions in the constitutive model affect the behavior.

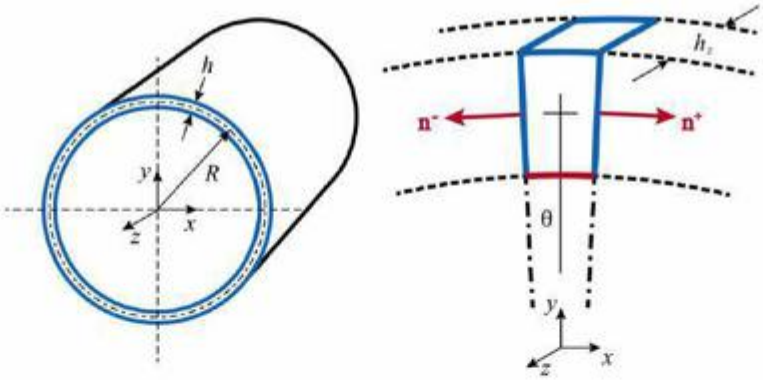

Figure 1: Boundary value problem for the internal pressurization of a cylinder in plane strain.

BOUNDARY VALUE PROBLEM

We consider the internal pressurization of an aluminum cylinder as shown in Figure 1. The problem is modeled using continuum finite elements. We enforce plane strain in the axial direction; with $R/h = 100$ the state of stress is nearly plane stress. The material is 2090-T3 Al which has been parameterized for the Yld2004-18p model by Barlat et. al. [3]. The parameterization is used to fit the Tresca, von Mises, and Hosford yield surfaces in such a way that the yield stress is matched in uniaxial tension. The Hill yield surface is also fit so that the yield stresses are the same in uniaxial tension and shear relative to the principal material directions. The material models are implemented in Sandia National Laboratories' Sierra Solid Mechanics code [5], which is used to solve the boundary value problem. The finite element model is loaded through a prescribed radial displacement on the inner surface of the cylinder and the internal pressure is calculated from the reaction forces and the current geometry. This is necessary so that a solution can be found through the maximum load.

* Corresponding author. Email: wmscher@sandia.gov.

MODELING RESULTS

The internal pressure is plotted in Figure 2 as a function of the radial displacement for models using the Barlat, Hill, and von Mises yield surfaces. The Barlat and Hill yield surfaces are two choices one can choose for an anisotropic model, but they give significantly different results; the results using the Hill model have a maximum pressure that is approximately 15% higher than that calculated with the Barlat model. This shows a significant difference in behavior for two models that, to the extent that they can, model the same material behavior.

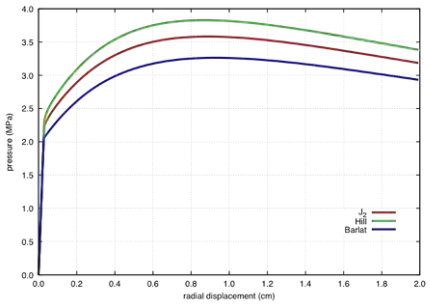

Figure 2: The pressure vs. radial displacement curve for the internally pressurized cylinder showing significantly different results for 2090-T3 Al.

We analyze the results to understand the influence of the yield surface on the structural loads. The stress paths are plotted in plane stress space in Figure 3. For this load path the effect of the yield surface is obvious. While the yield stress in the circumferential direction is the same for all three models, and the yield stress in the axial direction is the same for the two orthotropic models, the results are very different, even for the orthotropic models. The shape of the yield surface between the two material directions along with the different plastic flow directions leads to significant differences in the results.

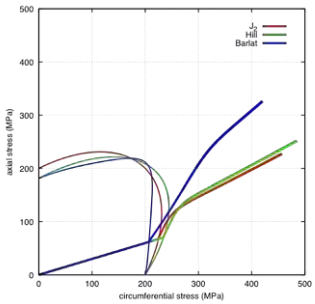

Figure 3: The pressure vs. radial displacement curve for the internally pressurized cylinder showing significantly different results for 2090-T3 Al.

We have many choices for plasticity models, and many aspects of a plasticity model - including the hardening model, temperature dependence, and rate dependence - are important. The yield surface, however, is often overlooked. As shown in this work, significantly different results can be obtained for models that ostensibly capture the same behavior.

References

[1] Hosford W. F.: A generalized isotropic yield criteria. *J. Applied Mech* **39(2)**:607-609, 1972.

[2] Hill R.: A theory of the yielding and plastic flow of anisotropic metals. *Proc. Roy. Soc. London A* **193**:281-297,1948.

[3] Barlat F., Aretz H., Yoon J. W., Karabin M. E., Brem, J. C., Dick R. E.: Linear transformation-based anisotropic yield functions. *Int. J. Plasticity*, **21**:1009-1039, 2005.

[4] Karafillis A. P., Boyce M. C.: A general anisotropic yield criterion using bounds and a transformation weighting tensor. *J. Mech. Phys. Solids*, **41(12)**:1859-1886, 1993.

[5] Sierra/SM Development Team: Sierra/SM 4.36 User's Guide. SAND2015-2199, Sandia National Laboratories, 2015.

MICROSTRUCTURAL EFFECTS IN NICKEL-BASED ALLOYS DAMAGE DURING PLASTIC LOADING

Shakhrukh Ismonov, Monica Soare
General Electric Global Research, Niskayuna, NY, USA

Summary It was experimentally observed in the literature that damage during low cycle fatigue of polycrystalline nickel-based alloys initiates in the areas with highly localized plastic strains. In our study alloy-R88DT with densely populated annealing twins, the interface between the twin and the parent grain is especially prone to local damage since it coincides with the slip planes. This is more evident when the interface is characterized by high Schmid factors and low elastic modulus grain. Crystal plasticity simulations are performed in order to identify numerically the microstructural factors, such as crystalline orientation of the grain–twin pair, elastic properties of the grain and twin, twin geometry, promoting high total stain in the material and thus high probability of damage. Maps indicating the strain localization are provided in the space defined by grains/twins orientations at high temperatures where multiple types of slip systems are activated.

Introduction

R88DT material is a precipitation strengthened polycrystalline superalloy used in the gas turbine disks due to its excellent elevated temperature properties such as high tensile strength, superior creep resistance, and high resistance to fatigue crack growth. The crack nucleation process at the microscale was studied experimentally [1,2] and location of damage was identified. For this material with high annealing twin density, the interface between the twin and the parent grain appeared to be the weakest link, especially if it is characterized by a high Schmid factor and high discrepancy in the elastic modulus of the two sides of the interface. Using crystal plasticity models, the current study identifies the orientations (of the grain and associated twin) for which the interface may experience high plastic deformations and thus high probability of failure. First a micro-structurally informed crystal plasticity model was developed at high temperature. Single crystals with representative microstructures were created and mechanically tested under different crystallographic orientations for model calibration. The model calibrated on single crystal data was then used in a polycrystalline structure to predict the macroscopic stress-strain response. Once validated, the model was applied for various grains/twin orientations in order to identify the high interface strains scenarios.

MECHANICAL TESTS, CHARACTERIZATION AND MODEL DEVELOPMENT

Tensile and compressive tests of representative material, single crystal oriented in 3 different directions ([100], [110], [111]) were conducted at 1200°F. Tensile tests were performed at a strain rate between 1e-3 to1e-4/s while compression tests were performed at constant strain rate of 1e-3/s. Selected specimens were deformed to rupture, while others were interrupted around 7% strain for microstructure characterizations. The mechanical tests were followed by TEM characterization for deformation mechanisms understanding. Mechanisms as plastic slip alongside primary and secondary octahedral systems, stacking-faults formation and precipitate shearing have been observed. Their activation was highly dependent on crystal orientation. Figure 1 shows the dominant mechanisms for [100] and [111] loading direction. Interestingly strong tension-compression asymmetry has been observed at tested temperature in [111] orientation.

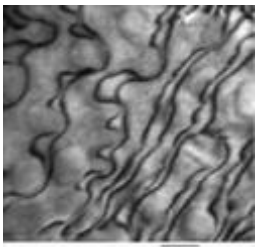

a) [100] tension sample Pairs of {111}½[011] dislocations shearing the precipitates

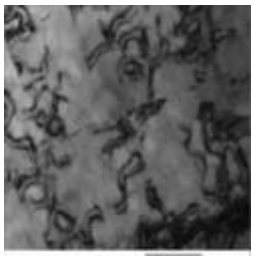

b) [111] tension sample. Pairs of 1/6[211] partials

Figure1. TEM observations for single grain specimens. Strongly coupled {111}½[011] dislocation pairs observed for [100] oriented sample (a)), dislocation activity in {111}1/6[211] observed for [111] oriented sample (b)) (Courtesy of Mallikarjun Karadge, GE Global Research)

The observed mechanisms have been incorporated in a viscoplastic constitutive model and implemented in a finite element code based on framework proposed by Lee [4, 5]. The model was able to distinguish the activation of octahedral primary and secondary slip systems for different crystallographic orientations, to capture the tension compression asymmetry and to predict very well the initial yield values. Applied on the actual samples geometries (cylindrical with circular cross-section)

[a)] Corresponding author. Email: soare@ge.com.

the model captured the ellipsoidal deformed cross section of the tension samples and extensive shearing of the compression samples.

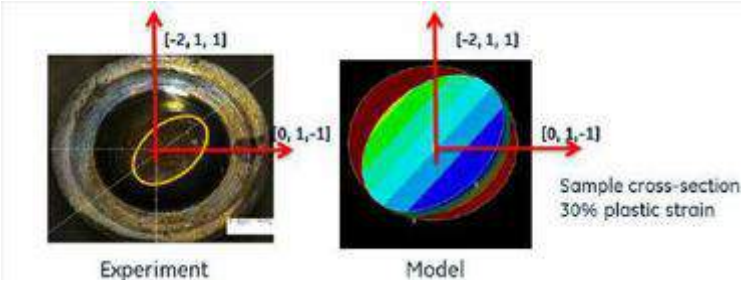

Figure 2 Deformed cross-section of the [111] tensile sample as observed in the experiment and predicted by the crystal plasticity model

RESULTS AND CONCLUSIONS

Experimental observations presented in the literature [1, 2] showed correlations between the the high damage probability locations and high strains locations (which are most often at the interface between grains at their associated annealing twins). Due to the FCC structure of the studied alloy, the interface grain- coherent twin is always in a {111} type of plane. Using the calibrated visco-plastic model, we constructed a contour map of the maximum projected strains at the grain –twin interfaces, in a sphere representing the grain orientation (Figure 3c).This type of map can provide a rapid estimation of the damage probability when comparing various grains orientation. We observed numerically that the high strains locations are cumulated effect of high Schmid factor (Figure 3a)) locations and high grain/twin difference in elastic modulus (Figure 3b), in agreement with the experimental observations. The method can be efficiently applied (and maps reconstructed) for various stress and temperature levels.

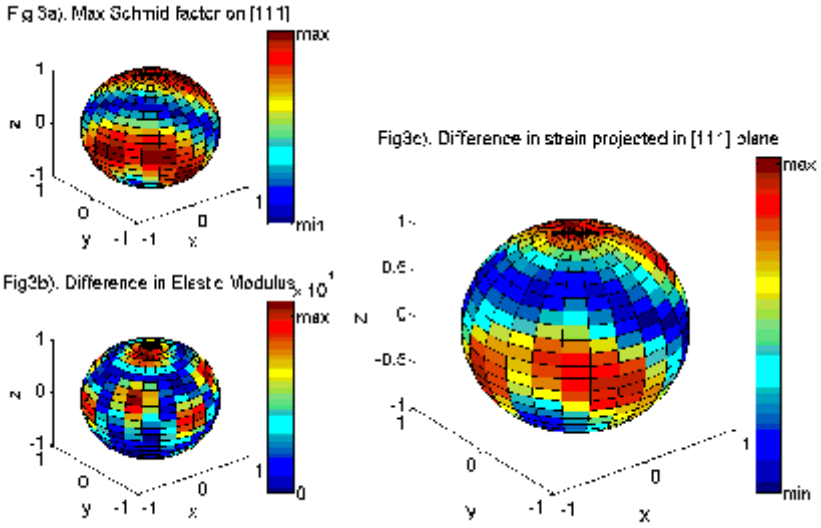

Figure 3 Contour maps of the elastic modulus difference, maximum [111] Schmid factor difference and projected strain difference between a grain and its associated annealing coherent twin. Each point on the sphere represents a loading direction. Figure 3c – gives a first order indication of the orientations with higher probability of failure (red areas)

The authors would like to acknowledge Shenyan Huang and Mallikarjun Karadge (General Electric Global Research) for their contributions to the experimental and microstructural characterization parts.

References

[1] Stinville J. C., Echlin M.P., Texier D., Bridier F., Bocher P., Pollock T.M.: Sub-Grain Scale Digital Image Correlation by Electron Microsopy for Polycrystalline Materials during Elastic and Plastic Deformation. *Experimental Mechanics*: 1-20, 2015.

[2] Miao J., Pollock T.M., Jones J.W.: Fatigue Crack Initiation in Nickel-based Superalloy Rene 88DT at 593ºC. *Superalloys* 589-597, 2008.

[3] Lee E.H. Elastic-plastic deformation at Finite strains. *J. Appl. Mech*. 36:1, 1969

[4] Maniatty A., Yu J-S. Effect of Elasticity on slip system activity in face-centered cubic crystals: a numerical study, *IJSS* 33(8):1069-1082, 1996

AN ELASTIC-VISCOPLASTIC CRYSTAL PLASTICITY MODELING AND STRAIN HARDENING FOR PLANE STRAIN DEFORMATION OF PURE MAGNESIUM

Weidong Song[a)]
School of Mechatronical Engineering, Beijing Institute of Technology, Beijing, China

Abstract A rate-dependent elastic-viscoplastic constitutive model is proposed to simulate the plane strain deformation of pure magnesium crystal. The basal, prismatic and pyramidal slip systems in the parent grain, compressive twinning (CT) and tensile twinning (TT) are incorporated in the model. The constitutive descriptions of CT and TT are distinguished to better characterize their effects on the overall hardening of magnesium single crystals. The plane strain numerical schemes of seven different orientations for loading and fixed boundary are considered and their various mechanisms and characteristics of plastic deformation are discussed. These computational predictions are carefully compared with their corresponding macroscopic experimental observations and other numerical results. These results prove that it is necessary to distinguish different twinning systems and their associated hardening laws for the plastic deformation of magnesium and its alloy.

MODELING THEORY

Geometric kinematics

According to the assumption of pseudo slip for the deformation twinning, the plastic part of crystal velocity gradient tensor is co-produced by the slip in the matrix (un-twinned region), twinning in the matrix and slip in the twinned region [1].

$$L^P = \left(1-\sum_{\beta}^{N^{tw}} f^{\beta}\right)\sum_{\alpha}^{N^{sl}} \dot{\gamma}_{sl}^{\alpha}\left(n_{sl}{}^{\alpha} \otimes m_{sl}{}^{\alpha}\right) + \sum_{\beta}^{N^{tw}} \dot{\gamma}_{tw}^{\beta}\left(n_{tw}{}^{\beta} \otimes m_{tw}{}^{\beta}\right) + \sum_{\beta}^{N^{tw}} f^{\beta} \sum_{\mu}^{N^{sl-tw}} \dot{\gamma}_{sl-tw}^{\mu}\left(n_{sl-tw}^{\mu} \otimes m_{sl-tw}^{\mu}\right) \tag{1}$$

where the $\dot{\gamma}_{sl}^{\alpha}$ denotes the shear rate on the slip system α ; f^{β} and $\dot{\gamma}_{tw}^{\beta}$ represent the volume fraction and shear rate on the twin system β respectively; $\dot{\gamma}_{sl-tw}^{\mu}$ denotes the shear rate on the slip system μ produced in the twinned region; N^{tw}, N^{sl} and N^{sl-tw}, respectively, denote the total number of twin systems, slip systems and slip systems in the twinned region; n^{*} and m denote the direction of slip or twinning and the normal to the slip or twin plane; $\otimes$ denotes the tensor product.

The total Cauchy stress is superimposed by the volume fraction of twinning with the Cauchy stresses of slip and twinning.

$$\sigma = \left(1-\sum_{\beta}^{N^{tw}} f^{\beta}\right)\sigma^{sl} + \sum_{\beta}^{N^{tw}} f^{\beta}\sigma^{tw} \tag{2}$$

Hardening theory

The deformation of CT prefers the Hall-Petch mechanism. It is clear that the twinning boundary is similar to the grain boundary and it reduces the length of the slip in the Hall-Petch mechanism. So the growth of CT will promote the hardening of whole grain. However, when the volume fraction of CTs reaches a saturation value, there are some decreases for strain hardening rate. A simplified expression was adopted to describe the hardening of CT by considering the nucleation and growth of CT.

$$\dot{s}^{\beta}{}_{\_} = h_{ct}\left(\sum_{=1}^{ct} f^{m}\right)^{b} \cdot \dot{\gamma}^{\beta} \tag{3}$$

where h_{ct} and b are both the parameters to control the hardening rate of CT.

Because there are wider dislocation cores in TT than CT, TT can nucleate and grow up more easily and saturate faster. This phenomenon is consistent with latent hardening by dislocation transmutation and incompatible with the Hall-Petch effect. It is very similar to the mode of hardening of slip system, so the hardening rate of twinning from the influence of TT on itself is substituted by a form of resembling the hardening rate of slip.

$$\dot{s}_{\_} = h_{tt}^{\beta} \sec h^{2}\left|\frac{h_{tt}^{\beta}\bar{\gamma}_{tt}}{\tau^{\beta}{}_{\_} - \tau_{0-tt}^{\beta}}\right| \cdot \dot{\gamma}^{\beta} \tag{4}$$

where h_{tt}^{β} is the initial parameter of hardening rate on TT system β ; τ_{0-tt}^{β} and $\tau^{\beta}{}_{\_}$ denote the critical resolved shear stress and saturated stress on TT system β respectively; $\bar{\gamma}_{tt}$ is the cumulative shear strain on all the TT.

[a)] Corresponding author. Email: swdgh@bit.edu.cn.

CRYSTAL PLASTICITY SIMULATION MODEL

Kelley and Hosford [2] conducted a detailed study for the plane strain deformation of magnesium whose initial directions have been determined in the experiments under loads of different directions. They adopted a channel-die experimental test: the sample was compression in one direction, while the second one was constrained by a fixed rigid wall and the third one was free. The identical schedule is used in the simulations of present paper. Seven different loads and fixed directions are adopted. Graff et al. [3] performed their model to simulate the seven orientations with Voce hardening. But they did not consider the pyramidal slip <a> and CT for deformation of magnesium. Zhang and Joshi [4] also made a similar simulation. The predicted results of this paper will be compared with the experimental data and their simulation results.

RESULTS AND DISCUSSIONS

The parameter values are calibrated for constitutive equations by comparing with the experimental data. The parameters for each slip or twinning system will keep fixed in all the cases. Only orientations E and F will be presented for the limitation of page [2]. The $\{10\bar{1}2\}$ twinning is the first deformation mode to be activated for the orientation E and F. The grains are reoriented while the volume fraction of TT reaches a critical value. The CT and non-basal slip (i.e. pyramidal<c+a>slip in case E, prismatic and pyramidal<a> slip in case F) in the reoriented material are required to accommodate the further strain. The Euler angles of orientation E are changed from (90°, 90°, 60°) to (-90°, 5.56°, 60°). This orientation is only 5.56° away from case B. So the deformation mechanisms of post-TT are CT and pyramidal<c+a>slip which are same to the orientation B. The Euler angles of orientation F are from (90°, 90°, 30°) to (-5.11°, 33.58°, -91.95°). The CT, prismatic and pyramidal<a> slip become the dominate deformation modes for orientation F after the implementation of the TT.

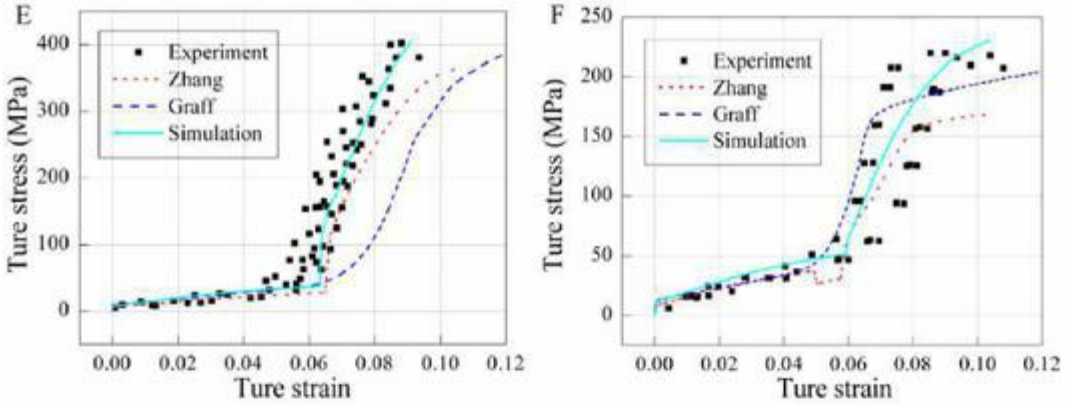

Fig. 1. Comparison of stress-strain curves from plane-strain compression predictions with experiments and other simulations (orientations E and F).

CONCLUSIONS

A rate-dependent CPCM was presented to simulate the plane-strain deformation of magnesium single crystals. The differences between tensile and compressive twins are distinguished. The crystallographic reorientation due to twinning is considered. And the numerical simulations of seven orientations are carried out. The activity and influence of each deformation mechanism are identified.

References

[1] Kalidindi, S.R.: Incorporation of deformation twinning in crystal plasticity models. J. Mech. Phys. Solids 46:267–271, 1998.
[2] Kelley, E.W., Hosford, W.F.: Plane-strain compression of magnesium and magnesium alloy crystals. Trans. Met. Soc. AIME 242:5–13, 1968.
[3] Graff, S., Brocks, W., Steglich, D.: Yielding of magnesium: From single crystal to polycrystalline aggregates. Int. J. Plast. 23:1957–1978, 2007.
[4] Zhang, J., Joshi, S.P.: Phenomenological crystal plasticity modeling and detailed micromechanical investigations of pure magnesium. J. Mech. Phys. Solids 60:945–972, 2012.

AN INFLUENCE OF CYCLIC LOADING ON STRESS COMPONENT REDUCTION IN THE TRANSVERSAL DIRECTION

Tadeusz Szymczak[1a)], Zbigniew Kowalewski[2]
[1]*Centre for Material Testing, Motor Transport Institute, Warsaw, Poland*
[2]*Department for Strength of Materials, Institute of Fundamental Technological Research, Warsaw, Poland*

Summary The paper reports results of tests where monotonic deformation was conducted in assistance of cyclic straining in the perpendicular direction. Two variants of strain signals combinations were applied, i.e. monotonic tension with torsion cycles and monotonic torsion with tension-compression cycles. The amplitudes of cyclic strain were lower than ±1%, frequency levels were selected within the range from 0.005 to 1 Hz. Independently of the cyclic strain direction applied the material response was similar. A stress reduction with the cyclic strain amplitude increase was obtained for direction of monotonic loading.

INTRODUCTION

An effect of cycles on material subjected simultaneously to monotonic loading was investigated with special emphasis to find possible application for technological forces reduction. Such approach is widely used by research groups trying to modify the so called KOBO method, [1, 2]. This technique enables to produce tubes, rods and other types of profiles at lower forces, than those necessary during conventional processes execution, [3]. In typical procedures an application of the KOBO technique enforces large deformation in direction of cyclic loading [1, 2]. However, as it has been shown by other researches [4, 5] the same effect can be achieved using cyclic loading of significantly lower strain amplitude. Such aspect of analysis is not sufficiently recognized as yet. Therefore, the main aim of this paper is to study variations of stress-strain curve due to monotonic deformation assisted by cyclic loading under a range of strain amplitudes and different frequencies.

EXPERIMENTAL PROCEDURE

The experimental procedure contained three stages. Firstly, monotonic tension and monotonic torsion tests were carried out. Afterwards, monotonic tension assisted by cyclic torsion (symmetrical cycles) with step increasing strain amplitude was performed. The third stage was planned to have step increasing strain amplitude of tension-compression cycles superimposed on monotonic torsion. All tests were performed at room temperature using thin-walled tubular specimens of: 60 mm – total length; 15.7 mm – gauge length; 0.75 mm – wall thickness, Fig. 1. Axial and shear strain components in the form of monotonic and sinusoidal functions were used to control the loading programme, Fig. 2a. In the case of torsion-reverse-torsion cycles the following magnitudes of shear strain amplitude were taken: ±0.1, ±0.2, ±0.4, ±0.8%, while frequency was equal to 1Hz. The tests to identify a frequency effect were conducted for values lower than 1Hz under constant strain amplitude equal to ±0.4%. An influence of tension-compression cycles on monotonic torsion was investigated for axial strain amplitude equal to: ±0.1, ±0.15, ±0.3 and ±0.75%.

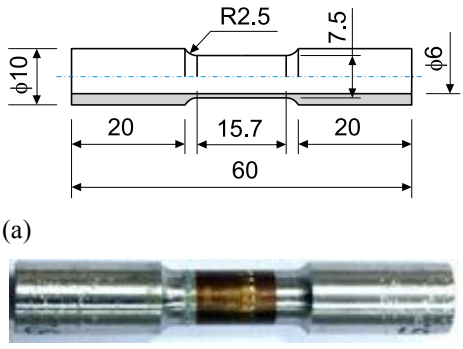

Fig. 1. Thin-walled tubular specimen: (a) geometry and dimensions, (b) zone for location of strain gauges

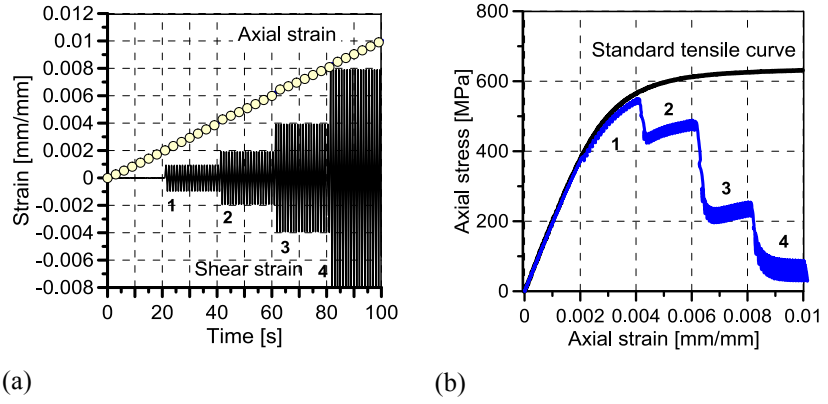

Fig. 2. Test details: (a) loading programme, (b) comparison of standard tensile characteristic to the responses under combined loading programme illustrated in Fig. 2a

[a)] Corresponding author. Email: tadeusz.szymczak@its.waw.pl

RESULTS AND THEIR ANALYSIS

The 14 MoV 6-3 steel commonly applied in automotive industry was selected for testing. It is used to produce car elements, engine parts and suspensions. Tensile parameters of the steel were as following: Young's modulus - 1.9×10^5 MPa; yield point - 523 MPa; ultimate tensile stress - 653 MPa. The representative results from tests are presented in Figs. 2÷4. As it is shown in Fig. 2, the steel in tension direction exhibited significant stress reduction due to presence of torsion cycles. This effect became to be stronger with the increase of shear strain amplitude. The tensile stress drop attained 90% for the highest strain amplitude considered. Similar effect has been observed during monotonic torsion assisted by tension-compression cycles, Fig. 3. Again, with the increase of the cyclic strain amplitude, the shear stress magnitudes diminished dramatically. Shear stress drop attained the level of ~30, ~150 and ~200 MPa for cyclic strain amplitude equal to ±0.15, ±0.3, ±0.75%, respectively.

In the final step of the experimental programme an influence of cyclic torsion frequency on the monotonic tension was investigated. Three levels of frequency were taken into account: 0.005, 0.05 and 0.5 Hz. In each test the cyclic strain amplitude was the same: ±0.4%. The results are summarized in Fig. 4. As it can be seen, the axial stress lowered around 250 MPa for the lowest frequency considered. For the higher values of this parameter, i.e. 0.05 Hz and 0.5 Hz, such drop was equal to 370 MPa and 470 MPa, respectively.

The experimental observations were modelled using the three surface model proposed by Mróz and Maciejewski [6].

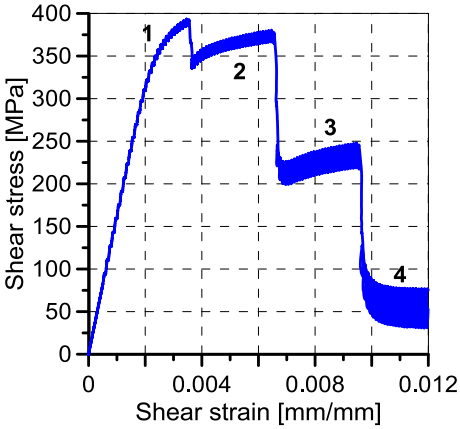

Fig. 3. Variations of shear stress due to presence of step increasing amplitude of tension-compression cycles: 1 - 0.1%; 2 - 0.15%; 3 - 0.3%; 4 - 0.75 %, frequency 1Hz

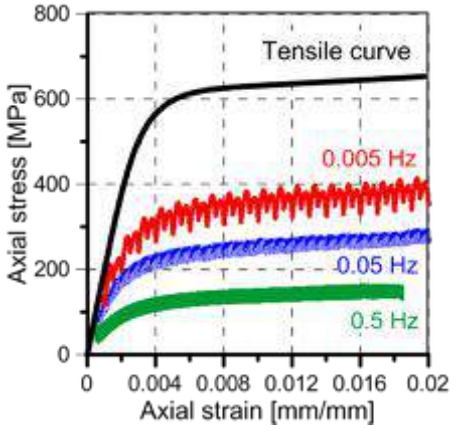

Fig. 4. Effect of cyclic torsion frequency on tensile curves

SUMMARY

Stress occurred during monotonic deformation can be significantly reduced by application of cyclic strain in the transversal direction. This effect was visible for small values of cyclic strain amplitude and frequency, below ±1 % and 0.5 Hz, respectively. In comparison to the initial state even 90 % stress reduction during monotonic loading can be achieved when assisted by cycles.

References

[1] Kong L.X., Lin L., Hodgson P.D.: Material properties under drawing and extrusion with cyclic torsion, *Materials Science and Engineering*, **A308**:209-215, 2001.

[2] Bochniak W., Korbel A., Szyndler R., Hanarz R., Stalony-Dobrzański F., Błaż L., Snarski P.: New forging method of bevel gears from structural steel, *J. Mat. Proc. Tech.*, **173**:75-83, 2006.

[3] Korbel A., Szyndler R.: The new solutions in the domain of metal forming - contribution of the Polish engineering idea, *Metal Forming*, **XXI(3)**, 203-216, 2010.

[4] Szymczak T., Kowalewski Z.L.: Variations of mechanical parameters and strain energy dissipated during tension-torsion loading, *Archives of Metallurgy and Materials*, **57(1)**:193-197, 2012.

[5] Kowalewski Z.L., Szymczak T., Maciejewski J.: Material effects during monotonic-cyclic loading, *International Journal of Solids and Structures*, **51(3-4)**: 740-753, 2014.

[6] Maciejewski J., Mróz Z.: Modelling of plastic deformation of metals at complex loading paths (in Polish), *the I Congress of Polish Mechanics*, Warsaw, 28-31 August 2007, Poland.

E PERIMENTAL RESEARCH OF CREEP RECOVER AND FRACTURE PROCESSES OF ASPHALT CONCRETE UNDER TENSION

Alibay Iskakbayev[1], Bagdat Teltayev[2a)], Femistokl Andriadi[2],
Kayrat Estayev[2], Elena Suppes[2] & Ainur Iskakbayeva[3]
[1]*al-Faraby Kazakh National University, Almaty, 050040, Kazakhstan*
[2]*Kazakhstan Highway Research Institute, Almaty, 050061, Kazakhstan*
[3]*Caspian University, Almaty, 050012, Kazakhstan*

Summary There are given results of experiments over fine grained asphalt concrete on mode of direct tension under constant stress, staged and cyclic loading at temperature of 20°C. Curves of creep and long-term strength have been constructed. Essential influence of magnitude, duration of loading and resting between loadings on asphalt concrete failure time has been stated. Only 6-7% of strain recovers after removing of the load.

INTRODUCTION

Asphalt concrete is one of the main materials to construct road pavements. Mechanical properties of asphalt concrete depend on temperature, magnitude and duration of loading [1]. Under actual road condition, load magnitude of vehicles' wheels on asphalt concrete pavement surface and loading duration change in wide range. Therefore practical importance is determination of the mechanical behavior of asphalt concrete taking into consideration changes in mentioned above factors.

In this paper there are presented results of experiments over samples (size: 5x5x16 cm) of fine grained asphalt concrete prepared using bitumen (grade of 100-130) on scheme of direct tension in different loading regimes at 20 °C temperature. 70 samples of asphalt concrete were tested.

CONSTANT STRESS

Testing under constant stress (creep) is one of the basic methods for determine behavior of viscoelastic material [2]. Testing of asphalt concrete samples was carried out on special constructed equipment. Obtained results showed that under all stresses asphalt concrete samples were failed. Asphalt concrete creep curves have three characteristic sites (Fig.1): the site I of unstabilized creep with decreasing rate, the site II of stabilized creep with constant (minimum) rate and the site III of accelerating creep with increasing rate which precedes failure. Average relative durations of these sites are equal to 13 %, 63 % and 24 % respectively.

Constructed curve of asphalt concrete long-term strength is satisfactorily approximated by power function. Stress change per one order causes changes in failure time of tree orders.

STAGED LOADING

Under actual road conditions vehicles with different weight parameters move on roads. Their axial loads vary in wide range. Sequence of its application also essentially changes. Therefore there were tested asphalt concrete samples according to staged loading scheme to estimate influence of loading sequence and its value on asphalt concrete failure.

The first sample was loaded by stress equal to 2.29 kg/cm^2 (39.4 % from strength) during 40 seconds (loading rate 0,0573 kg/(cm^2·s) which had not changed for 60 s. Then with the same loading rate the stress was reduced till 1.57 kg/cm^2 which was constant till the sample failure. The sample failure time was 1987 s.

The second sample was loaded firstly by stress equal to 1.7 kg/cm^2 (27.0 % from strength) with the same loading rate which was constant during 60 s. Then the stress was increased till 2.29 kg/cm^2 with the same loading rate which was constant till the sample failed. The sample failure time was 1024 s.

There was established that changes in small and big tension stresses sequences essentially influence on the asphalt concrete failure time. In the case when the sample was firstly loaded by big stresses and then by small ones the failure time increases almost for two times than the sample was loaded firstly by small stresses and then by big ones. This fact can be explained by the fact that in the first case the duration of acting of big stress is essentially less than duration of acting of small stresses.

C CLIC LOADING

There are relaxation periods with different durations between loading sequences on roads. The sample of asphalt concrete was tested according to the certain scheme to estimate relaxation effect. Firstly the sample was loaded by stress equal to 1.38 kg/cm^2 (23.8% from strength) with rate equal to 0.0626 kg/(cm^2·s) which was constant during 120 s. Then

[a)]Corresponding author. Email:bagdatbt@yahoo.com

the sample was unloaded fully with the same rate and it rested during 300 s. That regime of loading-unloading-rest was carried out five times. The stress was constant after the 6th time of loading till the sample failure (Fig. 2). Next sample of asphalt concrete was tested under constant stress equal to 1.38 kg/cm^2 till it failure. The times of the samples failure were 14 916 s and 5 836 s respectively.

LOADING WITH CONSTANT RATE

It was established that the asphalt concrete under investigated regimes of loading and temperature has essential plasticity: only 6-7% of strain recovers; relaxation between serial loadings essentially increase the failure time - five time relaxation with 300 s duration of each increased the failure time for 2.6 times.

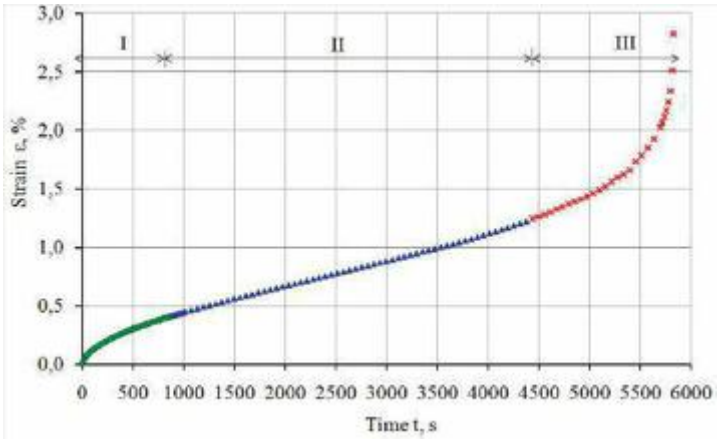

F Creep curve of the asphalt concrete

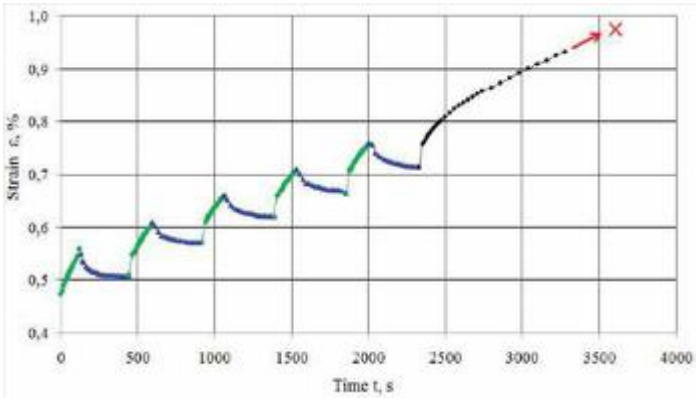

F 2 Curve of the asphalt concrete deforming at staged loading

Next samples of asphalt concrete were tested by loading with constant rate till failure. The results showed that dependence of strain from stress is nonlinear. The influence of loading rate on asphalt concrete strength was found.

CONCLUSIONS

Experimental research of fine grained asphalt concrete samples at different regimes of loading showed, that: a creep curve has tree stages of deforming; the curve of long-term strength is discribed by the power function; at big loads dependence of stress from strain is nonlinear and plasticity is occurs.

References

[1] Levenberg E.: Modelling asphalt concrete viscoelasticity with damage and healing. International Journal of Pavement Engineering. 2015: 1-13.

[2] Cristensen R.M.: Theory of viscoelasticity: an introduction, Academic Press, NY 1971.

SM14 - Stability of Structures

TS.SM14-1.01	Bigoni, Davide - Flutter and dissipation instabilities in structures subject to dry friction follower forces (INVITED)	2766
TS.SM14-1.02	Zippo, Antonio - Experimental investigation of dynamic behaviour of pre-compressed circular cylindrical shell	2768
TS.SM14-1.03	Ford, Matthew - Buckling and collapse of the bicycle wheel	2770
TS.SM14-1.04	Formica, Giovanni - Nanocomposite microbeams for sensing applications	2772
TS.SM14-1.05	Galich, Pavel - Elastic wave propagation in highly deformable layered materials	2774
TS.SM14-1.06	Hadrien, Bense - Instabilities in dielectric elastomer plates	2776
TS.SM14-2.01	Paidoussiss, Michael P. - Dynamics of long tubular cantilevers in axial flow (INVITED)	2778
TS.SM14-2.02	Hamouche, Walid - Non-linear dynamic actuation of multistable shells ***(Paper Confidential – to be disclosed at later date)***	
TS.SM14-2.03	Hoang, Tuan - Stability and buckling of a flat circular, intrinsically curved filament spanned by a fluid film	2780
TS.SM14-2.04	Kochmann, Dennis - Transition waves in periodic multi-stable mechanical systems	2782
TS.SM14-2.05	Lazarus, Arnaud - Modal analysis of structures in periodic states	2784
TS.SM14-2.06	Lestringant, Claire - Instabilities of a compressed hyper elastic prism: Competition between wrinkles and creases	2786
TS.SM14-3.01	Shrivastava, Suresh - Plastic bifurcation paradox for circular and rectangular plates	2788
TS.SM14-3.02	Martin, Maverick - Tape spring rod model as a regularised Ericksen's bar involving propagating instabilities	2790
TS.SM14-3.03	Mora, Serge - Gravity driven instability in horizontal elastic layers	2792
TS.SM14-3.04	Plucinsky, Paul - Interplay of wrinkling and microstucture in nematic elastomer membranes	2794
TS.SM14-3.05	Psarra, Erato - Instability of MRE film - substrate block under magneto - mechanical loadings	2796
TS.SM14-3.06	Qu, Shaoxing - Wrinkling behavior of an inflated dielectric elastomer balloon	2798
TS.SM14-4.01	Reis, Pedro - Defect-controlled buckling of depressurized elastic shells (INVITED)	2800
TS.SM14-4.02	Tanaka, Hiro - Transformation shift of periodic cellular structure by controlling internal stiffness	2802
TS.SM14-4.03	Wehmeyer, Steven - Non-linear response of elastic snap-through structures	2804
TS.SM14-4.04	Wen, Guangyang - Dynamic Stability of Biaxially Strained Thin Sheets Under High Strain-Rates	2806
TS.SM14-4.05	Xu, Fan - On axisymmetric/diamond-like mode transitions in core-shell cylinders under axial compression.	2808
TS.SM14-4.06	Yu, Tian - Multi-stability and bifurcations of thin bands	2810
PO.SM14-1.01.305	Aranda-Iglesias, Damian - Oscillatory behaviour of compressible hyperelastic shells subjected to dynamic inflation	2812
PO.SM14-1.02.306	Borkowski, Łukasz - Numerical analysis of dynamic stability of plate by using tools used in dynamics	2813
PO.SM14-1.03.307	Cottanceau, Emmanuel - A finite element/quaternion/asymptotic numerical method for the 3D simulation of flexible cables	2815

PO.SM14-1.04.308	Darabi, Mehdi - Dynamic Instability of Antisymmetric Cross-ply Laminated Composite Cylindrical Shell	2817
PO.SM14-1.05.309	Hollenbeck, Derek - Effect of Non-Linear Constitutive Law on Column Buckling	2819
PO.SM14-1.06.310	Kento, Okui - Study on desigining the superior crushing response of lightweight egg-box panel	2821
PO.SM14-1.07.311	Kesari, Haneesh - Enhancement of buckling strength in the tapered skeletal elements of marine sponges	2823
PO.SM14-1.08.312	Lerbet, Jean - Kinematic structural stability	2825
PO.SM14-1.09.313	Li, Bo - Stability analysis of uniform deployable structure in compression	2827
PO.SM14-1.10.314	Liu, Yang - Post-buckling analysis of a hyperelastic layer-substrate structure under compression	2829
PO.SM14-1.11.315	Liu, Yuanpeng - Torsional wrinkling behaviour of annular thin elastic sheets	2831
PO.SM14-1.12.316	Renaud, Sylvain - A new approach to assess the dynamic sliding stability of structures: Application to concrete dams	2833
PO.SM14-1.13.317	Seraj, Saemul - Dynamic instability of doubly-tapered rotating laminated composite beams	2835
PO.SM14-1.14.318	Singler, Timothy - Thin film wrinkling: A solid-liquid interface instability	2837
PO.SM14-1.15.319	Slesarenko, Viacheslav - Formation Of Wavy Interfaces In Layered Visco-Hyperelastic Composites	2839
PO.SM14-1.16.320	Tao, Qiang - Bending capacity of inflated mesh-reinforced-membrane beam	2841
PO.SM14-1.17.321	Vaziri, Ashkan - Highly deployable multifunctional cellular structures with hierarchy	2843
PO.SM14-1.18.322	Yin, Jie - Harnessing directed buckling for switchable conductive pathway	2844
PO.SM14-1.19.323	Zheng, Bin - Buckling distortion of aluminum plates under non-uniform welding stress field	2846
PO.SM14-1.20.324	Zou, Shibo - Unfolding process of coiling fibers made by instability-assisted fused deposition modeling	2848

FLUTTER AND DISSIPATION INSTABILITIES IN STRUCTURES SUBJECT TO FRICTION FOLLOWER FORCES

Davide Bigoni[1], Oleg Kirillov[2], Diego Misseroni,[1] Giovanni Noselli,[3] Mirko Tommasini[1]
[1]*DICAM, University of Trento, Trento, Italy*
[2]*Russian Academy of Sciences, Steklov Mathematical Institute, Moscow, Russia*
[3]*SISSA, International School for advanced Studies, Trieste, Italy*

Summary Flutter and divergence instabilities are theoretically and experimentally analyzed in elastic structures with internal and external damping. Despite of the fact that only the former (and not the latter) was believed to be a destabilizing effect, it is theoretically demonstrated that the external damping plays a role similar to internal damping, so that both yield a pronounced destabilization paradox (in the Ziegler sense). This finding and other features of the Beck and Pflueger columns are substantiated by an experimental campaign in which the follower forces are obtained via dry friction with a newly designed experimental apparatus.

INTRODUCTION

Flutter and divergence instabilities may occur in elastic structures subject to tangential follower loads and well-known examples are the Ziegler double pendulum and the Beck and Pflueger columns [1, 2]. A key point in these mechanical frameworks is the realization of the follower force, which has been long debated and often considered of impossible practical realization, as discussed in detail by Elishakoff [3].
The controversy about the realization of the force was definitively solved by Bigoni and Noselli [4], who showed how to realize a follower tangential force in the Ziegler pendulum via Coulomb friction. Their idea, sketched in Fig. 1, was to provide the follower force through a wheel of negligible mass mounted at the end of the Ziegler double pendulum and constrained to slide against a frictional plane.

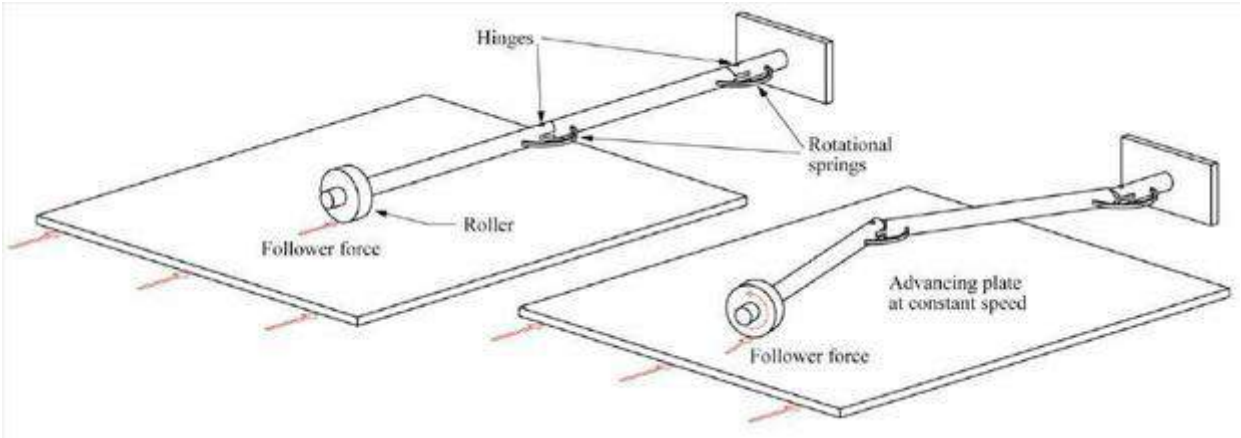

Fig. 1 Sketch of the experimental setup to realize a follower tangential force in the Ziegler double pendulum (figure adapted from [4])

THE EXPERIMENTAL REALIZATION OF THE BECK'S COLUMN

The experimental realization by Bigoni and Noselli was found unsuitable for the analysis of the Beck and the Pflueger columns, because if the ellipse of inertia of the cross-section of the rod to be tested is elongated, lateral torsional buckling occurs and if the ellipse of inertia of the cross-section of the rod is a circle, flexure involves large deformation, too large to produce the force necessary to flutter. Therefore, a new apparatus has been designed, following the scheme reported in Fig. 2 and realized.

The new experimental setup allows the first realization of follower tangential forces on elastic structures and allows a systematic investigation of flutter, divergence, and dissipation-induced instabilities. In these experiments, internal and external damping play a chief role, so that the effects associated to these two types of damping have been thoroughly

[a] Corresponding author. Email: davide.bigoni@unitn.it

investigated. From theoretical point of view it is shown that external damping plays a destabilizing role qualitatively similar to internal damping [5], a feature previously not believed, and which is now also experimentally confirmed.

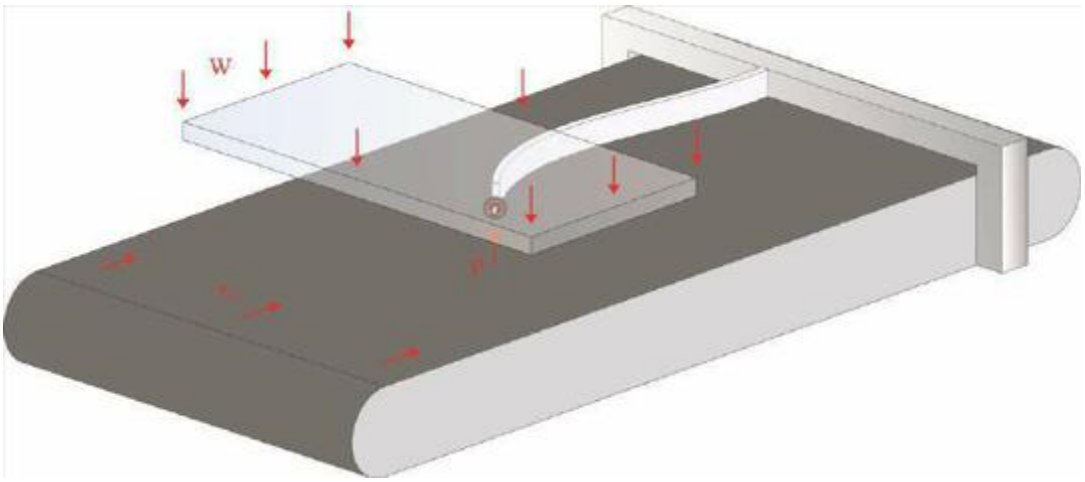

Fig. 2 Sketch of the experimental setup to realize a follower tangential force in the Beck's column

The experimental realization of the follower force also permits the investigation of the so-called 'Ziegler destabilization paradox', where the critical force for flutter instability decreases by an order of magnitude when the coefficient of internal damping becomes infinitesimally small. This instability is important since it represents an example of dissipation-induced instability (in the sense explained in [6]) and the experimental setup allows for the first systematic investigation of this instability.

CONCLUSIONS

A theoretical framework and an experimental setup have been proposed for the investigation of flutter and divergence instabilities in elastic continuous structures, in the presence of internal and external damping. Results confirm theoretical results that were demonstrated a long time ago, but never experimentally verified and pave the way to the realization of self-oscillating mechanisms of completely new design.

ACKNOWLEDGEMENT

The authors gratefully acknowledge financial support from the ERC Advanced Grant 'Instabilities and nonlocal multiscale modelling of materials' FP7-PEOPLE-IDEAS-ERC-2013-AdG (2014-2019).

References

[1] Beck, M. Die Knicklast des einseitig eingespannten, tangential gedruckten Stabes. *Z. angew. Math. Phys.* **3**:225, 1952.

[2] Pflueger, A. Zur Stabilitat des tangential gedruckten Stabes. *Z. angew. Math. Mech.* **35**:191, 1955.

[3] Elishakoff, I. Controversy associated with the so-called "follower force": critical overview. *Appl. Mech. Rev.* **58**:117-142, 2005.

[4] Bigoni, D, Noselli, G. Experimental evidence of flutter and divergence instabilities induced by dry friction. *J. Mech. Phys. Solids* 59:2208–2226, 2011.

[5] Tommasini, M., Kirillov, O., Misseroni, D., Bigoni, D. The destabilizing effect of external damping: Singular flutter boundary for the Pflueger column with vanishing external. *Submitted*.

[6] Krechetnikov, R. Mrsden, J.E. Dissipation-induced instabilities in finite dimensions. *Rev. Modern. Phys.* **79**:519-553, 2007.

EXPERIMENTAL INVESTIGATION OF DYNAMIC BEHAVIOUR OF PRE-COMPRESSED CIRCULAR CYLINDRICAL SHELL

Antonio Zippo*[1], Francesco Pellicano[1], Marco Barbieri[1], and Matteo Strozzi[2]

[1]*Dipartimento di Ingegneria "Enzo Ferrari", Università di Modena e Reggio Emilia*
[2]*Dipartimento di Scienze e Metodi dell'Ingegneria, Università di Modena e Reggio Emilia*

Summary Circular cylindrical shells are very efficient structures that have many applications and plays as key elements in several engineering fields. Shells usually exhibit a complicated dynamic behaviours because the curvature will effectively couple the flexural and in-plane deformations together as the three displacement fields simultaneously appear in each of the governing partial differential equations and boundary conditions. Therefore, it is understandable that the axial constraints can have direct effects on a predominantly radial modes. For instance, it has been shown that the natural frequencies for the circumferential modes of a simply supported shell can be noticeably modified by the constraints applied in the axial direction. In this paper the results of experimental tests on pre-compressed circular cylindrical shell will be presented: different combinations of preload and harmonic external axial load have been tested but for brevity only few results are shown.

SETUP AND TEST DESCRIPTION

The system under investigation consists of a circular cylindrical shell, made of aluminium, clamped both base and top sides by means of two rings at two rigid supports (see Figure 1).The bottom support is an aluminium alloy circular disk rigidly bolted to the shaker. The top disk is connected to the frame by means of a dynamic load cell, a stinger, and a static load cell. The stinger is introduced in order to reduce the effects of misalignments. The frame provides an axial compression load and the shaker provides a dynamic excitation: a sine step signal is generated by an ad hoc Matlab$^{\bigcirc}$ script. A laser vibrometer is used to measure the vibration of the side of the shell and its output is routed both to the spectrum analyser and to the controller. The control system is open-loop in order to avoid control instabilities induced by nonlinear behaviour of the tested structures.

MODAL ANALISYS

The aim of the experimental modal analysis is to experimentally find the modes and corresponding eigenfrequencies which characterise the dynamic behaviour of the structure. A complete preliminary modal analysis has been carried out for better understand the shell behaviour and to identify natural frequencies, damping ratios and modal shapes of the modes by an impact modal test with an impact hammer. More in details, three complete modal analysis between $1100Hz$ and $2000Hz$ have been performed on the shell with three different level of preload at $0N$, $50N$ and $100N$. All experimental datas was post processed in order to obtain the synthesised FRF and reconstructed with a dedicated Matlab$^{\bigcirc}$ script, the modal shapes was identified with the study in 3D representation and as map for better understand the shell properties. The effect of preload reflects a reduction of the natural frequencies in all the considered modes.

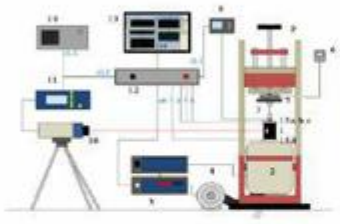

Figure 1: system setup: (1) structure under test (2) shaker (3) shaker amplifier (4) air cool system (5) static load cell (6) digital load gauge (7) force transducer "pcb m231b" (8) force transducer amplifier (9) press system to apply static preload (10) laser vibrometer (11)laser controller (12) shaker control system (13) pc (14) spectrum analyzer "ono-sokki cf-5220" (15a.b.c) 3 top accelerometers (15d) Base accelerometer

2.5cm

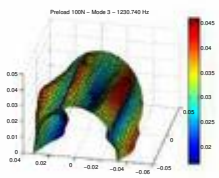

Figure 2: Modal Shape - $100N$ preload - 3D

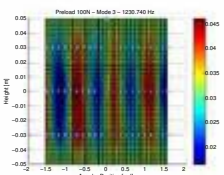

Figure 3: Modal Shape - $100N$ preload - map

*Corresponding author. Email: antonio.zippo@unimore.it

EXPERIMENT RESULTS

The experimental analysis was carried out with an open loop by a sine step from 1100Hz to 2000Hz, with a step frequency of 1.0 Hz (in some tests reduced to 0.1Hz to better refine the study). Each run starting from the highest frequency (2000Hz) towards the lower frequency (1100Hz) and backwards, each time varying the magnitude of the oscillations generated from the shaker, from 0.1 V with regular steps of 0.1 V up to the maximum value of 1.0 V. These sweeps were repeated, both the power supplied to the shaker and axial static load P_0 are varied. The press system allows to vary the static axial load from a minimum value $P_0 = 0N$ up to a maximum value $P_0 = 250N$ (safety limit to avoid shaker damage). Results are presented for preload values of $100N$ and for different voltage levels. Symbols *"d"* and *"u"* mean decreasing (d, down) and increasing (u, up) frequency sweep . The dynamic axial load, the lateral vibration and the accelerations at top and base of the shell are measured to better highlight the dynamic behaviour.

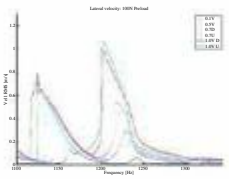

Figure 4: Amplitude-frequency diagram of lateral velocity - 100N

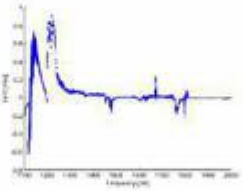

Figure 5: Bifurcation Diagram of lateral velocity drive voltage $1.0V$ d

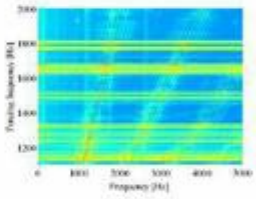

Figure 6: Waterfall of lateral velocity drive voltage $1.0V$ d

Table 1: Poincare maps, phase diagrams, spectrum and time history at $100N1.0VDW2$

Poincaré map	Phase portrait	Spectrum	Time history
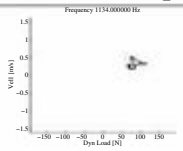	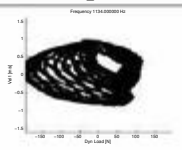	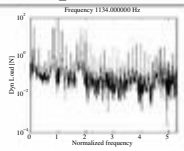	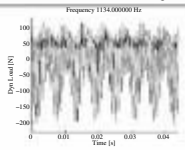

(i) $100N1.0VDW2$ - $1134.00Hz$ - Velocity vs Dynamic Load

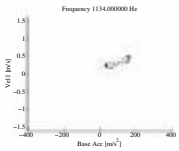
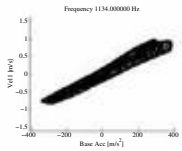
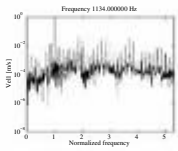
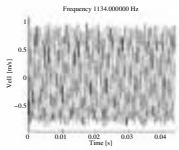

(ii) $100N1.0VDW2$ - $1134.00Hz$ - Velocity vs Base Acceleration

CONCLUSIONS

An ad hoc setup has been developed in order to measure both the dynamic load and the amplitude of vibration on the shell surface; tests are performed at different preloads and different amplitudes of the axial dynamic excitation, they have shown the existence of non linear behaviour in certain instability ranges. Chaos is found and a very well defined softening behaviour can be observed together with a quasi periodic and multiple periodicity. Non linear dependence of the response on the preload parameter is observed. Further experiments and correlation with numerical and theoretical models need to be performed in order to fully understand the observed phenomena.

References

[1] Francesco Pellicano, Marco Barbieri, Complex dynamics of circular cylindrical shells, International Journal of Non-Linear Mechanics, Volume 65, October 2014, Pages 196-212, ISSN 0020-7462

[2] F. Pellicano, M. Amabili, Dynamic instability and chaos of empty and fluid-filled circular cylindrical shells under periodic axial loads, Journal of Sound and Vibration, Volume 293, Issues 1–2, 30 May 2006, Pages 227-252, ISSN 0022-460X

BUCKLING AND COLLAPSE OF THE BICYCLE WHEEL

Matthew Ford *[1], Li Zhang[2], and Oluwaseyi Balogun[1, 2]
[1]*Department of Mechanical Engineering, Northwestern University, Evanston, IL, USA*
[2]*Department of Civil Engineering, Northwestern University, Evanston, IL, USA*

Summary A bicycle wheel is a prestressed structure; the tensioned spokes hold the rim under compression. It can buckle due to the elastic energy stored during construction or from external loads. This buckling mode, known as a "taco" or "potato chip" due to its saddle-like shape, can result from either of two related failure mechanisms: (1) elastic buckling under uniform spoke tension, and (2) dynamic collapse when loaded through the hub. Dynamic failure initiates from local buckling of the rim near the road contact. We derive an analytical expression for the buckling tension for an unloaded wheel and simulate wheel collapse using non-linear finite-element calculations. We present a lower bound for the load at which spokes will buckle. We find that increasing spoke tension increases the failure load, unless the spoke tension is close to the buckling tension, in which case the wheel will collapse under even a small disturbance.

ANALYSIS AND DISCUSSION

The rim of a conventional bicycle wheel is connected to the hub by a set of slender spokes. Each spoke exerts a restoring force on the rim proportional to the deflection of the rim at that point. If the spokes are closely spaced, the rim can be modeled as a curved beam on a continuous elastic foundation [1]. The foundation stiffness in the radial and lateral directions are

$$k_{rr} = \frac{n_s E_s A_s}{2\pi R L_s}\cos^2\alpha \quad , \quad k_{uu} = \frac{n_s E_s A_s}{2\pi R L_s}\sin^2\alpha \tag{1}$$

where n_s is the number of spokes, E_s and A_s are the Young's modulus and cross-sectional area of a spoke, R is the rim radius, L_s is the length of a single spoke, and α is the inclination angle of a spoke out of the center plane of the wheel.

Elastic buckling under uniform spoke tension

We first derive an analytical solution for the critical tension based on the principle of stationary potential energy. The strain energy is decomposed into components for rim bending, torsion, spoke deformation, and a non-linear contribution from the compressive force in the rim, $U = U_{bend} + U_{tors} + U_{spokes} + U_{nonlinear}$ [2]. Decomposing the deformation into a series of sinusoidal modes and setting the second variation $\delta^2 U = 0$ leads to an expression for the critical buckling tension.

$$T_{max} = \frac{2\pi EI}{n_s R^2}\left(\frac{\mu(n^2-1)^2}{1+\mu n^2} + \frac{k_{uu}R^4}{EIn^2}\right) \tag{2}$$

where EI is the rim bending stiffness, μ is the ratio of the torsion to bending stiffness GJ/EI, and n is the mode number.

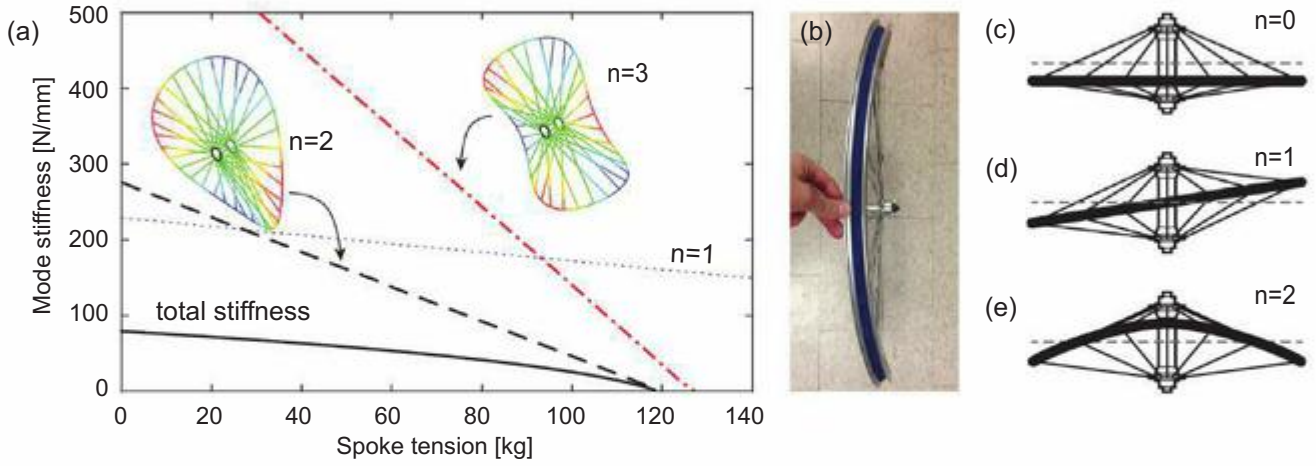

Figure 1: (a) Mode stiffness for the first three rim modes and the overall wheel stiffness. The wheel buckles when the stiffness of mode n=2 goes to zero. (b) Buckled wheel viewed from above. (c-d) Sinusoidal deformation modes.

*Corresponding author. Email: mford@u.northwestern.edu

Dynamic collapse of a loaded bicycle wheel

When a bicycle wheel supports a vertical load, the load is supported by shortening of a few spokes underneath the hub [3]. If the load is great enough to cause spokes in this zone to lose tension entirely leaving the rim unsupported laterally, the wheel will buckle locally which leads to catastrophic failure. Dynamic finite-element simulations of wheel collapse reveal a failure process very similar to that which was qualitatively described by Brandt [4]. The failure process is modeled in ABAQUS Explicit using beam elements for the rim and spokes (Figure 2).

The load-displacement curve for a loaded wheel exhibits non-linearity due to buckling of individual spokes underneath the hub. We model this behavior by including a foundation yield stress, $f_y = n_s T/2\pi R$ in the continuum elastic foundation model. The yield stress represents the average line load at which the spoke loses tension. We implement this model using a custom non-linear finite-element code (Figure 2 (c)). A lower bound for the onset of spoke buckling is given by

$$P_{crit} = 2 f_y \sqrt[4]{4EI/k_{rr}}\,. \tag{3}$$

The collapse load depends on the rim and spoke properties, as well as the spoke tension. Increasing spoke tension generally increases the buckling load because the spoke system can bear a higher load before detensioning (note the non-linear behavior in Figure 2 (c)). However, if the spoke tension is close to the critical buckling tension predicted by Equation 2, even a small disturbance will lead to failure.

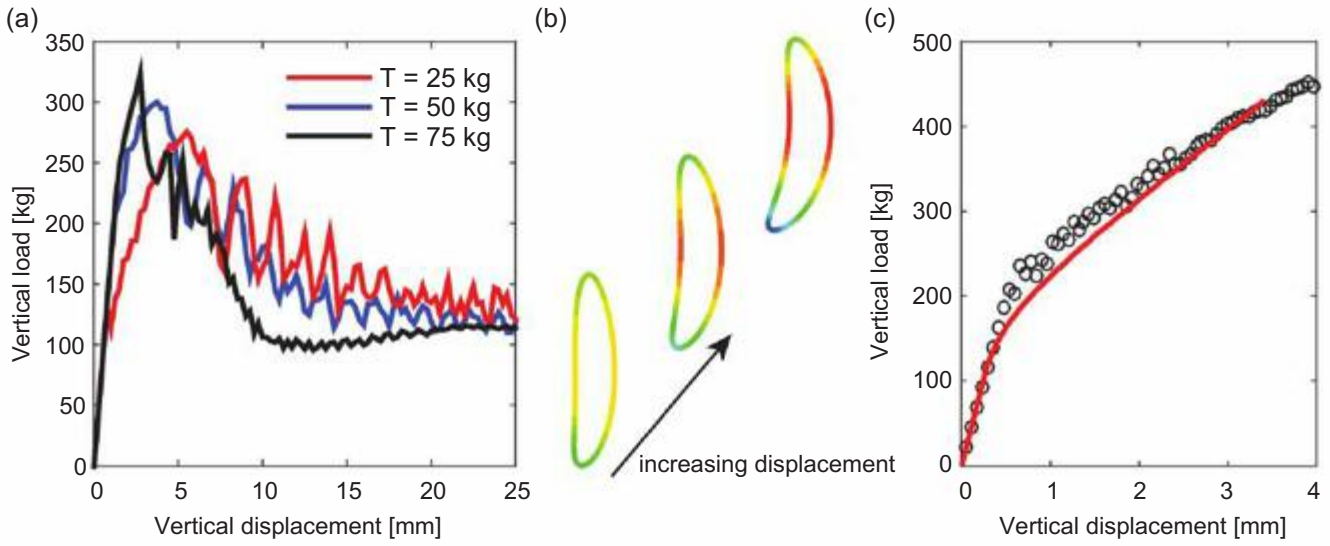

Figure 2: (a) Load-displacement curve for wheels with different spoke tensions. (b) Snapshots from a simulation of wheel collapse. Spokes are hidden for clarity. (c) Comparison between direct numerical solution with ABAQUS Explicit (circles) and continuum beam on elastic-plastic foundation model (red line).

CONCLUSIONS

The strength of a bicycle wheel is optimized through cooperativity between the rim and the spoke system. The spokes must be tight enough to resist detensioning when the wheel is loaded and the rim must be stiff enough to distribute the load over several spokes. Tightening the spokes beyond the critical tension described by Equation 2 will cause the wheel to buckle without any external load. We described the mechanism of wheel collapse through numerical simulations and derived a lower bound for the critical load for spoke buckling in Equation 3. These results can be used by designers and wheelbuilders to optimize wheel strength for different riders and conditions.

References

[1] Pippard A.J.S, Francis W.E., On a Theoretical and Experimental Investigation of the Stresses in a Radially Spoked Wire Wheel under Loads applied to the Rim, *Philosophical Magazine*, **11**(69), pp. 233-285, 1932.

[2] Pi Y. L. and M. A. Bradford M. A., Elastic flexural-torsional buckling of continuously restrained arches, *Int. J. Sol. Struct.*, **39**, pp. 2299-2322, 2002

[3] Burgoyne C. J. and Dilmaghanian R., Bicycle Wheel as Prestressed Structure, *J. Eng. Mech.*, **119**, pp. 439-455, 1993.

[4] Brandt J., *The Bicycle Wheel*, Avocet, Palo Alto, 1993.

NANOCOMPOSITE MICROBEAMS FOR SENSING APPLICATIONS

Marek Cetraro[1], Walter Lacarbonara [*1], and Giovanni Formica[2]
[1]*Department of Structural and Geotechnical Engineering, Sapienza University of Rome, Rome, Italy*
[2]*Department of Studies on Structures, Rome Tre University, Rome, Italy*

Summary The nonlinear dynamic behavior of nanocomposite microbeams excited near the primary resonance of the lowest modes is investigated towards wide-band mass sensing applications. The aim of the study is to exploit and expand the frequency bandwidth of the microdevice taking into account both the nonlinear bending effect of the frequency response and the significant frequency shift of the frequencies due to the variation of carbon nanotubes (CNTs) volume fraction, a control parameter in the process design of the nanocomposite material. A nonlinear inextensible Euler-Bernoulli model is employed to describe the large bending motions [1], and the Ehelby-Mori-Tanaka theory [2] is used to obtain an equivalent elastic law for the employed two-phase material. The nonlinear equation of motion is discretized via the Galerkin method, the eigenvalues analysis is carried out to detect the frequency shift and the nonlinear frequency response is unfolded and characterized using a pathfollowing technique.

INTRODUCTION

A great deal of research is being focused on the design and manufacturing of microdevices such as accelerometers, gyroscopes, microswitches for electronic circuits, gas sensors, miniaturized devices for structural health monitoring and signal filtering. A lot of these microelectromechanical (MEMS) devices can be realized using microbeams designd to operate under static or dynamic conditions near resonances.
An example of a micromechanical resonant gas sensor was proposed in [3] to perform high-quality measurements of the level of matter in rarefied chemical vapors. The microcantilever was designed so that a portion of its surface could absorb a specific type of molecules (matter) which, in turn, shifts the resonance frequency. Thus the frequency shift is used as indirect measure of the level of matter in the gas in which the beam oscillates. A nonlinear study of a gas sensor was presented in [4] where both the static and dynamic behaviors of the electrostatically actuated device were studied to avoid the pull-in which would prevent the sensor from working.

EQUATION OF MOTION

For an inextensible Euler-Bernoulli nanocomposite beam (see Fig. 1 left), the full nonlinear equation of motion expanded up to third order is given by the following nondimensional integral-partial-differential equation [1]:

$$\begin{aligned}
&\ddot{v}\left(1-\frac{1}{2}(\partial_s v)^2\right)+\partial_s v\int_0^s\left((\partial_{\xi_1}\dot{v})^2+\partial_{\xi_1}v\partial_{\xi_1}\ddot{v}\right)d\xi_1-\partial_{ss}v\int_s^1\left(\int_0^{\xi_2}\left((\partial_{\xi_1}\dot{v})^2+\partial_{\xi_1}v\partial_{\xi_1}\ddot{v}\right)d\xi_1-\ddot{v}\partial_{\xi_2}v\right)d\xi_2+\\
&+2\zeta\omega_{01}\partial_t v+k(\phi_{\mathrm{C}},\,E_{\mathrm{M}},\,\nu_{\mathrm{M}},\,E_{\mathrm{C}},\,\nu_{\mathrm{C}})\partial_{ss}\left(\partial_{ss}v+\frac{1}{2}(\partial_s v)^2\partial_{ss}v\right)-k(\phi_{\mathrm{C}},\,E_{\mathrm{M}},\,\nu_{\mathrm{M}},\,E_{\mathrm{C}},\,\nu_{\mathrm{C}})\partial_{ss}v\int_s^1(\partial_{\xi_2\xi_2}v\partial_{\xi_2\xi_2\xi_2}v)\,d\xi_2\\
&=f_1\left(1-\frac{1}{2}(\partial_s v)^2\right)+\partial_{ss}v\int_s^1(f_1\partial_{\xi_2}v)\,d\xi_2
\end{aligned}\tag{1}$$

where v represents the bending displacement, k is the equivalent nondimensional bending stiffness that is a nonlinear function of the CNTs volume fraction ϕ_c, the Young modulus and Poisson coefficients of the polymer hosting matrix (E_{M}, ν_{M}) and CNTs (E_{C}, ν_{C}). The 3D constitutive equations for the nanocomposite reduced to a plane stress state (Saint-Venant conjecture) are used to obtain the generalized stress resultants in terms of the beam generalized strains.

EIGENVALUE AND FREQUENCY RESPONSE ANALYSIS

The eigenvalue problem was first solved varying the volume fraction of CNTs. The results in Fig. 1 show that the frequencies increase with increasing CNTs volume fraction while no appreaciable differences exist using different polymeric matrices such as PEEK or Epoxy.
The frequency-response curves for the lowest three modes, for different excitation levels, are reported in Fig. 2 portraying a hardening behavior of the first mode and a softening behavior of the second mode. Moreover, Fig. 2 (right) shows a number of frequency-response curves obtained, at a given excitation amplitude, for various volume fractions. The peaks of the resonance curves decrease with the growth of CNTs volume fraction. A closed-form formula, useful for design, that predicts the peak resonance amplitudes was obtained. The (dashed) curve shown in Fig. 2 is an excellent approximation of the microbeam behavior also in the nonlinear range.

*Corresponding author. Email: wlater.lacarbonara@uniroma1.it

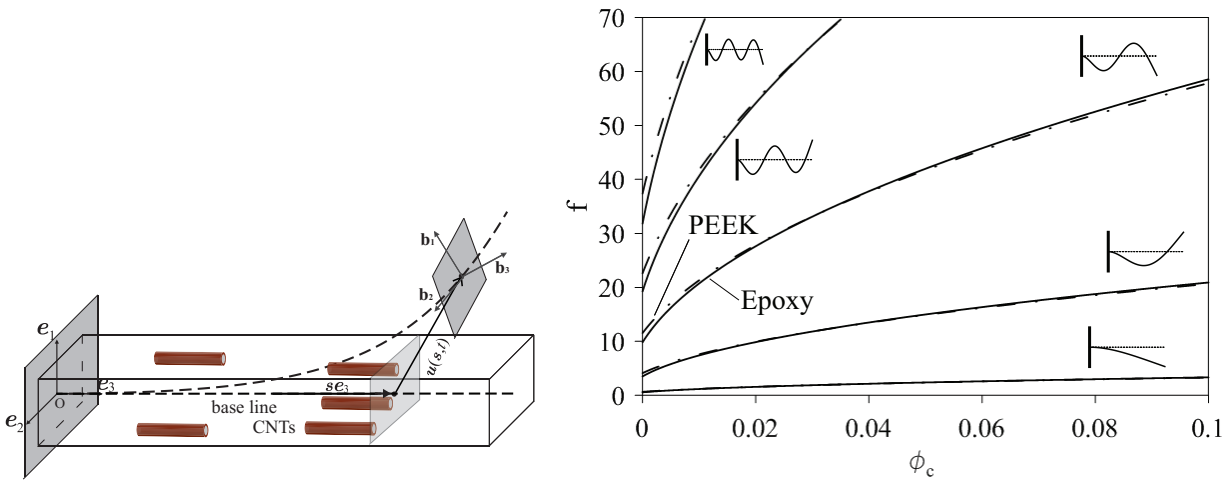

Figure 1: Carbon nanotube composite microbeam model (left). Variation of the lowest five nondimensional beam frequencies with the CNTs volume fraction. The solid line indicates Epoxy nanocomposite microbeams, while the dotted-dashed line describes PEEK nanocomposite microbeams.

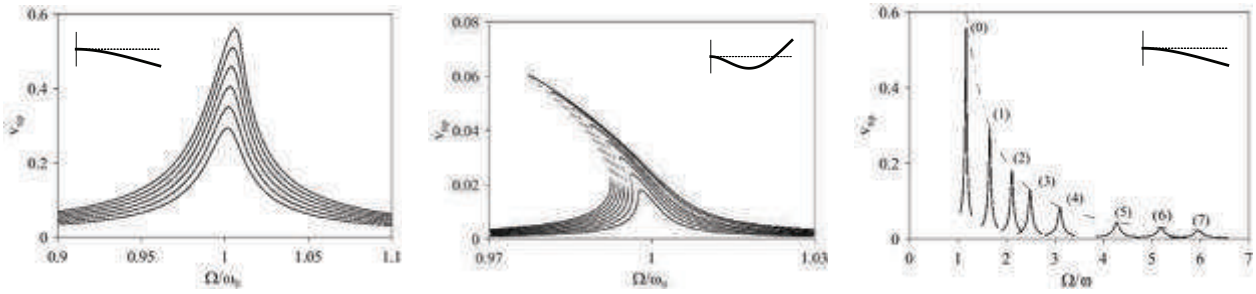

Figure 2: Frequency-response curves of the lowest two modes of the micro cantilever for fixed values of CNTs volume fraction ($\phi_c = 0.1\%$), for different excitation amplitudes (left). ω_0 is the first natural frequency, Ω is the excitation frequency.

CONCLUSIONS

The eigenvalue and path following analyses of nanocomposite microbeams in large-amplitude bending showed that the frequency bandwidth of the device, thought as a microresonator sensor, can be expanded using both the frequency shift due to variations of CNTs volume fraction and the nonlinear bending of the frequency-response curves. Experimental work is being carried out starting from the fabrication of arrays of microbeams.

References

[1] Lacarbonara W.: Nonlinear structural mechanics: theory, dynamical phenomena and modeling. Springer Science & Business Media, 2013.

[2] Formica G., Lacarbonara W., Alessi R.: Vibrations of carbon nanotube-reinforced composites. Journal of sound and vibration 329:1875-1889, 2010.

[3] Yu F., Yu H., Xu P., Li X.: Precise extension-mode resonant sensor with uniform and repeatable sensitivity for detection of ppm-level ammonia. Journal of Micromechanics and Microengineering 24, 2014.

[4] Nayfeh A.H., Ouakad H.M., Najar F., Choura S., Abdel-Rahman E.M.: Nonlinear dynamics of a resonant gas sensor. Nonlinear Dynamics 59: 607-618, 2010

ELASTIC WAVE PROPAGATION IN HIGHLY DEFORMABLE LAYERED MATERIALS

Pavel I. Galich*[1] and Stephan Rudykh[1]
[1]*Department of Aerospace Engineering, Technion – Israel Institute of Technology, Haifa, Israel*

Summary Elastic wave propagation in highly deformable layered matter with compressible neo-Hookean phases is investigated. The explicit relations of the phase and group velocities in the finitely deformed incompressible layered materials are derived by utilizing an exact analytical solution for the finitely deformed incompressible laminates. Moreover, based on the expressions of the phase velocities for the finitely deformed compressible homogeneous material, the phase velocities of pressure and shear waves propagating orthogonally to the layers in the finitely deformed compressible laminates are estimated.

INTRODUCTION

Elastic waves have been treated in detail due to doubtless significance for many fields: ranging from seismology to medicine. The change in the media properties, stress-strain state and stiffening effects [1] can significantly transform elastic wave propagation. Remarkably, even relatively simple homogeneous materials can be utilized to achieve acoustic functionalities such as disentangling of pressure and shear waves by application of the certain deformation [2]. Recently, fabricated materials (referred as acoustic metamaterials) have attracted considerable attention due to acoustic properties which are not commonly observed in natural materials, i.e. negative elastic moduli or/and mass density (which can result in a negative refractive index, for example). Particular case of these metamaterials is capable of large deformations materials, referred as the soft metamaterials, which open the promising opportunities of manipulating the acoustic properties by deformation. Thus, elastic waves can be tuned by designing microstructures, which can be further actively controlled by external stimuli, for example, by mechanical loading [3], electric or magnetic field.

The heterogeneity of the matter together with the deformations can stimulate the development of elastic instabilities [4, 5]. These sudden and reversible geometry transformations can be employed to change the acoustic characteristics [3]. On the other hand, mechanical stimulus applied to the inhomogeneous media influences elastic waves by the change in the local properties, for example, local softening/hardening. We show that the local deformations significantly influence elastic wave propagation even if the geometry of the material does not tangibly change [6].

ANALYSIS

In this work, we focus on the metamaterials with the periodic microstructures (i.e. phononic crystals), which have attracted considerable attention recently due to possibility of phononic band gaps (BGs). A specific case of the generic periodic materials is the class of layered structures (see Fig. 1). Layered phononic crystals are easy to build in contrast to sophisticatedly microstructured ones, while ,as we will show later, they can produce similar acoustic characteristics, actively tuned by the application of deformation.

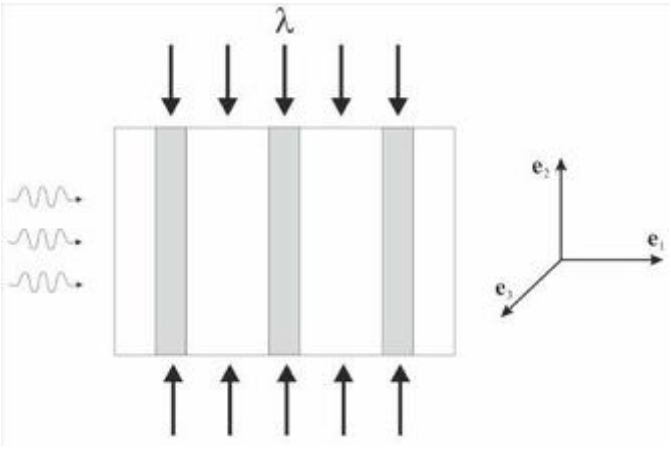

Figure 1: Schematic representation of the periodic layered material made out of two alternating phases with volume fractions v_a and $v_b = 1 - v_a$.

*Corresponding author. Email: galich@technion.ac.il

To account for the finite deformation non-linear effects as well as for the material non-linearity, we analyse the wave propagation in terms of the incremental small-amplitude motions superimposed on a finitely deformed state. By utilizing an exact analytical solution for the finitely deformed incompressible laminates, we derive explicit relations of the phase and group velocities in the finitely deformed layered materials. Moreover, based on the expressions of phase velocities for the finitely deformed compressible homogeneous material, we estimate the phase velocities of pressure and shear waves propagating orthogonally to the layers in the finitely deformed compressible laminates.

The explicit relations for phase and group velocities simplify construction of the slowness and energy curves clarifying behaviour of elastic waves in the finitely deformed laminates. The example of slowness and energy curves for in-plane (with polarization lying in plane $\mathbf{e}_1 - \mathbf{e}_2$) shear wave in the laminate undergoing in-plane deformation (the average deformation gradient is equal to $\mathbf{F} = \lambda^{-1}\mathbf{e}_1 \otimes \mathbf{e}_1 + \lambda \mathbf{e}_2 \otimes \mathbf{e}_2 + \mathbf{e}_3 \otimes \mathbf{e}_3$) are presented on Fig. 2. Specifically, in-plane extension decreases phase velocity of the in-plane shear wave propagating orthogonally to the layers, and increases it in case when the wave propagates along the layers; while the in-plane compression influences phase velocity of the in-plane shear wave in an opposite way. Slowness and energy curves on Fig. 2 clearly indicate that the elastic wave propagation strongly depends on the

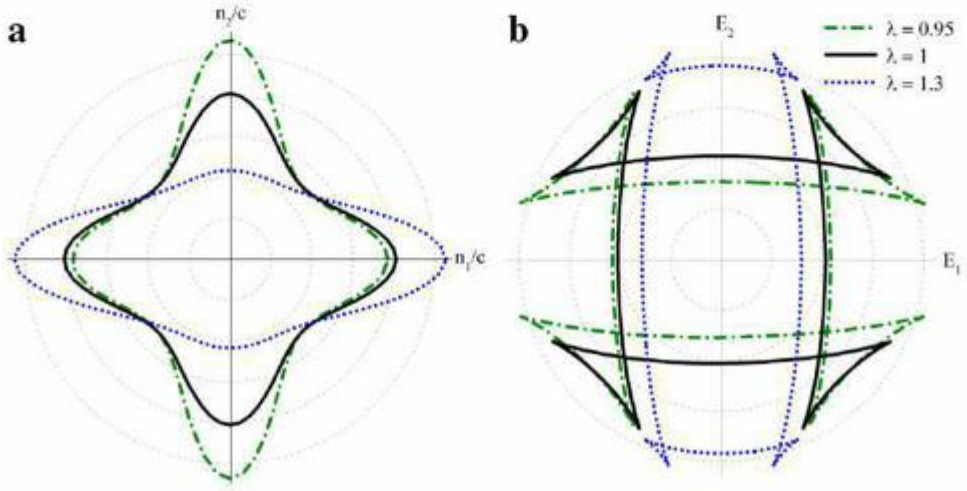

Figure 2: a) Slowness curves for the in-plane shear wave in the laminate undergoing in-plane deformation ($v_a = 0.1, \mu_a/\mu_b = 20, \rho_{0a}/\rho_{0b} = 1$, where μ_a and μ_b are the corresponding shear moduli of each layer, ρ_{0a} and ρ_{0b} are the corresponding initial densities of each layer). Scale is 0.4 per division, slowness is normalized by $\sqrt{\mu/\rho_0}$, where $\mu = v_a\mu_a + v_b\mu_b$ and $\rho_0 = v_a\rho_{0a} + v_b\rho_{0b}$. b) Energy curves for the in-plane shear wave in the laminate undergoing in-plane deformation ($v_a = 0.1, \mu_a/\mu_b = 20, \rho_{0a}/\rho_{0b} = 1$). Scale is 0.3 per division, where group velocity is normalized by $\sqrt{\rho_0/^-}$.

applied deformation and direction of wave propagation in the layered materials, however, considerable transformations in the geometry are absent.

CONCLUSIONS

We analysed elastic wave propagation in the finitely deformed layered materials with compressible neo-Hookean phases, and estimated the phase velocities of pressure and shear waves propagating orthogonally to the layers. For the finitely deformed incompressible laminates, we derived exact relations of the phase and group velocities for the in-plane and out-of-plane shear waves for all directions of wave propagation.

References

[1] Galich P. I., Rudykh S.: Influence of Stiffening on Elastic Wave Propagation in Extremely Deformed Soft Matter: From Nearly Incompressible to Auxetic Materials. Extreme Mechanics Letters. 4:156-161, 2015.

[2] Galich P. I., Rudykh S.: Comment on "Disentangling Longitudinal and Shear Elastic Waves by Neo-Hookean Soft Devices" [Appl. Phys. Lett. 106, 161903 (2015)]. Appl. Phys. Lett. 107:056101, 2015.

[3] Rudykh S., Boyce M. C.: Transforming Wave Propagation in Layered Media via Instability-Induced Interfacial Wrinkling. Phys. Rev. Lett. 112:034301, 2014.

[4] Rudykh S., deBotton G.: Instabilities of Hyperelastic Fiber Composites: Micromechanical versus Numerical Analyses. Journal of Elasticity. 106:123147, 2012.

[5] Li Y., Kaynia N., Rudykh S., Boyce M.C.: Wrinkling of Interfacial Layers in Stratified Composites. Advanced Engineering Materials. 2013, 15(10), 921926.

[6] Galich P. I., Rudykh S.: Wave Propagation in Highly Deformable Layered Phononic Crystals. In preparation, 2016.

INSTABILITIES IN DIELECTRIC ELASTOMER PLATES

Hadrien Bense[1a)], José Bico[1], Benoît Roman [1], Miguel Trejo[1], Etienne Reyssat[1]
[1]PMMH, UMR 7636 ESPCI 10 rue Vauquelin, 75321 Paris Cedex 05, France

Summary We use dielectric elastomers to mimic artificial inhomogeneous growth to observe and study mechanical instabilities.

Dielectric elastomers are part of a class of electro-active polymers that exhibit mechanical deformations when stimulated by an electric voltage. Potential applications are numerous, ranging from sensors to actuators, displays or even energy harvesting systems. The principle of dielectric elastomers is relatively simple [1]: an insulating polymeric sheet is covered on both sides with a stretchable conductive layer (e.g. carbon black), which results into a deformable capacitor. When a voltage is applied, the conductive layers convey charges with opposite signs, and are attracted to each other (fig.1). Electrostatic forces tend to squeeze the elastic sheet across its thickness, which induces lateral extension as a result of incompressibility (Poisson ratio close to ½). Such systems, when pre-stretched, have exhibited change in surface area up 200% upon the application of a uniform high voltage [2].

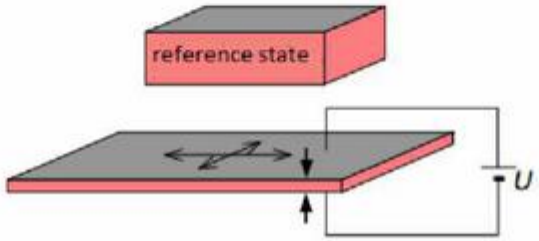

Figure 1: Principle of actuation: applying an electric field through a soft dielectric sheet compresses the material along the field and extends it in the other directions.

In most cases [1] the elastomer is strongly stretched and clamped, or submitted to large dead loads before the voltage is applied. Here, we are interested in similar systems, but without any prestrain and investigate the effect of a spatially non uniform voltage. We find that the membranes under non-uniform load undergo mechanical instabilities. Such buckling-like instabilities are not observed in other studies because of large tensile loading, but they are common in thin plates with internal stresses (such as non-uniform plastic deformation in a torn ductile plate [4] or differential growth in hydrogels [5]).
As a first step, we propose to study simple geometries, where the sample is only partially covered with the conductive coating. A disk where only the central zone or a peripheral annulus is growing would be a first example (fig. 4). These systems, despite their apparent simplicity, display surprising features. The threshold buckling is surprisingly high and the buckling pattern of the disk is strongly localized inside the active part (fig. 2). Secondary instability presenting radial wrinkles may even be observed for high voltages (fig. 3). Predicting the threshold of buckling and the main characteristics of the pattern (wavelength, extension) is complex, even in simple geometries. Linear stability analysis is not sufficient to describe our experimental observations. A non-linear analysis is indeed necessary to capture, at least qualitatively, the behavior of such systems from the buckling threshold to the evolution of the observed patterns.

[a)] Corresponding author. Email: hadrien.bense@espci.fr.

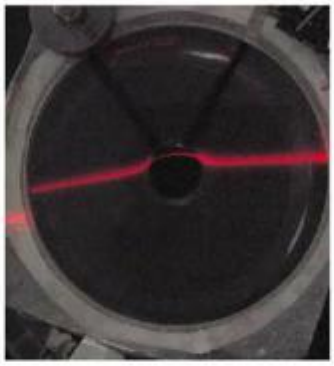

Figure 2: *Buckling of a disk. The central black region: active part (here subjected to a 4kV voltage) is surrounded by a large passive zone with clamped edges by a PVC frame. The red line is a laser sheet in razing incidence allowing us to observe the buckling. It is clear that the buckling is very strongly localized in the active region.*



Figure 3: *Secondary instability of a disk (around 5kV): apparition of radial wrinkles*



Figure 3: *Buckling of a peripheral annulus (V=3kV). When voltage is applied, the active part (black annulus here) increases its area, but as it is constrained inside a passive part (appearing pink here) the system is unstable. For a high enough voltage, we observe a buckling instability, resulting, for an annulus, in oscillations along the active zone.*

References

[1] Z. Suo, Theory of dielectric elastomers, Acta Mechanica Solida Sinica 23, 549-578 (2010).

[2] J. Huang et al., Giant, voltage-actuated deformation of a dielectric elastomer under dead load, Applied Phys. Lett., 100, 041911 (2012) [2] T. Singh, Mechanics of Materials, Springer, Berlin, 2012.

[3] B. Audoly and A. Boudaoud, Phys. Rev. Lett. 91, Self-similar structures near boundaries in strained systems, 086105 (2003)

[4] E.Sharon, B.Roman, S. Smith and H.Swinney Geometrically induced buckling cascade observed in free sheets. Phys.Rev.E 75, 046211 (2007).

[5] Zi Lang Wu et al., Three-dimensional shape transformations of hydrogel sheets induced by small-scall modulation of internal stresses. Nat Commun. 2013;4:1586. doi: 10.1038/ncomms2549.

[a)] Corresponding author. Email: hadrien.bense@espci.fr**.**

DYNAMICS OF LONG TUBULAR CANTILEVERS IN AXIAL FLOW

Michael P. Païdoussis *

Department of Mechanical Engineering, McGill University, Montreal, Québec, Canada

Summary The dynamics of slender cylinders in axial flow is considered, including very long cylinders. Both the conventional flow configuration, with the flow from the supported end towards the free one, and the reverse flow case are discussed. The system is subject to both static and dynamic instabilities.

INTRODUCTION

Among the many engineering applications involving long cylinders in axial flow, here we mention two: (i) the 'acoustic streamers' used in underwater oil and gas exploration and (ii) pre-assembled pipelines towed underwater for installation at a desired location. Such systems are very slender and flexible and they are subject to static and dynamic instabilities if the axial flow velocity is sufficiently high.

The first combined experimental and linear theoretical study of the system dynamics has been done by Païdoussis in 1966 and 1973 [1,2]. The dynamics has been re-examined by nonlinear theory in 2002 [3,4]. The nonlinear dynamical behaviour is qualitatively similar to that predicted by linear theory [4].

DYNAMICS

Consider a cylinder of cross-sectional area A, length L, diameter D, mass per unit length m, and flexural rigidity EI, in a fluid of density ρ flowing axially around the cylinder with flow velocity U. Figure 1 shows the system under consideration, with a drogue at the free end. Placing the origin at the downstream end, for a horizontal system, neglecting pressurization and gravity effects as well as dissipative forces, the simplest non-dimensional form of the linear equation of motion [5] is

$$\frac{\partial^4\eta}{\partial\xi^4}+\frac{\partial}{\partial\xi}\left[u^2\left(1-\tfrac{1}{2}c_b+\tfrac{1}{2}\varepsilon c_T\xi\right)\frac{\partial\eta}{\partial\xi}\right]+\frac{1}{2}\varepsilon c_T\left(\frac{c_N}{c_T}-1\right)u^2\frac{\partial\eta}{\partial\xi}$$

$$\overline{2}\varepsilon c_T\left(\frac{c_N}{c_T}\right)\beta^{1/2}u\overline{\partial\tau}+2\beta^{1/2}u\frac{\partial^2\eta}{\partial\xi\partial\tau}+\overset{2}{\partial\tau^2}=0, \tag{1}$$

where $u=(\rho A/EI)^{1/2}UL$ is the dimensionless flow velocity, $\eta=y(x,t)/L,\ \xi=x/L,\ \beta=\rho A/(\rho A+m)$, $\varepsilon=L/D,\ \tau=\{EI/(\rho A+m)\}^{1/2}t/L^2$; c_N and c_T are the coefficients of the viscous forces acting on the cylinder in the normal and longitudinal direction, respectively, and c_b a base drag coefficient.

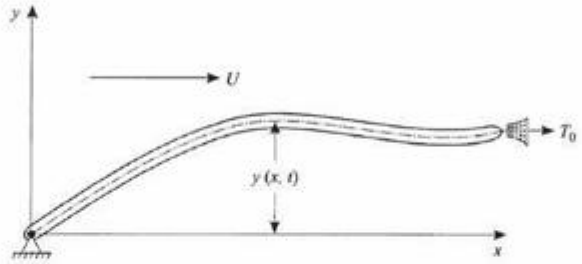

Figure 1: Pinned-free cylinder in axial flow.

The free end of the cylinder is supposed to be terminated by a short ogival end-piece of length $x_e << L$. The forces on that end-piece result in a non-zero shear force, giving rise to the boundary condition

$$\left[\frac{\partial^3\eta}{\partial\xi^3}+fu\left(\beta^{1/2}\frac{\partial\eta}{\partial\tau}+u\frac{\partial\eta}{\partial\xi}\right)\right]_{\xi=0}=0, \tag{2}$$

*

where $\chi_e = x_e/L$. The parameter f is related to the degree of streamlining of the free end. Thus, $f \to 1$ for a well-streamlined end, and $f \to 0$ for a blunt one; generally, $f < 1$. It is also supposed that the bending moment at the free end is approximately equal to zero: $(\partial^2\eta/\partial\xi^2)_{\xi=0} = 0$.

If the flow past the cylinder is laterally confined, the added mass is no longer ρA but $\chi\rho A$, where $\chi = [(D_{ch}^2+D^2)/(D_{ch}^2 \nearrow D^2)] > 1$, D_{ch} being the diameter of the confining flow channel, and equations (1) and (2) need to be slightly modified; e.g., the first term in square brackets in (1) becomes $\chi u^2(\partial\eta/\partial\xi)$ rather than $u^2(\partial\eta/\partial\xi)$. With increasing χ the cylinder is generally less stable.

Typically, the system with a pinned upstream end develops stationary yawing and divergence at low flow velocities and flexural instabilities at higher ones (Figure 2). For a clamped rather than pinned upstream end, stationary yawing does not arise, but the flexural instabilities do. An interesting feature of the dynamics is that there is a location along the cylinder where the flow-induced tension vanishes, and downstream of that point the cylinder is under compression [5].

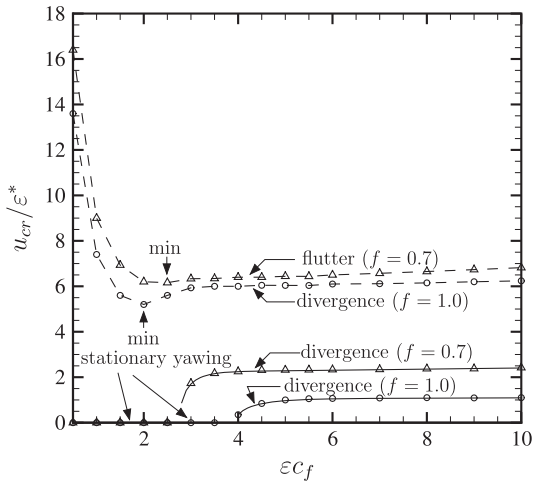

Figure 2: The dimensionless critical flow velocity u_{cr} for divergence and flutter, divided by $\varepsilon^* = \frac{1}{2}\varepsilon c_f$, where $c_f = c_N = c_T$ is the frictional drag coefficient.

Early work suggested that the system remains stable for all flow velocities if it is sufficiently long. More recently, however, it was found that flutter may occur even for very long systems [5,6], provided that the free end is not too blunt, as seen in Figure 2. The oscillatory motion is concentrated near the free end.

The theoretical predictions of the dynamics and stability are in good agreement with experimental observations.

Interesting dynamics is also displayed by the 'reverse flow' system, where the flow is from the free downstream end towards the supported end [7,8]. Flutter-like motions occur at low flow velocities ($u = 0.3 \nearrow 0.$). At higher flow velocities, the oscillation ceases, and eventually a static divergence takes place. Agreement between theory and experiment is good qualitatively, and reasonably good quantitatively.

CONCLUSION

The dynamics of a cantilevered cylinder (truly cantilevered or with the upstream end pinned) in forward and reverse axial flow has been studied, and it is shown that the system is subject to both static and dynamic instabilities, with the static ones occurring first for forward flow and last for reverse flow.

Support of this research by the NSERC of Canada and SMRI is gratefully acknowledged.

References

[1] Païdoussis M.P.: J. Fluid Mech 26:717-736 and 737-751, 1966.
[2] Païdoussis M.P.: J. Sound Vib 29:365-385, 1973.
[3] Lopes J-L., Païdoussis M.P., Semler C.: J. Fluids Struct 16:715-737.
[4] Semler C., Lopes J.-L., Augu N., Païdoussis M.P.: J. Fluids Struct 16:739-759.
[5] de Langre E., Païdoussis M.P., Doaré O., Modarres-Sadeghi Y.: J. Fluid Mech 571: 371-389, 2007.
[6] Kheiri M., Païdoussis M.P.: J. Fluids Struct 55:204-217, 2015.
[7] Rinaldi S., Païdoussis M.P.: J. Fluids Struct 28:167-179, 2012.
[8] Païdoussis M.P.: Fluid-Structure Interactions, Vol. 2, 2nd edition, Academic Press, 2016.

STABILITY AND BUCKLING OF FLAT CIRCULAR CONFIGURATIONS OF A CLOSED, INTRINSICALLY CURVED FILAMENT SPANNED BY A FLUID FILM

T. M. Hoang and Eliot Fried*

Okinawa Institute of Science and Technology Graduate University, Onna, Okinawa, Japan 904-0495

Summary We study stability and buckling behavior of generic flat circular configurations of flexible but inextensible loops made from filaments with intrinsic curvature and spanned by liquid films. Three dimensionless parameters govern stability and buckling. Of these, the dimensionless surface tension of the liquid film and the ratio of torsional rigidity to flexural rigidity of the filament are familiar from previous works. The remaining parameter, namely the dimensionless intrinsic curvature of the filament, captures the influence of the curvilinear rest configuration. In-plane and out-of-plane buckling modes corresponding to stable solution branches that bifurcate from the branch of flat circular solutions are found to exist. The critical value of the dimensionless surface tension needed to induce out-of-plane buckling is found to be less than that needed to induce in-plane buckling. The destabilizing influence of the intrinsic curvature can nevertheless be countered by increasing the torsional rigidity relative to the flexural rigidity.

PRELIMINARIES

Consider a flexible loop made from a filament, with uniform circular cross section and mechanical properties, spanned by a liquid film. Let the filament be modeled as an inextensible and unshearable rod with midline C. Suppose that the rod has intrinsic curvature κ_0, bending rigidity $a > 0$, and twisting rigidity $c > 0$. Additionally, let the liquid film be modeled as a surface S endowed with uniform tension $\sigma > 0$. Assume that the curve C has no points of self-contact, that the surface S is orientable, and that the midline C of the rod and the boundary ∂S of S coincide, so that $C = \partial S$.

Let $\boldsymbol{t}$ denote a unit vector field to C and introduce a consider field $\boldsymbol{d}$ satisfying

$$|\boldsymbol{d}| = 1 \qquad \text{and} \qquad \boldsymbol{d} \cdot \boldsymbol{t} = 0. \tag{1}$$

Consistent with the special Cosserat theory of rods, the orthonormal triad $\{\boldsymbol{t}, \boldsymbol{d}, \boldsymbol{t} \times \boldsymbol{d}\}$ provides a material frame for C. By $(1)_2$, $\boldsymbol{d}$ lies in the cross-section of the rod and admits a representation

$$\boldsymbol{d} = \cos\psi\, \boldsymbol{p} + \sin\psi\, \boldsymbol{b} \tag{2}$$

in terms of the normal and binormal elements $\boldsymbol{p}$ and $\boldsymbol{b}$ of the Frenet frame $\{\boldsymbol{t}, \boldsymbol{p}, \boldsymbol{b}\}$ of C. Using a prime to denote differentiation with respect to arclength along C, consider the curvature vector $\boldsymbol{\kappa}$ and the twist density ω of C, as defined by

$$\boldsymbol{\kappa} = \boldsymbol{t}' \qquad \text{and} \qquad \omega = (\boldsymbol{d} \times \boldsymbol{d}') \cdot \boldsymbol{t}. \tag{3}$$

Let $\boldsymbol{n}$ denote a unit normal field for S, in which case the mean curvature S by given by

$$H = -\frac{1}{2}\mathrm{div}_S \boldsymbol{n}, \tag{4}$$

where div_S denotes the surface divergence operator on S.

Bearing in mind the foregoing assumptions and notation, suppose that the total free-energy E of the system is of the particular form

$$E = \int_C \frac{1}{2}(a|\boldsymbol{\kappa} - \kappa_0 \boldsymbol{d}|^2 + c\omega^2) + \int_S \sigma. \tag{5}$$

On denoting the radius of the loop by R, simple considerations lead to three potentially significant dimensionless parameters:

$$\alpha = \frac{c}{a} > 0, \qquad \beta = R\kappa_0 \geq 0, \qquad \eta = \frac{\sigma R^3}{a} > 0. \tag{6}$$

EQUILIBRIUM CONDITIONS

Granted that the system is mechanically isolated, the equilibrium conditions can be derived by requiring that the first variation δE of E obeys $\delta E = 0$. These amount to a condition

$$H = 0 \tag{7}$$

on S along with two conditions

$$(a((\kappa - \kappa_0 \cos\psi)\boldsymbol{p})' - c\omega\kappa\boldsymbol{b} - c(\kappa^{-1}\omega'\boldsymbol{b})' - \lambda\boldsymbol{t})' + \sigma\boldsymbol{t} \times \boldsymbol{n} = \boldsymbol{0} \qquad \text{and} \qquad c\omega' = a\kappa_0\kappa\sin\psi, \tag{8}$$

on C. In (8), λ is a Lagrange multiplier needed to ensure that the constraint of inextensibility $|\boldsymbol{t}| = 1$ holds, $\kappa = |\boldsymbol{\kappa}|$. The equilibrium conditions (7)–(8) are satisfied for any flat circular configuration of the system. For $\kappa_0 = c = 0$ the equilibrium conditions (7)–(8) reduce to those of Giomi & Mahadevan [1] and Chen & Fried [2]. For $\kappa_0 = 0$ the equilibrium conditions (7)–(8) become those of [3].

*Corresponding author. Email: eliot.fried@oist.jp

STABILITY RESULT

An equilibrium state in which S has unit normal $\boldsymbol{n}$ and C has unit tangent $\boldsymbol{t}$, unit normal $\boldsymbol{p}$, director $\boldsymbol{d}$ with the form (2), and curvature κ and twist density ω determined by $(3)_2$ is stable if and only if the second variation $\delta^2 E$ of E obeys

$$\delta^2 E = \int_C a((1-\kappa_0\kappa^{-1}\cos\psi)|\boldsymbol{u}''|^2 + \kappa_0(\kappa^{-1}\cos\psi\,(\boldsymbol{p}\cdot\boldsymbol{u}'')^2 + 2\sin\psi(\boldsymbol{p}\cdot\boldsymbol{u}'') + \kappa\cos\psi(\delta\psi)^2))$$
$$+ \int_C \lambda|\boldsymbol{u}'|^2 + c((\delta\omega)^2 - \omega\boldsymbol{t}\cdot(\boldsymbol{u}'\times\boldsymbol{u}'') - \omega'\delta(\kappa^{-1}\boldsymbol{b})\cdot\boldsymbol{u}'') + \int_S \sigma((\mathrm{div}_S\boldsymbol{u})^2 - \mathrm{tr}\,((\nabla_S\boldsymbol{u})^2) + |(\nabla_S\boldsymbol{u})\boldsymbol{n}|^2) \geq 0 \quad (9)$$

for all $\boldsymbol{u} = \delta\boldsymbol{r}$, where $\boldsymbol{r}$ denotes any parameterization $\boldsymbol{r}$ of S with restriction to C satisfying $\boldsymbol{r}' = \boldsymbol{t}$. For a loop made from an intrinsically straight filament, $\kappa_0 = 0$ and (9) simplifies to a condition derived by Biria & Fried [4]. In particular, the stability condition (9) is satisfied for a flat circular configuration of the system if the following inequalities hold:

$$0 \leq \eta \leq \min\left\{3, 6\left(1 - \frac{(\alpha+\beta)\beta}{4\alpha+\beta}\right)\right\}, \qquad 0 \leq \frac{(\alpha+\beta)\beta}{4\alpha+\beta} \leq 1. \quad (10)$$

When $\kappa_0 = 0$, (10) reduces to the condition $\eta = 3$ obtained by Giomi & Mahadevan [1], Chen & Fried [2], and Biria & Fried [4]. Hereafter, we assume that $\kappa_0 > 0$.

BIFURCATION RESULT

Buckling occurs if and only if the linearization of the equilibrium equations (7)–(8) about a trivial solution (i.e. a flat circular configuration) has a nonvanishing solution. This yields to the following results:

A stable bifurcation from the flat circular solution branch to a flat noncircular solution branch occurs at $\eta = 3$ if the intrinsic curvature κ_0 satisfies

$$\kappa_0 \leq \frac{1}{2R}\left(\sqrt{\alpha^2+7\alpha+\frac{1}{4}} - \alpha + \frac{1}{2}\right). \quad (11)$$

From (11), the maximum allowable value of κ_0 corresponding to the onset of bifurcation occurs increases monotonically with the ratio $\alpha = c/a$. Increasing c relative to a therefore increases the value of κ_0 at which the bifurcation from the trivial solution branch to the flat noncircular solution branch occurs.

Alternatively, a stable bifurcation from the flat circular solution branch to a saddle-like out-of-plane solution branch occurs at $\eta = 6\big(1 - \frac{(\alpha+\beta)\beta}{4\alpha+\beta}\big) < 3$ if the intrinsic curvature κ_0 satisfies

$$\frac{1}{2R}\left(\sqrt{\alpha^2+7\alpha+\frac{1}{4}} - \alpha + \frac{1}{2}\right) \leq \kappa_0 \leq \frac{1}{2R}\left(\sqrt{\alpha^2+14\alpha+1} - \alpha + 1\right). \quad (12)$$

Since the critical value of η in this case increases monotonically with α for any choice of $\beta > 0$ but decreases monotonically with $\beta > 0$ for any choice of α, and since the permissible range of κ_0 determined by (12) increases monotonically with α, it follows that the destabilizing influence of κ_0 can be countered by increasing c relative to a.

CONCLUSIONS

We synopsized results concerning the stability and buckling behavior of a generic flat circular configuration consisting of a liquid film spanning a flexible loop made from a filament with a curvilinear rest configuration characterized by the presence of intrinsic curvature. We found in-plane and out-of-plane buckling modes. The critical value of the dimensionless surface tension required to induce out-of-plane buckling is less than that required to induce in-plane buckling. However, the destabilizing influence of the intrinsic curvature of the filament can be neutralized by increasing the torsional rigidity relative to the flexural rigidity.

References

[1] Giomi L., Mahadevan L.: Minimal surfaces bounded by elastic lines. P. Roy. Soc. Lond. A Mat. 468:1851–1864, 2012.

[2] Chen Y.-C., Fried E.: Stability and bifurcation of a soap film spanning a flexible loop. J. Elasticity 116:75–100, 2014.

[3] Biria A., Fried E.: Buckling of a soap film spanning a flexible loop resistant to bending and twisting. P. Roy. Soc. Lond. A Mat. 470:20140368, 2014.

[4] Biria A., Fried E.: Theoretical and experimental study of the stability of a soap film spanning a flexible loop. Int. J. Eng. Sci. 94:86–102, 2015.

TRANSITION WAVES IN PERIODIC MULTI-STABLE MECHANICAL SYSTEMS

Dennis M. Kochmann*[1], Neel Nadkarni[1], and Vidyasagar Vidyasagar[1]
[1]*Graduate Aerospace Laboratories, California Institute of Technology, Pasadena, CA 91125, USA*

Summary Multistable mechanical systems possess more than one stable equilibrium configuration; examples include buckling structures as well as crystalline solids undergoing solid-solid phase transitions or ferroelectric switching. Under external loading, such systems can produce strongly-nonlinear transition waves that switch between equilibria; this process is commonly accommodated by interfacial motion (e.g., of phase boundaries or domain walls). We will derive the fundamental underlying dynamic theory and demonstrate – through simulations and experiments – that it applies equally to the snapping of periodic buckled structures and ferroelectric ceramics.

INTRODUCTION: INSTABILITY-INDUCED TRANSITION WAVES

Instabilities in solids and structures are ubiquitous across length and time scales, and our engineering design principles commonly aim to prevent those. In recent years, engineering mechanics has undergone a paradigm shift towards taking advantage of instabilities. At the core of all instabilities lies a non-convex energy landscape that is responsible, e.g., for phase transitions, localization, and structural buckling. Among others, such systems can give rise to strongly nonlinear transition waves that switch between stable configurations (e.g., between phases or between buckling modes). Understanding the underlying dynamic phenomena enables us to understand the physics of various microscale phenomena as well as to create new interesting mechanical systems that exploit the effects of instability. Therefore, we have developed the underlying theory and studied its application to selected examples including periodic snapping structures for mechanical logic and nonlinear diodes, and domain switching in ferroelectric ceramics.

UNDERLYING THEORY OF NONLINEAR DYNAMICS

We consider a periodic lattice whose elastically-connected elements are attached to nonlinear multi-stable potential energy landscapes. Examples of this scenario include periodic chains of elastically-coupled masses attached to buckled beams [1, 2] as well as ferroelectric ceramics whose potential energy is multi-welled with respect to the atomic-scale polarization [3]. As a result, phase or domain boundaries exist which separate regions of homogeneous configurations. Under external loads, those boundaries move, thereby producing a kink transition wave whose propagation gradually switches the system locally from one stable configuration into another. This process is observed in a myriad of physical systems spanning length and time scales from atomistics to macroscopic structures. Based on the nature of the physical process, such systems are characterized as non- or weakly-dissipative, dissipative, or diffusive. Non- or weakly-dissipative models have been used to explain phenomena such as dislocation motion, ferromagnetic domain wall motion, dynamics of CNT foams, or lattices of bistable structures [1]. By contrast, diffusive or dissipative kinetics play an essential role in describing the physics of, e.g., ferroelectric domain switching, magnetic flux propagation in Josephson junctions with tunneling losses, pulse propagation in cardiophysiology and neurophysiology, sliding friction, or under-damped commensurate phase transition to name but a few (see [4] and references therein). Although numerous theoretical studies have been devoted to characterizing the motion of phase boundaries particularly in 1D periodic physical, chemical or biological systems, the lessons learned almost exclusively apply to special cases only, owing to the variety of nonlinear interaction potentials and non-convex on-site potentials. Here, we present a surprisingly simple universal energy law that applies to all of the above dissipative and diffusive systems and uniquely links speed and profile of transition waves to the energetics and kinetics of the periodic system. In non- or weakly-dissipative systems, the energy is described well by its Hamiltonian which remains approximately constant as the wave propagates. However, energy transport in dissipative or diffusive lattices is not well understood at present. Therefore, we focus on the dynamics of diffusive and dissipative systems and derive an explicit energy transport law for such lattices [4].

APPLICATIONS: SNAPPING STRUCTURES AND FERROELECTRIC SWITCHING

We consider two particular applications. On the one hand, mechanical transition waves are found in structures undergoing coordinated snap-buckling. Such a scenario arises, e.g., in periodic chains of elastically-coupled masses, where each mass is exposed to a bistable on-site potential (e.g., because it is attached to a pre-buckled membrane, as shown in Fig. 1). Despite the highly-complex geometry and the strongly-nonlinear interactions between the individual masses and the nonlinear potentials of the buckled members, the resulting transition wave obeys a surprisingly simple linear scaling law which relates the kinetic energy of the wave, the wave speed, the linear damping inherent in the system, and the difference in potential energy between the two buckled states of the bistable elements.

*Corresponding author. Email: kochmann@caltech.edu

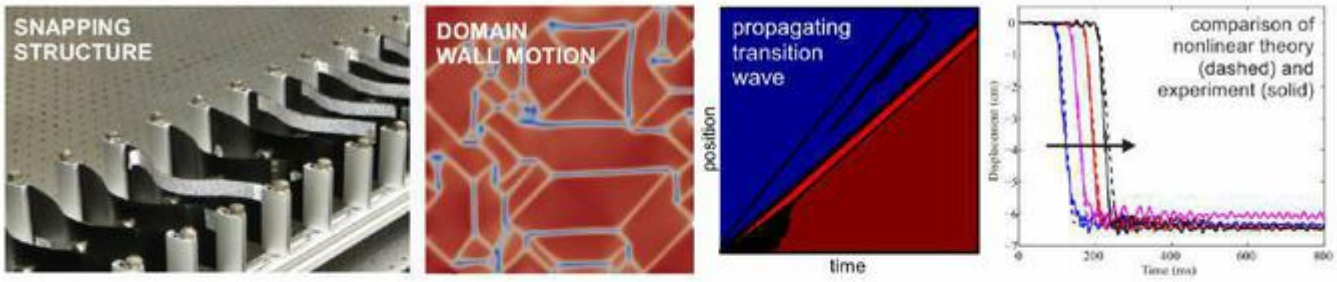

Figure 1: Demonstration of nonlinear transition waves in periodic structures (shown here is a chain of elastically-coupled snapping membranes [2]) and in ferroelectric ceramics (shown is a phase-field-simulated domain structure). Upon excitation by means of an impulse or an applied electric field, both systems produce nonlinear transition waves whose dynamics are described by the model presented here.

On the other hand, we consider domain switching in ferroelectric ceramics (such as $BaTiO_3$ or PZT whose domain switching characteristics have been examined in our laboratory [5]). This process accommodates the (re)poling of ferroelectrics under large applied electric fields; Fig. 1 illustrates a simulated domain structure under quasistatic conditions in PZT. The motion of a planar domain wall can be regarded as a transition wave in the very same way as the snapping structures above, and the same fundamental theory applies. Therefore, we will show how our theory predicts the domain wall speed, among others, and provides insight into the microstructural kinetics which are hardly accessible through experiments.

CONCLUSIONS

We present a fundamental theory of transition waves in dissipative and diffuse periodic systems that apply across scales and, in particular, that apply equally to microstructural processes such as ferroelectric domain switching and macroscopic structural phenomena such as the collective snapping motion of coupled bistable elastic members. The new theory is verified numerically and experimentally for a variety of systems.

References

[1] Nadkarni N., Daraio C., Kochmann D.M.: Dynamics of a periodic structure containing bistable elastic elements: from elastic to solitary wave propagation. Phys. Rev. E 90:023204, 2014.

[2] Nadkarni N., Arrieta A.F., Chong C., Kochmann D.M., Daraio C.: Unidirectional Transition Waves in Bistable Lattices. Under review, 2016.

[3] Zhang W., Bhattacharya K.: A computational model of ferroelectric domains. part i: model formulation and domain switching. Acta Mater. 53:185-198, 2005.

[4] Nadkarni N., Daraio C., Abeyaratne R., Kochmann D.M.: A universal energy transport law for dissipative and diffusive phase transitions. Under review, 2016.

[5] Wojnar C.S., le Graverend J.-B., Kochmann, D.M.: Broadband control of the viscoelasticity of ferroelectrics via domain switching. Appl. Phys. Lett. 105:162912, 2014.

MODAL ANALYSIS OF STRUCTURES IN PERIODIC STATES

Barend Bentvelsen[1,2] and Arnaud Lazarus *[1,2]
[1]*Sorbonne Universités, UPMC Univ Paris 06, UMR 7190, Inst Jean Le Rond d'Alembert, F-75005, Paris, France*
[2]*CNRS, UMR 7190, Inst Jean Le Rond d'Alembert, F-75005, Paris, France*

Summary This presentation focuses on the numerical computation of linear vibrational modes, or Floquet Forms, of mechanical systems in periodic states such as rotating machineries with imperfections or any structures that are in compressive or tensile periodic states. To make our point, we present an original spectral method through the fundamental example of the oscillations of a 2D bi-articulated bar submitted to a periodic compressive load at its end. We show that Floquet Forms generalize the concept of classic modal analysis for structures in equilibrium states. Because of the complexity of the frequency spectrum of Floquet Forms as compared to the classic harmonic modes of vibration, the type of instabilities encountered by periodically-varying structural systems is naturally much richer than systems in equilibrium.

CONTEXT AND NEED

Modal analysis is a key concept in structural mechanics and is today commonly used by engineers in various fields such as Civil Engineering, automotive, aerospace or rotor-dynamics industries. It especially allows to reveal intrinsic vibrational properties of structures in equilibrium states, as well as their local stability, and it is therefore often a necessary step in the design of structures.

Thanks to Floquet theory [1], it should be possible to extend this modal approach to structures in periodic states, i.e. structures with mechanical or geometrical properties that vary periodically with time. Modal analysis of structures in periodic states could be of practical interest for many problems in mechanical engineering including the vibrational behavior of rotating machineries with imperfections, the design of structures submitted to periodic compression or tension loadings or the stability analysis of structures undergoing large oscillations [2]. Surprisingly, to the best knowledge of the authors, this generalization of modal analysis has never been completely and clearly implemented. Due to the conceptual complexity of the vibrational analysis of structures in periodic states, the developed numerical methods mostly focused on dynamic stability [3, 4], neglecting the modal informations that are either ignored, inaccurate or even inaccessible from the computations. As a consequence, the natural link between modal analysis of equilibrium and periodic states yet suggested by Floquet remains largely unknown by the structural engineer and researcher community.

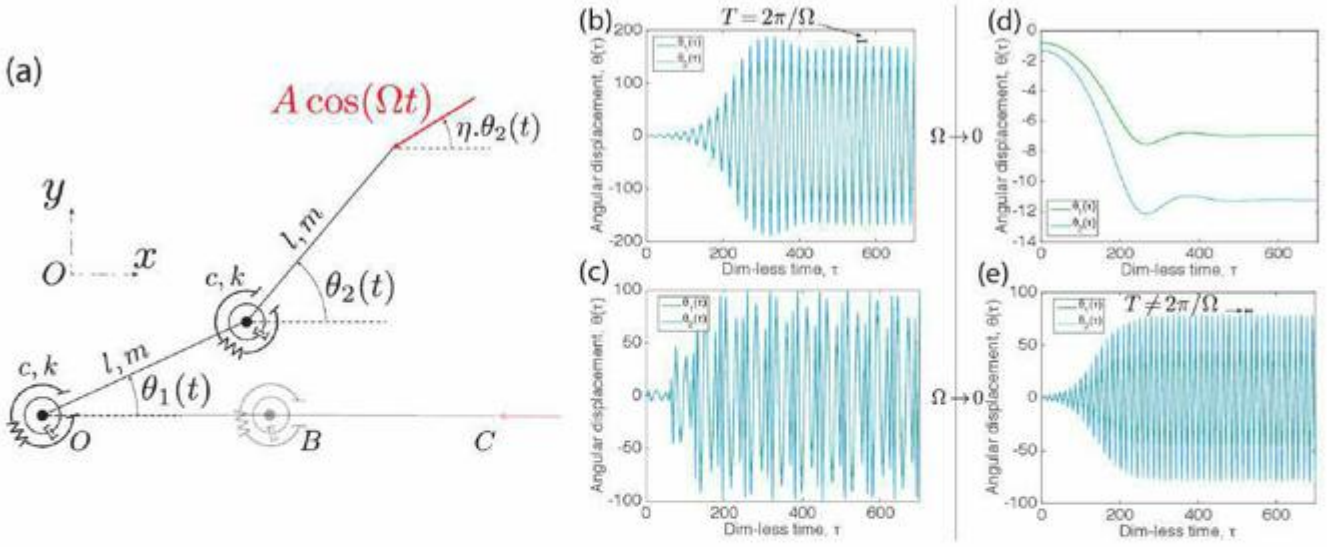

Figure 1: (a) The system under study is a bi-articulated bar submitted to a compressive load with a period $T = 2\pi/\Omega$ at its end. The load is either periodically conservative ($\eta = 0$, i.e. horizontal force) or non conservative ($\eta = 1$, i.e. following force). (b) Steady-state bifurcation on a T-periodic orbit ($\Omega \neq 0$ and $\eta = 0$). (c) Neimark-Sacker bifurcation on a almost-periodic orbit ($\Omega \neq 0$ and $\eta = 1$). (d) Static bifurcation on a new equilibrium state ($\Omega \to 0$ and $\eta = 0$). (e) Hopf bifurcation on a T-periodic stationary state with $T \; / \quad \pi/\Omega$ ($\Omega \to 0$ and $\eta = 1$).

*Corresponding author. Email: arnaud.lazarus@upmc.fr

TASK AND FINDINGS

Here, through the archetypal example of a $2D$ bi-articulated bar submitted to a periodic compressive load at its end as illustrated in Fig.1.a, we present an original and accessible spectral numerical framework that generalizes the modal analysis of structures in equilibrium to structures in periodic states. Although apparently simple, this fundamental system encounters all the classic instabilities of 2-dimensional dynamical systems that can be easily sorted depending on the fundamental frequency of the state Ω and the parameter η as illustrated in Fig.1.b-e.

Thanks to a single algorithm based on the sorting of the eigenvalue spectrum of Hill's matrix [5], our method allows to compute Floquet forms (FFs) of periodically conservative or non conservative systems. FFs are almost periodic modal entities reducing to classic harmonic vibrational modes for the particular case of structures in equilibrium states (for a system such as the one illustrated in Fig.1.a, FFs are simply the 2 modes of vibration of the originally straight bi-articulated bar). Like for classic modal analysis, FFs carry the intrinsic vibrational signature of the structure and their spectrum allows to assess the linear stability of the periodic state as illustrated in Fig.2.b-e. In the general case when $\Omega = 0$, the almost-periodicity of FFs as well as the dependency of their frequency spectrum on Ω can cause the periodic state to lose stability and consequently lead to steady-state, period doubling or Neimark-Sacker bifurcations as illustrated in Fig.1.b,c and Fig.2.b,c. In the particular cases when $\Omega \to 0$, FFs reduce to harmonic eigenmodes and the equilibrium state can eventually become statically or dynamically unstable depending on the loading parameter A as shown in Fig.1.d,e and Fig.2.d,e. Like in classic modal analysis, since FFs are first order perturbations of stationary states, they carry the kinematic shape and temporal signature of the bifurcated nonlinear vibrational responses such as illustrated in Fig.1.b-e. Their computation and analysis is therefore crucial for the design of structures in periodic states.

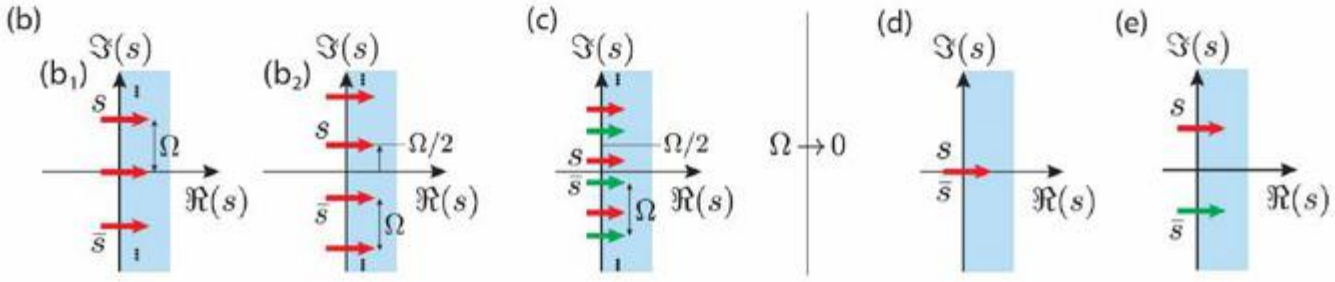

Figure 2: Argand representation of the spectrum s and s of the 2 Floquet Forms of the system shown in Fig.1.b-e at the onset of bifurcation. (b_1) Steady state bifurcation. (b_2) Flip or period-doubling bifurcation. (c) Secondary Hopf, or Neimark-Sacker bifurcation. (d) Steady-state bifurcation or buckling. (e) Dynamic instability or flutter leading to a Hopf bifurcation.

CONCLUSIONS AND PERSPECTIVES

The algorithm presented in this article is a unified method to perform modal analysis of conservative or non conservative systems in periodic states, including equilibria. This unique framework emphasizes the natural link between vibrational behavior of standstill and periodically-varying systems that are common in mechanical engineering. Like for classic modal analysis, this generalized modal approach should allow to design a broader range of structures by computing and analyzing FFs which give better physical insight and understanding on the linear stability of nonlinear dynamical systems. This first study on a simple archetypal 2 dof system will pave the way to the modal analysis of real structures in periodic state with a large number of degrees of freedom. Due to the linear nature of those entities, the interesting properties of classic vibrational modes should remain with FFs which could be promising candidates for modal reduction for structures in periodic states or predictors in nonlinear algorithm such as Newton-Raphson method to compute nonlinear periodic orbits of vibrating structures.

References

[1] G. Floquet. Sur la théorie des équations différentielles. Annales scientifiques de l'Ecole Normale Supérieure, 8: 3-132, 1879.

[2] V. V. Bolotin. The dynamic stability of elastic systems. Holden Day, 1964.

[3] R. Castelli and J.-P. Lessard. Rigorous numerics in Floquet theory: computing stable and unstable bundles of periodic orbits. SIAM Journal on Applied Dynamical Systems, 12: 204-245, 2013.

[4] J. Zhou, T. Hagiwara and M. Araki. Spectral characteristics and eigenvalues computation of the harmonic state operators in continuous-time periodic systems, Systems & Control Letters, 53: 141-155, 2004.

[5] A. Lazarus and O. Thomas. A harmonic-based method for computing the stability of periodic solutions of dynamical systems. Comptes Rendus Mecanique, 338: 510-517, 2010.

INSTABILITIES OF A COMPRESSED HYPER ELASTIC PRISM: COMPETITION BETWEEN WRINKLES AND CREASES

Claire Lestringant *[1], Corrado Maurini[1], Arnaud Lazarus[1], and Basile Audoly[2]

[1]*UPMC Univ Paris 06, CNRS, UMR 7190, Institut Jean Le Rond d'Alembert, F-75005 Paris, France*
[2]*Laboratoire de Mecanique des Solides, CNRS, Ecole polytechnique, Palaiseau, France*

Summary We study the stability of a long hyper elastic prism whose cross-section is an isosceles triangle, subjected to axial compression. Experiments reveal extended buckling modes (wrinkles) when the ridge angle ϕ is smaller than $\approx 90°$, and localized modes (creases) when ϕ is larger than $\approx 90°$. The compression of a neo-Hookean half-space, which is known to produce creases, appears as a particular case of our system ($\phi = 180°$). With this aim to explain the competition between the extended vs. localized buckling modes, we carry out a linear stability analysis based on a neo-Hookean (hyperelastic) model using the finite-element method. The first buckling mode and the associated critical strain ϵ_c are obtained as a function of the angle ϕ at the apex. The simulations reproduce the different types of behaviors depending on the ridge angle ϕ as seen in the experiments.

We investigate the buckling of a prism having a triangular basis made of a soft elastic polymer (Vynilpolysiloxane - VPS), when subjected to axial compression. In our experiments, the prism is a ridge attached to a parallepipedic block. We used VPS casting in a mold realized by rapid prototyping (laser cutter) to produce the samples. The block is then subjected to a compressive load P which forces the prism to shrink longitudinally, see Figure 1a.

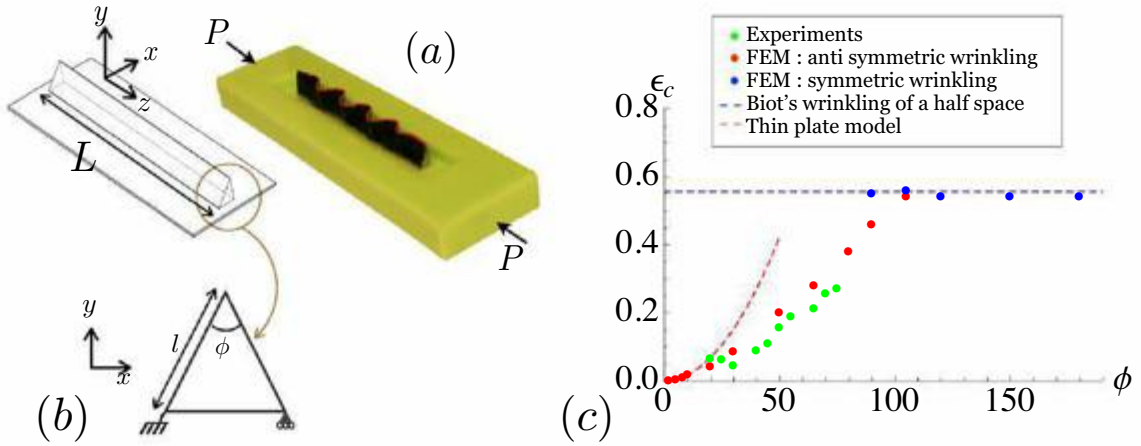

Figure 1: (a): Geometry of undeformed sample and wrinkling mode under axial compressive load P: photo of the experiment with ridge angle $\phi = 20°$ and side length $l = 13\,\mathrm{mm}$. (b): sketch of the undeformed cross-section and boundary conditions used in the simulation. (c): Buckling strain as a function of the ridge angle ϕ. Numerical results are shown using red dots for the anti symmetric wrinkling (ASW) mode and blue dots for the symmetric wrinkling (SW) mode. Prediction of a thin plate model with varying thickness (dashed red line), and Biot strain corresponding the surface wrinkling instability of the lateral faces (dashed blue line). Experimental results are shown with green dots.

For a sufficiently compressive load P, the prism buckles. The buckling mode observed in the experiments depends on the ridge angle ϕ: it is an extended mode (wrinkles, as in Figure 1a) when the ridge angle is smaller than $\approx 90°$, and a localized mode (creases) when ϕ is larger than $\approx 90°$. The well-studied compression of a neo-Hookean half-plane appears as a particular case of our system ($\phi = 180°$): our experiments reveal a transition from localized creases to extended wrinkles when the ridge angle ϕ is decreased.

With the aim to explain these observations, we have set up a linear stability analysis of the compressed prism using the finite-element method. The stability analysis is formulated in an original manner, namely as a polynomial eigenvalue problem in the triangular cross-sectional domain, with the axial wavenumber q entering as the eigenvalue. This formulation allows to address the case of an infinitely long prism with optimal numerical efficiency.

In the simulation, the first buckling mode and the associated critical strain ϵ_c are obtained as a function of the ridge angle ϕ. The critical strain ϵ_c is small for slender cross-sections ($\epsilon_c \to 0$ for $\phi \to 0$). A stability analysis based on the von Karman equations for thin plates (with varying thickness) accurately captures the dependence of ϵ_c on ϕ for $\phi \to 0$ as $\epsilon_c \sim \phi^2$ (see dashed red line in Figure 1b, which is asymptotically consistent with the FEM results).

*Corresponding author. Email: claire.lestringant@gmail.com

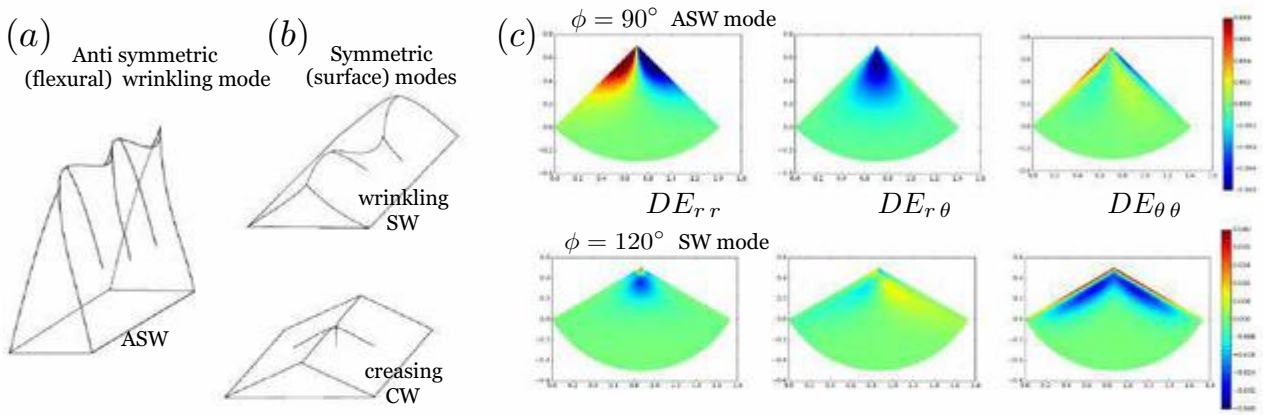

Figure 2: (a): Sketch of the anti symmetric wrinkling (ASW) buckling mode predicted by the simulation for values of ϕ below $\approx 105^\circ$. (b): Sketch of the symmetric wrinkling (SW) buckling mode predicted by the simulation for values of ϕ above $\approx 105^\circ$ (above). Sketch of the symmetric creasing (SC) buckling mode obtained in the experiments for values of ϕ above $\approx 90^\circ$ (below). (c): Visualization of the first buckling mode in the cross-sectional plane: incremental radial strain DE_{rr}, shear strain $DE_{r\theta}$ and hoop strain $DE_{\theta\theta}$ for a ASFW mode (top row, $\phi = 90^\circ$) and a SSW mode (bottom row, $\phi = 120^\circ$). Here, r and θ are the polar coordinates in the plane of the cross-section. Note that the modes have a harmonic dependence on the axial variable, not shown.

The buckling mode predicted by the plate model is an anti symmetric (flexural) wrinkling (ASW) mode, making the ridge bend out of the plane of symmetry of the prism (see Figure 2a). A mode of this type is indeed predicted by the FEM analysis, for all ridge angles below $\phi \approx 105^\circ$ (red dots in Figure 1 and top row in Figure 2c).

When ϕ reaches $\approx 105^\circ$, the critical strain ϵ_c of the edge mode becomes larger than the value 0.55 corresponding to the surface wrinkling instability in a neo-Hookean half-plane [1]. Consistently, when ϕ is larger than $\approx 105^\circ$ the first buckling mode predicted by the FEM analysis is a symmetric mode living on the surface of the lateral faces of the prism (see blue dots and blue dashed line in Figure 1, and bottom row in Figure 2). For this mode, our linear analysis can only predict a wrinkling mode having an harmonic dependence on the axial coordinate z, but it is known that modes of this type appear concurrently with all possible wavelengths, and that the non-linear coupling between them gives rise to a creasing mode [2], [3]. In view of this, the wrinkles living on the faces of the prism predicted by our linear analysis (SW modes) are consistent with the creasing modes (SC) observed in the experiments. Buckling strain for creasing instability in a neo-Hookean half-plane ϵ_C is known to be lower than buckling strain for wrinkling: $\epsilon_C < \epsilon_B$ [3], this probably explains why edge mode maintains up to bigger ϕ in simulations (105°) than in experiments (90°).

An elastic prism under axial compression is an interesting system that features a competition between creasing modes for large ridge angles, like Biot's Neo-Hookean half-space, and wrinkling modes for small ridge angles. We have observed this competition in experiments, and explained it by a buckling analysis.

References

[1] Biot M.: Mechanics of Incremental Deformations. Wiley, 1965.

[2] Hohlfeld E., Mahadevan L.: Unfolding the sulcus. Physical Review Letters, 2011.

[3] Cao Y., Hutchinson J. W.: From wrinkles to creases in elastomers: the instability and imperfection-sensitivity of wrinkling. Proceedings of the Royal Society A: Mathematical, Physical and Engineering Sciences, 2011.

PLASTIC BIFURCATION PARADOX FOR CIRCULAR AND RECTANGULAR PLATES BONDED TO ELASTIC FOUNDATIONS IN BIAXIAL LOADINGS

Suresh Shrivastava[1], Andre Bahous, and Bob Munlemvo
Department of Civil Engineering and Applied Mechanics
McGill University, Montreal, Quebec, Canada

Summary Exact bifurcation analyses are performed for circular and rectangular plates bonded to elastic foundations. The stresses before bifurcation are biaxial for rectangular plates and equibiaxial for circular ones. Rival theories of strain hardening plasticity model the plate material. For circular plates, the theories yield almost the same results regardless of the foundation. For rectangular plates, the results are similar for equibiaxial loading. Large differences emerge for non-equibiaxial loadings.

1. INTRODUCTION

Buckling of plates on elastic foundations has relevance to delamination in sandwich or composite plates. Elastic plate buckling has been presented in [1] for circular plates. Here such buckling for circular and rectangular plates is presented when the plate is in the strain-hardening range [2] and [3] under biaxial loads. The foundation resistance is linear elastic.
Plastic buckling has a history of paradoxes. The column paradox was resolved by Shanley by showing that no unloading occurs in plastic bifurcation. For plates, paradoxes persist. Generally, bifurcation loads from the incremental theory (the right theory) are higher, even absurdly, than from the deformation theory (the wrong theory). Experiments support the latter.

2. CONSTITUTIVE RELATIONS

As bifurcation is an incremental phenomenon, relations connecting the stress increments to strain increments due to bifurcation are needed. The moduli for the incremental relations are dependent on the pre-bifurcation stresses. These stresses for the present biaxial case are: $\sigma^0_{yy} = \alpha\sigma^0_{xx}$ with the equivalent stress $\sigma^0_{eq} = \sqrt{(3/2)s^0 s^0} = (1-\alpha+\alpha^2\ \sigma^0_{xx}$

The plane stress J_2 deformation theory relations are [2, 3]: $\sigma_{xx} = B\varepsilon_{xx} + C\varepsilon_{yy}, \sigma_{yy} = C\varepsilon_{xx} + D\varepsilon_{yy}, \sigma_{xy} = 2F\varepsilon_{xy}$ where

$B = E\ \Delta\ \lambda + \ + e + \lambda\alpha\ \alpha -\quad C = E\ \Delta\ \quad +\alpha^2\ \lambda - \ + \ \nu\ + \alpha\ \ + e - \lambda - \ \nu$

$D = E\ \Delta\ \alpha\ \lambda + \ + e\ - \lambda\ \alpha -\quad F = \quad + \ \nu + e$

$\Delta = (1 - \ + \ ^2\ \lambda\ + e - \ \nu\ - \ - \nu\ \ + \alpha\ - \ + e\ \ - \nu$

In the above $\lambda = E_t\ \ E\ e = E_s\ \ E - 1.\ E_s, E_t$ are the secant and tangent moduli from a uniaxial $\sigma - \varepsilon$ material curve at the stress level $\sigma = \sigma^0_{eq}$. Taking $e = 0$ yields the J_2 incremental theory relations. $\lambda = \ \ e = \$ give the elastic relations.

3. GOVERNING EQUATIONS

For circular plates, the governing equilibrium equation (and boundary conditions) follows from the principle of virtual work together with Kirchhoff hypothesis, and Shanley's concept of no unloading. For equibiaxial stresses $\sigma_{rr} = \sigma_{\theta\theta} = P\ \ t$, $\alpha = 1,$ the moduli are $2\ \ + \ \ = D = B = \ \ \lambda + \ + e\ \ \ \ + \ - \nu\ \ + \nu + e$ and the governing equation is

$$(Bt\ \ /12)\nabla^4 w + \ \nabla\ \ + \ \ = 0$$

where w is the deflection, ∇^2, ∇^4 the harmonic and biharmonic operators in $r - \theta$ coordinates, P the load per unit length at the periphery $\ = \ \ ,$ and k the foundation modulus. $k = 0$ when foundation is absent (a) outside or (b) inside $\ = \ \ .$

For rectangular plates, the prebuckling stresses are biaxial. The above procedure yields the governing equation:

$$\frac{t^3}{12}\{B\frac{\partial^4 w}{\partial x^4} + 2(2\ \ + \ \ )\frac{\partial^4 w}{\partial\ \partial^{\ 2}} + D\frac{\partial^4 w}{\partial y^4}\} + P\ \frac{\partial^2 w}{\partial x^2} + \alpha\frac{\partial^2 w}{\partial y^2}) + kw = 0.$$

For equibiaxial loading, $\alpha = 1$, the above becomes $(Bt\ \ /12)\nabla^4 w + \ \nabla^2\ \ + \ \ = 0$ where $\nabla^2\ \ \nabla^4$ are in $\ - \$ system.

4. SOLUTION AND RESULTS FOR CIRCULAR PLATES

Solution $w\ \xi\ \theta\ = W\ \xi\ \ \ \ n\theta$ where $r = \xi\ \ ,$ n = number of nodal diameters, gives for foundation inside:

$W_1\ \xi\ = A_1 J_n\ s_2\xi\ + A_2 I_n\ s_1\xi\quad W_2\ \xi\ = A_3 J_n\ \mu\xi\ + A_4 Y_n\ \mu\xi\ + A_5\xi\ + A_6\xi^{-n}$ for $0 < \xi < c$ and $c < \xi < 1.$

[1] Corresponding author. Email: **suresh.shrivastava@mcgill.ca**

$s_2^2\ \ s^2 = \frac{1}{2}(\sqrt{\mu^4 - 4\gamma^4} \pm \mu^2), \gamma^4 = 12kr \quad Bt \quad \mu^2 = 12P_{cr}R^2 \quad Bt$ For axisymmetric mode $n = 0$, ξ^{-n} is replaced by $\ln \xi$. For foundation outside: $W_1\ \xi\ = A_1 J_n\ \mu\xi\ + A_2 \xi^n$, $W_2\ \xi\ = A_3 J_n\ s_2\xi\ + A_4 Y_n\ s_2\xi\ + A_5 I_n\ s_1\xi\ + A_6 K_n\ s_1\xi$ Matching of the solutions at the common boundary requires equality of the functions and their three derivatives. Support conditions at = are (i) simple $W = \ _{rr} = \ \frac{d\ W}{dr^2} + C\frac{dW}{rdr} = 0,$ or (ii) fixed $W = \frac{dW}{dr} = 0$. Thus, one gets six homogeneous equations in six constants. Vanishing of the determinant of these equations is the bifurcation condition.

The plate material is an Al alloy: $\varepsilon = \sigma \quad + \quad \sigma \quad ^7 \sigma$ in MPa, $\nu = 0.33,$ and the valid plasticity range is 170-310 MPa. The k values are for foam like material. For calculations, $D = 610$ mm. For simply supported plates, the graphs and table below show that the incremental theory results match the deformation theory results within 1% regardless of the foundation. For fixed plates (not shown) the loads are higher by ≈ 10% at the upper end of the plasticity range.

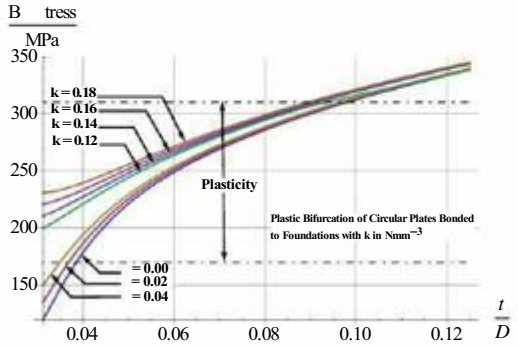

Incremental vs Deformation Theory (Dia = 610 mm Full Foundation)	
k in Nmm^{-3}	$Max\left(\frac{\sigma_{cr}^i}{\sigma_{cr}^d}\right)$
0.00	338.56/335.42
0.02	339.28/336.13
0.04	340.00/336.85
0.12	338.25/337.12
0.14	343.71/340.53
0.16	344.47/341.29
0.18	345.24/342.05

5. SOLUTION AND RESULTS FOR RECTANGULAR PLATES

A solution $w = A_{mn} \sin(\ \pi\ /\ )\sin(\ \pi$ where $a\ b$ are lengths, and m, n are number of buckles, gives

$$\sigma_{cr} = [k + \frac{t^3}{12}\{B\frac{m^4\pi^4}{a^4} + 2(2\ \ +\ )\frac{m^2n^2\pi^4}{a\ b} + D\frac{n^4\pi^4}{b^4}\}]/(t\frac{m^2\pi^2}{a^2} + \alpha t\frac{n^2\pi^2}{b^2})$$

For square plates (=) in equibiaxial loads $\alpha = 1)$: $\sigma_{cr} = B\frac{\pi^2 t^2}{12a^2}(m^2 +\ ^2) + \frac{ka^2}{\pi^2 t\ m^2 +\ ^2)}, m = \ = 1$ for low k. For incremental theory, the loads are ≈ 15% higher for thick plates. For equal compression tension: $B = D = (3\lambda +\ + e\ E\ \Delta$ $C = (3\lambda -\ -\ +\ \nu\ E\ \Delta\ F = E\ \ \ +\ \nu +\ e$ and $\Delta = (2 +\ -\ \nu\ \ \lambda -\ +\ \nu$ .Here $\alpha = -\ \ n = \ \ m = 2$ for square plates. Dramatic divergence occurs between the two theories. Thin plates bifurcate at high plasticity for the incremental theory. In contrast for the deformation theory, the bifurcation occurs at low plasticity and at low loads regardless of plate thickness.

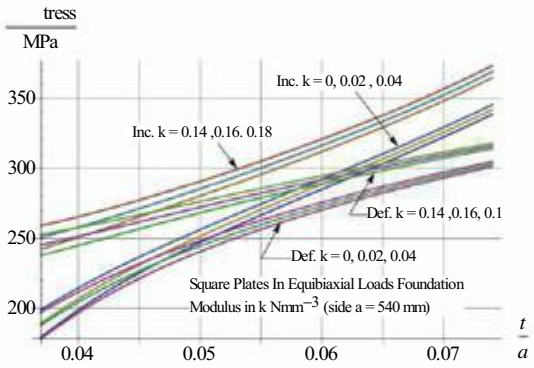

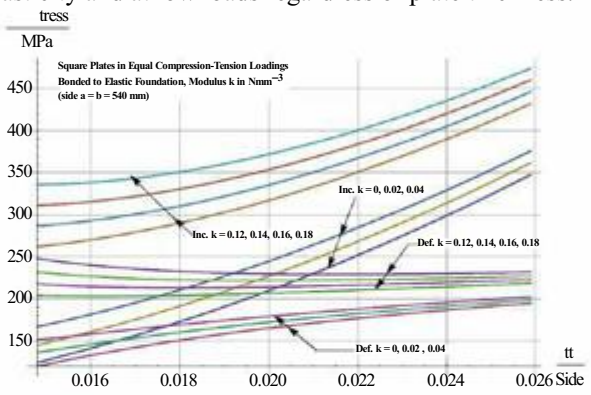

CONCLUSIONS

In equibiaxial compression, the paradox is muted; for SS circular plates it disappears. It emerges strongly in equal compression-tension; the bifurcation loads are either too low or too high. The results call for more experimental and theoretical researches, especially the former, to resolve the paradox.

References

[1] Wang, C.Y , On the Buckling of Circular Plate on an Elastic Foundation, *Journal of Applied Mechanics*, vol.72, 2005, pp. 795-796.

[2] Bahous, André, Plastic Buckling of Circular Plates on Elastic Foundations, *M. Eng. Thesis*, McGill University, Montreal, Canada 2014.

[3] Munlemvo, Bob, Plastic Buckling of Rectangular Plates Bonded to Elastic Foundation in Biaxial Loading, *M. Eng. Project*, McGill, Montreal, Canada 2012.

TAPE SPRING ROD MODEL AS A REGULARISED ERICKSEN'S BAR INVOLVING PROPAGATING INSTABILITIES

Maverick Martin*[1,2], Stéphane Bourgeois[1], Bruno Cochelin[1], and François Guinot[2]
[1]*LMA, Centrale Marseille, CNRS, UPR 7051, Aix-Marseille Univ, F-13451 Marseille, France*
[2]*Thales Alenia Space, Cannes, France*

Summary This paper focuses on a tape spring rod model with an up-down-up elastic bending constitutive equation that explains the creation of localised folds which involve propagating instabilities. A simplified version of a recently published planar rod model with flexible cross-section is presented and analysed as a regularised Ericksen's bar problem. This simplified model allows to estimate the characteristic length of the transition zones that govern numerical simulations.

THE BENDING-FLATTENING MODEL FOR PURE BENDING TEST

An original model of tape spring has been recently proposed by Guinot *et al.* [1]. This model is based on the reduction of a classical shell model into a thin-walled planar rod model with flexible cross-section. This model has been improved by Picault *et al.* [2] and extended to 3D motions [3]. It has been implemented in a finite element software and simulations have demonstrated its ability to account for complex behaviour of tape springs such as the creation of localised folds. However, a fine mesh is required to obtain reliable results whereas the use of coarse mesh leads to numerical issues that generate perturbations on the overall response. In order to investigate these numerical troubles, a simplified version of the planar rod model developed in [2] is presented in this work. Considering the pure bending test, additional assumptions lead to a model with only two kinematic variables : the opening angle β^e of the cross-section (Figure 1(a)) and the rotation angle θ of the cross-section assumed to remain orthogonal to the centerline (Figure 1(b)). Only two coupled phenomena are kept : the bending of the centerline and the flattening of the cross-section. Let s_1 be the normalised curvilinear abscissa along the centerline. The strain energy of the rod model is expressed with the normalised longitudinal curvature $\tilde{\theta}_{,1}$[a] and the normalised transverse curvature $\tilde{\beta}^e$:

$$u_e(\tilde{\theta},\tilde{\beta}^e) = 2D\,(\beta_0^e)^2 \int_0^l \frac{1}{2}\left[\left(1+\eta(\tilde{\beta}^e)^2\right)(\tilde{\theta}_{,1})^2 + \left(\tilde{\beta}^e \nearrow 1\right)^2 + \frac{2(1\nearrow\nu)}{3}\left(\tilde{\beta}^e_{,1}\right)^2 \nearrow 2\nu\tilde{\theta}_{,1}\left(\tilde{\beta}^e \nearrow 1\right)\right] s_1 \qquad (1)$$

$$\text{with } \eta = \frac{12a^2\,(\beta_0^e)^2\,(1\nearrow\nu^2)}{5h^2}, \qquad (2)$$

in which a is the half-length of the cross-section, h its thickness, $l = L/a$ is the normalised length of the tape spring, β_0^e is the initial opening angle. $D = \frac{Eh^3}{12(1-\nu^2)}$ is the shell flexural rigidity with E the Young's modulus and ν the Poisson's ratio.

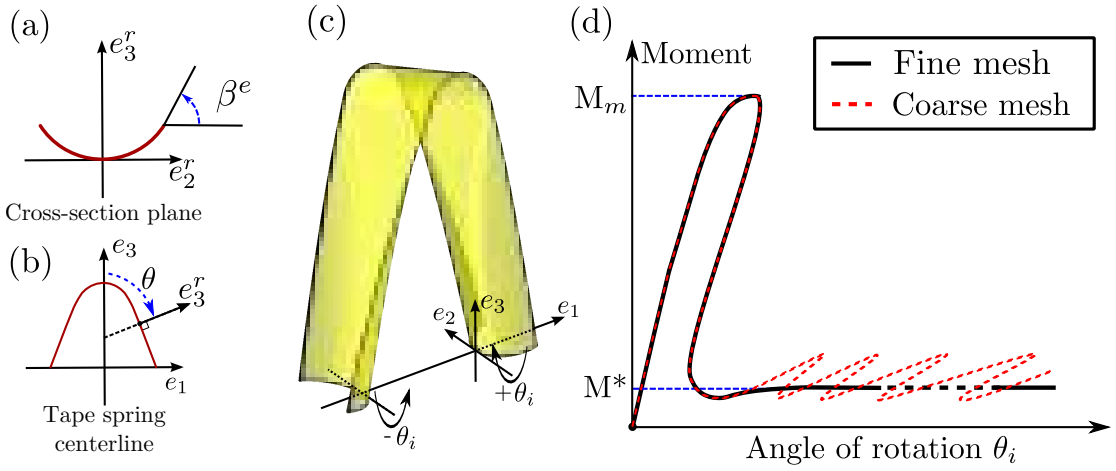

Figure 1: (a) and (b) definitions of variables β^e and θ. (c) Tape spring deformed shape for an *opposite-sense* bending test and (d) the related moment-rotation curve obtained with an arclength continuation method for both coarse and fine mesh.

*Corresponding author. Email: martin@lma.cnrs-mrs.fr
[a] $X_{,1}$ refers to the derivative of X over the curvilinear abscissa s_1.

The pure *opposite-sense* bending test described by Seffen and Pellegrino [4] consists in applying two opposite rotations θ_i around $\boldsymbol{e_2}$ at ends. During this test, a localised fold appears and the deformed shape involves three distinct zones : the folded area where the cross-section is flattened ($\beta^e = 0$), the non-deformed zones ($\beta^e = \beta_0^e$) and the transition ones. The moment-rotation curve obtained with an arclength continuation method is plotted in Figure 1(d) for both coarse and fine mesh. The plateau results from propagating instabilities that occur during the growth of the fold at the constant *propagating fold moment* M^*. This plateau is affected by oscillations which amplitude and frequency depend on the mesh density.

LINK WITH THE ERICKSEN'S BAR PROBLEM

Taking the curvatures $\tilde{\theta}_{,1}$ and $\tilde{\beta}^e$ as constants along s_1 leads to the up-down-up law shown in Figure 2(a), which can be seen as the local constitutive bending equation. This kind of law generates jumps between two deformation states at M^* (Maxwell load) corresponding to the equality of energies represented by areas A_1 and A_2 in Figure 2(a).

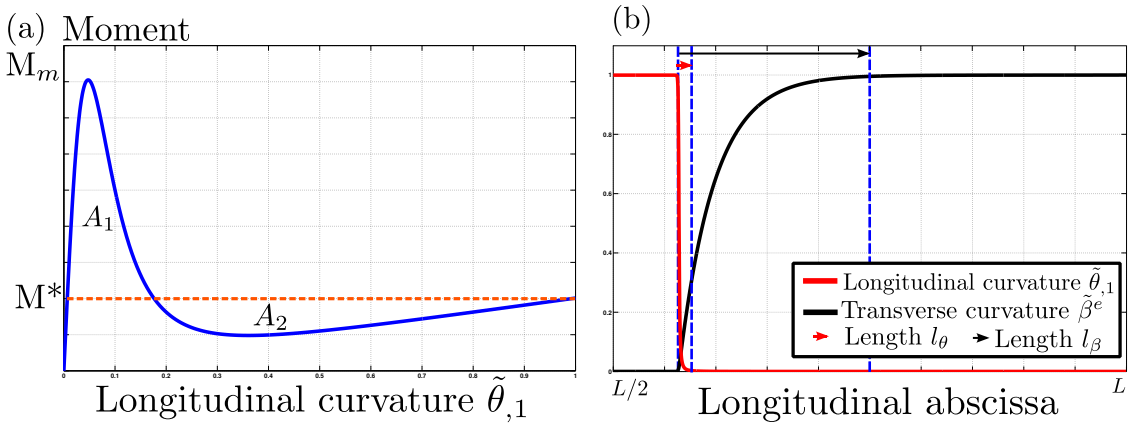

Figure 2: (a) Up-down-up behaviour law and corresponding *propagating fold moment* M^*. (b) Value of longitudinal curvature $\tilde{\theta}_{,1}$ (red) and opening angle $\tilde{\beta}^e$ along a half tape spring and associated characteristic lengths l_θ and l_β.

Considering the equilibrium of a bar with an up-down-up constitutive equation, Ericksen [5] has shown that the continuum problem has an infinity of solutions, and that jumps occur for the mesh-dependent discrete problem. Truskinovsky [6] has introduced high-order terms that regularise the problem in order to obtain a unique solution. Regarding equation (1), one can see the presence of the first derivative of the transverse curvature $\tilde{\beta}^e$ which has a regularising effect on the model. Because of this term, jumps of solution are replaced by rapid transitions over some short characteristic lengths. As illustrated in Figure 2(b), estimates of characteristic lengths l_θ and l_β linked to $\tilde{\theta}_{,1}$ and $\tilde{\beta}^e$ are found with the simplified proposed model. A reliable solution for the discrete problem is obtained when the size of elements is smaller than l_θ, which is found to be shorter than l_β.

CONCLUSION

Starting from a complete planar rod model with flexible cross-section, a simplified bending-flattening model has been created. This model helps to point out the origin of numerical instabilities which are observed during finite element simulations with coarse mesh. The presence of the first derivative of the transverse curvature $\tilde{\beta}^e$ introduces characteristic lengths related to transition zones where propagating instabilities occur. Numerical issues are avoided when the length of elements is shorter than the smallest characteristic lengths. Because numerical issues have been solved, authors are now able to determine the optimal mesh density to perform finite element simulations.

References

[1] Guinot, F., Bourgeois, S., Cochelin, B., Blanchard, L.: A planar rod model with flexible thin-walled cross-sections. application to the folding of tape springs. International Journal of Solids and Structures (2011)

[2] Picault, E., Marone-Hitz, P., Bourgeois, S., Cochelin, B., Guinot, F.: A planar rod model with flexible cross-section for the folding and the dynamic deployment of tape springs: Improvements and comparisons with experiments. International Journal of Solids and Structures 51(18), 3226-3238 (2014)

[3] Picault, E., Bourgeois, S., Cochelin, B., Guinot, F.: A rod model with thin-walled flexible cross-section: extension to 3D motions and application to 3D foldings of tape springs. Accepted in International Journal of Solids and Structures (2016)

[4] Seffen, K.A., Pellegrino, S.: Deployment dynamics of tape springs. Proceedings of the Royal Society of London A 455, 10031048 (1999)

[5] Ericksen, J.L.: Equilibrium of bars. Journal of Elasticity 5(3-4), 191201 (1975)

[6] Truskinovsky, L., Zanzotto, G.: Ericksens bar revisited : Energy wiggles. Journal of the Mechanics and Physics of Solids 44(8), 13711408 (1996)

GRAVITY DRIVEN INSTABILITY IN HORIZONTAL ELASTIC LAYERS

Serge Mora*[1], Ty Phou[2], Jean-Marc Fromental[3], and Yves Pomeau[4]

[1]*Laboratoire de Mecanique et de Génie Civil de Montpellier. Université Montpellier and CNRS. Place Eugène Bataillon. F-34095 Montpellier Cedex, France.*

[2,3]*Laboratoire Charles Coulomb. Université Montpellier and CNRS. Place Eugène Bataillon. F-34095 Montpellier Cedex, France.*

[4]*University of Arizona, Department of Mathematics, Tucson, USA.*

Summary We demonstrate the instability of the free surface of a soft elastic layer facing downwards. Experiments are carried out using a system consisting in a gel of constant density ρ and shear modulus μ, put in a rigid cylindrical dish of depth h. When turned upside down, the free surface of the gel undergoes a normal outgoing acceleration g. It remains perfectly flat for $\rho g h/\mu < \alpha^*$ with $\alpha^* \simeq 6$, whereas a steady pattern spontaneously appears in the opposite case. This phenomenon results from the interplay between the gravitational energy and the elastic energy of deformation of the system.

Many materials such as biological tissues can withstand huge elastic deformations of more than several hundred percent. Specific and fascinating patterns, reminiscent of those that can be seen in hydrodynamics, can then occur with these materials [2, 1].

Out of the many instabilities experienced by liquids, the Rayleigh-Taylor instability (RTI)[4, 5] is outstanding because it is easy to understand, not too difficult to rationalize and also important in many technological and physical situations. The dispersion relation for regular gravity waves on a deep ocean reads $\omega = \sqrt{gk}$, where g is the downward gravity acceleration, $\omega/(2\pi)$ is the wave frequency and k its horizontal wave number. As often noticed, if one turns the gravity upward, that is if one changes the sign of g, ω becomes purely imaginary $\pm i\sqrt{-gk}$, showing the existence of fluctuations growing exponentially with time. These fluctuations do not saturate and yield ultimately fingers of liquids in free fall. If one considers, as we do below, a soft solid in air with its surface turned downward, there are a priori good reasons to believe that some sort of RTI will set in.

In the experiments [3], we use aqueous polyacrylamide gels consisting in a loose permanent polymeric structure immersed in water. The density of this incompressible elastic material is almost equal to that of water. It behaves as an elastic solid for strains up to several hundreds of percent. The shear modulus can be tuned over a wide range by varying the concentrations in monomers and crosslinkers, or the temperature. In our experiments, it lies between 30 and 150 Pa. The reagents generating

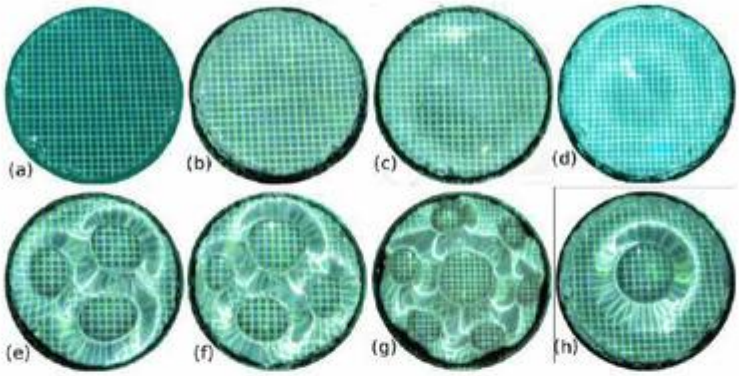

Figure 1: **Views of the downwardly facing free surface of gels with different shear modulii**. (a) $\mu = 78\pm$ 0.5 Pa; (b) 44 $\pm$ 0.5 Pa; (c) 43.3 $\pm$ 0.5 Pa; (d) 42.8 $\pm$ 0.5 Pa; (e) 41.0 $\pm$ 0.5 Pa; (f,g,h) 40.0 $\pm$ 0.5 Pa. The cylindrical dish is 18 cm diameter and 2.75 cm deep. (a-g) Steady patterns obtained just after reversal. (h) The sample temperature was 50 degrees when reversed. The snapshoot is taken after the sample has cooled to room temperature.

the gel are dissolved in ultrapure water and poured into the brim in a cylindrical dish. After the gel is made and its shear modulus measured, the dish is inverted upside down. We observe that the surface of the thinnest and hardest samples remains perfectly flat (Fig.1-a). In a narrow range of shear moduli and heights non propagating undulations grow spontaneously at the free surface of the gel and remain permanently (Fig.1-b,c,d). For lower shear moduli or greater thicknesses, several cuvettes appear next to each other at the surface, and remain permanently. Their number (from one to seven in our experiments) and

*Corresponding author. Email: serge.mora@umontpellier.fr

their size depend on the shear modulus (Fig.1-e,f,g) and of the thickness. Flipping again the container (so that the free surface is horizontal and upward) leads to the perfectly flat surface we started from.
To obtain quantitative information about the surface deformation, a regular light grid is projected about the free surface (Fig. 2-a). If the free surface is flat, the image of the grid is not distorded (Fig.1-a). It is warped if the free surface is deformed, this distorsion is the bigger the surface is more deformed (Fig.1-b-g). To measure the distortion, a rectangular lattice is fitted with the recorded images (Fig. 2-b). The deviation is plotted as a function of $\alpha = \rho g h/\mu$ in Fig.2-c. Fitting functions $a + b(\alpha \nearrow \alpha^*)^c$ with these data gives $\alpha^* = \ .05 \pm 0.25$, demonstrating the existence of an instability threshold at α^* (Fig. 2-c). The elastic layer remains flat for $\alpha < \alpha^*$, and it is unstable in the opposite case.
A linear analytic calculation taking into account the interplay between elasticity and gravity yields an instability threshold

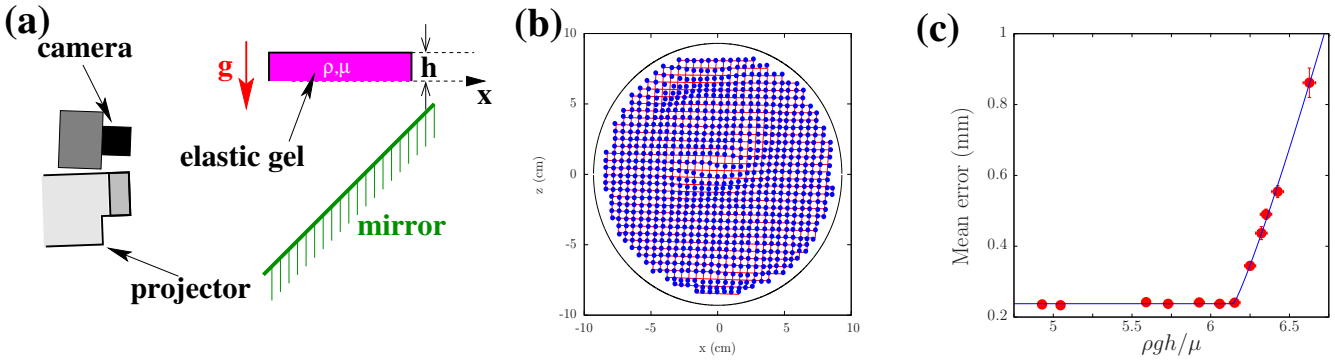

Figure 2: **Quantitative analysis of the surface distortion.** **(a)** Experimental setup. **(b)** Full circles: intersections of the distorted lines of the grid observed on a sample ($\mu = \ 1.5 \pm 0.5$ Pa). Solid lines defined the grid that best fits the observed one. **(c)** Square root of the mean squared error with the grid that best fits the observed one as a function of $\alpha = \rho g h/\mu$ with $g = 9.81 m \cdot s^{-2}$ (full circles). The solid line is the best fit with the power law $a + b(\alpha \nearrow \alpha^*)^c$. We find $\alpha^* = \ .05 \pm 0.25$.

for $\rho g h/\mu = \ .223\cdots$, in nice agreement with the experiments.

A surprising and striking non linear feature of the instability (well beyond the threshold) is the difference in the observed patterns between snapshots (f), (g) and (h) of Fig.1, all the three corresponding to the same shear modulus with the same container size. The first two are directly obtained from a gel of $\ 0 \pm 0.5$ Pa at room temperature. The third one is obtained after cooling sample of Fig.1-(f,g) upside down from 50 degrees down to room temperature. The shear modulus correspondingly decreases from $\ \pm 0.5$ Pa to $\ 0 \pm 0.5$ Pa. The cooling takes place gradually from the boundaries towards the center of the sample, resulting in shear modulus gradients until thermal equilibrium is reached. The dramatic difference between the observed patterns highlights the existence of several equilibrium configurations. This must be related to a complicated energy landscape with several local minima far from the instability threshold, providing a particularly interesting challenge for non linear physics and morphogenesis. Somehow the notion of instability as introducing a kind of free choice in the evolution of a system shows up here. It implies that the ultimate state reached after such an instability depends not only on the growth of the unstable structure itself but also on uncontrollable or at least hard to control small effects, like various inhomogeneities in space and time. This is clearly evidenced in our experiment.

These results open the way for further fundamental studies, for instance concerning the dynamic formation and the large-scale organization of the patterns, which are both of great importance for non linear physics and morphogenesis. RTI in solids should also be found in more complex situations, such as biology, geology and industrial processing, with visco-plastic, visco-elastic or non-isotropic materials. Moreover, the instability is expected to occur to structures subjected to more extreme conditions (high accelerations, strong and non-uniform gravitational fields) where the direct observation is hardly possible.

References

[1] S. Mora, C. Maurini, T. Phou, J. M. Fromental, B. Audoly, and Y. Pomeau. Solid drops: Large capillary deformations of immersed elastic rods. *Phys. Rev. Lett.*, 111:114301, 2013.

[2] S. Mora, T. Phou, J. M. Fromental, L. M. Pismen, and Y. Pomeau. Capillarity driven instability of a soft solid. *Phys. Rev. Lett.*, 105:214301, 2010.

[3] S. Mora, T. Phou, J. M. Fromental, and Y. Pomeau. Gravity driven instability in solid elastic layers. *Phys. Rev. Lett.*, 113:178301, 2014.

[4] L. J. Rayleigh. Investigation of the character of the equilibrium of an incompressible heavy fluid of variable density. *Proc. London. Math. Soc.*, 14:170–177, 1883.

[5] G. I. Taylor. The instability of liquid surfaces when accelerated in a direction perpendicular to their planes. *Proc. London. Math. Soc. Series A*, 210:192–196, 1950.

INTERPLAY OF WRINKLING AND MICROSTRUCTURE IN NEMATIC ELASTOMER MEMBRANES

Paul Plucinsky[1] and Kaushik Bhattacharya *[1]

[1]*Engineering and Applied Sciences, California Institute of Technology, Pasadena, CA 91125, USA*

Summary Nematic elastomers are rubbery solids which have liquid crystals incorporated into their polymer chains. These materials are characterized by unusual mechanical properties due to their ability to form fine-scale microstructure. In this work, we study thin membranes made of nematic elastomers. Such membranes feature two potential instabilities – the formation of fine-scale material microstructure and the formation of fine-scale wrinkles. We develop a theoretical framework to study thin membranes of nematic elastomers that accounts for both instabilities, and we implement this framework numerically. Using both analytic and numerical studies, we show that the nematic elastomers can suppress wrinkling. This has important implications on space and other engineering applications where there is a pressing need to combat wrinkling in membrane structures.

INTRODUCTION

Membrane structures – often with thickness of the order of micrometers and lateral dimension of the order of meters – are increasingly being exploited in space applications due to their high surface to volume ratio, light weight, and easy deployability. However, membranes offer little resistance to out-of-plane deformation and wrinkle under the typical (non-ideal) boundary conditions required to pull membranes taut (see Figure 1(left)). This is undesirable. For instance, the effectiveness of solar sails, which exploit large surface area to capture radiation pressure for propulsion, is diminished – by as much as 5 to 15% – by wrinkling. This has motivated a number of structural mechanisms to suppress wrinkling such as catenaries and shear compliant borders. Nevertheless, wrinkling continues to be a challenge in the design of these systems.

Our current work is motivated by an alternative approach to suppressing wrinkles by exploiting the peculiar features of nematic liquid crystal elastomers. This material couples the finite deformation elasticity of a cross-linked polymer network with the anisotropy of liquid crystals pendent to this network. This marriage results in a solid with many novel features, one being the ability to form microstructure under mechanical deformation. This is seen, for instance, in the clamped stretch experiments of Kundler and Finkelmann [5] provided in Figure 1(right). Here, the average direction of the liquid crystal molecules (represented by a director field n mapping to a unit vector) is uniform and aligned vertically in the undeformed nematic elastomer sheet. Upon deforming the sheet via a stretch of the clamped boundary, microstructure is induced in the form of fine-scale planar oscillations in this orientation. Importantly, wrinkling is not apparent in these experiments. This is in stark contrast to conventional isotropic sheets, where one would expect wrinkling due to clamped stretching deformation.

MODELING NEMATIC ELASTOMER MEMBRANES: THEORY AND NUMERICAL STUDIES

Nematic elastomers are rubbery solids which have liquid crystals incorporated into their polymer chains. The liquid crystals spontaneously align giving rise to a nematic director below a critical temperature. This alignment is accompanied by a spontaneous stretch along and contraction transverse to the director (characterized by an anisotropy parameter $r \geq 1$ with $r = 1$ the degenerate case of no spontaneous deformation). As the director reorients, so does the spontaneous deformation; conversely deformation leads to reorientation of the director. This emerges naturally from a theory of statistical physics for nematic elastomers which leads to a free energy density with nematic-elastic coupling [1]. This free energy density predicts

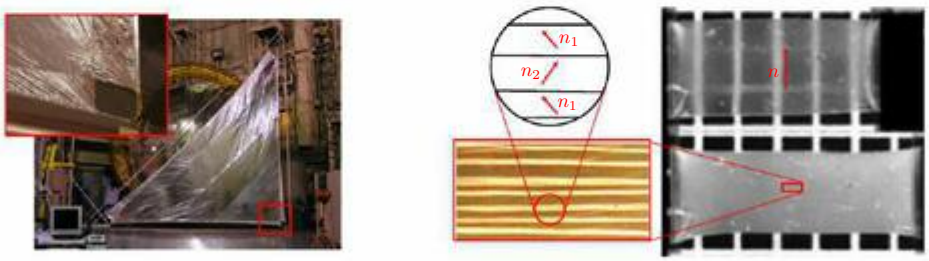

Figure 1: Solar sail with shear compliant border, NASA Langley Research Center (left). Clamped stretching of nematic elastomer sheet by Kundler and Finkelmann [5] and depiction of microstructure (right).

*Corresponding author. Email: bhatta@caltech.edu

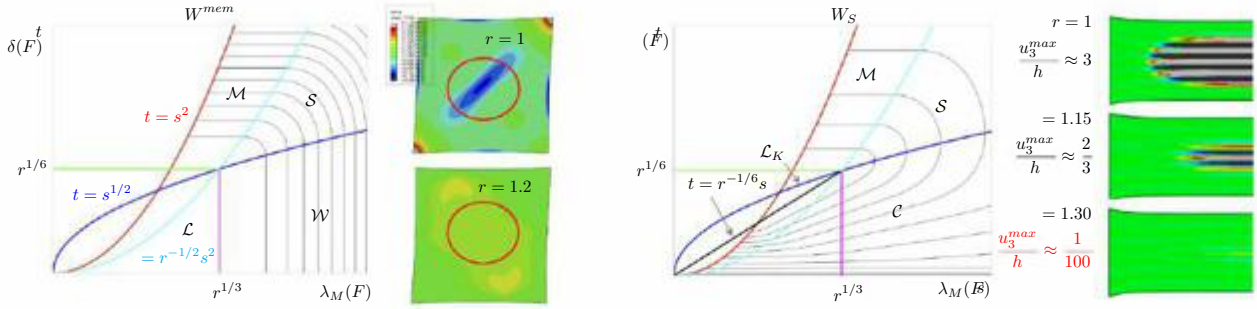

(a) Effective membrane energy and membrane simulations

(b) Planar part of Koiter model and shell simulations

Figure 2: Energy densities for nematic elastomer membranes and corresponding simulations

the emergence of microstructure including stripe domains in Figure 1(right), and explains many unusual features observed in these materials [4, 3].

We start from this free energy density and *rigorously derive and characterize an effective membrane theory* for nematic elastomers W^{mem} as the Γ-limit of the bulk theory in the limit of small thickness. The behavior of these membranes is characterized by four regimes depending on the principal stretch $\lambda_M(F) := \sup_{e\in\mathbb{S}^1} |Fe|$ and the areal stretch $\delta(F) := |\text{adj}F|$ of effective planar deformation (Figure 2a): one denoted $\mathcal{W}$ where wrinkling leads to uniaxial tension, a second $\mathcal{M}$ where nematic oscillations lead to equi-biaxial tension, a third $\mathcal{L}$ where wrinkling and microstructure reduces the effective membrane energy and stress to zero, and a fourth $\mathcal{S}$ with no fine scale features and biaxial tension. While the regions $\mathcal{W}, \mathcal{S}, \mathcal{L}$ are similar to usual elastic membranes, the region $\mathcal{M}$ is special to nematic elastomers. Remarkably, this region has *zero shear stress* even in the presence of shear strain.

We implemented W^{mem} in Abaqus/Standard via a user material model for plane stress elements, and used it to subject an initially square membrane to displacement boundary conditions which mimic the non-ideal conditions seen in space applications (equibiaxial stretch in circled red region followed by shear). We find that the nematic membrane (r=1.2) remains entirely in the regions $\mathcal{M}$ and $\mathcal{S}$, characteristic of strictly planar deformation (Figure 2a, right-bottom). This is in marked contrast with that of a normal elastic membrane (r=1, Figure 2a, right-top) that shows a significant region in $\mathcal{W}$ indicative of wrinkling. Therefore, these simulations suggest that *nematic elastomer membranes can suppress wrinkling*.

To study this further, we *formally derive a generalized Koiter-type theory* where we allow nematic microstructure to form freely (i.e. relax against microstructure), but penalize wrinkling through bending. The resulting theory has a planar energy density W_S (Figure 2b) at $O(h)$ and bending energy at $O(h^3)$. We implement (a slightly modified version of) this theory in Abaqus/Standard via a user material model for shell elements and study the stretch of a long rectangular strip with clamped ends (following Zheng [6]). The panel on the right of 2b shows the results for various values of r. For usual elastic membranes ($r = 1$), we observe significant amounts of wrinkling in agreement with the observations of Zheng [6]. In contrast, for nematic elastomers ($r = 1.3$), we observe no wrinkling in agreement with the observations of Kundler and Finkelmann [5]. We once again see that *nematic elastomer membranes can suppress wrinkling*.

CONCLUSION

We have derived a theoretical framework to study thin membranes of nematic elastomers that are characterized by two potential instabilities – the formation of fine-scale material microstructure and the formation of fine-scale wrinkles. We have shown through a combination of analytic and numerical studies that the presence of microstructure can suppress wrinkling. This has important implications as there is a pressing need to combat wrinkling in many engineering system incorporating membrane structures.

References

[1] P. Bladon, E.M. Terentjev and M. Warner, *Phys. Rev. E.* **47** R3838-R3840 (1993)

[2] P. Cesana, P. Plucinsky and K. Bhattacharya, *Arch. Rational Mech. Anal.* **218** 863-905 (2015)

[3] S. Conti, A. DeSimone and G. Dolzmann, *J. Mech. Phys. Solids* **50** 1431-1451 (2002)

[4] A. DeSimone and G. Dolzmann, *Arch. Rational Mech. Anal.* **125** 184-204 (2002)

[5] I. Kundler and H. Finkelmann, *Macromol. Chem. Rapid Commun.* **16** 679-686 (1995)

[6] L. Zheng, *Thesis* 1-177 (2009)

INSTABILITY OF MRE FILM – SUBSTRATE BLOCK UNDER MAGNETO–MECHANICAL LOADINGS

Erato Psarra [*1], Laurence Bodelot[1], and Kostas Danas[1]

[1] *Solid Mechanics Laboratory (LMS), Ecole Polytechnique, Palaiseau, France*

Summary The present study pertains to the bifurcation modes of a MRE film bonded on a non–linear elastic and highly compliant substrate. The motivation derives from the increasing development of the magneto–sensitive elastomers and the magnetically trigered instabilities, possibly applicable in actively controlled haptic systems, where a transverse magnetic field induces desirable surface patterns. The present investigation aims at the active control of a surface roughness by exploiting the unstable regime of a critically stable MRE stiff film–soft foundation. Being inspired by biological processes (e.g., skin wrinkling), a stable post–bifurcation mode of finite and controllable wavelength is obtained. In order to do so, the boundary value problem and the post–bifurcation evolution have to be numerically solved, so as to determine the constitutive material properties and the critical loads needed to trigger and control the instability. Novel manufacturing and experimental procedures have to be put in place, driven by the simulation (FE) analysis and the analytical study of the film–substrate problem. The present study introduces a fully featured magneto–mechanical experiment that yields the MRE film finite wrinkling, being activated by low magnetic fields and proper pre–straining of the film–substrate system.

INTRODUCTION

Magneto–rheological elastomers (MRE) are ferromagnetic particle impregnated elastomers, whose mechanical properties are altered by the application of external magnetic fields. The reversibility and repeatability of their response, combined with a strong multi-physics coupling, render them applicable in sensors and actuators. However, one of the most restrictive parameters in finding new applications – or widen the already known – is the usually high magnetic fields required to achieve an efficient active control.

A primary structure, which is relatively easy to cope with analytically and fabrication wise, is the stiff film–soft substrate block. Literature provides several examples of such bilayers that buckle under purely compressive mechanical loads[1]. However, the present study aims at exploiting the magneto–elastic coupling of such a system, since wrinkling can be a result of coupled magneto–mechanical loadings[2]. Hence, the basic idea is to mechanically bring the structure near (but not at) a critically stable state and then destabilize it with a tiny magnetic field (Figure 1a).

THEORY & NUMERICAL INVESTIGATION

The continuum formulation proposed is a Langrangian variational approach. It pertains to the minimization of a potential energy function, which yields all the appropriate governing equations and boundary/interface conditions[3]. At the heart of the analytical theory lies a phenomenological isotropic free energy density that depends on both elastic (i.e., deformation gradient tensor **F**) and magnetic (i.e., magnetic field **B**) properties of the materials.

To numerically account for the magnetic energy of the air in the potential energy formulation, it is required to mesh the surrounding space. The finite element analysis (FEA) considers an isotropically particle filled film laying upon an elastic substrate, for given substrate-to-film thickness ratios, H_s/H_f. The magnetic field is always applied in the direction of the film thickness, while the stretch is applied along the interface direction (Figure 1b). Three external loading cases are studied: a purely mechanical ($\lambda \neq 1, b = 0$), a purely magnetic ($\lambda = 1, b \neq 0$) and a combined magneto-mechanical ($\lambda \neq 1, b \neq 0$). Figure 1c shows the critical value of the dimensionless applied magnetic field $b_c/\mu_0 m_s$ (where, μ_0 is the vacuum permeability and m_s the saturation magnetization), as a function of the substrate-to-film shear modulus ratio G_s/G_f, in the absence of stretching ($\lambda = 1$).

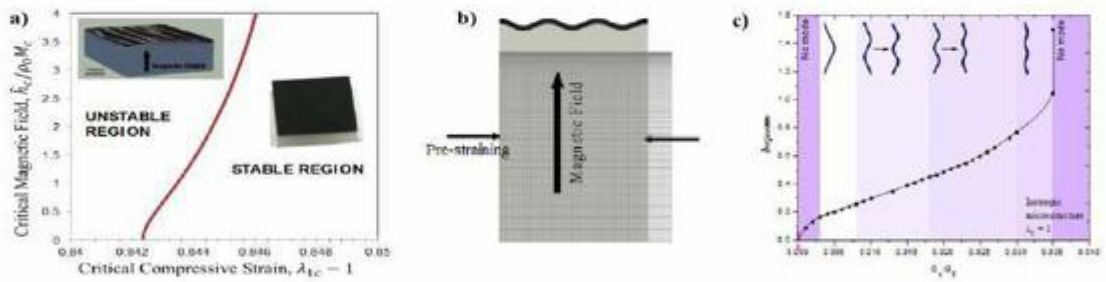

Figure 1: (a) Pre and post-bifurcation regime of a MRE film-substrate block after the application of magneto–mechanical loadings; (b) Directions of load application and (c) Critical value of the dimensionless applied magnetic field $b_c/\mu_0 m_s$ as a function of the substrate-to-film shear modulus ratio G_s/G_f, in the absence of stretching ($\lambda = 1$).

*Erato Psarra. Email: erato.psarra@gmail.com

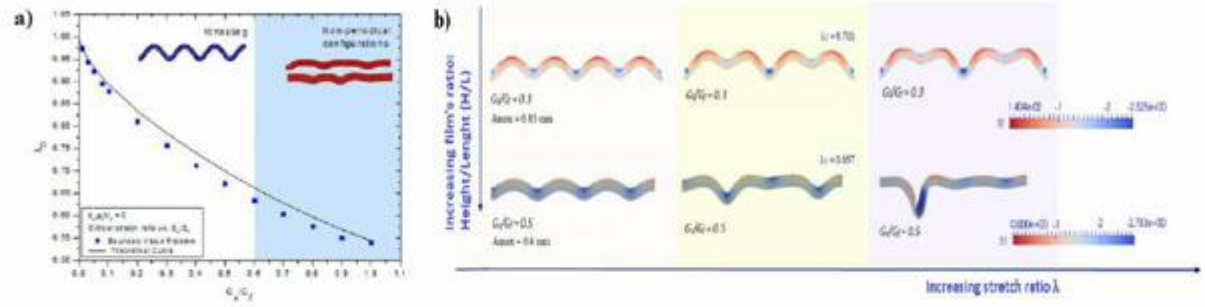

Figure 2: (a) Critical value of the stretch ratio λ_c as a function of the substrate-to-film shear ratio G_s/G_f, in the absence of external magnetic field ($b = 0$) and (b) Different shape configurations as a function of the substrate-to-film shear ratio G_s/G_f and the compressive load λ, in the absence of external magnetic field. A_m denotes the maximum wrinkle amplitude.

Figure 2a shows the critical value of the stretch ratio λ_c as a function of the substrate-to-film shear ratio G_s/G_f, in the absence of external magnetic field ($b = 0$). A finite wavelength wrinkling is observed for $G_s/G_f \leq 0.6$, while for higher than this threshold values, the post–bifurcated configuration becomes non–periodic, indicating possible initiation of creases. Figure 2b reveals the rich morphological post–bifurcated evolutionary behavior of the system, in the parameter space of λ loading and G_s/G_f ratio.

FABRICATION & EXPERIMENTS

The substrate and the film are fabricated using standard silicones (e.g., ECOFLEX Shore). The reinforcing spherical particles are in form of carbonyl iron powder. The materials are manufactured in the absence of magnetic field, hence leading to isotropic MREs (Figure 3a,b,c). Different filler volume fractions are tested. The manufacturing process is a typical cross–linked polymer obtained by 3 min mixing and 7 min degassing. To cast the material into the $40\ x\ 40\ x\ 40\ (mm^3)$ aluminum mold, first we pour the film and immediately after the substrate on the top of the film. The bilayer is subjected to a 60 min thermal processing at 70^oC.

Purely mechanical, purely magnetic and combined magneto–mechanical tests are carried-out to experimentally reveal the wrinkling effect. The magneto–mechanical experiment takes place into a 0.8 T maximum amplitude electro–magnet, while the pre–stretch is applied by a $3D$ printed compression device, able to be incorporated into the magnet. Figure 3d shows wrinkling at a critical magnetic field $b = 0.29\ T$ and a critical pre–strain $\lambda = 0.85$. The experiments are found to be in accordance with the numerical and the analytical results.

CONCLUSIONS

The study involves the development of novel fabrication techniques and experimental testing procedures, combined efficiently with advanced theoretical and numerical models and tools. These altogether allow for the in-depth analysis and understanding of the coupled nonlinear structure–property relation of the MREs, whereby we guide the design of a combined magneto–mechanical wrinkling surface pattern.

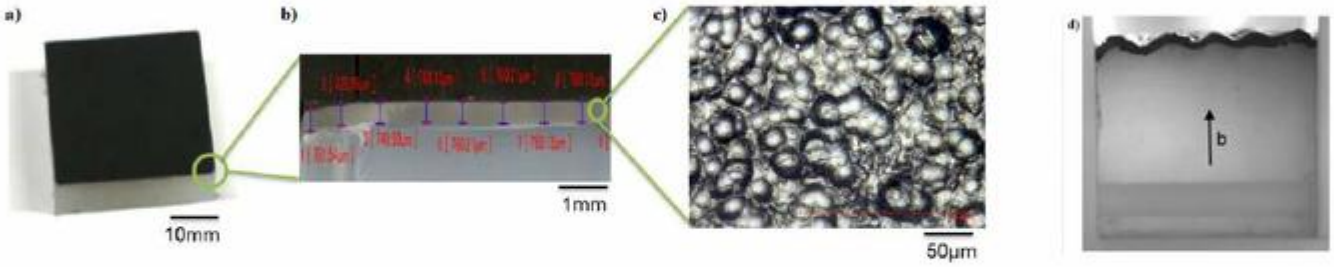

Figure 3: (a) Macroscopic view of the MRE film–substrate block; (b) Microscopic topography of the MRE film–substrate block; (c) MRE film microstructural mophology by Keyence Microscopy, c=30% particle volume fraction and (d) Instability of the Shore-0050/c=25% CIP MRE film adhered on the Shore-0010 substrate for $40\ x\ 40\ x\ 28\ (mm^3)$ block, of $0.8\ mm$ film thickness, pre-stretched with $\lambda = 0.85$ and $b_c = 0.29\ T$, giving 5 wrinkles along its length.

References

[1] Audoly B., Boudaoud, A.: Buckling of a stiff film bound to a compliant substrate. Part I. Formulation, linear stability of cylindrical patterns, secondary. J. Mech. Phys. Solids 56:24012421, 2008.

[2] Danas K., Triantafyllidis, N.: Instability of a magnetoelastic layer resting on a non-magnetic substrate. J. Mech. Phys. Solids 69:6783, 2014.

[3] Kankanala S., Triantafyllidis, N.: Magnetoelastic buckling of a rectangular block in plane strain. J. Mech. Phys. Solids 56:11471169, 2008.

WRINKLING BEHAVIOR OF AN INFLATED DIELECTRIC ELASTOMER BALLOON

Guoyong Mao, Xiaoqiang Huang, Junjie Liu, Mazen Diab & Shaoxing Qu[a)]
Department of Engineering Mechanics, Zhejiang University, Hangzhou, Zhejiang, China

Summary Wrinkles are often observed in a dielectric elastomer membrane when it is pre-stretched, inflated and then electromechanically activated. In this study, a hybrid experimental and analytical study is conducted to investigate the role of various parameters, i.e., the initial pre-stretch, initial inflation pressure and applied voltage, on the wrinkling behavior of an inflated dielectric elastomer balloon, such as the nucleation sites, critical voltage and type of wrinkles. Snap-through instability and electrical breakdown of the activated membrane are also analysed. Three-dimensional phase diagrams that delineate the different operation conditions of the activated dielectric elastomer membrane are constructed to aid designing soft actuators.

INTRODUCTION

Dielectric elastomer (DE) as one kind of electroactive polymers, has attracted extensive studies in the field of smart materials and structures, due to its superior properties, such as voltage-induced large deformation, fast response, quiet operation, high energy density, light weight and low cost. DE is widely used as a soft transducer with unique electromechanical property [1]. A typical DE transducer is composed of a DE membrane sandwiched between two compliant electrodes (such as carbon grease). When subjected to a high voltage, the DE membrane contracts out-of-plane and extends largely in-plane.

Usually, a DE membrane undergoing large deformation can experience three types of failure: mechanical, electrical and pull-in instability. This electromechanically-induced large deformation needs to be studied and understood in order to control it and tailor it to suit the applications as soft transducer. Generally speaking, instabilities, including pull-in instability, snap-through instability, wrinkling and creasing, may lead to the failure of DE structure. Therefore, suppression of such instabilities is very important. On the other hand, mechanical instabilities accompanied by large deformation can, if rationally harnessed, pave the way for new functions and applications.

Recently, we conducted experimental and theoretical studies to investigate the wrinkling instability of a pre-stretched DE membrane subject to a combination of internal pressure and high voltage [2]. We set up the analytical model for the inflated DE membrane and study the wrinkling instability of the balloon considering the effect of pre-stretch, initial inflation pressure and applied voltage [2]. We then create a bifurcation diagram that delineates homogenous zone, snap-through instability and wrinkle instability for the DE membrane.

EXPERIMENT

The experimental setup is schematically shown in Fig. 1 of our previous publication [2]. Wrinkles are observed when a step voltage is applied on the inflated DE balloon. The substantial observations are summarized in the following. (i) The geometric characteristics of the wrinkle morphology and the nucleation sites depend on the inflation pressure, the applied voltage, and the prestretch. (ii) The critical voltage to nucleate wrinkle decreases as the inflation pressure increases. (iii) The location to nucleate the wrinkle shifts from the center to the boundary of the membrane as the inflation pressure increases. (iv) The wrinkle morphology changes from stripe-like wrinkles to labyrinth-like wrinkles when increasing the voltage. (v) The nucleation sites and types of wrinkles with initial pre-stretch near 1 are different from the above observations with larger pre-stretches.

THEORETICAL PREDICTIONS

The experimental results showed that the nucleation sites and pattern are dominated by the initial inflation pressure and the voltage. Moreover, pre-stretching the DE membrane can affect wrinkling instability of the inflated DE balloon. In the following, analytical study is necessary to predict the wrinkling behavior of the DE membrane as a function of the pre-stretch, initial inflation pressure and voltage. In our study, the DE membrane is modeled using the membrane theory, and the key assumptions in deriving the analytical model are stated as follows: (i) The shape change of the DE membrane during charging is assumed to be negligible; (ii) The total stress ($\boldsymbol{S}^{+}$) in the current configuration is the sum of the mechanical stress ($\boldsymbol{S}^{-}$) due to the mechanical loading and the compressive Maxwell stress ($-\boldsymbol{S}^{+M}$) induced by the electric field; (iii) If either of the two in-plane stress components, S_i^{+} (i = 1, 2) becomes negative, the membrane wrinkles immediately12. If $s_2^{+} < 0$ and $\left|s_1^{+}\right| < 0.5\left|s_2^{+}\right|$, stripe-like wrinkles along the circumferential direction nucleate. If $s_1^{+} < 0$, $s_2^{+} < 0$ and $\left|s_1^{+}\right| \geq 0.5\left|s_2^{+}\right|$, labyrinth-like wrinkles emerge. We developed the governing equations for this problem [2].

[a)] Corresponding author. Email: squ@zju.edu.cn.

RESULTS

The experimental and analytical predictions show that the nucleation sites and patterns of the wrinkles of an inflated dielectric elastomer membrane are dependent on the initial inflation pressure, the voltage applied, and the prestretch. As the inflation pressure increases, the critical voltage to nucleate wrinkle decreases, while the location to nucleate the wrinkle shifts from the center to the boundary of the membrane. Moreover, by increasing the amplitude of the applied voltage, wrinkle morphology changes from stripe-like wrinkles to labyrinth-like wrinkles. The nucleation sites and types of wrinkles with initial pre-stretch near 1 are different from the above observation, i.e., those with larger pre-stretches, i.e., ≥ 2. While wrinkles are more spread throughout the surface in the former case, they are localized either near the edge or the apex of the inflated balloon in the latter. We also discuss and analyze snap-through instability and electrical breakdown of the activated membrane. As shown in Figure 1, three-dimensional phase diagrams that delineate the different operation conditions of the activated dielectric elastomer membrane are constructed.

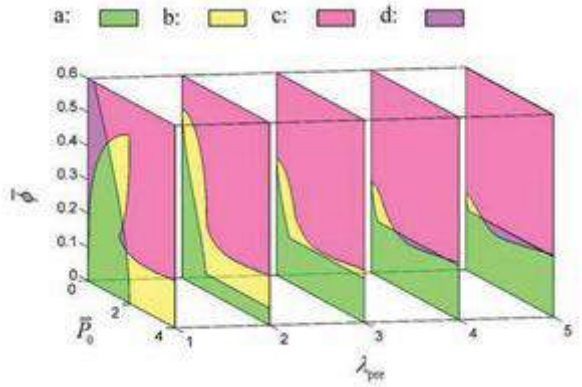

Figure 1 3D phase diagram of pre-stretched DE membrane subject to electromechanical loads. (a) Safe area. (b) Snap-through may occur if the DE balloon is inflated within this area. (c) Wrinkles occur if the DE balloon is subject to a step voltage. (d) Cross area of (a) and (c). The pre-stretch ratio is varied as $\lambda_{pre} = 1, 2, 3, 4, 5$.

CONCLUSIONS

Results obtained from both experiment and analytical model show that various parameters, i.e., the pre-stretch, initial inflation pressure and applied voltage, have significant effects on the wrinkling behavior of an inflated dielectric elastomer balloon. The critical conditions for wrinkle nucleation conditions and patterns can be tuned by prestretch, initial inflation pressure, and the voltage. Snap-through instability and electrical breakdown of the activated membrane were also determined. Three-dimensional phase diagrams that delineate the flat state, wrinkle state or snap-through zones are also presented.

References

[1] Zhao X., Wang Q.: Harnessing Large Deformation and Instabilities of Soft Dielectrics: Theory, Experiment and Application. *Applied Physics Reviews* **1**: 021304, 2014.

[2] Mao G., Huang X., Diab M., Li T., Qu S., Yang W.: Nucleation and Propagation of Voltage-driven Wrinkles in an Inflated Dielectric Elastomer Balloon. *Soft Matter* **11**: 6569-6575, 2015.

DEFECT-CONTROLLED BUCKLING OF DEPRESSURIZED ELASTIC SHELLS.

Pedro M. Reis[1,2], Anna Lee[1], Francisco López Jiménez[2], Joel Marthelot[2], and John Hutchinson[3]
[1]*Department of Civil & Environmental Engineering, MIT, Cambridge, MA 02139, USA*
[2]*Department of Mechanical Engineering, MIT, Cambridge, MA 02139, USA*
[3]*School of Engineering and Applied Sciences, Harvard University, Cambridge, MA 02138 USA*

Summary We revisit the classic problem of buckling of spherical elastic shells under pressure loading, with an emphasis on determining the role that engineered imperfections have on the critical buckling pressure. Since the 1960's numerous theoretical and computational studies have addressed this canonical Mechanics problem, but there is a striking lack of precision experiments to corroborate these predictions. We perform an experimental investigation where thin shells of nearly uniform thickness are fabricated by the coating of hemispherical molds with a polymer solution, which upon curing yields the elastic structure. Moreover, our manufacturing technique allows us to introduce a single dimple-like defect with controllable geometric properties. By systematically varying the amplitude of this defect (smaller than the thickness of the shell) we study the effect that these imperfections have on the buckling strength of our spherical shells. Small deviations from the spherical geometry result in large reductions in the buckling pressure and our experimental results agree well with existing theories. We then perform a broader exploration for other classes of defects, for which theoretical predictions are yet to be developed.

FABRICATION OF OUR THIN ELASTIC SHELLS

We have developed of a coating technique to fabricate nearly uniform hemispherical thin elastic shells that is analogous to the traditional recipe to make chocolate eggs. We start with volume of liquid solution – Vinylpolysiloxane (VPS) or Polydimethylsiloxane (PDMS) – and pour it onto a rigid spherical mold (inset of Fig. 1a). Gravity induces drainage and viscosity of the fluids resists it. The drainage dynamics is such that it leads to uniform coatings frozen in time as the polymer cures, which are subsequently peeled off from their mold. We have studied how the curing of the polymer affects the drainage dynamics and eventually selects the final shell thickness, h_f, and sets its uniformity (approximately 7% standard deviation in h_f between the pole and the equator). Using this technique we have fabricated shells in the range $30 < h_f\,[\mu\quad] < 800$.

A series of experiments has been performed where we have systematically varied material (VPS and PDMS, at different temperatures) and geometric (radius of the mold, R) parameters. The results are plotted in Fig. 1a, where we find that the shell thickness scales as $h_f \sim R^{1/2}$. The square-root dependence of h_f on R can be rationalized by balancing the characteristic curing time, τ_c, of the polymer solution against the characteristic drainage time, $\mu_0 R/(\rho g h_f^2)$, obtained when balancing the viscous stresses and gravity in the lubrication layer, to yield $h_f \sim \sqrt{\mu_0 R/[\rho g \tau_c]}$, where μ_0 is a characteristic viscosity of the polymer, ρ its density, and g is the acceleration of gravity. The fact that all the data collapse onto a master curve (irrespective of the polymer and curing temperature, over a wide range of R) supports this scaling analysis. We have also developed a more formal lubrication theory for the flow field that takes the rheology of the polymer into account, which is able to even more accurately predict the experimental results.

The robustness of the coating technique and its flexibility, two critical features for providing a generic fabrication framework, are shown to be an inherent consequence of the flow field (memory loss). Moreover, the shell structure is both independent of initial conditions and tailorable by changing a single experimental parameter: the waiting time between the preparation of the polymer solution and the pouring onto the mold.

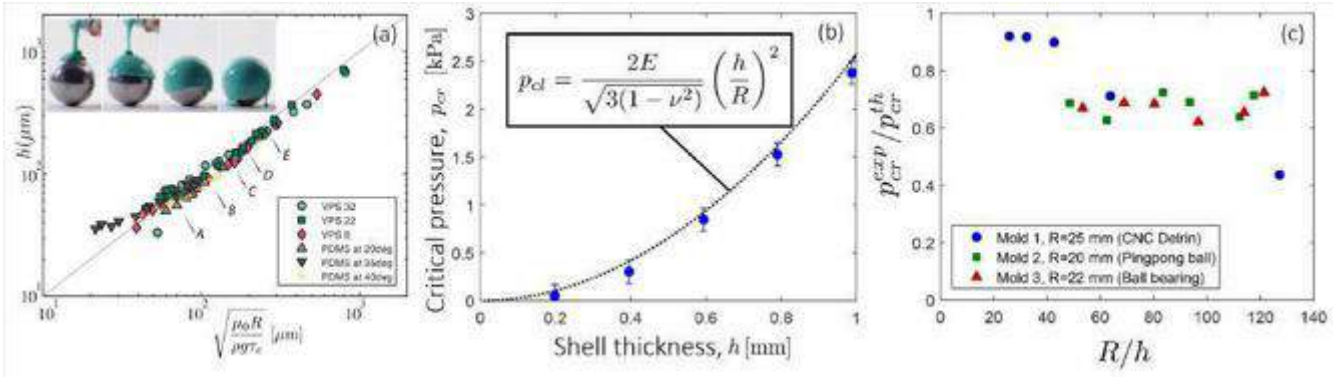

Figure 1: (a) Final thickness of the elastic shells fabricated using a coating technique (inset). The solid line corresponds to the scaling $h_f \sim \sqrt{\mu_0 R/[\rho g \tau_c]}$. (b) Critical buckling pressure as a function of shell thickness. The dashed line corresponds to the classic prediction, Eq. (1). (c) Knockdown factor as a function of R/h for three different shells (see legend).

CRITICAL BUCKLING PRESSURE AND KOCKDOWN FACTORS

We proceed by performing mechanical tests on shells that were fabricated using the mechanism described in the previous section. In Fig. 2b, we plot the experimentally measure critical pressure for the onset of buckling (imposed volume conditions), and compare the results with the classic prediction [1]:

$$p_{cl} = \frac{2E}{\sqrt{3(1 \nearrow \nu^2)}} \left(\frac{h}{R}\right)^2, \tag{1}$$

where E is the Young's modulus of the polymer and $\nu \approx 0.5$ its Poisson's ratio. The classic theory consistently underpredicts the data, as expected due to the presence of material imperfections. In Fig. 1c, we plot the ratio of the critical pressures measured experimentally and the prediction from Eq. (1), as a function of R/h and observe knockdown factors of approximately 30%, consistently with classic experimental results in the literature. These knockdown factors can be attributed to material imperfections (e.g. small air bubbles trapped during the curing of the polymer).

TUNING THE CRITICAL BUCKLING PRESSURE THROUGH GEOMETRIC IMPERFECTIONS

The fabrication protocol described above was modified to produce thin shells containing engineered geometric imperfections at the pole. The starting point is a thick VPS shell fabricated using the original method, which is itself used as a flexible mold (light green in Fig. 2a). Fresh liquid polymer is then poured onto this spherical mold (dark green in Fig. 2a), and the ensemble is immediately placed under an Instron machine to apply an indentation displacement, w. This indentation load deforms the flexible mold such that the final thin shell (upon curing and after pealing it from the mold) has a 'dimple-like' geometric imperfection with an amplitude that can be accurately set by varying w. In Fig. 2b, we present the angular profile of the imperfection (calculated with Finite Element Modeling for an indentation scenario during fabrication identical to the experiments, in the range $30 < w\,[\mu \quad] < 2\ \ 0$) and find that our shells have a profile similar to the "Type 1" defects considered in the seminal paper by Koga and Hoff [2]. This now enables us to establish a direct connection to the predictions by Hutchinson [3], which, to the best of our knowledge, had to date not been directly compared to experimental data. In Fig. 2c, we plot the experimental critical buckling pressure, normalized by the classic prediction Eq. (1), as a function of the dimensionless amplitude of the geometric defect, $\delta = w/h$. Our data closely follows the theoretical predictions, which do however provide a consistent over-prediction. These findings have motivated us to consider the possibility that non-axisymetric considerations at the onset of buckling may be important to more accurately describe the process.

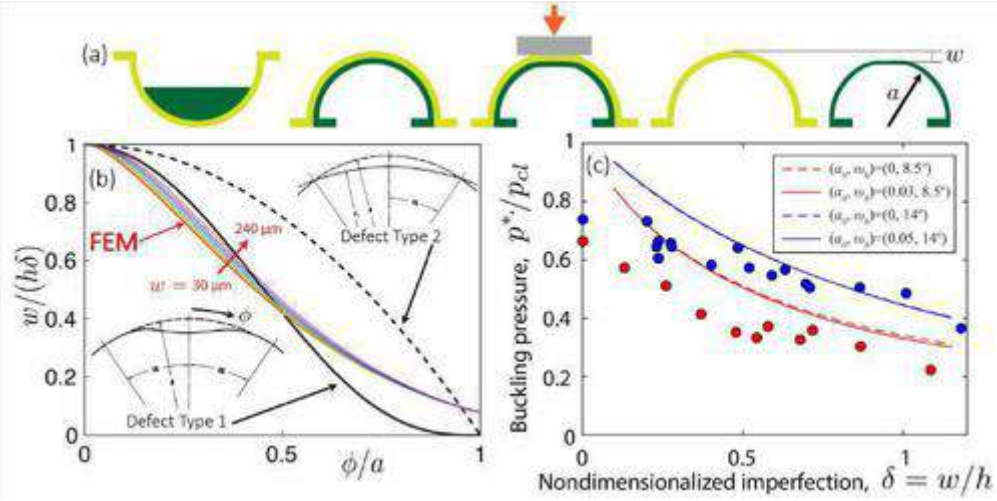

Figure 2: (a) Schematic of the experimental protocol used to fabricate nearly spherical shells with a well defined geometric imperfection at its pole. (b) Angular profile of the geometric defects of our shells compared with for Type 1 and Type 2 defects previously considered by Koga and Hoff (image adapted from Ref. [2]). (c) Kockdown factor as a function of the amplitude of the imperfection. The lines are theoretical prediction from axisymmetric buckling theory [2, 3].

References

[1] R. Zoelly, " Uber ein Knickungsproblem an der Kugelschale." Dissertation, Zurich (1915).

[2] T. Koga and N.J. Hoff, "The axisymmetric buckling of initially imperfect complete shells", *Int. J. Solids Structures*, **5**, 679-697 (1969).

[3] J.W. Hutchinson, "Imperfection sensitivity of externally pressurized spherical shells", *J. App. Mech*, **34**(1), 49-55 (1967).

TRANSFORMATION SHIFT OF PERIODIC CELLULAR STRUCTURE BY CONTROLLING INTERNAL STIFFNESS

Hiro Tanaka*[1], Tofu Nakanishi[1], and Yoji Shibutani[1]
[1]*Department of Mechanical Engineering, Osaka University, Suita, Osaka, Japan*

Summary In some instability phenomena as typified by Euler buckling, the pre-bifurcation deformation is infinitesimal. Engineers are used to make a design to prevent the structure from falling down because of such unstable deformation. In this study, we propose a novel bifurcation system for two-dimensional cellular structure, which shows that the pre-bifurcation deformation is not small. We previously developed the structural unit, the geometry of which exhibits eight-fold rotational symmetry. Controlling the point of loading, the system can switch between two types of auxetic transformation; the structure transforms into diamond cells or square cells. We here newly model a modified structure by inserting linear springs between periodic unit cells and demonstrate the large deformation analyses under uniform compression, which show the switching mechanism for the two different motions after the structure undergoes some extent of cell deflection. We also discuss about the analogy mechanism of a linkage structure.

TRANSFORMATION SHIFT OF A PERIODIC STRUCTURE WITH CELL DEFLECTION

We consider the periodic assembly with a cell unit in the fashion of a square lattice [1, 2], as shown in Fig. 1(a). The periodic cells are pivotally connected at their vertices on the boundaries. Additionally, a linear spring is periodically inserted between adjacent cells. We assume all cell walls have a dimension of ℓ, stretching stiffness EA and bending stiffness EI. Then, the couples of cells of same color are welded and the couples of cells of different color are pinned, respectively. We here define a dimensionless parameter as $\tilde{k} \equiv k\ell^3/EI$, where k is the constant of a half-length spring.

By applying the finite element method with beam elements [2], we perform the large deformation analyses of the proposed structure for a change in $\tilde{k}$ under uniform compression load W. Figures 1(b) and (c) show the obtained stress–strain curves for $\tilde{k} = 10.5$ and 11.0, respectively, The two curves clarify that there is a bifurcation point between $\tilde{k} = 10.5$ and 11.0 and that the structural deformation shifts to a square patterned cell parallel to the loading direction when $\tilde{k} \leq 10.5$ and does to a diamond patterned cell when $\tilde{k} \geq 11.0$ (see the insets in Figs. 1(b) and (c)). We hereafter call the former motion as Motion II and the latter as Motion I. In this structural system, increasing $\tilde{k}$ changes the distortion of the internal square cells against compression, which shifts the balance point of the resultant moment inside the squares. That is the switching mechanism whether the squares rotate in the direction of Motion I or II.

The switching mechanism obtained provides the additional interpretation that the deformation of the finite-sized structure with $\tilde{k} \approx 11.0$ strongly depends on the boundary conditions of the external loading. In other words, there is a possibility of selecting the two types of deformations at will to control the boundary conditions, which might be useful in engineering applications.

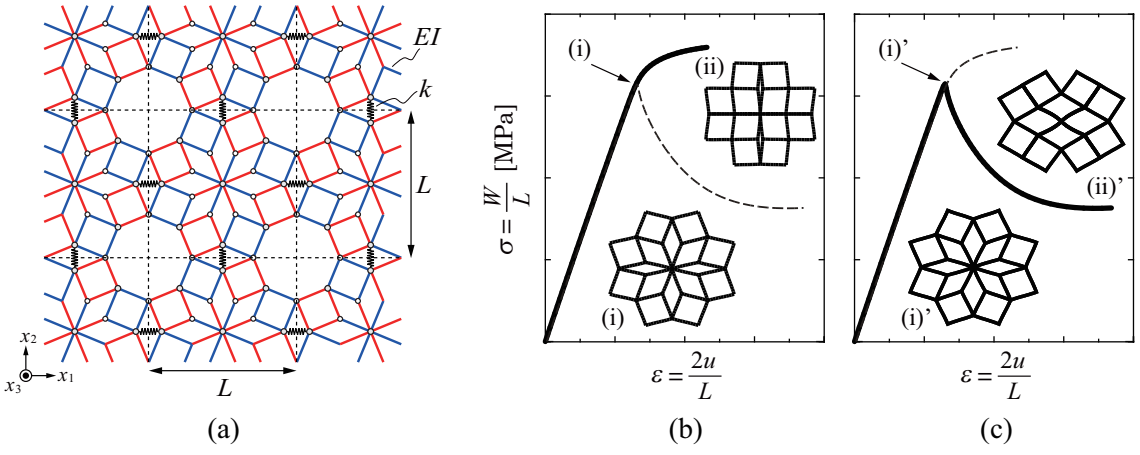

Figure 1: (a) The periodic cellular structure [2]; the two equilibrium paths calculated by the compression analyses: (b) Motion II for $\tilde{k} = 10.5$ and (c) Motion I for $\tilde{k} = 11.0$.

*Corresponding author. Email: htanaka@mech.eng.osaka-u.ac.jp

THE MECHANICAL ANALOGY OF LINKAGE STRUCTURE

It is well known that there is an energy equivalence between structural mechanics and molecular mechanics [3]. In a two-dimensional beam structure, the strain energy of a uniform beam under pure axial force and pure bending moment can be respectively described as

$$U_A = \frac{1}{2}\frac{EA}{\ell}(\Delta\ell)^2 \ \text{ and } \ U_M = \frac{1}{2}\frac{EI}{\ell}(2\alpha)^2, \tag{1}$$

where $\Delta\ell$ is the axial stretching deformation and α is the rotational angle at the ends of the beam. In comparison with atomic structure, a direct relationship between the structural mechanics parameters EA, EI and the molecular mechanics parameters is obtained as follows:

$$\frac{EA}{\ell} = k_r \ \text{ and } \ \frac{EI}{\ell} = k_\theta, \tag{2}$$

where k_r and k_θ are the bond stretching force constant and bond angle bending force constant, respectively. According to the relationship between structural and molecular mechanics, we here represent the cell deflection with the bending angle of a bond to construct the bar-and-joint framework with flexible squares linked by rotational springs as shown in Fig. 2(a). Let the stiffness of the rotational springs be r and the linear spring constant be k, respectively, we redefine the dimensionless parameter as $\tilde{k} = kL^2/r$.

We perform the large deformation analyses of the linkage structure subjected to uniform compression loading W for $\tilde{k} = 4.6$ and 4.7. Figure 2(b) shows the calculated stress–strain curves and it can be observed that the structure behaves as Motion II for $\tilde{k} = 4.6$ and does Motion I for $\tilde{k} = 4.7$. The bifurcation of the transformations is located at $\varepsilon \approx 0.4$. The shifting mechanism obtained here is similar with that of the proposed cellular structure with cell deflection. Thus, the distortion of the linked square induced by a change in the bonding angle shifts the equilibrium state of the moment, which causes switching to Motion I or II. This suggests that the linkage structure has a wide range of applications from molecules to architecture and that the simple mathematical model might allow the derivation of the exact solution of our proposed bifurcation system.

Acknowledgements

This work was supported by the JSPS KAKENHI for Young Scientists (A) and for Scientific Research (A) (grant nos. 25709001 & 26249002).

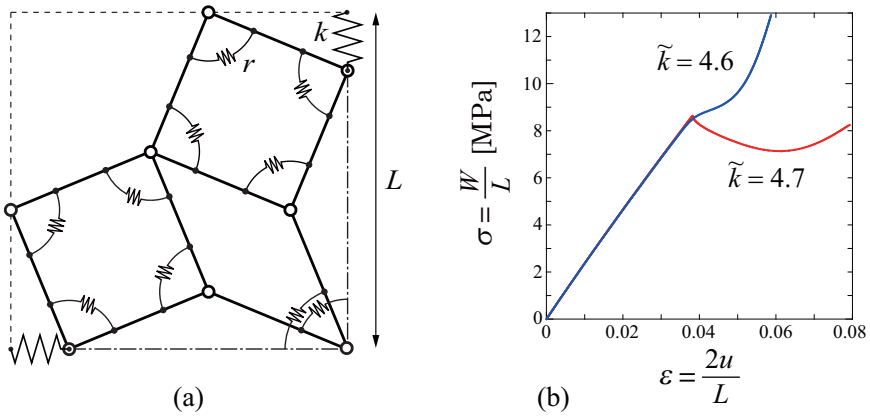

Figure 2: (a) The first of the eight structural elements of the proposed periodic linkage structure; (b) The calculated stress–strain curves of the deformed structures under uniform compression. The structure transforms to Motion II for $\tilde{k} = 4.6$ and to Motion I for $\tilde{k} = 4.7$.

References

[1] Tanaka H.: Bi-stiffness Property of Motion Structures Transformed into Square Cells. Proc. R. Soc. A 469:20130063, 2013.

[2] Tanaka H., Nakanishi T., Shibutani Y.: Switching Between Two Types of Auxetic Behavior of Two-dimensional Periodic Cells with Square Rotation. Phys. Stat. Sol. (b) (accepted).

[3] Li C., Chou T.-W.: A Structural Mechanics Approach for the Analysis of Carbon Nanotubes. Int. J. Solid. Struct. 40:2487-2499, 2003.

NON-LINEAR RESPONSE OF ELASTIC SNAP-THROUGH STRUCTURES

Steven Wehmeyer[1], Matthew R. Begley *[1,2], Francis W. Zok[2], Christopher Eberl[3], and Peter Gumbsch[3]

[1]*Mechanical Engineering, University of California, Santa Barbara, California*
[2]*Materials, University of California, Santa Barbara, California*
[3]*IWM, Freiburg, Germany*

Summary Moderate rotation beam theory is used to map out a complete quasi-static analytical solution. Insight from the quasi-static solution is exploited to derive a single degree-of-freedom dynamic model. Complete regime maps are presented for the macroscopic lattice stress and strain associated with snap-through, stable configurational changes, and the peak strains in the struts before and after snap-through. It is demonstrated that snap-through behavior can only be achieved without densification by including struts in the loading direction that are twice the lattice spacing. The paper concludes with a brief discussion of lattice concepts that enable exploitation of these behaviors.

INTRODUCTION

While topology optimization of linear behavior appears to be well in hand, the understanding and exploitation of non-linear behaviors associated with large lattice deformation is far less established. This is particularly true for lattices that experience large deformation yet small strains, which exhibit highly non-linear behavior despite the fact that members remain elastic. Such behaviors are critical for lattices with very low relative density since elastic buckling of the members is prevalent, as opposed to higher relative density lattices that are governed by inelastic deformation in stretch-dominated members.

Many have analyzed the structure presented here for load-deflection response [1], as well as used the highly non-linear response as a benchmark test for different non-linear solution techniques for finite element analysis [2]. Figure 1A shows one lattice concept for which the derived governing equations are applicable; this concept is motivated by the fact that the geometry is arguably the simplest cellular lattice topology that will exhibit snap-through behaviors. The lattice material consists of slender members oriented at an angle with respect to the global (X_1, X_2) coordinate system. For compression in one direction and suitable constraint in the other, one obtains a variety of behaviors, as shown in Figures 1B and 1C. Depending on the strut angle and slenderness ratios, one can obtain: (*i*) non-linear but purely monotonic behaviors with no snap-through, (*ii*) bi-directional snap-through (Figure 1B), and (*iii*) snap-through that leads to a second stable equilibrium configuration upon unloading (Figure 1C). Referring to Figure 1, the inclusion of finite-sized 'nodes' at strut intersections is motivated by the fact that certain behaviors would otherwise be influenced by densification (self-contact), because such transitions occur at large displacements relative to the projected length of the struts in the loading direction.

RESULTS

This work presents a comprehensive analytical solution that elucidates the combinations of geometry and loading that produce each type of behavior (Figure 2). These governing equations can be used in designing non-linear structures through examination of relative density, macroscopic strains before and after snap-through, etc (see Figure 3). The full dynamic equations, and insights generated by the quasi-static solutions, are used to develop an idealized single degree of freedom non-linear model, which is used to elucidate the nature of structural damping and identify scenarios in which quasi-static behaviors are sufficient to infer cyclic response (Figure 4). This enables rapid computation of complete regime maps indicating the type of behavior expected, as well as contour maps of the critical loads, deflections and strut strains associated with unstable transitions in lattice configurations.

Hysteresis in a loading-unloading cycle is typically inferred from the instability points identified with *quasi-static* solutions. This implicitly assumes that there is sufficient damping in the material (or boundary conditions) to suppress dynamic oscillations during snap-through. While sometimes true, it is not clear from prior treatments when such assumptions are valid. To gain general insight into the hysteresis introduced by unstable transitions, this work adopts a Kelvin-Voight viscoelastic constitutive law, which serves a simple purpose: it introduces a dissipative time-scale that governs the transition from the quasi-static time scale associated with slow loading rates to the much faster inertial time-scale triggered by an instability. This can be used to accurately determine instances in which quasi-static solutions yield acceptable estimates of hysteretic losses.

References

[1] William F. W.: An approach to the non-linear behaviour of the members of a rigid jointed plane framework with finite deflections. The Quarterly Journal of Mechanics and Applied Mathematics 17(4):451-469, 1964.

[2] Wood R.D., Zienkiewicz O.C.: Geometrically nonlinear finite element analysis of beams, frames, arches, and axisymmetric shells. Computers & Structures. 7(6):725-735, 1977.

*Corresponding author. Email: begley@engr.ucsb.edu

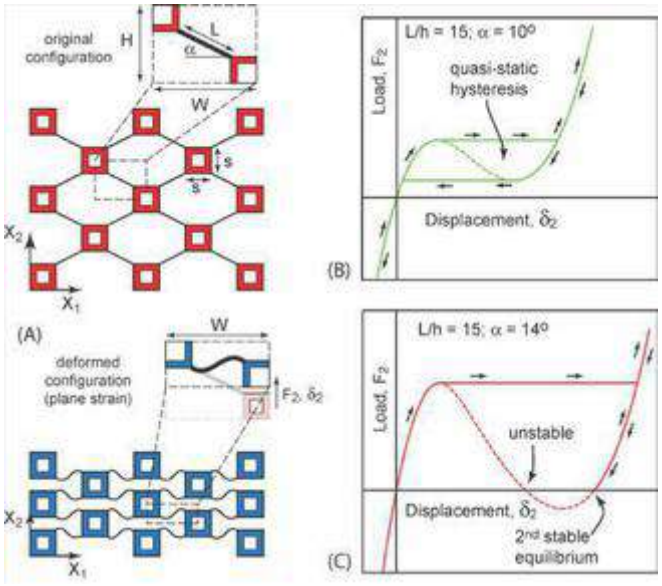

FIG 1. Lattices formed from straight-sided struts. For some configurations, bistable behaviors can only be achieved by using finite-sized strut connections that eliminate self-contact at large deformation.

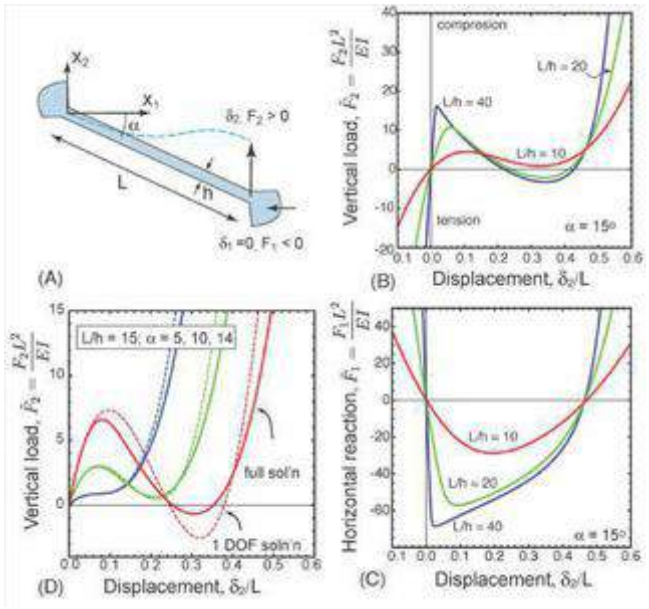

FIG. 2. Typical plane strain (e1 = 0) behaviors of angled struts: (A) a comparison of full solutions and approximate solutions, B) inferred quasi-static response for cycling under load control with constant hysteresis, (C) inferred quasi-static response for cyclic under load control where shakedown occurs after the first cycle, due to a second stable equilibrium state.

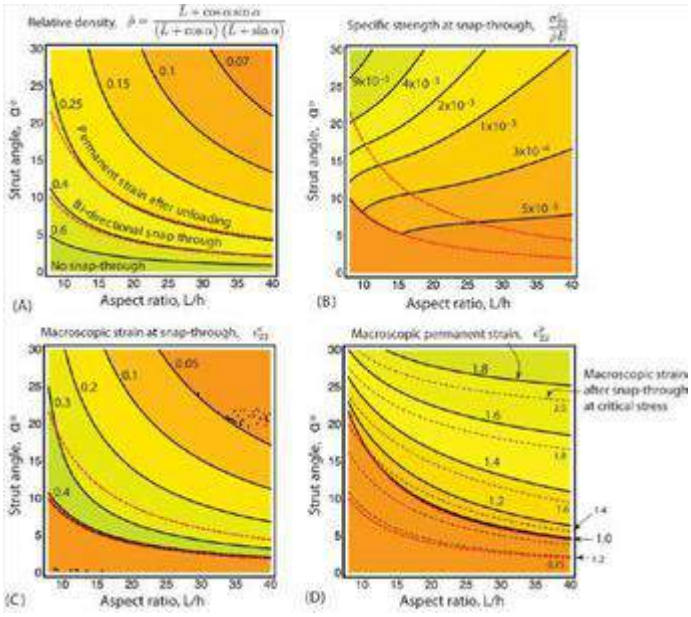

FIG 3. Regime maps for design of bistable lattices. Three regimes include no snap-through, bi-directional snap-through, and permanent strain after unloading.

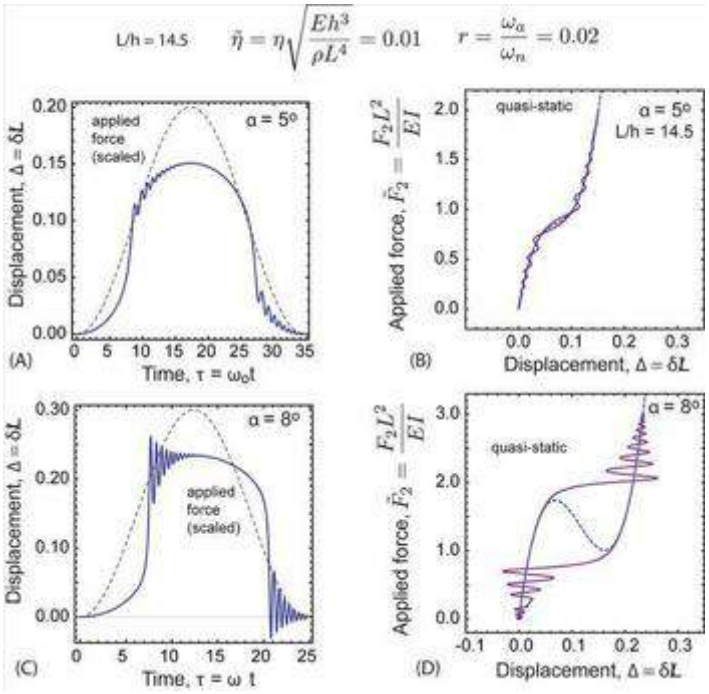

FIG 4. Typical plane strain dynamic behaviors of angled struts with low-frequency applied force. On the left, the dashed line is a scaled plot of the applied force as a function of time; on the right, the dashed line is the quasi-static force-displacement relationship (assuming displacement control).

DYNAMIC STABILITY OF BIAXIALLY STRAINED THIN SHEETS UNDER HIGH STRAIN-RATES

G. Wen*[1] and N. Triantafyllidis[1,2,3]
[1]*Laboratoire de Mecanique des Solides, C.N.R.S. UMR7649*
Ecole Polytechnique, FRANCE
[2]*Département de Mecanique, Ecole Polytechnique, FRANCE*
[3]*Aerospace Engineering Department & Mechanical Engineering Department (emeritus)*
The University of Michigan, USA

Summary This work pertains to the stability of structures under rapid loading rates when inertia is taken into account. In contrast to the widely used approach using modal analysis to determine the structure's fastest growing eigenmode — meaningful only for slow loading rates — the present study analyzes the time-dependent response to spatially localized perturbations in structures, in order to understand the initiation of the corresponding failure mechanisms. This approach is followed here to study the stability of rapid biaxial stretching of thin plates. The nonlinear time evolution of a such a perturbation is studied numerically and it is shown that these structures are stable until the time when the condition for the loss of ellipticity is reached. An analytical method, based on linearization, is used to define the size of the influence zone of a point-wise perturbation and we study its dependence on constitutive laws and loading conditions.

BACKGROUND

The issue of dynamic stability of structures is an important engineering problem and a substantial amount of work has been done to investigate the response of structures to impulse or time-dependent loads. As a result, and due to the many possible definitions for the stability of time-dependent systems, the term *dynamic stability* encompasses many classes of problems and different physical phenomena and has many interpretations, with inertia being the only common denominator.

In the absence of inertia, the processes of failure by a bifurcation instability mode in elastic solids and structures is well understood and a general asymptotic methodology based on modal analysis has been developed; this approach has also been used for the dynamic stability problem of elastic structures. Another idea, popular in fluid mechanics, has also been used for the dynamic stability analysis of solids with more general constitutive laws under high rates of loading, according to which one seeks the solid's fastest growing eigenmode, or the wavelength associated with lowest necking strain. This method has been repeatedly applied in the study of dynamic stability of various elastoplastic structures (bars, rings, plates, shells e.t.c.) under high loading rates where the failure pattern and size of fragments is of interest.

However, experimental evidence from rapidly expanding electromagnetically loaded metallic rings by [4] shows no dominant wavelength at the necked pattern of the rings. Moreover, there is no evidence of influence of strain rate on the necking strains, which are consistent with maximum force criterion of a rate independent constitutive law (Considère criterion). Motivated by these observations, [3] have recently studied the dynamic stability of an incompressible, nonlinearly elastic bar at different strain-rates by following the evolution of localized small perturbations introduced at different times. The same approach is followed here for the biaxial stretching of rapidly expanding thin plates, where we follow the time evolution of spatially localized perturbations and their interactions, using linearized stability analysis and fully nonlinear numerical calculations.

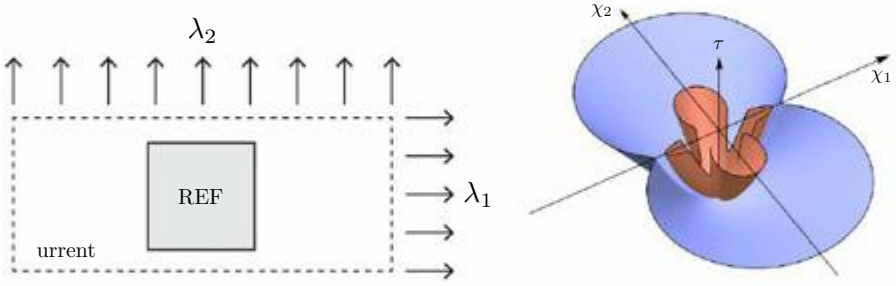

Figure 1: Left: Schematic diagram of a biaxially strained plate; Right: Typical influence cone of an initial ($\tau = 0$) perturbation at the origin ($\mathbf{X} = 0$) showing the evolution of the influence zones χ_- (in red) and χ_+ (in blue) of the slow and fast wave speeds along the corresponding radial direction.

*Corresponding author. Email: guangyang.wen@polytechnique.edu

PROBLEM SETTING AND RESULTS

The novel idea here is to analyze the evolution of spatially localized perturbations of time-dependent, rapidly strained plates under biaxial tension in order to understand the initiation of the corresponding failure mechanisms. We study a 2D, incompressible, elastoplastic (rate-independent) plate, using a nonlinear constitutive law makes sense for real structures since no unloading occurs until a point in the structure reaches the loss of ellipticity condition, at which point our calculations are terminated.

Using a finite strain deformation theory of plasticity (based on logarithmic strain), we follow the time evolution of spatially localized perturbations and their interactions. The nonlinear time evolution of such a perturbation is studied numerically using FEM and it is shown that these structures are stable until the time when the condition for the loss of ellipticity is reached. An analytical method, based on linearization, is used to define the size of the influence zone of a point-wise perturbation and we study its dependence on constitutive laws and loading conditions. More specifically we determine the extent of the influence zones χ_+ and χ_-, corresponding to the faster and slower wave speeds ν_+ and ν_- along a direction inclined by ϕ with respect to the horizontal axis at dimensionless time τ. A 3D plotting of the two influence cones for the case of a uniaxial stretching (load angle $\tan\psi = -1/2$) of a power law material with uniaxial yield strain $\epsilon_y = 0.002$ and hardening exponent $n = 0.22$ is shown in Figure 1.

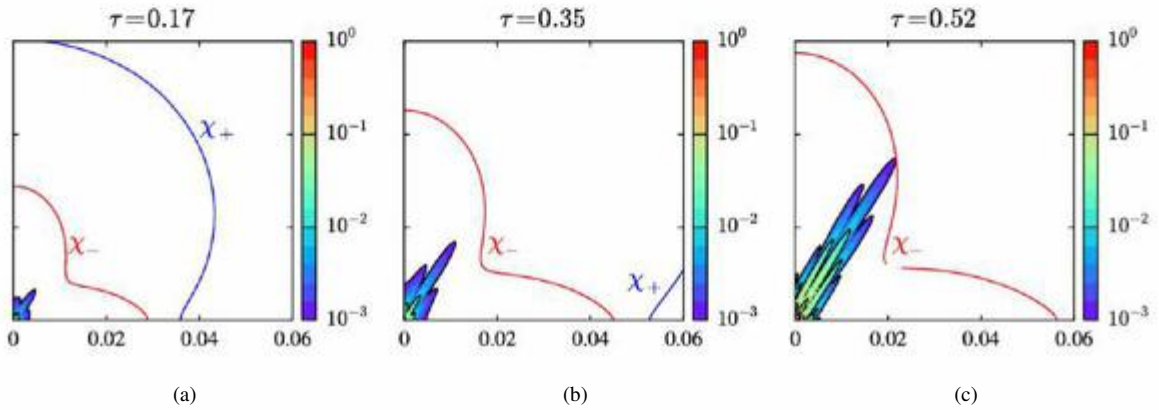

Figure 2: Green-Lagrange strain perturbation contours $\Delta E(\boldsymbol{\chi}, \tau)$ at three different dimensionless times a) $\tau = 0.17$, b) $\tau = 0.35$ and c) $\tau = 0.52 = \tau_m$, where only contours of $\Delta E \geq 10^{-3}$ are shown in color. The extent of the influence zones $\chi_-(\phi, \tau)$ and $\chi_+(\phi, \tau)$ for the slowest and fastest wave speeds ν_- and ν_+ respectively, are also shown in these figures. Results calculated correspond to a hyperelastic constitutive law with a piecewise power law uniaxial curve ($\epsilon_y = 0.002$, $n = 0.22$) and a loading angle $\tan\psi = -1/2$.

The numerical calculation of the time evolution of the time evolution of an initial ($\tau = 0$) perturbation at the origin ($\mathbf{X} = 0$) for three different dimensionless times τ is shown in Figure 2, where the last time corresponds to the onset of loss of ellipticity along one direction (the one along which the strongly localized pattern of deformation appears) in the plate.

The proposed approach is useful for the stability analysis of more realistic structures under high strain rates. As one such example we cite the recent work by [2] on the stability of a pressurized thin ring at high rates, where it is shown that for small values of the applied loading rate, the structure fails through a global mode, while for large values of the applied loading rate the structure fails by a localized mode of deformation, as also found recently in the experiments of [1]. Our study also shows the sensitivity of the size of minimum and maximum influence zones with respect to the constitutive model used, and hence the caution needed in using such calculations to predict failure patterns.

References

[1] A. Mainy and K. Ravi-Chandar. Dynamic buckling of thin metallic rings under external pressure. *MS thesis;*, 2012.

[2] T. Putelat and N. Triantafyllidis. Dynamic stability of externally pressurized elastic rings subjected to high rates of loading. *International Journal of Solids and Structures*, 51:1–12, 2014.

[3] K. Ravi-Chandar and N. Triantafyllidis. Dynamic stability of a bar under high loading rate: Response to local perturbations. *International Journal of Solids and Structures*, 58:301–308, 2015.

[4] H. Zhang and K. Ravi-Chandar. On the dynamics of necking and fragmentation – I. real-time and post-mortem observations in al 6061-O. *International Journal of Fracture*, 142:183–217, 2006.

ON AXISYMMETRIC/DIAMOND-LIKE MODE TRANSITIONS IN CORE-SHELL CYLINDERS UNDER AXIAL COMPRESSION

Fan Xu*[1] and Michel Potier-Ferry[2]

[1]*Dept. of Mechanics and Engineering Science, Fudan University, Shanghai, P.R. China*
[2]*LEM3, UMR CNRS 7239, Université de Lorraine, Metz, France*

Summary Recent interests in curvature- and stress-induced pattern formation and pattern selection motivate the present study. Surface morphological wrinkling of a cylindrical shell supported by a soft core subjected to axial compression is investigated based on a nonlinear 3D finite element model. The post-buckling behavior of core-shell cylinders beyond the first bifurcation often leads to complicated responses with surface mode transitions. The proposed finite element framework allows predicting and tracing these bifurcation portraits from a quantitative standpoint. The occurrence and evolution of 3D instability modes including sinusoidally deformed axisymmetric patterns and non-axisymmetric diamond-like modes will be highlighted according to critical dimensionless parameters. Besides, the phase diagram obtained from theoretical analyses and numerical results could be used to guide the design of core-shell cylindrical systems to achieve the desired instability patterns.

INTRODUCTION

Broad interests in surface morphological instabilities of a soft material with a stiff thin surface layer have motivated numerous research studies during past years. Recent investigations reveal that wrinkling patterns may also vary with the substrate curvature and the wrinkling process under curvature constraints becomes promising techniques for micro/nano-scale surface patterning fabrication as well as adaptive aerodynamic drag control. Curvature-induced wrinkling pattern formation and mode selection are only lately being pursued [1, 2], which demonstrates the important role played by the topological constraints of curved surfaces on instability patterns. Nevertheless, the prediction and tracing of the whole pattern evolution on the equilibrium path and the mode transition on curved surfaces in core-shell cylindrical structures represents a challenging numerical issue due to its complicated nonlinear responses and merits much further efforts.

This study aims at exploring the occurrence and post-buckling evolution of 3D wrinkling patterns in core-shell soft cylindrical structures subjected to axial compression, through applying advanced numerical methods from a quantitative standpoint. A theoretical analysis based on the nonlinear Donnell–Mushtari–Vlassov (DMV) shell equations is first carried out to qualitatively determine the critical dimensionless parameters that influence the instability patterns. Spatial pattern formation is then quantitatively investigated based on a nonlinear 3D finite element model associating geometrically nonlinear shell formulations for the surface layer and linear elastic solids for the core. The model incorporates Asymptotic Numerical Method (ANM) as a robust path-following technique to predict a sequence of secondary bifurcations on their post-buckling evolution path as the load is increased. In this work, we consider geometrically perfect core-shell cylinders without any imperfection. The numerical path-following method is employed to trace the whole post-buckling evolution in bifurcation diagrams and to describe the phase diagrams (axisymmetric/diamond-like modes) according to those critical dimensionless parameters.

THEORETICAL ANALYSIS

The theoretical analysis is conducted within the framework of the DMV shell equations that appears to be the simplest model for cylindrical thin-walled structures. It is known that this model offers good results in the cases of short-wavelength instability, which generally occurs under axial compression situation. To find the critical parameter that determines the axisymmetric/diamond-like instability patterns, a dimensional analysis is performed. By introducing some dimensionless coordinates and kinematic variables, after the manipulation of shell energy and core energy, a dimensionless parameter that is a measure of the core stiffness compared with the shell membrane stiffness can be obtained:

$$C_s = \frac{E_s}{E_f}\left(\frac{R}{h_f}\right)^{3/2}, \tag{1}$$

where the thickness of the shell and the radius are denoted by h_f and R, respectively. Young's moduli of the shell and the core are respectively expressed by E_f and E_s. The critical parameter C_s can determine a phase diagram (see Fig. 1) on pattern selection, *i.e.* axisymmetric or diamond-like mode, which well agrees with the analytical solution in [1] and our numerical results.

*Corresponding author. Email: fanxu@fudan.edu.cn

RESULTS

The 3D core-shell cylindrical system is modeled in a rather classical way, the surface layer being represented by a thin shell model to allow large rotations while the core being modeled by small strain elasticity. Indeed, the considered instabilities are governed by nonlinear geometric effects in the stiff material, while these effects are much smaller in the soft material. The model incorporates the ANM as a robust path-following technique to predict and trace a sequence of secondary bifurcations on their complicated post-buckling evolution path (see Fig. 1). The occurrence and evolution of sinusoidally deformed axisymmetric patterns and non-axisymmetric diamond-like modes are detected in the post-buckling range. Most importantly, the transition from sinusoidally deformed axisymmetric patterns to non-axisymmetric diamond-like modes is quantitatively captured according to the critical dimensionless parameter C_s.

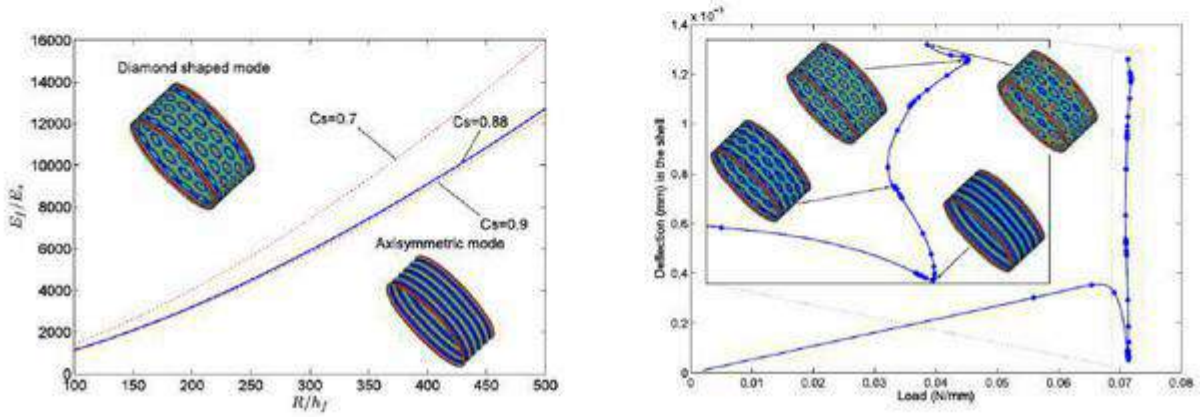

Figure 1: The left figure shows a phase diagram on pattern selection defined by Eq. (1). The blue solid curve is determined by the critical parameter $C_s = 0.88$, which corresponds to the two critical ratios, R/h_f and E_f/E_s, respectively chosen as (125, 1600) and (200, 3200) in [1]. The two red dash-dot curves give the upper and lower bounds obtained through numerical calculations. When the critical parameter $C_s \geqslant 0.9$, the instability mode is axisymmetric; whereas at a smaller value $C_s \leqslant 0.7$, the system may branch into the diamond shaped mode. The pattern selection in the narrow region $0.7 < C_s < 0.9$ appears to be quite sensitive in the numerical results. The right figure presents a bifurcation curve (axisymmetric/diamond-like mode transition) and the associated representative wrinkling modes on the post-buckling evolution path.

CONCLUSIONS

Pattern formation and post-buckling evolution of core-shell soft cylindrical systems were investigated theoretically and numerically. The critical parameter C_s that determines post-buckling pattern selection has been found qualitatively through dimensional analysis of the DMV shell equations. The further quantitative investigation is performed numerically based on a 3D finite element model. As for planar film/substrate systems, uniaxial compression generally leads to 1D sinusoidal surface wrinkles perpendicular to the loading direction [3, 4, 5]. As for core-shell cylindrical structures under uniaxial compression, buckling and post-buckling behavior mainly depends on the core stiffness measured by the dimensionless parameter C_s. Precisely, for a stiff core ($C_s \geqslant 0.9$), the buckling pattern is axisymmetric and post-bifurcation solutions are stable; whereas for a soft core ($C_s \leqslant 0.7$), the bifurcated solution branch is often subcritical and the associated instability modes are diamond shaped after secondary bifurcations.

References

[1] Zhao, Y., Cao, Y., Feng, X., Ma, K.: Axial compression-induced wrinkles on a core-shell soft cylinder: Theoretical analysis, simulations and experiments. J. Mech. Phys. Solids 73: 212–227, 2014.

[2] Stoop, N., Lagrange, R., Terwagne, D., Reis, P.M., Dunkel, J.: Curvature-induced symmetry breaking determines elastic surface patterns. Nat. Mater. 14: 337–342, 2015.

[3] Xu, F., Potier-Ferry, M., Belouettar, S., Cong, Y.: 3D finite element modeling for instabilities in thin films on soft substrates. Int. J. Solids Struct. 51: 3619–3632, 2014.

[4] Xu, F., Koutsawa, Y., Potier-Ferry, M., Belouettar, S.: Instabilities in thin films on hyperelastic substrates by 3D finite elements. Int. J. Solids Struct. 69-70: 71–85, 2015.

[5] Xu, F., Potier-Ferry, M.: A multi-scale modeling framework for instabilities of film/substrate systems. J. Mech. Phys. Solids 86: 150–172, 2016.

MULTI-STABILITY AND BIFURCATIONS OF THIN BANDS

Tian Yu[1] and James Hanna *[1]
[1]*Engineering Mechanics Program, Department of Biomedical Engineering and Mechanics, Virginia Tech, U.S.A.*

Summary Thin band- or strip-like structures are common motifs in flexible and deployable systems [1], serving as integrated connectors [2], hinges, and umbilicals. We experimentally investigate a simple configuration representing the above type, a thin elastic band with end constraints on position and orientation. These constraints correspond to a combination of compression and shear with respect to a flat rectangular rest configuration. We vary the aspect ratio of the band, and the position and clamping angle at its ends. The buckled structure remains developable up to limiting deformations that approach one of two types of state, each dominated by two singularities. At intermediate deformations, the structure may adopt many distinct stable states. Transitions between these states can be smooth or violent, and depend strongly on constraints such as the clamping angle.

In our presentation, we will relate our results to prior work on twisted strips [3, 4], and analytical models of anisotropic rods.

We employ $0.005''$-thick polyester shim stock bands of dimensions L and W. First the W-ends are displaced towards each other by a fixed distance ΔL and clamped at a fixed angle θ (see Figure 1a). Then these ends are displaced laterally by a variable distance ΔW, shearing the buckled band. The clamps are oriented vertically to minimize the effects of gravity. Shearing is performed quasi-statically, and the process is often halted so that the band can be manually manipulated into other local minima inaccessible by the shearing process.

At a limiting value of shear displacement $\Delta W = \sqrt{L_D^2 + (L - \Delta L)^2}$, where $L_D^2 = W^2 + L^2$, the band's diagonal straightens and two conical singularities begin to form at its ends. Further deformation requires stretching rather than pure bending. We characterize these limiting states as S-like or U-like, depending on whether the band lies on both sides or on one side of the plane between the clamped ends (see Figure 1).

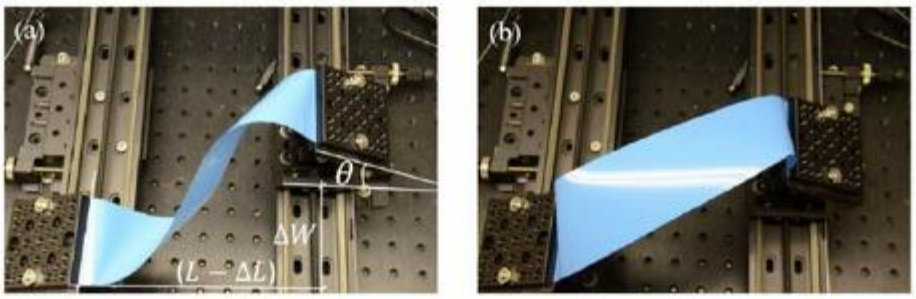

Figure 1: (a) S and (b) U configurations near the developable limit.

At intermediate values of shear displacement ΔW, a band may adopt many intermediate stable states, as shown in figure 2. States named with $+$ or $-$ are symmetric pairs, so there are nine distinct states, which degenerate into five when the clamping angle $\theta = 0°$. Our initial attempt to classify these states uses geometric features such as inflection points.

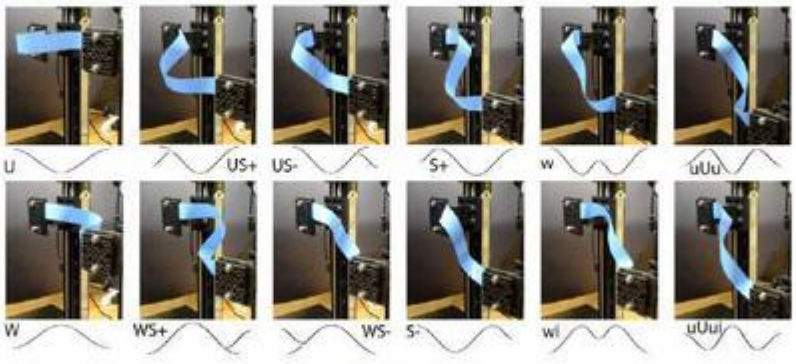

Figure 2: Twelve stable configurations of a strip with aspect ratio $W/L = 0.125$, normalized compression $\Delta L/L = 0.5$, and clamping angle $\theta \approx 5°$.

*Corresponding author. Email: hannaj@vt.edu

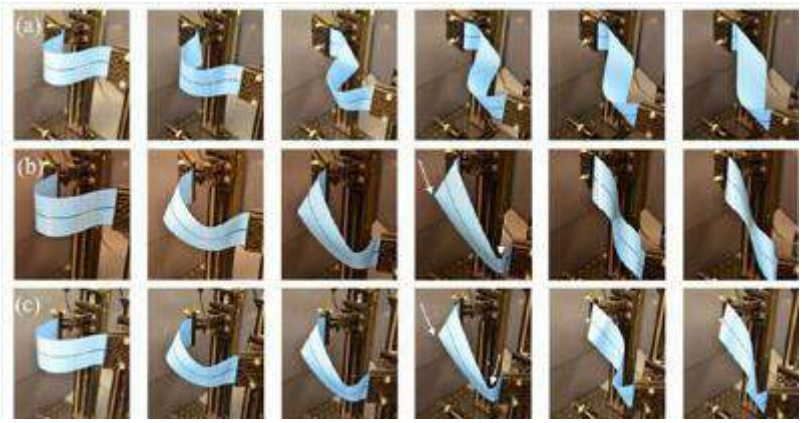

Figure 3: Shearing a band of aspect ratio $W/L = 0.25$ and normalized compression $\Delta L/L = 0.5$, with different clamping angles. Three time series from left to right. (a) $\theta = 15°$, smooth transition from U to US+ ; (b) $\theta = 30°$, snap-through from U to WS- ; (c) $\theta = \ 5°$, snap through from U to uUui.

Figure 3 shows the effect of clamping angle on the response of a band to shear. At low angles, a smooth transition to an S-like state is observed. At slightly larger angles, the transition is a violent snap-through. At still larger angles, the system snaps to a higher-mode shape. Prior to a snap, elastic energy is focused at two points on the structure (white arrows); this is relaxed upon snapping.

Figure 4 shows the landscape of stable states and transitions for the examples in Figure 3 (a) and (c). The normalized shear displacement $\Delta W/W_{max}$ serves as a bifurcation parameter. Red lines show paths (one hysteretic and one not) traced by sweeping the parameter up and down, beginning in the U state. In some cases (not shown), the system returns to a W state rather than a U state. Gravity in the vertical orientation causes asymmetry between some $+$ and $\nearrow$states. Snap-through can involve significant inertia.

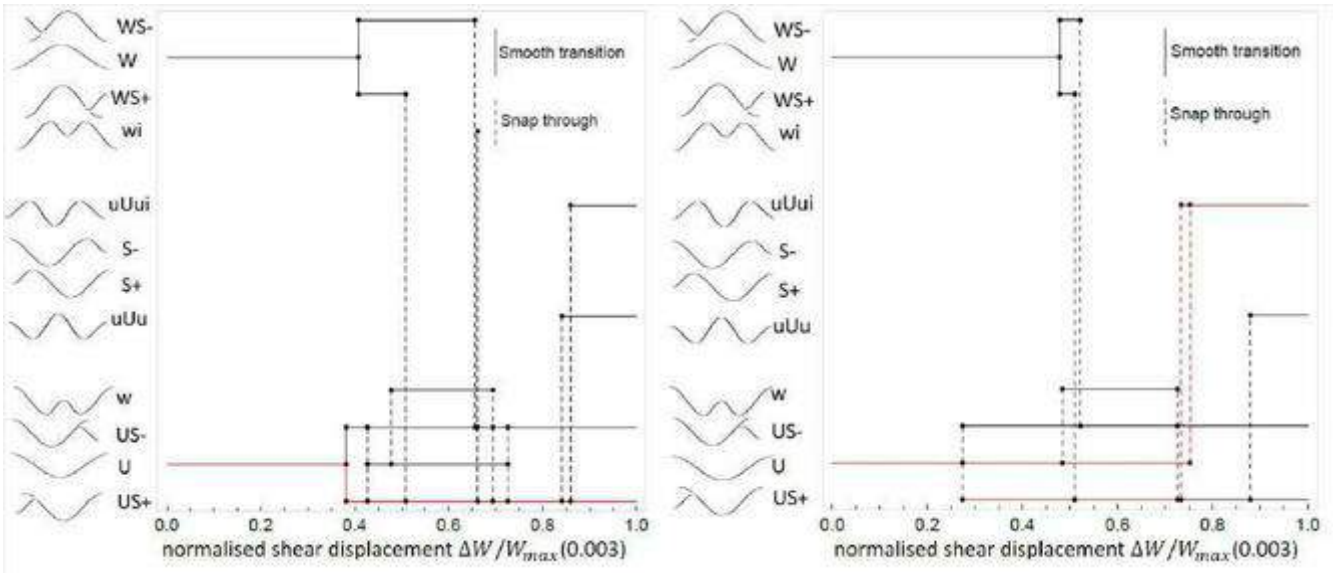

Figure 4: Bifurcation diagrams corresponding to Figure 3(a) (left) and (c) (right).

References

[1] M. Arya, N. Lee, and S. Pellegrino. In 2nd AIAA Spacecraft Structures Conference, Kissimmee, FL, USA, 2015.
[2] D.-H. Kim, R. Ghaffari, N. Lu, and J. A. Rogers. Annu. Rev. Biomed. Eng., 14:113128, 2012.
[3] J. Chopin and A. Kudrolli. Phys. Rev. Lett. 111 174302, 2013.
[4] E. L. Starostin and G. H. M. van der Heijden. J. Elasticity, 119:67112, 2015.

Oscillatory behaviour of compressible hyperelastic shells subjected to dynamic inflation: A numerical study

D. Aranda-Iglesias*, G. Vadillo, and J. A. Rodríguez-Martínez

Department of Continuum Mechanics and Structural Analysis. University Carlos III of Madrid. Avda. de la Universidad, 30. 28911 Leganés, Madrid, Spain

Summary This paper is concerned with the role played by material compressibility in the oscillatory behaviour of Mooney-Rivlin spherical shells subjected to dynamic inflation. For that purpose we carried out a comprehensive numerical analysis using: (1) a finite differences MacCormack's scheme implemented in MATLAB and (2) a finite elements model implemented in ABAQUS/Explicit.

ABSTRACT

The oscillatory behaviour of a thick-walled spherical shell, due to the application of a step pressure in the inner face, is investigated. The shell material is taken to be isotropic and compressible within the framework of finite nonlinear elasticity. For that purpose we have developed two different numerical methodologies. The first one is a finite differences MacCormack's scheme first proposed by [1]. The second one is a finite elements model aimed to systematically verify and complement the outcomes of the aforementioned finite differences method. We have detected that numerical dispersion and diffusion impose limits to the capacity of the computational simulations to describe the shock wave that emanates from the inner surface of the shell due to the application of the inflation pressure. Nevertheless, both numerical approaches capture the essential features which describe the oscillatory behaviour of the shell, including the maximum stretch of the oscillation. Furthermore, we have conducted a parametric study to assess the role played by applied pressure, material compressibility and shell thickness in the oscillatory motion of the shell. Systematic comparison with the analytical solution for the incompressible limit first proposed by [2] is carried out. We have shown the interplay between the maximum amplitude of the oscillation and the applied pressure, and obtained the critical pressure for which the oscillatory behaviour is lost, leading to an unbounded expansion of the sphere. Moreover, our calculations have revealed that the wave propagation within the specimen plays a key role in the dynamic response of the shell. The phase portraits used to represent the oscillatory motion of the sphere show a characteristic sawtooth shape that is accentuated with the increase of material compressibility and shell thickness.

ACKNOWLEDGEMENTS

The authors are indebted to the *Ministerio de Economía y Competitividad de España* (Project EUIN 2015-62556) for the financial support which permitted to conduct this work.

References

[1] Janele P., Haddow J.B., Mioduchowski A.: Finite amplitude spherically symmetric wave propagation in a compressible hyperelastic solid. Acta Mechanica 79:25-41, 1989.

[2] Zhong-Heng, G., Soleki, R.:Free and forced finite-amplitude oscillations of an elastic thick-walled hollow sphere made of incompressible material. Archiwum Mechaniki Stosowanej 15:427-433, 1963.

*Corresponding author. Tel. +34 916248809; Fax: +34 916249430. E-mail address: faranda@ing.uc3m.es

NUMERICAL ANALYSIS OF DYNAMIC STABILITY OF PLATE BY USING TOOLS USED IN DYNAMICS

Łukasz Borkowski[1a)], Zbigniew Kołakowski[2]
[1,2]*Department of Strength of Materials, Lodz University of Technology, Lodz, Poland*

The aim of the study is to analyze an isotropic plate in terms of its dynamic stability (or its instability), by using tools that are mainly used in the vibrations theory of dynamical systems e.g. in the theory of bifurcation and chaos. The results achieved by using tools such as phase portraits, Poincaré maps, FFT analysis, Lyapunov exponents will be compared with the results obtained by using the Volmir criterion.

In this presentation was examined a square isotropic plate with dimensions b=l=100mm, h=1mm and the material constants E=200GPa, ν=0,3, joint supported on the all edges (Fig. 1). Dynamic compressive load was included in the plane of the plate.

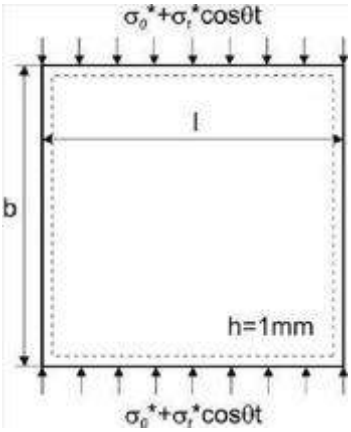

Fig. 1. Analyzed plate

Using research done by Volmir [1], the above plate can be described by following equation:

$$\ddot{\zeta}+\Omega^2(1-k\cos\theta t)\zeta+\eta\zeta^3=0 \tag{1}$$

where: $k=\dfrac{\sigma_t^*/\sigma_{kr}^*}{1-\sigma_0^*/\sigma_{kr}^*}$, $\Omega^2=\omega_0^2(1-\dfrac{\sigma_0^*}{\sigma_{kr}^*})$, ζ - deflection of the plate, ω_0 - natural frequency, σ_{kr} - critical stress, σ_0 - medium stress, σ_t - stress amplitude, η - parameter which is dependent on the boundary conditions.
Transform the equation (1) to dimensionless form we get:

$$\ddot{x}+a(1-k\cos\psi\tau)x+bx^3=0 \tag{2}$$

where: $a=1-\dfrac{\sigma_0^*}{\sigma_{kr}^*}$, $b=\dfrac{\eta}{\omega_0^2}$, $\ddot{x}=\dfrac{1}{\omega_0^2}\ddot{\zeta}$, $x=\zeta$, $x^3=\zeta^3$, $\psi=\dfrac{\theta}{\omega_0}$, τ – dimensionless time.

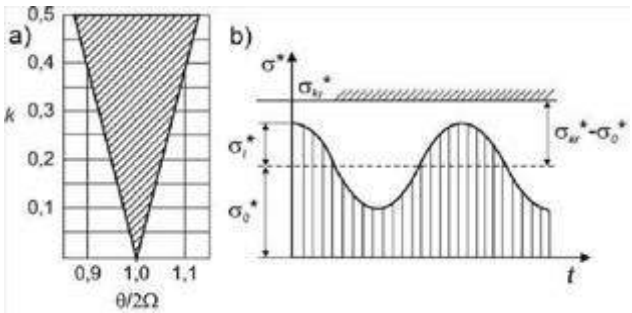

Fig. 2. The graph of dynamic stability and instability of the plate (a) and the timing diagram of stress (b) [1].

[a)] Corresponding author. Email: lukasz.borkowski@p.lodz.pl.

An analysis of dynamic stability consists of changing parameters σ_0 and σ_t (Fig. 2b), which in turn allowed to create the graph of dynamic stability and instability of the plate (Fig. 2a).

Comparison of the results obtained by phase portraits, Poincaré maps, FFT analysis and Lyapunov exponents [2] with the results shown in Fig. 2a was made for the two values of the parameters k and $\theta/2\Omega$: an area of dynamic stability (k=0,3, $\theta/2\Omega$=0,9), an area of dynamic instability (k=0,45, $\theta/2\Omega$=1,1).

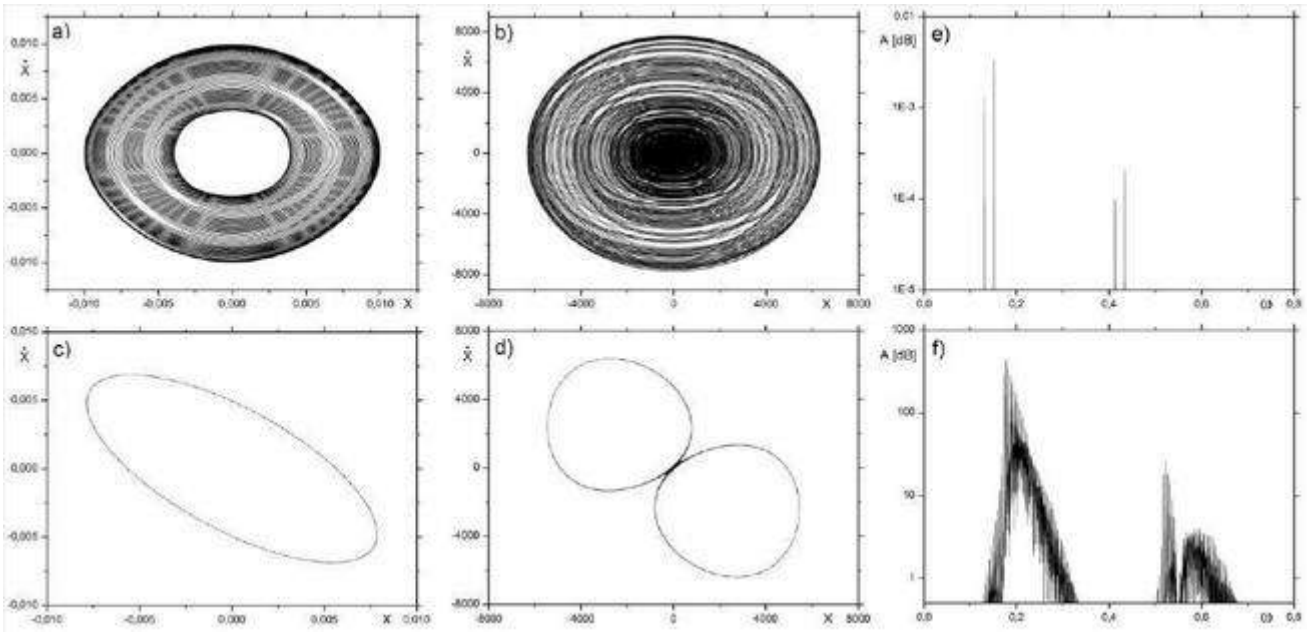

Fig. 3. Phase portraits (a, b), Poincaré maps (c, d), FFT analysis (e, f) for the stability solution (a, c, e) and the instability solution (b, d, f).

Summing up the results, it can be concluded that using tools used in dynamics it is possibile to designate the areas of stability and instability for the study system. For phase portraits (Figs 3a, 3b) and Poincaré maps (Figs 3c, 3d) loss of stability associated with a significant increase in the value of displacement and velocity (all studies have been done for the initial conditions equal to x=0,01, $\dot{x}$=0,00) and the nature of the resulting solutions. On the graphs of the FFT analysis, during the transition into the area of instability, a signal spectrum is continuous (specification of dominant frequencies is impossible) and significantly increased their amplitude. Using the Lyapunov exponents cannot precisely described when the loss of stability take place. Both of the stability (k=0,3, $\theta/2\Omega$=0,9) and instability (k=0,45, $\theta/2\Omega$=1,1) areas we get the two Lyapunov exponents equal to zero – a quasiperiodic solution (two disproportionate to each other frequency, so-called a 2D torus). However, the use of the Lyapunov exponents is useful for the larger values of parameter k, which are not shown in Fig. 2a. For k=1,60, $\theta/2\Omega$=1,1 the largest Lyapunov exponent reaches a positive value, the analyzed system goes into a chaotic solution. This solution can be also observed in the Poincaré map (Fig. 4).

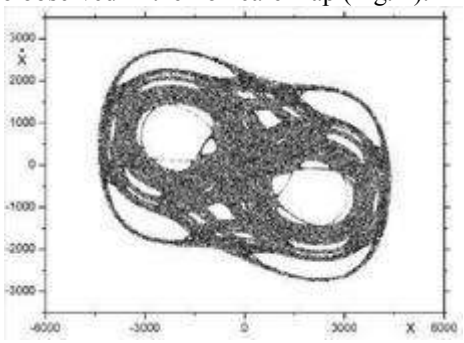

Fig. 4. Poincaré maps for the chaotic solution.

References

[1] Volmir, S.A., (1972). Nonlinear Dynamics of Plates and Shells. Science, Moscow (in Russian)

[2] Borkowski, L., Perlikowski, P., Kapitaniak, T., & Stefanski, A. (2015). Experimental observation of three-frequency quasiperiodic solution in a ring of unidirectionally coupled oscillators. *Physical Review E*, *91*(6), 062906.

A FINITE ELEMENT/QUATERNION/ASYMPTOTIC NUMERICAL METHOD FOR THE 3D SIMULATION OF FLEXIBLE CABLES.

Emmanuel Cottanceau[1,2], Olivier Thomas *[1], Philippe Véron[1], Marc Alochet[2], and Renaud Deligny[2]
[1]*Arts et Metiers ParisTech, LSIS UMR CNRS 7296, 8 bd. Louis XIV 59046 Lille, France*
[2]*Technocentre Renault, 1 av. du Golf 78084 Guyancourt, France*

Summary A flexible cable is modeled by a geometrically exact beam model with 3D rotations described using quaternion parameters. The boundary value problem is then discretized by the finite element method. The use of an asymptotic numerical method to solve the problem, requiring quadratic equations, is well suited to the quaternion parametrization. This combination of methods leads to a fast, robust and accurate algorithm very well-adapted for the simulation of the assembly process of cables. This is proved by running many examples involving complicated solutions.

INTRODUCTION



Figure 1: Cable harnesses.

The use of numerical tools for design is crucial in automotive industry. Indeed, they allow to limit the mock-up phases and thus reduce the design duration and the manufacturing costs. Most of the car pieces being rigid body solids, CAD software are nowadays widely used. However, these tools are not able to accurately predict the behavior of flexible pieces. In particular, cables simulation represents an outstanding challenge for the assembly process departments. Their structure is complex : a wire is made up of copper filaments wrapped in an elastomer duct. These wires are most of the time gathered in bundles which are themselves surrounded by various protections such as tape, PVC tube... All these features lead to very complex geometries. In addition, the large displacements undergone by cables, due to their flexibility, bring geometric nonlinearities. Furthermore, design departments require fast computation algorithms such that several design configurations can be tried. The current commercial softwares using computationally costly 3D elements are thus not adapted. In this context, we propose to build a dedicated tool in which the cables are modeled by the geometrically exact beam theory and simulated by an original combination of techniques: the finite element method for discretization, the quaternion parameters to describe rotations and an asymptotic numerical method (ANM) to compute the branches of solution.

TECHNIQUES USED

Beam formulation

The slender geometry of cables and their flexibility make a beam model with large displacements/large rotations and small strains really appropriate. These geometrically exact beam models consist in giving the position of the centerline of the beam and the rotation of the sections. They have been widely studied during the last decades but are still of interest for research, mainly because of the difficulty to describe 3D rotations. Indeed, they are not unique and among the main parametrizations existing, most of the papers have been focusing on rotational vector-like formulation, highlighting the use of only 3 parameters [1]. However, it has been proved that at least 4 parameters are necessary to avoid any singularities. Consequently, quaternions based on Euler parameters seem an optimal choice (least parameters avoiding singularities). Beyond their computational efficiency they also offer an alternative description of rotations avoiding trigonometric functions, that we found very well-adapted to be coupled with an ANM.

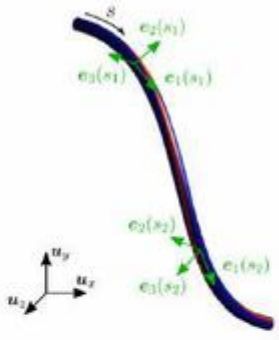

Figure 2: Beam kinematics.

Finite element analysis

Several authors have recently used the quaternions coupled with both finite element methods (FEM) [2] and finite difference methods [3], leading to promising results. For the purposes of our application, we preferred the use of the former. Indeed, the FEM is really convenient for the simulation of complicated geometries, featuring easy assembly of multibody systems (such as piecewise cables). Our FE formulation is obtained from the weak formulation of the beam. As recommended in [2], in numerical purposes, we added a Lagrangian multiplier to keep the unity of quaternions, seen as a supplementary variable. In our code, we have used isoparametric elements with a linear interpolation which seems sufficient if enough elements are employed.

*Corresponding author. Email: olivier.thomas@ensam.eu

Asymptotic Numerical Method

To solve the nonlinear algebraic problem obtained from the FEM $\boldsymbol{f}_{\text{int}}(\boldsymbol{u}) = \lambda \boldsymbol{f}_{\text{ext}}$ (with internal force vector $\boldsymbol{f}_{\text{int}}$, external force vector $\boldsymbol{f}_{\text{ext}}$, unknowns vector $\boldsymbol{u}$, load parameter λ), predictor-corrector algorithms are usually used. However, these algorithms require the delicate choice of a step size which has to be small enough to get convergence but not too small to keep efficiency. Besides, the convergence toward the equilibrium solution is never assured. An alternative is to use an asymptotic numerical method [4] [5]. Such a method principle is, starting from a solution point, to seek the branch of solution as an asymptotic expansion of an arc length measure, leading to a semi-analytical solution. The range of validity of the series expansion is automatically computed and allows to define a new starting point for the next branch. The full equilibrium diagram can then be computed iteratively. This method features 3 main advantages : the user does not have any parameter to tune, it requires less computation time than a classical predictor-corrector method and it is not concerned by convergence problems [4]. The main difficulty using this method is to put the system of equations under the quadratic form $\mathcal{R}(\boldsymbol{u}) = \boldsymbol{f}_{\text{int}}(\boldsymbol{u}) - \lambda \boldsymbol{f}_{\text{ext}} = \mathcal{C} + \mathcal{L}(\boldsymbol{u}) + \mathcal{Q}(\boldsymbol{u}, \boldsymbol{u}) = \boldsymbol{0}$ (with $\mathcal{C}$, $\mathcal{L}$ and $\mathcal{Q}$ respectively constant, linear and quadratic operators). However, the use of quaternions instead of the usual trigonometric functions leads to polynomial expressions which makes the quadratization process very straightforward. Using both quaternions and the ANM is thus a very good combination.

RESULTS AND CONCLUSION

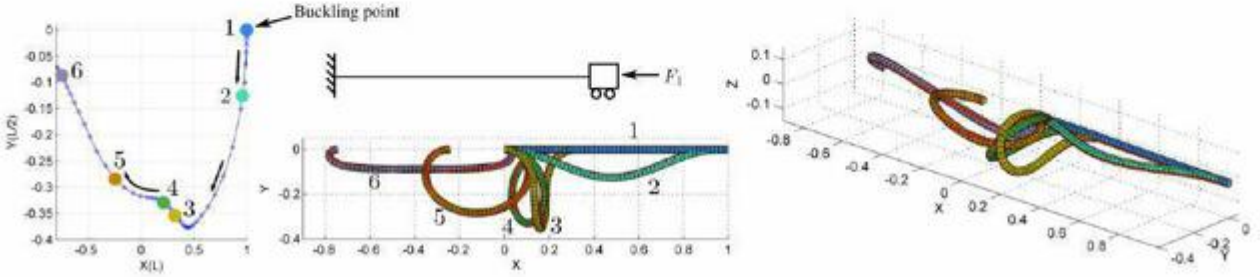

Figure 3: Post-buckling of a clamped-clamped beam. Equilibrium curve (left) and corresponding deformed shapes.

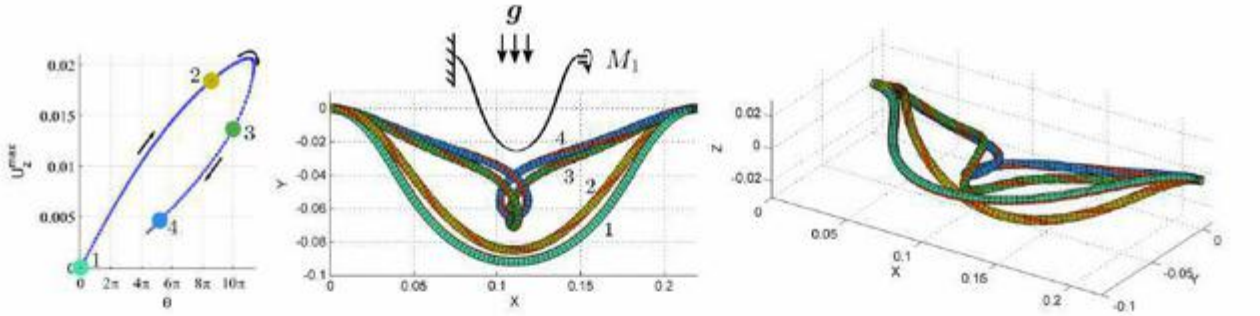

Figure 4: Formation of a plectoneme [3]. Equilibrium curve (left) and corresponding deformed shapes.

The full method has been implemented in Matlab. To solve the quadratic system $\mathcal{R}(\boldsymbol{u}) = 0$ with the ANM, use of the free online package ManLab [6] has been made. Several standard examples of the literature for which an analytical solution is known [1] [2], as well as examples featuring a more intricate bifurcation diagram have been run. On figure 3, the post-buckling of a clamped-clamped beam is illustrated. On figure 4, the experiment of [3] is reproduced numerically : it shows the appearance of a plectoneme (loop) on a cable undergoing gravity by the sole rotation of the right end-section. These results demonstrate the accuracy and the robustness of the method for a simple cable (one piece). They will lead our future developments which will consist in testing the method on a great variety of cables and on more complex geometries. In particular, we will focus on bundle-type structures whose cross-sections contain several wires. If concluding, this will allow to simulate accurately the assembly process of cables and will constitute a very useful tool for industry.

References

[1] Géradin M., Cardona A.: Flexible Multibody Dynamics. 2001.

[2] Zupan E. et al.: On a virtual work consistent 3D Reissner Simo beam formulation using the quaternion algebra. Acta Mech. 224: 1709-1729, 2013.

[3] Lazarus A. et al.: Continuation of equilibria and stability of slender elastic rods using an asymptotic numerical method. JMPS 61-8: 1712-1736, 2013.

[4] Damil N., Potier-Ferry M.: A new method to compute perturbed bifurcation: application to the buckling of imperfect elastic structures, International Journal of Engineering Sciences 26: 943-957, 1990.

[5] Cochelin B.: A path-following technique via an asymptotic-numerical method. Computers & Structures 53-5:1181-1192, 1994.

[6] Arquier, R., Karkar, S., Lazarus, A., Thomas, O., Vergez, C., Cochelin, B. Manlab 2.0 : an interactive path-following and bifurcation analysis software. Tech. rep., Laboratoire de Mecanique et d'Acoustique, CNRS, http ://manlab.lma.cnrs-mrs.fr, 2005-2015.

DYNAMIC INSTABILITY OF ANTISYMMETRIC CROSS-PLY LAMINATED COMPOSITE CYLINDRICAL SHELLS

Mehdi Darabi [a], Rajamohan Ganesan
Concordia Centre for Composites, Department of Mechanical and Industrial Engineering, Concordia University, Montreal, Quebec, Canada

Summary In the present work, the non-linear dynamic instability of thin laminated composite cylindrical shells under periodic axial loading is investigated. In particular, antisymmetric cross-ply laminates are considered. Donnell's shallow-shell theory with von Karman-type of nonlinearity are considsered in equations of motion. Galerkin's technique is then applied to solve the non-linear larg deflection shallow-shell eequations of motion and it leads to a system of nonlinear Mathieu-Hill equations. Using Bolotin's method the instability regions and both stable and unstable solutions amplitude of the steady-state vibrations are obtained. The effects of diffrent lamination schemes on the instability regions and parametric resonance particularly the steady-state vibrations amplitude are examined. The present formmulation shows good agreement with that available in the literature for linear instability analysis.

INTRODUCTION

The interest to study the dynamic stability behavior of engineering structures dates back to the text by Bolotin [1] which addresses numerous problems on the stability of structures under pulsating loads. A comprehensive literature review covering the period 2003- 2013 on non-linear vibrations of shells has been done by Alijani and Amabili [2].

To the present authors' knowledge most of the works on dynamic instability are based on linear analysis and so lead to dynamic instability regions. Stability analysis based on classical linear theories provided only an outline of the parameter regimes where nonlinear effects are of importance. In the present work, the instability regions as well as steady-state amplitudes of stable and unstable solutions are determined based on nonlinear large deflection shallow-shell equations of motion which lead to a system of nonlinear Mathieu-Hill equations.The effects of different lamination schemes of antisymmetric cross-ply laminated shells on both instability regions and ampiltude of steady-state vibrations are investigated.

SYSTEM MODELLING AND SOLUTION

A thin simply supported laminated composite cylindrical shell, having length L and radius R with respect to the curvilinear coordinates (X, θ, Z) which are assigned to the mid-surface of the shell is considered. The cylindrical shell is subjected to a periodically pulsating load in the axial direction with the axial loading per unit length given by:

$$F_{xx}(t) = F_s + F_d cosPt \tag{1}$$

The non-linear von Karman strains associated with large deflections and curvatures according to Donnell's theory are considered. Introducing Airy's stress function and neglecting the inertia forces in X and θ directions, Galerkin's technique is then applied to the problem. It leads to a system of non-linear Mathieu equation as follow:

$$M_{mn}\ddot{q}_{mn}(t) + K_{mn}q_{mn}(t) - (F_s + F_d \cos pt)Q_{mn}q_{mn}(t) + \eta_{mn}q_{mn}^3(t) = 0 \tag{2}$$

where M_{mn}, K_{mn} , $Q_{mn}$and η_{mn} are matrices in terms of extensional, bending, bending-extensional coupling stiffnesses, shell's geometry properties and wave numbers for the studied laminate composite cylindrical shell.

Using Bolotin's [1] method for parametric vibration, the solution of period $2T$ considering the first approximation is given by the following equation:

$$q(t) = a \sin\frac{Pt}{2} + b \cos\frac{Pt}{2} \tag{3}$$

By substitution of Eq. (3) into Eq. (2) a system of two homogeneous linear equations with respect to a and b can be obtained. This system has solutions that differ from zero only in the case where the determinant composed of the coefficients is equal to zero:

$$\begin{vmatrix} 1 + \mu_{mn} - n_{mn}^2 + \frac{3\gamma_{mn}}{4\Omega_{mn}^2}A^2 & 0 \\ 0 & 1 - \mu_{mn} - n_{mn}^2 + \frac{3\gamma_{mn}}{4\Omega_{mn}^2}A^2 \end{vmatrix} = 0 \tag{4}$$

where A is the amplitude of steady-state vibrations and is given by:

$$A = \sqrt{a^2 + b^2} \tag{5}$$

and

$$\omega_{mn} = \sqrt{\frac{K_{mn}}{M_{mn}}} \quad , \gamma_{mn} = \frac{\eta_{mn}}{M_{mn}}, \; N_* = \frac{K_{mn}}{Q_{mn}} \; , \Omega_{mn} = \omega_{mn}\sqrt{1 - \frac{F_s}{N_*}} \; , \quad \mu_{mn} = \frac{F_d}{2(N_* - F_s)} \tag{6}$$

Expanding the determinant and solving the resulting equation with respect to the amplitude, A, two solutions are obtained for A which are called stable-solution and unstable-solution corresponding to $+\mu_{mn}$ and $-\mu_{mn}$ respectively. Also the dynamically unstable regions are determined by setting $A = 0$ in equation (4).

[a] Corresponding author. Email: m_darab@encs.concordia.ca

RESULTS AND DISCUSSION

The material properties used in the present analysis are : $E_1/E_2 = 40$, $G_{12}/E_2 = 0.5$ and $\upsilon_{12} = 0.25$. For laminated circular cylindrical shells, the critical static buckling load is approximated as [3]

$$N_{cr} = \frac{E_2 h^2}{R\sqrt{[3(1-\nu_{12}\nu_{21})]}} \tag{7}$$

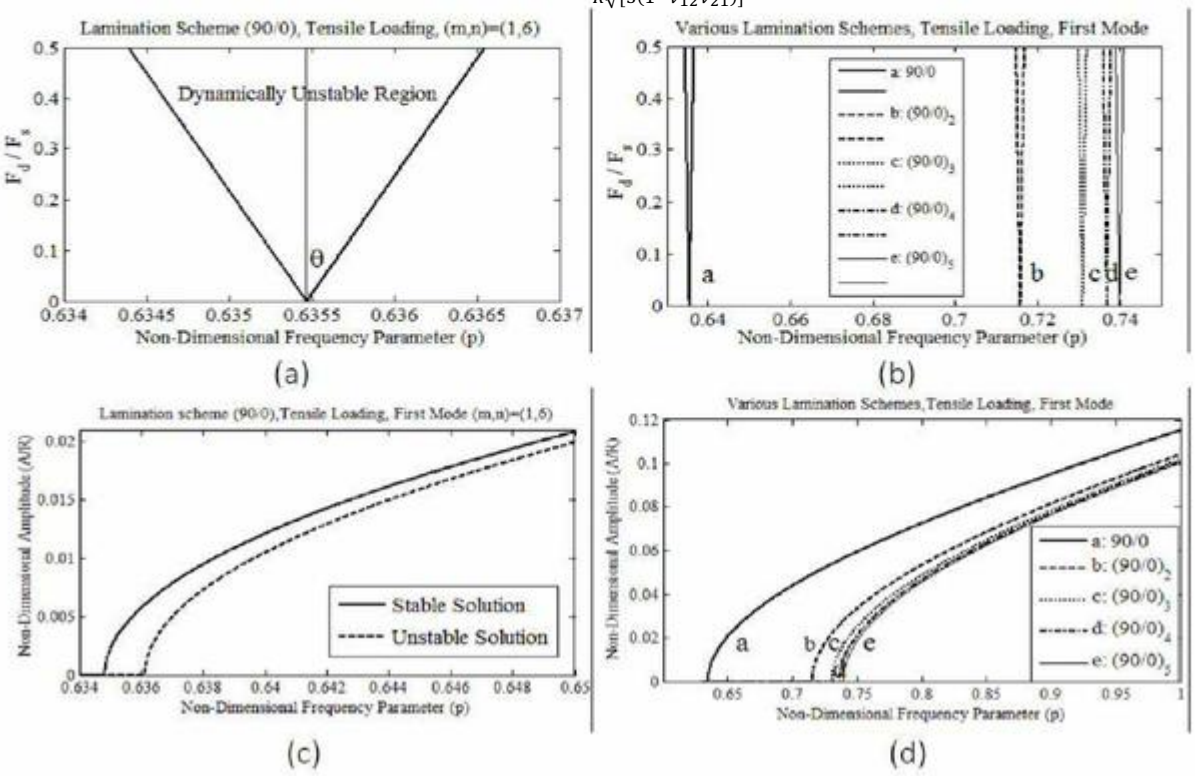

Fig.1. (a) First dynamically unstable region, (b) variation of the first mode unstable regions with different lamination schemes, (c) stable- and unstable-solutions amplitudes, (d) variation of the first mode stable-solution amplitude of steady-state vibrations with various lamination schemes.

Figure 1 displays the dynamically unstable regions and both stable- and unstable-solutions amplitudes of steady-state vibrations for an antisymmetric cross-ply laminated cylindrical shell having aspect ratios of / = 2 and / = 200 subjected to tensile loading of $F_s = 0.1N_{cr}$. As can be observed from Figure 1(a) each unstable region is separated by two lines which are not completely straight and they curved slightly outward with a common point of origin. Figure 1(c) shows both stable and unstable solutions of amplitude-frequency relation of steady-state vibrations for a two-layered $(90^o/0^o)$ laminate corresponding to $F_d = 0.3F_s$. It is observed from Figure 1(b) and 1(d) that unstable regions and amplitude of steady-state vibrations shift to the right along the frequency axis having higher frequencies of excitation. This shifting to the right of the frequency axis is reduced once the number of layers is doubled and appears to converge at a certain value as the unstable regions and amplitudes of steady-state vibrations of eight- and ten-layered laminates almost coincide with each other.

CONCLUSION

The present work has shown that there is vibration with steady-state amplitude in the instability region which approaches almost constant amplitude when the excitation frequencies are increased. Hence, for more perfect and complete studies of dynamic instability, the nonlinear analysis presented here is required to determine both the stable and unstable vibration amplitudes in addition to instability regions. It has been shown that the amplitude of steady-state vibrations are decreased, corresponding dynamically-unstable regions shift to the right along the frequency axis having higher frequencies of excitation, and the widths of the instability regions are decreased when the number of plies are increased and further, convergence is achieved at a specific number of plies in each case.

References

[1] Bolotin, V. V.;, The dynamic stability of elastic systems, San Francisco: Holden-Day, 1964.Icer D.F., Adams J.A.: Mathematical Elements for Computer Simulation. Montreal, Canada 1977.

[2] Alijani, Farbod; Amabili, Marco;, "Non-linear vibrations of shells: A literature review from 2003 to 2013," *Non-linear Mechanics,* vol. 58, pp. 233-257, 2014.

[3] Liew, K. M.; Hu, Y. G.; Zhao, X.; Ng, T. Y.;, "Dynamic stability analysis of composite laminates cylindrical shells via the mesh-free kp-Ritz method," *Cmput. Methods Appl. Mech. Eng. ,* vol. 196, pp. 147-160, 2006..

EFFECT OF NON-LINEAR CONSTITUTIVE LAW ON COLUMN BUCKLING

Derek Hollenbeck*[1], Soheil Fatehiboroujeni[1], and Sachin Goyal[1]
[1]*Department of Mechanical Engineering, University of California, Merced, CA, USA*

Summary Columns with linear constitutive laws in bending can sustain higher than critical buckling load after buckling. In other words, they have stable post-buckling behavior. However, a class of materials such as redwood exhibits cubic nonlinearity in the constitutive law with softening effect. An analysis with simple idealized model reveals that such cubic nonlinearity in the constitutive law diminishes the domain of post-buckling stability, and lead to catastrophic collapse. This work further investigates the finding by taking into account the nonlinear constitutive law into beam theory.

It is known that certain materials such as redwood exhibit cubic constitutive law of the form [1]

$$\sigma = E_1\epsilon + E_2\epsilon^3 \tag{1}$$

where E_1, E_2 are constants, σ is the axial stress and ϵ is the axial strain. This nonlinearity translates into a similar nonlinearity in the constitutive law for bending

$$q = E_1 I_1 \kappa + E_2 I_2 \kappa^3 \tag{2}$$

where q is the bending moment having restoring effect on the curvature κ, and I_1 and I_2 are the second and fourth moments of cross-sectional area respectively. Accounting for the above nonlinearity in the Euler equation, and using perturbation analysis for a clamped-free case, Haslach [2] showed that the post-buckling behavior becomes unstable beyond a critical value of E_2. Szymczak and Mikulski [3] refined this analysis further with the tangent modulus theory, and found that even the buckling load is reduced.

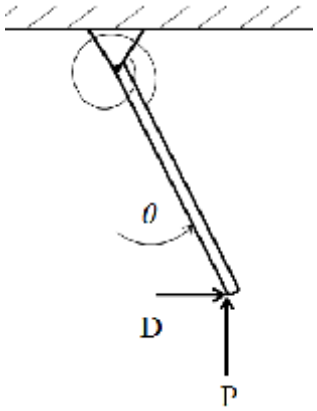

Figure 1: Idealized model of buckling of a clamped-free column. The torsional spring at the hinge captures lumped bending stiffness as $M = k_1\theta + k_2\theta^3$, where k_1 and k_2 are constants and M is the restoring moment of the spring.

However, an analysis with simple idealized model, such as shown in Fig. 1, with the cubic nonlinearity in the constitutive law reveals that the post-buckling behavior does not abruptly change from being stable to being unstable as the cubic nonlinearity in the constitutive law is increased. Instead, the domain of stability diminished smoothly as shown in the bifurcation diagrams in Fig. 2. In other words, the post-buckling behavior is stable at the onset, but after at a critical value of θ, it becomes unstable and the column collapses catastrophically. The critical value of θ does depend on the cubic nonlinearity factor k_2.

Motivated by this observation, we further investigated the post-buckling stability using a nonlinear beam theory. By including higher order terms in the perturbation analysis of the beam, we observed similar trends as observed in the idealized model. Therefore, we conclude that it is necessary to include higher order terms in the perturbation analysis that were ignored in [2], to capture important trends in the post-buckling stability of the columns with nonlinear constitutive laws.

*Corresponding author. Email: dhollenbeck@ucmerced.edu

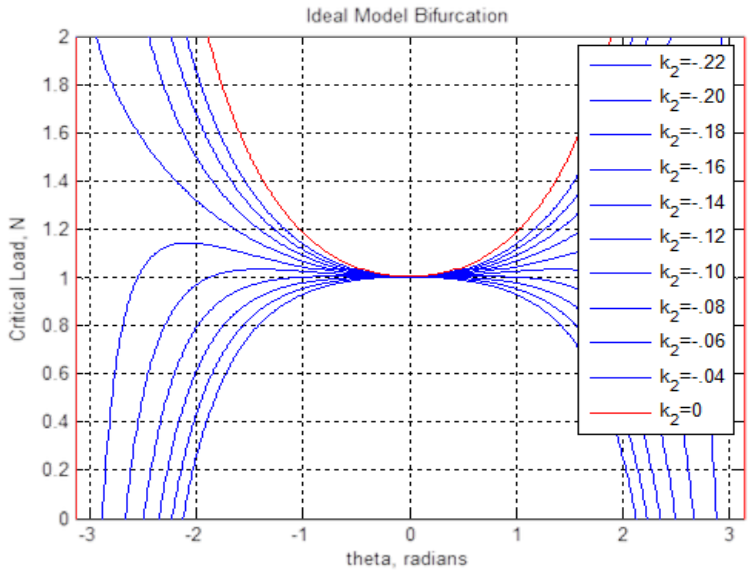

Figure 2: Normalized critical buckling load is plotted against θ for several values of k_2 while keeping k_1 constant. The red curve corresponds to the trajectory of the critical load for a linear constitutive law ($k_2 = 0$). The stable post-buckling domain is shrinking as $|k_2|$ is increasing.

References

[1] J. Bodig and B. A. Jayne, Mechunics oJ Wood and Wood Composites. Van Nostrand, New York (1982).

[2] Haslach, H. W., 1985. "Post-buckling behavior of columns with non-linear constitutive equations". International Journal of Non-Linear Mechanics, 20(1), pp. 53 - 67.

[3] Szymczak, C., and Mikulski, T., 1990. "On post-buckling behavior of columns with cubic constitutive equations". International Journal of Non-Linear Mechanics, 25(1), pp. 117 - 121.

STUDY ON DESIGINING THE SUPERIOR CRUSHING RESPONSE OF LIGHTWEIGHT EGG-BOX PANEL

Kento Okui[1] and Kuniharu Ushijima *[2]
[1]*Department of Mechanical Engineering, Graduate School of Engineering, Tokyo University of Science, Tokyo, Japan*
[2]*Department of Mechanical Engineering, Faculty of Engineering, Tokyo University of Science, Tokyo, Japan*

Summary In this paper, study on designing the superior crushing response of lightweight egg-box panel is carried out which consisted of a conical frusta and the base, by a using finite element method. There exists three kinds of deformation stages, and the compressive load-displacement curve for each stages, can be evaluated from that for semisphere and conical frusta proposed by other researchers, where the strain-hardening effect can be relatively small. However, if the strain-hardening of material increases, the deformation behavior changes, and the conventional estimation technique cannot be used. In order to take the strain hardening effect into consideration, instead of using yield stress, one has to use an energy equivalent flow stress defined by the work-hardening exponent (n-value), and evaluate the compressive load. Further, a controlling technique for the ideal compressive load-displacement curve is proposed by introducing the basement and changing the length of the basement and the cone angle.

INTRODUCTION

It is confirmed by many researchers until now that egg-box used as a reinforcement board of the bonnets of the cars has superior absorption properties. For example, the Deshpande and others (Deshpande and Fleck,2003) consider egg-box panel is cone with the cover (conical frusta in the following) and build a movement hinge model to evaluate crush properties of the conical frusta theoretically. Furthermore, we clarify a geometric condition which do not cause elastic buckling and collapse. This give guidance to design a conical frusta as an energy absorption material in a crush process. However, there are few geometry shape used for the examination of the egg-box panel and materials properties, and the coverage of the theoretical model is not clear. Therefore, in this study we degined a model to have a shape and materials characteristic of real egg-box and evaluate the shock absorption characteristic of the egg-box panel while analyzing numerical value of simulation based on a finite element method.

METHODS OF NUMERICAL ANALYSIS

The commercial Finite Element analysis software, Msc.Marc, is used to evaluate the crushing response of elasto plastic egg-box panel. As for the finite element mesh, a four node, thick-shell element is used for the 3D shell model and discretized. For geometry the egg-box was represented by a periodic 3D shell model (Fig.1). The boundary condition defines as in fig. 2. In fig.2, we locate two rigid bodies between the egg box panel, the lower rigid body is static and the upper rigid body is bring close to egg-box panel and crush it. The friction between the rigid board and egg-box panel dose not consider it then.

Next, explanation on material properties. As a strain hardening characteristic of elasto plasticity materials, supposed all elements with a homogeneous elasto plasticity body. Unless stated, the annealed Al 1050 H111 aluminium alloy was modelled by isotropic Von Mises plasticity theory, with the uniaxial tensile response given by the stress-strain curves (Zupan et al,2003). Young's modulus E=70[GPa] of materials, Poisson ratio $\nu = 0.3$, yield stress Y=30[MPa]. Also in our calculation, the Mises' yield criterion and the updated Lagrangian method are used for formulating the nonlinear problem, and the Newton-Raphson numerical method is applied for finding the root effectively.

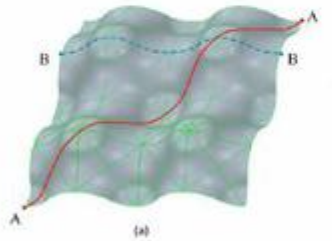

Fig.1 Geometries of egg-box panel.

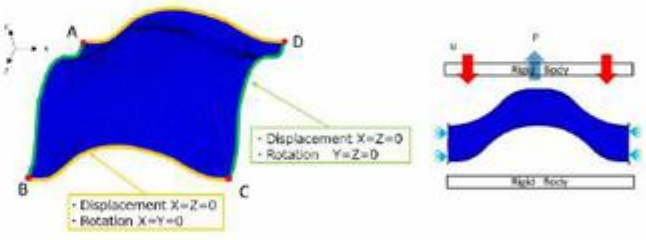

Fig.2 Boundary conditions applied in FEM.

*Corresponding author. Email: kuniharu@rs.tus.ac.jp

RESULTS AND DISCUSSIONS

Fig.3(a) shows FEM result and experiment result (Zupan et al,2003) and both results are in good agreement. As can be seen from fig.3(a), crush response of egg-box panel can be divided into three stages, stage1:elastic deformation of conical cover, stage2:plastic deformation of conical cover, stage3:plastic deformation of the cone. Among these three stages, we will evaluate stage2 to stage3 which the affect crush response of egg-box panel. Fig.3(b) shows the compressive load during these stages can be approximated by equation (1) and (2) which proposed by Oliveria and Deshpande respectively. The large difference between equation (1) and FEM result is due to effect of strain hardening of the material. Therefore, the effect of strain hardening coefficient on the deformation behavior for model with angle $\omega = 60°$ and thickness t=1mm, is shown in fig.3(c). For large strain hardening coefficient E_h the slope expands to the outside while cone deformed inside. As the slope expand to the outside, strain energy caused by the expansion of strain at the circumference occurs, but this is ignored in equation (1) and (2) as it considers only strain energy by the bending.Thus, it is concluded that the theoritical solution of equation (1) and (2) becomes smaller than FEM result of egg-box.

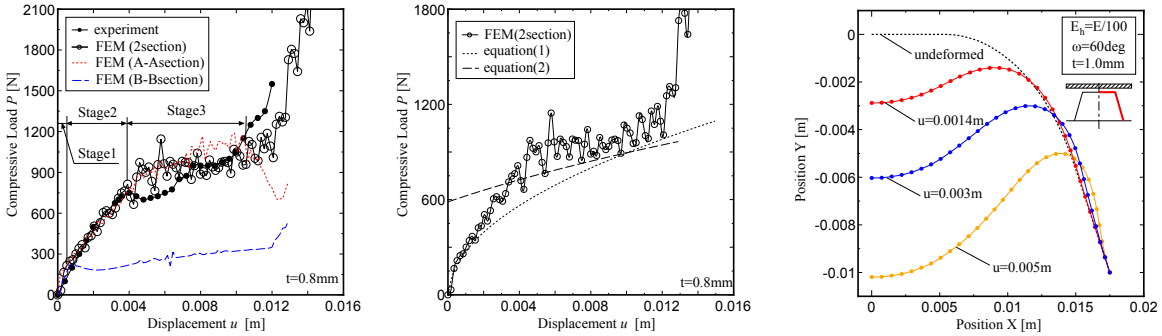

(a) (b) (c)

Fig.3 (a) Comparisons of FEM result and experiment result. (b) Comparisons of FEM result and analysis result. (c) Deformation behaviours for egg-box with different hardening modulus $E_h/E = 1/100$.

$$\frac{u}{t} = \frac{4}{43}\left(\frac{P}{\pi\sigma_{fl}t^2} + 1\right)^2 - \frac{3P}{16\pi\sigma_{fl}t^2} \tag{1}$$

$$\frac{P}{\sigma_{fl}t^2} = \frac{2\sqrt{2}\pi\omega\tan\omega\sqrt{\cos\omega}}{(2\omega - \sin 2\omega)^2} \cdot \left(\frac{a}{t} + \frac{u}{t}\cot\omega\right)^{\frac{1}{2}} \quad , \quad \sigma_{fl} = \sqrt{\frac{Y\sigma_u}{1+n}} \tag{2}$$

$$\sigma = \begin{cases} E\varepsilon & (\sigma < Y) \\ Y + \dfrac{EE_h}{E - E_h}\varepsilon_p & (\sigma > Y) \end{cases} \tag{3}$$

CONCLUSIONS

In this paper, study on designing the superior crushing response of lightweight egg-box panel is carried out which consisted of a conical frusta and the base, by a using finite element method (FEM). It is found that there exists three kinds of deformation stages.However, if the strain-hardening of the constituent material increases, the deformation behavior changes, and the conventional estimation technique cannot be used effectively. So in order to take into consideration the strain hardening effect of the material properties, one has to use an energy equivalent flow stress σ_{fl} defined by the work-hardening exponent (n-value), and evaluate the compressive load P by using σ_{fl} instead of yield stress Y. Further, a controlling technique for the ideal compressive load-displacement curve is proposed by introducing the basement and changing the length of the basement and the cone angle.

References

[1] Deshpande V.S., Fleck N.A.: Ehergy absorption of an egg-box material, Journal of the Mechanics and Physics of Solids, Vol.51(2003), pp.187–208.

[2] Zupan M., Chen C., Fleck N.A.: The plastic collapse and energy absorption capacity of egg-box panels, International Journal of Mechanical Science, Vol.45(2003), pp.851–871.

[3] Chung J.G., Chang S.H.: Sutcliffe, M. P. F., Deformation and energy absorption of composite egg-box panel, Composites Science and Technology, Vol.67(2007), pp.2342–2349.

[4] Oliveira J.G., Wierzbicki T.: Crushing analysis of rotationally symmetric plastic shells, Journal of Strain Analysis, Vol.17, No.4(1982), pp.229–236.

[5] Wierzbicki T., Abramowicz W.: The mechanics of deep plastic collapse of thin-walled structures, In Jones, N., and Wierzbicki, T. editors, Structural Failures, John Wiley(1989).

ENHANCEMENT OF BUCKLING STRENGTH IN THE TAPERED SKELETAL ELEMENTS OF MARINE SPONGES

Michael A. Monn[1] and Haneesh Kesari [*1]
[1]*Brown University School of Engineering, Brown University, Providence, Rhode Island, USA*

Summary Biological structures, such as stems and bones, possess some very distinct mechanical designs. By comparing variants of these designs using synthetic materials, scientists have shown that bio-inspired designs can lead to an enhancement of the materials' properties. However, a major criticism of pursuing bio-inspired engineering has been that there are scarcely any examples of structural biomaterials that have been rigorously shown to contain a close-to-optimal design. To address this criticism, we discuss the skeletal elements of the marine sponge *Tethya aurantia* called spicules, which are monolithic silica rods that are 1–2 mm long, 30–50 μm thick. The spicules' mechanical effectiveness is primarily limited by their buckling strength. Spicules possess a distinct taper along their length. Using recent mathematical results, mechanical testing and computational modeling we show that the spicules' tapered shape is very close to the shape that has the greatest buckling strength.

INTRODUCTION

Structural biomaterials (SBs), such as bones and shells, possess some remarkable mechanical properties, such as high specific toughness and stiffness [1, 2]. Underlying the SBs' remarkable properties are the structures' unique mechanical designs, which are a consequence of millions of years of evolution. These distinct designs have serendipitously inspired engineers to come up synthetic materials that possess enhanced mechanical properties [3]. Currently, engineers are interested in making the process of discovering new ideas and designs from nature more systematic. However, these efforts are being excessively undermined by the idea that evolutionary adaptations do not create perfect designs, but rather only provide enhancements to make biological materials perform well enough. Furthermore, there are scarcely any examples of SBs that have been rigorously shown to contain a close to optimal design. For this reason, it is natural to wonder whether evolution is even capable of producing a "perfect" structure.

To provide a balanced perspective on the benefits of looking to nature for inspiration we discuss the form and function of the skeletal elements of the marine sponge *Tethya aurantia*. These elements, called spicules, are axisymmetric, monolithic silica rods that are 1–2 mm long, and 30–50 μm thick. The spicules are distributed in the sponges' compliant collagenous body to enhance its stiffness [4]. These spicules possess a distinct taper along their length, which we found be a highly uniform feature across individual specimens. The spicules are internally homogeneous and we found that their deformation is linearly elastic and that they break cleanly into two pieces in an abrupt, brittle fashion. From these two observations and the slender nature of the spicules, we infer that they primarily fail through a buckling instability, which is triggered by the compressive tractions that are distributed along their lengths.

The spicules most certainly experience various, complex compressive traction distributions along their length. However, we show that of all possible compressive load distributions the case where the forces are concentrated at the ends is the most critical. Furthermore, we found using numerical modeling that the compressive loads on the sponge body mostly appear as concentrated forces on the spicule ends. Thus, the spicule's performance is limited by the maximum compressive force that it can support on its ends prior to encountering the buckling instability. It was proven only recently that columns that possess what we term the Clausen profile can withstand the largest compressive end forces for a given volume of material before buckling [5]. We found that the tapered profiles of the spicules are very close to the Clausen profile. In addition to maximizing the buckling strength, we also show that small imperfections in the Clausen profile result in only minor decreases in the critical buckling load. This design is therefore not only optimal, but also robust against potential fabrication constraints. Thus, our results demonstrate that in at least some cases evolution can be powerful enough to lead us to the best solutions.

HYPOTHESIS AND SPICULE SHAPE MEASUREMENTS

Buckling is a phenomenon that occurs when an, often slender, element under compressive forces transitions from a purely compressed state to a state characterized by large lateral deflections. This sudden transition, or "bifurcation", in the deformation behavior results in a loss of the structure's capacity to transmit loads and is characterized by increased compliance and the presence of tensile stresses due to bending.

For an axisymmetric column with radius r that can vary with the position z along its length L. Of all possible $r(z)$ over $[0, L]$, for which the total volume V is constant, the shape $\hat{r}(z)$ that results in the maximum load transmitted before the onset of buckling is given by

[*]Corresponding author. Email: Haneesh_Kesari@brown.edu

$$\hat{r}(\theta) = L\alpha \quad \mathrm{n}(\theta) \tag{1a}$$

$$z(\theta) = \frac{L}{\pi}\left(\theta \nearrow \frac{1}{2} \quad \mathrm{n}(2\theta)\right) \tag{1b}$$

where the parameter θ varies from 0 to π, and α is the column's aspect ratio [5]. This shape provides a 33% enhancement to the critical buckling load over that of an equal volume cylindrical column.

The Clausen profile is a very gradually tapered shape; a feature that serves as the motivation for our study of the spicules. Specifically, we hypothesize that the taper of the spicules maximizes structural support provided to the sponge by maximizing their critical buckling load.

To test our hypothesis, we quantify the taper of 32 spicules by extracting the boundary of the spicule profile from stitched SEM images. We consider four candidate models – constant cross-section (CCS), ellipsoid, double-cone, and the Clausen profile – to describe the shape of the spicules. For each spicule measured, we fit the four models to the boundary data points using the aspect ratio as the fitting parameter and minimizing the sum of squared errors (SSE) between the data and the model. In order to select the best fit model we compute Akaike's Information Criterion (AIC) for the four candidates for each spicule [6]. We find that of the four candidate models considered, there is very strong support that Clausen profile is the best descriptor of the spicule shape. This similarity between the Clausen profile and the measured taper of the spicules reinforces our hypothesis that the tapered shape of the spicules is an adaptation for making the sponge body stiffer.

Table 1: Summary of model comparison metrics across the 32 spicules

	$SSE \times 1000$		AIC	
	mean	SD	mean	SD
Clausen (1)	0.16 $\pm$	0.08	-3608.3 $\pm$	160.8
ellipsoid	0.28 $\pm$	0.17	-3475.7 $\pm$	187.8
CCS	0.77 $\pm$	0.40	-3205.6 $\pm$	145.9
double cone	2.13 $\pm$	0.84	-2932.9 $\pm$	102.9

ROBUSTNESS OF THE CLAUSEN PROFILE

Finally, we investigate the sensitivity of the enhancement in buckling load to deviations from the perfect Clausen column shape. Specifically we perturb the Clausen profile while enforcing the constraint that the volume of the perturbed and unperturbed columns must be equal. We numerically compute the buckling load for the perturbed shape and compare it to the critical buckling load of the unperturbed Clausen profile. By generating 10^4 different randomly perturbed shapes, we estimate the worst case reduction of the critical buckling load as a function of the magnitude of the perturbation.

We repeat this process for an equal volume CCS column and show that the critical buckling load of the Clausen profile is affected less by imperfections in its cross-sectional area.

References

[1] Barthelat, F., & Rabiei, R. (2011). Toughness amplification in natural composites. Journal of the Mechanics and Physics of Solids, 59(4), 829-840.

[2] Weiner, S., & Wagner, H. D. (1998). The material bone: structure-mechanical function relations. Annual Review of Materials Science, 28(1), 271-298.

[3] Munch, E., Launey, M. E., Alsem, D. H., Saiz, E., Tomsia, A. P., & Ritchie, R. O. (2008). Tough, bio-inspired hybrid materials. Science, 322(5907), 1516-1520.

[4] Nickel, M., Bullinger, E., & Beckmann, F. (2006). Functional morphology of Tethya species (Porifera): 2. Three-dimensional morphometrics on spicules and skeleton superstructures of T. minuta. Zoomorphology, 125(4), 225-239.

[5] Keller, J. B. (1960). The shape of the strongest column. Archive for Rational Mechanics and Analysis, 5(1), 275-285.

[6] Burnham, K. P., & Anderson, D. R. (2002). Model selection and multimodel inference: a practical information-theoretic approach. Springer Science & Business Media.

KINEMATIC STRUCTURAL STABILITY

Jean Lerbet*[1], François Nicot[2], Noël Challamel[3], and Félix Darve[4]
[1]*IBISC, Université d'Evry Val d'Essonne, Evry, France*
[2]*IRSTEA, ETNA, Grenoble, France*
[3]*LITMAB, Université de Bretagne Sud, Lorient, France*
[4]*3SR, Université de Grenoble-Alpes, Grenoble, France*

Summary This paper provides an update on a recent sequence of results [4],[5],[6],[7],[8],[9],[10] concerning stability of non conservative discrete systems which led to the emergence of the original concept of Kinematic Structural Stability (ki.s.s). This concept deals with the property for a system (more accurately for an equilibrium configuration) to preserve or not its (linear) stability domain when it is subjected to additional kinematic constraints. Conservative systems show a universal ki.s.s. whereas nonconservative elastic systems show a conditional divergence ki.s.s. according to the second order work criterion. Flutter ki.s.s has not been characterized by a simple algebraic condition.

DEFINITION OF KI.S.S.

It is well-known that non conservative systems may exhibit some paradoxical behaviors like the well-known destabilizing effect by additional damping (see [3] for example for a modern point of view). However, it is less reported that a similar destabilizing effect may occur by additional kinematic constraint(s). To the best of our knowledge, it has been first mentioned by J.J Thompson in [2] but it has never been really investigated until the last five years.
Ignoring then thisThompson's work, authors of the present paper started in 2009 to investigate the links between stability and the so-called second-work criterion first introduced by Hill [1] in a complete different framework, and more recently used by considering stability of discrete systems under mixed perturbations. Coming back to the usual Lyapounov stability namely stability under perturbations of initial conditions, the authors then questioned the property a stable equilibrium to remain stable when the system is constrained by additional kinematic constraints. More accurately, suppose Σ a mechanical system described by a finite family of coordinates $q = (q_1, \ldots, q_n)$ subjected to a load system which is described for the sake of simplicity by a loading parameter p. Let q^e an equilibrium configuration so that it is not removed with an increasing of p. We then question the stability of q^e when p is increasing and more accurately, using only a linear framework, we assume that the motion about q^e is governed by:

$$M\ddot{X} + K(p)X = 0 \tag{1}$$

where $M, K(p) \in \mathcal{M}_n(\mathbb{R})$ are respectively the mass and stiffness matrices (at q^e) of Σ and $X = (q - q^e)^T \in \mathcal{M}_{n1}(\mathbb{R})$. We suppose that for $p = 0$, Σ is conservative stable and that the domain of stability of this equilibrium q^e is $[0, p^*[$ with eventually $p^* = +\infty$.
A family of m linear kinematic constraints is a family $\mathcal{C} = (C_1, \ldots, C_m)$ of linear forms identified by the scalar product with column vectors so that these constraints are equivalent to a matrix $C = mat(C_1 \ldots C_m) \in \mathcal{M}_{nm}(\mathbb{R})$. The constrained system will be denoted by $\Sigma_{\mathcal{C}}$ and q^e is then supposed to be still an equilibrium position of $\Sigma_{\mathcal{C}}$. Analogously, $[0, p^*_{\mathcal{C}}[$ is the stability interval of the configuration 0 for $\Sigma_{\mathcal{C}}$.
The main question reads: what is the relationship between p^* and $p^*_{\mathcal{C}}$? More accurately, do we have $p^* \leq p^*_{\mathcal{C}}$ as it always happens for conservative systems? If not, can we explain why and can we find (or build) a family of constraints $\mathcal{C}$ so that $p^*_{\mathcal{C}} < p^*$.

Definition 1 *If $p^* \leq p^*_{\mathcal{C}}$ $\forall \mathcal{C}$ we say that the system (more accurately the equilibrium position of the system) Σ is universally kinematically structurally stable or that its kinematical structural stability (ki.s.s) is universal. If there is a value $p^*_k (< p^*)$ such that $p^*_k \leq p^*_{\mathcal{C}}$ $\forall \mathcal{C}$, the ki.s.s. is only conditional. If there is no such p^*_k, the ki.s.s is any. According to the mode of linear stability (divergence or flutter) we also speak about divergence or flutter ki.s.s.*

RESULTS ABOUT KI.S.S.

The results may be so summarized:

- Using Rayleigh quotient, an usual well-known result (Courant's Theorem) claims that for conservative systems the ki.s.s. is universal.

*jlerbet@gmail.com

- For nonconservative systems leading to (1) with a non symmetric matrix $K(p)$, the divergence ki.s.s. is conditional. More accurately, $p^*_{k,div} = p^*_{sw} (< p^*)$ is the lowest positive root of the symmetric part $K_s(p)$ of $K(p)$. In other words, as long as the second order work criterion holds, no kinematic constraint $\mathcal{C}$ may destabilize $\Sigma_{\mathcal{C}}$. Moreover, the number $m < n$ of constraints is not significant. Finally, for $p = p^*_{sw}$, the destabilizing constraint $\mathcal{C} = (U) = \begin{pmatrix} a_1 \\ \vdots \\ a_n \end{pmatrix}$ such that $\Sigma_{\mathcal{C}}$ is divergence unstable (the constraint then reads $a_1 x_1 + \ldots + a_n x_n = 0$) must be chosen so that the vector U is on the invert image by $K(p^*_{sw})$ of the isotropic cone of $K_s(p^*_{sw})$ (because of $p^*_{sw} < p^*_{div}$, $K(p^*_{sw})$ is invertible).

- For nonconservative systems, the flutter ki.s.s is any: there is a systematic analytical method for finding $p^*_{k,fl}$ by use of calculations on Grassmmann manifolds but, according to the three degree of freedom systems Σ, $p^*_{fl} \leq p^*_{k,fl}$ or $p^*_{fl} > p^*_{k,fl}$ may occur.

References

[1] R. Hill, "A general theory of uniqueness and stability in elastic-plastic solids", Journal of the Mechanics and Physics of Solids, 6 (1958), 236-249

[2] J. M. T. Thompson, " 'Paradoxical' mechanics under fluid flow", Nature, 5853, vol. 296, 135-137, (1982)

[3] O.N. Kirillov and F. Verlhust, Paradoxes of dissipation-induced destabilization or who opened Withney's umbrella? Z. Angew. Math. Mech., 90, 6, 462-488, 2010

[4] N. Challamel, F. Nicot, J. Lerbet and F. Darve, Stability of non-conservative elastic structures under additional kinematic constraints, Engineering Structures, 32, 3086-3092, (2010)

[5] Nicot F., Challamel N., Lerbet J., Prunier F. and Darve F.: Some insights into structure instability and the second-order work criterion. Int. J. of Solids and Structures, Vol. 49, (2012), pp. 132-142.

[6] J. Lerbet, M. Aldowaji, N. Challamel, F. Nicot, F. Prunier, F. Darve, P-positive definite matrices and stability of nonconservative systems, ZAMM, 92, No.5, pp 409-422, (2012)

[7] Lerbet J., Kirillov O., Aldowaji M., Challamel N., Nicot F. and Darve F., Additional Constraints may soften a non conservative structural system: buckling and vibration analysis., Int. J. of Solids and Structures, Vol. 50 (2013), pp 363-370

[8] F. Nicot, J. Lerbet, F. Darve : Divergence and flutter instabilities of some constrained two-degree-of-freedom systems. J. of Eng. Mec. 140(1) pp 47-52 (2014)

[9] J. Lerbet, N. Challamel, F. Nicot, F. Darve Variational Formulation of Divergence Stability for constrained systems, Appl. Math. Modell. doi:10.1016/j.apm.2015.02.052 (2015)

[10] J. Lerbet, G. Hello, N. Challamel, F. Nicot, F. Darve, 3-Dimensional Flutter Kinematic Structural Stability, Nonlinear Analysis: Real World Applications, http://dx.doi.org/10.1016/j.nonrwa.2015.10.006

STABILITY ANALYSIS OF UNIFORM DEPLOYABLE STRUCTURE IN COMPRESSION

Bo Li[1,2 a)], Sanmin Wang[1], Viliam Makis [2a)], Xiang-Zhen Xue [1]
[1]*School of Mechanical engineering, Northwestern Polytechnical University, Xi'an, China*
2Department of Mechanical and Industrial Engineering, University of Toronto, Toronto, Ont., Canda

Summary In order to obtain the buckling load of deployable structure based on Scissor-like Element (SLE) in compression, its stability is analyzed and discussed. In the process of analysis, the stability model of SLE is established based on the analysis of the elastic deformation of bar, which can be applied to a linear array deployable structure with n SLEs. In the sequel of this process, the effect of various parameters that affect the instability of the structure, such as the number of units, bar length and degree of deployment is being investigated, and the theoretical analysis results are verified through comparing with the simulation results in ANSYS, which show that the new stability model proposed here can predict the buckling load of scissor deployable structure. It can be concluded that the critical load of each unit should be considered and the minimum value is chosen as the buckling load of this structure.

INTRODUCTION

A lot of spacecraft, such as large-diameter antenna, solar sail and solar power satellites, should be constructed in space, which will evidently involve the dynamics and stability of deployable structure. The deployable structure researched in this paper is one of the linear deployable mechanisms where scissor-like element (SLE) with the movement contractive function is the basic unit, which consists of pairs of straight bars connected by pivots. Also, the analysis of deployable structure can be divided into three stages in the time domain: start-up phase, steady expansion stage, unfolding end and locking phase[1]. In the first and second stage, the dynamic response and dynamic stress of the system obtained using the multi flexible body system dynamics method are the main purpose of the study, while in the third stage, the objective is to obtain the critical buckling load in advance to avoid structural instability, which can also be applied to the design of deployable structure.

Dynamics of deployable structures have attracted many scholars' and research institutions' attention. Also, a considerable amount of experimental and theoretical works associated with clearance joints have been the subjects of many investigations[2,3]. However, there are very few studies on the stability and critical load of deployable structure. Actually, since the elastic curve and the buckling load of the slender column were expounded by Euler, the influence of the stability on the structure performance has already attracted wide attention of scholars [4]. When the applied service loading exceeds the critical value but does not reach the yield limit, the structure will be destroyed and its shape and accuracy will not be assured due to the instability. Therefore, the stabilization of deployable structure is worth of further studying. For the stability analysis of large space structures after unfolding and locking phase, the structure can be decomposed into a large number of cells in the space domain. Then, the sub structure theory can be integrated into the stability analysis, which can be utilized periodically to simplify the analysis process. Finally, the instability condition of the whole structure can be obtained by analyzing the results of each substructure. In this paper, an SLE is taken for mechanical analysis and the results are extended to any unit. Afterwards, a stability model obtained to compute the buckling load can be used to determine whether the structure is unstable. Also, the theoretical results are verified in ANSYS.

MECHANICAL ANALYSIS OF DEPLOYABLE STRUCTURE BASED ON SLE IN COMPRESSION

Deployable structure consists of units and each unit is composed of pairs of bars connected to each other at their midpoints by a sheer-resisting pivot. A number of identical scissor units arrayed along axis x form a linear array structure, namely an SLE pantographic mechanism, which is shown in Figure 1(a). In the SLE pantographic mechanism, the ends of a bar are hinged to the end points of the other SLE from right to left and the two nodes in the first SLE are subjected to horizontal lateral loads, P. The deformation of An SLE is shown in Figure 1(b).

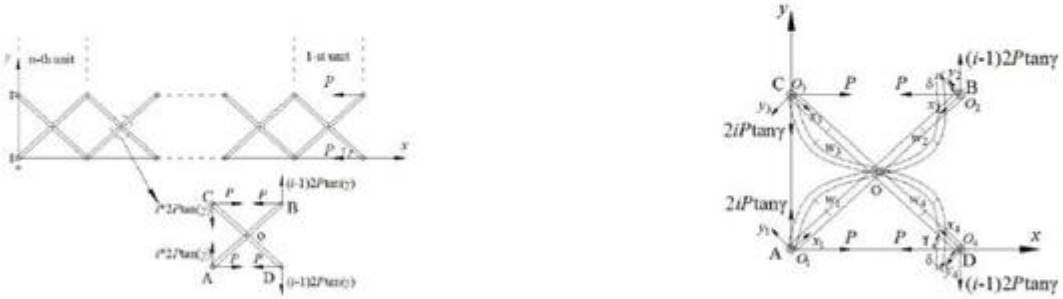

(a) Mechanical analysis of an SLE (b) Structural stability analysis of an SLE

Figure 1 Mechanical and structural stability analysis of an SLE pantographic mechanism under lateral loads

[a)]Corresponding author. yunfenglibo@126.com; makis@mie.utoronto.ca (V. Makis)

Because of the symmetry of the SLE and force depicted in Figure 1(b), the stability of the whole structure can be represented by a bar. Considering the force and bending of the structure, the deflection of the end node can be obtained as

$$\delta = \sigma - \frac{(2i-1)\sin\gamma}{\gamma - i - \quad \gamma \quad \gamma} - \frac{\beta}{\beta}\left[\alpha \quad \alpha \quad \sigma - \frac{(2i-1)\sin\gamma}{\cos\gamma + i \quad \gamma \quad \gamma}) + \frac{(2i-1)\sin\gamma}{\cos\gamma + i \quad \gamma \quad \gamma} + \frac{(2i-1)\sin\gamma}{\cos\gamma - i - \quad \gamma \quad \gamma}\right] \tag{1}$$

When the deflection δ tends to infinity the corresponding critical load can be written as

$$\begin{cases} P_1 = \dfrac{\pi^2 EI}{L \quad \gamma - i - \quad \gamma \quad \gamma} \\ P_2 = \dfrac{\pi^2 EI}{L^2(\cos\gamma + i \quad \gamma \quad \gamma} \end{cases} \tag{2}$$

In Equation (2), the smaller values of P_1 and P_2 are chosen as the critical loads of deployable structure.

SIMULATION AND DISCUSSION

The deployable mechanism under consideration is composed of three basic units. It is subjected to the lateral load P in the first unit, and the degree of deployment γ between the units and the horizontal plane is taken as 60°. As the analysis of the deployable structure is carried out in space, the gravity effect is neglected. The cross-sectional shape of the bar is a circular tube and the outer diameter and inner diameter are 0.244 m and 0.228 m, respectively. The length of a bar is L = 4m, and the elastic modulus is taken as $E = 2e \quad P_a$. Substituting the above parameters into the stability model (2), when γ=60°, the corresponding minimum instability load of deployable structure is $P_{cr} = 5.3687e^5 N$.

In order to verify the correctness of the theoretical model, scissor deployable structure is established in ANSYS according to the physical parameters, and the corresponding load-displacement curves can be obtained, as seen in Figure 2.

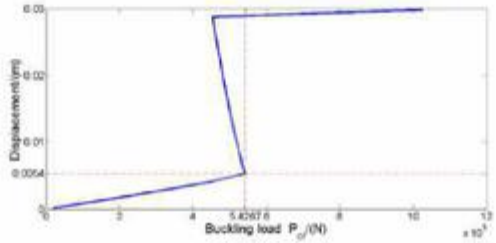

Figure 2 Load - displacement curve of the scissor linear structure

It can be seen from Figure 2 that when the load gradually increased to $5.4267e^5 N$, the deformation of the deployable structure increased sharply, which indicates that the deployable structure has collapsed and is no longer capable of bearing load. At this point, the load is exactly what we need, that is, the buckling load. The simulation result and the theoretical result calculated in the formula (2) are compared yielding the relative error about 1.08%, which is acceptable.

CONCLUSION

In this work, we have studied the stability of a linear array deployable structure based on SLE and derived a new stability model to calculate the buckling load. The theoretical values and simulation results are in good agreement, which confirm the correctness of the proposed method. Also, this result can be extended to the linear array deployable structure with n units, which provides a basis for study of the stability of subsequent complex deployable structures.

Moreover, it can be concluded that the number of units, bar length, and degree of deployment jointly affect the critical load of deployable structure. In the study of stability, the critical load of each unit should be considered and the minimum value is chosen as the buckling load of this structure.

References

[1] Hu HY, Tian Q, Zhang W, et al. Nonlinear dynamics and control of large deployable space structures composed of trusses and meshed. Adv Mech 2013; 43: 390-414.

[2] Li B, Wang SM, Yuan R, et al. Dynamics analysis method study based on linear array deployable structure symmetry of Scissor-Like Element. Journal of Northwestern Polytechnical University, 2015, 33(4): 665-671.

[3] Li B, Wang SM, Yuan R, et al. Dynamic characteristics of planar linear array deployable structure based on scissor-like element with joint clearance using a new mixed contact force model. Proceedings of the Institution of Mechanical Engineers, Part C: Journal of Mechanical Engineering Science 0954406215607903,first published on September 21, 2015

[4] Raskin I and Roorda J. Nonlinear analysis of uniform pantographic columns in compression. Journal of engineering mechanics 1999; 125(12): 1344-1348.

Post-buckling analysis of a hyperelastic layer-substrate structure under compression

Yang Liu[1] and Hui-Hui Dai [*2]

[1]*Department of Mechanics, School of Mechanical Engineering, TianJin University, TianJin, China*
[2]*Department of Mathematics, City University of Hong Kong, Hong Kong SAR*

Summary The compression of a hyperelastic layer-substrate structure is considered in our paper. We consider the whole structure is relatively thin so that it will buckle when the external loads reach certain critical value. Considering the effect of Young's modulus between layer and substrate, the asymptotic model equations are obtained by use of the combined series-asymptotic expansion method. Both the linear and weak non-linear analysis are carried out in this paper. The good agreements of critical stretch from our model and the exact one shows the validity of our model. Then, we unitizing the solvability condition technique to obtain the analytic solutions of two cases, i.e., the ratio of Young's modulus between layer and substrate is of O(1) or large. Corresponding numerical solutions verified that our approach can obtain quite good results and from the analytic formulas of strains, deflections, one can easily see how the parameters affect the quantities.

METHODS AND MODEL

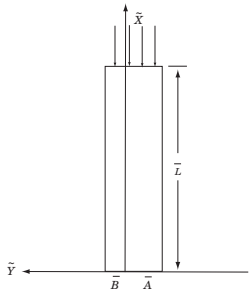

Figure 1: The geometry of the problem.

The geometry together with the Cartesian coordinates system for the current problem is shown in figure 1. The incremental governing equations for the system with traction free boundary conditions for a static problem is well-known, one can refer to (1) and (2) for details. Due to the complexity of the equations themselves, we adopt the combined series-asymptotic expansion method (see also (3)) to derive the asymptotic model equations and the results are as following

$$\begin{cases} h_1 W + h_{31} W^2 + h_{32} G^2 + h_{33} W^3 + h_{13} W G^2 + h_{38} G^4 + h_{39} W^2 G^2 + h_{40} W^4 + B(h_3 G_{,X} + h_6 G W_{,X} + h_7 W G_{,X} \\ +h_{14} W W_{,X} G + h_{15} W^2 G_{,X} + h_{16} G^2 G_{,X}) + B^2(h_2 W_{,XX} + h_{34} W_{,X}^2 + h_9 W W_{,XX} + h_{35} G_{,X}^2 + h_{11} G G_{,XX}) = \Delta\gamma, \\ h_{17} G + h_{20} W G + h_{36} G^3 + h_{27} W^2 G + h_{41} W G^3 + h_{42} W^3 G + B(h_{18} W_{,X} + h_{21} W W_{,X} + h_{22} G G_{,X} \\ +h_{28} W^2 W_{,X} + h_{29} W_{,X} G^2 + h_{30} W G G_{,X}) + B^2(h_{19} G_{,XX} + h_{23} G W_{,XX} + h_{37} G_{,X} W_{,X} + h_{25} W G_{,XX}) = \Delta q, \end{cases} \tag{1}$$

where $h_i (i = 1, 2, \cdots)$ are related to m_1, e (the Young's modulus ratio), $\overline{\nu}$ and r (the thickness ratio). W and G denote the leading order axial and shear strain. $\Delta\gamma$ and Δq denote the incremental stress along X and Y directions, respectively.

POST-BIFURCATION ANALYSIS

We consider two cases, i.e., e is of O(1) or large. The weak non-linear analysis can be conducted by use of the solvability condition and we directly show the results here. The two-terms asymptotic solutions are

$$W \approx b\zeta(W_0 + \zeta W_1) = \pm \frac{B h_3 \lambda_1}{B^2 h_2 \lambda_1^2 - h_1} \sqrt{-\Delta\gamma} \sqrt{\frac{\phi_0}{\phi_1}} \cos(\lambda_1 X) + \frac{\Delta\gamma}{h_1} + \frac{\phi_0(d_1 + d_2)\Delta\gamma}{2 h_1 \phi_1} - c_2 \frac{\phi_0}{\phi_1} \Delta\gamma \cos(2\lambda_1 X), \tag{2}$$

$$G \approx \zeta(G_0 + \zeta G_1) = \pm \sqrt{-\Delta\gamma} \sqrt{\frac{\phi_0}{\phi_1}} \sin(\lambda_1 X) - c_3 \frac{\phi_0}{\phi_1} \Delta\gamma \sin(2\lambda_1 X). \tag{3}$$

*Corresponding author. Email: mahhdai@cityu.edu.hk

Thus the leading order asymptotic solutions are

$$W \approx \zeta^{\frac{7}{5}} W_0 = \pm e^{-\frac{7}{5}} \sqrt[4]{-\Delta\gamma e^{\frac{3}{5}} \frac{\phi_0}{\phi_1}} \frac{Bq_3\lambda_1}{B^2 q_2 \lambda_1^2 - q_1} \cos(\lambda_1 X), \quad G \approx \zeta^{\frac{7}{5}} G_0 = \pm e^{-\frac{7}{5}} \sqrt[4]{-\Delta\gamma e^{\frac{3}{5}} \frac{\phi_0}{\phi_1}} \sin(\lambda_1 X). \tag{4}$$

Where the coefficients are related to the material and geometrical parameters.

Note that the validity of analytic formulas have been verified by the corresponding numerical results. With the obtained analytic solutions, the deflection of the structure can be easily deduced and we find that both the curves of critical stretch and the amplitude with Young's modulus ratio are not monotone, which suggest a possible way to control the structure's stability and deflection. Fig.2 shows that when the whole displacement is fixed, we can use bilayer replace a single layer so as to achieve the ideal deflection (adjust the material or geometrical parameters).

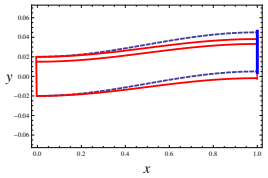

(a) Dashed line is a single layer and solid line is a bilayer.

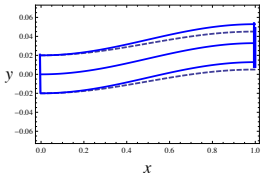

(b) Dashed line is a single layer and solid line is a bilayer.

CONCLUSIONS

The post-bifurcation analysis for a layer-substrate structure are studied both analytically and numerically. By constructing certain small geometrical parameters, the complicated governing equations are reduced to two coupled nonlinear ODEs through the combined series-asymptotic expansions method. Then we solve the two coupled equations by use of the solvability condition technique at the near-critical loads. Two cases are considered, i.e., e is of $O(1)$ or large. Through the systematically asymptotic analysis, it is found that, when e is of $O(1)$, the nature of bifurcation is supercritical and the two-terms approximate solutions for the leading order axial and shear strain are obtained, when e is large, the nature of bifurcation is subcritical and the leading order approximate solutions are obtained. All the analytic results are verified by the numerical ones.

The obtained analytic formulas for the post-buckling solutions can give us useful insights about how the geometrical and material parameters affect the post-buckling states. Further, our results can give people certain insights when designing a structure. one can control the stability and deflection amplitude of a composite layer by specifying the geometrical and material parameters into certain domains.

References

[1] R. W. Ogden: Non-linear elastic deformations. New York: Ellis Horwood, 1984.

[2] Y. Liu, H. H. Dai : International Journal of Engineering Science 80: 74-89 2014.

[3] H. H. Dai, Y. B. Wang, F. F. Wang: Primary and second bifurcations of a compressible hyperelastic layer: Asymptotic model equations and solutions. International Journal of Non-linear Mechanics.

TORSIONAL WRINKLING BEHAVIOUR OF ANNULAR THIN ELASTIC SHEETS

Changguo Wang[1a)], Yuanpeng Liu[1], Huifeng Tan[1]
[1] *Center for Composite Materials and Structures, Harbin Institute of Technology, Haerbin, China*

Summary Torsional deformations in annular thin sheets is a challenging problem in theoretical mechanics due to destabilizing torsional shearing stresses that result in wrinkling. Determining the location, pattern, and evolution of wrinkles in these problems has important applications in design and is an area of increasing interest in the fields of physics and engineering. In this work, nondimensional nonlinear von Karman buckling equations are established, which are solved by the finite difference method to acquire the post-wrinkling characteristics. The proposed theoretical model can accurately predict the critical wrinkling behavior and post-wrinkling characteristics of the annular thin sheets, which are verified by the experimental measurement based on the digital image correlation (DIC) technique.

INTRODUCTION

Recently, thin film wrinkling has provoked extensive research owing to its importance in a wide variety of applications, ranging from deployable gossamer spacecraft, biological tissues, to nanoscale devices [1]. Note that wrinkling, on one hand, is a nuisance in some cases and, on the other hand, wrinkling may also be used as an efficient way of tuning the properties. However, little attention has been paid to the theoretical studies on the post-wrinkling behavior of a thin elastic sheet, mainly owing to the difficulties in the mathematical modeling and solution towards this mechanical problem [2]. Thus, in this work, we aim to develop a nonlinear theoretical analysis on the torsional wrinkling behavior and conduct a non-contact experiment to verify the correctness of our theory.

MATHEMATICAL MODEL

We consider a model of an annular thin sheet under inner torsion and outer tension. Thin elastic sheet wrinkling is generally regarded as a typical nonlinear out-of-plane deflection, which can be derived from the non-dimensional large deflection von Kàrmàn equations. For the annulus under inner torsion, the shape function of linear buckling can be expressed as follows:

$$\bar{w}(\rho,\varphi) = W_1(\rho)\cos(n\varphi) + W_2(\rho)\sin(n\varphi) \tag{1}$$

As to the wrinkling problem, the shape in Eq. (1) is considered as an initial configuration which is substituted in von Kàrmàn equations to obtain the stress function Φ. The stress function comprises two parts, namely a general solution, Φ^* and a particular solution Φ^{**}. The general solution, Φ^*, corresponds to the non-dimensional pre-bifurcation stress state and the particular solution Φ^{**} can be obtained as:

$$\Phi = \Phi_1(\rho) + \Phi_2(\rho)\cos(2n\varphi) + \Phi_3(\rho)\sin(2n\varphi) \tag{2}$$

Subsequently, Eq. (2) is substituted in von Kàrmàn equations, where $\Phi_1(\rho)$, $\Phi_2(\rho)$ and $\Phi_3(\rho)$ satisfy the following non-homogeneous differential equation groups with varied coefficients, where $\mathcal{L}_1$ and $\mathcal{L}_2$ are the operators:

$$\begin{cases} \mathcal{L}_1[\Phi_1(\rho)] = \rho^4 \mathcal{F}_1(\rho) \\ \mathcal{L}_2[\Phi_2(\rho)] = \rho^4 \mathcal{F}_2(\rho) \\ \mathcal{L}_2[\Phi_3(\rho)] = \rho^4 \mathcal{F}_3(\rho) \end{cases} \tag{3}$$

Eq. (3) can be solved by using a compound series method. Further, the stress state induced by the out-of-plane deflection of the wrinkled thin sheet $\sigma^{**}_{\alpha\beta}(\rho,\varphi)$ can be obtained. The variable stress $\sigma^{**}_{\alpha\beta}(\rho,\varphi)$ intimately associated with the wrinkle configuration should be considered in $\sigma^{w}_{\alpha\beta}(\rho,\varphi)$ which is relevant to two variables, ρ and φ. Therefore, for arbitrary $\varphi=\varphi_i$, $\sigma^{w}_{\alpha\beta}(\rho,\varphi)$,($\alpha,\beta=\rho,\varphi$) is only a function of the radial parameter ρ. Here, the solution, $W^{w}(\rho)_{\varphi=\varphi_i}$, to the fourth-order ordinary differential equation is obtained. Then, for the nonlinear wrinkling problem, we can obtain:

$$w^{w}(\rho,\varphi_i) = \mathbf{Re}\left[W^{w}(\rho)_{\varphi=\varphi_i}\right]\cos(n\varphi_i) + \mathbf{Im}\left[W^{w}(\rho)_{\varphi=\varphi_i}\right]\sin(n\varphi_i) \tag{5}$$

EXPERIMENT AND NUMERICAL RESULTS

The wrinkle configuration of the annular thin sheet in the post-wrinkling stage is obtained by using the VIC-3D instrument based on the digital image correlation (DIC) technique. It has been proven experimentally that the DIC technique is a highly efficient and reliable method for acquiring the wrinkle configuration with a satisfactory accuracy. In a typical experiment, an annular thin film of polyurethane with 0.1 mm thickness is fixed on the torsion test device, and a pair of CCD cameras is installed in front of the specimen, as shown in **Fig. 1(a)**. During testing, a torsion shearing is applied on the annular thin film by gradually rotating the central rigid disc, and a photo is taken on the wrinkle configuration (with speckles) of the annular thin film resulting from rotation. **Fig. 1(b)** compares the experimental and theoretical results of the wrinkle patterns under 2 M_{min} torsions. Here, M_{min} represents the minimum torque corresponding to the critical buckling load factor, λ_{min}. It can be ambiguously observed that the experimental and theoretical results are in good agreement with each other.

(a) (b)

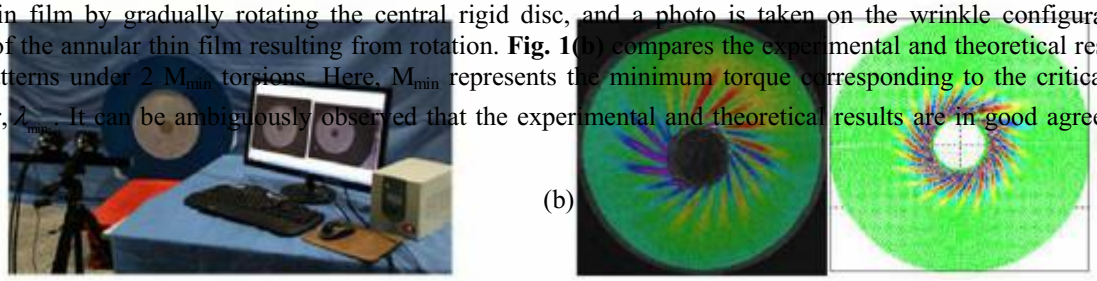

Fig. 1. The wrinkling test device and the wrinkle patterns: (a) the wrinkling test device ; (b) the experimental and theoretical results.

The enveloping lines of the in-plane post-wrinkling stress within one period are plotted in **Fig. 2**. It can be found that the overall stress level in the post-wrinkling stage is much higher than that in the pre-buckling stage. The stress along the wrinkle direction is dominant and concentrated around the inner boundary in a petal type. Such a stress distribution is intimately associated with the wrinkle configuration in the post-wrinkling stage.

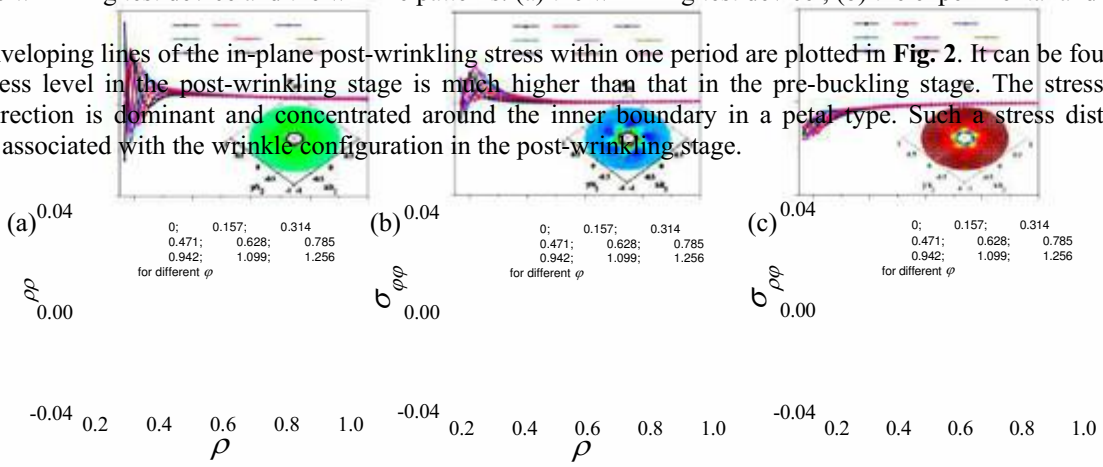

Fig. 2. The post-wrinkling stress distribution: (a) the radial stress, (b) the hoop stress and (c) the shearing stress.

CONCLUSIONS

In this work, the post-wrinkling stress and wrinkle configuration of an annular thin sheet, under inner torsion, are theoretically solved by using the finite difference method based on the nonlinear von Karman buckling theory. The nonlinear post-wrinkling characteristics of the thin sheet are predicted by using the proposed theoretical model and subsequently verified by non-contact experimental tests. The wrinkle configuration is mainly sustained by the post-wrinkling stress in the post-wrinkling stage, and a close interaction between them is revealed. The wrinkle evolution is dominated by the hoop post-wrinkling stress along the wrinkle texture direction of the annular thin film. These results suggest that the linearized Donnell-von Karman bifurcation theory is unable to accurately capture the interaction between the wrinkle configuration and the post-wrinkling stress owing to the presence of a pre-buckling stress.

References

[1] Li, B., Cao, Y., Feng, X., Gao, H., 2012. Mechanics of morphological instabilities and surface wrinkling in soft materials: a review. Soft Matter 8, 5728.

[2] Huang, Z.Y., Hong, W., Suo, Z., 2005. Nonlinear analysis of wrinkles in a film bonded to a compliant substrate. J. Mech. Phys. Solids 53(9), 2101-2118.

A NEW APPROACH TO ASSESS THE DYNAMIC SLIDING STABILITY OF STRUCTURES: APPLICATION TO CONCRETE DAMS

Sylvain Renaud[1], Najib Bouaanani *[1], and Benjamin Miquel[2]

[1]*Department of Civil, Geological and Mining Engineering, Polytechnique Montréal, Montréal, Québec, Canada*
[2]*Division of Expertise in Dams, Hydro-Québec, Montréal, Québec, Canada*

Summary This paper proposes a new numerical technique to assess the dynamic sliding stability of structures. First, special finite elements are developed to account for the effects of cohesive contact and tensile strength along interfaces regardless of the complexity of their geometric irregularity. The developed elements can account for sliding, rocking and degradation of the mechanical properties along contact interfaces during dynamic excitation. For illustration purposes, the proposed methodology is applied to an existing concrete dam subjected to earthquakes. Based on the results, the simplifying assumptions commonly adopted in this type of analyses are criticized and are shown to be unconservative in some cases.

INTRODUCTION

Sliding stability assessment of structures is crucial to ensure their safety against extreme dynamic loads such as earthquakes. Structures usually contain joints, which may constitute weakness zones where cracking, sliding and/or rocking may occur under extreme loads [1-3]. The mechanical behaviour at a joint can be generally characterized by interface geometry, friction angle ϕ, cohesion c, and tensile strength f_{t}. However, it is common in simplified stability analyses to: (i) oversimplify irregular joint interfaces, and (ii) neglect the effects of c and f_{t}. In this paper, an original and efficient numerical technique is developed to assess the dynamic sliding stability of structures while accounting for the effects irregular interfacial geometry, friction angle ϕ, cohesion c, and tensile strength f_{t}.

PROPOSED TECHNIQUE

Two types of nonlinear behavior can occur after cracking at a bounded structural joint: uplift and sliding. Sliding can be divided into two phases: (i) the first, occurring when the joint basic frictional strength is exceeded; and (ii) the second, which is triggered when the strength of the bounded joint interface, characterized by the cohesion c, is exceeded. When the second sliding phase occurs, cracking is considered and $c = 0$. In the same manner, uplift can be divided into two phases: (i) the first, corresponding to uplift of cohesionless joint interfaces; and (ii) the second which occurs as soon as the strength of the bounded interface, characterized by tensile strength f_{t}, is exceeded. When the second phase of uplift is active, cracking is considered and $f_{\mathrm{t}} = 0$. When $c = f_{\mathrm{t}} = 0$, uplift and sliding at the interface is modeled using basic frictional contact finite elements related to the friction angle ϕ as shown in Fig. 1 (a). To model c and f_{t}, two types of interface elements are introduced in Fig. 1 (a), denoted by TECs and TETs, i.e. abbreviations for Truss Element for Cohesion and Truss Element for Tensile strength, respectively. The TECs are constrained to remain parallel to the joint interface while the TETs are constrained to remain perpendicular to this interface during dynamic motion. When the first phase of sliding is triggered, a deformation $\Delta^{(\mathrm{TEC})}$ is induced in the TEC, which starts to sustain a force $F^{(\mathrm{TEC})}$ as shown in Fig. 1 (b). This deformation increases until $\Delta^{(\mathrm{TEC})}_{\mathrm{max}}$ where it reaches the ultimate strength of the TEC, which is related to cohesion c. At this level of strain, the joint is cracked parallel to the interface, the TEC disappears and $c = 0$. When the first phase of uplift is triggered, the TET deforms by $\Delta^{(\mathrm{TET})}$ and starts to sustain a force $F^{(\mathrm{TET})}$ as shown in Fig. 1 (c). This deformation increases until $\Delta^{(\mathrm{TET})}_{\mathrm{max}}$ where it reaches the ultimate strength of the TET related, which is related to tensile strength f_{t}. At this level of strain, the joint is cracked perpendicularly to the interface, the TET disappears and $f_{\mathrm{t}} = 0$. Therefore, the ultimate strengths of the TECs and the TETs are governed by

$$k^{(\mathrm{TEC})}\,\Delta^{(\mathrm{TEC})}_{\mathrm{max}} = \big[\,\tau - \sigma\tan(\phi)\,\big]\,S = c\,S \qquad k^{(\mathrm{TET})}\,\Delta^{(\mathrm{TET})}_{\mathrm{max}} = -\sigma\,S = f_{\mathrm{t}}\,S \tag{1}$$

where $k^{(\mathrm{TEC})}$ and $k^{(\mathrm{TET})}$ are the rigidity of the TEC and the TET, respectively, S is the tributary area associated with each TEC or TET, τ is the shear stress, and σ is the normal stress at the joint. Truss elements are adopted because they are basic finite elements available on most finite element software or can be easily programmed. They are implemented using bilinear materials including a rupture option that causes their disappearance as soon as their ultimate strength is reached. The proposed modeling procedure was successfully verified against analytical predictions based on Mohr-Coulomb failure criterion.

*Corresponding author. Email: najib.bouaanani@polymtl.ca

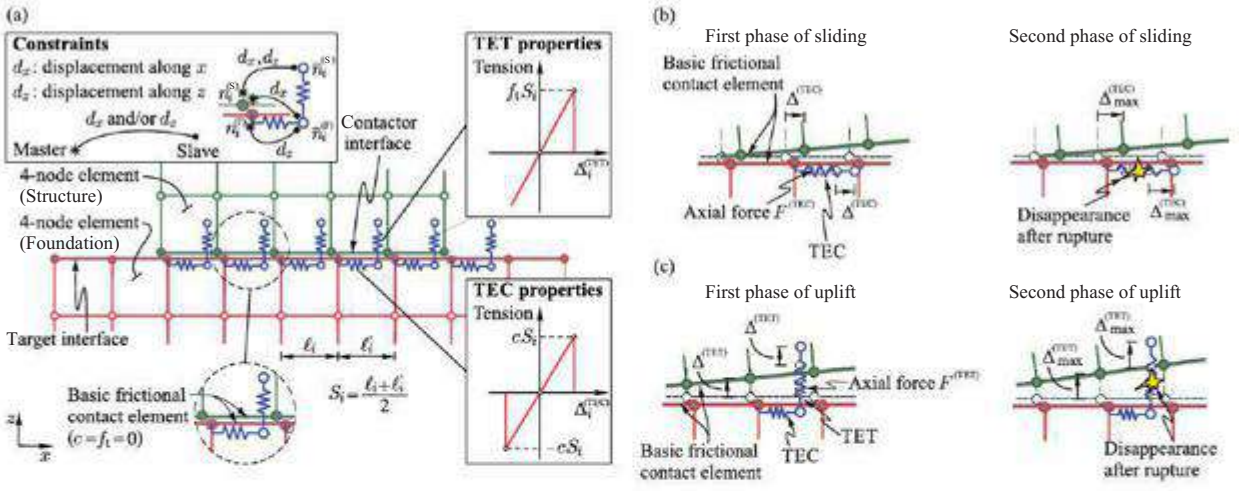

Figure 1: Proposed finite elements at a contact interface: (a) properties; (b) TEC to model c; and (c) TET to model f_t.

APPLICATION TO AN ACTUAL CONCRETE DAM

The proposed methodology is applied to an actual gravity dam with subjected to various earthquake-induced loads as shown in Fig. 2. The following main conclusions could be drawn: (i) A simplified dam-rock geometry should be used with caution as is may lead to inaccurate results for sliding safety factors and residual displacements; (ii) The values of cohesion c and friction angle ϕ are as critical for dam stability assessment as dam-rock geometry; (iii) tensile strength f_t should be accounted for in seismic stability assessment; and (iv) Stress distributions at contact interface are substantially sensitive to dynamic motion. The analyzes also demonstrate the importance of appropriately modeling contact at structural joints and of selecting relevant mechanical parameters. This process calls for caution from the analyst who bears the responsibility of assessing the conservatism or unconservatism of the obtained results with respect to safety evaluation of each structure studied.

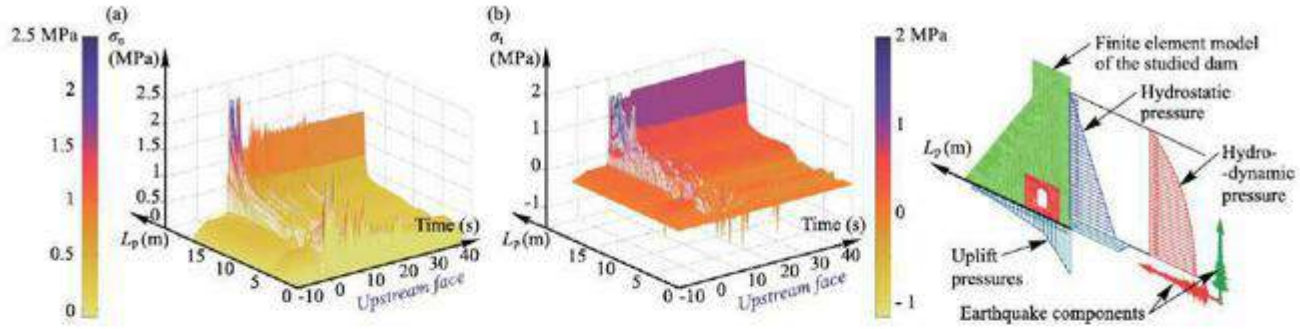

Figure 2: Seismic response at dam-rock interface of the studied dam: (a) normal stresses; (b) tangential stresses.

CONCLUSION

This paper proposed an efficient numerical procedure to assess the dynamic sliding stability of structures. The proposed technique uses special finite elements developed to account for the effects of cohesion and tensile strength along irregular contact interfaces. For illustration purposes, the proposed methodology was applied to an existing concrete dam subjected to strong ground motions. The developed approach was used to assess and criticize simplifying assumptions commonly adopted in dynamic stability analyses. Although the application of the procedure was illustrated for concrete dams, it can indeed be used to assess the dynamic stability of other types of structures comprising interfacial joints than can potentially slide or uplift.

References

[1] Nuss, L. K., Matsumoto, N., and Hansen, K. D. (2012). "Shaken, but not stirred - Earthquake performance of concrete dams." *32nd Annual USSD Conference*, USA.

[2] CDA. (2006). *Dam safety guidelines*, Edmonton, Alberta, Canada.

[3] ICOLD. (2004). *Sliding Safety of Existing Gravity Dams - Final Report.*

DYNAMIC INSTABILITY OF DOUBLY-TAPERED ROTATING LAMINATED COMPOSITE BEAMS

Saemul Seraj[1a] and Rajamohan Ganesan[1]
[1]*Department of Mechanical and Industrial Engineering, Concordia University, Montreal, Quebec, Canada*

Summary The dynamic instability of doubly-tapered rotating cantilever laminated composite beams due to periodic rotational velocity is investigated. The Rayleigh-Ritz method in conjunction with the classical lamination theory is used to obtain the system mass and stiffness matrices for the case of out-of-plane bending vibrations. Bolotin's method is applied to determine the instability regions. The combined effects of width and thickness taper on the dynamic instability of the rotating laminated beam are studied. In addition, to verify the instability analysis results, time responses are investigated at different locations of the instability region by using the Runge-Kutta method.

INTRODUCTION

A rotating structure can experience dynamic instability due to periodic rotational velocity. When a cantilever beam swings periodically, that is, oscillates about the axis of rotation, the dynamic bending stiffness varies harmonically that causes transverse vibrations with gradually increasing amplitudes that are often called dynamic instability. This large amplitude vibration could damage the rotating structure. Particularly in an aircraft engine or in a wind turbine, rotating blade experiences periodic aerodynamic load. This periodic aerodynamic load converts the constant rotational velocity to the pulsating rotational velocity. The excitation frequency of the pulsating load may coincide with the natural frequency of free vibration and blade becomes dynamically unstable from the nominal equilibrium position. In the present work, the dynamic instability problem caused by periodic rotational velocity of the doubly-tapered laminated composite beam is studied.

System description

A doubly-tapered laminated composite beam is shown in Figure 1(a), which can be designed by using four different taper configurations as shown in Figure 1(b). The beam is attached to a hub. The hub rotates about its axis at periodic rotational velocity $\Omega(t)$. The periodic rotational velocity can be written in terms of static and dynamic rotational terms and parametric resonance frequency as:

$$\Omega(t) = \Omega_0 + \beta\,\Omega_0 sin\ {}_p t \tag{1}$$

Here, Ω_0 is mean rotational velocity, β is amplitude factor, ${}_p$ is parametric resonance frequency and t is time.

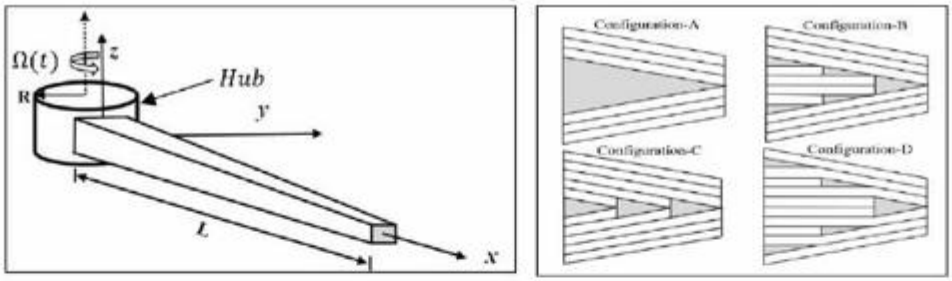

(a) (b)

Figure 1: (a) Doubly-tapered rotating beam, (b) Thickness taper configurations

The equations of motion for this physical system with periodic rotational velocity can be written in matrix form as:

$$[M]\{\ddot{q}\} + ([K] + \Omega^2(t)[K^C])\{q\} = \{0\} \tag{2}$$

where, $[M], [K], [K^C]$ and $\{q\}$ are mass matrix, stiffness matrix, stiffness matrix due to centrifugal action and system displacement vector respectively. Equation (2) represents the dynamic instability problem, and it can be solved by using Bolotin's first approximation [1] to obtain the eigenvalue system for the boundary between stable and unstable regions.

Results and discussion

In Figure 2, the instability region for a doubly-tapered (considering four different taper configurations) rotating composite beam and for a uniform rotating composite beam have been illustrated, where the vertical axis represents parametric ratio, which is the resonance frequency of the parametric exciting system divided by the doubled fundamental frequency, and the horizontal axis represents the amplitude factor. The beam length is 25 cm and width is 2 cm at the fixed side. The mean value of rotational velocity is 50 rad/s. The hub radius is taken as 0.025 m. The ply thickness is 0.125 mm and stacking sequence is $[0/90]_{9s}$. The doubly-tapered beams are obtained by dropping-off 18 plies and by considering 0.2 cm width at the free side. Drop-off plies are replaced by the resin material. NCT-301 Graphite/Epoxy Prepreg has been selected to conduct the numerical analysis, which is available in the laboratory of the Concordia Centre for Composites (CONCOM).

[a)] Corresponding author. Email: saemseraj@gmail.com.

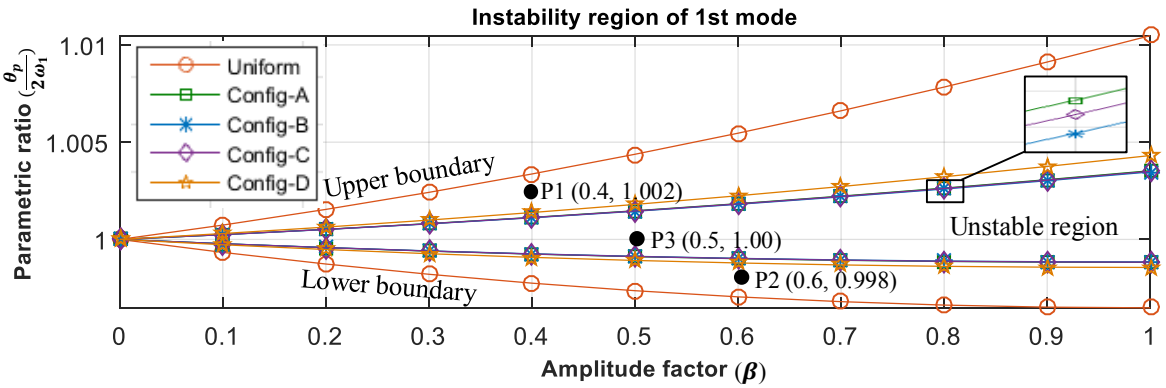

Figure 2: Instability region for 1st out-of-plane bending mode of doubly-tapered and uniform composite beams

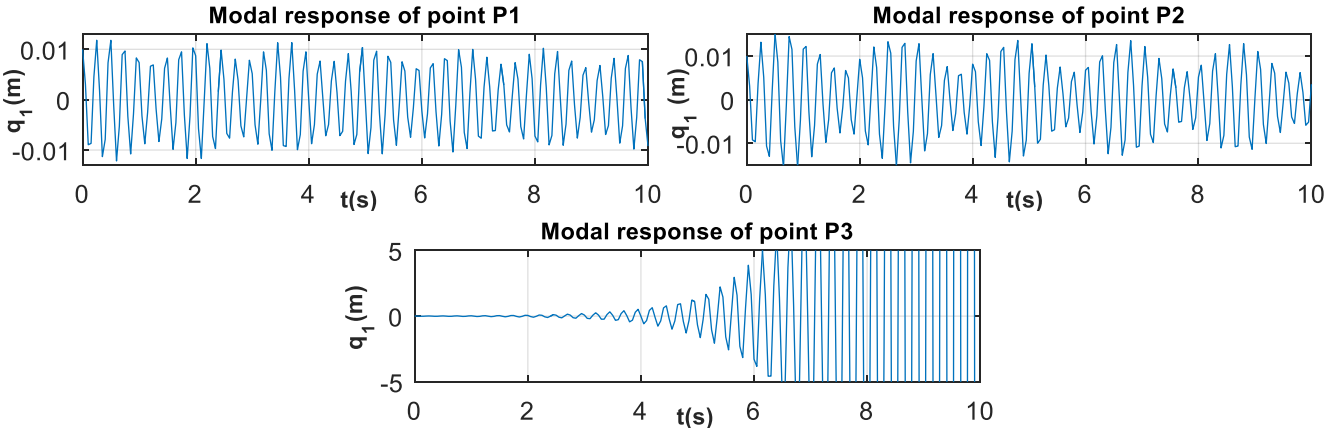

Figure 3: Modal response $q_1(t)$ for the parametric points P1, P2 and P3

In Figure 2, the area inside the upper and lower boundary lines is an unstable region where the width of instability region increases with the amplitude factor. Compared to the uniform composite beam, the width of instability region for the doubly-tapered (Configuration-D) beam is 53.03% (for $\beta = 0.5$) less. Also, it can be understood from Figure 2, that beam with taper Configuration-B has the smallest width of the instability region and beam with taper Configuration-D has the largest width of the instability region among all the taper configurations considered.

If any parametric point $(\beta, \theta_p/2\omega_1)$ of the structural system is in the unstable region, the system becomes dynamically unstable. In order to verify such a statement, the modal response $q_1(t)$ corresponding to any parametric point can be determined after solving the state-space form of equation (2) by using the Runge-Kutta method [3]. The modal response should keep increasing with time when the beam is unstable. In Figure 3, modal responses of three different points (P1, P2 and P3 shown in Figure 2) are given for 1st vibration mode, where points P1 ($\theta_p = 1814.2$ rad/s, $\beta = 0.4$) and P2 ($\theta_p = 1806.3$ rad/s, $\beta = 0.6$) are located in the stable region and point P3 ($\theta_p = 1810.4$ rad/s, $\beta = 0.5$) is located in the unstable region of the doubly-tapered beam of taper Configuration-A. The modal responses of points P1 and P2 are confined within a scope of about 0.01 m, while that of point P3 increases rapidly and exceeds 5 m within the same time duration. Hence, the structural system corresponding to point P1 and point P2 is dynamically stable, but that corresponding to point P3 is dynamically unstable.

CONCLUSIONS

The combined effects of width and thickness taper on the dynamic instability behavior of laminated composite beam are significant. The double tapering significantly reduces the risk of dynamic instability caused by periodic rotational velocity. An increase in the amplitude of periodic rotation increases the possibility of dynamic instability.

References

[1] V.V. Bolotin, *The Dynamic Stability of Elastic System*, Holden-Day, INC., San Francisco, London, Amsterdam, 1964.

[2] K. He, S. V. Hoa and R. Ganesan, "The Study of Tapered Laminated Composite Structures: A Review," *Com. Sc. & Tech.*, 2000.

[3] S. S. Rao, *Mechanical Vibration*, Pearson Education, Inc., 2004.

[4] R. L. Bielawa, *Rotary Wing Structural Dynamics and Aeroelasticity*, Reston, VA: American Institute of Aeronautics and Astronautics.

THIN FILM WRINKLING: A SOLID-LIQUID INTERFACE INSTABILITY

Ali Davoodabadi, Congrui Jin, Timothy J. Singler*

Mechanical Engineering Department, State University of New York at Binghamton, NY 13902, USA

Summary When a small mercury (*Hg*) droplet is gently placed on a gold (*Au*) thin film deposited on a glass substrate, a complex process ensues. The spreading of the *Hg* on the *Au* substrate under the action of an uncompensated Young force and the simultaneous penetration of the *Hg* through the *Au* film via intergranular penetration comprise the first part of the process. This penetration allows *Hg* to reach the *Au*/glass interface. The sustained transport of *Hg* from the drop on top of the film to the *Au*/glass interface, and its subsequent flow along this interface serve to delaminate the *Au* film from the glass substrate and comprises the second part of the process. The delaminated film is unstable to wrinkling and secondary finger-like growth of the wrinkles.

EXPERIMENTAL PROCEDURE

Different thicknesses of *Au* thin films (400*nm*, 700*nm*, and 1000*nm*) are deposited on pre-cleaned glass substrates using an E-beam evaporator apparatus at room temperature. The sample is then placed on a platform equipped with three synchronized cameras capable of capturing top, bottom and side view videos. A small droplet of *Hg* is gently placed on the *Au* film. The mass of the *Hg* droplet is varied between tenths of a milligram to several milligrams to assess the effect of droplet size on the wrinkling instability.

EXPERIMENTAL RESULTS

When the *Hg* droplet is placed on the *Au* thin film, it wets the top surface and establishes a stable contact line while simultaneously penetrating into the film underneath. With continued penetration, the entire volume of *Hg* on the top surface of the film is transported to the *Au*/glass interface and starts spreading out, delaminating the thin *Au* film from the glass substrate. Wrinkling instabilities are observed during this spreading process, as shown in Fig. 1. Data for contact angle, penetration time, interfacial spreading rate, and morphology of the *Au* film's wrinkles and secondary finger-like growth of the wrinkles can be acquired and analyzed from repeated experiments. Here we focus on the evolution of the wrinkles and fingers as a result of structural instability. We observed that by varying the thickness of the *Au* film, the evolution of the instability changes drastically. For a 400*nm* thick film (Fig. 1(a)), a dome-shaped axisymmetric delamination occurs in the beginning of the spreading. Small corrugations then begin to appear around the rim of this region. These corrugations subsequently grow radially to form fingers that are susceptible to tip splitting as they grow radially. The dome-shaped delaminated region also exists in case of a 700*nm* thick film, but unlike the 400*nm* case, corrugations occur almost immediately (Fig. 1(b)). But as the film thickness is increased to 1000*nm*, the dome-shaped region disappears and finger-like growth is the only observable morphology (Fig. 1(c)). We observe that the number of fingers per unit length of the circumference (wave number) deceases significantly as the thickness of the film is increased, as shown in Fig. 2. Moreover, spreading slows down significantly with increasing film thickness, as shown in the time stamps in Fig. 1.

DISCUSSION AND THEORETICAL MODEL

The pressure at the forefront of the wetted region where the mercury, gold film, and glass meet (triple line) plays a prominent role in determining the morphology of the instability's evolution. In fact, for the spreading to continue at any point, the liquid pressure must be great enough to be able to deform the thin film and proceed. Thus we suggest that one of the reasons for transformation from axisymmetric to more stable non-axisymmetric finger-like spreading observed in Figs. 1 ((a)-(b)) is for the liquid to compensate its pressure drop caused by friction forces by creating an additional capillary pressure inside the large surface curvature narrow fingers. Tip splitting can be explained by the same argument since the fingers resulting from branching are narrower. The formation of initial corrugations around the rim can be rationalized by considering the well-confirmed fact that once a thin film is subjected to large tensile stresses in one direction, it buckles in a perpendicular direction to minimize the total energy and stabilize the situation[1-3]. In this experiment, deflections of the thin film to accommodate a large amount of liquid result in exceedingly large stretching in radial direction that induces buckling in azimuthal direction. A theoretical model to simulate the whole process has been proposed. For the solid membrane, the

*Corresponding Author Email: singler@binghamton.edu

well-known Föppl–von Kármán equations, widely used to analyze membranes subjected to large deflections[1-4], have been adopted to simulate the deformation of the *Au* film, accounting for both stretching and bending effects. The flow of the fluid is described by the Reynolds lubrication equation. The fluid and solid equations are coupled because the pressure in the Föppl–von Kármán equations depends on the pressure in the fluid.

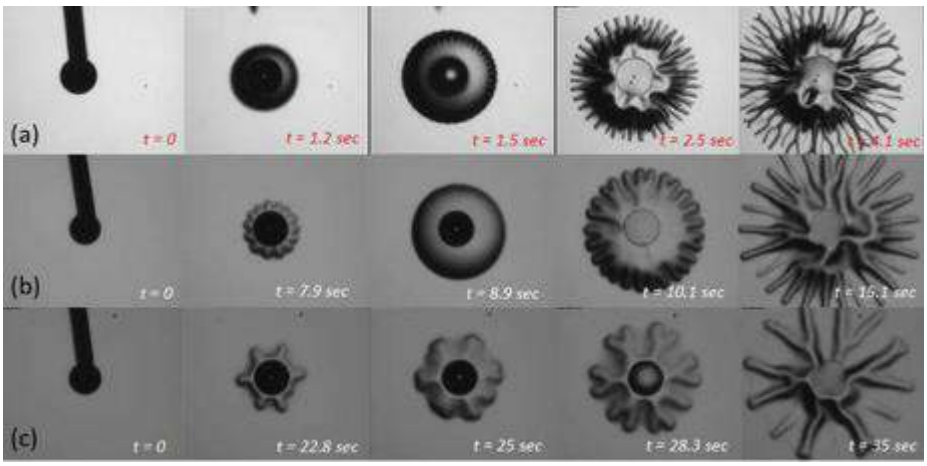

Figure 1. Effect of thickness on evolution of the instability, (a) thickness=400 nm, droplet mass=0.89 mg; (b) thickness=700 nm, droplet mass=1.11 mg; (c) thickness=1000 nm, droplet mass=0.65 mg.

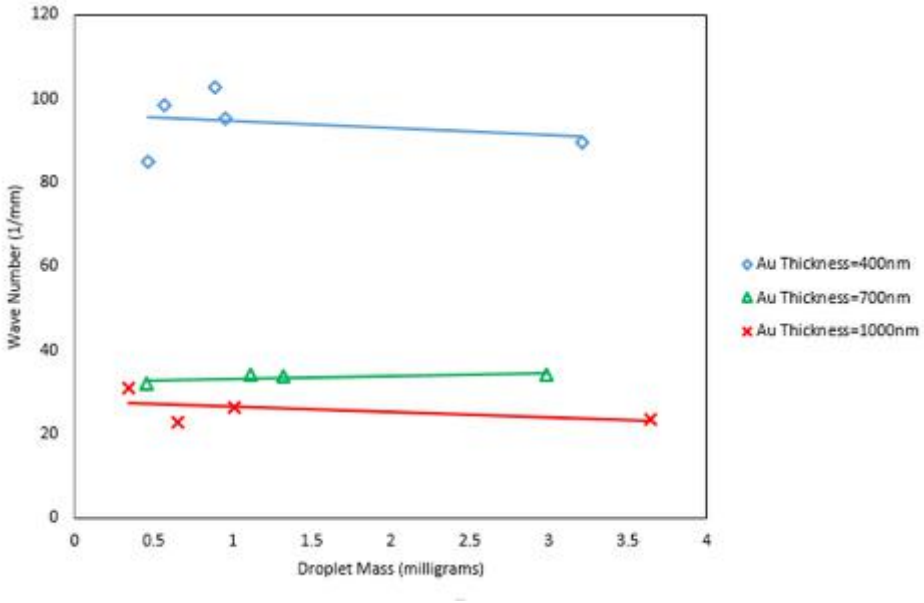

Figure 2. Wave Number drops significantly as the thickness of the film is increased.

CONCLUSION

It has been observed that spreading of liquid *Hg* at the *Au*/glass interface resulted in a wrinkling instability in which its evolution (both temporal and spatial) strongly depends on the film thickness. A theoretical model has been proposed to simulate this complex process.

References

[1] Timoshenko S.P., Gere J.M., Theory of Elastic Stability, McGraw-Hill Kogakusha, New York, USA, 1961.

[2] Huang J., Juszkiewicz M., de Jeu W.H., Cerda E., Emrick T., Menon N., Russell T.P.: Capillary Wrinkling of Floating Thin Polymer Films, *Science*, **317**, 650, 2007.

[3] Cerda E., Mahadevan L.: Geometry and Physics of Wrinkling, *Phys*. *Rev*. *Lett*., **90**, 074302, 2003.

[4] Pihler-Puzovic D., Russell R.M., Juel A., Heil M.: Modelling the Suppression of Viscous Fingering in Elastic-Walled Hele-Shaw Cells. *J*. *Fluid Mech*. **731**, 162, 2013.

FORMATION OF WAVY INTERFACES IN LAYERED VISCO-HYPERELASTIC COMPOSITES

Viacheslav Slesarenko[a] & Stephan Rudykh
Faculty of Aerospace Engineering, Technion, Haifa, Israel

Abstract We study the buckling behavior of soft layered composites with visco-hyperelastic constituents. We show that critical strain and the post-bifurcation geometry in such composites are defined by not only geometrical parameters, but also by rate-dependent properties of constituents. This allows us to experimentally and numerically prove the possibility to tune amplitude of the post-bifurcation wavy patterns in wide range by applying different loading rates. Moreover, we reveal the existence of optimal strain level, for which the tuning effect is the most pronounced. Therefore, the composites with viscoelastic constituents can be directly tailored to achieve required microstructure tunability, which may be useful for the various practical applications from elastic wave propagation to optical camouflage.

Rationally chosen microgeometry allows scientists and engineers to design and manufacture materials with enhanced properties, which combine excellent strength and toughness [1] or flexibility and protection [2]. It was shown that internal microstructures define not only mechanical but optical, acoustical, electromechanical or magnetic properties. Therefore possessing control of geometry one becomes capable to tune the performance of materials and structures. This effect can be amplified by the instability-induced microstructure transformations [3], the phenomenon which is frequently used in nature designed materials. The ability to trigger dramatic geometric transformations opens exciting opportunities to design soft reconfigurable materials and structures with tunable microstructures to achieve control over a large variety of material properties. It was shown, that soft layered composites under compression demonstrate buckling phenomenon, which leads to the formation of wavy patterns [4]. The wavelength as well as amplitude of such patterns at a particular strain level are exclusively defined by the composite microstructure and by the contrast in the elastic moduli of the phases. It means that for specific deformed state it is possible to achieve only one exclusive post-bifurcation geometry. This imposes restrictions on admissible microstructure, and, as a result, the tunability of the material properties and functionalities is drastically limited. In this study, we overcome this issue and show that it is possible to create various wavy microstructures in soft layered composites with rate-dependent constituents. This will allow us to design the instabilities by controlling the governing properties of the constituents through the deformation rate.

In order to prove the possibility to control post-bifurcation geometry we designed soft layered composites and manufactured them by means of 3D printing. Basing on mechanical tests of raw resins, available for Polyjet technology, we choose the combination of soft TangoPlus (TP) and more rigid FL9795-DM (DM) materials. Pronounced rate-dependent behavior of latter, which shear modulus varies 8-10 times depending on the applied strain rate, allowed us to increase the range of contrasts in elastic moduli of stiffer and softer constituents and, hence, to achieve an enhanced tunability of the composite microstructures. Guided by theoretical and numerical predictions of buckling behavior in rate-independent composites, we examined the composite with stiff phase volume fraction of 15 %. The thickness of the stiffer layers was 0.75 mm and the distance between them was 4.25 mm, while the width, height and out-of-plane depth were 85 mm, 35 mm and 8 mm, respectively. The specimens were constrained by special fixtures to eliminate out-of-plane deformation and maintain the plane strain conditions. The composite was subjected to compression up to 75 % of initial height at the strain rates of 10^{-4}, 10^{-3}, 10^{-2} and 10^{-1} s^{-1}. Numerical simulations were performed with a help of finite element software COMSOL. We used simple neo-Hookean model to describe the behavior of TP matrix materials, while more complex Quasi-Linear Viscoelastic model (QLV) [5], which is able to capture hyperelasticity as well as rate-dependent properties, was chosen to approximate the behavior of DM layer material.

Experimental observations together with numerical simulations show that studied composite undergoes buckling, however the value of critical strain, when bifurcation occurs, strongly depends on the applied strain rate [6]. Figure 1 shows the variety of observed wavy patterns for the same strain value of 15% but for different strain rates. It is easy to see that due to the rate-dependent behavior of constituents one is able to achieve the post-bifurcation patterns with different amplitudes,

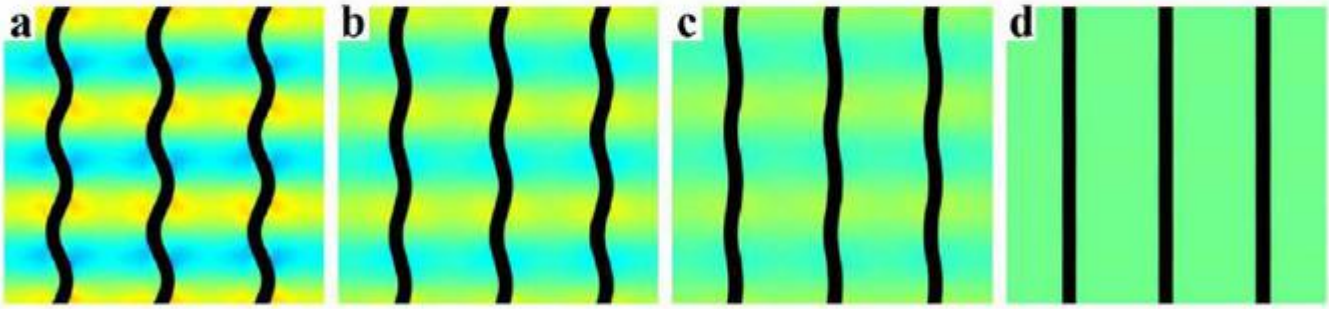

Figure 1 Post-bifurcation wavy patterns for strain level of 15 % and strain rates of **(a)** 10^{-1}, **(b)** 10^{-2}, **(c)** 10^{-3} and **(d)** 10^{-4} s^{-1}

[a] Corresponding author. Email: slslesarenko@technion.ac.il, slslesarenko@gmail.com

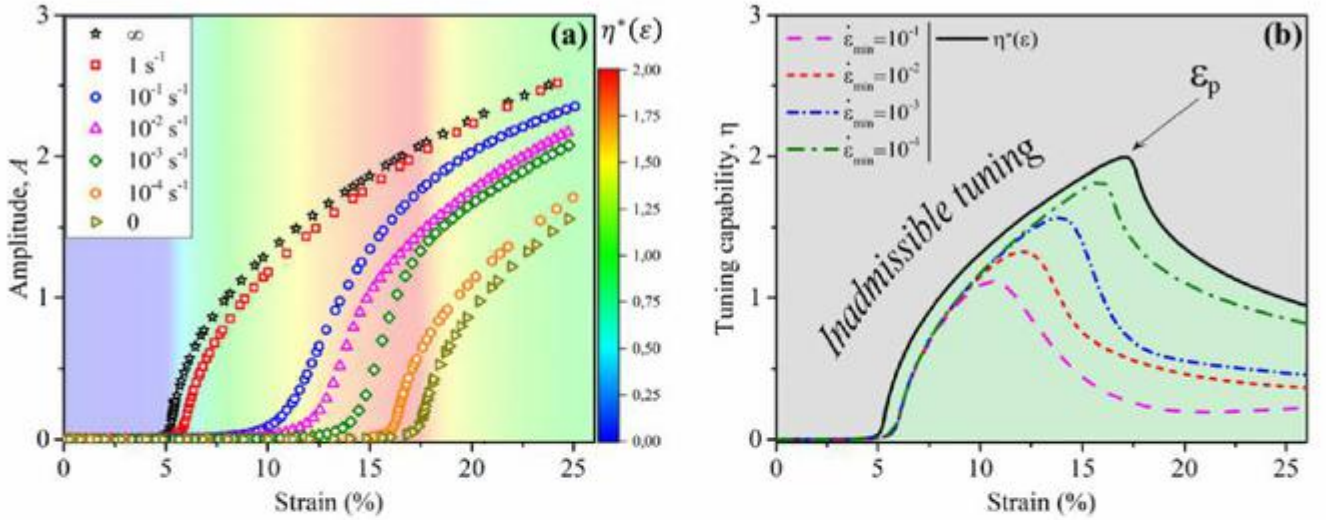

Figure 2 (a) - dependence of amplitude $A(\varepsilon)$ on strain for different strain rates. The amplitude is normalized by the stiffer layer thickness. The background color corresponds to the value of the tunability function, $\eta^*(\varepsilon)$. **(b)** - dependence of tuning capability $\eta(\varepsilon, \dot{\varepsilon}_{min}, \dot{\varepsilon}_{max})$ on strain for different $\dot{\varepsilon}_{min}$ and $\dot{\varepsilon}_{max} = 1$ s^{-1} [6]

depending on the applied strain rate. Finite element analysis allows us to follow the evolution of patterns amplitude during loading (Figure *2a*). We observe a rapid increase in the wrinkling amplitude directly after the bifurcation; however, after the formation of the wavy patterns, the corresponding curves flatten with further increase in compressive loading. Obviously, at each macroscopic strain level, different amplitudes can be induced by managing the strain rate. At the same time, considering the strain rates which is slower than 1 s^{-1} (red squares on Figure *2a*) and faster than 0.1 s^{-1} (blue circles), one may notice that variety of achievable amplitudes for strain of 10% is much wider ($0.1 < A(\varepsilon) < 1.1$) in comparison with strain of 20 % ($1.9 < A(\varepsilon) < 2.1$). To quantify this tunability phenomena, we introduce function, $\eta(\varepsilon, \dot{\varepsilon}_{min}, \dot{\varepsilon}_{max})$, which describes the tuning capability for specific strain value ε and for strain rates range $[\dot{\varepsilon}_{min}, \dot{\varepsilon}_{max}]$ and defines by equation

$$\eta(\varepsilon, \dot{\varepsilon}_{min}, \dot{\varepsilon}_{max}) \equiv A(\varepsilon)|_{\dot{\varepsilon}=\dot{\varepsilon}_{max}} - A(\varepsilon)|_{\dot{\varepsilon}=\dot{\varepsilon}_{min}}$$

The defined tuning capability function can be expanded to capture any possible strain rates. In this case, previous equation is modified as

$$\eta^*(\varepsilon) \equiv \eta(\varepsilon, 0, \infty) = A(\varepsilon)|_{\dot{\varepsilon}\to\infty} - A(\varepsilon)|_{\dot{\varepsilon}\to 0}$$

Figure *2b* show the dependence of the function $\eta(\varepsilon, \dot{\varepsilon}_{min}, \dot{\varepsilon}_{max})$ on the strain for the various ranges of strain rates $[\dot{\varepsilon}_{min}, \dot{\varepsilon}_{max}]$. We observe that the tuning capability is non-monotonic function, and it reaches the maximum for a particular strain level $\varepsilon_p(\dot{\varepsilon}_{min}, \dot{\varepsilon}_{max})$. The overall performance of composite is limited by instantaneous and infinitely slow loading, so the area under black curve on Figure *2b*, representing $\eta^*(\varepsilon)$ function, encloses the admissible values of the tuning capability in layered composites. While the tuning capability is limited by the value of η^* function, the exact value of ε_p is defined by the material constants, in particular, by the Prony series constants of QLV model, capturing the rate-dependent behavior of constituents. Consequently, by combining different materials pairs for composite constituents one may achieve maximal tunability for the specific strain ranges.

Thus, we find that the combination of the elastic instability and visco-hyperelastic phenomena leads to a significant increase the admissible range of tunable microstructures in soft layered composites. We found that the tuning capability reaches its maximum for particular strain level, which, in turn, depends on the composite microstructure as well as on the material properties of the constituents. Consequently, the composites with viscoelastic constituents can be directly tailored to achieve required microstructure tunability. This can provide powerful means to control the material performance and achieve new functionalities.

References

[1] L. S. Dimas et. al: Tough composites inspired by mineralized natural materials: Computation, 3D printing, and testing. *Adv. Funct. Mater.* **23:**4629–4638, 2013.

[2] S. Rudykh and M. C. Boyce: Analysis of elasmoid fish imbricated layered scale-tissue systems and their bio-inspired analogues at finite strains and bending. *IMA J. Appl. Math.* **79**:830–847, 2014.

[3] A. J. Crosby: Why should we care about buckling? *Soft Matter.* **6**:5660, 2010.

[4] Y. Li, et.al: Wrinkling of Interfacial Layers in Stratified Composites. *Adv. Eng. Mater.* **15:**921–926, 2013.

[5] R. De Pascalis et.al: On nonlinear viscoelastic deformations: a reappraisal of Fung's quasi-linear viscoelastic model. *Proc. R. Soc. A.* **470**:20140058, 2014.

[6] V. Slesarenko and S. Rudykh: Harnessing viscoelasticity and instabilities for tuning wavy patterns in soft layered composites. *(submitted)*, 2016.

BENDING CAPACIT OF INFLATED MESH-REINFORCED-MEMBRANE BEAM

Changguo Wang[1], Qiang Tao[1a)], Zhimin Xie[1], Huifeng Tan[1]
[1]*Center for Composite aterials, arbin Institute of Technology, arbin, China*

Summary In this paper, an inflated MRM beam was fabricated, theoretical and experimental analysis were carried out to study its bending capacity. Experimental results verified that an inflated MRM beam has higher load-carrying efficiency than a pristine membrane beam. The inflated MRM beam performed novel wrinkling characteristics obtained by VIC-3D technique. This provides a useful way to resist wrinkling for membrane structures. Theoretical analysis based on a Shell-Membrane Model was also validated by experiments.

INTRODUCTION

Inflated membrane beams are the major load-carrying components of the space inflatable structures. Load-carrying capacity is the major concerned issue on inflatable beam. Gossamer Space Inflatable Structures[1-2] such as isogrid inflatable boom[3] were developed for their low packing volume, reduced mass and high load-carrying efficiency. Wang et al.[4] proposed a Mesh-Reinforced-Membrane (MRM) concept. Numerical modelling and experiment were both carried out and revealed that MRM has a higher load-carrying efficiency than pristine membrane.

In this paper, bending capacity of an inflated beam with MRM wall material will be studied. Theoretical analysis based on Shell-Membrane Model will be firstly introduced when an inflated MRM beam subjected to a tip bending load. Then experiments will be carried out to verify theoretical prediction.

THEORETICAL ANAL SIS

Membrane Model and Thin-walled Shell Model[5] are two main methods which are used to predict bending properties of inflated beam. Combined these two models together, we a Shell-Membrane Model was developed to predict the bending performance of an inflated MRM beam.

According to Shell-Membrane Model, the critical wrinkle force and collapse force of an inflated MRM beam are as follows:

$$ {}^{sm}_{w} = \frac{\alpha \cdot \ \pi^{\ 3}}{l} \qquad \alpha = \frac{\theta_w}{2\pi} $$

$$ {}^{sm}_{coll} = \frac{\alpha \cdot \ \pi^{\ 3}}{l} + \frac{2\sqrt{2}}{9}\frac{\pi t^2 r E_1}{l}\sqrt{\frac{E_2}{E_2}}\sqrt{\frac{1}{1-\nu_{12}\nu_{21}} + 4\frac{(\ -\ )^2}{E_2}} $$

where: t , E , ν , r , represents thickness, Elastic modulus, Poisson's ratio of membrane and radius, length of inflated beam, respectively; represents modifying factor; θ_w is the actual wrinkle angle in the experiment; In this case, r =0.03m, l =0.6m, $t^{\ ap}$ =25μm, $E^{\ ap}$ =3GPa, $\nu^{\ ap}$ =0.31. MRM is treated as an orthotropic material. t =50μm, E_1 =6.94GPa, E_2 =4.30GPa, ν_{12} =0.34, ν_{21} =0.30.

E PERIMENTAL ANAL SIS

In order to elucidate the load-carrying efficiency, both pristine membrane beam and MRM beam were fabricated. Here MRM is fabricated by using glass fiber tape (GFT) to reinforce Kapton membrane. Fig.1 shows layouts of the bending experiments. The experimental deflection-load curves at internal pressure 10kPa and wrinkling patterns captured by VIC-3D technique are shown in Fig.2, Fig.4. Seen from Fig.2, the critical wrinkle load and collapse load for inflated MRM beam are 1.04N, 2.57N, respectively, while 0.88N, 1.47N for inflated Kapton beam. Mesh structure formed by GFT will undoubtedly improve bending capacity of inflated beam, but will inevitably increase structure weight. Therefore define the specific load calculated from the equation to evaluate the structure's load-carrying efficiency. Fig.3 shows the comparison results of specific load between inflated Kapton beam and inflated MRM beam. From the view point of the specific load, inflated MRM beam has higher load-carrying efficiency. Comparison theoretical results with experimental results shown in Table 1 revealed Shell-Membrane Model is valid for predicting the critical wrinkle force and collapse force of inflated MRM beam. As shown in Fig.4, the inflated MRM beam performed novel wrinkling characteristics. Wrinkles dispersed in several meshes on the membrane, and were confined in these meshes. So GFTs play the role of “obstacles” during the wrinkle propagation process. This provides a useful way to resist wrinkling for membrane structures.

a) Corresponding author. Email: taoqiang@hit.edu.cn

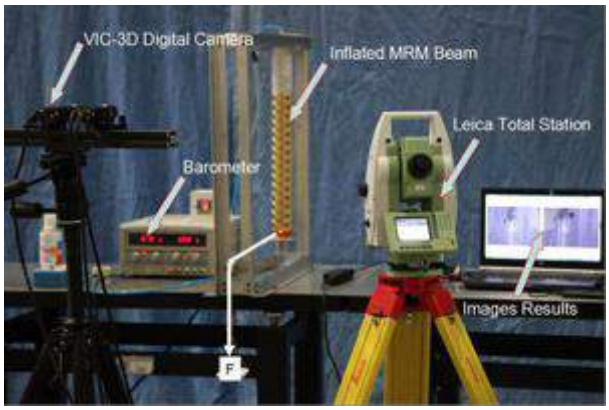

Fig.1 Layouts of bending experiments

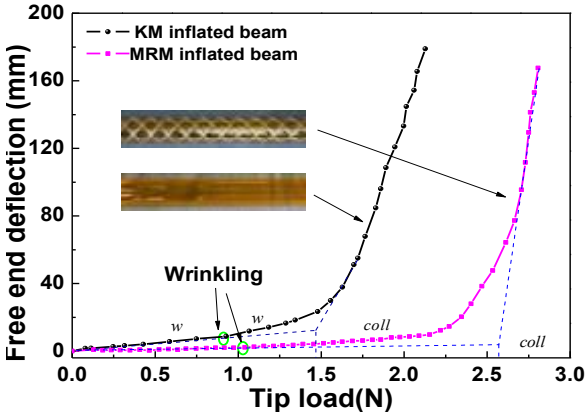

Fig.2 The experimental load-deflection curves

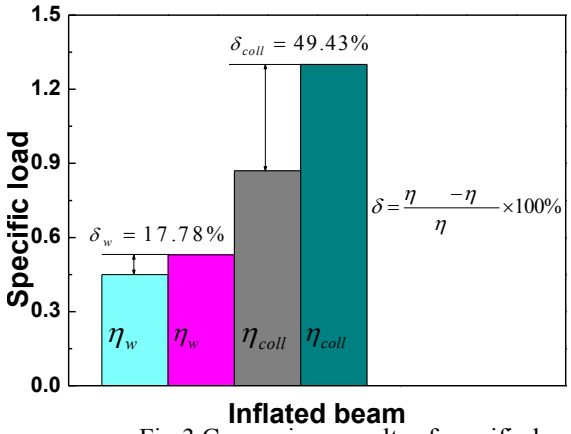

Fig.3 Comparison results of specific load

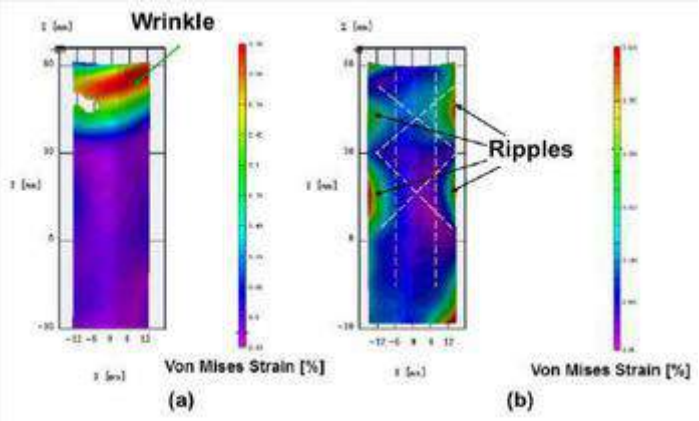

Fig.4 Wrinkling patterns

Table 1 Comparison theoretical results with experimental results

Tip Load	Theoretical results (N)	Experimental results (N)	Difference (%)
w	0.93	0.88	5.68
$coll$	1.35	1.47	-8.16
w	0.94	1.04	-9.62
$coll$	2.66	2.57	3.50

COMMENTS

An inflated MRM beam was fabricated, theoretical and experimental analysis were carried out to study its bending capacity. Experimental results verified an inflated MRM beam has higher load-carrying efficiency than a pristine membrane beam. The Shell-Membrane Model was validated by experiments. The inflated MRM beam performed novel wrinkling characteristics. This provides a useful way to resist wrinkling for membrane structures.

References

[1] David P. Cadogan, Stephen E. Scarborough et al. Shape Memory Composite Development for Use in Gossamer Space Inflatable Structures. 43rd AIAA/ASME/ASCE/AHS/ASC Structures, SDM Conference, Denver, Colorado 2002.

[2] Wang C. G., Du X. W., Tan H. F., He X. D.: A new computational method for wrinkling analysis of gossamer space structures. Int. J. Solids Struct. 46 (6):1516-1526, 2009.

[3] Lin John K.H and George H. Inflatable rigidizable isogrid boom development.: 43rd AIAA/ASME/ASCE/AHS/ASC Structures, Structural Dynamics, and Materials Conference, Denver, Colorado 2002.

[4] Wang C., Zhang L., Tan H., Wan Z.: Mesh Reinforced Membrane and Its Wrinkling Characteristics. International Conference on Textile Composites and Inflatable Structures, STRUCTURAL MEMBARNES 2013.

[5] Veldman S.L., Bergsma O.K., Beukers A.: Bending of anisotropic inflated cylindrical beams. Thin-Walled Struct. 43(3): 461-475, 2005.

HIGHLY DEPLOYABLE MULTIFUNCTIONAL CELLULAR STRUCTURES WITH HIERARCHY

Hamid Ebrahimi[1], Babak Haghpanah[2], Davood Mousanezhad[1], Ranajay Ghosh[1], and Ashkan Vaziri[1a)]
[1]*Department of Mechanical and Industrial Engineering, Northeastern University, Boston, MA, USA*
[2]*Department of Mechanical and Aerospace Engineering, University of California, Irvine, CA, USA*

Summary In the present work we propose a new class of cellular structures with square and triangular grids, which are capable of dramatic but controlled shape and size change through alteration of their underlying topological hierarchy. This high degree of geometrical change can yield a correspondingly wide bracket of mechanical and multifunctional behavior of these structures.

ABSTRACT

The properties of traditional materials are fixed by their atomic or molecular arrangements and typically difficult to alter further due to the constraints of sub continuum forces and relatively closely packed microstructure. Thus developing and engineering new materials with either extreme properties or a non-traditional combination of behavior becomes extremely challenging. This fundamental limitation of the properties can however be challenged by first noting that the overall properties of a given material originate not just from the atomic constituents but their mutual arrangements, for instance, their lattice structure.

Therefore, although coal, graphite, diamond and graphene are allotropes of carbon, their properties are strikingly different. Taking the analogy of allotropy further, an adroit control of topological distribution of matter can be used to engineer novel properties even at a larger scale. In this context, cellular materials, whose structure is made up through scaling up of a fundamental geometrical unit cell can be seen as analogs of natural crystals and thus serve as an excellent template for metamaterial development. More importantly, the meso-level organization and large free spaces inside cellular structures make imparting geometrical changes in their underlying structure much easier compared to traditional materials or composites. Since the overall properties of cellular materials are directly linked to the geometry of the underlying unit cell, it becomes possible to herald materials capable of reversible change of properties through physical stimuli hitherto impractical at large scale except in special cases such as piezoelectric, shape memory or specially designed glass materials.

In the present work we propose cellular structures with square or triangle grids, which are capable of dramatic but controlled shape and size change through alteration of their underlying topological hierarchy. This high degree of geometrical change can yield a correspondingly wide bracket of mechanical and multifunctional behavior since the overall properties of cellular materials are intrinsically tied to their underlying topology. We are particularly interested in investigating the elastic, as well as the phononic behaviour of these structures. We carry out an energy-based method to obtain closed-form expression of Young's modulus for hierarchical structures with underlying square-grid topology with changing hierarchy. Furthermore, finite element (FE) based band structure calculations were employed to obtain the phononic bandgap (i.e., frequency ranges of strong wave attenuation) evolution of these structures at different levels of hierarchy. We find that the change in shape and size of these hierarchical structures can significantly affect the static and dynamic responses, and they can be effectively used to tune the stiffness and bandgaps of these multifunctional hierarchical cellular structures.

[a)] Corresponding author. Email: vaziri@coe.neu.edu

HARNESSING DIRECTED BUCKLING FOR SWITCHABLE CONDUCTIVE PATHWAY

Gaojian Lin[1], Dengteng Ge[2], Shu Yang[2] & Jie Yin[1a)]
[1]*Department of Mechanical Engineering, Temple University, Philadelphia, PA, U.S.A*
[2]*Department of Materials Science and Engineering, University of Pennsylvania, Philadelphia, PA, U.S.A*

Summary Extensive studies have been conducted on buckling induced pattern transformation in free-standing structures while little attention in constrained structure. Here we study the swelling-induced buckling of arrays of thin stripes with their bottom fixed to the substrate, as well as their potential applications in switchable conductive pathway. We find that unlike the classical buckling of free-standing thin plate stripe only showing one global half wave, multiple local waves are generated on the top through bottom constrained buckling. The explicit analytical solutions for predicting buckled geometry are developed and validated by both finite element method (FEM) simulation and experiments. Moreover, we demonstrate the use of buckling-induced controllable contacts in enabling design of switchable conductive pathway in electricity, which opens up a wide range of novel application possibilities in conductive pathway, photonic/phonic wave guiding, and among others.

INTRODUCTION

Deterministic order is highly desired in surface patterning [1] and structural reconfiguration in metamaterials [2] through deformation. However, buckling deformation, which can either bend up or down is energetically equivalent, often induces geometrical frustration in structures and thus disordered configuration [3], presenting a challenge for structural ordering in reconfigurable metamaterials. To control the ordered buckling configurations, we carried out a combined experimental and numerical method to create large area of ordered and deterministic patterns of arrays of ridges with their bottom constrained through directed buckling strategy. The deterministic control of buckling configurations is demonstrated in ridges consisting of both hydrogel and Polydimethylsiloxane (PDMS) at multiple length scales.

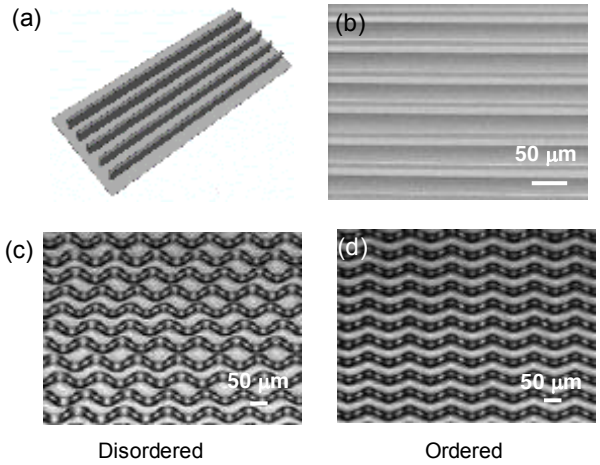

Fig. 1 (a) Schematic illustration of array of ridges with bottom constrained to substrate. (b) Tilted SEM images of hydrogel micro-ridges before deformation. (c) SEM images of disordered buckling pattern in ridges after swelling-induced buckling. (d) SEM images of ordered buckling pattern after directed buckling

RESULTS AND DISCUSSIONS

Fig. 1b shows the tilted SEM image of an array of undeformed hydrogel micro-ridges. Upon swelling, the free swelling of ridges is constrained by their clamped bottoms to non-swelling rigid substrates, which renders the ridges under compression and thus induces lateral buckling when beyond a critical strain. Despite the same buckled sinusoidal wavy shape in each single ridge, a disordered buckled structural configuration is observed with randomly shifted phase angles between ridges (Fig. 1c) owing to the bistability in each wave, where it can equivalently bend upward or downward and thus the buckling direction is indeterminate. In contrast, after directed buckling, the disordered pattern transits to a long-range ordered one showing the same phase angle in (Fig. 1d).

The well-controlled phase angle of buckled waves in ridges can be used for enabling the new function in potentially activating the switchable electrical conductive pathway through controllable buckling-induced ridge contacts. Fig. 2a shows that for buckled ridges with the same phase angle, there is no contact after buckling between ridges since buckled ridges are parallel to each other no matter how close they are. However, when ridges are shifted to certain distance, after buckling, the physical contacts between buckled ridges are enabled due to their mismatched phase angles (Fig. 2b). Using this way, the

[a)] Corresponding author. Email: jieyin@temple.edu.

connections between ridges after buckling is established through buckling-induced contact. To demonstrate this new function we apply conductive coating to the hydrogel ridges. Proof-of-concept experiments show that a Domino-like conductive pathway in series can be reversibly activated through swelling-induced buckling and evaporation induced de-swelling of ridges on rigid substrates (Fig. 2c). The lit LED light proves the success of the activation.

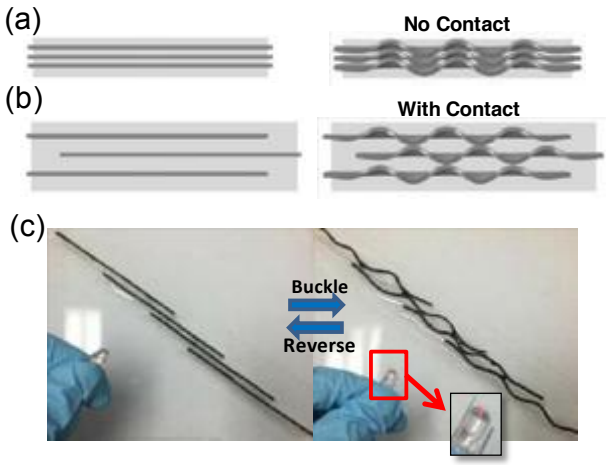

Fig. 2 (a) Schematic illustration of buckled parallel ridges without physical contact due to identical phase angles (b) After phase angle shifting, contacts between parallel buckled ridges are enabled. (c) Proof-of-concept experiment on demonstrating of activating switchable conductive pathway in array of ridges through buckling driven contacts. LED light is on after buckling.

CONCLUSIONS

The directed buckling strategy opens a new avenue for creating highly ordered and deterministic buckled structural configurations, where the original disordered buckling patterns with random distributed phase angle of buckle waves transit to ordered one with the same phase angle. The directed buckling leads to the physical contacts between ridges, and thus enables the functionality in activating switchable conductive pathway, which may find great potential applications in environmental hazard sensors, display, electric circuits, phononic and photonic waveguiding, and active micro-fluid channels, and among others.

References

[1] Yin, J., Yagüe, J. L., Eggenspieler, D., Gleason, K. K. & Boyce, M. C. Deterministic Order in Surface Micro-Topologies through Sequential Wrinkling. *Adv. Mater*. **24**, 5441-5446, 2012.

[2] Zheludev, N. I. & Kivshar, Y. S. From metamaterials to metadevices. *Nat Mater* **11**, 917-924, 2012.

[3] Kang, S. H. *et al*. Complex Ordered Patterns in Mechanical Instability Induced Geometrically Frustrated Triangular Cellular Structures. *Phys. Rev. Lett*. **112**, 098701, 2014

BUCKLING DISTORTION OF ALUMINUM PLATES UNDER NON-UNIFORM WELDING STRESS FIELD

Bin Zheng[1,2], Haidong Yu[2] & Xinmin Lai [1,2]

[1]*Key Laboratory of Mechanical System and Vibration, Shanghai Jiao Tong University, Shanghai, China*

[2]*Shanghai Key Laboratory of Digital Manufacture for Thin-walled Structures, Shanghai Jiao Tong University, Shanghai, China*

Summary Thin aluminum plate is prone to buckle after welding. The buckling distortion is induced by the non-uniform welding stresses. To predict the critical stress in the buckling distortion accurately, a rational analysis is presented in this paper. The non-uniform welding stresses is represented by mathematical equations. Then, the prediction model of critical buckling stress is established to predict the critical stress.

WELDING INDUCED BUCKLING ANALYSIS

The amount of the buckling distortion is large which significantly influences the dimensional accuracy and the assembly process. Besides, it cannot be pushed back mechanically in general, once a plate has buckled. Thus, the welding induced buckling is widely focused by many researchers. Masubuchi [1] investigated the buckling distortion in long steel strips after welding. The critical buckling stresses under various boundary conditions were calculated by engineers at Kawasaki Heavy Industries [2]. Frank [3] calculated the critical buckling force where the welding residual stresses are equivalent to the uniform welding stresses. Actually, the welding residual stresses are non-uniform. In this paper, the critical residual stresses are calculated by employing the non-uniform welding stresses.

NON-UNIFORM WELDING STRESS

The longitudinal compressive residual stresses generated by welding is the key factor leading to the buckling distortion in welded structure. In Refs. [2-3], the longitudinal residual stresses are simplified to uniform stresses, as shown in Fig. 1a, which is beneficial to the calculation of the critical buckling force. However, the welding residual stresses are non-uniform in the welded structure, as shown in Fig. 1b. Here, the longitudinal residual stresses are represented as

$$N_x = N_0(\alpha y^2 + \beta y + \gamma) \tag{1}$$

where, N_0 is the average stress. α, β, and γ are coefficients.

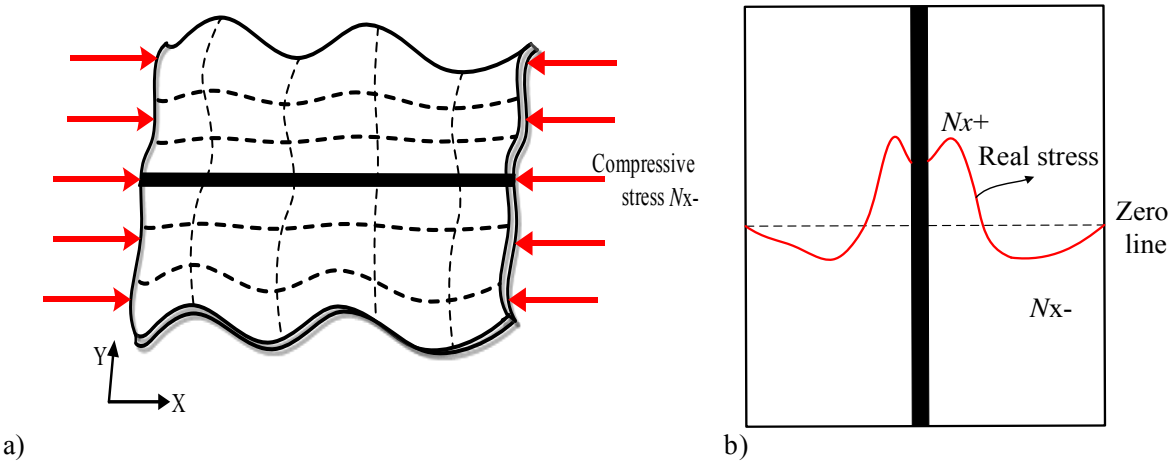

a) b)

Fig. 1 Welding residual stresses applied in the critical stress calculation

CRITICAL RESIDUAL BUCKLING STRESS

The residual welding stresses can be divided into compressive stress and tensile stress. For compressive stress, the basic equation can be written as

$$\frac{\partial^4 w}{\partial y^4} + 2\frac{\partial^4 w}{\partial x^2 \partial y^2} + \frac{\partial^4 w}{\partial x^4} = -\frac{1}{D} N_x \frac{\partial^2 w}{\partial x^2} \tag{2}$$

where w is the deflection, D is the flexural rigidity of the plate, N_x is the mid-plane load in X direction. In the basic equation, the body forces are ignored. For compressive stress, the basic equation can be written as

[a] Corresponding author. Email: hdyu@sjtu.edu.cn.

$$\frac{\partial^4 w}{\partial y^4}+2\frac{\partial^4 w}{\partial x^2\partial y^2}+\frac{\partial^4 w}{\partial x^4}=\frac{1}{D}N_x\frac{\partial^2 w}{\partial x^2} \tag{3}$$

The boundary conditions of the buckled plate after welding can be given as

$$\frac{\partial^2 w}{\partial y^2}+\upsilon\frac{\partial^2 w}{\partial x^2}=0,\ \frac{\partial^3 w}{\partial y^3}+(2-\upsilon)\frac{\partial^3 w}{\partial x^2\partial y}=0 \tag{4}$$

$$w_T=w_C,\ \frac{\partial w_T}{\partial y}=\frac{\partial w_C}{\partial y}$$

$$\frac{\partial^2 w_T}{\partial y^2}+\upsilon\frac{\partial^2 w_T}{\partial x^2}=\frac{\partial^2 w_C}{\partial y^2}+\upsilon\frac{\partial^2 w_C}{\partial x^2} \tag{5}$$

$$\frac{\partial^3 w_T}{\partial y^3}+(2\text{-}\upsilon)\frac{\partial^3 w_T}{\partial x^2\partial y}=\frac{\partial^3 w_C}{\partial y^3}+(2\text{-}\upsilon)\frac{\partial^3 w_C}{\partial x^2\partial y}$$

The equilibrium equation is given as Eq. (4). The continuity condition at the boundary of the tensile and compressive stresses is written as Eq. (5). The critical buckling stresses can be solved with Eqs. (2-5).

CONCLUSIONS

The non-uniform welding stresses is represented in this paper. Then, the critical buckling stresses can be solved with the basic equation and the boundary conditions. The study in this paper can help the critical stress predition.

ACKNOWLEDGEMENTS

The authors appreciate the financial supports by the National Basic Research Program of China (Grant No. 2014CB046600), the National Natural Science Foundation of China (Grant No. 51275292).

References

[1] Masubuchi K.: Analysis of Welded Structures. Oxford, England 1980.
[2] Terai K.: Study on Prevention of Welding Deformation in Thin-Skin Plate Structure. *Kawasaki Technical review* **61**:61-66, 1978.
[3] Frank P. K.: Buckling Distortion of Thin Aluminum Plates during Welding. *Master Thesis*, MIT Mech. Eng. Dept., Boston, 1975.

UNFOLDING PROCESS OF COILING FIBERS MADE BY INSTABILITY-ASSISTED FUSED DEPOSITION MODELING

Shibo Zou, Daniel Therriault & Frédérick P. Gosselin[a]
Laboratory for Multiscale Mechanics, École Polytechnique de Montréal, Montréal, Québec, Canada

Summary Microstructured fibers with sacrificial bonds fabricated by instability-assisted fused deposition modeling (IFDM) exhibit high toughness and stretchability. However, early breakage of backbone hinders the fiber from achieving higher toughness. Finite element analysis using ANSYS was performed to analyse the unfolding process of a single coiling loop under uniaxial force. Results show that maximum von Mises stress is found at the inner side of the previous top loop, which corresponds with the location of fiber breakage from experiments. Bending continues to be the dominant factor for maximum stress during the unfolding process. Torsion contributes more to maximum stress with decreasing fiber slenderness. The stress analysis of the unfolding process would help to optimize the fiber production by reducing maximum von Mises stress to avoid early breakage of backbone. We hope that microstructured fibers made with IFDM could one day be used for safety-critical applications, such as safety harness or bulletproof vests.

INTRODUCTION

By depositing either a thin filament of Newtonian viscous fluid [1, 2] or a slender elastic rod [3, 4] onto a moving belt, periodic patterns are generated. These instability phenomena are known as the fluid mechanical sewing machine (FMSM) and the elastic sewing machine (ESM), respectively. The patterns generated with the FMSM and the ESM are highly similar indicating the dominance of the geometry of the problem over the constitutive relation of the material used [3]. Passieux et al.[5] harnessed a similar instability phenomenon occurring in a fused deposition modeling (FDM) 3D printer to create patterned fibers. Passieux et al.[5] demonstrated that this instability-assisted fused deposition modeling (IFDM) could be used to tailor the mechanical properties of the fibers by picking the right patterns to make fibers with more or less toughness and rigidity. However, early breakage of the fiber for some fabrication parameter values remains a big obstacle to increase the fiber's toughness. Previous experiments show that the location of breakage changes from the top of the loop to the site of broken sacrificial bonds where stress concentration are generated depending on the fiber size and pattern. Therefore, a comprehensive stress analysis of the unfolding process of a single coiling loop needs to be done to understand the cause of early breakage.

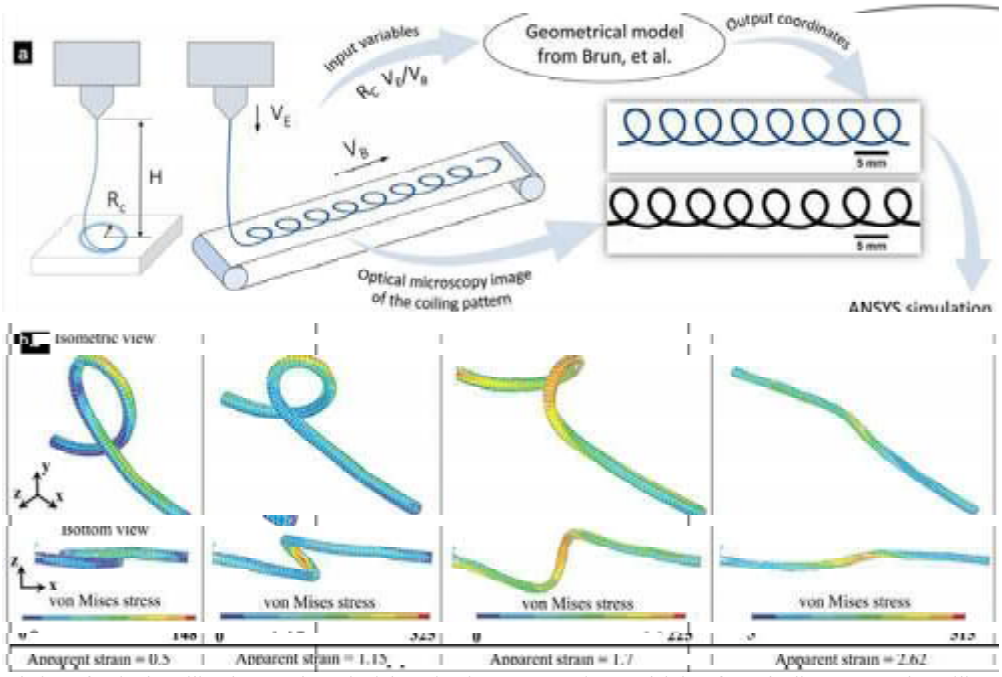

Figure 1. Simulation of a single coiling loop under uniaxial tension in ANSYS using model data from the literature: **a**, the coiling pattern in the optical microscopy image was fabricated using the speed ratio (V_E/V_B) of 3.616 under a deposition height of 10 mm, which corresponds to the steady coiling radius of 2.55 mm. Same parameters were used in this paper, including the geometrical model inputs and ANSYS simulation model. **b**, uniaxial tension was simulated in ANSYS by fixing the left end of the fiber in the isometric view, and extending the right end. Apparent strain was obtained by dividing the displacement of the right end by the initial distance between the left and right end.

[a] Corresponding author. Email: frederick.gosselin@polymtl.ca.

A finite element analysis (FEA) of a single coiling loop was built based on the geometrical model for FMSM patterns from the literature. Nonlinear analysis was carried out based on beam elements by FEA in ANSYS. Axial, bending, torsional shear and von Mises stresses were calculated from FEA to provide a comprehensive stress analysis of the unfolding process.

METHODS AND RESULTS

Finite element model for single coiling loop

Brun, et al. [2] developed a geometrical model for FMSM patterns containing three coupled non-linear ordinary differential equations. Although the fiber material we used in the experiment is a shear thinning fluid [6] rather than a Newtonian fluid, the geometric results based on this model match well with experiment results. Symmetry was utilized to generate z coordinates of the fiber pattern according to the diameter of the filament. The three-node beam element BEAM 189 was used to model the unfolding of a single coiling loop with the geometric nonlinearities taken into account.

Finite element analysis results

Nonlinear analysis was carried out for the single coiling loop in ANSYS. The simulated coiled fiber is shown in Fig. 1 as it is extended. Maximum von Mises stress is found at the inner side of the previous top loop, which corresponds with the location of fiber breakage from experiments.

The preliminary results of Fig. 2 allow to understand the effect of slenderness on different stress components during the unfolding process. In general, von Mises stress goes down with increasing slenderness. For bigger slenderness, torsional shear stress is much smaller as expected, which is due to the reduction of torque for slenderer fiber. While mid-way bending peak becomes more obvious for bigger slenderness, and the slenderer the fiber is, the longer the bending mid-way peak continues. Thus, bending should be taken more care of when we choose slenderer fiber to minimize von Mises stress.

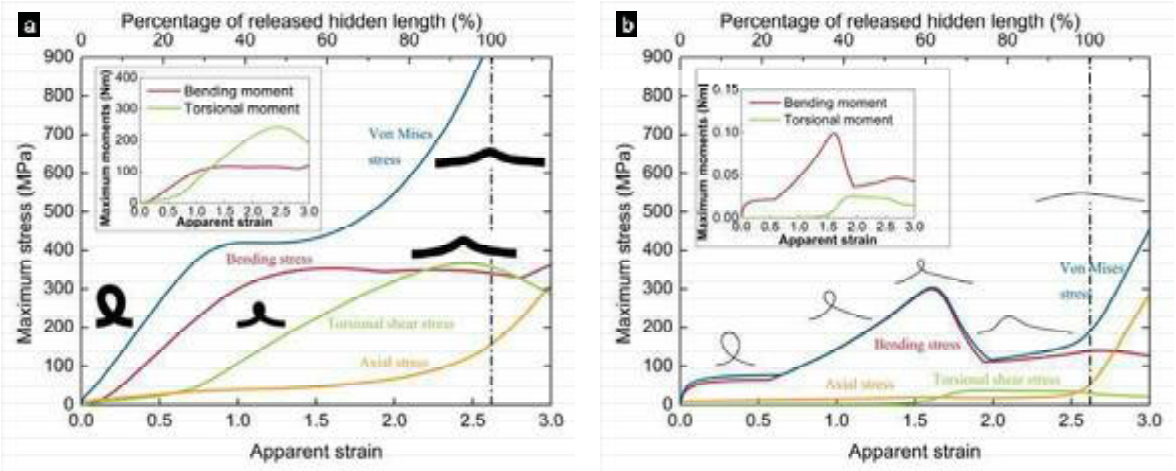

Figure 2. Maximum stress during the unfolding process of a fiber with wavelength λ = 5.23 mm and slenderness ratio: **a**, λ/d = 3.49; **b**, λ/d = 34.87. Maximum bending and torsional moments are plotted versus strain in the insets.

CONCLUSIONS

Although torsion could be reduced by using slenderer fiber, bending continues to be a key factor for the fluctuation of maximum stress during the unfolding process of coiling loop. Therefore, strategies which reduce the bending stress could be practised to avoid early breakage of backbone and optimize the fiber production.

References

[1] Welch R. L., Szeto B., Morris S. W.: Frequency Structure of the Nonlinear Instability of a Dragged Viscous Thread. *Physical Review E* **85**: 066209, 2012.

[2] Brun P.-T., Audoly, B., Ribe N. M., et al.: Liquid Ropes: A Geometrical Model for Thin Viscous Jet Instabilities. *Physical Review Letters* **114**: 174501, 2015.

[3] Jawed M. K., Da F., Joo J., et al.: Coiling of Elastic Rods on Rigid Substrates. *PNAS* **111**(41): 14663-14668, 2014.

[4] Jawed M. K., Brun P.-T., Reis P. M.: A Geometric Model for the Coiling of an Elastic Rod Deployed Onto a Moving Substrate. *Journal of Applied Mechanics* **82**: 121007, 2015.

[5] Passieux R., Guthrie L., Rad S. H., et al.: Instability-Assisted Direct Writing of Microstructured Fibers Featuring Sacrificial Bonds. *Adv. Mater* **27**(24): 3676-3680, 2015.

[6] Othman N.: Rheology and processing of poly(lactides) and their enantiomeric copolymers and blends. *PhD Thesis*, UBC, Vancouver, Canada 2012.

SM15 - Computational Solid Mechanics

TS.SM15-1.01	Djaka, Komlan Senam - A FFT method for continuum dislocation mechanics with heterogeneous elasticity (INVITED)	2853
TS.SM15-1.02	Alleman, Coleman - Distribution-enhanced homogenization: Theory and application	2855
TS.SM15-1.03	Goenezen, Sevan - Non-destructive characterization of heterogeneous solids from limited surface measurements	2857
TS.SM15-1.04	Cui, Yi - Molecular dynamics study of the interfacial debonding due to cylindrical nano-inclusion	2859
TS.SM15-1.05	Hallberg, Håkan - Microstructure evolution in Cu thin films, investigated by ab-initio and level set modeling	2561
TS.SM15-1.06	Cailletaud, Georges - Multiscale modeling of DS alloys applied to material element and structural calculations	2863
TS.SM15-2.01	Reese, Stefanie - Anisotropic damage coupled with plasticity - model development and comparison with experiments (INVITED)	2865
TS.SM15-2.02	Cheng, Long - Modeling of porous materials with isotropic-kinematic hardenable matrix under cyclic loading	2867
TS.SM15-2.03	Tralli, Antonio - Fast kinematic limit analysis of masonry vaults: A new ga-nurbs based approach	2869
TS.SM15-2.04	Nagarajan, Anand - Conform to Interface Structured Adaptive Mesh Refinement (CISAMR)	2871
TS.SM15-2.05	Uetsuji, Yasutomo - Multiscale Numerical Study on Polycrystalline Ferroelectric Solids	2873
TS.SM15-2.06	Lee, James - Sequential and concurrent multiscale modeling: From molecular dynamics to continuum mechanics	2875
TS.SM15-3.01	Upadhyay, Manas - Lattice strain evolution during biaxial loading: A fe-fft multiscale modelling approach (INVITED)	2877
TS.SM15-3.02	Knezevic, Marko - Transitioning rate sensitivities across multiple length scales in crystal plasticity	2879
TS.SM15-3.03	Kochmann, Julian - Two-scale, FE-FFT- and phase-field-based computational homogenization	2881
TS.SM15-3.04	Luscher, Darby - Continuum transport of dislocations during shock response of crystals	2883
TS.SM15-3.05	Mastorakos, Ioannis - Investigation of single crystal deformation with continuum dislocation dynamics	2885
TS.SM15-4.01	Suquet, Pierre - Model reduction for composite materials and polycrystals	2887
TS.SM15-4.02	Alian, Ahmed - Multiscale modelling of carbon nanotube– Reinforced polymer composites	2889
TS.SM15-4.03	Frydrych, Karol - Modelling Microstructure Evolution in SPD Processes in the Framework of Crystal Plasticity Theory	2891
TS.SM15-4.04	Kobayashi, Takuya - Piezoelectric and dielectric properties of barium titanate polycrystals	2893
TS.SM15-4.05	Ozturk, Deniz - Crystal plasicity FE study of the role of microtexture on Dwell Fatigue Response of Ti-6242	2895
TS.SM15-4.06	Zhang, Xiaohan - A continuum model for discrete dislocation dynamics	2897

TS.SM15-5.01	Dornisch, Wolfgang - Dual basis functions for isogeometric solid mechanics	2899
TS.SM15-5.02	Papoulia, Katerina - Non-differentiable energy minimization for cohesive fracture	2901
TS.SM15-5.03	Paggi, Marco - A computational framework for nonlinear contact between deformable excitable biological cells	2903
TS.SM15-5.04	Waddad, Yassine - A multi-scale model for contact mechanics of rough surfaces	2905
TS.SM15-5.05	Pierreux, Gerrit - Realistic RVE-geometries generation for Non-Crimp Fabric composites	2907
TS.SM15-6.01	Ghaisas, Niranjan - Unified treatment of shocks and material interfaces in hyperelastic solids and fluids	2909
TS.SM15-6.02	Polyzois, Ioannis - Simulating the microstructural failure mechanism of shear bands in steel	2911
TS.SM15-6.03	Fan, S C - Strain-rate-dependent cohesive law in modelling breakup of earth covered magazine	2913
TS.SM15-6.04	Vidyasagar, Vidyasagar - Spectral Methods for Electromechanical Coupling in Ferroelectrics	2915
TS.SM15-6.05	Sattarpanah Karganroudi, Sasan - Validation and verification of a non-rigid part inspection method	2917
TS.SM15-7.01	Gabriel, Dusan - Searching for local contact constraints in isogeometric contact analysis	2919
TS.SM15-7.02	Talamini, Brandon - A parallel computational framework for simulating fracture in shells	2921
TS.SM15-7.03	Wang, Qingguo - Improvement of weight-efficiency for a vehicle component based on the U* theory	2923
TS.SM15-7.04	Lee, Ming-Hsiao - Structural analysis of 3D printing parts	2925
TS.SM15-7.05	Chauvin, Rémi - A cell centered finite volume method for solving hyperelasticity equations	2927
PO.SM15-1.01.194	Batoz, Jean-Louis - On the mechanics of bio-inspired stiffened shell structures	2929
PO.SM15-1.02.195	Belov, Aleksander - Computer modeling of dynamics of 3-D elastic solids with coupled fields	2931
PO.SM15-1.03.196	Cheng, Zhuang - a study on particle stress evolution in biaxial test	2933
PO.SM15-1.04.197	Ipatov, Aleksandr - Study of wave propagation in poroviscoelastic solid using boundary element approach	2935
PO.SM15-1.05.198	Ke, Hang - Phase field modeling of additive manufacturing in metals	2937
PO.SM15-1.06.199	Liu, Ning - Peridynamic Modeling of Beam Vibration and Impact Damage Concerning Different Deformation Scale	2939
PO.SM15-1.07.200	Lund, Erik - Gradient based post-buckling optimization of laminates using Koiter's method	2941
PO.SM15-1.08.201	Ma, Hang - Formulation of boundary integrals with eigenstrains in 3-D eigenstrain bie	2943
PO.SM15-1.09.202	Markov, Ivan - A Laplace domain BEM formulation for dynamic problems of anisotropic elasticity	2945
PO.SM15-1.10.203	Molavi Nojumi, Mohamad - Evaluation of modified finite elements with spatially varying elastic parameters for FGMs	2947
PO.SM15-1.11.204	Pejhan, Khashayar - Load transfer analysis of a vehicle component with u* index theory	2949

PO.SM15-1.12.205	Rezaei Mianroodi, Jaber - Comparison of methods for discontinuous and smooth inhomogeneous elastostatics	2951
PO.SM15-1.13.206	Sadeghifar, Morteza - FE modeling and optimization of cutting temperature in orthogonal turning	2953
PO.SM15-1.14.207	Wang, Jizeng - A wavelet-based method with arbitrary high order of accuracy for nonlinear problems in mechanics	2955
PO.SM15-1.15.208	Wu, Wenwang - Stress Fields Induced by Dislocation Loops in Isotropic Cunb Film-substrate System	2957
PO.SM15-1.16.209	Yin, Shengwen - Gegenbaur series expansion with interval, fuzzy and random variables	2959

A FFT METHOD FOR CONTINUUM DISLOCATION MECHANICS WITH HETEROGENEOUS ELASTICITY

Komlan Sénam Djaka[1], Vincent Taupin[1] & Stéphane Berbenni[1a)]
[1]*Laboratoire d'Etude des Microstructures et de Mécanique des Matériaux, LEM3, UMR CNRS 7239, Université de Lorraine, Ile du Saulcy, 57045 Metz, France*

Summary A Fast Fourier Transform (FFT) method is developed to solve the elasto-static equations of the field dislocation mechanics for periodic media with heterogeneous linear elasticity. After prescribing a Nye's dislocation density tensor, the incompatible and compatible parts of the elastic distortion are obtained, respectively, from the resolution of a Poisson-type equation and a Lippmann-Schwinger integral equation with incompatibilities. Both equations are solved through an iterative basic scheme based on intrinsic discrete Fourier transforms with centered and rotated finite difference schemes, respectively. For a single pixel regularization of the dislocation density within the dislocation core, the elastic fields due to dislocations with elastic heterogeneities are accurately obtained by the present method without Gibbs oscillations.

INTRODUCTION

The elastic theory of continuously distributed dislocations initiated by Kröner [1] and recently revisited by Acharya [2] through the so-called Field Dislocation Mechanics (FDM) leads to a rigorous description of the incompatibility of the elastic strain due to the presence of dislocations in crystalline solids. The elasto-static equations of FDM were recently solved for linear elasticity within a FFT framework [3, 4]. In the latter, the equations for the incompatible elastic distortions and the balance of momentum are solved in the Fourier space, while the resulting elastic fields are obtained in the real space by using the inverse Fourier transform. An extension of this spectral approach to field dislocation and generalized-disclination mechanics (FDGDM) was proposed in [4]. The elasto-static field equations of FDM in a linear heterogeneous medium yield a Lippmann-Schwinger integral equation with incompatibilities arising from the presence of polarized (or geometrically necessary) dislocation densities. The FFT scheme based on the iterative basic scheme (BS) allows solving the classic Lippmann-Schwinger integral equation of the periodic boundary-value problem by the introduction of a modified Green's function associated with a well-chosen reference medium [5]. The presence of elastic incompatibilities needs a two-step numerical procedure starting from the resolution of Poisson-type equation. Motivated by the accuracy and the efficiency of the FFT-based iterative scheme for heterogeneous elastic materials, we propose in this paper to extend the work described in [4] to study the interactions between elastic heterogeneities and dislocations for periodic media. Special attention will be paid to the control of the Gibbs phenomenon by using discrete Fourier transforms (DFT) together with centered finite differences for the Poisson-type equation [4], and, with rotated finite differences for the Lippmann-Schwinger equation [6].

RESULTS AND DISCUSSIONS

The assessment of the present approach is conducted by comparisons with the analytical solutions [7] in the case of a single edge dislocation of Burgers vector magnitude $b=4.05\times10^{-10}$m restricted to a single pixel located in the centre of a circular inclusion embedded in a matrix phase of unit cell dimension 900b×900b. As an example of simulation results, the composite material is discretized using a 2D FFT grid constituted of 2048×2048 pixels and the circular inclusion is ten times softer than the matrix assuming isotropic heterogeneous elasticity. In this case, Figure 1(a) shows the occurrence of spurious Gibbs oscillations regarding local stress field T_{11} (normalized by the shear modulus of the matrix μ_M) when using the classical discrete approximation of the continuous Fourier transform to solve both the Poisson-type equation (P) and the implicit Lippmann-Schwinger integral equation (BS) [5], here denoted by P- BS procedure. In contrast, a good approximation is obtained with the centered finite difference scheme together with DFT to compute the Poisson-type equation (P_C) and the rotated finite difference scheme (BS_R) together with DFT to solve the Lippmann-Schwinger equation, here denoted by P_C- BS_R procedure. Indeed, it is shown (Figure 1(b)) that the local stress field inside the inclusion and around the "core region" of the dislocation obtained with the present iterative basic scheme well matches the analytical solution (AS). The combination of centered differences with DFT to compute the Poisson-type equation (P_C) and the classic FFT approximation for Lippmann-Schwinger equation (BS) denoted here by P_C- BS procedure also leads to satisfying results for such mechanical contrast (Figure 1(b)). However, careful comparisons between the P_C- BS_R and the P_C- BS procedures reveal the occurrence of little Gibbs oscillations in the P_C- BS solution contrary to the P_C- BS_R one (see Figure 1(c)). These observations reinforce the conclusions given in the case of homogeneous elasticity [4]: such an intrinsic DFT scheme constitutes a suitable way to solve Poisson-type equations without any Gibbs oscillations especially when the dislocation density is restricted to a single pixel. On the other hand, as reported in [6], the DFT with rotated finite difference scheme to compute the modified Green tensor improves the accuracy of the FFT method, in comparisons with [5]. The present FFT method is also suitable to simulate more

[a)] Corresponding author. Email: stephane.berbenni@univ-lorraine.fr

physical cases of interest in crystalline materials such as dislocation density dipoles constrained at discontinuity interface between the matrix and the inclusion or located in the matrix phase of the composite material.

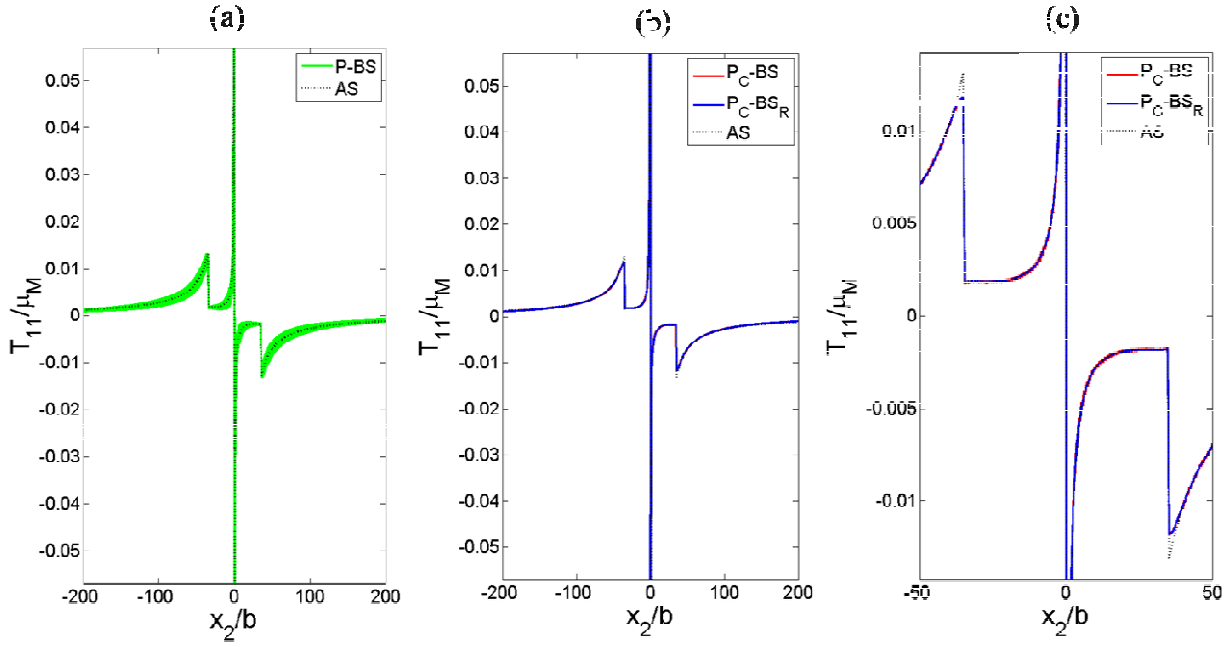

Figure 1: Stress profile T_{11} (normalized by the shear modulus of the matrix μ_M) obtained in the case of an edge dislocation density located in a single pixel at the centre of a soft circular inclusion ($\mu_I = 2.3001\times10^3$ MPa, $\nu_I = 0.3647$) with radius 40b embedded in a hard matrix ($\mu_M = 10\,\mu_I$, $\nu_M = \nu_I$) discretized using 2D FFT grid of 2048×2048 pixels: P-BS solution (green solid lines) vs. analytical solutions (dashed lines) (a), P_C-BS solution (red solid lines) and P_C-BS_R solution (blue solid lines) vs. analytical solutions AS (dashed lines) (b), and zoom of Fig. 1b in the inclusion and near the matrix/inclusion interface revealing Gibbs oscillations with the P-BS solution contrary to the P-BS_R solution (c).

CONCLUSIONS

The FDM elasto-static equations with heterogeneous linear elasticity are solved with a spectral method based on the FFT basic scheme and the solution of the incompatibility problem solved through a Poisson-type equation in the Fourier space. Accurate and stable results are obtained by using a centered difference scheme with DFT to compute the Poisson-type equation (P_C) and the finite difference rotated scheme (BS_R) for the modified Green's operator, here introduced as the P_C- BS_R procedure. Further studies will be focused on the implementation of a spectral framework for the complete elastoplastic FDM field equations by coupling the present FFT method to the transport of dislocation density numerically solved by a filtered-spectral approach [8].

References

[1] Kröner E.: Continuum theory of defects In: Balian R et al (Eds), Physics of defects Les Houches Session 35 North Holland. New York 1981.

[2] Acharya A.: A model of crystal plasticity based on the theory of continuously distributed dislocations. *J. Mech. Phys. Solids* **49:** 761-784, 2001.

[3] Brenner R., Beaudoin A. J., Suquet P., Acharya A.: Numerical implementation of static field dislocation mechanics for periodic media. *Philos. Mag.* **94 (16):** 1764-1787, 2014.

[4] Berbenni S., Taupin V., Djaka K. S., Fressengeas C.: A numerical spectral approach for solving elasto-static field dislocation an g-disclination mechanics. *Int. J. Solids Struct.* **51** 4157-4175, 2014.

[5] Moulinec H., Suquet P.: A numerical method for computing overall response of nonlinear composites with complex microstructures. *Comput. Methods Appl. Mech. Eng.* **157:** 69-94, 1998.

[6] Willot F.: Fourier-based schemes for computing the mechanical response of composites with accurate local fields. *C. R. Mecanique* **343**: 232–245, 2015.

[7] Dundurs J., Sendeckyj G. P.: Edge dislocation inside a circular inclusion. *J. Mech. Phys. Solids* **13**: 141–147, 1965.

[8] Djaka K. S., Taupin V., Berbenni S., Fressengeas C.: A numerical spectral approach to solve the dislocation density transport equation. *Modell. Simul. Mater. Sci. Eng.* **23**: 065008 (27pp), 2015.

[a] Corresponding author. Email: stephane.berbenni@univ-lorraine.fr

DISTRIBUTION-ENHANCED HOMOGENIZATION: THEORY AND APPLICATIONS

Coleman Alleman*[1], Somnath Ghosh[2], D.J. Luscher[3], and Curt Bronkhorst[3]
[1]*Mechanics of Materials Department, Sandia National Laboratories, Livermore, California USA*
[2]*Department of Civil Engineering, Johns Hopkins University, Baltimore, Maryland USA*
[3]*Solid Mechanics and Fluid Dynamics, Los Alamos National Laboratory, Los Alamos, New Mexico USA*

Summary Multiscale modeling offers a tractable means to model sufficiently large spatial domains of heterogeneous media without the prohibitive computational overhead incurred by high-resolution modeling of microscopic scales. The present study proposes a novel homogenization-based approach to achieve the transfer of information between the scales of representation. The *distribution-enhanced homogenization* (DEH) framework presented here associates a non-uniform microscale field variable to a macroscopic material region by incorporating moments of microscale field variable distributions in the macroscale constitutive calculations, which are formulated by constructing series expansions in terms of these moments. Using DEHF, it is possible to derive a set of macroscale constitutive relations that represent the microscale behavior exactly in the limit, without constructing effective macroscale parameters by fitting the macroscopic behavior to the average microscopic behavior.

The success of multiscale models lies in their ability to retain the effects of microscale heterogeneity on the macroscale response without recourse to full micromechanical calculations. The fundamental problem of multiscaling is the transfer of information between the scales of representation. The present study proposes a novel alternative approach to this problem, the *distribution-enhanced homogenization* (DEH) framework, where the macroscale constitutive model is formulated in terms of moments of microscale field variable distributions. In DEH, models of the microscale constitutive response are sufficient to construct the effective macroscale constitutive relations, without any fitting to a known macroscale response. Instead, the macroscale constitutive relations in DEH operate on a set of macroscale moment-based descriptors of distributions of microscale field variables. Formally, the k-th moment $\mu^k_{q_1^{p_1}\cdots q_n^{p_n}}$ of the field variable $\mathbf{q}$ is given by

$$\mu^k_{q_1^{p_1}\cdots q_n^{p_n}} = \langle q_1^{p_1}\cdots q_n^{p_n}, \phi_\Omega(\mathbf{q})\rangle = \int_{\mathbb{R}^n} q_1^{p_1}\cdots q_n^{p_n}\phi_\Omega(\mathbf{q})\,dq_1\cdots dq_n \tag{1}$$

where $\phi_\Omega(\mathbf{q})$ can be interpreted as the density of $\mathbf{q}$ in a neighborhood Ω. Taking $\mathbf{q}$ as a microscale field variable, $\mu^k_{q_1^{p_1}\cdots q_n^{p_n}}$ is a macroscale variable that carries some quantitative information about the microscale field. Standard homogenization frameworks operate on low-order moments (typically just order one). The general theory of DEH extends the macroscale formulation to include moments of arbitrary order. Conceptually, this extension relaxes the assumption that the microscale response is represented by a set of constitutive relations operating on a uniform microscale. DEH enables the calculation of macroscale constitutive response of the moment-based variables by constructing series expansions that relate these variables and their rates. In general, for a vector-valued function $\mathbf{r}(\mathbf{q})$ of a microscale vector field $\mathbf{q}$, the macroscale variable $\mu^1_{\mathbf{r}}$ is given as a function of the macroscale variables $\mu^k_{\mathbf{q}}$ and the partial derivatives of $\mathbf{r}(\mathbf{q})$ in the *moment expansion*, [1]

$$\mu^1_{\mathbf{r}} = \mathbf{r}(\mathbf{0}) + \mu^1_{q_j}\mathbf{r}_{,j}(\mathbf{0}) + \cdots + \frac{1}{k!}\mu^k_{q_{j_1}\cdots q_{j_k}}\mathbf{r}_{,j_1\cdots j_k}(\mathbf{0}) + \cdots \tag{2}$$

Truncations of these expansions result in approximations that converge to an exact representation of the microscale response with increasing order.

The application of the DEH framework to the mechanics of elasto-plasticity is studied for problems involving non-uniform geometry or material properties in Alleman et. al. [1] For these problems, the macroscale stress is defined as a functional acting on the microscale stress density functions as $\boldsymbol{\Sigma}_1 \triangleq \mu^1_{\boldsymbol{\sigma}} = \langle \boldsymbol{\sigma}, \phi_\Omega(\boldsymbol{\sigma})\rangle$. The DEH treatment of the macroscale problem proceeds by relating the macroscale plastic strain rate $\dot{\Xi}^p_1 = \langle \dot{\boldsymbol{\epsilon}}^p, \phi_\Omega(\dot{\boldsymbol{\epsilon}}^p)\rangle$ to the moments of the stress field. In the first example, uniaxial tension is simulated in a specimen of non-uniform cross-section with minimum diameter D_B in the gauge section, and grip section diameter D_A. The loading produces a heterogeneous microscale stress field, and the macroscale constitutive relations are written in terms of the moments of this stress distribution and the moments of the inverse of the cross-sectional area $A(x)$ as

$$\dot{\Xi}^p_1 = \sum_{k=2}^{\infty}\frac{1}{(k-1)!}\mu^{k-1}_{\boldsymbol{\sigma}}\circ\left.\frac{\partial^{k-1}\dot{\boldsymbol{\epsilon}}^p}{\partial\boldsymbol{\sigma}^{k-1}}\right|_{\boldsymbol{\sigma}=\mathbf{0}}, \quad \frac{d}{dt}\mu^k_{\boldsymbol{\sigma}} = k\left(\frac{|\Omega|}{L}\right)^k \mu^k_{A\ 1}(\boldsymbol{\Sigma}_1)^{k-1}\mathbb{C}:\left(\dot{\Xi}_1 - \dot{\Xi}^p_1\right) \tag{3}$$

The tenth-order moment approximation is compared to the DNS results in Figure 1a, where it is seen that the macroscale DEH results are in very good agreement with the macroscale average of the DNS results.

*Corresponding author. Email: callema@sandia.gov

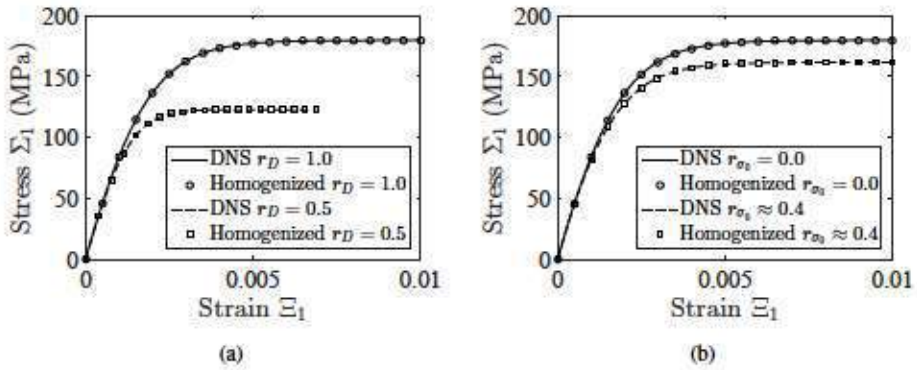

Figure 1: Comparison of macroscale stress-strain response generated by microscale DNS and DEH simulations of a bar of (a) non-uniform cross-section and (b) non-uniform material properties.

The DEH framework is also applied to a microscale problem of a tensile bar of uniform cross-section, with material property σ_0 varying along the length of the bar. The macroscale constitutive relations for this problem are:

$$\dot{\Xi}_1^p = \sum_{k=0}^{\infty} \frac{1}{k!} \sum_{j=0}^{k} \mu_{\sigma_0}^{k-j} \left(\boldsymbol{\Sigma}_1\right)^j \circ \left. \frac{\partial^k \dot{\epsilon}^p}{\partial \boldsymbol{\sigma}^j \partial \sigma_0^{k-j}} \right|_{\boldsymbol{\sigma}=\mathbf{0}, \sigma_0=0}, \quad \dot{\boldsymbol{\Sigma}}_1 = \left(\mu_{\mathbf{C}\ 1}^1\right)^{-1} : \left(\dot{\Xi}_1 - \dot{\Xi}_1^p\right) \tag{4}$$

The simulation results for representative values of $r_{\sigma_0} = \hat{\mu}_{\sigma_0}^2 / \left(\mu_{\sigma_0}^1\right)^2$ are plotted in Figure 1b, where it is seen that the agreement between DNS and DEH calculations is very good. Qualitatively, both examples illustrate the enhancement of plastic flow for heterogeneous microscale fields, and DEH accurately quantifies this effect without any parameter fitting.

The DEH framework is also applied to problems in finite-deformation elasto-viscoplasticity in Alleman [2] to study the evolution of damage in body-centered cubic tantalum under dynamic loading. Key features of the DNS results for an elastic deformation of the voided volume shown in Figure 2a are accurately reproduced by DEH, as shown in Figure 2b. Current work is focused on applying this implementation of DEH to study ductile failure in tantalum flyer-plate specimens.

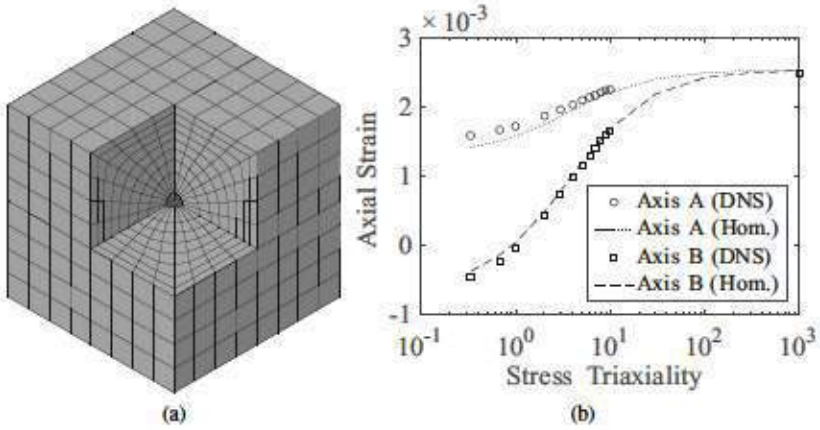

Figure 2: (a) Explicit geometric representation of voided microstructure for DNS and (b) Comparison of changes in ellipsoidal void shape in responses based on the microscale DNS and the DEH macroscale simulations.

References

[1] Alleman C., Luscher D.J., Bronkhorst C., Ghosh S.: Distribution-enhanced homogenization framework and model for heterogeneous elasto-plastic problems. J. Mech. Phys. Solids 85:176-202, 2015.

[2] Alleman C.: Distribution Enhanced Methods of Homogenization for Heterogeneous Materials and Multi-scale Crystal Plasticity Modeling. PhD Thesis, Johns Hopkins University Civil Eng. Dept., USA, 2015.

NON-DESTRUCTIVE CHARACTERIZATION OF HETEROGENEOUS SOLIDS FROM LIMITED SURFACE MEASUREMENTS

Yue Mei[1] & Sevan Goenezen [1 a)]
[1]*Department of Mechanical Engineering, Texas A&M University, College Station, TX, USA*

ABSTRACT

We present a novel methodology to characterize the linear elastic property distribution of a heterogeneous solid non-destructively from measured surface deformations (for example from Digital Image Correlation measurements) and mathematical model in linear elasticity. In this paper, we show the feasibility of this methodology on a theoretical heterogeneous sample with a stiff inclusion surrounded by a softer background. The algorithms are based on finite element techniques and the elastic properties are unknowns on mesh nodes and interpolated in the problem domain with linear shape functions. We observe that a rich set of surface deformation fields is sufficient to recover the elastic property distribution uniquely, i.e., the inclusion is clearly reconstructed and the contrast in the elastic property distribution is close to the target contrast in the presence of noisy displacement data. This methodology could have important applications in detecting defects in aerospace structures or as a novel screening approach for breast tumors.

INTRODUCTION

Characterizing the heterogeneous elastic properties of solids non-destructively requires measurement of displacement data [1, 2] and robust inverse algorithms [3-6]. Measuring displacement fields from ultrasound data has been well developed and used to map the elastic property distribution of soft tissues [7-9]. This has shown great potential in breast cancer screening and diagnosis [7]. Alternatively, displacement data can be acquired using magnetic resonance imaging.

Recently, digital cameras were used to determine surface displacement fields of specimens, widely known as digital image correlation (DIC). These systems are commercially available and allow the user to determine surface strains to potentially infer inhomogeneity in the specimen's interior. This type of analysis may help to analyse materials for inhomogeneity, assuming that they are supposed to be homogeneous. This, however, has the disadvantages that 1) it may not be simple to locate the inhomogeneity from surface strains, and 2) many materials are heterogeneous and thus strain measurements on the surface cannot directly be related to the interior heterogeneity. In this paper, we will show that DIC systems could potentially be used to recover the full spectrum of the heterogeneous elastic properties. As investigated in [10] the feasibility of this technology depends on a rich surface data set and efficient physics-based algorithms to robustly solve mathematically ill-posed partial differential equations.

METHODS

The inverse problem is posed as a constrained minimization problem, where the objective function given by

$$F = \sum_{i=1}^{k} \sum_{j=1}^{N_i} w_{ij} \left\| \mathbf{u}_j^i(\mu) - \mathbf{u}_{j\ meas}^i \right\|^2 + \alpha \int_\Omega \sqrt{|\nabla \mu|^2 + c^2}\, d\Omega \tag{1.1}$$

is minimized with respect to the unknown shear modulus distribution μ. Equation (1.1) is subject to the constraint of the forward elasticity problem, solved via finite element methods. The first summation in Equation (1.1) accommodates a total of k surface displacement sets and the second summation minimizes the difference between the j-th measured surface displacement point $\mathbf{u}_{j\ meas}^i$ and computed displacement point $\mathbf{u}_j^i(\mu)$ for the i-th measurement set. We note that the number of measured surface displacement points may vary between different data sets i, thus we denote the total number of measured displacement points by N_i. Further, w_{ij} denotes the weight for data set i and point j and depends on the finite element mesh discretization [10]. The second term represents the total variation diminishing regularization term, ensuring a smooth overall solution of the shear modulus distribution, while preserving sharp interfaces between objects in the problem domain. The regularization factor α is chosen according to the noise level in the measurements using Morozov's principle or a smoothness criteria, and the constant c is chosen to be a small number to avoid singularities. The nodal computed displacement of the j-th data set $\mathbf{u}_j^i(\mu)$ satisfies the forward elasticity problem. We assume that the material is incompressible, implying that an additional

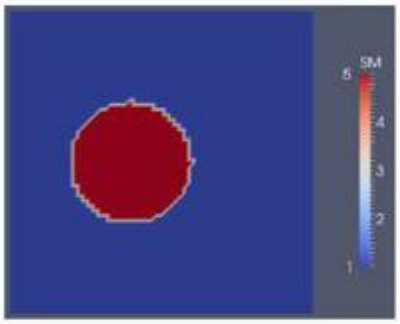

Figure 1: Target shear modulus μ distribution for the given problem domain

[a)] Corresponding author. Email: sevangoenezen@gmail.com.

pressure variable is introduced and an incompressibility constraint imposed. Equation (1.1) is minimized with the limited BFGS method using the adjoint equations [3, 4, 10] to calculate the gradient of the objective function with respect to the shear modulus.

We will test this approach with theoretical noisy surface displacement, created by solving the forward finite element problem. To this end the problem domain in Figure 1 consisting of a stiff inclusion ($\mu = 5$) embedded in a soft background ($\mu = 1$) is meshed with linear triangular elements and 61x61 uniformly distributed mesh nodes. The bottom edge is fixed in vertical direction and indentations are applied on the top edge. Then the specimen is rotated by 90 degrees clockwise and counter clockwise and indentations are applied for each rotation. Each indentation induces surface deformations extracted on three edges, excluding the edge with vertically fixed nodes. About 2% white Gaussian random noise is added to the surface displacement nodes to simulate noisy measured displacement data and used to recover the target shear modulus distribution.

RESULTS AND DISCUSSIONS

Shear modulus reconstructions using a set of 3, 9, and 15 noisy surface displacement sets (recall that each corresponds to an indentation) are shown in Figure 2, left, middle, and right image, respectively. It is observed that the contrast in μ approaches the target shear modulus contrast with increasing number of data sets. Further, the shape of the inclusion becomes slightly more circular as the data set is increased from 3 to 15. We note that the indentations are imposed as displacement indentations and no traction boundaries are used. This implies that these shear modulus reconstructions are determined only up to a multiplicative factor. Thus, future work will involve simulations with force indentations to test this methodology to recover μ absolutely and uniquely. Further, future work will compromise to test 1) smaller inclusions, 2) heterogeneous problem domain in 3D, and 3) limited surface displacement data on a more confined boundary, e.g., on one single face/edge.

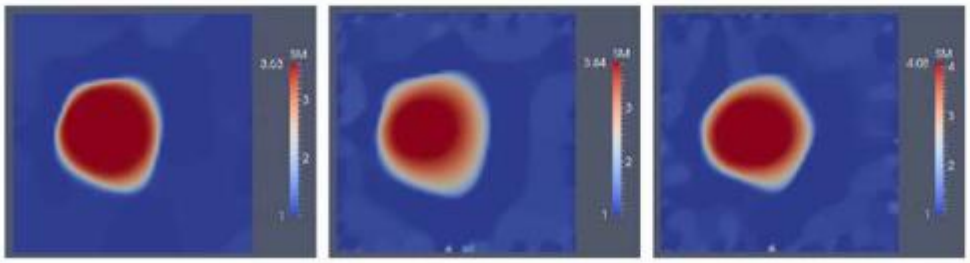

Figure 2: Reconstruction of μ with 3, 9, and 15 indentations.

CONCLUSIONS

We have presented a novel approach to recover the interior shear modulus distribution from surface displacements only. The results show that this method is robust in the presence of noisy data and leads to a unique μ reconstructions for a proper data set. This work has great importance in that it requires only a set of digital cameras to acquire surface displacement data and map the specimen's interior. Further studies are needed to investigate uniqueness and data requirements. Also, a proof of concept with experimental data is essential. Even though the noise level in the synthetic surface displacement data is of the order being reported for data from DIC systems, the nature of experimentally acquired surface displacement noise may be different than the synthetically added white Gaussian random noise.

References

1. Barbone, P., A.A. Oberai, J.C. Bamber, G.P. Berry, J. Dord, E.R. Ferreira, S. Goenezen, and T. Hall, Biomechanical imaging: elastography beyond Young's modulus. CRC Handbook of Imaging in Biological Mechanics, 2014.
2. Hall, T., P.E. Barbone, A.A. Oberai, J. Jiang, J. Dord, S. Goenezen, and T. Fisher, Recent results in nonlinear strain and modulus imaging. Current Medical Imaging Reviews, 2011. **7**(4): p. 313-327.
3. Goenezen, S., Inverse problems in finite elasticity: An application to imaging the nonlinear elastic properties of soft tissues. PhD Dissertation, 2011.
4. Goenezen, S., P. Barbone, and A.A. Oberai, Solution of the nonlinear elasticity imaging inverse problem: The incompressible case. Computer Methods in Applied Mechanics and Engineering, 2011. **200**(13-16): p. 1406-1420.
5. Mei, Y. and S. Goenezen, Spatially weighted objective function to solve the inverse problem in elasticity for the elastic property distribution, in Computational Biomechanics for Medicine: New Approaches and New Applications B.J. Doyle, et al., Editors. 2015, Springer NY.
6. Mei, Y., S. Kuznetsov, and S. Goenezen, Reduced boundary sensitivity and improved contrast of the regularized inverse problem solution in elasticity. Journal of Applied Mechanics, 2015. **83**(3).
7. Goenezen, S., J.F. Dord, Z. Sink, P. Barbone, J. Jiang, T.J. Hall, and A.A. Oberai, Linear and nonlinear elastic modulus imaging: An application to breast cancer diagnosis. IEEE Trans Med Imaging, 2012. **31**(8): p. 1628-37.
8. Goenezen, S., A.A. Oberai, J. Dord, Z. Sink, and P. Barbone, Nonlinear elasticity imaging Bioengineering Conference (NEBEC), 2011 IEEE 37th Annual Northeast 2011: p. 1 - 2
9. Oberai, A.A., N.H. Gokhale, S. Goenezen, P. Barbone, T. Hall, A.M. Sommer, and J. Jiang, Linear and nonlinear elasticity imaging of tissue in-vivo: Demonstration of feasibility. Physics in Medicine and Biology, 2009. **54**: p. 1191-1207.
10. Mei, Y., R. Fulmer, V. Raja, S. Wang, and S. Goenezen, Estimating the non-homogeneous elastic modulus distribution from surface deformations. International Journal of Solids and Structures, in print., 2016.

MOL CULAR YNAMICS STUDY O THE INTERFACIA DEBONDING DUE O CY INDERIC L NANO-INCLUSIO

Yi Cui, Zengtao Chen [a)]
De artment of echanical En ineering, University of Al erta, Edmonton, AB T6G H9, Canada

Summary The corresponding s ress-strain relation and the nucl ated void volu e fraction of t e composite m terial are monitored during uniaxial loading using the modif ed embedded atom model (ME M). Due to the presence of the inclusion-matrix interface, both he effect of energy minimiz tion and confi uration relaxati n are investigated to ensure an initial physical bonding of the two materials. During the stretching of si ulation box, the localized decohesion tends to initiate on the portion of the interfacial circu ference facing the loading direction. The simulation results also reveal tha the simulation size and strain rate influence t e onset of interfacial decohesion while the thickness of the imulation box has virtually no i pact. The largest simulation size contains an inclusion up to 105. nm in diameter with a total of 10.6 million a oms. An enlarg d simulation size not only lower the yield stress but also the strain of decohesion nitiation

INT ODUCTIO

It is of gr at importanc to understand the interfacial debonding and related material fracture due to the i-material interfaces in o der to model he mechanical response of broad range f engineering materials [1]. For example, the silicon or aluminium-oxide inclusio s are found to be fatigue crack nucleation sites in Al-Si astings [2]. As for ductile fracture, the void initiation from the second-phase particles or other i purities is the first stage o the void evol tion during t e damage accumulation. Broek [3] pointed out that large second hase particles can determine the moment and location of ductile fracture, but they are not essential to th fracture process itself. O the contrary, he concluded that smalle particles appeared to govern the fra ture process. Therefore it is not only e onomic but also physically important for the MD simulation to tart with the case of interfacial debonding from nano-inclusions. As for the MD sim lation for the composite material, most reported simulations focuse on the planar debonding or the nanocryst lline composi es.

M DELS, RES LTS AND DISCUSSION

As illustra ed in Fig. 1, he periodical simulation bo is employed to represent uniformly-distr buted silicon inclusions inside the alu inum matrix. The axis of the cylindrical i clusion is in the z direction. The volume f action of the ylindrical inclusions is ixed as 20%. The atomisti interaction i considered y the modifi d embedded atom method (MEAM). Applied uniaxial loading is strain-control ed in the x direction. Energy minimization and suitab e relaxation teps were applied to attain a perfect initial bonding at the silicon-al minum interf ce.

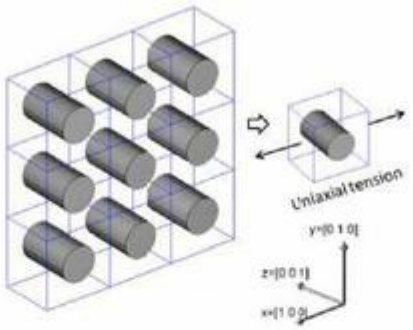

ig. 1 Periodic l simulation box with Si inc usion (gray) i Al matrix

As shown in Fig. 2(a), t e ultimate str ngth of the c mposite mate ial relates to the initiation of decohesion ather than the dislocatio emission. In Fig. 2(a), the initiation of dislocation emission only occurs some point after the ultimate strength and has limited im act on the de ohesion process. However, these conclusions are subject to the geom try of the inclusion. From the simulation regardin spherical inclusion not displayed here, both the interfacial debo ding and dislocation e ission happen before the ultimate strength. The slight trace of the dislocation line in Fig. 2(b) marks the beginning of dislocation e ission. The subsequent de elopment of the dislocatio structure inside the matri is fairly similar to the simulation r sults of typical FCC metals (add a reference here). s shown in Fig. 2(b), the localized decohesion te ds to initiat on the portion of the int rfacial circu ference faci g the loadin direction. It has been experimentall evidenced t at void initi tion happens earlier by the larger inclusions. The o jective of Fi . 3 is to investigate the size effect and associated i terfacial debonding. The le gth of the simulation cell is increased fro 52.1 nm to 208.2 nm, hich gives t e size range of inclusion f om 26.3 nm to 105.1 nm in diameter. I Fig. 3(a), o ly a clear decrease of the yield stress can be seen from the smallest size compared to the larger sizes. owever, a strong strain

[a)] Correspondin author. Email: zengtao.chen@u lberta.ca (ZT Chen).

hardening feature not only ffsets the decrease of the yield stress bu also even el vates the ulti ate strength. From the largest three size cases in ig. 3(a), the radual enhan ing of the st ain hardening can be reco nized. In Fig. 3(b), the increasing simulation size r sults in a slig tly earlier de ohesion of the interface. T e largest sim lation size also leads to considerably l wer growth pace of the initiated void.

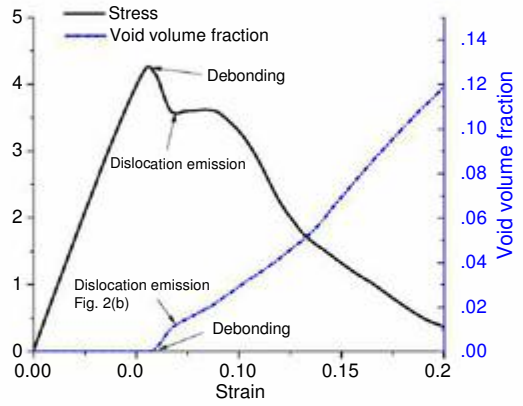



(a) Stress-strain and void volu e fraction cu ve (b) Onset of dislocation emission

Fig. 2 The st ess-strain relation, void vol me fraction a d dislocation emission under a simulation size of 58.3×58.3×3.24 n with a cylin rical inclusio sized 14.7 n in diameter embedded und r a strain rate of 2×10^{9} s^{-1}

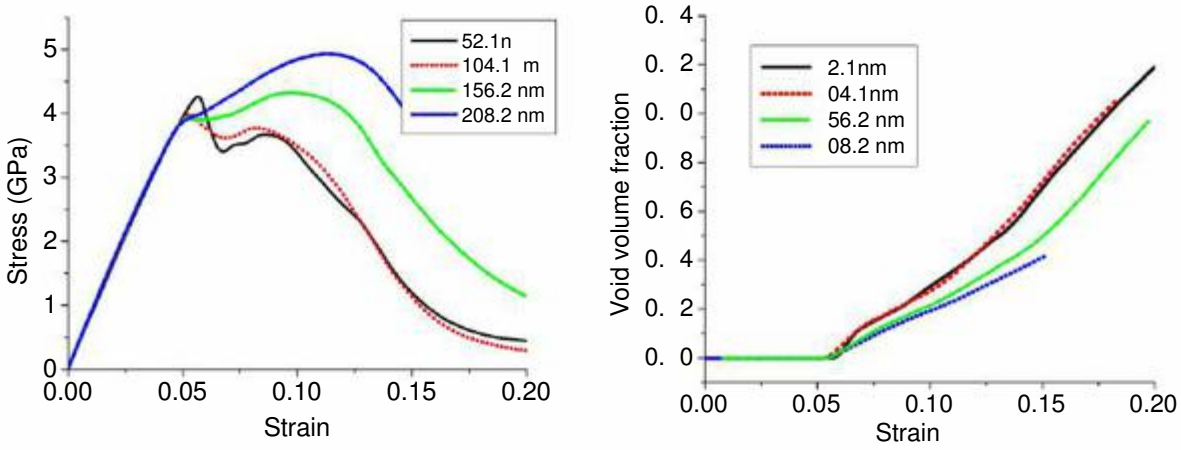

(a) Stress-strain relation (b) The gro th of the initiated void

Fig. 3 Stress-strain relation and growth o the initiated oid under dif erent simulati n size (length of the simulation cell) with 20% inclusion volume fraction

CO CLUSIONS

MEAM potential is empl yed to study the interfacial ebonding via MD simulatio . Due to the presence of the inclusion-matrix interface, both the effect of energy minimization an configuration relaxation are investigated to ensure an initial physical bonding of th two material . The decreas ng strain rate not only lowers the debonding strain but also accelerates the void growth. Durin the stretchin of simulatio box, the localized decohesion tends to i itiate on the ortion of the interfacial circumference facing the loading direction. he simulation esults also reveal that the simulation size and strain rate in luence the onset of interfacial decohesio while the thickness of the si ulation box has virtually no impact. Enlarged simulation ize lowers both the yield tress and the strain of decohesion initiation lightly. A strong strain hardening feature d e to the increasing of the simulation size elevates the p edicted ultima e strength.

References

[1] K. Gall, M.F. orstemeyer, M. an Schilfgaarde, M.I. Baskes, J. Mech. Phys. Solids. 48 (2000) 2183-2212.
[2] K. Gall, N. Yang, M. Horsteme er, D. McDowell, J. Fan, Metall. Mater. Trans. A 30 1999) 3079-3088.
[3] D. Broek, Eng. Fract. Mech. 5 (1973) 55-66.

MICROSTRUCTURE EVOLUTION IN CU THIN FILMS, INVESTIGATED BY *AB-INITIO* AND LEVEL SET MODELING

Håkan Hallberg[1a)], Pär A.T. Olsson[2]
[1]*Division of Solid Mechanics, Lund University, P.O. Box 118, SE-221 00, Lund Sweden*
[2]*Materials Science and Applied Mathematics, Malmö University, SE-205 06, Malmö, Sweden*

Summary The microstructure of Cu thin films may evolve significantly from the as-deposited state by self-annealing, also at room temperature. These microstructure alterations are of importance as they have a profound impact on both electrical and mechanical film properties. In the present study, the microstructure developments during self-annealing are studied by means of combining *ab-initio* and mesoscale level set modeling. This allows investigation of relative and combined effects of anisotropic grain boundary energy, mobility and stored energy distribution on the evolution of both grain structure and texture. Variation of grain boundary energy is evaluated by density functional theory calculations and is used as input for the mesoscale level set model. Based on the numerical simulations, observations are made related to, for example, the stability of the (111) texture which is dominant in the as-deposited state, to the prerequisites for abnormal grain growth and to the influence of stored energy heterogeneities.

MODELING OF SELF-ANNEALING IN CU THIN FILMS

Background

Electrical wiring in integrated circuits is commonly achieved by deposition of thin Cu films. These electroplated films are, however, metastable directly following the deposition and significant changes may occur in the material due to self-annealing. This process can continue for hours or days after deposition, also at room temperature. The process causes substantial changes to the microstructure. For example in terms of crystallographic texture, grain size and grain size distribution. Due to the extensive alterations of the microstructure, also bulk thermomechanical and electrical properties of the film change. Self-annealing in thin Cu films has been investigated for several years but there is still, however, some dispute on the origins of the process and on the actual mechanisms which are involved. The phenomena has been in focus for numerous experimental investigations, but considerably less attention has been given to numerical modeling approaches which permit further studying of the microstructure evolution during self-annealing in thin Cu films. Such numerical modeling is in focus of the present study.

Modeling framework

In the present work, microstructure evolution in thin Cu films during room temperature self-annealing is investigated by means of a mesoscale level set model. This allows very accurate representation of the grain boundary network in the polycrystalline microstructure. The model is formulated in such way that the relative, or collective, influence of anisotropic grain boundary energy, mobility and heterogeneously distributed stored energy can be investigated. Related research has also been presented previously in [1-3]. The consideration of anisotropic grain boundary properties is achieved by allowing misorientation-dependent grain boundary quantities to be evaluated locally in the microstructure with high precision. *Ab-initio* density functional theory (DFT) calculations are also performed to provide input to the mesoscale model in terms of the variation of grain boundary energy for different grain boundary configurations. The stability of the predominant (111) fiber texture in the as-deposited state is studied as well as the stability of some special low-Σ grain boundaries. Further, the numerical model allows tracing of the grain size distribution and any triggering and evolution of abnormal grain growth during self-annealing.

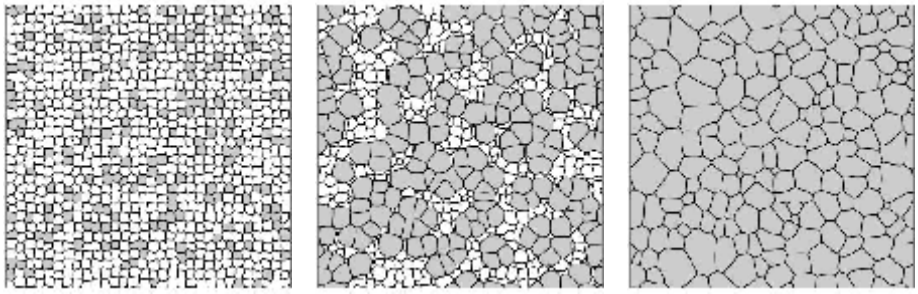

Figure 1: Abnormal growth, from left to right, of (001) grains (gray) at the expense of the (111) texture component (white). The abnormal growth of (001) grains is triggered by a lower stored energy content in this texture component.

CONCLUSIONS

[a)] Corresponding author. Email: hakan.hallberg@solid.lth.se.

A mesoscale level set model of microstructure evolution in polycrystalline materials is established. Using results from *ab-initio* DFT calculations, the level set model is shown to be a competent tool for tracing microstructure evolution during room temperature self-annealing in Cu thin films.

It is found that abnormal grain growth depends mainly on stored energy variations, whereas anisotropic grain boundary energy or mobility is insufficient to trigger abnormal growth in the model. However, texture dependent grain boundary properties contribute to an increased content of low-Σ boundaries in the annealed microstructure. Texture evolution is also caused by stored energy variations, since the coexisting (111) and (001) texture components in the as-deposited state evolve into a (001)-dominated texture after sufficient annealing time, cf. Figure 1. Further, it is found that whereas stored energy variations promote the stability of the (001) texture component, anisotropic grain boundary energy and mobility tend to work the other way and stabilize the (111) component at the expense of (001) grains.

References

[1] Hallberg, H.: A modified level set approach to 2D modeling of dynamic recrystallization. *Model. Simul. Mater. Sci. Eng.* **21**(8): 085012, 2013.

[2] Hallberg, H.: Influence of anisotropic grain boundary properties on the evolution of grain boundary character distribution during grain growth - A 2D level set study. *Model. Simul. Mater. Sci. Eng.* **22**(8):085005, 2014.

[3] Hallberg, H., Zhu, Y.: Stability of grain boundary texture during isothermal grain growth in UO2 considering anisotropic grain boundary properties. *J. Nuc. Mater.* **465**:664-673, 2015.

MULTISCALE MODELING OF DS ALLOYS APPLIED TO MATERIAL ELEMENT AND STRUCTURAL CALCULATIONS

Florent Coudon[1,3], Georges Cailletaud [*1], Alain Koster[1], Jonathan Cormier[2], and Lionel Marcin[3]

[1]*MINES ParisTech, PSL Research University, Centre des matériaux, UMR 7633, 91003 Evry, France*
[2]*Institut P', UPR CNRS 3346, ISAE-ENSMA, 86961 Futuroscope Chasseneuil, France*
[3]*SAFRAN Tech, rue des jeunes bois, 78117 Chateaufort, France*

Summary The purpose of this paper is twofold. A first section deals with the development and calibration of a multiscale model able to describe the anisotropic viscoplastic behaviour of a directionally solidified material. The model is applied to a Nickel-Base superalloy used in turbine blades. The second part proposes a solution to estimate the scatter observed between several components due to the fact that the grain size is not small with respect to the component size.

MULTISCALE MODELLING

Directionnally solidified materials have a very specific columnar microstructure, with all the grains sharing one crystallographic direction. In the present case, the material is FCC, and the axes of the cylindrical grains (namely the x_3 direction in the laboratory frame) correspond to the crystallographic $\langle 001 \rangle$ direction, generating a strong elastic and plastic anisotropy. The resulting material has an initial transverse isotropy, and can be represented by means of macroscopic models with the relevant symmetries [1, 2]. It is nevertheless difficult to follow the way the material hardening will develop with this type of models, this is why we used crystal plasticity, in the framework of a mean field model, to represent the material.

In the present work, the so called β-model is used and adapted to account for elastic anisotropy and the subsequent viscoplastic flow [3, 4]. The single crystal model takes into account both isotropic and kinematic hardening [5]. The transition rule describing the way local stress can be obtained from the macroscopic stress introduces a state accommodation variable β^g for each crystallographic orientation g, the role of which is to represent a non linear accomodation term in each crystallographic phase. The specificity of the model is then to have the same response as the Kröner model at the onset of plastic flow, then to follow the response of a self consistent model, but with an explicit accomodation tensor, that increases the numerical efficiency. The rule involves specific parameters that have to be calibrated from an external computation. This is made here by means of Finite Element Crystal Plasticity on a material element [6]. This calculation is made with a synthetic aggregate generated by Voronoï tesselation, loaded in tension and shear. The comparison between the model and FECP results is made on the macrosopic response, but also on the averaged responses in each crystallographic phase (Fig.1).

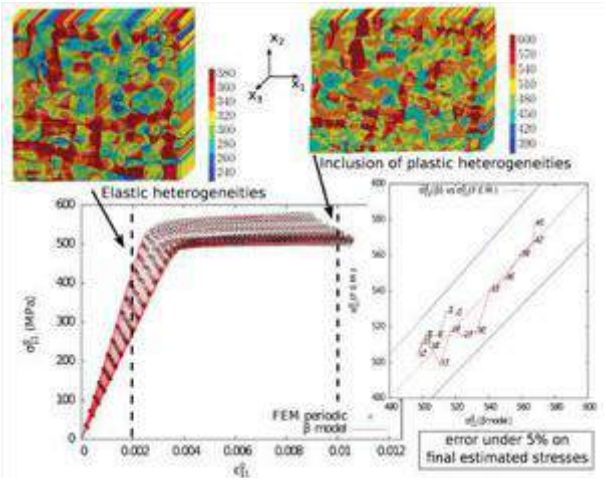

FIGURE 1 – Contour of the local tensile stress in the elastic and plastic regime, and the corresponding tension curves for each crystal orientation. The mean field model is in agreement with the average of 20 realizations obtained with the full field model (less than 5%error).

*Corresponding author. Email : georges.cailletaud@mines-paristech.fr

STRUCTURAL CALCULATIONS

The DS materials are often used in components which size is not large with respect to grain size, so that the assumption of scale separability, needed to safely apply the scale transition rules is not verified. In such conditions, an unique macroscopic calculation is far from giving a reasonable information. The averaging process linked to the use of the macroscopic model may hide important local overstress in case of non compatible local deformation schemes. A calculation that introduces the mean field model at each integration point does not meet the response of the individual specimen. The only satisfactory solution seems to use the "brute force" to compute every component as a very new structure. Obviously, this solution is not manageable in an industrial environment. A statistical approach is then needed. This section introduces a numerical strategy to estimate the scatter in a given component by means of a reduced number of calculations using the basic "one shot" response delivered by the β-model and subsequent calculations on a limited number of time steps with a full field approach. As an example, Figure 2 shows the full field response (von Mises equivalent stress) on a cruciform specimen under an equi-biaxial loading. Both upper and lower faces are shown. The field presents an important heterogeneity, which is due to the grain shape and distribution. The proposed method allows to estimate the mean value of each critical variable in each geometrical point of the component, and the local scatter. A series of tests is planned on this type of specimen.

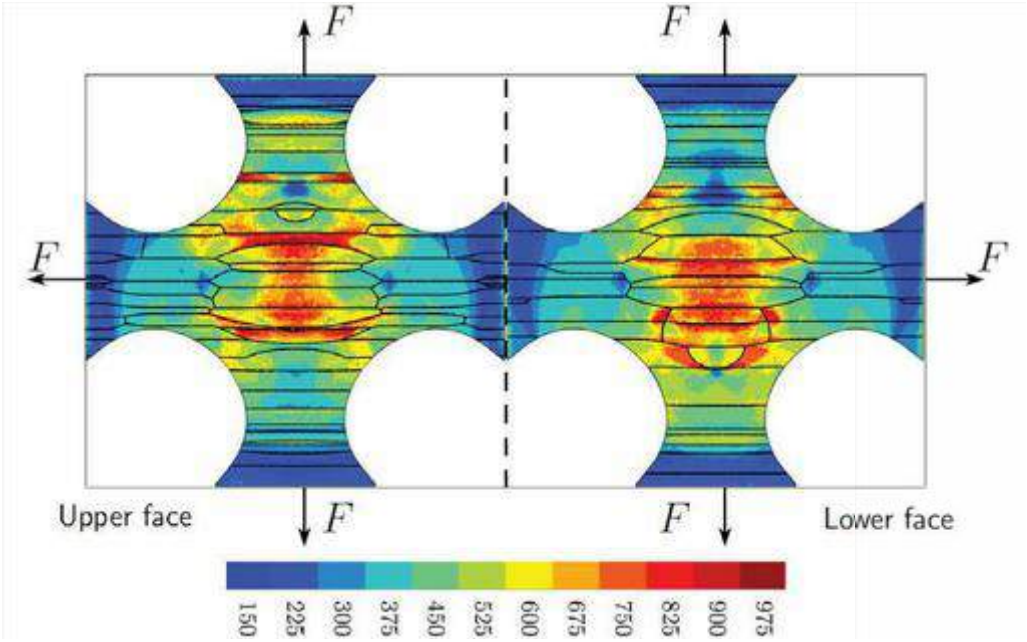

FIGURE 2 – Von Mises stress contour on the upper and lower faces of a cruciform specimen made of DS material, under equi-biaxial loading. The grain shape and orientation has a predominant influence on the local result.

REFERENCES

[1] M. Shenoy, D. McDowell, and R. Neu, "Transversely isotropic viscoplasticity model for a directionally solidified Ni-base superalloy," *Int. J. of Plasticity*, vol. 22, pp. 2301–2326, 2006.

[2] M. Yaguchi, M. Yamamoto, T. Ogata, and N. Ohno, "An anisotropic constitutive model for a directionally solidified superalloy," *Key Eng. Mater.*, vol. 22, pp. 901–906, 2007.

[3] G. Cailletaud and P. Pilvin, "Utilisation de modèles polycristallins pour le calcul par éléments finis," *Revue Européenne des Éléments Finis*, vol. 3, no. 4, pp. 515–541, 1994.

[4] K. Sai, G. Cailletaud, and S. Forest, "Micro-mechanical modeling of the inelastic behavior of directionally solidified materials," *Mech. of Materials*, vol. 38, pp. 203–217, 2006.

[5] L. Méric, P. Poubanne, and G. Cailletaud, "Single crystal modeling for structural calculations. Part 1 : Model presentation," *J. of Engng. Mat. Technol.*, vol. 113, pp. 162–170, 1991.

[6] F. Coudon, G. Cailletaud, J. Cormier, and L. Marcin, "A multi-scale strategy for the numerical modeling of directionally solidified ni-base superalloys at high temperature," in *Int. Symposium on Plasticity 2016*, (Kona, HI, USA), January 3–9, 2016.

ANISOTROPIC DAMAGE COUPLED WITH PLASTICITY - MODEL DEVELOPMENT AND COMPARISON WITH EXPERIMENTS

Stefanie Reese[1], Marek Fassin[1], Shahed Rezaei[1]& Stephan Wulfinghoff[1]
[1]*Institute of Applied Mechanics, RWTH Aachen University, Aachen, Germany*

Summary In the present contribution, a new anisotropic and coupled damage-plasticity model is developed. It is based on a second order damage tensor and applies two potentials, one for the plasticity and one for the damage part. The formulation includes only very few material parameters and can be easily transferred to large deformations. Example computations and comparison with experimental results show that the model yields physically reasonable results whereas it is numerically still feasible.

Basic modeling steps in the context of small deformation

In contrast to isotropic damage based on a scalar damage variable D, the modeling of anisotropic damage requires to work either with a second-order or a fourth-order damage tensor. Approaches of the first kind can be found e.g. in [1,2]. Models based on a fourth-order damage tensor are presented e.g. in [3,4]. In the present work, we start the derivation by formulating the Helmholtz free energy function ψ as isotropic function of a second-order damage tensor $\mathbf{D}$ and the elastic strain tensor $\boldsymbol{\varepsilon}_e$. As such we let depend ψ on the ten invariants of $\mathbf{D}$ and $\boldsymbol{\varepsilon}_e$ (J_1, ..., J_{10}). Inserting the ansatz into the Clausius-Duhem inequality we finally come to defining two potentials, one for the plasticity and one for the damage part. Using these, the evolution equations for the plastic strain tensor $\boldsymbol{\varepsilon}_p$, the damage tensor $\mathbf{D}$ and the two hardening variables (plastic and damage part) are formulated in an associated form.

The damage potential includes two functions f_d and q_d (hardening part) which allow to adjust the damage evolution over time as well as the stress-strain curve quite well. A good correlation with experiments can be achieved. Interestingly, the model can be well adapted to metallic materials but also to non-metallic materials such as concrete or composites.

The concrete choice of the Helmholtz free energy function is leaned on the work of Lemaitre (see e.g. [5,6]) where we, however, slightly modify the suggestion of the mentioned authors in such a way that ψ is a function of the invariants J_1, ..., J_{10}. In this way, the material tensor obtains with respect to the orthotropic frame an orthotropic structure which can be well exploited to determine the material parameters hidden in ψ.

Further important is the fact that we can introduce one or several "drivers" for the damage. Suitable drivers are the strain tensor, the plastic strain tensor, the continuum mechanical stress tensor or the effective stress tensor. Tension-compression asymmetry is included by considering only the positive eigenvalues of these drivers (Macaulay bracket).

Numerical issues

At the Gauss point level of the finite element implementation, several challenging numerical problems have to be tackled. First of all, we need to robustly manage the case differentiation into (1) elastic, (2) only damage, (3) only plastic, (4) coupled plastic damage behaviour. For the integration of the sophisticated evolution equations suitable algorithms shall be used, e.g. the backward Euler algorithm. This leads to a set of highly non-linear equations the solution of which can be e.g. performed by means of Newton-Raphson's method. The associated tangent is here computed numerically. Further, the algorithm has to recognize non-physical cases, e.g. D_A ($A = 1,2,3$) (eigenvalues of $\mathbf{D}$) <0 or >1.

Since anisotropic damage modeling is per se elaborate it is important to keep the numerical effort at the finite element level as low as possible. In the present contribution a special reduced integration finite element technology is suggested which works with only one Gauss point. An important issue is the hourglass stabilization which has to be developed in such a way that the anisotropic material behaviour is taken into account.

Some example computations, striving for a comparison of algorithms (fully implicit and partially explicit) are shown below.

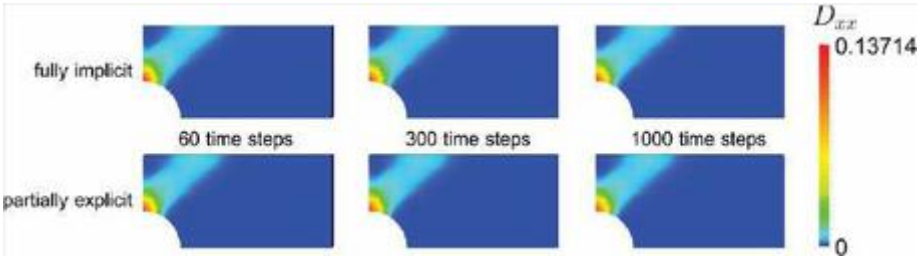

[a] Corresponding author. Email: s.reese@tu-bs.de

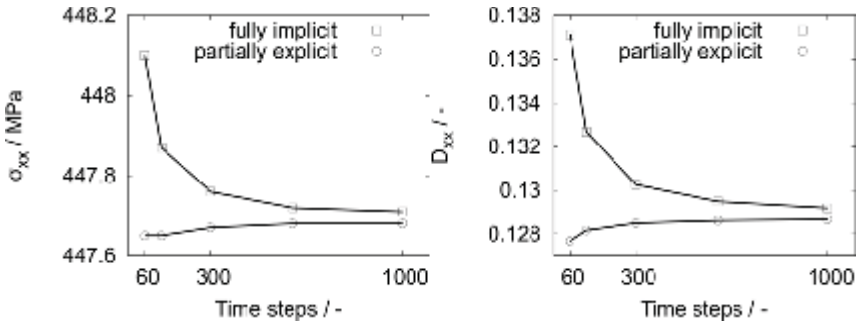

Extension to large deformations

The extension of the modeling approach to large deformations is certainly not easy but follows the same methodology as described above. A new point is the aspect that the damage tensor **D** is considered to live in the intermediate configuration. It is then possible to define the Mandel stress tensor which turns out to be symmetric. Finally, evolution equations for $\mathbf{C}_p$ (plastic right Cauchy-Green tensor) and $\mathbf{D}_r$ (damage tensor with respect to the reference configuration) are formulated. There are no additional material parameters. Also the damage potential can be taken over. See also [7,8] for more information.

References

[1] R. K. Abu Al-Rub, G. Z. Voyiadjis, International Journal of Solids and Structures 40 (2003) 2611-2643

[2] N. Challamel, C. Lanos, C. Casandjian, International Journal of Mechanical Sciences 47 (2005) 459-473

[3] J. L. Chaboche, P. M. Lesne, J. F. Maire, International Journal of Damage Mechanics 4 (1995) 5-22

[4] J. J. C. Pituba, G. R. Fernandes, Journal of Engineering Mechanics 137 (2011), 610-624

[5] J. Lemaitre, R. Desmorat, M. Sauzay, European Journal of Mechanics A/Solids 19 (2000) 187-208

[6] R. Desmorat, S. Cantournet, International Journal of Damage Mechanics 17 (2008) 65-96

[7] I. N. Vladimirov, M. P. Pietryga, S. Reese, International Journal for Numerical Methods in Engineering 75 (2008) 1-28.

[8] I. N. Vladimirov, M. P. Pietryga, Y. Kiliclar, V. Tini, S. Reeese, International Journal of Damage Mechanics 23 (2014) 1096-1132

MODELING OF POROUS MATERIALS WITH ISOTROPIC-KINEMATIC HARDENABLE MATRIX UNDER CYCLIC LOADING

Long Cheng *[1], Kostas Danas[1], and Djimédo Kondo[2]

[1]*Laboratoire de Mécanique des Solides, CNRS UMR7649 & Département de Mécanique, École Polytechnique, F91128 Palaiseau Cedex, France*

[2]*Institut Jean Le Rond d'Alembert, CNRS UMR7190, Université Pierre et Marie Curie, 4 place Jussieu, F75005 Paris, France*

Summary The main objective of this work is to investigate the response of the ductile porous material subjected to cyclic loading. To this end, by adopting the non-linear homogenization theory proposed in [2], we first formulate a new constitutive model for porous materials with hardenable matrix. An isotropic hardening law as well as kinematic one are considered. The resulting elasto-plastic model at macroscopic scale is then numerically implemented based on the algorithm described in [1]. Finally, the prediction of the proposed elasto-plastic model is validated by comparing with the Finite Elements results.

HOMOGENIZATION OF THE POROUS MATERIAL WITH A HARDENABLE PLASTIC MATRIX

Constitutive model

Let us consider a porous material whose microstructure is assumed to be statistically uniform and represented by a "Representative Volume Element (RVE)", denoted Ω. The latter one is composed of the domain $\Omega^{(1)}$ occupied by the matrix and void spaces $\Omega^{(2)}$, which are considered to be in the form of ellipsoid randomly distributed in the matrix. The latter $\Omega^{(1)}$ is made of an elasto-plastic material with an isotropic and a linear kinematic hardening law, while voids are assumed to change their volumes, shapes and orientations under finite plastic deformation. The local plastic criterion reads then:

$$\phi_M(\boldsymbol{\sigma}, \boldsymbol{X}) = \sqrt{\frac{3}{2}(\boldsymbol{\sigma}' \nearrow \boldsymbol{X}) : (\boldsymbol{\sigma}' \nearrow \boldsymbol{X})} \nearrow \sigma_0(\varepsilon^p_{eq}) \leq 0 \quad \text{with} \quad \boldsymbol{\sigma}' = \boldsymbol{\sigma} \nearrow \frac{1}{3} tr(\boldsymbol{\sigma}) \mathbf{1} \tag{1}$$

where $\boldsymbol{\sigma}$ is the Cauchy stress tensor. As classically, $\boldsymbol{X}$ denotes the back stress tensor in the matrix and is deviatoric by definition. ε^p_{eq} is the local equivalent plastic strain while σ_0 is the cohesion of the matrix.

Furthermore, the internal variables describing the microstructures of the RVE is denoted $s = \left\{\varepsilon^p, f, w_1, w_2, \boldsymbol{n}^{(1)}, \boldsymbol{n}^{(2)}, \boldsymbol{n}^{(3)}\right\}$, in which f is the porosity, w_1, w_2 the aspect ratios of the representative ellipsoid void, $\boldsymbol{n}^{(i)}, i = 1, 2, 3$ the orientations of the principal axes.

By constructing a "Linear Comparison Composite (LCC)" (see for instance [2]) for the considered porous materials, the macroscopic yield criterion is derived as:

$$\widetilde{\Phi} = \frac{(\bar{\boldsymbol{\sigma}} \nearrow \bar{\boldsymbol{X}}) : \widetilde{\mathbb{M}}^p : (\bar{\boldsymbol{\sigma}} \nearrow \bar{\boldsymbol{X}})}{1 \nearrow f} \nearrow \sigma_0^2(\varepsilon^p_{eq}), \quad \text{with} \quad \widetilde{\mathbb{M}}^p = \frac{3}{2}\mathbb{K} + \frac{3}{1 \nearrow f}\hat{\mathbb{Q}}^{-1} \tag{2}$$

where $\widetilde{\mathbb{M}}^p$ is the effective plastic compliance tensor of the incompressible matrix, expressed by means of the fourth order deviatoric tensor $\mathbb{K}$ and the microstructural tensor $\hat{\mathbb{Q}}(w_1, w_2, \boldsymbol{n}^{(i)})$. $\bar{\boldsymbol{X}}$ is the instantaneous macroscopic back stress tensor.
It is important to indicate that, as opposed to the case of heterogeneous composites (see [3]) , the isotropic hardening in the matrix will not induce any kinematic hardening in the macroscopic response of the porous materials; this is due to the fact that the stress field is null in the pore.

Numerical implementation of the proposed macroscopic model

The macroscopic strain tensor is written as:

$$\bar{\boldsymbol{D}} = \bar{\boldsymbol{D}}^e + \bar{\boldsymbol{D}}^p, \qquad \bar{\boldsymbol{D}}^e \text{ and } \bar{\boldsymbol{D}}^p \text{ are respectively macroscopic elastic and plastic strain rate} \tag{3}$$

In the present study, the elastic and plastic responses of the porous material are treated independently and then combined to numerically compute the full elasto-plastic response. The elastic strain rate reads $\bar{\boldsymbol{D}}^e = \tilde{\mathbb{M}}^e : \overset{\circ}{\bar{\boldsymbol{\sigma}}}$ (see also [1]), where $\overset{\circ}{\bar{\boldsymbol{\sigma}}}$ is the Cauchy stress co-rotating with the spin of the voids and $\tilde{\mathbb{M}}^e(\boldsymbol{s})$ the effective elastic compliance tensor, while the plastic one $\bar{\boldsymbol{D}}^p$ is obtained from the normality law:

$$\bar{\boldsymbol{D}}^p = \dot{\Lambda}\frac{\partial \bar{\Phi}}{\partial \bar{\boldsymbol{\sigma}}} = \dot{\Lambda}\boldsymbol{N} = \frac{2\dot{\Lambda}}{1 \nearrow f}\tilde{\mathbb{M}}^p : \left[\bar{\boldsymbol{\sigma}} \nearrow \bar{\boldsymbol{X}}\right) \tag{4}$$

*Corresponding author. Email: cheng@lms.polytechnique.fr

in which the plastic multiplier $\Lambda \mapsto \Lambda(\boldsymbol{s}, \mathcal{C})$ can be calculated from the consistency conditions $\widetilde{\Phi} = 0$. It depends on the internal variables $\boldsymbol{s}$ and the kinematic hardening parameter $\mathcal{C}$ (such as $\boldsymbol{X} = \frac{2}{3}\mathcal{C}\boldsymbol{D}^p$).

Combining the elastic and plastic constitutive relations, the Jaumann derivative of the stress tensor $\overset{\triangledown}{\boldsymbol{\sigma}}$ is expressed in function of the elasto-plastic Jacobian L^{ep} for the finite plastic deformation problem:

$$\overset{\triangledown}{\boldsymbol{\sigma}} = \mathbb{L}^{ep}(\boldsymbol{s}, \mathcal{C}) : \boldsymbol{D} \tag{5}$$

VALIDATION OF THE PROPOSED MODEL WITH FINITE ELEMENTS COMPUTATIONS

The macroscopic model (5) is firstly implemented and applied to a sample subjected to cyclic loading. Then, the predictions are compared to the Finite Elements solutions obtained by using Abqaus software on a REV containing 20 spherical voids.

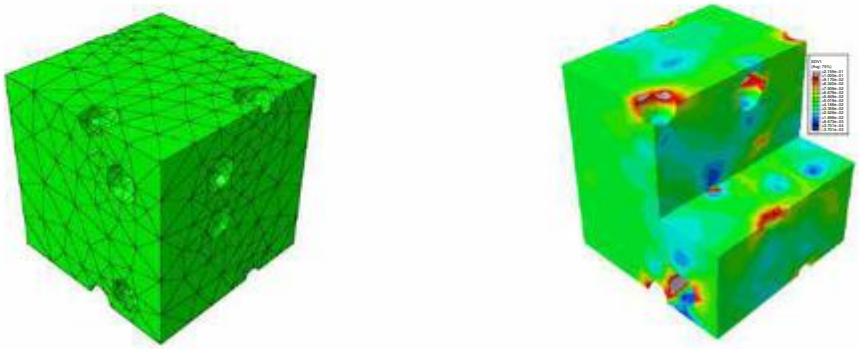

(a) (b)

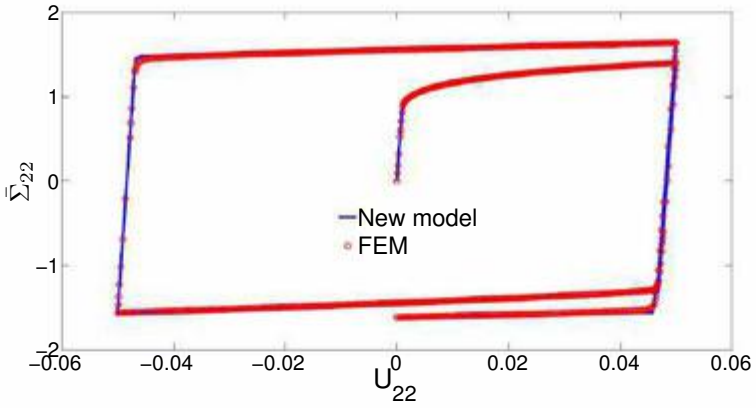

(c)

Figure 1: (a): Geometry of REV; (b):Contour of the equivalent Von Mises stress and (c): Uniaxial stress Σ_{22} as a function of uniaxial displacement U_{22}

Fig.1 displays the geometry of the REV (Fig.1(a)), the contours of the Von Mises equivalent stress after uniaxial loading and unloading (Fig.1(b)) and the uniaxial stress Σ_{22} as a function of uniaxial displacement U_{22} (Fig.1(c)). Except for the slight difference in the elastic-plastic transition zones, probably due to the decoupling between elastic and plastic responses, there is an excellent agreement between the prediction of the non-linear homogenization model and the FEM solutions. This validates the proposed macroscopic model of the porous material having a plastic hardenable matrix.

References

[1] Aravas, N., Ponte Castañeda, P.: Numerical methods for porous metals with deformation-induced anisotropy. Computer methods in applied mechanics and engineering, 193, 3767-3805, 2004.

[2] Ponte Castañeda, P.: The effective mechanical properties of nonlinear isotropic composites. J. Mech. Phys. Solids 39, 45-71, 1991.

[3] Suquet P.: Effective properties of nonlinear composites. Continuum Micromechanics. CISM Lecture Notes N0 377. Springer-Verlag. Wien. 1997. pp 197-264.

FAST KINEMATIC LIMIT ANALYSIS OF MASONRY VAULTS: A NEW GA-NURBS BASED APPROACH

Andrea Chiozzi[1a], Gabriele Milani[2] & Antonio Tralli[1]
[1]*Department of Engineering, University of Ferrara, Ferrara, Italy*
[2]*Department of Architecture, Built Environment and Construction Engineering (A.B.C.), Technical University of Milan, Milan, Italy*

Summary The present paper proposes a new Genetic Algorithm NURBS-based approach for the homogenized limit analysis of masonry vaults based on an upper bound formulation. A given masonry vault geometry can be represented by a NURBS (Non-Uniform Rational B-Spline) parametric surface and a NURBS mesh of the given surface can be generated. Each element of the mesh is a NURBS surface itself and can be idealized as a rigid body. An upper bound limit analysis formulation, which takes into account the main characteristics of masonry material is deduced, with internal dissipation allowed exclusively along element edges. It is proved that, even by using a mesh constituted by very few elements, a good estimate of the collapse load multiplier is obtained provided that the initial mesh is adjusted by means of a Genetic Algorithm (GA), in order to enforce that element edges accurately approximate the actual failure mechanism.

INTRODUCTION AND MOTIVATION

It can be affirmed that the modern theory of limit analysis of masonry structures, which has been developed mainly by [1], is the most reliable tool to assess the ultimate load bearing capacity of masonry vaults. According to [1], limit theorems of plasticity, i.e. static (lower bound) theorem and kinematic (upper bound) theorem, can be applied to masonry structures provided that the some basic assumptions are made on the masonry material [1].

In the present paper, a novel NURBS-based approach for the homogenized limit analysis of masonry vaults based on the upper bound theorem is proposed. Vaults geometry can be described by a NURBS representation of their mid-surface, which can be generated within any commercial free form modeler, together with information about the local thickness at each point of the surface. By exploiting the properties of NURBS functions [2], a mesh of the given surface, which still provides an exact representation of the vaulted surface, can be obtained. Each element of the mesh is a NURBS surface itself and is idealized as a rigid body. Starting from the obtained rigid bodies assembly, an upper bound limit analysis problem with very few optimization variables can be devised, which takes into account the main aspects of masonry material through homogenization and in which dissipation is allowed along element edges only. Due to the very limited number of rigid elements used, the quality of the collapse load so found depends on the shape and position of the interfaces, where dissipation is allowed. Mesh adjustments are therefore needed, but the utilization of SLP (which would be really cumbersome in presence of curved surfaces, as already pointed out) can be here easily circumvented, adopting a simple meta-heuristic (like a standard Genetic Algorithm GA) approach of mesh adjustment. In the GA-NURBS approach proposed, each individual forming the population is represented by a mesh. For small-to-medium populations (from 5 individuals up to 100), each iteration requires the solution of a Linear Programming problem for each individual. Thanks to the extremely reduced number of NURBS elements used in the discretization (and hence the number of variables of the Linear Programming problem), the computational effort required at each iteration is almost negligible.

The strength of the proposed GA-NURBS method lies in the fact that even by using a mesh made of very few elements (which therefore require a negligible computational time to have an estimate of collapse loads), it is possible to obtain accurate load multipliers and failure mechanisms, thus exhibiting an edge over existing methods for the collapse analysis of masonry vaults in terms of computational efficiency. Several numerical simulations obtained by the proposed procedure have been carried out and are hereafter briefly described.

NUMERICAL RESULTS

For the sake of brevity, the details of the upper-bound formulation used for the kinematic limit analysis and of the Genetic Algorithm are not reported. Nevertheless, it has to be made clear that the kinematic limit analysis procedure constitute the basis for the cost function used within the Generic Algorithm. In other words, to each individual of the selected population (i.e. to each mesh formed by NURBS rigid elements describing the vaulted surface) correspond a cost, which is given by the collapse load multiplier for the assigned mesh. Individuals are than ranked in terms of their cost and only the best individuals (i.e. with the least cost) can deliver offspring to the next generation.

Three numerical examples of GA-NURBS based kinematic limit analyses of masonry vaults have been carried out in order to evaluate the applicability of the proposed method.

A first analysis has been performed on the parabolic barrel vault belonging to Prestwood Bridge, a single-span masonry arch bridge located in Preston, Staffordshire (UK). The bridge has a net span of 6550mm, a rise of 1428mm and a section depth of 220mm and was tested up to collapse in [3] with a load applied across the bridge at quarter of the span. The initial

[a)] Corresponding author. Email: andrea.chiozzi@unife.it

NURBS mesh of the vaulted surface is composed by three quadrangular elements only. The interface between the second and the third element is fixed and is placed at quarter of net span, where a vertical point live load applied. The interface between the first and the second element is mobile and its position is governed by the genetic algorithm. The genetic algorithm allows to evaluate the optimal position of the unloaded interface between elements, in order to minimize the collapse load multiplier and therefore obtain the actual collapse mechanism for the arch. Due to symmetry and the type of applied load, the position of this interface is defined by only one parameter. Collapse load multiplier and collapse mechanism are in agreement with both the results contained in [4] and by using the open source code ArchNURBS [5].

The second analysis concerns a hemispherical dome with an inner radius of 1150 mm and a thickness of 120 mm, which was experimentally tested by [6]. In [6] a vertical load was applied to the upper crown and the load was increased until failure occurred. The initial NURBS mesh of the vaulted surface is composed by sixteen quadrangular elements only. The genetic algorithm allows to evaluate the optimal position of the middle parallel of the mesh, in order to minimize the collapse load multiplier and therefore obtaining the actual collapse mechanism. Again, the unknown position of the mesh, due to symmetry, is governed by one parameter. A graphical representation of the process is given in Fig. 1. Good agreement with both experimental results and the results obtained with the method proposed in [7] is found, for both the collapse mechanism and the collapse load.

In the third numerical simulation, the proposed GA-NURBS approach is applied to the skew circular arch experimentally tested in [8]. The arch has a clear square span of 3000 mm, a rise of 750 mm and a skew of 45 degrees. A concentrated live load is applied at the three quarter span mid-width of the arch barrel. The initial NURBS mesh of the vaulted surface is composed by four quadrangular elements only. Due to the point load presence, the position of the active interfaces is governed by three parameters: two parameters fix the extremes of the unloaded interface, whereas a third parameter fixes the position of the loaded interface (since this interface is bound to pass though the load application point). The genetic algorithm allows evaluating the optimal position of the two active interfaces. Good agreement with both experimental results and the results obtained with the method proposed in [7] is found, for both the collapse mechanism and the collapse load.

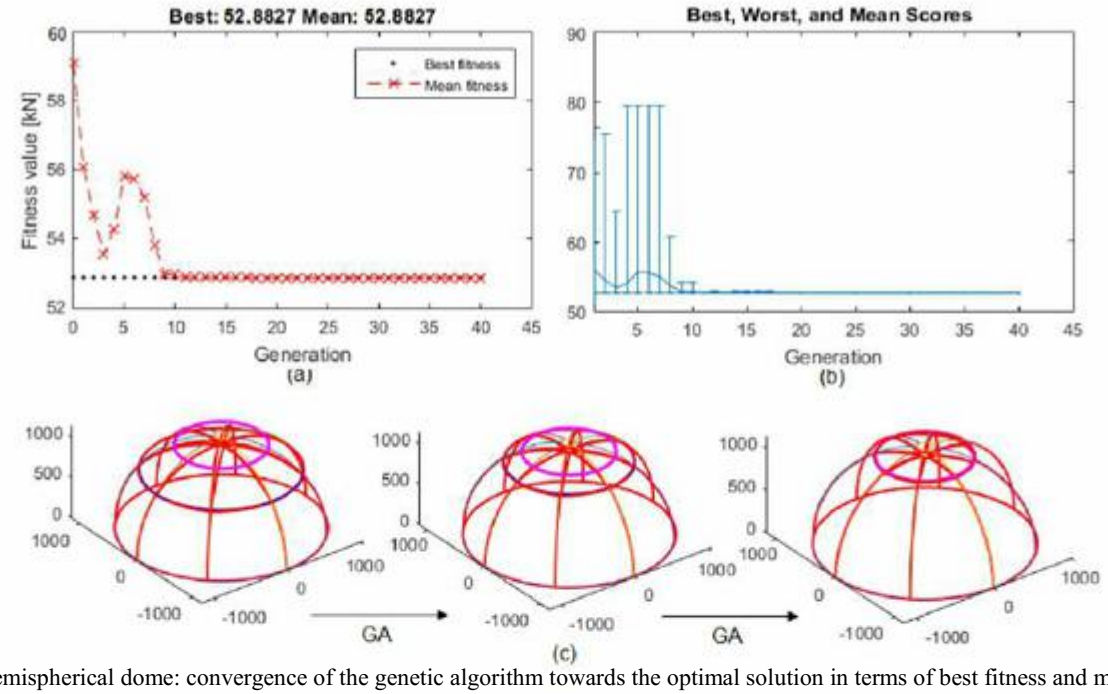

Fig. 1: Hemispherical dome: convergence of the genetic algorithm towards the optimal solution in terms of best fitness and mean value.

References

[1] Heyman, J.: The stone skeleton. Cambridge University Press, 1997.

[2] Piegl, L., Tiller, W.: The NURBS Book. Springer, Berlin, 1995.

[3] Page, J.: Load tests to collapse on two arch bridges at Preston, Shropshire and Prestwood, Staffordshire. *TRRL Res. Rep.*, 1987.

[4] Cavicchi, A., Gambarotta, L.: Lower bound limit analysis of masonry bridges including arch–fill interaction. *Eng. Struct.*, **29**:3002-3014, 2007.

[5] Chiozzi, A., Malagù, M., Tralli, A., Cazzani, A.: ArchNURBS: NURBS-Based Tool for the Structural Safety Assessment of Masonry Arches in MATLAB. *J. Comput. Civ. Eng.*, published on-line, 2015.

[6] Foraboschi, P.: Masonry structures externally reinforced with FRP strips: tests at collapse. Proc. 1st National Conference "Experimental tests on materials and Structures", Venice, Italy, 2006.

[7] Milani, G.: Upper bound sequential linear programming mesh adaptation scheme for collapse analysis of masonry vaults. *Adv. Eng. Softw.*, **79**:91-110, 2015.

[8] Wang., J., Melbourne, C.: The 3-Dimensional Behaviour of Skew Masonry Arches. The British Masonry Society, London, 1996.

CONFORM TO INTERFACE STRUCTURED ADAPTIVE MESH REFINEMENT TECHNIQUE (CISAMR)

Anand Nagarajan[1] and Soheil Soghrati *[1,2,3]

[1]*Department of Mechanical and Aerospace Engineering, The Ohio State University, Columbus, OH, USA*
[2]*Department of Materials Science and Engineering, The Ohio State University, Columbus, OH, USA*
[3]*Simulation Innovation and Modeling Center (SIMCenter), Columbus, OH, USA*

Summary A novel algorithm named Conform to Interface Structured Adaptive Mesh Refinement (CISAMR) is introduced for the automated finite element modeling of materials with complex microstructures. This algorithm transforms a structured grid, into a conforming mesh composed of both quadrilateral and triangular elements. The background grid is first subjected to an appropriate level of Structured Adaptive Mesh Refinement (SAMR) along the interface and in the vicinity of the domain boundaries. An r-adaptivity algorithm is then applied to relocate selected nodes of the background mesh to the intersection points between materials interfaces and element edges. The elements deformed by the r-adaptivity process are further subdivided to create triangular children elements with aspect ratios smaller than 3. The sub-triangulation is also expanded to neighboring elements and those affected by the SAMR to eliminate potential hanging nodes.

METHODOLOGY

Simulating problems such as design optimization and uncertainty analysis, requires the construction of multiple finite element (FE) models of the problem throughout the solution process. However, the complexities and labor costs associated with transforming Computer-Aided Design (CAD) drawings or imaging data into conforming meshes present a significant challenge. These problems have been addressed in the past via mesh-independent numerical techniques such as the Boundary Element Method (BEM) [1] or Mesh Free Methods (MMs) [2]. However, these methods do not provide the flexibility of the FEM for modeling a wide range of governing equations. Alternatively, advanced FEM-based techniques such as the eXtended/Generalized FEM (X/GFEM) [3] and the Hierarchical Interface-enriched FEM (HIFEM) [4, 5] have been developed, which allow using simple structured meshes for modeling the problem via enhancing the approximate field in nonconforming element with appropriate enrichment functions. However, in addition to imposing a higher computational cost than the standard FEM, successful implementation of such methods require additional treatments for accurate numerical integration, applying Dirichlet boundary conditions, and avoiding the high condition number of the stiffness matrix, as well as further considerations for the accurate recovery of the gradient field (e.g., stress field) along materials interfaces.

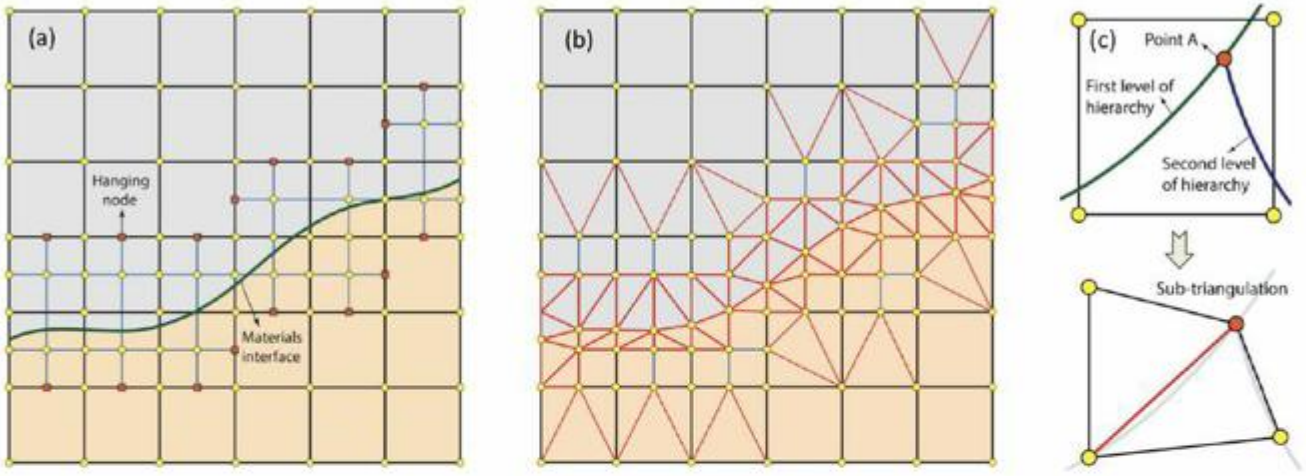

Figure 1: Evolution of the background mesh in the CISAMR: (a) SAMR of elements in the vicinity of the materials interface; (b) r-adaptivity of elements cut by the interface and construction of conforming sub-triangles with proper aspect ratios; (c) Hierarchical r-adaptivity of the element cut by two intersecting materials interfaces.

The CISAMR technique introduced in this work aims at transforming a structured background mesh into a conforming mesh with appropriate element aspect ratios (less than three) for modeling problems with highly complex microstructures. This process, which is schematically illustrated in Figure 1 for modeling a bimaterial domain discretized using a 6×6 background mesh, is composed of three main phases: (i) Structured Adaptive Mesh Refinement (SAMR) of the structured

*Corresponding author. Email: soghrati.1@osu.edu

background grid, to achieve the desired level of refinement in the vicinity of materials interfaces to reduce the geometric discretization error and improve the approximation of the field; (ii) Applying r-adaptivity to the nonconforming elements cut by the materials interface, which relocates selected nodes of the nonconforming mesh to intersection points between the interface and edges of background elements; (iii) Creating a conforming mesh by sub-triangulating the quadrilateral elements affected by the r-adaptivity process, as well as those with hanging nodes due to applying the SAMR.

While the SAMR phase of the CISAMR is an optional step for most elements of the background mesh, it is essential to implement this step in elements located along the domain boundaries or cut by multiple materials interfaces to assure that final conforming elements have proper aspect ratios. However, regardless of such algorithmic considerations, refining the elements in such regions is also necessary to assure the finite element solution can accurately capture the sharp gradients of the field in the vicinity of materials interfaces. The r-adaptivity phase of the CISAMR is applied to certain nodes of the nonconforming elements based on their distances to the materials interface. Only some of these nodes are then snapped to the interface and the rest are remain intact, such that after the sub-triangulation process the resulting triangular sub-elements (Figure 1b) have aspect ratios of smaller than three. As shown in Figure 1c, a hierarchical r-adaptivity algorithm is also developed to handle intersecting or branching materials interfaces similar to those observed in polycrystalline materials. The extra effort and computational cost associated with this r-adaptivity process, however, is compensated during the construction of conforming triangular sub-elements. The CISAMR only requires diagonal sub-division of elements cut by the interface, which can significantly facilitate its implementation compared to the algorithm needed for creating integration elements in mesh-independent methods such as the X/GFEM.

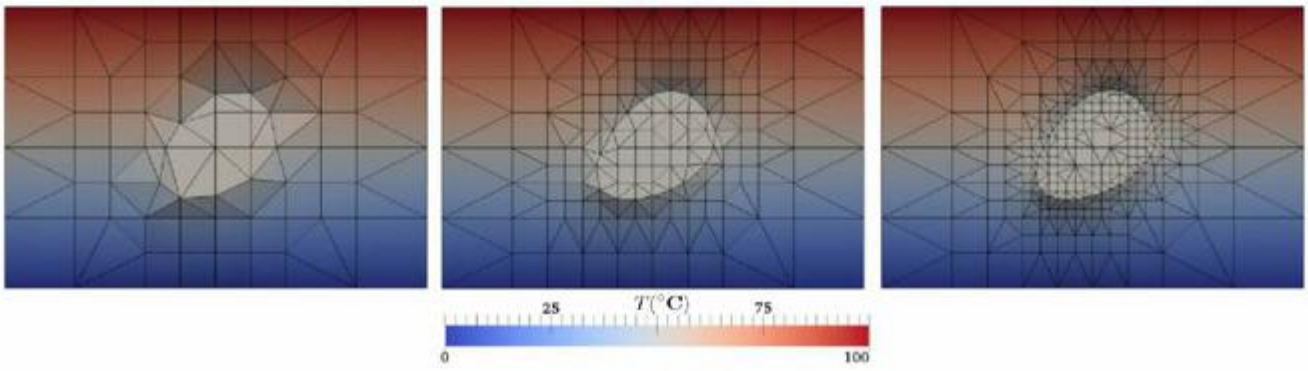

Figure 2: Preliminary results of the CISAMR for simulating the thermal response of a bimaterial domain using different levels of the SAMR in the vicinity of the materials interface.

Figure 2 illustrates preliminary results on the application of the CISAMR for simulating the steady-state thermal response of a rectangular domain with an embedded inclusion represented using a Non-Uniform Rational B-Spline (NURBS) function. The thermal conductivity ratio of the inclusion to that of the matrix in this example is 1000:1. The domain is subjected to Dirichlet boundary conditions of $T_t = 100\,^{\circ}\text{C}$ and $T_b = 0\,^{\circ}\text{C}$ along the top and bottom edges, respectively, while the side edges are insulated. As shown in this figure, the CISAMR can easily create a conforming mesh with desired level of refinement along the materials interface by transforming the original 6×4 background mesh. The presentation will further expand these results by demonstrating the CISAMR ability for modeling heterogeneous materials with highly intricate microstructures, including simulations of the nonlinear damage evolution in particulate and fiber-reinforced composites.

References

[1] Y. J. Liu, S. Mukherjee, N. Nishimura, M. Schanz, W. Ye, A. Sutradhar, E. Pan, N. A. Dumont, A. Frangi, and A. Saez. Recent advances and emerging applications of the boundary element method. *Applied Mechanics Reviews*, 64(3):1001, 2011.

[2] T. Belytschko, Y. Krongauz, D. Organ, M. Fleming, and P. Krysl. Meshless methods: an overview and recent developments. *Computer methods in applied mechanics and engineering*, 139(1):3–47, 1996.

[3] T. Belytschko, R. Gracie, and G. Ventura. A review of extended/generalized finite element methods for material modeling. *Modeling and Simulation in Material Science and Engineering*, 17:043001, 2009.

[4] Soghrati S. Hierarchical interface-enriched finite element method: An automated technique for mesh-independent simulations. *Journal of Computational Physics*, 275:41–52, 2014.

[5] Soheil Soghrati and Hossein Ahmadian. 3D hierarchical interface-enriched finite element method: Implementation and applications. *Journal of Computational Physics*, 299:45–55, 2015.

MULTISCALE NUMERICAL STUDY ON POLYCRYSTALLINE FERROELECTRIC SOLIDS

Yasutomo Uetsuji [1a)] & Tatsuya Oka [2]
[1]Department of Mechanical Engineering, Osaka Institute of Technology, Osaka, Japan
[2]Graduate School, Osaka Institute of Technology, Osaka, Japan

Summary A multiscale finite element modelling is presented for polycrystalline ferroelectric materials with MPB (morphotropic phase boundary). The purpose of this study is to reveal nonlinear behaviors caused by domain switching and structural phase transition. The homogenization theory was employed for scale-bridging between macrostructure and microstructure. Crystal morphologies, which were characterized as an inhomogeneous structure composed of many grains and domains with individual orientations, were modeled at a microscopic scale. Then nonlinear response of the macrostructure was evaluated through monitoring microstructural crystal morphology change. The proposed simulation was applied to a polycrystalline PZT (lead zirconate titanate) at MPB.

INTRODUCTION

Ferroelectric solids, especially polycrystalline PZT is used widely for actuators and sensors of electromechanical devices and it has multiple crystal systems [1]. Although PZT outputs large piezoelectricity, it shows a complicated hysteresis behavior caused by domain switching and structural phase transition at MPB. It is important for development and improvement of biocompatible lead-free piezoelectric materials to understand the mechanism of huge piezoelectricity in PZT. Many numerical and computational models have been developed to analyze macroscopic hysteresis behaviors and physical properties of ferroelectric materials. Their models are reviewed perfectly by some literatures [2]. Although macroscopic hysteresis behaviors depend on microstructural crystal morphology, there is no application of scale-bridging techniques to polycrystalline ferroelectric solids at MPB in perfect consideration with domain switching and structural phase transition. In this study, a multiscale simulations based on asymptotic homogenization theory is proposed to understand ferroelectric hysteresis behaviors.

NUMERICAL METHOD AND RESULTS

Figure 1 shows the proposed multiscale nonlinear simulation of polycrystalline ferroelectric solids. The asymptotic homogenization theory is employed for scale-bridging between macrostructure and microstructure [3]. We utilize an incremental form of fundamental constitutive law in consideration with physical property change caused by domain switching and structural phase transition [4, 5]. Crystal morphologies, which are characterized as an inhomogeneous structure composed of many grains and domains with individual orientations, are modeled at a micro scale. Then the homogenized material properties of macrostructure can be estimated with perfect correlation to microstructural changes such as domain switching and structural phase transition.

The proposed multiscale finite element method was applied to a polycrystalline PZT, and the relation between the macroscopic properties and microscopic domain switching and structural phase transition were investigated. Especially the difference among tetragonal single phase, rhombohedral single phase and their dual phases were discussed. Their comparison revealed the advantageous effect of MPB on macroscopic piezoelectric response.

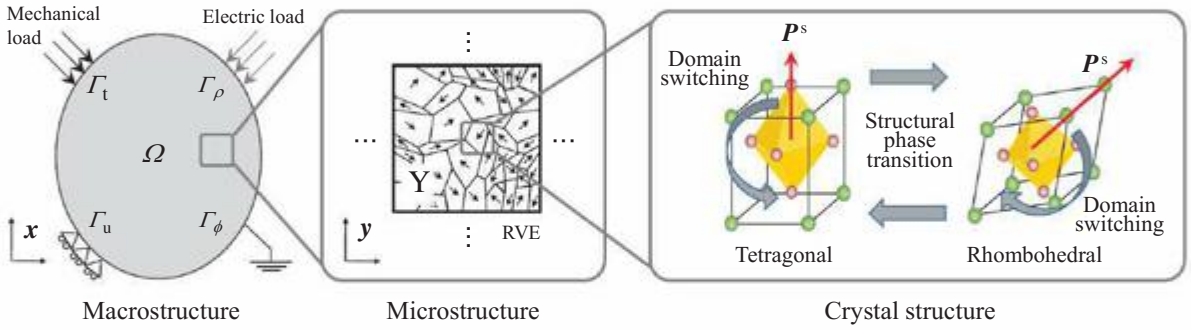

Figure 1 Multiscale modeling of polycrystalline ferroelectric solids.

a) Corresponding author. Email: yasutomo.uetsuji@oit.ac.jp.

ACKNOWLEDGMENTS

One of the authors (Y. Uetsuji) was financially supported by a Grant-in-Aid for Scientific Research (C) (Grant Number 26420030) from the Ministry of Education, Culture, Sports, Science and Technology of Japan.

References

[1] Hindrichsen C. G.: Advantages of PZT Thick Film for MEMS Sensors. *Sensors and Actuators* A**163**: 9-14, 2010.

[2] Potnis P.R., Tsou, N.T., Huber, J.E.: A Review of Domain Modelling and Domain Imaging Techniques in Ferroelectric Crystals. *Materials* **4**: 417-447, 2011.

[3] Uetsuji Y., Kuramae H., Tsuchiya K.: Two-Step Homogenization Simulation for Multidomain and Multigrain Structures in Piezoelectric Materials. *Acta Materialia* **61**:7304-7312, 2013.

[4] Uetsuji Y., Hata T., Kuramae H., Tsuchiya K.: Homogenization Modeling of Domain Switching in Ferroelectric Materials. *Acta Mechanica* **225**:2969-2986, 2014.

[5] Uetsuji Y., Hata T., Kuramae H., Tsuchiya K.: Multiscale Simulation of Domain Switching Behavior in Polycrystalline Ferroelectric Materials. *Computational Materials Science* **106**:100-110, 2015.

SEQUENTIAL AND CONCURRENT MULTISCALE MODELING: FROM MOLECULAR DYNAMICS TO CONTINUUM MECHANICS

James D. Lee*[1], Jiaoyan Li[2], and Zhen Zhang[1]
[1]*Department of Mechanical and Aerospace Engineering, George Washington University, Washington, DC, USA*
[2]*School of Engineering, Brown University, Providence, RI, USA*

Summary Molecular dynamics has become a powerful tool in simulating material system viewed as a collection of discrete atoms/particles, while continuum mechanics has been successfully used to study continuum medium. The fundamental difference between these two disciplines leads to the challenges in constructing a multiscale method aiming at bridging the gap between atomistic description to continuum description either sequentially or concurrently. In this work, we have proposed a novel multiscale method from atoms, modeled by molecular dynamics (MD), to genuine continuum, modeled by classical continuum mechanics (CM). The philosophy is that a solution region can be decomposed into critical region and non-critical far-field, where MD is used in critical region to capture the key phenomena such as cracks, dislocations, etc., and a newly formulated coarse-grained MD and finite element method are used in non-critical far-field. The size of the simulated material system can be significantly increased, which overcomes the well-known size limitation of MD.

INTRODUCTION

Nowadays, due to the development of massively parallel computers, numerical simulation has emerged as a powerful tool to investigate material and structural behaviors. Basically, there exist two fundamental physical models, discrete and continuous, that provide foundations for all material modeling. At nano-scale, the material body is viewed as a collection of discrete particles moving under the influence of their mutual interactive forces. Unfortunately, due to large number of particles involved as well as complex nature of atomistic interactions, the application of MD over a realistic range of length and time scales is not feasible. Even worse, the occurring time of concerned physical event is too far away in the future comparing with the small time step needed in MD simulations. On the other hand, at macro-scale, materials are modeled by continuum physics, which is simply invalid for material systems at nanoscale because, to say the least, stress-strain relation cannot replace interatomic potential and the treatment of temperature is totally different than that in MD. From a practical viewpoint, simulation of strongly coupled multiscale systems becomes necessary. Therefore, a new unified theory and associated computational methods for such strongly coupled system have to be developed.

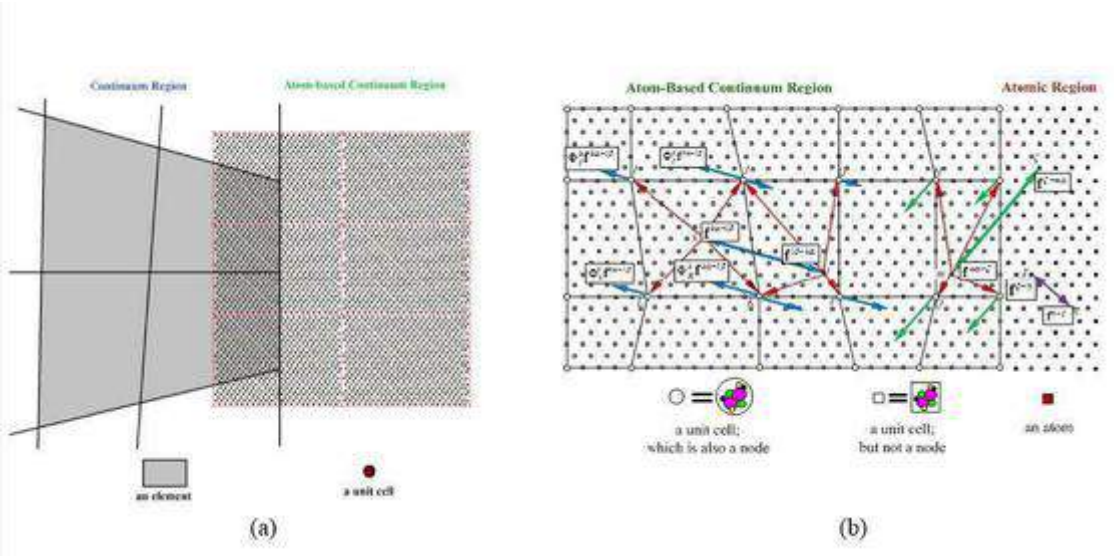

Figure 1: (a) Schematic diagram of coarse-grained MD model in the ABC region and continuum mechanics in continuum region; (b) Schematic diagram of MD model in the atomic region and coarse-grained MD model in the ABC region [6,7].

*Corresponding author. Email: jdlee@gwu.edu

METHOD

Several concurrent multiscale techniques have been developed, such as handshaking domain method [1], bridging-scale method [2], heterogeneous multiscale method [3], quasicontinuum method [4], and multiscale field theory [5]. Those multiscale techniques provide simulations for atomistic/microscale coupling system. However, it remains a challenge to extend the simulations to macroscale scale. In this work, we construct a multiscale modeling theory from atoms, modeled by molecular dynamics (MD), to genuine continuum, modeled by classical continuum mechanics (CM).

The basic strategy for multiscale modeling may be described as follows. Suppose we have a solution region, in which there are several critical sub-regions where cracks, dislocations or other critical physical phenomena occur. We choose concurrent multiscale modeling: use atomistic model for the critical regions and large-scale model for the non-critical far field. We have successfully incorporated MD and coarse-grained MD for co-existing atomic region and atom-based-continuum (ABC) region (cf. Fig. 1b) in a single theoretical framework. We now proceed to add genuine continuum (GC) region, modeled by continuum theory, into the picture (cf. Fig. 1a).

Atoms in the atomic region, modeled by MD, simply follow the Newtons law of motion. Temperature in the atomic region is calculated based on the velocity field; but it is not controlled through any thermostat. For the ABC region, we set up a mesh, consisting of nodes and elements (cf. Fig. 1b), similar to the one used in classical finite element method. It is noticed that, in the ABC, each node represents a unit cell, which consists of n atoms, not necessarily the same kind. Atoms in the ABC act as followers and messengers: they follow the nodes according to shape functions and serve as messengers to pass the interatomic forces to the corresponding nodes. In the GC region, each node only has three degrees of freedom for displacements (or two if 2D plane problem is treated) and one degree of freedom for temperature, because in continuum mechanics there are three equations for equilibrium and one for energy. The material properties include stress-strain relations, thermal expansion coefficient, heat conductivity, and heat capacity. We will find those properties from pure MD simulations, i.e., sequential multiscale modeling. At the interface, a group of nodes in ABC corresponds to a node in GC as shown in Figure 1a. Here, we make two assumptions: (1) A node in GC is anchored at the mass center of the corresponding group in ABC and (2) The sum of heat fluxes into the node in GC and the group in ABC is zero. We also set the target temperature of the group in ABC to be the temperature of the node in GC. Thus we can formulate the interface conditions between ABC region and GC region. This enables one to perform concurrent multiscale modeling.

RESULTS AND CONCLUSIONS

We have successfully developed a MD computer code, which is capable of simulating material systems, such as rocksalts, perovskites, and even complex polycrystalline structures, in thermal, mechanical and electromagnetic applications. An atomistic simulation methodology, based on the energy release rate, is introduced as a tool to unveil the fracture mechanism of graphene at nanoscale. This methodology can be easily extended to any other atomistic material system. Phonon dispersion relation subject to strains at various levels are investigated. We also investigated the heat conduction phenomena at nanoscale by reformulating the Nose-Hoover thermostat for MD and CGMD simulation. Moreover, we have developed both force-based and stiffness-based coarse-grained MD models to show that mechanical wave can propagate through the interface between the Atomic region and ABC region smoothly. More results will be shown and discussed in details during the presentation.

References

[1] Rudd R.E., Broughton J.Q.: Concurrent coupling of length scales in solid state systems. Phys. Status Solidi B, 217: 251291, 2000.

[2] Wagner G.J., Liu W.K.: Coupling of atomistic and continuum simulations using a bridging scale decomposition. J. Comout.Phys, 190: 249-274, 2003.

[3] E W., Engquist B., Li X., Ren W., Vanden-Eijnden E.: The heterogeneous multiscale method. A review. Comm. Comp. Phys, 23: 367-450, 2007.

[4] Knap J., Ortiz M.: An analysis of the quasicontinuum method. J. Mech. Phys. Solids, 49: 1899-1923, 2001.

[5] Chen Y., Lee J.D.: Atomistic formulation of a multiscale theory for nano/micro physics. Philos. Mag., 85: 4095-4126, 2005.

[6] Li J., Wang X., Lee J.D.: Multiple time scale algorithm for multiscale material modeling. Computer Modeling in Eng. and Sci., 85: 463-480, 2012.

[7] Li J., Lee J.D.: Stiffness-based coarse-grained molecular dynamics. J. Nanomech. Micromech, 4: 1-8, 2014.

LATTICE STRAIN EVOLUTION DURING BIAXIAL LOADING: AN FE-FFT MULTISCALE MODELLING APPROACH

Manas V. Upadhyay[1a)], Tobias Panzner[2], Steven Van Petegem[1], Helena Van Swygenhoven[1,3] & Ricardo Lebensohn[4]
[1]*Swiss Light Source, Paul Scherrer Institute, Villigen, Switzerland*
[2]*Laboratory for Neutron Scattering, NUM, Paul Scherrer Insittute, Villigen, Switzerland*
[3]*NXMM, IMX, Ecole Polytechnique Fédérale de Lausanne, Lausanne, Switzerland*
[4]*MST, Los Alamos National Laboratory, Los Alamos NM, USA*

Summary: In this work, we use a multiscale modelling approach to understand the role of lattice strain evolution during biaxial loading of cruciform shaped samples of 316L steel. Finite element simulations performed on cruciform samples provide correct macroscopic boundary conditions to drive the meso-scale elasto-viscoplastic fast Fourier transform model. Lattice strains are predicted along one of the principal directions of the cruciform sample and compared with in-situ neutron diffraction experiments. Results show that at the macroscopic scale uniaxial load on cruciform sample results in biaxial stress state in the gauge area. This contributes to kinks observed in lattice strain evolution from diffraction peaks. During equibiaxial loading the spread in lattice strain evolution is much lower than in uniaxial loading. This implies that elastic anisotropy of 316L steel does not play a significant role in lattice strain evolution in the in-plane direction during equibiaxial loading.

INTRODUCTION

Metals and alloys used for engineering purposes are typically subjected to multiaxial stress states during processing or under service conditions. Their mechanical behaviour can be significantly different depending on the type of applied stress state. These differences originate at the microstructural level and manifest themselves in the form of variations in inter (type II) and intra-granular (type III) stresses. To that end, in a recent work [1] in-situ neutron diffraction experiments were carried out during biaxial mechanical testing of cruciform shaped 316L stainless steel samples. In the present work, we propose to use a multiscale modelling approach to simulate these experiments in order to obtain a deeper understanding of the mechanical behaviour of the 316L steel during biaxial loading. The multiscale modelling approach combines macroscale finite element simulations to model the cruciform shaped samples in order to provide realistic boundary conditions for the meso-scale elasto-viscoplastic fast Fourier transform (EVP-FFT) model [2].

SIMULATION SETUP AND VALIDATION

At the macroscopic scale, finite element simulations of the cruciform sample geometry (see figure 1a) are performed using ABAQUS/Standard software. The sample is assigned homogeneous isotropic elastic properties. The plastic behaviour is modelled using a combined non-linear isotropic and kinematic hardening model with 5 backstresses. The finite element simulations are validated by comparing surface strains (E_{11} and E_{22}) predicted in the gauge region (4 x 4 x 2.5 mm^3) with those obtained experimentally using the in-situ digital image correlation. As can be seen in figure 1b an excellent match is obtained. Then, the predicted engineering stress (S_{11} and S_{22}) components (shown in figure 1c) are volume averaged in the gauge region and supplied as macroscopic boundary conditions to drive the EVP-FFT model.

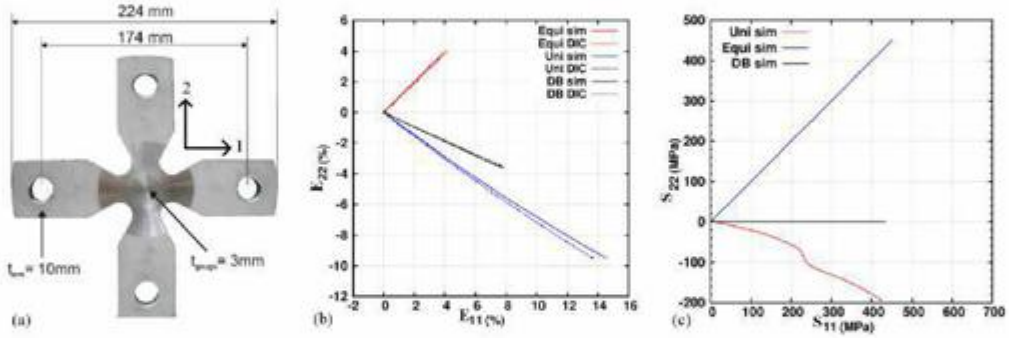

Figure 1: (a) Cruciform sample geometry, (b) comparison of DIC strains with those predicted from FE simulations and (c) stress components averaged over the gauge region for tensile loading in dog bone samples (DB), and uniaxial (UNI) and equibiaxial (EQUI) loading in cruciform samples.

For the EVP-FFT model, a representative volume element of 2500 randomly oriented grains is discretized into a grid of 64 x 64 x 64 equi-spaced voxels. Each voxel is assigned single crystal elastic and plastic properties of the face centred cubic

[a)] Corresponding author. Email: manas.upadhyay@psi.ch

316L stainless steel. The material hardening behaviour is modelled using a Voce isotropic hardening law. Lattice strains ($\mathbf{g}\cdot\boldsymbol{\varepsilon}\cdot\mathbf{g}$; $\boldsymbol{\varepsilon}$ = local strain tensor and $\mathbf{g}$ is the normalized diffraction vector) are predicted along one of the principal cruciform directions. For each grain family σ_{VM}, the von Mises (VM) equivalent of averaged stress tensor over all grains, is computed. Results are compared for uniaxial loading in dog bone samples, and uniaxial and equibiaxial loading cruciform samples.

During in-situ neutron diffraction measurements, the sample is held at constant displacement due to which stress relaxations occur in the gauge area. According to the usual practice, Voce parameters are fitted to these relaxed stress values whereas for the macroscopic model plastic parameters are fitted to the real hardening curve. This results in a constant off-set in the lattice strain results.

RESULTS

Figure 2 shows the lattice strain and stress evolution for the grain families 111, 200, 220 and 311. During tensile loading in dog bone samples, the macroscopic stress state is uniaxial. In the elastic regime, the differences in slopes of the lattice strains are due to the elastic anisotropy of the steel. The 200 grain family is the most compliant while the 111 is the stiffest.

During uniaxial loading in cruciform shaped samples, the stress state in the gauge region is biaxial with a non-linearly evolving tension-compression components along in-plane directions. The macroscopic stress ratio S_{22}/S_{11} changes from -0.23 in the elastic regime to -0.42 during the elastic-plastic transition regime. This results in the kink observed in lattice strain evolution in figure 2b. For uniaxial cruciform loading, a larger variation in lattice strain and $\bar{}_{VM}$ evolution is obtained. Equibiaxial loading, in comparison with dog bone samples, results in much smaller variations. For this type of loading, one may assume that any of the 4 grain families is representative of the average polycrystalline response. Going from a load ratio of S_{22}/S_{11} = -0.42, -0.23, 0 to 1, the role of elastic anisotropy of 316L steel is found to play a decreasingly significant role.

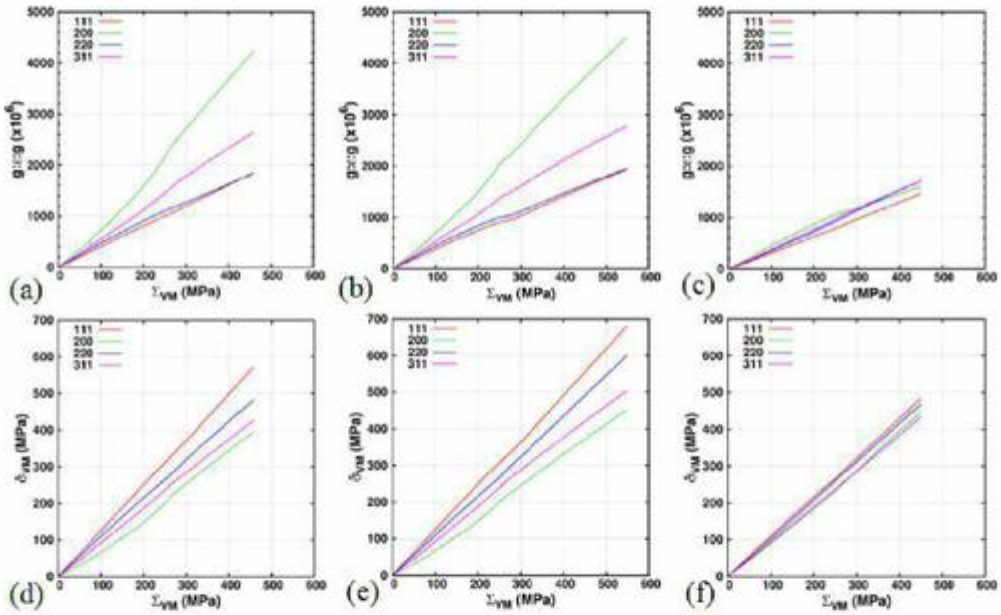

Figure 2: Lattice strain evolution (a, b, c) and $\bar{}_{VM}$ (d, e, f) in different grain families during uniaxial loading of dog bone sample (a,d), uniaxial cruciform loading (b, e) and equibiaxial cruciform loading (c, f) as a function of the macroscopic VM stress Σ_{VM}.

CONCLUSIONS

The role of elastic anisotropy on the lattice strain evolution along the in-plane loading direction in 316L stainless steel decreases going from a uniaxial tensile stress state to an equibiaxial tensile stress state.

References

[1] Van Petegem S., Wagner J., Panzner T., Upadhyay M.V., Trang T.T.T., Van Swygenhoven H.: In-situ neutron diffraction during biaxial deformation. Acta Mater. *105*:404-416, 2016.

[2] Lebensohn R.A., Kanjarla K.K., Eisenlohr P.: An elasto-viscoplastic formulation based on fast Fourier transforms for the prediction of micromechanical fields in polycrystalline materials. Int. J. Plast. *32-33*:59-69, 2012.

TRANSITIONING RATE SENSITIVITIES ACROSS MULTIPLE LENGTH SCALES IN CRYSTAL PLASTICITY

Marko Knezevic[1a)], Miroslav Zecevic[1], Rodney J. McCabe[2] & Irene J. Beyerlein[3]
[1]*Department of Mechanical Engineering, University of New Hampshire, Durham, NH 03824, USA*
[2]*Theoretical Division, Los Alamos National Laboratory, Los Alamos, NM 87545, USA*
[3]*Materials Science and Technology Division, Los Alamos National Laboratory, Los Alamos, NM 87545, USA*

Summary A finite-element based plasticity model is developed for polycrytals deforming at high-strain-rates. The model is multi-scale, covering from thermally activated dislocation motion on a specific crystallographic slip system, to single crystal plasticity, to polycrystalline plasticity, and ultimately heterogeneous deformation of the macro-scale sample. Within the model, the rate dependence in macro-scale response arises solely from the characteristic stress to activate dislocation motion. This is accomplished by introduction of a novel methodology, used at the intermediate length scales, to remove any extraneous rate dependencies occurring as a result of the visco-plastic rate sensitive flow rule, commonly associated with crystal plasticity formulations. Simulation results are presented for the deformation of high-purity zirconium in a Taylor impact cylinder test. The variation in sample shape changes, texture evolution, and deformation twin fraction after the test are experimentally measured. These same quantities are calculated using the model and good agreement is achieved in all aspects.

INTRODUCTION

The deformation response of zirconium (Zr), like other hexagonal metals, depends sensitively on which slip and twinning modes are activated throughout the history of deformation. Each mode acts on a particular slip or twinning plane and in a specific direction. Over the temperature and strain rate regimes of interest (77 K to 800 K and 10^{-4} /s to 10^{5} /s), slip and twinning on these systems are carried by the motion of dislocations, and this motion is thermally activated [1]. Thus, the stresses needed to these mechanisms depend on strain rate and temperature and evolve with strain level as dislocations interact and become stored in the crystal. As the structural characteristics of the dislocations are different, each mode has its own separate evolution law with strain and function with strain rate and temperature.

A Taylor impact cylinder test was devised in efforts to develop constitutive laws for polycrystalline metals over a wide range of strain rates in one single test [2]. This deceptively simple test involves propelling a cylindrical specimen at a rigid target and measuring the changes in sample shape and microstructure after the test. The resulting strain rate and stress fields are non-varying along the cylinder axis and can vary widely depending on the material and parameters of the test. Heterogeneous deformation in both time and space can result in gradients in the plastic deformation response and underlying microstructural evolution. For a metal, such as Ta, with a high symmetry body centred cubic (BCC) crystal structure, a finite element model employing simple constitutive laws based on yield surfaces were sufficient to understand and model the shape changes resulting from the test [3]. For a low symmetry metal like Zr, it was pointed out similar modeling approaches were not sufficient and there is a need to account for the evolution of texture and the specific deformation mechanisms underlying plastic deformation.

The objective of this work is to develop a multi-scale finite-element (FE) based model for the rate-sensitive constitutive response of a hexagonal metal, Zr, which deforms by multiple slip and twinning modes. We introduce a formulation that removes the rate sensitivity that enters via the power-law exponent n, while still retaining the visco-plastic flow rule. As such, all the rate sensitivity can be embodied in the characteristic activation stresses for the individual slip and twinning systems.

APPROACH

We employ a vosco-plastic self-consistent (VPSC) model to relate the deformation of an aggregate to the deformation of its constituent grains. The VPSC model operates at each FE integration point of a macro-scale model. The constitutive response requires a hardening model for slip/twin resistances that dictates how they evolve with strain, temperature, and strain-rate. In all calculations here, we employ within this FE-VPSC model, a dislocation density based hardening law which is governed by thermally activated rate laws for dislocation storage. It is physical and thus desirable in modeling the macro-scale deformation response to account for the strain-rate dependence solely by a functional form of strain-rate. However, in most mulitscale modeling techniques, rate sensitivity can additionally enter in via the visco-plastic power-law flow rule and its parameter n, which is used at the single-crystal scale. Typically used values for the exponent n lie in the range of 1 to 50 and with these values, the flow rule can have a significant, superfluous effect on the rate sensitivity of the macro-scale response. In principle, the larger the exponent n the smaller the rate sensitivity is, and so only in the limit of n approaching infinity can a power-law rate-insensitive response be achieved. Then, rate sensitivity in material response will only be a consequence of the rate dependence of the slip resistance, which is desired. This paper will describe the methodology for decreasing or eliminating the overall rate sensitivity effect of the power-law exponent allowing us to simulate high-rate

[a)] Corresponding author. Email: marko.knezevic@unh.edu.

deformation during the Taylor impact test of Zr. The approach is integrated in Abaqus through a User MATerial (UMAT) subroutine.

RESULTS

The FE-VPSC model is applied to calculate the deformation of high-purity Zr in the Taylor impact test. It is known that the strain rate distribution generated during this test is highly heterogeneous, giving rise to a variation in the plastic deformation response and microstructural evolution throughout the sample. To date, this test has been a challenge to model comprehensively and across many scales from the macroscale response to the underlying microscopic deformation mechanisms. This test represents a good check for the model developed here. We use the dynamic implicit FE code called Abaqus standard dynamic. The simulation microstructure was initialized with this starting measured texture. Every integration point was represented by a VPSC polycrystal with 150 orientations. Figure 1 shows the time evolution of the equivalent strain rate that develops during the simulation and the shape change after the impact. The calculations indicate that the strain rate develops heterogeneously along the sample length, with peak rates rising substantially to excess of 10^4/s. The peak position travels from the foot, where impact first occurs, to the end of the sample. During its excursion, the peak decreases in intensity.

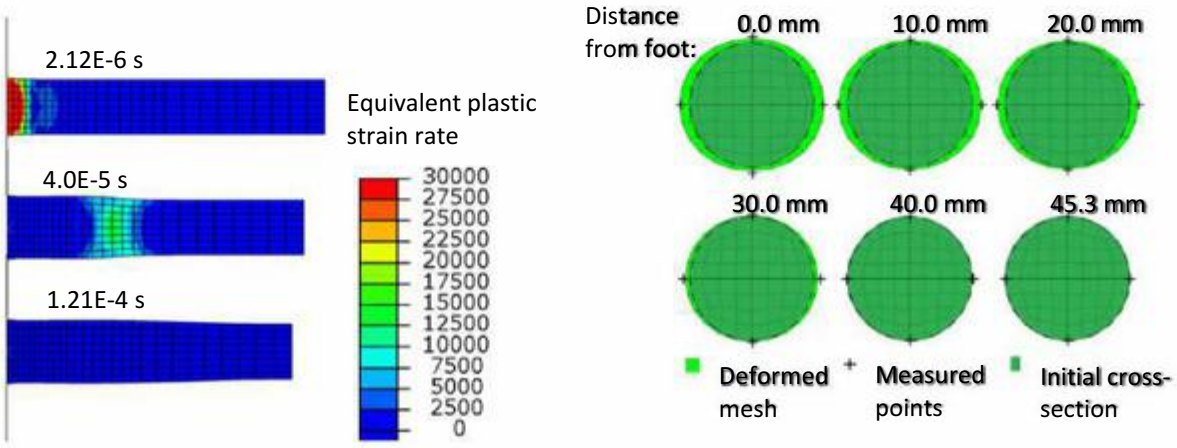

Figure 1. Equivalent plastic strain rate contours developed during the impact simulation of the Zr Taylor cylinder. Cross-sections after the impact as a function of the distance from the foot predicted by FE-VPSC along with the experimentally measured points superimposed over the FE mesh. The initial cross-sectional geometry is shown to illustrate the extend of plastic deformation from the foot towards the tail. It can be seen that the cross-sections 40 mm and 45.3 (the actual tail cross-section) from the foot do not show any permanent shape change.

CONCLUSIONS

In this work, we have developed a finite element based multi-scale constitutive model for polycrystals that can deform by multiple slip and twinning systems. The model is novel in that rate sensitivities in material response are a consequence solely of dislocation motion on active crystallographic slip systems. We develop a methodology that removes the rate sensitivities that are introduced while not increasing computational time and still retaining use of the visco-plastic power-law formulation. We also develop a UMAT for strain-rate-imposed boundary conditions, overcoming the limitation of prior FE-VPSC approaches that were stress-imposed and less numerically stable. Through these two chief advancements, the scale transitions from crystal plasticity to polycrystalline plasticity and from polycrystalline plasticity to the finite-element UMAT are adequately treated. With the model, the shape changes, texture evolution, and twin fractions are calculated for Zr in a Taylor impact cylinder test and all aspects achieve very good agreement with measurements.

References

[1] Knezevic M., Zecevic M., Beyerlein I.J., Bingert J.F., McCabe R.J.: Acta Materialia **88**: 55-73, 2015.

[2] Maudlin P., Bingert J., House J., Chen S.: International Journal of Plasticity **15**: 139-166, 1999.

[3] Maudlin P., Gray G., Cady C., Kaschner G.: Philosophical Transactions of the Royal Society of London A: Mathematical, Physical and Engineering Sciences **357**: 1707-1729, 1999.

TWO-SCALE, FE-FFT- AND PHASE-FIELD-BASED COMPUTATIONAL HOMOGENIZATION

Julian Kochmann*, Stephan Wulfinghoff, Stefanie Reese[1] and Bob Svendsen[2]

[1]*Institute of Applied Mechanics, RWTH-Aachen University, Aachen, Germany*
[2]*Chair of Material Mechanics, RWTH Aachen University, Aachen, Germany*

Summary The purpose of this work is the development of a two-scale, FE-FFT- and phase-field-based computational model to link macroscopic deformation processes to microstructural modifications and peripheral and surface zone properties of polycrystalline materials. The macroscopic BVP is solved using finite element (FE) methods and the solution of the microscopic BVP, which is embedded as an RVE in each integration point, is found exploiting fast Fourier transform (FFT), augmented Lagrangean and fixed-point methods. Non-conserved phase-fields are introduced to characterize the local material composition and model changes in the crystal structure. As a first example, the proposed methodology is applied to the modeling of martensitic phase transformations subjected to macroscopic deformation processes. For simplicity, attention is restricted to the linearly geometric, isothermal and isochemical case and quasi-static processes.

INTRODUCTION

Surface layer properties such as the state of eigenstress or the hardness of the material affect the durability and functionality of processed materials to a large extent, but are difficult to predict, in general. On the one hand, this is due to the fact that these properties are determined by microstructural features such as the grain size, distribution or morphology. On the other hand, different processes are characterized by different and complex loading and boundary conditions. Thus, to capture both, a two-scale approach might be considered. Recently, [1] proposed a two-scale and RVE-based computational approach of elastic phase-field- and FFT-based modeling of microstructure evolution and FE-based modeling of structural behavior. In this work, this model is extended to viscoplastic constitutive modeling, texture evolution and macroscopic contact problems.

MATERIAL MODEL FRAMEWORK

The proposed model is two-scale, FE-FFT- and homogenization-based in nature [1, 2]. In what follows, macroscopic quantities are denoted by the index "M", whereas their microscopic counterparts are characterized by no index.

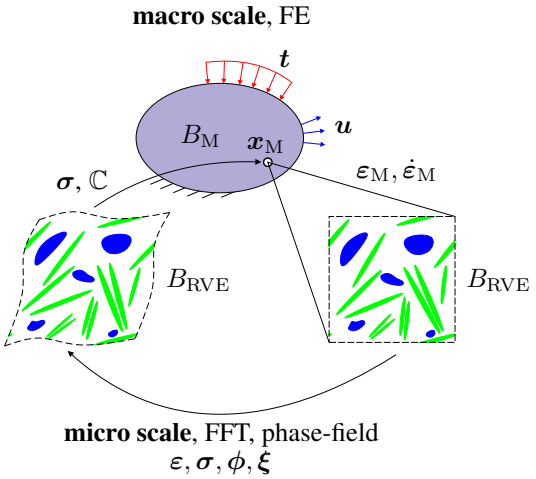

Macroscopic relations and scale separation
Let us introduce the macroscopic strain $\boldsymbol{\varepsilon}_{\mathrm{M}} = \operatorname{sym} \nabla \boldsymbol{u}_{\mathrm{M}}$ and stress $\boldsymbol{\sigma}_{\mathrm{M}}$, which is assumed to fullfill the quasi-static balance of linear momentum $\operatorname{div} \boldsymbol{\sigma}_{\mathrm{M}} = \boldsymbol{0}$ defined at each integration point $\boldsymbol{x}_{\mathrm{M}}$ of the macroscopic structure B_{M} with boundary ∂B_{M}. The constitutive relation is determined by the solution of the microscopic BVP, which is embedded as a RVE $\boldsymbol{x} \in B$ in each $\boldsymbol{x}_{\mathrm{M}} \in B_{\mathrm{M}}$. The handshake between both scales is accomplished through $\boldsymbol{\varepsilon}_{\mathrm{M}} = \frac{1}{V} \int_V \boldsymbol{\varepsilon}(\boldsymbol{x}; \boldsymbol{x}_{\mathrm{M}})\, dV(\boldsymbol{x})$ and $\boldsymbol{\sigma}_{\mathrm{M}} = \frac{1}{V} \int_V \boldsymbol{\sigma}(\boldsymbol{x}; \boldsymbol{x}_{\mathrm{M}})\, dV(\boldsymbol{x})$, respectively. The macroscopic BVP is solved using an implicit reduced FE formulation yielding one integration point per element. The algorithmic tangent operator $\mathbb{C} = \partial_{\boldsymbol{\varepsilon}_{\mathrm{M}}} \boldsymbol{\sigma}_{\mathrm{M}}$, which is required for the linearization procedure, is computed by numerical differentiation.

Microscopic field relations
Consider a heterogeneous microstructure, which is composed of multiple grains $g = 1, \ldots, n_{\mathrm{gr}}$ with orientation $\boldsymbol{R}_g$, (coexisiting) phases $a = 1, \ldots, n_{\mathrm{ph}}$ with residual strains $\boldsymbol{\varepsilon}_{ra}$ and slip systems $s = 1, \ldots, n_{\mathrm{sl}}$ associated with the crystal symmetry of phase a. The local material composition and microstructure evolution is modeled by means of a non-conserved phase-field ϕ and its gradient $\nabla \phi$. The specific form of the Helmholtz free energy density $\psi := \psi(\boldsymbol{\varepsilon}, \phi, \nabla \phi, \boldsymbol{\xi})$ is adapted from [6], where $\boldsymbol{\xi} = \{\gamma, \boldsymbol{\alpha}\}$ represents a set of internal variables associated to plastic slip γ_s and kinematic hardening $\alpha_s = |\gamma_s|$. The quasi-static balance of linear momentum $\operatorname{div} \boldsymbol{\sigma} = \boldsymbol{0}$ and Allen-Cahn equation $\dot{\phi}\, m_\phi^{-1} = \partial_\phi \psi - \operatorname{div}(\partial_{\nabla \phi} \psi)$ form the microscopic BVP in $\boldsymbol{x} \in B$ with periodic boundary conditions for $\boldsymbol{u}$ and ϕ on ∂B. The plastic strain rate $\dot{\boldsymbol{\varepsilon}}_p$ is assumed to take the standard form from crystal plasticity $\dot{\boldsymbol{\varepsilon}}_p = \dot{\gamma}_0 \sum_{s=1}^{n_{\mathrm{sl}}} \boldsymbol{m}_s \left(|\tau_s| / \tau_s^c\right)^p \operatorname{sgn}(\tau_s)$ where $\dot{\gamma}_0, \dot{\gamma}_s, \tau_s^c, p$ and $\boldsymbol{m}_s$ are the normalization factor, shear rate, critical resolved shear stress, rate-sensitivity exponent and symmetric Schmid tensor. The system of microscopic equations is solved in a fully staggered fashion based on FFT-, augmented Lagrangean- and fixed-point methods (e.g., [4]) for viscoplastic polycrystals (e.g., [5]) and implicit time integration in Fourier space.

*Corresponding author. Email: julian.kochmann@rwth-aachen.de

COMPUTATIONAL EXAMPLE

The proposed methodology is applied to the modeling of martensitic phase transformations in polycrystals subjected to a macroscopic indentation process. In each macroscopic integration point a random microstructure with 100 grains of random crystallographic orientations was generated by using DAMASK (www.damask.mpie.de). The model was implemented into the open-source finite element program FEAP (www.ce.berkeley.edu/projects/feap/), the FE-results were visualized using PARAVIEW (www.paraview.org) and the local fields at the RVE-level using OVITO (www.ovito.org). The material parameters were adapted from [3] and [6], respectively.

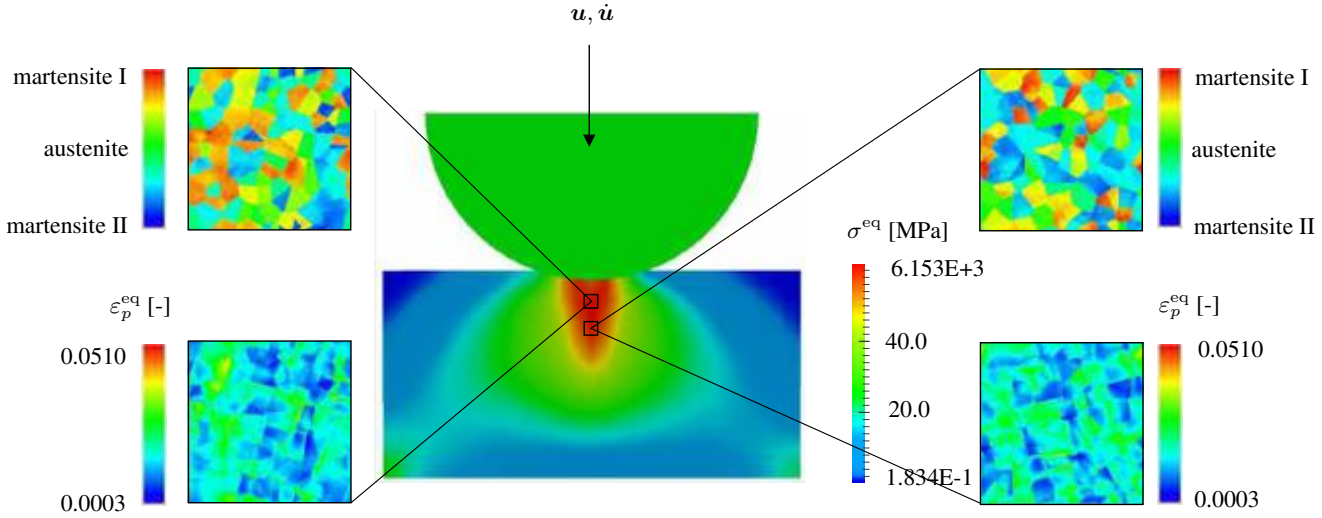

Figure 1: **Indentation problem**: Visualization of volume fraction of retained austenite and plastic strain distribution of different integration points at a different depth with respect to the surface

The von-Mises equivalent stress distribution in the macroscopic structure is visualized in Fig. 1 as well as local fields (phase composition and equivalent plastic strain) of the two elements, which are highlighted in black. With increasing load, shear bands form and the volume fraction of martensite twin variants increases in grains with specific crystallographic orientations. The evolution of martensitic variants is coupled to crystal plasticity based on [6], which captures the inheritance of plastic slip during the phase transformation.

CONCLUSION

The proposed two-scale model represents an efficient alternative to the classical multiscale FE method. Quadratic convergence can be observed at the FE-level for each load step and a high fidelity representation of local fields is possible using FFT- and Green function methods. Compared to FE- and Newton-based solvers, the microscopic FFT-solver requires much more iterations. However, each of these iterations only takes seconds. The proposed methodology captures macroscopic boundary and loading conditions as well as the evolution of the microstructure and texture and microstructural characteristics such as the grain morphology and size. Therefore, the proposed model represents a promising approach to link macroscopic processes to microstructural modifications and surface layer properties. Future development will focus on the identification and quantification of material parameters and the extension to thermo-mechanically coupled processes.

Acknowledgements: Financial support of Subproject M03 of the Transregional Collaborative Research Center SFB/TRR 136 by the German Research Foundation (DFG) is gratefully acknowledged.

References

[1] J. Kochmann, J. Rezai Mianroodi, S. Wulfinghoff, B. Svendsen and S. Reese, CMAME, pp. 89–110 (**305**), 2016.
[2] J. Spahn, H. Andrae, M. Kabel and R. Müller, CMAME, pp. 871–883 (**268**), 2014.
[3] J. Kochmann, S. Wulfinghoff, B. Svendsen and S. Reese, Proceedings of the YIC GACM, 2015.
[4] J. C. Michel, H. Moulinec and P. Suquet, IJNME, pp. 139–160 (**52**), 2001.
[5] R. A. Lebensohn, A. K. Kanjarla and P. Eisenlohr, IJP , pp. 59–69 (**32-33**), 2012.
[6] R. Schmitt, C. Kuhn, R. Müller and K. Bhattacharya, Technische Mechanik, pp. 23–38 (**34**), 2014.

CONTINUUM TRANSPORT OF DISLOCATIONS DURING SHOCK RESPONSE OF CRYSTALS

D.J. Luscher[1a], Jason Mayeur[1], Hashem Mourad[1], Abigail Hunter[2], Mark Kenamond[2]
[1]*Theoretical Division, Los Alamos National Laboratory, Los Alamos, New Mexico, U.S.*
[2]*Computational Physics Division, Los Alamos National Laboratory, Los Alamos, New Mexico, U.S.*

Summary We present a modeling framework that couples continuum dislocation transport, nonlinear thermoelasticity, crystal plasticity, and consistent internal stress and deformation fields to simulate the single-crystal level response of materials to extreme dynamic conditions. Dislocation transport is modeled by enforcing dislocation conservation at a slip-system level through the solution of advection-diffusion equations. The configuration of geometrically necessary dislocation density gives rise to a back-stress that inhibits or accentuates the flow of dislocations. Associated with this internal stress field is an internal strain field. The paper will describe each theoretical component of the framework, key aspects of the constitutive theory, and details of implementation into a 1-D research code and 3-D production hydrocode. Results from single- and poly-crystal plate impact simulations will be discussed in order to highlight the role of dislocation transport and pile-up in shock loading regimes.

OVERVIEW OF MODEL FRAMEWORK

Mesoscale modeling and simulation can provide a physical connection between important microstructural processes (e.g. plasticity, damage nucleation, phase transformation, twinning) occurring under extreme dynamic environments and macroscale models of engineered performance. In the case of polycrystalline materials, this connection can be established via theoretical and numerical mesoscale models of polycrystal response, only if such models include accurate descriptions of the underlying single-crystal physics. In addition, mesoscale simulation results can assist in the interpretation of experimental observations in many cases. Together, mesoscale modeling and experiments with high-resolution diagnostics can inform the development of improved macroscale damage and plasticity models. A predictive modeling capability for phenomena occurring at material interfaces during shock loading of solids demands a proper, physics-based treatment of the fundamentally nonlocal interactions involving dislocations and interfaces.

Our modeling approach is outlined in Figure 1 and explained in more detail in Ref. [1]. Crystal plasticity is modeled as a coupled initial- and boundary-value problem (IBVP), consisting of three sub-problems: deformation momentum balance (DMB), continuum dislocation transport (CDT), and dislocation-deformation compatibility (DDC). The DMB sub-problem reflects classical continuum deformation field theory, with the displacement field as the primary unknown variable. This sub-problem is governed by the principle of conservation of momentum under the applied loading. The CDT sub-problem is governed by conservation laws for the densities of dislocation populations, which are treated as primary field variables. The DDC sub-problem reconciles evolving dislocation fields from CDT with the deformation and stress fields of DMB. Specifically, solving the DDC sub-problem is necessary to identify the internal stress field, and associated strain field, attributed to the distribution of geometrically necessary dislocations in the lattice. The coupling between these sub-problems reflects (i) that plastic deformation (DMB) is accommodated by dislocation motion (CDT), (ii) the redistribution of dislocations (CDT) within a crystalline material is driven by stress (DMB, DDC), and (iii) a net polarity in the dislocation density fields (CDT) gives rise to long-range internal, residual stresses (DDC).

DISLOCATION MOTION UNDER SHOCK LOADING

Simulations of a flyer plate impact experiment are presented in an effort to highlight the intended applicability of the model. In one considered case (cf. Figure 2) a shock wave transits a target specimen driving dislocation motion. Figure 2a depicts the situation in this toy problem. The target plate comprises a bi-crystal with grain boundary aligned perpendicular to the direction of shock wave at the mid-thickness of the specimen. In this case, the grain boundary is assumed to be perfectly impenetrable to dislocation motion. A flyer plate (not shown) impacts the bi-crystal specimen at $t = 0$. A compressive wave travels through the thickness of the specimen until reaching the free surface on the right hand side. At the same time, the flyer plate has separated from the target specimen such that two release waves travel towards each other ultimately interacting to generate a state of large tensile stress nominally aligned with the interface between the two crystals. As the shock wave moves through the material the compressive stress state behind the elastic precursor wave drives dislocation motion. Dislocations of opposite polarity travel in opposite directions on a given slip plane giving rise to an evolving geometrically necessary dislocation (GND) density field depicted in Figure 2b. In this case, the impenetrable (i.e. zero dislocation flux) grain boundary inhibits crystallographic slip in the vicinity of the grain boundary. Other cases considered include restricted, but non-zero dislocation transmission through the boundary in various 1D and 3D simulations of bi-crystal and polycrystal test cases.

[a)] Corresponding author. Email: djl@lanl.gov

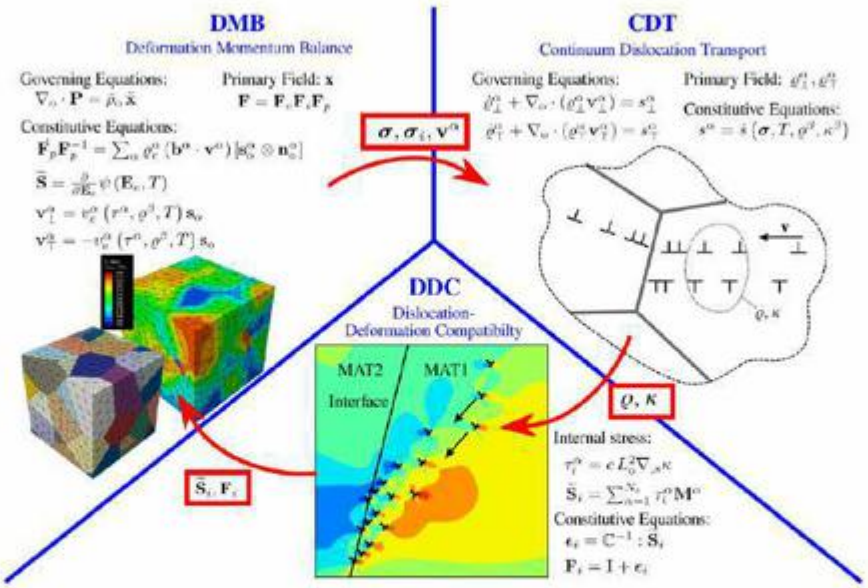

Figure 1. Overview of coupled multi-physics approach for modeling crystal plasticity.

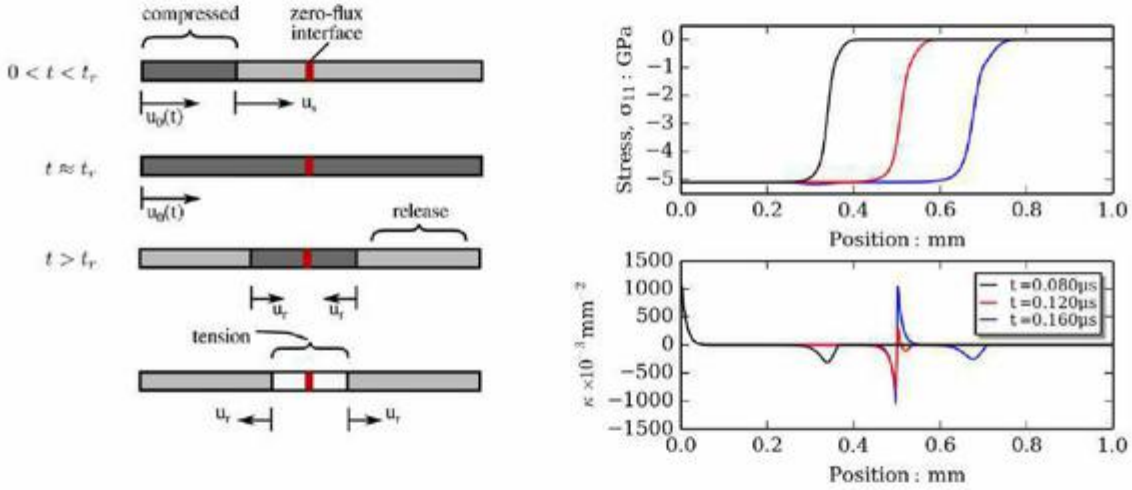

(a) Bi-crystal toy problem (b) axial stress and corresponding GND distribution

Figure 2. Illustration of test problem, i.e. shock transmission through a bi-crystal with grain boundary perfectly impenetrable to dislocation motion. Diagram at left (a) highlights the 1D geometry and sequence of compression and release waves and resulting tensile pulse. Plot at right (b) depicts evolving stress wave and the corresponding distributions of geometrically necessary dislocation density.

CONCLUSIONS

In order to highlight the utility and applicability of the framework developed (cf. Ref. [1]), results from simulations of a toy model problem with interface is presented here. While the selected case is idealized for illustrative purposes, the model parameters used here are generally consistent with the shock loading of single crystal copper along a [100] surface normal. We believe the theoretical framework and modeling approach presented here will prove instrumental for simulating the effects of interfaces within single- and poly-crystals subjected to shock and impact loading. We have demonstrated the approach for plane wave impact loading of single crystals and bi-crystals. The extension to polycrystals is conceptually straightforward and the approach enables direct introduction of interfacial constitutive relations or boundary conditions via the dislocation velocity and source models that can depend upon interface characteristics, which, in general, may evolve throughout the solution. While recent results highlighting these aspects are omitted here for brevity, they are included in the accompanying presentation.

References

[1] Luscher D.J., Mayeur J.R., Mourad H.M., Hunter A., Kenamond M.A., Coupling continuum dislocation transport with crystal plasticity for application to shock loading conditions. *I. J. Plasticity. 76*:111-129, 2016.

INVESTIGATION OF SINGLE CRYSTAL DEFORMATION WITH CONTINUUM DISLOCATION DYNAMICS

Navid Kermanshahimonfared[1], Ioannis Mastorakos[1a)] & Hussein Zbib[2]
[1] *Department of Mechanical & Aeronautical Engineering, Clarkson University, Potsdam, New York, USA*
[2] *School of Mechanical and Materials Engineering, Washington State University, Pullman, Washington, USA*

Summary Continuum dislocation dynamics (CDD) is a method to predict the behavior of material under load. In this study CDD is used to find dislocation density in desired domain. By pairing CDD with Orowan constitutive law, the shear strain rate under unidirectional load is investigated and the plastic strain rate is obtained. Then, the plastic strain rate is used to calculate and plot the Stress – Strain relation.

INTRODUCTION

The goal of this study is to predict the plastic behavior of crystals based on a continuum dynamic (CDD) dislocation method. The CCD is used to find the Stress – Strain curve and using these data in crystal plastic model. Most of previous works in this area have been done for only a single crystal by using discrete dynamic dislocation method (DDD) [1]. The DDD framework uses molecular dynamics to simulate the dislocation behavior so it can be using for small grain.

METHOD

The CDD method uses crystal plasticity to predict the behavior of grains. In this technique, stress could be found by evaluating shear strain rate. The constitutive law for shear strain rate could be found by using Orowan relation [2].

$$\dot{\gamma}^{(\alpha)} = \rho_M^{(\alpha)} b V_g^{(\alpha)} \tag{1}$$

Where $\rho_M^{(\alpha)}$ is the mobile dislocation density of slip system α, b is the Burgers vector and $V_g^{(\alpha)}$ is the glide velocity in respective slip system. The glide velocity is expressed by a power law function based on $\tau^{(\alpha)}$ resolved shear stress and $\tau_0^{(\alpha)}$ slip resistance of the slip system α [3]. The slip resistance of slip system α, $\tau_0^{(\alpha)}$, is a combination of reference resistance τ_0 from internal friction and hardening resistance $\tau_{dh}^{(\alpha)}$. The reference resistance can be obtained from experimental data. The hardening resistance is due to slip resistance between dislocations on different slip systems. It is function of interaction matrix $\Omega^{(\alpha)(m)}$, Burgers vector b, shear modulus μ, dislocation densities and Baily – Hirsch factor α [4].

In CDD, the evolution of mobile dislocation density (both positive and negative) is composed of eight terms with different physical meaning [3]. The first is term is dislocation flux term and it is responsible for the moving of dislocation in the direction of glide velocity. The second mechanism is production, growth and multiplication of mobile dislocation in each slip system. The third term shows the annihilation of two mobile dislocations with opposite Burgers vector. The fourth mechanism is formation of locks. This mechanism happens when any type of mobile dislocation turns into immobile dislocation due to interaction between dislocations. The fifth mechanism describes the mobilization of immobile dislocation due to breakup of junctions or dipoles. The fifth term will activated at a critical stress condition. This means the immobile dislocation starts to move if resolved shear stress is larger than critical stress. The sixth mechanism is about cross slip. Cross slip means that dislocation starts to move on some slip system then jumps or glide into another slip system. This phenomenon is stochastics and depends on temperature. The seventh term is annihilation between mobile and immobile dislocation. The eighth term is dipole formation. By adding all of these mechanisms together, the evolution rate of dislocation is

$$\dot{\rho}_+^{(\alpha)} = V_g^{(\alpha)} \nabla_x \rho_+^{(\alpha)} + (\alpha_1 - \alpha_3) \frac{V_g^{(\alpha)}}{l} \rho_+^{(\alpha)} - 2(\alpha_2 + \alpha_7) R_c V_g^{(\alpha)} \rho_+^{(\alpha)} \rho_-^{(\alpha)} + \alpha_4 \frac{V_g^{(\alpha)}}{l} \left(\frac{|\tau^{(\alpha)}|}{\tau^*} \right)^r \rho_I^{(\alpha)} + \alpha_5 \sum_\beta^N p^{(\alpha)(\beta)} \rho_+^{(\alpha)} V_g^{(\alpha)} - \alpha_6 R_c^3 V_g^{(\alpha)} \rho_I^{(\alpha)^2} \rho_+^{(\alpha)} \tag{2a}$$

$$\dot{\rho}_-^{(\alpha)} = -V_g^{(\alpha)} \nabla_x \rho_-^{(\alpha)} + (\alpha_1 - \alpha_3) \frac{V_g^{(\alpha)}}{l} \rho_-^{(\alpha)} - 2(\alpha_2 + \alpha_7) R_c V_g^{(\alpha)} \rho_-^{(\alpha)} \rho_+^{(\alpha)} + \alpha_4 \frac{V_g^{(\alpha)}}{l} \left(\frac{|\tau^{(\alpha)}|}{\tau^*} \right)^r \rho_I^{(\alpha)} + \alpha_5 \sum_\beta^N p^{(\alpha)(\beta)} \rho_-^{(\alpha)} V_g^{(\alpha)} - \alpha_6 R_c^3 V_g^{(\alpha)} \rho_I^{(\alpha)^2} \rho_-^{(\alpha)} \tag{2b}$$

$$\dot{\rho}_I^{(\alpha)} = \alpha_3 \frac{V_g^{(\alpha)}}{l} \left(\rho_+^{(\alpha)} + \rho_-^{(\alpha)} \right) - 2\alpha_4 \frac{V_g^{(\alpha)}}{l} \left(\frac{|\tau^{(\alpha)}|}{\tau^*} \right)^r \rho_I^{(\alpha)} + \alpha_6 R_c^3 V_g^{(\alpha)} \rho_I^{(\alpha)^2} \left(\rho_+^{(\alpha)} + \rho_-^{(\alpha)} \right) + 4\alpha_7 R_c V_g^{(\alpha)} \rho_+^{(\alpha)} \rho_-^{(\alpha)} \tag{2c}$$

[a)] Corresponding author. Email: imastora@clarkson.edu

The first equation indicates the positive mobile dislocation; second on shows the negative mobile dislocation and third equation is immobile dislocation rate equation. By solving above system of equation one could find dynamic dislocation and using these results help we to obtain the shear strain rate.

RESULTS AND DISCUSSION

In order to find the dislocation densities a first order forward time scheme is chosen and for space gradient a central difference method is implemented. After discretizing the equation, a structured mesh grid is generated. In this study, we assumed that the grains are cubic. The only thing is left to do is evaluating each terms at every nodes then obtaining shear strain rate and plastic strain rate and finally updating stress at each time step. After calculating stress at each time step, the Stress – Strain curve will be plotted. Periodic function was chosen for initial conditions for each equation. In this research, the crystal type is fcc (so slip system is also known) and all of the properties are in table 1. The grid resolution is $1^{\mu m}$. In this study a fixed boundary is chosen on all boundaries.

Figure 1a shows the initial condition of positive mobile dislocation that is used in this case. Figure 1b illustrates the contour plot of positive mobile dislocation densities when the strain rate reaches to 0.5. This shows some band is forming. This band shows that the dislocations are trying to make some group. Figure 1c exhibits the Stress – Strain curve for this plot. The first segment of this plot is elastic relation between stress and strain. In this region the glide velocity of dislocations is zero which means that dislocation are not moving in any direction; in this region dislocations are only growing or annihilating. After yielding point, dislocation start to move and plastic strain rate is not zero any more. The fluctuations in this curve are due to numerical error and they could be diminishing by picking smaller time step which is a tradeoff between accuracy and speed of simulation.

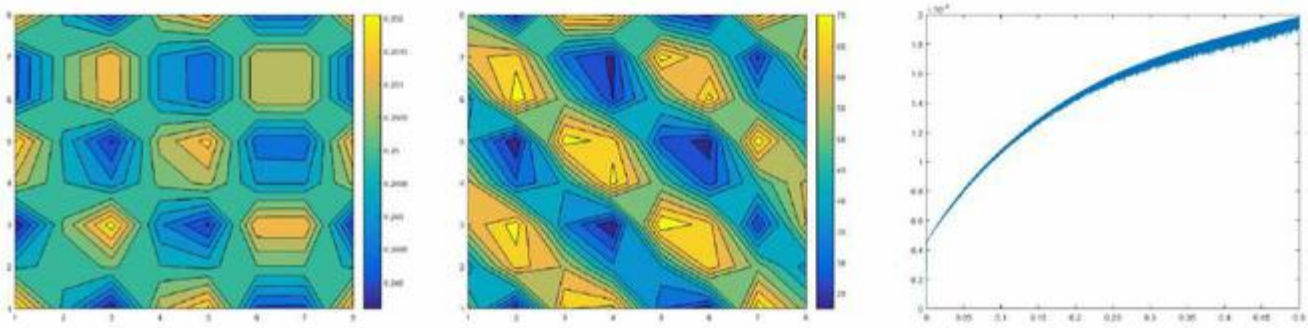

(a) (b) (c)

Figure 1: (a) Periodic initial condition of positive mobile dislocation, (b) Positive mobile dislocation distribution after 50 % strain, (c) Stress – Strain curve

CONCLUSIONS

The purpose of this study is to predict the plastic behavior of single crystal based on continuum dislocation dynamic (CDD) and plotting Stress – Strain relation. At first CDD model and significant mechanism were introduced. In next step, the evolution rate equations were numerically solved for different cases. By investigating the result for different cases it is concluded that regardless of initial condition, the Stress – Strain curve remains unchanged. Time step plays great role on accuracy.

Reference

[1] Zbib H., Rhee M., Hirth J.P., On plastic deformation and the dynamics of 3D dislocations. International Journal of mechanical Science 40, 113- 127, 1998.

[2] Orowan E., Problems of plastic gliding. Proceedings of the physical society 52, 8, 1940

[3] Li D., Zbib H., Sun X., Khaleel M., Predicting plastic flow and irradiation hardening of iron single crystal with mechanism – based continuum dislocation dynamics. International Journal of Plasticity 52. 3 – 17, 2014.

[4] Ohashi T., Numerical modeling of plastic multislip in metal crystal of fcc type. Philosophical magazine A – physics of condensed matter structure defects and mechanics properties 70, 793 – 803, 1994.

MODEL REDUCTION FOR COMPOSITE MATERIALS AND POLYCRYSTALS

Pierre Suquet *[1], Rodrigue Largenton[2], and Jean-Claude Michel[1]

[1] *Laboratoire de Mécanique et d'Acoustique, CNRS, Marseille, France.*
[2] *MMC, EDF R&D Site des Renardières, Avenue des Renardières, 77818 Moret sur Loing, France*

Summary The present study is devoted to the generalization of the Nonuniform Transformation Field Analysis (NTFA), a model-reduction approach introduced by the authors. First, the local fields of internal variables are decomposed on a reduced basis of modes. Second, the dissipation potential of the phases is replaced by its tangent second-order (TSO) expansion. The reduced evolution equations of the model can be entirely expressed in terms of quantities which are pre-computed once for all.

REDUCED-ORDER MODELS

A common engineering practice in the analysis of composite (or polycrystalline) structures is to use *effective* or *homogenized* material properties instead of taking into account all details of the individual phase properties. Unfortunately when the individual constituents are nonlinear, the exact description of the effective constitutive relations requires the determination of the local fields (at the microscopic scale). For structural computations, the consequence of this theoretical result is that the two levels of computation, the level of the structure and the level of the unit-cell, remain intimately coupled. The nested resolution of these coupled problems (known as FE^2 analysis) is so far limited by their formidable size.

It is therefore quite natural to resort to *model-reduction techniques* achieving a compromise between analytical approaches, which are costless but often very limited by nonlinearity, and full-field simulations which resolve all complex details of the exact solutions, but come at a very high cost.

Individual constituents

The composite materials considered in this study are comprised of individual constituents undergoing partly reversible and partly irreversible transformations modelled by a finite number of *internal variables* $\boldsymbol{\alpha}$. It is further assumed that the stress derives from a *free-energy* function $w(\boldsymbol{\varepsilon}, \boldsymbol{\alpha})$ and that the evolution of the variables $\boldsymbol{\alpha}$ is governed by the driving forces $\boldsymbol{\mathcal{A}}$ associated with $\boldsymbol{\alpha}$. It is often the case (but not always) that this last relation can be expressed with the help of a dissipation potential φ and the constitutive relations take the compact form,

$$\boldsymbol{\sigma} = \frac{\partial w}{\partial \boldsymbol{\varepsilon}}(\boldsymbol{\varepsilon}, \boldsymbol{\alpha}), \quad \frac{\partial w}{\partial \boldsymbol{\alpha}}(\boldsymbol{\varepsilon}, \boldsymbol{\alpha}) + \frac{\partial \varphi}{\partial \dot{\boldsymbol{\alpha}}}(\dot{\boldsymbol{\alpha}}) = 0. \tag{1}$$

Composites and polycrystals

A representative volume element (r.v.e.) V of the composite is comprised of phases occupying domains $V^{(r)}$. The spatial averaging over V is denoted by $\langle . \rangle$. Each individual phase is governed by the above differential equation with potentials $w^{(r)}$ and $\varphi^{(r)}$ in $V^{(r)}$. The r.v.e. V is subjected to a path of macroscopic strain $\overline{\boldsymbol{\varepsilon}}(t)$ and periodicity conditions are assumed on ∂V. The local problem to be solved to determine the local fields $\boldsymbol{\sigma}(\boldsymbol{x}, t)$, $\boldsymbol{\varepsilon}(\boldsymbol{x}, t)$ and $\boldsymbol{\alpha}(\boldsymbol{x}, t)$ consists of a generalized thermoelastic problem, in which the field of internal variables $\boldsymbol{\alpha}(\boldsymbol{x})$ is fixed, coupled with the differential equation (1) at every point $\boldsymbol{x}$ in the volume element. The *homogenized* (or effective) response of the composite along this path $\{\overline{\boldsymbol{\varepsilon}}(t), t \in [0, T]\}$ is the history of average stress $\{\overline{\boldsymbol{\sigma}}(t), t \in [0, T]\}$ where $\overline{\boldsymbol{\sigma}}(t) = \langle \boldsymbol{\sigma}(\boldsymbol{x}, t) \rangle$.

Nonuniform Transformation Field Analysis (NTFA)

In order to avoid the full-field resolution of the local problem, Michel and Suquet ([1, 2, 5]) have introduced a decomposition of the fields of internal variables on a finite set of pre-determined shape functions (NTFA decomposition) $\boldsymbol{\alpha}(\boldsymbol{x}, t) = \sum_{k=1}^{M} \xi^{(k)}(t)\, \boldsymbol{\mu}^{(k)}(\boldsymbol{x})$, where the fields $\boldsymbol{\mu}^{(k)}(\boldsymbol{x})$ are the *modes* and the $\xi^{(k)}$ are the *reduced variables*. It can then be shown that the overall response of the composite is governed by two potentials

$$\overline{\boldsymbol{\sigma}} = \frac{\partial \widetilde{w}}{\partial \overline{\boldsymbol{\varepsilon}}}(\overline{\boldsymbol{\varepsilon}}, \boldsymbol{\xi}), \quad \frac{\partial \widetilde{w}}{\partial \boldsymbol{\xi}}(\overline{\boldsymbol{\varepsilon}}, \boldsymbol{\xi}) + \frac{\partial \widetilde{\varphi}}{\partial \dot{\boldsymbol{\xi}}}(\dot{\boldsymbol{\xi}}) = 0, \quad \widetilde{w}(\overline{\boldsymbol{\varepsilon}}, \boldsymbol{\xi}) = \inf_{\langle \boldsymbol{\varepsilon} \rangle = \overline{\boldsymbol{\varepsilon}}} \langle w(\boldsymbol{\varepsilon}, \boldsymbol{\alpha}) \rangle, \quad \widetilde{\varphi}(\dot{\boldsymbol{\xi}}) = \langle \varphi(\dot{\boldsymbol{\alpha}}) \rangle, \tag{2}$$

where $\boldsymbol{\alpha}$ is given by the NTFA decomposition. In many cases of interest, the effective free-energy $\widetilde{w}$ can be expressed in terms of pre-computed quantities and the difficulty lies in the evaluation of the effective dissipation potential $\widetilde{\varphi}$ in terms of $\dot{\boldsymbol{\xi}}$ without computing "on-line" the local fields $\dot{\boldsymbol{\alpha}}$.

*Corresponding author. Email: suquet@lma.cnrs-mrs.fr

VISCOELASTIC PHASES AND TANGENT SECOND-ORDER LINEARIZATION (TSO)

When the individual phases are linear viscoelastic and Maxwellian, the only internal variable is the viscous strain $\boldsymbol{\alpha} = \boldsymbol{\varepsilon}_{\mathsf{v}}$ and the dissipation potential for the individual phases is $\varphi\ \boldsymbol{\alpha}) = (1/2)\dot{\boldsymbol{\alpha}} : \boldsymbol{L}_{\mathsf{v}} : \dot{\boldsymbol{\alpha}}$. Largenton *et al* [4] have shown that φ can be obtained explicitly as $\varphi(\boldsymbol{\xi}) = (1/2)\boldsymbol{\xi}.\boldsymbol{\mathcal{L}}_{\mathsf{v}}.\boldsymbol{\xi}$, where the effective viscosity tensor $\mathcal{L}_{\mathsf{v}}^{(k\ell)} = \langle \boldsymbol{\mu}^{(k)} : \boldsymbol{L}_{\mathsf{v}} : \boldsymbol{\mu}^{(\ell)} \rangle$ can be pre-computed "off-line".

When the constituents are nonlinear the hybrid formulation of [3] (although not rigorously equivalent to the exact formulation (2)) is used. An additional (and essential) step is achieved by replacing the force potential ψ dual of φ by its second-order expansion in each individual phases ([5]). This linearization permits to reduce the problem to an homogenization problem for a composite with linear viscoelastic phases.

SAMPLE EXAMPLES

Three-phase linear viscoelastic composites

Mixed oxide (a nuclear fuel) can be modelled as a three-phase composite composed of three linear viscoelastic phases. The modes are generated by the snapshot Proper Orthogonal Decomposition along a few learning loading paths. The reduced model is validated by comparison with full-field simulations along validation paths, different from the learning paths. The agreement is seen to be excellent (figure 1b). The speed-up is in the order of 10^4.

Creep of polycrystalline ice

Ice, as a single crystal, is an hexagonal material. A crystal plasticity model for ice has been proposed in [6]. The above reduced model has been applied to the simulation of creep tests on polycrystals of ice and compared with full-field simulations and experiments. The agreement is seen to be quite satisfactory (figure 1d). The speed-up is in the order of 10^2.

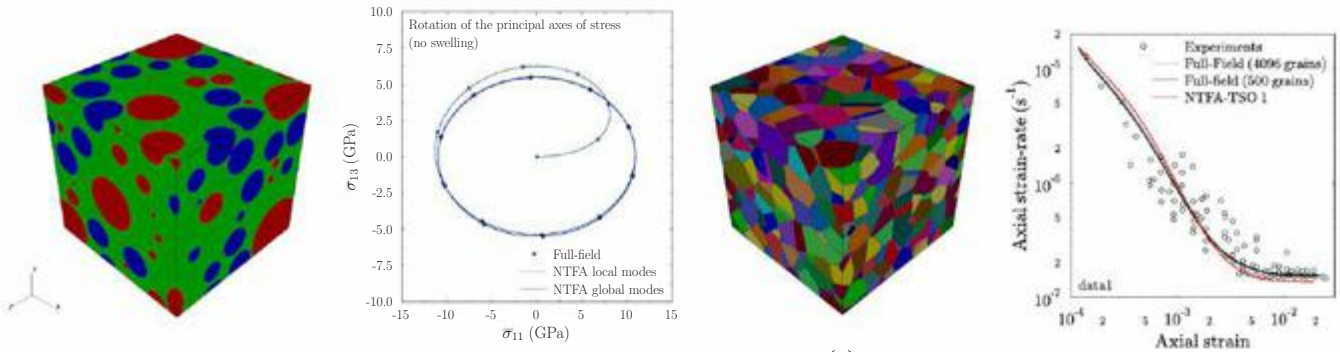

(a) (b) (c) (d)

Figure 1: *Sample examples. (a) and (b): Three-phase composite comprised of two inclusion phases (red, blue) dispersed in a matrix phase (green). (a): configuration. (b) Reduced model vs full-field simulations along a validation path including rotation of the principal axes of macroscopic stress. (c) and (d) Polycrystalline ice. (c): configuration used in the full-field simulations. (d) Creep test. Reduced model vs full-field simulations and experiments.*

References

[1] Michel, J.C., Suquet, P., 2003. Nonuniform Transformation Field Analysis. Int. J. Solids Structures **40**, 6937–6955.

[2] Michel, J.C., Suquet, P., 2004. Computational analysis of nonlinear composite structures using the Nonuniform Transformation Field Analysis. Comput. Meth. Appl. Mech. Engrg. **193**, 5477–5502.

[3] Fritzen, F., Leuschner, M., 2013. Reduced basis hybrid computational homogenization based on a mixed incremental formulation. Comput. Methods Appl. Mech. Engrg. 260, 143–154.

[4] R. Largenton, J.C. Michel, and P. Suquet, 2014. Extension of the nonuniform transformation field analysis to linear viscoelastic composites in the presence of aging and swelling. Mechanics of Materials, **73**, 76–100.

[5] Michel, J.C., Suquet, P., 2015. A model-reduction approach to the micromechanical analysis of polycrystalline materials. *Comput. Mech.* Accepted for publication.

[6] P. Suquet, H. Moulinec, O. Castelnau, N. Lahellec, M. Montagnat, F. Grennerat, P. Duval, and R. Brenner, 2012. Multi-scale modeling of the mechanical behavior of polycrystalline ice under transient creep. *Procedia IUTAM*, **3**, 76–90.

MULTISCALE MODELLING OF CARBON NANOTUBE–REINFORCED POLYMER COMPOSITES

A. R. Alian, S. I. Kundalwal & S. A. Meguid[a)]
MADL, Department of Mechanical and Industrial Engineering, University of Toronto, Toronto, Ontario, Canada

Abstract In this article, a multiscale modelling that combines molecular dynamics (MD) with micromechanics and homogenisation techniques was developed to determine the effect of carbon nanotube's (CNT) waviness and agglomeration on the bulk properties of CNT-reinforced thermoset composites. MD simulations were first conducted to determine the effective elastic modulus at the nanoscopic level using a constant-strain energy minimization technique. To account for the marked discrepancy in the literature between existing modelling predictions and experimental findings, CNTs of different curvatures and bundle sizes were appropriately considered in our simulations. To scale up the elastic properties to the microscopic level, micromechanics approach of the Mori-Tanaka type was then used. The predictions of the current multiscale model are in good agreement with existing experimental findings indicating that waviness and agglomeration of CNTs limit their reinforcement effect and thus explain the reasons for the marked discrepancy between existing grossly idealised models and the experimental findings.

INTRODUCTION

Owing to their remarkable mechanical and physical properties, a few weight percentages of CNTs can significantly improve the mechanical, electrical, and thermal properties of CNT-reinforced polymer composites [1-4]. The presence of CNT agglomerates limits the reinforcement effect of the CNTs due to their slippage within the bundle [2]. This slippage limits the stress transfer between the CNTs within the bundle as well as between the CNTs and the surrounding polymer matrix [2]. Due to their extremely high aspect ratio and very low bending stiffness, CNTs tend to curve when dispersed in polymer matrices, resulting in a nanocomposite with properties that vary significantly in different directions [1]. Earlier models that considered polymer nanocomposites reinforced with isolated well-dispersed straight CNTs predicted mechanical properties that are much higher than the experimental measurements [2, 3]. To overcome these simplified models, we developed a multiscale model, based on molecular dynamics simulations and micromechanical modeling techniques, to evaluate the effect of CNT waviness and agglomeration on the elastic properties of CNT-polymer nanocomposites. First, MD simulations of a wavy CNT embedded in an epoxy matrix was conducted to determine the effective elastic moduli at the nanoscale level. Then, Mori-Tanaka micromechanical technique was used to scale up the nanoscale properties to the microscale level. The obtained numerical results were validated with recently obtained experimental findings. Our results reveal the detrimental effects of CNTs waviness and agglomeration on bulk properties.

MULTISCALE MODELING

All MD simulations were conducted with large-scale atomic/molecular massively parallel simulator (LAMMPS). Interactions between the CNT and the polymer molecules were nonbonded interactions that originate from the van der Waals (vdW) and electrostatic forces. Epoxy matrix based on DGEBA resin and TETA curing agent was used in the current study. The properties of the neat epoxy were taken from our earlier study [2]. MD simulations were conducted for RVEs reinforced with either well dispersed or agglomerated wavy CNTs of different waviness (curvatures). To study the effect of CNT waviness, CNTs were considered to have a sinusoidal shape; as defined by:

$$y = \mathrm{a}\cos\left(\frac{\pi z}{2\lambda}\right) with\ z \in [0,\lambda] \tag{1}$$

where a and λ are the amplitude and the quarter wavelength of the wavy CNT, respectively. The parameter α=a/λ is used as a shape parameter that defines the degree of curvature of the CNT. Seven curved single wall CNTs were generated and equilibrated before using them as reinforcements in the RVE of the nanocomposites. Armchair (5, 5) CNTs of length 256 Å were considered for all the simulations. The combined influence of CNT waviness and agglomeration was examined by considering RVEs reinforced with individual and agglomerated bundles of wavy CNTs, as shown in Fig. 1. Curved CNTs have reinforcement effects on both the chord and the transverse directions. Therefore, in order to determine the properties of a nanocomposite reinforced with wavy CNTs, the RVEs were assumed to be orthotropic. Accordingly, nine independent material constants are required to fully define the elastic stiffness matrix of the RVE. A series of MD simulations were carried out to determine the elastic moduli of the RVEs using the constant-strain energy minimization method. Predefined displacements were applied on the MD unit cell and the obtained viral stress tensor was then used to determine its effective stiffness constants. The averaged stress tensor of the MD unit cell was defined in the form of a virial stress [2]; as follows:

$$\sigma = \frac{1}{V}\sum_{i=1}^{N}\left(\frac{m_i}{2}v_i^{\,2} + F_i\, r_i\right) \tag{2}$$

[a)] Corresponding author. Email: meguid@mie.utoronto.ca.

where V is the volume of the RVE; v_i, m_i, r_i and F_i are the velocity, mass, position and force acting on the ith atom, respectively. The obtained stiffness tensors of the RVEs from the MD simulations were then used as an input to the micromechanical model to aid in the determination of the bulk properties.

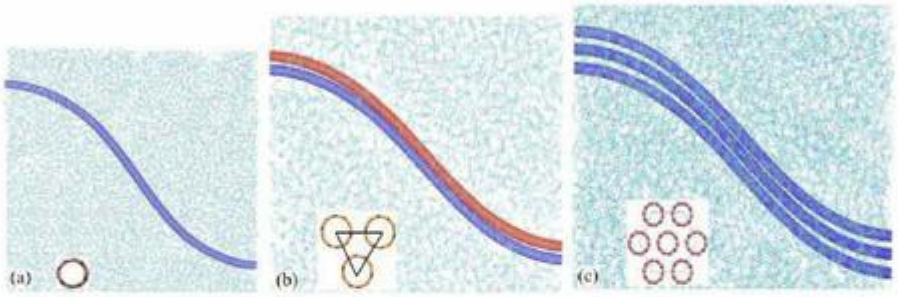

Fig. 1. MD unit cells representing RVEs reinforced with (a) single CNT (α=0.54), (b) bundle of three CNTs (α=0.54), and (c) bundle of seven CNTs (α=0.54).

RESULTS AND DISCUSSION

Figure 2(a) shows the predicted variation of Young's modulus of nanocomposites reinforced with randomly oriented wavy CNTs. The model predicts that the bulk elastic properties of the nanocomposite are reduced significantly with increasing the CNT curvature. However, the effect of waviness stabilizes after α=0.75, due to a reduction in the longitudinal and the simultaneous increase in the transverse elastic constants of the effective fiber upon reaching this curvature. Figure 2(b) shows the variation of the effective Young's modulus of the nanocomposite with the CNT loading for the three agglomeration cases, the well-dispersed straight case, and the experimental results for a similar nanocomposite system obtained from the literature [4]. The results indicate that the CNT agglomeration has a significant effect on the bulk elastic properties of the nanocomposite and this effect increases with the increase in the number of CNTs in the bundle.

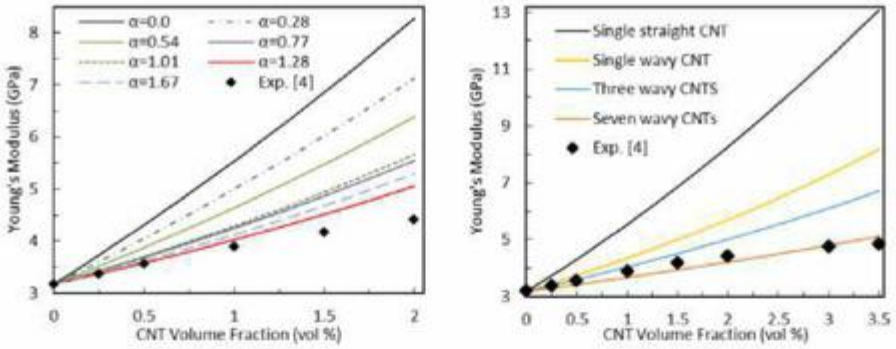

(a) (b)

Fig. 2. Effect of CNT (a) waviness and (b) agglomeration on the bulk Young's modulus of CNT-epoxy composites.

CONCLUSIONS

We developed a multiscale model to determine the effect of CNT waviness and agglomeration on the bulk elastic properties of CNT-reinforced epoxy composites. The results show good agreement between the developed model and the reported experimental results; thus validating the modeling procedures developed in this study and emphasizing the importance of the inclusion of CNT waviness and agglomeration in future models.

ACKNOWLEDGEMENT: This work was supported by the Natural Sciences and Engineering Research Council of Canada (NSERC) and the Discovery Accelerated Supplement of NSERC.

References

[1] Dastgerdi J.N., Marquis G., Salimi M.: Micromechanical modeling of nanocomposites considering debonding and waviness of reinforcements. *Compos. Struct.* **110**, 1–6, 2014.

[2] Alian A.R., Kundalwal S.I., Meguid, S.A.: Multiscale modeling of carbon nanotube epoxy composites. *Polymer* **70**, 149–160, 2015.

[3] Wernik J.M., Meguid S.A.: Multiscale micromechanical modeling of the constitutive response of carbon nanotube–reinforced structural adhesives. *International Journal of Solids and Structures* **51**, 2575–2589, 2014.

[4] Omidi M., Rokni D.T.H., Milani A.S., Seethaler R.J., Arasteh R.: Prediction of the mechanical characteristics of multi-walled carbon nanotube/epoxy composites using a new form of the rule of mixtures. *Carbon* **48**, 3218–3228, 2010.

MODELLING MICROSTRUCTURE EVOLUTION IN SPD PROCESSES IN THE FRAMEWORK OF CRYSTAL PLASTICITY THEORY

Karol Frydrych* and Katarzyna Kowalczyk-Gajewska

Institute of Fundamental Technological Research, Polish Academy of Sciences, Warsaw, Poland

Summary Grain refinement and texture evolution has been analysed using two modelling approaches, namely the three-scale crystal plasticity model and the crystal plasticity finite element method. The first approach combines the Taylor iso-strain model and the visco-plastic self-consistent (VPSC) model. The second approach consists in embedding crystal plasticity constitutive equations at each integration point of the finite element mesh.

STATE OF THE ART

Modelling of texture evolution and grain refinement is currently a subject of intensive research. The evolution of crystallographic texture can be captured using mean-field models such as Taylor or VPSC [1] models. However, such approaches are unable to predict grain refinement. Therefore these classical formulations are enhanced by some addittional features. Although the developed proposals are usually physically motivated, they still do not reproduce this phenomenon sufficiently well and/or are very computationally expensive. Some potential for modelling both phenomena lies in the use of the crystal plasticity finite element method (CPFEM). Modelling twinning, which seems very important in grain refinement of many metals and alloys, is also at the stage of development. Two models presented below are developed in order to propose efficient and reliable tools for modelling the microstructure evolution of metals and alloys in severe plastic deformation (SPD) processes.

MODELLING APPROACH

The Three Scale Crystal Plasticity model

In the mean-field Three Scale Crystal Plasticity (3SCP) model [2], there are three levels, namely the macroscale level, the upper microscale level and the lower microscale level. The lowest level corresponds to a part of a grain (a cell block) with initially slightly different orientation than the nominal parent grain orientation. The parent grain is an aggregate of such cell blocks and the interactions between blocks are managed through the VPSC model. The macroscale level represents the representative volume element RVE, which is the material point of the deformed sample. The current deformation gradient is applied to the RVE and the material response is analysed assuming relevant crystal plasticity framework at the lowest level.

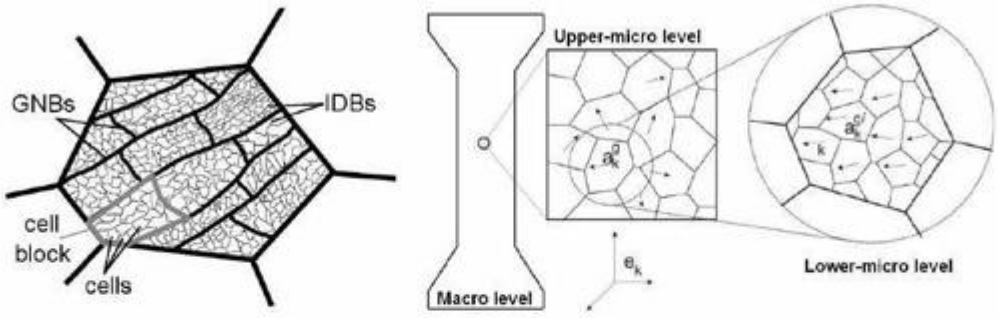

Figure 1: a) The basis for the idea of the 3SCP model - the schematic drawing of the dislocation induced cell substructure of a grain observed in fcc materials for small to medium accumulated plastic strain. b) Its representation by a three-scale model, cf. [2].

The Crystal Plasticity Finite Element Method

The CPFEM is now well established tool to model the material behaviour at various scales and in application to diverse processes, cf. e.g. the monograph by Roters et al. [3]. In the presented research twinning has been incorporated in the existing CPFEM procedures on the basis of the Probabilistic Twin Volume Consistent (PTVC) scheme [4]. The developed numerical model is applied to analysis of the SPD processes. By modelling a given polycrystal grain by a number of finite elements it is straightforward to account for in-grain strain inhomogeneities and the resulting grain refinement.

*Corresponding author. Email: kfryd@ippt.pan.pl

RESULTS

Results of simulations using the two abovementioned modelling approaches will be compared with each other. Their validity in view of the available experimental data will be discussed. Figure 2 shows some preliminary results obtained using the two models.

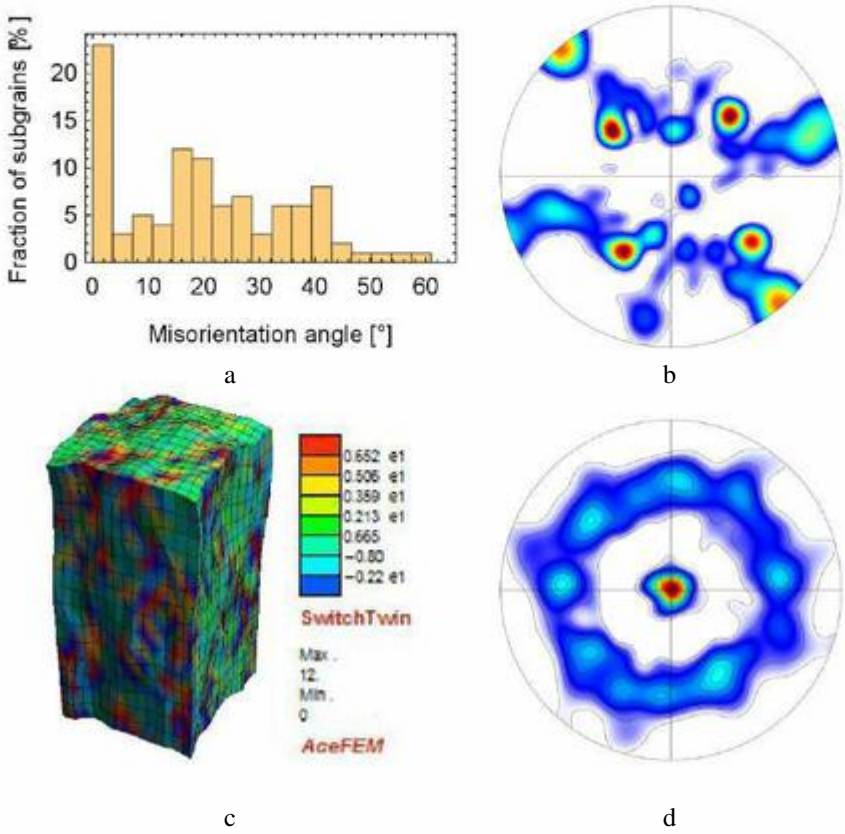

Figure 2: Preliminary results obtained with the use of both modelling approaches. a) Misorientation angle distribution and b) (111) pole figure in the fcc metal subjected to simple shear in 3SCP simulation of ECAP process for polycrystalline aggregate composed of 100x100 orientations with random initial texture. c) Deformed mesh with twinned domains and d) {111} pole figure obtained from the CPFEM simulation of the Hadfield steel subjected to uniaxial tension with periodic boundary conditions for a polycrystalline aggregate composed of 125 grains with random initial texture. The PTVC reorientation procedure was applied in c and d. Pole figures graphics by JTEX - Software for Texture Analysis, J.J. Fundenberger, B, Beausir. Universite de Lorraine - Metz 2015.

ACKNOWLEDGEMENT

The research is partially supported by the project of the National Science Center (NCN) 2013/09/B/ST8/03320.

References

[1] R. A. Lebensohn and C. N. Tomé. A self-consistent anisotropic approach for the simulation of plastic deformation and texture development of polycrystals: Application to zirconium alloys. *Acta Metall. Mater.*, 41:2611–2624, 1993.

[2] K. Frydrych and K. Kowalczyk-Gajewska. A three-scale crystal plasticity model accounting for grain refinement in fcc metals subjected to severe plastic deformations (submitted to Mater. Sci. Eng. A). 2016.

[3] F. Roters, P. Eisenlohr, and T. R. Bieler nad D. Raabe. *Crystal Plasticity Finite Element Methods*. WILEY-VCH Verlag GmbH & Co. KGaA, Weinheim, 2010.

[4] K. Kowalczyk-Gajewska. Micromechanical modelling of metals and alloys of high specific strength. *IFTR Reports 1/2011*, pages 1–299, 2011.

PIEZOELECTRIC AND DIELECTRIC PROPERTIES OF BARIUM TITANATE POLYCRYSTALS

Fumio Narita[1a], Takuya Kobayashi [1] & Yasuhide Shindo [2]
[1]*School of Engineering, Tohoku University, Sendai, Miyagi, Japan*
[2]*Tohoku. Polytechnic College, Kurihara, Miyagi, Japan*

Summary This work deals with the electromechanical problems of poled barium titanate ($BaTiO_3$) polycrystals with oxygen vacancies. A phase field model is developed for ferroelectric polycrystals, coupled with the time-dependent Ginzburg-Landau theory and the oxygen vacancies diffusion, to demonstrate the interaction between oxygen vacancies and domain evolutions. To generate grain structures, the phase field model for grain growth is also used. The strain vs stress curve and strain vs electric field curve are calculated, and the effects of grain size and oxygen vacancy density on the piezoelectric and dielectric properties of the $BaTiO_3$ polycrystals are discussed.

INTRODUCTION

Piezoelectric materials have been recognized for their potential utility in energy harvesters[1)]. In particular, lead zirconate titanate (PZT) materials are candidates for use as piezoelectric devices such as sensors, actuators and harvesters. However, due to lead toxicity, the introduction of legislation in Europe to limit the usage of lead in electronic products has led to a worldwide search for lead-free compounds. $BaTiO_3$ is one of the basic and widely applied lead-free ferroelectric materials[2)]. Recently, Zheng et al.[3)] studied experimentally the grain size effect on the dielectric and piezoelectric properties of the $BaTiO_3$ ceramics. Huan et al.[4)] also prepared the $BaTiO_3$ ceramics with different grain sizes by two-step sintering method, and explored the effect of grain size on the piezoelectric properties. In the above two papers, it was shown that the dielectric and piezoelectric properties increase with the reduction of the average grain size and reach the maximum at about 1 μm. On the other hand, it is well known that the electrical properties and microstructures of the $BaTiO_3$ ceramics depend on the oxygen partial pressure[5,6)]. Although grain size and oxygen activity have been found to play a significant role in piezomechanical properties of ferroelectric ceramics, it is difficult to find the optimal conditions experimentally.

Phase field approach can serve as an efficient tool for the purpose of microstructural analysis of ferroelectric materials[7)]. In this paper, we develop the phase field simulation framework for studying the effects of grain size and oxygen vacancy density on the electromechanical behavior of $BaTiO_3$ polycrystals. This information is essential for establishment of optimal processing conditions, such as temperature, time of annealing and gas phase composition, of $BaTiO_3$ polycrystals.

PHASE FIELD MODEL

Let us now consider the global rectangular Cartesian coordinates x_i (O-$x_1x_2x_3$). The temporal evolution of the component of polarization vector P_i and thus the domain structure is governed by the following time-dependent Ginzburg-Landau (TDGL) equation:

$$\frac{\partial P\ x\ t}{\partial t} = -M\frac{\delta F}{\delta P\ x\ t} \qquad (i = 1,2,3) \tag{1}$$

where F is the total free energy of the ferroelectric polycrystal, M is the kinetic coefficient related to the domain mobility, and t is the time. The total free energy is given by

$$F = \int_V (f_{\text{bulk}} + f_{\text{grad}} + f_{\text{elas}} + f_{\text{elec}})dV \tag{2}$$

where f_{bulk} is the local bulk free energy density, f_{grad} is the gradient energy density which is only non-zero around domain walls and grain boundaries, f_{elas} is the elastic strain energy density, f_{elec} is the electrostatic energy density, and V is the volume of the polycrystal.

The oxygen vacancy density N_{d} is governed by the following diffusion equation[8)]:

$$\frac{\partial N_{\text{d}}}{\partial t} = \nabla\cdot\left[\beta_{\text{d}}N_{\text{d}}\nabla\left(\frac{\partial W_{\text{d}}}{\partial N_{\text{d}}} + eZ\phi\right)\right] \tag{3}$$

where $\beta_{\text{d}} = 5\times10^5$ m^2/sJ is the defect's mobility, W_{d} is the contribution to the free energy due to defects, $e = 1.6021773\times10^{-19}$ C is the coulomb charge per electron, $Z = 1$ is the valency of donors (oxygen vacancies), and ϕ is the electric potential. If the mole fraction of vacancies is very small, Eq. (3) is simplified to

$$\frac{\partial N_{\text{d}}}{\partial t} = \nabla\cdot\ \beta \qquad \nabla\ _{\text{d}} + \beta_{\text{d}}eZN_{\text{d}}\nabla\phi) \tag{4}$$

[a)] Corresponding author. Email: narita@material.tohoku.ac.jp

where k_B = 1.3807 10^{-23} J/K is the Boltzmann constant.

To study the effect of the grain size on the dielectric and piezoelectric properties, a phase field model for grain growth is used and a two-dimensional grain structure is generated. Here, we employ the grain growth model developed by Krill III and Chen[9].

DISCUSSION

We consider a plane strain rectangular $BaTiO_3$ polycrystal of dimensions 3.3 3.3 μm. Fig. 1 shows the images of $BaTiO_3$ polycrystal with average grain radius d = 1.03 μm. Table 1 lists the piezoelectric coefficient d_{33} of $BaTiO_3$ polycrystals for oxygen vacancy densities N_d = 0, 100, 500, 1000 ppm and average grain radii d = 0.89, 1.03 μm. As the oxygen vacancy density increases, the piezoelectric coefficient increases reaching a peak and then decreases. Fig. 2 shows the piezoelectric coefficient versus average grain radius for various oxygen vacancy densities. The piezoelectric coefficient increases with increasing average grain radius and may have some peaks. The grain radius at which the peak occurs depends on the oxygen vacancy density.

Table 1. Piezoelectric coefficients d_{33} of barium titanate with oxygen vacancies.

N_d(ppm)		0	100	500	1000
$d_{33}(\times 10^{-12}\mathrm{m/V})$	$d = 0.89\ \mu m$	98.3	132	243	161
	$1.03\ \mu m$	99.1	148	157	115

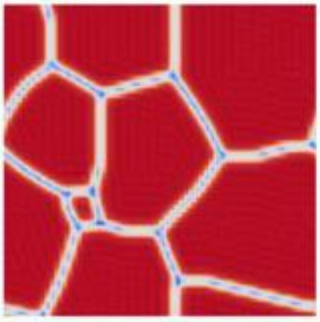

Fig. 1 Image of $BaTiO_3$ polycrystal (d = 1.03 μm)

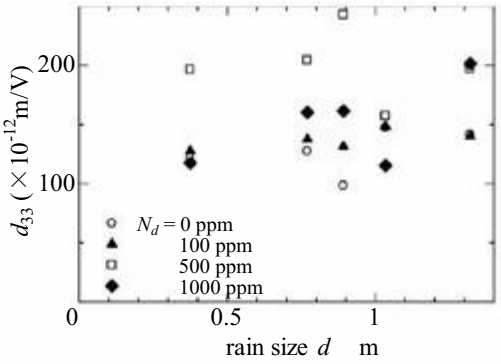

Fig. 2 Piezoelectric coefficient d_{33} vs grain size d

References

[1] Y. Shindo and F. Narita, Dynamic bending/torsion and output power of S-shaped piezoelectric energy harvesters, Int. J. Mech. Mater. Des., 105 (2014) 305-311.

[2] F. Narita and Y. Shindo, Piezoelectric detection and response characteristics of barium titanate unimorph cantilevers under AC electric fields, Int. J. Metal. Mater. Eng., in press.

[3] P. Zheng, J.L. Zhang, Y.Q. Tan, C.L. Wang, Grain-size effects on dielectric and piezoelectric properties of poled BaTiO3 ceramics, Acta Mater. 60, 5022 (2012).

[4] Y. Huan, X. Wang, J. Fang and L. Li, Grain size effect on piezoelectric and ferroelectric propertiesof BaTiO3 ceramics, J. Eur. Ceram. Soc. 34, 1445 (2014).

[5] Q. Feng, C. J. McConville, D. D. Edwards, D. E. McCauley and M. Chu, Effect of oxygen partial pressure on the dielectric properties and microstructures of cofired base-metal-electrode multilayer ceramic capacitors, J. Am. Ceram. Soc. 89, 894 (2006).

[6] H. T. Langhammer, D. Makovec, Y. Pu, H.-P. Abicht and M. Drofenik, Grain boundary reoxidation of donor-doped barium titanate ceramics, J. Eur. Ceram. Soc. 26, 2899 (2006).

[7] Y. Su and G. J Weng, Phase field approach and micromechanics in ferroelectric crystals, Handbook of Micromechanics and Nanomechanics, S. Li and X.-L. Gao (Eds), pp.73-140 (2013).

[8] Y. Xiao and K. Bhattacharya, A continuum theory of deformable, semiconducting ferroelectrics, Arch. Rational Mech. Anal. 189, 59-95 (2008).

[9] C. E. Krill III and L.-Q. Chen, Computer simulation of 3-D grain growth using a phase-field model, Acta Mater. 50, 3057-3073 (2002).

CRYSTAL PLASTICITY FE STUDY OF THE ROLE OF MICROTEXTURE ON DWELL FATIGUE RESPONSE OF TI-6242

Deniz Ozturk[1], Shravan Kotha[2], and Somnath Ghosh *[3]
[1,2]*Graduate Research Assistant, Department of Civil Engineering, Johns Hopkins University, U.S.A.*
[3]*M. G. Callas Professor, Departments of Civil and Mechanical Engineering, Johns Hopkins University, U.S.A.*

Summary The fatigue performance of the aero-space alloy Ti-6242 is strongly dependent on its microstructural design. In particular, micro-textured regions (MTRs) are known to be critical features for dwell crack formation. In this work, a Crystal Plasticity FE model and an experimentally validated dwell crack nucleation model of Ti-6242 are used to study the effect of MTRs on dwell fatigue performance of Ti-6242. A wavelet-based multi-time-scale integration method is used in calculating the material response over fatigue cycles. It is shown that the presence of MTRs results in increased accumulation of local plastic strain, higher stress concentration grain boundaries, and early dwell crack nucleation. Microstructures without MTRs show significantly better fatigue performance. The level of microtexture is characterized by statistical measures which are used as microstructural parameters for structural-scale homogenized models of fatigue damage. Micro-mechanical modeling of fatigue along with homogenization may help understand and predict the structural-scale response in relation to the microstructural-level material design.

INTRODUCTION

Ti-6242 is a near-α Titanium alloy preferred in aerospace applications for its high strength to weight ratio, high fracture toughness and corrosion resistance at elevated temperatures. Despite these attractive properties, this alloy suffers from earlier fatigue failure under dwell loading, compared to cyclic loading with no hold time. Dwell fatigue crack initiation sites are characterized by faceted cracks within the α grains, oriented within 10 degrees of the crystallographic basal plane[1]. α-Titanium exhibits high resistance for plastic deformation and high elastic stiffness along the crystallographic [0001] direction. While faceted α grains are unfavorably oriented for plastic slip, they are observed to be surrounded by grains that are suitably oriented for plastic deformation by basal and/or prismatic slip[1]. This combination of neighboring soft and hard grains is thought to trigger a time-dependent stress redistribution mechanism called load shedding, leading to early crack initiation under dwell fatigue.

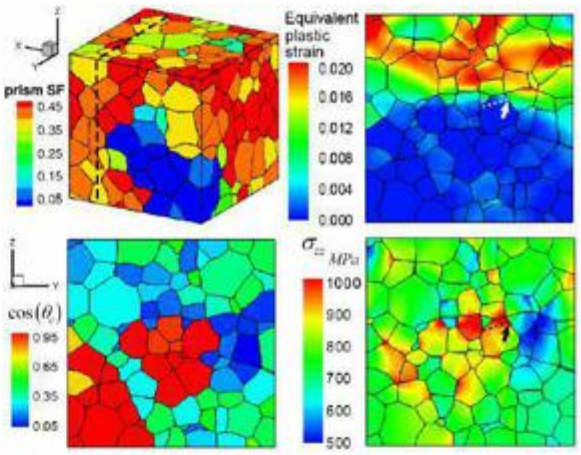

Figure 1: Local strain and stress fields and dwell crack nucleation in microtextured Ti-6242. Left: Clusters of grains with similar orientations forming MTRs. Dashed line, arrow: crack plane and the location of initiation

Experimentally calibrated and validated rate- and size-dependent crystal plasticity finite element (CPFE) models of Ti-6242 have been developed[2] to show the effect of time-dependent stress relaxation on the soft grains leading to stress concentration on the hard grain. The stress concentration on the hard grain has a large normal tensile component on the basal plane, which progressively increases with the number of dwell cycles. An experimentally validated microstructure-dependent crack nucleation model has been developed by Anahid et al.[3, 4] to predict the microstructural location and cycles to crack nucleation for Ti alloys under dwell loading. The criterion is based on the pile-up of dislocations at the soft grain boundary and the development of stresses in the adjacent hard grain, opening a microcrack in the hard grain:

$$R > R_c \quad \text{where } R = \sqrt{c}\sqrt{\langle T_n \rangle^2 + \beta T_t^2} \text{ and } R_c = K_c/\sqrt{\pi}$$

Here, R is the dwell crack nucleation variable, R_c is the critical value for nucleation, c is the wedge crack opening length calculated from the Nye's dislocation tensor, and $\langle T_n \rangle$ and T_t are the normal tensile and shear components of the traction vector on the potential crack surface at the hard grain.

Using the size- and rate-dependent crystal plasticity model of Ti-6242 developed in Refs.[2] and dwell crack nucleation model developed previously[3, 4], this work is based on a recent paper[5] and studies the effect of the presence and size of micro-textured regions on the dwell fatigue life of Ti-6242. Micro-textured regions (MTR) has been identified as critical microstructural features that control early fatigue failure and facilitate early short crack propagation[6]. These are regions of similarly oriented α grains that nucleate from the same prior-β grain, whose presence and size depend on the thermo-mechanical processes adopted during manufacturing. Adjacent MTRs with easy and hard orientations for plastic slip are critical regions in dwell fatigue, initiating faceted cracks on the grains within the hard MTR.

*Corresponding author. Email: sghosh20@jhu.edu

SIMULATION RESULTS AND DISCUSSION

To study the effect of microtexture on dwell fatigue response, two 3D polycrystalline models of bimodal Ti-6242 were created with and without MTRs, by the following procedure: A set of grain orientations based on X-Ray Diffraction macrotexture measurements from a forged bimodal Ti-6242 specimen[2] are assigned to both models. Using an iterative algorithm the crystallographic orientations are swapped between randomly selected grain pairs in order to either (1) obtain clusters of similarly oriented grains representing MTRs in microstructure MS_{MTR} (See Fig 1); and (2) obtain highly-misoriented grain pairs in MS_{mis}, therefore resulting in a microstructure devoid of MTRs.

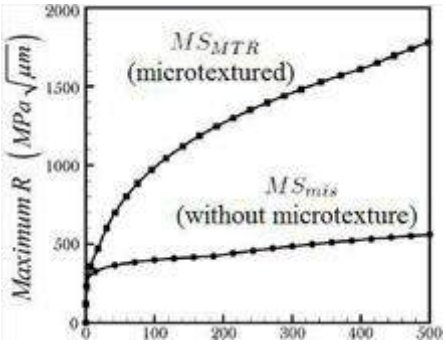

Figure 2: Effect of micro-texture on the evolution of the crack nucleation parameter R.

Dwell fatigue simulations are conducted at peak load level of 750 MPa and load ratio R=0.1[5]. A wavelet-based multi-time scaling method WATMUS[3] is used for efficient calculation of the local material response over the fatigue cycles. Investigation of both microstructures MS_{MTR} and MS_{mis} reveals significant differences in their micro-scale responses. Fig 1 shows the distributions of the local plastic strain and stress, the predicted location of crack nucleation and crack plane in the microtextured model MS_{MTR} after 500 dwell fatigue cycles. The response of microtextured model is characterized by: (i) significant plastic strain accumulation within the micro-textured regions that are favorably oriented for plastic slip, (ii) confinement of plastic deformation to these microtextured regions, ending at the boundaries of hard microtextured regions, and (iii) stress concentration due to load shedding predominantly at boundaries of the hard microtextured regions. These features result in a dwell crack nucleation at the boundary of a hard micro-textured region, neighboring a soft region as shown in Fig 1 indicated with the arrow and the dashed line. The microstructure without MTRs exhibits milder and less variable response of local plasticity and stress compared to the micro-textured model[5]. The lack of clustered soft grains, and the grain-scale alternation of plastic anisotropy results in a composite strengthening effect, suppressing plastic strain accumulation in the grains. Consequently, load shedding is less pronounced in this microstructure. The evolution of the maximum dwell crack nucleation variable R over the fatigue cycles is given in Fig. 2, for both microstructures. MS_{MTR} shows a rapid accumulation of the nucleation variable, while MS_{mis} shows limited accumulation, i.e. better dwell fatigue resistance. The critical region for crack nucleation in MS_{MTR} is located at the boundary of a 'hard' MTR with low Schmid factor that exhibits cycle-dependent stress concentration due to load shedding mechanism. This MTR is adjacent to a 'soft' MTR with high prismatic Schmid factor that exhibits high plastic strain accumulation. The crack initiates within the hard MTR, and crack plane normal is within 20 degrees of the load axis, consistent with the experimental observations[1]. These results are verified by repeating simulations with different macrotextures: models with MTRs consistently show poor dwell fatigue performance.

Hierarchical Multi-scaling of Crystal Plasticity Simulations for Structural-scale Constitutive and Damage Models

The CPFE model presented above is used to develop structural-scale elastic-plastic constitutive and damage models using parametric homogenization. A rigorous sensitivity analysis is performed to identify the important statistical parameters of the microstructure that control the macroscopic elastic-plastic behavior. CPFE simulations on polycrystals with different grain morphologies and textures are performed under various loading conditions. The macroscopic constitutive equations are then derived in terms of the microstructural statistical parameters. As macroscopic response is influenced by microstructural variability, a probabilistic extension of the parametric homogenization is being developed to predict structural-scale response.

The presence and spatial extent of MTRs are characterized by statistical measures such as grain misorientation distribution and spatial auto-correlation of orientations. These measures are used as microstructural parameters for structural-scale models of fatigue damage. Micro-mechanical modeling of deformation and fatigue along with multi-scale homogenization may help understand and predict the structural-scale response in relation to the material design at the microstructural-level.

References

[1] V. Sinha, M. J. Mills, and J. C. Williams. Determination of crystallographic orientation of dwell-fatigue fracture facets in Ti-6242 alloy. *Journal of Materials Science*, 42(19):8334–8341, 2007.

[2] Dhyanjyoti Deka, Deepu S. Joseph, Somnath Ghosh, and Michael J. Mills. Crystal plasticity modeling of deformation and creep in polycrystalline Ti-6242. *Metallurgical and Materials Transactions A*, 37(5):1371–1388, 2006.

[3] M Anahid, P Chakraborty, D S Joseph, and S Ghosh. Wavelet decomposed dual-time scale crystal plasticity FE model for analyzing cyclic deformation induced crack nucleation in polycrystals. *Modelling and Simulation in Materials Science and Engineering*, 17(6):064009, sep 2009.

[4] Masoud Anahid, Mahendra K. Samal, and Somnath Ghosh. Dwell fatigue crack nucleation model based on crystal plasticity finite element simulations of polycrystalline titanium alloys. *Journal of the Mechanics and Physics of Solids*, 59(10):2157–2176, oct 2011.

[5] Deniz Ozturk, Ahmad Shahba, and Somnath Ghosh. Crystal Plasticity FE Study of the Effect of Thermo-Mechanical Loading on Fatigue Crack Nucleation in Titanium Alloys. *Fatigue & Fracture of Engineering Materials & Structures*, (in press), 2016.

[6] V. Sinha, J. E. Spowart, M. J. Mills, and J. C. Williams. Observations on the faceted initiation site in the dwell-fatigue tested ti-6242 alloy: Crystallographic orientation and size effects. *Metallurgical and Materials Transactions A*, 37(5):1507–1518, 2006.

A CONTINUUM MODEL FOR DISCRETE DISLOCATION DYNAMICS

Xiaohan Zhang*[1], Amit Acharya[2], Noel Walkington[3], and Jacobo Bielak[2]

[1]*Mechanical Engineering, Stanford University, Palo Alto, C.A., U.S.*
[2]*Civil and Environmental Engineering, Carnegie Mellon University, Pittsburgh, P.A., U.S.*
[3]*Department of Mathematical Sciences, Carnegie Mellon University, Pittsburgh, P.A., U.S.*

Summary This work reports on a 2-d edge dislocation model within the framework of a PDE-based continuum dislocation mechanics theory (Field Dislocation Mechanics) [1] . We numerically explore such physical phenomena as Peierls stress, dislocation pile-ups, dislocation annihilation & dissociations, supersonic dislocations (even in 2-d); Within the same framework,'self-healing', an important tectonic phenomena that cannot be predicted by the mostly used crack-based dynamic rupture models, is also modelled.

INTRODUCTION: SIMULATIONS OF SOME KEY PROBLEMS IN PLASTICITY

- *Peierls' stress effects in a translationally-invariant continuum theory as FDM* is commonly believed to [2] vanish since the system energy is translationally-invariant. However, the fact that classical models treat dislocations as rigid objects fails to account for the possibility that Peierls stress could be affected by shape change of dislocations. Representing dislocations with tensor fields (Nye tensor), FDM serves as an appropriate tool to probe such problems. As a matter of fact, FDM can predict that there exists a finite magnitude applied load that cannot set the dislocation in motion (Fig. 2), i.e., Peierls stress exists due to the dislocation core effects.

- *Quasi-static behaviours of individual or a few dislocations* are approached here as equilibrium configurations of the dynamical model. The corresponding non-singular stress distribution obtained from modelling these problems is a true equilibria of a dynamic theory corresponding to a local minima of the free energy of a body. The solutions of [3] have no such thermodynamic status. A larger implication is that FDM can serve as a *model* for studying questions related to equilibrium and dynamic evolution (at realistic time-scales) of core structures of single and interacting dislocations under loads, utilizing input from finer length-scale models like Density Functional Theory and Molecular statics. As examples, Fig. 3 shows dislocations pile up against the left boundary under shear load; Fig. 4 shows the initial, intermediate and final states of the quasistatic process where a perfect dislocation dissociates into two partials, simply due to energetical preference wiht no ad-hoc rules inserted to carry out the nonlinear process of dissociation.

- *The velocity of dislocation versus applied load with the presence of material inertia* is analyzed, with special emphasis on investigating velocity of sub-inter-supersonic regime. The MD experiment of [4] has revealed the nonlinear relationship between the dislocation velocity and the applied load. FDM qualitatively reproduces those effects, as shown in Fig. 5. A supersonic dislocation forming (behind the dislocation) a nonsymmetric Mach cone of Cauchy stress wave is also observed and analyzed.

- *'self-healing' traction profiles behind slip fronts in rupture dynamics* is a conclusion deduced from observations of many earthquake records [5] which says that the slip duration at any given point through which a rupture front has propagated is relatively short compared to the duration of the whole earthquake. It is demonstrated that FDM can be used as a modelling tool for rupture dynamics. Most importantly, FDM can predict the 'self-healing' behaviour, which is out of the reach of mostly used slip-weakening, crack-based rupture models. Fig. 6 shows the agreement of transverse displacement field across the rupture layer produced by FDM with that inferred from Parkfield earthquake (from Aki, 1968; copyright by the American Geophysical Union).

MODEL SETUP AND SOME KEY RESULTS

We reduce the small deformation FDM theory, a complete discription of which can be found in [6], to a 2-d composite layer model. The geometry concerned in this paper is illustrated by Fig. 1. The body is made of two elastic parts and a plastic layer where dislocation plasticity is active. To ensure non-negative dissipation we choose the dislocation velocity in the direction of driving force (as is standard in thermomechanics). The reduced governing equations take the form of,

$$\begin{cases} \rho \dfrac{\partial^2 u_i}{\partial t^2} = \dfrac{\partial T_{ij}}{\partial x_j} \quad \text{in } \Omega \\ \dfrac{\partial \phi}{\partial t} = \dfrac{1}{B_m\, l^{m-1}} \left| \dfrac{\partial \phi}{\partial x_1} \right|^{2-m} \left(\tau \nearrow \dfrac{\partial \eta}{\partial \phi} + \epsilon \dfrac{\partial^2 \phi}{\partial {x_1}^2} \right) \quad \text{in } L \end{cases} \tag{1}$$

*Corresponding author. Email: xzhang11@stanford.edu

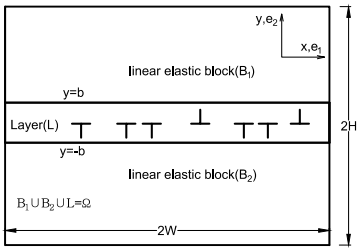

Figure 1: Geometry of the 2-d edge dislocation model. Dislocation plasticity is only active in layer L. All dislocations are assumed to be of edge type and move only in e_1 direction.

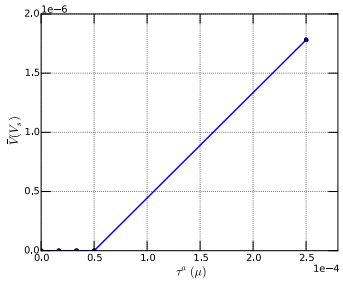

Figure 2: A single edge dislocation under investigated remains still for smaller shear traction loads, showing a Peierls stress $= 5 \times 10^{-5}\mu \sim 1MPa$.

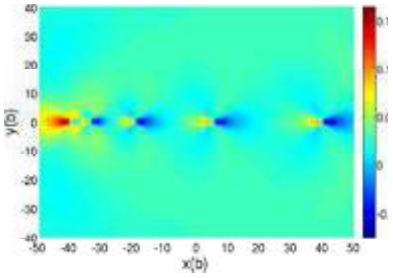

Figure 3: Shear stress: initially evenly distributed array of dislocations pile up against the leftmost fixed dislocation under shear load then get equilibrium.

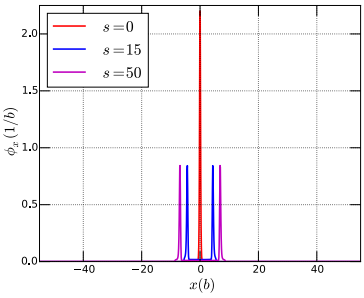

Figure 4: An example of modeling dislocation dissociation. The perfect dislocation energetically preferred to become partials.

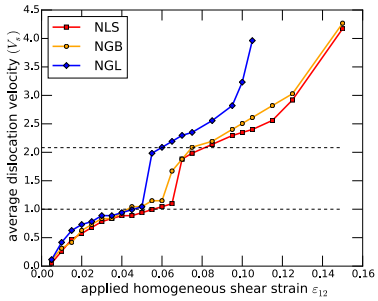

Figure 5: FDM reproduce MD simulations of dislocation kinetic with inertia. Horizontal dashed lines indicate relevant acoustic wave speeds.

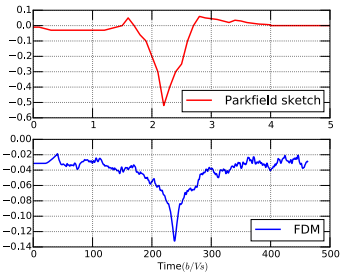

Figure 6: Transverse displacement at a fixed point in the rupture passage calculated by FDM model compared with sketch of the observed data recorded in Parkfield earthquake.

where m is a scalar parameter that shows up in the dislocation velocity function and can be chosen to probe different types of behaviours. $\phi(x,t) := U_{12}^p$ is the plastic distortion; $\tau(x,t)$ is a stress averaged over the plastic layer thickness. B_m is the drag coefficient and ϵ is the scalar diffusion parameter. The system of equations are solved with a Finite Elemenet method coupled with an upwinding Finite Difference scheme in a staggered formulation.

References

[1] Xiaohan Zhang, Amit Acharya, Noel J. Walkington, Jacobo Bielak.: A single theory for some quasi-static, supersonic, atomic, and tectonic scale applications of dislocations. Journal of the Mechanics and Physics of Solids, 2015.

[2] R. Peierls.: The size of a dislocation. Proceedings of the Physical Society, 52(1):3437, 1940.

[3] Wei Cai, Athanasios Arsenlis, Christopher R Weinberger, and Vasily V Bulatov.: A non-singular continuum theory of dislocations. Journal of the Mechanics and Physics of Solids, 54(3):561587, 2006.

[4] Peter Gumbsch and Huajian Gao.: Dislocations faster than the speed of sound. Science, 283(5404):965968, 1999.

[5] Thomas H. Heaton.: Evidence for and implications of self-healing pulses of slip in earthquake rupture. Phys. Earth Planet. Inter. 64 (1), 120, 1990.

[6] Amit Acharya, Xiaohan Zhang.: From dislocation motion to an additive velocity gradient decomposition, and some simple models of dislocation dynamics. In: Li, Ta.-Tsien, Ciarlet, Ph.G. (Eds.), Proceedings of the International Conference in honor of Luc Tartar on Nonlinear and Multiscale Partial Differential Equations: Theory, Numerics and Applications; Series in Contemporary Applied Mathematics. Higher Education Press, Beijing and World Scientific, Singapore, 2014.

DUAL BASIS FUNCTIONS FOR ISOGEOMETRIC SOLID MECHANICS

Wolfgang Dornisch*[1] and Ralf Müller [1]

[1]*Institute of Applied Mechanics, University of Kaiserslautern, Kaiserslautern, Germany*

Summary The main paradigm of isogeometric analysis is the use of a common set of basis functions for design and analysis. Thus, the basis functions of a Computer-Aided-Design (CAD) application are used for the analysis with the Finite-Element-Method (FEM). In this work the basis functions of Non-Uniform Rational B-splines (NURBS), which is the prevailing geometry definition in CAD industry, are used. The defining characteristic of dual basis functions is that the integral of their product with their associated standard basis functions yields the Kronecker delta property with respect to indices. In the case of NURBS the definition of dual basis functions is non-trivial and several possibilities exist. This work shows and compares different approaches for the dual basis functions. They are applied within the isogeometric mortar method, which is used to couple non-conforming NURBS meshes. An outlook on further applications is given.

INTRODUCTION

This works shows and compares different approaches for the computation of dual basis functions for Non-Uniform Rational B-splines (NURBS) with the intention to use them in the isogeometric mortar method. Isogeometric analysis simplifies a tighter integration between design and analysis [1] by using the NURBS geometry description and the NURBS basis functions for the analysis. Furthermore, the employed NURBS basis functions exhibit higher continuity as standard Lagrange basis functions and are able to exactly represent complex geometries.

NURBS AND ISOGEOMETRIC ANALYSIS

The i-th B-spline basis function of order p with $i = 1, \dots, n$ is defined by the Cox–de Boor algorithm

$$N_i^p(\xi) = \frac{\xi \nearrow \xi_i}{\xi_{i+p} \nearrow \xi_i} N_i^{p-1}(\xi) + \frac{\xi_{i+p+1} \nearrow \xi}{\xi_{i+p+1} \nearrow \xi_{i+1}} N_{i+1}^{p-1}(\xi) \quad \text{with} \quad N_i^0(\xi) = \begin{cases} 1 & \text{if } \xi_i \le \xi \le \xi_{i+1} \\ 0 & \text{otherwise} \end{cases} \tag{1}$$

and has local support on the interval $[\xi_i, \xi_{i+p+1})$, where ξ is the parametric coordinate and the knot values ξ_i are taken from the knot vector $\boldsymbol{\Xi} = [\xi_i]_{i=1,\dots,n+p+1}$. The control points $\boldsymbol{B}_i = [x_i, y_i, z_i w_i]^T = \begin{bmatrix} \boldsymbol{X}_i^T & w_i \end{bmatrix}^T$ with $i = 1, \dots, n$ are used as nodes for the finite element discretization, and the NURBS basis functions

$$N_I(\xi) := \frac{N_i^p(\xi) w_i}{\sum_{\hat{i}=1}^{n_{en}} N_{\hat{i}}^p(\xi) w_{\hat{i}}} \tag{2}$$

are used as ansatz functions for the displacements $\boldsymbol{u} = \sum_{I=1}^{n_{en}} N_I \boldsymbol{u}_I$ and as virtual test functions. Here only the 1D case which is used for curves is displayed. Higher-dimensional cases can be found e.g. in [1].

DUAL AND APPROXIMATE DUAL BASIS FUNCTIONS

The dual functional f_i is defined by

$$f_i(N_j) := \int_{\boldsymbol{\Xi}} N_j \lambda_i \quad s = \delta_{ij}\,, \tag{3}$$

where λ_i denotes the dual basis functions. By definition, the dual functional $f_i(N_j)$ is equal to the Kronecker delta δ_{ij}. Approximate dual basis functions do not fulfill the Kronecker delta property exactly but approximately by

$$f_i^{approx}(N_j) \approx \begin{cases} 1 & \text{if } i = j \\ 0 & \text{if } i \neq j \end{cases} \tag{4}$$

and were introduced by Chui et al. [2]. An important property of dual or approximate dual basis functions λ_i is their ability to exactly reproduce polynomials of degree r by

$$x^r = \sum_{j=1}^{n} c_j^r N_j \quad \text{with} \quad c_j^r = \int_I x^r \lambda_j \quad s\,. \tag{5}$$

This property is not fulfilled by all choices for the dual basis functions, especially this is not the case for the dual basis functions of de Boor which are used in [3]. Another important property is the support of the dual basis functions. Here the most unfavorable approach is to use the inverse Gram matrix as proposed in [4] as this yields global support for each basis function. A more detailed comparison of potential dual basis functions can be found in [5].

*Corresponding author. Email: dornisch@rhrk.uni-kl.de

EXEMPLARY APPLICATION: ISOGEOMETRIC MORTAR METHOD

The mortar method was initially proposed by Bernardi et al. [6] in order to couple domains with non-conforming discretization. The mortar method as proposed by Bernardi et al. uses constrained approximation spaces to enforce the equality of deformations along the interface and maintains the positive definiteness of the global system of equations. The use of the mortar method to couple non-conforming NURBS patches in an isogeometric framework was proposed in [4]. The basic idea of the mortar method is to decompose the domain into two complementary subdomains Ω^1 and Ω^2, in which the standard equations, here exemplary for linear elasticity

$$\mathrm{v}\,\boldsymbol{S} + \boldsymbol{b} = \boldsymbol{0} \quad \text{in } \Omega = \Omega^1 + \Omega^2\,, \quad \boldsymbol{t} = \bar{\boldsymbol{t}} \quad \text{on } \mathrm{y}_N = \mathrm{y}_N^1 + \mathrm{y}_N^2 \quad \text{and} \quad \boldsymbol{u} = \boldsymbol{0} \quad \text{on } \mathrm{y}_D = \mathrm{y}_D^1 + \mathrm{y}_D^2\,, \tag{6}$$

are established. The equality of deformations $\boldsymbol{u}^1 = \boldsymbol{u}^2$ along the interface y_c is fulfilled by choosing a constrained solution space $\mathcal{S}$ with the properties

$$\mathcal{S} := \left\{ \boldsymbol{u} \in H^1\left(\Omega^1 \cup \Omega^2\right) \,\middle|\, \boldsymbol{u} = \boldsymbol{0} \text{ on } \mathrm{y}_D\,,\ \int_{\Gamma_c} \left(\boldsymbol{u}^1 - \boldsymbol{u}^2\right) \cdot \delta\boldsymbol{\lambda}\,\mathrm{d}s = 0 \quad \forall\, \delta\boldsymbol{\lambda} \in L^2\left(\mathrm{y}_c\right) \right\} \tag{7}$$

for the discretization of the problem stated in Eq. (6). The numerical results of [5] show that the approximate dual basis functions are the most promising candidate for the use in the isogeometric mortar method. Their properties, which combine local support with high continuity and an sufficient polynomial reproduction, entail numerical results of which neither accuracy nor computational costs noticeably deviate from computations with conforming meshes. This does not hold for all other concepts for the computation of dual basis functions. The results of non-conforming computations of a curved shell structure with kink are given in Fig. 1. The results clearly show the superior properties of the approximate dual basis functions. For more details, and for results using the de Boor dual basis functions we refer to [5].

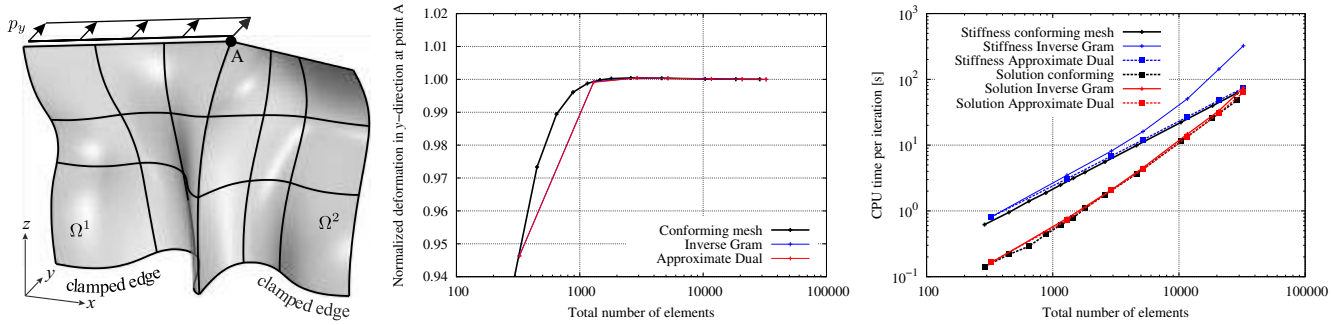

(a) System sketch. (b) Study of deformation convergence. (c) Comparison of computational costs.

Figure 1: Free form surface with kink: Comparison of deformation convergence behavior and computational costs between Inverse Gram and Approximate Dual basis functions for computations of non-conforming meshes with $15j : 12j$-refinement along the interface.

CONCLUSION

This works presents different concepts for the computation of dual basis functions for splines. They are applied as test functions within the isogeometric mortar method. Further applications which make use of the advantageous properties of approximate dual basis functions seem to be possible.

References

[1] Hughes T.J.R., Cottrell J.A., Bazilevs Y.: Isogeometric analysis: CAD, finite elements, NURBS, exact geometry and mesh refinement. Comput. Meth. Appl. Mech. Engrg., 194:4135-4195, 2005.

[2] Chui C.K., He W., Stöckler J.: Nonstationary tight wavelet frames, I: Bounded intervals. Appl. Comput. Harmonic Anal., 17(2):141-197, 2004.

[3] Schumaker L.L.: Spline functions: Basic theory, Cambridge mathematical library, Cambridge University Press, Cambridge and New York, 2007.

[4] Dornisch W., Vitucci G., Klinkel S.: The weak substitution method – An application of the mortar method for patch coupling in NURBS-based isogeometric analysis. Int. J. Numer. Meth. Engng., 103(3):205-234, 2015.

[5] Dornisch W., Müller R.: Dual and approximate dual basis functions for B-splines – Comparison at the example of mortar patch coupling in isogeometric analysis. submitted to Comput. Meth. Appl. Mech. Engrg., 2015.

[6] Bernardi C., Maday Y., Patera A.T.: Domain Decomposition by the Mortar Element Method. In Kaper H.G., Garbey M., and Pieper G.W. (eds.), Asymptotic and Numerical Methods for Partial Differential Equations with Critical Parameters, 269-286. Springer Netherlands, Dordrecht, Netherlands, 1993.

NON-DIFFERENTIABLE ENERGY MINIMIZATION FOR COHESIVE FRACTURE

Katerina D. Papoulia*[1], M. Reza Hirmand[2], and Stephen A. Vavasis[3]

[1]*Department of Applied Mathematics, University of Waterloo, Waterloo, Ontario, Canada*
[2]*Department of Mechanical and Mechatronics Engineering, University of Waterloo, Waterloo, Ontario, Canada*
[3]*Department of Combinatorics and Optimization, University of Waterloo, Waterloo, Ontario, Canada*

Summary A potential-based formulation for an initially rigid cohesive fracture model is proposed. The key feature is a term for the energy stored in the cohesive interfaces that is nondifferentiable at the origin. A consequence of this formulation is that the activation computation necessary in previous initially rigid formulations is now replaced by the computation of a minimizer of a nondifferentiable objective function. This immediately makes the method more amenable to implicit time stepping, since the activation criterion no longer interacts with the nonlinear solver for the next time step. The algorithm also sidesteps the complexities of time-discontinuity and traction-locking previously observed in relation to initially rigid models. The optimization problem is reformulated as a nonlinear second-order cone programming problem. This reformulation allows the nondifferentiability created by the square-root terms in the potential to be treated in a well-understood conic programming framework and addressed with an interior point method.

COHESIVE FRACTURE AS AN ENERGY MINIMIZATION PROBLEM

Initially rigid cohesive interface models exhibit no discontinuity until a traction criterion is reached, arguably a desirable property of a fracture model in a continuum setting. In numerical solutions, this constraint is imposed by adaptive insertion of an interface finite element at the time of activation, weakly through a penalty initial stiffness, or through a discontinuous Galerkin formulation. The activation criterion is a separate entity from the traction-displacement relationship, hence initially rigid cohesive interface models are also called *extrinsic* models. These models exhibit a discontinuity in the traction-displacement relationship, i.e., the interface traction is a discontinuous function of the displacement jump $[[\boldsymbol{\phi}]]$. Indeed, the traction vector imparted by the interface at activation will almost certainly be unequal to that imparted by the bulk material prior to activation [5, 7]. Termed a *time discontinuity*, this is a discontinuity of the governing equations in the displacements at the time of activation of an interface. Differential equations which are discontinuous in the solution variable are known to suffer from lack of a solution or nonuniqueness of solution [3]. Time discontinuity can create undesirable effects including nonphysical vibrations, nonconvergence or slow convergence of the method as the time step size is decreased, and overactivation of interfaces in the resulting computations unless the activation criterion is formulated in a very special (and perhaps nonintuitive) manner [5, 7]. Initially rigid models are not appropriate for implicit calculations, as would typically occur in a quasistatic problem, because the activation criterion interacts with the nonlinear solver for the next time step.

We propose a novel formulation of initially rigid cohesive models that dispenses with both the activation criterion and the explicit use of a traction-displacement relationship. Instead, the main ingredient of the proposed method is an energy functional, in which one term is energy stored in the interfaces. Variational solutions in the current literature such as the ones which, based on the variational setting of Eshelby, introduce a fracture criterion in terms of configurational forces [4] are typically obtained from a weak form. In the case of an initially rigid cohesive model, a weak form is not equivalent to minimizing an energy functional because the energy function corresponding to the interface is not Fréchet-differentiable in the displacements. A *global* minimization principle is employed in [1], in which the crack is described as a field in order to regularize the functional. This leads to a smeared crack with a sharp crack obtained in the limit as the mesh size goes to zero. Based on the notion of eigendeformation, Schmidt *et al.* perform energy minimization to obtain the optimal crack set [8]. The proposed functional corresponds to the Barenblatt approach of cohesive fracture. The crack geometry follows our analysis in [6].

The crucial mathematical property of this functional is that it is nondifferentiable at the origin (zero interface opening), which gives the interfaces the property that they do not activate until a certain level of traction is reached. This critical traction is incorporated in the construction of the energy functional rather than appearing as an explicit activation criterion. In addition, the proposed functional is non convex. Overall the proposed energy functional takes the form

$$E = \int_{V_0} W \, dV_0 + \int_{S_0} (\phi(\delta; \delta_{\max}) + \theta(\delta_n)) \, dS_0, \tag{1}$$

where V_0 is the initial (undeformed) volume of the body and S_0 is the union of potential cohesive surfaces; W denotes a hyperelastic potential; The two functions ϕ and θ are functions of the displacement discontinuity as follows: δ is a norm of the displacement discontinuity vector, e.g., $\delta = \sqrt{\quad \mathrm{x}(0,\delta_n)^2 + \beta^{-2}(\delta_2^2 + \delta_3^2)}$, where δ_n is the normal opening displacement, the other two components δ_2, δ_3 being tangent to the cohesive surface; $\delta_{\max}$ is an internal variable that characterizes

*Corresponding author. Email: papoulia@uwaterloo.ca

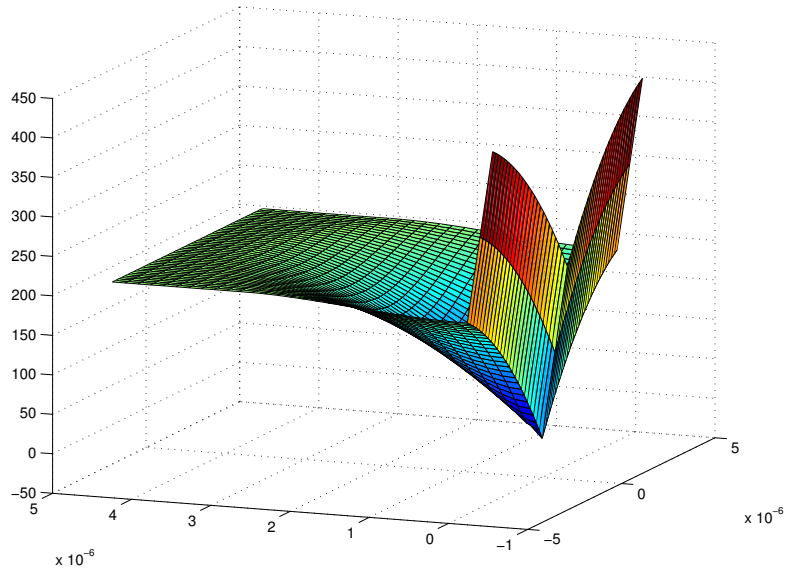

Figure 1: The potential surface $\phi(\delta) + \theta(\delta_n)$ in first loading, i.e., $\delta_{\max} = \delta$, in the two dimensional case.

irreversibility and is defined as the largest relative displacement attained through the history of the interface. In the dynamic case we solve the optimization problem

$$\begin{array}{ll} \text{n} & 8E(\bar{\mathbf{u}}) + (\mathbf{v}^{i+1} \nearrow \mathbf{v}^i)^T M (\mathbf{v}^{i+1} \nearrow \mathbf{v}^i) \\ \text{s.t.} & \frac{\Delta t}{4}(\mathbf{v}^{i+1} \nearrow \mathbf{v}^i) = \bar{\mathbf{u}} \nearrow \mathbf{u}^i. \end{array} \tag{2}$$

OPTIMIZATION ALGORITHM

The optimization problem has been solved in previous work using a continuation method. In this approach, the nondifferentiable objective function is approximated with a differentiable function that can then be solved by classical methods of nonlinear programming. The particular methods used in the previous work are the augmented Lagrangian method to handle the nonlinear constraints coupled with a trust region solver to minimize the resulting unconstrained subproblem.

The new optimization algorithm directly captures the nondifferentiability in a general purpose method for *nonlinear second-order cone programming* [2]. Second-order cone programming is a special case of semidefinite optimization in which, in addition to linear constraints, some of the constraints have the form $\|\mathbf{x}\| \leq y$, where $\mathbf{x}$ and y are variables of the problem. These constraints define convex sets, so the problem is overall a convex optimization problem and is usually solved by interior point methods. However, nonlinear second-order cone programming allows the treatment of nonconvex problems through the incorporation of additional nonlinear equality constraints. Extensions of interior point methods to the nonconvex case use various elements of traditional nonlinear programming.

References

[1] B. Bourdin, G. A. Francfort, and J.-J. Marigo. Numerical experiments in revisited brittle fracture. *Journal of the Mechanics and Physics of Solids*, 48(4):797–826, 2000.

[2] S. Boyd and L. Vandenberghe. *Convex Optimization*. Cambridge University Press, 2004.

[3] E. Hairer, S. P. Nørsett, and G. Wanner. *Solving Ordinary Differential Equations I: Nonstiff Problems*, vol. 8. *Springer Ser. Comput. Math*, 1993.

[4] C. Miehe, E. Gürses, and M. Birkle. A computational framework of configurational-force-driven brittle fracture based on incremental energy minimization. *International Journal of Fracture*, 145(4):245–259, 2007.

[5] K. D. Papoulia, C.-H. Sam, and S. A. Vavasis. Time continuity in cohesive finite element modeling. *Int. J. Numer. Methods Eng.*, 58(5):679–701, 2003.

[6] K. D. Papoulia, S. A. Vavasis, and P. Ganguly. Spatial convergence of crack nucleation using a cohesive finite element model on a pinwheel-based mesh. *Int. J. Numer. Methods Eng.*, 67(1):1–16, 2006.

[7] C.-H. Sam, K. D. Papoulia, and S. A. Vavasis. Obtaining initially rigid cohesive finite element models that are temporally convergent. *Eng. Frac. Mech.*, 72(14):2247–2267, 2005.

[8] B. Schmidt, F. Fraternali, and M. Ortiz. Eigenfracture: an eigendeformation approach to variational fracture. *Multiscale Modeling & Simulation*, 7(3):1237–1266, 2009.

A COMPUTATIONAL FRAMEWORK FOR NONLINEAR CONTACT BETWEEN DEFORMABLE EXCITABLE BIOLOGICAL CELLS

Marco Paggi*[1] and Alessio Gizzi[2]

[1]*IMT School for Advanced Studies Lucca, Lucca, Italy*
[2]*Università Campus Bio-Medico di Roma, Rome, Italy*

Summary Excitable deformable cells act as cooperative structures and show emergent behaviors from their interactions. The theoretical modeling and numerical simulation of such an interaction is far from being fully unveiled though information transmission mismatches have been shown to underline severe pathological conditions. In this study we provide a novel contact mechanics computational framework simulating the cooperative interaction among cardiac myocytes.

INTRODUCTION

Cardiac tissue is a complex heterogeneous and anisotropic medium characterized by nonlinear, multiscale and stochastic dynamics. Imperfect mechanotransduction in the cardiac tissue, converting mechanical deformation into a change in cell growth or remodeling, is a cutting edge research topic [1] since it can lead to a variety of diseases. In order to describe the dominant mechanisms occurring at different scales within a constitutive framework for the cardiac tissue, microstructural properties have to be properly described, including mechano-regulated interactions occurring among the tissue constituents. In particular, modeling and simulation of contact interactions between myocytes is a topic still unchallenged today and a progress in this field would allow the study of emergent phenomena considered at the forefront of research in cardiovascular biomechanics. In this perspective, in the present contribution, a novel constitutive and computational framework for the simulation of contact between cardiac myocytes is proposed.

METHODS

Computational model of active myocytes

The kinematics of myocytes is framed within the classical description of continuum mechanics under finite elasticity assumptions and specialized for two-dimensional domains. The boundaries $\partial\Omega$ of the myocytes are assumed to be smooth with $\partial\Omega = \partial\Omega_D \cup \partial\Omega_N \cup \partial\Omega_C$, where $\partial\Omega_D$, $\partial\Omega_N$ are the portions with Dirichlet and Neumann boundary conditions, while $\partial\Omega_C$ is the boundary interacting with the extra-cellular matrix or with neighboring cells (see Fig.1).

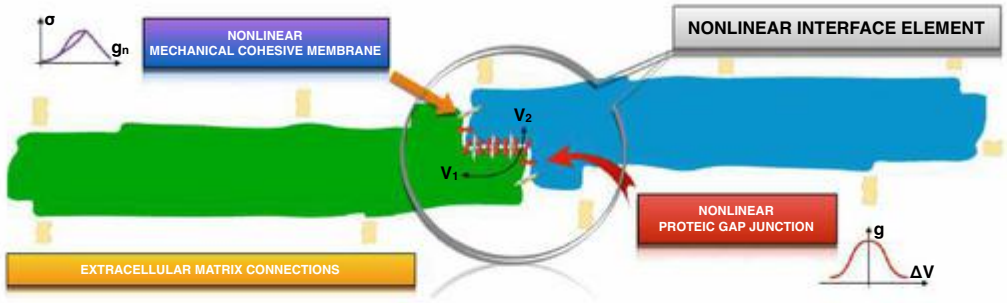

Figure 1: Schematic representation of the nonlinear contact modeling of excitable deformable cells.

In order to encompass the nonlinear coupling between the electrophysiological dynamics and the hyperelastic material response induced by the excitation-contraction mechanisms in cardiomyocytes [2], the multiplicative decomposition of the deformation gradient into an elastic and inelastic part is assumed [3, 4]. Specifically, the inelastic active deformation gradient, $\mathbf{F}_a$, is provided by the subcellular calcium/voltage dynamics, while the elastic deformation gradient is computed as is customary.

As far as the electrophysiological model for myocytes is concerned, in the present work the minimal model [5] is adopted, which has been demonstrated to capture the main features of the action potential spatio-temporal dynamics of the phenomenon with a reduced mathematical complexity. The resulting strong form of the problem is then:

$$\left\{\begin{array}{rl} -\nabla\cdot\mathbf{P}(\mathbf{u},\gamma) & = 0 \\ \mathrm{d}_t\gamma - f_\gamma(\mathbf{u},\gamma,s) & = 0 \end{array}\right. \quad \bigcup \quad \left\{\begin{array}{l} \partial_t V = \mathrm{div}\,(\mathbf{D}(\mathbf{u})\,\nabla V) + f_V(V,g_1,g_2,s) \\ \mathrm{d}_t g_1 = f_{g_1}(V,g_1), \quad \mathrm{d}_t g_2 = f_{g_2}(V,g_2), \quad \mathrm{d}_t s = f_s(V,s) \end{array}\right. \tag{1}$$

*Corresponding author. Email: marco.paggi@imtlucca.it

equipped with generalized boundary conditions describing the interaction of the myocyte with the extracellular matrix and with other cells. In this framework, the field variables are the displacement vector $\mathbf{u}$, the diffusive membrane voltage field V, the local electrophysiological gating fields g_1, g_2 and s, and the local fiber activation field γ. In Eq. (1), $\mathbf{P}$ denotes the second Piola-Kirchhoff stress tensor and the terms f_i are nonlinear functions of the field variables used to mathematically describe the corresponding reaction-diffusion partial differential equations.

For the solution of the above differential problem, a monolithic fully coupled isoparametric finite element formulation is proposed, extending and generalizing similar approaches [6]. Due to the strong nonlinearity of the resulting set of algebraic equations obtained by the semi-discretized finite element formulation in space, a fully implicit solution scheme is adopted. Hence, the implicit backward Euler time stepping technique is used and the incremental-iterative Newton-Raphson method is employed at each time step to achieve quadratic convergence of the numerical scheme.

Mathematical formulation of the interface model for myocytes interactions

Physiological quantities, mechanical tractions, and electric signals are exchanged at the boundaries between adjacent cells in contact, but also between a single cell and its extracellular matrix. Hence, a novel generalized interface element to be used along the whole myocyte boundary is proposed, thus to model both cell-cell and the cell-matrix interactions. As far as the mechanical field is concerned, the interface interactions are assumed to be of different type depending on the relative normal displacement, taking into account contact interactions with partial slip frictional effects in compression, and adhesive interactions in the case of separation. As regards the other fields, jumps in the transjunctional voltage and in the kinetic variables transmitted at the interface are allowed. The corresponding current and fluxes are assumed to obey nonlinear Fickian constitutive relations whose expression is determined from experimental measurements reported in the literature and obtained from cell-on-chip testing [1, 7]. The resulting formulation is implemented in a novel interface finite element for multi-field computations, in line with previous applications to mechanics and thermo-elasticity [8, 9]. Also for the interface, a monolithic fully coupled formulation is exploited and a fully implicit solution scheme is pursued, paying attention to the derivation of the tangent operators for the Newton-Raphson method.

RESULTS AND CONCLUSIONS

The proposed novel constitutive model, validated against experimental evidences, reproduces static and dynamic observed behaviors with particular attention to (i) length and slope of contact boundary, (ii) maximum tractions at the interface, (iii) cell width-length ratio, and (iv) propagation rate of action potential between adjacent myocytes. Simplified geometries are analyzed reproducing the microfluidic cell cultures adopted in the experiments in [1]. The proposed computational contact framework opens a new micro-scale level of analysis within the context of nonlinear interaction among biological objects. Forthcoming contributions will target different biomedical applications, e.g., crosstalk-based cardiovascular diseases, low energy defibrillation devices, and microfluidic chip design and optimization.

ACKNOWLEDGEMENTS

The present work has received funding from the European Research Council under the European Union's Seventh Framework Programme (FP/2007-2013) / ERC Grant Agreement n. 306622 (ERC Starting Grant "Multi-field and multi-scale Computational Approach to Design and Durability of PhotoVoltaic Modules" - CA2PVM).

References

[1] McCain M.L., Lee H., Aratyn-Schaus Y., Klber A.G., Parker K.K.: Cooperative coupling of cell-matrix and cell-cell adhesions in cardiac muscle. PNAS 109:9881–9886, 2012.

[2] Ambrosi D., Arioli G., Nobile F., Quarteroni A.: Electromechanical coupling in cardiac dynamics: the active strain approach. SIAM J Appl Math 71:605–621, 2011.

[3] Ruiz-Baier R., Gizzi A., Rossi S., Cherubini C., Laadhari A., Filippi S., Quarteroni A.: Mathematical modeling of active contraction in isolated cardiac myocytes. Math Med Biol 31:259–283, 2014.

[4] Gizzi A., Cherubini C., Filippi S., Pandolfi A.: Theoretical and numerical modeling of nonlinear electromechanics with applications to biological active media. Comm Comput Phys 17:93–126, 2015.

[5] Bueno-Orovio A., Cherry E.M., Flavio F.H.: Minimal model for human ventricular action potentials in tissue. J. Theor Biol 253:544–560.

[6] Wong J., Göktepe S., Kuhl E.: Computational modeling of chemo-electro-mechanical coupling: A novel implicit monolithic finite element approach. Int J. Numer Meth Biomed Engng 29:1104–1133, 2013.

[7] Hurtado D.E., Castro S., Gizzi A. Computational modeling of non-linear diffusion in cardiac electrophysiology: A novel porous-medium approach, Comput Methods Appl Mech Eng 300:70–83, 2016.

[8] Paggi M., Wriggers P.: Stiffness and strength of hierarchical polycrystalline materials with imperfect interfaces. J. Mech Phys Sol 60:557–572, 2012.

[9] Reinoso J., Paggi M.: A consistent interface element formulation for geometrical and material nonlinearities. Comput Mech 54:1569–1581, 2014.

A MULTI-SCALE MODEL FOR CONTACT MECHANICS OF ROUGH SURFACES

Yassine Waddad *[1], Vincent Magnier[1], Philippe Dufrénoy[1], and Géry De Saxcé[1]
[1]*Laboratoire de Mecanique de Lille, Université Lille 1, Lille, France*

Summary An efficient methodology is proposed for the analysis of contact between rough surfaces. First, a micro-contact model is defined depending on surface topography and material properties. Second, the parameters issued from the model are integrated into a macro-scale numerical model following a specific method. An example of this method is presented to show its robustness. Comparing to a numerical model where surface topography is explicitly meshed, this strategy provides good results and saves considerably computation time.

INTRODUCTION

Contact mechanics is of big interest in many mechanical systems such as friction brakes where the real contact area evolves constantly and influence drastically the system's performance. Indeed, contact interface is an important parameter to be considered because it plays a key role on many physical aspects such as stiffness, strength localisation, wear etc.
Consequently and given the scale where contact phenomena occur, it is nearly impossible to consider them in a macro-scale model without thinking on a multi-scale technique that transforms all the rules governing the micro-scale behaviour of contact interface into some sort of simplified laws that can be integrated into macro-scale models.
Accordingly, a multi-scale strategy is proposed to consider micro-contact phenomena's. First, for each considered contact phenomena, a micro-model is briefly described. Second, the multi-scale strategy of contact modelling is explained. Finally an example is presented and compared to a numerical model, where a real contact interface is explicitly modelled.

MICRO-CONTACT MODELS

Considering a rigid plan making contact with an elastic body having a rough surface. Roughness can be seen as a random set of parabolic asperities (see fig.1). When contact occurs, surface asperities deform elastically and contact forces are distributed among them, and thus, contact stresses and displacements in each point are given by a combination of all contact forces. Contact zones are almost elliptic and pressure have a semi-elliptic shape. If the elastic body is considered is homogeneous, Hertz theory is used to describe pressure and displacements following an approach based on potential theory and developed in ([1],[2]). If the body have an elastic properties varying with the depth; the latter approach is no longer valid. For this case, a model have been developed using the Hankel transform [3] and transfer matrix techniques[5].
The latter models describe the elastic squeezing of asperities under normal forces. Now if the plan is sliding, shear stresses lead to an expansion of contact zones. Additionally, due to wear effect, a part of the debris issued from the interface are compacted and form a relatively smooth and flat contact zones, namely called "contact plateaus" (see fig.2), that have an arbitrary geometry. These zones are discretized into many square patches. The contact is mainly concentrated on these zones and the remaining asperities. The problem is solved using an optimization technique to minimize the system's energy ([4]), as well as the FFT technique to accelerate the solving scheme.

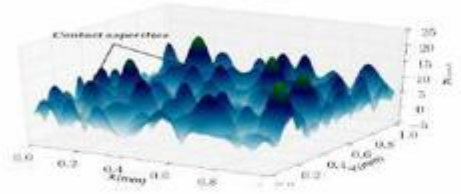

Figure 1: Schema of a surface containing asperities

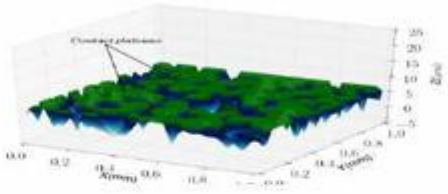

Figure 2: Schema of a surface containing plateaus

MULTI-SCALE STRATEGY

The aim of this strategy is to integrate the microscopic behaviour of an interface in a macroscopic numerical model. Indeed surface roughness will not be represented physically in the model but only included via a parameter namely called contact stiffness K_n. Indeed, within finite element framework, contact problems are solved using regularization methods, such as the penalty method. More precisely, this technique consists on pairing up contact pressure p_n to the gap g_n by a stiffness K_n: $p_n = K_n.g_n$. If the contact is perfect, theoretically g_n should be equal to zero, but practically, K_n is chosen to be very large to ensure a very small gap. However, this is not the case of real surfaces. In a real interface g_n evolves continuously considering

*Corresponding author. Email: waddad.yassine@gmail.com

roughness effect. To fulfil the strategy's objective, contact stiffness K_n will be chosen depending on surface roughness. Practically, contact surface is divided into many zones, where each zone has its proper geometry and roughness. On the one hand, micro-contact models give an information on how real displacement is related to contact pressure, and on the other hand, one can calculate the elastic displacement corresponding to perfect contact situation. The gap is then deduced by a simple subtraction of these displacements from real displacement, and automatically stiffness is calculated by derivation. This operation is done for all surface zones so that each zone has its local stiffness.

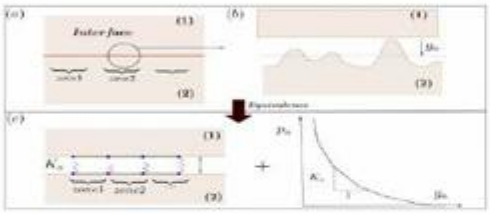

Figure 3: Schema of the proposed strategy

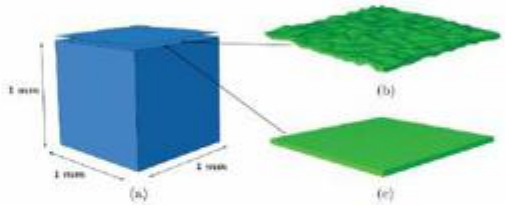

Figure 4: Numerical models

EXAMPLE : CONSIDERATION OF ASPERITIES

Considering a homogeneous elastic cube and a rigid plan (see fig.4(a)). The plan is moved vertically against the cube with a given vertical motion δ. Roughness is modelled by asperities. Two numerical models are proposed:

- Numerical reference model: A first model where asperities are explicitly meshed (see fig.4(b));
- Embedded numerical model: In the second model, the interface is flat. The surface is divided into 25×25 square zones. For each zone, the contact interface is embedded with a local contact stiffness using a semi analytic model considering elliptic asperities and the strategy described above (see fig.4(c)).

In fig.5, the evolution of contact mean pressure vs δ is presented for both numerical models and micro-model. The results obtained from embedded models match with the reference model and the semi analytic micro-model. In fig.6, contact pressure distribution is shown for different models. In fig.(a) and (b), it is clear that the number of contact zones, their shape and their orientation are consistent with the numerical reference model. In the embedded models (fig.6(c)), contact stresses distribution correspond to the contacting zones and depend on the size of each zone and its geometry. These zones are the ones where asperities are in contact, hence each zone describes macroscopically the micro mechanical behaviour of the asperities standing inside it. As regards the computational time, It has been reduced significantly. For the numerical reference model, the computational time is 3h whereas it does not exceed 15min for the embedded models and 10min for the semi-analytic model.

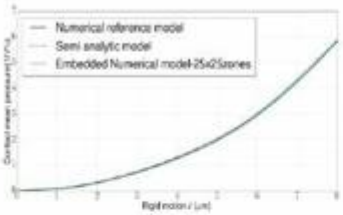

Figure 5: Mean pressure vs displacement

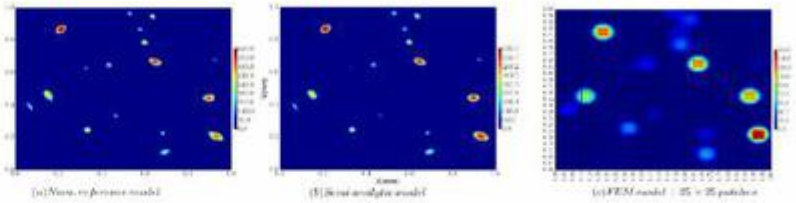

Figure 6: Contact pressure distribution (MPa) for different models

CONCLUSIONS

In conclusion, various contact models of rough surfaces have been presented. Also a strategy to integrate these models into macroscopic models have been proposed. Numerical analysis shows consistent results and the computational time have been reduced remarkably.

References

[1] Ciavarella, M.; Delfine, V. & Demelio, G. *A re-vitalized Greenwood and Williamson model of elastic contact between fractal surfaces*. J Mech Phys Solids 2006;54:256991.

[2] Johnson, K. L. *Contact mechanics*. Cambridge university press, 1987

[3] Sneddon, I. N. *The relation between load and penetration in the axisymmetric boussinesq problem for a punch of arbitrary profile*. Int. J of Eng Science, 1965, 3(1):47-57.

[4] Willner, K *Fully coupled frictional contact using elastic halfspace theory*. ASME Journal of Tribology, 130:0314051/8, 2008.

[5] Yue, Z. Q. *Elastic field for eccentrically loaded rigid plate on multilayered solids*. Int. journal of solids and structures, 1996, 33, 4019-4049.

Realistic RVE-geometries generation for Non-Crimp Fabric composites

G. Pierreux[1,2], D. Van Hemelrijck[1], Lincy Pyl[1], T.J. Massart[2]
[1]*MeMC Department, Vrije Universiteit Brussel (VUB), Brussels, Belgium*
[2]*BATir Department, Université Libre de Bruxelles (ULB), Brussels, Belgium*

Summary Non-Crimp Fabric composites (NCFs) are characterized by their high specific mechanical properties and enhanced delamination resistance. To extend their use in car and airplane applications, predictive damage models are necessary. Damage phenomena initiation, however, may be strongly influenced by stress concentrations, which requires a realistic geometrical modelling to capture accurately stress states at damage initiation sites. Yet, current models remain geometrically simplified, and/or would require the actual manufacturing of the NCF specimen each time another NCF configuration needs to be investigated. Using principles developed in [1] and extended with NCF features, a RVE generator was developed that allows producing realistic geometrical models in a computational efficient and automated way. This abstract discusses the RVE generation principles, illustrating that arbitrary shapes of NCFs can be obtained for different stitching parameters. Next, the geometrical models are discretized and used to investigate the influence of different stitching parameters on stress concentrations.

INTRODUCTION

The geometrical complexity of the reinforcement in Non-Crimp Fabric composites (NCFs) is due to the stitching process. Initially presented in unidirectional (UD) lamina, fibers are pushed aside by the penetration and tensioning of stitching yarns, resulting in mesoscopic and microscopic changes in the fibers configuration. Mesoscopic configuration changes may be classified in two categories, stitching holes and nesting, with different undulations directions. Stitching holes are typically linked to in-plane undulations of fibers, while, nesting, defined as the penetration of fibers of a given lamina into stitching holes of neighboring laminae, is accompanied by out-of-plane undulations. Microscopic changes in fibers configuration, additionally, need to be accounted for changes in the local fiber volume fractions and the local fiber directions.

As compared to straight unidirectional laminae; undulated laminae and local changes in the fiber configuration need to be included in geometrical models to obtain predictive damage models. These geometrical side-effects may initiate early damage, as they may act as stress concentrators. Undulated laminae may act as favorite places for delamination with increased volume fractions causing early crack initiation in the surrounding matrix. Additionally, straightening of undulated fibers upon loading may increase further the stress concentrations in their surroundings. A lack of account for these geometrical side-effects may cause inaccurate stress concentration prediction and, thus, inaccurate prediction of damage initiation.

Current geometrical models are usually based on simplifications or require the actual NCF specimen for each NCF configuration to be investigated. Geometrical model generators as WiseTex and TexGen assume NCFs as straight lamina in which "elliptical holes" are introduced via CAD geometries [2]. Alternatively, geometrical models can be based entirely on analytical descriptions of the contours of fiber bundles [3], for which the size and shape can be obtained via computed tomography, rendering the last approach a time consuming process. However, simplifications and/or time consuming processes make current methodologies cumbersome to investigate systematically the influence of stitching parameters on the stress concentrations. A new geometrical generation procedure that allows reproducing the complex geometrical features of NCFs in a computationally efficient way, has therefore been developed. The geometrical and meshing generation procedures will be described in the following.

RVE GENERATION PROCEDURE

The *geometrical generation* procedure consists of three successive operations (Fig.1):
(1) Initially, a set of straight in-plane lines represent the fiber configuration inside UD laminae (Fig. 1a), where its contour represents the UD lamina itself. Given the in-plane lines having a chosen diameter and considering geometrical contact conditions, the in-plane lines near stitching positions may be pushed away by the inflation of zero-thickness perpendicular lines representing the stitching yarns, to its final stitching yarn diameter (Fig. 1b). After inflation, a geometrical tensioning procedure straightens the lines in different stages (Fig. 1c). The number of lines discretisations and the amount of geometrical tensioning stages determine the final configuration of the set of discretized lines.
(2) contouring operations, acting on the final configuration of discrete lines, are implemented to obtain a 3D discrete volume entity for each lamina individually – stitching yarns are simplified as lines with circular cross section, as such, only contouring of laminae is needed. In the contouring operation, first, tetrahedral elements are created between the points of the discretized lines using a Delaunay 3D triangulation. Afterwards, tetrahedral elements inside stitching hole regions, as well as on possible concave borders of the lamina, are removed. Finally, by extracting the outer triangles from the remaining tetrahedral elements, a discretized contour of the lamina including possible holes is obtained (Fig. 1d).

(3) a level set-based post-processor is implemented to suppress possible interpenetrations, which may be present due to the discretization of lines into vertices. The implemented post-processor, as prescribed in [1], is based on distance calculations between the discrete contouring triangles and a regular grid, on which the level set field is created. A contouring function in MatLab allows extracting a set of triangles representing the contour of the final geometry (Fig. 1e).

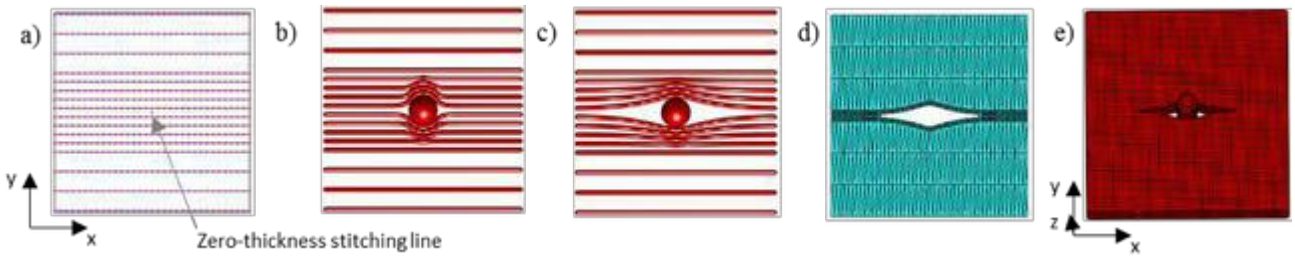

Fig. 1. Successive steps of the RVE generation procedure, illustrated on a UD lamina [0] penetrated by a straight stitch in its center: (a,b,c) set of discretized lines representing lamina and stitching yarn, respectively, at initial stage, after inflation and after geometrical tensioning (d) contouring of the discretized set of lines; (e) final geometry produced by a post-process level set-based procedure.

The *meshing generation* procedures can be performed in any general purpose meshing tool, such as GMSH [4], as the contours are constituted of a set of triangles that can easily be exploited. The set of triangles are representing boundaries of the fibrous rich regions. After surrounding these fibrous rich regions with a rectangular box, the boundaries of the matrix rich regions are obtained by subtracting the fibrous rich areas from the box. Using the "Compound Surfaces" tool in GMSH, sets of triangles are reparametrized in the meshing procedure, therefore avoiding ill-shaped elements . Successively, the regions are meshed with tetrahedral elements.

The generated RVEs can be used in any general purpose FE code, in which the fiber volume fractions and directions can be explicitly taken into account by exploiting the discretized lines configuration form the geometrical model. Considering linear elastic material models, the influence of the stacking sequence and stitching parameters on the stress concentrations will be illustrated.

RESULTS

Geometrical models of NCFs with different stitching parameters and stacking sequence can easily be obtained with the parametrized RVE generator. As an illustration, the in-plane and out-of-plane undulations of fiber bundles, in a RVE presenting a NCF with stacking sequence [90/+45/0], can be reproduced by the generator (Fig 2). Current geometrical models, on the contrary, would consists of straight lamina with a constant shape of the stitching hole across the thickness, or would be based on CAD geometries requiring the actual NCF specimen. The importance of these geometrical side-effects on the stress concentrations will be emphasized.

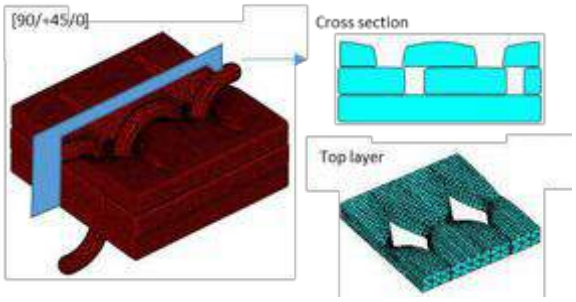

Fig. 2. shape of fiber bundles in NCF obtained by the computational generation procedure.

References

[1] Sonon, Bernard, and Thierry J. Massart. "A Level-Set based Representative Volume Element generator and XFEM simulations for textile and 3D-reinforced composites." Materials 6.12 (2013): 5568-5592.

[2] Verpoest, Ignaas, and Stepan V. Lomov. "Virtual textile composites software WiseTex: Integration with micro-mechanical, permeability and structural analysis." Composites Science and Technology 65.15 (2005): 2563-2574.

[3] Zeng, Xuesen, et al. "Geometrical modelling of 3D woven reinforcements for polymer composites: Prediction of fabric permeability and composite mechanical properties." Composites Part A: Applied Science and Manufacturing 56 (2014): 150-160.

[4] Geuzaine, Christophe, and Jean- François Remacle. "Gmsh: A 3- D finite element mesh generator with built- in pre- and post- processing facilities." International Journal for Numerical Methods in Engineering 79.11 (2009): 1309-1331.

UNIFIED TREATMENT OF SHOCKS AND MATERIAL INTERFACES IN HYPERELASTIC SOLIDS AND FLUIDS

Niranjan S. Ghaisas*[1], Akshay Subramaniam[2], and Sanjiva K. Lele[1,2]

[1]*Center for Turbulence Research, Stanford University, Stanford, California, USA*
[2]*Dept. of Aeronautics & Astronautics, Stanford University, Stanford, California, USA*

Summary Treatment of discontinuities like shockwaves and interfaces pose a challenge for numerical simulations. Here, we present a novel treatment of shockwaves and material interfaces in the context of high-order Eulerian simulations of hyperelastic solids, liquids and gases using a 10th order spectral-like compact finite difference scheme [1] and an adaptation of the standard LAD scheme [2]. The method is suitable for solving high energy density problems in a single phase as well as problems involving interactions between different phases. Particular emphasis is laid on the scaling of the model constants in the LAD scheme for different problems. We demonstrate the applicability of the method using 1D stationary shock, shock tube and impact problems.

INTRODUCTION

High energy density materials undergoing large deformations occur in various engineering applications such as Inertial Confinement Fusion (ICF), cavitation and metal welding, which can benefit from a detailed understanding of the underlying physical processes, afforded by numerical simulations. An Eulerian method is well suited to such simulations since they involve large deformations. The Eulerian equations tracking elastic and plastic flows in a hyperelastic material were developed by [3]. The aim of the current work is to extend a high-order compact finite-difference scheme previously used for shock-capturing simulations of gases to liquids and solids.

FORMULATION

The basic framework comprises of equations governing transport of mass, momentum, energy and elastic components of the inverse deformation gradient tensor [4], with plasticity incorporated as described in [5]. The hyperelastic separable equation of state (EOS), with parameters γ, p_∞ and μ [4] is used. Gases, liquids and solids are described by a single EOS, since setting $\mu = 0$ reduces the material to a stiffened gas (or liquid), and further setting $p_\infty = 0$ leads to the ideal gas EOS.

The system of equations is solved using a 10th order compact finite-difference scheme with th order Runge-Kutta time stepping. A key component enabling the use of high-order centered schemes is the addition of numerical dissipation to capture shocks that might arise in the solution stably. The localized artificial diffusivity (LAD) scheme of [2], involving artificial shear and bulk viscosities and artificial conductivity, with coefficients C_μ, C_β and C_κ, respectively, is used here. Typical values used previously for ideal gases are $C_\mu = 0.002$, $C_\kappa = 0.01$, and $C_\beta \sim 2.0$.

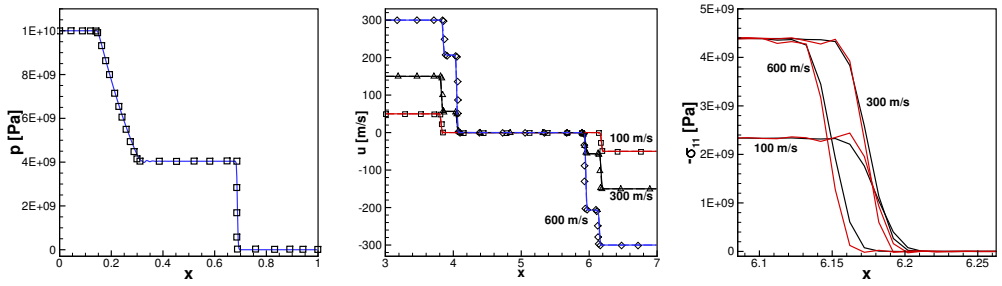

(a) (b) (c)

Figure 1: (a) Shock tube problem in water ($\gamma =$. , $p_\infty = 0.$ GPa, $\mu = 0$ Pa [6]) at 51 μs using $C_\beta =$ .0. Current results: line, exact solution: symbols. (b) Elastic-plastic impact problem in steel ($\gamma = 2.8$, $p_\infty =$ 0 GPa, $\mu =$ GPa [7]) half-spaces for three impact velocities at 0.2 ms. Current results: lines, ref. [7]: symbols. (c) Close-up view around the elastic shock of negative axial stress showing large oscillations when $C_\beta = 2$ (red lines) and oscillations damped out when $C_\beta \sim 10$ (black lines).

*Corresponding author. Email: nghaisas@stanford.edu

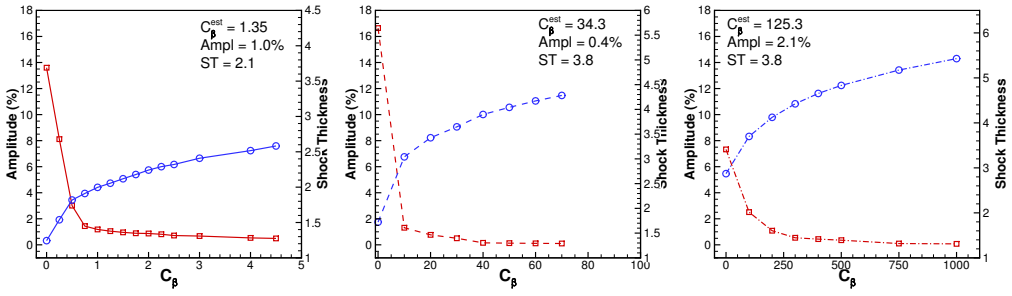

(a) (b) (c)

Figure 2: Amplitude (red lines) and shock thickness (blue lines) as a function of artificial bulk viscosity coefficient C_β in stationary shocks in (a) air ($\gamma = 1.$, $p_\infty = 0$ Pa, $\mu = 0$ Pa, pressure jump $p_R/p_L =$ .5), (b) water ($p_R/p_L =$ 0) and (c) steel ($p_R/p_L = 2$ 0). The text in the figures indicates coefficients predicted by a dynamic procedure and corresponding amplitudes and shock thicknesses.

RESULTS

Figure 1(a) shows an application of the proposed methodology to the classical shock tube problem in water with pressures on two sides of the interface at $x = 0.5$ equal to 10^{10} Pa and 10^5 Pa. The solution at $t = 51$ μs agrees well with the analytical solution. The value $C_\beta =$ had to be used in order to capture the shock smoothly in this case. Figures 1(b-c) demonstrate problems involving impacts of two steel half-spaces [7]. Elastic-plastic shocks arise depending on the impact velocities, and the velociy profiles obtained from our method agree with the reference results [7]. $C_\beta =$ ~ 11 had to be used for these results. The proposed methodology successfully captures shocks and provides stable solutions in gases, liquids and hyperelastic solids, provided the coefficient C_β is adapted to the problem and material parameters.

Figure 1(c) demonstrates that the value used previously for ideal gases leads to oscillations when applied to solids. The dependence of C_β on material and problem parameters has not yet been explored systematically since the range of EOS variation considered was small. Finding a scaling for C_β is imperative for a unified treatment of shocks using LAD. To explore this issue, 1D stationary normal shock simulations are carried out for various parameter values, and the variation of the amplitude of wiggles in the pressure profile expressed as a percentage of the pressure jump and numerical shock thickness normalized by the grid spacing (computed as in [2]), with C_β is shown in Figure 2. It is again clear that a single value of C_β is unsuitable, and C_β needs to be varied drastically in order to capture shocks smoothly across the three continuum media.

A dynamic method to auto-tune the coefficient is proposed, and the coefficient values estimated by the dynamic method, along with the resulting amplitudes and thicknesses are mentioned in the text in Figure 2. The method is based on order of magnitude estimates of the advection and diffusion terms in the momentum equation, and modifies the coefficient according to shock strength, material properties, as well as the numerical discretization method. Details of the dynamic method will be included in the final paper. We note that the method produces reasonable estimates that lead to wiggle amplitudes less than or close to 1% without excessive smearing of the shock in gases, liquids as well as solids.

SUMMARY AND FURTHER WORK

A high-order compact finite-difference numerical framework with the LAD scheme, previously applied to ideal gases, is successfully extended to shocks in liquids and solids. A dynamic method to auto-tune the artificial coefficients appearing in the LAD scheme is proposed, and will be described in detail in the final paper. Further single-material demonstration problems and extension to multi-material interfaces will also be included in the final paper.

This work was supported by Grant B612155 from Lawrence Livermore National Laboratory, U.S. Department of Energy.

References

[1] Lele, S.K.: Journal of computational physics, 103(1), pp.16-42, 1992.
[2] Kawai, S. and Lele, S.K.: Journal of Computational Physics, 227(22), pp.9498-9526, 2008.
[3] Plohr, B.J. and Sharp, D.H.: Advances in Applied Mathematics, 13(4), pp.462-493, 1992.
[4] Gavrilyuk, S., Favrie, N. and Saurel, R.: Journal of Computational Physics, 227, pp.2941-2969, 2008.
[5] Favrie, N. and Gavrilyuk, S.: Philosophical Transactions of the Royal Society A, 369, pp.2864-2880, 2011.
[6] Farhat, C., Rallu, A. and Shankaran, S.: Journal of Computational Physics, 227, pp.7674-7700, 2008.
[7] Kluth, G. and Després, B.: Continuum Mechanics and Thermodynamics, 20, pp.173-192, 2008.

SIMULATING THE MICROSTRUCTURAL FAILURE MECHANISM OF SHEAR BANDS IN STEEL

Ioannis Polyzois[1a)], Nabil Bassim[1]
[1]*Department of Mechanical and Manufacturing Engineering, University of Manitoba, Winnipeg, Manitoba, Canada*

Summary High strain rate plastic deformation of metals results in the formation of localized zones of severe shear strain known as adiabatic shear bands (ASBs), which are a precursor to shear failure. The formation of ASBs in AISI 4340 steel was examined experimentally and through simulations. Testing parameters included heat treatment temperatures, testing temperature, and impact momentum using the Direct Impact Hopkinson Pressure Bar (DIHPB). Using experimental stress strain response data, a two dimensional axi-symmetric simulation model was developed in Matlab and explicit FEA software LSDYNA to simulate ASB formation in AISI 4340 steel. The model uses the Voronoi tessellation to generate the prior austenite grain structure of the steel, and also generates geometry for the martensite sub-grain lath blocks and a grain boundary geometry representative of the cross section of the specimens. The model was discretized using a meshless Lagrangian formulation. Simulation results closely matched experimental findings.

EXPERIMENTAL INVESTIGATION

An experimental program was designed to determine (a) the effect heat treatment on the grain size of AISI 4340 steel, and (b) the conditions that lead to the formation of ASBs. The following parametric variations were selected: Type of steel (AISI 4340); Heat Treatments (800˚C, 900˚C, 1000˚C / 30min, oil quenching, & tempering at 400˚C /90min and 550˚C /90min); Impact Momenta (30kgm/s, 45kgm/s, 49kgm/s, 52kgm/s); and Testing Temperatures (20°C, 428°C). Specimens were cut in lengths of 9.5mm from high strength low-alloy AISI 4340 normalized steel rods with a diameter 9.5 mm. The specimens were tested under impact using the DIHPB. A total of 48 specimens were tested.

In studying martensitic steel AISI 4340, the accepted measure of grain size is the size of the crystallographically coherent block or the prior austenite grain which is formed when the steel is austenized at elevated temperatures. Impacted steel specimens were etched with a picric acid solution mixed with small amounts of HCl and heated to 80ºC, to reveal the prior austenite grains and martensite lath blocks. Grain sizes were calculated using the ASTM grain size number, G, and a modified Hyen Intercept Method. This method uses randomly positioned concentric circles of known circumference that is overlaid on the micrograph and the number of intersections of grain boundaries with the circumference is calculated (Fig.1). The number of grain boundaries that intercept the circles was meticulously counted and recorded and used to determine the grain size according to ASTM E112-10 [1]. The key findings from the experimental program are summarized as follows [2,3]. a) Prior austenite grain size increased by an average of 7µm per 100ºC increase in austenization temperature. b) Prior austenite grain size did not change with tempering temperature. c) Prior austenite grain sizes away from the location of ASBs did not change with impact momentum. d) Under deformation, grains reoriented themselves and elongated in the direction of maximum shear. e) ASBs formed more readily at higher impact momenta. f) Deformed ASBs are characterized by the reorientation and severe elongation of grains in the direction of maximum shear, while transformed ASBs are characterized by the reorientation, elongation, and sudden refinement of grains inside the band. g) Prior austenite and martensitic block grain sizes did not change with testing temperature.

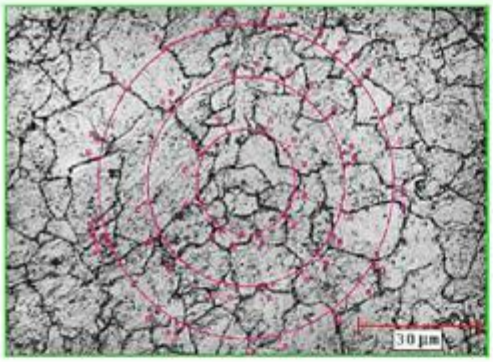

Fig. 1. Micrograph of AISI 4340 specimen heat treated at 800°C, tempered at 400°C and impacted at 52 kgm/s showing area used to calculate ASTM grain size

THEORETICAL INVESTIGATION

Using measurements of AISI 4340 steel grain size at various heat treatments as well as dynamic stress-strain data, a finite element model was developed in Matlab and explicit dynamic software LSDYNA, by Polyzois [2,4], to simulate the microstructural deformation of grains under high strain rate impact, through the cross-section of a specimen. The model approximates the complex heterogeneous grain microstructure of AISI 4340 steel by simulating grains in 2D using the Voronoi Tessellation algorithm. It takes into account prior austenite grain size, martensite lath block grain size, and the associated microstructural material property inhomogeneity between the grains and grain boundaries. The model takes advantage of the Lagrangian formulated Smooth Particle Hydrodynamics meshless discretization to simulate highly localized deformation as well as the high strain rate Johnson-Cook Plasticity material model for defining the properties of the steel at various heat treatments. Simulation results show the heterogenetic material property dependence on nucleation and

[a)] Corresponding author. Email: umpolyzo@myumanitoba.ca

propagation of ASBs in AISI 4340 steel, more accurately and realistically, compared to a homogeneous model, for a wide range of heat treatment and testing conditions.

A simulation of the progression of strain propagation for steel heat treated at 800ºC/30 minutes and tempered at 400ºC/90 minutes, subject to an impact momentum of 52 kgm/s, is shown in Fig 2. The model is comprised of large prior austenite

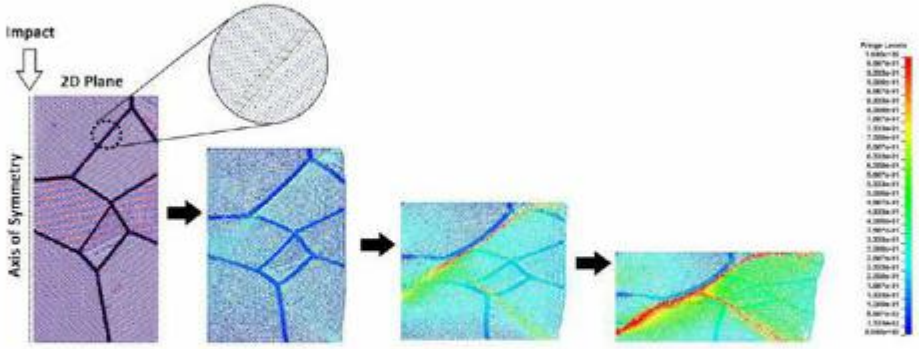

Fig. 2. Progressive effective plastic strain response of a heterogeneous material Grain Model of AISI 4340 steel with heat treatment (800°C/30 min & 400°C/ 90min) impacted at 52 kgm/s

grains, which are themselves comprised of long martensite lath blocks. The prior austenite grain boundaries are also modeled to have a specific thickness based on the size of the grains. Grain size and material properties of the microstructural constituents were calculated from extensive impact testing and micro indentation hardness tests of the AISI 4340 steel specimens at various heat treatments. Fig. 2 shows ASB localization nucleating from the grain boundary and propagating outwards in the direction of maximum shear. The figure also shows that when a grain boundary is not present near the maximum shear direction, localization will occur through the grain, but to a lesser extent, and initiate from an impact face.

The results of various simulations showed that ASBs formed in two distinct ways. Firstly, thick localized zones of severe shear strain surrounded by a reorientation and elongation of the surrounding matrix were found to nucleate from the impact face and propagate through the grains. This is indicative of the formation of “deformed” ASBs found in softer steels heat treated to have large prior austenite grains, and which exhibit a large plastic zone during deformation. Secondly, thinner more prominent zones of severe localization were found to nucleate at the prior austenite grain boundaries and propagate outward along the lines of maximum shear. This is indicative of severely localized “transformed” ASBs which were found in harder, stronger steels heat treated to have smaller grain sizes. Based on the results, it can be said that localization is more severe in steels that have a higher prior austenite grain boundary density, which act as nucleation points along the lines of maximum shear. The prior austenite grain boundaries tend to be low energy zones between grains, to which hard solute particles segregate. These hard particles can be said to be the initiators from which ASBs form.

In all simulations, grains were shown to rotate and elongate in the direction of shear. In severely localized zones of shear, SPH elements were found to break down into smaller groups of nodes or individual nodes, indicative of micro-cracking or grain refinement. In experimentation, grains, several times smaller (x10) than the parent prior austenite grain, were observed within the formation of severely localized ASBs [2,3] indicating the possibility of grain refinement as a mechanism within the formation of ASBs.

CONCLUSIONS

Experimental and simulation results showed that the formation and severity of localization under impact in AISI 4340 steel is highly dependent on prior austenite grain size (controlled by heat treatment) and the prior austenite grain boundary density. Severe localization formed by nucleating at the prior austenite grain boundaries and propagating outwards along the lines of maximum shear. A higher grain boundary density creates more nucleation sites for ASB formation. A reduction in observed grain size within the formation of ASBs, both experimentally and through simulations, indicate that grain refinement is a possible mechanism within the formation of ASBs in AISI 4340 steel.

References

[1] ASTM E112-10: Standard Test Methods for Determining Average Grain Size. *ASTM International*, 2010.
[2] Polyzois I.: Prediction of the Formation of Adiabatic Shear Bands in High Strength Low Alloy 4340 Steel Through Analysis of Grains and Grain Deformation. *PhD Thesis*, University of Manitoba Mech. Eng. Dept., Winnipeg, 2014.
[3] Polyzois I., Bassim N.: An Examination of the Formation of Adiabatic Shear Bands in AISI 4340 Steel Through Analysis of Grains and Grain Deformation. *Mater. Sci. Eng. A*, **631**:18-26, 2015.
[4] Polyzois I., Bassim N.: Microstructural Simulation of Adiabatic Shear Band Formation in AISI 4340 Steel Using Voronoi Tessellation. *Computational Materials Science*, **109**:157-171, 2015.

STRAIN-RATE-DEPENDENT COHESIVE LAW IN MODELLING BREAKUP OF EARTH COVERED MAGAZINE

Q J Yu[1], S C Fan[1a)], & C K Lee[2]
[1]*School of Civil & Environmental Engineering, Nanyang Technological University, Singapore*
[2]*School of Engineering and Information Technology, University of New South Wales Canberra, Australia*

Summary Numerical simulation has been carried out to study the breakup of earth covered magazine due to internal detonation. As experimental study of such problem is very expensive, time consuming and with many limitations in scaling, data collections and analyses, numerical simulation using advanced modelling techniques provides a valuable alternative approach. In this study, the commercial dynamic solver LS-DYNA [1] is adopted to carry out the simulations of the magazine breakup by using the cohesive element model. The *MAT_COHESIVE_TH model in LS-DYNA is strengthened by implementing the strain-rate dependent characteristics of the concrete cohesive law. The simulation results are comparable with the test results.

INTRODUCTION

Upon accidental internal explosion, an ammunition magazine will break up and debris formed will be ejected out at high speed. The debris could impact on the neighbouring structures or people and may cause damages and causalities. The size of the hazard zone due to ejected debris is a critical factor to meet the design requirements of minimum safe clear distance to the nearby inhabited buildings or facilities. Due to the nature of the problem, full-scale or scaled experimental study on the high speed debris trajectories is deemed to be very costly. A feasible alternative is to harness the power of the modern computing technology to conduct numerical simulations, together with verification by a limited number of field tests. In numerical simulation, a physics-based modelling procedure has to be established to simulate the dynamic response and the breakup process of the earth covered magazine (ECM). These simulations were based on the general dynamic analysis package LS-DYNA [1] which has been used extensively in solving dynamic problems (impact, crash, penetration, explosion, etc.). However, when using it to simulate the strain-rate-dependent material behaviour and response during the breakup of an ECM, further development is needed.

BREAKUP MODELLING

The present simulation involves quite a few simulation aspects: blast loading, fluid solid interaction, structural breakup, etc. The breakup modelling is critical to determine the debris distribution and their flight distances. In the finite element (FE) method, the fracture simulation is achieved mainly by an approach through element erosion. In LS-DYNA, nodal-splitting is an alternative approach to simulate the fracture. In which, the FE mesh is shattered into separate element-sized pieces, and the nodes at the same location are bundled together by a nodal constraint. The bundled nodes will be released after a pre-defined strain-based criterion is met. Prior to the event of nodal split, the elements perform integrally as in a continuum structure and the nodal displacements are continuous. Upon occurrence of nodal split, free fractured/cracked surface will be formed along the element mesh interface. While the nodal splitting is easy to be implemented, such approach comes with many shortcomings. Obviously, fractured surfaces through the split node in all directions will be created at the same instant when the strain criterion is met. Furthermore, the strain-based splitting criterion has less physical meaning. To alleviate these shortcomings, cohesive law and cohesive elements are introduced to simulate the reinforced-concrete (RC) structural breakup. In the latter approach, discrete elements are connected to each other through inter-element faces by cohesive elements instead of the nodal constraint. These cohesive elements, sometimes referred as "interface element", are inserted along all element interfaces. Fractured surface will be formed along FE interface once the in-between cohesive element fails. In this case, a pseudo-material model is needed for these cohesive elements to simulate their responses and failures. This pseudo-material model is normally referred as the cohesive law (or the traction-separation law).

IMPLEMENTATION OF STRAIN-RATE-DEPENDENT COHESIVE LAW

In this study, a *MAT_COHESIVE_TH cohesive model in LS-DYNA is used for concrete material. As the thickness of cohesive element is zero, the common definition of strain rate is not applicable. So the crack opening or separation velocity is chosen to be defined as a rate-relevant parameter. As the cohesive law constitutes cohesive strength and fracture energy, the rate effect can be divided into two parts. The first part is the rate-dependent cohesive strength for the loading stage. The second part is the rate-dependent fracture energy for the softening stage. As such, the relationship of cohesive strength and fracture with the opening velocity should be established. In this study, a simple model (see Fig.1) is built to study the relationship between the cohesive strength and the opening velocity. It includes two solid bulk material elements and one cohesive element with elements size of 0.01m. The bottom is fixed and the top four nodes are subjected to tension.

[a)] Corresponding author. Email: cfansc@ntu.edu.sg

Responses to 6 different loading rates are investigated and the results are shown in Table 1. Fig.2 shows the fitted Dynamic Increase Factor (DIF) for cohesive strength against the opening velocity. For the rate-dependent fracture energy, the results of Harald [2] are adopted. Fig.3 shows the DIF of fracture energy against the opening velocity.

Table 1 Relationship between cohesive strength DIF and opening velocity

Case	Strain rate(1/s)	Strength peak(MPa)	DIF	Opening velocity (m/s)
1	0.1	4.15	1.0375	1.42e-4
2	1	4.47	1.1175	0.0014
3	10	7.23	1.8075	0.015
4	50	12.8	3.2000	0.08
5	100	15.4	3.8500	0.18 during loading; 0.4 upon yielding and unloading
6	500	30.0	7.5000	0.8 (average) during loading; 4.5 upon softening till fail

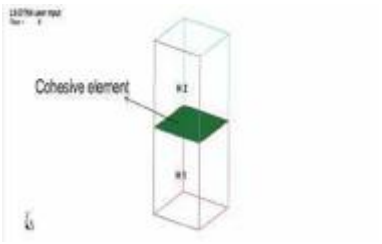

Fig.1 Simple model

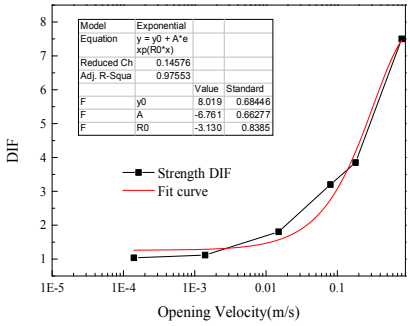

Fig.2 Strength DIF

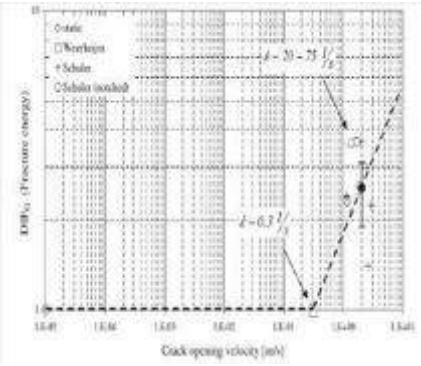

Fig.3 Fracture energy DIF (Harald [2])

RESULTS IN AN ECM BREAKUP

In an ECM 2/5th scaled ECM explosion test, the structural internal dimensions of the RC cubic box are 2.0m×2.0m×1.6m. Wall and roof thicknesses are 200mm and they are reinforced with Ø 10-mm bars at 100-mm spacing in two directions and double layers. Fig.4 shows the FE model for half of the ECM. Under a high loading density of 20 kg/m^3, the cohesive elements almost all failed if rate-independent cohesive law is used. Upon implementing the current rate-dependent cohesive law, the breakup results are found to very different as shown in Fig.5, which shows very big pieces of debris formed from the side walls, rear wall and the roof, and such outcomes agreed very well with site test results.

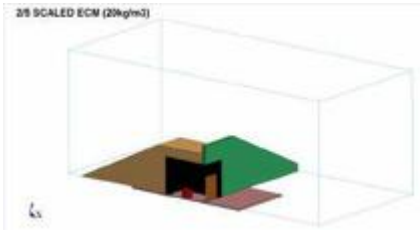

Fig.4 FE model for 2/5th scaled ECM

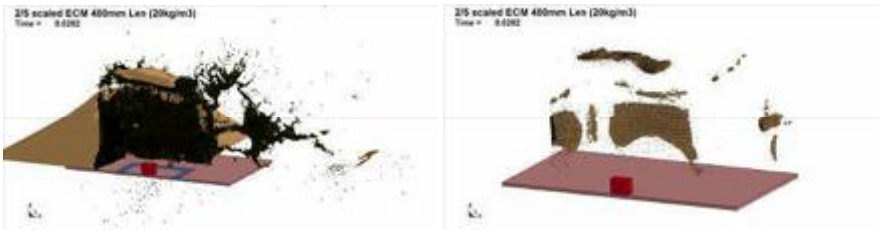

(a) The half structure (b) The remained cohesive elements

Fig.5 Breakup simulation results with rate-dependent cohesive law

References

[1] LS-DYNA Keyword User's Manual, Version 971. Livermore Software Technology Corporation (LSTC), USA, 2007.

[2] Harald S., Christoph M., and Klaus T.: Spall experiments for the measurement of the tensile strength and fracture energy of concrete at high strain rates. *International Journal of Impact Engineering* **32**:1635-1650, 2006.

SPECTRAL METHODS FOR ELECTROMECHANICAL COUPLING IN FERROELECTRICS

Vidyasagar A.[1 a)], Felix Göküzüm[2], Wei-Lin Tan[1] & Dennis Kochmann[1]
[1]*Graduate Aerospace Laboratories, California Institute of Technology, Pasadena, CA 91125, USA*
[2]*Institut für Mechanik (Bauwesen) Lehrstuhl I, Universität Stuttgart, Pfaffenwaldring 7, 70550 Stuttgart, Germany*

Summary Recent advances in fast numerical methods to compute the mechanical response of heterogeneous microstructures have allowed the solution of hitherto intractable systems. In particular the use of an iterative Fourier Spectral Method as opposed to the traditional Finite Element Method has gained significant interest in the periodic homogenisation of microstructures. In this paper, a method is presented to solve a periodic boundary value problem involving electromechanical coupling in a polycrystalline ferroelectric microstructure. In addition to the mechanical response of the structure, this method provides insight into the kinetics of domain wall motion in a complex microstructure. Time hysteresis curves for the electric displacement and strain evolution resulting from a saw-tooth electric loading are presented, and are shown to qualitatively match experimental results. An overview of the diverse applications of this method is also provided.

INTRODUCTION

Piezoelectrics are a class of materials which demonstrate strong electromechanical coupling behaviour. The application of an external electric field results in a spontaneous strain in a given sample; conversely, the application of a strain results in the generation of an electric field. Ferroelectrics are a subset of piezoelectrics which exhibit spontaneous electric polarisation, demonstrate domain switching and consequently possess a remnant strain [1]. Ferroelectric materials such as PZT, Barium Titanate and PMN-PT have been widely used in engineering applications. Examples of the use of ferroelectrics include sensors, actuators, transducers and energy harvesting devices.

However, the primary use of ferroelectrics lies in the linear regime, where they behave with piezoelectric properties. In order to advance the use of the non-linear regime, further study is required into the kinetics of domain wall motion and thermos-electromechanical coupling in ferroelectrics [1]. This would also allow for tunable electrical and mechanical systems which exploit the memory effect due to non-linearity of the strain hysteresis. In this context, the problem of simulating and understanding microstructural evolution with dynamic thermo-electromechanical loading is complex and numerically expensive using a traditional Finite Element framework. In this paper, a Fourier Spectral implementation is presented, which allows for solution of hitherto intractable periodic boundary value problems involving electromechanical coupling in ferroelectrics.

OVERVIEW OF THE SPECTRAL METHOD FRAMEWORK

Spectral methods which utilise the Fast Fourier Transform have been introduced in computational solid mechanics over the past two decades by Moulinec, Suquet, Lebensohn and others [2, 3, 4]. Lebensohn et al. have developed an algorithmic framework for solving coupled problems involving thermoelasticity and viscoplasticity [3]. The iterative spectral method developed scales quasilinearly (as opposed to quadratic or cubic) in computational cost with the number of degrees of freedom and avoids the assembly of large stiffness matrices. Hence this framework allows for solution of polycrystals with a large number of grains. The limitation of this technique is that the initial problem has to be periodic for convergence of the Fourier inversion. Subsequently, the solution is subject to periodic boundary conditions. The spectral framework developed takes advantage of this fact, solving for a periodic Representative Volume Element (RVE). An example of a periodic polycrystalline microstructure, together with a simulated heterogeneous non-linear elastic RVE under uniaxial strain are shown in Figure 1.

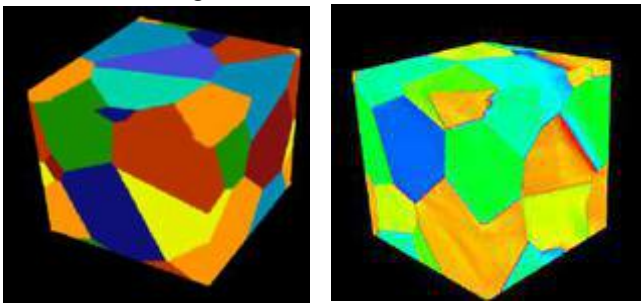

Figure 1: *Periodic polycrystalline model and stress distribution of a simulated polycrystal during non-linear elastic test*

Following this work, a numerical implementation for the solution of coupled electromechanical periodic boundary value problems has been developed. The governing model and associated scaling parameters are obtained from Zhang and Bhattacharya and recast within this spectral framework [5]. The spectral framework itself can be described as an explicit, time-stepped Fast Fourier Transform-based scheme. The τ perturbation method is used to convert the governing mechanical

[a)] Corresponding author. Email: vvidyasa@caltech.edu

and electrical equilibrium equations into the iterative equations. Polarisation distributions are updated using an evolution equation or kinetic law and external electric load stepping is performed. The external electric field is applied to the sample through a saw-tooth function and the coupled electric and mechanical response is obtained at each step of the loading.

SIMULATION RESULTS & COMPARISON TO EXPERIMENTS

A simplified two dimensional homogeneous microstructure is simulated to observe the generation of a polarisation wave that propagates across the body resulting in domain switching. This is used to produce the curves of electric displacement and strain with the electric loading, and shown in Figure 2.

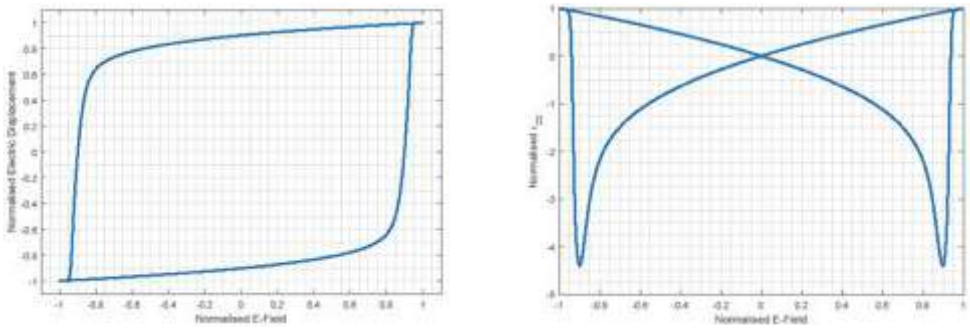

Figure 2: *Normalised simulation results for switching in a single crystal under saw-tooth electric loading*

Experimental material characterization was performed on commercial samples of polycrystalline PZT-5A with 1mm thickness. SEM analysis indicates average grain sizes of ~2μm. Typical electrical displacement hysteresis curves below were obtained by applying a through-thickness electric field of -2kV to 2kV with a triangular wave profile. Simultaneous in-plane strain measurements were taken using a 3D digital image correlation (DIC) system.

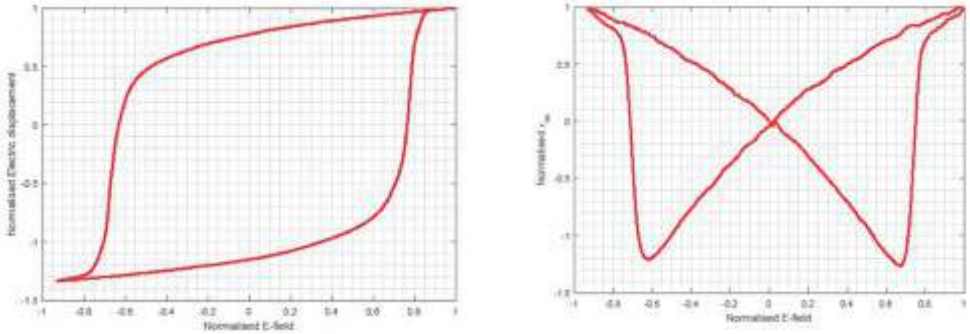

Figure 3: *Normalised experimental results for electromechanical response under saw-tooth cyclic electric loading*

Figure 3 shows a typical electrical displacement response of PZT-5A with applied electric field. Switching occurs at coercive field of 1.5kV/mm. The corresponding ε_{xx} (in-plane) strain curve indicates abrupt transition from extension to compression at the coercive field. Positive values indicate extension. These experimental measurements show qualitative agreement with the normalised plots of electric displacement and strains obtained using our spectral framework.

CONCLUSIONS

This work has shown promise in providing new insight into the complex mechanics of domain wall motion and electromechanical response of ferroelectrics. The advantage of the Spectral Method implementation over using Finite Elements is the computational efficiency in simulating large and complex microstructures. Further work is to be done in understanding and incorporating further effects such as thermal dependence and improving the kinetic relations for domain switching [1].

References

[1] Wojnar S. C.: Exploring the Kinetics of Domain Switching in Ferroelectrics for Structural Applications. *PhD Thesis*, GALCIT Caltech, 2015.

[2] Moulinec H., Suquet, P.: Comparison of FFT-based methods for computing the response of composites with highly contrasted mechanical properties. *Physica B*, 338:58–60, 2003

[3] Lebensohn R. A.: N-site modeling of a 3D viscoplastic polycrystal using Fast Fourier Transform, *Acta Materialia*, 49: 14: 2723-2737, 2001.

[4] Diehl M.: A spectral method using fast Fourier transform to solve elastoviscoplastic mechanical boundary value problems. *Dip. Thesis*, TU München, 2010.

[5] Zhang W., Bhattacharya K.: A computational model of ferroelectric domains. Part I: model formulation and domain switching, *Acta Materialia*, 53:1:185-198, 2005.

VALIDATION AND VERIFICATION OF A NON-RIGID PART INSPECTION METHOD

Sasan Sattarpanah Karganroudi[1a)], Jean-Christophe Cuillière[1], Vincent Francois[1] & Souheil-Antoine Tahan[2]
[1]*Équipe de Recherche en Intégration Cao-CAlcul (ÉRICCA), Université du Québec à Trois-Rivières, Trois-Rivières, Québec, Canada*
[2]*Laboratoire d'ingénierie des produits, procédés et systèmes (LIPPS), École de Technologie Supérieure, Montreal, Québec, Canada*

Summary: This paper investigates a statistical approach for the validation of a new non-rigid registration method aimed at automating the inspection of non-rigid parts in a free-state condition. This non-rigid registration method is based on generating, filtering sample points and finite element analysis. Validation of the registration method uses Kolmogorov-Smirnov test to accept or reject estimated defects with respect to nominal defects at a desired risk level.

INTRODUCTION

Computer aided inspection (CAI) methods speed up the geometric dimensioning process and increase the inspection accuracy of manufactured parts by eliminating human intervention and its unavoidable errors. CAI methods for fixtureless inspection of non-rigid parts aim at scanning these parts in a free-state condition (without conformation) and compare data with the nominal CAD model in a common coordinate system and common state of deformation, which allows identifying and estimating defects on these parts. Non-rigid (flexible) manufactured parts (e.g. parts with a very thin thickness) deform to an extent in free-state which is beyond the dimensional and/or geometrical tolerances on designed parts. In this study the *generalized numerical inspection fixture* (GNIF) [1] method is applied to generate, for a given part, a set of corresponding sample points between the nominal CAD model and the scanned model in a free state. These points are evenly distributed over both models and then used to deform the CAD model to conform to scanned data, through finite element non-rigid registration (FENR). In [2, 3] an automatic sample point filtering method based on two metrics: von-Mises stress criteria and curvature criteria is developed. The developed inspection method filters GNIF corresponding sample points that are suspected to be close to defect areas, which makes that associated defects on manufactured non-rigid part can be identified and measured accurately. Validation and verification (ASME V&V) approaches on computational simulated models allow assessing accuracy and reliability of simulation methods [4]. Verification is the assessment of accuracy of the solution to a computational model while validation is the assessment of accuracy of a computational simulation if compared with experimental data. In this paper a validation approach in accordance with the ASME V&V10.1-2006 recommendations is applied to corroborate the estimated results of fixtureless inspection obtained from our improved method based on filtering GNIF sample points [2, 3].

VALIDATION OF NON-RIGID COMPUTER AIDED INSPECTION

The investigated validation method is presented herein on a case study based on measuring an aerospace aluminum skin panel with the following approximate dimensions: 1.5°m length, 1°m width and 1°mm thickness. For this part, Fig. 1a shows the nominal CAD model and Fig. 1b shows the scanned mesh, which is deformed (representing free-state deformation) and features three defects (bumps). Fig. 1c illustrates nominal maximum amplitude and area for these 3 bumps whereas Fig. 1d illustrates estimated maximum amplitude and area for these bumps.

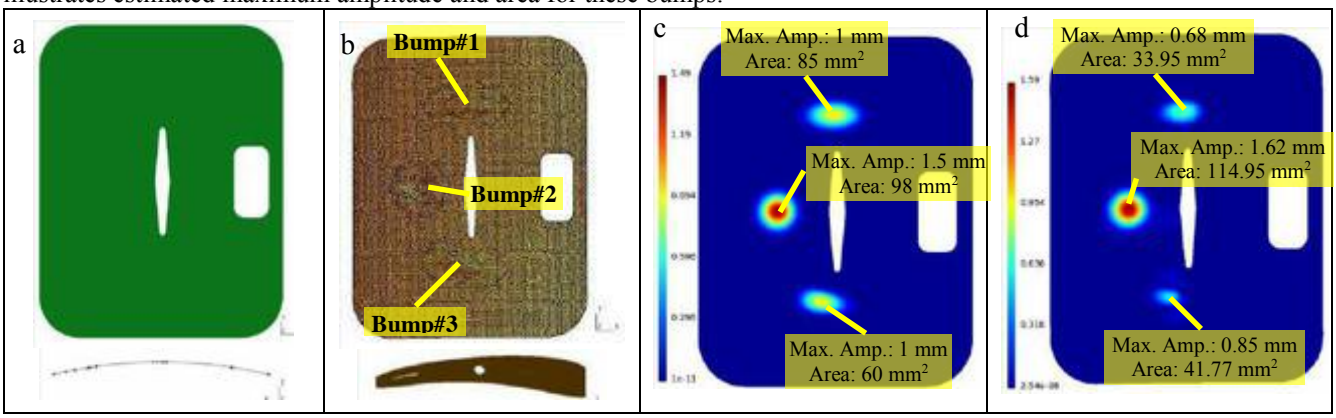

Figure 1: A non-rigid aluminum panel a) front and top views of the CAD model b) front and top views of the scanned part in a free-state c) nominal distance distribution d) estimated distance distribution.

The nominal inspection result of distance distribution, as shown in Fig. 1c, is a comparison between the CAD model and scan model before flexible deformation. This model (before deformation) thus only features the 3 bumps and represents scan model in the actual assembly state. The area of a defect is based on assessing the portion of the defect that exceeds the tolerance, as

[a)] Corresponding author. Email: Sattarpa@uqtr.com.

specified on the drawing. In this paper, we considered a 0.4°mm tolerance, which is a usual representative profile tolerance value for this type of thin-walled aerospace parts. Applying non-rigid fixtureless inspection based on filtering corresponding sample points, the area and amplitude of defects on the scanned model are estimated. The estimated inspection result is presented as a distance distribution, as shown in Fig. 1d. This distribution is based on calculating distances between the scan model (including both defects and flexible deformation) and deformed CAD model using our improved non-rigid registration method (based on filtering sample points). Then, a further investigation of these results consists in using V&V to assess similarity between shapes of estimated and nominal defects (without free-state deformation). The boundary and shape of a given defect is defined, either for nominal or estimated defects, with respect to sets of nodes for which the distance between shape with and without defect exceeds a certain threshold. We studied three thresholds: 100% (0.4° mm), 30% (0.12° mm) and 10% (0.04° mm) of the specified tolerance (defects are illustrated in red in Fig. 2).

Defect shape threshold	**(10% tolerance) 0.04 mm**	**(30% tolerance) 0.12 mm**	**(100% tolerance) 0.4 mm**
Nominal inspection result			
Estimated inspection result			

Figure 2: Shape of defects for different distance thresholds.

Distances between shape with and without defects measured on the nodes of each triangulation provides us with two sample data referred to as nominal and estimated distance distributions. Similarity between these distributions is assed using, among many other statistical tests, the Kolmogorov-Smirnov (K-S) test [5]. This test is applied to evaluate the difference between the cumulative distribution functions (CDFs) of the two sample data mentioned above at a desired significance level. The failure in the decision of K-S test is interpreted that the two shapes of defects are different enough. In contrast, the K-S test decision is passed when the two sample data have sufficiently similar statistical distribution. We have implemented K-S tests at a 5% significance level in MATLAB®. Meanwhile, we studied the robustness of our improved non-rigid inspection method by adding synthetic noise into scan data. In Table 1, the K-S test decision for inspection results associated with noise-free scan models as well as inspection results including noise is presented, for the three thresholds introduced above. The added noise in the scan data is form Gaussian distribution with mean value of 0 mm and standard deviation of 0.03 mm.

Table 1: Results obtained with K-S tests at a 5% significance level (Error type I (α) = 0.05).

Defects:	**BUMP1**		**BUMP2**		**BUMP3**	
Noise inclusion status: / **Defect shape threshold**	Noise-free	With noise	Noise-free	With noise	Noise-free	With noise
(10% tolerance) 0.04 mm	Pass	Pass	Pass	Fail	Pass	Pass
(30% tolerance) 0.12 mm	Fail	Fail	Pass	Pass	Pass	Pass
(100% tolerance) 0.4 mm	Fail	Fail	Pass	Pass	Pass	Pass

CONCLUSIONS

In this work, a nonparametric statistic hypothesis test, namely Kolmogorov-Smirnov test, is applied to validate the estimation of defects that are detected using our improved fixtureless inspection method for flexible parts. A positive K-S test decision is interpreted as meaning that an estimated defect shape is sufficiently similar to that of the nominal defect or not. An interesting aspect of this V&V approach is that it can easily be generalized to many other geometric feature identification and assessment processes.

References

[1] H. Radvar-Esfahlan and S.-A. Tahan, "Nonrigid geometric metrology using generalized numerical inspection fixtures," Precision Engineering, vol. 36, pp. 1-9, 2012.

[2] S. S. Karganroudi, J.-C. Cuillière, V. François, and S.-A. Tahan, "An improvement of fixtureless inspection for non-rigid parts based on filtering sample points" in Proceedings of the 25th Canadian Congress of Applied Mechanics (CANCAM 2015), London, Ontario, Canada, 2015.

[3] S. S. Karganroudi, J.-C. Cuillière, V. François, and S.-A. Tahan, "Automatic fixtureless inspection of non-rigid parts based on filtering registration points" submitted to The International Journal of Advanced Manufacturing Technology (2015).

[4] ASME, 2006, Guide for Verification & Validation in Computational Solid Mechanics, ASME V&V 10-2006, The American Society of Mechanical Engineers, New York, NY.

[5] Haldar, A., and Mahadevan, S., 2000, Probability, Reliability, and Statistical Methods in Engineering Design, Wiley, New York.

SEARCHING FOR LOCAL CONTACT CONSTRAINTS IN ISOGEOMETRIC CONTACT ANALYSIS

Dušan Gabriel *[1], Ján Kopačka[1], Radek Kolman[1], and Jiří Plešek[1]
[1]*Institute of Thermomechanics of the CAS, v. v. i., Czech Academy of Sciences, Prague, Czech Republic*

Summary In this paper, the performance of local searching procedure was tested in proposed isogeometric contact algorithm. Recent study on the assessment of various unconstrained optimization methods for computing the closest point projection in local contact search was followed up and extended to problems discretized by spline representation (Bezier, B-spline, NURBS, etc.). It was shown that the sphere and the torus approximation methods significantly increase the robustness of the local contact search procedure in isogeometric contact algorithm.

INTRODUCTION

The main difficulty in the contact analysis is a non-smoothness of contacting surfaces. It arises from inequality constraints as well as from geometric discontinuities induced by spatial discretization. The contact analysis based on traditional finite elements utilizes element facets to describe a contact surface. Unfortunately, the facet interfaces are only C^0 continuous so that normal surface vectors may experience jump across element boundaries, which may lead to artificial oscillations of contact forces.

A remedy to this geometric discontinuity may be provided by isogeometric formulation [1]. In this approach, the known geometry is accurately described by the Non-Uniform Rational B-Splines (NURBS) basis functions, which serve at the same time as the element basis functions. The isogeometric analysis provides some additional advantage, which is especially attractive to contact analysis [2], namely, preserving geometric continuity, facilitating patch-wise contact search, supporting a variationally consistent formulation, and having a uniform data structure for the contact surface and the underlying volumes.

LOCAL CONTACT SEARCHING

In isogeometric contact analysis well-established contact searching procedures originally developed for classical finite element method are usually utilized [3]. This procedures were designed mainly for linear finite elements. Therefore, their direct employment in isogeometric analysis requires sampling of free-form surface patches, which is rather computationally expensive. Local searching represents the calculation of the closest point projection of a contactor/slave point onto a given target/master segment. In other words, measuring penetration of slave point through the counterpart's object master surface is required. It is necessary first to define the outward normal and then to compute its intersection with a curved surface, establishing minimum distance. The condition of minimum distance leads to the solution of the following equations

$$\begin{aligned} \frac{\partial \mathbf{x}(r,s)}{\partial r} \cdot (\mathbf{x}(r,s) \nearrow \mathbf{x}_s) &= 0 \\ \frac{\partial \mathbf{x}(r,s)}{\partial s} \cdot (\mathbf{x}(r,s) \nearrow \mathbf{x}_s) &= 0 \end{aligned} \tag{1}$$

where the isoparametric coordinates r, s of the contact point $\mathbf{x}(r,s)$, defined as the point on the master surface closest to the given slave node $\mathbf{x}_s$, have to be found. Although appearing trivial at first glance the numerical solution process is far from being easy, especially when dealing with severely distorted surfaces. Recently, several unconstrained optimization methods for the solution of non-linear algebraic systems (1) were thoroughly tested in Reference [4]: the Newton-Raphson method, the least square projection, the sphere and torus approximation method, the steepest descent method, the Broyden method, the BFGS method, and the simplex method. The effectiveness and robustness of these methods was tested by means of a proposed benchmark problem discretized by a three-dimensional quadratic serendipity elements. It is obvious that the local search procedure strongly influences the robustness, accuracy and computational cost of the contact analysis.

In this paper, we followed conclusions drawn in Reference [4] and extended this work to problems discretized by spline representation (Bezier, B-spline, NURBS, etc.) In proposed isogeometric contact algorithm [5] the attention was focused on the geometric approximation methods which turned out to be the most promising methods in local contact search. The simplest geometric approximation is the least square projection method [4]. This method utilizes plane as the approximation surface and therefore it is also denoted as the first order algorithm. In the second order algorithm proposed in Reference [6] the surface is approximated by a sphere. The example of osculating sphere is shown in Figure 1. A more advantageous approximation surface is given by a torus patch [7].

*Corresponding author. Email: gabriel@it.cas.cz

The principle of these method is as follows: the slave point $\mathbf{x}_s$ is projected onto the contact surface which is replaced by the selected approximation surface described by the plane, sphere or torus in every iteration. Next, the projection of the slave point $\mathbf{x}_s$ is mapped onto this alternative surface. Finally, the resulting projected point is considered as a new approximation of the solution and the process is repeated until the convergence is reached.

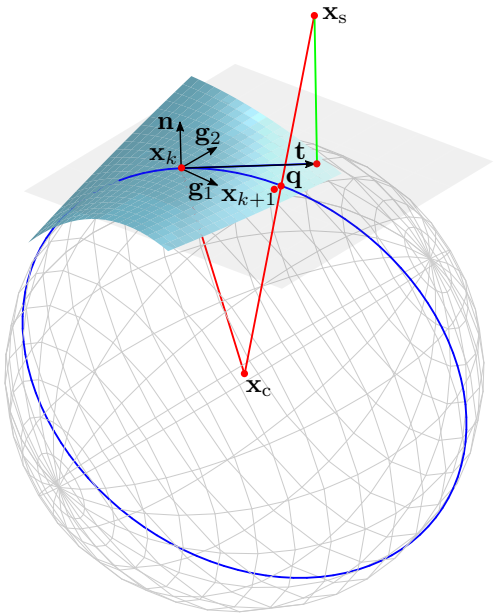

Figure 1: Sphere approximation method.

CONCLUSIONS

In this paper, the performance of local searching procedure was tested in proposed isogeometric contact algorithm. Several unconstrained optimization methods were thoroughly tested: the Newton-Raphson method, the least square projection, the sphere and torus approximation method, the steepest descent method, the Broyden method, the BFGS method, and the simplex method. The effectiveness and robustness of these methods was tested by means of a benchmark problem involving impact of two tubes discretized by the NURBS splines. It was shown that the sphere and the torus approximation methods significantly increase the robustness of the local contact search procedure in isogeometric contact algorithm.

ACKNOWLEDGEMENTS

The work was supported by the GACR projects GAP101/12/2315 and 15-20666S with institutional support RVO:61388998.

References

[1] Hughes T.J.R., Cottrell J.A., Bazilevs Y.: Isogeometric analysis: CAD, finite elements, NURBS, exact geometry and mesh refinement. Comput. Methods in Appl. Mech. Eng. 194:4135-4195, 2005.

[2] De Lorenzis L., Wriggers P., Hughes T.J.R.: Isogeometric contact: a review. GAMM-Mitteilungen. 37:85-123, 2014.

[3] Benson D.J., Bazilevs Y., Hsu M.C., Hughes T.J.R.: Isogeometric shell analysis: The Reissner-Mindlin shell. Comput. Methods in Appl. Mech. Eng. 199:276-289, 2010.

[4] Kopačka J., Gabriel D., Plešek J., Ulbin M.: Assessment of methods for computing the closest point projection, penetration, and gap functions in contact searching problems. Int. J. Numer. Meth. Eng. doi: 10.1002/nme.4994, 2015.

[5] Kopačka J., Gabriel D., Kolman R., Plešek J.: On the contact pressure oscillations of an isogeometric contact-impact algorithm. YIC/GACM 2015, Aachen, Germany, 2015.

[6] Hu S.M., Wallner J.: A second order algorithm for orthogonal projection onto curves and surfaces. Computer Aided Geometric Design. 22:251-260, 2005.

[7] Liu X.M., Yang L., Yong J.H., Gu H.J., Sun J.G.: A torus patch approximation approach for point projection on surfaces. Computer Aided Geometric Design. 26:593-598, 2009.

A PARALLEL COMPUTATIONAL FRAMEWORK FOR SIMULATING FRACTURE IN SHELLS

Brandon Talamini*[1] and Raúl Radovitzky[1]
[1]*Department of Aeronautics and Astronautics, Massachusetts Institute of Technology, Cambridge, Massachusetts, USA*

Summary We propose a new computational framework for simulating deformation and fracture in large shell structures that is well-suited to parallel computation. In contrast to many existing methods, the framework is able to model fracture driven by transverse shear, in addition to combined bending and in-plane stretching. The essential ingredients of this framework are a discontinuous Galerkin discretization of a Reissner-Mindlin type shear-flexible theory and a interface element-based cohesive zone model of fracture.

APPROACH

Plate and shell elements remain in wide use in the practical design of large thin structures such as aircraft fuselages, ship hulls, automobiles, submarines, and pressure vessels. In many applications, fracture is a critical design concern, and thus the ability to numerically predict crack propagation in shells is a highly desirable goal. There has been considerable progress on this front in the last 10-15 years; however, in this manuscript we wish to draw attention to two important aspects that have received relatively attention. First, many existing computational shell fracture methods are not scalable, in the sense of parallel computing, and consequently simulation of large structures remains out of reach. Second, while most existing approaches treat in-plane tensile failure, modeling fracture due to transverse shearing is often omitted.

Scalability problems typically arise from the introduction of new degrees of freedom on the fly to describe crack propagation. A recently developed remedy has been proposed that is composed of two elements: (i) a discontinuous Galerkin (DG) discretization of the body, and (ii) a cohesive zone model (CZM) of fracture implemented through interface elements. The combined DG-CZM methodology, initially proposed in the context of three-dimensional solids, has the unique advantage that scalability in parallel computation is achieved almost automatically; see [1, 2]. We adopt this methodology and formulate a new discontinuous Galerkin method for shear-flexible shells.

In adopting a DG-CZM method, our framework is similar to the work of Becker et al. [3, 4] for Kirchhoff-Love (i.e., thin) shells. The distinction of our work is that it is based on a *shear-flexible* shell theory, which brings us to the second point raised above. An obvious domain of shear-flexible theories is the modeling of relatively thick shells. Another, perhaps less obvious, is in modeling of highly impulsive loads for both thick and thin shells. High-rate loadings, such as impacts and blasts, increase the influence of transverse shearing on the response, even in shells that could be considered "thin" in a quasi-static scenario. In highly impulsive events, the duration of the loading is short compared to the characteristic flexural response time of the structure, essentially shortening the span (and increasing the effective "stubbiness") of loaded material during the initial response. Shear-off type failure near supports or stiffeners is favored in such cases. In thin shell theories, the transverse shear stress resultants are indeterminate, and are related to a derivative of a generalized force. In practical terms, this means that the shear resultants are not readily available in a computer implementation to use in a fracture criterion. Furthermore, as there is no elastic energy storage of shear deformation in thin shell theories, even if a shear-off fracture were modeled, there would be no energy release from the structure into the fracture process zone that provides the essential driving force in fracture mechanics. On the contrary, the shear-flexible theory underlying the proposed framework allows the modeling of transverse shear-off type failures, in addition to in-plane tearing type fractures.

By way of illustration, we show numerical results of beam blast experiments originally conducted in [5]. In these experiments, planar explosive charges were affixed to the top face of a clamped aluminum beam and detonated; the delivered impulse was controlled by varying the thickness of the charge. In the left of Figure 1, the experimental results are shown in order of increasing impulse, top to bottom. At small impulses, the beam experiences permanent deflection due to bending and stretching without fracture. At intermediate levels of impulse, the beam shows necking and tensile failure at the supports after large deflections have been sustained. Finally, at large impulses, the beam undergoes shear-off at the supports with little permanent deformation. Each of these regimes has been captured in our numerical results, shown at right for three representative impulse values.

Locking is a well-known problem in numerical analysis of shear-flexible shells; here, the inherent flexibility afforded by DG methods in the choice of approximation spaces is exploited to prevent locking naturally, without recourse to mixed methods or reduced integration. Hence, the DG discretization imultaneously furnishes remedies for locking, consistent enforcement of compatibility, and parallel scalability in an elegant manner.

The scalability of the method can be exploited to simulate deformation and fracture in large engineering-scale structures. As a demonstration, in Figure 2 we show snapshots from an idealized simulation of explosive decompression in a modern

*Corresponding author. Email: talamini@mit.edu



Figure 1: *Left*: Impulsively loaded aluminum beam experiments of Menkes and Opat (1973). These post mortem photographs show the transition from tensile failure to shear-off with increasing impulse. Image source: Menkes and Opat [5]. *Right*: Numerical results, top to bottom: Case 1, small impulse, final static position of the beam. Case 2, intermediate impulse, snapshot soon after the beam has fractured. Case 3, large impulse, the beam shears off virtually instantaneously.

commercial airliner. The skin of the entire fuselage was modeled, employing approximately 650 000 elements distributed over 208 processors. The ability of the proposed method to capture realistic effects such as skin buckling, fragmentation, and petalling is evident.

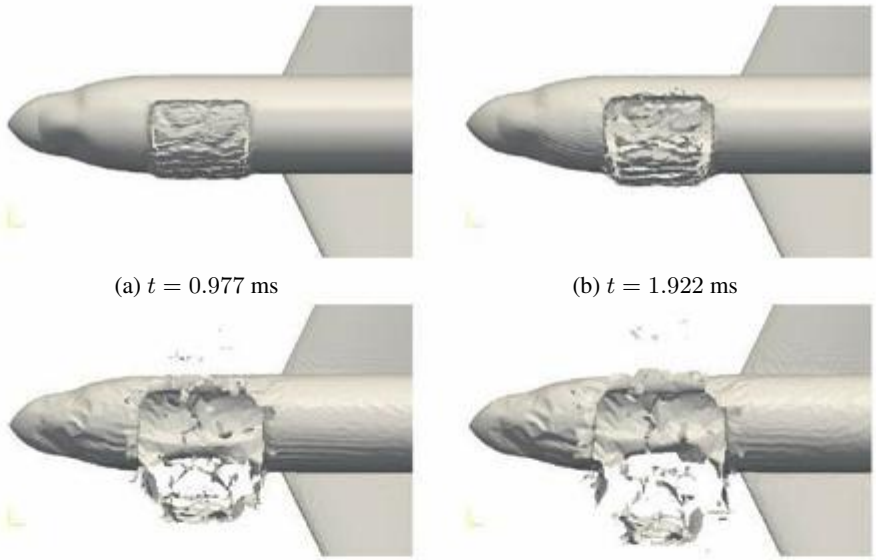

(a) $t = 0.977$ ms (b) $t = 1.922$ ms

(c) $t = 6.806$ ms (d) $t = 9.712$ ms

Figure 2: Snapshots of simulation results for the explosive decompression of an airliner fuselage.

References

[1] A. Seagraves, R. Radovitzky, Dynamic Failure of Materials and Structures, Springer, 2009, Ch. 12 Advances in Cohesive Zone Modeling of Dynamic Fracture, pp. 349–405.

[2] R. Radovitzky, A. Seagraves, M. Tupek, L. Noels, A scalable 3D fracture and fragmentation algorithm based on a hybrid, discontinuous Galerkin, Cohesive Element Method, Computer Methods in Applied Mechanics and Engineering 200 (2011) 326–344.

[3] G. Becker, C. Geuzaine, L. Noels, A one field full discontinuous Galerkin method for Kirchhoff-Love shells applied to fracture mechanics, Computer Methods in Applied Mechanics and Engineering 200 (45-46) (2011) 3223–3241.

[4] G. Becker, Numerical simulations of brittle and elasto-plastic fracture for thin structures subjected to dynamic loadings, Ph.D. thesis, University of Liège (2012).

[5] S. B. Menkes, H. J. Opat, Broken beams, Experimental mechanics 13 (11) (1973) 480–486.

IMPROVEMENT OF WEIGHT-EFFICIENCY FOR A VEHICLE COMPONENT BASED ON THE U* THEORY

Qingguo Wang[1a], Khashayar Pejhan, Igor Telichev, Christine Q. Wu
[1]*Dpartment of Mechanical Engineering, University of Manitoba, Winnipeg, Manitoba, Canada*

Summary In this paper, a method was proposed based on the U* theory to decrease the weight while improve the load transfer performance of the vehicle structure. Based on the proposed method, material removal and structural modifications were conducted to a vehicle component. Compared to the original, the modified design makes the structure lighter and performs better in terms of load transfer. Meanwhile, the overall rigidity of the modified structure is not declined due to the weight reduction.

INTRODUCTION

To satisfy the demand of high weight-efficiency for structures, it is essential to understand the structure from the viewpoint of load transfer. Load transfer index (U^*) was introduced as the indicator of the load transfer within the structure [1]. The U* theory suggests that the parts with highest U^* values transfer the main portion of the load. Load transfer analysis based on the U^* theory has been developed to be a new design paradigm for lightweight structures. It has been used in vehicle design by automotive manufacturers like Honda. However, a study on the feasibility and the effectiveness of the U^* theory with respect to the weight reduction of the structure is still lack. In this paper, based on the U^* theory, a method was proposed to reduce the weight of the structure without impairing its overall rigidity. A parcel rack strut of a multiple passenger vehicle was used as the sample structure to demonstrate the effectiveness of the method. In the method, the distribution of the U^*_{sum} index is used to evaluate the load transfer efficiency of the structure, where the stability of the load transfer in the structure is analyzed based on the variation of the U^* index. The material removal and structural modifications were conducted to the sample structure based on the U^*_{sum} and U^* indexes. Compared to the original, the modified structure is 10% lighter while the overall rigidity of the structure is not declined due to the weight reduction. Meanwhile, the efficiency and the stability of the load transfer in the structure are improved.

METHODOLOGY

The U* index and load paths

The U^* index indicates the internal stiffness between the loading point and an arbitrary point in the structure. The "internal stiffness" represents the strength of the connection between any two points in the structure. The parts with higher U^* values carry more load in the structure. Fig. 1 shows a linear elastic, isotropic, and homogeneous structure with the loading point (Point *A*), the supporting point (Point *B*), and an arbitrary point (Point *C*). The springs are used to represent the internal stiffness between any two points in the structure and the U^* index is defined as [1]:

$$U^* = 1 - \frac{U}{U'} \tag{1}$$

where *U* is the total strain energy stored in the structure when Point *C* is unconstrained and *U'* is the total strain energy of the structure with Point *C* constrained as shown in Fig. 1.

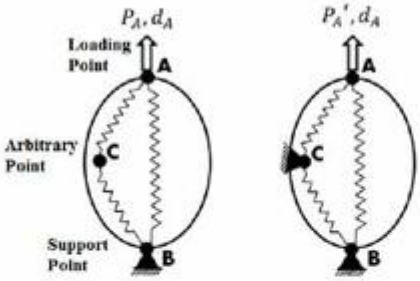

Fig. 1: The system for U* calculation

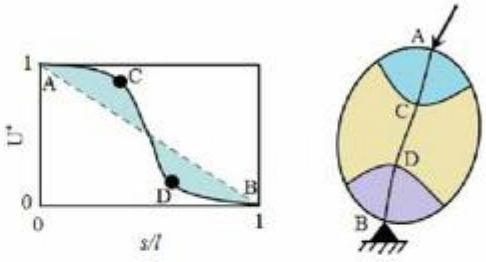

Fig. 2: Illustration of the uniformity of U* variation

Load transfer stability

The degree of the uniformity of the U^* variation can be used to evaluate the load transfer stability of the structure. The uniform U^* variation leads to the stable load transfer for the structure, while the non-uniform U^* variation causes the load transfer of the structure unstable. As shown in Fig. 2, the solid line shows the U^* variation along a load path of the sample structure, while the dash line depicts the U^* variation of a desirable structure.

Load transfer efficiency

Fig. 3 present the definition of the U^*_{sum} index [2]. The areas with lower U^*_{sum} values are considered as non-important for load transfer, while the areas with higher U^*_{sum} values are over stiff. Then, the material of those two kinds of area can be reduced to improve the load transfer efficiency of the structure. The load transfer efficiency represents the weight efficiency of the structure with respect to the load transfer. In a structure with ideal load transfer efficiency like a linear spring, the

[a)] Corresponding author. Email: wangq311@myumanitoba.ca.

U^*_{sum} index is consistent throughout the structure. The degree of consistency of the U^*_{sum} index is set as the criterion to evaluate the load transfer efficiency of the structure.

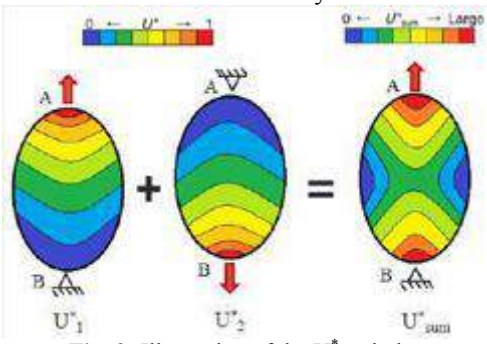

Fig. 3: Illustration of the U^*_{sum} index

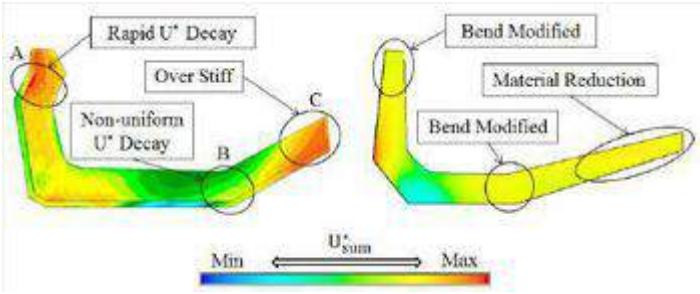

Fig. 4: U^*_{sum} distributions and design modifications of the strut

RESULTS

A parcel rack strut was used as the sample structure to be modified as shown in Fig. 5. Based on the U^* theory, three structural issues were detected for the strut and then the corresponding modifications were conducted as shown in Fig. 4. The modified strut is 10% lighter than the original as can be seen from Tab. 1. Meanwhile, the overall rigidity of the structure is not declined due to the weight reduction. The overall deformation of the modified strut is 5% smaller than the original. Though having lighter weight, the modified strut accomplishes better stability of the load transfer compared to the original design. It can be seen from Fig. 6 that the U^* variation of the modified strut (solid line) is much more uniform than the original (dash line). It has to be pointed out that the marked area of the strut is the failure location in the force testing as shown in Fig. 6. On the other hand, the modified strut performs better than the original from the viewpoint of the load transfer efficiency. As can be seen from Fig. 4, the degree of the consistency of the U^*_{sum} index in the modified strut (on right) is much higher than the original (on left) when comparing the U^*_{sum} distribution of both struts (same colour indicates same U^*_{sum} value).

Tab. 1: Computational data of the strut

Model	Material	Young's Modulus (GPa)	Service Loading (N)	Maximum Deformation (mm)	Maximum Stress (MPa)	Mass (g)
Original Strut	Nylon	2.5	1921	2.49	20.6	1403
Modified Strut				2.37	15.2	1265

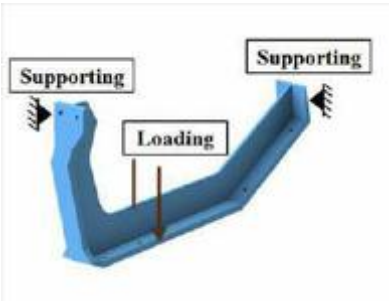

Fig. 5: Model of the parcel rack strut

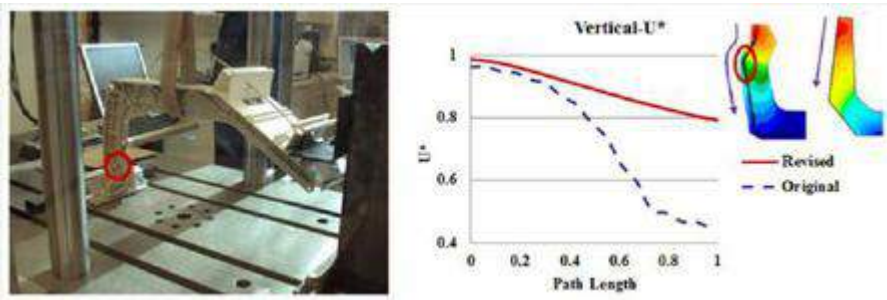

Fig. 6: Force testing and the U* variation of the strut

CONCLUSIONS

Design modifications were conducted for a vehicle component based on the proposed method. Compared to the weight of the original, the modified structure is 10% lighter (Tab. 1). Meanwhile, the overall rigidity of the modified structure is not declined due to the weight reduction (Tab. 1). Furthermore, the load transfer performance of the modified structure is improved not only in terms of stability (Fig. 6) but also from the viewpoint of efficiency (Fig. 4). The results of the design modifications demonstrate that the proposed method is effective on designing advanced vehicle structures with lighter weight and better load transfer performance.

References

[1] Akima S., Omiya M., et al.: Load Transfer of Passenger Car Compartment for Improvement of Structural Performance in Side Impact. No. 15-0209, 2015.

[2] Pejhan K., Wu C. Q., Telichev I.: Comparison of load transfer index (U*) with conventional stress analysis in vehicle structure design evaluation. *Int. J. of Vehicle Design*, 68(4): 285-303, 2015

STRUCTURAL ANALYSIS of 3D PRINTING PARTS

Ming-Hisao Lee[1a)], Chau-Yi Chou[1], Shou-I Chen[2], Keng-Liang Ou[3,4,5,6]
[1]*National Center for High-performance Computing, Taiwan*
[2]*Instrument Technology Research Center, NARL, Taiwan*
[3]*Research Center for Biomedical Implants and Microsurgery Devices, Taipei Medical University, Taiwan*
[4]*Research Center for Biomedical Devices and Prototyping Production, Taipei Medical University, Taiwan*
[5]*Department of Dentistry, Taipei Medical University-Shuang Ho Hospital, Taiwan*
[6]*School of Dentistry, College of Oral Medicine, Taipei Medical University, Taiwan*

Summary 3D printing is a promising way for product manufacturing. However, some problems rising during 3D printing processes could decrease the accuracy and quality of the printed parts. In order to solve those problems, the printing processes need to be evaluated in advance to avoid likely defects. Although FEM is well adopted to do engineering simulations, finite element meshes for irregular objects always are irregularly distributed that the element meshes cannot match the horizontally-growing shapes of the parts during the additive process. Hence, FEM cannot be easily adopted for this type of simulation. On the contrary, the proposed method based on so-called meshless method doesn't need element meshes, so its analysis models can be designed to match the horizontally-growing shapes to simulate the parts' behaviors during printing processes. Furthermore, the proposed method adopts STL geometry, which is the main format used in 3D printing industry, as the only analysis model.

INTRODUCTION

3D printing has become a promising and popular way to produce parts in various fields, for it can produce almost any kinds of shapes, even extremely irregular. However, during implementing 3D printing to produce parts, some issues which could decrease the accuracy and quality of the printed parts may rise, such as warpage of parts after cooling, collapse due to inadequate support during printing, etc. In order to tackle those problems and reduce the manufacturing cost due to repetitive tries, the printing processes need to be evaluated in advance and improved when defects could happen. Numerical simulation is one of the efficient ways for evaluating engineering problems; especially, the Finite Element Method (FEM) has been considered a powerful tool to do the simulation. Nevertheless, the FEM models, i.e. element meshes, for irregular objects always are irregularly distributed that the element meshes cannot match the growing shapes of the parts in the middle of the growing additive process. As a result, the FEM doesn't seem to be a suitable tool for simulating 3D printing processes. In contrast, the proposed method based on the so-called meshless method [1] doesn't need element meshes, so its analysis models can be designed to match the growing shapes for simulating the parts' behaviors during printing processes.

Geometry data in STL (Stereo-Lithography) format has been adopted by the 3D printing industry as a De facto standard format to transfer geometry data between different software systems, e.g. sending a CAD data in STL format to a 3D machine to print it out. The geometry in STL format (simply called STL geometry) has higher capability and flexibility to represent irregular geometry, especially those data obtained with scanning equipment such as CT-scanners and 3D scanners. Therefore, the proposed method adopts STL geometry as the analysis model that no other analysis model-building work is needed. To achieve that, this method includes several schemes to handle the STL geometry so that the STL geometry can be directly used for the simulation. This STL-based way can largely reduce the time and effort for building the analysis models. To demonstrate the effectiveness and efficiency of the proposed method, a structural analysis of a mandible bone with irregular-shaped geometry has been conducted.

METHOD

3D printing simulation

A 3D printing machine prints parts in a layer-by-layer (additive) way that the printed parts are growing horizontally. In order to simulate the horizontally-growing situation, the analysis models must meet the same condition, i.e. horizontally-growing. Unfortunately, the finite element meshes for parts with irregular shapes always are irregularly distributed that they cannot match the horizontally-growing condition. As a result, it is hard to generate a suitable analysis model for doing simulation. In contrast, the proposed method [2][3] based on so-called meshless method doesn't need any element meshes, so its analysis models can be designed to match the horizontally-growing shapes, as shown in Fig. 1. Hence the proposed method can be used to simulate the growing processes in 3D printing.

Geometry in STL format (STL geometry)

a) Corresponding author. Email: mhlee@nchc.narl.org.tw

STL geometry has been adopted by the 3D printing industry as a De facto standard format to transfer geometry data between different software systems. In STL geometry, The triangularized surface geometry is employed to represent the boundary surfaces of the objects, i.e. the surfaces of the three-dimensional objects are represented by certain number of tiny triangular facets. This type of geometry data has higher capability and flexibility to represent irregular geometry, especially those objects obtained with scanning tools such as CT-scanners and 3D scanners, e.g. medical parts. Currently, most computer-aided tools support this type of format. Therefore, the proposed method adopts STL geometry as the analysis model; besides, no other manually model-building work is needed for the proposed method that the analysis process directly proceeds with the STL geometry to do simulations. To achieve that, several geometry-related schemes has been designed to treat the STL geometry that the STL geometry data becomes the only analysis model data needed for the simulation.

CONCLUSIONS

Evaluating printing processes in advance is necessary to assure the product's quality. Nevertheless, the FEA becomes difficult to use due to the requirement of finite element meshes which cannot meet the horizontally-growing condition easily. On the contrary, with the proposed method based on the meshless method, the analysis model with only nodes can be designed to meet that condition easily. Moreover, the proposed method adopts the STL geometry, which is a De facto standard in 3D printing industry for transferring product geometry, as the analysis model. As a result, the user can directly use the already-ready geometry model to be the analysis model that no extra model-building work is needed; the analysis process can become much simpler and straightforward.

References

[1] Belytschko, T.; Lu, Y.Y.; Gu, L.: Element-Free Galerkin Method. *International Journal for Numerical Methods in Engineering*, **37**: 229-256, 1994.

[2] Chen, W. H. and Lee, M. H.: A Novel Meshless Analysis Procedure for Three-dimensional Structural Problems with Complicated Geometry. *Computer Modeling in Engineering & Sciences*, **93(2)**:149-166, 2013.

[3] Lee, M. H. and Chen, W. H.: Geometry related treatments for three-dimensional meshless method, *Computer Modeling in Engineering & Sciences*, **61(3)**: 249-271, 2010.

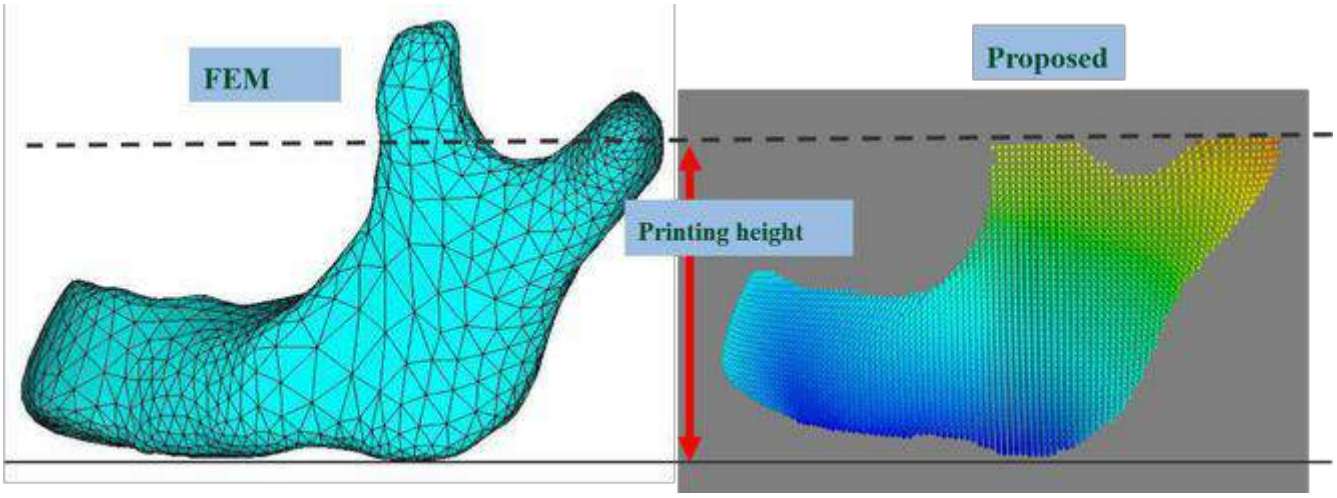

Fig. 1 Analysis model comparison between the FEA and the proposed method

A CELL CENTERED FINITE VOLUME METHOD FOR SOLVING THE MULTIDIMENSIONAL COMPRESSIBLE HYPERELASTICITY EQUATIONS

Rémi Chauvin[1], Isabelle Bertron[1], Patrick Le Tallec[2], Pierre-Henri Maire *[1], and Renaud Motte[3]
[1]*CEA/CESTA, Le Barp, France*
[2]*Ecole Polytechnique, Palaiseau, France*
[3]*CEA/DIF, Arpajon, France*

Summary We describe a cell-centered Finite Volume space discretization of the multidimensional compressible hyperelasticity equations written under Lagrangian form. The main features of the numerical method relies on its capability, at the discrete level, to ensure not only the Geometric Conservation Law but also the Clausius-Duhem imbalance (entropy inequality), while conserving the total energy. Numerous representative test cases assess the accuracy and the robustness of this novel Finite Volume method.

CONTEXT AND MOTIVATIONS

The numerical modelling of fast transient dynamics phenomena characterized by large deformations and high strain rates is a topics of great importance for industrial applications such as high velocity impacts. Nowadays, the development of Finite Volume (FV) discretizations for Lagrangian solid dynamics seems to be a promising alternative to the traditional Finite Element approaches. For instance, in [6, 7, 1] FV algorithms are provided for simulating the dynamic response of hyperelastic materials for which the constitutive law satisfies the principle of material frame indifference and is consistent with the second law of thermodynamics, refer to [4]. Furthermore, cell-centered Lagrangian FV discretizations of the so-called Wilkins hypoelastic model [14] have been also recently proposed [8, 12]. In this framework, standard infinitesimal elastoplasticity models are extended to the finite strain range by formulating constitutive law in terms of frame invariant stress rates. In spite of its simplicity this approach arises two main difficulties [11, 3, 9]. First, the definition of objective stress rates is somewhat arbitrary and not unique, further it leads to an evolution equation for the deviatoric stress which cannot be written under conservative form for multi-dimensional flows. This flaw renders the mathematical analysis of discontinuous solutions such as shock waves questionable. Second, hypoelastic based models are characterized by a dissipative behavior within the elastic regime. In other words, reversible transformations of an elastic material are characterized by a non-zero rate of entropy. This shows that the Wilkins hypoelastic model is thermodynamically inconsistent. Up to our knowledge, the traditional shock wave hydrocode community has not paid attention to these problems. It is certainly due to the fact that the Wilkins model is good enough for most engineering purposes for highly unsteady problems, if one turns material parameters to match experimental results. However, the issues related to the non uniqueness of the objective stress rate and the thermodynamical inconsistency are very troubling from both theoretical and numerical perspectives, particularly when one is dealing with flows containing shear and shock waves. On the other hand, the established computational mechanics community is careful about these issues but it typically does not deal with shock waves.

To cure the aforementioned flaws of the hypoelastic approach in the context of fast solid dynamics, we present a cell-centered FV methodology that solves the conservation laws of continuum mechanics (mass, momentum and total energy) for isotropic materials characterized by an hyperelastic constitutive law. Since the proposed numerical scheme will keep the same structure as the one developed for the Wilkins hypoelastic model [8], we shall be able to perform rigorous comparisons between the hyperelastic and the hypoelastic modelling. Indeed, using the same FV framework, we shall assess precisely hypoelastic model weaknesses against representative test cases in which shock and shear waves are present.

LAGRANGIAN HYPERELASTICITY IN TOTAL LAGRANGIAN FORM AND UPDATED LAGRANGIAN FORM

We consider the conservation laws of continuum mechanics written under total Lagrangian form, refer to [4]. The material constitutive law is derived according to the principle of material frame-indifference (objectivity) and consistently with the second law of thermodynamics. Assuming an elastic isotropic material, its constitutive response is defined by a free energy function expressed in terms of the principal invariants of the left Cauchy-Green tensor and the absolute temperature [5]. The first Piola Kirchhoff stress tensor and the Cauchy stress tensor are determined by means of the derivative of this free energy function with respect to the left Cauchy-Green tensor. In addition, to facilitate the comparison with the hypoelastic Wilkins model, we introduce a decomposition of the free energy function into an isochoric and a volumetric part, which implies the decomposition of the Cauchy stress tensor into a spherical part (pressure) and a deviatoric part (shearing). The time evolution of the deformation gradient, required to update the left Cauchy-Green tensor, is governed by the Geometric Conservation Law (GCL). A special attention is given to the compatibility condition associated to the GCL and its link with the Piola

*Corresponding author. Email: pierre-henri.maire@cea.fr

condition [13]. These equivalent conditions are of major importance since they allow to transform the foregoing conservation laws written under total Lagrangian form to their counterparts written under updated Lagrangian form. In this representation, the Cauchy stress terms uniquely depends on the left Cauchy-Green tensor and the GCL amounts to write that the Olroyd derivative of the left Cauchy-Green tensor is equal to zero. The characterization of discontinuous solutions (shock waves) by means of the Rankine-Hugoniot jump conditions will be briefly reviewed in both total Lagrangian frame and updated Lagrangian frame.

CELL-CENTERED LAGRANGIAN FINITE VOLUME DISCRETIZATION

The FV discretization of the foregoing conservation laws in both total Lagrangian and updated Lagrangian representations are detailed in bidimensional geometry employing a cell-centered placement of the physical variables. The numerical flux computation relies on a node-centered approximate Riemann solver which allows to compute not only the nodal velocities but also the subcell traction forces. This FV algorithm is the natural but non-trivial extension to solid dynamics of the method initially introduced in the context of gas dynamics in [10]. The numerical flux approximation ensures the compatibility with the GCL at the discrete level. The subcell force expression in terms of the cell-centered stress tensor, the nodal velocity and the cell-centered velocity has been derived to enforce a local entropy inequality at the semi-discrete level ensuring the conversion of kinetic energy into internal energy through irreversible processes such as shock waves. We also note that this discretization guaranties the conservation of total energy and momentum. The second-order time and space discretization is obtained by means of an acoustic Generalized Riemann Problem (GRP) approach [2, 10]. The piecewise linear space time reconstruction of the state variables is performed in each computational cell and in each time interval following the characteristic equations. More precisely the time derivative of the physical variables are eliminated in terms of the spatial derivatives through the use of a Lax-Wendroff method. The monotonicity of the discrete solution is enforced employing a frame-invariant limiting procedure which applies to scalar as well as to vectors and tensors.

CONCLUSION AND PERSPECTIVES

After having defined and validated a nominally second-order FV discretization of the non linear elasticity equations for isotropic hyperelastic materials, we plan to extend its capability to cope with the numerical simulation of elastic-plastic flows of isotropic solids at large deformations.

Acknowledgment

This work was partially supported by l'Agence Nationale de la Recherche, France (grant number ANR-14-ASTR-0016-01).

References

[1] Aguirre M., Gil A.J., Bonet J., Lee C.H.: An upwind vertex centred Finite Volume solver for Lagrangian solid dynamics. Journal of Computational Physics 300:387-422, 2015.

[2] Ben-Artzi M., Falcovitz J.: Generalized Riemann Problem in Computational Fluid Dynamics. Cambridge Monographs on Applied and Computational Mathematics, 2003.

[3] Gavrilyuk S.L., Favrie N., Saurel R.: Modelling wave dynamics of compressible elastic materials. Journal of Computational Physics 227:2941-2969, 2008.

[4] Gurtin M.E., Fried E., Anand L.:The Mechanics and Thermodynamics of Continua. Cambridge University Press, 2009.

[5] Holzapfel G.A.:Nonlinear Solids Mechanics. John Whiley & Sons, LTD, 2010.

[6] Kluth G., Després B.: Discretization of hyperelasticity on unstructured mesh with a cell-centered Lagrangian scheme. Journal of Computational Physics 229:9092-9118, 2010.

[7] Lee C.H., Gil A.J., Bonet J.: Development of a cell centred upwind finite volume algorithm for a new conservation law formulation in structural dynamics. Computers and Structures 118:13-38, 2013.

[8] Maire P.-H., Abgrall R., Breil J., Loubère R., Rebourcet B.: A nominally second-order cell-centered Lagrangian scheme for simulating elastic-plastic flows on two-dimensional unstructured grids. Journal of Computational Physics 235:626-665, 2013.

[9] Maire P.-H., Le Tallec P., Rebourcet B., Abgrall R.: A Simple Elasticity Model at Large Deformations or where does come the Wilkins model from? Multimat Conference 2013, website https://multimat13.llnl.gov/.

[10] Maire P.-H.: A high-order cell-centered Lagrangian scheme for two-dimensional compressible fluid flows on unstructured meshes 228:2391-2425, 2009.

[11] Plohr B., Plohr J.: Large deformation constitutive laws for isotropic thermoelastic materials. Los Alamos National Laboratory, Report LA-UR-05-5471, 2005.

[12] Sambasivan S.K., Shashkov M.J., Burton D.E.: A finite volume Lagrangian hydrodynamics approach for solids in general unstructured grids 72:770-810, 2013.

[13] Vilar F., Maire P.-H., Abgrall R.: A discontinuous Galerkin discretization for solving the two-dimensional gas dynamics equations written under total Lagrangian formulation on general unstructured grids 276:188-234, 2014.

[14] Wilkins M.L.:Calculation of elastic-plastic flows. Methods in Computational Physics, Academic Press, 1964.

ON THE MECHANICS OF BIO-INSPIRED STIFFENED SHELL STRUCTURES

Jean-Louis Batoz[1a], Pascal Lardeur[1], Eduard Antaluca[2], Fabien Lamarque[2], Salim Bouabdallah[3]
[1]*Sorbonne University, Université de Technologie de Compiègne, UMR 6253 Roberval, 60205 Compiègne,*
[2]*Sorbonne University, Université de Technologie de Compiègne, EA 7284, 60205 Compiègne, France*
[3]*Altair Engineering France, 5 Rue de la Renaissance, 92160 Antony, France*

Summary The paper deals with the 3D finite element modelling of structures obtained by assemblages of thin shell parts. The whole structure represents a complex geometry inspired by vegetable nature and plants such as a maple leaf in the present study. This type of structure can become a bio-inspired architectural project at human scale. In the present study some challenging finite element analyses are discussed related to the complete integrated modelling: 3D scanning, geometrical model, appropriate finite element model for linear and nonlinear static and dynamic analysis of the stiffened 3D shell structures subjected to gravity and pressure loading. New finite element models are developed in the research project.

INTRODUCTION

Nature has always been a source of inspiration for scientists and engineers in various domains, from ancient civilizations to nowadays. The geometry of plants, trees, branches and leaves has been the subject of interest and applications from the point of view of mathematicians and computer graphics specialists [1]. Wood and bones have been deeply studied from a material science point of view but also for their mechanical properties pertinent for the use in construction (for wood) or for biomechanics, or bioengineering applications (for bones) [2]. The structure of plants has been studied and has been an inspiration for design in architectural and mechanical engineering. One famous example is the Gaudi architecture in Barcelona as discussed in many documents such as [2]. In [3], chapter 8 and in [4], chapter 5, the authors (Andres, Ortega and Paloto) discussed the funicular polygon and the homeostatic model based on a biological principle that can be generated by the simultaneous action of thermal and mechanical loads on thermoplastic materials to design free form shapes. Natural structures such as wood and bones have also been the source of structural design and shape optimisation algorithms to reduce stress concentrations or to optimize the fibres orientations in composite man-made materials. Several books and papers have been published on the subject of optimization mechanics in nature such as [4] including a very interesting chapter on the structural efficiency of trees.

The present paper is part of a general project related to the mechanics of plants in order to understand the mechanical behaviour under gravity and wind pressure loading in various situations of plant types and scale (trees, branches, leaves, flowers), in various space and life time conditions (behaviour of a deciduous leaf from spring to fall for example). The project is limited to the mechanical aspects, without coupling with the genetic bio-chemistry ones (which are essential for the explanation of the growth and attribution of material properties of any natural object). This means that the geometry and material properties relevant for the present mechanical analysis must be assumed for a given space and time situation. The project is also "biomimesis" oriented since we will analyse, design and possibly optimize engineering man-made structures inspired by nature.

More precisely the present paper deals with the mechanics of a 3D structure with the shape of a maple leaf at a given stage of development (end of summer, say), Figure 1. The paper concentrates on the different models (geometry and physics) based on the Finite Element Method [5].



Figure 1. A typical maple leaf on the ground in the fall season.

[a)] Corresponding author. Email: batoz@utc.fr.

THE FINITE ELEMENT MODELS

We first collect a maple leaf of about 30 cm maximum length. The average thickness of the leaf is 0,18 mm. The mimetic structure to be analysed will have the same dimensions multiplied by a factor of 5, and the material properties will be those of an elastic isotropic steel with E=210 GPa, ν=0.3 and Yield stress σ_Y = 400 MPa.
The first step is to identify the shape of the contour, the main cantilevered beam connecting the leaf to the branch and all the ribs we can identify with a criteria of diameter more than 1,5 times the leaf thickness. That step can be performed by different means including laser scanning. The ribs of circular cross section are represented as stiffeners and are assumed to be non-eccentric with respect to the middle surface. There are around 20 secondary ribs per leaf with varying diameters. The main connecting beam has a diameter of 1,5 mm and a length of 5 cm. The leaf will be clamped at its root (cantilevered main beam in Figure 2).

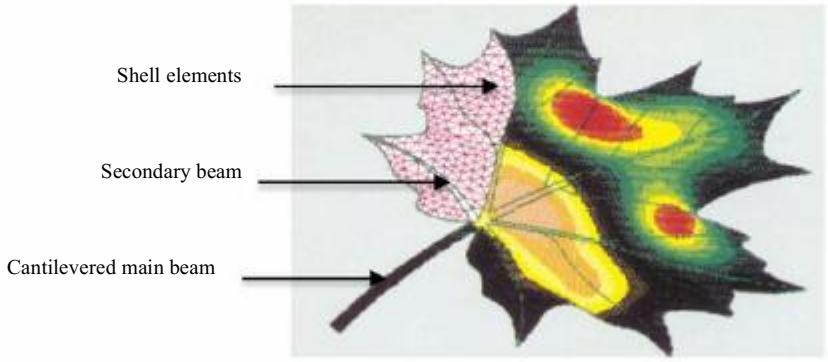

Figure 2. A finite element model of a maple leaf

The different finite element models considered in the present study are:

- the classical thin shell triangular and quadrilateral DKT18 and DKQ24 elements with 6 dof/node developed by the first author and colleagues [5], compatible with the classical 3D beam elements representing the ribs. This type of analysis can be performed with commercial finite element packages,
- new shell elements with one rotation per mid side [6], with a new representation for the beam stiffeners,
- rotation free shell elements as discussed in different papers [7],[8].

The different analyses performed are:

- linear static analyses considering gravity and pressure loadings, for different mesh densities and for different shell formulations (as defined above),
- dynamic analyses (frequencies and vibration modes) for a clamped leaf and a free leaf in space.

Results include displacements and stresses distributions, frequencies and natural modes (figure 2 as example).

CONCLUSIONS

The mechanics of a complex ribbed shell structure bio-inspired by a maple leaf has been studied in this paper using several finite element models. The objective is to understand the behaviour of the leaf structure under gravity and wind loads and to evaluate the stress distribution at any point. One difficult aspect of the study was the construction of relevant meshes for the different finite element models. The present study includes the development of new rotation free finite element shell models in the perspective of future works: dynamic and geometrical non-linear analysis.

References

[1] P. Prusinkiewicz, A. Lindenmayer: The algorithmic beauty of plants, Springer-Verlag, 1990.
[2] J. Bassegoda I Nonell, P. Vivas, R. Pla: Gaudi, toutes les oeuvres, Triangle Postal, 2014
[3] M.W. Collins, M.A. Atherton, J.A. Bryant, Editors: Nature and design, WIT Press, 2005.
[4] M.W. Collins, D.G. Hunt, J.A. Bryant, Editors: Optimisation mechanics in nature, WIT Press, 2004.
[5] J.L. Batoz, G. Dhatt: Modélisation des structures par éléments finis. Vol. 2, Poutres et plaques, Vol. 3, Coques. Hermes Editeurs. Paris, 1992.
[6] J.L. Batoz, C.L. Zheng, F. Hammadi: Formulation and evaluation of new triangular, quadrilateral, pentagonal and hexagonal Discrete Kirchhoff plate/shell elements, *International Journal for Numerical Methods in Engineering.* Vol. 52, pp. 615-630, 2001.
[7] E.M. Meghlat, M. Oudjene, H. Ait-Aider, J.L. Batoz: A new approach to model nailed and screwed timber joints using the finite element method, *Construction and Building Materials*, Vol. 41, pp. 263-269, 2013.
[8] Y.X. Zhou, K.Y. Sze: A geometric nonlinear rotation-free triangle and its application to drape simulation, *International Journal for Numerical Methods in Engineering*, Vol. 89, pp. 509-536, 2012.

COMPUTER MODELING OF DYNAMICS OF 3-D ELASTIC SOLIDS WITH COUPLED FIELDS

Aleksander Belov[1a)], Leonid Igumnov[1], Andrey Petrov[2], Svetlana Litvinchuk[1]
[1]*Research Institute for Mechanics of Lobachevsky State University of Nizhni Novgorod, Nizhny Novgorod, Russia*
[2]*Research and Education Center «Materials», Don State Technical University, Rostov-on-Don, Russia*

Summary The dynamic three-dimensional linear boundary-value problems of elasticity theory with coupled physical and mechanical fields are considered based on the boundary elements methods. Obtained calculation results are compared with the corresponding results from other authors and numerically-analytic solutions. High precision of the results is obtained and presented in this paper.

INTRODUCTION

Studies of the dynamic problems of elastic solids with coupled mechanical and non-mechanical fields (porosity, electricity, temperature) are highly demanded. The integral approach is one of the universal approach of numerically-analytical analysis of dynamic boundary-value problems of solid mechanics. A Boundary Elements Method [1] can be outlined from a variety of discrete schemes of this approach. The approximated singular integral equations are used to get the numerically-analytical solutions of boundary-value problems of the dynamics of anisotropic elastic solids. Dual Reciprocity theorem [2, 3] is used to get these equations. The alternative approach is based on regular integral equations of the first type [1, 4]. Both approaches promoting rejection of the traditional formulations of singular integral equations method. One of the main reason is not effective scheme to calculate the kernels of these equations. Kernels may be transformed using the Radon representation [5] to resolve this issue. In addition, usage of the effective numerical schemes of computer modeling for dynamic [6] and static [7] parts of the kernels allow us to use the classical formulation of the solution of dynamic problems. First solutions were found for scattering of elastic waves [8, 9]. The development of this approach for boundary-value dynamic problem of three-dimensional solids with physicomechanical fields is presented in this paper. Examples of this kind of boundary elements solutions may be found in [10, 11]. Traditionally, the numerical solution of the time-domain boundary integral equations may be found with usage of integral transformation or stepped algorithms. Convolution quadrature methods [12] allow to use stepped schemes for thermoelasticity and poroelasticity boundary-value problems where Green's matrices can't be written in time domain. Boundary elements schemes are based on Green-Betti-Somigliana formula. The development of boundary-elements method is done by usage of time-step method for numerical Laplace transform inversion and Butcher tableau notation for Runge-Kutta method for computer modeling of solids dynamics. The results of numerical experiments are presented.

MATHEMATICAL AND DISCRETE MODELS

Field interaction models correspond to poroelasticity, thermoelasticity and electro-magneto-elasticity. For porous materials characterization Biot's model is used. Green's matrices and, based on it, boundary integral equations are written for basic differential equations in private derivatives. Discrete analogue are obtained by applying the collacation method to a regularized boundary integral equation. The collocation nodes coincide with the approximate nodes of the intital boundary functions. Boundary element schemes follow time-step method of numerical Laplace transform inversion with classical and modified Durbin's method and Convolution Quadrature Method with modifications. To improve the accuracy and effectiveness of warking schemes of the BEM decisions are based on time units of the schemes of Runge-Kutta methods.

THE RESULTS OF NUMERICAL STUDIES

The effectiveness of the developed boundary-element approach is demonstrated on a number of boundary-element analyses of dynamic deformation of 3-D poroelastic bodies: modeling surface waves of a homogeneous and a compound poroelastic body; investigating the effect of the properties of a poroelastic material on the propagation velocities of surface waves. A two- and three-component media are considered with four and five basic functions, respectively, describing the wave process. In accordance with Biot's analogues of poroelasticity problems with four basic functions and a thermoelasticity problem makes it possible to consider one of the theories. Using as an example the problem of the effect of an axial force upon the end of a prismatic body in the form of Heaviside time function, a comparative study of the wave propagation in completely or partially saturated porous media is done. In problems of a half-space, the effect of attenuating cavities on the wave processes is shown. Boundary-element evaluations of poroelastic solutions of the problems considered are obtained, using both drained and non-drained material models. The wave process in a poroelastic material is characterized by the appearance of a third wave. In what follows, some illustrations of the results of numerical experiments

[a)] Corresponding author. Email: belov_a2@mech.unn.ru

are given by way of studying this phenomenon. Figs.1 and 2 demonstrate the third wave in the responses of pore flow and pressure. Fig. 1 presents the results of numerically analyzing the effect of the appearance of the slow longitudinal wave in a 9 *m*-long poroelastic cantilever prismatic body made of a completely saturated material with the following parameters: $K = 4.8\cdot10^9 H\ \ m^2$, $G = 7.2\cdot10^9 H\ \ m^2$, $\rho =\ \ kg\ \ m^3$, $\varphi = 0.19$, $K_s = 3.6\cdot10\ \ H\ \ m^2$, $\rho_f =\ \ kg\ \ m^3$, $K_f = 3.3\cdot10^9 H\ \ m^2$, $\kappa = 1.9\cdot10^{-7} m^4/(H\cdot s)$, where K, G are the related elastic moduli, ρ, ρ_f are total density and filler density, φ is porosity coefficient, $K_s\ K_f$ are elastic bulk moduli of the skeleton and the filler, κ is pore permeability coefficient. The dynamic process is generated by axial end force $F = H\ \ m^2$. Numerical inversion of Laplace transform, implementing a time-step method on the nodes of Lobatto scheme of Runge-Kutta family, is used in calculations. A stepped scheme with a key, generated by quadrature formula strongly oscillating functions, is used. A numerical-analytical solution is presented for the response of pore pressure and flow at a distance of $1{,}5\ m$ from the loaded end. Fig.1 also depicts the results of analyzing the convergence (dotted lines) of the stepped scheme on the nodes of Lobatto method when calculating the related pore flow. Fig. 2 presents the results of analyzing the problem of the effect of an axial force of the value $F = 1H/м$ upon the end of a 3m-long poroelastic cantilever prismatic body made of partially saturated material with the following parameters: $K = 1.02\cdot10^9 H\ \ m^2$, $G = 1.44\cdot10^9 H\ \ m^2$, $\phi = 0.23$, $\rho_s =\ \ kg\ \ m^3$, $\rho_f =\ \ kg\ \ m^3$, $\rho_a = 1.10 kg\ \ m^3$, $K_s = 3.55\cdot10\ \ H\ \ m^2$, $K_f = 2.25\cdot10\ \ H\ \ m^2$, $K_a = 1.10\cdot10^5 H\ \ m^2$, $\kappa = 2.5\cdot10^{-12} m^2$, $\eta_f = 1.0\cdot10^{-3} H\cdot s\ \ m^2$, $\eta_a = 1.8\cdot10^{-5} H\cdot s\ \ m^2$, where ρ_s, ρ_a, ρ_f densities of the components (skeleton, gas, liquid), $K_s\ K_a\ K_f$ are elastic bulk moduli of the components, $\eta_a\ \eta_f$ is viscosity of the components, κ is pore permeability coefficient. Saturation coefficient S_w is set equal to 0.9. The response of displacements at the loaded end of the cantilever is presented. Numerical inversion of Laplace transform with a time-step method is used, with the step of $\Delta t = 0.000015$. A stepped scheme with a key, generated by quadrature formulas for strongly oscillating functions, is used.

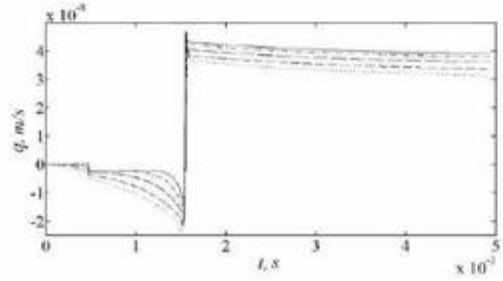

Fig. 1

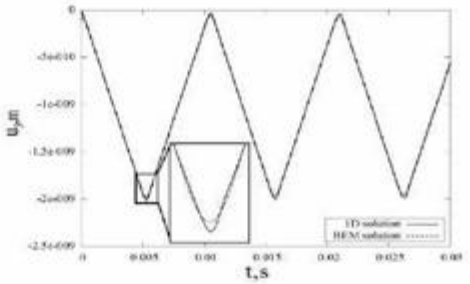

Fig. 2

Solutions of a series of electroelastic dynamic problems on the combined effect of a load in the form of Heaviside time function and an electric potential on homogeneous electroelastic bodies are given in comparison with a FEM solution.

The work was done with financial support from RFFI Grants (Projects №15-08-02814-a; №15-08-02817-a; 15-48-02333), the calculations on three-component medium were done with financial support from RNF (Project № 14-19-01096).

References

[1] Bazhenov V.G., Igumnov L.A. BIE and BE methods for analyzing 3-D problems of dynamic elasticity with coupled fields. M.: Fizmatlit, 2008. 352 p.

[2] Gaul L., Kogl M., Wagner M. Boundary Element Methods for Engineers and Scientists. Berlin Springer, 2003. 488p.

[3] Nardini D., Brebbia C.A. A New Approach to Free Vibration Analysis Using Boundary Elements. *In Boundary Element Methods. (Brebbia C.A., Ed.). Springer-Verlag*: Berlin, 1982. P.312-326.

[4] Babeshko V.A. A novel method for analyzing boundary-value problems of continuum mechanics and mathematical physics for non-classical fields. *Reports of AS.* 1985. V.284, № 1. P. 73-76.

[5] Wang C.Y., Achenbach J.D. Three-dimensional time-harmonic elastodynamic Green's functions for anisotropic solids. *Proceedings of the Royal Society of London A 1995*; 449:441– 458.

[6] Dravinski M., Zheng T. Numerical evaluation of three-dimensional time-harmonic Green's functions for a nonisotropic full-space. *Wave Motion 2000*; 32:141–151.

[7] Wilson R.D., Cruse T.A. Efficient implementation of anisotropic three-dimensional boundary-integral equation stress analysis. *Int. J. Numer. Meth. Engng*, 1978. 12, 1383-1397.

[8] Niu Y., Dravinski M. Three-dimensional BEM for scattering of elastic waves in general anisotropic media. *Int. J. Numer. Meth. Engng*. 2003. P.979-998.

[9] Niu Y., Dravinski M. Direct 3D BEM for scattering of elastic waves in a homogeneous anisotropic half-space. *Wave Motion. 2003*. P.165-175.

[10] Igumnov L.A., Markov I.P., Rataushko Ya.Yu. Modeling the dynamics of 3-D elastic anisotropic solids using boundary element method. *Advanced Materials Research*. Vol.1040. 2014. P.633-637.

[11] Igumnov L.A., Markov I.P. Modeling the dynamics of 3-D homogeneous electroelastic bodies using boundary element method. P*roblems of Strength and Plasticity*. Inter-University Collection. Nizhniy Novgorod: NNSU Publishers. 2014. Issue. 76(3). P.191-197.

[12] Lubich C. Convolution Quadrature and Discretized Operational Calculus. II. *Numerische Mathematik*. 1988. № 52. P. 413-142.

A STUDY ON PARTICLE STRESS EVOLUTION IN BIAXIAL TEST

Zhuang Cheng[a)], Jianfeng Wang
Department of Architecture and Civil Engineering, City University of Hong Kong, Kowloon, Hong Kong

Summary This paper examines the evolution of particle stress inside uncrushable granular materials in biaxial test using DEM and probabilistic method. It is found that the magnitude of normalized maximum shear stress inside particles have a nearly unified probability distribution at different loading stages, while the orientation shows increasing anisotropy with the rising of stress ratio. For samples with different initial void ratios but the same grading, the magnitude of normalized maximum shear stress probability density function can be approximately expressed by a two-parameter Weibull distribution function, in which the scale parameter and shape parameter are affected by sample grading, showing better grading samples having lower probability of high maximum shear stress. Second order Fourier series can be used to approximate probability density functions of the maximum shear stress orientation.

INTRODUCTION

Inter-particle contact forces in granular media systems play a key role in particle scale behaviours such as particle movement and breakage. Several failure criterions have been proposed in DEM to model the behaviour of crushable granular materials based on contact forces, including maximum contact force, multiple contact force induced maximum tensile stress, and multiple contact force induced maximum shear stress, etc.[1-3] On the basis of these criterions, statistic approaches also have been used to quantify the failure probability of particles inside granular materials in different boundary conditions including single particle crushing and one dimensional compression test. In particular, after Marketos and Bolton[4], who proposed a probabilistic model to predict particle breakage probability in one dimensional compression tests based on the maximum contact force, our previous work by Zhou et al[5] presents a new probabilistic model which takes multiple contact forces into consideration by using maximum tensile strength criterion.

As an extended work, this paper examines the evolution of maximum shear stress inside particles in granular materials in a more complex boundary condition, the biaxial test using DEM and probabilistic method. The results would further our understanding of granular material behaviours and study on particle breakage probability in biaxial test.

NUMERICAL MODEL

Biaxial tests are performed using PFC2D (Itasca, 2008) and all samples are with a size of 10mm in width and 20mm in height. Samples of linear distribution grading with d_{min}=0.20mm (the minimum size) and d_{max}=2.00mm (the maximum size), d_{min}=0.30mm and d_{max}=1.20mm, d_{min}=0.50mm and d_{max}=1.00mm, d_{min}=0.67mm and d_{max}=1.00mm, are tested respectively with both initial void ratio 0.17 and 0.25. During the biaxial tests, isotropic compression are firstly applied on samples to reach a pressure of 200kPa, and then the left and right boundaries maintain this pressure on samples, while top and bottom boundaries moves towards each other at a constant rate of 0.5mm/s until the axial strain reaches to 0.2. All biaxial tests are conducted using a group of typical parameters with particle density of 2600kg•m^{-3}, inter-particle friction coefficient μ=0.5, wall friction coefficient μ_{wall}=0.0, particle normal and shear stiffness of 5×10^8 N/m and wall normal stiffness of 5×10^7 N/m.

MAXIMUM SHEAR STRESS DISTRIBUTION AND ORIENTATION

Probability distribution of normalized maximum shear stress magnitude $\bar{\tau}$ (defined as the shear stress index by Eqs. (1) and (2)) and orientation θ_s (Determined according to Eq. (3)) inside each sample during shearing are examined, which is shown in Fig.1(a) and (b) as discrete symbols and solid lines in Fig. 2, respectively. The symbols in Fig.1 (a) contain DEM results from samples with different grading and initial void ratios of both $e_0 = 0.17$and $e_0 = 0.25$, at different loading stages including stress ratio / ′=0.0, 0.2, 0.4, 0.6, 0.8 and axial strain of 4%, 8% 12%. More detailed results showing probability distribution evolution of shear stress index during biaxial test are given in Fig.1 (b) for samples with the best grading tested. In this short paper, only orientation θ_s probability distribution for sample with d_{min}=0.67mm and d_{max}=1.00mm sheared at stress ratio of 0.0, 0.4, 0.8 are given in Fig. 2. It should be noted that the probability here is defined as the mass of particles with the specified normalized maximum shear stress magnitude or orientation divided by the total mass of particles inside the sample.

$$\bar{\tau} = \frac{\tau}{\langle\tau\rangle}\ , \tag{1}$$

$$\tau = \frac{1}{2}\sqrt{(\sigma_{11}-\sigma_{22})^2 + 4\sigma_{12}^2}\ , \tag{2}$$

$$\theta_s = \frac{1}{2}arctan\left(\frac{2\sigma_{12}}{\sigma_{11}-\sigma_{22}}\right) + \frac{\pi}{4}\ , \tag{3}$$

where τ and $\langle\tau\rangle$ are the maximum shear stress and the average maximum shear stress within a sample; respectively; and σ_{11}, σ_{12} and σ_{22} are 2D stress components within a particle.

a) Email: zhuangcheng1810@gmail.com

As can be seen in Figs. 1(a) and (b), a nearly unified pattern can be found in the probability density function of the normalized maximum shear stress in biaxial test at different loading stages. Samples with different initial void ratios and the same grading are examined. A two-parameter Weibull distribution model can be used to approximately describe the *pdfs* of $\bar{\tau}$ within a particle in a biaxial test, with better graded samples showing a lower probability of high stress index. (See the fitted curves in Figs. 1(a) and (b)).

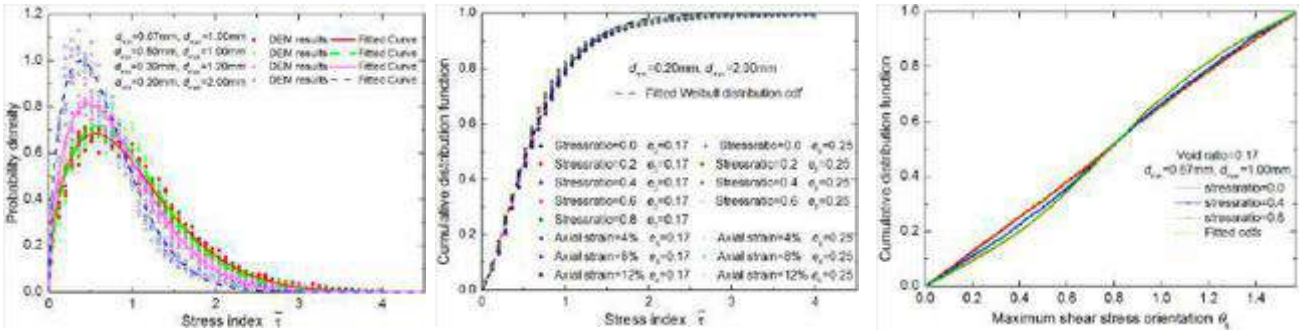

(a) (b)

Fig.1 *pdfs* (a) and *cdfs* (b) of stress index magnitude in biaxial test

Fig.2 *cdfs* of maximum shear stress orientation in biaxial test

For samples at different loading stages in a biaxial test, second order Fourier series expressed by Eq. (4) can be used to approximate the probability distribution function of maximum shear stress orientation $f(\theta_s)$,

$$f(\theta_s) = \frac{2}{\pi} + a_s cos4(\theta_s - \theta_0) \quad . \tag{4}$$

$f(\theta_s)$ in Eq. (4) is composed of a linear part and a nonlinear part. The coefficient a_s of the nonlinear part reflects the degree of anisotropy of θ_s and implies a complete isotropy when $a_s = 0$. θ_0 is a parameter denoting the most possible orientation. a_s and θ_0 can be determined by a nonlinear regression of the corresponding *cdf*. The fitted *cdfs* using Fourier series are shown with dash lines in Fig. 2.

For the samples tested, an obvious trend of increasing anisotropy can be found with the increase of stress ratio, from the start of shearing to the peak state.

CONCLUSIONS

This paper examines the evolution of the maximum shear stress in uncrushable granular materials in biaxial tests using DEM and probabilistic method. We found that for both loose and dense samples with the same grading, the magnitude of normalized maximum shear stress inside particles during biaxial test have a nearly unified probability density function and can be approximately described by a two-parameter Weibull probability distribution function. For the same material tested, the distribution function is affected by the change of grading during biaxial test, with better grading showing a lower probability of maximum shear stress, while the void ratio have little effect on the distribution. However, the anisotropy of the maximum shear stress increases with the rising of stress ratio. Second order Fourier series can be used to approximately express the probability density function of maximum shear stress orientation.

ACKNOWLEDGEMENT

The study presented in this article was supported by the General Research Fund CityU122813 from the Research Grant Council of the Hong Kong SAR, National Science Foundation of China Grant No. 51379180 and Shenzhen Basic Research Grant No. JCYJ20150601102053063.

References

[1] Lobo-Guerrero, S. and Vallejo, L. Discrete Element Method Evaluation of Granular Crushing Under Direct Shear Test Conditions. *Journal of Geotechnical and Geoenvironmental Engineering* 131.10: 1295-1300, 2005.

[2] Tsoungui, O., Vallet, D. and Charmet, J.C. Numerical Model of Crushing of Grains Inside Two-dimensional Granular Materials. *Powder technology* 105.1: 190-198, 1999

[3] McDowell, G.R., and de Bono., J.P. On The Micro Mechanics of One-dimensional Normal Compression. *Géotechnique* 63.11: 895, 2013.

[4] Marketos, G., and Bolton, M. D. Quantifying the Extent of Crushing in Granular Materials: A Probability-based Predictive Method. *Journal of the Mechanics and Physics of Solids* 55.10:2142-2156, 2007

[5] Zhou, B., Wang, J. and Wang, H. A New Probabilistic Approach for Predicting Particle Crushing in One-dimensional Compression of Granular Soil. *Soils and Foundations* 54.4:833-844, 2014

STUDY OF WAVE PROPAGATION IN POROVISCOELASTIC SOLID USING BOUNDARY ELEMENT APPROACH

Aleksandr Ipatov[a], Leonid Igumnov & Aleksandr Belov
Research institute for Mechanics of National Research Lobachevsky State University of Nizhni Novgorod, Nizhny Novgorod, Russia

Summary The present paper is dedicated to numerical solving of three dimensional boundary-value problems in poroviscoelastic formulation. The poroviscoelastic formulation is treated as a combination of Biot's theory of poroelasticity and elastic-viscoelastic correspondence principle. Boundary element method (BEM) and boundary integral equation (BIE) method are applied to obtain Laplace domain solution of three-dimensional boundary-value problem. Modified Durbin's algorithm of numerical inversion of Laplace transform is used to perform solutions in time domain.

INTRODUCTION

Wave propagation in dispersed media is a great interest of many disciplines. Mechanics of advanced materials, such as poro-, visco- or poroviscoelastic materials, is relevant to such disciplines as geophysics, geo- and biomechanics, seismology, physical chemistry, petroleum engineering etc. The implementation of the solid viscoelastic effects in the theory of poroelasticity was first introduced by Biot [1, 2]. The viscoelastic deformations in solid skeleton of poroelastic media may be accounted through the use of correspondence principle [3]. Although many significant achievements have been made on wave motion in porous media [4], because the complexity of the inertial viscosity and mechanical coupling in porous media most transient response problems can only be solved via numerical methods. There are two major approaches to dynamic processes modeled by means of BEM: solving BIE system directly in time domain or in Laplace or Fourier domain followed by the respective transform inversion. Classical formulations for BIE method with their discretized realization and traditional BEM are successful approaches for solving three-dimensional problem [5, 6].

SOLUTION METHOD

The set of differential equations of poroelasticity for displacements $\hat{}_i$ and pore pressure $\hat{}$ in Laplace domain (s – transform parameter) take the following form [4]:

$$G\hat{}_{i,jj}+\left(K+\frac{1}{3}G\right)\hat{}_{j,ij}-(\alpha-\beta)\hat{}_{,i}-s^2(\rho-\beta\rho_f)\hat{}_i=-\hat{F}_i\,,\qquad \frac{\beta}{s\rho_f}p_{,ii}-\frac{\phi^2 s}{R}p-(\alpha-\beta)su_{i,i}=-a$$

$$\beta=\frac{k\rho_f\phi^2 s^2}{\phi^2 s+s^2k(\rho_a+\phi\rho_f)},\ R=\frac{\phi^2K_fK_s{}^2}{K_f(K_s-K)+\phi K_s(K_s-K_f)}$$

where G, K – material constant from elasticity, ϕ – porosity, k – permeability, α – Biot's effective stress coefficient, ρ, ρ_a, ρ_f – bulk, apparent mass and fluid densities respectively, $\hat{F}_i$, $\hat{}$ – bulk body forces per unit volume.

Following types of boundary conditions for Ω are considered:

$u_l(x,s)=f_l(x,s),\ u_4(x,s)=p(x,s)=f_4(x,s), x\in\Gamma^u,\ t_l(x,s)=g_l(x,s),\ t_4(x,s)=q(x,s)=g_4(x,s),\ x\in\Gamma^\sigma,\ l=\overline{1,3}$.

Direct approach of boundary integral equations method is given [4-6]:

Displacement vector at internal points is connected with boundary displacements and tractions as follows:

$$u_l(x,s)=\int_{\Gamma_k}U^s_{lj}(x,y,s)t_j(y,s)d_yS-\int_{\Gamma_k}T^s_{lj}(x,y,s)u_j(y,s)d_yS,\ l=1,2,3,\ \ x\in\Omega.$$

U_{lj} and T_{lj} – components of fundamental and singular solution tensors.

Poroviscoelastic solution is obtained from poroelastic solution by means of the elastic-viscoelastic correspondence principle, applied to skeleton's elastic constants K and G in Laplace domain. Forms of $K(s)$ and $G(s)$ in case of model with weakly singular kernel (Abel type) are following: $G=\dfrac{G}{1+hs^{\alpha-1}}$, $K=\dfrac{K}{1+hs^{\alpha-1}}$,

Integral representation and BIE with integral Laplace transform are used. Fundamental and singular solutions are considered in term of singularity isolation. Realization of boundary element approach for solving problems of poroviscoelasticity needs in a special calculating method [4]. Numerical scheme is based on the Green-Betti-Somigliana formula. To perform numerical results double accuracy calculations are used. Regularized BIE are considered in order to introduce BE discretization [6]. Shape functions are quadratic polynomials of interpolation. Unknown boundary fields are

[a] Corresponding author. Email: sansan.com@inbox.ru

integrated by interpolation node values. The problem is solved in Laplace domain. Durbin's method [7] with variable integrating step is used to obtain solution in time domain.

NUMERICAL RESULTS

Problem of a prismatic poroviscoelastic column clamped at one end and subjected to a Heaviside type load at another and is considered. Poroelastic material is Berea sandstone. Material constants are: $K = 8 \cdot 10^9\ N/m^2$, $G = 6 \cdot 10^9\ N/m^2$, $\rho = 2458 kg/m^3$, $\phi = 0.66$, $K_s = 3.6 \cdot 10^{10}\ N/m^2$, $\rho_f = 1000\, kg/m^3$, $K_f = 3.3 \cdot 10^9\ N/m^2$, $k = 1.9 \cdot 10^{-10}\ m^4/(N \cdot s)$. Displacements, pore pressure and tractions are obtained at points B (Fig.1) for different values of viscoelastic parameters (Fig.2 – Fig.4).

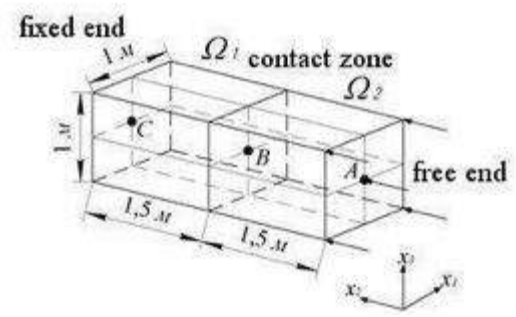

Fig.1 Problem statement.

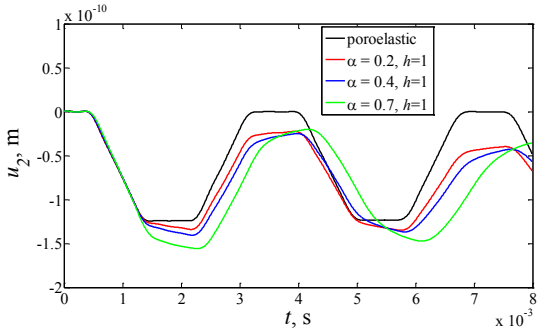

Fig.2 Displacements.

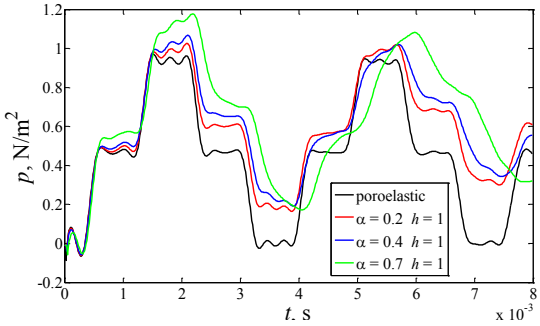

Fig.3 Pore pressure.

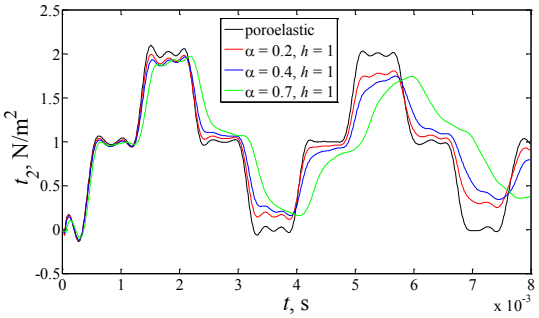

Fig.4 Tractions.

CONCLUSIONS

An influence of viscoelastic parameters on dynamic responses is demonstrated on the example of a problem of the prismatic poroviscoelastic solid under Heaviside-type load (Fig.2 – Fig.4) by boundart element approach. The poroviscoelastic media modelling is based on Biot's theory of porous material in combination with the elastic-viscoelastic corresponding principle. Viscous properties are described by model with weakly singular kernel.

ACKNOWLEDGMENT

The work was supported by RFBR under grants Nos. 14-08-00811, 15-08-02814, 15-48-02333 and 16-31-00450.

References

[1] Biot M. A.: Theory of propagation of elastic waves in a fluid-suturated porous solid. *J. Acoust. Soc. Am.*, vol. 28(2), 168-191, 1956.

[2] Biot M. A.: Theory of deformation of a porous viscoelastic anisotropic solid. *J. Acoust. Soc. Am.*, vol. 27, 459-467,1956.

[3] Cristensen R.: Introduction to the theory of viscoelasticity, Mir, Moscow, Russia, 1974.

[4] Schanz M.: Wave Propagation in Viscoelastic and Poroelastic Continua, Springer, Berlin, Germany, 2001.

[5] Ugodchikov A.G., Hutoryanskii N.M.: Boundary element method in deformable solid mechanics, Kazan State University, Kazan, Russia, 1986.

[6] Bazhenov V.G., Igumnov L.A.: Boundary Integral Equations & Boundary Element Methods in treating the problems of 3D elastodynamics with coupled fields. PhysMathLit, Moscow, Russia, 2008.

[7] Durbin F.: Numerical inversion of Laplace transforms: an efficient improvement to Dubner and Abate's method. *The Computer Journal*. vol. 17, 371-376, 1974,

PHASE FIELD CRYSTAL MODELING OF ADDITIVE MANUFACTURING IN METALS

Hang Ke [a] & Ioannis Mastorakos
Department of Mechanical and Aeronautical Engineering, Clarkson University, Potsdam, NY, United States

Summary Additive manufacturing, also known as the 3D printing, is rising popularity for the past few years due to its widely application in various areas. However, not enough emphasize is drawn to the microstructures of the "build" material, which is actually really significant to the property and performance of the product. In this paper, we showed that the phase field crystal (PFC) model could be applied to identify and predict the microstructures during the solidification of the metals in additive manufacturing. Using this model, we can control and optimize the process parameters for microstructures in order to get the desired materials that we need.

PHASE FIELD CRYSTAL MODEL

Compared with the conventional phase field model, PFC model introduces phase fields which are periodic by including a free energy scalar that is minimized by periodic solutions and is also rotationally invariant[1]. The basic equation for PFC model was actually derived from Swift-Hohenberg equation to calculate problems in thermal convection. The free energy of the model can be written as a function of the density field ϕ,

$$F' = \int_V \left\{\frac{1}{2}\phi[\alpha + \lambda(+_0^2 + \nabla^2)^2]\phi + \frac{g}{4}\phi^4\right\} d\boldsymbol{r} \quad (1)$$

In the equation, α0λ0+$_0$0and g are constants. The density field ϕ can be minimized by periodic functions for solid state and a constant density value for liquid state. To simplify the calculation process, we revise our equation into a dimensionless form as below:

$$F = \int_V \left\{\frac{1}{2}\psi[-\varepsilon + (d + \nabla^2)^2]\psi + \frac{1}{4}\psi^4\right\} d\boldsymbol{x} \quad (2)$$

Where $\varepsilon = -\frac{\alpha}{\lambda q_0^4}$, $\psi = \phi\sqrt{\frac{g}{\lambda q_0^4}}$, $\mathbf{x} = +_0\boldsymbol{r}$, and $F = \frac{g}{\lambda^2 q_0^5}F'$. And the dynamics for this model is of the Cahn-Hilliard model:

$$\frac{\partial\psi}{\partial t} = \nabla^2\frac{\partial F}{\partial\psi} \quad (3)$$

The periodic density field can be obtained from the reciprocal lattice vectors **G** by the following equation:

$$\psi = \overline{\psi} + \sum_{\boldsymbol{G}} \eta_{\boldsymbol{G}} e^{i\boldsymbol{G}\cdot\boldsymbol{x}} + c.g.g \quad (4)$$

where $\overline{\psi}$ is the average density in solid state, η_G is the amplitude of the reciprocal lattice vector, and c.c. represents complex conjugates. Here, we prepare to model a two-dimensional (2D) solution system, and the **G** can be written as the following:

$$\mathbf{G} = k_1\boldsymbol{q}_1 + k_2\boldsymbol{q}_2 \quad (5)$$

Where both k_1 and k_2 are integers. For 2D hexagonal system, we finally get the dimensionless density field as:

$$\psi = \overline{\psi} + A(cos + x cos\frac{qy}{\sqrt{3}} - \frac{1}{2}cos\frac{2qy}{\sqrt{3}}) \quad (6)$$

where A is a constant and $q = \frac{2\pi}{a}$. Substituting (6) into (2) and minimizing free energy with respect to A and q leads to $\overline{\psi} = \frac{\sqrt{-r}}{2}$, $q = \frac{\sqrt{3}}{2}$, and $4 = \frac{4}{5}\alpha\overline{\psi} + \frac{1}{3}\sqrt{-d5r - 36\overline{\psi^2}})$

SIMULATIONS AND RESULTS

For the simulation, we used the PFC model suggested by Elder[2]. Our simulation experiments are achieved using a square box of size Nx=Ny=4096. The time step (dt) and the grid size (dx=dy) are 0.5 and π/4, respectively. We set a range of r from −0.20 to −0.32 to study the temperature effects on the grain growth. Also, the average density $\overline{\psi} = -0.285$.

To start the simulations, two small circular seeds were placed at the left side of the simulation box. Then the crystallites will grow and impinge on other crystallites, and grain boundaries between seeds will formed. The results of the evolution of the seed growth are shown in Fig. 1. From these graphs, we can see clearly the so-called columnar structure, which matches the real growth in the additive manufacturing experiment.

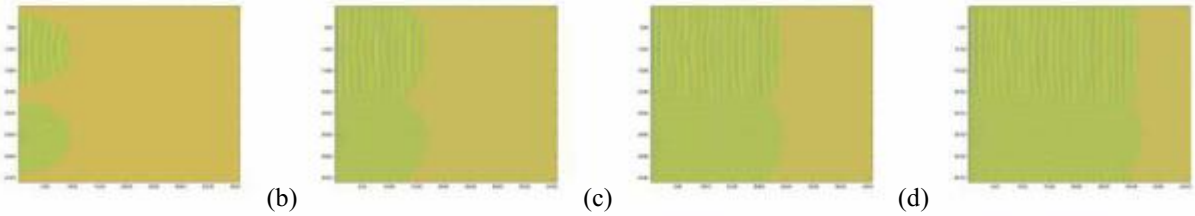

(a) (b) (c) (d)

Fig. 1. Time evolution of the seeds at r= −0.24 at four different time steps: (a) t=2500; (b) t=5000; (c) t=7500; and (d) t=10000.

[a] Corresponding author. Email: keh@clarkson.edu

One of the most important process parameters during the solidification is the temperature difference, which can be denoted by the model parameter r. We run a range of r cases to show its effects. Fig. 2 shows the correlation between the average grain growth and temperature difference. Fig. 3 shows the relationship between temperature difference and growth velocity (the slope of the lines in Fig.2). It can be observed that the velocity of the grain growth increased with r (absolute value). As we stated before, the bigger r (absolute value) means a much larger temperature difference, which will result in a faster grain growth. Furthermore, the effect of ambient temperature and seed-seed distance has been investigated.

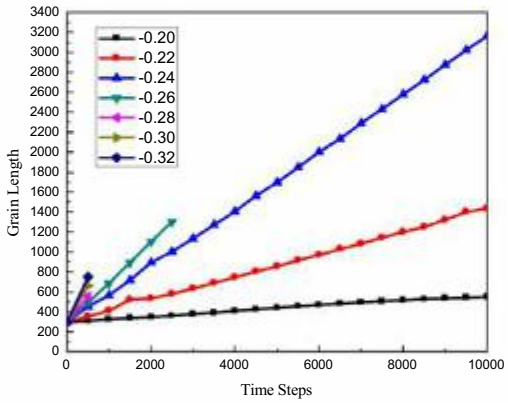

Fig. 2. The grain length for different temperatures

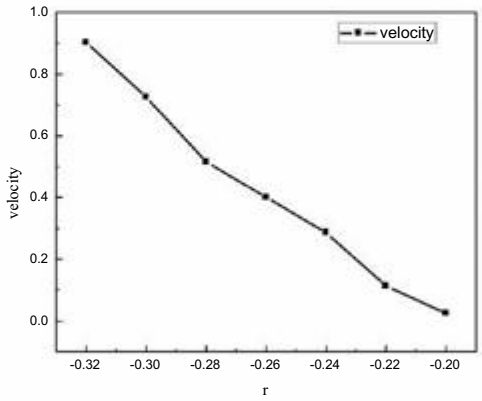

Fig. 3. Growth velocity for different temperatures

Finally, we find that crystal defects exist in the grain structures (Fig. 4). As can be seen in the graph, the dislocations showed periodic arrangement in the grain boundary. The residue stress of the crystal can be derived using eigenstresses field theory similar to that described in Akarapu's paper[3].

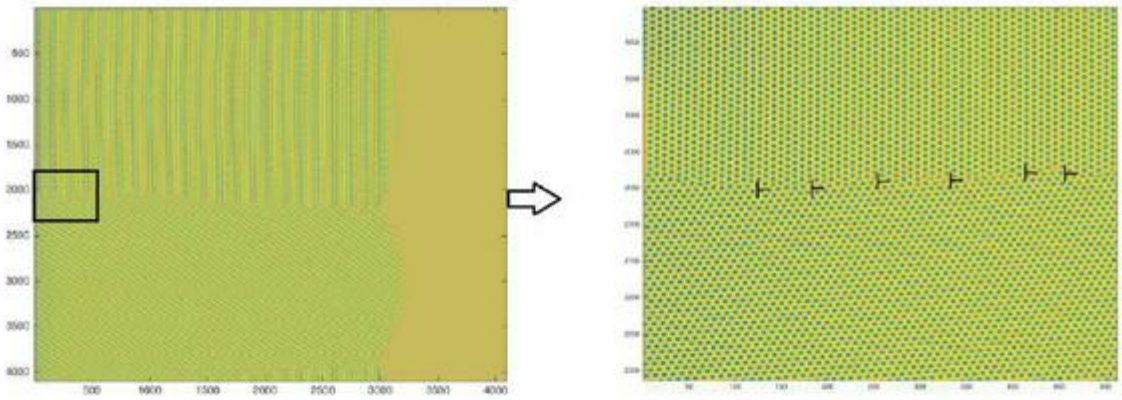

Fig. 4. Grain boundary mismatch between two seeds for r=−0.24

CONCLUSIONS

In conclusion, we have presented a PFC model for the crystal growth in the solidification process during additive manufacturing, which is one of the most promising technologies in the near future. Using PFC simulations and solid-liquid coexistence approach, the evolution of the growth microstructure shows the columnar grain structure, which is in reasonable agreement with the real experiments. Since our model is based on atomistic length and diffusive time scales, it is much faster compared with other approaches, such as molecular dynamics. Overall, this model could provide a fast and effective tool for analyzing the microstructures during additive manufacturing technology.

References

[1] N. Provatas, K. Elder.: Phase-Field Methods in Materials Science and Engineering. Wiley, US 2010.
[2] K. Elder, M. Grant.: Physical Review E 70, 051605, 2004.
[3] S. Akarapu, H.Zbib.:Int J Mech Mater Des 4, 399–406, 2008.

PERIDYNAMIC MODELING OF BEAM VIBRATION AND IMPACT DAMAGE CONCERNING DIFFERENT DEFORMATION SCALE

Ning Liu[1a)], Guolai Yang [1]
[1] *School of Mechanical Engineering, Nanjing University of Science and Technology, Nanjing, China*

Summary A revised bond-based peridynamic approach is proposed to study the beam vibration and impact damage with different deformation scale. In order to predict the beam vibration with small deformation correctly, a surface correction factor is introduced to eliminate the peridynamic inherent "soft" material problem near the boundary. The large deformation induced crack propagation in the beam under impact load is studied subsequently with the uniform peridynamic model. The numerical results indicate that the peridynamic solutions for beam vibration analysis and dynamic fracture behaviour are almost identical to the results based on classical beam theory and experimental investigations.

INTRODUCTION

The peridynamic (PD) theory was first proposed by Silling [1] as a nonlocal theory for modeling the deformation of solid materials subjected to mechanical loading. It reformulates the basic equations of motion in such a form that the internal forces are evaluated through an integral formulation that does not require the evaluation of a stress tensor field or its spatial derivatives. Damage is incorporated naturally in the theory at the level of these two particle interactions. However, bond-based peridynamic model, in their simplest form, shows a boundary effect leading to an effectively "softer" material near the boundary if we keep the distribution of micro-modulus for the points on or close to the boundary to be the same as that for points in the bulk. Besides, the ordinary bond-based peridynamics uses the constant micro-modulus function in the horizon, i.e., the effect of the distance between particles on the stiffness of the bond is ignored so that the intensity forces between particles keeps the same within the horizon. Nevertheless, it does not match the physical nature of non-local theory well. In the present contribution, a revised bond-based peridyanmic model is proposed to solve the aforementioned problems. We provides a complete solution for the deformation and impact damage of elastic peridynamic beams.

BOND-BASED PERIDYNAMIC THEORY

In peridynamic theory, the state of any material point is determined by its pairwise interaction with the points that are located within a finite distance, called the horizon, which is symbolized by δ. The equation of motion of a material point at position x in the reference configuration is written as:

$$\rho\ddot{u}(x,t)=\int_{H_x} f(u'-u,x'-x)\,dV_{x'}+b(x,t) \tag{1}$$

where $\boldsymbol{f}$ is the pairwise force exerted on particle $\boldsymbol{x}$ in the peridynamic bond that connects particle $\boldsymbol{x}$ to $\boldsymbol{x}$'. In most of previous studies the pairwise force is given linearly dependent on the bond stretch [1]. However, the forces acting among bodies decrease with increasing distances in real life problems and examples of such forces can be atomic interactions, gravity and Lorentz force [2]. In the present work, another form of the pairwise force is adopted as follows

$$\boldsymbol{f}(\boldsymbol{\eta},\boldsymbol{\xi})=c(\boldsymbol{\xi})\cdot s(\boldsymbol{\eta},\boldsymbol{\xi})\cdot\frac{\boldsymbol{\eta}+\boldsymbol{\xi}}{|\boldsymbol{\eta}+\boldsymbol{\xi}|}\cdot e^{-(|\boldsymbol{\xi}|/\delta)^2} \tag{2}$$

The numerical procedure involves discretization of the domain of interest into subdomains. During the discretizing process, if one simply assumes the micro-elastic modulus drops to zero outside of the physical domain, there will be an unreasonable reduction in material stiffness near the free surfaces. In this study the stiffness inaccuracies is revised numerically by a parameter termed surface correction factor G, as explained in literature [3]. Thus, the discrete form of the equations of motion given in Eq. (1) can be written as

$$\rho\ddot{u}_i^n=\sum_{j=1}^{N}G_{ij}f(u_j^n-u_i^n,x_j-x_i)V_j+b_i^n \tag{3}$$

where G_{ij} is the correction factor for a peridynamic bond between material points x_i and x_j.

NUMERICAL EXAMPLES

Free vibration of a simple supported beam

We first carry out the elastic vibration analysis of a simply supported beam with small deformation. The geometric and material properties considered for the beam are: length L=0.1 m, thickness h=0.005 m, width b=0.005 m, E=71GPa, ρ=2700 kg/m^3, as shown in Fig. 1.

[a)] Corresponding author. Email: liunieng@gmail.com.

The transverse displacement of the midpoint (point C in Fig.1) is shown in Fig. 2. In order to investigate the effect of surface correction factor on PD solution, the result without surface correction factor is also shown in Fig. 2. It is obvious that considering surface correction factor the peridynamic solution is almost identical to that of classic continuum mechanics. However, the result without considering surface correction factor shows the "soft boundary effect" which leads to a longer vibration period of the beam.

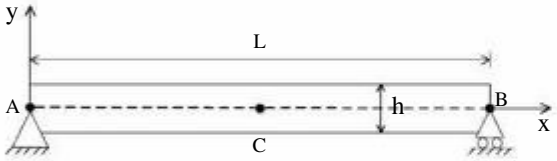

Fig.1. Schematic of a simple supported beam

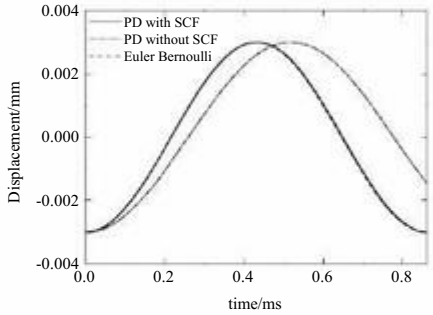

Fig.2. Beam midpoint transverse displacement response.

Impact damage of a three-point bending beam with offset notch

A beam specimen of PMMA with size of 220 mm × 45 mm is cut with an initial notch of 6 mm depth at the bottom boundary as shown in Fig. 3. The relative location of the notch (denoted by γ) is defined by the offset distance, a, from the midspan to the notch divided by half-length of the beam, i.e. γ=2a/L. A drop hammer with weight of m=5 kg is used to introduce a vertical impulsive loading in the center of the top surface with an impact speed of v_0=2.3 m/s. The large deformation goes through beam leading to the crack initiation and growth until ultimate failure of the sample.

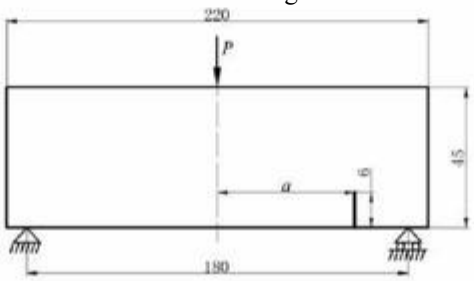

Fig.3. Edge-cracked three-point bending beam with offset notch under impact loading (all dimensions in mm)

We carry out the PD calculations with the notch location of γ=10/110, 20/110, 30/110, 40/110 and 50/110, respectively. Fig.4. (a) shows the PD predicted crack propagation paths with different initial notch locations. The experiment results are presented simultaneously for comparison, as shown in Fig.4 (b). We can see that the PD predictions of the crack propagation behaviors agree reasonably well with the experimental result.

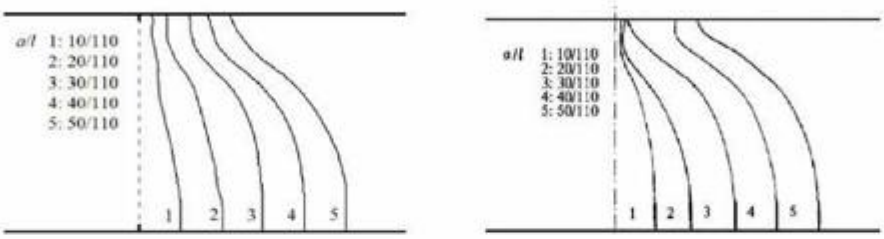

(a) PD results (b) Experimental results

Fig.4. Predicted and experimental crack paths with different notch locations

CONCLUSIONS

A revised bond-based peridynamic model is proposed by considering the effect of the distance between particles on the the pairwise force and the peridynamic inherent surface effect. Numerical results show that the model could accurately predict the vibration response of elastic beams and the dynamic crack propagation in structure.

References

[1] Silling S.A., Askari E., A meshfree method based on the peridynamic model of solid mechanics. Computers & Structures, 83, 17, 1526-1535, 2005.

[2] Kilic B., Madenci E., Structural stability and failure analysis using peridynamic theory, International Journal of Non-Linear Mechanics, 44, 8, 845-854, 2009.

[3] Madenci E., Oterkus E. Peridynamic theory and its applications. Springer, New York, 2014.

GRADIENT BASED POST-BUCKLING OPTIMIZATION OF LAMINATES USING KOITER'S METHOD

Søren R. Henrichsen[1], Paul M. Weaver[2], Esben Lindgaard[1], and Erik Lund [*1]
[1]*Department of Mechanical and Manufacturing Engineering, Aalborg University, Denmark*
[2]*Department of Aerospace Engineering, University of Bristol, United Kingdom*

Summary Laminated composite structures are typically thin-walled structures that are prone to buckling, when compressed. To fully utilize the capabilities of such structures, the post-buckling response should be considered and optimized in the design process. This work presents a novel method for gradient based design optimization of the post-buckling performance of such structures. The post-buckling analysis is based on Koiter's asymptotic method. The design sensitivities of the Koiter factors are derived using the direct differentiation method and new design optimization formulations based on the Koiter factors are presented. The proposed optimization formulations are demonstrated on a square laminated composite plate and a curved panel where the post-buckling stability is optimized.

INTRODUCTION

Fiber reinforced laminated composite structures allow a high degree of tailoring of the structural response, and in several cases such a structure has a design load close to the buckling load. In these cases the performance of the structure in the post-buckling regime is of interest, and it is the aim of this work to develop gradient based optimization methods for improving the post-buckling performance. Detailed post-buckling analysis is computationally expensive, as it involves nonlinearities, and often a path following solution algorithm like the arc length method is used to trace the equilibrium curve. One method to reduce the complexity and extract the most important properties of the post-buckling response is to use asymptotic methods. The methods substitute the full and complex response by a series of simpler problems [1]. Much research within asymptotic post-buckling analysis is based on the work by Koiter [2], see also [3, 4] for an exhaustive description of the analytical approach to Koiter analysis. Recently, [5] demonstrated Koiter analysis combined with the Differential Quadrature Method. Asymptotic methods extract the essential properties of the considered problem. For bifurcation buckling, these properties relate to the type of buckling i.e., symmetric/asymmetric and the stability of the post-buckling response. In asymptotic methods the response is assumed to develop in a self-similar manner, and it cannot capture effects not included in the asymptotic expansion. Regardless of these limitations, asymptotic methods have demonstrated their applicability for post-buckling analysis of structures.

In the standard Koiter analysis only the first two terms in the expansions are of interest as these describe the stability in the vicinity of the critical point and the type of stability. If the response further in the post-buckling regime is of interest, more terms are needed in the expansion. The primary interest in this work is in the initial response, thus Koiter's method is applied. Assuming that the load and deformation for the distinct critical bifurcation point ^{c} are known, the initial post-buckling response is represented by a Taylor-like expansion, where the expanded load factor λ, displacements $\boldsymbol{u}$, strains $\boldsymbol{\epsilon}$, and stresses $\boldsymbol{\sigma}$ are extrapolated into the post-buckling regime as

$$\lambda = \lambda_c + a\lambda_c\xi + b\lambda_c\xi^2 + c\lambda_c\xi^3 + \dots \tag{1}$$

$$\boldsymbol{u} = {}^0\boldsymbol{u}\lambda + {}^1\boldsymbol{u}\xi + {}^2\boldsymbol{u}\xi^2 + {}^3\boldsymbol{u}\xi^3 + \dots \tag{2}$$

$$\boldsymbol{\epsilon} = {}^0\boldsymbol{\epsilon}\lambda + {}^1\boldsymbol{\epsilon}\xi + {}^2\boldsymbol{\epsilon}\xi^2 + {}^3\boldsymbol{\epsilon}\xi^3 + \dots \tag{3}$$

$$\boldsymbol{\sigma} = {}^0\boldsymbol{\sigma}\lambda + {}^1\boldsymbol{\sigma}\xi + {}^2\boldsymbol{\sigma}\xi^2 + {}^3\boldsymbol{\sigma}\xi^3 + \dots \tag{4}$$

Here a superscript ^{0} defines a pre-buckling quantity, whereas all higher quantities are related to the post-buckling state. λ is the post-buckling load factor normalized with respect to the applied load, λ_c is the critical buckling load factor, a, b, and c are the first three Koiter factors which are non-dimensional, ${}^0\boldsymbol{u}$ is the pre-buckling displacement field, ${}^1\boldsymbol{u}$ through ${}^3\boldsymbol{u}$ are the post-buckling displacement fields, and ξ is the perturbation variable. ${}^{0\dots3}\boldsymbol{\epsilon}$ and ${}^{0\dots3}\boldsymbol{\sigma}$ are the expanded strains and stresses with ^{0} being the pre-buckling quantities. The expansions for λ, $\boldsymbol{u}$, $\boldsymbol{\epsilon}$, and $\boldsymbol{\sigma}$ are assumed to be valid asymptotically as $\xi \to 0$.

FINITE ELEMENT BASED ANALYSIS AND OPTIMIZATION

Koiter analysis has been implemented within a finite element framework in previous work such as [6–10], where shell and beam elements have been used. In this work the finite element implementation is based on 9-node equivalent single layer isoparametric shell elements using first order shear deformation theory, see details in [11].

The objective is to maximize the post-buckling stability of laminated composite structures by gradient-based optimization techniques. Thus, the design sensitivities of the Koiter factors, a and b, and the critical buckling load factor λ_c are needed. The

*Corresponding author. Email: el@m-tech.aau.dk

direct differentiation method has been used to derive semi-analytical design sensitivities. A number of different optimization formulations have been implemented and investigated in order to handle both asymmetric post-buckling and symmetric post-buckling responses. The Koiter factors are used to optimize the initial post-buckling response of all structures considered, and in order to have a benchmark on the performance of the considered structures, maximization of the critical buckling load factor is also performed.

When the bifurcation is symmetric the Koiter a-factor is zero and the initial post-buckling response is governed by the Koiter b-factor. To maximize the post-buckling stability maximization of the Koiter b-factor is applied in such cases. This formulation only considers the post-buckling curvature factor i.e., the Koiter b-factor, in the objective as this factor defines the post-buckling stability. An alternative approach is to maximize the $b\lambda_c$ product, as the product is present in the expansion of the load factor.

When an asymmetric post-buckling response is present the Koiter a-factor is non-zero. Consequently the initial post-buckling response is unstable. In order to minimize the asymmetry the a-factor should be as close to zero as possible. In such cases the absolute value of the a-factor is minimized.

The gradient based optimization formulations are demonstrated on two different examples i.e., a simply supported square plate and a curved panel, see details in [11]. The parameterization is based on elementwise fiber angles but other laminate parameterizations like the Discrete Material Optimization parameterization have been implemented within the presented framework.

CONCLUSIONS

The proposed post-buckling optimizations successfully optimize the post-buckling stability even in the considered cases where the pre-buckling response is nonlinear, resulting in structures with increased post-buckling stability. The post-buckling optimization method operates directly on the physical phenomenon related to post-buckling stability. Consequently, the proposed method enables the possibility of obtaining a better performance of the laminated composite structure in the post-buckling regime.

References

[1] C. M. Bender and S. A. Orszag. *Advanced Mathematical Methods for Scientists and Engineers*. McGraw-Hill, 1978. ISBN 9780070044524.

[2] W. T. Koiter. *The Stability of Elastic Equilibrium*. PhD thesis, Technische Hooge School Delft, 1945. Translated by E. Riks.

[3] B. Budiansky. Theory of buckling and post-buckling behavior of elastic structures. *Advances in Applied Mechanics*, 14: 1–65, 1974. ISSN 0065-2156.

[4] E. Byskov. *Elementary Continuum Mechanics for Everyone*. Springer-Verlag, Berlin, 1st edition, 2013. ISBN 9789400757653.

[5] S.C. White, G. Raju, and P.M. Weaver. Initial post-buckling of variable-stiffness curved panels. *Journal of the Mechanics and Physics of Solids*, 71:132–155, 2014.

[6] J. F. Olesen and E. Byskov. Accurate determination of asymptotic postbuckling stresses by the finite element method. *Computers & Structures*, 15(2):157–163, 1982. ISSN 0045-7949.

[7] J. Arbocz and J.M.A.M. Hol. Koiter's stability theory in a computer-aided engineering (CAE) environment. *International Journal of Solids and Structures*, 26(910):945–973, 1990. ISSN 0020-7683.

[8] A. D. Lanzo and G. Garcea. Koiter's analysis of thin-walled structures by a finite element approach. *International Journal for Numerical Methods in Engineering*, 39(17):3007–3031, 1996. ISSN 1097-0207.

[9] G. Garcea, A. Madeo, G. Zagari, and R. Casciaro. Asymptotic post-buckling FEM analysis using corotational formulation. *International Journal of Solids and Structures*, 46(2):377–397, 2009. ISSN 0020-7683.

[10] T. Rahman and E.L. Jansen. Finite element based coupled mode initial post-buckling analysis of a composite cylindrical shell. *Thin-Walled Structures*, 48(1):25–32, 2010.

[11] S.R. Henrichsen, P.M Weaver, E. Lindgaard, and E. Lund. Post-buckling optimization of composite structures using Koiter's method. *International Journal for Numerical Methods in Engineering*, submitted, 2016.

FORMULATION OF BOUNDARY INTEGRALS WITH EIGENSTRAINS IN 3-D EIGENSTRAIN BIE

Hang Ma[1a)] & Jicheng Zhou[2]
[1]*Deaprtment of Mechanics, College of Sciences, Shanghai University, Shanghai 200444, China*
[2]*Shanghai Institute of Applied Mathematics and Mechanics, Shanghai University, Shanghai 200072, China*

Summary The formulations of the three dimensional boundary integrals with eigenstrains assumed to be polynomial distributions are derived from the corresponding domain integrals in the eigenstrain boundary integral equations (BIE) by making use of the properties of integral kernels or the fundamental solutions. By comparing the results of numerical integrations of the corresponding two integrals over a volume element and its boundary, the validity of the formulations is checked and verified.

INTRODUCTION

The eigenstrain solution in solid mechanics is pioneered by Eshelby [1] in the middle of the last century, which can correspond to a wide variety of physical and engineering problems such as thermal mismatch, lattice mismatch, phase transformation, microstructural evolution, quantum dot [2] and intrinsic strains [3] or eigenstrains [4] in residual stress problems, etc. As the distributions of eigenstrain in structure are in general inconstant, the use of internal cells is indispensable by dividing domain integrals for the analysis of residual stresses with the eigenstrain boundary integral equation (BIE) based numerical method [5]. To get rid of this deficiency, by assuming the polynomial distribution of eigenstrain and making use of the properties of the integral kernels or the fundamental solutions, the boundary integrals can be derived from the corresponding domain integrals [6]. In this way, the residual stress analysis can be carried out without the use of internal cells using the eigenstrain BIEs [7]. In the present work, the three dimensional formulation of the boundary integrals with polynomial eigenstrains is derived from the corresponding domain integrals in the eigenstrain BIE by making use of the properties of the integral kernels or the fundamental solutions and comparing the numerical integrations over a volume element and its boundary.

FORMULATIONS

The eigenstrain boundary integral equations

The displacement and the stress BIEs with eigenstrains, ε_{ij}^0, distributed over the domain Ω are written as follows [7]

$$C_{ij}u_j(p)=\int_\Gamma \tau_j(q)u_{ij}^*(p,q)d\Gamma(q)-\int_\Gamma u_j(q)\tau_{ij}^*(p,q)d\Gamma(q)+\int_\Omega \varepsilon_{jk}^0(q)\sigma_{ijk}^*(p,q)d\Omega(q) \tag{1}$$

$$\sigma_{ij}(p)=\int_\Gamma \tau_k(q)u_{ijk}^*(p,q)d\Gamma(q)-\int_\Gamma u_k(q)\tau_{ijk}^*(p,q)d\Gamma(q)+\int_{\Omega-\Omega_\varepsilon} \varepsilon_{kl}^0(q)\sigma_{ijkl}^*(p,q)d\Omega(q)+O_{ijkl}^*\varepsilon_{kl}^0(p) \tag{2}$$

where the two points p and q represent the source and the field points, respectively. Suppose that the eigenstrains can be approximated by polynomials as follows

$$\varepsilon_{ij}^0(q)\approx \sum_{m=0,n=0,l-0}^{m+n+l=N} \chi_{ij}^{mnl}x_1^m(q)x_2^n(q)x_3^l(q) \tag{3}$$

As noticed that all the kernels in (1) and (2) are two point functions, any term in the eigenstrain polynomials should also be written in the form of two point variable by defining $x_k=x_k(q)-x_k(p)$ before the derivation can be carried out from domain integrals to boundary integrals

$$\chi_{ij}^{mnl}\int_\Omega x_1^m(q)x_2^n(q)x_3^l(q)\sigma_{ijk}^*d\Omega=\chi_{ij}^{mnl}\sum_{s=0}^m\sum_{t=o}^n\sum_{u=0}^l\frac{m!n!l!}{(m-s)!(n-t)!(l-u)!s!t!u!}\ x_1^{m-s}(p)x_2^{n-t}(p)x_3^{l-u}(p)\int_\Omega x_1^sx_2^tx_3^u\sigma_{ijk}^*d\Omega \tag{4}$$

$$\chi_{ij}^{mnl}\left\{\int_\Omega x_1^m(q)x_2^n(q)x_3^l(q)\sigma_{ijkl}^*d\Omega+x_1^m(p)x_2^n(p)x_3^l(p)O_{ijkl}^*\varepsilon_{kl}^0(p)\right\}$$

$$=\chi_{ij}^{mnl}\left\{\sum_{s=0}^m\sum_{t=o}^n\sum_{u=0}^l\frac{m!n!l!}{(m-s)!(n-t)!(l-u)!s!t!u!}x_1^{m-s}(p)x_2^{n-t}(p)x_3^{l-u}(p)\int_\Omega x_1^sx_2^tx_3^u\sigma_{ijkl}^*d\Omega+x_1^m(p)x_2^n(p)x_3^l(p)O_{ijkl}^*\varepsilon_{kl}^0(p)\right\} \tag{5}$$

Formulations of boundary integrals in the displacement equation

The kernel σ_{ijk}^*, or the stress fundamental solution, in equation (1) is the stress at the point q owing to a unit force acting on the point p in i direction, which obeys Cauchy's relation $\sigma_{ijk}^*(p,q)n_k(q)=\tau_{ij}^*(p,q)$ and equilibrium equation $\sigma_{ijk,k}^*(p,q)+\delta_{ij}\delta(p,q)=0$ from which an integral relation can be derived as

a) Corresponding author. Email: hangma@staff.shu.edu.cn.

$$\int_\Omega \left\{ m x_1^{m-1} x_2^n x_3^l \delta_{1k} + n x_1^m x_2^{n-1} x_3^l \delta_{2k} + l x_1^m x_2^n x_3^{l-1} \delta_{3k} \right\} \sigma_{ijk}^*(p,q)\, d\Omega(q) = \int_\Gamma x_1^m x_2^n x_3^l \tau_{ij}^*(p,q)\, d\Gamma(q) \tag{6}$$

Based on the above integral identity and comparing the results of the numerical integration in both the two sides of (6) over a volume element Ω and its boundary Γ, respectively, the explicit formulations of boundary integrals can be obtained

$$\int_\Omega x_1^m x_2^n x_3^l \sigma_{kkj}^* d\Omega = \frac{1}{m+n+l+1} \int_\Gamma x_1^{m+\delta_{j1}} x_2^{n+\delta_{j2}} x_3^{l+\delta_{j3}} \tau_{kk}^* d\Gamma \tag{7}$$

$$\int_\Omega x_1^m x_2^n x_3^l \sigma_{jkk}^* d\Omega = \frac{1}{m\delta_{k1} + n\delta_{k2} + l\delta_{k3} + 1} \int_\Gamma x_1^{m+\delta_{k1}} x_2^{n+\delta_{k2}} x_3^{l+\delta_{k3}} \tau_{kk}^* d\Gamma$$
$$- \frac{m\delta_{j1} + n\delta_{j2} + l\delta_{j3}}{(m\delta_{k1} + n\delta_{k2} + l\delta_{k3})(m+n+l+1)} \int_\Gamma x_1^{m-\delta_{j1}+2\delta_{k1}} x_2^{n-\delta_{j2}+2\delta_{k3}} x_3^{l-\delta_{j3}+2\delta_{k3}} \tau_{jj}^* d\Gamma \; - \frac{\left| m e_{1jk} + n e_{j2k} + l e_{jk3} \right|}{m\delta_{k1} + n\delta_{k2} + l\delta_{k3}} \int_\Gamma x_1^{m-|e_{1jk}|+\delta_{k1}} x_2^{n-|e_{j2k}|+\delta_{k2}} x_3^{l-|e_{jk3}|+\delta_{k3}} \sigma_{123}^* d\Omega \tag{8}$$

where j, k=1,2,3 with no summation, except a special term which can be derived in a recurrence form with the aid of the high order fundamental solutions and Gaussian divergence theorem

$$\int_\Omega x_1^m x_2^n x_3^l \sigma_{123}^{(N)} d\Omega = \int_\Gamma x_1^m x_2^n x_3^l \frac{\partial}{\partial n} \sigma_{123}^{(N+1)} d\Gamma - \int_\Gamma \frac{\partial}{\partial n} \left(x_1^m x_2^n x_3^l \right) \sigma_{123}^{(N+1)} d\Gamma + \int_\Omega \left(x_1^m x_2^n x_3^l \right)_{,kk} \sigma_{123}^{(N+1)} d\Omega \tag{9}$$

where $\sigma_{123}^{(N)} = \sigma_{123}^{(N+1)}{}_{,kk}$ and $\sigma_{123}^* = \sigma_{123}^{(N)}$ when N=1.

Formulations of boundary integrals in the stress equation

The boundary integrals with eigenstrains in the stress equation (2) can also be derived from the corresponding domain integrals by making use of the following derived constitutive relation between kernels

$$\sigma_{ijkl}^*(p,q) = -\mu \left\{ \beta \delta_{ij} \sigma_{skl,s}^* + \sigma_{ikl,j}^* + \sigma_{jkl,i}^* \right\}$$

where μ is the shear modulus and $\beta = 2\nu/(1-2\nu)$ and ν is Poisson's ratio. The boundary integrals with eigenstrains in the stress equation are presented as follows

$$\frac{1}{\mu} \int_\Omega x_1^m x_2^n x_3^l \sigma_{ijkl}^* d\Omega = -\int_\Gamma x_1^m x_2^n x_3^l \left\{ \beta \delta_{ij} \sigma_{skl}^* n_s + \sigma_{ikl}^* n_j + \sigma_{jkl}^* n_i \right\} d\Gamma + \beta \delta_{ij} \int_\Omega \left\{ m x_1^{m-1} x_2^n x_3^l \sigma_{1kl}^* + n x_1^m x_2^{n-1} x_3^l \sigma_{2kl}^* + m x_1^m x_2^n x_3^{l-1} \sigma_{3kl}^* \right\} d\Omega$$
$$+ \int_\Omega \left\{ \left(m x_1^{m-1} x_2^n x_3^l \delta_{1j} + n x_1^m x_2^{n-1} x_3^l \delta_{2j} + m x_1^m x_2^n x_3^{l-1} \delta_{3j} \right) \sigma_{ikl}^* + \left(m x_1^{m-1} x_2^n x_3^l \delta_{1j} + n x_1^m x_2^{n-1} x_3^l \delta_{2j} + m x_1^m x_2^n x_3^{l-1} \delta_{3j} \right) \sigma_{jkl}^* \right\} d\Omega$$
$$(m \ge 0, n \ge 0, l \ge 0, m+n+l \ge 0) \tag{10}$$

Combining with (7), (8) and (9), all domain integrals at the right hand side of (10) can be written in the form of boundary integrals, which can be reduced into the following integral relations of kernels [8] if the constant eigenstrains are assumed

$$\int_\Omega \sigma_{ijk}^*(p,q)\, d\Omega(q) = = \int_\Gamma x_k \tau_{ij}^*(p,q)\, d\Gamma(q), \quad \int_\Omega \sigma_{ijkl}^*(p,q)\, d\Omega(q) + O_{ijkl}^*(p,q) \varepsilon_{kl}^0(p) = \int_\Gamma x_l \tau_{ijk}^*(p,q)\, d\Gamma(q) \tag{11a, b}$$

CONCLUSIONS

The formulations of the 3D boundary integrals with polynomial eigenstrains are derived from the corresponding domain integrals, which are expected to be used for the numerical analysis of problems with non-constant eigenstrains with the eigenstrain BIEs.

Acknowledgment: The work was supported by the National Natural Science Foundation of China (11272195, 11172159).

References

[1] Eshelby J.D.: The determination of the elastic field of an ellipsoidal inclusion and related problems. Proc. Royal Soc. London, **A241**:376-396, 1957.

[2] Pan E.: Elastic or piezoelastic fields around a quantum dot: fully coupled or semicoupled model? J. Appl. Phys., **91**(6):3785-3796, 2002.

[3] Ueda Y., Jirn Y., Yuan M.: Determination of residual stresses based on the sources of their formation. Trans. Japan Weld. Soc., **6**(1): 59-64, 1986.

[4] Korsunsky A.M, Regino G.M, Latham D., Liu J., Nowell D., Walsh M.: Eigenstrain analysis of synchrotron X-ray diffraction measurement of residual strains in machined nickel alloy plates. J. Strain Anal., **41**(5): 381-395, 2006.

[5] Ma H., Deng H.L.: Nondestructive determination of welding residual stresses by boundary element method. Adv. Eng. Software, **29**: 89-95, 1998.

[6] Ma H., Kamiya N., Xu S.Q.: Complete polynomial expansion of domain variables at boundary for two-dimensional elasto-plastic problems. Eng. Anal. Bound. Elem., **21**(3):271-275, 1998.

[7] Ma H., Wang Y., Qin Q.H.: Determination of welding residual stresses by inverse approach with eigenstrain formulations of BIE. Applicable Anal., **91**:807-821, 2012.

[8] Ma H., Fang J.B., Qin Q.H.: Simulation of ellipsoidal particle-reinforced materials with eigenstrain formulation of 3D BIE. Adv. Eng. Software, **42**:750-759, 2011.

A LAPLACE DOMAIN BEM FORMULATION FOR DYNAMIC PROBLEMS OF ANISOTROPIC ELASTICITY

Leonid Igumnov[a)], Ivan Markov, Igor Vorobtsov & Alexander Konstantinov
Research Institute for Mechanics, National Research Lobachevsky State University of Nizhni Novgorod, Nizhny Novgorod, Russia

Summary This paper presents a Laplace domain direct boundary element formulation for three-dimensional problems of linear anisotropic elasticity, based on the integral representations of the dynamic fundamental solutions. Special technique for approximation of both static and dynamic parts of the displacement fundamental solution (and its spatial derivative) over the boundary elements is employed along with a parallelization scheme in order to improve computational efficiency. Modified Durbin's method is used to obtain time domain solutions. To validate the proposed formulation numerical results are compared with results of dynamic experiment and finite element solutions.

INTRODUCTION

The Boundary Element Method (BEM) is known to be a very efficient numerical approach for solving dynamic problems of linear isotropic elasticity. As is well known, boundary element formulations are strongly dependent on the availability of the corresponding fundamental solutions. This becomes a major impediment to developing a conventional direct BEM approach when general anisotropic materials are considered since the corresponding dynamic fundamental solutions are not available in the closed form. One way to overcome this drawback is to employ the Dual Reciprocity Method first formulated by Nardini and Brebbia [1]. However, internal collocation nodes are often required to achieve desirable accuracy of the solution.

In this research, a three-dimensional direct boundary element formulation is presented which uses integral representations of Laplace domain dynamic fundamental solutions derived by Wang and Achenbach [2]. Validity of the present formulation is confirmed through the comparison of the obtained numerical solution with results of dynamic experiment and finite element simulation.

BEM FORMULATION

The Somigliana identity for problems of linear anisotropic elasticity yields the displacements at any point inside the domain Ω when both displacements and tractions on the boundary $\Gamma = \partial\Omega$ are known:

$$\overline{u}_i(\mathbf{x},s) = \int_\Gamma \left(\overline{g}_{ij}(\mathbf{x},\mathbf{y},s)\overline{t}_j(\mathbf{y},s) - \overline{h}_{ij}(\mathbf{x},\mathbf{y},s)\overline{u}_j(\mathbf{y},s)\right)\mathrm{d}\Gamma(\mathbf{y}), \quad \mathbf{x}\in\Omega. \tag{1}$$

where superposed bar denotes a Laplace transformed variable and s is the Laplace parameter. $\mathbf{x}$ and $\mathbf{y}$ are the source and field points, $\overline{u}_i$ and $\overline{t}_i$ are displacements and tractions, respectively. $\overline{g}_{jk}$ and $\overline{h}_{jk}$ are the displacement and traction Laplace domain fundamental solutions.

Following standard boundary element procedure, we obtain the boundary integral equation:

$$c_{ij}\overline{u}_j(\mathbf{x},s) = \int_\Gamma \overline{g}_{ij}(\mathbf{x},\mathbf{y},s)\overline{t}_j(\mathbf{y},s)\mathrm{d}\Gamma(\mathbf{y}) - \text{p.v.}\int_\Gamma \overline{h}_{ij}(\mathbf{x},\mathbf{y},s)\overline{u}_j(\mathbf{y},s)\mathrm{d}\Gamma(\mathbf{y}), \quad \mathbf{x}\in\Gamma, \tag{2}$$

where c_{ij} is the free terms, p.v. denotes that the integral is to be interpreted in the Cauchy principal value sense.

As the first step of numerical implementation, we approximate boundary geometry by eight-node quadrilateral elements with quadratic shape functions. Spatial discretization of Eq. (2) is based on the point collocation scheme with the mixed boundary elements with linear and constant approximation of the displacements and tractions, respectively. Such splitting of the collocation points allows to deal with the natural discontinuities of the tractions while continuously approximating the displacements. Displacement fundamental solution is obtained by taking the Laplace transform of the time domain representation derived by Wang and Achenbach:

$$\overline{g}_{jk}(\mathbf{x},\mathbf{y},s) = \overline{g}_{jk}(\mathbf{r},s) = \overline{g}^S_{jk}(\mathbf{r}) + \overline{g}^R_{jk}(\mathbf{r},s), \quad \mathbf{r} = \mathbf{y}-\mathbf{x},\ r = |\mathbf{r}|, \tag{3}$$

$$\overline{g}^R_{jk}(\mathbf{r},s) = -\frac{1}{8\pi^2}\int_{\substack{|\mathbf{n}|=1\\ \mathbf{n}\cdot\mathbf{r}>0}} \sum_{m=1}^{3}\frac{k_m E_{jm}E_{km}}{\rho c_m^2} e^{-k_m|\mathbf{n}\cdot\mathbf{r}|}dS(\mathbf{n}), \tag{4}$$

[a)] Corresponding author. Email: igumnov@mech.unn.ru

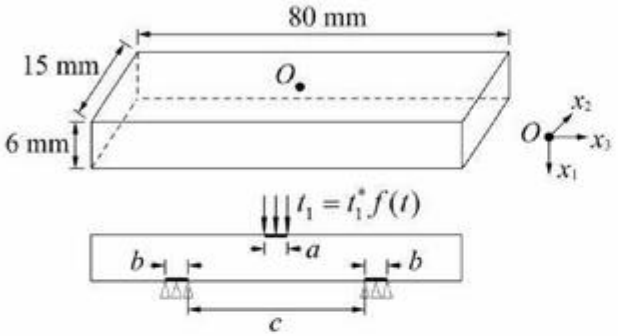

Figure 1. Analysis model.

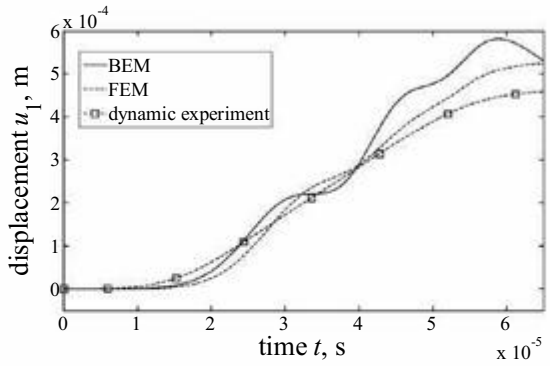

Figure 2. Displacement $u_1(t)$ at the point (0, 0, 0) m.

$$\overline{g}^S_{jk}(\mathbf{r}) = \frac{1}{8\pi^2 r} \int_{|\mathbf{d}|=1} \Gamma^{-1}_{jk}(\mathbf{d}) dL(\mathbf{d}), \tag{5}$$

where superscripts *R* and *S* denote the dynamic and the static parts, respectively.

The traction fundamental solution can be written as:

$$\overline{h}_{jm}(\mathbf{x}, \mathbf{y}, s) = C_{ijkl} \overline{g}_{km,l} n_i(\mathbf{y}), \tag{6}$$

where $n_i(\mathbf{y})$ denotes the unit outward normal vector at the field point.

Since fundamental solutions cannot be expressed in a closed form, their computation, which is required for each integration point, greatly increase overall computation time. Therefore, for calculating the displacement fundamental solution (and its derivative) we use linear Lagrangian interpolation for the static part and approximation over five-node quadrilateral element for the dynamic part [3]. In addition, parallelization scheme using the OpenMP is implemented. Modified Durbin's scheme [4] for numerical inversion of the Laplace transform is employed to obtain time domain solutions.

NUMERICAL RESULTS

Transient problem shown in Fig. 1 is solved by the proposed method. Prismatic solid is simply supported at the bottom face on two rectangular areas located symmetric with respect to the x_1x_2 plane. These areas have width b = 1.5 mm and the distance between them is c = 45 mm. A uniform surface pressure $t_1 = t_1^* f(t)$, $t_1^* = -9.724 \cdot 10^7$ Pa is applied on the area with width a = 1.4 mm in the middle of the top face. Considered material is orthotropic. In Fig. 2 obtained BEM solution for the displacement $u_1(t)$ at the point (0, 0, 0) m is compared with the results of dynamic experiment and corresponding finite element analysis. As it can be observed, these results are in a good agreement.

CONCLUSIONS

In this work a Laplace domain three-dimensional boundary element formulation for transient dynamic analysis of general anisotropic elastic solids was presented. The difficulties arising from the use of dynamic fundamental solutions in their integral representations are dealt with by using approximation techniques and parallelization scheme. Reliability of the proposed boundary element formulation is confirmed by the provided numerical results. The reported study was funded by RFBR, according to the research project No. 16-38-60097 mol_a_dk and by the Russian Science Foundation under grant No.14-19-01096 in a part concerning the dynamic experiment.

References

[1] Nardini D., Brebbia C.A.: A new approach to free vibration analysis using boundary elements. *Appl. Math. Modelling* **7**:157-162, 1983.

[2] Wang C.Y., Achenbach J.D.: Elastodynamic fundamental solution for anisotropic solids. *Geophys. J. Int.* **118**:384-392, 1994.

[3] Matsumoto T., Tanaka M., Ogawa Y.: A simple technique for efficient evaluations of boundary integrals of time-harmonic elastodynamic BEM analyses for anisotropic solids. *Proceedings Second MIT Conference on Computational Fluid and Solid Mechanics.* 2071-2073, 2003.

[4] Zhao X.: An efficient approach for the numerical inversion of Laplace transform and its application in dynamic fracture analysis of a piezoelectric laminate. *Int. J. Solids. Struct.* **41**:3653-3674, 2004.

EVALUATION OF MODIFIED FINITE ELEMENTS WITH SPATIALLY VARYING ELASTIC PARAMETERS FOR FUNCTIONALLY GRADED MATERIALS

Mohamad Molavi Nojumi[a)], Xiaodong Wang
Department of Mechanical Engineering, University of Alberta, Edmonton, Alberta, Canada

Summary This paper represents a new discussion on the contribution of graded elements in providing better estimation in comparison with conventional homogeneous elements. This comparison relies on the stress/strain variation through graded and conventional elements. The piecewise homogeneous modelling of functionally graded materials (FGMs) by normal elements is challenged with specific examples. Static nodal equilibrium equations are derived based on the traditional finite element formulation for a 9-node graded quadrilateral element in which elastic constants change spatially. The superiority of graded elements over conventional elements is proved by producing more accurate results with less efforts. Moreover, it is indicated that errors may happen in the estimation of the local field behaviour of FGMs which are modeled with normal elements. The validity of the solution with graded elements is demonstrated by comparison with analytical works.

INTRODUCTION

In determining stress field in FGMs the idea of considering the elastic property as a function of the coordinate system in the traditional finite element formulation was suggested by Lee and Erdogan [1]. Giannakopoulos et al. developed a subroutine for describing the elastic and plastic properties of FGMs at the element level [2]. Then, Kim and Paulino compared the performance of graded elements to conventional elements in some boundary value problems [3]. Although previous works established a good background for understanding graded elements, however, there is still no detailed discussion on potential issues when conventional homogeneous elements are applied for studying FGMs. The importance of the current work is to explain the mechanism through which graded elements produce more accurate, efficient and reliable solutions, and to introduce the root of the dissimilarity in results obtained with graded and normal elements through specific examples. To probe this issue, a 9-node linear elastic isotropic graded element is considered which is more accurate for investigating the stress/strain variation through the element in comparison with the previously discussed 4 and 8-node graded elements [3]. Investigating when these two types of elements leads to different results or in agreement is a key point to analyze their performance in modelling FGMs. In the following discussion, the variation of the stress/strain through graded and homogeneous elements is scrutinized and differences in solutions are justified with respect to the dissimilar behavior of the FGM and homogeneous structures.

FORMULATION OF THE PROBLEM

The focus of the work is to study the influence of the material variation on the static structural behaviour of linear elastic isotropic FGMs by using the finite element method. Applying the varying elasticity matrix in traditional finite element formulation is the main characteristic of graded elements. The elasticity matrix under the plane strain condition is given in Eq.(1). N_k represent shape functions for isoparametric 9-node quadrilateral elements. In comparison conventional elements have a constant elastic property.

$$[D]=\frac{\sum_k N_k E_k(x,y)}{(1+\sum_k N_k \nu_k(x,y)).(1-2\sum_k N_k \nu_k(x,y))}\begin{bmatrix}1-\sum_k N_k\nu_k(x,y) & \sum_k N_k\nu_k(x,y) & 0\\ \sum_k N_k\nu_k(x,y) & 1-\sum_k N_k\nu_k(x,y) & 0\\ 0 & 0 & (1-2\sum_k N_k\nu_k(x,y))/2\end{bmatrix}. \quad (1)$$

By applying the well-known principle of the virtual work or the theory of minimum total potential energy the equilibrium equation can be reached, from which nodal displacements (a^e) can be obtained,

$$F^e = K^e a^e, \left(K^e = \int_{A^e} B^T D B \, dA\right). \quad (2)$$

The local stress/strain field obtained by this procedure will be evaluated for graded and normal elements. Based on the validated data for structural response of FGMs, it will be checked whether homogeneous elements agree or disagree with graded elements in presenting the true estimation.

NUMERICAL RESULTS AND DISCUSSION

Two sample examples are selected to investigate the effectiveness, accuracy and reliability of the introduced 9-node graded element. First, the validity of the solution is demonstrated in Fig. 1 by comparing it with the analytical Saint-Venant solution for a cantilever bi-directional FGM beam in which Young's modulus varies exponentially ($E(x,y)=E_0e^{\alpha x+\beta y}$) [4]. Dimensions and loading conditions of the problem are the same with those applied in the referenced work. The axial stress profile along the thickness of the FG beam is drawn in Fig. 2 for different non-homogeneity indexes. Fig. 3 shows FG and normal element solutions for axial stresses with non-homogeneity constant being $\beta h = 1.25$. It can be observed that FG

[a)]Corresponding author. Email:molavino@ualberta.ca.

elements are more accurate also converge faster. In addition, it is clear that the stress follows a wrong trend at the homogeneous elements represented by scatter points (each three scatter points represent one homogeneous element). The axial stress σ_{xx} in FGM experiences an increasing trend, whereas, it is decreasing for homogeneous normal elements as shown in Fig. 2 and Fig. 3. This will cause the error so that even by averaging between common nodes in adjacent elements, the stress still does not match the true solution except for very fine mesh.

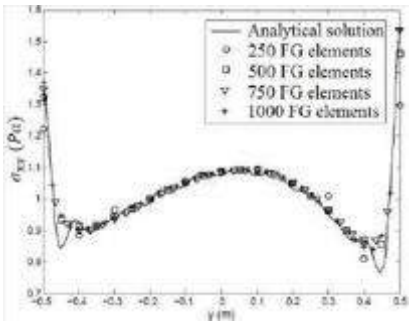

Fig. 1. The comparison of the axial stress along the thickness direction at $x = 0$ between the FEM and analytical solution for $\alpha h = 0.01,\ \beta h = 1$.

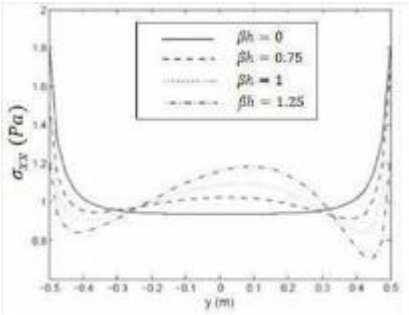

Fig. 2. The stress contour along the beam thickness at $x = 0$ for different indexes of material variation $\beta h (\alpha = 0)$.

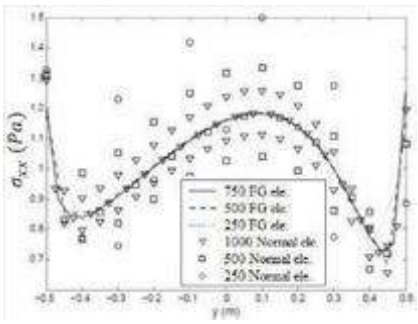

Fig. 3. The comparison of the axial stress along the thickness direction at $x = 0$ obtained with FEM between FG and normal elements for $\beta h = 1.25$.

The second example is the indentation of a rigid flat punch to a FG substrate as exhibited in Fig. 4. The width and height of the FGM are L_x and L_y, the width of the flat rigid punch is a, and the indentation depth is d, with $L_x/a = 2, L_y/a = 1, d/a = 10^{-4}$. The elastic constants of the FGM substrate vary exponentially in the y direction, and a reference value of 200 GPa is considered for the Young's modulus at the bottom, while, the Poisson's ratio ν has the constant value of 0.3. The problem is solved under the plane strain condition. The distribution of normal strains along $x = 1$ is depicted in Fig. 5 in which the distinction in the behaviour of homogeneous and FGM elements is clear. This issue is assessed by inspecting the strain convergence shown in Fig. 6. It is found that strains achieved by FG elements converge with 100 elements, but for conventional elements it will take place with higher number of elements. Furthermore, similar to the previous example it can be justified that the piecewise homogeneous modelling of the problem with normal elements may not produce reliable results.

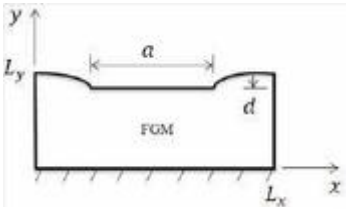

Fig. 4. A FGM substrate indented by a flat rigid punch.

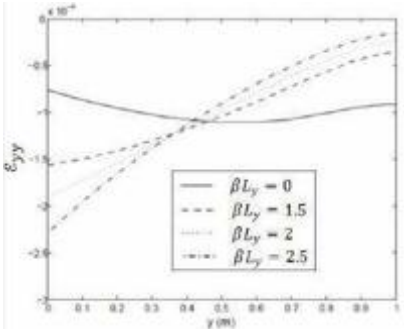

Fig. 5. The strain contour along the defined pass for different indexes of material gradient βL_y.

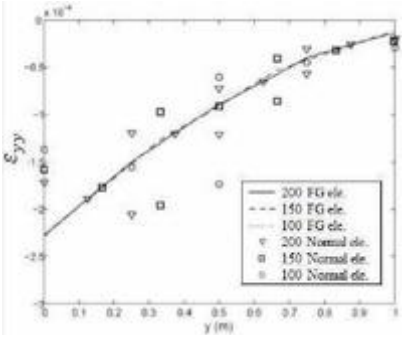

Fig. 6. The comparison of the normal strain along the defined pass between the FG and normal elements for $\beta L_y = 2.5$.

CONCLUSION

A general finite element procedure was reviewed for modelling linear elastic isotropic FGMs with 9-node graded and homogeneous elements. Solving two sample problems, it was revealed that 9-node graded elements are more accurate and effective. Furthermore, the reliability of the piecewise homogeneous modelling of the problem with normal elements for local stress/strain field was challenged as they may produce inaccurate estimation except for very fine mesh.

References

[1] Lee Y. –D, Erdogan F.: Residual/thermal stresses in FGM and laminated thermal barrier coating *.Int. J.Fract.***69**:145-165, 1995.

[2] Giannakopoulos A.E., Suresh S.: Indentation of solids with gradients in elastic properties: Part I. point force *.Int. J.Solids.Struct.***34**:2357-2392, 1997.

[3] Kim, J.-H., Paulino G. H.:Isoparametric Graded Finite Elements for Nonhomogeneous Isotropic and Orthotropic Materials *.J.Appl.Mech.***69**:502-514, 2002.

[4] Zhao L., Chen W.Q., Lu C.F.: Symplectic elasticity for bi-directional functionally graded materials.*Mech. Mater.***54**:32-42, 2012.

LOAD TRANSFER ANALYSIS OF A VEHICLE COMPONENT WITH U* INDEX THEORY

Khashayar Pejhan[1a], Qingguo Wang[1], Christine Wu [1] & Igor Telichev[1]
[1]*Mechanical Engineering Department, University of Manitoba, Winnipeg, Manitoba, Canada*

Abstract Engineering structures are designed to transfer external loads to the supports. Therefore, it is necessary to study this process of load transfer. The U* index method has been introduced to follow the load path in the structure. The U* index value at each point corresponds to its significance in the load carrying process. The U* index theory has been used as a new design criteria in lightweight vehicle structures but there have been few studies that apply this method to real vehicle components under working loading conditions. In this study, a major load carrier component of a multiple passenger vehicle is studied from the load transferring perspective, using the U* index theory. A detailed design evaluation is also performed, based on the U* index analysis and design modification are suggested based on the evaluation.

INTRODUCTION

Load transfer analysis has opened a new door to structural analysis in mechanical engineering. While the conventional stress analysis provides failure criteria by searching for local mechanical features, the load transfer analysis provides a general awareness regarding the performance of the structure. Combinations of these two paradigms can lead a global understanding of the structure. Load path is defined as the course taken by a unit of applied load within a structure, beginning at the point of application and ending at the equilibrating boundary constraint [1]. The U* index theory for load transfer was introduced in 1995 [2] as an approach for detecting load paths in the structure. The U* index value of each point in the structure represents its significance in load transfer process and thus, the U* index distribution in the structure can be used to detect the main load paths in the structure [3]. Moreover, the U* index has evolved so much in the last twenty years and some useful design criteria have been derived from this theory. These features have been used in several studies in literature (e.g. [4] and [5]). However, to expand the application of theory it still necessary to apply the U* index theory to real world problems. Therefore, objective of this study is to evaluate a real load carrying member of a multiple passenger vehicle using the U* index theory.

METHODOLOGY

The U* index theory introduces an indicator for load transfer in the structure. This index can be calculated using the total strain energy of the system under different loading conditions. Fig. 1a shows a sample structure. If we illustrate the whole structure with three linear springs (Fig. 1b) the strain energy of the system can be calculated using Eq. 1. Then, as shown in Fig. 1c, by fixing the arbitrary point C, and applying the initial d_A at point A (Loading point) the strain energy of the system will change and can be calculated with Eq. 2.

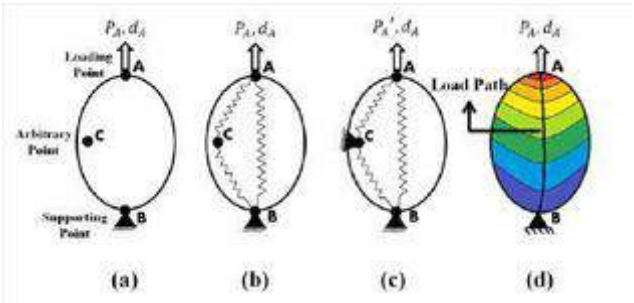

Figure 1) Sample structure for U* analysis: (a) Original structure, (b) Spring model and (c) Modified constraints (d) U* distribution

$$U = \frac{1}{2}\int P_A d_A = \frac{1}{2}\int (K_{AA}d_A + K_{AC}d_C)d_A \qquad \text{(Eq. 1)}$$

$$U' = \frac{1}{2}\int P_A' d_A = \frac{1}{2}\int (K_{AA}d_A)d_A \qquad \text{(Eq. 2)}$$

where P_A and P_A' represent the loading magnitude in original and modified systems, respectively; and d_A is the displacement at the loading point. K_{ij} (i, j=A, B, C) is the internal stiffness between the any two points in the structure. Then following the approach introduced in [2] the U* index can be calculated by the presented formula in Eq. 3

$$U_1^* = 1 - \frac{U}{U'} = \left(1 - \frac{2U}{(K_{AC}d_c).d_A}\right)^{-1} \qquad \text{(Eq. 3)}$$

where U is the strain energy of the original system U′ is the strain energy of the modified system and U^*_1 is the load transfer index for the imposed loads. Figure 1d shows the U^*_1 distribution in the sample structure along with the detected load path based on the U* theory. Following the similar approach and index of U^*_2 can be defined and calculated for the reaction forces that are going to be transferred in the structure. Combination of these two indices provides a new measure for load transfer in the structure. This index is called U^*_{sum} and the value of this index at any point in the structure is proportional to the significance of that point in the load carrying process.

CASE STUDY- WINDOW PILLAR OF A MULTIPLE PASSENGER VEHICLE

To verify capabilities of the U* index theory in real life problems, the window pillar of a multiple passenger vehicle was selected for this study. Figure 2a shows the modelled window pillar. The loading and boundary condition for modelling was extracted from an analysis on a full vehicle model.

[a] Corresponding author. Email: pejhank@myumanitoba.ca.

RESULTS AND DISCUSSION

The results of the conventional stress analysis and the load transfer analysis for the imposed load (U^*_1) and the reaction forces (U^*_2) are shown in Fig 2. Following the two load paths of U^*_1 and U^*_2 explains the reason behind the visible stress concentration in Fig 2b. Predicted load paths show that the major portion of the loading is passing through the edge of the interface between the horizontal and vertical bars. Thus a detailed analysis of this section can show the weak points and the potentials for improvement in the design. Figure 2e shows the U^*_{sum} distribution in the structure and Fig. 3depicts a details analysis on the intersection of horizontal and vertical bars.

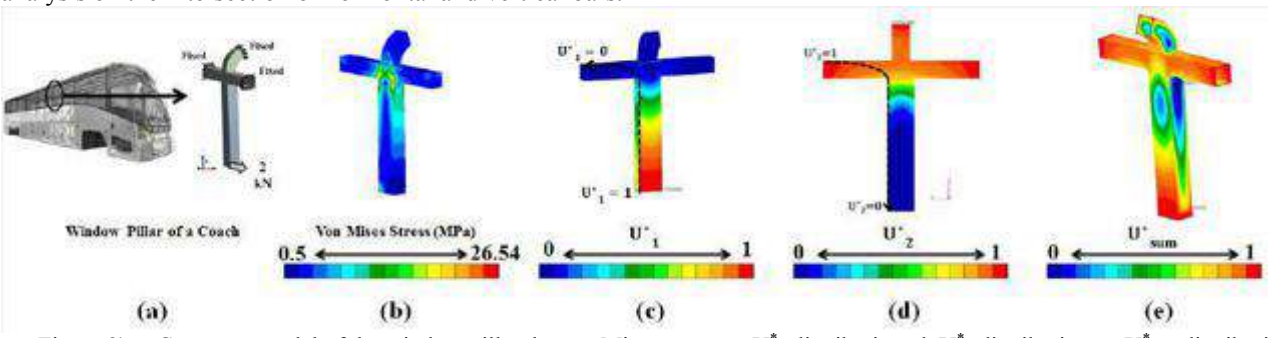

Figure 2) a: Computer model of the window pillar, b: von-Mises stress, c: U^*_1 distribution, d: U^*_2 distribution, e: U^*_{sum} distribution

As shown in Fig.2e side part of the vertical bar is not contributing in the load transfer, which leads to poor load transfer as shown in Fig 3d. Figures 3b and 3c highlights the jump in the stiffness value of the structure at the area which is experiencing stress concentration in Fig 3a. Therefore, design modifications like adding a stiffener in the marked location can improve the performance of this structure. Such modification, based on the predicted load transfer, will reduce the stress concentration and lowers the risk of failure.

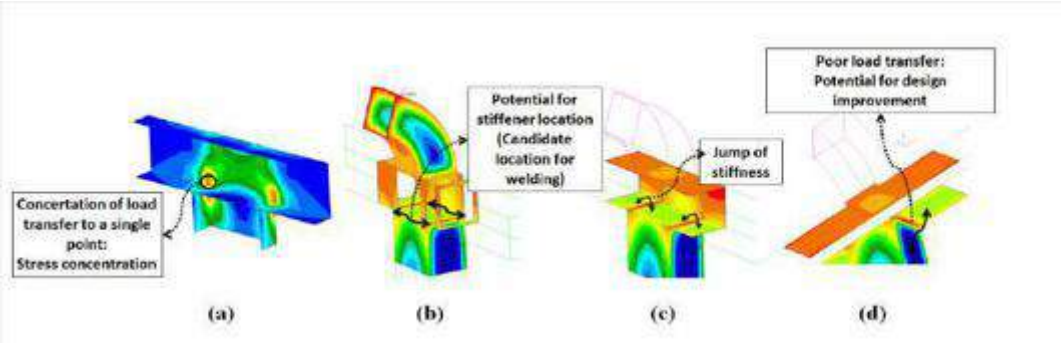

Figure 3) Detailed analysis of the intersection (a) stress concentration, (b) candidates for stiffener (welding) , (c) stiffness jump – weak point and (d) poor load transfer

CONCLUSION

In this study the load transfer of a vehicle component was studied using the U^* index theory. It was shown that U^* index can provide a reasonable justification for the complicated stress distributions and more importantly design evaluation was done on the structure using this theory. Using U^* index theory potential locations for design improvement was found in the structure, based on the assessed load transfer of the design. This application of U^* index theory in a real world problem enhances further development of this relatively new concept in structural analysis.

References

[1] D. W. Kelly and M. Elsley, "A Procedure for Determining Load Paths in Elastic Continua," *Engineering Computations*, vol. 12, no. 5, pp. 415-424, 1995.

[2] M. Shinobu, D. Okamoto, S. Ito , H. Kawakami and K. Takahashi, "Transferred Load and Its Course in Passenger Car Bodies," *JSAE Review*, vol. 16, no. 2, pp. 145-150, 1995.

[3] K. Takahashi and T. Sakurai, "Expression of Load Transfer Paths in Structures," *Transactions of Japan Society of Mechanical Engineers Series A*, vol. 71, no. 708, pp. 1097-1102, 2005.

[4] K. Pejhan, C. Q. Wu and I. Telichev, "Comparison of load transfer index (U*) with conventional stress analysis in vehicle structure design evaluation," *International Journal of Vehicle Design*, vol. 68, no. 4, pp. 285-303, 2015.

[5] T. Naito, H. Koboyashi, Y. Urushiyama and K. Takahashi, "Introduction of the New Concept of U*sum for Evaluation of Weight- Efficient Structure," *SAE International Journal of Passenger Cars- Electronic and Electrical Systems*, vol. 4, no. 1, pp. 30-41, 2011.

COMPARISON OF METHODS FOR DISCONTINUOUS AND SMOOTH INHOMOGENEOUS ELASTOSTATICS

Jaber Rezaei Mianroodi [*1], Pratheek Shanthraj[2,3], and Bob Svendsen[1,2,3]
[1]*Material Mechanics, RWTH Aachen, Aachen, Germany*
[2]*AICES, RWTH Aachen, Aachen, Germany*
[3]*Microstructure Physics and Alloy Design, Max-Planck-Institut fur Eisenforschung GmbH, Dusseldorf, Germany*

Summary In this work, a number of computational methods for the numerical solution of boundary-value problems (BVPs) for inhomogeneous elastostatics are investigated and compared. This includes algorithmic formulations, discretization methods, and numerical solution schemes. The inhomogeneity of interest is the classic case of an inclusion embedded in a matrix. Both discontinuous (i.e., classic) and smooth stiffness distributions are treated, the latter via phase-field modeling of the matrix-inclusion composite as a two-phase system. For simplicity, attention is restricted to the strong form of mechanical equilibrium. With the help of the analytic solutions in the one-dimensional context, a number of principle issues related to numerical solution of the BVP are investigated. Besides being of interest in its own right, the general lack of commutativity of differentiation and interpolation motivates as well the investigation and comparison of both displacement- and the more classic strain-based algorithms. A number of examples will be discussed.

BASIC ALGORITHMIC RELATIONS

For brevity, only the mechanical part of the coupled BVP for the mechanical and phase fields (i.e., in the case of a smooth stiffness) is summarized here. For simplicity, attention is restricted to the case of geometric and physical linearity. Let $\boldsymbol{u}$, $\boldsymbol{E} = \quad \nabla\boldsymbol{u}$, $\boldsymbol{T}$, and C represent the displacement, strain, stress, and elastic stiffness fields, respectively, in the matrix-inclusion (MI) system. As usual, in the discontinuous case, formulation of the BVP is based on additional compatibility and equilibrium conditions at the matrix-inclusion interface. Perhaps the most well-known class of algorithms developed for inhomogeneous elastostatics is that based on the equivalent homogeneous medium [e.g., 2, 3]. Let $\mathsf{C}_{\rm H}$ be the corresponding homogeneous stiffness and $\boldsymbol{G}_{\rm H}$ the Green function of the elliptic operator $\nearrow \quad \mathrm{v} \circ \mathsf{C}_{\rm H} \circ \nabla$. On this basis, $\boldsymbol{E} = \bar{\boldsymbol{E}} \nearrow \boldsymbol{\Gamma}_{\rm H} * \boldsymbol{T}_{\rm P}$ is a (formal) strain-based solution of the mechanical BVP determined by mean strain $\bar{\boldsymbol{E}}$, the Lippmann-Schwinger operator $\boldsymbol{\Gamma}_{\rm H}$ induced by $\nabla\boldsymbol{G}_{\rm H}$, and the "polarization" stress $\boldsymbol{T}_{\rm P} := \boldsymbol{T} \nearrow \mathsf{C}_{\rm H}\nabla\boldsymbol{u}$. This is exploited for fixed-point iteration in a number of algorithms or "schemes". In particular, the "basic" scheme [e.g., 1, 3] utilizes the algorithmic (i.e., algebraic) forms $\widehat{\nabla\boldsymbol{u}} = \hat{\boldsymbol{u}} \otimes \imath\boldsymbol{k}$, $\widehat{\mathrm{v}\,\boldsymbol{T}} = \hat{\boldsymbol{T}}\imath\boldsymbol{k}$, $\hat{\boldsymbol{G}}_{\rm H}^{-1}\boldsymbol{a} = \mathsf{C}_{\rm H}[\boldsymbol{a}\otimes\boldsymbol{k}]\boldsymbol{k}$ and $\hat{\boldsymbol{\Gamma}}_{\rm H}\boldsymbol{A} = \quad \hat{\boldsymbol{G}}_{\rm H}\boldsymbol{A}(\boldsymbol{k}\otimes\boldsymbol{k})$ for the corresponding quantities obtained via (continuous) Fourier transformation (FT) in terms of (continuous) wavenumber $\boldsymbol{k}$ with $\imath = \sqrt{\nearrow 1}$. In order to (low-pass) filter Gibbs-related oscillations occuring in the case of discontinuous C, resulting in improved convergence behavior and robustness, [1, 4] developed alternatively "accelerated" algorithms or schemes. Rather than on FT of the "exact" quantities, these are based on FT of finite-difference approximations $\nabla_{\mathbf{h}}\boldsymbol{u}$ and $\mathrm{v}_{\mathbf{h}}\boldsymbol{T}$ to $\nabla\boldsymbol{u}$ and $\mathrm{v}\,\boldsymbol{T}$, respectively, in physical space depending on the grid spacing $\mathbf{h} = (h_1, \ldots)$. Any of these can be expressed in the general forms $\widehat{\nabla_{\mathbf{h}}\boldsymbol{u}} = \hat{\boldsymbol{u}} \otimes \boldsymbol{q}_{\mathbf{h}}$, $\widehat{\mathrm{v}_{\mathbf{h}}\boldsymbol{T}} = \hat{\boldsymbol{T}}\boldsymbol{q}_{\mathbf{h}}^{*}$, $\hat{\boldsymbol{G}}_{\rm H}^{-1}\boldsymbol{a} := \mathsf{C}_{\rm H}[\boldsymbol{a}\otimes\boldsymbol{q}_{\mathbf{h}}]\boldsymbol{q}_{\mathbf{h}}^{*}$, $\hat{\boldsymbol{\Gamma}}_{\rm H}\boldsymbol{A} = \quad \hat{\boldsymbol{G}}_{\rm H}\boldsymbol{A}(\boldsymbol{q}_{\mathbf{h}}^{*}\otimes\boldsymbol{q}_{\mathbf{h}})$, with $\boldsymbol{q}_{\mathbf{h}}^{*}$ the complex conjugate of $\boldsymbol{q}_{\mathbf{h}}$. In particular, for forward-backward-difference (FBD)-based acceleration, $q_{\mathbf{h}m} = h_m^{-1}(e^{\imath k_m h_m} \nearrow 1)$ for $m = 1, \ldots, d$ in d dimensions. On the other hand, in the case of central-difference (CD)-based acceleration, $q_{\mathbf{h}m} = \imath\, h_m^{-1} \quad \mathrm{n}\, k_m h_m$. These compare with $q_m = \imath k_m$ holding in the case of the basic scheme just discussed. In the current work, the above "conventional" strained-based algorithms are compared with analogous displacement-based algorithms in the context of the (formal) solution $\boldsymbol{u} = \bar{\boldsymbol{E}}\boldsymbol{x} + \boldsymbol{G}_{\rm H} * \quad \mathrm{v}\,\boldsymbol{T}_{\rm P}$ of the mechanical BVP.

EXAMPLE RESULTS IN ONE DIMENSION

In what follows, five different algorithms are compared for the case of discontinuous C. The first three are based on Fast Fourier Transformation (FFT) and include the basic scheme (FFT-basic), accelerated CD (FFT-C) and accelerated FBD (FFT-FB). The other two represent direct forward-backward- (FB) and central- (C) based finite-difference schemes in the physical space. As shown in Figure 1 (left), the inclusion lies in the region $0.25 < x < 0.\ 5$ and is 100 times stiffer than the matrix. Results for $\mathrm{v}\,\boldsymbol{T}_{\rm P}$ from the three FFT-based algorithms are shown in Figure 1 (right). In particular, the Gibbs oscillations resulting from the jump in C at the MI interface are visible in the results from the basic approach (green curve). In contrast, the filtering in the accelerated schemes filter these out. Here, the FFT-FB scheme is the most effective. This is due at least in part to the fact that forward-backward differencing couples even and odd computational nodes, whereas central differencing does not. This can be seen most clearly in the displacement-based results in Figure 2 (right). The analogous strain-based results in Figure 2 (left) are insensitive to this. Note that the Gibbs oscillations of $\mathrm{v}\,\boldsymbol{T}_{\rm P}$ in Figure 1 (right) for the FFT-basic case

*Corresponding author. Email: jaber.rezaeimianroodi@rwth-aachen.de

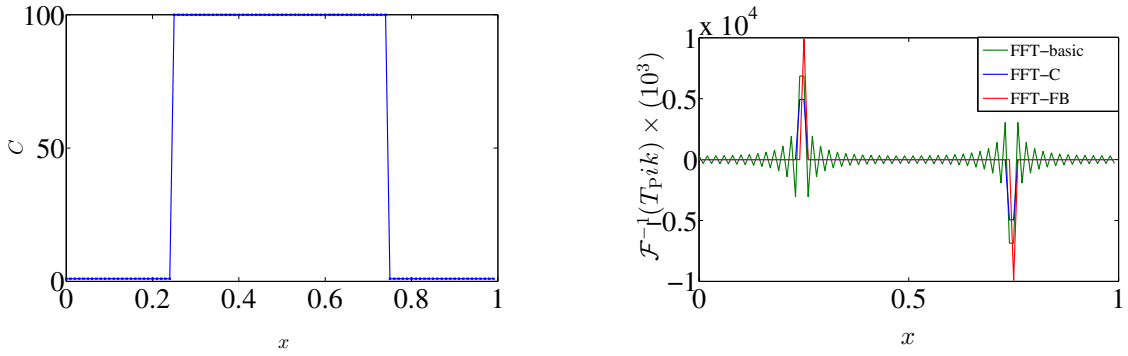

Figure 1: Left: stiffness distribution in the MI system. Right: v $\boldsymbol{T}_{\mathrm{P}}$ from the three FFT-based algorithms.

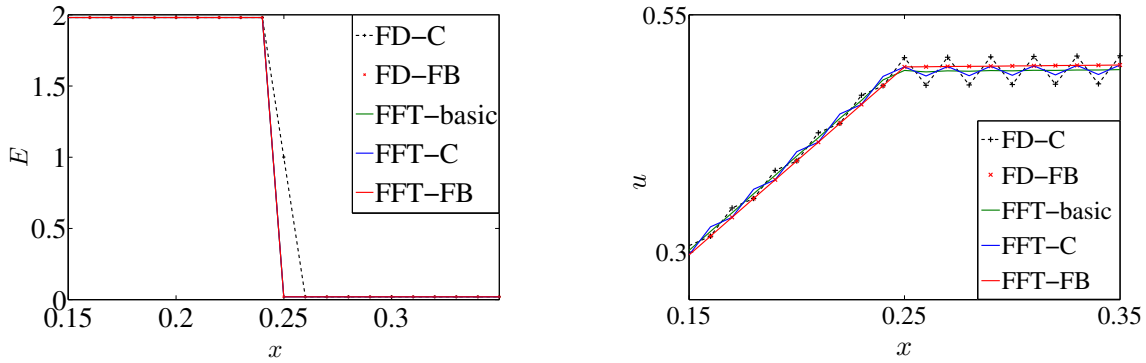

Figure 2: Strain (left) and displacement (right) results near the MI interface at $x = 0.25$. The points shown are grid points.

(green curve) have been largely filtered out by the Green function in the corresponding displacement results (green curve) in Figure 2 (right). This filtering effect of the Green function can also be seen in the reduction in the FFT-C results (blue curve) of the oscillations in the FD-C results (black dashed curve) due to the odd-even node decoupling mentioned above. On the other hand, perfect agreement is obtained between the FD-FB (red crosses) and FFT-FB (red curve) results because of node coupling in this case.

CONCLUSIONS

Displacement-based solutions provide a much more detailed picture of differences among the respective algorithms examined than the strain-based approach. Gibbs oscillations due to the stiffness jump at the interface affect the polarization stress and displacement results, but not the strain results. Central-difference-based accelerated algorithms filter out these oscillations, but result in additional fluctuations due to decoupling of odd and even computational nodes. Forward-backward-difference-based accelerated algorithms restore such coupling, resulting in perfect agreement between displacement results.

References

[1] Moulinec, H., Silva, F., 2014. Comparison of three accelerated fft-based schemes for computing the mechanical response of composite materials. International Journal for Numerical Methods in Engineering 97, 960–985.

[2] Mura, T., 1987. Micromechanics of Defects in Solids. Martinus Nijhoff, Dordrecht.

[3] Suquet, P., 1997. Continuum Micromechanics. Vol. 377 of CISM International Center for Mechanical Sciences. Springer, Berlin.

[4] Willot, F., 2015. Fourier-based schemes for computing the mechanical response of composites with accurate local fields. Comptes Rendus Mécanique 343 (3), 232–245.

FE MODELING AND OPTIMIZATION OF CUTTING TEMPERATURE IN ORTHOGONAL TURNING

M. Sadeghifar[1,a], R. Sedaghati[1] , V. Songmene[2]
[1]*Department of Mechanical and Industrial Engineering, Concordia University, Montreal, Quebec, Canada*
[2]*Department of Mechanical Engineering, École de Technologie Supérieure, Montreal, Quebec, Canada*

Abstract Cutting difficult-to-machine materials has always been a challenging task for the industry. It is known that that high cutting temperature leads to inaccuracies in component dimensions, phase transformation, and tensile residual stresses, while large cutting forces cause high tool wear and power consumption of turning machines. Accordingly, the present study aims at the design optimization of machining parameters including cutting speed, feed rate, edge radius and rake angle using a combination of Genetic Algorithm (GA) and Sequential Quadratic Programming (SQP) technique in order to accurately capture the global minimum value for the cutting temperature against the cutting force constraint. The results demonstrate that low feed and edge radius along with a roughly small magnitude of cutting speed and an intermediate value of rake angle lead to the smallest cutting temperature when the resultant cutting force is limited to a specific value.

INTRODUCTION

Difficult-to-machine materials are extensively employed in the aerospace industry such as in landing gear and engine rotors of aircrafts. These materials show severe work hardening together with low thermal conductivity, leading to high cutting forces and temperatures during machining. In most optimization studies on metal cutting processes, the objective function was often based on surface roughness, material removal rate, and production cost/time/rate [1]. There are a few research works on the optimization of cutting temperature as the objective function. Pretea et al. [2] presented an optimization procedure using AdvantEdge software for orthogonal turning of Waspaloy. They sought the optimal machining parameters including feed rate, cutting speed and rake angle to maximize the material removal rate as the objective function subjected to the constraints of cutting temperature and forces using genetic and simulated annealing algorithms.

FINITE ELEMENT MODELING

In order to obtain accurate Finite Element (FE) results, not only should reliable material, frictional, and chip formation models be used, but also the FE model and especially the element size (number) and arrangement and adaptive remeshing parameters must be properly fine tuned. In this study, the simulation is conducted using Abaqus/Explicit software and 4-node element CPE4RT is used to mesh the workpiece and tool. The Johnson-Cook material constitutive model, Zorev frictional model, and also pure deformation method with adaptive remeshing and rezoning/remapping techniques for chip formation, are employed. In addition, the optimal number (size) and arrangement of elements are obtained as those displayed in Fig. 1, and 'Frequency=5' and 'Remeshing sweeps per increment=8' are found as optimized remeshing magnitudes. The cutting and thrust forces in turn in the cutting and feed directions along with the resultant force direction are illustrated in Fig. 1. The validity of the FE model is verified by comparing the cutting forces and temperature of the present work with those presented by Ref. [3] in Table 1, in which good agreement between the results is observed. The distribution of the cutting temperature in the workpiece and tool is also shown in Fig. 1.

OPTIMIZATION PROBLEM STRATEGY AND FORMULATION - RESULTS

It is known that there is no absolute guarantee for GA to obtain accurate global point because GA searches the design space based on random number generation using natural selection [4]. From the other side, SQP is a powerful gradient-based mathematical method capable of catching the local optimum point around the initial point accurately. As a result, if SQP is provided with an initial point given by GA, it is guaranteed that the local point obtained by SQP is the true global point. This optimization strategy is utilized in this work. Response Surface Method (RSM) is employed to relate input parameters including cutting conditions and tool geometry to output quantities namely cutting temperature and resultant cutting force via approximate, efficient response functions. Then, using these predictive explicit functions as the objective

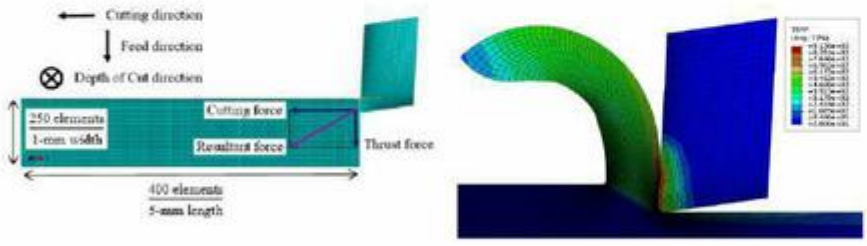

Fig. 1. Left: Cutting force directions and arrangement of elements, Right: Distribution of cutting temperature in the workpiece and tool

Table 1. Comparison of average cutting temperature $T_{chip}(^oC)$, cutting force $F_c(N)$, and thrust force $F_t(N)$.

	$T_{chip}(^oC)$	$F_c(N)$	$F_t(\ )$
Present: Simulation	922	482	178
Ref. [3]: Experiment	-	514	204
Ref. [3]: Simulation	949	455	133

[a] Corresponding author. Emails: mor_sade@encs.concordia.ca ; sadeghifar.morteza@gmail.com.

and constraint functions, the optimization is carried out in order to accurately capture the global optimum point for the cutting temperature against the resultant force constraint. It needs mentioning that the virtual design of experiment is based on L'16 Taguchi's orthogonal Array, the factors-levels and the matrix of experiments of which are given in Tables 2 and 3, respectively. The predicted cutting temperatures and resultant cutting forces are also presented in Table 3. The temperature and resultant force are formulated in terms of cutting velocity V, feed f, edge radius r_β, and rake angle γ_0 by the second-order polynomial regression model as follows:

$$T = -1818 + 0.7525V + 5723f + 39789r_\beta - 54.7\gamma_0 + 1.7Vf + 1.2Vr_\beta - 0.006264V\gamma_0 - 134580fr_\beta + 269f\gamma_0 + 921r_\beta\gamma_0 - 0.0001194V^2 - 28960f^2 - 336764r_\beta^2 + 0.8332\gamma_0^2 \quad (1\text{-}1)$$

$$F_r = -3403 + 1.1840V + 6105f + 59609r_\beta - 107\gamma_0 + 0.0617Vf + 0.0172Vr_\beta + 0.0021V\gamma_0 - 150860fr_\beta + 437f\gamma_0 + 274r_\beta\gamma_0 - 0.0001468V^2 - 2435f^2 - 505407r_\beta^2 + 1.691\gamma_0^2 \quad (1\text{-}2)$$

The coefficients in Eqs. (1-1) and (1-2) are calculated using the Least Square technique. The coefficients of determination, i.e. R^2 values, calculated for Eqs. (1-1) and (1-2) are in turn 0.9916, 0.9983, showing that these quadratic response models are very good approximations of both temperature and force. Using these functions, the optimization problem is formulated as: Find V, f, r_β, and γ_0 To minimize $OF=T/T_{min}$ Subject to $CF=(F_r/F_{r,min})\leq 0$, where OF and CF are the normalized objective and constraint functions, and $T_{min}=757\ ^oC$ and $F_{r,min}=253\ N$ are the minimum values of the temperatures and resultant forces presented in Table 3, respectively. The upper and lower bounds and optimal values of the design variables are provided in Table 4. Also, the objective and constraint functions are equal to 0.8960 and -0.0036, respectively. This represents that the optimization process furnishes a decline of about 10.4% in the cutting temperature, i.e. from 757 to 678 ^{o}C. This also indicates that the cutting force diminishes slightly by 0.36%, which can be attributed to the opposing behavior of temperature and force during cutting. In fact, cutting force constraint is nearly active from the lower side. It is also worth noting that the sensitivity of the design variables to the upper and lower bounds is not similar. The cutting speed and rake angle approach one of the intermediate values between their upper and lower bounds, whereas the feed and edge radius converge to their lower bounds. None of the design variables approaches their upper bounds, denoting that the upper bounds are inactive side constraints and have less influence on the optimum solution.

CONCLUSIONS

In the present research, a FE model and an optimization strategy were developed to simulate dry orthogonal turning of AISI 4340 steel. Special attention was given to optimizing machining parameters including cutting speed, feed rate, edge radius, and rake angle using a combination of GA and SQP technique. The results demonstrated that small feed and edge radius together with a roughly small value of cutting speed and a middle magnitude of rake angle in the given bounds provided the lowest cutting temperature in the presence of a confined cutting force.

Table 2. Factors and levels used for virtual design of experiment

Level	Factor			
	$V[m/\min]$	$f[mm]$	$r_\beta[\mu m]$	γ_0[deg]
1	200	0.1	25	0
2	240	0.14	30	3
3	275	0.16	40	6
4	300	0.2	50	10

Table 4. Upper and lower bounds and optimum values of the design variables

Design variable	$V[m/\min]$	$f[mm]$	$r_\beta[\mu m]$	γ_0[deg]
Upper bound	300	0.2	50	10
Lower bound	200	0.1	25	0
Optimum value	216	0.1	25	5

Table 3. Design of experiment based on orthogonal array of L'16 and cutting temperature and resultant cutting force

	Level of machining factors				Simulation results	
Exp. No.	Cutting speed	Feed	Edge radius	Rake angle	Temp. $T_{chip}(^oC)$	Force $F_r(N)$
1	1	1	1	1	758	318
2	1	2	2	2	806	375
3	1	3	3	3	853	414
4	1	4	4	4	807	466
5	2	1	2	3	757	253
6	2	2	1	4	788	336
7	2	3	4	1	850	452
8	2	4	3	2	828	545

Table 3. Design of experiment based on orthogonal array of L'16 and cutting temperature and resultant cutting force (*continued*)

	Level of machining factors				Simulation results	
Exp. No.	Cutting speed	Feed	Edge radius	Rake angle	Temp. $T_{chip}(^oC)$	Force $F_r(N)$
9	3	1	3	4	794	275
10	3	2	4	3	956	375
11	3	3	1	2	877	426
12	3	4	2	1	920	544
13	4	1	4	2	835	325
14	4	2	3	1	912	435
15	4	3	2	4	852	400
16	4	4	1	3	870	505

References

[1] Yusup N., Zain A.M., Hashim, S.Z.M.: Evolutionary techniques in optimizing machining parameters: Review and recent applications. Expert Syst Appl 39: 9909-9927, 2012.

[2] Del Pretea A., Primo T., Franchic R.: Super-Nickel orthogonal turning operations optimization. Procedia CIRP 8: 164-169, 2013.

[3] Arrazola P.J., Ozel T.: Investigations on the effects of friction modeling in finite element simulation of machining. Int J Mech Sci 52: 31-42, 2010 .

[4] Arora J.S.: Introduction to optimum design. 3rd ed. Elsevier, 2012.

A WAVELET-BASED METHOD WITH ARBITRARY HIGH ORDER ACCURACY FOR NONLINEAR PROBLEMS IN MECHANICS

Jizeng Wang[1a)], Lei Zhang[1], Xiaojing Liu[1] & Youhe Zhou[1]
[1]*College of Civil Engineering and Mechanics, Lanzhou University, Lanzhou, Gansu, China*

Summary A high-order wavelet-based solution method is developed for general nonlinear boundary value problems in mechanics. This method is established based on a Coiflet (a typical wavelet) approximation of *n*-tuple integrals of interval bounded functions combined with an accurate and adjustable boundary extension technique. Accuracy order of the proposed method is proven to be any positive even number *N* as long as the Coiflet with *N* vanishing moment is adopted. And most interestingly, this accuracy is independent of the highest order of derivatives in the equation to be solved. Error analysis and numerical examples of a wide range of nonlinear mechanical problems have demonstrate that the proposed wavelet method has a much better accuracy and efficiency than most major existing methods.

METHOD

Nonlinear boundary value problems arise from almost every scientific and engineering field, especially structural mechanics [1-4]. Commonly, the nonlinear boundary value problems can be written into a general form

$$\mathbf{T}\left(x, y, \frac{dy}{dx}, \cdots, \frac{d^n y}{dx^n}\right) = 0, \quad x \in a\ b \tag{1}$$

with the corresponding boundary conditions, where **T** is a nonlinear operator, and *y* is an unknown function of *x*. Although there exist many alternative methods for solving the nonlinear boundary value problems (1), yet these methods may only suitable for specific types of these problems and their accuracy can be limited by concrete characteristics of the equations to be solved, for example, their highest order of derivatives in these equations. In this study, we develop a solution method for general boundary value problems with adjustable arbitrary high accuracy of order *N* corresponding to the number of shifted vanishing moments of the adopted Coiflet scaling function. This *N* can be chosen as any positive even integers.

Approximation of *n*-tuple integral of a function

The multi-resolution analysis of wavelet theory state that the function space $\mathbf{L}^2(\mathrm{R})$ can be divided to a sequence of nested subspaces $\{0\}\cdots \subset \mathrm{V}_0 \subset \mathrm{V}_1 \subset \cdots \subset \mathrm{V}_j \subset \mathrm{V}_{j+1} \subset \cdots \subset \mathbf{L}^2(\mathrm{R})$. A set of orthogonal basis of subspace V_j can be formed by $\phi_{j\,k}\ x = {}^{j}\phi\ {}^{j} -)$, $k \in \mathbf{Z}$. A function $f\ x \in \mathbf{L}^2\ R$ can be approximated by projecting this function from $\mathbf{L}^2(\mathrm{R})$ to V_j as

$$f\ x \approx \mathbf{P}^j f\ x = \sum_k c_{j\,k}\phi_{j\,k}\ x$$

where $\phi\ x$ is the orthogonal scaling function, and $c_{j,k} = \int_{-\infty}^{\infty} f\ x\ \phi_{j,k}\ x\ dx$. for the Coiflet-type wavelet with *N* the number of vanishing moments. The corresponding scaling function has the unique property of shifted vanishing moments:

$$\int_{-\infty}^{\infty} (t - M_1\ {}^{k}\phi\ t\ dt = 0, \quad 1 \le\ <$$

where M_1 is the first-order moment of the scaling function, which can be a positive integer. Based on this unique property, one has

$$c_{j,k} \approx 2^{-j/2} f[(\ +\ _1)/2^j] \triangleq 2^{-j/2} f_{M_1+k},$$

such that the approximation of the function can be written as

$$f\ x \approx \mathbf{P}^j f\ x = \sum_{k=-\infty}^{\infty} f_{M_1+}\ \phi(2^j\ -\ ).$$

We define the *n*-tuple integral of the function *f*(*x*) as $f^{\int}\ x = \int \int^{\xi_n} \cdots \int_0^{\xi_2} f\ \xi_1\ \ \xi_1\ \xi_2 \cdots d\xi_n$. Then we have

$$f^{\int}\ \ x \approx \sum_{k=-\infty}^{\infty} f_{M_1+}\ \phi^{\int_n}\ \ x \tag{2}$$

where $\phi_{j\,k}^{\int_n}\ x = \int \int^{\xi_n} \cdots \int_0^{\xi_2} \phi(2^j \xi_1 -\ \ \xi_1\ \xi_2 \cdots d\xi_n$. We have proved that if $f\ x \in \mathbf{L}^2\ \mathbf{R}\ \ \mathbf{C}^N\ \mathbf{R}$, then the accuracy of this approximation (2) can be estimated as

$$\left\| f^{\int}\ x\ f_{\mathbf{P}^j}^{\ \int}\ x \right\|_{L^2[0,1]} \sim 2^{-jN} \ \text{ and } \ | f^{\int_n} - f_{\mathbf{P}^j}^{\ \int_n} | \sim 2^{-jN}.$$

This result shows that the integral tuple *n* does not affect the approximation accuracy. And *N* can be adjusted to any high value as long as the Coiflet with compact support [0, 3*N*-1] is chosen, which can be realized following a standard procedure.

Solution method for general boundary value problems

a) Corresponding author. Email: jzwang@lzu.edu.cn.

Defining the derivatives of the unknown function as new functions and considering $x \in [0,1]$, then Eq. (1) can be converted to

$$\begin{cases} \mathbf{T}\left(x \;\; y_0 \;\; y_1 \;\; \cdots \;\; y_n\right) = 0 \\ y_0 = \int_0^x \int_0^{\xi_n} \cdots \int_0^{\xi_2} y_n \;\; \xi_1 \;\; \xi_1 \;\; \xi_2 \cdots d\xi_n + \sum_{i=0}^{n-1} \frac{x^i}{i!} y_i(0) \\ y_1 = \int_0^x \int_0^{\xi_{n-1}} \cdots \int_0^{\xi_2} y_n \;\; \xi_1 \;\; \xi_1 \;\; \xi_2 \cdots d\xi_{n-1} + \sum_{i=1}^{n-1} \frac{x^{i-1}}{i-} y_i(0), \quad x \in [0,1], \\ \vdots \\ y_{n-1} = \int_0^x y_n d\xi + \;\; _{n-1}(0) \end{cases} \tag{3}$$

where y_i is denoted as $d\ y\ dx^i$, and $y_i(0)$ can be determined by the boundary conditions. This procedure provides a significant computational advantage that all boundary conditions have been included in the equations.

We approximate the newly defined functions y_0, y_1,…, y_{n-1} based on Eq. (2), then submit the approximations to the transformed governing equations, eventually we use conventional collocation method to solve the resulting equations. For a linear version of Eq. (3), we have theoretically proven that accuracy of such a solution method can be $o(2^{-jN})$, and most interestingly, this accuracy is independent of the highest order of derivatives in the equation.

EXAMPLES AND CONCLUSIONS

Typical numerical examples including the large deformation bending of plate structures have been considered to justify the proposed method. All the results show that accuracy order of the proposed method could reach about 7.0 when the Coiflet basis with compact support of [0, 17] was adopted, and this accuracy order is unchanged for nonlinear differential equations with different highest orders of derivatives.

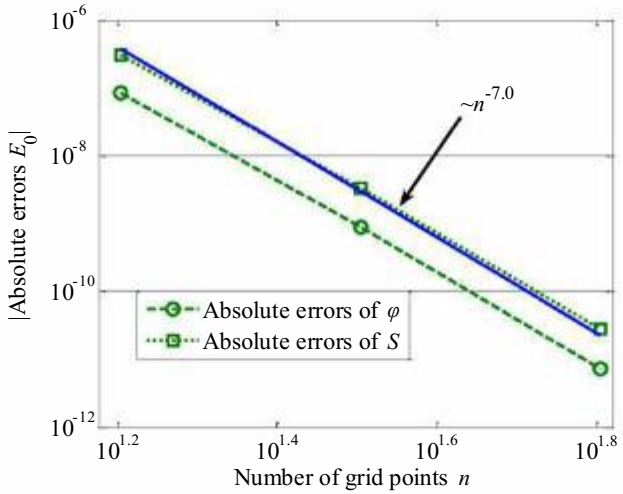

Fig.1. Absolute errors E_0 at x=1/2 as function of the number of grid points n under normalized load Q=50 (corresponding to resolution level j, through relation $n=2^j+1$) for the large deformation bending of circular plate, where φ and S are dimensionless deflection and internal axial force.

References

[1] Liu X., Zhou Y., Wang, X., Wang, J.: A wavelet method for solving a class of nonlinear boundary value problems. *Comm. Nonlin. Sci. Num. Simu*. **18**:1939-1948, 2013.

[2] Zhang L., Wang J., Zhou Y. H.: Wavelet solution for large deflection bending problems of thin rectangular plates. *Arch. Appl. Mech.* **85**:355-365, 2014.

[3] Wang X., Liu X., Wang J., Zhou Y.H.: A wavelet method for bending of circular plate with large deflection. *Acta Mech. Solida Sinica* **28**:83-90, 2015.

[4] Zhang L., Wang J., Zhou Y.H.: Large deflection and post-buckling analysis of non-linearly elastic rods by wavelet method. *Int. J. Non-Lin. Mech.* **78**:45-52, 2015.

STRESS FIELDS INDUCED BY DISLOCATION LOOPS IN ISOTROPIC CUNB FILM-SUBSTRATE SYSTEM

Wenwang Wu[1a)], Guian Qian[2], Shucai Xu[1] & Jinhuan Zhang[1]
[1]*State Key Laboratory of Automotive Safety and Energy, Tsinghua University, Beijing PR China*
[2]*Nuclear Energy and Safety Department, Paul Scherrer Institute, Villigen PSI, Switzerland*

Summary Based on linear superposition rules and fast discrete Fourier transformation, a semi-analytical solution is developed for calculating the elastic fields induced by dislocation loops in an isotropic thin CuNb film-substrate system. The elastic field problem of thin film-substrate system is decomposed into two sub-problems: bulk stress due to a dislocation loop in an infinite space, and correction stress induced by free surface and interface of the film-substrate system. Thus, continuous displacement and traction stress across the interface plane of the perfectly-bounded film-substrate system are generated. Elastic fields of dislocation loops within Cu film and Nb substrate of the Cu–Nb film-substrate system are analyzed, and it is found that the elastic fields of dislocation loop are influenced remarkably by film thickness.

INTRODUCTION

Film-substrate structures and systems are widely used in micro-chips, smart electronics, micro-sensors and manipulators, protective coatings, etc. Study of the dynamic behaviours of dislocations are of critical importance for understanding the microstructure evolution, plastic deformation process of thin film-substrate systems. Solutions to the elasticity field induced by dislocations within film-substrate system are important, because the elasticity solution provides a direct means of determining the Peach-Koehler force acting on dislocations, which is of direct relevance in understanding the microstructure evolution and mechanical behaviours of these film-substrate systems. Making use of mirror dislocation concept and potential theory, Head [1, 2] analyzed the changes in the stress field of a straight screw/edge dislocation caused by differences in the shear modulus on either side of bimetallic medium. Kelly et al. [3] studied the stress field induced by an edge dislocation of arbitrary orientation in both the surface layer and substrate medium of the layer-substrate system. The objective of this paper is to develop an efficient and accurate method to calculate the stress due to dislocation loops in an isotropic thin film–substrate system, and it is found that film thickness has a remarkable impact on the elastic fields of dislocation loops within film-substrate system.

STRESS FIELDS INDUCED BY DISLOCATION LOOP IN FILM–SUBSTRATE SYSTEM

In this section, a semi-analytical solution is proposed to solve the elastic fields due to dislocation loops within thin film or substrate of perfect bonding film-substrate system. The elastic properties of the film and substrate medium are assumed to be $(\lambda_f, \mu_f, \nu_f)$ and $(\lambda_s, \mu_s, \nu_s)$, respectively. Accordingly, $-h \le z^+ \le h$ is valid for the upper thin film A, and $z^- \le 0$ is valid for the lower substrate B. Elastic field of perfect bonding film-substrate system can be decomposed into two sub-problems: bulk stress due to a dislocation loop in an infinite space, and correction stress induced by the free surface and interface of the film-substrate system. As shown in Fig. 1(a), perfect bonding film-substrate system is decomposed into thin film A containing dislocation loops L1 and substrate B containing dislocation loop L2. Bulk traction elastic field $\{\sigma_{i3}\}_A^{\infty}$ and $\{\sigma_{i3}\}_B^{\infty}$ on the top free surface and interface plane can be calculated out. As shown in Fig. 1(b), correction traction stress $\{\sigma_{i3}\}_A^{\text{correction}}$ and $\{\sigma_{i3}\}_B^{\text{correction}}$ are linearly superimposed onto the bulk elastic fields. As shown in Fig. 1(c), after linear superposition of bulk stress and correction stress, displacement and traction stress continuity across the interface plane are satisfied.

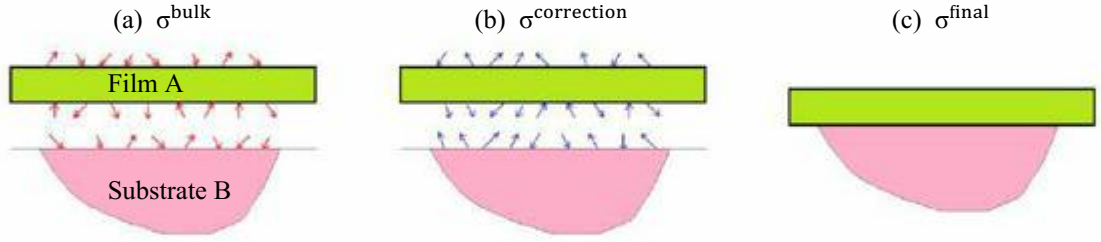

Figure. 1: Diagram of decomposition of film-substrate system containing dislocation loops $\mathbf{L_1}$ within the upper thin foil **A** and dislocation loops $\mathbf{L_2}$ with the lower layer **B** into a two-step linear superposition problem: (a), bulk stress; (b), correction traction stress; (c), continuous displacement and traction stress are generated at interface plane; and free traction boundary conditions are satisfied on the top surface planes of the film-substrate system.

Similar to the solutions for the image stress of half space developed by Weinberger et. al [4], an arbitrary correction elastic field written in the form of Fourier series with unknown coefficients (A, B, C, D, E, F) and (K_1^-, K_2^-, K_3^-) are employed.

a) Corresponding author. Email: ictam2016papers@legendconferences.com.

Considering the displacement and traction stress continuity requirements for the perfect bonding film-substrate system, following relation stands for each (k_x, k_y) Fourier mode.

Free traction stress on the free surface plane of the perfect bonding film-substrate system should be satisfied:

$$\{\hat{\sigma}_{i3}\}^{\infty}_{z^+=+h} + \{\hat{\sigma}_{i3}\}^{correction}_{z^+=+h} = 0 \quad (1)$$

Interface traction stress and displacement continuity across the interface plane of the perfect bonding film-substrate system should be satisfied:

$$\{\hat{\sigma}_{i3}\}^{\infty}_{z^+=-h} + \{\hat{\sigma}_{i3}\}^{correction}_{z^+=-h} = \{\hat{\sigma}_{i3}\}^{\infty}_{z^-=0} + \{\hat{\sigma}_{i3}\}^{correction}_{z^-=0} \quad (2)$$

and

$$\{\hat{u}_i\}^{\infty}_{z^+=+h} + \{\hat{u}_i\}^{correction}_{z^+=+h} = \{\hat{u}_i\}^{\infty}_{z^-=0} + \{\hat{u}_i\}^{correction}_{z^-=0} \quad (3)$$

Then, unknown coefficient (A, B, C, E, F, G) and (K_1^-, K_2^-, K_3^-) of correction displacement can be solved from Eqs. (1)–(3), and the correction elastic field of the film medium **A** and substrate medium **B** can be generated.

SIMULATION RESULTS

In this subsection, effects of film thickness on the displacement and interface traction stress fields are investigated for CuNb film-substrate system, and the elastic modulus are treated with Voigt isotropy [5, 6]. The thin Cu film thickness is assumed to be: t= 30, 40 and 50 nm, and the dislocation loop is situated in the middle of the upper thin Cu film. The simulation results are shown in Fig. 2. It can be concluded from Fig. 2 that: with the decrease of film thickness, bulk elastic field at interface plane are changed more remarkable by correction stress.

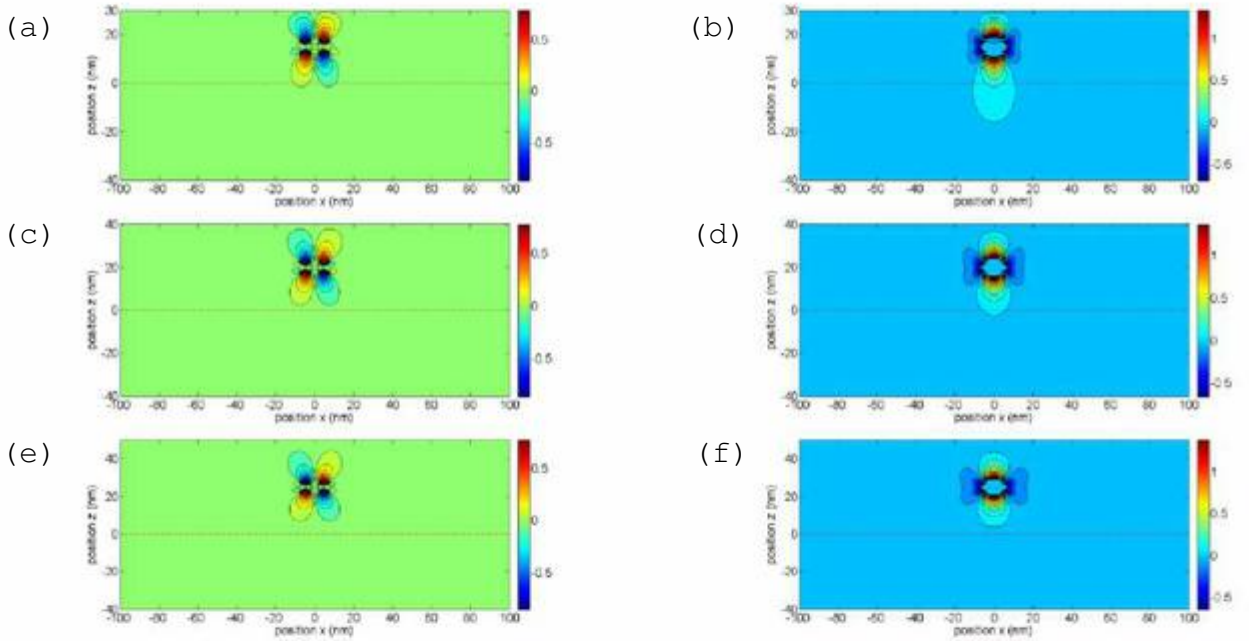

Figure. 2: Film thickness effect on elastic fields due to a dislocation loop in the upper Cu film of the Cu–Nb film-substrate system. Traction stress field σ_{xz}^{final} and σ_{zz}^{final}: (a)–(b), $t = 30$ nm; (c)–(d), $t = 40$ nm; (e)–(f), $t = 50$ nm.

CONCLUSION

A semi-analytical calculation approach based on 2D discrete FFT is developed for studying the elastic field due to dislocation loop in perfect bonding thin film-substrate system. Effects of film thickness on the elastic field are analyzed, demonstrating that film thickness have a significant impact on the elastic fields of dislocation loops in the thin film.

References

[1] Head A. K.: The interaction of dislocations. Phil. Mag. 44: 92–94, 1953.

[2] Head A. K.: Edge dislocations in inhomogeneous media. Proc. Phys. Soc. B 66: 793–801, 1953.

[3] Kelly P. A., O'Connor J. J., Hills D. A.: The stress field due to dislocation in layered media. J. Phys. D 28: 530–534, 1995.

[4] Weinberger C. R., Aubry S., Lee S. W., Nix W. D., Cai W.: Modelling dislocations in a free-standing thin film. Modelling Simul. Mater. Sci. Eng. 17: 075007, 2009.

[5] Bower A.F.: Applied Mechanics of Solids. CRC Press, London, 2012.

[6] Voigt W.: Ueber die Beziehung zwischen den beiden Elasticitätsconstanten isotroper Körper. Ann. Phys. 274: 573–587, 1889.

GEGENBAUR SERIES EXPANSION WITH INTERVAL, FUZZY AND RANDOM VARIABLES

Shengwen Yin, Dejie Yu[a], Hui Yin, Baizhan Xia
State Key Laboratory of Advanced Design and Manufacturing for Vehicle Body,
Hunan University, Changsha, Hunan, China

Summary For uncertain problem with interval, random and fuzzy uncertainties, a unified orthogonal polynomial approximation method is developed using *Gegenbauer series expansion*(GSE). A simple numerical example is presented to investigate the accuracy of GSE with different value of polynomial parameter λ. Based on the numerical analysis, the optimal λ for GSE with fuzzy and random variable is determined.

INTRODUCTION

As the response prediction of uncertain models is computational expensive in many engineering cases, there is a growing demand for the development of more efficient and accurate methods for propagating uncertainties. Due to the good performance in accuracy and efficiency, the orthogonal polynomial approximation method has received much attention lately. A lot of well-established orthogonal polynomial approximation methods are available for random, fuzzy and interval analysis[1,2,3]. However, these methods are developed based on different types of polynomials. As a result, the choice of a suitable polynomial for various uncertain models has become an important issue in the application of orthogonal polynomial on uncertainty analysis. The aim of this paper is to develop a unified orthogonal polynomial approximation method for uncertain problem with random, fuzzy and interval parameters. In order to construct the unified framework, the *Gegenbauer series expansion*(GSE)[3] which has been successfully used for random analysis is introduced and then adapted for interval and fuzzy analysis.

FUNDAMENTAL THEORY OF GSE AND ITS APPLICATION FOR RANDOM PROBLEMS

Based on the Gegenbauer polynomials, a continuous function $f(\xi)$ defined on $\xi \in [-1,\ 1]$ can be approximated as the *n*th-order GSE

$$f(\xi) \approx p_n(\xi) = \sum_{i=0}^{n} f_i G_i^{\lambda}(\xi) \tag{1}$$

Where f_i is the *i*th ($i = 0,1,...,n$) constant coefficient which can be estimated by Gauss-Gegenbauer integration, n denote the retained order of GSE. $G_n^{\lambda}(\xi)$ is the parametric Gegenbauer polynomials of *n* degree. λ is the polynomial parameter which satisfies $\lambda > 0$. Recently, the GSE has been developed for bounded random problems. The premise of GSE with random variable is to use the random variables following λ-PDFs or their derivative PDFs to approximate original random variables. By using a suitable transformation of random variable, the GSE can be adopted to approximate any mono-peak or mono-valley PDFs according to the practical needs of engineering. More details about the application of GSE for bounded random problems can be found in the literatures[3] and [4]. Obviously, the GSE is based on the parametric polynomial, thus it may have the potential to solve the interval and fuzzy problems by using a suitable λ. The GSE for the approximation of uncertain problems with random, interval and fuzzy variable is presented hereafter. In particular, the optimal value of λ for the interval and fuzzy uncertainty analysis is fully discussed.

GSE WITH INTERVAL VARIABLES

In the orthogonal polynomial approximation method, the weight function is always used to minimize the residual error of the polynomial expansion. As a result, the weight function may have a great influence on the accuracy of the polynomial expansion. In order to investigate the effect of the weight function on the accuracy of GSE, the third-order GSE is used to approximate a simple function $y = f(x) = 1/(1+x^2)$, and different values of λ are considered. The error yielded by GSE is plotted in Fig.1. For a comparison, the weight function of GSE with different λ is plotted in Fig.2. By a comparison of Fig.1 and Fig.2, we can find that GSE will lead to large errors at the region where the weight value is approach to zero. Furthermore, we can observe that when $\lambda = 0.5$, the error yielded by GSE is much larger at the bounds of interval. However, the weight value of GSE is the same over the interval when $\lambda = 0.5$. It indicates that a relatively large weight value of GSE should be assigned at the bounds of interval if we want to achieve the same accuracy over the whole interval. As regarding the engineering cases, the minimum or maximum of the response is always attained at the bounds of interval. In order to improve the accuracy of GSE at the boundary points, the λ of GSE can be set as arbitrary small value that is a little less than 0.5. In this paper, the λ of GSE with interval random is set as $\lambda = 0.1$.

[a)]Corresponding author. Email: djyu@hnu.edu.cn.

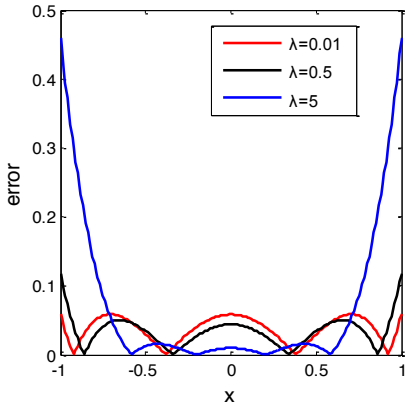

Fig.1 The error yielded by GSE

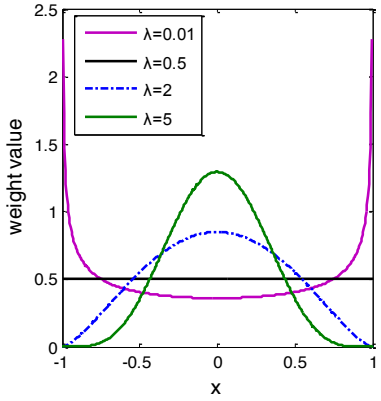

Fig.2 The weight function of GSE

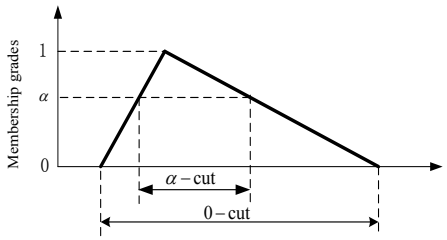

Fig.3 A typical membership function

GSE WITH FUZZY VARIABLES

Generally, the fuzzy uncertainty propagation can be converted into a set of nested interval evaluations by the $\alpha-$cut technique[2]. The $\alpha-$cut denotes the interval cut from the range of variation of fuzzy variables. When $\alpha_1 > \alpha_2$, there is $\alpha_1-\text{cut} \subseteq \alpha_2-\text{cut}$. Fig. 3 shows a typical membership function of fuzzy variable. Based on the $\alpha-$cut technique, the GSE for fuzzy uncertainty analysis contains two main steps: (1) constructing the GSE for the response at the $0-$cut of interval parameter; (2) calculating the minimal/maximal of response at each $\alpha-$cut through the $0-$cut GSE, which can avoid multiple approximations at all $\alpha-$cuts. As the minimal/maximal of the response at each $\alpha-$cut is calculated through the $0-$cut GSE, it is more important to ensure the accuracy of $0-$cut GSE over the whole interval. Fig.1 and 2 indicate that when $\lambda = 0.5$, the GSE can converge more rapidly at the bounds of interval. In this case, the error yielded by using GSE for interval analysis at $0-$cut may be smaller than that at any other $\alpha-$cuts. In order to ensure the accuracy of the $0-$cut GSE for the interval analysis at any other $\alpha-$cuts, the GSE with $\lambda \geq 0.5$ is employed for fuzzy analysis. However, when λ ? 0.5, a very high retained order of GSE is required to achieve a desirable accuracy for interval analysis at $0-$cut. Therefore, the λ of GSE with fuzzy variable is set as $\lambda = 1$.

CONCLUSIONS

GSE can provide a unified approximation for the response of uncertain problems with random, fuzzy and interval uncertainties. The polynomial parameter λ of GSE depends on the nature of the uncertainty: for the random problems, λ is determined according to the original PDFs; for the interval problems, λ is set as an arbitrary small value that is a little smaller than 0.5; for the fuzzy variable λ is set as 1. Through the unified GSE which is a simple function, the random, fuzzy and interval analysis can be efficiently implemented by many numerical solver.

References

[1] Xiu D, Karniadakis GE. The wiener-askey polynomial chaos for stochastic differential equations. *Siam. J. Sci. Comput.* **24**: 619-644, 2003.

[2] S. Adhikari, H. HaddadKhodaparast. A spectral approach for fuzzy uncertainty propagation in finite element analysis. *Fuzzy Sets Syst*.**243**: 1-24, 2014.

[3] Ma XP, Wu CL, Fang T. A complementary note on Gegenbauer polynomial approximation for random response problem of stochastic structure. *Probabilist. Eng. Mech*. **21**: 410-419, 2006.

[4] Liu J, Sun X, Han X. Dynamic load identification for stochastic structures based on Gegenbauer polynomial approximation and regularization method. *Mech. Syst. Signal Pr*. 35-54, 2015.

SM16 - Vibrations and Control of Structures

TS.SM16-1.01	Matveenko, Valerii - Optimization of dynamic characteristics of smart-systems based on piezoelements	2963
TS.SM16-1.02	Araumi, Naoto - Fifth Order Analysis in Simply Supported Beam Subjected to Parametric Excitation	2965
TS.SM16-1.03	Brack, Tobias - Monitoring the Viscoelastic Behavior of Complex Fluids Using Multi-Frequency Resonance Tracking	2967
TS.SM16-1.04	Hajdu, David - Robust stability of milling processes	2969
TS.SM16-1.05	Krenk, Steen - Calibration of tuned mass or inerter based vibration absorbers	2971
TS.SM16-1.06	Majewski, Tadeusz - Two Possible Excitations for the Bristle Robot	2973
TS.SM16-2.01	Hobeck, Jared - Metastructures for vibration suppression (INVITED)	2975
TS.SM16-2.02	Lu, Zeqi - Mechanical Vibration Isolation with Stochastic Resonance	2977
TS.SM16-2.03	Mesh, Mikhail - Efficient algorithm for a nonlinear transient vibration problem	2979
TS.SM16-2.04	Michailidis, Georgios - Modal basis approaches in shape and topology optimization of frequency response problems	2981
TS.SM16-2.05	Perlikowski, Przemyslaw - Novel type of tuned mass damper with inerter	2983
TS.SM16-3.01	Keogh, Patrick - Control of contact events in active rotor dynamic systems (INVITED)	2985
TS.SM16-3.02	Reshmin, Sergey - Time-Optimal Control for Pendulum-Like Systems in Case of Large Control Bounds	2987
TS.SM16-3.03	Mal, Ajit - Semi-analytical modeling of substrate loss of miniature resonators	2989
TS.SM16-3.04	Tang, You-Qi - Parametric and internal resonance of axially accelerating viscoelastic beams	2991
TS.SM16-3.05	Tyrell, Nathan - Attitude control via structural vibration	2993
TS.SM16-4.01	Xu, Jian - The optimal parameters of time-delayed control quasi-zero-stiffness vibration isolation system (INVITED)	2995
TS.SM16-4.02	Warminski, Jerzy - Nonlinear vibration control of a rotating composite beam with an embedded active element	2997
TS.SM16-4.03	Weder, Mario - Damping of waves in a layered structure composed of two elastic plates coupled by a viscous liquid	2999
TS.SM16-4.04	Yamane, Saeha - Identification of fractional order of viscoelastic materials by feedback control	3001
TS.SM16-4.05	Yang, Haolin - Shake table test of an isolated bridge with cable-sliding friction aseismic bearing	3003
PO.SM16-1.01.211	Asokanthan, Samuel - Uncertainty quantification for a class of vibratory MEMS gyroscopes	3005
PO.SM16-1.02.212	Ben Lassoued, Mohamed Amin - Vibration energy localisation in inhomogenous beam structure	3007
PO.SM16-1.03.213	Bognash, Mohamed - Mass anomaly and random rate fluctuation effects on vibratory gyroscope dynamics	3009
PO.SM16-1.04.214	Dourado Guerra Silva, Arinan - Uncertainty analysis of rotating machines using fuzzy logic approach	3011
PO.SM16-1.05.215	Farid, Mehrdad - Nonliner vibrations of FGM shallow shells subjected to random excitation in thermal environment	3013
PO.SM16-1.06.216	Hernandez, Eric - Equivalent viscous damping of a cylinder moving transversly	3015

	through sand: Experimental Results	
PO.SM16-1.08.218	Rafiee, Mohammad - Vibration of rotating multiscale nanocomposite cantilever beams	3017
PO.SM16-1.09.219	Rai, Amit - Vibration of a Simply Supported Circular Plate under Moving Points Loads	3019
PO.SM16-1.10.220	Szyszkowski, Walerian - FE simulation of active vibrations attenuation in structures	3021
PO.SM16-1.11.221	Tarlakovskiy, Vladimir - Non-stationary coupled electromagnetic elastic oscillations of spherical shells	3023
PO.SM16-1.12.222	Yu, Haidong - Dynamic behavior of gripper cylinder in TBM with variable stiffness	3025
PO.SM16-1.13.223	Zhang, Wei - Multi-pulse chaotic motions of equivalent circular cylindrical shell	3027
PO.SM16-1.14.224	Zhang, Yi - Damage localization for operational modal analysis via random decrement technique	3029
PO.SM16-1.15.225	Zhou, Chunyan - Micro-dynamic characterization of modal parameters for a honeycomb plate structure	3031
PO.SM16-1.16.226	Zhu, Jiang - Robust, smooth and fast ASMC - applications to robot manipulators	3033

OPTIMIZATION OF DYNAMIC CHARACTERISTICS OF SMART-SYSTEMS BASED ON PIEZOELEMENTS

Valerii Matveenko, Natalya Sevodina, Nataliia Yurlova, Dmitriy Oshmarin,
Maksim Yurlov, Aleksey Ivanov
Institute of Continuous Media Mechanics of the Ural Branch
of Russian Academy of Sciences, Perm, Russia

Summary We consider the electroelastic systems consisting of an elastic deformable elements, some of which has piezoelectric properties. Electric series circuits are connected to the piezoelectric elements. The purpose of research is to establish effective methods of mathematical modeling, makes possible to find the parameters of the external electric circuit elements providing at predetermined resonant frequencies the maximum damping properties of electroelastic body. A problem of natural vibrations is offered to select effective schemes of solving the given problem. Some options of equivalent circuits of the elastic system with piezoelectric elements are suggested as the most effective approaches to calculate the required parameters of an electric circuit for maximum damping. The justification of the most reliable equivalent circuits is carried out on the basis of the problem of natural vibrations. Numerical results are given.

INTRODUCTION

With the variety of options for control dynamic characteristics of smart-structures with piezoelements, it is practically impossible to find optimal decisions without mathematical modeling. As a rule, when simulating damping properties of smart systems are estimated according to the value of the amplitude at the resonance mode or speed transients. In the first case, the problem about forced steady-state oscillations is solved, in the second one - the dynamic problem with initial conditions. The applications of these tasks to find optimal parameters of piezo elements and external electrical circuits are coupled with a number of problems. In particular, a multiple solution to the problem at different frequencies of external actions is required to get an amplitude at the resonant modes based on the solution of the problem about the forced steady-state oscillations. When using the problem about the forced steady-state oscillations or the problem with initial conditions the found optimal solutions are associated with the simulated option of load of the studied system.
In this paper, it is suggested to use the problem of natural vibrations and equivalent circuits in order to optimize the dynamic characteristics of smart-systems based on piezoelements and external electrical circuits.

OPTIMIZATION OF PARAMETERS OF AN EXTERNAL ELECTRIC CIRCUIT BASED ON THE PROBLEM OF NATURAL OSCILLATIONS

We consider a piecewise homogeneous body with a volume $V = V_1 + V_2$, where the volume V_1 consists of uniform elastic parts, and the volume V_2 - of piezoelectric elements. Power and voltage generators and RLC-circuits of any structure, consisting of resistance, capacitance and inductance, can be connected to the piezoelectric elements through the electroded part of surface. The problem of natural vibrations is related to finding with homogeneous boundary conditions, solutions in the form

$$_{i} = \overline{}_{i} \rightarrow \omega, \qquad \varphi(x\,t) = \overline{\varphi}\ \vec{x}\ e^{\omega}$$

where $\omega = \omega_R + i\omega_I$ - a complex natural vibration frequency, at the same time ω_R determines the resonance frequency, ω_I characterizes rate of vibrations damping, $\overline{u}_i\ \vec{x}$, $\overline{\varphi}\ \vec{x}$ - determines the vibration modes of displacements components and electric potential. A variational equation for the problem of natural vibrations is formulated. Numerical implementation of the task is performed by the finite element method. The solution to this problem gives the values of the complex natural frequencies. Based on these results, one can build an optimization algorithm associated with finding the values of the parameters of the external circuit (R, L, C), which provide maximum damping (maximum value ω_I) of the respective vibration modes, except for those in which the potential on the electroded surfaces of the piezoelements is zero.

VERIFICATION OF PARAMETERS OF EXTERNAL ELECTRIC CIRCUITS BASED ON EQUIVALENT CIRCUITS

In these electromechanical processes a piezoelement demonstrates capacitive properties and forms a series RLC-resonant circuit (fig. 1a) with the external circuit, which leads to appearance of additional natural frequency. Maximum

[a)]Corresponding author. Email: mvp@icmm.ru

damping of the corresponding vibration mode is achieved when this vibrations frequency coincides with one of the natural frequency of an electroelastic body.

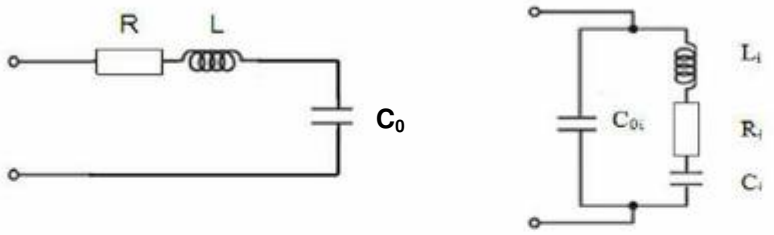

a b

Fig.1. Equivalent circuit

A number of studies suggest, as an electrical analog of a piezoelement, using its elementary model, consisting of a capacitor with a constant capacity C_0. Then, on the basis of the relations describing the behavior of the current and voltage in the series oscillatory electric circuit, it is possible to obtain expressions for the real and imaginary parts of the natural oscillation frequency

$$\omega_{Re} = \frac{1}{2\pi}\sqrt{\frac{1}{LC_0} - \frac{R^2}{4L^2}} \qquad \omega_{Ie} = -\frac{1}{\pi}\frac{R}{L}$$

The numerical results allow to conclude that the piezoelectric behaves as a capacitor with a constant capacitance C_0 only at frequencies well far from resonance frequencies of the original system (a plate with a piezoelement), that is why, the obtained parameters *R* and *L* do not provide maximum damping.

For a more adequate description of piezoelectric equivalent models are used composed of electrical elements with fixed parameters. One of these models shown in figure 1b. Equivalent resistor R_i in the series resonant circuit RLC_i corresponds to energy losses in the structure due to the viscoelastic properties of the material. If a piezoelectric is made of piezoceramics, which is a elastic material, then the resistance R_i can be neglected. In this model, the capacitance of the piezoelement is not constant. Here, the piezoelement behaves like a conventional capacitor with a capacitance of C_{0i} only at frequencies far from resonance. The parameters of the equivalent circuit C_i, L_i - the dynamic capacitance and inductance - appear only in the vibrations at a frequency close to the resonance frequency of a piezoelectric itself. The algorithm for calculating the parameters of the circuit is based on the equations describing oscillatory processes in the given equivalent circuit. The results of numerical experiments display the efficiency of the electrical equivalent model consisting of elements with lumped parameters.

CONCLUSION

A statement of the problem of natural oscillations of piecewise-homogeneous elastic bodies, a part of which has piezoelectric properties and is connected through the electrode surface with external serial circuits, consisting of resistance, inductance and capacitance. The possibility of using the problem of natural vibrations of electroelastic bodies with external electric circuits to select the its parameters, which providing at a predetermined resonant frequency the highest rate of damping vibrations is demonstrated in the numerical example.

Two options of the equivalent electrical circuits of a piecewise-homogeneous elastic body, containing piezoelements are considered: based on the capacitor with a constant capacitance and a circuit composed of electric elements with fixed parameters.

It is shown that a replacement of a piecewise homogeneous body, containing a piezoelement, with a constant value capacitance capacitor, gives only a minor error at frequencies far from resonance. The second scheme considered shows high accuracy of the entire frequency range.

The reliability and efficiency of the use of the equivalent circuits to calculate the required parameters of the elements of the external electrical circuits is proved by comparing the obtained results with the calculations based on the problem of natural oscillations of deformable elastic bodies with piezoelements and external circuits.

This work was supported by RFBR (grants №14-01-96003- r_ural-a, № 15-01-03976-a).

FIFTH ORDER ANALYSIS IN SIMPLY SUPPORTED BEAM SUBJECTED TO PARAMETRIC EXCITATION

Naoto Araumi[1] and Hiroshi Yabuno*[1]

[1]*Graduate School of Systems and Information Engineering, University of Tsukuba, Tsukuba, Ibaraki, Japan*

Summary The nonlinear response in a simply supported beam subjected to parametric excitation is investigated. Taking into account the fifth order nonlinearity of curvature of beams and using Hamilton's principle, the governing equation of the beam in the lateral direction is derived. Different from usual third order analysis, the accuracy of fifth order for the hysteresis phenomenon in frequency response curve is performed in this presentation. Employing the method of multiple scales, amplitude equation is obtained and the bifurcations in the frequency response curve is clarified.

INTRODUCTION

There have been many studies on parametric resonance because it has very large response amplitude compared to the excitation amplitude and resonates only in a narrow band. Due to these features, parametric resonance can be applied as an energy harvester [1] which derives energy from vibration and as a mechanical filter [2]. Towards the efficient application, more accurate analysis of the motion of the parametric resonance is required.

In this presentation, we theoretically analyze the nonlinear response in a simply supported beam subjected to parametric excitation. The governing equation of the system in the accuracy of fifth order of the lateral deflection is derived by using Hamilton's principle and is analyzed by the method of multiple scales. Yabuno and Nayfeh investigated the nonlinear normal modes of a vertical cantilever beam excited by a principal parametric resonance theoretically [3]. They derived the third order approximation of the lateral deflection. Utilizing this method to express the nonlinear normal mode of this third order approximation, we obtain the amplitude equation. Different from the frequency response curve in the third order approximation, the frequency response curve has hysteresis due to the fifth order geometric nonlinear elasticity. The stability and the bifurcation points of these steady state amplitudes are analyzed theoretically.

ANALYTICAL MODEL AND GOVERNING EQUATION

We consider the analytical model of a beam with a tip mass and a movable end subjected to parametric excitation in the axial direction, as shown in Figure 1 where v describes the displacements of the elastic component in the y directions. We introduce a static Cartesian coordinate system $x-y$ and a coordinate s along the axis of the beam. Here, M is the tip mass at the movable end, and $\xi(=b\cos\Omega t)$ is the axial periodic excitation.

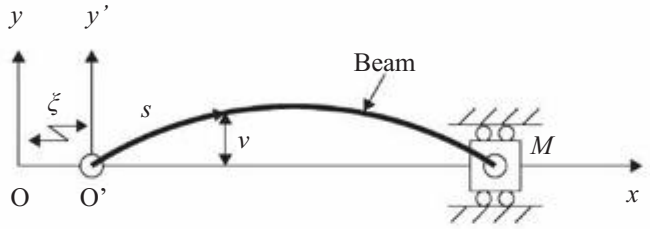

Figure 1: Analytical model of simply supported beam under axially periodic excitation.

Under the inextensibility condition [4], we can obtain the non dimensional governing equation and the associated boundary conditions in the accuracy of fifth order of the lateral deflection v as follows:

$$
\begin{aligned}
&\ddot{v} + \mu\dot{v} + (v'''' + v''^3 + 4v'v''v''' + v'^2v'''' + 6v'^2v''^3 + 8v'^3v''v''' + v'^4v'''') \\
&+ \left\{ -\left(v' + \frac{1}{2}v'^3\right) + (1+M-s)\left(v'' + \frac{3}{2}v'^2v''\right) \right\}\xi \\
&- M\left(v'' + \frac{3}{2}v'^2v''\right)\int_0^1 \left(v'^2 + v'v' + \frac{3}{2}v'^2v'^2 + \frac{1}{2}v'^3v'\right) ds \\
&+ \left(v' + \frac{1}{2}v'^3\right)\int_0^s \left(v'^2 + v'v' + \frac{3}{2}v'^2v'^2 + \frac{1}{2}v'^3v'\right) ds \\
&+ \left(v'' + \frac{3}{2}v'^2v''\right)\int_1^s\int_0^s \left(v'^2 + v'v' + \frac{3}{2}v'^2v'^2 + \frac{1}{2}v'^3v'\right) dsds = 0,
\end{aligned}
\tag{1}
$$

*Corresponding author. Email: yabuno@esys.tsukuba.ac.jp

$$v|_{s=0} = v''|_{s=0} = v|_{s=1} = v''|_{s=1} = 0, \tag{2}$$

where $(\dot{})$, $(')$ are the derivatives with respect to t and s, respectively. In Eq. (1), μv is the effect of linear viscous damping, v'''' is the linear stiffness of the beam, the terms of $v''^3 + 4v'v''v''' + v'^2v'''' + 6v'^2v''^3 + 8v'^3v''v''' + v'^4v''''$ are the nonlinear stiffness of the beam, and the terms proportional to ξ are the effect of excitation in the axial direction and induce the parametric resonance. The terms of $M\left(v'' + \frac{3}{2}v'^2v''\right)\int_0^1 \left(v'^2 + v'v' + \frac{3}{2}v'^2v'^2 + \frac{1}{2}v'^3v'\right) ds$ are the nonlinear inertia force due to the tip mass, and others of the terms are the nonlinear inertia force of the beam.

FREQUENCY RESPONSE CURVE DERIVED BY FIFTH ORDER ANALYSIS

By applying the method of multiple scales, we can obtain the approximate solution as follows:

$$\begin{aligned} v = a\cos\left(\frac{\Omega}{2}t - \gamma\right)\sin\pi s + \frac{1}{4}a^3\cos\left(\frac{\Omega}{2}t - \gamma\right)h_{11}(s) + ab\cos\left(\frac{\Omega}{2}t + \gamma\right)h_{12}(s) \\ + ab\cos\left(\frac{3\Omega}{2}t - \gamma\right)h_{31}(s) + \frac{1}{4}a^3\cos\left(\frac{3\Omega}{2}t - 3\gamma\right)h_{32}(s) + O(a^5), \end{aligned} \tag{3}$$

where $0 < \epsilon \ll 1$ and $h_{11}(s)$, $h_{12}(s)$, $h_{31}(s)$, $h_{32}(s)$ are the mode functions derived from boundary conditions and conditions that these functions are orthogonal to the first mode function. We can also obtain the frequency response curve, as shown in Figure 2 where σ is the detuning parameter of the excitation frequency ($\Omega = 2\omega + \sigma$, ω is the first natural frequency of the beam) and a_{st} is the steady state amplitude, "3rd" and "5th" lines stand for the steady amplitudes derived by third and fifth order analysis respectively, and the solid and dashed lines indicate the curves for stable and unstable steady state amplitudes respectively. As a_{st} becomes large, "5th" lines separate from "3rd" lines and their slopes change from negative to positive through the inflection points.

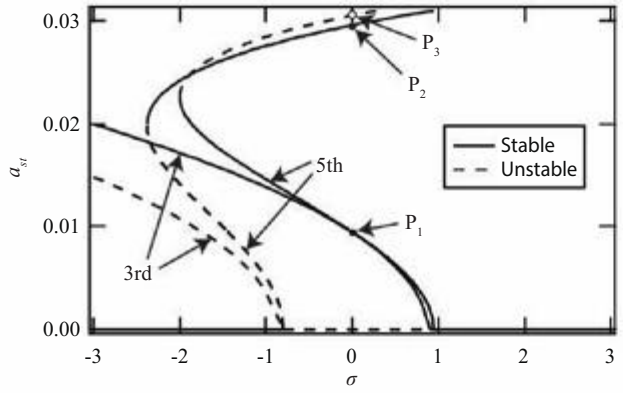

Figure 2: Theoretical frequency response curve.

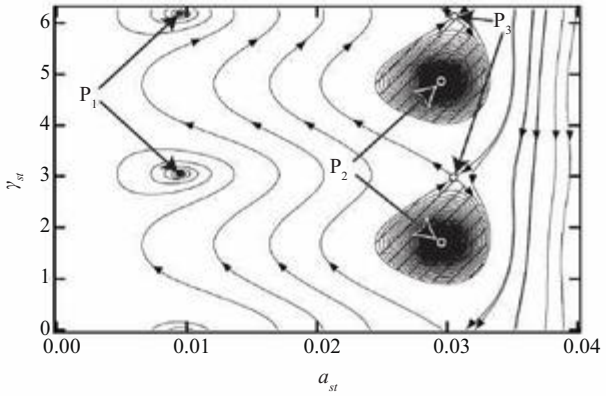

Figure 3: Phase plane at $\sigma = 0$.

In Figure 3, we show a phase plane at $\sigma = 0$ where a_{st} is the steady state amplitude and γ_{st} is the steady state phase of the beam. Points P_1 and P_3 are stable foci, and point P_2 are saddle points. The arrows indicates the direction of the motion of the points. All initial conditions in the unshaded area lead to the points P_1 which are lower steady state amplitudes, while all initial conditions only in the shaded area lead to the points P_3 which are higher steady state amplitudes.

CONCLUSIONS

In this presentation, we derived the governing equation of a simply supported beam subjected to parametric excitation considering fifth order nonlinearity of the lateral deflection. By using the nonlinear normal modes of third order analysis and obtaining the solvability condition of fifth order solution, we described the frequency response curve with the effect of the fifth order geometric nonlinearity of the beam. For a particular excitation frequency at which there are two nontrivial and steady state amplitudes, we showed the trajectories in the phase plane and the initial conditions determine which steady state amplitude is realized. In the near future, we will do experiments by various initial conditions and confirm the theory.

References

[1] M. F. Daqaq, D. Bode, Exploring the parametric amplification phenomenon for energy harvesting, *P I MECH ENG I-J SYS* 225 (14) (2011) 456-466.

[2] J.F. Rhoads, S.W. Shaw, K.L. Turner, R. Baskaran, Tunable microelectromechanical filters that exploit parametric resonance, *J VIB ACOUST*, 127 (5) (2005) 423-430.

[3] H. Yabuno, A. H. Nayfeh, Nonlinear normal modes of a parametrically excited cantilever beam, *NONLINEAR DYNAM* 25 (1-3) (2001) 65-77.

[4] C. C. Glynn, M. R. M. Crespo da Silva, Nonlinear flexural-flexural-torsional dynamics of inextensional beams, *J. Struct. Mech.* 6 (1978) 437.

MONITORING THE VISCOELASTIC BEHAVIOR OF COMPLEX FLUIDS USING MULTI-FREQUENCY RESONANCE TRACKING

Tobias Brack *[1] and Jurg Dual[1]
[1]*Institute for Mechanical Systems, Department of Mechanical and Process Engineering, ETH Zurich, Zurich, Switzerland*

Summary This paper presents a resonance sensor that is able to monitor shear storage and shear loss modulus of a complex fluid. Using a frequency tracking control loop, the dynamic properties of a vibrating circular tube that is in contact with the fluid are evaluated. An analytical sensor model allows to relate the dynamic properties of the coupled system tube-fluid with the mechanical properties of the fluid itself. By simultaneously controlling multiple resonance modes of the oscillator, a discrete spectrum of the complex moduli can be monitored. As an example, a viscoelastic xanthan gum solution is characterized at five discrete frequencies between 2 kHz and 20 kHz. The measurements are combined with a conventional mechanical rheometer representing the lower frequency range from 10 to 300 Hz. The results are compared to measurements obtained by diffusing-wave spectroscopy (DWS).

INTRODUCTION

In modern applications, a lot of sensors exist that use the dynamic parameters (e.g. resonance frequency) of a vibrating system to determine the magnitude of external influences. This may be the mass of an additional load [1] or the mechanical properties of a fluid [2]. Usually, control loops are used to maintain the vibration at resonance which allows to continuously monitor the measurement parameters. However, this method is typically limited to one single frequency. But especially in rheology, the evaluation of several frequencies is necessary. Until now, this has been overcome by using multiple resonators [3] or by consecutively tracking different resonance frequencies [4].
The sensor presented in this paper uses multiple parallel control loops that are each responsible for the tracking of one resonance frequency of a continuous mechanical oscillator. This allows to simultaneously evaluate a discrete frequency spectrum of external influences by using one single oscillator.

SENSOR DESIGN AND OPERATION MODE

The experimental setup of the sensor presented in this paper is depicted in Fig. 1. The vibrating structure, colored in red, is a fixed-free brass tube system with a free length of 227 mm. Approximately half of the free vibrating length is in contact with the fluid. An electromagnetic transducer excites the system at the free end to torsional oscillations.
Since the phase shift between an excitation signal and the corresponding response is a unique indicator for both resonance frequency and damping, the response of the system is measured optically and a phase-locked loop is used as control method to achieve the frequency tracking. This allows to continuously measure the resonance frequency as well as the damping of the oscillator with or without fluid influence [5]. As described in [6], a parallel arrangement of multiple PLL subsystems can be used for the simultaneous tracking of multiple frequencies. Thereby, each PLL is responsible for the phase control and generation of one single frequency, while the sum of all PLL outputs is led to the oscillator as excitation.

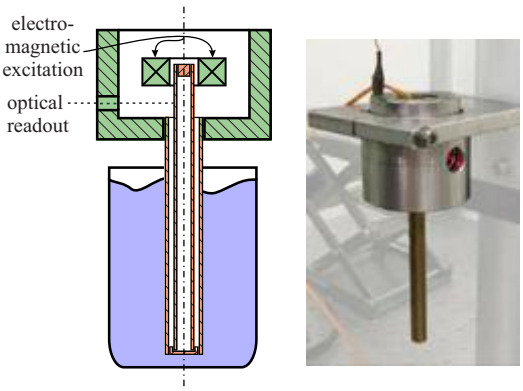

(a) (b)

Figure 1: Experimental setup of the sensor. - a) Section view: Moving parts are colored red, fixed parts are green. (b) Photo of the sensor.

In the vicinity of a resonance frequency the torsional oscillator can be described by a linear, single degree of freedom oscillator. If the sensor is immersed into a fluid, an external shear force influences the sensor. Due to this force, both resonance frequency and the damping will alter. The shear force can be described by a non-linear, complex function F_f that is dependent on the fluid properties, i.e. the density and complex viscosity $\eta = \eta' \nearrow i\eta''$, the sensor dimensions, the vibration frequency ω and a mode-dependent factor that includes uncertain parameters like the fluid level or the influence of the fixation [2]. It is assumed that all parameters except the two viscosity parameters are known a-priori or by means of calibration. Hence, the measurement of two parameters, namely the resonance frequency and modal damping, is sufficient to evaluate the complex viscosity and thus shear storage and shear loss modulus G' and G'' of the fluid at the resonance frequency.

*Corresponding author. Email: brack@imes.mavt.ethz.ch

It can be shown that the additional damping is proportional to the real part and the shift of the resonance frequency is proportional to the imaginary part of the fluid influence F_f [2]. However, the formulation for the frequency and damping shift cannot be analytically solved for η' and η'' due to the complexity of the function F_f. Therefore, the shift of both resonance frequency and damping is numerically calculated for a given set of complex viscosities using an analytic model of the sensor. The resulting data points are then used to relate the measured values of frequency shift and damping shift with the complex viscosity.

RESULTS

As a sample fluid a solution of 0.5% kg/m^3 xanthan gum in deionized water is used. Here, the five first torsional modes of the sensor are used, covering a frequency range from 2 kHz to 20 kHz. The measurement results are compared with diffusing-wave spectroscopy (DWS) measurements provided by LS Instruments AG. Measurements with a conventional mechanical rheometer are performed as well. The result depicted in Fig. 2 shows a very good agreement between the different methods. The error for mode 5 is due to the digital control loop that operates near at its maximum frequency of 24 kHz.

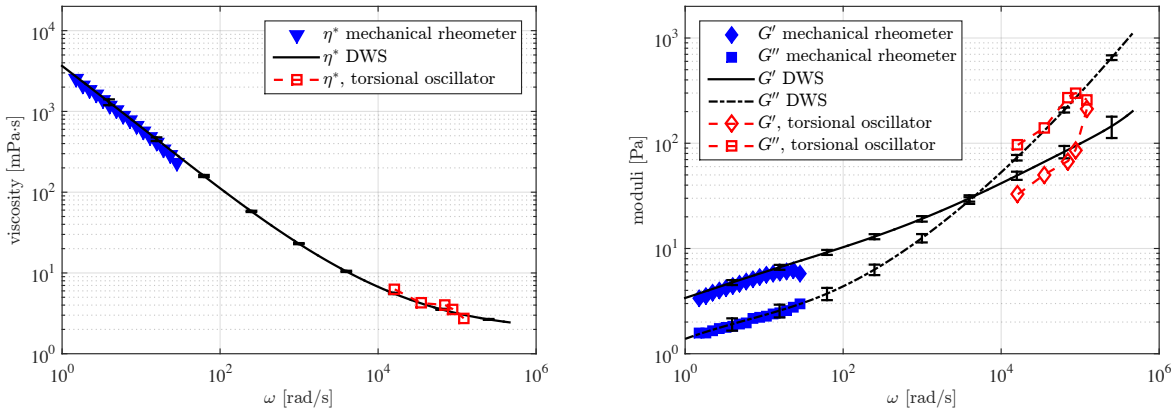

Figure 2: Complex viscosity $\eta^* = \sqrt{\eta'^2 + \eta''^2}$ and complex shear moduli G' and G'' of 0.5 w% xanthan solution measured by conventional rheometry, DWS and the torsional oscillator.

CONCLUSIONS

In this paper a resonance sensor has been presented that is able to measure the viscoelastic properties of a complex fluid by using multiple resonance frequencies of a vibrating structure. In contrast to other existing methods this approach allows to monitor viscoelastic parameters in the laboratory as well as in industrial applications. Here, five frequencies between 2 kHz and 20 kHz have been used. Since a full calibration is not possible, the calculation of the complex viscosity is performed based on an analytic model of the sensor. Measurement results of xanthan solution show a very good agreement to other methods, hence proving the correctness of the measurement method.
Since only one oscillating structure as well as one sensor/actuator pair is necessary, the presented method is very flexible. By varying the design and the controller hardware, the range and the number of the used frequencies can easily be adapted.

References

[1] Kharrat C., Colinet E., Voda A.: H∞ loop shaping control for PLL-based mechanical resonance tracking in NEMS resonant mass sensors. *IEEE Sensors Conference*: 1135 – 1138, 2008.

[2] Dual J., O'Reilly O.: Resonant torsional vibrations: an application to dynamic viscometry. *Archive of Applied Mechanics* **63**(7): 437–451, 1993.

[3] Blom C., Mellema J.: Torsion pendula with electromagnetic drive and detection system for measuring the complex shear modulus of liquids in the frequency range 80-2500 Hz. *Rheologica Acta* **23**: 98–105, 1984.

[4] Stokich T. M., Radtke D. R, White C. C., Schrag J. L.: An instrument for precise measurement of viscoelastic properties of low viscosity dilute macromolecular solutions at frequencies from 20 to 500 kHz. *Journal of Rheology* **38**(4): 1195–1210, 1994.

[5] Kern D. Brack T. and Seemann W.: Resonance Tracking of Continua Using Self-Sensing Actuators. *Journal of Dynamic Systems, Measurement, and Control* **134**(5): 051004, 2012.

[6] Brack T., Vujanic R., Dual J.: Simultaneous phase control of multiple frequencies of multi-degree-of-freedom systems. *SAGE Journal of Vibration and Control*, submitted 2015.

ROBUST STABILITY OF MILLING PROCESSES

David Hajdu*[1], Tamas Insperger[1], Daniel Bachrathy[1], and Gabor Stepan[1]

[1]*Budapest University of Technology and Economics, Budapest, Hungary*

Summary Prediction of machine tool chatter requires the characterization of the dynamics of the machine-tool-workpiece system by means of frequency response functions (FRFs). Uncertainties of the measured FRFs implies uncertainties of the calculated stability diagrams, therefore robust stability analysis against perturbations of the FRF is of high importance. In this work, a method is presented to calculate robust stability boundaries based on uncertain FRFs using a combination of the multi frequency solution and the concept of stability radius defined by μ-values.

INTRODUCTION

In the 1960s, the work of Tobias and Tlusty highlighted the importance of the so-called surface regenerative effect in machine tool vibration. Past vibrations of the cutting affects the actual cutting force acting on the tool tip, therefore the process can be described by delay-differential equations (DDE). Stability properties of the machining processes are depicted by the so-called stability lobe diagrams, which plot critical depths of cut versus spindle speed. These diagrams provide a guide to the machinist to select the optimal technological parameters in order to achieve maximum material removal rate without chatter. Although there are several efficient numerical techniques to the stability analysis of the underlying DDEs, the predicted stability lobe diagrams often do not match experimental cutting tests. One reason for this is the uncertainties of the measured FRF.

DYNAMICAL MODEL OF MILLING OPERATIONS

The governing equation of milling operations involves time-periodic coefficients, which implies the existence of a periodic solution. The stability properties of the perturbed variational system around the periodic motion can be determined according to the extended Floquet theory. The simplest model is used here, where the dynamical properties of the tool are reduced to a single-degree-of-freedom system (SDoF), and a straight-fluted milling tool is considered with constant pitch angle, i.e., the principal period is identical to the tooth-passing period. This model is described by a linear periodic delay-differential equation in the form

$$\ddot{x}(t) + 2\zeta\omega_{\mathrm{n}}\dot{x}(t) + \omega_{\mathrm{n}}^2 x(t) = \quad (t)\,(x(t \nearrow \tau) \nearrow x(t))\,, \tag{1}$$

where $\tau = \quad 0N/\Omega$ is the regenerative delay (tooth passing period), N is the number of teeth and Ω is the revolution of the spindle given in rpm. The τ-periodic function $\quad(t)$ is called directional factor, which can be calculated as

$$G(t) = Q\sum_{j=1}^{N} g_j(t) \quad \mathrm{n}\,\varphi_j(t)\left(\frac{K_t}{K_r} \qquad \varphi_j(t) + \quad \mathrm{n}\,\varphi_j(t)\right), \tag{2}$$

where $Q = a_{\mathrm{p}} q f_{\mathrm{z}}^{q-1} K_{\mathrm{r}}/m$ is the specific cutting-force coefficient, m, k and c are the modal mass, stiffness and damping, respectively, $\omega_{\mathrm{n}} = \sqrt{k/m}$ is the undamped natural angular frequency, $\zeta = c/(2m\omega_{\mathrm{n}})$ is the damping ratio, a_{p} is the axial depth of cut, f_{z} is the feed per tooth, K_{r} is the radial- and K_{t} is the tangential cutting coefficient, $\varphi_j(t)$ is the angular position of tooth j and $g_j(t) \in \{0, 1\}$ is a screen function indicating whether the tool is in the cut ($g_j(t) = 1$) or not ($g_j(t) = 1$) [1].

Extended multi frequency solution

The mathematical background of the multi frequency method and its extension is detailed in [2, 3]. The solution implies a Fourier-series expansion of the periodic functions and gives a Hill's infinite matrix in the form

$$\begin{bmatrix} \vdots \\ p_{-1} \\ p_0 \\ p_1 \\ \vdots \end{bmatrix} = \begin{bmatrix} \ddots & & & & & \\ & A_{-1,0} & A_{-1,-1} & A_{-1,-2} & & \\ & A_{0,1} & A_{0,0} & A_{0,-1} & & \\ & A_{1,2} & A_{1,1} & A_{1,0} & & \\ & & & & \ddots & \end{bmatrix} \begin{bmatrix} \vdots \\ p_{-1} \\ p_0 \\ p_1 \\ \vdots \end{bmatrix} = \mathbf{\Phi} \begin{bmatrix} \vdots \\ p_{-1} \\ p_0 \\ p_1 \\ \vdots \end{bmatrix}, \quad A_{m,n} = H(m\Omega + \omega_c) G_n(\ ^{-i(m\Omega+\omega_c)\tau} \nearrow 1), \tag{3}$$

*Corresponding author. Email: hajdu@mm.bme.hu

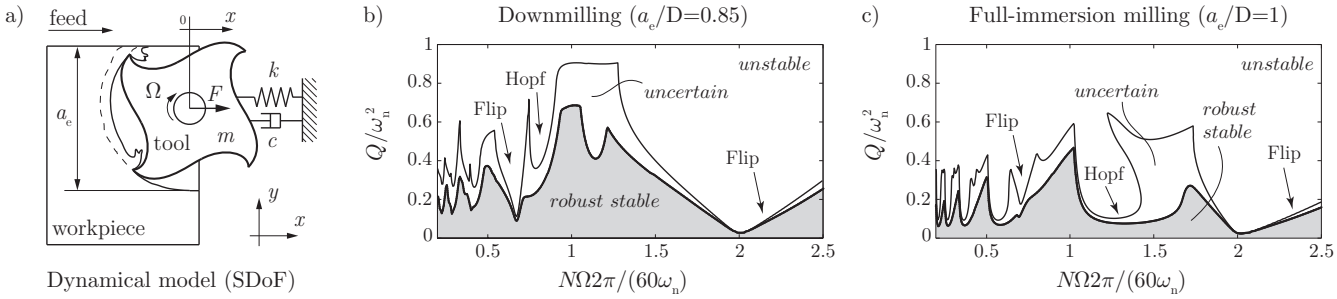

Figure 1: Milling operations: a) Dynamical model b) Robust stability diagram of a downmilling operation with radial immersion ratio 85% (relative error is $r(\omega) = 0.2|H(\omega)|$) c) Robust stability diagram of a full-immersion milling operation (relative error is $r(\omega) = 0.2|\bar{H}(\omega)|$).

which corresponds to the perturbed motion around the periodic solution, where G_n is the nth-order Fourier component of the periodic function (t). Hill's infinite matrix can be factorized as $\mathbf{\Phi} = \mathbf{HEW}$, where $\mathbf{H} = (H(m\Omega + \omega_c))$, $\mathbf{E} = (\ ^{-i(m\Omega+\omega_c)\tau} \nearrow 1)$, and $[\mathbf{W}]_{mn} = G_{(m-n)}$. After truncation to the first $\pm l$ harmonics, the indices are reduced to $m \in \{\nearrow, \ldots, l\}$ and $n \in \{\nearrow, \ldots, l\}$. The existence of a periodic solution around the stationary motion requires that $(\mathbf{I} \nearrow \mathbf{\Phi}) = 0$.

ROBUST STABILITY

Due to imperfect excitation, the changes in the environment and the complexity of the machine-tool structure, the measured FRFs are usually loaded by noise. In practice, the measurements are repeated several times and the average of the individual measurements is used for the construction of stability diagrams. This technique does not take into account the uncertainty of the measurements. Here we assume that the FRF is decomposed into two parts, an averaged frequency response function $\bar{H}(\omega)$ and a perturbation $\delta H(\omega)$, i.e. $H(\omega) = \bar{H}(\omega) + \delta H(\omega)$. The maximum size of the perturbation is described by the uncertainty radius $r(\omega)$ such that $|\delta H(\omega)| \leq r(\omega)$. This definition of the perturbation gives complex disks on the Nyquist diagram. Condition for a periodic solution for the perturbed system can be given as

$$(\mathbf{I} \nearrow (\bar{\mathbf{H}} + \delta\mathbf{H})\mathbf{EW}) = 0 \quad \Longleftrightarrow \quad (\mathbf{I} \nearrow \mathbf{EW}(\mathbf{I} \nearrow \bar{\mathbf{H}}\mathbf{EW})^{-1}\delta\mathbf{H}) = 0. \tag{4}$$

Robust stability analysis is performed using the concept of stability radius, which defines the distance from the stability limit in terms of perturbations. Following [4], the formula for the stability radius can be given using the so-called μ-values in the form

$$r_\delta = \left(\operatorname*{p}_{\omega_c \geq 0} \mu(\mathbf{M}) \right)^{-1}, \tag{5}$$

where $\mathbf{M} = \mathbf{EW}(\mathbf{I} \nearrow \bar{\mathbf{H}}\mathbf{EW})^{-1}$. The μ-values are then approximated as $\mu(\mathbf{M}) \leq \rho(\tilde{\mathbf{M}}\mathbf{R})$, where ρ is the spectral radius, $\mathbf{R} = (r(m\Omega + \omega_c))$ and $[\tilde{\mathbf{M}}]_{mn} = |[\mathbf{M}]_{mn}|$ (for further details, see [4]).

Results are presented in Fig. 1 b) and c) for a straight-fluted milling tool with $N = 2$, where 20% uncertainty was assumed in the FRF in the form $|\delta H(\omega)| \leq r(\omega) = 0.2|\bar{H}(\omega)|$. Robust stability boundaries show that, for certain parameter regions, the uncertainties of the FRF can strongly affect the stability of the process. Machining parameters should be selected from the robust stable region in order to avoid the possibility of producing chatter.

Acknowledgment

This work was supported by the Hungarian National Science Foundation under grant OTKA-K105433. The research leading to these results has received funding from the European Research Council under the European Unions Seventh Framework Programme (FP/2007-2013) / ERC Advanced Grant Agreement n. 340889.

References

[1] Insperger T., Stepan G.: Semi-discretization for time-delay systems. Applied Mathematical Sciences 178, Springer, New York, 2011.

[2] Altintas Y, Budak E.: Analytical prediction of stability lobes in milling. CIRP Annals - Manufacturing Technology 44, 357362, 1995.

[3] Bachrathy D., Stepan G.: Improved prediction of stability lobes with extended multi frequency solution. CIRP Annals - Manufacturing Technology 62, 411-414, 2013.

[4] Karow M., Hinrichsen D., Pritchard A.J.: Interconnected systems with uncertain couplings: explicit formulae for μ-values, spectral value sets and stability radii. SIAM J. Control Opt. 45(3), 856-884. 2006.

CALIBRATION OF TUNED MASS OR INERTER BASED VIBRATION ABSORBERS

Steen Krenk* and Jan Høgsberg
Department of Mechanical Engineering, Technical University of Denmark, Kongens Lyngby, Denmark

Summary It is becoming increasingly common to use vibration absorbers on civil and mechanical engineering structures, due to increased flexibility of these structures. The flexibility of the structure generates a non-trivial interaction between the structure and the absorber, that may severely influence the optimal calibration of the device. A common calibration procedure for mass and inerter based devices is developed, based on a simplified system in which the effect of the structure flexibility is represented by two contributions: a quasi-static flexibility and a quasi-dynamic inertial term. This system is used to develop an equivalent resonant absorber device, and an explicit calibration procedure is developed, in which the equivalent system is calibrated first, and the equivalent parameters then recalculated for the real device parameters. Examples illustrate the near optimal balance of the frequency response attained by this calibration.

INTRODUCTION

The concept of the tuned mass damper, in which the structural vibration generates a resonance in the device consisting of a suspended mass, was developed in the forties [1] and has found increased use with the development of more slender and flexible structures. The tuned mass absorber is mounted at a single point and reacts to the absolute motion. Much more recently a similar device, but based on the relative motion of two points of fixture, has been developed in the form of absorbers with an inertial element in the form of an inerter [2, 3]. As it turns out a common format and calibration procedure can be developed for mass and inerter based vibration absorbers. These vibration absorbers target a specific vibration mode, and due to the local mounting of the device the motion and the forces associated with the structure-device interaction will be influenced by contributions from other modes. A common calibration procedure is described, in which the effect of the non-resonant modes is accounted for by two coefficients, associated with flexibility and inertia, respectively.

EQUIVALENT DEVICE-STRUCTURE SYSTEM

When mounting a device on a structure, the interaction can be described by a displacement component $u = \mathbf{w}^T\mathbf{u}$ in which $\mathbf{u}$ denotes the displacement components of the structure, and $\mathbf{w}$ is an integer array with one or two entries that identify the degree(s) of freedom connected to the device. A key point of the present procedure is an approximate representation of the response u to a device force f in the form

$$u \simeq \left[\begin{array}{cc} \omega_r^2 & 1 \\ \omega_r^2-\omega^2 & k_r \end{array}\right] + \left[\begin{array}{cc} 1 & 1 \\ k_r' & -\ k_r''\ \omega^2 \end{array}\right] \omega_r^2 \Big] f. \tag{1}$$

This is a modification of the standard modal response formula in which ω_r and k_r are the frequency and modal stiffness of the resonant mode r, while the additional two terms are an approximate representation of the response from the non-resonant modes. The coefficients k_r' and k_r'' represent a flexible and an inertial coupling between the resonant modal displacement and the device. These coefficients can be determined from the structure stiffness and mass matrices by standard matrix operations, without the need for a full modal analysis, as demonstrated in [4]. Seen in relation to the device these two terms correspond to a spring with stiffness k_r' and an inerter type term with equivalent mass $m_r' = k_r''/\omega_r^2$ as illustrated for the tuned mass absorber in Fig. 1a.

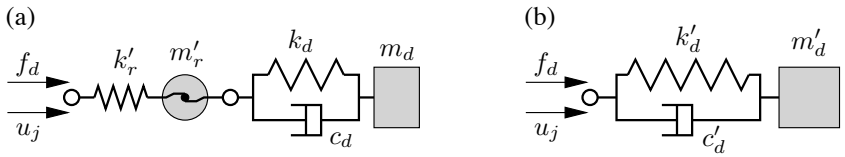

Figure 1: (a) Tuned mass absorber with structural corrections k_r' and m_r'. (b) Equivalent device with parameters k_d', m_d', c_d'.

The tuned mass absorber with stiffness k_d, mass m_d and damping parameter c_d can be calibrated in an optimal sense if acting on a single mass structure by use of the poles of the quartic characteristic equation [5]. It furthermore turns out, that the dynamic amplification of the amplitude of the structure is closely equal to the reciprocal of the optimal damping ratio of the

*Corresponding author. Email: sk@mek.dtu.dk

absorber. Thus, for the basic structure-absorber system a simple explicit calibration procedure is available based on selection of the target amplification around resonance [5].

In the present case with flexibility and inertia effects from the non-resonant modes an explicit calibration procedure can be obtained by establishing an equivalent tuned mass absorber in which the background flexibility and inertia effects are represented via equivalent stiffness, mass and damping parameters k'_d, m'_d and c'_d, as illustrated in Fig. 1b. The design procedure starts with the selection of the dynamic amplification factor, and setting this equal to the reciprocal of the equivalent device damping ratio ζ'_d. When selecting this to be the optimal damping, this determines the equivalent device mass and stiffness m'_d and k'_d. The relations defining the equivalent resonant absorber parameters are now inverted to yield the stiffness k_d, mass m_d and damping c_d of the actual device.

EXAMPLE

The efficiency of tuned mass/inerter absorbers and the efficiency of the calibration procedure are illustrated by the simple example of an 10 storey building represented as a shear frame with identical stiffness of all storeys. For the lowest vibration modes a good location of a tuned mass damper is at the top floor, while the inerter based device connects the ground floor and ceiling. Both devices are calibrated for an amplification factor around resonance of 10, corresponding to an equivalent device damping ratio of $\zeta'_d = 0.1$. Figure 2 shows the dynamic amplification for loading with the mode 2 vertical distribution, and thus the effect of the non-resonant modes is solely due to the non-resonant displacements resulting from the local interaction with the device. Three calibration procedures are compared: simple calibration without effects from non-resonant modes, effect of non-resonant modes via a low-frequency flexibility correction, and the present procedure with a combined flexibility-inertia correction. As seen from the figure the present procedure leads to a regular frequency response curve closely matching the maximum amplification factor of 10 used in the design, while the other two calibration procedures handle one of the devices satisfactorily, while the other is quite unbalanced.

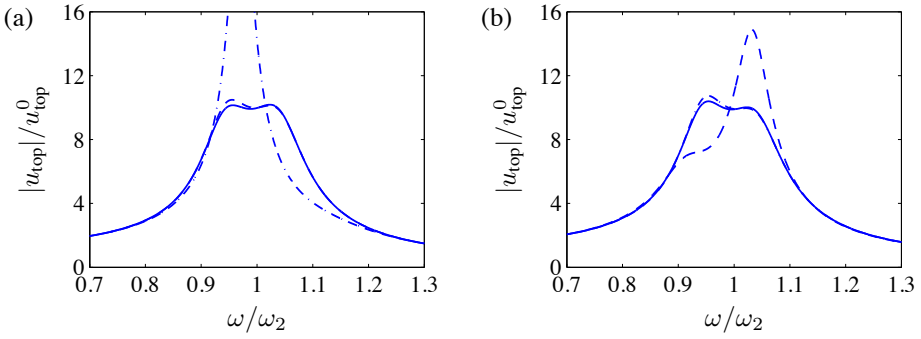

Figure 2: Second mode amplification of shear frame structure. Absorber with (a) mass, (b) inerter. Simple (dashed), quasi-static (dashed-dotted), quasi-dynamic (solid).

CONCLUSIONS

An explicit procedure has been developed for the calibration of resonant vibration absorbers with an inertia element from either a suspended mass or an inerter. The procedure incorporates the structure-device interaction effects into a simple equivalent resonant mass/inerter based system, which is then calibrated by established methods, followed by subsequent evaluation of the parameters of the actual device. The structure is represented by the appropriate modal mass and natural frequency, plus two new parameters characterizing the additional flexibility and inertia effects of the interaction between structure and device. Examples demonstrate high accuracy of the calibration procedure, which attains a balanced frequency response curve with specified level of amplification with high accuracy.

References

[1] Den Hartog, J.P.: *Mechanical Vibrations* (4th edn). McGraw-Hill, NY, 1956. (Reprinted by Dover, NY, 1985)

[2] Smith, M.C.: Synthesis of mechanical networks: The inerter. IEEE Trans. Automat. Control 47:1648–1662, 2002.

[3] Chen, M.Z.Q., Papageorgiou, C., Scheibe, F., Wang, F.C., Smith, M.C.: The missing mechanical circuit. IEEE Circuits Syst. Mag. 9:10–26, 2009.

[4] Krenk, S., Høgsberg, J.: Tuned resonant mass or inerter-based absorbers: unified calibration with quasi-dynamic flexibility and inertia correction. Proc. R. Soc. A 472:20150718, 2016.

[5] Krenk, S.: Frequency analysis of the tuned mass damper. J. Appl. Mech. 72:936–942, 2005.

TWO POSSIBLE EXCITATIONS FOR THE BRISTLE ROBOT

Tadeusz Majewski[1], Dariusz Szwedowicz[2] & Maciej Majewski [3]
[1]*Universidad de las Americas Puebla, Mexico*
[2]*Centro Nacional de Investigacion y Desarrollo Tecnologico-Cuernavaca, Mexico*
[3]*Power Alstom, Poland*

Summary The paper presents the vibratory robot with two different excitations. One excitation acts in the vertical and the other in the horizontal plane. The dynamic model of the robot locomotion is given and the behaviour of the robot is analysed. The deformation of the bristle and the change of the friction between the bristle and the supporting plane are defined as a function of the robot vibrations and the slip velocity of the bristle tip. The difference in the behaviour of the robot for both excitations is shown and indicates which excitation is more efficient. The locomotion velocity as a function of the frequency is given for both excitations.

INTRODUCTION

The robots which imitate the motion of small or very small animals have different principles of working than larger robots that usually have wheels or they walk. The latter are very complicated; there may be problems with their stability and control, but they are very useful in many industrial applications. Small animals move by crawling, jumping, changing their shape, using their wings, etc; worms and caterpillars periodically swell their bodies, snakes periodically change the distance between scales and their angle on the bottom of their body. The periodic motion of some organs (the swelling of their bodies, the motion of their tails, the upward/downward movement of their wings) generatevariable forces which are responsible for the animal locomotion. The average of periodic force is called vibratory force and it is responsible for the motion. The average velocity stabilizes when the vibratory force is zero.

DESCRIPTION OF THE ROBOT

The vibratory robot is shown in Fig.1. It consists of the base 1, two motors DC 2, 3 with the static imbalance, the bristles 4, 5 in two rows, and the remote control of the robot´s motion. The rotor´s imbalances can rotate in the vertical or horizontal plane. The centrifugal forces generate vibrations of the robot and variable normal and friction forces at contact with the base. The components of the centrifugal forces in the direction *x* and the friction force at the bristle´s tips are responsible for the robot locomotion. When the motor spins with the same velocity the robot moves straight. The direction of the robot´s motion is controlled by the motor´s spin velocities.

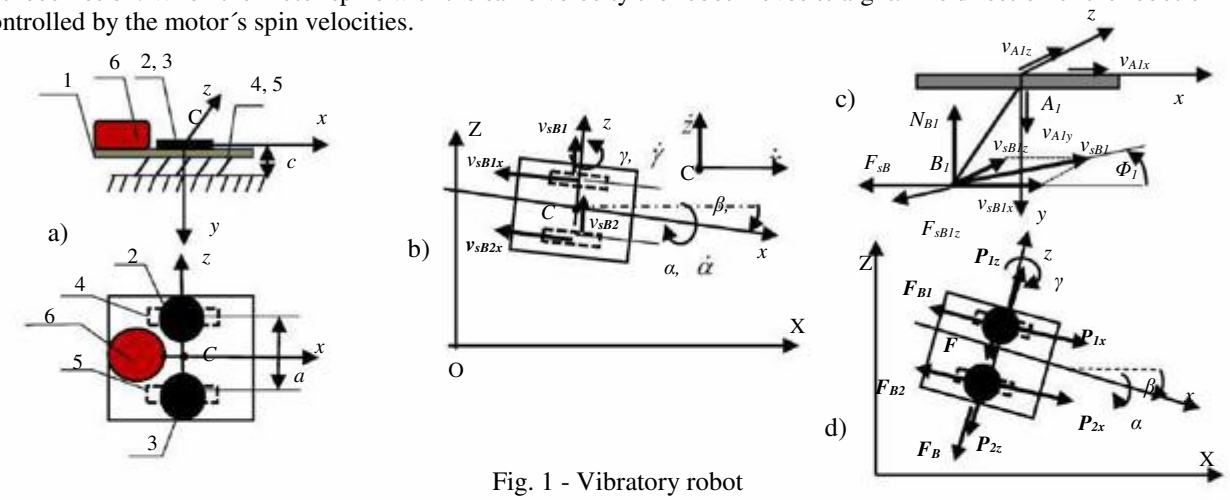

Fig. 1 - Vibratory robot
a) side and top view, b, c) components of the slipping velocity and the forces at the tip,
d) forces acting on the robot in the horizontal plane
1-base of the robot, 2, 3 – motors, 4, 5 - bristles, 6- battery

The friction forces at the tips B_1 and B_2 depend on the vertical vibration of the robot and its locomotion velocity. The contact of the bristle with the base and the forces acting on it are shown in Fig. 2.

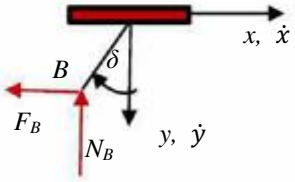

Fig.2. Forces at the tip B

[a)] Corresponding author. Email: tadeusz.majewski@udlap.mx

Without friction the normal reaction is a function of vertical displacement of the robot and the rigidity of the bristles as $N = ky/tan^2\gamma$. The friction force increases or decreases the normal force depending on the direction of the slipping velocity. $N_B = ky_B/(sin\gamma(sin\delta + \mu \cdot cos\delta \cdot sign(v_B)))$, where v_B is the slip velocity of the bristle´s tip.

BEHAVIOR OF THE ROBOT

The motion of the robot in the reference frame OXYZ is defined by the following equations
translation $M\ddot{\boldsymbol{q}}_\mu = \boldsymbol{Q}_{\boldsymbol{q}\mu} + \boldsymbol{F}_{\boldsymbol{q}\mu}$ and rotation in *Cxyz* frame $\boldsymbol{I}\ddot{\boldsymbol{q}}_\mu = \boldsymbol{Q}_{\boldsymbol{q}2} + \boldsymbol{F}_{\boldsymbol{q}2}$.
where $\boldsymbol{q}_1=[x, y, z]^T$, - defines the position of the mass center C in the XYZ reference frame,
$\boldsymbol{q}_2=[\alpha, \beta, \gamma]^T$ – defines the robot´s angular position in the Cxyz reference frame,
$\mathbf{Q_{q1}}$, $\mathbf{Q_{q2}}$ – forces from the motors and their moments about the axis x, y, z,
$\mathbf{F_{q1}}$, $\mathbf{F_{q2}}$ –friction forces and their moments around the axis Cxyz.

Some results are presented in Fig.3

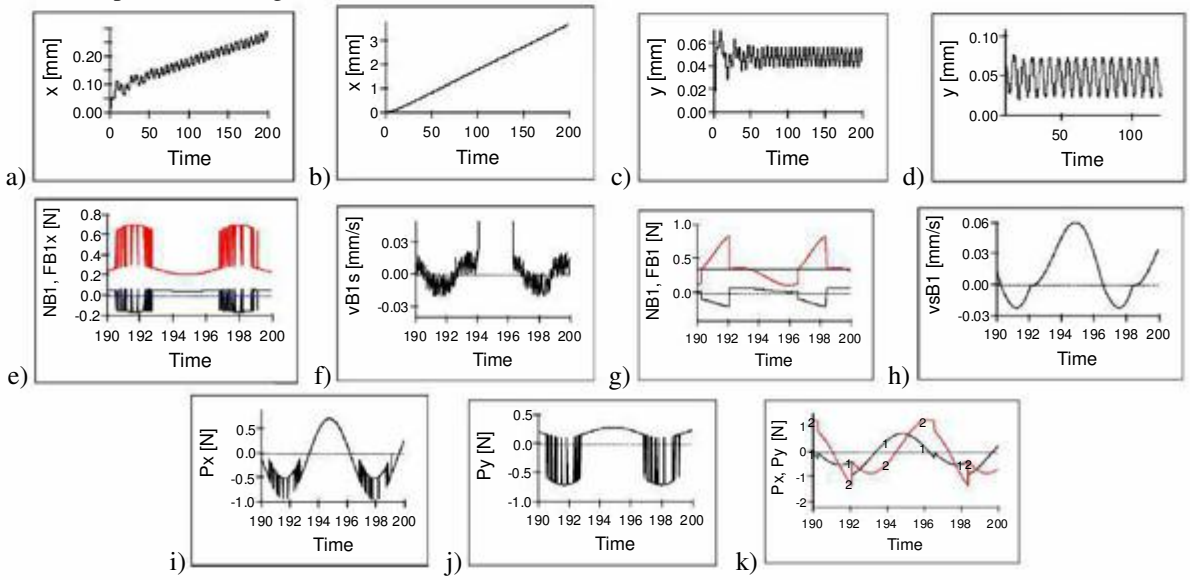

Fig. 3. Some properties of the robot
a, b) displacement of the robot for horizontal (HE) and vertical (VE) excitation, c, d) vertical vibration for HE and VE, e, f) normal, friction force and slip velocity of the tip B_1 for HE, g, h) normal, friction force and slip velocity of the tip B_1 for VE, i, j) components of vibratory force for HE, k) components of vibratory force for VE

For vertical excitation the normal reaction is higher than for horizontal excitation which results in higher friction force in the direction x. Therefore the velocity of locomotion of the robot with vertical excitation is higher as is shown in Fig.4. Changing the angular velocity of the motors one can control the trajectory of the robot.

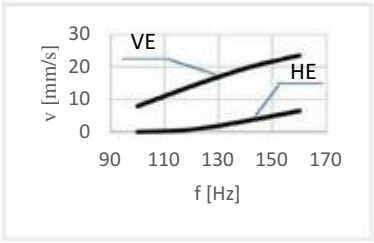

Fig.4. Locomotion velocity as a function of the motor speed

CONCLUSIONS

The inertial excitation and asymmetrical friction generates vibratory force which pushes the robot. The excitation in the vertical plane generates greater friction forces and therefore higher velocity of locomotion. For greater imbalance the robot can move by jumping/hopping. The inertial excitation needs less energy than other exciters of vibration. The bristle robot can be made very small.

References

[1] T. Majewski, D. Szwedowicz, Behavior of the robot with vibratory excitation, *IFToMM-FeIbIM International Symposium on Multibody Systems and Mechatronics,* Mechanism and Machine Science 25, 2014, Springer, ISSN 2211-0984, ISBN 978-3-319-09857-9, DOI 10.1007/978-3-319-09858-6
[2] F. Becker, et al., An approach to the dynamics of a vibration-driven robot, *Proc. Of the 19th CISMIFToMM Symposium,* Vol.19, 2006, pp.299-308

METASTRUCTURES FOR VIBRATION SUPPRESSION

Jared D. Hobeck and Daniel J. Inman
Department of Aerospace Engineering, University of Michigan, Ann Arbor, MI, USA

Summary Traditional damping methods such as viscoelastic treatments as well as the more recent metamaterial inspired approaches are not scalable, fail at low frequency, are temperature sensitive and are relatively narrowband. This talk examines the expansion of the metamaterial concept of repeated cells to address the aforementioned issues. This talk examines a metamaterial inspired approach to creating new structural systems with superior vibration damping properties by embedding inserts into a structure to create a system with low frequency, broadband-damping and vibration suppression properties across multiple scales. In addition to optimizing chiral based meta material configurations, two novel insert configurations combined with a magnetic field to produce nonlinear inserts that greatly improve the design space of metamaterial inspired structures are illustrated. These new configurations are scalable from micrometers to meters. Simple analytical models are presented, 3-D printed examples are manufactured and the models validated against experiments.

METASTRUCTURE BACKGROUND

Here we use the term "metastructure" rather then metamaterial to underscore that we are interested in low frequency vibration and are looking at man made structures, not man made materials. This effort builds off of previous research in two, seemingly disparate areas of mechanics. The first is the field of metamaterials, the area of research based on inserting periodic anomalies into structures to create materials and structures with new features (e.g. Fok, et. al., 2008, Craster and Guenneau, 2013). The second significant background involves mechanics developed by the author in creating low frequency, high bandwidth oscillators while researching piezoelectric based, vibration energy harvesters (e.g. Erturk and Inman, 2011; Karami and Inman, 2011a, b, c). While the two areas seem unrelated the mechanics of energy harvesting devices are extremely relevant because energy harvesting devices can also serve as actuators, sensors and vibration absorbers. In fact, much of the early work in piezoelectric based energy harvesting was performed by the community working on piezoelectric shunt damping (Lesieutre, 1998). There are numerous research results in metamaterials and correspondingly large bodies of literature. Here we focus just on the most relevant previous work.

The most relevant previous work in metamaterials is that of Baravelli and Ruzzene (2013a, 2013b) who addressed the problem of low frequency vibration suppression using inserts that act as vibration absorbers. Their method consisted of chiral lattice inserts used as internal resonators. This work shows that the proposed effort has a good possibility of success by illustrating clearly that a finite sized beam with proper inserts can reduce global vibration levels. In addition they showed that using graded chiral inserts improved vibration reduction and band gap performance.

SAMPLE RESULTS

A lumped mass model of the metastructure bar is assembled. A base line bar is established with a uniform distribution of mass and no absorbers. Next a bar with the absorbers is printed (see Fig. 1) and modelled with inserts that constitute internal vibration absorbers making up a metastructure. Note that the metastructure is designed to have the same mass as the base line bar. The response of the two systems is compared for a number of cases with varying physical parameters and geometries. Fig. 2 shows both the (steady state) frequency response of each structure and the (transient) time response to an impulsive load for both the base line structure and the metastructure. It is clear from both response plots that the metastructure has superior vibration suppression qualities along a range of frequencies.

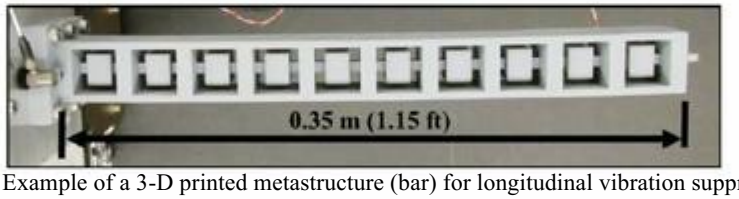

Figure 1 Example of a 3-D printed metastructure (bar) for longitudinal vibration suppression.

The situation can be made broadband by introducing magnetic components into the metastructure and these results are also presented. The results can also be optimized as presented in Fig. 3 to further enhance vibration suppression qualities.

[a] Corresponding author. Email: daninman@umich.edu.

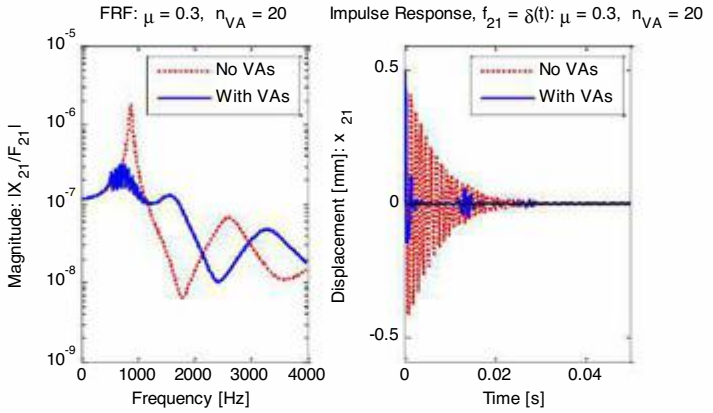

Figure 2 Comparison of the frequency and time response of solid bar (No VAs) with a metastructure bar of equal mass (with Vas).

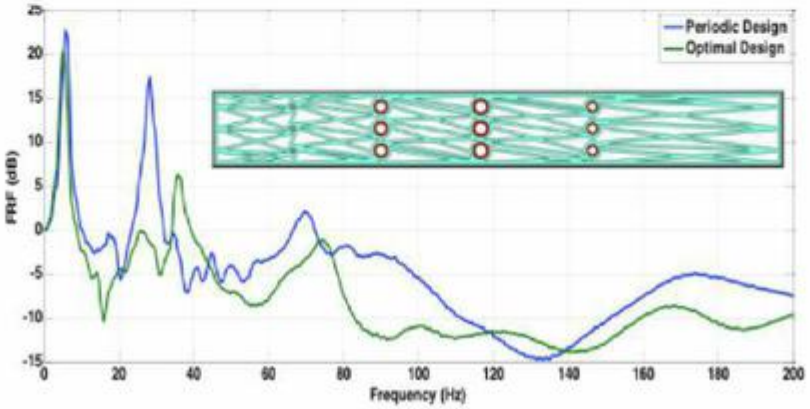

Figure 3 Optimal design of chiral-based metastruture [10]

CONCLUSIONS

An introduction to vibration suppression using metastructure concepts illustrating broadband vibration suppression and scalability has been presented. The examples presented here show that this design of a metastructure can produce a favorable dynamic response. Keeping the mass constant between a plain bar and a metastructure is an important design constraint because typical add on absorbers may increase the mass of the system by as much as 25%, which is unacceptable in aerospace applications.

Acknowledgement

This work is supported in part by the US Air Force Office of Scientific Research under the grant number FA9550-14-1-0246 ‘’Electronic Damping in Multifunctional Material Systems’’ monitored by Dr. BL Lee.

References

[1] Baravelli, E. and Ruzzene, M., 2013a, “High Stiffness - High Damping Chiral Metamaterial Assemblies for Low-Frequency Applications”, *Proceedings SPIE,* 8695, Health Monitoring of Structural and Biological Systems; doi:10.1117/12.2009712

[2] Baravelli, E., and Ruzzene, M., 2013b, "Internally resonating lattices for bandgap generation and low-frequency vibration control." *Journal of Sound and Vibration*. Vol 332, No. 25 ,pp. 6562-6579.

[3] Craster, R. V. and Guenneau, S., ed., 2013 *Acoustic Metamaterials*, Springer Series in Materials Science, New York.

[4] Erturk, A, and Inman, D. J. 2011. *Piezoelectric Energy Harvesting*, John Wiley & Sons, Ltd., Chichester, West Sussex, UK.

[5] Fok, L., Ambati, M. and Zhang, X., 2008, “Acoustic Metamaterials”, MRS Bulletin, Vol. 33, pp. 931-934.

[6] Karami, M. A., Yardimoglu, Y., Inman, D. J., 2010. “Coupled Out of Plane Vibrations of Spiral Beams for Micro-scale Applications,” *Journal of Sound and Vibration,* Vol. 329, pp. 5584–5599.

[7] Karami, M. A., and Inman, D. J., 2011a, "Parametric study of zigzag micro-structure for vibrational energy harvesting," *IEEE/ASME Journal of Microelectromechanical Systems*, Vol. 21, No. 1, pp. 145-160, DOI: 10.1109/JMEMS.2011.2171321

[8] Karami, M. A., and Inman, D. J., 2011b. “Analytical Modeling and Experimental Verification of the Vibrations of the Zigzag Micro-Structure for Energy Harvesting,” *ASME Journal of Vibration and Acoustics*, Vol. 133, No. 1, 011002 (10 pages) doi:10.1115/1.4002783

[9] Karami, M. A., and Inman, D. J., 2011c. “Electromechanical Modeling of the Low-Frequency Zigzag Micro-Energy Harvester,” *Journal of Intelligent Material Systems and Structures*, Vol. 22, No. 3, pp. 271-282.

[10] Abdeljaber, O, Avici O. and Inman, D. J., 2016, “Genetic Algorithm use for Internally Resonating Lattice Optimization: Case of a Beam-like Metastructure*”, Journal of Sound and Vibration*, in press.

Mechanical Vibration Isolation with Stochastic Resonance

Ze-Qi Lu[1], Li-Qun Chen[1]
[1]*Shanghai Institute of Applied Mathematics and Mechanics, Shanghai University, Shanghai, China*

Summary Stochastic resonance is observed by a mechanical experimental apparatus, it is found that addition of noise can lead to an improved SNR-the ratio of signal to noise for the response. This paper challenges the vibration isolation to embrace the definition of stochastic resonance in terms of signal processing "noise benefits", and to design of the nonlinear isolator aimed at verifying that unpredictable fluctuations can play a functional role in the force transmission. The nonlinear vibration isolation system could be implemented by connecting a vertical springs in parallel with two additional horizontal springs, which are configured so that the potential energy of the system has a double-well. SNR of transmitted force is used to analysis this isolation system. It can be seen that the stochastic resonance peak can shift to the higher noise intensity as excitation frequency is increased, and as excitation amplitude is increased the SNR can be increased at any noise intensity.

INTRODUCTION

In certain nonlinear systems, increasing the noise level causes an increase, rather than a decrease, in the quality of signal transmission[1]. A vibration isolation model consisting of three springs [2-3] is used to demonstrate the usage of stochastic resonance in vibration isolation.

EXPERIMENTAL OBSERVATION OF STOCHASTIC RESONANCE

Fig. 1 shows the schematic and photograph of the experiment rig. It consists of a cantilever beam and two magnets, which attract the tip of the beam. The cantilever beam is made of steel (GCr15SiMn) with total length 0.2 m, Cross-sectional area $0.008\times0.001\text{m}^2$, thickness 0.001m, Young's modulus 206GN/m^2, mass density 2700kg/m^3. The magnets each have intensity 0.2T were positioned close to the beam tip to ensure that the system was bi-stable, symmetric and the static displacement of the beam due to the magnetic attraction was 0.0089 m. The amplitude of the sinusoidal signal supplying the shaker was maintained at a constant level 0.5 V and the frequency 1 Hz. The ratio of input signal to noise $\text{SNR}_{\text{linear}}$ is the controlled parameter. In this experiment $1/\text{SNR}_{\text{linear}}$ was varied from 20% to 40%, and the time series of the response was recorded for each setting. Fig. 1(c) shows the SNR of response varying with input SNR. It is clearly that as increasing noise intensity, the SNR is increased at some noise. At $1/\text{SNR}_{\text{linear}}$=0.3, The system jumps randomly between two wells when only subject to random excitation, then put a weak periodic that cannot drive the system from one well to another well into the system, noise induced hopping between the potential wells can become synchronized with the weak periodic forcing, and the red line shows periodic and its period equals 1 seconds.

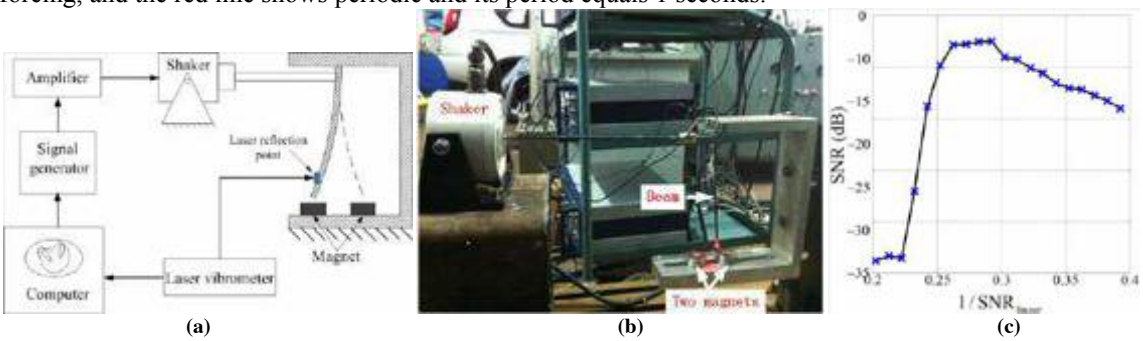

(a) **(b)** **(c)**

Fig. 1 Stochastic resonance experiment rig; (a) Schematic experiment device, (b) actual experiment rig. (c)Ratio of output signal to noise changing with $1/\text{SNR}_{\text{linear}}$, harmonic excitation voltage is fixed at 0.5V.

VIBRATION ISOLATION WITH STOCHASTIC RESONANCE

Fig.2(a) shows a simple lumped parameter model of a nonlinear vibration isolation system. It consists of a vertical stiffness k_v and linear damping coefficient c, and two additional horizontal springs each with stiffness k_h which can act as negative stiffness in the vertical direction. The mass *m*, is excited by both harmonic random force. The three springs are configured so that the potential energy of the system has a double-well. The equation of motion for the system can be rewritten in non-dimensional form as

$$\hat{x}'' + 2\zeta\,\hat{x}' + \alpha\hat{x} + \gamma\hat{x}^3 = \hat{F}_e\cos(\Omega\tau) + \sigma\hat{\eta}_e(\tau) \tag{1}$$

[a] Corresponding author. Email: luzeqi@shu.edu.cn.

where, $\hat{x} = x \ \ x_s$, $x_s = l_o^2 - l$) , $\zeta = c \ \ m\omega_n$, $\omega_n = \sqrt{k_v \ \ m}$, $\alpha = - \ \ l - \ \ \hat{k}$, $\gamma = (1 - l \ \ k \ \ l^3$, $\Omega = \omega \ \ \omega_n$, $\tau = \omega_n t$, $\hat{F}_e = F_e \ \ k_v x_s$, $\langle \hat{\eta}_e \ \tau \ \rangle = \ $, $\langle \eta_e \ \tau \ \eta_e \ \tau - \Delta\tau \ \rangle = \hat{D}\delta \ \Delta\tau$, $\sigma = \sqrt{\hat{D}} = \sqrt{D} \ \ k_v x_s$, $\cdot' = \ \cdot \ \ \tau$.

Stochastic differential equation in the form of Euler-Maruyama, results in

$$\begin{cases} x^{n+1} = x^n + hv^n + \ ^n \\ v^{n+1} = v \ + h \ \hat{f} \ x^{n+1} \ + \hat{f} \ x^n \ \ - \ \ \zeta \ ^n + \sqrt{h}\sigma\lambda_1^{\ n} - 2\zeta A^n \end{cases} \tag{2}$$

where, $A^n = h^2 \ \hat{f} \ x^n \ - \ \zeta v^n) / 2 + h^{3/2} \ \lambda_1 \ \ + \lambda_2^{\ n} / 2\sqrt{3})$, $\hat{x}^n$ is the numerical approximation of $x \ nh$, $\hat{v}^n$ that of $v \ nh$ and ($\lambda_1^{\ n}$, $\lambda_2^{\ n}$) are independent Gaussian variables. The procedure to obtain the SNR is as follows: (1) The power spectrum that contains the harmonic component and the noise, is determined by way of the PSD of the displacement time response. The total power is the area under the curve; (2) The background noise power spectrum in the single frequency that has been removed can be determined by the linear interpolation; (3)Subtracting background noise power from total power to get the harmonic component power; (4) he SNR of the output signal of the system can be determined by the ratio of the harmonic power to the noise power. The SNR of the transmitted force is shown in Fig. 2(b, c). For a low level of random noise, the system jumps between the two potential wells, the displacement response exhibits stochastic switching between positive and negative displacements, so the total response is increased but the line spectrum at the excitation frequency of the periodic force is almost the same. This corresponds to the stochastic anti-resonance in the SNR plot. For moderate levels of random noise, the system jumps between the two wells periodically and the displacement response exhibits some regularity. It can be seen that the response at the excitation frequency increases sharply. Effects of varying the amplitude and frequency of the excitation are also shown in Fig. 2(b, c). Fig. 2(b) shows the SNR when the excitation amplitude is fixed at 0.04, and when the non-dimensional excitation frequency is changed. It can be seen that the stochastic resonance peak shifts to the right as frequency is increased, and the stochastic anti-resonance peak magnitude is increased. Fig. 2(c) illustrates the effect when the non-dimensional excitation frequency is fixed at 0.01 and the non-dimensional excitation amplitude is varied. It can be seen that in this case as the amplitude is increased the SNR is increased. Generally, it can be observed that for the parameters chosen, the stochastic anti-resonance occurs at almost the same noise intensity when either the excitation frequency or excitation amplitude are changed.

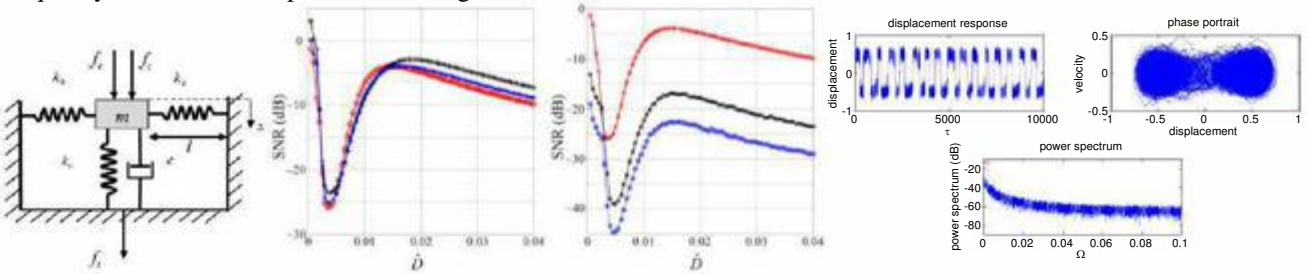

Fig.2 (a) Nonlinear isolator behaving as a double-well system (b, c) SNR of the nonlinear isolation system: (b) the amplitude is fixed to 0.04 with changing frequency: red 'o': 0.01, blue '×': 0.015, green '+': 0.02; (c) the frequency is fixed to 0.01 with changing amplitude: red '+': 0.04, black '×':0.008, blue 'o': 0.004. (d) Response to harmonic excitation with moderate random noise level.

CONCLUSIONS

Stochastic resonance in the nonlinear mechanical vibration system has been observed experimentally. Then this paper concerns the usage of the stochastic resonance in nonlinear vibration isolation system to improve the component of the transmitted force. The model of vibration isolation system comprising three springs when subject to random excitation with additional periodic driving was constructed. It was found that the stochastic resonance peak shifts to the right as the excitation frequency is increased, and as the excitation amplitude is increased the SNR is increased at any noise intensity.

Acknowledgments

The work was supported by the National Natural Science Foundation of China (Project Nos. 11232009 and 11502315)

References

[1] McDonnell M.D., Abbott D., What Is Stochastic Resonance? Definitions, Misconceptions, Debates, and Its Relevance to Biology, *PLoS Computational Biology*, 5(5), (2009), e1000348.

[2]Carrella A., Brennan M.J., Waters T.P., V. Lopes Jr., Force and displacement transmissibility of a nonlinear isolator with high-static-low-dynamic-stiffness, International Journal of Mechanical Sciences, 55(1), (2012), 22-29.

[3] Lu Z., Brennan M.J., Yang T., Li X., Liu Z., An investigation of a two-stage nonlinear vibration isolation system, Journal of Sound and Vibration, 322 (4-5), (2013), 1456-1464.

EFFICIENT ALGORITHM FOR A NONLINEAR TRANSIENT VIBRATION PROBLEM

Mikhail Mesh[a)]
Sandia National Laboratories, Albuquerque, New Mexico, USA

Summary The Galerkin method is a powerful computational tool that is successfully applied to many engineering problems. In the recently published monograph [1] consistent treatment of the nonlinear periodic vibration problems based on the application of the Newton-Kantorovich approach to linearize nonlinear operators and the Galerkin method to solve the resulting linear problem is proposed.
In this paper, we seek to combine the above technique with the method to solve linear transient problem [1] to develop a method for the solution of a nonlinear transient vibration problem. First, we derive equations of the linearized problem using the Newton-Kantorovich method. A system of linear equations resulting from the projection conditions of the Galerkin method is derived and solved numerically. The solution is used to perform the next step of the Newton-Kantorovich method.

NEWTON-KANTOROVICH METHOD FOR A NONLINEAR VIBRATION PROBLEM

For simplicity, the method will be presented as it applies to the damped vibration of a single degree of freedom system with nonlinear stiffness subjected to an external force. An extension to more complex systems is straightforward. We seek to find a solution to the initial value problem:

$$\ddot{u} + g\dot{u} + c(u) - p = 0, \tag{1}$$

where $u = u(t)$ – mass displacement, t – time, $p = p(t)$ – applied force, $g\dot{u}$, $c(u)$, p – are ratios of the damping force, nonlinear force in the spring, and external force, respectively, to the mass. For convenience, Eq.(1) is replaced by a system of the two equations with appropriate initial conditions:

$$\begin{matrix} \dot{u} - v = 0, \\ \dot{v} + gv + c(u) - p = 0 \end{matrix} \quad \begin{pmatrix} u(0) \\ v(0) \end{pmatrix} = \begin{pmatrix} U \\ V \end{pmatrix} \tag{2}$$

which can be written in compact form as,

$$\dot{w} = L(w), \quad L(w) = A(w) + f \tag{3}$$

$$w = \begin{pmatrix} u \\ v \end{pmatrix}, \; f = \begin{pmatrix} 0 \\ p \end{pmatrix}, \; A(w) = \begin{pmatrix} v \\ -c(u) - gv \end{pmatrix} \tag{4}$$

We also introduce $F(w) = \dot{w} - L(w)$ so that the Eq. (3) takes the form:

$$F(w) = 0 \tag{5}$$

The Newton-Kantorovich method [2] is employed to reduce the solution of the nonlinear Eq. (5) to a sequence of linear problems. Ensuing the Newton-Kantorovich method, the following iterative process is constructed,

$$F(w_n) + F'(w_n)(w_{n+1} - w_n) = 0, \tag{6}$$

where $F'(w_n)$ denotes Frechet derivative of the operator $F(z)$ and

$$F'(w_n)w_{n+1} = \dot{w}_{n+1} - L'(w_n)w_{n+1} = \begin{pmatrix} \dot{u}_{n+1} \\ \dot{v}_{n+1} \end{pmatrix} - \begin{pmatrix} 0 & 1 \\ -c'(u_n) & -g \end{pmatrix} \begin{pmatrix} u_{n+1} \\ v_{n+1} \end{pmatrix}, \quad c' = \frac{dc(u)}{du} \tag{7}$$

The iterative process defined by the equations will, under certain conditions [2], converge to the solution of Eq. (5). After substituting (3), (4), and (7), Eq. (6) takes form:

$$\begin{pmatrix} \dot{u}_{n+1} - v_{n+1} \\ \dot{v}_{n+1} + c(u_n) + c'(u_n)(u_{n+1} - u_n) + gv_{n+1} \end{pmatrix} = \begin{pmatrix} 0 \\ p \end{pmatrix} \tag{8}$$

The linearized equations above can be solved numerically using ordinary differential equation solution methods. We use the Galerkin method to solve the system in Eq. (8). A main motivation is the ability to obtain a functional form of the solution.

GALERKIN METHOD FOR THE LINEARIZED EQUATION

The solution of the linearized equation (8) needs to be determined at each step of the iterative procedure. Application of the Galerkin method for that purpose was extensively studied by Krasnoselskii et al [3]. In the case of periodic oscillations, it is convenient to construct the solution as a Fourier series and use Galerkin projection conditions to find unknown coefficients in the expansion. Unfortunately, that idea can't be applied directly to the case of transient vibration.

A modification of the method for the case of linear transient vibration was proposed in [1], where new unknown functions were introduced in a way that allowed recasting the problem in a form suitable for the application of the Galerkin method. We use that approach to solve the initial value problem for the linearized system in (6). First, new functions $\varphi(t)$, $\psi(t)$ are introduced:

$$\varphi(t) = u(t)e^{-qt}; \quad u(t) = \varphi(t)e^{qt} \; and \; \psi(t) = v(t)e^{-qt}; \; v(t) = \psi(t)e^{qt}, \; q > 0 \tag{9}$$

Initial conditions for the newly introduced functions are still the same:

[a)] Corresponding author. Email: mmesh@sandia.gov

$$\varphi(0) = U; \quad \psi(0) = V \tag{10}$$

The transient problem can be solved for a finite but sufficiently large interval $[0;T]$. On that finite, interval functions $\varphi(t)$, $\psi(t)$ and external force can be represented by a Fourier series

$$\varphi(t) = \sum_{m=-M}^{M} \varphi^m e^{im\omega t}, \varphi^m = \frac{1}{T}\int_0^T e^{-im\omega t}\,\varphi(t)\,dt \tag{11}$$

$$\psi(t) = \sum_{m=-M}^{M} \psi^m e^{im\omega t}, \psi^m = \frac{1}{T}\int_0^T e^{-im\omega t}\,\psi(t)dt\,, \quad \omega = 2\pi/T \tag{12}$$

The Galerkin method is used to determine coefficients in the expansions (11) and (12). A special choice of the test function proposed in [1] for the linear problem is employed here as well and projection conditions for Eq.(8) are written as:

$$\frac{1}{T}\int_0^T e^{-(q+im\omega)t}\left[\frac{d(\varphi_{n+1}(t)e^{qt})}{dt} - (\psi_{n+1}(t)e^{qt})\right]dt = 0 \tag{13}$$

$$\frac{1}{T}\int_0^T e^{-(q+im\omega)t}\left[\frac{d(\psi_{n+1}(t)e^{qt})}{dt} + c(\varphi_n(t)e^{qt}) + c'(\varphi_n(t)e^{qt})((\varphi_{n+1}(t) - \varphi_n(t))e^{qt})\right]dt +$$
$$+\frac{1}{T}\int_0^T e^{-(q+im\omega)t}[g\psi_{n+1}(t)e^{qt} - p(t)]dt = 0 \tag{14}$$

$$p^m = \frac{1}{T}\int_0^T e^{-(q+im\omega)t}\,p(t)dt \tag{15}$$

The integrals in Eq. (13) and (14) that contain derivatives with respect to time are evaluated by integration by parts, for example:

$$\frac{1}{T}\int_0^T e^{-(q+im\omega)t}\left[\frac{d(\varphi_{n+1}(t)e^{qt})}{dt}\right]dt = \frac{1}{T}[\varphi_{n+1}(T) - \varphi_{n+1}(0)] + \frac{(q+im\omega)}{T}\int_0^T e^{-im\omega t}\varphi_{n+1}(t)dt = 0 \tag{16}$$

As stated in [1], because of (9), $\varphi_{n+1}(T)$ can be made as small as desired in almost any problem by proper choice of q and T. Using the expansion (11) and initial condition (10), the integral in (16) can be reduced to

$$\frac{1}{T}\int_0^T e^{-(q+im\omega)t}\left[\frac{d(\varphi_{n+1}(t)e^{qt})}{dt}\right]dt = -\frac{U}{T} + (q + im\omega)\varphi_{n+1}^m \tag{17}$$

The second term in Eq.(14) is computed as

$$\frac{1}{T}\int_0^T e^{-(q+im\omega)t}[-(\psi_{n+1}(t)e^{qt})]dt = -\frac{1}{T}\int_0^T e^{-im\omega t}\psi_{n+1}(t))dt = -\psi_{n+1}^m \tag{18}$$

After evaluating the integrals in (16) in a similar manner and using c^m, d^{k-m} and r^{k-m} to denote their values, we arrive at the following system of the $2M$ equations for the unknown coefficients ψ_{n+1}^m, φ_{n+1}^m

$$(q + im\omega)\varphi_{n+1}^m - \psi_{n+1}^m - \frac{U}{T} = 0, \quad m = 1, \dots, M \tag{19}$$

$$-\frac{V}{T} + \left(q + im\omega + \frac{g}{T}\right)\psi_{n+1}^m + c^m + \sum_{k=-M}^{M} \varphi_{n+1}^k d^{k-m} - \sum_{k=-M}^{M} \varphi_n^k r^{k-m} = p^m, \quad m = 1, \dots, M \tag{20}$$

This system has some special properties that allow for efficient implementation and simplified numerical calculations. After the solution of the system is found, a new step in the iterative process (6) is performed. The procedure is continued until desired covergence is achieved.

CONCLUSIONS

We have developed a method for a solution of the nonlinear transient vibration based on the combination of the Newton-Kantorovich iterations and the Galerkin projection procedure. Unlike conventional numerical methods, this method allows to develop functional form of the solution. Implementation of the method is straightforward and efficient.

ACKNOWLEDGMENTS

We would like to thank V.M. Fridman for bringing to our attention to the methods described in the paper and suggesting applying them to the nonlinear transient vibration problem and V. Babuska and B. Owens for reviewing the paper.
Sandia National Laboratories is a multi-program laboratory managed and operated by Sandia Corporation, a wholly owned subsidiary of Lockheed Martin Corporation, for the U.S. Department of Energy's National Nuclear Security Administration under contract DE-AC04-94AL85000. The views expressed herein are those of the authors and should not be interpreted as necessarily representing the official policies or endorsements, either expressed or implied, of Sandia or the U.S. Government.

References

[1] Fridman, V.M. Theory of Elastic Oscillations: Equations and Methods, Nauka, 2014 (in Russian)

[2] Lusternik L.A., Sobolev, V.J. Elements of Functional Analysis, Frederick Ungar Publishing Co, 1961

[3] M. Krasnoselskii, G. Vainikko, P. Zabreyko, and Y. Rutitskii (1972) Approximate Solution of Operator Equations, Wolters-Noordhoff Pub, 1972

MODAL BASIS APPROACHES IN SHAPE AND TOPOLOGY OPTIMIZATION OF FREQUENCY RESPONSE PROBLEMS

Grégoire Allaire[1], Georgios Michailidis [*1], and Nicole Spillane[1]

[1]*CMAP, Ecole Polytechnique, 91128 Palaiseau Cedex, France*

Summary The optimal design of mechanical parts subject to periodic excitations within a large frequency interval is quite challenging. Mechanical intuition in such problems is very limited and although Shape and Topology (S&T) optimization techniques could provide an answer in the conceptual design phase, the necessary computational time using traditional techniques is prohibited, mainly due to the costly adjoint analysis. In this work, we present two non-adjoint approaches for treating frequency response problems in S&T optimization. In the first method, we propose to use an approximation of the objective function and its shape derivative via a modal decomposition of the direct and adjoint states. In the second, we use the modal decomposition both to formulate the problem and to approximate the shape derivative of eigenvectors, in order to evitate the solution of an adjoint equation for every eigenvector. We present numerical examples for the minimization of the dynamic compliance.

PROBLEM DESCRIPTION

Consider a structure that vibrates under the application of a periodic harmonic load $f(t)$. The time-harmonic part of the displacement field $u(x,t)$, solves the equation: $M\ddot{u}(x,t)+C\dot{u}(x,t)+Ku = f(t)$, where M, C and K are the mass, damping and stiffness matrices and the symbol ($\dot{}$) denotes derivation with respect to the time. Using complex instead of real numbers, i.e. considering $\widetilde{f} = \widetilde{F}e^{i\omega t}$ and $\widetilde{u} = \widetilde{U}e^{i\omega t}$, where $\widetilde{F} = f_{Re} + if_{Im}$, $\widetilde{U} = u_{Re} + iu_{Im}$ and ω denotes the excitation frequency, the previous equation reads

$$\left[K + i\omega C \nearrow \omega^2 M\right] \widetilde{U} = \widetilde{F}. \tag{1}$$

We search to find a shape Ω, belonging to an admissible domain $\mathcal{U}_{ad}$ that minimizes the dynamic compliance (C_{dyn}) in a range of frequencies $[\omega_1, \omega_2]$, i.e. the optimization problem reads

$$\min_{\Omega \in \mathcal{U}_{ad}} J(u_{Re}, u_{Im}) = \int_{\omega_1}^{\omega_2} \int_{\Gamma_N} (f_{Im} u_{Re}(\omega) \nearrow f_{Re} u_{Im}(\omega)) ds\, d\omega, \tag{2}$$

where Γ_N is the part of the boundary on which the external loads are applied.

NON-ADJOINT METHODS FOR FREQUENCY RESPONSE PROBLEMS

The discretization of (2) and the solution of equation (1) for every excitation frequency requires an unrealistic computational time for industrial examples with large number of DOFs. The most common remedy to this problem consists of using a modal decomposition of $\widetilde{U}$. However, using a classical adjoint analysis for the calculation of derivatives with respect to design variables also requires a significant computational time, since a large number of eigenvalues is required for an accurate approximation of $\widetilde{U}$ and a linear system needs to be solved for each eigenvalue. Therefore, there is a great interest on developping non-adjoint methods to render S&T optimization applicable on industrial frequency response problems.

Such an approach has appeared in [2], using Padé approximants. In this work, we propose two methods to accelerate significantly the optimization process for frequency response problems, using a classical modal decomposition method. In this way, we avoid numerical issues related to the calculation of Padé approximants while using numerical tools that are standard in industry. We use the level-set method for S&T optimization [1], thus in every iteration of the optimization algorithm we compute a notion of shape derivative to advect the shape.

Modal decomposition of the direct and adjoint states

A first approach consists of taking the exact shape derivative of (2), then using a modal decomposition for the direct and adjoint states. More specifically, the shape derivative of (2) reads

$$\begin{aligned} J'(\Omega)(\theta) = \int_\Gamma (\theta \cdot n) \int_{\omega_1}^{\omega_2} \quad & (\nearrow \omega^2 \rho u_{Re} q_{Re} \nearrow \omega c u_{Im} q_{Re} + Ae(u_{Re}) e(q_{Re}) \\ & \nearrow \omega^2 \rho u_{Im} q_{Im} + \omega c u_{Re} q_{Im} + Ae(u_{Im}) e(q_{Im})) d\omega\, ds, \end{aligned} \tag{3}$$

where A denotes the elasticity tensor and $\widetilde{Q} = q_{Re} + iq_{Im}$ is the complex amplitude of the adjoint state, solving equation

$$\left[K \nearrow i\omega C \nearrow \omega^2 M\right] \widetilde{Q} = i\widetilde{F}. \tag{4}$$

*Corresponding author. Email: michailidis@cmap.polytechnique.fr

Instead of solving equations (1) and (4) for every frequency in the discretized set of $[\omega_1, \omega_2]$, we can use a modal approximation as $\widetilde{U} = \sum_{j=1}^{\infty} \widetilde{a}^j r_j$ and $\widetilde{Q} = \sum_{j=1}^{\infty} \widetilde{a}_Q^j r_j$, where (ω_j^2, r_j) are solutions of the eigenvalue problem $\left[K \nearrow \omega_j^2 M\right] r_j = 0$ and $\widetilde{a}^j, \widetilde{a}_Q^j$ are the coordinates of $\widetilde{U}$ and $\widetilde{Q}$ in the modal base.

Modal decomposition of eigenvectors shape derivative

A second approach consists of expressing directly (2) as a function of (ω_j, r_j), i.e. writing $J(\Omega) = J\left(u_{Re}(\omega_j, r_j), u_{Im}(\omega_j, r_j)\right)$, then compute its shape derivative which reads

$$J'(\Omega)(\theta) = \sum_{j=1}^{\infty} \left[\frac{\partial J}{\partial u_{Re}} \left(\frac{\partial u_{Re}}{\partial \omega_j} \Omega_j(\theta) + \frac{\partial u_{Re}}{\partial r_j} U_j(\theta) \right) + \frac{\partial J}{\partial u_{Im}} \left(\frac{\partial u_{Im}}{\partial \omega_j} \Omega_j(\theta) + \frac{\partial u_{Im}}{\partial r_j} U_j(\theta) \right) \right], \tag{5}$$

where $\Omega_j(\theta), U_j(\theta)$ stand for the eulerian derivatives of ω_j and r_j respectively. Assuming that eigenvalue ω_j is of multiplicity one, in order to avoid complications realted to the crossing of eigenvalues, $\Omega_j(\theta)$ is classical in literature. In order to avoid an adjoint analysis for each $U_j(\theta)$, we first consider the corresponding lagrangian derivative of r_j as $V_j = U_j + \nabla r_j \theta$ and approximate it, using the same eigenbasis, as $V_j = \sum_{k=1}^{\infty} a_{V_j}^k r_k$.

NUMERICAL RESULTS

Consider a classical 2d cantilever, clamped at its left boundary and with a unitary vertical force applied at the middle of its right side (see Figure 1). Minimizing the volume of the structure under a constraint on the static compliance, we result in the optimized shape of Figure 1 (right). For this shape, the dynamic compliance for an excitation force of the type $f(t) = cos(\omega t)$ for $\omega \in [0.1, 0.2]$ Hz takes the value $C_{dyn} = 2\ .5$. Adding a further constraint on C_{dyn} in the previous problem, the optimized shapes for the different approaches appear in Figure 2.

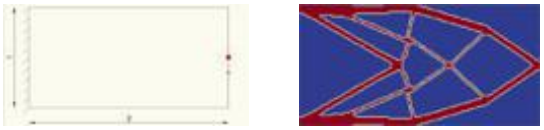

Figure 1: Left: boundary conditions; right: optimized shape for the static compliance.

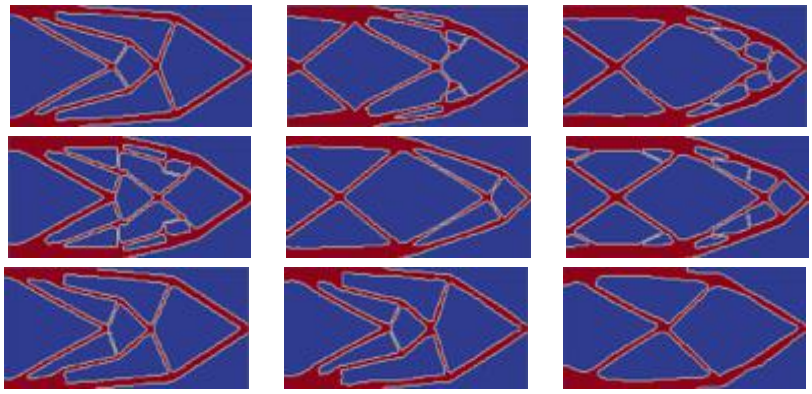

Figure 2: Optimized shapes for: $C_{dyn} \leq 15$ (left column); $C_{dyn} \leq 10$ (middle column); $C_{dyn} \leq 5$ (right column), using the: adjoint method (upper row); modal decomposition of the direct and adjoint states (middle row); modal decomposition of eigenvectors shape derivative (lower row).

References

[1] G. Allaire, F. Jouve, and A.-M. Toader. Structural optimization using sensitivity analysis and a level-set method. *Journal of computational physics*, 194(1):363–393, 2004.

[2] J.S. Jensen. Topology optimization of dynamics problems with padé approximants. *International Journal for Numerical Methods in Engineering*, 72(13):1605–1630, 2007.

NOVEL TYPE OF TUNED MASS DAMPER WITH INERTER

Piotr Brzeski[1], Tomasz Kapitaniak[1], and Przemyslaw Perlikowski[1a]
[1]*Division of Dynamics, Lodz University of Technology, Stefanowskiego 1/15 Lodz, Poland*

Summary In this paper we propose the novel type of tuned mass damper. Characteristic feature of the device is that it contains a special type of inerter equipped with a continuously variable transmission and gear-ratio control system which enables stepless and accurate changes of inertance. We use the frequency response curves to present how considered devices influence the dynamics of one degree of freedom system. Numerical results show excellent level of vibration reduction in an extremely wide range of forcing frequencies.

Introduction

Effective damping of unwanted oscillations of mechanical and structural systems have always been a big challenge for engineers. One of the first attempts to absorb energy of vibrations and in consequence reduce the amplitude of motion is a tuned mass damper (TMD) [1,2]. In this paper, we propose new design of TMD based on a special type of an inerter. Inerter by Smith [3] - is a two terminal element which has the property that the force generated at its ends is proportional to the relative acceleration of its terminals. It's constant of proportionality is called inertance and is measured in kilograms. The theoretical studies are confirmed with experiment showing that suspension layouts with inerter are more effective than classical designs with dampers and springs only [4].

Design of the tuned mass damper

We propose the TMD construction layout that is schematically presented in Fig. 1(a). It consists of inertial component (1) that is coupled via elastic link (2) and inerter (3) to support (4) that allows fixing the device to the damped structure. Inertial element can move in vertical direction. In the device presented in Fig. 1(a) solid bodies are used as the inertial element (1) and support (4) along with helical spring (2) that is an elastic link between them. Characteristic feature of the device is the presence of the inerter (3) which contains in its construction a continuously variable transmission (CVT) and gear-ratio control system which enables stepless and accurate changes of the inertance value. Thanks to the presence of inerter with the CVT and gear-ratio control system one can easily change the natural vibrations frequency of the device. The formula that describes how the natural frequency of the TMD depends on inertance value is the following: $\omega_{TMD} = \sqrt{k/(m+I)}$, where: k is the stiffness of linear spring ((2) in Fig.1(a)), m is the mass of the inertial element ((1) in Fig.1(a)) and I is the controllable parameter that describes current value of inertance.

Model of the system

The analyzed system is shown in Fig. 1(b). It consists of two oscillators that can move in vertical direction. The first oscillator is connected to the support and forced by harmonic excitation. The second oscillator is connected to the first one and represents the TMD of the design described in previous Section. In order to better imitate real device characteristics we assume that the TMD contains a viscous damper that models damping that is always present in the system due to internal damping, friction and motion resistance introduced by the presence of CVT.

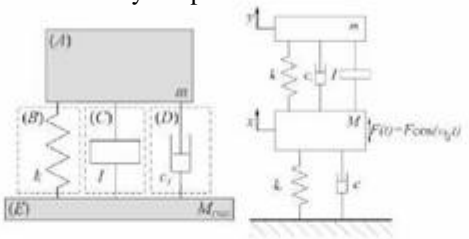

Figure 1. (a) Scheme of the proposed TMD design and (b) model of the system and notation of system's parameters.

Introducing dimensionless time $\tau = t\omega$ ($\omega = \sqrt{k_1/M}$) and the reference length $l_0 = 1.0[m]$ one can write equations in dimensionless form:

$$\ddot{x}' + x' + c_D\dot{x}' + I_D(\ddot{x}' - \ddot{y}') + k_D(x' - y') + c_{TD}(\dot{x}' - \dot{y}') = F_D\cos(\omega'\tau),$$
$$m_D\ddot{y}' - I_D(\ddot{x}' - \ddot{y}') - k_D(x' - y') - c_{TD}(\dot{x}' - \dot{y}') = 0,$$

where $x' = x/l_0$, $\dot{x}' = \dot{x}/(l_0\omega)$, $\ddot{x}' = \ddot{x}/(l_0\omega^2)$, $y' = y/l_0$, $\dot{y}' = \dot{y}/(l_0\omega)$, $\ddot{y}' = \ddot{y}/(l_0\omega^2)$, $c_D = c/(M\omega)$, $I_D = I/M$, $k_D = kl_0^2/(M\omega^2)$, $c_{TD} = c_T/(M\omega)$, $m_D = m/M$, $F_D = F/(Ml_0\omega^2)$, $\omega' = \omega_0/\omega$ and $\omega'_{TMD} = \omega_{TMD}/\omega$. In numerical calculations we use the following values of base oscillator parameters: $M = 10$ [kg], $k_1 = 9810$ [Nm] and $c = 61.62$ [kg/s] which is equal to 5% of critical damping. Amplitude of forcing is equal to $F = 98.1$ [N].

Numerical results

In order to show damping properties of the proposed TMD design we analyze the response of the base oscillator. Additionally, to emphasize the versatility of introduced TMD layout we consider four representative devices characterized by given sets of parameters. In Fig. 2(c) we present parameters and ranges of accessible dimensionless natural frequencies

[a)] Corresponding author. Email: przemyslaw.perlikowski@p.lodz.pl

ω_{TMD} of four analyzed TMD embodiments. First set of parameters (No. I) contains the following values: m = 1.0 [kg], k = 2943.0[Nm], $c_T = 0.8859$ [Nsm] and inertance I in the range from I=0.5[kg] to I=11[kg]. After transformation to dimensionless values we get: m_D=0.1, k_D=0.3, c_{TD}=0.002828 and $I_D \epsilon \langle 0.05, 1.1 \rangle$. In the second case (No.II) we consider the TMD with increased stiffness of the spring and changed accessible range of inertance (see Fig. 2(c)). In the third (No. III) and fourth (No. IV) case the mass of TMD is increased twice and both stiffness and ranges of accessible inertance are changed. Parameters of all investigated TMDs are chosen so that in each case the range of accessible dimensionless natural frequencies of the device is $\omega_{TMD} \epsilon \langle 0.5, \sqrt{2} \rangle$. We assume that damping properties should be preserved in a wide range of excitation frequencies. The best measurable indicator of amplitude decrease is comparison of frequency response curves (FRC) of base oscillator without and with TMD. For that reason for each considered set of TMD parameters we pick 200 equally spaced values of I_D from the accessible range of inertance and for each of them calculate the FRC using continuation method (AUTO-07p package [5]). Next, we superimpose received curves and find minimum amplitudes of the base structure for $\omega \epsilon (0.5, \sqrt{2})$. As a result we obtain the curve that can be used to evaluate damping effectiveness of the proposed TMD and present them in Fig. 2(a,b). Dashed lines in Fig. 2(a,b) demonstrate the response of the base oscillator without TMD. In Fig. 2(a) we show changes of the base structure response when No. I set of parameters of TMD is used. In Fig. 2(a) gray lines correspond to FRCs of base oscillator with the TMD for equally spaced values of inertance I_D from the accessible range $I_D \epsilon \langle 0.05, 1.1 \rangle$ (we plot every tenth from 200 FRCs to do not blur the figure). Analyzing the shape of the FRCs one can say that parameter I_D significantly influences the response of the structure and determines the position of the minimum along FRC. Therefore, to fully present benefits from the changeable inertance we plot the black solid line that is created as a connection of points where we observe minimum values of the base oscillator amplitude. Procedure described above was performed also for Nos. II, III and IV of TMD parameters' sets. Results of the computations are presented in Fig. 2(b). Comparing the shapes of FRCs obtained for four considered TMDs realizations one can say that changes of mass and spring stiffness of TMD strongly affects its damping properties. The difference in the systems response is especially visible for $\omega \epsilon (0.5, 1.1)$. For TMDs with smaller oscillator's mass $m_D = 0.1$ (Nos. I and II) we do not observe any peak along FRCs while for increased mass $m_D = 0.2$ (Nos. III and IV) one spike emerges around ω=0.6. Using smaller mass we can decrease the base oscillator amplitude for all excitation frequencies. Reduction of the amplitude is the more noticeable the larger ω. Simultaneously, TMDs with higher mass are more effective in mitigation of base structure motion for all ω except for the small range near the peak on the FRC. In that range $\omega \epsilon (0.582, 0.623)$ for No. III and $\omega \epsilon (0.640, 0.680)$ for No. IV usage of TMD increases the base structure amplitude instead of mitigating its motion. Hence, for further improvement of damping efficiency by increasing the mass of the TMD one has to be reconciled with the fact that for some ω the amplification of base structure motion may occur instead of its reduction. TMDs with smaller spring stiffness (Nos. I and III) provides better damping efficiency in the whole considered range of excitation frequency.

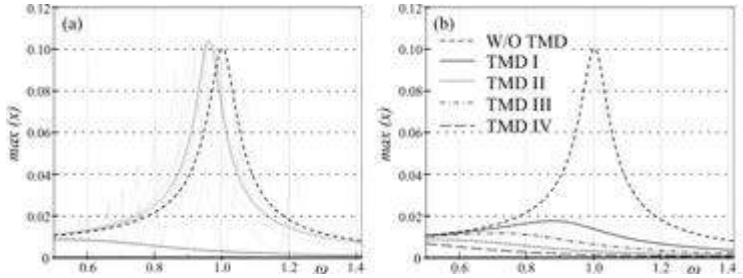

(c)

No.	Dimensionless parameters				
	c_{TD}	m_D	k_D	I_D	ω'_{TMD}
I	0.28	0.1	0.3	< 0.05, 1.1 >	< 0.5, $\sqrt{2}$ >
II		0.1	0.4	< 0.1, 1.5 >	< 0.5, $\sqrt{2}$ >
III		0.2	0.5	< 0.05, 1.8 >	< 0.5, $\sqrt{2}$ >
IV		0.2	0.6	< 0.1, 2.2 >	< 0.5, $\sqrt{2}$ >

Figure 3: FRCs of the base structure with linear stiffness and attached TMD. Subplot (a) presents in details results obtained for the No. I set of TMD parameters, on subplot (b) comparison between all four TMD embodiments (Nos. I-IV) is presented. The black dashed line corresponds to the FRC of system without TMD, gray lines show the FRC for system with TMD for different I_D values. Table (c) values of parameters in simulations.

Conclusions

In this paper we present and analyze properties of new TMD design that is characterized by the presence of inerter with controlled CVT that enables stepless changes of inertance. To prove the versatility of the device we check damping performance of four TMD embodiments characterized by different sets of parameters. For all considered sets of TMD's parameters one can observe a significant decrease of amplitude of motion in wide range of excitation frequencies. Results presented in this paper prove that introduced construction of TMD provides remarkable damping properties in a notably wide range of vibration frequencies. For detailed studies see [6].

References

[1] Frahm H., Device for damping vibrations of bodies, 1909.
[2] Den Hartog J. P., Mechanical Vibrations, McGraw-Hill, New York, 1934.
[3] Smith M., Synthesis of mechanical networks: the inerter, IEEE T Automat Contr, **47**:1648–1662, 2002
[4] Wang F.-C., Su W.-J., Inerter nonlinearities and the impact on suspension control, in American Control Conference, 2008.
[5] Doedel E. J., AUTO-07P: Continuation and bifurcation software for ordinary differential equations. Montreal, Canada, 2006.
[6] P. Brzeski et. al.: Novel type of tuned mass damper with inerter which enables changes of inertance, J Soun Vibr **349**:56-66, 2015.

CONTROL OF CONTACT EVENTS IN ACTIVE ROTOR DYNAMIC SYSTEMS

Patrick Keogh
Department of Mechanical Engineering, University of Bath, Bath BA2 7AY

Abstract
Spinning rotors are ubiquitous components that are essential for power generation, propulsion, gas compression, vacuum generation, machining, and other energy driven processes. Higher rotational speeds enable smaller, hence more power dense machines, to be developed. Active rotor dynamic systems include those where rotors are levitated by controllable active magnetic bearings. In principle, the rotor is levitated in a contact-free condition, which is efficient for high speed operation. However, abnormal overload events or transient faults may give rise to a loss of functionality and cause a rotor to come into contact with emergency touchdown bearings. This may result in excessive vibration at a level that may cause structural damage to the system. It is important to understand the mechanisms that drive these persistent nonlinear dynamics in order that control of contact-free rotor levitation may be restored. This paper will explore the options that are available.

INTRODUCTION

The principles of operation of rotor/active magnetic bearing (AMB) systems are well-known [1]. A typical layout is shown in Figure 1. In the vertical axis through the AMB coils, electrical currents (i_U, i_L) may be adjusted for levitation control of the rotor and to maintain clearance between the rotor and the AMB. However, excessive external influences or faults conditions may cause the rotor to make contact with a touchdown bearing (TDB), which is in place to prevent excessive rotor dynamic excursions. When the rotor is in contact with the TDB, radial (normal) and tangential (friction) forces are introduced into the rotor dynamic behaviour. These forces may be large and may become persistent and undesirable [2, 3]. If control functionality is still available from an AMB or an active TDB, it may be possible to restore the rotor to a desirable contact-free state. An understanding of the contact dynamics is required.

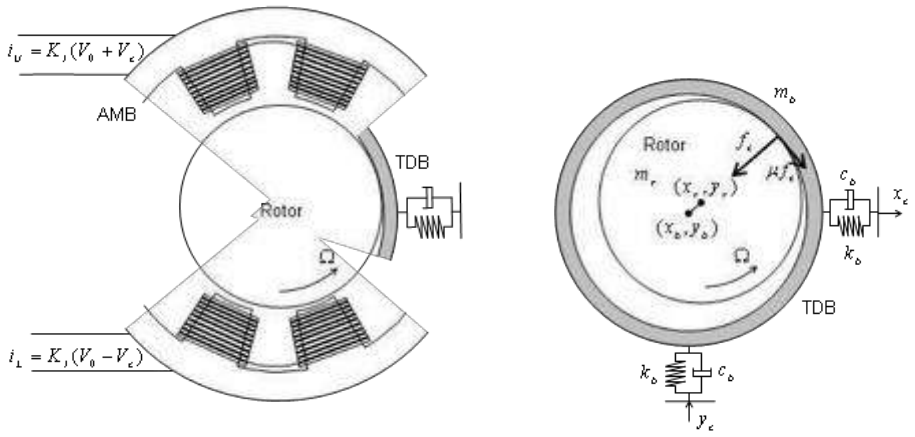

Figure 1. Spinning rotor within an AMB showing possible contact with a TDB

CONTROL OF PERSISTENT ROTOR CONTACT MODES

Figure 2 shows an example of bistable responses driven by rotor unbalance. In case A, the rotor whirls in a circular contact-free condition within the clearance space of the AMB. In case B, a bouncing mode solution is also possible. In the left hand side diagram it is seen that the response of orbit B is lagging slightly behind the rotating unbalance vector, while the orbit A is almost in anti-phase with the unbalance vector. This effect is caused by the 'hard' boundary of the TDB. The phases of the orbits are seen more clearly in the rotating frame view of the right hand side diagram in which orbit A is represented by a single point and orbit B becomes a small loop on the TDB boundary.

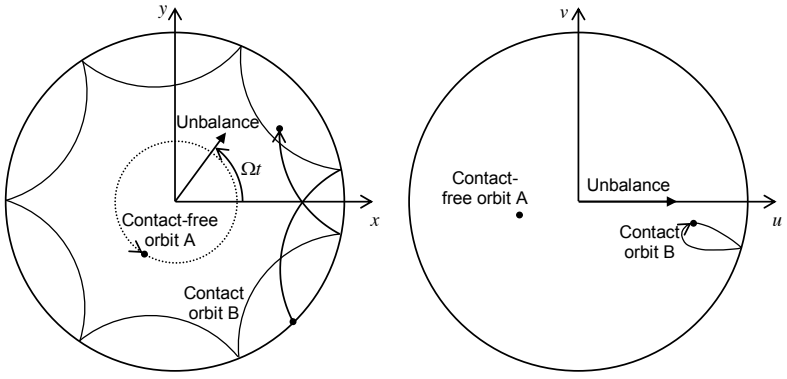

Figure 2. Bistable contact-free (A) and bouncing contact (B) motions in inertial (x, y) and synchronously rotating (u, v) frames of reference.

[a] Corresponding author. Email: p.s.keogh@bath.ac.uk.

Persistent contact is problematic since the contact force levels are typically large and in excess of the magnitude of the unbalance force vector. These may cause structural damage to the TDB and the rotor. Furthermore, frictional forces at a contact zone will be high, which will induce significant thermal inputs to the TDB and the rotor, resulting in thermal distortion and thermal bending, respectively.

There are a multitude of contact responses that may coexist with a contact-free orbit A. Figure 3 shows other bouncing modes (B1-B4) together with full forward whirl rub orbits, C1 and C2. In each case, the equations of motion were solved analytically with different initial conditions and the solutions were obtained with a fully functional AMB and the same unbalance vector.

Another response, not shown, is that of backward whirl. Under a fully developed backward whirl, the frequency of rotor vibration is scaled by R/c, the rotor radius to clearance ratio. This amplifies the contact force to a level that is usually destructive.

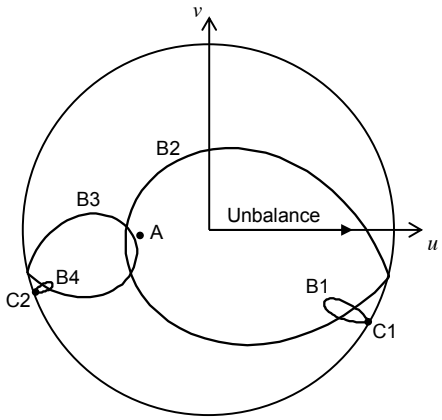

Figure 3. Further contact orbits viewed in a synchronously rotating (u, v) frame of reference.

Control using AMB feedback

The operation of an AMB utilises displacement feedback of the rotor orbit. In principle, if the effective unbalance vector could be cancelled, say through AMB control action, all contact orbits, together with the contact-free orbit would degenerate to the origin at the centre of the AMB. In order to achieve this ideal case, the control system would be required to assess the dynamic content of the displacement signals in order to:

(a) Deduce whether contact has occurred, for example, due to a change in the rotor unbalance condition.
(b) Ascertain which contact orbit has been excited.
(c) Evaluate the source unbalance (magnitude and phase).
(d) Apply a synchronous force through the AMB to cancel out the source unbalance.

It is also necessary to account for the fact that a rotor must be considered as a multimode vibrational system and that multi-point contact with more than one TDB is possible.

Control through an active TDB

It is also possible to activate a TDB, moving it in response to rotor contact. For such control:

(a) The TDB motion must be a fraction of the radial clearance.
(b) The actuation must be able to overcome high dynamic contact forces under positional control.
(c) It is possible for TDB control to be applied under open-loop action, or under closed loop control.
(d) The TDB may be moved in response to rotor motion, in anticipation of approaching contact to reduce contact force levels or to avoid unnecessary contact.
(e) Once contact-free conditions have been achieved in a stable manner, further TDB control is not required.

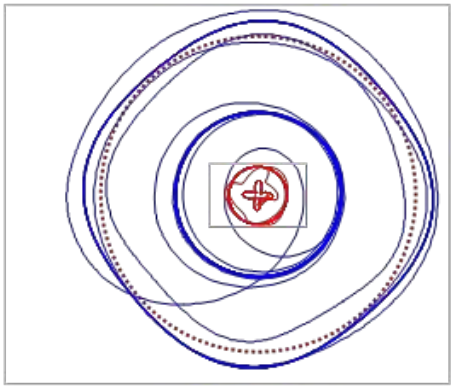

Figure 4. Active TDB motion (red) to induce a rotor out of a persistent rub contact mode (blue). Viewed in an inertial (x, y) frame of reference.

References

[1] Magnetic Bearings: Theory, Design, and Application to Rotating Machinery, edited by Gerhard Schweitzer, Eric H. Maslen, Springer, ISBN 978-3-642-00496-4, 2009.

[2] Keogh, P.S. and Cole, M.O.T. Rotor Vibration with Auxiliary Bearing Contact in Magnetic Bearing Systems Part 1: Synchronous Dynamics, *Proc.I.Mech.E., Part C, Journal of Mechanical Engineering Science*, **217**, 377-392, 2003.

[3] Enemark, S. and Santos, I.F. Nonlinear Dynamic Behaviour of a Rotor-Foundation System Coupled Through Passive Magnetic Bearings with Magnetic Anisotropy - Theory and Experiment. *Journal of Sound and Vibration*, **363**, 407-427, 2016.

TIME-OPTIMAL CONTROL FOR PENDULUM-LIKE SYSTEMS IN CASE OF LARGE CONTROL BOUNDS

Sergey Reshmin[1a)]
[1]Laboratory of Mechanics of Systems, Institute for Problems in Mechanics RAS, Moscow, Russia

SummaryA time-optimal control problem for a pendulum-like system is considered. The system describes the dynamics of an inertial object under the action of a bounded control force and an external force which is periodic in coordinate. The terminal set consists of points on the abscissa axis of the phase plane, and the distance between two neighboring points is equal to the period of the external force. We suggest a numeric procedure that allows one to find an exact estimate for the amplitude of the control for which the time-optimal feedback control has the simplest structure: the number of switchings is not greater than one for any initial conditions. We consider the coordinate of the first terminal point as a parameter and find such estimate for different terminal positions in case of pendulum and earth satellite control problems.

DESCRIPTION OF THE SYSTEM

We consider a nonlinear controlled dynamical system

$$\ddot{\varphi} = \varepsilon(\varphi) = u. \qquad (1)$$

We will call the scalar control $u(t)$ an admissible control if it satisfies the two conditions: $u(t)$ is a piecewise continuous function of time; for all $t \in [0, +\infty)$, we have

$$|u(t)| \le k, \quad k = \text{const}. \qquad (2)$$

The function $\varepsilon(\varphi)$ is periodic in coordinate with a period of 2θ and continuously differentiable for all $\varphi \in (-\infty, +\infty)$. Without loss of generality, we assume $|\varepsilon(\varphi)| \le 1$.
The initial states of system (1) at the time $t = 0$ are arbitrary, and the terminal conditions at some time $t = T$ ($T > 0$) are given as

$$\varphi(T) = \varphi_T + 2\theta n, \quad \dot{\varphi}(T) = 0, \qquad (3)$$

where $\varphi_T \in [0, 2\theta)$ is a fixed value and n is an arbitrary integer. The time T when the system hits the terminal set (3) is not fixed and depends on the control $u(t)$.

TIME-OPTIMAL CONTROL PROBLEM

Problem. For a given positive parameter k, it is required to construct a feedback control $u(\varphi, \dot{\varphi})$ satisfying constraint (2) and bringing system (1) from an arbitrary initial state into terminal state (3) in a minimum time T.

Problem can be solved numerically using the Pontryagin maximum principle. This principle implies that the optimal control takes the values $u = \pm k$. There are no singular controls, see [1]. To obtain the feedback optimal control $u(\varphi, \dot{\varphi})$, it suffices to find "switching curves" and "dispersal curves" in the plane $\varphi\dot{\varphi}$, which bound the domains where $u = +k$ and $u = -k$. The control pattern is periodic with respect to φ.
Optimal control for pendulum-like systems was considered in [2-5] for large admissible control bounds k. The following theorem was proved in [4].

Theorem. There exists a number $\tilde{k} > 1$ such that the time-optimal control in Problem has no more than one switching for $k \ge \tilde{k}$ and any initial conditions.

An explicit expression for $\tilde{k}$ was obtained in [4] as a function of half-period θ. Constant $\tilde{k}$ can be considered as an upper estimate for the exact threshold value k^* (bifurcation value). If $k > k^*$ then the number of switching is not greater than one. If $k \le k^*$ then optimal trajectories with two switchings appears in the phase plane.
We present a numeric procedure for finding bifurcation value k^*, which in general case depends not only on the half-period θ but also on the coordinate φ_T in (3) and function $\varepsilon(\varphi)$ in (1). The mentioned procedure was described briefly in [5]. It uses necessary optimality condition jointly with the equation of the indifferent curve. Below, we demonstrate numerical results obtained for a nonlinear pendulum and artificial earth satellite moving on a circular orbit (see [3]).

NUMERICAL RESULTS

Normalized motion equation of nonlinear pendulum or artificial earth satellite [3] can be written in the following form

$$\ddot{\varphi} = \sin\varphi = u,$$
$$|u| \le k, \quad k = \text{const}.$$

[a)]Corresponding author. Email:reshmin@ipmnet.ru.

The terminal set is given by

$$\varphi(T) = \varphi_T + 2\pi n, \quad \varphi_T \in [0,2\pi),$$

in case of the pendulum control or by

$$\varphi(T) = \varphi_T + 4\pi n, \quad \varphi_T \in [0,4\pi),$$

in case of the earth satellite control. We obtained numerically bifurcation values $k^*(\varphi_T)$ and compare it with the absolute value of gravitational moments at the same terminal angles, see figures 1 and 2. In addition, we found coordinates of the bifurcation point in the phase plane (where additional switching curves appear) as a functions of φ_T. Note that bifurcation values for the equilibrium states of the pendulum were calculated earlier by the author, i.e. $k^*(0) \approx 1.04$ and $k^*(\pi) \approx 0.80$. By the way, a small mistake is found in paper [3], where estimate $\tilde{}(0) = 1$ is incorrect in the problem of optimal transfer of an artificial earth satellite to a gravitationally stable equilibrium position. It turns out that $k^*(0) \approx 1.09 > 1$.

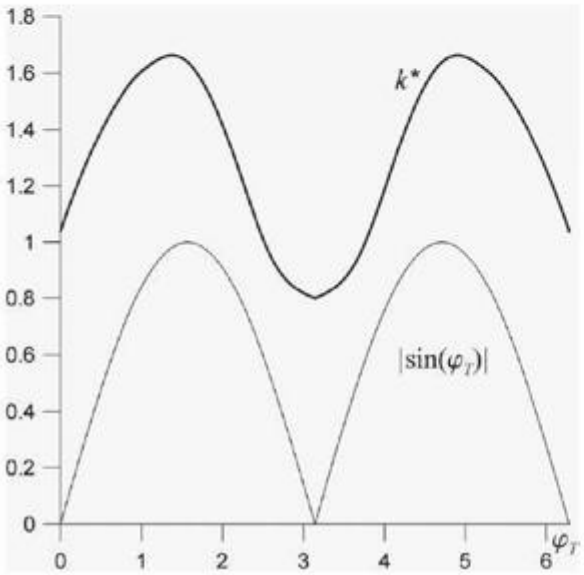

Figure 1: pendulum control problem.

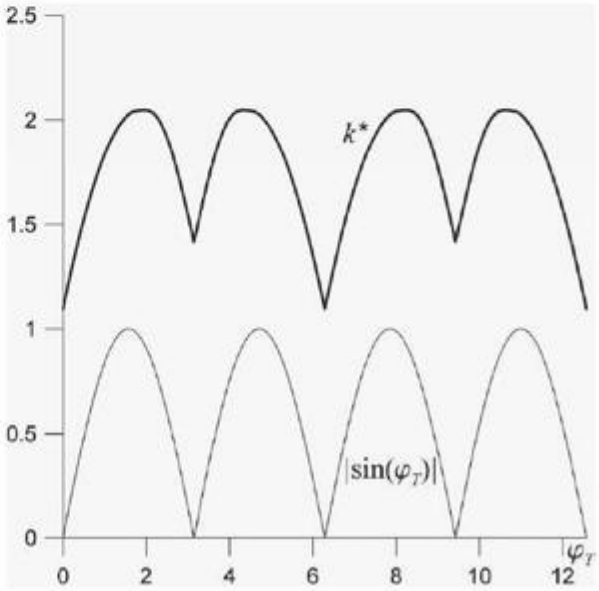

Figure 2: earth satellite control problem.

CONCLUSIONS

For the pendulum-like systems, we propose fast and reliable numerical procedure that finds a threshold value (bifurcation value) of control bounds as a function of terminal position (angle). We assume that for every terminal state, an admissible control amplitude is sufficiently large and exceeds the corresponding bifurcation value. In this case, the time-optimal feedback control has the simplest structure without two or more switchings for all initial and terminal conditions.

The terminal position is not necessary equilibrium state of the considered systems. Thus, we can compare the obtained bifurcation values with the absolute values of external force acting in the corresponding terminal position. Numerical results confirm an essential relationship between these two dependences in case of a nonlinear pendulum and earth satellite control. In other words, they have a similar behaviour. It turns out that in both cases the obtained bifurcation values greater than modulus of gravitational moments acting in the corresponding terminal angles.

ACKNOWLEDGEMENTS

This work was supported by the Russian Foundation for Basic Research (project nos. 14-01-00476 and 14-08-00606). Author is also thankful to Mr. Stepan Yudin for the help in obtaining numerical results.

References

[1] Lee E.B., Markus L.: Foundations of Optimal Control Theory. Wiley, New York, 1967.

[2] Garcia Almuzara J.L., Flügge-Lotz I.: Minimum time control of a nonlinear system. *J. Differen. Equations***4**(1):12–39, 1968.

[3] Beletskii V.V.: Optimal transfer of an artificial earth satellite to a gravitationally stable position. *Cosmic Research***9:**337, 1971.

[4] Reshmin S. A., Chernousko F. L.: Properties of the time-optimal feedback control for a pendulum-like system. *Journal of Optimization Theory and Applications***163**(1):230−252, 2014.

[5] Reshmin S. A.: Properties of the time-optimal control for Lagrangian single-degree-of-freedom systems. *IEEE Transactions on Automatic Control***60** (12):3350-3355, 2015.

SEMI-ANALYTICAL MODELING OF SUBSTRATE LOSS OF MINIATURE RESONATORS

Christoph Schaal [*1], Ajit Mal[2], and Robert M'Closkey[2]

[1]*Department of Mechanical Engineering, California State University, Northridge, CA, USA*
[2]*Mechanical and Aerospace Engineering Department, University of California, Los Angeles, CA , USA*

Summary In this paper, a new semi-analytical technique for estimating the energy loss in a miniature resonator mounted on a substrate is presented. Recent high quality factor resonators typically have resonant frequencies up to several hundred kilohertz, and therefore, the substrate is best treated as a plate. The only traveling waves in a plate are Lamb waves, which leads to a simplified characterization of the energy carried away from a vibrating source on the plate surface. In the presented approach, absorbing boundary elements of standard finite element (FE) models are replaced with the analytical expressions for Lamb waves. The method of stitching together the FE model and analytical expressions is extended to include modal analysis in order to determine quality factors of the resonator modes. The semi-analytical approach is demonstrated for a cantilever bonded to a plate, and eigenmode parameters are determined. Good agreement with conventional FE simulations is shown.

MOTIVATION

For the resonator designer, it is crucial to have an efficient method for determining the quality factors of the resonator at an early stage. Resonator energy loss due to interaction with its substrate (so called anchor loss) has been widely studied, but most treatments have assumed a semi-infinite medium due to the small dimensions of the resonator compared to the substrate thickness. Recent high quality factor resonators, though, typically have resonant frequencies from a few kilohertz up to several hundred kilohertz, and in these cases, due to the wavelengths involved, the substrate is more accurately treated as a plate, not as a semi-infinite medium. Typically, a model of the resonator that includes a small segment of the plate is created with a finite element (FE) software in conjunction with absorbing boundary elements [1]. In this paper, an approach is presented in which the absorbing boundary elements are replaced with the analytical expressions for Lamb waves.

MODAL ANALYSIS APPROACH

Using a FE software, the resonator as well as a small segment of the plate is modeled, as shown in Fig. 1. At the plate boundaries of the FE model, continuity between FE and analytical solution has to be satisfied [2]. A lossless material is assumed as well as harmonic motion of the form $^{-\mathrm{i}\omega t}$, where $\omega = 2\pi f$ is the angular frequency. Introducing the subscripts I and B denoting a DOF in the interior and on the interface boundary (cf. Fig. 1), the FE equations are written in the form

$$\left(\underbrace{\begin{bmatrix} \boldsymbol{K}_{\mathrm{II}} & \boldsymbol{K}_{\mathrm{IB}} \\ \boldsymbol{K}_{\mathrm{BI}} & \boldsymbol{K}_{\mathrm{BB}} \end{bmatrix}}_{\boldsymbol{K}} \nearrow \omega^2 \underbrace{\begin{bmatrix} \boldsymbol{M}_{\mathrm{II}} & \boldsymbol{M}_{\mathrm{IB}} \\ \boldsymbol{M}_{\mathrm{BI}} & \boldsymbol{M}_{\mathrm{BB}} \end{bmatrix}}_{\boldsymbol{M}} \right) \begin{bmatrix} \bar{\boldsymbol{u}}_{\mathrm{I}} \\ \bar{\boldsymbol{u}}_{\mathrm{B}} \end{bmatrix} = \begin{bmatrix} \boldsymbol{0} \\ \boldsymbol{f}_{\mathrm{B}} \end{bmatrix} , \tag{1}$$

where $\bar{(\cdot)}$ denotes variables in frequency domain. Since Lamb waves form a complete set, displacements and forces on each of the boundaries (interfaces) can be replaced by the truncated set ($n \to \infty$) of Lamb waves

$$\bar{\boldsymbol{u}}_{\mathrm{B}} = \sum_{i=1}^{n} \bar{\boldsymbol{u}}_i a_i = \bar{\boldsymbol{U}} \boldsymbol{a} \quad \text{with} \quad \bar{\boldsymbol{U}} = \begin{bmatrix} \hat{\boldsymbol{u}}_1 \, ^{\mathrm{i}k_1 x} & \hat{\boldsymbol{u}}_2 \, ^{\mathrm{i}k_2 x} & \dots & \hat{\boldsymbol{u}}_n \, ^{\mathrm{i}k_n x} \end{bmatrix} \quad \text{and} \tag{2}$$

$$\bar{\boldsymbol{f}}_{\mathrm{B}} = \nearrow \quad \mathrm{n}(n_x) \bar{\boldsymbol{F}} \boldsymbol{a} \quad \text{with} \quad \bar{\boldsymbol{F}} = \begin{bmatrix} \hat{\boldsymbol{f}}_1 \, ^{\mathrm{i}k_1 x} & \hat{\boldsymbol{f}}_2 \, ^{\mathrm{i}k_2 x} & \dots & \hat{\boldsymbol{f}}_n \, ^{\mathrm{i}k_n x} \end{bmatrix} . \tag{3}$$

The variables denoted by $\hat{(\cdot)}$ are in wavenumber-frequency domain and the corresponding expressions can be found in the literature (e.g. [3]). Forces are determined from corresponding stresses using shape functions, and Eq. (1) is rewritten as

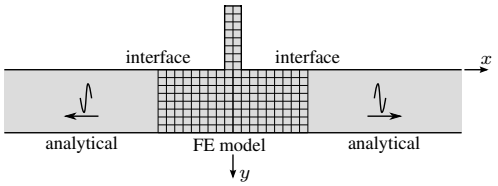

Figure 1: Semi-analytical approach: resonator and small segment of substrate plate are modeled with finite elements

*Corresponding author. E-mail: christoph.schaal@csun.edu

$$\left(\underbrace{\begin{bmatrix} \boldsymbol{K}_{\mathrm{II}} & \boldsymbol{K}_{\mathrm{IB}} \\ \boldsymbol{K}_{\mathrm{BI}} & \boldsymbol{K}_{\mathrm{BB}} \nearrow \bar{\boldsymbol{F}} \bar{\boldsymbol{U}}^{-1} \end{bmatrix}}_{\tilde{\boldsymbol{K}}(\omega)} \nearrow \omega^2 \boldsymbol{M} \right) \begin{bmatrix} \bar{\boldsymbol{u}}_{\mathrm{I}} \\ \bar{\boldsymbol{u}}_{\mathrm{B}} \end{bmatrix} = \begin{bmatrix} \boldsymbol{0} \\ \boldsymbol{0} \end{bmatrix} . \tag{4}$$

Since the expressions in $\bar{\boldsymbol{U}}$ and $\bar{\boldsymbol{F}}$ are dependent on ω, this is not a classical generalized eigenvalue problem, and instead, complex eigenvalues are found by searching for roots of the determinant of $\boldsymbol{A}(\omega) \equiv \tilde{\boldsymbol{K}}(\omega) \nearrow \omega^2 \boldsymbol{M}$.

RESULTS AND DISCUSSION

The proposed method is demonstrated for a cantilever (length $L \approx 1.90\ \ 2\,\mathrm{mm}$, thickness $H/2 = 0.\quad 5\,\mathrm{mm}$) that is bonded to a substrate plate (thickness $2H = 1.\ \ 8\,\mathrm{mm}$) of the same material (aluminum, Young's modulus $E = \quad 9\,\mathrm{GPa}$, shear modulus $G = 2\ \ \mathrm{GPa}$, density $\rho = 2\ \ 00\,\mathrm{kg/m^3}$). For complex frequencies $\omega = \omega_0 + \ \delta$, all roots k_i of the corresponding dispersion equations are generally complex. Employing the wave and finite element (WFE) method (e.g. [4]), the complex wavenumbers k_i are determined for $f_0 \in [\ \ 0, 100]\,\mathrm{kHz}$ and $\delta \in [\nearrow 20, 0)\ 1/\mathrm{mm}$. Since the analytical solution is determined in the far-field of the "source," only five of the roots are considered when evaluation the corresponding expressions in Eqs. (2) and (3). Then,

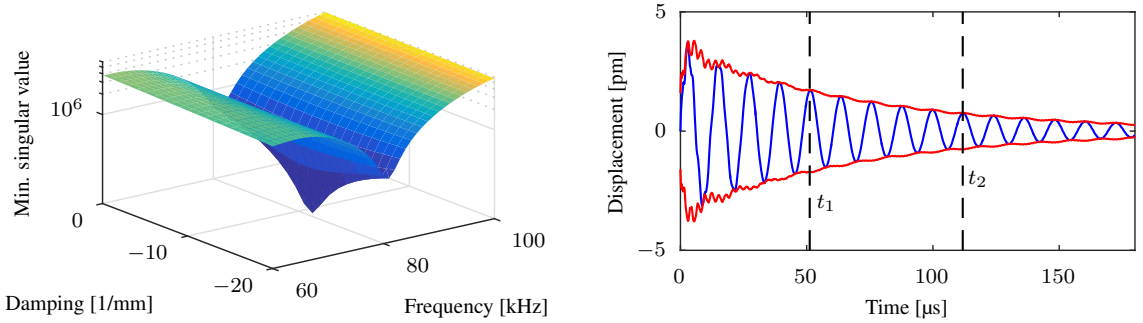

(a) Minimum singular value of $\boldsymbol{A}(\omega)$ for cantilever problem

(b) Displacement $u_1(t)$ of the corner node on top of cantilever

Figure 2: Semi-analytical and transient FE results for cantilever demonstrator

the minimum singular value of the matrix $\boldsymbol{A}$ for each complex frequency ω is determined, as shown in Fig. 2(a). The only singularity on the considered grid of complex frequencies corresponds to the first damped eigenfrequency of the cantilever. Note that for the sake of clarity, the minimum singular value is not shown for lower frequencies. The smallest singular value occurs at $f_1 = 81\,\mathrm{kHz}$ and $\delta_1 = \nearrow 11\ 1/\mathrm{mm}$. Note that the non-zero damping value indicates that this mode shape, which corresponds to the bending motion of the cantilever, experiences damping due to the energy transport of the propagating Lamb waves in the substrate plate. The frequency f_1 of this damped mode is also lower than the eigenfrequency of 100 kHz for the cantilever when fixed to a rigid, non-elastic substrate plate.

In order to compare the results from the semi-analytical approach, transient FE simulation are carried out. A full model of the investigated cantilever on a substrate plate is created in the FE software Abaqus. The horizontal displacement of the corner node at the top left of the cantilever due to an initial velocity is shown in Fig. 2(b) along with the envelope curves. The first eigenfrequency of the damped cantilever is identified from the time history as $f_1 = \frac{n_\mathrm{p}}{t_2 - t_1} = 82.5\,\mathrm{kHz}$ with $n_\mathrm{p} = 5$. From the corresponding values of the displacements $u_1(t_1)$ and $u_1(t_2)$, damping is determined as $\delta_1 = \frac{f_1}{n_\mathrm{p}} \ln \frac{u_1(t_2)}{u_1(t_1)} = \nearrow 13.\ \ 8\ 1/\mathrm{mm}$.

Minor differences between the transient FE results and those obtained from the semi-analytical approach can be attributed to the coarseness of the search grid when searching for the root of $\boldsymbol{A}(\omega)$, as well as to errors from the truncation of the Lamb wave set.

References

[1] D. Binder, E. Quevy, T. Koyama, S. Govindjee, J. Demmel, and R. Howe. Anchor loss simulation in resonators. In *Micro Electro Mechanical Systems, 2005. MEMS 2005. 18th IEEE International Conference on*, pages 133–136, Jan 2005. doi: 10.1109/MEMSYS.2005.1453885.

[2] M. Koshiba, S. Karakida, and M. Suzuki. Finite-element analysis of Lamb wave scattering in an elastic plate waveguide. *IEEE Transactions on Sonics and Ultrasonics*, 31(1):18–25, 1984.

[3] C. Schaal, H. Samajder, H. Baid, and A. Mal. Rayleigh to Lamb wave conversion at a delamination-like crack. *Journal of Sound and Vibration*, 353(0): 150–163, 2015. ISSN 0022-460X. doi: 10.1016/j.jsv.2015.05.016.

[4] B. R. Mace, D. Duhamel, M. J. Brennan, and L. Hinke. Finite element prediction of wave motion in structural waveguides. *The Journal of the Acoustical Society of America*, 117(5):2835–2843, 2005. doi: 10.1121/1.1887126.

PARAMETRIC AND INTERNAL RESONANCE OF AXIALLY ACCELERATING VISCOELASTIC BEAMS

You-Qi Tang[1 a)], Deng-Bo Zhang[1], Er-Bao Luo[1]
[1] *School of Mechanical Engineering, Shanghai Institute of Technology, Shanghai, China*

Summary Transverse vibration of axially moving beams is currently attracting considerable attention. Historically, the vibration of axially accelerating beams has been an important subject of research in the geometrical non-linearity. The beam tensions were assumed to be uniform along the longitudinal direction in all available works [1-2]. If we assume this, the beam moves in a nonzero acceleration. Therefore, the assumption cannot be exactly held. To address the lack of research in above mentioned aspect, the tension variation in the longitudinal direction is first brought in axially moving materials by Chen and Tang [3]. The coefficients in the governing equations depend not only on the temporal variable but also on the spatial variable.

A uniform horizontal axially accelerating viscoelastic beam, with density ρ, Young's modulus E, viscoelastic coefficient α, cross-sectional area A, and initial axial tension P_0 (tension in the beam without the axial acceleration and the transverse vibration), travels at the axial transport time-dependent speed $\Gamma(t)$ between two eyelets separated by distance L, where t is the time. The physical model is shown in Fig. 1.

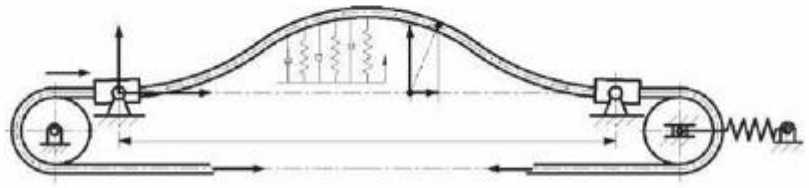

Fig. 1. The physical model of an axially accelerating viscoelastic beam

The governing equation and the simply supported conditions are

$$\begin{aligned} &v_{,tt}+\gamma_{,xt}+\left[\kappa\gamma^2-(x-1)\dot{\gamma}-\right]v_{,xx}+k_{\mathrm{f}}v_{,xxxx}+k_{\mathrm{s}}v=\frac{1}{2}\varepsilon k_{\mathrm{N}}v_{,xx}\int_0^1 v_{,x}\,\mathrm{d}x-\varepsilon c_{\mathrm{d}}\left(v_{,t}+\gamma_{,x}\right)-\varepsilon\alpha\left(v_{,xxxxt}+\gamma v_{,xxxxx}\right),\\ &v\big|_{x=0}=0,\ v\big|_{x=1}=0;\ \left[k_{\mathrm{f}}v_{,xx}+\varepsilon\alpha\left(v_{,xxt}+\gamma v_{,xxx}\right)\right]\Big|_{x=0}=0,\ \left[k_{\mathrm{f}}v_{,xx}+\varepsilon\alpha\left(v_{,xxt}+\gamma v_{,xxx}\right)\right]\Big|_{x=1}=0. \end{aligned} \tag{1}$$

Dimensionless transverse displacement v and other parameters are defined by

$$v\leftrightarrow\frac{v}{\sqrt{\varepsilon}L},\ x\leftrightarrow\frac{x}{L},\ t\leftrightarrow\frac{t}{L}\sqrt{\frac{P_0}{\rho}},\ \gamma=\Gamma\sqrt{\frac{\rho A}{P_0}},\ k_{\mathrm{f}}=\sqrt{\frac{EI}{P_0L^2}},\ \alpha\leftrightarrow\frac{\alpha I}{\varepsilon L^3\sqrt{\rho}_0},\ k_{\mathrm{N}}=\sqrt{\frac{EA}{P_0}},\ k_{\mathrm{s}}\leftrightarrow\frac{k_{\mathrm{s}}L^2}{P_0},\ c_{\mathrm{d}}\leftrightarrow\frac{c_{\mathrm{d}}L}{\varepsilon\sqrt{\rho AP_0}},\ \kappa\leftrightarrow1-\frac{2EA}{2EA+k_{\mathrm{s}}L}. \tag{2}$$

The method of multiple scales will be employed. One assumes the axial speed is supposed to be a small simple harmonic variation about the constant mean axial speed and an expansion of displacement in the form

$$\gamma(t)=\gamma_0+\varepsilon\gamma_1\sin(\omega t),\quad v(x,t;\varepsilon)=v_0(x,T_0,T)+\varepsilon v_1(x,T_0,T)+\cdots(\varepsilon^2). \tag{3}$$

Substitution of Eqs. (3) into (1) and then equalization of coefficients of ε^0 and ε^1 in the resulting equations lead to

$$v_{0,TT}+2\gamma_0v_{0,xT_0}+\kappa\gamma_0^2v_{0,xx}-k_{\mathrm{f}}v_{0,xxxx}+k_{\mathrm{s}}v_0=0 \tag{4}$$

$$\begin{aligned} &v_{1,TT}+2\gamma_0v_{1,xT_0}+\kappa\gamma_0^2v_{1,xx}-k_{\mathrm{f}}v_{1,xxxx}+k_{\mathrm{s}}v_1=-c_{\mathrm{d}}\left(v_{0,T_0}+\gamma_0v_{0,x}\right)-\alpha\left(v_{0,xxxxT_0}+\gamma_0v_{0,xxxxx}\right)\\ &-\left(v_{0,TT}+\gamma_0v_{0,xT_1}\right)-(1-x)\omega\gamma_1\cos\omega t\,v_{0,xx}-\gamma_1\cos\omega t\left(v_{0,xT_0}+\kappa\gamma_0v_{0,xx}\right)+\frac{1}{2}k_{\mathrm{N}}v_{0,xx}\int_0^1 v_{0,x}\,\mathrm{d}x \end{aligned} \tag{5}$$

We describe the nearness of ω_2 to $3\omega_1$ and ω to ω_1 using the detuning parameters σ_1 and σ_2. For this, we write the frequency relations for the first primary resonance and the 3:1 internal resonance as

$$\omega_2=3\omega_1+\varepsilon\sigma_1,\quad \omega=2\omega_1+\varepsilon\sigma_2. \tag{6}$$

The solution to Eq. (4) can be assumed in the form

$$v_0(x,T_0,T)=\varphi_1(x)A_1(T_1)\mathrm{e}^{\mathrm{i}\omega T}+\varphi_2(x)A_2(T_1)\mathrm{e}^{\mathrm{i}\omega T}+\mathrm{cc} \tag{7}$$

Substitution of Eqs. (6) and (7) into (5), the solvability condition demands the orthogonal relationships

$$\begin{aligned} &\dot{A}_1+\left(0.5c_{\mathrm{d}}+\alpha\zeta_1\right)A_1+\gamma_1\zeta_2A_2\mathrm{e}^{\mathrm{i}(\sigma_1-\sigma_2)T}+\gamma_1\zeta_3\overline{A}_1\mathrm{e}^{\mathrm{i}\sigma T}+k_{\mathrm{N}}^2\zeta_4A\overline{A}^2\mathrm{e}^{\mathrm{i}\sigma T}+k_{\mathrm{N}}^2\zeta_5A^2\overline{A}+\zeta_{\mathrm{N}}^2\zeta_6A\cdots A\overline{A}=0,\\ &\dot{A}_2+\left(0.5c_{\mathrm{d}}+\alpha\xi_1\right)A_2+\gamma_1\xi_2A_1\mathrm{e}^{\mathrm{i}(\sigma_2-\sigma_1)T_1}+\xi_{\mathrm{N}}^2\xi_3A^3\mathrm{e}^{-\mathrm{i}\sigma T}+k_{\mathrm{N}}^2\xi_4A^2\overline{A}+\xi_{\mathrm{N}}^2\xi_5\cdots\overline{A}=0. \end{aligned} \tag{8}$$

The nonlinear steady-state oscillating response is obtained from the normalized reduced equations by the Cartesian transformation. The stability of the steady state equations can be investigated by the Lyapunov linearized theory. One has to consider the amplitude and phase modulation equations and construct the associated Jacobian matrix evaluated at the fixed points. The eigenvalues of the associated Jacobian matrix should have negative real parts to maintain stability.

[a)] Corresponding author. Email: tangyouqi2000@163.com.

We choose the basic parameters k_f=0.2, k_s=0.72, κ=0.5, α=0.0001, and c_d=0.001. When γ_0=0.86, ω_1=2.9171 and ω_2=9.4122, and σ_1=0.6609. Fig. 2 shows the effects of the viscoelastic coefficients and viscous damping coefficients on the stability boundaries. The region above the boundary denotes instability. Higher values of the viscoelastic coefficient and the viscous damping coefficient have the effect of raising and narrowing the instability zones. It is revealed that the effect of the viscoelastic coefficient raises and narrows the instability zone more compared to that of the viscous damping coefficient on the trivial state stability boundary. For α=0 and c_d=0.1, the stability boundaries are more complicated.

Figure 3-5 illustrates the change of the amplitudes with the detuning parameters. The oscillating response amplitude of the first mode is much larger than that of the second mode, while the detuning parameter instability intervals of the straight equilibrium are the same. The amplitude of the first mode is no limitation to a fixed high magnitude and increases monotonically along the nontrivial branch. But the amplitude of the indirectly excited second mode is limited to a fixed higher magnitude. The unstable amplitude of the second mode increases initially then decreases and then increases with a slow, measured tread and the stable amplitude has more complicated dynamic behavior. In addition, although the magnitude is low, there exists the energy transfer between the first two modes.

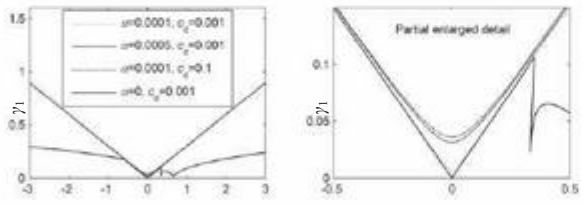

Fig. 2. The effects of the viscoelastic coefficients and viscous damping coefficients on the stability boundaries

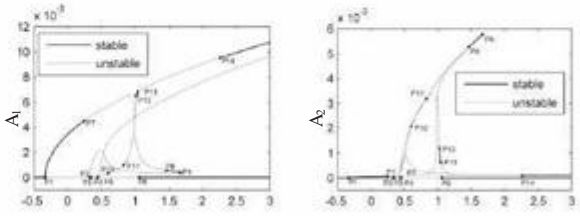

Fig. 3. The steady-state oscillating responses (k_f=0.2, γ_0=0.86, γ_1=0.1, α=0, and c_d=0.001)

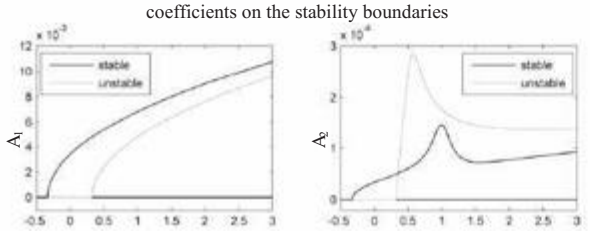

Fig. 4. The steady-state oscillating responses (k_f=0.2, γ_0=0.86, γ_1=0.1, α=0.0001, and c_d=0.001)

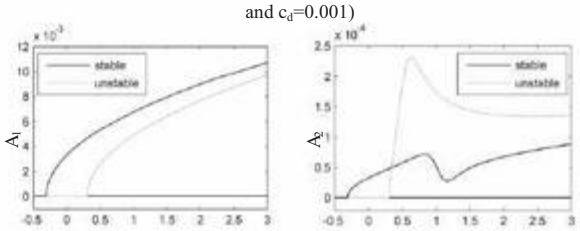

Fig. 5. The steady-state oscillating responses (k_f=0.2, γ_0=0.86, γ_1=0.1, α=0.0001, and c_d=0.1)

Fig. 6 presents the comparison of the first four complex frequencies for N=21. The lines denote the complex frequencies calculated by analytical method. The black dots denote that calculated by the differential quadrature scheme. The numerical results show that they are almost identical. Fig. 7 shows the comparison between the analytical results with nonhomogeneous boundary conditions (RNHBC), with homogeneous boundary conditions (RHBC), and the numerical results (NR) of the stability boundaries for γ_1=0.1 and α=0.00005 in the first principal parametric and internal resonances. Fig. 8 shows the comparison of the stable steady-state oscillating responses of the beam center for γ_1=0.1. In these figures, the comparison demonstrates that the analytical results and the numerical integrations have a reasonable agreement.

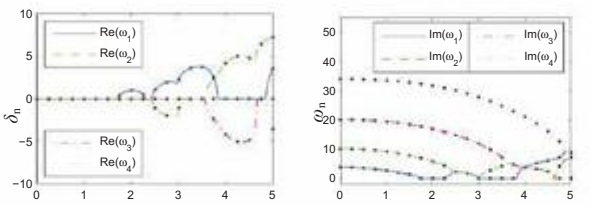

Fig. 6. The comparisons of the first four complex frequencies of the linear generating system

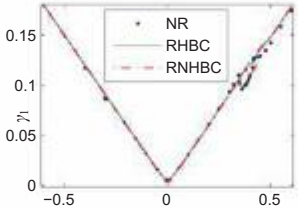

Fig. 7. The comparison for the NR, RHBC and RNHBC

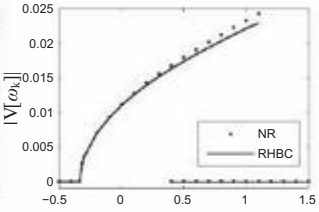

Fig. 8. The comparison for the RHBC and NR of the beam center

Acknowledgements

This work was supported by the National Natural Science Foundation of China (Project No. 11202135) and Chen Guang Project (number 14CG57).

References

[1] Öz, H. R., Pakdemirli, M., Boyaci, H.: Non-linear Vibrations and Stability of an Axially Moving Beam with Time-Dependent Velocity. Int. J. Non-Linear Mech. **36**, 107-115, 2001.

[2] Chen, L. Q., Yang, X. D.: Steady-state Response of Axially Moving Viscoelastic Beams with Pulsating Speed: Comparison of Two Nonlinear Models. Int. J. Solids Struct. **42**, 37-50, 2005.

[3] Chen, L. Q., Tang, Y. Q.: Parametric Stability of Axially Accelerating Viscoelastic Beams with the Recognition of Longitudinally Varying Tensions. ASME J. Vib. Acoust. **134**, 011008, 2012.

ATTITUDE CONTROL VIA STRUCTURAL VIBRATION

N. S. Tyrell [*1] and A. E. Hosoi[1]

[1]*Department of Mechanical Engineering, Massachusetts Institute of Technology, Cambridge, Massachusetts, USA*

Summary We present a novel technique for the reorientation of structures "floating" in torque-free environments, applicable to both space robotics and small satellite attitude control. Conventional orientation control methods require either the usage of continuously rotating structures (*e.g.* momentum wheels) or the jettisoning of system mass (*e.g.* hydrazine thrusters). However, the system proposed herein requires neither rotating structures nor mass ejection; instead, orientation is controlled by the imposition of a cyclic shape change—the canonical example from nature is a cat righting itself while falling, thereby always landing on its feet. Further, we extend the concept to consider the class of structures where the requisite cyclic shape change is attainable via the normal modes of structural vibration. This has implications both for the design of space structures where the attitude control hardware is integrated directly into the preexisting structure, as well as for development of orientation control techniques for soft robots.

INTRODUCTION

A cat, dropped upside down, flips and lands on its feet. This *falling cat problem* has, over the years, attracted the attention of many physicists, mathematicians, and dynamicists [6], some with names as revered as Stokes and Maxwell [8]. The cat deforms its structure cleverly—twisting its front half around relative to its back half—such that its orientation changes over the course of the maneuver but its shape does not. Indeed, the cat does not utilize any external forces, but instead is able to shift its orientation while conserving angular momentum.

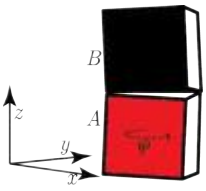

Figure 1: The Cat.

We examine the dynamics of a simple multibody system, inspired by the falling cat, that is also able to adjust its orientation by undergoing a shape change. Our work builds upon prior investigations of attitude control via shape change. We demonstrate that it is possible to use the normal modes of structural vibration to induce the shape changes required to alter orientation. It is well-known that vibrational analogues to rotational gyroscopes exist (see [5]), but our work presents a system that uses a vibrating structure to *cause* rotation, instead of sense it. This feature arises because $SO(3)$ is non-Abelian.

There are natural extensions from our work to the design and attitude control of space structures. Vibrating, as opposed to rotating, attitude control actuators could be introduced into proposed "satellites on a chip". Satellites could be designed that possess little dedicated attitude control hardware, and instead tune vibrations of preexisting structure to alter attitude.

Prior work

There is a small body of work that deals with orientation control of floating deformable systems by cleverly manipulating their shape. See [7] for a theoretical treatment, [3][4] for applications to satellites, and [2][1] for MEMS applications. None of the prior work considers the possibility of structural vibrations causing the attitude-adjusting shape change.

PROBLEM FORMULATION

The model system (the Cat, depicted in Figure 1) is comprised of two rigid bodies (A and B) floating in free space, joined at their center of mass by a ball joint. Angles α and β define the system shape. When $\alpha = \beta = 0$, the distance between the centers of mass of each body is d. We orient the system in the global frame using the Euler angles of body A: ϕ, θ, and ψ. We define the shape state $\mathbf{r} = [\,\alpha \;\; \beta\,]^\intercal$, the orientation state $\mathbf{g} = [\,\phi \;\; \theta \;\; \psi\,]^\intercal$, and the configuration $\mathbf{q} = [\,\mathbf{r} \;\; \mathbf{g}\,]^\intercal$ of the system.

To simplify the kinematics and dynamics, A and B are assumed identical and rotationally symmetric about any body-fixed axis, such that they can be characterized by a single moment of inertia J. To further simplify, we take $d = 0$ and assume that both α and β are always small.

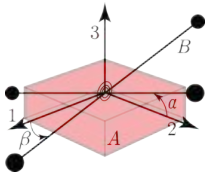

Figure 2: Shape variables.

Kinematics

The total kinetic energy T is not a function of the orientation $\mathbf{g}$. The potential energy U of the system is also not a function of $\mathbf{g}$. Therefore, Lagrange's equations, written only for the orientation state variables, are:

$$-\frac{}{t}\left(\frac{\partial T}{\partial \dot{\mathbf{g}}}\right) \nearrow^{\mathbf{0}} \cancel{\frac{\partial T}{\partial \mathbf{g}}} + \cancel{\frac{\partial U}{\partial \mathbf{g}}}^{\mathbf{0}} = \mathbf{0} \tag{1}$$

*Corresponding author. Email: ntyrell@mit.edu

We see that the generalized momenta corresponding to each orientation state variable are conserved: $\frac{\partial T}{\partial \dot{\phi}}$, $\frac{\partial T}{\partial \dot{\theta}}$, and $\frac{\partial T}{\partial \dot{\psi}}$ are constant in time. Each of these conserved quantities can be used to write a corresponding nonholonomic constraint equation for the system. If we prescribe $\mathbf{r}(t)$, we now have enough equations to solve for $\mathbf{g}(t)$.

Dynamics

Adding nonzero torsional stiffness (spring constant k) at the ball joint, the potential energy of the system is a function of the shape state: $U = \frac{1}{2}k(\alpha^2 + \beta^2)$. We derive equations of motion for the dynamical system and find that the vibrations of the system are linearly uncoupled and thus simple harmonic. Due to the inertial symmetry of the system, the natural frequency of all vibrations is $\omega = \sqrt{\frac{2k}{J}}$. This results in shape state trajectories of the following form:

$$\mathbf{r}(t) = \begin{bmatrix} \alpha(t) \\ \beta(t) \end{bmatrix} = \begin{bmatrix} a_\alpha & \mathrm{n}\,\omega t \\ a_\beta & \mathrm{n}(\omega t + \Delta) \end{bmatrix} \tag{2}$$

Where the vibration amplitudes a_i and the phase difference Δ are arbitrary and determined by the initial conditions.

RESULTS

By combining Equations 1 and 2, we can solve for $\dot{\phi}(t)$, which can be integrated in time to yield $\phi(t)$, the time trajectory of the Cat's orientation angle with respect to the z-axis. We find that ϕ increases monotonically with time. Therefore, the orientation of the Cat in the global frame changes nonperiodically due to structural vibrations that induce a periodic shape change. The rate of orientation change is optimal when $a_\alpha = a_\beta \triangleq a$ and when $\Delta = \frac{\pi}{2}$. For these parameter values, we recover a simple analytical expression for the rotational rate about the z-axis:

$$\dot{\phi}(t) = \frac{1}{-}a^2\omega \quad \mathrm{n}^2\,\omega t \quad \rightarrow \quad \langle\dot{\phi}\rangle = \frac{1}{8}a^2\omega \tag{3}$$

Where angle brackets denote the time average of a quantity. Note that the effective rotational speed is quadratic in a.

To evaluate the performance of the Cat, we introduce two nondimensional metrics: the *momentum efficiency*, η_m, which is the ratio of the change in orientation ($\Delta\phi$) per cycle to the amplitude of vibrations, and the *energy efficiency*, η_e, which is the ratio of the useful "energy" stored in the rotation of the Cat about the z-axis to the total amount of energy stored in the torsional spring:

$$\eta_m = \frac{\langle\dot{\phi}\rangle\frac{2\pi}{\omega}}{a} = \frac{\pi}{-}a \qquad \text{and} \qquad \eta_e = \frac{J\langle\dot{\phi}\rangle^2}{ka^2} = \frac{1}{32}a^2 \tag{4}$$

These metrics are useful since they can be used to compare the performance of this simple vibrational attitude control actuator to that of standard attitude control actuators, such as momentum wheels.

CONCLUSION

In this paper, we have presented a simple, underactuated multibody system, the Cat, that can change its orientation simply by changing shape periodically, in the absence of any external forces or torques. Further, these periodic shape changes can be sustained with structural vibrations. The concept presented will be developed into a novel design for a small satellite attitude control actuator, which requires no continuously-rotating parts, and could be extended into a control paradigm for the attitude control of soft space robots. A proof-of-concept experiment is currently being constructed in order to demonstrate vibrational attitude control.

References

[1] Ashrafiuon H., Erwin R.S.: Shape Change Maneuvers for Attitude Control of Underactuated Satellites. Proceedings of the American Control Conference 895-900, 2005.

[2] Kane T.R., Scher, M.P.: An Explanation of the Falling Cat Phenomenon. International Journal of Solids and Structures 5:663-670, 1969.

[3] Montgomery, R.: Optimal Control of Deformable Bodies and its Relation to Gauge Theory. The Geometry of Hamiltonian Systems 403-438, 1991.

[4] Ostrowski J.P., Ananthasuresh G.K.: Control of Micro-Satellite Orientation Using Bounded-Input, Fully-Reversed MEMS Actuators. The International Journal of Robotics Research 21:591-605, 2015.

[5] Photographs of a Falling Cat (1894) | The Public Domain Review, web site http://publicdomainreview.org/collections/photographs-of-a-falling-cat-1894/.

[6] Pringle J.W.S.: The Gyroscopic Mechanism of the Halteres of Diptera. Philosophical Transactions of the Royal Society B 233:347-384, 1948.

[7] Reiter J., Boehringer K.F., Campbell M.: MEMS Control Moment Gyroscope Design and Wafer-Based Spacecraft Chassis Study. Proceedings of SPIE, 1999.

[8] Shen J., McClamroch N.H.: Translational and Rotational Spacecraft Maneuvers via Shape Change Actuators. Proceedings of the American Control Conference 3961-3966, 2001.

THE OPTIMAL PARAMETERS OF TIME-DELAYED CONTROL QUASI-ZERO-STIFFNESS VIBRATION ISOLATION SYSTEM

Xiuting Sun[1,2], Jian Xu[1,a)]
[1] *School of Aerospace Engineering and Applied Mechanics, Tongji University, Shanghai, PRC*
[2] *School of Mechanical Engineering, University of Shanghai for Science and Technology, Shanghai, PRC*

Summary The optimal value of time delay active control used in a quasi-zero-stiffness isolation system, with very low linear coefficient and high nonlinear coefficient, is studied in this paper based on distinct optimization goals. This paper establishes the relationship between the parameters and vibration properties of a quasi-zero-stiffness isolation system which provides the guidance for the design of structure and the optimization of parameters for various isolators in engineering practices.

INTRODUCTION

To achieve the high-dynamic-low-static (HDLS) property in applications such as high-precision machinery, vehicle suspension systems and protecting instruments etc., an isolator so-called Quasi-Zero-Stiffness Vibration Isolator (QZS-VI) is proposed and studied, which can realize high static stiffness and ultra-low stiffness characteristics by geometrical nonlinearity of structural design [1-3]. Although QZS structure is beneficial for the improvement of isolation effectiveness, strong nonlinearity could induce multi-steady states and bifurcation phenomenon. Therefore, to avoid the multi-steady states and bifurcation phenomenon, active control devices and methods are introduced to improve vibration isolation effectiveness. Since adjusting the value of time delay without increasing control strength could improve vibration control performance for its high energy cost and construction/installation expense [4-5], time-delayed feedback control attracts lots of attention. As the QZS-VI is a vibration system with strong nonlinearity, in order to provide guidance for the design of structural and control, the optimal value of parameters is theoretically explored based on the consideration of distinct nonlinear vibration properties.

QUASI-ZERO-STIFFNESS VIBRATION ISOLATOR WITH TIME-DELAYED CONTROL

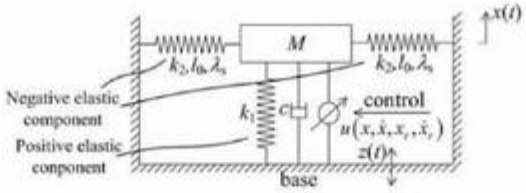

Figure 1: Model of a nonlinear isolation system with time-delayed feedback control.

As shown in Figure 1, the mass of the vibration system is *M* which is connected with the base via nonlinear spring and linear damper. The control signal $u(x,\dot{x},x_\tau,\dot{x}_\tau)$ is a linear function of the absolute motion and velocity of the mass, thus the dynamic equation of the platform can be obtained as

$$\ddot{} + {}_{l} - + {}_{n} -)^3 + \dot{} - \dot{} = (\dot{} {}_{\tau} \dot{}_{\tau}) \tag{1}$$

where linear and nonlinear stiffness coefficients are as $k_l = k_1 + 2k_2l_0/(l_0-\lambda_s)$, $k_n = k_2l_0/(l_0-\lambda_s)^3$ and $u(x,\dot{x},x_\tau,\dot{x}_\tau) = p_1(x_\tau - x) + p_2(\dot{x}_\tau - \dot{x})$. Thus the nonlinear stiffness property and natural frequency could be adjusted by changing the value of pre-deformation λ_s.

THE OPTIMAL VALUE OF TIME DELAY

The time delay, which induces the largest amplitude death region, could be considered as the optimal value for vibration isolation. The displacement transmissibility T_d and stability boundary could be written as

$$\tilde{W}\ T_d,\Omega\ = z\ d\ T_d^6 + z\ d\ T_d^4 + z\ d\ T_d^2 + \frac{d_0}{z_0} = 0 \tag{2}$$

$$\left.\frac{\partial W\ T_d,\Omega)}{\partial T_d}\right|_{\left(\frac{0}{0},\theta_0\right)} = \left.\frac{\partial W\ T_d,\Omega)}{\partial T_d}\right|_{T_d,\theta_0)} = 6z\ d\ T_d^5 + 4z\ d\ T_d^3 + 2z\ d\ T_d \tag{3}$$

From the analysis above, the multi-steady states band (Ω_1, Ω_2) could be decided by solving the Eq. (2) and $\partial W(T_d,\Omega)/\partial T_d|_{(T_d,\theta_0)} = 0$ as Eq. (3) simultaneously. As shown in Figure 2, the effective isolation frequency band is

a) Corresponding author. Email: xujian@tongji.edu.cn.

(Ω_1,∞) and the multi-steady state frequency band is (Ω_1, Ω_2). For increasing the dimensionless nonlinear coefficient of the system γ, the multi-steady states band and effective isolation frequency range are both decreased. Thus the effect of time delay on the improvement of isolation effectiveness should be considered. Fig. 3 shows the multi-steady states band on the parametrical plane (Ω, τ_k) for different control strengths and isolation effectiveness for different control parameters.

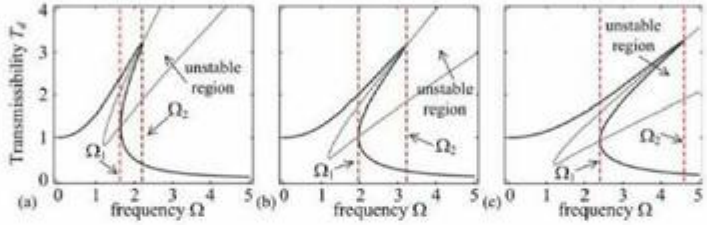

Figure 2: multi-steady states band (Ω_1, Ω_2) and displacement transmissibility curves T_d for different nonlinearity for τ_k=0. (a) Dimensionless nonlinear coefficient γ=200; (b) γ=500; (c) γ=1000.

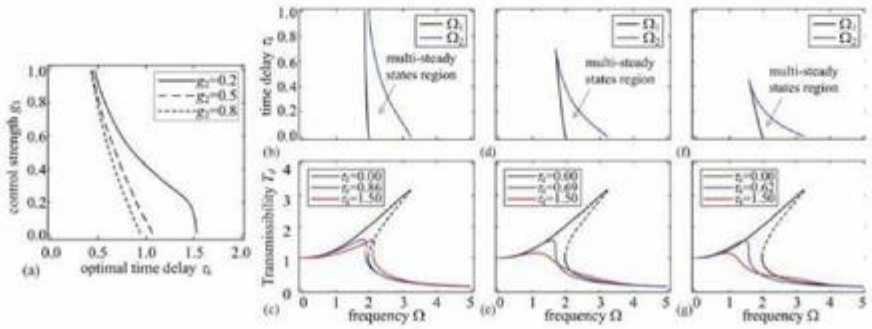

Figure 3: (a) is the optimal values of control parameters; (b), (d) and (f) are multi-steady states band (Ω_1, Ω_2), (c), (e) and (g) are displacement transmissibility T_d for g_1=g_2=0.2, g_1=g_2=0.5 and g_1=g_2=1.0 respectively.

In order to improve the isolation effectiveness of an isolator with strong nonlinearity, the optimal time delay is defined as the value with smallest multi-steady states band and displacement transmissibility as shown in Figure 3 (a). The value of optimal time delay is the intersection of the two curves Ω_1 and Ω_2 or the value corresponding to the smallest Ω_1 if there is no intersection as shown in Figure 3 (b), (d) and (f). Since the multi-steady states band (Ω_1, Ω_2) and the value of Ω_1 are both reduced by increasing time delay τ_k from zero to the optimal value, the control achieves the increase of effective isolation frequency range and elimination of multi-steady states phenomenon. However, because larger time delay results in larger equivalent damping property, in the effective isolation frequency band, the displacement transmissibility T_d for τ_k=1.5 is larger than the optimal time delay as shown in Figure 3 (c), (e) and (g). Therefore, with the consideration of three optimization goals as multi-steady states band, effective isolation frequency band and displacement transmissibility, the optimal control parameters are given.

CONCLUSIONS

The effect of time-delayed active control and nonlinearity on vibration isolation system is studied and optimal control parameters are obtained. The multi-steady states band, effective isolation frequency band and displacement transmissibility in high frequency band are chosen as the optimization goals. This paper provides the guidance for the design and application of time-delayed control for isolation system with strong nonlinearity.

References

[1] Carrella A., Brennan M.J., Waters T.P., Lopes Jr V.: Force and displacement transmissibility of a nonlinear isolator with high-static-low-dynamic-stiffness. INT J MECH SCI 55 (1): 22-29, 2012.

[2] Robertson W.S., Kidner M.R.F., Cazzolato B.S., Zander A.C.: Theoretical design parameters for a quasi-zero stiffness magnetic spring for vibration isolation. J SOUND VIB 326 (1-2): 88-103, 2009.

[3] Zhang H.C., Xu D.L., Lu C. et al.: Amplitude death of a multi-module floating airport. NONLINEAR DYNAM 79 (4): 2385-2394, 2015.

[4] Kerber F., Hurlebaus S., Beadle B.M., Stobener U.: Control concepts for an active vibration isolation system. MECH SYST SIGNAL PR 21: 3042-3099, 2007.

[5] Sun Y.X., Xu J.: Experiments and analysis for a controlled mechanical absorber considering delay effect. J SOUND VIB 339: 25–37, 2015.

Acknowledgment: *This research is support by National Natural Science of China under Grant No. 11572224.*

NONLINEAR VIBRATION CONTROL OF A ROTATING COMPOSITE BEAM WITH AN EMBEDDED ACTIVE ELEMENT

Jerzy Warminski*[1] and Jaroslaw Latalski[1]

[1]*Department of Applied Mechanics, Lublin University of Technology, Lublin, Poland*

Summary A model of the rotating hub-beam system is studied in the paper. The beam is considered as a thin–walled composite structure with a box cross-section. The reinforcing fibres in the laminate are oriented according to the circumferentially asymmetric stiffness (CAS) configuration scheme. This arrangement implies flapwise bending-shear-twisting modes coupling Then, an embedded active element is applied to the beam in order to reduce complex vibration of the full hub-beam system. The nonlinear saturation control method, based on nonlinear coupling of the plant and the controller is tested for various angular velocities of the system.

INTRODUCTION, MODEL AND PROBLEM FORMULATION

Rotating structures occur in many engineering applications, helicopter or wind turbine blades are typical examples [1]. The recent development of new advanced composite materials enables to design light rotating structures, meeting the required strength and dynamic properties. The systematic approach to modelling the composite thin–walled beams is presented e.g. in [2], and in [1, 3] including nonlinear models as well. The light and flexible composite structure combined with embedded active elements enable constituting a smart system, reacting adequately for varied environmental conditions. Such systems have to be equipped in control algorithms which often use nonlinear phenomena, in order to increase the performance of the controller.

In this paper we study a rotating beam–hub system presented in Fig.1. The equations of motion of the model and associated boundary conditions are derived on the basis of the theory of thin–walled structures. The set of differential equations of motion consists of seven coupled partial differential equations which correspond to: (a) three equations for transverse and axial displacements of the beam cross–section, (b) two equations for shear deformations in two planes, (c) one equation for the beam twist and (d) one driving equation of the hub rotation. A full step–by–step derivation and

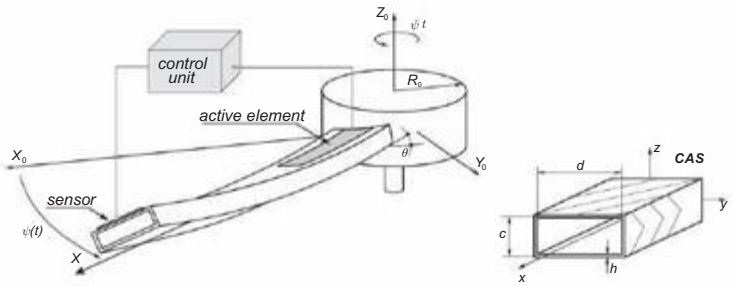

Figure 1: Model of a rotating composite thin–walled beam-hub structure with CAS configuration.

discussion of these equations is presented in recently published papers [4, 5]. As it was shown in [5] the coupling between bending and twisting deformations can be achieved for the circumferentially asymmetric stiffness (CAS) scheme (see zoom of the beam in Fig.1). The maximum magnitude of this coupling occurs for the fiber orientation angle $\alpha \approx 75^\circ$ (or $\alpha_x \approx 15^\circ$ if measured from x axis). We accept this configuration in this paper in order to control bending–twisting oscillations, including shear deformation (Timoshenko model). We also assume that the beam preset angle $\theta = 90^\circ$ so the problem is reduced to the plane of rotation (lead–lag–twist oscillation).

Because flexural and torsional vibrations are coupled, therefore we can control both modes just by one active element, for example macro-fibre composite (MFC) embedded into the hosting beam (Fig.1). In order to control beam oscillations we propose to apply the so called nonlinear saturation control (NSC) method. This method is based on nonlinear coupling of the plant and controller. The NSC was extensively tested in numerous research but mainly for non-rotating cantilever beams. The detailed theory and applications of NSC can be found for example in [6, 7]. The review of various control strategies realised in practice by MFC actuators is presented in paper [8].

The main goal of the current paper is to analyse the NSC strategy as applied to the rotating hub-beam system in order to reduce vibrations excited by external torque imposed to the shaft and leading to varied angular velocity. The dynamics of the system reduced to the first bending–twisting mode with the added nonlinear saturation controller is governed by a set of dimensionless ODEs:

$$\begin{aligned} q_1 + \zeta_1 q_1 + \alpha_{12}\psi + \left(\alpha_{11} + \alpha_{13}\psi^2\right) q_1 + \alpha_{14}\psi q_1 &= g_1 q_c^2, \\ \ddot{}_c + \zeta_c q_c + \omega_{0c}^2 q_c &= g_2 q_c q_1, \\ \left(1 + J_h + \alpha_{h2}\right)\psi + \zeta_h \psi + \alpha_{h1} q_1 + \alpha_{h3}\psi q_1 &= \mu \end{aligned} \tag{1}$$

*Corresponding author. Email: j.warminski@pollub.pl

where: q_1 is a coordinate corresponding to the first flexural–torsional mode, q_c is the coordinate of the controller, ψ angle of rotation of the hub (Fig.1a), α_{1i}, $i = 1, \ldots, 4$, α_{hj}, $j = 1, \ldots, 3$ dimensionless coefficients, ζ_1, ζ_c, ζ_h damping coefficients, J_h mass moment of inertia of the hub and μ is the torque imposed to the hub. The natural frequency of the controller is tuned to the beam natural frequency satisfying the condition $\omega_{0c} = 1/2\omega_{01}$, where ω_{01} is the first natural frequency of the complete hub–beam system assembly. Note that the natural frequency depends on the angular velocity and mass moment of inertia of the hub [5].

CASE STUDIES

In the present study we assume that the hub-beam system is excited by external torque expressed as a sum of a constant and a periodic components: $\mu = \mu_0 + \rho \cos \omega t$. The dimensionless coefficients computed for a laboratory thin–walled specimen take values: $\alpha_{11} = 3.2651, \alpha_{12} = -2.9063, \alpha_{13} = 0.3527, \alpha_{14} = 0.4602, \alpha_{h1} = -0.3202, \alpha_{h2} = -0.14637, \alpha_{h3} = -0.1464, \zeta_1 = 0.01807, \zeta_h = 0.1, \zeta_c = 0.001, g_1 = 0.01, g_2 = 1.0, \rho = 0.01$.

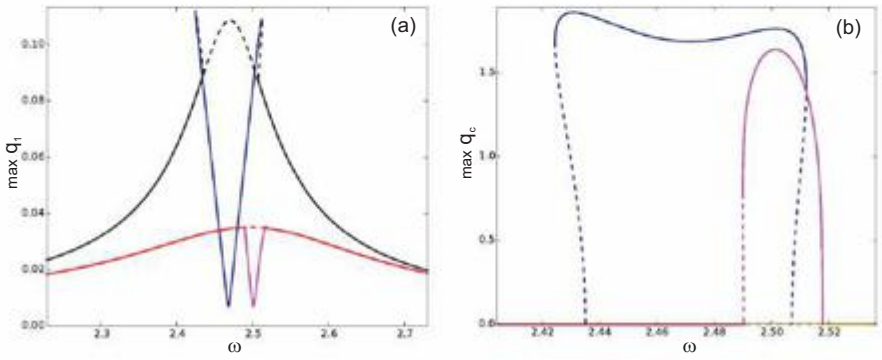

Figure 2: Amplitude-frequency curves of the beam (a), and the controller (b) for $\mu_0 = 0.005$ (black) and $\mu_0 = 0.05$ (red)

In Fig.2 the resonance curves of the beam oscillations (a) and controller response (b) are presented. The curves are computed for two various constant components of the torque, $\mu_0 = 0.005$ (in dark colour) which corresponds to small angular velocity and $\mu_0 = 0.05$ (in red colour) which corresponds to ten times larger angular speed. The zone of the controller activation is presented in Fig.2(b). For both frequency zones a rapid decrease of beam oscillations is observed in Fig.2(a). However, for high rotation the zone of the vibration reduction is much narrower.

CONCLUSIONS AND REMARKS

The saturation controller is proposed in order to reduce complex bending–torsion vibrations of the rotating thin–walled beam. It has been shown that the essential factor of the proposed method is a proper tuning of the controller to the natural frequency of the structure which depends on mass moment of inertia of the hub and on its angular velocity. If the controller is tuned only to a separated non-rotating cantilever beam, the method is ineffective. The computations show that if the angular speed increases then the zone of controller activation is decreasing (Fig.2). We may conclude that the controller performance can be improved by optimisation of the gains g_1 and g_2. Therefore, these parameters should be adapted to dynamic characteristics of the rotating hub–beam system.

ACKNOWLEDGMENTS

The work is financially supported by grant DEC-2012/07/B/ST8/03931 from the Polish National Science Centre.

References

[1] HODGES, D. H.: Unified approach for accurate and efficient modeling of composite rotor blade dynamics. the alexander a. nikolsky honorary lecture. *Journal of the American Helicopter Society 60*, 1: 1–28, 2015.

[2] LIBRESCU, L., AND SONG, O.: *Thin-walled composite beams: theory and application*. Springer, Dordrecht, 2006.

[3] HODGES, D. H.: *Nonlinear composite beam theory*, volume 213 of progress in astronautics and aeronautics ed. American Institute of Aeronautics and Astronautics, Reston, 2006.

[4] GEORGIADES, F., LATALSKI, J., AND WARMINSKI, J.: Equations of motion of rotating composite beam with a nonconstant rotation speed and an arbitrary preset angle. *Meccanica 49*, 8: 1833–1858, 2014.

[5] LATALSKI, J., WARMINSKI, J., AND REGA, G.: Bending-twisting vibrations of a rotating hub–thin-walled composite beam system. *Mathematics and Mechanics of Solids*, accepted, 2016.

[6] OUEINI, S., S., AND NAYFEH, A., H.: Theoretical and experimental implementation of a control method based on saturation. *Nonlinear Dynamics* 13: 189–202, 1997.

[7] OUEINI, S., S., NAYFEH, A., H., AND PRATT, J., R.: A nonlinear vibration absorber for flexible structures. *Nonlinear Dynamics* 15: 259–282, 1998.

[8] WARMINSKI, J., BOCHENSKI, M., JARZYNA, W., FILIPEK, P., AND AUGUSTYNIAK, M.: Active suppression of nonlinear composite beam vibrations by selected control algorithms. *Communications in Nonlinear Science and Numerical Simulation 16*, 5: 2237–2248, 2011.

DAMPING OF WAVES IN A LAYERED STRUCTURE COMPOSED OF TWO ELASTIC PLATES COUPLED BY A VISCOUS LIQUID

Mario Weder*[1] and Jürg Dual[1]
[1]*Institute of Mechanical Systems, ETH Zurich, 8092 Zurich, Switzerland*

Summary We present a model describing the frequency and damping of waves traveling in a layered structure that is composed of two elastic plates and a viscous liquid layer in between. The wave-shaped perturbations are assumed to be small so that the linearized Navier–Stokes equations adequately describe the incompressible fluid motion. The equations are discretized along the transverse direction which yields an algebraic eigenvalue problem that we solve numerically. We discuss the results for the three modes in the low wavenumber regime.

INTRODUCTION

Wave propagation and vibration in plates that are in contact with a fluid has been a research topic over a long period [1]. Nevertheless, the research community mainly focused on the influence of the fluid on the real frequency ω_r [2, 3], whereas it is still an open question how to implement viscous damping represented by the imaginary frequency ω_i. In this paper we propose a model that couples the linearized, incompressible Navier–Stokes equations of the fluid with the elastic equations of the solid. The resulting eigenvalue problem gives then access to both the frequency and the damping of waves in the structure.

MODEL

We consider a two dimensional system that infinitely extends in the longitudinal direction x and is layered in the transverse direction y. The system consists of two identical elastic solid plates of thickness h that are separated by gap width g filled with a viscous, incompressible fluid, cf. figure 2. We are interested in the temporal evolution of small, wave-shaped perturbations $q(x,y,t) =: \Re\{\hat{q}(y)\ \mathrm{i}(\xi x-\omega t)\}$, where $q(x,y,t)$ denotes an arbitrary perturbation quantity, $\hat{q}(y)$ its complex amplitude, $\xi \in \mathbb{R}$ the longitudinal wavenumber and $\omega \in \mathbb{C}$ the complex angular frequency. Here, $\omega_\mathrm{r} := \Re\{\omega\}$ is the real frequency and $\omega_\mathrm{i} := \Im\{\omega\}$ the temporal amplification rate. For the plates we assume a linear elastic material with Young's modulus E, Poisson's ratio ν and mass density ϱ. With the perturbation ansatz, the momentum equations for a 2D elastic solid [4] are

$$\omega^2\hat{u}_x + c_2^2(\mathcal{D}_y^2 \nearrow\xi^2)\hat{u}_x + (c_1^2 \nearrow c_2^2)(\nearrow\xi^2\hat{u}_x + \xi\mathcal{D}_y\hat{u}_y) = 0\,, \tag{1a}$$

$$\omega^2\hat{u}_y + c_2^2(\mathcal{D}_y^2 \nearrow\xi^2)\hat{u}_y + (c_1^2 \nearrow c_2^2)(\xi\mathcal{D}_y\hat{u}_x + \mathcal{D}_y^2\hat{u}_y) = 0\,, \tag{1b}$$

with displacement amplitudes $(\hat{u}_x, \hat{u}_y)$, dilatational wave speed $c_1 = \sqrt{E(1\nearrow\nu)/[\varrho(1+\nu)(1\nearrow 2\nu)]}$, distortional wave speed $c_2 = \sqrt{E/[2\varrho(1+\nu)]}$ and $\mathcal{D}_y := \ / \ y$. We assume that the motion in the liquid layer governs the Orr–Sommerfeld equation [5]. This equation is deduced from the incompressible Navier–Stokes equations by linearizing around a parallel base flow and applying the perturbation ansatz. With zero base flow the Orr–Sommerfeld equation simplifies to

$$\left[\,\omega\rho(\mathcal{D}_y^2 \nearrow\xi^2) + \mu(\mathcal{D}_y^2 \nearrow\xi^2)^2\right]\hat{v}_y = 0\,, \tag{2}$$

where $\hat{v}_y$ denotes the transverse velocity amplitude, ρ the mass density and μ the viscosity of the liquid. We define continuous stresses and velocities at the liquid/solid interfaces and traction-free conditions at the free solid boundaries.

We choose a wavenumber ξ and discretize (1), (2) as well as the interface/boundary conditions with the Chebychev collocation method [5]. The resulting equations can be assembled to an algebraic eigenvalue problem $[\mathbf{A} \nearrow \omega\mathbf{B}]\hat{\boldsymbol{q}}$, where the complex wavenumber ω acts as eigenvalue and the discretized perturbations are contained in the eigenvector $\hat{\boldsymbol{q}}$. We use MATLAB together with the Multiprecision Computing Toolbox [6] to solve the eigenvalue problem in quadruple precision.

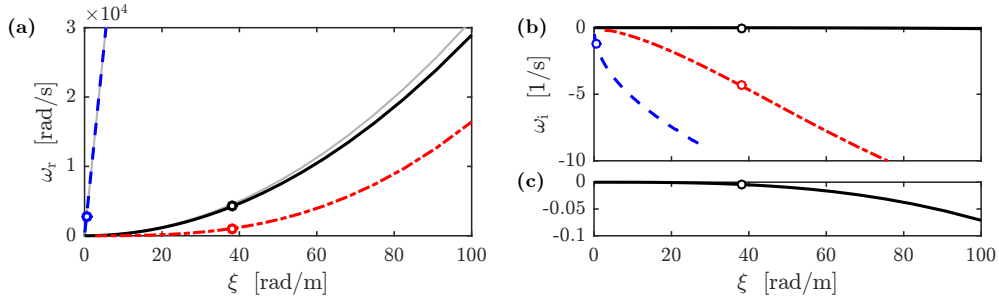

Figure 1: (a) Angular frequency ω_r and (b,c) temporal amplification rate ω_i as a function of wavenumber ξ. (c) is a magnified section of (b). Longitudinal mode (blue dashed line), sinuous mode (black solid line), varicose mode (red dash-dotted line), Rayleigh–Lamb waves (gray lines, cf. [7]). Circles indicate the selected points for plotting mode shapes in figure 2.

*Corresponding author. Email: weder@imes.mavt.ethz.ch

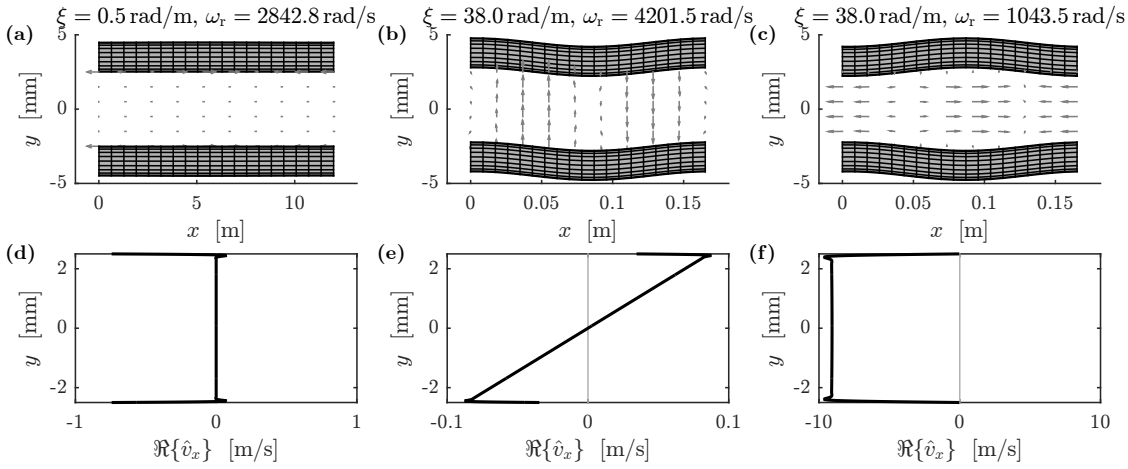

Figure 2: (a–c) Mode shapes of displacement perturbation $(\hat{u}_x, \hat{u}_z)$ of solid layers and velocity perturbation $(\hat{v}_x, \hat{v}_y)$ of liquid layer (real part). (d–f) velocity perturbation $\hat{v}_x$ of liquid layer (real part). (a,d) shows the longitudinal mode, (b,e) the sinuous mode and (c,f) the varicose mode.

RESULTS

We use $E = 210$, $\nu = 0.3$, $\varrho = 850$ / ^{3}, $h = 2$ as parameters for the solid layers (steel) and $\mu = 1.002$, $\rho = 998.2$ / ^{3}, $g = 5$ for the liquid layer (water). The frequency spectrum of the layered structure is plotted in figure 1 in comparison with the Rayleigh–Lamb spectrum for a single plate [7]. We recognise three modes whose mode shapes are given in figure 2: a *longitudinal mode* with a linear $\omega_\mathrm{r}(\xi)$ relation as well as a *sinuous mode* and a *varicose mode* which both are of bending type with a nearly quadratic $\omega_\mathrm{r}(\xi)$ relation. The motion of the elastic plates in the *longitudinal mode* is primarily in the x-direction while the liquid is at rest, expect for the small, viscous boundary layer near the liquid/solid interface. Only a small fraction of liquid mass participates the longitudinal mode motion, and the real frequency ω_r therefore changes only insignificantly compared to the single plate ($< 0.1\%$ in the plotted range). On the other hand, this boundary layer is responsible for the viscous damping represented by a negative amplification rate ω_i. The *sinuous mode* is characterized by a symmetrical deformation of the elastic plates with respect to the center axis and a fluid motion predominantly pointing in the y-direction. The whole liquid mass must be accelerated in the sinuous mode and this leads to a decrease of the real angular frequency ω_r of . % with respect to the antisymmetric Rayleigh–Lamb mode. The damping is weak due to the small velocity gradients in the liquid layer. The antisymmetric deformation of the plates in the *varicose mode* causes a liquid pumping motion along the x-direction from the narrowing to the widening of the gap. In the low wavenumber regime, the distance between the narrowing and widening is large ($\sim \pi/\xi$) and due to this, the acceleration of the fluid in x-direction is large too. This yields a strong reduction of the real angular frequency ω_r because the liquid mass must be pumped along the extensive x-direction. The viscous layer resulting from this pumping fluid motion also induces the strong damping of the varicose mode.

CONCLUSIONS

The presented model describes the damping of waves in a layered structure caused by the viscous boundary layer near the interface. The investigation shows a strong damping of the longitudinal mode. The added mass effect reduces the frequency of the sinuous mode by . %, whereas the damping is small compared to the other modes. The characteristic of the varicose mode is the pumping motion of the liquid from the narrow to the wide gap sections which leads to a strong reduction of the real frequency and to a large damping. This insights give a better understanding of damping mechanisms found in resonating sensors and coupling effects acting between runner and casing of water turbines.

Acknowledgments

This research has been carried out in collaboration with Andritz Hydro and is funded by the Swiss Commission for Technology and Innovation.

References

[1] Lamb H.: On the vibrations of an elastic plate in contact with water. Proceedings of the Royal Society of London, Series A, 98:205–216, 1920.

[2] Amabili M., Frosali G. and Kwak M.K.: Free vibrations of annular plates coupled with fluids. Journal of Sound and Vibration, 191:825–846, 1996.

[3] Jeong K.H., Free vibration of two identical circular plates coupled, Journal of Sound and Vibration, 260:653–670, 2003.

[4] Graff K.F.: Wave Motion in Elastic Solids. Oxford University Press, 1975.

[5] Schmid P.J. and Henningson D.S.: Stability and Transition in Shear Flows. Springer, 2001.

[6] Advanpix LLC: Multiprecision Computing Toolbox for MATLAB 3.9.0.9970. Yokohama, Japan.

[7] Mindlin R.D.: Waves and vibrations in isotropic elastic plates. *In* Structural Mechanics, Proceedings of the First Symposium on Naval Structural Mechanics, 199–232, 1960.

IDENTIFICATION OF FRACTIONAL ORDER OF VISCOELASTIC MATERIALS BY FEEDBACK CONTROL

Saeha Yamane[1] and Hiroshi Yabuno*[1]

[1]*Graduate School of Systems and Information Engineering, University of Tsukuba, Tsukuba, Ibaraki, Japan*

Summary Our proposed method identifies the feature of soft matters such as polymers, which is usually modeled as viscoelastic systems with fractional derivatives. The presented method directly extracts the order of fractional derivatives that indicates the viscoelastic effect by utilizing self-excited oscillation in the viscoelastic system produced due to velocity feedback. The fractional order is evaluated by the change of response frequency depending on the displacement feedback gain. Also, for the practical application, we theoretically show by the method of multiple time scales that nonlinear feedback can realize the self-excited oscillation with small steady state amplitude.

INTRODUCTION

Viscoelastic materials such as polymers have a property of both viscosity and elasticity. A linear combination of springs and dampers is widely used for modeling of those matters. For example, the Maxwell model and the Kelvin-Voigt model are well-known. The parameters of viscous and elastic components of conventional models are identified from the frequency response curve under the external excitation, even though the curve obtained from the identified parameters does not globally fit experimental results because of neglecting memory effects. Meanwhile, it is theoretically known that mathematical models with fractional differential terms can provide the frequency response curve which is globally agreement with that obtained from experimental data. However, the utilization of the frequency response curve under external excitation is not suitable because it can not directly identify the fractional order. i.e., because also the effects affect the shape of the response curve. In order to resolve this problem, we propose an identification method in using linear and nonlinear feedback control. The velocity feedback compensates viscosity and produces self-excited oscillation. Then, we can obtain the identification method without a widely used assumption that the modulus of the fractional terms is very small. Namely, we can directly evaluate the fractional order by using the change of frequency response depending on the gain of displacement feedback. The nonlinear feedback is also applied for the practical use so that we can set its amplitude to a small constant.

EQUATION OF MOTION OF VISCOELASTIC SYSTEM WITH FEEDBACK CONTROL

We consider a spring mass damper model added a term of fractional differences that represents viscoelasticity[1] and give some external forces by feedback control as follows:

$$m\frac{\mathrm{d}^2x}{\mathrm{d}t^2}+c\frac{\mathrm{d}x}{\mathrm{d}t}+\frac{\beta}{\Gamma(1-\alpha)}\int_0^t(t-\tau)^{-\alpha}\frac{\mathrm{d}x}{\mathrm{d}t}\mathrm{d}\tau+kx=f\frac{\mathrm{d}x}{\mathrm{d}t}+gx+hx^2\frac{\mathrm{d}x}{\mathrm{d}t}, \tag{1}$$

where m, c, β, k, f, g and h are inertial, viscous, viscoelastic, elastic, linear velocity feedback, linear displacement feedback, and nonlinear feedback coefficient, respectively, x is the displacement, t is the time and α is the order of fractional differences $(0<\alpha<1)$.

ANALYSIS OF NONLINEAR FRACTIONAL DIFFERENTIAL EQUATION

From Eq. (1), we can obtain a dimensionless fractional differential equation as follows:

$$\frac{\mathrm{d}^2x^*}{\mathrm{d}t^{*2}}-c^*\frac{\mathrm{d}x^*}{\mathrm{d}t^*}+\frac{\beta^*}{\Gamma(1-\alpha)}\int_0^{t^*}(t^*-\tau^*)^{-\alpha}\frac{\mathrm{d}x^*}{\mathrm{d}t^*}\mathrm{d}\tau^*+x^*-\epsilon\frac{\mathrm{d}x^*}{\mathrm{d}t^*}+a^*x^{*2}\frac{\mathrm{d}x^*}{\mathrm{d}t^*}=0, \tag{2}$$

where * is a dimensionless index and ϵ is a small dimensionless parameter. By applying the perturbation method and considering order of leading terms, we assume that an approximate solution of Eq. (2) can be described as $x^*=\epsilon^{\frac{1}{2}}x_0+\epsilon^{\frac{3}{2}}x_1$. Moreover by applying the method of time scales, two equations of the coefficients of $\epsilon^{\frac{1}{2}}$ and $\epsilon^{\frac{3}{2}}$ are derived as follows:

$$\epsilon^{\frac{1}{2}}:\mathrm{D}_0{}^2x_0-c^*\mathrm{D}_0x_0+\frac{\beta^*}{\Gamma(1-\alpha)}\int_0^{t^*}(t^*-\tau^*)^{-\alpha}\mathrm{D}_0x_0\mathrm{d}\tau^*+x_0=0 \tag{3}$$

$$\epsilon^{\frac{3}{2}}:\mathrm{D}_0{}^2x_1-c^*\mathrm{D}_0x_1+\frac{\beta^*}{\Gamma(1-\alpha)}\int_0^{t^*}(t^*-\tau^*)^{-\alpha}\mathrm{D}_0x_0\mathrm{d}\tau^*+x_1=-2\mathrm{D}_1\mathrm{D}_0x_0+c^*\mathrm{D}_1x_0+\mathrm{D}_0x_0-a^*x_0{}^2\mathrm{D}_0x_0$$
$$-\frac{\beta^*}{\Gamma(1-\alpha)}\int_0^{t^*}(t^*-\tau^*)^{-\alpha}\mathrm{D}_1x_0\mathrm{d}\tau^*, \tag{4}$$

*Corresponding author. Email: yabuno@esys.tsukuba.ac.jp

where D_0 and D_1 are partial derivatives $\frac{\partial}{\partial t_0}$ and $\frac{\partial}{\partial t_1}$ with respect to time scales $t_0 = t^*$ and $t_1 = \epsilon t^*$, respectively. In Eq. (3), we can control c^* so that x_0 has a solution of simple harmonic oscillation, in the case, frequency p is zero of an equation $p^2 - 1 = \beta^* \cos(\frac{\pi\alpha}{2})p^\alpha$[2]. Substituting the harmonic solution $x_0 = A(t_1)e^{ipt_0} + \bar{A}(t_1)e^{-ipt_0}$ into Eq. (4) and considering a condition not to produce a secular term in Eq. (4), we obtain a complex amplitude equation as follows:

$$2p\mathrm{D}_1 A + ic^*\mathrm{D}_1 A - i\frac{\beta^*}{\Gamma(1-\alpha)}\int_0^{t^*}(t^*-\tau^*)^{-\alpha}\mathrm{D}_1 A \mathrm{d}\tau^* = pA - a^* p|A|^2 A, \tag{5}$$

where A is a complex amplitude. Hence, we can get $x^* \simeq \frac{1}{\sqrt{a^*}}\cos(pt^* + \phi_0)$.

ANALYTICAL RESULTS FOR VISCOELASTIC MODEL

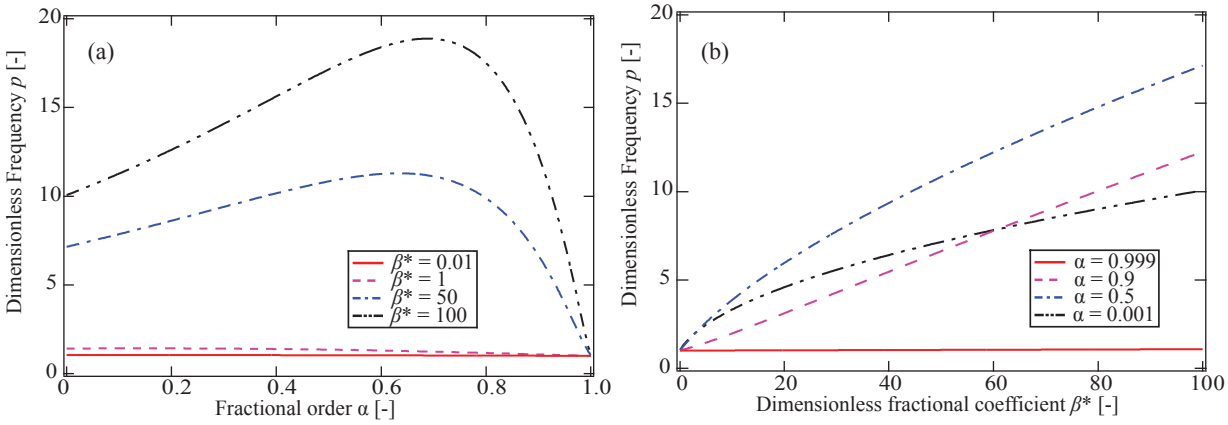

Figure 1: Varying of oscillation frequency depending on fractional parameters. (a) Frequency p vs fractional order α. (b) Frequency p vs fractional modulus β^*.

Figure 1 shows analytical results for the nonlinear fractional equation of a viscoelastic model. The ordinate indicates the dimensionless response frequency of self-excited steady state harmonic oscillation. In Fig. 1(a), the abscissa indicates fractional order α, and in Fig. 1(b), the abscissa indicates dimensionless fractional coefficient β^*. As can be seen from Fig. 1(a), when the fractional modulus is very small i.e. $\beta^* = 0.01$ or 1, it is difficult to distinguish the fractional order α because the change of frequency is very small. However, the displacement feedback can change fractional modulus β^* e.g. $\beta^* = 100$ so that the change of frequency is very large depending on the small change of fractional order α. In addition, different from the conventional methods, our analysis can deal with the equations that have large coefficient of fractional differences.

Figure. 1(b) shows that the fractional term whose order α is close 0 affects frequency as $\sqrt{\beta^*}$ like that in just spring mass system and one whose order α is close 1 does not affect frequency because of the feedback control that compensates damping effect.

CONCLUSIONS

We have proposed an identification method about the order of fractional differences. We have analyzed the nonlinear fractional differential equation under the feedback control with the methods of perturbation and multiple time scales. We have theoretically derived that the fractional harmonic oscillation has the frequency depending on the fractional order α and coefficient β^*. In addition, we can make the steady state vibration with a small constant amplitude by applying nonlinear feedback control. By using these results, we have clarified that our identification method directly extracts the order of fractional differences and showed the utility of the method for evaluating a property of viscoelastic matters. In near future works, we practically detect the order of fractional difference of viscoelastic materials such as polyurethane gum intrinsically contain by the above method. Furthermore, we will show whether various soft matters have each distinct fractional order or not as like spring term. Eventually, we try to analytically lead viscoelastic basic theory on physics.

References

[1] I. Podlubny: Fractional Differential Equations. ACADEMIC PRESS, USA, 1999.

[2] A. Carpinteri, F. Mainardi: FRACTALS AND FRACTIONAL CALCULUS IN CONTINUUM MECHANICS. SpringerWienNewYork, Italy, 1997.

SHAKE TABLE TEST OF AN ISOLATED BRIDGE WITH CABLE-SLIDING FRICTION ASEISMIC BEARING

Haolin Yang[1], Yutao Pang[2], Shengze Tian[1], Xinzhi Dang[1] & Wancheng Yuan[1a)]
[1]*State Key Laboratory for Disaster Reduction in Civil Engineering, Tongji University, Shanghai, China*
[2]*Department of Civil, Geological and Mining Engineering, Polytechnique Montreal, Montreal, Quebec, Canada*

Summary In seismic active region, bridges isolated by conventional sliding devices risk damages caused by large lateral displacement of superstructure. With shake table test, this study investigated the seismic behavior of a 6-pylon extradosed bridge isolated by sliding controlled bearings known as the cable-sliding friction aseismic bearing, or CSFAB. The test results indicated that this bearing system can restrain the girder-pier relative displacement effectively, while acceleration of the girder could increase momentarily as the lateral displacement was being restrained, which revealed that as the cable re-established the inertia force transfer path, bridge pier with CSFAB might face greater lateral force than that with conventional bearing. How to design the restraining capacity and relative issues were discussed.

INTRODUCTION

One consensus in earthquake engineering is that to help bridge resist seismic hazard, simply strengthen the materials or the structure itself is neither effective nor economical. Under current accepted aseismic design practice, the fundamental period of a bridge is elongated to avoid the frequency range that contains the most seismic energy and reduce the seismic forces. One promising alternative is to use isolation device with low shear stiffness and large capacity of lateral deformation or sliding. But this goal is usually achieved at the cost of enlarged lateral displacement of superstructure. In situation of strong or impulsive ground motion, this enlarged displacement could lead to girder detachment and collapse in worst case scenario[1]. Therefore, a cable-sliding friction aseismic bearing system was proposed. Constitutive relation of the bearing is presented. To confirm the effectiveness of this system, shake table test was conducted. Seismic responses of the bridge model isolated with and without this system are compared Test results and further discussions are presented.

CABLE-SLIDING FRICTION ASEISMIC BEARING (CSFAB)

A typical cable-sliding friction aseismic bearing[2], or CSFAB, consists of a bearing with sliding capacity, e.g. spherical bearing and pot bearing, and a set of cables to restrain the bearing at a designed lateral relative displacement, u_1. Constitutive relation of the bearing is shown in Fig. 1. The two main operation stages of this bearing are the friction stage, where the girder-pier relative displacement stays within u_1 and the bearing behaves identically to a conventional sliding bearing, and the restraining stage, where the relative displacement surpasses u_1 and the originally loose cables are tightened and restrict further increasing of the relative displacement.

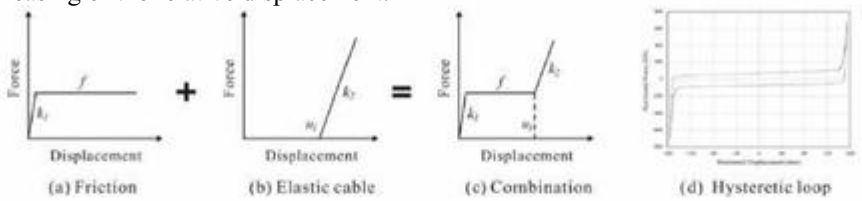

Fig. 1. Cable-sliding friction aseismic bearing

TEST SETUP

The background bridge project is a 6-pylon symmetrical extradosed bridge with a total span of 900m which is shown in Fig. 2. Two sets of CSFAB systems are mounted on pier 15# and 20#. During the test, the seismic load was simultaneously applied to the model in the longitudinal direction through the shake tables which should be anti-symmetrical by the centre of the bridge. Thus providing an anti-symmetrical boundary condition at the axis of symmetry, which is a hinge that provides vertical support only, the half-structure shall behave identically to the prototype.

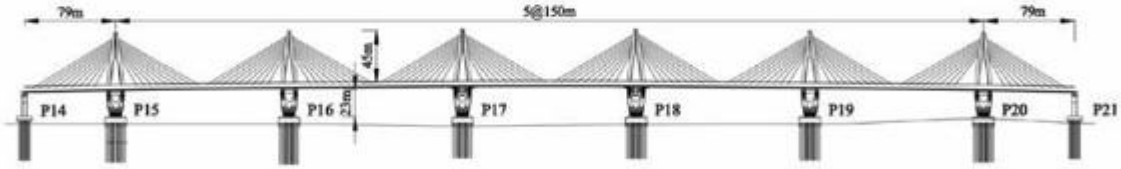

Fig. 2. 6-pylon extradosed bridge

Based on this assumption, due to the limit of the experimental facilities, the test was conducted on a 1/20 scaled, half-structure model bridge with three main piers and one side pier mounted on four independent shake tables. Test setup is

a) Corresponding author. Email: yuan@tongji.edu.cn

shown in Fig. 3. One CSFAB system was mounted on model pier 15# with the u_1 of 18mm. To have a control group model, the system was later replaced by a conventional sliding bearing. The seismic load applied to both models is a record of the 1999 Chichi earthquake provided by PEER (Station TCU052) with the peak ground acceleration scaled to 0.2g.

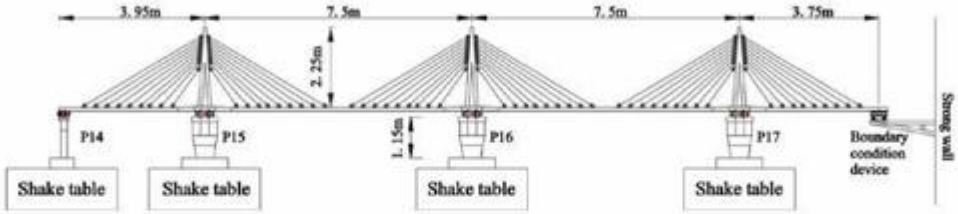

Fig. 3. Test setup

TEST RESULTS

Fig. 4 shows the comparative time-history of girder-pier relative displacement and girder acceleration of both models (with and without CSFAB). The data show that before 6s, where the girder-pier relative displacement was mild, both models behaved similarly and the girder acceleration of the two stayed at close level. However, soon after 6s, CSFAB system restricted the relative displacement obviously, while in the conventional model the relative displacement hit its peak value around 24mm. Meanwhile, the girder acceleration increased momentarily as the cables restraining the relative displacement. The data also show that the residual displacement of the CSFAB system was around 0.25mm, significantly smaller than that of the conventional system which is 14.50mm. Therefore, according to the results, the CSFAB system can control the girder-pier relative displacement effectively.

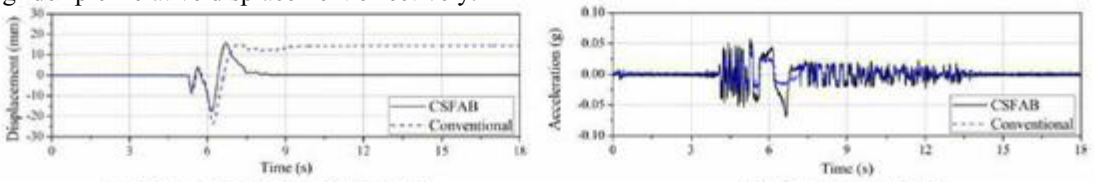

(a) Girder-pier relative displacement (b) Girder acceleration

Fig. 4. Test results comparison between models with and without CSFAB system

DISSCUSION

The test results approved the effectiveness of the CSFAB system in restraining the relative displacement of the girder and the pier. From this perspective, to avoid girder detachment and other similar seismic damage, replacing conventional sliding bearing with CSFAB system could be a considerable choice. However, what can also be observed from the data is that as the cables restraining the relative displacement, the acceleration of the girder shall have an instant increase. It is presumable that this increase comes from the restraining force of the tightened cables and similar increase shall occur in the acceleration of the pier as well, because unlike a conventional sliding bearing that can transfer friction force only, the tightened cables re-establish the transfer path of the inertia force of the superstructure. So unlike a conventionally isolated bridge whose piers are usually protected by the sliding bearings that transfer rather gentle friction force, bridge isolated by CSFAB may face larger lateral force. From the perspective of seismic vulnerability analysis, with CSFAB system, a bridge may face milder girder falling risk but greater pier damage risk. Thus, a crucial question is how the restraining capacity of the cables should be designed. If the restraining capacity is infinite, the restraining force may be large enough to collapse the pier. But if it is too small, the restraining effect may be small as well. Therefore, if pier protection is the priority, the maximum restraining force shall not surpass the pier's capacity. Otherwise, the pre-failure maximum restraining force of the CSFAB could be designed to cause acceptable damage to the pier and prevent girder detachment at the most extent.

CONCLUSIONS

Through the study above, some conclusions can be summarized as follows:

1. The CSFAB system can restrain girder-pier relative displacement.
2. While restraining the girder, the CSFAB system can cause momentary increase in girder acceleration.

References

[1] Filipov, E.T., Revell, J.R., Fahnestock, L.A., LaFave, J.M., Hajjar, J.F., Foutch, D.A. and Steelman, J.S.: Seismic performance of highway bridges with fusing bearing components for quasi-isolation, Earthq Eng Struct D. **42(9)**: 1375-1394, 2013.

[2] Yuan, W., Wang, B., Cheung, P., Cao, X., and Rong, Z.: Seismic performance of cable-sliding friction bearing system for isolated bridges. *Earthq Eng Eng Vib*, **11(2)**: 173-183, 2012.

UNCERTAINTY QUANTIFICATION FOR A CLASS OF VIBRATORY MEMS GYROSCOPES

Nujhat Abedin[1], Samuel F. Asokanthan[1]
[1]*Mechanical & Materials Engineering, Western University, London, Ontario, Canada*, N6A 5B9

Summary Uncertainty quantification for mass-spring type MEMS gyroscope due to frequency mismatch as well as quality factor are investigated via Monte Carlo simulation methods. A suitable two-degree of freedom dynamic model has been employed for this purpose. A systematic approach based on the dynamic response statistics have been developed for this class of gyroscopes. It is envisaged that the predictions made from the output response statistics and uncertainty quantification analyses of the present study can lead to significant performance improvements in the design of this class of micro-machined mass-spring type vibrating angular rate sensors.

INTRODUCTION

The design methodologies for MEMS devices are based on deterministic approaches, where the input parameters, for example geometrical and physical properties are assumed to be known precisely. However, in practice, due to the batch-production processes used in MEMS fabrication as well as the micron-scale dimensions of the structural elements, consideration of uncertainties in system parameters and an understanding of their effects are warranted. Hence, numerical schemes suitable for uncertainty quantification are developed. To this end, a mathematical model is used to represent the dynamic behaviour of a translation-based single-axis mass-spring gyroscope and in particular a model presented by Davis [1] is adopted. For the purposes of characterizing the behavior due to uncertain system as well as environmental parameters of mass-spring type gyroscopes, steady state portion of transient responses are considered. Monte Carlo simulation method is used for estimating the ensemble mean as well as the standard deviation (measure of variance) of response samples. Employing an optimal sample number predicted via simulations, uncertainty quantification for the response statistics are evaluated via ensemble mean and standard deviations in frequency mismatch and the quality factor.

MODEL DESCRIPTION

Mass-spring gyroscope model used in the present paper is based on the equations developed by Davis [1] and later presented by Tianfu Wang [2] and Ye Tian [3] who considered application of this class of gyroscopes for active vehicle roll control applications. The gyroscope configuration consists of a lumped point mass (proof mass) of mass m_p at the centre and four support springs with equivalent stiffness k_x and k_y, respectively, along and x and y axes. In order to achieve maximum sensitivity, the proof mass is excited along the x-axis in steady-state (driving direction) with a periodic external force of magnitude F_0 and frequency which is set to be the same as the natural frequency ω_x associated with non-rotating system along the x-axis. The system is then subjected to an input angular rate Ω about the z-axis (input axis) which is orthogonal to the driving axis. Owing to the Coriolis Effect that result from velocity along the x-axis and frame rotation rate Ω along the z-axis, the lumped proof mass oscillates along the direction of y-axis which is referred to as the sensing axis. Governing equations in terms of the generalized coordinates q_1 and q_2 that represent motion along x and y axes are:

$$\begin{bmatrix}1 & 0\\ 0 & 1\end{bmatrix}\ddot{\boldsymbol{q}}+\begin{bmatrix}0 & -2\Omega\\ 2\Omega & 0\end{bmatrix}\dot{\boldsymbol{q}}+\begin{bmatrix}\omega_x/Q_x & 0\\ 0 & \omega_y/Q_y\end{bmatrix}\dot{\boldsymbol{q}}+\begin{bmatrix}\omega_x^2-\Omega^2 & 0\\ 0 & \omega_y^2-\Omega^2\end{bmatrix}\boldsymbol{q}=\begin{bmatrix}(F_0/m_p)sin\,\omega_x t\\ 0\end{bmatrix}, \quad (1)$$

where, $\boldsymbol{q}=[q_1\ q_2]^T=[x\ y]^T$,$\omega_x^2=k_x/m_p$, $\omega_y^2=k_y/m_p$, $Q_x=m_p\omega_x/c_x$, $Q_y=m_p\omega_y/c_y$ while ω_x and ω_y represent the natural frequencies of the non-rotating system in the x and y axes, respectively.

Equation (1) is employed for the purposes simulating the time response analysis for fixed system parameter values such as the input angular rate, damping and frequency/stiffness mismatch. In addition, these equations are also modified in the first order form that is suitable for numerical integration of the ODE's to accommodate uncertainties via random variation of parameters to aid uncertainty quantification. The simulation is performed via the fourth-order Runge-Kutta scheme available within the MATLAB computing environment.

RESULTS AND DISCUSSION

Uncertainties in input angular speed are introduced in the mathematical model considering drift and noise terms and the resulting dynamic response simulations are used to obtain optimal number of points along time axis and optimal number of samples along path axis. For the purposes of uncertainty quantification, the noise term in the model is introduced as a random variable with Normal (Gaussian) distribution. At a certain temporal point which lies after 3900 points along time sample, 50 samples are taken along sample path axis for the application of Monte Carlo simulation based on the dynamic

[1)] Samuel F. Asokanthan Email: sasokant@uwo.ca

response. This enables prediction of response statistics in the form of standard deviation of output response for different cases which are presented in the work by Nujhat Abedin [4].

In order to introduce frequency mismatch ϑ in equation (1), the natural frequencies of the stationary gyroscope, namely ω_x and ω_y ,are considered unequal and these frequencies are related via: $\omega_y = \omega_x(1+\vartheta)$. It is evident from Figure 1 that Standard deviations of output response increases in a nonlinear fashion with varying frequency mismatch and the magnitude of the output response standard deviation shows a diverging trend when the quality factor increases (i.e. damping ratio decreases). In order to quantify uncertainties in quality factor, for different fixed frequency mismatch, standard deviations from 50 with an increment of 50 up to 500 while the mean is fixed at 1000, quantification is performed and presented in Figure 2. It is evident that, for 0.01% and 0.02% frequency mismatch, output response statistics show a significantly different trend when compared with higher mismatch values. It may be attributed to the fact that for lower frequency mismatch the two natural frequencies are likely to be close to each other. As a result, the response statistics may take large values as a result of internal resonance. For the lower values of frequency mismatch, when the quality factor increases, the output standard deviations increase and seem to have converging trend. Further, in order to illustrate the effect of large frequency mismatch on the performance of mass-spring gyroscope, 10% and 20% frequency mismatch are used in the numerical simulation. The figure also shows that for large frequency mismatch, magnitudes of output standard deviations do not have notable variation as internal resonance may not play a significant role.

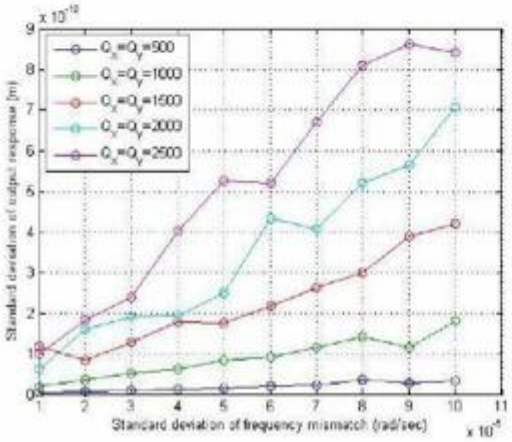

Figure 1. Standard deviation of frequency mismatch vs. standard deviation of output response, ($\Omega = 2\pi$)

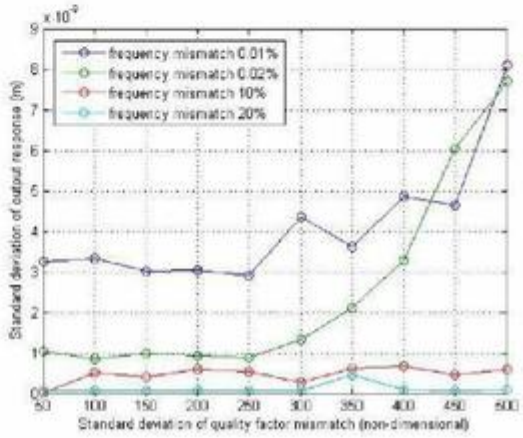

Figure 2. Standard deviation of quality factor mismatch vs. standard deviation of output response for different frequency mismatch ($\Omega = 2\pi$)

CONCLUSION

A dynamic model and numerical simulation procedures suitable for uncertainty quantification predictions for a class of MEMS gyroscopes are developed. Propagation of uncertainties in frequency mismatch as well as quality factor are investigated by considering optimal temporal sample paths via Monte Carlo simulation methods and response statistics for the mean as well as the standard deviation have been quantified. To the best of authors' knowledge, this systematic approach for predicting the dynamic response statistics have not been performed for this class of gyroscopes and it is hoped that this approach paves the way for performing uncertainty quantification when these systems are subjected to various other uncertainties that may be present in practice. It is envisaged that the predictions made from the output response statistics and uncertainty quantification analyses of the present study can lead to significant performance improvements in the design of this class of micro-machined mass-spring type vibrating angular rate sensors.

References

[1] Davis, W. O :Mechanical Analysis and Design of Vibratory Micromachined Gyroscopes, *Ph.D. Thesis,* University of California, Berkeley, USA, 2001.

[2] Asokanthan, S. F. and Wang, T: Instabilities in a MEMS Gyroscope subjected to Angular Rate Fluctuations*, Journal of Vibration and Control*, 15(2), 299-320.

[3] Tian, Y: Active Roll Control of Heavy Road-vehicles employing MEMS Angular Rate Sensors, MESc Thesis, University of Western Ontario, 2005.

[4] Abedin, N.: Uncertainty Quantification for a Class of MEMS-based Vibratory Angular Rate Sensors, *MESc Thesis,* University of Western Ontario, London, Ontario, Canada, 2014.

VIBRATION ENERGY LOCALIZATION IN INHOMOGENOUS BEAM STRUCTURE

Mohamed Amin Ben Lassoued[12a)], Guilhem Michon[1]& Annie Ross[2]
[1]*Université de Toulouse, CNRS, ICA, ISAE, Toulouse, France*
[2]*LAVA, Department of Mechanical Engineering, EcolePolytechniquede Montreal, Montreal, Quebec, Canada*

*Summary*In this paper, we studied the effect of an exponential distribution of the Young's modulus and the density in monolith and sandwich beams. Such a distribution of property shows a localization of the vibration in the low stiffness and low density part of the structure. A finite element model is compared to analytical approach based on WKB method for inhomogeneous wave guide for a better understanding of the parameters governing energy localisation in these structures.

INTRODUCTION

To have a better dissipation of energy in vibrating structures, dissipation systems must be designed for a certain frequency band. The band, however, does not always cover the entire frequency range to be attenuated. One solution is to have a dissipative system for each band. In order to make this idea efficient, the main system must distribute different frequency bands at different positions on the structure. The phenomenon of energy focussing was discovered by Von Bekesy[1]. It occurs for example in the cochlea in the inner ear of mammals. The inhomogeneity of the mechanical characteristics of the basilar membrane acts as a frequency filter which allows exciting different nerves for different sound frequency. This phenomenon called tonotopy was reproduced by Foucaud [2] for a metallic beam with linear geometric variation immerged in a fluid duct. He used the WKB method including evanescent wave for more accurate results. Another way to disperse energy in beams is to use an acoustic black hole [3]. It is based on an exponential decrease of the thickness of the beam which leads to amplification of high frequency modes at the thin extremity of the beam.The purpose of this paper is to show that the phenomenon also appears when beam mechanical properties are exponentially varied, instead of geometrical properties such as width or thickness. This will allow obtaining energy focussing without changing the beam bulk dimensions.

METHODOLOGY

The studied structures are clamped-free beams with constant cross sections. First, a monolithic metal beam is used as a simple structure to validate the approach and to know the influence of each parameter on energy focussing. Next, a sandwich composite beam was considered; in this case, vibration attenuation is more relevant because of the high beam stiffness. The variable parameters in this paper are the density and/or the Young's modulus of the monolithic beam or the core of the sandwich beam (fig.1). We used an exponentially decreasing law (eq.1) where X_0 is the material property at the clamped edge,α is a parameter that controls the axial decrement, and L is the beam length. Finite element models were created using Euler-Bernoulli beam formulation, and linear eigenvalue and eigenmode extraction was performed to obtain the flexural mode shapes of the beams.

$$X_i = X_0 e^{(\alpha\left(-\frac{x}{L}\right))} \qquad (1)$$

RESULTS

Modal extraction from the finite element models shows that the displacement amplitude of high frequency modes is highest at the free edge, where the variable property is minimal. Fig.2 presents the first, eighth and twentieth modal shapes of a constant parameter (left) and a variable parameter beam (right). This figure shows that for the first mode we have the same modal deformation for the structures with constant and variable properties. The difference in mode shape is observable from the eighth mode and is accentuated for higher eigenvalues. Energy concentration is more pronounced above a certain frequency, as it occurs in geometrically non uniform beams [2]. This behaviour is explained by a decrease of the wave propagation velocity in an exponentially variable medium. The wave slows down and stops as the variable parameter approaches zero [4].

[a)]Corresponding author. Email:mohamed-amin.ben-lassoued@isae.fr

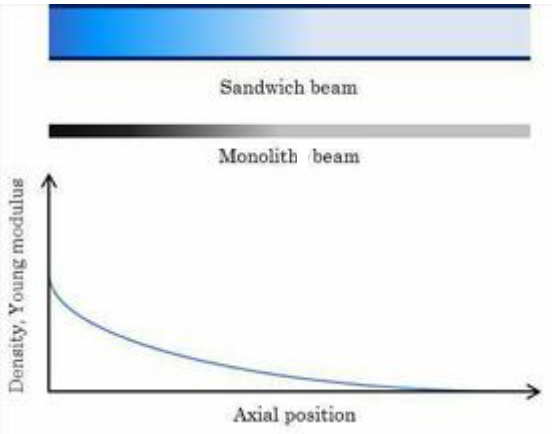

Figure.1 Parameter repartition in beams (color gradient represents property gradient)

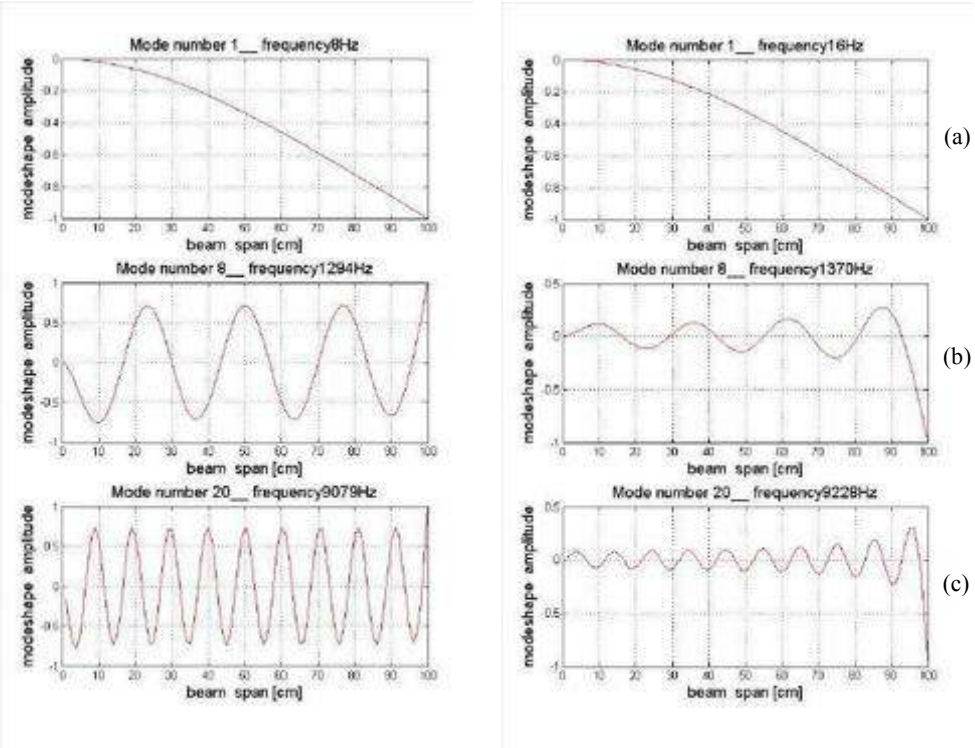

Figure.2 Mode shapes for a monolithic beam with constant properties (left) and exponentially variable properties (right) : (a) mode 1, (b) mode 8, (c) mode 20.

CONCLUSION

At this point, the acoustic black hole phenomenon was reproduced with other means than changing the beam geometry. Application of this approach on more complex models, and its combination with other means of mode concentration such as coupled systems with structural irregularity, can provide better understanding of the energy focussing phenomenon.

References

[1] Von Bekesy, G: Simplified Model to demonstrate the Energy Flow and Formation of Traveling Wave Similar To Those Found in cochlea, Proceedings of the National Academy of Sciences of the United States of America 42:930-944, 1956

[2] Foucaud S. M. G .P. G: Artificial Cochlea and Acoustic Black Hole Travelling Waves Observation: Model and Experimental Results, J. Sound and Vibration 333:3428-3439, 2014

[3] Denis.V.A.F.B.: *Modal Overlap Factor of a Beam with an Acoustic Black Hole Termination* , *J.Sound and Vibration* **333**:2475-2488, 2014

[4] Mironov M : Propagation of flexural wave in a plate whose thickness decreases smoothly to zero in a finite interval, Soviet Physics: Acoustics34(3) 318-319,1988

MASS ANOMALY AND RANDOM RATE FLUCTUATION EFFECTS ON VIBRATORY GYROSCOPE DYNAMICS

Soroush Arghavan[1] , Mohamed Bognash[1] , Jihyun Cho[2], Samuel F. Asokanthan[1]
[1]*Mechanical & Materials Engineering, Western University, London, On., Canada, N6A 5B9* [2]*Aercoustics Engineering Ltd., Toronto, Ontario, Canada, M9W 1B3*

Summary Experiments have been conducted in order to investigate the linearity of system response and system behavior of a macro-scale ring-type vibratory gyroscope. Particular emphasis is placed on examining the effects of environmental fluctuation in angular rate, mass mismatch and the linearity of system response. It is shown that the system natural frequency decreases with input angular rate and mass mismatch. It is also revealed that the system exhibits a more efficient dissipative behavior when subjected to stochastic angular rate fluctuations with fixed intensity at higher input angular rates.

INTRODUCTION

The operation of ring-type vibratory gyroscopes relies on excitation of the second ring flexural mode and detection of modal shift due to Coriolis' effect [1, 2]. However, complications may arise during typical operating conditions and inaccuracies due to fabrication processes. Device stability and detection limitation at low angular rate are caused by environmental fluctuations and imperfections of mass distribution, respectively [3]. The experimental investigations for studying vibratory characteristics are quite cumbersome, and to date only a few studies have been performed (see, e.g., [4]). In order to investigate the system behaviour due to these effects, experiments have been conducted using a macro-scale prototype [5] which exhibits similar dynamic characteristics of a vibratory ring-type MEMS gyroscope.

EQUATIONS OF MOTION

A homogenous, isotropic ring is chosen for the angular rate sensor. For the purposes of illustrating the dynamic behaviour of a ring gyroscope, governing equations for the system developed in studies [1, 6] are adopted. The equations of motion in terms of the generalized coordinates associated with the flexural coordinates q_1 and q_2 are given by

$$\begin{bmatrix}1 & 0\\ 0 & 1+\delta m\end{bmatrix}\begin{bmatrix}\ddot{q}_1\\ \ddot{q}_2\end{bmatrix}+\left[\begin{bmatrix}0 & -2\Omega\gamma\\ -2\Omega\gamma & 0\end{bmatrix}+\begin{bmatrix}2\zeta\omega_{01} & 0\\ 0 & 2\zeta\omega_{02}\end{bmatrix}\right]\begin{bmatrix}\dot{q}_1\\ \dot{q}_2\end{bmatrix}+\begin{bmatrix}\kappa_1+\kappa_2\Omega^2 & -\dot{\Omega}\gamma\\ -\dot{\Omega}\gamma & \kappa_1+\kappa_2\Omega^2\end{bmatrix}\begin{bmatrix}q_1\\ q_2\end{bmatrix}=\begin{bmatrix}f_1 cos\omega t\\ 0\end{bmatrix}, \quad (1)$$

where $(\dot{})$ denotes the time derivative. The gyroscopic term, $2\Omega\gamma$, and the stiffness term, $\kappa_1+\kappa_2\Omega^2$, are functions of input angular rate as well as the geometrical and materials properties of the ring and the supporting springs [1,7]. An external excitation term $f_1 cos\omega t$ which is instrumental for the excitation of the second flexural mode is also included. The terms ω_{01} and ω_{02} represent the natural frequencies of the second flexural modes. The imperfection in the ring is considered via a parameter δm together with small modal damping [1]. For the purposes of characterizing the fluctuation effects, the nominal input angular velocity Ω_0 is subjected to a white noise fluctuation of magnitude.

EXPERIMENTAL RESULTS AND DISCUSSION

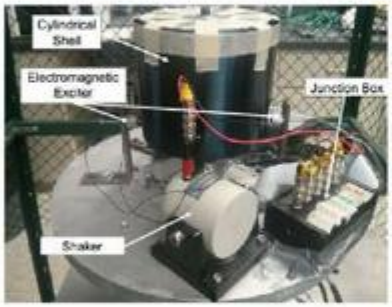

Figure 1: Experimental Setup of Rotating Cylindrical Structure

The experimental setup consists of a circular cylindrical structure, sensors and actuators, and a sensor driver which are placed on a test base which is attached to the IDEAL AEROSMITH 1291BR Precision Single-Axis Rate table as shown in Figure 1 [3, 5]. The cylinder is *92.5mm* in diameter, has an average thickness of *0.1mm*, and an average axial length of *150mm*. It is made of blue-tempered steel (C1095) is attached on the centre of the test base, while two electromagnets are arranged on an anti-nodal line to excite the free cylinder end. Two Eddy-current displacement sensors are arranged on the other anti-nodal line and one of the nodal lines. The rate table equipped with a built-in slip ring for signals routing to and from sensors and exciters is employed to produce accurate constant angular speed. A National Instruments data acquisition device and LabView software are used for the acquisition and data analysis. A KCF shaker system paired with a KCF PA5100 Signal Generator/Power Amplifier has been employed for the purpose of simulating environmental white noise fluctuation. The shaker is mounted on the rate table and connected to the rate table axis through a welded steel beam. The ring is excited using a linear sinusoidal wave frequency sweep in order to determine the natural frequencies of the ring associated with second flexural mode for stationary/rotating ring. A reduction in the natural frequency is noted as the rotation rate is increased.

[1)] Samuel F. Asokanthan. Email: sasokant@uwo.ca

The vibration amplitude at nodal and at anti-nodal points are compared for this purpose. When the excitation frequency is chosen to be close to the natural frequency of the stationary ring, variation of vibration amplitudes with angular rate are captured and shown in Figure 2. It can be seen that the device exhibits high non-linearity which may be attributed to the low natural frequency of the system, *10.4 Hz,* as well as high vibration amplitudes. It has been found that the linearity of the device is highly dependent on the excitation frequency. This results in a high angular rate to natural frequency ratio as opposed to typical MEMS sensors which are designed with high natural frequencies in the *kHz* range and detection angular rates of *0~2 rad/s*.

In order to investigate the effects due to mass mismatch, mass anomalies are placed on the ring at different locations and with different percentages of the total mass of the ring. The sensor outputs are measured at a range of frequencies to determine the natural frequency of the first configuration associated with the second flexural mode. Figure 3 displays the effects of the quantity of localized mass at different locations on the ring. It can be seen that increasing the mass of the anomaly results in a decrease in the natural frequency. Furthermore, the figure shows that the effect of mass concentration is larger when the mass is located in the vicinity of anti nodal points.

Experiments conducted on both rotating and stationary ring with white noise fluctuation revealed that the effect of high frequency fluctuation is less visible for the rotating ring compared to a stationary ring. This effect may be a result of the changes in system stiffness due to rotation. Further, low frequency fluctuations are more visible with the absence of high frequency noise. The angular rate input to the system is subjected to uniformly distributed white noise fluctuations introduced via the shaker. The fluctuation magnitude is held constant while the angular rate is varied to monitor the ability of the system in damping unwanted fluctuations. Twenty vibration cycles are documented for each angular rate both with and without the presence of noise. Figure 4 shows the standard deviation with 95% confidence intervals for different input angular rates at fixed fluctuation magnitudes and depicts a reduction in the amount of visible fluctuation on the output vibratory sensor data. This reduction may be associated with the lower relative noise-to-nominal angular rate ratio. Furthermore, an increase in angular rate results in variations in system natural frequency, as well as effective system stiffness and damping mostly due to centrifugal forces.

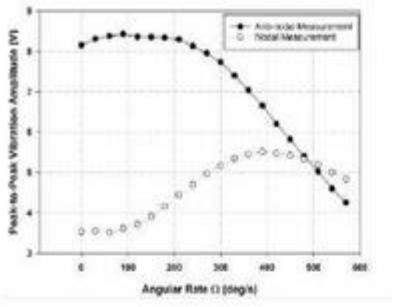

Figure 2: Linearity of nodal and anti-nodal measurements.

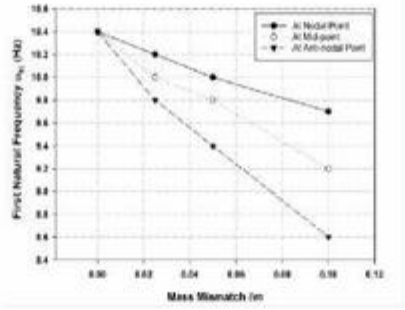

Figure 3: Variation of natural frequency with mass mismatch.

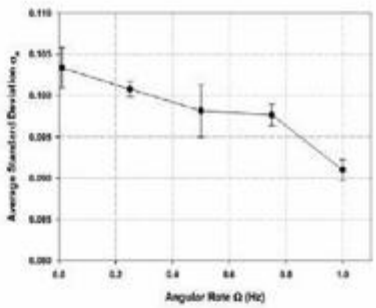

Figure 4: Variation of output standard deviation with angular rate.

CONCLUSIONS

An experimental macro-scale ring-type gyroscope has been developed in order to study the dynamic behaviour of ring-type vibratory gyroscopes. The device exhibits high non-linearity which may be attributed to the low natural frequency of the system as well as high vibration amplitudes. Increasing mass mismatch reduces the natural frequency of the system for nodal, anti-nodal and mid-point locations. When the system is under white noise angular rate fluctuation, the system exhibits a more efficient dissipation of fluctuations when subjected to lower noise to fluctuation amplitude ratios.

References

[1] Asokanthan, S. F. and Cho, J. :Dynamic stability of ring-based angular rate sensors, *Journal of Sound and Vibration*, 295, 571-583, 2006.

[2] Eley, R., Fox, C. H. J. and McWilliam, S. :Coriolis coupling effects on the vibration of rotating rings, *Journal of Sound and Vibration*, 238(3), 495-480, 2000.

[3] Arghavan, S. :Stochastic Stability and Uncertainty Quantification of Ring-Based Vibratory Gyroscopes. *M.Sc. thesis*, Western University, 2015.

[4] Evensen, D. A. :Nonlinear flexural vibrations of thin circular rings, *Journal of Applied Mechanics*, 33, 553-560, 1966.

[5] Cho, J. and Asokanthan, S. F.: Nonlinear Dynamic Response of Harmonically Driven Rotating Thin Circular Rings, *Proceedings of 7th European Nonlinear Dynamics Conference (ENOC),* Paper #MS-04, Rome, Italy, July 2011.

[6] Huang, S. C. and Soedel, W.: Effects of Coriolis acceleration on the free and forced in-plane vibrations of rotating rings on elastic foundation. *Journal of Sound and Vibration*, 115(2):253–274, 1987.

[7] Canchi, S. V and Parker, R. G.:Parametric Instability of a Rotating Circular Ring with Moving, Time-Varying Springs, ASME Journal of Vibration and Acoustics, 128, 231-243, 2006.

UNCERTAINTY ANALYSIS OF ROTATING MACHINES USING FUZZY LOGIC APPROACH

Valder Steffen Jr, Aldemir Ap Cavalini Jr & Arinan D Guerra Silva
LMEst – Structural Mechanics Laboratory, Federal University of Uberlândia, School of Mechanical Engineering, Av. João Naves de Ávila, 2121, Uberlândia, MG, 38408-196, Brazil.

Summary The present contribution is dedicated to the analysis of uncertainties affecting the dynamic behaviour of flexible rotors. For this aim, according to the literature, a stochastic method has been extensively used to model uncertain parameters, namely the so-called Monte Carlo simulation. However, in the present contribution, the inherent uncertainties of various parameters of the system (i.e., geometry, material, oil viscosity, and radial clearance of oil film bearings) are modelled by using a fuzzy based analysis. This alternative methodology seems to be more appropriate when the stochastic process that models the uncertainties is unknown. The dynamic analysis includes both time and frequency domains, as given by the unbalance responses and orbits. A comparison between Monte Carlo simulation and fuzzy analysis is performed. Finally, experimental tests are made to illustrate the validity of the methodology conveyed.

INTRODUCTION

Uncertainty analysis of dynamic systems has been studied by applying stochastic techniques based on three different stochastic approaches, namely the probability theory, in which uncertainty is dealt with by stochastic modelling; interval analysis, where uncertainty is modelled as represented by predefined intervals; and fuzzy set theory, in which uncertainty is described as incomplete and inaccurate information. Reference [1] brings a review about the main issues in fuzziness and probability. The contextualization of the stochastic approach within the structural dynamics scope through the Stochastic Finite Element Method (SFEM) and the so-called Polynomial Chaos Expansion (PCE) technique is presented in [2]. In [3] the fuzzy set theory to uncertainty structural analysis was introduced. Concerning rotor dynamics associated problems, [4] used SFEM and PCE techniques to investigate the quantification of the effects of uncertainties in the variability of the rotating system response. In [5] the SFEM approach was applied to a flexible rotor with uncertain parameters modelled as homogeneous Gaussian random fields discretized by the Karhunen-Lòeve series expansion. Following the fuzzy theory, [6] analysed the dynamics of flexible rotors under uncertain parameters. In [7] the dynamic behaviour of a flexible rotor with three rigid discs, supported by two fluid film bearings was evaluated.

In this context, the present work proposes the application of a straightforward approach to demonstrate the effectiveness of fuzzy approach for uncertainty analysis of rotating machines. Thus, fuzzy uncertain parameters are mapped onto the model with the aid of the so-called α-level optimization [3]. Additionally, the Differential Evolution algorithm is used to solve the optimization problem in the fuzzy analysis [9]. For comparison purposes, the Monte Carlo simulation combined with Latin Hypercube sampling is used to generate the envelope of responses of the stochastic rotor system. Experimental tests are made to illustrate the validity of the methodology conveyed.

FUZZY LOGIC APPROACH

Fuzzy logic is the term used to the intuitive formulation proposed by [9] that generalize the membership notion of an element in a mathematical set, creating a graded notion represented by a membership function. In the fuzzy set theory, the uncertainties are described as fuzzy inputs and the mathematical model is represented as a fuzzy function that maps those inputs by using the so-called α-level optimization. In this case, the fuzzy inputs are discretized by means of α-cuts creating a crisp subspace that is the search space of an optimization problem. The optimization process is carried out in order to finding the minimum and maximum values of the model output for each α-level (i.e., lower and upper limits of the correspondent α-level).

APPLICATIONS

The proposed uncertainty analysis was first applied to a horizontal rotating machine, which is shown in Fig. 1a. The finite element model is composed by a flexible steel shaft with 780 mm length and 12 mm diameter, two rigid discs of steel, and two cylindrical hydrodynamic bearings, each one with 25 mm diameter, 10 mm length, and radial clearance of 50 μm [10]. In this case, the uncertainty analysis is dedicated to evaluate the influence of uncertainties on the oil viscosity of both bearings of the rotating system (i.e., oil temperature). Figures 1b and 1c show the responses obtained along the horizontal direction at the disc #8, for the rotor operating under a linear run-down condition (3200 to 100 rev/min in 30 sec). The instantaneous radius of the orbit obtained at the bearing #4 was considered as being the objective function for the minimization and maximization problems associated to the fuzzy analysis. Considering the Monte Carlo simulation, it has been considered 200 samples. Note that both uncertainty analyses provided similar results.

[a)] Arinan Dourado Guerra Silva. Email: arinandourado@ufu.br

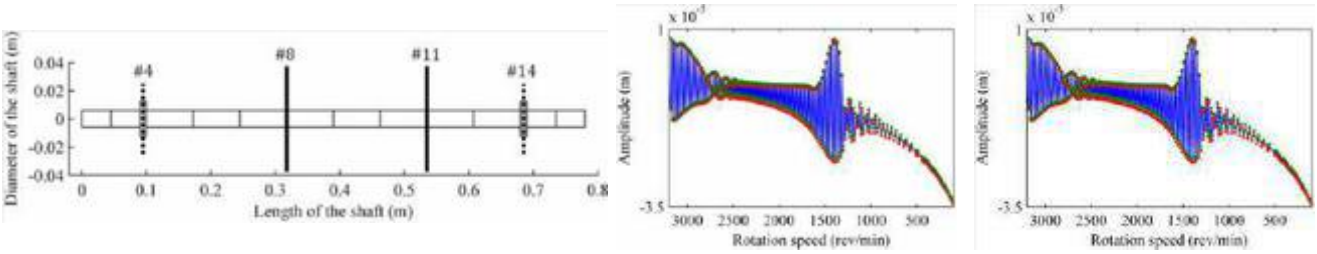

a) FE model of the rotor (····· bearing; —— disc). b) Fuzzy analysis. c) Stochastic analysis.

Figure 1 – Numerical analysis applied in a horizontal rotating machine
(•••• lower limit; •••• upper limit; ---- nominal).

The experimental tests were applied to a horizontal rotating machine modeled by using 35 Timoshenko beam elements, which is shown in Fig. 2. The finite element model is composed by a flexible steel shaft with 840 mm length and 19.05 mm diameter, three rigid discs of steel, and two cylindrical hydrodynamic bearings, each one with 19.05 mm diameter and 12.8 mm length. The uncertainty analysis is dedicated to evaluate the influence of uncertainties on the radial clearance of both bearings. Note that the displacements determined by applying the uncertainty scenario in the FE model can predict satisfactorily the dynamic behaviour of the rotor. Only the fuzzy approach was used in this application.

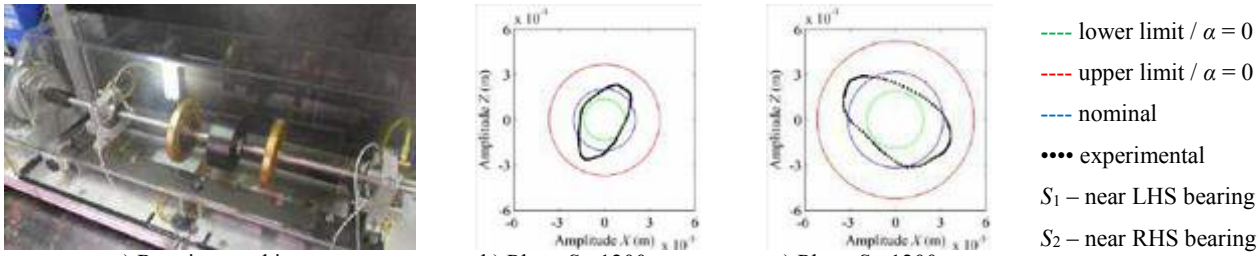

a) Rotating machine. b) Plane S_1; 1200 rpm. c) Plane S_2; 1200 rpm.

Figure 2 – Experimental analysis applied in a horizontal rotating machine.

CONCLUSIONS

In this paper two uncertainty approaches were used to evaluate the dynamic responses of a flexible rotor supported by oil film bearings, namely fuzzy and stochastic analyses. The applications show that both uncertainty approaches led to similar results. However, the fuzzy analysis seems to be more adequate when the stochastic process that models the uncertain parameters of the bearings is not well defined. Finally, the proposed strategy demonstrates the relevance of introducing uncertainties in the design variables from the design perspective of rotating machinery.

ACKNOWLEDGEMENTS

The authors are thankful to the Brazilian Research Agencies FAPEMIG and CNPq (INCT-EIE) and also to CAPES for the financial support provided to this research effort.

References

[1] Kosko, B., 1990, "Fuzzyness vs. Probability", International Journal of General Systems, Vol. 17, pp. 211-240.
[2] Ghanem, R.G. and Spanos, P.D., 1991, "Stochastic Finite Elements – A Spectral Approach", Spring Verlag.
[3] Möller, B. and Beer, M., 2004, "Fuzzy Randomness, Uncertainty in Civil Engineering and Computational Mechanics", Springer-Verlag.
[4] Didier, J., Faverjon, B. and Sinou, J.J., 2011, "Analysing the Dynamic Response of a Rotor System Under Uncertain Parameters Polynomial Chaos Expansion", Journal of Vibration and Control, Vol. 18, pp. 712-732.
[5] Koroishi, E.H., Cavalini Jr, A.A., de Lima, A.M.G., and Steffen Jr, V., 2012, "Stochastics Modeling of Flexible Rotors", Journal of the Brazilian Society of Mechanical Sciences and Engineering, Vol. 34, pp. 597-603.
[6] Lara-Molina, F.A., Koroishi, E.H. and Steffen Jr, V., 2015, "Uncertainty Analysis of Flexible Rotors Considering Fuzzy and Fuzzy Random Parameters", Latin American Journal of Solid and Structures, Vol. 12, No. 10.
[7] Cavalini Jr., A.A., Lara-Molina, F.A., Sales. T.P., Koroishi, E.H., and Steffen Jr, V., 2015, "Uncertainty Analysis of a Flexible Rotor Supported by Fluid Film Bearings", Latin American Journal of Solids and Structures, Vol. 12, No. 8, pp. 1487-1504.
[8] Price, K.V., Storn, R.M. and Lampinen, J.A., 2005, "Differential Evolution a Practical Approach to Global Optimization", Springer-Verlag.
[9] Zadeh, L., 1965, "Fuzzy Sets", Information and Control, Vol. 8, pp. 338-353.
[10] Lallane, M. and Ferraris, G., 1998, "Rotordynamics Prediction in Engineering", John Wiley and Sons, Second Edition.

NONLINER VIBRATIONS OF FGM SHALLOW SHELLS SUBJECTED TO RNDOM EXCITATION IN THERMAL ENVIRONMENT

Hassan Parandvar and Mehrdad Farid[a]
School of Mechanical Engineering, Shiraz University, Shiraz, Iran

Summary In this paper, nonlinear vibrations of functionally graded (FGM) shallow shells under random excitation in thermal environment are studied using multimodal finite element method (FEM). The material properties which are function of temperature, vary in the thickness direction based on a simple power law distribution. The equations of motion are obtained first in the structural node degrees of freedom (DOF) based on higher order shear deformation theory (HST) using an improved element. Then using modal reduction method the order of equations of motion are reduced. Three buckled equilibrium positions (BEPs) are obtained for FGM shallow shells under uniform temperature rise. The effects of various parameters including sound pressure level (SPL), initial condition, and radii of curvature on the nonlinear behavior of the system are studied. It is shown that FGM shallow shells demonstrate a snap through behavior under random load in thermal environment.

INTRODUCTION

Plates and shallow shells as common structural components can fatigue under strong acoustical loads in thermal environment. Many researchers studied FGM plates and shallow shells subjected to various loadings such as static, harmonic, and step loads [1-5]. However, few studies on the large amplitude vibrations of FGM shallow shells subjected to random excitation in thermal environment appeared in the literature. Dogan [6] and Parandvar and Farid [7] studied nonlinear vibration of FGM plates in thermal environment based on the classical and first order shear deformation theories, respectively. In the present paper, the nonlinear vibrations of FGM shallow shells under random excitation in thermal environment are investigated.

FORMULATIONS

In this study, the equations of motion of FGM shallow shells are obtained using FEM. In order to use HST, Mindline plate element (MIN3) [8] is modified by adding warping DOF introduced by Shankara [9]. Therefore, there are seven DOF at each node of the modified MIN3 element which can be presented by $U = [w \quad \psi_x \quad \psi_y \quad \phi_x \quad \phi_y \quad u \quad v]^T$, where u, v, and w are deflections in x, y, and z directions, respectively, while ψ_x and ψ_y are rotations and ϕ_x and ϕ_y are warping DOF. The equations of motion of the system in structural node DOF can be obtained and written in the following form.

$$\begin{bmatrix} M_b & 0 \\ 0 & M_m \end{bmatrix} \begin{Bmatrix} \ddot{U}_b \\ \ddot{U}_m \end{Bmatrix} - q \begin{bmatrix} K_b^{\Delta T} & 0 \\ 0 & 0 \end{bmatrix} \begin{Bmatrix} U_b \\ U_m \end{Bmatrix} + q \begin{bmatrix} K_b & K_{bm} \\ K_{mb} & K_m \end{bmatrix} \begin{Bmatrix} U_b \\ U_m \end{Bmatrix} + \left(q \begin{bmatrix} K1_b & K1_{bm} \\ K1_{mb} & 0 \end{bmatrix} + \begin{bmatrix} K2_b & 0 \\ 0 & 0 \end{bmatrix} \right) \begin{Bmatrix} U_b \\ U_m \end{Bmatrix} = q \begin{Bmatrix} F_b \\ 0 \end{Bmatrix} + \begin{Bmatrix} F_b^{\Delta T} \\ F_m^{\Delta T} \end{Bmatrix} \quad (1)$$

where subscripts b and m show the bending and membrane DOF, respectively. By neglecting the in-plane inertia terms ($\ddot{U}_m = 0$) , the in-plane DOF can be obtained in terms of bending DOF from the in-plate part of equation (1). By inserting them in the bending part of equation (1), the equations of motion of FGM shallow shells can be written in the following compact form.

$$[M_b]\{\ddot{U}_b\} - [K_b^{\Delta T}]\{U_b\} + [\bar{K}_b]\{U_b\} + [\bar{K}1_b]\{U_b\} + [\bar{K}2_b]\{U_b\} = \{F_b\} + \{F_b^{\Delta T}\} \quad (2)$$

The order of equations (2) can be reduced using the modal reduction method ($\{U_b\} = \sum_{i=1}^{n} q_i \{\varphi\}_i$, in which $\{\varphi\}_i$ are eigenvectors of linear part of equation (2)). The equations of motion in the generalized coordinates (q_i) can be presented as

$$[\tilde{M}]\{\ddot{q}\} + [\tilde{K}_q]\{q\} + [\tilde{K}1_q]\{q\} + [\tilde{K}2_q]\{q\} = \{\tilde{F}_b\} + \{\tilde{F}_b^{\Delta T}\} \quad (3)$$

RESULTS

A simply supported double curved FGM shallow shell with immovable edges and dimensions 0.2 m × 0.2 m × 0.002 m is considered. The results are obtained for three different radii of curvature: R = 2 m, R=3 m, and R = 10 m. The FGM shallow shell is made of SUS304 and Si_3N_4 with volume fraction exponent n=1. The order of equations of motion is reduced by first five symmetric dominant bending modes (DBM). A modal damping is also included in the reduced equations of motion. The modal damping ratio is selected to be 0.004 for all generalized coordinates. Fig (1) shows non-dimensional maximum deflection (W_{max}/h) versus uniform temperature rise (ΔT) for different radius. As can be seen, after a critical temperature depending on the radius, there are three different BEPs: stable positive, stable negative, and unstable negative ones. In all previous researches, only the stable positive BEP was reported for each pair of radii of curvature. Now, for uniform temperature rise ΔT=30 ^{0}C, the aforementioned FGM shell is additionally subjected to a truncated Gaussian white noise pressure in the frequency range [0, 1500] Hz. Figs (2-5) show the central deflection of the FGM shallow shell for different SPLs, radius of curvature, and initial conditions. As can be seen, the FGM shallow shell shows a snap-through behavior under

[a] Corresponding author. Email: farid@shirazu.ac.ir.

random excitation in thermal environment. It is worth mentioning that for larger radius, the snap through behavior becomes sharper.

CONCLUSIONI

The dynamic response of FGM shallow shells in thermal environment subjected to random excitation was studied and the effects of initial conditions, radii of curvature, and SPL were investigated. It was shown that when the FGM shallow shell is initially at the equilibrium position in the negative stable BEP it vibrates about it during a very short time interval, and then jumps to the positive stable BEP. But if the shell is initially at its positive BEP, it vibrates about this configuration for small SPLs, while for big SPLs the snap-through behaviors occur.

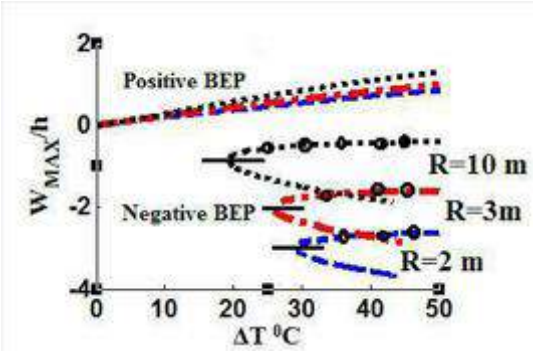

Fig (1). BEPs versus temperature rise for immovable FGM shallow shell ● unstable branch

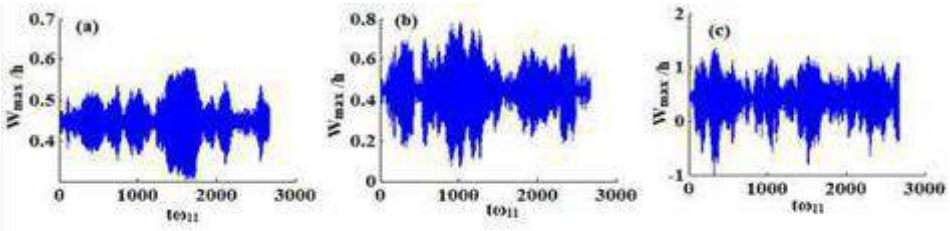

Fig (2) The positive BEP as initial condition, R=2 m, SPL= a) 160 dB, b) 170 dB, c) 180 dB

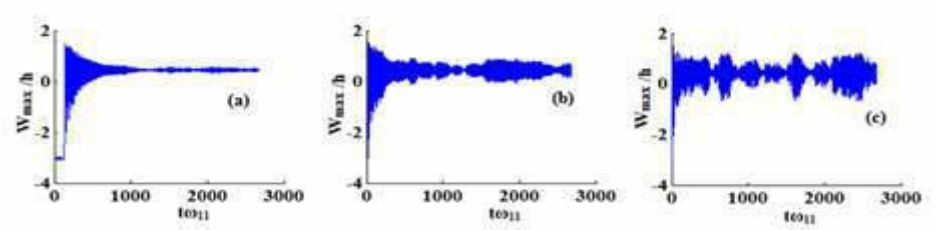

Fig (3) The negative BEP as initial condition, R=2 m, SPL= a) 160 dB, b) 170 dB, c) 180 dB

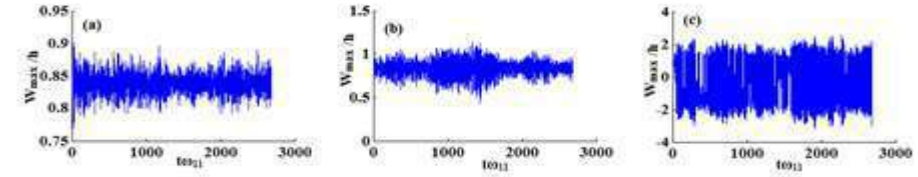

Fig (4) The positive BEP as initial condition, R=10 m, SPL= a) 160 dB, b) 170 dB, c) 180 dB

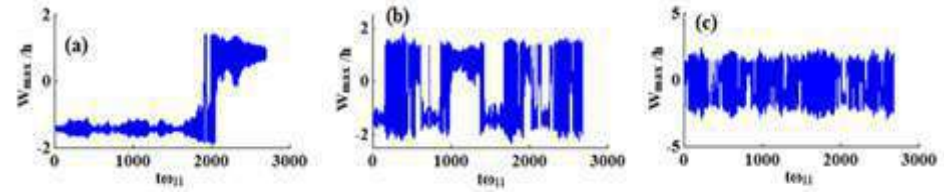

Fig (5) The positive BEP as initial condition, R=10 m, SPL= a) 160 dB, b) 170 dB, c) 180 dB

REFERENCESI

[1]-Alijani, F., Amabili, M., Bakhtiari-Nejad, F. "Thermal effects on nonlinear vibrations of functionally graded doubly curved shells using higher order shear deformation theory." Composite Structures 93, no. 10 (2011): 2541-2553.

[2]-Alijani, F., Bakhtiari- Nejad, F., Amabili, M." Nonlinear vibrations of FGM rectangular plates in thermal environments." International journal of Nonlinear Dynamics and Chaos in Engineering Systems 66 (2011): 251-270.

[3]-Pradyumna, S., Nanda, N., Bandyopadhyay, J. N. "Geometrically nonlinear transient analysis of functionally graded shell panels using a higher-order finite element formulation." Journal of Mechanical Engineering Research 2, no. 2 (2010): 39-51.

[4]-Alijani, F., Amabili, M., Karagiozis, K., Bakhtiari-Nejad, F. "Nonlinear vibrations of functionally graded doubly curved shallow shells." Journal of Sound and Vibration 330, no. 7 (2011): 1432-1454.

[5]-Ribeiro, P. "On the influence of membrane inertia and shear deformation on the geometrically non-linear vibrations of open, cylindrical, laminated clamped shells." Composites Science and Technology 69, no. 2 (2009): 176-185.

[6]-Dogan, V." Nonlinear vibration of FGM plates under random excitation." Composite Structures 95 (2013): 366–374.

[7]-Parandvar, H., & Farid, M., "Nonlinear reduced order modeling of functionally graded plates subjected to random load in thermal environment. Composite Structures, no.126 ((2015). 174-183.

[8]- Tessler, A. "A C^0-anisoparametric three-node shallow shell element." Computer methods in applied mechanics and engineering 78.1 (1990): 89-103.

[9]-Shankara, C. A., Iyengar, N. G. R. "A C0 Element for the free vibration analysis of laminated composite plates "Journal of Sound and Vibration 191.5 (1996): 721-738.

EQUIVALENT VISCOUS DAMPING OF A CYLINDER MOVING TRANSVERSELY THROUGH SAND: EXPERIMENTAL RESULTS

Eric M. Hernandez*[1], Elizabeth Richards[1], and Steven Bellavance[1]
[1]*School of Engineering, University of Vermont, Burlington, Vermont, USA*

Summary This paper presents experimental results regarding the equivalent viscous damping induced by a cylinder moving transversely through sand with varying degree of water content. The experimental set up consists of a flexible steel frame with an attached cylinder which moves in free vibration inside a container with sand. Various conditions are examined which include cylinder embedded length, water-to-sand ratio and initial displacements. It is shown that the proposed set-up significantly increases the effective damping of the frame.

INTRODUCTION

Damping has a significant effect on the dynamic response of structures, specially in free vibration and near resonance. Most large structures have a damping which is less than 5 percent of critical and thus engineers typically look for ways to increase damping with additional devises. A variety of devises have been proposed with varying costs, complexity and effectiveness. This paper reports on experimental results aimed at identifying the equivalent viscous damping ratio of a SDOF system that uses sand as supplemental means to add damping. The paper examines various cases including dry, saturated and over saturated sand. Specifically we test the damping imparted by a cylinder moving in the transverse direction through sand. The experimental setup can be seen in Fig.1.

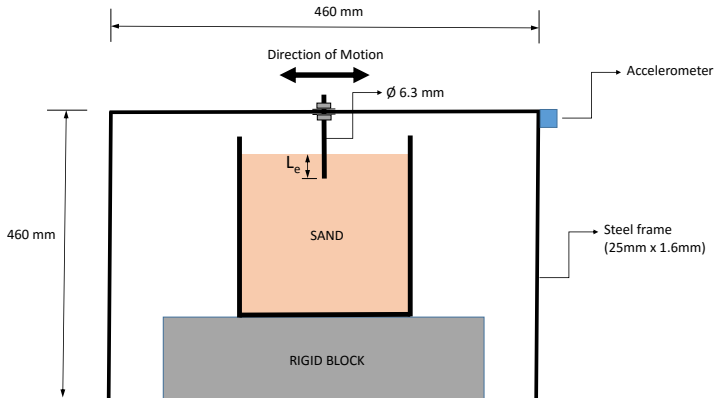

Figure 1: Experimental set-up.

THEORETICAL BACKGROUND

The free vibration response of a linear, viscously damped single degree of freedom system is governed by

$$m\ddot{x} + c\dot{x} + kx = 0 \tag{1}$$

with solution given by [1]

$$x(t) = e^{-\xi\omega t}\left(\frac{v_o + \xi\omega x_o}{\omega_d} \quad \mathrm{n}\,\omega_d t + x_o \quad \omega_d t\right) \qquad \xi = \frac{c}{2m\omega} \qquad \omega = \sqrt{\frac{k}{m}} \qquad \omega_d = \omega\sqrt{1 \nearrow \xi^2} \tag{2}$$

where $\xi < 1$ is the damping ratio and ω is the natural circular frequency. If the response is measured and we wish to identify the equivalent value of ξ from the tests, we can use the so-called log decrement test. The logarithmic decrement δ is defined as

$$n\delta = 1 \quad \frac{X_i}{X_{i+n}} \tag{3}$$

*Corresponding author. Email: eric.hernandez@uvm.edu

where X_i is the response at the ith peak and X_{i+n} is the response at the nth peak after i. It can be shown that the damping ratio is given by

$$\xi = \frac{\delta}{\sqrt{\pi^2 + \delta^2}} \tag{4}$$

To reduce the effect of measurement noise, the estimated damping ratio is averaged across multiple sequential peaks.

IDENTIFICATION RESULTS

This section presents the estimated sand-induced damping ratio results under a combination of conditions. So far we have examined 3 water-to-sand ratios, 3 different initial displacements (x_o), 3 different embedded lengths (L_e) and 2 different natural frequencies. Due to space constraints we only show a subset of results. In each case 10 tests (10 seconds long) where conducted and a summary of the results is presented in the table below. The acceleration response of the system was measured using PCB-333B30 accelerometers. The sampling rate was ,09 Hz. Prior to using the raw acceleration data for identification a low-pass Butterworth filter and re-sampled at 100 Hz.The frequency and damping ratio of the steel frame in free vibration (without any added damping) were identified at 5. Hz and 0.003 respectively. Saturated sand exhibited a moisture content between 10 and 15 percent. Over-saturated sand exhibited a moisture content around 25 percent.

Table 1: Estimated damping ratio and natural frequency for $L_e = 10mm$.

	$x_o = 10mm$		$x_o = 20mm$		$x_o = 30mm$	
	ξ	$f_n(Hz)$	ξ	$f_n(Hz)$	ξ	$f_n(Hz)$
Dry	0.078	5.38	0.0435	5.18	0.02	5.10
Saturated	0.058	5.38	0.032	5.18	0.03	5.15
Over-Saturated	0.038	5.19	0.029	5.10	0.021	5.05

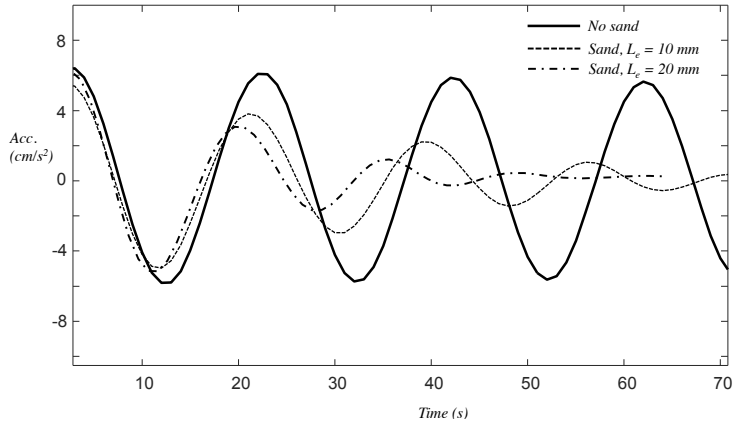

Figure 2: Time history of free-vibration acceleration response with rod embedded at various lengths.

CONCLUSIONS

The effective damping induced by a rigid cylinder moving in free-vibration transversely through sand was investigated experimentally. The main trends were as follows: (1) The effective damping in all conditions is significantly larger than the intrinsic damping of the structure without the added damping, (2) The effective damping imparted by the cylinder moving transversely in sand decreases with water content and with the amplitude of the motion. The effective natural frequency also exhibits the same trends however with a smaller sensitivity. Future work on this topic will look at the effective damping under various types of forced excitation such as harmonic and seismic-induced ground motion.

References

[1] Chopra A.: Dynamics of Structures, 4th Edition, 2012. Prentice Hall.

VIBRATION OF ROTATING MULTISCALE NANOCOMPOSITE CANTILEVER BEAMS

Mohammad Rafiee[1a)], Fred Nitzsche[2] & Michel Labrosse[1]
[1]*Department of Mechanical Engineering, University of Ottawa, Ottawa, Canada*
[2]*Department of Mechanical and Aerospace Engineering, Carleton University, Ottawa, Canada*

Summary We studied the linear free vibrations of thin-walled carbon nanotubes/fibre/polymer laminated multiscale composite beams. A set of nonlinear intrinsic equations describing the response of rotating cantilever composite beams undergoing large deformations was discretized by the Galerkin method and solved for natural frequencies and mode shapes. Halpin–Tsai equations and fibre micromechanics were used to predict the bulk material properties of the multiscale nanocomposite. The carbon nanotubes (CNTs) were assumed to be uniformly distributed and randomly oriented through the epoxy resin matrix. The weight percentages of single-walled and multi-walled carbon nanotubes (SWCNTs and MWCNTs) were investigated through a detailed parametric study for their effects on the natural frequencies. It was found that natural frequencies are significantly influenced by a small percentage of CNTs.

INTRODUCTION

It is known that addition of a small amount of carbon nanotubes (CNTs) can considerably improve the mechanical, electrical and thermal properties of polymeric composites. CNTs-reinforced composites have attracted considerable attention in recent years due to their unique properties [1]-[5]. The incorporation of such advanced high-performance materials is likely to expand the use and capabilities of thin-walled beam structures.

In recent years researchers have investigated the dynamic behavior of the thin-walled beams made of isotropic or advanced composite materials. An intrinsic formulation developed by Hodges and his co-workers [6]-[7] covers the anisotropic beams with large deformations and small strains. Ghorashi and Nitzsche [8] studied the nonlinear dynamic response of an accelerating composite rotor blade using perturbations. Patil and Althoff [9] and Althoff et *al*. [10] developed a nonlinear model based on the Galerkin method to investigate the nonlinear response of rotating composite blades using intrinsic equations. The nonlinear response of multiscale nanocomposites and CNT-reinforced non-rotating composite beams and beam-type structures is also discussed in the literature. A significant contribution in this area was made by Rafiee and his coworkers [1-3],[11-12]. Recently, He et al. [2] developed a study to investigate the large amplitude vibration of fractionally damped viscoelastic CNTs/fibre/polymer multiscale composite (CNTFPC) beams.

Even though the nonlinear analysis of rotating composite beams made of advanced materials is of a great importance, to date, no mathematical model has been available for the vibration analysis of CNTs-reinforced rotating composite thin-walled beams or blades.

THEORETICAL FORMULATION

The nonlinear, intrinsic, mixed equations for the dynamics of a general (nonuniform, twisted, curved, anisotropic) beam undergoing small strains and large deformations are given below based on the generalized Timoshenko beam model [9]

$$\begin{aligned} &\mathbf{F}' + \left(\tilde{\mathbf{k}} + \tilde{\boldsymbol{\kappa}}\right)\mathbf{F} + \mathbf{f} = \dot{\mathbf{P}} + \tilde{\boldsymbol{\Omega}}\mathbf{P}, \quad \mathbf{M}' + \left(\tilde{\mathbf{k}} + \tilde{\boldsymbol{\kappa}}\right)\mathbf{M} + \tilde{\mathbf{e}}_1 + \tilde{\boldsymbol{\gamma}}\right)\mathbf{F} + \mathbf{m} = \dot{\mathbf{H}} + \tilde{\boldsymbol{\Omega}}\mathbf{H} + \tilde{\mathbf{V}}\mathbf{P}, \\ &\mathbf{V}' + \left(\tilde{\mathbf{k}} + \tilde{\boldsymbol{\kappa}}\right)\mathbf{V} + \left(\tilde{\mathbf{e}}_1 + \tilde{\boldsymbol{\gamma}}\right)\boldsymbol{\Omega} = \dot{\boldsymbol{\gamma}}, \quad \boldsymbol{\Omega}' + \left(\tilde{\mathbf{k}} + \tilde{\boldsymbol{\kappa}}\right)\boldsymbol{\Omega} = \dot{\boldsymbol{\kappa}} \end{aligned} \tag{1}$$

where the prime denotes the partial derivative with respect to the undeformed beam reference line defined by the curvilinear coordinate x, the over dot denotes the partial derivative with respect to the time t ; and internal forces $\mathbf{F} = [F_1\ F_2\ F_3]^T$, internal moments $\mathbf{M} = [M_1\ M_2\ M_3]^T$, generalized force strains $\boldsymbol{\gamma} = [\gamma_{11}\ 2\gamma_{12}\ 2\gamma_{13}]^T$, generalized moment strains $\boldsymbol{\kappa} = [\kappa_1\ \kappa_2\ \kappa_3]^T$, generalized curvatures $\mathbf{K} = [K_1\ K_2\ K_3]^T$, linear momentums $\mathbf{P} = [P_1\ P_2\ P_3]^T$, angular momentums $\mathbf{H} = [H_1\ H_2\ H_3]^T$, linear velocities $\mathbf{V} = [V_1\ V_2\ V_3]^T$, angular velocities $\boldsymbol{\Omega} = [\ \Omega_1\ \Omega_2\ \Omega_3]^T$, and external forces $\mathbf{f} = [f_1\ f_2\ f_3]^T$; and external moments $\mathbf{m} = [m_1\ m_2\ m_3]^T$; γ_{11} is the extensional strain measure, and $2\gamma_{12}$ and $2\gamma_{13}$ are the transverse shear measures; and, finally, the tilde over certain terms denotes an skew-symmetric matrix (pseudovector) of the components of the column matrix of the same name.

The effective material properties of the three-phase CNTs/fibre/polymer multiscale laminated composite were predicted according to Rafiee *et al*. [1-3]. The equations (1) are discretized by expanding $\mathbf{V}$, $\boldsymbol{\Omega}$, $\mathbf{F}$ and $\mathbf{M}$ using the shifted Legendre polynomials [9-10]. Using the Galerkin method [1-3], the linear natural frequencies of the nanocomposite beam can be obtained by using the linearized eigenvalue problem in steady state.

NUMERICAL RESULTS AND DISCUSSIONS

In this section, we analyse the eigenvalues of rotating CNTs/fibre/polymer laminated multiscale composite beams. The effect of SWCNTs weight percentages on the fundamental linear natural frequency of the cantilever rotating and non-rotating CNTFPC blades was investigated and the results are listed in Tables 1 - 2. Our findings suggest that a small amount

a) Corresponding author. Email: mrafiee@uottawa.ca, mrafiee20@gmail.com

of single-walled carbon nanotubes (5%) can significantly increase the natural frequencies of the fibre reinforced laminated composite beams. Another observation is that the rise in fundamental natural frequency of beams due to addition of CNTs is more significant in nonrotating rather than the rotating cases.

Table 1. Effect of SWCNTs weight percentages w^{CN} on the fundamental natural linear frequency of the cantilever rotating and non-rotating CNTFPC blades.

Case	Ω_3 = 0 rad/s			Ω_3 = 10 rad/s		
	w^{CN}			w^{CN}		
	0%	5%	10%	0%	5%	10%
Strip	24.2744	28.7979 [18.63%]	32.4403 [33.64%]	26.4403	30.6478 [15.91%]	34.0946 [28.95%]
Box	154.9875	210.513 [35.83%]	232.879 [50.26%]	155.3577	210.788 [35.68%]	233.116 [50.05%]

Table 2. Effects of aspect ratio and type of the nanotubes on the fundamental natural linear frequency of the cantilever rotating and non-rotating CNTFPC blades.

Case	ℓ^{CN} / d^{CN}	Ω_3 = 0 rad/s			Ω_3 = 10 rad/s		
		SWCNTs	MWCNTs	Difference	SWCNTs	MWCNTs	Difference
Strip	100	26.6496	24.5043	[-8.05%]*	28.6383	26.6530	[-6.93%]
	10000	28.7794	24.5128	[-14.83%]	30.6304	26.6608	[-12.96%]
Box	100	187.0501	159.0431	[-14.97%]	187.3596	159.4047	[-14.92%]
	10000	210.3223	159.1685	[-24.32%]	210.5982	159.5299	[-24.25%]

The effects of aspect ratio and type of the nanotubes are shown in Table 2. One can observe that the fundamental natural frequency of the CNTFPC beams increases with an increase in CNT percentage and this increase is more significant in SWCNTs than MWCNTs. In other words, single walled carbon nanotube reinforced composite beams exhibit better resistance to flexural deflection and vibration in comparison with multi-walled carbon nanotube reinforced beams.

CONCLUSIONS

Free vibration analysis of rotating multiscale nanocomposite beams was investigated in this study. The governing equations of motions were discretized by the Galerkin method, and the natural frequencies were determined. Numerical results showed that the natural frequencies significantly increase with a small content of CNTs. It was also found that the SWCNTs reinforcement produces more pronounced effect on the natural frequencies of the beam in comparison with MWCNTs. This may be attributed to the defect-free structure of SWCNTs.

References

[1] Rafiee M., He X. Q., Mareishi S., Liew K. M., Modeling and stress analysis of smart CNTs/fiber/polymer multiscale composite plates. *International Journal of Applied Mechanics*, **6** (03) (2014), 1450025.

[2] He X. Q., Rafiee M., Mareishi S., Liew K. M., Large amplitude vibration of fractionally damped viscoelastic CNTs/fiber/polymer multiscale composite beams. *Composite Structures*, **131**(2015) 1111-1123.

[3] Rafiee M., Liu X. F., He X. Q., Kitipornchai S., Geometrically nonlinear free vibration of shear deformable carbon nanotube/fiber/polymer multiscale laminated composite plates. *Journal of Sound and Vibration*, **333**(14) (2014) 3236-3251.

[4] Bekyarova E., Thostenson E.T., Yu A., Kim H., Gao J., Tang J., Hahn H. T., Chou T. W., Itkis M. E., Haddon R. C., Multiscale carbon nanotube-carbon fiber reinforcement for advanced epoxy composites, *Langmuir*, **23** (2007) 3970-3974.

[5] Kim M., Park Y. B., I.Okoli O., Zhang C., Processing, characterization, and modeling of carbon nanotube-reinforced multiscale composites. *Composites Science and Technology*, **69**(3) (2009) 335-342.

[6] Hodges D. H., A mixed variational formulation based on exact intrinsic equations for dynamics of moving beams. *International journal of solids and structures*, **26**(11) (1990) 1253-1273.

[7] Hodges D. H., Atilgan A. R., Cesnik C. E. S., and Fulton M. V., On a simplified strain energy function for geometrically nonlinear behavior of anisotropic beams, *Compos*. *Eng*. **2**:5–7 (1992) 513–526.

[8] Ghorashi M., Nitzsche F., Nonlinear dynamic response of an accelerating composite rotor blade using perturbations. *Journal of Mechanics of Materials and structures*, **4**(4) (2009) 693-718.

[9] Patil M. J., Althoff M., Energy-consistent, Galerkin approach for the nonlinear dynamics of beams using intrinsic equations. *Journal of Vibration and Control*, **17**(11) (2010) 1748-1758.

[10] Althoff M., Patil M. J., Traugott J. P., Nonlinear modeling and control design of active helicopter blades. *Journal of the American Helicopter Society*, **57**(1) (2012), 1-11.

[11] Rafiee M., Yang J., Kitipornchai S., Large amplitude vibration of carbon nanotube reinforced functionally graded composite beams with piezoelectric layers. *Composite Structures*. **96**(2013) 716–725.

[12] He X. Q., Rafiee M., Mareishi S., Nonlinear dynamics of piezoelectric nanocomposite energy harvesters under parametric resonance. *Nonlinear Dynamics*, **79**(3) (2015) 1863-1880.

VIBRATION OF A SIMPLY SUPPORTED CIRCULAR PLATE UNDER MOVING POINTS LOADS

Arpit Sharma[1], Amit Kumar Rai[1]&Shakti S. Gupta[1a)]
[1]*Mechanics and Applied Mathematics Group, Department of Mechanical Engineering, Indian Institute of Technology Kanpur, Kanpur, India*

*Summary*Here, undamped dynamical response of a circular simply supported plate at the periphery due to an arbitrary moving point loading is obtained in the closed form using Green's function approach. The plate material is taken to be linear elastic, homogeneous and isotropic. Specifically, in this paper the transverse response of the plate due to a single point load q moving circularly at the fixed radius with constant angular velocity is calculated. Subsequently, the response due to three $q/3$ loads moving circularly at the same radius and same angular velocity but with 120^0 phase is compared with the previous calculation. The FFT of time response in both the cases contains the spectral lines at the natural frequencies, however, in the later case other than the first mode all other modes are quenched significantly.

INTRODUCTION

Vibration of structures subjected to moving point loads is an important problem in engineering. Structures in the field of transportation, e.g. bridges, guide ways, overhead cranes, cableways, rails, sleepers, roadways and runways are subjected to moving point loads. Dynamic response of a thin rectangular plate resting on a Winkler elastic foundation, subjected to a moving harmonic line and point loads has been obtained by Sun [1] using Green's function approach. Weiner [2] also used Green's function approach and studied response of a circular plate subjected to moving loads of several types but not the one due to moving point loads. Mote [3] studied the transverse response and stability of a centrally clamped and peripherally free plate circular plate subjected to circularly moving point loads. Stanisic and Lafayette [4] also studied the similar system as that by Mote [3] and deduced stability criterion for an arbitrarily moving point load. In this paper we have obtained dynamical response of a circular plate simply supported at the periphery, due to an arbitrary point loading which to the best of our knowledge has not been addressed in the open literature.

MATHEMATICAL FORMULLATION

The governing equation of transverse motion of a thin circular plate due to a time dependent pressure loading given in [5] is nondimensionalized using the following transformations: $r' = r/b$, $v = w/h$, $\tau = t/T$, where $T^2 = b^4\rho/D$. The resulting equation of motion is as follows

$$\nabla^{\pi} v + \alpha v_{\tau\tau} = q'(r', \phi, t), \tag{1}$$

$$\text{where, } \alpha = \frac{\pi b^4}{T^2 D} \text{ and } q'(r', \phi, t) = \frac{b^4}{hD} q(r', \phi, t). \tag{2}$$

The parameter D is called as the bending stiffness and is given by $Eh^3/12(1-\nu^2)$. The appropriate nondimensional boundary conditions for simply supported edge are

$$v(r', \varphi, t) = 0, \text{and } v_{r'r'} + \nu\left(\frac{v_{r'}}{r'} + \frac{v_{\phi\phi}}{r'^2}\right) = 0 \quad \text{at } r' = 1. \tag{3}$$

Green function of Eq. (1) is derived and is given as follows

$$G(r', \phi, \tau; r'_0, \phi_0, \tau_0) = \sum_{m=0}^{\infty}\sum_{n=1}^{\infty} \frac{b^4}{Dh} R_{mn}(r_0)\cos m\phi_0 \frac{\sin \omega_{\pi\, n}(\tau-\tau_0)}{\omega_{\pi\, n}} H(\tau-\tau_0) R_{mn}(r'), \tag{4}$$

where m and n are the nodal diameter and nodal circle, respectively, and R_{mn} are the eigen functions corresponding to simply supported boundary conditions.

Using Eq. (4) response of the plate for an arbitrary loading distribution $q(r', \phi, t)$ becomes

$$v(r,' \phi, t) = \int_0^{\tau}\int_0^{2\pi}\int_0^1 G(r', \phi, \tau; r'_0, \phi_0, \tau_0) q(r'_0, \phi_0, \tau_0) r'_0 dr'_0 d\phi_0 d\,\phi_0. \tag{5}$$

To determine the response due to a circularly moving point load at r'_0 with an angular velocity Ω we substitute $q(r'_0, \phi_0, \tau_0) = Q(\tau)\delta(r' - r'_0)\delta(\phi - \Omega\tau_0)$ in Eq. (5). Thus the calculated response is

$$v(r,' \phi, t) = \frac{b^4}{Dh}\sum_{m=0}^{\infty}\sum_{n=0}^{\infty} r'_0\, R_{mn}(r'_0) R_{mn}(r') \cos m\emptyset (A_{mn}(\tau)\sin(\omega_{mn}\tau) - B_{mn}(\tau)\cos(\omega_{mn}\tau)), \tag{6}$$

$$\text{where, } A_{mn}(\tau) = \int_0^{\tau} Q(\tau_0)\frac{\cos m\Omega\tau_0}{\omega_{\pi\, n}}\cos\omega_{mn}\tau_0\, d\tau_0 \text{ and } B_{mn}(\tau) = \int_0^{\tau} Q(\tau_0)\frac{\cos m\Omega\tau_0}{\omega_{\pi\, n}}\sin\omega_{mn}\tau_0\, d\tau_0.$$

Similarly, response for three point load moving at a phase difference of $2\pi/3$ will be

$$v(r,' \phi, t) = \frac{b^4}{Dh}\sum_{m=0}^{\infty}\sum_{n=0}^{\infty} r'_0\, R_{mn}(r'_0) R_{mn}(r') \cos m\emptyset (A_{mn3}(\tau)\sin(\omega_{mn}\tau) - B_{mn3}(\tau)\cos(\omega_{mn}\tau)), \tag{7}$$

[a)]Corresponding author. Email:ssgupta@iitk.ac.in

where $A_{d\ n3}(\tau) = \int_0^\tau Q(\tau_0) \frac{\cos d\ \Omega\tau_0 + \cos d\ \left(\Omega+\frac{2\pi}{3}\right)\tau_0 + \cos d\ \left(\Omega+\frac{4\pi}{3}\right)\tau_0}{3d_{\ mn}} \cos \omega_{d\ n}\tau_0\ d\tau_0$, and

$B_{d\ n3}(\tau) = \int_0^\tau Q(\tau_0) \frac{\cos d\ \Omega\tau_0 + \cos d\ \left(\Omega+\frac{2\pi}{3}\right)\tau_0 + \cos d\ \left(\Omega+\frac{4\pi}{3}\right)\tau_0}{3d_{\ mn}} \sin \omega_{d\ n}\tau_0\ d\tau_0$, respectively.

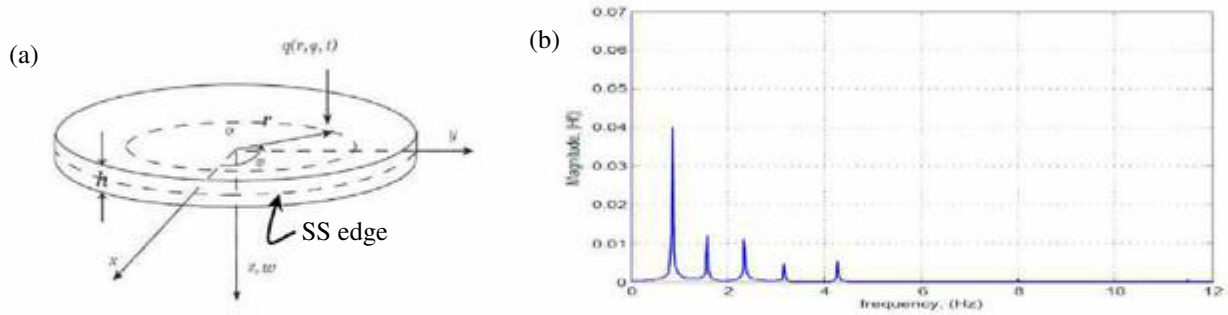

Figure 1: (a) Single point load q moving on circular plate. (b) FFT of time response obtained at (r' = 0.75, ϕ = 0), due to single point load rotating at r'=0.43(nodal circle corresponding to m = 0, n = 2) with Ω = 1.59 Hz.

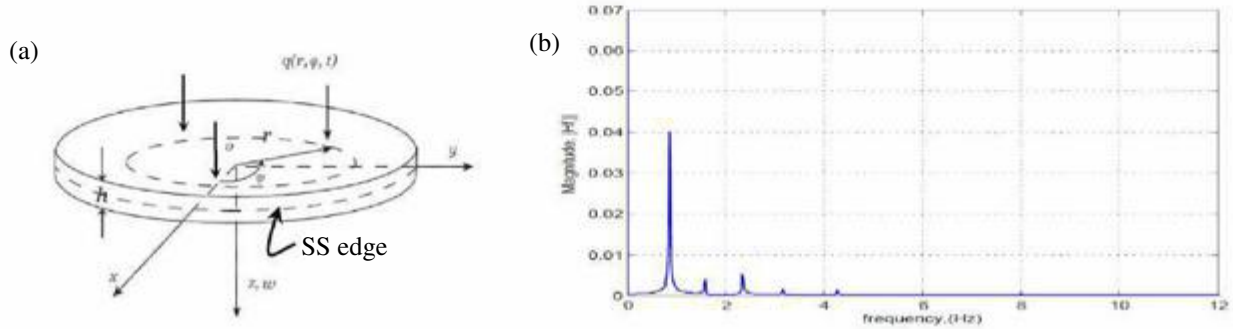

Figure 2: (a) Three point loads moving on circular plate at a phase difference 2π/3, (b) FFT of time response obtained at (r' = 0.75, ϕ = 0) , due to three point load rotating at r'=0.43 (nodal circle corresponding to m = 0, n = 2) with Ω = 1.59 Hz.

RESULTS AND DISCUSSION

Firstly, we find the first six eigen values for a plate made of the material with E = 180 GPa, ρ = 7860 Kg/m^3 and ν = 0.3. These are as follows: (ω_{01} = 0.87 Hz, ω_{02} = 4.9 Hz, ω_{11} = 2.4 Hz, ω_{12} = 7.99 Hz, ω_{21} = 4.3 Hz, ω_{22} = 11.5 Hz). For a single load q = 10 N rotating with 1.59 Hz on the nodal circle corresponding to m = 0 and n = 2, the FFT of time response is shown in Fig. 1(b). In this we clearly note that the (0,2) mode is missing and the response has a significant contribution from (0,1) mode. However, when we split the load into three equal parts and move them 120^0 apart on the same nodal circle with the same velocity we note in Fig. 2(b) that the contribution from the fundamental mode remains the same but that from other modes drops significantly.

CONCLUSIONS

Closed form solution for transverse vibration of a simply supported circular thin plate subjected to transverse moving point loads is obtained. The formulation can be used for any arbitrary motions of a point load. In the example presented, splitting a angularly separating circular moving point load helps in quenching higher modes and may be a desirable option in a machinery.

References

[1] Sun L.: Dynamics of the Plate Generated by Moving Harmonic Loads. *J Appl Mech T ASME* **72**, 2005.
[2] Weiner R. S.: Transient Motion of a Circular Elastic Plate Subjected to Impulse and Moving Loads. *Bell Syst Tech J* **44**,2409-2431,1965.
[3] Mote C. D. JR.: Stability of Circular Plate Subjected to Moving Loads. *J Franklin I* **290**, 1970.
[4] Stanisic M. M., Lafayette W.: A Contribution to the Stability of Circular Plates. *Ing Arch* **46**, 383-388, 1977.
[5] Hagedorn P., Dasgupta A.: Vibration and waves in Continuous systems. *John Willey and Sons Ltd.*2007.

SIMULATION OF ACTIVE VIBRATIONS ATTENUATION IN STRUCTURES BY COMBINING THE FE AND OPTIMAL CONTROL METHODOLOGIES

Simon Woods[1], Walerian Szyszkowski[1a)]
[1]*Department of Mechanical Engineering, University of Saskatchewan, Saskatoon, SK, Canada*

Summary A method of simulating optimal vibrations attenuation in elastic continuous mechanical systems by discrete actuators is presented. Such systems are inherently under-actuated and involve second-order non-holonomic constraints. The approach applies Pontryagin's Principle to the system modeled by the finite elements (FE) with a large number of DOFs, in which several significant vibration modes are controlled by a small number of discrete actuators. For an assumed set of actuators the complete dynamic response of the system is obtained (including the forces to be generated by particular actuators), as well as the rate and effort parameters to evaluate efficiency of the whole attenuation process. The method is intended to help the engineers in analyzing, designing, and optimizing active vibration control systems.

THE METHOD AND ILLUSTRATING EXAMPLES

An elastic mechanical system (Figure 1) represented by vector $X(t)$ with a large number of DOFs is to be controlled by n_a independent actuators denoted by vector $F_a(t)$. The system's behavior is governed by:

$$M\ddot{X} + C\dot{X} + KX = BF_a \tag{1}$$

where M, C, K are mass, damping, and stiffness matrices, and matrix B assigns the actuation forces to DOFs. The task of the actuators is to bring the system from a disturbed vibrating state to the resting configuration in an optimal way by minimizing the task [1]:

$$J = \tfrac{1}{2}\int_o^{t_f} (aX^T KX + b\dot{X}^T M\dot{X} + c(BF_a)^T K^{-1} BF_a)dt \to \min \tag{2}$$

where a, b, and c are weights for the system's strain energy, kinetic energy, and actuators' power respectively (note that in (1-2) both vectors X and F_a are unknown). The problem defined by (1) and (2) can be re-defined in terms of the modal variables η and the modal controls U by applying the conversion $X = \phi\eta$ and $U = \phi^T BF_a$, where matrix ϕ represents M-normalized modal shapes.

It is assumed that n_m significant modes (where $n_m \geq n_a$) will be controlled. These modes are not independent since they have to satisfy $n_r = n_m - n_a$ generally non-holonomic constraints [2]. Vector v of n_r time-dependent Lagrange multipliers is introduced to handle such constraints.

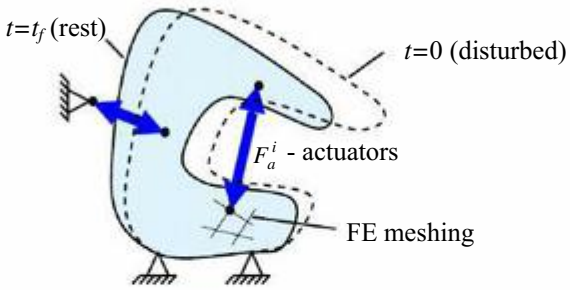

Figure 1. Actively controlled vibrating system

By applying the Pontryagin Principle the optimality equations for the problem are derived as [3]:

$$\begin{gathered}\hat{R}\eta + (2\Omega\hat{R} - \hat{Q}_v - \hat{R}\Delta^2)\eta + (\hat{R}\Omega^2 + \hat{Q}_d)\eta - (A^T\ddot{v} - \Delta A^T\dot{v} + \Omega A^T v) = 0 \\ AU = (I\ddot{\eta} + \Delta\dot{\eta} + \Omega\eta) = 0\end{gathered} \tag{3}$$

[a)] Corresponding author. Email: ictam2016papers@legendconferences.com.

where matrices $\hat{R}$, $\hat{Q}_v$, $\hat{Q}_d$, Δ, Ω, and A are determined in terms of matrices M, C, K, B, and parameters a, b, c. Matrix A (called the matrix of constraint), which depends only on the actuators' placement and the system's frequency spectrum, plays a crucial role in the analysis. Performance of a particular control setup can be evaluated by using the terms of this matrix to form two indicators representing the rate of attenuation and the actuators effort. These indicators appear to be convenient quantitative measures when comparing effectiveness of different configurations of actuators.
The set of $n_m + n_r$ equations (3) is to be solved for n_m unknown modal variables η and n_r Lagrange multipliers in vector v. In the procedure we used ANSYS for any FE calculation (such as matrix ϕ, frequency spectrum, etc), while Eq. (3) were handled automatically by MAPLE. Open or closed loop control schemes can be simulated. For verification, the forces F_a obtained from (3) are substituted back into equation (1) to run the system's transient response, this also checks for any possible spillover effects.

The method will be illustrated by two examples. In the first example four modes of vibrations (Figure 2a) of a 2-D three bays frame structure supporting a heavy plate on the top are to be attenuated in closed loop control either by one or two actuators at various locations/configurations. As mentioned, the most suitable setup can be selected by comparing the rate of attenuation and the actuators effort for the configurations considered. Interestingly, actuator F_1 placed between nodes 7 and 25 appears to be quite effective both in terms of the attenuation rate and the actuation effort.

In the second example the mast structure shown in Figure 2b and consisting of 12 bays, each 140 mm high, composed of steel bars is considered (more details on the mast, as well as on some experimental results are available in [1]). Its vertical members form the points of an equilateral triangle when viewed in the z-direction. Active members, representing piezoelectric linear actuators F_1 and F_2, are shown as thick black lines (the frequencies and shapes of the three lowest vibration modes are also indicated).

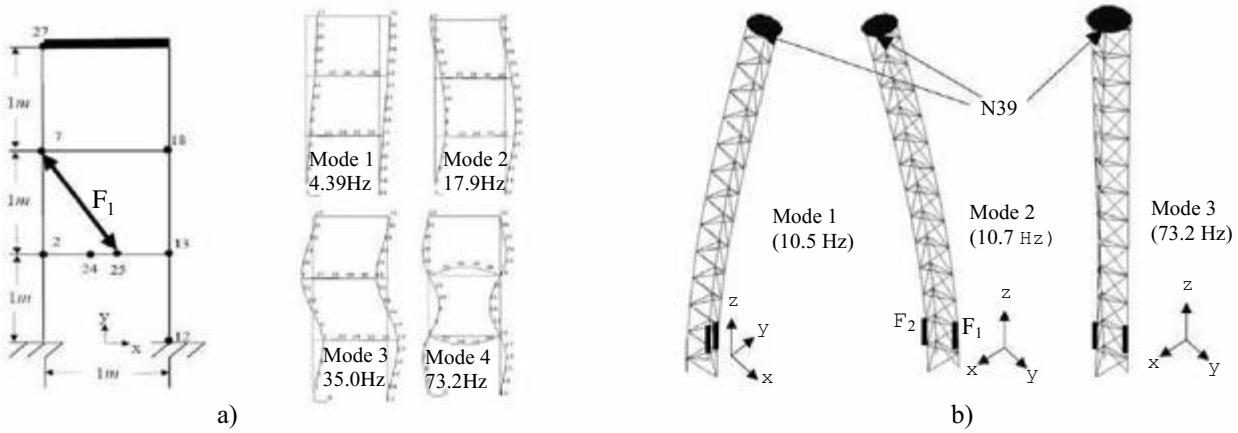

Figure 2. FE models of the structures considered: a) 2-D frame, b) 3-D mast.

The deflections of the mast's top (node 39, labeled as N39) is monitored. First the solution of a fully actuated problem considered in [1], with actuators F_1 and F_2 controlling two bending modes of vibrations, was closely recreated. For this case both vibration modes attenuate with an identical active damping ratio of about 0.69 (i.e. $\xi_1 = \xi_2 = 0.69$), and about 7kN maximum force is required in both actuators. Next, in order to examine the control performance in the situation of one of the actuators failing, only actuator F_2 is employed to control the same first two modes of vibration. For such a case actuator F_2 of similar maximum force produces the active damping ratios of $\xi_1 = 0.69$ for the first mode but only $\xi_2 = 0.011$ for the second mode. Clearly, depending on the application, this level of vibration control may still be considered adequate and therefore adding an extra actuator to handle such an emergency situation may be not necessary.

Finally, if two actuators F_1 and F_2 are used to control two bending modes and the third torsional mode, then the actuation forces of about 40kN are required to produce the active damping ratios of order of 0.1.

References

[1] A. Preumont, 2002, Vibration control of active structures. 2nd edn., Kluwer Academic Publishers, Dordrecht, Boston.

[2] I. Fantoni, and R. Lozano, 2002, Non-linear Control for Underactuated Mechanical Systems, Springer Verlag, London,.

[3] S. Woods, W. Szyszkowski, W., 2009, "Simulating Active Vibration Attenuation in Under-actuated Spatial Structures," Journal of Guidance, Control, and Dynamics, Vol. 32, No. 4, pp. 1246-1253,

NON-STATIONARY COUPLED ELECTROMAGNETIC ELASTIC OSCILLATIONS OF SPHERICAL SHELLS

Vladimir Vestvak[1]. Dmitry Tarlakovskii[2a)]
[1]*Department of Mathematical Modeling Moscow Aviation Institute (National Research University), Moscow, Russia*
[2]*Institute of Mechanics Lomonosoy Moscow State University), Moscow, Russia*

Summary The present work studies related non-stationary axially symmetrical problems of propagation of waves in spherical shells filled with isotropic conductor. Initial boundary value problems include linearized equation systems, zero initial and boundary conditions. Required functions are expanded in terms of Legendre and Gegenbauer polynomials, as well as in serials with respect to a small parameter describing the link between electromagnetic and mechanic fields.

PROBLEM DESCRIPTION

It is assumed that spherical shells (thick-wall sphere, spherical cavity or ball) are filled with isotopic conductor. Non-stationary coupled axially symmetric process is described by non-dimensional linear equations of motion with its right side in the form of Lorenz force linearized generalized Ohm's law, as well as by conclusion from Maxwell's equation in a spherical coordinate system $r,\theta,\vartheta\ (r\ge 0,\ 0\le\theta\le\pi,\ -\pi<\vartheta\le\pi)$ [1]:

$$\ddot{u}=\left(1-\eta^{-2}\right)\frac{\partial I_1}{\partial r}+\eta^{-2}\left\{\Delta u-\frac{2}{r^2}\left[\frac{1}{\sin\theta}\frac{\partial}{\partial\theta}\left(v\sin\theta\right)+u\right]\right\}+\alpha\left[\rho_{e0}E_r+\rho_e E_{0r}+\gamma\left(j_{0\theta}H+j_\theta H_0\right)\right],$$

$$\ddot{v}=\frac{1}{r}\left(1-\eta^{-2}\right)\frac{\partial I_1}{\partial\theta}+\eta^{-2}\left[\Delta v+\frac{1}{r^2}\left(2\frac{\partial u}{\partial\theta}-\frac{v}{\sin^2\theta}\right)\right]+\alpha\left[\rho_{e0}E_\theta+\rho_e E_{0\theta}-\gamma\left(j_{0r}H+j_r H_0\right)\right],$$

$$I_1=\frac{\partial u}{\partial r}+\frac{1}{r}\left(\frac{\partial v}{\partial\theta}+2u+v\operatorname{ctg}\theta\right),\ \Delta=\frac{1}{r^2}\left[\frac{\partial}{\partial r}\left(r^2\frac{\partial}{\partial r}\right)+\frac{1}{\sin\theta}\frac{\partial}{\partial\theta}\left(\frac{\partial}{\partial\theta}\sin\theta\right)\right];$$

$$j_r=E_r+H_0\dot{v}+\rho_{e0}\dot{u}/\gamma,\ j_\theta=E_\theta-H_0\dot{u}+\rho_{e0}\dot{v}/\gamma;$$

$$\eta_e^2\left(\ddot{H}+\gamma\dot{H}\right)=\Delta\dot{H}-\frac{\dot{H}}{r^2\sin^2\theta}+\frac{\eta_e^2}{r}\left[\frac{\partial\left(r\rho_{e0}\ddot{v}\right)}{\partial r}-\frac{\partial\left(\rho_{e0}\ddot{u}\right)}{\partial\theta}\right]-\frac{\gamma\eta_e^2}{r}\left[\frac{\partial\left(r\ddot{u}H_0\right)}{\partial r}+\frac{\partial\left(\ddot{v}H_0\right)}{\partial\theta}\right];$$

$$\eta_e^2\left(\dot{E}_\theta+\gamma E_\theta\right)=-\frac{1}{r}\frac{\partial\left(rH\right)}{\partial r}+\eta_e^2\left(\gamma H_0\dot{u}-\rho_{e0}\dot{v}\right),\ \eta_e^2\left(\dot{E}_r+\gamma E_r\right)=\frac{1}{r\sin\theta}\frac{\partial\left(H\sin\theta\right)}{\partial\theta}-\eta_e^2\left(\gamma H_0\dot{v}+\rho_{e0}\dot{u}\right);$$

$$\dot{\rho}_e+\gamma\rho_e=-\frac{1}{r^2}\frac{\partial}{\partial r}\left[r^2\left(\rho_{e0}\dot{u}+\gamma H_0\dot{v}\right)\right]-\frac{1}{r\sin\theta}\frac{\partial}{\partial\theta}\left[\left(\rho_{e0}\dot{v}-\gamma H_0\dot{u}\right)\sin\theta\right].$$

Here u and v are radial and tangential displacements; E_r, E_θ and j_r, j_θ are corresponding components of electric field vectors and current density; H is non-zero coordinate of electric field vector; ρ_e - surface charge density; α, η, γ, η_e are non-dimensional physical parameters; time derivatives are dotted, lower index "0" corresponds to the initial values. The following values are taken as units of measurement: R and E_* are describing linear size and electric field; R/c_1 where c_1 is velocity of the waves of tension and compression; ρR^3 where ρ is density of material.

Initial conditions are zero, the required functions are limited, initial density of magnetic field is absent. The methods of solutions in the above mentioned areas and various boundary conditions are identical. Such methods can be exemplified in a ball of r_1 radius with displacement and intensity of electrical field set at the boundary.

EXPANSION AND INTEGRAL REPRESENTATION OF SOLUTION

Let the required functions as well as the right sides of the boundary conditions be expanded in terms of Legendre polynomials $P_n\left(\cos\theta\right)\left(n\ge 0\right)$ and in products $\sin\theta C_{n-1}^{3/2}\left(\cos\theta\right)\left(n\ge 1\right)$ where the second factor is a Gegenbauer polynomial (coefficients are marked by lower index "n"). Then, the Laplace time transformation is applied (with upper index "L" corresponding representation in time, s, corresponding parameter). The study of the resulted initial boundary value problem shows that its analytical solution is pretty much difficult. Therefore, the problem is expanded in series with respect to small parameter α which is describing relatedness of the problem (only a part of functions indicated):

[a)] Corresponding author. Email: tdvhome@mail.ru

$$u_n=\sum_{m=0}^{\infty}u_{nm}\alpha^m,\ v_n(r,\tau)=\sum_{m=0}^{\infty}v_{nm}(r,\tau)\alpha^m,\ H_n(r,\tau)=\sum_{m=0}^{\infty}H_{nm}(r,\tau)\alpha^m,E_{rn}(r,\tau)=\sum_{m=0}^{\infty}E_{rnm}(r,\tau)\alpha^m.$$

The result is a recurrent (by m index) system of boundary value problems. Let their solution be written in integral form (relations are shown partially; g_u, g_v and l_H are known functions):

$$u^L_{nm}(r,s)=\int_0^{r_1}G^L_{uun}(r,\xi,s)f^L_{un,m-1}(\xi,s)d\xi+\int_0^{r_1}G^L_{uvn}(r,\xi,s)f^L_{vn,m-1}(\xi,s)d\xi,$$

$$v^L_{nm}(r,s)=\int_0^{r_1}G^L_{vun}(r,\xi,s)f^L_{un,m-1}(\xi,s)d\xi+\int_0^{r_1}G^L_{vvn}(r,\xi,s)f^L_{vn,m-1}(\xi,s)d\xi, \quad (1)$$

$$f^L_{un,m-1}(\xi,s)=\rho_{e0}(\xi)E^L_{rn,m-1}(\xi,s)+E_0(\xi)\rho^L_{n,m-1}(\xi,s),\ f^L_{vn,m-1}(\xi,s)=\rho_{e0}(\xi)E^L_{\theta n,m-1}(\xi,s)-\gamma E_0(\xi)H^L_{n,m-1}(\xi,s);$$

$$H^L_{nm}(r,s)=-\eta_e^2 s\int_0^{r_1}G^L_{Hn}(r,\xi,s)l_H\left[u^L_{nm}(\xi,s),v^L_{nm}(\xi,s)\right]d\xi,\ rl_H(u,v)=(r\rho_{e0}v)'+\rho_{e0}u\,. \quad (2)$$

The kernels of these representations are Green functions, i.e. limited solutions of the corresponding boundary value problems. They are represented explicitly which allows for precise finding originals through expansion in serials with regard to exponents [2]. For instance, G^L_{uu0} in (1) is represented as ($h(x)$, a Heaviside's function, other functions are not given here because of space limitation):

$$G^L_{uu0}(r,\xi,s)=\xi^2\left[F^L_{uu0}(r,\xi,s)h(\xi-r)+F^L_{uu0}(\xi,r,s)h(r-\xi)\right],$$

where

$$F^L_{uu0}(r,\xi,s)=\frac{\Lambda_{01}(rs)E_{110}(\xi s,r_1 s)}{2\xi^2r^2s^3\Lambda_{01}(r_1 s)}e^{(\eta+1)r_1 s},\ \Lambda_{01}(z)=(1-z)e^z-(1+z)e^{-z},\ E_{110}(x,y)=(1+x)(1-y)e^{y-x}-(1-x)(1+y)e^{x-y}.$$

In the same way the dominant functions in (2) can be represented, as well as in integrations of other components of electromagnetic field. However, calculation of their originals implies significant difficulties due to the small value of η_e parameter. To this reason they are substituted by quasi-static analogues where

$$G^L_{Hn}(r,\xi,s)=G^c_{Hn}(r,\xi)=\xi^2\left[F^c_{Hn}(r,\xi)H(\xi-r)+F^c_{Hn}(\xi,r)H(r-\xi)\right],\ F^c_{Hn}(r,\xi)=-\frac{(n+1)r_1^{2n+1}+n\xi^{2n+1}}{(n+1)(2n+1)\xi^{n+1}r_1^{2n+1}}r^n.$$

This allows to write the original representations (2) in the form of single interval (without time convolutions):

$$H_{nm}(r,\tau)=-\eta_e^2\int_0^{r_1}F^c_{Hn}(r,\xi)l_H\left[\dot u_{nm}(r,\tau),\dot v_{nm}(r,\tau)\right]d\xi\,. \quad (2)$$

Recurrent system of equations (1), (2) is solved through numerical integration.

CONCLUSIONS

The algorithm developed will allow for studying mutual influence of non-stationary mechanical and electromagnetic fields in bodies limited by spherical surfaces. Such approach can also be applied to bodies of other geometry (for instance, semi-plane, round cylinder).

This work was done with financial support of the Russian Foundation for Basic Research (project code 15-08-00788).

References

[1] Tarlakovskii D.V., Vestyak V.A., Zemskov A.V. *Encyclopedia of Thermal Stresses* (Springer, Dordrecht, Heidelberg, New York, London), 2014.

[2] Gorshkov A.G., Tarlakovskiy D.V. Transient Aerohydroelasticity of Spherical Bodies. Berlin-Heidelberg-New York: Springer-Verlag, 2001.

DYNAMIC BEHAVIOR OF GRIPPER CYLINDER IN TBM WITH VARIABLE STIFFNESS

Lin Li[1], Haidong Yu[1, 2a)], Jianfeng Tao[1], Chengliang Liu[1]
[1)] *State Key Laboratory of Mechanical System and Vibration, Shanghai Jiao Tong University, No.800 Dongchuan Road, Shanghai 200240.*
[2)] *Shanghai Key Laboratory of Digital Autobody Engineering, Shanghai, 200240, China*

Summary: The lumped parameters dynamic model of gripper cylinder in Tunnel Boring Machines is established in which the interaction with the rock and the variable stiffness of structures are considered. The correlation between the dynamic behavior and the variable stiffness of the cylinder due to interaction with the rock, the oil, the seals, the copper guide sleeve and the length of piston rod is numerical discussed. The results show that the natural frequency of the gripper cylinder is mainly affected by the equivalent stiffness of the seals and the oil. The fluctuation of the loads between the cylinder and piston rod is investigated, which provides the guide for the damage analysis of the gripper cylinder in TBM.

DYNAMIC MODEL OF GRIPPER CYLINDER

The Tunnel Boring Machine (TBM) is widely used in hard rock tunnel construction. The gripper cylinder provides enormous supported load force for the TBM during the excavation shown in Fig.1a and Fig.1b. The vibration performance of the gripper cylinder is important because the damage usually is caused such as the pitting of piston, fracture of the seals and fatigue of the cooper guide sleeve. It easily results in the blockage serious accidents. Consequently, it is important to study the dynamic model and the vibration characteristic influenced by the uncertainties of gripper cylinder.

A lumped parameter dynamic model of gripper cylinder system is illustrated in Fig.1c. The cylinder barrel and the piston rod are modelled as the beams with the mass m_b and m_r. The mass of seals and the copper guide sleeve are m_s and m_c. The length of the barrel and the rod are L_b and L_r while their bending moments are $I_{cgb}=1/2m_bL_b^2$ and $I_{cgr}=1/2m_rL_r^2$, respectively. And a_1 represents the distance between the centre of the barrel and the seals, a_2 is the distance between the centre of the rod and the copper guide sleeve. The interaction between the gripper and the rock would change the boundary condition of the vibration model, which is defined as the equivalent stiffness of the rock k_r. In addition, the equivalent stiffness of the seals, the copper guide sleeve, the oil and the bending stiffness of the gripper are denoted as k_s, k_c, k_o and k_g, respectively. The axial displacements of barrel and rod are denoted as x_1 and x_2, the radial displacements of the barrel and rod are denoted by y_1 and y_2, and the rotation displacements are θ_1 and θ_2.



Fig.1. A lumped parameter model of gripper cylinder in TBM

According to the Lagrange equations:

$$\frac{dy}{dt}\left(\frac{\partial L}{\partial \dot{q}_i}\right)-\frac{\partial L}{\partial q_i}=Q_i \quad i=1,2,\cdots,n \qquad L=T-V \tag{1}$$

where T is the kinetic energy, V is the potential energy and q_i is the generalized coordinate of the whole systems. The dynamic equations of the gripper cylinder system can be written as:

$$\mathbf{M}\ddot{\mathbf{q}}+\mathbf{K}\mathbf{q}=\mathbf{0} \qquad \mathbf{M}=\begin{bmatrix} M_{11} & M_{12} \\ M_{12} & M_{22} \end{bmatrix} \qquad \mathbf{K}=\begin{bmatrix} K_{11} & K_{12} \\ K_{21} & K_{22} \end{bmatrix} \qquad M_{11}=\begin{bmatrix} m_b & & \\ & m_b & \\ & & I_{cgb} \end{bmatrix} \qquad M_{12}=M_{21}=0$$

$$M_{22}=\begin{bmatrix} m_r+m_c+m_s & 0 & 0 \\ 0 & m_r+m_c+m_s & m_cL_r/2-m_sL_r/2 \\ 0 & m_cL_r/2-m_sL_r/2 & I_{cgr}+L_r^2m_c/4+L_r^2m_s/4 \end{bmatrix} \qquad K_{11}=\begin{bmatrix} k_o+k_s+k_c & 0 & 0 \\ 0 & k_o+k_s+k_c & -a_1k_s+L_bk_c/2 \\ 0 & -a_1k_s+L_bk_c/2 & a_1^2k_s+L_b^2k_c/4 \end{bmatrix} \tag{2}$$

$$K_{12}=\begin{bmatrix} -(k_o+k_c+k_s) & 0 & 0 \\ 0 & -(k_o+k_c+k_s) & a_1k_s-L_bk_c/2 \\ 0 & -a_2k_c+L_rk_s/2 & -a_1L_rk_s/2-a_2L_bk_c/2 \end{bmatrix} \qquad K_{21}=K_{12}^{\mathrm{T}}$$

$$K_{22}=\begin{bmatrix} k_r+k_o+k_c+k_s & 0 & 0 \\ 0 & k_s+k_c-k_o+k_r & -L_rk_s/2+a_2k_c \\ 0 & -L_rk_s/2+a_2k_c & k_g+a_2^2k_c+L_r^2k_s/4 \end{bmatrix}$$

[a)] Corresponding author. Email: hdyu@sjtu.edu.cn.

where **q** is a vector containing the system coordinates while **M** and **K** stand for mass matrix and stiffness matrix, respectively.

RESULTS AND DISCUSSIONS

A six degree dynamic model of gripper cylinder can be obtained when the copper guide sleeve and the seals have the same velocity with the rod illustrated in Fig.1c. The rod of the gripper cylinder extends to a designed length to provide support force when the TBM is working. The influence on the dynamic behaviour due to the gripper and the rock, the equivalent stiffness of the seals, the oil, and the copper guide sleeve is numerical studied by using Matlab2015.

The correlations of the natural frequency and the equivalent stiffness are illustrated in Fig. 2. The natural frequency decreases with the extension of the rod increasing. The natural frequency of the gripper cylinder is 34.8 Hz when the piston rod is extended to the maximal length (Fig.2a). The natural frequency has the positive correlation with the equivalent stiffness of the oil, the seals, the copper guide sleeve (CGS) and the rock (Fig. 2b, Fig. 2c, Fig. 2d and Fig. 2e). It can be found that the relationships between the natural frequency and the variable equivalent stiffness are nonlinear because the stiffness due to variable factors is coupled. The natural frequency increases 33.3% with the equivalence stiffness of the seals changing from 0.01 GN/m to 0.15 GN/m and it has the same increment with the equivalence stiffness of the oil changing from 0.3 GN/m to 1.2 GN/m. It increases 12.8% with the equivalence stiffness of the copper guide sleeve changing from 0.2 GN/m to 6 GN/m. The nature frequency changes 1.1% when the equivalent stiffness of the rock varies from 20 GN/m to 120 GN/m. It can be concluded that the equivalence stiffness of the seals and the oil have greater influence on the natural frequency of the gripper cylinder.

The vibration is unavoidable for the copper guide sleeve. The loads between the cylinder barrel and the copper guide sleeve were studied and the frequency was achieved by FFT shown in Fig.3. The load has an oscillation between -30kN and 30 kN and it has a complex frequency spectrum.

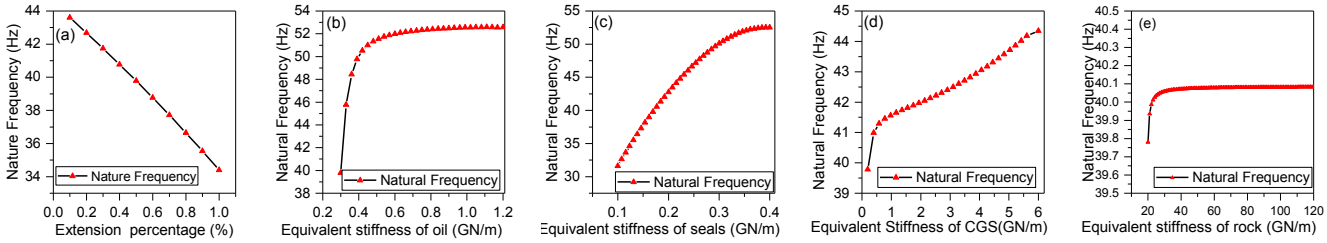

Fig.2. Nature frequency of the gripper cylinder changing with equivalent stiffness of the copper guide sleeve, the oil, the seals and the extension of piston

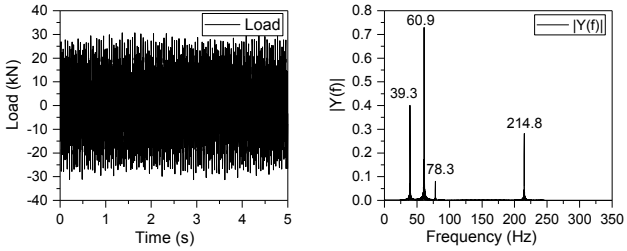

Fig.3. Loads between the cylinder barrel and the copper guide sleeve

CONCLUSIONS

The dynamic model of the gripper cylinder in TBM considering variable stiffness is established. The dynamic performance of the gripper cylinder is numerically studied by considering the variable factors. The results show that the equivalent stiffness of the seals and the oil play the most important role in the natural frequency of the gripper cylinder. The natural frequency decreases with the extension of the piston rod. Based on the dynamic characteristics of the gripper cylinder, the loads between the cylinder barrel and the copper guide sleeve are calculated, which may be used in the damage analysis of the gripper cylinder. Meanwhile, it is useful in the fault diagnosis and the life prediction of the gripper cylinder in TBM.

ACKNOWLEDGEMENTS

The authors appreciate the financial supports by the National Basic Research Program of China (2013CB035403) and National Natural Science Foundation of China (51275292).

MULTI-PULSE CHAOTIC MOTIONS OF EQUIVALENT CIRCULAR CYLINDRICAL SHELL

Wei Zhang[1], Ying Sun[1] , Qian Wang[1] & JieYu Ding[1,2]
[1] *College of Mechanical Engineering, Beijing University of Technology, Beijing, China*
[2]*College of Mathematical sciences, Qingdao University, Qingda , Shangdong, China*

Summary The multi-pulse heteroclinic orbits and chaotic dynamics of an equivalent circular cylindrical shell for the circular mesh antenna are investigated in the case of 1:2 internal resonance in this paper for the first time. Applying the method of averaging, the four-dimensional averaged equation in the Cartesian form is obtained. The theory of normal form is used to reduce the averaged equation to a simpler form. Based on the simplified system, the energy phase method is employed to investigate the heteroclinic bifurcations and the Shilnikov type multi-pulse chaotic dynamics. The results obtained here show the existence of the Shilnikov type multi-pulse chaotic motions of the circular mesh antenna. Numerical simulations are used to find multi-pulse chaotic motions. The results obtained by the theoretical analysis and numerical simulation are qualitatively agree.

EQUATIONS OF MOTION

With the rapid development of space science and technology, the requirement of new type satellite antenna is increasing constantly. The design and dynamic analysis of antenna structures are directly related to the quality of the satellite work. The circular mesh antenna is a new type of satellite antenna, which is designed to be the foldable and deployable structure to overcome the volume and weight limitations of the launch vehicle. The shell structures have wildly been used in the aeronautic and astronautic engineering. Many investigators studied the nonlinear vibrations and chaos motions of circular cylindrical shells. In the past two decades, researches on the global bifurcations and chaotic dynamics of high-dimensional nonlinear systems have been at the forefront of nonlinear dynamics.

The equivalent shell is subjected to the thermal excitation in changing thermal environment. A cylindrical coordinate system (O, x, θ, z) is introduced, in which Ox, $O\theta$ and Oz are in the axial, circumferential and radial directions, respectively, as shown in Figure 1.

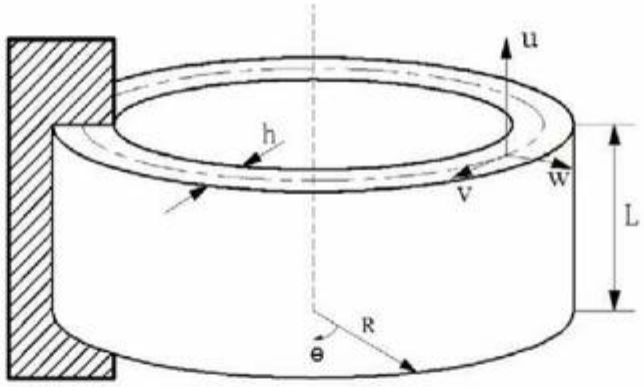

Figure 1 The model of equivalent circular cylindrical shell is presented.

Based on reference [1], the dimensionless governing differential equation of the nonlinear breathing vibrations for the equivalent circular cylindrical shell is obtained as follows

$$\ddot{w}_1 + \mu_1\dot{w}_1 + \omega_1^2 w_1 + \gamma_{11} f_T \cos(\Omega t) w_1 + \gamma_{12} w_2 + \gamma_{13} {w_1}^3 + \gamma_{14} {w_1}^2 w_2 + \gamma_{15} w_1 {w_2}^2 + \gamma_{16} {w_2}^3 = \gamma_{17} + \gamma_{18} f_T \cos(\Omega t), \quad (1a)$$

$$\ddot{w}_2 + \mu_2\dot{w}_2 + \omega_2^2 w_2 + \gamma_{21} f_T \cos(\Omega t) w_2 + \gamma_{22} w_1 + \gamma_{23} {w_2}^3 + \gamma_{24} {w_2}^2 w_1 + \gamma_{25} w_2 {w_1}^2 + \gamma_{26} {w_1}^3 = \gamma_{27} + \gamma_{28} f_T \cos(\Omega t), \quad (1b)$$

The method of averaging is used to analyze the nonlinear breathing vibrations of the equivalent circular cylindrical shell. We obtain the four-dimensional averaged equation in the Cartesian form as follows

$$\dot{x}_1 = -\frac{1}{2}\mu_1 x_1 - (\sigma_1 - f_1) x_2 - \frac{3}{4}\gamma_{13} x_2 \left({x_1}^2 + {x_2}^2\right) - \frac{1}{2}\gamma_{15} x_2 \left({x_3}^2 + {x_4}^2\right), \quad (2a)$$

$$\dot{x}_2 = (\sigma_1 + f_1) x_1 - \frac{1}{2}\mu_1 x_2 + \frac{3}{4}\gamma_{13} x_1 \left({x_1}^2 + {x_2}^2\right) + \frac{1}{2}\gamma_{15} x_1 \left({x_3}^2 + {x_4}^2\right), \quad (2b)$$

$$\dot{x}_3 = -\frac{1}{2}\mu_2 x_3 - \frac{1}{2}\sigma_2 x_4 - \frac{3}{8}\gamma_{23} x_4 \left({x_3}^2 + {x_4}^2\right) - \frac{1}{4}\gamma_{25} x_4 \left({x_1}^2 + {x_2}^2\right), \quad (2c)$$

$$\dot{x}_4 = -f_2 + \frac{1}{2}\sigma_2 x_3 - \frac{1}{2}\mu_2 x_4 + \frac{3}{8}\gamma_{23} x_3 \left({x_3}^2 + {x_4}^2\right) + \frac{1}{4}\gamma_{25} x_3 \left({x_1}^2 + {x_2}^2\right). \quad (2d)$$

ENERGY PHASE METHOD

[a] Corresponding author. Email: sandyzhang0@yahoo.com

The key point of using the energy-phase method to demonstrate the existence of the Shilnikov type multi-pulse heteroclinic orbits is the calculation of the energy difference function. Based on the general expression derived by Haller and Wiggins [2-4] for the classical systems, the energy difference function for the dissipative system is given as follows

$$\Delta^n\hat{H}_D(\gamma)=\hat{H}_D(h,\gamma+n\Delta\gamma)-\hat{H}_D(h,\gamma)\ -n\int_A\left[\frac{d}{du_1}g^{u_1}(u_1,u_2,I_r,\gamma)+\frac{d}{du_2}g^{u_2}(u_1,u_2,I_r,\gamma)\right]du_1du_2-n\int_{\partial A_1}g^I d\gamma\,, \tag{3}$$

where

$$\hat{H}_D(h,\gamma+n\Delta\gamma)-\hat{H}_D(h,\gamma)=-n\bar{\mu}_2I_r\Delta\gamma+\bar{f}_2\left[\cos(\gamma+n\Delta\gamma)-\cos\gamma\right], \tag{4}$$

$\Delta\gamma$ is the phase difference, A denotes the area enclosed by a pair of heteroclinic orbits in plane (u_1,u_2) and ∂A_1 is the boundary of the area A.

We use the energy phase method to investigate the heteroclinic bifurcations and multi-pulse chaotic dynamics of the equivalent circular cylindrical shell for the circular mesh antenna in the case of 1:2 internal resonance.When there are the dissipative perturbations in the system, the center type singular point changes a hyperbolic sink or a saddle-focus. In the following studies, we mainly find out the homoclinic multi-pulse orbits to the saddle-focus. In fact, when the dissipative perturbations exist, Shilnikov type multi-pulse orbits are negatively and positively asymptotic to the saddle-focus itself in full four-dimensional phase space. Studies show that the existence of N-pulse Shilnikov orbits results in the chaotic dynamics in the sense of the Smale horseshoes.

We choose the averaged equation (2) to conduct numerical simulations. A numerical approach through the computer software Matlab is utilized to explore the existence of the Shilnikov type multi-pulse chaotic motions in the equivalent circular cylindrical shell. Figure 2 indicates the existence of the multi-pulse chaotic motion of the equivalent circular cylindrical shell

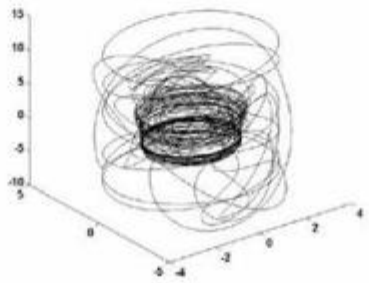

Figure 2 the phase portraits in the three dimensional space (x_1,x_2,x_3).

CONCLUSIONS

The analysis of the multi-pulse heteroclinic orbits for the equivalent circular cylindrical shell demonstrates that the unperturbed integrable Hamiltonian system contains a normally hyperbolic invariant two-dimensional manifold near the resonance. The resonance leads to a circle of fixed points on the two-dimensional manifold. Two different points on the circle of fixed points are connected by a heteroclinic orbit. The dissipative perturbation can severely change the dynamic behaviors near the circle of fixed points. The analysis also shows that the existence of heteroclinic orbits depend only on an energy-phase criterion. In order to verify the theoretical prediction, Numerical simulations are used to examine the chaotic motions of the equivalent circular cylindrical shell. It is found from the numerical results that there exist different shapes of the chaotic motions in the nonlinear breathing vibrations of the equivalent circular cylindrical shell under different excitations, parameters and initial conditions. Therefore, the parameters and initial conditions impact on the shapes of the multi-pulse chaotic motions.

References

[1] Zhang. W., Chen. J., Sun. Y.: Nonlinear breathing vibrations and chaos of a circular truss antenna with 1:2 internal resonance, submitted to International Journal of Bifurcation and Chaos, 2015.

[2] Wiggins. S.: Global Bifurcations and Chaos-Analytical Methods, Springer-Verlag, New York, 1988.

[3] Haller. G.: Chaos Near resonance, Springer-Verlag, New York, 1999.

[4] Yao M. H., Zhang. W.: Multiples heteroclinic orbits and chaotic dynamics of the laminated composite piezoelectric rectangular plate, Discrete Dynamics in Nature and Society 2013, ID 958219-27, 2013

DAMAGE LOCALIZATION FOR OPERATIONAL MODAL ANALYSIS VIA RANDOM DECREMENT TECHNIQUE

Y. Zhang[1], H.W. Song[1a)] & D. Bernal[2]
[1]*School of Aerospace Engineering and Applied Mechanics, Tongji University, Shanghai, P. R. China*
[2]*Civil and Environmental Engineering Department, Northeastern University, Boston, USA*

Summary An approach to localize damage from response of wide band excitation with the help of undamaged model is presented. The wide band response is transferred to a free decay response via random decrement technique. The free decay response is regarded as two parts, a forced response related with damage and a free decay response of undamaged system. If the second part can be eliminated, the residual should belong to a span related with damage. However, the second part cannot be extracted directly because the initial condition is not measurable for all system coordinates with limited sensors. Therefore, we employ the null space of free decay response span based on undamaged model to eliminate it. The fact that subspace angle between the treated free decay response and columns in transfer matrix selected by correct damaged pattern should be zero is used in final localization.

INTRODUCTION

The identification module is often the weak link in damage characterization schemes. This paper presents a damage localization scheme that operates without identification and holds whenever it is possible to extract free-vibration signals from the damaged state. Random decrement technique, which can extract free response from random response[1], helps to extend our application for ambient response. The principle of damage localization based on subspace analysis between damaged and undamaged system[2]. The difference with previous papers is that we only take a vector from damaged state rather than the vector of difference between damaged state and undamaged state.

There is no direct relationship between free decay damaged response vector and the subspace related with damage. However, we regard the free decay damaged response as a summation of a free decay response of undamaged system and a forced response cause by damage. To eliminate the free decay response of undamaged system part, null space of free decay response is constructed with the help of undamaged model. The relationship is built up by multiplying the null space to the free decay damaged response vector.

This paper is organized as: 1) the theory of damage localization from free decay response; 2) description of random decrement technique; 3) numerical example.

DAMAGE LOCALIZATION FROM FREE DECAY RESPONSE

Consider a system with damage treated as a change in the stiffness matrix $\Delta\mathbf{K}$. The equation that governs the response to an arbitrary initial condition is $\mathbf{M}\ddot{\mathbf{x}}_d(t)+\mathbf{C}\dot{\mathbf{x}}_d(t)+(\mathbf{K}-\Delta\mathbf{K})\mathbf{x}_d(t)=0$,which can be written as $\mathbf{M}\ddot{\mathbf{x}}_d(t)+\mathbf{C}\dot{\mathbf{x}}_d(t)+\mathbf{K}\mathbf{x}_d(t)=\Delta\mathbf{K}\mathbf{x}_d(t)$. Let $\mathbf{x}_d(t)$ be divided in two parts $\mathbf{x}_d(t)=\mathbf{x}'_d(t)+\mathbf{x}''_d(t)$, where they are

$$\begin{aligned}&\mathbf{M}\ddot{\mathbf{x}}'_d(t)+\mathbf{C}\dot{\mathbf{x}}'_d(t)+\mathbf{K}\mathbf{x}'_d(t)=\Delta\mathbf{K}\mathbf{x}_d(t) \qquad \mathbf{x}'_d(0)=0 \qquad \dot{\mathbf{x}}'_d(0)=0\\ &\textit{and}\\ &\mathbf{M}\ddot{\mathbf{x}}''_d(t)+\mathbf{C}\dot{\mathbf{x}}''_d(t)+\mathbf{K}\mathbf{x}''_d(t)=0 \qquad \mathbf{x}''_d(0)=\mathbf{x}_d(0) \qquad \dot{\mathbf{x}}''_d(0)=\dot{\mathbf{x}}_d(0)\end{aligned} \tag{1}$$

Since the initial conditions in the first equation are zero, a Laplace transform leads to $\mathbf{x}'_d(s)=\mathbf{G}(s)\Delta\mathbf{K}\mathbf{x}_d(s)$, where $\mathbf{G}(s)=\left(\mathbf{M}s^2+\mathbf{C}s+\mathbf{K}\right)^{-1}$, and $\mathbf{x}''_d(s)=\mathbf{C}_u(s\mathbf{I}-\mathbf{A}_u)^{-1}\begin{Bmatrix}\mathbf{x}_0\\ \dot{\mathbf{x}}_0\end{Bmatrix}$, where $\mathbf{A}_u$ is the transition matrix, $\mathbf{C}_u$ is the observation matrix and $\mathbf{I}$ is the identity matrix . The principle for damage localization is $\mathbf{x}'_d(s)$ belongs to the subspace of $\mathbf{G}(s)\Delta\mathbf{K}$. If we can eliminate $\mathbf{x}''_d(t)$ from $\mathbf{x}_d(t)$, it become possible to localize damage.

With the help of undamaged model, it is not difficult to get the left null space of $\mathbf{C}_u(s\mathbf{I}-\mathbf{A}_u)^{-1}$, which is assumed as $\mathbf{Q}$. Multiply $\mathbf{Q}$ on both sides of $\mathbf{x}_d(s)=\mathbf{x}'_d(s)+\mathbf{x}''_d(s)$ to get $\mathbf{Q}\mathbf{x}_d(s)=\mathbf{Q}\mathbf{x}'_d(s)$. Consequently, we have $\mathbf{Q}\mathbf{x}_d(s)=\mathbf{Q}\mathbf{C}_u\mathbf{G}(s)\Delta\mathbf{K}\mathbf{x}_d(s)$, which means the subspace angle between $\mathbf{Q}\mathbf{x}_d(s)$ and $\mathbf{Q}\mathbf{C}_u\mathbf{G}(s)\Delta\mathbf{K}$ should be zero with the correct damage pattern. Considering the number of sensors is always less than number of DOFs in practice, it is impossible to make $\mathbf{C}_u(s\mathbf{I}-\mathbf{A}_u)^{-1}$ column full rank with signal s-values. Therefore, we take multiple s-values to construct the null space $\mathbf{Q}$ as well as to calculate $\mathbf{Q}\mathbf{C}_u\mathbf{G}(s)\Delta\mathbf{K}$.

[a)] Corresponding author. Email: hwsong@tongji.edu.cn.

RANDOM DECREMENT TECHNIQUE (RDT)

Because free vibration is often difficult to realize one often must extract the signals from forced vibration response. One way that does not require system identification be carried out is using the Random Decrement Technique, which is a method to obtain free vibration from random response. The principle of this method is to average segments in random response. The segments start at special instants under a condition like $C = \left\{ t_i \,\middle|\, y_p(t_i) = a\,,\, \dot{y}_p(t_i) > 0 \right\}$.

It was shown in [3] that this condition often leads to residual spectra with a peak at the first modal frequency. To avoid it, a minimum gap between two adjacent instants of the fundamental period is suggested.

In addition, one limitation of RDT is that it provides a short length faithful free decay response. This leads to error in Fourier transform. To deal with this drawback, the rule that the duration of RD signal taken into Fourier transform depends on s-values is studied.

NUMERICAL EXAMINATIONS

This approach is illustrated by the 5 DOFs lumped system in Fig.1. Damage is simulated as some percent loss of stiffness in spring #4. In addition, there are sensors at coordinates [1 2 4 5] measuring accelerations and 20 dB measured noise in random response.

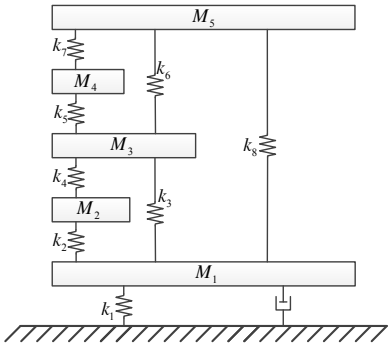

Fig. 1 System of numerical example

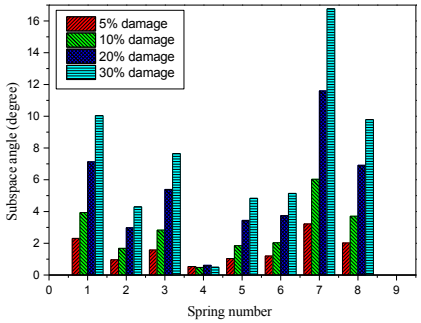

Fig. 2 Comparison of different damage extents

To show the efficiency for different damage extents, we illustrates the numerical results in Fig. 2. As one intuitively expects, the contrast realized between the undamaged and the damaged location increases as the extent of damage increases.

In addition, we also verified this approach under different SNRs and model error. As it is discussed in [4], the noise in RDT mainly depends on averaged times rather than SNRs. As a result, the comparison of subspace angles shows little difference with various SNRs but great improvement with increasing of averaged time. And a 5% model error is tolerable for this example. Further calculation shows the tolerance would decrease with bigger system.

CONCLUSIONS

The paper presents a technique for damage localization that operates with ambeint response from the damaged state and a model of the healthy state. The scheme operates without the need to perform identification and does not impose any significant constraints on the input, namely: it requires that the input be reasonably broad band and of long duration so that sufficiently accurate free vibration signals can be extracted from the measurements using the random decrement technique.

A feature of the approach is we do not need the response from undamaged state. The localization comes from tranfer matrix and free decay response of damaged system (both left multiply the the null space of free response for undamaged system. It seems like the model should be highly accurate. In the numerical example, a maximum model error of 5% is obtained. As limited length RD signal is faithful, the Fourier tranform will be inaccuracy with a uniform langth for every s-values. We suggest the length of RD signal should depond on specific s-value, which can be obtained form analytical Fourier transform.

References

[1] H.A. COLE, On-the-line analysis of random vibrations, AIAA Paper, (1971).
[2] D. Bernal, Load vectors for damage location in systems identified from operational loads, Journal of engineering mechanics, 136 (2009) 31-39.
[3] Y. Zhang, H. Song, Non-overlapped random decrement technique for parameter identification in operational modal analysis, J Sound Vib, (2015).
[4] Y. Zhang, L.J. Wu, H.W. Song, Triggering expectation and residual excitation of distributed random decrement technique, J Sound Vib, 340 (2015) 368-382.

MICRO-DYNAMIC CHARACTERIZATION OF MODAL PARAMETERS FOR A HONEYCOMB PLATE STRUCTURE

Chaofan Wang, Chunyan Zhou[a)]

School of Aerospace Engineering, Beijing Institute of Technology, Beijing, China

Summary Results of this paper are presented from an experimental investigation of a honeycomb plate structure under micro-dynamics. The dynamic response of the honeycomb plate structure was characterized in terms of modal parameters at different micro-vibration level. Two main sweep test methods were established on the ground to measure the FRF curves of a combined plate structure jointed by bolts, over a range of vibration acceleration from 10^{-1} g to 10^{-6} g, by which the natural frequencies and damping ratios were obtained. The results showed that the variances of the first three natural frequencies were less than 1% on different acceleration levels, and the variances of damping ratios for the first three modes are less than 25%.

INTRODUCTION

Micro-vibration of the spacecraft means the vibration with amplitude below 0.1g caused by normal functioning of on-board equipment such as reaction wheels [1]. For high-precision spacecraft such as the space telescopes and navigation satellites, the micro-vibration environment will affect seriously the accuracy and stability of the cameras or antenna, which reduces the important indicators including resolution. It is therefore necessary to obtain the dynamic characteristics of spacecraft under micro-vibration [2]-[3]. In this article, two honeycomb plates jointed by bolts and inserts are designed and manufactures as a typical substructure of a spacecraft [4]-[5]. An experimental system is set up to isolate environment vibration, to provide subtle excitations and to measure the weak responses. The FRF curves are obtained over a range of vibration acceleration from 10^{-1} g to 10^{-6} g. Natural frequencies and damping ratios for the first three modes are analyzed for different vibration level.

TEST INSTRUMENTATION

The measured specimen is a combined structure made up of a two aluminium honeycomb sandwich plates with gross dimension of 300×400×20mm. The two plates are connected by three bolts through inserts imbedded to the honeycomb plates. Two excitation mathods are used in the tests. The first one is a Model 2007E electrodynamic shaker, providing force which is measured by the PCB piezotronics force sensor model 208C01 as shown in Fig.1(a). The other is a TA0505D024W piezoelectric chip produced by THORLABS as an actuator as shown in Fig.1(b), which is controled by piezotronics controller (MDT693B). It offers a maximum displacement of 2.8μm±15% with drive voltage range is from 0 to 75 V. To measure the small vibration response, a Polytec portable digital vibrometer PDV 100, is used for non-contact measurement of surface vibration velocities. When piezoelectric chip is chosed as exciter, the force is derived from acceleration of the chip measured by another Polytec vibrometer PDV 100. A LMS Scadas II system is used to control the tests, acquire data and analysis the results.These sensors and actuators are chosen because they are the best to meet the requirements defined by the objectives of the experiment, because they can excite vibration and provide measurements from which vibration acceleration could be diminished to 10^{-6}g with relatively good signal to noise ratio.



(a) (b)

Fig.1 Experimental setup: (a) excitation with shaker and (b)excitation with piezoelectric chip

TEST PROCEDURE AND EXPERIMENTAL RESULTS

Three sweep frequency bands are set to cover the first three natural frequencies, which are 180Hz to 200Hz, 340Hz to 360Hz, and 420Hz to 440Hz, respectively. For each frequency band, sweep tests were performed on the different constant

[a)] Corresponding author. Email: cyzhou@bit.edu.cn.

force (0.2N, 0.1N, 0.05N, 0.01N, 0.05N, 0.001N), provided by the Model 2007E electrodynamic shaker, which excited the specimen to vibrate with acceleration level from 10^{-1}g to 10^{-4}g. Sweep tests by the piezoeletric chip can further lower the acceleration level to 10^{-6}g. To guarantee repeatability of the test results, five tests were conducted for each condition.

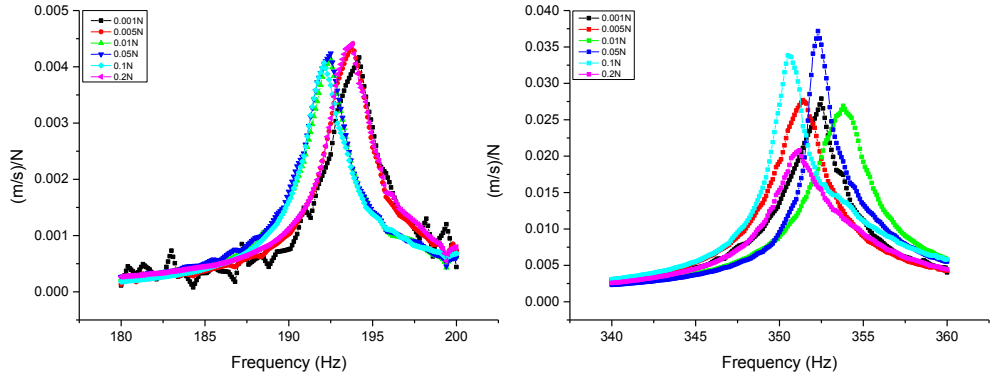

Fig.2 The FRF curves of the first and the second frequency bands under different excitation forces

As shown in Fig. 3, modal damping ratios and natural frequencies for the first three modes of the combined structure were obtained at various acceleration levels through FRF curves measuered.

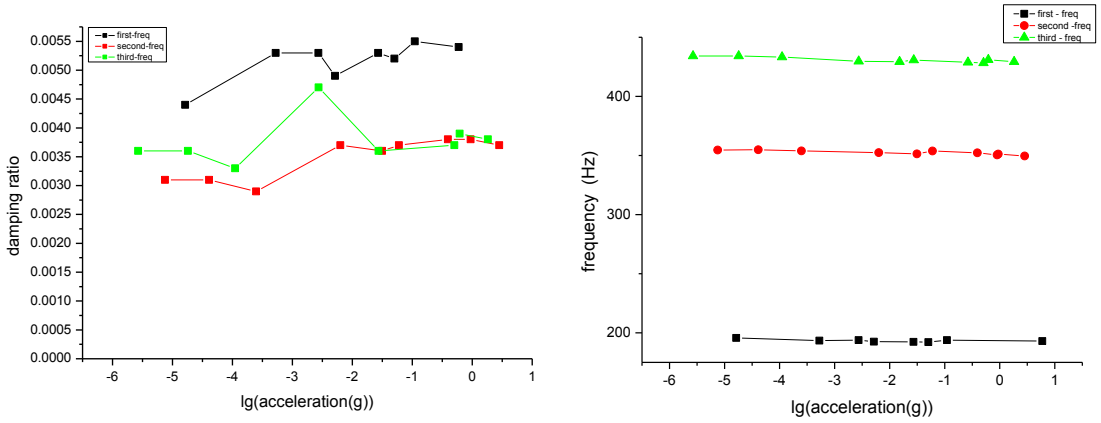

Fig.3 (a) Modal damping ratio and (b) natural frequencies vs acceleration level

The results showed that the first three frequencies matian almost constants and variances were less than 1%. Lower damping ratios were observed for lower vibration level whereas the variances of damping ratios for the first three modes are less than 25%.

References

[1] Ingham M.D., Crawley E.F.: Microdynamic Characterization of Modal Parameters for a Deployable Space Structure. AIAA Journal, 39:331-338, 2001.

[2] Crawley E. F.: Experimental measurement of passive material and structural damping for flexible space structures. Acta Astronautica. 10(5):381-393, 1983.

[3] Ting J.M., Crawley E.F.: Characterization of damping of materials and structures from nanostrain levels to one thousand microstrain. AIAA Journal, 1992, 30(30):1856-1863.

[4] Wang P.P, Chen C.Y, Luo W.B: Analysis and test of the frequency shift for satellite with honeycomb sandwich. Journal of Harbin Institute of Technology. 38(1):74-73, 2006.

[5] Liu L.J., Zhang Y.S., Tang C.Y., Wang W.F.: Research for Drilling Holes on Embedded Parts of Honeycomb Board with High Quality and Efficiency. Aerospace Manufacturing Technology 06:44-47, 2014.

ROBUST, SMOOTH AND FAST ASMC - APPLICATIONS TO ROBOT MANIPULATORS

Jiang Zhu[1] and Karim Khayati *[1]

[1]*Dept of Mechanical and Aerospace Engineering, Royal Military College of Canada, Kingston, Ontario, Canada*

Summary In this contribution, we discuss different designs based on the concept of sliding mode control (SMC) to deal with uncertain robotic dynamics in general. We demonstrate the effectiveness of a recently proposed adaptive sliding mode control (ASMC) design with a novel switching gain dynamics, called integral/exponential adaptation law and referred to as IEG-ASMC hereafter. An adjusting term to improve the robustness of this gain adaptation during the reaching phase will be discussed. The proposed design does not require *a priori* knowledge of the upper bounds of perturbations. These perturbations are not necessarily assumed to be bounded. Tested with different constant-gain-based SMC and ASMC schemes, the simulation results on a five-link robot manipulator dynamics show chatter elimination on control actions, faster responses and better tracking error performances of the new IEG-ASMC design.

INTRODUCTION

Rigid manipulators are basically characterized by high nonlinearities, modeling errors, uncertainties and external disturbances making their dynamics partially or largely unknown [1, 2, 3]. Then, robust variable structure control methods are investigated accordingly to deal with their lumped uncertainties of supposedly known and unknown bounds [1, 3]. In particular, with the ASMC design, the gain is dynamically compensating for the lumped uncertainties (see [1, 2, 4] and references cited therein). However, the slow response to the uncertainties and the relatively large chattering phenomenon during the adaptation process remain inherent weaknesses of the integral adaptation [5, 6]. The objective of this contribution (that will be presented in form of a poster) is to apply the new adjustable IEG-ASMC approach modified from [5] for robotic systems. We validate the improvements of this gain law compared to conventional SMC and ASMC laws in terms of fast response, smaller trajectory variation and reduced chattering level. Samples of the simulation results are shown below.

PROBLEM STATEMENT

In general given $q \in \mathbb{R}^n$ a vector of joint angles and $u \in \mathbb{R}^n$ the input torque, the dynamics of an n-link rigid robotic manipulator is written as $M(q)\ddot{q} + N(q,\dot{q}) = u + d(t)$ [3]. The inertia matrix $M(q)$ and the vector of Coriolis, centrifugal forces and gravitational forces $N(q,\dot{q})$ counts for nominal terms and unknown modeling uncertainties (*i.e.*, parameter variations, unknown loads *etc.*) [3]. Let $q_d \in \mathbb{R}^n$ be any desired trajectory and $e = q - q_d$ the corresponding trajectory error. Defining a measurable $\sigma(e,\dot{e},t) \in \mathbb{R}^n$, called "*sliding* variable" [4, 5]. Given the time derivative of σ along the system error dynamics as: $\dot{\sigma}(x,t) = \Psi(x,t) + \mathrm{y}(x,t)\cdot u$, with $x \equiv \left[e \quad \dot{e}\right]^T$ the error state vector, $\psi \in \mathbb{R}^n$ and $\mathrm{y} \in \mathbb{R}^{n\times n}$ are nonlinear time-varying smooth functions containing parametric uncertainties and external disturbances [4]. From such robot dynamics, the norm of the perturbation $\Psi(x,t)$ can be considered upper-bounded with some polynomial function in the norm of state vector x of unknown constants, and the norm of the uncertain term $\mathrm{y}(x,t)$ is positive definite in the wider sense meaning [7].

CONTROL DESIGN AND APPLICATION

The control applied to these uncertain dynamics consists of two parts. An equivalent control u_{eq}, to deal with known dynamics by maintaining the movement of the system on the targeted sliding surface. The details of this nominal compensation term are omitted here due to lack of space. The second term u_s, derived from a discontinuous switching control, drives the system trajectory to reach such a sliding surface and then to reduce the effect of lumped uncertainties [1, 2, 3]. By implementing the nominal control u_{eq}, the tracking error problem is transformed into σ-dynamics in u_s, that is, the control objective turns to find a feedback switching law u_s such that the output σ converges to zero. We define the unit switching control as $u_s = K \cdot \frac{\sigma}{\|\sigma\|}$ for $\sigma \neq 0$ (note $u_s = 0$ elsewhere) [4, 5]. To deal with the lumped uncertainties upper-bounded with some polynomial functions in the norm of state vector x of unknown constants, the switching gain K is derived from [5] as $\dot{\breve{K}} = \left(\frac{1+\gamma\|\sigma\|}{1+\|\sigma\|}\right)\alpha\cdot\|\sigma\|$ and $K = \breve{K} + \beta\left(e^{\|\sigma\|} - 1\right)$ for $\alpha > 0$, $\beta \geq 0$ and $0 < \gamma \leq 1$. In fact, for any $\|\sigma(0)\| \neq 0$ the sliding variable σ converges to the hypersurface $\sigma = 0$ in finite time [5]. Each of the three parameters α, β and γ has a specific role within the algorithm. The term in β (*i.e.*, exponential term) speeds up the gain adaptation to overpower the lumped uncertainty, while the term $\alpha\|\sigma\|$ guarantees the finite time convergence of the error dynamics. Finally, the adjustable fraction term in β tends to slow down the increase rate of the integral term $\breve{K}$ when the lumped uncertainties are compensated and the sliding dynamics σ tends to reach its target manifold.

*Corresponding author. Email: karim.khayati@rmc.ca

Alternatively, among the numerous variable structure control methods, we distinguish the two main classes of conventional SMC with constant gains and varying ones. Under the first category, we recall the conventional constant-gain-based SMC (CG-SMC), where the switching gain K is selected a priori based on the upper-bound value of the lumped uncertainties [3]. On the one hand, the terminal sliding mode (TSM) based SMC (TSM-SMC) as well as its continuous nonsingular form, referred to as NSTSM-SMC have been also applied to robot control systems [1]. These techniques are basically characterized by their terminal sliding surfaces where the error dynamics converges in finite time within these surfaces. Suffering from the problem of singularity when the tracking error e approaches zero, a boundary layer TSM design can be implemented to overcome this issue. Alternatively, the NSTSM-SMC avoids this constraint by an equivalent modified version of the sliding surface dynamics [1]. Either conventional TSM-SMC and NSTSM-SMC assume bounded lumped uncertainties and require knowledge of their upper-bounds (of constant or affine functions in the states). The number of design parameters characterizing these two schemes remains high and the procedure to select properly these parameters is critical. On the other hand, IEG-ASMC belongs to the techniques with switching gains dynamically varying. The IG-ASMC represents the basis of a such design where the lumped assumptions are only assumed to be bounded with unknwon limit values [4]. The high order integral-type adaptation law designed in [2] for nonlinear systems with uncertainties bounded by some high order polynomial functions with unknown parameters is referred to as MIG-ASMC. The latter extends the IG-based design by using multiple state-dependent integral adaptation laws to compensate for the perturbations bounded with affine functions in such states. The number of adaptation dynamics and design parameters is drastically high in MIG-based design [2]. Both IG-ASMC [4] and MIG-ASMC [2] emphasize relatively slow responses and/or high level of chattering. An ϵ-tunning procedure tends to reduce such effects in real sliding mode design. Given a 5-link robot structure designed using SimMechanics in Matlab, we compare the performance of the IEG-ASMC scheme with the older controls discussed above, CG-SMC, TSM-SMC, NSTSM-SMC, IG-ASMC and MIG-ASMC [1, 2, 3, 4], respectively applied with different sine and quintic curves. A sample is shown below. The errors are computed in $\%$ of the maximum displacement.

CONCLUSIONS

The design of ASMC with integral/exponential gain law is successfully tested on complex robotic manipulator dynamics. The results clearly demonstrate the effectiveness of the proposed scheme in terms of chatter reduction and fast response.

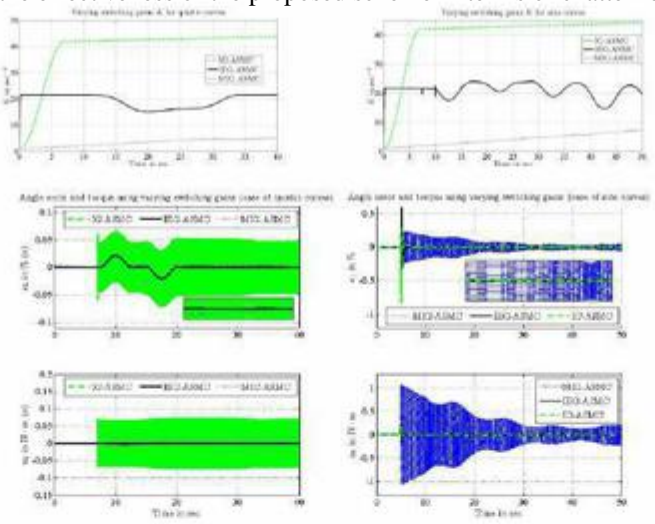

References

[1] Yu S., Yub X., Shirinzadehc B., Mand Z.: Continuous Finite-Time Control for Robotic Manipulators with Terminal Sliding Mode. Automatica, 41(11): 1957–1964, 2005.

[2] Cheng C.C., Chien S.-H., Shih F.-C.: Design of Robust Adaptive Variable Structure Tracking Controllers with Application to Rigid Robot Manipulators. IET Control Theory and Applications, 4(9): 1655–1664, 2010.

[3] Spong M.W., Hutchinson S., Vidyasagar M.: Robot Modeling and Control. Wiley, NJ, 2005.

[4] Plestan F., Shtessel Y., Bregeault V., Poznyak A.: Sliding Mode Control with gain adaptation – Application to an Alectropneumatic Actuator. Control Engineering Practice, 21:679–688, 2013.

[5] Zhu J., Khayati K.: A New Approach for Adaptive Sliding Mode control: Integral/Exponential Gain Law. Transactions of the Insitute of Measurement and Control, DOI: 10.1177/0142331215583328, 2015.

[6] Zhu J., Khayati K.: Adaptive Sliding Mode Control – Convergence and Gain Boundedness Revisited. International Journal of Control, DOI: 10.1080/00207179.2015.1101491, 2015.

[7] Marcus M., Minc H.: A Survey of Matrix Theory and Matrix Inequalities. Dover Publications, NY, 2010.

FS01 - Acoustics

TS.FS01-1.01	Mao, Yijun - Convective vector wave equation of aeroacoustics (INVITED)	3037
TS.FS01-1.02	Mongeau, Luc - Mechanical characterization of collagen I fibrils through 3-point bending using AFM (INVITED)	3039
TS.FS01-1.03	Page, John - Acoustic bubble metascreen for broadband superabsorption of waterborne acoustic waves (INVITED)	3041
TS.FS01-1.04	Sánchez-Dehesa, José - Rainbow trapping of torsional waves in a chirped rectangular beam (INVITED)	3043
TS.FS01-1.05	Abaid, Nicole - Passive Localization Inspired by Bats in Silent Flight	3045
TS.FS01-1.06	Attendu, Jean-Michel - Time-domain NAH as a means to prevent exposition to harmful industrial impact noises	3047
TS.FS01-2.01	Buchta, David - Mechanisms of jet crackle	3049
TS.FS01-2.02	Fotsing, Edith Roland - Acoustic properties of porous PLA monoliths produced via nonsolvent induced phase separation	3051
TS.FS01-2.03	Gregory, Alastair - Modelling biological phenomena with rocket balloon buzz	3053
TS.FS01-2.04	Reichert, Peter - Acoustophoretic Handling of C. elegans in Microfluidic Channels	3055
TS.FS01-2.05	Rodriguez-Lopez, Eduardo - Flow Field and Acoustic Study of the Flow in Various Wall-Mounted Porous Fences	3057
TS.FS01-2.06	Schmidt, Oliver - Global stability and resolvent analysis of sound emission in a high-Reynolds number turbulent jet	3059
TS.FS01-3.01	Lamprecht, Andreas - 3D characterization of acoustofluidic force fields in the fN range	3061
TS.FS01-3.02	Bailly, Christophe - Experimental investigation and modelling of the boundary-layer wall pressure spectrum	3063
TS.FS01-3.03	Noiray, Nicolas - Stochastic aspects of thermoacoustic instabilities in combustion chambers (INVITED)	3065
TS.FS01-3.04	Illingworth, Simon - Robust feedback control of thermoacoustic oscillations	3067
TS.FS01-3.05	Juniper, Matthew - Combined experimental and adjoint-based sensitivity analysis in thermoacoustics	3069
TS.FS01-3.06	Bennewitz, John - Periodic Partial Extinction in Acoustically Coupled Fuel Droplet Combustion	3071
PO.FS01-1.01.326	Baasch, Thierry - Simulating acoustofluidic particle interactions and unilateral contacts	3073
PO.FS01-1.02.327	Guillermic, Reine-Marie - PDMS-based acoustic impedance-matched material in water	3075
PO.FS01-1.03.328	Hu, Gengkai - Broadband pentamode acoustic cloak using single phase solid	3077
PO.FS01-1.04.329	Langthjem, Mikael - Flow-acoustic interaction in an expansion chamber-pipe system	3079
PO.FS01-1.05.330	Misawa, Ryota - A Biem for Transmission Resonance Problems for Elastic Waveguides	3081
PO.FS01-1.06.331	Qu, Yegao - Nonlinear vibration and sound radiation from skin/core debonded sandwich plates	3083
PO.FS01-1.07.332	Schifferli, Yasna - Atmospheric and Cosmic Infrasound Detection Techniques.	3085
PO.FS01-1.08.333	Sugimoto, Nobumasa - Asymptotic theories of nonlinear thermoacoustic waves in a gas-filled channel	3087

PO.FS01-1.09.334	Wang, Yue-Sheng - Enhanced acousto-optical coupling of surface waves in an air-slot phoxonic crystal cavity	3089
PO.FS01-1.10.335	Xu, Chen - Passive control of flow and noise around a circular cylinder covered with porous material	3091

CONVECTIVE VECTOR WAVE EQUATION OF AEROACOUSTICS

Yijun Mao[a)]
[1]*School of Energy and Power Engineering, Xi'an Jiaotong University, Xi'an, Shaanxi, China*

Summary This paper extends the vector wave equation of aeroacoustics to consider the effect of uniform mean flow, and the corresponding acoustic velocity formulation is deduced. By employing the acoustic pressure and acoustic velocity formulations suitable for uniform mean flow, the classic exponent law of acoustic power output from the stationary point/compact source is corrected by considering the effect of mean flow on sound propagation.

INTRODUCTION

The FW-H equation and its integral formulations are usually used to compute the acoustic pressure radiated from flow interaction with solid surfaces. Recently, a vector wave equation of aeroacoustics and the corresponding acoustic velocity formulations have been deduced [1-3], which show an advantage in visually displaying the acoustic energy flow path from sources and around scattering surfaces. All the above-mentioned investigations assumed sound propagation in quiescent medium, however, acoustic radiation and scattering phenomena widely exist in moving medium. For sound radiated from sources in uniform mean flow, the convective FW-H equation and the corresponding acoustic pressure formulations have been deduced [4, 5], but acoustic power cannot be computed from these formulations. For sound scattered by rigid surfaces in uniform mean flow, the acoustic velocity boundary condition $u_n = 0$ rather than the acoustic pressure gradient boundary condition $\partial p'/\partial = 0$ should be employed on the rigid scattering surface. Owing to the above requirements, an acoustic velocity formulation taking into account of the convective effect is meaningful to analyze the acoustic power output and the acoustic scattering in uniform mean flow. The paper presents a convective vector wave equation, which is an extension of the convective FW-H equation [4, 5] and the vector wave equation of aeroacoustics [3].

CONVECTIVE VECTOR WAVE EQUATION OF AEROACOUSTICS

It is assumed that a permeable data surface surrounding the acoustic source is defined by $f\ \mathbf{x}\ =$ and $\mathbf{U}_\infty$ is the velocity of uniform mean flow with arbitrary direction. The flow velocity at each location is $\mathbf{U}_\infty\ \mathbf{u}$, where $\mathbf{u}$ is the local perturbation velocity of fluid. Note that $\mathbf{u}$ is the acoustic velocity outside the nonlinear flow region. The generalized continuity and momentum equations that consider the effects of the boundary and uniform mean flow are as follows [4, 5]

$$\frac{D[(\rho-\rho_0\ H\ f}{Dt}+\frac{\partial[\rho u_j H\ f}{\partial x_j}=Q\delta\ f \tag{1}$$

$$\frac{D[\rho u_i H\ f}{Dt}+\frac{\partial[(\rho u_i u_j+\ \delta_{ij}-\sigma_{ij}\ H\ f}{\partial x_j}=L_i\delta\ f \tag{2}$$

Performing the spatial derivative $\partial/\partial x_i$ of Eq. (1) and the material derivative D/Dt of Eq. (2), and using some mathematical manipulations and the approximation of $\rho\mathbf{u}\approx\rho_0\mathbf{u}$ outside the nonlinear region, we can deduce the following convective vector wave equation in which the quadrupole volume source term is ignored

$$\begin{aligned}\frac{1}{c_0^2}\frac{D\ \ H\ f\ \rho_0\mathbf{u}}{Dt^2}-\nabla^2\ H\ f\ \rho_0\mathbf{u}\ &=-\nabla\ Q\delta\ f\\ &+\frac{D\ \mathbf{L}\delta\ f}{c_0^2\ Dt}+\int_0^t\ \nabla\times\ \nabla\times\ \mathbf{L}\delta\ f\quad dt^*\end{aligned} \tag{3}$$

The integral solutions of Eq. (3) can be deduced by employing the convective Green's function [4, 5]. Here, we only present the time-domain acoustic velocity formulation for the monopole source in arbitrary motion as follows

$$\begin{aligned}4\pi\rho_0 u_{Ti}\ \mathbf{x}\ t\ =&\int_{f=0}\left[\frac{\dot{Q}\hat{R}_i}{c_0R^*(1-M_R)^2}+\frac{Q\ \hat{R}_i^*-M_i)}{R^{*2}(1-M_R)^2}+\frac{Q\hat{R}_i(R^*\dot{M}_R+c_0\ M_{R^*}-M^2))}{c_0R^{*2}(1-M_R)^3}\right]_{\text{ret}}\mathrm{d}S\\ &-\int_{f=0}\left[\frac{Q\hat{R}_i(M_{R^*}M_R+\gamma^2(M_{\infty M}^2-M_{R^*}^2))}{R^{*2}(1-M_R)^3}+\frac{Q(M_R\hat{R}_i^*+\gamma^2(M_{\infty M}M_{\infty i}-M_{R^*}\hat{R}_i^*))}{R^{*2}(1-M_R)^2}\right]_{\text{ret}}\mathrm{d}S\end{aligned} \tag{4}$$

with $\hat{R}_i^*=\partial R^*/\partial\ _i=r\ \hat{r}_i+\gamma^2M_\infty\ M_{\infty i})/\gamma\ R$, $\hat{R}_i=\partial\ /\partial\ _i=\gamma^2(\hat{R}_i^*-M_{\infty i})$, $\gamma=\sqrt{1/(1-M_\infty^2)}$, M_∞ is the Mach number of uniform mean flow. Numerical cases are carried out to validate Eq. (4) but we don't present them in this paper.

a) Corresponding author. Email: maoyijun@mail.xjtu.edu.cn.

ACOUSTIC POWER OUTPUT FROM THE STATIONARY SOURCE IN MEAN FLOW

The instantaneous acoustic intensity in uniform mean flow is defined by [6]

$$\mathbf{I} = (p'/\rho_0 \quad \mathbf{u} \ \mathbf{U}_\infty)(\rho_0\mathbf{u} + \rho'\mathbf{U}_\infty) \tag{5}$$

In the far field outside the nonlinear region, there is $p' = \rho' c_0^2$. The corresponding active acoustic intensity is

$$\tilde{} = 0.5\tilde{} \ \tilde{}^{\dagger} + 0.5\tilde{} \ \tilde{} \ ^{\dagger}\mathbf{M}_\infty / \rho_0 c_0 + 0.5\rho_0 c_0 \tilde{} \ \tilde{}^{\dagger} \quad _\infty + \quad \tilde{}'\mathbf{M}_\infty \ \tilde{\mathbf{u}}^{\dagger} \ \mathbf{M}_\infty) \tag{6}$$

where superscript † means the complex conjugate. Since the last three terms only exist for uniform mean flow, Eq. (6) reduces to the conventional definition of the active acoustic intensity at $\mathbf{M}_\infty = 0$. In order to analyze the convective effect on the acoustic power output, a non-dimensional acoustic power ratio is defined as follows

$$\sigma = W_{M_\infty} / W_0 \tag{7}$$

where W_0 and W_{M_∞} are acoustic power output from the stationary source with the same source strength in quiescent and moving medium, respectively. Based on this definition, the acoustic power level (SWL) is computed by

$$\mathrm{SWL}_{M_\infty} = \mathrm{SWL}_0 + 10\log \ (\sigma) \tag{8}$$

Here, the term $10\log \ (\sigma)$ can be regarded as the correction of acoustic power level accounting for the convective effect. It is observed from Figure 1 that a correction of the acoustic power output should be taken into account at high Mach number. Note that this correction is independent of the sound frequency.

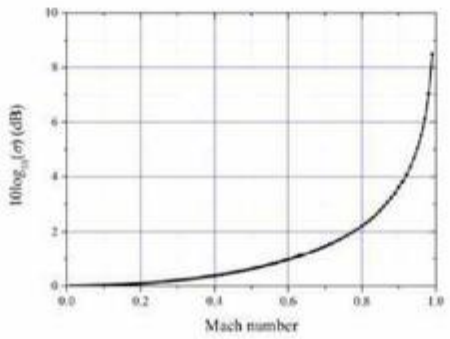

Figure 1 Variation of $10\log \ (\sigma)$ with the Mach number of uniform mean flow for the stationary monopole point source

CONCLUSIONS

In this paper, a convective vector wave equation and its integral formulation are developed by starting from the generalized continuity and momentum equations. By employing the acoustic pressure and acoustic velocity formulations accounting for uniform mean flow, the acoustic power output from sources in uniform mean flow with a high Mach number should be corrected from the classic exponent law. The developed acoustic velocity can also be directly used as a boundary condition for predicting acoustic scattering from solid surfaces in uniform mean flow.

ACKNOWLEDGMENTS

The research is supported by the National Natural Science Foundation of China (Nos. 51476123, 51511130075 and 51206127).

References

[1] Ghorbaniasl, G., Carley, M., Lacor, C. Acoustic velocity formulation for sources in arbitrary motion. *AIAA J* **51**: 632-642, 2013.
[2] Mao, Y., Zhang, Q., Xu, C., Qi, D. Two types of frequency-domain acoustic-velocity formulations for rotating thickness and loading sources. *AIAA J* **53**: 713-722, 2015.
[3] Mao, Y., Tang, H., Xu, C. Vector wave equation of aeroacoustics and acoustic velocity formulations for quadrupole source. *AIAA J*. Accepted for publication, 2016.
[4] Najafi-Yazdi, A., Bres, G.A., Mongeau, L. An acoustic analogy formulation for moving sources in uniformly moving media. *P Roy Soc A-Math Phy* **467**, 144-165, 2011.
[5] Ghorbaniasl, G. & Lacor, C. A moving medium formulation for prediction of propeller noise at incidence. *J Sound Vib* **331**, 117-137, 2012.
[6] Goldstein, M.E. *Aeroacoustics*. New York, McGraw-Hill International Book Company, 1976.

MECHANICAL CHARACTERIZATION OF COLLAGEN I FIBRILS USING AFM

Meisam Asgari*[1], Neda Latifi [1], Hossein K. Heris [2], Ruixiang Sun[1], and Luc Mongeau[1,2]

[1]*Department of Mechanical Engineering, McGill University, Montreal, Quebec, Canada*
[2]*Department of Bioengineering, McGill University, Montreal, Quebec, Canada*

Summary Collagen fibrils are the most abundant proteins in the extracellular matrix of biological soft tissue. They contribute to tensile strength as well as mechanical stability, cohesiveness, cellular migration regulation, and remodelling. Collagen fibrils have a characteristic D-banding periodicity of 67 nm. They are synthesized by the assembly of collagen molecules, which have a length of 300 nm and a diameter of 1.4 nm. In the present study, tropocollagen molecules were fibrilized, and 3-point bending tests were performed on ten different samples to evaluate the elastic stiffness of the fibrils. Linear isotropic elasticity was assumed. The Young's modulus of the collagen fibrils was found to be around 2-3 MPa.

INTRODUCTION AND METHODS

Many biological soft tissues are comprised of extra-cellular matrix (ECM) embedded in a fluid substrate. The ECM includes different protein-made structures such as elastin and collagen fibrils [1]. Collagen is one of the most abundant proteins in the ECM. It provides its structural strength. There are many applications for collagen such as in manufacturing cosmetics, glue and gelatin. It is used to produce biomaterials [1, 2]. Various types of collagen have been identified in soft tissues. Among them, collagen type I is believed to be the most significant tension-bearing component of the ECM [3, 4].

The structure of each collagen fibril incorporates a hierarchical arrangement. Laterally packed, triple-helical monomeric tropocollagen molecules with a thickness of 1.5 nm and a length of 300 nm [2], are organized in fibrillar units with a diameter of 4–5 nm, in turn forming larger micrometer sized fibrils. One feature of collagen structure is its D-banding periodicity of 67 nm, resulting from the quarter-staggered alignment of collagen chains during fibrillogenesis [1].

Various methods have been used to measure the mechanical stiffness of collagen fibrils [1]. In the present study, 3-point bending tests were performed using atomic force microscope (AFM) to evaluate the bending stiffness of collagen fibrils. Collagen fibrils were laid over fabricated micro-channels with 2.5 μm width, and 10 μm depth. The AFM tip then exerts a load on the fibril over the micro-channel, while recording the force-deflection curve, from which the value of Young's modulus of the fibrils was obtained.

Sample preparation

The collagen molecules to be fibrilized were obtained from commercially available human placenta (Advanced BioMatrix Inc., CA) and kept in an acidic solution. To fibrilize the collagen molecules, the following materials were used: 6 μL sterile, de-ionized water, 20 μL disodium phosphate (Na_2PO_4), 10 μL potassium chloride (KCl), and 4 μL collagen molecules (human placenta). These materials were mixed in a small plastic vial on a vortex mixer at 300 rpm for five minutes. The solution was well mixed to be homogeneous. The vial was then incubated at 37°C for 4 hours, after which the mixture appeared cloudy.

Imaging and force measurement

To prepare a sample for imaging and force spectroscopy purposes, 20 μL of the fibrilized collagen was placed on a glass slide, or the micro-channels. After the sample dried for about 15 minutes, it was gently washed with deionized water to eliminate the salt residues. For force spectroscopy, the glass slide was replaced with the prepared micro-channels. Collagen fibrils have a high attraction to other surfaces, due to the electrostatic attraction of charged amino acids. Hence, the fibrils

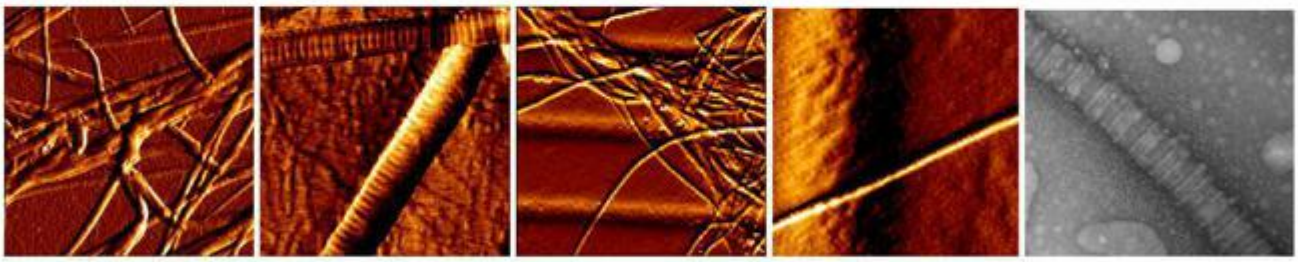

Figure 1: AFM and TEM Images of collagen fibrils, and their positioning on fabricated parallel micro-channels.

*Corresponding author. Email: meisam.asgari@mcgill.ca

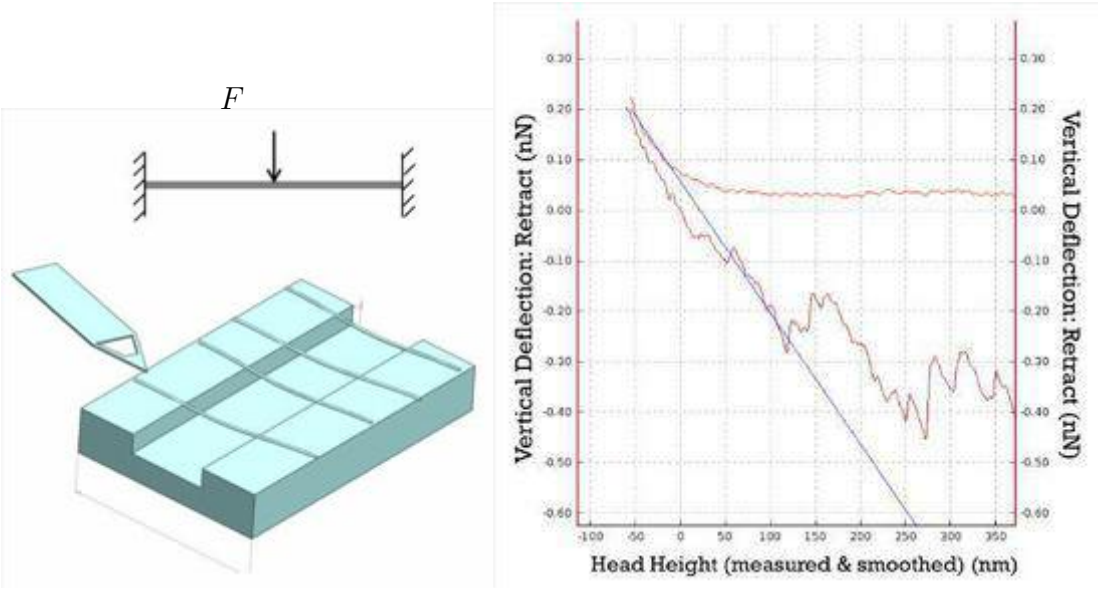

Figure 2: Schematics of collagen fibrils crossing a micro-channel. The AFM cantilever applies the lateral force on the midpoint of the fibril, and deflection versus piezo displacement curves are obtained from which the elastic modulus is calculated.

adhered strongly to the micro-channels, resulting in a clamped or fixed boundary condition on both sides for the fibril. Thus, the fibril was treated as a beam with fixed-fixed boundary conditions. Collagen fibrils are relatively long, and thus, to maintain consistency for the bending test, it is preferable to have a fibril lay over several channels. For these reasons, micro-channels needed to be constructed with relatively small widths and gaps between channels. Conversely, the channels need to be wide enough for the length of the fibrils to be significantly greater than the diameter of the fibrils. Hence, a channel width of 5 μm was used and the space in between fibrils were also chosen to be 5 μm. These dimensions were confirmed using AFM during the imaging process. A depth of 10 μm (twice the width) was selected. The AFM probe applied a point load at the midpoint of the fibril (relative to the edges of the channel), causing a deflection. The magnitude of the deflection depends on the applied load, as well as the boundary conditions.

RESULTS AND DISCUSSION

An appropriately-positioned fibril was located to perform force measurements. Only fibrils clearly traversing multiple channels were used to ensure reproducibility of the results by applying the cantilever on the same fibril, but over different channels to ensure consistency. Prior to applying the force, a drop of phosphate buffer solution (PBS) was added to the sample to hydrate the fibrils. The cantilever was applied at the midpoint and along the length of the fibril over the channel and force-displacement curves were obtained. Further, bending was performed for multiple times at the same point for consistency as well as ensuring that the fibrils were not permanently deformed. The boundary conditions of the fibrils were assumed to be clamped on both sides. Images were taken of the fibrils before and after the bending process to ensure that the fibrils have not moved. It is known that if the fibrils slide while being bent by the AFM probe, causes the force-deflection curve to be nonlinear. Thus, the linearity of the data was checked. The deflection of the midpoint of the collagen fibril was obtained in terms of the applied lateral force F, as $\delta = FL^3/192EI$ with L and I being the length and the area moment of inertia of the cross-section of the fibril, respectively. The Young's modulus was then obtained as $E = \frac{F}{\delta}\left(\frac{L^3}{192I}\right)$. The bending test yields the value F/δ to 806 pN/μm. The length of the fibril was found to be 2.5 μm, and the radius of the cross-section was 75 nm. These measurements gives the value of the Young's modulus of the fibrils to be 2.6 ± 0.2 MPa.

References

[1] Yang, L., Fitie, C., van der Werf, K. O. Bennink, M., Dijkstra, P., Feijen, J. 2008, "Mechanical properties of single electrospun collagen type I fibrils,"*Biomaterials*, Vol(29), pp. 955–962.

[2] Bozec, L., van der Heijden, G., Horton, M. 2007, "Collagen fibrils: nanoscale ropes,"*Biophysical Journal*, Vol(92), pp. 70–75.

[3] Wenger, M. P. E., Bozec, L., Horton, M. A., Mesquida, P. 2007, "Mechanical properties of collagen fibrils,"*Biophysical journal*, Vol(93), pp. 1255–1263.

[4] Radmacher, M. 2002, "Measuring the elastic properties of living cells by the atomic force microscope," *Methods in cell biology*, Vol(68), pp. 67–90.

ACOUSTIC BUBBLE METASCREEN FOR BROADBAND SUPERABSORPTION OF WATERBORNE ACOUSTIC WAVES

John H. Page[1,a)], Valentin Leroy[2], Anatoliy Strybulevych[1], Maxime Lanoy[3], Eric J.S. Lee[1], Reine-Marie Guillermic[1], Fabrice Lemoult[1,3] and Arnaud Tourin[3]

[1]*Department of Physics and Astronomy, University of Manitoba, Winnipeg, Manitoba, Canada*
[2]*Laboratoire MSC, Université Paris-Diderot, CNRS (UMR 7057), Paris France*
[3]*Institut Langevin, ESPCI Paris Tech, PSL Research University, CNRS, Paris, France*

Summary: We show that a superabsorbing metamaterial for waterborne acoustic waves can be constructed by optimizing the structure of a bubble metascreen containing a single layer of bubbles embedded in a soft solid in contact with a rigid reflector. The optimization is guided by a simple analytical model, which not only facilitates the optimization but also gives insight into the underlying physics. The predictions of the model are confirmed by finite element simulations and experiments, which demonstrate very large energy absorption (> 91%) over a broad bandwidth extending over a factor of two in frequency, with a maximum absorption of nearly unity at a frequency near the lower edge of this absorption band. This work shows that ultrathin coatings made from bubble metascreens can turn acoustic reflectors into perfect absorbers.

INTRODUCTION

Recently, there has been growing scientific and engineering interest in materials that efficiently absorb acoustic or electromagnetic waves. In practice, one wants the absorber to be as small and light as possible, motivating the use of thin metamaterials, which are ideally much thinner than a wavelength. In acoustics, much of the previous research has focused on airborne sound, and has investigated either narrowband superabsorption in subwavelength metalayers or broadband absorption for larger metastructures [1-3]. Broadband absorption has also been demonstrated for different acoustic waveguide geometries [4]. In this presentation, we show how superabsorption over a wide frequency range can be achieved for waterborne acoustic waves using an acoustic metalayer that consists of a single layer of monodisperse bubbles embedded in a soft solid [5]. We call this metalayer a bubble metascreen. Our acoustic metamaterial capitalizes on the strong low-frequency acoustic resonance of bubbles, which occurs when the radius of the bubbles is much smaller than the wavelength (by as much as hundreds of times).

OPTIMIZING ACOUSTIC ABSORPTION IN AN ISOLATED BUBBLE METASCREEN

Achieving strong absorption with a bubble metascreen requires that the structure of the bubble layer be optimized, since if the spacing between the bubbles is too large, the transmission is high and the incident waves can easily pass through the layer with almost no absorption, whereas if the spacing is too small, the incident waves are almost entirely reflected and again are not significantly absorbed. To optimize the structure, we take advantage of a simple analytic model [6] that accurately predicts the reflection and transmission coefficients of a bubble monolayer, and gives considerable insight into how these properties can be tuned for maximum absorption. One of the strengths of the model is that it successfully describes the coupling between the resonating bubbles, an effect which is often neglected in research on metamaterials but which is crucial to understanding how superabsorption can be realized in our system. In particular, the model predicts that at the minimum of the transmission, the absorption of acoustic energy is maximized when the dissipative damping of the resonating bubbles, δ, is equal to the superradiative damping, Ka, where $K = 2\pi/(kd^2)$, k is the incident wavevector, d is the separation between bubbles and a is the bubble radius. For bubbles in a soft solid matrix, dissipative damping is generally dominated by viscous effects, $\delta_{dis} = 4\eta/(\rho\omega a^2)$, where η and ρ are the viscosity and density of the medium in which the bubbles are embedded and ω is the angular acoustic frequency. Thus, the

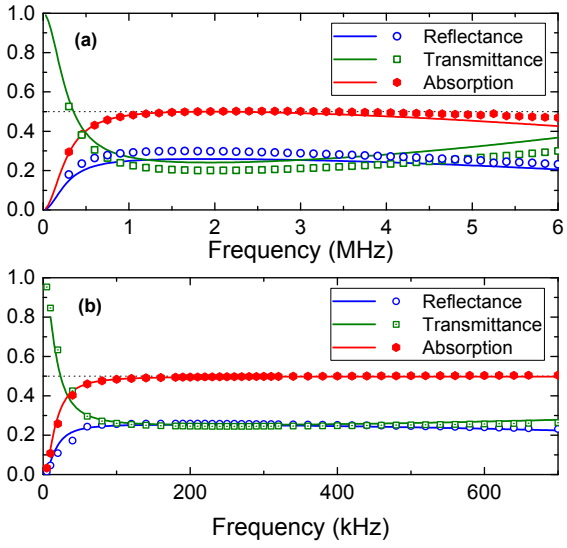

Figure 1 Transmission, reflection and absorption predicted by the model (lines) and finite element simulations (symbols) for two bubble metascreens with $\eta = \eta^*$. Here t and r are the amplitude transmission and reflection coefficients, and $A = 1 - |r|^2 - |t|^2$ is the absorption. The bubbles were arranged in a square array. (**a**): $a = 8$ μm, $d = 50$ μm, and $\eta = 0.32$ Pa s. (**b**): $a = 50$ μm, $d = 240$ μm, and $\eta = 5.1$ Pa s.

a) Corresponding author email: john.page@umanitoba. ca

condition $\delta = Ka$ for maximum absorption will be satisfied when the acoustic and geometric parameters of the bubble metascreen are such that the viscosity $\eta = \eta^* = (\pi Z a^3)/(2d)^2 \propto a^3/d^2$, where Z is the acoustic impedance. Note that since both δ and Ka are inversely proportional to the angular frequency ω, the condition for maximum absorption is met for a wide range of frequencies. When this critical coupling condition is satisfied, the model predicts that 50% of the incident energy is absorbed, as is shown in Fig. 1 for two different metascreens with different bubble sizes and spacings, and different matrix viscosities.

ACHIEVING SUPERABSORPTION USING A BUBBLE METASCREEN

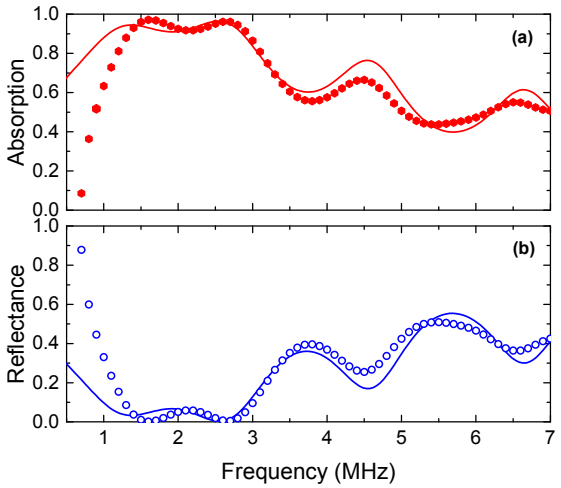

Figure 2 Experimental measurements (symbols) and model calculations (lines) for the (**a**) absorption and (**b**) reflectance of a bubble metascreen on a steel block. The metascreen consists of a 230-μm-thick slab of PDMS (η = 0.3 Pa s) containing a single layer of 10.5-μm-radius bubbles separated by d = 120 μm. The oscillations are due to reflections caused by the acoustic impedance mismatch between PDMS and water, an effect which can be satisfactorily accounted for by the model but which we are currently working towards eliminating in new experiments.

While the maximum absorption that can be realized with a single metascreen is only 50%, superabsorption approaching 100% can be achieved when the metascreen is placed on a rigid reflector. In this case, the total reflection is the result of interferences between waves reflected from the layer of bubbles, which undergo a π shift in phase, and waves reflected from the perfect reflector, which have zero phase shift. Providing that the bubble layer is much closer to the reflector than a wavelength, and the reflector is perfect, it is easy to show that the total reflection is zero when the amplitude reflection coefficient from the bubble layer alone is $r = -1/3$; then, all the incident energy is absorbed. This condition is fulfilled when $\eta = 2\eta^*$. An example of experimental results and model predictions for an optimized superabsorbing metascreen is shown in Fig. 2. These experiments demonstrate peak absorption greater than 97% and broadband absorption greater than 91% over a range of frequencies that extends over a factor of two in frequency. At the maximum of absorption, the reflectance is nearly zero (< 0.2%). Thus, a nearly perfect rigid reflector can become almost invisible to waterborne acoustic waves when coated with such an optimized bubble metascreen.

There is another configuration in which a bubble metascreen can be used to achieve superabsorption. This is the case of a "coherent perfect absorber" in which a metalayer is illuminated coherently by two oppositely propagating incident beams [7]. Metascreens such as shown in Fig. 1 should be ideal candidates for demonstrating this effect for acoustic waves, as we are currently investigating via simulations, model calculations and experiments. We have already achieved the important first step of developing an impedance-matched soft matrix into which the single layer of bubbles will be embedded, so that the water-matrix reflection can be eliminated (see Fig. 2). Results will be shown in the presentation by R-M Guillermic at this conference. This implementation of a coherent perfect absorber using a bubble metascreen offers the potential for achieving 100% broadband absorption in a single deeply subwavelength metalayer.

.

CONCLUSIONS

We have demonstrated that a broadband superabsorbing metamaterial for acoustic waves can be constructed by coating a rigid reflector with a bubble metascreen, whose properties are optimized by designing the structure of the bubble layer (bubble size and separation) to match the viscosity of the thin soft solid layer in which the bubbles are embedded. Our experiments also show that reflection below 1% can be achieved over a narrow frequency range. Both experiments and simulations support the predictions of the model that we have developed to guide the optimization of the metascreen.

References

[1] J. Mei, G. Ma, M. Yang, W. Wen, and P. Sheng, *Nat. Commun*. **3**, 756, 2012.
[2] G. Ma, M. Yang, S. Xiao, Z. Yang, and P. Sheng, *Nat. Mater*. **13**, 873, 2014.
[3] J. Christensen et al., *Sci. Rep*. **4**, 4674, 2014.
[4] V. Romero-Garcia, G. Theocharis, O. Richoux, A. Merkel, V. Tournat and V. Pagneux, arXiv:1501.00191.
[5] V. Leroy, A. Strybulevych, M. Lanoy, F. Lemoult, A. Tourin, and J.H. Page, *Phys. Rev. B* **91**, 020301(R), 2015.
[6] V. Leroy, A. Strybulevych, M. G. Scanlon, and J.H. Page, *Eur. Phys. J. E* **29**, 123, 2009.
[7] P. Wei, C. Cröenne, S.T. Chu and J. Li, *Appl. Phys. Lett*. 104, 121902, 2014.

RAINBOW TRAPPING OF TORSIONAL WAVES IN A CHIRPED RECTANGULAR BEAM

A. Arreola-Lucas[1,2], G. Baez[1], F. Cervera[2], A. Climente[2], R.A. Mendez-Sánchez[1] & José Sánchez-Dehesa[2a]
[1]*Departamento de Ciencias Básicas, Universidad Autónoma Metropolitana-Azcapotzalco, México DF, México*
[2]*Wave Phenomena Group, Dept. of Electronics Engineering, Universitat Politècnica de Valencia, Valencia, Spain*

Summary This work presents the demonstration of the rainbow trapping effect for torsional waves propagating in an aluminum beam with rectangular cross section. The beam contains a chirped structure that is machined with notches separated with the rule $\lambda = (a_j - a_{j-1})/a_j$, where a_j is the size of the cavity defined between notches j-1 and j, and λ is the chirp intensity parameter. We have observed the temporarily trapping of waves at positions in the beam that depend of the central frequency of the wave packet. This demonstration for torsional waves is encouraging and opens the possibility of its extension to more complex elastic waves.

INTRODUCTION

The control of wave propagation through materials is a long-standing field of research due to its potential applications in industry and technology. For example, vibrational energy trapping is a subject of considerable interest because of its importance in designing mechanical devices like oscillators. The phenomenon of "rainbow trapping" was characterized in optical metamaterials, where each frequency component of a wave packet was trapped at different positions inside a tapered left-handed heterostructure[1]. This phenomenon was later characterized for other type of waves, like acoustic waves[2,3]. Thus, trapping of broadband acoustic waves was demonstrated in designed gradient subwavelength structures. The trapping positions can be predicted because of the interplay between the acoustic resonance inside individual apertures and the mutual coupling among them. Bloch oscillations are a phenomenon strongly related with rainbow trapping and has been demonstrated in acoustics using chirped structures[4]. For mechanical waves, however, the complexity associated to polarization mixing and the difficulty of selectively measure the modes has delayed the observation of rainbow trapping for elastic waves.

This work reports experiments showing that mechanical waves can be slowdown in chirped structures. Particularly, we demonstrate rainbow trapping of torsional waves propagating in a beam with rectangular cross section. The waves are temporarily trapped at different depths in the structure for different frequencies.

NUMERICAL SIMULATIONS

We have considered a finite length aluminum beam with rectangular cross section. The beam has free boundary ends and it is made of a uniform part and a chirped structure. The chirped structure consists of notches separated by the rule $\lambda = (a_j - a_{j-1})/a_j$, where a_j is the size of the cavity defined between notches j-1 and j, and λ is the chirp intensity parameter. The periodic structure is obtained for $\lambda=0$. When $\lambda\neq0$ the chirped structure is obtained. The cells defined between notches become smaller with the j-index. First, the band structure of the chirped structure was calculated. With no chirp ($\lambda=0$) the first gap of the locally periodic structure is located between 6,5 kHz and 9,5 kHz. The last frequency defines the starting point of the second passband, which ends at around 13,5 kHz. For chirped structures ($\lambda\neq0$) the levels in each band separate, the bands becoming wider and the gaps narrower with increasing values of λ.

The evolution of a wave packet has been numerically studied using the transfer matrix formalism[6]. The wave packet has been expanded in around 250 normal-mode wave amplitudes for both cases; the locally periodic structure and the chirped structure. The predicted dynamics by the numerical simulations is reported in Fig. 1. For the periodic structure ($\lambda=0$) it is observed that the wave packet is completely reflected when its central frequency (f_C) lies in the gap (see Fig. 1a) while it is completely transmitted when its central frequency lies in the passband (see Fig. 1b). For the chirped structure with $\lambda=0,03$ the wave packet is reflected at different positions in the beam depending of the frequency f_C (see Figs. 1c, 1d, 1e, 1f). This behavior represents the *mechanical rainbow trapping effect*.

EXPERIMENTS

The theoretical predictions have been experimentally confirmed using a beam with the same dimensions than that employed in the simulations. In addition to the chirped aluminum beam, the experimental setup consists of signal generator, a high-fidelity audio amplifier, an electromagnetic-acoustic transducer (EMAT) and a 500V laser Doppler vibrometer. In brief, torsional waves are generated in the uniform part of the beam are sent to the chirped part. The waves traveling in the opposite direction are almost completely absorbed using a homemade passive vibration isolation system which dissipate efficiently the waves for frequencies higher than 1500 Hz. The excited Gaussian wave packet has a spatial width of 0.875 m

[a)] Corresponding author. Email: jsdehesa@upv.es

in the uniform region of the beam. Figure 2 reports the measured dynamics, showing that the predicted behaviour is supported by the experimental observation.

CONCLUSIONS

In summary, we have reported numerical simulations and measurements showing "rainbow trapping" of torsional waves propagating in a quasi-one-dimensional elastic structure. Experimental data corroborated the simulations based on transfer matrix formalism. Our finding foresees that other well-known phenomena in quantum mechanics and photonics can be attainable also for mechanical waves, opening the possibility of vibration control in automotive, building and aeronautic industries.

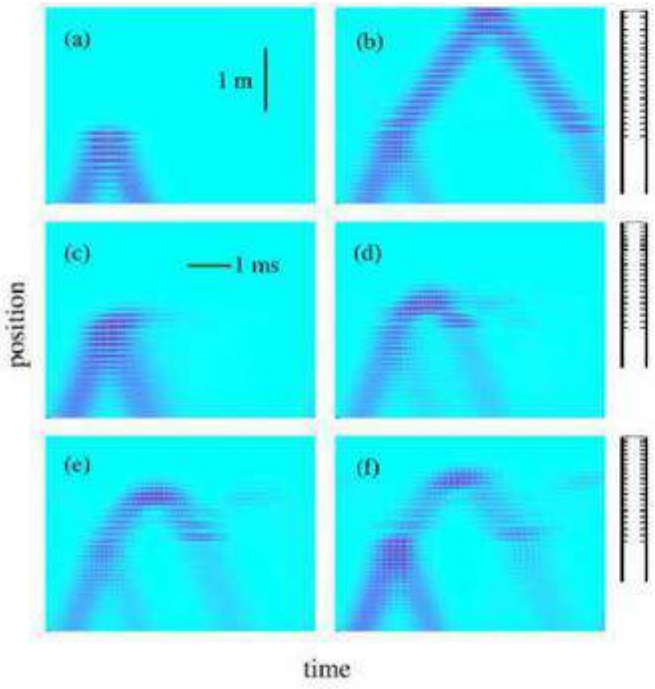

Figure 1.- Calculated dynamics of the wave packet. The plots are obtained using the transfer matrix method. The position of the wave packet is given as a function of time for a beam with a locally periodic structure (λ=0) and central frequencies lying in (a) the gap f=8kHz; (b) in the band, f=11.5 kHz. For the beam with a chirped structure (λ=0,03) the evolution is given for the following central frequencies: (c) f=9 kHz, (d) f_C=10kHz, (e) f_C=11kHz and (f)f_C=12 kHz.

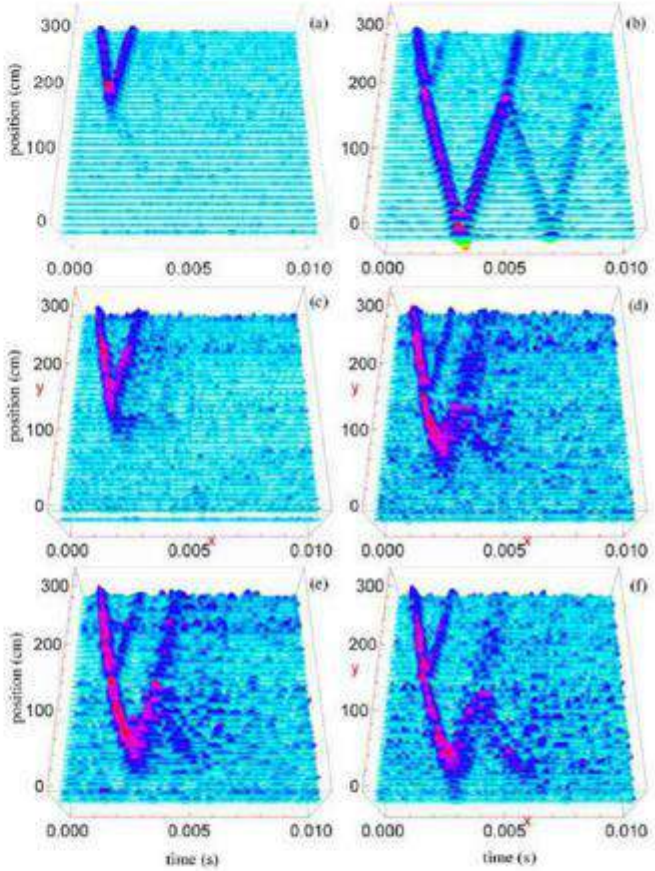

Figure 2.- Measured dynamics of the wave packet using the same parameters than in Figure 1. Notice that the beam here is oriented in the opposite direction. In other words, the structured part is in the right-hand side of the beam. Now, the propagation goes from the left (upper part in this plot) to the right (lower part in this plot).

Acknowledgements.- This work was supported by DGAPA-UNAM under project PAPIIT IN103115 and by CONACYT. RAMS received support from DGAPA-UNAM under program PASPA.. F.C, A.C. and J. S-D. acknowledge the support of the Spanish MINECO under the contract with Ref. TEC2014-53088-C3-1-R

References

[1] Tsakmakidis, K. L., Boardman, A.D., and Hess, O.: trapped rainbow" storage of light in metamaterials, *Nature*, **450**, 397-401 (2007)
[2] Zhu, J. *et al.*: Acoustic rainbow trapping. Sci. Rep. **3**, 1728 (2013).
[3] Romero-García, V, Picó, R., Cebrecos, A., Sánchez-Morcillo, V. and Staliunas, K.: Enhancement of sound in chirped sonic crystals. *App. Phys. Lett.* **102**, 091906 (2013).
[4] Ni, X. *et al.*: Acoustic rainbow trapping by coiling up space. *Sci. Rep*. **4**, 7038 (2014).
[5] Sanchis-Alepuz, H., Kosevich, Y.A., Sánchez-Dehesa, J.: Acoustic Analogue of Electronic Bloch Oscillations and Resonant Zener Tunneling in Ultrasonic Superlatticces. *Phys. Rev. Lett.*, **98**, 134301 (2007).
[6] Morales, A., Flores, J., Gutierrez, L., Mendez-Sánchez, R.A.: Compressional and torsional wave amplitudes in rods with periodic structures. *J. Acoust. Soc. Am.* , **112**, 1961 (2002).

PASSIVE LOCALIZATION INSPIRED BY BATS IN SILENT FLIGHT

Masoud Jahromi Shirazi[1] and Nicole Abaid *[1]
[1]*Biomedical Engineering and Mechanics, Virginia Tech, Blacksburg, Virginia, United States*

Summary Bats use echolocation to build a three-dimensional map of their environment by emitting ultrasounds and interpreting the echoes from objects near them. The distance to such objects can be estimated by the time difference between the sent signal and received echo times half of the speed of sound. This approach is an example of active sensing, since bats actively echolocate to localize objects, rather than passively receiving an existing environmental signal. Studies on pairs of bats show that one of them may cease echolocation to prevent signal jamming. This behavior suggests that only passively listening to the echo from another bat is enough for garnering sufficient information about the location of obstacles in the environment. This paper studies the possibility of passive localization through numerical simulation and demonstrates a strategy to passively use echolocation signals for localization. This work paves the way for energy optimization in a robot swarm.

INTRODUCTION

Since the word "echolocation" was used for the first time by Griffin in 1958, numerous studies have shown how this sensing method enables bats to search the environment, detect objects and classify them, track and catch a prey while avoiding obstacles, and more capabilities crucial for survival [1]. From an engineering point of view, these capabilities are far beyond that of the man-made ultrasonic sensors. Thus, understanding bat behavior can inspire engineering research and technological developments. In particular, based on the highly social nature of many bat species, we are interested in how echolocation behaviors are adapted in the presence of many individuals, which can yield applications for engineered multi-agent systems.

In 2008, Chiu et al. observed that, 76% of the times that two bats were located within one meter of each other, one of them stopped echolocation for more than 0.2 seconds. The authors hypothesized that bats ceased echolocation to prevent signal jamming with the other bat, yet it raised the question that how the environment can be perceived during that silent flight. One possible answer is to get localization cues by passively eavesdropping on the echo coming from another bat's sound [2].

Active sensing is easier and more accurate than passive sensing, but it costs more, especially for a swarm of robots. In active sensing, each robot consumes energy to send its own signal. Besides, as the number of robots increases, it may increase the chance of signal jamming. By integrating passive sensing based on eavesdropping, it is not necessary for all the robots to send signals, which can save energy and increase the operation time of the swarm. In this paper, the possibility of object localization using passive sensing via eavesdropped signals is investigated by simulation of the acoustic field.

ACOUSTIC FIELD SIMULATION

We simulate a robot which senses its 2D environment passively by interpreting echoes from sounds generated by a fixed beacon. The domain is limited by walls which reflect sounds. The beacon is equipped with a speaker as an emitter and the robot with two microphones as receivers. Passive localization is based on the sound received by each microphone. Therefore, for simulation purposes, it is necessary to model sound propagation in the air and sound reflection from the walls to calculate the sound pressure level at a robot's microphone position. For simplicity, the robot's microphones and beacon's speaker are assumed to be omni-directional. Also, the sound pressure level of the beacon's signal is assumed to be constant and known by the robot. The walls are assumed to be rigid and therefore reflect all the acoustic power back in a mirror-like reflection. By these assumptions, the acoustic wave equation has an analytic solution for the sound pressure level at any position and time.

PASSIVE LOCALIZATION

It is enough to estimate the distance and direction of a sound source relative to robot to localize it. The distance can be estimated by measuring the sound pressure level recorded by microphones. Since the robot knows the pressure level of the sound produced by the beacon and the sound pressure level decay for an omni-directional source is related to the inverse of the distance, it is possible to find the estimated distance of the source location.

The direction of the source is mainly estimated by a localization cue called Interaural Time Difference (ITD). It is applicable when two auditory receivers are available (as in animals with two ears). ITD is the difference in the sound's arrival time between two ears as a result of different distances between the source and two ears and it is the main cue for far field localization [3]. Finding the direction of the source (or an echo that acts as a virtual source) by ITD is illustrated in Figure 1. In this figure, θ is the angle between source and the robot's head, θ_h is the robot's head angle relative to its body, and L is the distance between microphones. If the source is located far enough from the robot, one can find its direction as

*Corresponding author. Email: nabaid@vt.edu

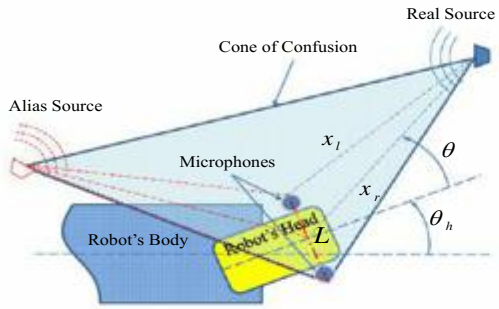

Figure 1: Schematic of the robot and the source. This figure shows how ITD can estimate the sound's direction and the concept of cone of confusion, shown as the shaded triangle

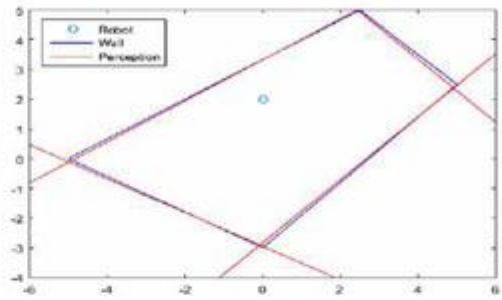

Figure 2: Passive localization of the walls of the room. The beacon is on the robot, but the robot does not know the location of the beacon nor the time sounds are emitted

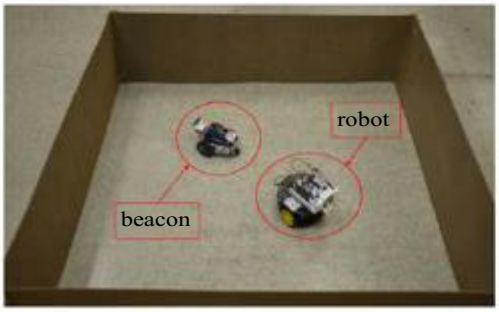

Figure 3: The experimental setup to verify the simulation as future work

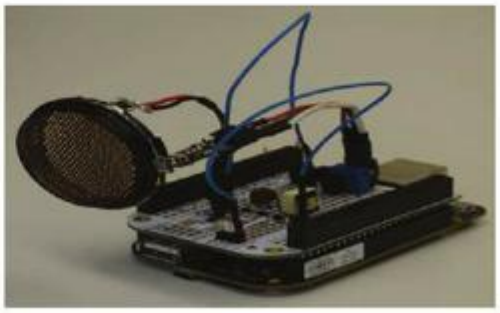

Figure 4: The SonicBeagle, a frequency modulated ultrasonic sensor inspired by bat echolocation [4]

$\sin(\theta) = \frac{x_r - x_l}{L} = \frac{c \cdot ITD}{L}$, where c is the speed of sound. The locus of all the points with the same distance to the left and right microphones is a cone with the line between the microphones as its axis, shown as the bold shaded triangle in Figure 1. This cone is known as the cone of confusion. One way to resolve the true position of the beacon in the cone is to tilt the head and estimate the direction of sound again. The direction of the real source should not change by the head motion. Figure 2 shows the simulation result of a robot passively perceiving the locations of walls of a room using this strategy to resolve the cone of confusion. Simulation results show a strong correspondence between the true and perceived locations of the walls.

CONCLUSIONS

Although active sensing is easier and more accurate than passive sensing, exploiting the free acoustic information makes passive sensing an energy saver especially for a large group of robots. In addition, switching to passive sensing in critical times may help a swarm to avoid jamming in the same way that is observed in bats. In this paper, the functionality of using passive sensing to localize obstacles is verified by simulation.

The next step in this work is to experimentally verify this approach to solve a mapping problem. The experimental setup is shown in Figure 3, in which one robot acts as beacon and the other one passively detects the walls. We have developed the SonicBeagle (Figure 4), an ultrasonic sensor that can create modulated frequency sounds and record the echo, mimicking bat's sonar [4]. It will be integrated on all the robots to let them move around and sense the environment like bats.

References

[1] Surlykke A., Nachtigall P. E., Fay R. R., Popper A. N.: Biosonar. Springer, 2014.

[2] Chiu C., Moss C. F.: Flying in Silence: Echolocating Bats Cease Vocalizing to Avoid Sonar Jamming. Proceeding of the National Academy of Science 105:13116-13121, 2008.

[3] Stecker, G. C. and Gallun, F. J. (2012). Binaural Hearing, Sound Localization, and Spatial Hearing, in Translational Perspectives in Auditory Neuroscience: Normal Aspects of Hearing, edited by Tremblay, K. L., and Burkard, R. F. (Plural Publishing, Inc., San Diego), 383433, 2012.

[4] Kepa K., Abaid N.: Development of a Frequency-Modulated Ultrasonic Sensor Inspired by Bat Echolocation. Proc. SPIE 9429, Bioinspiration, Biomimetics, and Bioreplication, March 2015.

TIME-DOMAIN NEAR-FIELD ACOUSTICAL HOLOGRAPHY AS A MEANS TO PREVENT EXPOSITION TO HARMFUL INDUSTRIAL IMPACT NOISES

Jean-Michel Attendu[1a)] & Annie Ross[1]
[1]*Mechanical Engineering, École Polytechnique de Montréal, Montréal, Québec, Canada*

Summary Time-domain near-field acoustical holography is a method used to visualize non-stationary sound radiation. It is based on the use of a microphone array and fast-Fourier transform based convolution. However, current methods are subject to spectral leakage and wrap-around errors. A new formulation based on the time and spatial representation of the transfer function is presented in this paper. The errors are suppressed when this formulation is used in conjunction with linear convolution. It is also shown that the method can be used to monitor impact noises obtained experimentally. Such visualization is an asset in passive noise control for the correction of harmful impact noises often found in industrial environments.

INTRODUCTION

According to the *World Health Organisation*, 360 million people (over 5% of the world's population) have disabling hearing loss [1], which involves detrimental social and functional consequences on their lives. A major cause of deafness is exposition to excessive noise, which is particularly predominant in industrial environments. Often, the loudest and most damageable noises are related to impacts, such as in riveting or hammering. In this proceeding, a new formulation for time-domain near-field acoustical holography (TD-NAH) is used to monitor impact noises. A pressure field is produced experimentally by impacting of a metallic rod on a plate. Such sound mapping can be used for noise diagnosis and can be a major asset for establishing passive noise corrections on the source. In the next sections, the theory behind the proposed formulation for TD-NAH is summarized, followed by an experimental analysis and conclusions.

TIME AND SPACE DOMAIN NEAR-FIELD ACOUSTICAL HOLOGRAPHY

In NAH, the sound field is acquired in the near-field of the source using an array of microphones. This acts as a boundary condition to solve the wave equation using Green's method, in order to represent the sound field in three-dimensions. The standard formulation supposes a stationary sound field, and the problem is solved in the frequency domain [2]. For non-stationary signals, adaptations of the original formulation were proposed in order to represent the sound field in the time-domain [3-5]. However, unlike other existing TD-NAH formulations, the formulation proposed here eliminates wrap-around and leakage errors by expressing the Green's function in the space and time domains before performing linear convolution. Consequently, the representation of the sound field with the proposed method is more accurate, even after its propagation dozens of centimetres away from the source.

The pressure field is acquired on the measurement plane at $z = z_0$. Then, by convolving the measured pressure field with the Green's function expressed in Eq. 1, the sound field can be reconstructed on other parallel planes. The convolution is performed over the x, y and time dimensions.

$$g(t,x,y,d) = \frac{d}{2\pi}\left(\frac{1}{R^2}\frac{\partial}{\partial t} + \frac{c}{R^3}\right) \cdot \delta\left(t - \frac{R}{c}\right) \tag{1}$$

In Eq. 1, d is the distance between the measurement plane and the forward reconstruction plane and R is expressed as $R = \sqrt{x^2 + y^2 + d^2}$. The geometry of the problem is illustrated in Fig. 1.

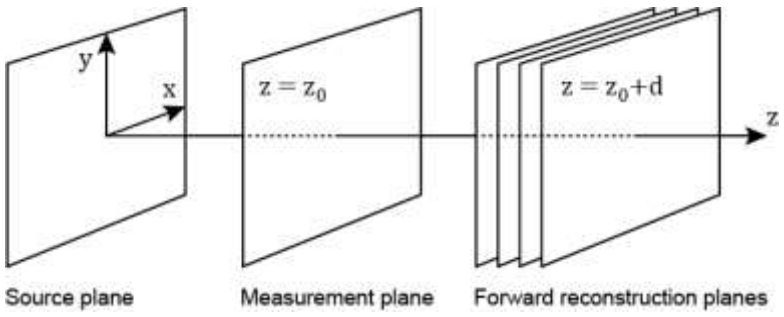

Fig. 1 *Propagation of the sound field from the measurement plane to reconstruction planes*

In practice, since the measurements are performed over a finite and discrete aperture, special care must be given to the discrete convolution process in order to avoid signal processing errors. First, linear convolution must be applied, as the non-

a) Corresponding author. Email: jean-michel.attendu@polymtl.ca.

stationary signal is not periodic over x, y or t. Linear convolution can be obtained by performing circular convolution using the Fast Fourier Transform (FFT), after zero-padding both signals over each dimension [6]. It must also be ensured that both the pressure field at $z = z_0$ and the Green's function are entirely included in the spatial domain, as the linear convolution supposes that the signals are null outside of their domain of definition. Since the span of g over x and y increases with d, it is important to fix the spatial domain large enough in order to avoid truncation errors. Finally, the sampling frequency and the noise level must be controlled in order to avoid errors due to the differential operator in the time domain. Fourth order finite element differentiation is used in this case. In the case of low *SNR*, regularization algorithm was successfully applied with the proposed method to avoid considerable differential errors.

EXPERIMENTAL RESULTS

Experimental measurements were performed in an anechoic environment in order to study the pressure field radiated from the impact of an aluminum rod with a 50 by 30 *cm* Plexiglas plate. The measurement apparatus consists in 64 aligned class-1 microphones distanced by one *cm* center to center. A slide allows the translation of the line of microphones over the scanning surface (91 *cm* by 63 *cm*), with an increment of 1 *cm*. The impact is repeated for each measurement position by releasing the rod with an electro-magnet, and the measurements are phased by using a 65th fixed reference microphone. The sampling frequency is 200 *kHz*, and the acquisition is performed with a 24-bit resolution. Measurements were performed in the near-field at 65 *mm* from the plate.

Fig. 2a) presents the sound pressure obtained 100, 200 and 300 *mm* away from the measurement plane on the central orthogonal axis. Each signal has a null amplitude until the sound field reaches its position, and as expected, the maximum amplitude decreases with the distance from the source. The pressure field at evolution at $z = 300$ *mm* and at $t = 1.2$ *ms* is presented in Fig. 2b). The main wave front travels radially away from the impact point. Other high frequency wave fronts are present due to the dispersion of the bending waves in the plate.

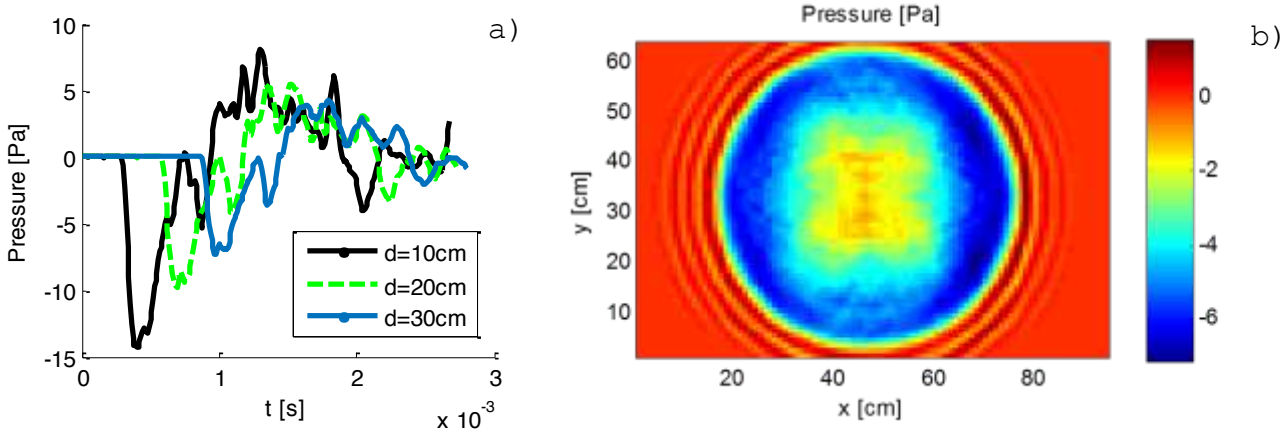

Fig. 2 *Forward reconstruction of the transient acoustic field. a) Time evolution of the pressure on the central orthogonal axis at 10, 20 and 30 cm from the measurement plane. b) Spatial representation of the sound field at t=1.2 ms and z=30 cm.*

DISCUSSION AND CONCLUSION

The proposed method is accurate in the calculation of the sound field for any propagation distance *d* representative of normal working distances in industrial environments. It is thus suitable for the monitoring of transients in industrial environment, where sound mapping can be used as a diagnosis tool to control harmful noise emissions with, for example, passive damping. The key elements of the proposed method are the time and spatial domain formulation of the Green's function which allows the application of a linear convolution and the definition of the spatial domain of the Green's function which increases with respect to the propagation distance *d*. The authors would like to thank NSERC for supporting this research.

References

[1] World Health Organisation, Deafness and hearing loss, Fact sheet N°300 (March 2015). Retrieved January 13, 2016, from http://www.who.int/

[2] J. D. Maynard, E. G. Williams, and Y. Lee (1985). "Nearfield acoustic holography: I. Theory of generalized holography and the development of NAH". Journal of the Acoustical Society of America 78 (4), 1395–1413.

[3] J.F. Blais, A. Ross, (2009). "Forward projection of transient sound pressure fields radiated by impacted plates using numerical Laplace transform". Journal of the Acoustical Society of America 125 (5), 3120-3128.

[4] J-H Thomas · V Grulier · S Paillasseur · J-C Pascal · J-C Le Roux (2010). "Real-time near-field acoustic holography for continuously visualizing nonstationary acoustic fields". Journal of the Acoustical Society of America 128 (6), 3554-3567.

[5] Hald, J. (2001)," Time domain acoustical holography and its applications". Sound and Vibration, 35 (2), 16-25.

[6] A. V. Oppenheim, R. W. Schafer, *Digital Signal Processing*. Prentice-Hall, 1975.

MECHANISMS OF JET CRACKLE

David A. Buchta *[1] and Jonathan B. Freund[2]
[1]*Mechanical Science & Engineering, University of Illinois at Urbana-Champaign, Illinois, USA*
[2]*Mechanical Science & Engineering and Aerospace Engineering, University of Illinois at Urbana-Champaign, Illinois, USA*

Summary Crackle is a particularly intense and annoying characteristic of the noise radiated by high-speed (supersonic) jets. Pressure traces show evidence of relatively strong compression in the sound field and more extreme positive than negative pressure fluctuations thus leading to positive skewness. To study its mechanisms, a turbulent free shear flow and its near acoustic field is directly simulated without modeling approximations. The simulations confirm that the 'footprint' of pressure skewness originates close to or within the turbulence. A supersonic flow which includes weak gas dynamic nonlinearities over a wavy-wall, with characteristics set to match scales of the turbulence, suggest a basic mechanism that potentially underlies the generation of crackle's near-field pressure fluctuations.

BACKGROUND

Military aircraft and other jet engines operating with high-specific thrust $M_j \gtrsim 1.5$ radiate a particularly intense and distinct sound that has become known as 'crackle'. The root mechanisms of crackle are not fully understood, though it is thought to involve nonlinear acoustics because the sound waves appear steepened. They also have a positive pressure skewness,

$$S_k(p') = \frac{\langle (p')^3 \rangle}{\langle (p')^2 \rangle^{3/2}}, \tag{1}$$

with more extreme pressure maxima than minima. Ffowcs Williams *et al.*[1] first identified crackle as a distinct phenomenon and found that its perception correlates with $S_k(p') \gtrsim 0.$. Pressure signals have periods made up of steepened shock-like waves followed by weaker, longer, rounded rarefaction regions, but to what extent this character originates at the turbulent source or arises from propagation effects is unclear. We investigate a potential mechanism leading to these peculiar pressure fluctuations.

APPROACH AND OBJECTIVES

Simulations are designed to represent the thin, weakly curved turbulent shear layers near the nozzle exit, and there provide a detailed description of the turbulence mechanisms, including any near-field acoustic nonlinearity that leads to crackle. The simulations resolve all the energetic scales with no modeling approximations. Figure 1 shows an x-y plane of the three-dimensional simulation configuration. Following previous work,[2] the turbulence was initially seeded with broadbanded, solenoidal velocity perturbations. Velocity spectra at the centerline confirm that the solution is well resolved and that it develops to have realistically broadbanded turbulence matching experimental measurements. Linear, 'wavy-wall' analogies have been relatively successful in predicting some aspects noise radiated by high-speed flows;[3] however, linear analysis precludes the finite S_k of crackle. Weakly nonlinear effects can be included in models of irrotational flow over wavy walls, and we invoke these to examine possible mechanisms leading to finite S_k.

RESULTS

For $M \geq 2.5$ flows, the near-field ($|y| > \delta_{99}$ in figure 1) is seen to be teeming with weak, shock-like structures. There the pressure signal has intense, sharp peaks with rounded, shallow valleys. The corresponding S_k in figure 2 shows $S_k \gtrsim 0.$ for $M \geq 2.5$. Skewness appears unchanged over the distances simulated. The detailed budget of pressure skewness suggests a balance between local nonlinear interactions and entropy production through a viscous diffusion term. Simulations at higher Reynolds number confirm insensitivity to viscosity and suggest that large-scale structure dynamics are important in its generation.

We compare the DNS near field to results for nonlinear supersonic flow over an impenetrable wavy wall. The wall shape in figure 3 is parameterized by the turbulence integral length scales, l_x and l_z, in the x- and z-directions, respectively, from the DNS of the free-shear layers. The wall height (ϵ) is set so as to reproduce the v'_{rms} at the midplane of the turbulent mixing layer. We observe that nonlinear mechanisms lead the fluid to compress more intensely above the wall troughs with weaker expansions over the wall crests, so the pressure fluctuations radiate from the surface with more intense peaks than valleys. Due to convective effects[4] the pressure waves then steepen into thin, weak, shock-like waves. Figure 4 shows that skewness

*Corresponding author. Email: buchta1@illinois.edu

increases with relative speed. $S_k \gtrsim 0.4$ is observed for $U_r \gtrsim 0.6\Delta U$ suggesting that loud, crackle events arise from instances of large structures convecting faster than their average $\Delta U/2$ speed. Experimental observations support that the geometry of intense wave events correlate to apparent source speeds larger than $\Delta U/2$.[5]

CONCLUSIONS

The near field of temporally-developing turbulent shear layers exhibit the salient features of jet crackle with pressure skewness $S_k(p') \gtrsim 0.4$ for speeds $M \geq 2.5$. Pressure skewness is insensitive to Reynolds number, for the range simulated, and also appears constant in the near field, confirming that the root of jet crackle is near or within the turbulence. A wavy-wall model matching turbulence scales reproduces comparable near-field skewness to high-speed free-shear-flow turbulence and shows a similar wave pattern. (Support from AFOSR and ONR is greatly appreciated)

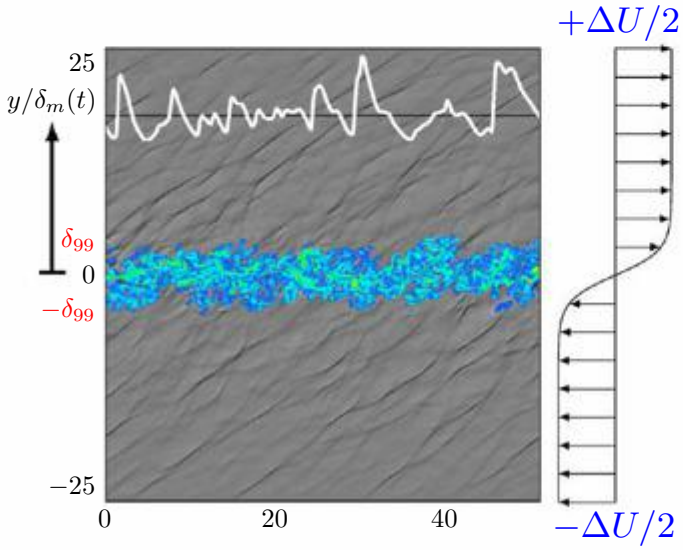

Figure 1. Shear layer configuration of an x-y plane at $z = L_z/2$ with $\nabla \cdot \mathbf{u}$ in gray and $|\nabla \times \mathbf{u}|$ in color. The trace shows the typical near-field pressure fluctuation p' associated with crackle.

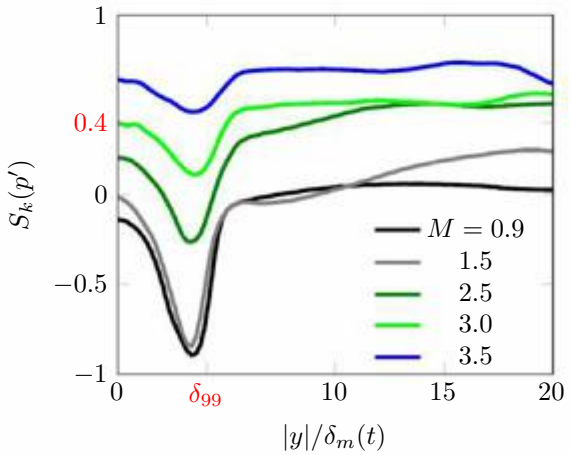

Figure 2. Turbulence: Pressure skewness with distance from the mixing layer midplane.

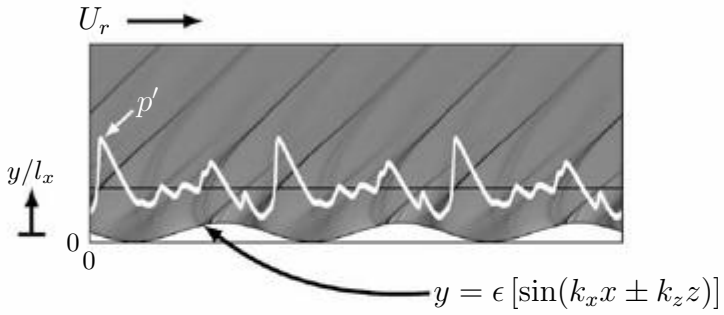

Figure 3. Supersonic flow over a wavy surface designed to reflect turbulence statistics. Contours of $\nabla \cdot \mathbf{u}$ in an x-y plane at $z = L_z/2$.

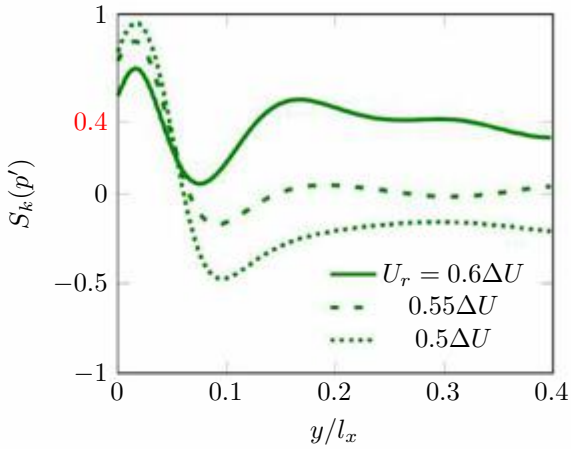

Figure 4. Wavy wall: Pressure skewness with distance from the wall, with $M = 2.5$ flow characteristics at potential U_r speeds.

References

[1] Ffowcs Williams, J. E., Simson, J. and Virchis, V. J., 'Crackle': An annoying component of jet noise. Journal of Fluid Mechanics, 1975.
[2] Kleinman, R. and Freund, J. B., The sound from mixing layers simulated with different ranges of turbulence scales. Physics of Fluids, 2008.
[3] Tam C. K. W., Directional acoustic radiation from a supersonic jet generated by shear layer instability. Journal of Fluid Mechanics, 1971.
[4] Lighthill M. J., Viscosity effects in sound waves of finite amplitude. Surveys in Mechanics. Editors Batchelor & Davies, 1956.
[5] Oertel, H., Kinematics of Mach waves inside and outside supersonic jets. In Recent Developments in Theoretical and Experimental Fluid Mechanics, 1979.

ACOUSTIC PROPERTIES OF POROUS PLA MONOLITHS PRODUCED VIA NONSOLVENT INDUCED PHASE SEPARATION

E.R. Fotsing[1a)], E. Rezabeigi[2], A. Dubourg[1], A. Ross[1], P.M. Wood-Adams[2], R.A.L. Drew[2]
[1]*Department of mechanical engineering, École Polytechnique, Montreal, Quebec, Canada*
[2]*Department of mechanical and industrial engineering, Concordia University, Montreal, Quebec, Canada*

Summary The acoustic properties of porous PLA monoliths used as bone scaffold were characterized using an impedance tube. This broadband absorbing material was produced by controlling the microstructure of pores through an innovative synthesis process. Despite its lightness, the obtained PLA foam with mesopores was shown to be an excellent sound barrier whereas the absorption effect was more important for foams with macropores interconnected by mesopores. These results can pave the way for new applications in various fields of engineering.

INTRODUCTION

Polylactic acid (PLA) is a biodegradable thermoplastic which is categorized as saturated aliphatic polyester. Relatively high melting point (~ 170 °C); recyclability and good mechanical properties have made PLA attractive for various areas including biomedical engineering, transportation and aerospace. PLA has successfully replaced some of the non-biodegradable industrial polymers and its applications are increasing, because new mass production techniques are making this polymer inexpensive and more available in various molecular weights and properties [1,2]. In this study, we designed a versatile foaming route, *nonsolvent induced phase separation (NIPS)*, which is able to produce highly porous (up to 91%) PLA foams with no gas or sacrificial phases involved. Based on the Flory-Huggins theory, the addition of a nonsolvent to a polymer solution increases the Gibbs free energy of the system which may result in phase separation (liquid-liquid or solid-liquid) [3,4]. Depending on the initial PLA-solvent-nonsolvent composition and the phase separation standing temperature, various pore morphologies are formed in situ as a result of this phase separation. The flexibility of this foaming method provides the opportunity of tailoring the characteristics of the PLA foams according to their applications. Also, the shape of the final foam can be determined by the shape of the mold wherein the phase separation and gelation occur. These ultralight NIPS-derived PLA foams have a great potential in aerospace and transportation applications where fuel efficiency is very important both for financial and environmental reasons. In fact, porous materials are widely used for noise control in high-speed trains, cars and under certain requirements, as new materials for novel turbofan acoustic liners.This article reports the correlation between the acoustic properties and the microstructure of porous PLA monoliths produced by nonsolvent induced phase separation.

PROCEDURES

Fabrication of PLA foams

In order to fabricate the foams, PLA (NatureWorks LLC, Ingeo™ Biopolymer 4032D) with a high average molecular weight (Mn = 97000, Mw/Mn = 2) and 1.6 % D-lactide content; dichloromethane (DCM, Fisher Chemical; Stabilized/Certified ACS, ≥99.5) as solvent and hexanes (Fisher Chemicals; Certified ACS, ≥98.5 %) as nonsolvent were used [2,3]. First, some systems were selected from the liquid-liquid (hexane/DCM volume ratio = 1) [2] and solid-liquid (hexane/DCM volume ratio = 1.25) phase separated regions of the PLA-DCM-hexane phase diagram. These ternary systems were produced by preparing PLA-DCM solutions with certain concentrations followed by the gradual incorporation of hexane at room temperature under vigorous stirring. The systems were allowed to phase separate at room temperature or -23° C (in a freezer) until complete gelation which was followed by 24 hours aging. The PLA foams were characterized after a thorough solvent exchange in methanol for 30 hours and then drying under ambient conditions.

Measurement of acoustic properties

Acoustic properties (absorption coefficient, acoustic impedance and transmission loss (TL)) of the manufactured foams were measured using an impedance tube, in absorption (two microphones) and transmission configuration (four microphones). In the tube, the speaker generates plane waves in the tube that travel forward and backward after reflecting onto the specimen at the end of the tube. The measurement of the acoustic pressures by the microphones along the tube lead to determination of the absorption coefficient and the acoustic impedance. The samples are small cylinders of NIPS derived PLA foams having a 30 mm diameter and thickness varying between 10 mm and 30 mm.

RESULTS

PLA foams with various crystallinity, mechanical properties and mesoporous or meso/macroporous morphologies were produced. Fig. 1a represents a foam with mesopores and Fig.1b shows a foam with a combination of meso and macropores. A density of 0.14 g/cm^3 and 0.17 g/cm^3 has been reported for mesoporous and meso/macroporous foams, respectively. In general, porous materials can be classified in two groups: open cells which are intereconnected not only over the entire material but also connected to the surrounding environment; and closed cells which are discrete and isolated from each other and from the outside [5]. Interconnections between macropores through mesopores (Fig.1b) suggest that this type of PLA

[a)]Corresponding author. Email:edith-roland.fotsing@polymtl.ca.

foam may have interesting acoustic properties and can be used as broadband absorbing material. The airborne noise dissipation and absorption capacity are achieved through successive interactions and viscous friction of the moving air within the cavities of the material.

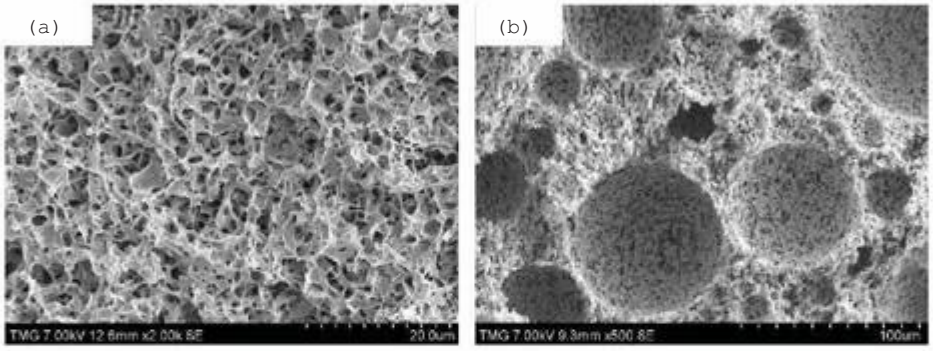

Fig.1. Examples of mesoporous (a) and meso/macroporous (b) morphologies of the NIPS-derived PLA foams prepared at room temperature.

Results obtained from impedance tube showed that foam with mesopores is more resistive. The real part of the acoustic impedance particularly high in the 500-2500Hz range (Fig. 2a). The absorption coefficient is less than 0.1, and the transmission loss (TL) is greater than 30dB for frequencies below 3500Hz (Fig. 2b), suggesting that the foam acts more as sound barrier and less as noise absorbing material. This finding is therefore interesting since the sound wave is almost completely reflected back by a lightweight porous material, whereas the low frequency performance of sound barriers is usually correlated with the mass of the material. On the other hand, foams with macropores are less resistive and the absorption coefficient is increased over a broad frequency range.

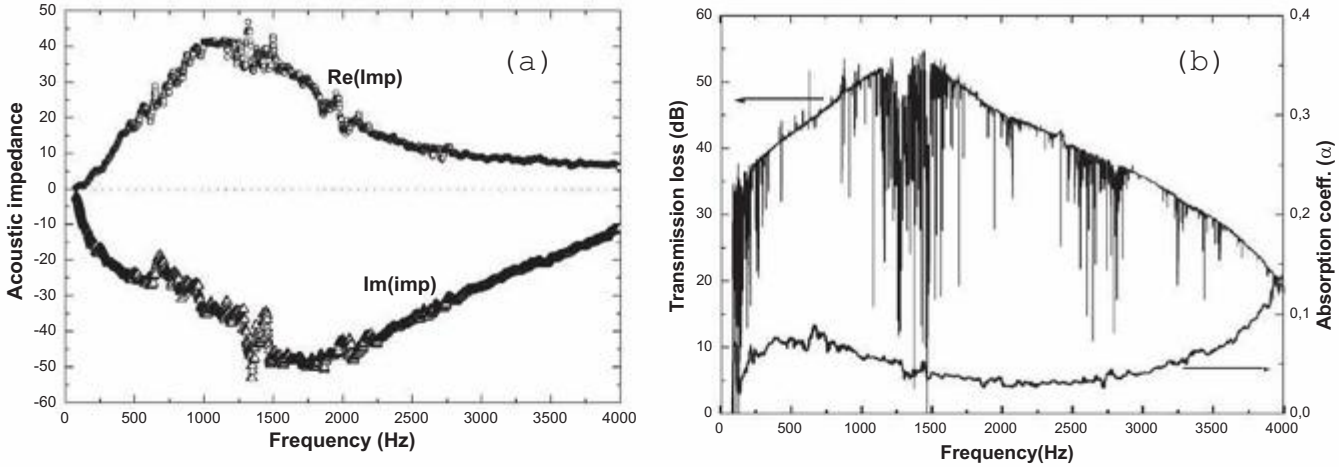

Fig.2. Acoustic properties of mesoporous PLA foam: Impedance (a), Transmission loss and absorption coefficient (b).

CONCLUSIONS

The acoustic properties of PLA foams produced by *nonsolvent induced phase separation (NIPS)* are correlated with their microstructure. The lightweight foam with mesopores behaves surprisingly as a low and medium frequency sound barrier. The foam is a standard absorbing material when pore dimensions reach the macrometric range.

References

[1] Nampoothiri K. M., Nair N. R., John R. P.: An overview of the recent developments in polylactide (PLA) research. *Bioresource Technology,* 101: 8493-8501, 2010.

[2] Rezabeigi E., Wood-Adams P.M., Drew R.A.L.: Production of porous polylactic acid monoliths via nonsolvent induced phase separation. *Polymer*, 55:6743 – 6753, 2014.

[3] Rezabeigi E., Wood-Adams P.M., Drew R.A.L.: Isothermal ternary phase diagram of the polylactic acid-dichloromethane-hexane system. *Polymer*, 55:3100 – 3106, 2014.

[4] Xin Y., Fujimoto T., Uyama H.: Facile fabrication of polycarbonate monolith by non-solvent induced phase separation method. *Polymer,* 53:2847–2853, 2012.

[5] Ishizaki K., Komameni S., Nanko M.: Porous materials process technology and applications. Kluver Academic Publishers, Netherlands 1998.

MODELLING BIOLOGICAL PHENOMENA WITH ROCKET BALLOON BUZZ

Alastair Gregory*[1], Pavel Kahout[1], and Anurag Agarwal[1]

[1]*Department of Engineering, University of Cambridge, Cambridge, United Kingdom*

Summary The flow of air through the exit tube of a rocket balloon produces a characteristic buzzing sound. It provides a novel fluid structure interaction problem that is investigated experimentally. The work is a part of ongoing efforts to better understand the mechanisms of sound production in diseased lungs, and so allow more specific diagnoses to be made using auscultation. The buzzing sound from a rocket balloon is produced by a large-amplitude oscillation of the exit tube. Scaling laws are desired for the dominant frequency of oscillations and for the critical speed for the onset of oscillations.

INTRODUCTION

The oscillation of rocket balloon exit tubes, producing a characteristic buzzing sound, provides a novel fluid structure interaction problem, with applications to medical diagnosis. We believe that the mechanism for wheezing sounds and flatulence is similar to buzzing in rocket balloons. Better understanding of the wheezing mechanism will improve the specificity of diagnosis [4]. The instability of flow through tubes has been investigated using starling resistors [1, 3], however, in much of this work the density ratio of the wall to the fluid is large, and wall inertia is frequently neglected (water has been used as the working fluid), which does not match conditions in the lung. The aim of this work is to improve this situation, working towards the development of a stethoscope for the 21st century. To this end, air was forced though rubber tubing and the resulting oscillations were observed (see fig. 1) as flow rate and tube parameters were varied.

EXPERIMENTAL SETUP

Three rubber tubes were investigated, all with an inner diameter of and a wall thickness of 0. . The tubes were pulled over a nozzle downstream of an air supply and flow conditioner. The video stills in fig. 1 show the tube only. Different tube lengths were attained by pulling the tubes over the nozzle to a greater or lesser extent, and length was measured from the end of the nozzle to the end of the tube. Time averaged flow rate was measured with a rotameter upstream of the tube, and sound recordings were taken with a Linear X M51 microphone at a distance of 1 away from the tube exit, and a polar angle of 0° from the axis of symmetry of the microphone (downstream). High speed video was also taken of particular oscillation modes using a Fastcam-ultima APX 120K high speed camera.

RESULTS AND DISCUSSION

When the flow rate is small, the tube remains open and stationary. There is a critical flow rate as flow is increased at which self excited oscillations are first observed. As flow is further increased the amplitude of the oscillations is seen to increase, and the frequency increases slightly. The initial oscillations usually involve small movements of the tube walls about an oval configuration. At higher flow rates the movement transitions to the kind of motion illustrated in fig. 1 in which the tube collapses completely in alternating orthogonal directions. The dominant frequencies shown in fig. 2b correspond to the first onset of visible vibration.

Characterising the Sound Source

We postulate that there are two main mechanisms by which sound is projected into the far-field. The movement of the tube wall will produces a sound field similar to that of a quadrupole, and oscillations in mass flux out of the tube will produce a sound field similar to that of a monopole. Observing the tube motion shown in fig. 1, we see that for every cycle of the tube wall, the area of the tube exit will go through two cycles, so we expect sound produced by the monopole to be at twice the frequency of sound produced by the quadrupole. Quadrupoles are less efficient at radiating sound than monopoles [2], and so we predict that the second harmonic of the sound measured will be louder than the first harmonic. Figure 2a shows an example where this is indeed the case.

*Corresponding author. Email: alg57@cam.ac.uk

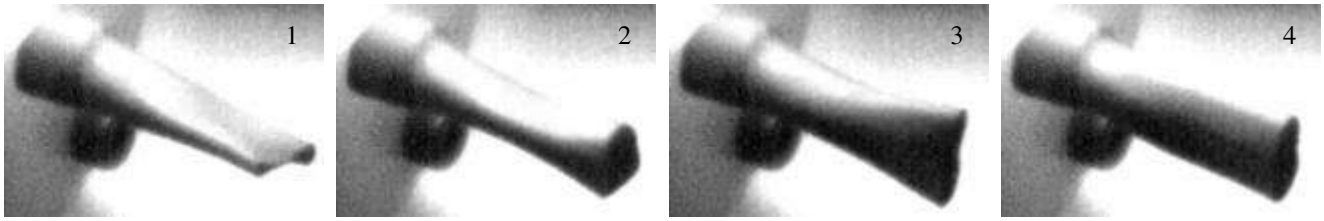

Figure 1: Tube oscillation images from high speed video ($\Delta t =$).

(a) Sound source characterisation.

(b) Scaling of frequency with length.

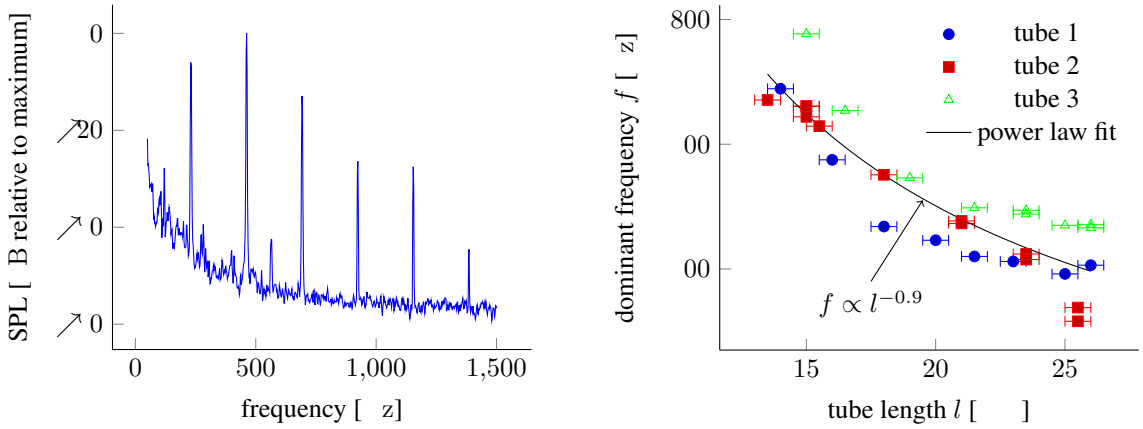

Figure 2: Results.

Scaling of Frequency with Tube Length

The frequency of oscillation is assumed to be primarily set by the normal mode of the flexible tube. There is some evidence that this is indeed the case in the lung [5]. Furthermore, we assume that the restoring force in the tube is primarily due to bending. This leads to the approximate scaling law,

$$\omega \sim \frac{h}{rl}\sqrt{\frac{E}{\rho(1 \nearrow \nu^2)}}. \tag{1}$$

where h is the wall thickness, l is the length, r is the radius, E is the Young's modulus, ρ is the wall density, and ν is Poisson's ratio. Figure 2b shows the dominant frequency of oscillation at onset as a function of tube length. There is good agreement with this scaling law.

CONCLUSIONS

Progress has been made towards characterising the mechanism of sound production in rocket balloons. Wall movement and unsteady mass flux have been considered as sources, and the scaling of the dominant frequency with tube length has been observed. Future work will investigate the effect of wall thickness and diameter of tube, and measure the directionality of sound produced. Experiments are also under way using a fixed downstream boundary condition, rather than an open one.

References

[1] C. D. Bertram. Experimental Studies of Collapsible Tubes. In P. W. Carpenter and T. J. Pedley, editors, *Flow past Highly Compliant Boundaries and in Collapsible Tubes*, pages 51–65. Kluwer Academic Publishers, 2003.

[2] A. P. Dowling and J. E. Ffowcs Williams. *Sound and Sources of Sound*. Ellis Horwood Limited, Chichester, 1983.

[3] M. Heil and O. E. Jensen. Flows in deformable tubes and channels. In P. W. Carpenter and T. J. Pedley, editors, *Flow past Highly Compliant Boundaries and in Collapsible Tubes*, pages 15–49. Kluwer Academic Publishers, 2003.

[4] N. Meslier, G. Charbonneau, and J. L. Racineux. Wheezes. *Eur. Respir. J.*, 8(11):1942–1948, Nov. 1995.

[5] Y. Shabtai-Musih, J. B. Grotberg, and N. Gavriely. Spectral content of forced expiratory wheezes during air, He, and SF6 breathing in normal humans. *J. Appl. Physiol.*, 72(2):629–635, Feb. 1992.

ACOUSTOPHORETIC HANDLING OF C. ELEGANS IN MICROFLUIDIC CHANNELS

Peter Reichert[1,a)], Thierry Baasch[1], Gamuret Hack[1], Nadia Vertti Quintero[2], Jürg Dual[1]
[1]*Institute of Mechanical Systems, Swiss Federal Institute of Technology Zurich, Zurich, Switzerland*
[2]*Chemical and Biological Systems Engineering Laboratory, Swiss Federal Institute of Technology Zurich, Zurich, Switzerland*

Summary *Caenorhabditis elegans* (*C. elegans*) is a model organism for research in the field of molecular and developmental biology. Microfluidic chips have improved the handling capabilities and have made high-resolution imaging and fluorescent scanning of *C. elegans* possible by immobilization with special geometries, cooling or gasses [1]. Bulk acoustic wave (BAW) acoustophoresis is proposed to be a new contactless handling tool for un-anesthetized *C. elegans* with ultrasound. Acoustophoresis has been used to position or rotate particles in a fluid [2]. Here we show the abilities of this method for the contactless and harmless immobilization of *C. elegans*. The *C. elegans* are injected into a silicon microchanel and immobilized by focussing them in the pressure nodal lines of a standing acoustic wave. Switching between two fluid resonance modes is used to sort *C.elegans* in two separate outlets. Moreover, a 3D numerical simulation shows the physical princples of *C. elegans* manipulation.

MOTIVATION

Controlled handling of *C. elegans* for imaging purposes in microfluidic chips is a challenging task due to their active behaviour (swimming, bending and rolling). For laser screening applications it is important to straighten the *C. elegans* to scan its whole length. If the contour is not defined (rolled up or bended) it is not possible to use fluorescent intensity data for biological studies if the exciting laser source has a spot size in the range of the width of an adult *C. elegans*. Also *C. elegans* can block the channel and a synchronization with a later sorting system at high throughput can fail [3]. Acoustophoresis as a contactless handling tool can eliminate these problems and lead to reliable biological experiments.

EXPERIMENTAL SETUP AND SIMULATION

The experimental setup shown in fig. 1(a) consists of a silicon/glass chip with microfluidic channels and a high-speed camera. Syringe pumps are used to inject wildtype *C. elegans* in a M9 buffer carrier fluid into the chip. For acoustophoresis, a piezoelectric transducer for the excitation of harmonic bulk acoustic waves is glued to the back side of the device. The transducer is excited by a function generator and an amplifier at the frequency of a fluid resonance inside the channel. A peltier element for temperature control is connected with a thermally conductive foam.

To understand the physical principles of the observed phenomena in the experiment, a simulation with the FEM software Comsol Multiphysics is conducted. Fig. 1(b) shows the simulated 3D model and the pressure distribution inside the device at a frequency of 3 MHz. To set the material properties of the *C. elegans*, the speed of sound has to be approximated. Pre-experiments with polystyrene particles of known material properties are used to evaluate the pressure distribution in a microfluidic channel [4]. A *C. elegans* is moved to the pressure node in the same channel and by fitting the simulation with the resulting experimental trajectory a speed of sound of 1600 m/s is achieved, which is similar to the speed of sound of human skin [5]. It is then possible to simulate the forces acting on a *C. elegans*, the influence on the acoustic field and the trajectories inside the channel for different frequencies.

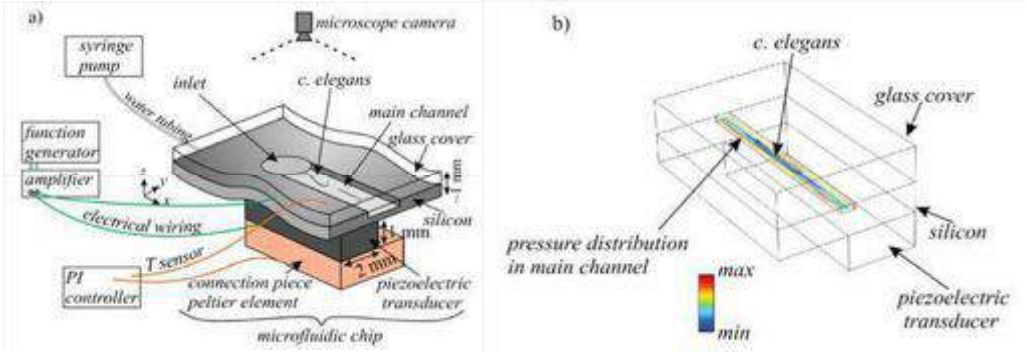

Fig. 1. Sketch of the experimental setup, the microfluidic device and the simulated device. In (a) The main channel has a depth of 90 µm, a length of >8 mm and a width of 200 µm or 700 µm. A piezoelectric transducer Pz26 (Ferroperm) is mounted to the back side of the chip. The chip is connected to a peltier element by a thermally conductive foam. The simulated 3D model in (b) shows the absolute pressure amplitude at a frequency of 2.8 MHz inside a chip with a modelled *C. elegans* in the middle.

a) Corresponding author. Email: reichert@imes.mavt.ethz.ch.

RESULTS

Immobilization of a *C. elegans* is shown in the image sequence from a high-speed recording in fig. 2. An adult *C. elegans* flows in a bent state through the microfluidic chip. After a visual detection ultrasound is switched on and the *C. elegans* is straightened and focussed in the middle of the channel. In this position e.g. a laser can detect fluorescent proteins along the length or a motion detection software can be used for a length measurement. After a duration of 60 ms the ultrasound is switched off and the *C. elegans* bends again which shows its viability.

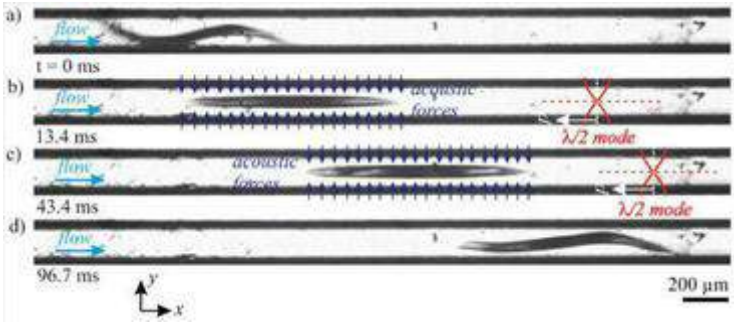

Fig. 2. Straightening and immobilization of an adult *C. elegans* for optical scanning purposes. a) No ultrasound, a moving *C. elegans* flows with a speed of 25 mm/s. In b) and c) an excitation pulse (time 60 ms) at a frequency of 3.56 MHz at an amplitude of 17 Vpp straightens the *C. elegans* in the pressure node of the half wavelength (λ/2) fluid resonance mode in the channel middle. The *C. elegans* is slowed down to 9 mm/s due to acoustic forces in x- direction. In d) the negative control without ultrasound shows the bent *C. elegans*.

Sorting in fig. 3 is performed by switching between two fluid resonance modes and guiding the *C. elegans* either in the middle outlet or in one of the remaining outlets of the trifurcation (outlet 1.1 or outlet 1.2). Dependent on the size, the viability (image analysis) or a detected fluorescent threshold it is possible to sort *C. elegans* into two categories.

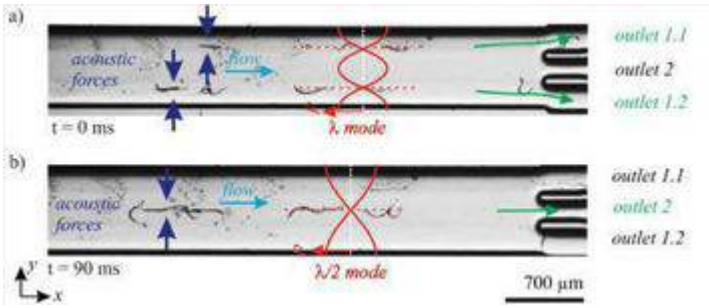

Fig. 3. Sorting of *C. elegans* with an average length of 350 µm (L 3 stage) at a flow speed of 1.6 mm/s. (a) Excitation at 2.165 MHz generates a λ mode, which deflects *C. elegans* to the upper or bottom outlet. (b) In a next time step, the piezoelectric transducer is excited at a frequency of 970 kHz ((λ/2), *C. elegans* are moved to the channel middle and are sorted to the outlet in the middle of the trifurcation. An amplitude of 28 Vpp is used. By switching between the λ- and λ/2 resonance mode sorting in two different outlets becomes possible.

CONCLUSIONS

The microfluidic handling tool BAW acoustophoresis enables immobilization and sorting of living *C. elegans*. With this method contactless and un-anesthetized handling of *C. elegans* at low flow rates in wide channels becomes possible. In the high kHz frequency range a temperature controlled acoustic actuation is harmless for living organisms. Acoustophoresis is seen as a handling tool for biological researchers which is harmless, versatile (immobilization and sorting), with a simple chip fabrication and is applicable for *C. elegans* in every stage of its life cycle. Furthermore, new experimental ideas become possible, e.g. the evaluation of the fitness of a *C. elegans* (comparing simulation and experiment) or the imaging at low flow rates.

References

[1] A. San-Miguel and H. Lu *Microfluidics as a tool for C. elegans research. WormBook*, http://www.wormbook.org, (2013).

[2] H. Bruus, et al. *Forthcoming Lab on a Chip tutorial series on acoustofluidics: Acoustofluidics—exploiting ultrasonic standing wave forces and acoustic streaming in microfluidic systems for cell and particle manipulation.* Lab on a Chip 11(21), p. 3579-3580 (2011).

[3] Y. Yan, et al. *A continuous-flow C. elegans sorting system with integrated optical fiber detection and laminar flow switching*. Lab on a Chip 14(20), p. 4000-4006 (2014).

[4] R. Barnkob, et al. *Measuring the local pressure amplitude in microchannel acoustophoresis.* Lab on a Chip 10, p. 563-570 (2010).

[5] C.M. Moran et al. *Ultrasonic propagation properties of excised human skin*, Ultrasound in Medicine & Biology 21, p. 1177-1190 (1995).

FLOW FIELD AND ACOUSTIC STUDY OF THE FLOW IN VARIOUS WALL-MOUNTED POROUS FENCES

Eduardo Rodríguez-López *[1], Laurent E. Brizzi[2], Paul J.K. Bruce[1], Oliver R.H. Buxton[1], and Vincent Valeau[2]

[1]*Departments of Aeronautics, Imperial College London, London, United Kingdom.*
[2]*Institut P′, Université de Poitiers, Poitiers, France*

Summary An extensive experimental characterization of the flow past wall-mounted single- and multi-scale porous fences is presented. Results are shown using hot-wires, PIV, fluctuating wall pressure and a microphone array. There is evidence that both the mechanism of formation of the far field boundary layer and of sound generation depend strongly on the grid geometry. Results will be presented involving wall-flow correlations in order to characterize the distinct influences of the grids' wake in the near-wall region.

INTRODUCTION AND EXPERIMENTAL SET-UP

Wall-mounted porous fences (both single- and multi-scale) are widely employed for industrial flows in which a wall-bounded flow needs to be passively controlled. More fundamentally, the turbulence generated by the grid interacts with the turbulent boundary layer (TBL) modifying its properties and influencing its development further downstream [1]. The present paper will study both the near and far field behaviours of TBL generated downstream of porous fences. Special attention is paid to (i) the influence of the wake turbulence on the near-wall region and (ii) the acoustic performance of the wall-mounted fences which may make them unsuitable for certain applications.

Hot-wire measurements were performed at Imperial College London using constant temperature anemometry with an in-house etched wire of diameter $5\,\mu$m. This is a closed loop wind tunnel with a square section $0.91 \times 0.91\,\mathrm{m}^2 \times 4.8\,\mathrm{m}$ long. It was run at a constant freestream speed of $U_\infty = 10\,$m/s with a background turbulence intensity of $\lesssim 0.05\%$. Further details for this wind tunnel are reported in [1]. A flat plate was mounted spanning the whole test section and the different grids were mounted at $x_0 = 2\,$m downstream of its leading edge where the thickness of the boundary layer $\delta = 73\,$mm.

Particle Image Velocimetry (PIV) coupled with fluctuating wall pressure was conducted at the University of Poitiers in the $3/4$ open BETI wind tunnel built inside an anechoic chamber. The end of the contraction is $0.7 \times 0.7\,\mathrm{m}^2$ and a square collector of $0.9 \times 0.9\,\mathrm{m}^2$ is located $1.5\,$m downstream. A flat plate was mounted spanning the gap between contraction and collector; grids were placed at $x_0 = 288\,$mm where $\delta \approx 20\,$mm. An Underbrink multi-arm spiral array of 31 microphones (mounted $1.3\,$m above the flat plate) allowed the measurement of the radiated sound pressure level, SPL, $\Phi = 10\log(P'/M^6)$, where P' stands for the Power Spectral Density of the sound pressure, p'; and M is the Mach number. The location of acoustic sources was also measured to determine where the radiated noise was generated with a resolution of $\approx 3\,$cm for intermediate frequencies $\mathcal{O}\,(6\text{ kHz})$.

Four different geometry grids were tested in both wind tunnels; all of them were $100\,$mm high with $800\,$mm span and blockage ratio $\sigma = 0.3$. The different grids were formed by a basic pattern repeated until achieving the desired span. Fractal grid was based on the fractal square pattern described in [2] with thickness ratio $t_r = 5$ and $t_0 = 5\,$mm. Cross grid was based on the fractal cross pattern described in [2] with $t_r = 5$ and $t_0 = 5.6\,$mm. Multiscale grids have been extensively studied in the past decade because of their characteristic dissipation behaviour [3] and they have been previously employed in wall-mounted fences [4]. Following Townsend's attached eddy hypotheses, one can generate a grid such that the size of the generated eddies scales with the wall-normal coordinate to mimic the expected behaviour of the boundary layer; hence, Attached grid was made of squares of different sizes with their length equal to the wall-normal location of their centre. Finally, for comparison purposes a Regular grid of the same blockage was made of bars of thickness $t_0 = 5\,$mm separated $33\,$mm.

RESULTS

Experiments conducted at Imperial College: The flow in the vicinity of the grids is dominated by the different distributions of blockage. Although this dependence decays with downstream distance, the furthest measurement station is not far enough as to get a self similar state in which there is no dependence on the grid. This suggests that different grids present distinct mechanisms of evolution from initial conditions entailing different adaptation regions for the canonical state of the TBL, in agreement with results shown in [1]. This hypothesis is also sustained by the spectral measurements and the turbulence intensity profiles (not shown for brevity), which show a lack of collapse for the outer region of the flow.

Experiments at Poitiers University: The far field SPL shown in fig 1 does not display any preferential frequency for the Attached and Regular grids (and arguably for the Cross grid at $f/U_\infty \lessapprox 200$). However, there is a clear broadband peak for the Fractal case at $f/U_\infty \approx 200$. This peak may be related with the shedding of the smallest bars (with a thickness of $1\,$mm their Strouhal number, $St \approx 0.2$, is reasonable for vortex shedding). The spectra for different velocities collapse with the M^6 non-dimensionalization. This implies that the sound formation mechanisms behave as dipoles rather than quadrupoles; i.e., the importance of the sound radiated by the obstacle immersed in the flow is higher than the sound generated by the turbulence activity downstream of it.

*Corresponding author. Email: eduardo.rodriguez-lopez12@imperial.ac.uk

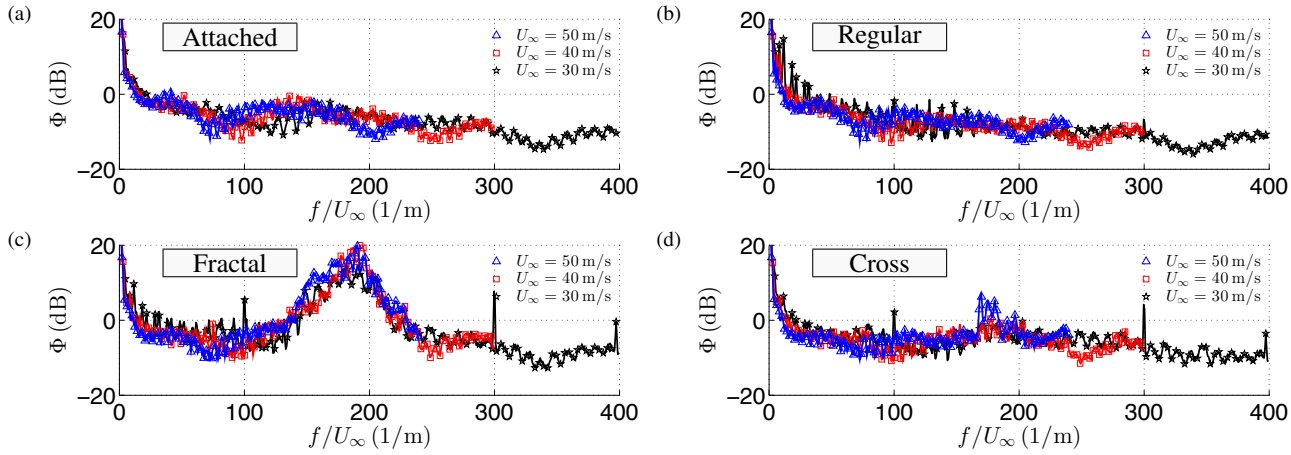

Figure 1: Sound spectra, Φ, in the far field for Attached (a), Regular (b), Fractal (c) and Cross (d) grids at various velocities.

Moreover, one can perform a detection of acoustical sources using a conventional delay-and-sum beamforming followed by a CLEAN-SC deconvolution algorithm [5]. It confirms the aforementioned result, where the acoustical sources are located on the grid plane and not in their turbulent wake. Fig 2 shows that for the cases where the spectra showed a peak for a given $St \approx 0.2$ (i.e. Fractal and Cross grids) the sound is mainly generated in regions with a high concentration of the smallest iterations and it is not uniform along the span of the grid. This contrasts with the Regular case in which there is not a preferential location of the sound sources along the span of the grid. This effect may be caused by the non-uniform blockage in the spanwise direction which forces the flow to concentrate along the regions where this blockage is smaller (hence the velocity is larger); consequently the noise generation is bigger in regions with a higher population of small iterations which entail a smaller blockage.

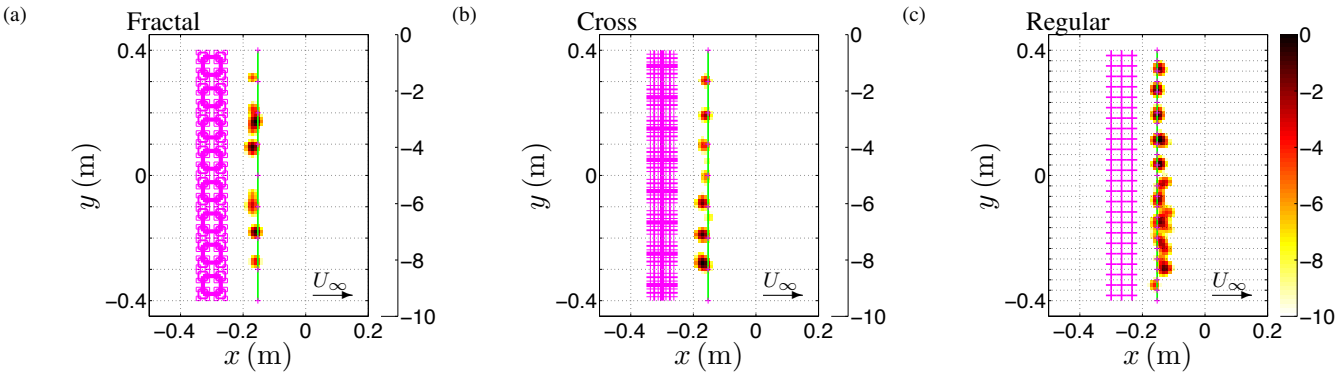

Figure 2: Acoustic source plot at 7200 Hz and $U_\infty = 40$ m/s for Fractal (a), Cross (b) and Regular (c) grids. Solid green line shows the location of the grid normal to the measurement plane. Note that the grid is only presented as a reference sketch. $(x, y) = (0, 0)$ is the projection of the microphone array centre on the measurement plane located at 50 mm above the wall.

In order to explore the sound generation mechanisms and the influence of different grids on the near field development of the boundary layer, coupled PIV and wall pressure fluctuations are being processed and will be presented showing the different formation mechanisms of the turbulence and sound in the near wakes of the various grids. In particular, correlations between the fluctuating wall-pressure and velocity fields will be presented in order to study the influence of distinct motions generated by bars of different sizes and orientations on the near-wall region. The change in thickness of the incoming TBL for both experimental campaigns will also be tested and discussed along with the development of the flow further downstream.

References

[1] Rodríguez-López E., Bruce P.J.K. and Buxton O.R.H.: On the formation mechanisms of artificially generated high Reynolds number turbulent boundary layers. Boundary Layer and Meteorology. *Accepted for publication*. 2016.

[2] Hurst D. and Vassilicos J.C.: Scalings and decay of fractal-generated turbulence. Physics of fluids 19(3):035103. 2007.

[3] Vassilicos J.C.: Dissipation in Turbulent Flows. Annual review of fluid mechanics 47:95-114. 2015.

[4] Keylock C.J., Nishimura K., Nemoto M. and Ito Y.: The flow structure in the wake of a fractal fence and the absence of an 'inertial regime'. Environmental Fluid Mechanics 12(3):227-250. 2012.

[5] Sijtsma P.: CLEAN based on spatial source coherence. International Journal of Aeroacoustics 6(4):357-374. 2007.

GLOBAL STABILITY AND RESOLVENT ANALYSIS OF SOUND EMISSION IN A HIGH-REYNOLDS NUMBER TURBULENT JET

Oliver T. Schmidt*[1], Aaron Towne[2], and Tim Colonius[1]
[1]*California Institute of Technology, Pasadena, CA, USA*
[2]*Stanford University, Stanford, CA, USA*

Summary Global stability and resolvent mean flow analyses of a Mach 0.9 high Reynolds number turbulent jet are conducted. The global modes are compared with wave packets distilled from a high-fidelity LES data base. The near-field and acoustic radiation of the linear global modes compare favorably with the simulation. Super-directive as well as multi-directive radiation patterns are observed. Since all global modes are stable, we conduct a resolvent analysis to characterize the noise amplifier behavior of the jet.

INTRODUCTION

It is widely accepted that large scale coherent structures or wave packets play an important role in the super-directive noise generation mechanism of fully turbulent jets at high Reynolds numbers [5]. It has also been established that these structures can be described as instability waves, i.e. normal waveform solutions of the linearized governing equations [3]. In the past, local parallel or weakly non-parallel stability analyses, and later calculations based on the parabolized stability equations (PSE) were conducted to model linear instability waves in jets. A first global stability analysis of a cold supersonic jet was performed by Nichols & Lele [4], and a first resolvent or input-output analysis by Garnaud et al. [2].

In this work, we calculate spectra and corresponding global modes based on the mean flow of a carefully validated large eddy simulation (LES) of a turbulent Mach 0.9 jet at Re=1×10^6 issuing from a convergent-straight nozzle [1]. The main focus is on the acoustic radiation of the global modes, and comparison with the LES data. In addition, optimal forcing distributions and responses are calculated from a singular value decomposition of the resolvent operator, i.e. the transfer function between the forced linear system, and an output quantity of choice.

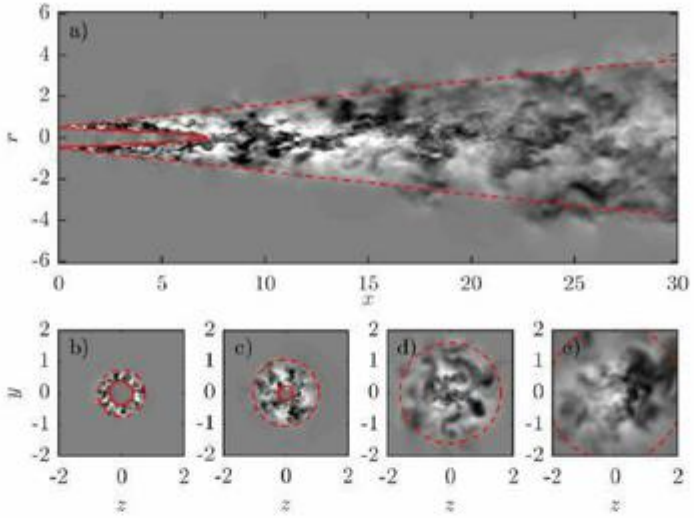

Figure 1: Instantaneous perturbation (grayscale) and mean (—— $u = 0.95$; - - - $u = 0.05$) flow field of the LES in terms of the streamwise velocity component: (a) streamwise plane; (b-e) transverse planes at x =2, 5, 10 and 15, respectively.

Figure 1 shows an instantaneous flow field and contours of the mean streamwise velocity. The vast range of scales involved at such high Reynolds numbers is apparent, and the existence of large scale coherent structures is far from obvious. Apart from the Kelvin-Helmholtz type shear-layer instability, the potential core supports trapped acoustic modes which give rise to tones frequently observed in experiments. Unlike a PSE computation, the following global mode analysis gives insight into how the latter two instability mechanism and the overall acoustic radiation of the combined linear wave packet are connected.

RESULTS

Figure 2 compares global modes of different azimuthal wave numbers m and dimensionless frequencies St to selected Fourier modes of the LES data of approximately the same frequency. It can be seen that the emitted acoustic radiation

*Corresponding author. Email: oschmidt@caltech.edu

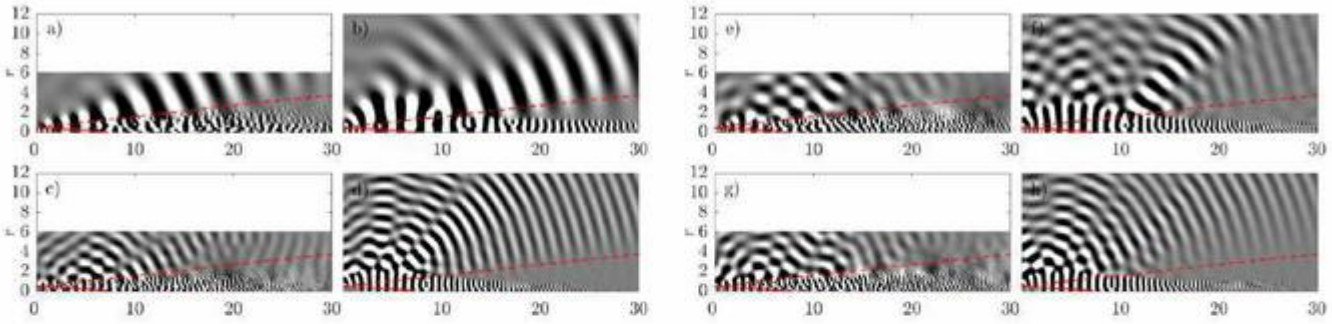

Figure 2: Pairs of temporal Fourier modes of the LES data (a,c,e,g) and linear global modes (b,d,f,h) of comparable frequency in terms of the perturbation pressure (grayscale): (a,b) $m = 0$, $St \approx 0.4$; (c,d) $m = 0$, $St \approx 0.8$; (e,f) $m = 1$, $St \approx 0.6$; (g,h) $m = 2$, $St \approx 0.8$. The perturbation pressure contours are individually saturated to highlight the acoustic radiation, and the mean streamwise velocity is indicated in red as in figure 1 above.

of the global modes closely resembles that observed in the simulation. Most notably, only the symmetric wave packet at $St \approx 0.4$ depicted in 2(a,b) exhibits a strictly super-directive radiation pattern, whereas all other modes emit in a multi-directive fashion. This observation is of particular interest regarding the standard two source model of jet noise that attributes high-angle (w.r.t. the jet axis) radiation to purely stochastic turbulent fluctuations.

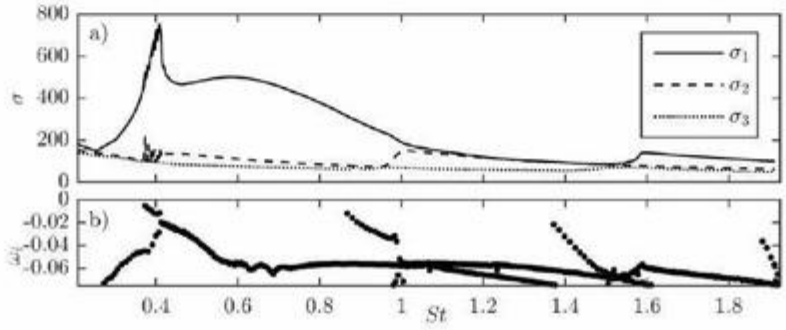

Figure 3: Comparison between resolvent and classical linear stability analysis for $m = 0$: (a) optimal gain σ_1, and leading sub-optimal gains, σ_2 and σ_3; (b) eigenvalues of the global linear stability operator.

Results of the resolvent analysis and linear stability theory (LST) are compared in figure 3 in terms of (sub-) optimal gains and the LST eigenvalue spectrum, respectively. It can seen that even though all modes appear damped, significant energy amplification can be attained. Most intriguingly, the highest gain is observed in the region of the least stable branch of modes. This suggests a pseudo-resonance mechanism in which external stochastic forcing, e.g. provided by the shear-layer turbulence, promotes linear instability wave packets. The good resemblance between the theoretically predicted and the observed structures as seen in figure 2 strongly supports this conjecture.

References

[1] G. .A Brès, P. Jordan, T. Colonius, M. Le Rallic, V. Jaunet, and S. K. Lele. Large eddy simulation of a mach 0.9 turbulent jet. In *Center for Turbulence Research Proceedings of the Summer Program*, page 221, 2014.

[2] X. Garnaud, L. Lesshafft, P. J. Schmid, and P. Huerre. The preferred mode of incompressible jets: linear frequency response analysis. *Journal of Fluid Mechanics*, 716:189–202, 2013.

[3] P. Jordan and T. Colonius. Wave packets and turbulent jet noise. *Annual Review of Fluid Mechanics*, 45:173–195, 2013.

[4] J. W. Nichols and S. K. Lele. Global modes and transient response of a cold supersonic jet. *Journal of Fluid Mechanics*, 669:225–241, 2011.

[5] C. K. W. Tam, K. Viswanathan, K. K. Ahuja, and J. Panda. The sources of jet noise: experimental evidence. *Journal of Fluid Mechanics*, 615:253–292, 2008.

3D CHARACTERIZATION OF ACOUSTOFLUIDIC FORCE FIELDS IN THE fN RANGE

Andreas Lamprecht *[1], Stefan Lakaemper[1], Iwan A.T. Schaap[2], and Jurg Dual[1]

[1]*Institute for Mechanical Systems, ETH Zurich, Zurich, Switzerland*
[2]*Institute of Biological Chemistry, Biophysics and Bioengineering, Heriot Watt University, Edinburgh, UK*

Summary One of the multifaceted techniques to handle functionalized beads and cells in "Lab on a Chip" devices is acoustic particle manipulation. The characterization of the formed acoustic potential inside the micro channels is inaccessible by common methods, like microphones or pressure sensors. Therefore we developed an unique direct and contactless force sensor based on an optical trap to measure the acoustic forces on a single micro particle. A force resolution of 12 fN was reached for 2.06 μm silica particles at 180 mW laser power. Up to 680 measurement points were realized and led to a 3D distribution of the acoustic force vector on a micro particle inside microfluidic channels and chambers.

INTRODUCTION AND THEORY

Investigations on standardization and smaller probe volumes in bio-chemical research have accelerated the development of "Lab on a Chip" devices in the last few years. In particular, the use of bulk acoustic standing waves (BAW) and surface acoustic waves (SAW) has received increasing attention, the expanding ability to manipulate objects, like solid particles, functionalized beads, cells, etc., has laid base to tremendous advances. The total acoustic force on a micro particle inside the device consists, in general, of two different components, due to (a) acoustic radiation and (b) drag induced by acoustic streaming.

The acoustic radiation force is a time-averaged acoustic effect and drives the motion of particles within an acoustic manipulation device. Acoustic radiation forces will be present if an incident standing wave is scattered at the micro objects. The strength and direction of the acoustic force is directly related to the acoustic pressure distribution and particle properties within the manipulation device. The acoustic radiation force $\boldsymbol{F}_{rad}$ on a rigid and compressible sphere can be described for an inviscid fluid as a gradient force of the potential U, defined by Gorkov [1] as

$$\boldsymbol{F}_{rad} = \nabla U \quad \text{with} \quad U = 2\pi r_s^3 \rho_f \left(\frac{1}{3} \frac{\langle p^2 \rangle}{\rho_f^2 c_f^2} f_1 - \frac{1}{2} \langle |\boldsymbol{v}^2| \rangle f_2 \right) \tag{1}$$

where p is the acoustic pressure field, $\boldsymbol{v}$ is the acoustic velocity field and $\langle \dots \rangle$ indicates the time-average over one wave cycle. The compressibility factor f_1 and density factor f_2, are defined as

$$f_1 = 1 - \frac{k_s}{k_f} \qquad \text{and} \qquad f_2 = \frac{2(\rho_s - \rho_f)}{2\rho_s + \rho_f} \tag{2}$$

where c is the speed of sound, k is the compressibility and ρ the density, the index f and s indicate the fluid and particle properties. In a viscous fluid, with dynamic viscosity μ, a standing BAW in a microfluidic channel forms an acoustic boundary layer $\delta = \sqrt{\frac{\mu}{\rho_f \omega}}$, due to the zero slip condition at the fluid boundaries [2]. The angular excitation frequency is described by ω. The velocity gradient inside this boundary layer generates an additional time-averaged effect called acoustic streaming, which is a constant non-zero fluid velocity $\boldsymbol{v}_{str}$ inside the fluid channel. The resulting force on the micro particles is the Stokes drag and can be written as, $\boldsymbol{F}_{str} = 6\pi r_s \mu (\boldsymbol{v}_{str} - \boldsymbol{v}_s)$, where $\boldsymbol{v}_s$ is the particle velocity.

Force Sensor

One possibility to measure $\boldsymbol{F}_{rad}$ and $\boldsymbol{F}_{str}$ inside acoustofluidic channels is to combine an optical tweezer with an acoustic manipulation device. The physical principle of the optical trap was invented by Askin[3] and an adapted experimental setup has been described by Lakaemper *et al.*. The laser beam of the optical system traps a particle in its focus and the thermal energy of the trapped particle can be measured by observing its Brownian Motion with quadrant photo detectors (QPDs) located after the microscope condenser. The analysis of the fluid submerged particle dynamics leads to a quantitative analysis of the trapping potential (without BAW or SAW) and the diagonal optical trapping stiffness matrix $\boldsymbol{\kappa_{xyz}}$ can be derived. If a BAW or SAW propagates in the fluid medium, the total force $\boldsymbol{F}_{tot}$, defined as $\boldsymbol{F}_{tot} = \boldsymbol{F}_{rad} + \boldsymbol{F}_{str}$, displaces the trapped particle relative to its equilibrium position inside the optical trapping potential. The displacement $\boldsymbol{u}$ can be detected in all 3 directions by observing the intensity change of the particle interference pictures on the QPDs and $\boldsymbol{F}_{tot}$ is calculated as $\boldsymbol{F}_{tot} = \boldsymbol{\kappa_{xyz}} \boldsymbol{u}$. A force resolution of 12 fN was reached for 2.06 μm silica particles at 180 mW laser power by repeating the same measurement for 50 times to consider signal noise and changes of the experimental acoustic and thermal environment.

*Corresponding author. Email: lamprecht@imes.mavt.ethz.ch

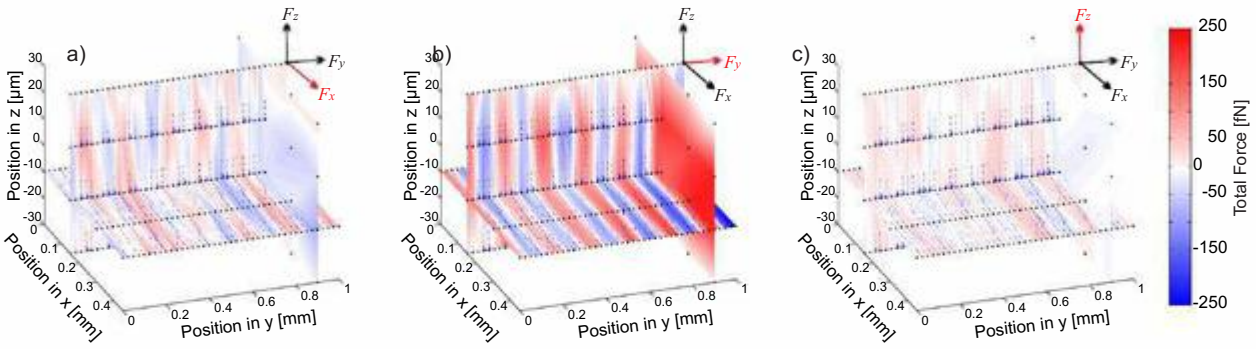

Figure 1: 3D spatial distribution of the total force on a 2.06 μm particle inside a 4 mm wide, 120 μm high and 76 mm long fluid channel[4] filled with water. The excitation frequency is at 3822 kHz with 10V$_{pp}$ excitation amplitude. a), b), c) show the x-, y- and z forces on the particle at the xy-, yz- and xz-plane of the device specific coordinate system

RESULTS

The analysis of the global total force field gives an overview about the 3D spatial homogeneity of the 3D force field in microfluidic devices. A glass-silica-glass device with a 4 mm wide, 120 μm high and 76 mm long fluid channel[4] was used and filled with water and 2.06 μm silica particles. This experiment contained 296 measurement points (controlled by LabView) that are shown as solid black dots in Fig.1. The points define 3 force analysis planes, one in the xy-, yz- and xz-plane of the device specific coordinate system, which has its reference point in the channel center in front of the piezoelectric transducer. The excitation frequency was chosen at a fluid cavity resonance of 3822 kHz with 10 V$_{pp}$ excitation amplitude. Fig.1 shows linear interpolated data between the neighboring measurement points. The acoustic y-forces F_y in the xy-plane of Fig.1b, appeared in a repeating pattern of positive and negative forces in wave propagation direction, as it is the typical force field for an eigen mode. The zero force lines define the pressure nodes and anti nodes of the standing wave field in y-direction. The F_y field in the xz-plain showed along the z-coordinate a constant force distribution. This property shows that the acoustic wave field is parallel to the channel walls and the spatial variance of the forces can be related to non-ideal scattering effects and structural vibrations of the device structure. The F_y closer to the channel walls at $z = \pm 30$ μm starts to loose slightly the homogeneity of the plane wave and a 38% decrease of the amplitudes is observable. The sinusoidal distribution of F_y had a spatial force amplitude variation of $111 fN$ $\pm$46 fN and a constant force wavelength of 181 μm $\pm$11 μm. The averaged force curves can be related by Eq.1 to an acoustic pressure amplitude of 685 kPa. Fig.1a corresponds to the acoustic x-force F_x across the described spatial planes. The x-forces are about 56% smaller than F_y and have local peaks of -84 fN and 90 fN. At the pressure nodes of the standing wave a purely positive F_x is present and F_x is mainly constant in z-direction. The negative force areas indicate the particle concentration change along the particle lines formed by F_y. Fig.1c shows the z-forces F_z inside the channel. The force amplitudes are about five times smaller than F_y and have a sinusoidal like distribution along y on the xy-plane at $z = 0$ (data not shown). In the xz-plane a sign change of F_z can be observed. This could be an indication for a streaming vortex but a higher spatial y- and z-resolution is necessary to resolve the vortex in more detail.

CONCLUSION AND OUTLOOK

The results show a good agreement of the device specific force field between theory and experiment. The 3D force data gave a so far new input to the field of acoustic particle manipulation and gave a clear image about the complexity of experimental acoustofluidic devices. The derived acoustic pressure amplitudes were in a good agreement with indirect measurement methods [5] that are related to analytical models. So far only the total force $\boldsymbol{F}_{tot}$ was measured and the extraction of acoustic radiation force and Stokes drag induced streaming forces will be the future work. Beside that, this method allows to derive further effects, e.g. near-wall or sharp-edge acoustics, which were so far inaccessible for quantification.

References

[1] Gor'kov L. P.: On the forces acting on a small particle in an acoustical field in an ideal fluid, Sov. Phys. Dokl., 6: 88-91, 1962.

[2] Sadhal S. S.: Acoustofluidics 13: Analysis of acoustic streaming by perturbation methods, Lab Chip, 12: 2292-2300, 2012.

[3] Askin A.: Acceleration and trapping of particles by radiation pressure, PRL, 24, 156, 1970.

[4] Lakaemper S., Lamprech A., Schaap I. A. T.,Dual J.: Direct 2D measurement of time-averaged forces and pressure amplitudes in acoustophoretic devices using optical trapping, Lab Chip, 15:290-300, 2015.

[5] Barnkob R., Augustsson P., Laurell T., Bruus H.: Acoustic radiation-and streaming-induced micro particle velocities determined by micro particle image velocimetry in an ultrasound symmetry plane, Phys. Rev. E, 86: 056307, 2012.

EXPERIMENTAL INVESTIGATION AND MODELLING OF THE BOUNDARY-LAYER WALL PRESSURE SPECTRUM

Christophe Bailly*[1], Edouard Salze[1], and Daniel Juvé[1]

[1]*Laboratoire de Mecanique des Fluides et d'Acoustique*
Ecole Centrale de Lyon et UMR CNRS 5509, Ecully, France

Summary Wall pressure fluctuations beneath a turbulent boundary layer, and the modelling of the wall pressure spectrum, are investigated in this study. Various experimental conditions have been studied, such as the presence of a mean pressure gradient achieved by changing the ceiling angle of a rectangular channel designed for flow-acoustic measurements. Wall pressure spectra are measured by using a pinhole microphone in conjunction with a high-frequency-calibration procedure. A direct measurement of the wall pressure wavenumber-frequency spectrum is also performed with the use of a rotating linear antenna of remote microphones. Both aerodynamic and acoustic components of the wavenumber-frequency spectrum can thus be identified and are investigated. A short overview of the results is first reported and discussed. These experimental data, including the characterization of the turbulent boundary layer, are then systematically used to inform a wall pressure spectrum model.

INTRODUCTION

The understanding of vibrations and noise induced by wall pressure fluctuations is of great importance in hydroacoustics [12, 3], in aeronautics [13, 6, 10] and more recently in automotive applications [8, 5] to predict interior noise. Turbulent boundary layer excitation can be characterized by its wall pressure wavevector-frequency spectrum including both aerodynamic and acoustic components. The aerodynamic part is associated with the indirect contribution to cabin noise through panel vibration while the acoustic part represents a direct contribution to this noise. They have thus a distinct influence on the sound transmitted owing to the structural response.

Various models have been developed in the past for the root-mean-square wall pressure fluctuations, the one-point and wavevector-frequency spectra, motivated in particular by underwater applications. Good reviews can be found in the references mentioned above, and also by Bull [4]. It must be however recognized that reported experimental data are often scattered [7], even for zero-pressure-gradient turbulent boundary layers. Furthermore, only a fragmented view is currently offered regarding pressure gradient effects or the compressible part of spectra. The necessary small separation distance between sensors, and the large difference in energy between the two components, make this experimental identification quite tricky [1, 2, 5]. In a previous study [2], a rotating microphone array was used to deduce the wall pressure wavenumber-frequency spectrum through an original post-processing. Results have been reported for a turbulent boundary layer at a Reynolds number $\mathrm{Re}_{\delta_1} = u_\tau \delta_1/\nu = 5.5 \times 10^4$ and at a moderate velocity $U_\infty = 44$ m.s^{-1}. The feasibility to estimate wavevector spectra by this original approach was demonstrated. In these expressions, u_τ denotes the friction velocity, δ_1 the displacement thickness and U_∞ the free stream velocity of the boundary layer, and ν is the kinematic viscosity of the fluid.

Wall pressure fluctuations beneath a turbulent boundary layer submitted to an external mean pressure gradient have been investigated in a more recent study [11], with a significantly improved experimental approach. A new channel has been developed for flow-acoustic measurements, in which the ceiling of the test section can be inclined, to generate an accelerated or decelerated mean flow over a flat plate. A new rotating microphone array, mounted on a rigid flat disk, has also been designed to enhance the spectral resolution of the wavevector-frequency spectra of wall pressure fluctuations, and 2-D wavevector-frequency spectra have been directly measured in various flow conditions.

Some experimental results are first briefly reported and discussed in a first section. A modelling of the wall pressure spectrum is then investigated, based on a formulation developed by Lysak [9]. Each step of the model is however revisited. Experimental data are systematically used to inform the model, as the one-dimensional velocity spectra measured in the log-region of the boundary layer. Concluding remarks are finally provided.

OVERVIEW OF EXPERIMENTAL RESULTS

The experiments were conducted in the main subsonic wind tunnel of the Centre Acoustique at Ecole Centrale de Lyon in France. A detailed description of the channel can be found in Salze *et al.* [11], including a characterization of the longitudinal mean pressure distribution, mean velocity profiles, turbulent velocity spectra and wall pressure spectra measured in various configurations. The most original results have been obtained for wavenumber-frequency pressure spectra using the new microphone array, and a specific post-treatment of signals. As an illustration, the normalized wavenumber-frequency pressure spectrum is plotted in Fig. 1 for a zero-pressure-gradient boundary layer and for different frequencies. The turbulent or

*Corresponding author. Email: christophe.bailly@ec-lyon.fr

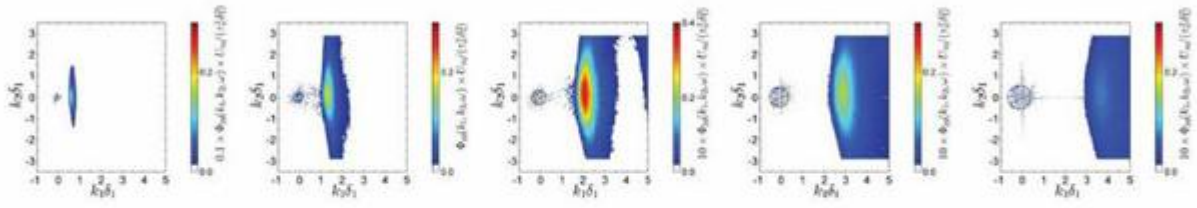

Figure 1: Wavenumber-frequency spectrum $\Phi_{pp}(\boldsymbol{k},\omega)$ in dB as a function of the wavenumber $(k_1\delta_1, k_2\delta_1)$, for a zpg boundary layer at $U_\infty = 76\text{m.s}^{-1}$ and $\text{Re}^+ \simeq 3500$, and for frequencies $f = 2, 4, 6, 8$ and 10 kHz.

aerodynamic part, centered around the convective wavenumber $k_1 = \omega/U_c$ where U_c is the convection velocity, is clearly seen with its characteristic elongated shape in the k_2 direction. The dissymmetry in the k_1 direction is also apparent. The acoustic component is seen as an ellipse, plotted in dashed line, given by the geometrical acoustic dispersion relation $c_\infty^2 k^2 - (k_1 U_\infty - \omega)^2 = 0$ where c_∞ is the speed of sound.

MODELLING OF THE WALL PRESSURE SPECTRUM

The analytical wall pressure spectrum model retained in this study is based on the linear Poisson equation for the pressure [9]. Under reasonable assumptions regarding the turbulent flow, but this point will be discussed during the talk, the wall pressure spectrum $S_{pp}(\omega)$, corresponding to the integration of $\Phi_{pp}(\boldsymbol{k},\omega)$ over $\boldsymbol{k}$, can be expressed as

$$S_{pp}(\omega) \simeq 8\pi^2\rho^2 \int_0^\delta \left(\frac{\partial \overline{U}_1}{\partial x_3}\right)^2 \frac{\omega^2}{\overline{U}_1^3} \left\{ \int_{-\infty}^{+\infty} \frac{e^{-2k\xi_3}}{k^2} \phi_{33}(\boldsymbol{k},\xi_3,0) dk_2 \right\}_{k_1=\omega/\overline{U}_1} d\xi_3$$

All these quantities, namely the velocity profile, turbulence intensity profiles and some components of the spectral tensor ϕ_{ij} have been measured by hot-wire anemometry. Predictions of the wall pressure spectra will be discussed with respect to other similar models, and compared to measurements.

CONCLUDING REMARKS

The prediction of wall pressure fluctuations is of great interest to predict interior noise, but the modelling of pressure spectra from a partial knowledge of the turbulent velocity field remains difficult. In the present study, critical assumptions made in the models are identified, and a more rational approach is developed with the aim to include the influence of an external pressure gradient.

Aknowledgment
This research has been funded by the Agence Nationale de la Recherche through the ANR-2011- BS09-035-02 project SONOBL, and by the Labex CeLyA of Université de Lyon, operated by the French National Research Agency (ANR-10-LABX-0060/ ANR-11-IDEX-0007).

References

[1] Abraham, B. M. & Keith W. L., 1998, Direct measurements of t.b.l. wall pressure wavenumber-frequency spectra, *J. Fluid Eng.*, **120**, 29-39.
[2] Arguillat, B., Ricot, D., Bailly, C. & Robert, G., 2010, Measured wavenumber-frequency spectrum associated with acoustic and aerodynamic wall pressure fluctuations, *J. Acoust. Soc. Am.*, **128**(4), 1647-1655.
[3] Blake, W. K., 1986, Essentials of turbulent wall-pressure fluctuations, in Mechanics of flow-induced sound and vibration, Vol. II Complex flow-structure interactions, *Academic Press Inc.*, Orlando, Florida.
[4] Bull, M. K., 1996, Wall-pressure fluctuations beneath t.b.l.: some reflections on forty years of research, *J. Sound Vib.*, **190**(3), 299-315.
[5] Gabriel, C., Müller, S., Ullrich, F. & Lerch, R., 2014, A new kind of sensor arry for measuring spatial coherence of surface pressure on a car's side window, *J. Sound Vib.*, **333**, 901-915.
[6] Graham, W.R., 1997, A comparison of models for the wavenumber-frequency spectrum of t.b.l. pressures, *J. Sound Vib.*, **206**(4), 430-454.
[7] Keith, W.L., Hurdis, D.A. & Abraham, B.M., 1992, A comparison of turbulent boundary layer wall-pressure spectra, *J. Fluids Eng.*, **114**, 338-347.
[8] Leclercq, D.J.J. & Bohineust, X., 2002, Investigation and modelling of the wall pressure field beneath a t.b.l. at low and medium frequencies, *J. Sound Vib.*, **257**(3), 477-501.
[9] Lysak, P.D., 2006, Modeling the wall pressure spectrum in pipe flows, *J. Fluids Eng.*, **128**, 216-222.
[10] Miller, T. S., Gallman, J. M. & Moeller, M. J., 2012, Review of turbulent boundary-layer models for acoustic analysis, *J. Aircraft*, **49**(6), 1739-1754.
[11] Salze, E., Bailly, C., Marsden, O., Jondeau, E. & Juvé, D., 2014, An experimental characterization of wall pressure wavenumber-frequency spectra in the presence of pressure gradients, AIAA Paper 2014-2909.
[12] Sevik, M. M., 1986, Topics in hydro-acoustics, in *Aero- and Hydro-Acoustics*, Springer-Verlag Berlin, 285-308.
[13] Wilby, J. F., 1996, Aircraft interior noise, *J. Sound Vib.*, **190**(3), 545-564.

Stochastic aspects of thermoacoustic instabilities in combustion chambers

Nicolas Noiray*[1] and Alexey Denisov[2]

[1] *CAPS Lab., Mechanical and Process Engineering Dep., ETH Zürich, Switzerland*
[2] *Paul Scherrer Institute, Villigen, Switzerland*

Summary The stochastic nature of combustion instabilities in practical land-based gas turbines and aeroengines combustors has seldom been investigated. It is shown here that a wealth of information about the constructive acoustic-flame interactions can be gained by scrutinizing the effects of the inherent turbulence-induced noise which forces the nonlinear thermoacoustic dynamics. In particular, one presents a method, based on the Fokker-Planck formalism, to identify from dynamic pressure signals the linear growth rates, the type of flame response nonlinearity and the potential defining the system acoustic energy. It is applied to and validated against experimental data measured in a lab-scale combustion chamber.

Due to the lack of cost-effective actuators, passive damping technologies constitute the vast majority of thermoacoustic instability control systems in practical combustors. It has been shown that robust design of these dampers requires the knowledge of the thermoacoustic linear growth rates [1]. Up to now, only linear decay rates providing stability margin could be quantified, because common output-only system identification (SI) methods used to process pressure data necessitate linearly stable system. Recently, it has been shown that one can take advantage of the presence of inherent turbulent combustion noise to extract linear growth rates from limit cycle data [2, 3]. This SI is based on the work of Friedrich and co-workers [4].

A cylindrical combustion chamber operated at atmospheric pressure is used. The thermal power is approximately 30 kW. The turbulent swirled V-flame is anchored at the rim of a lance equipped with an axial swirler. The acoustic pressure in the combustion chamber is measured by using a calibrated water-cooled microphone. When the equivalence ratio is varied from 0.47 to 0.5 by increasing the fuel mass flow, the acoustic level in the combustion chamber sharply increases due to the constructive interaction between the flame and one of the longitudinal acoustic modes (Fig. 1a). At condition c_3, the acoustic pressure probability density function $P(p)$ exhibits a bimodal distribution, which is typical of stochastic limit cycle oscillation. In contrast, at condition c_1, the PDF has a gaussian like distribution which is characteristic of randomly excited linearly stable oscillator. High speed Particle Image Velocimetry is performed at condition c_3 and proper orthogonal decomposition (POD) is computed from 2 seconds data (see Fig. 1b and 1c). The first two POD modes, exhibiting an axially shifted pattern of coherent structures typical of coherent vortex shedding and advection, carry nearly 20 % of the kinetic energy. The corresponding axisymmetric roll-up of vortices from the burner exit occurs at the thermoacoustic mode frequency around 150 Hz.

Starting from the acoustic wave equation with heat release rate source term, one can derive a Langevin equation for the acoustic pressure envelope $A(t)$, where the acoustic pressure is defined by $p = A(t)\cos(\omega t + \phi(t))$. This derivation is based on the following assumptions, which are valid for many practical situations: (i) a single thermoacoustic mode resulting from the constructive acoustic-flame interaction dictates the flow dynamics, (ii) the flame heat-release-rate fluctuations can be decomposed into a coherent and a noisy part $\widehat{q} = \widehat{q}_c + \widehat{q}_n$, the former resulting from the acoustically driven heat release rate fluctuations and the latter from the intense turbulence pertaining to practical combustion chambers, (iii) the coherent flame response to acoustic perturbations exhibits a sigmoid type saturation when the acoustic level increases, which is approximated

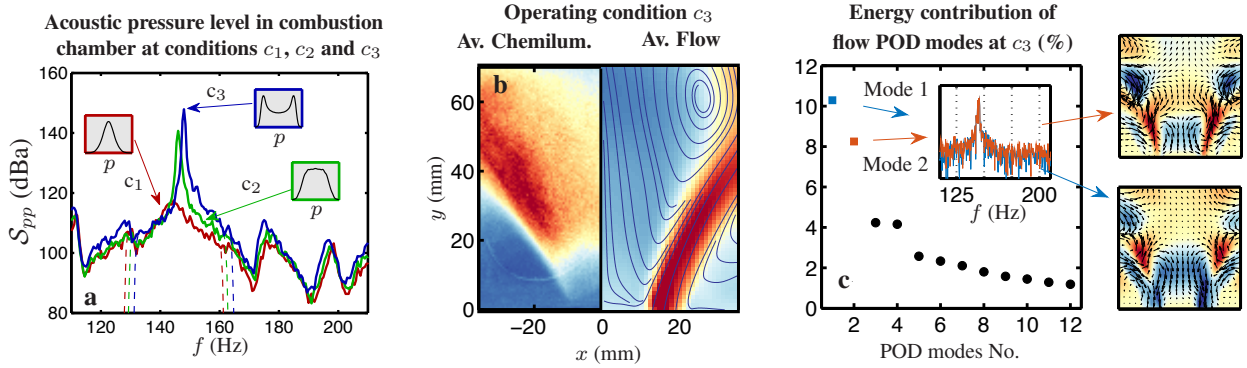

Fig. 1: **(a)** Acoustic power spectral density from signals measured in the atmospheric-pressure combustion chamber at different equivalence ratios ($\simeq$ 30 kW thermal power), and corresponding acoustic pressure probability density functions P_p. **(b)** Averaged OH* chemiluminescence from the turbulent V flame, and averaged axial velocity field from -8 (blue) to 15 m/s (red) at self-oscillating condition c_3. **(c)** Energy contribution of the first 12 POD modes deduced from 2 seconds data (294 acoustic cycles) at condition c_3, and POD modes 1 and 2 (blue and red for negative and positive axial displacement). Also shown, the Fourier transforms of the POD modes amplitudes.

*Corresponding author. Email: noirayn@ethz.ch

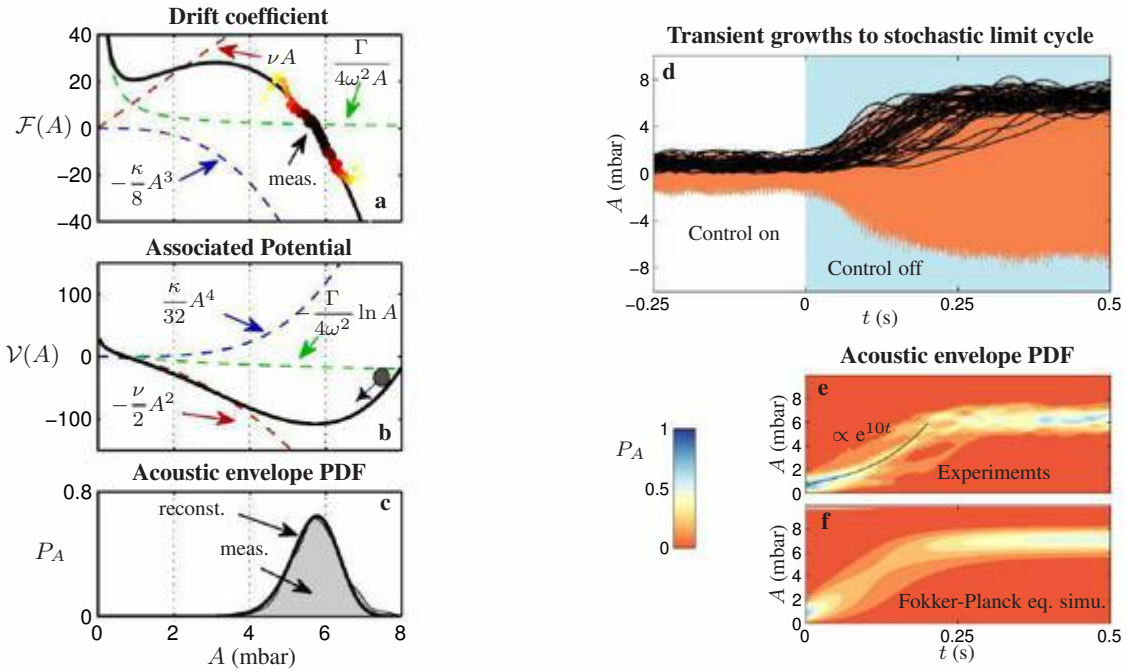

Fig. 2: Processing of the statistics of the acoustic pressure envelope A at operating condition c_3. **(a)** 1st transition moment of the amplitude A processed from the envelope of the 30 seconds limit-cycle acoustic pressure data (symbols coloured by P_A) and corresponding best fit (thick line). The parameters Γ, ν and κ are optimised using the assumed theoretical model. Also included as thin dotted lines the identified linear, nonlinear and stochastic contributions. **(b)** Potential defining the system acoustic energy deduced from the output-only system identification process. **(c)** PDF reconstructed from the identification process using theoretical model superimposed on the one directly computed from the acoustic signal. **(d)** 100 superimposed transient growths around control-switch-off instants for conditions c_3. **(e)** corresponding PDF. **(f)** Simulation of the Fokker-Planck equation (1) using the parameters obtained from the output-only SI method, with initial condition taken from the experimental PDF shown at $t = 0$ in (e).

by a cubic type nonlinearity $q_c = \beta\eta - \kappa/3\,\eta^3$ on a range of acoustic amplitudes, where η is the acoustic mode amplitude. In the ideal deterministic case, when the source term β exceeds the mode linear damping α, it yields an exponential amplification of perturbations at a growth rate $\nu = (\beta - \alpha)/2$. The resulting Langevin equation with additive forcing ζ of intensity $\Gamma/2\omega^2$ and the associated Fokker-Planck equation describing the evolution of the probability $P(A,t)$ are given below:

$$\dot{A} = -\frac{\partial \mathcal{V}}{\partial A} + \zeta, \quad \text{and} \quad \frac{\partial}{\partial t}P_{A,t} = -\frac{\partial}{\partial A}\big(\mathcal{F}(A)P_{A,t}\big) + \frac{\Gamma}{4\omega^2}\frac{\partial^2}{\partial A^2}P_{A,t}, \tag{1}$$

where the potential $\mathcal{V}(A) = \nu/2\,A^2 + \kappa/32\,A^4 - \Gamma/4\omega^2 \ln A$, is linked to the drift coefficient as $\mathcal{F}(A) = -\partial\mathcal{V}/\partial A$. The potential defines the acoustic energy of the system because for standing oscillations, the latter is proportional to the square of the acoustic pressure envelope A measured at a given location. Considering that $\mathcal{F}(A) = \lim_{\tau\to 0}\frac{1}{\tau}\int_{-\infty}^{\infty}(a - A)\,P^{\tau}_{A|a}\,da$, one computes the drift coefficient by acoustic-pressure-records binning, and subsequently perform model-based fit to extract the governing parameters, especially the linear growth rate ν (see Fig. 2a-c). The results from this SI approach are then validated using an active control system allowing us to periodically trigger transient growths to the stationary stochastic limit cycle. The Fokker-Planck equation fed with the identified parameters is numerically integrated and one can see in Fig. 2d-f that the simulation results are in remarkable agreement with the measured ones, which validates the SI method.

This methodology constitutes a significant step forward for practical applications, because it can be applied to validate low-order thermoacoustic network models used for stability analysis, and also to reliably design effective damping systems.

References

[1] N. Noiray and B. Schuermans. Theoretical and experimental investigations on damper performance for suppression of thermoacoustic oscillations. *Journal of sound and vibration,*, 331(12):2753–2763, 2012.

[2] N. Noiray and B. Schuermans. Deterministic quantities characterizing noise driven hopf bifurcations in gas turbine combustor. *Int. J. Non-linear Mechanics*, 50:152–163, 2013.

[3] N. Noiray and B. Schuermans. On the dynamic nature of azimuthal thermoacoustic modes in annular gas turbine combustion chambers. *Proc. Roy. Soc. A*, 469(20120535), 2013.

[4] R. Friedrich, J. Peinke, M Sahimi, and M. R. R. Tabar. Approaching complexity by stochastic methods: From biological systems to turbulence. *Phys. Reports*, 506:87–162, 2011.

ROBUST FEEDBACK CONTROL OF THERMOACOUSTIC OSCILLATIONS

Simon J. Illingworth*[1], Alessandro Orchini[2], Bernhard Semlitsch[2], Matthew P. Juniper[2], and Ann P. Dowling[2]

[1]*Mechanical Engineering, University of Melbourne, VIC 3010, Australia*
[2]*Department of Engineering, University of Cambridge, UK*

Summary This study investigates the feedback control of nonlinear thermoacoustic oscillations. A particular aim is to investigate the efficacy of feedback control when the system's nonlinear dynamics are rich. Specifically, we investigate a flame model which exhibits significant changes in both the gain and the phase of its response to harmonic fluctuations. The flame is modelled by the kinematic G-equation. We model the experimental geometry of Balachandran *et al.* [1], accounting for a spatially non-uniform flow field, curvature corrections on the flame speed and equivalence ratio fluctuations at the injection point. Robust control techniques are used to design a controller which is then applied to both the linear and fully nonlinear system.

Thermoacoustic oscillations can occur whenever combustion takes place inside an acoustic resonator. Unsteady combustion is an efficient acoustic source, and combustors tend to be highly resonant systems. Therefore for suitable phase between unsteady combustion and acoustic perturbations, large-amplitude self-excited oscillations can occur. Most recent studies of combustion oscillations have focused on low NO_X premixed gas turbine combustors, which are particularly susceptible to thermoacoustic instability [2].These studies typically assume linear acoustics: the low Mach number means that the acoustic pressure fluctuations are small even when the acoustic velocity fluctuations are large [3]. The heat release is therefore treated as the only nonlinear element in the coupled system.

Figure 1 (*a,b*) shows the steady state amplitude, a_s, for two types of nonlinear behaviour that we expect to find. The first is a supercritical bifurcation, in which the limit cycle amplitude grows gradually as the control parameter, P, increases past P_l (P_l denotes the Hopf bifurcation, at which point the system becomes linearly unstable). The second is a subcritical bifurcation, in which the limit cycle amplitude grows suddenly as P increases past P_l, and for which there are two stable solutions in the region $P_c \leq P \leq P_l$.

Limit cycles can be found in the frequency domain using a Flame Describing Function (FDF), which involves measuring the flame's response to harmonic forcing for different forcing frequencies and forcing amplitudes. By assuming that the flame's response to a given forcing frequency is predominately at that frequency (i.e. by discarding higher harmonics), the FDF provides the flame's gain and phase as a function of forcing frequency and forcing amplitude. Dowling [4] calculated the FDF for a kinematic model of a premixed ducted flame and found that the limit cycle amplitude of the coupled system was determined by the amplitude-dependence of the gain. Noiray et al. [5] measured the FDF of a premixed flame experimentally and find that the limit cycle amplitude of the coupled system was determined by the amplitude-dependence of both the gain and the phase of the flame's response.

Let us now relate the describing function analysis (in particular, its description of the variations in the flame's gain and phase with forcing amplitude) to the supercritical and subcritical bifurcations seen in Fig. 1 (*a,b*). If the flame's phase does not change with forcing amplitude, then one would expect to find only supercritical bifurcations (provided that the flame's gain decreases with increasing forcing amplitude, which is a sensible assumption). This is because as the forcing amplitude

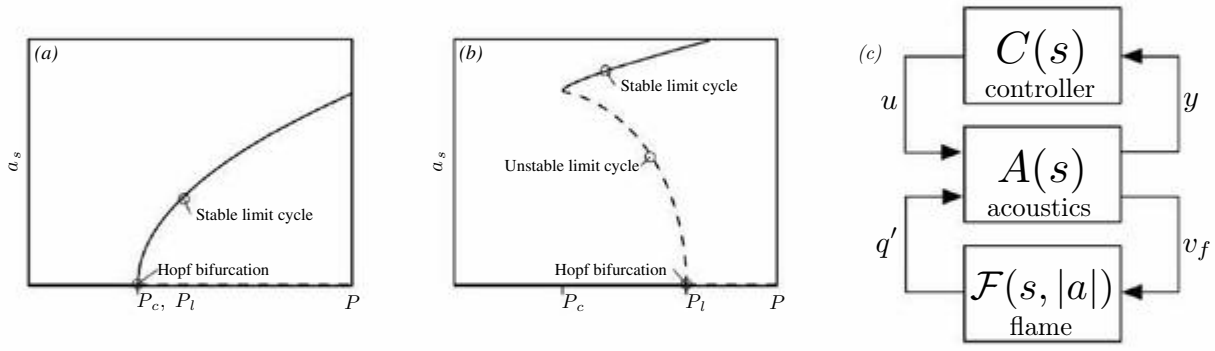

Figure 1: (*a,b*) The limit cycle amplitude, a_s, as a function of a control parameter, P, for (*a*) a supercritical bifurcation and (*b*) a subcritical bifurcation. P_l is the Hopf point, where the system becomes linearly unstable. P_c is the point below which no oscillations can be sustained. (*c*) Feedback control arrangement: v_f is the velocity at the flame; q' is the unsteady heat release rate; and u and y depend on the feedback control arrangement.

*Corresponding author. Email: sillingworth@unimelb.edu.au

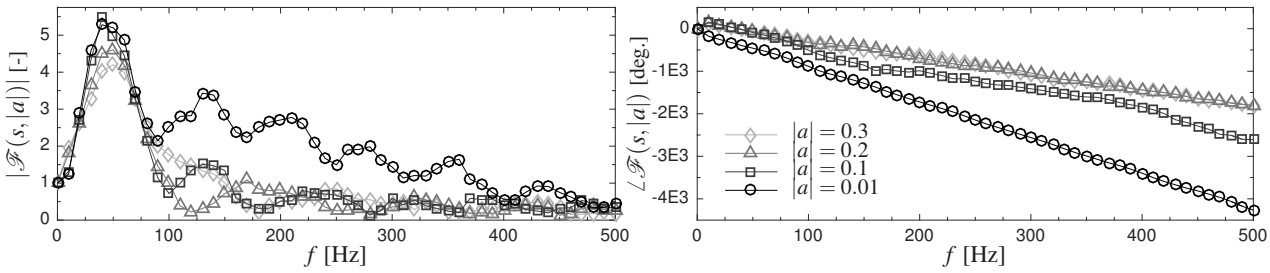

Figure 2: The flame describing function, $\mathcal{F}(s, |a|)$, for four forcing amplitudes: (a) gain and (b) phase.

increases, the positive feedback between unsteady heat release and acoustics can only weaken, since the flame's gain is decreasing, while the phase between them remains fixed. If both the gain and the phase vary, however, then both supercritical and subcritical bifurcations are possible. In this case, even if we assume that the flame's gain decreases with increasing forcing amplitude as before, variations in phase can actually lead to stronger positive feedback between unsteady heat release and acoustics. Now relating these considerations to previous studies: the variations in the flame's phase with forcing amplitude seen by Dowling are either zero [3] or small [4], and so only supercritical behaviour is seen; while in Noiray *et al.* [5], the experimentally-determined FDF exhibits significant changes in both gain and phase, and so both types of bifurcation behaviour are seen (and predicted).

As well as looking at the effect of a simple saturation nonlinearity on the *dynamics* of thermoacoustic oscillations, Dowling [3] also looked at implications for feedback control. It was found that a linear feedback controller, as well as stabilizing the linear system, was also stabilizing when applied from an already-established limit cycle. A describing function analysis was used to explain why the controller was still successful when applied to the limit-cycling system. It is important to remember here that, due to the relatively simple nature of the flame's nonlinearity, there was no amplitude dependence of the flame's phase response, and therefore the subcritical bifurcations shown in Fig. 1 (*b*) could not occur. In more recent work, the amplitude dependence of the flame's phase response has been shown to play an important role for the *dynamics* of the coupled system. In particular, the subcritical bifurcations depicted in Fig. 1 (*b*) can occur. However, none of these studies has looked at the implications of this more complex nonlinear dynamics on their *feedback control*. That is the focus of this work.

This study investigates the feedback control of nonlinear thermoacoustic oscillations. A particular aim is to investigate the efficacy of feedback control when the system's nonlinear dynamics are rich. Specifically, we investigate a flame model which exhibits significant changes in both the gain and the phase of its response to harmonic fluctuations. The flame is modelled by the kinematic G-equation. We model the experimental geometry of Balachandran *et al.* [1], accounting for a spatially non-uniform flow field, curvature corrections on the flame speed and equivalence ratio fluctuations at the injection point. The flame describing function for this model (gain and phase) is plotted in Fig. 2, which has been determined by forcing the flame in simulations over a wide range of frequencies and amplitudes. Crucially, we see that both the gain and the phase vary with forcing amplitude, $|a|$. This means that bifurcations of both the supercritical and subcritical type (see Fig. 1) are possible. The acoustic response of the geometry is modelled using LOTAN [7]. This coupled system is in turn coupled to a feedback controller (whose objective is to completely eliminate oscillations), as shown in Fig. 1 (*c*).

Our task therefore is to design a controller that is sufficiently robust to provide closed-loop stability even in the presence of the flame's changes in gain and phase—and the changes in the dynamics of the coupled system that this will cause. This is shown in Fig. 1 (*c*): the coupled thermoacoustic system is represented by the two lower blocks. Notice that the flame dynamics, $\mathcal{F}(s, |a|)$, is a function of both the Laplace variable, s, and the forcing amplitude, $|a|$. The feedback controller (top block in Fig. 1 (*c*)) is denoted by $C(s)$ and is designed using robust control techniques [6] to stabilize both the linear and fully nonlinear system. The final presentation will present results for control applied to both the linear and fully nonlinear system.

References

[1] Balachandran, R., Ayoola, B. O., Kaminski, C. F., Dowling, A. P. and Mastorakos, E., Experimental investigation of the nonlinear response of turbulent premixed flames to imposed inlet velocity oscillations. *Combust. Flame* **143** (1), 37–55, 2005.

[2] Richards, G. & Janus, M., Characterization of oscillations during premix gas turbine combustion. *J. Eng. Gas Turbines Power* **120** (2), 294–302, 1998.

[3] Dowling, A. P., Nonlinear self-excited oscillations of a ducted flame. *J. Fluid Mech.* **346**, 271–290, 1997.

[4] Dowling, A. P., A kinematic model of a ducted flame. *J. Fluid Mech.* **394**, 51–72, 1999.

[5] Noiray, N. and Durox, D. and Schuller, T. and Candel, S., A unified framework for nonlinear combustion instability analysis based on the flame describing function. *J. Fluid Mech.* **615** (1), 139–167, 2008.

[6] Vinnicombe, G., Uncertainty and Feedback: $\mathcal{H}_\infty$ loop-shaping and the ν-gap metric. *Imperial College Press*, 2000.

[7] Stow, S. R. and Dowling, A. P., A Time-Domain Network Model for Nonlinear Thermoacoustic Oscillations. *J. Eng. Gas Turbines Power* **131** (3), 2009.

COMBINED EXPERIMENTAL AND ADJOINT-BASED SENSITIVITY ANALYSIS IN THERMOACOUSTICS

Matthew Juniper *[1], Nicholas Jamieson[1], José Aguilar[1], and Georgios Rigas[1]

[1]*Department of Engineering, University of Cambridge, CB2 1PZ, Cambridge, UK*

Summary Thermoacoustic oscillations are a persistent problem in gas turbine engines. Adjoint-based sensitivity analysis of a thermoacoustic model shows, in a single calculation, how the growth rate of an eigenvalue is affected by every parameter of the model. These predictions are tested with automated experiments, which forces careful revision of the models. This paper contains results from one experiment and three models of increasing complexity, to show how this technique could be used in design optimization.

INTRODUCTION AND MOTIVATION

The goal of rocket and gas turbine manufacturers is to design an engine that is linearly stable to thermoacoustic oscillations over the operating regime. Currently, this is achieved through (i) extensive testing, which is expensive, (ii) the avoidance of certain engine operating regimes, which reduces flexibility, and (iii) the retro-fitting of passive dampers such as Helmholtz resonators, which add weight [1]. A systematic method to identify and then stabilize thermoacoustic oscillations would speed up testing, eliminate dangerous operating points, and either determine the optimal placement of passive dampers or remove the need for them entirely. Such a method can exploit three convenient facts: (i), the requirement is for linear stability, meaning that the tools of linear analysis can be used; (ii), usually only a handful of thermo-acoustic modes are unstable; (iii), usually many parameters of the system can be altered. An ideal solution is to combine adjoint methods with a standard thermoacoustic stability analysis [2]. The stability analysis identifies the handful of unstable eigenvalues. The adjoint methods then show, in a single calculation for each eigenvalue, how each eigenvalue is affected by every parameter in the system. While this can be achieved with finite difference calculations, this would require a single calculation for each parameter, which is too expensive.

This optimization process relies on the model and gradient information being accurate. Experiments often test over a range of operating points and model coefficients are sometimes tweaked to match the experiments. The novelty in this paper is to test the gradients around the operating points, performed through automated experiments. This provides a much more stringent test of numerical models than is currently practiced and forces us to carefully revise inadequate parts of a model.

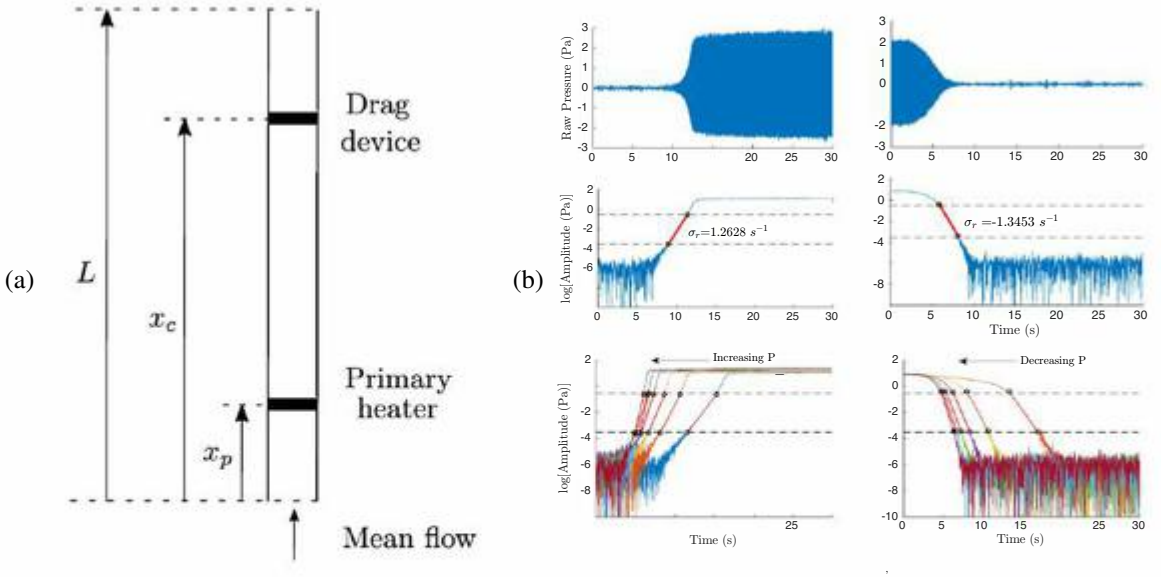

Figure 1: (a) Diagram of the Rijke tube, which contains a primary heater at x x

*Corresponding author. Email: mpj1001@cam.ac.uk

EXPERIMENTAL CONFIGURATION AND NUMERICAL MODELS

This paper compares an experiment on a vertical hot wire Rijke tube [3] with three thermoacoustic models of increasing complexity, whose adjoints are used to derive the sensitivity of the eigenvalue (i.e. the linear growth rate and frequency of thermoacoustic oscillations) to changes in the models. Figure 1(a) shows a diagram of the experimental rig. A primary heater is placed at position x_p and a drag device at x_c. When the primary heater is switched on, thermoacoustic oscillations increase in amplitude, as shown in Fig. 1(b) (top-left). The pressure signal's instantaneous amplitude and phase is extracted with a similar process, shown in Fig 1(b) (right). This processes is automated and repeated several hundred times.

The first model is a Galerkin model [4]. The acoustic momentum and energy equations are discretized by projecting solutions onto a basis containing the acoustic modes of the system. This is simple and easy to adjointize but suffers from the Gibbs phenomenon at the hot wire. The second model is a network model in which acoustic waves are modelled as they propagate upstream and downstream. Reflection coefficients are defined at the ends and a nonlinear eigenvalue problem is defined from the jump conditions for pressure and velocity at the hot wire. This is relatively easy to adjointize and can easily account for the mean temperature jump across the hot wire. The third model is a Helmholtz solver with heat release. The heat release into the region of space around the wire is assumed to be proportional to the velocity at the wire, with a pre-defined

RESULTS

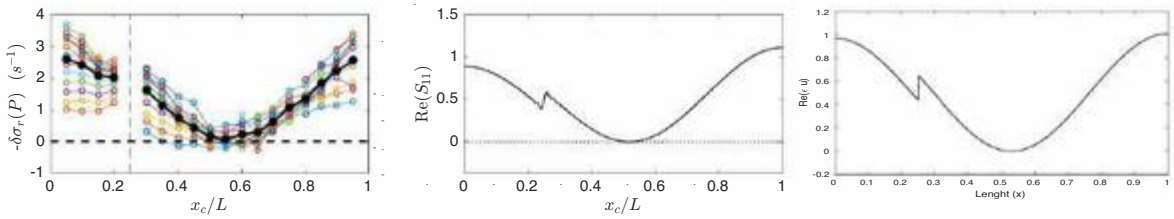

Figure 2: Left: experimentally-measured increase in the decay rate caused by placing the drag device at position x_c/L, relative to the case with no drag device; the black line is the mean of measurements at 12 primary heater powers. Centre: increase in the decay rate predicted from the Galerkin model. Right: increase in the decay rate predicted from the network model.

The direct and adjoint models give, in a single calculation, the shift in the growth rate as a function of any perturbation to the system. In this paper, we consider the influence of a drag device, defined as a device that gives a force in the opposite direction to the flow. We consider its influence on the growth/decay rate of thermoacoustic oscillations.

In the experiments, we measure the growth rate of oscillations with and without the drag device, following the procedure shown in Fig. 1, and subtract one from the other. The shift in the growth rate is shown in Fig. 2 (a) for different positions, x_c, of the drag device, and for different primary heater powers (coloured lines). The average for all primary heater powers is shown in black. This can be compared with the growth rate shift that as calculated from the different models, such as for the Galerkin model, Fig. 2(b), and the network model, Fig. 2(c). For the growth rate, the comparison is very good, certainly in a of gradients around operating points provides a much more stringent test of numerical models than is currently practiced.

Models of thermoacoustic systems are generated firstly to understand the physics and secondly to aid design. In the case of gas turbines, the aim is to eliminate thermoacoustic oscillations across the operating range. Having gradient information of a model greatly speeds up the design optimization process, but only if the gradient information and the model itself are reliable. The combination of adjoint-based sensitivity analysis and parallel automated experiments presented here provides the mechanism and the data to improve models that can be used in design optimization of thermoacoustic systems.

References

[1] Richards G., Strauss D., Robey E.: Passive Control of Combustion Dynamics in Stationary Gas Turbines. J. Prop. Power 19:795-810, 2003.

[2] Luchini P., Bottaro A.: Adjoint Equations in Stability Analysis. Ann. Rev. Fluid Mech. 46:492-517, 2014.

[3] Rigas G., Jamieson N., Li L., Juniper M.: Experimental sensitivity analysis and control of thermoacoustic systems. J. Fluid Mech. 787:R1. 2016.

[4] Magri L., Juniper M.: Sensitivity Analysis of a Time-delayed Thermoacoustic System via an Adjoint-based Approach. JFM 719:183-202, 2013.

PERIODIC PARTIAL EXTINCTION IN ACOUSTICALLY COUPLED FUEL DROPLET COMBUSTION

John W. Bennewitz[1], Miguel A. Plascencia[1], Dario Valentini[1], Owen I. Smith[1] and Ann R. Karagozian[1a]

[1]*Department of Mechanical and Aerospace Engineering*
UCLA Henry Samueli School of Engineering and Applied Science
Los Angeles, CA 90095-1597, USA

Summary This experimental study investigates the response of burning liquid fuel droplets exposed to one-dimensional standing waves created within an acoustic waveguide. Building upon prior droplet combustion studies[1] quantifying mean and temporal flame response of several alternative fuels to moderate acoustic excitation, the present work extends recent studies[2] pertaining to the discovery of periodic partial extinction of flames during exposure to higher amplitude acoustic forcing. This investigation explores several alternative liquid fuels exposed to a range of acoustic forcing conditions (frequencies and amplitudes) creating sustained oscillatory combustion, periodic partial extinction, and full extinction. Phase-locked OH* chemiluminescence imaging and local temporal pressure measurements allow quantification of the combustion-acoustic coupling through the local Rayleigh index as well as temporal oscillations in the flame standoff distance. An estimation of the oscillatory strain rates experienced by the flames during excitation helps to explain specific relationships among acoustic, chemical, and fluid mechanical/straining time scales that can lead to periodic flame extinction.

BACKGROUND AND CONTEXT OF PRESENT STUDIES

Acoustically coupled combustion instabilities have been a major challenge in the development of liquid rocket engines (LREs) and gas turbine engines over many decades. Typically, these instabilities are spontaneously excited, and are characterized by large-scale, self-sustained pressure oscillations corresponding to a natural acoustic mode of the combustion chamber. The onset of combustion instabilities is attributed to a feedback cycle among temporal velocity oscillations u', pressure oscillations p', and oscillatory heat release q', resulting in instability when the latter two parameters are in phase, or nearly so, per the well-known Rayleigh criterion[3]. Conversely, when pressure and heat release oscillations are out of phase with respect to one another, there is suggested to be a dampening of the instability[4]. For a reactive system, combustion instability can be mathematically described over an acoustic period T using the Rayleigh index G at a given location x:

$$G(x) = \frac{1}{T}\int_T p'(x,t)q'(x,t)dt \qquad (1)$$

where a positive G value denotes in-phase fluctuations of pressure and heat release and hence instability, while out-of-phase p' and q' lead to a negative G value and presumably stable combustion. Although the Rayleigh criterion has shown to predict naturally occurring thermo-acoustic instabilities in a large number of combustion systems[5], relating the bulk properties of the reactive system to the detailed acoustically-coupled flame dynamics is still a topic of great interest, especially for alternative fuels.

The single isolated burning fuel droplet represents a heterogeneous reactive process that provides a fundamental means to investigate condensed phase combustion. Over the past decade our group has examined burning fuel droplets within a controlled acoustic environment to investigate fundamental acoustically-coupled combustion processes[1,2,6], where global flame properties (e.g., Rayleigh index G and mean droplet burning rate constant K) as well as temporally oscillatory parameters (e.g., acoustic pressure p' and flame chemiluminescent intensity I') could be quantified throughout the acoustic cycle via phase-locked OH* chemiluminescence imaging. Bulk flame deflection characteristics are qualitatively consistent with the notion of a spatially variable acoustic radiation force[7] causing the flame to deflect away from the pressure node (PN). For both alcohol fuels (ethanol, methanol) and sooting hydrocarbons (JP-8, Fischer-Tropsch synfuel), the strongest degree of flame-acoustic coupling for moderate excitation (pressure perturbation amplitudes at or below 150 Pa) occurred for droplets situated near a PN at relatively low frequency excitation (332 Hz). More recent studies[2] show that at higher amplitude excitation conditions, exceeding perturbation pressure amplitudes of 200 Pa, ethanol droplets can experience periodic partial extinction of the oscillating flame structure. The present study extends this exploration to alternative excitation conditions and fuels to enable a more fundamental understanding of acoustically-coupled flame dynamics.

EXPERIMENTAL APPROACH AND SAMPLE RESULTS

The current study investigates the behavior of several alternative fuel droplets, including ethanol and JP-8, burning within a closed optically-accessible cylindrical waveguide with loudspeakers situated at each end. The burning droplet is continuously fed through a glass capillary by a syringe pump and fixed in place at the geometrical center of the waveguide. The acoustic drivers are forced at frequencies low enough to create effectively one-dimensional longitudinal waves to which

[a] Corresponding author. Email: **ark@seas.ucla.edu**

the droplets are exposed. When the loudspeakers operate out of phase, standing acoustic waves with a PN mid-way between the speakers can be created. The speakers may be moved relative to the geometrical center of the waveguide, with a fixed distance between them to enable effective alteration of the droplet location relative to the PN. Forcing frequencies f_a of 332 Hz, 586 Hz, 898 Hz and 1500 Hz are explored, corresponding to resonant conditions for two different waveguide lengths. Phase-locked OH* chemiluminescence imaging is performed using a high-speed ICCD camera equipped with a U-330 bandpass filter and UV lens, and simultaneous pressure measurements within the waveguide are obtained via miniature pressure transducers. Further details on the experimental test facility may be found in earlier papers[1,6].

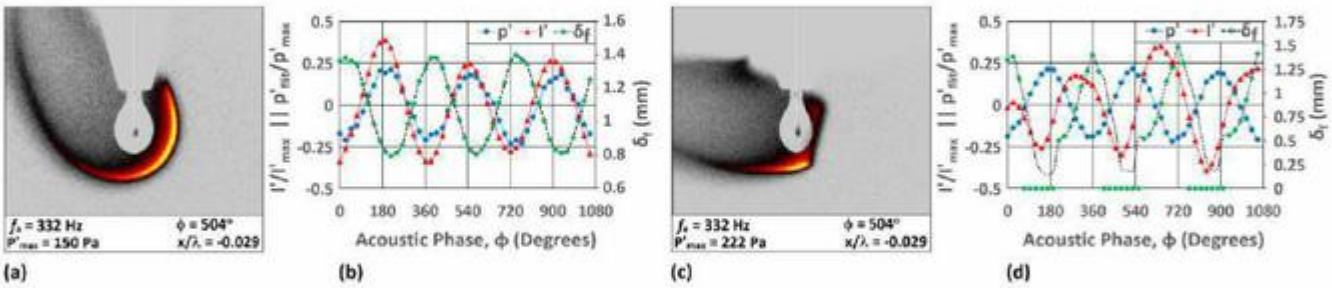

Figure 1: Instantaneous OH* chemiluminescence images of burning ethanol droplets situated at 0.29 wavelengths to the left of the PN during acoustic forcing at f_a = 332 Hz for (a) p'_{max} = 150 Pa and (c) 222 Pa. Nondimensionalized measurements of local p', integrated chemiluminescent intensity I', and horizontal flame standoff distance δ_f are plotted as a function of the acoustic phase for the same forcing conditions, at (b) p'_{max} = 150 Pa and (d) 222 Pa.

Sample results contrasting sustained combustion and periodic partial flame extinction for an ethanol droplet exposed to f_a = 332 Hz forcing at two different pressure perturbation amplitudes p'_{max} are shown in Figure 1. Instantaneous OH* chemiluminescence images show a flame deflected away from the PN (to the left) for both forcing amplitudes 150 Pa and 222 Pa, in Figs. 1(a) and (c), respectively, but partial extinction of the flame and a larger degree of flame deflection is seen in the latter case. The associated phase-locked measurements of local perturbation pressure p', integrated chemiluminescent intensity I', and horizontal flame standoff distance δ_f are plotted as a function of the acoustic phase in Figs. 1(b) and (d) for the lower and higher amplitude forcing conditions, respectively. Fig. 1(b) shows that the temporal/phase-locked variation in p' and I' are in phase for 150 Pa forcing, consistent with more vigorous burning as the diffusion flame periodically approaches the droplet surface, thus producing a positive Rayleigh index G. This type of coupling is seen for a range of fuels at moderate excitation amplitude in the vicinity of the PN[1]. But at higher amplitude excitation at 222 Pa, Fig. 1(d) shows out-of-phase variation in p' and I', resulting from localized extinction as the flame approaches the droplet surface, although reignition occurs as the flame periodically moves away from the droplet surface. This out of phase oscillation typically creates a negative Rayleigh index G, which theoretically suggests stable combustion, despite clear oscillatory flame behavior. For ethanol droplet combustion at f_a = 332 Hz, full extinction is observed for pressure perturbation amplitudes exceeding approximately 235 Pa.

Similar behaviors to those documented in Fig. 1 are observed for fuel droplets exposed to higher frequency forcing but at even higher amplitudes. In general, the flame shows a greater response to low-frequency excitation, where the acoustic time scales ($T_a = 1/f_a$) are large compared to the kinetic/reaction times scales for diffusion-limited combustion processes. Moreover, large periodic velocity perturbations u' at the PN create larger amplitude periodic strain fields to which flames are exposed. As in a counterflow configuration, the stagnation region of the droplet's flame is exposed to periodic straining of the form $\varepsilon = \varepsilon_s + \varepsilon' \sin(2\pi f t)$, where ε_s is the mean strain and ε' is the oscillatory strain amplitude. Estimating these parameters for the present configuration suggests that ε' exceeds ε_s for conditions producing periodic partial extinction, consistent with oscillatory flame theory[8]. Thus, differences among the various chemical, acoustic, and fluid mechanical time scales can provide insights into different flame responses and hence into the fundamental nature of combustion instabilities.

References

[1] Sevilla-Esparza C.I., Wegener J.L., Teshome S., Rodriguez J.I., Smith O.I., Karagozian A.R.: Droplet Combustion in the Presence of Acoustic Excitation. *Combustion and Flame* **161**: 1604–1619, 2014.

[2] Valentini D., Tran P.H., Lopez B., Ekmekji A., Smith O.I., Karagozian A.R.: Partial Extinction and the Rayleigh Index in Acoustically Driven Fuel Droplet Combustion. *Bulletin of the American Physical Society*, **59**:16, 2014.

[3] Rayleigh J.: The Explanation of Certain Acoustical Phenomena. *Nature* **18**: 319-321, 1878.

[4] Putnam A.: *Combustion-Driven Oscillations in Industry*. New York, USA 1971.

[5] Candel S.M.: Combustion Instabilities Coupled by Pressure Waves and their Active Control. *Proc. . Comb. Inst.*, **24**:1277-1296, 1992

[6] Dattarajan, S., Lutomirski, A., Lobbia, R., Smith, O. I., and Karagozian, A. R. Acoustic excitation of droplet combustion in microgravity and normal gravity. *Combustion and Flame*, **144**:299–317, 2006

[7] Tanabe M., Kuwahara T., Kimiyoshi S., Fujimori T., Sato J., Kono M.. Droplet Combustion in Standing Sound Waves. *Proc. Comb. Inst.*, **30**:1957–1964, 2005

[8] Ghoniem A.F., Soteriou M.C., Knio O.M., Cetegen B.: Effect of Steady and Periodic Strain on Unsteady Flamelet Combustion. *Proc. .Comb. Inst.*, **24**:223-230, 1992

SIMULATING ACOUSTOFLUIDIC PARTICLE INTERACTIONS AND UNILATERAL CONTACTS

Thierry Baasch[1a)], Jürg Dual[1]
[1]*Institute for Mechanical Systems, Swiss Federal Institute of Technology, Zurich, Switzerland*

Summary Determining the trajectories of particles in acoustic fields is one of the major challenges of numerical acoustophoresis. Previous work has only focused on determining the trajectory of one single particle or cell in an acoustic field[1]. Although the forces between multiple small spherical particles can be obtained analytically[2], previous research failed to address the unilateral contacts in the trajectories of multiple interacting particles. The aim of this work is to present a method, which allows to compute trajectories of multiple interacting particles in an acoustic field. This goal is achieved by combining acoustic force simulations with a Moreau type time integrator[3]. The model requires acoustic forces to be determined at each time-step, two different methods are applied and compared. The presented algorithm allows to simulate the motion of particle clumps, effectively explaining phenomena such as particle chain formation and particle clump rotation.

MOTIVATION

In Lab-on-a-Chip technology acoustic waves can be used for the contactless handling of particles and cells.
Bulk acoustic wave devices use acoustic resonance modes to achieve high acoustic pressure and force amplitudes. The Gorkov theory has become a reliable tool to predict the stable and unstable equilibria positions of single particles in the acoustic fields, valid for spherical particles much smaller than the acoustic wavelength. However it fails to fully explain certain phenomena observed in recent experiments such as particle clump rotation and particle pattern formation as seen in figure 1.
Particle clump rotation has been performed by Thomas Schwarz[4]. Here the presence of unilateral contacts between the particles has to be acknowledged in order to fully understand and simulate the particle trajectories.
Particle line-up or chain formation has been known for a while and was observed by Ivo Leibacher et al. [5,6,7] using aluminum disk and core-shell particles. Not only do the particles line up in chains, but the chains seem also to repel each other, thus forming a grid.
Better understanding of these phenomena can also lead to further advances in micro assembly applications. The presented algorithm allows to simulate the complete trajectories of spherical particles in these systems. The method does not limit itself to spherical particles and can be expanded for particles of more complicated shapes (work in progress).

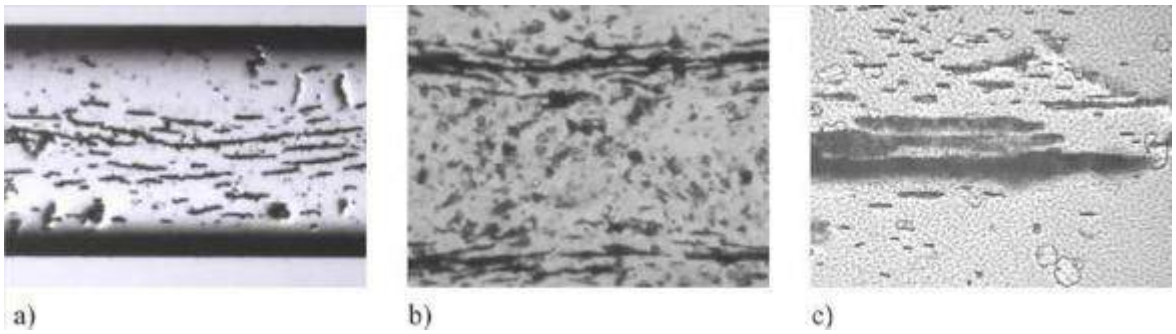

Fig. 1. Line-up and stack formation of a) core-shell particles[6,7], b) c) aluminum disks in a one dimensional pressure wave[5,7] (Videos available).

NUMERICAL SET UP

The acoustic forces acting on the particles can be calculated in various ways. It is possible to use the algorithm in combination with a semi-analytical approach as presented by Silva et al.[2] or to combine it with a finite element software package such as Comsol Multiphysics. Comsol Multiphysics can be accessed through the Matlab Livelink and the forces can be determined by performing a scattering simulation at each time-step. One main advantage of this method is it not being limited in the particle shapes and sizes. Both methods have been applied during our numerical studies.

In order to include the unilateral contacts and the inelastic impacts in the simulation, a Moreau type time integrator with an additional drift correction step has been used. The Moreau time-stepping algorithm involves performing a collision

[a)] Corresponding author. Email: *baasch@imes*.mavt.*ethz*.ch.

detection and solving a normal cone inclusion problem. A projected over relaxed Gauss Seidel scheme is used to solve the inclusion problem[8].

RESULTS

The particle line-up mechanism is shown in fig. 2. Small particles with a radius of 50 µm were simulated in a one dimensional standing wave situation. Here the acoustic interaction forces have been calculated applying the approach presented by Silva et al.[2] for perfectly rigid particles. The particles have been assumed to instantaneously reach terminal velocity, which has been determined using the Stokes drag.
The particles move into the minimum of the Gorkov potential, which is shown in blue. While moving the particles interact with each other, repelling or attracting each other, ultimately forming three repelling particle chains.

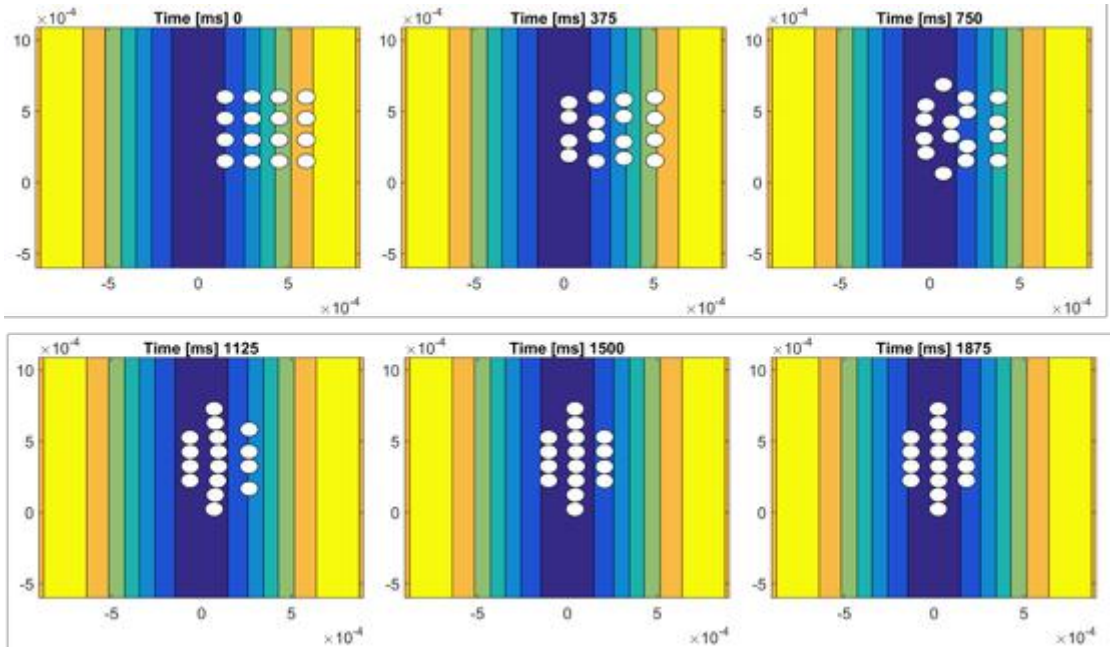

Fig. 2. Line-up and stack formation of rigid particles in an acoustic field due to secondary acoustic forces. In the background the Gorkov potential for one single particle in a one-dimensional acoustic field is shown, blue marking its minimum and yellow its maximum. Although the Gorkov theory is only valid for single particles, the particles move into the minimum of the Gorkov potential. The particles also form chains which seem to repel each other (Video available).

CONCLUSION AND OUTLOOK

Using the presented algorithm it is possible to simulate complete particle trajectories in realistic acoustofluidic multi-particle systems. The algorithm includes acoustic interaction (Bjerknes) forces, unilateral contacts and impacts. The possibility to combine it with Comsol Multiphysics allows to perform a pre-simulation calculating the pressure field in a complex device[1] and then using this pressure field as a background field in the following scattering simulations. The algorithm can also be expanded to allow for more complex particle shapes (work in progress).

References

[1] Philipp Hahn et al. *Numerical simulation of acoustofluidic manipulation by radiation forces and acoustic streaming for complex particles* Lab Chip, 2015, 15, 4302-4313

[2] Glauber T. Silva and Henrik Bruus *Acoustic interaction forces between small particles in an ideal fluid* Phys. Rev. E 90, 063007

[3] Moreau, J. *Unilateral contact and dry friction in finite freedom dynamics*. *In: J.J. Moreau and P.D. Panagiotopoulos*. Vol. 302 of International Centre for Mechanical Sciences, Courses and Lecture. Springer, Verlag, 1988.

[4] Thomas Schwarz *Rotation of Particles by Ultrasonic Manipulation* Phd. Thesis Diss. ETH No. 21572

[5] Ivo Leibacher et al**.** *Acoustophoresis of disk-shaped microparticles: A numerical and experimental study of acoustic radiation forces and torques* J. Acoust. Soc. Am. 138 (5), November 2015

[6] Ivo Leibacher et al**.** *Acoustophoresis of hollow and core-shell particles in two-dimensional resonance modes* Microfluid Nanofluid (2014) 16:513–524

[7] Provided by Ivo Leibacher and used with permission

[8] Gabriel Nützi *Non-Smooth Granular Rigid Body with Application to Chute Flows* (unpublished Phd. Thesis)

PDMS-BASED ACOUSTIC IMPEDANCE-MATCHED MATERIAL IN WATER

Reine-Marie Guillermic[1a)], Anatoliy Strybulevych[1] & John H. Page[1]
[1]*Department of Physics and Astronomy, University of Manitoba, Winnipeg, Manitoba, Canada*

Summary We have created a composite material that has the same longitudinal acoustic impedance as water using Polydimetylsiloxane (PDMS) and TiO_2 particles. To predict the concentration of particles needed in the PDMS matrix to obtain impedance matching to water, we used a Coherent Potential Approximation (CPA) model for dispersed particles in an elastic matrix [1]. This model predicts the shear and longitudinal moduli of the final composite system. We discuss the validity and limitation of the model and show experimentally that it is possible to achieve perfect impedance matching for longitudinal waves by adding submicron particles to a soft solid, here PDMS, and to measure its shear mechanical properties.

Acoustic probing of materials underwater in the ultrasonic frequency range is a common technique, due to the convenience of immersion transducer technology, which can avoid a difficult to reproduce direct contact bond between the transducer and the material of interest and enable spatially resolved measurements to be easily made. If the material to be probed is liquid or is not able to keep its shape, it needs to be confined in a cell, between walls. Having walls that are acoustically "transparent" in water can be an asset in such an example. In a more fundamental point of view, an acoustically impedance-matched medium can be also used as a matrix for the creation of novel complex materials containing particles or bubbles, reducing some impedance matching problems that can occur at the interface between the sample and the surrounding water [2]. It is possible in practice to create such a material by dispersing the right type and amount of filler particles in a soft solid matrix in order to tailor its acoustic effective medium properties. For this approach to work well, it is important that the matrix be soft, so that its shear modulus is low enough not to complicate the acoustic properties but still rigid enough to have useful mechanical properties for these types of applications.

The prediction of the behaviour of a soft composite material composed of an elastic medium with a dispersion of submicron fillers is done with a Coherent Potential Approximation (CPA) model [1]. Knowing the shear and longitudinal complex moduli (μ and β), and the densities (ρ) of the matrix and particles, the model predicts the composite material moduli and therefore the longitudinal velocity $v = \sqrt{\beta/\rho}$. To obtain a water impedance-matched material, the longitudinal velocity and the density should be chosen in order to obtain an acoustic impedance $Z = \rho v$ equal to the impedance of water (1.5 MRay). Initially the impedance of the PDMS used (RTV615) is 1.04 MRay. The addition of TiO_2 particles increases the density of the final material considerably while having a much smaller effect on the sound velocity for concentrations of these inclusions up to 60%, thus enabling the ideal impedance-matched material to be created. Some predictions of the model are shown in Figure 1.

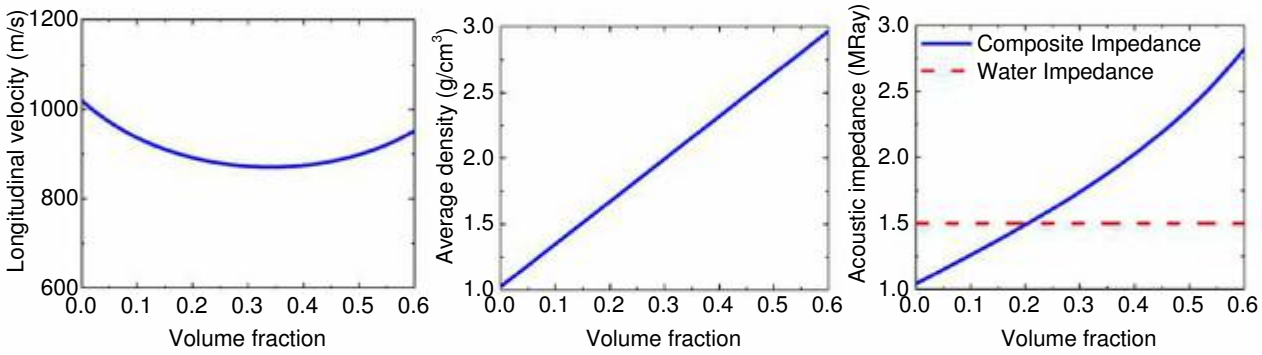

Figure 1: Longitudinal velocity, average density and acoustic impedance of a PDMS-TiO_2 composite material calculated with the CPA model as a function of the volume fraction of TiO_2 particles. The model predicts impedance-matching to water when the volume fraction of TiO_2 particles in the PDMS matrix is 20.6%.

Experimentally, we prepared different PDMS-TiO_2 composite materials, with different amounts of crosslinker or TiO_2 particles, chosen according to the model predictions. We measured experimentally the acoustic properties of the PDMS-TiO_2 samples created. By using different pairs of transducers of different central frequencies face-to-face in a water tank,

[a)] Corresponding author. Email: guillermic@physics.umanitoba.ca.

we show that the impedance can be tuned by the concentration of TiO_2 particles, and that when the amount of particles is ideal no significant reflection can be observed. Some absorption can also be quantified. Using a shear wave device [3,4] – an acrylic prism and a shear transducer centered around 400 kHz – we measured the shear moduli of the PDMS-TiO_2 materials. The mechanical properties of the composite material can be further tuned by using silica particles and by changing the amount of PDMS crosslinker. We will discuss the agreement between the CPA model and the experimental results.

We demonstrated that it is possible to create a home-made impedance-matched material using PDMS and particles (TiO_2 in this case). We showed that the CPA model helps in choosing the concentration of particles necessary to achieve this goal, and discussed the agreement between the theoretical predictions and experimental measurements for the shear and longitudinal properties. The composite material can be cured in a mold to achieve desired sample shape in the same way as with classic PDMS, which makes it very easy to handle and to use. This material, which prevents acoustical reflections, can be used as a cell or for walls around a sample to allow the sample's acoustical properties to be probed. We plan to use this material to improve the performance of bubble metascreens for broadband superabsorption of acoustic waves in water [2].

References

[1] P.Sheng, Introduction to wave scattering, localization and mesoscopic phenomena, 2nd edition, Springer, 2006.

[2] Leroy V., et al., Super-Absorption of Acoustic Waves with Bubble Meta-Screens. *Phys. Rev. B* **91**:020301, 2015

[3] Y. Longin, et al., Dynamic shear rheology of high molecular weight polydimethylsiloxanes: comparison of rheometry and ultrasound. *J. Non-Newtonian Fluid Mech.* **76**: 213–232, 1998.

[4] Leroy V., et al., The complex shear modulus of dough over a wide frequency range. *J Non-Newtonian Fluid Mech.* **165**:475-478, 2010

BROADBAND PENTAMODE ACOUSTIC CLOAK USING SINGLE PHASE SOLID

Yi Chen, Xiaoning Liu & Gengkai Hu[a)]
School of Aerospace Engineering, Beijing Institute of Technology, Beijing, China

Summary Pentamode acoustic cloak using single phase solid is designed with detailed microstructure. Resonance scattering induced by shear standing wave in the cloak, due to imperfection of practically designed pentamode unit cells, is found to damage the expected broadband property. By increasing perfection level, the resonance frequency is found to shift toward zero with narrowed bandwidth, which can be suppressed by introducing damping effect.

INTRODUCTION

Like fluids, Pentamode (PM) materials are degenerated elastic solids bearing only one state of stress, not necessarily hydrostatic[1]. They can be made approximately from conventional solids with careful designed microstructure. Inviscid fluids can be regarded as natural isotropic PM materials, while PM materials with solid microstructures are able to support off-axis shear. This property makes it very promising in acoustic wave control, particularly with the advance of transformation acoustics theory based on pentamode materials [2-4].

Because of broadband and solid material nature, acoustic cloak using PM materials is thought to be more realistic for practical application, compared to that based on anisotropic density fluid. However, the inherent microstructure and stability requirement render ideal solid pentamode material almost impossible, and weak shear resistance always presents in solid pentamode materials. Few works have been done with practical realization of PM cloak with solid microstructure [4]. In this work, we will design PM unit cells with targeted material property and assemble them into a microstructure cloak with single phase solid PMs. The designed invisibility function will be demonstrated through numerical simulation, and impact of imperfection in the PM unit cells on the overall performance of the cloak will also be examined.

MATERIAL AND METHODS

Fig.1(a) shows the proposed basic microstructure of PM unit cell with five dimensionless parameters, length ratio $\bar{m}=m/l$, topology angle β, slenderness ratio $\bar{t}=t/l$, rectangular width $\bar{w}=w/(l\sin\beta)$ and height $\bar{h}=h/(m+l\cos\beta)$. Since only quasi-static property is needed here, the effective density of the unit cell is simply taken as volume average, while elastic constants, K_r, K_θ, $K_{r\theta}$ and $G_{r\theta}$, are computed from wave velocity along different directions. Imperfection of the PM unit cell is defined by two PM characteristic parameters $\pi=|K_{r\theta}|/(K_rK_\theta)^{1/2}$ and $\mu=|G_{r\theta}|/(K_rK_\theta)^{1/2}$. Due to static stability requirement, one can only expect π and μ to approach 1 and 0 as much as possible. Using built-in optimization algorithms in Matlab, we get geometric parameters of the above unit cells with the targeted PM property. By integrating optimized 12 different PM unit cells along radial direction and duplicating the segment along circumferential directions in a cylinder coordinate, a microstructure PM cloak based on a single-phase solid is finally obtained. Fig.1(b) shows a quarter of the designed microstructure PM cloak with 2600 honeycomb unit cells. Since strong anisotropy near the inner boundary is necessary for guiding wave to go around the cloaking region, the topology angle β for unit cells near the inner boundary is almost 90° as indicated by the inset figure.

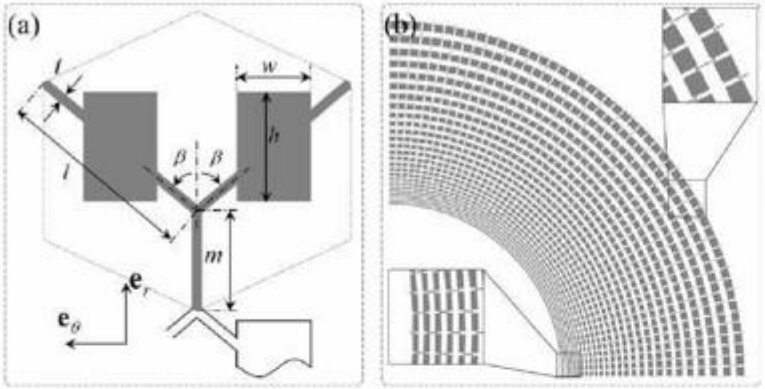

Fig.1 (a) PM unit cell with rectangular weight block. (b) Quarter of geometric model of designed 12 layers microstructure PM cloak.

RESULT AND DISSCUSSIONS

[a)] Corresponding author. Email: hugeng@bit.edu.cn.

After determining the microstructure of the PM cloak, numerical simulation with a plane incident wave is conducted with COMSOL to verify its broadband property. As shown in Fig.2(a), TSCS (Total Scattering Cross Section) of the designed microstructure cloak matches well with the layered perfect PM case, and is significantly reduced compared to that of a rigid cylinder for the frequency range ka/π=0~1. However, many TSCS peaks are also observed, which has also been verified using a layered imperfect PM material model, i.e. homogenized parameters for the corresponding microstructure,

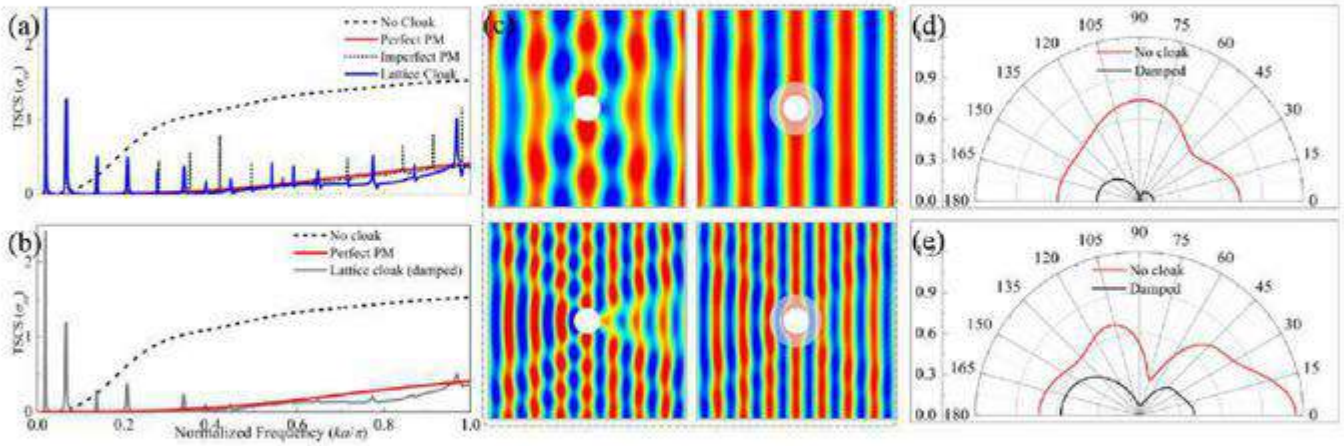

Fig.2 (a)(b) TSCS versus frequency for different cases; (c) Pressure patter for uncloaked and cloaked cases at ka/π=0.5, 1.0; (d)(e) Far field form function for uncloaked and cloaked cases at ka/π=0.5, 1.0.

especially at low frequency when wavelength in the background fluid is much larger than PM unit cells. Further investigation on the TSCS peak frequencies reveals that, these peaks are induced by shear standing wave confined in the cloaking layer generated due to the imperfection of the PM unit cells. The narrow resonance peaks can be well suppressed through introduction of structure damping, and the broadband property (Fig2.(b)) is obtained. Snapshots (Fig2.(c)) of pressure field at two frequencies demonstrate clearly the wave steering ability of the designed cloak. Far-field pattern also illustrates a significant reduction in all directions compared to that of a rigid cylinder. The far-field scattering coefficients for backward direction are decreased by 6dB and 2dB for the examined two frequencies, respectively.

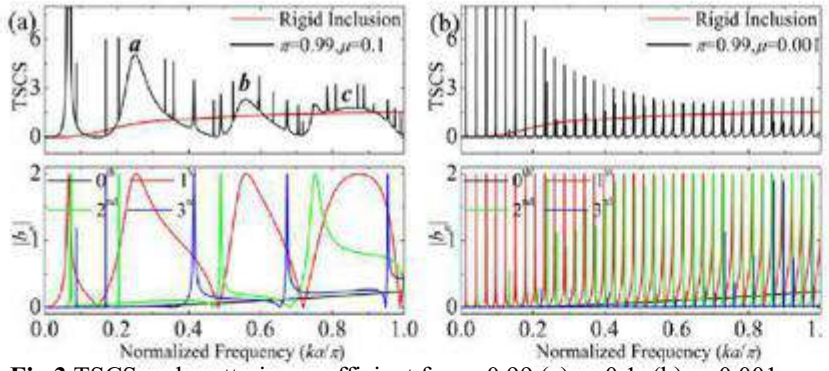

Fig.3 TSCS and scattering coefficient for π=0.99 (a) μ=0.1; (b) μ=0.001.

The resonance scattering induced by imperfect PM material is further investigated by developing a semi-analytical acoustic scattering model of gradient orthotropic elastic shells. It is seen that reduction in shear modulus of the imperfect PM material (Fig.3) shifts resonance frequencies towards zero with narrowed resonance peak width. Reduction of the parameter π shows the similar result because the two parameters both determine shear wave velocity. It is concluded, when the imperfection approaches to zero, all resonance frequency will be compressed to zero and broadband property without resonance is able to achieve. This implies that the imperfection of PM unit cells and structure damping in the matrix material should be both considered in order to achieve broadband acoustic invisibility.

CONCLUSIONS

Acoustic cloak based on PM material is realized with concrete PM unit cells, its broadband cloaking performance is examined by numerical simulation. Resonance scattering at low frequency is explained by shear standing wave and it can be suppressed by introducing weak structure damping. A semi-analytical acoustic scattering model of gradient orthotropic elastic shells is also developed to explain the impact of PM imperfection on the cloaking effect.

References

[1] Milton G.W., Cherkaev A.V.: Which elasticity tensors are realizable? J. ENG MATER-T ASME **117**:483-493, 1995.
[2] Norris A.N.: Acoustic cloaking theory. P. ROY SOC A-MATH PHY **464**:2411-2434, 2008.
[3] Kadic M., Bückmann T. et al.: On the practicability of pentamode mechanical metamaterials, APPL PHYS LETT **100**:191901, 2012.
[4] Chen Y., Liu X.N., Hu G.K.: Latticed pentamode acoustic cloak, SCI REP-UK **5**:15745, 2015.

FLOW-ACOUSTIC INTERACTION IN AN EXPANSION CHAMBER-PIPE SYSTEM

M. A. Langthjem *[1] and M. Nakano[2]

[1]*Faculty of Engineering, Yamagata University, Jonan 4-cho-me, Yonezawa, Japan*
[2]*Institute of Fluid Science, Tohoku University, 2-1-1 Katahira, Aoba-ku, Sendai, Japan*

Summary The paper is concerned with the generation of sound by the flow through a closed, cylindrical expansion chamber, followed by a long tailpipe. The sound generation is due to self-sustained flow oscillations in the expansion chamber which, in turn, may generate standing acoustic waves in the tailpipe. The main interest is in the interaction between these two sound sources. An analytical, approximate solution of the acoustic part of the problem is obtained via the method of matched asymptotic expansions. The sound-generating flow is represented by a discrete vortex method, which is modified to include the effects of acoustic feedback. It is demonstrated that lock-in of the self-sustained flow oscillations to the resonant acoustic waves in the tailpipe can take place.

INTRODUCTION

Expansion chambers (mufflers) are used in connection with silencers in engine exhaust systems, with the aim of attenuating the sound waves through destructive interference. But the gas flow through the chamber may generate self-excited oscillations, thus becoming a sound generator rather than a sound attenuator. Similar geometries and thus similar sound generation problems may be found in, for example, solid propellant rocket motors, valves, and in corrugated pipes. The aim of the present work is to contribute to the understanding of the interaction between the flow field and the acoustic field.

The paper considers a simple axisymmetric 'silencer model' consisting of an expansion chamber followed by a tailpipe, as shown in Fig. 1(a).

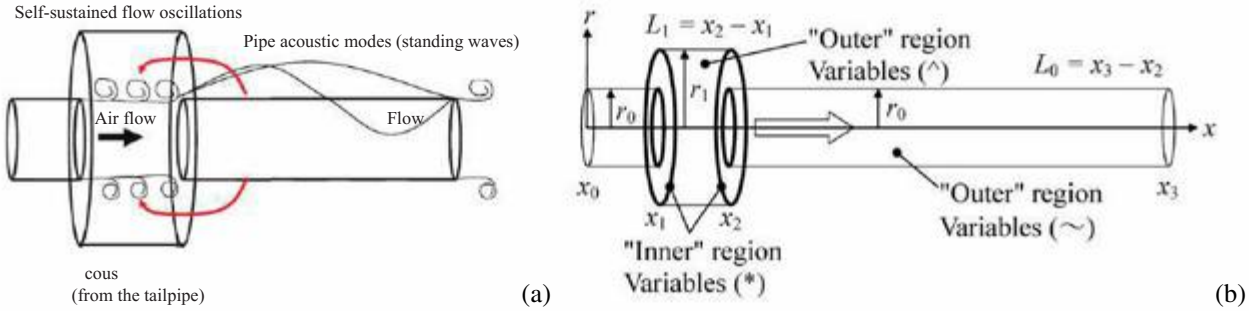

Figure 1: (a) Sketch of the expansion chamber-tailpipe problem. (b) Definition sketch for the acoustic problem, with indication of coordinates used in the matched asymptotic expansions solution.

As indicated in Fig. 1(a), perfect axisymmetry is assumed, and a mathematical model is formulated in terms of the cylindrical axisymmetric coordinates (x, r), see Fig. 1(b). It is assumed that the flow field can be separated into an incompressible, rotational part, referred to as the flow problem, with flow velocity $\mathbf{v}$ and vorticity $\boldsymbol{\omega} = \nabla \times \mathbf{v}$, and a compressible, irrotational part, referred to as the acoustic problem, with acoustic velocity $\mathbf{u}$.

THE FLOW-ACOUSTIC COUPLING PROBLEM

Modeling of the acoustic problem

The compressible, irrotational acoustic field is assumed to be governed by the linearized, inhomogeneous Euler equation

$$\frac{\partial \mathbf{u}}{\partial t} + \frac{1}{\rho}\nabla p = -\,\mathfrak{L}\, H(x - x_1)H(x_2 - x), \tag{1}$$

together with the continuity equation $\kappa \partial p/\partial t = -\nabla \cdot \mathbf{u}$, where $\kappa = (\rho c_0^2)^{-1}$. Here p is the acoustic pressure, t is the time, ρ is the fluid density, $\mathfrak{L} = \boldsymbol{\omega} \times \mathbf{v}$ is the vortex force, also known as the Lamb vector [1], and $H(s)$ is the Heaviside step function, which equals 0 for $s < 0$ and 1 for $s > 0$. Finally, c_0 is the speed of sound.

This acoustic problem is *solved* (with respect to p and $\mathbf{u}$) by taking advantage of characteristic length-scales in the different regions of the problem: (i) tailpipe region, (ii) step (cross section change) regions, and (iii) cavity region, as indicated in Fig. 1(b). The tailpipe radius-to-length ratio $\epsilon = r_0/L_0$ acts a small parameter in a perturbation approach. The simplified analytical solutions for these three regions are then coupled by employing the method of matched asymptotic expansions [2]. In this way we have obtained analytical expressions for (i) the acoustic pressure inside, and downstream from, the tailpipe and (ii) the acoustic feedback velocity (generated by the pressure oscillations in the tailpipe) within the cavity.

*Corresponding author. Email: mikael@yz.yamagata-u.ac.jp

Modeling of the flow problem

The source field, i.e., the sound-generating incompressible 'background flow', is assumed to be governed by the Euler equation $\partial \mathbf{v}/\partial t + \rho^{-1}\nabla p_h = \nearrow \mathbf{v} \cdot \nabla \mathbf{v}$, where p_h is the 'hydrodynamic' fluid pressure. Adding the acoustic velocity $\mathbf{u}$ to this equation gives $\partial\left(\mathbf{v}+\mathbf{u}\right)/\partial t + \left(\mathbf{v}+\mathbf{u}\right)\cdot\nabla\left(\mathbf{v}+\mathbf{u}\right) = \nearrow \rho^{-1}\nabla p_h$. Taking the curl on both sides eliminates p_h, and the (last) equation can be written as

$$D\boldsymbol{\omega}/Dt = \boldsymbol{\omega}\cdot\nabla\mathbf{w} + \kappa\boldsymbol{\omega}\partial p/\partial t, \tag{2}$$

where $\mathbf{w} = \mathbf{v} + \mathbf{u}$, $D/Dt = \partial/\partial t + \mathbf{w}\cdot\nabla$, and p (without an index) is again the acoustic pressure. Eq. (2) is solved numerically in terms of a discrete vortex method, by discretizing the cylindrical shear layer of the jet into a series a vortex rings. Inspired by the viscous splitting algorithm used in viscous vortex methods [3], where the Navier-Stokes equation is split up into a convection part and a diffusion part, (2) is split up into the convection part $D\left(\omega_\theta/r\right)/Dt = 0$ and a part which 'infuses' vorticity, $\partial\left(\omega_\theta/r\right)/\partial t = \left(\omega_\theta/r\right)\kappa\partial p/\partial t$. Here ω_θ is the azimuthal component of $\boldsymbol{\omega}$, the only non-zero component by axisymmetry. In terms of the discrete vortex method, the last of these two equations can be solved, to give the strength (circulation) of the mth vortex ring as $\mathrm{y}_m(t) = \mathrm{y}_{0m}(r_m(t)/r_0)\ \ \mathrm{xp}(\kappa(p(t) \nearrow p(t^m_{\mathrm{rel}}))$, where $r_m(t)$ is the vortex ring radius at time t, and t^m_{rel} is the time where the ring is released at the nozzle (of radius r_0), at position x_1 (see Fig. 1(b)).

Thus acoustic problem and the flow problem are complete coupled.

NUMERICAL EXAMPLES

Figure 2 shows the frequency spectrum of the flow velocity fluctuations in the shear layer, at position x_2 (see Fig. 1(b)) near the 'end plate' (i.e. at the downstream end of the cavity), for three different mean flow speeds, U_0 = 9, 10, and 11 m/s. The results in the upper row (parts a, b, c) are without acoustic feedback, while it is included by those in the lower row (parts d, e, f). The resonance frequency of the tailpipe is f_{pipe} = 200 Hz (in mode $n = 1$, one half-wave), and it is seen that inclusion of acoustic feedback results in lock-in of the self-sustained flow oscillations to this frequency.

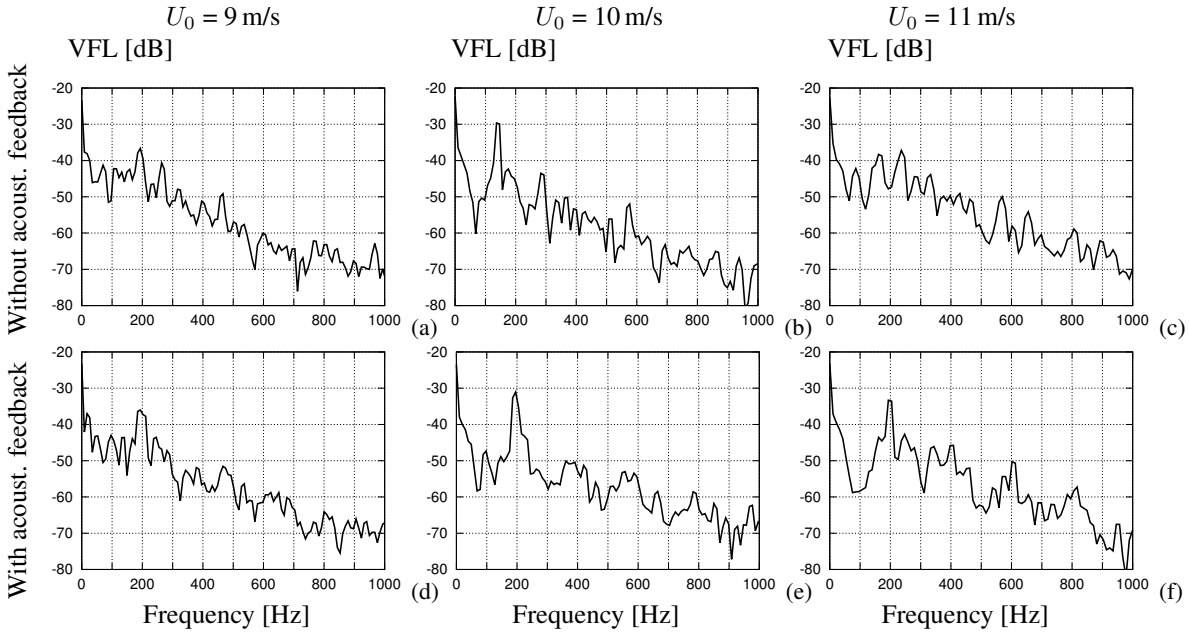

Figure 2: Frequency spectrum of the flow velocity fluctuations in the shear layer at position x_2 in Fig. 1(b).

CONCLUSIONS

The main contribution of the present work is (i) the formulation and solution in analytical (albeit approximate) form of an inherently coupled flow-acoustic problem within the framework of the classical acoustic analogy approach, and (ii) successful demonstration of lock-in of the self-sustained flow oscillations to resonant acoustic oscillations.

References

[1] M. S. Howe, Acoustics of Fluid-Structure Interactions, Cambridge University Press, Cambridge, 1998.

[2] M. B. Lesser, J. A. Lewis, Applications of matched asymptotic expansion methods to acoustics. I. The Webster horn equation and the stepped duct, J. Acoust. Soc. Am. 51:1664-1669, 1972.

[3] Cottet, G.-H., Koumoutsakos, P. D.: Vortex Methods: Theory and Practice. Cambridge University Press, Cambridge, 2000.

A BIEM FOR TRANSMISSION RESONANCE PROBLEMS FOR ELASTIC WAVEGUIDES

Ryota Misawa[1], Kazuki Niino[1], and Naoshi Nishimura*[1]

[1]*Department of Applied Analysis and Complex Dynamical Systems, Kyoto University, Yoshida-honmachi, Sakyo-ku, Kyoto, 606-8501, Japan*

Summary A BIEM (Boundary Integral Equation Method) for computing resonance frequencies for elastic waveguides is presented. We show that Müller's integral equation may suffer from *complex* fictitious eigenfrequencies although this equation is known to be without *real* ones. We propose a new BIE formulation which resolves this problem and show numerical examples of resonance frequencies obtained with this formulation.

INTRODUCTION

Determining resonance frequencies in waveguides is of interest because they affect the behaviour of the solution considerably. This study considers a numerical solver for resonance problems for time harmonic (with $e^{-i\omega t}$) SH waves in waveguides with inclusions. Mathematically, the resonance frequencies are complex eigenvalues (ω's) at which there exist non-trivial solutions to the homogeneous boundary value problems. Real resonance frequencies as well as leaky ones with ω's having small imaginary parts are of interest.

Boundary Integral Equation Method (BIEM) is considered to be one of advantageous solvers for waveguide problems because it requires no truncation of the domain thus requiring no special techniques to avoid reflections from artificial boundaries introduced by the truncation. The long standing inefficiency problem of BIEM is now almost solved with the development of so called fast BIEMs such as FMM (Fast Multipole Method). With BIEM, however, one has to solve non-linear eigenvalue problems for discretized BIEs in order to determine resonance frequencies. This non-linear eigenvalue problem, however, can now be solved efficiently with the SS method [1] as has been verified successfully in [2].

However, one has to be careful in solving transmission problems with BIEs because some known integral equations without real fictitious resonance frequencies may have complex ones when one considers leaky modes [2]. This paper proposes a new BIE with which one can distinguish true resonance frequencies from fictitious ones, which we validate with some numerical examples. These examples clearly show that resonance frequencies are related to the behaviour of energy transmittances.

FORMULATION

Let P be an infinite strip given by $P=[-1/2,1/2]\times\mathbb{R}$ which is a model of a traction free waveguide. Also, let $\Omega_2\subset P$ be a finite domain (inclusion), $\Gamma=\partial\Omega_2$ be its boundary and $\Omega_1=P\setminus\overline{\Omega_2}$. We consider the following homogeneous transmission problem: find u which satisfies Helmholtz' equation

$$\Delta u+k_i^2u=0\quad\text{in }\Omega_i\ (i=1,2),$$

boundary conditions

$$u^+=u^-,\quad \mu_1\frac{\partial u^+}{\partial n}=\mu_2\frac{\partial u^-}{\partial n}\quad\text{on }\Gamma,\qquad \frac{\partial u}{\partial x_1}=0\quad\text{on } x_1=\pm\frac{1}{2}$$

and the outgoing radiation condition for u as $x_2\to\pm\infty$ in P, where $k_i=\omega\sqrt{\rho_i/\mu_i}$ is the wavenumber, ρ_i is the density and μ_i is the shear modulus in Ω_i $(i=1,2)$, respectively. Also, the superscript $+(-)$ stands for the trace to Γ from Ω_1 (Ω_2), $\partial/\partial n$ for the normal derivative and $\boldsymbol{n}$ for the unit normal vector on Γ directed towards Ω_1, respectively.

A standard BIE for this problem is the Müller formulation given as follows:

$$\begin{aligned}
&\frac{\mu_1+\mu_2}{2}u(\boldsymbol{x})-\int_{\partial\Omega}\left(\mu_1\frac{\partial G_1(\boldsymbol{x},\boldsymbol{y})}{\partial n_y}-\mu_2\frac{\partial G_2(\boldsymbol{x},\boldsymbol{y})}{\partial n_y}\right)u(\boldsymbol{y})ds_y+\int_{\partial\Omega}\left(G_1(\boldsymbol{x},\boldsymbol{y})-G_2(\boldsymbol{x},\boldsymbol{y})\right)t(\boldsymbol{y})ds_y=0\\
&\frac{\mu_1+\mu_2}{2\mu_1\mu_2}t(\boldsymbol{x})-\int_{\partial\Omega}\left(\frac{\partial^2G_1(\boldsymbol{x},\boldsymbol{y})}{\partial n_x\partial n_y}-\frac{\partial^2G_2(\boldsymbol{x},\boldsymbol{y})}{\partial n_x\partial n_y}\right)u(\boldsymbol{y})ds_y+\int_{\partial\Omega}\left(\frac{1}{\mu_1}\frac{\partial G_1(\boldsymbol{x},\boldsymbol{y})}{\partial n_y}-\frac{1}{\mu_2}\frac{\partial G_2(\boldsymbol{x},\boldsymbol{y})}{\partial n_y}\right)t(\boldsymbol{y})ds_y=0
\end{aligned}\tag{1}$$

where G_1 is the Green function for the waveguide and G_2 is the fundamental solution for Ω_2 given as follows:

$$G_1(\boldsymbol{x},\boldsymbol{y})=\sum_{l=0}^{\infty}f_l\frac{e^{-\sqrt{(l\pi)^2-k_1^2}|x_2-y_2|}}{\sqrt{(l\pi)^2-k_1^2}}\cos l\pi\left(x_1+\frac{1}{2}\right)\cos l\pi\left(y_1+\frac{1}{2}\right),\ G_2(\boldsymbol{x},\boldsymbol{y})=\frac{i}{4}H_0^{(1)}(k_2|\boldsymbol{x}-\boldsymbol{y}|).\tag{2}$$

*Corresponding author. Email: nchml@i.kyoto-u.ac.jp

In (2), f_l is 1 for $l \neq 0$ and 1/2 for $l = 0$ and $H_n^{(\nu)}$ stands for the Hankel function of the ν-th kind, respectively. The branches of square roots in G_1 are taken so that the summand decays as $l \to \infty$. The integral equation in (1) is known to have no real fictitious eigenfrequencies. Namely, solving (1) is equivalent to solving the transmission problem if ω is a real number.

We next consider the transmission resonance problem which finds complex ω's at which the above transmission problem has non-trivial solutions. We call such ω's resonance frequencies and the corresponding non-trivial solutions eigenmodes, respectively. These eigenmodes are outgoing and the resonance frequencies have non-positive imaginary parts.

To solve the transmission resonance problem we search complex ω's such that (1) has non-trivial solutions (u, t). This is a non-linear eigenvalue problem for ω which is solved with SS method[1]. The SS method uses path integrals with respect to ω in the complex plane, thus requiring the analytic continuation of BIE to complex ω. We can carry out this continuation using an integral representation of the Green's function in (2). We thus identify a continuous spectrum extending from $k_1 = n\pi,\ n \in \mathbb{N}$ and we can take the paths of integrations for SS method so that they do not touch the continuous spectrum. See Misawa et al.[2] for further details.

Unfortunately, this method may suffer from fictitious resonance frequencies when we consider leaky modes. In fact, we can show that the fictitious eigenvalues of (1) are leaky eigenfrequencies of a certain transmission problem in the free space $\mathbb{R}^2$ with the wavenumbers of the interior and exterior interchanged.

A remedy for this problem is simply to use the incoming fundamental solution $-(i/4)H_0^{(2)}(k_2|\boldsymbol{x} - \boldsymbol{y}|)$ for G_2 in (1) instead of the outgoing fundamental solution in (2). In fact, we can show that this remedy moves the fictitious eigenvalues to the upper complex plane while keeping true resonance frequencies unchanged. We can thus distinguish fictitious eigenvalues from true resonance frequencies since true ones have non-positive imaginary parts.

NUMERICAL EXAMPLE

We consider 2 circular inclusions in the waveguide, each having a radius of 0.4 and whose centers are $(0, 0),\ (0, -2)$, respectively. We set $\rho_1 = 1$, $\rho_2 = 0.34$, $\mu_1 = 1$ and $\mu_2 = 0.16$ (we assume quartz inclusions within an iron waveguide). We solved the non-linear eigenvalue problem with an FMM accelerated BIEM and SS method and plotted obtained eigenvalues with symmetric eigenmodes in the upper part of Fig.1. We see that the fictitious eigenvalue can be distinguished clearly from the true ones if we use incoming fundamental solution for G_2. We can thus check the effectiveness of our method. The lower part of Fig.1 shows the energy transmittance in response to a symmetric incident wave $e^{ik_1x_2}$ from the negative x_2 side. We can find peaks or dips in the transmittance curve at locations corresponding to eigenvalues with non-positive imaginary parts. We also see that the smaller the imaginary parts of the eigenvalues the sharper the corresponding changes of the transmittance. We thus see that all the true eigenvalues in Fig.1 actually have relevance to the resonance phenomena.

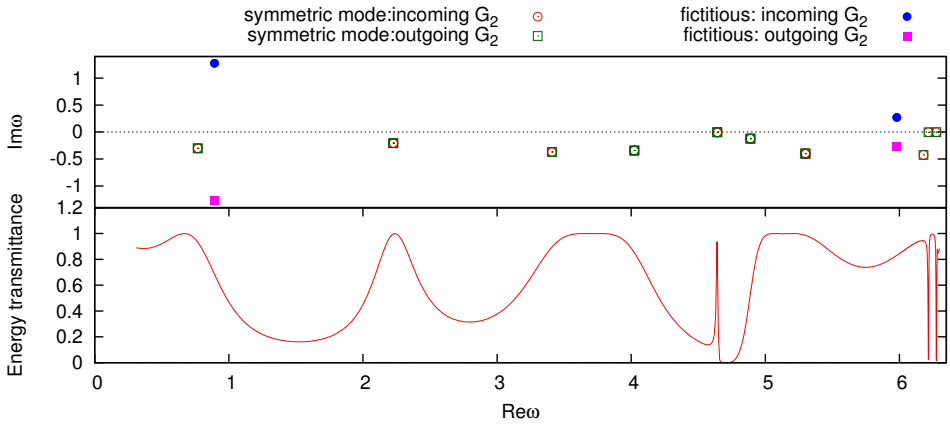

Figure 1: Eigenvalues with symmetric modes (upper) and energy transmittance for incident $e^{ik_1x_2}$ (lower). Solid symbols stand for fictitious resonance frequencies.

Acknowledgement This work has been supported by JSPS KAKENHI Grant Number 14J03491.

References

[1] J. Asakura, T. Sakurai, H. Tadano, T. Ikegami and K. Kimura: A numerical method for nonlinear eigenvalue problems using contour integrals, JSIAM Letters, Vol. 1, No. 0, pp. 52–55, 2009.

[2] R. Misawa, K. Niino and N. Nishimura: An FMM for waveguide problems of 2-D Helmholtz' equation and its application to eigenvalue problems, http://dx.doi.org/10.1016/j.wavemoti.2015.12.006, Wave Motion, 2016. (accepted)

NONLINEAR VIBRATION AND SOUND RADIATION FROM SKIN/CORE DEBONDED SANDWICH PLATES

Yegao Qu[1,2a)], Hongguang Li[1], Fucai Li[1], Guang Meng[1]
[1]*State Key Laboratory of Mechanical System and Vibration, Shanghai Jiao Tong University, Shanghai, China*
[2]*Department of Biomedical Engineering and Mechanics, Virginia Polytechnic Institute and State University, Blacksburg, Virginia, USA*

Summary The nonlinear structural and acoustic responses of debonded sandwich plates are analysed by using a time-domain finite element/boundary element method. The nonlinear contact/impact constraints on the interfaces of debonded parts are taken into account by the augmented Lagrange method. The time-domain Burton-Miller integral equation is employed to evaluate the radiated sound from debonded plates. Effect of interface contact/impact on the vibro-acoustic responses of debonded plates under impulsive and harmonic loads are examined.

INTRODUCTION

Sandwich plates with thin, stiff face-sheets and a lightweight, compliant core are commonly used in aerospace and marine industries. One of the most common damages of sandwich plates is a partial separation between the face-sheet and the core along their interface. The presence of interface debonding in a sandwich plate may reduce the overall plate stiffness and strength, and as a consequence may alternate the vibro-acoustic behaviour of the plate.

The dynamic behaviour of a debonded sandwich plate is intrinsically nonlinear due to the local contact/impact between the interfaces of the debonded parts. Attempts have been made by many researchers to study the nonlinear vibration of delaminated composite laminated plates and sandwich plates; see Marjanović et al. [1], Chandrashekhar and Ganguli [2], and Burlayenko and Sadowski [3]. The nonlinear vibration of debonded sandwich plates with complex debonded interfaces were mostly analysed by the finite element method. The literature related to the acoustic problem of debonded sandwich plates is rather limited, though considerable attention has been paid to analysis of acoustic radiation from intact plates. The objectives of this study are twofold: one is to develop a time-domain nonlinear finite element/boundary element model for the vibro-acoustic analysis of debonded sandwich plates; the other is to explore the effect of nonlinear contact/impact on the vibration and acoustic responses of debonded plates under impulsive and harmonic loads.

THEORY AND FORMULATION

The structural model of a debonded sandwich plate is formulated by using the finite element method. The principle of virtual work is used to develop the finite element model of the plate, given as

$$\int_\Omega \delta \boldsymbol{u}\cdot\rho\ddot{\boldsymbol{u}}d\Omega+\int_\Omega \delta \boldsymbol{u}\cdot c\dot{\boldsymbol{u}}d\Omega+\int_\Omega \delta\boldsymbol{\varepsilon}:\boldsymbol{\sigma}d\Omega-\int_{\Gamma_t}\delta\boldsymbol{u}\cdot\bar{\boldsymbol{t}}dS-\delta W_c=0 \tag{1}$$

where $\boldsymbol{u}$, $\dot{\boldsymbol{u}}$ and $\ddot{\boldsymbol{u}}$ are the displacement, velocity and acceleration, respectively. ρ is the mass density, and c is a viscous damping coefficient. $\boldsymbol{\sigma}$ and $\boldsymbol{\varepsilon}$ are the Cauchy stress tensor and the infinitesimal strain tensor respectively, which are related by a fourth-order stiffness tensor $\boldsymbol{C}$ as: $\boldsymbol{\sigma}=\boldsymbol{C}\boldsymbol{\varepsilon}$. The mass density ρ and the elements of the stiffness matrix $\boldsymbol{C}$ may take different values for different material layers. $\bar{\boldsymbol{t}}$ is the surface traction. δW_c is the virtual work related to contact/impact between debonded regions, given as: $W_c=\int_{\Gamma_c}(\lambda_n g_n+\kappa_n g_n^2/2)dS$, where λ_n is the field of Lagrange multipliers, g_n is the normal gap function and κ_n is the penalty parameter. Eight-noded solid elements with three degrees of freedom at each node are employed to discretize the sandwich plates, and the finite element equations of motion for debonded plates are given as:

$$\boldsymbol{M}\ddot{\boldsymbol{q}}(t)+\boldsymbol{C}\dot{\boldsymbol{q}}(t)+\boldsymbol{K}\boldsymbol{q}(t)=\boldsymbol{F}_{ext}-\boldsymbol{F}_{cont} \tag{2}$$

where $\boldsymbol{q}$, $\dot{\boldsymbol{q}}$ and $\ddot{\boldsymbol{q}}$ are the displacement, velocity and acceleration vectors, respectively. $\boldsymbol{M}$, $\boldsymbol{C}$ and $\boldsymbol{K}$ are the global mass, damping and stiffness matrices, respectively. $\boldsymbol{F}_{ext}$ and $\boldsymbol{F}_{cont}$ are the global vectors of external and contact forces.

The time-domain Burton–Miller integral equation is adopted to evaluate the acoustic field of sandwich plates, which is obtained by taking a linear combination of the time and normal derivatives of the Kirchhoff integral equation, written by [4]:

$$(1-\alpha)\left\{D(\dot{\varphi}(\boldsymbol{x},t))-S\left(\frac{\partial\dot{\varphi}}{\partial n_x}(\boldsymbol{x},t)\right)-\frac{\dot{\varphi}(\boldsymbol{x},t)}{2}\right\}+\alpha c_0\left\{\frac{\partial}{\partial n_x}D(\varphi(\boldsymbol{x},t))-\frac{\partial}{\partial n_x}S\left(\frac{\partial\dot{\varphi}}{\partial n_x}(\boldsymbol{x},t)\right)-\frac{1}{2}\frac{\partial\varphi(\boldsymbol{x},t)}{\partial n_x}\right\}=0 \tag{3}$$

where φ is the velocity potential of the acoustic field. α is a coupling parameter, $\alpha\in(0,1)$. The detail expressions of $D(\dot{\varphi})$ and $S(\partial\dot{\varphi}/\partial n_x)$ are given in Ref. [4]. Piecewise constant flat elements are used to discretized the surface of the plate, and the velocity and acceleration are evaluated at the centre of the external surface of each structural element. The sound field are calculated by using the following equation: $\varphi(\boldsymbol{x},t)=D(\varphi)-S(\partial\varphi/\partial n_x)$. The sound pressure is related to the velocity potential as: $p=-\rho_f\dot{\varphi}$, where ρ_f is density of the fluid.

a) Corresponding author. Email: quyegao@vt.edu.

RESULTS AND DISCUSSION

A cantilever rectangular 0°/90°/0°/core//0°/90°/0° plate ('//'indicates the location of debonded interface) subjected to a rectangular impulsive pressure load (see Fig.1; $f = 500\text{Pa}$, for $t \le 0.02\text{s}$; $f = 0$, for $t > 0.02\text{s}$) is examined. The material properties of the face layers are: $E_1 = 140\,\text{GPa}, E_2 = E_3 = 10\,\text{GPa}, G_{12} = G_{13} = 4.6\,\text{GPa}, G_{23} = 3.8\,\text{GPa}, \mu_{12} = \mu_{23} = \mu_{13} = 0.3$, $\rho = 1650\,\text{kg/m}^3$, and the thickness of these layers are the same, given as: $h_f = h_c / 6$. The material and geometrical data of the core are: $E_c = 0.05\,\text{GPa}, \mu_c = 0.1905, \rho = 52\,\text{kg/m}^3, \; h_c = 0.008\text{m}$. Figure 1 shows the comparison of the vibration and acoustic responses of the debonded and intact plates. The vibration responses are evaluated at the centre of the top surface of the plates and the radiated sound is measured at ($x = 0.15\text{m}$, $y = 0\,\text{m}$, $z = 2\text{m}$). The density and speed of sound of the fluid (air) are 1.23kg/m^3 and 340m/s, respectively. The results show that the presence of the interface debonding increases the amplitudes of vibration and acoustic responses of the plate. The frequency signal of the radiated sound from the debonded plate is characterized by wider peaks in comparison with those of the intact plate.

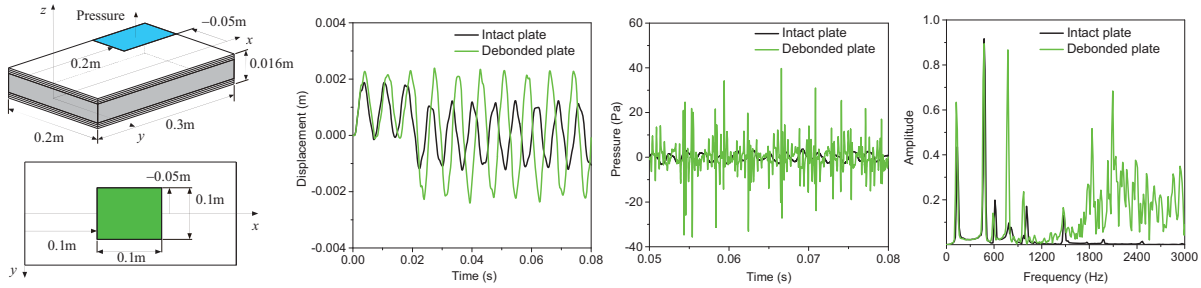

Fig.1 Comparison of vibration and acoustic responses of intact and debonded sandwich plates under rectangular impulsive load: (a) plate model; (b) transversal displacement; (c) radiated sound pressure; (b) FFT of sound pressure

Figure 2 shows the comparison of the vibration and acoustic responses of the intact and debonded plates under a harmonic force, which is applied at the centre of the top surface of the plate, given as: $f = 100[\sin(2\pi f_1 t) + \sin(2\pi f_2 t)]$, $f_1 = 1000\text{Hz}$ and $f_2 = 1700\text{Hz}$. The vibration and acoustic responses are evaluated at the same points as the previous case.

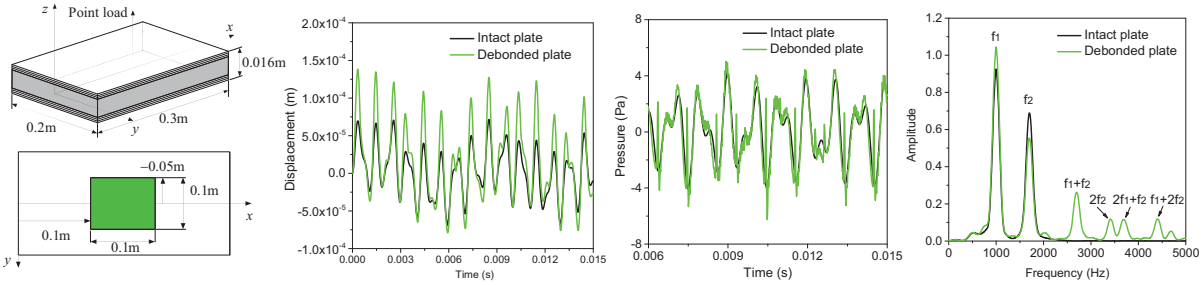

Fig.2 Comparison of vibration and acoustic responses of intact and debonded sandwich plates under a harmonic load: (a) displacement; (b) FFT of displacement; (c) radiated sound pressure; (b) FFT of sound pressure

As shown in Fig.2, the debonded sandwich plate exhibits complex motions, which not only include the harmonic motions of the driving frequencies, but also include the quasi-harmonic and super-harmonic motions. The latter two types of motions are due to the intermittent contact between the detached interfaces.

CONCLUSIONS

A time-domain nonlinear finite element/boundary element model is developed for vibro-acoustic analysis of debonded sandwich plates. The existence of debonded interface increases the amplitudes of vibration and acoustic responses of the plate. The spectral analysis for the time signals of the structural and acoustic responses of the intact and debonded plates reveal that their frequency contents differ considerably.

References

[1] Marjanović M., Vuksanović D., Meschke, G.: Geometrically nonlinear transient analysis of delaminated composite and sandwich plates using a layerwise displacement model with contact conditions. Compos Struct **122**: 67–81, 2015.

[2] Chandrashekhar M., Ganguli R.:Large deformation dynamic finite element analysis of delaminated composite plates using contact-impact conditions. Comput Struct **144**:92–102, 2014.

[3] Burlayenko V.N., Sadowski T.: Finite element nonlinear dynamic analysis of sandwich plates with partially detached face sheet and core. Finite Elem Anal Des **62**: 49-64, 2012.

[4] Chappell D.J., Harris P.J., Henwood D., Chakrabarti R.: A stable boundary element method for modeling transient acoustic radiation. J. Acoust. Soc. Am. **120**: 74-80, 2006.

ATMOSPHERIC AND COSMIC INFRASOUND DETECTION TECHNIQUES.

Yasna Schifferli[1]
[1] *Department of Electrical Engineering, University of Santiago of Chile, Santiago, Chile.*

Abstract. By using the current infrasonic techniques and technologies, it is possible to effectively and efficiently detect signals generated by meteors, bolides and other sources. The geolocalization of the explosion source is the result of the intersection of infrasonic signals generated by the bolide obtained in more than one infrasonic station. It is also possible to relate the periods of such signals with the energy source of the fireball. Auroras are other phenomena that are detected by infrasonic arrays. The recently discovered infrasonic waves are those generated in the depths of sidereal space and they are the lowest-frequency sounds ever found in the universe. It has been developed an early-universe sound simulation software using the data obtained by the scientists of the Wilkinson Microwave Anisotropy Probe, WMAP. Moreover, the Laser Interferometer Space Antenna, LISA, space mission, may be able to detect very low frequency gravitational acoustic waves produced in the space.

THE INTERNATIONAL MONITORING SYSTEM (IMS) INFRASOUND NETWORK.

The work at IMS in order to ensure compliance with the Comprehensive Nuclear-Test-Ban Treaty (CTBT) comprises 321 seismic, infrasonic, hydroacoustic and radionuclide monitoring stations, distributed as uniformly as possible on the Earth's surface. Most of IMS infrasonic stations have been constructed with arrays of 7 or 8 units and all the stations have been installed with arrays of tubes in order to guarantee an effective noise reduction as it is shown on Figure 1.

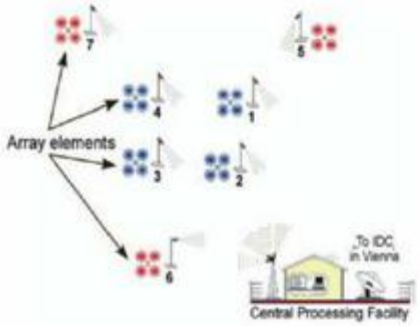

Figure 1.

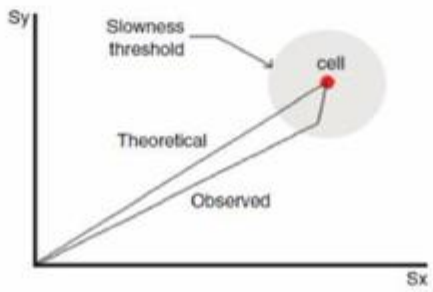

Figure 2.

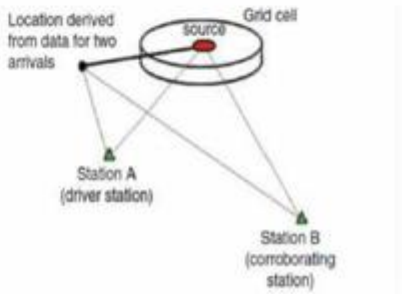

Figure 3.

Detection methods.

The CTBTO Preparatory Commission International Data Centre, IDC, located in Vienna, receives and processes in near-real time the data from the seismic, hydroacoustic, infrasonic and radionuclide stations. Once received the data of time-series at the IDC from all these stations, the data are stored in the IDC database, organized in time blocks and automatically processed at the station processing level, where the system attempts to detect signals and extracts their characteristics as back azimuth, horizontal trace velocity, frequency content, amplitude, and duration at individual stations. The infrasound data are processed using the Progressive Multichannel Correlation, PMCC, and mean cross-correlation maximum, MCCM, algorithms. Then, the network processing stage associates the signal detections at individual IMS stations with events and provides localization and a magnitude for them. At this stage, all relevant infrasonic detections are combined with detections from seismic and hydroacoustic technologies. The localization algorithm utilized at IDC is an iterative non-linear minimum square regression that includes the azimuth and slowness observations. The association of arrivals is done using an event hypothetic seeds search grid. The arrival detected at the closest station to the grid cell calls a driver that provides the observed slowness, corresponding to the predicted value ± one standard deviation (Figure 2). The driver is used to predict the time at the other IMS stations. The stations that are consistent with the driver are added to the seed event (Figure 3). In the current configuration, automatic seed events are created with arrivals detected by stations that use the same technology. For each seed event, the association with other technologies is done through the prediction of the phase characteristics at the other stations; the detections that meet the expected time, azimuth and slowness criteria are added to the event and may contribute to the localization solution. The resulting candidate events of the automatic association process are analyzed and validated by an acceptance test, based in the weighted count of defining phases: all time, azimuth and slowness weightings for each observation are added at the associated stations. The events with a minimum total weighting of 3.55 are stored in the automatic bulletins called Standard Event Lists (SELs). Given these criteria, infrasonic arrivals observed in two arrays are sufficient to constitute an automatic event.

Yasna Schifferli. Email: **yasna.schifferli@usach.cl**

INFRASOUND WAVES FROM A SUPERMASSIVE BLACK HOLE.

On September 9th, 2003, acoustic waves have been found, for the first time, coming from a supermassive black hole, which is located in the Perseus Galaxy Cluster, located at 250 million light-years from the Earth (Figure 4). This event has been registered by the NASA's Chandra X-ray Observatory, a telescope in orbit. These waves correspond to acoustic waves that travelled hundreds of thousands light-years from the black hole located at the center of the cluster. For many years, astronomers have been wondering why most of the gas inside the galaxy clusters is hot. It is believed that the reason is the acoustic waves that propagate through the gases are finally absorbed, transforming their energy into heat. This may regulate the formation rate of new stars. In consequence, these waves may have implications in galaxies and galaxy clusters evolution. Thus, through the tremendous quantity of energy transported by these acoustic waves, may be solved an astrophysics issue that has persisted for a long time: the understanding of galaxy cluster growth.

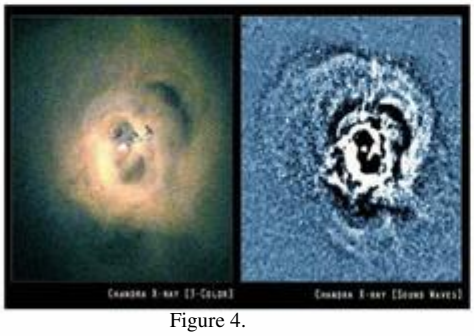

Figure 4.

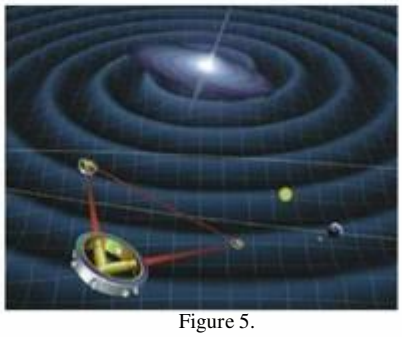

Figure 5.

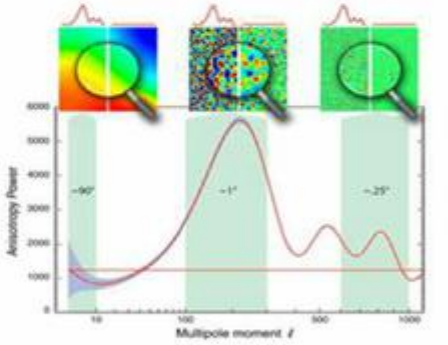

Figure 6.

THE LASER INTERFEROMETER SPACE ANTENNA, LISA.

LISA is a space mission that would be able to detect some gravitational waves as a huge astronomical microphone. LISA will place three spaceships in orbit around the Sun that will travel in a triangular configuration (Figure 5). When a gravitational wave approaches, the ripples generated in space will slightly push the spaceship. However, the ultrasensitive laser beams that interconnect the three spaceships will measure this small movement. LISA may facilitate the understanding of Universe evolution.

THE WMAP MISSION.

The WMAP mission launched its spaceship during summer 2001 and finished the registration of scientific data the 19th August, 2010. WMAP reveals the early universe conditions by measuring the small temperature variations of cosmic microwave background (CMB) radiation, a fossil record of the acoustic waves present in space during the first 380000 years of the universe. The scientists of WMAP mission obtained the curve shown on Figure 6, where a "meseta" is shown at large angular (or longitude) scales, and then, a series of coherent peaks at scales progressively smaller. These characteristic are generated by different physical process that release different quantities of energy (temperature) at different angular scales.

CONCLUSIONS.

The efficient and effective techniques and methods used by the IMS network to detect infrasonic signals generated by auroras, meteors, bolides and other sources in order to localize events and characterize their sources were presented on this paper. The detection of large bolides in a regular basis is possible through the 60 IMS infrasonic array stations composed by sensors globally distributed on the Earth's surface. Finally, it is worth to highlight the importance of cosmic infrasound detections for the understanding of the past, present and future of the universe.

References.

[1] HEASARC and the Astrophysics Science Division at NASA/GSFC, Build a Universe with the CMB Power Spectrum Analyzer, 2011.
[2] LE PICHON, A.; BLANC, E.; HAUCHECORNE, A. *Infrasound Monitoring for Atmospheric Studies*, Dordrecht Heidelberg, London, New York, USA: Springer Science+Business Media B.V., cop. 2010.
[3] NASA's Goddard Space Flight Center, *Interpreting the 'Song' Of a Distant Black Hole*, 2003.
[4] NASA SCIENCE, National Aeronautics and Space Administration, BLACK HOLE SOUND WAVES, 2003.
[5] National Aeronautics and Space Administration, NASA, Wilkinson Microwave Anisotropy Probe, 2011.
[6] The Space Place, *LISA mission gives humans a sixth sense*, USA, 2011.

ASYMPTOTIC THEORIES OF NONLINEAR THERMOACOUSTIC WAVES IN A GAS-FILLED CHANNEL

Nobumasa Sugimoto

Department of Pure and Applied Physics, Kansai University, Suita, Osaka, Japan

Summary This paper introduces two asymptotic theories for nonlinear thermoacoustic waves in a gas-filled channel subject to temperature gradient. On the basis of a narrow-tube approximation, the theories exploit, as an asymptotic parameter, the ratio of a typical thickness of thermoviscous diffusion layer to a channel width. If the ratio is large enough, thermoviscous effects are confined in a boundary layer so that they affect lossless propagation in a core outside of the boundary layer through a velocity component normal to the channel wall at the outer edge of the boundary layer. If the ratio is small enough, propagation is described by a nonlinear diffusion-wave (advection) equation. Even for an intermediate value of the ratio, it is expected that either asymptotic theory will be able to describe propagation of nonlinear thermoacoustic waves.

BACKGROUND OF THE PROBLEM

Thermoacoustic heat engines have attracted much attention from a viewpoint of energy and environmental problems. They exploit thermoacoustic phenomena, in which a gas in contact with a solid wall subject to temperature gradient becomes unstable to oscillate spontaneously, if a gas-filled system has a resonance mode of oscillations. The oscillations that ensue are nonlinear ones and the pressure level of oscillations attains the order of 10% of a mean pressure. Then there appear various nonlinear phenomena such as harmonic generation, acoustic and thermoacoustic streaming, emergence of an acoustic shock wave, flow separation, vortex shedding and so on. These nonlinear effects act to deteriorate both power and efficiency of the heat engines.

The thermoacoustic heat engines are very simple in structure in comparison with any conventional engines, and essential parts of the engines lie in a stack or a regenerator subject to temperature gradient. The stack means a "stack" of thin plates of ceramics and consists of many narrow flow passages, while the regenerator is made of metal wires or pins, and consists of many, narrow, tortuous flow passages. In other words, a span length of the passage in the stack is wider than a thermoviscous diffusion layer, while narrower in the regenerator. To design the heat engines suitably to achieve high performance, it is important to understand how the nonlinear effects affect the acoustic field as well as flow and thermal fields. While CFD methods have recently been begun to be used [1-3], they do not provide us with physical insight into a behaviour of a gas in the stack or regenerator.

To deal theoretically with the behaviour of the gas therein, the author has developed nonlinear theories for thermoacoustic waves from a viewpoint of an asymptotic theory in terms of the ratio of a typical thickness of a thermoviscous diffusion layer to the span length. Because the asymptotic theories are originally valid only in the cases of extremely large or small values of the ratio, it may be thought that they would fail for an intermediate value of the ratio. However, it is expected that a whole range of the ratio would rather be covered substantially by either one of the theories.

OUTLINE OF THE THEORY

In developing the theory, at the outset, a narrow-tube approximation is assumed in the sense that a typical axial length L is much longer than a channel width H, i.e., $H \quad L \ll 1$, and that terms of order $H \quad L^{2}$ are neglected. It then follows that the gas temperature T_e in a quiescent state may be set equal to the wall temperature T_w and that the pressure of gas in motion may be regarded as being uniform in a spanwise direction. Assuming the channel is long enough axially to ignore end effects, there are three parameters associated with propagation of thermoacoustic waves. Letting a typical angular frequency of a disturbance to be ω, one is the ratio of a typical thickness of viscous diffusion layer $\sqrt{\nu \quad \omega}$ to the channel width, ν being a typical kinematic viscosity, another the ratio of an adiabatic sound speed a to a typical propagation speed ωL, and the other the ratio of a typical magnitude of pressure disturbance Δp to a uniform pressure p_0, defined, respectively, by

$$\delta = \frac{\sqrt{\nu \quad \omega}}{H}, \quad \chi = \frac{a}{\omega L} \quad \text{and} \quad \varepsilon = \frac{\Delta p}{p_0} \ll 1. \tag{1}$$

Although δ may be defined based on a typical thermal diffusion layer $\sqrt{\kappa \quad \omega}$ κ being a typical thermal diffusivity, it is represented by the viscous one because the Prandtl number $= \nu \quad \kappa$ is comparable with unity for usual gases like air, e.g. 0.7. The second parameter χ takes a value of order unity but it tends to take a large value when the channel width becomes very narrow. The third parameter measures the order of nonlinearity, which is assumed to be much smaller than unity, e.g. 0.1 to 0.01 in practice.

On the other hand, the solid wall is assumed to have a large heat capacity so that no temperature variations take place. Then the boundary conditions on the wall require no slip and no temperature fluctuation. The latter assumption is not always valid especially when the wall is thin. Then a heat conduction in the solid wall must be solved simultaneously by imposing continuity of heat fluxes, and a study on this influence will be a next target. Exploiting the narrow-tube approximation and using the parameters in (1), fluid dynamical equations for the ideal gas are approximated asymptotically and reduced to simpler equations.

[a] Corresponding author. Email: n_sugimo@kansai-u.ac.jp; sugimoto@me.es.osaka-u.ac.jp

Asymptotic theory for the case of a thin diffusion layer

When δ takes a small value, the thermoviscous diffusion layer may be treated as the boundary layer. This is depicted in Fig. 1 as domains between broken curves and the solid walls. In the core outside of the boundary layer, lossless, nonlinear plane wave propagation may be assumed. The solid curve with label (*a*) shows the profile of the axial velocity component, which varies rapidly across the boundary layer but may be treated as being uniform in the core. Averaging the fluid dynamical equations over the core and assuming the linear theory for the boundary layer, the thermoviscous effect appears on the right-hand side of the equation of continuity through a velocity v_b at the edge of the boundary layer directed normal to the wall into the core as [4,5]

$$\frac{\partial \rho}{\partial t} + \frac{\partial}{\partial x}(\rho u') = \frac{\rho v_b}{H}, \tag{2}$$

with t and x being, respectively, the time and the axial coordinate along the channel, where ρ is a mean density and v_b is given in terms of the axial velocity component u' in the core as

$$v_b = \sqrt{\nu_e}\left[C \frac{\partial^{1/2}}{\partial t^{-1/2}}\left(\frac{\partial u'}{\partial x}\right) + \frac{C_T}{T_e}\frac{\mathrm{d}T_e}{x}\frac{\partial^{-1/2}u'}{\partial t^{-1/2}}\right], \tag{3}$$

with the derivative of minus half order define by $\dfrac{\partial^{-1/2}u'}{\partial t^{-1/2}} = \dfrac{1}{\sqrt{\pi}}\displaystyle\int_{-\infty}^{t} \frac{'\ \tau}{\sqrt{t-\tau}}\ \tau$ (4)

where ν_e denotes a local kinematic viscosity at the temperature T_e x C C_T being constants. The one-dimensional equation of motion, i.e. Euler equation, and that of energy representing the adiabatic process for each gas particle are used. It is shown that this system of equations can describe a transient behaviour of instability of a helium gas column subject to temperature gradient and emergence of self-excited Taconis oscillations [4,5]. This theory is expected to be applicable for a gas in the stack.

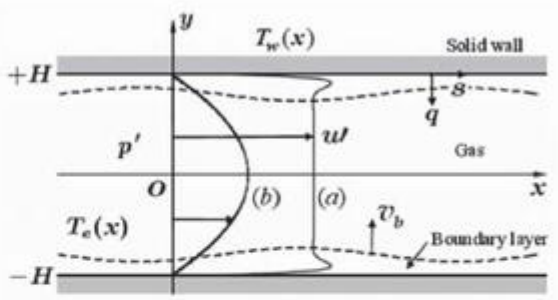

Figure 1: Illustration of a flow field in a channel of width 2*H*, where the excess pressure p' is uniform in a spanwise direction, and the solid curves (a) and (b) represent the profiles of the axial velocity component over the span, respectively, for the case of a thin diffusion layer and that of a thick diffusion layer, v_b, s and q being, respectively, the velocity at the edge of the boundary layer directed normal to the wall into the core, the shear stress acting on the gas and the heat flux flown into it.

Asymptotic theory for the case of a thick diffusion layer

When δ takes a large value, the thermoviscous diffusion layer fills out the channel spanwise. As shown in Fig. 1 by the solid curve with label (*b*), the profile of the axial velocity is simply the one of Poiseuille flow in spite of compressibility of the gas to the lowest order where no temperature fluctuation occurs in the gas. Then the acoustic waves can no longer be propagated but diffused. When the temperature gradient is present, however, it is shown that the wave is not only diffused but also propagated (or advected) in the direction of the positive temperature gradient. For $\delta^{-2} \sim \chi^{-2} \sim \ll 1$, the behaviour of the excess pressure p' over the pressure p_0 is governed by a following nonlinear diffusion-wave (advection) equation given by [6]

$$\frac{\partial p'}{\partial t} - \frac{\partial}{\partial}\left({}_e \frac{\partial p'}{\partial x}\right) + \frac{\alpha_e}{T_e}\frac{\mathrm{d}T_e}{x}\frac{\partial p'}{\partial x} + \left[\frac{6}{5}\gamma - \gamma - \right]\frac{\alpha_e}{a_e^2}\frac{\partial^2 p'}{\partial^2} - \frac{2}{5} + \frac{\alpha_e H^2}{\nu_e T_e}\frac{T_e}{\partial}\frac{\partial^2 p'}{\partial}\frac{}{\partial} - \frac{p'}{0}\frac{\partial}{\partial t}\frac{'}{} - \frac{\alpha_e}{p_0}\left(\frac{\partial p'}{\partial x}\right)^2 = 0, \tag{5}$$

with the diffusivity α_e given by $p_0 H^2$ μ_e μ_e, a_e and γ being, respectively, a shear viscosity, an adiabatic sound speed and the ratio of specific heats. The first three terms in (5) constitute the lowest equation, while the fourth and fifth terms reflect finite effects of the channel width. The last two nonlinear terms stem from the advection term of the density in the equation of continuity. Although the channel is considered here for the sake of geometrical simplicity, the lowest diffusion-wave (advection) equation would be valid even for a case of a tortuous flow passage, provided the diffusivity α_e would be available by any means.

CONCLUSION

The two asymptotic theories have been presented for the extreme cases of the thickness of the thermoviscous diffusion layer relative to the channel width. While their application to derive linear marginal conditions of instability in thermoacoustic devices is done [7], both theories are expected to describe propagation of nonlinear thermoacoustic waves over a whole domain in the heat engines.

References

[1] Lycklama à Nijeholt, J. A., Tijani, M. E. H., Spoelstra, S. *J. Acoust. Soc. Am.*, **118**:2265-2270, 2005.
[2] Tijani, M. E. H., Spoelstra, S. *J. Appl. Phys*., **110**:093519 1-6, 2011.
[3] Scalo, C., Lele, S. K., Hesselink, L. *J. Fluid Mech*., **766**:368-404, 2015.
[4] Sugimoto, N., Shimizu, D. *Phys. Fluids*, **20**:104102 1-11, 2008.
[5] Shimizu, D., Sugimoto, N. *J. Appl. Phys*., **107**:034910 1-11, 2010.
[6] Sugimoto, N., submitted to *J. Fluid Mech.*
[7] Hyodo, H., Sugimoto, N. *J. Fluid Mech*., **741**:585-618, 2014.

ENHA CED AC USTO-OPTICAL C UPLING F SURF CE WAV S IN AN IR-SLOT PHOXON C CRYST L CAVI Y

Yue-She g Wang [1a)], Tian-Xue M [1] & Chuanzeng Zhang [2]
[1]Institute o Engineerin Mechanics, Beijing Jiao ong University, Beijing 100044, Chin
[2]Depart ent of Civil Engineering, University of Siegen, Sie en, D-5706 , Germany

Summary In his paper, a two-dimensional air-slot phoxon c crystal cavity is designed to confine the a oustic and optical surface wa es simultaneously. The enhanced acousto-optical coupling of the acoustic and o tical surface c vity modes is discussed by including the moving interface and hotoelastic eff cts. The frequency modulations of the phot nic cavity modes induced by the phononic cavity modes re calculated. The results show the dependence o the acousto-op ical coupling st ength on the width of the air- s ot.

I TRODUCT ON

A phoxo ic crystal (PxC) is a kind of periodic co posite material which behaves simultaneously like a hotonic crys al (PtC) and p ononic crystal (PNC), (f r instance, xhibiting si ultaneous p otonic band aps (PTBGs and phono ic bandgaps (P BGs)), and t erefore can simultaneousl manipulate light and sound [1]. It has p tential applications in desi n of dual-funct onal (optical and acoustic) devices such as cavities, w veguides, se sors and mo e converters, etc. Particula ly, it can be used as a promising platform o enhance acousto-optical (AO) or optomechanical (M) couplings in micro- a d nano-structures because it an confine p otons and phonons in the same region simultaneously.

Recently the present authors desi ned a two-dimensional (2D) PxC h tero-structur cavity whi h can confine simultaneous surface optical wave (SO) and surface acoustic wave (SAW), a d discussed he AO coupling between the acoustic and optical surface cavity m des [2]. In this paper, w will provid a way to enhance the O coupling y introducing an air-slot structure. It is known that air-slot structures can provide igh optical q ality factors and small mode volumes bec use of a large discontinui y of the elec ric field at high index-contrast (air/diel ctric) interfaces [3]; and the air/dielectric interface can sustain SA which is hi hly localized within a sm ll region ne r the interface. Therefore, in such a structure, the photon-phonon oupling may be strength ned. Here i the present paper, we ill discuss the dependence f the AO cou ling on the slot width.

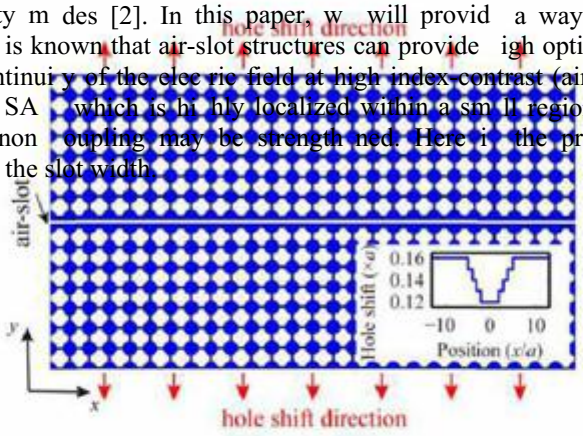

ig.1. Proposed air-slot phoxo ic crystal structure with a het ro-structure ca ity

AIR-SL T PHOXO IC CRYST L CAVITI S AND SURFACE WAVE MODES

The proposed air-slot xC cavity is formed by setting two identical surface mode caviti s [2] close t each other, as shown in Fig. 1. The struc ure is made f silicon with distributed holes. The hol s in each col mn are shift d slightly away from the slot, as indicated y arrows in ig. 1, to crea e a hetero-str cture cavity ased on the ode gap effect [4]. The in set in Fig. 1 plots the amount of the holes' hifting along the y-axis. T e in-plane mode is consid red for the acoustic waves in dielectric media (silicon), which cannot radiate into the air region (i.e. the pho onic cavity odes in the pper and lo er structures are independent). The transverse electric mode is consid red for the o tical waves. The analysis is performed y using the finite element method based on the software of COMSOL Multiphysi s. The perfe t matched la ers (PMLs) re applied at the boundaries of the computation domain for absorbing the radiating aves without reflection.

Computa ions show th t there are 4 phononic cavity modes, a ong which t o are of od symmetry with respect to *y*-axis and two are of even s mmetry. Th two even ca ity modes are symmetrically excited on upper and lower parts of t slot cavity, leading to an e en-even pho onic mode distribution, see Fig. 2a. The surface optic l modes are dependent on t width of the slot. In this ork we only consider the cavity modes hich fall in he mode gaps. Generally there are seve al optical cavit modes appe ring in the m de gaps. Those optical mo es whose ca ity modal distributions (e.g. the one sho n in Fig. 2b) near the slot region are hig ly overlapped with the acoustic cavity modal distri utions may enhance the O coupling and will be consi ered in this paper.

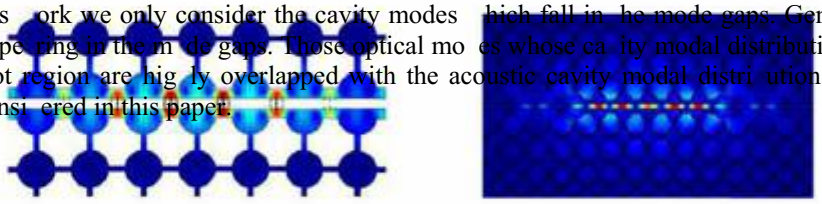

( ) (b)

Fig.2. Modal distributions of typical c vity modes for acoustic (a) and optical (b) su face waves

COUSTO-OPTICAL C UPLING A D NUMERICAL RESU TS

We examine the AO c upling strength from the modulation of the photonic resonant frequency during one period of t phononic cavity mode. Two mechanisms of the AO coupling, the oving interface and photo lastic effects, are consider d. The moving interface effect is owing t the motion f the air/diel ctric interfaces induced b the acoustic waves; and t photoelastic ffect is due t the variatio of the refractive index of he dielectric materials wit the elastic d formation. T frequency m dulations of various phot nic cavity m des induced by different hononic cavity modes are calculated. T results show that the movi g interface e fect dominat s the AO coupling while the photoelasti effect results in a very sm frequency shift. The movi g interface effect will be ignificantly enhanced whe the phononic and photonic cavity modes are confined in the same small region near the air sl t. It is also s own that the coupling strength is dependent on the slot width. The p esent analysi is relevant t design of P C slab cavities with strong AO interacti n which can e used as du l-functional devices.

ACK OWLEDGEMENTS

Support y the National Natural Science Foundation under grant number 11372031 is gratefully ack owledged. T second auth r is grateful to China Scholarship Cou cil (CSC) f r the financi l support of the research at the Chair of Structural M chanics, Uni ersity of Sie en, Germany.

References

[1] Pennec Y., Laude V., Papani olaou N., Djafar -Rouhani B., Ou ich M., El Jallal ., Beugnot J.C., scalante J.M., and Martínez A.: *N nophotonics* **3**: 4 3-440, 2014.

[2] Ma T.X., Zou K., Wang Y.S., Zhang Ch., and u X.X.: *Opt. Express* **22**: 28443-28 51, 2014.

[3] Almeida V.R., Xu Q., Barrio C.A., and Lipso M.: *Opt. Lett*. **29**: 1209-1212, 200 .

[4] Song B.S., oda S., Asano T., and Akahane Y.: *Nat. Mater*. 4, 2 7-210, 2005.

PASSIVE CONTROL OF FLOW AND NOISE AROUND A CIRCULAR CYLINDER COVERED WITH POROUS MATERIAL

Chen Xu, YijunMao[a)]
School of Energy and Power Engineering, Xi'an Jiaotong University, Xi'an, Shaanxi, China

Summary This paper presents a numerical study to investigate flow and noise around a cylinder surface covered by porous material. The large eddy simulation and acoustic analogy are employed to predict the cylinder flow and noise, respectively. Three-dimensional instantaneous flowfield inside the porous zone is simulated by using a volume-averaged method. The flow information on different permeable data surfaces is successively employed to predict the aerodynamic noise. The result obtained from unsteady flow simulation reveals that the porous material postpones the alternating vortex shedding from the cylinder, not only reducing the pressure drag but also suppressing the pressure fluctuation on the cylinder surface. The aeroacoustics prediction results confirm that the porous material significantly reduces the aerodynamic noise of the cylinder flow.

INTRODUCTION

Porous materials, such as open-cell metal foams, show an appealing application potential in control of flow and noise. Experimental study of Sueki et al.[1] has shown that the noise radiated from flow past a cylinder can be significantly reduced by covering the porous material. This paper conducts a numerical study to validate the flow and noise prediction methods related to porous material and aims to reveal the mechanism of noise control.

NUMERICAL SIMULAITON

The numerical case corresponds to an experiment conducted by Sueki et al. [1].The length and the diameter of the bare cylinder are l=600mm and d=25mm, respectively. In the present simulation, the cases of the bare cylinder and the cylinder covered with open-cell porous material, which correspond to the types of A and D in Ref [1], are computed. The surface of the bare cylinder is covered with the porous material with the uniform thickness of t=10mm, and the outside diameter of the cylinder is 45mm. The porosity of the porous material is 97% and the pores per inch are approximately 13, corresponding to the equivalent diameter of the pore 2mm. The uniform flow velocity at the inlet is 27.7m/s, it can be obtained that the flow Mach number is 0.08, the inflow Reynolds number is 8.3×10^4 based on the outside diameter of the porous cylinder and porous flow Reynolds number is 3.7×10^3 based on the pore diameter of the porous material.

At this flow condition, the flow outside as well as inside the porous material can be regarded as fully turbulent. The porous material is assumed to be homogenous and the permeability and porosity are uniform in each direction. The flow inside and outside the porous zone is computed using the continuum approach. The incompressible continuity and Navier-Stokes equations are employed to describe the flow outside the porous zone. For the flow inside the porous region, the Ergun's equation is employed to consider the viscous and inertial effects of the porous material, and the macroscopic flow inside the porous region is solved by using the volume-averaged method.

Aeroacoustics prediction is also carried out by using Formulation 1A of Farassat [2], where two different permeable cylindrical surfaces with different diameters (45mm and 65mm) are selected as the input data surfaces. The numerical results obtained from these two permeable surfaces include both the contributions from the loading source on the bare cylinder surface and the near-field quadrupole source inside the date surface.

NUMERICAL RESULTS

Figure 1 compares the time history of lift and drag coefficients between the bare cylinder and the porous cylinder. The result shows that the amplitude of the lift fluctuation for the porous cylinder is much smaller than that for the bare cylinder, and the averaged drag coefficient for the porous cylinder is also smaller than that for the bare cylinder. This feature implies that porous material is beneficial to reduce the noise and the flow drag as well.

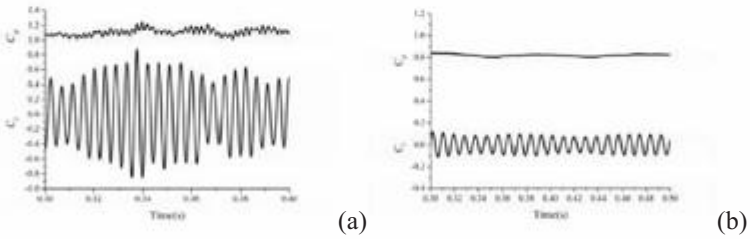

(a) (b)

Figure 1 Time history of lift and drag coefficients: (a) bare cylinder; (b) porous cylinder

a)Corresponding author. Email:maoyijun@mail.xjtu.edu.cn.

Figure 2 displays instantaneous contours of the velocity magnitude for the bare and porous cylinders. Alternating vortex shedding from the bare cylinder is observed, and this phenomenon causes a low-pressure region downstream the bare cylinder, as shown in Figure 3(a). However, the alternating vortex shedding is postponed by the porous cylinder and there is an obvious low-speed region downstream the porous cylinder (Figure 2(b)). The above flow feature causes that the pressure drag of the porous cylinder is much smaller than that of the bare cylinder, as shown in Figure 3(b).

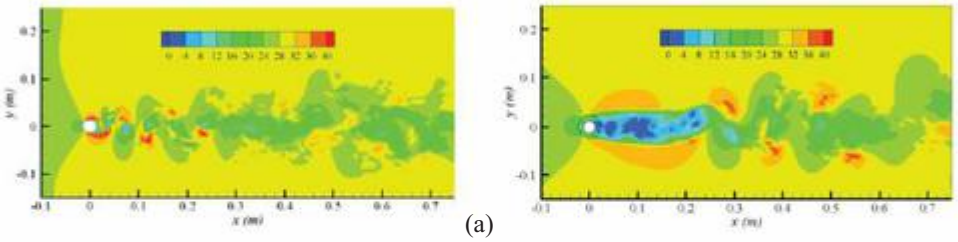

(a) (b)

Figure 2 Instantaneous contours of the velocity magnitude: (a) bare cylinder; (b) porous cylinder

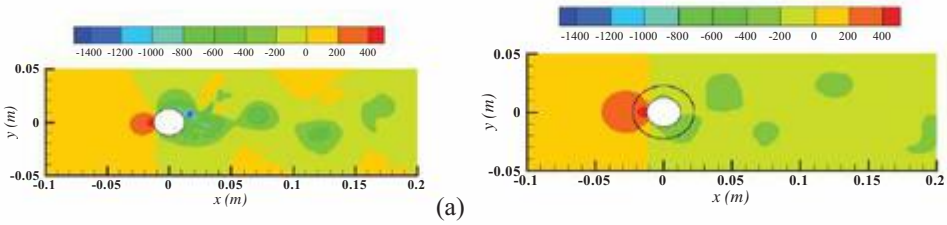

(a) (b)

Figure 3 Instantaneous contours of the static pressure:(a) bare cylinder; (b) porous cylinder

Figure 4 presents A-weighted sound pressure level spectra of the bare and porous cylinders. The numerical results obtained from different data surfaces are in reasonable agreement with the experimental data. All the results validate that the porous material significantly reduces the noise radiated from the cylinder.

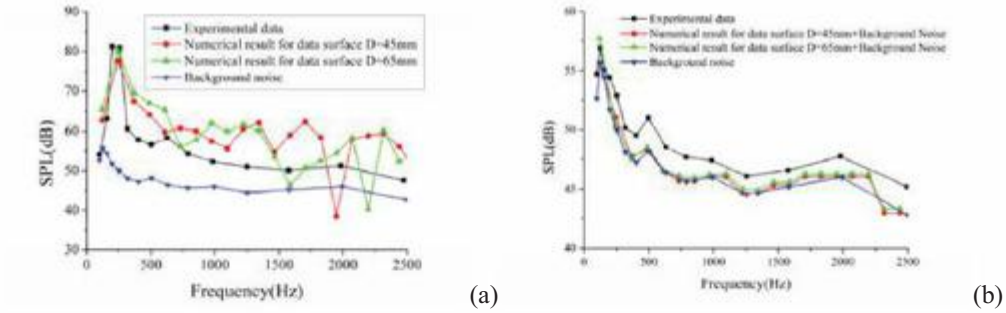

(a) (b)

Figure 4 A-weighted SPL spectra: (a) bare cylinder; (b) porous cylinder

CONCLUSIONS

A numerical study is carried out to analyze the effect of the porous material on the cylinder flow and noise. Result shows that porous material postpones the alternating vortex shedding from the cylinder surface. This phenomenon brings the following two benefits: (1) the lift fluctuation on the cylinder surface is suppressed and noise radiated from cylinder surface is reduced as well; (2) the flow drag is also diminished because the obvious low-pressure region downstream the cylinder disappears.

ACKNOWLEDGEMENTS

The research has been supported by the National Natural Science Foundation of China (No. 51476123 and No.51206127).

References

[1] Sueki, T., Takaishi, T., Ikeda, M. & Arai, N. Application of porous material to reduce aerodynamic sound from bluff bodies. *Fluid Dyn Res,* **42**, 015004, 2010.
[2] Farassat, F. Derivation of Formulations 1 and 1A of Farassat. NASA/TM 2007-214853, 2007.

FS02 - Exascale Computing

TS.FS02-1.01	Ghattas, Omar - Big data meets big models: Towards exascale Bayesian inverse problems (INVITED)	3094
TS.FS02-1.02	Alexeev, Dmitry - An HPC framework for Bayesian uncertainty quantification of flows across scales (INVITED)	3096
TS.FS02-1.03	Hori, Muneo - Earthquake Hazard and Disaster Simulation Using Urban Area Model of 10.7 10^9 Degree-Of-Freedom	3098
TS.FS02-1.04	Yoshimura, Shinobu - Full scale seismic response simulation of nuclear power plant subjected to strong earthquake	3100
TS.FS02-1.05	Konduri, Aditya - Implementation of exascale asynchronous solvers for PDEs	3102
TS.FS02-1.06	Kawai, Hiroshi - Subdomain local FE solver implementation using iterative solver in domain decomposition method	3104
TS.FS02-2.01	Idomura, Yasuhiro - Computational challenges towards exa-scale fusion plasma turbulence simulations (INVITED)	3106
TS.FS02-2.02	Chen, Jackie - Towards Exascale Simulation of Turbulent Combustion (INVITED)	3108
TS.FS02-2.03	Uzawa, Ken - Parallel performance of FrontFlow/Violet-Cartesian with wall-modelled LES capability	3109
TS.FS02-2.04	Adams, Darren - Petascale DNS using the fast Poisson solver PSH3D	3111
TS.FS02-2.05	Schumacher, Jörg - Supercomputations of low-Prandtl-number convection flows	3113
TS.FS02-2.06	Wu, Xiaohua - “Turbulent Spot” Deep Inside the Turbulent Boundary Layer with Exascale Simulation	3115
PO.FS02-1.01.337	Ostilla Monico, Rodolfo - AFiD: A multipurpose and versatile tool for turbulence simulations	3117
PO.FS02-1.02.338	Subramaniam, Akshay - Petascale simulations of shock-induced multi-material mixing	3119
PO.FS02-1.03.339	Trikuta Srinath, Ashwin - A novel strategy for compact finite difference evaluation on gpu-accelerated clusters	3121
PO.FS02-1.04.340	Yamada, Tomonori - Balancing domain decomposition method on additive Schwartz framework	3123

BIG DATA MEETS BIG MODELS: TOWARDS EXASCALE BAYESIAN INVERSE PROBLEMS

Omar Ghattas*[1], Tobin Isaac[2], Noémi Petra[3], and Georg Stadler[4]
[1]*Institute for Computational Engineering & Sciences and Departments of Geological Sciences and Mechanical Engineering, The University of Texas at Austin, Austin, Texas, U.S.A.*
[2]*Computation Institute, University of Chicago, Chicago, Illinois, U.S.A.*
[3]*School of Natural Sciences, University of California, Merced, Merced, California, U.S.A.*
[4]*Courant Institute for Mathematical Sciences, New York University, New York, New York, U.S.A.*

Summary Predictive models of complex systems often contain numerous uncertain parameters. Rapidly expanding volumes of observational data present opportunities to reduce these uncertainties via solution of inverse problems. Bayesian inference provides a systematic framework for inferring model parameters with associated uncertainties from (possibly noisy) data and any prior information. However, solution of the Bayesian inverse problem via conventional Markov chain Monte Carlo methods remains prohibitive for expensive models and high-dimensional parameters. Despite the large size of observational datasets, typically they provide only sparse information on model parameters. Based on this property we design MCMC methods that adapt to the structure of the posterior probability and exploit an effectively-reduced parameter dimension. We apply the methodology to an inverse problem for Antarctic ice sheet flow.

One of the greatest challenges in computational science and engineering today is how to combine complex data with large-scale models to create better predictions. This challenge cuts across every application area within CS&E, from the geosciences to materials to chemical systems to biological systems to astrophysics to engineered systems in aerospace, transportation, buildings, and biomedicine, and beyond. At the heart of this challenge is an inverse problem: we seek to infer unknown model inputs (parameters, source terms, initial or boundary conditions, model structure, etc.) from observations of model outputs. The critical need to quantify the uncertainty in the solution of such inverse problems has gained increasing recognition in recent years. This can be carried out in a systematic manner by casting the problem as one in Bayesian inference. Here, uncertain observations and uncertain models are combined with available prior knowledge to yield a probability density as the solution of the inverse problem, thereby providing a rational means of quantifying uncertainties in the model parameters. The resulting uncertainties in model parameter are then propagated forward through the model to yield predictions with associated uncertainty.

Unfortunately, solution of Bayesian inverse problems for systems governed by large-scale, complex computational models with large-scale, complex data has traditionally been intractable. However, a number of advances over the past decade have brought this goal much closer. First, improvements in scalable forward solvers for many classes of large-scale models have made feasible the repeated evaluation of model outputs for differing inputs. Second, the exponential growth in high performance computing capabilities has multiplied the effects of the advances in solvers. Third, the emergence of MCMC methods that exploit problem structure has radically improved the prospects of sampling probability densities for inverse problems governed by expensive models. And fourth, recent exponential expansions of observational capabilities have produced massive volumes of data from which inference of large computational models can be carried out.

To overcome the prohibitive nature of Bayesian methods for large-scale inverse problems, we exploit the fact that, despite the large size of observational data, they typically provide only sparse information on model parameters. This implicit dimension reduction is provided by low rank approximations of the Hessian of the data misfit functional, which is typically a compact operator due to ill-posedness of the inverse problem. The low rank approximation of the Hessian can be extracted efficiently in a matrix-free manner by a randomized SVD method, requiring a number of matrix-vector products that scales only with the rank of the Hessian, and not its overall size. Each Hessian-vector product amounts to one linearized forward and one adjoint solve. By exploiting the structure of the inverse problem as represented by the data misfit Hessian, we are able to substantially reduce the effective parameter dimension (often by three orders of magnitude) at a cost, measured in (linearized) forward/adjoint PDE solves, that is independent of both the parameter and data dimensions.

The specific problem we address here is the flow of ice from polar ice sheets such as Antarctica and Greenland, which is the primary contributor to projected sea level rise in the 21st century. The ice is modeled as a creeping, viscous, incompressible, non-Newtonian shear-thinning fluid. One of the main difficulties faced in modeling ice sheet flow is the uncertain spatially-varying Robin boundary condition that describes the resistance to sliding at the base of the ice. Satellite observations of the surface ice flow velocity, along with a model of ice as a creeping incompressible shear-thinning fluid, can be used to infer this uncertain basal boundary condition. We cast this ill-posed inverse problem in the framework of Bayesian inference, which allows us to infer not only the basal sliding parameters, but also the associated uncertainty. We demonstrate scalability with respect to state dimension, parameter dimension, data dimension, and number of processor cores. The largest forward problems solved have over two billion unknowns on up to 128K cores, and the largest Bayesian inverse problems solved have over one million uncertain parameters.

*Corresponding author. Email: omar@ices.utexas.edu

References

[1] K. Wang, T. Bui-Thanh, and O. Ghattas, A randomized maximum a posteriori method for posterior sampling of high dimensional nonlinear Bayesian inverse problems, submitted, 2016.

[2] H. Zhu, N. Petra, G. Stadler, T. Isaac, T.J.R. Hughes, and O. Ghattas, Inversion of geothermal heat flux in a thermomechanically coupled nonlinear Stokes ice sheet model, submitted, 2015.

[3] H. Zhu, S. Li, S. Fomel, G. Stadler, and O. Ghattas, A Bayesian approach to estimate uncertainty for full waveform inversion with a priori information from depth migration, submitted, 2015.

[4] A. Alexanderian, N. Petra, G. Stadler, and O. Ghattas, A fast and scalable method for A-optimal design of experiments for infinite-dimensional Bayesian nonlinear inverse problems, *SIAM Journal on Scientific Computing*, 2015, to appear.

[5] J. Rudi, A.C.I. Malossi, T. Isaac, G. Stadler, M. Gurnis, P.W.J. Staar, Y. Ineichen, C. Bekas, A. Curioni, O. Ghattas, An Extreme-Scale Implicit Solver for Complex PDEs: Highly Heterogeneous Flow in Earths Mantle, *Proceedings of IEEE/ACM SC15*, 2015.
http://dx.doi.org/10.1145/2807591.2807675

[6] T. Isaac, G. Stadler, and O. Ghattas, Solution of nonlinear Stokes equations discretized by high-order finite elements on nonconforming and anisotropic meshes, with application to ice sheet dynamics, *SIAM Journal on Scientific Computing*, 37(6):B804B833, 2015.
http://dx.doi.org/10.1137/140974407

[7] T. Isaac, C. Burstedde, L.C. Wilcox, and O. Ghattas, Recursive algorithms for distributed forests of octrees, *SIAM Journal on Scientific Computing*, 37(5):C497–C531, 2015.
http://arxiv.org/abs/1406.0089

[8] N. Petra, J. Martin, G. Stadler, and O. Ghattas, A computational framework for infinite-dimensional Bayesian inverse problems. Part II: Stochastic Newton MCMC with application to ice sheet flow inverse problems, *SIAM Journal on Scientific Computing*, 36(4):A1525–A1555, 2014.
http://dx.doi.org/10.1137/130934805

[9] A. Alexanderian, N. Petra, G. Stadler, O. Ghattas, A-optimal design of experiments for infinite-dimensional Bayesian linear inverse problems with regularized ℓ_0-sparsification, *SIAM Journal on Scientific Computing*, 36(5):A2122–A2148, 2014.
http://dx.doi.org/10.1137/130933381

[10] T. Isaac, N. Petra, G. Stadler, O. Ghattas, Scalable and efficient algorithms for the propagation of uncertainty from data through inference to prediction for large-scale problems, with application to flow of the Antarctic ice sheet, *Journal of Computational Physics*, 296(1):348–368, 2015.
http://dx.doi.org/10.1016/j.jcp.2015.04.047

[11] J. Worthen, G. Stadler, N. Petra, M. Gurnis, and O. Ghattas, Towards adjoint-based inversion for rheological parameters in nonlinear viscous mantle flow, *Physics of the Earth and Planetary Interiors*, 234:23–34, 2014.
http://dx.doi.org/10.1016/j.pepi.2014.06.006

[12] T. Bui-Thanh, O. Ghattas, J. Martin, and G. Stadler, A computational framework for infinite-dimensional Bayesian inverse problems. Part I: The linearized case, with applications to global seismic inversion. *SIAM Journal on Scientific Computing*, 35(6):A2494-A2523, 2013.
http://dx.doi.org/10.1137/12089586X

[13] N. Petra, H. Zhu, G. Stadler, T.J.R. Hughes, O. Ghattas, A scalable adjoint-based inexact Newton method for inversion of basal sliding and rheology parameters in a nonlinear Stokes ice sheet model, *Journal of Glaciology*, 58(211):889903, 2012.
http://dx.doi.org/10.3189/2012JoG11J182

[14] J. Martin, L.C. Wilcox, C. Burstedde, and O. Ghattas, A Stochastic Newton MCMC method for large-scale statistical inverse problems with application to seismic inversion, *SIAM Journal on Scientific Computing*, 34(3):A1460-A1487, 2012.
http://dx.doi.org/10.1137/110845598

[15] T. Bui-Thanh, C. Burstedde, O. Ghattas, J. Martin, G. Stadler, and L.C. Wilcox, Extreme-scale UQ for Bayesian inverse problems governed by PDEs, *Proceedings of IEEE/ACM SC12*, 2012.
http://dx.doi.org/10.1109/SC.2012.56

[16] T. Isaac, C. Burstedde, and O. Ghattas, Low-Cost Parallel Algorithms for 2:1 Octree Balance, *International Parallel and Distributed Processing Symposium (IPDPS 12)*, 426–437, IEEE Computer Society, 2012.
http://doi.ieeecomputersociety.org/10.1109/IPDPS.2012.47

[17] H.P. Flath, L.C. Wilcox, V. Akcelik, J. Hill, B. van Bloemen Waanders, and O. Ghattas, Fast algorithms for Bayesian uncertainty quantification in large-scale linear inverse problems based on low-rank partial Hessian approximations, *SIAM Journal on Scientific Computing*, 33(1):407-432, 2011.
http://dx.doi.org/10.1137/090780717

[18] C. Burstedde, L.C. Wilcox, and O. Ghattas, p4est: Scalable algorithms for parallel adaptive mesh refinement on forests of octrees, *SIAM Journal on Scientific Computing*, 33(3):1103–1133, 2011.
http://dx.doi.org/10.1137/100791634

AN HPC FRAMEWORK FOR BAYESIAN UNCERTAINTY QUANTIFICATION OF FLOWS ACROSS SCALES

Petros Koumoutsakos*[1], Diego Rossinelli[1], Lina Kulakova[1], Dmitry Alexeev[1], Sergey Litvinov[1], Panagiotis Angelikopoulos[1], Panagiotis Hadjidoukas[1], and Costas Papadimitriou[2]
[1]*Computational Science and Engineering Laboratory, ETH Zürich, Zurich, Switzerland*
[2]*Department of Mechanical Engineering, University of Thessaly, Volos, Greece*

Summary Predictive computational science implies the integration of models driven by physical understanding, discretised with appropriate numerical algorithms with experimental/real world data that can take advantage of extreme scale HPC architectures. Here we discuss large scale flow simulations across scales and their integration with experimental data through a Bayesian framework. Bayesian inference stands amongst the prevalent Uncertainty Quantification and Propagation (UQ+P) techniques. It is used for quantifying and calibrating engineering models, to achieve data-driven, robust predictions of system performance, reliability and safety. We assess the role of imperfections (numerical, experimental, observational) in developing and selecting models with predictive capabilities while incorporating both expert knowledge and experimental data. We demonstrate the capability to efficiently harness extreme scale computational resources for the proposed Bayesian UQ+P framework, ushering its applicability to large scale engineering problems.

INTRODUCTION

Simulations of fluid flows in extreme scale HPC architectures have enabled us to understand transport rates of water in Carbon nanotubes [1], the separation blood and tumor cells in high-throughput microfluidics [2] and insight into the cavitation collapse of tens of thousands of bubbles in two phase flows [4]. An important aspect of these simulation are the uncertainties involved in the model parameters and their inference from experimental data. We present the development of such effective inference techniques using a Bayesian Uncertainty Quantification and Propagation (UQ+P) framework. Bayesian UQ+P tools involve the solution of global optimization problems, sampling from probability distributions, as well as evaluating high dimensional integrals. It is used for quantifying and calibrating uncertainty models in engineering simulations, to achieve data-driven, robust predictions of system performance, reliability and safety. The computational challenge of Bayesian tools comes from the large number of model evaluations required, specifically in cases of complex engineering models with high time to solution and resources requirements.

COMPUTATIONAL CHALLENGES AND PROPOSED SOLUTION

A modest number of parallel software frameworks for uncertainty quantification studies are currently available to the scientific community, with a non-exhaustive list containing DAKOTA [5] and QUESO [6]. The parallelization of these systems has been mostly based on MPI and either follows a master-worker approach or applies domain decomposition to construct processor groups where simulations are assigned for execution. Most systems exploit only one level of parallelism, otherwise they rely on cumbersome implementations that apply hard partitioning of processing units. In addition, they do not take into account heterogeneous computing architectures, and, finally, they lack runtime support for asynchronous nested task-based parallelism and adaptive load balancing. Consequently, these systems cannot counteract the increasing number of sources of load imbalance, such as variable processing power and simulation time, hardware and software faults and the irregularity of UQ algorithms.

Our Bayesian UQ+P computational framework Π4U [7] addresses these issues. Within this framework, we implement population based sampling methods and evolutionary algorithms for optimization, such as Transitional Markov Chain Monte Carlo (TMCMC) [8] and the Covariance Matrix Adaptation Evolution Strategy [9] respectively. All the algorithms implemented have highly parallel task graphs and thus are ideally suited for distributed and parallel computing. The framework is based on the TORC task-parallel library for clusters [10], which is designed to provide unified programming and runtime support for computing platforms that range from low-cost desktop machines to large-scale HPC environments. TORC combines efficient exploitation of multilevel task-based parallelism with ease of programming, hiding low-level parallelization details and thus facilitating algorithm development using a highly portable and platform-agnostic approach.

RESULTS

We used our framework to orchestrate thousands of full molecular dynamics simulations regarding the calibration of their interatomic potentials and to reveal traditional calibration shortcomings resulting to large prediction uncertainty [11]. We performed model selection amongst different constitutive force-displacement laws for granular materials simulations [12].

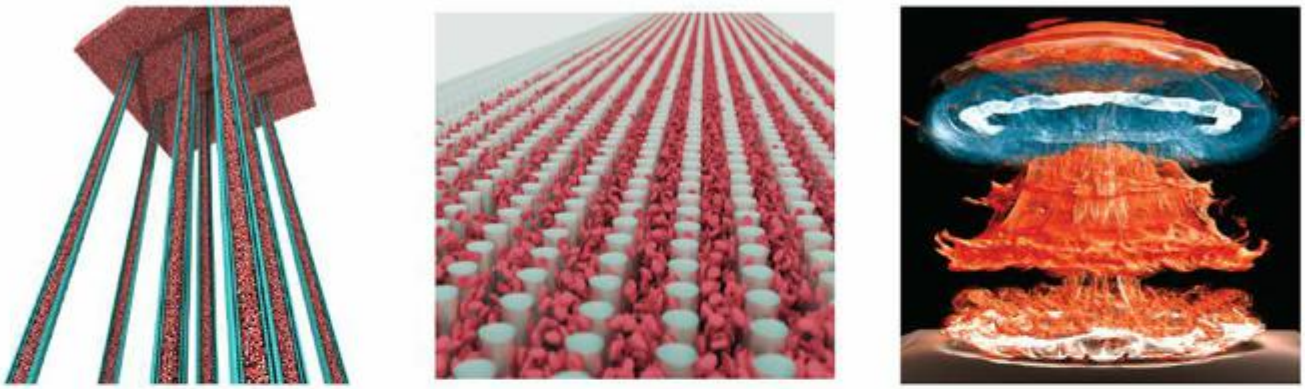

Figure 1: Large scale simulations at nano-, meso- and macro-scale: molecular dynamics of water flow through μm long Carbon Nanotubes [1](left), microfluidics at cell resolution [2](middle) and shock-bubble interactions [3](right).

We present two examples that showcase the effectiveness of Π4U run on the Piz Daint Cray-XC30 HPC system at CSCS (Swiss National Supercomputing Center). The first example regards the estimation of the force-field parameters that dictate the intermolecular interactions between atoms in bulk water using molecular dynamics simulations. We used GROMACS, a molecular simulation code that involves GPU-accelerated kernels as well as multithreading and MPI. The TMCMC method within Π4U achieved an overall parallel efficiency of more than 90% despite the highly variable time-to-solution between simulations with different interaction parameters. The second example applies TMCMC to the calibration of Red-Blood-Cell model parameters in a stretching experiment. The simulations were performed with our in-house uDeviceX software which relies on CUDA and MPI to run efficiently on petascale GPU-accelerated supercomputers [2]. We used 1024 samples per stage and 128 nodes of the Piz Daint cluster, resulting into 15 hours of wall-clock time.

CONCLUSIONS

The development of HPC software for UQ+P on complex multi-physics problems is of paramount importance for exascale computing and the advancement of predictive computational science. With their aid, we envisage that Bayesian UQ will become an indispensable part of predictive engineering.

References

[1] Walther J.H., Ritos K., Cruz-Chu E., Megaridis C.M., Koumoutsakos P.: Barriers to superfast water transport for carbon nanotube membranes, Nano Letters 13(5):1910–1914, 2013.

[2] Rossinelli D., Tang Y., Lykov K., Alexeev D., Bernaschi M., Hadjidoukas P., Bisson M., Joubert W., Conti C., Karniadakis G., Fatica M., Pivkin I., Koumoutsakos P.: The in-silico lab-on-a-chip: petascale and high-throughput simulations of microfluidics at cell resolution, Intl. Conf. on High Performance Computing, Networking, Storage and Analysis (SC '15), 2015. (ACM Gordon Bell Prize Finalist)

[3] Rossinelli D., Hejazialhosseini B., Cont C., Koumoutsakos P.: High throughput software for direct numerical simulations of compressible two-phase flows, Intl. Conf. on High Performance Computing, Networking, Storage and Analysis (SC '12), 2012.

[4] Rossinelli D., Hejazialhosseini B., Hadjidoukas P.E., Bekas C., Curioni A., Bertsch A., Futral S., Schmidt S.J., Adams N.A., Koumoutsakos P.: 11 PFLOP/s simulations of cloud cavitation collapse, Intl. Conf. on High Performance Computing, Networking, Storage and Analysis (SC '13), 2013. (ACM Gordon Bell Prize Winner)

[5] Adams B., Bohnhoff W., Dalbey K., Eddy J., Eldred M., Gay D., Haskell K., Hough P., Swiler L.: DAKOTA, a multilevel parallel object-oriented framework for design optimization, parameter estimation, uncertainty quantification, and sensitivity analysis: Version 5.3. User's Manual SAND2010-2183, Sandia Technical Report, May 2013.

[6] Prudencio E., Cheung S.H.: Parallel adaptive multilevel sampling algorithms for the Bayesian analysis of mathematical models. International Journal for Uncertainty Quantification, 2(3):215–237, 2012.

[7] Hadjidoukas P.E., Angelikopoulos P., Papadimitriou C., Koumoutsakos P.: Π4U: A high performance computing framework for Bayesian uncertainty quantification of complex models. J. Comput. Phys., 284:1–21, 2015.

[8] Ching J.Y., Chen Y.C.: Transitional Markov chain Monte Carlo method for Bayesian model updating, model class selection, and model averaging. Journal of Engineering Mechanics-ASCE, 133(7):816–832, 2007.

[9] Hansen N., Muller S.D., Koumoutsakos P.: Reducing the time complexity of the derandomized evolution strategy with covariance matrix adaptation (CMA-ES). Evolutionary Computation, 11(1):1–18, 2003.

[10] Hadjidoukas P., Lappas E., Dimakopoulos V.: A runtime library for platform-independent task parallelism. 20th Intl. Conf. on Parallel, Distributed and Network-Based Processing (PDP), pages 229–236. Euromicro, 2012.

[11] Angelikopoulos P., Papadimitriou C., Koumoutsakos P.: Data driven, predictive molecular dynamics for nanoscale flow simulations under uncertainty. J. Phys. Chem. B, 117, 14808–14816, 2013.

[12] Hadjidoukas P., Angelikopoulos P., Rossinelli D., Alexeev D., Papadimitriou C., Koumoutsakos P.: Bayesian uncertainty quantification and propagation for discrete element simulations of granular materials. Comput. Methods Appl. Mech. Engrg. 282:218–238, 2014.

EARTHQUAKE HAZARD AND DISASTER SIMULATION USING URBAN AREA MODEL OF 10.7×10^9 DEGREE-OF-FREEDOM

Muneo Hori*[1,2], Tsuyoshi Ichimura[1], Kohei Fujita[2], and Lalith Wijerathne[1]
[1]*Earthquake Research Institute, The University of Tokyo, Bunkyo, Tokyo, Japan*
[2]*Advanced Institute for Computational Science, RIKEN, Kobe, Hyogo, Japan*

Summary Earthquake hazard and disaster simulation for an urban area is carried out by numerically solving non-linear wave equations. A finite element method with a fast iterative solver is developed, and its performance is examined on the Japanese supercomputer. Tokyo Metropolis is simulated using a model of 10.7×10^9 degree-of-freedom. Complicated distribution of seismic ground and structural responses are computed as consequence of the physical processes that are expressed by the wave equations.

INTRODUCTION

Earthquake is a menace of modern civilization, as it induces various damage and malfunctioning in an urban area. The physical processes of seismic wave propagation and structural response are expressed by non-linear wave equations for solid continuum. For the estimation of a possible earthquake hazard and disaster, therefore, it is most straightforward to solve this equation using a suitable urban area model[1].

The scale of the wave equation is huge; spatial and temporal resolutions required are 10^{-1} m and 10^{-1} s, and the size of the urban area and the earthquake duration is $10^{4\sim5}$ m and $10^{1\sim2}$ s. Configuration of ground structure influences local concentration of ground motion, and hence high fidelity is essential for the analysis model.

To numerically solve the wave equations for an urban area model of high fidelity, we are developing a finite element method (FEM)[2]. The degree-of-freedom (DOF) and the time step of the numerical analysis exceed 10^9 and 10^4, respectively. A fast solver is a key element for this FEM.

DEVELOPMENT OF FAST SOLVER

A solver is designed to solve a 10^9-dimensional matrix equation at 10^4 times steps. On the K computer, the fastest parallel computer in Japan, each time step must be solved in 1.44 s in order to simulate the physical processes of an earthquake in 12 h. In view of the K computer characteristics, we adopt a preconditioned conjugate gradient (PCG) method[3], and seek a moderate preconditioner with less computation cost and high scalability.

The following five features are implemented in the solver that is being developed: 1) a predictor which predicts an initial solution using the Adams-Bashforth method; 2) an adaptive CG method in which an approximate solution is first obtained, and then an accurate solution is obtained using the approximate solution as a preconditioner; 3) a multigrid method which uses low and high resolution models to obtain approximate and accurate solutions, respectively; 4) mixed-precision arithmetic which uses single- and double-precision arithmetic for low and high resolution models, respectively; and 5) an element-by-element method which is applied to the matrix-vector operation of the high resolution model, without storing the huge matrix.

Both the low and high resolution models are divided into a set of submodels, each of which one compute node is assigned and OpenMP parallelization is applied on the node. Hence, the whole process of the solver is computed by MPI-OpenMP hybrid parallelization.

NUMERICAL EXPERIMENT FOR PERFOMANCE EXAMINATION

The performance of the developed FEM on the K computer is examined; the K computer consists of 82,944 compute nodes with 8 cores and peak performance of 128 GFLOPS, and its ideal peak performance is 10.6 PFLOPS. A two-layered ground structure is used as a test model, with an element size being 0.44 m. The actual wave observed in 1995 Kobe Earthquake is used, with time increment of 0.002 s.

We examine size-up and speed-up efficiencies. A small or large model of 1.5 or 5.27×10^9 DOF is analyzed in 1.42 s using 36,864 CPU cores or 1.63 s using 663,552 CPU cores, respectively. This leads to a size-up efficiency of 87.1%. A model of 12×10^9 DOF is analyzed in 4.92 s using 73,728 CPU cores or in 1.56 s using 294,912 CPU cores. This leads to a speed-up efficiency of 38.9%.

Since most of process time is used by a solver, high size-up efficiency and low speed-up efficiency are the characteristic of the developed solver; note that FEM is categorized as unstructured grid computation, and, generally, both the efficiencies are low. Higher band-width ratio is needed for further speed-up of the developed solver.

*Corresponding author. Email: hori@eri.u-tokyo.ac.jp

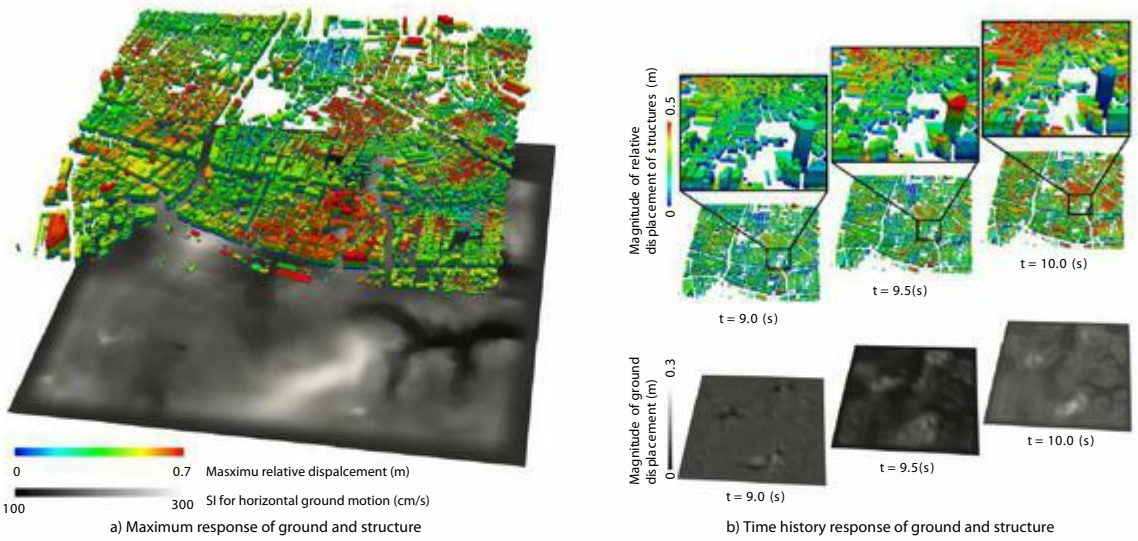

Figure 1: Seismic ground and structural responses in a central part of Tokyo Metropolis for given earthquake.

EARTHQUAKE HAZARD AND DISASTER SIMULATION FOR TOKYO METROPOLIS

The developed FEM is used to simulate earthquake processes in a central part of Tokyo Metropolis, in which 13,275 buildings exist. The dimension of a ground model consisting of three soil layers is 2,000×2,000×100 m. A high resolution model of 10.7×10^9 DOF is constructed for the ground, and a structure model of $10^{1\sim3}$ is constructed for each building. 1995 Kobe Earthquake is used as input earthquake. The time increment and the number of time steps are 0.001 s and 30,000.

On the K computer, it takes 41,521 s to compute 30,000 time steps, which implies 1.38 s for each time step. Most of the computation time is spent by the solver. It is seen that adequate speed-up of the solver enables such a large-scale computation. For the first 1,000 time steps, the performance of the solver is 0.421 PFLOPS (8.93% of the peak performance of the K computer), and the performance of the whole program is 0.358 PFLOPS.

Figure 1 shows the seismic ground response on the surface and the seismic structural response induced by in-site ground motion; an SI-value and relative displacement, typical indices used for ground motion and structural damage, are displayed. It is seen that the spatial distribution of the seismic ground and structural responses are complicated due to the topographical effects and the diversity in the natural frequencies of the buildings.

The results presented in Fig. 1 demonstrates the usefulness of FEM analysis of a high fidelity model to predict earthquake hazard and disaster. It should be noted that higher SI does not necessary induce larger relative displacement. In earthquake engineering, it is known that resonance of local ground and a building is critical for structural damage. The present FEM analysis is able to examine the occurrence of resonance for each building subjected to in-site ground motion.

CONCLUSIONS

We have developed a solver based on the PCG method to carry out FEM analysis for the prediction of earthquake hazard and disaster in an urban area. On the K computer, the solver shows adequate performance, and the FEM analysis is made for Tokyo Metropolis, demonstrating the usefulness of solving the wave equations for an urban area model of high fidelity.

It is still necessary to increase the size of the analysis domain so that the whole Tokyo Metropolis is simultaneously simulated[4]. Also, it is necessary to account for the uncertainty of a possible earthquake as well as the ambiguity of urban area information such as inventory of buildings and infrastructures. Ensemble computing that uses many earthquake scenario and stochastic modeling will solve this problem.

References

[1] Hori, M.: Introduction to computational earthquake engineering (2nd ed.), Imperial College Press, 2011.

[2] Ichimura, T., Fujita, K., Tanaka, S., Hori, M., Maddegedara, L., Shizawa, Y., Kobayashi, H.: Physics-based Urban Earthquake Simulation Enhanced by 10.7 BlnDOF X 30 K time- step Unstructured FE Non- linear Seismic Wave Simulation, SC14, 2014.

[3] Saad, Y.: Iterative methods for sparse linear systems (2nd ed.), *SIAM*, 2003.

[4] Ichimura, T., Fujita, K., Quinay, P.E.B., Maddegedara, L., Hori, M., Tanaka, S., Shizawa, Y., Kobayashi, H. and Minami, K.: Implicit Nonlinear Wave Simulation with 1.08T DOF and 0.270T Unstructured Finite Elements to Enhance Comprehensive Earthquake Simulation, SC15, 2015.

FULL SCALE SEISMIC RESPONSE SIMULATION OF NUCLEAR POWER PLANT SUBJECTED TO STRONG EARTHQUAKE

Shinobu Yoshimura[1a)], Tomoshi Miyamura[2], Tomonori Yamada[3] & Hiroshi Kawai[4]
[1]*Department of Systems Innovation, The University of Tokyo, Tokyo, Japan*
[2]*Department of Computer Science, Nihon University, Fukushima, Japan*
[3]*RACE, The University of Tokyo, Chiba, Japan*
[4]*Department of Mechanical Engineering, Tokyo University of Science-Suwa, Nagano, Japan*

Summary Recent strong earthquakes attacking some Japanese nuclear power plants such as the Great East Japan Earthquake (GEJE) of 9.0 Mw on March 11, 2011 recalled the importance of seismic design of existing nuclear power plants seriously. Latest high-performance computational mechanics simulation is a promising approach that gives us the ability to predict complicated future scenarios quantitatively and to take adequate measures for preventing and mitigating potential damages. In this paper, we explain some key technologies, i.e. the Hierarchical Domain Decomposition Method (HDD) with Balancing Domain Decomposition (BDD) preconditioner, of our developing parallel finite element software ADVENTURE and its application to a seismic response simulation of an actual nuclear power plant subjected to GEJE during 140 seconds using 200 million DOFs mesh on the K computer.

INTRODUCTION

The Great East Japan Earthquake (GEJE) centered off the Pacific cost of Tohoku occurred on March 11, 2011. The magnitude was 9.0 Mw and it was the greatest earthquake recorded in the history of Japan. The consequent Tsunami inflicted immense damage on the Pacific coast area near the focal region in the east of Japan. Most of the large industrial plants including nuclear power plants (NPPs) located along the focal Pacific coast were damaged by the seismic loading and the subsequent Tsunami. In case of NPPs, 11 units among 14 units of 4 facilities located along the Pacific coast were under operation. These 11 units were safely shutdown with automatic scram systems. At Tokyo Electric Power Company's (TEPCO) Fukushima Dai-ichi NPP facilities, Units 1, 2 and 3 under operation were also shutdown with automatic scrum systems just after the earthquake occurred, and the emergency core cooling system started up. However the subsequent Tsunami of 15m height far exceeding a design limit caused long-term station blackout (SBO). As a result, nuclear fuels in the reactor core and the used fuel storage pool were not cooled down sufficiently, which led to extremely serious problems, i.e. meltdown, failure in containing radioactive materials inside, and emission of radioactive materials outside of the facilities [1]. Even today, five years after the accident, the evacuation of local residents still continues and the shortage of electricity supply due to the halt of almost all NPPs across the country is a common problem. There is still a big controversy whether the earthquake caused any failure in the containment function of Unit 1 before the arrival of the Tsunami. It is very hard to precisely investigate actual situation of damaged NPPs by so-called Plant Walk-down in a heavily contaminated environment. A NPP is a large-scale and very complex system, and a small leakage of radioactive material somewhere and failure of some important system, structure and component might cause heavy contamination of the whole plant. Today, over 440 NPPs are under operation to provide electricity in worldwide. At the same time, a huge number of earthquakes occur everywhere in the world.

Latest high-performance computational mechanics simulation is a promising approach that gives us the ability to predict complicated future scenarios quantitatively and to take adequate measures for preventing and mitigating potential damages. In this paper, we explain some key technologies of our developing parallel finite element software ADVENTURE [2-5] and its application to perform seismic response simulation of an actual NPP subjected to GEJE of 9.0Mw during 140 seconds using 200 million DOFs mesh on the K computer [6].

PARALLEL FINITE ELEMENT ANALYSIS USING HDDM WITH BDD PRECONDITIONER

Leading supercomputers offer the computing power of petascale, and exascale systems are expected to appear in the end of this decade. Supercomputers with more than tens of thousands of computing nodes, each of which has many cores, cause serious problems in practical finite element software. Not only the time consuming hot spots of the algorithms but also the entire algorithms must be well tuned and parallerized. For example, K-computer, a Japanese Petaflops machine consists of 88,128 processing nodes and 705,024 cores, and achieves peak performance of 10.5 Peta FLOPS [6]. Latest HPC machines require the following three-layered parallelisms, i.e. (1) Speedup within core, (2) Parallelism in inter-node : Increase parallel efficiency in multicore calcuation considering memory band width, and (3) Parallelism in intra-node : Increase parallel efficiency in intra-node calculation considering intra-node communication speed.

Since 1997, we have been developing a unique open source parallel finite element software known as ADVENTURE [2-5], which enables very precise analyses of practical structures and machines using over 100 million to billions DOF mesh. The parallel solution algorithm employed is the Hierarchical Domain Decomposition Method (HDDM) [3-5] with Balancing Domain Decomposition (BDD) [4,5,7] as preconditioner. Figure 1 illustrates the schematic analysis flow of the HDDM-

a) Corresponding author. Email: yoshi@sys.t.u-tokyo.ac.jp.

BDD algorithm. In addition, we have developed a generalized parallel IO system, a Hierarchical Domain Decomposition module [8], and parallel and walkthrough visualization modules. Recently, we have tuned the software on the K computer, and have achieved 40 % better execution efficiency compared to theoretical peak performance when using 4,096 nodes (32,768 cores), and 10 % above peak performance when using 32,768 nodes (262,144 cores).

SIMULATION MODEL AND RESULTS

As one of various application problems, we have been studying seismic response and structural integrity evaluation of existing NPPs atacked by strong earthquake exceeding design limit [9]. Using the latest version of ADVENTURE system on the K computer, we have been performing a precise investigation on how the Unit 1 of TEPCO's Fukushima Dai-ichi NPP facilities responded during 140 seconds to GEJE of 9.0 Mw. Figure 2 shows its CAD model. The finite element model of the pressure boundaries consists of 211,606,180 four-node tetrahedral elements, 44,215,124 nodes and 132,645,372 degrees of freedom (DOFs), while that of the building consists of 141,151,977 elements, 25,691,899 nodes and 77,075,697 DOFs. The total of the DOFs of the combined model is about 200 million DOFs. The time increment Δt is 0.01 second, and the duration of the event is 140 seconds. Figure 3 shows a snapshot of simulated stress distribution of the combined model.

CONCLUSIONS

We shows how to solve a realistic and large scale structural model of 100 million – 10 billion DOFs mesh using the K computer which has a huge number of nodes and cores. HDDM with BDD preconditioner is robust and very suitable to handle such large scale problems on petaflops machines. We have been investigating any seismic damage onto Unit 1 of Fukushima Dai-ichi NPP attacked by GEJE on March 11, 2011 before the arrival of the huge Tsunami. Such petascale simulation technology is a very powerful tool to obtain the best estimate of quake proof capability of existing NPPs attacked by strong earthquake.

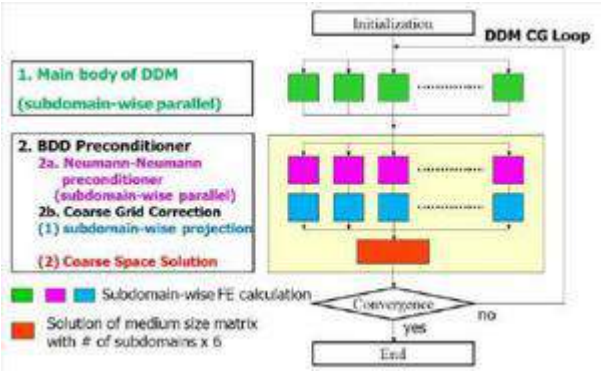

Figure 1 Analysis flow of HDDM with BDD

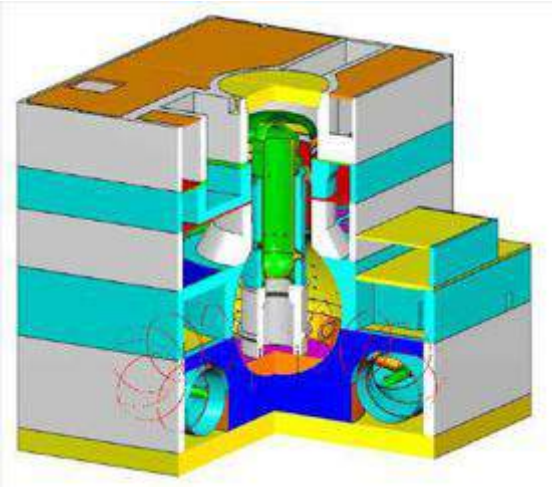
Figure 2 CAD model of NPP

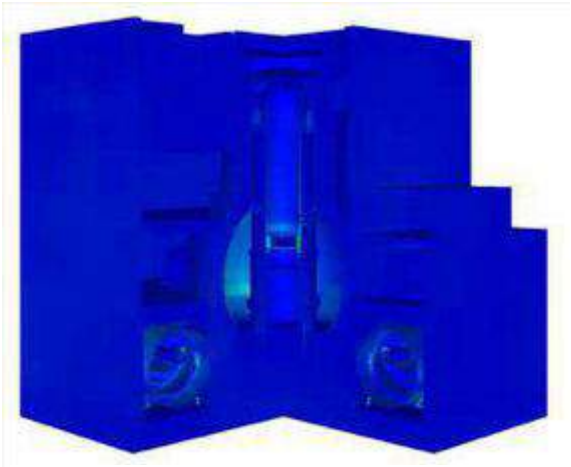
Figure 3 Snapshot of seismic response analysis (equivalent stress)

References

[1] Narabayashi, T., Sugiyama, K.: Fukushima 1st NPPs Accidents and Disaster Caused by the Pacific Coast Tsunami of Tohoku Earthquake : Lessons from Evaluation of the Fukushima 1st NPPs Accidents. *Journal of the Atomic Energy Society of Japan* **53**(6):387-400, 2011. (in Japanese)

[2] http://adventure.sys.t.u-tokyo.ac.jp/

[3] Yoshimura, S., Shioya, R., Noguchi, H., Miyamura, T.: Advanced General-Purpose Computational Mechanics System for Large-Scale Analysis and Design. *Journal of Computational and Applied Mathematics* **49**:279-296, 2000.

[4] Ogino, M., Shioya, R., Kawai, H., Yoshimura, S.: Seismic Response Analysis of Full Scale Nuclear Vessel Model with ADVENTURE System on the Earth Simulator. *Journal of the Earth Simulator* **2**:41-54, 2005.

[5] Yoshimura, S.: Virtual Demonstration Tests of Large-Scale and Complex Artifacts Using an Open Source Parallel CAE System ADVENTURE. *Journal of Solid State Phenomena* **110**:133-142, 2006.

[6] http://www.aics.riken.jp/en/k-computer/about/

[7] Mandel, J.: Balancing Domain Decomposition. Communications on Numerical Methods in Engineering. 9:233-241, 1993.

[8] Murotani, K., Sugimoto, S., Kawai, H., Yoshimura, S.: Hierarchical Domain Decomposition with Parallel Mesh Refinement for Billions-of-DOF Scale Finite Element Analyses. *International Journal of Computational Methods* **11**:1350061, 2014.

[9] Yoshimura, S., Kobayashi, K., Akiba, H., Suzuki, S., Ogino, M.: Seismic Response Analysis of Full-Scale Boiling Water Reactor Using Three-Dimensional Finite Element Method. *Journal of Nuclear Science and Technology*. **52**(4):546-567, 2015.

IMPLEMENTATION OF EXASCALE ASYNCHRONOUS SOLVERS FOR PDEs

Konduri Aditya[1,2], Diego A. Donzis *[1], and Lawerence Rauchweger[3]

[1]*Department of Aerospace Engineering, Texas A&M University, Texas, United States of America*
[2]*Combustion Research Facility, Sandia National Laboratories, California, United States of America* †
[3]*Department of Computer Science and Engineering, Texas A&M University, Texas, United States of America*

Summary To overcome the challenges likely to be present in exascale systems we recently developed novel asynchrony-tolerant numerical schemes for partial differential equations which relax the need for synchronization between processing elements at a mathematical level. The advantages of such schemes can only be realized if their implementation also aims at alleviating the limiting factors at exascale in terms of hardware, software, and programing frameworks. We present two such implementations with different degrees of asynchrony and their corresponding tradeoffs between numerical accuracy and performance. Analysis and numerical experiments demonstrate their respective potential to increase scalability of solvers in future exascale systems.

INTRODUCTION

In the view of the challenges in scalability of solvers likely to be present on future exascale systems, we recently proposed [2] an asynchronous computing method for partial differential equations (PDEs) based on finite differences. This method relaxes data synchronization between processing elements (PEs) at a mathematical level, which potentially can reduce the communication time and improve scalability. An important conclusion from our work is that the numerical properties of those schemes also depend on the characteristics of the hardware and software on a particular system in addition to standard numerical and physical parameters. While the mathematical foundation of asynchronous methods has been established in [2, 1], a number of alternatives open up in terms of implementation of solvers for simulations at extreme scales on real exascale systems. Different choices in implementation can have an impact on, among others, communication patterns, contention on subsystems, and the potential degree of computations-communication overlap. In this work, we present two implementations which result in two broad families of schemes to highlight their capabilities in terms of numerical accuracy and computational performance. As we show, in both cases there is a trade-off between performance and accuracy. The focus on the comparison between implementations will shed light on how to quantitatively strike the right balance in realistic simulations.

CONCEPT

Consider the one-dimensional linear advection-diffusion equation, given by $\partial u/\partial t + c\partial u/\partial x = \alpha\partial^2 u/\partial x^2$, where c and α are constants, discretized with an Euler scheme in time and a second order central difference in space: algebraic equation:

$$\frac{u_i^{n+1} - u_i^n}{\Delta t} + c\frac{u_{i+1}^n - u_{i-1}^n}{2\Delta x} = \alpha\frac{u_{i+1}^n - 2u_i^n + u_{i-1}^n}{\Delta x^2} + \mathcal{O}(\Delta x^2, \Delta t) \tag{1}$$

The solution is evolved in time for given initial and boundary conditions. When the domain is decomposed into multiple PEs, the computation of spatial derivatives near PE boundaries need u values from neighboring PEs. Thus, at each time step, these computations cannot proceed unless communications between PEs is completed, thus enforcing synchronization.

This synchronization, however, can be relaxed by allowing schemes to compute spatial derivatives using function values that are not current but from delayed time levels. This modifies the nature of the finite difference equation, affecting also its numerical properties. The mathematical feasibility of this method has been studied in [2] where we found that though standard schemes remain stable under asynchrony, their accuracy is significantly affected. In [1] we derived families of asynchrony-tolerant (AT) schemes of arbitrary order under asynchronous conditions. An example of a second-order AT scheme is

$$\frac{\partial^2 u}{\partial x^2} \approx \frac{u_{i+1}^n - 2u_i^n + (k+1)u_{i-1}^{n-k} - ku_{i-1}^{n-k-1}}{\Delta x^2}, \tag{2}$$

where k is the delay in the latest available time level at the grid point $i-1$, which can be set deterministically or randomly depending on the implementation. This difference is the basis for selecting the implementations presented here. The maximum delay can be restricted to L time levels (i.e. $k \in \{0, 1, \ldots, L-1\}$), providing a knob to control error. We define $\mathcal{T}$ as the number of asynchronous time levels that a particular scheme needs, which in the case of Eq. (2) is $\mathcal{T} = 2$, corresponding to the time levels $\{n-k, n-k-1\}$. The average error due to asynchrony can be then shown [1] to be proportional to $(P/N)\Delta x^a \sum_{m=1}^{\mathcal{T}} \gamma_m \overline{k^m}$, where γ_m are some constants, and P, N and a are the number of PEs, the number of grid points and the order of accuracy of the AT scheme, respectively. An overbar is an ensemble average. This result clearly shows that the accuracy of asynchronous schemes at exascale depends not only on the numerical scheme but also on architectural details of the system (through statistics of the delays $\overline{k^m}$) as well as the manner in which problems are scaled up (through P/N).

*Corresponding author. Email: donzis@tamu.com
†Current affliation of KA.

IMPLEMENTATIONS OF NUMERICAL SCHEMES WITH DELAYS

We present two implementations with different communication algorithms. In the first one, which will be referred as communication minimizing (CM) implementation, communication of data with synchronization is not carried out at every time step in a simulation, but after a given number of time steps. This reduces the number of messages that are sent during a simulation to improve scalability. Specifically, communications are done during $\mathcal{T}$ time levels after which computations continue without communications for $L - \mathcal{T}$ time levels. The process then repeats. Note that the delay k varies in a deterministic manner in this implementation. For a given physical problem represented by a PDE, error control is based on the particular AT scheme used and the value of L. They also have an impact on size, frequency and number of messages during communications. We show how one can predictably trade performance and accuracy with these parameters.

The second implementation is based on asynchronous communications, in which communication between PEs is initiated at every time step but no explicit synchronization is enforced as long as $k < L - 1$, where L is set based on accuracy requirements. We refer to this as the weakly synchronous (WS) implementation. The scalability of solvers is then improved by overlapping computations and communications which is possible due to the removal of explicit synchronizations at every time step. In such an implementation, message arrivals are in general random and so is the delay k.

RESULTS AND CONCLUSIONS

To evaluate the performance of our asynchronous methods we have conducted simulations of the advection-diffusion equations, which represent a widely used case for a PDE with realistic physical content. As a reference case, we choose the standard synchronous scheme in Eq. (1). The results show that the CM and WS implementations give rise to different moments of the delay k. This has a first order effect on the error incurred. As we show in this work, in both implementations we can control the error using L though the effect is different. An example of the numerical convergence of both implementations is shown in Fig. 1(a) as grid resolution is increased. When compared to the standard synchronous case (black line), the error incurred by using a standard (non-AT) scheme asynchronously is much greater and converges at a lower rate (red line). However, this effect is relieved by using the AT scheme in Eq. (2), as seen in the figure (green line).

Performance at extreme scales will also depend on the particular scheme, the statistics of the delay, and L at which synchronization is enforced. We show how these elements combine in each implementation. An example of the computational performance is shown in the strong scaling graph in Fig. 1(b). The computational effort per PE used in these simulations is similar to the expected values at exascale. We see that the standard synchronous case scales poorly as we increase the PE count, due to the dominance of communication time. When the communication synchronization is relaxed using e.g. WS implementation, a nearly ideal scaling is obtained. A similar behaviour is also observed in the case of CM implementation.

In conclusion, this work combines recent advances in the mathematical understanding of AT schemes with elements on the actual implementation on real architectures and its consequences in accuracy and performance. We demonstrate how specific implementations of AT schemes can provide a path towards true exascale simulations of problems governed by PDEs. We also note that since the complexity in writing asynchronous exascale codes (especially in high dimensional space and with complex geometries) is expected to be extremely high, a framework that provide mechanisms in which asynchronous schemes can be expressed and analyzed efficiently [3] will be extremely valuable.

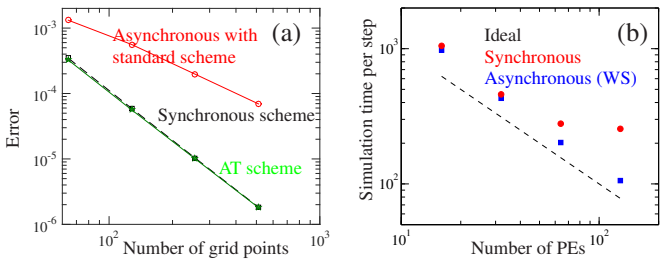

Figure 1: (a) Convergence of error with increase in grid resolution. (b) Strong scaling graph.

References

[1] K. Aditya. *Highly scalable asynchronous computing method for partial differential equations: a path towards Exascale*. PhD thesis, TAMU, 2015.

[2] D. A. Donzis and K. Aditya. Asynchronous finite-difference schemes for partial differential equations. *J. Comp. Phys.*, 274(0):370 – 392, 2014.

[3] M. Zandifar et al. Composing algorithmic skeletons to express high-performance scientific applications. In *Proceedings of ICS*, pages 415–424, 2015.

SUBDOMAIN LOCAL FE SOLVER IMPLEMENTATION USING ITERATIVE METHOD IN DOMAIN DECOMPOSITION METHOD

Hiroshi Kawai[1], Masao Ogino[2], Ryuji Shioya[3], Tomonori Yamada[4] & Shinobu Yoshimura[5]
[1]*Department of Mechanical Systems Engineering, Tokyo University of Science-Suwa, Nagano, Japan*
[2]*ITC, Nagoya University, Aichi, Japan*
[3]*Faculty of Information Science and Arts, Toyo University, Saitama, Japan*
[4]*RACE, The University of Tokyo, Chiba, Japan*
[5]*Department of Systems Innovation, The University of Tokyo, Tokyo, Japan*

Summary As the hardware architecture of modern supercomputers is getting more and more complicated, it is more and more difficult to achieve high performance in real production-level application codes. To obtain, not only inter-node parallel performance using MPI, but also higher intra-node thread-parallel performance, more efficient utilization of processor cache memory and SIMD vectorization should be considered. In case of the domain decomposition method (DDM), one obvious performance bottleneck is the subdomain-wise local FE solver. Here in this presentation, performance benchmark of subdomain local FE solvers implemented using preconditioned conjugate gradient solvers will be demonstrated. The strength of this implementation is that the working set of local solver just fits in the processor cache memory. They are tested on modern multi-core scalar based supercomputers, such as RIKEN K Computer, Fujitsu PRIMEHPC FX100, Intel Haswell and Knights Corner.

INTRODUCTION

Exa-scale supercomputers will appear around 2020-2022. The total number of processor core in a system is already reaching the order of millions, as already demonstrated in RIKEN K Computer at Kobe [1]. Also, to obtain high intra-node performance, efficient utilization of processor cache memory and SIMD instruction set should be considered. Drastically new design and implementation approaches will be required in the post-peta-scale as well as the exa-scale eras. The traditional memory access-intensive approach, which prefers less computing and more storage on main memory, might not be effective for supercomputers in near future. As a result, the gap between the full potential of the HPC hardware architectures and the actual performance of a particular simulation code, written by an ordinary researcher or a developer, could be wider and wider.

The Domain Decomposition Method (DDM) is one of the effective parallel finite element schemes. We have been developing an FE-based parallel structural analysis code, ADVENTURE_Solid [2] [3], based on DDM, with the Balancing Domain Decomposition (BDD) pre-conditioners. It was successfully applied on a vector-type supercomputer, The Earth Simulator (ES) [4]. However, the performance of multi-core scalar-type supercomputers has already surpassed vector-type machines. To switch hardware platform from high Byte / FLOPS environments like ES to relatively low B/F one like multi-core PC clusters, BlueGene and K Computer, we need to re-design some performance sensitive kernels in our DDM code, especially the subdomain local FE solver.

In this paper, various types of performance tuning approaches for the DDM-based structural analysis code, ADVENTURE_Solid, on peta-scale massively parallel supercomputers are presented. Here in this paper, we focus our attention on the intra-node performance of a supercomputer. In case of a DDM code, this means the parallelization and performance tuning of the subdomain local FE solver based on multi-thread programming models, such as OpenMP, compiler-based auto-parallelization and utilization of thread-enabled libraries.

SUBDOMAIN LOCAL FE SOLVER IN DDM

The Domain Decomposition Method (DDM) is a numerical scheme for solving a partial differential equation (PDE) based on a kind of "divide and conquer" approach. Assuming structural analysis using FEM, the flow of a basic DDM algorithm is shown in Fig. 1. First, displacement boundary condition is assumed along the interface between neighboring subdomains. For each subdomain, a finite element analysis is carried out by the subdomain local FE solver, and reaction force can be evaluated along the interface, where displacement values are enforced. There still remains some amount of reaction force unbalance along the interface between subdomains. Then, using this unbalance information, the assumed displacement boundary conditions can be modified somehow so that the amount of the unbalance is reduced. Typically, this process naturally introduces an iteration of Richardson, Gauss-Siedel, SOR or CG. This can be further accelerated by the introduction of DDM pre-conditioner, such as BDD and FETI. The iteration is repeated until acceptable convergence along the interface is obtained. It is notified that FE analyses of subdomain local problems can be executed independently and in parallel.

[a] Corresponding author. Email: kawai@rs.tus.ac.jp.

Although the subdomain local FE solver itself runs on a single MPI process and it is not yet parallelized within a computational node, various types of design and implementation of subdomain local solvers have already been investigated in our previous work. The choice of linear equation solver (direct or iterative) and usage pattern of main memory (matrix storage-free or not) are two main issues. If it is iterative solver-based, further, the type of pre-conditioner and utilization of element-by-element techniques may be additional points. They have been roughly categorized into four, DS (Direct solver-based matrix Storage), DSF (Direct solver-based matrix Storage-Free), IS (Iterative solver-based matrix Storage) and ISF (Iterative solver-based matrix Storage-Free). Of them, except the first one, DS, other three approaches consume significantly less memory and can be used for solving a very large scale problem. Also, they may be able to utilize processor cache memory more efficiently. Actually it was identified that, in terms of execution time, they perform comparably well against DS approach. On some low B/F environments, they even run faster than DS.

In this work, an on-cache iterative solver based on the DDM framework is developed. The subdomain local FE solver in DDM code is based on IS-type design described above, employing pre-conditioned CG solvers, such as diagonal scaling, SSOR and ICT. They are also parallelized using OpenMP. By adjusting the subdomain size so that the footprint fits within the last-level cache of processor, this DDM code can be considered as a kind of an on-cache iterative solver. Some performance benchmark results are shown on various kinds of HPC platform, such as Haswell, Knights Corner, RIKEN K Computer and Fujitsu PRIMEHPC FX100.

CONCLUSIONS

As a preliminary benchmark result, about 10 % of peak FP performance is obtained on RIKEN K Computer using 32768 nodes. The implementation will be introduced to the future version of open-source CAE system, ADVENTURE.

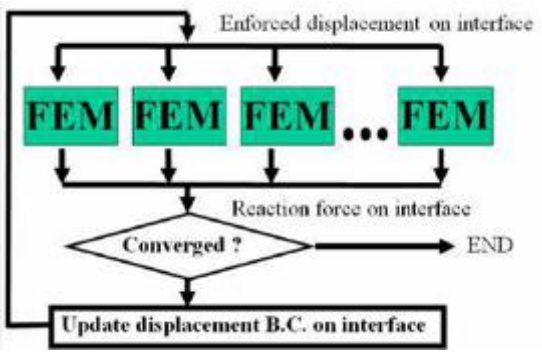

Fig.1: Flow of DDM algorithm.

References

[1] http://www.aics.riken.jp/en/k-computer/about/

[2] http://adventure.sys.t.u-tokyo.ac.jp

[3] Yoshimura, S., Shioya, R., Noguchi, H., Miyamura, T.: Advanced General-Purpose Computational Mechanics System for Large-Scale Analysis and Design. Journal of Computational and Applied Mathematics 49:279-296, 2000

[4] Ogino, M., Shioya, R., Kawai, H., Yoshimura, S.: Seismic Response Analysis of Full Scale Nuclear Vessel Model with ADVENTURE System on the Earth Simulator. Journal of the Earth Simulator 2:41-54, 2005.

COMPUTATIONAL CHALLENGES TOWARDS EXA-SCALE FUSION PLASMA TURBULENCE SIMULATIONS

Y. Idomura *, Y. Asahi, T. Ina, and S. Matsuoka

Japan Atomic Energy Agency, Kashiwa, Chiba 277-0871, Japan

Summary Turbulent transport in fusion plasmas is one of key issues in ITER. To address this issue via the five dimensional (5D) gyrokinetic model, a novel computing technique is developed, and strong scaling of the Gyrokinetic Toroidal 5D Eulerian code GT5D is improved up to ~ 0.6 million cores on the K-computer. The computing technique consists of multi-dimensional/multi-layer domain decomposition, overlap of communication and computation, and optimization of computing kernels for multi-core CPUs. The computing power enabled us to study ITER relevant issues such as the plasma size scaling of turbulent transport. Towards the next generation burning plasma turbulence simulations, the physics model is extended including kinetic electrons and multi-species ions, and computing kernels are further optimized for the latest many-core architectures.

Fusion energy has a significant potential as a widely available energy source with essentially unlimited supply and manageable environmental impact. One of the most promising approaches to a fusion reactor is magnetic confinement fusion, in which high temperature fuel plasmas with ~ 10 are confined by torus magnetic fields. So far, deuterium plasma experiments in two major devices in Japan and in EU achieved the so-called breakeven condition, where the fusion gain factor Q, the ratio of (estimated) fusion power to the power required for the operation, becomes unity. To demonstrate the scientific and technological feasibility of magnetic confinement fusion, the next generation experimental reactor, ITER, is designed to keep burning plasmas at $Q = 10$ for $\sim$ 00 . In achieving this target, one of key issues is to understand and predict turbulent transport, which dictates the performance of energy confinement, thus, an amount of auxiliary heating required to sustain and control burning plasmas. Compared with deuterium experiments in existing devices, burning plasma experiments in ITER have the following differences. Firstly, the plasma size is several times larger than existing devices. Secondly, burning plasmas contain multi-species ions, deuterium, tritium, helium, and other impurities. Thirdly, plasma heating due to fusion born α particles becomes dominant, while deuterium plasmas are sustained by external heating. Although ITER was designed based on an extrapolation of experimental database from existing devices, the above new features make quantitative predictions very difficult. Therefore, first principles based fusion plasma turbulence simulations are expected to play critical roles in improving the credibility of operation scenarios in ITER.

Turbulence is characterized by chaotic behavior and turbulent mixing leading to much larger transport than diffusion processes. In addition, fusion plasma turbulence is even more complex because of the following features. Firstly, multiple fluids (electrons and multi-species ions) with considerably different mobility are coupled through electromagnetic fields and weak collisional interactions. Secondly, strong confinement fields provide highly anisotropic turbulent structures. Thirdly, inhomogeneities in density, temperature, and magnetic fields excite multiple micro-instabilities over wide spectral ranges. Finally, because of weak collisionality in high temperature plasmas, a particle distribution function is deviated from a local thermodynamic equilibrium, and kinetic effects such as wave-particle resonant interactions and particle orbit effects play essential roles. Because of this collisionless character, conventional three dimensional (3D) fluid models such as a magnetohydrodynamics (MHD) model becomes insufficient, and kinetic descriptions of a plasma in 5D phase space are needed. Here, the standard first principle model of fusion plasma turbulence is given by a 5D gyrokinetic model, which is derived from a 6D Boltzmann equation by eliminating fast gyro-motion of charged particles in magnetized plasmas. Although experimentally relevant turbulence simulations based on the 5D gyrokinetic model have been prohibitive for a long time, developments of modern supercomputers and advanced computing techniques dramatically expanded capabilities of 5D gyrokinetic simulations [1].

The latest Peta-scale machines are characterized by relatively low memory size and bandwidth compared with Flops, complicated hierarchy of hardware architecture in computing nodes and interconnects, and extreme concurrency reaching at million cores. In addition, future Exa-scale machines may be based on many-core processors and accelerators, which have complicated hierarchy also within them. In order to overcome such technical requirements, we have developed novel computing techniques [2]. Firstly, multi-dimensional/multi-layer domain decomposition is designed by fully utilizing the physics symmetry and the high dimensional property of the 5D gyrokinetic model, and process mapping is optimized for interconnect topologies. Secondly, communication overheads are minimized by overlapping communication and computation via communication threads, which are implemented by using OpenMP, and are applicable to any kind of MPI communication including (blocking/non-blocking) point-to-point and collective communications. Thirdly, within computing nodes, arithmetic intensity of computing kernels is improved by optimizing OpenMP thread scheduling so that data loaded by different threads are reused on a shared cache in multi-core processors. By applying the above computing techniques, the strong scaling of the Gyrokinetic Toroidal 5D Eulerian code GT5D [3, 4] is improved up to $\sim 0.$ million cores on the K-computer with keeping the sustained performance of $\sim 10\%$.

*Corresponding author. Email: idomura.yasuhiro@jaea.go.jp

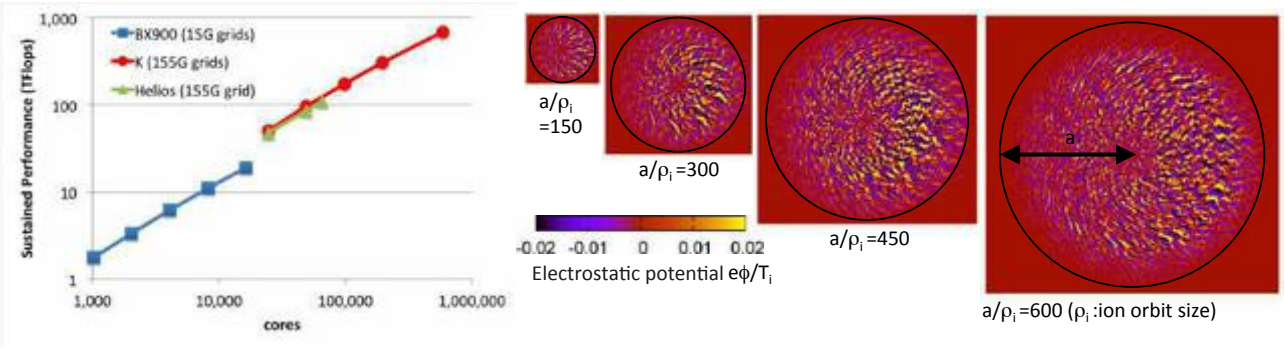

Figure 1: The strong scaling of GT5D on the BX900 (JAEA), the Helios (IFERC) and the K (Riken). Problem sizes for an existing device ($N_R \times N_\zeta \times N_Z \times N_{v\parallel} \times N_{v\perp} = 2\ \ 0\times\ \ \times 2\ \ 0\times 128\times 32 \sim 1.5\times 10^{10}$) and ITER ($\ \ 8\times\ \ \times\ \ \ 8\times 128\times 32 \sim 1.5\times 10^{11}$) are used (left). The turbulent electrostatic potential in the plasma size scan of global ion turbulence simulations ranging from existing device sizes, $a/\rho_i < 300$, to the ITER regime, $a/\rho_i =\ \ 00$ (right).

The strong scaling dramatically expanded the capability of GT5D both in time scales and in problem sizes, and enabled us to access ITER relevant parameter regimes. In turbulent fusion plasmas, the spatio-temporal scales of plasma turbulence are characterized by $\Delta r \sim 1\ \ \ $ and $\Delta t \sim 10\mu$, while those of plasma profiles are given as $a \sim 1\ \ \ $ and $\tau \sim 100\ \ \ $. Here, Δt and Δr are turbulent correlation time and length, respectively, a is the plasma radius, and τ is the energy confinement time. In the conventional δf simulations for relatively short time scales $< 1\ \ \ $, the scale gap has been treated by assuming scale separation, where the total particle distribution f is separated into a macroscopic equilibrium distribution f_0 and a microscopic turbulent perturbation δf, and only the latter is evolved under prescribed f_0. On the other hand, with increasing computing power, full-f simulations, which compute f for longer time scales $\sim \tau$ without any scale separation, have been established. Thanks to the multi-scale feature, full-f simulations disclosed the so-called self-organized critical phenomena of avalanche-like non-local transport [4], which is induced by an interaction between turbulence and plasma profiles, and it was shown that such non-local transport significantly affects the plasma size scaling of turbulent transport [5]. Since ITER is several times larger than existing devices, its confinement performance will be affected by the plasma size scaling. Although full-f simulations at ITER size have been prohibitive for a long time, the K-computer enabled us to study the plasma size scaling up to the ITER regime, $a/\rho_i =\ \ 00$ ($\sim 10^{11}$ grids), where ρ_i is the ion gyro-radius (see Fig.1 right). Conventional plasma transport theories predicted that for $a/\rho_i > 300$, finite plasma size effects such as the plasma boundary effect disappear, and the heat diffusivity χ_i approaches a local diffusion theory, $\chi_i \sim \chi_L \sim \Delta r^2/\Delta t$. However, the numerical results showed that even in large devices, χ_i increases with the plasma size, $\chi_i \sim \chi_L a/\rho_i$, due to the nonlocal heat transport [6]. This finding provides a new physics ingredient, which is essential for the prediction of the confinement performance in ITER.

Towards Exa-scale burning plasma simulations, GT5D is extended from deuterium plasmas to burning plasmas by introducing multi-species ions, and kinetic electrons. Since these extensions require two orders of magnitude larger computational cost, Exa-scale computation is essential. To this end, the computing kernel is further optimized for the latest Tera-Flops class many-core architectures such as the Fujitsu FX100, the Intel Xeon Phi, and the Nvidia Tesla, and the suitability of the current numerical approache to different many-core architectures is examined [7].

The computation in this work was performed on BX900 (JAEA), Helios (IFERC), FX10 (Univ. Tokyo), Tsubame (Tokyo Tech.), FX100 (NIFS) and K-computer (hp120011,hp150027,hp150279). This work was supported by the JAEA-NIFS-NU collaboration program and by the MEXT, Grant for HPCI Strategic Program Field No.4: Next-Generation Industrial Innovations, Grant for Post-K priority issue No.6: Development of Innovative Clean Energy, and Grant No. 22686086.

References

[1] Garbet X., Idomura Y., Villard L., Watanabe T.-H.: Gyrokinetic simulations of turbulent transport. Nuclear Fusion 50:043002, 2010.

[2] Idomura Y., Nakata M., Yamada S., et al.: Communication-overlap techniques for improved strong scaling of gyrokinetic eulerian code beyond 100k cores on the K-computer. International Journal of High Performance Computing Applications 28:73-86, 2014.

[3] Idomura Y., Ida M., Kano T., et al.: Conservative global gyrokinetic toroidal full-f five-dimensional Vlasov simulation. Computer Physics Communications 179:391-403, 2008.

[4] Idomura Y., Urano H., Aiba N., et al.: Study of ion turbulent transport and profile formations using global gyrokinetic full-f Vlasov simulation. Nuclear Fusion 49:065029, 2009.

[5] Jolliet S., Idomura Y.: Plasma size scaling of avalanche-like heat transport in tokamaks. Nuclear Fusion 52:023026, 2012.

[6] Idomura Y., Nakata M.: Plasma size and power scaling of ion temperature gradient driven turbulence. Physics of Plasmas 21:020706, 2014.

[7] Asahi Y., Latu G., Ina T., et al.: Optimization of stencil-based fusion kernels on Tera-flops many-core architectures. SC15, Austin, USA, 2015.

TOWARDS EXASCALE SIMULATION OF TURBULENT COMBUSTION

Jacqueline H. Chen[1], *, Giulio Borghesi[1], Ankit Bhagatwala[1] and Sean Treichler[2], Mike Bauer[2], Alex Aiken[2]

[1]*Sandia National Laboratories, Livermore, CA*
[2]*Stanford University, Palo Alto, CA*

Summary Combustion currently provides 85% of the US energy needs. In fact, the continued demand for abundant combustion fueled energy will persist well into this century. This places enormous pressure to improve the combustion efficiency in engines for transportation and power generation while simultaneously developing more diverse fuel streams, including carbon neutral biofuels. Ultimately, to shorten the design cycle of new fuels optimally tailored to work with novel fuel efficient, clean engines requires fundamental advances in combustion science. One key avenue of study in this area is the development of predictive models for engineering design. These predictive models couple chemistry with turbulent transport under real world conditions. Exascale computing will enable first principles direct numerical simulation (DNS) of turbulent combustion science at higher Reynolds number, higher pressure, and with greater chemical complexity.

One of the primary challenges to achieving exascale computing is designing new architectures that will work under the enormous power and cost constraints. The mission of co-design within the Center for Exascale Simulation of Combustion in Turbulence (ExaCT) is to absorb the sweeping changes necessary for exascale computing into software and ensure that the hardware is developed to meet the requirements to perform these real world combustion computations. ExaCT performs multi-disciplinary research required to iteratively co-design all aspects of combustion simulation including math algorithms for partial differential equations, asynchronous programming environments, scientific data management and analytics for in situ uncertainty quantification.

I will present recent results from petascale DNS focusing on mixed regimes of combustion in compression ignition engine environments. I will then present computer science research highlights in ExaCT in the areas of programming environment and runtimes and in situ data analytics. I will conclude with a discussion of prospects for DNS of turbulent combustion at the exascale.

Direct numerical simulation of turbulent combustion is an important tool for understanding fuels used in internal combustion engines. Recent results from petascale direct numerical simulation using S3D [1] of a realistic primary reference fuel blend of iso-octane and n-heptane, involving 171 chemical species and 861 chemical reactions and from a n-dodecane diesel jet flame are presented. The key to excellent weak and strong scaling performance in S3D is using a task-based programming model called Legion [2, 3]. Legion automates details of scheduling tasks and data movement, and separates specification of tasks/data from the mapping onto a machine. It will be shown that these properties have profound implications for programmer productivity, shortening activities previously requiring weeks to hours. Performing the DNS and the in situ analysis on heterogeneous supercomputers with hybrid cpu-gpu configurations required changes in functionality ports to multiple supercomputers, 2D vs. 3D and low vs. high resolution runs. Each variation altered both work and communication, sometimes radically, but remapping required minimal human effort. The result is a robust, easily modified PRF implementation that is also over five times faster than the current production code.

In a second DNS performed using Legion, direct numerical simulation of a turbulent, self-igniting temporal mixing layer between n-dodecane and diluted air was performed to clarify the coupling between turbulence, mixing and ignition chemistry in diesel engine combustion [4]. The thermodynamics conditions were selected to result in a two-stage ignition event, in which low- and high-temperature chemical reactions play an equally important role during the ignition process. Jet parameters were tuned to yield a target ignition Damkohler number of 0.4, a value representative of conditions found in diesel spray flames. Chemical reactions were described by a 35-species reduced mechanism, including both the low- and high-temperature reaction pathways of n-dodecane. The present work focuses on the influence of low-temperature chemistry on the overall ignition transient. Previous studies have demonstrated that ignition is most likely to occur in those regions where scalar dissipation is low and the mixture composition is close to the most reactive one, e.g. the composition for which, in an homogeneous reactor, the ignition delay is the shortest. The present study focuses on whether this picture remains valid when low-temperature reactions are important, and how the ignition delay and location are affected by these low-temperature processes.

References

[1] Chen, J. H., Choudhary, A., de Supinski,B., DeVries, M., Hawkes, E. R., Klasky, S., Liao, W. K., Ma, K. L., Mellor-Crummey, J., Podhorszki, N., Sankaran, R., Shende, S., and Yoo, C. S., Terascale direct numerical simulations of turbulent combustion using S3D. Computational Science and Discovery, page 015001, 2009.

[2] Bauer, M., Treichler,S., Slaughter, C. and Aiken, A. Legion: Expressing locality and independence with logical regions. In Supercomputing (SC), 2012.

[3] Bauer, M., Treichler, S., and Aiken, A., Singe: Leveraging warp specialization for high performance on GPUs. In Symposium on Principles and Practice of Parallel Programming, Feb. 2014.

[4] Borghesi, G. and Chen, J. H., A DNS investigation of turbulent n-dodecane / air autoignition. Submitted to the Western States Section of the Combustion Institute Conference, Seattle, WA 2016.

*Corresponding author. Email: jhchen@sandia.gov

PARALLEL PERFORMANCE OF FRONTFLOW/VIOLET-CARTESIAN WITH WALL-MODELLED LES CAPABILITY

Ken Uzawa[1] & Kenji Ono[1, 2]
[1] *Institute of Industrial Science, The University of Tokyo, Meguro-ku, Tokyo, Japan*
[2]*Advanced Institute for Computational Science, RIKEN, Kobe, Hyogo, Japan*

Summary We have developed Cartesian-based high-performance parallel flow solver FrontFlow/Violet-Cartesian (FFV-C) by implementing wall-modelled LES. In this work, parallel performance of FFV-C is examined by choosing NACA0012 airfoil as a validation model. As a result, excellent scalability was observed. It was also found that the computational cost in the model is only 20 percent larger than that without the wall model. This shows potential to perform computation of high Reynolds number flows with much less expense than DNS.

INTRODUCTTION

Computational Fluid Dynamics (CFD) based on structured/unstructured grids plays an important role in development and improvement of industrial products. Conventionally, unstructured grids are often used to analyze the flow around industrial products with high accuracy. However, as the performance of computers increases, computational geometry to be solved become more and more complex and it demands a lot of time to prepare computational grids in comparison with calculation time itself. This tendency becomes remarkable in coming Exascale computing. Because of this situation, we have developed Direct Numerical Simulation (DNS) solver FrontFlow/Violet-Cartesian (FFV-C) [1,2]. The significant feature of FFV-C is the use of the Cartesian grid system, therefore it enables us to make arbitrary size of computational grids instantaneously and robustly. Up to now, over 90 percent of weak-scalability with 82,944 nodes on the K-computer is achieved and there is a track record of flow calculations around an automobile by 29 billion cells at $R_e = 10^6$.

However, as the Reynolds number increases up to the order of 10^7, a massive computational grid is required near wall boundaries to resolve vertical vortices that are the main cause of momentum transfer. From simple estimation, the computational grid that is proportional to $R_e^{9/4}$ and $R_e^{1.9}$ is needed in DNS and wall-resolved Large Eddy Simulation (LES), respectively [3]. For example, if the Reynolds number is the order of 10^7, 10 trillion grids are required even in wall-resolved LES. It is impossible to achieve this huge-scale calculation on the latest supercomputer. To overcome this difficulty, we develop a simplified wall-modelled LES in which dynamics in the inner layer is modelled and examine its validation.

WALL-MODELLED LES

The model consists of the immersed boundary method and LES models with the Spalding law and is formulated without dependency on the position of the image points and the boundary cells compared to previous studies. Furthermore, increase of the flow rate toward streamwise direction is suppressed by satisfying the streamwise momentum conservation. For subgrid-scale (SGS) models, Coherent Smagorinsky (CSM) model [4] and wall-adapting local eddy-viscosity (WALE) model [5] are employed. These models are local eddy viscosity models that determine positive model coefficient locally and avoid data communication among extra-neighboring nodes, therefore we can guarantee FFV-C's high-performance and scalability. We have performed validation for channel flow with viscous Reynolds number from 150 to 650 and found that validated results are well in agreement with results by resolved LES and existing DNS database [6]. In this work, we examine parallel performance for high Reynolds number flow around streamlined structure.

PARALLEL PERFORMANCE

Here, NACA0012 airfoil [7] is employed as a validation model. The computational domain and the airfoil are shown in Figure1. The computation size is (L_x, L_y, L_z) = (16.0, 4.0, 1.0) [m], the chord line of the airfoil is $l = 2.0$ [m], the angle of attack is 0 [deg], the inlet velocity is $u = 23.6$ [m/s], the kinematic viscosity is $\nu = 1.46 \times 10^{-5}$[m^2/s]. We examine four different cases for total cell size N, i.e., N = 262K, 2.1M, 16.7M and 134M. The numbers of MPI and thread processes are chosen to 32 and 8, respectively.

The instantaneous streamwise velocity normalized by the inlet velocity in the wall-modelled LES is illustrated in Figure2. The cell size is (*a*) 16.7M and (*b*) 134M. The Kármán's vortex street is observed in both cases and numerically stable even when the Reynolds number increases. In Figure3, the averaged computational time par one step for different cell sizes in the wall-modelled LES is compared with that of original FFV-C. The horizontal and vertical axes represent the total cell size and the averaged computational time par one step. Favourable scalability is observed in both cases and it is also found that computational cost in the wall-modelled LES is only 20 percent larger than that without the wall model.

[a)] Corresponding author. Email: uzawa@iis.u-tokyo.ac.jp

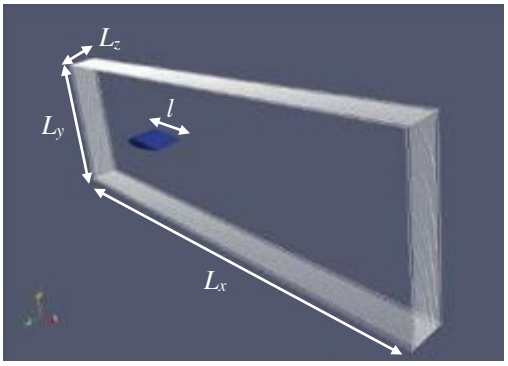

Figure1 The computational domain and the NACA0012 airfoil.

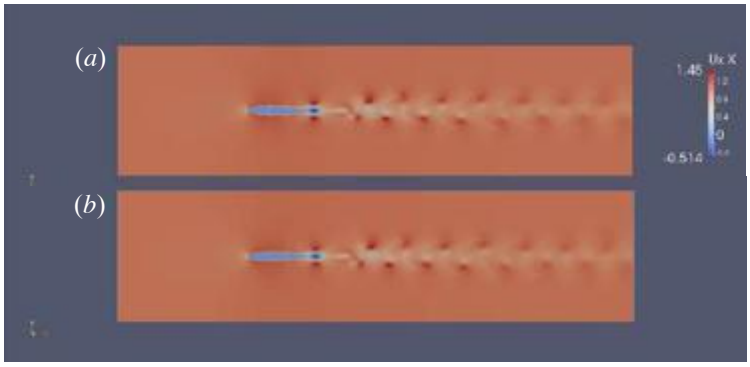

Figure2 Comparison of the instantaneous streamwise velocity. The cell size is (*a*) 16.7M and (*b*) 134M.

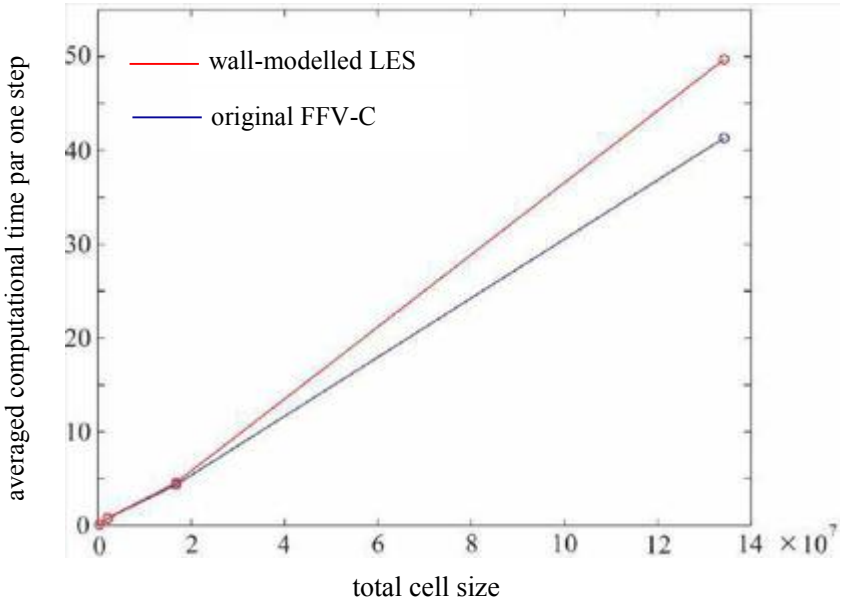

Figure3 The averaged computational time par one step for different cell sizes.

CONCLUSIONS

We have developed Cartesian-based high-performance parallel solver FFV-C by implementing wall-modelled LES. In this work, parallel performance of FFV-C is examined by choosing a NACA airfoil as a validation model. As a result, favourable scalability is observed and also found that computational cost in the model is only 20 percent larger than that in the DNS. Considering that wall-modeled LES can save total cell size drastically, reduction of the computational cost for high Reynolds number calculation is achieved.

References

[1] http://avr-aics-riken.github.io/ffvc_packege

[2] https://github.com/avr-aics-riken/FFVC

[3] Chapman D.R.: Computational aerodynamics development and outlook, *AIAA Journal* 17, 1293-1313, 1979.

[4] Kobayashi H.: The subgrid-scale models based on coherent structures for rotating homogeneous turbulence and turbulent channel flow, *Phys. Fluids* 17, 045104-1-045104-12, 2005.

[5] Nicoud F. *et al*.: Subgrid-scale modelling based on the square of the velocity gradient tensor, *Flow, Turbulence, and Combustion* 62, 183-200, 1999.

[6] Uzawa K. and Ono K.: Validation of local SGS models implemented in high-performance CFD solver: FFV-C, ASME-JSME-KSME Joint Fluids Engineering Conference, 2015.

[7] Jacobs E.N, *et al*.: The characteristics of 78 related airfoil sections from tests in the variable-density wind tunnel, NACA report No.460, 1-59, 1933.

PETASCALE DNS USING THE FAST POISSON SOLVER PSH3D

Darren Adams[1], Michael Dodd[2] & Antonino Ferrante *[2]
[1]*The National Center for Supercomputing Applications (NCSA), University of Illinois, Urbana, IL, USA*
[2]*William E. Boeing Department of Aeronautics & Astronautics, University of Washington, Seattle, WA, USA*

Summary Direct numerical simulation (DNS) of high Reynolds number ($Re = \mathcal{O}(10^5)$) turbulent flows requires computational meshes of $\mathcal{O}(10^{12})$ grid points. Thus, DNS requires the use of petascale supercomputers. DNS often requires the solution of a Helmholtz (or Poisson) equation for pressure, which constitutes the bottleneck of the solver. We have developed and implemented a parallel solver of the Helmholtz equation in 3D called petascale Helmholtz 3D (PSH3D). The numerical method underlying PSH3D combines a parallel 2D Fast Fourier transform (P2DFFT) and a parallel linear solver (PLS). Our numerical results show that PSH3D scales up to at least $262{,}144$ cores. PSH3D has a peak performance $6\times$ faster than 3D FFT-based methods (e.g., P3DFFT) when used with the partial-global optimization. We have verified that the use of PSH3D with the partial-global optimization in our DNS solver does not reduce the accuracy of the numerical solution when tested for the Taylor-Green vortex flow.

INTRODUCTION AND NUMERICAL METHODS

DNS of turbulent flows, e.g. for solving the incompressible Navier-Stokes equations, using the pressure correction method [1], requires a solution to the Poisson equation for pressure at each time integration step. The Poisson solver is the bottleneck of such DNS codes. The current work extends the terascale parallel Poisson solver developed by [3, 4] based on [6], which uses 1D domain decomposition (1DD), to a petascale solver using 2D domain decomposition (2DD).

The key aspect of this method that enabled the advance toward a petascale implementation is the parallel Helmholtz/Poisson solver and is described briefly here. The general 3D Helmholtz equation

$$\nabla^2 p - \lambda^2 p = q. \tag{1}$$

is discretized using second-order finite differences on a uniform Cartesian mesh. $p_{(i,j,k)}$ and $q_{(i,j,k)}$ are unknowns and knowns, respectively, located at grid point (i, j, k). Applying a 2D FFT to the discrete form of Eq. (1) results in a system of tri-diagonal linear equations,

$$p^*_{(m,n,k-1)} - \alpha p^*_{(m,n,k)} + p^*_{(m,n,k+1)} = q^*_{(m,n,k)} \Delta z^2 \tag{2}$$

for each set of Fourier wavenumbers (m, n), where $p^*_{(m,n,k)}$ and $q^*_{(m,n,k)}$ are the Fourier transforms of $p_{(i,j,k)}$ and $q_{(i,j,k)}$, respectively and

$$\alpha = 2 + (\lambda^2 + \lambda_{(m,n)})\Delta z^2 \tag{3}$$

and

$$\lambda_{(m,n)} = \frac{2(1 - \cos(\frac{2\pi m}{N_x}))}{\Delta x^2} + \frac{2(1 - \cos(\frac{2\pi n}{N_y}))}{\Delta y^2}. \tag{4}$$

Solutions to Eq. (2) yield the second-order accurate $p^*_{(m,n,k)}$ to which an inverse 2D FFT is applied to obtain $p_{(i,j,k)}$.

Applying the 2DD, the grid $(N_x \times N_y \times N_z)$ is partitioned into N sub-domains $(N_x \times \frac{N_y}{P_y} \times \frac{N_z}{P_z})$ where the total number of processors is: $P_y \times P_z$ and $P_y \leq N_y$, $P_z \leq N_z$ and $P_y \leq \frac{N_x}{2} + 1$. The complex linear system in Eq. (2) is now sub-divided across P_z domain partitions, where $P_y \leq \frac{N_x}{2} + 1$. A divide-and-conquer strategy, developed by Schumann and Strietzel [7], leads to a PLS algorithm that only involves nearest neighbor communication *except* for a boundary correction step which must satisfy the following constraint equation

$$r_n R_{\kappa-1} - (\alpha + 2r_2)R_\kappa + r_n R_{\kappa-1} = q_1^\kappa - p_n^\kappa - p_2^\kappa. \tag{5}$$

where $\kappa = 1, 2, .., P_z$.

*Corresponding author. Email: ferrante@aa.washington.edu

RESULTS AND CONCLUSIONS

The total PSH3D execution time on a 8192^3 mesh was studied for various 2DD layouts on up to $262{,}144$ processor cores of Blue Waters. Dependence on 2DD layout and full strong scaling results are presented in Figure 1. We first tested a version in which we perform global reductions for all vectors; we refer to this as the "all-global" variant (PSH3D-AG). Next, we implemented a "local-only" version of the PLS, dubbed "no-global" (PSH3D-NG) . The NG simplification avoids the costly global reduction step demanded by the full algorithm and demonstrates the maximum possible level of scaling and performance; only limited by the P2DFFT operation. Finally, we investigate our novel hybrid approach, dubbed "partial-global" (PSH3D-PG), in which we assess the diagonal dominance in Eq. (5) and construct a parallel reduction scheme that applies only to vectors at locations where the ratio of diagonal to off-diagonal terms are above a prescribed tolerance. When optimized through the use of MPI-3 non-blocking collectives, this method shows much better performance relative to all-global while maintaining the second order accuracy expected by the full DNS algorithm.

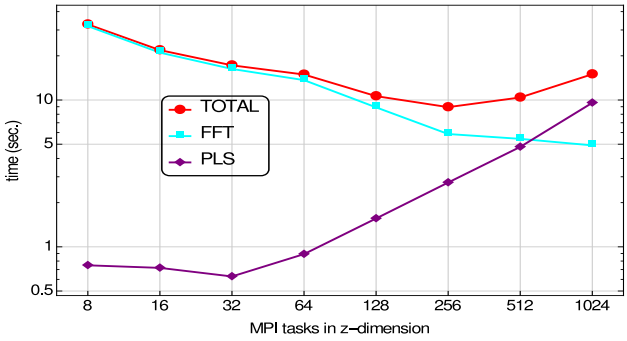

(a) Total Poisson-time and constituent FFT and PLS times vs. P_z for PSH3D-AG using a series of 2DD layouts on $16{,}384$ processors.

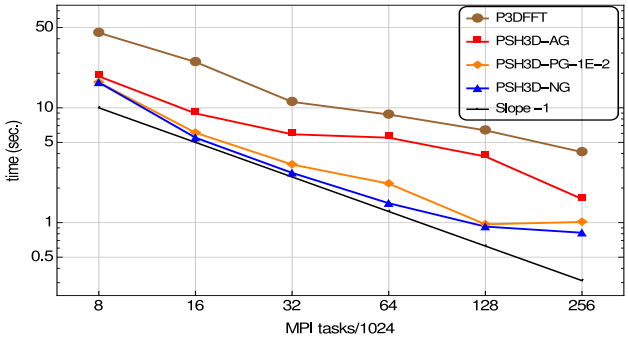

(b) Strong scaling of total wall-clock time to solve the Poisson equation in 3D for variations of PSH3D and P3DFFT solvers [5].

Figure 1: Execution times for parallel Poisson solutions on an 8192^3 mesh using Cray XE6 compute nodes on Blue Waters. The PSH3D-AG method computes global reduction operations for *all* Fourier wave-numbers: (m, n). The PSH3D-PG-"tol" results solve the global reduction for fewer and fewer (m, n) as tol increases. The PSH3D-NG method avoids global reduction operations *completely*.

Performance of PSH3D-PG is shown in Figure 1b for a tolerance value of 10^{-2}. Larger values of the PG-tolerance reduce the number of global solutions that now require a solution, thus creating a more lightweight global-reduction step. The most dramatic improvement using this technique, was observed on 128k processors where the original AG wall-clock time was reduced from about 4 to 1 sec. Our numerical tests show that the method retains second-order accuracy for PG-tolerance values of up to 10^{-1}.

We have developed a new petascale solver for the Helmholtz 3D equation (PSH3D) and tested it on Blue Waters up to $262{,}144$ MPI ranks. The novelty of this method stands in performing a parallel 2DFFT in two spatial directions and a parallel linear solver in the third spatial direction rather than a fully parallel 3D FFT, and in the special "partial-global" treatment in implementing the global correction step. The results show that the PSH3D, when used with the AG PLS, is 30% to 40% faster than P3DFFT [5], and with the optimized PG PLS is more than 6 times faster and 4 times faster than P3DFFT on 128k and 262k MPI ranks of Blue Waters, respectively. We have then extended our DNS solver [2] from 1DD to 2DD and used PSH3D as its Poisson solver. The DNS code has been verified using this highly optimized solver (PG-PLS) by comparing the DNS results with the analytical solution of the Taylor-Green vortex flow [8].

References

[1] A. J. Chorin, *A numerical method for solving incompressible viscous flow problems*, J. Comput. Phys. **2** (1967), no. 1, 12–26.

[2] M. S. Dodd and A. Ferrante, *A fast pressure-correction method for incompressible two-fluid flows*, J. Comput. Phys. **273** (2014), 416–434.

[3] A. Ferrante, *Reduction of skin-friction in a microbubble-laden spatially developing turbulent boundary layer over a flat plate*, Ph.D. thesis, University of California, Irvine, 2004.

[4] A. Ferrante and S. Elghobashi, *On the physical mechanism of two-way coupling in particle-laden isotropic turbulence*, Phys. Fluids **15** (2003), no. 2, 315–329.

[5] D. Pekurovsky, *P3DFFT: A framework for parallel computations of Fourier transforms in three dimensions*, SIAM J. Sci. Comput. **34** (2012), no. 4, C192–C209.

[6] H. Schmidt, U. Schumann, and H. Volkert, *Three dimensional, direct and vectorized elliptic solvers for various boundary conditions*, Rep. 84-15, DFVLR-Mitt, 1984.

[7] U. Schumann and M. Strietzel, *Parallel solution of tridiagonal systems for the Poisson equation*, J. Sci. Comput. **10** (1995), no. 2, 181–190.

[8] G. I. Taylor, *On the decay of vortices in a viscous fluid*, Philos. Mag. **XLVI** (1923), 671–674.

SUPERCOMPUTATIONS OF LOW-PRANDTL-NUMBER CONVECTION FLOWS

Jörg Schumacher[1] and Janet D. Scheel[2]

[1]*Department of Mechanical Engineering, Technische Universität Ilmenau, Ilmenau, Germany*
[2]*Department of Physics, Occidental College, Los Angeles, USA*

Summary Massively parallel supercomputations are an important analysis tool to study the fundamental local and global mechanisms of heat and momentum transfer in turbulent convection. We discuss the perspectives and challenges in this vital field of fundamental turbulence research for the case of convection at very low Prandtl numbers.

MOTIVATION AND SIMULATION MODEL

Turbulent convection is an important area of present research in fluid dynamics with applications to diverse phenomena in nature and technology. The turbulent Rayleigh-Bénard convection (RBC) model is at the core of all these turbulent flows. It can be studied in a controlled manner, but has enough complexity to contain the key features of turbulence in heated fluids. This flow in cylindrical cells has been investigated intensively over the last few years in several laboratory experiments all over the world [1]. In RBC, a fluid cell or layer is kept at a constant temperature difference $\Delta T = T_{bottom} \nearrow T_{top}$ between top and bottom plates which are separated by a vertical distance H. The Rayleigh and Prandtl numbers are given by

$$Ra = \frac{g\alpha H^3 \Delta T}{\nu\kappa} \qquad \text{and} \qquad Pr = \frac{\nu}{\kappa}\,. \tag{1}$$

The parameter Ra characterizes the thermal driving in convective turbulence with the acceleration due to gravity, g, the thermal expansion coefficient, α, the kinematic viscosity, ν, and the thermal diffusivity, κ. The hard turbulence regime in RBC is established for $Ra \geq 10^6$. The Prandtl number Pr characterizes the molecular properties the working fluid. The aspect ratio Γ, which is the ratio of cell diameter or cell length and cell height H, is the third input parameter. In this contribution, we will focus on the specific turbulence properties of convection at very low Prandtl numbers and the resulting challenges for supercomputer simulations.

The three-dimensional Boussinesq equations (2)–(4) are used to model Rayleigh-Bénard convection. They are given in dimensionless form by

$$\nabla \cdot \mathbf{u} = 0\,, \tag{2}$$

$$\frac{\partial \mathbf{u}}{\partial t} + (\mathbf{u}\cdot\nabla)\mathbf{u} = \nearrow\!\nabla p + \sqrt{\frac{Pr}{Ra}}\nabla^2\mathbf{u} + T\mathbf{e}_z\,, \tag{3}$$

$$\frac{\partial T}{\partial t} + (\mathbf{u}\cdot\nabla)T = \frac{1}{\sqrt{RaPr}}\nabla^2 T\,. \tag{4}$$

The variable $\mathbf{u}(\mathbf{r},t)$ is the velocity field, $p(\mathbf{r},t)$ is the pressure, and $T(\mathbf{r},t)$ is the temperature. We use no-slip velocity boundary conditions along all walls of the closed cylindrical cell. The temperature field obeys insulating sidewalls and constant values along the top and bottom plates. A spectral element method (SEM) is applied which is based on the Nek5000 software package [2]. The order of the Lagrangian interpolation polynomials for the expansion on each element (see the element mesh in the left panel of figure 1) which is used in each space direction is as high as $N \nearrow 1 = 13$. This code is a pure MPI code which scales very well up to $\sim 10^6$ MPI tasks. Numerical details and comprehensive resolution tests are found in Scheel et al. [3]. The SEM is preferred if the fine-scale structure, i.e. gradients of the turbulent fields have to be analyzed.

TURBULENT CONVECTION AT VERY LOW PRANDTL NUMBERS

Compared to the vast number of investigations of turbulent convection in air or water, the very-low-Pr regime appears almost as a "Terra incognita" despite many applications. Turbulent convection in the Sun is present at Prandtl numbers $Pr < 10^{-3}$, in the liquid metal core of the Earth one finds $Pr \sim 10^{-2}$. Convection flows as present in material processing, nuclear engineering, or liquid metal batteries have Prandtl numbers between 5×10^{-3} and 2×10^{-2}. One reason for significantly fewer studies of convection at low Prandtl numbers is that laboratory measurements have to be conducted in opaque and aggressive liquid metals when Pr should become much smaller than 0.1.

Direct numerical simulations (DNS) are currently the only way to gain access to the full three-dimensional convective turbulent fields in low-Pr convection. However, these simulations become very demanding when the small-scale structure of turbulence has to be studied, even for moderate Rayleigh numbers Ra. To give an example: a simulation for convection

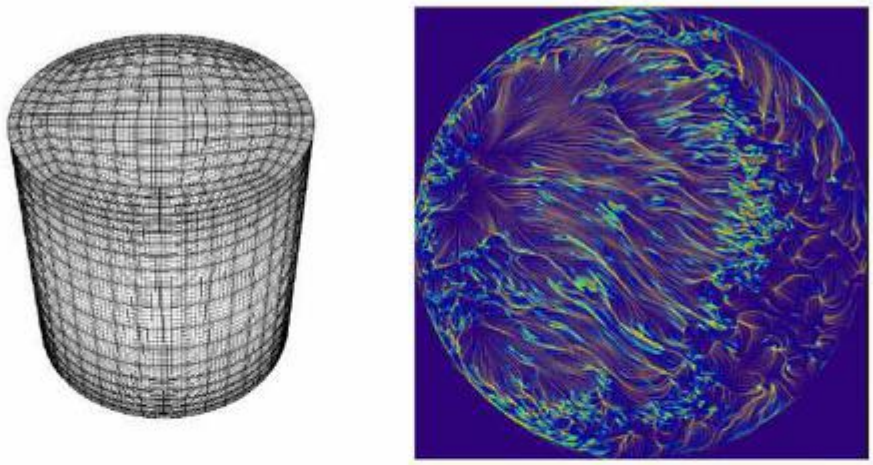

Figure 1: Left: Spectral element grid for the RBC cell. Right: Snapshot of the dynamics in the vicinity of the bottom plate of the convection cell. We show field lines of the wall shear stress field and isocontours of the magnitude of the wall-normal vorticity component. The snapshot is for convection in liquid mercury at $Pr = 0.021$ at $Ra = 10^8$.

in liquid sodium at $Ra = 2.38 \times 10^6$ and $Pr = 0.005$ required the same SEM mesh of 4.1×10^9 cells as a simulation for convection in air at $Ra = 10^{10}$ and $Pr = 0.7$. The latter Rayleigh number is almost four orders of magnitude larger than in sodium. Both runs were conducted with 65,536 MPI tasks on BG/Q.

What makes these simulations so expensive? While the heat transport is reduced in low–Pr convection, the production of vorticity and shear are enhanced significantly. We found that this in turn amplifies the small-scale intermittency in these flows and makes them more comparable to classical Kolmogorov turbulence [4]. We have also shown in [4] that the cascade of the fluid turbulence is extended at the large-scale and small-scale end with decreasing Prandtl number thus enhancing the flow Reynolds number and consequently the turbulent momentum transport in the convection flow. The more vigorous fluid turbulence enhances in the enstrophy production in the fluid. Since the Rayleigh-Bénard fluid is confined, tiny boundary layers of the temperature and velocity fields form in the vicinity of the walls. Figure 1 (right) displays a snapshot of the velocity boundary layer dynamics at the bottom plate for our biggest simulation in liquid mercury with 131,072 MPI tasks on BG/Q. This figure and our comprehensive analysis suggest that turbulence is also strongly amplified in the boundary layers although the Rayleigh number seems to be moderate. An increase from the present value of $Ra = 10^8$ to $Ra = 5 \times 10^8$ requires 1.3×10^{10} mesh cells and 524,288 MPI tasks for a well-resolved run. We will also discuss the increasing challenges in the data analysis which one faces for these big simulations.

Our research topic demonstrates clearly that supercomputing has become an essential tool for revealing the secrets of turbulence, and especially those of turbulent convection.

ACKNOWLEDGEMENTS

The work of JS is supported by the Deutsche Forschungsgemeinschaft. We want to thank the John von Neumann-Institute for Computing for the support with supercomputing resources by projects HIL07 and HIL09 as well as the Scientific Big Data Analytics Project SBDA003. This work is also supported by the DOE INCITE projects RayBen (2014) and LiquidGaNa (2016).

References

[1] Chillà F. and Schumacher J.: New perspectives in turbulent Rayleigh-Bénard convection. Eur. J. Phys. E 35: no. 58, 2012.

[2] Nek5000 Website: https://www.nek5000.mcs.anl.gov/

[3] Scheel J. D., Emran M. S. and Schumacher J.: Resolving the fine-scale structure in turbulent Rayleigh-Bénard convection. New J. Phys. 15: no. 113063, 2013.

[4] Schumacher J., Götzfried P. and Scheel J. D.: Enhanced enstrophy generation for turbulent convection in low–Prandtl number fluids. Proc. Natl. Acad. Sci. USA 112: 9530–9535, 2015.

"TURBULENT SPOT" DEEP INSIDE THE TURBULENT FLAT-PLATE BOUNDARY LAYER IDENTIFIED FROM VERY-LARGE SCALE DIRECT SIMULATION

Xiaohua Wu[1], Parviz Moin[2] & James Wallace[3]
[1]*Royal Military College of Canada, Kingston, Ontario, Canada*
[2]*Center for Turbulence Research, Stanford University, California, USA*
[3]*Department of Mechanical Engineering, University of Maryland, Maryland, USA*

Summary Zero-pressure-gradient flat-plate boundary layer (ZPGFPBL) beneath a continuous flow of freestream nearly-isotropic turbulence (FST) from momentum thickness Reynolds number 80 to 3000 has been computed with direct numerical simulation (DNS) on 4 billion grid points. The thoroughly validated DNS data reveal an intriguing unknown flow physics feature: In the fully turbulent region after transition, the near-wall layer (log-layer and below) is populated with hairpin-packed turbulent "turbulent spot". Although less distinct due to their existing in a chaotic turbulent environment, these turbulent "turbulent spots" nevertheless bear certain similarities to the commonly known transitional turbulent spots which are also packed with hairpin vortices. In the outer forty percent of the boundary layer, the flow is populated by large-scale hairpin forest. Both features persist until the end of the computational domain at momentum thickness Reynolds number 3000.

INTRODUCTION

Coherent structures in the zero-pressure-gradient flat-plate boundary layer have remained a fundamental subject of interest in fluid mechanics research since the early 1950s. Based on the hydrogen bubble visualization by Kline and others in the 1960s, it has been widely believed that the dominant near-wall coherent structure in the ZPGFPBL is streamwise streak and the related vertical structure is quasi-streamwise vortex. However, it is unclear what the relative length is between the streak and the quasi-streamwise vortex. The observed streaks are of the order of boundary layer thickness or longer: Are the near-wall quasi-streamwise vortices about the same length? Since the 1980s, there have been reported indirect experimental observations and models from Adrian, Marusic and others suggesting the existence of a hierarchy of hairpin packets in the ZPGFPBL. But this was not supported by the early DNS of Spalart, and was further challenged by the more recent DNS results of several European groups. Our DNS data to be presented at the 2016 IUTAM reveal both near-wall and outer layer ZPGFPBL coherent structures and their dynamics in remarkable detail than achieved before.

In the present study, the DNS domain size is $21562.5\theta_0$, $2250\theta_0$ and $843.75\theta_0$, where θ_0 is the inlet momentum thickness. The boundary layer grows to $\mathrm{Re}_\theta = 3018$ at $x = 21562.5\theta_0$. The grid size is $16384 \times 500 \times 512$. At $\mathrm{Re}_\theta = 3000, \delta = 309\theta_0$. The continuous freestream flow above the boundary layer has an inlet FST level of 3%, which was generated separately using a large set of independent computations on the incompressible isotropic grid turbulence. The reliability of the boundary layer simulation results is thoroughly verified by comparing the skin-friction coefficient, mean and second-order statistics with existing data. For example, we found that the DNS skin-friction result falls almost exactly on to the Blasius solution over an extended region ($0 < x < 700\theta_0$, $80 < \mathrm{Re}_\theta < 180$) prior to laminar layer breakdown. This suggests that the present free-stream perturbation near the inlet is mild and well-controlled and the present simulation accuracy at the laminar end is good. During transition, the present skin-friction follows the trend of the T3A bypass transition experimental data. Further downstream, our DNS skin-friction coefficient result in the fully-turbulent region agrees well with classical experimental data for the turbulent ZPGFPBL. We also found that after the completion of transition, the profiles of the rate of dissipation for turbulence kinetic energy exhibit the -1 slope dependence on inner wall unit when normalized by the viscous scaling, in excellent agreement with the theory of Tennekes and Lumley for high Reynolds number ZPGFPBL.

Figure 1 presents iso-surfaces of swirling strength in the near-wall region of $0 < y/\delta < 0.15$ over the streamwise range of $2800 < \mathrm{Re}_\theta < 2900$. The corresponding wall unit range is approximately $0 < y^+ < 150$. The iso-surfaces are colored by wall distance with blue indicating locations closest to the wall $0 < y/\delta < 0.01$. The full spanwise dimension is shown in the figure and is approximately 3δ locally. The existence of hairpin packed turbulent "turbulent spots" is evident. The smallest size of the hairpin vortices forming the spots observed from the figure is approximately 20 wall units in width. In the figure, the largest hairpin vortex is less than 0.12δ in height. The hairpin forest in the outer region is not visible in Figure 1 since all the outer grid points higher than 0.15δ have been stripped away so that the near-wall coherent structures can be made visible. It is also clear from the figure that is a lack of very-long quasi-streamwise vortices. The observed streamwise vortices seem to be only of the order of 0.1δ. Overall, we believe that the presently discovered hairpin-packed turbulent "turbulent spot" is an important element in near-wall turbulence dynamics of the ZPGFPBL.

[a] Corresponding author. Email: Xiaohua.Wu@rmc.ca

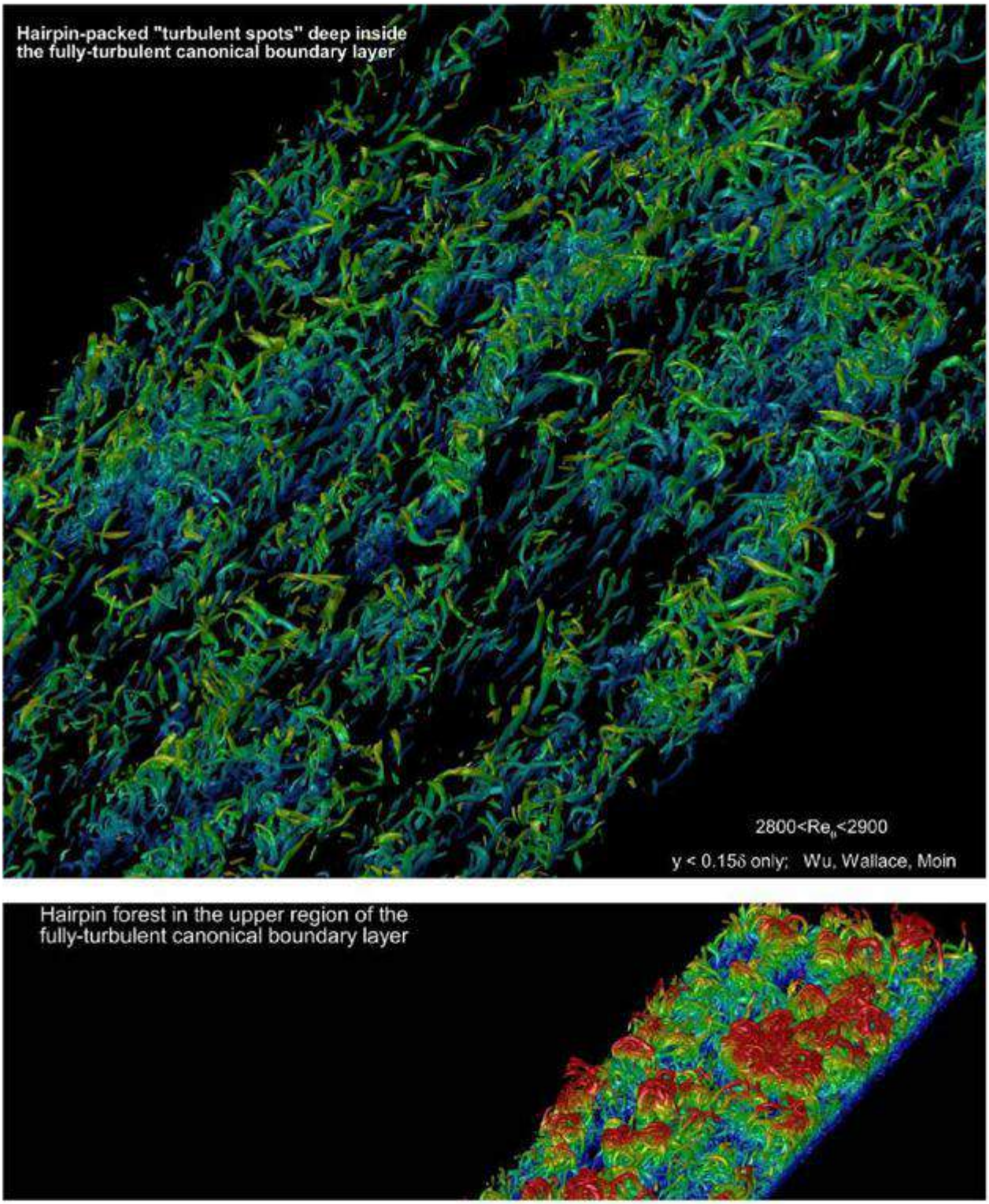

Figure 1: Hairpin-packed turbulent “turbulent spots” deep inside the fully-turbulent, zero-pressure-gradient, flat-plate boundary layer and the hairpin forest in its outer region.

AFID: A MULTIPURPOSE AND VERSATILE TOOL FOR TURBULENCE SIMULATIONS

J. Donners[1], M. Fatica[2], D. Lohse[3], R. Ostilla-Mónico*[4], E. Phillips[2], E. P. van der Poel[3], G. Ruetsch[2], V. Spandan[3], R. J. A. M. Stevens[3], R. Verzicco[3,5], Y. Yang[3], and X. Zhu[3]

[1]*SURFSara, Amsterdam, The Netherlands*

[2]*NVIDIA Corporation, Santa Clara, California, USA*

[3]*Physics of Fluids, University of Twente, Enschede, The Netherlands*

[4]*School of Engineering and Applied Sciences, Harvard University, Massachusetts, USA*

[5]*Dipartimento di Ingegneria Industriale, University of Rome "Tor Vergata", Rome, Italy*

Summary A code named AFiD has been developed for the direct numerical simulation (DNS) of turbulence. We focus on the problem of thermal convection, but AFiD can be used for a variety of fluid dynamical cases. AFiD is a hybrid MPI-OpenMP parallelization of an energy conserving staggered second-order finite difference scheme geared towards high Reynolds number flows. The code is based on ideas of 2DECOMP, and uses a pencil-type domain decomposition. AFiD allows for one non-uniform dimension in the grid distribution, which is advanced in time semi-implicitly. Both uniform directions are advanced fully explicitly, which reduces the number of communications. AFiD builds on 2DECOMP with new data transposes based on `MPI_ALLTOALLW` calls. A multiple-resolution strategy allows the efficient solution of advection/diffusion equations for low diffusivity scalar fields, which leads to wall time and memory savings. A GPU port is also detailed, and its present performance is compared to the current CPU code.

INTRODUCTION

Direct numerical simulations (DNS) provide a valuable tool for studying in detail the underlying, and currently not fully understood physical mechanisms behind turbulence. Turbulence is a dynamic and high dimensional process, in which energy is transferred (cascades) from large vortices into progressively smaller ones, until the scale of the energy is so small that they are dissipated by viscosity. DNS requires solving all of the flow scales, and to adequately simulate a system with very large size separation between the largest and the smallest scale, immense computational power is required.

Efficient code parallelization is essential to obtaining scientific results. Here we detail the parallelization of an energy-conserving second-order finite-difference scheme (FDS) based on Ref. [1]. FDS present several advantages, they are very flexible, allowing for complex boundary conditions and/or structures interacting through the immersed boundary method with relative ease. Because lower-order schemes are computationally very inexpensive, the grid resolution can in general be larger for the same computational cost compared to higher order schemes, although one has to consider the higher memory bandwidth over FLOPS ratio. In our applications, we focus on Rayleigh-Bénard (RB) convection, the flow in a fluid layer between two parallel plates; one heated from below and cooled from above, with the aim of achieving a high enough thermal driving (Rayleigh number) to enter the "ultimate" regime, of relevance to geo- and astro-physics, and to help understand the discrepancies between high-Rayleigh number experiments. However, our code can be easily extended to any wall-bounded flow which is bounded in only one dimension, i.e. Channel flow and Taylor-Couette flow.

PARALLELIZATION AND I/O

AFiD was designed with high Reynolds number simulations in mind, and it uses this to its advantage, as efficient parallelization is deeply tied to the underlying numerical schemes. As the CFL stability condition for the convective terms becomes more restrictive at high driving than the stability condition for the viscous terms in the wall-parallel directions, their implicit integration is no longer required. Thus, we only need to solve implicitly the wall-normal direction. Using a two-dimensional (pencil) decomposition aligned in the wall-normal direction avoids the communication of non-local information to a process for the computation of implicit derivatives in wall-parallel directions. This decreases the number of all-to-all communications per time-step to six, all found in the pressure correction (Poisson solver). The MPI parallelization of AFiD is based on, and extends 2DECOMP, which only has four transposes available (no x-to-z or z-to-x) with two new data transposes based on `MPI_ALLTOALLW` calls, as all six possible data transposes are required. Figure 1(a) shows the code's strong scaling, which is very good up to at least 64K cores on the CURIE (CEA) supercomputer. The weak scaling also shows very good performance.

Data output in AFiD uses parallel HDF5. Due to the scale of our simulations, we generate petabytes of raw data in every run. Most data is not preserved. Every time-step advance generates a new flow field gigabytes large, and thousands of time steps are advanced every day to obtain statistical convergence in the mean quantities. In our research, we focus on the transitions in the scaling laws relating heat flux and driving, focusing on temporally- and spatially averaged statistics of the temperature and velocity fields, which are calculated on-the-fly. In addition, 2D cuts of the whole volume are also saved, as these require less space and are also used for other analysis, i.e. studying the morphology of the small scale fluctuations. A few snapshots of the full flow field are also saved, which for the largest cases are as large as 300 GB. We are currently developing tools for a-posteriori parallel analysis of full flow fields, to study the 3D underlying structures.

*Corresponding author. Email: rostillamonico@g.harvard.edu

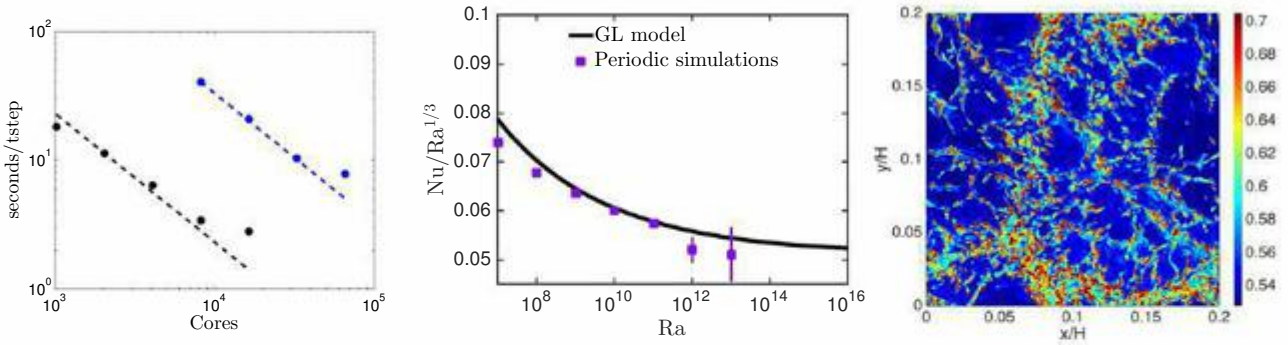

Figure 1: Left: Strong scaling in CURIE for 2048^3 (black) and 4096^3 (blue) grids. Middle: Compensated Nusselt against Rayleigh for the current simulations and from the theoretical prediction of the GL model. Right: Pseudocolour of temperature inside the thermal boundary layer at $Ra = 10^{13}$. The small scale temperature fluctuations, that are required to be properly resolved can be seen.

MULTIPLE RESOLUTION APPROACH

AFiD can use a grid for the scalars with a higher spatial resolution than that of the momentum, as integrating both fields on a single grid tailored to the most demanding variable produces an unnecessary computational overhead. In order to advect the scalar, the velocity field must be however carefully interpolated onto the scalar mesh. As the arrangement of the grid is staggered, if not careful, one could end up with a non-solenoidal velocity field, which does not conserve mass (or energy). The full details of the strategy are described in Ref. [3]. A multiple resolution approach is used also in the time integration in order to maintain the stability of the scalars on the finer grid. The method is the more advantageous the less diffusive the scalar is with respect to momentum. However, even in the case of equal diffusivities, at high drivings the present procedure gives significant wall time ($4\times$) and memory occupation ($2.6\times$) savings, due to the more intermittent behaviour of the scalars when compared to momentum.

GPU OPTIMIZATION

Moving with the current trends in high-performance computing, a GPU port of AFiD in CUDA Fortran has been carried out. One of the main objectives was to have a source code as close as possible to the original, so kernel loop directives (CUF kernels) have been extensively used and just few routines have been manually written. On Piz-Daint (CSCS), the current GPU version can solve a 1024^3 mesh on 48 K20x GPUs (the minimum number required for memory) in 2.7s per time step, while with 512 GPUs, we measured 0.37s per time step. As a comparison, with the same resolution, a time step with 1024 CPU nodes on the Cartesius (SURFSara) supercomputer takes 2.2s, and for 4096 CPUs it takes 0.56s. Planned optimizations focused on overlapping the GPU/CPU transfers with network traffic should further speed up the code.

SUMMARY AND PROSPECTS

In this manuscript we have summarized the current work in developing a thermal convection code. Using the present day version of AFiD with only the semi-implicit integration, Rayleigh numbers of $Ra = 10^{13}$ have already been achieved. A sample the results obtained are seen in figures 1(b,c). The combined approaches of multiple resolution strategies, semi-implicit integration, and porting to GPUs will allow for even higher Rayleigh number simulations, in the hope of finally achieving the driving parameters for entering the "ultimate" regime of thermal convection and understanding the discrepancies between experiments. AFiD is open source and available for download at `www.afid.eu`.

References

[1] R. Verzicco, P. Orlandi: A finite-difference scheme for three-dimensional incompressible flows in cylindrical coordinates, J. Comp. Phys. 123(2):402-414, 1996.

[2] N. Li, S. Laizet: 2DECOMP&FFT - A highly scalable 2D decomposition library and FFT interface, Cray User Group 2010 conference, Edinburgh, 2010.

[3] R. Ostilla-Monico, Y. Yang, E. P. van der Poel, D. Lohse, R. Verzicco: A multiple-resolution strategy for Direct Numerical Simulation of scalar turbulence, J. Comp. Phys. 301:308-321, 2015.

[4] E. P. van der Poel, R. Ostilla-Monico, J. Donners, R. Verzicco: A pencil distributed finite difference code for strongly turbulent wall-bounded flows, Computers and Fluids 116:10-16, 2015.

PETASCALE SIMULATIONS OF SHOCK INDUCED MULTI-MATERIAL MIXING

Akshay Subramaniam [*1] and Sanjiva K. Lele[2]

[1,2]*Department of Aeronautics & Astronautics, Stanford University, Stanford, California, USA*

Summary The Richtmyer-Meshkov instability arises when a shock wave interacts with an interface separating two fluids. In this work, high fidelity simulations of shock induced multi-material mixing between N_2 and CO_2 in a shock tube are performed for a Mach 1.55 shock interacting with a planar material interface that is inclined with respect to the shock propagation direction. In the current configuration, unlike the classical perturbed flat interface case, the evolution of the interface is non-linear from early time onwards. The computational domain is setup to match experiments performed by McFarland et. al. [4]. Simulations at multiple grid resolutions upto 4.3 billion grid points were performed on upto $65,536$ processors on the Blue Waters system. Comparison with experiments show that the simulations adequately represent the experimental results. Turbulence statistics before and after re-shock are presented.

INTRODUCTION

The Richtmyer-Meshkov Instability (RMI) is a hydrodynamic instability that is caused by the interaction of a shock-wave with a material interface. Like in the Rayleigh-Taylor instability where gravity acts to produce vorticity at the material interface, baroclinic vorticity generation due to the interaction of the interface with the shock wave renders the interface unstable to perturbations. Equation 1 governs the evolution of the vorticity.

$$\frac{\partial \boldsymbol{\omega}}{\partial t} + (\boldsymbol{u}\cdot\nabla)\boldsymbol{\omega} = \underbrace{\cancel{\boldsymbol{\omega}(\nabla\cdot\boldsymbol{u})}}_{\text{vortex-dilatation}} + \underbrace{(\boldsymbol{\omega}\cdot\nabla)\boldsymbol{u}}_{\text{vortex stretching}} + \underbrace{\frac{1}{\rho^2}\nabla\rho\times\nabla p}_{\text{baroclinic generation}} + \underbrace{\nabla\times\left(\frac{1}{\rho}\nabla\cdot\boldsymbol{\tau}\right)}_{\text{viscous term}} \tag{1}$$

where $\boldsymbol{\omega}$ is the vorticity, $\boldsymbol{u}$ is the velocity, ρ is the density, p is the pressure and $\boldsymbol{\tau}$ is the viscous stress tensor. In Equation 1, the baroclinic vorticity generation term given by $(\nabla\rho\times\nabla p)/\rho^2$ is active when there is a misalignment of the density and pressure gradients.

RMI is an important phenomenon in many engineering and science applications involving material mixing. It is important in supersonic combustion as an enhancer of mixing between fuel and oxidizer. It is important in astrophysical applications, especially in the physics of supernovae to explain the lack of stratification in supernova remnants. It is also a major roadblock in achieving sustained fusion in Inertial Confinement Fusion (ICF) and can cause reduced yield and potentially inhibit startup.

NUMERICAL MODEL

We solve the three dimensional multi-species compressible Navier Stokes equations in the mass fraction formulation. Details of the equations solved are given in [1]. The Miranda code [1] developed at the Lawrence Livermore National Laboratory (LLNL) was used for the simulations shown here. Miranda employs a 10th order compact differencing scheme for the spatial derivatives that gives a spectral-like resolution [2]. A 5 step th order Runge-Kutta scheme is used for the time integration. An 8th order compact filter is applied to the conserved variables after each time step to remove the top 10% of the resolvable wavenumbers as partial de-aliasing and to ensure numerical stability. This choice of numerical scheme gives high order accuracy as well as minimal dissipation in regions where the solution is smooth. For regularization of steep numerical gradients that appear at regions of solution discontinuity (shocks, interfaces, etc.), the molecular transport coefficients are augmented locally by artificial fluid properties. Formulae for the artificial properties are given in [3].

PROBLEM SETUP

The interaction of a shock wave with an inclined material interface separating N_2 and CO_2 is considered. The problem setup is based on the inclined shock tube experiments performed at the Georgia Tech Shock Tube and Advanced Mixing Laboratory (STAML) [4]. A schematic of the problem setup is given in Figure 1.

The domain extends from $0\ cm$ to $11.\ cm$ in the y direction, $0\ cm$ to $2.85\ cm$ in the z direction and from $.23\ cm$ to $251.\ cm$ in the x direction. An adiabatic no-slip wall boundary condition is applied at the right end of the shock tube. In the y direction, slip wall boundary conditions are used to mimic the kinematic blocking effect of the walls. In the z direction, periodic boundary conditions are used since the z direction is homogeneous except wall effects which are expected to be negligible in the bulk of the domain. The domain is discretized using four different isotropic cartesian grids with 128, 25 , 512 and 102 grid points in the y direction. The largest case has a total of $\sim$ $.3$ billion grid points.

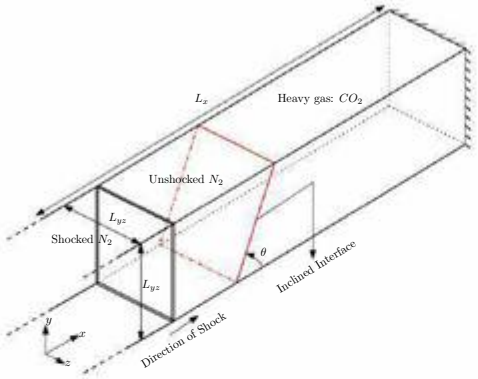

Figure 1: Schematic of the problem setup

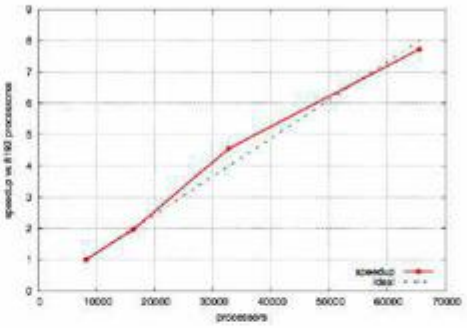

Figure 2: Strong scaling for Miranda (from [1]).

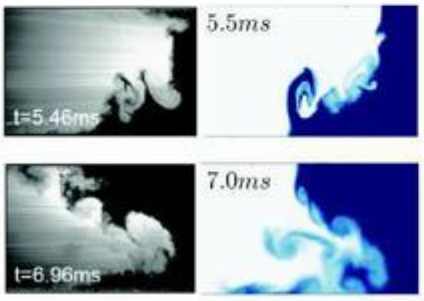

Figure 3: Qualitative comparison of the simulation and experiment at different times.

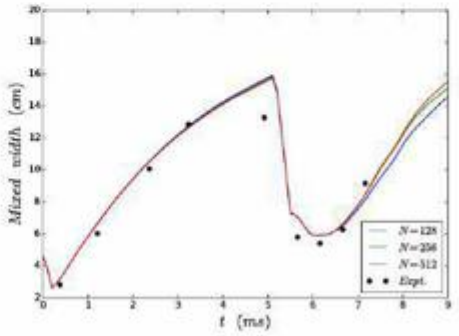

Figure 4: Evolution of the mixed width with time. Solid lines are simulations and solid circles are from the experiment.

RESULTS

Due to the large range of scales present in this problem, the resolution requirements for numerical simulations are very high. Hence, simulations of these types of flows require massive computational resources to be able to capture the physics of the problem adequately. Figure 2 shows that Miranda scales virtually perfectly up to 65,536 processors. We performed simulations of up to 4.3 billion grid points on up to $65,536$ processors on Blue Waters and found virtually perfect scaling.

Figure 3 shows that the simulations compare well qualitatively with the experiment at the two times shown. The mixed width is defined as $\int 4(1 - \langle Y_{CO_2} \rangle) \langle Y_{CO_2} \rangle \, dx$ where $\langle Y_{CO_2} \rangle$ is the CO_2 massfraction averaged in the y and z directions. Figure 4 shows the evolution of the mixed width with time from three simulation grids and from the experiment. It is seen that the simulations (a) are grid converged at the highest resolutions and (b) capture the experimental mixed width evolution very well.

SUMMARY AND FUTURE WORK

Petascale simulations of shock induced multi-material mixing were performed and shown to compare well with experiments. The parallel efficiency of the code was also demonstrated and shown to be very good. Further details on the parallel algorithms used and turbulence statistics such as TKE, Reynolds Stress anisotopy, turbulent mass flux, etc. will be presented at the conference talk. We also carefully assess the grid-sensitivity of the computed quantities.

We acknowledge computer time provided by the NSF PRAC award titled “Multi-material shock induced mixing” on the NCSA Blue Waters system. We also acknowledge code support provided by Lawrence Livermore National Laboratory.

References

[1] Cook, A. W., Cabot, W. H., Williams, P. L., Miller, B. J., Supinski, B. R. D., Yates, R. K., & Welcome, M. L.: In Proceedings of the 2005 ACM/IEEE conference on Supercomputing (p. 60), IEEE Computer Society, 2005.

[2] Lele, S.K.: Journal of computational physics, 103(1), pp.16-42, 1992.

[3] Kawai, S. and Lele, S.K.: Journal of Computational Physics, 227(22), pp.9498-9526, 2008.

[4] McFarland, J., Reilly, D., Creel, S., McDonald, C., Finn, T. and Ranjan, D.: Experiments in fluids, 55(1), pp.1-14, 2014.

A NOVEL STRATEGY FOR COMPACT FINITE DIFFERENCE EVALUATION ON GPU-ACCELERATED CLUSTERS

Ashwin Srinath[1], Daniel Livescu[2], and Richard S. Miller *[3]
[1,3] *Department of Mechanical Engineering, Clemson University, Clemson, SC 29634-0921*
[2]*Los Alamos National Laboratory, Los Alamos, NM 87544, USA*

Summary In this work, we present a novel strategy to solve the tridiagonal systems arising in such numerical schemes as compact finite differences and alternating direction implicit methods on graphics processing units (GPUs). We demonstrate the impact of the simple matrix structure on the *cyclic reduction* algorithm, and show that precomputation of coefficients appearing in the algorithm becomes feasible and efficient. We demonstrate that an implementation using our approach is able to outperform the NVIDIA CUSPARSE and multithreaded Intel MKL solvers on GPU and CPU, respectively. We apply this tridiagonal solver to the solution of compact finite differences on multiple GPUs distributed in a cluster, and show scaling for up to 64 GPUs.

Compact finite difference schemes [1,2] are widely used in computational fluid dynamics (CFD) for their ability to resolve the high-wavenumber fluctuations associated with turbulent flows. In CFD codes using compact schemes, this generally constitutes a significant portion of the runtime. The high computational cost associated with compact finite difference schemes arises from the fact that they require the solution of tridiagonal linear systems. Classically, the Thomas algorithm has been used to solve such linear systems. But with multi-core CPUs, graphics processing units (GPUs), and more recently, architectures such as the Intel Many Integrated Core (MICs) expected to be mainstays in scientific computing, such sequential algorithms need to be replaced by algorithms more suited to these architectures. In this study, we develop an algorithm to solve the tridiagonal systems arising in compact finite difference evaluation and similar numerical schemes. Our approach is based on *cyclic reduction*, an extremely successful algorithm for solving multiple tridiagonal systems on GPUs. Our work fills two existing gaps in the literature. First, whereas current efforts to develop tridiagonal solvers are focused on single GPUs (e.g., [3–7]) we develop an approach for *multiple* GPUs in a distributed system (GPU-accelerated clusters). Second, we specialize the cyclic reduction for the case of *near-Toeplitz* tridiagonal systems, a special class of systems arising in numerical schemes such as compact finite differences, alternating direction implicit methods, line relaxation methods, and others.

If f_i represents the value of a uniformly sampled function with spacing dx, evaluated at the ith sample point, the first derivative f_i' can be approximated from a relation of the form:

$$f_i' + \alpha(f_{i-1}' + f_{i+1}') = a\frac{f_{i+1} \nearrow f_{i-1}}{dx} + b\frac{f_{i+2} \nearrow f_{i-2}}{dx} + c\frac{f_{i+3} \nearrow f_{i-3}}{dx} + \ldots \tag{1}$$

The derivative is defined implicitly, requiring the solution of a linear system to solve for the derivative at all points i simultaneously. An example of such a scheme is the fourth-order accurate Padé scheme, which yields the following system:

$$\begin{bmatrix} 1 & 2 & & & & \\ 1/ & 1 & 1/ & & & \\ & \ddots & & & & \\ & & \ddots & & & \\ & & & \ddots & & \\ & & & & 2 & 1 \end{bmatrix} \begin{bmatrix} f_1' \\ f_2' \\ \vdots \\ \vdots \\ f_{n-1}' \\ f_n' \end{bmatrix} = \begin{bmatrix} \frac{-5f_1+4f_2+f_3}{2dx} \\ \frac{3(f_3-f_1)}{4dx} \\ \vdots \\ \vdots \\ \frac{3(f_n-f_{n-2})}{4dx} \\ \frac{5f_n-4f_{n-1}-f_{n-2}}{2dx} \end{bmatrix} \tag{2}$$

We note the *near-Toeplitz* nature of the tridiagonal system, i.e., constant diagonal coefficients except near the boundaries. The cyclic reduction algorithm consists of two phases, each containing $log_2(N) \nearrow 1$ steps. At each step of the *forward reduction* phase, the odd-indexed equations are eliminated, yielding eventually a 2-by-2 system. At each step of the *backward substitution* phase, the odd-indexed equations are solved from the known solutions of the even-indexed equations. Cyclic reduction is well-suited to highly threaded processors such as GPUs [8], as the individual equations can be processed in parallel.

*Corresponding author. Email: rm@clemson.edu

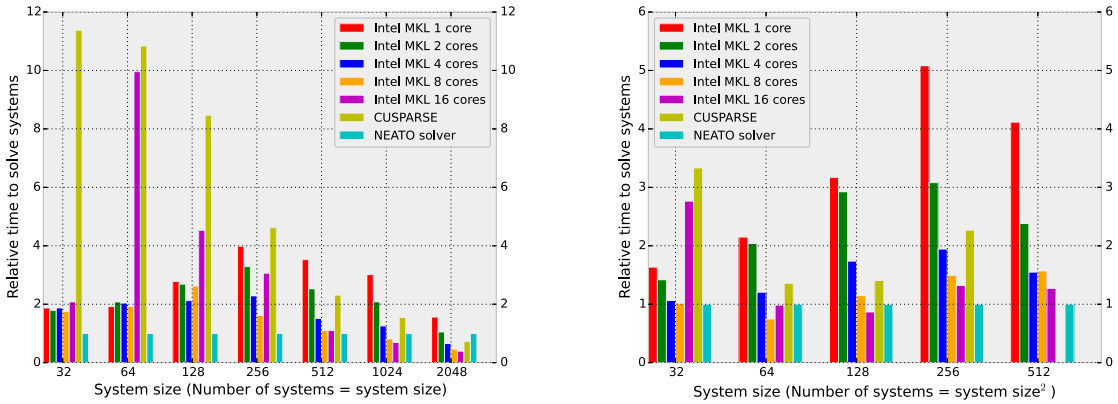

Figure 1: Relative solver performance for 2-D (left) and 3-D (right) problems. Relative solver time defined as: Time taken by solver/Time taken by NEATO solver

When cyclic reduction is applied to *near-Toeplitz* tridiagonal systems, we make the important observation that each forward reduction step preserves the near-Toeplitz nature of the linear system, i.e., the elimination of the odd-indexed equations at each step yields a new linear system that has exactly the same near-Toeplitz structure. This makes it feasible to precompute and store the coefficients of each linear system, significantly reducing the amount of computation required. As it turns out, this approach also ameliorates several GPU architecture-specific issues relating to memory access patterns. To extend the above approach to multiple GPUs, we adapt the algorithm described by Mattor et. al [9] to GPUs. Our implementation ensures that each step of this algorithm is performed on the GPU, avoiding memory transfers to and from the CPU entirely. In Fig. 1, we compare the performance of our GPU tridiagonal solver for near-Toeplitz systems (NEATO), with the equivalent library solvers from Intel MKL (CPU) and NVIDIA CUSPARSE (GPU). Here we solve the tridiagonal system in Eq. (2) for sizes N and multiple right hand sides N_{rhs}. We present results for two cases, $N_{rhs} = N$, (representative of 2-D problems) and $N_{rhs} = N^2$ (3-D problems). On the GPU, we are consistently able to obtain better performance than the CUSPARSE solver. Our GPU solver also outperforms the MKL solver running on up to 16 CPU cores for large 3-D problems. We have also investigated the strong and weak scaling for a multi-GPU compact finite difference application. Here, we solve for the derivatives of a 3-D function in a domain distributed among multiple GPUs in a cluster. We are able to show both strong and weak scaling for up to 64 GPUs (the largest problem investigated).

References

[1] Sanjiva K Lele. Compact finite difference schemes with spectral-like resolution. *Journal of Computational Physics*, 103(1):16–42, 1992.

[2] Christopher A Kennedy and Mark H Carpenter. Several new numerical methods for compressible shear-layer simulations. *Applied Numerical Mathematics*, 14(4):397–433, 1994.

[3] Dominik Göddeke and Robert Strzodka. Cyclic reduction tridiagonal solvers on GPUs applied to mixed precision multigrid. *IEEE Transactions on Parallel and Distributed Systems (TPDS), Special Issue: High Performance Computing with Accelerators*, 22(1):22–32, January 2011.

[4] Andrew Davidson and John D. Owens. Register packing for cyclic reduction: A case study. In *in Workshop on General Purpose Processing on Graphics Processing Units*, pages 1–6, 2011.

[5] Vahid Esfahanian, Behzad Baghapour, Mohammad Torabzadeh, and Hossain Chizari. An efficient GPU implementation of cyclic reduction solver for high-order compressible viscous flow simulations. *Computers & Fluids*, 92:160–171, 2014.

[6] Bulent Tutkun and Firat Oguz Edis. A GPU application for high-order compact finite difference scheme. *Computers & Fluids*, 55:29–35, 2012.

[7] Di Zhao and Jinhang Yu. Efficiently solving tri-diagonal system by chunked cyclic reduction and single-GPU shared memory. *The Journal of Supercomputing*, 71(2):369–390, 2015.

[8] Yao Zhang, Jonathan Cohen, and John D. Owens. Fast tridiagonal solvers on the GPU. *SIGPLAN Not.*, 45(5):127–136, January 2010.

[9] Nathan Mattor, Timothy J Williams, and Dennis W Hewett. Algorithm for solving tridiagonal matrix problems in parallel. *Parallel Computing*, 21(11):1769–1782, 1995.

BALANCING DOMAIN DECOMPOSITION METHOD ON ADDITIVE SCHWARTZ FRAMEWORK

Tomonori Yamada[1a)] & Shinobu Yoshimura[2]
[1]RACE, The University of Tokyo, Chiba, Japan
[2]Department of Systems Innovation, The University of Tokyo, Tokyo, Japan

Summary Computing performance of the balancing domain decomposition (BDD) method on additive Schwartz framework is described in this paper. BDD family is one of the most effective approaches for parallel computing of large scale structural finite element analyses. In the balancing domain decomposition by constraints (BDDC), the coarse grid correction procedure is applied in an additive manner, while it is applied multiplicatively in BDD. Here, BDD with additive Schwartz framework is implemented and computing performance is evaluated with numerical examples.

INTRODUCTION

The leading supercomputers are offering peta-scale computing capability in the world and further exa-scale systems are expected to be available by 2020[1]. Because the performance of each computing core is physically limited, the peta-scale computing systems contain hundreds of thousands of cores. As an application software in the field of solid mechanics for K computer (Japanese peta-scale computing system developed by MEXT), Japan Atomic Energy Agency and ADVENTURE project[2, 3] have been conducting a research project entitled "next generation seismic analysis of large plants in its entirety". Here, the safety requirement of large industrial plants such as nuclear power plants under seismic events is extremely high enough to perform real experiments to evaluate the structural integrity of mechanical components. However, such experiments are performed on the independent sets of components because the ability of experimental facilities is limited. Hence, a numerical simulation, which can treat full-scale large industrial plants, attracts more and more attention with the growing computational technologies. In our research project, simulation technologies have been developed to realize the full-scale simulation of large industrial plants on K computer.

The balancing domain decomposition(BDD) method[4], which is a combination of non-overlapping domain decomposition method, Neumann-Neumann preconditioner[5] and coarse grid correction, is one of the most effective simulation technologies for the large scale structural finite element analyses. However, the computing performance of BDD for extremely large scale analysis, more than a billion degrees of freedom, is not enough because the size of coarse problem exceeds the limit of direct solution approach such as parallel LU decomposition. In the BDD by constraints (BDDC)[6], the coarse grid correction is applied in an additive manner, while it is applied multiplicatively in BDD, and this additive framework(called additive Shwartz framework) drastically reduces the size of coarse problem to be solved with direct solution approach. Hence, computing performance of the BDD method with additive Schwartz framework is described in this paper.

FORMULATION OF BDD METHOD

Conventional formulation

The linear algebraic equations to be solved can be described as follows;

$$\mathbf{K}\mathbf{u} = \mathbf{f}, \tag{1}$$

where $\mathbf{K}$ is a positive, definite and symmetric matrix, $\mathbf{u}$ is the solution vector and $\mathbf{f}$ is a given right hand side vector. In primal substructuring approach, the analysis domain is decomposed into non-overlapping subdomains. In each subdomain, the subdomain boundary, the local unknown vector and local stiffness matrix can be denoted as Γ_i, $\mathbf{u}_i$ and $\mathbf{K}_i$, respectively. The global stiffness matrix and local stiffness matrix can be converted with appropriate conversion matrix, $\mathbf{R}_i$, which is a (0,1) integer matrix.

$$\mathbf{K} = \sum_{i=1}^{N} \mathbf{R}_i^{\mathrm{T}} \mathbf{K}_i \mathbf{R}_i, \tag{2}$$

where $\mathbf{N}$ is the number of subdomains. Each element in local vector and matrix is classified as interface element, which is allocated on the boundary of subdomain, Γ_i, and interior element, which is not allocated on the boundary. The local vectors and matrix are represented as follows;

$$\mathbf{K}_i = \begin{bmatrix} \mathbf{K}_{\mathrm{II}i} & \mathbf{K}_{\mathrm{IB}i} \\ \mathbf{K}_{\mathrm{BI}i} & \mathbf{K}_{\mathrm{BB}i} \end{bmatrix}, \quad \mathbf{u}_i = \begin{Bmatrix} \mathbf{u}_{\mathrm{I}i} \\ \mathbf{u}_{\mathrm{B}i} \end{Bmatrix}, \quad \mathbf{f}_i = \begin{Bmatrix} \mathbf{f}_{\mathrm{I}i} \\ \mathbf{f}_{\mathrm{B}i} \end{Bmatrix}, \tag{3}$$

where subscripts I and B denote the interior elements and boundary elements, respectively. By eliminating the interior elements of local stiffness matrices, the reduced system of Equation (3) is obtained.

a) Corresponding author. Email: yamada@race.u-tokyo.ac.jp

$$\mathbf{S}\mathbf{u}_B = \mathbf{g}, \tag{4}$$

where $\mathbf{S}$ is the Schur complement of $\mathbf{K}$, $\mathbf{u}_B$ is the unknown vector on the interface of all the subdomains, and $\mathbf{g}$ is the corresponding given vector. This reduced system is called as interface problem and generally preconditioned conjugate gradient method is applied for its solution procedure. The preconditioned conjugate gradient method contains the following auxiliary problem.

$$\mathbf{M}\mathbf{z} = \mathbf{r}, \tag{5}$$

where $\mathbf{M}$ is a preconditioning matrix and $\mathbf{r}$ is a residual vector in each iterative step of the conjugate gradient method. The Neumann-Neumann preconditioner in BDD method is described as follows;

$$\mathbf{M}_{\mathrm{N-N}}^{-1} = \sum_{i=1}^{N} \mathbf{R}_{Bi}^{T} \mathbf{D}_i^{T} \mathbf{S}_i^{+} \mathbf{D}_i \mathbf{R}_{Bi}, \tag{6}$$

where $\mathbf{S}_i^{+}$ is a generalized inverse of $\mathbf{S}_i$, and $\mathbf{D}_i$ is a weight matrix.

Finally, the preconditioning matrix for BDD method is introduced as follows;

$$\mathbf{M}_{\mathrm{BDD}}^{-1} = \mathbf{R}_0 \mathbf{S}_C^{-1} \mathbf{R}_0^{\mathrm{T}} + \left(\mathbf{I} - \mathbf{R}_0 \mathbf{S}_C^{-1} \mathbf{R}_0^{\mathrm{T}} \mathbf{S}\right) \mathbf{M}_{\mathrm{N-N}}^{-1} \left(\mathbf{I} - \mathbf{S}\mathbf{R}_0 \mathbf{S}_C^{-1} \mathbf{R}_0^{\mathrm{T}}\right), \tag{7}$$

where $\mathbf{S}_C$ and $\mathbf{R}_0$ are a coarse matrix and restriction matrix to construct coarse matrix. The coarse problem is a Galerkin projection of original structural problem on a coarse space derived from rigid body motion of each subdomain.

Proposed BDD on additive Schwartz framework

The formulation of BDD method on additive Schwartz framework is as follows;

$$\mathbf{M}_{\mathrm{BDD\_ADIDITIVE}}^{-1} = \mathbf{R}_0 \mathbf{S}_C^{-1} \mathbf{R}_0^{\mathrm{T}} + \mathbf{M}_{\mathrm{N-N}}^{-1} \tag{8}$$

Hence, the implementation is very simple and the great advantage of this additive Schwartz framework is the hierarchical implementation is straight forward.

NUMERICAL EXAMPLE

For a numerical example, a self-gravity analysis of Pantheon model illustrated in Fig. 1 is conducted. This benchmark model consists of 1,329,027 elements (3D Quadratic Tetrahedrons) and 2,002,285 nodes and conducted on four machines (Intel Core i7-2600, 4 cores for each) with only MPI implementation. Computing performance of conventional BDD implementation is illustrated in Fig.2 and that of proposed method with a diagonal scaling[7], instead of Neumann-Neumann preconditioner, and hierarchical implementation is also illustrated in Fig.2. Drastic improvement of computing performance is observed.



Fig.1 A decomposed Pantheon Model

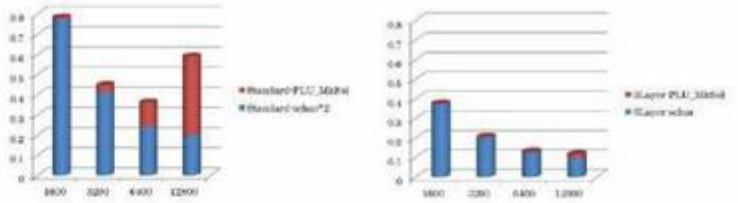

Fig.2 Computing Performance of Conventional BDD(left) and Proposed One(right)

CONCLUDING REMARKS

Computing performance of the BDD method with additive Schwartz framework is described in this paper. Even with middle scale model, benchmark results show good improvement with our proposed approach. Because of its hierarchical implementation, computing performance of BDD with additive Schwartz framework for extremely large scale analyses on peta-scale computers will improve drastically.

References

[1] Dongarra, J. et. al, International Journal of High Performance Computing Applications, 25, pp. 3-60 (2011).
[2] http://adventure.sys.t.u-tokyo.ac.jp/
[3] S. Yoshimura, R. Shioya, H. Noguchi and T. Miyamura, Journal of Computational and Applied Mathematics, 49, pp.279–296 (2000).
[4] J. Mandel, Communications on Numerical Methods in Engineering, 9, pp.233–241 (1993).
[5] Y. Roeck, P. LeTallec, Fourth International Symposium on Domain Decomposition Methods for Partial Differential Equations, pp. 112–128 (1991).
[6] C. R. Dohrmann, SIAM J. Sci. Comput., Vol.25, No.1, pp.246-258 (2003).
[7] M. Ogino, R. Shioya, H. Kanayama, JCST, Vol.2, pp.150-161 (2008).

FS03 - Experimental Methods in Mechanics

TS.FS03-1.01	Cobelli, Pablo - New developments in space- and time-resolved measurements of free-surface water waves (INVITED)	3126
TS.FS03-1.02	Vetrano, Maria Rosaria - Experimental characterisation of ln2 sloshing by means of non-intrusive optical techniques	3128
TS.FS03-1.03	Lu, Hua - Determination of Critical Loads for Embedded RF PA Assembly (INVITED)	3130
TS.FS03-1.04	Csernák, Gábor - Evaluation of mechanical contact between metallic surfaces	3132
TS.FS03-1.05	Hartmann, Stefan - Strain and strain-rate dermination using digital image correlation	3134
TS.FS03-1.06	Ma, Shaopeng - Are commercial CCD/CMOS cameras trustable for photomechanics?	3136
TS.FS03-2.01	Volk, Romain - A shadow PTV technique for particle tracking in an inhomogeneous turbulent flow (INVITED)	3138
TS.FS03-2.02	Kopp, Gregory A. - Evaluation of mean pressure field above a roof using PIV data and a 2D interpolation algorithm	3140
TS.FS03-2.03	Tripuraneni, Rajasekhar - Real-time measurement of biaxial modulus of GEanode for li-ion batteries	3142
TS.FS03-2.04	Trachsel, Mathis - Friction measurements on small journal bearings	3144
TS.FS03-2.05	Stepan, Gabor - Digital Effects in Hardware-in-the-Loop Experiments of Stick-Slip Phenomena	3146
TS.FS03-2.06	Wojnar, Charles - Measuring the dynamic electromechanical response of ferroelectrics	3148
TS.FS03-3.01	Xie, Huimin - Micro-speckle/grating by FIB deposition and their application to deformation measurement (INVITED)	3150
TS.FS03-3.02	Wang, Wei-Chung - A modulo pi temporal phase unwrapping theory in photoelasticity (INVITED)	3152
TS.FS03-3.03	Xu, Chaochen - An experimental investigation on interfacial properties of graphene: Size effect	3154
TS.FS03-3.04	Qiu, Wei - Residual stress analysis in si-based multi-layer heterostructure by micro-raman	3156
TS.FS03-3.05	Wu, Shangquan - Cell viability and rapid screening anti-cancer drug based on nanomechanical fluctuation	3158
TS.FS03-3.06	Pakrashi, Vikram - Scaled Experiments on Tuned Liquid Column Damper-Wind Turbine-Soil Interaction	3160
PO.FS03-1.01.342	Mikkelsen, Lars - Residual strains and their relation to the fatigue damage evolution in composite materials	3162
PO.FS03-1.03.344	Shang, Yibo - In-situ SEM study of short fatigue crack propagation behavior in a dissimilar metal welded joint of nuclear power plant	3164

NEW DEVELOPMENTS IN SPACE- AND TIME-RESOLVED MEASUREMENTS OF FREE-SURFACE WATER WAVES

Pablo Cobelli*[1], G. Lagubeau[2], T. Bobinski[3], A. Maurel[4], V. Pagneux[5], and P. Petitjeans[3]
[1]*Departamento de Física, Facultad de Ciencias Exactas y Naturales, Universidad de Buenos Aires and IFIBA, CONICET, Buenos Aires, Argentina*
[2]*Departamento de Física, Universidad de Santiago de Chile, Santiago, Chile*
[3]*Institut Langevin, UMR 7587, Paris, France*
[4]*Laboratoire d'Acoustique de l'Université du Maine, UMR CNRS 6613, Le Mans, France*
[5]*Physique et Mécanique des Milieux Hétérogènes PMMH, UMR CNRS 7636-ESPCI-UMPC Univ. Paris 6-UPD Univ. Paris 7*

Summary We present here a novel experimental technique for the space- and time-resolved measurement of the free-surface dynamics. We discuss recent enhancements on this technique, as well as its characteristics, capabilities and overall performance. Finally, we show recent results of its application to the study of gravity-capillary wave turbulence.

A NOVEL TECHNIQUE FOR MEASURING THE FREE-SURFACE DYNAMICS

Standard fluid measuring techniques for free-surface deformations are usually limited to point measurements, employing either one or an array of synchronized sensors. Furthermore, many of these methods involve the use of surface-piercing elements (such as resistive or capacitive probes) which are intrinsically intrusive. In any case, such methods only allow for a small number of discrete localized measurements, so that the information on the detailed spatial aspects of the free-surface deformation and the propagation of disturbances is incomplete. This limitations have led us to develop a novel measurement technique for the accurate measurement and tracking of the three-dimensional topography of the free-surface [1-2].

This optical profilometric technique is based on the principle employed in fringe projection profilometry. A fringe pattern of known spatial frequency is projected onto the free surface and its image is recorded by a camera. The topography of the free surface introduces a frequency modulation in the observed pattern, which is also modified by the perspective due to the relative positioning and orientation of the projection-recording system. The deformed fringe patter is later compared to the undeformed (reference) one, leading to a phase map from which the local free-surface height can be reconstructed. In order to be able to project images onto the liquid surface, its light diffusivity is enhanced by the addition of TiO_2 powder, which was carefully selected in order to provide sufficient contrast without altering the rheology of the working liquid [3].

Fringe projection on the free-surface is achieved by the use of a high-resolution videoprojector, allowing for the projection of wavelength-controlled sinusoidal-profile fringe patterns, which considerably increases the overall performance of the technique and the quality of the reconstruction. Moreover, as the technique poses no restrictions on the time-tracking of the free-surface deformation (other than that arising from exposure time), the obtention of time-resolved measurements of the free-surface dynamics is only limited by the capturing system's sampling rate.

Recently, we enhanced the capabilities of this fringe projection profilometry technique by introducing the empirical mode decomposition profilometry technique (EMDP). This new fringe analysis algorithm, based on the empirical mode decomposition, is free of spatial filtering and specially apt for measuring free-surface height fields characterized by a broadband spectrum of deformation. We have shown, both numerically and experimentally, that the free-surface wave fields reconstructed by EMDP are both spectrally and statistically accurate, which renders it particularly suitable for the study of weakly nonlinear water-wave phenomena [4].

APPLICATION TO GRAVITY-CAPILLARY WAVE TURBULENCE

In our experiments, water waves are generated by two piston-type wavemakers (20 cm wide, 1 cm inmersed) in a (180×80) cm^2 tank filled with water with depth at rest of 5 cm. Each wavemaker is independently controlled by a servomotor, which provides a random signal within the (broadband) frequency range of 0–4 Hz. The forcing amplitudes were varied between 1–30 mm. Employing our free-surface measuring technique, we have performed a full space-time characterization of the free-surface (vertical) velocity field in the context of wave turbulence [5]. The inspected field is 45×45 cm^2 with 968^2 pixels and the measurements are performed at a sampling rate of 250 Hz.

Figure 1 shows several snapshots of the free-surface vertical velocity field, $v_\perp(x, y, t)$, as determined by our measuring technique. Each data set considered in this study consisted on 6000 snapshots such as those shown in the figure. Based

*Corresponding author. Email: cobelli@df.uba.ar

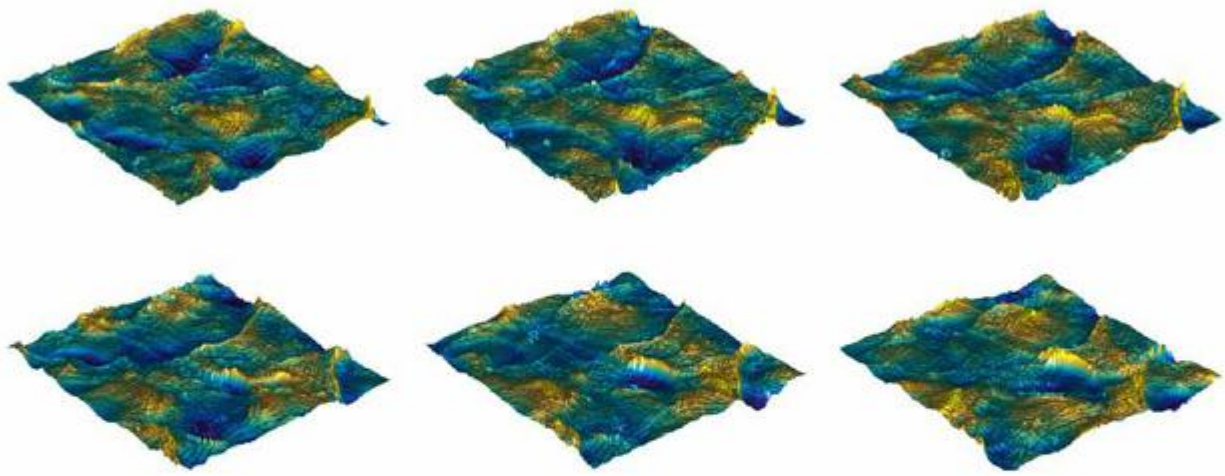

Figure 1: Snapshots of the free-surface (vertical) velocity for the gravity-capillary wave turbulence study presented in this work (time evolves from left to right, and from top to bottom). Each field shown spans an area of 45×45 cm^2, and consists of 968^2 equispaced data points. The time interval between each frame is 40 ms.

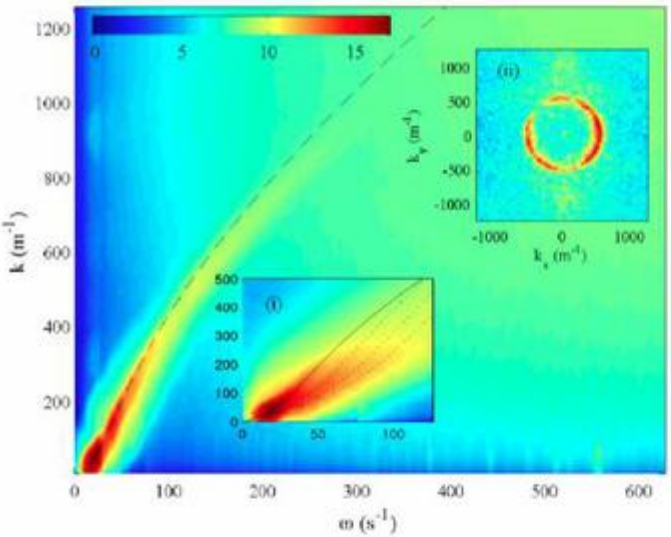

Figure 2: Power spectrum $|\eta(k,\omega)|^2$ at low-amplitude forcing (A =3 mm). Inset (i) shows a zoom on the spectrum, in the gravity wave regime and at high amplitude forcing ($A = 22$ mm). The solid line shows the linear dispersion relation and the dotted lines depict the dispersion relation of bound waves. Inset (ii) illustrates the isotropy in the (k_x, k_y) space for $\omega = 138$ rad/s ($A = 3$ mm).

on those, the space-time power spectra of the free-surface vertical velocity $|v_\perp(k,\omega)|$ are computed by a multidimensional Fourier transform, allowing for the calculation of the full 3D spectrum (in k_x, k_y, ω). The isotropy of these spectra in k-space is illustrated in the inset of Figure 2 for a fixed value of ω, although we have checked that the isotropy is preserved at all frequencies. By virtue of this isotropy, an angular average in wavenumber space led us to the wave energy spectrum $|\eta(k,\omega)|^2$, shown in the main panel of Figure 2. The wave spectrum reveals that the energy appears to be mainly concentrated on the linear dispersion relation for gravity-capillary waves. Nevertheless, the wave energy is shared between the resonant part of the wavefield on the linear dispersion relation and a non-resonant part composed of bound waves. Finally, the (k,ω) power spectra give the usual energy density spectra, which compare well with most results of laboratory experiments on water-wave turbulence.

References

[1] P. Cobelli, A. Maurel, V. Pagneux, P. Petitjeans. *Experiments in Fluids*, **46**, 1037 (2009).

[2] A. Maurel, P. Cobelli, V. Pagneux, P. Petitjeans. *Applied Optics*, **48**(2), 380 (2009).

[3] A. Przadka, B. Cabane, V. Pagneux, A. Maurel, P. Petitjeans. *Experiments in Fluids*, **52**, 519 (2012).

[4] G. Lagubeau, P. Cobelli, T. Bobinski, A. Maurel, V. Pagneux, P. Petitjeans. *Applied Optics*, **54**(32), 9409 (2015).

[5] P. Cobelli, A. Przadka, P. Petitjeans, G. Lagubeau, V. Pagneux, A. Maurel. *Physical Review Letters*, **107**, 214503 (2011).

EXPERIMENTAL CHARACTERISATION OF LN2 SLOSHING BY MEANS OF NON-INTRUSIVE OPTICAL TECHNIQUES

Alessia Simonini [1], Laura Peveroni [1]& Maria Rosaria Vetrano [1a)]

[1] *Von Karman Institute for Fluid Dynamics, 72 Chaussée de Waterloo, 1640 Rhode-st-Génèse, Belgium*

Summary The main goal of this work is to present the possibility to characterize the free surface shape and the velocity field of liquid nitrogen contained in a partially filled cylindrical transparent vessel during cryogenic (LN_2) sloshing. The results obtained will be compared with the one already performed using water as test fluid in order to verify semi-empirical formulas generally used for fluid sloshing.

INTRODUCTION

The motion of the free liquid surface is called "sloshing"[1]. This phenomenon is particularly important during the management of conventional and cryogenic propellants on spacecraft: it can affect the normal operating condition, compromising the full space mission [2]. Being able to understand the behaviour of the propellant subjected to extreme environmental conditions means being able to predict its position and topology inside the tank, for a given external and gravitational acceleration and a determined thermodynamic condition. An example of cryo-sloshing can be seen in Figure 1. The prediction and control of this motion is far to be understood due to the different parameters playing a role in the dynamic system such as the geometry of the container, the type of external excitation (shape, frequency content and amplitude), the level of the liquid and finally the kind of liquid. Therefore the creation of a reliable and consistent experimental database is crucial for assessing the accuracy and the range of validity of existing theoretical and numerical models for cryogenic sloshing. Unfortunately today there is a lack of database able to provide at the same time quantitative information on fluid velocity and interface shape due to both the complexity in handling the cryogenic fluid and to the difficulty in applying standard techniques. It is in this framework that the work here presented can be placed.
Indeed, the main goal of this work is to present the characterization of the free surface shape and the velocity field of LN_2, contained in a partially filled cylindrical transparent vessel, during sloshing using non intrusive optical based techniques. More specifically, the free surface shape of LN_2 will be determined, tracking low density particles floating on the gas/liquid interface using the so called LeDaR (Level Detection and Recording) technique [3].
To determine the fluid velocity, particles possessing a density comparable the one of the fluid are mixed to LN_2 to perform PIV (Particle Image Velocimetry) and/or PTV (Particle Tracking Velocimetry). PIV is a well-establish technique which, when applied to cryogenic liquids, is still in development regarding the seeding selection and procedures [4]. It will be shown in this work that the use of glass hollow spheres as tracer for PIV is possible provided a proper seeding procedure. The results obtained will be compared with the one already performed using as test fluid water in order to verify semi-empirical formulas generally used for fluid sloshing.

EXPERIMENTAL SET-UP

The experimental set-up used is mainly constituted by a cryostat containing a fully transparent cell, in which LN_2 is stored, a sloshing table used to generate the sloshing excitation and a time resolved PIV system. The cell is constituted by a hexahedral quartz piece possessing a cylindrical hole up to ¾ of its height and is placed in the cryostat sample volume. The cryostat is provided of five quartz windows in order to have a full optical access to the fluid during sloshing. Cryogenic temperature sensors (RTDs) and pressure transducers are used to monitor temperature and pressure in different locations of the sample room and the cell during the whole experiment. The displacement of the sloshing table is measured using an Optical Device Sensor (ODS). Finally the PIV system is constituted by a low-power continuous laser, a laser sheet generator and a CCD camera (30 fps). A picture of the experimental set-up is shown in Figure 2.

EXPERIMENTAL CONDITIONS

In order to decouple thermal and dynamic behaviour the sloshing fluid in the cell is kept at saturation conditions. During this study, sinusoidal harmonic excitations with amplitude of 1.5 mm and a frequency of 2 Hz and 2.5 Hz are used to generate fluid sloshing. For the LeDaR technique the particles used are 3M K46 glass bubbles (density 460 Kg/m3 and mean size of 40 μm). Their density is almost half of the one of liquid nitrogen at ambient pressure (807 Kg/m3 at 106 Pa). Phase locked images, i.e. images taken at the same phase position of different excitation cycles, of the particles are acquired.

Particle Image Velocimetry is applied taking into account the standard rules for PIV seeding in liquids and the selection criteria presented by Fonda [5]. The evaluation of the seeding characteristics, the particle response time and the PIV processing algorithm will be presented in the final paper. Commercial particles (Cospheric hollow glass sphere) possessing

[a)] Corresponding author. Email: vetrano@vki.ac.be.

a density of density 830 Kg/m3 and mean size of 40 μm have been used to seed the flow. In order to have density match between the particles and the fluid, the LN_2 is set to the temperature of 70.3 K and the particle displacement in absence of external excitation is measured to verify the absence of buoyant forces. For both the techniques, the amount of particles added to the fluid corresponds to a volume ratio between the fluid and solid of about 40000 and ice crystal formation due to the humidity of the particles, is prevented by means of successively purging cycles (vacuum and gas nitrogen).

EXAMPLE OF RESULTS

Figure 3a presents a LeDaR image obtained during sloshing where the interface position is highlighted by means of the floating particles. This image is the result of the average between 200 phase locked images. Using a specific image-processing algorithm the location of the particles on the surface can be determined and the free surface position can be then extrapolated as shown in Figure 3b.

An example of instantaneous velocity field obtained by Particle Image Velocimetry, for an excitation phase close to the one presented in Figure 3, is shown in Figure 4.

CONCLUSIONS

In conclusion in this work it will be shown how non-intrusive measurement techniques can be used to characterize sloshing of cryogenic fluids. The protocols to properly seed the cryogenic fluid will be described and evaluated, the results obtained both for liquid/gas interface position and fluid velocity will be compared with the ones achieved using water as test-fluid. A first attempt in the validation of the semi empirical correlations for frequency behaviour of fluid will also be presented.



Figure 1 Example image of sloshing



Figure 2 Picture of the experimental setup mounted on the sloshing table

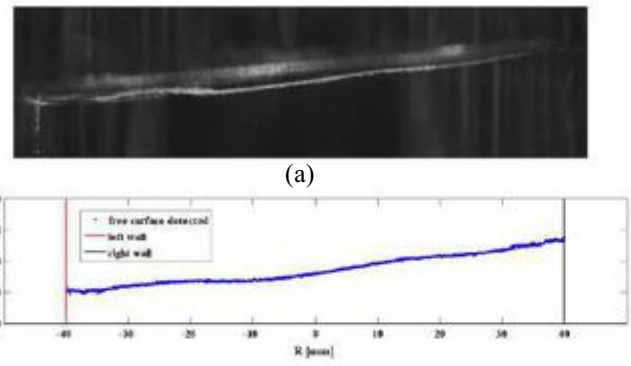

(a)

(b)

Figure 3 Image of the particles floating on the LN_2 liquid gas interface during sloshing, (b) Interface determination by image processing

Figure 4 Example of PIV vector field extracted for a fixed positions of sinusoidal excitation for LN_2 sloshing

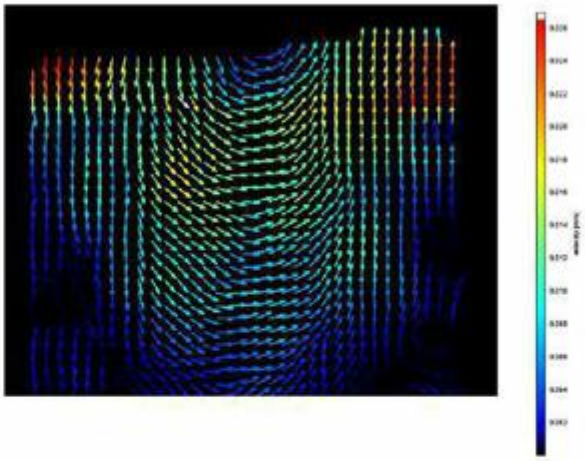

References

[1] R. Ibrahim, Liquid sloshing dynamics: theory and applications, Cambridge University Press, 2005.

[2] H. Abramson, The dynamic behavior of liquids in moving containers with applications to space vehicle technology., Washington: National Aeronautics and Space Administration, 19666.

[3] B. Tóth, Two-phase flow investigation in a cold-gas solid rocket motor model through the study of the slag accumulation process, Rhode-Saint-Gènese: von Karman Institute, 2008.

[4] E. Fonda, K. R. Sreenivasan and D. P. Lathrop, "Liquid Nitrogen in fluid dynamics: visualization and velocimetry using frozen particles.," Review of Scientific Instruments, vol. 83, 2012.

[5] E. Fonda, PhD Thesis: Visualization of classical and quantum turbulence in cryogenics fluids., Trieste: University of Trieste, 2012.

DETERMINATION OF CRITICAL LOADS FOR EMBEDDED RF PA ASSEMBLY

Hua Lu[1a)]
[1]*Department of Mechanical and Industrial Engineering, Ryerson University, Toronto, Canada*

Abstract Presented is an experimental mechanics based methodology and a case study exemplifying a novel, effective and efficient reliability evaluation for a package. Under the study is a prototype of an advanced embedded RF (radio frequency) PA (power amplifier). The study focuses on determining its tolerance to thermal loads and mechanical bending. The reliability attributes are the key specifications for the package qualification, which characterize the assembly's safe operation limits. Localized sites of structural weakness in a new design are identified first backed by theories of interfacial mechanics. Novel opto-mechanistic based metrological techniques including optical imaging and shadow moiré are applied to measure strains in these areas leading to quantitatively determined failure critical parameters of the package, which thus facilitate the design evaluation, modification and optimization.

INTRODUCTION

High power RF PA is a popular yet critical and costly component for wireless and satellite communication applications. The coin construction in conjunction with the back-attached heat sink is a proving solution to accelerating the heat dissipation from the PA, thus is a key technology ensuring the RF PA's thermal reliability. Driven by increasing signal processing speed and demand for reducing the assembly thickness and cost, the embedded PA architecture emerges to mitigate the elevated overall thickness of the coin structure. Due to the rapid market shift a timely assessment for the assembly's mechanical and thermal reliability is imperative for a speedy design concept verification and optimization. The new method integrates the reliability testing and the experimental stress analyses, which effectively tackled the challenges.

STRUCTURE FEATURES AND RELAIBILITY CONCERNS

The assembly has a novel architecture of a three-dimensional embedded coin construction (Fig. 1), which enables a fast heat spread from the PA while keeping a low overall thickness. On the coin's top and bottom surfaces a PA component and a copper heat sink are attached respectively via reflow soldering. The coin construction is embedded in a cavity of the ceramic-epoxy made PCB via the coin's tab locks with a conductive silver-particle filled epoxy adhesive. To reduce thermal impedance between the heat sink and the coin, a thin shim is inserted in between the contacting surfaces. The elements are tightly bolted together in reflow processing. The coin-PCB bonding strength is critical since any mechanically or thermally caused de-bonding could possibly damage the nearby electric routines. Considering also the high mismatch in the CTE (coefficient of thermal expansion) and Young's modulus across the interfaces (the laminate CTE is measured at 44 ppm/^{o}C as opposed to 17 ppm/^{o}C for the coin material), high thermal and mechanical stress concentrations are expected in the area. As such, the theory of interfacial fracture provides needed guidance to the assessment, though it can barely reach quantifiable results given the complex structural features and largely uncertain materials' behavior. A quick global structural inspection indicates that the heat sink attachment (Fig. 2) introduces in-plane compression to the PCB due to CTE mismatch, which in turn causes the PCB to bend. The stresses at multi-material interfaces are thus highly concentrated considering the co-existence of both material property discontinuities (CTE and E) and geometric discontinuities around local interface corners.

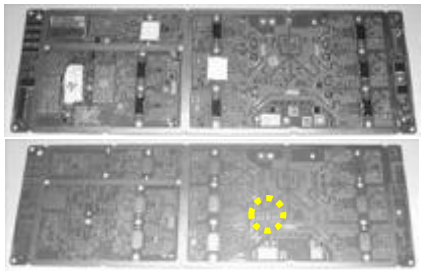

Fig. 1a PCB with PA components (top) and a bare PCB (bottom) with embedded coins.

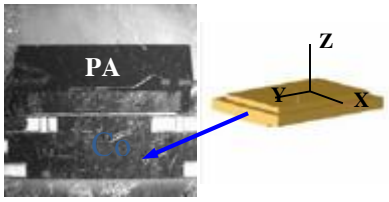

Fig. 1b Cross section view of PA and heat sink of a coin (left), and the coin geometry (right).

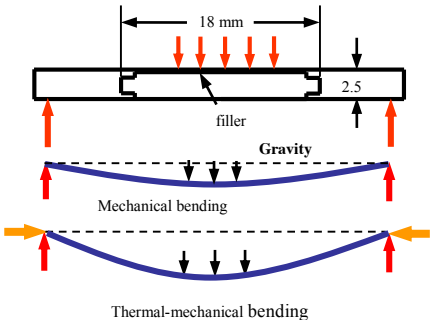

Fig. 2 PCB bending

METHODOLOGY AND EVALUATION

The mechanistic analysis as adopted can avoid costly and time consuming full-scale testing. The properties of the PCB and adhesive material are viscoelastic and dependent on the glass-transition, geometric scale and processing conditions. Nonetheless a simple two-dimensional linear-elastic modeling can qualitatively outline patterns of strain/stress distribution (Fig. 3). As revealed, the weak structural links highlighted by areas of shear strain concentrations match well with the mechanistic-based analysis. The results of the qualitative analysis guide the microscopic strain measurement which is aimed to quantitatively determine the package's critical failure parameters such as the critical de-bonding temperature. Visual failure detection is followed upon completion of the measurement in a temperature ramping-up process. The method, the setups and the application approaches of the digital speckle correlation can be found in the references [1, 2]. A test sample with a bolt-

[a)] Corresponding author. Email: hlu@ryerson.ca.

connected thick heat sink attachment is schematically shown (Fig 4). Shadow moiré method is applied to determine the coin's edge-to-center warpage and the filler thickness is decided based on the image correlation obtained strain results. The strains at anticipated critical locations are measured in separate tests at room and elevated temperatures (Fig. 5, 6). Test samples are grouped according to the different tests arranged to investigate temperature/mechanically induced interface strains in bare PCBs, PCBs with heat sink and the component-to-board joints.

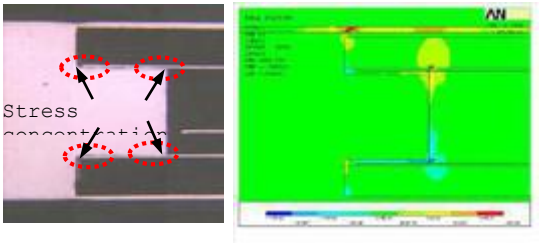

Fig. 3 FEA obtained shear strain concentration

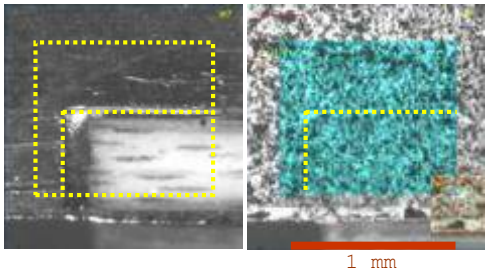

Fig. 5 Local interfacial area prepared for optical imaging correlation measurement before (left) and after (right) speckles are applied.

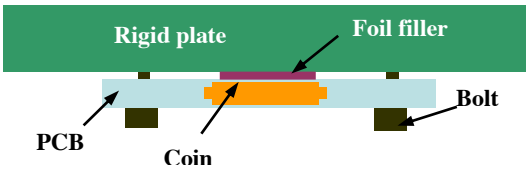

Fig. 4 Schematic for test sample used in strain measurement for coin construction.

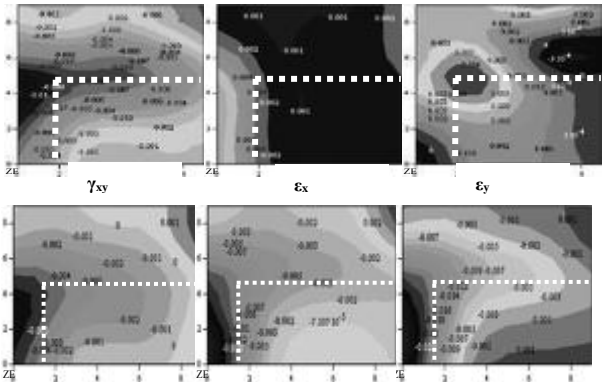

Fig. 6 Mechanical strains at room temperature (top) and thermal-mechanical strains at 120 °C (bottom).

RESULTS AND CONCLUSIONS

The shear strain in a horizontal-vertical interface corner (Fig. 7) typically experiences a substantial increase when the heat sink is attached or shim layer inserted. The visual inspection indicates the cracks grow exclusively along the horizontal interfaces as the tab locks and the PCB laminate debond. The thermal-mechanical shear strain in the case of 3-mil filler (Fig. 8) reveals a recovery at 117 °C, signifying the initiation of de-bonding at that temperature. The crack initiation revealed by the unloading thus leads to the determination of the critical temperature or the safe operation criterion for the 3-mil filler case.

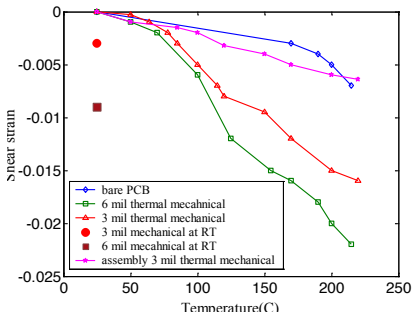

Fig. 7 Variation of maximum shear strain in a vertical interface site.

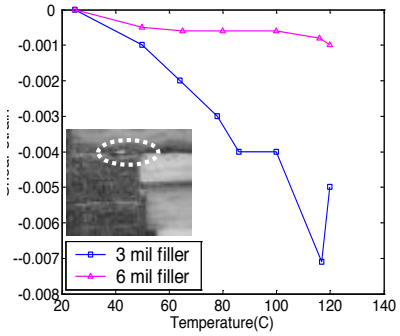

Fig. 8 Critical de-bonding temperature determined via strain measurement and visual inspection.

ACKNOWLEDGEMENT

The author acknowledges the financial support to the fundamental study of microelectronic packaging reliability funded by NSERC (Natural Science and Engineering Research Counsel of Canada) and the technical support by Ming Zhou.

References

[1] H. Lu, H. G. Shi and M. Zhou, 2005, "Thermally Induced and Deformation of Solder Joints in Real Packages: Measurement Analysis," submitted for publication to *Microelectronics Reliability*, accepted and in press.

[2] H. Lu, J. Zhou and M. Zhou, 2005, "Hybrid Reliability Assessment for Packaging Prototyping," *Microelectronics Reliability*, Vol. 45, pp 609, March 2005.

EVALUATION OF MECHANICAL CONTACT BETWEEN METALLIC SURFACES

Gábor Csernák *, Richárd Wohlfart, Roland Zana, Bálint Magyar, Gábor Hénap, Gábor Stépán
Department of Applied Mechanics, Budapest University of Technology and Economics, Budapest, Hungary

Summary In case of machines or other metallic structures the internal damping is usually negligible compared to the dissipation due to micro-slips at frictional contacts between machine parts. Consequently, one of the most challenging problems in modal analysis is the proper evaluation of the effects of contact properties on the modal damping. The frictional dissipation strongly depends on the actual contact patch, which is hard to determine in case of macroscopically matching surfaces. In the present paper, an experimental technique is proposed for the evaluation of the contact pattern by the measurement of electric field potentials.

INTRODUCTION

Even well-machined surfaces are rough on a microscopic scale. Consequently, the real area of contact is extremely small [1]. It means that the pressure – defined as the ratio of the load and the nominal area – does not provide first-hand information about the real normal stress distribution on the rough surface of the materials. However, the distribution of the compressing force on a sufficiently small grid can be used for the evaluation of the mechanical contact of surfaces. The contact models in the literature usually provide relations between the compressing force and the number and size of local contacts. One of the most popular models was set up by Greenwood and his co-authors [2, 3], who showed that in nominally flat surfaces the individual contacts are dispersed, while in case of curved surfaces the individual contact areas are often clustered. Our primary goal is the macroscopic evaluation of contacts such that the clustering of contact areas can be identified (see Figure 1). Even a coarse discretization may reveal the possibly adverse asymmetries in the contact pressure or the differences between seemingly identical contacts. Moreover, the force distribution on the contact area may be used for the reliable prediction of energy dissipation due to dry friction [4]. Since there is physical connection between electrical resistance and the properties

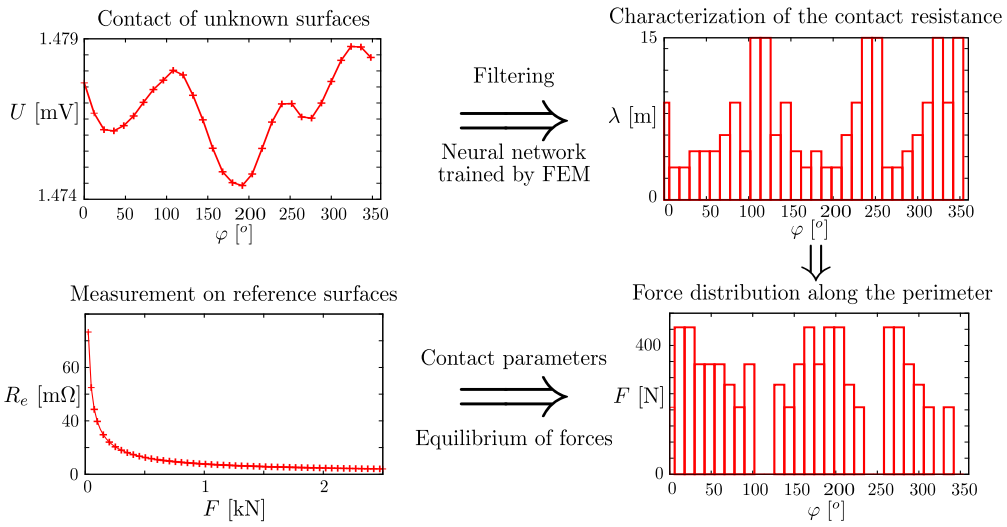

Figure 1: Block diagram of the evaluation algorithm. The force distribution shows three disjoint contact areas.

of mechanical contact [2], it is possible to evaluate the mechanical contact pattern based on the measurement of resistance. According to the authors' knowledge, no such methods were published yet, however, there is an extensive body of literature about the inverse problem, i.e., the determination of electrical contact resistance R_e based on the characteristics of contacting surfaces [5].

MEASUREMENT LAYOUT AND ALGORITHM

At the present stage of the research, the case of line contact is considered, i.e., the nominal contacting surface is narrow compared to its length. According to the results obtained so far, the method can be extended to the evaluation of real 2D contacts, as well. The block diagram of the developed algorithm is shown in Figure 1. In the first step, a constant current

*Corresponding author. Email: csernak@mm.bme.hu

is kept flowing between the contacting machine parts at a certain contact force, while the voltage (U) is measured along the contact line between probes on either side (see Figure 2). Due to the large internal resistance of the voltmeter, the contact resistance at the probes does not influence the results. In the second step, a discretized resistivity distribution is calculated along the contact. This step is accomplished by a neural network, trained using the output of a finite element model. The model is based on the introduction of a layer between the contacting surfaces. The contact resistance on a short segment can be characterized by the thickness λ of an equivalent hypothetical steel layer.

Once the resistivity distribution is known, the pressure distribution can be calculated, based on simple models from the literature [2]. For the determination of the necessary material parameters, standard contact resistance measurements are performed on reference surfaces (step 3). Finally, in step 4, the scaling of the force distribution can be accomplished by taking into account the equilibrium of forces.

During the first experiments, the contact of two thin-walled tubes along their perimeter was evaluated at various values of normal load. The test rig is shown in Figure 2. To make sure that the test rig is reliable and the results are repeatable,

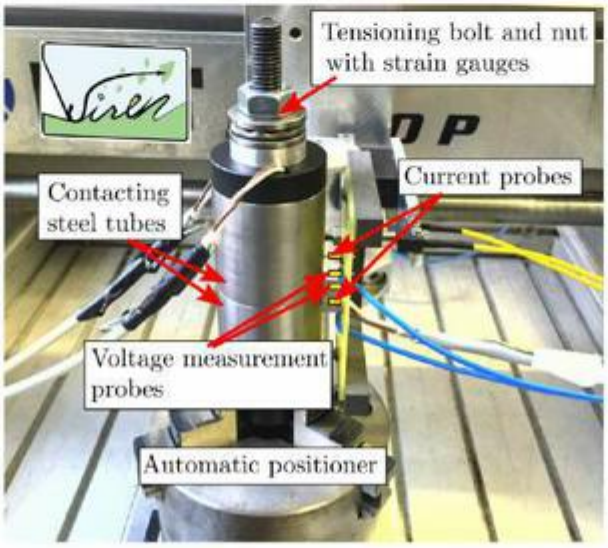

Figure 2: The contacting tubes with the probes.

three thin copper wires were placed between the tubes. Thus, practically the electric current flew at these three points, only. The contacting regions were clearly identifiable by our method. Similar curves were obtained without the copper wires, too, indicating the clustering of contacting regions – see Figure 1.

CONCLUSIONS

The performed measurements proved that a contact pattern between metallic surfaces can be identified on the basis of measured electric voltage, at a broad range of the normal load. The fitted voltage curves changed with the load, but the overall pattern stayed the same, indicating that the pattern recognition can be performed with ease. According to the results we claim that a practically useful contact evaluation method is proposed that will be further elaborated in the near future.

ACKNOWLEDGEMENTS

The research leading to these results has received funding from the European Research Council under the European Union's Seventh Framework Programme (FP/2007-2013) / ERC Advanced Grant Agreement n. 340889.

References

[1] Archard J. F.: Elastic Deformation and the Laws of Friction. Proc. Roy. Soc. A 243: 190-205, 1957.
[2] Greenwood J. A. and Williamson J. B. P.: Contact of Nominally Flat Surfaces, Proc. Roy. Soc. A 295:300-319, 1966.
[3] Greenwood J. A. and Wu J. J.: Surface Roughness and Contact: An Apology, Meccanica 36:617-630, 2001.
[4] Barber J. R., Davies M. and Hills D. A.: Frictional Elastic Contact with Periodic Loading, Int. Journal of Solids and Structures 48:2041-2047, 2011.
[5] Barber J. R.: Bounds on the Electrical Resistance Between Contacting Elastic Rough Bodies, Proc. Roy. Soc. A 459:53-66, 2003.

STRAIN AND STRAIN-RATE DETERMINATION USING DIGITAL IMAGE CORRELATION

Stefan Hartmann*[1], Susana Rodriguez[1], and Carmen Sguazzo[1]
[1]*Institute of Applied Mechanics, Clausthal University of Technology, Clausthal-Zellerfeld, Germany*

Summary Digital Imaging Correlation systems for full-field strain analysis are based on traditional approaches to determine strains and strain-rates on the basis of the motion of discrete points in space and time. Both the theoretical background and concepts to verify the codes are missing for three-dimensional curved surfaces under large strains. In this presentation, we discuss various possible approaches for determining different strain measures and the possibility of obtaining the strain-rate as well. This discussion is performed in view of verification examples, where homogeneous and inhomogeneous deformations are prescribed. It turns out that under certain circumstances the strain determination might be inaccurate. Additional aspects, for example, real experimental data and the comparison to finite element results are treated as well.

INTRODUCTION

Full-field determination of displacements and strains is an increasing measurement technology for two- and three-dimensional surface deformations. Two different systems are explained in [2] and [6]. Commonly, these devices are applied for full-field measurement and both the displacements as well as the strains are used for the interpretation of the deformation characteristics of a part, for the comparison of numerical models with experimental observations, or for the purpose of material parameter identification. The system detects coordinates of points on the surface (two coordinates for 2D- and three coordinates in 3D-camera systems) and follow them during the deformation in the experiment. In the two-dimensional case no essential problems occur. However, for the case of curvilinear surfaces, the theory increases to be more complex because the deformation of curvilinear surfaces has to be studied. In this case, we follow the abstract ideas of [3, 5] and concretize these concepts to the problem under consideration. Unfortunately, the approaches in [2] and [6] circumvent an explanation how the strains are determined in detail. This leads to a number of questions:

- What kind of approach is possible to determine the strain and the strain-rates in a curvilinear surface for a given set of points?
- What accuracy can we obtain using different methods for determining strains, and which advantages and disadvantages do these methods have?
- Are there verification examples so that the systems can be investigated in view of their accuracy? (in view of the terminology of verification of programs, see [1], which is adapted to the strain analysis of DIC-systems)
- Can we adapt the models to further problems?

In this presentation, we will address the issue mentioned above and provide new theoretical concepts for strain analysis. Furthermore, the methods are studied in view of their advantages and disadvantages at various verificiation examples as well as real experimental data.

SURFACE STRAIN ANALYSIS

The full-field deformation analysis system provides coordinates in the surface of a specimen in the reference and in the current configuration, see as an example, Fig. 1(a). These points at time t can be described by surfaces, which are necessary for specific interpolation concepts. In [6] the coordinates of a subset of points of the entire surface in the reference configuration and for each displacement component is applied leading to four interpolations with a least-square method. In [4] shape functions from finite elements are chosen requiring only two interpolation, which are based on pure function evaluations. The latter is based on in-plane deformation gradient

$$\hat{\mathbf{F}} = \frac{\partial \theta_{\mathrm{R}}^{\alpha}}{\partial \Theta^{\beta}} (\vec{a}_{\alpha} \otimes \vec{A}^{\beta}), \quad \alpha = 1,2, \quad \beta = 1,2, \tag{1}$$

where $\vartheta^{\alpha} = \theta_{\mathrm{R}}^{\alpha}(\Theta^{\beta})$ defines the surface motion of the surface parameters Θ^{β} (material surface coordinates), and ϑ^{α} the surface parameters in the current configuration. $\vec{a}_{\alpha} = \hat{\vec{x}}_{,\alpha} = \partial \hat{\vec{x}} / \partial \vartheta^{\alpha}$ and $\vec{A}_{\alpha} = \hat{\vec{X}}_{,\alpha} = \partial \hat{\vec{X}} / \partial \Theta^{\alpha}$ define the tangential vectors in the current and in the reference configuration, $\vec{A}^{\alpha} = A^{\alpha\beta} \vec{A}_{\beta}$ symbolize the gradient vectors. In [4] convective coordinates are chosen, $\vartheta^{\alpha} = \Theta^{\alpha}$, whereas in [6] $\Theta^1 = X$ and $\Theta^2 = Y$ (using the constraint $Z = f(X,Y)$ are applied.

*Corresponding author. Email: stefan.hartmann@tu-clausthal.de

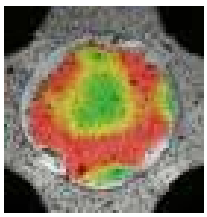

(a) Biaxial tensile test

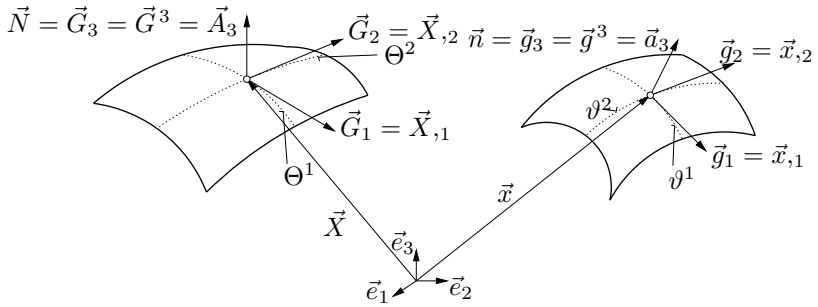

(b) Kinematical description of the deformation

Figure 1: Illustrative example of surface deformations

We propose two additional approaches using non-convective coordinates combining the advantages of both existing methods. Thus, different methods have different accuracies and computational efficiencies.

Having the in-plane deformation gradient $\hat{\mathbf{F}}$, the in-plane right Cauchy-Green tensor $\hat{\mathbf{C}} = \hat{\mathbf{F}}^T\hat{\mathbf{F}}$ and related principal stretches, which are of interest in industrial applications, can be determined.

The whole concept of strain analysis can also be adapted to finite elements surface deformations, so that for arbitrary finite element programs strains on the surface can be determined at any place and a comparison of experimental and numerical results is possible.

VERIFICATION EXAMPLES

Numerical methods have to be verified. Thus, the presented methods are verified at analytical examples of simple shear (plane problem), tension combined with torsion (curvilinear surface) and an analytical description of a deep drawing process (complex three-dimensional deformation) so that a code verification and a sensitivity analysis of the proposed schemes can be investigated.

REAL EXAMPLES

Finally, a real experimental example is chosen to show the applicability of the methods. Furthermore, the surface strain analysis is also adapted to a fully three-dimensional finite element simulation, so that both a comparison of experimental data and simulation is possible as well as material parameter identification on the basis of finite element simulations can be performed.

References

[1] Babuska, I. and Oden, J. T.: Verification and validation in computational engineering and science: basic concepts Computer Methods in Applied Mechanics and Engineering, 193: 4057-4066, 2004.

[2] GOM: Aramis – User Manual: The basics of strain. GOM – Gesellschaft für optische Messtechnik, Braunschweig, Germany, 2011.

[3] Gurtin, M. E. and Murdoch, A. I.: A continuum theory of elastic material surfaces. Archive of Rational Mechanics and Analysis, 57:291–323, 1975.

[4] Hartmann, S. and Sguazzo, C.: Strain Analysis in Sandwich Structures using Digital Image Correlation. in: Fortschrittsberichte der Materialforschung und Werkstofftechnik / Bulletin of Materials Research and Engineering, 1, Shaker Verlag, Aachen, Germany, 61-71, 2015.

[5] Javili, A., McBride, A., and Steinmann, P.: Thermomechanics of solids with lower-dimensional energetics: on the importance of surface, interface and curve structures at the nanoscale. A unifying review. Applied Mechanics Review, 65(1):1–31, 2013.

[6] Sutton, M. A., Orteu, J.-J., and Schreier, H.-W.: Image correlation for shape, motion and deformation measurements. Springer, New York, 2009.

IS COMMERCIAL CCD/CMOS CAMERAS TRUSTABLE FOR PHOTOMECHANICS?

Chao Wang, Qinwei Ma, Hao Gu, Shaopeng Ma[a)],
School of Aerospace Engineering, Beijing Institute of Technology, Beijing, China

Summary The parasitic deformation of the images from a digital camera in long-time measurements is investigated, and the heat-induced image expansion and pixel motion are observed. The start-up time differences of multiple high-speed cameras with synchronous triggering are measured, and the possibility of occurrence of unneglectable start-up time differences is calculated. The measuring results show that commercial CCD or CMOS cameras cannot faithfully record the image data in photomechanics measurements with high-precision requirements. The systematic errors from image recording should be compensated.

INTRODUCTION

Commercial CCD or CMOS cameras are very popular equipment for image acquisition in daily life and industrial applications. After compensation of the lens distortion, cameras are thought to be capable to record the real scenes and then are trustable in these circumstances. In the previous applications of photomechanics, this is also thought to be true. The raw image data consisting of the pixel grey matrix series and corresponding time series for imaging are directly used for deformation field evaluation and further mechanical analysis. Recently, some studies [1-3] reported that the image captured by commercial CCD or CMOS cameras might contain slight systematic errors. For long-time measurements, it is found that there is a parasitic expansion to the image because of the self-heating or/and the environment temperature increasing [4-6]. Although it is slight enough and could be neglect in most other applications, it may produce apparently systematic errors on photomechanics methods. For high speed measurements, it is observed that there may exist start-up difference among multiple high-speed cameras even though when they are triggered simultaneously. This may produce apparent errors on time for the high-speed images series when multi-cameras are used, for example the stereo-vision applications. This paper introduces the two kinds of errors firstly and then confirms that the commercial CCD/CMOS cameras are not trustable for photomechanics if the compensation techniques are not considered.

HEAT INDUCED IMAGE ERRORS OF CAMERAS IN LONG-TIME MEASUREMENTS

In the long-time measurements, temperature of the camera may vary because of the self-heating and/or the variation of the environment temperatures (as shown in Fig. 1a). Fig.1b shows that the temperature variation could induce the structural deformation of the camera, leading to the change of the equivalent optical path (as shown in Fig. 1c). The image deformation caused by the optical path changing is investigated as follows: 1) Capturing the speckle images of an unloaded board using IMPERX 12M-3L digital camera, and recording the temperatures of the camera simultaneously. 2) Analysing parasitic displacement and strain fields from the images. Fig. 2a shows that the self-heating could induce a strain error of 200 με with about 12 °C temperature increment (about 15 με/°C). The displacement errors (see Fig. 2b) is up to 0.5 pixels, which is partially caused by the image expansion expressed by the parasitic strain and also result from the heat induced rigid motion of the CCD chip (see Fig. 2c).

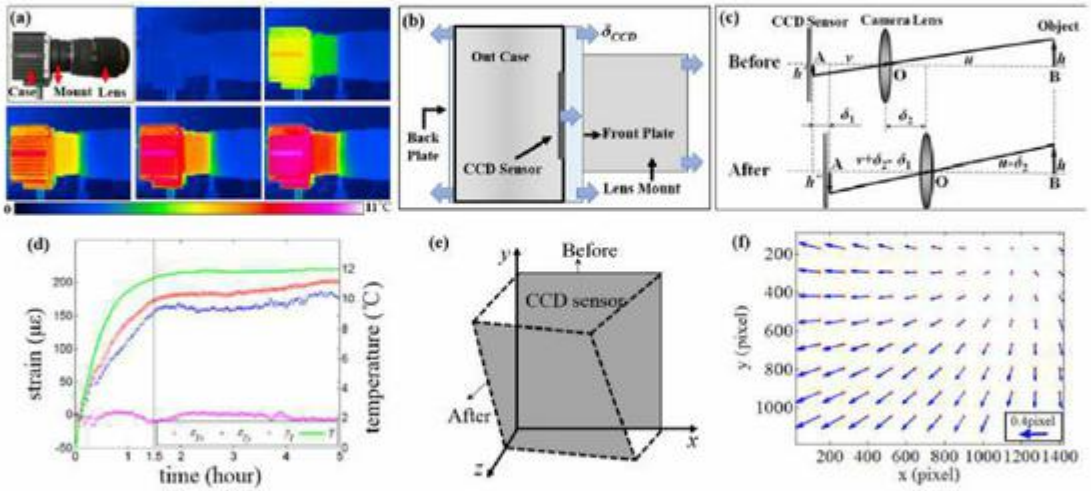

Fig.1 Heat induced image error of CCD/CMOS camera. (a) the temperature variation of the camera case, mount and lens within 5 hours, (b) the motion of the different parts of the camera, (c) the changes of the equivalent optical path, (d) the parasitic strain, (e) the typical parasitic displacement field, and (f) the schematic of the rigid motion of the CCD chip.

[a)] Corresponding author. Email: masp@bit.edu.cn.

START-UP TIME DIFFERENCE ERROR FOR MULTIPLE HIGH-SPEED CAMERA SYSTEM

In a high-speed stereo-vision system, dual high-speed cameras are used. The two cameras are triggered simultaneously and then is regarded starting recording images at the same time. A system as shown in Fig. 3a is used to check if the two cameras are exactly synchronized. It is found that sometimes there exists start-up time differences (STD), which means that the two cameras do not start recording the images simultaneously with a certain probability. For a typical high-speed cameras pairs (two Photron SA1.1 cameras manufactured in different years), systematic investigation shows that the possibility of occurrence of apparent start-up time difference is about 13%, and the STD is up to several hundreds microseconds (as shown in Fig. 4a). This error is not very critical for other applications, but it is unacceptable for photomechanics. As shown in Fig. 4b, the possibility of the occurrences of STD of different dual-camera imaging system is counted according to the similarity of the two cameras. The lower similarity, the greater of possibility of occurrence of STD. Synchronizing cable is helpful for reducing the percentage of occurrence of STD but cannot eliminate STD completely.

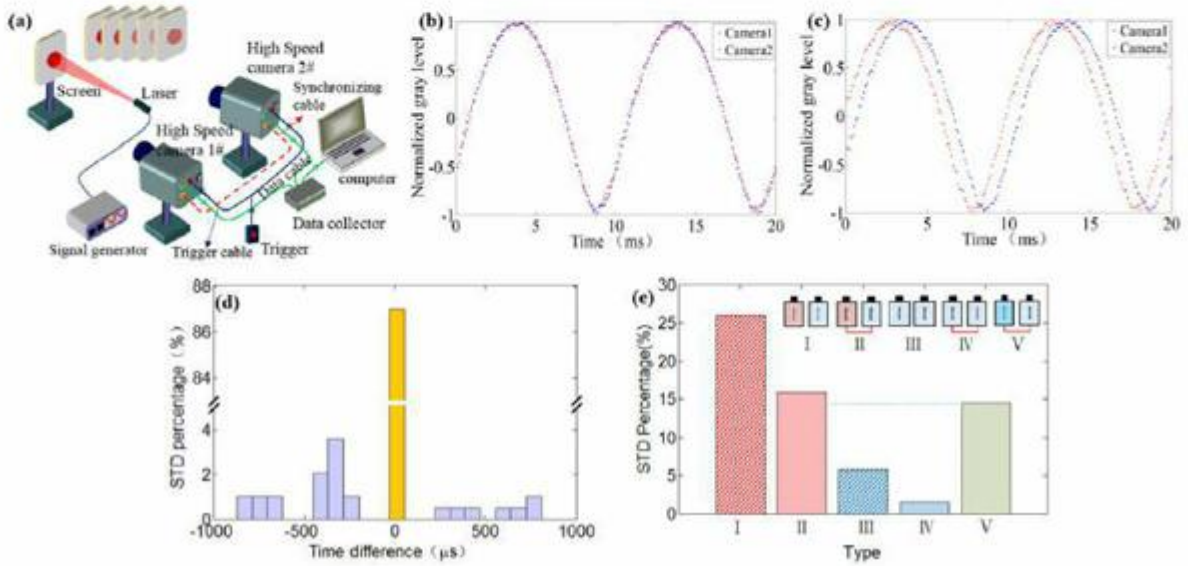

Fig.2 STD measurement and statistic for dual high-speed camera system: (a) the schematic of the experimental setup triggering the two cameras simultaneously and capturing the laser point with the sinusoidal intensity changing, (b-c) two typical intensity variation analysed from image series recorded by the two cameras, (d) distribution of STD for one dual high-speed camera system, and (e) percentage of STD for different assemblies of Photron high-speed cameras (I: SA1.1-SA2; II: SA1.1-SA2 with synchronizing cable; III: SA5-SA5; IV: SA5-SA5 with synchronizing cable; V: SA1.1 (made in 2009) - SA1.1 (made in 2013) with synchronizing cable).

CONCLUSIONS

For standard digital camera used in long-time measurements, there exists the heat-induced image expansion as well as the pixel motion. The strain error induced by the image expansion is up to tens με per °C, and the displacement error could be up to pixel level. For dual high-speed cameras used in stereo vision system, there exists start-up time difference and thus error on the time history of the image series from the two cameras, even though when they are triggered simultaneously. Images are the raw information of photomechanics measurements, thus the errors consisting of the parasitic deformation and the mismatching of time history of the image series could inevitably produce measurement errors with photomechanics methods. Therefore, commercial CCD or CMOS camera are not trustable enough for photomechanics. To perform reliable photomechanics measurements, the errors should be evaluated and the image data should be corrected. For the heat-induced image error, an unloaded specimen placed in the same field of view with the measured specimen could be used to eliminate the errors. For the high-speed measurement using multi-cameras, a specially designed independent, high-frequency timer may be used to align the different image series.

References

[1] Beyer H. A.: Geometric and Radiometric Analysis of a CCD-Camera Based Photogrammetric Close-Range System. *PhD Thesis*, Institut fur Geodasie und Photogrammetrie, ETH, Zurich, 1992.

[2] Podbreznik P., Potocnik B.: Influence of temperature variations on calibrated cameras. *Mach. Vision Appl.* **23**: 953-966, 2012.

[3] Handel H.: Analyzing the influences of camera warm-up effects on image acquisition. *IPSJ Trans. Comput. Vis. Appl.* **1**: 12-20, 2009.

[4] Ma S. P., Pang J. Z., Ma Q. W.: The systematic error in digital image correlation induced by self-heating of a digital camera. *Meas. Sci. Technol.* **23**: 025403, 2012.

[5] Yu Q. F., Chao Z. C., Jiang G. W., Shang Y., Fu Y. H., Liu X. L., Zhu X. W., Liu H. B.: The effects of temperature variation on videometric measurement and a compensation method. *Image Vision Comput.* **32**: 1021-1029, 2014.

[6] Ma Q. W., Ma S. P.: Camera self-heating induced systematic error for photomechanic methods and its compensation. *Opt. Express* **6**: 7686-7698, 2013.

A SHADOW PTV TECHNIQUE FOR PARTICLE TRACKING IN AN INHOMOGENEOUS TURBULENT FLOW.

Peter Huck[1], Nathanael Machicoane[2], and Romain Volk *[1]
[1]*Laboratoire de physique, Ecole Normale Suéprieure de Lyon, CNRS et Université de Lyon, France*
[2]*Laboratoire FAST, CNRS et Université Paris-Sud 11, Orsay, France*

Summary We use a Shadow Particle Tracking Velocimetry technique (S-PTV) with collimated light to investigate the dynamics of a turbulent von Kármán (VK) flow of water. Such a PTV technique, easy to calibrate as apparent particle position on the images do not depend on the camera-particle distance, allows to track small objects (100 μm particles, fibers, ...) with low power LEDs as light sources. Investigating the dynamics of Lagrangian tracers, we observe the flow produced in a square tank is bistable, the two states having a life time of several minutes so that the high speed recordings appear as snapshots of one of the two states that can be reconstructed from the particle trajectories. We show the two states topologies strongly differ from the one of the mean flow, and how the bistability affects the dispersion of tracers.

INTRODUCTION

Turbulent flows play a major role in mixing, chemical process in reactors, and transport of pollutants in the atmosphere. In this context, because the Lagrangian point of view which describes the fluid flow properties along the trajectories is the most natural, Particle Tracking Velocimetry has grown a lot in the past decade [1, 2, 3]. Using an ensemble of fast cameras, PTV allows to track small particles ($10-100$ μm large) in turbulent flows with Reynolds numbers $R_\lambda > 100$ with a temporal resolution of the order of the Kolmogorov frequency $f_K = \sqrt{\epsilon/\nu} \sim 1-10$ kHz, ϵ being the injected power per mass unit, and ν the fluid viscosity. However when developing a PTV setup with classical illumination, one has to face several difficulties: the quality of images strongly depends on the particles characteristics (refraction index, size), it needs a complex 3d calibration in order to achieve stereo-matching between the different views [4], and it requires powerful light sources (high power LEDs, or a high power laser) when tracking small objects. To overcome these difficulties we have developed a new optical setup inspired from [5] which allows to track particles' shadows produced when using parallel lighting.

EXPERIMENTAL SETUP AND RESULTS

The experimental apparatus is a von Kármán flow identical to the one used in [5]. The flow is produced in a cylinder with square section using two bladed discs, with radius $R = 7,1$ cm, which counter rotate at constant frequency Ω (figure 1 a)). Their spacing is equal to 15 cm, which is also the length of the tank section. Using a water-Ucon mixture 8 times more viscous than water, this setup produces an intense turbulence with a Taylor based Reynolds number $R_\lambda = 200$ and a dissipative length $\eta = 90$ microns. We perform particle tracking of Lagrangian tracers (200 μm polystyrene particles) in a large volume $8 \times 7.6 \times 7.6$ cm^3 centered around the geometrical centre ($(x, y, z) = (0, 0, 0)$) of the flow with 2 high-speed video cameras (Phantom V.12, Vision Research, 1Mpix@7kHz) with a resolution 800×768 pixels, and a frame rate $f_s = 12$ kHz. The camera arrangement, inspired from reference [5], is depicted in figure 1 b). It consist of 2 arms forming an angle $\theta = 90°$ with parallel lighting. Both arms are identical and use a small LED imaged in the focus of a large parabolic mirror (15 cm diameter, 50 cm focal length). This large parallel ray of light then reflects on a beam splitter and intersects the flow volume before being collected onto the camera using a doublet consisting of a large lens (15 cm in diameter) and the camera objective. As this arrangement requires some precision in the mounting, all optical elements are aligned using large (home made) reticules also used to measure precisely the magnification in each arm. When placing an object in the field of view, it appears as a black shadow on a white background corresponding to the parallel projection of the object on the sensor. When particles are tracked, camera 1 will then provide their (x_1, z_1) 2d positions while camera 2 will measure their (y_2, z_2) positions, the z coordinate being perfectly redundant (we have $z_2 = az_1 + b$). 3d tracking is then performed by first tracking particles independently on the movies corresponding to the 2 views before trajectories with $z_1(t) \simeq z_2(t)$ are identified using the relation $z_2 = az_1 + b$ as shown in figure 1 c). This relation is obtained by self-calibration with a dilute ensemble of particles that is tracked within a pair of movies recorded by cam1 and cam2 (here the parameters are $a = 0.96$, $b = 2.7$ pixels). Together with the pixel to mm magnification of one of the cameras, it provides all informations about particle positions in world coordinates.

Because the measurement volume $8 \times 7.6 \times 7.6$ cm^3 is twice larger than the integral length-scale $L = 3$ cm of the turbulence, the flow properties are not homogeneous in space. We thus record 200 pairs of movies with duration 1.3 seconds per Reynolds number with $\mathcal{O}(100)$ particles in the measurement volume, leading to a very large ensemble of $\mathcal{O}(4.\ 10^5)$ trajectories with mean duration $\langle t \rangle \sim 0.25/\Omega$ so the Lagrangian statistics can be conditioned in space. However we discovered that whatever the number of movies randomly chosen, we always found that the x and y component of the velocity had

*Corresponding author. Email: romain.volk@ens-lyon.fr

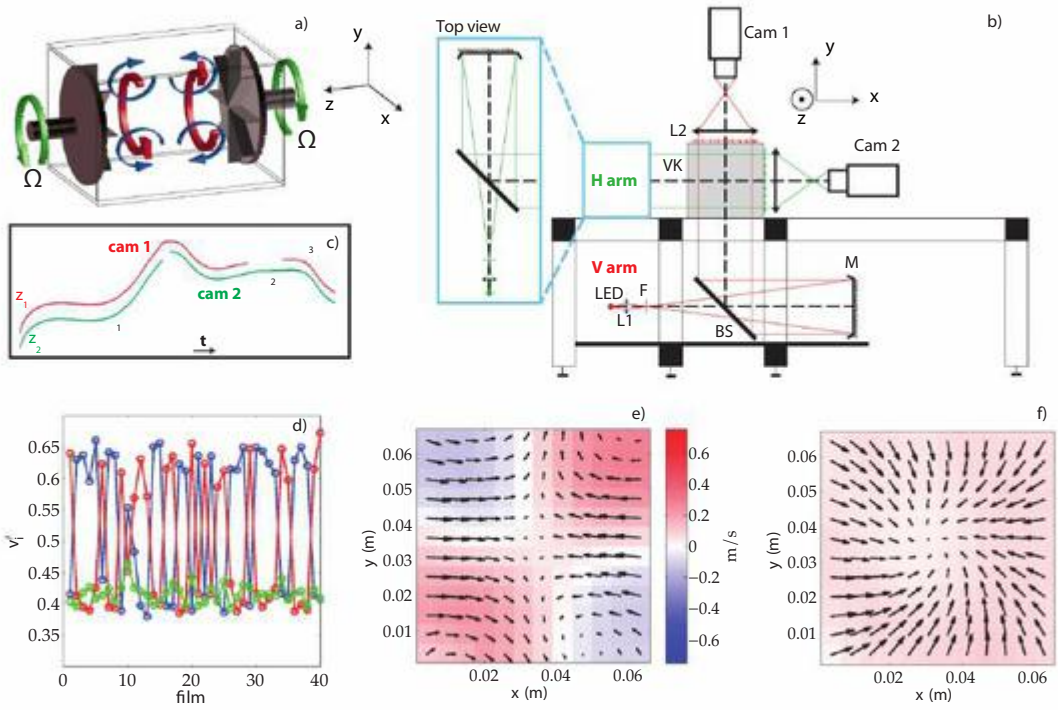

Figure 1: a) Sketch of the counter-rotating von Kármán flow. Arrows indicate the topology of the mean flow. b) Optical arrangement for S-PTV with 2 identical arms forming an angle $\theta = 90$ degrees (only the vertical arm is described).The 1W LED source is imaged in the focus of a parabolic mirror to form a large collimated beam. Light is propagating through the flow volume using beam splitter (BS) before being collected using a 15 cm large lens whose function is to redirect the light into the camera objective of the camera. The optical system [L_2+objective] is focussed on the output face of the vessel marked with a dashed-dotted line. c) time evolution of the z (redundant) coordinate of the same particle as obtained with 2d tracking with cam1 and cam2. d) rms velocities of the averaged of the particles (v'_x, v'_y, v'_z) for 40 consecutive movies and a rotating frequency $\Omega = 5.5$ Hz, which corresponds to $Re_\lambda = 200$. (symbol, v'_x-blue, v'_y-red, v'_z-green). e,f) reconstructed mean flow in the plane $z = 0$. Arrows indicate $(\langle v_x \rangle(x, y, z = 0), \langle v_y \rangle(x, y, z = 0))$ while colors indicate $\langle v_z \rangle(x, y, z = 0)$. e) as obtained by conditioning on the v_x dominant state. f) as obtained with the same number of movies from each state.

different statistics, which is in contradiction with the symmetries of the setup. This can be observed in figure 1 d), which displays the changes of the rms value of the velocity components (v'_x, v'_y, v'_z) obtained using all the trajectories whitin one movie. Indeed one always find $v'_z \sim 0.4$ with very different values for v'_x and v'_y which take randomly the values 0.4 and 0.65 m/s. This behavior, observed whatever the frequency of rotation in the fully turbulent regime, indicates that the large scale flow is bistable with one transverse component dominating over the other. This is confirmed when investigating the mean flow conditioned on the x-dominant state (corresponding to $v'_x > 0.55$) measured in the mid-plane $(z = 0)$ in figure 1 d). In the x-dominant state, $\langle v_x \rangle(x, y, z = 0)$ is much larger than $\langle v_y \rangle(x, y, z = 0)$ with a non zero component $\langle v_z \rangle(x, y, z = 0)$. The global symmetries of the flow are broken so that the mean flow is not invariant under a rotation of an angle $\pi/2$ around the z-axis. As shown in figure 1 f), the symmetries of the mean flow are only recovered when averaging over the same number of realizations of both x-dominant and y-dominant states. This type of bistability, for which the two states exchange under a discrete rotation on a time-scale of several minutes (estimated from flow visualization with bubbles), is different from the one already observed in von Kármán flows with circular section [6]. Indeed the present bistability, which has important consequences concerning the transport of particles in the flow, may be due to the interaction between corner vortices on the flat walls that can have complex interactions with the flow.

References

[1] Virant M., and Dracos T., 3D PTV and its application on Lagrangian motion, Measurement science and technology, **8**, (1997).

[2] Ouellette N. T., Xu H. , Bourgoin M., and Bodenschatz E., Small-scale anisotropy in Lagrangian turbulence, New J. Phys., **8**, (2006).

[3] Springer Handbook of Experimental Fluid Dynamics, ed. C. Tropea, A. L. Yarin, and J. F. Foss, pp. 789-799 (Springer-Verlag, 2007)

[4] Tsai, R., IEEE T. Robot. Autom., A versatile camera calibration technique for high accuracy 3d machine vision metrology, **RA-3**, (1987)

[5] Machicoane N., Bonaventure J., and Volk R.,, Melting dynamics of large ice balls in a turbulent swirling flow, Physics of fluids, , (2013)

[6] de la Torre, A. and Burguete, J., Slow Dynamics in a Turbulent von Kármán Swirling Flow, Physical Review Letters, **99**(5), (2007)

EVALUATION OF MEAN PRESSURE FIELD ABOVE A ROOF USING PIV DATA AND A 2D INTERPOLATION ALGORITHM

Chieh-Hsun Wu[1a)], Abul Fahad Akon[1] & Gregory A. Kopp[1]
[1]*Boundary Layer Wind Tunnel Laboratory, Faculty of Engineering, University of Western Ontario, London, ON, Canada*

Summary A 2D interpolation method is applied to integrate the pressure gradient data obtained from PIV measurement for the flow above a building roof. The reconstructed pressure field is smooth and matched the measured surface pressures reasonably well in terms of distribution. This method also allows users to remove the bad input data points.

INTRODUCTION

In order to better understand the mechanism how the atmospheric boundary layers affect the wind loads on buildings (i.e., surface pressures), particle image velocimetry (PIV) has been used to measure the velocity field together with the surface pressures. The PIV method can render deeper insights if we can infer the pressure field information from the measured flow field data. For 2D flow field, the gradient of mean pressure coefficient can be found by taking the time average of the Navier-Stokes equation, i.e.

$$\left(\overline{Cp}\right)_x = -2\cdot\left\{\overline{u}\left(\overline{u}\right)_x + \overline{v}\left(\overline{v}\right)_y + \left(\overline{u'u'}\right)_x + \left(\overline{u'v'}\right)_y - \nu\left[\left(\overline{u}\right)_{xx} + \left(\overline{u}\right)_{yy}\right]/U_{ref}\right\} \tag{1a}$$

$$\left(\overline{Cp}\right)_y = -2\cdot\left\{\overline{u}\left(\overline{v}\right)_x + \overline{v}\left(\overline{v}\right)_y + \left(\overline{u'v'}\right)_x + \left(\overline{v'v'}\right)_y - \nu\left[\left(\overline{v}\right)_{xx} + \left(\overline{v}\right)_{yy}\right]/U_{ref}\right\}, \tag{1b}$$

where the overbar denotes the time averaging; $(\bullet)'$ denotes the fluctuation; $(\bullet)_x$ and $(\bullet)_y$ are the x and y derivatives respectively; v is the kinematic viscosity. The pressure coefficients, Cp, in Eq. (1) are defined as the division of gauge pressure to a reference dynamic pressure $0.5\rho U_{ref}^2$. Therefore, the velocity components, u and v, are non-dimensional and defined as division of actual velocity to U_{ref}.

Gurka et al. (1999) [1] used the pressure Poisson equation and Neumann type of boundary condition to solve the pressure field from PIV data. More recently, van Oudhensden et al. (2007) [2] obtained the 2D velocity field around a square prism via PIV. They integrated the pressure field directly from the gradient data via a line-wise, downstream marching scheme with the inlet boundary pressure prescribed by Bernoulli's equation. Although this integration scheme is straightforward and fast, the measured gradient data needs to be curl free, such that the value obtained by integration along any arbitrary path is independent [3]. However, if a measured gradient data is not perfect, due to either measurement error or noise, the error will be propagated along the integration path, leading to distorted results. Ettl et al. (2008) [3] presented an alternative for integrating gradient data using generalized Hermite interpolation approach with analytic radial basis functions. This method is aimed to solve the problems described earlier. We have been finding this method useful in integrating our pressure gradient data obtained from PIV. So this algorithm is briefly introduced and the results of application will be shown in the following sections.

2D ANALYTIC INTERPOLATION

This method first assumes that the estimated pressure coefficient Cp^* at location $\mathbf{x}$ can be represented as linear spatial superposition of analytic function [3], i.e.

$$Cp_*(\mathbf{x}) = \sum_{i=1}^{N}\left[\alpha_i\Phi_x(\mathbf{x}-\mathbf{x}_i) + \beta_i\Phi_y(\mathbf{x}-\mathbf{x}_i)\right], \tag{2}$$

where α_i and β_i denote the appropriate coefficients for the analytic support Φ centered at i-th grid point. Wenland's function was selected in [3] and therefore here for the analytic support. This function is symmetric about its centre and resembles a bell shaped surface for $r \le 1$, where r is the radial distance from the support center. For regions of $r > 1$ values of zeros are padded. The range of influence for the support is denoted here as support size and set as unity. In order to find the coefficients for the spatial superposition, the gradient of Cp^*, is taken and matched with the measured gradient data obtained from Eq. (1). Once the linear system is formed as a result of this procedure, the coefficients can be simply solved by matrix inversion.

RESULTS AND DISCUSSIONS

The PIV data obtained from the flow field above the roof of a 1/50 scale model of Texas Tech University "WERFL" Building [4] was used to demonstrate the application of the proposed method. This modelled building has plane dimensions of 18.4 cm × 27.5 cm and a height of 7.8 cm. A row of 9 taps were placed on the model's roof surface for pressure measurement. This pressure measurement system was synchronized with a Time-Resolved Particle Image Velocimetry (TR-PIV) system. The model was placed on the high speed test section of Wind Tunnel-II at the University of Western Ontario.

[a)] Corresponding author. Email: cwu283@uwo.ca.

An ‘open’ terrain was used as the roughness condition of the simulated atmospheric boundary layer. At the building roof height, the corresponding turbulence intensity is 17% with an integral length scale of about 11 times of the building height. Akon and Kopp (2015) [4] addressed the turbulence characteristics in terms of the statistics of the time averaged velocity field. Those results were used as the input for the right hand side of Eq. (1) to determine the gradient of mean Cp.

Data were obtained on the two frames shown in Fig. 1(a), i.e., the frame in front of building is denoted as frame 1 and the frame above roof is denoted as frame 2. The resulting gradient field of mean Cp is also shown in Fig. 1(a) for the region close to the leading edge. Note that bulk wind direction is in the positive x direction. The x-axis denotes the distance from the leading edge of roof and y-axis denotes the vertical distance above the (tunnel) floor. High-gradient vectors are found to be pointing out near radially from the leading edge, therefore large pressure gradients can be anticipated in this region. The little red boxes near the roof and wall are used to denote locations with bad data points. The gradient vectors at these points were found to be either unreasonably large or pointing into reverse direction when compared to the adjacent vectors. Thus, these ‘noise’ vectors are not shown in Fig 1(a). In order to apply the interpolation method for pressure integration, the size of analytic support is chosen to be 2.5 cm, which is around 14 times of the grid spacing ($\Delta x = \Delta y = 0.18$ cm). At the upper left corner of the frame 1 (x = -12.5 cm, y = 15 cm), the mean pressure is assumed to be the same as ambient value (i.e. Cp = 0), which is used as constant of integration for pressure reconstruction on frame 1. For frame 2, the pressure reconstruction was first obtained with an arbitrary value of integration constant. The reconstructed pressure were then adjusted by a constant through minimizing the difference between values obtained in frame 1 and frame 2 but within the overlapped region. The ‘integrated’ mean Cp as a result of considering all gradient data is shown in Fig. 1(b) (‘All data’) for locations along a horizontal line near roof height (i.e., $y \approx 7.8$ cm). Although a constant underestimation ($\Delta Cp \approx 0.2$) can be observed between measurement and integrated data, the slopes of Cp distributions generally match well. The constant underestimation may be due to the different reference velocities used in PIV analyses and surface pressure measurement, while the local spikes are due to noisy data points. Once this noise is excluded in the reconstruction procedure, the integrated Cp becomes smooth, as shown by the dots in Fig. 1(b) (‘Corrected’). The corresponding field of integrated Cp is shown in Fig. 1(c), along with streamlines of mean separated flow. Smooth distribution of mean Cp field can be observed.

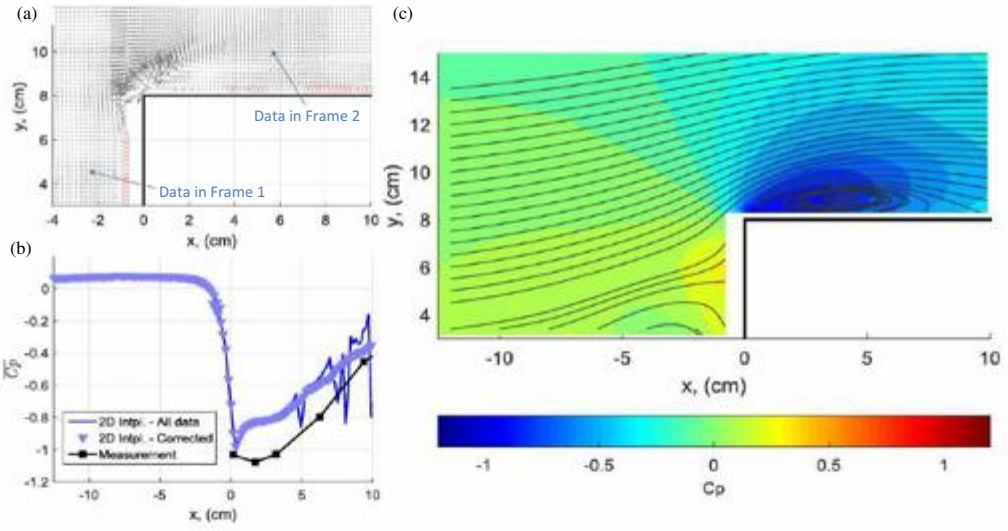

Figure 1:
(a) Gradient vector of mean Cp;
(b) Integrated mean Cp at roof height;
(c) Contour of integrated mean Cp using inputs excluding bad points.

CONCLUSIONS

A 2D interpolation method is applied to integrate the pressure gradient data obtained from PIV measurement for the flow above a building roof. The reconstructed pressure field is smooth and matched the direct measurement well in terms of distribution. This method also allows the user to remove the bad inputs data points for pressure reconstruction.

References

[1] Gurka R, Liberzon A, Hefetz D, Rubinstein D, Shavit U.: Computation of pressure distribution using PIV velocity data. In: 3rd International workshop on PIV, Santa Barbara, 101–106, 1999.

[2] van Oudheusden, B. W., Scarano, F., Roosenboom, E.W.M., Casimiri, E.W.F., Souverein, L. J .: Evaluation of integral force and pressure fields from plannar velocimetry data for incompressible and compressible flows. Exp. Fluids *43*: 153-162, 2007.

[3] Ettl, S., Kaminski, J., Knauer, M. C., Häusler, G.: Shape reconstruction from gradient data. Applied Optics 47: 153-162, 2008.

[4] Akon, A. F., Kopp, G. A.: Fluctuating pressures and flow characteristics within separation bubbles on surface-mounted prisms. In: Proceedings of 25th CANCAM, London, Ontatiao, Canada, 2015.

REAL-TIME MEASUREMENT OF BIAXIAL MODULUS OF GE ANODE FOR LI ION BATTERIES

Rajasekhar Tripuraneni, Siva Nadimpalli [a)]
Micro and Nano Mechanics Lab
Mechanical Engineering, New Jersey Institute of Technology, New Jersey, USA

Abstract An in situ measurement of biaxial modulus evolution of germanium as a lithium ion battery anode material is presented. Thin films of germanium are cycled in a half-cell configuration with lithium metal foil as counter/reference electrode, with 1M $LiPF_6$ in ethylene carbonate, diethyl carbonate, dimethyl carbonate solution (1:1:1, wt. %) as electrolyte. At various capacity levels the germanium thin films were loaded/unloaded by small lithiation/delithiation steps, the slope of stress-strain curve during this load/unload portion provides the modulus data. It was observed that biaxial modulus changed from 45 GPa for $Li_{0.45}Ge$ to 30 GPa for $Li_{3.75}Ge$. Understanding variations in biaxial modulus is essential for predicting the stresses accurately and designing fracture resistant germanium electrodes.

INTRODUCTION

Germanium (Ge) and its alloys are among the promising materials as negative electrodes which have significantly higher charge capacities compared to that of graphite (e.g., Ge have theoretical capacities of 1625 mAh/g[1] compared to 372 mAh/g for graphite) . Germanium electrodes however, pose some unique challenges because of volume expansion induced stresses due to lithiation is as high as 0.83 Gpa[2] and can influence the electrochemical processes. These stresses are the primary driving force for fracture and effects the durability of Ge electrodes. Understanding the mechanical property and stress evolution in Ge due to lithiation, is important for designing innovative fracture resistant microstructures to avoid premature failure. The modulus data will enable the mechanics based models to predict the electrode behavior more accurately which helps not only in estimating the battery losses due to fracture of electrodes but also in designing fracture/failure resistant Ge electrodes. The objective of this study is to carryout real-time biaxial modulus measurement of Ge thin films during lithiation/delithiation cycling using the substrate curvature method.

EXPERIMENTAL PROCEDURE

Electrodes were prepared by sputter depositing 5 nm of titanium (Ti), 200 nm of copper (Cu), and 100 nm of Ge films on 2-inch double-side polished fused silica substrates (525 µm thick, and 50.8 mm diameter). Planar thin film geometry without binder eliminates assumptions and complexities associated with the composite behavior; hence, this thin film configuration provides ideal conditions for measuring stress and other fundamental mechanical properties of lithiated Ge. Stress evolution in the amorphous Ge (a-Ge) films during lithiation and delithiation was measured by monitoring the substrate curvature with the MOS setup (k-Space Associates). The system consists of a laser source that generates a single focused beam, two etalons, whose rotation axes are arranged orthogonally to each other in order to generate a 2 x 2 array of beams, and a CCD camera to capture the reflected beam-array from the sample surface as shown in Fig.1. The relative change in the distance between the laser spots on the CCD screen gives the sample curvature, κ. The array of reflected spots enables curvature measurement in two orthogonal directions. Biaxial film stress is related to substrate curvature through the Stoney equation3

$$\sigma = \sigma_r + \frac{E_s t_s^2 \kappa}{6 t_f (1-\upsilon_s)} \quad \text{.....Eq.1}$$

where σ_r is residual stress in the film due to sputter deposition. E_s, υ_s, and t_s are Young's modulus, Poisson ratio, and thickness of the substrate, respectively. The t_f is the film thickness of Ge which evolves continuously during lithiation and delithiation processes. Liang *et al*.[4] reported a 260% increase in volume of spherical Ge nanoparticles upon full lithiation. Hence, a linear variation of thickness with State of Charge (SOC) during lithiation is assumed for Ge and the resulting equation for film-thickness as a function of SOC in Ge is given as

$$t_f = t_f^o(1 + 2.6z) \quad \text{..... Eq.2}$$

where t_f^o is the initial film thickness, z is SOC which varies between 0 and 1; z =1 corresponds to a capacity of 1625 mAh/g and a volumetric strain of 2.6.[4] The in-plane strain change (Δε) is given by $\Delta\varepsilon=\Delta\sigma/Y+\Delta\varepsilon^*$, where σ is the biaxial film stress, Y is biaxial modulus of film E is young's modulus and υ poission's ratio.

$$\varepsilon^* = (1 + 2.6z)^{1/3} - 1 \quad \text{..... Eq.3}$$

And, due to substrate constraint ε_0 is 0 and biaxial modulus can be given by $Y = -\Delta\sigma/\Delta\varepsilon^*$.[5]During delithiation-relithiation the change in stress $\Delta\sigma$ is measured from substrate curvature change and $\Delta\varepsilon^*$ is calculated from Eq. 3.

Electrochemical experiments were carried out using a Solartron 1470 E Potetntiostat. The Ge thin-film electrodes were subjected to a series of galvanostatic lithiation(5 µA/cm^2), 1 hr open circuit, 8 min delithiation sequences at various levels of

[a)] Corresponding author. Email: siva.p.nadimpalli@njit.edu

state of charge as shown in Fig.2. The slope of stress-strain response corresponding to these lithiation/delithiation steps provides the modulus value.

RESULTS AND DISCUSSION

Note from Figure 2 that during lithiation compressive stresses increases representing loading of film which are relaxed during the following open circuit condition. Stress increases in the opposite direction during delithiation representing unloading. The stress-strain data during elastic loading and unloading is considered to measure the biaxial modulus of Li-Ge system. Biaxial modulus measured by using $Y = -\Delta\sigma/\Delta\varepsilon^*$ does not consider formation of solid electrolyte interface layer which when considered will underestimate modulus during lithiation and overestimate it during delithiation. Hence an average of these two modulus values,i.e., from loading and unloading curve should be considered as the actual modulus. Note that the modulus decreased as the lithium concentration increased. Using a rule of mixtures biaxial modulus as a function of x can be estimated as

$$Y_{est} = \frac{x_{Lx}E_{Lx}+x_{Ge}E_{Ge}}{1-(x_{Lx}\upsilon_{Lx}+x_{Lx}\upsilon_{Lx})} \quad \text{.....Eq.4}$$

where x_{Li} , x_{Ge} are the fraction of li and Ge in $Li-Ge$ system, $\upsilon_{Li}, \upsilon_{Li}$ are Poission's ratio and E_{Li}, E_{Ge} represents Young' s modulus of Li and Ge. Biaxial modulus as a function of x in Li_xGe estimated from rule of mixtures seems to agree with the experimentally measured values for higher lithium concentration as shown in Figure 3.

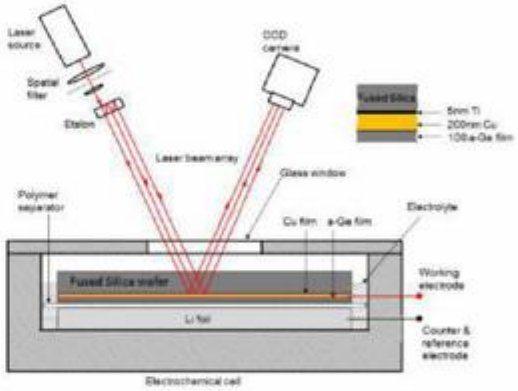

Figure 1: Schematic of experimental setup. Inset shows details of thin film layers

CONCLUSION

Germanium thin film electrodes were cycled against Li foil counter/reference electrode. Real-time modulus evolution in planar a-Ge film electrodes is measured during galvanostatic lithiation/delithiation using substrate curvature technique. It was observed that biaxial modulus reduces from 45Gpa for $Li_{0.45}Ge$ to 30Gpa for $Li_{3.75}Ge$.

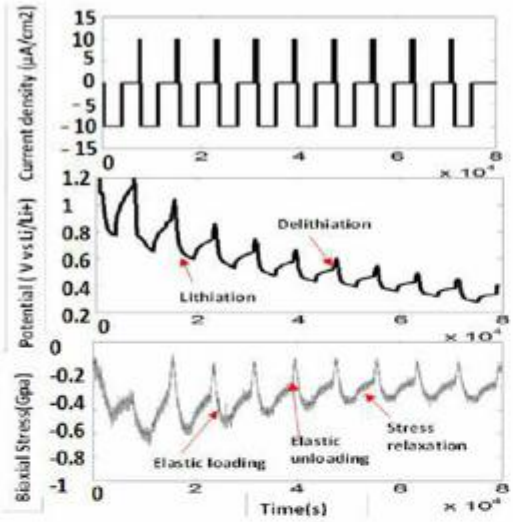

Figure 2: Current density, Potential and stress from in-situ measurements as function of time

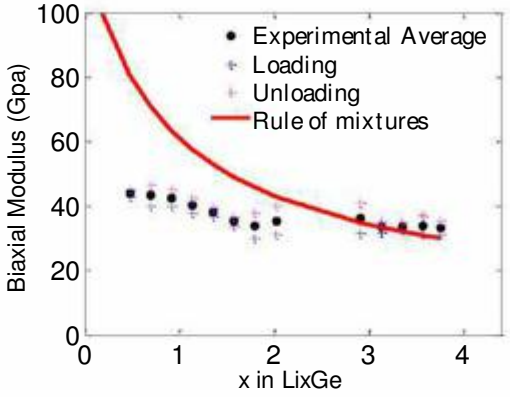

Figure 3: Biaxial modulus of a-Ge thin film as function of x in Li_xGe

REFERENCES

[1] Loïc Baggetto; Notten, P. H. L., Journal of The Electrochemical Society 2009, 156 (3), A169.

[2] Nadimpalli, Siva PV, Rajasekhar Tripuraneni, and Vijay A. Sethuraman., Journal of The Electrochemical Society 162.14 (2015): A2840-A2846.

[3] L. B. Freund; Suresh, S., Thin Film Materials: Stress, Defect Formation and Surface Evolution. 2004.

[4] Wentao Liang; Hui Yang; Feifei Fan; Yang Liu; Xiao Hua Liu; Jian Yu Huang; Ting Zhu; Zhang, S., Tough Germanium Nanoparticles under Electrochemical Cycling. ACS Nano 2013, 7 (4), 3427.

[5] Sethuraman, V. A., Chon, M. J., Shimshak, M., Van Winkle, N., & Guduru, P. R., Electrochemistry Communications 12.11 (2010): 1614-1617.

FRICTION MEASUREMENTS ON SMALL JOURNAL BEARINGS

Mathis Trachsel*[1,2], Jürg Dual[1], and Raniero Pittini[2]
[1]*Institute of Mechanical Systems, ETH, 8092 Zurich, Switzerland*
[2]*maxon motor ag, 6072 Sachseln, Switzerland*

Summary The setup described in this work allows precise friction measurements on small bearings for various shaft-speeds, radial loadings, lubricants and gap widths. The system is able to capture simultaneously the friction, as well as the relative displacement between shaft and bearing which reveals the displacement trajectory and the dynamic behavior, mainly half-frequency whirling with critical speeds. If displacement is considered for the friction measurement, an improvement in measurement accuracy is achieved when compared to previously reported techniques. Geometrical tolerances are identified by two measurements and corrected.

INTRODUCTION

Friction measurements in the range of $\mu\mathrm{Nm}$ are extremely sensitive to external forces and kinematic constraints which favor or prevent a fluid film to separate the two sliding bodies. Experiments therefore, should reproduce the common case of a radial load and an unconstrained displacement. In this work, the friction force is captured at the bearings and transmitted by a band to a precise balance as shown in Fig. 1. A similar technique was applied in [1, 2, 3]. This method is very precise and is thus sensitive to tolerances which are identified and corrected by two measurements in opposite direction of rotation. The relative displacement between shaft and bearing is a key parameter as identified by Reynolds in 1886 and later by Sommerfeld. But today experimental work is still scarce and only available for bigger shaft diameters [4, 5, 6]. To determine the friction torque at the shaft, the horizontal component Δx of bearing eccentricity has to be considered, which is new for this type of measurement and leads to higher friction at values of high eccentricity. Dynamic phenomena can be investigated and whirling can be detected in the displacement-data. All parameters involved can be changed easily.

MECHANICAL SETUP

A steel shaft of $3\,\mathrm{mm}$ diameter is driven at a controlled speed by an electric motor and lies on a V-shaped support built of hardened steel. The two bearings to be measured are aligned on a steel needle and pressed in a steel cylinder. The friction force is transmitted to a balance (METTLER, $PH403S$, $1\,\mathrm{mg}$ resolution) by a band. The total radial loading F_r can be varied by changing the weight F_w. On the side of the balance the friction force is either added or subtracted to the force of the static equilibrium, depending on the direction of rotation.

F_r therefore depends on friction and on the direction of rotation. Considering the mass of the cylinder m_z, a simplified value $F_r = F_w + F_b + m_z g$ is used here. To assure high accuracy and constant distance of the forces F_b and F_w from the axis of rotation, a stainless steel band of $10\,\mu\mathrm{m}$ thickness is applied. Previous work using ropes did not allow precise measurements and reproducibility. The system resolution is further increased from the nominal $50\,\mathrm{nNm}$ by taking average values at each speed. Data are digitally ($RS232$) transmitted to a PC, data acquisition is controlled by *LabVIEW*. Two laser systems *ILD2300LL* by *Micro-Epsilon* capture the displacement of one bearing in x- and y- direction. Results illustrating this technique are shown for porous journal bearings *Sint-B50* having 20% porosity and using non-Newtonian *CX-2000* by Klueber as lubricant, with variable speed and $5\,\mu\mathrm{m}$ radial gap between shaft and bearing.

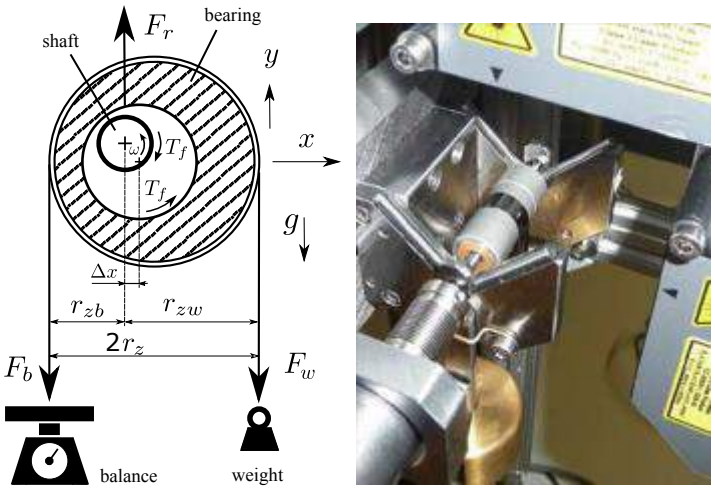

Fig. 1: Principle and photo of the measurement setup built with a balance, weight, rotating shaft and bearings considering tolerances.

DATA ANALYSIS AND PROCESSING

The friction torque T_f acting on the shaft is calculated from the data F_b, acquired from the mentioned balance, the known weight F_w and the radius r_{zb} of the imperfect cylinder on the side of the balance and on the side of the weight r_{zw}:

$$T_f = r_{zw}\, F_w - r_{zb}\, F_b \tag{1}$$

*Corresponding author. Email: trachsel@imes.mavt.ethz.ch

Considering tolerances Δr in cylinder-bearing concentricity and horizontal displacement Δx, the friction torque T_f from (1) is written with variable parameters $r_{zw} = r_z + \Delta r + \Delta x$ and $r_{zb} = r_z - \Delta r - \Delta x$.

Correction of friction data by identification of geometric tolerances (calibration)

At high speed hydrodynamic friction is not expected to depend on the direction on rotation. According to measurements and well known theory [8], the shaft is well centered in the bearings and effects of horizontal displacement Δx are negligible. The friction torque (1) of two measurements in opposite direction of rotation (cw: clockwise, ccw: counterclockwise) is set equal at maximum speed and $\Delta x = 0$. By solving for Δr the tolerances are identified with high accuracy:

$$\Delta r = r_z \cdot \frac{2F_w - F_{b,ccw} - F_{b,cw}}{2F_w + F_{b,ccw} + F_{b,cw}}. \tag{2}$$

The effect and importance of the calibration Δr and displacement measurement Δx is illustrated in Fig. 2 at $F_r = 0.52\,\mathrm{N}$. A value of $\Delta r = 8.38\,\mu\mathrm{m}$ was found in this case. The horizontal Δx and the vertical displacement are shown in Fig. 3.

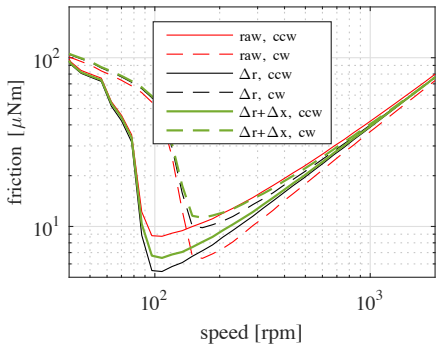

Fig. 2: Friction data considering calibration Δr and Δx from measurement.

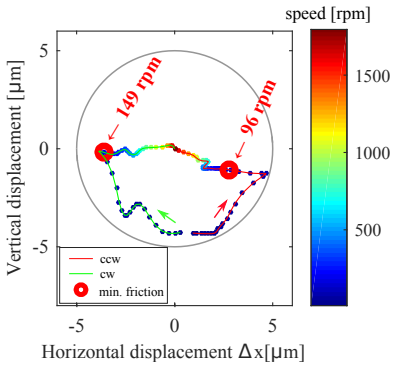

Fig. 3: Displacement for cw and ccw direction shown for increasing speed.

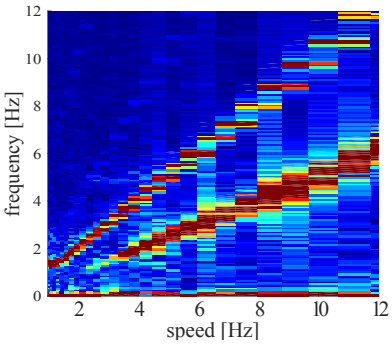

Fig. 4: Campell-diagramm of Δx: $F_r = 0.33\,\mathrm{N}$, critical speed at 3.5 Hz.

Influence of the direction of rotation

A dependance of the friction measurements on the direction of rotation was noted at low speeds. With reference to Fig. 1, this could be explained by the fact that in ccw-rotation the cylinder can easily move up, lift the weight and a fluid film is built. In cw-rotation however the band is held fixed to the balance resulting in higher friction at the transition to the hydrodynamic domain and a shift of minimum friction towards higher speeds can be noted as shown in Fig. 2.

Additional insight

The bearing trajectory does not follow the theory by Sommerfeld for all speeds as already found via numerical investigations carried out in [5]: A lift off is detected at the point of minimum friction or just before. At this point the displacement changes direction and moves towards a concentric position. Domains of mixed- and hydrodynamic lubrication can be distinguished. In Fig. 4 an analysis in the frequency domain at low radial loading reveals the dynamic behavior and the well known half-frequency whirling [8] starting at some specific critical speed and comes along with a slight increase in friction.

CONCLUSION

A new setup was developed to study the performance of small bearings. Simultaneous detection of friction and displacement improves the precision of friction data and leads to a profound understanding of the fluid-structure interaction which allows further optimization of parts involved according to specific application.

References

[1] Brenner, W. ; The measurement of minimotors and micromotors torque-characteristic using min. cable brake. Microsystem Technologies, 1997.
[2] Tao, Y M and Yao; Precision metrology of micro-workpieces on their tribological performance with an error compensation method, 2002.
[3] Kim, Hyung Jin and Park, In Kyum and Seo; International Journal of Precision Engineering and Manufacturing, 15(2):267-273, 2014.
[4] Dubois, George B; Analytical derivation and experimental evaluation of short-bearing approximation for full journal bearing, 1953.
[5] Balasoiu, Ana Maria; A self-circulation porous bearing with a wrapped-around reservoir. Dissertation, 2012.
[6] L.Costa and Miranda; Temperature, Flow, and Eccentricity Measurements in a Journal Bearing. Lubrication Science, 167-180, 2001.
[7] Yao, Zhenqiang and Zhang, Qi and Tao; Tribology International, 33(7): 485-489, 2000.
[8] Stachowiak, Batchelor, Engineering Tribology, 2014.

DIGITAL EFFECTS IN HARDWARE-IN-THE-LOOP EXPERIMENTS OF STICK-SLIP PHENOMENA

Gabor Stepan*, Zsolt Veraszto

Department of Applied Mechanics, Budapest University of Technology and Economics, Hungary

Summary The topic of this study is the analysis of one degree of freedom (DoF) oscillatory systems subjected to the friction force generated at moving surfaces of mixed dry and viscous friction. The stick-slip phenomenon arising on partially lubricated surfaces can be critical in many engineering systems. This study aims to present the theoretical considerations behind the use of the hardware-in-the-loop (HIL) method and to report on possible experimental implementation. We compare the results of the global dynamical analysis with the numerical results of the simulations. The mathematical model of the HIL experiment considers idealised control, but takes into account the delay related to the digital effects like sampling. The analytical and numerical analysis of the corresponding discrete model leads to results validated by the measurements. The conclusions of the theoretical, numerical and experimental study call the attention on the limitations of HIL experiments when the system is strongly nonlinear.

MOTIVATION

There is a set of historical dynamical problems in engineering that causes permanent difficulties in the design on certain machines, machine parts. One common feature of these systems is that the desired steady-state behavior of the machine may become unstable at certain speed ranges. While systems can be tuned to stable parameter domains with reasonable reliability, they can still exhibit undesired dynamical behavior when large perturbations occur. Machine tool vibrations [1], wheel shimmy [2], stick-slip [3] or even traffic dynamics [4] belong to this set of problems. The fundamental reason of the unpredictable occurrence of undesired oscillations is the subcritical sense of the Hopf bifurcations at the loss of stability of the desired steady states. It is a rule of thumb that delay tends to destabilize dynamical systems, also, it tends to make bifurcations subcritical. Delay exists in many of the models of the mentioned industrial problems, except the stick-slip phenomenon, which has simple, even single degree-of-freedom (DOF) nonlinear models while it still performs subcritical Hopf bifurcation.

Since the design of these systems cannot guarantee the avoidance of undesired oscillations, extensive numerical simulation is needed for large sets of parameters and initial conditions, which still does not substitute expensive tests on prototypes. A promising way to reduce the costs of this development process is the application of hardware-in-the-loop (HIL) experiments [5], in other words real-time substructuring [6] when some parts of the system is substituted by actuators and computer simulation. Digital effects are introduced into these systems when HIL experiments are performed [7]. The discretization in time (sampling) and space (round-off) may lead to somewhat modified dynamical behavior than the real system [8]. These limitations of the HIL experiments are studied for the simplest nonlinear model of stick-slip phenomenon.

MATHEMATICAL MODEL AND TEST RIG OF STICK-SLIP HIL EXPERIMENT

The stick-slip phenomenon can be described by a 1 DoF damped oscillator subjected to the so-called Stribeck force:

$$\ddot{x}(t) + 2\zeta\omega_{\rm n}\dot{x}(t) + \omega^2 x(t) = F_{\rm Str}(\dot{x}(t_j-\tau))/m\,, \quad t\in[t_j, t_j+\tau), \quad t_j = j\tau, \quad j=1,2,\dots\,.$$

$$F_{\rm Str}(\dot{x}) = \left(C + (C_0 - C)\mathrm{e}^{-c_{\rm v}|v_0-\dot{x}|}\right)\mathrm{sgn}(v_0-\dot{x}) + b_{\rm Str}(v_0-\dot{x})\,,$$

where the oscillatory system is characterized by its undamped angular natural frequency $\omega_{\rm n}$, damping ration ζ and modal mass m. The Stribeck force describes the mixed viscous-dry friction between the body and a moving surface of velocity v_0 resulting the relative velocity $v_0 - \dot{x}$ between the surfaces. There are several parameters in the force $F_{\rm Str}$ among which the sticking friction force C_0 and the sliding friction force C can easily be identified. The HIL experiment can run with certain sampling frequency only. This is taken into account by means of the sampling time τ. Due to the piece-wise constant force $F_{\rm Str}$, the above system can be transformed into a 3-dimensional nonlinear discrete system.

A HIL experiment was compiled where the damped oscillator consisted of an elastic beam and a block, while the Stribeck force was emulated by an electromagnetic actuator controlled by a processor that calculated the force according to the formula of $F_{\rm Str}$. The test rig is shown in Fig. 1 together with its mechanical model. The deformation of the spring (the elastic beam) was sensed to obtain the signals of position x and velocity $\dot{x}$, and the control force was created by means of a PI control of the current I that was also measured at the actuator. The signal was sent to the actuator by means of pulse width modulation (pwm).

*Corresponding author. Email: stepan@mm.bme.hu

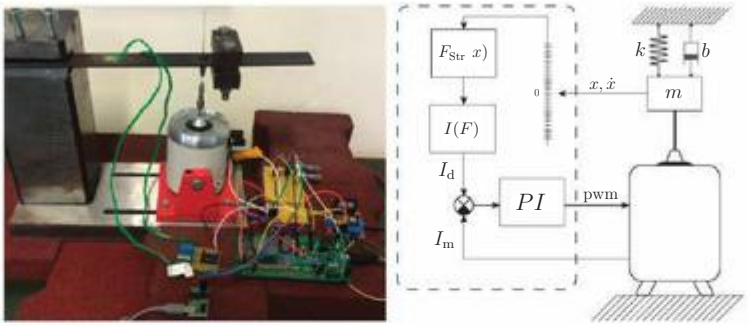

Figure 1: HIL experiment: test rig and sketch.

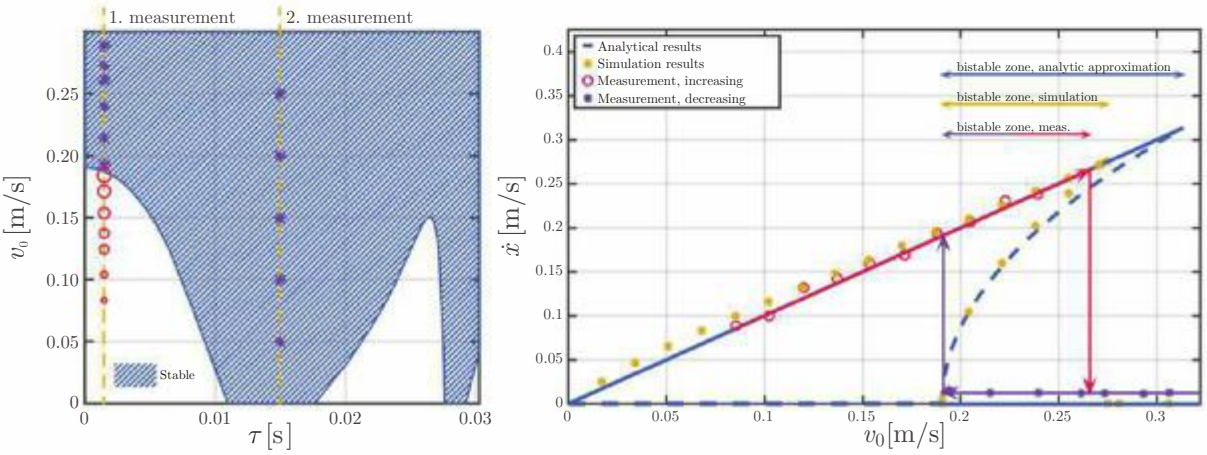

Figure 2: Stability chart with test results at $\tau = 2$ ms and 15 ms, and bifurcation diagram for $\tau = 2$ ms.

CONCLUSIONS

The dynamic behaviors of the original continuous system ($\tau = 0$) and the digital system ($\tau > 0$) are not exactly the same as it can be followed in Fig. 2. For small sampling time $\tau = 2$ ms, the linear stability limit is almost correct, the unstable limit cycle exists and the stable limit cycle appears as a weakly chaotic attractor, while the size of the bistable zone is reduced. However, for sampling time $\tau = 15$ ms, the unstable limit cycle disappeared in the experiments, and linear stability survived even for low speeds v_0, which was confirmed by the linear stability calculation of the discrete system as shown in the strange stability chart of Fig. 2. This calls the attention of the possibly unacceptable effect of time delays in the HIL experiments.

Acknowledgement

The research leading to these results has received funding from the European Research Council under the European Unions Seventh Framework Programme (FP/2007-2013) / ERC Advanced Grant Agreement n. 340889.

References

[1] Stepan G: Modelling non-linear regenerative effects in metal cutting. Philosophical Transactions of the Royal Society 359:739-757, 2001.
[2] Takacs D, Orosz G, Stepan G: Delay effects in shimmy dynamics of wheels with stretched string-like tyres. European J of Mech A 28:516-525, 2009.
[3] Leine RI, van Campen DH, de Kraker A, van den Steen L: Stick-Slip Vibrations Induced by Alternate Friction Models. Nonl Dynamics 16: 4154, 1998.
[4] Orosz G, Stepan G: Subcritical Hopf bifurcations in a car-following model with reaction-time delay. Proc Roy Soc A 462:2643-2670, 2006.
[5] Tsiotras P, Jung D: Modeling and hardware-in-the-loop simulation for a small unmanned aerial vehicle. Proc AIAA Guidance Conf, pages 1-13, 2007.
[6] Kyrychko YN, Blyuss KB, Gonzalez-Buelga A, Hogan SJ, Wagg DJ: Real-time dynamic substructuring in a coupled oscillatorpendulum system. Proc Roy Soc A 462:1271-1294, 2006.
[7] Haller G, Stepan G: Micro-chaos in digital control. J Nonl Sci, 6:415-448, 1996.
[8] Ayasun S, Monti A, Dougal R, Fischl R, Vallieu S, On the stability of hardware in the loop simulation. Proc. 7th Int. Conf. Model. Simul. Elect. Mach., Convert. Syst., pages 185-191, 2002.

MEASURING THE DYNAMIC ELECTROMECHANICAL RESPONSE OF FERROELECTRICS

Charles S. Wojnar*[1]

[1]*Department of Mechanical and Aerospace Engineering, Missouri University of Science and Technology, Rolla, Missouri, USA*

Summary To better understand the dynamic response of thermo-electro-mechanically coupled materials, in particular stiffness and mechanical damping, an experimental method called Broadband Electromechanical Spectroscopy (BES) was developed. The motivation for BES was to study ferroelectric materials over wide ranges of frequencies of simultaneously applied electric fields and mechanical stresses under temperature control. By precisely controlling electric fields and mechanical loading, the effect of microstructural changes, in particular domain switching in ferroelectrics, on the dynamic mechanical response is measured. Experiments show large increases in mechanical damping during domain switching that can be tuned by appropriate electrical loading. Results obtained using the new capabilities brought by BES can be used to better understand the damping associated with domain wall motion to be able to create ceramic materials with both high stiffness and high damping – an elusive combination of properties in typical engineering materials.

INTRODUCTION

Various approaches can be taken to reduce vibrations in structures in order to mitigate fatigue. Passive methods involve combining high damping materials into structures, which results in a compromise of stiffness and damping. Alternatively, active methods involve actuating structures in such a way to cancel out vibrations. This is typically achieved by piezoelectric actuators. Piezoelectric materials exhibit a linear relationship between applied stress and resulting charge accumulation on the surface (electric displacement). This phenomenon is used in shunted piezoelectrics where charge accumulation is dissipated by connecting surface electrodes with a resistor [1]. But this approach is also highly frequency dependent. The converse relationship (linear relationship between applied electric field and strain) is what is used in piezoelectric actuators where an applied electric field is carefully controlled to generate strains in such a way to cancel out vibrations.

The approaches using piezoelectrics, however, only utilize their linear response. Piezoelectrics like the widely used material lead zirconate titanate (PZT) are also ferroelectric. That is, they exhibit a spontaneous polarization that can be reoriented by applying sufficiently large electric fields and/or stresses. The process of polarization reorientation, or so-called domain switching, is a dissipative process [2]. Nonetheless, there are only a limited number studies on using domain switching as an alternative mechanism for mechanical damping. This is in part due to a lack of experimental methods for its characterization. We close this gap by presenting an experimental setup and method called Broadband Electromechanical Spectroscopy (BES) for measuring the dynamic mechanical response (i.e. stiffness and damping) of ferroelectrics (and other materials) while applying sufficiently large electric fields to induce domain switching. Using BES, the stiffness and damping of a particular ferroelectric, viz. PZT, was measured over a wide range of bending and torsional frequencies.

MATERIALS AND METHODS

The apparatus developed for BES is based on Broadband Viscoelastic Spectroscopy (BVS) [3]. That is, cantilevered beam specimens are tested in bending and/or torsion using contact-less techniques. A magnet is attached to the free end of the specimen such that when placed between a pair of Helmholtz coils, the magnetic field from the coils applies a bending and/or torsional moment to the specimen as shown in Fig. 1. The resulting deflection and/or twist of the specimen is measured via a laser detector setup; an incoming laser beam reflects off of a mirror attached to the specimens free end into a laser position sensor. Thus, changes in the specimens deflection angle and/or twisting angle are captured by the movement of the reflected laser beam in the sensor. Going beyond current BVS setups, we add the capability to simultaneously apply electric fields to specimens via surface electrodes while applying bending and/or torsional moments. Furthermore, the experimental setup is placed inside a vacuum chamber to reduce parasitic damping.

RESULTS

To measure the dynamic Young modulus and loss tangent, specimens were subjected to bending moments at 75 Hz by using the vertical pair of coils in the BES setup. Simultaneously, a slowly varying triangle wave electric field with an amplitude of 1.95 MV/m was applied from 0.01 to 1 Hz for all experiments. The resulting electric displacement is shown in Fig. 2(a).

*Corresponding author. Email: wojnarc@mst.edu

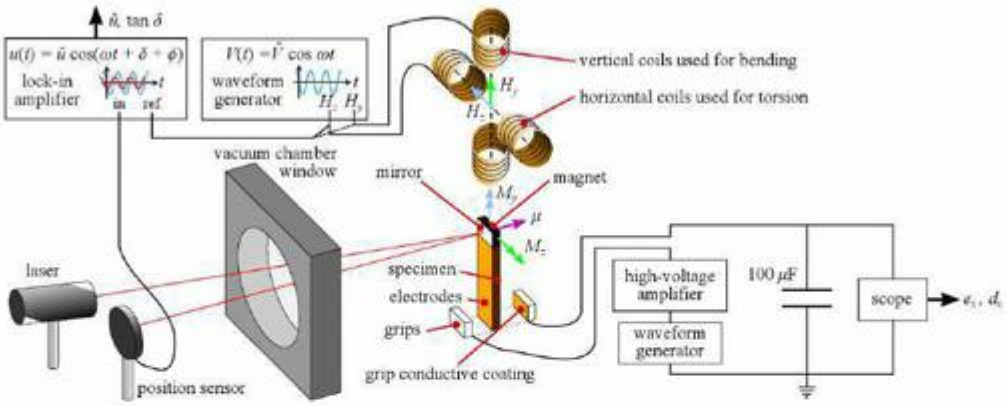

Figure 1: Schematic of Broadband Electromechanical Spectroscopy setup.

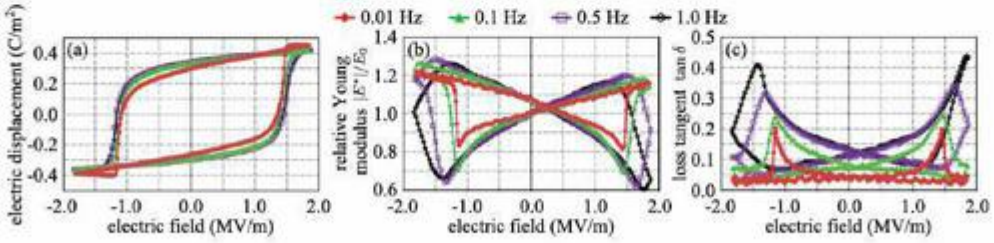

Figure 2: Experimental measurements of (a) electric displacement, (b) dynamic Young modulus, and (c) mechanical loss tangent for different electric field frequencies.

dependence of the elastic constants [4]. Further softening in the Young modulus during domain switching.

in the loss tangent during domain switching (by almost an order of magnitude for the case of 1 Hz). The motion of domain walls dissipates energy [2] and causes an increase in the macroscopic loss tangent.

CONCLUSIONS

moduli and loss tangent of PZT. Softening of the Young and shear moduli as well as large increases in their associated loss

were achieved.

References

1991.

1980.

[3] Lakes R. S.: Viscoelastic measurement techniques. Rev. Sci. Instrum. 75:797-810, 2004.

[4] Fu R., Zhang T.-Y.: Effects of an electric field on the fracture toughness of poled lead zirconate titanate ceramics. J. Am. Ceram. Soc. 83:1215-1218, 2000.

[5] Wang Q.-M., Zhang T., Chen Q., Du X.-H.: Effect of DC bias field on the complex materials coefficients of piezoelectric resonators. Sensor Actuat. A: Phys. 109:149-155, 2003.

MICRO-SPECKLE/GRATING BY FIB DEPOSITION AND THEIR APPLICATION TO DEFORMATION MEASUREMENT

Ronghua Zhu[1], Huimin Xie[1a)], Dan Wu[1] & Yanjie Li[2]
[1]*AML, School of Aerospace, Tsinghua University, Beijing, 100084, China*
[2]*School of Civil Engineering and Architecture, University of Jinan, Jinan, 250022, China*

Summary Deformation carriers-speckle and grating are essential components for deformation measurement using the digital image correlation (DIC) and moiré techniques. In order to promote the application of DIC and moiré techniques in micro-deformation measurement, new techniques for fabricating the micro-speckle/grating are in urgent need. In this study, with aid of the FIB-EB dual beam system, a novel micro-speckle/grating fabrication technique with FIB deposition was proposed. The speckle or grating structures can be generated by the gas-assisted deposition in the dual beam system. The successful results verify that the technique is feasible and can be used for micro-speckle or grating fabrication, and the minimum feature size can reach submicron level. From the results of this study, we can find that this technique owns several advantages, such as accurate positioning, adjustable view filed and carrier pattern, good adaptability for different surface, no damage on the specimen surface.

INTRODUCTION

With the rapid development of the micro-device and microsystem, the study of the mechanical behaviour of microstructures has drawn great attention from the researchers in related fields, and while analysis of deformation field of the measured object will offer a great help for understanding the mechanical behaviour. From the available reports, we know that DIC and the moiré techniques are the powerful approaches for deformation measurement. And the methods already achieved great progresses in the application of macro-deformation measurement. However, analysis on the research results illustrate that there are some difficulties for their application to micro-deformation measurement due to the shortage of techniques for fabricating deformation carriers in a micro-region. The objective of this research is to develop new fabrication techniques for micro-deformation carrier by FIB deposition method. The technique procedures are introduced in detail, and the key parameters which influence the quality of the carrier are also studied. As applications, the optimized micro-scale speckle patterns or gratings are utilized to measure the deformation fields incurred by releasing residual stress and thermal deformation around a crack, respectively.

EXPERIMENT AND RESULTS

In this study, a commercial FIB-EB dual beam system (FEI DB 235) is utilised (Figure 1). The FIB system takes a role as a manufacturing tool, and while the EB system is used for high resolution observation and accurate positioning. In the experiment, at first the fabrication process starts with template generation of grating or speckle by software. And then place the specimen on the sample stage to select an area of interest. And after that, start deposition according to the template once the FIB controlling parameters are determined. Finally, speckle or grating pattern can be fabricated on the specimen surface (Figure 2).

In the process of fabrication, the major factors which affect the quality of the speckle or grating pattern are dwell time, current intensity of the ion beam, and total deposition time. As for the dwell time, our experimental result verifies that the choice of 10 μs is a suitable value and can effectively avoid the elongation or over-etching of the pattern. Moreover, an appropriate intensity value of ion beam current could make a balance between the spatial resolution and the deposition efficiency, and thus it should be adjusted according to the pattern size and the total deposition time. The lower current intensity of ion beam and shorter total deposition time should be an ideal choice for a smaller size of view field. For instance, the current intensity of 30 pA and total deposition time of 2 min was chosen for pattern with the size of 10×10 μm, while current intensity was 100 pA and total deposition time was 5 min when the pattern had a size of 20×20 μm.

As applications, in figure 3, the optimized micro-speckle patterns are deposited onto the surface of the laser shock peened metallic glass. With the slot milling by focused ion beam, the deformation normal to the slot can be measured after the stress release. And then the residual stress can be calculated according the measured deformation. In figure 4, the micro-gratings produced by this method were used to measure the thermal deformation around a crack in an aluminium film supported by PDMS substrate. The deformation during the crack propagation was measured and the results indicate that this method is feasible to measure the deformation of thin film at micro-scale.

[a)] Corresponding author. Email: xiehm@mail.tsinghua.edu.cn.

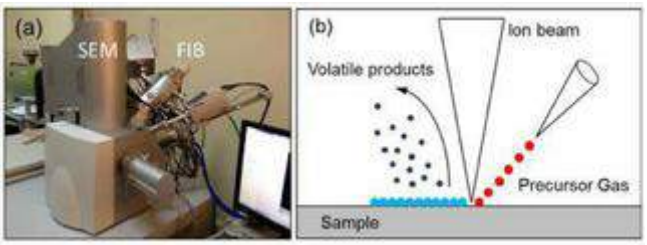

Figure 1. (a) The dual-beam microscope (FIB-EB) used in the experiment. (b) Schematic diagram of gas-assisted deposition [3]

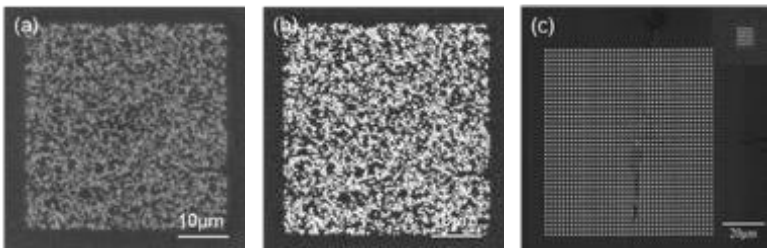

Figure 2. SEM images of speckle and grating patterns in two modes. Speckle patterns fabricated by FIB deposition(Pt) in (a) SEI mode and (b) BEI mode [1, 3] (c) A micro-grating deposited on the Al film. [2]

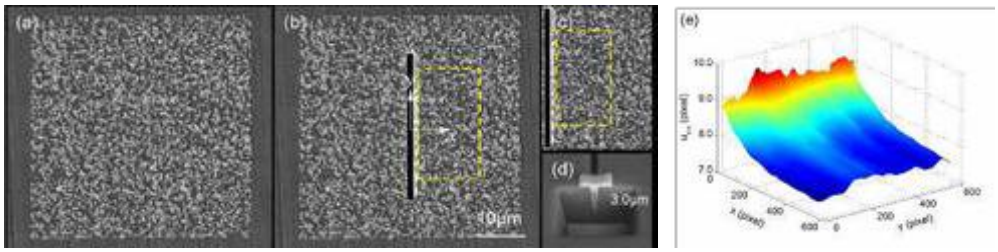

Figure 3. (a) and (b) are SEM images of the speckles before and after the milling step, respectively. (c) The region in the yellow dotted box is cropped for DIC calculation. (d) The trench after ion milling is with a depth of 3.0 μm. (e) The deformation normal to the slot after the stress release. [3]

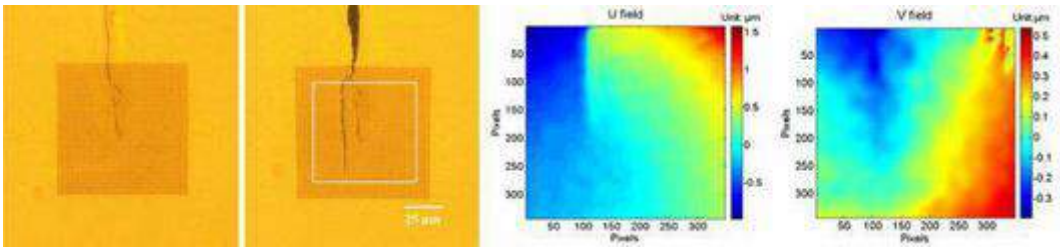

Figure 4. Crack propagation in Al film with a temperature rise of 70°C. The displacement fields in the front of the crack tip before crack propagation are calculated. [2]

CONCLUSIONS

The dual beam (FIB-EB) system can be successfully utilized in the fabrication of different micro-deformation carriers. As applications, the residual stress on the metallic glass surface and the displacement fields in the front of the crack tip were measured. The results demonstrate that FIB-EB dual-beam system is a useful tool with the integrated function of deposition, milling, imaging, and we believe this proposed carrier fabrication method has a good potential to promote the further application of DIC and moiré techniques in micro-deformation measurement.

References

[1] Y. J. Li, H. M. Xie, et al. Fabrication technique of micro/nano-scale speckle patterns with focused ion beam. *Sci. China Phys. Mech.* **55**:1037–44, 2012.

[2] D. Wu, H. M. Xie, et al. A novel method to fabricate micro-gratings applied for deformation measurement around a crack in a thin film, *Meas. Sci. Technol.* **25(2)**: 025012, 2014.

[3] R. H. Zhu, H. M. Xie, et al. Fabrication of speckle patterns by focused ion beam deposition and its application to micro-scale residual stress measurement. *Meas. Sci. Technol.* **26(9)**: 095601, 2015.

A MODULO PI TEMPORAL PHASE UNWRAPPING THEORY IN PHOTOELASTICITY

Wei-Chung Wang[1a)], Po-Chi Sung[1] & Te-Heng Hung[1]
[1]*Department of Power Mechanical Engineering, National Tsing Hua University, Hsinchu, Taiwan*

Summary In this paper, a temporal phase unwrapping theory (TPUT) was proposed to retrieve the corresponding stress value of the modulo π isochromatic retardation to the correct stress value interval. The proposed TPUT uses three wrapped stress values at three wavelengths to determine the correct stress value by judgement conditions and the least squares method. A specimen made of PSM-1 photoelastic material under tensile test was used for verifying the feasibility and availability of the proposed modulo π TPUT.

INTRODUCTION

In the manufacturing process of the flexible display, the flexible substrate may suffer large stress so that the warpage may be generated. Therefore, the relationship between the stress in flexible substrate and the degree of warpage of the flexible display is urgently needed to help manufacturers inspect the quality of the flexible display and further improve the manufacturing process.

Digital photoelasticity [1] is an effective and efficient approach for the analysis of the stress in the specimen. The isochromatic retardation is proportional to the in-plane principal stress difference. However, the isochromatic retardation appertains to wrapped phase. A phase unwrapping theory is required to retrieve the wrapped phase to the unwrapped phase when the retardation to be measured is over the value interval of the wrapped phase.

Recently, the authors developed a technique called transmissivity extremities theory of photoelasticity (TEToP) [2, 3] to determine the low-level in-plane principal stress difference in low birefringent materials. To determine the higher level stress, i.e. the large stress in the flexible substrate, the suitable phase unwrapping algorithm is needed. In practice, the stress value obtained by using TEToP belongs to the modulo π wrapped phase. Besides, due to the use of the spectrometer in TEToP, the information at multi-wavelength can be acquired simultaneously. Therefore, this paper proposed a temporal phase unwrapping theory (TPUT) for modulo π phase. The proposed TPUT utilizes the information at three wavelengths and the correlation between transmissivity extremities linear equations [2, 3] to retrieve the wrapped stress value to the correct stress value. In addition, the TPUT is performed without using iterative methods. The phase can be directly unwrapped by using judgment conditions and least squares method. Most importantly, in the past three-wavelength unwrapping algorithms, the values of three employed wavelengths have to satisfy particular conditions. On the contrary, the three wavelengths can be arbitrarily chosen in the TPUT. Furthermore, the TPUT can also be applied to unwrap the modulo π isochromatic phase map obtained by other photoelastic techniques as long as the modulo π isochromatic phase is converted into stress value by stress-optic law [1]. In this paper, a specimen was manufactured from the 5.8mm thick photoelastic material PSM-1 (Vishay Precision Group Inc., Micro-Measurements). By implementing the tensile test, the parameters of the PSM-1 material were obtained by TEToP. Both simulation and experimental values of the modulo π wrapped stresses of the PSM-1 specimen at three wavelengths were unwrapped for verifying the feasibility and availability of the proposed TPUT.

CONCEPT OF PRINCIPLE

In TEToP, the relationship between the corresponding wrapped stress values of the modulo π isochromatic phases at three wavelengths and the original stress value can be expressed as follows [3]

$$\begin{aligned} S &= i_{\lambda_1} A\lambda_1 + \;) \pm {}_{w\lambda_1} \\ S &= i_{\lambda_2} A\lambda_2 + B) \pm {}_{w\lambda_2} \\ S &= i_{\lambda_3} A\lambda_3 + B) \pm {}_{w\lambda_3} \end{aligned} \tag{1}$$

where $S_{w\lambda_1}$, $S_{w\lambda_2}$ and $S_{w\lambda_3}$ denote the three wrapped stress values at wavelengths λ_1, λ_2 and λ_3, respectively. S denotes the original stress value. i_{λ_1}, i_{λ_2} and i_{λ_3} denote the integer fringe orders of the corresponding retardations of S at wavelengths λ_1, λ_2 and λ_3, respectively. In Eq. (1), there are seven unknowns, i.e. S, i_{λ_1}, i_{λ_2}, i_{λ_3} and three undetermined signs. Consequently, these seven unknowns cannot be directly solved. However, there is a regularity between $S_{w\lambda_1}$, $S_{w\lambda_2}$ and $S_{w\lambda_3}$. Through converting $S_{w\lambda_2}$ and $S_{w\lambda_3}$ into particular value intervals, the regularity can be established. Thus, the number of unknowns can be reduced from seven to two and then the S can be solved from Eq. (1).

UNWRAPPED RESULTS OBTAINED BY SIMULATION AND EXPERIMENT

[a)] Corresponding author. Email: wcwang@pme.nthu.edu.tw .

Figure 1(a) shows the simulation data of S as well as $S_{w\lambda_1}$, $S_{w\lambda_2}$ and $S_{w\lambda_3}$ at wavelengths of 670nm, 650nm, and 630nm, respectively. In Fig. 1(a), the black dotted-line represents S. The red, green, and blue lines represent $S_{w\lambda_1}$, $S_{w\lambda_2}$ and $S_{w\lambda_3}$, respectively. By implementing the proposed TPUT, the wrapped stress values were retrieved as the continuous stress value expressed in yellow line. Obviously, the retrieved stress value is equal to S. Figure 1(b) displays the experimental data of S (black dotted-line) as well as $S_{w\lambda_1}$ (red line), $S_{w\lambda_2}$ (green line) and $S_{w\lambda_3}$ (blue line) at wavelengths of 690nm, 650nm and 610nm, respectively. The yellow line shows the unwrapped result by using the proposed TPUT. It can be seen that most of the regions of wrapped stress value can be appropriately unwrapped except the regions near the extremities of $S_{w\lambda_1}$, $S_{w\lambda_2}$ and $S_{w\lambda_3}$. That is because experimental values of $S_{w\lambda_1}$, $S_{w\lambda_2}$ and $S_{w\lambda_3}$ have larger deviation near their extremities. Two means can be used to effectively remove the unwrapped deviation near extremities, i.e. the pre-processing of normalized wrapped stress values and the post-processing of spatial smoothing of unwrapped results. The purple line in Fig. 1(b) shows the processed results after implementing post-processing of spatial smoothing. It is clear that the unwrapped deviation is almost removed and the processed results match the values of S. Therefore, the feasibility and availability of the proposed TPUT were verified.

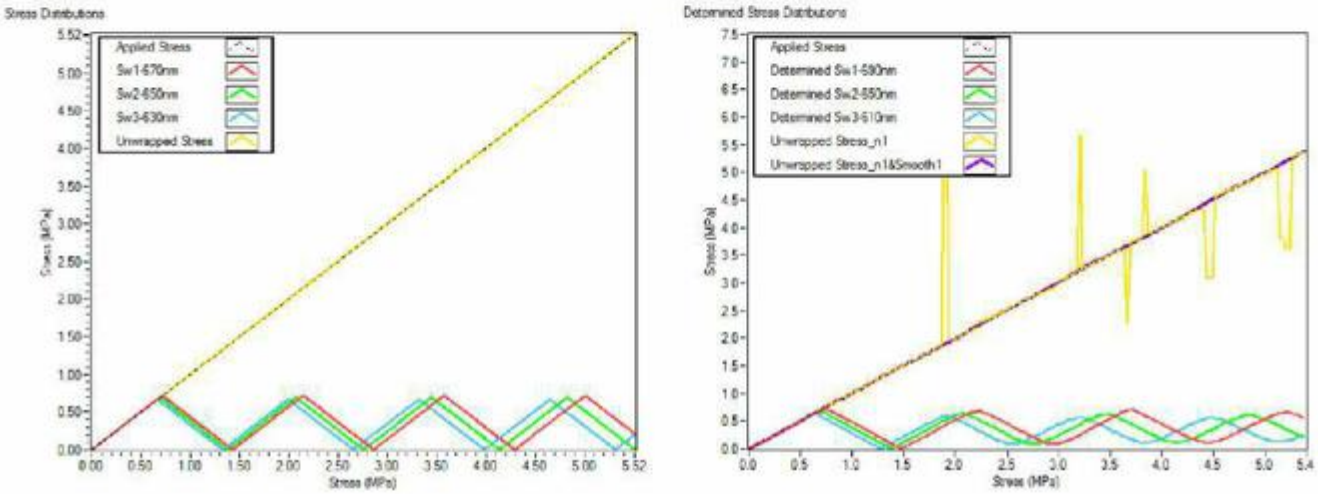

(a) Unwrapped results of the simulation data (b) Unwrapped results of the experimental data

Figure 1. Unwrapped results by using the proposed TPUT

CONCLUSIONS

By using the information at three wavelengths, a TPUT was proposed in this paper to unwrap the modulo π phase. Not only the simulation values but also the experimental values of the wrapped stresses at three wavelengths obtained by TEToP can be appropriately unwrapped through the proposed TPUT. Theoretically, the proposed TPUT can also be applied in other photoelastic techniques to acquire the modulo π isochromatic retardation. Moreover, it can also be used in other optical methods as long as the modulo π phase is proportional to the determined physical quantities with the linear function of the wavelength, e. g., the thin film interferometry. More applications of the proposed TPUT are expected.

ACKNOWLEDGEMENTS

This paper was supported in part by the Ministry of Science and Technology, Taiwan (Grant no. MOST 103-2221-E-007-014-MY3).

References

[1] Ramesh K.: Digital Photoelasticity: Advanced Techniques and Applications. Springer-Verlag, Berlin, 2000.

[2] Sung P. C., Wang W. C., Chiang Y. A., Hung T. H.: Investigation of Systematic Relationship between Spectrometry and White Light Photoelasticity by Regression Analysis. *J. Strain Anal. Eng. Des.* **50**:252-263, 2015.

[3] Sung P. C.: Investigation of Novel Photomechanics Methods for Inspecting Stress and Thickness of Materials. *PhD Dissertation*, Department of Power Mechanical Engineering, Hsinchu, Taiwan, 2014.

AN EXPERIMENTAL INVESTIGATION ON INTERFACIAL PROPERTIES OF GRAPHENE: SIZE EFFECT

Chaochen Xu[1], Wei Qiu[1] & Yilan Kang[1a)]
[1]*Department of Mechanics, Tianjin University, Tianjin, China*

Summary The size-dependent mechanical properties and the edge effect of the tangential interface between graphene and a polyethylene terephthalate substrate (PET) are investigated. The interfacial mechanical parameters of graphene with seven different lengths (50μm-1cm) are measured by in-situ Raman spectroscopy experiments. The three bonding status (adhesion, slide and debond) of the interface between the graphene and the substrate results are identified. New phenomena are observed in the interfacial stress/strain transfer process, such as the existence of the edge effect and the length of the edge of the interface can be affected by the size of graphene. Additionally, the interfacial shear stress exhibits a size effect, with its value significantly decreasing with an increase of the length of graphene, hence the interface between large-sized graphene and PET is relatively weak. However, the ultimate stiffness and failure strength of the interface are size-independent as they are constant regardless of the length of graphene.

INTRODUCTION

Varisized graphene materials have been widely applied to the new domain of microelectronic devices, such as flexible electronic components and strain sensors. [1] The quality and performance of these devices are often limited by the mechanical properties and the deformation transmission efficiency of the interface between graphene and the substrate or surrounding material. [2] However, there have only been a few experimental studies on the interfacial mechanical properties of graphene, and these experimental studies have mainly focused on small-sized graphene samples that are a few to dozens of microns in length. Therefore, the studies on the interfacial performance of graphene on the macro- to micro-scales and the size effects on the performance are insufficient. Herein, we focus on the size effect of graphene, and investigate the size-dependent mechanical properties of the tangential interface between multi-sized graphene and PET substrate.

TECHNIQUES

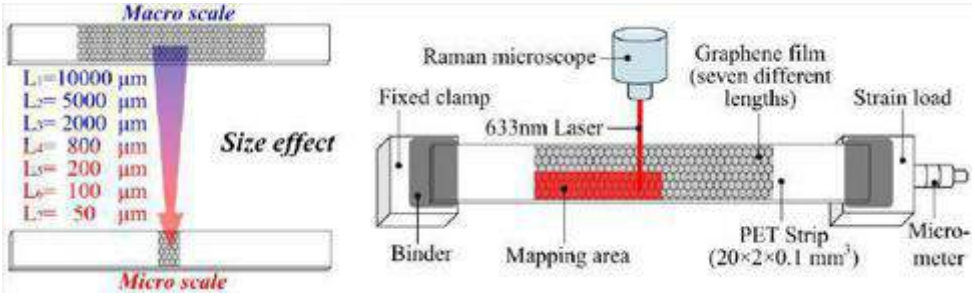

FIG.1 Sketch of the seven graphene/PET specimens with different lengths (not to scale) and schematic diagram of the experimental setup (micro-Raman system and graphene/PET specimen, not to scale).

To explore the size effect of graphene, seven graphene/PET specimens are designed. The lengths of graphene range from the macro (L_1=1cm) to micro (L_7=50μm) scales, as shown in Fig.1, and the width of graphene is identical (W=2mm). The graphene sheet is produced by CVD method (chemical vapor deposition) and is physically adsorbed on the PET substrate by Van der Waals forces at the interface. These forces guarantee that the graphene can be deformed simultaneously as the PET substrate is subjected to a uniaxial tensile displacement-controlled loading process by an ingenious micro-loading device, and the in-situ Raman spectroscopy is employed to measure the whole-field deformation of graphene, as shown in Fig.1. [3-5]

RESULTS

To explore the size-dependent interfacial mechanical behaviors, Fig.2 provides the variations of strain along the centerline of the longest (L_1) and shortest (L_7) graphene for PET tensile strains (ε_P) of 0%–2.5% during the loading process. The evolution of the strain across the entire graphene can be divided into three stages. In the adhesion stage ($\varepsilon_P \leqslant 0.5\%$), the strain of the entire graphene, except for the edge, equals the strain of PET. In the sliding stage ($0.5\% < \varepsilon_P \leqslant 2\%$), the graphene strain is less than the PET strain because the Van der Waals force is not sufficiently strong. In the debonding stage ($\varepsilon_P > 2\%$), the curves of graphene strain do not change even as the PET strain keeps increasing indicating the damage of the interface. The critical PET strain at which the interface begins to debond is defined as the failure strength of the interface and the maximum strain that can be transferred to the graphene before the interfacial failure is defined as the ultimate stiffness of the interface. As Fig.2 shows, these two mechanical parameters of the interface is hardly affected by the size of graphene.

[a)] Corresponding author. Email: tju_ylkang@tju.edu.cn (Kang Yilan)

The variations of strain along the centerline of graphene with two different lengths are both composed of two areas at every PET strain. These are the central region, where the strain is stable, and the edge region, which is controlled by the interfacial edge effect that exhibits the strain gradient. However, the lengths of the edge region are different depending on the size of graphene. If the length of this edge region, in which the graphene strain rises from 0% to approximately 90% or 100% of the plateau value, is defined as the 'critical length', l_c, [6] then the ratio of the critical length to total length, l_c/l, is defined as the 'relative critical length', ϑ, which can represent the extent that the interface is influenced by the edge effect, where the smaller the ϑ, the smaller the extent. From Fig.2, the longer the graphene, the smaller the relative critical length, and hence the smaller the extent that the interface is influenced by the edge effect.

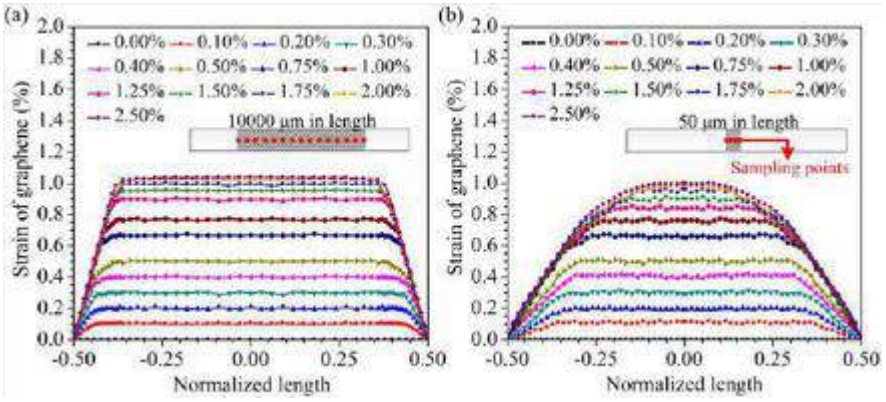

FIG.2 Variations of the strain along the centerline of (a) the longest 10000-μm-long graphene (L_1) and (b) the shortest 50-μm-long graphene (L_7) at 13 different levels of PET tensile strain during the loading process. (Inset) Schematic showing the locations of the sampling points along the centerline of graphene (the length of graphene is normalized and the fractional coordinate is used).

To systematically discuss the size-dependent interfacial performance of graphene, Table I gives the experimental results on the graphene with seven different lengths, including five interfacial mechanical parameters, are included in, where the deformation parameters, such as the failure strength and stiffness of interface, are size-independent, while the critical length, relative critical length and maximum interfacial shear stress are size-dependent. The relative critical length, ϑ, is considered as a dimensionless parameter to evaluate the interfacial edge effect of graphene. As the scaling factor tends toward being constant, the size of graphene reaches the macroscopic scale and the interfacial edge effect is no longer influenced by the size of graphene.

TABLE I. The interfacial mechanical parameters of graphene with seven different lengths.

Graphene length l/	(μm)	50	100	200	800	2000	5000	10000
Failure strength of interface/$\varepsilon_{m//}$	(%)	2	2	2	2	2	2	2
Stiffness of interface/$\varepsilon_{max//}$	(%)	0.988	0.988	0.988	1.00	1.013	1.013	1.013
Critical length/l_c	(μm)	40	70	116	280	400	1000	2000
Relative critical length ϑ		0.80	0.70	0.58	0.35	0.20	0.20	0.20
Maximum interfacial shear stress τ_{max}/	(Mpa)	0.237	0.158	0.089	0.055	0.022	0.009	0.003

CONCLUSIONS

We experimentally investigated the size-dependent mechanical properties and edge effect of the tangential interface between graphene and a PET substrate. The experiments on graphene with seven different lengths show that the edge effect in the interface is affected by the size of graphene, and this size effect can be described by the scaling factor, that is, the relative critical length (defined as the ratio of the critical length to total length). This scaling factor decreases with an incremental change of the graphene length and tends toward being constant when the graphene reaches the macroscopic level. Additionally, we show that the interfacial shear stress is size-dependent, and its value significantly decreases with an increase of the graphene length, hence the interface between large-sized graphene and PET is weak. However, the ultimate stiffness and failure strength of the interface are size-independent.

References

[1] Qiu W.: The use of a carbon nanotube sensor for measuring strain by micro-Raman spectroscopy. *Carbon* **53**:161-168, 2013.

[2] Xu C.: An experimental investigation on the mechanical properties of the interface between large-sized graphene and a flexible substrate. *J. Appl. Phys.* **117**:164301, 2015.

[3] Qiu W.: Mechanical behavior study of microdevice and nanomaterials by Raman spectroscopy: a review. *Chin. Sci. Bull.* **59**:2811-2824 1, 2014.

[4] Kang Y.: An application of Raman spectroscopy on the measurement of residual stress in porous silicon. *Opt. Laser. Eng.* **43**:847-855, 2005.

[5] Li Q.: Micro-Raman spectroscopy stress measurement method for porous silicon film. *Opt. Laser. Eng.* **48**:1119-1125, 2010.

[6] Xu C.: An experimental investigation on the tangential interfacial properties of graphene: Size effect. *Mater. Lett.* **161**: 755-758, 2015.

RESIDUAL STRESS ANALYSIS IN SI-BASED MULTI-LAYER HETEROSTRUCTURE BY MICRO-RAMAN

Lu-Lu Ma[1], Qiu Li[2], Dong-Hui Fu[1],Cui-Li Cheng[1], Yu-Cheng Zhao[1]&Wei Qiu[1a)]
[1]*Department of Mechanics, Tianjin University, Tianjin 300072, China*
[2]*Tianjin Key Laboratory of High Speed Cutting and Precision Machining, Tianjin University of Technology and Education, Tianjin 300222, China*

Summary: Si-based multilayer semiconductor heterostructures are widely used in microelectronics. Inhomogeneous residual stress is induced during their preparation. In this work, a methodological study on the residual stress measurement in Si-based multi-layer heterostructure was presented. The geometric parameters of the multilayer structure was measured by using scanning electron microscopy (SEM) and transmission electron microscopy (TEM). Meanwhile, the relationship between the Raman spectrum and the internal stress on the [100] and [110] crystal orientations for silicon and germanium silicon was determined to enable surface and cross-section residual stress analyses, respectively. Based on the Raman mapping results, the distribution of residual stress along the depth of the multi-layer heterostructure was successfully obtained

INTRODUCTION

Strain is introduced into Si-based semiconductor devices to effectively promote carrier mobility and reduce thermal energy consumption [1]. Nevertheless, intrinsic and/or processing residual stresses are always introduced during the manufacture of Si-based structures coincident with the artificial strain[2]. Because semiconductor materials usually have good Raman activity and Raman sensitivity to strain and stress, micro-Raman spectroscopy (MRS) has been regarded as an effective method of residual stress measurement on the micro-scale[3-5]. Although several works have attempted to characterize the mechanical behavior of Si-based materials using Raman spectroscopy, there still remains a lack of systematic investigation of a method for measuring internal mechanical behavior, especially the distribution of residual stress near internal interfaces inside the multilayer heterostructures.

EXPERIMENT

Materials and samples

The multilayer structure, shown in Fig.1a, was manufactured by means of reduced pressure chemical vapor deposition (RPCVD). The cross-section samples, shown in Fig.1b, were prepared to allow the accurate investigation of the internal material properties and mechanical behaviors.

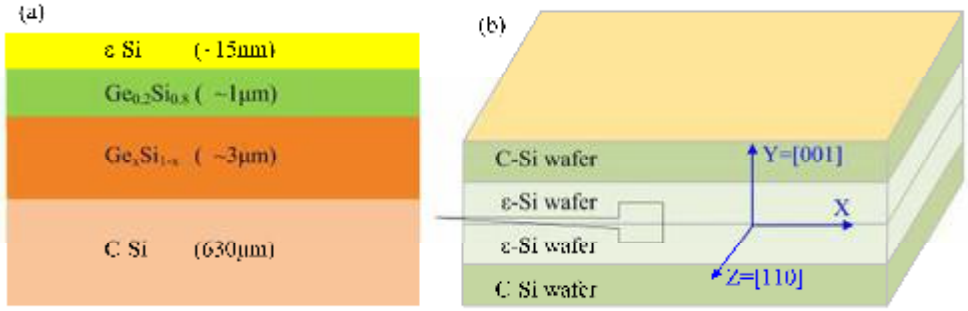

Fig. 1. Schematic of (a) multi-layer structure and (b) cross-section sample

Raman-Mechanical Relationship of Silicon-Based Semiconductor Materials

For the backscattering measurements on the cross-section, it was essential to understand the Raman-mechanical relationship on the crystal orientation before further analysing the Raman results. Eq. (1) shows the wavenumber-stress/strain relationship for [110] crystal orientation applicable to evaluate the residual stress of monocrystalline silicon (C-Si) and germanium silicon alloy (Ge_xSi_{1-x}), respectively, where x is the mol content of Ge in alloy.

$$\text{C-Si: } \begin{cases} \sigma = -1825.56\Delta w_3 \ (\text{MPa}) \\ \varepsilon_X = -10.81\times10^{-3}\Delta w_3 \end{cases}; \qquad \text{Ge}_x\text{Si}_{1-x}\text{: } \begin{cases} \sigma = -\dfrac{1000}{0.548+0.241x}(\Delta w_Z + 62x)\ (\text{MPa}) \\ \varepsilon_X = -\dfrac{5.92+1.305x}{0.548+0.241x}\times10^{-3}(\Delta w_Z + 62x) \end{cases} \tag{1}$$

a)Corresponding author. Email:qiuwei@tju.edu.cn

Characterization methods

The material properties and mechanical behaviours of the cross-section samples were measured at different spatial scales using experimental techniques including SEM, TEM, and micro-Raman spectroscopy. The Raman spectroscopy experiments utilized a Renishaw InVia microscopic confocal Raman spectroscope. A UV laser with 325nm wavelength, was used to analyze the surface of the ε-Si wafer. For the cross-section sample, spectral data from a 40 μm × 20 μm region in the vicinity of the multilayers was obtained through Raman mapping (streamline) whose step lengths were 1.2 μm and 0.1 μm along the X and Y directions, respectively. A 532nm laser and a 50× object lens (NA= 0.80) were used, giving an incident laser spot size of about 1μm in diameter.

RESULTS

Fig.2a shows a SEM image of the cross-section sample. The interface between the silicon substrate and the graded germanium silicon (Ge_xSi_{1-x}) buffer layers clear, straight, continuous and complete. The thicknesses of the graded and relaxed germanium silicon ($Ge_{0.2}Si_{0.8}$) buffer layers are 2.7 μm and 0.9 μm, respectively. The strained silicon (ε-Si) layer is too thin to be observable by SEM. The UV Raman spectrum from the ε-Si surface has a single, strong, and narrow peak near 500cm^{-1}, indicating that the ε-Si was primarily in monocrystalline state, which is in good agreement with the result of the TEM. The residual stress of ε-Si is about 1.70 GPa. For the backscattering measurements on the [110] cross-section, the wavenumber distribution along the depth direction is shown in Fig.2b. By using Eq. (1), the residual stress of sampling spots in the C-Si substrate and germanium silicon layers can be obtained, respectively. The experimental results show that the residual stress inhomogeneously distribute inside the material. Near the ε-Si/$Ge_{0.2}Si_{0.8}$ interface, it is about 2.45 GPa.

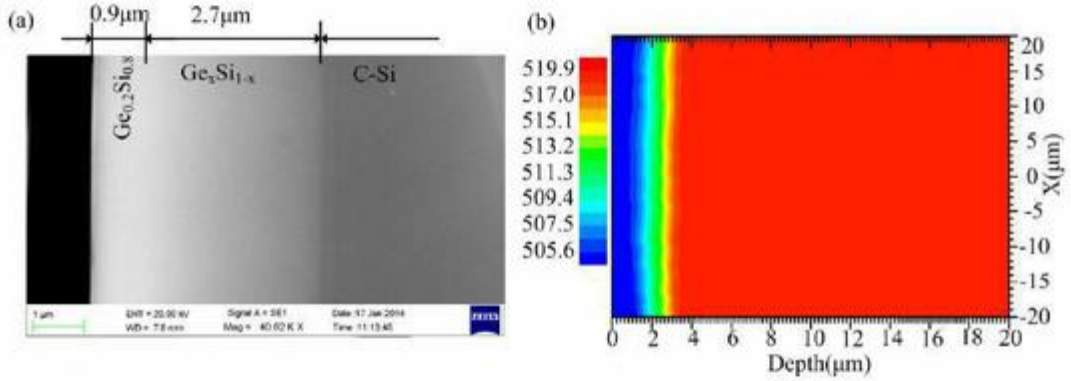

Fig.2. (a) SEM image of a cross-section sample (b)Measured wavenumber distribution along the depth direction for the cross-section sample.

CONCLUSIONS

Taking ε-Si/$Ge_{0.2}Si_{0.8}$/Ge_xSi_{1-x}/C-Si as an example, this paper presented a methodological study of residual stress measurement in Si-based multi-layer semiconductor heterostructure. The distribution of residual stress along the depth of the multi-layer heterostructure can be determined by combining the experimental and theoretical results. The geometric and material properties measured by SEM, TEM, MRS and/or EDS experiments are all essential parameters for the determination of the Raman to stress/strain relationship to evaluate the residual stress and its distribution.

ACKNOWLEDGMENTS

This work is financially supported by the National Basic Research Program of China (No.2012CB937504), the National Natural Science Foundation of China (grant Nos. 11422219, 11302149, 11227202and 11272232).

REFERENCE

[1] JacobsenR.S., AndersenK.N., BorelP.I., et al: Strained silicon as a new electro-optic material. Nature441:199-202,2006.
[2] GogotsiY., BaekC.,Kirscht F.: Raman microspectroscopy study of processing-induced phase transformations and residual stress in silicon. Semiconductor Science & Technology14:936-944,1999.
[3] KangY.L., QiuY., LeiZ.K., HuM.: "An application of Raman spectroscopy on the measurement of residual stress in porous silicon", Optics and Lasers in Engineering43:847-855,2005.
[4] LiQ., QiuW., TanH.Y., GuoJ.G., KangY.L.:"Micro-Raman spectroscopy stress measurement method for porous silicon film", Optics and Lasers in Engineering48:1119-1125,2010.
[5] QiuW., KangY.L.:Mechanical behaviorstudy of microdevice and nanomaterials by Raman spectroscopy", Chin. Sci. Bull59:2811-2824,2014.

CELL VIABILITY AND RAPID SCREENING ANTI-CANCER DRUG BASED ON NANOMECHANICAL FLUCTUATION

Qingchuan Zhang [a)], Shangquan Wu, Xiaoping Wu
Department of Modern Mechanics, University of Science and Technology of China, Hefei, China

Summary We present an approach of utilizing a nanomechanical fluctuation based highly sensitive microcantilever sensor, which is capable of characterizing the viability of cells and quantitatively screening (within tens of minutes) their responses to a drug with the obvious advantages of real-time and in-situ assay. The microcantilever sensor operated influctuation mode was used in evaluating the paclitaxel effectiveness on breast cancer cell line MCF-7. This study demonstrated that the nanomechanical fluctuations of the microcantilever sensor are sensitive enough to detect the dynamic variation in cellular force which is provided by the cytoskeleton, using cell metabolism as its energy source, and the dynamic instability of microtubules plays an important role in the generation of the force. We propose that cell viability consists of two parts: biological viability and mechanical viability. This new method provides a new concept and strategy for the evaluation of cell viability and the screening of anti-cancer drugs.

INTRODUCTION

Cell viability assays have been gaining attention due to their strategic importance in both fundamental science and clinical medicine. Various techniques, such as flow cytometry (FCM), direct immunofluorescence staining, clonogenic assays, colorimetry and microscopic imaging have been used to investigate cell viability and its change under drug treatment [1-4]. However, most of the current approaches are either relatively expensive or unable to quantifiably evaluate cell viability and are only able to distinguish between live and dead cells. In addition, some of these methods require chemiluminescent, fluorescent, or radioactive labeling steps which often involve destruction of the physiological function of cells and the loss of certain important biological information on viable cells. Thus, label-free, real-time, noninvasive, inexpensive and fast methods to quantify cell viability and its change under drug treatment are essential in cancer management, especially in anti-cancer drug discovery and screening. However, as a highly sensitive sensor, cantilevers have not yet been used in the quantification of cell viability, especially in quantifying the viability of cancer cells, which plays an important role in anti-cancer drug screening. When we used a cantilever sensor to detect the presence of cancer cells, we found that the deflection and resonance frequency shift of the cantilever was detected as expected, and additionally, found that the presence of cancer cells on the cantilever produced a larger fluctuation of the microcantilever (Fig. 1), which was also been found in the presence of normal mammalian cells and bacteria [5]. The energy released from the metabolism of cells may drive the fluctuations of the cantilever. Therefore, in the present study, we developed a methodology to monitor the viability of cancer cells in a label-free and real-time manner using the fluctuations of a microcantilever. The amplitude of the fluctuation reflects the viability of the cancer cells, and thus we quantified the viability of cancer cells by calculating the variance of the deflection curves. Based on this feature, we exploited the microcantilever sensor in a fluctuation mode to characterize the viability change in breast cancer cells (MCF-7) subjected to various doses of an anti-cancer drug, and thus anti-cancer drug screening can be realized in a rapid and quantitative manner.



Fig. 1. Schematic representation of the fluctuation mode measurement set-up. (A) Real-time nanomechanical deflection of the microcantilever with MCF-7 cells adhered to it. Illustration: optical micrograph of a microcantilever, on which several adherent cells can be observed. (B) Corresponding results for the naked microcantilever without cells. Illustration: optical micrograph of a microcantilever. (C) Schematic representation of the microcantilever sensor experimental setup. (D) Depiction of nanomechanical fluctuation caused by adherent cells on the microcantilever surface.

RESULTS AND DISCUSSION

The experimental setup used to detect microcantilever fluctuations was a home-built microcantilever sensing system which measured the deflection of the microcantilever tip in the nanometer scale [6-9] and is described in detail in the Methods section. When the cells (MCF-7) had adhered to the microcantilever in the incubator (micrograph in Fig. 1A), the microcantilever was mounted in the liquid cell and the deflection of the microcantilever was measured in real-time (Fig.

[a)] Corresponding author. Email: zhangqc@ustc.edu.cn

1C). The mechanical movements driven by the metabolic energy of the cell produced a larger fluctuation of the cantilever (Fig. 1A and 2A), while the microcantilever fluctuated very little for the naked microcantilever in PBS without cells (Fig. 1B).

We investigated the characteristics of microcantilever fluctuation in the MCF-7 cell line treated with different concentrations of paclitaxel which can inhibit cell viability [10] and is one of the most effective natural anticancer agents usually used in clinical practice for the medical treatment of ovarian, breast and non-small cell lung cancers [11]. We next evaluated the effect of paclitaxel exposure on MCF-7 cells in the measurement process. To understand the origin of the fluctuations, the morphology of adherent cells (MCF-7) was observed in-situ using conventional optical microscopy (Supporting Information section S6). We observed both live and dead cells which died due to lack of culture medium (Supporting Information Video 1 and 2). It can be seen from the microscope videos that live cells moved continuously and dead cells was relatively motionless. For a deeper insights of the origin of the fluctuation, the Cell Counting Kit-8 (CCK-8) which provides a sensitive colorimetric assay of the biological viability of cells was conducted.

CONCLUSIONS

In this study, we demonstrated the capability of a fluctuation-based nanomechanical sensor for monitoring the micromotions of live cells under various conditions. We proved that the microcantilever sensor is capable of quantifying cell viability by measuring nanoscale fluctuations of the microcantilever and calculating the variance of the fluctuation curve when cancer cells were exposed to different concentrations of anti-cancer drug. Compared with existing methods, this new mode based on fluctuations of the microcantilever has obvious advantages in cell viability monitoring and anti-cancer drug screening due to the rapid, label-free, quantitative, noninvasive, real-time and in-situ assay of cell viability within tens of minutes instead of days or weeks. This presents the successful use of nanomechanics for anti-cancer drug screening, namely that of characterizing the viability change of cancer cells (MCF-7) subjected to various doses of anti-cancer drug.

The experiments show that fluctuations of the microcantilever with cancer cells (MCF-7) adhered to it decreased with increasing concentrations of paclitaxel. The experiments demonstrate that the nanomechanical fluctuations are driven by the force generated from the cytoskeleton, using cell metabolism as an energy source, and the dynamic instability of microtubules plays an important role in this process. We propose that cell viability consists of two parts: biological viability and mechanical viability. The results show that paclitaxel has little effect on biological viability which can be estimated by existing biological methods such as the CCK-8, but has a significant effect on mechanical viability which was estimated by the nanomechanical method. The technique can not only determine the biological viability of cells, but can also quantify mechanical viability in the pN range, which cannot be determined by existing methods. This will be particularly useful for anti-cancer drugs which cannot be screened out by existing methods. One might consider the nanomechanical approach as being more direct than the electrical and optical methods. This new method provides a new concept and strategy for the evaluation and assay of cell viability and the screening of anti-cancer drugs.

References

[1] Banasiak, D., Barnetson, A.R., Odell, R.A., et al, Comparison between the clonogenic MTT, and SRB assays for determining radiosensitivity in a panel of human bladder cancer cell lines and a ureteral cell line, Radiat. Oncol. Investi. 7, 77-85. 1999.

[2] Ilkow, C.S., Marguerie, M., Batenchuk, C., et al, Reciprocal cellular cross-talk within the tumor microenvironment promotes oncolytic virus activity, Nat. Med. 21, 530-536, 2015.

[3] Park, C., Suh, Y., Cuervo, A.M., Regulated degradation of Chk1 by chaperone-mediated autophagy in response to DNA damage, Nat. commun. 6, 6823. 2015.

[4] Zhang, S., Bai, H., Pi, J., Yang, P., Cai, J., Label-Free Quartz Crystal Microbalance with Dissipation Monitoring of Resveratrol Effect on Mechanical Changes and Folate Receptor Expression Levels of Living MCF-7 Cells: A Model for Screening of Drugs, Anal. Chem. 87, 4797-4805. 2015.

[5] Kasas, S., Ruggeri, F.S., Benadiba, C., et al, Detecting nanoscale vibrations as signature of life2015. Proc. Natl. Acad. Sci. U.S.A. 112, 378-381.

[6] Tan, W.M., Huang, Y., Nan, T.G., et al, Development of Protein A Functionalized Microcantilever Immunosensors for the Analyses of Small Molecules at parts per trillion Levels， Anal. Chem. 82, 615-620. 2010.

[7] Wu, S.Q., Nan, T.G., Xue, C.G., et al, Mechanism and enhancement of the surface stress caused by a small-molecule antigen and antibody binding, Biosens. Bioelectron. 48, 67-74. 2013.

[8] Xue, C.G., Zhao, H.W., Liu, H., et al, Development of sulfhydrylated antibody functionalized microcantilever immunosensor for taxol, Sens. Actuators B-Chem. 156, 863-866. 2011.

[9] Zhao, H.W., Xue, C.G., Nan, T.G., et al, Detection of Copper Ions Using Microcantilever Immunosensors and Enzyme-linked Immunosorbent Assay, Anal. Chim. Acta 676, 81-86. 2010.

[10] Jordan, M.A., Toso, R.J., Thrower, D., et al, Mechanism of mitotic block and inhibition of cell proliferation by taxol at low concentrations, Proc. Natl. Acad. Sci. U.S.A. 90, 9552-9556. 1993.

[11] Murphy, W.K., Fossella, F.V., Winn, R.J., Shin, D.M., Hynes, H.E., Gross, H.M., Davilla, E., Leimert, J., Dhingra, H., Raber, M.N., Krakoff, I.H., Hong, W.K., Phase II Study of Taxol in Patients With Untreated Advanced Non-Small-Cell Lung Cancer, J. Nat. Cancer Inst. 85, 384-388. 1993.

SCALED EXPERIMENTS ON TUNED LIQUID COLUMN DAMPER-WIND TURBINE-SOIL INTERACTION

Phoebe Watson[1], Tadhg Buckley[1], Paul Cahill[1, 2], Vesna Jaksic[1, 2] & Vikram Pakrashi[1,2,3, a]
[1]*Dynamical Systems & Risk Laboratory (DSRL), Ireland*
[2]*MaREI, Environmental Research Institute, University College Cork, Ireland*
[3]*School of Mechanical and Materials Engineering, University College Dublin, Ireland*

Summary This paper presents scaled experimentation of a wind turbine interacting with soil at its base and investigates the dynamic responses of the scaled experimental turbine for different excitation frequencies with and without a tuned liquid column damper. The natural frequency of the wind turbine is a function of its interaction with soil. It is observed that small-scale experiments can be useful for inexpensive demonstration and assessment of passive control of wind turbine towers in the presence of varying soil conditions.

INTRODUCTION

Control of unwanted structural vibrations can lead to a longer life of wind turbines by decreasing stress and fatigue [1], reduction of gearbox faults [2] and reduced load on foundation. Studies into the use of Tuned Liquid Column Dampers (TLCDs) have indicated that TLCDs may be a reasonable way to reduce wind turbine tower vibrations [3]. When coupled with a wind turbine, the success of TLCDs depend on their tuning to the natural frequency of the turbines, which in turn is linked to the boundary condition created by its interaction with soil [4] Such soil properties change with respect to the loading, increasing the complexity in understanding the long behaviour of the turbine and thereby introducing the risk that the natural frequency may change gradually over time [5]. This paper investigates the influence of soil conditions on the control performance of a TLCD coupled with a wind turbine.

EXPERIMENTAL SETUP

Experimental Design

Modelling the system as a cantilever connected to springs related to soil conditions at the boundaries [5] and applying relevant non-dimensional parameters, a 1:100 geometrically scaled experimental setup was created [Figure 1]. For the construction of the TLCD, piping with a diameter of 20*mm* and 16*mm*, inner and outer respectively, was chosen. This was guided by the mass-ratio of the TLCD to the primary system, with a ratio of 5% being desirable [6]. To determine the TLCD damping effects, two orifice sizes, of 8*mm* and 12*mm*, were investigated resulting in a varying head-loss coefficient.

In order to eliminate grain size effect in scaling, the ratio between the average grain size and the pile diameter is kept larger than 88 [7]. The set-up was measured using a wireless accelerometer and the soil was standard garden soil whose grain size falls between sand (coarse) and kaolin (fine). For the monitoring of the experimentation, an X-Bee Waspmote 3D accelerometer was utilized, consisting of a Waspmote board, an X-Bee Series-2 radio, an SD card and battery pack. The accelerometer was placed at the top of the experimental model turbine, on the opposing side to the TLCD.



Figure 1. Image of scaled experimental wind turbine with attached TLCD.

[a] Corresponding author. Email: Vikram.Pakrashi@ucd.ie

Experimental Procedure

To determine the effects of the TLCD on the model wind turbine, responses due to impulse forces of equal magnitude were recorded for varying levels of water column in the TLCD. A baseline case was initially established for the system with no water in the TCLD, i.e. model wind turbine with no control. Subsequent to this, liquid was added to the system at increasing 15ml volumes and identical testing was conducted for each liquid column height.

EXPERIMENTAL RESULTS

It was determined from the baseline case that the natural frequency of the wind turbine with no control was 8.4Hz. From this, the optimal water column length can be calculated, which proved to be 278mm for the chosen experimental TLCD, equalling a total volume of water of 0.056L. This equates to 5.2% of the mass of the primary structure above the level of the soil. At a water column height of 278mm, it was observed that the response of TLCD the controlled wind turbine to an impulse response was significantly mitigated when compared to the uncontrolled, baseline case [Figure 2]. It was determined that the influence of the optimised TLCD resulted in a 48.5% reduction compared to the TLCD not being present. It was found that the level of response is significantly sensitive to the change in length of column, and hence the volume and weight, of water around the optimum value. With an increase of 1ml of water, from 55 ml to 56 ml, the response amplitude in the frequency domain dropped significantly, with a 28.57% reduction being observed. When this optimum volume of 56 ml was surpassed by 1 ml, the response quickly returned to the magnitude of response observed at for 1 ml below the optimal value.

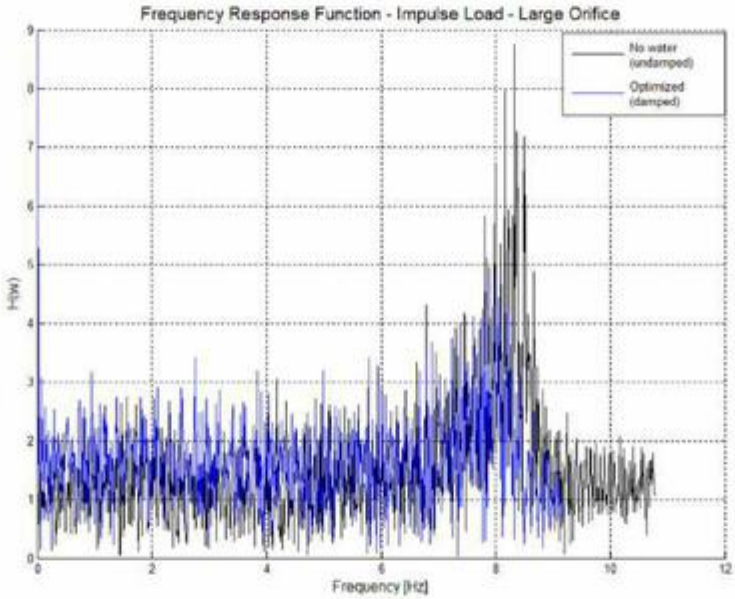

Figure 2. Experimental results for top soil with a 12 ml orifice for TLCD comparing controlled and uncontrolled situation.

CONCLUSIONS

This paper presents a study on TLCDs deployed to control vibrations of wind turbine towers while considering the interaction of the tower and the foundation soil through small scale model experimentation. It was found that the introduction of a TLCD with the model wind turbine resulted in a reduction in vibrations. The largest reduction in vibration was found to be valid for a relatively short domain of frequency range. Such experimentation may be extended to assess TLCD control in future with variations in TLCD design and for other soil or structural conditions.

References

[1] Liu X.: Bo L.: Luo H. Dynamic measurement system for wind turbine fatigue load. *Renew. Energy*, 86, 909-921, 2016.

[2] Jianu O.: Rosen M. A.: Naterer G. Noise pollution prevention in wind turbines; status and recent advances. *Sustainability*, 4(6), 1104-1117, 2012.

[3] Jaksic V.: Wright C.: Murphy J.: Afeef C.: Ali S. F.: Mandic D. P.: Pakrashi V. Dynamic response mitigation of floating wind turbine platforms using tuned liquid column dampers. *Phil. Trans. R Soc. A*, 373: 20140079, 2015.

[4] Adhikari S.: Bhattacharya S. Vibrations of wind-turbines considering soil-structure interaction. *Wind Struct.,* **14**(2), 85, 2011.

[5] Bhattacharya S.: Adhikari S. Experimental validation of soil-structure interaction of offshore wind turbines. *Soil Dyn. Earthq. Eng.,* 31(5), 805-816, 2011.

[6] Yalla S.: Kareem A. Optimum Absorber Parameters for Tuned Liquid Column Dampers. *J. Struct. Eng.*, 126(8), 906-915, 2000.

[7] Klinkvort R. T.: Leth C. T.: Hededal O. Centrifuge modelling of monopoles in dense sand at the Technical University of Denmark. *Eurofuge 2012,* Delft, Netherlands, 2012.

RESIDUAL STRAINS AND THEIR RELATION TO THE FATIGUE DAMAGE EVOLUTION IN COMPOSITE MATERIALS

Lars P. Mikkelsen[1a)], Gilmar Pereira[1] & Kristine M. Jespersen[1]
[1]*Department of Wind Energy, Technical University of Denmark, Roskilde, Denmark*

Summary The fatigue performance of unidirectional glass fibre reinforced epoxy is found to be highly dependent on at which curing temperature the composite is manufactured. Performing the curing at 110C instead of at 40C is found to reduce the life-time dramatically with a factor of 10. Even though, the volumetric shrinkage of the epoxy at the two curing cycles is identical, the resulting residual strain in an embedded optical fibre measured using fibre Bragg Grating is found to be increased with a factor of 3. Together with, 3D x-ray tomography of partly fatigued test specimens there is an indication of a link between the measured increased residual strains with the governing fatigue damage mechanism.

INTRODUCTION

In the attempt of making wind turbines cost-competitive, size matters. By increasing the size of wind turbines from less than 20 meters as the dominant design for more than 30 years ago to the present turbines with a turbine diameter on more than 120 meters, the cost of energy has been reduced with more than a factor of 6. A reduction, which have made the electricity price for electricity coming from onshore wind turbines comparable with electricity coming from conventional energy sources. Throughout the life-time, the load carrying laminates inside a wind turbine blades experience load cycles in the order of 10^8-10^9 cycles and the material fatigue resistance is together with the material stiffness considered as one of the key material design parameters when designing new wind turbine blade [1]. Therefore, improving the material fatigue resistance will make it possible to design larger or lighter wind turbine blade and thereby reducing the cost of energy.

Another way to reduce the blade price is by reducing the mould time of the wind turbine blade during the production. Nevertheless, in the present study it will be demonstrated that this will have a significant influence on the fatigue life time. Test-laminates are typically manufactures using a so-called 2-stage cure cycle which include a low temperature curing for at least 16-24 hours followed by a post-cure sequence performed at an elevated temperature. Manufacturing large wind turbine blade under such conditions will results in un-realistic long mould time and wind turbine blade is therefore often manufactured at an elevated temperature throughout the full curing cycles which here will be called a 1-stage cure cycle.

In the present study, an optical in fibre Bragg gratings sensor system are used in order to extract the residual stress experience by the glass fibre reinforcement during different curing cycles as suggested by [2]. In here, one optical fibre are placed in the neat epoxy resin and based on the strains experience by the optical fibre Bragg Grating sensor, the residual stresses in the composite can be back-calculated. Some composite material test specimens are manufactured prescribing the same cure cycle. Those test specimens is loaded in fatigue, and the corresponding fatigue S-N curves during a tensile-tensile fatigue loading are extracted. Some of the fatigue tests are stopped before the final failure and 3D X-ray technique are used exploring the fatigue damage evolution.

MATERIAL SYSTEM

A representative unidirectional glass fibre reinforced epoxy matrix composite which could have been used in the wind turbine industry are used in the study. The composite layup is given by $[\pm45/b/0/b/0]_s$ where the skin-layer, ±45, is a biax 600 g/m^2 woven fabric while the internal part is build-up of a non-crimp UD 1150 g/m^2 fabric with a biax100 g/m^2 as the backing. The orientation of the backing in the layup is indicated by the b in the 0/b sequence. After the stacking, the dry fibre fabric is epoxy impregnated with Araldite LY 1564SP/XB3486 from Huntsman by vacuum infusion. Following this, the laminate is cured using one of the following two curing cycles; 40ºC in minimum 18 hours followed by a post-curing sequence at 75 ºC in minimum 5 hours or a fast curing cycle on 110 ºC in 2 hours. In the following, those two different curing sequence will be denoted 40C and 110C, respectively. Both curing cycles will results in a fully cured laminate with a final thickness on approximately 4.5mm.

For the neat epoxy resin, some additional test was performed curing the epoxy in silicon bags where there central in the silicon bag was mounted an optical fibre Bragg Grating sensor system. This system was cured one of the two temperature profiles mention above.

RESULTS

The neat resin will independent on the curing sequence results in the same overall volumetric shrinkage. Nevertheless, the response from the fibre Bragg Grating will show a change going from 0.4% strain for the 40C curing sequence to a 1.2% strain for the 75C curing sequence. The 110C curing sequence are resulting in a residual strain somewhere between those to

[a)] Corresponding author. Email: lapm@dtu.dk.

values and this lower value for an even higher curing temperature is believed to be linked to some non-linear effects going in due to some very high exothermic reactions going on at this high temperature. Static test of the neat resin is found to results in nearly identical stress versus strain curves. This is also the case for the static stress versus strain curve for the composite material. Nevertheless, testing the composite material cured at the two different temperature profiles in fatigue are leading to very different fatigue resistance as seen in Fig. 1. Going from a curing temperature on 40C to 110C the life-time is seen to be reduced with a factor of 10. Additional test was also performed for a curing temperature on 75C. This was resulting in a curve which was only slightly above the 110C curve.

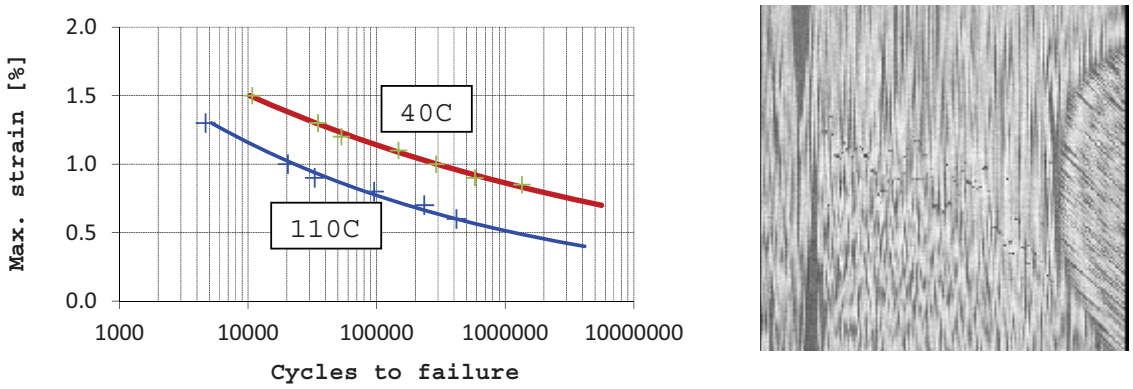

Fig. 1 The fatigue curves for the laminates manufactured at different curing temperatures and example on typical damage failure inside a fatigued sample.

Based in scanning electron microscopic pictures of fatigue specimens, Hansen [3] has postulated a fatigue damage mechanism where the fibre failure in the load carrying fibres are introduced from transverse cracks in the off-axis backing layers. This is a failure mechanism, which is expected to be sensitive to the magnitude of the residual stresses. The slide of a 3D X-ray scan shown in Fig 1, is taken after 67,000 cycles loaded to 1% strain at 1 Hz of a damage region. The region is identified using thermography during the testing looking for hot-spot at the surface. After this, a full test sample width 15x15mm scan is performed of a hotspot region. From the large field of view scan, a localized damage region can be observed which subsequently has been scanned in a zoom field of view scan of a 2.5x2.5 mm region. The localized damage region is seen to be align with the backing bundle direction shown to the right in the figure. Observations, which may indicate that the backing bundles are controlling the fibre failure of the load carrying fibers. Opposite to [4], it has not been necessary to make any physical cuts in the specimen and therefore, the cyclic fatigue loading can be continued afterwards exploring the growth of the observed damage region.

CONCLUSIONS

There has been observed a large influence of the curing cycle on the fatigue resistance of a glass fibre epoxy matrix composite. Curing cycles which is seen to results in different levels of residual strains. In addition, X-ray scan show fibre failures which are aligned with the backing bundles in the non-crimp unidirectional fabric. An observation which indicate that backing bundle transverse cracking are influencing the final fatigue damage evolution. A fatigue damage mechanism which are believed to be sensitive to the present of residual stresses.

References

[1] P. Brøndsted, Composite materials for wind power turbine blades, *Annu. Rev. Mater. Res.*, vol. 35, pp. 505–538, 2005.
[2] M. Harsch, Monitoring of Cure-Induced Strain of an Epoxy Resin by Fiber Bragg Grating Sensor, *J. Appl. Polym. Sci.*, 107, 719–725, 2008.
[3] J. Z. Hansen, Fatigue damage propagation in unidirectional glass fibre reinforced composites made of a non-crimp fabric, *J. Compos. Mater.*, 2013.
[4] K. M. Jespersen, Micromechanical Time-Lapse X-Ray Ct Study Of Fatigue Damage In Uni-Directional Fibre Composites,in *20th Int. Conf. on Composite Materials*, 2015.

IN-SITU SEM STUDY OF SHORT FATIGUE CRACK PROPAGATION BEHAVIOR IN A DMWJ

Yibo Shang[1], Huiji Shi[1a)], Zhaoxi Wang[2] & Guodong Zhang[3]
[1]*AML, School of Aerospace Engineering, Tsinghua University, Beijing, China*
[2]*CPI Nuclear Power Institute, Beijing, China*
[3]*Suzhou Nuclear Power Research Institute, Suzhou, China*

Summary In-situ SEM fatigue experiments were carried out to study short fatigue crack propagation behavior of various regions (weld zone, interface region and heat affected zone) in a dissimilar metal welded joint (DMWJ). The local microstructural effect on short fatigue crack initiation and propagation behavior was investigated with its influence on both the material fatigue and structure fatigue analyzed. The fatigue crack propagation rate of each region was compared and analyzed.

INTRODUCTION

Dissimilar metal welded joints (DMWJs) are typically used in the primary system of nuclear power plant (NPP) to connect the pipe-nozzles to the safe-ends. The fatigue loading is an important concern for the failure of DMWJ. Knowledge of fatigue crack initiation and propagation behavior in each region of DMWJ is essentially important for the safety design and integrity assessment of NPP. However, fatigue crack propagation (FCP) investigations of DMWJ in NPP are mainly focused on the macroscale regime nowadays, and the microstructural effect on the FCP is far less completely understood.

In order to investigate the short FCP mechanism of various regions in DMWJ (A508/309L/308L/316L), in-situ low cycle FCP experiments (f=10Hz, R=0.1, T=320℃) were carried out under SEM with single edge notched specimens taken from the weld zone (one specimen FCP direction is parallel to the columnar grain, the other one is perpendicular to the columnar grain) and interface region (weld/316L interface and weld/A508 interface), see Fig.1. The microstructural effect on the FCP path and rate of each region was compared and analyzed.

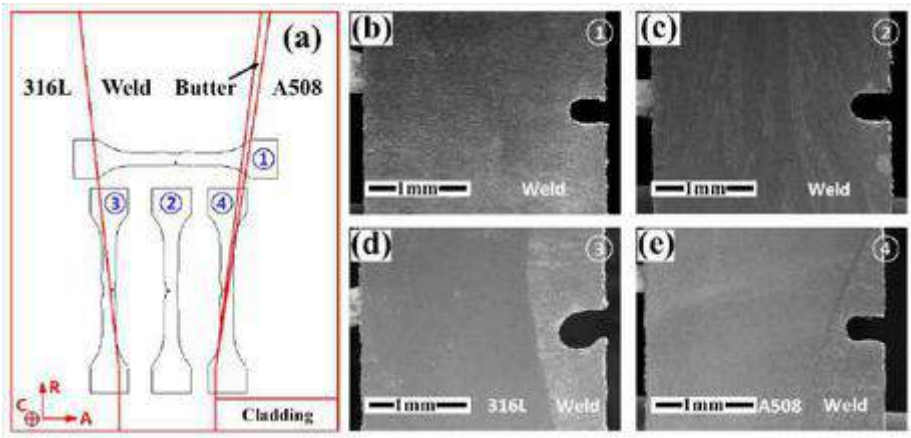

Fig.1. (a) Illustration of sampling location (b-e) specimens of various regions (the SEM images were taken before fatigue experiments)

RESULTS

Fig.2 shows the short FCP modes in various regions of DMWJ. In the weld region, the FCP is mainly influenced by the duplex microstructure of γ austenite dendrite, δ ferrite and γ/δ interface. It can be concluded that the crack propagates preferably along the slip lines of γ austenite dendrite, δ ferrite and γ/δ interface [1-4], and the grain boundary may be an obstacle for crack propagation. For the structural fatigue of weld/316L interface region, the weld/316L interface may have resistance to the FCP by changing its direction with the influence of the local γ austenite dendrite structure. After penetrating the interface, the crack tends to propagate along the slip lines of various grains and coalesce with the secondary cracks formed by slip lines of various directions in the 316L region. For the structural fatigue of weld/A508 interface region, the weld/A508 interface without buttering (namely a mixed martensite and austenite zone) may also have resistance to the FCP by crack deflection and second crack initiation. After penetrating the interface, the crack propagates or branches along the coarse martensite transgranularly within the coarse grain in A508 HAZ.

[a)]Corresponding author. Email: shihj@mail.tsinghua.edu.cn

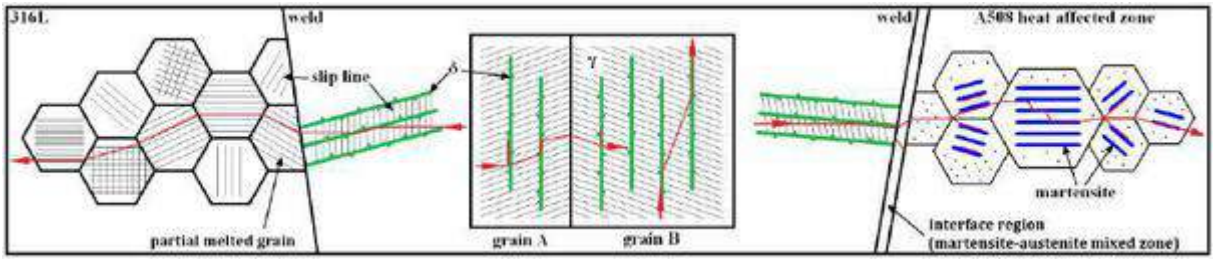

Fig.2. Schematic of short fatigue crack propagation modes in various regions of DMWJ

Fig.3 shows the fatigue crack growth rates of each specimen. In the weld region, when propagating perpendicular to the columnar grain, the crack tends to deflect and branch due to the vertical grain boundary, γ austenite dendrite, δ ferrite and δ/γ interface and results in a much fluctuant FCP rate; when propagating parallel to the columnar grain, the crack propagates preferably along the δ ferrite and penetrates the austenite, resulting in a decreased but less fluctuant FCP rate. In the weld/316L interface region, the FCP rate decreases significantly when deflecting at the 316L/weld interface, indicating the 316L/weld interface has a resistance to the structure fatigue failure. In the weld/A508 interface region, the strength of weld/A508 interface of mixed martensite and austenite is much higher than the weld region and A508. Therefore, when the crack tip plastic region reaches the weld/A508 interface, the FCP rate stagnates or even decreases. It can be concluded that the high strength martensite zone at the weld/A508 interface is beneficial for the structural fatigue failure. When the crack propagates in the A508 HAZ region, due to the coarse grain and lathy martensite structure, the FCP rate decreases when the crack penetrating the martensite, branching at the martensite or initiating the second crack.

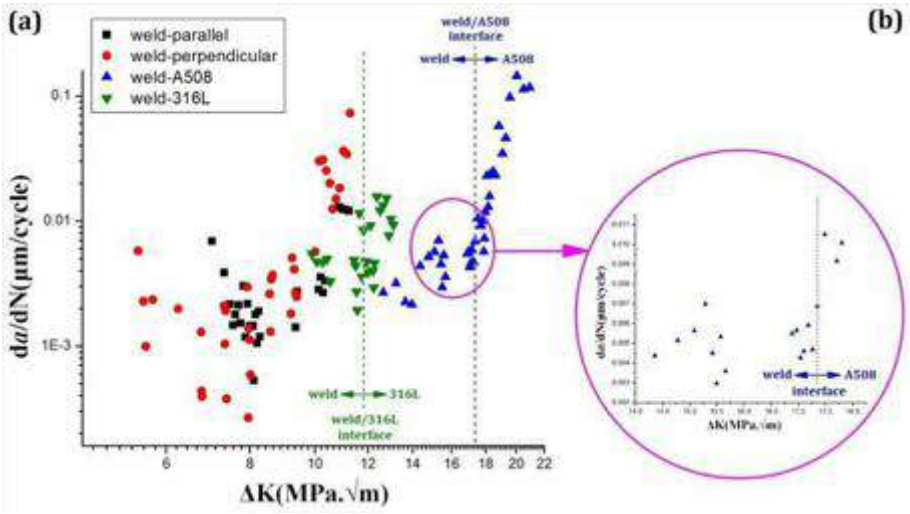

Fig.3. Fatigue crack growth rates of each specimen

CONCLUSIONS

In-situ SEM fatigue experiments were carried out to study short fatigue crack propagation behavior of various regions in DMWJ. In the weld region, the FCP is mainly influenced by the duplex microstructure of γ austenite dendrite, δ ferrite and γ/δ interface. The weld/316L interface and weld/A508 interface have resistance to the FCP. The crack propagates or branches along the coarse martensite transgranularly within the coarse grain in A508 HAZ.

References

[1] Jang C., Cho P.Y., Kim M., Oh S.J., Yang J.S.: Effects of microstructure and residual stress on fatigue crack growth of stainless steel narrow gap welds. Mater. Des. 31: 1862-1870, 2010.

[2] Hong H.U., Rho B.S., Nam S.W.: A study on the crack initiation and growth from δ -ferrite/γ phase interface under continuous fatigue and creep-fatigue conditions in type 304 L stainless steels. Int. J. Fatigue 24: 1063-1070, 2002.

[3] Rho B.S., Hong H.U., Nam S.W.: The effect of δ-ferrite on fatigue cracks in 304 L steels. Int. J. Fatigue 22: 683-690, 2000.

[4] Rho B.S., Hong H.U., Nam S.W.: The fatigue crack initiation at the interface between matrix and δ-ferrite in 304 L stainless steel. Scr. Mater. 39: 1407-1412, 1998.

FS04 - Chaos and Pattern Formation

TS.FS04-1.01	Peitz, Sebastian - Reduced Order Model based Multiobjective Optimal Control of Fluids (INVITED)	3167
TS.FS04-1.02	Revzen, Shai - Why we need more degrees of freedom (INVITED)	3169
TS.FS04-1.03	Hikihara, Takashi - Power Packet Dispatching and Dynamics in Network (INVITED)	3171
TS.FS04-1.04	Taira, Kunihiko - Complex network analysis of unsteady fluid flows	3173

REDUCED ORDER MODEL BASED MULTIOBJECTIVE OPTIMAL CONTROL OF FLUIDS

Sebastian Peitz*[1], Sina Ober-Blöbaum[2], and Michael Dellnitz[1]
[1]*Department of Mathematics, University of Paderborn, Warburger Str. 100, D-33098 Paderborn*
[2]*Department of Engineering Science, University of Oxford, Parks Road, Oxford OX1 3PJ, UK*

Summary In this article, we show how to combine reduced order modeling and multiobjective optimal control techniques in order to efficiently solve multiobjective optimal control problems constrained by PDEs. Using Galerkin projection and Proper Orthogonal Decomposition (POD), the underlying PDE is replaced by a system of ordinary differential equations, thereby drastically reducing the computational effort. We develop a gradient based algorithm by using an adjoint approach in combination with a scalarization method and the numerical results are illustrated with the example of the two-dimensional incompressible flow around a cylinder.

INTRODUCTION

In a wide range of applications it is desirable to optimally control a dynamical system with respect to concurrent, potentially competing goals. This gives rise to a multiobjective optimal control problem where, instead of computing a single optimal solution, the set of optimal compromises, the so-called Pareto set, has to be approximated. When the problem under consideration is described by a partial differential equation (PDE), as is the case for fluid flow, the computational cost rapidly increases and makes its direct treatment infeasible. Reduced order modeling (ROM, see e.g. [1]) is a very popular method to reduce the computational cost, in particular in a multi query context such as uncertainty quantification, parameter estimation or optimization. In the following, we present a method for the solution of multiobjective optimal flow control problems. The velocity field $U(x,t)$ is described by the 2D incompressible Navier Stokes equations within the domain Ω (Fig. 2). Dirichlet boundary conditions (BC) with a constant horizontal velocity are imposed on the inflow as well as on the upper and lower boundary, whereas a standard no-shear Neuman BC is imposed on the outflow boundary. On the cylinder we prescribe a time dependent Dirichlet BC such that it performs a rotation with the angular velocity $\gamma(t)$. The system is controlled by $\gamma(t)$ and the aim is to compute the *Pareto set* of optimal compromises for the conflicting objectives *minimization of flow field fluctuations* $u(x,t) = U(x,t) \nearrow \langle U(x) \rangle$ around the mean flow field $\langle U(x) \rangle = \frac{1}{T}\int_0^T U(x,t)\,dt$ and *control cost* for the flow around a cylinder at $Re = 200$:

$$\min_{U,\gamma} \widehat{J}(U,\gamma) = \min_{U,\gamma} \begin{pmatrix} \int_{t_0}^{t_e} \|u(\cdot,t)\|_{L^2}^2\,dt \\ \|\gamma\|_{L^2}^2 \end{pmatrix}. \tag{1}$$

A more detailed description and derivation of the algorithms can be found in [2].

REDUCED ORDER MODELING

Reduced order models obtained by Galerkin projection and POD [3] have been very successful in the past for the analysis of coherent structures in fluid flow. In the context of flow control, ROMs have been investigated by many researchers (see [2] for an overview). Here, we follow the procedure in [4] to derive a ROM for a system with non-homogeneous, time-dependent BC. The flow field is decomposed into the mean value $\langle U(x) \rangle$, a so-called control function $U_c(x)$ and a fluctuating field $u(x,t)$ in such a manner that $u(x,t)$ possesses homogeneous BC. The Galerkin Ansatz $U(x,t) \approx \langle U(x) \rangle + \gamma(t)U_c(x) + \sum_{i=1}^{l} \alpha_i(t)\Psi_i(x)$ is inserted into the weak formulation of the Navier-Stokes equations, resulting in the following *optimality system* (see [2] for details):

$$\begin{aligned} \dot{\alpha} &= \mathcal{A} + \mathcal{B}\alpha + \mathcal{C}(\alpha) + \mathcal{D}v + (\mathcal{E} + \mathcal{F}\alpha)\gamma + \mathcal{G}\gamma^2, & \dot{\gamma} &= v, \\ \dot{\lambda} &= -\frac{\partial \overline{J}}{\partial \alpha} - \left(\mathcal{B} + \frac{\partial \mathcal{C}(\alpha)}{\partial \alpha} + \mathcal{F}\gamma\right)^T \lambda, & \dot{\mu} &= -\frac{\partial \overline{J}}{\partial \gamma} - (\mathcal{E} + \mathcal{F}\alpha + 2\mathcal{G}\gamma)^T \lambda, \\ 0 &= \frac{\partial \overline{J}}{\partial v} + \mathcal{D}^T\lambda + \mu, \\ \alpha(0) &= \alpha_0,\ \lambda(T) = 0,\ \mu(0) = 0,\ \mu(T) = 0, \end{aligned} \tag{2}$$

with ordinary differential equations for the states α and γ as well as for the adjoint variables λ and μ. Note that by introducing a new control function $v = d\gamma/dt$ (v is the time derivative of the angular velocity), the actual control γ is now formally a state variable. The optimality condition (2) is only satisfied by an optimal control function, otherwise it provides a descent direction for the optimization algorithm.

*Corresponding author. Email: speitz@math.upb.de

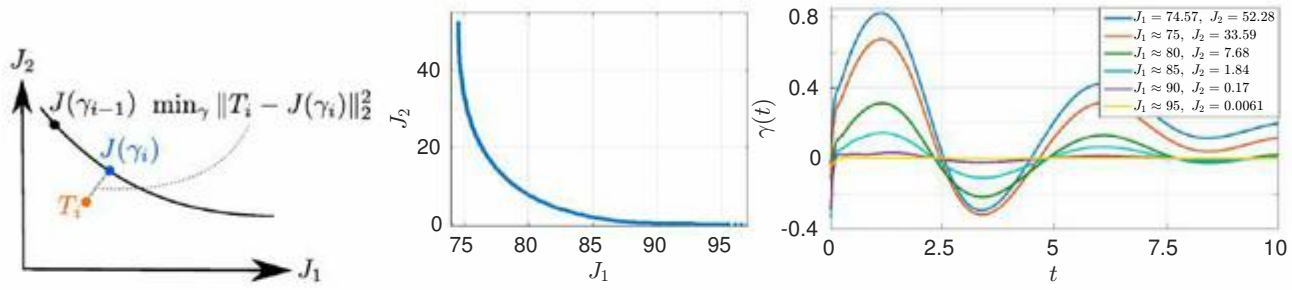

(a) (b) (c)

Figure 1: (a) Scalarization of (1) using target points T. (b) Pareto set of optimal compromises between fluctuation energy (J_1) and control cost (J_2). (c) Comparison of different Pareto optimal controls.

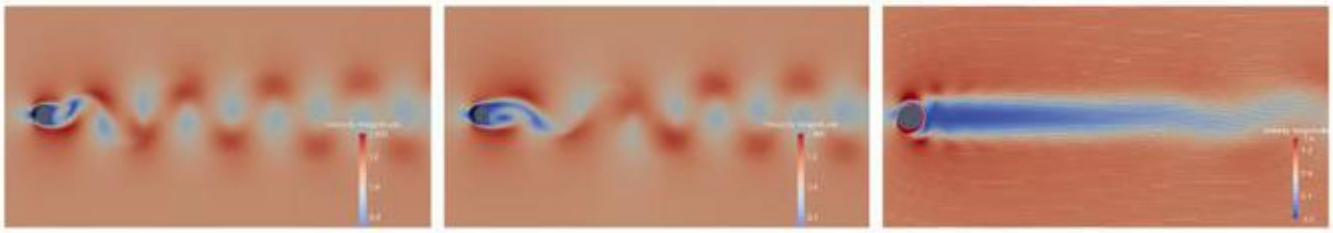

(a) (b) (c)

Figure 2: (a) Solution for $\gamma(t) = 0$: *von Kármán vortex street*. (b) Solution corresponding to maximal stabilization after $T = 10$ seconds. (c) Solution corresponding to maximal stabilization after $T = 60$ seconds using a periodic control [5].

RESULTS

Problem (1) can now be expressed in terms of the reduced model ($J_1 = \int_{t_0}^{t_e} \int_\Omega \| \sum_{i=1}^{l} \alpha_i(t)\psi_i(x)\|_2^2 \, dx \, dt$ and $J_2 = l \int_{t_0}^{t_e} \gamma^2(t) \, dt$, where l is the dimension of the ROM) and transformed into a scalar optimization problem with the objective to minimize the euclidean distance between a feasible point (J_1, J_2) and an infeasible target point (T_1, T_2) in image space (cf. Fig. 1a) such that the optimal solution (J_1^*, J_2^*) is on the boundary of the feasible set in image space and hence Pareto optimal (i.e. there does not exist a feasible point J with $J_1 \leq J_1^*$ and $J_2 \leq J_2^*$).

The resulting Pareto set and a selection of Pareto optimal controls are depicted in Fig. 1 (b, c), indicating that a tradeoff between flow stabilization and control cost is almost exclusively achieved by varying the amplitude whereas the oscillatory behavior is changed only marginally. The reason for this is very intuitive: the control has to counteract the natural oscillations of the *von Kármán vortex street* (cf. Fig. 2a). The uncontrolled solution and the solution corresponding to a strong stabilization are shown in Fig. 2. Note that due to the relatively short time interval, the effect is restricted to the immediate wake region behind the cylinder. For longer time intervals, the effect becomes more evident [5].

For future work, we intend to investigate error estimates for multiobjective optimal control problems constrained by PDEs. Moreover, we will extend our method to systems of coupled nonlinear PDEs, for instance the coupling of the Navier-Stokes and scalar transport equations, e.g. for the temperature, in order to solve multiobjective optimal control problems for HVAC applications.

References

[1] Kunisch, K., Volkwein, S. Galerkin Proper Orthogonal Decomposition Methods for a General Equation in Fluid Dynamics. SIAM Journal on Numerical Analysis 40(2):492-515. 2002.

[2] Peitz S., Ober-Blöbaum, S., Dellnitz, M. Multiobjective Optimal Control Methods for Fluid Flow Using Model Order Reduction. arXiv:1510.05819

[3] Holmes, P., Lumley, J. L., Berkooz, G. Turbulence, coherent structures, dynamical systems and symmetry. Cambridge University Press. 1998.

[4] Bergmann, M., Cordier, L., Brancher, J. P. Optimal rotary control of the cylinder wake using proper orthogonal decomposition reduced-order model. Physics of Fluids 17(097101):1-21. 2005.

[5] Peitz, S., Dellnitz, M. Multiobjective Optimization of the Flow Around a Cylinder Using Model Order Reduction. PAMM15:613-614. 2015.

*Corresponding author. Email: speitz@math.upb.de

Why we need more Degrees of Freedom

Shai Revzen*[1] and Daniel E. Koditschek[2]
[1]*Electrical Engineering and Computer Science & Ecology and Evolutionary Biology, University of Michigan, Ann Arbor, MI, USA*
[2]*Electrical and Computer Engineering, University of Pennsylvania, Philadelphia, PA, USA*

Summary The mechanical systems encountered in biology have many degrees of freedom (DOF). Even the relatively rigid arthropods and crustaceans have at least 5 DOF in each limb; tentacles and human hands have many more. Here we present a theoretical argument why multiuse mechanical systems in the natural world have many DOF. Under the assumption that they are power and force limited, and must furthermore resist environmental disturbances to their state, we derive a limit on the rate of the mechanical system to express multiple distinct states needed for different uses. As a consequence, higher DOF systems would intrinsically out-compete lower DOF systems.

BACKGROUND

One of the mysteries of the natural world is the staggering structural complexity of organisms. Why does nature select for mechanisms so much more complex than those we build? In this short paper we offer a motivating argument for why a high DOF count is an inevitable consequence of requiring versatility. To do so, we must combine ideas from computer science, theoretical mechanics, and pure mathematics.

Borrowing from computer science[2], let us define sufficient versatility as the ability to express any string in a language Σ^* generated by a set of symbols Σ. By "expressing a symbol σ" we will mean the system needs to maintain its configuration close enough to some nominal configuration that represents $\sigma \in \Sigma$. By abuse of notation we will take $\Sigma \subseteq \mathtt{Q}$ to be a discrete finite subset of the configuration space $\mathtt{Q}$ of our mechanism, and the configuration space to be embedded in a real space $\mathtt{Q} \subseteq \mathrm{R}^N$ which we will use to induce a norm on $\mathtt{Q}$. A symbol σ is expressed if the state $q(t)$ remains within distance ρ from σ for an interval of time of length δt, i.e. symbol σ was expressed at time t is equivalent to:

$$\forall s \in [t \nearrow \delta t, t] : \|q(s) \nearrow \sigma\| \leq \rho \tag{1}$$

We add some mechanical assumptions, and assume that our mechanism has a finite maximal velocity V_{max} when changing configurations by exercising its degrees of freedom. In robotics and biology such velocity limits are usually due to power limitations and the interaction of intrinsic limits of the motors or muscles with dissipation arising from friction or fluid dynamics. We shall also assume our mechanism can only exert a force of F_{max} or less because of limitations on its material properties and actuators. Finally, we assume that the environment introduces arbitrary disturbances of bounded energy ΔE.

If a state is maintained without exercising an active DOF, it must be a local minimum of the potential energy. To resist our postulated disturbances and maintain the state in a neighborhood of a symbol σ, requires introducing a potential energy well that is at least ΔE deep. Doing so with a force limited to F_{max} requires a ball of radius $r := \Delta E / F_{max}$ or larger around σ to be contained within the potential well, otherwise the mechanical work done by the potential energy is insufficient to neutralize some disturbances. Thus to meet the requirement that symbols can be reliably expressed at all, our mechanism must satisfy $\rho \geq r$.

Let us now examine the switching time between some pair of symbols α and β. To switch between symbols, our mechanism must escape the potential well of α and enter the expression ball of β. As a consequence of the previous paragraph we may conclude

$$\forall \alpha, \beta \in \Sigma : \|\alpha \nearrow \beta\| > 2\rho \tag{2}$$

However, because there are non-intersecting balls of radius ρ around each symbol, that is a severe underestimate. Instead, one must look to mathematical theory to estimate the density of packing of hyper-spheres[1]. As as a crude underestimate, since hyper-spheres are measurable sets with the standard Borel measure $\mu(\cdot)$, one may safely estimate an upper bound using volumes. We use $\#$ to denote set cardinality, and $B_r(x)$ is a "ball" $\{y \mathrm{R}^N | \|x \nearrow y\| < r\}$:

$$\forall x \in \mathrm{R}^N : \#(\Sigma \cap B_R(x)) < \frac{\mu(B_R(0))}{\mu(B_r(0))} = \frac{\mu(B_1(0))R^N}{\mu(B_1(0))r^N} = (R/r)^N \tag{3}$$

Let us choose a τ to indicate the maximal inter-symbol delay, i.e. our mechanism is to express $\#\Sigma$ symbols at a rate of at least one for each $\delta t + \tau$ units of time. Even if the distubances placed us at the most convenient state within $B_\rho(\alpha)$, the transition to $B_\rho(\beta)$ requires a configuration change travel distance of at least $\|\alpha \nearrow \beta\| \nearrow 2\rho$. Thus, for a given α, if we require the ability to travel to any $\sigma \in \Sigma$, then $\|\sigma \nearrow \alpha\| < 2\rho + \tau V_{max} =: R$. Choosing R in this way gives $\Sigma \subseteq B_R(\alpha)$ and $\#\Sigma < (R/r)^N$.

*Corresponding author. Email: shrevzen@umich.edu

Main result

By manipulating the last expression we may therefore conclude:

$$\begin{aligned} N &> (\mathrm{l} \quad (2\rho + \tau V_{max}) \nearrow \mathrm{l} \quad r)/\mathrm{l} \quad (\#\Sigma) \\ &> \mathrm{l} \quad (2+\xi)/\mathrm{l} \quad (\#\Sigma) \\ \xi &:= \frac{\tau}{r} V_{max} = \frac{F_{max} V_{max}}{\Delta E/\tau} \end{aligned} \tag{4}$$

Thus, there is a **minimal number of DOF required to express a language** in the presence of disturbances, velocity and force limits. That dimension grown with the logarithm of the ratio maximal device power to average disturbance power per symbol.

ILUSTRATIVE EXAMPLE

Let us consider a case of 1, 2, and 3 DOF systems, with parameters $F_{max}, \Delta E, V_{max}$ all set to 1, and $\tau = 2$. For all these systems, each symbol must be surrounded by a unit ball associated with it. For the 1 DOF system, only 3 unit balls (intervals) can be within τV_{max} of each other, and therefore at our desired rate $\tau = 2$, only 3 symbols at most can be expressed reliably. If we relax τ, the number of symbols will grow linearly with τ.

For a 2 DOF system, at most 7 unit balls (discs) can be within τV_{max} of each other, and therefore at our desired rate $\tau = 2$, 7 symbols at most can be expressed reliably. If we relax τ, the number of symbols will grow quadratically with τ.

Holding the number of symbols and τ constant, we must conclude that a mechanical system that needs to express more than 7 symbols must have at least 3 DOF.

CONCLUSION

The argument we present is very elementary, and includes many simplifying assumptions. We make no claim that these assumptions correctly describe the constraints placed on real world systems. Many of our assumptions can be relaxed to be even more realistic without changing the essence of our result, and were made in the current form for ease of exposition. For example, the assumption of bounded disturbance can be replaced with a suitably low probability of large disturbances, and a requirement for bounded probability of symbol expression failure.

The core of our observation is that expressing symbols in manner robust to noise implies a packing problem for the stability basins of the symbols, and that the limits of packing bound the rate of expression of such symbols. The consequence is that at a given symbol rate and noise, the number of distinct symbols that can be expressed is bounded by an exponential in the number of DOF. Thus a high number of DOF is an essential requirement for expressing many distinct symbols rapidly and robustly.

Our astute reader may wonder why organisms would need to express many symbols in the sense we describe here. The inspiration for this notion comes from looking at locomotion and manipulation[3]. In both cases, organisms must rapidly and deftly adopt a set of contacts that transfer the required forces the ground or object being manipulated. While that problem requires only few DOF with flat ground, or spherical objects, it seems to require many distinct specialized configurations when manipulating complex objects or when small animals move through complex terrain. One may thus envision that the life of a mouse critically depends on escaping predators through the clutter of a forest floor, and requiring many distinct, complex, rapid, and deft foot placement choices. Thus, the mouse with many effective DOF in its feet out-competes the one whose feet are simpler, and allow fewer ways to interact with the substrate rapidly and reliably.

Finally, we draw the reader's attention to the fact that nowhere in this calculation did we presume an inertia for the system, nor did our bounds depend on the value of δt required to express a symbol. This means that our conclusion applies equally to mechanical systems at all scales, and without regard to how briefly they are required to express their symbols, provided our remaining assumptions apply. The implication is that for systems of all scales, at high levels of environmental noise, if we want the ability to rapidly express many distinct mechanical configurations, we invariably need more Degrees of Freedom.

References

[1] Y. STOYAN AND G. YASKOV, *Packing congruent hyperspheres into a hypersphere*, Journal of Global Optimization, 52 (2012), pp. 855–868.

[2] J.-P. TREMBLAY AND P. SORENSON, *Compiler Writing*, McGraw-Hill Book Co, 1985.

[3] S. VOGEL, *Comparative biomechanics: life's physical world, 2nd Ed*, Princeton University Press, 2013.

POWER PACKET DISPATCHING AND DYNAMICS IN NETWORK

Takashi Hikihara *, Shinya Nawata, and Ryo Takahashi

Department of Electrical Engineering, Kyoto University, Katsura, Nishikyo, Kyoto 615-8510, Japan

Summary Electric power distribution has been a continuous power flow system from high potential energy sources to low potential loads. Recently we realized a power packet dispatching system and demonstrated. It may change power distribution completely different from the conventional in low power network. In the system a packet is a quantized power delivered from potential nodes to others. The packet is also attached an information to identify the direction of power and so on. The dynamics of quantized distribution form is discussed.

OUTLINE

The power packet is defined as a wave of power with information[1, 2]. As for the physical layer, various configurations are possible with keeping this concept. However, the substantial characteristic is that the power is quantized and transferred by the density distribution in a duration of time between two nodes. That is, power is digitized and quantized. In the quantized form, the spatially transferred power is decided between nodes. Wave equation isa form of relationship in neighboring elements. Single power packet, which corresponds to a quantized power, is exactly a wave between nodes. The relationship does not include the long distance over the next node. In and out flow of power at a node corresponds to a density of packet. The deference of the densities implies the stored power at the node and loss. As for the link, the power is kept between nodes. We would like to represent the system based on the coupling of resonators and quantum mechanics[3].

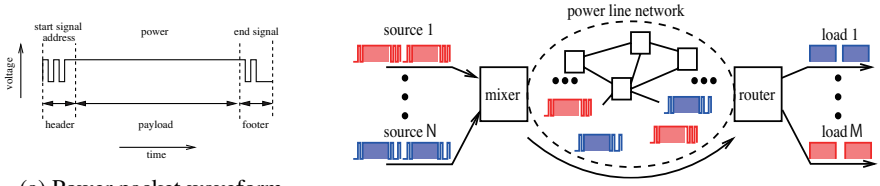

(a) Power packet waveform.

(b) Network[1]

Figure 1: Power Packet dispatching system

Here, we define the density (probability) [4] of power packet by $\sigma(n,t)$ at a node n in the s-th time duration $[t_s, t_s+\Delta t_s)]$, $v(n,t)$ is set as the voltage of packet, and $i'(n,t)$ the current between nodes by the packet. The energy $u(n,s)$ is given in the duration by the following relation:

$$u(n,s) = \int_{t_s}^{t_s+\Delta t_s} \sigma(n,t)\cdot v(n,t)\cdot i'(n,t)\mathrm{d}t. \tag{1}$$

Hereafter, the system is normalized by an appropriate base.

The total flow of power from the k-th node depends on the total flow into the node. The spatial node index is given by subscript. If there is no storage at the node, the energy conservation law at t_s is represented by $\sum_{i\in\{i\to k\}} u_i^k(s) = \sum_{j\in\{j\leftarrow k\}} u_k^j(s)$. The density of packet in a time duration gives the energy flow as follows:

$$u_k(s) = -\int_{t_s}^{t_s+\Delta t_s} \sigma_k(t)\cdot v_k(t)\cdot i_k(t)\mathrm{d}t. \tag{2}$$

Here, assume the single connection of nodes, then the energy flow by packets is defined between node k and $(k+1)$ as $u_k^{k+1}(s) = -u_{k+1}(s) + u_k(s)$. In the connection, $u_k^{k+1}(s) = 0$ implies lossless line. Between nodes, the relationship holds:

$$u_k^{k+1}(s) = -\int_{t_s}^{t_s+\Delta t_s} \{\sigma_{k+1}(t)\cdot v_{k+1}(t)\cdot i_{k+1}(t) - \sigma_k(t)\cdot v_k(t)\cdot i_k(t)\}\mathrm{d}t, \tag{3}$$

The power packet is quantized in voltage. At the setting, $v_{k+1}(s) = v_k(s)$. When $\sigma_{k+1}(s) = \sigma_k(s)$, the transferred energy from node k to $k+1$ at t_s becomes

$$u_k^{k+1}(s) \sim -v_k(s)\int_{t_s}^{t_s+\Delta t_s} \sigma_k(t)\cdot\{i_{k+1}(t) - i_k(t)\}\mathrm{d}t. \tag{4}$$

*Corresponding author. Email: hikihara.takashi.2n@kyoto-u.ac.jp

The relationship implies that the the energy between nodes depends on the current through the neighboring loop.

$$\sigma_k = \int_{t_s}^{t_s+\Delta t_s} \sigma_k(t)\mathrm{d}t \tag{5}$$

gives the temporal rate of packet.

The total energy of the system is give by $U(s)$. It normalizes the system as

$$j_k^{k+1}(s) = -\frac{u_k^{k+1}(s)}{U(s)} \sim \frac{A\sigma_k}{K} v_k(s) \cdot \{i_{k+1}(s) - i_k(s)\} \tag{6}$$

Here A is the normalizing coefficient and K the coupling inductance. The Γ-shaped radder connection of L and C is the unit element of distribution line. Then, $i_{k+1}(s) - i_k(s) = v_k(s) \cdot \mathrm{i}\omega C$. Here the current can be replaced by voltages of nodes. Real value v_k can be replaced by using complex conjugate voltage $v_k^c + v_k^{c*}$. And the current

$$j_k^{k+1}(s) \sim \frac{\mathrm{i}\omega CA\sigma_k}{K}(v_k^c(s) + v_k^{c*}(s))\{(v_k^c(s) - v_{k+1}^c(s)) - (v_k^{c*}(s) - v_{k+1}^{c*}(s))\} \tag{7}$$

n the time duration Δt_s, we set that there exists a single packet at duty ratio 0.5. $p_k(s) = 1$. The packet has a dc averaged value and a fundamental component with the period $\Delta t_s/2$. The frequency is set as $\omega(s)$. The average of $j_k^{k+1}(s)$ becomes

$$J_k^{k+1}(s) \sim \frac{\mathrm{i}\omega A'}{2K}[v_k^{c*}(s)(v_k^c(s) - v_{(k+1)}^c(s)) - v_k^c(s)(v_k^{c*}(s) - v_{(k+1)}^{c*}(s))] \tag{8}$$

Where $A' = CA\sigma_k$. There the components with $2\omega(s)$ and higher are neglected because of averaging in the duration.

The differential form can be rewrite as $v_k^c(s) - v_{k+1}^c(s) = \Delta v/\Delta x$. At a limit of $k+1$ to k, Δx goes to 0. $J_k^{k+1}(s)$ converges to $J(x)$ and $\Delta v/\Delta x$ to $\mathrm{d}v/\mathrm{d}x$.

$$J(x) = \frac{\mathrm{i}\omega A'}{2K}(v^c \cdot \frac{\mathrm{d}v^{c*}}{\mathrm{d}x} - v^{c*} \cdot \frac{\mathrm{d}v^c}{\mathrm{d}x}) \tag{9}$$

Then

$$\frac{\mathrm{i}\omega A'}{2K}\frac{\mathrm{d}}{\mathrm{d}x}\int_x |v^c(x)|^2\mathrm{d}x = J(x) \tag{10}$$

holds. This formulation corresponds to the representation by Schrödinger wave equation [3]. The averaged energy between nodes is defined generally.

$$\frac{\mathrm{i}\omega A'}{2K}\frac{\mathrm{d}}{\mathrm{d}x}\int_{x_1}^{x_2} |v^c(x)|^2\mathrm{d}x = J(x_2) - J(x_1) \tag{11}$$

CONCLUSION

The power packet dispatching system is described as a classical realization of quantized power distribution. In the formulation, the power distribution is defined as a density of power packet in the network spatially and temporally. This formulation includes the conventional swing dynamics in a conventional power system. It will give us a clue to develop the power delivery system into multi-scale system with various network.

ACKNOWLEDGEMENT

The author appreciate Professor M.Kitano and his research group for fruitful discussion about quantum mechanics. This research is partially supported by the Cross-ministerial Strategic Innovation Promotion Program supported by NEDO.

References

[1] T.Takuno, M.Koyama, and T.Hikihara: In-home Power Distribution Systems by Circuit Switching and Power Packet Dispatching, 1st IEEE International Conference on Smart Grid Communications, 4-6 Oct. 2010, Maryland, USA.

[2] R.Takahashi, K. Tashiro, and T. Hikihara, Router for Power Packet Distribution Network: Design and Experimental Verification, IEEE Trans. on Smart Grid, Vol. 6, No. 2, 618–626 (2015).

[3] Masao Kitano, Fundamentals of Quantum Mechanics (Kyoritsu Shuppan, 2010), Chap. 10 (in Japanese).

[4] Norbert Wiener, Nonlinear Problems in Random Theory (MIT Press, 1966).

COMPLEX NETWORK ANALYSIS OF UNSTEADY FLUID FLOWS

Kunihiko Taira *[1], Aditya G. Nair[1], and Steven L. Brunton[2]

[1]*Department of Mechanical Engineering, Florida State University, Tallahassee, Florida, USA*
[2]*Department of Mechanical Engineering, University of Washington, Seattle, Washington, USA*

Summary Unsteady fluid flows have rich dynamics generated from the nonlinear interactions that take place over a broad range of spatial and temporal scales. We can view these interactions to be present between vortical elements in physical space or between modal structures in wave space. To characterize these interactions, the use of network analysis that combines graph theory, operator theory, and dynamical systems theory is considered in our work. We show that network theory is able to capture the important vortical or modal interactions present in the flow field to provide physical insights beyond those from conventional analyses. The current approach enables the identification of key interactions and the examination of the resilience of the global interaction network to external disturbances. Moreover, we can derive the sparsified dynamics models that preserve conservation properties, using concepts from graph theory. Applications of network-based analysis to vortex dynamics, turbulence, and separated flows are presented.

INTRODUCTION

Network theory studies the underlying mathematical structure of a network (graph), consisting of individual units, or nodes, with their own local dynamics, as well as their connectivity and mutual influence, given by edges [2, 1, 4]. Collectively, this system is described by a dynamical system on a graph [5]. These fields of study are fundamental in nature, and have impacted a wide range of applications, including social networks, biological and artificial neural networks, epidemiology, and cyber security [5]. Network theory can reveal the structural connectivities amongst a set of elements and analyze their collective dynamics.

While there has been a wealth of studies performed to examine unsteady fluid flows from a variety of perspectives, there have been limited attempts to capture the vortical interactions using advanced mathematical toolsets. Network analysis is ideal for the modeling and control of large-scale fluid dynamics systems with high-dimensionality, multi-scale coherence, and nonlinearity. The vortices or modal structures present in the flow field can be viewed as graph nodes and the interactions among them can be seen as graph edges. The objective of the present work is to capitalize on these unique capabilities of network theory to perform network-based characterization and modeling of vortical interactions in unsteady fluid flows. In what follows, we briefly describe our recent findings from examining unsteady fluid flows with network-theoretic analyses.

NETWORK-BASED ANALYSIS OF FLUID FLOWS

Vortex dynamics network

To demonstrate the strength of network-theoretic analysis for fluid flow applications, we consider the dynamics of a set of discrete point vortices [3]. We characterize the network by taking individual point vortices as the network nodes and the vortical induced velocities as the edge weights based on the Biot–Savart law. This leads to the vortical interaction network to be described by a complete graph with a range of edge weights. With the mathematical formulation established for the vortical interaction network, we employ graph theory based sparsification techniques [8] to significantly reduce the number of edges to model the dynamics without altering the collective behavior of the vortices. This approach gives rise to the sparsified-dynamics model that has a sparse state operator while preserving physical conservation properties. The model problem with discrete vortices not only demonstrates the unique capabilities of network and graph theories to extract important vortical interaction network but also lays the pathways for extensions to the other problems below.

Turbulence network

We examine the dense vortex interactions in two-dimensional isotropic turbulence and find that the vortical interaction network can be characterized by a (weighted) scale-free network. Cartesian spatial cells can be viewed as nodes in this example with interaction strength determined by the vorticity of each cell. Shown in Figure 1 are the turbulent vortical interaction network, network node strengths s, and probability distribution of the strength $P(s) \sim s^{-2.7}$. Such scale-free network structure is representative of airline, internet, and social networks and plays an important role in modeling collective network behavior and designing control strategies for uninterrupted services or for combatting disease transmissions [5]. In two-dimensional turbulence, we found that the turbulent flow network retains its scale-free behavior until the characteristic value of circulation reaches a critical value. Furthermore, we show that the two-dimensional turbulence network is resilient against random perturbations but can be greatly influenced when forcing is focused towards the vortical structures that are categorized as network hubs. These findings can serve as a network-analytic foundation to examine complex geophysical and thin-film flows.

*Corresponding author. Email: ktaira@fsu.edu

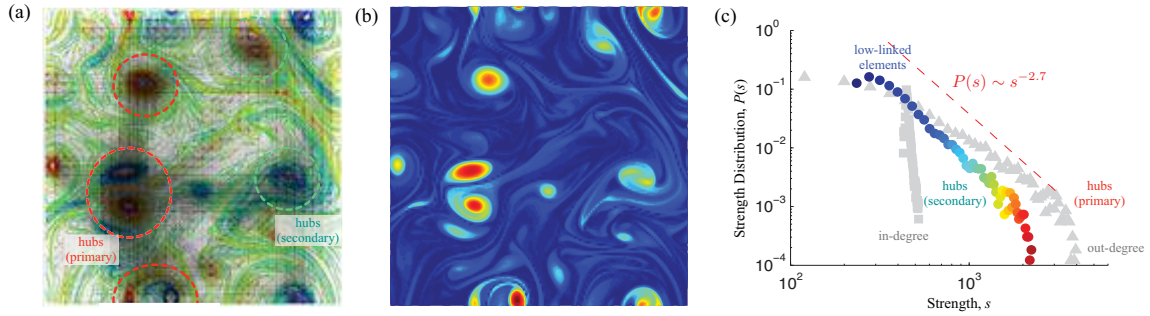

Figure 1: Vortical interactions in two-dimensional isotropic turbulence described by a scale-free network [9]. (a) Turbulence network. (b) Node strength. (c) Scale-free strength distribution.

Modal interaction network

We can also gather physical insights associated with modal interactions. Network analysis can play a key role in the identification of these nonlinear interactions amongst modes. In addition, network analysis highlights interaction dynamics which can be subsequently used for modification (control) of the flow. In this work, we focus on interactions between modes in terms of energy pathways. We utilize the Galerkin-projection based reduced-order modeling technique [6] and modal analysis based on finite-time thermodynamics [7] for network-based representation of nonlinear modal interaction. This formulation enables us to show energy transfer between modes, as presented in Figure 2. In this example of separated flow over a cavity, we find that the interaction network highlights the dominant Rossiter mode and the nonlinear energy transfer to its higher harmonics but not to the energetic hydrodynamic modes. We also note that there are network-theoretic metrics that can reveal important modal nodes for energy transfer analyses.

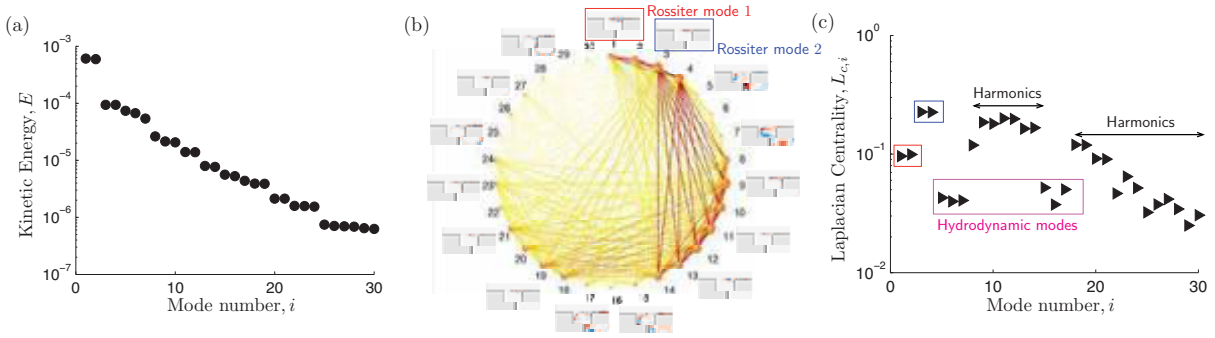

Figure 2: (a) POD modes arranged based on energy contents, (b) network model (normalized) of nonlinear modal interactions for cavity flow, and (c) Laplacian centrality of cavity flow network. The edge color indicates edge weights and the size of the node represents the node strength.

CONCLUSIONS

We considered the utilization of network theory to establish a novel formulation of analyzing and modeling the vortical and modal interactions present in unsteady fluid flows. This approach is able to capture the underlying structure of nonlinear interactions and can produce a sparse representation of the essential interaction physics. The presented formulation opens up a promising avenue in interaction-based studies of a wide variety of unsteady fluid flows complementing classical analysis techniques. We foresee that network theory and graph theory can provide new insights into the behavior of fluid flows and provide means for new techniques for modeling and controlling complex unsteady flows.

References

[1] Albert R., Barabási A.-L.: Statistical Mechanics of Complex Networks. Rev. Mod. Phys. 74: 47-97, 2002.
[2] Bollobás B.: Modern graph theory. Springer, 1998.
[3] Nair A. G., Taira K.: Network-Theoretic Approach to Sparsified Discrete Vortex Dynamics. J. Fluid Mech. 768:549-571, 2015.
[4] Newman M. E. J.: The Structure and Function of Complex Networks. SIAM Rev. 45(2):167-256, 2003.
[5] Newman M. E. J.: Networks: An Introduction. Oxford Univ. Press 2010.
[6] Noack B. R., Afanasiev K., Morzyński M., Tadmor G., Thiele F.: A Hierarchy of Low-Dimensional Models for the Transient and Post-Transient Cylinder Wake. J. Fluid Mech. 497:335-363, 2003.
[7] Noack B. R., Schlegel M., Ahlborn B., Mutschke G., Morzyński M., Comte P., Tadmor G.: A Finite-Time Thermodynamics of Unsteady Fluid Flows. J. Non-Equilib. Thermodyn. 33:103-148, 2008.
[8] Spielman D. A., Teng S.-H.: Spectral Sparsification of Graphs. SIAM J. Sci. Comput. 40(4):981, 1025, 2011.
[9] Taira K., Nair A. G., Brunton S. L..: Network Structure of Two-Dimensional Isotropic Turbulence. In Review 2016.

FS05 - Porous Media

TS.FS05-1.01	Vandamme, Matthieu - Influence of the hydric state on the elastic and creep properties of self-standing clay films	3176
TS.FS05-1.02	Abousleiman, Younane - Micromechanical characterization of a natural organic rich composite porous medium (INVITED)	3178
TS.FS05-1.03	Pellenq, Roland - The bottom-up modeling approach to cement paste (INVITED)	3180
TS.FS05-1.04	Shikhmurzaev, Yulii - Non-Washburn imbibition: Modelling results and emerging issues (INVITED)	3182
TS.FS05-1.05	Worster, Grae - Freezing solutions and colloidal suspensions (INVITED)	3184
TS.FS05-1.06	Prevost, Jean - Intersecting Faults Simulations for Reservoir-geomechanical Models	3186
TS.FS05-2.01	Carmeliet, Jan - Multiscale investigation of imbibition, drainage and drying in macroporous media	3188
TS.FS05-2.02	Chen, Mingyang - A multi-scale study on adsorption induced deformation of hybrid porous materials	3190
TS.FS05-2.03	Hellmich, Christian - Liquid crystal interface micromechanics	3192
TS.FS05-2.04	Gamnitzer, Peter - Numerical simulation of surface subsidence and heave in water saturated/unsaturated soil	3194
TS.FS05-2.05	Laouafa, Farid - Modeling of salt and gypsum dissolution processes	3196
TS.FS05-3.01	Louge, Michel - Tension and tomographic measurements while draining water from a granular sample	3198
TS.FS05-3.02	Schrefler, Bernhard - Shear and mixed mode fracture in disordered saturated porous media	3200
TS.FS05-3.03	Shang, Zhihao - Competitive adsorption of gas mixtures in fractal slit nanopores	3202
TS.FS05-3.04	Shao, Jianfu - A micro-macro mechanical model for porous rock-like materials with a pressure-sensitive matrix	3204
TS.FS05-3.05	Huang, Zhangfeng - Effect of local porous coating on the stability of boundary layer	3206
PO.FS05-1.01.228	Beaudoin, Anthony - Transport equation for the concentration gradient	3208
PO.FS05-1.02.229	Budyn, Elisa - Bone healing in Live Allograft Biological Systems	3210
PO.FS05-1.03.230	Karmakar, Timir - Lifting a large object from an anisotropic porous bed	3212
PO.FS05-1.04.231	Lasseux, Didier - Macroscopic modeling of slightly compressible gas slip flow in homogeneous porous media	3214
PO.FS05-1.05.232	Li, Xiying - Controllable Capillary Flow and Direct Oil Recovery in Carbon Nanotube Sponges	3216
PO.FS05-1.06.233	Lundström, Staffan - Stereoscopic particle image velocimetry for the study of turbulent flow in a packed bed of spheres	3218
PO.FS05-1.07.234	Zhang, Chi - Hygromechanical behavior of hemicellulose and s2 cell wall layer of wood	3220
PO.FS05-1.08.235	Zu, Yingqing - Pore scale modeling of CO_2 migration in porous rocks under conditions of saline aquifers	3222

INFLUENCE OF THE HYDRIC STATE ON THE ELASTIC AND CREEP PROPERTIES OF SELF-STANDING CLAY FILMS

Benoit Carrier[1], Matthieu Vandamme[1a)], Roland J.-M. Pellenq[2,3,4], Michel Bornert[1], Eric Ferrage[5], Fabien Hubert[5], & Henri Van Damme[2,3,4]

[1]*Laboratoire Navier (UMR 8205 CNRS, ENPC, IFSTTAR), Université Paris-Est, Champs-sur-Marne, France*
[2]*Department of Civil and Environmental Engineering, Massachusetts Institute of Technology, Cambridge, Massachusetts, United States*
[3]*Centre Interdisciplinaire des Nanosciences de Marseille, CNRS (UPR 7251), Marseille, France*
[4]*<MSE>2, UMI 3466, CNRS-MIT, Cambridge, Massachusetts, United States*
[5]*UMR 7285 IC2MP, Université de Poitiers/CNRS, Poitiers, France*

Summary Better understanding the hydromechanical behavior of clay-based materials is of interest for a variety of applications in petroleum or civil engineering. Here we study self-standing clay films whose thickness is of a few dozen microns. We characterize how the elastic and creep properties of those porous systems depend on relative humidity or, equivalently, water content: the dependence is very significant, and the relationship between stiffness and water content exhibits no hysteresis. The characterized mechanical properties also depend on the cation present in the interlayer water, from which we infer that the mesostructure of the films must play a significant role on their mechanical behavior.

INTRODUCTION

Clay-based materials are known to be sensitive to water: for instance, upon drying, a clayey soil cracks. This sensitivity is a direct consequence of the fact that clay is porous. Better understanding the influence of water on the mechanical properties of clays (i.e., their hydromechanical behavior) is of interest for nuclear waste storage, since, in France, the future underground storage center will be implemented in an argillite, which is a clayey rock. It is also of interest for a variety of applications in civil or petroleum applications, e.g., stability of buildings built on clay rich soils, or stability of boreholes drilled through clayey cap rocks.

Clay-based materials are also known to be heterogeneous and multi-scale, which makes it more complex to understand their hydromechanical behavior at the macroscopic scale. Therefore, here, we work with relatively simple systems made of pure clay since, in clay-based materials, clay is the phase that is the most sensitive to water. The systems considered are self-standing clay films with a thickness of a few dozen microns. The basic building units of those films are the same as for any clay-based material, i.e., nanometer-thick clay solid layers. For most clays (and in particular for the montmorillonite clay here tested), those layers are negatively charged. In order to ensure electroneutrality, the interlayer water between adjacent clay layers contains cations, whose nature is known to influence the hydromechanical behavior of the clay.

Here, we characterize the elastic and creep properties of montmorillonite clay films with various interlayer cations. We characterize how those properties depend on the hydric state. First, we present the materials and methods. Then we present and discuss the elastic and creep results, before concluding.

MATERIALS AND METHODS

The films here studied were manufactured with the montmorillonite clay SWy-2, which naturally contains both calcium and sodium interlayer cations. We homoionized part of the material with sodium cations, and part of the material with calcium cations, so that we could eventually manufacture films with 3 types of interlayer cations: only sodium, only calcium, and a mix of both. The films were manufactured by evaporation of a clay suspension on a polyethylene surface. After drying, the solid film was just peeled off from the substrate. The films were a-few-dozen-microns-thick and highly ordered (see Fig. 1).

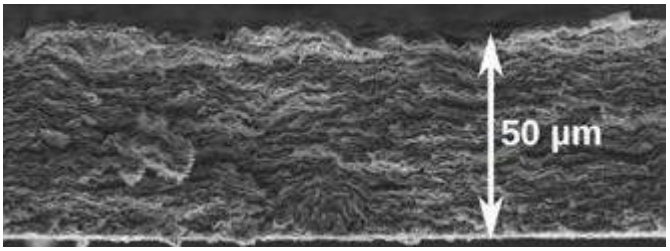

Figure 1: ESEM picture of the edge of one of the manufactured films (credits: L. Wang).

Elastic and creep properties were characterized by tensile testing (see Fig. 2a). The samples were cut from the manufactured films into rectangles with a width of 9.3 mm and a length of 80 mm. All experiments were performed at room

[a)] Corresponding author. Email: **matthieu.vandamme@enpc.fr**

temperature in a controlled environment: humidity was varied from 5% to 90% for the elastic characterization and from 50% to 99% for the creep characterization. Strains were measured by digital image correlation, which is a contact-free technique, with the in-house software CMV.

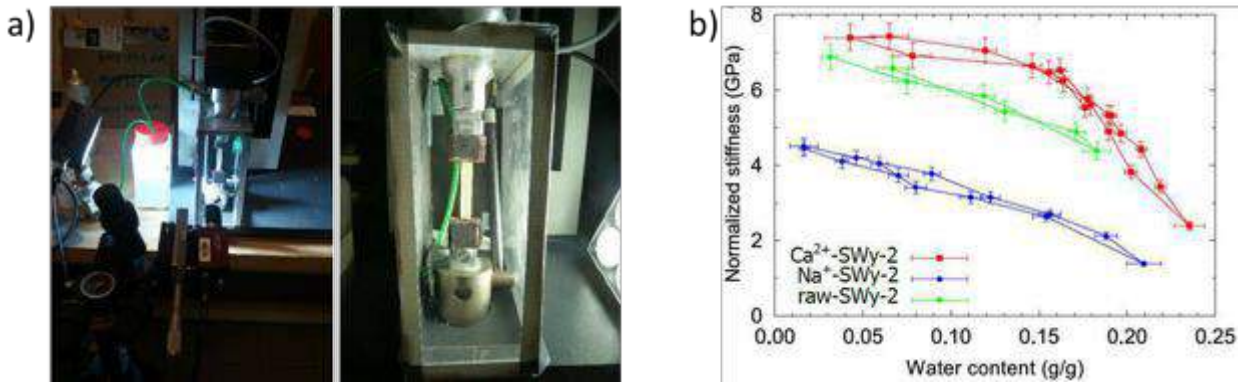

Figure 2: Measurement of elastic stiffness: a) Pictures of setup and b) Results.

We also characterized the adsorption isotherms of the films, by weighing the films after equilibration at various relative humidities. Thus, we can display next the mechanical properties of the films versus relative humidity as well as versus water content.

RESULTS AND DISCUSSION

In terms of elastic properties, at given water content, the normalized Young's modulus of the films depended on the interlayer cation (see Fig. 2b). When the relative humidity or water content increased, the stiffness of all films decreased. On a full cycle of relative humidity, stiffness displayed a hysteretic behavior when plotted versus relative humidity, but no hysteretic behavior when plotted with respect to water content (see Fig. 2b), suggesting that the natural parameter on which elastic properties of the films depend is the water content, not the relative humidity.

All films exhibited a creep strain which, after a transient period, increased logarithmically with respect to time. We introduce a creep parameter κ (expressed in Pa^{-1}) defined as $\kappa = (bd/F)\, d\varepsilon/d(\ln t)$, where b is the width of the film, d is its dry thickness, F is the load applied to the film, and $\varepsilon(t)$ is the measured creep strain. This creep parameter κ depended on the interlayer cation and was very much sensitive to water: over the whole range of relative humidities considered, this parameter was an exponential function of the water content.

The results obtained on those films can be compared with results we obtained previously at the scale of the clay layer by molecular simulations [2]. In particular, for what concerns elastic properties, molecular simulations showed that the stiffness of the clay layer does not depend on the interlayer cation. Therefore, the dependence observed on our films must stem from a scale greater than that of the clay layer: the mesostructure of the films, i.e., how clusters of clay layers are arranged with respect to each other in space, must play a significant role on their mechanical properties.

CONCLUSIONS

Here we characterized the elastic and creep properties of self-standing thin clay films. With increasing relative humidity, independent of the cation, the films creeped more and were softer. At given water content, the interlayer cation played a significant role on those properties: the mesostructure of the films must play a significant role on their mechanical properties. Hysteresis disappeared when stiffness was displayed versus water content rather than versus relative humidity. Also, all films exhibited a creep strain that evolved logarithmically with respect to time, which is reminiscent of the logarithmic creep observed on macroscopic clay samples: this logarithmic feature must originate from the scale of the films or from a lower scale.

The gathered data, on top of having made it possible to shed some light on the effect of water or of the interlayer cation on mechanical properties of clay, can be of interest for researchers aiming at performing bottom-up approaches and upscaling the hydromechanical behavior by starting from the scale of the clay layer: the results that we here gathered on our films provide a set of data on which those researchers can validate a first step of their upscaling scheme.

References

[1] Carrier B., Vandamme M., Pellenq R. J.-M., Bornert M., Ferrage E., Hubert F., Van Damme H.: Effect of Water on Elastic and Creep Properties of Self-Standing Clay Films, *Langmuir*, just accepted.

[2] Carrier B., Vandamme M., Pellenq R. J.-M., Van Damme H.: Elastic Properties of Swelling Clay Particles at Finite Temperature upon Hydration, *J. Phys. Chem. C* **118**:8933−8943, 2014.

MICROMECHANICAL CHARACTERIZATION OF A NATURAL ORGANIC RICH COMPOSITE POROUS MEDIUM

Y. N. Abousleiman[1a)] & K. L. Hull[2]
[1]*Geology & Geophysics, Petroleum & Geological Engineering, Integrated PoroMechanics Institute, University of Oklahoma, Norman, Oklahoma, United States of America*
[2]*Aramco Research Center-Houston, Aramco Services Company, Houston, Texas, United States of America*

Abstract Composite porous materials have been the subject of micro-scale experimental and theoretical mechanics for decades, with their mineral and organic composite matter well defined a priori. However, natural composites in geomaterials with organic and mineral content, e.g., energy source shale, are inhomogeneous and anisotropic multi-phase components at all scales. Kerogen is lenticular and woven within the mineral clay and non-clay porous matrix, making the source shale hard to mechanically characterize. In this study, composite porous shale samples were manufactured as micro-pillars and micro-beams using a Focused Ion Beam and loaded in situ to failure in a Scanning Electron Microscope. Results show the polymer nature of kerogen-rich shale has a tensile elastic behaviour with a tensile "modulus of toughness" greater than any known natural geomaterial. Also, kerogen acted like a cross-linked polymer with substantial tensile strength and large tensile modulus of toughness, when compared to the brittle behaviour of kerogen-free shale.

INTRODUCTION

Organic-rich shale is a nonhomogeneous multi-phase composite termed as "source rock." This shale got its famous reputation recently from the oil and gas industry in the fracking business in search of more economical resources of fossil energy [1]. The fracking consisted of huge volumes of low-viscosity water (2-3 million gallons) pumped with some sand proppant to keep the fracture open. These practices met with very challenging outcomes, in particular large pumps in series, at huge cost, in addition to economical production per fractured wellhead lasting less than 20 months in best case scenarios. The problem was clearly the "tight" low permeability, organic-rich shale. Mechanical characterization was back to square one, in terms of the Representative Elementary Volume (REV) of organic-rich shale problem domains and their intricate multi-porosity systems [2, 3]. Early micro-mechanical testing conducted by Ulm and Abousleiman [4] attempted to isolate the REV of shale using the nanoindenter. Their results showed that 100's of nm are the scale at which porous organic-rich shale exhibited its full upscaling mechanical characteristics. However, the tensile characteristics and the large tensile "modulus of toughness" were not discovered in the previous suite of nanoindentation and micromechanical characterization.

In this work, new methods for testing and characterizing organic-rich shale were thought of by manufacturing shale micro-beams and micro-pillars using a Focused Ion Beam (FIB). Using nanotechnology techniques and equipment, the micron-sized geometries were milled via the FIB in a scanning electron microscope (SEM), then loaded to failure via nanoindentation in the SEM. The associated loads/forces in micro-Newtons and failures at displacements in the range of 100s of nanometers have shown the true nature of the failure mechanisms, in compression and tension, of the composite polymer nature behavior of the organic-rich shale.

EXPERIMENTAL PROTOCOL AND RESULTS

Micro-cantilever beam and micro-pillar sample production: A sample with dimensions of 1 x 1 x 0.4 cm was cut from a preserved shale sample and an FIB was used to clean the surface for better sample imaging as well as to prepare the desired micro-beams geometries shown in Fig 1. A Hysitron Pi-85 picoindenter was used to load the micro-beams under displacement control mode at a rate of 15 nm/s all the way to sample failure. Similarly, prismatic micro-pillars, with minimal taper, were manufactured in the FIB instrument (Quanta 3D FEG) with successively lower beam currents. The aspect ratio (micro-pillar height divided by width) was set close to 3:1. These dimensions are not perfect for the shale samples seen in Fig. 2 (a), and they may vary slightly during FIB milling. A different Hysitron indenter was used to uni-axially compress the micro-pillars using a diamond flat punch tip indenter, with 60° conical, and a 10 μm diameter flat tip, as shown in Fig. 2 (c). The micro-pillars were loaded, following the micro-cantilever beams, at a predetermined displacement rate of 15nm/s until failure.

[a)] Corresponding author. Email: **yabousle@ou.edu.**

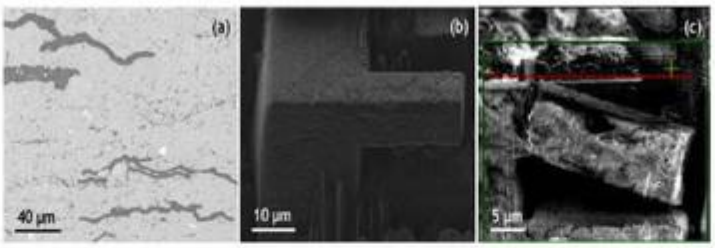

Fig. 1 The micro-cantilever beam from sample to failure, Micro-Beam, T3

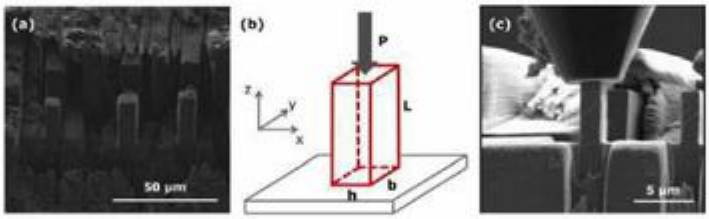

Fig. 2 The three FIB milled micro-pillars in (a); loading configuration in (b) and (c)

Results and Discussion: Four micro-cantilever beams were tested. The results are illustrated for three micro-beams in Fig. 3. Observe the brittle failure of micro-beam T3 when compared to micro-beam T1 that exhibited strain softening, while micro-beam T2 showed strain hardening before failure. While loading is in pre-yield from the elastic response, the estimated Young's moduli of the micro-beams were very close to their macro-scale values [5]. However, it is the post-yield behaviour that is not typical of a granular cohesive and frictional porous media when tested unconfined. Post yield behaviour is typical of fibre reinforced porous material, such as reinforced concrete beams.

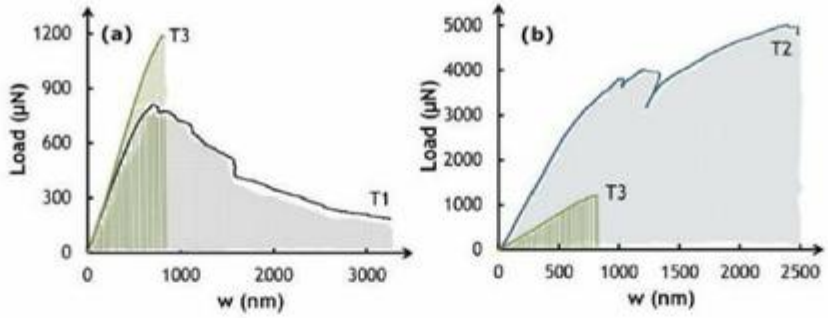

Fig. 3 The load/displacement curves of the three micro-cantilever beams tests, T1, T2 and T3

CONCLUSIONS

These experimental results show that the composite nature of the organic-rich shale has tensile strength characteristics such as the modulus of rupture that can be more relevant and problematic to fracking and optimizing field applications. An obvious question is why for the past decade or so in rock mechanics testing we did not pick up on the tensile attributes of the organic rich shale as a fiber composite porous media? The answer is simply that these tensile characteristics of composite porous polymers, like kerogen (organic matter), are easily masked when practicing the recommended ASTM and ISRM standard testing methods for macroscale geomechanics material characterization, such as the Brazilian test and/or other recommended tensile strength measurements for rocks.

References

[1] Turcotte D., Moores E., Rundle J.: Super Fracking. Physics Today, August 2014.

[2] Slatt R., Abousleiman Y.: Merging sequence stratigraphy and geomechanics for unconventional gas shales. The Leading Edge 30(3):274-282, 2011.

[3] Mehrabian A., Abousleiman Y.: Generalized Biot's theory and Mandel's problem of multiple-porosity and multiple-permeability poroelasticity. J Geo. Res., 2014.

[4] Ulm F-J., Abousleiman Y.: The nano granular nature of shale. Acta Geotecnica, 1(2):77-88, 2006.

[5] Abousleiman Y., Hull K., Muntasheri G., Hosemann P., Parker S., Howard C.M.: The granular and polymer composite nature of kerogen-rich shale. Acta Geotechnica, in press 2016.

THE BOTTOM-UP MODELING APPROACH TO CEMENT PASTE

Katerina Ioannidou[1], Emanuela Del Gado[2], Franz Ulm[3], Roland J.-M. Pellenq[1,3,4, a)]
[1] "Multi-Scale Materials Science for Energy and Environment", <*MSE*>[2], the CNRS-MIT Joint Laboratory, Massachusetts Institute of Technology, Cambridge, Massachusetts, United States
[2] Department of Physics and Institute for Soft Matter Synthesis and Metrology, Georgetown University, Washington DC, United States
[3] Department of Civil and Environmental Engineering, Massachusetts Institute of Technology, Cambridge, Massachusetts, United States
[4] Centre Interdisciplinaire des Nanosciences de Marseille, CNRS, Aix-Marseille Université, France

Summary Strength and other mechanical properties of cement paste and concrete rely upon the formation of Calcium–Silicate–Hydrates (C–S–H) during cement hydration. Here we propose a novel description of the C–S–H meso-scale texture with an opportunity to translate results from the fundamental (nano) scale to the macro-scale of engineering properties. We use simulations that combine information of the nano-scale building units of C–S–H and on their effective interactions, obtained from atomistic simulations and experiments, into a statistical physics framework for aggregating nanoparticles. We compute small angle scattering intensities, pore size distributions, local densities, indentation modulus of the material, providing a new quantitative understanding of different experimental investigations. Our results lead to a quantitative insight into how the heterogeneities developed during the early stages of hydration persist in the structure of C–S– H and impact the mechanical performance of the hardened cement paste.

.

INTRODUCTION

Controlling the structure and properties of the C–S–H phase is still a challenge, due to the complexity of this hydration product and of the mechanisms that drive its precipitation from the ionic solution upon dissolution of cement grains in water. Departing from traditional models that are mostly focused on length-scales above the micrometer, recent research has addressed the molecular structure and properties of C–S–H. However, small angle neutron scattering, electron-microscopy imaging and mechanical nanoindentation experiments, all suggest that an even more important role may be played by the mesoscale organization of the C–S–H structure that extends over hundreds of nanometers. In this paper, we illustrate the bottom-up modeling effort applied to C–S–H and provide a mesoscale picture of cement paste that results from fundamental interactions between grains gained at the atomistic level.

COMPUTATIONAL METHODS

We have used a statistical physics approach to gain new insight into the C–S–H at the scale of hundreds of nanometers, based on the knowledge developed at the nanoscale [1]. The effective interactions between C–S–H nanograins at the end of setting (hardened paste) are modelled with a generalized Lennard-Jones potential:

$$V(r)=6\epsilon\left[\left(\frac{\sigma}{r}\right)^{2\gamma}-\left(\frac{\sigma}{r}\right)^{\gamma}\right] \quad (1)$$

where r is the inter-particle distance, ε is the strength of the attraction between two particles with diameter σ and γ=12. The temperature was T=0.15 in reduced units and the particles size σ was randomly distributed between 3.78 and 9.2 nm. The simulations have been performed with box size L = 585.54 nm containing up 6.1·105 particles (total packing fraction η = 0.33 and 0.52) with at least 5 independent samples. Simulations of C–S–H precipitation were performed using a hybrid scheme of Grand Canonical Monte Carlo (GCMC) and Molecular Dynamics (MD). A GCMC cycle consists of NMC attempts of particle insertion or deletion followed by NMD = 100 MD steps in the NVT ensemble. The pore size distribution (PSD) was obtained from the distribution of diameters of the largest spheres (non-overlaping with the solid particles) that can be accommodated in the void regions. The local packing fractions ηlocal were computed in a spherical region of radius 35 nm around each C–S–H spherical particle. or the small angle scattering I(q), we first generated a digitized 3D image of the structure with a voxel size of 0.571 nm, much smaller than the minimum particle diameter 3.78 nm and well below the box size. Having computed the two points fluctuation auto-correlation function $\eta(r)^2$, the scattered intensity, I(q), was deduced in absolute scale using the following relation:

$$I(q)=-\frac{2\pi(\Delta\rho)^2}{q}\frac{d(Re(\tilde{\eta}^2(q))}{dq} \quad (2)$$

where Δρ is the scattering length density contrast and $\tilde{\eta}(q)^2$ the 1D Fourier transform of $\eta(r)^2$. The stiffness of the interaction between two particles of size σ is defined as the curvature of the generalized Lennard-Jones potential and at the local equilibrium distance $r_m = \varepsilon / (444\sigma^2)$. By assuming that the cohesive strength between particles is the same as for the

a) Corresponding author. Email: pellenq@mit.edu

calcium-silicate layers within a C–S–H grain, we express the inter-particle stiffness as Y A/r_m, where Y is the Young modulus of solid C–S–H (68.4 GPa from atomistic simulations of few nanometers C– S–H grains with Ca/Si= 1.7 [2]) and $A=\pi r_m^2$ is the cross section of the applied force. All this leads to a unit pressure $\varepsilon/\sigma^3 = 0.51$GPa. The C–S–H configurations were relaxed to zero stress before computing indentation modulus M and hardness H. To compute M, we slightly deform the simulation box in the three axial directions and the three shear planes. The range of strain for the elastic deformation is ±0.005. The indentation modulus M was computed as a linear combination of the bulk K and shear modulus G, *M=4G(3K+G)/(3K+4G)*.

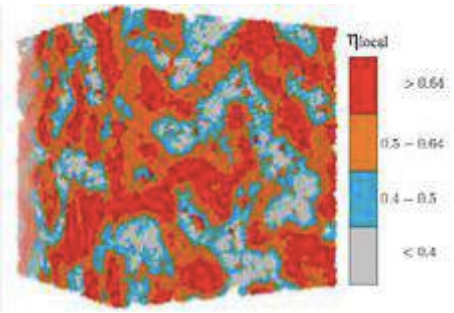

Figure 1: The mesoscale model of C–S–H (at η=052) showing the local packing fractions distribution

RESULTS AND DISCUSSION

In our model, the complex pore network and the structural heterogeneities naturally emerge from the short range cohesive interactions typical of nanoscale cement hydrates and from the non-equilibrium conditions under which C–S–H densifies during cement setting. The scattering intensity, pore size distribution (related to water and nitrogen adsorption/desorption exp.), local volume fractions, indentation modulus obtained from our simulations are compared with experiments, and provide a first consistent characterization of the elusive meso-scale structure of C–S–H.

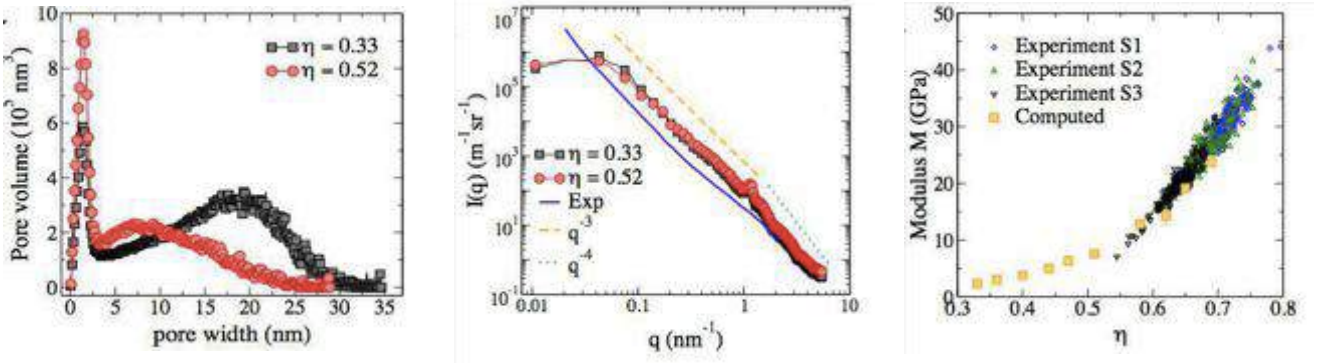

Figure 2: (left) Pore size distributions, (center) Small–Angle Scattered intensity, (c) Nanoindentation modulus for mesoscale model of C–S–H at various packing fractions

CONCLUSIONS

Calcium-silicate-hydrate nanoscale gel (C–S–H) is the main binding agent in cement and concrete, crucial for the strength and the long-term evolution of the material. We use a statistical physics framework for aggregating nanoparticles and numerical simulations to obtain a first quantitative model for such a complex material. The extensive comparison with experiments ranging from SANS, adsorption/desorption of N_2 and water to nano-indentation provide new, fundamental insights into the microscopic origin of the properties measured. Unraveling such links in cement hydrates can be groundbreaking and controlling them can be the key to smarter mix designs of cementitious materials.

References

[1] K. Ioannidou, K. J. Krakowiak, M. Bauchy, C. G. Hoover, E. Masoero, S. Yip, F. Ulm, P. Levitz, R. J.-M. Pellenq and E. Del Gado, *Proceeding of the National Academy of Science of the United States*, accepted

[2] M.J. Abdolhosseini Qomi, K.J. Krakowiak, M. Bauchy, K.L. Stewart, R. Shahsavari, D. Jagannathan, D.B. Brommer, A. Baronnet, M.J. Buehler, S. Yip, F.-J Ulm, K.J. Van Vliet, R.J-.M. Pellenq, *Nature Communication*, 2014, 5:4960 | DOI: 10.1038/ncomms5960 |

NON-WASHBURN IMBIBITION: MODELLING RESULTS AND EMERGING ISSUES

Yulii Shikhmurzaev[1]
[1]*School of Mathematics, University of Birmingham, Birmingham, United Kingdom*

Summary As discovered experimentally two decades ago, the wetting front propagating through some porous media can exhibit two very different regimes distinctly visible in the log-log plot: the front covers two thirds of its eventual propagation distance in just a few minutes and then it takes many hours for it to advance over the remaining third. The first of these regimes is well described by any of the Washburn-type models, with the differences between them being insignificant on the log-log plot, whilst the second one is different both quantitatively and qualitatively. A new approach to the modelling of the dynamics of wetting fronts in porous media is formulated which makes it possible to describe simultaneously both regimes as well as the transition between them. A fundamental issue with Darcy's law for essentially 2D flows is brought to light and a new class of models required to address it is discussed.

INTRODUCTION

In essence, the problem of the Darcy-scale description of how a wetting front propagates through a porous medium boils down to formulating the dynamic boundary condition on the free interface confining the domain where the bulk equations, namely Darcy's law and the continuity equation, operate. The kinematic boundary condition stating that the interface propagates with the (volume-averaged) velocity of the fluid is obvious, so it is only the dynamic boundary condition that is required to complete the problem formulation. This problem is conventionally addressed by relating the fluid's velocity to the capillary pressure at the surface of the menisci which collectively form the wetting front. The origins of this approach can be traced back to Washburn's 1921 paper [1], where the author considered the Poiseuille flow driven by the pressure gradient between the supply reservoir and the meniscus whose surface is bent to meet the wall of the capillary at a prescribed contact angle. Variants of this approach include the use of velocity-dependent (dynamic) contact angle in the Poiseuille formula instead of the static one used by Washburn as well as longitudinally profiled (as opposed to cylindrical) capillaries. These models collectively referred to as Washburn-type models have broadly similar properties and adequately describe a host of phenomena observed in experiments [2].

However, experiments show that in some porous media, notably in the sandstone-like ones in controlled experiments represented by porous matrices made of densely packed spherical beads [3, 4], there appears another regime of the wetting front propagation. Pictorially, it looks as follows: after a very short period of rapid advancement, when the wetting front covers approximately two thirds of its eventual propagation distance, its motion slows down so that it takes many hours for the front to cover the remaining third and reach its equilibrium position. Importantly, in this last regime the Darcy-scale propagation of the wetting front consists of 'stick-slip' unsteady motion of individual menisci. This 'anomalous' regime of the wetting front propagation holds the key to such phenomena as the trapping of ganglia of oil or carbon dioxide sequestration by a porous matrix and the problem of removing the former and retaining the latter. With regard to the anomalous dynamics of the wetting front the Washburn-type models not only appear to be inadequate, the very approach offers no conceptual framework that would allow one to generalize these models to describe the regime in question.

A NEW APPROACH

The key idea of the new approach to the modelling of wetting fronts in porous media is to consider the modes of motion that the individual menisci collectively forming the wetting front go through as the front advances on the Darcy scale. The two main modes of motion are: (a) the wetting mode, where in essence the meniscus moves as a whole until the contact line formed at the intersection of the free surface and the pore wall gets pinned by asperities or at the throat-chamber junction, and (b) a threshold mode, where, with the pinned contact line, the meniscus bends as the pressure on the free surface mounts until some critical values of the meniscus' parameters are reached and it is released back into the wetting mode. Schematically, the modes of motion are illustrated in Figure 1. The Darcy-scale propagation of the wetting front results from the 'dynamic average' of the pore-scale advancements of individual menisci which intermittently go through different modes of motion with the main contribution coming from the mode in which menisci spend more time. From the viewpoint of the new approach, all Washburn-type models appear as variations on the wetting mode of motion and hence unable to describe the phenomenon where, as observed experimentally, the pinning and de-pinning of the contact lines of individual menisci play the key role. The new approach provides a conceptual framework for incorporating processes occurring on the pore scale and, importantly, offers a methodology for constructing mathematical models of increasing complexity. The main difficulty in the way is the averaging in the situations where more than two mode of motion are to be considered and non-isotropic porous matrices are involved.

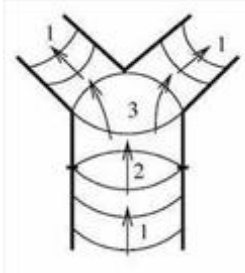

Figure 1. 2D illustration of modes of motion. 1: wetting mode; 2: threshold mode.

The parallel treatment of the wetting and threshold modes means that one has to consider simultaneously the direct and the conjugate problem where the latter is needed to calculate the 'termination pressure' and contact angle, i.e. the maximum values of the pressure and the contact angle corresponding to the threshold mode. To describe the anomalous regime of the wetting front propagation [3], the simplest model developed in the framework of the new approach [5] was generalized to account for the possibility of the menisci's release from the threshold back into the wetting mode as a result of fluctuations of pressure on their surfaces coming, for example, from the motion of the neighbouring menisci. This effect is accounted for by assuming that, for subcritical values of the contact angle, the time spent by the meniscus in the threshold mode is proportional to the difference between the critical and the maximum value the contact angle reaches in the threshold mode for the current position of the wetting front. Figure 2 shows the application of the resulting model to one of the sets of data from [3]. One can clearly see the two distinct regimes of the wetting front propagation with the data indicating that no simple empirical power-law dependence would be able to describe them. In contrast, the developed theory, where the interface formation model [6] is used for the dynamic wetting process on the pore scale and the spherical-cap approximation for the meniscus' shape is applied for both the wetting and the threshold mode, describes the whole experimental curve, from the onset of the motion in the Washburn regime to the moment when the interface reaches its equilibrium state.

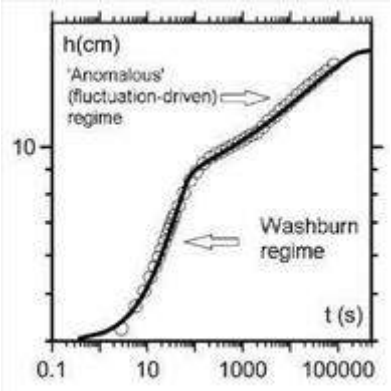

Figure 2. Open circles: experimental data for the capillary rise through the packed 253 micron-sized beads [3]; solid line: theory.

AN EMERGING CLASS OF MODELS/PROBLEMS

The developed theory is straightforward to apply for unidirectional flows for which most experiments are performed but when it comes to essentially 2D and 3D problems, it highlights an issue with the classical Darcy model itself in its application to such flows. In the case where, on the Darcy scale, a fraction of the wetting front moves while the neighbouring fraction remains at rest it becomes necessary to consider flows in domains with corners greater than 180 degrees. Such problems also occur, for example, in a situation where a drop sitting on a porous substrate is imbibed into the latter: the free surface of the drop and the boundary of the substrate will then form a corner of 270 degrees and the fluid will pass round it. In such cases, the classical Darcy model gives rise to singularities in the velocity field. Although integrable, such singularities become unacceptable from the physical standpoint for the problems involving moving interfaces since it is the velocity and not its integral that features in the boundary conditions on such interfaces. Therefore, these singularities have to be regularized by generalizing the model used to describe the bulk flow. The issue here is that the singularity in question occurs solely due to the flow geometry so that no generalization, like Brinkman's model, which would alter the Darcy model for unidirectional flows would be acceptable.

An analysis of the issue has shown that the only generalization that would (a) remove the singularity and (b) preserve the Darcy model for unidirectional flows for which it is well justified is a model where the permeability of the porous matrix is a function of the curvature of the streamlines of the flow that passes through this matrix. By considering a flow in a bent channel as a representative analogy of the flow in a porous medium, one can show that, indeed, the permeability decreases as the curvature of the streamlines goes up. It can be shown that an algebraic decrease is sufficient to regularize the flow velocity. This analysis introduces a new class of models/problems for the fluid flows in essentially 2D and 3D configurations where, for a given porous matrix, the permeability is not a prescribed constant but a function to be found simultaneously with the flow. A simple example illustrating this class of problems is considered.

References

[1] Washburn, E.W.: The dynamics of capillary flow. *Phys. Rev.* **17**:273-283, 1921.

[2] Alava, M., Dubé, M., Rost, M.: Imbibition in disordered media. *Adv. Phys.* **53**:83-175, 2004.

[3] Delker, T., Pengra, D.B., Wong, P.-z.: Interface pinning and the dynamics of capillary rise in porous media. *Phys. Rev. Lett.* **76**:2902-2905, 1996.

[4] Lago, M., Araujo, M.: Capillary rise in porous media. *J. Colloid & Interf. Sci.* **234**:35-43, 2001.

[5] Shikhmurzaev, Y.D., Sprittles, J.E.: Wetting front dynamics in an isotropic porous medium. *J. Fluid Mech.* **694**:399-407, 2012.

[6] Shikhmurzaev, Y.D.: Capillary Flows with Forming Interfaces/ Boca Raton, USA 2007.

FREEZING SOLUTIONS AND COLLOIDAL SUSPENSIONS

M. Grae Worster *[1], J.S. Wettlaufer[2, 3, 4], and S.S.L. Peppin[2]
[1]*Department of Applied Mathematics and Theoretical Physics, University of Cambridge, CMS Wilberforce Road, Cambridge CB3 0WA, UK*
[2]*Yale University, New Haven, CT 06520, USA*
[3]*Mathematical Institute, University of Oxford, Oxford OX2 6GG, UK*
[4]*Nordita, Royal Institute of Technology and Stockholm University, SE-10691 Stockholm, Sweden*

Summary We present a theoretical model of solidification of a colloidal suspension when a partially frozen region (mushy layer) forms. The relative motion between solvent and colloidal particles within the mushy layer can be described as diffusion of particles, as regelation of the particles or as flow of the interstitial solvent through the porous matrix of particles driven by a cryosuction pressure. We illustrate these ideas using similarity solutions of the governing equations.

INTRODUCTION

When mixtures are frozen, their constituents tend to become segregated. This is equally true whether the mixture is a molecular solution or a suspension of solid particles. The physical character of the segregated, partially frozen material can differ markedly between solutions and suspensions (figure 1), though similar structures to those produced from solutions (figure 1a) are sometimes seen when the suspension is dilute and colloidal (figure 1b).

Any segregation requires relative motion (transport) between the constituents. In the case of solutions, such relative motion is typically described by Fickian diffusion, with fluxes proportional to concentration gradients. In the case of dense suspensions, particularly those near to being close-packed, such relative motion is typically described by Darcy's law of fluid motion through porous media, with fluxes proportional to pressure gradients. For example, in the case illustrated by figure 1c, water must flow from the upper layer of original, colloidal suspension, through the intermediate porous medium formed by the compacted suspension, whether unfrozen or partially frozen, to form the ice lenses below.

Peppin, Elliott & Worster [1] showed that Fickian diffusion and Darcy flow are equivalent and are end members of a unified thermodynamic model of relative motion. They used their formulation [2] to calculate freezing rates and segregation at planar interfaces of ice growing from suspensions of different particle sizes, representing the two extremes of dilute solutions and concentrated suspensions. Both are prone to constitutional supercooling in a layer of rejected solute (colloid), which can lead to morphological instability of the interface [3, 4], as originally quantified for solutions by Mullins & Sekerka [5].

Here we extend this unified thermodynamic approach to the solidification of mixtures by analysing the formation of mushy layers from colloidal suspensions, simply using a phase diagram appropriate for colloidal suspensions and following the approach established for solutions [6]. The unified approach allows connections to be made between studies of solidification of binary alloys and studies of freezing in soils through the intermediate cases of colloidal suspensions, particularly the equivalence of solute diffusion to regelative fluxes in partially frozen systems.

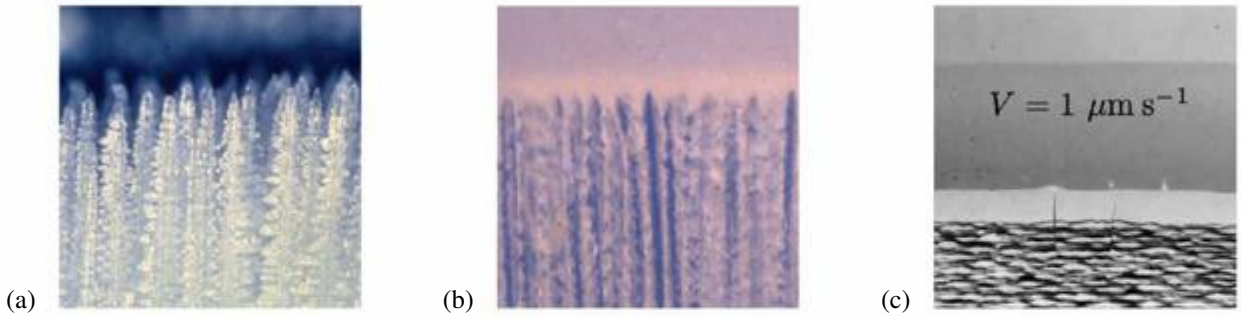

Figure 1: Segregation during solidification upwards of solutions and suspensions. (a) Dendritic microstructure of ammonium chloride solidifying from aqueous solution (photo MA Hallworth). (b) Dendritic microstructure of ice solidifying from a dilute aqueous suspension of bentonite (5% by mass) (photo SSL Peppin). (c) From bottom to top, there is a layer of ice lenses (dark coloured) separating lenses of frozen colloid (light coloured); a continuous layer of frozen colloid (also light coloured); a thicker layer of unfrozen, compacted colloid (dark grey); all forming from an aqueous suspension of alumina (27% by volume of approximately 3μm particles) (uppermost, light grey layer)[7].

*Corresponding author. Email: mgw1@cam.ac.uk

MATHEMATICAL FORMULATION

Central to the mathematical formulation is an expression for the osmotic pressure

$$\Pi(\phi, R) = \phi \frac{k_B T_m}{v_p(R)} z(\phi), \tag{1}$$

where ϕ is the volume fraction of solute (colloid), k_B is Boltzmann's constant, T_m is the absolute freezing temperature of the solvent, $v_p = \frac{4}{3}\pi R^3$ is the (effective) particle volume for each element of the solute of (effective) radius R and $z(\phi)$ is a dimensionless 'compressibility factor' that accounts for particle–particle interactions. From the osmotic pressure, the equilibrium freezing temperature (liquidus) is calculated from the Clausius-Clapeyron equation and the diffusion coefficient is determined from the generalised Stokes-Einstein relation as

$$T_f(\phi, R) = T_m \left[1 \nearrow \frac{\Pi(\phi, R)}{\rho L}\right] \qquad \text{and} \qquad D(\phi, R) = \phi \frac{k}{\mu} \frac{\partial \Pi(\phi, R)}{\partial \phi} \tag{2}$$

respectively, where $k(\phi, R)$ is the permeability of the suspension, μ is the dynamic viscosity of the solvent, ρ is density and L is the latent heat of fusion. The solute flux, both in unfrozen and partially frozen (mushy) colloid, can be written in three equivalent forms as

$$\nearrow \mathcal{D}(\phi) \frac{\partial \phi}{\partial z} = \phi \frac{k}{\mu} \frac{\partial p}{\partial z} = \phi \frac{k}{\mu} \frac{\rho L}{T_m} \frac{\partial T_f}{\partial z}, \tag{3}$$

where χ is the volume fraction of unfrozen colloid and $p = P \nearrow \Pi$ is the 'pervadic pressure' [1], which is the difference between the bulk pressure P and the osmotic pressure and can be interpreted as the pore pressure in a close-packed colloid or porous medium. In solutions and dilute colloidal suspensions, it is convenient to work with and think in terms of the diffusive flux (3a) but as the close-packed limit is approached the diffusivity diverges while the concentration gradient tends to zero and it is more convenient to work with and think in terms of the Darcy Flux (3b). Within a mushy region $T = T_f$ and the diffusive flux is equal to the regelative flux (3c) driven by 'thermodynamic buoyancy' [8].

RESULTS

We have used these fundamental ideas to determine similarity solutions for solidification from a cooled boundary within partially frozen colloidal suspensions (e.g. figure 2). As particle size increases, the interfacial concentration increases and the concentration more quickly reaches the close-packed limit within the mushy layer.

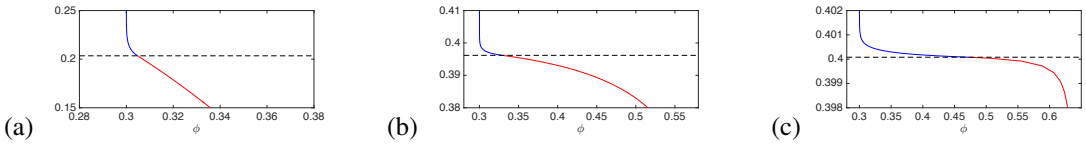

Figure 2: p l v l f n (l n n n) f n n f v l p n f p l z ( ) 0 5n , (b) 2n n ( ) 10n n v n f –l q n f (l n): b l w ( ); nf z n ll b v (bl) N ff n x l

CONCLUSIONS

Regelation within a partially frozen colloidal suspension or soil results from a balance between thermodynamic buoyancy, driving particles towards warmer temperatures, and viscous drag forces associated with flow through the partially frozen porous medium. It is fundamentally equivalent to diffusion of solute or of particles within a molecular solution or dilute suspension of small particles. We have developed a unified model that illustrates this equivalence and provides a means of computing the characteristics of freezing colloids of arbitrary particle size and concentration.

References

[1] Peppin, S.S.L., Elliott, J.A.W. & Worster, M.G.: Pressure and relative motion in colloidal suspensions. Phys. Fluids 17(5), art. no. 053301, 2005.
[2] Peppin, S.S.L., Elliott, J.A.W. & Worster, M.G.: Solidification of colloidal suspensions. J. Fluid Mech. 554, 147–166, 2006.
[3] Peppin, S.S.L., Worster, M.G. & Wettlaufer, J.S.: Morphological instability in freezing colloidal suspensions. Proc. Roy. Soc. A 463, 723–733, 2007.
[4] Peppin, S.S.L., Wettlaufer, J.S. & Worster, M.G.: Experimental verification of morphological instability in freezing aqueous colloidal suspensions. Phys. Rev. Lett. 100(23), 238301, 2008.
[5] Mullins, W. W. & Sekerka, R. F.: Stability of a planar interface during solidification of a dilute binary alloy. J. Appl. Phys. 35, 444–451, 1964.
[6] Worster, M.G.: Solidification of an alloy from a cooled boundary . J. Fluid Mech. 167, 481–501, 1986.
[7] Anderson, A.M. & Worster, M.G.: Periodic ice banding in freezing colloidal dispersions. Langmuir 28(48), 16512–16523, 2012.
[8] Rempel, A.W., Wettlaufer, J.S. & Worster, M.G.: Interfacial premelting and the thermomolecular force: thermodynamic buoyancy. Phys. Rev. Lett. 8708(8), 8501, 2001

INTERSECTING FAULTS SIMULATION FOR RESERVOIR_GEOMECHANICAL MODELS

[1]Zahra Loftian, [1]Jean H. Prevost[(a)] and [2]N. Sukumar
[1]*Department of Civil and Environmental Engineering, Princeton University, Princeton, NJ, USA*
[2]*Department of Civil and Environmental Engineering, UC Davis, Davis, CA, USA*

Summary The proposed approach is a marked departure from the FEM for the modeling of three-dimensional faults. Significant meshing difficulties arise when faults (multiple) are modeled using the FEM, where the mesh has to conform to the geometry of the fault(s) and hence a structured mesh cannot be used. Unstructured mesh generation (triangles in 2D and tetrahedra in 3D) is needed for the FEM. On using the X-FEM, a structured mesh suffices and the faults can arbitrarily cut the elements in the mesh. This advantage of the X-FEM has been leveraged for many applications in fracture mechanics, and in [2] we have shown that it is equally advantageous for modeling faults. In this paper we focus on modeling intersecting faults.

ABSTRACT

Faults are geological entities with thicknesses (of the order cm) several orders of magnitude smaller than the grid blocks (of the order 10 m) typically used to discretize reservoir and/or over-under-burden geological formations. Introducing faults in a complex reservoir and/or geomechanical mesh therefore poses significant meshing difficulties. In this paper, we consider the strong-coupling of solid displacement and fluid pressure in a three-dimensional poro-mechanical (reservoir-geomechanical) model. We introduce faults in the mesh without meshing them explicitly, by using the extended finite element method (X-FEM) in which the nodes whose basis function support intersects the fault are enriched within the framework of partition of unity [1]. For the geomechanics, the fault is treated as an internal displacement discontinuity that allows slipping to occur using a Mohr-Coulomb type criterion. For the reservoir, the fault is either an internal fluid flow conduit that allows fluid flow in the fault as well as to enter/leave the fault or is a barrier to flow (sealing fault). For internal fluid flow conduits, the continuous fluid pressure approximation admits a discontinuity in its normal derivative across the fault, whereas for an impermeable fault, the pressure approximation is discontinuous across the fault. Equal-order displacement and pressure approximations are used.

The proposed approach is a marked departure from the FEM for the modeling of faults. Significant meshing difficulties arise when faults (multiple) are modeled using the FEM, where the mesh has to conform to the geometry of the fault(s) and hence a structured mesh cannot be used. Unstructured mesh generation (triangles in 2D and tetrahedra in 3D) is needed for the FEM. On using the X-FEM, a structured mesh suffices and the faults can arbitrarily cut the elements in the mesh. This advantage of the X-FEM has been leveraged for many applications in fracture mechanics, and in [2] we have shown that it is equally advantageous for modeling faults.

In the X-FEM, only the nodes whose basis function support intersects the fault are enriched. Modeling many (tens or even hundreds) faults is relatively straightforward since the faults are never meshed and hence they can be placed within the reservoir mesh by simply identifying their plane(s). However, as we pointed out in [2], there existed a limitation in our implementation at the time, namely, we could not accommodate nonplanar faults in 3D, which presents significant additional challenges. This has been the subject of ongoing research and we have now succeeded in overcoming this limitation, and this is the focus of this communication.

As an example, we consider a three-dimensional cube $40\ \text{m} \times 40\ \text{m} \times 40\ \text{m}$ that is cut by two intersecting faults at angles $\alpha_1 = -35^0$ and $\alpha_2 = 55^0$, respectively. The rock permeability used is $k_{\text{rock}} = 3.33 \times 10^{-14}\ \text{m}^2$, and a uniform inflow fluid flux $q_f = 10^{-6}\ \text{m}^3/\text{s}$ is prescribed on the top boundary. No flow is assumed to take place on all lateral boundaries, and a free-flow boundary is used at the bottom where the fluid pressure $p_f = 0$. Both fault are assumed as acting as flow conduits, and are assigned a thickness $t = h \times 10^{-2} = 0.02\,\text{m}$ and their transverse and longitudinal permeability are chosen as $k_n = 10^{-3} k_{\text{rock}}$ and $k_t = 10^3 k_{\text{rock}}$, respectively. The structured mesh is shown in Fig.1a, and contains 1,337 nodes and 1,000 hexahedral elements. The unstructured mesh is shown in Fig. 2a and contains 3,223 nodes and 16,281 tetrahedral elements. The resulting Darcy fluid velocities are shown in Fig. 1b and Fig. 2b. Note that most of the flow is taking place along the fault planes of both faults due to their high longitudinal permeability (and low transverse permeability).

[a)] Corresponding author. Email: prevost@princeton.edu

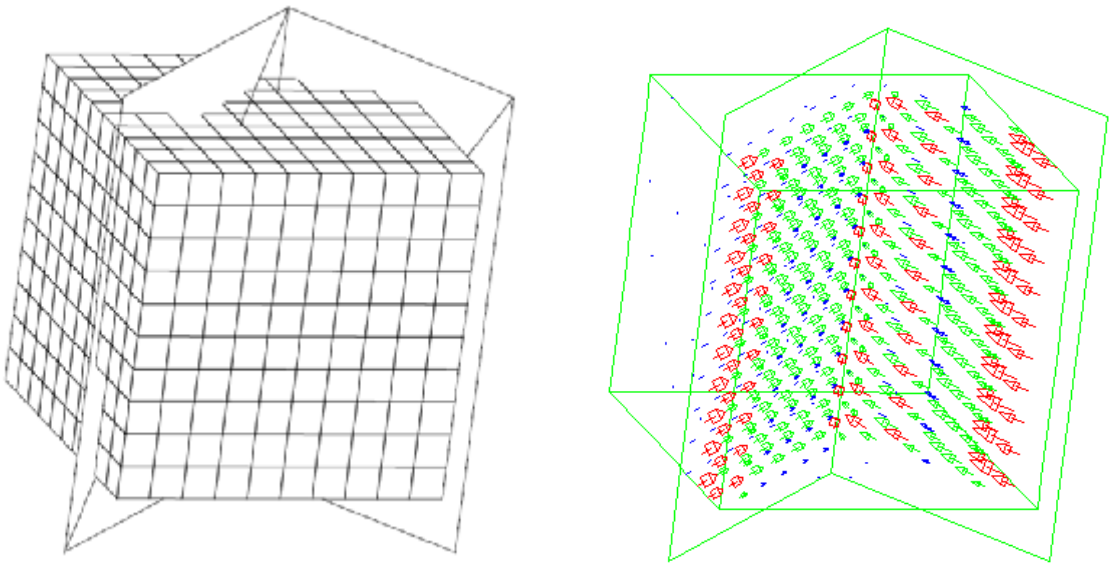

Fig. 1: Extended FE solution for the fluid flow in a 3D domain. (a) Structured mesh (two intersecting faults are present); (b) Darcy velocities; maximum velocity is 4.5×10^{-10} m/s.

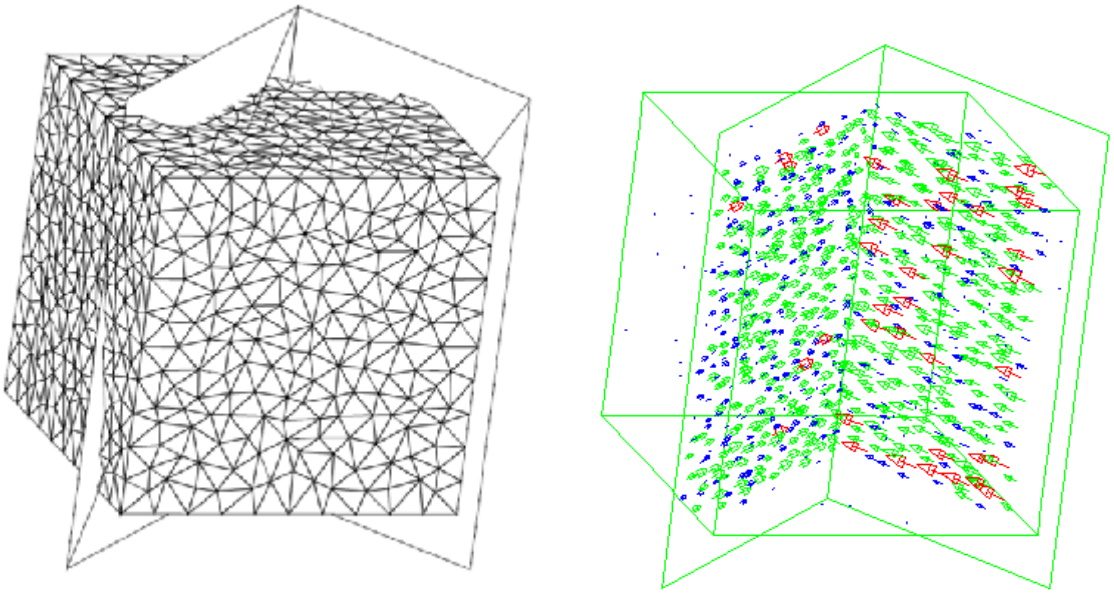

Fig. 2: Extended FE solution for the fluid flow in a 3D domain. (a) Unstructured mesh (two intersecting faults are present); (b) Darcy velocities; maximum velocity is 4.5×10^{-10} m/s.

References:

[1] Melenk, J.M., Babuška, I., 1996. The partition of unity finite element method: Basic theory and applications. *Computer Meth. Appl. Mech. Eng.* 139, 289-314.

[2] Prevost, J.H., Sukumar, N., 2016. Faults simulations for three-dimensional reservoir-geomechanical models with the extended finite element method. *J. Mech. Phys. Solids*. 86, 1-18.

MULTISCALE INVESTIGATION OF IMBIBITION, DRAINAGE AND DRYING IN MACROPOROUS MEDIA

Sreeyuth Lal[1,2 a)], Lily Poulikakos[3], Manfred Partl[3], Dominique Derome[1] & Jan Carmeliet[1,4]
[1]*Laboratory for Multiscale Studies in Building Physics, Empa, Switzerland.*
[2]*Department of Civil, Environmental and Geomatic Engineering, ETH Zurich, Switzerland.*
[3]*Laboratory for Road Engineering/Sealing Components, Empa, Switzerland.*
[4] *Chair of Building Physics, ETH Zürich, Switzerland.*

Summary We present the investigation of imbibition, drainage and drying in porous asphalt (PA), a macroporous material with a wide range of pore sizes ranging from microns to millimeters. In macroporous media, due to the presence of large pores, gravity becomes the most important driving force for liquid transport and consequently the transport behavior of PA is very different from that of microporous materials. To obtain a fundamental understanding of a highly complex media like PA, experiments, simulations and modeling are performed at a variety of material scales to investigate the physics of air and water transport during imbibition, drainage and drying in PA with an overall objective of predicting the residence time of water in PA under specific environmental conditions.

INTRODUCTION

A comprehensive understanding of fluid transport in porous media is of great commercial, built and natural environmental and scientific interest. A variety of commercial activities like enhanced oil recovery from seabed reservoirs, drying of paper pulp, water management in polymer electrolyte membrane fuel cells, cooling by porous heat exchangers etc. are directly dependent on the accurate prediction of transport properties in porous media. From a scientific point of view, transport in porous media is a challenging area to understand due to the co-occurrence of many physical, thermal, chemical and biological processes.

In macroporous media, due to the presence of large pores in the range of millimeters, gravity becomes the most important driving force for liquid transport. Additionally, in the large pores, gaseous transport is enhanced and consequently, continuum-scale transport properties such as permeability curves cannot be calculated in a straightforward manner without considering additional complexities. Moreover, pore space characteristics such as pore size distribution, tortuosity, connectivity etc. can influence both the rate of evaporation of the liquid within the material and the subsequent transport of the evaporated gas by diffusion and convection, but the degree of their influences may be different in microporous and macroporous media.

This study focuses on the investigation of imbibition, drainage and drying in porous asphalt (PA), a macroporous material with a wide range of pore sizes ranging from microns to millimeters. PA is used as the surface layer of roads to allow the seepage of water and thereby prevent aquaplaning and splash-spray effects during and after rain events. PA has a porosity of approximately 20% and is a composite material made from fine and coarse mineral aggregates, a bituminous binder and air voids. Due to its high permeability, a large area of the internal structure of PA is exposed to water after a rain event. This leads to an accelerated deterioration of the material since water destroys the adhesion between the bitumen and the aggregates, a phenomenon called stripping. Therefore, in order to design longer lasting PA pavements, it is imperative to obtain a comprehensive understanding of the residence time of water in PA under typical environmental loadings.

METHODOLOGY

The occurrence of typical transport phenomena such as gravity-driven drainage, capillary uptake [1], forced convective drying [2] and thermal drying is experimentally investigated by subjecting PA to downscaled recreations of various environmental loadings in laboratory conditions. Neutron radiography (NR) imaging is used to visualize the spatial and temporal distributions of water in PA during these experiments. The three-dimensional pore space of all the PA specimens used in these experiments is characterized by high-resolution X-ray microcomputed tomography (X-ray μ-CT). Various pore space characteristics such as pore diameter distribution, connectivity and tortuosity are clearly identified from the 3D images. By carefully combining the moisture content distribution in the specimens as observed from NR images with the 3D structure of the specimens as observed from X-ray μ-CT images, a deeper understanding of the physics of moisture flow in PA is obtained.

From the NR experiments, a macroscopic picture of the influence of high wind speeds on drying in PA is obtained. However, further investigations are required to conclusively establish the role of wind. It is known that wind flow above a wet macroporous material can accelerate the drying of the material in two ways: by thinning the air boundary layer and by air penetration into the material. To investigate the first phenomenon i.e. boundary layer above the air-PA interface, wind tunnel experiments are carried out on large slabs of PA [2]. Particle imaging velocimetry (PIV) is used to visualize the wind

[a)] Corresponding author. Email: lals@ethz.ch

boundary layer as well as the turbulent structures that are active just above the air-PA interface at different wind speeds. To investigate the second phenomenon i.e. air entrainment into PA, single-phase computational fluid dynamics (CFD) simulations of airflow above a real PA geometry are performed. The results from some of the investigations are presented in figure 1.

Having obtained a clear picture of the transport mechanisms that are critical to predict the residence time of water in PA, the next step is to model the drainage and drying behaviors of a fully saturated PA using pore network models, in which the pore space of PA, obtained from X-ray μ-CT scans, is converted to an idealized geometry in which the large voids, the pores, are connected to each other by constrictions, the throats. Multiphase flow is modeled in this idealized geometry to calculate macroscale transport properties such as relative permeability curves and capillary pressure curves. These macroscale properties are then used as input parameters for modeling the drying of PA as a continuum process which has the major advantage of being computationally inexpensive for carrying out various parametric studies.

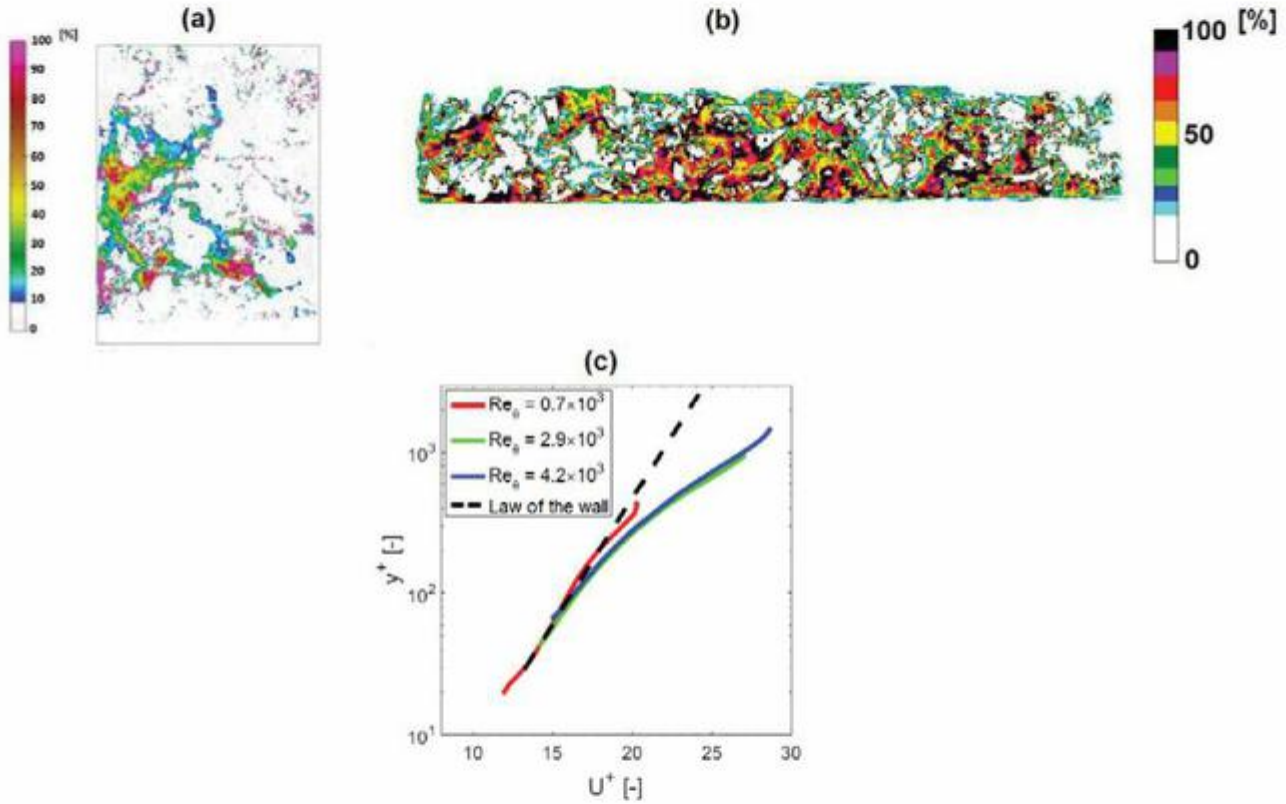

Figure 1: Investigation of transport phenomena in PA at various material scales; (a) capillary uptake in a PA specimen of dimensions 45×25×10 mm^3, (b) gravity-driven imbibition in a PA specimen of dimensions 180×35×12 mm^3 and (c) wind boundary layer above a PA specimen of 2400×400×30 mm^3.

References

[1] Lal, S., Poulikakos, L.D., Gilani, M.S., Jerjen, I., Vontobel, P., Partl, M.N., Carmeliet, J.C. and Derome, D., 2014. Investigation of Water Uptake in Porous Asphalt Concrete Using Neutron Radiography. Transport in Porous Media, 105(2), pp.431-450.

[2] Lal, S., Lucci, F., Defraeye, T., Poulikakos, L., Partl, M., Derome, D. and Carmeliet, J., 2015. Convective drying of a macroporous medium: a comparison of original porous asphalt geometry with randomized Kelvin cells. Bulletin of the American Physical Society, 60.

A MULTI-SCALE STUDY ON ADSORPTION INDUCED DEFORMATION OF HYBRID POROUS MATERIALS

Mingyang Chen[1,2a)], Robert A. Guyer[3], Dominique Derome[2], Jan Carmeliet[1,2]
[1] *ETH Zürich, Swiss Federal University of Technology Zürich, Zürich, Switzerland*
[2] *EMPA, Swiss Federal Laboratories for Materials Science and Technology, Dübendorf, Switzerland*
[3] *Solid Earth Geophysics Group, Los Alamos National Laboratory, New Mexico, United States*

Summary In this paper, the coupled effect between adsorption and deformation of hybrid porous materials are studied with the help of a multi-scale model. The Grand Canonical Monte Carlo (GCMC) [1] and Molecular Dynamic (MD) [2] simulations are employed to characterize the micro-pores. On the other hand, the meso-pores are modelled by the Derjaguin-Broekhoff-de Boer (DBdB) theory. Then the macroscopic properties of the material are modelled using the Dependent Domain Theory (DDT). The result shows that strong coupling effect between adsorption and deformation exists in the hybrid porous materials and it has significant influence on the macroscopic behaviour of the materials.

INTRODUCTION/METHODOLOGY

Adsorption originates at the molecular scale from the interactions between the atoms of the solid skeleton and the molecules of the fluid. When the size of the pores is in the order of the range of the molecular interactions (micro or nano-porous materials), a mechanical pressure arises orthogonal to the porous interface leading to sorption induced deformations. Besides, in a pore of nanometer size, fluid molecules are not in their bulk state anymore since they interact with the atoms of the solid. For such microporous media, conventional poro-mechanics breaks down. To address this problem, a multi-scale model is constructed to investigate the coupled behaviour between adsorption and deformation of hybrid porous materials which contain both micro-pores and meso-pores. For the micro-pores, the adsorption-deformation character is modelled using atomistic modelling method, including Grand Canonical Monte Carlo (GCMC) [1] and Molecular Dynamic (MD) [2] simulations. For the meso-pores, the adsorption-deformation character is modeled using the Derjaguin-Broekhoff-de Boer (DBdB) theory [3]. Then the macroscopic properties of the material are assembled using the Dependent Domain Theory (DDT), in which the material behavior is considered to be the global outcome of the interaction of elements with different pore characteristics (size, orientation)[4]. Based on the results acquired from atomistic modelling and DBdB theory, the behavior of each element is modelled using a coupling matrix between the mechanical variables (stress and strain) and the adsorption parameters (chemical potential and fluid content).

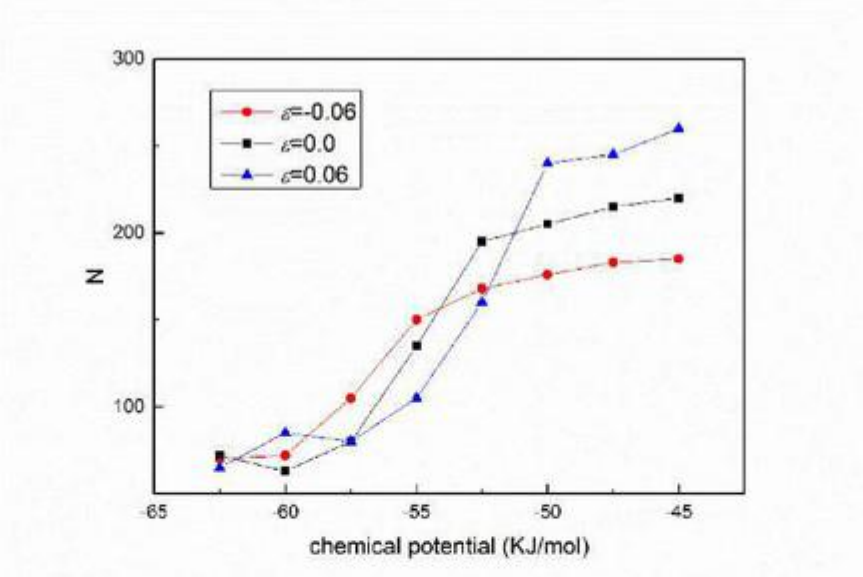

Figure 1: Adsorption isotherms acquired from hybrid GCMC/MD simulation

SIMULATION RESULTS

Figure 1 shows the adsorption isotherms of a single micro-pore under different strains, from which we can derive the relationship between strain and critical chemical potential. Figure 2 shows the relationship between the strain and adsorption amount and adsorption induced stress. With the help of above relationships, we have derived the coupling matrix between the

[a)] Corresponding author. Email: mingyang.chen@arch.ethz.ch.

mechanical variables and the adsorption parameters for micro-pores. By combining with the DBdB theory for meso-pores, the constitutive relationship for basic element of DDT theory can be determined. The simulated macroscopic behaviour of the material is shown in Figure 3.

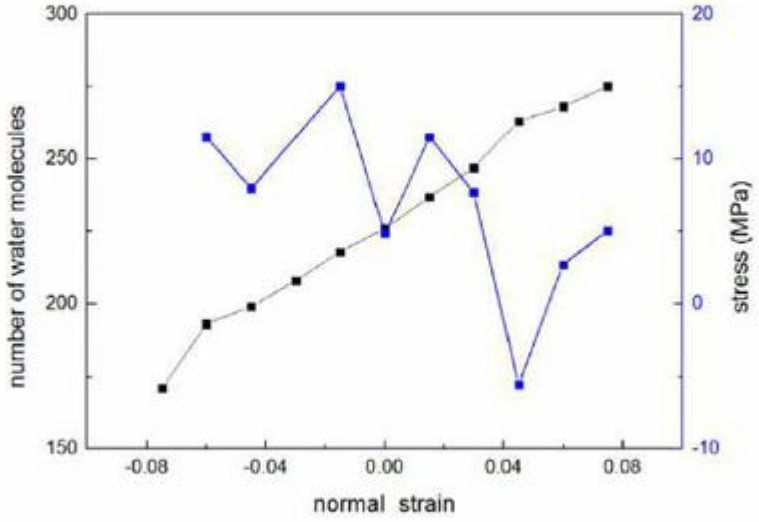

Figure 2: Influence of deformation on the adsorption amount and adsorption induced stress

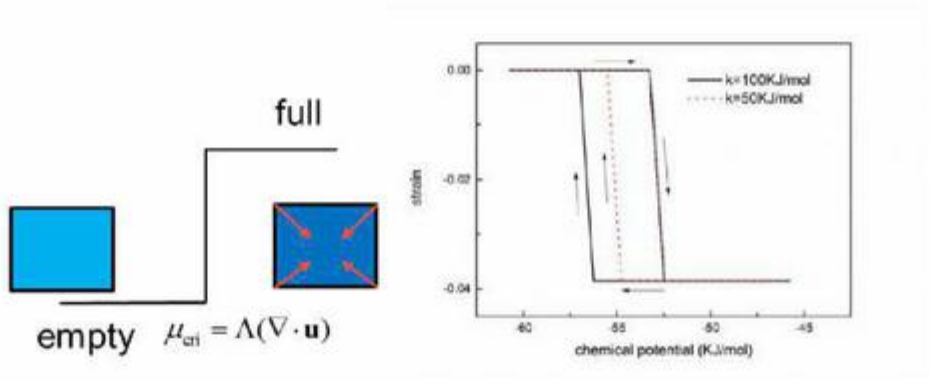

(a) (b)

Figure 3 (a) Basic element is Dependent Domain Theory. (b) Isotherms for adsorption induced strain.

CONCLUSIONS

The simulation results show both the adsorption induced deformation and mechano-sorptive effect. In addition mechanical and adsorption hysteresis are observed. It is shown that the hysteresis originates from capillary condensation for meso-pores and from coupled behaviour at lower scale for micro-pores. Strong coupling effects between adsorption and deformation are present in the hybrid porous materials and have a significant influence on the macroscopic behaviour of the materials.

References

[1] Bonnaud, P. a, Coasne, B. and Pellenq, R. J.-M. Molecular simulation of water confined in nanoporous silica. J. Phys. Condens. Matter 22, 284110, 2010.

[2] Kulasinski, K., Guyer, R., Derome, D. and Carmeliet, J. Poroelastic model for adsorption-induced deformation of biopolymers obtained from molecular simulations. Phys. Rev. E 92, 022605, 2015.

[3] Neimark, A. V & Ravikovitch, P. I. Capillary condensation in MMS and pore structure characterization. Microporous Mesoporous Mater. 44-45, 697–707, 2001.

[4] Guyer, R. a., Kim, H. A., Derome, D., Carmeliet, J. and Tencate, J. Hysteresis in modeling of poroelastic systems: Quasistatic equilibrium. Phys. Rev. E - Stat. Nonlinear, Soft Matter Phys. 83, 1–13, 2011.

LIQUID CRYSTAL INTERFACE MICROMECHANICS

Christian Hellmich[1a)], Viktoria Vass[1], Claire Morin[2], Mehran Shahidi[3] & Bernhard Pichler[1]

[1]*Institute for Mechanics of Materials and Structures, TU Wien – Vienna University of Technology, Vienna, Austria*

[2]*Centre for Biomedical and Healthcare Engineering, Ecole Nationale Supérieure des Mines de Saint-Etienne, Saint-Etienne, France*

[3]*Institute of Structural Engineering, BOKU – University of Natural Resources and Life Sciences, Vienna, Austria*

Summary: Liquid crystals within interfaces embedded in material micro- and nanostructures are key to the creep and plastic behavior of many geo- and biomaterials. We here review latest developments in continuum micromechanics-based upscaling of viscous interface-to-creeping bulk material behavior; and we present novel results concerning the plastic effects at the bulk material scale, arising from inelastic frictional behavior of the type of interfaces mentioned before.

Inelastic deformations (such as creep or plastic strains) in hydrated geo- and biomaterials often stem sliding events in very thin layers of layered viscous fluids in an otherwise elastic matrix [10]. Recent explicit micromechanical homogenization schemes [5-7, 9] allow for upscaling the liquid crystal behavior confined to 2D interfaces, up to the 3D creep behavior of the overall bulk material. These schemes are based on limit cases of the Eshelby-type solution for eigenstressed ellipsoidal inclusions in infinite matrices [1-3] together with the compatibility requirements fulfilled in so-called Mori-Tanaka schemes [11]. They have been developed for interfaces with identical size and viscosity [5], as well as for such varying sized and viscosities [6-7, 9].

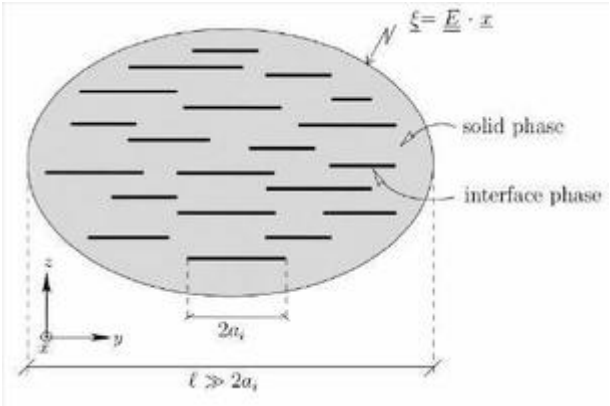

Figure 1: Representative Volume Element of flat interfaces embedded into a solid matrix

It turns out that there exists a full analogy between the customarily used spring and damper parameters of classical rheological models of the Maxwell and Kelvin-Voigt types, and the interface sizes and viscosities. In particular, the parameters related the Kelvin-Voigt representation, i.e. a serial arrangement of one spring and one damper each being positioned in parallel, appear as naturally related to the interface properties; each spring-damper unit is uniquely related to one interface family [7]. This allows for retrieval of intrinsic interface properties from a series of macroscopic creep on different bio- or geomaterials, such as bone [4] or concrete [8].

In the present contribution, we discuss the extension of this concept to elastoplasticity, the source of which is the inelastic sliding of opposite interface lips once the interface traction exceeds a critical threshold value, namely the cohesion value c. Even if this threshold is constant, the overall elastoplastic behavior turns out to be of the hardening type, as ongoing sliding events also result in increasing „frozen“ energy in the elastic matrix in-between the plastic interfaces. Interestingly, the

a) Corresponding author. Email: Christian.Hellmich@tuwien.ac.at.

corresponding macroscopic hardening modulus $\mathcal{H}$ depends on the interface density d and the Poisson's ratio v of the elastic matrix, but neither on the elastic modulus of the latter, nor on the interface size, see Figure 2.

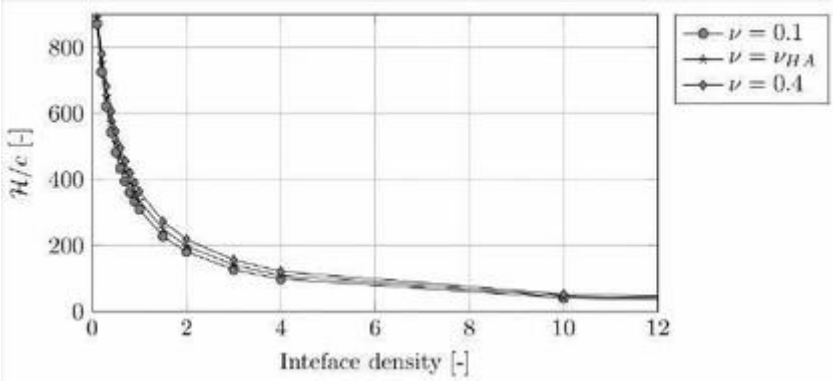

Figure 2: Dimensionless hardening modulus-interface density relation in dependency of the Poisson´s ratio of the matrix v

References

[1] Dvorak G. J., Benveniste Y.: On Transformation Strains and Uniform Fields in Multiphase Elastic Media. *Proceedings of Royal Society London A* **437**: 291-310, 1992.

[2] Pensée V., Kondo D., Dormieux L.: Micromechanical Analysis of Anisotropic Damage in Brittle Materials. *J. of Engineering Mechanics* **128**: 889-897, 2002.

[3] Pichler B., Hellmich C.: Estimation of Influence Tensors for Eigenstressed Multiphase Elastic Media with Nonaligned Inclusion Phases of Arbitrary Ellipsoidal Shape. *J. of Engineering Mechanics* **136**: 1043-1053, 2010.

[4] Qu T., Verma D., Shahidi M., Pichler B., Hellmich C., Tomar V.: Mechanics of organic-inorganic biointerfaces—Implications for strength and creep properties. *MRS Bulletin* **40**: 349-358, 2015.

[5] Shahidi M., Pichler B., Hellmich C.: Viscous interfaces as source for material creep: A continuum micromechanics approach. *European J. of Mechanics A/Solids* **45**:41-58, 2014.

[6] Shahidi M., Pichler B., Hellmich C.: Interfacial Micromechanics Assessment of Classical Rheological Models. I: Single Interface Size and Viscosity. *J. of Engineering Mechanics* 10.1061/(ASCE)EM.1943-7889.0001012, 2015.

[7] Shahidi M., Pichler B., Hellmich C.: Interfacial Micromechanics Assessment of Classical Rheological Models. II: Multiple Interface Sizes and Viscosities. *J. of Engineering Mechanics* 10.1061/(ASCE)EM.1943-7889.0001013, 2015.

[8] Shahidi M., Pichler B., Wendner R., Scheiner S., Hellmich C.: Interfacial Micromechanics Assessment of Rheological Chain Models and Their Application to Early-Age Creep of Concrete. *10th International Conference on Mechanics and Physics of Creep, Shrinkage, and Durability of Concrete and Concrete Structures*, Vienna, 2015.

[9] Shahidi M., Pichler B., Hellmich C.: How interface size, density, and viscosity affect creep and relaxation functions of matrix-interface composites: a micromechanical study. *Acta Mechanica* **227**:229-252, 2016.

[10] Vlahinić I., Thomas J. J., Jennings H. M., Andrade J. E.: Transient creep effects and the lubricating power of water in materials ranging from paper to concrete and Kevlar. *J. of Mechanics and Physics of Solids* **60**:1350-1362, 2012.

[11] Zaoui A.: Continuum Micromechanics: Survey. *J. of Engineering Mechanics* **128**: 808-816, 2002.

NUMERICAL SIMULATION OF SURFACE SUBSIDENCE AND HEAVE IN WATER SATURATED/UNSATURATED SOIL

Peter Gamnitzer and Günter Hofstetter*
Department of Basic Sciences in Engineering Science, Innsbruck University, Innsbruck, Austria

Summary A multi-phase model for predicting surface subsidence and heave caused by changes of the groundwater table is presented. The employed multi-phase model allows considering the interactions between the air flow and water flow in the water saturated/unsaturated soil regions and the nonlinear response of the unsaturated/saturated soil. Special attention is paid to the implementation of the model into a parallelized multi-phase FE code and to the efficient iterative solution of the resulting nonlinear system of equations. The application of the model is demonstrated by a large-scale 3D numerical simulation of subsidence induced by groundwater withdrawal.

MULTI-PHASE MODEL

Numerical models of different complexity and capabilities have been used for predicting surface subsidence and heave caused by changes of the groundwater table [1,2]. In the present contribution the benefits of a multi-phase model for predicting subsidence in unsaturated and saturated soil due to changes of the groundwater table are addressed. It is characterized by taking into account water and/or air flow within a deformable porous solid skeleton and coupling effects between the three phases solid, water and air [3,4,5].

The governing equations of the multi-phase model consist of (i) the linear momentum equations for the three-phase mixture, formulated in terms of the total stresses, (ii) the linear momentum equations for the fluid phases, from which Darcy's law for the artificial velocity of a particular fluid phase, relative to the soil skeleton, is derived, (iii) the kinematic equations for the soil skeleton, relating the displacements of the soil skeleton to the strains in the soil skeleton, (iv) the mass balance equations for the fluid phases, describing the balance between the inflow of a particular fluid phase into a volume element and storage of the latter in the volume element by an increase of the degree of saturation of the respective fluid phase and/or an increase of the volumetric strain of the soil skeleton and/or by an increase of the density of the respective fluid phase and (v) a number of constitutive equations, which describe the volumetric behavior of the fluid phases, the relationship between matric suction and the degree of water saturation, the permeabilities in terms of the degree of water saturation and last but not least the nonlinear behavior of the soil skeleton. The latter is represented by a multi-surface plasticity model for water saturated/unsaturated soils, which is formulated in terms of the generalized effective stress and matric suction, allowing a straightforward transition from unsaturated to saturated conditions. The smooth yield surface (Fig. 1) is formulated in terms of the effective stress with I_1^{eff} and $||s||$ denoting the first invariant of the effective stress and the norm of the deviatoric stress tensor, respectively, and p^c representing matric suction. The soil model is described in detail in [6]. Three material parameters determine the elastic behavior of the soil skeleton, five parameters are required for defining the yield surface with two further parameters describing the dependence of the yield surface on the Lode angle, four material parameters are required for defining the hardening law and four parameters determine the soil water retention behavior. Particular emphasis is placed on the efficient implementation using only single-surface projections due to the smoothness of the yield surface and on the robustness by employing problem-fitted start-up procedures for the stress update based on investigations of the non-linear projection equations.

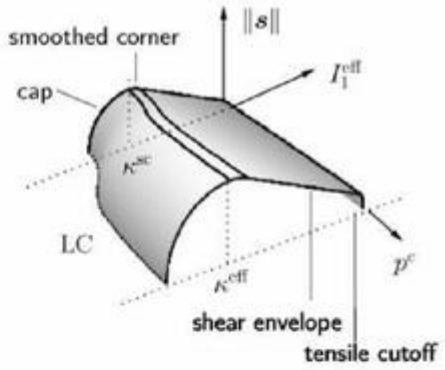

Fig. 1: Smooth yield surface of the cap model

The numerical formulation of the multi-phase model is derived within the framework of the finite element method (FEM), placing particular emphasis on the efficiency of the developed parallel FE-code for solving 3D large-scale multi-phase problems.

IMPLEMENTATION ASPECTS

The MPI [7] parallelized object oriented FE-program contains implementations of three-phase elements with the nodal unknowns, consisting of the displacement vector of the soil skeleton, matric suction and excess air pressure. The complex elasto-plastic constitutive model for unsaturated soils requires storage of a relatively large number of internal variables at the integration points. Furthermore, compared to ordinary displacement-based structural FE-problems, the additional unknowns reduce the sparsity of the system matrix. Thus, memory requirements are quite demanding and special care was

*) Corresponding author. Email: Guenter.Hofstetter@uibk.ac.at

taken during program development to have at all times a fully distributed storage of graphs, system matrices, system vectors, node data, and element data. The graph partitioning is also done in parallel using ParMETIS [8].

The resulting nonlinear system of equations for the mass balance of the water phase, the linear momentum balance of the three-phase continuum, and the mass balance of the air phase is solved using Newton's method. For problems of moderate size, solutions of the linearized system of equations can be obtained easily using parallel direct solvers like MUMPS [9], for instance. For larger systems, iterative solution methods can be advantageous. The success of these methods however heavily depends on the use of a good preconditioner, which due to the special matrix structure described above is not straightforward to design. The developed multi-phase finite element code provides an interface for the iterative solution of the linearized system using block preconditioning strategies and multigrid methods provided by the TRILINOS package [10,11,12]. Solution methods provided by the PETSc package [13] are supported as well.

APPLICATION TO A LARGE-SCALE 3D PROBLEM

A large-scale fully-coupled solid-fluid 3D numerical simulation of two-phase flow and of the associated ground settlements due to groundwater withdrawal is presented. To this end one quarter of a cylindrical domain, characterized by a radius of 80 m and a depth of 40 m, is discretized by 72.447 finite elements with quadratic serendipity shape functions for displacements and linear shape functions for air pressure and matric suction with altogether 1.082.735 degrees of freedom. The arrangement of the soil layers, the properties of the soil layers and the initial conditions and boundary conditions are omitted here because of the limited space. Groundwater is withdrawn from several pumping wells, which are located close to the center of the discretized domain. In this simulation, the drawdown of the groundwater table is caused by setting pressure boundary conditions for the wells. Fig. 2 depicts the employed FE-mesh together with the computed lowered groundwater table and the distribution of the volumetric plastic strain in the soil skeleton. Further results like the surface settlements, the deviation of the air pressure from the atmospheric pressure and the water pressure fluctuations in the course of groundwater withdrawal are also obtained from the multi-phase simulation. These results allow the study of short-term pressure responses to pumping which have previously been studied only in the fully saturated, elastic context.

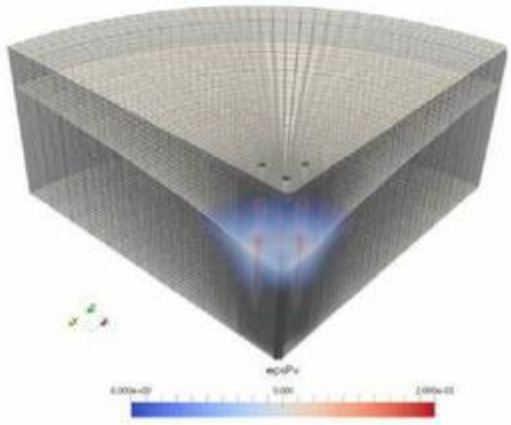

Fig. 2: FE-mesh, lowered groundwater table and volumetric plastic soil strains (epsPv)

References

[1] Galloway D.L., Burbey T.J.: Review: Regional land subsidence accompanying groundwater extraction, *Hydrogeology J.* **19**: 1459–1486, 2011.

[2] Jiao J.J., Guo H.: Airflow induced by pumping tests in unconfined aquifer with a low-permeability cap. *Water Resources Research.* **45**: W10445, 2009.

[3] Schrefler B.A.: Mechanics and thermodynamics of saturated/unsaturated porous materials and quantitative solutions, *Appl Mech Rev*. 55: 351–388, 2002.

[4] Ehlers W., Graf T., Ammann M.: Deformation and localization analysis of partially saturated soil, *Comput Methods Appl Mech Engrg.* **193**: 2885–2910, 2004.

[5] Gamnitzer P., Aschaber M., Hofstetter G.: Multi-phase Models in Structural Engineering. *Computational Engineering*, G. Hofstetter (ed.), Springer, 113-149, 2014.

[6] Gamnitzer P., Hofstetter G.: A smoothed cap model for variably saturated soils and its robust numerical implementation. *Int. J. Numer. Anal. Meth. Geomech.* **39**:1276-1303, 2015.

[7] Message Passing Interface Forum: MPI: A Message-Passing Interface standard (version 3.1), Technical Report, `http://www.mpi-forum.org`, 2015.

[8] Karypis G., Schloegel K.: ParMETIS parallel graph partitioning and sparse-matrix ordering. Library Version 4.0, University of Minnesota, 2011.

[9] Amestoy P.R., Guermouche A., L'Excellent J.-Y, Pralet S.: Hybrid scheduling for the parallel solution of linear systems, *Parallel Computing.* **32:** 136-156, 2006.

[10] Heroux M.A., Bartlett R.A., Howle V.E., Hoekstra R.J., Hu J.J., Kolda T.G., Lehoucq R.B., Long K.R., Pawlowski R.P., Phipps E.T., Salinger A.G., Thornquist H.K., Tuminaro R.S., Willenbring J.M., Williams A., Stanley K.S.: An overview of the Trilinos project, *ACM Trans. Math. Softw*. **31**: 397-423, 2005.

[11] Gee M.W., Siefert C.M., Hu, J.J., Tuminaro, R.S., Sala, M.G.: ML-5.0 smoothed aggregation user's guide, Technical Report SAND2006-2649, Sandia National Laboratories, 2006.

[12] Cyr E.C., Shadid J.N., Tuminaro R.S.: Stabilization and scalable block preconditioning for the Navier-Stokes equations. *J. Comput. Phys*., **231**:345-363, 2012.

[13] Balay S., Abhyankar S., Adams M.F., Brown J., Brune P., Buschelman K., Eijkhoutt V., Gropp W.D., Kaushik D., Knepley M.G., Curfman McInnes L., Rupp K., Smith B.F., Zhang H.: PETSc User's Manual ANL-95/11 - Revision 3.5, Argonne National Laboratory, 2014.

MODELING OF SALT AND GYPSUM DISSOLUTION PROCESSES

Farid Laouafa[1], Michel Quintard[2]
[1] *Institut National de l'Environnement Industriel et des Risques, Verneuil-en-Halate, France*
[2] *Université de Toulouse ; INPT, UPS; Institut de Mécanique des Fluides de Toulouse, Toulouse, France & CNRS; IMFT, Toulouse, France*

Summary Extraction of salt by leaching process is used intensively nowadays. In this analysis about cavity dissolution modeling, we consider the case of a binary system characterized by a chemical solute corresponding to the solid that is dissolved by a "solvent". Salt dissolution is controlled by thermodynamic equilibrium at the interface, i.e., equality of the chemical potentials. In this paper, a local non-equilibrium Diffuse Interface Model and an explicit treatment of the brine-salt interface are introduced in order to solve such dissolution problems. Equations are obtained by upscaling micro-scale equations for a solid-liquid dissolution problem using a volume averaging theory. Based on this mathematical formulation, dissolution test cases are presented. We introduce and discuss the main features of the method. Illustrations of the interaction between natural convection and forced convection in dissolution problems are presented and the time and space evolution of the rock salt-fluid interface is shown through several examples.

INTRODUCTION

Dissolution of porous media or solids is widely concerned in many industrial fields, e.g., acid injection into petroleum reservoirs, dissolution of rocks caused by underground water, etc. In the latter, rock dissolution creates underground cavities of different shapes and sizes, which induce a potential risk of collapse as shown in Fig.1. In most applications, modeling such liquid/solid dissolution problems is of paramount importance.

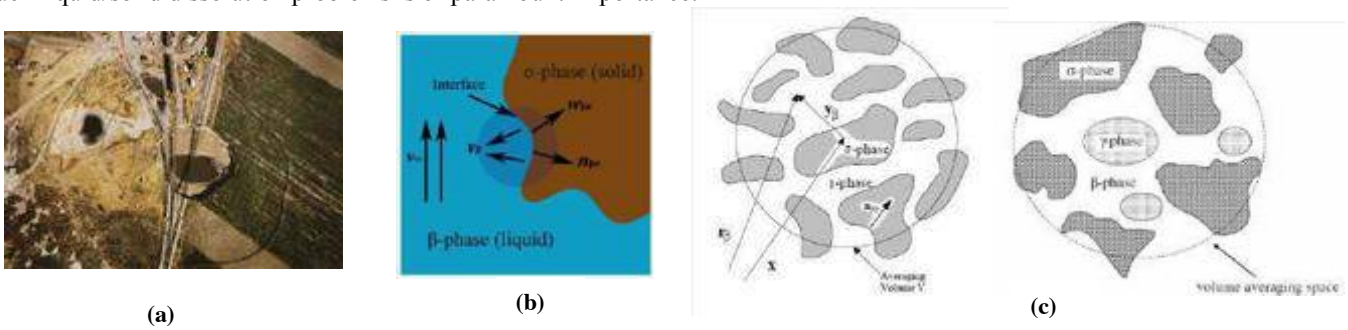

(a) **(b)** **(c)**

Fig. 1: Land Subsidence in Central Kansas Related to Salt dissolution (a), explanation of the variables at the local level to the interface (b) and averaging volume at pore scale level with material point position vector and 3-phases model (the third phase may be insoluble species for instance) (c).[1]

Among all methods used for modeling dissolution process, we present two generic ways for simulating such problems. The first one is a direct treatment of the evolution of the fluid-solid interface, for instance using an ALE (Arbitrary Lagrangian-Eulerian) method. The second uses a Diffuse Interface Model (DIM) to smooth the interface with continuous quantities [1, 3, 6], like the liquid phase volume fraction, species mass fractions, etc.

MATHEMATICAL MODEL

According to [1], the Darcy-scale diffuse interface model for Solid/Liquid dissolution problems in a binary system includes the 3 following balance equations: the mass balance for the β-phase, the mass balance for the σ-phase, the mass balance for species A.

$$\varepsilon_\beta \rho_\beta^* \frac{\partial \Omega_{A\beta}}{\partial t} + \rho_\beta^* \boldsymbol{V}_\beta \cdot \nabla \Omega_{A\beta} = \nabla \cdot \left(\varepsilon_\beta \rho_\beta^* \boldsymbol{D}_{A\beta}^* . \nabla \Omega_{A\beta} \right) + \rho_\beta^* \alpha \left(1 - \Omega_{A\beta}\right)\left(\omega_{eq} - \Omega_{A\beta}\right)$$

$$\frac{\partial \varepsilon_\beta \rho_\beta^*}{\partial t} + \nabla \cdot \left(\rho_\beta^* \boldsymbol{V}_\beta \right) = \rho_\beta^* \alpha \left(\omega_{eq} - \Omega_{A\beta} \right)$$

$$-\rho_\sigma \frac{\partial \varepsilon_\sigma}{\partial t} = \rho_\sigma \frac{\partial \varepsilon_\beta}{\partial t} = \rho_\beta^* \alpha \left(\omega_{eq} - \Omega_{A\beta} \right)$$

[a] Corresponding author. Email: farid.laouafa@ineris.fr

where ε_β is the volume fraction of β-phase, $\Omega_{A\beta}$ is the mass fraction of species A in the β-phase, ω_{eq} is the equilibrium mass fraction at the σ–β interface, α is the mass exchange term, ρ_β^* and ρ_σ are respectively the β-phase and σ-phase densities, and $\boldsymbol{D}_{A\beta}^*$ is the effective diffusion tensor for species A. $\boldsymbol{D}_{A\beta}^*$ is the macroscopic diffusion/dispersion coefficient, ρ_β^*: such that $\left\langle \rho_\beta \omega_{A\beta} \right\rangle = \varepsilon_\beta \rho_\beta^* \Omega_{A\beta}$ and α(is the mass exchange coefficient between the two phases. The macroscopic diffusion/dispersion coefficient and the mass exchange coefficient are obtained by solving "closure problems" over representative unit cells of the pore-scale geometry, characterized by two boundary value problems for two "mapping variables" (closure variables In the DIM model, there is no "pure liquid phase" since ε_β is used continuously to represent the fluid as well as the solid regions. Therefore, the Navier-Stokes equations are no longer suitable for this situation. Instead, we can adopt a Darcy-Brinkman model to take the place of Navier-Stokes equations for the momentum equations,

$$\frac{\mu_\beta\left(\Omega_{A\beta}\right)}{\varepsilon_\beta}\Delta \boldsymbol{V}_\beta - \left(\nabla P_\beta - \rho_\beta^* \boldsymbol{g}\right) - \mu_\beta\left(\Omega_{A\beta}\right)\boldsymbol{K}^{-1}\cdot\boldsymbol{V}_\beta = 0$$

where $\boldsymbol{K}$ is a permeability function of ε_β. The Darcy-Brinkman equation will approach Stokes equation when $\boldsymbol{K}$ is very large and will simplifies to Darcy's law when $\boldsymbol{K}$ is very small. If inertia terms are not negligible, a similar penalization of Navier-Stokes equations may be used by adding Darcy-Forchheimer contributions.

NUMERICAL MODELLING

Whenever density variation is present in the fluid phases, gravity (buoyancy force) plays an important role in mass and heat transports, through natural convection mechanisms. This natural convection phenomenon, often called salt fingering, is well illustrated by our model Figures 2 [2].

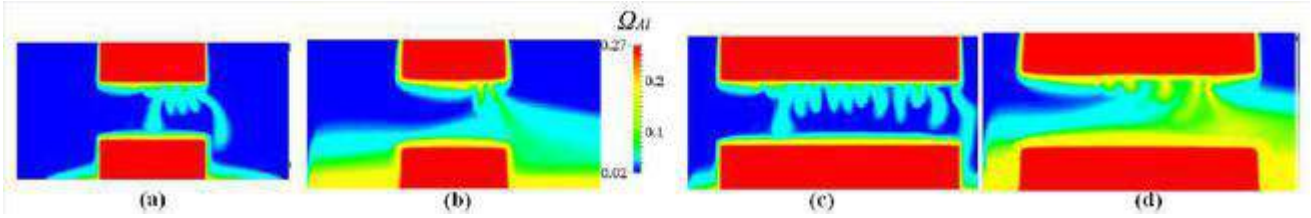

Fig 2: Examples of concentration plumes for a 2D simulation with gravity at time 100 s (a) and 1000 s (b) and salt block size 8 mm, and for a salt (c) and (d) block size 16 mm (from [2]).

The second illustration deals with the modeling of an experimental leaching test performed in a salt layer (Fig. 3). The numerical model was extended to gypsum material and one can observe the significant difference in terms of rate of dissolution (at the beginning of the test there was no cavity).

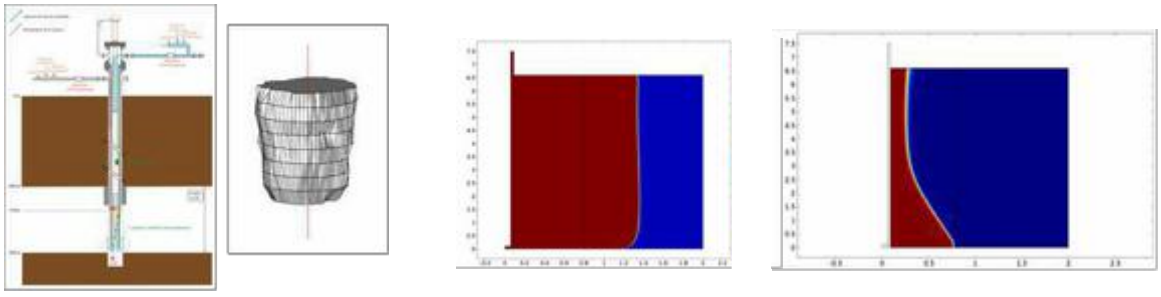

Fig 3: From left to right: experimental dissolution-leaching test (and final cavity shape) in a salt layer, cavity after in salt after 12 day and then cavity shape in case of gypsum material after 3years. (The cavity is in red and the solid material in blue).

References

[1] H. Luo, M. Quintard, G. Debenest, and F. Laouafa (2012). Properties of a diffuse interface model based on a porous medium theory for solid–liquid dissolution problems. *Computational Geosciences*, 16:913–932, 2012.

[2] H. Luo, F. Laouafa, G. Debenest and M. Quintard (2015). Large scale cavity dissolution: From the physical problem to its numerical solution. European Journal of Mechanics B/Fluids 52, 131–146

TENSION AND TOMOGRAPHIC MEASUREMENTS WHILE DRAINING WATER FROM A GRANULAR SAMPLE

Jin Xu[1], Theis Solling[2], Thomas McKay[2], and Michel Y. Louge*[1]

[1]*Mechanical Engineering, Cornell University, Ithaca, NY, USA*
[2]*Maersk Oil Research & Technology Centre, Doha, Qatar*

Summary We report simultaneous measurements of capillary pressure and water distribution in an unsaturated bed of glass beads subject to evaporation-induced drainage using xray computed tomography (CT) and a tensiometer. The data reveal that drainage can occur with or without pressure jumps. In the statistical mechanics framework of Xu and Louge [PRE 92:062405, 2015], these observations suggest that the drainage phase transition involves reversible periods punctuated by irreversible avalanches.

BACKGROUND

Unsaturated porous media are familiar features of industrial and geophysical systems such as fuel cells, oil deposits and soils. Recently, Xu and Louge [1] proposed a statistical mechanics that regards permeable solids as an ensemble of interconnected pores exhibiting geometrical "frozen disorder", which they characterized by the distribution of two parameters α and λ measuring, respectively, the specific areas of neck cross section and wettable pore surface relative to pore volume. In that framework, these authors attributed drainage and imbibition to irreversible collective first-order phase transitions occurring at capillary pressures ψ and degrees of saturation in wetting fluid S predictable from known distribution of α and λ and surface energies. They showed how hysteresis in the "retention curves" plotting S vs ψ is an inevitable consequence of collective interactions among pores, like other systems where statistical mechanics applies, such as magnetic materials [2]. After calculating the "latent" energies released in the draining and wetting transitions, they attributed sudden "Haines" jumps in ψ and S to the viscous dissipation of those energies by rapid fluid motion. They then devised a simple model reproducing the time-history of fluid speed jumps observed in an ordered pore network [3].

In those experiments, Armstrong and Berg [3] noted the limited extent of domains where pores interact collectively. Xu and Louge [1] called them "mesoscopic domains", and estimated their size in terms of S. Following Preisach [6], they showed that, if capillary pressure is applied on boundaries located farther than the mesoscopic size, then retention curves may no longer be unique. For example, upon reversing the rate of change of ψ, a new curve may invade the region in (ψ, S) between the two "main" hysteretic retention curve of drainage and imbibition [5]. This "return-point" hysteresis is also commonly observed in magnetization [2].

Recalling the numerical simulations of Ji and Robbins [4], Xu and Louge [1] also recognized that "avalanches" can follow the main drainage phase transition, particularly if the degree of geometrical pore disorder, measured as the standard deviation of α relative to the mean λ, exceeds a critical value. Like the main drainage phase transition, these avalanches should be irreversible, perhaps contributing, once again, to "return-point" hysteresis.

Therefore, an important question arising in the theoretical framework of Xu and Louge [1] is whether a sample of mesoscopic size but relatively weak disorder also experiences irreversible avalanches as it loses wetting fluid following the draining transition and, conversely, whether any fluid drainage can ever occur reversibly.

OBSERVATIONS

To inform this question, we carried out experiments on an open DELRIN plastic tube tightly fitting the $5\,\mathrm{mm}$ outer diameter of a T5x tensiometer with -160 to $+100\,\mathrm{kPa}$ pressure range and $\pm 0.5\,\mathrm{kPa}$ accuracy manufactured by UMS GmBH (Munich), holding glass beads (65% SiO_2, 25% Na_2O, 8% CaO, 1% K_2O, Potters MIL-PRF 9954-5) with diameter in the range 300 to $425\,\mu\mathrm{m}$ to a height of about $20\,\mathrm{mm}$, initially saturated with degassed, deionized water. This relatively small sample was on the order of the mesoscopic domain size [1]. A micro-CT scanner manufactured by Australian National University operating in the double-helix mode with a General Electric nano-focus x-ray source at $80\,\mathrm{keV}$ and $100\,\mu\mathrm{A}$ produced 9000 counts on the detector in $1.3\,\mathrm{s}$ with a $0.8\,\mathrm{mm}$-thick aluminum filter [7]. Three-dimensional tomographic reconstructions were achieved using the MANGO software package from 1440 projections acquired in approximately $30\,\mathrm{min}$. Segmentation between air, water and glass was relatively straightforward (Fig. 1). To find the capillary pressure ψ_- where drainage transition occurs (a.k.a. the air-entry potential), we also evaporated the same beads over ten days in the much larger HYPROP kit of UMS GmbH with a cylindrical vessel of $80\,\mathrm{mm}$ diameter and $50\,\mathrm{mm}$ height. Air entry occurred after about 4 hours at $\psi_- \simeq 1.2\,\mathrm{kPa}$ (Fig. 1, bottom left).

As Fig. 1 suggests, drainage from the smaller CT sample exhibited no jump in ψ above noise for the first 4 hours. Then, near (likely after) the phase transition, significant pressure jumps occurred between long periods of gradual adjustment. During the latter, B and C had visible changes in water and air conformation from the previous scan, but without jump. This suggests that some changes in saturation can occur reversibly, as Berg, et al [8] implied. Conversely, irreversible

*Corresponding author. Email: MYL3@cornell.edu

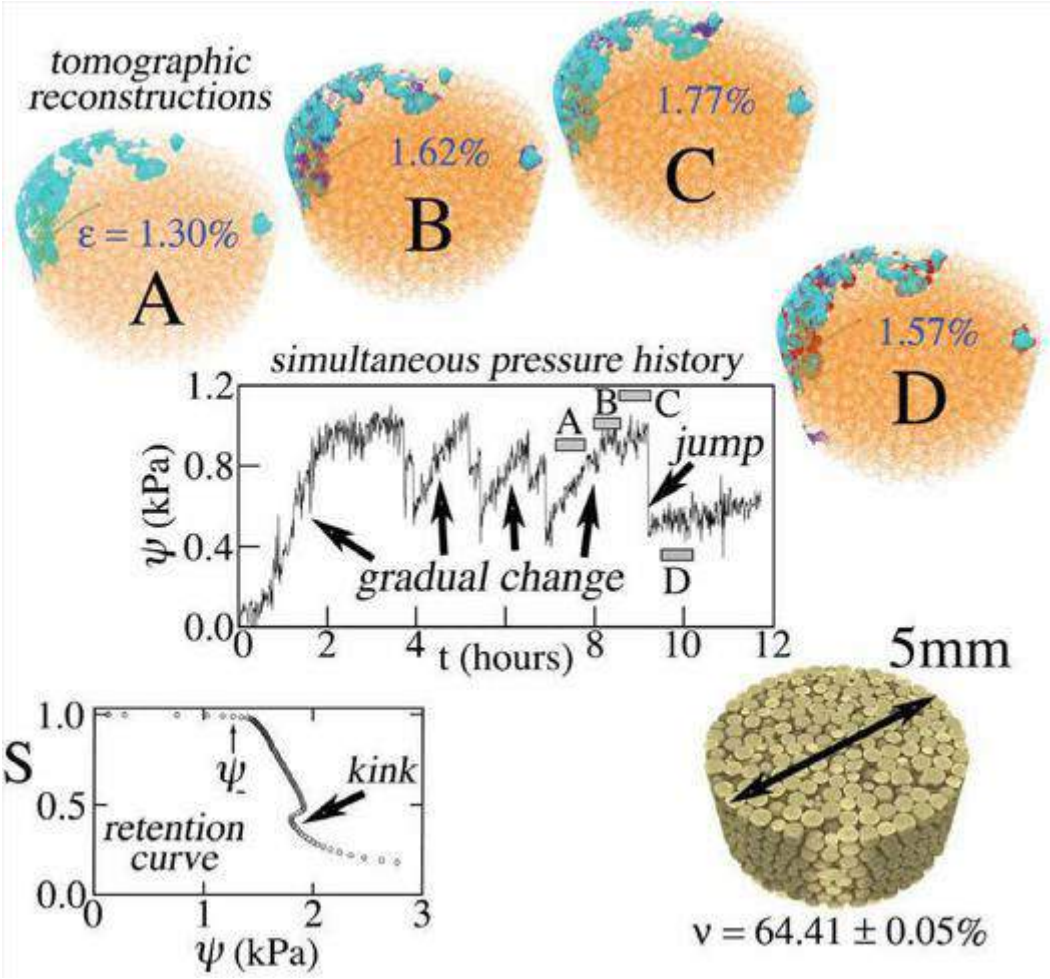

Figure 1: Top: tomographic reconstruction of scans A to D; light blue is air without discernible motion from the previous scan. Deep blue and red are, respectively, advancing and receding air; ϵ is air volume fraction. Middle: capillary pressure ψ vs time; segments show scan duration. Bottom right: glass beads shown without surrounding air or water; ν is solid volume fraction. Bottom left: drainage retention curve $S \equiv 1 - \epsilon/(1-\nu)$ vs ψ measured in the larger UMS HYPROP.

ψ-jumps occurred around the drainage transition, again with detectable changes in water and air conformation. (However, it is unclear what role the cylindrical wall played). Meanwhile, because the retention curve had a obvious "kink" in ψ (Fig. 1, bottom left), we suspect that the sample holder of the HYPROP was much larger than the mesoscopic domain size, thereby allowing the (ψ, S) region between the main curves of drainage and imbibition to be invaded [1, 6], possibly leading to irreproducible return-point hysteresis, albeit yielding a smoother retention curve.

In short, our simultaneous tomographic reconstructions and tension measurements suggest that the drainage phase transition predicted by Xu and Louge [1] is accompanied by irreversible "avalanches" [2, 4] interspersed with reversible periods of gradual changes in saturation. In future, faster synchrotron CT-scans should be conducted to observe these avalanches as they redistribute liquid on msec timescales [1, 3], while simultaneously recording their pressure jumps.

This paper was made possible by the support of NPRP grant 6-059-2-023 from the Qatar National Research Fund.

References

[1] Xu J., Louge M.Y.: Statistical Mechanics of Unsaturated Porous Media. Phys. Rev. E 92:062405, 2015.
[2] Sethna J.P., Dahmen K., Kartha S., Krumhansl J.A., Roberts B.W., Shore J.D.: Hysteresis and Hierarchies: Dynamics of Disorder-Driven First-Order Phase Transformations. Phys. Rev. Lett. 70:3347, 1993.
[3] Armstrong R.T., Berg S.: Interfacial Velocities and Capillary Pressure Gradients During Haines Jumps. Phys. Rev. E 88:043010, 2013.
[4] Ji, H., Robbins, M.O.: Transition from Compact to Self-Similar Growth in Disordered Systems: Fluid Invasion and Magnetic-Domain Growth. Phys. Rev. A 44:2538-2542, 1991.
[5] Poulovassilis A.: Hysteresis of Pore Water, an Application of the Concept of Independent Domains. Soil Science 93:405-412, 1962.
[6] Preisach, F.: Über die magnetische Nachwirkung. Zeitschrift für Physik 94:277-302, 1935.
[7] Sheppard A., Latham S., Middleton J., et al.: Techniques in Helical Scanning, Dynamic Imaging and Image Segmentation for Improved Quantitative Analysis with X-ray micro-CT. Nuclear Instruments and Methods in Physics Research B 324:49, 2014.
[8] Berg S., Ott H., Klapp S.A., et al: Real-time 3D Imaging of Haines Jumps in Porous Media Flow. PNAS 110:3755, 2013.

SHEAR AND MIXED MODE FRACTURE IN DISORDERED SATURATED POROUS MEDIA

Enrico Milanese[1], Okan Yılmaz[2], Jean-François Molinari[2], Bernhard A. Schrefler[1a]
[1]*Civil, Architectural and Environmental Engineering Department, University of Padua, Padua, Italy*
[2]*Civil Engineering Institute, Materials Science and Engineering Institute,*
Ecole Polytechnique Federale de Lausanne (EPFL), Lausanne, Switzerland

Summary We investigate shear fracture and mixed mode fracture in inhomogeneous fully saturated porous media with a 2D central force lattice model. For this purpose we adopt the extended Biot's theory. The bars of the lattice break only under traction. This breaking process is simulated with a continuous damage model where after a partial failure event spring elements get a new failure threshold sampled from a uniform distribution. We investigate avalanche behaviour of the breaking events as well as the pressure evolution and the existence of pressure jumps linked to the breaking events in the disordered medium. It is found that the behaviour under pure shear loading is brittle while under mixed mode loading overall elasto-plastic behaviour is recovered as was previously observed under biaxial tension loading.

INTRODUCTION

We have analysed crack propagation in inhomogeneous media under dry and fully saturated conditions in prevailing mode I conditions under different loading conditions adopting a 2D central force lattice model [1]. For this purpose we have adopted the extended Biot's theory and developed a special element, shown in Figure 1. The bars of the lattice break only under traction. This breaking process is simulated with a continuous damage model where after a partial failure event spring elements get a new failure threshold sampled from a uniform distribution which implies an annealed disorder in the system. The loading conditions investigated were boundary traction, assigned pressure and assigned flow. We have investigated avalanche behaviour and the connected power law behaviour [2, 3]. We have found that the existence of fluid itself does not destroy this power-law behaviour except when the following condition is satisfied: the length scales introduced in the model through fluid flow become effective which happens when the value of the increment per step of the external loading (pressure or flow) increases above a certain threshold. Moreover we have found the confirmation that crack tip advancement is step-wise and that pressure rises or drops at crack tip advancement according to the applied loading condition [4]. This behaviour has been explained with Biot's theory.

We extend now the study to shear fracture and to mixed mode fracture. It has been found that the behaviour strongly depends on the sample size and the boundary conditions. For a square sample, by imposing a relative horizontal displacement between the top and bottom sides a 45° crack is obtained at failure, shown in Figure 2. This is typical for a shear test on a small sample. For periodic boundary conditions at the vertical edges (horizontal strip) for the same loading conditions a crack parallel to the horizontal side develops at failure, shown in Figure 3. In both cases the failure is sudden (brittle behaviour) without a stepwise development of the fracture which on the contrary was observed in case of mode I type fractures. Avalanches of the breaking events of the bars in the domain are still observed in both cases. Also pressure fluctuations in the samples are observed. Careful examination of the snapshots of the deformed configuration evidences that these pressure oscillations happen each time a broken bar results in some opening in the lattice which corresponds to a sudden increase of the volumetric strain. This is consistent with Biot's theory. Both examples show a strong pressure jump at failure. This is depicted in Figure 4 for the blue point of Figure 3. For both cases the behaviour is brittle as opposed to the overall elasto-plastic behaviour of the mode I type case. When a horizontal traction is added at the vertical sides, which corresponds to mixed mode behaviour, pressure oscillations as well as overall elasto-plastic behaviour, typical for mode I type situations, are recovered, see Figure 5. The avalanches (number of broken bars for a time step) for such a mixed mode case are shown in Figure 6. The number of loading steps to reach failure in case of pure shear loading is roughly ten times that for prevailing mode I and mixed mode loading.

CONCLUSIONS

It has been shown that fracturing in disordered fully saturated porous media at mesoscopic level under shear loading differs substantially from mode I type fracturing, while mixed mode fracturing recovers some of the features of mode I type fracturing. The former is clearly brittle; the latter shows overall elastoplastic behaviour.

References

[1] Milanese E.. Yılmaz O., Molinari J.F., Schrefler B.A.: Avalanches in dry and saturated disordered media at fracture, to appear
[2] Zapperi S., Vespignani A., Stanley H.E.: Plasticity and avalanche behavior in microfracturing phenomena. *Nature* 388: 658 – 660, 1997.
[3] Zapperi, S., Ray P., Stanley H.E., Vespignani A.: Avalanches in breakdown and fracture processes. *Physical Review E* 59(5): 5049 – 5057, 1999.

[a)] bernhard.schrefler@dicea.unipd.it

[4] Schrefler, B.A., Secchi S., Simoni L. On adaptive refinement techniques in multi-field problems including cohesive fracture. *Computational Methods in Applied Mechanics and Engineering* 195: 44, – 461, 2006.

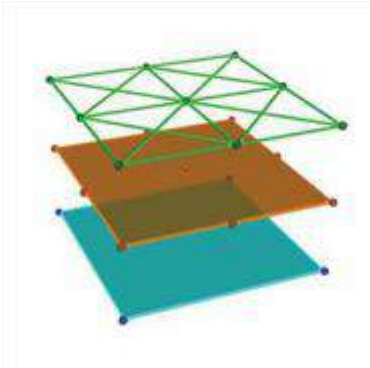

Figure 1. The three-layer finite element of the model. From the bottom to the top: the fluid pressure 4-node plane element (blue), the coupling 9-node plane element (orange) and the solid skeleton made of 20 2-node trusses (green). The layers are superposed on the same plane.

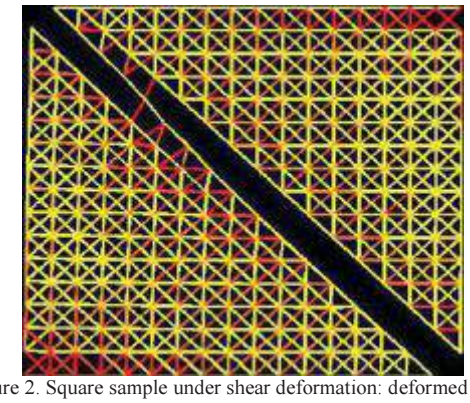

Figure 2. Square sample under shear deformation: deformed shape at failure. The red bars are damaged, the yellow ones undamaged.

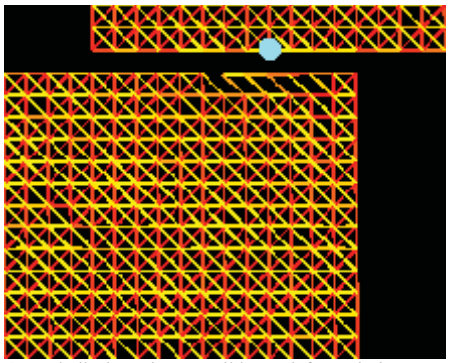

Figure 3. Periodic boundary conditions: deformed shape at failure. The blue dot is the point where the pressure evolution of Figure 4 is recorded. The red bars are damaged, the yellow ones undamaged.

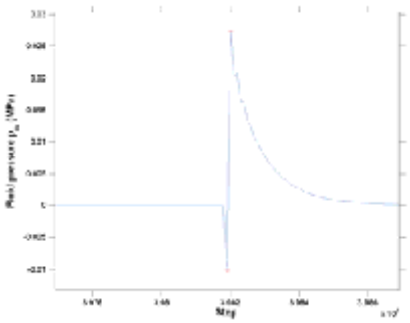

Figure 4. Periodic b.c., pressure oscillation at the breaking event recorded at the blue point of Figure 3.

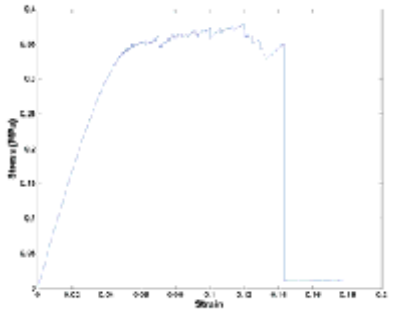

Figure 5. Mixed mode loading: Average stresses in the trusses versus equivalent strain

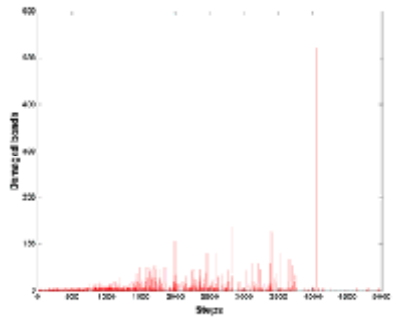

Figure 6. Mixed mode loading: Avalanche distribution versus loading steps for the simulation of Figure 5.

COMPETITIVE ADSORPTION OF GAS MIXTURES IN FRACTAL SLIT NANOPORES

Zhihao Shang[1], Li-Sha Niu*[1], Hui-Ji Shi[1], and Liang Dong[1]

[1]*Department of Engineering Mechanics, Tsinghua University, Beijing, China*

Summary Fractal slit nanopore is a ubiquitous pore structure in porous media such as shale. Gas in rough pores exhibits different adsorption characteristics from that in smooth pores. In this study, graphite slit nanopores with different roughness (quantified by fractal dimension) were created using random midpoint displacement method to model the most common pore structure in shale, and the competitive adsorption of CH_4/N_2 and CH_4/CO_2 mixtures was investigated through grand canonical Monte Carlo simulation, which elucidated the effects of roughness on the selective adsorption capacity of the nanopores. The result of this study is helpful not only for understanding the microscopic mechanism of competitive adsorption of gas mixtures in rough nanopores with fractal characteristics but also for estimating the separation efficiency of methane from other components of shale gas.

INTRODUCTION

Shale gas, as a clean and high-efficient energy, has been attracting more and more attention from all over the world. Because shale gas is mainly stored in adsorbed state, adsorption is a key factor in the gas-in-place reserve estimation and in separating of methane from other components of shale gas.[1] In addition, according to experimental observation, the pore wall of shale has obvious fractal characteristics, with fractal dimension ranging from 2.5 to 2.9 and fractal regime from 0.5 nm to 2,500 nm, indicating that even at atomic scale it also shows fractal irregularity.[2, 3, 4] On the other hand, in shale, most of the pores have slit pore shape,[5] and the diameters of most pores are at nanoscale.[6, 7] In summary, the study of competitive adsorption in fractal slit nanopores is representative for reveling the effects of roughness on adsorption in shale. To our best knowledge, most studies focused on the comparison between smooth and rough effects on adsorption, and there have been few reports about the effects of quantified roughness on adsorption using a mathematical description. Therefore, this study may throw some new lights on understanding the effects of roughness on competitive adsorption behavior.

COMPUTATIONAL MODELS AND METHODOLOGY

A series of fractal Brownian surfaces with different fractal dimension was created using random midpoint displacement method characterized by the following three parameters: (1) the initial standard deviation σ, (2) the iteration number N, and (3) the Hurst parameter $H = 0.9, 0.8 \ldots, 0.1$. In terms of the relation between the fractal dimension and the Hurst parameter $D = 3 - H$, the roughness of the pores is quantified by the fractal dimension $D = 2.1, 2.2 \ldots 2.9$ respectively. A smooth surface ($D = 2$) was also created as reference. Then the slit nanopore models were generated by cutting a graphite bulk using two identical surfaces with corresponding roughness. (Figure 1)

TraPPE force field was adopted to the gases to describe all the interatomic interactions.[8, 9] Grand canonical Monte Carlo simulations under 298 K were performed from using Multipurpose Simulation Code (Music) 4.0.[10] The partial fugacity, ranging from 0.001 to 18 MPa, was taken equal for each component of the gas mixtures. Periodic boundary conditions were applied on the two directions that are perpendicular to the pore width direction. In total, 100 million trials were performed for each simulation: the initial 50 million trials for system equilibration, and the remaining 50 million trials for the calculation pVT properties.

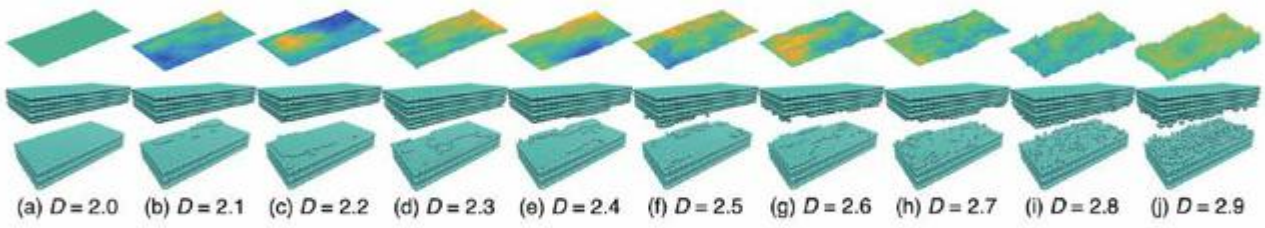

Figure 1: Fractal Brownian surfaces and corresponding slit nanopore models with different roughness quantified by fractal dimension of the pore wall.

*Corresponding author. Email: niulsh@mail.tsinghua.edu.cn

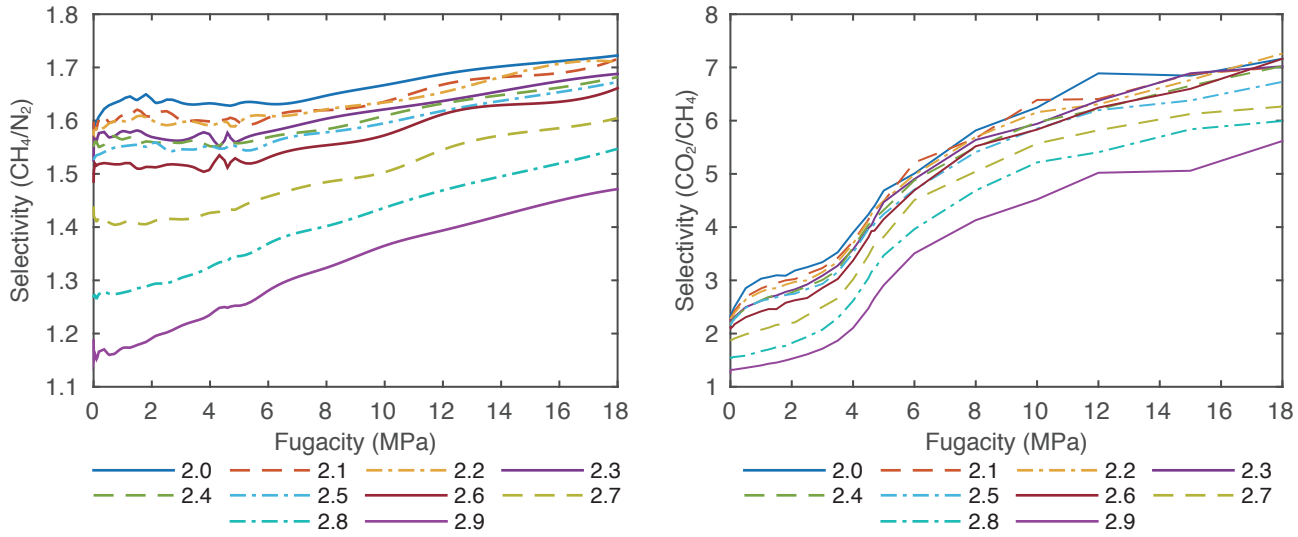

Figure 2: Selectivity coefficient of CH_4/N_2 and CO_2/CH_4 mixtures.

RESULTS AND DISCUSSION

Roughness has significant effects on the selectivity of the gas mixtures. (Figure 2) The selectivity coefficient decreases with increasing roughness, which means the smoother pore has higher efficiency to separate the gas component that has stronger interaction from the gas mixture. On the other hand, under the simulation conditions, the physical properties of CH_4 and N_2 are similar, so the selectivity of CH_4/N_2 is between 1 and 2, indicating that the pore has no obvious selective adsorption capacity on the two gas components. However, as CO_2 liquefies but CH_4 turns into supercritical fluid state at high pressure, the selectivity coefficient of CO_2/CH_4 can reach 7.

The cause of the decrease of the selectivity coefficient with roughness is that the density of the adsorption layer decreases with roughness increasing. Moreover, as roughness increases, the difference of the adsorption layer density between the gas components also decreases. This is because with roughness increasing, the interaction between gas molecules and the pore wall descends, so the number of adsorption sites decreases. If roughness is large enough, the adsorption layer disappears and thus the pore will no longer has the capacity to adsorb gas molecules.

CONCLUSIONS

Roughness has obvious effects on the competitive adsorption behavior of gas mixtures. The selective adsorption capacity decreases with increasing roughness, indicating that roughness is an unfavorable factor in the separation of gas mixtures, which could help us to understand the mechanism in the process of shale gas transportation and displacement.

References

[1] Ambrose R. J., Hartman R. C., Diaz-Campos M., Akkutlu I. Y., Sondergeld C. H.: Shale Gas-in-Place Calculations Part I: New Pore-Scale Considerations. *SPE Journal* **17**: 219 – 229, 2012.

[2] Krohn C. E.: Fractal Measurements of Sandstones, Shales, and Carbonates. *J Geophys Res* **93**: 3297, 1988.

[3] Bahadur J., Radlinski A. P., Melnichenko Y. B., Mastalerz M., Schimmelmann A.: Small-angle and Ultrasmall-angle Neutron Scattering (SANS/USANS) Study of New Albany Shale: a Treatise on Microporosity. *Energy Fuels* **29**: 567 – 576, 2015.

[4] Liu X., Xiong J., Liang L.: Investigation of Pore Structure and Fractal Characteristics of Organic-Rich Yanchang Formation Shale in Central China by Nitrogen Adsorption/Desorption Analysis. *J Nat Gas Sci Eng* **22**: 62 – 72, 2015.

[5] Wang Y., Zhu Y., Chen S., Li W.: Characteristics of the Nanoscale Pore Structure in Northwestern Hunan Shale Gas Reservoirs Using Field Emission Scanning Electron Microscopy, High-Pressure Mercury Intrusion, and Gas Adsorption. *Energy Fuels* **28**: 945 – 955, 2014.

[6] Loucks R. G., Reed R. M., Ruppel S. C., Jarvie D. M.: Morphology, Genesis, and Distribution of Nanometer-Scale Pores in Siliceous Mudstones of the Mississippian Barnett Shale. *J Sediment Res* **79**: 848 – 861, 2009.

[7] Mastalerz M., Schimmelmann A., Drobniak A., Chen Y.: Porosity of Devonian and Mississippian New Albany Shale across a Maturation Gradient: Insights from Organic Petrology, Gas Adsorption, and Mercury Intrusion. *AAPG Bull* **97**: 1621 – 1643, 2013.

[8] Martin M. G., Siepmann J. I.: Transferable Potentials for Phase Equilibria. 1. United-Atom Description of *n*-Alkanes. *J Phys Chem B* **102**: 2569 – 2577, 1998.

[9] Potoff J. J., Siepmann J. I.: Vapor-Liquid Equilibria of Mixtures Containing Alkanes, Carbon Dioxide, and Nitrogen. *AIChE J* **47**: 1676 – 1682, 2001.

[10] Gupta A., Chempath S., Sanborn M. J., Clark L. A., Snurr R. Q.: Object-oriented Programming Paradigms for Molecular Modeling. *Mol Simul* **29**: 29 – 46, 2003.

A MICRO-MACRO MECHANICAL MODEL FOR POROUS ROCK-LIKE MATERIALS WITH A PRESSURE-SENSITIVE MATRIX

W Q n[1] n J *[1]

[1]*LML, UMR CNRS 8107, University of Lille, 59655 Villeneuve d'Ascq, France.*

Summary In this work, a micro-macro mechanical model is proposed to describe elastic-plastic behaviors of porous geomaterials. The studied material is considered as a porous medium composed of a solid matrix and spherical pores. The solid matrix exhibits a pressure-dependent plastic behavior which is described by an associated plastic model based on a Mises-Schleicher yield criterion. A macroscopic yield criterion is firstly presented, explicitly taking into account effects of porosity. With an appropriate plastic hardening law, the micro-mechanical model is then formulated and implemented in a finite element code. The proposed model is then applied to describe mechanical behaviors of two representative porous rocks, sandstone and chalk.

MACROSCOPIC CRITERION FOR POROUS MEDIA WITH MISES-SCHLEICHER MATRIX

f q n l n n n v n n n ppl n l n xpl n, n n n n , l p b l , q n f l 2 n , w w ll p p l b n l b v f p l l p p f b n n n n l l xp n f p l n, ll w p w p *f* n l x b n p n p n v pl , w b l l n [2]:

$$f(\boldsymbol{\sigma}) = \sigma_{eq}^2 + 3\alpha\sigma_0\sigma_m \nearrow \sigma_0^2 \leq 0 \tag{1}$$

B n p l n n n q n [3, 1], p l n f p l w l x fin ll v n b :

$$\Phi = \frac{\frac{\Sigma_{eq}^2}{\sigma_0^2}}{\left(\frac{1-f}{1-\Gamma}\right)^2 \nearrow 3\alpha\frac{1-f}{(1-\Gamma)^2}\frac{\Sigma_m}{\sigma_0}} + 2\mathrm{y} \qquad \left(A\ln\left(1 \nearrow 3\alpha\frac{\Sigma_m}{\sigma_0}\right)\right) \nearrow 1 \nearrow \mathrm{y}^2 = 0 \tag{2}$$

n w $\mathrm{y} = \left[\alpha^2 W^2(fp) + 2\alpha^2 W(fp)\right]^A$, $A = sign(\Sigma_m)\dfrac{1 \nearrow \frac{1-\alpha^2W^2(fp)-2\alpha^2W(fp)}{9}}{2\alpha}$

FORMULATION OF THE CONSTITUTIVE MODEL AND NUMERICAL IMPLEMENTATION

B n p f n , p n (2) p n w w bl pl n n l w b pl f n f p , xpl l n n n ff f p *f* n pl p b l f l x n pl fl w l p n fin b n l l : $\boldsymbol{D}^p = \dot{\lambda}\frac{\partial\Phi}{\partial\boldsymbol{\Sigma}}$ w $\boldsymbol{D}^p$ n p pl n pl l pl $\dot{\lambda}$ n b n b l l pl n n n n:

$$\dot{\Phi}(\boldsymbol{\Sigma}, f, \alpha, \bar{\sigma}) = \frac{\partial\Phi}{\partial\boldsymbol{\Sigma}} : \dot{\boldsymbol{\Sigma}} + \frac{\partial\Phi}{\partial f} : \dot{f} + \frac{\partial\Phi}{\partial\bar{\sigma}} : \dot{\bar{\sigma}} = 0 \tag{3}$$

n ll , n :

$$\dot{\lambda} = \frac{\frac{\partial\Phi}{\partial\boldsymbol{\Sigma}} : \mathbb{C} : \boldsymbol{D}}{\frac{\partial\Phi}{\partial\boldsymbol{\Sigma}} : \mathbb{C} : \frac{\partial\Phi}{\partial\boldsymbol{\Sigma}} \nearrow \frac{\partial\Phi}{\partial f}\left[(1 \nearrow f)\frac{\partial\Phi}{\partial\Sigma_m} \nearrow 3\alpha\frac{\boldsymbol{\Sigma}:\frac{\partial\Phi}{\partial\boldsymbol{\Sigma}}}{2\bar{\sigma} - 3\alpha\frac{\Sigma_m}{1-f}}\right] \nearrow \frac{\partial\Phi}{\partial\bar{\sigma}}\frac{\partial\bar{\sigma}}{\partial\varepsilon_{eq}^p}\frac{\boldsymbol{\Sigma}:\frac{\partial\Phi}{\partial\boldsymbol{\Sigma}}}{(1-f)(\bar{\sigma}^2 - \frac{3}{2}\alpha\bar{\sigma}\frac{\Sigma_m}{1-f})}\sqrt{\bar{\sigma}^2 \nearrow 3\alpha\bar{\sigma}\frac{\Sigma_m}{1-f}}} \tag{ }$$

n v l f $\dot{\lambda}$, n n l pl p f p l n b n f ll w :

$$\mathbb{L} = \begin{cases} \mathbb{C} & \text{f } \Phi \leq 0, \dot{\Phi} < 0 \\ \mathbb{C} \nearrow \dfrac{\left(\mathbb{C} : \frac{\partial\Phi}{\partial\boldsymbol{\Sigma}}\right) \otimes \left(\frac{\partial\Phi}{\partial\boldsymbol{\Sigma}} : \mathbb{C}\right)}{H^G} & \text{f } \Phi = 0, \dot{\Phi} > 0 \end{cases} \tag{5}$$

n p p n l l pl l pl n n fin l n (b q) v b n b n n l p pl p pl l f l l n n p n

*Corresponding author. Email: jian-fu.shao@polytech-lille.fr

VALIDATION OF THE PROPOSED MODEL FOR POROUS GEOMATERIAL

The proposed micro-mechanical model is now applied to the description of mechanical behaviors of two representative porous rocks: sandstone and chalk. The efficiency of the model is assessed by comparing numerical results and experimental data for hydrostatic and triaxial compression tests with different confining pressures. A good agreement is observed (Figure 1 and 2).The main aspects of mechanical behaviors of the studied porous rocks have been correctly described.

Application to sandstone

As a first application, the Vosges sandstone will be considered which is mainly composed of quartz grains (93%). The average porosity is about 22%. Concerning the plastic hardening function $\bar{\sigma}$ of the solid matrix used in (2), an isotropic hardening law is here considered: $\bar{\sigma} = \sigma_0 + H(\varepsilon^p_{eq})^m$.

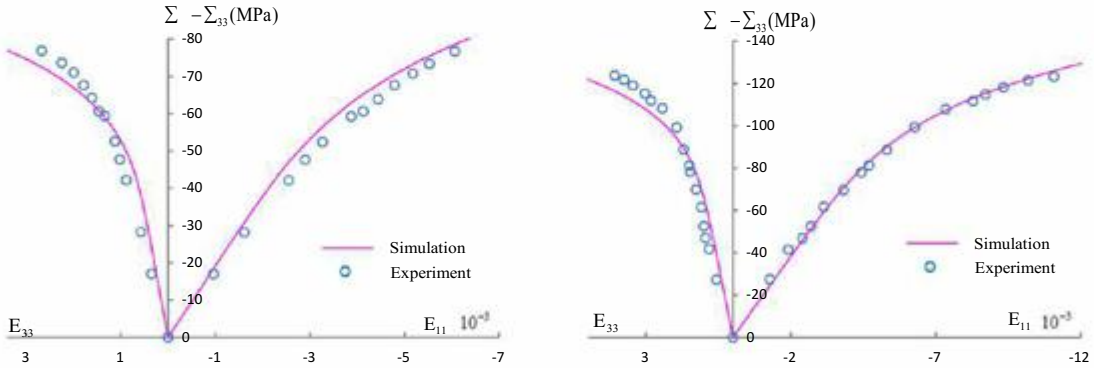

(a) $10MPa$ confining pressure (b) $40MPa$ confining pressure

Figure 1: Simulation of a triaxial compression test on Vosges sandstone with different confining pressure.

Application to chalk

For the second application example of the proposed model, the Lixhe chalk will be studied whose average porosity is $f = 43\%$. Based on experimental data, the following form is chosen for the plastic hardening function of the solid matrix: $\bar{\sigma} = \sigma_0 \left(1 + b(\varepsilon^p_{eq})^m + c(e^{n\varepsilon^p_{eq}} - 1)\right)$.

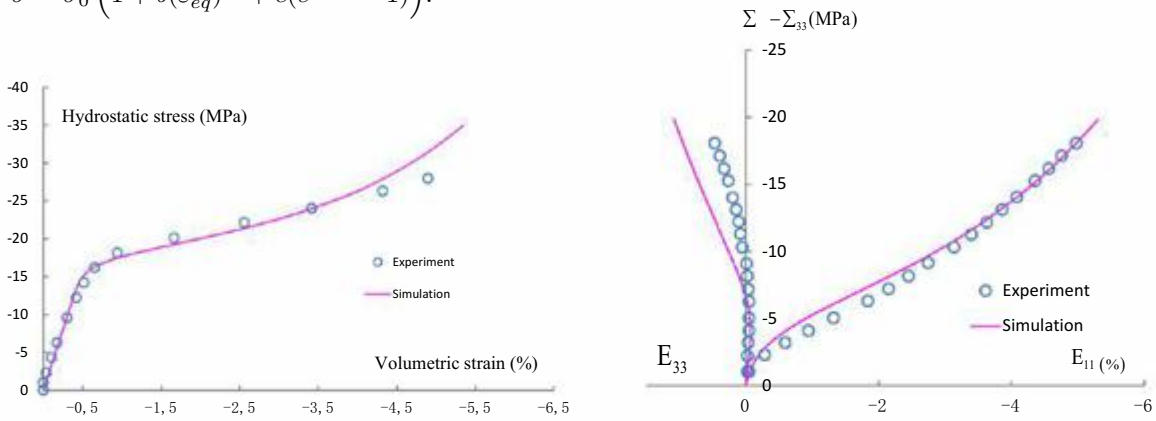

(a) hydrostatic compression test (b) $17MPa$ confining pressure

Figure 2: Simulation of hydrostatic and triaxial compression test on Lixhe chalk.

References

[1] V. Monchiet and D. Kondo. Exact solution of a plastic hollow sphere with a mises-schleicher matrix. *International Journal of Engineering Sciences*, 51:168–178, 2012.

[2] F. Schleicher. Der spannungszustand an der fließgrenze (plastizitatsbedingung). zamm. *Journal of Applied Mathematics and Mechanics - Zeitschrift fur Angewandte Mathematik und Mechanik*, 6:199–216, 1926.

[3] W.Q. Shen, J.F. Shao, D. Kondo, and G. De Saxce. A new macroscopic criterion of porous materials with a mises-schleicher compressible matrix. *European Journal of Mechanics A/Solids*, 49:531–538, 2015.

EFFECT OF LOCAL POROUS COATING ON THE STABILITY OF BOUNDARY LAYER

ZhangFeng Huang *[1], JingGang Mao[1], and Xuesong Wu[1,2]

[1]*Department of Mechanics, Tianjin University, Tianjin 300072, China*
[2]*Department of Mathematics, Imperial College London, London, SW7 2AZ, UK*

Summary A local scattering approach (LSA) was introduced to study the effect of local porous coating on the stability of an incompressible boundary layer. The prediction by LSA was verified by direct numerical simulation (DNS), and was compared to that by linear stability theory (LST) in order to check the validity of the latter. A systematic parametric study was performed, and the results show that local porous coating significantly enhances Tollmien-Schlichting (T-S) waves, and the effects can be quantified naturally by a transmission coefficient, which is an intrinsic physical property of the problem.

INTRODUCTION

Porous coating is a passive control of boundary-layer transition, and its effects on supersonic flows over flat plates and cones have been studied by means of theoretical analyses [1], experiments [2, 3] and numerical simulations [4, 5, 6, 7]. Almost all previous work focussed on the case of extended coating, for which the effects of coating can be understood from viewpoint of the local linear stability theory (LST). It was found that the second mode growth is massively reduced, but the first mode growth is moderately increased. However, for local porous coating over a streamwise width comparable with the wavelength of the instability of the unperturbed flow, conventional LST becomes invalid, because even though the disturbances far upstream and downstream are essentially eigen modes, the fluctuation near the porous coating is not and can indeed be rather complex. In this case, the effects of abrupt change (local coating or of rigid-porous junctions) must be accounted for by a local scattering approach (LSA) [8, 9]. In this paper, the effect of local porous coating on the stability of incompressible boundary layer on flat plate will be studied in this framework, which is both efficient and accurate numerically.

PROBLEM DESCRIPTION AND METHOD

This problem is illustrated in figure 1. A T-S wave approaches a local porous coating centred at x_c and having a width d. The local porous coating is modelled mathematically by the relation between blowing-suction velocity and the pressure: $v' = \lambda p'$, where $\lambda = \lambda_m \exp(i\varphi) f(x)$ with $f(x) = 0.5\cos[2\pi(x - x_c)/d] + 0.5$, when $|x - x_c| \leq 0.5d$; here λ_m is the coating porosity, φ represents the phase delay between the velocity and pressure, and the function $f(x)$ characterizes the distribution of impermeability. The propagation of the T-S wave through the region of coating should be formulated as a local scattering problem (LSP)[9] and can be solved by local scattering approach (LSA)[9], in which the disturbance is written in the form $Q'(x, y, t) = q(x, y)\exp(-i\omega t) + c.c.$, and the linearized Navier-Stokes equations are solved subject to inlet and outlet boundary conditions respecting the flow physics. The key concept of LSA is the transmission coefficient[8], defined as the ratio of the amplitude of the instability wave after the porous coating to that before the coating, and it is a natural characterization of the effect on stability. If the non-parallel effect of the mean flow is ignored, LSP can be formulated as an eigenvalue problem, in which the transmission coefficient appears as the eigenvalue, and the resulting prediction will be referred to as EVF (eigenvalue formulation).

RESULT

Figure 2 shows the evolution of the amplitude and local growth rate obtained by LSA, LST, EVF and DNS. The predictions by LSA and DNS agree quite well, which verifies the validation of LSA. The result obtained by EVF with a parallel-flow

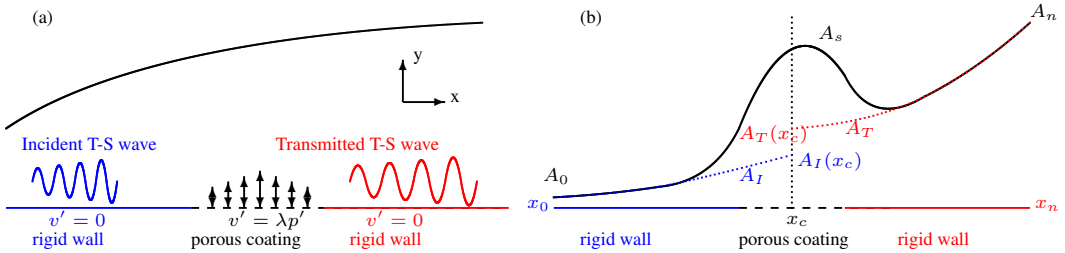

Figure 1: Diagrammatic illustration of (a) local scattering problem and (b) transmission coefficient $Tr = A_T(x_c)/A_I(x_c)$

*Corresponding author. Email: hzf@tju.edu.cn

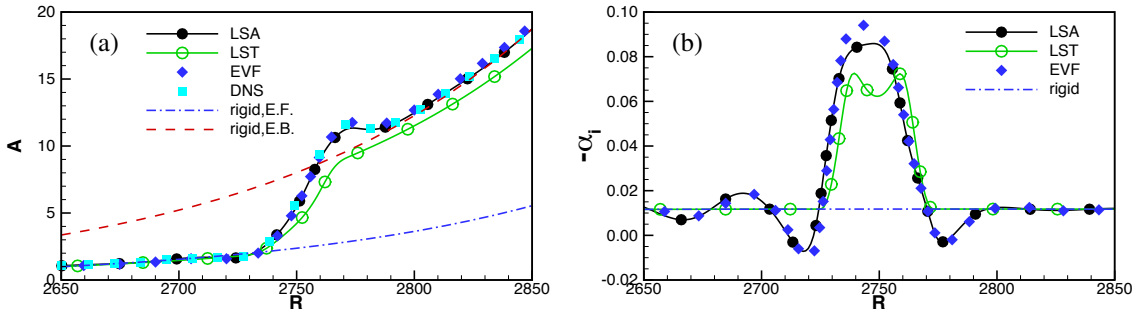

Figure 2: The evolution of (a) amplitude and (b) growth rate, where $R_c = 2750$, $d = 32$, $\lambda_m = 1$, $\phi = 0^0$, $F = 20$.

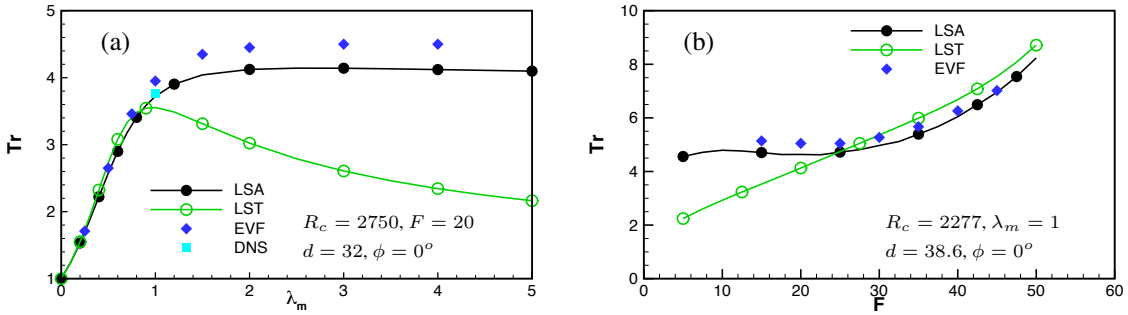

Figure 3: Variation of transmission coefficient with (a) porosity λ_m and (b) frequency F.

assumption is in good agreement with that by LSA, which includes non-parallelism, implying that the non-parallelism of the mean flow is a weak effect compared to that of local porous coating. There is a sharp increase of the amplitude in the region over the porous coating, and the corresponding transmission coefficient is $Tr \approx 3.8$, indicating that local porous coating significantly enhances the T-S wave. The evolution of the amplitude and growth rate obtained by LSA is non-monotonic, indicating that LSA, being of elliptic nature mathematically, captures the upstream and downstream influences of local porous coating. In contrast, LST only predicts variation within the porous section even though it captures also the overall enhanced amplification.

Figure 3 shows the variation of the transmission coefficient with the porosity and frequency. The transmission coefficient predicted by EVF is in good qualitative agreement with those by LSA and DNS, with a quantitative difference of 5% due to the non-parallelism of the mean flow, indicating that the abrupt change of porosity is the dominant effect. Significant deviations between LST and LSA arise for large porosity or for small frequencies. LST fails as it does not capture the upstream or downstream influence of the porous coating.

CONCLUSION

The effect of local porous coating on the stability of an incompressible boundary layer on a flat plate was studied by using LSA. The approach was validated by DNS, and the prediction by LSA, which includes the non-parallelism of the mean flow, is compared to that by EVF and LST. The non-parallel effect of the mean flow is found to be very weak compared to that of local porous coating. T-S waves are significantly destabilized by local porous coating and the enhancement can quantitatively be characterized by a transmission coefficient. LST is inadequate except for very weak porosities.

Acknowledgments This work was supported by the National Natural Science Foundation of China (11332007), the Tianjin Natural Science Foundation (15JCYBJC19500) and an open fund from the State Key Laboratory of Aerodynamics (SKLA201401).

References

[1] Fedorov A.V., Malmuth N.D., etc: Stabilization of hypersonic boundary layers by porous coatings. AIAA J. 39(4), 605, 2001.
[2] Shiplyuk A.N., Burov E.V., etc: Effect of porous coatings on stability of hypersonic boundary layers, J. Appl. Mech. Tech. Phys. 45(2),286,2004.
[3] Fedorov A.V., Kozlov V.F., etc: Stability of hypersonic boundary layer on porous wall with regular microstructure, AIAA J. 44(8), 1866, 2006.
[4] Chokani N., Bountin D.A., etc: Nonlinear aspects of hypersonic boundary-layer stability on a porous surface, AIAA J. 43(1), 149, 2005.
[5] Egorov I.V., Fedorov A.V., etc: Receptivity of a hypersonic boundary layer over a flat plate with a porous coating, J. Fluid Mech. 601,165,2008.
[6] Sandham N.D., Ludeke H.: Numerical study of Mach 6 boundary-layer stabilization by means of a porous surface, AIAA J. 47(9), 2243, 2009.
[7] Wang X., Zhong X.: The stabilization of a hypersonic boundary layer using local sections of porous coating, Phys. Fluids 24, 034105, 2012.
[8] Wu X., Hogg L. W.: Acoustic radiation of Tollmien-schlichting waves as they undergo rapid distortion. J. Fluid Mech., 550:307-347, 2006.
[9] Huang Z.F., Wu X.: A local scattering approach for the effect of abrupt changes on boundary-layer instability and transition: a numerical method, AIAA-2015-2623.

TRANSPORT EQUATION FOR THE CONCENTRATION GRADIENT

Anthony Beaudoin[1], Jean-Raynald de Dreuzy[2], and Serge Huberson[1]

[1]*Institute of Pprime, Department D2, HYDEE team, University of Poitiers, Poitiers, France.*
[2]*Géosciences de Rennes - 263 Avenue du Général Leclerc, 35042 Rennes, France*

Summary The organization and dynamic of the concentration in the heterogeneous porous media are key physical factors driving the chemical reactivity. At equilibrium, the chemical reactivity depends not only on the concentration distribution but also on concentration gradients for a simple precipitation. We derive the transport equation for concentration gradient and set up an adapted diffusion velocity method to approximate them numerically. The numerical results give optimal predictions of the chemical reactivity.

INTRODUCTION

A precipitate P dissolves yielding two solute species A and B, $P \Leftrightarrow A + B$. Solute concentrations c_A and c_B are related through the equilibrium constant $K = c_A c_B$. The reactive rate r between the two species A and B is given by :

$$r = \frac{2K}{((\delta c)^2 + K)^{3/2}} \nabla(\delta c) D \nabla(\delta c) \quad \text{with} \quad \delta c = c_A \nearrow c_B \tag{1}$$

Reactivity does not depend only on the concentration distribution but also on the local diffusive dynamic of concentration mixing [Le Borgne et al., 2010]. Concentration gradients follow complex spatial and temporal dynamics as they are created by velocity gradients through elongation and shear stress of the mixing fronts and dissipated by diffusion [Le Borgne et al., 2015]. Numerical methods should give accurate approximations of both concentration distributions and concentration gradients. The transport equation for concentration gradients is derived and solved with a particle method based on a diffusion velocity scheme [Beaudoin et al., 2003]. The particle methods are frequently used to solve the transport equation in porous and fractured media [Beaudoin et al., 2013] [Robinet et al., 2013]. When transport by advection largely dominates dispersion and diffusion processes, the particle methods offer a relevant alternative to Eulerian methods [Zhang et al., 2007]. Furthermore, particle methods can handle a large panel of inert as well as chemical and biological particle types [Tartakovsky et al., 2007].

TRANSPORT EQUATION OF CONCENTRATION GRADIENTS

The transport equation of concentration gradient $\nabla \delta c$ i obtained by applying ∇ to the transport equation :

$$\nabla \left(\frac{\partial \delta c}{\partial t} \nearrow \nabla \cdot (D\mathbf{g}) + \nabla \cdot (\mathbf{u} \delta c) \right) = 0 \quad \text{with} \quad \mathbf{g} = \nabla \delta c \tag{2}$$

where D is the diffusion coefficient, g the concentration gradient and u the flow velocity. Using the properties of vector operators and the assumptions of incompressible and irrotational flow, the previous equation becomes :

$$\frac{\partial \mathbf{g}}{\partial t} \nearrow \nabla \cdot (\nabla (D\mathbf{g})) + (\mathbf{g} \cdot \nabla)\mathbf{u} + \nabla \cdot (\mathbf{u} \otimes \mathbf{g}) = 0 \tag{3}$$

The last step consists in writing the diffusion term of equation (3) as an advection term by means of the diffusion velocity :

$$\frac{\partial \mathbf{g}}{\partial t} + \nabla \cdot ((\mathbf{u_d} + \mathbf{u}) \otimes \mathbf{g}) + (\mathbf{g} \cdot \nabla)\mathbf{u} = 0 \quad \text{with} \quad \mathbf{u_d} \otimes \mathbf{g} = \nearrow \nabla (D\mathbf{g}) \tag{4}$$

where u_d is the diffusion velocity. The transport equation of g (Eq. 3) is then transformed in a purely convective equation with a source term (Eq. 4). The expression of u_d is derived by means of a simple identification between equations (3) and (4).

NUMERICAL RESULTS

The transport of a concentration difference δc between two species is studied in a 2D heterogeneous flow field, see Figure 1. The porous medium is defined by a rectangle with the dimensions Lx = 2048 m and Ly = 512 m. The mean flow direction is the x axis. The permeability field K, assumed isotropic and heterogeneous, is characterized by a stationary log-normal probability distribution $Y = ln(K)$, defined by a zero mean and a covariance function given by $C(r) = \sigma^2 exp(\nearrow |r|/\lambda)$ where σ^2 and λ are the variance and the correlation length of Y. σ^2 and λ are fixed to 4 and 10 m. The classical laws governing the steady flow in a porous medium are mass conservation and Darcy law, $u = \nearrow K \nabla P$ and $\nabla \cdot u = 0$ with P the

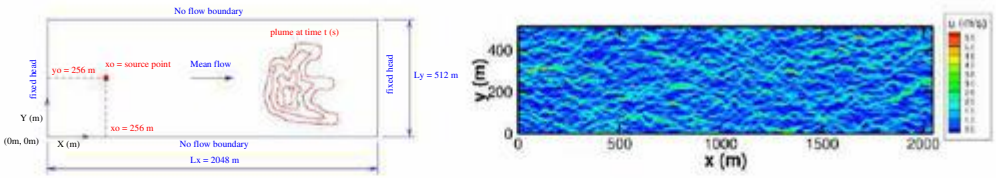

Figure 1: Scheme of problem considered (left) and horizontal component of the flow velocity (right).

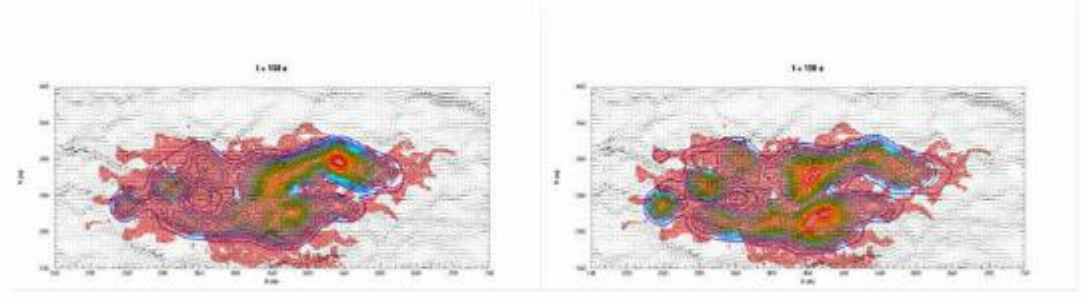

Figure 2: Concentration difference δc (left, colored contour lines) and its gradient norm $|g|$ (right, colored contour lines) with the set of numerical particles (full red circles) at time t = 150 seconds. The black arrows show the flow field.

hydraulic head. Boundary conditions are homogeneous Neumann on upper and lower sides, and Dirichlet P = 0 on left side and $P = Lx$ on right side. To characterize the mass transport, the Peclet number is defined by $Pe = \lambda|u|/D$. The norm of the mean flow velocity $|u|$ is equal to 1 m/s. Thus the Peclet number Pe is equal to 10000 for a diffusion coefficient D = 0.001 m^2/s. At the initial time, the concentration difference δc is injected at the source point Xo = (256 m, 256 m). The numerical simulation is stopped at time t = 150 seconds. The set of numerical particles is initialized by using a gaussian function. Figure 2 shows the concentration difference δc (left) and its gradient norm $|g|$ (right) with the set of numerical particles at time t = 150 seconds. We can observe that the negative values do not appear on the field of δc. Thus the chemical mechanisms can be simulated efficiently. The fields of δc and $|g|$ follow the flow. The zones of high values and low values are the same for the two quantities. The gradient particle method seems to simulate correctly the effects of the heterogeneous flow on the transport of the concentration, mixing and spreading. These two mechanisms are important for evaluating the impact of the heterogeneous flow on the chemical reactivity. These first results, obtained from the context of modelling groundwater flow and mass transport, allow to show how the gradient particle method can be used for simulating the reactive transport in high heterogeneous porous media.

REFERENCES

- Beaudoin A., Huberson S. and Rivoalen E., (2003), Simulation of anisotropic diffusion by means of a diffusion velocity method, Journal of Computational Physics, 186 122-135.
- Beaudoin A. and de Dreuzy J.R., (2013), Numerical assessment of 3D macro dispersion in heterogeneous porous media, Water Resources Research, vol. 49, 1-8.
- Le Borgne T., et al. (2010), Non-Fickian mixing: Temporal evolution of the scalar dissipation rate in heterogeneous porous media, Advances in Water Resources, 3(12), 1468-1475.
- Le Borgne T., et al. (2015), The lamellar description of mixing in porous media, Journal of Fluid Mechanics, 770, 458-498.
- Tartakovsky A.M., et al. (2007), Simulations of reactive transport and precipitation with smoothed particle hydrodynamics, Journal of Computational Physics, 222(2), 654-672.
- Roubinet D., et al., (2013), Particle-tracking simulations of anomalous transport in hierarchically fractured rocks, Computers and Geosciences, 50(0), 52-58.
- Zhang Z. and Chen Q., (2007), Comparison of the Eulerian and Lagrangian methods for predicting particle transport in enclosed spaces, Atmospheric Environment, 41(25), 5236-5248.

BONE HEALING IN LIVE ALLOGRAFT BIOLOGICAL SYSTEMS

Elisa Budyn*[1,4], Morad Bensidhoum[2], Samantha Sanders[1], Willy Haik[1], Romeo Antier[1], Florian Mainnemare[1], Thibault Marsan[1], Eric Schmidt[4], Patrick Tauc[3], and Hervé Petite[2]

[1]*Department of Mechanical Engineering, LMT Laboratory CNRS UMR 8535, ENS Cachan, Paris-Saclay University, Cachan, France*

[2]*Department of Biology, B2OA Laboratory UMR CNRS 7052, Paris Diderot University, Paris, France*

[3]*Department of Biology, LBPA Laboratory CNRS UMR 8113, ENS Cachan, Paris-Saclay University, Cachan, France*

[4]*Department of Mechanical Engineering, University of Illinois at Chicago, Chicago, Illinois, USA*

Summary Bone healing is observed in Live Allograft Biological Systems (LABS) where human mesenchymal stem cells that have been reseeded on human cortical and trabecular bone. After 15 days a collagenous matrix is produced and after 39 days hydroxyapatite crystals are produced by the cells that are undergoing differentiations into osteocytes. The tissues produced after 109 days exhibits nearly a third of the stiffness of mature bone tissue.

INTRODUCTION

With increasing life expectancy in the US and in Europe, bone pathologies related to massive bone loss occurring later in life following a cancer resection or a massive trauma on osteoporotic bone carry $5-10$ billion financial burden on the health-care system. Human Haversian cortical bone is a complex heterogeneous tissue resulting from continuous remodeling that resorb microdamage by osteoclasts before tubular multi-lamellar structures (osteons) are formed by osteoblast cells issued from differentiated mesenchymal stem cells (progenitor osteocytes) laying collagen fibrils mineralizing with hydroxyapatite crystals that are glued together with non-collagen proteins and proteoglycans. Trapped osteoblasts further differentiate into mechano-sensitive mature osteocytes sensing stimulation from microdamage through 40 to 60 cytoplasmic processes extending into canaliculi to create an extensive syncytial network with the neighboring cells. Because osteocytes regulate healthy bone turnover, it is essential to quantify the relationship between in situ mechanical stimulations and the cell biological response to improve allograft bone treatments.

MATERIALS AND METHODS

Live Allograft Bone Systems (LABS) were created using human donor bone tissues and bone cells from human patients to study the osteocyte in situ mechanobiology. Micro mechanical tests were conducted on the live systems bearing characteristic micro cracks that are controled stress concentrators [2]. Hybrid experimental and numerical top-down investigations are applied to image the growth of the controled nascent sub-microscopic damage near live progenitor (hMSCs) and mature (MLOY4s) osteocytes [3]. UV, fluorescent and laser confocal microscopies coupled to a hierarchical multi-level numerical simulations fed the assumed multi-scale local constitutive fracture mechanisms that were validated through scale by scale identifications after the balance of the energies between the global and local scales [1]. The model includes the mineralization heterogeinities of the osteons, the cohesive interfaces between the lamellae, and the diffuse damage mechanism inside the lamellae. The finite element discretization of the bone tissue morphology was explicit and the Dirichlet boundary conditions were calculated by digital image correlation.

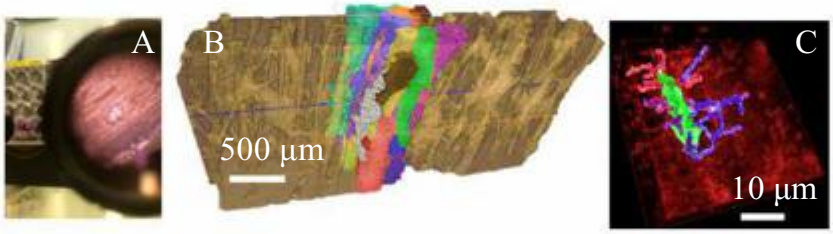

Figure 1: A- Live Allograft Biological Systems of human reseeded with human cells, B- 3D morphology reconstructions of the human bone tissue from micro CT images and C- 3D morphology of mature human osteocytes extracted from laser confocal imaging.

*Corresponding author. Email: ebudyn@ens-cachan.fr

RESULTS AND DISCUSSION

The model evaluates the in situ stress field near the cells and quantified the nascent diffuse damage thresholds within osteon lamellae and confirmed the known brittle/ductile fracture behavior of bone. The osteocyte morphology was reconstructed from confocal microscopy images that were demultiplied to account for the information of finite thickness planes that had been compressed into single images of the 3D plane segmentation. The canaliculi were traced by tubular geodesics and the edges of the contours of the cell body were detected by contrast enhancement techniques [3]. The cell meshing was built through a customized 3D meshing algorithm adequate to interpolate geometrical elements for complex morphologies exhibiting lack of information. The in situ cell 3D environment were numerically reconstructed from micro CT imaging parallel planes segmentations with a 5 micron resolution. The highly irregular tubular structures of the osteons were interpolating with a 10 microns resolutions [4]. The live systems mechanically behaved in agreement with the known behavior of fresh human bone. The mature osteocytes undergo a stable intake of cytoplasmic calcium under loading, nearly 1 to 13 nM under 124 pN local micro force. This is observed with CFSE and Calcium dye specific. The mixture of progenitor and differentiated osteocytes release a significant amount of calcium, 7 to 64 nM under 31 pN local micro force and regain about a third of its lost calcium after successive micro loading cycles. The progenitor and mature osteocytes reorganized in vitro as they are in vivo after 10 days. After 15 days a collagenous matrix is produced and after 39 days hydroxyapatite crystals are produced by the cells that are undergoing differentiations into osteocytes. The tissues produced after 109 days exhibits nearly a third of the stiffness of mature bone tissue.

CONCLUSIONS

A successful bone on chip has been implemented to measure osteocyte mechano-biology ate different stages of their differentiation for period of at least 170 days. The *in situ* cell biological response to mechanical load in particular its cytosolic calcium circulation was tracked by two fluorochromes and showed that the calcium membrane exchange rate adapts to the expected in vivo mechanical load seen by the cells through their differentiation. The created LABS are able to heal micro cracks in producing a mineralizing collagenous matrix of significant stiffness.

ACKNOWLEDGMENT

The authors are grateful for the support from NSF CMMI BMMB 1214816, the Farman Institute for the project OLA!, the Fulbright Scholar Program and the company CC contact.

References

[1] Jonvaux J., Hoc T. and Budyn E., Analysis of micro fracture in human Haversian cortical bone under compression, International Journal in Numerical Methods in Biomedical Engineering, 28(9):974-998, 2012.

[2] Budyn E., Bensidhoum M., Tauc P., Deprez E., Petite H., How the morphlogy of osteocytes contributes to their mechanotransduction near microdamage, MRS Fall meeting 2014 Proceeding, 1-5 December 2014, Boston, USA, 8 pages. DOI: http://dx.doi.org/10.1557/opl.2015.598

[3] Budyn E., Bensidhoum M., Marsan T., Mainnemare T., Tauc P., Sasnouski S., Schmidt E., Deprez E., Petite H., Mechano-Transduction of Osteocytes in Live Allograft Bone Systems (LABS), CMBE 2015, P. Nithiarasu E. Budyn (Eds.) E. Boileau, I. Sazonov, X. Xie (co-Eds.), ZetaComputational Resources Ltd., vol. 1, p. 124-127, 2015, ISBN 978-0-9562914-3-1

[4] Sanders S., Bensidhoum M., Budyn E., Explicit 3-Dimensional Modelling of Human Haversian Cortical Bone Failure, CMBE 2015, P. Nithiarasu E. Budyn (Eds.) E. Boileau, I. Sazonov, X. Xie (co-Eds.), ZetaComputational Resources Ltd., vol. 1, p. 132-135, 2015, ISBN 978-0-9562914-3-1

LIFTING A LARGE OBJECT FROM AN ANISOTROPIC POROUS BED

Timir Karmakar[1] and G.P. RajaSekhar *[1]

[1]*Department of Mathematics, Indian Institute of Technology Kharagpur, Kharagpur-721 302, India*

Summary Considering the porous nature of a seabed, lift-up problem has been studied theoretically. It is assumed that the seabed is anisotropic in nature and the pore flow is governed by Brinkman equation and the gap flow is governed by Stokes equation. An analytical series solution is obtained for the flow inside the gap and the seabed in terms of stream function via separation of variables. It is shown that increasing of vertical permeability enhances the vertical flow, hence decreases the lift-up force. Breakout phenomenon in terms of the anisotropic ratio and the width of the gap has been discussed.

MATHEMATICAL FORMULATION

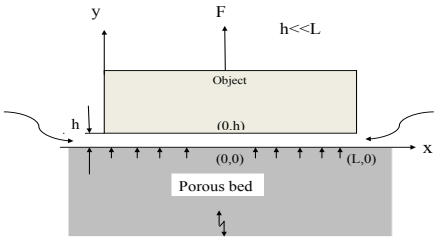

Figure 1: Schematic of the lift up problem

The lift-up process in general is a slow process and involves a slowly increasing gap between the bottom of the object (to be uplifted) and the porous bed until a turning point when it detaches itself from the porous bed. This point sometimes is referred as breakout point (see Mei[1], Chang et al.[2]). The relevant two-dimensional domain of interest is shown in Fig. 1. In this model we assumed that the gap width is less than the size of the pore and hence the gap flow initially comes from the pore of the rigid porous bed. We further assumed that the gap flow is governed by Stokes equation and the pore flow is governed by Brinkman equation together with the equation of continuity given as follows

$$-\nabla p + \mu\nabla^2\vec{u} - B\frac{\mu\varphi}{\mathbf{K}}\vec{u} = 0, \qquad \nabla.\vec{u} = 0 \tag{1}$$

where $B = 0$ for the gap region and $B = 1$ for the porous region. $\vec{u}$ is the velocity, φ is the porosity, p is the fluid dynamic pressure, $\mathbf{K}$ is the permeability tensor given by $\mathbf{K} = \begin{pmatrix} K_1 & 0 \\ 0 & K_2 \end{pmatrix}$ (see Kohr et al. [4]).

Boundary conditions

We use $\vec{u} = (u, v)$ with superscript (1), (2) correspond to the fluid and porous regions respectively. **Gap region/ Fluid region:** No-slip condition at the flat bottom of the object ($u^{(1)} = 0,\ v^{(1)} = V$) at $y = h$; symmetry about y-axis ($u^{(1)} = 0,\ \frac{\partial v^1}{\partial x} = 0$) at $x = 0$; parallel flow at the periphery of the gap ($\frac{\partial u^{(1)}}{\partial x} = 0,\ v^{(1)} = 0$) at $x = L$; negligible of pressure effect at the periphery $p^1 = 0$ at $x = L$.

Porous region: Symmetric condition about y-axis ($u^{(2)} = 0,\ \frac{\partial v^{(2)}}{\partial x}$) at $x = 0$; finiteness at the bottom of the porous medium, i.e., $u^{(2)},\ v^{(2)}$ is finite at $y = -\infty$; below the periphery of the gap parallel flow condition and negligible pressure, i.e., $\frac{\partial u^{(2)}}{\partial x} = 0,\ v^2 = 0,\ p^{(2)} = 0$ at $x = L$.

At the porous liquid interface, we have, (i) Continuity of velocity component: $u^{(1)} = \varphi u^{(2)},\ v^{(1)} = \varphi v^{(2)}$ at $y = 0$ (ii) Continuity of stress: $\tau_{xy}^{(1)} = \tau_{xy}^{(2)},\ \tau_{yy}^{(1)} = \tau_{yy}^{(2)}$ (refer Song and Huang [3]). We introduce the corresponding non-dimensional variables: $\psi = \frac{\psi}{VL},\ x = \frac{x}{L},\ y = \frac{y}{h},\ p = \frac{p}{\frac{\mu V}{\sqrt{K_1/\varphi}}},\ \varepsilon = \frac{h}{L},\ Da_x = \frac{K_1}{L^2},\ Da_y = \frac{K_2}{L^2}$. Da_x and Da_y are the corresponding Darcy numbers along horizontal and vertical directions respectively which represent the ease at which flow can percolate through the pores. Since it is assumed that the gap flow initially is vertical from

*Corresponding author. Email: timir@maths.iitkgp.ernet.in

the porous medium, increasing vertical permeability enhance the gap flow. Hence our primary interest is the case $Da_y \geq Da_x$. After introducing the non-dimensional parameters the corresponding governing equations in terms of stream function reduce to

Fluid region:$(0 \leq y \leq 1)$

$$\frac{\partial^4 \psi}{\partial y^4} + 2\varepsilon^2 \frac{\partial^4 \psi}{\partial x^2 \partial y^2} + \varepsilon^4 \frac{\partial^4 \psi}{\partial x^4} = 0. \tag{2}$$

Porous region:$(-\infty < y \leq 0)$

$$\frac{\partial^4 \psi}{\partial y^4} + 2\varepsilon^2 \frac{\partial^4 \psi}{\partial x^2 \partial y^2} + \varepsilon^4 \frac{\partial^4 \psi}{\partial x^4} - \varepsilon^4 \frac{\varphi}{Da_y} \frac{\partial^2 \psi}{\partial x^2} - \varepsilon^2 \frac{\varphi}{Da_x} \frac{\partial^2 \psi}{\partial y^2} = 0. \tag{3}$$

We have solved Eqs. 2 and 3 analytically subject to the boundary conditions mentioned above. We have discussed the breakout phenomenon in terms of anisotropic ratio $\xi = Da_y/Da_x$ and the gap width ε.

RESULTS AND DISCUSSION

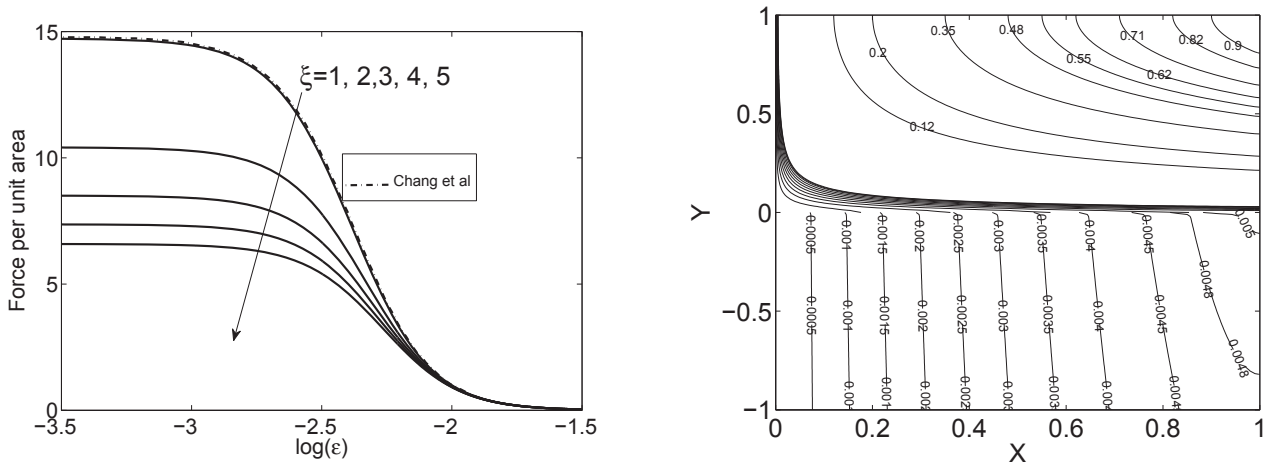

(a) (b)

Figure 2: (a) Force per unit area for different values of anisotropic ration for $Da_x = 1.02 \times 10^{-8}$, $V = 2.3 \times 10^{-5}$m/s (b) Streamlines near the interface region for $Da_x = 10^{-8},\ \xi = 1,\ \varepsilon = 10^{-1.5}$.

Fig. 2(a) shows the force per unit area with respect to the ratio of the gap width and the object length (ε) for different anisotropic ratio ξ. For an imposed constant velocity, force decreases with the anisotropic ratio. One may note that increase in the anisotropic ratio (i.e., increase of vertical permeability) assists more flow to come from the porous bed. This initiates increase in the gap ratio and reduces the lift-up force. This process indicates that an object can be lifted easily when the anisotropic ratio is high. Fig. 2(a) shows that force remains constant before the first turning point and reduces to zero at the breakout point ($\varepsilon = 10^{-1.7}$). Our results agree with Chang et al. [2] for $\xi = 1$, i.e., for corresponding isotropic situation. Initially when the gap width is less than the pore size the gap flow mainly comes vertically from the porous seabed. Flow from the periphery of the gap play a vital role for larger gap-width. Fig. 2(b) shows that when the breakout occurs ($\varepsilon = 10^{-1.5}$), most of the gap flow comes from the periphery of the gap.

References

[1] Mei Chiang C., Ronald W. Yeung, Ko-Fei Liu.: Lifting of a large object from a porous seabed. J. Fluid Mech 152, 203-215, 1985.

[2] Chang Y., L.H. Huang., F.P.Y. Yang.: Two-dimensional lift up problem for a rigid porous bed. Physics of fluids, 27, 2015.

[3] Song. C.H., Liang-Hsiung Huang.: Laminar poroelastic media flow. Journal of engineering mechanics, 126, 358-366, 2000.

[4] Kohr Mirela., RajaSekhar. G.P., John R. Blake.: Green's function of the Brinkman equation in a 2D anisotropic case. IMA journal of applied mathematics, 73, 374-392, 2008.

MACROSCOPIC MODELING OF SLIGHTLY COMPRESSIBLE GAS SLIP FLOW IN HOMOGENEOUS POROUS MEDIA

Didier Lasseux*[1], Francisco J. Valdés-Parada[2], and Mark Porter[3]
[1]*CNRS - Univ. Bordeaux, I2M - UMR 5295, Esplanade des Arts et Metiers - 33405 Talence Cedex - France*
[2]*Universidad Autónoma Metropolitana-Iztapalapa - Av. San Rafael Atlixco 186 - 09340 Mexico D.F. - Mexico*
[3]*Earth Systems Observations, MS D462 Los Alamos National Laboratory Los Alamos, NM 85745 - USA*

Summary A macroscopic model for slightly compressible gas slip flow in homogeneous porous media is derived by upscaling the microscopic boundary-value problem. A Darcy-like macroscopic momentum equation is obtained first, where the apparent permeability tensor, $\mathbf{K}_s$, is non intrinsic and features a non linear behavior with respect to the Knudsen number, $\overline{Kn}$. A further development is carried out using an expansion in $\xi\overline{Kn}$, ξ being related to the tangential momentum accommodation coefficient. All the macroscopic coefficients in this model are obtained from intrinsic and coupled closure problems. The upscaled model, up to the first order in $\overline{Kn}$, coincides with the classical Darcy-Klinkenberg law for an ideal gas. As illustrated from numerical solutions on model porous structures, validated from analytic solutions, higher-order terms of the expansion are required in order to recover the non-linear behavior of $\mathbf{K}_s$ versus $\overline{Kn}$.

INTRODUCTION

The interest for studying slightly compressible gas slip-flow in porous media for which the characteristic pore-size is comparable to the gas mean free path at the pressure and temperature under consideration is tremendous for many applications that encompass characterization of low permeable porous materials [4, 3, 6] involved in processes ranging from gas production [2], gas or nuclear waste storage, filtration and separation [1], to composite manufacturing [7], among many others. Consequently, a great deal of interest may also be focused on the prediction and estimation of the coefficients governing the physics of gas transport at the macroscale. This can be carried out by best-fitting experimental or numerical simulations. An alternative is to derive the upscaled model and to predict the associated coefficients. In this work, we follow this last alternative using the volume averaging method, which also allows identifying the corresponding length scale constraints and assumptions that support the model.

MACROSCOPIC MODEL

Using the volume averaging method, the macroscopic model is derived in which the momentum balance equation is given by $0 = -\nabla \langle p_\beta \rangle^\beta - \mu_\beta \mathbf{K}_s^{-1} \cdot \langle \mathbf{v}_\beta \rangle$ in which $\langle p_\beta \rangle^\beta$ is the intrinsic average of the gas pressure and $\langle \mathbf{v}_\beta \rangle$ the superficial (or filtration) velocity in the gas phase of dynamic viscosity μ_β. The apparent permeability, $\mathbf{K}_s$, can be predicted by solving a closure problem and is non intrinsic as it depends on the mean free path, $\overline{\lambda_\beta}$, in the gas phase. This closure problem was solved on periodic unit cells of model porous structures made of arrays of parallel cylinders arranged on a regular square pattern or randomly distributed cylinders (see Fig. 1). The resulting apparent permeabilities predicted from solving the closure problem on these structures are represented in Fig. 2 versus $\xi\overline{Kn} = \xi\overline{\lambda_\beta}/\ell_\beta$, for different values of the porosity, ε, ℓ_β being the characteristic pore size and ξ a parameter related to the tangential momentum accommodation coefficient of the gas-solid system.

Clearly, the apparent permeability depends non-linearly on $\overline{Kn}$, even though this number remains characteristic of the slip-flow regime, and this effect becomes more significant as porosity increases.



a) *b)* *c)*

Figure 1: Velocity fields on unit cells of 2D model porous structures. Unit pressure gradient along $\mathbf{e}_x$. *a)* and *b)* Square array of parallel cylinders - $\varepsilon = 0.8$ - $\xi\overline{Kn} = 1.8510^{-4}$ (*a*)) and $\xi\overline{Kn} = 0.185$ (*b*)). *c)* Randomly distributed parallel cylinders - $\varepsilon = 0.804$ - $\xi\overline{Kn} = 0.0185$.

*Corresponding author. Email: didier.lasseux@ensam.eu

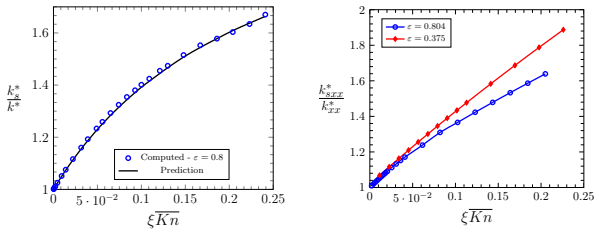

Figure 2: Apparent to intrinsic permeability ratio versus $\xi\overline{Kn}$. Left: square pattern of parallel cylinders - $\varepsilon = 0.8$. The solid line corresponds to an analytic solution. Right: random distribution of parallel cylinders.

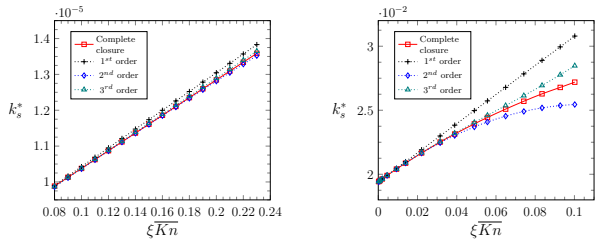

Figure 3: Dimensionless apparent permeability computed from the complete closure problem and using the expansion up to the 3rd order. Square pattern of parallel cylinders. Left: $\varepsilon = 0.25$. Right: $\varepsilon = 0.8$.

To further elucidate the non linear dependence of the velocity upon the pressure gradient versus the Knudsen number, the closure problem yielding $\mathbf{K}_s$ was developed using an expansion in $\xi\overline{Kn}$. This allows expressing the macroscopic momentum equation, up to the mth order in $\overline{Kn}$, under the form $\langle \mathbf{v}_\beta \rangle \simeq \nicefrac{1}{\mu_\beta}\mathbf{K} \cdot \left(\mathbf{I} + \sum_{j=1}^{m} \left[\!\left[\xi \right]\!\right]_\beta^j \mathbf{S}_j \right) \cdot \nabla \langle p_\beta \rangle^\beta$.

In this expression, $\mathbf{K}$ is the intrinsic permeability tensor, while $\mathbf{S}_j$ is the slip correction tensor at the jth order, $\mathbf{I}$ being the unit tensor. The tensors $\mathbf{K}$ and $\mathbf{S}_j$ can be predicted from their corresponding closure problems having all the same structure but coupled together. Up to the first order ($m = 1$), for which the corresponding apparent permeability remains linear in $\overline{Kn}$, the classical Darcy-Klinkenberg model is recovered if the gas is assumed to be ideal, as was already reported in a previous work [5]. The higher order terms allow recovering the non-linear behavior observed in the original model prior to the expansion. This is highlighted in figure 3 representing the apparent permeability versus $\xi\overline{Kn}$ that was computed from the solution of the closure problems up to the 3rd order on unit cells of the porous structure reported in Fig.1a. A careful analysis of the slip-like boundary condition in the closure problem at the jth order indicates that it contains an explicit dependence upon the curvature of the solid-fluid interface that is, however, filtered out for $j = 1$, explaining why, for a structure like the one in Fig.1a, the first-order apparent permeability becomes more inaccurate as porosity increases since curvature scales as $(1 - \varepsilon)^{-1/2}$.

CONCLUSIONS

Upscaling of slightly compressible gas slip flow in homogeneous porous media was carried out using the volume averaging method yielding a macroscopic momentum balance equation having a Darcy-like form in which the apparent permeability depends non-linearly on the Knudsen number in the general case. Using an expansion in the Knudsen number, the apparent permeability was expressed in terms of the intrinsic permeability and slip-correction tensors, all of them being determined from closure problems intrinsic to the microstructure of the medium. A thorough analysis indicates that the non-linear dependence of the apparent permeability on the Knudsen number is related to the curvature of the solid-fluid interface.

References

[1] R. D. Chmielewski and S. L. Goren. *Environ. Sci. Technol.*, 6(13):1101–1105, 1972.
[2] H. Darabi, A. Ettehad, F. Javadpour, and K. Sepehrnoori. *J. Fluid Mech.*, 710:641–658, 2012.
[3] Y. Jannot and D. Lasseux. *Rev. Sci. Instrum.*, 83(1):015113, 2012.
[4] D. Lasseux, P. Jolly, Y. Jannot, E. Sauger, and B. Omnes. *J. Pressure Vessel Technol.*, 133(4):041401, 2011.
[5] D. Lasseux, F. J. Valdes Parada, J. A. Ochoa Tapia, and B. Goyeau. *Phys. Fluids*, 26(5):053102, 2014.
[6] S. Profice, D. Lasseux, Y. Jannot, N. Jebara, and G. Hamon. *Petrophysics*, 53:430–438, 2012.
[7] T. Zhang, P. Zhang, C. K. Law, and F. Qi. *Chem. Vap. Deposition*, 15:274–280, 2009.

CONTROLLABLE CAPILLARY FLOW AND DIRECT OIL RECOVERY IN CARBON NANOTUBE SPONGES

Xiying Li[1], Yahui Xue[1], Anyuan Cao[2], Huiling Duan[1, a)]
[1] *State Key Laboratory for Turbulence and Complex Systems, Department of Mechanics and Engineering Science, College of Engineering, Peking University, Beijing, P. R. China*
[2] *Department of Materials Science and Engineering, College of Engineering, Peking University, Beijing, P. R. China*

Summary: Nanoscale fluid transport with high controllability and efficiency is highly desired in developing high performance nanofluidic materials and systems. In this work, fast and elaborately controllable fluid flow in carbon nanotube (CNT) sponges has been achieved. Based on the electrocapillary effect, the affinity between the electrolyte and the CNT surfaces can be regulated by applying low electric potentials, which produces or diminishes the capillary pumping pressure inside the sponge, leading to controllable fluid flow. Prefilled oil in the sponge is directly extractable with high recovery by electrically switching CNT surfaces from oleophilic to hydrophilic assisted by surfactant. Moreover, it is possible to build deformable imbibition media with desired pore sizes since the bulk sponges can be compressed to different degrees while maintaining the imbibition function.

INTRODUCTION

Nanoscale fluid transport is a phenomenon widely presents in processes such as energy conversion and water desalination. Enabling controllable, efficient fluid transport through predefined channels is an important consideration in developing high performance nanofluidic systems for biological and environmental applications [1]. The spontaneous imbibition of fluids in nanoporous hydrophilic media is one issue of present interest. The imbibition dynamics are determined by the geometry of the porous host, the fluid-wall interaction, the fluidity and capillarity of the liquid imbibed. Those properties are static or hardly externally changeable during the transport process, rendering a flexible, active control of the fluid flow very challenging. Recently, the electrocapillary effect was utilized to accelerate the liquid flow through a conductive media (nanoporous gold) under low operating voltages (e.g., −1 V) [2]. However, more elegant control of the fluid flow in nanoporous gold requires preloading of another organic solution (e.g., cyclohexane). In addition, flexible nanofluidic systems with tailored pore sizes are also highly desired for many applications.

Carbon nanotube (CNT) sponges, readily fabricated by chemical vapour deposition, are macroscopic assemblies of nanotubes with high porosity, intrinsic hydrophobicity, electrical conductivity, and mechanical flexibility [3]. In this work, we show that these CNT sponges could serve as an electrocapillary imbiber to achieve efficient water imbibition under low voltages and on–off switchability. Moreover, electrocapillary water imbibition can displace adsorbed oil in the porous sponge and extrude oil out smoothly and completely.

ELECTROCAPILLARY IMBIBITION IN CARBON NANOTUBE SPONGES

Sponge samples and experiment setup

Sponge samples supported by copper wires were used for imbibition test under electric potential. As illustrated in Figure 1A, the sponge sample in contact with an electrolyte solution was hung from a microbalance to monitor the instantaneous mass change. A three-electrode potentiostat was used to control the electric potential of the system with the sponge as the working electrode, a commercial Ag/AgCl (in 3 M KCl) as the reference electrode, and another sponge as the counter electrode in the electrolyte solution [4]. The electrolyte solution was 1 M KOH.

Electrolyte imbibition in empty CNT sponges

We first probed the possibility to render CNT sponges from intrinsically hydrophobic to hydrophilic by applying electric potential so as to initialize the electrolyte imbibition. The mass change monitored by the microbalance keeps almost constant in potential range from −0.1 to −0.52 V, indicating no electrolyte was sucked inside the pores, as an as-grown CNT sponge is hydrophobic and water cannot enter its pores spontaneously. Right after this threshold voltage, imbibition was initiated with a detectable change of m which kept increasing upon more negative potentials. By applying two voltages (-1.2 V and -0.13 V) alternatively, controlled on-off switching is demonstrated (Figure 1B). This means that the liquid front is completely arrested within the pores in the absence of a proper negative potential. The flow velocity can be adjusted by applied voltage as well. This on-off switchable imbibition rate is over 20-fold higher than in the oil-pre-saturated nanoporous gold.

[a)] Corresponding author. Huiling Duan: hlduan@pku.edu.cn;

Oil imbibition in compressed CNT sponges

We investigated how compression affects the capacity and effect pore size of CNT sponges using cyclohexane imbibition. The saturation mass value is found to decrease significantly in compressed sponges, and the imbibition capacity can be tailored over nearly an order of magnitude by mechanical compression. Intriguingly, the liquid invasion velocity initially drops for the sponge compressed to 38% of original volume, but then starts to increase under further compression. This may be related the well-known phenomenon in CNT systems, i.e., liquid slippage, which shows faster fluid transport through smaller CNT pores.

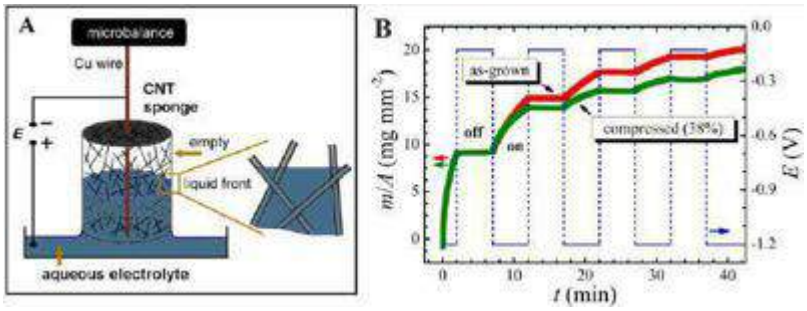

Figure 1. (A) Experiment setup of the imbibition in CNT sponges. (B) On-off switching during the imbibition of 1M KOH into as-grown and unidirectionally compressed CNT sponges, respectively.

Direct oil recovery in CNT sponges

If the CNT sponge is saturated with organic solvent, the electrolyte imbibition is suppressed even when a relatively large voltage is applied. To solve the problem, a regime of surfactant-assisted electrocapillary imbibition is adopted. With the help of surfactant, electrolyte is imbibed into the CNT sponge and the organic solvent is extracted out smoothly and completely by applying a low voltage. The process is repeatable and the capacity of oil imbibition and oil displacement is maintained. Organic solvents in a wide range of viscosities can be extracted, and the recovery of the organic solvents can go up to 95%.

CONCLUSIONS

We have demonstrated a high-performance CNT sponge-based nanoporous imbiber utilizing its 3D conductive network and highly porous structure. Compared to traditional porous materials, the CNT sponges show distinct advantages such as easy on–off control, fast imbibition and high capacity, as well as being compressible and pore-size tunable. A simple and efficient electrocapillary method to recover adsorbed oil from saturated CNT sponges in controlled manner has been developed. More than 95 % of adsorbed oil could be directly recovered, and the CNT sponges can be reused for many cycles with high capacity.

References

[1] Whitby, M., Quirke, N.: Fluid flow in carbon nanotubes and nanopipes. *Nat. Nanotechnol.* **2**: 87-94, 2007.

[2] Xue Y., Markmann J., Duan H., WeissmüllerJ., Huber P.: Switchable imbibition in nanoporous gold. *Nat. Commun.* **5**:4237, 2014.

[3] Gui X. Wei J., Wang K., Cao A., Zhu H., Jia Y., Shu Q., Wu D.: Carbon Nanotube Sponges. *Adv. Mater.* **22**, 617-621, 2010.

[4] Xue Y., Yang Y., Sun H., Li X., Wu S., Cao A., Duan H.: A Switchable and Compressible Carbon Nanotube Sponge Electrocapillary Imbiber. *Adv. Mater.*, **27**, 7241-7246, 2015.

STEREOSCOPIC PARTICLE IMAGE VELOCIMETRY FOR THE STUDY OF FLOW DYNAMICS IN A PACKED BED

Shervin Khayamyan, Per Gren, Henrik Lycksam, T. Staffan Lundström and J. Gunnar I. Hellström

Division of Fluid and Experimental Mechanics, Luleå University of Technology, Luleå, SE-971 87, Sweden

ABSTRACT

Stereoscopic particle image velocimetry has been used to investigate the flow dynamic in a randomly packed bed of mono sized spherical particles. By using an index matched fluid the studied bed is optically transparent and measurements can be performed within the bed. The velocity field observations are done for particle Reynolds numbers between 30 and 4000. Results show that in porous media the dynamics of flow can vary significantly from pore to pore. Also in the studied plane a considerable amount of the fluid moves in the perpendicular directions to the main flow direction and the averaged magnitude of the velocity in the main direction is only about 40 % of the magnitude of the total velocity. This percentage is only weakly dependent on Re_p.

INTRODUCTION

Fluid motion within porous media takes place in geological, biological and technical processes. Due to the vast amount of applications the area has been in focus for more than a century. Still the knowledge of some fundamental issues is lacking. This includes information about the detailed flow as the Reynolds number increases and the flow becomes inertia dominated or even turbulent. To disclose the details of the flow experimentally, tomographic or optical techniques may be applied. Tomographic techniques include Magnetic Resonance Imaging (MRI) (Baldwin et al. **1996**; Sederman et al. **1997** and **1998**; Ogawa et al. **2001** and Suekane et al. **2003**), Particle Emission Tomography (PET) (Khalili et al. **1998**), Nuclear Magnetic Resonance (NMR) imaging (Baldwin et al. 1996 and Johns and Gladden 1999), Gamma attenuation and X-ray. The drawbacks of these techniques are that they require rather expensive test facilities and may give poor spatial and temporal resolution (Kutsovsky et al. **1996**; Chang and Watson **1999** and Gladden et al. **2006**).

In contrast to the tomographic techniques, the relative simplicity and low cost of optical techniques such as particle image velocimetry (PIV) make them attractive. Usage of such optical techniques in porous media require all phases to be transparent and refractive index matched (RIM) (Johnston et al. **1975**; Yarlagadda and Yoganathan **1989**; Stephenson and Stewart **1986**; Peurrung et al. **1995**; Moroni and Cushman **2001**; Rashidi et al. **1996**; Huang et al. 2008; Lachhab et al. 2008 and Patil and Liburdy 2013). One result from a recent study (Khayamyan et al, 2014, 2015) with PIV on packed beds is that measurements of all velocity components are required to get a full understanding of the flow.

EXPERIMENTAL

The studied packed bed is made from a randomly packing of Plexiglas (PMMA) spherical particles with a diameter D_p = 12.5 mm. The bed has a square cross section of 100 × 100 mm^2 and its length is 310 mm. The bed width to particle diameter ratio is consequently 8. This is about two times larger than the bed width to particle diameter ratio used by Patil and Liburdy 2013. This ratio is large enough to avoid major effects of channeling near the confining walls on bed overall porosity and permeability (Chu and Ng 1989). The bed overall porosity (ϕ) which is the ratio of void volume to bed volume is about 0.414 from direct geometrical calculations. All PIV measurements were performed at the mid-section of this porous bed. The fluid is circulated in a closed loop with a centrifugal pump, Tapflo HTM15PP, from an atmospheric pressure storage tank where the temperature of the fluid is regulated and kept at 20 ± 0.1 $^{\circ}$C with a temperature control unit. The fluid is pumped through an electromagnetic flowmeter from ABB, ProcessMaster FEP300, to the Plexiglas box and finally back to the storage tank in a completely closed system. The pressure difference over the porous bed was recorded with pressure transducers from General Electric, GE PTX5012.

As already mentioned the Plexiglas box is longer than the bed to enable a uniform flow entering and leaving the bed. To fulfill this requirement the jet entering the box is broken and pushed towards the side walls by a baffle plate. After the baffle plate the flow passes through a net and a honeycomb to reduce its level of fluctuations and also to break down large scale eddies. The net has square openings with a mesh size of 2 × 2 mm^2 and the cells in the honeycomb have a circular cross-section with a diameter of 2 mm. The thickness of the honeycomb in the flow direction is 25 mm. The inlet to the packed bed is 150 mm downstream the honeycomb. To have optical access to the flow field within the bed, the bed has to transmit light rays without distortion. To have such a medium the refractive index of the working fluid is matched to that of the spheres in the bed.

A commercial PIV system from LaVision GmbH was used for imaging. This system is based on a double pulsed Nd:YAG laser at a wavelength of 532 nm with a maximum frequency of 100 Hz, a minimum inter-frame time for image pairs of 5 μs, and two LaVision double-frame FlowMaster Imager Pro cameras with spatial resolution of 1280 × 1024 pixels per frame with pixel size of 12 × 12 μm^2. Two Nikon AF Nikkor 105 mm lenses were used, with an f-stop of 2.8. The time

[a] Corresponding author. Email: staffan.lundstrom@ltu.se.

delay between image pairs was adjusted to restrict seeding particles mean displacements between 6 to 8 pixels. The laser and camera were mounted on a 3D traversing system so that the laser sheet and camera can be moved up to 500 mm in the *x*-, *y*- and *z*-directions. Hollow glass spheres with a diameter of 10 µm from Dantec were used as seeding particles. The PIV software DaVis 7.2.2 based on a cross-correlation algorithm was used to derive velocity vectors. A multi-step correlation processing algorithm with decreasing window size was used to evaluate recorded images with a final window size of 32 × 32 pixels. The overlap of windows was constant at 50 % for all steps. This final window size gives a vector spacing of 0.28 mm or 44 vectors per particle diameter. Vectors, for which, RMS exceeds 1.5 times of the neighboring vectors RMS were recognized as false vectors and were removed. At the end a 3 × 3 Gaussian kernel was used to smooth the vector field. All velocity data presented here are located in the x-y plane near the center of the bed. Stereoscopic PIV consists of two cameras capturing the particles in the light sheet from two different directions giving a stereo vision in the same fashion as the human eyes.

RESULTS

Time-averaged velocity fields at two Re are presented in Figure 1. Since the main flow is in the x-direction u_x is mostly positive while u_y and u_z take up a fair amount of negative values. Statistical analysis yields that u^* covers a narrower range at $Re_p \approx 1460$ due to less pronounced recirculation zones probably caused by turbulent flow. A comparison between the velocity vector field at $Re_p \approx 300$ and 1460 shows the same trend, a more uniform flow being aligned in the axial direction of the pores like flow fields in channel flow. Also the rotational part of the flow decreases significantly with Re_p.

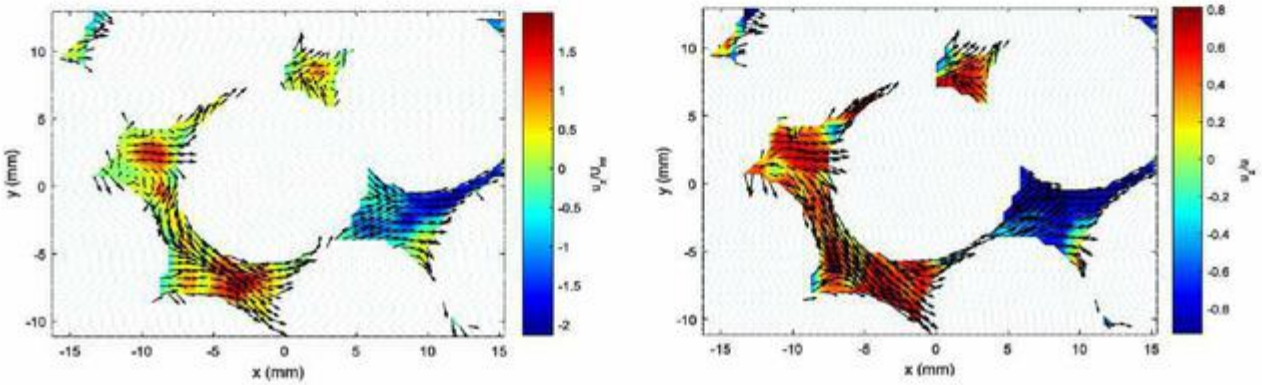

Figure 1. Velocity vector field consist of u_x and u_y components and u_z contour plot at $Re_p \approx 300$ and 1460.

References

[1] Agelinchaab, M., M. F. Tachie, et al. (2006). "Velocity measurement of flow through a model three-dimensional porous medium." Physics of Fluids **18**(1): 17105-1-11.

[2] Baldwin, C. A., Sederman, A. J., Mantle, M. D., Alexander, P., & Gladden, L. F. (1996). Determination and characterization of the structure of a pore space from 3D volume images. *Journal of Colloid and Interface Science, 181*(1), 79-92. .

[3] Chang, C., & Watson, A. T. (1999). NMR imaging of flow velocity in porous media. *AIChE Journal, 45*(3), 437-444.

[4] Chu, C., & Ng, K. (1989). Flow in packed tubes with a small tube to particle diameter ratio. *AIChE Journal, 35*(1), 148-158.

[5] Gladden, L., Akpa, B., Anadon, L., Heras, J., Holland, D., Mantle, M., et al. (2006). Dynamic MR imaging of single-and two-phase flows. *Chemical Engineering Research and Design, 84*(4), 272-281.

[6] Huang, A. Y., Huang, M. Y., Capart, H., & Chen, R. (2008). Optical measurements of pore geometry and fluid velocity in a bed of irregularly packed spheres. *Experiments in Fluids, 45*(2), 309-321.

[7] Khalili, A., Basu, A., & Pietrzyk, U. (1998). Flow visualization in porous media via positron emission tomography. *Physics of Fluids (1994-Present), 10*(4), 1031-1033.

[8] Khayamyan, S., & Lundström, T. S. (2015b). Interaction between the flow in two nearby pores within a porous material during transitional and turbulent flow. *Journal of Applied Fluid Mechanics, 8*(2), 281-290.

[9] Khayamyan, S., Lundström, T. S., & Gustavsson, L. H. (2014). Experimental investigation of transitional flow in porous media with usage of a pore doublet model. *Transport in Porous Media, 101*(2), 333-348.

[10] Kutsovsky, Y., Scriven, L., Davis, H., & Hammer, B. (1996). NMR imaging of velocity profiles and velocity distributions in bead packs. *Physics of Fluids (1994-Present), 8*(4), 863-871.

[11] Lachhab, A., Zhang, Y., & Muste, M. V. (2008). Particle tracking experiments in Match-Index-Refraction porous media. *Groundwater, 46*(6), 865-872.

[12] Moroni, M., & Cushman, J. H. (2001). Statistical mechanics with three-dimensional particle tracking velocimetry experiments in the study of anomalous dispersion. II. experiments. *Physics of Fluids (1994-Present), 13*(1), 81-91.

[13] Ogawa, K., Matsuka, T., Hirai, S., & Okazaki, K. (2001). Three-dimensional velocity measurement of complex interstitial flows through water-saturated porous media by the tagging method in the MRI technique. *Measurement Science and Technology, 12*(2), 172.

[14] Patil, V.A., Liburdy, J.A., "Optical measurement uncertainties due to refractive index mismatch for flow in porous media" Experimental in fluids, 53:1453–1468 (2012)

[15] Patil, V. A., & Liburdy, J. A. (2013). Flow characterization using PIV measurements in a low aspect ratio randomly packed porous bed. *Experiments in Fluids, 54*(4), 1-19.

[16] Peurrung, L. M., Rashidi, M., & Kulp, T. J. (1995). Measurement of porous medium velocity fields and their volumetric averaging characteristics using particle tracking velocimetry. *Chemical Engineering Science, 50*(14), 2243-2253.

[17] Rashidi, M., Peurrung, L., Tompson, A., & Kulp, T. (1996). Experimental analysis of pore-scale flow and transport in porous media. *Advances in Water Resources, 19*(3), 163-180.

[18] Sederman, A., Johns, M., Alexander, P., & Gladden, L. (1998). Structure-flow correlations in packed beds. *Chemical Engineering Science, 53*(12), 2117-2128.

[19] Sederman, A., Johns, M., Bramley, A., Alexander, P., & Gladden, L. (1997). Magnetic resonance imaging of liquid flow and pore structure within packed beds. *Chemical Engineering Science, 52*(14), 2239-2250.

[20] Stephenson, J., & Stewart, W. (1986). Optical measurements of porosity and fluid motion in packed beds. *Chemical Engineering Science, 41*(8), 2161-2170.

[21] Suekane, T., Yokouchi, Y., & Hirai, S. (2003). Inertial flow structures in a simple-packed bed of spheres. *AIChE Journal, 49*(1), 10-17.

[22] Yarlagadda, A., & Yoganathan, A. (1989). Experimental studies of model porous media fluid dynamics. *Experiments in Fluids, 8*(1-2), 59-71.

HYGROMECHANICAL BEHAVIOR OF HEMICELLULOSE AND S2 CELL WALL LAYER OF WOOD

Chi Zhang[1,2a)], Karol Kulasinski[1], Dominique Derome[2], Jan Carmeliet[1,2]
[1]*Chair of Building Physics, ETH Zürich, Swiss Federal Institute of Technology Zürich, Zürich, Switzerland*
[2] *Laboratory for Multiscale Studies in Building Physics, Empa, Swiss Federal Laboratories for Materials Science and Technology, Dübendorf, Switzerland*

Summary Molecular dynamics (MD) simulations are conducted to investigate arabinoglucuronoxylan (AGX), one of the major hemicellulose in softwood. Mechanical tests and structural analyses reveal that mechanical weakening happens with the increasing of moisture content until saturation point, due to the loss of interpolymer hydrogen bonds. Thermal softening and glass transition temperature are also discussed. These results will help improve our atomic model of wood cell wall S2 layer to unravel the underlying mechanism of hygromechanical behaviour of wood cell wall.

INTRODUCTION

The wood cell wall S2 layer, a nanoporous composite material that strongly interacts with moisture, is the thickest cell wall layer which plays a key role in the hygromechanical behavior of wood. It consists of cellulose, hemicelluloses and lignin. Xylan is the most common hemicellulose and the second most abundant biopolymer in plant[1]. The aim of this study is to investigate the hygromechanical properties of the S2 layer, more especially to understand its swelling and moisture-induced shape memory effect. The understanding of this behavior is important with respect to the paper, pharmaceutical, cosmetic, biofuel and food industries.

Molecular dynamics simulations, where the time evolving trajectory of a set of interacting atoms is presented by integrating the equations of motion, is applied in this study. Simulations capture the system behavior across a subtle spatiotemporal domain—length scales up to thousands of angstroms, and timescales up to milliseconds, at femtosecond resolution.

HYGROMECHANICAL BEHAVIOR OF AGX

In this study, we investigate a major hemicellulose in softwood: arabinoglucuronoxylan. We model the AGX according to the reported chemical composition and stereochemical structure[2], and then randomly add water molecules to the bulk dry material thus mimicking the adsorption phenomenon. Mechanical tests as well as comprehensive structural analyses are conducted to identify the sorption isotherm, the bulk and shear stiffness, the free swelling, the diffusion coefficient, as well as porosity changes and hydrogen bonding breakage, as the moisture content increases. With the increasing of moisture content, the AGX material swells in a linear and isotropic way with an almost constant swelling coefficient. The diffusion coefficient increases with moisture content which is mainly related to an increase of porosity and a decrease of tortuosity. The stiffness decreases with increasing moisture content until around 30% (mass by mass), after which no further weakening is observed. The weakening is attributed to the breakage of hydrogen bonds. At moisture contents higher than 30%, no hydrogen bond breakage occurs explaining the constant mechanical properties above fiber saturation point as observed in macroscopic experiments. Finally, we also studied the glass transition temperature for dry and wet materials and the important thermal softening of the material.

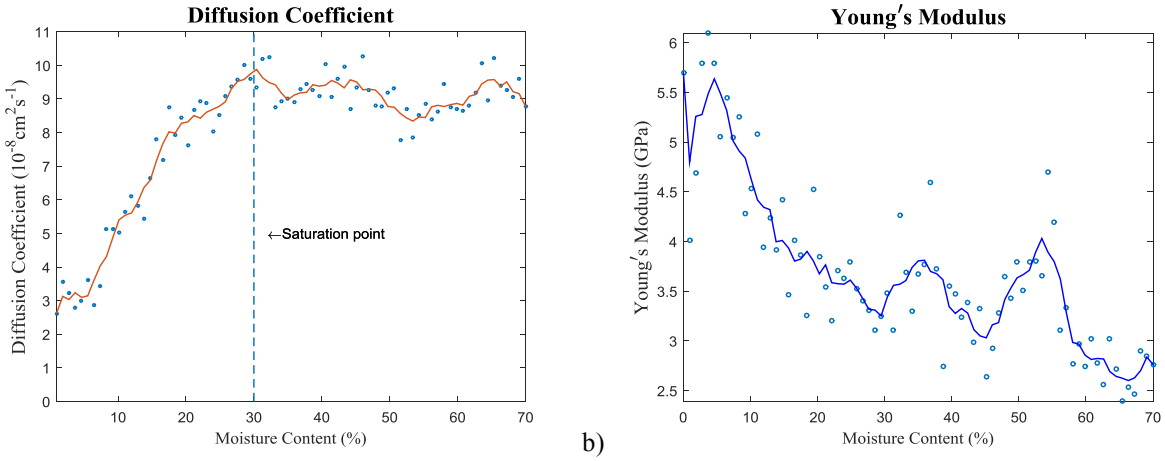

Fig. a) Diffusion coefficient of water; b) average Young's modulus.

[a)] Corresponding author. Email: zhangchi@student.ethz.ch

In a next step, AGX is combined with cellulose[3], galactoglucomannan[4] and lignin, to form a representative system of wood cell wall S2 layer. Different representative systems are studied to identify its main hygromechanical properties as well as the bonding between the microfibrils and the matrix. Special attention is paid to the so-called hot spots connecting different microfibrils [5]. The final goal of this study is to upscale the MD-identified hygromechanical behavior into a poro-mechanical finite element model allowing also to unravel the underlying mechanism of sorption hysteresis and moisture-related shape memory effect [6].

References

[1] Stephen A. M., in: "The Polysaccharides", G. O. Aspinall, Ed., Academic, San Diego, CA, 1983, pp. 98–193

[2] Aspinall, G. O., and K. M. Ross., "315. The degradation of two periodate-oxidised arabinoxylans", Journal of the Chemical Society (Resumed), 1963, pp. 1681-1686.

[4] Kulasinski K., Guyer R., Derome D., and Carmeliet J., "Impact of Moisture Adsorption on Structure and Physical Properties of Amorphous Biopolymers", Macromolecules, 2015, 48, pp. 2793−2800.

[4] Kulasinski, K., Keten, S., Churakov, S. V., Derome D., and Carmeliet J., "A comparative molecular dynamics study of crystalline, paracrystalline and amorphous states of cellulose", Cellulose, 2014, 21(3), pp.1103–1116.

[5] Cosgrove D J. "Re-constructing our models of cellulose and primary cell wall assembly", Current opinion in plant biology, 2014, 22, pp. 122-131.

[6] Derome D, Rafsanjani A, Patera A, Guyer R, Carmeliet J., "Hygromorphic behaviour of cellular material: hysteretic swelling and shrinkage of wood probed by phase contrast X-ray tomography, Philosophical Magazine, 92, pp. 3680-3698

PORE SCALE MODELING OF CO_2 MIGRATION IN POROUS ROCKS UNDER CONDITIONS OF SALINE AQUIFERS

Y.Q. Zu[1, a)]

[1]*Department of Mechanics and Engineering Science, Fudan University, Shanghai, 200433, China*

Abstract In this paper, CO_2 migration in porous rocks under conditions of saline aquifers is numerically simulated with lattice Boltzmann method (LBM). An improved LBM model has been given to minimize the unphysical interfacial current. Using the newly formulated LBM model, brine-CO_2 two phase flow past through real rock geometry under the conditions of CO_2 storage in saline aquifers is numerically simulated in pore scale. Through the simulation, the effects of different parameters on the permeability of the pores rocks are analysed and discussed.

INTRODUCTION

Geological storage of CO_2 in saline aquifers is presently one of the most promising technologies for reducing the emissions of CO_2 into the atmosphere [1]. So far, numerical investigations of CO_2 transport in porous media have been conducted using two different types of models, i.e. continuum field-scale models [2] and pore-scale models [3]. The continuum field-scale models can only provide information under average conditions and rely heavily on the knowledge of the effective properties of the rock such as relative permeability and capillary pressure functions, which depend critically on the geometry and topology of the pore space and the interaction between the fluids and the pore boundaries. Thus, it is necessary to conduct the pore-scale modeling to identify key parameters or physical processes that control macroscopic phenomena but which are not captured by continuum field-scale models. In this paper, a new LBM method is developed to simulate brine-CO_2 two-phase flow past through porous rocks in pore scale.

METHODOLOGY

LBE for Interface Capturing

According to the phase-field theory, an interface-capturing equation is formulated as [4],

$$\partial_t \phi + \nabla \cdot (\phi \mathbf{u}) = M \nabla^2 \mu_\phi \tag{1}$$

where $\mathbf{u}$ and t are the velocity and time respectively; and M is a diffusion parameter named as mobility, μ_ϕ is a chemical potential, ϕ acts as an order parameter to distinguish the different fluids.

A LBE for interface capturing of Zheng et al. [5] is introduced below to recover the Cahn-Hilliard equation,

$$f_\alpha(\mathbf{x}+\mathbf{e}_\alpha \delta t, t+\delta t) - f_\alpha(\mathbf{x},t) = (1-q)[f_\alpha(\mathbf{x}+\mathbf{e}_\alpha \delta t, t) - f_\alpha(\mathbf{x},t)] - [f_\alpha(\mathbf{x},t) - f_\alpha^{(eq)}(\mathbf{x},t)]/\tau_f \tag{2}$$

where, $\mathbf{x}$ is the space coordinate; $\mathbf{e}_\alpha$ is discrete velocity vector in the αth direction; δt is the time step during which the particles travel the lattice spacing; τ_f is a dimensionless relaxation time; $f_\alpha(\mathbf{x},t)$ is a distribution function for the order parameter ϕ, while $f_\alpha^{(eq)}(\mathbf{x},t)$ is its corresponding equilibrium state, $q = 1/(\tau_f + 0.5)$ is a constant

Eq. (2) was initially proposed to track the interface of two phase flow in 2D [5]. In this study, it is extended to solve 3D problem by developing new equilibrium distribution function $f_\alpha^{(eq)}(\mathbf{x},t)$. On the basis of three-dimensional fifteen-velocity (D3Q15) lattice structure [6], $f_\alpha^{(eq)}(\mathbf{x},t)$ is developed as

$$f_\alpha^{(eq)} = \begin{cases} \varphi - (1-\omega_0)\xi\mu_\varphi / c_s^2, & \alpha = 0 \\ \omega_\alpha[\xi\mu_\varphi + (\mathbf{e}_\alpha \cdot \mathbf{u})\varphi]/c_s^2, & \alpha = 1-14 \end{cases} \tag{3}$$

Where c_s is the sound speed for an ideal fluid, ω_α is the weighting coefficient in the αth direction, ξ is a constant controlling the strength of mobility, $M = q(q\tau_f - 1/2)\xi\delta t$. ϕ is computed by $\phi = \sum_\alpha f_\alpha$.

LBE for Velocity and Pressure

A LBE for velocity and pressure fields of He et al. [7] is introduced to solve the velocity and pressure field,

$$\begin{aligned} &g_\alpha(\mathbf{x}+\mathbf{e}_\alpha \delta t, t+\delta t) - g_\alpha(\mathbf{x},t) = -[g_\alpha(\mathbf{x},t) - g_\alpha^{(eq)}(\mathbf{x},t)]/\tau_g + \\ &[(2\tau_g - 1)/(2\tau_g)](\mathbf{e}_\alpha - \mathbf{u})[\Gamma_\alpha(\mathbf{u})(\mathbf{F}+\mathbf{G}) + (\Gamma_\alpha(\mathbf{u}) - \Gamma_\alpha(0))\nabla(\rho c_s^2)]\delta t \end{aligned} \tag{4}$$

a) Corresponding author. Email: yzu@fudan.edu.cn.

where, **F** is the force associated with surface tension, τ_g is a relaxation time related to fluid kinetic viscosity, and **G** is the body force. g_α is the distribution function for pressure and velocity, $g_\alpha^{(eq)}$ is its equilibrium states given by

$$g_\alpha^{(eq)}(\mathbf{x},t) = \Gamma_\alpha(0)p + [\Gamma_\alpha(\mathbf{u}) - \Gamma_\alpha(0)]\rho c_s^2 \quad , \Gamma_\alpha(\mathbf{u}) = \omega_\alpha[1 + \frac{\mathbf{e}_\alpha \cdot \mathbf{u}}{c_s^2}(\mathbf{e}_\alpha \cdot \mathbf{u}) + \frac{(\mathbf{e}_\alpha \cdot \mathbf{u})^2}{2c_s^4} - \frac{\mathbf{u} \cdot \mathbf{u}}{2c_s^2}] \tag{5}$$

Hydrodynamic pressure p and the macroscopic velocity $\mathbf{u}$ are computed by,

$$p = \sum_\alpha g_\alpha - \frac{1}{2}\mathbf{u} \cdot \nabla \rho c_s^2 \delta t \quad , \qquad \mathbf{u} = [\sum_\alpha \mathbf{e}_\alpha g_\alpha + \frac{1}{2}(\mathbf{F} + \mathbf{G})c_s^2 \delta t] / \rho c_s^2 \tag{6}$$

NUMERICAL SIMULATION

The sandstone rocks from Bramhope [8] are studied. Samples of the rocks are scanned using the X-ray computed micromotography (CMT) and digital images with a size of 1mm×1mm×1mm are produced, an example of which is shown in Fig. 1. It is assumed that the fluid flow through rocks is laminar and fluid parameters used in the LBM simulations are: ρ_{brine}/ρ_{CO2} =2, μ_{brine}/μ_{CO2} =8 and contact angle is set as 30°. The fluids flow is driven by the pressure gradient and gravity along the vertical (upward) direction and the periodic boundary condition is imposed on the top and bottom faces. Two layers of voids are added on top and bottom faces to enable the boundary conditions to be applied. The side surfaces are made symmetric boundary conditions. Fig. 2 shows the preliminary results of time dependent phase distributions when the situation of brine=0.79.

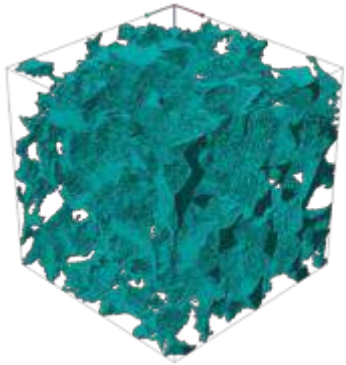

Fig. 6. Digital image of a rock reproduced by the CMT.

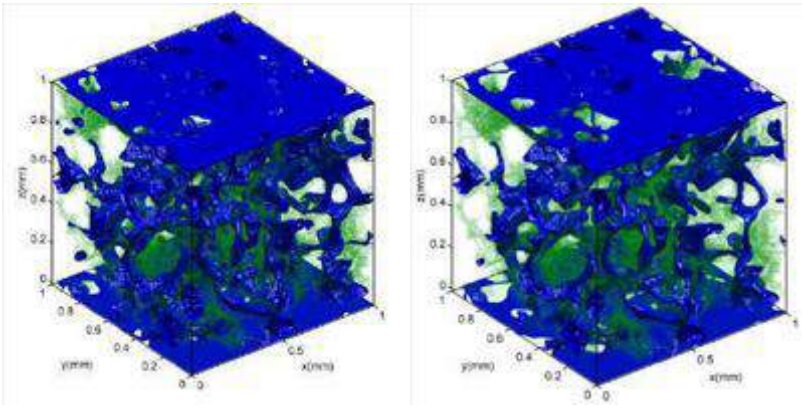

(a) t=400s; (b)t=500s

Fig. 7. Evolution of phase distribution with brine saturation of 0.79 (green: solid; blue: supercritical CO_2; clear: saline water).

CONCLUSIONS

In this paper, CO_2 migration in porous rocks under conditions of saline aquifers is numerically investigated using LBM in pore scale. A new LBM method has been developed. Using the newly formulated LBM model, brine-CO_2 two phase flow past through real rock geometries is numerically simulated. CO_2 and saline-water properties under conditions of CO_2 storage in saline aquifers are used in the simulation. Through the simulation, the effects of different parameters on the permeability of the pores rocks have been analysed and discussed.

References

[1] IPCC Special Report on Carbon Dioxide Capture and Storage. Cambridge University Press, Cambridge, UK; IPCC, 2005.
[2] Jiang X. A review of physical modelling and numerical simulation of long-term geological storage of CO2. Appl Energ. 2011;88:3557-66.
[3] Ellis JS, Bazylak A. Dynamic pore network model of surface heterogeneity in brine-filled porous media for carbon sequestration. Phys Chem Chem Phys. 2012;14:8382-90.
[4] Zu YQ, He S. Phase-field-based lattice Boltzmann model for incompressible binary fluid systems with density and viscosity contrasts. Physical Review E. 2013;87.
[5] Zheng HW, Shu C, Chew YT. Lattice Boltzmann interface capturing method for incompressible flows. Physical Review E. 2005;72:056705.
[6] Yan YY, Zu YQ. A lattice Boltzmann method for incompressible two-phase flows on partial wetting surface with large density ratio. J Comput Phys. 2007;227:763-75.
[7] He XY, Chen SY, Zhang RY. A lattice Boltzmann scheme for incompressible multiphase flow and its application in simulation of Rayleigh-Taylor instability. J Comput Phys. 1999;152:642-63.
[8] Lamy-Chappuis B, Angus D, Fisher Q, Grattoni C, Yardley BWD. Rapid porosity and permeability changes of calcareous sandstone due to CO2enriched brine injection. Geophys Res Lett. 2014;41:399-406.

FS06 - Fluid Structure Interactions

TS.FS06-1.01	Nové-Josserand, Clotilde - Converting wave energy from fluid-elasticity interactions	3226
TS.FS06-1.02	Boucher, Jean-Philippe - Optimal design of rectangular fins for underwater propulsion	3228
TS.FS06-1.03	Dias, Frederic - A potential-flow model of viscous dissipation for the oscillating wave surger converter	3230
TS.FS06-1.04	Ducloué, Lucie - Multiple bubble propagation modes in elasto-rigid models of airway reopening	3232
TS.FS06-1.05	Medraj, Mamoun - Water Droplet Impingement Erosion: Testing, Mechanisms and Improved Representation	3234
TS.FS06-2.01	Hanna, James - Catenaries in viscous fluid	3236
TS.FS06-2.02	Kamrin, Ken - Eulerian Method for FSI Based on the Reference Map	3237
TS.FS06-2.03	Labbé, Romain - Mist harvesting with vertical fibers	3239
TS.FS06-2.04	Luzzatto-Fegiz, Paolo - Entrainment models of turbine wakes, wind farms, and flow adjustment in canopies	3241
TS.FS06-2.05	Griffith, Martin - Energy-harvesting from flow-induced vibration of circular and elliptical cylinders	3243
TS.FS06-3.01	Michelin, Sebastien - Fluid-solid-electric couplings of piezoelectric flags	3245
TS.FS06-3.02	Modarres-Sadeghi, Yahya - A model for wall shear stress estimation in abdominal aortic aneurysms using POD	3247
TS.FS06-3.03	Nave, Gary - Wake stiffness and its application: Tethered cylinders and flying snakes	3249
TS.FS06-3.04	Mittal, Sanjay - Resonance-forever in laminar flow regime	3251
TS.FS06-3.05	Olivier, Mathieu - On the deviation motion of self-propelled flexible flapping wings	3253
PO.FS06-1.01.237	Amar, Luc - Passive control of fluter applicated to a 3DOF airfoil	3255
PO.FS06-1.02.238	Blanchard, Antoine - Resonance capture in vortex-induced vibration of a cylinder with a rotator	3257
PO.FS06-1.04.240	Chen, Weimin - Multi-Frequency Vortex-Induced Vibrations of a long Cylinder in Shear Flow	3259
PO.FS06-1.05.241	Frey, Raphael - Modelling and Experimental Characterization of Diaphragm Pumps and Tubing	3261
PO.FS06-1.06.242	Furquan, Mohd - Flow induced vibrations of cylinder with flexible splitter plate	3263
PO.FS06-1.07.243	Hassani, Masoud - Large deformation of chiral rods and ribbons subjected to wind	3265
PO.FS06-1.08.244	Jaiman, Rajeev - Partitioned iterative and dynamic subgrid-scale methods for vibrating offshore structures	3267
PO.FS06-1.09.245	Kay, Edmund - A vibrating membrane model for mitral valve honks	3269
PO.FS06-1.10.246	Lv, Jinan - Investigation on aeroelastic response of a hypersonic wind tunnel experiment model	3271
PO.FS06-1.11.247	Ma, Ruiqiang - Study on vibration characteristics of the inflatable boom filled with gas	3273
PO.FS06-1.13.249	Paraz, Florine - Thrust generation by a heaving flexible foil	3275
PO.FS06-1.14.250	Tubaldi, Eleonora - Nonlinear response of shells conveying pulsatile flow	3277

PO.FS06-1.15.251	Tulchinsky, Arie - Transient dynamics of elastic hele-shaw cell due to external forces	3279
PO.FS06-1.16.252	Vedeneev, Vasily - Nonlinear panel flutter at variable transonic flow speed	3281
PO.FS06-1.17.253	Xing, Jing - Mixed FE-SP method for nonlinear structure-water interactions with freak waves	3283

CONVERTING WAVE ENERGY FROM FLUID-ELASTICITY INTERACTIONS

Clotilde Nové-Josserand[1], Frederico Castro Hebrero[2], William Megill[3], Caroline Cohen[4], Ramiro Godoy-Diana[1] & Benjamin Thiria[1]

[1]*PMMH UMR 7636 CNRS-ESPCI-UPMC-UDD, Paris, France*

[2]*Laboratorio de Fluido Dinamica, UBA, Buenos Aires, Argentina*

[3]*Faculty of Technology and Bionics, Rhine-Waal University of Applied Sciences, Germany*

[4]*MSC, UMR 7057 CNRS-UDD, Paris, France*

Summary Aquatic plants are known to protect coastal lines and riverbeds from erosion by damping waves and fluid flow. These flexible structures are able to absorb the energy of an incoming fluid by deforming mechanically. Although this natural phenomenon is well accepted in the literature, it is not yet well understood. Our research focuses on the mechanisms involved in these fluid-elasticity interactions in order to develop an efficient energy harvesting system. The system consists of a forest of flexible rods interacting collectively. We investigate the role of different parameters (that concern both the system characteristics and the environmental conditions) on the ability of our system to absorb energy from the flow. In these first experiments, we vary the spatial distribution of the rods, their flexural rigidity, the frequency and amplitude of incoming waves.

INTRODUCTION

Understanding the mechanisms involved between fluid flow and vegetation reconfiguration has been the focus of a number of recent studies [1][2]. This is particularly interesting when looking at particle transport and coastal erosion. It has been observed that when flow passes through a vegetation field, the kinetic energy of the fluid is transferred to the plant through mechanical bending, which results in a damping of the flow. This mechanical energy can then be returned to the fluid or could instead be harvested and converted into useful electrical energy. In this study, we investigate the potential energy which could be extracted from such fluid-structure interactions.

EXPERIMENTAL SETUP

The studied system consists of a field of flexible beams made from silicone (Polyvinyl siloxane (PVS)). Two different flexibilities were tested: a first silicone with a Young's Modulus ranging between 200 – 300 kPa, and a second silicone with a Young's Modulus ranging between 600 – 700 kPa. The beams were moulded into 12cm long and 1.9cm diameter cylinders, which were then onto a plexiglass base of thickness 1cm. The base has 10 x 10 holes with a regular spacing of 2.6cm.

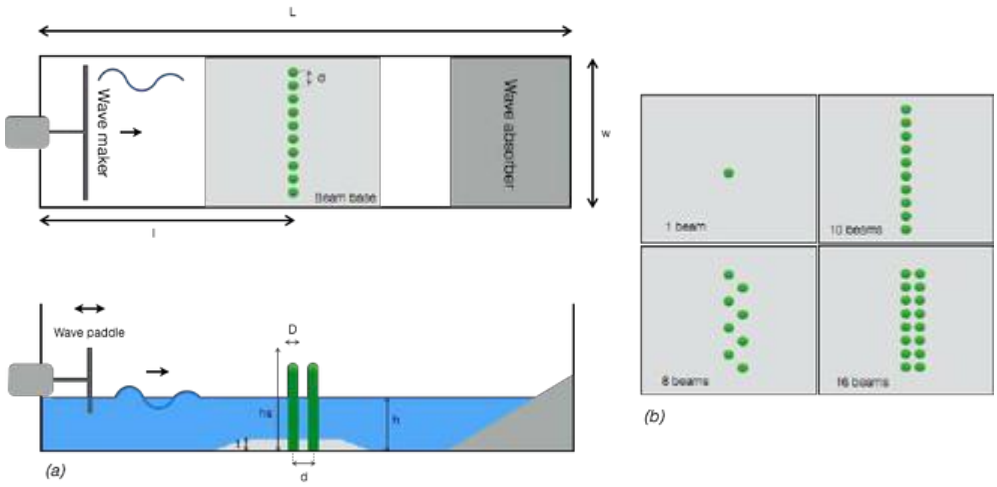

Figure 1: Experimental setup. (a) Schematic of the flume. (b) Tested configurations.

Several configurations were explored for both rigidities: no beams (« 0 beams »), a single beam (« 1 beam »), two rows of 4 beams each off set from one another (« 8 beams »), a row of 10 beams (« 10 beams »), and two rows of 8 beams parallel to each other (« 16 beams ») (see Fig. 1).

Experiments were conducted in a small scale flume at the PMMH laboratory. A schematic of the setup is given in Figure 1. The dimensions of the flume are 1.8m long (L) and 0.6m wide (w). The flexible beams were placed in the center of the flume onto the acrylic base, which possesses a 1 to 5 ramp on either side in order to minimize any effects of the change in

[a] Corresponding author. Email: clotilde.nove-josserand@espci.fr

water depth. A linear driven wave paddle was used to produce continuous waves of various frequencies and amplitudes.

The method used for measuring the surface waves is Fourier Transform Profilometry (FTP). The optical profilometric technique developed at the PMMH laboratory by Cobelli et al. [3] uses global measurement of free-surface deformations. In this system, a video-projector is used to project a fringe pattern of known characteristics onto the free surface of the flume and its image is registered by a digital camera. This image then serves as a reference image and is compared to the deformed images for which the deformed fringe pattern can be analyzed and the free surface reconstructed.

RESULTS

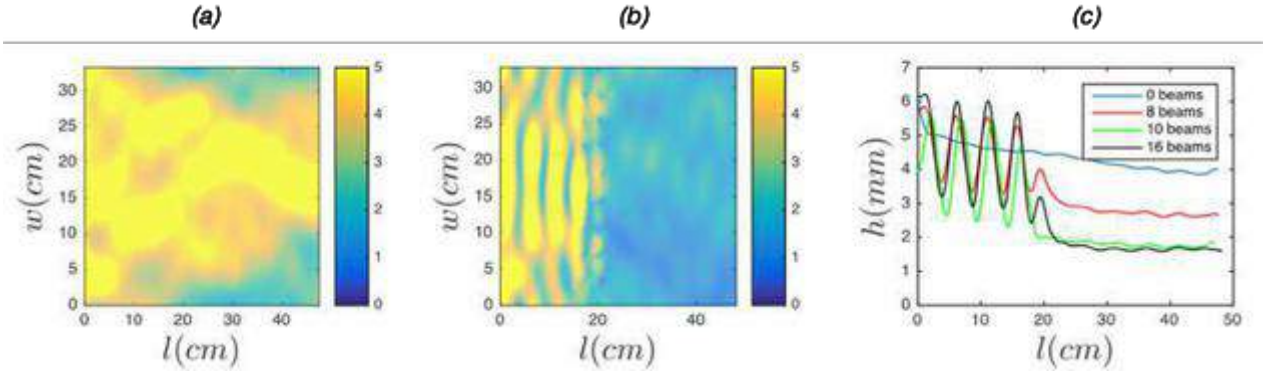

Figure 2: (a) Surface deformation map for "0 beams" configuration. (b) Surface deformation map for "16 beams" configuration. (c) Comparison of wave height for the tested configurations.

Fig 2 displays a typical comparison between unperturbed and controlled wave energy maps. The beam configuration in this example consists in a double array of 8 beams dispatched along the span (see Fig. 1 (b) bottom right) corresponding to the "best" configuration in terms of energy absorption. In Fig (a) and (b), the square of the local height integrated in time (over 80 periods) is shown as a function of space. As can be seen, the presence of the beams (located at x = 18cm in Fig 2(b)) have a strong effect on the incoming wave energy where up to 60% of dissipation can be achieved for this case. Fig. (c) summarizes the progressive effect of the beam density for three different configurations. Here the wave energy has been integrated along the transversal coordinate and displayed as a function of x for the sake of clarity.

CONCLUDING REMARKS & FUTURE WORKS

The first results shown in Fig. 2 confirm the strong ability of this system to control the transmitted energy beyond the artificial vegetation. We have been conducting an extensive parametrical study as a function of beam rigidity and spatial configuration in order to highlight optima. This point will be discussed in terms of wave interaction and beam mechanical response.

As seen on Fig. 2, this system is undeniably efficient for the prevention of coast erosion, we shall now determine to what extent it is also efficient in harvesting energy. Future works will focus on such systems involving this time mechanical loading to mimic energy harvesting.

References

[1] H. Nepf. Flow and transport in regions with aquatic vegetation. *Annual Review of Fluid Mechanics*, **44** :123-142, 2012.

[2] E. De Langre. Effects of Wind on Plants. *Annual Review of Fluid Mechanics*, **40** :141-68, 2008.

[3] P. J. Cobelli, A. Maurel, V. Pagneux, P. Petitjeans. Global measurement of water waves by Fourier transform profilometry. *Exp Fluids,* **46**:1037-1047, 2009.

OPTIMAL DESIGN OF RECTANGULAR FINS FOR UNDERWATER PROPULSION

Jean-Philippe Boucher[1] and Christophe Clanet *[1]

[1]*Laboratoire d'Hydrodynamique (LadHyX), Ecole polytechnique, Palaiseau 91128 France*

Summary Inspired by fish swimming, the propulsion of crafts with flexible plates has recently regained interest. In this experimental study, we look at the effect of geometry on the propulsive performance of rectangular flexible fins subjected to an oscillatory forcing. The optimal design of a rectangular fin appears to be only dictated by its resonant frequency.

INTRODUCTION

In a world in which the impact of the climate change on our societies is more and more sensitive, the propulsion of crafts and floats with flexible plates set into motion by water waves appears like an attractive alternative to conventional means of propulsion. It has indeed been observed that a flexible plate forced to oscillate vertically at one edge propels itself horizontally. This experimental study is mainly focused on the understanding of the physical mechanisms at stake in this kind of high Reynolds number propulsion in order to design fins with optimal shapes and mechanical properties.

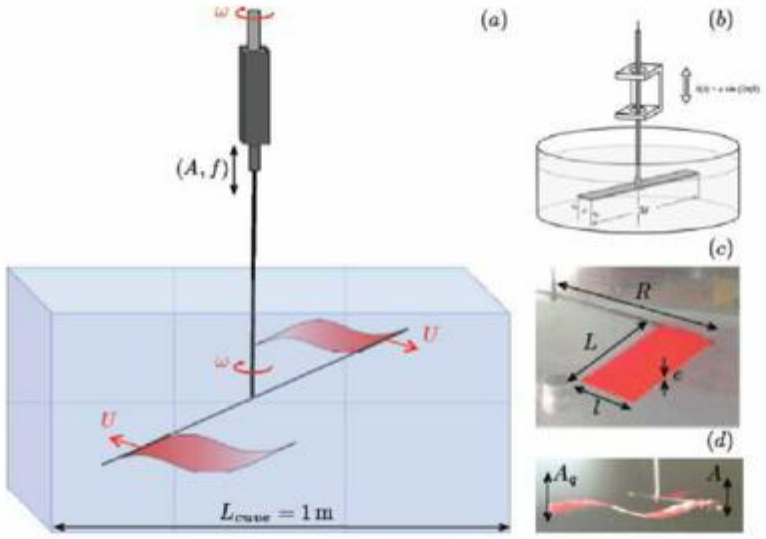

Figure 1: (a) Schematic of the experimental set-up. (b) Experimental set-up used by [1] and [2]. (c) Rectangular flexible plate of length L, width l, thickness e ($e \ll l < L$) and Young's modulus $E \sim 2GPa$. (d) Picture of an oscillating plate : the leading edge oscillates at the frequency f with the amplitude A, whereas the trailing edge oscillates with the amplitude A_q and a phase difference Φ.

We use the experimental set-up presented in Figure 1-(a), which is inspired from [1] and [2] (see Figure 1-(b)). Two identical rectangular flexible plates are attached at the extremities of a rod on either side. This rod has its center linked to a vertical axis which is set into motion by an electromagnetic linear actuator and is free to rotate about the vertical direction. When the system oscillates, it spontaneously starts rotating. With this set-up, we measure the propulsion speed U and the propulsive force F that drives the motion for different amplitudes A and forcing frequencies f as well as for different geometries of the plate (Figure 1-(c)). As we observe that the speed U is related to the propulsive force F, we focus in the following on the propulsive force characterization.

EXPERIMENTAL RESULTS

Figure 2-(a) illustrates the typical evolution of the propulsive force with the forcing frequency for plates of different lengths: one can observe, for a given plate, that this force reaches a plateau at a characteristic frequency. Video recordings of the deformation of the plate in this forcing regime show that the appearance of the plateau corresponds to the resonance of the

*Corresponding author. Email: clanet@ladhyx.polytechnique.fr

plate. Equivalently, we observe that the propulsive force is proportional to the trailing edge amplitude squared A_q^2, as predicted by Lighthill [3]. The length of the plate has a significant effect on this plateau as an increase in the length decreases the force reached at the plateau as well as the resonant frequency. As a result, a compromise is needed to achieve high propulsive force with a low forcing frequency. Considering plates of different length L, width l and thickness e, we show that the resonant frequency f_r scales like $\sqrt{Ee^3/(\rho L^4 l)}$ (with E the Young's modulus of the plate and ρ the density of water), while the plateau force F_r can be written as $Ee^3A^4/(L^4 l)$. Figure 2-(b) shows the evolution of the force F, rescaled by F_r, with the forcing frequency f, rescaled by the resonant frequency f_r, for different lengths, widths and thicknesses of the plate. All the data collapse for $f/f_r \lesssim 1$ proving the validity of both scales.

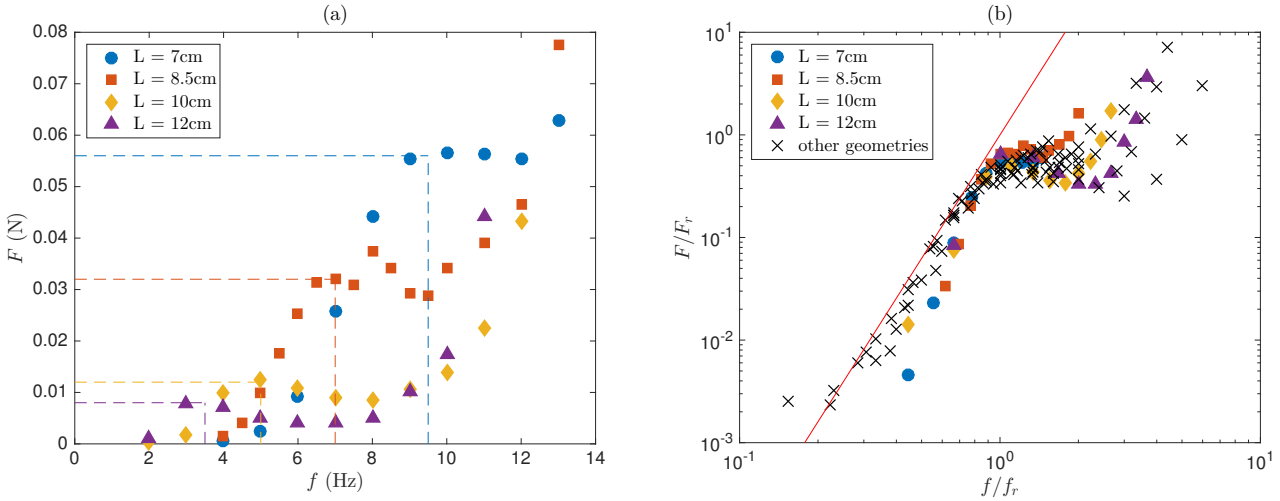

Figure 2: (a) Propulsive force F as a function of the forcing frequency f for four plates of different length L but same width ($l = 5\ cm$) and same thickness ($e = 1\ mm$). The four data sets show the appearance of a plateau indicated by the horizontal dotted lines (corresponding force noted F_r) and reached at the resonant frequency f_r of the plate (highlighted by the vertical dotted lines). (b) Propulsive force rescaled by the plateau force F_r as a function of the frequency rescaled by the resonant frequency f_r for the four data sets plotted in (a) and for plates with varying length, width and thickness. The red line represents the function $f(x) = x^4$.

In order to build a model to account for these observations, the flow field around the rectangular plate is characterized using flow visualization with fluorescein and Particle Image Velocimetry (PIV). In the model, both the friction force due to the vortices shed at the trailing edge and the added mass effect are considered. The resulting numerical model gives close results to the experimental ones and also predicts qualitatively the same deformation of the plate.

CONCLUSION

These experimental results provide a straight forward way of predicting the optimal shapes of a rectangular flexible plate for a given forcing. As $F_r \sim \rho A^4 f_r^2$, the crucial parameter in the design of optimal rectangular fins appears to be the resonant frequency. Moreover, with this set-up, we also looked at the effect of a wall or of a free surface on the propulsive performance of such fins. For further work, it would be of great interest to look at the propulsion of other geometries of fins such as triangular or streamlined shapes.

References

[1] Vandenberghe N., Zhang J., Childress S.: Symmetry breaking leads to forward flapping flight. Journal of Fluid Mechanics, 2004.

[2] Vandenberghe N., Childress S., Zhang J.: On unidirectional flight of a free flapping wing. Physics of Fluids, 2006.

[3] Lighthill, M. J.: Note on the swimming of slender fish. Journal of fluid Mechanics, 1960.

A potential-flow model of viscous dissipation for the oscillating wave surger converter

Cathal Cummins*[1] and Frederic Dias[1,2]

[1]*UCD School of Mathematics and Statistics, University College Dublin, Belfield, Dublin D04 N2E5, Ireland*
[2]*CMLA, Ecole Normale Supérieure de Cachan, 94235 Cachan, France*

Summary A mathematical model of an oscillating wave surge converter is developed to study the effect that viscous dissipation has on the behaviour of the device. Recent theoretical and experimental testing have suggested that the standard treatment of viscous drag (e.g., Morison's equation) may not be suitable when the effects of diffraction dominate the wave torque on the device. In this paper, a new model of viscous dissipation is presented and explored within the framework of linear potential flow theory, and application of Green's theorem yields a hypersingular integral equation for the velocity visco-potential in the fluid domain. The hydrodynamic coefficients in the device's equation of motion are then calculated, and used to examine the effect of dissipation on the device's performance. A special focus is given to the effects of dissipation on the performance of a device that is tuned to resonate with the incoming waves.

INTRODUCTION

The oscillating wave surge converter (OWSC) belongs to a family of wave energy converters (WECs) known as 'flap-type' WECs [6]. In its simplest form, the OWSC comprises a buoyant flap that is hinged to the seabed, and typically operates in the nearshore environment where its pitching motion couples with the surge component of the incident waves [9]. Recent theoretical and experimental studies have shown that OWSCs can achieve high levels of power capture in commonly occurring seas [9]. This has prompted researchers to develop new mathematical models of the OWSC in order to better understand its hydrodynamic behaviour. To date, considerable understanding has been achieved primarily through the use of semi-analytical models to examine the hydrodynamic performance of the OWSC [4, 5], an array of OWSCs [3], and a farm of OWSCs [7].

In each of these studies, the fluid is deemed to be inviscid, and hence the effects of viscous dissipation are neglected. However, recent experimental wave tank tests and computational fluid dynamics simulations have found that flow separation occurs at the flap's tips [8]. In this paper, we assess the effect that viscous dissipation has on an OWSC by modifying the semi-analytical theory of [4] to include the effects of viscous dissipation near the flap's edge. We achieve this by applying an effective pressure discharge in the vicinity of the flap's tips. The equation of motion of the flap is solved in the frequency domain, and the solution to which is used to quantify the effect of viscous dissipation on the device's performance.

MATHEMATICAL MODEL

Consider an OWSC in an open ocean of constant water depth h', where the prime indicates a quantity with a physical dimension. The OWSC is represented as a buoyant box-shaped flap of width w' and thickness $2a'$, hinged at a depth d' on a rigid platform of height $h' \nearrow d'$ as shown in figure 1. Monochromatic waves of amplitude A_I' and period T' are normally incident upon the flap, which set the device oscillating about its hinge line. Let $\theta'(t')$ be the pitching amplitude of the device and let t' denote time. We define the reference system of coordinates $O'(x', y', z')$ with x' pointing in the opposite direction to the incoming waves, let the y'-axis lie along the width of the device and the z'-axis points upwards from the still water level. The origin O' is located in the middle of the device at the still water level.

The fluid is deemed to be inviscid and incompressible and the flow irrotational. Hence, there exists a scalar potential $\Phi'(x', y', z', t')$ for the velocity field $\boldsymbol{v}' = \nabla'\Phi'$ that satisfies the following equations (and invoking $2a' \ll w'$ [4, 5, 7]):

$$\nabla'^2\Phi' = 0, \quad (x', y', z') \in V', \tag{1a}$$

$$\Phi'_{,t't'} + g\Phi'_{,z'} = 0 \text{ at } z' = 0 \quad \text{and} \quad \Phi'_{,z'} = 0 \text{ at } z' = \nearrow h', \tag{1b}$$

$$\Phi'_{,x'} = \nearrow \theta'_{,t'}(t')(z' + d') \text{ Heaviside}(z' + d'), \quad x' = \pm 0, \quad |y'| < \tfrac{1}{2}w', \tag{1c}$$

where V' is the fluid domain, g the acceleration due to gravity, and we have assumed that the behaviour of the system is linear [4] – a subscripted comma indicates differentiation. In order to incorporate the dissipative effects due to viscosity, we introduce a 'dissipative surface' $\mathcal{D}'$ close to the flap's edge, as shown in figure 1(*b*). Across $\mathcal{D}'$, we impose a pressure discharge $\Delta P'$, which is a function of the local velocity component ($v_n' = \Phi'_{,n}$) along the outward unit normal vector $\boldsymbol{n}$ to $\mathcal{D}'$

$$\Delta P' = f\left(\Phi'_{,n}\right), \quad x = \pm 0, \quad \tfrac{1}{2}w' < |y'| < \tfrac{1}{2}\left(w' + \ell'\right); \quad \Delta P'(y', z', t') = P'(\nearrow 0, y', z', t') \nearrow P'(+0, y', z', t'), \tag{2}$$

where P' is the hydrodynamic pressure in the fluid. The relationship (2) represents the energy loss due to vortex shedding near the flap's edge [1], previously reported in simulations and laboratory tests of the OWSC [8]. The function f typically takes the form of a linear [1] or quadratic function [2] of the flow velocity. We consider a linear law, with $\bar{\epsilon}$ the linear coefficient measuring the strength of viscous dissipation; setting $\bar{\epsilon} = 0$ gives equivalence to existing inviscid models of the OWSC [5].

*Corresponding author. Email: cathal.cummins@ucd.ie

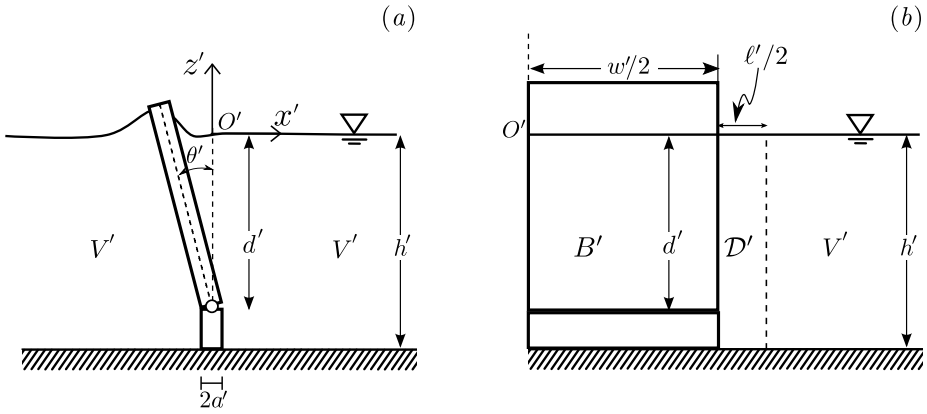

Figure 1: The geometry of the surface-piercing OWSC with dissipative surface $\mathcal{D}'$: (a) section (b) front view.

THE RESULTS

Using the model formulated in [5], we find that the capture factor (the ratio of captured to available wave power) curve contains a spike near the flap's resonant period; however, including a small amount of dissipation removes this spike. Figure 2 reveals the effect that increasing dissipation has on the resonant peak ($T' \approx 9$ s). We find that increasing $\bar{\epsilon}$ to 0.01 is sufficient to reduce the resonant peak to below the level of the peak corresponding to maximum exciting torque ($T' \approx 2.2$ s).

The capture factor curve of an OWSC contains an unphysical spike when standard inviscid linear potential theory is used. We show that the inclusion of dissipation in the form of a pressure discharge in the vicinity of the flap's tips is sufficient to eliminate this spurious behaviour, and give a more realistic prediction of the hydrodynamic performance of the OWSC.

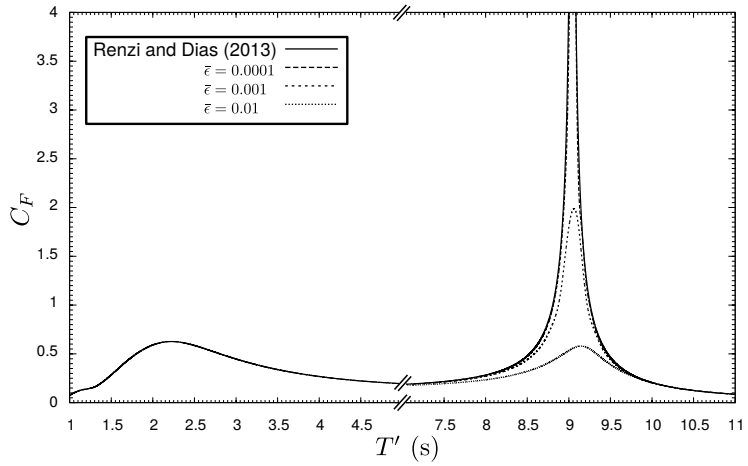

Figure 2: The influence of dissipation on the capture factor of an OWSC with spike at the resonant wave period at $T' \approx 9$ s.

References

[1] X. B Chen, F. Dias, and W. Y. Duan. Introduction of dissipation in potential flows. In *Proceedings of the 7th International Workshop on Ship Hydrodynamics*, Shanghai, China, 2011.

[2] O. M. Faltinsen, R. Firoozkoohi, and A. N. Timokha. Steady-state liquid sloshing in a rectangular tank with a slat-type screen in the middle: quasilinear modal analysis and experiments. *Phys. Fluids*, 23:042101, 2011.

[3] E. Renzi, A. Abdolali, G. Bellotti, and F. Dias. Wave-power absorption from a finite array of OWSCs. *Renew. Energ.*, 63:55–68, 2013.

[4] E. Renzi and F. Dias. Resonant behaviour of an OWSC in a channel. *J. Fluid Mech.*, 701:482–510, 2012.

[5] E. Renzi and F. Dias. Hydrodynamics of the OWSC in the open ocean. *Eur. J. Mech. B/Fluids*, 41:1–10, 2013.

[6] E. Renzi, K. Doherty, A. Henry, and F. Dias. How does Oyster work? The simple interpretation of Oyster mathematics. *Eur. J. Mech. B/Fluids*, 47:124–131, 2014.

[7] D. Sarkar, E. Renzi, and F. Dias. Wave farm modelling of OWSCs. *Proc. R. Soc. Lond.* A, 470(2167):20140118, 2014.

[8] Y. Wei, A. Rafiee, A. Henry, and F. Dias. Wave interaction with an OWSC, Part I: Viscous effects. *Ocean Eng.*, 104:185–203, 2015.

[9] T. Whittaker and M. Folley. Nearshore OWSCs and the development of Oyster. *Phil. Trans. R. Soc. Lond.* A, 370(1959):345–364, 2012.

MULTIPLE BUBBLE PROPAGATION MODES IN ELASTO-RIGID MODELS OF AIRWAY REOPENING

Lucie Ducloué[1 a)], Andrew Hazel[2] & Anne Juel[1]
[1]*School of Physics and Astronomy and Manchester Centre for Nonlinear Dynamics, University of Manchester, Manchester, United Kingdom*
[2]*School of Mathematics and Manchester Centre for Nonlinear Dynamics, University of Manchester, Manchester, United Kingdom*

Summary We study experimentally the effect of vessel compliance on the propagation of a two-phase flow in a confined geometry. The experimental set-up consists of a rigid, thin-gapped rectangular channel topped with an elastic membrane. The injection of air in the oil-filled channel leads to the steady propagation of an air finger. Depending on the initial profile of the membrane and the bubble speed, different propagation modes can be observed, characterized by the bubble shape and pressure. We show that for weakly collapsed membrane shapes, the propagation mode is predominantly governed by the dynamic local membrane vertical displacement at the bubble tip, whereas for strong levels of initial collapse the initial (static) non-uniform channel cross-section plays a major role.

INTRODUCTION

The first breath after birth is an important physiological event in which air first enters the collapsed fluid-filled lungs [1]. A related process can occur later in life, when reopening accidentally collapsed regions of the lungs through artificial ventilation. Understanding the mechanics of this process is fundamental in designing ventilation strategies that quickly reopen the airways while minimizing lung damage [2].

The mechanical problem of airway reopening is complex: during air propagation the airway changes shape in response to fluid motion inside it as well as external forces (bronchoconstriction). To understand the reopening of a single airway, pioneering experiments [3] have investigated the coupling of a tube deformation to a two-phase flow inside it by studying air injection in a fluid-filled, initially collapsed elastic tube. The results have shown the existence of a variety of air propagation modes as the tube reopens. Among those, air fingers that propagate at higher speed and lower air pressure are of particular biological interest [4]. Those fingers are only observed for high levels of initial collapse and take a surprising "pointed" shape in which the tip of the finger propagates in the thin layer of liquid in the middle of the collapsed tube cross-section. These experiments have demonstrated the strong influence of the initial (static) level of collapse of the tube on the observed propagation modes. However, the role of the shape of the cross-section and the dynamic tube geometry changes in response to fluid motion to select the propagation mode remains unclear. Here we propose to experimentally investigate the effect of vessel compliance on the propagation of a two-phase flow by designing a simpler compliant channel in which the cross-section geometry is partially decoupled from wall elasticity. With this system, we aim to understand the selection of the propagation modes observed in the collapsed tube, and assess their generality.

EXPERIMENTAL SET-UP

Control over the vessel's cross-section and its compliance is achieved by designing an elasto-rigid channel. A long, rigid, thin-gapped rectangular Hele-Shaw channel is milled from a block of Perspex. Only the top wall of the channel is made of an elastic membrane which can be inflated or deflated by a uniform pressure loading. The injection of air at a given flow rate in the initially oil-filled channel leads to the propagation of a steady bubble. During propagation, a differential pressure sensor records the bubble pressure, while a first camera placed vertically well above the channel allows us to monitor the bubble speed and shape. The vertical deformation of the membrane during propagation is imaged by a second camera recording the position of a laser line shone on the membrane across the width of the channel. This set-up allows us to precisely control the shape of the membrane in the initial statically collapsed state, as well as monitor the dynamic changes in the cross-section during air injection. This is essential to understand how fluid motion couples with the membrane displacement to select the shape of the air finger.

RESULTS

Influence of the level of initial collapse at fixed bubble speed

For a given bubble speed, we show that two different modes of propagation can be obtained depending on the level of initial collapse. For moderate initial collapse (finite measurable channel depth in the middle of the cross-section), the static depth of the channel prior to air injection is smoothly reduced towards the middle of the cross-section (see figure 1-*a*). A single centered air finger is observed, which resembles the one first observed by Saffman and Taylor [5] for two-phase flow in an entirely rigid thin-gapped rectangular channel. However, the finger in the elasto-rigid channel is always wider than the

[a)] Corresponding author. Email: lucie.ducloue@manchester.ac.uk.

one observed under the same conditions in a rigid cell. We show that membrane deflection at the tip of the propagating bubble is responsible for this modification in the selection of the finger width.

At high levels of collapse, a thin layer of a few dozens of microns of liquid separates the membrane from the channel bottom along most of the cross-section, and is matched to the rigid edges by two wedges of liquid at the sides (see figure1-*b*). This results in the selection of a completely different mode of propagation in which the air finger is very wide and exhibits an unusual 'flat-tipped' shape. This propagation mode seems to be selected by the extreme shape of the channel cross-section.

Reopening dynamics from initially strongly collapsed states

We also discuss the role of bubble speed on finger selection for high levels of initial collapse, which is a case of particular interest to the problem of airway reopening. It is also the limit in which the biologically relevant "pointed finger" can be obtained in collapsed elastic tubes. In the elasto-rigid channel, we show that the flat-tipped bubble disappears below a critical speed and, after a short region of bi-stability, is replaced at low speeds by a propagation mode in which two long air fingers travel down the deeper sides of the channel. This transition due to the extreme shape adopted by the channel cross-section at high levels of collapse seems to be general and the equivalent of the transition to the propagation of the pointed bubble in elastic tubes [3,4]. The simpler constitutive law of the elasto-rigid channel leads to a simplified phase diagram compared to the tube case. We take advantage of this more easily controlled geometry to investigate the mechanisms underlying this transition.

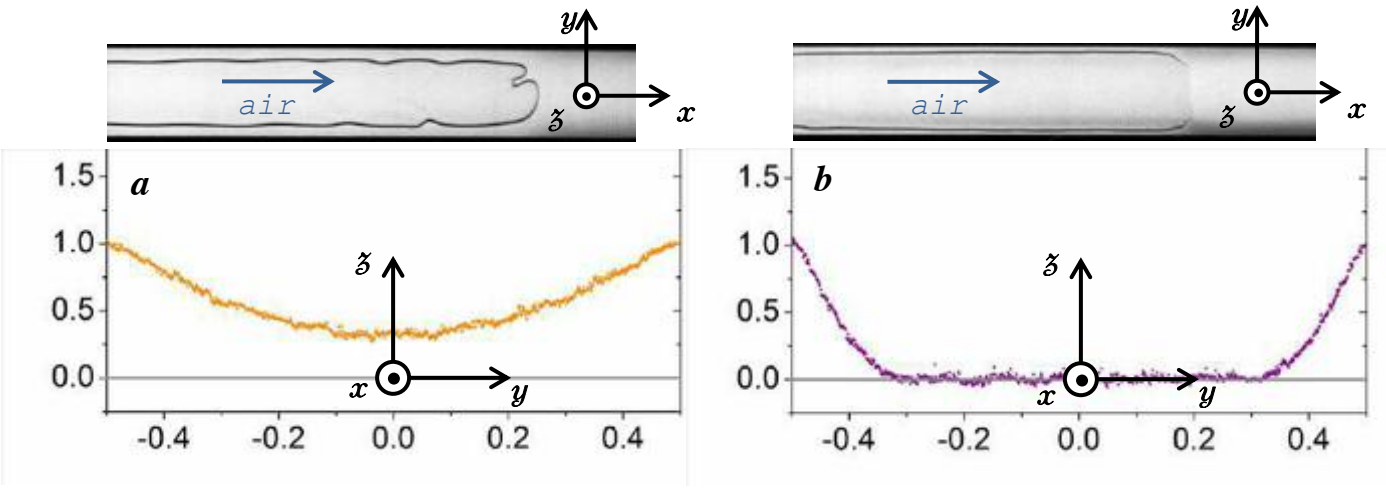

FIGURE 1: Typical shape of the channel cross-section imposed prior to air injection for (*a*) a moderately collapsed state and (*b*) a highly collapsed state. The channel rigid bottom lies at z=0. The vertical height has been scaled by the channel depth (1 mm), and the transverse length by the channel width (30 mm). Top pictures show the shape of the finger obtained for propagation at the same speed in the two cases.

References

[1] Hodson W. A.: The first breath, in *The Lung: scientific foundations*, edited by R. G. Crystal, J. B. West, P. J. Barnes and E. R. Weibel, Lippincott, Williams and Wilkins, New-York, 1991.

[2] Dos Santos C.C., Slutsky A.S.: Mechanisms of ventilator-induced lung injury: a perspective, *J. Appl. Physiol*, **89**, 1645-1655, 2000.

[3] Heap A, Juel A.: Anomalous bubble propagation in elastic tubes. *Phys. Fluids*, **20**, 081702, 2008.

[4] Heap A, Juel A.: Bubble transitions in strongly collapsed elastic tubes, *J. Fluid Mech.*, **633**, 485-507, 2009.

[5] Saffman, P. G., Taylor, G.: The penetration of a fluid into a porous medium or Hele-Shaw cell containing a more viscous liquid. *Proceedings of the Royal Society of London A: Mathematical, Physical and Engineering Sciences*, **245**, 312-329, 1958.

WATER DROPLET IMPINGEMENT EROSION: *TESTING, MECHANISMS AND IMPROVED REPRESENTATION*

Hany Kirols[1], Mohammad S. Mahdipoor[1], Dmytro Kevorkov[1] & Mamoun Medraj[1,2a)]

[1]*Mechancial and Industrial Engineering Department, Concordia University, Montreal, Quebec, Canada*
[2]*Mechanical and Materials Engineering Department, Masdar Institute, Abu Dhabi, UAE*

Summary Water Droplet Impingement Erosion (WDIE) is a result of liquid/solid interaction at high speeds (sub/supersonic speeds). Extensive research is carried out at the TMG lab at Concordia University to further understand this phenomenon. It is of great concern to the power generation and aerospace industries and leads to failure of multiple airplanes components, when flying in the rain, steam turbine blades, and gas turbine compressor blades. In this article, WDIE mechanisms of Martensitic 12% Cr stainless steel, TiAl4V and TiAl, widely used alloys in the power generation and aerospace fields, are discussed. In addition, a unified energy intensity method to represent WDIE results is presented.

EXPERIMENTAL PROCEDURE

WDIE experiments were performed using a state of art erosion rig, which was designed based on the ASTM G73 standard. A schematic of WDIE rig is presented in Figure 1-a. In a vacuum chamber, the disk rotates at speeds up to 20,000 rpm, which corresponds to 500 m/s linear impact speed. Liquid/solid impingement parameters including impact speed, impact angle, droplet size, and number of impacting droplets are controlled in this test rig. In addition, different types of nozzles (single-ray, multi-ray and shower-head) can be used, as shown in Figure 1-b and 1-c. In this work, a single-ray nozzle generating 460 µm droplets was used. Moreover, the generated droplets impact the surface of samples at relative speeds of 300 and 350 m/s. It is worthy to note that the generated water droplets were shielded against the turbulence occurring inside the chamber to ensure the straightness of water ray with minimum aerodynamic distortion of the droplets until impacting the rotating sample.

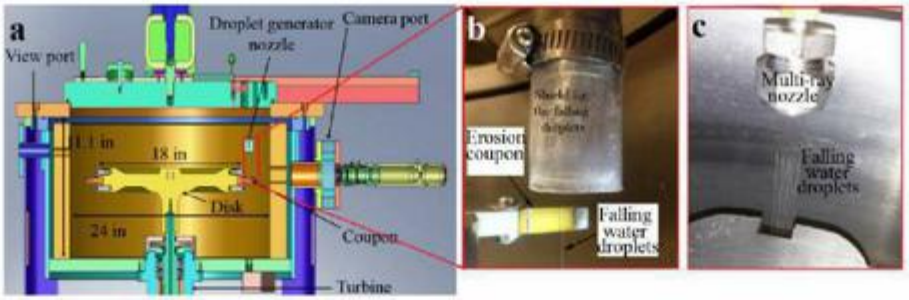

Figure 1. (a) Schematic of water droplet erosion rig, (b) Droplets generated using single-ray nozzle, (c) Droplets generated using multi-ray nozzle.

RESULTS

Erosion performance of structural alloys in aerospace industries

Figure 2 presents the results of a set of experiments performed using a single-ray nozzle for three different alloys: Ti6Al4V, TiAl and 12% Cr stainless steel. In Figure 2-a, the superiority of TiAl could be observed when tested at 300 m/s. As the impact speed increases, TiAl loses its superiority to stainless steel. At 350 m/s, the WDIE performance of the 12% Cr stainless steel becomes superior to both Ti6Al4V and TiAl. It can be concluded that the erosion performance of solid surfaces is a function of many interacting parameters representing the mechanical properties of the solid and the impingement conditions. Figure 2-c shows the evolution of solid damage due to liquid droplet impingements in the case of TiAl.

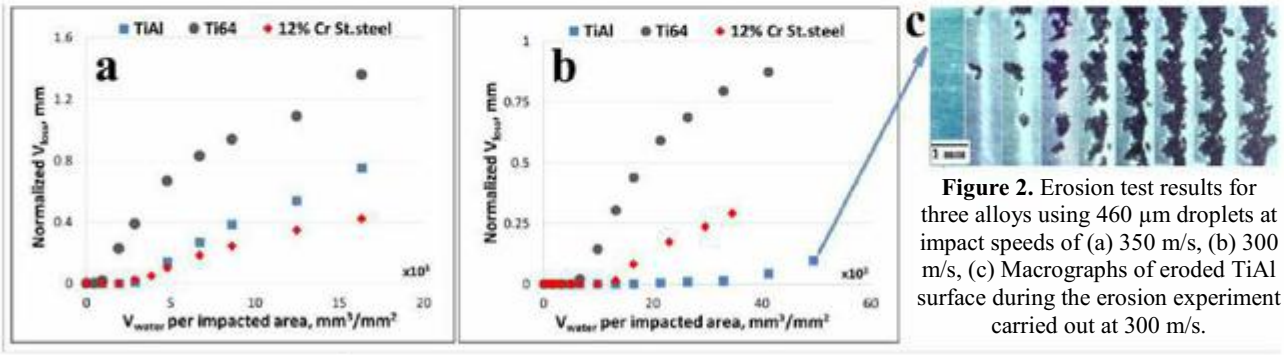

Figure 2. Erosion test results for three alloys using 460 µm droplets at impact speeds of (a) 350 m/s, (b) 300 m/s, (c) Macrographs of eroded TiAl surface during the erosion experiment carried out at 300 m/s.

a) Corresponding author. Email: **mmedraj@masdar.ac.ae**

Unified energy intensity method

The erosion representation method used in Figures 2-a and 2-b is applicable when comparing the results of WDIE tests carried out using the same experimental procedure, especially when using the same erosion test rig. Different WDIE test rigs have various factors that may influence the erosion results, for instance, the pressure in the rig, the direction of water droplets injection, the amount of water droplets impacting the surface of the sample per cycle, etc. A new method of representation should be developed to directly link the experimental results to the impingement conditions and their physical meanings. If the underlying physical principles are uncovered, experimental results performed using different erosion rigs could be compared accurately, and the differences between test rigs can be accounted for. The physical quantity that could include most of these parameters is the kinetic energy of the impacting water droplets. Therefore, experimental results were re-presented in Figure 3 as curves between the volume loss per unit impacted area and the intensity of the applied kinetic energy. The kinetic energy intensity is calculated using the impingement speed, droplet size and the number of impinging particles. Using kinetic energy intensity as the x-axis is a novel method to represent WDIE test results. The dashed arrow lines in Figure 3-b represent a specific amount of applied kinetic energy, and it is clear that the Ti6Al4V response varies at different test speeds. Understanding the reasons of such variation is the topic of our current and future work. Our most recent findings in this regard will be presented in this conference.

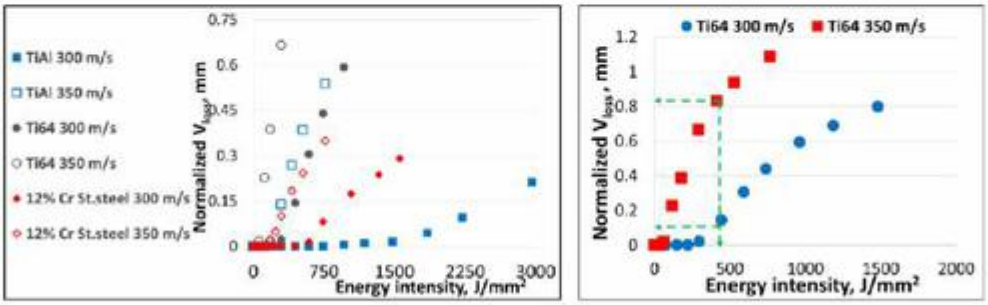

Figure 3. WDIE curves represented using the unified energy intensity method for (a) Ti6Al4V, TiAl and 12%Cr St. Steel, (b) Ti6Al4V.

Erosion damage mechanism

WDIE damage initiation mechanism is a function of erosion severity (liquid/solid interaction conditions) and dynamic mechanical properties of the target. Figure 4 shows a schematic for liquid behaviour and solid response in the case of high speed impingements. Figure 5 demonstrates SEM images of slightly eroded martensitic stainless steel and TiAl alloys within their incubation period. In the case of stainless steel, after initial droplet impacts shallow depressions appeared on the surface, as shown in Figure 5-a. Such depressions led to the generation of surface asperities which became a trigger for material loss initiation. The localized depressions imply that impact pressure of hitting droplets would be higher than the dynamic yield strength of stainless steel. On the other hand, TiAl as a semi-brittle material did not show surface depression. However, large amount of micro plasticity in the forms of miro-slips and twinning was detected on the surface of eroded TiAl, as shown in Figure 5-b. The formed asperities and the raised micro-slips are considered as the surface irregularities, which could be cracked and detached from the surface as shown in Figure 4.

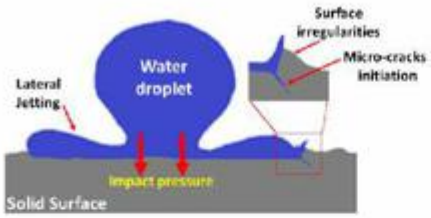

Figure 4. Schematic for the liquid/solid interaction during WDIE initiation

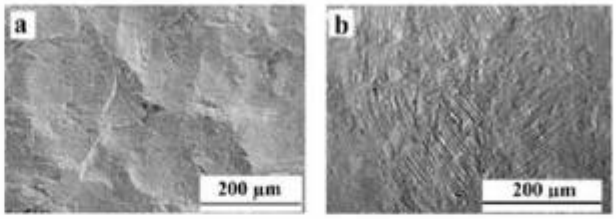

Figure 5. Slightly eroded surface in the incubation period of (a) Stainless steel and (b) TiAl.

CONCLUSION

Water droplet impingement erosion of three structural alloys were investigated. Their response to sub/supersonic impacts of water droplet were characterized. Microstructure of the solid materials and their mechanical properties in relation to impact pressures played notable role in damage evolution. A novel approach for representing WDIE results has been developed in this work. Introducing applied energy intensity as a new measure of erosion exposure and presenting erosion results in terms of applied energy intensity was found to be a comprehensive approach, as it covers most of impingement parameters. This approach enabled comparing results obtained using the same rig for different materials as well as comparing results from different rigs.

References

[1] Heymann F.J.: Survey of clues to the relationship between erosion rate and impact conditions, 2nd Meersburg Conference on Rain Erosion and Allied Phenomena, Bondensee, Fedreal German Republic, 1967.

[2] Mahdipoor M.S., Kirols H.S., Kevorkov D., Jedrzejowski P., Medraj M.: Influence of impact speed on water droplet erosion of TiAl compared with Ti6Al4V. Sci Rep **5**, 2015.

[3] Kirols H.S., Kevorkov D., Uihlein A., Medraj M.: The effect of initial surface roughness on water droplet erosion behaviour, Wear **342-343**:198-209, 2015.

[4] Mahdipoor M.S., Kevorkov D., Jedrzejowski P., Medraj M., Water droplet erosion mechanism of nearly fully-lamellar gamma TiAl alloy. Mater Des **89**: 1095-1106, 2016.

CATENARIES IN VISCOUS FLUID

James Hanna*[1] and Brato Chakrabarti[2]

[1]*Engineering Mechanics Program, Department of Biomedical Engineering and Mechanics, Virginia Polytechnic Institute and State University, Blacksburg, VA, USA*

[2]*Department of Mechanical and Aerospace Engineering, University of California, San Diego, CA, USA*

Summary This work explores a simple model of a slender, flexible structure in a uniform flow. We present analytical solutions for the translating, axially flowing equilibria of strings subjected to a uniform body force and drag forces linear in the velocities. This is an extension of the classical catenaries to a five-parameter family of shapes, represented as trajectories in angle-curvature "phase space". A sixth parameter affects the tension in the curves. Limiting cases include neutrally buoyant towed cables and freely sedimenting flexible filaments.

The catenary, or hanging chain, is one of the oldest problems in analytical mechanics. As shapes, the catenaries are a family of curves with a single scaling parameter that can effectively describe the length of a string hung, or arching, between two points. Additional axial flow along the tangents of the curve serves only to increase the tension in the string, leaving shape equilibria intact. Here we extend these classical results to include the effects of linear, anisotropic drag forces, such as would arise if the translating, axially flowing catenary were immersed in a highly viscous fluid. The presence of fluid breaks multiple symmetries and turns the one-parameter family of catenary curves into a five-parameter family. The additional parameters beyond scaling are the magnitude and direction of the translational velocity, the magnitude of the axial velocity, and the anisotropy of the drag forces. A sixth parameter, the inertial mass of the system, affects only the tension in the catenaries, not their shapes.

Our augmented catenaries are generically planar curves, and admit an analytical description as a first-order dynamical system for the tangential angle θ, with arc length s as the independent variable. Figure 1 shows several curves along with their phase portrait representations and locations in parameter space. Further details may be found in [1].

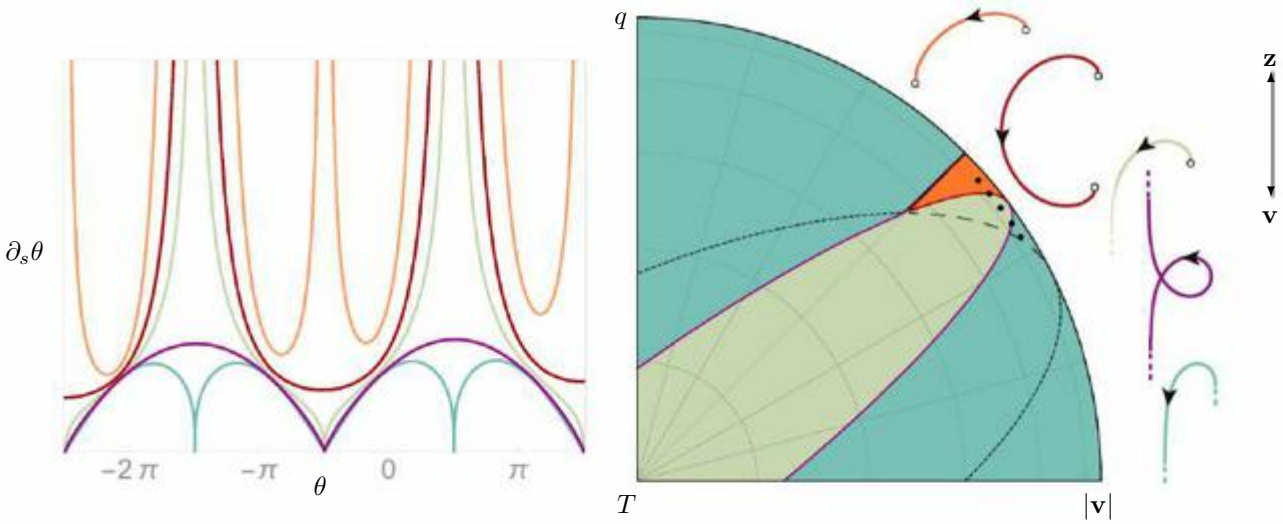

Figure 1: Five catenaries taken from the dotted locations on the central diagram, where $|\mathbf{v}|$, q, and T are the normalized magnitudes of the translational velocity, body force, and axial velocity, such that $|\mathbf{v}|^2 + q^2 + T^2 = 1$. The curves translate at an angle of $-89.9°$ with respect to the horizontal, in response to a body force oriented at $-90°$. The ratio of tangential to normal drag coefficients on the body is 0.5, and material is flowing along the catenary axis at a normalized velocity of 0.2. The other two parameters vary, and are given by $|\mathbf{v}| = (0.83, 0.81, 0.78, 0.76, 0.74)$ and $q = (0.52, 0.55, 0.59, 0.62, 0.64)$. The configurations (right), and several periods of orbits (left), correspond to a generic π-subtending heteroclinic connection, a 2π-subtending heteroclinic special case, a generic π-subtending single-sided blow up solution, a 2π-subtending double-sided blow up special case, and a generic π-subtending double-sided blow up solution. Dashed ends indicate that the configuration extends indefinitely, while a dot on the end of a curve indicates that the configuration terminates at finite length.

References

[1] B Chakrabarti and J A Hanna. Catenaries in viscous fluid. [arXiv:1509.01282].

*Corresponding author. Email: hannaj@vt.edu

Eulerian Method for FSI Based on the Reference Map

Ken Kamrin *[1], Chris H. Rycroft[2], and Chen-Hung Wu[1,2]
[1]*Department of Mechanical Engineering, MIT, Cambridge, MA*
[2]*School of Engineering and Applied Sciences, Harvard, Cambridge, MA*

Summary We present a new method for FSI based on discretizing the inverse of the motion function, known as the reference map. By storing and updating this field, finite-deformation solid constitutive relations can be implemented numerically in Eulerian frame. Together with an Eulerian-frame method for the fluid motion, the two phases can be represented on a single, fixed background grid, with interfaces between phases resolved using level-sets. The universally Eulerian nature of the method removes certain computational costs and simplifies issues such as resolving contact between (submerged) solids and as well as implementation of incompressibility conditions. We demonstrate the method in problems involving one to twenty submerged hyperelastic solids interacting within low and moderate Reynolds fluid flows, both compressible and incompressible. We demonstrate the ability to model plastic media and capture shocks by way of discretizing the system in conservative form.

BASICS

This talk discusses a new Eulerian-frame method for simulating fluid-structure interaction problems on a single fixed grid. Central to the method is the use of the newly proposed Reference Map Technique (RMT), which permits the simulation of large-deformation solid mechanical behaviors, such as hyperelasticity, in a straightforward Eulerian finite-difference framework [1, 2]. In the fluid phase, our approach transitions naturally into a Navier-Stokes solver. A level-set is used to distinguish the fluid and solid phases, and two methods to treat the interfacial conditions are employed. The first is a sharp-interface method utilizing ghost-point extrapolations of the stress and velocity to guarantee proper jump conditions. The second method is a blurred interface technique in which these jumps are implicitly upheld. Thanks to the single-fixed-grid nature of our approach, FSI solutions can be calculated rapidly with this technique, as will be demonstrated. Of note, our method can be applied to situations where fluids induce large, continuous solid deformations, such as the interaction of fluid with soft, hyperelastic bodies.

RMT is based on advection of the reference map field on a finite-difference grid. The reference map $\mathbf{X} = \boldsymbol{\xi}(\mathbf{x}, t)$ is a spatial vector field, which indicates the original position $\mathbf{X}$ of material current;y at $\mathbf{x}$. Because the original location of a material point does not change, the evolution of the reference map obeys

$$\boldsymbol{\xi}_t + \mathbf{v} \cdot \nabla \boldsymbol{\xi} = \mathbf{0} \tag{1}$$

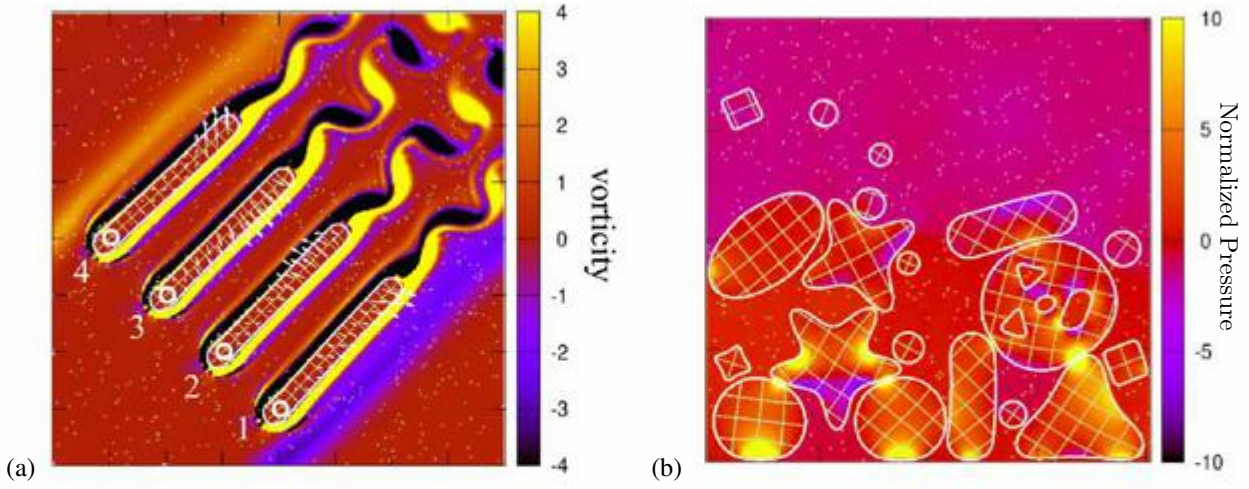

Figure 1: Reference Map Technique for FSI. Deformed grid lines indicate solid deformation, dots are fluid tracers. (a) Inflow from the lower left passes four elastic anchored rods inducing vortex-shedding and rod vibrations. (b) Twenty neo-Hookean hyperelastic objects of differing sizes, shapes, and topologies interact with each other while settling in a stirred fluid low-viscosity fluid ($Re = 1000$).

*Corresponding author. Email: kkamrin@mit.edu

The ability to simulate large-deformation solid constitutive relations results from the kinematic identity

$$\mathbf{F} = (\nabla \boldsymbol{\xi})^{-1} \tag{2}$$

where $\mathbf{F}$ is the deformation gradient tensor. By storing and evolving $\boldsymbol{\xi}(\mathbf{x}, t)$ on a fixed Cartesian grid, a spatial finite-difference gradient can be conducted to obtain the needed kinematic variable, $\mathbf{F}$, for the stress in solid mechanics. In this talk we will primarily be concerned with hyperelastic relations, whose constitutive relation has the form

The above formulation can be included within an explicit discretization of momentum conservation in order to update the spatial velocity field $\mathbf{v}(\mathbf{x}, t)$. Hence, each grid point stores two vectorial quantities, the reference map and the velocity, with each having a consistent rule for time-step updating.

Note that this routine for solids is very similar to that of a fluid solver, with the exception that the numerical reference map gradient is utilized in calculating the shear stress rather than the gradient of velocity. This duality is taken advantage of to produce a rapid, explicit (or semi-implicit) FSI routine.

INTERFACIAL TREATMENT AND SOLID CONTACT

Here, we employ a level-set to distinguish the phases. Because solid interfaces are a persistent material set, the reference map can be used to 'correct' the level set field to ensure the solid mass is always conserved. utilize two different approaches to maintain continuity between the fluid and solid phases at the interface. The sharp-interface approach ensures satisfaction of the continuity of normal traction and normal velocity at the interface through subgrid calculation of the zero level-set. A simpler blurry interface approach permits the fluid and solid properties to switch over gradually, over the course of several grid spacings. The added simplicity of the latter approach enables us to add certain additional capabilities. Recently, we have demonstrated the ability to simulate fluid-solid-solid interaction; i.e. solid-solid contact under fully submerged conditions. The contact interaction is simulated by using the difference of the two solid level-set fields as a measure of relative distance between the two solid interfaces.

INCOMPRESSIBILITY

The method can be implemented for both compressible and incompressible materials. To implement incompressible material relations, for the solid and fluid, we can append a projection step to the update procedure, which calculates the pressure from the solution of a Poisson equation, as solved with a multi-grid method. This approach for implementing incompressibility is rather straightforward as it is a linear constraint on the spatial velocity gradient, and serves as one of the benefits of the Eulerian framework.

References

[1] Kamrin, Ken, Chris H. Rycroft, and Jean-Christophe Nave. "Reference map technique for finite-strain elasticity and fluidsolid interaction." Journal of the Mechanics and Physics of Solids 60.11 (2012): 1952-1969.

[2] Valkov, Boris, Chris H. Rycroft, and Ken Kamrin. "Eulerian method for multiphase interactions of soft solid bodies in fluids." Journal of Applied Mechanics 82.4 (2015): 041011.

MIST HARVESTING WITH VERTICAL FIBERS

Romain Labbé[1], Christophe Clanet[1], and Camille Duprat*[1]
[1]*Laboratoire d'Hydrodynamique (LadHyX), Ecole polytechnique, Palaiseau 91128 France*

Summary In some arid regions an important source of water is fog. The method used to collect water from mist consists in erecting a large net on which the droplets carried in the mist can impact. The two main issues involved in this process are the impact of the drop on the fibers and the drainage of the fluid from the fibers to the tank below the net. In this work we consider a system with only vertical parallel fibers and aim at optimizing its design to maximize the drainage. We experimentally study this fluid-structure interaction problem with a wind mist tunnel and characterize the collecting efficiency of the fibers array. We develop theoretical models considering the interaction of wind, drops, wetting of the fibers and deformations of the fibers in order to identify and characterize the physical mechanisms at play.

INTRODUCTION

In some arid regions like Chile, fog is an important resource of fresh water. Historically, people raise large meshes (fish nets) to collect this water. When the mist passes through the net, some drops impact the fibers, slide along them and are collected bellow the net. This water is then used as drinking water, crop irrigation and livestock beverage. This simple and cheap method is widely used around the world and allows collection of up to ten litres of water per day per square meter of net [1].

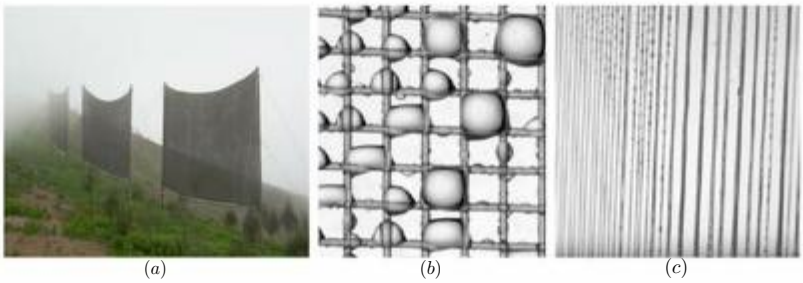

Figure 1: (a) Fog collector deployed in the Chilean mountain. (©Anne Lummerich) (b) An example of square mesh with droplet deposit on it. (c) A structure with only parallel vertical fibers .

Many questions arise around the collection of mist water. The main questions are the impact of the drops on the fibers and the conditions under which drops adhere to the fibers or are re-entrained in the flow [2]. An additional question is the drainage; if the drainage is not efficient, large droplets can appear on the mesh and obstruct the flow (figure 1.b). We propose a new system to limit this clogging effect as well as the re-entrainment by considering an array of vertical parallel fibers (figure 1.c). We study the collection efficiency of this structure with wind tunnel experiments, as well as a model drainage experiment.

EFFICIENCY OF MIST COLLECTION ON AN ARRAY OF PARALLEL FIBERS

In order to have an homogeneous laminar flow of mist, we have built a custom environmental wind tunnel. The water drops are created with piezoelectric membranes that vibrates the air-water interface of a water tank. With this system, we obtain drops of uniform size around 3 μm, similar to the drop size in natural fog. The drops are mixed in air in a turbulent chamber to obtain an homogeneous mist, that is then pushed through a convergent and laminarized with an honeycomb structure. We obtain a uniform mist flow of speed v ($0.3 < v < 5$ ms^{-1}). At the exit of the wind-mist tunnel, we place a small structure on which the fibers grating is attached. At the bottom of this structure there is a container where the water caught by the fibers is collected. The structure is suspended in the mist flow and attached to a force sensor that measures the total mass of the structure (and thus of the collected water) in time. The density of water droplets in the mist is highly dependant on the environmental conditions, we thus use a reference net for all experiments. We define a dimensionless quantity, the relative efficiency, as the ratio of the collection rate of the structure to the collection rate of the reference net.

We first study a regular array of well spaced rigid fibers, and vary the size of the structure and the diameter of the fibers. We then vary the distance between fibers in order to study their interaction and in particular the effect of the formation of capillary bridges between fibers on the water collection efficiency.

*Corresponding author. Email: camille.duprat@ladhyx.polytechnique.fr

We then study the effect of the fibers elasticity on the collection. In particular, adjacent fibers can collapse under capillary forces when bridges are formed between them [3]. This results in the formation of long liquid columns (Figure 1.c ,[4]). The probability of column formation and the resulting shape of the deformed fibers depend on the inter-fiber distance, tension in the fibers and on the fibers oscillations under the forcing of the wind. We study the effect of this column formation on the overall efficiency of collection. We can thus identify an optimal structure for water collection, but we have to understand the role of the drainage on the collection efficiency and the fibers deformation.

INFLUENCE OF THE DRAINAGE

The drainage is also modified by the fibers elasticity. In order to investigate this effect, we have built a model experiment consisting in two nylon fibers between which liquid is drained at a constant flow rate Q (figure 1.a). We adjust the tension in the fibers by varying the mass M. As the liquid front advances between the fibers, we observe the formation of a large drop at the front suspended by thin liquid film (figure 2.b.1). The drop volume increases until the drop reaches a critical size, at which capillary forces can not balance the weight of the drop any more and the drop falls while the liquid film recedes. A new drop is then created, this phenomenon appears at a constant frequency as a function of the flow rate Q.

We can define two dimensionless parameters, $N^\star = \frac{Mgl_c}{2\gamma H^2}$ with l_c the capillary length, that compares the capillary forces holding the drop to the tension within the fibers and a geometric parameter $L^\star_{init} = L/2l_c$. At hight tension (large $N^\star$) or large distance $L^\star_{init}$, the fibers are only weakly deformed and the dynamics is similar to the rigid cases (figure 2.b.1). At low tensions (small $N^\star$) or small distance $L^\star_{init}$, the fibers are strongly deformed and part of the fibers collapse on each other forming a liquid column (figure 2.b.3). In these two regimes the drop falls at a constant frequency, similar to the rigid case. Finally, there is an intermediate regime where the system oscillates between large and small deformation of the fibers (figure 2.b.2). In that case the frequency at witch the drop falls is irregular. We obtain a phase diagram figure 2.c as function of the two dimensionless parameters.

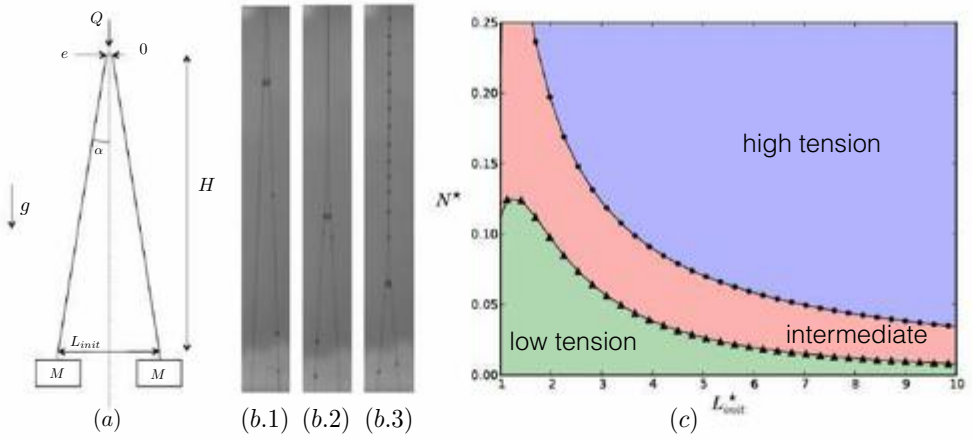

Figure 2: (a) sketch of the experimental setup (b.1) Typical picture of an experiment at high tension (b.2) typical picture of an experiment at intermediate tension (b.3) typical picture of an experiment at low tension (c) Phase diagram in the space $N^\star$ and $L^\star_{init}$.

We develop a simple model by considering two rigid beams in rotation undergoing a torque from the fluid (surface tension) and a torque from the tension in the fiber. With this model we predict the shape of the deformed fibers, the dynamics and the boundaries between the different regime in good agreement with experimental values. We combine these results with previous considerations in order to understand and model the overall liquid collection from mist.

References

[1] O. Klemm, R. S. Schemenauer, A. Lummerich, P. Cereceda, V. Marzol, D. Corell, J. van Heerden, D. Reinhard, T. Gherezghiher, J. Olivier, P. Osses, J. Sarsour, E. Frost, M. J. Estrela, J. a. Valiente, and G. M. Fessehaye. Fog as a fresh-water resource : overview and perspectives. Ambio, 41(3) :22134, May 2012.

[2] K.-c. Park, S. S. Chhatre, S. Srinivasan, R. E. Cohen, and G. H. Mckinley. Optimal Design of Permeable Fiber Network Structures for Fog Harvesting. Langmuir, 29 :1326913277, 2013.

[3] C. Duprat and H. A. Stone. Elastocapillarity. In C. Duprat and H. A. Stone, editors, Fluid Structure Interactions in Low-Reynolds number Flows. RSC publishing, 2015.

[4] S. Protiere, C. Duprat, and H. A. Stone. Wetting on two parallel fibers : drop to column transitions. Soft Matter, 9 :271276, 2013.

ENTRAINMENT MODELS OF TURBINE WAKES, WIND FARMS, AND FLOW ADJUSTMENT IN CANOPIES

Paolo Luzzatto-Fegiz*[1], Samaneh Sadri[1], and Colm-cille Caulfield[2]

[1]*Department of Mechanical Engineering, University of California at Santa Barbara, Santa Barbara, California, USA*

[2]*BP Institute for Multiphase Flow and Department of Applied Mathematics and Theoretical Physics, University of Cambridge, Cambridge, UK*

Summary In this conference presentation, we build on the turbulent entrainment hypothesis to develop models for flow past individual wind turbines, large wind farms, and other canopy flows. The entrainment hypothesis consists of a concise turbulence model, which has been widely used in geophysical fluid mechanics. We develop models for the wake of a single wind turbine, as well as for fully-developed flow in a large wind farm, inclusive of atmospheric stratification. We next consider flow adjustment at the front of a canopy, which may be rigid (for wind farms) or flexible (for vegetation). The resulting theories, based on this general turbulence model, agree with field and laboratory measurements without the need for introducing flow-specific parameters. Finally, this framework can be used to yield a limit for the output of large wind farms, which we find to be an order of magnitude larger than the performance of current designs.

AN ENTRAINMENT MODEL FOR WIND TURBINE WAKES

Simple models for turbine wakes have been used extensively in the wind energy community, both as independent tools for engineering calculations, as well as to complement more refined and computationally-intensive techniques. Jensen [6] developed a model assuming that the wake radius grows linearly with distance x, and approximating the velocity deficit with a top-hat profile. This model has been widely implemented in the wind energy community; however, recently Ref. [1] showed that this theory does not conserve momentum. Ref. [1] proposed a momentum-conserving theory, which assumed a Gaussian velocity deficit and retained the linear-spreading assumption, significantly improving agreement with experiments and Large Eddy Simulations of turbine wakes.

While the linear spreading assumption facilitates conceptual modeling, it requires empirical estimates of the spreading rate, and does not readily enable generalizations to other turbine designs. Furthermore, field measurements show sub-linear wake growth with x in the far-wake, consistently with results from fundamental turbulence studies, and with similarity solutions that are expected to hold in the very far wake [8].

We develop an integral model, for a turbine wake, by relying on a simple and general turbulence parameterization, namely the entrainment hypothesis, which has been used extensively in other areas of geophysical fluid dynamics [7, 3]. Without assuming similarity, we derive an analytical solution for a circular turbine wake, which predicts a far-wake radius increasing with $x^{1/3}$, and is consistent with field measurements and fundamental turbulence studies.

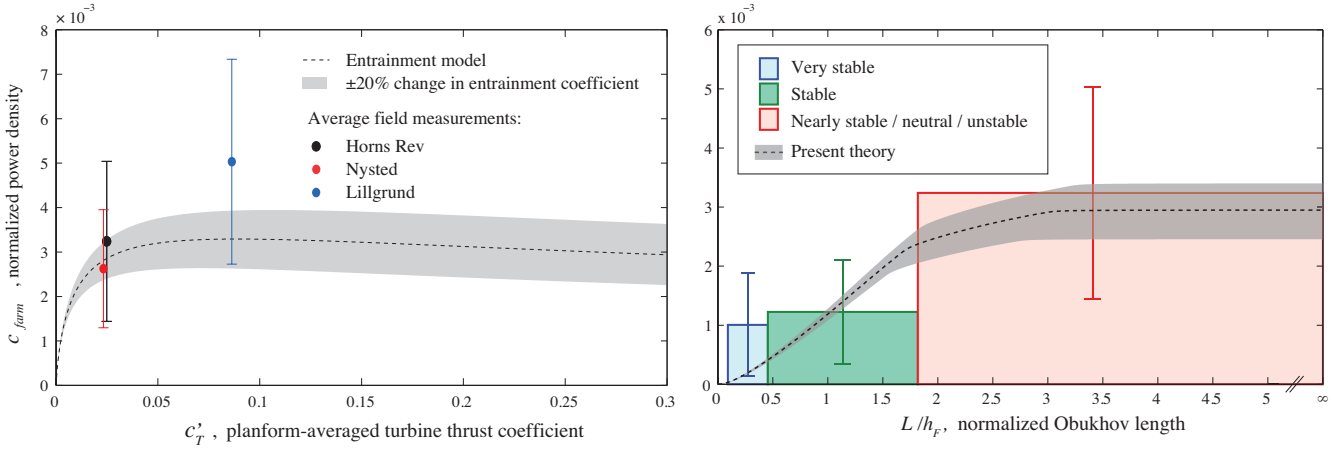

Figure 1: (Left): power density (corresponding to power per unit planform area), in a large wind farm, versus planform-averaged turbine thrust coefficient. (Right): power density versus atmospheric stability, expressed by Obukhov length.

*Corresponding author. Email: fegiz@engineering.ucsb.edu

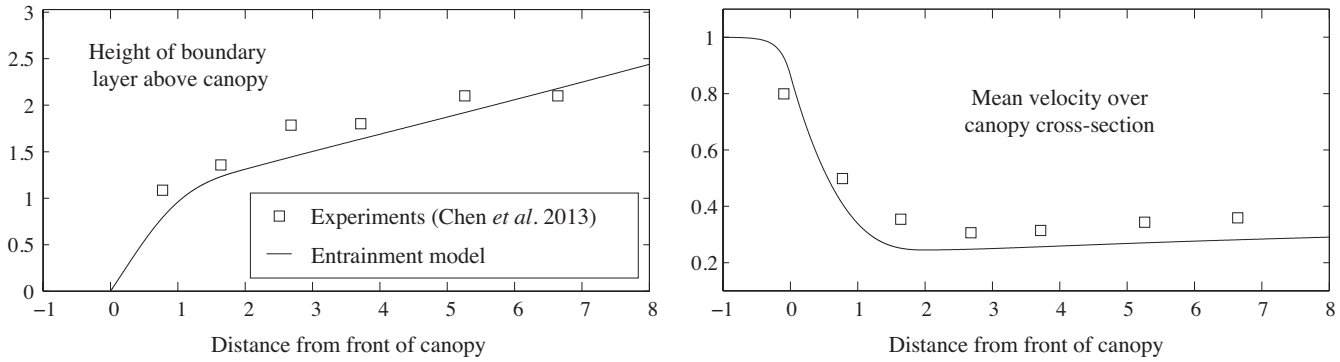

Figure 2: Flow adjustment for a model canopy of vertical cylinders. (Left): height of the developing boundary layer over the canopy. Right: flow velocity, averaged over the canopy cross section.

AN IDEAL LIMIT FOR POWER OUTPUT IN LARGE WIND FARMS

Wind turbines are often deployed in arrays of hundreds of units, where interactions lead to drastic losses in power output. Remarkably, while the theoretical "Betz" maximum has long been established for the output of a single turbine, no corresponding theory appears to exist for a generic, large-scale energy extraction system, although models exist for specific turbine designs and layouts. Recent work with vertical-axis turbines indicates that large performance gains may be achievable [5], making the search for a theoretical upper bound even more compelling.

By building on the turbulent entrainment hypothesis, we develop a model for an array of energy-extraction devices of arbitrary design and layout, focusing on the fully-developed regime. When tailoring our model to reflect current wind farm designs, the predicted power output is consistent with field measurements, as shown on the left-hand-side of Fig. 1. Furthermore, by considering a suitable ideal limit, we establish an upper bound on the performance of a large wind farm. This is found to be an order of magnitude larger than the output of existing arrays, thus supporting the notion that performance improvements may be possible. In addition, by making use of an entrainment parameterization from geophysical measurements of stratified turbulence, we extend our model to account for the effect of atmospheric stability. Our model is consistent with field data for large wind farms, as shown in the right-hand panel of Fig. 1.

FLOW ADJUSTMENT IN RIGID AND FLEXIBLE CANOPIES

At the front of a canopy, flow deceleration is associated with strong vertical fluxes of mass and momentum. Accurately describing this region is important in many applications, including terrestrial and aquatic vegetation, as well as wind farms. Simple models can provide a framework to analyze these flows, thereby guiding and complementing more refined and computationally intensive tools. Belcher *et al.* [2] introduced a linearised model that describes the flow field through sparse canopies, albeit at the cost of solving a PDE. A simpler approach involves vertically integrating the governing equations across the canopy, yielding scalings that relate key variables (e.g. [4]), which in turn can be used to construct empirical fits.

We build a simple and complete theory, by extending our model for fully-developed canopies. We account for upstream pressure variations, retain nonlinear advective terms, and neglect pressure gradients inside the canopy. Our entrainment-based model quantitatively describes the flow velocity and boundary layer height in developing canopy flows, as shown in Fig. 2. Finally, we extend our theory to account for effects of flexibility in vegetation canopies.

References

[1] M. Bastankhah and F. Porté-Agel. A new analytical model for wind-turbine wakes. *Renewable Energy*, 70(C):116–123, 2014.

[2] S.E. Belcher, N. Jerram, and J.C.R. Hunt. Adjustment of a turbulent boundary layer to a canopy of roughness elements. *J. Fluid Mech.*, 488:369–398, 2003.

[3] C. Cenedese and C. Adduce. A new parameterization for entrainment in overflows. *J. Phys. Oceanogr.*, 40:1835–1850, 2010.

[4] Z. Chen, C. Jiang, and H. Nepf. Flow adjustment at the leading edge of a submerged aquatic canopy. *Water Resour. Res.*, 49(9):5537–5551, 2013.

[5] J. O. Dabiri. Potential order-of-magnitude enhancement of wind farm power density via counter-rotating vertical-axis wind turbine arrays. *J. Renew. Sust. Energy*, 3(4):043104, 2011.

[6] I. Katic, J. Højstrup, and N. O. Jensen. A simple model for cluster efficiency. In *Proceedings of the European Wind Energy Association Conference and Exhibition*, pages 407–410, Rome, Italy, 1986. A. Raguzzi for the Italian Section of the International Solar Energy Society.

[7] B. R. Morton, G. Taylor, and J. S. Turner. Turbulent gravitational convection from maintained and instantaneous sources. *Proc. Roy. Soc. A*, 234:1–23, 1956.

[8] S. B. Pope. *Turbulent Flows*. Cambridge University Press, 2000.

ENERGY-HARVESTING FROM FLOW-INDUCED VIBRATION OF CIRCULAR AND ELLIPTICAL CYLINDERS

Martin D. Griffith and Justin Leontini

Department of Mechanical Engineering and Product Design, Swinburne University, Hawthorn VIC 3122, Australia

Summary A parameter space study is presented of the flow past an elastically-mounted cylinder constrained to oscillate in the cross-stream direction, where the cylinder is also forced to rotationally oscillate. The focus is on enhancing the cross-stream heaving response with the intent of harvesting energy. Linear damping is applied to the heave to simulate power extraction. The variation of power output with damping coefficient and geometry is investigated, with circular, elliptical and aerofoil cross-sections tested. Of interest is the variation of the flow and configuration parameters for the optimal case for each geometry. For these optimal cases, an increase in power output, cylinder displacement and wake width is observed with increasing cross-section aspect ratio, while a roughly constant driving frequency of 0.180 is observed for aspect ratios greater than 1.0.

Harvesting energy from flow-induced oscillation of bodies in a freestream has been a focus of renewable energy research. [1, 2, 3]. With regard to cross-sectional shape, the focus for this problem has been on aerofoils; this study seeks to explore the effect of geometry and aspect ratio and to also consider the role of vortex-induced vibration, more commonly associated with circular cross-sections. Of interest will be the changes in flow behaviour and power output across a range of cross-sectional shapes; more specifically, the elliptical cross-section, of aspect ratio, $1.0 < \Gamma < 6.0$ and more standard aerofoils. Are there common factors between the flows with optimal configurations for energy-harvesting for circular, elliptical and aerofoil geometries?

PROBLEM DEFINITION AND METHOD

The study investigates flows for rotationally-oscillating geometries ranging from the circular cylinder to the aerofoil, where energy is extracted via a damper on the passive heaving motion. The harmonic oscillator equation governing the heaving motion is:

$$M\left(\ddot{y} + \frac{c}{M}\dot{y} + (2\pi f_n)^2 y\right) = F_y, \tag{1}$$

where $\ddot{y}$, $\dot{y}$ and y are respectively the acceleration, velocity and displacement of the cylinder perpendicular to the freestream, F_y is the lift force on the cylinder, M is the mass of the cylinder, m^* is the ratio of the mass of the cylinder to the mass of the equivalent volume of fluid, c is the damping coefficient and f_n is the natural structural frequency of the system. The

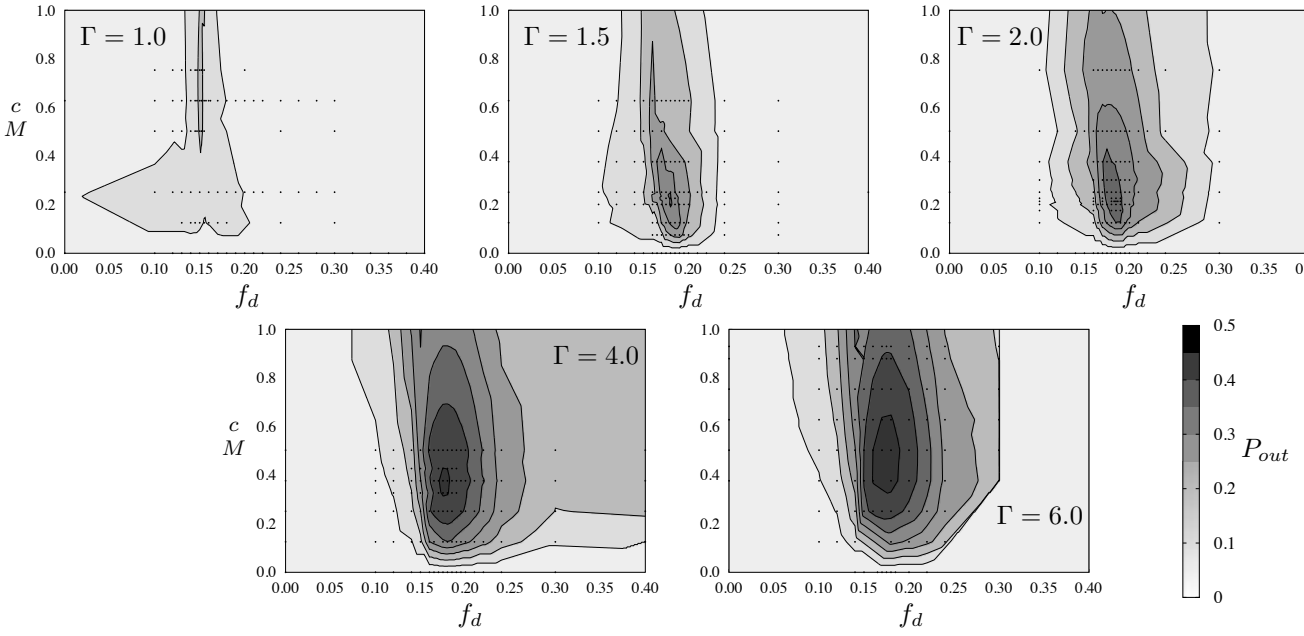

Figure 1: Contour maps of output power, P_{out}, for aspect ratios, $\Gamma = 1.0$, 1.5, 2.0, 4.0 and 6.0, over the driving frequency, f_d, normalized damping coefficient, $\frac{c}{M}$, parameter space. Axis ranges and contour scales are constant across the five maps.

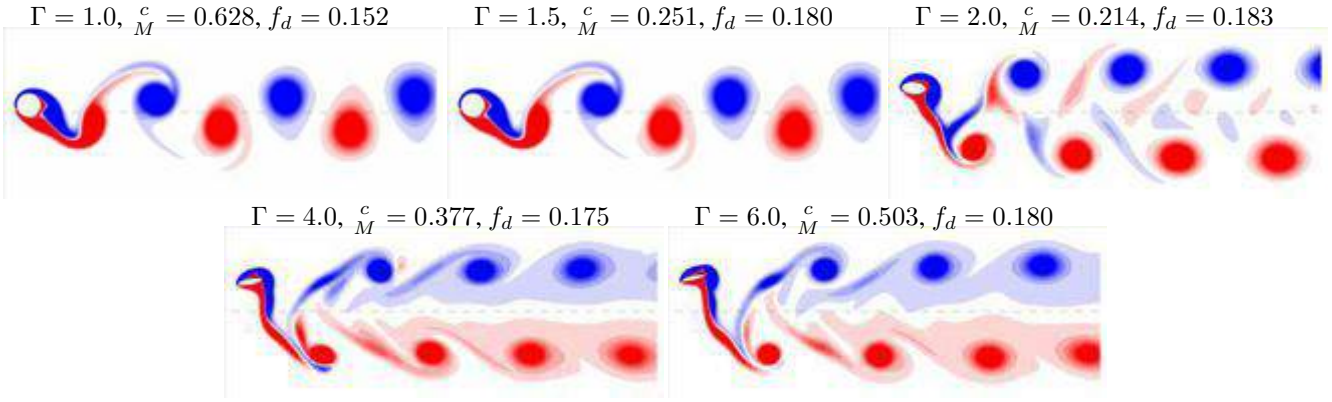

Figure 2: For the optimal power output cases of figure 1 for aspect ratios, $\Gamma = 1.0$, 1,5, 2.0, 4.0 and 6.0, the vorticity fields at the moment of maximum body displacement.

natural structural frequency is chosen to be close to the vortex shedding frequency for a stationary circular cylinder, that is, $f_n = 0.20$. Active control is implemented via a pitching motion, with $\theta = A\sin(2\pi f_d)$, where θ is the angular displacement, f_d is the driving frequency and A is the pitching amplitude. An amplitude of $A = \pi$ is chosen; although large compared with other studies of similar problems, for elliptical cross-sections this pitching amplitude results in the major and minor axes of the geometry both presenting fully-perpendicularly to the freestream during the oscillation. This makes the pitching amplitude $A = \pi$ a fundamental starting point for the parameter space. The driving frequency of the pitching motion is varied by $0.00 \leq f_d \leq 0.40$. Optimal power output is explored by also varying the damping of the system, c. A constant ratio of body density to fluid density is chosen as, $m^* = \rho_{body}/\rho_{fluid} = 5.0$. All times and distances are non-dimensionalized by D/U and D respectively, where D is the major axis of body cross-section and U is the freestream velocity. The Reynolds number is defined as $Re = UD/\nu$, where ν is the kinematic viscosity; all simulations were run with $Re = 200$.

Simulations are carried out using an immersed boundary method to represent the moving circular and elliptical bodies on an underlying Cartesian grid, on which the flow is solved using a finite-difference scheme[4]. The pitching motion of the body is controlled, while the heaving motion is solved with equation 1 using a Newmark-β method.

RESULTS & CONCLUSIONS

Figure 1 presents contour maps of power output, $P_{out} = c\dot{y}^2$, as function of both driving frequency, f_d, and the damping coefficient normalized by the cylinder mass, $\frac{c}{M}$, for five elliptical cross-sections of aspect ratios, $\Gamma = 1.0$, 1.5, 2.0, 4.0 and 6.0, where Γ is the ratio of the major axis of the cross-section to the minor axis, with $\Gamma = 1.0$ corresponding to a circular section. The axis ranges and contour scale are constant across the five plots. The limiting case $f_d = 0.00$ represents the case with no rotational forcing. The plots show that across the geometries an increase in power output from the unforced case is possible. For the five geometries, the cases of maximum power output are grouped in the range of driving frequencies, $0.150 \leq f_d \leq 0.200$, below the natural structural frequency of the system, $f_n = 0.200$. The heave response in this region is periodic, with a single dominant frequency. An increase in the magnitude of power output is observed with increasing aspect ratio. This can be partially explained by the change in mechanism by which the rotation of the body transfers energy to the flow. For the circle of aspect ratio, $\Gamma = 1.0$, energy from the rotation is transferred only via viscosity; for an ellipse, for sections of the surface, the rotation contributes to a velocity component normal to the surface. Energy is then also transferred via pressure. The elliptical shape does also result in a greater power required to produce the rotation; however, incorporating a P_{in} does not significantly affect the results of figure 1.

Figure 2 plots the vorticity fields for each case of maximum power output from figure 1, with the cylinder in each case at maximum displacement. The maximum displacement of the cylinder and the width of the wake increase with aspect ratio. The fields for aspect ratios $\Gamma = 4.0$ and 6.0 are qualitatively similar; the geometry converges to a flat plate with increasing aspect ratio, so some convergence in behaviour is expected. The variation of the flows for these geometries and for those of aerofoils of equal aspect ratio is the subject of further work, as well as consideration of the effect of pitching axis location.

References

[1] Xiao Q., Zhu Q.: A Review on Flow Energy Harvesters Based on Flapping Foils. J. Fluids Struct. 46:174-191, 2014.

[2] Kinsey T.,Dumas G.: Parametric Study of an Oscillating Airfoil in a Power-Extraction Regime. AIAA Journal 46(6):13181330, 2008.

[3] Young J., Lai C. S. L., Platzer, M. F.: A Review of Progress and Challenges in Flapping Foil Power Generation. Prog. Aerospace Sci. 67:2-28, 2014.

[4] Mittal R., Dong H., Bozkurttas M., Najjar F. M., Vargas A, von Loebbecke A.: A Versatile Sharp Interface Immersed Boundary Method for Incompressible Flows with Complex Boundaries. J. Comp. Phys. 227:4825-4852, 2008.

FLUID-SOLID-ELECTRIC COUPLINGS OF PIEZOELECTRIC FLAGS

Sébastien Michelin*[1], Yifan Xia[1], and Olivier Doaré[2]
[1]*LadHyX – Département de Mécanique, Ecole Polytechnique – CNRS, Palaiseau, France*
[2]*IMSIA, ENSTA ParisTech – EDF – CNRS, Palaiseau, France*

Summary Flow-induced vibrations such as the flag instability can be used to harvest energy from fluid flows when coupled to an electric generator (e.g. piezoelectric materials). Focusing on piezoelectric flags, we investigate here the coupling of the fluid-solid mechanical system to the electric output circuit, and resulting energy transfers. In particular, a new fluid-solid-electric lock-in mechanism is identified that greatly enhances the harvesting efficiency of the system. Finally, we investigate the synchronization of two piezoelectric flags under the combined effect of hydrodynamic and electrodynamic interactions.

PIEZOELECTRIC FLAGS AS ELECTRIC GENERATORS

Flow-induced instabilities such as the flutter of flexible plates in axial steady flows generate spontaneous vibrations of solid bodies. When coupled to an electric generator, these flow-induced vibrations effectively act as flow energy harvesting mechanisms that can power an output circuit. A piezoelectric flag consists in a flexible plate covered by pairs of piezoelectric patches: during the flapping motion, the periodic stretching and compression of these patches result in periodic charge displacements that can power an output circuit (Figure 1). These elements also introduce a feedback of the electric circuit on the solid dynamics: the voltage applied to the piezoelectric electrodes generates an additional mechanical torque on the flag. An essential property is the piezoelectric coupling factor α that is a measure of the electromechanical energy transfer.

In this work, we present a fully-coupled model for the nonlinear dynamics of the fluid, solid and electric systems, and investigate the influence of fluid-solid-electric couplings and energy exchanges on the harvesting efficiency, defined as the ratio of the power effectively used in the output circuit to the kinetic energy flux through the flow section occupied by the flag [1, 2].

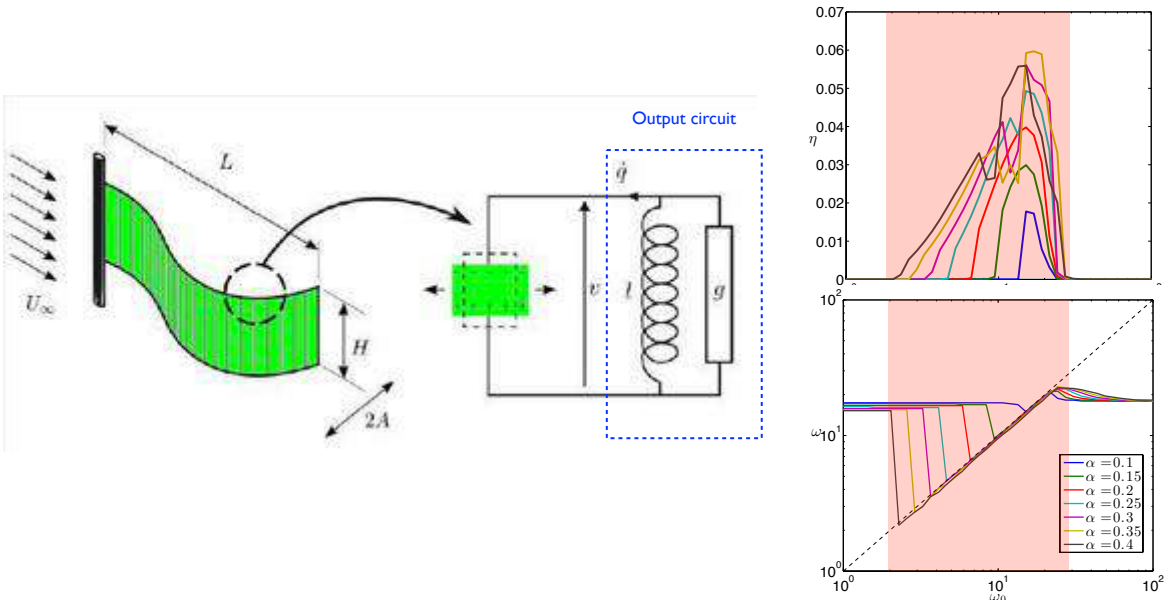

Figure 1: (Left) Piezoelectric flags in an axial flow. Each piezoelectric pair is connected to an output circuit consisting of a resistor (where the energy is harvested) and an inductor. (Right) Fluid-solid-electric lock-in: when the fundamental frequency of the circuit ω_0 is comparable to the flag's spontaneous flapping frequency, the motion of the flag locks onto the circuit dynamics, resulting in high output efficiency.

*Corresponding author. Email: sebastien.michelin@ladhyx.polytechnique.fr

FLUID-SOLID-ELECTRIC LOCK-IN AND HARVESTING EFFICIENCY

Piezoelectric components have an intrinsic capacitance. For purely resistive circuits, a tuning of the flapping frequency to the characteristic time scale of the RC circuit results in maximum efficiency of the energy transfer [2]. When the output circuit also includes an inductive component, the circuit has resonance properties that greatly enhance the harvesting performance, regardless of the intensity of the piezoelectric coupling [3]. Further, for strongly-coupled systems (large α), we demonstrate the existence of a fluid-solid-electric lock-in phenomenon: within an extended range of parameters (i.e. characteristic frequency of the circuit, flow velocity...), the electric circuit is able to prescribe its characteristic frequency ω_0 to the flapping motion. This results in a permanent forcing of the output circuit at its resonance frequency: the energy transfer and harvesting efficiency is then maximized (Figure 1, [4]).

ELECTRO- VS. HYDRODYNAMIC COUPLINGS OF TWO PIEZOELECTRIC FLAGS

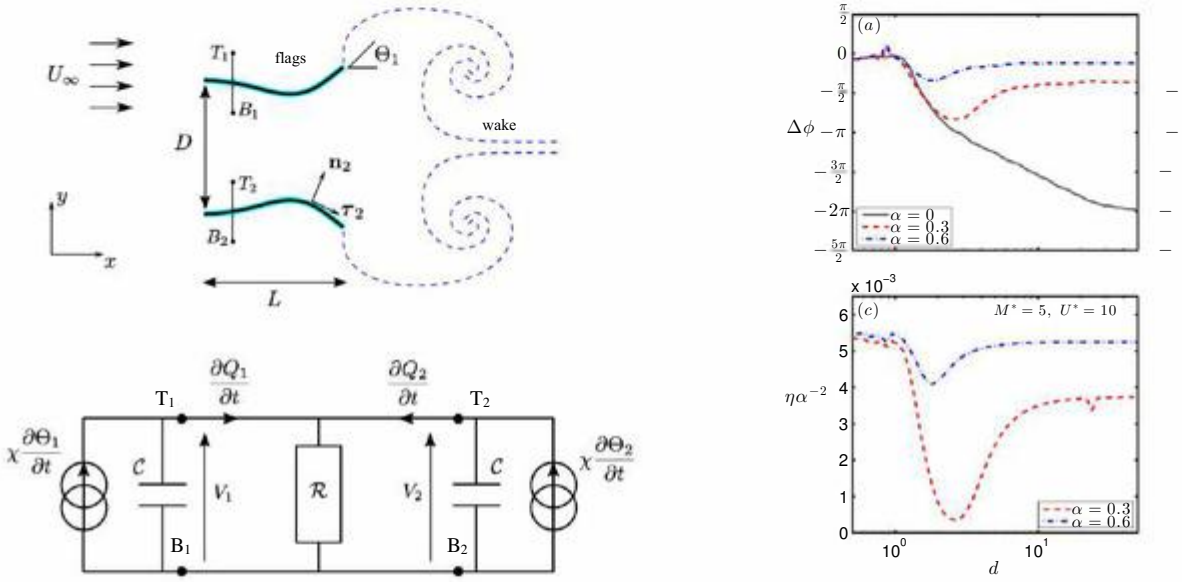

Figure 2: (Left) Electro-hydrodynamic coupling of two parallel flags: each flag is covered by one single pair of piezoelectric

the efficiency of the assembly with their relative distance: at large distance, piezoelectric coupling overcomes hydrodynamic

synchronization fundamentally alters the efficiency of the assembly (Figure 2).

References

Struct. 27:1357-1375, 2011.

[3] Y. Xia, S. Michelin, O. Doaré: Resonance-induced enhancement of the energy harvesting performance of piezoelectric flags. Appl. Phys. Lett.

A MODEL FOR WALL SHEAR STRESS ESTIMATION IN ABDOMIAL AORTIC ANEURYSMS USING PROPER ORTHOGONAL DECOMPOSITION

Gary Han Chang[1], Yahya Modarres-Sadeghi[1a)]
[1]*Mechanical Engineering, University of Massachusetts, Amherst, Amherst, Massachusetts, USA*

Summary In this work, a reduced-order model (ROM) is constructed to study the physiological flow and wall stress conditions for abdominal aortic aneurysms. The method of snapshot Proper Orthogonal Decomposition (POD) is used to construct the reduced-order bases based on a series of CFD results, which are then improved using a QR-factorization technique to satisfy the various boundary conditions in physiological flow problems. This method can effectively construct a computationally efficient FSI model, which allows us to examine a large range of physiological flow parameters.

INTRODUCTION

Simulating physiological flows remains to be computationally expensive and difficult for clinical usage. This is not only because of the geometrical complexity involved in these kinds of flow simulations, but also because one might be interested in a parametric study of several physiological flow parameters (for example, asymmetry of the inflow, and its flow velocity and frequency) for a given model. Here we focus on an abdominal aortic aneurysm. A reduced order model (ROM) of this system, which is very highly nonlinear and geometrically non-uniform, can replace the full, nonlinear model with a low-degrees of freedom ROM model, thus reduce the overall computational cost. In the present problem, we utilize the ROM by Proper Orthogonal Decomposition (POD) method to estimate the flow-induced wall shear stress (WSS) and pressure loading of a simplified abdominal aortic aneurysm (AAA) based on a decoupled fluid structure approach. This method allows us to investigate a wide range of different physiological flow parameters without conducting CFD simulations repetitively.

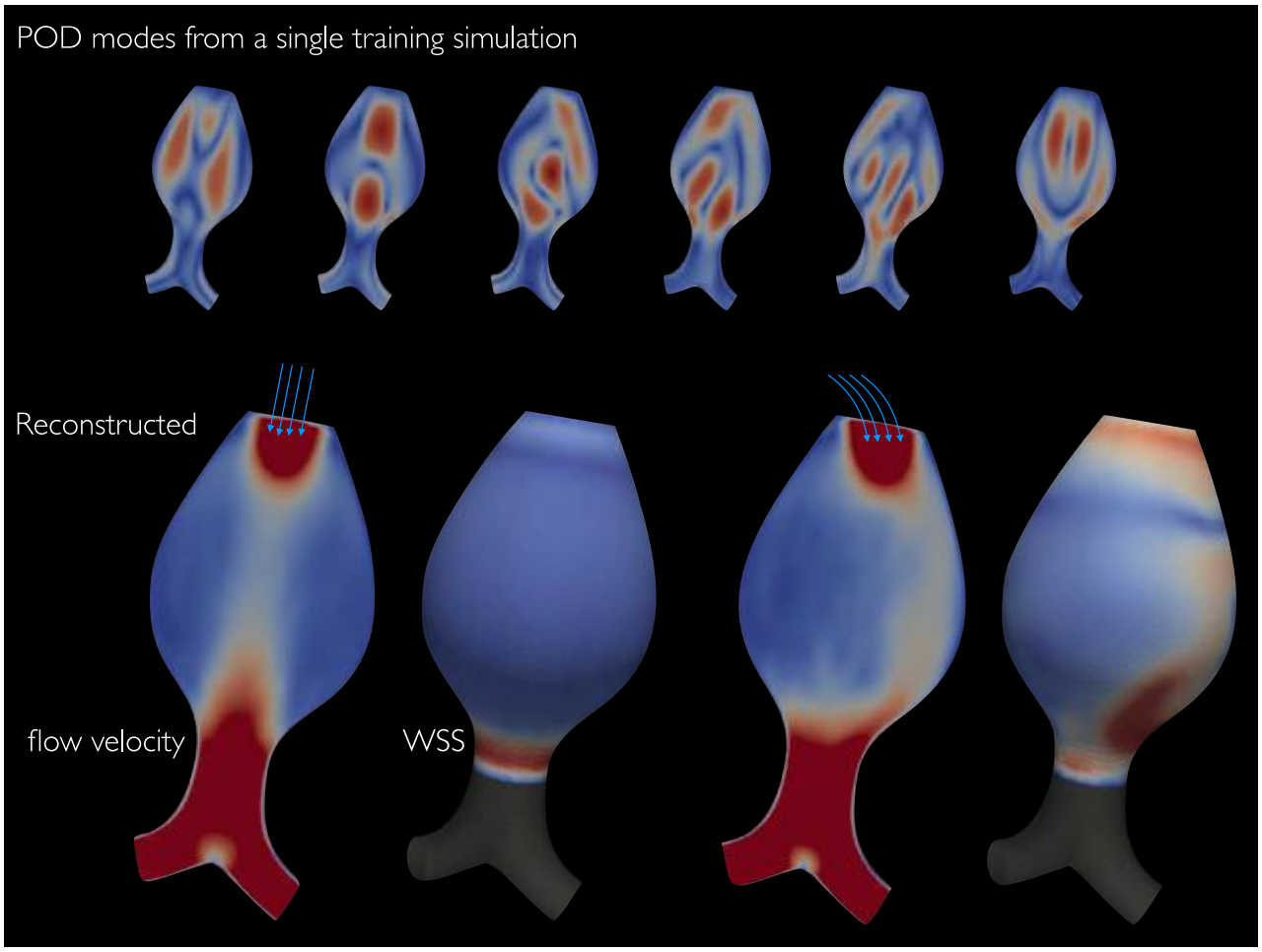

Figure 1: The POD modes from a training set and the reconstructed flow velocities and WSS distributions for different inflow angles

[a)] Corresponding author. Email: modarres@engin.umass.edu.

SNAPSHOT POD WITH TIME-DEPENDENT BOUNDARY CONDITIONS

The snapshot POD method is used here to construct the ROM model [1]. Assume the incompressible Navier-Stokes equations are solved in the abdominal aneurysm's flow domain with time-dependent inflow velocity and outflow pressure boundary conditions. The resulting time series are sampled at a fixed time interval and are called a set of snapshots. Because each snapshot is divergence free due to the incompressible flow condition, a linear combination of these snapshots will also be divergence free, thus only the discretized Navier-Stokes equations are required to be satisfied. The POD modes are found by calculating the time-correlation coefficients between each two snapshots, and repetitive information is filtered out. This can be confirmed by recognizing that the energy stored (or the eigenvalue) in each POD mode decays rapidly as the mode number increases. Because the flow is strongly driven by the time-dependent pressure, pressure POD modes are directly used to model the pressure distribution without additional pressure-velocity equation [2].

To adapt the unsteady boundary conditions of the physiological flow on multiple inlets and outlets of the computational flow domain, the method discussed in [3], using the QR decomposition algorithm, is utilized. A series of N snapshots is generated from a simulation, containing multiple time-dependent boundary conditions, which can be separated into K spatial and temporal components. Several different boundary conditions can exist in the same section of the boundary. For example, a Womersley flow profile defined on a circular inlet can be expressed as a superposition of a parabolic flow profile and a reverse flow profile. The temporal components can then be decided such that they satisfy the overall flow profile based on various Womersley numbers.

The flow velocity is subsequently approximated by the combination of a series of eigenmodes, chosen by the POD technique, to ensure that the dominating dynamic behavior is captured with a relatively small number of modes. The eigenmodes consist of N particular and N-K homogenous modes. The particular modes have non-zero values for the inflow and traction on the boundaries, and are used to satisfy the prescribed inflow condition and the solved boundary traction condition. The number of particular modes equals to the number of discretized boundary conditions. Consequently, a limited number of particular flow modes are capable of satisfying multiple boundary conditions, which are continuous functions in spatial coordinates. The homogenous modes have zero velocity or traction values on the boundaries, and are used to satisfy the reduced order model using Galerkin's technique to discretize the Navier-Stokes equation.

TRAINING SET AND RECONSTRUCTION WITH VARIOUS FLOW PARAMETERS

To construct a reduced order model that is capable of predicting a wide range of behavior of different systems, we obtain a set of snapshots from a flow simulation with multiple variable parameters. The created set of snapshots is called the training set. The training set should be simulated by changing the parameters of interest as widely as possible, to create the richest dynamic behavior for the snapshots and thus to make the POD model a more closely representative model of the full system. In order to estimate the reliability of the reduced order model, one seeks to compare the results of the reconstructed solution to the exact simulated solution. One method to estimate the relative error in a POD solution without the knowledge of the exact solution is by calculating the POD solution's residual of the Galerkin method. We show that both the velocity and pressure distributions are well reconstructed when compared with the exact simulated values with relatively small number of modes (Figure 1). A meshless shell model is used to estimate the aneurysm sidewall's in-plane stresses. Sidewalls with non-uniform thickness are considered to model the influence of local weakness on the aneurysm's risk of failure. It is found that the sensitivity of the material's strength to the local weakness depends on the aneurysm's sidewall's Gaussian curvature, the curvature to thickness ratio, and the distribution of the flow loading. We have pinpointed the locations where the aneurysm's sidewall is most sensitive to the local weakness.

CONCLUSIONS

A reduced-order model (ROM) is constructed to study the physiological flow in abdominal aortic aneurysms. The method of snapshot Proper Orthogonal Decomposition (POD) is used to construct the reduced-order bases based on a highly robust training CFD simulation, thus a rich dynamic behavior can be captured by the POD modes. Reconstructed distribution of flow velocities, pressure and wall shear stress are calculated based on a wide range of physiological flow parameters and show excellent agreement with the exact simulated solutions, while keeping the ROM runs computationally efficient.

References

[1] J. Burkardt, M. Gunzburger, H.-C. Lee, POD and CVT-based reduced-order modeling of Navier–Stokes flows, Computer Methods in Applied Mechanics and Engineering. 196 (2006) 337–355. doi:10.1016/j.cma.2006.04.004.

[2] T. Lassila, A. Manzoni, A. Quarteroni, G. Rozza, Model Order Reduction in Fluid Dynamics: Challenges and Perspectives, in: Reduced Order Methods for Modeling and Computational Reduction, Springer International Publishing, Cham, 2014: pp. 235–273. doi:10.1007/978-3-319-02090-7_9.

[3] M.D. Gunzburger, J.S. Peterson, J.N. Shadid, Reduced-order modeling of time-dependent PDEs with multiple parameters in the boundary data, Computer Methods in Applied Mechanics and Engineering. 196 (2007) 1030–1047. doi:10.1016/j.cma.2006.08.004.

WAKE STIFFNESS AND ITS APPLICATION: TETHERED CYLINDERS AND FLYING SNAKES

Gary Nave *[1], Mark Stremler[1], and Shane Ross[1]

[1]*Department of Biomedical Engineering and Mechanics, Virginia Tech, Blacksburg, Virginia, United States*

Summary Wake stiffness is the tendency of the wake of an upstream body to pull a downstream body toward the centerline of the wake. Here, we investigate and discuss the validity of applying the wake stiffness model to the dynamics of a tethered pair of cylinders in a uniform flow. We find that wake stiffness provides an effective simplified model for tethered cylinders, but does not explain the whole behavior, particularly for cylinder spacings above 3.5 diameters. We also explore the extension of the wake stiffness concept to modeling the underlying mechanics of flying snakes.

WAKE STIFFNESS IN THE MOTION OF TANDEM, TETHERED CYLINDERS

When considering cylinder oscillations in the wake of an upstream cylinder submerged in a uniform flow, several researchers have found that oscillations persist and even amplify beyond the lock-in region for single cylinders in a flow [2][4]. Assi et al. [1] have proposed an explanation for the effect of the upstream wake that they refer to as "wake stiffness". They demonstrate in their experimental system that the wake of the upstream cylinder acts as a linear spring, pulling the downstream cylinder toward the centerline of the wake.

To understand the behavior of tandem bluff bodies and investigate this concept of wake stiffness, we focused our experimental efforts on investigating tandem circular cylinders. Using a free surface water channel at Virginia Tech, we conducted experiments over a range of cylinder spacings, $x_0/D \in [3.0, 5.0]$, and a range of Reynolds numbers, $Re \in (4\times10^3, 1.1\times10^4)$. In our experiments, the upstream cylinder is fixed and the trailing cylinder is tethered to this fixed cylinder; that is, the downstream cylinder is constrained to move along a circular path around the upstream cylinder, as pictured in Figure 1(a) and shown schematically in Figure 1(c). The trailing cylinder is displaced to angular amplitudes up to 22.1°, giving a nearly transverse cylinder motion. Since the majority of the literature considers transverse oscillations [1][2][4], we will compare with such experiments.

In their investigations of wake induced vibration of tandem cylinders, Assi et al. [1] conducted experiments on a fixed upstream cylinder with a transversely constrained downstream cylinder on air bearings. They found that steady oscillations of the trailing cylinder persisted when they removed the structural restoring force from their experiments, and they introduce

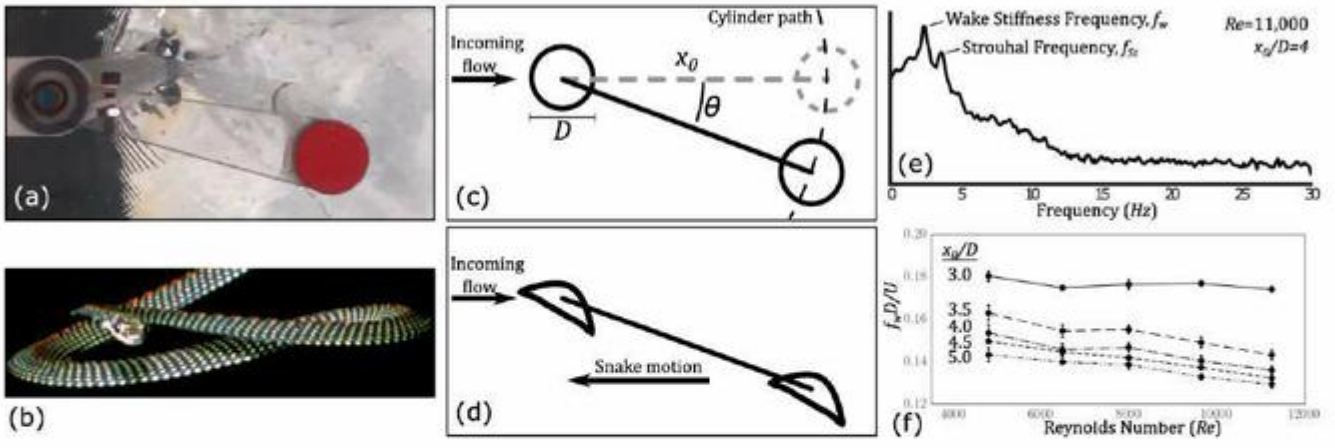

Figure 1: (a) Photo of experimental setup, including grey upstream PVC cylinder and red-capped downstream acrylic cylinder (b) Front view of *C. paradisi* in flight. From Socha [6]. (c) Configuration of the tandem, tethered cylinder system. The trailing cylinder is constrained to move around the upstream cylinder along the "cylinder path." (d) Schematic of side view of tandem wing model of flying snakes. The wings move together and are constrained to a constant distance, giving the similarity to tethered cylinders. (e) Power spectral density (PSD) of dynamic response for cylinder spacing $x_0/D = 4$, showing frequency peaks corresponding to Strouhal frequency and wake stiffness frequency. (f) Apparent Wake Stiffness, f_wD/U, for tandem, tethered cylinders at various spacings. Wake stiffness effects decrease for $x_0/D \geq 3.5$, but remain constant for $x_0/D = 3.0$.

*Corresponding author. Email: gknave@vt.edu

wake stiffness to explain the frequency of oscillations that they measure. As the cylinder is displaced from the wake centerline, the average magnitude of the coefficient of lift increases, giving the overall wake a stiffness-like behavior for quasi-steady dynamics. The wake stiffness is generated by the mean pressure difference between the surrounding flow and passing vortices shed from the upstream cylinder, providing an approximately linear dependence on displacement.

Since our experiments have no structural restoring force, any forces on the cylinders are due solely to fluid forces. For cylinder separations of $x_0/D \in [3.5, 5]$, the power spectrum of cylinder motion is dominated by two frequencies: a lower power, higher frequency component consistent with the corresponding Strouhal frequency for a stationary cylinder at that flow velocity; and a higher power, lower frequency component that we associate with the wake stiffness, as shown in Figure 1(e). When $x_0/D = 3$, the power spectrum shows one frequency peak. Based on results from the literature [7], this behavior lies within the little-studied gap-flow switching regime for tandem cylinders, which occurs for spacings $x_0/D < 3.5$ according to [7]. As the trailing cylinder is displaced, flow around the cylinders is redirected through the gap, causing the cylinder to be forced back toward the centerline. Assi et al. [1] did not conduct experiments in the gap-flow switching regime.

In the present study, we non-dimensionalize the measured frequency of oscillation by flow velocity and diameter to calculate an apparent wake stiffness, which we define as the stiffness necessary to give the measured frequency. Our experimental results support the use of the wake stiffness model in our tethered cylinder system. Figure 1(f) shows that apparent wake stiffness decreases slightly as Reynolds number increases for all cases within the wake induced vibration regime for which Assi et al. [1] initially postulated wake stiffness. This decreasing relative frequency is also shown in the original paper. In contrast, in the gap-flow switching regime the apparent wake stiffness remains essentially constant throughout the tested range, suggesting that the wake stiffness model is even more applicable to this regime than to the parameter range proposed in [1].

APPLYING WAKE STIFFNESS TO A MODEL OF FLYING SNAKES

A tandem wing model of flying snakes provides an opportunity to extend wake stiffness to tethered, non-circular bluff bodies. Five species of arboreal snakes native to Southeast Asia, most notably *Chrysopelea paradisi*, are able to flatten their bodies into a symmetric airfoil-like shape and glide through the air, as pictured in Figure 1(b). They continue to undulate their bodies throughout the flight much as snakes do on the ground, leading to complex flight mechanics. The flow structure around their bodies is unknown, but Holden et al. [3] have investigated the fluid forces on a representative cross-sectional body shape and have found that the cross-section is a bluff body with a vortex wake at every angle of attack.

In the investigation of flying snakes, work has been done to represent the essential components of the mechanics of gliding with simplified models. One such model, developed by Jafari et al. [5], uses the mean lift and drag forces on the snake body shape from experiments by Holden et al. [3] to influence a tandem wing model, considering the wings as rigidly connected, aerodynamically decoupled bodies, as shown in Figure 1(d). Each wing represents an approximately straight segment of the snake that is transverse to the incoming flow, which is a bluff body at any angle of attack. The tethered cylinder experiments provide a connection between previous cylinder experiments and the rigidly connected snake model. Therefore, we assume that we can apply the concept of wake stiffness to the model, and thereby achieve a first order improvement over the initial model. We find that wake stiffness affects glide stability and distance for the tandem wing model of the snake.

CONCLUSIONS

We examined the validity of the concept of wake stiffness, first introduced by Assi et al. [1], on a tethered cylinder configuration, fixing the distance between the cylinders rather than the direction of oscillation. We found that wake stiffness is a suitable framework for predicting these oscillations, but does not hold completely constant for increasing Reynolds number. The cylinder experiments lay a foundation for exploring the implications of extending the wake stiffness model to a non-circular pair of bluff bodies, such as the cross-sectional body shape of flying snakes.

References

[1] Assi G.R.S., Bearman P.W., Carmo B.S., Meneghini J.R., Sherwin S.J., Willden R.H.J.: The role of wake stiffness on the wake-induced vibration of the downstream cylinder of a tandem pair. J. Fluid Mech 718:210-245, 2013.

[2] Assi G.R.S., Bearman P.W., Meneghini J.R.: On the wake-induced vibration of tandem circular cylinders: the vortex interaction excitation mechanism. J. Fluid Mech 661:365-401, 2010.

[3] Holden D., Socha J.J., Cardwell N.D., Vlachos P.P.: Aerodynamics of the flying snake Chrysopelea paradisi: how a bluff body cross-sectional shape contributes to gliding performance. J. Exp Biol 217:382-394, 2014.

[4] Hover F.S., Triantafyllou M.S.: Galloping response of a cylinder with upstream wake interference. J. Fluid Struct 15:503-512, 2001.

[5] Jafari F., Ross S.D., Vlachos P.P., Socha J.J.: A theoretical analysis of pitch stability during gliding in flying snakes. Bioinspir Biomim 9, 2014.

[6] Socha J.J.: Gliding flight in Chrysopelea: turning a snake into a wing. Integr Comp Biol 51:969-982, 2011.

[7] Zdravkovich M.M.: Review of interference-induced oscillations in flow past two parallel circular cylinders in various arrangements. J. Wind Eng Ind Aerod 28:183-199, 1988.

RESONANCE-FOREVER IN LAMINAR FLOW REGIME

Navrose*[1] and Sanjay Mittal[1]
[1]*Indian Institute of Technology Kanpur, Kanpur, India*

Summary The phenomenon of *infinite-lock-in/resonance-forever* is investigated at low Reynolds numbers. It corresponds to the situation where the structure exhibits large amplitude oscillation up to infinite reduced speed (U^*). Computations have been carried out for various mass ratios (m^*) to obtain the critical value, m^*_{crit}, that demarcates the synchronized and desynchronized response at $U^* = \infty$. The study brings out significant differences between high Reynolds number and $2D$ flow regime.

INTRODUCTION

Unsteady aerodynamic forces arising from vortex shedding from a bluff body may lead to its vibrations. There is a strong interdependence between the motion of the body and the wake structure associated with it. Free-vibrations are often associated with *resonance/synchronization/lock-in*, wherein the structure exhibits relatively large amplitude of oscillation [1]. The range of reduced speed over which lock-in occurs increases with decrease in the mass-ratio of the cylinder [2]. The mass ratio is defined as the ratio of the mass of the oscillating structure to the mass of the displaced fluid. Experimental studies carried out at large Reynolds numbers regime show that below a critical value of mass ratio (m^*_{crit}), the range of lock-in extends up to infinite reduced velocity [3]. This situation is referred to as *infinite-lock-in/resonance-forever*. In this work the critical mass phenomenon is explored in the laminar regime. Compared to high-Re regime, significant differences are noted in the response of the fluid-structure system in the laminar flow regime. The differences have been investigated in detail.

COMPUTATIONAL DETAILS

The Navier-Stokes equations in primitive variable form are used to model the incompressible fluid flow. The structure is modeled as a rigid cylinder mounted on linear spring. To encourage high amplitude oscillations, the structural damping coefficient is set to zero. Only transverse oscillations are considered. A stabilized space-time finite element formulation has been utilized to carry out the computations. The details of the formulation along with the boundary conditions and the mesh employed for the study has been presented in our earlier works [4]. The reduced speed is defined as $U^* = U/f_n D$, where, U is the free stream speed, D is the diameter and f_n is the natural frequency of the oscillator *in-vacuo*. The Reynolds number is based on U and D. Computations have been carried out over a wide range of reduced speed and for $U^* = \infty$. For computations at $U^* = \infty$, the natural frequency of the oscillator is assigned zero value in the equations governing the motion of the oscillator.

RESULTS

Figure 1(a) and (b) shows the variation of the amplitude of cylinder oscillation with reduced speed (U^*) at $Re = 150$ and 100 for different values of mass ratio. Also shown is the response of the cylinder corresponding to $U^* = \infty$. The amplitude has been non-dimensionalized with the diameter of the cylinder. At $Re = 150$, the response of the cylinder for $m^* > 0.1$ is associated with two jumps at the two ends of the lock-in boundary with respect to U^*. Outside the lock-in regime, the cylinder exhibits low amplitude oscillation. The reduction of mass ratio to $m^* = 0.1$ results in an interesting situation. The cylinder exhibits large amplitude oscillation up to $U^* = 100$, the largest finite reduced speed for which the computations have been carried out. The amplitude of cylinder oscillation for $U^* = 100$ is found to be very similar to that at $U^* = \infty$. The difference in the two amplitude values for all mass ratios is less than 1%. It therefore, appears that for $m^* = 0.1$, the extent of lock-in regime persists up to $U^* = \infty$. At $U^* = \infty$ the amplitude of cylinder oscillation shows a sharp increase as the mass ratio is reduced to $m^* = 0.1$. This jump is associated with the transition of the response of the fluid-structure system from desynchronization to lock-in. Therefore, the critical mass ratio for $Re = 150$ is 0.1.

For $Re = 100$, the response of the cylinder for $m^* = 10.0$ is similar to that at $Re = 150$. It is associated with two jumps. However, for $m^* < 2.0$, only one jump is observed. Unlike, at $Re = 150$, the amplitude of cylinder oscillation at $U^* = \infty$, increases smoothly with decrease in mass ratio. Therefore, the critical mass ratio, based on the criteria of jump in the amplitude of cylinder oscillation at $U^* = \infty$, does not exist for $Re = 100$. In this situation, a frequency based criteria is used to identify m^*_{crit}. At the critical mass ratio the frequency of cylinder oscillation at $U^* = \infty$ achieves its lowest value. This definition is found to be consistent with the conventional definition of m^*_{crit} that is based on the jump in amplitude at U^*_∞. Detailed computations show that for $Re > 111$, the critical mass phenomenon is associated with amplitude jump at m^*_{crit}, while for $Re \leq 111$, the amplitude at $U^* = \infty$ decreases smoothly across m^*_{crit}.

*Corresponding author. Email: navrose@iitk.ac.in

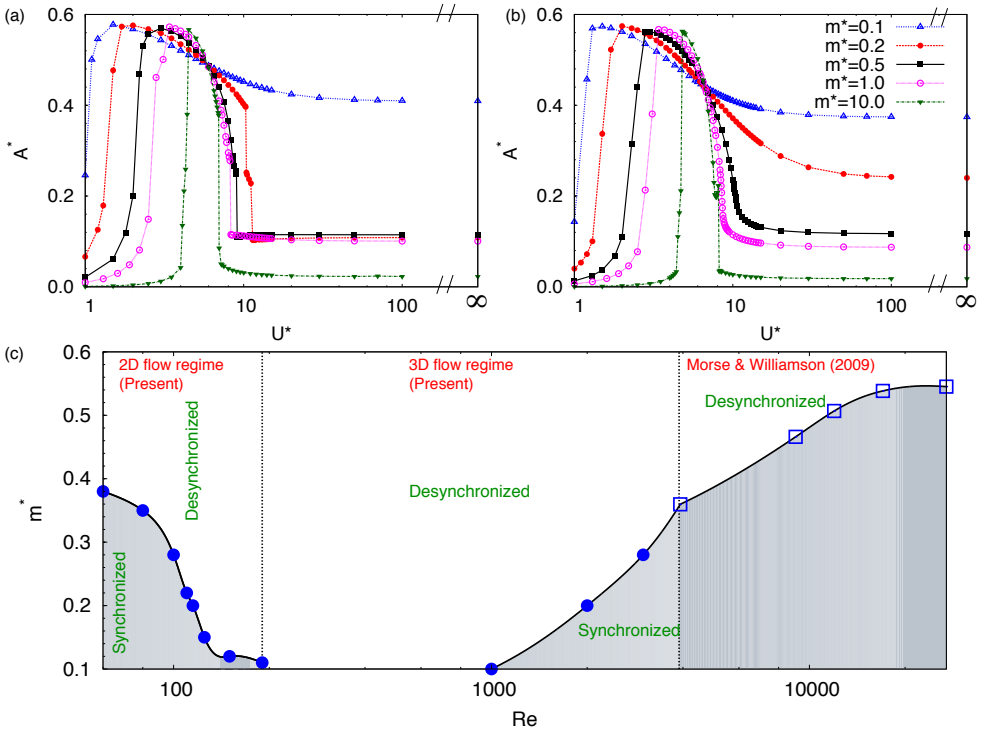

Figure 1: Flow past a free vibrating cylinder: variation of non-dimensional amplitude with reduced for various mass ratios for (a) $Re = 150$, and (b) $Re = 100$. Also shown is the amplitude corresponding to $U^* = \infty$. (c) Variation of critical mass ratio with Re.

Earlier studies at large Reynolds number have shown that during lock-in the mode of vortex shedding at $U^* = \infty$ is $2P$. In the $2P$ mode two pairs of counter-rotating vortices are shed per cycle of cylinder oscillation. The present study shows that, in the laminar flow regime, the vortices are shed in $2S$ pattern at $U^* = \infty$. In this mode, two vortices of opposite circulation are shed in one cycle of cylinder oscillation. Figure 1(c) shows the variation of m^*_{crit} with Reynolds number. It is observed that in the laminar flow regime, m^*_{crit} increases with increase in Re. This is different from observation made at large Re, where m^*_{crit} decreases with increase in Re. A few computations were carried out beyond the $2D$ flow regime also. These points are shown in the figure.

CONCLUSIONS

The phenomenon of *resonance-forever* is investigated in the laminar flow regime. Computations have been carried over a wide range of U^* and $U^* = \infty$. The response of the cylinder for $U^* = 100$ is found to be nearly the same as the response at $U^* = \infty$. For $Re > 111$, the amplitude of cylinder below critical mass ratio jumps from desynchronized response to locked-in state at $U^* = \infty$. On the other hand, for $Re \leq 111$, the amplitude of cylinder oscillation for $U^* = \infty$, increases smoothly with decrease in mass ratio from no lock-in to lock-in. Unlike large Re, the value of critical mass ratio decreases with increase in Re in the $2D$ regime.

References

[1] Blevins R. D.: Flow induced vibrations. 2nd edn. Krieger, 1990.

[2] Govardhan R. N., Williamson C. H. K.: Modes of vortex formation and frequency response of a freely vibrating cylinder. J. Fluid Mech, 420, 85-130, 2000.

[3] Govardhan R. N., Williamson C. H. K.: Resonance forever: existence of a critical mass and an infinite regime of resonance in vortex-induced vibration. J. Fluid Mech, 473, 147-166, 2002.

[4] Prasanth, T. K., Mittal, S.: Vortex-induced vibrations of a circular cylinder at low Reynolds numbers. J. Fluid Mech, 594, 463-491, 2008.

ON THE DEVIATION MOTION OF SELF-PROPELLED FLEXIBLE FLAPPING WINGS

Mathieu Olivier [*1]
[1]*Department of Mechanical Engineering, Laval University, Quebec City, Quebec, Canada*

Summary This paper presents a numerical study of the deviation motion of 2D flexible flapping in propulsion regime. The wing evolves in an incompressible flow at low Reynolds number and is subject to large structural deformations. It is shown that the deviation motion amplitude and phase are influenced by the wing inertia as well as by two feathering mechanisms.

INTRODUCTION

The study of flapping wings has received much attention in the last several years. This subject is of great interest in life sciences since insects, birds, and many aquatic animals use flapping wings or fins to move. Interest is also growing in the engineering community as flapping wings constitutes an interesting alternative to conventional aerodynamic principles (fixed or rotary wings) when it comes to design a lift or propulsion system for small scale devises such as micro air vehicles. In this context, this paper presents a study of self-propelled flexible flapping wings. The study focuses specifically on the deviation motion of such wings with different masses and flexibilities.

PROBLEM DEFINITION

The self-propelled flexible flapping wing investigated in this paper is assimilated to a flat plate of chord c whose profile is modeled by an Euler-Bernoulli beam model. The beam model is formulated to take into account geometrical nonlinearities since the wing undergo significant deformations even though the internal strains remain small. The flow field surrounding the wing is modeled by the incompressible Navier-Stokes equations. A harmonic pitching motion given by $\theta = \theta_0 \quad \mathrm{n}(2\pi ft)$ as well as a harmonic vertical heaving motion given by $h = h_0 \qquad (2\pi ft)$ are imposed at the leading edge of the wing which is let free to move horizontally (see Fig. 1). The heaving amplitude is $h_0 = c$, the pitching amplitude is $\theta_0 = 30°$, f is the motion frequency. Since the horizontal velocity is a priori unknown, the Reynolds number is defined as $Re = h_0 fc/\nu$, where ν is the kinematic viscosity of the fluid. The Reynolds number is set to $Re = 200$ throughout this study. The other relevant dimensionless parameters are:

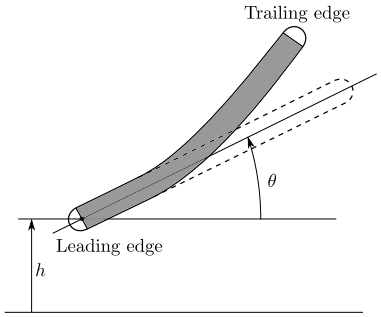

Figure 1: Geometry and motion description of the flat plate wing considered here. The grayed region is flexible.

$$\Sigma = \frac{\rho_f h_0}{\rho_s e}, \quad \delta_P^* = \frac{\rho_f (h_0 f)^2 c^3}{EI'},$$

where ρ_f and ρ_s are respectively the fluid and the solid densities, E is the solid rigidity, e is the wing thickness, and I' is the inertia of the wing frontal section per unit span given by $I' = e^3/12$. Σ represents the ratio of pressure forces over inertia forces that act on the wing structure. On the other hand, δ_P^* represents the dimensionless flexibility of the wing with respect to pressure forces. As such, δ_P^* provides an estimation of the trailing edge relative displacement with respect to the leading edge. Lastly, it is worth pointing out that the deviation motion is defined as the horizontal back and forth motion of the wing with respect to a point that moves at the wing average velocity.

NUMERICAL METHODS

The 2D flexible flapping wing scenario described above is a fluid-structure interaction problem. In order to obtain a numerical solution for such problem, a partitioned algorithm is used. That is, the fluid flow and the structural deformations are computed by two dedicated tools while the interaction is realized by transferring loads and velocities through the boundary conditions on the wing itself. The fluid flow is solved with a second-order finite-volume code based on the *OpenFOAM* library. The code uses an iterative PISO algorithm and the mesh motion is handled by inverse-weighting interpolation. On the other hand, the beam model is implemented using an in-house finite-element code that uses Hermite shape functions and Newton-Raphson iterations. The two solvers are embedded in a fixed point iterative loop to ensure full implicitness of the temporal scheme upon convergence. Because such coupling scheme is unstable when the fluid-solid interaction is strong [1], a stabilization strategy based on artificial compressibility similar to [2] was implemented. The numerical method is presented in more details and is thoroughly validated in [3].

*Corresponding author. Email: mathieu.olivier@gmc.ulaval.ca

RESULTS AND DISCUSSION

Numerical simulation results show that both flexibility and mass produce significant effects on the deviation motion of a flexible flapping wing. Fig. 3a shows the deviation motion of rigid wings. It clearly appears that decreasing the mass of the wing (increasing Σ) increases the amplitude of the deviation motion. This is simply explained by the fact that heavier wings undergo a smaller acceleration at a given aerodynamic force. As such, the motion of heavier wing and their general behavior resembles that of fully-constrained flapping wings (i.e., with an imposed horizontal velocity). On the other hand, the deviation motion of light wings has a feathering effect that levels and reduces the magnitude of aerodynamic forces.

The effect of wing flexibility on light wings ($\Sigma = 50$) is illustrated in Fig. 3b. It is observed that increasing flexibility reduces the amplitude of the deviation motion. This is attributable to another feathering effect, this time caused by wing flexibility. Indeed, when Σ is high, the wing shape of flexible wings tends to align itself with the local velocity field since the wing deformation is govern mainly by pressure forces. This behavior is clearly visible in Fig. 2a. Moreover, increasing flexibility also has an effect on the phase of the deviation which alters the openness of the figure-of-eight pattern. The effect on the phase is attributable to thrust peaks that are damped out by flexibility. While aerodynamic forces do not significantly influence the trajectory of heavy wings, Fig. 3c shows that increasing the flexibility of such wings increases the magnitude of the deviation motion that would be mostly nonexistent otherwise. This increase in deviation is explained by the fact that heavy wings deform at the extremities of their vertical course at which points, the trailing edge is pulled downward or backward because of its high inertia (see Fig. 2b). When the deformation is large, the trailing edge displacement also has a significant forward component that has the effect of pulling the leading edge backward so that the center of mass position remains mostly unchanged, hence the increase in the amplitude of the deviation motion.



(a)

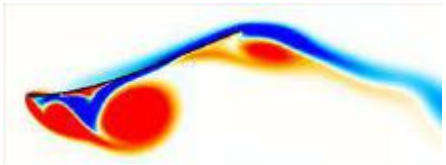

(b)

Figure 2: Vorticity field surrounding very flexible wings at $ft = 0$. (a) $\Sigma = 50$, and (b) $\Sigma = 0.1$.

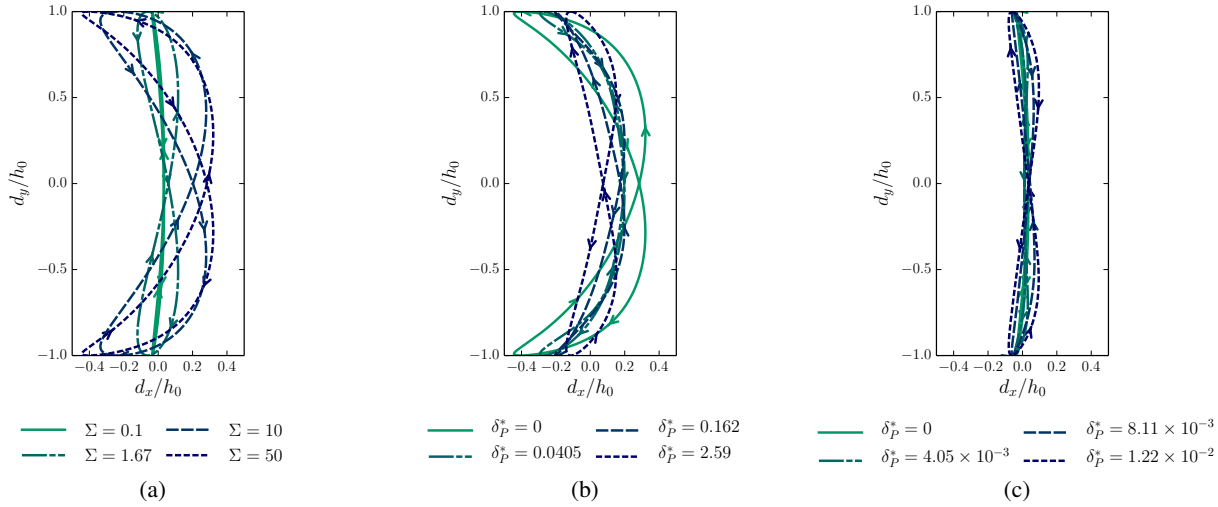

Figure 3: Deviation motion of flapping wings. (a) Rigid wings for different values of Σ, (b) Flexible light wings ($\Sigma = 50$), and (c) Flexible heavy wings ($\Sigma = 0.1$). d_x and d_y are respectively the x- and y-components of the leading edge relative displacement.

References

[1] P. Causin, J.F. Gerbeau, and F. Nobile. Added-mass effect in the design of partitioned algorithms for fluid-structure problems. *Computer Methods in Applied Mechanics and Engineering*, 194:4506–4527, 2005.

[2] J. Degroote, A. Swillens, P. Bruggement, R. Haelterman, P. Segers, and J. Vierendeels. Simulation of fluidstructure interaction with the interface artificial compressibility method. *International Journal for Numerical Methods in Biomedical Engineering*, 26:276–289, 2010.

[3] M. Olivier. *A Fluid-Structure Interaction Partitioned Algorithm Applied to Flexible Flapping Wing Propulsion*. PhD thesis, Université Laval, 2014.

PASSIVE CONTROL OF FLUTER APPLICATED TO A 3DOF AIRFOIL

Luc Amar[12], Guilhem Michon[1], Eric Laurendeau[2] & Sébastien Prothin[3]
[1]Université de Toulouse, CNRS, ICA, ISAE, DMSM, Toulouse, France
[2]Department of Aerodynamic, Ecole Polytechnique Montrel, Montreal, Quebec, Canada
[3]Université de Toulouse, ISAE, DAEP, ISAE SUPAERO, Toulouse, France

Summary This paper presents numerical simulations of passive control of flutter applied to a two dimensional airfoil-aileron configuration. The geometric model is composed of two joint solids: a main airfoil which can pitch (α) and plunge (h), and a hinged Control Surface (β). Under potential flow, low angle and frequency hypothesis, a linearization of the aeroelastic system reaches out a strongly coupled formulation. The time-domain expression of the Theodorsen unsteady aerodynamic model is computed using R.T. Jones approximation the Wagner function. This work focuses on three strategies to shift the critical speed. Firstly, the called "Linear Vibration Absorber" (LTVA) is a tuned mass damper (TMD), placed inside the airfoil, which oscillates in the plunge direction. Secondly, the "NES" is a nonlinear damper, based on the Nonlinear Ensegy Sink technology. Thirdly, the named "Cubic Control Surface" (CCS) configuration consist nonlinear hinge jointure featuring cubic restoring forces.

PRESENTATION OF THE PROBLEM AND METHODS

Dynamic aeroelasticity issues are contemporary research topics given their dangerous, hard to predict and their long, expensive certification stages [1]. The Tuned Vibration Absorbers technology (TVA) [2], consisting in adding a light {mass, spring, damper} (Fig. 1) device in the structure, is usually used by dynamists to passively transfert energy to a small subsystem. This method has been widely used to control bridge flutter but less on the airfoil application [3]. More recently oscillators with a cubic nonlinear stiffness (NES and NLTD) have shown interesting capacity in energy sinking and robustness [4], [5].

The goal of the study is to improve the understanding of adding such devices to an airfoil-aileron configuration (Fig. 2). According to potential aeroelasticity hypothesis, the Theodorsen model can be written in the compact, strongly coupled form [6] (eq. 1), where u is a general generalised coordinate vector containing unsteady aerodynamic informations and $\tilde{}_{nl}$ is the nonlinear restoring force vector. In the case where jointures are fully linear, reduced natural pulsations Ω and modal damping ratios ζ of normal modes can be computed with the eigenvalues "λ" (2). Thus, the sign of the aeroelastic damping is opposite to the eigenvalues real part. Linear reduced flutter speed is reached when the damping ratio becomes negative. At the uncontrolled configuration, the flutter speed is $6.25\,rad^{-1}$ (Fig. 3).

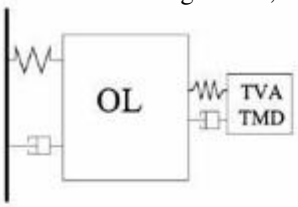

Figure 1. Tuned Mass Damper Attached to a Linear Oscillator

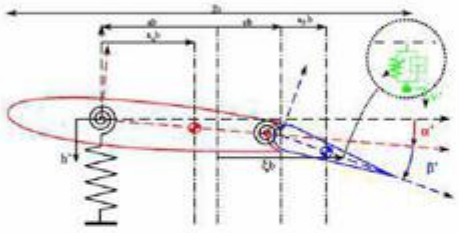

Figure 2. Aileron-Airfoil configuration with an Attached TMD

$$\tilde{\ddot{\boldsymbol{u}}} + \tilde{\boldsymbol{K}}\boldsymbol{u} = \tilde{\boldsymbol{f}}_{\boldsymbol{nl}} \quad (1)$$

$$\Omega^2 = |\lambda|^2 \quad \zeta = -\Re(\lambda) \quad (2)$$

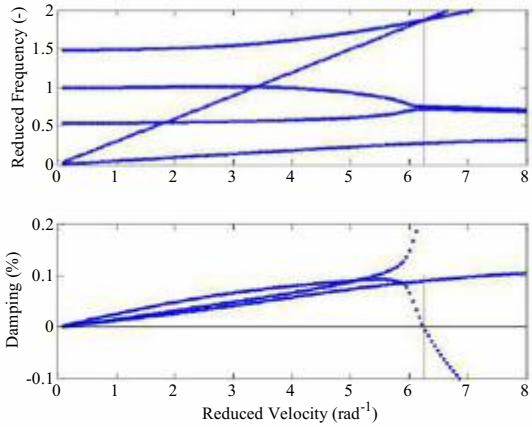

Figure 3. Flutter Diagram of the airfoil without passive control device.

a) Corresponding author. Email: ictam2016papers@legendconferences.com.

RESULTS AND CONCLUSIONS

Three passive technologies have been considered to shift flutter. The linear TMD, the Nonlinear Energy Sink TMD (NES), inside the airfoil, and a control surface including cubic restoring force (CCS). A frequency domain analysis coupled with a section method allows fast computation of the flutter speed (Fig. 4). Two areas show increasing of the flutter speed over 10%. Since the mass is a critical parameter in the aeronautical industry, the optimal position is at the trailing edge for an added mass around 2%. A fall of the flutter speed around the center of the airfoil is observed and goes behind 90%. Hence, it is important that the linear TMD keeps its position during the flight.

The indicator of efficiency of the nonlinear devices has been chosen as the ratio between the permanent root mean square amplitude and the initial condition (eq. 3). Hence, when the indicator equal 1, it means that the amplitude RMS is ten times under the initial condition.

$$indicator = -\log_{10}(\alpha_{rms}/\alpha_0) \qquad (3)$$

Figure 5 shows the indicator as function of the position and the reduced nonlinear term of the added NES 5% over the linear flutter speed. The NES mass is 5% of the airfoil. The optimal position is at the leading edge for high nonlinear stiffness. Around the small extremum, the NES configuration decreases the aeroelastic behaviour.

Figure 6 shows the indicator as function of the flutter velocity ration and the reduced nonlinear term of the CCS. The flutter speed increases as the cubic stiffness. If the nonlinear term is below 1E6, no flutter shift is observed. According to the parameter mapping, the CCS device can increase the flutter velocity of 7%.

This work confronted two nonlinear damping technologies to 'well known' linear TMD for flutter control. The linear absorber appears to be the most efficient (10%) for a light increasing of the mass (2%). However, the CCS device looks very interesting since it can increase the flutter speed of 7% without mass addition. The nonlinear TMD appears to be the less efficient method. In a future work, it would be interesting to verify the robustness of nonlinear methods and to continue the parametrical study with focusing on the TMD's damping ratio.

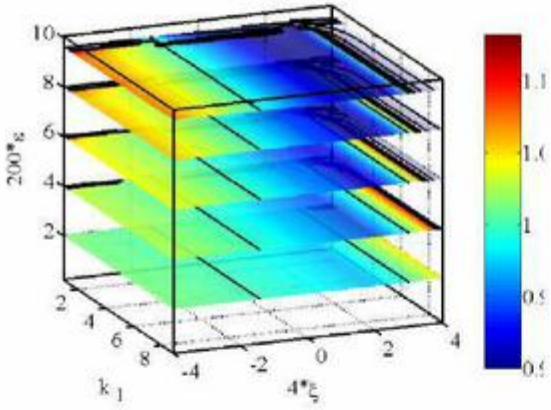

Figure 4. Flutter speed increasing as function of the reduced position, stiffness and mass of the linear

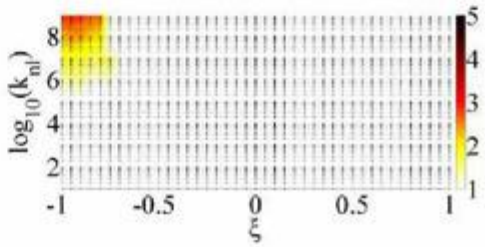

Figue 5. Indicator as function of the reduced nonlinear stiffness and the position 5% over the linear flutter speed for the "NES" configuration. $\epsilon = 5\%$.

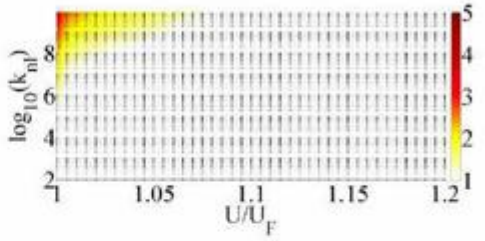

Figue 6. Indicator as function of the reduced nonlinear stiffness and wind velocity for the "CCS" configuration.

References

[1] Henshaw M. & al. : Non-linear aeroelastic prediction for aircraft applications, *Progress in Aerospace Sciences*

[2] Frahm H. : Device for damping vibrations of bodies, *US Patent 989,958,* 18 april 1911

[3] Karpel : Design for Active and Passive Flutter Suppression and Gust Alleviation, *NASA report,* 1981

[4] **G**. Habib : Passive flutter suppression using a nonlinear tuned vibration absorber *IMAC XXXIII – A Conference and Exposition on Structural Dynamics*, Orlando, Florida, 2015

[5] Y. Lee : Suppressing aeroelastic instability using broadband passive targeted energy transfers, part 2: experiments, *AIAA Journal,* vol. 45, n110, pp. 2391--400, 2007.

[6] L. Amar : Unsteady Vortex Lattice Method of an Aeroelastic Airfoil with Aileron Structural Nonlinearities, *CASI - AERO15*, Montreal, 2005

RESONANCE CAPTURE IN VORTEX-INDUCED VIBRATION OF A CYLINDER WITH A ROTATOR

Antoine B. Blanchard*[1], Oleg V. Gendelman[2], Lawrence A. Bergman[1], and Alexander F. Vakakis[3]
[1]*Department of Aerospace Engineering, University of Illinois at Urbana-Champaign, USA*
[2]*Faculty of Mechanical Engineering, Technion, Israel Institute of Technology, Israel*
[3]*Department of Mechanical Science and Engineering, University of Illinois at Urbana-Champaign, USA*

Summary At the intermediate Reynolds number $Re = 100$, a two-dimensional, linearly-sprung, circular cylinder restricted to move in the cross-flow direction and incorporating a rotational nonlinear energy sink (NES; consisting of a mass freely rotating about the cylinder axis and whose angular motion is restrained by a linear viscous damper) can undergo repetitive cycles of slowly decaying oscillations — which can lead to significant vortex street elongation with partial stabilization of the wake — interrupted by chaotic bursts. We construct a reduced-order model of the fluid-structure interaction dynamics and employ analytical techniques to show that the strongly modulated response is the manifestation of a resonance capture into a slow invariant manifold (SIM) that leads to targeted energy transfer from the cylinder to the rotator. Capture into the SIM corresponds to transient cylinder stabilization, and escape from the SIM to chaotic bursts.

FORMULATION OF THE FLUID-STRUCTURE INTERACTION PROBLEM

We consider a two-dimensional circular cylinder of mass $M_{\rm cyl}$ and diameter D, immersed in an incompressible fluid of density $\rho_{\rm f}$ and kinematic viscosity ν, mounted on a linear spring of stiffness $K_{\rm cyl}$, and allowed to move only in the direction transverse to the free stream. A pendulum of mass $M_{\rm NES}$ is attached to the cylinder and freely rotates at constant radius r_0 about the cylinder's generatrix (*cf.* Fig. 1). Inertial coupling allows energy to be transferred from the cylinder to the rotator, part of which is dissipated by a linear rotational viscous damper about the axis of rotation of the NES [1]. The Reynolds number $Re = UD/\nu$ is based on the cylinder diameter and on the free-stream velocity. We define a dimensionless time $\tau = tU/D$, scale the length, velocity and pressure by D, U and $\rho_{\rm f}U^2/2$, respectively, and introduce the dimensionless quantities $y = Y/D$, $\bar{r}_0 = r_0/D$, $m^* = \rho_{\rm b}/\rho_{\rm f}$ as well as a mass ratio $\epsilon_{\rm r} = M_{\rm NES}/(M_{\rm cyl} + M_{\rm NES})$. The equations governing the motion of the two coupled oscillators are then expressed in non-dimensional form as

$$\ddot{y} + \omega_{\rm r}^{*2} y = \epsilon_{\rm r}\bar{r}_0 \frac{}{\tau}(\dot{\theta} \quad {\rm n}\,\theta) + \frac{2C_{\rm L}}{\pi m^*} \qquad \text{and} \qquad \ddot{\theta} + \lambda_{\rm r}\dot{\theta} = \frac{\ddot{y}}{\bar{r}_0} \quad {\rm n}\,\theta, \tag{1}$$

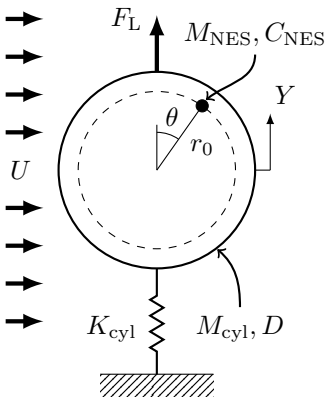

Figure 1: Circular cylinder in cross-flow with rotational NES.

where $\dot{(\,)} = \quad (\,)/\ \tau$ and $\rho_{\rm b}$ is the density of the cylinder with the NES [2]. The lift force $F_{\rm L}$ has been scaled in favor of a dimensionless lift coefficient $C_{\rm L} = 2F_{\rm L}/(\rho_{\rm f}U^2D)$, while the natural frequency of the linear spring supporting the cylinder has been non-dimensionalized as $\omega_{\rm r}^{*2} = (2\pi f_{\rm n}^*)^2 = D^2K_{\rm cyl}/[U^2(M_{\rm cyl} + M_{\rm NES})]$, and a dimensionless damping coefficient has been defined as $\lambda_{\rm r} = DC_{\rm NES}/(UM_{\rm NES})$. The density ratio m^* is set equal to 10, and the Reynolds number to $Re = 100$. The natural frequency $f_{\rm n}^*$ of the linear spring is chosen close to the normalized shedding frequency of a stationary circular cylinder at $Re = 100$, which is equal to the Strouhal number $St = 0.1 \quad$. The cylinder is initially at rest, while the NES initial conditions are selected as $\theta(0) = \pi/2$ and $\dot{\theta}(0) = 0$. Our computational approach is based on the spectral-element code Nek5000 [3]. The Navier-Stokes equations are cast in an arbitrary Eulerian-Lagrangian frame and integrated forward in time in a staggered fashion, together with (1) governing the motion of the two coupled oscillators.

PHYSICAL PHENOMENA FOR FINITE MASS RATIOS

For NES parameters $\epsilon_{\rm r} = 0.33$, $\lambda_{\rm r} = 0.002 \quad 5$ and $\bar{r}_0 = 0.\ 58$, the dynamics is characterized by successive cycles of regular motion of the cylinder and the NES interspersed by chaotic bursts. During periods of regular motion, the cylinder oscillation amplitude gradually decreases and the NES becomes locked in a regime of steady rotation that corresponds to 1:1 resonance capture with the cylinder. As the slowly decaying cycle progresses, the amplitudes of the lift and drag coefficients reduce drastically, while the cylinder, NES and lift coefficient are in clear 1:1:1 resonance, dominated by a single frequency that slowly decreases and reaches a minimum right before the dynamics transitions toward instability. More interesting, as the lift coefficient approaches zero and the drag coefficient tends to a minimum, the structure of the flow aft of the cylinder changes noticeably. The attached vorticity is considerably elongated and straightened, suggesting that the steady, symmetric solution (unstable at $Re = 100$) is partially stabilized due to the indirect action of the NES on the flow (*cf.* Fig. 2) [2, 4].

*Corresponding author. Email: ablancha@illinois.edu

ORDER REDUCTION OF THE DYNAMICS AND NUMERICAL VALIDATION

We analytically study the dynamics of the system governed by (1) in the aforementioned regime of resonance [4]. The cylinder interacts with the surrounding fluid *only* through the lift coefficient C_{L}, for which numerical data provides enough information to formulate an *ansatz* C_{L} for the asymptotic analysis. In order to apply classical complexification-averaging techniques, we impose the condition of 1:1:1 resonance and formally introduce the slowly varying instantaneous frequency $\omega = \omega(\tau)$ that depends on the amplitude of cylinder oscillations. We then use a slow-fast partition of the dynamics by letting $R(\tau)\mathrm{e}^{\mathrm{j}\zeta(\tau)} = \dot{y} + \omega(\tau)y$ and $\theta = \pm\zeta(\tau) + \psi(\tau)$. The instantaneous frequency ω and "fast" phase ζ are related through $\zeta(\tau) = \omega(\tau)$. We assume an *ansatz* lift coefficient of the form $C_{\mathrm{L}} = B(\tau)\sin[\zeta(\tau) + \eta(\tau)]$. In the above expressions, R, ψ, B and η are slowly varying functions of time. These steps are consistent with the numerical results in that they incorporate the essential assumption that, in the regime of 1:1:1 resonance, the NES, the cylinder and the lift coefficient are dominated by a single, slowly varying frequency ω and, consequently, that additional small-amplitude harmonics may be neglected.

Traditional averaging procedure yields the complex slow-flow equations, from which we extract the expression of the slow invariant manifold (SIM) of the problem, given by $R\cos\psi = -2\lambda_{\mathrm{r}} r_0$. The SIM is composed of two branches (the one stable, the other unstable), and breaks down by the mechanism of saddle-node bifurcation. Past this point, the slow flow leaves the regime of 1:1:1 resonance and enters a different regime of dynamics. At the super-slow scale, on the stable branch of the SIM, further approximations and algebraic manipulations allow us to reduce the dynamics down to a system of one nonlinear ordinary differential equation governing the slow modulation of the fast oscillations of the cylinder during the slowly decaying cycle, $R = f(R, \omega)$; and one algebraic equation relating the frequency of the cylinder oscillation to its amplitude, $\omega = g(R)$. The asymptotic analysis is validated by comparing the analytical predictions to numerical data obtained with Nek5000. Figure 2 shows the "sliding" of the trajectories on the stable branch of the slow invariant manifold. In the absence of a stable fixed point on the SIM, the "sliding" of the dynamics continues until the trajectory escapes the SIM and transitions into intermittent chaos, after which the dynamics is again captured on the stable branch of the SIM, and the previous cycle starts anew.

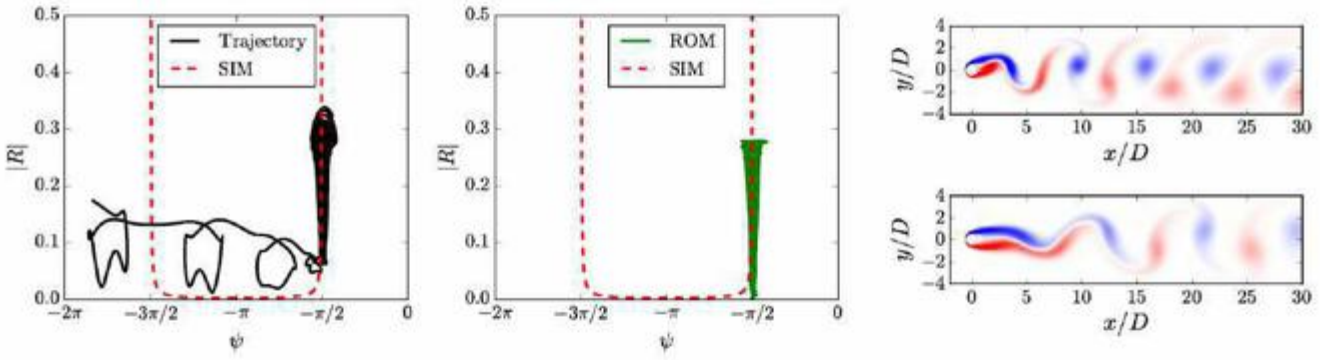

Figure 2: Capture into the 1:1 slow invariant manifold, for NES parameters $\epsilon_{\mathrm{r}} = 0.33$, $r_0 = 0.458$ and $\lambda_{\mathrm{r}} = 0.002745$. From left to right: comparison between the raw data obtained by direct numerical simulation and the analytical prediction resulting from integration of the reduced-order slow-flow model (ROM); and spanwise vorticity field at the beginning (top right) and end (bottom right) of the slowly decaying cycle highlighting significant elongation of the attached vorticity.

CONCLUSIONS

The mechanism of passive VIV suppression of a sprung cylinder in cross-flow with a rotational NES characterized by successive cycles of regular, slowly decaying motion interrupted by chaotic bursts, is proven to be the result of a resonance capture into the stable branch of a slow invariant manifold. This clarifies the action of the rotator on the resonance dynamics of the fluid-structure interaction problem, including the partial wake stabilization observed for finite mass ratios.

References

[1] O. V. Gendelman, G. Sigalov, L. I. Manevitch, M. Mane, A. F. Vakakis, L. A. Bergman, Dynamics of an eccentric rotational nonlinear energy sink, Journal of Applied Mechanics 79 (1) (2012) 011012.

[2] R. K. R. Tumkur, A. J. Pearlstein, A. Masud, O. V. Gendelman, L. A. Bergman, A. F. Vakakis, Wake Modification, Vibration Suppression, and Chaos at Intermediate Reynolds Number for Flow past a Sprung Circular Cylinder with a Nonlinear Rotational Dissipative Element, (submitted) (2015).

[3] P. Fischer, J. Kruse, J. Mullen, H. Tufo, J. Lottes, S. Kerkemeier, Nek5000 — Open-source Spectral Element CFD Solver, Argonne National Laboratory, Mathematics and Computer Science Division, Argonne, IL. See https://nek5000.mcs.anl.gov.

[4] A. B. Blanchard, O. V. Gendelman, L. A. Bergman, A. F. Vakakis, Slow-invariant-manifold capture in the fluid-structure interaction of a sprung cylinder with an essentially nonlinear internal rotator at intermediate Reynolds number, (submitted) (2016).

MULTI-FREQUENCY VORTEX-INDUCED VIBRATION OF A LONG CYLINDER IN SHEAR FLOW

Weimin Chen[1], Yilun Li[2], Min Li[3a)] & Yiqing Fu[1]
[1] *Key Laboratory of Mechanics in Fluid Solid Coupling System, Institute of Mechanics, Chinese Academy of Sciences, Beijing, China*
[2] *Sino-French Engineering School, Beihang University, Beijing, China*
[3] *School of Aeronautics Sciences and Engineering, Beihang University, Beijing, China*

Summary Multi-frequency vortex-induced vibrations of a slender cylinder in non-uniform flow are explored based on finite element simulations. A hydrodynamic model taking account of the interaction between fluid and structural dynamics is developed and combined with the finite element method so as to carry out multi-frequency vortex-induced vibration (VIV) of a slender cylinder in shear flow. Our numerical results shows that multi-frequency VIV may occur due to participations of several excited modes. As the towing speed (or the maximum speed of the linearly sheared flow) increases, the average RMS stress progressively rises and the spectral contents of the mixed standing-traveling wave structural responses become wider; but the displacement amplitude changes just a little. The region of first-dominant frequency shrinks because more and higher-order modes are involved into the responses.

1. INTRODUCTION

Vortex-induced vibration of long flexible cylinders such as riser, tension leg and pipeline of deep water platform experiencing ocean current (or wave) become more complicated as water depth increases. The dynamic characteristics of slender cylinder usually presents low-frequency and high-density natural modes due to large structural flexibility. The distribution of fluid field is no longer uniform. Several modes, rather than a single mode, are often excited during cylinder's VIV[1,2]. Further understanding and development of practical prediction model of the VIV for long cylinder like deep water riser experiencing non-uniform flow are significantly challenging.

2. HYDRODYNAMIC MODEL AND FINITE ELEMENT SIMULATION

For a long cylinder undergoing VIV, to get the theoretical solution is pretty difficult. Thus a numerical method based on a hydrodynamic model and finite element method is used here. First, based on our understanding of VIV and observations on experimental results[3,4], particularly in large-scale fields, along with CFD simulations, we found the lift force expression during lock-in would be more accurate and reasonable if the coupling between structural and fluid dynamics are taken into accounts. A third-order polynomial of the structure velocity, instead of the previous constant lift coefficient C_L, is proposed to model the vortex-induced lift force $f_L(z,t)$ as:

$$f_L(z,t) = (1/2)\rho V^2 D(C_{L0}\sin(\omega t) + C_1\dot{y}(z,t) + C_2\dot{y}^2(z,t) + C_3\dot{y}^3(z,t)) = p_f C_L(\dot{y}(z,t)) \quad (1)$$

where *z, y* and are respectively the axial position and transverse displacement of the cylinder and t is the time. *V* and ρ are the velocity and density of the fluid. *D* is the diameter of the cylinder. The values of the coefficients in Eq.(1) can be derived by fitting experimental data[4,5]. Observing Eq. (1), we may say it can capture, to some extents, features of VIV. For examples: the feature of self-excitation is represented by the first and second term; self-limitation is represented by the nonlinear terms; span coherence behavior is automatically captured because of the axially varying amplitude of structure's velocity.

Then the dynamic response of the cylinder undergoing VIV can be obtained by combining the presented hydrodynamic force model with the finite element method. The cylinder is uniformly divided into N elements which are normal two-node Euler beam element. The vortex-induced lift force and the drag force exerted by the ambient fluid are applied at the nodes respectively in the excitation and damping region. Regarding the nonlinear load, the Newmark-Beta direct numerical integration is used to solve the dynamic equations.

3. MULTI-FREQUENCY VIV RESPONSES AND DISCUSSIONS

The VIV responses of a 90-meter tension cable in linearly sheared flow at ten towing speeds were simulated by our FEM simulations and compared with the experiments[5]. Here selected results, at two towing speeds of 0.54m/s and 1.14m/s, are presented in Fig.1.

3.1 RMS and temporal-spatial evolution of displacement

Fig.1a and c show that the calculated RMS displacement and the dominating modes give acceptable agreements with the experiments. Observing the evolution of displacement versus time and cylinder span, see Fig.1b and d, the response is a mix of standing wave and travelling wave. Standing wave dominates the two regions closer to top or bottom ends where it is easier for the excited wave to meet the reflected wave and form a standing wave. Travelling wave becomes more obvious at higher towing speed (1.14m.s) because the damping effect is faster for the modes with higher modal order.

a) Corresponding author. Email: limin@buaa.edu.cn.

3.2 Influences of speed on the displacement and stress

The temporal power spectral densities (PSD) of displacements at the maximum RMS displacement are plotted in Fig. 2. They present the vibrations at multiple frequencies and the structural responses differ in the participating mode: as the towing speed increases, the highest modal order increases, while the band width of mainly excited frequencies broadens. Interestingly, more and/or higher-order participating modes do not necessarily mean larger displacement, see Fig.3, since different modes participate into (or drop out of) dynamic response and the excitation region for a certain mode change too. However, the stress obviously rises, see Fig.3, because new modes with higher-order number are excited. The higher level of stress with higher frequencies will inevitably impact the fatigue performance of structure.

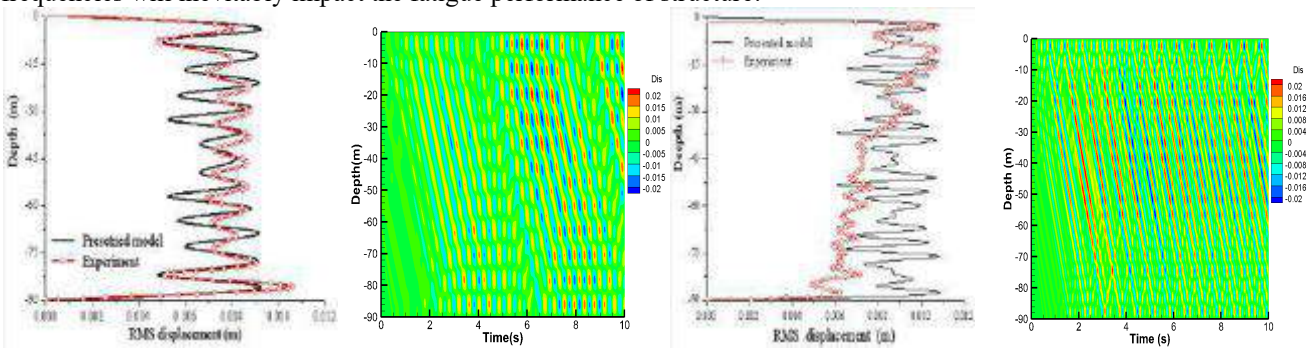

a RMS displacement **b** Temporal-spatial evolution **c** RMS displacement **d** Temporal-spatial evolution

Figure 1 VIV of flexible cylinder in shear flow respectively at towing speed 0.54m/s (a and b) and 1.14m/s (c and d).

3.3 Distributions of dominating frequencies along cylinder span

The distributions of dominant frequencies along cylinder length are presented in Fig.4. It is noted that the distributions along cylinder span, in terms of the band width and length of dominant frequencies, varies as the towing speeds rises. The band width of dominant frequencies gets wider and the first-dominant region gets smaller while the second and other dominant frequencies share more region along the span. It is partly because there are more participating modes into the dynamic response as the towing speed gets larger, the modal competition gets fiercer. This phenomena of multi-frequency dominance along cylinder span was also reported in Ref.[6,7].

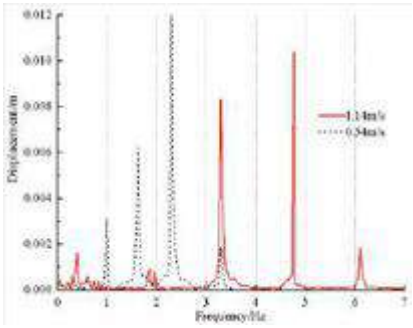

Figure 2 Frequency spectrum of the point with maximum displacement

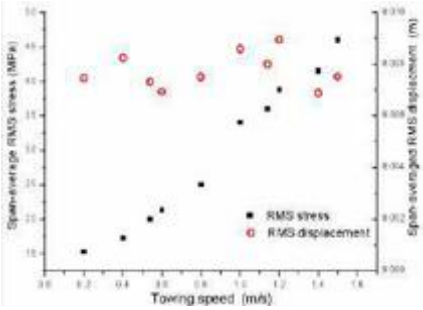

Figure 3 Effects of towing speed on VIV response

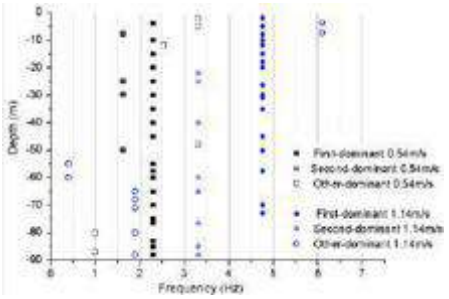

Figure 4 Distributions of dominant frequencies along the cylinder span

CONCLUSIONS

More and higher-order modes take part in the dynamic response as the towing speed increases. And, the average displacement slightly changes while the stress progressively increases, approximately linear, with the increase of towing speed. High-level of stress at higher frequency could be a concern owing to fatigue problem. There are different dominant frequencies distribute along cylinder span, and the length of the first dominant frequency gets smaller due to larger shear parameter along with more intense competition between participating modes.

References

[1] Vandiver JK, Allen D, Li L.: Journal of Fluids and Structures Mechanics, 10: 555-561, 1996.
[2] Sarpkaya T. A.: Journal of Fluids and Structures Mechanic, 19: 389-447, 2004.
[3] Gopalkrishnan R.: Vortex induced forces on oscillating bluff cylinders. *Ph.D.Thesis*. MA, USA: MIT, Cambridge, 1993.
[4] Lie H, Kaasen H K.: Journal of Fluids and Structures Mechanics. 22: 557-575, 2006.
[5] Chen WM, Li M, Zheng ZQ.: Ocean Engineering 42: 7-12, 2012.
[6] Bourguet R, Karniadakis GE, Triantafyllou M S.: Journal of Fluids and Structures Mechanics. 41: 33-42, 2013.
[7] Lucor D, Karniadakis GE.: European J. of Mech.-B/Fluids 23 (1): 41-49, 2004.

MODELLING AND EXPERIMENTAL CHARACTERIZATION OF DIAPHRAGM PUMPS AND TUBING

Raphael Frey *[1] and Jürg Dual[1]
[1]*Institute of Mechanical Systems, ETH Zurich, 8092 Zurich, Switzerland*

Summary The following work presents the basic components of fluid systems containing liquid diaphragm pumps. First, the elastic components of liquid diaphragm pumps are isolated and a mathematical representation for these elements is introduced. Then a formalism for the behaviour of polymer tubing is presented, which is then combined with the model of the diaphragm pump and other simple fluid system components. Measurements of such fluid systems are then compared with simulation results.

INTRODUCTION

Models of pumps which are connected to pipes have been treated in a variety of works [1, 2]. However, the elastic pump components are mostly represented with a linear model and pipes are modelled according to a linear elastic material behaviour. Both assumptions cannot represent small liquid diaphragm pumps whose elastic components consist of rubber and are connected to polymer tubes. In this paper we propose a model for the representation of the non-linear behaviour of the elastic components of a diaphragm pump and introduce an existing model for the viscoelastic material behaviour of tubes [3].

ELASTIC PUMP COMPONENTS

The flow–pressure behaviour of a working and resonating diaphragm in liquid diaphragm pumps can be represented with the following equation

$$Q = \frac{dp}{dt}\left(c(p) + \frac{dc(p)}{dp}p\right) \tag{1}$$

, where Q is the flow generated by a certain pressure change in such a diaphragm. The pressure dependent hydraulic capacity $c(p)$ can be determined with help of the geometrical constraints and the material properties of a specific diaphragm, according to non-linear plate theories [4]. A possible representation of the variable $c(p)$ is:

$$c(p) = w_0(p)\frac{\pi a^2}{3p} \tag{2}$$

where a is the radii of the clamped diaphragm, p the pressure acting on this diaphragm and w_0 the maximal deflection of this diaphragm, according to the approximative expression developed by Timoshenko [4]. Solving equation (1) for dp/dt yields two differential equations one for the pressure inside the working chamber and one for the pressure in the resonating chamber of the pump. These equations can then be solved numerically. Measurements of these non-linear pressure-volume relationships show good agreement with the established theoretical models, as can be seen in figure 1

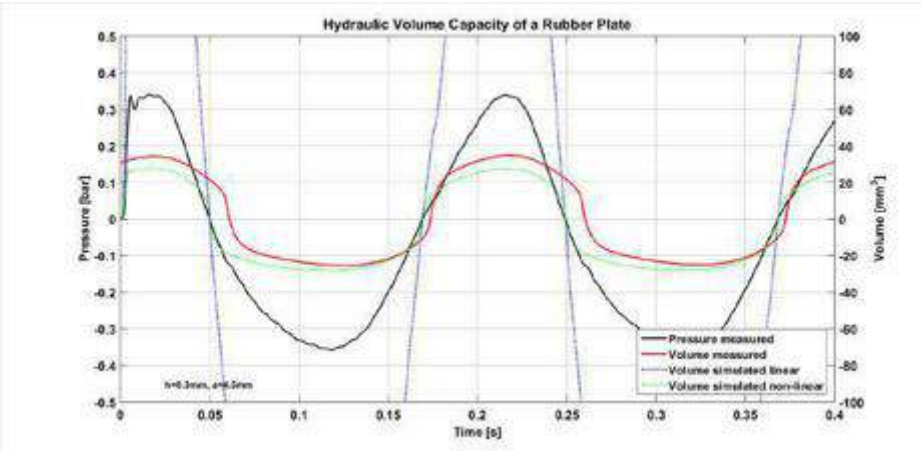

Figure 1: Measured volume depending on pressure for a rubber plate with a thickness of 0.3mm. Black solid line: Measured pressure acting on the resonating diaphragm. Red solid line: Measured volume displaced by the resonating diaphragm. Blue dotted line: Simulated volume curve according to linear plate theories. Green dotted line: Simulated volume curve according to non-linear plate theories

*Corresponding author. Email: frey@imes.mavt.ethz.ch

TUBING

The behaviour of fluids flowing in tubes can be represented with a set of two partial differential equations (continuity and momentum equation). In the one dimensional case these partial differential equations can be transformed to a set of ordinary differential equations with help of the method of characteristics. These equations can then be solved numerically. Furthermore steady and unsteady friction and the viscoelastic material behaviour of tubes can be integrated into the equations which are describing the tube flow [3].

FLUID SYSTEM MEASUREMENTS AND MODEL VALIDATION

For the solution of this set of differential equations describing the tube flow, boundary conditions at the tube ends are needed. At the end of the upstream tube and at the beginning of the downstream tube the model of a diaphragm pump serves as boundary condition. Reservoirs with a constant liquid level at the other ends of the tubes serve as boundary conditions at these ends. Measurements on a liquid diaphragm pump are compared to a model of this pump. The results of this comparison are shown in figure 2

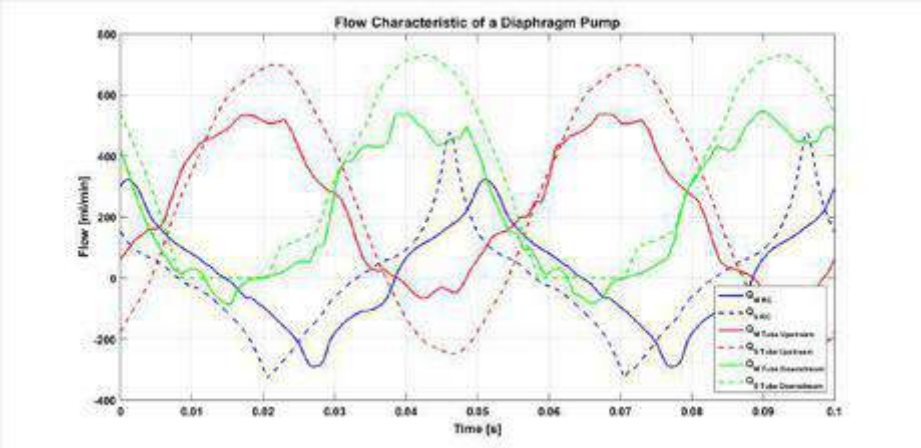

Figure 2: Measured (solid lines) and simulated (dashed lines) flow rates in the upstream and downstream tube as well as in the resonating chamber of a diaphragm pump

The overall flow characteristic, especially the characteristic in the resonating chamber, of the measured pump is in relatively good agreement with the simulation. Flow rate peaks are overestimated for the flow in the upstream and downstream tube as well as in the resonating chamber (RC). This could be due to cavitation which may occur for this measurement situation. Furthermore there is a shift of about 5ms between measured and simulated flow rates in the resonating chamber. If vapour pressure is reached this will act like a supplementary capacity, which could cause this shift. The viscoelastic property of rubber could be another explanation.

CONCLUSIONS

The presented non-linear models for the elastic pump components, show relatively good agreement to measurements and provide good insights in the behaviour of such pump elements. It is therefore possible to use these models, to design new pumps with a specific flow–pressure behaviour, for example.

References

[1] Shu J–J., Burrows C.R.: Pressure pulsations in reciprocating pump piping systems – Part1: modelling. Proc. Inst. Mech. Eng. 211:229–237, 1997.

[2] Richter M.: Modellierung und experimentelle Carakterisierung von Mikrofluidsystemen un deren Komponenten. PhD Thesis, Universität der Bundeswehr München, München, 1998.

[3] Covas D.: The dynamic effect of pipe-wall viscoelasticity in hydraulic transients. Part II–model development, calibration and verification. J. Hydraul. Res. 43:56–70, 2005.

[4] Timoshenko S., Woinowsky–Krieger S.: Theory of plates and shells. McGraw-Hill, 1959.

FLOW INDUCED VIBRATIONS OF CYLINDER WITH FLEXIBLE SPLITTER PLATE

Mohd Furquan *[1], Tulsi Ram Sahu[1], and Sanjay Mittal[1]

[1]*Department of Aerospace Engineering, Indian Institute of Technology Kanpur, Uttar Pradesh, India*

Summary Flow past rigid cylinders with an attached flexible splitter plate is investigated for low Reynolds numbers. Cross-sections with corners (square) as well as without any corner (circle) are considered. An isolated circular cylinder with flexible splitter plate is mounted on spring. The effect of flexibility of plate on suppression of vibrations is considered. The rigid plate is found to be more effective for suppressing the vibrations. The interference between two square cylinders with splitter plates is considered for side-by-side configuration for different values of stiffness of the plate. Large amplitude of vibrations is observed for the cases in which dominant frequency of the plate vibrations locks–in with the first natural frequency of its bending oscillations.

INTRODUCTION

Flow past a bluff body with a flexible splitter plate is a classic problem in fluid-structure interaction. The interaction of the separated shear layers with the vibrating plate leads to interesting dynamical phenomena. Splitter plates/filaments are commonly used as devices for controlling vortex shedding and vibrations associated with bluff bodies. Several researchers have studied the effect of rigid [1, 2] as well as flexible [3] splitter plates on the vortex shedding from a stationary circular cylinder. However, the effect of splitter plates on multiple cylinders and on oscillating cylinders has not been studied in detail. In this paper, the effect of flexible splitter plates on flow past two square cylinders and on elastically mounted single circular cylinder is studied.

COMPUTATIONAL METHOD

The fluid flow problem over the deforming domain is solved by using the SUPG/PSPG stabilized space-time approach known as DSD/SST [4]. The movement of the mesh in the deforming domain is modeled as a linear elastic pseudo-solid. The nonlinear elastic structural dynamics calculations are carried out via an open-source program [5] based on the standard Galerkin FEM in a total Lagrangian framework. The fluid and structure dynamics is coupled using a block iterative technique.

RESULTS AND DISCUSSION

Results for the flow past two square cylinders with splitter plates in a side-by-side arrangement are presented. The cylinder centers are separated by a distance twice the edge length (L) of the cylinders. Each plate is of length of 4L and 0.06L thickness. Reynolds number based on edge length of the cylinder is 100. The flexibility of the plate, characterized by the non-dimensionalized Young's modulus $Ae(= E/\rho_f U_\infty^2)$, is varied from $\times 10^5$ to 32×10^5. The ratio between the densities of the structure and the fluid is 84.746. Initially, the flow is allowed to develop over the rigid structure for a fixed period of time. As the flexibility is switched on, the plates exhibit small amplitude oscillations while moving out-of-phase with each other. However, over a period of time depending on Ae, the motion of the plates eventually becomes in-phase. The frequency and amplitude of the fully developed response varies with the flexibility of the plates. Figure 1(a) shows the variation of the amplitude and frequency of vibration of the plates with Ae. The filled blue circles correspond to the amplitude, while the frequency of vibration is shown with triangles. Also shown, for reference is the variation of natural frequency of the plates with Ae using a continuous red curve. As seen from the figure 1(a), relatively large amplitudes are observed for the cases wherein the frequency of oscillation of the plates is close to their first natural frequency. These cases correspond to 'lock-in'. During lock-in a well defined closed orbit exists in the phase portraits drawn between tip displacements of the two plates. Figures 1(b) and 1(c) show the vorticity fields for a lock-in and a no lock-in case, corresponding to Ae equal to $\times 10^5$ and 12×10^5 respectively, at a time instant corresponding to the maximum deflection of the plates. During lock-in, the wake is wider and vortices are released further downstream as compared to the no lock-in case.

Next, the results for the flow past an elastically mounted circular cylinder with splitter plate are presented. The Reynolds number based on the cylinder diameter (D) is 150. The plate is $3.5D$ long and $0.2D$ thick. The value of the parameter Ae is $8\ 35$, while the ratio of structure and fluid densities is 10. The natural frequencies, non-dimensionalized by U_∞ and D, of the rigid body and bending oscillations are 0.1 and $0.0\ \ 8$ respectively. Figure 2 shows the vorticity fields for – (a) an isolated cylinder, (b) cylinder with an attached rigid plate and (c) cylinder with an attached flexible plate, each having the same natural frequency of rigid body oscillations. For cases (b) and (c), splitter plate interacts with the shear layers separated from the cylinder, while inhibiting communication between the two sides of the cylinder. This leads to changes in the frequency of vortex shedding and amplitude of vibration. The cylinder with the deformable plate has Strouhal number St equal to

0.1664, which is slightly more than the value of St for an isolated cylinder. However, for the cylinder with a rigid plate St is 0.1166, which is much less than the other two cases. The presence of plates delays the release of shed vortices to a relatively downstream location in the wake. The delay is more pronounced in the case of the rigid plate than the compliant one. The reduction in amplitude of cylinder oscillations is also significantly more for the rigid plate than the flexible one. This suggests that the rigidity of the splitter plate plays an important role in suppressing vortex induced vibrations.

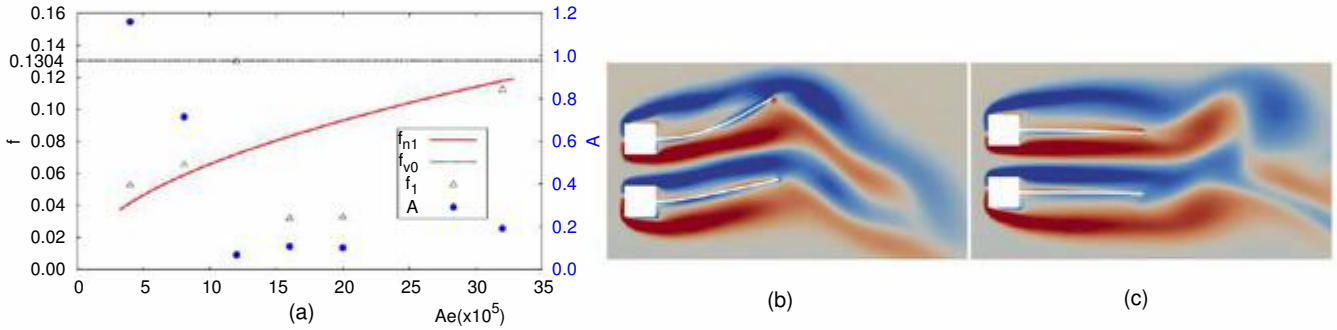

Figure 1: $Re = 100$ flow past two square cylinders with flexible splitter plates: (a) variation of frequency and amplitude of displacement with Ae (b) instantaneous vorticity field with $Ae = 4 \times 10^5$ and (c) $Ae = 12 \times 10^5$. The plate are in their maximum deflection configuration.

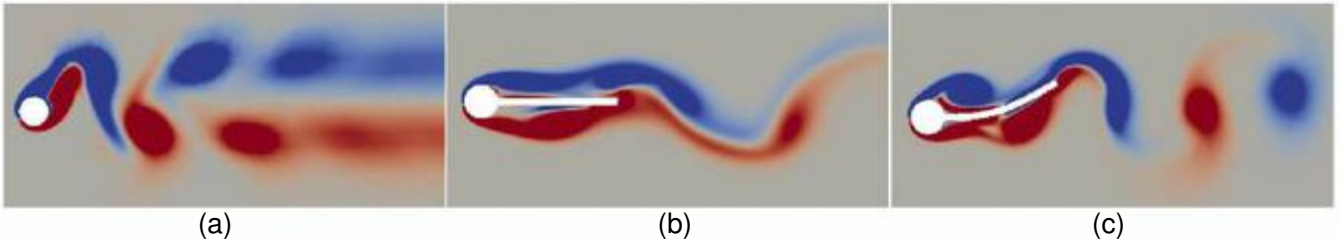

Figure 2: $Re = 150$ flow past an elastically mounted circular cylinder instantaneous vorticity field for: (a) isolated cylinder case (b) rigid plate case and (c) flexible plate case.

CONCLUSIONS

In this study, results have been presented for the flow induced vibration of flexible plates attached behind rigid cylinders. In the case of flow past two square cylinders, the two plates initially exhibit out-of phase vibrations, but eventually get synchronized with each other and show in-phase fully developed response. The lock-in of the frequency of plate oscillations with the first natural frequency of bending oscillations is observed for certain values of stiffness. The lock-in cases show relatively large amplitudes of oscillations, which is consistent with the well studied behavior of isolated cylinders at lock-in. For the case of elastically mounted cylinder with splitter plate, the rigidity of the plate is found to play an important role in reducing both amplitude and frequency of the cylinder oscillations.

References

[1] Mansingh V., Oosthuizen P.H.: Effect of splitter plates on the wake flow behind a bluff body. AIAA. J., 28:778-783, 1990

[2] Kwon K., Choi H.: Control of laminar vortex shedding behind a circular cylinder using splitter plates. Phys. Fluids, 8:479-486, 1996.

[3] Lee J. and You D.: Study of vortex-shedding-induced vibration of a flexible splitter plate behind a cylinder. Phys. Fluids 25(11),110811, 2013.

[4] Tezduyar T.E., Behr M., Mittal S., Liou J.: A new strategy for finite element computations involving moving boundaries and interfaces-the deforming-spatial-domain/space-time procedure: II. Computation of free-surface flows, two-liquid flows, and flows with drifting cylinders. Comput Meth. Appl. Mech. Eng.,94(3):353-71, 1992.

[5] Dhondt G.: Calculix: A free software three-dimensional structural finite element program http://www.calculix.de/

LARGE DEFORMATION OF CHIRAL RODS AND RIBBONS SUBJECTED TO WIND

Masoud Hassani[1], Simon Molgat-Laurin[1], Njuki W. Mureithi[1], and Frédérick P. Gosselin [*1]

[1] *Department of Mechanical Engineering, École Polytechnique de Montréal, Montréal, Québec, Canada*

Summary In the present work, we seek to understand the reconfiguration of plants with a chiral morphology by experimental and theoretical modeling of the large deformation of flexible chiral rods under wind. Test specimens are made of ABS plastic and polyurethane foam reinforced with nylon fibers. Wind tunnel tests are performed to evaluate the effect of chirality on flow-induced reconfiguration. A theoretical model is developed by coupling the Kirchhoff rod theory with a semi-empirical formulation for aerodynamic loading evaluation. A range of geometrical and material properties and flow velocity is studied in the experimental and theoretical model. It is shown that chirality reduces the effect of the loading direction on deformation.

INTRODUCTION

In general, plants and vegetation are flexible and are prone to significant deformation under fluid loading, their own weight or precipitation load. The deformation of plants in flow is usually accompanied by a drag reduction which is termed reconfiguration [1]. The reconfiguration of plants has been studied fundamentally by modeling them as simple mechanical structures such as bending beams, fibers and plates [2, 3]. Although these aforementioned models can simplify the two-dimensional deformation of plants, they are not representative for all forms of plants' reconfiguration. For instance, some species of plants grow with a chiral morphology which cannot be modeled by a bending beam. Plants with erect slender leaves such as typha latifolia usually demonstrate a level of chirality [4]. It has been argued in several studies that chirality renders plants less vulnerable to wind-induced deformation and buckling [4, 5, 6]. The effect of chirality on the stability of plants against buckling has been studied by modeling them as upward pre-twisted beams [4, 5]. However, the role of chirality in the three-dimensional reconfiguration of plants under transverse loading is missing from the literature. The goal of this work is to study the mechanisms underlying the reconfiguration of chiral biological structures in the flow by modeling them as a chiral rod. We seek to understand the effect of chirality on the ability of plants to withstand the fluid loading.

METHODOLOGY

Experimental Procedure and Materials

The tests on flexible specimens with chiral morphology are performed in a wind tunnel. A 6-axis force balance is used in the present experiments to measures the aerodynamic forces and moments. The specimens are clamped to the force balance at one end using a mast to subtract the effect of boundary layer from the measurements and they are free at the other end. The measurements represent the time-averaged values of fluctuating loads within the stable region of the test specimens.

Two types of flexible specimens are used in the experiments: circular rods and flat ribbons. The circular rods are made using polyurethane foam and are internally reinforced with nylon fibers as detailed in [7]. The fibers are positioned along one diameter of the circular rod and twist around its centerline to form a rotating material frame $(\mathbf{e}_x, \mathbf{e}_y, \mathbf{e}_z)$ with anisotropic rigidity $\lambda = (EI)_y/(EI)_x < 1$ (see Fig. 1a). This geometry is used in order to simplify the fluid loading evaluation in the theoretical model. The bending rigidity of the rods is evaluated from a three-point bending test. The flat ribbons on the other hand have intrinsic directional rigidity due to their less-than-unity thickness to width ratio (Fig. 1b). They are made of ABS plastic and twisted along their length with a range of pre-twist angles φ. Annealing at 100 for several hours is performed to make the twisted state of the rods their stress-free state (Fig. 1c,d). For a chiral ribbon, fluid loading depends on the alignment of its sections with respect to the flow direction i.e. the local angle of incidence ψ. In the tests, the directional rigidity gives rise to a three-dimensional deformation in asymmetric bending. The clamped end of each specimen is rotated around its centerline to have different values of angle of incidence at the clamped end ψ_0. Eleven rod specimens are made for a range of natural twist φ from 0 to 720 degree and a variety of bending rigidity ratio λ.

Theoretical Model

The three-dimensional reconfiguration is modeled theoretically using the Kirchhoff theory of rods. In the model, a rod is represented by a deforming three-dimensional and inextensible curve with the assumption of small strains [7, 8]. It is also assumed that each cross section of the rod remains planar and normal to the centerline. Bending moments and the twisting moments are proportional to the curvatures, $(\kappa_x\ ,\ \kappa_y)$ and the twist (τ), respectively. In this model, the rotation of the material frame around the centerline is considered by coupling the derivatives of the direction cosines to the Kirchhoff equations. A semi-empirical formulation of the pressure drag force on an oblique cylinder is also used to evaluate the aerodynamic loading

[*]Corresponding author. Email: frederick.gosselin@polymtl.ca

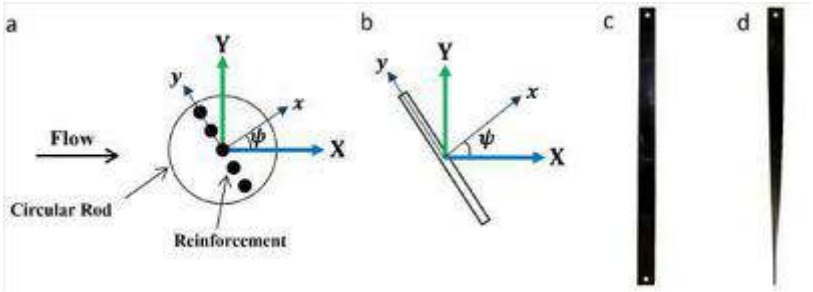

Figure 1: A section of a) circular reinforced rod and b) a chiral ribbon. c) A ribbon made of ABS d) A ribbon with 90 degree of pre-twist angle φ after annealing.

on the deformed specimens [7]. For the ribbon, lift and drag are evaluated based on the sectional angle of incidence and the normal component of the flow velocity to the ribbon's centerline. The lift and drag coefficients are evaluated from the wind tunnel tests on a rigid metallic ribbon with the same aspect ratio as the flexible specimens. The governing equations are solved using Matlab as a boundary value problem.

RESULTS AND CONCLUSIONS

A static bending test is performed on the foam rods by hanging them horizontally under their own weight. Figure 2a shows the variation of the maximum tip deflection of the hanged rods as a function of ψ_0 for three value of φ. It is found that by increasing φ from 0 to 720 degree, the deformation becomes less dependent to the loading direction. Figure 2b illustrates the drag for two ribbons for different angles of incidence, one without twist and the other with a natural twist angle of 360 degree. The results show that chirality decreases the dependency of the drag to the flow direction. This is in agreement with the results from the static bending test. Moreover, the drag generally decreases for a naturally twisted ribbon compared to a straight one. Both of these conclusions support the hypothesis that a chiral morphology could provide an evolutionary advantage to plants in reducing drag load and making their properties more isotropic.

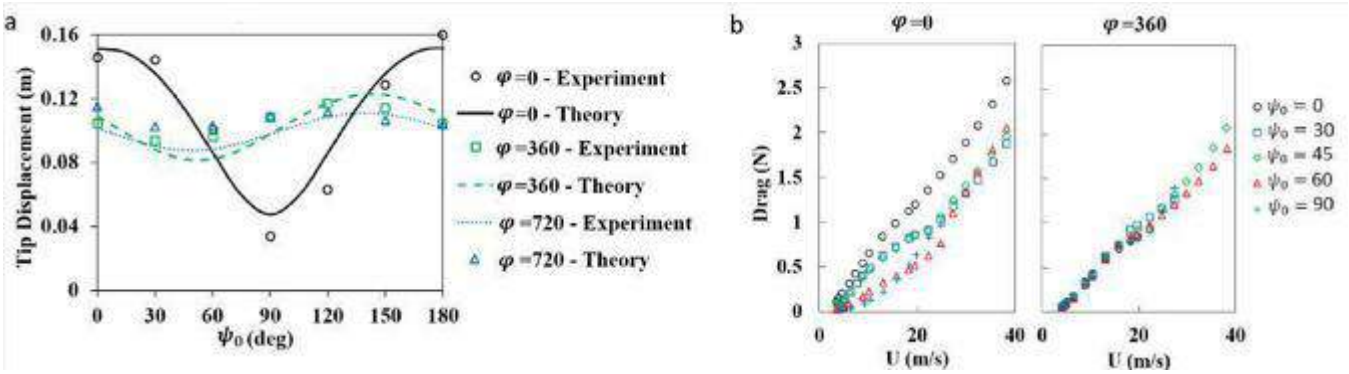

Figure 2: a) Maximum vertical deflection of a horizontally hanged beam for a range of ψ_0. Here, the angle of incidence is measured with respect to the gravity direction. b) Drag measurement for two ribbons with a natural twist of 0 and 360 degree for different values of angle of incidence ψ_0

References

[1] Vogel S.: Drag and flexibility in sessile organisms. American Zoologist 24 (1), (1984), 37-44.

[2] Alben S., Shelley M., Zhang J.: Drag reduction through self-similar bending of a flexible body. Nature 420 (6915), (2002), 479-481.

[3] Gosselin F. P., de Langre E., Machado-Almeida, B. A.: Drag reduction of flexible plates by reconfiguration. Journal of Fluid Mechanics 650 (2010) 319.

[4] Schulgasser K. and Witztum A.: Spiralling upward. Journal of theoretical biology 230.2 (2004), 275-280.

[5] Zhao ZL et al.: Analysis of bending and buckling of pre-twisted beams: A bioinspired study. Acta Mechanica Sinica 30.4 (2014), 507-515.

[6] Rowlatt U. and Morshead H.: Architecture of the leaf of the greater reed mace. Botanical journal of the Linnean Society 110.2 (1992), 161-170.

[7] Hassani M., Mureithi N. W., Gosselin F. P.: Large Coupled Bending and Torsional Deformation of an Elastic Rod Subjected to Fluid Flow, Accepted for publication in the Journal of Fluids and Structures, 2016.

[8] Dill E. H.: Kirchhoff's theory of rods. Archive for History of Exact Sciences, 44(1) (1992) 1-23.

PARTITIONED ITERATIVE AND DYNAMIC SUBGRID-SCALE METHODS FOR FREELY VIBRATING OFFSHORE STRUCTURES IN TURBULENT FLOW

R.K. Jaiman *[1], P. S. Gurugubelli[2], M. Z. Guan[3], and T. P. Miyanawala[4]
[1]*Department of Mechanical Engineering, National University Singapore, Singapore*

Summary Fully-implicit combined field scheme proposed in [1, 2] has been extended to model flow-induced vibration of 3D offshore structure in a turbulent flow. We employ a partitioned iterative and dynamic subgrid-scale (SGS) schemes for solving coupled fluid-rigid body interaction using unstructured grid. The iterative scheme relies on the so-called non-linear interface force correction formulation to stabilize the variational coupled system based on the filtered Navier-Stokes equations. The interface corrections provide the force equilibrium with arbitrary accuracy while maintaining the velocity continuity condition along the fluid-structure interface. We show that our second-order scheme is stable for both VIV and galloping instabilities found in a freely vibrating square cylinder with strong added-mass effects. We demonstrate the SGS-based large-eddy simulation solver for 3D multicolumn semi-submersible floater subjected to flow-induced motions at Reynolds number Re = 20000. The transverse amplitude and the Strouhal number of the offshore floater are validated against the experimental data.

INTRODUCTION

Coupled dynamical fluid-structure systems undergo a great variety of flow-induced vibrations (FIV), both useful and destructive manners in numerous engineering applications. In particular, ocean environments are full of such self-excited instabilities, which constitute an interesting problem for the numerical modeling and can have a significant impact on the systems used in ocean and offshore engineering, including moorings, risers, subsea pipelines, large floating structures. Offshore structures interacting with ocean currents are inevitably subject to fluid forces and they may undergo FIV at certain conditions [4]. Square shaped columns are widely used in offshore floating structures such as semi-submersible. Predicting FIV in column floaters is a challenging task due to complex wake interference, vortex-induced vibrations and galloping and several other self-excited instabilities. These coupled instabilities associated with rhythmic oscillations are undesirable for the riser and mooring fatigue. The motivation of this study is to understand the fundamental FIV behavior of multicolumn configurations employed in semi-submersible structures. This numerical study focuses on the wake flow fields and vibration characteristics of the single and multicolumn floating structure. We develop a partitioned iterative procedure to couple the filtered Navier-Stokes solver with rigid-body dynamics. To account for fluid-body interaction, a partitioned iterative scheme so-called nonlinear interface force correction (NIFC) has been developed to rigid-body coupling for capturing flow-induced vibration. The coupled fields are advanced explicitly and the interface force correction is constructed at the end of each fluid subiteration.

We introduce a new variational formulation along the fluid-body interface through combined interface [5] and nonlinear iterative force corrections [2]. We provide a modified form of the interface force correction which can be applied with arbitrary solid dynamics. In addition, we construct a dynamic sequence parameter for stabilizing the interface force along fluid-structure interface through nonlinear sub-iterations. We show that the geometric extrapolations with the nonlinear iterative force correction and the CIBC corrections can provide stable solution fluid-structure interaction with strong added-mass effects. We perform systematic flow-induced vibration study of a square cylinder vibrating freely for the range of reduced velocity $U_r \in [1, 20]$ and mass ratio $m^* \in [0.1, 10]$. The developed dynamic LES scheme is then validated for the vortex shedding benchmark problem of an incompressible fluid flow at high Reynolds number ($Re = 22000$) flow past a squared cylinder. For the first time, the NIFC procedure based on CIBC corrections has been extended for turbulent flow calculation using the LES technique. The motion and forces of the floater is discussed as a function of structural damping and reduced velocity. The numerical results are validated with the recent towing test in the ocean basin [6]. In our numerical study, we demonstrate that flow-induced vibrations must be considered during the design process of column floater.

REPRESENTATIVE RESULTS

This section reports a set of numerical experiments to understand flow-induced vibrations of the column deep draft semi-submersible. All the geometry parameters of the semi-submersible model is adopted from [6]. The model is scaled at 1:70 to the real operational semi-submersible with the sharp cornered columns, as shown in Fig. 1a. The model has four columns with four pontoons and in the full-load and deep draft condition and is elastically mounted and free to oscillate in the in-line and transverse directions. The mesh consists of about 1.7 million nodes and 10 million linear tetrahedral elements for capturing the turbulent wake using the dynamic subgrid LES model. Figure 1b presents the relationship between the reduced velocity and the transverse vibration amplitude. The "lock-in" region of VIV happens at $U_r \in [\ , 15]$, which changes into the galloping mode after increasing the reduced velocity further.

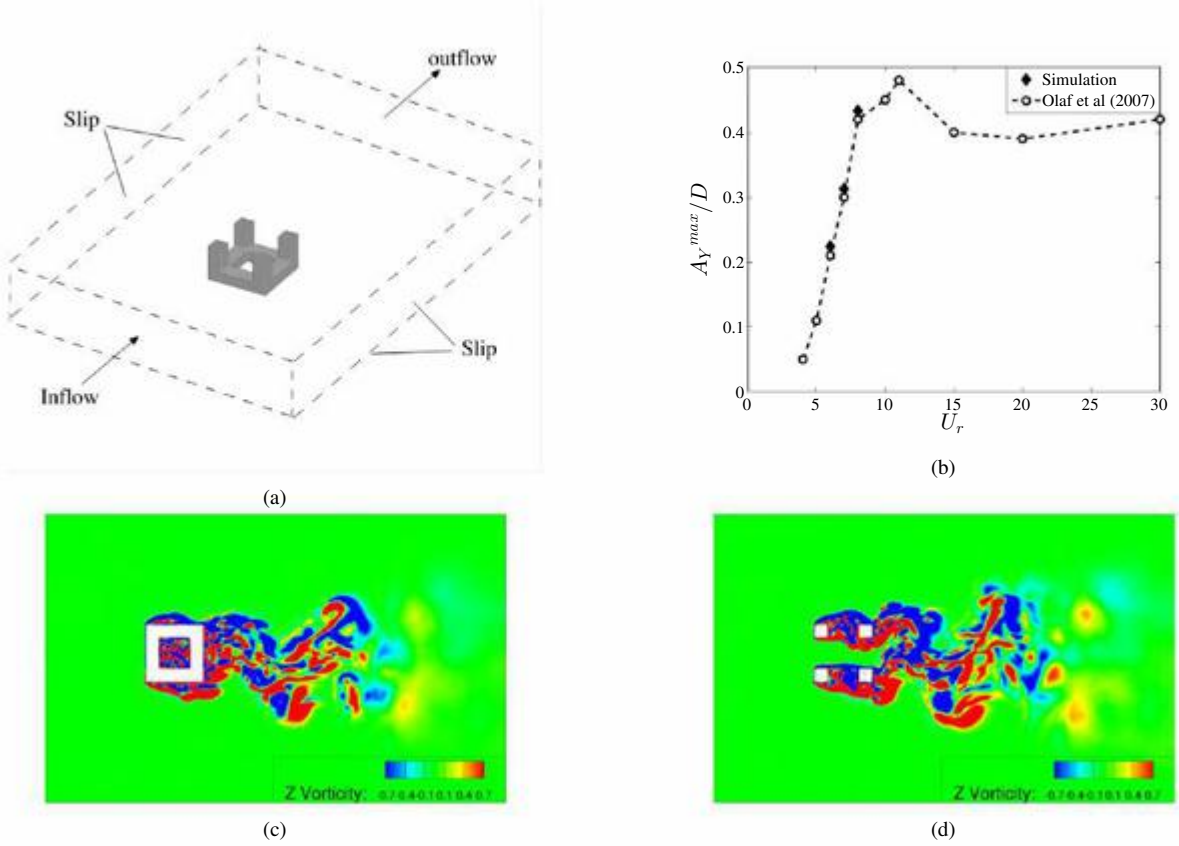

Figure 1: Semi-submersible structure with four pontoons in deep draft condition: (a) Detail of the dimension of semi-submersible, (b) Comparison of response amplitude A_Y^{max}/D between experimental data and computational results, (c,d) Vorticity contour plots at 2D cross-section at pontoon level

CONCLUSIONS

To overcome the deficiencies in the partitioned scheme, we have employed a sub-iteration based nonlinear iterative force correction procedure for fluid-structure interactions. Second-order temporal accuracy of the NIFC scheme has been confirmed through a systematic analysis of flow-induced vibration. Three-dimensional semi-submersible platform model is then simulated to investigate flow-induced vibration at $Re = 20000$ and $m^* = 0.83$ for range of reduced velocity corresponding to the VIV branch. The transverse amplitude and the Strouhal number agreed reasonably well with the model test conduced in the ocean basin. This study confirms that the partitioned iterative scheme can handle flow-induced vibration of low mass offshore structure at higher Reynolds number. In future, the effects of flow incidence and wave-current interactions on semi-submersibles will be considered.

References

[1] R.K. Jaiman, S. Sen, and P. Gurugubelli. A fully implicit combined field scheme for freely vibrating square cylinders with sharp and rounded corners. *Computers and Fluids*, 112:1–18, 2015.

[2] R.K. Jaiman, N.R. Pillalamarri, and M.Z Guan. A stable second-order partitioned iterative scheme for freely vibrating low-mass bluff bodies in a uniform flow. *Computer Methods in Applied Mechanics and Engineering*, 301:187–215, 2016.

[3] M. Paidoussis, S. Price, and Emmanuel de Langre. *Fluid-structure interactions: cross-flow-induced instabilities*. Cambridge University Press, UK, 2011.

[4] R. K. Jaiman, P. Geubelle, E. Loth, and X. Jiao. Combined interface condition method for unsteady fluid-structure interaction. *Comp. Meth. Appl. Mech. Engrg.*, 200:27–39, 2011.

[5] O.J. Waals, A.C. Phadke, and S. Bultema. Flow-induced motions of multi-column floaters. In *ASME Offshore Mechanics and Arctic Engineering OMAE07-29539 CP*, 2007.

A VIBRATING MEMBRANE MODEL FOR MITRAL VALVE HONKS

Edmund Kay*[1] and Anurag Agarwal[1]

[1]*Engineering Deparmtent, University of Cambridge, United Kingdom*

Summary A novel flow-structure interaction that simulates mitral valve vibration in the heart, is investigated experimentally. The mitral valve is modelled by a thin latex rubber membrane and its vibrations are modelled by the Föppl-von Karman equations for the motion of thin plates. Scaling analyses are used to determine the deflection of the membrane under a given pressure difference, the frequency of vibration and the critical pressure difference for the onset of oscillation.

INTRODUCTION

A flow-structure interaction is investigated for air flowing over a semi-circular latex rubber membrane as shown in figure 1. When the pressure difference across the membrane is increased above a critical value (dependent on membrane thickness) the membrane starts to vibrate with large amplitude. Investigating this phenomenon should help give an insight into the production mechanism for the "precordial honk", a tonal heart sound heard in some patients with mitral valve regurgitation [1–3]. The "precordial honk" is believed to be caused by valve vibration [3, 4]. In this paper we will look to describe the motion of the membrane by determining non-dimensional relationships from the governing equations.

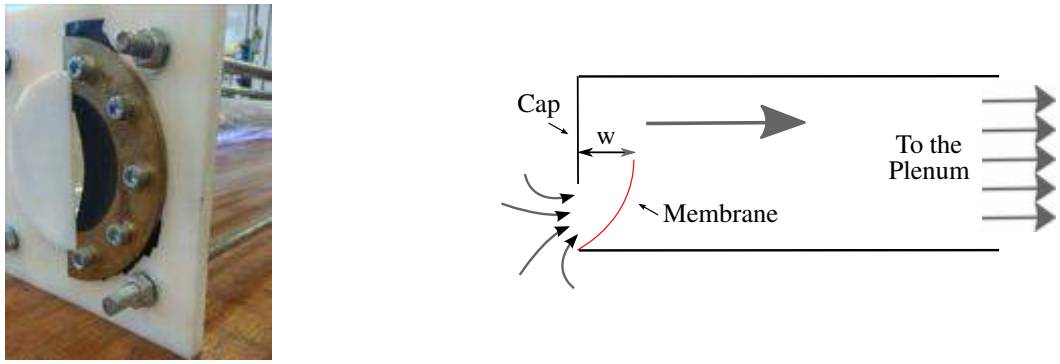

Figure 1: Photo and schematic of the experimental apparatus

EXPERIMENTAL APPARATUS

The experimental apparatus and a schematic representation are shown in figure 1. Air is sucked from atmosphere through the opening between the cap and the membrane and then along a pipe to a plenum. The cap overlaps the edge of the membrane by mm, the tube has a diameter of 9 mm, so the semi-circular membrane has a radius of 3 .5 mm . The steady-state velocity through the tube is measured by a venturi tube downstream of the membrane.

MATHEMATICAL MODEL

The motion of the membrane may be described by the Föppl-von Karman equations for the motion of thin plates (equations 1 and 2). The bending stiffness of all membranes tested is negligible. The material law is given by

$$\frac{1}{E}\Delta^2\phi = w_{,xy}^2 \nearrow w_{,xx}w_{,yy} \tag{1}$$

where E is the Young's modulus Δ is the Laplacian operator, ϕ is the Airy stress function, and w is the deflection of the membrane. The equation of motion for the membrane is given by

$$\frac{\rho}{h}\ddot{w} = \phi_{,yy}w_{,xx} \nearrow 2\phi_{,xy}w_{,xy} + \phi_{,xx}w_{,yy} + \frac{\Delta p}{h} \tag{2}$$

where ρ is the density of the membrane, h is the thickness, and Δp is the pressure difference across the membrane. The amplitude of vibration of the membrane is large and so these equations cannot be further simplified.

*Corresponding author. Email: ek360@cam.ac.uk

RESULTS

The equations describing the large amplitude vibrations are non-linear and difficult to solve. Therefore, the analysis is restricted to scaling arguments.

Static Analysis

A static analysis is performed to determine how the deflection of the membrane varies with the pressure difference across it. Equation 1 gives

$$\phi \sim EW^2 \tag{3}$$

Using this in equation 2 gives

$$\frac{(Ehw^3)}{\Delta PL^4} \sim 1 \tag{4}$$

Membranes of 5 different thicknesses are tested at a variety of pressures (below the pressure required to cause them to vibrate) in order to test the non-dimensional relationship given in equation 4. The results are shown in figure 2, with the vertical lines indicating error bars which assume a maximum error of 1 mm in the reading of membrane deflection.

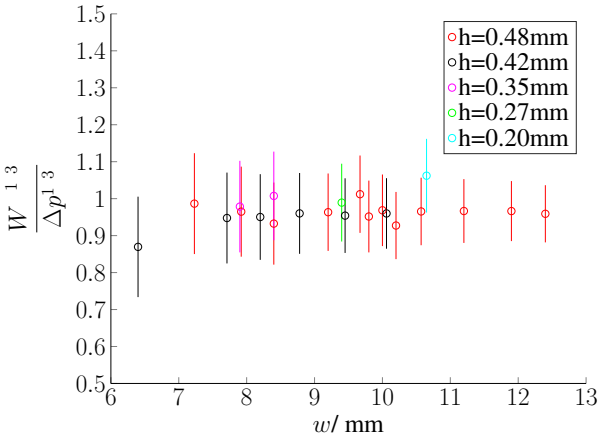

Figure 2: Verification of scaling relationship in equation 4

Unsteady Analyses

The vibration of the valve can be caused by two mechanisms. The first is if the unsteady pressure force oscillates at the same frequency as the natural frequency of the membrane, then this will cause the valve to vibrate. The second mechanism is if the pressure force is in-phase with the velocity of the membrane, for part of the oscillation cycle, then the pressure can provide a "negative damping" force where energy from the fluid is transferred to the membrane, causing it to become unstable. By analysing the functional form of the unsteady pressure force it is possible to determine which of these mechanisms is causing the vibration of the membrane.

CONCLUSIONS

A flow-structure interaction problem, modelling mitral valve vibration in the heart, has been investigated experimentally. Scaling analyses have been performed on the governing, Föppl-von Karman, equations to determine non-dimensional relationships for the deflection of the membrane under a given pressure difference, the frequency of vibration and the critical pressure difference for oscillation.

References

[1] V S Behar, R L Whalen, and H D Mcintosh. The Ballooning Mitral Valve in Patients with the "Precordial Honk" or "Whoop". *The American Journal of Cardiology*, 20:789–795, 1967.

[2] P Rizzon, G Biasco, and G Maselli-Campagna. The praecordial honk. *British Heart Journal*, 33:705–717, 1971.

[3] J M Felner, S Harwood, H Mond, W Plauth, D Brinsfield, and R C Schlant. Systolic Honks in Young Children. *Pediatric Cardiology*, 40:206–211, 1977.

[4] K Venkataraman, R Siegel, S J Kim, and J W Allen. Musical Murmurs: An Echo-Phonocardiographic Study. *The American Journal of Cardiology*, 41:439–452, 1978.

INVESTIGATION ON AEROELASTIC RESPONSE OF A HYPERSONIC WIND TUNNEL EXPERIMENT MODEL

Jinan Lv [1a)], Ding Chen[1], Chen Ji[1], Ziqiang Liu[1]
[1]*China Academy of Aerospace Aerodynamics (CAAA), Beijing, China*

Summary A coupling numerical simulation technology which combined computational fluid dynamics (CFD) method with computational structure dynamic (CSD) is developed. Several kinds of mode to exchange data for CFD/CSD coupled computation is designed. Aeroelastic response of hypersonic wing under Ma 5 wind tunnel experimental condition is calculated as an example. The coupling of bending and torsion mode is captured. The computed result indicates that CFD/CSD method of aeroelastic simulation is feasible and credible.

INTRODUCTION

In this paper, CFD/CSD coupling simulation method is used to predict the aeroelastic response of two wind tunnel experiment models. The aeroelastic response is simulated at the wind tunnel experimental condition, the influence of the coupling algorithm used in CFD/CSD coupling simulation is discussed. The CFD/CSD coupling simulation result is contrasted to the result predicted by piston theory. Finally, the simulation results are compared to the experiment data acquired by binocular vision measurement in hypersonic flutter wind tunnel.

NUMERICAL SIMULATION METHOD

CFD/CSD simulation method is adopted to predict the flutter boundary of hypersonic wind tunnel model. The procedure of data exchanged between CFD and CSD code is split up into three steps: pre-contact search, association and interpolation. In flux interpolation, the value is adapted to the element sizes to preserve the integral. In field interpolation, the values are kept to ensure a conservative transfer.

COMPUTATIONAL RESULTS

The wind tunnel experimental condition is used as the computational condition. Two kinds of wind tunnel model are analyzed which the thicknesses are 0.47mm and 0.58mm severally. The computational condition is Ma5, static temperature 60K.

Firstly, the steady CFD simulation is done and applied as the initial condition of unsteady CFD/CSD coupling simulation. Velocity initial condition is applied to the element nodes of finite element model, in this example it is set to be 1m/s. The wall-forces of the model are interpreted to the structural model as the force boundary condition. The displacements of boundary nodes of the structural model are interpreted and sent back to the flow field solver as the boundary condition. The unsteady flow field is calculated again under the new boundary condition and transfer new force data to the structural model.

The iteration continues in time domain. Four different dynamic pressures are used to capture the flutter boundary. Results of displacements in time domain are shown in Figure 1.

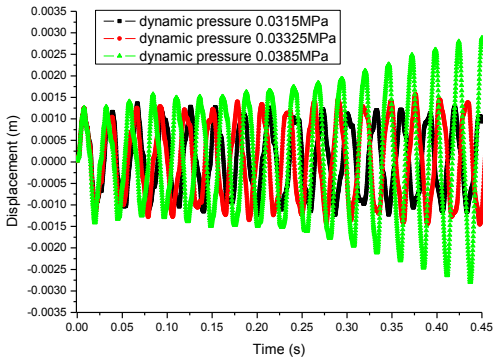

Figure 1: Deformed displacement of front node of the wing

For the model which the thickness is 0.47mm, the calculated results show that when the dynamic pressure grows from 0.0315MPa to 0.0385MPa, the vibration displacement of the wing appears divergent. The flutter appears in this region where the flutter dynamic pressure is between 0.0315MPa~0.03325Mpa. The amplitude of vibration of the wing is about 1.3mm.

[a)]Corresponding author. Email:madas1@126.com.

To obtain the vibration displacement, the optical binocular vision measurement system is applied to achieve the flutter model vibration displacement in hypersonic wind tunnel experiment (see Fig. 2.). The system is constituted with CCD camera, image acquisition card and control computer mostly. The morphologies of the flutter model are solved by self-made programs.



Figure 2: optical binocular vision measurement system in wind tunnel

For the model which the thickness is 0.58mm, the CFD/CSD simulation result is compared to the results which are obtained by optical binocular vision measurement system (see Fig. 3.).

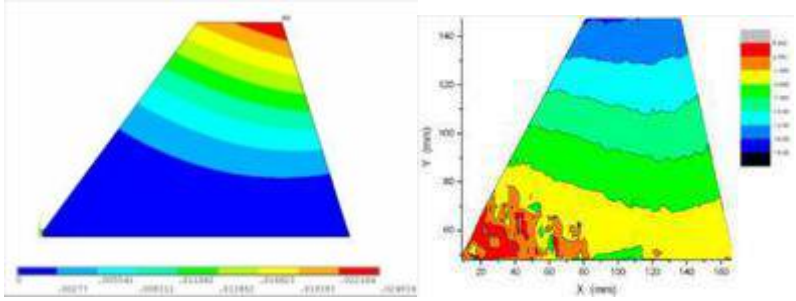

Figure 3: Contrast numerical simulation with experiment results

Because the displacement is plotted in time domain, the two pictures are somewhat different. The vibration frequencies acquired by simulation and optical binocular vision technique are 56Hz and 42Hz respectively. The reason is that the effect of reflect plate and wind tunnel wall is not be considered in simulation at present.

CONCLUSIONS

The CFD/CSD coupling numerical simulation method is introduced in this paper. The method is used for the simulation of the flutter problem of a hypersonic vehicle wing model. The flutter in time domain is simulated using this method and the physical phenomena of the coupling of bending and torsion mode is captured. The simulation results offer an efficient reference to the wind tunnel flutter experiment design.

References

[1] YANG Bing-yuan SHI Xiao-ming LIANG Qiang. Investigation and development of the multi-physics coupling dynamics on the hypersonic winged missiles. *STRUCTURE &ENVIRONMENT ENGINEERING*, 2008, 35(5).

[2] Yang Chao, Xu Yun, Xie Changchuan. Review of studies on aeroelasticity of hypersonic vehicles. *ACTA AERONAUTICA ET ASTRONAUTICA SINICA*, 2010, 31(1).

[3] Thuruthinattam B J, Friedmann P P, Powell K G, et al, Aeroelasticity of a generic hypersonic vehicle. AIAA-2002-1209, 2002.

[4] P.P. Friedmann, J.J. McNamara, B.J. Thuruthimattam and K.G. Powell,Hypersonic aerothermoelasticity with application to reusable launch vehicles, AIAA 2003-7014.

[5] Frederick W. Gibson, Flutter investigation of models having the planform of the north American X-15 airplane wing over a range of mach numbers from 0.56 to 7.3. NASA TM X-460.

STUDY ON VIBRATION CHARACTERISTICS OF THE INFLATABLE BOOM FILLED WITH GAS

Ruiqiang Ma[1], Jianzheng Wei[1a)], Huifeng Tan[1]
[1] *Center for Composite Materials and Structures, Harbin Institute of Technology, Haerbin, China*

Summary The inflatable membrane boom, as the support structure of space mission, has certain stiffness from the inner pressure. With more and more precise requirements of space mission, it is especially significant to predict the vibration characteristics of the boom accurately. Base on the study on fluid-structure coupling analysis, this paper establish a new method of the vibration characteristics of boom considering the influence of the in-tube gas. Taking the 1m inflatable tube for example, this paper investigates the effect of the in-tube gas for the vibration characteristics of the inflatable boom. This investigation can provide a theoretical basis for accurate calculation of the vibration characteristics of the inflatable structure.

INTRODUCTION

As the important support member of space structure, the pneumatic membrane structure required particular stiffness, and then it is often filled with the certain pressure gas. So, to improve the prediction accuracy of its vibration characteristic, a large quantity of pre-stress model analyses are investigated by domestic and foreign scholars. Base the Finite Element Methods, Pazhooh[1] and George[2] proposed a hexagonal membrane element and nine-node membrane element for the pre-stress model analysis. However, Pramila[3] found the natural frequencies of the inflation membrane structure come from the experiment measured increased 15 to 30% than from the pre-stress model. The natural frequency and damping ratio of the membrane model which had difference cable-net structure area ware investigate by Yang. This study verified the vibration characteristics of membrane would change due to the surrounding gas, and showed the gas would bring added mass and aerodynamic damping for this structure. Some approaches to solving the vibration characteristics of the membrane surrounding gas were proposed. Kassem first calculated the add mass by the potential flow theory, then solved the modal by applied the add mass to the membrane[4]. Moreover, the added mass could be solved by potential flow theory, also solved by numerical method. Deruntz and Geers applied the boundary element method to solve the added mass, and this reduced the amount of computation compared with the potential flow theory. In this paper, a new method is proposed by the earlier study of fluid-structure coupling, and the model and harmonic response of the boom is analysed base this method.

MATHEMATICAL MODEL

In view of shortcomings of virtual-density method, the fluid-structure coupling method is used to establish a new method for the model of the inflation boom has inner gas. As a kind of the finite element method, the model of both the inflatable boom and the gas field need be established. As you know, it is important for the set of the coupled boundary conditions for gas-membrane coupling. Whole cavity of the inflatable boom is filled with gas, and the gas in the boom is the compressible and inviscid.

Base the fluid-structure coupling method, the normal velocity of the wall on inflation booms and the air normal velocity nearby the wall of the inflation boom keep continuous on the contact boundary of the inflation booms and the air domain. The equation of contact can be written as：

$$v_{fn} = \vec{v}_f \cdot \vec{n} = \vec{v}_s \cdot \vec{n} = v_{sn} \tag{1}$$

Where, v_{fn}, v_{sn} are the normal direction velocity of the wall of booms and gas, respectively; $\vec{v}_f, \vec{v}_s$ are the velocity of the wall and the gas, respectively. The fluid momentum equation is projected to the normal direction of the wall, and be expressed

$$\frac{\partial p}{\partial n} + \rho_f \ddot{\vec{u}} \cdot \vec{n} = 0 \tag{2}$$

Where ρ_f and u is the gas density and the wall displacement respectively. Moreover, the coupling boundary demand the force continuity, so

$$\sigma_{ij} n_j = p_{si} n_j \tag{3}$$

Where σ_{ij} and p_{si} are the stress of the membrane and pressure of the gas. Base the dynamic equation of the structure, the dynamic equation of the inflation booms considering the inner gas can be express as

$$\begin{bmatrix} M_s & 0 \\ -Q^T & M_f \end{bmatrix} \begin{pmatrix} \ddot{u} \\ \ddot{p} \end{pmatrix} + \begin{bmatrix} K_s & \dfrac{Q}{\rho_f} \\ 0 & K_f \end{bmatrix} \begin{pmatrix} u \\ p \end{pmatrix} = \begin{pmatrix} F_s \\ 0 \end{pmatrix} \tag{4}$$

a) Corresponding author. Email: weijz@hit.edu.cn

In there, M_s and M_f are the mass matrix of the membrane booms and inner gas; K_s and K_f are its corresponding stiffness matrix; Q and F_s are the coupled matrix and load vector of inflatable booms. This equation shows the mass matrix and stiffness matrix of this structured system is unsymmetrical

RESULTS

The change curve of the boom natural frequency with the gas density and the sound velocity are showed in Fig.1. Form the lift diagram, one can obtain the fundamental frequency of the boom is 70.3HZ when the gas density is 0.8 kg/m^3. And the second natural frequency is the same as the fundamental frequency. Moreover, the first to the fourth natural frequency descends with the increase of the gas density. The fourth modal frequency decreases faster than the third natural frequency, and the two curves overlap while the gas density is 1.8 kg/m^3, then the frequency is 148HZ. When the inner gas density less than 1.8 kg/m^3, the third modal shape is expand and contract vibration. While the inner gas greater than 1.8 kg/m^3, the third modal shape is the same as the fourth modal shape, is wave motion. The right image sees the change law of the boom natural frequency with the increase of the sound speed. It shows the natural frequency of 1st mode and 4th mode keep remain constant, and the 3rd mode frequency is linear increased before 380 m/s. When the sound velocity exceeds 380 m/s, the 3rd mode frequency is the same as the 4th mode, and the frequency is 169.6HZ.

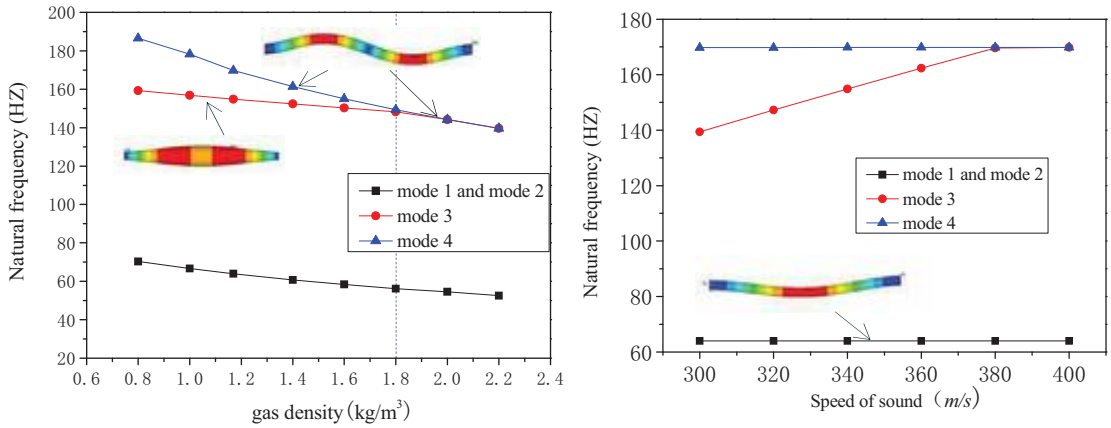

Fig.1 The change curve of the boom natural frequency with the gas parameters

CONCLUSIONS

In this paper, the in-tube gas effect on the vibration characteristics of the inflatable boom are investigated by the fluid-structure coupling method. The change law of the natural frequency with the gas parameter is obtained, and this result shows that the mode shape would change when gas parameters are within a certain range.

References

[1] Pazhooh M D, Dokainish M A, Ziada S, etcl. Experimental Modal Analysis of an Inflatable Selfrigidizing Toroidal Satellite Component. Experim- ental and Applied Mechanics,2011(6):187-198.

[2] George R B, John P. A finite element in elliptic coordinates with application to membrane vibration. Thin-Walled Structures,2005,43:1444-1454.

[3] Pramila A. Shell flutter and the interaction between sheet and air. TAPPI-Journal,1986,69:70-74.

[4] Kassem M. Dynamics of lightweight roofs. Dissertation of the University of Western Ontario, 1990.

THRUST GENERATION BY A HEAVING FLEXIBLE FOIL

Florine Paraz*[1], Lionel Schouveiler[2], and Christophe Eloy[2]
[1]*Okinawa Institute of Science and Technology, Okinawa, Japan*
[2]*Aix-Marseille Université, CNRS, Centrale Marseille, IRPHE UMR 7342, Marseille, France*

Summary In the context of swimming, flexibility of the fin has often been argued to be an advantage for the propulsion. Experimental and numerical studies have emphasized the role of the flexibility in propulsion. However, very few analytical works have been developed and are often limited in the linear regime. We will present a new analytical model of a flexible plate immersed in a flow. The model is weakly nonlinear and is based on the beam equation in vacuum for the structure and the coupling with the flow is made through linear potential theory. Comparison between experimental data and predictions are in excellent agreement. Predictions extended to the literature gives good results as well. This optimization study shows that the performance are always maximal when the system reach its resonance.

EXPERIMENTAL BACKGROUND

The experiment consists of a flexible plate of length $2c$ and bending rigidity b immersed in a uniform water flow u. The leading edge of the plate is actuated by a harmonic heave motion $a_{\rm LE}\cos(\omega t)$ where the amplitude $a_{\rm LE}$ and the angular frequency ω are controlled. The plate responds passively to the actuation and it deforms as a combination of beam eigenmodes. The amplitude of response at the trailing edge $a_{\rm TE}$ is then recorded and the relative amplitude $a_{\rm TE}/a_{\rm LE}$ is plotted as a function of the forcing frequency for different values of the experimental parameters. It appears that the only relevant parameters of the study is the forcing amplitude, which induces nonlinearities in the response of the plate. The force generated by the plate is measured by force sensors located the leading edge of the plate. The evolution of the force as a function of the forcing frequency and amplitude is also investigated. Resonance in amplitude and in thrust are evidence when the forcing frequency approaches the natural frequencies of the system plate and fluid. Experimental results are obtained from a previous study [1].

ANALYTICAL MODEL

An one-dimensional structure immersed in a two-dimensional potential flow is considered. The structure, actuated by a harmonic heave motion at the leading edge ($x=-1$), passively deform. The deflection of the plate h is decomposed into three eigenmodes of a beam in vacuum as follows

$$h(x,t)=\left(a_{\rm LE}+\sum_{i=1}^{N=3}a_i h_i(x)\right)\mathrm{e}^{\mathrm{i}\omega t}, \tag{1}$$

where a_i and h_i are the amplitude and the deflection of the ith eigenmode considered respectively [4]. The amplitude of actuation is imitated by a rigid motion of amplitude $a_{\rm LE}$. The model is weakly nonlinear and the asymptotic limit of small income flow velocity is considered. The coupling between the surrounding fluid and the flexible structure is modeled through the unsteady airfoil theory [3].

The governing equation of motion of the system fluid and structure is represented by the linearized Euler-Bernoulli equation. It is augmented by two linear damping terms from the visco-elastic dissipation ν and the fluid dissipation μ, a nonlinear transverse drag term c_D, which mimic the transverse motion of the plate due to the imposed motion and a pressure jump across the plate, given by the fluid. By inserting the modal decomposition (1), the governing equation becomes

$$(\mathrm{i}\omega\nu-\omega^2)(\alpha_i a_{\rm LE}+a_i)+(1+\mathrm{i}\omega\mu)\kappa_i^4 a_i+\mathrm{i}\omega^2\frac{c_D}{m}\frac{2}{3\pi}\int_{-1}^{1}h_i\left|a_{\rm LE}+\sum_{j=1}^{N=3}a_j h_j(x)\right|\left(a_{\rm LE}+\sum_{j=1}^{N=3}a_j h_j(x)\right)\mathrm{d}x$$
$$-\frac{\omega^2}{m}\left(\beta_{i0}a_{\rm LE}+\sum_{j=1}^{N=3}\beta_{ij}a_j\right)=0. \tag{2}$$

The clamped-free boundary conditions are added to the system in order to solve it. The coefficients of the linear dissipations have been measured independently in damped oscillations experiments. Whereas the constant value of the transverse coefficient c_D of the nonlinear term is adjusted manually to fit the experimental data.

*Corresponding author. Email: florine.paraz@oist.jp

From, the amplitude of each mode, the total thrust f_{T} generated by the moving plate is investigated. It is decomposed into the reactive force f_{P}, due to the pressure forces projected onto the direction of the flow, and the resistive force f_{R}, due to the nonlinear damping forces. Thus, f_{T} is expressed as

$$f_{\mathrm{T}} = f_{\mathrm{P}} + f_{\mathrm{R}} = -\frac{1}{2}\Re\int_{-1}^{1} p\,\partial_x h \mathrm{d}x - \frac{1}{2}\Re\int_{-1}^{1}\left(m\nu\partial_t h + \frac{4}{3\pi}c_D|\partial_t h|\partial_t h\right)\partial_x h \mathrm{d}x, \tag{3}$$

where $\Re$ stands for the real part and the overbar for the complex conjugate. The integration is performed over the length of the plate, *i.e.*, $-1 < x < 1$.

RESULTS AND DISCUSSION

Solutions of equation (2) give the amplitude of each modes as a function of the forcing frequency and amplitude. The relative amplitude given by the experimental data (markers) and the prediction (continuous curves) is plotted in figure 1(a) for two forcing amplitudes. Both exhibit peaks located at the resonant frequencies of the system. Amplitudes and frequencies are properly captured by the model regardless of a_{LE}, especially for the first resonance. The shape of the deformed plate is also well described by the model.

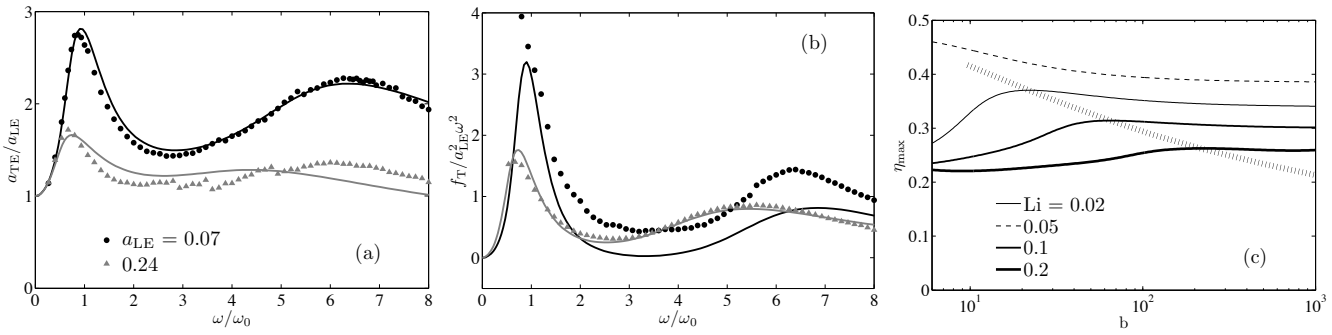

Figure 1: Comparison of the experimental data (symbols) with the predictions (continuous lines): (a) the relative amplitude $a_{\mathrm{TE}}/a_{\mathrm{LE}}$ and (b) the total thrust f_{T} for a plate of a given bending rigidity b in water. (c) Evolution of the Froude efficiency $\eta_{\max}$ as a function of the rigidity b. The dotted line represent the maxima of $\eta_{\max}$ for $\mathrm{Li} > 0.03$.

As the analytical force depends on the deflection at the trailing edge (equation (3)), one expects to have an agreement between the resonance in amplitude and the resonance in thrust. Figure 1(b) shows the evolution of the thrust for two forcing amplitudes as a function of the forcing frequency. Similarly to the amplitude, the predicted thrust are in agreement with the experimental data for the first resonance. The frequency at which the peak occurs matches the one in amplitude. Moreover, the model gives excellent results for the larger forcing amplitude regardless of ω/ω_0. Nevertheless, the trends for the smaller amplitude is correct despite the magnitude of the thrust. One possible explanation would be the constant value of the drag term c_D of the nonlinear term.

The evolution of the Froude efficiency $\eta_{\max}$ as a function of the bending rigidity b shows that the system reaches its maximal performance when the system is at its resonance (figure 1(c)). The Lighthill number, defined as $\mathrm{Li} = f_{\mathrm{T}}/u^2$, expresses the ratio between the desirable thrust and the typical achievable thrust.

To sum up, a weakly nonlinear, two-dimensional and inviscid analytical model has been developed to capture the behavior of the flexible plate immersed in a flow. Predictions for the kinematic and dynamic of the system have been compared with two different sets of experimental data and the results are in excellent agreement in both cases. The optimization process not only emphasize the role of the resonance to achieve maximal performances, but also the necessity of a well-defined expectation of the wanted system [2].

References

[1] Paraz F., Schouveiler L., Eloy C., "Experimental study of the response of a flexible plate to a harmonic forcing in a flow", C. R. Méc. **342**, 532-538 (2014).

[2] Paraz F., Eloy C., Schouveiler L., "Thrust generation by a heaving flexible foil: Resonance, nonlinearities, and optimality", Phys. Fluids **28** (1), 011903 (2016).

[3] Theodorsen T., "General theory of aerodynamic instability and the mechanism of flutter", Technical Report TR-496, NACA (1935).

[4] Wu, T. T.-T., "Swimming of a waving plate", J. Fluid Mech. **10**, 321-344 (1961).

NONLINEAR RESPONSE OF SHELLS CONVEYING PULSATILE FLOW

Eleonora Tubaldi[a)], Marco Amabili & Michael P.Paidoussis
Department of Mechanical Engineering, McGill University, Montreal, Quebec, Canada

Summary In deformable shells conveying pulsatile flow, oscillatory pressure changes cause local movements of the fluid and shell wall, which propagate downstream in the form of a wave. In this study, circular cylindrical shells described by the nonlinear Novozhilov shell theory with flexible boundary conditions conveying pulsatile flow and subjected to pulsatile pressure are investigated considering the pulse-wave propagation. Coupled fluid-structure Lagrange equations for a non-material volume with wave propagation in case of pulsatile flow are developed. The fluid is modeled as a Newtonian pulsatile flow; pulsatile viscous effects are taken into account. In the future, a more refined model of the one here presented will possibly be applied to reproduce the dynamic behavior of the human aorta and vascular prostheses used for repairing and replacing damaged and diseased thoracic aorta.

PROBLEM DESCRIPTION AND ANALYTICAL FORMULATION

Problem geometry

In this study, vascular prostheses currently used in aortic replacement surgery are modeled as isotropic linearly elastic shells via the nonlinear Novozhilov shell theory. The circular cylindrical shell under consideration is characterized by a mean radius *R*, a shell thickness *h* and a shell length *L*. The mechanical properties and the characteristics of the shell and of the fluid here studied can be found in [1]. In addition, *u* is the shell displacement in the axial *x*-direction, *v* is the shell displacement in the circumferential θ-direction and *w* is the shell displacement in the radial *r*-direction (taken positive outward). Flexible constraints to simulate connection with the remaining tissue, are applied at the shell ends [2].

Pulse-wave propagation of pulsatile velocity and pressure

In biomechanics, it is the propagation of the pulse that determines the pressure gradient during the flow at every location of the arterial tree. An input oscillatory pressure at the shell entrance propagates down the shell causing a wave motion within the shell where the pressure gradient and the flow velocity are functions of both the axial coordinate *x* and time *t*. If the wall thickness is small compared with the shell radius and if the effects of viscosity can be neglected, the wave speed c_0 is given approximately by the so called Moen-Korteweg formula

$$c_0 = \sqrt{\frac{E\,h}{2\,\rho_F\,R}}, \tag{1}$$

where *E* is the Young modulus of the shell and ρ_F is the constant fluid density. As a result, the pressure and flow velocity distributions within the shell are oscillatory both in space and time and they can be represented by a Fourier series as follows

$$(\ ,\ ) = \bar{\ } + \sum_{n=1}^{8}\left(a_{v\,n}\cos\left(n\,\omega\,(\ -\ /\ _0)\right) + b_{v\,n}\sin\left(n\,\omega(\ -\ /\ _0\right)\right)\ , \qquad _m(\ ,\ ) = \bar{\ }_m + \sum_{n=1}^{N}\left(a_{p\,n}\cos\left(n\,\omega\,(\ -\ /\ _0)\right) + b_{p\,n}\sin\left(n\,\omega(\ -\ /\ _0\right)\right)\ , \tag{2.a-b}$$

where ω is the heart rate, $\bar{p}_m$ and $\bar{U}$ represent the steady component of the pressure field and the pulsatile mean flow velocity, respectively, and *N* represents the number of terms in the series expansion. The coefficients a_n and b_n are the Fourier cosine and sine coefficients, respectively.

Fluid-Structure Interaction Model: Potential Flow Energy

The fluid is modeled as a Newtonian pulsatile flow. An unsteady perturbation potential Φ is introduced that satisfies the Laplace equation [2] . The total energy associated with the flow is given by

$$E_{TF} = \frac{1}{2}\rho_F\int_{\Gamma}\mathbf{v_F}\ \mathbf{v_F}\,\mathrm{d}\Gamma = \frac{1}{2}\rho_F\int_{\Gamma}\left(U+\nabla\Phi\ \cdot\ U+\nabla\Phi\right)\mathrm{d}\Gamma = \frac{1}{2}\rho_F\int_{\Gamma}\left(U^2+2U\frac{\partial\Phi}{\partial x}+\nabla\Phi\cdot\nabla\Phi\right)\mathrm{d}\Gamma = \frac{1}{2}\rho_F\int_{\Gamma}\ ^2\mathrm{d}\Gamma + \rho_F\int_{\Gamma}U\frac{\partial\Phi}{\partial x}\mathrm{d}\Gamma + \frac{1}{2}\rho_F\int_{\Omega}\Phi\frac{\partial\Phi}{\partial n}\,\Omega \tag{3}$$

where Γ is the cylindrical fluid volume inside the shell (delimitated by the length *L*) and the scalar product $\mathbf{v_F}\ \mathbf{v_F}$) has been expressed as a function of the undisturbed (pulsatile) blood flow velocity *U(x,t)* and the unsteady perturbation potential Φ*(x,t)*; Ω is the boundary surface of the Γ volume and *n* is the coordinate along the normal of the boundary. The integral associated to the constant term U^2 will be neglected since it doesn't give any time-varying contribution to the energy of the flowing fluid. The last integral on the right- hand term side of Eq. (3), can be divided in three terms: the reference kinetic energy T_F [2], the potential energy V_F and the gyroscopic energy E_G of the fluid respectively expressed as follows

$$V_F = -\frac{1}{2}\rho_F\int_0\int_0^L\sum_{m=}^{M}\sum_{=}^{M}\sum_{=}^{N}\sum_{k=}^{N}\frac{L}{m\pi}\frac{\mathrm{I}_n(m\,\pi\,R\ \ L}{\mathrm{I}_n(m\,\pi\,R\ \ L}U\ x\ t\ ^2\frac{\partial w_{m\,n}}{\partial x}\frac{\partial w_{l\,k}}{\partial x}\,dx\,R\,d\vartheta, \qquad E_G = \frac{1}{2}\rho_F\int_0\int_0^L\sum_{m=}^{M}\sum_{=}^{N}\sum_{=}^{M}\sum_{=0}^{N}\frac{U\ x\ t\ L}{m\pi}\frac{\mathrm{I}_n(m\,\pi\,R\ \ L}{\mathrm{I}_n(m\,\pi\,R\ \ L}\left(\dot{w}_{m\,n}\frac{\partial w_{l\,k}}{\partial x}+\dot{w}_{l\,k}\frac{\partial w_{m\,n}}{\partial x}\right)dx\,R\,d\vartheta. \tag{4a-b}$$

where I_n is the modified Bessel function of the first kind of order *n,* and I'_n is the derivative of $\mathrm{I}_n$with respect to its argument. In case of unsteady flow velocity *U(x,t)* with pulse-wave propagation, the expressions of V_F and E_G are time and

[a)] Corresponding author. Email: eleonora.tubaldi@mail.mcgill.ca

space dependent and because of that, new terms will appear in the Lagrange equations of motions.

Pulsatile Viscous Effects

The unsteady time-averaged Navier-Stokes equations are here employed to calculate the pulsatile viscous effects assuming that the flow is turbulent and fully developed. In case of unsteady flow, the pressure drop $\Delta P_{0,L}$ in the shell and the pulsatile axial friction traction force per unit area assume respectively the following expressions

$$\Delta P_{0,L} = P \quad t\ R\ -P\ L\ t\ R\ = \rho_f\ L\left(\frac{f}{4R}U\ x\ t\ ^2+\frac{\partial U\ x\ t}{\partial t}\right), \qquad \tau_x\ x\ t\ R\ = f\,\rho_f\,\frac{U\ x\ t\ ^2}{8}+\rho_F\,\frac{R}{2}\frac{\partial U\ x\ t}{\partial t}. \tag{5.a-b}$$

Coupled fluid-structure Lagrange equations for a non-material volume

The Lagrange equations of motion for open systems [3] here studied can be written as follows:

$$\frac{d}{dt}\left[\frac{\partial\left(\ _S+\ _F+\overline{\ }_G\right)}{\partial\dot{q}_j}\right]-\frac{\partial\overline{E}_G}{\partial q_j}+\frac{1}{2}\rho_F\int_\Omega\frac{\partial}{\partial\dot{q}_j}\ \mathbf{v_F}\ \mathbf{v_F}\quad\mathbf{v_F}\quad\mathbf{v_S}\big)\ \mathbf{n}\,\mathrm{d}s-\frac{1}{2}\rho_F\int_\Omega\ \mathbf{v_F}\ \mathbf{v_F}\big)\left(\frac{\partial\mathbf{v_F}}{\partial\ _j}-\frac{\partial\mathbf{v_S}}{\partial\dot{q}_j}\right)\cdot\mathbf{n}\,\mathrm{d}s+\frac{\partial\left(U_S+\overline{\ }_F\right)}{\partial q_j}=Q_j,\quad j=1...N_T \tag{6}$$

where T_S and U_S represent the kinetic and potential energy of the shell previously defined in [1]. The potential $\overline{V}_F$ and gyroscopic $\overline{E}_G$ energy of the flow are calculated not only on the shell wall Eq.(4a-b) but also on the inlet and outlet surfaces. Indeed, because of the pulse-wave propagation, the contribution of the integrals evaluated on these two surfaces doesn't cancel out. The vectors $\mathbf{v_F}$ and $\mathbf{v_S}$ are the velocity vector of the fluid and of the structure, respectively, and N_T is the number of degrees of freedom. The surface integrals are evaluated at the boundary surface Ω of the volume Γ and $\mathbf{n}$ denotes the outer normal unit vector at that surface. The generalized external forces Q_j are represented by

$$Q_j=-\rho_F\left(\frac{\partial}{q_j}\int_\Gamma U\frac{\partial\Phi}{\partial x}\mathrm{d}\ \right)\ \rho_F\left(\frac{\partial}{\dot{q}_j}\int_\Gamma U\frac{\partial\Phi}{\partial x}\mathrm{d}\Gamma\right)+\frac{\partial}{\partial q_j}\left(\int_0^{2\pi}\int_0^L\left[\left(\Delta P_{0,L}+p_m\right)w+\tau_x\ \right]\qquad\vartheta,\right)-\frac{1}{2}c\frac{\partial}{\partial\dot{q}_j}\left(\int_0^{2\pi}\int_0^L(\dot{u}^2+\ ^{\cdot 2}+\ ^{\cdot 2}\ dx\,R\,d\vartheta\right), \tag{7}$$

where the first two integrals on the right-hand side represent an effect of the pulse-wave propagation inside the shell and the second two integrals are related to the pulsatile viscous effects and the nonconservative damping forces assumed to be of viscous type (c is the viscous damping coefficient), respectively.

NUMERICAL RESULTS

The effects of the steady and the first harmonic component of physiological waveforms of velocity and pressure during the heart beating period [4] on the aorta prosthesis are presented through non-dimensionalized time responses of the shell displacement w for the angular coordinate $\vartheta=0$ and for different values of the axial coordinate x showing the pulse-wave propagation. Shell transverse sections are circular at any point since only axisymmetric modes are activated ($N_T=51$ [2]).

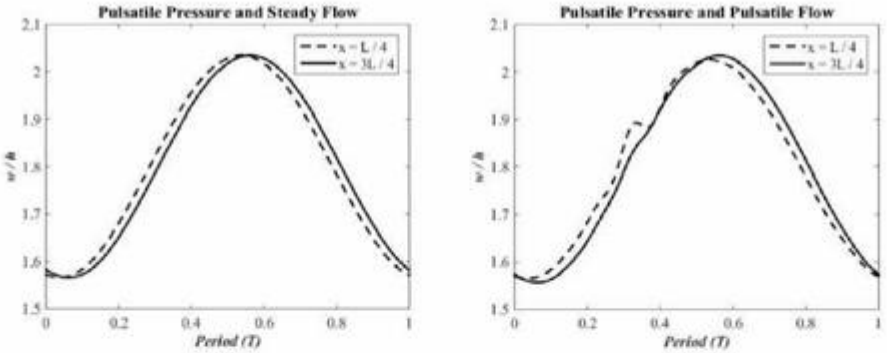

CONCLUSIONS

This study provides, for the first time in literature, a fully coupled fluid-structure interaction model of circular cylindrical shells subjected to pulsatile pressure and pulsatile flow with pulse-wave propagation. Specifically, this study represents the first attempt to describe the nonlinear behavior of vascular prostheses whose dynamic response can cause unwanted hemodynamic effects leading to their failure.

References

[1] E. Tubaldi, M. Amabili, M.P. Paidoussis, Fluid Structure Interaction for Nonlinear Response of Aorta Replacement, in: ASME 2015 International Mechanical Engineering Congress & Exposition, Houston, 2015.

[2] M. Amabili, K. Karazis, R. Mongrain, M.P. Païdoussis, R. Cartier, A three-layer model for buckling of a human aortic segment under specific flow-pressure conditions, International Journal for Numerical Methods in Biomedical Engineering, 28 (2012) 495-512.

[3] H. Irschik, H. Holl, The equations of Lagrange written for a non-material volume, Acta Mechanica, 153 (2002) 231-248.

[4] C. Mills, I. Gabe, J. Gault, D. Mason, J. Ross, E. Braunwald, J. Shillingford, Pressure-flow relationships and vascular impedance in man, Cardiovascular Research, (1970) 405-417.

TRANSIENT DYNAMICS OF ELASTIC HELE-SHAW CELL DUE TO EXTERNAL FORCES WITH APPLICATION TO IMPACT MITIGATION

Arie Tulchinsky[1] and Amir D. Gat *[1]

[1]*Faculty of Mechanical Engineering, Technion - Israel Institute of Technology, Haifa 3200003, Israel*

Summary We study the transient dynamics of a viscous liquid contained in a narrow gap between a rigid surface and a parallel elastic plate. The elastic plate is deformed due to an externally applied time-varying pressure-field. We model the flow-field via the lubrication approximation and the plate deformation by the Kirchhoff-Love plate theory. We obtain a self-similarity solution for the case of an external point impulse acting on the elastic plate. We examine a distributed external pressure, spatially uniform and linearly increasing with time, acting on the elastic plate over a finite region and during a finite time period, similar to the viscous-elastic interaction time-scale. The interaction between elasticity and viscosity is shown to reduce by order of magnitude the pressure within the Hele-Shaw cell compared with the externally applied pressure, thus suggesting such configurations may be used for impact mitigation.

DYNAMICS DUE TO EXTERNAL POINT IMPULSE

We study the transient dynamics of a viscous liquid contained in a narrow gap between a rigid surface and a parallel elastic plate. The elastic plate is deformed due to an external time-varying pressure-field applied perpendicular to the plate. We focus on configuration consisting of a shallow geometry, small ratio of transverse plate deformations to viscous film height, small Womersley number, negligible solid inertia and negligible membrane effects. Under the assumptions given, the upper elastic plate dynamics are governed by the Kirchhoff-Love equation and the viscous liquid by the lubrication approximation. Normalizing and combining the equations together with the no-slip and no penetration boundary conditions, we obtain a governing equation in terms of the pressure P

$$\frac{\partial P}{\partial T} \nearrow \nabla^6 P = \frac{\partial P_e}{\partial T} \tag{1}$$

where P_e is the external pressure. We focus on the viscous-elastic time scale, where there is no effect from the boundaries, thus prescribing $P(\boldsymbol{X} \to \infty) \to 0$.

The Green function for (1), in its Fourier integral form, is given by [1] . We utilize the symmetry of the transformation argument, thus converting it into a Hankel integral. We Express the Bessel function in a series form and integrate to obtain a closed form self-similar expression

$$G = \frac{\Psi(\eta)}{T^{\frac{1}{3}}}, \quad \eta = \frac{|\boldsymbol{X}|}{T^{\frac{1}{6}}}, \tag{2}$$

$$\Psi(\eta) = \frac{1}{12\pi}\left[\mathrm{y}\left(\frac{1}{3}\right) {}_0F_4\left(;\frac{1}{3},\frac{2}{3},\frac{2}{3},1;\nearrow\eta^6\right)\right.$$
$$\left. \nearrow 9\eta^2 \mathrm{y}\left(\frac{2}{3}\right) {}_0F_4\left(;\frac{2}{3},1,\frac{}{3},\frac{}{3};\nearrow\eta^6\right) + \frac{81}{}\eta^4 {}_0F_4\left(;\frac{}{3},\frac{}{3},\frac{5}{3},\frac{5}{3};\nearrow\eta^6\right)\right]. \tag{3}$$

While the function presented can be used by convolution to obtain a general solution, more insight may be obtained from a solution for the case of $P_e = \delta(\boldsymbol{X})\delta(T)$. This may be achieved without convolution by applying a time derivative on the green function equation to obtain an equation equivalent to (1). Thus, the pressure-field due to a unit point impulse is

$$G_p = \frac{\partial G}{\partial T} \tag{4}$$

IMPACT MITIGATION AND RESPONSE DYNAMICS TO EXTERNAL PRESSURES

We examine an external pressure, evenly distributed on a disk of radius L_e, linearly increasing in magnitude with respect to time until T_e and than decreases linearly until vanishing at $2T_e$, with a total impulse of 1. Convolving the external pressure with G_p, denoting $\eta_{L_e} = L_e/\ T^{1/6}$ and dividing by P_e yields the ratio of pressures at the center for $T \le T_e$

$$\frac{P(\boldsymbol{X}=0,T)}{P_e(T)} = \eta_{L_e}^6 G_{2,7}^{4,1}\left(\eta_{L_e}^6 \left| \begin{matrix} 0,1 \\ \nearrow\frac{2}{3},\nearrow\frac{1}{3},0,0,\nearrow 1,\nearrow\frac{2}{3},\nearrow\frac{1}{3} \end{matrix}\right.\right) \tag{5}$$

*Corresponding author. Email: amirgat@technion.ac.il

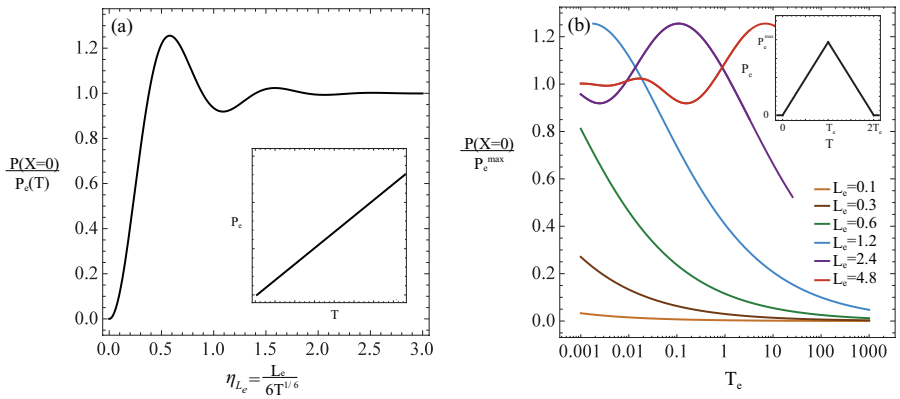

Figure 1: The liquid pressure at $\boldsymbol{X} = 0$ divided by the external pressure during application period as a function of the non-dimensional parameter η_{L_e} (a), and the time maximal magnitude of external pressure is reached T_e (b).

where $G^{4,1}_{2,7}$ is the Meijer G-function. Eq. (5) is presented in Fig. 1a. Three distinct periods are evident: I. An initial period, $2.5 \lesssim \eta_{L_e} < \infty$, where the fluidic pressure closely follows the external pressure, II. The interval, $0.5 \lesssim \eta_{L_e} \lesssim 2.5$, shows small oscillations of the pressure ratio going from mitigation to amplification and vise versa, and III. The period $0 \lesssim \eta_{L_e} \lesssim 0.5$ where mitigation occurs and grows with time. Fig. 1b shows the ratio of pressures at the time where maximal external pressure is reached (i.e. T_e). From Fig. 1b, it is evident that for any width of external pressure L_e, mitigation may be achieved if the application time is sufficiently long. Specifically, for the case of $L_e = 0.1$, mitigation of more than 90% is obtained for external pressures applied over the period of $2T_e = 10^{-3}$ or greater.

EXPERIMENTAL VERIFICATION

Experiments were conducted to illustrate and verify some of the theoretical results. The experimental setup (see Fig. 2a) consists of a $5mm$ width Polyurethane rubber plate floating over a mm silicon-oil film. The center of the plate is deformed due to application of a linear actuator connected to a load cell measuring the force applied on the elastic plate. The radial deformation profile created during force application is sampled by a laser profilometer. The theoretical deformation is

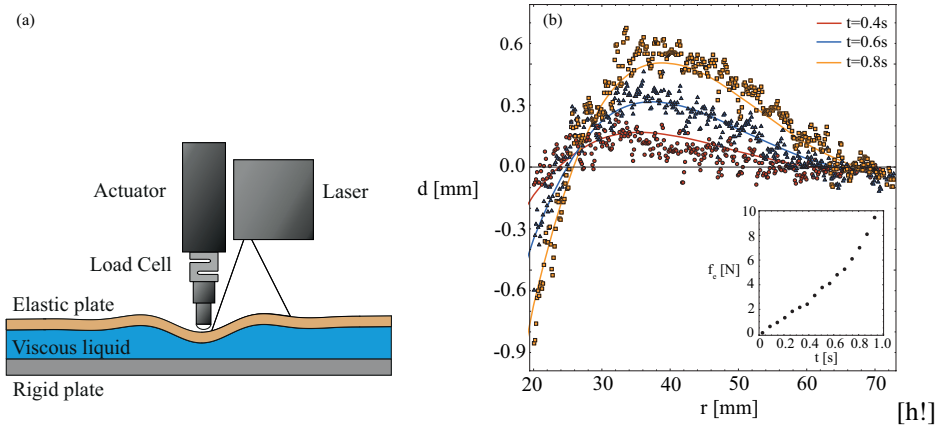

Figure 2: (a) Illustration of the experimental setup. (b) Experimental (markers) and theoretical (smooth lines) deformation d vs. r at $t = 0.\ s$ (red), $t = 0.\ s$ (blue) and $t = 0.8s$ (yellow), during the application of the external force f_e. The insert in part (b) shows force measurements f_e vs. time t.

obtained by convolution of the external force measurements.The radial location of the minimal radius measured by the laser profilometer was estimated by correlation to the analytic solution as $r = 20mm$. No other fitting parameters are used and good agreement between the analytical results and experimental data is evident (see Fig. 2b).

References

[1] Wanchak S and Amnuay K: The operator and its spectrum related to heat equation.Int. J. Pure and Applied Math., 54(1):141-152, 2009.

NONLINEAR PANEL FLUTTER AT VARIABLE TRANSONIC FLOW SPEED

Anastasia Shishaeva[1,2], Andrey Aksenov[2], and Vasily Vedeneev[*1]

[1]*Institute of Mechanics, Lomonosov Moscow State University, Moscow, Russia*
[2]*Tesis LTD, Moscow, Russia*

Summary We investigate nonlinear self-excited oscillations of elastic plate in transonic flow at unsteady flow conditions: the flow speed is variable in time. By observing unsteady plate behaviour, we detect bifurcations of limit cycle oscillations. In addition to previously known limit cycle types, new bifurcations of limit cycles are discovered. When increasing acceleration of the flow, some of the limit cycles disappear, because they do not have enough time to develop. However, flutter is not fully suppressed even for very high accelerations, though the most destructive higher-mode oscillations are missed.

INTRODUCTION

Aeroelastic instability of skin panels, known as panel flutter, has been intensively studied over decades [1, 2]. At high supersonic speeds the coupled-mode panel flutter occurs, while at low supersonic speeds the single-mode flutter is dominant [3]. Recent nonlinear study [4] has shown that at small supersonic flight speeds, different limit cycles can coexist at the same flight conditions, which is caused by linear growth mechanism and nonlinear interaction between growing eigenmodes. Some of the limit cycles include internal resonance between natural modes. Switches of panel oscillations from one limit cycles to another is accompanied by bifurcations of the aeroelastic dynamic system. In the present paper we study such bifurcations by means of varying the flow speed at different rates, and watching the unsteady panel response. This approach gives an explicit way to note the bifurcations in the limit cycles and reveals additional bifurcations not noticed before.

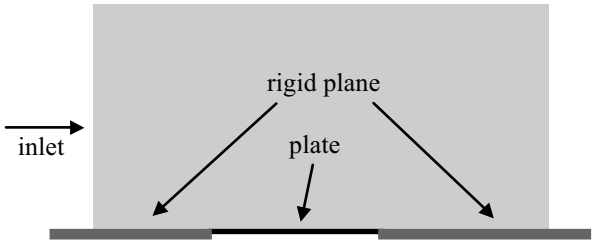

Figure 1: Simulation domain.

FORMULATION OF THE PROBLEM

Elastic plate is mounted into a rigid plane (Fig. 1) with the leading and trailing edges clamped. Inviscid gas flows over one side of the plate with variable Mach number $M(t)$. At the other side of the plate, a pressure equal to the undisturbed flow pressure is specified, such that the undisturbed pressure difference along the plate is zero. Linear increase of M in time with various increase rates $\Delta = (dM/dt) \times (L/a)$ (where L is the plate length, and a is the speed of sound) is considered. The plate-flow interaction is calculated using two coupled codes, Abaqus for simulating the plate, and FlowVision for simulating the gas flow. During each run a slight disturbing harmonic force is applied to the plate in order to enforce each bifurcation of the plate oscillations.

RESULTS

For sufficiently low acceleration of Mach number, $\Delta = 9.1 \times 10^{-5}$, several bifurcations are seen (Fig. 2a). First, at $M = 0.78$ the plate becomes unstable, and static divergence appears, which signifies pitchfork bifurcation. At transonic speed, $M = 1$, Hopf bifurcation occurs, resulting in the first-mode flutter of the plate. At slightly higher Mach number $M = 1.09$ transition from non-resonant to 1:2 resonant limit cycle occurs, which is expressed in the non-symmetry of the oscillations (Fig. 2), the appearance of the second mode in the plate shape and additional doubled frequency present in the spectrum. At $M = 1.41$ higher modes appear, and the oscillations become non-periodic. Finally, at $M = 1.7$ the oscillations damp out, and the plate becomes stable. At higher Mach numbers (not considered here) coupled mode flutter occurs.

*Corresponding author. Email: vasily@vedeneev.ru

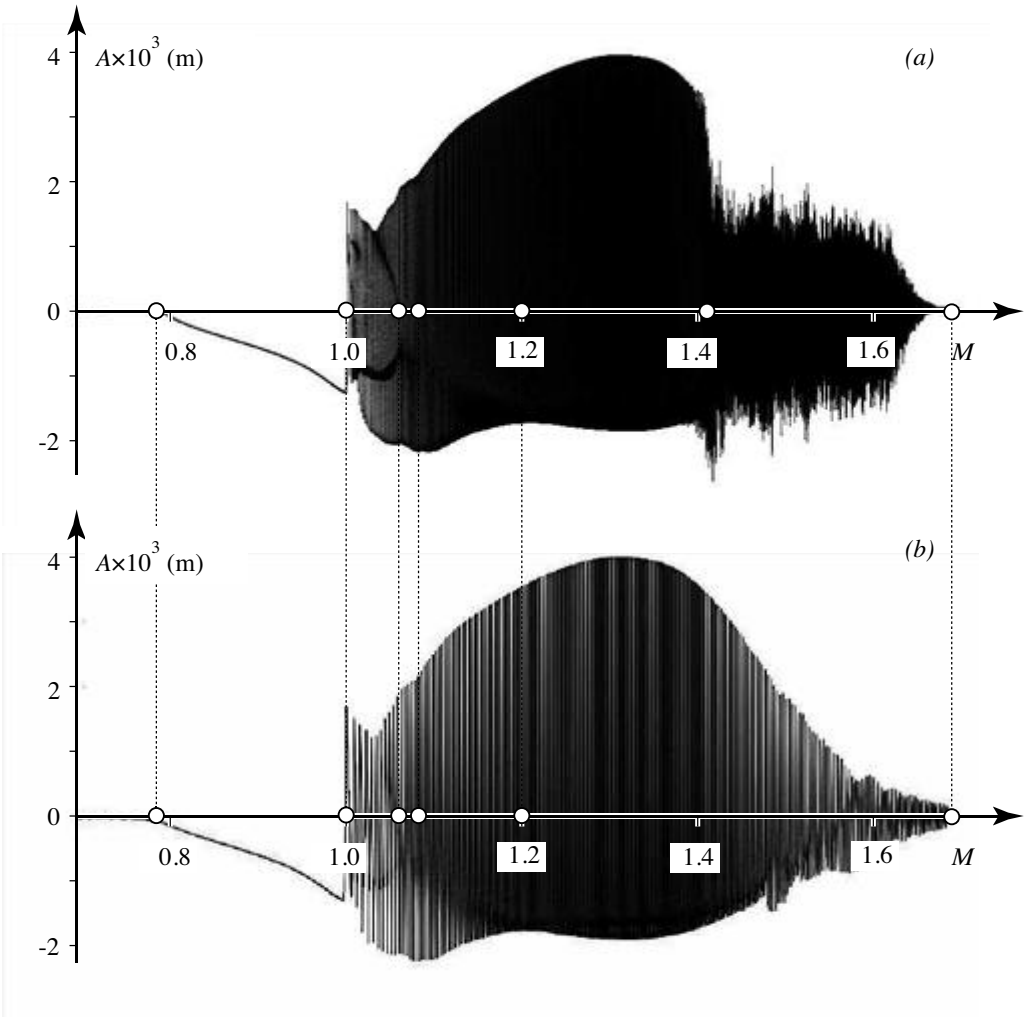

Figure 2: Vertical deflection of a plate point vs M, circles represent bifurcations of the limit cycle. Acceleration $\Delta = 9.1 \times 10^{-5}$ (a), $\Delta = 3.6 \times 10^{-4}$ (b).

The variety of limit cycles observed at transonic conditions are in agreement with [4], where flutter at constant flow speed was studied. Analysis of the problem with variable flow speed yields the detection of two minor bifurcations at $M = 1.07$ and $M = 1.2$, which are slightly visible in Fig. 2a by non-smoothness of $A(M)$ slope, and much better seen in the phase portraits. For each bifurcation, the change in the plate spectrum, phase portrait, and spatial oscillation mode are analyzed.

For faster increase of M, some of the limit cycles are not formed, since their formation periods are too large. For example, for $\Delta = 3.6 \times 10^{-4}$ (Fig. 2b) no non-periodic oscillations are observed. However, even for extremely fast increase of M, $\Delta = 1.8 \times 10^{-3}$ (for a plate of 0.3 m length in the air at normal conditions it corresponds to the acceleration of 660 m/s^2), first mode flutter oscillations are still formed, though more dangerous high-frequency oscillations are missed.

Thus the sufficiently high acceleration of a flight vehicle moving at transonic flow conditions is favourable not only because of shorter time passed in transonic flutter regime, but also because the most destructive limit cycle oscillations (involving higher modes) can be avoided.

The work is supported by grants MD-4544.2015.1 and MK-5514.2016.1.

References

[1] Dowell E.H.: Aeroelasticity of Plates and Shells. Kluwer Academic Publishers, 1974.

[2] Mei C., Abdel-Motagaly K., Chen R.R.: Review of Nonlinear Panel Flutter at Supersonic and Hypersonic Speeds. Applied Mechanics Reviews 10:321–332, 1999.

[3] Vedeneev V.V.: Panel Flutter at Low Supersonic Speeds. Journal of Fluids and Structures 29:79–96, 2012.

[4] Shishaeva A., Vedeneev V., Aksenov A.: Nonlinear single-mode and multi-mode panel flutter oscillations at low supersonic speeds. Journal of fluids and structures 56:205–223, 2015.

MIXED FE-SP METHOD FOR NONLINEAR STRUCTURE-WATER INTERACTIONS WITH FREAK WAVES

Jing Tang Xing[1a)], Kamal Djidjeli[2] & Zhe SUN [1,2]
[1]*FSI Group, FEE, University of Southampton, Southampton, UK*
[2]*CED Group, FEE, University of Southampton, Southampton, UK*

Summary This paper develops a mixed finite element – smoothing particle method for violent water-structure interactions involving freak waves and separation between structure and water. The structure undergoes a large rigid motion of 6 DOF with a small elastic deformation, so that its elastic displacement relative to the rigid motion can be represented a mode summation based on FE analysis. The water is assumed inviscid - incompressible and its motion governed by nonlinear N-S equation. On the coupling interface where no FS separation happens, the equilibrium and consistence conditions are required. The numerical iteration process is suggested to solve the nonlinear FSI equations, and validation examples are shown a good agreement with available experiment results.

GOVERNING EQUATIONS

As shown in Fig. 1, a sold in a material domain Ω_s of outside boundary normal vector ν_i, on which a traction force $\hat{T}_i$ and a displacement $\hat{U}_i$ are respectively given on boundary S_T and S_U, interacts on its wet interface Σ with water domain Ω_f, of which the dynamic pressure $p=0$ on free surface Γ_f, $v_i=0$ on Γ_b and possible given velocity $\hat{v}_i$ on boundaries Γ_v or Γ_v. Three coordinate systems are defined: $o-x_1x_2x_3$ with positive x_3 in the vertical direction is fixed in the space, $O-y_1y_2y_3$, of which axis $O-y_i$ parallels axis $o-x_i$, (i = 1,2,3), is a moving system fixed at the mass centre O of solid, and $O-X_1X_2X_3$ is a material system. A material point X_j at time $t=0$ moves to a new position x_j at time t, and its motion is denoted by a summation of a translation u_i of mass centre, rigid rotation θ_i about three axes and small elastic displacement U_j of structure. Using the notations of Cartesian tensors and summation convention [1], such as Kronecker Delta δ_{ij} and permutation symbol e_{ijk}, and denoting the rigid rotation by a tensor $\beta_{ij}(\theta_k)$ with its time derivative $\dot{\beta}_{ij}=e_{imk}\dot{\theta}_m\beta_{kj}$ and partial derivative $\partial\beta_{ij}/\partial\theta_m=e_{imk}\beta_{kj}$, we can derive the dynamic equations of the system as follows.

Solid: The position and velocity of particle X_j at time t respectively are

$$x_i=u_i+\beta_{ij}X_j+\beta_{ij}U_j,\qquad \dot{x}_i=\dot{u}_i+\dot{\beta}_{ij}X_j+\dot{\beta}_{ij}U_j+\beta_{ij}\dot{U}_j=\dot{u}_i+e_{imk}\dot{\theta}_m\beta_{kj}(X_j+U_j)+\beta_{ij}\dot{U}_j. \tag{1}$$

Introducing a transformation H_{ij} with its related generalised coordinate $\widetilde{U}_i$, which may be a *finite element interpolation function matrix* $\boldsymbol{H}_{ij}$ [2] *and node displacement vector*, or *a mode function matrix and generalised mode coordinate vector* [3], we denote the elastic displacement $U_i=H_{i\alpha}\widetilde{U}_\alpha$ and define $\widetilde{H}_{j\alpha}=\int_{\Omega_s}\rho_sH_{j\alpha}d\Omega$, $V_{jn\alpha\gamma}=\int_{\Omega_s}\rho_sH_{j\alpha}H_{n\gamma}d\Omega$, $S_{jn\alpha}=\int_{\Omega_s}\rho_sX_jH_{n\alpha}d\Omega$, $\widetilde{M}_{\alpha\gamma}=V_{jj\alpha\gamma}$, $(\alpha,\gamma=1,2,\cdots,N)$, so that the kinetic and potential energy of body are respectively calculated in the forms

$$\begin{aligned}
&T=0.5\{M\delta_{rs}\dot{u}_r\dot{u}_s+\widetilde{J}_{rs}\dot{\theta}_r\dot{\theta}_s+\widetilde{M}_{\alpha\gamma}\dot{\widetilde{U}}_\alpha\dot{\widetilde{U}}_\gamma+2A_{rs}\dot{u}_r\dot{\theta}_s+2B_{r\alpha}\dot{u}_r\dot{\widetilde{U}}_\alpha+2C_{r\alpha}\dot{\theta}_r\dot{\widetilde{U}}_\alpha\},\quad A_{rs}(\beta,U)=e_{rsk}\beta_{kj}\widetilde{H}_{j\alpha}\widetilde{U}_\alpha,\quad B_{r\alpha}(\beta)=\beta_{rn}\widetilde{H}_{n\alpha},\\
&\Pi=0.5\widetilde{K}_{\alpha\gamma}\widetilde{U}_\alpha\widetilde{U}_\gamma+gM\delta_{r3}u_r+g\delta_{i3}\beta_{ij}\widetilde{H}_{j\alpha}\widetilde{U}_\alpha-u_r\beta_{rl}\hat{F}_l-\widetilde{U}_\alpha\widetilde{F}_\alpha-\hat{\Gamma}+u_r\beta_{rl}P_l+\widetilde{U}_\alpha\widetilde{P}_\alpha+\Gamma_p,\quad \widetilde{K}_{\alpha\gamma}=\int_{\Omega_s}H_{i\alpha,j}E_{ijkl}H_{k\gamma,l}d\Omega,\\
&C_{r\gamma}(\beta,U)=e_{rki}\beta_{kj}\beta_{in}V_{jn\alpha\gamma}\widetilde{U}_\alpha,\quad \widetilde{J}_{rs}(\beta,U)=(J_{nn}\delta_{rs}-\beta_{rj}\beta_{sn}J_{jn})+[2\delta_{rs}S_{jj\alpha}-\beta_{rj}\beta_{sn}(S_{jn\alpha}+S_{nj\alpha})]\widetilde{U}_\alpha+(\delta_{rs}V_{jj\alpha\gamma}-\beta_{rj}\beta_{sn}V_{jn\alpha\gamma})\widetilde{U}_\alpha\widetilde{U}_\gamma,\\
&\hat{F}_l=\int_{S_T}\hat{T}_ldS,\quad \widetilde{F}_\alpha=\int_{S_T}H_{l\alpha}\hat{T}_ldS,\quad \hat{\Gamma}=\int_{S_T}X_l\hat{T}_ldS,\quad P_l=\int_\Sigma p\nu_ldS,\quad \widetilde{P}_\alpha=\int_\Sigma pH_{l\alpha}\nu_ldS,\quad \Gamma_p=\int_\Sigma pX_l\nu_ldS.
\end{aligned} \tag{2}$$

Here M is total mass of solid, $\widetilde{M}$ is generalised mass matrix, $\hat{F}_l$, $\hat{\Gamma}$ and $\widetilde{F}_r$ are resultant force, moment and generalised force, while the FSI forces involving fluid pressure p denotes by the last column in Eq. 3. We derive the dynamic equations of solid motion by using Hamilton equation [3], $d(\partial T/\partial\dot{q}_i)/dt-\partial T/\partial q_i+\partial\Pi/\partial q_i=0$, therefore, we have

$$\begin{bmatrix} M\delta_{rs} & A_{rs} & B_{r\alpha} \\ A_{sr} & \widetilde{J}_{rs} & C_{r\alpha} \\ B_{\gamma s} & C_{\gamma s} & \widetilde{M}_{\gamma\alpha} \end{bmatrix}\begin{bmatrix} \ddot{u}_s \\ \ddot{\theta}_s \\ \ddot{\widetilde{U}}_\alpha \end{bmatrix}+\begin{bmatrix} 0 & \dot{A}_{rs} & \dot{B}_{r\alpha} \\ \dot{A}_{sr} & \dot{\widetilde{J}}_{rs} & \dot{C}_{r\alpha} \\ \dot{B}_{\gamma s} & \dot{C}_{\gamma s} & 0 \end{bmatrix}\begin{bmatrix} \dot{u}_s \\ \dot{\theta}_s \\ \dot{\widetilde{U}}_\alpha \end{bmatrix}+\begin{bmatrix} 0 & 0 & 0 \\ 0 & 0 & 0 \\ 0 & 0 & \widetilde{K}_{\gamma\alpha} \end{bmatrix}\begin{bmatrix} u_s \\ \theta_s \\ \widetilde{U}_\alpha \end{bmatrix}$$
$$-\begin{bmatrix} 0 & 0 & 0 \\ \dot{\theta}_l\partial A_{sl}/\partial\theta_r & 0.5\dot{\theta}_l\partial\widetilde{J}_{ls}/\partial\theta_r & \dot{u}_l\partial B_{ls}/\partial\theta_r+\dot{\theta}_l\partial C_{l\alpha}/\partial\theta_r \\ \dot{\theta}_l\partial A_{sl}/\partial\widetilde{U}_\gamma & 0.5\dot{\theta}_l\partial\widetilde{J}_{l\alpha}/\partial\widetilde{U}_\gamma & \dot{\theta}_l\partial C_{l\alpha}/\partial\widetilde{U}_\gamma \end{bmatrix}\begin{bmatrix} \dot{u}_s \\ \dot{\theta}_s \\ \dot{\widetilde{U}}_\alpha \end{bmatrix}=\begin{bmatrix} -gM\delta_{r3} \\ -g\delta_{i3}\partial\beta_{ij}/\partial\theta_r\widetilde{H}_{j\alpha}\widetilde{U}_\alpha \\ -g\delta_{i3}\beta_{ij}\widetilde{H}_{j\eta} \end{bmatrix}+\begin{bmatrix} \beta_{rl}\hat{F}_l \\ u_m\partial\beta_{ml}/\partial\theta_r\hat{F}_l \\ \widetilde{F}_\gamma \end{bmatrix}-\begin{bmatrix} \beta_{rl}P_l \\ u_m\partial\beta_{ml}/\partial\theta_rP_l \\ \widetilde{P}_\gamma \end{bmatrix} \tag{3}$$

Fluid: The water motion is governed by *Lagrangian* Navier-Stokes equation for incompressible and inviscid fluid in association with corresponding boundary conditions [4-6]

$$\dot{v}_i=g\delta_{i3}-p_{,i}/\rho_f,\ \ v_{i,i}=0,\ \text{in }\Omega_f;\quad \rho_f(g\delta_{i3}+\ddot{U}_i)\nu_i=-p_{,i}\nu_i,\ \ v_i\nu_i=U_i\nu_i,\ \text{on }\Sigma;\quad p=0,\ \text{on }\Gamma_f;\quad v_i=\hat{v}_i,\ \text{on }\Gamma_v. \tag{4}$$

PARTITIONED ITERATION SOLUTION

Equations (3) and (4) include 3 rigid translations u_s, 3 rigid rotations θ_s and N generalised coordinates $\widetilde{U}_\alpha$, in which the rigid motions could be large but the elastic deformation is assumed small, so that the second order quantity of $\widetilde{U}_\alpha$ are neglected. It is convenience to use a commercial FE code to obtain the natural modes and frequencies of the solid as the input data for the code designed for the method

a) Corresponding author. Email: jtxing@soton.ac.uk.

proposed in this paper. The partitioned iteration is suggested to solve these FSI equations [7-8], starting from initial time $t = 0$, at which the state of the system are given, to calculate the solution at time $t + \Delta t$ in the following steps. i) *Initial calculations*: FE mode dada as input to generate related matrices; initial position, velocity, acceleration and pressure of the system. ii) *Fluid SPM solver*: based on the state of solid at time t to deliver fluid variables at time $t + \Delta t$ using the projection [9] method: a) with no pressure effect to calculate an intermediate velocity $\tilde{v}_i$ and location $\tilde{x}_i$ of particles, $\tilde{v}_i = v_i^t + \Delta t g \delta_{i3}$, $\tilde{x}_i = x_i^t + \Delta t \tilde{v}_i$; b) a pressure Poisson equation is solved to obtain the pressure, $p_{,ii}^{t+\Delta t} = \rho_f \tilde{v}_{i,i} / \Delta t + \psi \rho_f (n^0 - n^t) / (n^0 \Delta t^2)$, $\psi = | n^0 - n^t / n^0 | + \eta \Delta t | v_{i,i}^t |$, where $\eta = 1, 0$ respectively for $(n^0 - n^t) v_{i,i}^t \geq 0$, and $(n^0 - n^t) v_{i,i}^t \leq 0$, to identify compressed or expanded state of fluid; c) fluid velocity and position at time $t + \Delta t$ are calculated $v_i^{t+\Delta t} = \tilde{v}_i - \Delta t p_{,i}^{t+\Delta t} / \rho_f$, $x_i^{t+\Delta t} = x_i^t + \Delta t v_i^{t+\Delta t}$. iii) *Solid solver*: based on the fluid pressure to solve solid equation by time integration iteration to obtain the state variables of the solid. iv) *Convergence check*: calculating the displacement error norm on FSI interface to see if $\int_\Sigma | U_i^{t+\Delta t} - U_i^t | dS \leq \varepsilon$ then go to next time step $t + 2\Delta t$, otherwise, to repeat process ii) and iii) until convergence reached. A calculation flow chat is shown in Fig. 2, where n denotes an FSI iteration number and other notations are the state variables used in the computer code, for which some SPM particular treatment techniques, such as neighbour particle searching, particle interactions with shifting and collision handling, free surface particle identification and FS surface separation flag are considered [10-13].

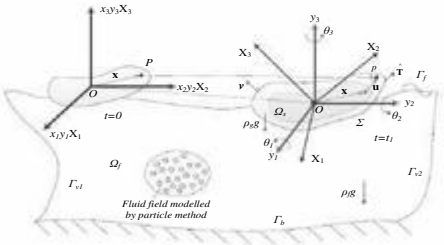

Fig.1 Scheme of FSI system

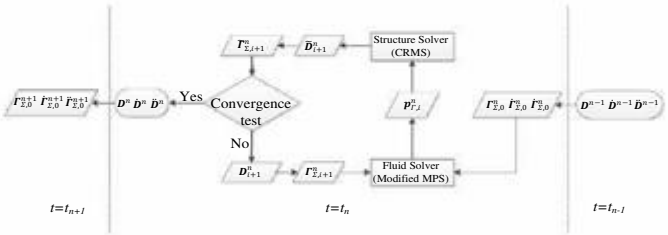

Fig. 2 Flow chart of FSI partitioned iteration process

VALIDATION AND APPLICATIONS

To validate the developed method, the numerical simulations [10-12] of rigid and elastic wedge dropping on the water surface have been completed and compared with available experiments [14-16], which are shown in Fig. 3.

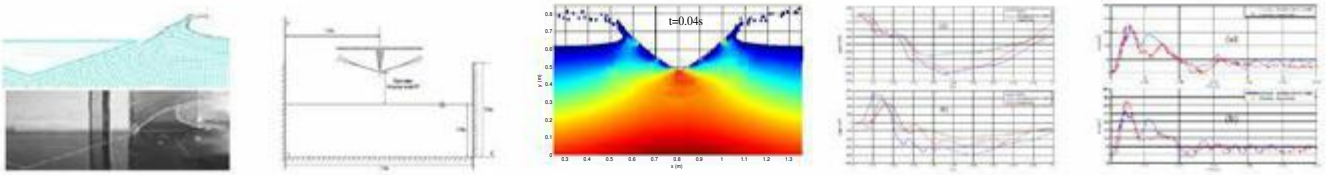

(i) (ii) (iii) (iv) (v)

Fig. 3 Wedge dropping simulations: (i) rigid one comparison with experiment photo [14][10]; (ii) elastic test arrangement [16]; (iii) numerical picture at time 0.04s [11-12]; (iv) comparison of strains at two points from wedge tip with experiments a) 30mm, b) 120mm [15]; (v) comparison of accelerations of elastic wedge with experiments a) case 1 (4.29m/s), b) case 2 (5.57m/s) [16].

It has been shown a very good agreement with experiments, which demonstrates that the proposed method is attractive to deal with strong nonlinear FSI involving freak waves or FS separations, which is difficult to be solved by mesh based methods. This type of problems have an important background in marine engineering, such as green water impacts concerned by ship designs and aircrafts landing on the water. The developed method and its integrated computer code is still developing to tackle more engineering application cases discussed in many books, such as [17-19]. It is noticed that the system involves chaos and bifurcations that may be met in FSI numerical simulations, which requires further investigations using nonlinear dynamic approaches, such as the developed energy flow method [20].

References

[1] Fung Y.C.: A first course in continuum mechanics. Prentice-Hall, 1977.
[2] Bathe K. J.: Finite Element Procedures in Engineering Analysis. Prentice-Hall, 1996.
[3] Meirovitch L.: Principles and techniques of vibrations. Prentice-Hall, 1997.
[4] Monaghan J J. 1992. Smoothed particle hydrodynamics. *Annual Review of Astr. and Astrophysics*, **30**:543-574.
[5] Monaghan, :Simulating Free Surface Flows with SPH. *Journal of Computational Physics* **110**: 399-406, 1994.
[6] Liu G. R., Liu M. B.: Smoothed particle hydrodynamics. World Scientific Publishing Co. 2003.
[7] Xing J. T., Price W. G., Chen Y. G.: A mixed finite element - finite difference method for nonlinear fluid-structure interaction dynamics, Part I: rigid structure-fluid interaction. *Proc. Royal Soc A* **459**: 2399-2430. 2003
[8] Xing J.T.: Developments of numerical methods for linear and nonlinear fluid-solid interaction dynamics with applications. *Advances in Mechanics* (in print), 2016.
[9] Chorin A.J.: A numerical method for solving incompressible viscous flow problems. *Journal of Computational Physics* **2**: 12-26, 1967.
[10] Sun F.: Investigations of smoothed particle hydrodynamics method for nonlinear fluid-rigid body interaction dynamics. *PhD thesis*, FEE, University of Southampton, 2013.
[11] Sun Z., Djidjeli K., Xing J.T., Cheng F.: Modified MPS method for the 2D Fluid Structure Interaction problems with free surface. *Computers & Fluids* **122**: 47-65, 2015.
[12] Sun Z., Djidjeli K., Xing J.T., Cheng F.: Coupled MPS-modal superposition method for 2D nonlinear fluid-structure interaction problems with free surface. *Journal of Fluids & Structures* **61**:295-323, 2016.
[13] Javed A., Djidjeli K., Xing J. T.: Shape adaptive RBF-FD implicit scheme for incompressible viscous Navier–Stokes equations. *Computer & Fluids*, **89:** 38-52, 2014.
[14] Zhao R., Faltinsen O., Aarsnes J.: Water entry of arbitrary two-dimensional sections with and without flow separation. *21st Symposium on Naval Hydrodynamics*,1997.
[15] Panciroli R., Abrate S., Minak G., Zucchelli A.: Hydroelasticity in water-entry problems: comparison between experimental and SPH results. *Comp Struc*, **94**: 532-539, 2012
[16] Panciroli R.: Hydroelastic Impacts of Deformable Wedges. *Solid Mechanics and Its Applications* **192**: 1-45, 2013.
[17] Morand H. J. P., Ohayon R.: Fluid structure interaction. John Wiley and Sons, Chichester, 1995.
[18] Païdoussis M. P.: Fluid-Structure Interactions: Slender Structures and Axial Flow. Academic Press. 2013.
[19] Païdoussis M. P., Price S. J., Langre E. D.: Fluid-Structure Interactions: Cross-Flow-Induced Instabilities. Cambridge University. 2011.
[20] Xing J.T.: Energy flow theory of nonlinear dynamical systems with applications. Springer, 2015.

FS07 - Actuating and Smart Materials

TS.FS07-1.01	Lynch, Christopher - Using piezoelectrics to electrically transfer momentum from a shock wave (INVITED)	3287
TS.FS07-1.02	Avakian, Artjom - Finite element simulation of magnetoelectric coupling in multiferroic composites	3289
TS.FS07-1.03	Bilal, Osama - Phononic transistors and mechanical calculators	3291
TS.FS07-1.04	Chatzigeorgiou, George - Thermomechanically coupled model for non-proportional loading in SMAs	3293
TS.FS07-1.05	Zhang, Yang - Remote bending control of liquid crystal polymer beams by light induced moment and shear forces	3295
TS.FS07-1.06	Dhote, Sharvari - A Compliant Orthoplanar Spring Based Piezoelectric Vibration Energy Harvester	3297
TS.FS07-2.01	Patoor, Etienne - Influence of phase transformation anisotropy on transformation surface around a crack tip (INVITED)	3299
TS.FS07-2.02	Zhou, Yue-Ting - The effect of surface waviness on contact behaviors in multiferroic structures	3301
TS.FS07-2.03	Jiang, Yunyao - The deformation mechanisms of new chiral structures	3303
TS.FS07-2.04	Lagoudas, Dimitris - Predicting the constitutive response of smas on the basis of composition and heat treatment	3305
TS.FS07-2.05	Lange, Stephan - Modeling ferromagnetic and multiferroic behavior based on a condensed method (CM)	3307
TS.FS07-3.01	Meraghni, Fodil - Cyclic loading effects on NiTi alloys under biaxial conditions	3309
TS.FS07-3.02	Wingen, Marius - Effects of switching processes in ferroelectrics on the temperature: A modeling approach	3311
TS.FS07-3.03	Srinivasan, Prashanth - Molecular Dynamics Simulations of Phase Transformations in NiTi Bicrystals	3313
TS.FS07-3.04	Tobushi, Hisaaki - Functionally-graded and composite shape memory actuation	3315
TS.FS07-3.05	Zhang, Xiaolong - Modeling of the Chemo-mechanical Behaviors of Reactive Materials	3317
PO.FS07-1.01.255	Chen, Fanlong - Design and simulation on a morphing marine propeller	3319
PO.FS07-1.02.256	Cramer, Mark - Numerical modeling of gas-expanded lubricants in hybrid bearings	3321
PO.FS07-1.03.257	He, Yongjun - High-frequency martensite reorientation in Ni-Mn-Ga — Temperature rise and its influence	3323
PO.FS07-1.04.258	Hobeck, Jared - Impedance Drift due to Thermal Cycling of Macro Fiber Composites	3325
PO.FS07-1.05.259	Hongqiu, Wei - Fabrication and characterization of epoxy based shape memory nano-composites	3327
PO.FS07-1.06.260	Tan, Yimin - Performance improvement of idm motor using nonlinear property of material	3329
PO.FS07-1.07.261	Wang, Yin - Application of an IHB method to the vibration of a dielectric elastomer balloon	3331
PO.FS07-1.08.262	Xia, Xiaodong - Nonuniform domain switching for interfacial crack subject to two-parameter crack tip fields	3333
PO.FS07-1.09.263	Xu, Yangguang - The magneto-induced stress relaxation of magnetorheological polymer gels	3335

PO.FS07-1.10.264 Yang, Zhengbao - A distributed-parameter model of a compressive-mode energy harvester 3337

USING PIEZOELECTRICS TO ELECTRICALLY TRANSFER MOMENTUM FROM A SHOCK WAVE

Christopher Roberts[1] & Christopher Lynch[2]
[1]*Department of Materials Science and Engineering, UCLA, Los Angeles, California*
[2]*Department of Mechanical and Aerospace Engineering, UCLA, Los Angeles, California*

Summary This research investigates the fundamental physics of smart materials under shock compression, and presents concepts that can be exploited for active shock mitigation. The results indicate momentum can be transferred through electro-magnetic field, not just mechanically. This enables new approaches to actively controlling the properties of materials subjected to impact or explosive generated shock.

Shock waves in solids arise from impact or explosive events. They travel at the speed of sound and impart momentum in their wake. Smart materials offer the ability to modify how a shock wave propagates through a material in the several microseconds that pass between the initial impact and the arrival of the shock. The speed of sound and the elastic modulus in a piezoelectric or ferroelectric material can be modified by changing the electrical boundary conditions (open vs. short circuit). How to use this property to electronically switch from a monolithic to a layered structure in linear piezoelectric materials has been under investigation as a means to spread the shock front. Even small changes in the width of the shock front result in considerable reductions in the acceleration it produces. This effect can be enhanced by taking advantage of the non-linear material behavior associated with domain wall motion and pressure induced phase transformations. This work addresses shock propagation in linear piezoelectric plates that make up the layers of an active 2-2 composite shock mitigation system. Simulations of the behavior of the plates were performed using the Sandia National Laboratory multiphysics shock modeling code ALEGRA-FE.

Layered structures provide an effective means to attenuate shockwaves through wave scattering at impedance-mismatched interfaces. The difference between the impedances of two dissimilar materials (density multiplied by speed of sound) determines how the shock wave is transmitted or reflected as it passes the interface. Impedance-mismatched layered structures have the ability to spread the shock front, thus reducing the associated acceleration. The effect depends on the geometry and the relative direction of shock propagation, i.e. normal or oblique to the 2-2 composite (layered plates) [1]. The shock viscosity (a measure of shock-front spreading and attenuation) of a heterogeneous material can be greatly increased by increasing the impedance mismatch of the constituents. [2,3,4] Layered piezoelectric structures can have their mechanical impedance changed by changing the electrical boundary conditions on the individual layers, offering the ability to rapidly switch from a homogeneous to a heterogeneous structure. The degree of heterogeneity indiced depends on the properties of the piezoelectric. In this work, PZT is considered.

PZT is a piezoelectric ceramic that, when poled, displays a remanent polarization. In a linear piezoelectric material the electric displacement is a function of both applied stress and electric field, i.e. $D=d\sigma+\varepsilon E$ where σ is the applied stress and d is the piezoelectric coefficient. At a boundary with an electrode, the normal component of electric displacement is equal to the surface charge density on the electrode. Under short circuit boundary conditions, stress causes charge to flow to keep the potential at the electrodes constant. Under open circuit conditions the charge density cannot change and thus the electric displacement is held constant and stress induces an internal electric field. Simulations indicate that these effects are not uniform in the transient case when a shock wave has travelled part way through the piezoelectric material.

The geometry for the shock propagation simulations was an electroded plate of PZT (fig. 1a) with initially homogeneous polarization. Prior to arrival of the shock, the surface charge density balances the internal dipole charges and there is no electric field (fig. 1b). As the shockwave traverses the element, the dipoles in the shocked region of the PZT are compressed, decreasing the electric displacement. Under open circuit conditions, in order to maintain zero electric displacement, an equal an opposite electric displacement εE is induced. As such, a compressive stress (negative) results in a positive electric field within the shocked material via the piezoelectric effect (fig. 1c). The electric field in the unshocked region remains zero, as there is no compressive stress to induce an electric field. The shockwave continues to traverse the element, until the entirety of the element is under shock compression and sustains an internal electric field approximately equal to $-d\,\sigma/\varepsilon$. The open circuit shock response is very similar to that of a non-piezoelectric material, with the exception that some energy is available as electrical energy. Under short circuit conditions, as the shockwave traverses the element the compressive stress results in a positive electric field within the shocked region. In this case, charge flows to balance the potential on the electrodes. This results in a negative electric field in the region ahead of the shock (fig. 1d). Depending on the mechanical boundary conditions, this can induce a corresponding tensile stress in the material ahead of the shock, effectively spreading out the shock front. The tensile stress induced by the negative electric field alters the unshocked PZT region in two ways. If the PZT element is rigidly bonded to the subsequent layers, the tensile stress will act to piezoelectrically-stiffen the PZT material. The amount of this stiffening can be tuned in real time by controlling the resistance between the two conductors. If the PZT element is not rigidly bonded to the subsequent layers, the tensile stress

[a] Corresponding author. Email: cslynch@seas.ucla.edu.

will cause the element to contract and separate, introducing a gap at the interface. This induced gap creates a new impedance-mismatched interface. Finally, if the back half of the PZT is replaced with PZT that has been poled in the opposite direction, the negative electric field will produce a compressive stress. This demonstrates the novel ability to transfer momentum from the shockwave forward into the unshocked material via electric field, inducing either compression or tension through composite design.

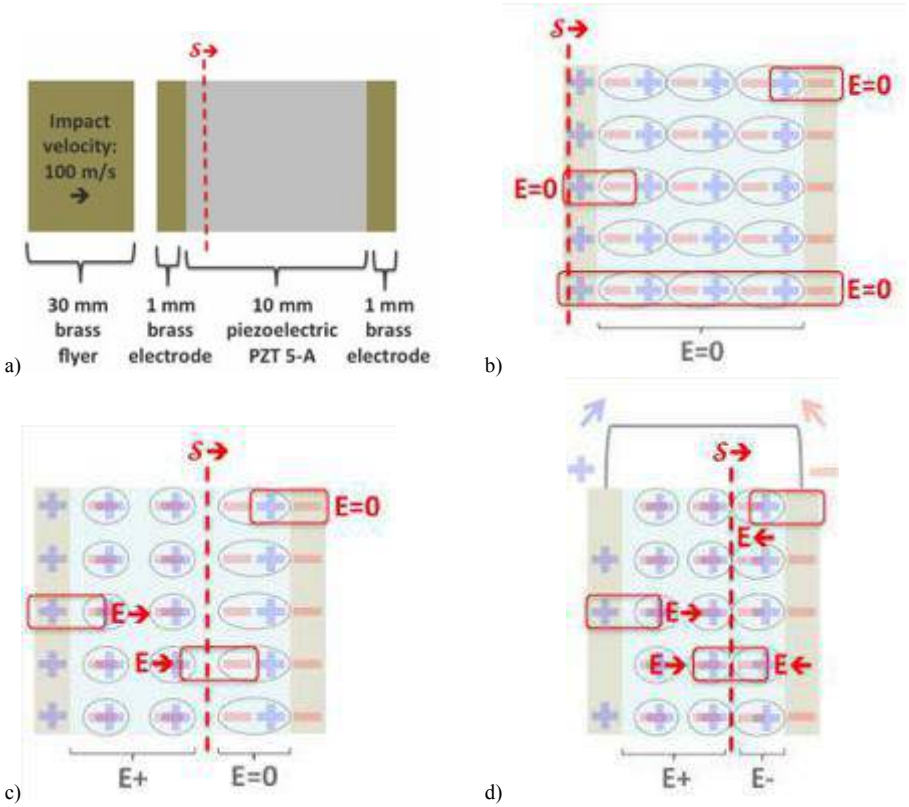

Fig 1). Schematic of representative volume element subjected to shock loading via plate impact (a). The shockwave will travel from left to right. Initially, all the dipoles are balanced and there is zero electric field within the PZT (b). As the wave traverses the PZT under open circuit conditions, an electric field develops in the shocked region due to the piezoelectric effect (c). No electric field develops in the unshocked region. Under short circuit conditions current flows to equilibrate conductor voltages, creating a negative electric field in the unshocked region (d). This field induces a tensile stress due to the converse piezoelectric effect.

References

[1] Zhuang, S., Ravichandran, G., Grady, D.: An experimental investigation of shock wave propagation in periodically layered composites, *J. Mech. Phys. Solids*, **51**, 2:245-265, 2003.

[2] Gardner, N., Wang, E., Shukla, A.: Performance of functionally graded sandwich composite beams under shock wave loading, *Comp. Struct*, **94**, 5: 1755-1770. 2012.

[3] Hosseini, H., Moosavi-Nejad, S., Akiyama, H., Menezes, V.: Shock wave interaction with interfaces between materials having different acoustic impedances, *Appl. Phys. Lett*., **104**:103701, 2014.

[4] Tsai, L., Prakash, V.: Structure of weak shock waves in 2-D layered material systems, *Int. J. Solids Struct*. **42**, 2: 727-750, 2005

FINITE ELEMENT SIMULATION OF MAGNETOELECTRIC COUPLING IN MULTIFERROIC COMPOSITES

Artjom Avakian[1a)] & Andreas Ricoeur[1]
[1]*Institute of Mechanics, University of Kassel, Kassel, Hessen, Germany*

Abstract In this paper, the constitutive modeling of nonlinear multifield behavior as well as the finite element implementation are discussed. Nonlinear material models describing the magneto-ferroelectric or electro-ferromagnetic behaviors are presented. Both physically and phenomenologically motivated constitutive models have been developed for the numerical calculation of principally different nonlinear magnetostrictive behaviors. Further, the nonlinear ferroelectric behavior is based on a physically motivated constitutive model. On this basis, the polarization in the ferroelectric and magnetization in the ferromagnetic and magnetostrictive phases, respectively, are simulated and the resulting effects analyzed. Additionally, the ferroelectric model accounts for damage due to microcrack growth. Numerical simulations focus on the calculation of magnetoelectric coupling and on the prediction of local domain orientations as well as damage evolution, microcrack growth and delamination of interfaces, going along with the poling process, thus supplying information on favorable electric-magnetic loading sequences.

THEORETICAL FRAMEWORK AND MODELS

The coupling of magnetic and electric fields due to the constitutive behavior of a material is commonly denoted as magnetoelectric effect. The latter is only observed in a few crystal classes exhibiting a very weak coupling, mostly at low temperatures, which can hardly be exploited for technical applications. Much larger coupling coefficients are obtained at room temperature in composite materials with ferroelectric and ferromagnetic constituents. The magnetoelectric effect is then induced by the strain of matrix and inclusions converting electrical and magnetic energies based on the piezoelectric and magnetostrictive effects.

Here, the constitutive frameworks of ferroelectric and reversible and irreversible ferromagnetic behaviors are summarized and compared to each other. Ferroelectric materials exposed to electromagnetic fields are described by the constitutive equations: $\sigma_{ij} = c_{ijkl}\left(\varepsilon_{kl} - \varepsilon_{kl}^{irr}\right) - e_{lij}E_l,\ D_l = e_{lij}\left(\varepsilon_{ij} - \varepsilon_{ij}^{irr}\right) + \kappa_{ln}E_n + P_l^{irr},\ B_k = \mu_{km}H_m$ [1]. Within a microphysical framework, the irreversible strain ε_{kl}^{irr} and polarization P_l^{irr} are due to domain wall motion. Considering plane problems, a grain consists of four domain species separated by 90° - and 180° - domain walls. The formulation of a nonlinear constitutive law thus requires at least four internal variables and associated evolution equations locally describing the switching of unit cells on the micro level. Due to intended applications within a multiferroic framework, the ferroelectric material is allocated a magnetic permeability expressed by the third equation relating the magnetic field H_m and the induction B_k. The elastic, piezoelectric, dielectric and magnetic permeability tensors c_{ijkl}, e_{lij}, κ_{ln} and μ_{km} also depend on the internal variables, giving rise to an additional source of nonlinearity, even in the magnetic properties. The other quantities are stress σ_{ij}, electric field E_l and electric displacement D_l.

Based on the same ideas as ferroelectric constitutive equations, the ferromagnetic constitutive equations read $\sigma_{ij} = c_{ijkl}\left(\varepsilon_{kl} - \varepsilon_{kl}^{irr}\right),\ D_l = \kappa_{ln}E_n,\ B_k = \mu_{km}H_m + M_k^{irr}$ [2, 3]. Here, local irreversible strain and magnetization M_k^{irr} are likewise governed by four internal variables describing Bloch wall motion due to magnetomechanical driving forces. The affinity to ferroelectricity on the macro- and mesoscales allows for a similar modeling of ferromagnetism covering the essential phenomena. In the constitutive framework the physical processes merge into an evolution law for the internal variables, which is based on the magnetoelastic or electroelastic energies, respectively, going along with the changes of the directions of magnetic or electric dipoles. In contrast to ferroelectricity, piezomagnetic coefficients relating magnetic field and stress or strain and magnetic induction are not involved, accounting for the saturation. As a second consequence, the irreversible strain does not directly induce a magnetic induction B_k. Magnetostriction is rather induced by the irreversible part of the strain, which in turn is controlled by the magnetic field but also by mechanical loads. The same way, a strain field has an impact on the magnetic induction via M_k^{irr}. Dielectric properties are allocated by the second equation which is linear only at the first glance, since the dielectric constants κ_{ln} are controlled by the internal variables in a nonlinear manner. Ferromagnetic materials exhibiting a significant electric conductivity are excluded by the model.

Whereas the previous ferromagnetic constitutive equations generate hysteresis loops, the constitutive equations of nonlinear reversible ferromagnetic behavior are given by $\dot{\sigma}_{ij} = c_{ijkl}(\varepsilon_{kl}, H_k)\dot{\varepsilon}_{kl} - q_{kij}(\varepsilon_{kl}, H_k)\dot{H}_k,\ \dot{D}_l = \kappa_{ln}\left(\varepsilon_{ij}, H_k\right)\dot{E}_n,\ \dot{B}_k = q_{kij}(\varepsilon_{ij}, H_m)\dot{\varepsilon}_{ij} + \mu_{km}(\varepsilon_{ij}, H_m)\dot{H}_m$ [2, 3], where a rate dependent depiction has been chosen. The nonlinearity is completely included in the material coefficients depending on the independent variables strain and magnetic field. Due to the reversibility of the constitutive behavior, these functions are unique, not involving any internal variables. The coefficient functions, now including the magnetostrictive tensor $q_{kij}(\varepsilon_{ij}, H_m)$, have to be chosen in a way to reflect experimental observations. A second requirement is to satisfy thermodynamical consistency by defining a thermodynamical potential yielding all the coefficient functions by differentiation. These purely phenomenological approaches involve several parameters, which are adjusted to specific material behaviors.

[a)] Corresponding author. Email: artjom.avakian@uni-kassel.de.

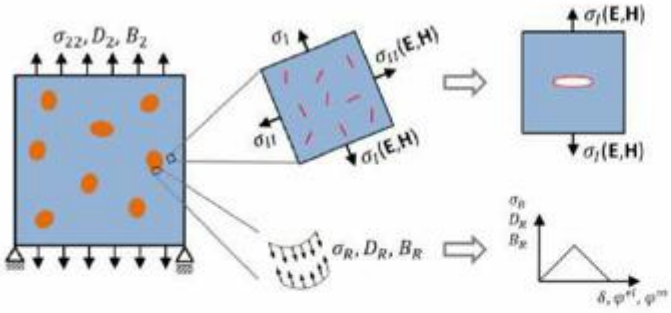

Fig. 1: Initiation of a microcrack perpendicular to the maximum principal stress σ_I and cohesive zone with restraining stress, electric displacement and magnetic flux σ_R, D_R and B_R for the modeling of delamination of inclusion and matrix

Damage is taken into account twofold, see Fig. 1. The cracking of the matrix is going along with microcrack growth driven by mechanical stresses predominantly being induced by magnetic and electric fields. Further, a generalized cohesive model accounts for the delamination of matrix and inclusion. Additional internal variables are introduced, their evolutions describing the onset and progress of damage. Due to the impact on effective properties, the magnetoelectric coupling will be degraded by crack growth.

RESULTS

In Fig. 2 the polarization in the ferroelectric matrix and the magnetization in the ferromagnetic inclusion are shown. Here, the initialization or poling process is finished and the composite is ready for magnetoelectric applications. A favourable configuration is going along with a smallest possible scatter of local orientations of polarization and magnetization around the preferred direction. Second, the residual stresses, being responsible for cracking as well as delamination and thus for functional as well as structural degradation, are of interest. According to Fig. 2a, the magnetization and polarization show a moderate scatter around the intended x_1-direction, leaving a sufficiently large potential for optimization. The tensile residual stresses, according to Fig. 2b, exhibit a maximum of approximately 100 MPa, certainly leading to cracking and delamination.

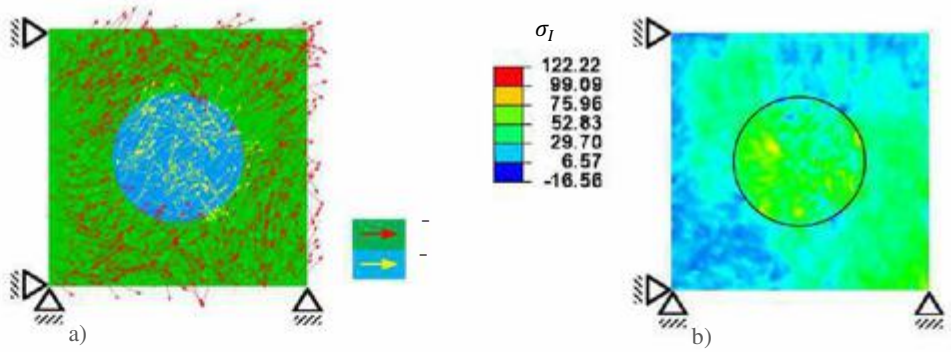

Fig. 2: Polarized and magnetized magnetoelectric composite with AlNiCo 35/5 – inclusion in a $BaTiO_3$ – matrix a) vectors of magnetization $\bar{}$ as well as polarization $\bar{}$ and b) maximum principal stress σ_I [MPa]

CONCLUSIONS

The constitutive models for ferroelectric materials and two types of constitutive models for ferromagnetic materials have been presented. The one of the ferromagnetic model produces irreversible hysteresis behaviour and the other exhibits nonlinear reversible features. Both characteristics are well-known from different ferromagnetic materials. Further, the ferroelectric model produces irreversible hysteresis behaviour. The material models have been implemented within a finite element context to be able to investigate complex boundary value problems. Finally, a multiferroic composite, consisting of a ferromagnetic inclusion in a ferroelectric matrix, has been investigated numerically, applying physically motivated constitutive models for both phases. Polarisation and magnetization of an initially unpoled composite have been simulated and the maximum principal stress has been calculated, being the basis for the prediction of magnetoelectric coupling coefficients and cracking.

References

[1] Avakian A., Gellmann R., Ricoeur A.: Nonlinear modeling and finite element simulation of magnetoelectric coupling and residual stress in multiferroic composites. Acta Mechanica *226 (8)*: 2789-2806, 2015.

[2] Avakian A., Ricoeur A.: Nonlinear numerical simulation of ferroelectric-ferromagnetic multifunctional composites. Proc. Appl. Math. Mech. *15*: 377 – 378, 2015.

[3] Avakian A., Ricoeur A.: Constitutive modeling of nonlinear reversible and irreversible ferromagnetic behaviors and application to multiferroic composites. J. of Intel. Mat. Sys. and Struct., 2015, revision submitted.

PHONONIC TRANSISTORS AND MECHANICAL CALCULATORS

Osama R. Bilal[1], André G. C. Foehr [1], and Chiara Daraio *[1,2]
[1]*Mechanical and process engineering, ETH Zurich, Zurich, Switzerland*
[2]*Division of Engineering and Applied Science, California Institute of Technology, Pasadena, California 91125, USA.*

Summary The realization of mechanical metamaterials analogous to electronics systems, like diodes, transistors and logic elements, opens new horizons towards the fabrication of advanced acoustic systems, smart actuators and adaptable vibration mitigating materials. Previous realizations of acoustic diodes and mechanical switches have employed nonlinearities to break transmission symmetry, but have not yet been able to demonstrate amplification or to execute complex logic operations. Our work harnesses the interaction between geometric nonlinearities and nonlinear magnetic potentials, to engineer frequency-agile band gaps in mechanical metamaterials. These gaps are utilized to demonstrate, both numerically and experimentally, the switching and amplification of a mechanical signal in a mechanical circuit board. The tunability of the proposed system in real-time enables the realization of the complete set of mechanical logic elements. We fabricate and test a mechanical metamaterial that utilizes interconnected phononic transistors to execute simple calculations.

Electronic transistors used in today's electronic devices are characterized by their ability to amplify or switch electronic signals. Conventional field effect transistors (FET) consist of at least three terminals: a source, a drain and a gate. The switching functionality takes place by applying a current at the gate to control the flow of electrons from the source to the drain. Due to the big difference in amplitude between the controlling signal (in the gate) and the controlled signal (flowing from the source to the drain), one can cascade or reproduce an electronic signal by connecting multiple transistors in-series to perform computations. The realization of a mechanical transistor analogous to a FET enables the switching and amplification of mechanical waves by mechanical waves (i.e., sound and vibrations). The challenge of building all-phononic circuits is the ability to switch and amplify phonons by phonons, while operating on a *single* frequency. This enables the reproduction of mechanical signals, without information loss due to frequency conversion. The possibility to create all-phononic transistors functioning at a single frequency, has been theoretically proposed [1], while switches and diodes [2] have already been shown both numerically and experimentally, as detailed in a recent review [3].

The idea of utilizing a mechanical computing-system has a long established history [4]. In fact, the first known calculators and computers were both mechanical; before electronics took over. Recently, with our growing ability to manipulate mechanical waves, the concept of *phononic computing* emerged [3]. That is, utilizing phononic metamaterials in basic logic operations. Phononic metamaterials are periodic systems composed of a basic building block, (i.e., unit cell), that repeats spatially. These materials exhibit distinct frequency characteristics, band gaps, which are frequency ranges where elastic/acoustic waves are prohibited from propagation. Applications of a phononic materials in computing can range from thermal computing (at small scales) to ultrasound and acoustic based computing (at larger scales).

In this work, we experimentally realize a phononic transistor analogous to an electronic FET device. The system we propose consists of an array of geometrically nonlinear unit cells (representing the metamaterial), connecting the source to the drain, as shown in the schematic (Fig.1). Each individual unit cell contains a magnet and is designed to have a subwavelength band gap, to decouple the frequency of operation from its characteristic size. An array of permanent magnets is positioned beneath the metamaterial and is used to tune the resonant response of the unit cells. To dynamically control the tuning (and provide a gating functionality), we coupled the permanent magnets to a driven, magnetic cantilever (herein referred to as the gate). When a relatively small mechanical signal passes through the gate, it induces a shift in the array of magnets, which in turn tunes the band gap frequency of the metamaterial, allowing the source energy to flow to the drain. Following a systematic design methodology, we utilize a configuration of four interconnected transistors to experimentally realize all existing electronic logic gates. We use a subset of these gates to build a phononic-circuit-board for a binary calculator.

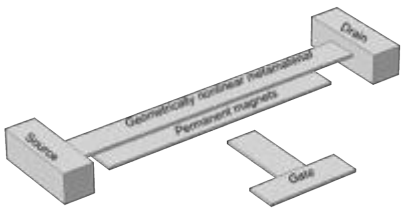

Figure 1: Schematic of the proposed concept for a mechanical transistor.

*Corresponding author. Email: daraio@ethz.ch

We calculate the band structure of an infinite array of unit cells using the finite element method, by solving the elastic wave equations and Bloch wave formulation and considering the wave propagation along the direction of periodicity (i.e., ΓX direction). We characterize the system experimentally by fixing one end of the finite metamaterial structure to the source (i.e., a mechanical shaker) and the other end to the drain (a fixed, rigid support). The signal at the drain is measured using a laser Doppler vibrometer. The numerically obtained dispersion curves of the infinite media is shown in Fig. 2 (left). The experimental characterization of the frequency response function of a 5 unit cell finite metamaterial is shown in Fig. 2 (right). Theory and experiments agree well, particularly in the band gap frequency range, highlighted in gray.

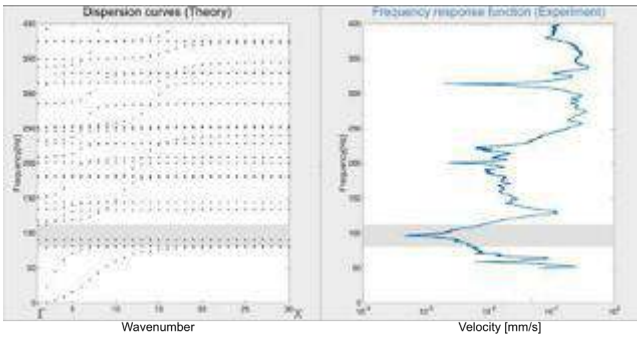

Figure 2: (Left) Numerically obtained dispersion curves in the Γ X direction of the metamaterial. (Right) Experimentally obtained frequency response function of a metamaterial consisting of 5 unit cells. The band gap region is highlighted in gray in both panels.

We demonstrate the switching ability of the fabricated system in Figure 3. We measure the mechanical signal at the drain when the gate is open, allowing the signal to pass, (Fig. 3 left) and when the gate is closed (Fig. 3 right). The amount of energy flowing from the source to the drain when the gate is closed is on the same order of magnitude as the laser vibrometer noise level, while the difference in magnitude between the two states, ON and OFF, is bigger than a factor of 5. It is important to mention that the switching response can be triggered dynamically, driving the gate cantilever at its resonant frequency. We also measure the signal amplification as a ratio of the amplitude of source signal to the gate signal. From numerical data and experimental results, not shown, the amplification reached by our system is 10. The combination of real-time switching and amplification shows the realization of a mechanical transistor analogous to an electronic FET. The realization of basic logic gates, namely, OR, AND, XOR, XNOR, NAND, NOR and NOT can easily follow. We utilize the proposed framework to realize the circuit board of a phononic calculator.

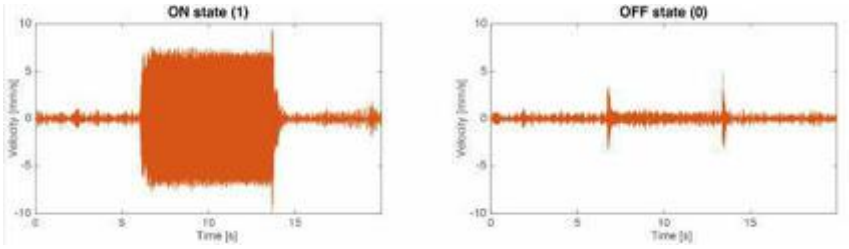

Figure 3: Time series of the mechanical signal at the drain when the system is ON (left) and OFF (right).

ACKNOWLEDGMENT: This work was partially supported by the ETH Postdoctoral Fellowship FEL-26 15-2 to the first author.

References

[1] Malishava M., and Ramaz K.: All-Phononic Digital Transistor on the Basis of Gap-Soliton Dynamics in an Anharmonic Oscillator Ladder. Phys Rev Lett 115.10 (2015): 104301. Liang, B., et al. "Acoustic transistor: Amplification and switch of sound by sound." Appl Phys Lett 105.8 (2014): 083510.

[2] Boechler, N., et al. "Bifurcation-based acoustic switching and rectification." Nature materials 10.9 (2011): 665-668. Devaux, Thibaut, et al.:Asymmetric acoustic propagation of wave packets via the self-demodulation effect. Phys Rev Lett 115.23 (2015): 234301.

[3] Sklan, S. R.: Splash, pop, sizzle: Information processing with phononic computing. AIP Adv 5.5 (2015): 053302.

[4] Freeth, Tony, et al.: Decoding the ancient Greek astronomical calculator known as the Antikythera Mechanism. Nature 444.7119 (2006): 587-591.

THERMOMECHANICALLY COUPLED MODEL FOR NON-PROPORTIONAL LOADING IN SMAS

Dimitris Chatziathanasiou[1], Yves Chemisky[1], George Chatzigeorgiou [*1], and Fodil Meraghni[1]
[1]*Arts et Métiers ParisTech, LEM3 UMR 7239 CNRS, France*

Summary In this work, a new 3D thermomechanically coupled phenomenological model is proposed for SMAs. SMA behavior is described through several strain mechanisms, each associated with its proper internal variables. Forward and reverse transformation are allowed to take place simultaneously with martensite variants reorientation. This model is built to capture the particular behavior of SMAs when subjected to complex loading, namely non-proportional thermomechanical loading. The effect of thermomechanical coupling, related to dissipation and latent heat is examined by means of conducting simulations under various thermal conditions. The validity of the model is demonstrated by approaching experimental results of complex thermomechanical loading paths of SMA structures.

INTRODUCTION

In this work, a new 3D phenomenological model for SMAs is presented. A physical interpretation of the processes occuring inside a SMA grain is intended to be approached to redefine the principles of reorientation, forward and reverse transformation. This leads to the introduction of independent scalar rate variables which drive each of the three strain mechanisms. Accordingly, a robust formalism is presented within a thermodynamical framework, and based on a Gibbs free energy potential. Each internal variable is designed to evolve linearly with respect to one of those three scalar variables.

The model is implemented based on an open-source numerical simulation library [3] to conduct simulations of complex loading paths. The material parameters are calibrated using advanced identification methods and the thermomechanical aspects of the thermodynamic modeling are examined by simulating various thermal loading paths, e.g. isothermal and adiabatic. Such thermomechanical coupling accounts for the dissipation phenomena related to the three mechanisms, namely forward and reverse transformation, and reorientation.

THERMODYNAMIC MODELING

In the framework of thermodynamic phenomenological modeling, a Gibbs free energy potential governing the whole material behavior is defined. The main internal variables selected are the martensitic volume fraction ξ and three parts of the total inelastic strain $\boldsymbol{\varepsilon^T}$, each driven by its respective inelastic mechanism. Forward transformation induces the evolution of $\boldsymbol{\varepsilon^F}$:

$$\dot{\boldsymbol{\varepsilon}}^{\boldsymbol{F}} = \dot{\xi}^F \boldsymbol{\Lambda}_{\boldsymbol{\varepsilon}}^{\boldsymbol{F}}(\boldsymbol{\sigma}) \tag{1}$$

Reverse transformation drives the evolution of $\boldsymbol{\varepsilon^R}$:

$$\dot{\boldsymbol{\varepsilon}}^{\boldsymbol{R}} = \dot{\xi}^R \left(\nearrow \frac{\boldsymbol{\varepsilon^T}}{\xi} \right) \tag{2}$$

The effect of reorientation is given by evolving $\boldsymbol{\varepsilon^{re}}$:

$$\dot{\boldsymbol{\varepsilon}}^{\boldsymbol{re}} = \dot{p}^{re} \boldsymbol{\Lambda}_{\boldsymbol{\varepsilon}}^{\boldsymbol{re}}(\boldsymbol{\sigma}, \boldsymbol{X}) \tag{3}$$

The martensitic volume fraction ξ is always found by updating the increasing (Forward) ξ^F and decreasing (Reverse) part ξ^R:

$$\dot{\xi} = \dot{\xi}^F \nearrow \dot{\xi}^R \tag{4}$$

The scalar $\dot{p}^{re}$ is the magnitude of the strain that evolves within the martensitic volume which remains intact during transformation. The quantities $\boldsymbol{\Lambda}_{\boldsymbol{\varepsilon}}^{\boldsymbol{F}}$ and $\boldsymbol{\Lambda}_{\boldsymbol{\varepsilon}}^{\boldsymbol{re}}$ are orientation tensors and depend on the direction of stresses $\boldsymbol{\sigma}$ and the history of loading, carried within the backstress $\boldsymbol{X}$.

It is clear that the three scalar rates $\dot{\xi}^F$, $\dot{\xi}^R$ and $\dot{p}^{re}$ are the driving variables of the three mechanisms. When they have zero values, the respective strains do not evolve, since the mechanisms are not activated. For forward transformation, the criteria and the evolution laws implemented in [1] are taken in mind. For reverse transformation, a suitable criterion to ensure return to zero transformation strain when all the martensitic volume is recovered. A criterion imposing kinematic hardening is considered for reorientation. The backstress $\boldsymbol{X}$ attributes the kinematic feature to the reorientation behavior.

[*]Corresponding author. Email: georges.chatzigeorgiou@ensam.eu

SIMULATION OF NON-PROPORTIONAL THERMOMECHANICAL LOADING

The validation of the model over experiments published in literature is performed. A thermomechanical loading consisting in tension, compression, torsion and temperature variation carried out on a NiTi thin-walled tube [2] has been simulated.

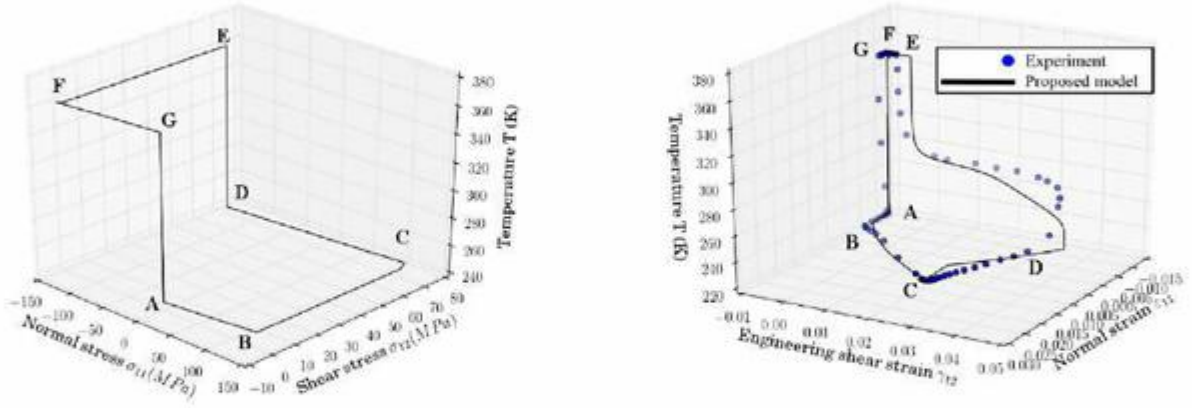

(a) Loading path

(b) Material and model response

Figure 1: Experimental results (points) and model reponse (continuous line) on the normal strain - shear strain - temperature diagram for the complex non-proportional thermomechanical loading taken from [2]

The implementation of the first law of thermodynamics has been carried out in the framework of multiple activated inelastic mechanisms. The effects of thermomechanical coupling are evident by comparing a simulation of a non-proportional loading under isotermal and adiabatic conditions. In the loading presented in Fig. 2, the initial temperature is 280K.

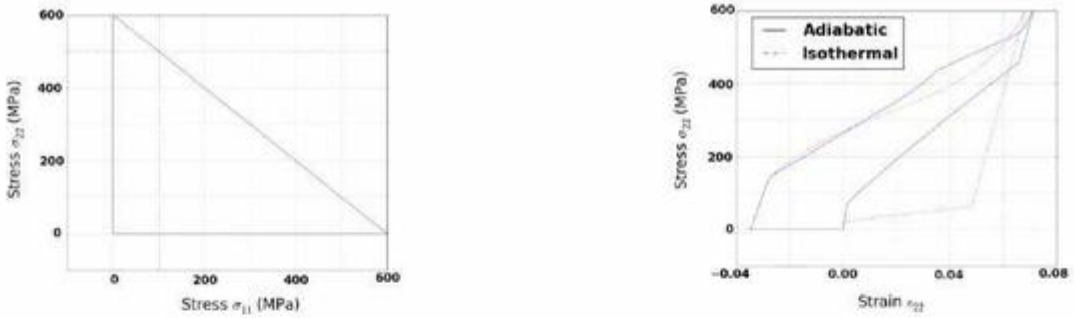

(a) Loading path

(b) Material and model response

Figure 2: Experimental results (points) and model reponse (continuous line) on the normal strain - shear strain - temperature diagram for the complex non-proportional thermomechanical loading taken from [2]

CONCLUSION

A novel thermomechanically coupled phenomenological model has been developped for SMAs. It succeeds in capturing material behavior under complex non-proportional thermomechanical loading, by taking in mind the simultaneous activation of transformation and reorientation. Its validity has been assessed in comparison with experimental results. The full implementation of the first law of thermodynamics allows the investigation of thermomechanical effects on the material response.

References

[1] Qidwai, M.A., Lagoudas, D.C.: On thermomechanics and transformation surfaces of polycrystalline NiTi shape memory alloy material. Int. J. Plast. 16, 13091343. 2000.

[2] Grabe, C., Bruhns, O.T.: Path dependence and multiaxial behavior of a polycrystalline NiTi alloy within the pseudoelastic and pseudoplastic temperature regimes. Int. J. Plast. 25, 513545. 2009.

[3] SMART+ development team: SMART+ Smart Materials Algorithms and Research Tools: A Scientific Library for the Analysis of the Thermomechanical Behavior of Heterogeneous Materials. 2012.

REMOTE BENDING CONTROL OF LIQUID CRYSTAL POLYMER BEAMS BY LIGHT INDUCED MOMENT AND SHEAR FORCES

Yang Zhang, Yue You & Yongzhong Huo[a)]
Department of Mechanics and Engineering Science, Fudan University, Shanghai, 200433 China

Summary Bending of beams made of chromic liquid crystal polymers can be remotely controlled by light illuminations and is modelled by Timoshenko beam theory due to the possible transversal shear induced by light. Both analytical solutions and finite element simulations have shown that the bending characteristics is controlled by the coupled action of opto-moment and opto-shear-force produced by light illumination. The effect of light induced shear could be very strong depending on the liquid crystal orientation and boundary conditions.

INTRODUCTION

Light induced contraction and bending have been reported and studied for crosslinked polymer materials with liquid crystal moieties and azo dyes [1,2]. The light induced actuation of such chromic liquid crystal polymers (LCPs) provides a unique means for remote controllability of smart devices. The classical Euler-Bernoulli beam theory (EBT) have been often used to study the light induced bending [3]. However, the photo-strain of LCPs is anisotropic, so a large transversal shear strain can be induced by light when the principal axes of photo-strain do not coincide with the directions of the beam axes. Thus, beam models considering shear effect such as the Timoshenko beam theory (TBT) should be applied and the light induced bending is controlled by the coupled action of opto-moment and opto-shear-forces as detailed in the following.

MODEL AND CALCULATION BASED ON TIMOSHENKO BEAM THEORY

Consider a LCP beam under light with director **n** of LC molecules as shown in Fig. 1, the photo-strain is,

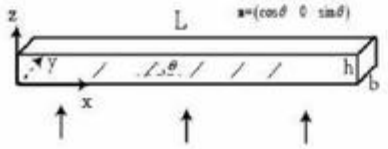

Fig. 1 LCP beam with light illumination. Unit vector **n** is the orientation of LC director

$$\begin{aligned}
&\boldsymbol{\varepsilon}^{ph} = \varepsilon_{-}^{ph}\mathbf{I} + (\varepsilon_{/}^{ph} - \varepsilon_{-}^{ph})\mathbf{n}\quad \mathbf{n}\\
&\text{With}\quad \mathbf{n} = (\cos\ ,0,\sin\ )^T\\
&\varepsilon_{xx}^{ph} = \varepsilon_{/}^{ph}((1+\nu^{ph})\cos^2\ -\ ^{ph})\\
&\gamma_{xz}^{ph} = \varepsilon_{/}^{ph}(1+\nu^{ph})\sin 2\theta
\end{aligned} \tag{1}$$

with the photo-contraction $\varepsilon_{/}^{ph} \le 0$ in //**n** and the photo-extention $\varepsilon_{-}^{ph} = -\nu^{ph}\varepsilon_{/}^{ph} \ge 0$ ($\nu^{ph} \approx 0.5$) in the perpendicular plane. Obviously, its shear component γ_{xz}^{ph} is nonzero except $\theta = 0$ or 90°, i.e. **n**//x or **n**//y. Hence, we propose to use the following model based on TBT for the light induced bending,

$$-\frac{d}{dx}\left(D_{xx}\frac{d\phi}{dx}\right)\quad K_s A_{xz}\left(\phi + \frac{dw}{dx}\right) = -\frac{dM_{xx}^{ph}}{dx} + Q_x^{ph} \quad \text{and} \quad -\frac{d}{dx}\left(K_s A_{xz}\left(\phi + \frac{dw}{dx}\right)\right) = -\frac{dQ_x^{ph}}{dx} \tag{2}$$

where the left hand sides are the standard forms of TBT as in [4]. The opto-moment $M_{xx}^{ph} = \iint_A E\varepsilon_{xx}\, z dz$ and opto-shear-force $Q_{xz}^{ph} = K_s \iint_A G\gamma_{xz}\, dA$ are shown in Fig. 2, M_{xx}^{ph} is monotonically decreasing and vanishes at $\theta_0^M = 54^\circ$, where $\varepsilon_{xx}^{ph} = 0$. However, Q_{xz}^{ph} vanishes at $\theta = 0$ and 90°, where $\gamma_{xz}^{ph} = 0$, but is nonmonotonic with a minimum at $\theta_m^Q \approx 37^\circ$.

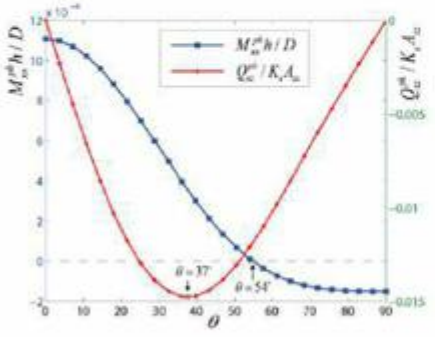

Fig. 2 Orientation dependence of opto-moment and opto-shear-force

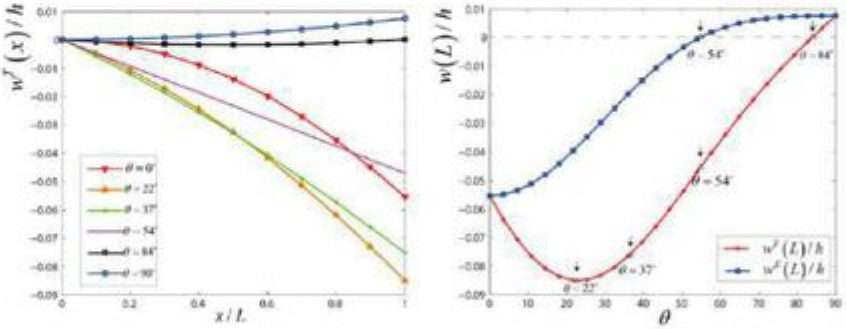

Fig. 3 Light induced deflection of cantilevers: (a) $w^T(x)$; (b) $w^T(L)$ *vs* $w^E(L)$

[a)] Corresponding author. Email: yzhuo@fudan.edu.cn

Analytical solutions for slender beams under uniform illumination

F-F ends: $w^T(x) = w^E(x) + C_1 + C_2$; **C-F ends**: $w^T(x) = w^E(x) - (M_{xz}^{ph}/K_s A_{xz})x$ with $w^E(x) = -M_{xx}^{ph}/2D_{xx}\, x^2$.

Thus, the bending curvatures are always the same for TBT and EBT. This is probably the reason why the effect of the opto-shear-force Q_{xz}^{ph} is often overlooked up to now. However, as shown in Fig. 3(a) for cantilevers, the two deflections can be quite different for **n** not parallel to x or y axis. Moreover, Q_{xz}^{ph} can produce a much larger end deflection $w^T(L)$ as shown in Fig. 3(b) and a rotation of the cross section as $\phi(x) = -w^T(x) + M_{xz}^{ph}/K_s A_{xz}$.

S-S ends: $w^T(x) = w^E(x) = M_{xx}^{ph}/2D_{xx}\, x(L-x)$ and $\phi(x) = -w^T(x) + M_{xz}^{ph}/K_s A_{xz}$;

C-S ends: $w^T(x) = w^E(x) + \alpha\left(Q_{xz}^{ph} - 3M_{xx}^{ph}\right)(L\,x(L-x) - L(L-x))$ with $w^E(x) = M_{xx}^{ph}/4D_{xx}L\,x(L-x)$

Although for S-S ends, TBT deflections are the same as EBT, the bending characteristics are very different for C-S ends beams. Fig. 4(a) depicts that for $\theta < \theta_0^M = 54^\circ$, $w^E(x)$ is positive and has a maximum at x=2L/3. For $\theta > \theta_0^M$, it becomes negative and has a minimum at x=2L/3. However, due to the opto-shear-force Q_{xz}^{ph}, $w^T(x)$ have two extremes for $0 < \theta < \theta_M^0 \approx 19^\circ$ and always has a negative minimum for $\theta > 0$ as in Fig. 4(b). Fig. 4(c) depicts the extreme values vs θ, EBT predicts a maximal light induced deflection at $\theta = 0$, i.e. **n//x** as its behavior is determined by M_{xx}^{ph}. However, much larger deflections are predicted by TBT due to the combined actions of M_{xx}^{ph} and Q_{xz}^{ph}. Therefore, an orientation of LC director **n** not along the beam axes can be very beneficial to maximize the light induced deflection.

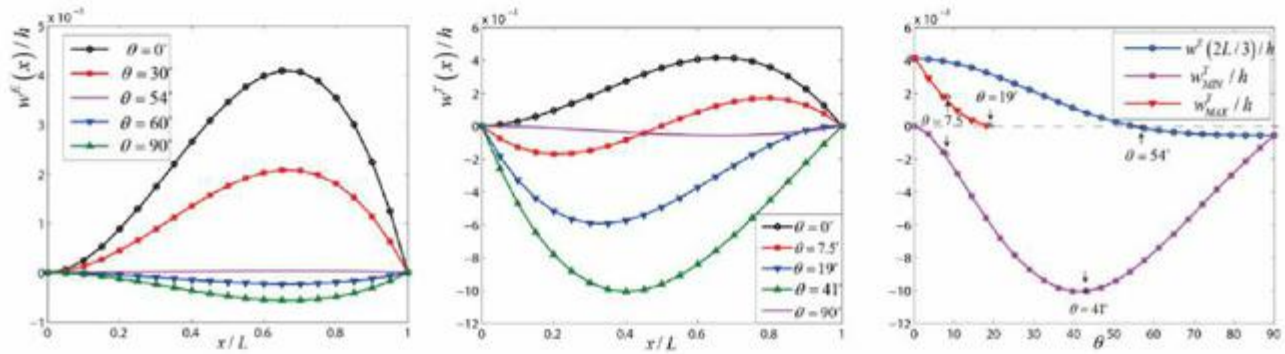

Fig. 4 Deflections for beam with one end clamped & the other simply supported, (a) EBT; (b) TBT; (c) Extreme values vs director angle

CONCLUSIONS

Timoshenko beam theory is applied to model the light induced bending of chromic liquid crystal polymer beams. When the liquid crystal molecules is not oriented along the beam axially or vertically, the light induced shear strain component is nonzero and can produce a large opto-shear-force in addition to opto-moment. For beams with two ends free and two ends simply supported, the light induced bending deflections are not affected by the opto-shear-force. However, for cantilever beams, the deflection can be much larger due to the coupled action of opto-moment and opto-shear-force. For beams with one end clamped and the other simply supported, the bending shapes are affected very strongly by the opto-shear-force. The results are confirmed by three-dimensional finite element simulations. Thus, the bending shapes of slender beams made of chromic liquid crystal polymers can be remotely controlled through light illumination. And beam models considering shear deformations should be applied in place of the classical beam theory to study the light induced bending behavior.

ACKNOWLEDGEMENT

The authors thank the support of the National Natural Science Foundation of China (No. 11461161008, 11272092).

References

[1] Finkelmann H., Nishikawa E., Pereira G.G., Warner M.: Phys Rev Lett 87:015501, 2001.

[2] Yu Y., Nakano M., Ikeda T. Nature 425:145, 2003.

[3] Warner M., Mahadevan L. Phys Rev Lett 92:134302, 2004.

[4] Wang CM, Reddy, JN, Lee CH, Shear deformable beams & plates, Elsevier, 2000

A COMPLIANT ORTHOPLANAR SPRING BASED PIEZOELECTRIC VIBRATION ENERGY HARVESTER

Sharvari Dhote *and Jean Zu

Deparment of Mechanical and Industrial Engineering, University of Toronto, Toronto,Ontario, Canada

Summary This paper presents the modeling and experimental analysis of a broad bandwidth piezoelectric harvester. The proposed harvester consists of a compliant orthoplanar spring (COPS) with piezoelectric plates attached at three different locations. The dynamic behavior of the harvester with a mass at the center is modeled numerically and characterized experimentally. The prototype is manufactured and experimentally investigated to study the effect of a mass on the bandwidth. The simulation and experimental results are in good agreement. The proposed PVEH has enhanced the performance of the energy harvester in terms of a wide frequency bandwidth and a high-voltage output under base excitations.

INTRODUCTION

Vibration-based energy harvester (VEH) provides a promising solution of maintenance free power to wireless sensor nodes. In the last decade, major research efforts have been focused on the design and development of novel harvesters generating a plethora of literature [1]. Ambient vibrations have wideband characteristics. The narrow bandwidth of resonance-based linear devices hinder commercialization of this technology. Nonlinear geometric structures are promising for energy harvesting because of the possibility to design a smaller device[1]. Various nonlinear geometric designs were investigated in the literature [2, 3].

Most of the multi-frequency VEHs proposed in the literature have used a close linear multiple modes to expand the bandwidth of an energy harvester. This paper investigates the piezoelectric vibration-based energy harvester (COPS-PVEH) vibration behavior through experiments and modeling.

DYNAMIC MODELING

In this paper, the equivalent circuit system is used to model and analyze the dynamic behavior of the designed harvester. The equations governing the motion of the COPS-PVEH are defined as follows:

$$M\ddot{X} + C\dot{X} + k_1 X + k_3 X^3 + \theta V = \nearrow M\ddot{Z}, \tag{1}$$

$$C_p\dot{V} + \frac{V}{R_l} \nearrow \theta\dot{X} = 0, \tag{2}$$

where $\ddot{Z} = Acos(\omega t)$ is input base acceleration and over dots describe differentiation with time. Here X represents the displacement of an inertial mass M, C is a linear viscous damping constant, k_1 and k_3 are the linear and nonlinear spring stiffness, θ represents the linear piezoelectric coupling coefficient, V is the voltage across the load resistance R_l for the piezoelectric harvesting part, and C_p refers a capacitance of the piezoelectric material. Eqs. 1 and 2 are converted to the non-dimensional governing equations. The ordinary differential equations are numerically solved using the Matlab ode45 solver.

EXPERIMENTAL SETUP AND PROTOTYPE

This section describes the experimental setup used for characterizing the vibration behavior of the COPS-PVEH. The proposed harvester consists of a COPS with piezoelectric plates attached at different locations. The spring is clamped between two aluminum rings. The diameter of the device is ϕ 52 $\times 10^{-3}$ m and thickness 5×10^{-3} m. The piezoelectric plate (PZT-5H) of $8 \times 5 \times 0.3$ mm^3 size with a wrap-up electrode is attached to the structure using a super glue. Figure 1(b) shows the piezoelectric plates attached to the prototype sample at three locations, and named as the end piezoelectric (EP) position, the middle piezoelectric (MP) position, and the center piezoelectric (CP) position. Figure 1(a) shows the experimental setup with the COPS-PVEH prototype mounted on a shaker. The designed harvester is clamped on the electrodynamic shaker, which provides a harmonic base excitation. The excitation signal is measured using an accelerometer. The electrical output voltage data are obtained using the Tektronix 3014 oscilloscope.

*Corresponding author. Email: sharvari.dhote@mail.utoronto.ca

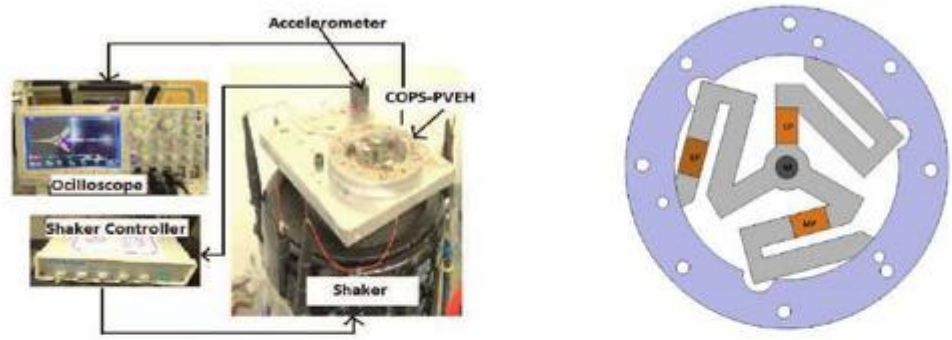

(a) (b)

Figure 1: (a) Experimental set-up and (b) designed prototype used to test the COPS-PVEH.

RESULTS

This section compares the simulation and the experimental results of the developed harvester. The frequency sweeps are carried out by increasing and decreasing the excitation frequency at a constant sweep rate of 0.5 Hz/s under a particular acceleration level. The prototype was tested by adding a single circular mass of 5×10^{-3} kg in the center and voltage outputs was measured at the EP position under 0.2g, 0.4g, 0.6g, and 0.8g excitations. Figure 2(a) shows the voltage-frequency response during the forward sweep experiment. The result shows the hardening nonlinearity and a distinct jump phenomena for the EP position. In the first mode, a duffing effect is observed due to large deflection of three fixed guided beams of the spring. This resulted in a wider frequency bandwidth. The derived governing equation of motion is a Duffing equation and model results are presented in figure 2(b). The voltage output at the EP position is compared between the experiment and simulation. The numerical model well predicted the frequency bandwidth, a jump frequency and the amplitude response at the EP position. The first vibration mode is also in closed agreement with the experiments.

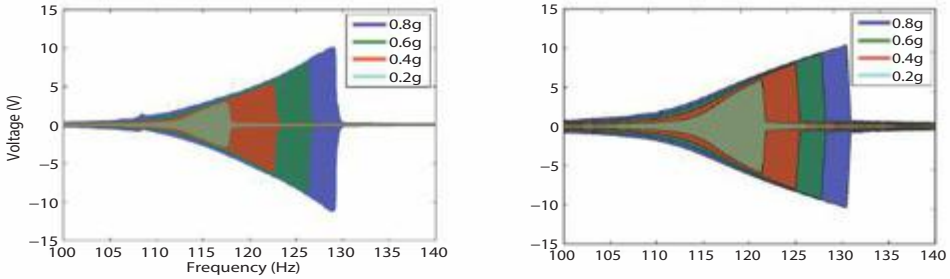

(a) (b)

Figure 2: Comparison of the open-circuit voltage response of the sample with an addition of 0.5×10^{-3} kg circular mass at the center under 0.2g, 0.4g, 0.6g, and 0.8g base excitations for the EP position (a) experiment (b) simulation.

CONCLUSIONS

This paper presents a model and experimental result for a wideband nonlinear compliant orthoplanar piezoelectric vibration-based energy harvester. It operates under a weak low-frequency excitations (<150 Hz). With one center mass, a typical hardening nonlinear response is observed. The developed model could predict a frequency jump, amplitude and resonance frequency of the prototype accurately. The COPS-PVEH has a wide bandwidth and a high-voltage output due to its unique compliant geometry design.

References

[1] Harne R.L., Wang K.W.:A review of the recent research on vibration energy harvesting via bistable systems.Smart materials and structures 22(2):023001,2013.

[2] Rezaeisaray M.,El Gowini M., Sameoto D., Raboud D, Moussa W.:Low frequency piezoelectric energy harvesting at multi vibration mode shapes. Sen. and Act. A: Physical 228:104-111,2015.

[3] Su W., Zu J., Zhu Y.: Design and development of a broadband magnet-induced dual-cantilever piezoelectric energy harvester. J. of Int. Mat. Sys. and Struct. 25(4):430-442,2013.

[4] Dhote S., Zu J., Zhu Y.,A nonlinear multi-mode wideband piezoelectric vibration-based energy harvester using compliant orthoplanar spring.App. Phy. Letters 106(16):163903,2015.

INFLUENCE OF PHASE TRANSFORMATION ANISOTROPY ON TRANSFORMATION SURFACE AROUND A CRACK TIP

Etienne Patoor[1,2,a)], Guillaume Mohara[1], Dimitris Chatziathanasiou[3],
Yves Chemisky[3], George Chatzigeorgiou[3] & Fodil Meraghni[3]
[1]*School of Mechanical Engineering, Georgia Institute of Technology, GT-Lorraine, Metz, France*
[2]*UMI 2958, Georgia Tech-CNRS, Metz, France*
[3]*Arts et Métiers Paris Tech, LEM3 UMR 7239 CNRS, Metz, France*

Summary A transformation criterion that includes the effect of tension-compression asymmetry and texture-induced anisotropy is used to describe the size of the transformation region surrounding the tip of an edge crack in a shape memory alloy. This analysis is made within the framework of the linear elastic fracture mechanics (LEFM). Different opening modes are considered. Transformation surfaces obtained are compared with those published by Lexcellent et al. (*Int. J. Fract.* **169**: 1-13, 2011) for the isotropic case to capture the influence of transformation anisotropy for different fracture modes.

INTRODUCTION

Shape memory alloys are nowadays used in a wide range of applications developed for a variety of industrial fields. However, the necessity to better understand the interaction between cracks and stress-induced martensitic transformation is only a recent concern [1, 2]. Based on the linear elastic fracture mechanics framework, Lexcellent et al. have recently derived [1, 3] the stress field around a crack tip and have determined the phase transformation zone. They have shown that this result is dependant of the loading mode. These authors have taken into account the tension–compression asymmetry observed in SMAs and established that this asymmetry is responsible for the "peanut shape" of the transformation region in Mode 1.

Most of SMA applications are made from NiTi sheets or wires produced by rolling or by drawing. These elements are usually strongly textured. The present work aims to consider the influence of the crystallographic texture-induced anisotropy on the shape of the transformation zone using the new anisotropic transformation criterion developed by Chatziathanasiou et al. (2015) [4].

ANISOTROPIC TRANSFORMATION CRITERION

In order to take into account the texture-induced anisotropy the notion of alteration of the axes of the stress space is used as introduced by Karafillis & Boyce [5]. A new space of stress **σ*** is considered that represents a distortion of the space of real stresses. In this way the expression of the original transformation criterion is kept and Chatziathanasiou et al. [4] have proposed the following expression:

$$\Phi(\sigma) = \sqrt{J_2(\sigma^*)}\left[1 + p\Big/\frac{J_3(\sigma^*)}{J_2^{3/2}(\sigma^*)}\right]^{\frac{1}{2}} - k_\sigma = 0$$

Transformation surfaces obtained in that way are presented in figure 1 for different values of parameter p.

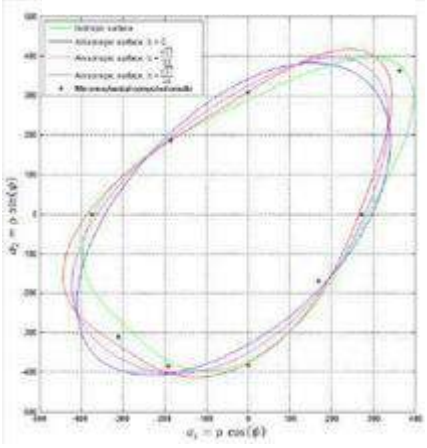

Figure 1 - Anisotropic Martensite Phase Transformation onset surface [4]

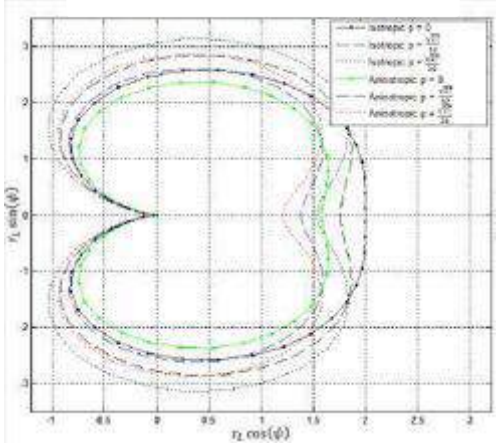

Figure 2 - Mode I, Anisotropic Martensite Phase Transformation onset surface under plane stress condition

a) Corresponding author. Email: etienne.patoor@georgiatech-metz.fr

DETERMINATION OF THE TRANSFORMATION ZONE AROUND A CRACK TIP

It is important to note that if the transformation is anisotropic we still assume that the elasticity remains isotropic. The determination of the transformation zone around a crack tip is then obtained considering the linear elastic fracture mechanics framework approach as proposed in [1]. The stress tensor $\boldsymbol{\sigma}^*$ is considered instead of the real stress tensor. The elastic stress field computed around the crack tip is investigated using the transformation criterion in order to determine the size and shape of the transformation surface. This is performed for different loading modes and different values of parameter p which characterizes the intensity of the asymmetry between tension and compression.

RESULTS

The onset zone limit for an anisotropic stress-induced transformation is determined for plane stress and plane strain conditions considering three different fracture modes. Results are compared with the isotropic ones presented in [1]. Material parameters are the same in both cases, only anisotropy differs. In Fig. 2 results for plane stress condition in Mode I are presented. Anisotropy generates a slightly smaller surface. Shape is globally conserved but it is shifted to the left. Surfaces obtained in Mode II are shown in Fig. 3. Here again, they are slightly smaller with respect to the isotropic ones, and is shifted downwards. The intersection of the three plots for a given configuration is not the same. For the isotropic case, the intersection is for $\psi = 0$, whereas it is around the (5;-1.5) coordinate for the anisotropic case. In Mode III the surface is a circular one as in the isotropic case (Fig. 4) but this surface is no longer independent of parameter p. This comes from the fact that the determinant of the anisotropic stress tensor is not equal to zero as this is the case for the isotropic one.

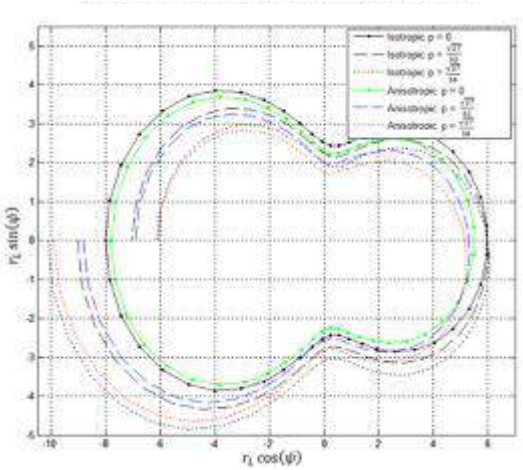

Figure 3 - Mode II, Anisotropic Martensite Phase Transformation onset surface for plane stress

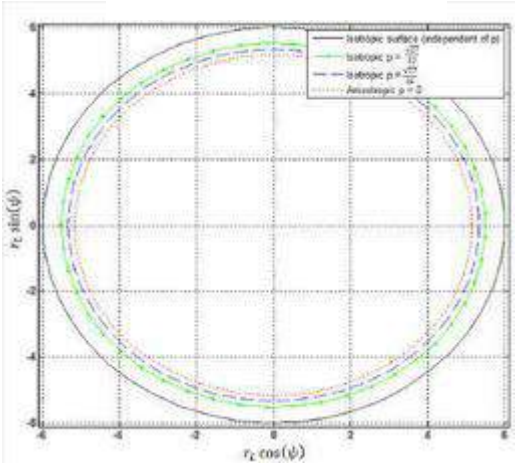

Figure 4 - Mode III, Anisotropic Martensite Phase Transformation onset surface for plane stress

CONCLUSIONS

The notion of alteration of the axes of the stress space to describe the influence of texture-induced anisotropy allows extending fracture analysis in SMAs. Prediction of the phase transformation onset zones around a crack tip is obtained for three loading modes in plane stress and plane strain conditions. It appears that anisotropic surfaces are slightly smaller than isotropic ones while still displaying the same trend. Moreover, a light but noticeable shift of theses surfaces can be observed for all modes.

References

[1] Lexcellent C., Laydi M.R., Taillebot V.: Analytical prediction of the phase transformation onset zone at a crack tip of a shape memory alloy exhibiting asymmetry between tension and compression. *Int. J. Fract.* **169**: 1-13, 2011.

[2] Baxevanis T., Parrinello A.F., Lagoudas D.C.: On the fracture toughness enhancement due to stress-induced phase transformation in shape memory alloys. Int. J. Plast. **50**: 158–169, 2013.

[3] Lexcellent C., Thiebaud F.: Determination of the phase transformation zone at a crack tip in a shape memory alloy exhibiting asymmetry between tension and compression. *Scripta Materialia* **59**: 321-323, 2008.

[4] Chatziathanasiou D., Chemisky Y., Meraghni F., Chatzigeorgiou G., Patoor E.: Phase transformation of anisotropic shape memory alloys: Theory and validation in superelasticity. *Shap. Mem. Superelasticity*, DOI 10.1007/s40830-015-0027-y, 2015.

[5] Karafillis A.P., Boyce M.C.: A general anisotropic yield criterion using bounds and a transformation weighting tensor. *J. Mech. Phys. Solids* **41**, (12): 1859-1886, 1993.

THE EFFECT OF SURFACE WAVINESS ON CONTACT BEHAVIORS IN MULTIFERROIC STRUCTURES

Yue-Ting Zhou[1] **Zheng Zhong** [1a)]

[1]*School of Aerospace Engineering and Applied Mechanics, Tongji University, Shanghai 200092, P R China*

Summary This work establishes a sliding rough interface model involving the multiferroic structures comprising of piezoelectric materials and magneto-electro-elastic materials with anisotropy. The interface is sliding at a constant velocity with the Galilean transformation used to address it. The partial contact between the two wavy surfaces of anisotropic piezoelectric materials and anisotropic magneto-electro-elastic materials is characterized as a sinusoidal function. Operator theory is applied to obtain the general solutions of the governing equations related to smart structures. Figures are drawn to reveal the influences of ket parameters, such as the gap at the crests of the wavy surfaces, on the rough contact behaviors.

INTRODUCTION

It is found that a wide class of crystals and emerging composite materials will possess simultaneously piezoelectric, piezomagnetic and magneto-electric effects, which are thereby classified as multiferroic solids [1]. These multiferroic materials have the ability of energy conversion among electric, magnetic and mechanical fields. In the practical engineering, multiferroic materials are often embedded as patches or, more conveniently, as embedded layers in multilayered structures. The roughness [2, 3] often arises among interfaces in multilayered structures from machining, wear, chemical polishing at different scales. Understanding the interaction of real rough surfaces in contact becomes an urgent issue in designing and applying multiferroi devices. There was little work on rough surface contact problem involving multiferroic materials due to the mathematic difficulty brought by the rough surface and the multi-field coupling.

PROBLEM DEFINITION

This study conducts an exact analysis of a dynamic rough surface contact problem of the multiferroic structures made of piezoelectric materials with superscript 1 and magneto-electro-elastic materials with superscript 2, between which the interface moves smoothly. Two groups of uniform pressures p at infinity make the two surfaces of anisotropic piezoelectric materials and anisotropic magneto-electro-elastic materials in partial contact. After using the Galilean transformation, the partial contact between the two wavy surfaces of anisotropic piezoelectric materials and anisotropic magneto-electro-elastic materials is described as

$$\frac{\partial\left[w^{(1)}(x,0)-w^{(2)}(x,0)\right]}{\partial x}=\frac{1}{2}g_0\sin(x),\qquad 0\le|x|<h_0, \tag{1}$$

where w denote the normal displacement, g_0 is the gap at the crests of the wavy surfaces, and h_0 is the half-length of the contact region.

Based on the general solutions of the anisotropic multiferroic governing equations and exact solution of the reduced dual series equations, the half-length of the contact region h_0 and the surface normal stresses can be given explicitly as follows:

$$h_0=\frac{L_0}{\pi}\operatorname{acos}\left(1-\frac{2p}{F_c}\right), \tag{2}$$

[a)] Corresponding author. Email: zhongk@tongji.edu.cn.

$$\sigma_{zz}^{(1)}(x,0)=\sigma_{zz}^{(2)}(x,0)=-\sqrt{2}F_c\cos\left(\frac{\pi x}{2L_0}\right)\sqrt{\cos\left(\frac{\pi x}{L_0}\right)-\cos\left(\frac{\pi h_0}{L_0}\right)},\quad 0\le|x|<h_0, \tag{3}$$

where $2L_0$ denote sinusoid wave length, and F_c is the critical loading to reach the full contact.

Numerical results are provided to investigate the effect of the gap g_0 at the crests of the wavy surfaces on various objectives (Fig. 1).

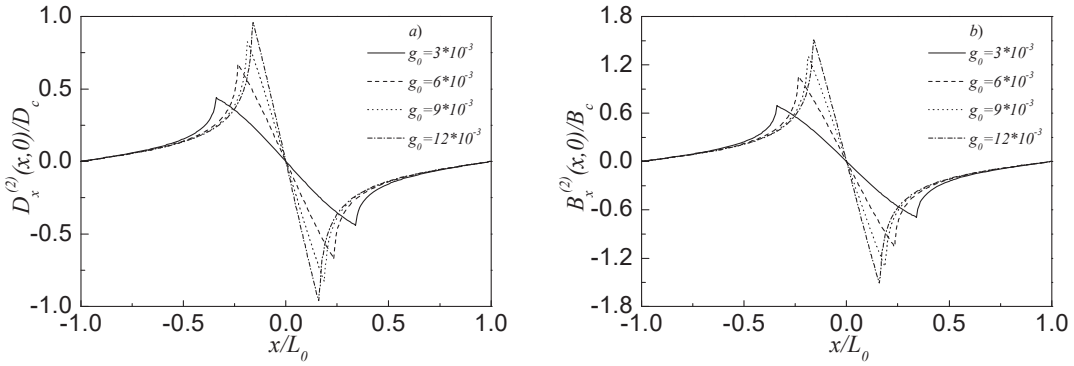

Fig. 1. The effect of the gap g_0 on: a) surface electrical displacement $D_x^{(2)}(x,0)/D_c$ with $D_c=e_{33}^{(2)}F_{c0}/c_{33}^{(2)}$, and b) surface magnetic induction $B_x^{(2)}(x,0)/B_c$ with $B_c=h_{33}^{(2)}F_{c0}/c_{33}^{(2)}$.

CONCLUSIONS

This article performs the dynamic periodic contact analysis involving the smart multiferroic structure comprising of anisotropic piezoelectric materials and anisotropic magneto-electro-elastic materials. The numerical tests have shown some interesting results, for example, an increasing of the gap at the crests of the wavy surfaces makes the largest magnitude bigger for both the surface electrical displacement and the surface magnetic induction.

References

[1] Nan C.W.: Magnetoelectric Effect in Composites of Piezoelectric and Piezomagnetic Phases. Phys Rev B **50**:6082-6088, 1994.

[2] Bhushan B.: Contact Mechanics of Rough Surfaces in Tribology: Multiple Asperity Contact. Tribo Lett **4**:1-35, 1998.

[3] Persson B.N.J.: Contact Mechanics for Randomly Rough Surfaces. Surf Sci Rep **61**:201-227, 2006.

THE DEFORMATION MECHANISMS OF NEW CHIRAL STRUCTURES

Yunyao Jiang & Yaning Li[a)]
Department of Mechanical Engineering, University of New Hampshire, Durham, NH03824, USA

Summary New chiral structures were designed to enlarge the auxetic effects and create new deformation mechanisms upon external stimuli. A rotational-spring-rigid-rod model was developed to predict the auxetic effects of the new chiral structures. Four new structures from this family were reported in this paper: (1) a regular chiral structure, (2) a chiral structures with hard core, (3) a chiral structure with soft hinges, and (4) a chiral structure with auxetic core. Finite element (FE) simulations and mechanical experiments on 3D-printed specimens were performed to study the mechanics of these structures. The results show that compared with the regular chiral structure, all other three new structures have a smaller Poisson's ratio. The smaller Poisson's ratio is attributed to larger rotational ratio between active and passive ribs in the chiral cells. More interestingly, the chiral structure with auxetic cores showed a unique sequential cell-opening mechanism.

Introduction

Due to the remarkable mechanical properties of auxetic chiral structures, there is a strong interest in the theoretical modelling and reformulation of several aspects of mechanics of chiral lattice. This theoretical interest must be accompanied by the design and fabrication of new chiral structures, so that the mathematical parameters in the theoretical model can be link to the physical parameters in real materials. The calibration of the parameters and the validation of the theoretical model are largely constrained by two facts that: (1) only a few chiral structures available in database, and (2) the limited capability of the traditional manufacturing technology on fabricating complex structures. To reduce the two constrains, efforts were made in this investigation by designing a new family of auxetic chiral structures, using 3D printing to fabricate the designs, and performing mechanical experiments.

The new family of auxetic chiral structures were inspired by the pioneering work on the two existing chiral structures: (1) a triangular lattice with central rings [1], and (2) the 'missing rib model' [2, 3]. The former one was first proposed by Prall and Lakes [1], and generated many interesting research [3-7] since then. However, due to the existence of middle rings, the deformation of this chiral structure is limited. Compared with the former one, the latter 'missing rib model' is more fundamental, more flexible to vary and have potential to accommodate larger deformation. Therefore it was chosen to serve as a base structure to develop the present family of chiral structures. The auxetic effects of this type of chiral structure were due to the rotational response of the chiral cells when subjected to uni-axial tension or compression.

This new family of auxetic chiral structures are robust and have deterministic chirality. Also, the behaviours of them can be well-controlled by the structures and material composition. They have potential broad applications in lightweight designs, energy absorption, smart biomedical materials and actuating devices, metamaterials and mechano-adaptive composites which provide multi-mission capability for air, space and land assets.

A ROTATIONAL-SPRING-RIGID-ROD MODEL FOR A CHIRAL CELL

The geometry of a typical chiral cell is shown in Fig. 1(left), in which each rib is perpendicular to the neighbouring ribs, and the length of all ribs are the same *a*. When the cell is subjected to uni-axial compression at *A* and *D*, the active ribs *B*-*O*-*C* will rotate clockwise with an angle φ_1, the ribs *F*-*O*-*G* will rotate passively with an angle φ_2. Since the auxetic effects of the chiral cells are due to the rotation of the ribs, the Poisson's ratio is directly related to the rotational ratio between the active ribs and passive ribs. In this model, the rotational ratio is defined as $R_r = \frac{\varphi_2}{\varphi_1}$. The ribs are assumed to be rigid.

To model the relative rotational flexibility of the ribs, one rotational spring with rotational stiffness K_ζ is introduced to the center *O*, and four rotational springs with rotational stiffness K_θ are introduced to corners *B*, *C*, *F*, and *G*. Thus the chiral cell becomes a system of rotational springs and rigid rods.

From the kinematics and equilibrium of the rotational-spring-rigid rod system, The Poisson's ratio ν of the cell can be derived as a function of the stiffness ratio between the rotational springs as $\nu = -\frac{K_\zeta/K_\theta}{K_\zeta/K_\theta+8}$. This relationship is plotted in Fig.1 (right), it can be seen that when the stiffness ratio increases, the Poisson's ratio decrease, and when the stiffness ratio changes from zero to infinity, the Poisson's ratio changes from zero to -1.

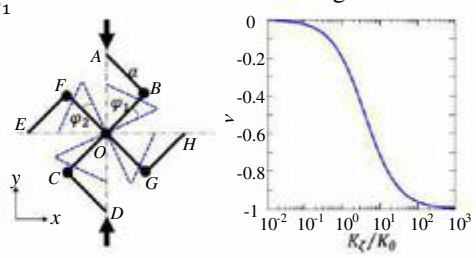

Fig.1 The rotational-spring-rigid-rod model for a chiral cell: the geometry (left), and the prediction on Poisson's ratio (right).

CHIRAL CELLS WITH HARD CORES AND SOFT HINGES

The analytical model shows the concept that larger auxetic effects (i.e. smaller Poisson's ratio) can be obtained by increasing K_ζ/K_θ. Based on this concept, two new chiral cells with larger auxetic effects were designed, as shown in Fig.2a: (1) a chiral cell with a hard core (to increase K_ζ), and (2) a chiral cell with soft hinges (to decrease K_θ).

a) Corresponding author. Email: yaning.li@unh.edu.

2D plane-strain Finite Element (FE) models were set up for three chiral cells: regular chiral cell (cell 1 in Fig.2a), chiral cell with core (cell 2 in Fig.2a), and chiral cell with soft hinges (cell 3 in Fig.2a). FE simulations were performed in ABAQUS 6.13 under uni-axial compression along y direction. Periodic boundary conditions (PBC) were applied on all four edges of each cell. Hyperelastic Mooney-Rivlin models were used for two materials in the FE models. The Poisson's ratio ν and ration ratio R_r were plotted as the function of the compressive strain, as shown in Figs. 2b and 2c.

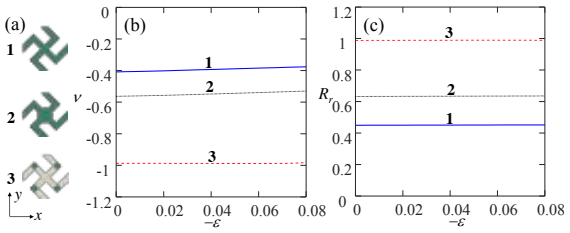

Fig. 2 (a) FE models, (b) Poisson's ratio, and (c) rotational ratio of three chiral cells.

It can be seem that the regular chiral cell gives a Poisson's ratio of ~-0.4, while the Poisson's ratios of the two new chiral structures are smaller than that of the regular one. The Poisson's ratio of the chiral cell with core is ~-0.58, and that of the chiral cell with soft hinges is ~-1. Fig.2c shows that the cells with smaller Poisson's ratio have a larger rotational ratio between the active and passive ribs.

A CHIRAL CELL WITH AUXETIC CORES

To further tailor the shape of the core, a new chiral structure with auxetic core was designed, and the representative volume element (RVE) of it is shown in Fig.3a. 2D FE simulations were performed for the RVE with PBCs under uniaxial tension. The ribs AB and CD are stiffened to avoid local buckling.

The Poisson's ratio of this new structure was compared with the regular chiral cell in Fig. 3b. The new structure shows a Poisson's ratio ~-0.58. The non-dimensional openings (current over the initial cell size) of both cells $R_d = d_i/d_{io}, (i = 1 \text{ or } 2)$ were plotted in Fig.3c. Interestingly, Fig.3c shows a unique sequential cell opening mechanism: step1, larger cells open, core cells only rotate; step 2, smaller cells open.

This new structure can be used to design smart medical bandage for sequentially releasing medicine particles with different sizes upon the degree of tension caused by different levels of inflammation.

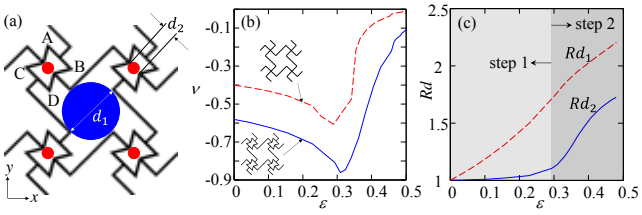

Fig. 3 (a) the new chiral cell with auxetic cores, (b) Poisson's ratio vs. tensile strain, (c) curves for sequential cell-opening.

3D PRINTING AND MECHANICAL EXPERIMENTS

The chiral structures designed were fabricated via a multi-material 3D printer (Objet, Connex 260). Mechanical experiments were performed to study the deformation mechanism of them. Digit Image Correlation (DIC) was used to quantify the strain in ribs during the overall deformation. FE simulations of the real 3D printed specimens were performed and compared with the experiments. Consistent results were obtained from FE simulations and mechanical experiments.

Fig.3 (left) shows the 3D printed specimens of the regular chiral structure, which was printed as TangoPlus materials in the 3D printer. The stress-strain behaviour of this material can be well captured by the Mooney-Rivlin model. Fig.3 (right) shows the DIC strain contour of this specimen under the overall strain of -10%. It can be seen that in most parts of the rib, the local strain is close to zero or much smaller than the overall strain. The strain mainly concentrated at the corners. This shows that the assumptions of the analytical model are reasonable.

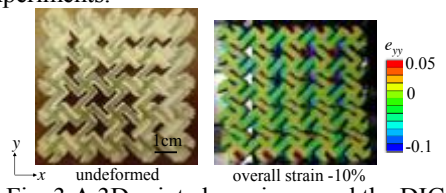

Fig. 3 A 3D printed specimen and the DIC results of it.

CONCLUSIONS

New chiral structures were designed based on the concept provided by an analytical rotational-spring-rigid-rod model. The deformation mechanisms of them were explored via 2D FE simulations and mechanical experiments on 3D printed specimens. The new chiral structure with a circular hard core was proved to have a Poisson's ratio of -0.58, and the one with soft hinges has Poisson's ratio close to -1. Compared with the regular chiral structure, the third new chiral structure with auxetic core not only provides a smaller Poisson's ratio (~-0.58), but also shows a unique sequential cell-opening mechanism. Those new chiral structures were proved to have robust auxetic effects and deterministic chirality. The new chiral structures can be used to design smart composites and actuating devices with applications in medical bandage for drug delivery, cellular camouflage, and sensors to respond to external stimuli.

References

[1] Prall D. and Lakes R. S.: Properties of a Chiral Honeycomb with a Poisson's Ratio of ν =−1. *Int. J. Mech. Sci.* **39**, 305–314, 1997.

[2] Smith C. W., Grima J. N. and Evans K. E.: A Novel Mechanism for Generating Auxetic Behaviour in Reticulated Foams: Missing Rib Foam Model. *Acta. Mater.* **48**, 4349-4356, 2000.

[3] Gaspar N., Ren X. J., Smith C. W., Grima J. N. and Evans K. E.: Novel Honeycombs with Auxetic Behaviour. *Acta. Mater.* **53**, 2439-2445, 2005.

[4] Spadoni A. and Ruzzene M.: Elasto-Static Micropolar Behavior of a Chiral Auxetic Lattice. *J. Mech. Phys. Solids* **60**, 156-171, 2012.

[5] Liu X. N., Huang G. L. and Hu G. K.: Chiral Effect in Plane Isotropic Micropolar Elasticity and Its Application to Chiral Lattices. *J. Mech. Phys. Solids* **60**, 1907-1921, 2012.

[6] Tee K. F., Spadoni A., Scarpa F. and Ruzzene M.: Wave Propagation in Auxetic Tetrachiral Honeycombs. *Journal of Vibration and Acoustics* **132**, 031007, 2010.

[7] Chen Y., Liu X. N., Hu G. K., Sun Q. P. and Zheng Q. S.: Micropolar Continuum Modelling of Bi-dimensional Tetrachiral Lattices. *Proc. R. Soc. A* **470**, 20130734, 2014.

PREDICTING THE CONSTITUTIVE RESPONSE OF SHAPE MEMORY ALLOYS ON THE BASIS OF COMPOSITION AND HEAT TREATMENT

Dimitris C. Lagoudas, Austin Cox, and Theocharis Baxevanis
Department of Aerospace Engineering, Texas A&M University, College Station, TX 77843-3409, USA

Summary A predictive microscale-informed model that takes into account the precipitate-shape memory performance relations and allows for the evaluation of the effective thermomechanical response of precipitated Ni-rich NiTi shape memory alloys on the basis of composition and heat treatment is presented. The model considers the structural effect of the precipitates (coherency stresses due to the lattice mismatch between the precipitates and the matrix material and precipitate volume fraction), as well as the effect of the Ni-concentration gradient in the matrix, resulting from Ni-depletion during precipitate growth. The predictive capability of the model is tested against experimental data obtained from $Ni_{50.7}Ti$ (at. %) that has been heat treated under different conditions and good agreement is shown.

INTRODUCTION

Near-equiatomic NiTi Shape Memory Alloys (SMAs) exhibit a reversible diffusionless solid to solid transformation from the high temperature phase B2 (austenite) to the low temperature phase B19′(martensite). Ni-rich near-equiatomic NiTi SMAs have received considerable attention because the phase transition temperatures can be adjusted through the Ni content. For many NiTi alloys, the material is subjected to solution annealing and subsequent aging to form a metastable stochiometric phase, Ni_4Ti_3, which precipitates coherently from the B2 phase. These precipitates significantly influence the martensitic transformation of NiTi due to the following important factors: the stress state around the precipitates and the Ni depletion in the matrix close to the precipitates. The stress field surrounding Ni_4Ti_3 precipitates affects the formation of the B19′ phase. Additionally, the local martensitic transformation temperature is strongly affected by the variation in Ni concentration in the matrix due to precipitation.

In the current work, the thermomechanical response of Ni-rich near-equiatomic NiTi SMAs is analyzed using Representative Volume Elements (RVEs) and validated with experimental results. The analysis take into account all the aforementioned precipitation effects.

PROBLEM FORMULATION & COMPUTATIONAL PROCEDURES

RVEs generated with random distributions of precipitates shaped as oblate spheroids with an assumed aspect ratio are used to approximate the microstructure of SMAs. An estimate of the precipitate volume fraction is required while constructing RVEs. This is calculated by a series of steps relating experimental data of pure and aged NiTi materials based on time–temperature–martensite transformation (TTT) maps (Figure 3b) and the phase transition temperatures of highly pure "solutionized" NiTi materials given by Frenzel et al. [1], as explained in [2].

The main aspects of the numerical analysis once the RVEs are constructed are briefly discussed below.

- **Coherency** – Eigenstrains corresponding to the lattice mismatch between the precipitates and the austenite phase are imposed on the precipitates to capture the coherency stress and strain fields.

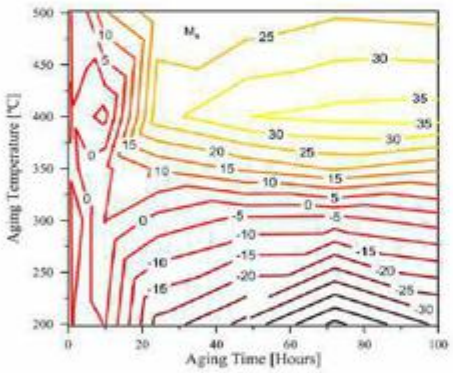

Figure 1: Contour plot relating martensitic transformation start temperature, M_s, to aging time and aging temperature for $Ni_{50.7}Ti$ alloy. Each contour represents a line of constant M_s.

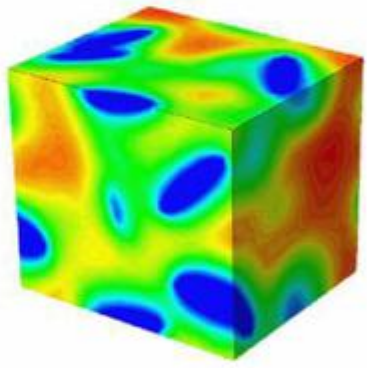

Figure 2: Diffused RVE showing periodic variation in Ni-content.

*Corresponding author. Email: lagoudas@tamu.edu

- **Ni-Distribution from Ni-Diffusion** – The Ni-concentration field in the RVE is calculated assuming Fickian's diffusion from the matrix through the precipitate boundaries. Starting with the initial concentration of Ni in the matrix, the Ni form the matrix is allowed to diffuse through the precipitate boundaries until an equivalent amount corresponding to the precipitate volume fraction is diffused.
- **Analysis of RVEs** – The obtained microstructure is subjected to thermomechanical loading paths under periodic boundary conditions to allow for the smallest necessary domain for extracting the effective response as the average response of different realizations of the microstructure. The precipitates are assumed elastic and non-transforming, whereas the matrix follows a constitutive law for SMAs with variable phase transition temperatures corresponding to the Ni-content distribution.

COMPARISON TO EXPERIMENTAL RESULTS

The predictions of the strain–temperature response of the thermally cycled $Ni_{50.7}Ti$ material aged at 300°C for 100hrs at 350°C for 48hrs under bias load levels of 150 and 200MPa are compared against experimental data in Figs 6 and 7. The predictions are able to reproduce quantitatively many of the precipitation-induced changes in the thermomechanical response. These include changes in transformation temperatures due to matrix compositional change and applied stress, increases in the width of transformation intervals (M_s-M_f), and reduction in transformation strain. The slopes of the predicted strain–temperature plots are lower than experimentally observed, *i.e.*, higher transformation hardening than observed. The observed discrepancy can be attributed to the differences in the detwinning behavior of compound twins and type II twins in martensite; the model does not capture the transition from type I and type II martensite twin formation in the solutionized NiTi SMAs to mostly (001)M type compound twin formation and thus the associated changes in the thermomechanical responses in precipitation hardened NiTi SMAs. In overaged cases, where the Ostwald ripening drastically reduces the precipitate surface to volume fraction ratio, the effect of compositional gradients becomes less prevalent and the matrix can be considered to be essentially homogeneously transforming in a very small temperature interval.

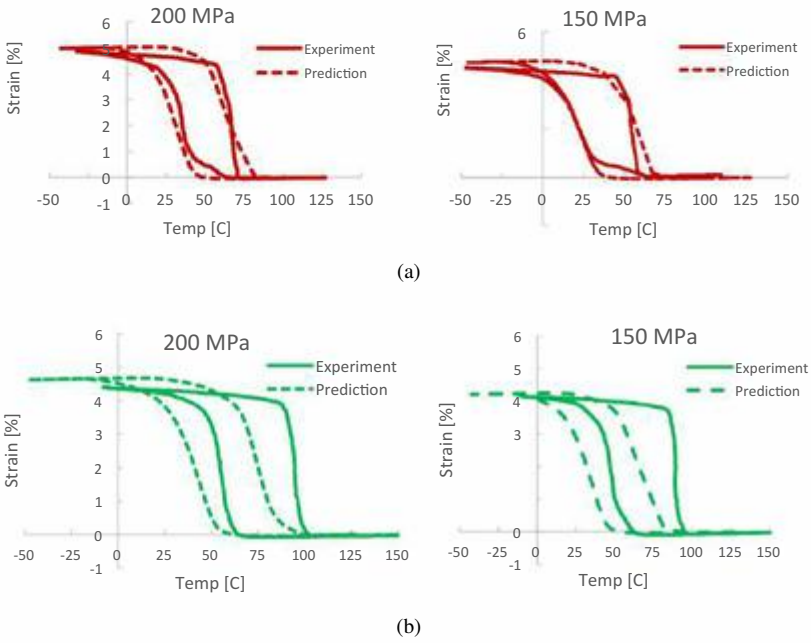

Figure 3: Comparison of predicted and experimentally determined isobaric thermomechanical responses of Ni50.7Ti SMA material (a) aged at 300°C for 100hrs, and (b) at 350°C for 48hrs.

CONCLUSIONS

A model for predicting the effective thermomechanical response of aged near-equiatomic Ni-rich NiTi SMAs on the basis of composition and heat-treatment conditions using a microscale-informed model is developed which in principle is transferable to other SMA systems. The model considers both the structural and chemical effects of the Ni_4Ti_3 precipitation process, *i.e.*, precipitate volume fraction, differences in elastic properties with the matrix, coherency stresses due to the lattice mismatch between the precipitates and matrix material, and Ni-distribution resulting from Ni-depletion during precipitate growth. The predicted overall effective thermomechanical response is shown to be in good agreement with experiments for initial composition $Ni_{50.7}Ti$ and two different heat treatments which result in relatively low precipitate volume fractions.

References

[1] Frenzel J., George E.P., Dlouhy A., Somsen C.M., Wagner F.-X., Eggeler E.: Influence of Ni on martensitic phase transformations in NiTi shape memory alloys. Acta Mat. 3444–3458, 2010.

[2] Cox A., Franco B., Wang S., Baxevanis Th., Karaman I., Lagoudas D.C.: Predictive modeling of the constitutive response of precipitation hardened Ni-rich NiTi SMAs. Submitted.

MODELING FERROMAGNETIC AND MULTIFERROIC CONSTITUTIVE BEHAVIOR BASED ON A CONDENSED METHOD (CM)

Stephan Lange [*1] and Andreas Ricoeur[1]

[1] *Chair of Engineering Mechanics / Continuum Mechanics, Institute of Mechanics, University of Kassel, Germany*

Summary Due to the multifunctional applicability, smart materials are of particular interest in the field of material modeling. Most of the developed models, describing the nonlinear behavior, are implemented within the framework of the Finite Element Method (FEM). However, most investigations are restricted to simple boundary value problems (BVP) under uniaxial loading and their goal is the calculation of hysteresis loops. Regarding this circumstance, the so-called condensed method (CM) is introduced to investigate the macroscopic polycrystalline ferroelectric material behavior at a global material point without any kind of discretization scheme. In the presented paper, the CM is extended towards ferromagnetic and multiferroic material behavior. Moreover, numerical results for a pure ferromagnetic behavior and a comparison between the magnetoelectric coupling coefficient calculated by the FEM and the CM are presented.

INTRODUCTION

Ferroelectric as well as ferromagnetic materials are widely used in smart structures and devices as actuators, sensors, etc. To model the nonlinear behavior, a variety of models has been developed in the past two decades, e.g. [1]. Most of the models that have been published were implemented within the Finite Element Method (FEM). The implementation of a discretization scheme is going along with a high computational effort and the solution of the boundary value problem (BVP) requires high computational costs. Concerning the material behavior, most investigations are restricted to simple BVP under uniaxial loading and their goal is the calculation of hysteresis loops. In [2] the so-called condensed method (CM) is introduced to investigate the macroscopic polycrystalline material behavior of tetragonal ferroelectrics at a global material point without any kind of discretization scheme. The CM is able to calculate hysteresis loops as well as residual stresses as a result of domain wall motion [2]. Since reliability and life time of smart structures are crucial features for their development and design and ferroelectric ceramics exhibit brittle failure characteristics, a high cycle fatigue model to predict the life time under combined electromechanical loading is introduced in [3]. Besides classical ferroelectrics, other fields of application of the CM have been exploited, e.g. ferromagnets or ferroelectric-ferromagnetic composites (s. [4]) or ferroelectrics with phase transition. In this paper the CM is extended towards ferromagnetic and multiferroic composites.

CONDENSED APPROACH FOR NONLINEAR FERROELECTRIC-FERROMAGNETIC COMPOSITES

The system under consideration is a multiferroic composite, where barium titanate ($\mathrm{B}\quad{}_3$) is supposed for the ferroelectric phase and cobalt ferrite ($\quad{}_2\quad{}_4$) for the ferromagnetic phase. The composite is a random dispersion of ferroelectric and ferromagnetic grains with variable volume fractions. Volume forces b_i and charges ω_V are neglected. Therefore, the static balance equations can be specified as $\sigma_{ij,j} = 0$, $D_{i,i} = 0$ and $B_{k,k} = 0$ with stresses σ_{ij}, electric displacement D_i and magnetic induction B_k. To describe the nonlinear behavior of a multiferroic composite, the thermodynamic potential of each phase is given as [2, 3, 5]

$$\Psi^{(\mathrm{FE})} = \frac{1}{2}C_{ijkl}\varepsilon_{kl}\varepsilon_{ij} \nearrow e_{lij}E_l\varepsilon_{ij} \nearrow \frac{1}{2}\kappa_{il}E_lE_i \nearrow \frac{1}{2}\mu_{km}H_mH_k \nearrow C_{ijkl}\varepsilon^{\mathrm{irr}}_{kl}\varepsilon_{ij} + e_{ikl}\varepsilon^{\mathrm{irr}}_{kl}E_i \nearrow P^{\mathrm{irr}}_i E_i, \tag{1}$$

$$\Psi^{(\mathrm{FM})} = \frac{1}{2}C_{ijkl}\varepsilon_{kl}\varepsilon_{ij} \nearrow \frac{1}{2}\kappa_{ln}E_nE_l \nearrow \frac{1}{2}\mu_{km}H_mH_k \nearrow C_{ijkl}\varepsilon_{kl}\varepsilon^{\mathrm{irr}}_{ij} \nearrow M^{\mathrm{irr}}_k H_k, \tag{2}$$

where C_{ijkl}, e_{ikl}, κ_{ln} and μ_{km} are the elastic, piezoelectric, dielectric and magnetic permeability tensors. ε_{kl}, E_i and H_m denote the independent variables strain, electric and magnetic field. $\varepsilon^{\mathrm{irr}}_{kl}$, P^{irr}_i and M^{irr}_k in Eqs. (1) and (2) identify the spontaneous strain, polarization and magnetization as results of domain wall motion [2, 5]. The associated variables are given by $\sigma^*_{ij} = \partial\Psi^*/\partial\varepsilon_{ij}$, $D^*_i = \nearrow\partial\Psi^*/\partial E_i$ and $B^*_k = \nearrow\partial\Psi^*/\partial H_k$, where $*$ distinguishes between the ferroelectric (FE) and ferromagnetic (FM) phases following Eqs. (1) and (2). In the presented model, each local material point has either ferroelectric or ferromagnetic properties. The domain wall motion is realized by either ferroelectric or ferromagnetic evolution laws for internal variables $\nu^{(n)}$, where $n = 1, \ldots,$ describe the domain species for a two-dimensional case [2, 4]. Switching occurs if $w^{\mathrm{diss}} > w^{\mathrm{crit}}$ is satisfied, where w^{diss} characterizes the dissipative work and w^{crit} the energy threshold. Next, the macroscopic constitutive equations of a representative multiferroic volume element (RVE), which is given as a global material point in the context of the CM, have to be determined. Assuming macroscopic values being microscopic volume averages of the 2-phase comnposite, homogeneous fields in a grain and grains with equal size, i.e. $V = MV^{(m)}$, macroscopic values $\langle\sigma_{ij}\rangle$, $\langle D_i\rangle$

[*]Corresponding author. Email: stephan.lange@uni-kassel.de

and $\langle B_k \rangle$ are obtained by a simple averaging method [2]. Furthermore, a generalized VOIGT approximation is assumed, where strain $\overline{\varepsilon}_{kl}$, electric field $\overline{E}_l$ and magnetic field $\overline{H}_m$ are kept constant in the RVE consisting of M grains. Applying the averaging method to the constitutive equations, given by partial derivatives of Eqs. (1) and (2), the macroscopic constitutive equations of a multiferroic composite yield:

$$\langle \sigma_{ij} \rangle = \langle C_{ijkl} \rangle \overline{\varepsilon}_{kl} \nearrow \langle e_{lij}^{(\mathrm{FE})} \rangle \overline{E}_l \nearrow \langle C_{ijkl}^{(\mathrm{FE})} \varepsilon_{kl}^{\mathrm{irr(FE)}} + C_{ijkl}^{(\mathrm{FM})} \varepsilon_{kl}^{\mathrm{irr(FM)}} \rangle, \tag{3}$$

$$\langle D_i \rangle = \langle e_{ikl}^{(\mathrm{FE})} \rangle \overline{\varepsilon}_{kl} + \langle \kappa_{il} \rangle \overline{E}_l \nearrow \langle e_{ikl}^{(\mathrm{FE})} \varepsilon_{kl}^{\mathrm{irr(FE)}} \rangle + \langle P_i^{\mathrm{irr(FE)}} \rangle, \tag{4}$$

$$\langle B_k \rangle = \langle \mu_{km} \rangle \overline{H}_m + \langle M_i^{\mathrm{irr(FM)}} \rangle. \tag{5}$$

Values with angled brackets in Eqs. (3), (4) and (5) denote macroscopic quantities. Angled brackets without the superscript (FE) or (FM) have contributions of both phases. Depending on the specific BVP the unknowns are chosen among the macroscopic quantities $\langle \sigma \rangle$, $\langle D_i \rangle$, $\langle B_k \rangle$, $\overline{\varepsilon}_{kl}$, $\overline{E}_l$ and $\overline{H}_m$. Assuming stress, electric and magnetic field as external loads, i.e. $\langle \sigma_{ij} \rangle = \sigma_{ij}^{\mathrm{ext}}$, $\overline{E}_l = E_l^{\mathrm{ext}}$ and $\overline{H}_m = H_m^{\mathrm{ext}}$, the strain $\overline{\varepsilon}_{kl}$ results from Eq. (3). The residual stress, e.g. for a local material point m of the ferroelectric phase, is given by:

$$\sigma_{ij}^{(m)} = C_{ijkl}^{(m)} \left(\langle C_{mnkl} \rangle^{-1} \left(\sigma_{mn}^{\mathrm{ext}} + \langle C_{mnop}^{(\mathrm{FE})} \varepsilon_{op}^{\mathrm{irr(FE)}} + C_{mnop}^{(\mathrm{FM})} \varepsilon_{op}^{\mathrm{irr(FM)}} \rangle + \langle e_{rmn}^{(\mathrm{FE})} \rangle E_r^{\mathrm{ext}} \right) \nearrow \varepsilon_{kl}^{\mathrm{irr}(m)} \right) \nearrow e_{lij}^{(m)} E_l^{\mathrm{ext}}. \tag{6}$$

Other quantities, e.g. $D_i^{(m)}$, $\langle D_i \rangle$, etc., can be determined likewise.

RESULTS

For the numerical investigations an RVE with $M = 30$ local material points is considered in the following. The external loads are the same as prescribed above. In Fig. 1(a) the strain and magnetization hysteresis loops for a ferromagnetic material are shown. The strain loop exhibits, in contrast to a ferroelectric material, the typical saturation for higher magnetic fields [5] since there is no linear piezoelectric or magnetostrictive contribution to $\sigma_{ij}^{(\mathrm{FM})}$. In Fig. 1(b) the numerical results for

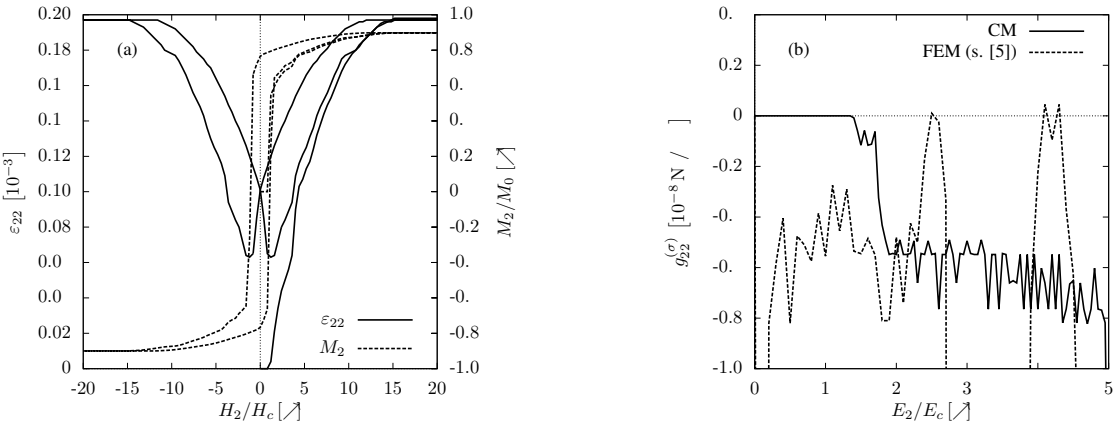

Figure 1: Numerical results of a pure ferromagnetic material ($_2$ $_4$) (a) and the magnetoelectric coupling coefficient of a composite ($0.8\,\mathrm{B}$ $_3$ ↗0.2 $_2$ $_4$) (b)

the magnetoelectric coupling coefficient $g_{22}^{(\sigma)}$ of the FEM (particle composite) and CM are presented for a ferroelectric - ferromagnetic composite with 80 % barium titanate and 20 % cobalt ferrite. The results of these entirely different methods are in a good accordance concerning the order of magnitude for the magnetoelectric coupling coefficient $g_{22}^{(\sigma)}$. Therefore, the CM is also a powerful tool to investigate ferromagnetic and multiferroic materials without a FEM framework.

References

[1] Hwang S. C., Lynch C. S., McMeeking R. M.: Ferroelectric / ferroelastic interactions and a polarization switching model. Acta Metall. Mater. 43: 2073-2084, 1995.

[2] Lange S., Ricoeur A.: A condensed microelectromechanical approach for modeling tetragonal ferroelectrics. Int. J. Solids Struct. 54: 100-110, 2015.

[3] Lange S., Ricoeur A.: High cycle fatigue damage and life time prediction for tetragonal ferroelectrics under electromechanical loading. Int. J. Solids Struct. 80: 181-192, 2016.

[4] Avakian A., Gellmann R., Ricoeur A.: Nonlinear modeling and finite element simulation of magnetoelectric coupling and residual stress in multiferroic composites. Acta Mech. 226: 2789-2806, 2015.

[5] Avakian A., Ricoeur A.: Constitutive modeling of nonlinear reversible and irreversible ferromagnetic behaviors and application to multiferroic composites. Revision submitted to J. Intel. Mat. Syst. Str., 2015.

CYCLIC LOADING EFFECTS ON NITI ALLOYS UNDER BIAXIAL CONDITIONS

Dimitris Chatziathanasiou[1], Nadine Bourgeois[2], Yves Chemisky[1], and Fodil Meraghni*[1]
[1]*Arts et Métiers ParisTech, LEM3 UMR 7239 CNRS , 4 rue Augustin Fresnel, F-57078 Metz - cedex 01, France*
[2]*Université de Lorraine, LEM3 UMR 7239 CNRS , 4 rue Augustin Fresnel, F-57078 Metz - cedex 01, France*

Summary In this work, the influence of the direction and the history of thermomechanical loading of NiTi shape memory alloys on the overall material behavior is experimentally investigated. In the first part, cyclic biaxial mechanical loading has been applied to cross-shaped specimens under constant temperature. The residual strains of selected points from the sample surface are extracted and analyzed. The second part of the study concerns thermomechanical testing of textured samples cut from a laminated plate under complex cyclic loading at different temperature levels. The evolution of residual strains and the transformation threshold are correlated to the history of loading and the amplitude of transformation strain. Anisotropic effects are studied by performing those same experiments on different directions according to the rolling direction of the laminated plate.

INTRODUCTION

Cyclic mechanical loading on NiTi shape memory alloys (SMA) induces a noticeable change in the actuation stroke – recoverable transformation strain and martensitic transformation stress limits. The general behavior under one-dimensional loading conditions depends on the temperature of the sample. This is a phenomenon commonly associated to transformation-induced plasticity [1], but retained martensite that can transform back at higher temperature is also present [2]. If such behavior is well understood for uniaxial tests, the anisotropic evolution of the SMA response upon cyclic has not been extensively studied. Moreover, SMAs are known to exhibit strong anisotropy for superelastic loading cases [3], since forming conditions induce texture in the polycrystal. This has a direct effect on the behavior under biaxial loading as well, as has been investigated in recent works [4].

In this paper, a series of thermomechanical cyclic tests on NiTi samples is presented. It aims at investigating the effect of three separate parameters of cyclic loading to the change of the material response, namely the evolution of residual strains and the transformation threshold in terms of stresses. These three parameters are the number of cycles, the magnitude of ultimate applied strain and the loading direction. The first part of this series concerns isothermal biaxial loading of cross-shaped specimens along their two directions. The evolution of the overall kinematic fields of the specimen surface is monitored using DIC. The second part concerns thermomechanical loading of one-dimensional specimens at different temperatures. A complex cyclic loading path is applied to observe the evolution of material properties, followed by heating to measure the recoverable residual strain.

THERMOMECHANICAL TESTING IN ONE DIMENSION

One-dimensional samples cut along the two directions of a rolled NiTi plate at 50.6% Ni atomic content were subjected to the following loading path: tension towards 3% strain and return to zero force, repeated 15 times in total. Then, tension to 5% strain and return to zero force. This sequence of 16 cycles is repeated a second time, followed by two last cycles to 3%. Tests were performed at a strain-rate up to $10^{-4}s^{-1}$ and the temperature was always controlled at 30, 40 or 50°C. At the end of the mechanical loading, the samples were heated up to 100°C to measure the recoverable residual strain. In the results presented in Figure 1, it seems to reach saturated values for the loading of 3%, but the 5% target in terms of strain induces further residual strain.

ISOTHERMAL NON PROPORTIONAL BIAXIAL TESTING

Cross-shaped samples are subjected to repeated biaxial loading at a temperature of 50°C. The first sequence is composed of tension cycles along the East-West direction and compression along the North-South direction. In the second sequence, the force is maintained at zero along East-West, whereas tension is applied in North-South. Two cycles of the first sequence are repeated during the third sequence. Figure 2 follows the overall force-displacement response for the specimen, as tracked by the test machine controller. Strain fields on the surface of the sample are tracked by Digital Image Correlation (DIC) [5].

CONCLUSION

The aspects of residual strain and transformation threshold are investigated experimentally for the superelastic behavior of NiTi alloys. Cyclic loading has been applied in one- and two-dimensional configurations. The effects of transformation strain magnitude and anisotropy have been studied and related to the material properties.

*Corresponding author. Email: fodil.meraghni@ensam.eu

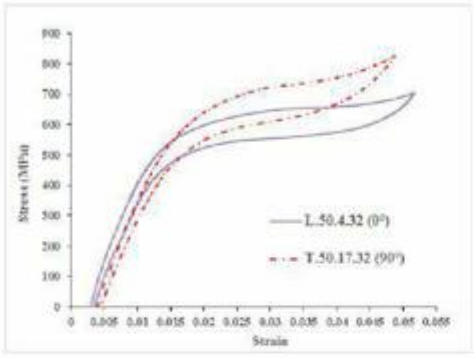

(a) Stress-strain diagram for the 32nd cycle

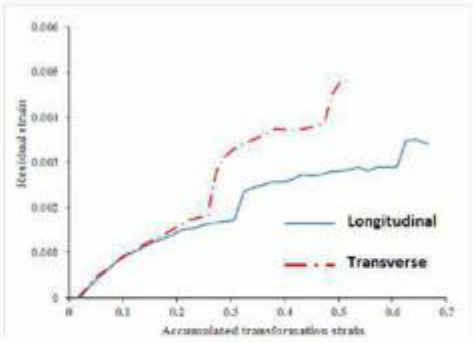

(b) Residual strains as a function of accumulated transformation strain

Figure 1: Mechanical material behavior (a) and evolution of residual strains (b) for two samples in the longitudinal and transverse direction of rolling, subjected to cyclic loading at 50°C.

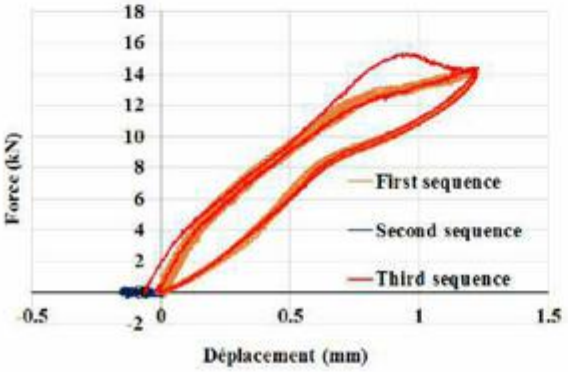

(a) East-West direction

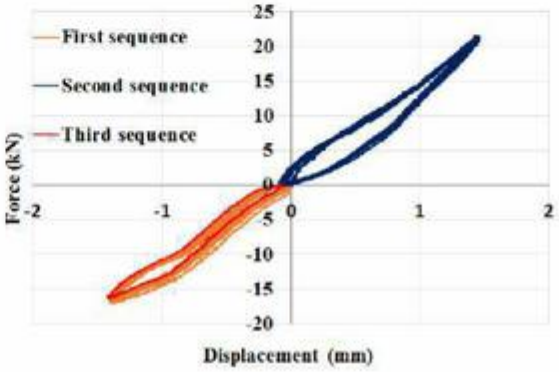

(b) North-South direction

Figure 2: Force-displacement diagrams for the overall behavior at 50°C of a cross-shaped specimen in its two directions.



(a) Cross-shaped NiTi specimen for biaxial tension test

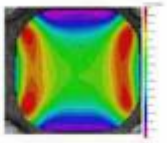

(b) DIC tracking for ε_{xx}

Figure 3: The NiTi biaxial sample used (a) and a experimental strain field ε_{xx} under tension-compression loading @50°C.

References

[1] Hartl, D. J., & Lagoudas, D. C. Constitutive modeling and structural analysis considering simultaneous phase transformation and plastic yield in shape memory alloys. Smart Materials and Structures, 18(10), 104017. 2009.

[2] Kumar, P.K., Caer, C., Atkinson, G., Patoor, E., Lagoudas, D.C.: The influence of stress and temperature on the residual strain generated during pseudoelastic cycling of NiTi SMA wires. Proc. SPIE 7978, Behavior and Mechanics of Multifunctional Materials and Composites, 79781E. 2011.

[3] Mehrabi, R., Andani, M. T., Elahinia, M., & Kadkhodaei, M. Anisotropic behavior of superelastic NiTi shape memory alloys; an experimental investigation and constitutive modeling. Mechanics of Materials, 77, 110–124. 2014.

[4] Chemisky, Y., Meraghni, F., Bourgeois, N., Cornell, S., Echchorfi, R., & Patoor, E. Analysis of the deformation paths and thermomechanical parameter identification of a shape memory alloy using digital image correlation over heterogeneous tests. International Journal of Mechanical Sciences, 96-97, 13–24. 2015.

[5] Pan, B., Qian, K., Xie, H., & Asundi, A. Two-dimensional digital image correlation for in-plane displacement and strain measurement: a review. Measurement Science and Technology, 20(6), 062001. 2009.

EFFECTS OF SWITCHING PROCESSES IN FERROELECTRICS ON THE TEMPERATURE: A MODELING APPROACH

Marius Wingen[1] and Andreas Ricoeur *[1]
[1]*Institute of Mechanics, University of Kassel, Kassel, Hessen, Germany*

Summary In this paper, the theoretical background and a Finite Element (FE) solution of a micromechanically and physically based constitutive model is presented. The model considers the mutual nonlinear coupling of thermal and electromechanical fields. Numerical calculations show the effects of temperature on the electromechanical field quantities and vice versa. They also reveal switching processes in ferroelectrics and associated heating or cooling.

THEORETICAL PRINCIPLES

Nonlinear thermo-electro-mechanical constitutive law

Based on the thermodynamical potential

$$\bar{\Omega} = \frac{1}{2} C_{ijkl} \epsilon_{kl}^{rev} \epsilon_{ij}^{rev} \nearrow \frac{1}{2} \kappa_{il} E_i E_l \nearrow \frac{1}{2} \gamma \theta^2 \nearrow e_{lij} E_l \epsilon_{ij}^{rev} \nearrow \beta_{ij} \theta \epsilon_{ij}^{rev} \nearrow k_l \theta E_l \nearrow P_i^{irr} E_i \nearrow \bar{S}^{irr} \theta, \tag{1}$$

with the material tensors $Cijkl$, κ_{il}, γ, e_{lij}, β_{ij} and k_l denoting the elasticity tensor, the dielectric tensor, the thermal coefficient, the piezoelectric tensor, the thermal stress and the pyroelectric coefficients, the constitutive equations of a nonlinear thermo-ferroelectric material are obtained as

$$\dot{\sigma}_{ij} = C_{ijkl}(\dot{\epsilon}_{kl} \nearrow \dot{\epsilon}_{kl}^{irr}) \nearrow e_{lij} \dot{E}_l \nearrow \beta_{ij} \dot{\theta}, \tag{2}$$

$$\dot{D}_i = e_{ikl}(\dot{\epsilon}_{kl} \nearrow \dot{\epsilon}_{kl}^{irr}) + \kappa_{il} \dot{E}_l + k_i \dot{\theta} + \dot{P}_i^{irr}, \tag{3}$$

$$\dot{\bar{S}} = \beta_{kl}(\dot{\epsilon}_{kl} \nearrow \dot{\epsilon}_{kl}^{irr}) + k_l \dot{E}_l + \gamma \dot{\theta} + \dot{\bar{S}}^{irr}, \tag{4}$$

where σ_{ij} and ϵ_{ij} are stresses and strains, D_i and E_i the electric displacement and electric field and θ and $\bar{S}$ the temperature and specific entropy. The superscript "rev" refers to reversible quantities and "irr" indicates irreversible changes of state.

Balance of energy

For describing a thermoelectromechanical three-field problem, a third field equation is required, which is obtained from the 1st law of thermodynamics. In the quasistatic case it reads

$$\dot{\bar{U}} = \dot{\bar{W}} + \dot{\bar{Q}} + \dot{\bar{\mathcal{X}}}, \tag{5}$$

postulating that the change of internal energy $\dot{\bar{U}}$ is equal to the sum of of the electromechanical work rate

$$\dot{\bar{W}} = \sigma_{ij} \dot{\epsilon}_{ij}^{rev} + E_i \dot{D}_i^{rev}, \tag{6}$$

the specific heat flow rate

$$\dot{\bar{Q}} = \dot{q}_v \nearrow \dot{q}_{j,j}^A, \tag{7}$$

where $\dot{q}_v$ is an internal heat source and $\dot{q}_{j,j}^A$ a heat flux across the boundary, and the dissipative work rate

$$\dot{\bar{\mathcal{X}}} = (\sigma_{ij} \dot{\epsilon}_{ij}^{irr} + E_i \dot{P}_i^{irr}) > 0 \tag{8}$$

due to ferroelectric domain switching. The term in braces is a simple approach to quantify the switching energy [1]. Switching events can also be interpreted as internal heat sources within a reversible control volume. According to Eq. (8), to $\dot{q}_v$ then applies

$$\dot{q}_v = \dot{\bar{\mathcal{X}}} = (\sigma_{ij} \dot{\epsilon}_{ij}^{irr} + E_i \dot{P}_i^{irr}). \tag{9}$$

Together with Fourier's law of heat conduction with the heat conduction coefficients λ_{ij} and the Gibbs fundamental equation for the internal energy

$$\dot{\bar{U}}(\dot{\epsilon}_{ij}, \dot{D}_i, \dot{\bar{S}}) = \sigma_{ij} \dot{\epsilon}_{ij} + E_i \dot{D}_i + T \dot{\bar{S}}, \tag{10}$$

Eqs. (4) and (5), excluding any irreversible entropy production inside the conservative control volume ($\dot{\bar{S}}^{irr}, \dot{\bar{\mathcal{X}}} = 0$), (6), (7) and (9) finally lead to the energy balance, where T is the constant absolute temperature within incremental changes of state:

$$\lambda_{ij} \theta_{,ij} = \beta_{ij} T \dot{\epsilon}_{ij}^{rev} + k_i T \dot{E}_i + \gamma T \dot{\theta} \nearrow \sigma_{ij} \dot{\epsilon}_{ij}^{irr} \nearrow E_i \dot{P}_i^{irr}. \tag{11}$$

*Corresponding author. Email: marius.wingen@uni-kassel.de

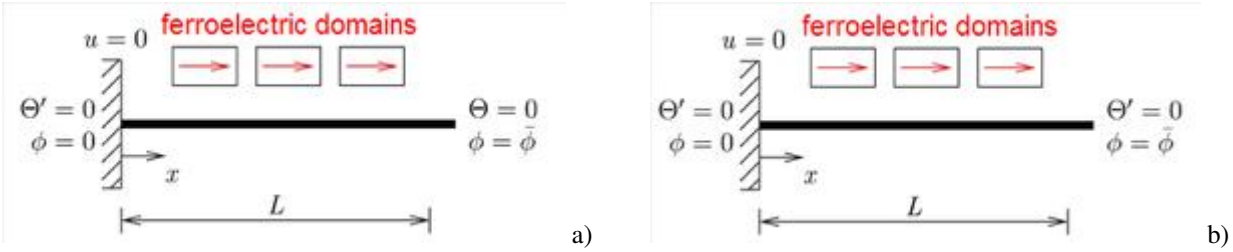

Figure 1: One-dimensional boundary value problem with **(a)** adiabatic (left boundary) and non-adiabatic (right boundary) boundary conditions and **(b)** adiabatic boundaries as numerical test examples

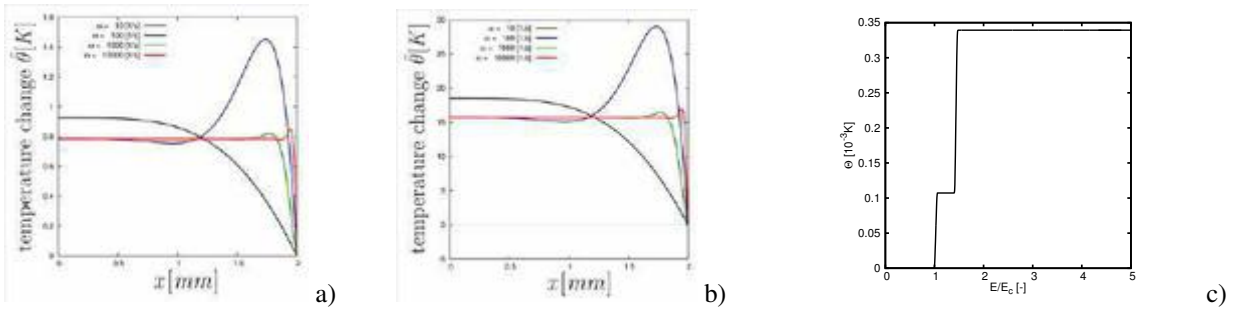

Figure 2: Analytical results for different loading frequencies with **(a)** $E = 1 \quad / \quad$ and **(b)** $E = 20 \quad / \quad$; **(c)** numerical result for the local evolution of the temperature at single switching event

SOME RESULTS

Numerical example

Assuming the switching process is dominant for heating, the elasto- and electrocaloric coupling effects are neglected in Eq. (11). The calculation, however, considers thermal expansion and the pyroelectric effect, which have an influence on electromechanical quantities. Fig. 2 (c) shows the temperature evolution for the boundary value problem in Fig. 1 (b) depending on the electric field strength. It shows a rising temperature during domain switching.

Analytical example

A Fourier transformation is applied to all time-dependent variables. As in the numerical solution, electro- and elastocaloric effects are neglected in Eq. (11). Fig. 2 (a) and (b) show results for the distribution of the temperature depending on the angular frequency ω for a stress-free ($\sigma_{ij} = 0$) one-dimensional boundary problem, as shown in Fig. 1 (a). Due to the adiabatic boundary condition at the left boundary ($x = 0$), the gradient of the temperature is zero there. At the right boundary ($x = L$), the heat flows out of the body. It is a pure heating effect caused by switching processes. Higher frequencies foster the homogeneity of the temperature in the rod.

Because of the relatively small electric field strength in Fig. 2 (a), this very simple calculation predicts results in an order of magnitude of $\theta = 10^0$, which is consistent with experiments in [2] and [3]. So-called thin film samples tolerate much higher electric field strengths than bulks, thus much larger effects can be produced (Fig. 2 (b)).

References

[1] S.C.Hwang, C.S. Lynch, R.M. McMeeking, Ferroelectric/ferroelastic interactions and a polarization switching model, Acta Metall. Mater. 43(5),2073-2084 (1995).

[2] J. Cui, Y. Wu, J. Muehlbauer, Y. Hwang, R. Radermacher, S. Fackler, M. Wuttig, I. Wuttig, I. Takeuchi, Demonstration of high efficiency elastocaloric cooling with large ΔT using NiTi wires, Applied Physics Letters 101, 073904 (2012); doi 10.1063/1.4746257.

[3] Y. Yang, W. Guo, K.C. Pradel, G. Zhu, Y. Zhou, Y. Zhang, Y. Hu, L. Lin, Z.L. Wang, Pyroelectric Nanogenerators for Harvesting Thermoelectric Energy, Nano Lett., 2012, 12(6), pp. 2833-2838.

MOLECULAR DYNAMICS SIMULATIONS OF PHASE TRANSFORMATIONS IN NITI BICRYSTALS

Prashanth Srinivasan *[1], Lucia Nicola[2], and Angelo Simone[1]
[1]*Faculty of Civil Engineering and Geosciences, Delft University of Technology*
Delft, The Netherlands
[2]*Faculty of Mechanical, Maritime and Materials Engineering, Delft University of Technology*
Delft, The Netherlands

Summary The influence of grain boundaries and grain misorientation on the nucleation and growth of martensite in an equi-atomic nickel-titanium (NiTi) shape memory alloy (SMA) is investigated by performing molecular dynamics (MD) simulations on bicrystals with a modified embedded atom method (MEAM) interatomic potential. Stress-induced martensitic transformations are simulated in bicrystals with mixed grain boundaries and the behavior of the bicrystal is compared to that of individual single crystals. Here, a particular bicrystal with $< 110 >$ and $< 111 >$ oriented austenite grains is chosen as an example. Results indicate that the mixed grain boundary in the austenite bicrystal acts as a nucleation site for stress-induced martensitic transformation in the grains. The deformation behavior and the transformation strain of the bicrystal fall in between those of the two corresponding single crystals.

INTRODUCTION

SMAs can exist in different phases depending on temperature and stress. This leads to interesting properties such as pseudo-elasticity and the shape memory effect. The reversible phase transformation happens between a high-symmetry B2 austenite phase, stable at high temperatures, and a low symmetry B19' martensite phase, stable at low temperatures. Under the application of a load at high temperatures, the austenite phase undergoes large reversible deformations up to a strain of 10 % by transforming into the martensite phase. This transformation is very sensitive to grain orientation [1], grain size [2] and grain boundaries (GBs) [3, 4, 5] which are known to influence the nucleation of martensite, the transformation stress and strain, and the type of variant in regions near the grain boundary. Since the martensitic transformation occurs rapidly, it is difficult to understand the precise role of various types of grain boundaries by performing experiments. This is why molecular dynamics is an important tool in understanding the underlying micro-structural changes during such phase transformations. So far, MD has been limited to study temperature and stress-induced transformations in single-crystal NiTi [6, 7]. In this work, we study the influence of mixed grain boundaries on stress-induced martensitic transformations by simulating differently oriented NiTi bicrystals.

METHODOLOGY

A specific bicrystal with a mixed high-angle grain boundary is chosen as an example to discuss method and results. A 3-D cell with periodic boundary conditions along all directions consisting of two grains of different orientation (Fig. 1(a)) is used. Overlapping atoms near the GB that are very close to each other are deleted. The two GBs, one in the middle of the cell and

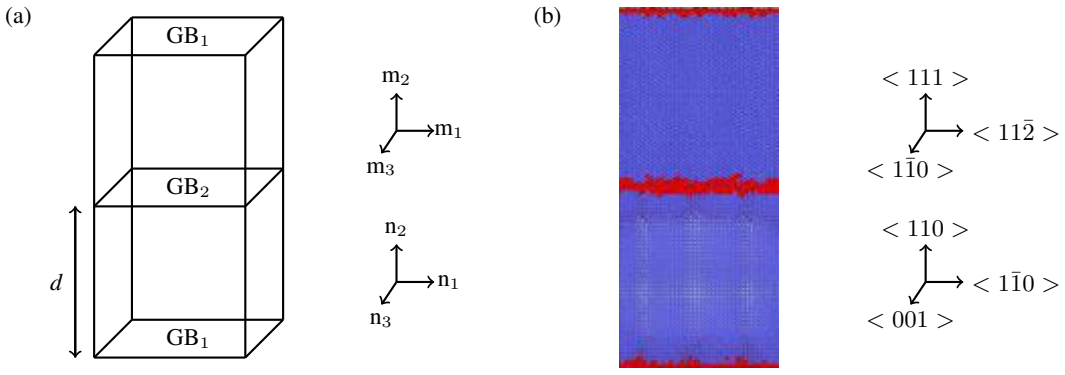

Figure 1: (a) Schematic of the 3-D periodic bicrystal simulation cell. (b) Sectional view of a relaxed bicrystal with a mixed grain boundary (atoms in red); orientation of individual grains is also shown.

*Corresponding author. Email: P.Srinivasan@tudelft.nl

one that arises because of periodicity are similar and the separation d between them is large enough to independently study the effect of the GB. In this work, we choose d =15 nm and 15 nm $\times$ 15 nm $\times$ 15 nm grains. The initial structure is austenite with the orientation of the two grains shown in Fig. 1(b).

An energy minimisation is performed to obtain the minimum energy GB structure. After that, the bicrystal is allowed to thermally equilibrate at 350 K. The loading axis is perpendicular to the GB plane. Tensile and compressive loading simulations are performed at a strain rate of 10^7 s^{-1}. To compare results with single crystal behaviour, bulk single crystals along $< 110 >$ and $< 111 >$ axis are subjected to the same boundary conditions. All simulations are performed with LAMMPS using the MEAM interatomic potential [8].

RESULTS AND DISCUSSION

Figure 2 shows the tensile (a) and compressive (b) stress-strain response of the B2 bicrystal shown in Fig. 1(b) and that of the individual single crystals loaded along the $< 110 >$ and $< 111 >$ axis at 350 K. In all cases, there are two regions of linear deformation, corresponding to phases B2 and B19', that are separated by a non-linear region – this implies the transformation and leads to super-elasticity. The stiffness of B2 and B19' and the strain associated with the stress plateau for the bicrystal are in between the corresponding single crystal values. Under both tension and compression, the GB acts as a nucleation site for the onset of martensitic transformation, starting in the bottom grain in Fig. 1(b). In this particular bicrystal, the GB does not affect martensite variant selection since the same variants are formed in each grain and in the individual single crystals (results not shown here).

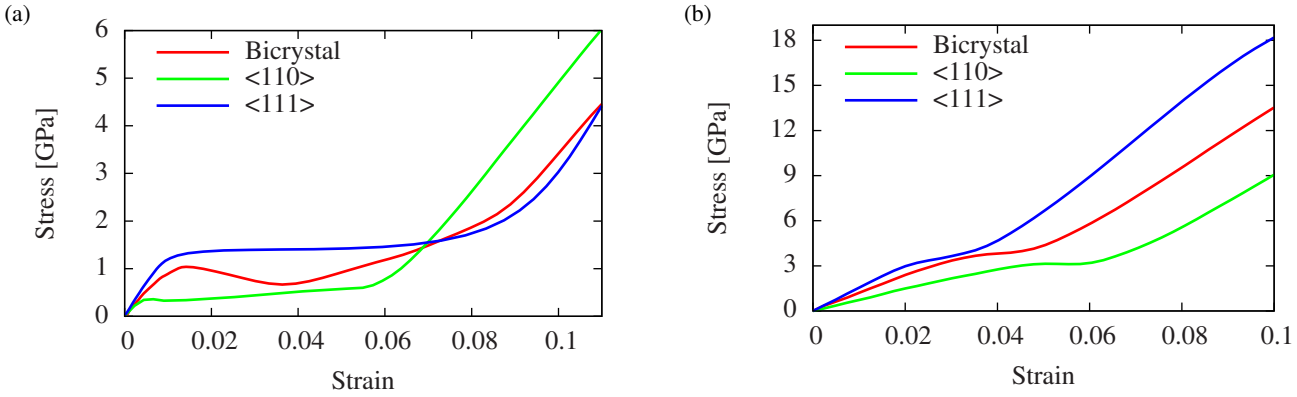

Figure 2: Isothermal stress-strain behavior of the bicrystal in Fig. 1(b) compared to individual bulk single crystals at 350 K under (a) tension and (b) compression.

References

[1] Pfetzing-Micklich J., Somsen C., Dlouhy A., Begau C., Hartmaier A., Wagner M.F.X., Eggeler G.: Acta Mater. **61**, 602-616 (2013).
[2] Waitz T., Spisak D., Hafner J., Karnthaler H.P.: Europhys. Lett. **71**, 98-103 (2005).
[3] Ueda M., Yasuda H., Umakoshi Y.: Science and Tech. of Adv. Mat. **3**, 4-9 (2002).
[4] Ueland S.M., Schuh C.A.,: J. App. Phys. **114**, 053503 (2013).
[5] Kato H., Miura S.: Mat. Sci Forum **394-395**, 205-208 (2002).
[6] Mutter D., Nielaba P.: European Phys. J. **84**, 109-113 (2011).
[7] Zhong Y., Gall K., Zhu T.: J. App. Phys. **110**, 033532 (2011).
[8] Ko W-S., Grabowski B., Neugebauer J.: Phys. Rev. B. **92**, 134107 (2015).

FUNCTIONALLY-GRADED AND COMPOSITE SHAPE MEMORY ACTUATION

Ryosuke Matsui [1a)], Kohei Takeda [1] & Hisaaki Tobushi [1]
[1]*Depertment of Mechanical Engineering, Aichi Institute of Technology, Toyota, Aichi, Japan*

Summary If the shape memory materials are applied into actuators, the novel intelligent shape memory actuators can be developed. In the present paper, the development of a functionally-graded shape memory alloy actuator, a functionally-graded shape memory polymer actuator and a shape memory composite actuator is discussed. The simple multi-way actuation can be developed by using the functionally-graded shape memory alloy. The functionally-graded shape memory polymer board, showing the close deformation property of the finger, can be applied to the elements coming into contact with body in the medical actuators. The three-way actuators can be developed by applying the shape memory composite with various kinds of shape-memory alloy and polymer.

INTRODUCTION

In the intelligent materials, the development of shape memory alloy (SMA) has attracted high attention because the unique properties of the shape memory effect (SME) and superelasticity (SE) appear. If we apply the recovery stress to the driving force, we can develop the novel SMA actuators. Shape memory polymer (SMP) has also been developed. In SMP, large recovery strain of more than 100 % can be obtained. We can use not only the shape recovery and shape fixity but also recovery stress. We can therefore develop the novel SMP actuators by using the recovery stress. Although elastic modulus and yield stress are large at high temperatures and small at low temperatures in SMAs, they are large at low temperatures and small at high temperature in SMPs. The dependence of rigidity and strength on temperature is therefore quite different between SMA and SMP elements. If the composite materials with SMA and SMP having different properties are developed, the new actuation properties of the material can be obtained. In the present paper, the functionally-graded SMA actuator, the functionally-graded SMP actuator and the three-way actuation of the shape memory composite (SMC) will be discussed.

FUNCTIONALLY-GRADED SMA ACTUATION

As an example of the functionally-graded shape memory alloy (FGSMA), we developed a new fabrication process that combines powder metallurgy and hot extrusion as shown in Fig. 1 to obtain the FGSMA wire that varies in transformation temperatures from high to low along the wire axis. First, a multilayered TiNi green compact in which the Ti–Ni compositions varied layer by layer was sintered using a spark plasma sintering process; the compact was then hot extruded into wires. We used a characteristic that the phase transformation temperature of TiNi SMA changes depending on the composition of Ti and Ni. Figure 2 shows the stress–local strain curves at three points of the hot extruded wire. The wire shows the SE at the position that correspond to a Ni content of 51.0at.% and the SME at the position of 50.4at.% Ni. These differences appear to be based on the different MT temperatures at each position. If the FGSMA wire and tape are developed, the temperature-dependent continuous actuation and the multi-way actuation can be obtained by using only one SMA wire or tape, resulting in a small and simple mechanism.

FUNCTIONALLY-GRADED SMP ACTUATION

The polyurethane SMP foam and sheet having different glass transition temperatures T_g were laminated and the FGSMP board was fabricated. The photograph and structure of the FGSMP board are shown in Fig. 3. Two SMP foams of thickness 5 mm with T_g = 298 K and two SMP sheets of thickness 2 mm with T_g = 308 K and 328 K were laminated. The indentation test was carried out for the FGSMP board. The relationship between force and displacement in five cycles obtained by the test for a maximum force of 5 N is shown in Fig. 4. In Fig. 4, the result for a finger is also shown. The relationship of the FGSMP board is close to that of the finger. The deformation properties of the body differ depending on the region. The FGSMP board corresponding to each region can be developed by the combination of the sheet and foam with appropriate thickness and glass transition temperature in the medical actuators.

THREE-WAY SHAPE MEMORY COMPOSITE ACTUATION

The SMC belt was fabricated by using two kinds of shape memory alloy tapes and three SMP tapes. The glass transition temperature of the SMP tape was between the phase transformation temperatures of the SMA tape and superelastic alloy (SEA) tape. The SMA tape and SEA tape were arranged facing in the opposite directions for the memorized round shape as

[a)] Corresponding author. Email: r_matsui@aitech.ac.jp

shown in Fig. 5. The SMP tape passed through the SMA tape and the SEA tape were sandwiched between two SMP tapes from upper and lower sides. The laminated material was set in the mold for heat-treating of the SMC belt. The photographs of the bending motion of the fabricated SMC belt during heating and cooling are shown in Fig. 6. The SMC belt bends to convex downwards (in the direction of the memorized round shape of the SEA tape) by the recovery force of the SEA tape during heating (1) – (2). It bends to convex upwards (in the direction of the memorized round shape of the SMA tape) by the higher recovery force of the SMA tape at higher temperature (2) – (3). It regains its original shape during cooling (3) – (4). As can be seen, the three-way (reciprocating) bending actuation can be obtained by a simple SMC structure.

CONCLUSIONS

In the present paper, the development of a functionally-graded shape memory alloy actuator, a functionally-graded shape memory polymer actuator and a shape memory composite actuator was discussed. The main points confirmed are as follows.

(1) The simple multi-way actuator can be developed by using the functionally-graded shape memory alloy.
(2) The functionally graded shape memory polymer board, showing the close deformation property of the finger, can be applied to the elements coming into contact with body in the medical actuators.
(3) With respect to the shape memory composite actuators, by the combination of various kinds of shape-memory alloy and polymer, the three-way actuation can be obtained.

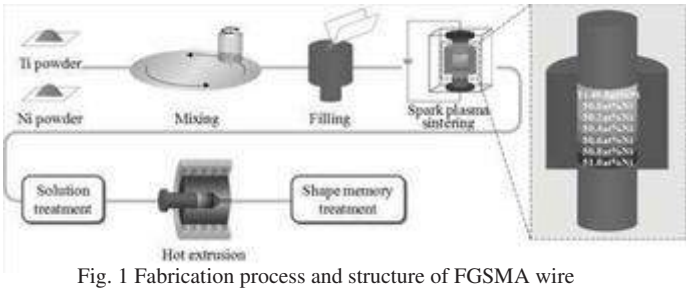

Fig. 1 Fabrication process and structure of FGSMA wire

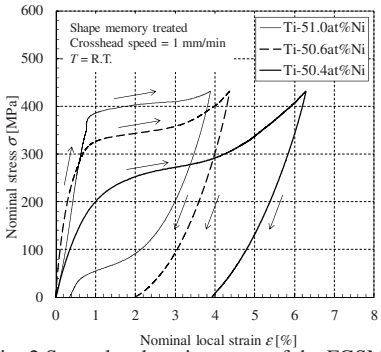

Fig. 2 Stress-local strain curves of the FGSMA wire at various Ni content positions

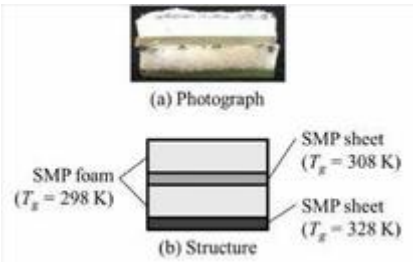

Fig. 3 Photograph and structure of FGSMP board

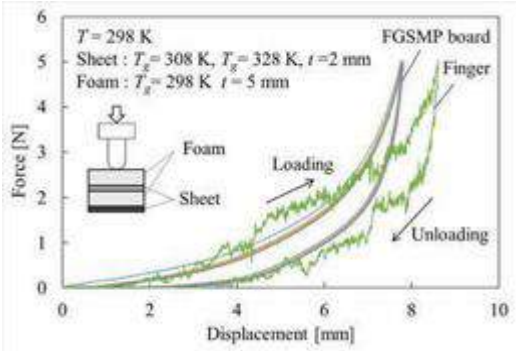

Fig. 4 Indentation curves of FGSMP board and finger

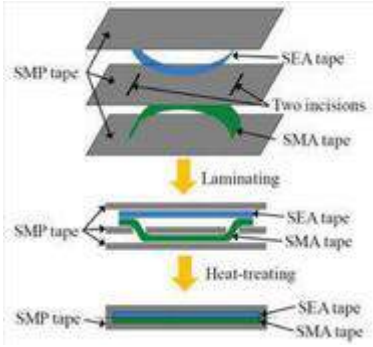

Fig. 5 Arrangement of SMA, SEA and SMP tapes for laminating and heat-treating of SMC belt

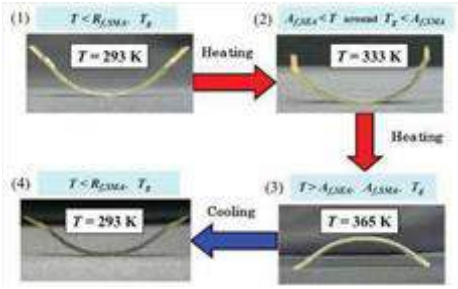

Fig. 6 Photographs of three-way bending motion of SMC belt during heating and cooling

MODELING OF THE CHEMO-MECHANICAL BEHAVIORS OF REACTIVE MATERIALS

Xiaolong Zhang, Zheng Zhong[a)]
School of Aerospace Engineering and Applied Mechanics, Tongji University, Shanghai, China

Summary To describe the transient behaviors of chemo-mechanical interactions in reactive materials, this paper formulate a continuum-mechanical model of the coupled mass transport, deformation and chemical reaction within the framework of nonequilibrium thermodynamics. By introducing a volumetric strain relation enforced as a constraint to the free energy function via a Lagrange multiplier, we consider separately the reaction dilation and the swelling due to imbibition of external molecules. The model is illustrated by two examples and the kinetic characters of these processes are analyzed under various ratios of characteristic time of diffusion and reaction.

INTRODUCTION

Chemo-mechanical interaction widely exists in materials such as hydrogel, shape memory alloys and chemical reactive substance as well as geomaterials and biological tissues. These materials respond easily to external stimulus like stretching, heating and chemical reactions, and some of which, particularly, possess the swelling ability and the chemical reactivity simultaneously. This compound trait results in complex material behaviours governed by the coupled mass diffusion, chemical reaction and mechanical deformation. From the engineering application viewpoint, there is a need to evaluate the coupling behaviour of these reactive swelling materials. Yet, most of the available theories are limited to the coupling of deformation and diffusion without chemical reaction or remain deficient in describing complex reaction-diffusion behaviours owing to treating the reaction dilation as a common swelling process and lack of reaction kinetics. Therefore, the purpose of the present work is to develop a model within the framework of nonequilibrium thermodynamics to describe the transient behaviours of a chemo-mechanical coupling system.

CONSERVATION LAWS AND THERMODYNAMIC IMBALANCE

Consider a macroscopically homogeneous body B bounded by the surface S with unit outward normal vector n_j. When all inertial effects and body forces are neglected, the macroscopic mechanical balance is described by:

$$\sigma_{ij\ j} = 0 \quad (in\ B\ ,\ \ \overline{f_i} = \sigma_{i\ j} n_j \quad on\ S_\sigma)\ ,\ \ u_i = \overline{u_i} \quad on\ S_u) \tag{1}$$

where, σ_{ij} is the Cauchy stress tensor, u_i is the displacement vector. $\overline{f_i}$ and $\overline{u_i}$ are respectively the prescribed force and surface displacement on the surface S. The mass conservation related to the αth component is expressed in the form:

$$\dot{c}_\alpha + \nabla \cdot \mathbf{J}_\alpha^m = \dot{r}_{\to\alpha} \tag{2}$$

where c_α is the number of molecules per unit volume of species α, $\dot{r}_{\to\alpha}$ is the rate of molecules formation or consumption and $\mathbf{J}_\alpha^m$ is the diffusion flux vector. In the framework of the irreversible thermodynamics, the second law takes the form of a local entropy imbalance. By introducing the Helmholtz free energy ψ, the chemical potential μ_α, the chemical affinity $A^\gamma = -\sum_\alpha \mu_\alpha v_\alpha^\gamma$ and the reaction rate $\ell^\gamma = \dot{r}_{\to\alpha}^\gamma\ v_\alpha^\gamma$ for the γth reaction with ℓ^γ and v_α^γ representing the reaction degrees and the stoichiometric coefficient respectively, the Clausius–Duhem inequality of the deformable reactive continua is given as:

$$\boldsymbol{\sigma}\ \ \dot{\boldsymbol{\varepsilon}} + \sum_\alpha \mu_\alpha \dot{}_\alpha - \quad \dot{} - \dot{\psi} + \frac{\mathbf{J}_q}{T} \cdot\ -\nabla T) + \sum_\alpha \mathbf{J}_\alpha^m \cdot\ -\nabla \mu_\alpha \big) + \sum_\gamma A^\gamma\ \ell^\gamma \ \geq 0 \tag{3}$$

where, $\boldsymbol{\varepsilon}$ is linear strain tensor, $\mathbf{J}_q$ is the heat flux, s and T are the entropy density and the absolute temperature respectively.

ISOTROPIC LINEAR CONSTITUTIVE REALTIONS AND KINETIC LAWS

For the isothermal case, under the considertaion that individual molecules are incompressible, we incorporate the volumetric difference between the reactants and the resultants with the chemical dialation coffiecient β. The volumetric strain is express as the sum of the swelling induced by diffusive speices and the dialation/shrinkage generated by reaction (in the form of simple case with single diffusive constituent, single reaction and superscript 0 refers to the reference state)

$$\varepsilon_{kk} = \Omega(\ -\ ^0\ +\ \beta\ell \tag{4}$$

where, Ω is the volume per small molecule. This condition can be enforced as a constraint to the free energy of the system with a field of Lagrange multiplier p. For an isotropic linear material with only one diffusive constituent β and single reation $\alpha_1\ s\ + \beta \to \alpha_2\ s\ $,we prescribe a particular form of the free-energy ψ as a function of independent variables

[a)] Corresponding author. Email: zhongk@tongji.edu.cn; Tel: 86-21-65983998; fax: 86-21-65983267.

ε_{kk} e c ℓ by choosing a quadratic expression (e_{ij} is the deviatoric strain tensor). By inserting ψ into the state equations derived from dissipation inequality with constraint (4), we obtain the linear constitutive relations as follows:

$$\begin{aligned} \sigma_{kk}-\sigma_{kk}^{0} &= \mathrm{K}\varepsilon_{kk}+R\,c-c^{0}-\mathrm{K}\beta\,\ell\quad \ell^{0}+p \qquad & \mu-\mu^{0} &= R\varepsilon_{kk}-N\,c-c^{0}-\varsigma\,\ell\quad \ell^{0})-\Omega, \\ -\,{}_{ij}^{0} &= \Lambda e_{ij} & A-A^{0} &= 3\,\mathrm{K}\,{}_{kk}+\varsigma(-{}^{0}+\ell\quad \ell^{0}) \end{aligned} \tag{5}$$

where, $s_{ij}=\sigma_{ij}-\sigma\ \delta\ /3$, K and Λ are the volumetric modulus and the shear modulus, R N ς and a are the mechanical-chemical coefficient, the chemical potential constant, the chemical potential-reaction coefficient and the chemical affinity constant, respectively. Let σ_1, σ_2 and σ_3 be the three principal stresses and set $R=0$ for a simplified case, we have

$$\sigma_i=\frac{E}{1+\nu}\left[\varepsilon_i+\left(\frac{\nu}{-\ \nu}-\frac{1+\nu}{E}\frac{N}{\Omega^2}\right)\theta\right]-\left(\frac{E\beta}{-\ \nu}+\frac{\varsigma}{\Omega}-\frac{3\beta N}{\Omega^2}\right)\ell-\frac{\mu-\mu^{0}}{\Omega} \tag{6}$$

where $i=1,2,3$, θ, E and ν are volumetric strain, the elastic modulus and the Poisson's ratio. Eqn.(6) can be further simplified to the standard swelling case when $\ell=0$ .The diffusion kinetics is given by the relation $\mathbf{J}_{\beta}^{m}=-\,c\ D\ kT\ \nabla\mu_{\beta}$. The reaction kinetics can be given by an additional evolving law, *i.e.* an Arrhenius type equation $A=\ \ell^{\,E_a\ RT}$ to satisfy dissipation inequality $\Phi\ =A\ell\geq 0$. However, a more practical way lies on introducing a differential form kinetics to link the reaction rate with reactant concentration: $\ell\quad=\quad{}_{\beta}^{\ n}$, where, k is rate constant and n is the reaction order.

TRANSIENT PROBLEMS

The theory described above is now applied to two numerical examples, one for a laterally constrained film fabricated on a rigid substrate (Fig. 1a) with the upper surface brought into contact with a diffusive species for which μ=0, and another for a film immersed in the same species (Fig. 1b). A first order reaction ($\partial\ell\ \partial\ =\quad$) between the film and the diffusive species is considered. For the freestanding film, it reacts with the species and swells in both in-plane and the thickness directions. The chemical potential $\mu\ z\ t$, the vertical displacement $u_z\ z\ t$ and the reaction degree change with time until both the diffusion and the reaction approach equilibriums. For the constrained film, it stretches in the thickness direction while the lateral stretches are constrained. The film thus develops a biaxial stress state with $\sigma_x\ z\ t\ =\sigma_y\ z\ t$ at $\varepsilon_x=\varepsilon_y=0$ .These problems are solved numerically with the definite conditions and a small part of the results are list as follows (Fig.1).

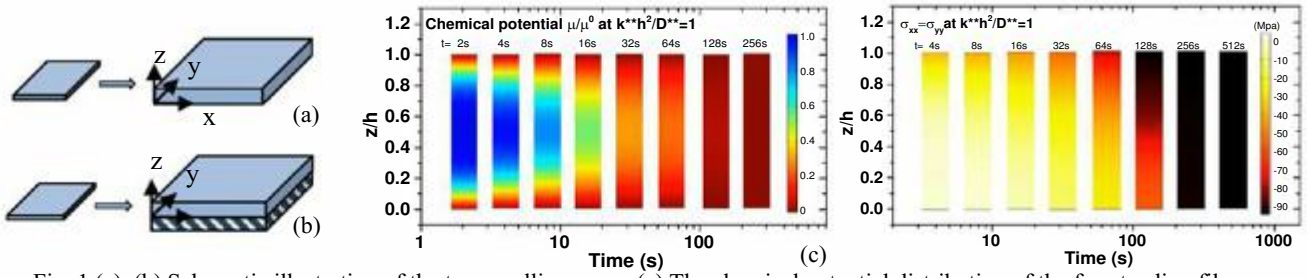

Fig. 1 (a), (b) Schematic illustration of the two swelling cases. (c) The chemical potential distribution of the freestanding film as a function of time. (d) The stress distribution of the constrained film as a function of time.

CONCLUSIONS

We developed a thermodynamically consistent model to describe the transient behaviors of reactive swelling material. The model is particularized by considering an isotropic free energy function and a single chemical reaction between the diffusive species and the material. Two transient problems exemplified the model application and the results illustrate the capability of the model to describe complex behaviors of chemo-mechanical systems.

References

[1] Hong W., Zhao X., et al.: A theory of coupled diffusion and large deformation in polymeric gels. *J. Mech Phys Solids* **56(5)**: 1779-1793, 2008.

[2] Loeffel K., Anand L.: A chemo-thermo-mechanically coupled theory for elastic–viscoplastic deformation, diffusion, and volumetric swelling due to a chemical reaction. *Int J Plasticity* **27:** 1409-1431, 2011.

[3] Hu S., Sheng S.: Non-equilibrium thermodynamics and variational principles for fully coupled thermal–mechanical–chemical processes. *Acta Mechanica* **224**: 2895-2910, 2013.

[4] Bouklas N., Huang R.: Swelling kinetics of polymer gels: comparison of linear and nonlinear theories. *Soft Matter* **8**: 8194-8203, 2012.

[5] Coussy O.: Poromechanics. John Wiley & Sons. Hoboken, NJ ,USA 2004.

DESIGN AND SIMULATION ON A MORPHING MARINE PROPELLER

Fanlong Chen[1], Liwu Liu[1 a)], Jian Sun[2], Yanju Liu[1], Jinsong Leng[2]
[1]*Department of Astronautic Science and Mechanics, Harbin Institute of Technology, Harbin, Heilongjiang, China*
[2]*Centre for Composite Materials and Structures, Harbin Institute of Technology , Harbin, Heilongjiang, China*

Summary Marine propellers play an important role in Marine Technology. However, the comprehensive performance of conventional marine propellers seems to be lower for advanced marine vehicles. Therefore, the improvement on the marine propeller catches and attracts increasing attentions of marine vehicle researchers. And this paper comes up with a novel method to design the marine propeller based on the morphing concept. The design scheme consists of three steps: the addition of active rotation flap (ARF) on the trailing edge of each propeller blade; design of suitable smart actuator to drive the flap; overall assembling of each member for the entire morphing propeller. The overall propeller can change its configuration with the flap's rotation. Then a simulation has been performed preliminarily for the acquisition of the dynamic properties of the morphing propeller. And the various dynamic properties have been obtained with different configurations of the propeller blades.

PREVIOUS WORK

The concept of the "active flap" stems from the wing flap of the airplane. On the taking-off stage of an airplane, the rotation of the flap on the trailing edge of the wing is conducted to increase the lift of the airplane wing. When transplanted this concept into the rotor of the helicopter, the active flap concept performs well on acoustic decrease and vibration attenuation as well as lift increase. However, few literatures focus on the active flap impacts on marine propellers but one master thesis [1], and in this thesis, the leading edge actuation system of marine propeller blade is fabricated and tested, the shape memory alloy actuating the active flap, with its effective results that the thrust force increases; the fabrication of the propeller is shown in Fig. 1.



Fig. 1 Leading Edge Actuation System Based on Shape Memory Alloy [1]

Theory

Before the design and simulation work, the statement of basic theory on fluid dynamics should be performed first. The work mainly embraces the conservation laws of the fluid, that is, mass and momentum conservation laws will relate to the calculation whose mathematical model are three groups of conservation equations; among them, the mass and momentum equations are mainly concerned in the work and they are as follows:

$$\frac{\partial u}{\partial x}+\frac{\partial v}{\partial y}+\frac{\partial w}{\partial z}=0 \tag{1}$$

$$\frac{\partial(\rho u)}{\partial t}+\frac{\partial(\rho u^2)}{\partial x}+\frac{\partial(\rho uv)}{\partial y}+\frac{\partial(\rho uw)}{\partial z}=-\frac{\partial p}{\partial x}+\frac{\partial \tau_{xx}}{\partial x}+\frac{\partial \tau_{yx}}{\partial y}+\frac{\partial \tau_{zx}}{\partial z}+F_x \tag{2-a}$$

$$\frac{\partial(\rho v)}{\partial t}+\frac{\partial(\rho uv)}{\partial x}+\frac{\partial(\rho v^2)}{\partial y}+\frac{\partial(\rho vw)}{\partial z}=-\frac{\partial p}{\partial y}+\frac{\partial \tau_{xy}}{\partial x}+\frac{\partial \tau_{yy}}{\partial y}+\frac{\partial \tau_{zy}}{\partial z}+F_y \tag{2-b}$$

$$\frac{\partial(\rho w)}{\partial t}+\frac{\partial(\rho uw)}{\partial x}+\frac{\partial(\rho vw)}{\partial y}+\frac{\partial(\rho w^2)}{\partial z}=-\frac{\partial p}{\partial z}+\frac{\partial \tau_{xz}}{\partial x}+\frac{\partial \tau_{yz}}{\partial y}+\frac{\partial \tau_{zz}}{\partial z}+F_z \tag{2-c}$$

[a)] Corresponding author. Email: liuliwu_006@163.com.

Among all these equations, ρ represents density, u、v、w means the velocities along x、y、z axes, p the pressure on the micro unit, $\tau_{xx}, \tau_{xy}, \tau_{xz}$ the component of viscous stress $\boldsymbol{\tau}$, F_x, F_y, F_z the components of body force $\boldsymbol{F}$.

STRUCTURE DESIGN OF MORPHING MARINE PROPELLER

A conventional marine propeller with two blades is designed firstly by SOLIDWORKS. Based on the model, the flaps, smart piezoelectric actuators and two sets of transmission mechanism are then designed and assembled in the propeller (Fig. 2). The actuators are set in the hub of the propeller, and each transmission mechanism in the corresponding blade.

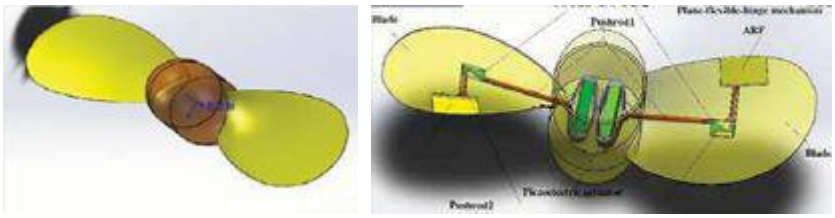

Fig. 2 The Design of Conventional (Left) and Morphing (Right) Marine Propellers.

SIMULATION OF 2D-HYDROFOIL WITH ACTIVE FLAP

In order to explore the relationship between force variation and flap rotation angle, a series of simulations are conducted with various flap angles (-6° ~6°) and advanced speeds (0.6~3.0 m/s). The simulation result curves are as Fig. 3.

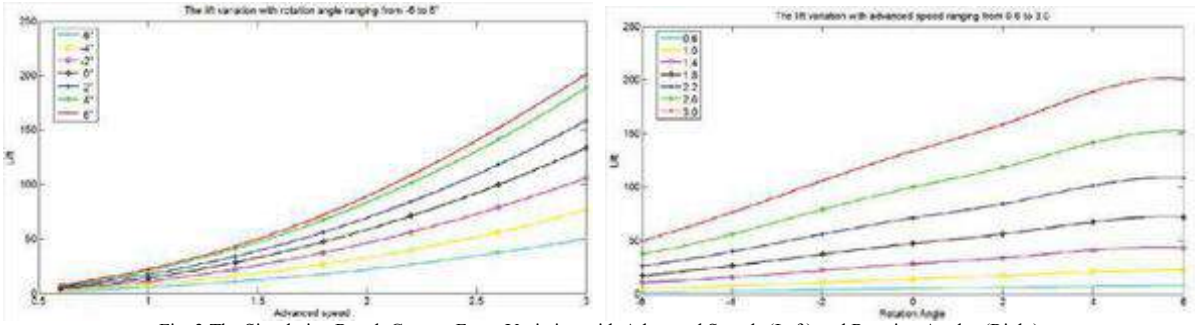

Fig. 3 The Simulation Result Curves: Force Variation with Advanced Speeds (Left) and Rotation Angles (Right)

CONCLUSIONS

The conventional and morphing marine propellers are designed and the preliminary simulations are conducted. The results show that the lift force will be changed with the various flap angles, which means that if the active flap technology was utilized on the propeller, the smart propeller can be obtained.

References

[1] Jonathan A. W.: Active Control of Underwater Propulsor Using Shape Memory Alloys. Master Thesis, Texas A&M University, 2005.

NUMERICAL MODELING OF GAS-EXPANDED LUBRICANTS IN HYBRID BEARINGS

Ssu-Ying Chien[1a)], Alexandrina Untaroiu[1], Mark S. Cramer[1]
[1]*Biomedical Engineering & Mechanics, Virginia Tech, Virginia, United States*

Summary A binary liquid mixture of synthetic oil and dissolved carbon dioxide could be a potential substitution of conventional lubricants. These smart-lubricants have the ability to provide a more efficient and reliable operation of turbomachinery through real-time adjustment of lubricant mixture properties. The goal of this study is to investigate the performance and phase behavior of these gas-expanded lubricants in a high-speed hybrid bearing using a three-dimensional CFD model. The results indicate that utilizing a smart-lubricant with altered properties results in lower power losses as compared to a bearing operating with pure oil. The resulting pressure and temperature distributions also indicate that two-phase behavior of carbon dioxide could trigger significant effects on bearing performance even under high ambient pressure condition.

INTRODUCTION

A smart lubricant, also called a gas-expanded lubricant (GEL), is a binary liquid mixture of synthetic oil and dissolved carbon dioxide (CO_2). The amount of gas dissolved can vary in time and can be correlated with the various operating conditions of the bearing. This provides direct control over the lubricant viscosity that could maximize bearing and rotor dynamic performance in real-time [1]. The lubricant properties of this binary mixture can be easily tuned by adjusting the mixture composition via the pressure inside the bearing housing as shown in Fig. 1(a). Although previous studies have evaluated the performance of GEL in high-speed rotating bearings, all of them were based on the two-dimensional form of generalized Reynolds equation with an assumption of a single-phase fluid, which does not account for the potential of dissolved CO_2 vaporizing or separating from lubricant oils [2]. Therefore, the objective of this study is to utilize three-dimensional numerical modelling to investigate the performance as well as the phase behavior of smart lubricants in a hybrid bearing under different operating environments. A series of single-phase simulations for different lubricants is performed to evaluate the potential two-phase behavior and bearing performance in terms of power loss, pressure and temperature distributions, as well as the corresponding mixture composition. These simulation results establish a foundation for further development of the two-phase model to study the complex fluid phase behavior inside high-speed rotating bearings under various operating conditions.

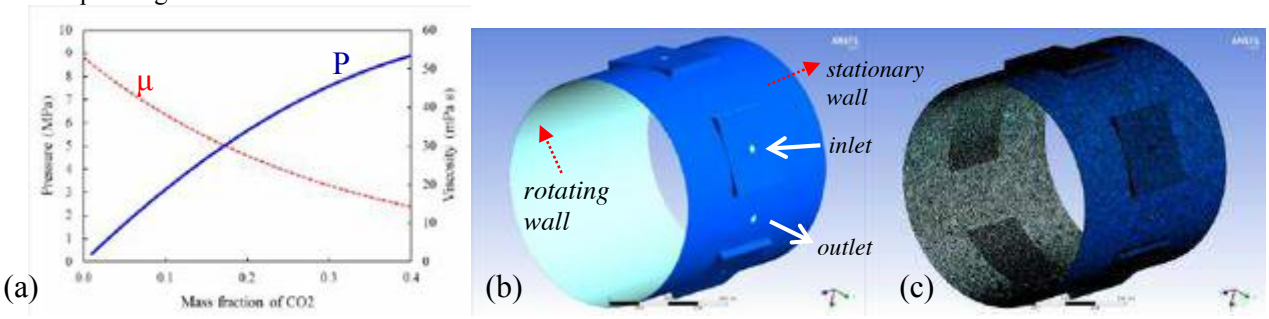

Fig. 1. (a) Smart lubricant viscosity adjustment potential, (b) Boundary conditions, and (c) CFD model of a hybrid bearing

METHODOLOGY

The high-speed hybrid bearing is selected from the literature and is shown in Fig. 1(b) [3]. It is 76.2 mm in diameter and 76.2 mm in axial length, has a radial clearance of 0.127 mm and 0.5 eccentricity ratio. The five square recesses on the stator are 27 mm in length and 0.254 mm in depth, each having a radially directed inlet orifice of 2.49 mm in diameter. There is one outlet port, as shown in Fig.1b). The operating speed is 24,600 rpm. The boundary conditions setup and lubricant properties are set according to previous work in [3]. The performance and phase behavior of GEL are first analysed using a three-dimensional single-phase model using ANSYS-CFX, which solves the Reynolds-averaged Navier-Stokes equations and the energy equation. The Shear Stress Transport turbulence model is selected. The boundary conditions include: adiabatic no slip walls, static pressure and temperature at the five inlet orifices, and static pressure at the outlet port. The lubricants analysed in this study included polyolester oil (POE) and smart lubricant (POE + 20% dissolved CO_2). The viscosity of POE and smart lubricant at 55°C are 34.04 mPa s and 22.4 mPa s, respectively. An empirical equation for solubility of CO_2 in POE based on experimental data from Hauk [4] was utilized to analyse the phase behavior: $P = a_1C + a_2CT + a_3C^2 + a_4C^2T + a_5C^2T^2$, where mass fraction of CO_2, C is described as a function of pressure, P and temperature, T; the empirical coefficients a_1 = -150.3, a_2 = 0.5926, a_3 = 525.1, a_4 = -3.317 and a_5 = 0.004917. The accuracy of the CFD model is demonstrated by comparing the simulated lift force with the experimental value from Franchek and Childs [5], and the relative error was approximately 4.3%.

a) Corresponding author. Email: armani23@vt.edu

RESULTS AND DISCUSSION

The effect of using POE and the smart lubricant on the performance of a hybrid bearing was numerically modelled considering the lubricant is fed into the bearing at a pressure of 7 MPa and temperature 55°C. The simulation results show that the bearing power loss produced by the smart-lubricant is 11.9 kW, resulting in a 13.1% reduction compared to the POE-lubricated case due to the lower viscosity.

Figure 2 (a) and (b) present the comparison of pressure and temperature profiles between a smart-lubricant delivered under two different conditions: (1) **low ambient pressure** with the supply pressure of 5.9 MPa, supply temperature of 40°C and outlet pressure of 0 MPa, and (2) **high ambient pressure** with the supply pressure of 6.4 MPa, supply temperature of 40°C and outlet pressure of 5.9 MPa. As can be seen, the peak pressure occurred on the side of the bearing between the applied load and the outlet orifice. Also, the wall boundary imposed at the axial ends of the bearing to mimic the effects of the pressure annular seals that isolate the bearing cavity induced a much higher temperature in these regions. Figure 2 (c) shows the calculated mass fraction of dissolved CO_2 based on the resulting pressure and temperature. These results indicate that the local pressure drop and the increased temperature can potentially result in the dissolved *CO_2 vaporized or separated* from the oil even under high ambient pressure condition. Further study will focus on the two-phase flow modelling to study the complex two-phase behavior of smart-lubricants in high-speed rotating bearings, as well as its implication on their performance under various operating conditions.

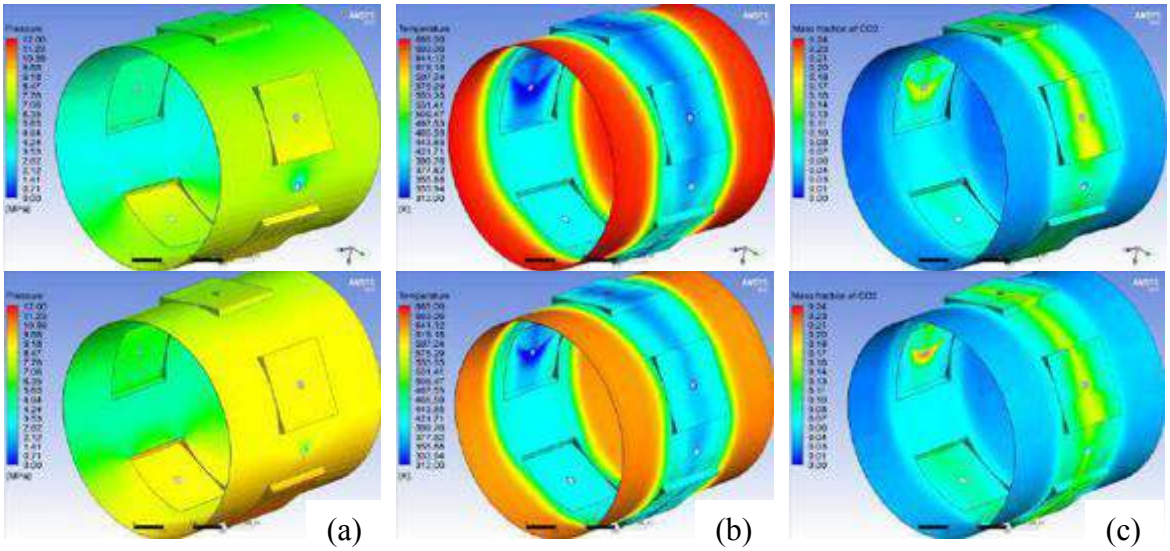

Fig. 2. (a) Pressure profile, (b) temperature profile and (c) mass fraction of dissolved CO_2 for a smart-lubricant delivered at low ambient pressure (1st row) and high ambient pressure (2nd row)

CONCLUSIONS

The performance and phase behavior of smart-lubricants in a high-speed hybrid bearing was investigated using a three-dimensional CFD model. The results indicated that utilizing a smart-lubricant with altered properties results in lower power losses as compared to a bearing operating with pure oil. The simulation results suggest that the two-phase flow could possibly exist inside a high-speed rotating bearing even under high ambient pressure. This is due to the decrease of local pressure and the rise of local temperature at the axial ends of bearing which are sealed. A two-phase flow model, therefore, should be developed in the future to investigate the potential vaporization or separation of dissolved CO_2 as well as its impacts on bearing performance under a variety of operating conditions.

References

[1] Clarens, A., Younan, A., and Wang, S.: Feasibility of Gas-Expanded Lubricants for Increased Energy Efficiency in Tilting-Pad Journal Bearings, *J. Tribology*, 132(3), pp. 031802-1-031802-8, 2010.

[2] Weaver, B.K., Younan, A. A., and Dimond, T. W.: Properties and Performance of Gas-Expanded Lubricants in Tilting Pad Journal Bearings, *Tribology Transactions*, 56, pp. 687-696, 2013.

[3] Weaver, B.K., Gen, F., Clarens, A. and Untaroiu A.: Performance Analysis of Gas-Expanded Lubricants in a Hybrid Bearing Using Computational Fluid Dynamics, Proceeding of the ASME International Mechanical Engineering Congress & Exposition, Texas, USA, 2015.

[4] Hauk, A. and Weidner, E.,: Thermodynamic and Fluid-Dynamic Properties of Carbon Dioxide with Different Lubricants in Cooling Circuits for Automobile Application, *Industrial & Engineering Chemistry Research*, 39(12), pp 4646–4651, 2000.

[5] Franchek, N., and Childs, D.: Experimental Test Results for Four High-Speed, High-Pressure, Orifice-Compensated Hybrid Bearings, *J. Tribology*, 116(1), pp. 147-153, 1994.

HIGH-FREQUENCY MARTENSITE REORIENTATION IN NI-MN-GA — TEMPERATURE RISE AND ITS INFLUENCE

Oana-Zenaida Pascan[1,2], Yongjun He [2a)], Ziad Moumni[1,2], Weihong Zhang[1]
[1] *Engineering Simulation and Aerospace computing, Northwestern Polytechnical University Xi'an, P.R.China*
[2] *IMSIA, ENSTA ParisTech, CNRS, CEA, EDF, Université Paris-Saclay, Palaiseau, France*

Summary: Ni-Mn-Ga Ferromagnetic Shape Memory Alloy (FSMA) has advantages in obtaining high-frequency large cyclic deformation with the magnetic-field driven martensite reorientation. However, most existing high-frequency tests on FSMA were conducted only for short time periods (a few seconds) to avoid temperature rise. In this work, we study the material's long-time (> 4 minutes) high-frequency dynamic behaviour. Particularly, the mechanism for the temperature rise and its influence on the dynamic output strain under different ambient conditions (with stagnant air and various ambient air flows) are investigated.
Keywords: Ferromagnetic Shape Memory Alloy, Magneto-thermo-mechanical coupling, High-frequency actuation.

Introduction

Ni-Mn-Ga Ferromagnetic Shape Memory Alloy (FSMA) is a promising candidate for actuators due to the high-frequency Magnetic-Field-Induced-Strain (MFIS) of its martensite reorientation [1,2]. In literature, there are reports on different aspects of the material's behaviours, such as the study on the microstructures of twins and magnetic domains [3,4], modelling of the magneto-mechanical coupling behaviours [5-7], and the dynamic effects (inertial effects) [3, 8]. However, most existing high-frequency tests on FSMA were conducted only for short time periods (e.g. only a few seconds in [3, 8]) because there was significant temperature rise in the dynamic tests. The temperature rise would change the material's performance since many of the material's properties are sensitive to temperature [9]. Recently, we measured the specimen's temperature rise and observed the twin morphology and found that the temperature rise was mainly due to the energy dissipation of the Type II twin boundary motion in slim specimens (eddy-current heating is ignorable) [10]. Based on the same dynamic setup, but with thicker specimens (with higher temperature rise), we conducted the tests under high-frequency long-time actuations in order to reveal the temperature influence on the output strain in current paper. In the following, the experimental setup and results are reported and some preliminary conclusions are drawn.

Experiment setup and material properties

The transformation temperatures of the single crystal $Ni_{50}Mn_{28.5}Ga_{21.5}$ (at. %) (from Goodfellow) M_s, M_f , A_s and A_f are 52.5°C, 51°C, 58.2°C and 59.8°C, respectively. The sample's dimensions are 2mm x 5mm x 20mm. All faces of the sample are parallel to the {1 0 0} planes of the austenite. A horizontal magnetic field (2 mm side) and a vertical compressive force (20 mm side) are applied (see Fig. 1). Before each test, the sample is largely compressed vertically to obtain a single variant with a vertical short-axis (so-called the stress-preferred variant). In the test, an initial compression stress (0.1 MPa) is set by the spring (of stiffness 15 kN/m) on the single variant. A field (0.6 Tesla of frequency 90 Hz) is applied to trigger cyclic martensite reorientation (switching between the stress-preferred variant and the field-preferred variant) leading to variation in the sample's length measured by a laser displacement sensor. The sample's temperature is measured with a thermocouple. In order to reduce the heat conduction from the sample to the fixtures, the sample holders are made of plexiglass with low heat conductivity. An air flow (with controllable velocity) is used to change the heat convection around the sample (i.e., change the characteristic heat transfer t_h [10]).

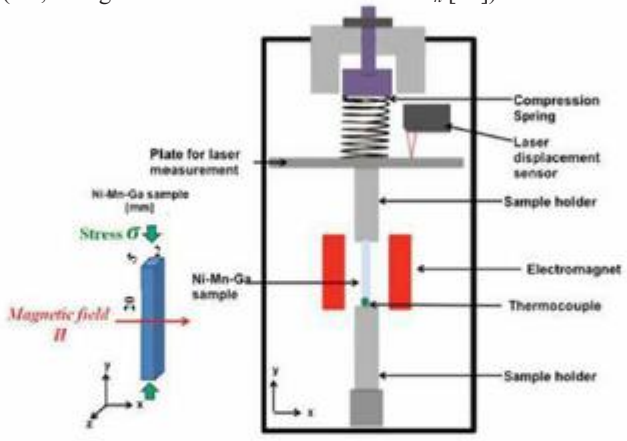

Fig. 1 Experimental setup for high-frequency magentic field indued martensite reorientation in Ni-Mn-Ga.

[a)] Corresponding author: Yongjun He . Email: yhe@ensta.fr

Experimental results

It is seen in Fig. 2, when the air flow velocity v increased from 0 m/s (stagnant air in Fig. (2a)) to 30 m/s (high-speed air flow in Fig. (2e)), the sample's steady-state temperature decreased from 51.3 °C to 28.6 °C while the steady-state output strain changed non-monotonically (increased from 0.8% in Fig. (2a) to 4.1% in Fig. 2(c), and then decreased to 3.1% in Fig. (2e)). Particularly, it is seen that there is a sudden drop in the output strain in Fig. (2a), where the sample's temperature reaches a high level close to the phase transformation temperature (note: the temperature is measured at the specimen's end by a thermocouple and the middle of the specimen might have higher temperature due to the localized dissipative twin boundary motion). One of the possible reasons for the strain drop is that phase transformation is triggered by the high temperature rise. However, to confirm this mechanism, further experiments and theoretical modelling about the heterogeneous twin boundary motion and the associated temperature evolution need to be developed.

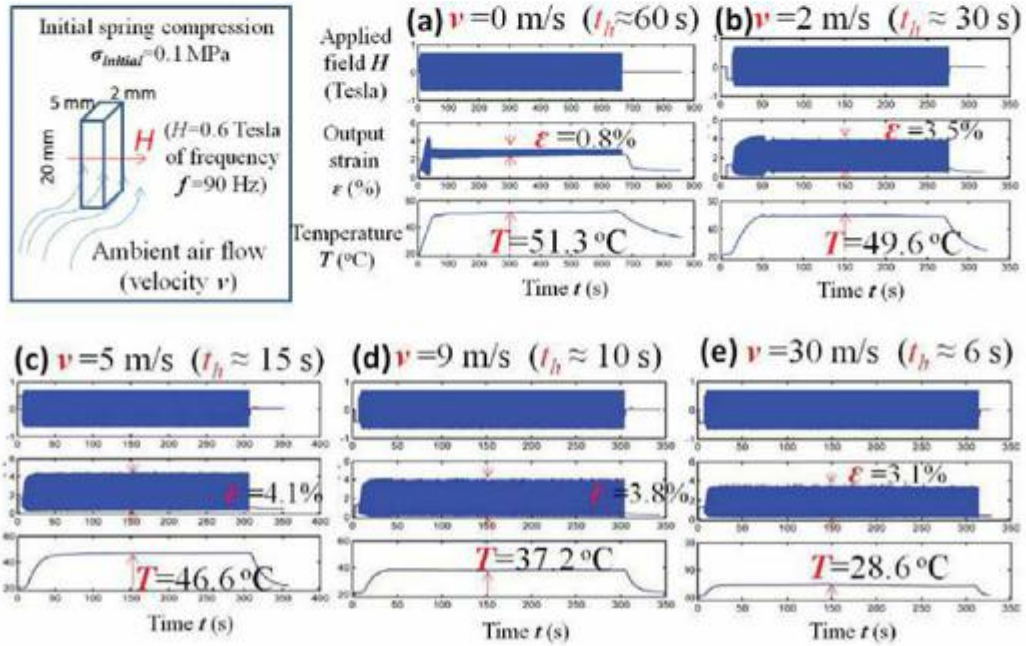

Fig. 2 The ambient-flow influence on the temperature evolution and output strain under the long-time actuation of a high-frequency magnetic field (0.6 Tesla of frequency 90 Hz).

CONCLUSIONS

- The ambient-flow significantly influences the sample's temperature which affects the output strain: the stable output strain changes non-monotonically with the ambient air velocity (or the characteristic heat transfer time t_h) while the stable (steady-state) working temperature decreases monotonically with increasing air flow (decreasing t_h).
- When the temperature rise is significant (close to phase transformation temperature), the sample doesn't stop deforming, but automatically adjusts its active zones to reduce the output strain (from ~4% to ~1%) in order to reduce the heat source to maintain its temperature below M_S (52.5 °C). In other words, long time actuation is still possible even in the cases of high temperature rise, e.g., stagnant air ambient, thick specimens, etc.
- Further questions and study: Did the phase transformation really occur in the high-frequency long-time actuation? How did the sample reduce the output strain to keep the temperature requirement (below M_S)?

References

[1] K. Ullakko, J. K. Huang, C. Kantner, R. C. O'Handley, and V. V. Kokorin, *Appl. Phys. Lett.* 69, 1966 (1996).

[.] S. J. Murray, M. Marioni, S. M. Allen, R. C. O'handley, and T. A. Lograsso, *Appl. Phys. Lett.* 77 886 (. 000)

[3] Y.W. Lai, Magnetic Microstructure and Actuation Dynamics of NiMnGa Magnetic Shape Memory Materials (Ph.D. thesis), Technical University, Dresden (. 009).

[4] Qi. Peng, Yongjun He, and Ziad Moumni, *Acta Materialia* 88, 13–. 4 (. 015).

[5] Kiefer, B.,Lagoudas,D.C.,. *Philos.Mag.*85,4. 89–43. 9 (. 005).

[6] Yongjun He, Xue Chen, Ziad Moumni. *J. Appl. Phys.* 11. , 03390. (. 01.).

[7] Xue. Chen, Ziad Moumni, Yongjun He, Weihong Zhang, *Journal of the Mechanics and Physics of Solids* 64 . 49–. 86 (. 014).

[8] C.P.Henry, Dynamic actuation properties of Ni-Mn-Ga ferromagnetic shape memory alloys. (Ph. D. thesis), MIT, USA (. 00.).

[9] L. Straka, A. Soroka, H. Seiner, H. Hänninen, and A. Sozinov. *Scripta Materialia* 67, . 5-. 8 (. 01.).

[10] Oana-Zenaida Pascan, Yongjun He, Ziad. Moumni and Weihong Zhang, *Scripta Materialia* 104, 71–74 (. 015).

IMPEDANCE DRIFT DUE TO THERMAL CYCLING OF MACRO FIBER COMPOSITES

Jared D. Hobeck[1a)], Robert B. Owen[2] & Daniel J. Inman[1]
[1]*University of Michigan, Department of Aerospace Engineering, Ann Arbor, MI, USA*
[2]*Extreme Diagnostics Inc., Boulder, Colorado, USA*

Abstract This paper summarizes results of a recent experimental investigation concerning the effects of long-term thermal cycling on macro fiber composite actuators. More specifically, this work focuses on how thermal cycling causes impedance measurements to drift and eventually stabilize after many cycles. This impedance drift may lead to significant implications for impedance-based structural health monitoring systems, strain sensing, and precision positioning devices that are implemented in dynamic temperature environments.

INTRODUCTION

Macro fiber composite (MFC) actuators are used by several industries in a wide variety of applications including: energy harvesting, structural health monitoring (SHM), precision optics, strain sensing, and active vibration suppression [1,2]. MFCs are composed of aligned rectangular fibers of piezoelectric ceramic material encased in a structural adhesive, layered with interdigitated electrodes, and sandwiched between two layers of polyimide film for electric isolation and additional structural reinforcement [3]. This unique design allows MFCs to be more flexible and durable compared to conventional single wafer piezoceramic actuators.

Bonding a MFC to a structure creates an electromechanically coupled system where electrical impedance of the MFC is influenced by the mechanical impedance of the structure. Any structural modification to this system (*e.g.*, damage or defects) changes its mechanical impedance, thus changing the electrical impedance measured with the MFC. Using these concepts to detect, locate, and assess damage from impedance measurements is the central goal of impedance-based SHM research. If significant changes in impedance are caused by anything other than structural damage (*e.g.*, thermal cycling) then the SHM system will fail unless proper compensation techniques are developed and implemented.

EXPERIMENTAL DETAILS

Impedance drift due to thermal cycling was first observed in a related study presented in 2014 by Faria *et al.* [4]. The current research builds on that of [4] by presenting results of a more rigorous experimental investigation. This was accomplished by testing multiple specimens in an isolated and controlled environmental chamber thus eliminating as many external variables as possible. Six identical specimens were made by bonding a MFC (model: M2814-P2-HT from Smart Material Corp.) to the base of a 6061-T6 aluminium cantilever beam having dimensions 127 x 19 x 1.59 mm with DP-460 structural adhesive following a standard vacuum bag bonding procedure. Three beams were placed in an environmental chamber and were exposed to repeated thermal cycling from -60°C to 90°C. Impedance measurements were taken at -60°C, 25°C, and 90°C during each cycle after allowing the system to achieve a steady state at each of the three temperature targets. Each cycle required 180 minutes to complete and total of 46 cycles were performed. The other three beams were placed outside the chamber and were used as reference or *control* specimens that were maintained at room temperature for the duration of the experiment.

All impedance measurements were carried out and managed by a LabVIEW program developed as part of this research. Measurements from this LabVIEW-based impedance analyzer were validated by comparing results with a proven technique. The analyzer generates a sine chirp signal to drive a MFC as the system input (X) which has user-defined start and stop frequencies, sample rate, and amplitude. The response signal (Y) is measured simultaneously at a user-defined sample rate. The frequency response function (FRF) is then calculated with $H = S_{xy} / S_{xx}$ where S_{xy} and S_{xx} are the cross- and auto- power spectrums respectively and H is the FRF. Given H, the reference resistance R_s and the input impedance of the data acquisition hardware, it is then possible to calculate the electromechanical impedance of the structure using fundamental circuit analysis techniques.

Given any two plots such as a pair of impedance measurements or FRFs, the difference between the two plots can be represented as a single value by calculating what will be referred to here as the *damage metric*. The damage metric used for this analysis is defined as,

$$CCD = 1 - \left| \frac{\sum_N \left(Z_b - \overline{Z}_b\right)\left(Z - \overline{Z}\right)}{\sqrt{\sum_N \left(Z_b - \overline{Z}_b\right)^2}\sqrt{\sum_N \left(Z - \overline{Z}\right)^2}} \right| \tag{1}$$

where Z_b is the baseline plot, Z is the new or damaged plot, N is the number of samples in each array, and the overbar denotes the mean value. This damage metric was used to make several comparisons between impedance measurements in the following results.

[a)] Corresponding author. Email: jdhobeck@umich.edu

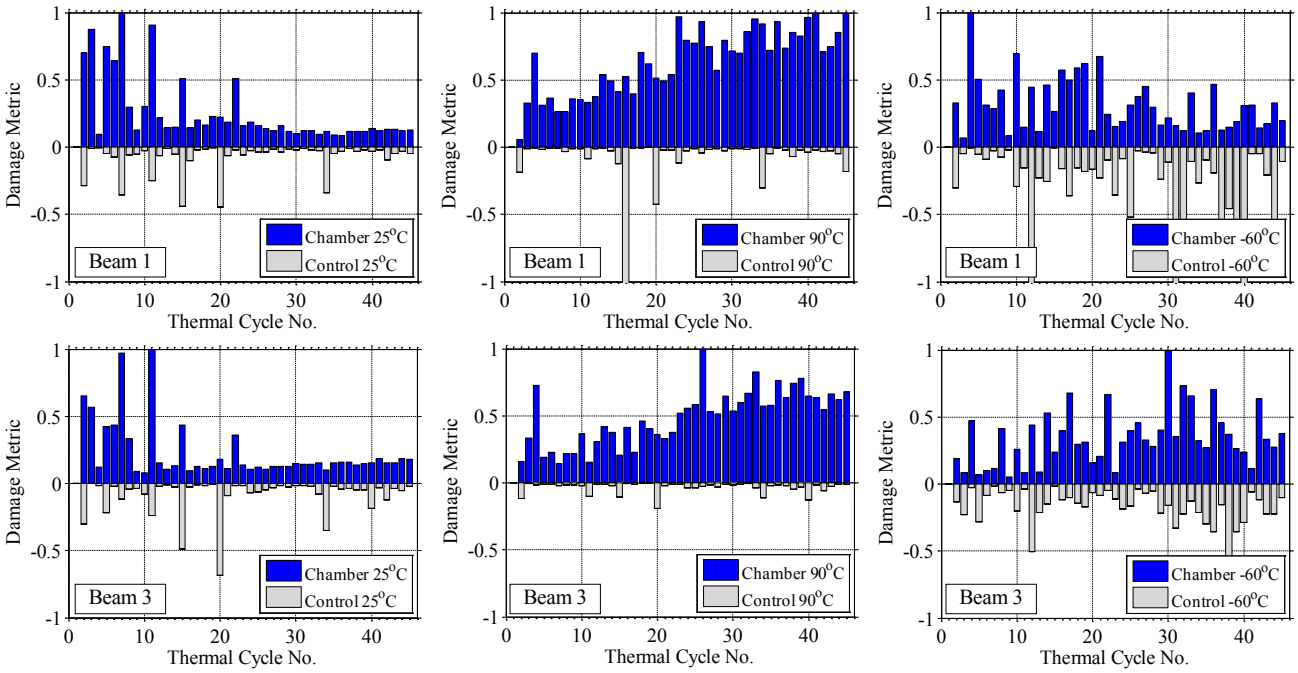

Figure 1. Summary of damage metrics for beam pairs 1 and 3 calculated from impedance measurements for the DP-460 specimens comparing the chamber beams (positive values) to the control beams (negative values).

RESULTS

Figure 1 shows a collection of damage metrics calculated for beam pairs 1 and 3 where the baselines were taken to be the first impedance measurements on the first temperature cycle for each beam pair. Results of beam pair 2 have been omitted due to a faulty connection that was discovered during testing. Each plot in Figure 1 was generated by first calculating the damage metrics for a chamber beam and the corresponding control beam. The damage metrics for each pair were then normalized by their maximum damage metric from all 46 cycles. The damage metrics for the chamber beams are plotted on the positive *y*-axis and the control beam damage is plotted on the negative *y*-axis. This was done to provide a direct comparison of the impedance drift between the chamber and control beams at each target temperature as a function of thermal cycle number.

The results in Figure 1 show that impedance measurements stabilize after approximately 25 cycles when measured at 25°C and 90°C; however, this stabilizing trend is not as apparent at -60°C. Also, the damage metric magnitude of the chamber beams at -60°C is similar to that of the control beams. This means that impedance measurements of thermally cycled beams at -60°C are approximately as stable and consistent as impedance measurements taken from beams that did not undergo thermal cycling.

CONCLUDING STATEMENTS

The authors present a brief summary of results from an experimental investigation focused on impedance drift in MFC actuators exposed to thermal cycling. Impedance measurements of a MFC bonded to an aluminium beam were taken at 25°C, 90°C, and -60°C during each cycle for a total of 46 cycles. Results show that the impedance appears to drift and be inconsistent before stabilizing after approximately 25 cycles. The cause of this drift is currently unknown; however, it is most likely due to long-term curing effects of epoxy or other construction materials within the MFC. Future work will focus on determining the exact cause of this drift followed by developing strategies to compensate for or eliminate it completely.

Acknowledgements

This research was funded in part by Extreme Diagnostics, Inc., (SBIR Phase I from NASA), "Macro-Fiber Composite-Based Actuators for Space" for which the authors would like to extend their sincere gratitude.

References

[1] Sodano, H.A., Park, G., and Inman, D.J., "An investigation into the performance of macro-fiber composites for sensing and structural vibration applications," *Mechanical Systems and Signal Processing* **18**(3), 683–697 (2004).

[2] Hagood, N., and Bent, A., "Development of piezoelectric fiber composites for structural actuation," in *AIAA/ASME/ASCE/AHS/ASC 34th Structures, Structural Dynamics, and Materials Conference* **1**, pp. 3625–3638 (1993).

[3] Wilkie, W.K., Bryant, R.G., Fox, R.L., Hellbaum, R.F., High, J.W., Jalink, A., Little, B.D., and Mirick, P.H., *Method of fabricating a piezoelectric composite apparatus*, US Patent 6,629,341 (2003).

[4] Faria, C.T., Owen, R.B., and Inman, D.J., "Macro-fiber composites performance under thermal cycling for impedance-based SHM applications," *Proceedings of SPIE - The International Society for Optical Engineering* **9057** (2014).

FABRICATION AND CHARACTERIZATION OF EPOXY BASED SHAPE MEMORY NANO-COMPOSITES

Hongqiu Wei[1], Yanju Liu[2] & Jinsong Leng[1a)]
[1]*Centre for Composite Materials and Structures, Harbin Institute of Technology, Harbin, Heilongjiang, China*
[2]*Department of Astronautic Science and Mechanics, Harbin Institute of Technology, Harbin, Heilongjiang, China*

Summary Epoxy based shape memory polymers (ESMPs) always present inherent brittleness and susceptible to fatigue due to the highly cross-linked network. To solve the above problems, in this study, we prepared a type of epoxy based shape memory nano-composites (ESMNCs) by introducing nano-carboxylic acrylonitrile butadiene rubber powder to ESMP matrix. The thermal, mechanical and shape memory behaviour of such ESMNCs were systemically investigated. Results demonstrated that the toughness of the fabricated materials greatly improved, without sacrifice of the Young's modulus and thermal properties. At the same time, the ESMNCs showed desirable shape memory behaviour with fast responsive speed, high shape fixing and recover ratio.

INTRODUCTION

Shape memory polymers (SMPs) as a kind of smart materials have obtained significant advancements in the past decades. SMPs feature the performance to recover the initial shape from the temporary shape upon exposure to suitable external stimulus [1, 2]. SMPs exhibit a plenty of merits, such as large deformation, lightweight, feasible manufacturability and low cost compared with shape memory alloys (SMAs) [2]. To date, many SMPs including epoxy based shape memory polymer (ESMPs), styrene based shape memory polymers (PSMPs), polyaspartimide-urea based shape memory polymers and shape memory polyurethanes (SMPUs) etc. have been reported [1]. Among them, ESMPs exhibiting high glass transition temperature (T_g), fine chemical stability, high hardness and superior shape memory behaviour. However, as a typical class of thermosetting SMPs, ESMPs always present inherent brittleness and susceptible to fatigue due to the highly cross-linked network, which greatly hinder their promising and practical applications, especially in engineering fields [3]. Some researches have focus on improving the toughness of ESMPs, however, the results lead to the sharp decrease in Young's modulus, and thermal properties [3, 4]. Therefore, to further enhance and broaden the applications of ESMPs in engineering areas, it is necessary to fabricate ESMPs with high toughness and excellent overall properties.

In this study, a kind of epoxy based shape memory nano-composites (E-SMNCs) were fabricated by introducing nano-carboxylic acrylonitrile butadiene rubber powder (CNBENP) to the polymer matrix. Through characterizations, we found that such materials possess superior mechanical, thermal and shape memory properties.

EXPERIMENTAL SECTION

Materials

ESMPs were fabricated as presented in our previous reports [5]. Nano carboxylic acrylonitrile butadiene rubber (Narpow VP-501) in powder form were obtained from SINOPEC, Beijing Research Institute of Chemical Industry (BRICI), China.

Preparation of the samples

The E-SMNCs were fabricated as following steps. To remove the influence of moisture, the obtained nano-rubber powder was dried at 50 ℃ for 24 h in an oven. After that, 100 phr and 8 phr nano-rubber were mixed by using a three-roll mill for three times. Then, curing agents and accelerators were added to the mixture and stirred at 80 ℃ for 30 min. The obtained mixture was degassed at a vacuum oven for 10 min at 80 ℃ and then casted into the pre-heated glass moulds. At last, the ESMNC blend was put into an oven for curing. The curing condition was set as 80 ℃ for 3 h, 100 ℃ for 3 h and 150 ℃ for 5 h. After cooling down to room temperature naturally, the ESMNCs were obtained.

RESULTS AND DISCUSSES

Thermal mechanical properties

Dynamical Mechanical Analyzer (DMA/SDTA861e, Mettler–Toledo) experiment was carried out to investigate the thermo-mechanical capabilities of the fabricated ESMNCs. The experiment was conducted in tension mode at a frequency of 1 Hz. The test temperature changed from 25 ℃ to 200 ℃ at a rate of 5 ℃/min. The result of the DMA test is shown in Fig. 1. It is clearly that the addition of nano-rubber into the ESMP matrix has little effect on the storage modulus and T_g as we expected.

a) Corresponding author. Email: lengjs@hit.edu.cn

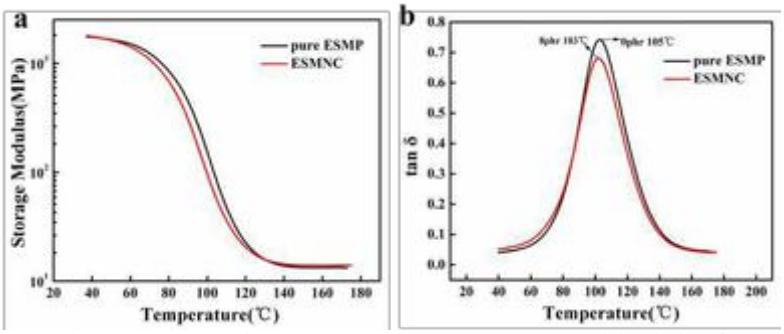

Fig. 1 DMA curves of pure ESMP and ESMNC (a) storage modulus (b) loss factor.

Mechanical properties

The mechanical properties were tested by Zwick/Roell Z010 (Zwick GmbH & Co. KG) instrument under tensional mode at room temperature and at T_g, respectively. The specimens were prepared according to the standard ASTM D638, Type IV. The strain rate was 5 mm/min. Fig.2 presents the original stress-strain curves. It can be obtained that, after introduction of nano-rubber, the elongation at break of ESMP improves at both low and high temperature. Although the facture stress show decreasing trend, the Young's modulus keep constant even a little increase at room temperature, which is an expected phenomenon in nano-rubber modified ESMP.

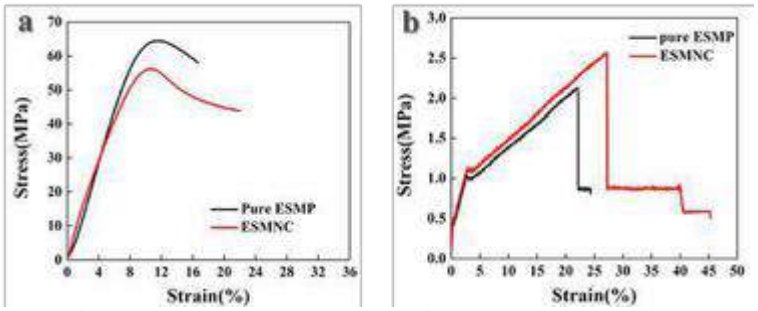

Fig. 2 The stress-strain curves of pure ESMP and ESMNC (a) at room temperature (b) at T_g.

Shape memory behavior

Shape memory behavior was investigated by a bending-recovery test. A straight specimen was treated as the original shape. Then, it was bended into a "U" shape as its temporary shape at T_g+20 ℃. The "U" shape bar could be fixed by cooling down the sample to room temperature. When deformed sample bar was re-heated above T_g +20 ℃, the specimen could recovery its original shape. Fig. 3 exhibit the visual demonstration of the shape recovery process of ESMNC. Clearly, the sample can recover its original strip shape from the temporary "U" shape with a fast responsive speed.



Fig. 4 Shape recovery process of ESMNC.

CONCLUSIONS

In this study, we fabricated a kind of epoxy based shape memory nano-composites (ESMNCs) with superior mechanical, thermal and shape memory properties. Combining the excellent overall properties and smart shape memory effect, the application of such materials will be much wider.

References

[1] Leng J. S., Lan X., Liu Y. J., Du S. Y.: Shape-memory polymers and their composites: Stimulus methods and applications. *Prog. Mater. Sci.* 56: 1077-1135, **2011**.
[2] Meng Q. H., Hu J. L.: A review of shape memory polymer composites and blends. *Compos. Part A-Appl. S.* 40: 1661-1672, **2009**.
[3] Rousseau I. A., Xie T.; Epoxy based shape memory polymer: composition, structure, properties and shape memory performances. *J. Mater. Chem.* 20: 3431-3441, **2010**.
[4] Leonardi A. B., Fasce L. A., Zucchi I. A., Hoppe C. E., Soule E. R., Perez C. J., Williams R. J. J.: Shape memory epoxies based on networks with chemical and physical crosslinks. *Eur. Polym. J.* 47: 362-369, **2011**.
[5] Leng J. S., Wu X. L., Liu Y. J.: Effect of a linear monomer on the thermomechanical properties of epoxy shape-memory polymer. *Smart Mater.Struct.*18: 095031, **2009**.

PERFORMANCE IMPROVEMENT OF IMPACT DRIVE MECHANISM MOTOR USING THE NONLINEAR PROPERTY OF THE DRIVING MATERIAL

Yimin Tan*[1], Zuguang Zhang [2], and Jean Zu[1]
[1]*Department of Mechanical and Industrial Engineering,University of Toronto, Toronto, Ontario, Canada*
[2]*Advanced Mechatronics of Toronto Inc., Mississauga, Ontario, Canada*

Summary Impact Drive Mechanism (IDM) motors, compromising the impact force and the friction to achieve the motion, have a great potential to be applied in the precision industry. Traditionally, to eliminate the complex behaviours of driving materials, these motors are majorly operated when the material is driven employing its linear property. The prevalent way of improving the performance of the IDM motors is to use the optimized driving waveform. However, using a complex waveform greatly increases the burden of driving hardware. The main objective of this work is to investigate the performance improvement of IDM motors utilizing the nonlinear property of the driving material. Experiments are conducted to explore the influence of Galfenol nonlinear property on the performance of IDM motors, whose nonlinear property is modulated using a bias DC current. The result indicates that the motor motion performance can be greatly improved using the quadratic nonlinear property of Galfenol.

INTRODUCTION

Impact Drive Mechanism (IDM)[1] has been applied in the development of various actuators and motors for the application in robotics and precision engineering industry. By applying a sawtooth driving waveform, the rapid elongation and slow shrinkage of the driving element can be achieved which results in a series of impact forces. When the impact force is larger than the static friction during the sudden deformation, the slip stage can be realized. While the driving material is experiencing the slow deformation, the generated inertia force is not large enough to overcome the friction force. Then, the motor does not exhibit an actuation. By repeating this step, a continuous slip-stick motion can therefore be realized. Existing IDM motors use the linear response of these driving materials for achieving the stick-slip motion to restrain the nonlinear property of the driving materials. Previous researchers[2] have made a lot of efforts to optimize the driving signal in order to achieve an improved motor performance. Unfortunately, because of the intrinsic complexity of the friction and the driving material property, the development of a comprehensive model consumes tremendous efforts. In addition, the optimized driving signal waveform varies significantly because of the motor application scenario. Also, as the optimized driving signal usually will not be in a regular type of waveform, generating and amplifying these signals requires more sophisticated hardware. In order to simplify the driving signal and the hardware, the objective of this work is to investigate the influence of the driving material nonlinear property on the performance of the IDM motors.

PROPELLING MECHANISM ANALYSIS AND EXPERIMENT VALIDATION

Piezoelectric materials have been prevalently employed in the development of IDM motors. In this study, a novel magnetostrictive material, Galfenol[3], is used to explore the effect of material nonlinear property on the performance of the IDM motors because of two reasons. First, different from the piezoelectric material that suffers from its brittle nature, Galfenol is known for the excellent mechanical property and thermal robustness. Second, Galfenol shows more controllable nonlinear effects than piezoelectric materials, which typically include the quadratic and saturation nonlinearity.

Figure 1 shows the prototype of the IDM motor for the experiment in this work. A permanent magnet is attached at the bottom of the motor mainbody to provide a constant bias magnetic field within Galfenol, whose strength is half of the saturation magnetic field strength. Figure 2 reveals the nonlinear relationship between the deformation of the Galfenol sample and the driving current. When the driving current amplitude exceeds 746 mA, the introduced driving magnetic field strength amplitude is larger than the bias magnetic field. Subsequently, the quadratic behaviour and saturation behaviour can be explicitly observed. This indicates that the quadratic nonlinearity and the saturation nonlinearity of Galfenol can be triggered individually by adjusting the bias magnetic field with a DC bias current while keeping a Pk-Pk current of 746 mA. When the DC current is negative, the quadratic nonlinearity can be the dominant phenomenon. Otherwise, the saturation nonlinearity is the dominant nonlinear effect.

Making an assumption that the response of Galfenol is absolutely linear against the driving signal, the inertia force generated by the motor is a continuous pulse signal with positive and negative spikes of a same amplitude. In order to improve the performance of IDM motors, the acceleration amplitude difference should be enlarged. The Figure 3 (a,b) and (c,d,e) shows two sets of Galfenol responses considering the saturation nonlinearity and the quadratic nonlinearity, respectively. In the quadratic nonlinearity dominating case, during the sudden change of the driving current, the material endures the process

*Corresponding author. Email: yimin.tan@mail.utoronto.ca

of demagnetizing and magnetizing in an extremely short period of time. Because of the rapid shrinkage generated by the demagnetization and the rapid re-elongation contributed by the magnetization, a large acceleration pulse in the positive direction is generated, which acceleration pulse is significantly larger than the pulse generated during the saturation dominating case. In this way, the self-propelling motion can be more easily achieved using the quadratic nonlinear effect. Experiment has been

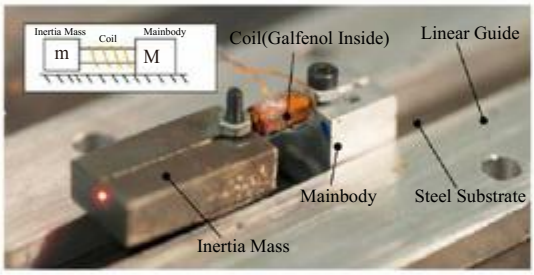

Figure 1: Experiment prototype (coil turns 180 AWG 31).

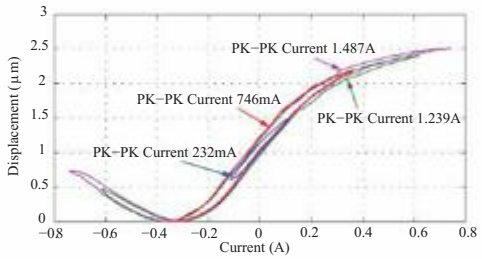

Figure 2: Nonlinear response of Galfenol vs. the driving current under the harmonic excitation(1Hz).

conducted to validate the analysis. The nonlinearity of Galfenol has been triggered individually by adjusting the bias magnetic field while a sawtooth current(constant Pk-Pk current) is applied. The bias magnetic field is modulated by applying a DC bias current. The relationship between the bias current strength and the moving velocity of the motor is shown in Figure 4. Indicated by the subfigure, when the bias current strength is positive, Galfenol reaches the saturation region, the motor does not reveal an explicit moving trend. It suggests that the inertia force generated is not large enough to improve the performance of the IDM motor. On the contrary, when the bias driving current is negative, the quadratic response is explicitly observed. From the subfigure on the top-left, the response of the motor in time-domain shows a re-elongation before the sudden deformation change. We can observe that as the bias current strength increases in the negative direction, the motor moves faster, which suggests that the quadratic nonlinear behaviour of Galfenol can improve the performance of the motor significantly. Also, for comparison, the blue line represents the deformation amplitude of the Galfenol bar. When a bias driving current is applied to the coil, the deformation of the material decreases. At the right side of the curve, the decrease of the deformation is mainly resulted from the saturation behaviour, while the decrease on the left side is because the driving power is applied to trigger the quadratic behaviour. When a negative bias driving current is applied, even though the deformation amplitude of Galfenol reduces, the quadratic behaviour can greatly improve the motor's ability to achieve the self-propelling movement. This finding suggests that modulating the quadratic nonlinearity of Galfenol accompanied by a fundamental sawtooth excitation is a new driving method for IDM motors instead of optimizing the driving signal waveforms.

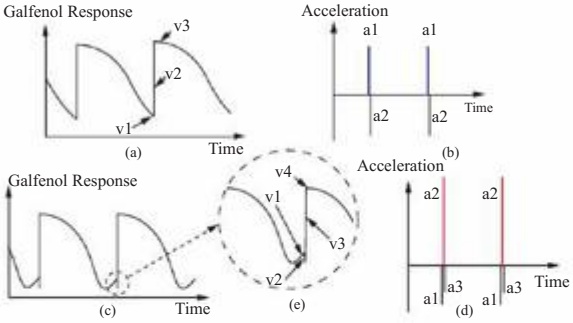

Figure 3: Generated acceleration using (a,b) the saturation response range and (c,d,e) the quadratic response range.

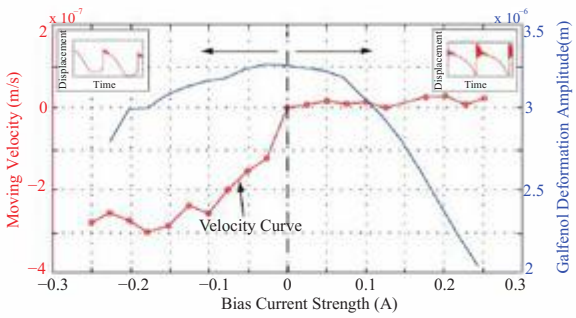

Figure 4: The motion velocity of the IDM motor vs. the bias current strength under the Pk-Pk driving current of 0.746A and the frequency of 1Hz.

References

[1] Yamagata Y. and Higuchi T.: A micropositioning device for precision automatic assembly using impact force of piezoelectric elements. IEEE International Conference on Robotics and Automation. Nagoya, Japan, 1995.

[2] Ha J.L., Fung R.F., Han Chang.F.: Optimization of an impact drive mechanism based on real-coded genetic algorithm. Sensors and Actuators A: Physical 121:488-493, 2005.

[3] Clark A., Restorff J.B., Wun-Fogle M., etc.: Magnetostrictive properties of body-centered cubic Fe-Ga and Fe-Ga-Al alloys. IEEE Transactions on Magnetics 36:3238-3240, 2000.

APPLICATION OF AN IHB METHOD TO THE VIBRATION OF A DIELECTRIC ELASTOMER BALLOON

Yin Wang[1], Na Ni[1], Fan Liu[1] and Jinxiong Zhou[1a)]
[1]*State Key Laboratory for Strength and Vibration of Mechanical Structures and School of Aerospace, Xi'an Jiaotong University, Xi'an, China*

Summary In this paper, an incremental harmonic balance method is employed to study the characteristics of the spherisymmetric vibration of dielectric elastomers. Subject to static pressure and voltage, a dielectric elastomer balloon will reach a state of equilibrium. If the voltage applied on the system becomes a sinusoidal function of time, the system exhibits strong nonlinearity, which leads to highly complex vibrational behaviours of the balloon. The incremental harmonic balance method coupled to an incremental arc-length method with a cubic extrapolation technique is adopted to successfully trace the amplitude-frequency relation of the balloon system with different damping factors.

INTRODUCTION

Dielectric elastomers (DEs) are increasingly promising for the applications of high-frequency oscillators, for example, acoustic equipment and pumps. The systems, which usually contain cubic or higher-order nonlinearities, exhibit strong nonlinearity. When a dielectric elastomer device works under high frequencies, the speed of motion maybe very fast, thus damping would be non-negligible and affect significantly the properties of the system. This paper makes use of an incremental harmonic balance (IHB) method coupled with an arc-length incrementation scheme to find possible steady state oscillatory solutions to the nonlinear vibration of an ideal dielectric elastomer balloon and reveals the influence of damping to the amplitude-frequency characteristics of the system. The results contribute to the building of theoretical foundations for the applications of dielectric elastomers in high-frequency occasions.

ANALYSIS

For a DE balloon subject to a static internal pressure p and a sinusoidal applied voltage $\Phi(t)=\Phi_{dc}+\Phi_{ac}\sin(\Omega t)$, the equation of motion [1] becomes

$$\frac{d^2\lambda}{dT^2}+2\lambda-2\lambda^{-5}+\widetilde{C}\frac{d\lambda}{dT}-\frac{pR}{\mu H}\lambda^2-2\frac{\varepsilon\Phi_{dc}^2}{\mu H^2}[1+\frac{\Phi_{ac}}{\Phi_{dc}}\sin(\widetilde{\Omega}T)]^2\lambda^3=0$$

where $\widetilde{C}=c/(4\pi RH\sqrt{\rho\mu})$ and c is the physical damping factor, $T=t/(R\sqrt{\rho/\mu})$ is the dimensionless time and $\widetilde{\Omega}=\Omega R\sqrt{\rho/\mu}$ is the dimensionless excitation frequency. For any initial conditions, this ordinary equation can be solved numerically by a lot of methods. However, we are more interested in the harmonic oscillation in steady states, for which the stretch ratio is assumed to be in such a form $\lambda=\lambda_{eq}+a\cos(\omega T)+b\sin(\omega T)$ and the balloon oscillates in a frequency that is equal to that of excitation, i.e. $\omega=\widetilde{\Omega}$. Note that λ_{eq} can be determined from static equilibrium and the amplitude-frequency characteristic can be obtained by solving a number of values of the sets $\{a, b, \omega\}$ from the equation. Substitution of λ into the equation will lead to an equation in the form of $f(\tau;a,b,\omega)=0$ where $\tau=\omega T$. An incremental harmonic balance (IHB) method (see [2]) includes a Galerkin process in which the following integrals are computed

$$\mathbf{F}(a,b,\omega)=\begin{bmatrix}F_1(a,b,\omega)\\F_2(a,b,\omega)\end{bmatrix}=\int_0^{2\pi}f(\tau;a,b,\omega)\begin{bmatrix}\cos\tau\\\sin\tau\end{bmatrix}d\tau$$

and a Newton process that solves $\mathbf{F}=\mathbf{0}$ iteratively. If the frequency ω is prescribed, $\mathbf{F}$ will be a function of a and b so that $\mathbf{F}=\mathbf{0}$ can be solved readily by a usual Newton routine. However, as will be shown in Fig. 1, the mapping from frequency to amplitudes is not one-to-one and as a result, an arc-length method needs to be employed in order to capture the meandering part of the amplitude-frequency curve. Suppose four points $\mathbf{x}_i=[a_i,b_i,\omega_i]^T, i=0,1,2,3$ have been available and an increment is going to be performed to yield the next point $\mathbf{x}_4$. An initial guess of $\mathbf{x}_4$ may be obtained by a cubic extrapolation technique, which provides:

$$\mathbf{x}_4=\sum_{i=0}^{3}\left(\prod_{j=0,j\neq i}^{3}\frac{t_4-t_j}{t_i-t_j}\right)\mathbf{x}_i$$

a) Corresponding author. Email: jxzhouxx@mail.xjtu.edu.cn.

in which $t_0 = 0, t_j = s_j + t_{j-1}$ and $s_j = \|\mathbf{x}_j - \mathbf{x}_{j-1}\| = \sqrt{(a_j - a_{j-1})^2 + (b_j - b_{j-1})^2 + (\omega_j - \omega_{j-1})^2}$ for $1 \le j \le 3$ and $s_4 = s_3 N_d / I_3$, where N_d is the desired number of iterations and I_3 is the actual number of iterations during the latest increment. Among the components of $\mathbf{x}_4 - \mathbf{x}_3 = [\Delta a, \Delta b, \Delta\omega]^T$, picks the one with maximum absolute value and fix the corresponding component of $\mathbf{x}_4$ as the initially guessed value. Afterwards the other two components will be updated by solving $\mathbf{F} = \mathbf{0}$ through a Newton routine. By incrementing a number of points, an amplitude-frequency characteristic curve can be produced.

RESULTS

By adopting the parameter $pR/(\mu H) = 0.1$, $\varepsilon\Phi_{dc}^2/(\mu H^2) = 0.1$ and $\Phi_{ac}/\Phi_{dc} = 0.1$, a family of amplitude ($\sqrt{a^2 + b^2}$)-dimensionless excitation frequency ($\Omega R\sqrt{\rho/\mu}$) characteristic curves based on different damping factors are obtained by means of the procedure outline above and plotted in Fig. 1. The zero-damping curve with C = 0 is basically the same with the one presented in [1], which indicates the effectiveness of the procedure. As the damping factor increases, the peak amplitude declines, which is similar to classical linear vibration systems. The jump phenomenon of the amplitude (see [1]) as the frequency increases from a small value still exists for all damping factors presented here, however, these curves demonstrate a trend that as the damping factor increases, the jump of amplitude is weakened and tends to vanish if damping grows further.

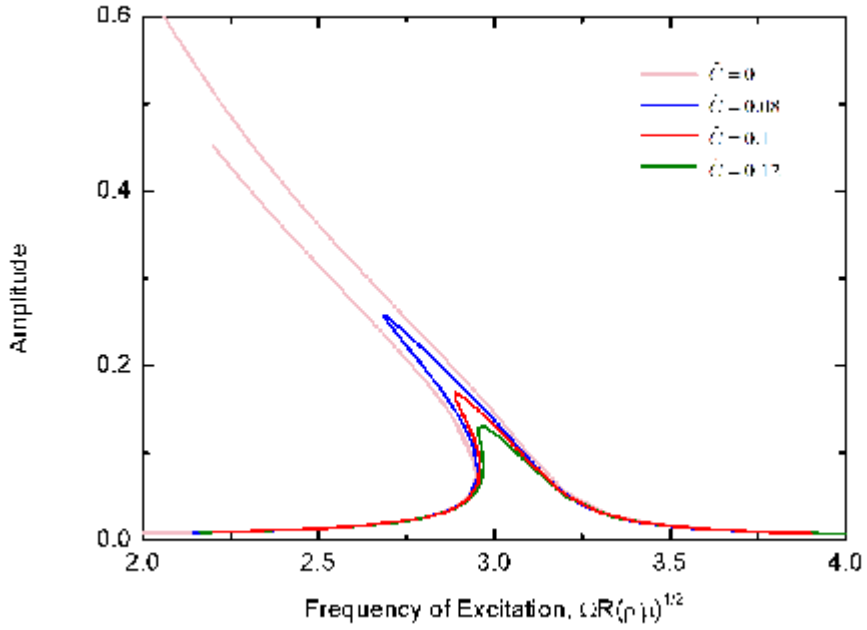

Fig. 1 The amplitude-frequency characteristics of the balloon with different dimensionless damping factors

Acknowledgement

This research is supported by Natural Science Foundation of China (11072185, 11102149 and 11372239).

References

[1] Zhu J., Cai S., Suo Z.: Nonlinear oscillation of a dielectric elastomer balloon. *Polym. Int.* **59**:378-383, 2010.

[2] Cheung Y.K., Chen S.H., Lau S.L.: Application of the incremental harmonic balance method to cubic non-linearity systems. *Journal of Sound and Vibration* **140**(2):273-286, 1990.

NONUNIFORM DOMAIN SWITCHING FOR INTERFACIAL CRACK SUBJECT TO TWO-PARAMETER CRACK TIP FIELDS

Xiaodong Xia[1] & Zheng Zhong [1a)]
[1] *School of Aerospace Engineering and Applied Mechanics, Tongji University, Shanghai, China*

Summary This paper deals with a mode III interfacial crack subject to anti-plane stress and in-plane electric fields under non-uniform ferroelectric-ferroelastic domain switching. The analysis focuses on the electric regulation effect of ferroelectric fracture properties. The electric field changes the size of asymmetric domain switching zone. Employing the weight function method, we obtain the switch toughening effect for stationary and quasi-static steady-state growing cracks, respectively. The research will give us ideas to control fracture properties of ferroelectric composites by altering the electric field.

INTRODUCTION

Discovery of ferroelectrics has led to a significant development in smart materials. However, electro-mechanical coupling effects are too weak in the existing single-phase ferroelectrics. Ferroelectric composites are designed by fabricating dissimilar ferroelectric layers for practical applications. Unfortunately, cracks and flaws inevitably emerge on the interface of ferroelectric composites during manufacture and service. Therefore, researches of the interfacial crack in ferroelectric composites are of great importance.

However, discrepancies between experimental results and theoretical predictions within the linear constitutive models imply that nonlinear phenomena of ferroelectric composites are of great significance. Ferroelectric materials can increase the fracture toughness through the domain switching process. To the best of the authors' knowledge, studies on the coupling ferroelectric-ferroelastic domain switching effect of the interfacial crack have not been addressed. The present paper deals with a mode III interfacial crack subject to anti-plane stress and in-plane electric fields while considering the domain switching effect.

DOMAIN SWITCHING ANALYSIS

Consider a semi-infinite interfacial crack subject to anti-plane mechanical loading and in-plane electric loading at the infinity, as illustrated in Fig 1(a). In this work, we assume that the ferroelectric constituents are modelled as elastically and dielectrically isotropic. The interaction between electric and stress fields near the crack tip is attributed to the ferroelectric-ferroelastic domain switching, and the interaction is weak outside the domain switching zone. Because of the orthogonality of tetragonal crystal, each mono-crystal of ferroelectrics possesses six types of probable orientations, as depicted in Fig. 1(b). The initial poling direction of ferroelectric mono-crystal is along the x_3-axis in the local coordinate. Mode 1 to mode 4 represent four types of 90° domain switching, and mode 5 represents one type of 180° domain switching. Only 90° switching needs to be considered, because 180° switching can be divided into two procedures of 90° switching. Actual domain switching process should proceed to release the maximum work, according to the minimum potential energy principle.

(a) (b)

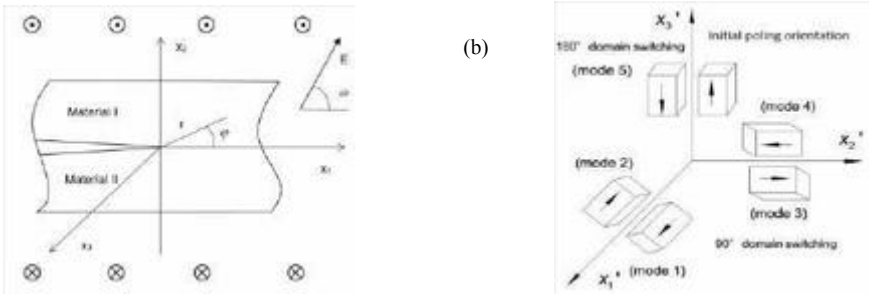

Fig. 1. (a) A semi-infinite interfacial crack subject to anti-plane stress loading and in-plane electric loading; (b) Schematic of domain switching of tetragonal crystal in the local coordinate.

Domain switching zone

In ferroelectric solids, only a part of ferroelectric crystals undergo the domain switching process. Based on the non-uniform ferroelectric-ferroelastic domain switching criterion [1], domain switching proceeds when the domains switching work exceeds the threshold. The shape of switching zone is shown in Fig. 2. The size of domain switching zone changes with respect to the electric loading, which is similar to the experimental results of Jiang et al. [2] about in-plane domain switching. For a crack embedded in a homogenous material, the switching zone decreases with respect to the magnitude of electric field under positive electric direction in Fig. 2(a), while it increases with respect to the magnitude of electric field

[a)] Corresponding author. Email: zhongk@tongji.edu.cn.

under negative electric direction in Fig. 2(b). In addition, an asymmetric domain switching zone is obtained in Fig. 2(c) for the interfacial crack in ferroelectric composites, due to the mismatch of bimaterial properties.

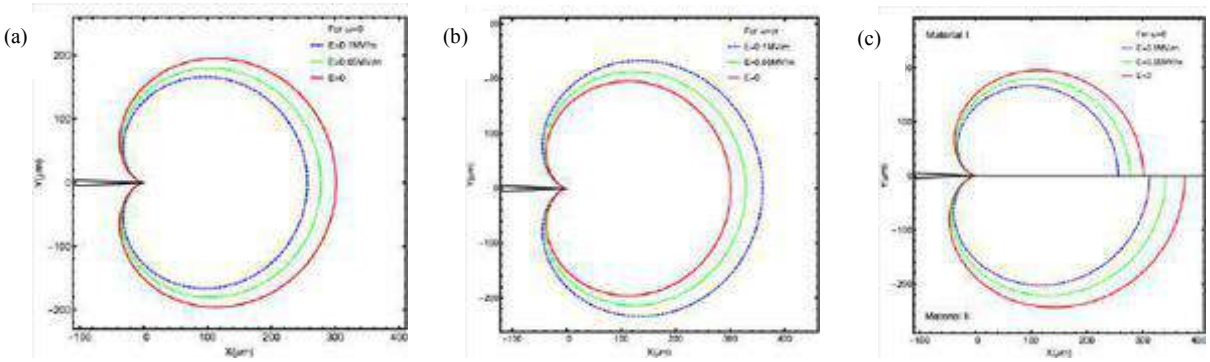

Fig. 2. The shapes of domain switching zone around a stationary crack tip versus the magnitude of electric field under different electric directions with $K_{app}=1\,\mathrm{MPa}\sqrt{\mathrm{m}}$, $\phi=0$: (a) in a homogeneous material with $\omega=0$; (b) in a homogeneous material with $\omega=\pi$; (c) in bimaterial composites with $\omega=0$, where K_{app} is the applied stress intensity factor, ϕ is the initial poling orientation.

NONUNIFORM SWITCHING TOUGHENING

Utilizing the crack tip field and domain switching zone obtained in previous sections, we will explore the switch toughening effect for a stationary crack and a quasi-static steady-state growing crack by calculating the interfacial crack tip stress intensity factor. Transformation strain induced by ferroelectric-ferroelastic domain switching is the source of toughening. The weight function method is applied here to quantify the interaction between the transformation strain and the interfacial crack [3]. The switch toughening effect can be achieved by a surface integral through the domain switching zone. For a stationary interfacial crack, the switch toughening effect is demonstrated as zero. For a quasi-static steady-state growing interfacial crack, the critical applied stress intensity factor varies with respect to the magnitude and direction of electric field, as shown in Fig. 3.

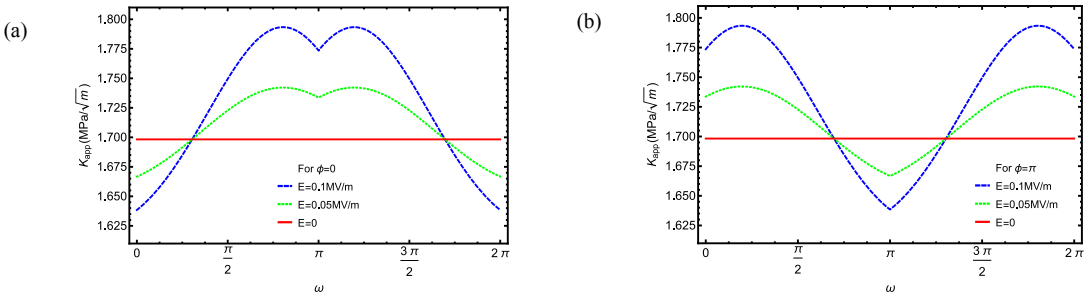

Fig. 3. Critical applied stress intensity factors of mono-domain quasi-static steady-state growing crack versus the magnitude and direction of electric field under different initial poling orientations: (a) $\phi=0$; (b) $\phi=\pi$.

CONCLUSIONS

This work deals with a mode III interfacial crack subject to anti-plane stress and in-plane electric fields while considering non-uniform ferroelectric-ferroelastic domain switching. We obtain the switch toughening effect for stationary and quasi-static steady-state growing interfacial cracks by employing the weight function method. The electric field plays a significant role in regulating the fracture toughness of ferroelectric composites. The conclusions can be reached from the analysis above: (i). For a stationary interfacial crack, the size of domain switching zone varies with respect to the electric loading. However, no toughening effect exists in spite of the electric loading; (ii). For a quasi-static steady-state growing interfacial crack, the critical applied SIF varies with respect to the magnitude and direction of electric field.

The research will give us ideas to control the fracture property of ferroelectric composites by altering the electric field.

References

[1] Cui Y., Zhong Z.: A novel criterion for nonuniform domain switching of tetragonal ferroelectrics, *Mech. Mater*,. **45**:61-71, 2012.

[2] Y. Jiang, D. Fang, F. Li: In situ observation of electric-field-induced domain switching near a crack tip in poled $0.62PbMg_{1/3}Nb_{2/3}O_3$–$0.38PbTiO_3$ single crystal, *Appl. Phys. Lett.*. **90**:222907, 2007.

[3] Xia X., Cui Y., Zhong Z.: A mode III interfacial crack under nonuniform ferro-elastic domain switching, *Thero. Appl. Fract. Mech.*, **69**:44-52, 2014.

THE MAGNETO-INDUCED STRESS RELAXATION OF MAGNETORHEOLOGICAL POLYMER GELS

Yangguang Xu*, Guojiang Liao & Qiang Wan
Institute of Systems Engineering, China Academy of Engineering Physics (CAEP), Mianyang, China

Summary The stress relaxation behaviors of magnetorheological polymer gels (MRPGs) under different magnetic field are investigated. An obvious magneto-induced effect on the stress relaxation of MRPGs is found, the stable relaxation modulus under a 243.7 mT magnetic field (213.98 kPa) is 534.95 times larger than that without magnetic field (0.4 kPa). For further analyzing the magneto-induced stress relaxation mechanism, a phenomenon model is established. It is found that the relaxation modulus of MRPGs induced by the mechanic-magnetic coupling effect plays an important role in the stress relaxation process.

INTRODUCTION

Magnetorheological polymer gel (MRPG) is a kind of magneto-sensitive smart materials prepared by dispersing micrometer sized magnetic particles into a polymer matrix without sufficient cross-linking. The magneto-induced microstructure evolution of the particles will change the rheological properties of MRPG remarkably, which indicates that the rheological properties of MRPG may be controlled by magnetic field more flexible. The mechanical-magnetic coupling mechanism is the key point for investigating the MR mechanism, and the characterization of viscoelasticity in the presence of magnetic field is the basis to describe the mechanical-magnetic coupling behaviors of MRPG. The time-dependent rheological properties actuated by different external loading, which mainly obtained from creep, stress relaxation, and the dynamic mechanical behavior under oscillatory loading, are the important characterizing parameters of viscoelasticity. The understanding of magneto-induced viscoelasticity only from dynamic mechanical property is not sufficient, the transient experiment under stepwise loading is also needed as complementarity. Stress relaxation is the foundation to investigate the complicated response of polymer under arbitrary actuating loadings, which are very important to describe the viscoelastic behaviors of polymer.

As far as we know, there have few public literatures about the stress relaxation behaviors of MRPG. To further understand the magneto-mechanical coupling mechanism and provide fully experimental data for theoretical analysis and engineering application, the magneto-induced stress relaxation behavior of MRPG is discussed in this paper.

RESULTS AND DISCUSSION

A commercial parallel-plate rheometer (Physica MCR 301, Anton Paar Co., Austria) with a magnetic field generator (as shown in Fig. 1a and 1b) is used to carry out the stress relaxation experiment of MRPG. The fabrication procedure can be found in our previous work. Fig. 1c shows the magneto-induced stress relaxation model, by which the stress relaxation experimental results of MRPG under different magnetic field can be further analyzed. The following equation can be used to describe the constitutive relationship of MRPG, the related parameters in this equation can be fitted from the experimental results.

$$\tau = \gamma_0\left(\frac{G_{m1}G_{m2}}{G_{m1}+G_{m2}} + G(H_0)\right) + \frac{\gamma_0 G_{m1}^2}{G_{m1}+G_{m2}} e^{-\frac{(G_{m1}+G_{m2})t}{\eta_{m2}}}$$

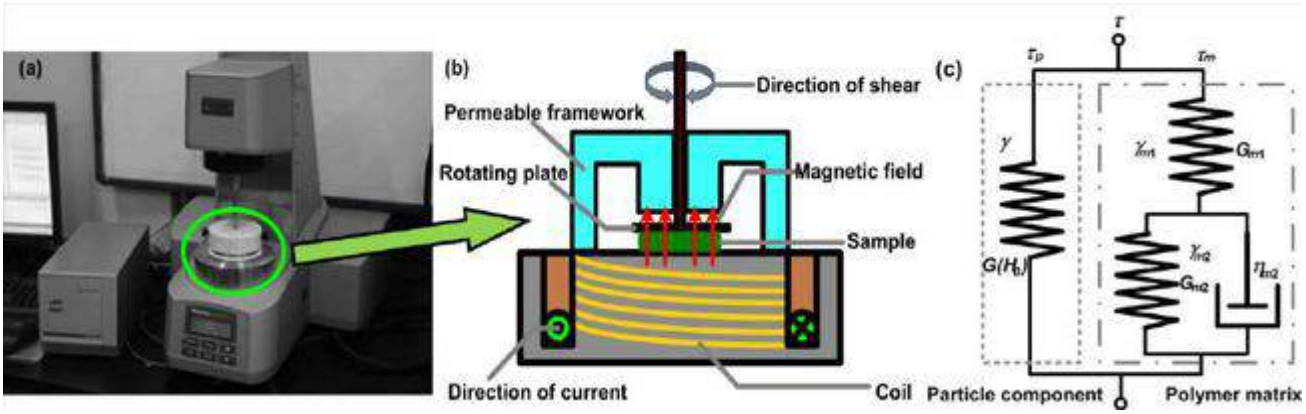

Fig. 1 The rheometer (a) with its magnetic field generator (b) and magneto-induced stress relaxation model (c).

[a] Corresponding author. Email: 412xuyg@caep.cn OR xyg@mail.ustc.edu.cn.

It is concluded from Fig. 2 that magnetic field has a great influence on the stress relaxation of MRPG. The relaxation stress increases gradually with the increasing magnetic field under the same stepwise strain. The calculating result by using the magneto-induced stress relaxation model is also shown in Fig. 2, which fits well with the experimental result. According to the fitting data, the stable relaxation modulus under a 243.7 mT magnetic field (213.98 kPa) is 534.95 times larger than that without magnetic field (0.4 kPa), which confirms that the magneto-sensitive effect on MRPG is obvious. This result is valuable for some applications which aim at controlling the rheological properties of MRPG by adjusting the magnetic field strength. The magneto-dependence of stress relaxation behaviors of MRPG indicates that the relaxation stress is induced by the particle chains, polymer matrix, and the coupling effect between magnetic particles and polymer chains, the particle chain strength and the coupling effect between magnetic particles chains and polymer matrix are significantly influenced by magnetic field.

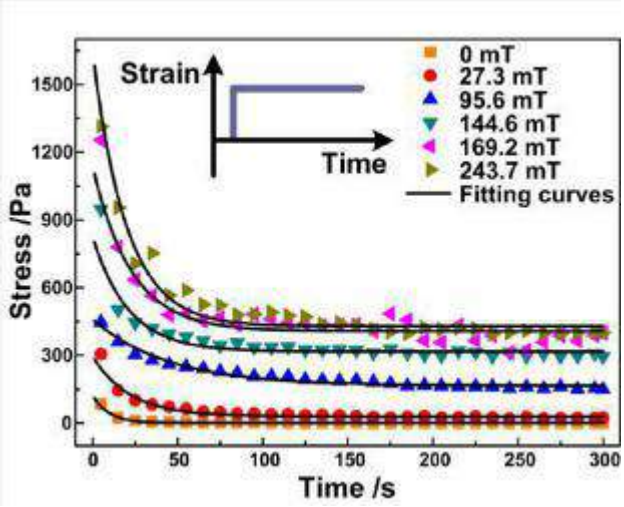

Fig. 2 The stress relaxation behaviors of MRPG under different magnetic field. The solid lines represent the fitting results by the magneto-induced stress relaxation model.

CONCLUSION

The stress relaxation experiment is a simple and efficient method to investigate the complex rheological behaviours of MRPG under different magnetic fields. With the increasing of magnetic field strength, both of the instantaneous modulus and stable modulus of MRPG will increase accordingly, which is originates from the magneto-mechanical coupling effect between magnetic particles and polymer matrix. This interpretation should be confirmed by building a more precise theoretical model in the future.

ACKNOWLEDGMENTS

The financial support of the National Natural Science Foundation of China (Grant Nos. 11502255, 11502256, 11372295) and the key subject "Computational Solid Mechanics" of China Academy of Engineering Physics are gratefully acknowledged.

References

[1] Xu Y. G., Gong X. L., Xuan S. H.: Soft Magnetorheological Polymer Gels with Controllable Rheological Properties. *Smart Materials and Structures* **22**: 075029, 2013.

[2] Xu Y. G., Gong X. L., Xuan S. H., Li X. F., Qin L. J., Jiang W. Q.: Creep and Recovery Behaviors of Magnetorheological Plastomer and its Magnetic-dependent Properties. *Soft Matter* **8**: 8483-8492, 2012.

[3] Li W. H., Du H., Chen G., Yeo S. H., Guo N. Q.: Nonlinear Rheological Behavior of Magnetorheological Fluids: Step-strain Experiments. *Smart Materials and Sructures*, **11**: 209-217, 2002.

A DISTRIBUTED-PARAMETER MODEL OF A HIGH-EFFICIENCY COMPRESSIVE-MODE PIEZOELECTRIC ENERGY HARVESTER

Zhengbao Yang *[1], Haitao Li[2], and Jean Zu[1]

[1]*Department of Mechanical and Industrial Engineering, University of Toronto, Toronto, Ontario, Canada*
[2]*Department of Engineering Mechanics, Northwestern Polytechnical University, Xian, China*

Summary Vibration energy harvesting is a promising technique to achieve self-powered operation of low-power wireless sensors and implantable devices. A plenty of research has been conducted recently to increase the power output and broaden the working bandwidth of energy harvesters. We proposed a high-efficiency compressive-mode energy harvester using piezoelectric materials, which exhibited a superior power-generation capability and nonlinearity-induced wide bandwidth. This study aims to develop a comprehensive electromechanical model for the proposed energy harvester. Specifically, using the Hamilton principle and the Euler-Bernoulli beam theory, we first obtained the governing equations of the electromechanical system. The model was then discretized using a Galerkin expansion and solved numerically. We finally compared the simulation results with the experimental data tested from a fabricated prototype. The developed distributed-parameter model gives us a deep insight into the dynamic characteristics of the system that can help further enhance the performance.

INTRODUCTION

Piezoelectric energy harvesters have the potential of replacing electrochemical batteries to achieve autonomous operation of electronic systems. In 2014, we proposed a high-efficiency compressive-mode piezoelectric energy harvester (HC-PEH) [1] which generated about one order of magnitude more power than the state of the art under the same conditions in experiments. Although a lumped-parameter model has been developed [2], we still need a comprehensive distributed-parameter model to gain a deeper insight into the strong nonlinear responses of the electromechanical coupling system. Therefore, here we for the first time present a distributed-parameter model for the nonlinear compressive-mode piezoelectric energy harvester .

As shown in Fig. 1 (a), the proposed HC-PEH consists of a flex-compressive center, two mass blocks and a pair of elastic beams. The flex-compressive center is composed of a piezo plate sandwiched by a pair of bow-shaped plates. While working, the base vibration energy is first absorbed by the flex-compressive center and proof mass. The vibration of proof mass then induces tensile stress along the elastic beams. Following that, the tensile stress in the elastic beams causes flexural motion of the bow-shaped plates, and further compression in the center piezo plate. Finally in the piezo plate, the mechanical energy is converted to electrical energy. Here in the process, force is deliberately amplified twice: first by the elastic beams; second by the bow-shaped plate. This novel two-stage force amplification mechanism and the employed compressive mode equip the HC-PEH with the high-power-output capability even under weak excitations.

The HC-PEH is a complex nonlinear electromechanical coupling system. Boundary connections are not rigid; Deformations are not in one direction; The electromechanical coupling in piezoelectric materials does not follow the common formulation in bending-mode energy harvesters. Therefore, the model for the HC-PEH is much more complicated than the general linear bending-mode ones. As illustrated in Fig. 1 (a), the transverse deflection and longitudinal deformation of the elastic beams are denoted by $w_1(x,t)$ and $u_1(x,t)$, respectively; and that are $w_2(x,t)$ and $u_2(x,t)$ for the transverse deflection and longitudinal deformation of the bow-shaped plate. The base excitation is expressed as $a(t)$. The Lagrangian of the system is expressed as $L = T \nearrow U + W_e$, where T is the kinetic energy, U is the potential energy and W_e is the electrical and electromechanical energy [3].

$$T = T_1 + T_2 + T_3 + T_M = 2 \times \frac{1}{2}\int_0^{L_1} m_1 \left((\dot{w}_1 + \dot{a})^2 + \dot{u}_1^2 \right)\ x + 2 \times \frac{1}{2} m_2 \int_0^{L_2} \left((\dot{u}_2 + \dot{a})^2 + \dot{w}_2^2 \right)\ y + \frac{1}{2} M_P (\dot{w}_1(L_1,t) + \dot{a})^2 + 2 \times \frac{1}{2} M \left((\dot{w}_1(L_1,t) + \dot{a})^2 + \dot{u}_1(L_1,t)^2 \right) , \quad (1)$$

where $m_1 = \rho_1 A_1 \left[H(x) \nearrow H(x \nearrow (L_a \nearrow L_b)) \right] + 2\rho_1 A_1 \left[H(x \nearrow (L_a \nearrow L_b)) \nearrow H(x \nearrow L_a) \right], m_2 = \rho_2 A_2$ are the mass per unit length of the elastic beams and the bow-shaped plates, respectively. $H(x)$ is a Heaviside function. L_a is the length of the elastic beams. L_b is the length of the fixing part of the elastic beams near to the proof mass, which area of the cross section is twice of that of the elastic beam. ρ_1 & ρ_2, L_1 & L_2, and A_1 & A_2 symbolize the density, length, and cross section of elastic beams and bow-shaped plates, respectively. M is the proof mass; M_P is the mass of the piezo plate.

*Corresponding author. Email: zbyang@mie.utoronto.ca

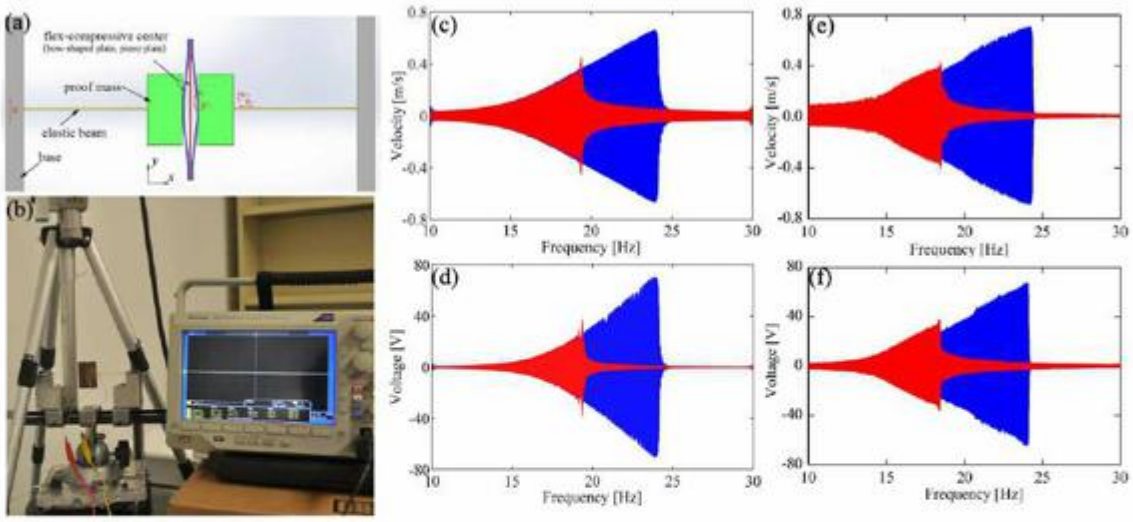

Figure 1: (a) schematic diagram of the proposed HC-PEH; (b) the experimental setup including a laser Doppler vibrometer, an oscilloscope, a shaker, an accelerometer and a holder; (c) velocity response of the center of the prototype from the simulation; (d) voltage response of the prototype from the simulation; (e) velocity response of the center of the prototype from the experiment; (f) voltage response of the prototype from the experiment. Blue lines denote the excitation frequency is ramped up gradually, while red lines denote the frequency ramped-down cases. The excitation is with an amplitude of 0.4 g (g=9.8m/s^2) and the external resistor is 100 KΩ.

The potential energy of the system is

$$\begin{aligned} U = U_1 + U_2 + U_3 + U_M = 2\left(\tfrac{1}{2}\textstyle\int_0^{L_1} E_1 I_1 \left(w''_1\right)^2 \mathrm{d}x + \tfrac{E_1 A_1}{2L_1}(\Delta x_1)^2 + \int_0^{L_1} m_1 \mathrm{g} w_1 \mathrm{d}x\right) + \\ 2\left(\tfrac{1}{2} E_2 I_2 \textstyle\int_0^{L_2} {w_2''}^2 \mathrm{d}y + 2\tfrac{E_2 A_2}{2L_2}(u_2\left(L_2/2, t\right))^2 + m_2 L_2 \mathrm{g} w_1(L_1, t)\right) + M_P \mathrm{g} w_1(L_1, t) + \\ \left(2\int\limits_{v_{Px}} \tfrac{1}{2}\sigma_{Px}\varepsilon_{Px}\mathrm{d}v_{Px} + \int\limits_{v_{Py}} \tfrac{1}{2}\sigma_{Py}\varepsilon_{Py}\mathrm{d}v_{Py}\right) + 2M\mathrm{g}w_1(L_1, t). \end{aligned} \tag{2}$$

where $(\cdot)$ and $(')$ indicate differentiation with respect to time and length. $E_1 I_1$ and $E_2 I_2$ represent the flexural rigidity of the elastic beams and bow beams. Δx_1 represents the axial deformation of the elastic beams. Note that Δx_1 is not equal to $u_1(L_1, t)$. The value of Δx_1 is determined by the geometric and force compatibility conditions at the connection point between the elastic beams and the bow-shaped plate. $\sigma_{Py}, \varepsilon_{Py}, \sigma_{Px}, \varepsilon_{Px}$ correspond to the stress and strain parallel and perpendicular to the poling direction in the piezo plate, respectively.

$$W_{\mathrm{e}} = 2\int\limits_{v_{Px}} (E_x D_{Px})\,\mathrm{d}v_{Px} + \int\limits_{v_{Py}} (E_x D_{Py})\,\mathrm{d}v_{Py} = 2\int\limits_{v_{Px}} \left(d_{33}\sigma_{Px}\tfrac{V}{h_3} + \varepsilon_{33}\left(\tfrac{V}{h_3}\right)^2\right)\mathrm{d}v_{Px} + \int\limits_{v_{Py}} \left(-d_{31}\sigma_{Py}\tfrac{V}{h_3} + \varepsilon_{33}\left(\tfrac{V}{h_3}\right)^2\right)\mathrm{d}v_{Py}. \tag{3}$$

where E_x is the electric field. D_{Px} and D_{Py} are the electric displacement components, corresponding to the edge parts bonded with the bow-shaped plates and the center part of the piezo plate, respectively. h_3 is the thickness of piezo plate a and V is the voltage generated from it.

Using the Hamilton principle, we derived the governing equations of the coupling system. The governing equations was then discretized using a Galerkin expansion and solved numerically. The solving process is same as those in literature. For simplicity, we do not show it here. The numerical results (Fig.1 (c) & (d)) agree well with the experimental data(Fig.1 (e) & (f)) . It is indicated that the developed model could accurately estimate both the velocity response and voltage response of the proposed nonlinear HC-PEH.

References

[1] Yang Z.B., Zu J.: High-efficiency compressive-mode energy harvester enhanced by a multi-stage force amplification mechanism. Energ. Convers. Manage. 88:829-833, 2014.

[2] Yang Z.B., Zhu Y., Zu J.: Theoretical and experimental investigation of a nonlinear compressive-mode energy harvester with high power output under weak excitations. Smart. Mater. Struct. 24:025028, 2015.

[3] Harne R.L., Wang K.W.: Axial suspension compliance and compression for enhancing performance of a nonlinear vibration energy harvesting beam system. J. Vib. Acoust. 138.1: 011004, 2016.

FS08 - Granular Materials and Flows

TS.FS08-1.01	Behringer, Robert - Identifying structure during shear jamming (INVITED)	3341
TS.FS08-1.02	Lagree, Pierre-Yves - Discharge flow of granular media from silos with lateral orifice: Experiments and simulations (INVITED)	3343
TS.FS08-1.03	DeGiuli, Eric - A Phase Diagram Unifies Energy Dissipation, Kinetics, and Rheology in Inertial Granular Flows (INVITED)	3345
TS.FS08-1.04	Maza, Diego - About the mass flow rate in silos (INVITED)	3347
TS.FS08-1.05	Barker, Thomas - Well-posed continuum modelling of granular flow	3349
TS.FS08-1.06	Bérut, Antoine - Microfluidic granular avalanches: A model for gravity detection in plants cells	3351
TS.FS08-2.01	Turnbull, Barbara - Ice as a granular material	3353
TS.FS08-2.02	Vidal, Valérie - Gas-induced fluidization in water-saturated sands	3355
TS.FS08-2.03	Clavaud, Cécile - Anomalous Low Friction Coefficient In Dense Suspensions	3357
TS.FS08-2.04	Dorostkar, Omid - CFD-DEM study of saturated granular media; applications to fault gouge	3359
TS.FS08-2.05	Forterre, Yoel - Impact in dense suspensions: Key role of pore-pressure	3361
TS.FS08-2.06	Henann, David - Size dependence of the yield threshold in dense granular materials	3363
TS.FS08-3.01	Umbanhowar, Paul - Controlling granular segregation patterns using unsteady flows	3365
TS.FS08-3.02	Jop, Pierre - Instability during the erosion of a cohesive granular heap	3367
TS.FS08-3.03	Kang, Wenting - Experimental and theoretical study about depth-dependent drag force in granular matter	3369
TS.FS08-3.04	Windows-Yule, Christopher - The Influence of Non-uniform Vibration on Granular Jamming, Segregation and Self-assembly	3371
TS.FS08-3.05	Lueptow, Richard - Modeling segregation in multidisperse granular flow	3373
TS.FS08-4.01	Marteau, Eloïse - Micromechanics of granular materials: An experimental investigation of shear behavior	3375
TS.FS08-4.02	Mathonnet, Jean-Eric - Singular behavior of a cohesive powder under horizontal vibrations	3377
TS.FS08-4.03	Maurin, Raphael - Granular rheology in bedload transport	3379
TS.FS08-4.04	Merceron, Aymeric - Reorganization of a granular medium around a localized transformation	3381
TS.FS08-4.05	Morize, Cyprien - How do fish hide in the sand? Erosion by an oscillating foil	3383
TS.FS08-5.01	Faug, Thierry - Hydrodynamics for standing granular jumps down inclines	3385
TS.FS08-5.02	Pouliquen, Olivier - Scaling Laws for the Segregation Forces in Sheared Granular Flows	3387
TS.FS08-5.03	Sano, Osamu - Solid-fluid transition and ripple in vertically vibrated thicker granular layer	3389
TS.FS08-5.04	Shatoff, Elan - Discontinuous shear thickening in dense suspensions: A force-space analysis	3391
TS.FS08-5.05	Xue, Kun - Numerical simulation of the formation of shock induced particle jets using DEM	3393
PO.FS08-1.01.266	Alvarez, Carlos - Density waves in the gravitational flow of grains in narrow pipes	3395

PO.FS08-1.02.267	Da Silva Maciel, Lucas - Wall-media interactions in vibrationally fluidized granular flows	3397
PO.FS08-1.03.268	Dalloz-Dubrujeaud, Blanche - Discharge Flow of a Granular Media from a Silo: Effect of the Packing Fraction and of the Geometry	3399
PO.FS08-1.04.269	Favier, Adeline - Particle stiffness influence on granular rheology	3401
PO.FS08-1.05.270	Haghgoo, Mohammad Reza - The role of the particle stress in the simulation of fluidized beds	3403
PO.FS08-1.06.271	Huang, Hao-Jie - Numerical Research on Wind-blown Sand with Semi-buried Checkerboard Sand Barriers Belt	3405
PO.FS08-1.08.272	Lattanzi, Aaron - A constant heat flux boundary condition for CFD-DEM simulations	3407
PO.FS08-1.09.273	Nonoyama, Hideto - Post-Failure Analysis of Slope by Smoothed Particle Hydrodynamics	3409
PO.FS08-1.10.274	Polezhaev, Denis - Ripple formation in a librating cylinder filled with fluid	3411
PO.FS08-1.11.275	Sirmas, Nick - Continuum description of Sirmas-Radulescu shock wave instability in dissipative gases	3413
PO.FS08-1.12.276	Vega Reyes, Francisco - Rheological properties of granular suspensions at moderate densities	3415

IDENTIFYING STRUCTURE DURING SHEAR JAMMING

R. P. Behringer[1] and Dong Wang
* 2

[1]*Department of Physics, Duke University, Durham, North Carolina, USA*
[2]*Department of Physics, Duke University, Durham, North Carolina, USA*

Summary There has been much recent interest in how granular materials jam, i.e. become mechanically stable. Recently, we have have shown that systems of frictional grains exhibit jamming phenomena that differ from the frictionless case[1, 2, 3]. In particular, a system of frictional particles can be sheared from a stress free state to produce a jammed state. Here, we consider the nature of shear jamming for frictional particles. We then consider the micromechanical processes that are involved, and why these processes should be different for the frictionless and frictional cases.

JAMMING BY SHEAR

We first consider jamming diagrams for frictionless and frictional systems, as in Fig. 1. Part a) shows a jamming diagram of shear stress, τ and packing fraction, ϕ, if the particles are frictionless. Part b) shows a sketch, after Bi et al.[2] for systems of frictional particles. Systems of frictionless grains are unjammed, i.e. mechanically unstable, below ϕ_J as in Fig. 1 a. Above

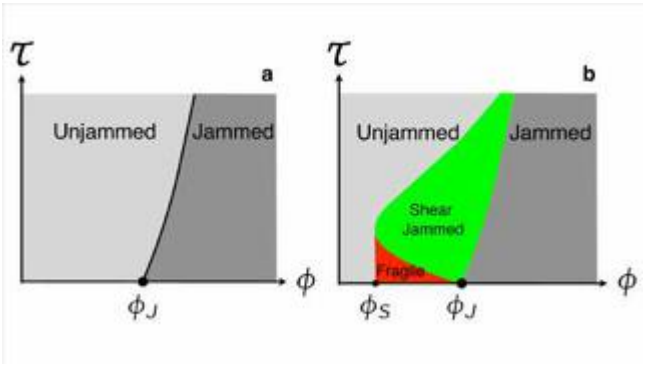

Figure 1: Schematics of jamming diagrams in a space of shear stress, τ and packing fraction, ϕ for a) frictionless particles and b) frictional particles.

ϕ_J, the system is jammed below the yield curve indicated by the positively sloping line separating dark and light gray regions. A frictionless system exhibits critical (e.g. power-law) behavior at ϕ_J, although ϕ_J itself is protocol-dependent. Above, ϕ_J, systems of frictional grains[2, 3, 1] have somewhat similar behavior as in Fig. 1 b, including power-law response at ϕ_J in some measures[3]. Necessarily, frictional systems have unjammed zero-stress states below ϕ_J, since every state of a frictionless system is also a state of a frictional system. However, if a frictional system is prepared in a zero-stress state in a packing fraction range $\phi_S \leq \phi \leq \phi_J$, and then subject to shear strain, it will arrive in the green region of Fig. 1, i.e. in a shear jammed state. It will arrive in that state after passing through a fragile regime characterized by *strong* force networks that are roughly aligned with the compressive direction of shear, and only weak networks in the dilation direction. Note that the fragile states are jammed[1, 2, 3], and the distinction between fragile and shear jammed is based on the anisotropic percolation of the strong force networks. The range $\phi_S \leq \phi \leq \phi_J$ is comparable to the range of packing fractions between random loose packing and random close packing.

By default, sheared jammed states are anisotropic, and have non-zero shear stress, τ. We demonstrate the difference between isotropically jammed and shear jammed states in Fig. 2, left and right, respectively. These two images are from experiments, described below, that involve photoelastic disks. In both cases, the forces are carried preferentially on force networks or force chains. But, the nature of the force networks differs substantially for the two images; in particular, the shear jammed state is characterized by a high degree of anisotropy.

In our experiments, e.g. Fig. 2, we use systems of photoelastic particles[4]. Photoelastic materials are birefringent under stress/strain. When particles made from a photoelastic material are subject to forces and viewed between crossed polarizers, they develop fringes that encode the forces they are experiencing. In a typical image, particles experiencing larger forces

*Corresponding author. Email: bobphy.duke.edu

appear brighter than particles experiencing smaller forces. The fact that the fringe patterns in the disks encode the forces means that it is possible to algorithmically determine the contact forces between grains, as first shown by Majmudar et al.[4]. Given the contact forces and other available geometric information, it is then possible to compute the full stress tensor for an experiment, as well as to determine other important measures, including fabric, density, etc. Note that a determination of the shear stress is essential for mapping out the jamming diagram, such as Fig. 1b.

The differences between jamming of frictional and frictionless systems immediately raises the questions: what are the micro-mechanical processes at work, and how are they differentiated by friction? The response of frictionless systems has been extensively explored in the context of foams and molecular-like models. For instance, structural evolution for the frictionless case is often modeled in terms of T1 and shear transformation zone (STZ) events. However, the highly anisotropic nature of shear jammed frictional states, with their long force chains indicates that different phenomena occur there. In this regard, it is important to note that the minimum average number of contacts per particle for a jammed state is $2N$ for frictionless particles, and only $N + 1$ for frictional particles. Thus for disks, 4 contacts are needed on average for a minimally jammed state of a frictionless system, vs. 3 for a frictional system. Although force chains in frictional systems might suggest that participating particles have only 2 contacts, in fact, many force chain particle experience 3 contacts, which is why they can be stable. The fact that frictionless systems of disks need 4 contacts per particle is a telling difference.

In order to capture the micro-mechanical response of our frictional systems, we need a small-scale measure that can depict the evolution of force chains, as well as other less obvious structures. Towards that end, we consider sequences of three contacting particles, which we refer to as trimers. We will show that the trimers give considerable insight into the microscopic response of a sheared (or otherwise strained) system. In particular, a force chain can be thought of as a sequence of partially overlapping trimers that deform in response to shear. In general, a system has many trimers, and a characterization of a system must involve statistical descriptions of trimer properties. The bulk of the associated presentation will focus on a number of different trimer properties.

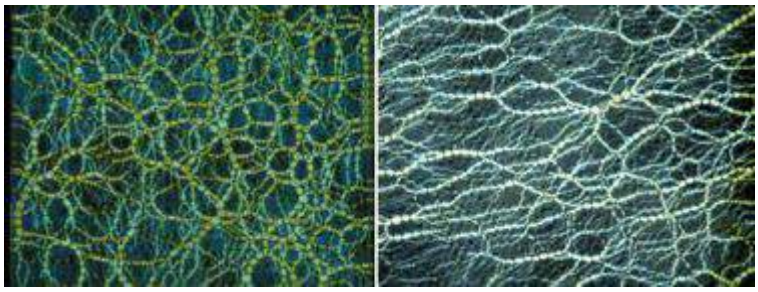

Figure 2: Photoelastic images which contrast an insotropic jammed state (left) and a shear jammed state (right). In these images, brighter particles carry larger forces. In the shear jammed state, the force network is highly anisotropic.

CONCLUSIONS

Recent work has shown that systems of frictional particles can jam under shear, starting from stress-free states. We provide a brief review of the macroscopic features of jamming by shear. We then turn to a micro-mechanical characterization of the processes at work during shear jamming. To this end we will consider the properties of 'trimers', sequences of three particles, that can be taken as the building blocks of force chains.

Acknowledgement. This work supported by NSF grants DMR1206351, DMS1248071, NASA grants NNX10AU01G,and NNX15AD38G, and by the William M. Keck Foundation.

References

[1] Zhang J., Majmudar T. S., Tordesillas A. and Behringer R.P. : Statistical Properties of a 2D Granular Material Subjected to Cyclic Shear. Granular Matter 12:159-172 ,2010.

[2] Bi D, Zhang J., Chakraborty B., and Behringer, R.P.: Jamming by Shear. Nature 480:355-358, 2011.

[3] Ren J., Dijksman J.A. and Behringer R.P.: Reynolds Pressure and Relaxation in a Sheared Granular System. Phys. Rev. Lett. 110:018302, 2013.

[4] Majmudar T. S. and Behringer R.P : Contact Force Measurements and Stress-Induced Anisotropy in Granular Materials, Nature 435:1079-1082 , 2005.

DISCHARGE FLOW OF GRANULAR MEDIA FROM SILOS WITH LATERAL ORIFICE : EXPERIMENTS, DISCRETE, AND CONTINUOUS SIMULATIONS

Yixian Zhou [1,3], Pierre-Yves Lagrée [*2], Stéphane Popinet[2], Pierre Ruyer[1], and Pascale Aussillous[3]

[1]*Institut de Radioprotection et de Sûreté Nucléaire (IRSN), PSN-RES, SEMIA, LIMAR, Cadarache, St Paul-Lez-Durance 13115, France*

[3]*Aix-Marseille Université, CNRS, IUSTI UMR 7343, Marseille 13013, France*

[2]*Sorbonne Universités, UPMC Univ Paris 06, CNRS UMR 7190, Institut ∂'Alembert, F-75005 Paris, France*

Summary We compare laboratory experiments, contact dynamics simulations and continuum Navier–Stokes with $\mu(I)$-rheology simulations of the granular flow through a silo with a lateral opening. For 3D and 2D simulations the Hagen-Beverloo law is obtained. For 3D shallow silos, the sidewalls have a crucial role, which has been added in an averaged version of $\mu(I)$-Navier-Stokes allowing to reproduce the deviation from Hagen-Beverloo due to this lateral friction.

INTRODUCTION

Marine sand glass has long been the main tool to measure time. Since then, granular flows outside silos remain always of great industrial interest in many fields (such as in food, pharmaceutical, energy, ... industry). Considering granular media stored in a tank, we want to understand the flow leaking outside it. This could be due to a lateral accidental tearing of the wall (this can represent very schematically a fuel rod in a nuclear power station during some hypothetical accidental conditions, in which case the orifice is lateral). The final modeled configuration is depicted on figure 1 left. In contrast, the usual silo configuration is symmetrical and has the orifice at the bottom. In this usual configuration, in case of a moderate opening of size D, the discharge flow rate Q is well known to follow the Hagen-Beverloo law (resp. in 3D and in 2D):

$$Q_{3D} \sim \rho\sqrt{gD^5} \quad \text{resp.} \quad Q_{2D} \sim \rho\sqrt{gD^3}.$$

Recently, there have been several papers reporting on the computation of a continuum flow ([6, 7] starting from a fluid description and [1] starting from a solid point of view) and comparing it to direct simulations of contact dynamics, the continuum theory being the $\mu(I)$-rheology ([4], [3]) in 2D, and the geometrical configuration the usual one. We propose here 2D simulations in a novel configuration and compare contact dynamics with 2D continuum simulations. We propose as well new 3D continuum simulations in order to find the scaling law of the discharge rate in this configuration with a lateral orifice, focussing on the friction of the walls.

EXPERIMENTS AND SIMULATIONS

Experiments

Experiments are performed with a rectangular silo fitted with spherical glass beads (see figure 1 left). The mass flow rate is measured by a precision balance; the top surface of particles is tracked by a fast camera. The controlled parameters are the size of particles d in the range [75μm-1300μm], the width of the silo W in the range [3.5mm-40mm] and the height of orifices D [2.7mm-35mm].

2D Contact Dynamics simulations

We use the LMGC 90 software implementation of the contact dynamics method [5]. The particles, interacting through a dense granular flow, are treated as perfectly rigid and inelastic. Contact dissipation is modeled in terms of a friction coefficient that we set to $\mu_p = 0.$ between particles and to $\mu_w = 0.5$ with the wall, further details may be found in [8].

2D, 3D, and averaged 2D numerical simulations

The Navier-Stokes simulations are performed with the free solver *Gerris* and its new version *Basilisk* under development. They both use finite volume, projection methods. As two phases are present: a passive surrounding gas and the granular fluid itself, a Volume of Fluid method is used to track the interface. *Basilisk* allows for a resolution of the fully-coupled Poisson–Helmholtz problem (the former code solved dimension by dimension). The simulations are in 2D and in 3D:

$$\underline{\nabla} \cdot \underline{u} = 0, \ \rho\frac{d\underline{u}}{dt} = \underline{\nabla} \cdot \underline{\sigma} + \rho\underline{g}, \quad \underline{\sigma} = \not{p}\underline{\underline{I}} + 2\eta\underline{\underline{D}} \quad \text{with} \ \underline{\underline{D}} = \frac{1}{2}(\underline{\nabla u} + \underline{\nabla u}^T),$$

*Corresponding author. Email: pyl@ccr.jussieu.fr

with the friction $\mu(I)$ depending on the inertial number I, ([4], [3]), see details in [6, 7] ($\mu_s = 0.$, $\Delta\mu$ = 0.28, I_0=0.4):

$$\eta = \frac{\mu(I)p}{\sqrt{2}D_2}, \text{ with } I = \frac{d\sqrt{2}D_2}{\sqrt{p/\rho}}, \quad \mu(I) = \mu_s + \frac{\Delta\mu}{I_0/I + 1}, \text{and} \quad D_2 = \sqrt{\underline{\underline{D}} : \underline{\underline{D}}}\,.$$

Modeling the friction on the wall (proportional to $\mu_w p$) is a problem with the fluid description as we can impose only no slip or slip for the velocity at the wall. To take into account this lateral friction, we average the momentum equation across the width of the silo (in the Hele-Shaw spirit, [2]). This adds $\nearrow 2(\mu_w p/W)(\vec{u}/|\vec{u}|)$ as an averaged additional force from the sidewalls in the momentum equation. We test these three models with both codes.

RESULTS

For the 2D configuration simulations we obtain a good agreement between contact dynamics and Navier–Stokes, and again we recover the Hagen–Beverloo 2D law. Interestingly enough, we found a simple analytical solution for the pressure field (a kind of Flamant solution plus lithostatic pressure), which describes well the initial times. For pure 3D continuum simulations with Navier-Stokes (with slip conditions at the wall), we obtain as well the Hagen–Beverloo 3D law for the flow for aspect ratio of order one and for square or round holes. Changing now the width W of the silo, from the experiments, we identify two regimes, which depend on the ratio of height to width of the orifice. When D/W is smaller than a critical value, $Q \sim D^{3/2}W$, when D/W is larger then $Q \sim W^{3/2}D$ (see figure 1 center). The same trend is observed for 2D cross-averaged simulations (with the additional sidewalls friction term), this is plotted on figure 1 right.

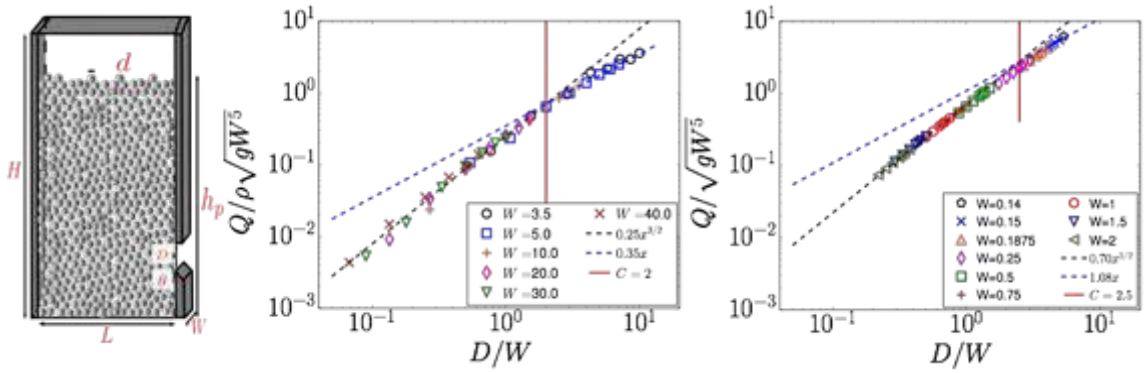

Figure 1: Left, the model configuration: an asymmetrical 3D silo with lateral orifice. When D/W is smaller than a critical value C, we have $Q \sim D^{3/2}W$, like the Hagen–Beverloo 2D scaling. When D/W is larger than C, we have $Q \sim W^{3/2}D$. The trends obtained from the experiments (center) are reproduced with the averaged Navier–Stokes with $\mu(I)$, (right).

CONCLUSIONS

The main result of this work is the identification, both experimentally and numerically, of a new flow regime for thin silos with a lateral opening, where the discharge rate is proportional to D, in contrast to the classical 2D behavior where the discharge rate is in power $3/2$, obtained for thick silos. This work also demonstrates that the continuum $\mu(I)$-rheology describes well granular flows compared to experiments and discrete simulations. It can thus be used as a tool to compute many industrial configurations.

References

[1] S. Dunatunga, K. Kamrin "Continuum modelling and simulation of granular flows through their many phases" JFM Vol 779, 2015, pp 483- 513

[2] P. Jop, Y. Forterre and O. Pouliquen, "Crucial role of sidewalls in granular surface flows: consequences for the rheology" JFM 541, 2005, 167-192

[3] P. Jop, Y. Forterre and O. Pouliquen, "A constitutive relation for dense granular flows", Nature, 2006, 44, 727-730,

[4] GDR MiDi (2004) "On dense granular flows" Eur. Phys. J. E 14, 341365

[5] F. Radjai and F. Dubois, "Discrete-element modeling of granular materials" Wiley-Iste, London, 2011, p. 425.

[6] L. Staron, P.-Y. Lagrée & S. Popinet (2012) "The granular silo as a continuum plastic flow: the hour-glass vs the clepsydra" Phys. Fluids 24, 103301 (2012); doi: 10.1063/1.4757390

[7] L. Staron, P.-Y. Lagrée, & S. Popinet (2014) "Continuum simulation of the discharge of the granular silo, A validation test for the μ(I) visco-plastic flow law" Eur. Phys. J. E (2014) 37: 5 DOI 10.1140/epje/i2014-14005-6

[8] Y. Zhou, P. Ruyer and P. Aussillous "Discharge flow of a bidisperse granular media from a silo: Discrete particle simulations" Phys Rev E 92, 062204 (2015)

A PHASE DIAGRAM UNIFIES ENERGY DISSIPATION, KINETICS, AND RHEOLOGY IN INERTIAL GRANULAR FLOWS

E. DeGiuli[a)1], J.N. McElwaine[2], and M. Wyart[1]
[1]*Institute of Theoretical Physics, Ecole Polytechnique Fédérale de Lausanne, Lausanne, Switzerland*
[2]*Department of Earth Sciences, Durham University, Science Labs, Durham, U.K.*

Summary Flows of hard granular materials depend strongly on the interparticle friction coefficient μ_p and on the inertial number $\mathcal{I}$, which characterizes proximity to the jamming transition where flow stops. Guided by numerical simulations, we derive the phase diagram of dense inertial flow of spherical particles, finding three regimes for $10^{-4} \lesssim \mathcal{I} \lesssim 0.1$: *frictionless, frictional sliding,* and *rolling*. These are distinguished by the dominant means of energy dissipation, changing from collisional to sliding friction, and back to collisional, as μ_p increases from zero at constant $\mathcal{I}$. The three regimes differ in their kinetics and rheology; in particular, the velocity fluctuations and the stress anisotropy both display non-monotonic behavior with μ_p, corresponding to transitions between the three regimes of flow. We characterize the scaling properties of these regimes, show that energy balance yields scaling relations for each of them, and explain why friction qualitatively affects flow.

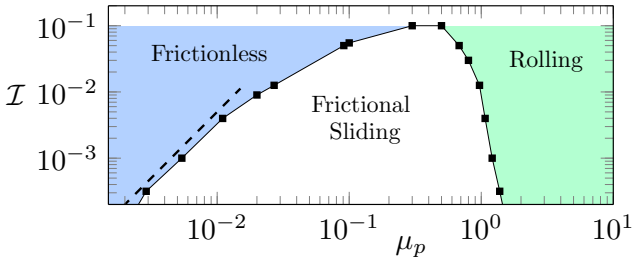

Figure 1: Phase diagram of dense homogeneous inertial frictional flow. In the frictionless and rolling regimes, most energy is dissipated by inelastic collisions, while in the frictional sliding regime energy dissipation is dominated by sliding. Along the phase boundary, grains dissipate equal amounts of energy in collisions and in sliding. The dashed line has slope 2.

In the last decade, progress has been made in describing dense flows of granular media by considering the limit of *perfectly rigid* grains, for which dimensional analysis implies that the strain rate $\dot{\epsilon}$, the pressure P and the grain density ρ can only affect flows via the inertial number $\mathcal{I} = \dot{\epsilon} D\sqrt{\rho/P}$, where D is grain diameter [7]. In particular, for stationary flows the packing fraction ϕ and stress anisotropy $\mu = \sigma/P$, where σ is the shear stress, are functions of $\mathcal{I}$. From the constitutive relations $\phi(\mathcal{I})$ and $\mu(\mathcal{I})$ the flow profile can be explained in simple geometries [5]. Here we focus on dense flows $\mathcal{I} \lesssim 0.1$ for which the networks of contacts between grains span the system and particle motion is strongly correlated [2], and do not consider the quasi-static regime $\mathcal{I} \lesssim 10^{-4}$ where flow appears intermittent [3]. In this intermediate range one finds

$$\mu(\mathcal{I}) = \mu_c + a_\mu \, \mathcal{I}^{\alpha_\mu}, \quad \phi(\mathcal{I}) = \phi_c \nearrow a_\phi \, \mathcal{I}^{\alpha_\phi}, \tag{1}$$

where μ_c and ϕ_c are non-universal and depend on details of the grains. Experiments on glass beads and sand find exponents $\alpha_\mu \approx \alpha_\phi \approx 1$, consistent with numerical simulations using frictional particles reporting $\alpha_\mu = 0.81$ and $\alpha_\phi = 0.8$ [9]. Despite their importance, constitutive laws Eq.1 remain empirical. Building a microscopic framework to explain them would shed light on a range of debated issues, including transient phenomena, non-local effects, and the presence of S-shaped flow curves when particles are soft.

To make progress, it is natural to consider the limiting case where particles are *frictionless*, a situation that has received considerable attention in the jamming literature [8, 11]. For hard particles, two geometrical results key for inertial flows are as follows. First, as the density increases, the network of contacts becomes more coordinated, implying that motion becomes more constrained. This leads to a divergence of the velocity fluctuations $\langle \delta V \rangle$ when constraints are sufficient to jam the material [6, 1]. Thus the contact network acts as a lever, whose amplitude is characterized by the dimensionless number $\mathcal{L} \equiv \langle \delta V \rangle / (\dot{\epsilon} D)$. At the same time, the rate at which new contacts are made increases, and the creation of each contact affects motion on a growing length scale. These effects imply that velocity fluctuations decorrelate on a strain scale ϵ_v that vanishes at jamming [4]. The theory of Ref. [4], which uses that dissipation can only occur in collisions for frictionless particles, predicts $\alpha_\mu = \alpha_\phi = 0.35$, $\mathcal{L} \sim \mathcal{I}^{-1/2}$ and $\epsilon_v \sim \mathcal{I}$. Encouragingly, these results agree with the numerics of Ref. [10], which found $\alpha_\mu \approx \alpha_\phi \approx 0.38$ and $\mathcal{L} \sim \mathcal{I}^{-0.48}$. However, α_μ and α_ϕ differ significantly from their values for frictional grains stated

a)Corresponding author. Email: eric.degiuli@epfl.ch

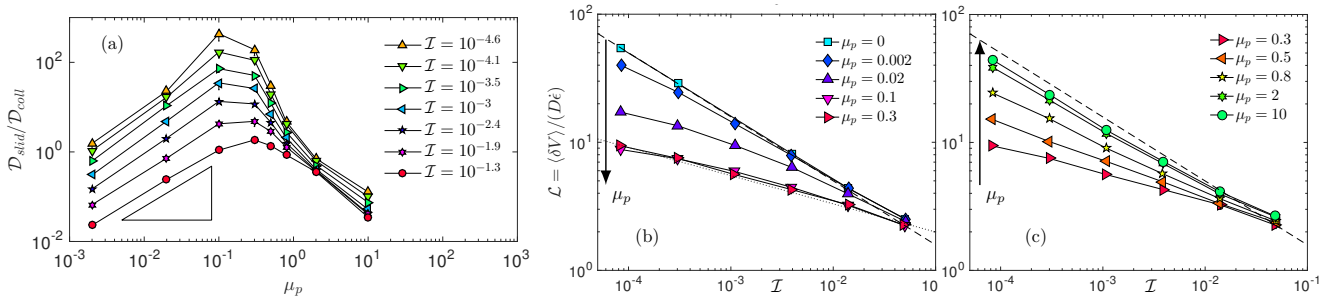

Figure 2: (a) Ratio of dissipation due to sliding, $\mathcal{D}_{slid}$, to sliding from collisions, $\mathcal{D}_{coll}$, vs μ_p. The triangle has slope 1. (b,c) Lever $\mathcal{L}$ vs $\mathcal{I}$, (b) for $\mu_p \leq 0.3$, and (c) for $\mu_p \geq 0.3$. The dashed lines are $\propto \mathcal{I}^{-1/2}$, while the dotted line is $\propto \mathcal{I}^{-0.22}$.

above, suggesting the presence of different universality classes. Currently, why friction qualitatively affects flows, how many universality classes exist, and what differs between them microscopically are unresolved questions.

In this contribution we use numerical simulations to answer these questions. We systematically study dense flows over a large range of $\mathcal{I}$ and particle friction coefficient μ_p. By focusing on the microscopic cause of dissipation, we show the existence of three universality classes, as illustrated in Figure 1. To derive this phase diagram, we note that frictional particles can dissipate energy either through inelastic collisions, at a rate $\mathcal{D}_{coll}$, or by sliding at frictional contacts, at a rate $\mathcal{D}_{slid}$. In steady state, dissipation must balance the work done at the boundaries. In simple shear, the energy input from the shear stress is $\Omega\sigma\dot{\epsilon}$, where Ω is the system volume, thus $\Omega\sigma\dot{\epsilon} = \mathcal{D}_{coll} + \mathcal{D}_{slid}$. To investigate which source of dissipation dominates, we consider the ratio $\mathcal{D}_{slid}/\mathcal{D}_{coll}$, shown in Fig.2a. As expected, collisional dissipation dominates in the frictionless limit, but sliding dissipation becomes more important as μ_p is increased, and becomes *dominant* at intermediate friction coefficients and small inertial number. Strikingly, the dependence on μ_p is non-monotonic: when μ_p reaches ≈ 0.2, this trend abruptly reverses, and $\mathcal{D}_{slid}/\mathcal{D}_{coll}$ *decreases* with μ_p, implying that collisional dissipation dominates as $\mu_p \to \infty$. We use the inertial number at which $\mathcal{D}_{slid}/\mathcal{D}_{coll} = 1$ to define phase boundaries, resulting in the phase diagram of Fig.1. From the non-monotonicity of $\mathcal{D}_{slid}/\mathcal{D}_{coll}$ with μ_p, this leads to two phase boundaries merging at $\mathcal{I} \approx 0.1$, where the dense flow regime ends [2]. We then show that this phase diagram correctly classifies other microscopic and macroscopic properties, such as the velocity fluctuations, which also display a non-monotonic behavior with μ_p, visible in Fig.2bc.

Our results are that at low friction, there exists a frictionless regime in quantitative agreement with the theory of Ref. [4], in particular we establish that $\epsilon_v \sim \mathcal{I}$. As the friction increases, one enters the *frictional sliding* regime, where dissipation is dominated by sliding at contacts instead of collisions, and for which $\epsilon_v \sim \mathcal{I}$ holds true but $\mathcal{L} \sim \mathcal{I}^{-b}$ with $b \approx 0.22$. We relate the exponent b to an exponent characterizing the density of sliding contacts. Finally, at even larger μ_p one enters a *rolling* regime where dissipation is once again dominated by collisions, and where exponents are consistent with those of frictionless particles, both for kinetic observables and constitutive laws. We derive the phase boundary between the frictionless and the frictional sliding regime. Overall, our work explains why friction qualitatively changes physical properties, and paves the way for a future comprehensive microscopic theory of dense granular flows.

References

[1] B. Andreotti, J.-L. Barrat, and C. Heussinger. Shear flow of non-brownian suspensions close to jamming. *Phys. Rev. Lett.*, 109:105901, Sep 2012.

[2] E. Azéma and F. Radjaï. Internal structure of inertial granular flows. *Physical review letters*, 112(7):078001, 2014.

[3] F. da Cruz, S. Emam, M. Prochnow, J.-N. Roux, and F. m. c. Chevoir. Rheophysics of dense granular materials: Discrete simulation of plane shear flows. *Phys. Rev. E*, 72(2):021309, Aug 2005.

[4] E. DeGiuli, G. Düring, E. Lerner, and M. Wyart. Unified theory of inertial granular flows and non-brownian suspensions. *Physical Review E*, 91(6):062206, 06 2015.

[5] Y. Forterre and O. Pouliquen. Flows of dense granular media. *Annual Review of Fluid Mechanics*, 40(1):1–24, 2008.

[6] E. Lerner, G. Düring, and M. Wyart. A unified framework for non-brownian suspension flows and soft amorphous solids. *Proceedings of the National Academy of Sciences*, 109(13):4798–4803, 2012.

[7] G. MiDi. On dense granular flows. *The European Physical Journal E: Soft Matter and Biological Physics*, 14(4):341–365, 2004-08-01.

[8] C. S. O'Hern, L. E. Silbert, A. J. Liu, and S. R. Nagel. Jamming at zero temperature and zero applied stress: The epitome of disorder. *Phys. Rev. E*, 68(1):011306–011324, Jul 2003.

[9] P.-E. Peyneau. *Etude du comportement et du compactage de pates granulaires par simulation numerique discrete*. PhD thesis, Ecole des Ponts ParisTech, 2009.

[10] P.-E. Peyneau and J.-N. Roux. Frictionless bead packs have macroscopic friction, but no dilatancy. *Physical review E*, 78(1):011307, 2008.

[11] M. Wyart. On the rigidity of amorphous solids. *Annales de Phys*, 30(3):1–113, 2005.

[a] Corresponding author. Email: eric.degiuli@epfl.ch

ABOUT THE MASS FLOW RATE IN SILOS

Diego Maza *, Karol Asencio, Sara Rubio-Largo, Ángel Garcimartín, Iker Zuriguel, and Raul Cruz Hidalgo
Granular Media Lab, University of Navarra, Irunlarrea S/N 31080 Pamplona, Navarra, Spain

Summary Despite the massive use of silos in the manipulation or processing of industrial materials, the expression used to predict the mass discharged through its outlet is basically an empirical fitting founded on dimensional arguments [1, 2]. However, the physical origin of this process –which has received renewed interest due to the recent advances of the numerical tools – has not been completely developed until very recently. Thereby, these new tools provide micro-mechanical arguments to link the mass flow rate passing through the silo exit with the dilatancy of the material near the outlet [4, 5, 6]. In this work we summarize these arguments and show its applicability to different practical situations.

INTRODUCTION

The bulk solids handling is intrinsic to industrial processing. Indeed, tons of particles are daily released through silos and hoppers under very different conditions. Despite the ubiquity of this situation, we lack of an expression that relate the micromechanical properties of the delivery material with the mass flow rate. Actually, the typically used expression to estimate the discharged mass through certain orifice is an empirical relationship founded in a simple dimensional analysis, generally enounced as Beveerlo "law".

Early in the sixties, W.A. Beverloo and coworkers[1] introduce an expression to relate the mass discharged through a flat bottom silo with an outlet orifice of diameter D:

$$W = C\rho_B\sqrt{g}[D \nearrow kd]^{5/2} \tag{1}$$

where ρ_B is the bulk density, g, is the gravity acceleration, d, the "typical" particle diameter, and C and k were fitting parameters. After the introduction of this expression, some authors attempted to introduce a microscopic interpretation of the meaning of the fitting constants, introducing concepts like the *empty annulus* or *vena contracta* and the *free fall arch*[2, 3], which remained as mere idealizations until very recently.

Notably, Eq.1 was introduced to fit a rather small range of experimental data (see Figure 1.a) and assuming that the *static* bulk density ρ_B is representative of the material bulk properties near the outlet orifice. Such assumptions were revised one decade ago by C. Mancok *et al.* [4] exploring a large range of orifice sizes under very precise experimental conditions, see Fig. 1.b.

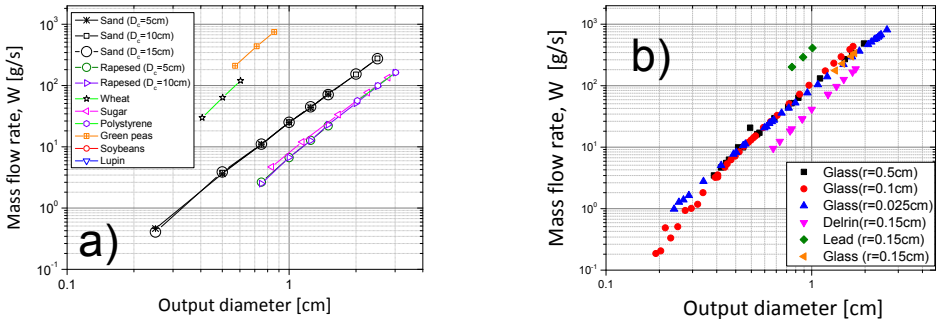

Figure 1: Comparison of the mass flow rate extracted from (a) the experimental results extracted from the Tables 5 and of Reference [1] and (b) using spherical beads of different diameters and materials with the same experimental conditions introduced in Reference [4].

Accordingly, these authors introduce an alternative expression to fit the long rage set of experimental results as:

$$W = C'\sqrt{g}[1 \nearrow \frac{1}{2}e^{-b(D-d)}][D \nearrow d]^{5/2} \tag{2}$$

where two important assumptions were proposed to fit the data: a) that the mass flow rate will be zero in $D = d$ and b) that the exponential term introduced in the expression is related with the dependence of the volume fraction near the exit orifice. After that, the dependence of the volume fraction in the silo discharge was explored experimentally in a 2D configuration confirming the exponential dependence introduced in Eq.2 [5].

*Corresponding author. Email: dmaza@unav.es

RESULTS

As both former expressions were postulated mainly under empiric considerations, we decided to explore numerically the micromechanical features of the same experimental situation introduced in figure 1.b. Under these conditions, we showed that the idealization of a "free fall arch" corresponds to a transition region were the collisional dissipation of energy is maximized and beyond which the particles flow almost freely [6]. Moreover, we showed how volume fraction and velocity profiles near the outlet have self-similar profiles depending only on the exit radius, R. Then, and only assuming that temporal correlations between velocity and volume fraction decay rapidly, it is possible to calculate the mass flow rate for a monodisperse granular material as:

$$W(R) = \int_o^{2\pi} \int_o^R \rho_o(R)\, v_o(R) r\, dr\, d\phi = C''\, \phi_\infty [1 \nearrow e^{-\beta R}] R^{5/2} \tag{3}$$

where C'' includes the physical and geometrical parameters of the problem (see reference [6] for the details), ϕ_∞ corresponds to the asymptotic volume fraction of the material near the orifice, β provides the typical scale where the dilatancy of the material becomes relevant. As Eq.3 does not depend explicitly on the particle radius it is possible to normalize the outlet size with the particle size to obtain:

$$W(R) = C''\, \phi_\infty [1 \nearrow e^{-\beta \frac{R}{r}}]\, \bar{R}^{5/2} r^{5/2} \tag{4}$$

Hence, Eq.4 can be used to collapse all the experimental results introduced in Figure 1 in a single master curve provided that a typical radius r can be introduced even for polydisperse materials like sugar or spinach seeds.

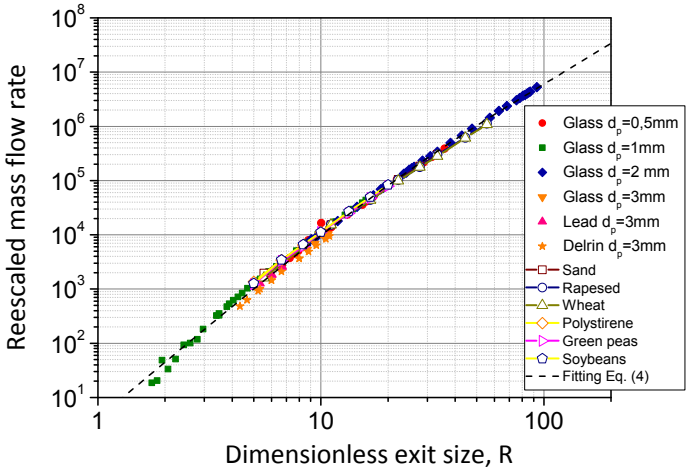

Figure 2: Collapsed experimental data extracted from references [1, 4] using Eq..

Hence, the mass flow rate can be analytically obtained if the right dependence of the volume fraction and velocity profiles just at the exit of a silo or hopper are introduced. Importantly, Eq. 3 does not depend on any empirical fitting constant related to concepts like the "empty annulus". Instead, the relevant scale to estimate the mass flow rate at small orifices is the scale β which characterizes the influence of the exit aperture on the dilatancy of the material.

References

[1] W. A. Beverloo, H. A. Leniger, and J. J. Van de Velde, *Chem. Eng. Sci.* **15**, 260 (1961).

[2] R.L. Brown and J.C. Richards, *Priciples of of powder mechanics*, Pergamon Press, 1970.

[3] R. M. Nedderman, *Statistics and kinematics of granular materials,* Cambridge University Press, 1992.

[4] C. Mankoc, A. Janda, R. Arévalo, M. Pastor, I. Zuriguel, A. Garcimartin and D. Maza, *Granular Matter* **9**, 407 (2007).

[5] A. Janda, I. Zuriguel and D. Maza, *Phys. Rev. Lett.* **108**, 248001 (2012).

[6] S.M. Rubio-Largo, A. Janda, D. Maza, I. Zuriguel, and R.C. Hidalgo, *Phys. Rev. Lett.* **114**, 238002-4 (2014).

WELL-POSED CONTINUUM MODELLING OF GRANULAR FLOW

Thomas Barker[1], David Schaeffer[2], Patricio Bohorquez[3], Nico Gray[1], and James Baker[1]
[1]*School of Mathematics, The University of Manchester, Manchester, U.K*
[2]*Duke University, Durham, North Carolina, USA*
[3]*Universidad Jaen, Jaen, Spain*

Summary By combining a plastic flow rule with co-linearity of stress and strain-rate, a viscosity is formed that is reflective of dissipation in flowing granular material. Unfortunately, if the ratio of shear and normal stress μ is taken to be a constant then the equations are always ill-posed [1]. Much experimental evidence is better fit by instead having $\mu = \mu(I)$ [2] where the inertial number I is a non-dimensional grouping of invariant particle and flow properties and is reflective of the deformation time-scales. We present a linear stability analysis of the resultant equations to show that this model is well-posed for intermediate values of I but exhibits unbounded growth of short-wavelength perturbations when flows vary too slowly or too quickly [3]. This makes reliable numerical solution impossible as grid-scale variations will dominate temporal solutions. It is possible to circumvent these issues by considering only steady or shallow flows [4] but additional physical effects should be included to ensure full regularisation.

FLOWS THAT WE WOULD LIKE TO MODEL

As shown in figure 1, many granular flows exhibit complex free surface shapes and may have either imposed or natural **time-dependent** behaviour. It is also noted that in these examples there is often a transition between static material and fluid-like flow and in some cases a further transition into grain-free or gaseous regions. As such, these flows cover a large range of inertial numbers.

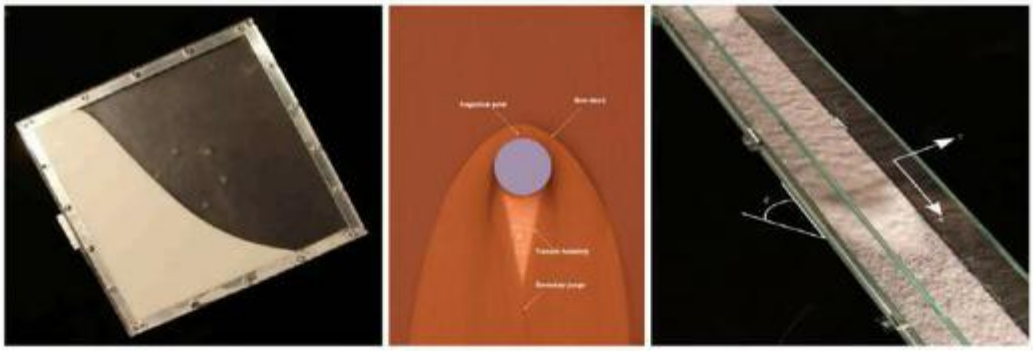

Figure 1: Typical granular flows with temporal variation. From left to right: rotating drums, flows past obstacles [5] & erosion and deposition waves [6]

ANALYSIS OF THE $\mu(I)$-RHEOLOGY

By **linearising** the governing equations and limiting consideration to **perturbations** of large wavenumber k, normal mode solutions can be found. This leads to a generalised eigenvalue problem for the growth rate λ. This problem is then solved analytically to give an analytic expression for λ in terms of the perturbation wavelength, direction and the flow and material properties. As this expression is quadratic in k, the growth rate tends to either $+\infty$ or $-\infty$ as the wavelength of perturbations is reduced.

Figure 2 shows regions for which the parameters give a positive value (white) which correspond to **ill-posedness** and the **well-posed** region (grey) where growth rates are negative. The analysis has been validated for both linear shear and inclined slope geometries. In the latter case, the analysis predicts a range of angles for which the flow is stable. Interestingly this range lies within but is smaller than the existing range for steady flow.

OPTIONS FOR REGULARISATION

At present, the model that has been analysed is two-dimensional, local, incompressible and time-dependent. It may be possible that the addition of finite-size effects, compressibility or limiting to steady flows may regularise the equations. It

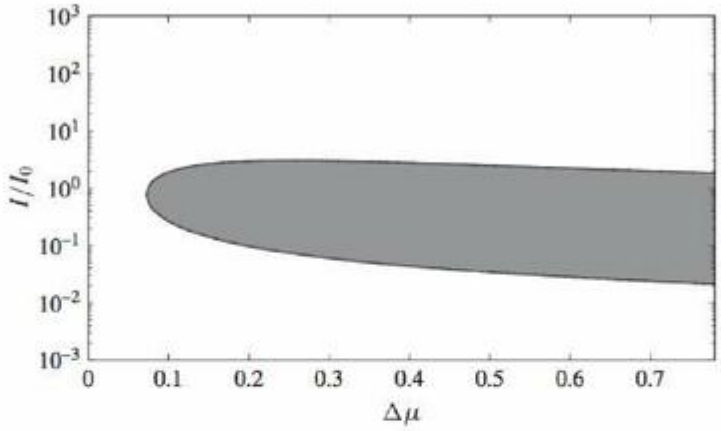

Figure 2: Stability diagram for the $\mu(I)$-rheology giving regions for which the equations are ill-posed (white) and well-posed (grey)

has also been found that depth-averaging the equations, assuming that flows are **shallow**, results in a well-posed system of equations for the range of steady flow angles. As shown in figure 3, this model is capable of predicting flow between frictional rigid sidewalls. Unlike standard shallow water models, this depth-averaged $\mu(I)$-rheology is able to capture the transition between roughly constant flow across the channel to the parabolic dependence seen for narrower flows.

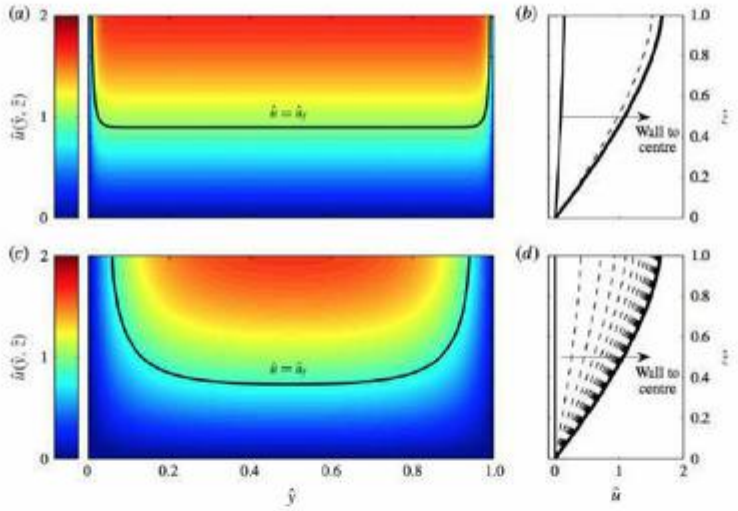

Figure 3: Flow profiles for an inclined chute with rigid frictional sidewalls for aspect ratio $\epsilon = 0.01$ (a,b) and a narrower channel with $\epsilon = 0.1$ (c,d).

References

[1] D. Schaffer, Instability in the evolution-equations describing incompressible granular flow (1987), J. Differ. Equ. 66, 19

[2] P. Jop, Y. Forterre & O. Pouliquen, A constitutive relation for dense granular flows (2006), Nature 44, 727

[3] T. Barker, D. G. Schaeffer, P. Bohorquez & J. M. N. T. Gray, Well-posed and ill-posed behaviour of the $\mu(I)$-rheology for granular flow (2015), J. Fluid Mech. 779, 794

[4] J. Baker, T. Barker & J. M. N. T. Gray, A two-dimensional depth-averaged $\mu(I)$-rheology for dense granular avalanches (2015), J. Fluid Mech. 787, 367

[5] X. Cui & J. M. N. T. Gray, Gravity-driven granular free-surface flow around a circular cylinder (2013), J. Fluid Mech. 720, 314

[6] A. N. Edwards & J. M. N. T. Gray, Erosion-deposition waves in shallow granular free-surface flows (2015) J. Fluid Mech. 762, 35

MICROFLUIDIC GRANULAR AVALANCHES: A MODEL FOR GRAVITY DETECTION IN PLANTS CELLS

Antoine Bérut*[1], Hugo Chauvet[1,2], Bruno Moulia[2], Valérie Legué[2], Olivier Pouliquen[1], and Yoël Forterre[1]
[1]*Aix-Marseille Université, CNRS, IUSTI UMR 7343, 13453 Marseille cedex 13, France.*
[2]*Clermont Université, Université Blaise Pascal, INRA, PIAF UMR 0547, F-63100 Clermont-Ferrand, France.*

Summary We study the avalanche dynamics of a granular media composed of microparticles (melamine resine, $5.17\,\mu\mathrm{m}$) in confined microfluidics systems. This experimental set-up allows us to mimic the behaviour of statoliths in plants cells, which are thought to be responsible for the plants' response to gravity. Moreover, contrary to real plants (*in-vivo*) experiments, our avalanches are done in a fully controlled environment, where the different roles of thermal fluctuations, non-Newtonian surrounding fluid, hydrodynamical and granular effects can be investigated. Comparison of this biomimetic system with measurements in wheat shoots suggest that fluctuations induced by cytoskeleton activity plays an important role in gravity detection by plants.

INTRODUCTION

Plants are able to adapt their growth to different directional environmental stimuli, such as light, gravity, moisture, etc. In particular plants can bend in response to gravity, so that the roots grow downward and the shoots upward (figure 1a). This gravitropism implies a way for plants to detect gravity, which has been widely studied by biologists [1]. The commonly accepted hypothesis states that the gravity detection is mediated by the movement of starch-accumulating amyloplasts (*statoliths*), that sediment toward gravity in gravity sensing cells (*statocytes*), see figure 1b. However, the exact biological mechanism for the intracellular detection and signalling is yet to be determined. Among the open questions, the role of biological activity in plants cells (e.g. actin cytoskeleton activity) remains unclear. Some studies states that it may enhance the gravity detection by agitating the statoliths, which could avoid sensor saturation [2], some others states that, on the contrary, plants with more cell activity are less sensitive to gravity [3], and finally a recent study considers the motion of statoliths as pure Brownian motion without effect of cell activity [4].

Recently we have shown, with macroscopic experiments, that plant shoots are only sensible to the direction of gravity, and not to its intensity [5]. This fact suggests that gravity sensing occurs mostly through detecting the position of a statoliths pile inside the statocytes. *In vivo* microscopic observations of wheat cells have also shown that statoliths piles relax to a zero-angle flat surface when the cells are subjected to a fast change of direction toward gravity (figure 1c). This behaviour is strikingly different from what is expected for a classical granular media, where an angle of repose exists. A key question is to know if the Brownian thermal agitation can explain this behaviour, or if the biological activity is needed to observe such a relaxation.

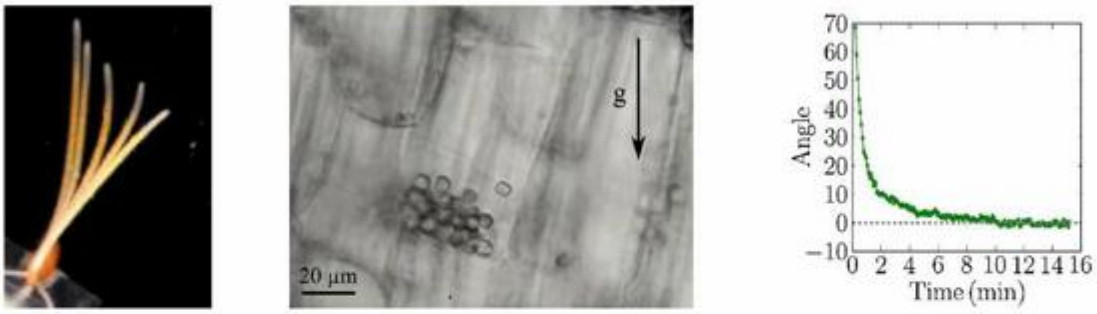

(a) (b) (c)

Figure 1: a) Images of a wheat coleoptile bending during $2\,\mathrm{h}$ of growth in response to gravity. b) A wheat coleoptile statocyte containing statoliths, observed with a $\times 40$ microscope objective. c) Relaxation of the angle of the statoliths pile's free surface after a rotation of 70°, averaged over several statocytes.

RESULTS

In first approximation, statoliths can be considered as a passive Brownian granular medium. However, the dynamics inside the statocytes is very complex: the statoliths are very confined, the surrounding fluid is non-Newtonian, and the plants cells show biological non-thermal activity. Moreover, *in vivo* experiments are difficult, due to the relatively short life-time of plants

*Corresponding author. Email: antoine.berut@univ-amu.fr

cells when placed between glass slide and cover slip for microscopic observations. To avoid these problems, we designed a biomimetic artificial system, where statoliths-like particles are embedded in plant cells-like microfluidic devices.

Our biomimetic devices are made of a matrix of small containers with dimensions close to those of wheat statocytes (approximatively $100\,\mu\mathrm{m} \times 30\,\mu\mathrm{m}$, and $50\,\mu\mathrm{m}$ depth). They are fabricated using classical microfluidic techniques: a negative master mould is created with SU-8 photoresist and a photolithography mask, then negative replicas are made using PDMS or agar-agar. The artificial statoliths are melamine resine microparticles ($5.17\,\mu\mathrm{m}$ in diameter), with a density of $1.51\,\mathrm{g/cm^3}$, which is close to starch density. The particles can be dispersed in bidistilled water (for simplicity) or other fluids with close density (to change the rheological properties). Hence, the particles show the same Brownian behaviour as real statoliths, because they have the same dimensionless number $\zeta \propto k_\mathrm{B}T/\Delta\rho R^4 g$ (where k_B is the Boltzmann factor, T the temperature, $\Delta\rho$ the difference of the particle's and fluid's densities, g the gravity on Earth, and R the particle's radius). ζ compares the strength of the thermal activity acting on the particle to it's own weight.

The system is observed with a customised microscope, placed horizontally, so that the gravity vector is contained in the observation plane (whereas gravity is perpendicular to the observation plane in an usual microscope). A picture of an *in vivo* sample is shown figure 2a, in comparison with one of our micro-fluidic devices in figure 2b. The sample is held on a rotation stage, which allows us to change rapidly its direction with respect to gravity. We observe the avalanches and subsequent relaxations of the microparticles piles in the confined geometry of the cells. The images recorded are then analysed to extract the fluctuations of the free surface, and in particular the mean angle between this surface and the gravity direction. The fact that we use a matrix of separate cells allows us to increase the statistics in a single experimental run.

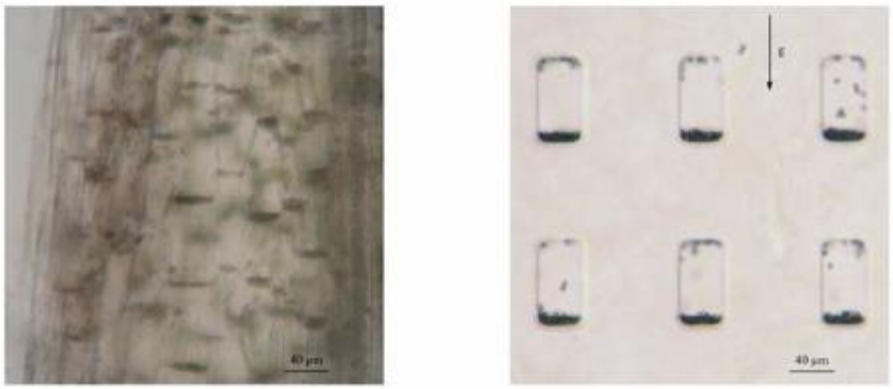

(a) (b)

Figure 2: Comparison between *in vivo* observation and artificial biomimetic device. a) A wheat coleoptile tissue with statocyte containing statoliths, observed with a $\times 10$ microscope objective. b) Agar-agar matrix of cells containing melamine resin microparticles, observed with a $\times 10$ microscope objective.

PERSPECTIVES

The use of artificial microfluidic devices with geometrical properties close to those of real plants cells allows us to study the motion of statolith-like particles in a fully controlled system, where rheological properties and thermal agitation are known. Preliminary results suggests that Brownian motion without cell activity is not enough to retrieve the relaxation observed with statoliths. By changing our particles' radius, we will be able to increase the influence of the thermal fluctuations to check for the equivalent agitation needed for gravity detection in plants cells.

This work was supported by the European Research Concil (ERC) under the European Unions Horizon 2020 research and innovation programme (grant agreement No. 647384) and by the French National Research Agency (ANR-13-BSV5-0005-01).

References

[1] M. Morita, Directional Gravity Sensing in Gravitropism, Annual Review of Plant Biology, vol. 61: 705-720 (2010).
[2] G. Leitz, B.-H. Kang, M. E.A. Schoenwaelder, and L. A. Staehelin, Statolith Sedimentation Kinetics and Force Transduction to the Cortical Endoplasmic Reticulum in Gravity-Sensing Arabidopsis Columella Cells, The Plant Cell, vol. 21, no. 3, 843-860 (2009).
[3] M. Nakamura, M.Toyota, M. Tasaka, and M. Morita, An Arabidopsis E3 Ligase, SHOOT GRAVITROPISM9, Modulates the Interaction between Statoliths and F-Actin in Gravity Sensing,The Plant Cell, vol. 23, no. 5, 1830-1848 (2011).
[4] Z. Zheng J. Zou, H. Li, S. Xue, Y. Wang, and J. Le, Microrheological Insights into the Dynamics of Amyloplasts in Root Gravity-Sensing Cells, Molecular Plant, 8 , 660-663 (2015).
[5] Article in preparation.

ICE AS A GRANULAR MATERIAL

Barbara Turnbull*[1], Michael Swift[2], and Richard Hill[3]
[1]*Faculty of Engineering, University of Nottingham, University Park, Nottingham, UK*
[2]*School of Physics & Astronomy, University of Nottingham, University Park, Nottingham, UK*
[3]*School of Physics & Astronomy, University of Nottingham, University Park, Nottingham, UK*

Summary Ice is a unique material, fundamental to vital processes on earth, in the atmosphere [1] and as planets and comets form [2]. In this work, we introduce two experiments investigating ice as a granular material, to provide snippets of insight into those processes. Initial investigations of ice particles in a granular flow show that the energy spent in collisions can generate localised surface wetting, even below the melting point [3]. This wetting reduces friction between granules, leading to acceleration of the bulk flow and in turn more wetting. The experiments described here are designed to show how even wetting invisible to an observer, can fundamentally alter the flow. The experiments also use the diamagnetic properties of ice to investigate how the outcome of high speed binary collisions, energetic enough to generate some melting, depends on this wetting.

Here we describe the development of two experiments: one investigating high speed binary collisions of ice in microgravity, the second creating a vibrating bed of ice particles to observe the transition from ostensibly dry granular behaviour to that of wetted granules.

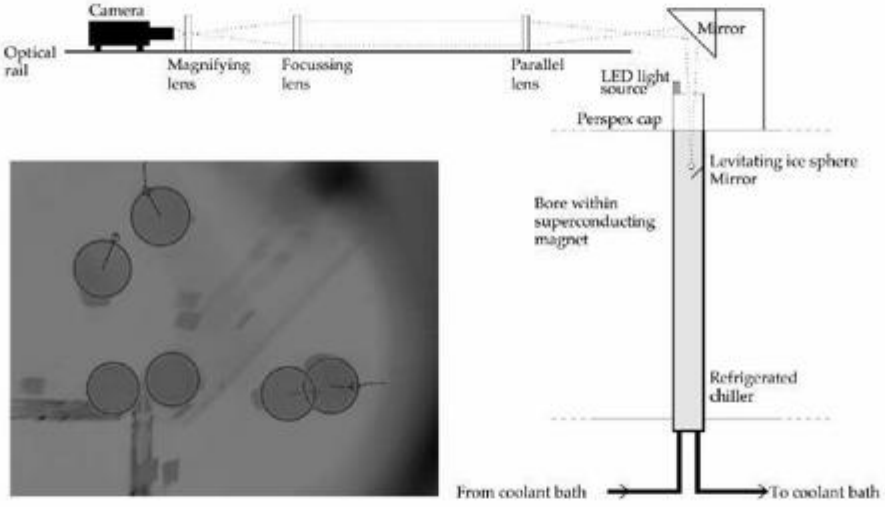

Figure 1: The configuration of an experiment with a single ice sphere levitated within the magnet bore. A combination of mirrors and lenses allows the trajectory of the levitated particle and any colliding particle to be recorded. A collision is created by dropping a second particle through a small hole in the top of the Perspex cap. Inset: Camera view after the collision of a dropped ice particle with a levitated ice particle. Centroid positions at collision are shown as circular markers, and centroid trajectory as lines. Here you see images of the pair of colliding particles, and their two perpendicular mirror images.

EXPERIMENTS

If we are to understand ice particle interactions in a variety of ambient conditions and with different particle geometries we need to be able to create a large number of binary collisions in a controllable environment. Here we introduce diamagnetic levitation [4] as a technique to investigate high speed ice collisions, where ambient conditions within the bore of a superconducting magnet can be controlled and the logistical constraints of parabolic flight or a drop tower [2], the chief alternatives, are removed. A refrigerated cylinder was inserted into the bore of a 19 Tesla superconducting magnet, cooled to -12°C. Ice particles were manufactured by dripping water from a syringe into a liquid nitrogen bath to form beads with diameters between 3 and 4 mm [3]. A single bead was placed at the levitation point in the magnet (fig. 1). A Perspex cap was placed over the magnet bore to stabilise the temperature within it and prevent convection. A 6 kHz camera was triggered to record as a second particle was dropped using tweezers through a small hole in the Perspex cap, vertically above the levitating particle. Since the

*Corresponding author. Email: barbara.turnbull@nottingham.ac.uk

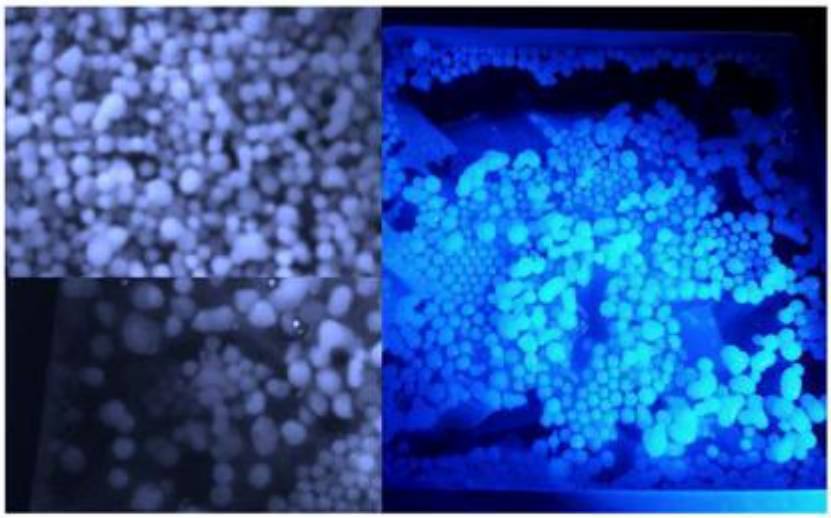

Figure 2: Ice granules in a closed glass cassette vibrated by an electromagnetic shaker, in a temperature controlled chamber at -3°C. Top left: A dry granular gas, after 5 minutes of shaking. Bottom left: After 20 minutes of shaking, larger coalesced particles appear alongside pockets of close packed particles. Right: Once all of the granules stopped moving after 65 minutes of shaking, the cassette was opened.

collision occurs along the camera axis, it was not possible to use the actual particle images to track collision trajectories and a pair of perpendicular mirrors were placed just below the levitation point allowing the full three-dimensional velocity field to be resolved (fig. 1 insert).

In a second experiment, ice particles (manufactured as previously described) were placed in a glass cassette (15 cm square, with a gap between base and top of 1.8 cm) that was shaken at $\omega = 50$ Hz with an amplitude $A = 0.87$ mm, providing a dimensionless peak acceleration $\tau = A\omega^2/g = 8.8$ [5]. The experiment was placed in a temperature controlled chamber at -3°C. Image sequences of the shaking ice particles were captured every 10 minutes, to identify changes to the bulk behaviour of the flow.

RESULTS

In a short space of time, 50 ice collisions were generated in the magnet bore, of which 22 were on-axis (thereby not generating spin). This compares with previous methods where only a few ice collisions have been possible under one set of conditions. Thus, large numbers of collisions can be created using diamagnetic levitation to generate statistically meaningful data on binary collisions, where we can control conditions such as impact speed and ambient temperature, and thus surface wetting, alongside additional parameters such as electrostatic charge and particle shape.

When ice was shaken at -3°C, the particles adopted an ostensibly dry granular flow (fig. 2). After 15 minutes, small changes could be observed, where some particles started to coalesce, and other small pockets of particles close to the centre of the cassette became clustered in a close packing formation. These patches of particles numbered up to approximately 10 until, after circa 65 minutes of shaking, all particles became spontaneously immobile. The majority, including the new larger, coalesced particles, clustering to the small patches of close packed pockets. At the end of the experiment, the granules still appeared dry. This spontaneous clustering behaviour is qualitatively very reminiscent of predictions from recent numerical simulations of wetted granular gases [5]. With enhanced diagnostics through e.g. capacitive liquid volume fraction measurements, this system should be capable of providing detailed verification of wetted materials that can currently only be explored numerically.

References

[1] Dash J. G., Rempel A. W., Wettlaufer J. S.: The physics of premelted ice and its geophysical consequences. Rev. Mod. Phys. 78(3):695, 2006.

[2] Heißelmann D., Blum J., Fraser H., Wolling K.: Microgravity experiments on the collisional behaviour of surturnian ring particles. Icarus 206(2):424–430, 2010.

[3] Turnbull B.: Scaling laws for melting ice avalanches. Phys. Rev. Lett. 107(25):258001, 2011.

[4] Hill R. J. A., Eaves, L.: Vibrations of a diamagnetically levitated water droplet. Phys. Rev. E 81(5):056312, 2010.

[5] Strauch S., Herminghaus, S.: Wet granular matter: a truly complex fluid. Soft Matter 8(32):8271-8280, 2012.

GAS-INDUCED FLUIDIZATION IN WATER-SATURATED SANDS

Valérie Vidal *[1], Gabriel Ramos[2], Raphaël Poryles[1], Jean-Christophe Géminard[1], and Germán Varas[2]
[1]*Laboratoire de Physique, École Normale Supérieure de Lyon - CNRS, Université de Lyon, France*
[2]*Instituto de Física, Pontificia Universidad Católica de Valparaíso, Chile*

Summary The morphology and dynamics of gas crossing a liquid-saturated granular bed has a drastic importance in natural and industrial processes. Due to the repetitive rise of gas through the bed, a fluidized zone is formed, which exhibits a parabolic shape at long times for a single injection point. This work investigates the fluidization of a liquid-saturated sand submitted to an ascending gas flow, in confined geometry. First, we focus on the fluidization dynamics from the initial state of a loose-packing, homogeneous bed. The stabilization time of the central air channel which is always formed in the stationary state is quantified, and its scaling inferred from an energy balance. Second, we investigate the global characteristics of the gas trapped in the system, in the stationary state. In particular, we show that the gas volume fraction in the fluidized zone is independent of the injection flow-rate and the grain diameter.

INTRODUCTION

Gas-induced fluidization of liquid-saturated sands is a process widely encountered, from geophysical to industrial processes. For instance, air sparging for soil remediation [1, 2], CO_2 sequestration [3] or catalytic processes [4] are among the numerous applications of these three-phase flows, which are still an active research topic. Indeed, due to the strong coupling between the gas, fluid and solid phase, the full understanding of the dynamics of such processes is still difficult to capture – in particular, the morphology and dynamics of the fluidized zone where the strong mixing between the three phases occurs. Many experiments have been developed in the laboratory to investigate the invasion dynamics of a fluid (liquid or gas) inside a liquid-saturated sand. In buoyancy-driven systems, where gas is injected from a single point at the base of a vertical cell, it has been shown that the gas rising through the grains forms a central fluidized zone at long times. Its stationary shape is parabolic, and a slow, global grain motion has been reported, with convective rolls following an upward motion close to the central air rise, and plunging downward close to the fluidized zone boundaries [5, 6]. In this work, we focus first, on the growth dynamics of the central fluidized zone, up to its stationary shape. Then, we investigate the dynamics of gas bubbles trapped in this central zone, and entrained by the granular convection rolls.

EXPERIMENTAL SETUP & DATA ANALYSIS

The experimental setup consists of a vertical Hele-Shaw cell ($\times$ 30 cm, gap 2 mm), filled with polydisperse, spherical glass beads immersed in water. In all the experiments, the height of the granular bed is $h_g = 20$ cm, and the liquid is filled up to a height $h_w = 2$ cm above the grains free surface. The grain diameter can be varied according to the following batches: $d = 218 \pm 1$ μm, $d = 318 \pm$ μm, $d = 31 \pm 3$ μm and $d = 802 \pm 8$ μm. At time $t = 0$ s, air is injected at the bottom of the granular bed from a central nozzle of inner diameter 1 mm, at constant flow-rate, Q. Direct visualization is achieved by means of a strong, homogeneous backlight (LED panel) and a camera (PixeLINK, 1280×800 px^2) acquiring at 0.1 Hz. Typically, the evolution of the system is followed up to 20 hrs.

The air invasion is analysed by stacking the successive image differences ($_{k+1} \nearrow _k$), according to the method detailled in [6]. We introduce first, the *flow density*, defined as $\rho_n(x,z) = \sum_{k=1}^{n-1} |\ _{k+1} \nearrow _k|$, and it normalized value $\bar{\rho}_n = \rho_n /$ x(ρ_n). To quantify the grain motion, we then define the horizontal and vertical cumulation, as $n_x(x,t) = \sum_x \rho_n(x,z)$ and $n_z(z,t) = \sum_x \rho_n(x,z)$, respectively, and their normalized value $\bar{n}_x$ and $\bar{n}_z$ over a given time series.

RESULTS

Growth dynamics of the fluidized zone

Figure 1a displays the flow density map in the system at different times. The fluidized zone starts forming from the grains free surface, then propagates downwards until reaching its stationary, parabolic shape (white dashed lines, Fig. 1a). The analysis of $\bar{n}_x$ and $\bar{n}_z$ makes it possible to quantify the stabilization time τ_s of the central air channel (white dashed line, Fig. 1b). The stabilization time is a decreasing function of the flow-rate (Fig. 1c), and this trend does not depend significantly on the grain size. A theoretical argument accounting for the grain motion, based on the balance between the energy injected in the system and the energy necessary to move grains over the system height h_g, gives $\tau_s \propto Q^{-2}$, in good agreement with the experimental observations (Fig. 1c). This result enhances the importance of the coupling between the grains, fluid and gas motion. Indeed, for a rigid porous network, a simple geometrical argument gives $\tau_s \propto Q^{-1}$, which does not fit the experimental trend (Fig. 1c).

*Corresponding author. Email: valerie.vidal@ens-lyon.fr

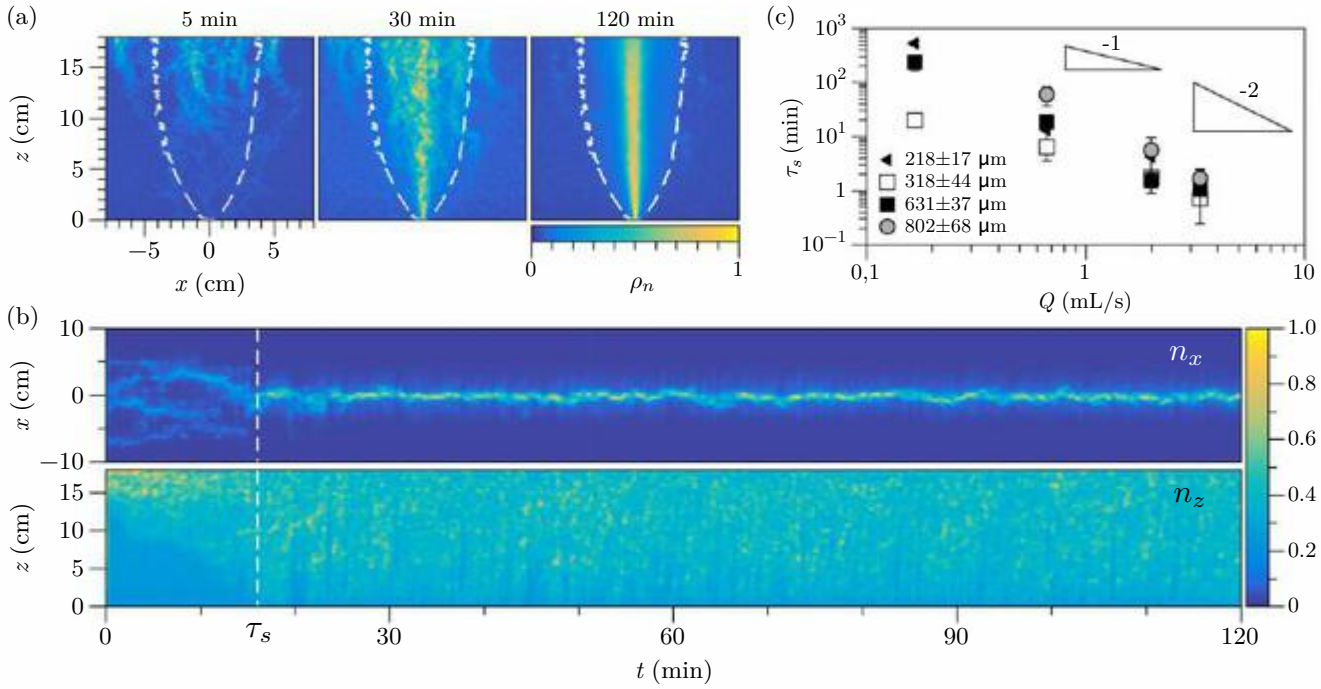

Figure 1: (a) Growth of the fluidized zone. The colors represent the normalized flow density ρ_n, representative of the motion in the system. At short times, the motion concentrates close to the surface, then the fluidized zone develops downward. After about 20 min, the air rise focuses on the center of the fluidized zone. The white dashed lines represent the border of the fluidized zone in the stationary regime, at long times [$Q = 0.66$ mL/s, $d = 318 \pm 44$ μm]. (b) Spatiotemporal diagram of the horizontal ($\bar{}_x$) and vertical (n_z) cumulation [same parameters than (a)]. The stabilization time, $\tau_s \sim 18$ min, is indicated by the white dashed line. (c) Characteristic time of the air channel stabilization, τ_s, as a function of the flow-rate Q, for different grain size. The triangles indicate $\tau_s \propto Q^{-1}$ et $\tau_s \propto Q^{-2}$ (see text) [$h_g = 20$ cm, $h_w = 2$ cm].

Gas volume fraction in the fluidized zone

In a second part, we focus on the stationary regime, and investigate the air volume fraction, ϕ_a, trapped in the central fluidized zone. Without any asumption on the final shape of the fluidized zone, we quantify its volume and show that it increases as $Q^{1/2}$. Interestingly, the air volume fraction ϕ_a in the fluidized zone is roughly constant when varying the air injection flow-rate, and does not depend significantly on the grain size.

CONCLUSIONS

This work summarizes experimental results on gas-induced fluidization in water-saturated sands. Interestingly, for a single injection point, the final parabolic shape of the fluidized zone is similar to the gas invasion pattern in a rigid porous medium [6]. We propose that the granular bed region initially explored by gas percolation becomes more fragile, and finally leads to the central fluidized zone. After quantifying the growth dynamics of the fluidized region, we have shown that the gas volume fraction trapped in the fluidized zone is constant and of about 2%. This last result is of importance in applications such as air sparging or catalytic reactors, as it demonstrates that increasing the injection flow-rate does not necessarily increases the fraction of gas in the region where the three phases mix.

References

[1] Reddy K. R., Kosgi S., Zhou J.: A review of In-Situ air sparging for the remediation of VOC-contaminated saturated soils and groundwater. Hazard. Waste Hazard. Mater. 12.97-118, 1995.

[2] Brooks M. C., Wise W. R., Annable M. D.: Fundamental changes in In Situ air sparging flow patterns. Ground Water Monit. Rem. 19:105-113, 1999.

[3] Kang Q., Tsimpanogiannis I. N., Zhang D., Lichtner P. C.: Numerical modeling of pore-scale phenomena during CO_2 sequestration in oceanic sediments. Fuel Process. Technol. 86:1647-1665, 2005.

[4] Biardi G., Baldi G.: Three-phase catalytic reactors. Catal. Today 52:223-234, 1999.

[5] Varas G., Géminard J.-C., Vidal V.: Air invasion in a granular layer immersed in a fluid: morphology and dynamics. Gran. Matt. 15:801-810, 2013.

[6] Ramos G., Varas G., Géminard J.-C., Vidal V.: Gas-induced fluidization of mobile liquid-saturated grains. Phys. Rev. E 92:062210, 2015.

ANOMALOUS LOW FRICTION COEFFICIENT IN DENSE SUSPENSIONS

Cécile Clavaud *[1], Antoine Bérut[1], Bloen Metzger[1], and Yoël Forterre[1]
[1]*Aix–Marseille Université, CNRS, IUSTI UMR 3 3, 13 53 Marseille Cedex 13, France*

Summary We study the friction coefficient of glass powders in water at low confining pressure, by measuring the pile slope angle in rotating drum flow experiments. We show that, at low rotation rates, the pile angle is about 10°, which is much lower than pile angles observed with larger glass beads in the same conditions ($\sim 25^\circ$). Changing the pH or salinity of the suspension restores the classical high slope angle, suggesting that physical and chemical interactions between particles are responsible for this observation. This result supports a recent scenario for the shear-thickening transition in such non-Brownian systems, where interparticle repulsive forces suppress friction at low confining pressure.

INTRODUCTION

Shear-thickening consists in a brutal increase in the viscosity of a dense suspension when the shear rate exceeds a critical value γ_c. The most famous example is a suspension of cornstarch in water. This phenomenon was first mentioned by Freundlich and Roder [1] in 1938 but remains ill-understood despite numerous studies. Recently, theoretical and numerical works [2, 3, 4] have proposed a new scenario for shear-thickening in non-Brownian suspensions. They suggest that it is due to a frictional transition induced by a repulsive force between the suspended particles. According to this model, at low confining pressure, repulsive particles should be nearly frictionless.

Testing this scenario would require to measure the friction coefficient μ_p between the grains in a suspension. However, this quantity is very difficult to obtain in classical rheological measurements using neutrally-buoyant suspensions. In this study, we use non-buoyant suspensions to indirectly measure μ_p through the pile slope angle θ_s in rotating drum flow experiments. In the quasi-static regime, $\theta_s =$ $\mathrm{n}(\mu)$, where μ is the macroscopic friction coefficient of the suspension, which itself depends on μ_p [5]. Therefore, measuring the pile slope angle θ_s should grant access to the interparticle friction at very low confining pressure ($P \sim \rho_p g d$ where ρ_p is the grains density and d their diameter). For repulsive particles and small enough d, we expect the pile angle to reflect the low frictional state of the system.

PROTOCOL

We studied the friction properties of glass powder in water. Glass in water is known to have a negative surface charge [6, 7], which should give rise to a repulsive force between the grains. We used small glass spheres, of diameter d such that $20\,\mu \lesssim d \lesssim 0\,\mu$, immersed in microfiltered deionized water. Larger glass beads ($d \sim 500\,\mu$) were also used as a standard granular suspension. For such large beads, the repulsive force is negligible compared to their weight, thus they should flow in a frictional state. The plexiglass rotating drums (diameter $D = 1.2$ and width $W = 3$ for the glass powder, $D =$ and $W = 8$ for the large beads, figure 1 a) are fixed on a vibration free rotating table controlled by a computer. The angular speed ω of the drum can be varied from $10^{-3\,\circ}\ ^{-1}$ to $90\,^\circ\ ^{-1}$. Both the light source and the camera used to take pictures are disconnected from the table bearing the experiment so they do not cause interfering vibrations. We took care not to contaminate the drum or the mixture. Indeed, the presence of ions dramatically changes the behavior of the system, as we evidenced by conducting the same experiment in salty water (1 $1\ ^{-1}$) and in a pH $= 10$ buffer solution. The experimental protocol was as follows: we rotated the drum at high speed ($90\,^\circ\ ^{-1}$) until the grains were suspended, then we set the angular speed to a chosen value. Time-lapse pictures were taken in order to determine the angle θ of the grains-water interface and its evolution in time.

RESULTS

Figure 1 b) shows the long time evolution of the interface angle θ for small glass spheres in microfiltered water, in a slowly rotating drum. We observe a steady regime with a low pile angle: $\theta_s \sim 10^\circ$. This angle seems independent of the angular speed ω, which suggests that it is the quasi-static pile slope angle of the suspension. To check the role of chemical and physical interactions between particles in this low angle, we changed the ionic force of the solution by adding salt or changing its pH. Figure 1 c) shows that in both cases, adding ions strongly increases the pile slope angle of the suspension to $\theta_s \sim 25^\circ$. This observation suggests that ions screen the repulsive force. The system thus transits from a frictionless to a 'standard' frictional granular medium. To test this hypothesis, we measured the pile angle of large glass beads of diameter $d \sim 500\,\mu$ at an angular speed of $5 \times 10^{-2\,\circ}\ ^{-1}$. As we can see (orange line in figure 1 c), they flow with a large pile angle of $\theta_s \sim 2\ ^\circ$,

*Corresponding author. Email: cecile.clavaud@univ-amu.fr

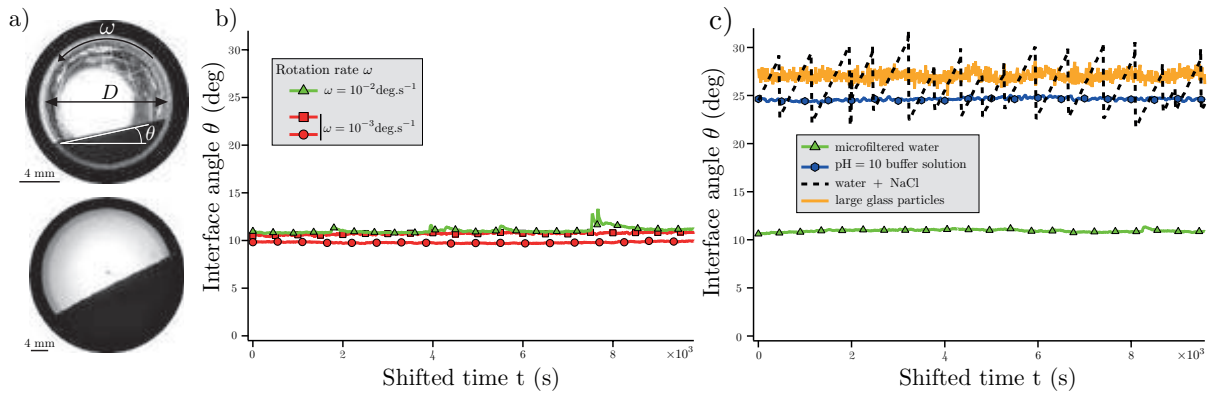

Figure 1: a) Pictures of the two rotating drums used in this study (top: for small beads, bottom: for large beads). Interface angle θ versus shifted time t: b) small ($20\,\mu \lesssim d \lesssim 0\,\mu$) glass beads in microfiltered water, comparison between two angular speeds, c) small glass beads in different suspending fluids and large ($d \sim 500\,\mu$) glass beads in microfiltered water. Time was shifted to simplify the presentation of the data, however this does not influence the discussion of the results.

which is close to that obtained with small beads in ionic solutions. This value is also compatible with previous experiments using large beads ($d \sim 230\,\mu$) [8]. This confirms our hypothesis: the small glass beads in microfiltered water are repulsive and subjected to a low confining pressure, therefore they flow with a low pile angle. The small beads in the buffer solution or in salty water, though subjected to a low confining pressure, are no longer repulsive because the presence of ions screens the repulsive force. The system thus becomes frictional. Finally, the large beads are forced into frictional contact by their weight, that overcomes the electric repulsion. They cannot be subjected to a low imposed confining pressure.

CONCLUSION

By performing rotating drum flow experiments, we demonstrate the existence of anomalous low pile angles of about 10° in suspensions of glass microspheres immersed in pure water. This is much lower than the pile angles observed in classical granular media and indicates an almost vanishing interparticle friction in these systems for low confining pressures. Modification of the ionic properties of the solution suggests that such a frictionless state arises due to short-range repulsive forces between particles that overcome the self weight of the first layers of beads.

This observation gives a first support to the recent scenario for the shear-thickening transition in non-Brownian suspensions, based on a frictional transition induced by short range interparticle repulsive forces. What remains to be asserted is that the glass powder suspension used in this study does shear-thicken in classical rheological configurations, as previously suggested [9]. It will also be interesting to adapt the rotating drum set-up to cornstarch suspensions, to see if a frictional transition occurs in this emblematical shear-thickening medium.

This work was supported by the European Research Concil (ERC) under the European Unions Horizon 2020 research and innovation programme (grant agreement No 647384).

References

[1] Freundlich H. and Roder H. L., Dilatancy and its relation to thixotropy, Trans. Faraday Soc. 34, 308–316, 1938.
[2] Seto R., Mari R., Morris J. F., and Denn M. M., Discontinuous shear-thickening of frictional hard-sphere suspensions, Phys. Rev. Lett. 111, 218301, 2013.
[3] Mari R., Seto R., Morris J. F., and Denn M. M., Shear-thickening, frictionless and frictional rheologies in non-Brownian suspensions, J. Rheol. 58, no. 6, 1693–1724, 2014.
[4] Wyart M. and Cates M. E., Discontinuous shear-thickening without inertia in dense non-Brownian suspensions, Phys. Rev. Lett. 112, 098302, 2014.
[5] Andreotti A., Forterre Y., and Pouliquen O., Granular media: between fluid and solid, Cambridge University Press, 2013.
[6] Vigil G., Xu Z., Steinberg S., and Israelachvili J., Interactions of silica surfaces, J. Colloid Interface Sci. 165, 367–385, 1994.
[7] Behrens S. H. and Grier D., The charge of glass and silica surfaces, J. Chem. Phys. 115, 6716–6721, 2001.
[8] Courrech du Pont S., Gondret P., Perrin B., and Rabaud M., Granular avalanches in fluids, Phys. Rev. Lett. 90, 044301, 2003.
[9] Boersma W. H., Laven J., and Stein H. S., Shear thickening (dilatancy) in concentrated dispersions, AIChE Journal, 36, 321–332, 1990.

CFD-DEM STUDY OF SATURATED GRANULAR MEDIA; APPLICATIONS TO FAULT GOUGE

Omid Dorostkar [1, 2a)], Paul A. Johnson [3], Robert A. Guyer[3], Chris Marone [4,5], Jan Carmeliet [1, 2]
[1]*ETH Zürich, Swiss Federal Institute of Technology Zürich, Switzerland*
[2]*EMPA, Swiss Federal Laboratories for Materials Science and Technology, Dübendorf, Switzerland*
[3]*Solid Earth Geophysics Group, Los Alamos National Laboratory, New Mexico, USA*
[4]*Pennsylvania State University, University Park, Pennsylvania, USA*
[5]*G3 Centre and Energy Institute, Pennsylvania State University, University Park, USA*

Summary In this paper, we present CFD-DEM simulations of stick-slip in dry and saturated granular media. The geometry of the CFD-DEM model is based on the loading geometry of the earthquake machine of Penn. State University, where granular layers under biaxial loading are tested. In our 3D CFD-DEM simulations, the particles are confined between two rough plates, compressed laterally, and sheared at constant velocity. The CFD-DEM results show nonlinear behavior of granular media caused by frictional weakening in the fault gouge leading to slip. We compare simulations in dry and saturated (drained) cases to characterize the influence of pore pressure and fluid-particle interactions. The macroscopic friction signal, kinetic energy, layer thickness, pore pressure and slip event rate, characteristics of the system, are recorded and analyzed. The aim is to characterize the influence of fluids on the frictional behavior of system during the stick-slip cycles.

INTRODUCTION/METHODOLOGY

There are many physical systems that store elastic energy and release it spontaneously. In earthquakes, the stored elastic energy is released abruptly through slips across the common plane of two sides of a fault [1, 2]. Granular materials (detritus) made from intact rocks due to erosion [3] are present in this common plane. It has been thought that earthquake physics is strongly controlled by the macro/micro scale behaviour of these granular materials [3]. Granular materials of fault gouge play a key role in inter-event time i.e. the time between each release of stored energy [1, 2]. Recent studies have shown that well before failure, the gouge material evolves into a so-called critical state [4, 5]. The main characteristics of this critical state is dilation, saturation in shear stress and mechanical weakening. The mechanical weakening is also manifested by the occurrence of precursors i.e. micro (small) shear failures, which can be recorded by acoustic emissions. However, most findings are done for dry media and the role of fluids with respect to critical state and slip failure are still less well studied. Use of CFD-DEM simulations helps us to understand the physics of frictional behaviour of saturated fault gouges at the grain scale. We use the so-called unresolved CFD-DEM method where particle size is smaller than the cell size in the CFD domain. Forces on the particles from solid-fluid interaction include drag force, viscous force and forces due to pressure gradient. The assembly of particles is first compressed vertically and then sheared horizontally at constant velocity. Figure 1 shows the assembly of particles, compacted between two corrugated plates before shearing. The fluid phase flow is obtained by solving the modified Navier-Stokes equation, taking into account the presence of granular materials in the fluid [6].

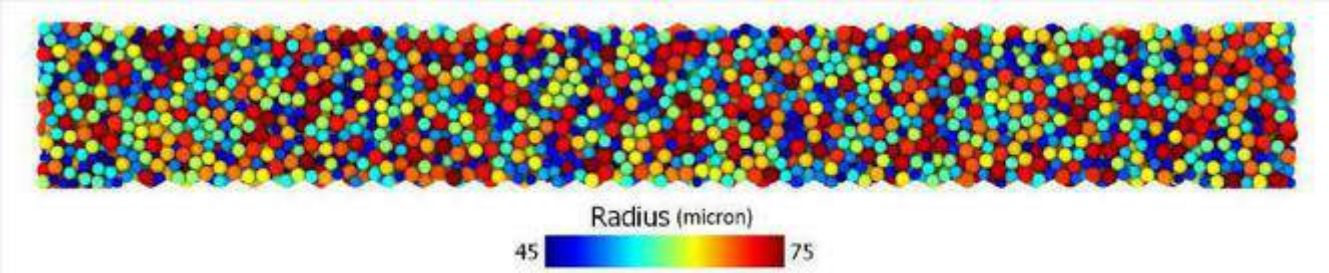

Figure 1: The assembly of particles compacted vertically between two corrugated plates before shearing stage. Periodic boundaries are applied at sides while front and back of sample are elastic walls (same material properties).

STICK-SLIP IN SATURATED GRANULAR MATERIALS

In Fig. 2, the simulation results for the drained saturated case are shown. Panel (a) in Fig. 2 gives the friction signal, where stick-slip cycles exhibit a non-linear behaviour of material. Associated with each slip event, we get an increase in kinetic energy signal (panel b, semi-log plot). In panels c to f, several stages of the velocity field in CFD domain are shown. Panel c shows the flow field in the stick phase where system is storing energy while being sheared, whereas panel e shows the chaotic behaviour of flow field during slip, where an abrupt movement of particles and associated release of kinetic energy occur. Precursors, i.e. micro-slips during the critical phase, are apparent from the friction signal before a large slip event.

[a)] Omid Dorostkar. Email: omid.dorostkar@empa.ch

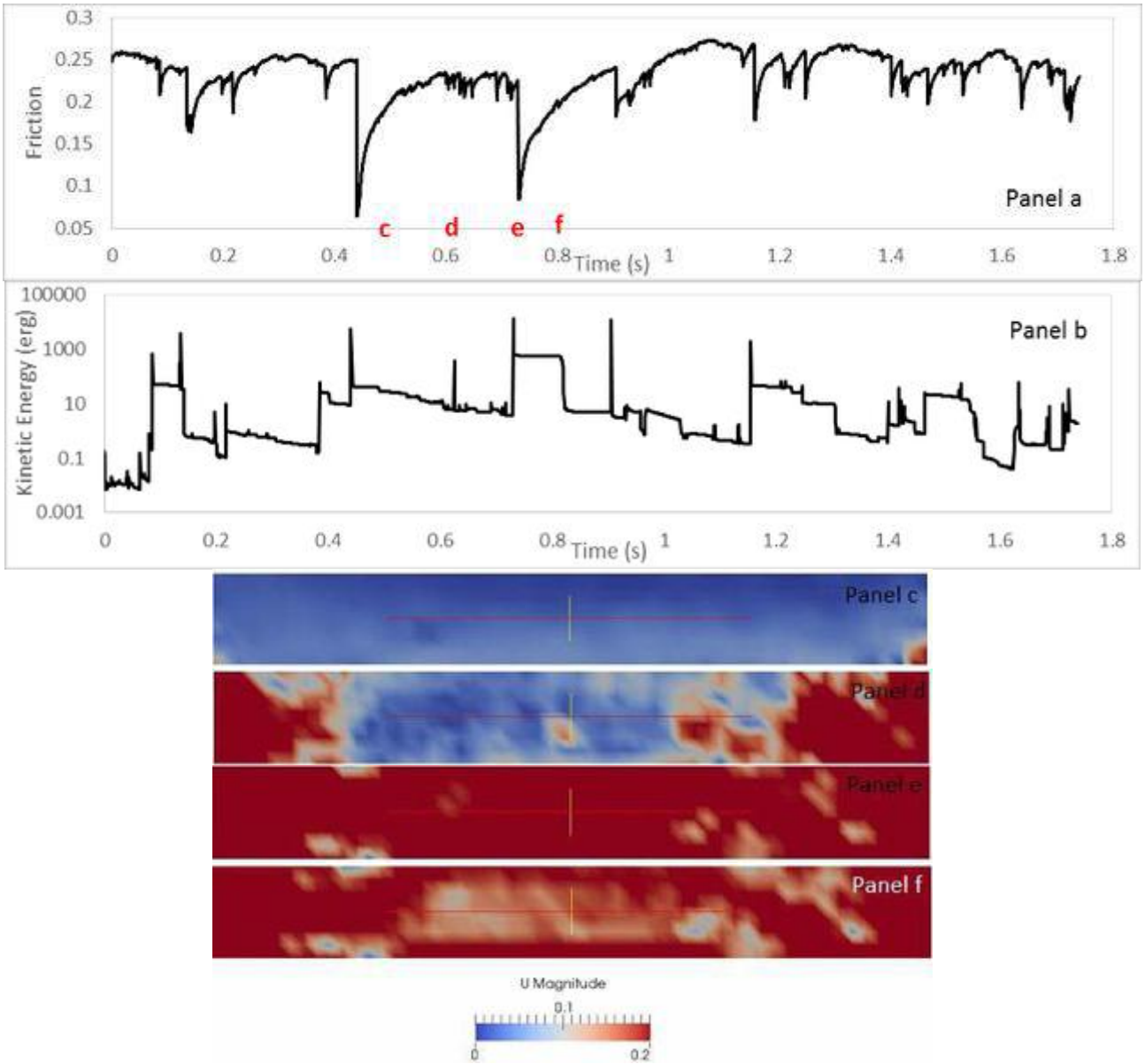

Figure 2: Simulation of saturated drained gouge in rather low viscosity. (a) friction signal (b) Kinetic energy in semi log plot. Panels (c) to (f) are fluid velocity field in stick, micro-slips, slip and after slip phases respectively. All units are in *cgs* unit system.

CONCLUSIONS

Fluids play a key role in failure mechanisms of granular materials. Our primary results show that fluids with high viscosity force the system to continuous sliding rather than to a stick-slip behaviour. Slip events either can occur locally related to small events or micro-slips or globally in whole domain associated with large slip events. We further show that fluid properties control this localization and general failure pattern.

References

[1] Brace, W. F. and Byerlee J. D.: Stick-Slip as a Mechanism for Earthquakes. Science 153 (3739), 990-992, 1966.

[2] Johnson, T., Wu F. T., Scholz C. H. , and Url S.: Source Parameters for Stick-Slip and for Earthquakes. Science 179 (4070), 278-280, 1973.

[3] Chester, F. M., Evans J. P. and Biegel R. L.: Internal structure and weakening mechanisms of the San Andreas fault. Journal of Geophysical Research: Solid Earth (1978-2012) 98 (B1), 771-786, 1993.

[4] Ferdowsi B., Griffa M., Guyer R. A., Johnson P. A., Marone C. and Carmeliet J.: 3D Discrete Element Modeling of triggered slip in sheared granular media. Physical Review E 89(4), 1-12, 2014.

[5] Johnson, P. A., H. Savage, M. Knuth, J. Gomberg, and C. Marone (2008). Effects of acoustic waves on stick-slip in granular media and implications for earthquakes. Nature 451 (7174), 57-60.

[6] Goniva, C., Kloss, C., Deen, N.G., Kuipers, J.A.M. and Pirker, S.: Influence of Rolling Friction Modelling on Single Spout Fluidized Bed Simulations, Particuology 10, 582-591, 2012.

IMPACT IN DENSE SUSPENSIONS: KEY ROLE OF PORE–PRESSURE

J John Soundar Jerome[1,2], Nicolas Vandenberghe[2], and Yoël Forterre [*1]
[1]*Aix–Marseille Université, CNRS, IUSTI UMR* 7343*,* 13453 *Marseille Cedex* 13*, France*
[2]*Aix–Marseille Université, CNRS, Centrale Marseille, IRPHE UMR* 7342*,* 13384 *Marseille Cedex* 13*, France*

Summary We investigate the impact of a freely-falling rigid sphere onto a granular pile immersed in a Newtonian liquid. Two very different behaviors are observed depending on the initial packing fraction of the pile. For initially loose packing, the ball readily sinks in the suspension as in a liquid whereas, for densely packed beds, the ball stops immediately as it hits the suspension. By combining local measurements of the interstitial fluid pressure and a simple impact model, we show that this liquid–solid transition is controlled by the coupling between the dilatancy of the pile and the pore–pressure generated by the impact. These results unify the description of impacts in various particulate media including cornstarch suspensions. They show that complex responses can arise from transient fluid–particle coupling rather than from the intrinsic rheology of the material.

INTRODUCTION

Impacts on particulate media like granular materials and suspensions have been the subject of an active research during the past decade, motivated by the question of the granular rheology and applications in astrophysics and ballistics (see a recent review in [1]). Depending on the experimental conditions, a very rich phenomenology is observed from the formation of permanent craters in dry granular media [2, 3] to the generation of fluid-like granular jets in fine powders in air [4, 5, 6]. Although these studies showed the importance of the air pressure or initial packing fraction in the impact response, the question of the physical mechanisms and control parameters that give rise to such a wide variety of phenomena is still largely open. Recently, studies on shear–thickening suspensions (cornstarch) show completely different behaviors. Above a critical velocity, an impacting object immediately stops, or in some cases generates cracks, as if hitting a solid [7, 8]. An important question is whether this impact-activated solidification is related to the complex rheology of the suspension or to more generic mechanisms involving jamming and/or the interaction between grains and fluid– a recurrent debate in the shear-thickening community [9]. In this study, we address this question by performing impact experiments on a model (non-buoyant) granular suspension [10], for which we can systematically control the initial volume fraction ϕ_0 (Fig. 1*A*).

RESULTS

Fig. 1*B* displays images captured during the impact on a suspension of water and glass beads of diameter $d = 170$ μm for an initially loose ($\phi_0 = 0.560$) and dense ($\phi_0 = 0.604$) packing. We observe two very distinct regimes. For loose packing, after impact the ball sinks in the suspension, giving rise to a collapsing cavity and a central jet similar to that observed in liquids or loose powders in air. By contrast, for dense packing, we observe that the ball stops abruptly within a few milliseconds as it hits the surface, as if the suspension hardened during impact. This solid-like behavior is strongly reminiscent of the impact-solidification observed when a solid object hits a shear-thickening suspension like cornstarch [7].

To explain how such a drastic change in behavior can occur with only a slight ($\sim 5\%$) change of volume fraction, we rely on a pore–pressure feedback mechanism: a coupling between Reynolds dilatancy and the pressure of the interstitial fluid between grains [12, 13]. When a dense granular packing starts to flow, it must dilate. However, if the medium is saturated with an incompressible liquid as in our case, this dilation induces a suction of the fluid and thus a drop in the interstitial fluid pressure (the pore–pressure), which in turn presses the grains against each other and transiently solidifies the medium. A loosely packed granular bed, on the other hand, tends to compact when it deforms. Therefore, a rise in pore–pressure is produced during impact, which can balance the weight of the grains and suppress the contact network, resulting in local or global fluidization. We proceed a direct verification of this mechanism via a pore–pressure measurement in the suspension (Fig. 1*C*). The transition between a positive peak and negative peak pore–pressure occurs at a critical volume fraction $\phi_c \simeq 0.585$, consistent with previous measurements with glass beads [13, 10].

To model these results, we combine the Darcy law [14] and an empirical law for Reynolds dilatancy [11], which gives the following scaling law for the pore–pressure: $P_f \sim -(\eta_f/\kappa)\Delta\phi V L$, where η_f is the fluid viscosity, $\kappa \propto d^2$ is the permeability of the pile, $\Delta\phi = \phi_0 - \phi_c$, V is the impact velocity and L the typical extent up to which deformation is experienced by the granular bed. Incorporating this relation in a simple impact model, and assuming a frictional rheology for the granular pile, predicts scaling laws for the ball penetration and pore–pressure in agreement with experiments for different impact parameters, grain sizes and fluid viscosities, thus validating our mechanism (Fig. 1*D*).

*Corresponding author. Email: yoel.forterre@univ-amu.fr

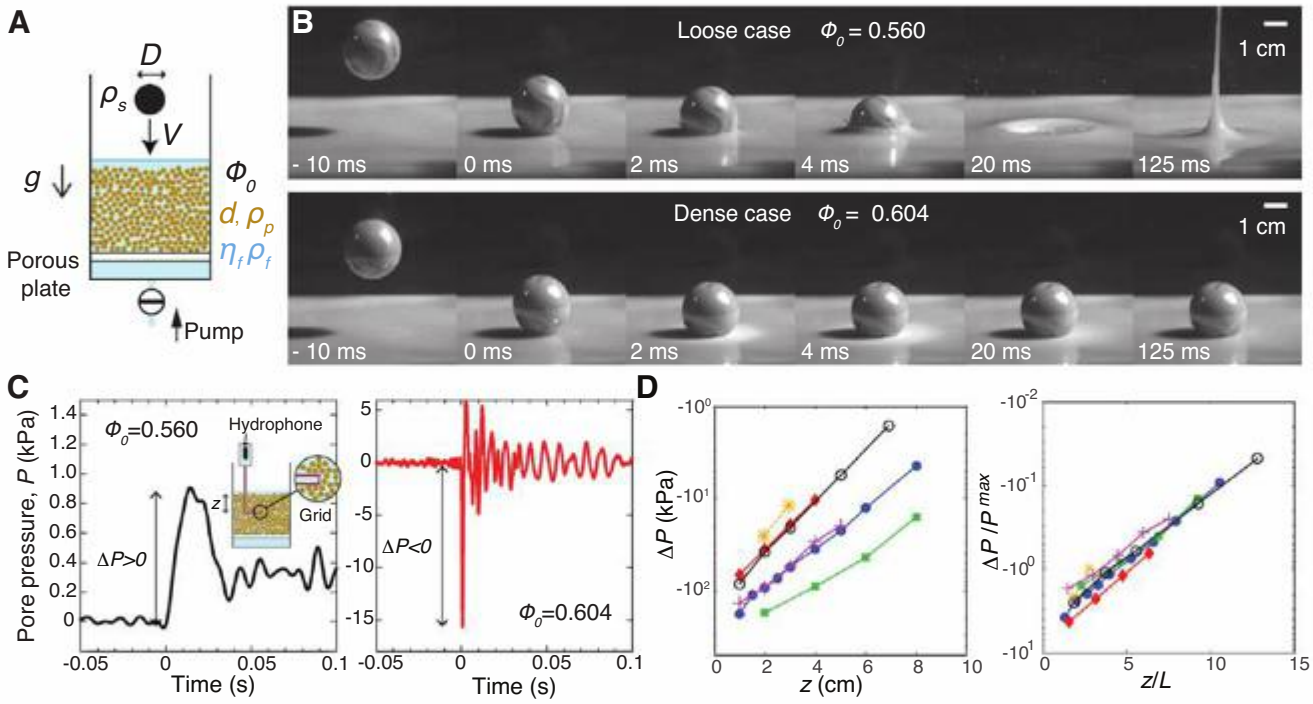

Figure 1: Liquid-solid transition after impact on a suspension of heavy particles. (*A*) Set-up. (*B*) Images sequence of a solid sphere (diameter $D = 25.2$ mm, speed $V = 2.35$ m s^{-1}) impacting on a loose (top) or dense (down) suspension of glass beads of diameter $d = 170$ μm in water. (*C*) Pore–pressure response in the loose (left) and dense (right) case. (*D*) Pore–pressure profile in the suspension right below the impact point for different impact conditions ($D = 16 - 25$ mm, $V = 1 - 5$ m s^{-1}), grain sizes ($d = 170 - 500$ μm) and fluid viscosities ($\eta_f = 10^{-3} - 10^{-2}$ Pa s) (left) rescaled by the model prediction (right).

CONCLUSIONS

In this study, we have shown that dramatic transition from fluid-like to solid-like impact response occurs in a mixture of grains and liquid close to jamming, due to a coupling between pile dilatancy and interstitial liquid flow. Our results can be easily extended to suspensions for which the interstitial fluid is not a liquid but a gas (like powders in air), by taking into account the fluid compressibility. They could also explain the impact–activated solidification observed in more complex shear-thickening media like cornstarch suspensions. In these systems, the critical volume fraction ϕ_c is expected to be function of the impact velocity [15, 16]. Thus, at high enough impact velocities, the suspension should become dilatant and solidify due to the pore–pressure feedback mechanism.

This work was supported by the French National Research Agency (ANR) through the program No. ANR-11-JS09-005-01 and by the Labex MEC (ANR-10-LABX-0092) and the A*MIDEX project (ANR-11-IDEX-0001-02) funded by the "Investissements d'Avenir" French Government program.

References

[1] Ruiz-Suàrez J.C. Penetration of projectiles into granular targets. Rep Prog Phys 76(6):066601, 2013.
[2] Walsh A.M, Holloway K.E, Habdas P, de Bruyn J.R. Morphology and scaling of impact craters in granular media. Phys Rev Lett 91(10):104301, 2003.
[3] Marston J.O, Li E.Q, Thoroddsen S.T. Evolution of fluid-like granular ejecta generated by sphere impact. J Fluid Mech 704:5–36, 2012.
[4] Thoroddsen S.T, Shen A.Q. Granular jets. Phys Fluids 13(1):4–6, 2001.
[5] Royer J.R. et al. Formation of granular jets observed by high-speed X-ray radiography. Nature Physics 1(3):164–167, 2005.
[6] Royer J.R. et al. The role of interstitial gas in determining the impact response of granular beds. Europhys Lett 93(2):28008, 2011.
[7] Waitukaitis S.R, Jaeger H.M. Impact-activated solidification of dense suspensions via dynamic jamming fronts. Nature 487(7406):205–209, 2012.
[8] Roché M, Myftiu E, Johnston M.C, Kim P, Stone H.A. Dynamic Fracture of Nonglassy Suspensions. Phys Rev Lett 110(14):148304, 2013.
[9] Brown E, Jaeger H.M. Shear-thickening in concentrated suspensions. Rep Prog Phys 77(4):046602, 2014.
[10] Boyer F, Guazzelli E, Pouliquen O. Unifying Suspension and Granular Rheology. Phys Rev Lett 107(18):188301, 2011.
[11] Andréotti B, Forterre Y, Pouliquen O. Granular media: between fluid and solid. Cambridge University Press, 2013.
[12] Iverson R.M. The physics of debris flows. Reviews of Geophysics. 35:245–296, 1997.
[13] Pailha M, Pouliquen O. A two-phase flow description of the initiation of underwater granular avalanches. J Fluid Mech 633:115–135, 2009.
[14] Jackson R. The dynamics of fluidized particles. Cambridge University Press, 2000.
[15] Seto R, Mari R, Morris J.F, Morton M.D. Discontinuous Shear Thickening of Frictional Hard-Sphere Suspensions. Phys Rev Lett 111:218301, 2013.
[16] Wyart M, Cates M.E. Discontinuous Shear Thickening without Inertia in Dense Non-Brownian Suspensions. Phys Rev Lett 112:098302, 2014.

SIZE DEPENDENCE OF THE YIELD THRESHOLD IN DENSE GRANULAR MATERIALS

Daren Liu[1] and David Henann *[1]
[1]*School of Engineering, Brown University, Providence, RI, USA*

Summary Yield of granular materials is typically modeled by local, pressure-dependent criteria, such as the Drucker-Prager condition, in which yield at a point is assessed based only on the stress. However, nonlocal effects lead to phenomena that cannot be captured with local yield conditions. For example, flows of thin layers of grains down an inclined surface exhibit a size effect whereby thinner layers require more tilt to begin flowing, and hence, sufficiently thin layers will not flow, even when the stress in the layer exceeds the yield condition. Recently, a new continuum model – the nonlocal granular fluidity (NGF) model – was successfully used to predict steady granular flow fields in a variety of flow configurations. In this work, we show that the NGF model is also capable of quantitatively describing the size-dependent strengthening of thin granular bodies – both in flow down an incline and in linear shear with gravity.

INTRODUCTION

Nonlocal effects in granular media manifest in myriad different ways. At the origin of the nonlocality is the finite size of the grains themselves, inducing cooperative behaviors that defy local rheological description. Examples include grain-size-dependent shear features in the steady flow profiles of granular media. A local rheology can be extracted from uniform simple shearing data of a granular media [1]; however, nonuniform steady flows of the same material can be seen to violate such a relation, as the grain-size sets up an internal length-scale that effectively penalizes variations in flow-rate over space [2].

One of the most compelling demonstrations of nonlocality in granular media can be observed in the behavior of grains on an inclined surface. Contrary to local rheological models, which predict a thickness-independent repose angle, experiments and discrete simulations verify that granular layers have a critical "stopping height" proportional to the grain size – layers thinner than this value come to a stop, whereas thicker layers admit steady flow down the incline [3].

Recently, a nonlocal rheological model based on the concept of "granular fluidity" has shown itself able to reconcile the issues of grain-size dependent shear features in granular media [4]. While these demonstrations pertain primarily to the way in which grain size influences spatial fields in materials that are driven to flow, nonlocality in the context of the flow threshold, i.e., whether a material flows at all, is of a relatively different nature. Despite this distinction, in this work we shall show that the nonlocal fluidity model is also capable of quantitatively describing the size-dependence of the yield threshold in two distinct geometries – inclined plane flow and linear shear with gravity.

INCLINED PLANE FLOW

In the inclined plane geometry, a layer of thickness H is inclined to an angle θ, shown schematically in the inset of Fig. 1(a). A simple consideration of equilibrium yields that the shear stress and normal pressure in the layer are $\tau = \rho G z \sin\theta$ and $P = \rho G z \cos\theta$, respectively, where G is the acceleration of gravity, ρ is the density of the granular material, and z is the distance beneath the surface. A local, pressure-dependent yield condition, such as Drucker-Prager, would dictate that the flow threshold is defined by a critical value of the ratio of the shear stress to the pressure, $\mu = \tau/P$, which we call $\mu_{\rm s}$. In inclined plane flow, we have that $\mu = \tan\theta$, so that any local yield condition would predict a universal angle of repose $\theta_{\rm r} = \arctan(\mu_{\rm s})$.

A signature of the cooperativity of granular motion is the fact that this universal repose angle is contradicted in experiments. As shown initially by Pouliquen [3] and verified by others, the angle at which an initially flowing layer of grains comes to a stop, $\theta_{\rm stop}$, depends sensitively on the thickness of the layer when H is small. Inverting, one can extract a function $H_{\rm stop}(\theta)$ for every granular media and substrate, which represents the critical thickness at which a flowing layer at a certain angle would arrest.

For inclined plane flow, the NGF model predicts that $H_{\rm stop}$ is given by

$$H_{\rm stop}(\theta) = \frac{\pi A d}{2}\sqrt{\frac{\mu_2 - \tan\theta}{(\mu_2 - \mu_{\rm s})(\tan\theta - \mu_{\rm s})}}, \tag{1}$$

where $\{\mu_{\rm s}, \mu_2, A\}$ are dimensionless material parameters and d is the grain size [5]. For a direct comparison, in Fig. 1(a), the above predicted form for $H_{\rm stop}(\theta)$, using previously-determined parameters for glass beads [4], is compared against Pouliquen's experimentally determined values using glass beads with a fully rough base. The quantitative agreement is excellent. It is worth pointing out that the model's result was obtained using the same continuum parameters that were used to successfully predict steady flow fields of glass beads in split-bottom cells and other geometries [4]. Yet here, the question is of a different nature, one of predicting input conditions for flow stoppage rather than velocity profiles in a flowing body.

*Corresponding author. Email: david henann@brown.edu

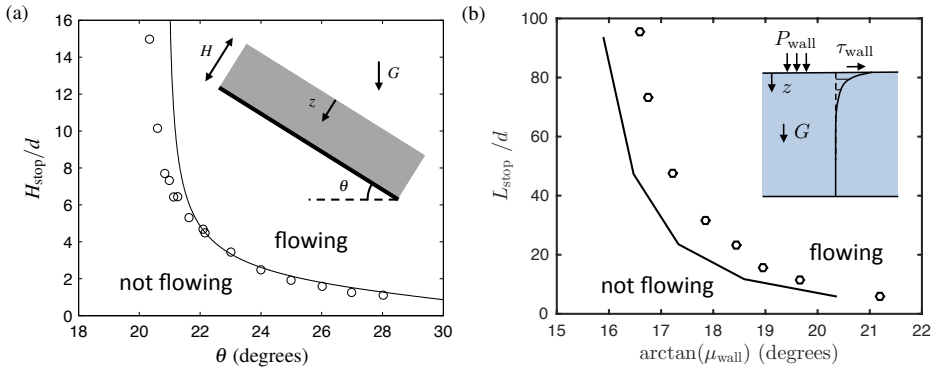

Figure 1: (a) Theoretically predicted $H_{\rm stop}$ locus ($-$) as calibrated for glass beads on a fully rough base, compared to experimentally determined values ($\circ$) from Pouliquen [3]. Inset: Schematic of the inclined plane flow geometry. (b) Theoretically predicted $L_{\rm stop}$ locus ($-$) as calibrated for frictional disks, compared to DEM-determined values ($\circ$). Inset: Schematic of the linear shear with gravity flow geometry.

LINEAR SHEAR WITH GRAVITY

In the case of linear shear with gravity, a rough plate is dragged horizontally across a deep bed (infinite half-space) of gravitationally-loaded granular material, shown schematically in the inset of Fig. 1(b). The weight of the plate imposes a pressure $P_{\rm wall}$ on the $z = 0$ surface, and its horizontal motion imposes a shear stress of $\tau_{\rm wall}$. For this flow configuration, the length-dimensioned "size" is given by $P_{\rm wall}/\rho G$, which we denote as L and is analogous to the layer thickness H in the previous configuration. Regarding the stress field in this configuration, the shear stress is spatially-constant and given by the shear stress imparted by the wall, $\tau = \tau_{\rm wall}$, and the pressure field is a combination of the wall pressure, $P_{\rm wall}$, and the gravitational pressure gradient, so that $P = P_{\rm wall} + \rho G z$. The stress ratio is then $\mu = \tau/P = \tau_{\rm wall}/(P_{\rm wall} + \rho G z)$, so that the maximum value of μ occurs directly under the plate ($z = 0$) and is $\mu(z = 0) = \mu_{\rm wall} = \tau_{\rm wall}/P_{\rm wall}$.

Again, as in the case of inclined plane flow, a local yield condition, such as Drucker-Prager, will predict a size-independent flow threshold of $\mu_{\rm wall} = \mu_{\rm s}$ with flow only occurring when this threshold is exceeded. In order to elucidate the geometric generality of the phenomena observed in inclined plane flow, we have performed two-dimensional discrete element method (DEM) calculations of linear shear with gravity for different "systems sizes," $L = P_{\rm wall}/\rho G$, and determined the flow threshold, $\mu_{\rm wall}$, in each case. In our DEM calculations, we utilize quasi-monodisperse frictional disks with an interparticle friction coefficient of 0.4. This granular system has been thoroughly studied, and its material parameters for the NGF model have been determined [6]. For each value of L, we determine the critical value of the wall stress ratio that corresponds to flow arrest. Inverted, we obtain a function $L_{\rm stop}(\mu_{\rm wall})$, which is plotted as circles in Fig. 1(b), showing a clear strengthening as the system size is decreased. We have plotted $L_{\rm stop}$ as a function of $\arctan(\mu_{\rm wall})$ so that the analogy to inclined plane flow is more clear. Note that the angle of repose, i.e., the vertical asymptote in Fig. 1, is different for 2D disks, $\theta_{\rm r} = 14.6^\circ$, than for glass beads, $\theta_{\rm r} = 20.9^\circ$.

For this flow configuration, the $L_{\rm stop}$ curve predicted by the NGF model cannot be derived analytically in closed form. Instead, we perform finite-element calculations using the nonlocal fluidity model to determine the $L_{\rm stop}$ locus predicted by the model. The predicted $L_{\rm stop}$ curve using previously determined material parameters [6] is also plotted in Fig. 1(b). Again, favorable quantitative agreement is obtained without any parameter fitting – only using parameters determined to describe flow fields in other geometries [6]. Hence, by comparing the model's predicted flow threshold in linear shear with gravity to 2D DEM calculations without parameter calibration, we have shown that the nonlocal fluidity model can be used to quantitatively model size-sensitive flow stoppage phenomena in geometries other than inclined plane flow.

References

[1] da Cruz F., Emam S., Prochnow M., Roux J.-N., Chevoir F.: Rheophysics of dense granular materials: Discrete simulation of plane shear flows. Phys. Rev. E 72:021309, 2005.

[2] Koval G., Roux J.-N., Corfdir A., Chevoir F.: Annular shear of cohesionless granular materials: From the inertial to quasistatic regime. Phys. Rev. E 79:021306, 2009.

[3] Pouliquen O.: Scaling laws in granular flows down rough inclined planes. Phys. Fluids 11:542–548, 1999.

[4] Henann D. L., Kamrin K.: A predictive, size-dependent continuum model for dense granular flows. Proc. Natl. Acad. Sci. 110:6730–6735, 2013.

[5] Kamrin K., Henann D. L.: Nonlocal modeling of granular flows down inclines. Soft Matter 11:179–185, 2015.

[6] Kamrin K., Koval G.: Effect of particle surface friction on nonlocal constitutive behavior of flowing granular media. Comp. Part. Mech. 1:169–176, 2014.

CONTROLLING GRANULAR SEGREGATION PATTERNS USING UNSTEADY FLOWS

Hongyi Xiao[1], David McDonald[2], Julio M. Ottino[1,3,4], Richard M. Lueptow [1,4] & Paul B. Umbanhowar[1]
[1]*Department of Mechanical Engineering, Northwestern University, Evanston, IL USA*
[2]*Department of Mechanical Engineering, Carnegie Mellon University, Pittsburgh PA USA*
[3]*Department of Chemical and Biological Engineering, Northwestern University, Evanston, IL USA*
[4]*The Northwestern Institute on Complex Systems, Northwestern University, Evanston, Illinois, USA*

Summary Unsteady flows of granular materials are ubiquitous yet remain largely unexplored. In this research, we apply unsteady flows to strongly segregating granular materials to control the segregation pattern and enhance mixing. Unsteady flows are generated by feeding size-bidisperse granular mixtures with large size ratios onto a quasi-2D bounded heap using alternating feed rates. With this flow modulation, large particles and small particles form stratified layers, which have better average mixing than the segregated patterns generated by steady feed rates. The mechanisms of layer formation under modulated flow differs from those observed during spontaneous stratification, and are related to changes in the repose angle and flowing layer depth with varying flow rate. The thickness and length of the stratified layers can be controlled by changing the flow rates and feed cycle durations, which is potentially useful for reducing segregation in industrial processes. Funded by NSF Grant CBET-1511450.

INTRODUCTION

Segregation and mixing of disperse granular materials (differing in size, density, etc.) have important implications in situations ranging from material handling in industry to natural phenomena. Most previous studies of granular segregation and mixing focused on steady granular flows. However, unsteady flows are ubiquitous and exhibit more complex phenomena due to their time-varying kinematics [1,2]. In this study, we intentionally generate unsteady flow to investigate the resulting kinematics, its influence on mixing and segregation, and the potential application of unsteady flow to enhanced mixing for strongly segregating materials.

FLOW MODULATION

To generate unsteady flow, we feed size bidisperse granular mixtures with large size ratios onto a quasi-2D bounded heap [3] using two distinct and alternating feed rates. Each feed cycle consists of two phases: a fast flow phase with feed rate Q_f for duration t_f and a slow flow phase with feed rate Q_s for duration t_s. Under this flow modulation, large particles and small particles form stratified layers, different from the segregated pattern generated by a steady equivalent mean feed rate, see Fig. 1. The modulated stratification is different from spontaneous stratification reported in previous studies [4,5], because it occurs at higher average flow rates and its pattern is controllable. To investigate the modulated stratification mechanism and the influence of input parameters on pattern formation, we conducted experiments in which the feed rates and cycle times were varied.

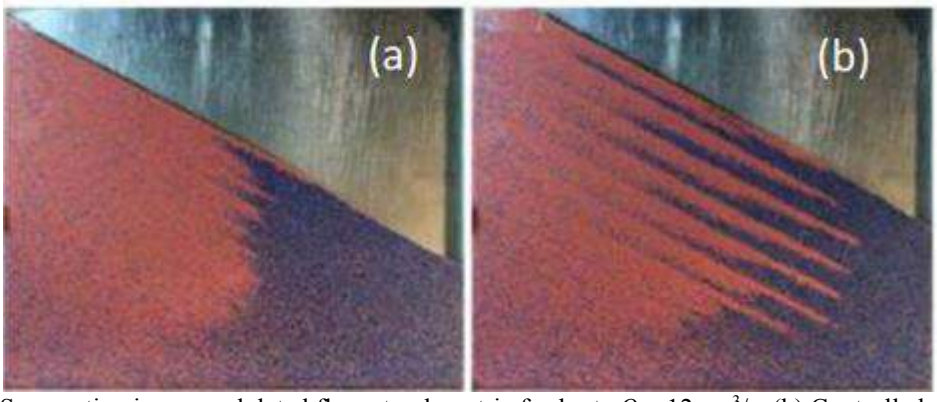

Figure 1. (a) Segregation in un-modulated flow at volumetric feed rate Q = 12 cm^3/s; (b) Controlled stratification in modulated flow at approximately the same mean feed rate as in the left figure (Q_s = 4.4 cm^3/s, t_s=12 s, Q_f = 18.4 cm^3/s, t_f =15 s, Q_{mean}=12.2 cm^3/s). Blue (dark): 3-mm glass spheres; red (light): 1-mm glass spheres.

[a] Corresponding author. Email: hongyixiao2016@u.northwestern.edu

RESULTS AND DISCUSSION

The experiments reveal that large particles flow over smaller ones during the fast flow rate phase but both smaller and larger particles flow down the slope during the slow flow rate phase. During the fast portion of the cycle, the layers of large particles form; during the slow portion of the cycle, the small particle strata progress further downstream under a moving layer of larger particles. The thickness of the repeating layers depends linearly on the total volume of the feed during each cycle, *V*, above a critical value, see Fig. 2. Below this critical value, the layer thickness is more variable, most likely because spontaneous avalanches occur at these slow flow rates [3]. The length of the layers of the strata depend in a more complex way on the flow rates and durations.

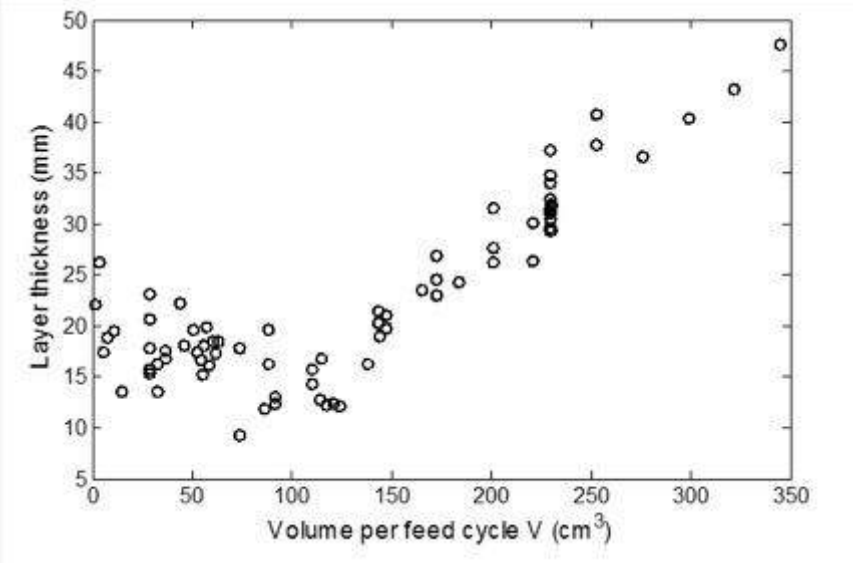

Figure 2. Layer thickness as a function of flow volume per feed cycle.

CONCLUSIONS AND ONGOING WORK

We demonstrate that stratified segregation patterns in bounded heap flow can be created at mean flow rates well above the steady flow rate where spontaneous stratification ends and that the wavelength and the streamwise extent of the layers of the segregation patterns can be controlled by changing feed rates and cycle duration time. We are conducting Discrete Element Methods (DEM) simulations to gain more insight into the kinematics of unsteady flows, and are optimistic that with this knowledge we will be able to design more complicated modulation approaches to achieve finer and more extended layered segregation patterns that further enhance mixing.

References

[1] Fiedor S.J., Ottino J.M: *J. Fluid Mech*., **533**:223-236, 2005.

[2] Pohlman N.A., Ottino J.M., Lueptow R.M.: *Phys. Rev. E*, **80**:031302, 2009.

[3] Fan Y., Boukerkour Y., Blanc T., Umbanhowar P.B., Ottino J.M., Lueptow R.M.:*Phys. Rev. E*, **86**:051305, 2012.

[4] Gray J.M.N.T., Hutter K.: *Continuum Mech. Therm*. **9**:341–345, 1997.

[5] Makse H.A., Havlin S., King P.R., Stanley H.E.: *Nature* **386**:379–382, 1997.

INSTABILITY DURING THE EROSION OF A COHESIVE GRANULAR PILE

Pierre Jop*, Gautier Lefebvre, and Aymeric Merceron
Surface du Verre et Interfaces, UMR 125 CNRS/Saint-Gobain,
39 quai Lucien Lefranc 93303 Aubervilliers, France

Summary The complex interplay between the topography and the erosion and deposition phenomena is a key feature to model granular flows such as landslides. Here, we investigated the instability that develops during the erosion of a wet granular pile by a dry dense granular flow. The morphology and the propagation of the generated steps are analyzed in relation to the specific erosion mechanism. The selected flowing angle of the confined flow on a dry heap appears to play an important role both in the final state of the experiment, and for the shape of the structures. We show that the development of the instability is governed by the inertia of the flow through the Froude number. We model this instability and predict growth rates that are in agreement with the experiment results.

INTRODUCTION

The situation where a cohesive granular media and a flowing granular layer interact encounters in the mixing processes of industrial applications or in some transport of sediment in nature. Erosion patterns are known to spontaneously develop at the bottom of the river bed depending on the coupling between the flow and the bed geometry through the erosion/transport laws [1, 2]. Granular flows such as landslides can also alter the underlying ground. However the erosion mechanisms are not clear when the granular material is dense. Thus recent studies have focused on the evolution of the interface between static and flowing dry granular layers, on the velocities and on the runout distances. Moreover the studies of instabilities in granular flows were generally focused on the flowing layer (roll waves, upward traveling waves). Finally, previous studies on the erosion rate of a cohesive media by a granular flow focused on the physical properties of the cohesive materials (e.g. [4]). Thus we explore here the coupling between a flow of dry granular material and a cohesive granular bed.

EXPERIMENTAL SET-UP

We performed experiments in a quasi-two-dimensional cell made of parallel vertical glass plates, whose gap width W was set at 6 and 12 mm. The same polydisperse glass beads of diameter 200-400 μm were used for both the cohesive granular bed and the flow. The cohesive material was obtained by mixing a small quantity of water with the beads to obtain a low water content of 1% wt, which corresponds to the formation of individual capillary bridges. This material was introduced and packed into the cell to form a heap with a planar free-surface of length ranging from 30 to 35 cm. We injected the dry granular material at the top left of the cell so a flowing layer would form above the wet heap [Fig. 1(a)]. The two remaining parameters are the initial inclination of the heap θ_i and the constant injected flow rate Q.

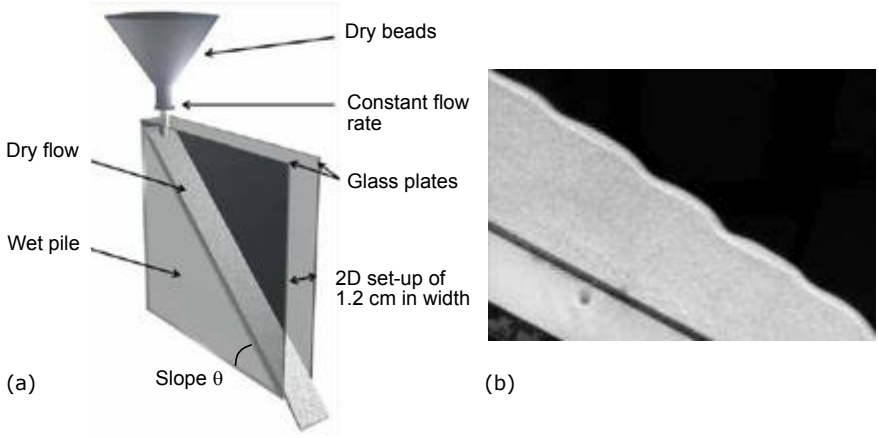

Figure 1: (a) Experimental set-up of the dry granular flowing on top of wet-cohesive granular pile. (b) Destabilization of the morphology of the pile during the erosion process, creating a succession of steps. The vertical scale is 12cm

.

*Corresponding author. Email: pierre.jop@saint-gobain.com

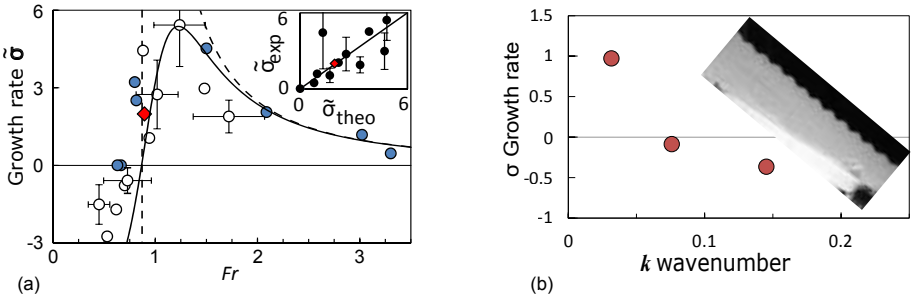

Figure 2: (a) Dimensionless growth rates of the steps as a function of the Froude number in experiments for glass beads in the mm channels (•) and 12 mm channel (○) and steel beads in 12 mm channel (◇). The curves correspond to a prediction of the theoretical model for a wavenumber in agreement with the experiment $h_0 k = 0.1$ at an inclination of $\theta_i = 30^o$. Inset: Direct comparison of growth rates using the measured wave numbers $\tilde{k}$ as a parameter. (b) Experimental growth rates for different imposed initial wavelengths. An example is shown on the inset.

RESULTS

With this low water content, we observe that erosion occurs at the interface between the cohesive pile and the granular flow, without deposition. Wet beads are slowly extracted by the action of the dry flow. Thus, the volume of the cohesive heap is gradually reduced during the experiment until it reaches a steady state in which the interface is flat and the dry granular material flows without eroding the wet bed. During this erosion process, two different behaviors can be observed. Either the eroded interface remains initially flat and parallel to the initial slope, or we observe the creation of step-shaped structures for rather high inclinations and high flow rates [Fig. 1(b)]. These steps grow and propagate upstream then disappear one after the other at the top of the channel. In both cases, the final interface is flat and forms an angle θ_f with the horizontal with $\theta_f < \theta_i$.

Due to the analogy with the shape and the propagation of the structures led by the pool and step instabilities in riverbeds [1], we expect to observe an inertial destabilization. The underlying mechanism would be the phase lag between the topography and the local erosion rate due to inertia. Such phase lag exists for step-pool formations between the erosion and the shape of the interface [1]. We expect therefore a stability criterion based on the Froude number $\mathrm{Fr} = u/\sqrt{gh \quad \theta_i}$, which compares the inertia with the gravity effects, where $g \quad \theta_i$ is the projection of the gravity perpendicular to the slope.

We compute the initial growth rates of the instability scaled by the measured erosion time scale. The figure 2(a) show the existence of a critical Froude number, around 0.8, above which the instability develops with positive growth rates. The negative values are obtained by following a step coming from the downstream boundary conditions that disappears.

We model the flow using a depth-averaged method with the now well-established rheology of dense granular flows [5]. We make the assumption, as in the fluid case, that the erosion rate is linked to the inertia of the grains. We then carry a linear stability analysis. We show that the previous assumptions are required to predict an instability of the interface above a critical Froude number. Moreover we are able to compare the theoretical growth rates for the observed wavelengths [Fig. 2(a)]. Finally we measure the growth rate for three initial wavy interfaces as shown on figure 2(b). These results show that a mechanism for the wavelength selection need now to be modeled.

CONCLUSIONS

We study a new erosion instability occurring with granular flows over a cohesive granular bed. Above a critical Froude number, the interface is unstable and the shape of the steps is governed by the properties of the granular flows. We model the mechanisms in the framework of a Saint-Venant approach. We finally identify that the inertia of grains governs the erosion mechanisms in dense granular flows. We believe that our results could lead to a better understanding of geophysical flows. On the other hand, for applications of mixing of grains and liquids such as building materials, our work represents a mechanism of homogenization of wet aggregates with dry grains in slow mixers.

References

[1] G. Parker and N. Izumi, J. Fluid Mech. 419, 203 (2000).
[2] B. Andreotti, P. Claudin, O. Devauchelle, O. Duran, and A. Fourriere, J. Fluid Mech. 690, 94 (2012).
[3] I. J. Hewitt, N. J. Balmforth, and J. N. McElwaine, J. Fluid Mech. 692, 446 (2012).
[4] L. Hsu, W. E. Dietrich, and L. S. Sklar, J. Geophys. Res. 113 (2008).
[5] P. Jop, Comptes Rendus Physique 16, 1, pp 62-72 (2015).

EXPERIMENTAL INVESTIGATION AND THEORETICAL ANALYSIS FOR DEPTH-DEPENDENT DRAG FORCE IN GRANULAR MATTER

Wenting Kang[1], Yajie Feng[1], and Caishan Liu *[1]

[1]*State Key Laboratory of Turbulence and Complex System, College of Engineering,Peking University, Beijing, 100871, China*

Summary A material testing machine was used to experimentally measure the quasistatic force acting on the bottom of cylinders that slowly and continuously move along its symmetric axis downwards into a granular medium. By utilizing different cylinders to plunge into different granular materials, we demonstrate that the normalized average pressure $[p_u]$ acting on the cylinder's bottom linearly increases with the penetration depth, while the linear scale-factor k_h just depends on the internal friction angle of the granular material. To theoretically figure this out, we employ Prandtl's Slip-Line(PSL) theory to analyze the stress field of the plastic region involved in the granular matter. The theoretical model also suggests that $[p_u]$ should be linearly related to the penetration depth, and k_h can be computed theoretically. Good agreement between the computed values and the experimental results of k_h sheds light on the way of the continuum description for the granular material behaviours.

EXPERIMENTAL STUDY

When a solid object slowly penetrates a granular material, it experiences a quasistatic vertical drag force that varies with penetration depth h. In general, the static drag force F_h can be reduced to a form as $F_h(h) = k_h h^\alpha$. Past experimental studies have found that the exponent α may vary with the intruder geometries and takes a value ranging from 1 to 1.8. Among these studies, Durian *et al.* experimentally confirmed, both from impact experiments[1] and quasi-static experiments[2], that the normalized average pressure $[p_u]$ seems to be linearly related to the penetration depth. This enables ones to unveil the reason underlying the diversity of the value of α involved in different geometries of the intruder. Until now, the understanding of this relationship is mainly from phenomenological analysis, rather than theoretical explanation. Meanwhile, how the physical properties of the granular medium affect the coefficient k_h is also desiderate to be resolved. In this paper we purpose to understand the static mechanical regime of granular material according to a combined investigation of experiments and theoretical analysis.

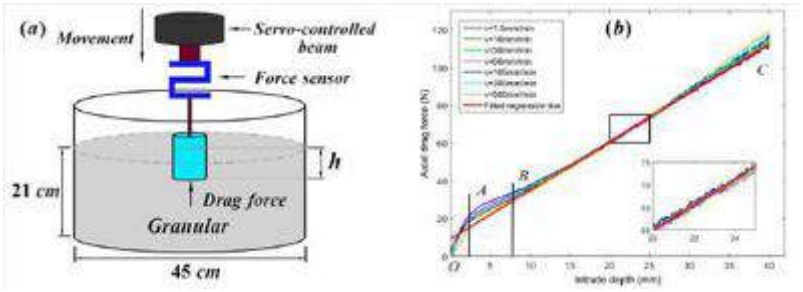

Figure 1: (a) The sketch of the experimental apparatus; (b) The reproducibility of the axial drag force for $D = 40mm$ cylinder penetrates sand with different velocities, and the raw data fit well with the fitted regression line (red) after point B.

We performed our experiments via an experimental apparatus sketched in Fig.1(a). A servo-control system drives a cylinder intruder to slowly and continuously plunge into a granular matter. A force sensor is adopted to measure the vertical resistance sensed by the intruder. The cylinder contacts the granular matter via its bottom surface so that the contact area remains unchanged during the whole process of the penetration. This enables us to conveniently scale the average pressure on the bottom of the cylinder. Four aluminous cylinders with the same height $50mm$, while their diameters D with values as $30mm$, $40mm$, $50mm$ and $70mm$, were tested in our experiments. We restrict the maximum of the penetration depth h to be less than $50mm$ so that the cylinders won't be buried in the medium at the end of the penetration process. The barrel is $45cm$ in diameter and is filled with granular matter of $21cm$ height. The size of the barrel is much larger than the cylinders which ensures the penetration process is free from the boundary effect. To figure out how the drag force relates to the granular characters, we use five different granular materials: air dry natural sand, millet, and three kinds of glass beads with different diameters. These granular materials cover different particle shapes, sizes and materials, consequently lead to different internal friction angles ranging from about 28° to 38°. Because the internal friction angle of the granular matter is very sensitive to

*Corresponding author. Email: liucs@pku.edu.cn

the state of the particles, we meticulously prepare the packings of the granular matter by the following procedure: before each test, we stir the granular matter vigorously and homogeneously at first and then gently level the surface with a flat metal spatula. Fig.1(b) shows the raw data for the cylinder with $D = 40mm$ moving in sand with different velocities ranging from $1.5mm/min$ to $500mm/min$. The high consistency among those different experiments confirms the reproducibility of our experiment, as well as the quasistatic state of the granular matter. Similar to the compression behaviors of metal materials, the curves in Fig.1(b) demonstrate that the granular matter will experience an elastic phase (OA), a transition phase (AB) and a plastic phase(BC), successively. Particularly, the plastic phase exhibits a good linear character for the relation between the quasi-static force and the penetration depth. A normalized average pressure, $[p_u] = \frac{F}{\rho_s g S} = C_0 + k_h h$, is defined to quantify all the data measured from our experiments. It turns out that the linear scale-factor k_h is only dependent on the physical property of granular material, yet independent of the size of cylinder.

THEORETICAL ANALYSIS

The quasistatic force exerted on the cylinder intruders essentially reflects the bearing capacity of the material at different depths. The bearing capacity is dominated by the stress strength of the granular material, and is affected by the stress boundaries of the granular matter. For the materials we use in our experiments, the onset of the material plasticity can be distinguished via the Mohr-Coulomb (MC) yield criterion [3], where $|\tau/\sigma_n| = \mu_0 \equiv \tan\phi$, τ is the shearing stress, σ_n is the associated normal stress, and ϕ is the internal friction angle of the granular material.

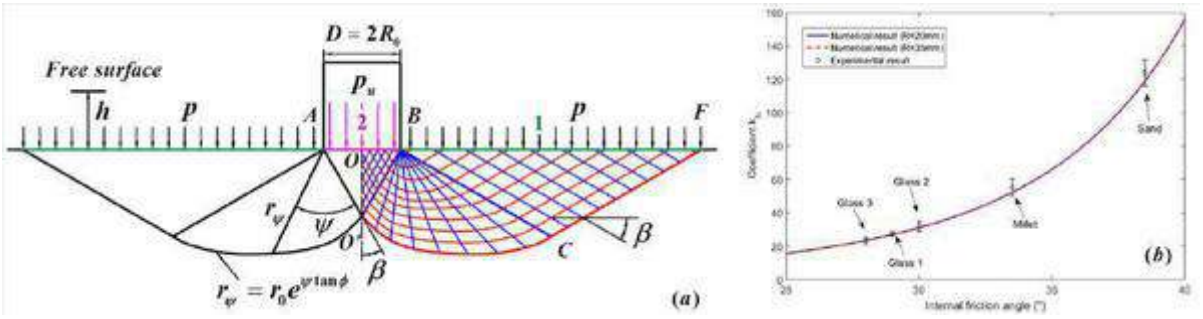

Figure 2: (a) Prandlt's slip-line (α-curves (red) and β-curves (blue)) together with the boundary conditions. (b) Numerical (lines) and experimental (markers) results of linear scale-factor k_h

Based on the MC criterion, together with the stress boundaries, we can use the PSL theory to analyse the plastic stress field as Fig.2(a) shows. By solving the differential equations of stress along the slip-lines and integrating the axial pressure over the whole area of the cylinder's bottom, we get the theoretical expression of linear scale-factor as $k_h(\phi) = \frac{2(1+\sin\phi)}{R_0^2(1-\sin\phi)} \exp(\pi\tan\phi) A(D,\phi)$, where $A(D,\phi)$ is an explicit formulation of cylinder diameter D and internal friction angle ϕ. Numerically solving $k_h(\phi)$, we find that the value of $k_h(\phi)$ just depends on ϕ and free from D. Fig.2(b) shows both the computed values of $k_h(\phi)$ and the experimental ones extracted from our experiments under different granular materials. Good agreement between them suggests that our theoretical model is suitable for characterizing the quasistatic state of the granular medium. In addition, we would mention that the value of $k_h(\phi)$ is sensitive to the small variation of the internal friction angle. This point indeed reflects the peculiar property of granular medium: the contact network between particles is so easily changed with the packing state, thus significantly alters the quasistatic force sensed by the intruder.

In summary, the static drag force sensed by a cylindrical intruder is linear to the penetration depth, and the linear scale-factor k_h is a reflection of the physical property of a granular material. The linear scale-factor k_h can be easily calculated numerically by our theoretical model. The good match between our theoretical model and experimental result means that the granular material can be treated as a uniform continuum whose plasticity is governed by the MC criterion.

References

[1] Katsuragi H, Durian D J.: Unified force law for granular impact cratering. J. Nature Physics 3:420-423, 2007.

[2] Brzinski T A, Mayor P, Durian D J.: Depth-Dependent Resistance of Granular Media to Vertical Penetration. J. Physical Review Letters 111:4977-4984, 2013.

[3] Pang Y, Liu C S.: Continuum description for the characteristic resistance sensed by a cylinder colliding against granular medium. J. Science China Physics Mechanics & Astronomy 56:1428-1436, 2013.

THE INFLUENCE OF NON-UNIFORM VIBRATIONAL EXCITATION ON THE JAMMING, SEGREGATION AND SELF-ASSEMBLY OF GRANULAR SYSTEMS

C. R. K. Windows-Yule *[1,2] and A. D. Rosato[3]
[1]*Multi-Scale Mechanics, Dept. of Mechanical Engineering, MESA+, University of Twente, The Netherlands*
[2]*School of Physics and Astronomy, University of Birmingham, UK*
[3]*Department of Mechanical and Industrial Engineering, New Jersey Institute of Technology, USA*

Summary Granular media exhibit many fascinating, and often unique, behaviours which are not only of considerable scientific interest, but may also prove highly impactful in various real-world processes – with both positive and negative consequences. The tendency of granular flows to 'jam' and become immobile, for example, can prove highly detrimental to the efficiency of various industrial processes. The predisposition of multicomponent mixtures to spontaneously 'segregate' into their individual constituents, meanwhile, can prove both extremely problematic or highly desirable in industry, and is also key to our understanding of various geological processes. Granular beds comprising aspherical particles also exhibit the ability to autonomously form complex, ordered patterns, reminiscent of those observed in colloidal or liquid crystal systems, making them valuable model systems for various thermodynamic and even biological systems. We demonstrate a means by which the vibrational excitation of granular systems may be harnessed to directly influence, and even control, these behaviours.

INTRODUCTION

Granular materials – assemblies of multiple discrete, macroscopic particles – are ubiquitous both in nature and industry; indeed, other than water, granular media are the most widely handled material on Earth, with over 10% of world energy resources expended on the processing of these materials. Yet despite their ubiquity and widespread relevance, the behaviours of these materials remain incompletely understood.

Granular materials, when exposed to an energy source, may exhibit a wide array of diverse phenomena. Of these phenomena, we focus on three examples with particular scientific and industrial significance: jamming, segregation, and self-assembly. *Jamming*, the term given to the phase transition of a fluid-like granular system to a rigid, solid-like state, is a well-known problem in many industrial processes, proving a considerable hinderance to the transport of granular materials. *Segregation* – the spontaneous separation of a granular mixture into its individual components – is in some instances (e.g. the separation of valuable ores in the mining industry) crucial, yet in other cases may prove highly problematic, or even dangerous – consider for instance the potential consequences of unwanted segregation during the mixing of excipients and active ingredients in the pharamceutical industry. The *self-assembly* of granular materials, meanwhile, is a burgeoning area of study which has only recently begun to receive considerable attention, as experimental and simulational techniques advance to a point where the accurate investigation and modelling of large systems of aspherical particles becomes feasible. This highly active new area of research has shown that granular materials subjected to vibrational excitation may exhibit ordered states and phase transitions (see Fig. 1) highly reminiscent of those observed in colloidal, liquid-crystal or even nanoscale systems. As such, it is hoped that such granular systems may be utilised as easily-studied 'models' for nanoscale or biological systems whose direct study may prove unfeasibly complex or expensive, making this a potentially highly valuable field of study.

We present data from vertically vibrated assemblies of spherical, spherocylindrical and mixed spherical-spherocylidrical particles, showing that by controlling the manner in which a particulate system is excited, its jamming and segregative behaviours [1, 2], configurational state and maximum achievable packing density [2, 3] may all be *dramatically altered*.

EXPERIMENTAL DETAILS

Our data are acquired through a combination of experiment and simulation. Our experimental data are obtained using Positron Emission Particle Tracking (PEPT), a technique capable of tracking particle motion with sub-millimetre accuracy and millisecond-scale temporal resolution in all three spatial dimensions, even deep within the bulk of large, dense and/or opaque systems. Additional data are produced using discrete particle method (DPM) simulations performed using the open-source software package *MercuryDPM*.

In both simulation and experiment, we explore a series of cuboidal containers of horizontal dimensions $L_x = L_y \in [\ 0, 120]$ mm and height $L_z = 200$ mm filled with between 2 and 12 layers of particles. The particle beds are excited by vertical vibrations of varying frequency, ω, and amplitude, A, thus producing a range of dimensionless driving strengths $\Gamma = \frac{\omega^2 A}{g} \in [1, 21]$. For each individual data set, data is acquired with a constant acceleration, Γ_0, being applied to the system; however, the bed may be initially prepared in one of three manners:

*Corresponding author. Email: c.r.windows-yule@utwente.nl

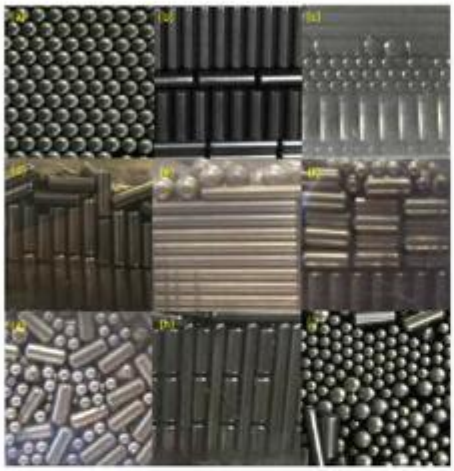

Figure 1: Examples of various configurational states which may be achieved by vibrated systems of spheres and spherocylinders.

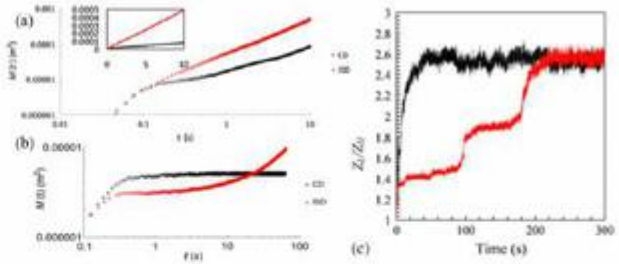

Figure 2: *Left:* Mean squared displacement plots showing (a) the faster dynamics of an initially strongly driven (ISD, method 1) system as compared to a continuously driven (CD, method 3) system and (b) the potential of method 1 to prevent jamming in otherwise identical systems. *Right:* time-evolution of the relative centre of mass, Z_L/Z_H, of light and heavy particle species for a pair of identical, bidisperse-by-density systems driven using method 1 (black) and method 3 (red). Images taken from our references [1, 2].

1. The bed is initially excited with an acceleration $\Gamma_i > \Gamma_0$ which is then pseudo-instantaneously reduced to Γ_0.
2. The bed is initially excited with an acceleration $\Gamma_i > \Gamma_0$ which is then linearly reduced to Γ_0 over a period of time Δt_r.
3. The bed is initially excited with an acceleration $\Gamma_i = \Gamma_0$, i.e. there is no change in the vibrational excitation.

By comparing otherwise identical systems prepared using methods 1, 2 and 3, we are able to analyse the hysteretic effects of initial driving on the system's subsequent behaviour.

RESULTS

Our results show that the initial excitation to which a system is exposed can impart a pronounced influence on its subsequent state and dynamics. A sharp decrease in driving acceleration (method 1) is observed to induce a *marked increase in the rate of segregation* (see Fig. 2(c)) as compared to method 3, the 'standard' manner in which a vibrated system is typically excited – even if the initial, strong excitation lasts only $\mathcal{O}(1\text{s})$. This increased segregation rate is accompanied by a *more homogeneous particle distribution* and *faster system dynamics* (see Fig. 2(a)). Under certain circumstances, this initial preparation method can also *increase the steady state compaction* achieved by the bed, or even *prevent the system from jamming* (see Fig. 2(b)) – both potentially highly valuable abilities in industry. Similar behaviours are observed for method 2, although the distinction from method 3 is considerably less emphatic. The differing initial excitation methods can also influence the final configurational state achieved by a system – for example a binary system of spherocylinders which forms an ordered, microphase-separated state (see, for example, Fig. 1(c)) when prepared using method 1 may instead form a bulk-separated state when prepared using method 2.

CONCLUSIONS

The history-dependent nature of granular media allows us to deliberately induce marked changes in the configuration, physical state and dynamical behaviours of a system solely through alterations in its initial excitation. This ability carries many, potentially highly valuable, applications in both academia and industry, where phenomena such as segregation, jamming, compaction and self-assembly are highly important.

References

[1] Windows-Yule, C. R. K., T. Weinhart, D. J. Parker, and A. R. Thornton, Physical Review Letters 112, no. 9 (2014): 098001.
[2] Windows-Yule, C. R. K., A. D. Rosato, N. Rivas, and D. J. Parker, New Journal of Physics 16, no. 6 (2014): 063016.
[3] Ratnaswamy, V., A. D. Rosato, D. Blackmore, X. Tricoche, N. Ching, and L. Zuo, Granular Matter 14, no. 2 (2012): 163-168.

MODELING SEGREGATION IN MULTIDISPERSE GRANULAR FLOW

Zhekai Deng[1], Austin Isner[1], Paul B. Umbanhowar[2] & Richard M. Lueptow[2,3a)]
[1] *Department of Chemical & Biological Engineering, Northwestern University, Evanston, IL USA*
[2] *Department of Mechanical Engineering, Northwestern University, Evanston, IL USA*
[3] *The Northwestern Institute on Complex Systems, Northwestern University, Evanston, Illinois, USA*

Summary As granular materials flow they can segregate due to particle size or density differences. The degree of segregation depends on the flow conditions and the differences between particles. We have developed an approach based on an advection-segregation-diffusion continuum equation to predict segregation for dense granular flows of particles with multiple particle sizes.

INTRODUCTION

Previous models for segregation of flowing granular materials due to particle size or density differences have focused on bidisperse systems of particles. However, most industrial and geophysical systems consist of particles with multiple sizes or densities. Here we extend our model for segregation in bidisperse particle systems to multidisperse systems and compare the results to experiments and Discrete Element Method (DEM) simulations.

THEORY

Our modelling approach is based on a continuum advection-diffusion equation for individual particle species with a semi-empirical segregation term. For a segregating 2D flow of multidisperse granular materials, the transport equation for each individual species within the flowing layer is:

$$\frac{\partial c_i}{\partial t} + \underbrace{\frac{\partial (u c_i)}{\partial x} + \frac{\partial (w c_i)}{\partial z}}_{\text{advection}} + \underbrace{\frac{\partial (v_{p,i} c_i)}{\partial z}}_{\text{segregation}} - \underbrace{\left[\frac{\partial}{\partial x}\left(D \frac{\partial c_i}{\partial x} \right) + \frac{\partial}{\partial z}\left(D \frac{\partial c_i}{\partial z} \right) \right]}_{\text{diffusion}} = 0$$

where (u,w) is the mean granular velocity in the streamwise (x) and surface-normal (z) directions, respectively . The first term in the equation is the rate of change of species concentration c_i, the second and third terms account for advection due to mean flow, the fourth term accounts for segregation due to the species specific percolation velocity $v_{p,i}$, and the bracketed terms account for collisional diffusion. A key aspect of the bidisperse model is the dependence of the percolation velocity of species i on the local shear rate γ and the local concentration of the other particle species. To date, we have applied this modelling approach to many flow geometries including steady quasi-2D [1,2] and 3D heap flows, steady quasi-2D chute flow, and transient and steady quasi-2D tumbler flow [3] for both size [1,2,3] and density [4] bidisperse particles. Here we demonstrate that the modelling approach is readily extended to multidisperse particle systems by generalizing the percolation velocity to a linear sum of the binary particle interactions so that the percolation velocity of species i depends on its interaction strength $S_{i,j}$ with species j such that $v_{p,i} = \sum S_{i,j}\, \gamma\, c_j$. A semi-empirical relation for $S_{i,j}$ can be obtained from DEM simulations of bidisperse particles with different size ratios [2]. The model also requires the diffusion coefficient D and the velocity profile $u(x,z)$, which can be determined from experiments, theoretical models, or DEM simulations.

RESULTS

Here we consider tridisperse chute flow, shown schematically below, where three different particle sizes that are initially well-mixed segregate in the normal z-direction as they flow down the sloped surface.

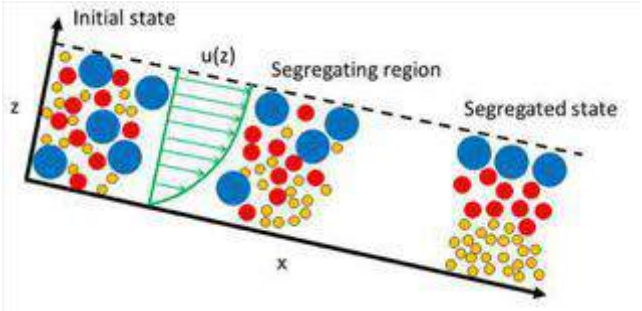

[a)] Corresponding author. Email: r-lueptow@northwestern.edu.

The concentration field in the flowing layer is shown below for a Bagnold velocity profile and equal initial concentrations of 1 mm (S-yellow), 1.7 mm (M-red), and 2.2 mm (L-blue) particles. The left side of the figure is the inlet where the particles are well-mixed; the bottom of the figure is the sloped surface; the top of the figure is the free surface of the flow; and the right side of the figure is where the particles exit the model domain at the characteristic length, which is defined as the streamwise displacement of the fastest segregating particle (here, a 1 mm particle among 2.2 mm particles) as it percolates from the top to the bottom of the flowing layer. Isocontours of particle concentration are shown as solid curves for small (black), medium (light blue), and large (green) particles.

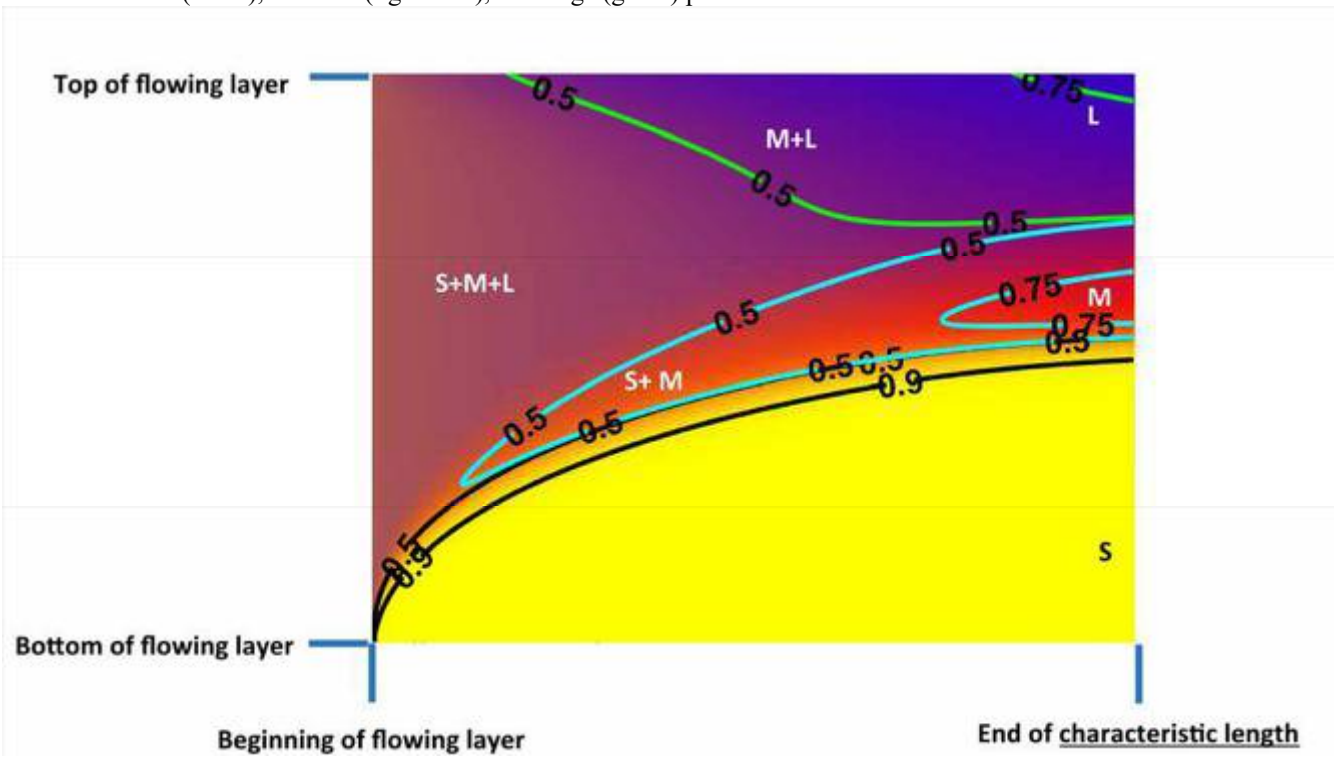

Shortly downstream of the inlet at the left side of the domain, the small 1 mm particles segregate quickly from the larger 1.7 mm and 2.2 mm particles due to the relatively large size ratios of 1.7 and 2.2, respectively. Because the medium and large particles are more similar in size (size ratio of 1.3), they only begin to segregate from one another further downstream (to the right). One characteristic length downstream, there are three layers of particles with the large particles at the top and the small particles at the bottom of the flowing layer, though the particles are not completely segregated. Segregation continues moving downstream (not shown).

CONCLUSIONS

We have shown that a simple advection-segregation-diffusion model for bidisperse particle segregation can be extended to multidisperse particle segregation. The approach can be further extended to model polydisperse particle segregation by considering a continuous distribution of particle sizes and replacing the sum in the expression for the percolation velocity used here with an integral [5].

Partially funded by the Dow Chemical Company.

References

[1] Fan Y., Schlick C.P., Umbanhowar P.B., Ottino J.M., Lueptow R.M.: *J. Fluid Mech.* **741**:252-279, 2014.
[2] Schlick C.P., Fan Y., Isner A.B., Umbanhowar P.B., Ottino J.M., Lueptow R.M.: *AIChE J.* **61**:1524-1534, 2015.
[3] C.P., Fan Y., Umbanhowar P.B., Ottino J.M., Lueptow R.M.: *J. Fluid Mech.* **765**:632-652, 2015.
[4] Xiao H., Umbanhowar P.B., Ottino J.M., Lueptow R.M.: *Proc. Royal Soc. A* Submitted, 2016.
[5] Schlick C.P., Isner A.B., Freireich B.J., Fan Y., Umbanhowar P.B., Ottino J.M., Lueptow R.M.: *J. Fluid Mech.* In revision, 2016.

MICROMECHANICS OF GRANULAR MATERIALS: AN EXPERIMENTAL INVESTIGATION OF SHEAR BEHAVIOR

Eloïse Marteau[1] and José E. Andrade *[1]
[1]*Division of Engineering and Applied Science, California Institute of Technology, Pasadena, USA*

Summary The macroscopic behavior of granular materials is governed by micro-scale mechanics, including inter-particle forces and kinematics. Although micromechanical tools have provided tremendous insight, they still lack quantitative accuracy and, associated with this, capacity to predict macroscopic behavior. We present here experiments in which we have successfully measured particle-scale kinematics and inter-particle forces in a two-dimensional idealized granular assembly subject to shear deformation. Kinematics are obtained using Digital Image Correlation (DIC). The inter-particle forces are inferred using the Granular Element Method (GEM), provided that average particle strains are measured and that the location of the contact points in the array is known. By seamlessly connecting particle-scale information to continuum scale experiments, we shed light into the multiscale mechanical behavior of granular assemblies under shear loading.

INTRODUCTION

Although granular media are constituted of discrete particles, forces and displacements within granular media are represented by continuous stresses and strains. Most stress-strain relationships, which describe the behavior of granular material, are derived from plasticity theory. However, plasticity theory is predicated on phenomenology, i.e. derived from macroscopic observations in the laboratory and the field. More recently, grain-scale methods have emerged and there is a strong interest in further understanding continuum models from micromechanics in order to escape phenomenology. For the last two decades, a tremendous amount of progress in advanced experimental methods has been made to access the kinematics of granular materials at the grain scale, i.e. particle displacements and rotations. Yet most of these grain scale techniques remain qualitative and continue to lack connection with the macroscopic framework.

EXPERIMENTAL SETUP

We present here a novel experimental device (see Figure 1) for investigating the continuum behavior of granular material by incorporating micromechanics. This mechanical apparatus is capable of reproducing (quasi-static) shear conditions over large deformation on a two-dimensional analogue granular assembly. The shear cell consists of a horizontal deformable parallelogram of size 50 cm by 50 cm in the undeformed configuration. The grains stand on a glass plate and are individually tracked by a camera that sits above the apparatus. A linear actuator composed of a brushless DC electric motor, linear guides and a ball screw provides the shear mechanism. Furthermore, a constant normal stress σ_n is applied using a system of pulleys and weights. We measure the shear angle γ and the strain in the y-direction ϵ_{yy} using, respectively, an angular and linear potentiometer, whereas the strain in the x-direction ϵ_{xx} remains equal to zero.

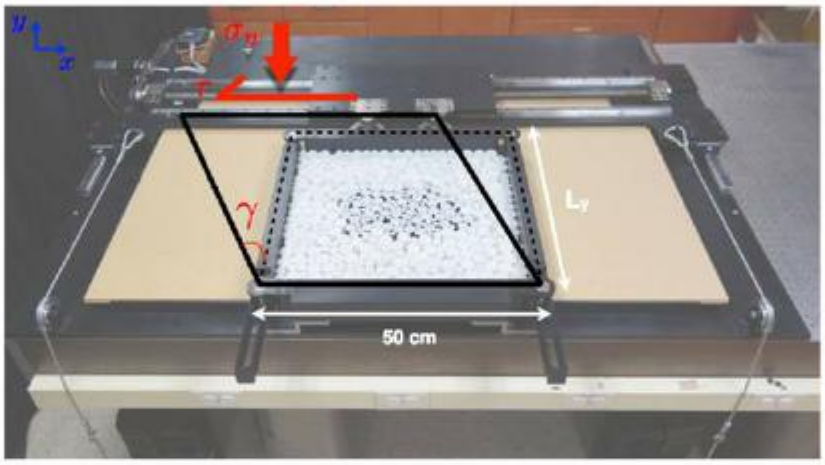

Figure 1: Experimental setup.

*Corresponding author. Email: jandrade@caltech.edu

We performed experiments on a two-dimensional analogue granular assembly composed of 400 cylinders of diameter of 20 and 30 mm and height of 25 mm. The grains are made of polyurethane that has a Youngs modulus of 20 MPa and a Poissons ratio of 0.5.

PRELIMINARY RESULTS

The Digital Image Correlation (DIC) technique is used to provide full-field displacements and strains by comparing the gray intensity changes of the grain surface before and after deformation. The figure below shows a typical image of the shear strain ϵ_{xy} at $\gamma = 25.2°$ in which clear force chains are observed.

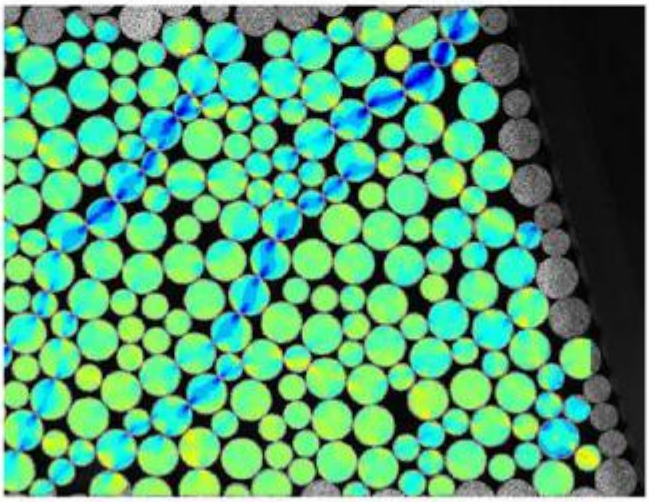

Figure 2: Experimental shear strain field ϵ_{xy} at $\gamma = 25.2°$

Furthermore, we use the Granular Element Method (GEM) to infer the inter-particle forces. The method takes as input the particle average stresses and the structure of the assembly, extracted from experimental techniques. This experimental data is then passed to GEM to reconstruct the force distribution.

References

[1] A.N. Schofield and P. Wroth. Critical state soil mechanics. McGraw-Hill, 1968.

[2] D.M. Wood. Soil Behaviour and Critical State Soil Mechanics. Cambridge University Press. 1991.

[3] B. Pan, K. Qian, H. Xie, A. Asundi. Two-dimensional digital image correlation for in-plane displacement and strain measurement: a review. Measurement Science and Technology 20, 062001. 2009.

[4] M.A. Sutton, J.J. Orteu, H. Schreier. Image Correlation for Shape, Motion and Deformation Measurements: Basic Concepts, Theory and Applications. Springer, 2009.

[5] J.E. Andrade and Avila, C.F. Granular element method (GEM): linking inter-particle forces with macroscopic loading. Granular Matter 14, 5161, 2012.

[6] R Hurley, E Marteau, G Ravichandran, and J.E. Andrade. Extracting inter-particle forces in opaque granular materials: Beyond photoelasticity. Geotechnique 29, 4765, 2014.

SINGULAR BEHAVIOR OF A COHESIVE POWDER UNDER HORIZONTAL VIBRATIONS

Jean-Eric Mathonnet*[1], Philippe Sornay[1], Blanche Dalloz-Dubrujeaud[2], and Maxime Nicolas[2]
[1]*CEA, DEN, DEC, SFER, LCU, Saint-Paul-Lez-Durance, France*
[2]*Aix-Marseille Université, CNRS, IUSTI UMR 7343, Marseille, France*

Summary We report the influence of horizontal vibrations on the time-evolution of the density of a very cohesive powder. For a wide range of vibration conditions, the kinetics of compaction presents a two time-scales behavior compared to model materials. A simple stochastic model, based on clusters of grains, has been developed to understand the compaction process, and a new empirical law proposed to describe the evolution of the packing fraction ϕ.

INTRODUCTION

Numerous studies have focused on the time-evolution of the compaction of non-cohesive granular system (monodisperse glass beads, rice grains ...) submitted to vibrations or vertical tapping. Through experiments, two main empirical laws have been proposed to describe the time evolution of the volume fraction ϕ with the number of taps or vibration cycles t.

The first one, based on a heuristics analysis, is an inverse logarithmic law [1, 2]:

$$\phi(t) = \phi_\infty \nearrow \frac{\phi_\infty \nearrow \phi_0}{1 + B\ln(t/\tau)} \tag{1}$$

with ϕ_0 the initial packing fraction, ϕ_∞, the final packing fraction, τ, a characteristic time, and B, a fitting parameter.

The second one is a modified Heckel equation [3] which has been written as a stretched exponential function with an exponent β and a characteristic time τ [4]:

$$\phi = \phi_\infty \nearrow (\phi_\infty \nearrow \phi_0)^{\ -(t/\tau)^\beta}. \tag{2}$$

These expressions may fit well the experimental results obtained with model materials, but many actual granular media used in industrial process are not made of monodisperse smooth spheres. As an exemple, in the nuclear industry, the shaping process of fuel pellets uses cohesive powders. Such a cohesive granular system is characterized by a very large angle of repose, difficulties for filling or emptying a silo, and a very small packing fraction due to the presence of macro-cavities, bulk holes and vaults.

Through long time experiments under horizontal vibration, we investigate the compaction kinetics of a very cohesive UO_2 powder mainly used in the nuclear industry. The UO_2 powder we use is a complex granular system constituted of sub-micron crystallites, aggregates around $0.\ \mu$m and agglomerates with a mean diameter $d = 30\ \mu$m. The powder was held in a vertical plane-parallel tank of different sections (15×15 mm^2, 25×25 mm^2, $0 \times\ 0$ mm^2 and $0 \times\ 0$ mm^2). The tank is vibrated horizontally with a permanent magnet shaker with a frequency range between 30 to 100 Hz, and with a normalized acceleration from 3 g to 9 g.

In order to compare our results on the cohesive UO_2 powder with non-cohesive and weakly cohesive materials, we have also investigated the compaction of monodisperse glass beads with a mean diameter $d = 130\ \mu$m, and an atomized alumina powder with a size-range $0.1 \nearrow\ 0\ \mu$m.

RESULTS

A typical experimental result of the compaction process under horizontal vibrations is shown on Figure 1. The time evolution of the UO_2 powder compactness presents two stages of compaction. During the first stage, the packing fraction increases rapidly and approaches a plateau value as observed with model non-cohesive materials. During the second stage, a second increase occurs, much more slowly: even after 10^7 cycles, the final state does not seem to be reached. We have also observed, through different characterizations (SEM, laser diffraction particle size analyzer, and mercury porosimetry), that the vibration process do not modify the agglomerates.

Our result on glass beads compaction showing only one compaction stage is similar to the results of the literature. For the alumina powder, we observe a weak second increase between 00 and 2×10^4 cycles. The two-stages compaction seems intrinsic to cohesive granular materials with a strong effect for highly cohesive powders. The expressions (1) and (2) are then not able to fit the experimental results on UO_2 and alumina powder.

The two-stages compaction process may be understood through a simple stochastic model. The model is a set of N unit grains shared out between N_c clusters of n grains each. Clusters and grains inside each cluster are randomly placed with a

*Corresponding author. Email: jean-eric.mathonnet@cea.fr

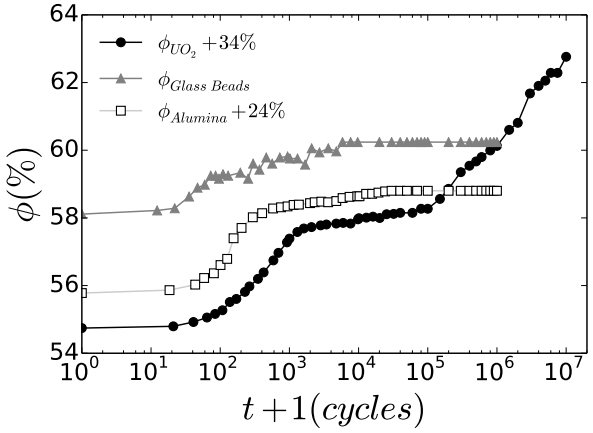

Figure 1: Examples of experimental results under horizontal vibrations at 100 Hz and g acceleration. The tank was 15×15 mm^2, and 2 0 mm height. The curves of UO_2 and alumina powders are shifted by 3 % and 2 % respectively.

linear fraction and without overlap. At each time step, the grains and the clusters may move according to probably laws p_g and p_c which are derived from normalized free volumes [5]. When a grain is allowed to move, it moves downward if the space below is free. When a cluster is allowed to move, it moves downward with a maximum falling distance of its size.

The results obtained with this simulation show a two-stages evolution analog to the experimental results of the UO_2 powder. The first stage (short-time) is related to the compaction of clusters. It mimics the collapse of macro-cavities and large holes in a cohesive granular system. The time-scale of this first stage is proportional to the clusters number. The second stage (long-time) is related to the compaction of the individual grains, with a time scale proportional to the number of individual grains.

The experimental and numerical results are well fitted by an extension of the equation (2) with two stretched exponentials:

$$\phi = \phi_\infty \nearrow (\phi_\infty \nearrow \phi_p)^{\ -(t/\tau_2)^{\beta_2}} \nearrow (\phi_p \nearrow \phi_0)^{\ -(t/\tau_1)^{\beta_1}} \tag{3}$$

with two characteristic times τ_1 and τ_2, two exponents β_1 and β_2, and a plateau packing fraction ϕ_p. One of the main result of our study is that the characteristic times are proportional to the number of objects (clusters or grains). This result is also confirmed experimentally. Indeed, we observe that the characteristic times are related to the initial height in the tank. It seems also that the exponents β_1 and β_2 are linked to the probability laws and characterize the compaction rates of each stage. While a double exponential fit has already been proposed [6], we provide a very different interpretation of this expression, with a short-time scale associated to large-scale structures and a long-time scale associated to small-scales (but numerous) grains.

CONCLUSION

Through experiments and a stochastic model, the compaction process of a cohesive powder is analyzed with a two-stages behavior. The time evolution of the volume fraction is very well fitted with a sum of two stretched exponential functions (3). While the physical origin of the exponents is still an open question, the characteristic time-scales are related to the number of moving structures (clusters or grains). The stochastic model may also be useful to describe the compaction of a non-cohesive granular material, and may be extended for multi-scales structures, leading to a multi-time-scales evolution of the packing fraction.

References

[1] Knight J. B., Fandrich C. G., Lau C. N., Jaeger H. M., Nagel S. R.: Density Relaxation in a Vibrated Granular Material. Phys. Rev. E 51(5):3957-3963, 1995.

[2] Nowak E. R., Knight J. B., Ben-Naim E., Jaeger H. M., Nagel S. R.: Density Fluctuations in Vibrated Granular Materials. Phys. Rev. E 57(2):1971-1982, 1998.

[3] Yu A.B., Hall J.S.: Packing of Fine Powders Subjected to Tapping. Powder Technology 78:247-256, 1994.

[4] Philippe P., Bideau D.: Compaction Dynamics of a Granular Medium Under Vertical Tapping. Europhys. Lett. 60 (5):677-683, 2002.

[5] Boutreux T., De Gennes P.-G.: Compaction of granular mixtures: a free volume model. Physica A 244:59-67, 1997.

[6] Barker G. C., Mehta A.: Transient phenomena, self-diffusion, and orientational effects in vibrated powders. Phys. Rev. E 47(1):184-188, 1993.

GRANULAR RHEOLOGY IN BEDLOAD TRANSPORT

Raphael Maurin *[1,2], Julien Chauchat[3,4], and Philippe Frey[1,2]

[1]*Irstea, Grenoble, UR ETGR*
[2]*Univ. Grenoble Alpes, Irstea*
[3]*CNRS, UMR 5519, LEGI*
[4]*Univ. Grenoble Alpes, LEGI*

Summary The granular rheology is analyzed locally in the framework of turbulent bedload transport simulations. Using a coupled fluid-discrete element model, the granular stress tensor is computed locally as a function of the depth, and the results are analyzed in the framework of the $\mu(I)$ rheology. Varying the Shields number, the specific density and the particle diameter, the data are shown to collapse over a wide range of inertial number and up to unexpectedly high values ($I \sim 3$). The results give a better understanding of the granular behavior in bedload transport and challenge the existing conceptions and parametrizations of the $\mu(I)$ rheology.

Considering a granular bed submitted to a surface fluid flow, bedload transport is classically defined by opposition to suspension as the part of the load in contact with the granular bed, i.e. in rolling, sliding or small jumping motions. This corresponds to particles for which the downward gravity force is on average much greater than the upward fluid force due to turbulent fluctuations. While being of fundamental interest for the prediction of riverbed evolution, bedload transport is also of interest in itself as a complex granular flow configuration. Indeed, the surface fluid shear stress induces a large variety of granular behavior as function of the depth, from dynamic at the top, to quasi-static inside the granular bed.
In the present contribution, the granular rheology in bedload transport is characterized locally as a function of the depth, and analyzed in the framework of the $\mu(I)$ rheology. To achieve this goal, turbulent bedload transport simulations are performed using a coupled fluid-discrete element model [1].

METHODOLOGY

A two-phase flow model is used, made of a three dimensional discrete element method (DEM) coupled with a one-dimensional fluid momentum balance. The model has been validated with experiments, both in terms of granular depth profiles and sediment transport rate. More details can be found in [1].
The gravity-driven system is made of an inclined channel filled with water, in which monodiperse spherical beads are deposited. The position of the water free-surface is imposed, and creates a turbulent, hydraulically rough, and supercritical fluid flow on the top of the granular bed. Bi-periodic boundary conditions are imposed for the DEM, and only steady uniform conditions are analyzed. Therefore, the unidirectional character of the problem allows to average spatially over the streamwise and spanwise directions, and to analyze the results only as a function of the depth. In order to study the granular rheology, the average granular stress tensor $\left\langle \sigma_{ij}^p \right\rangle$ is computed from DEM. For each slice of volume V, it reads [2]:

$$\left\langle \sigma_{ij}^p \right\rangle = \nearrow P^p \delta_{ij} + \tau_{ij}^p = \nearrow \frac{1}{V} \sum_{\alpha \in V} m^\alpha v_i^{'\alpha} v_j^{'\alpha} \nearrow \frac{1}{V} \sum_{c \in V} f_i^c b_j^c, \tag{1}$$

where the sums are respectively over the particles and the contacts contained in the volume V, $v_k^{'\alpha} = v_k^\alpha \nearrow \langle v_k \rangle$ is the k component of the spatial velocity fluctuation associated with particle α of mass m^α, $\mathbf{f}^c$ is the contact force applied by particle 1 on particle 2, and $\mathbf{b}^c$ is the branch vector from particle 1 to particle 2.

For each simulation, once at equilibrium, the data are averaged over 200 seconds. The stress tensor, the solid volume fraction and the shear rate profiles enable to compute the $\mu(I)$ rheology at each elevation and for each simulation.

RESULTS

Simulations of intense bedload transport are performed, at three different Shields number $\theta^* \sim 0.2, 0.$ and $0.$, where $\theta^* = \tau^f / ((\rho^p \nearrow \rho^f) g d)$ with τ^f the fluid bed shear stress, ρ^p and ρ^f the particle and fluid density, g the acceleration of gravity, and d the particle diameter. For each Shields number, the particle diameter and the specific density are also varied taking values of respectively $d = 3mm,\ \ mm$, $12mm$ and $\rho^p/\rho^f \nearrow 1 = 0.\ 5, 1.5, 3.$
Figure 1 shows the shear to normal granular stress ratio and the solid volume fraction as a function of the inertial number. The data collapse over a wide range of inertial numbers and show the relevancy of analyzing the granular rheology in bedload

*Corresponding author. Email: raphael.maurin@irstea.fr

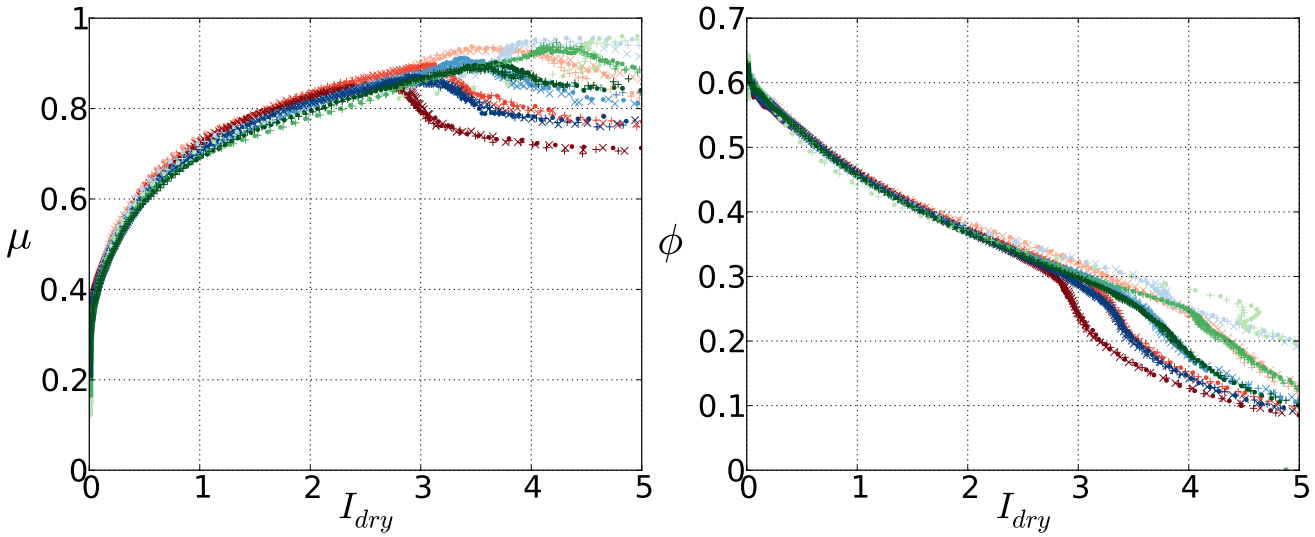

Figure 1: Shear to normal stress ratio $\mu = \tau^p_{xz}/\tau^p_{zz}$ and solid volume fraction ϕ as a function of the dry inertial number $I_{dry} = \dot{\gamma}d/\sqrt{\tau^p_{zz}/\rho^p}$ for different simulations with variation of Shields number, specific density and particle diameter.

transport in the framework of the $\mu(I)$ rheology. As can be seen from the good collaspe as a function of the dry inertial number, the effect of the interstitial fluid on the granular rheology is negligible, supporting recent work [3] suggesting the absence of a clear transition between the free-fall and the turbulent regime. In addition, the collapse as a function of the inertial number for both the solid volume fraction and the shear to normal stress ratio is observed up to unexpectedly high inertial numbers ($I \sim 3$), in regions showing an important dependency on the restitution coefficient [4]. While in contradiction with the classical view, similar high inertial number collapse have already been observed on steady non-uniform granular flows [5] and on local analysis of granular rolling waves instabilities [6]. Considering inertial number greater than $I \sim 3$, the different curves progressively show a decrease of the shear to normal stress ratio. The latter is similar to the one predicted by the kinetic theory [7] and suggests a transition to a granular gas behavior. Those results challenge the existing conceptions and parametrization of the $\mu(I)$ rheology, and suggest that the latter could be valid up to higher inertial number than classically thought.

References

[1] R. Maurin, J. Chauchat, B. Chareyre, and P Frey. A minimal coupled dem-fluid phase model for bedload transport. *Physics of Fluids*, 27, 2015.

[2] I. Goldhirsch. Stress, stress asymmetry and couple stress: from discrete particles to continuous fields. *Granular Matter*, 12(3):239–252, 2010.

[3] E. Izard, T. Bonometti, and L. Lacaze. Simulation of an avalanche in a fluid with a soft-sphere/immersed boundary method including a lubrication force. *The Journal of Computational Multiphase Flows*, 6(4):391–406, 2014.

[4] R. Maurin. *Investigation of granular behavior in bedload transport using an Eulerian/Lagrangian model*. PhD thesis, University Grenoble Alpes, 2015.

[5] A.J. Holyoake and J. N. McElwaine. High-speed granular chute flows. *Journal of Fluid Mechanics*, 710:35–71, 11 2012.

[6] T. Börzsönyi, R. E. Ecke, and J. N. McElwaine. Patterns in flowing sand: Understanding the physics of granular flow. *Phys. Rev. Lett.*, 103:178302, Oct 2009.

[7] Y. Forterre and O. Pouliquen. Flows of dense granular media. *Annual Review of Fluid Mechanics*, 40(1):1–24, 2008.

REORGANIZATION OF A GRANULAR MEDIUM AROUND A LOCALIZED TRANSFORMATION

Aymeric Merceron , Alban Sauret, and Pierre Jop
Surface du Verre et Interfaces, UMR 125 CNRS/Saint-Gobain

Summary Rearrangements of a two dimensional granular packing undergoing a local transformation are studied. We accurately track each particle of a model granular packing made of inert disks and of an intruder pulled out at constant speed. Long term displacements are similar to displacements for 2D quasi-static silos. Short term reorganizations are more heterogeneous in space and time. Structural evolutions exhibit a unique mechanism of rearrangement in terms of density variations whatever events amplitudes.

INTRODUCTION

Sintering, glass melting and other industrially relevant processes turn batches of grains into homogeneous end-products. Such processes involve complex coupled chemical and physical transformations of the granular packing through reorganizations of the contacts network. These transformations are of several and not exclusive natures : volume changes due to dilatation coefficients [1], phase transitions....

Several recent studies explore reactive granular materials but there are very few experimental systems ([2],[3]) mainly because of difficulties in monitoring grain transformations. Therefore, instead of having an entire packing in transformation, several authors have studied the granular packing behavior around an intruder ([4],[5]). Following the same approach, we use a single or a couple of intruders to destabilize our granular packing. Then, we analyze dynamics of rearrangements and structural evolutions thanks to image processing.

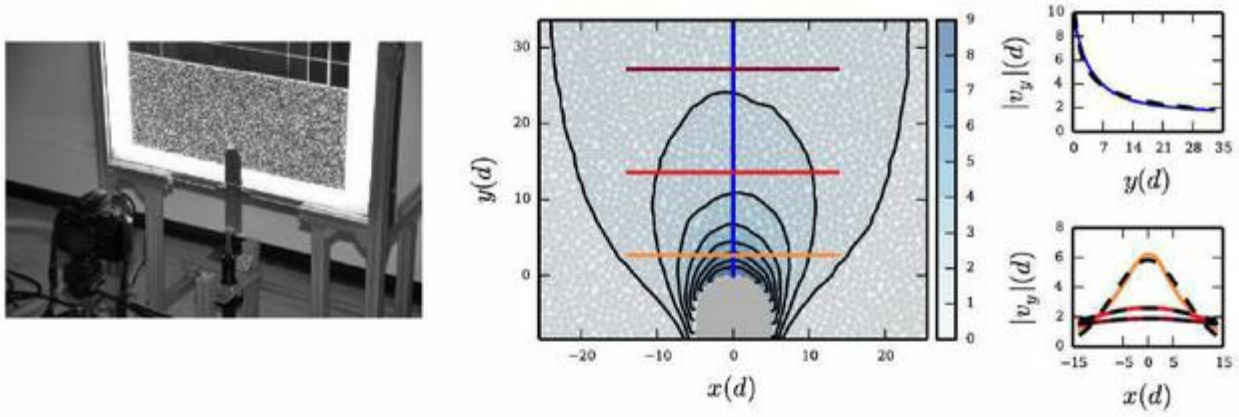

Figure 1: Left : picture of the setup. Middle : dimensionless displacement field expressed in d_{grain} between initial state and final state averaged over 100 experiments. Right : the blue line corresponds to experimental vertical displacements along x = 0d. Colored lines correspond to experimental vertical displacements along y = 2.7d, y = 13.6d and y = 27.1d. Dotted lines correspond to a model of 2D quasi static silos of [6].

EXPERIMENTAL SETUP

The setup (see Fig.1 left) is a quasi-two-dimensional cell made of two parallel glass plates of 300 mm height for 600 mm width separated by a gap of 3.1 mm. The packing is confined by three fixed PVC walls and by metallic weights at the top. The cell is horizontally filled with around 5000 bidisperse brass disks of 4 and 5 mm diameter (10:7) forming a dense and disordered assembly. At the middle bottom of the packing, an semi circular metallic intruder of 40 mm diameter (10 $d_{g_{min}}$) is horizontally inserted at the same moment. Then, we raise the cell vertically and we attached the intruder to a translation jack. The intruder is finally pulled down at low and constant speed (0.05 mm.s^{-1}) ensuring a quasi static evolution of the surrounding packing. The packing is photographed every 5 s with an high resolution reflex camera. We are able to segment our images to obtain the positions of disks with a subpixelic resolution of about 0.011 mm. Thanks to tracking and tessellation techniques, displacement fields, local and global densities are measured. 100 experiments have been performed to ensure a very good statistic.

*Corresponding author. Email: aymeric.merceron@saint-gobain.com

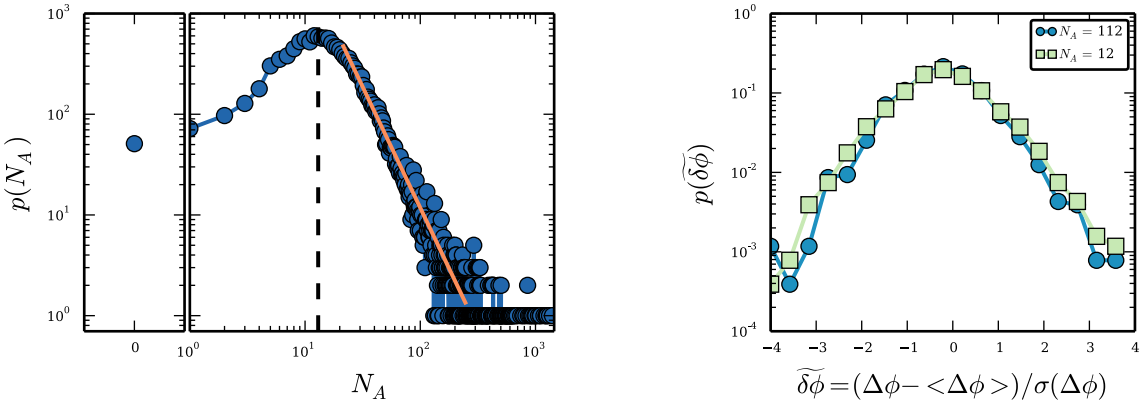

Figure 2: Left : probability density function of local density variations centered and renormalized by their means and their standard deviations for two events of different amplitudes. Right : log-log plot of the histogram for the avalanche sizes over 16000 events.

RESULTS

Long term displacements : a quasi-static 2D silo

The vertical displacement field of our experiment between the initial and the final state is plotted on Fig. 1 middle. The shape of such displacement field is qualitatively and quantitatively similar to fields observed in the literature on 2D silos. Indeed, some models describing 2D quasi-static granular silo-like flows for mining applications give a very good agreement with our displacements Fig 1 right.

Short term displacements : an avalanche-like system

Between two consecutive snapshots, the response of the granular medium is really heterogeneous and made of largely distributed spatio-temporal events. An avalanche size called N_A is defined as the number of disks that have an absolute displacement at least equals to the one of the intruder. The distribution of avalanche sizes for all experiments is plotted on Fig. 2 left. Largest events ($N_A > 13$) are power-law distributed that is characteristic of processes ruled by scale invariance. Finally, one can show that these largest events are not correlated in time.

Structural evolution

Analytical Voronoi tessellations have been performed on every picture in each experiment to get access to local and global density variations. We found that distributions of local density variations are linked to event amplitudes. Moreover, we can collapse each distribution by centering and renormalizing them by their means and their standard deviations respectively. This implies that there is a unique mechanism of rearrangement in terms of density variations see Fig. 2 right.

CONCLUSIONS

Long term and short term rearrangements are analyzed in a 2D granular medium in which an intruder is slowly pulled out. Long term displacements are very similar to displacements in a 2D quasi-static silo. Short term displacements have a behavior close to avalanche-like systems with events largely distributed in sizes and uncorrelated in time. Finally, the structural evolution at short terms is the result of a unique mechanism of rearrangement.

References

[1] Ludewig F., Vandewalle N., Dorbolo S., Pakpour M., Lumay G. : Bernal random loose packing through freeze-thaw cycling. Physical Review E 92, 010202 (2015)

[2] Dorbolo S., Ludewig F., Vandewalle N., Laroche C. : How does an ice block assembly melt ?Physical Review E 85, 051310 (2012)

[3] Turnbull B. : Scaling Laws for Melting Ice Avalanches, Physical Review Letters 107, 258001 (2011).

[4] Kolb E., Cixous P., Gaudouen N.,Darnige T. . : Rigid intruder inside a two-dimensional dense granular flow: Drag force and cavity formation, Physical Review E 87, 032207 (2013).

[5] Coulais C., Seguin A., Dauchot O. : Shear Modulus and Dilatancy Softening in Granular Packings above Jamming, Physical Review Letters 113, 198001 (2014).

[6] Melo F., Vivanco F., Fuentes C., Apablaza V. : On drawbody shapes: From BergmarkRoos to kinematic models, International Journal of Rock Mechanics and Mining Sciences 44, 77 (2007).

HOW DO FISH HIDE IN THE SAND? EROSION BY AN OSCILLATING FOIL

Cyprien Morize *[1], Alban Sauret[1,2], Guillaume Quibeuf[1], and Philippe Gondret[1]

[1]*Laboratoire FAST, Univ. Paris-Sud, CNRS, Univ. Paris Saclay, F-91405 Orsay, France*
[2]*Surface du Verre et Interfaces, UMR 125, CNRS/Saint-Gobain, 93303 Aubervilliers, France*

Summary Some bottom-dwelling fish generate a flow capable of resuspending sand, to bury themselves and avoid predators. By flapping their fins, they create vortices that lift the sand particles up and deposit them on top of their backs. A model experiment has been developed to characterize this situation: a rigid foil placed above a sand bed mimics the fin motion. We characterized the influence of the amplitude and frequency of the motion on the generated fluid flow. In addition, the onset of erosion was determined and these measurements were rationalized to predict the minimum velocity of the oscillation to erode the granular bed.

DESCRIPTION OF THE PROBLEM

The erosion or resuspension of a granular bed by fluid flows is a key phenomenon for the understanding of various natural and industrial situations. For instance, in geosciences, sand and sediments can be carried by wind during sand storms, or by water during a scour. Erosion can also be used in civil engineering to measure soil stability using the so-called *Jet Erosion Test* [1]. Some of the erosion processes can lead to catastrophic events. For instance, when a helicopter lands in sandy and dusty environments or when we step on a dusty ground, the flow generated can lead to the resuspension of harmful particles [2]. In contrast, some bottom-dwelling fish, such as flounders and stingrays, are able to cover themselves with resuspended sand to avoid predators. These fish come close to the seafloor and are able to generate vortices by flapping their fins. The vortices generate a recirculating flow that lifts the sand particles up and contribute to the deposition of the particles on top of the fish backs.

The oscillation of a foil is a non-stationary situation that can lead to the erosion of a granular bed by an oscillating motion and has been poorly studied in the literature contrary to the erosion by a stationary situation such as shear flows [3]. The interaction between the motion of the foil, the fluid and the granular material leads to a complex spatiotemporal evolution and a dynamic reorganization of the sand bed that can in turn modify the flow field. The objective of this study is to characterize experimentally the complex interplay between the oscillating foil, the fluid and the granular bed by first investigating the generated fluid flow and then its impact on the erosion of the granular bed.

EXPERIMENTAL SETUP

The model experiment developed to mimic this situation is sketched in Fig. 1(a). A disk of diameter D is oscillating at an amplitude A, a frequency f, and is located at a mean distance H from the granular bed. The motion of the disk generates vortices (Fig. 1(b)) [4]. The granular material used in this study is made of glass beads of diameter $d = 350\,\mu\mathrm{m}$ and density $\rho_g = 2500\,\mathrm{kg.m}^{-3}$ immersed in water. The instantaneous velocity fields, as illustrated in Fig. 1(c), are measured in a vertical plane located through the axis of the disk and are obtained from Particle Image Velocimetry (PIV). The fluid is seeded with neutrally buoyant small particles, and illuminated by a laser sheet, which allows us to track and quantify the fluid flow generated by the oscillation of the foil.

The erosion onset of the granular bed is determined by direct visualization (Fig. 1(d)). The onset depends on the gravity force that tends to keep a grain between its two neighbors and the fluid stress exerted by the flow leads to lift and drag forces on a particle. The ratio of the two effects is characterized by the Shields number: $Sh = \rho_f\, U^2/(\Delta\rho\, g\, d)$, where ρ_f is the density of the fluid, U the velocity close to the granular bed, g the gravity acceleration, $\Delta\rho = \rho_g - \rho_f$ and d is the mean particle diameter [5]. This expression of the Shields number is based on the fluid inertial stress, which is reasonnable since the particle Reynolds number, $Re_p = \rho_f U d/\eta$, where η is the dynamic viscosity of the fluid, remains much larger than one.

RESULTS

The velocity fields obtained by PIV measurements allow us to quantify the vortices generated by the foil oscillation. We fit the velocity profiles by a Lamb-Oseen vortex model where the radius of the vortices as well as the maximum velocity are extracted from the fit. We find that the radius of the vortices is proportional to the amplitude of the oscillations but does not depend on the frequency and on the radius of the foil. The maximum velocity is directly proportional to the maximum velocity of the foil $2\pi A f$.

*Corresponding author. Email: morize@fast.u-psud.fr

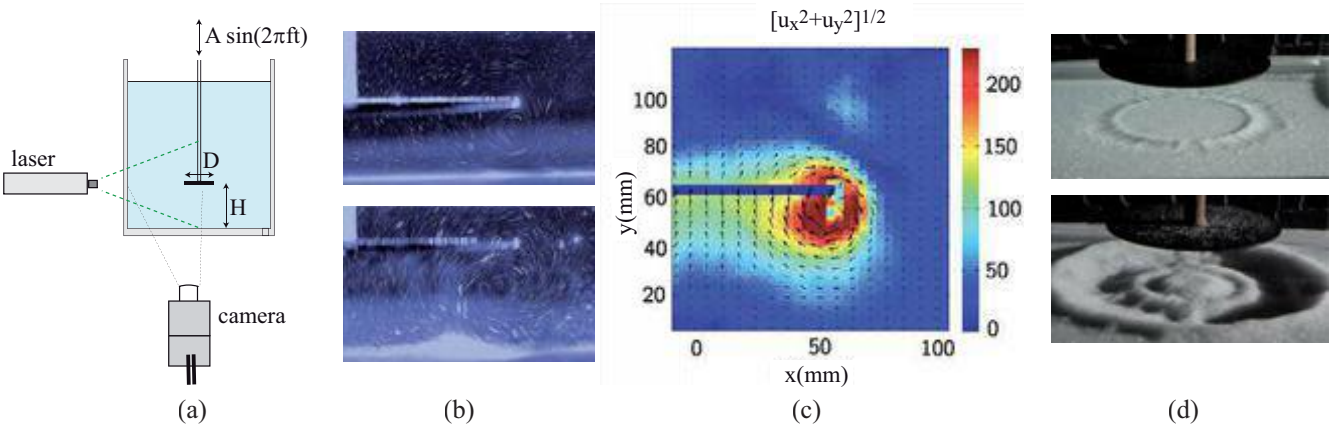

Figure 1: (a) Experimental set-up, (b) visualization of a vortex and the resuspension of the granular bed. (c) Typical velocity field obtained by PIV measurements. (d) Examples of erosion pattern.

We then systematically measure the erosion threshold for varying distance to the granular bed and we find that the larger the distance H is, the faster the oscillations need to be to reach the onset of erosion. We report in Fig. 2(a) the critical velocity of the foil V^c_{foil} at the onset of the erosion as a function of H. We observe that V^c_{foil} decreases for increasing A and decreasing H. Therefore, the relevant parameter to describe the erosion process is the minimum distance $H - A$ from the granular bed. In addition, the maximum velocity of the vortices is found to be proportional to the radius R of the foil, and therefore the relevant parameter to evaluate the critical velocity at the onset of the erosion, is the normalized minimum distance $(H - A)/R$ as confirmed by the collapse of the rescaled measurements shown in Fig. 2(b).

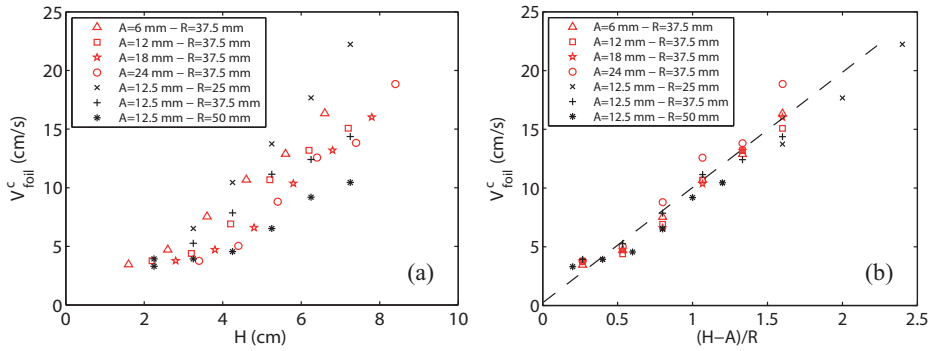

Figure 2: (a) Critical foil velocity V^c_{foil} as a function of the distance H to the granular bed for different amplitude of oscillation A and radius R of the foil and (b) V^c_{foil} as a function of the normalized minimum distance $(H - A)/R$.

CONCLUSION

In this study, we characterized the erosion of a granular bed by an oscillating foil. Coupling PIV methods and direct visualizations allowed us to show that the onset of the erosion for an oscillating disk at a distance H from a granular bed depends on a rescaled parameter $(H - A)/R$. This result suggests that the critical value of the global Shields number, based on V^c_{foil}, increases as $[(H - A)/R]^2$ for various experiments.

References

[1] Badr S., Gauthier G., Gondret P.: Erosion threshold of a liquid immersed granular bed by an impinging plane liquid jet. Phys. Fluids 26: 023302, 2014.

[2] Kubota Y., Higuchi H.: Aerodynamic particle resuspension due to human foot and model foot motions. Aerosol Sci. Technol. 47: 208-217, 2013.

[3] Ouriemi M., Aussillous P., Medale M., Peysson Y., Guazzelli E.: Determination of the critical Shields number for particle erosion in laminar flow. Phys. Fluids 19: 61706-63100, 2007.

[4] Shelley M. J., Zhang J.: Flapping and bending bodies interacting with fluid flows. Annu. Rev. Fluid Mech. 43: 449-465, 2011.

[5] Buffington J. M.: The legend of A. F. Shields. J. Hydraul. Eng. 125: 376-387, 1999.

HYDRODYNAMICS FOR STANDING GRANULAR JUMPS DOWN INCLINES

Thierry Faug*[1,2], Ségolène Méjean[1], Edward Wyburn[2], Philippa Childs[2], and Itai Einav[2,3]

[1]*Torrent Erosion, Snow and Avalanches Research Unit, Irstea − Univ. Grenoble-Alpes, Grenoble, France*
[2]*School of Civil Engineering, University of Sydney, Sydney, Australia*
[3]*Department of Civil Environmental and Geomatic Engineering, University College London, London, UK*

Summary The present paper addresses the problem of standing jumps formed in flows of granular materials down an incline. First, we show how a new analytic solution can be derived from depth-averaged hydrodynamics to predict the height of granular jumps. This solution is robust for a great number of available data on incompressible water flows and is then tested with success on recent experimental data for granular jumps.

INTRODUCTION

It is now well-established that flows of granular materials down inclines can produce sudden changes in height and velocity, namely granular jumps by analogy to hydraulic jumps, as for instance shown in one of the pionnering works on the topic proposed by Savage [1]. In a detailed experimental study [2], we have recently proposed a phase-diagram to show how the shape of standing granular jumps can drastically change if the slope and the mass discharge are varied (see Fig. 1). At low mass discharge, the granular flows are thin and dilute, and produce jumps characterized by a strong change in density across the jump. At high mass discharge, the granular flows are dense and thicker, and lead to nearly incompressible jumps. The shape of the latter jumps is remarkably influenced by the slope angle that controls the Froude number Fr_1 of the flow before the jump: the jumps are very steep at high slopes (high Fr_1), while they become much more diffuse at lower slopes (low Fr_1). Those experimental observations have proven that the one-to-one relation between the jump height relative the thickness of the incoming flow and the Froude number, which is tradionnally used in hydraulics, is not suitable for all situations encountered in the laboratory tests. In this paper, we present how an exact solution from hydrodynamics, which takes into account the influence of the forces acting within the jump volume (its weight and the friction force) and the density change across the jump, can convincingly reproduce the jump heights measured in the experiments.

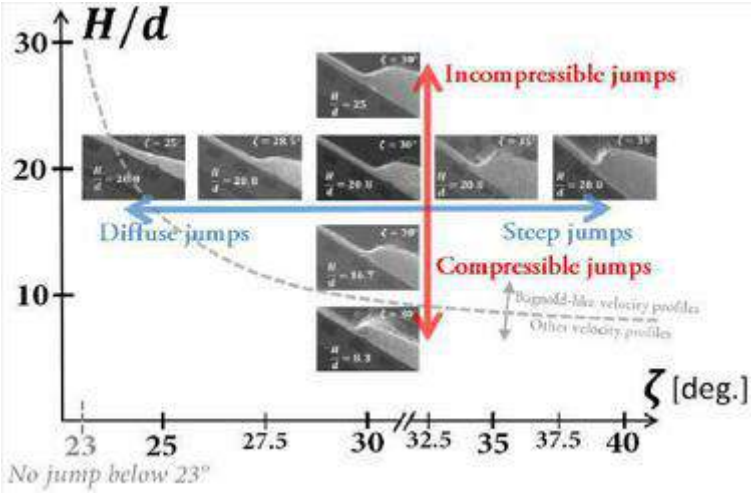

Figure 1: Phase-diagram for the shape of granular jumps down an incline proposed in Faug *et al.* [2]. H/d is the discharge height at the onset of the granular flows scaled by the grain diameter (glass beads) and ζ is the inclination angle of the granular chute. There exists a critical angle below which steady jumps can not form [2].

METHODS AND RESULTS

In order to derive an equation able to predict the jump height, we consider a control-volume surrounding the jump and apply the mass and momentum depth-averaged conservation equations. This yields the following hydrodynamic equation (see details in [3]):

*Corresponding author. Email: *thierry.faug@irstea.fr*

$$Fr_1^2 = \frac{1}{2}\left[\frac{\bar{\rho}_2}{\bar{\rho}_1}\left(\frac{h_2}{h_1}\right)^2 - 1 - \frac{\bar{K}L_*}{h_1}\left(1+\frac{\bar{\rho}_2}{\bar{\rho}_1}\frac{h_2}{h_1}\right)(\tan\zeta - \mu_e)\right]\left[\frac{1}{\left(1-\frac{1}{\frac{\bar{\rho}_2}{\bar{\rho}_1}\frac{h_2}{h_1}}\right)}\right], \quad (1)$$

where h_2/h_1 is the height of the jump relative to the thickness of the incoming flow, $\bar{\rho}_2/\bar{\rho}_1$ is the density change across the jump, ζ is the inclination angle, L_* is the jump length, $\bar{K}$ is a shape-coefficient (more details can be found in [3]), and μ_e corresponds to the basal depth-averaged friction within the jump volume.

This paper is firstly devoted to solve the above equation. The previous studies [2, 3] considered approximate solutions only. Eq.(1) can be put into the form of a cubic equation in h_2/h_1, which can be solved thanks to the Cardano method.

Then, we check the robustness of the physically meaningful solution of Eq.(1) by comparing it with success to a great number of available data with water flows ($\bar{\rho}_2/\bar{\rho}_1 = 1$ for water) under different conditions: horizontal smooth bottom ($\tan\zeta = 0$ and $\mu_e = 0$), horizontal rough bottom ($\tan\zeta = 0$ and $\mu_e \neq 0$), and inclined smooth bottom ($\tan\zeta \neq 0$ and $\mu_e = 0$). For the rough bottom, μ_e is calculated from the traditional empirical scaling for turbulent friction proposed by Strickler, which can be derived from the phenomenological theory of Kolmogórov [4].

Finally, under minimal assumptions regarding the law describing the depth-averaged granular friction force (μ_e in Eq.(1)), the physically meaningful solution of Eq.(1) is successfully compared to the experimental data on granular jumps by [2]. For the granular jumps down an incline, all the terms coming into play in Eq.(1) have to be considered: $\bar{\rho}_2/\bar{\rho}_1 > 1$, $\tan\zeta \neq 0$, and $\mu_e \neq 0$.

CONCLUSIONS

Our results show how depth-averaged hydrodynamics can convincingly reproduce the height of the standing jumps formed in flows of granular materials down inclines. It is worthy to note that Eq.(1) needs to be fed with the length of the jump and, to a lesser extent, an information on the shape of the jump (through the shape-coefficient $\bar{K}$). In all experiments considered in our study (both the water flows and the dry granular flows), this information was measured in the experiments and directly used for the computation of the solution of Eq.(1). A challenging question then arises: how to predict the length and the shape of the granular jumps?

ACKNOWLEDGMENTS

Thierry Faug is grateful to the financial support by the People Programme (Marie Curie Actions) of the European Unions Seventh Framework Programme under REA Grant Agreement No. 622899 (FP7-PEOPLE-2013-IOF, GRAINPACT). This work has also been supported by the LabEx Tec21 (Investissements d'Avenir: grant agreement No. ANR-11-LABX-0030).

References

[1] Savage S.B.: Gravity flow of cohesionless granular materials in chutes and channels. J. Fluid Mech. 92:53-96, 1979.

[2] Faug T., Childs P., Wyburn E., Einav I.: Standing jumps in shallow granular flows down smooth inclines. Phys. Fluids 27:073304, 2015.

[3] Faug T.: Depth-averaged analytic solutions for free-surface granular flows impacting rigid walls down inclines. Phys. Rev. E 92:062310, 2015.

[4] Gioia G., Chakraborty P.: Turbulent Friction in Rough Pipes and the Energy Spectrum of the Phenomenological Theory. Phys. Rev. Lett. 96:044502, 2006.

SCALING LAWS FOR THE SEGREGATION FORCES IN SHEARED GRANULAR FLOWS

François Guillard[1,2], Yoël Forterre[1], and Olivier Pouliquen [*1]

[1]*Aix Marseille University, CNRS, Marseille, France*
[2]*School of Civil Engineering, The University of Sydney, Sydney, Australia*

Summary In order to better understand the mechanism governing segregation in granular flows, the force experienced by a large particle embedded in a granular flow made of small particles is studied using discrete numerical simulations. Accurate force measurements have been obtained in a large range of flow parameters by trapping the large particle in an harmonic potential well to mimic an optical probe. An empirical expression of the segregation force is proposed as a function of the stress distribution.

INTRODUCTION

A rich phenomenology is observed in flows of polydispersed granular material. When flowing, large and small particles have a tendency to migrate in different regions, giving rise to complex patterns. This tendency to segregate is a major source of problems in many industrial applications involving mixing processes and is at the origin of geomorphological patterns observed in deposits of rock avalanches, landslides or pyroclastic flows. Important progresses have been made the last decade for describing polydispersed granular flows, and a relevant framework based on a mixture theory has been developed to describe the evolution of the species in many configurations (avalanches [1], flow in rotating drums [2], silo [3]). However, the segregation flux in those models remains mainly empirical and would benefit from a better understanding of the segregation phenomenon. Different physical explanations have been proposed in the literature to explain segregation. In the case of dilute collisional granular flows, segregation can be predicted within the framework of the kinetic theory [4]. This approach valid in the dilute regime failed to predict qualitatively the direction of segregation in the dense regime. Savage and Lun [5] in a pioneered work proposed a kinetic sieving mechanics to explained segregation in the dense regime for flows down an inclined plane. The picture is the following: during the flow, the fluctuating motion of the particles create holes. Large grains can fall only in large holes, while small grains can fall in both small and large holes. Segregation results from this asymmetry in the exchange of grains between layers. This pure kinematic picture turns out to be incomplete. Heavy enough particles can sink instead of rising up during the flow [6, 7], showing that gravity forces can overcome segregation. This suggests that a dynamics picture in terms of forces may more appropriate to describe segregation phenomenon. The objective of the present study is to precisely study the case of a single coarse particle in a bath of small particles, to understand in which condition segregation occurs and what control the forces experienced by the coarse particle.

METHODS

The configuration of interest is sketched in Fig 1a. A 2D granular medium made of slightly polydispersed disks of mean diameter d_s is sheared between two rigid rough plates. The discrete element simulations are made using the open source software LIGGGHTS.30, for soft, inelastic, frictional spheres [8]. A velocity V and a confining pressure P_0 are imposed at the top plate. Gravity can be imposed either in the vertical z direction, or in the horizontal x direction. In absence of gravity the system is symmetric and the velocity profil is linear (Fig. 1b). When gravity is switch on, the stress distribution is no longer uniform and the velocity profile becomes asymmetric (Fig. 1c and d). To study segregation, a particle of diameter d_c larger than d_s is introduced at different positions in the layer. To accurately measure the force experienced by the test particle, we mimic the existence of an optical trap in the z direction for the large particle only. In addition to the gravity and to the contact forces exerted by the other particles, an harmonic force $k * (z \nearrow z_0)$ is imposed to the large particle, where z is its vertical position and z_0 a reference position. The coarse particle is thus attached with a spring of stiffness k to the vertical position z_0, but is free to move horizontally with the flow. When the stationary regime is reached, the coarse particle flows with the bulk but remains in average at the same altitude. Its relative position to the reference position z_0 thus directly gives access to the segregation lift force F_z, i.e the force which would induced a migration in absence of the spring. We have checked that the results are independent of the spring stiffness k.

RESULTS

A large number of simulations have been carried out to investigate different flow conditions. The segregation force F_z (see Fig. 1a) has been measured for different confining pressure P_0, different shear velocity V, different position in the layer z_0, different coarse particle size (d_c). The main results are the following. First, the sign of the segregation force varies depending

*Email: olivier.pouliquen@univ-amu.fr

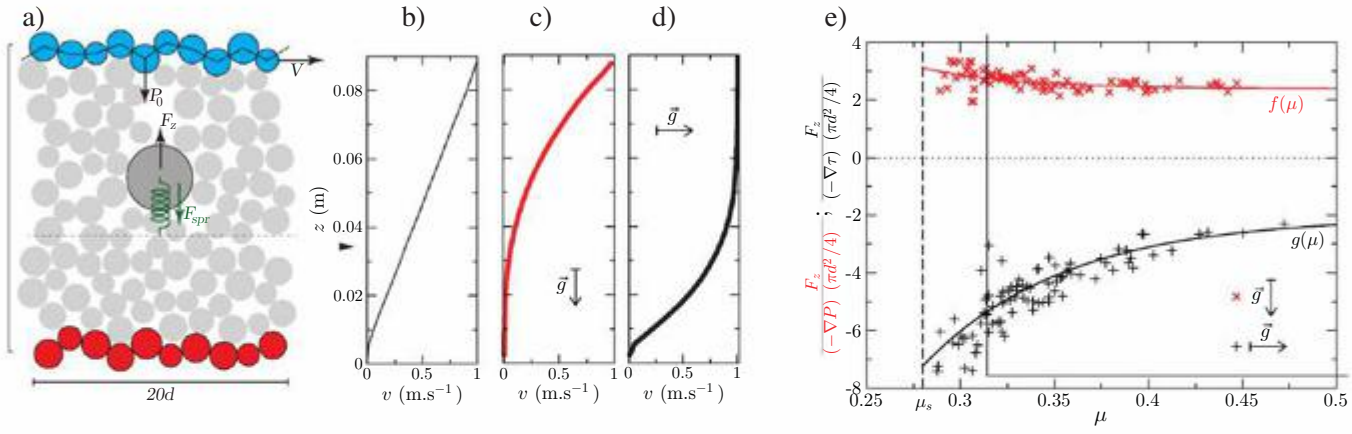

Figure 1: a) Sketch of the configuration: the coarse particle is vertically trapped in an harmonic potential; b) velocity profiles in the shear cell with no gravity, c) vertical and d) horizontal gravity; e) rescaled segregation force as a function of $\mu = \tau/P$.

on the origin of the asymmetry. When gravity points downward, a vertical pressure gradient $\frac{\partial P}{\partial z}$ exists (the shear stress τ is constant) and the lift force F_z is positive, meaning that a force exist opposite to the direction of gravity: the coarse particle would like to rise up at the top as observed in flows on inclined planes. When gravity is horizontal (Fig. 1d) a gradient of shear stress $\frac{\partial|\tau|}{\partial z}$ exists (but P is constant), and the segregation force is negative. The coarse particle has a tendency to sink, a situation that is reminiscent of what has been observed in silo [3]. The second main result is summarized in Fig. 1e. For the two configurations (vertical and horizontal gravity), the segregation force is proportional to the stress gradient, with a factor that varies with the ratio of the shear to normal stress $\mu = \tau/P$. All the data obtained for different flow parameters, at different positions, collapse on two main curves. The third result is obtained when imposing an inclined gravity or when simulating flows on inclined planes. In this case both a pressure gradient and a shear stress gradient exist, but we show that the segregation force is simply given by the sum of the two contributions measured in Fig. 1e. The last result is that the segregation force is a function of the size ratio d_c/d_s between the large particle and the small ones, with a maximum for $d_c/d_s \approx 2$. One can thus propose the following empirical law for the segregation force as a function of the stress distribution in the shear flow:

$$F_z = -\pi \frac{d^2}{4} a(d_l/d_s) \left(-f(\mu) \frac{\partial P}{\partial z} + g(\mu) \frac{\partial |\tau|}{\partial z} \right),$$

with $\mu = \tau/P$, $f(\mu)$ and $g(\mu)$ being the functions measured in Fig. 1e, and $a(d_l/d_s)$ a function we have measured (no shown here).

CONCLUSIONS

The segregation force experienced by a coarse particle flowing in a bath of small particles has been measured by means of extensive discrete element simulations. By changing the stress heterogeneity in the shear flow, it has been shown that a simple expression can be proposed for the segregation force as a function of the stress distribution. Such an expression may be useful when introduced in recent models for polydispersed flows. However, more studies are needed to better understand the physical origin of the measured segregation force.

References

[1] Gray J. M. N. T. and Thornton A. R. A theory for particle size segregation in shallow granular free-surface flows. Proc. R. Soc. Lond. A 461,1447, 2005.

[2] Schlick C.P. , Fan Y., Umbanhowar P.B., Ottino J.M. and Lueptow R.M., Granular segregation in circular tumblers: theoretical model and scaling laws, J. Fluid Mech. 765, 632-652, 2015.

[3] Hill, K. M., and Tan, D. S. Segregation in dense sheared flows: gravity, temperature gradients, and stress partitioning. J. Fluid Mech., 756, 54?88, 2014.

[4] Jenkins, J.T. and Mancini F., Kinetic theory for binary mixtures of smooth, nearly elastic spheres. Phys. Fluids A, 1, 2050-2057, 1989.

[5] Savage, S.B. and Lun, C.K.K. Particle size segregation in inclined chute flow of dry cohesionless granular solids. J. Fluid Mech. 199, 177-215,1989.

[6] Thomas, N. Reverse and intermediate segregation of large beads in dry granular media, Phys. Rev. E 62, 961?974, 2000.

[7] Tripathi A. and Khakhar D. V. Density difference-driven segregation in a dense granular flow. J. Fluid Mech., 717, 643, 2013

[8] Kloss C. , Goniva C. , Hager A. , Amberger S. , and Pirker S. , Models, algorithms and validation for opensource DEM and CFD-DEM. Prog. Comput. Fluid. Dyn. 12, 140-152, 2012.

SOLID-FLUID TRANSITION AND RIPPLE IN VERTICALL VIBRATED THICKER GRANULAR LA ER

Osamu Sano*

Professor Emeritus, Tokyo University of Agriculture and Technology, Koganei, Tokyo, Japan

Summary Collapse of the structure and the resultant flows in granular materials due to vertical oscillation are investigated. A thinner layer of granular material exhibits bending oscillation similar to an elastic plate, or *undulation*, over a certain range of forcing magnitude, where relative positions of the constituent particles remain within a distance of its diameter. With the increase of forcing magnitude, the structure of the material no longer holds, and the fluid-like behavior characterized by the surface wave, or *ripple*, appears. In a thicker granular layer, both the fluid-like and solid-like states coexist, whose regions change spatiotemporally. The upper part of the layer is relevant to ripple formation, whereas the lower part remains immobilized and transmits the momentum from the container bottom. Dependences of the above-mentioned solid-fluid transition and the flow characteristics on the magnitude of forcing and the layer thickness are elucidated.

INTRODUCTION

Granular layer vibrated vertically exhibits both solid-like and fluid-like behaviors depending mainly on the properties of the material (particle diameter d, density, friction and restitution coefficients), magnitude of the external forcing (amplitude a, frequency f), container size and the layer height h (or the number of the layer $N = h/d$), which adds difficulties in uniform mixing, control of transport or reaction processes, prediction of structural stability of the material, etc. Using assemblages of uniform spherical particles, we have already shown that

(1) collective motions are recognized for a layer number N larger than N_1 (nearly equal to 3), whereas they look random for $N < N_1$ [1],

(2) a layer of thickness between N_1 and a certain number N_2 (of the order of 10) exhibits

2a) solid-like collective motions (*undulation*) similar to the bending oscillation of an elastic plate under weaker external forcing [2-3],

2b) fluid-like wavy motions (*ripple*) with the increase of external forcing [4],

(3) in a layer thicker than N_2, only the upper part of the layer is fluidized under sufficiently large external forcing and contributes to ripple formation, whereas the lower part transmits the momentum applied at the collision with the bottom of the container [5-7],

(4) wavelength of the ripple is determined by the density wave refraction due to vertical variation of the number density of the particle, the latter of which is considerable over the effective thickness h^* near the upper surface, whereas it is almost constant in the lower part [6-8],

(5) aspect ratio of the height to wavelength of the undulation is determined by the product fa irrespective of the container size [9].

So far the details of the above item (3) are not fully understood, on which we shall cast a new light.

E PERIMENT

We performed an experiment on the vertically vibrated granular layer in a container, which consists of narrowly spaced transparent walls in one of the horizontal direction to allow observation of the quasi-two-dimensional particle motion from the side. We tested several granular materials in various sizes of the container. To avoid the complexity, however, we confine our attention to a series of experiments, in which single species of material (i.e., lead sphere of a diameter d=1 mm) is filled in a container of horizontal sizes L=100 mm (typical), W=10 mm and height H=100 mm. For the purpose of checking the effect of the boundary size, we also tested the one with L = 50 – 200 mm, whereas its height was chosen sufficiently large to keep the particles inside the container. The other horizontal size W was chosen to assure the quasi-two-dimensionality of motion as well as to assure the negligible effect of wall friction [1]. The container filled with particles was oscillated sinusoidally in vertical direction by the vibration generator with frequency f and amplitude a under atmospheric pressure.

* Corresponding author. Email: sano@cc.tuat.ac.jp

Observations were made by means of a high-speed video camera of typically 500 frames/s, with spatial resolution 0.1 mm. Particle positions were traced, and the type of collective motion of the granular layer is classified. Hereafter we denote solid phase by the assemblages of particles where relative positions remain within a particle diameter distance, and by fluid phase otherwise. Spatiotemporal changes of these phases are examined under systematically varied forcing conditions and the layer thicknesses.

RESULTS

We show an example of the ripple and its associated particle motion in a thicker granular in Fig.1. Figure 1(a) is a snapshot of the layer at t =283 ms (initial time is arbitrary), where surface contours at t =233, 258, 283 and 308 ms are superposed. Here, peak and valley regions alternate with a frequency $2/f$ (=$2T$), which is 100 ms in this case. Figure 1(b) shows the particle paths from t =258 ms to t =283 ms, which covers a time interval $T/2$. Note that the whole layer moves up-and-down, so that the relative positions of the particles with respect to a certain marker particle near the bottom are shown. In contrast to the conventional shallow water waves where fluid particles move throughout the fluid domain, the motion of the grains is recognized only in the upper part of the layer, whereas the lower part and the valley regions are immobilized or crystalized even in a free flight period of the layer. The layer number of the fluid phase is almost constant (but the thickness changes due to dilation and ripple formation) under a given forcing, whereas the layer number (and the thickness h_s) of the solid phase increases with the increase of the total layer number N (or the layer thickness h). Systematic results with varied f, a and h are obtained.

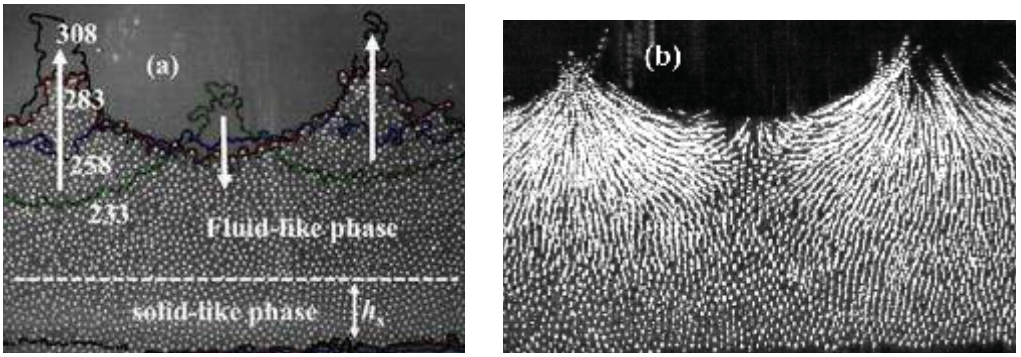

Fig.1. Particle motion during the growth of ripple (N=30, f=20 Hz, a=3.40 mm): (a) Snapshot , and (b) particle paths.

CONCLUSIONS

Spatiotemporal change in vibrating granular material is elucidated, and a pattern diagram is obtained, in which almost rigid-body phase, elastic phase characterized by undulation, fluid phase characterized by ripple, and coexisting phase, etc. are classified in terms of the forcing magnitude and the layer number.

References

[1] Kanai K., Ugawa A., Sano O.: Experiment on Vibration-Induced Pattern Formation of a Vertically Thin Granular Layer. J. Phys. Soc. Jpn. 74: 1457-1463, 2005.

[2] Ugawa A., Sano.O: Undulation of a Thin Granular Layer Induced by Vertical Vibration. J. Phys. Soc. Jpn. 72: 1390-1395, 2003.

[3] Sano O.: Dilatancy, buckling, and undulations on a vertically vibrating granular layer. Phys. Rev. E 72: 051302, 2005.

[4] Ugawa A., Sano.O: Dispersion Relation of Standing Waves on a Vertically Oscillated Thin Granular Layer. J. Phys. Soc. Jpn. 71: 2815-2819, 2002.

[5] Sano O.: Solid-fluid transition and the formation of ripples in vertically oscillated granular layers. AIP Conf. Proc. 1227: 100-114, 2010.

[6] Sano O.: Density Wave as a Mechanism of the Formation of Ripples in Vertically Oscillated Thicker Granular Layer. J. Phys. Soc. Jpn. 80: 034402, 2011.

[7] Sano O.: Wavelength Selection Mechanism of Ripples in Vertically Vibrated Thicker Granular Layer. J. Phys. Soc. Jpn. 81: 033401, 2012.

[8] Sano O.: Wavelength selection of ripples in a vertically vibrating dynamically thick granular layer due to density-wave refraction. Comptes Rendus Mecanique 342: 52-62, 2014.

[9] Sano O.: Aspect ratio of undulation in a vertically vibrating granular layer. to be published in Comptes Rendus Mecanique.

DISCONTINUOUS SHEAR THICKENING IN DENSE SUSPENSIONS: A FORCE-SPACE ANALYSIS

Elan Shatoff[1], Abhinendra Singh[2], Romain Mari[3], Jeff Morris[4], and Bulbul Chakraborty *[1]
[1]*Martin Fisher School of Physics, Brandeis University, Waltham, MA 02454*
[2]*Levich Institute, CUNY City College of New York, New York, NY 10031 USA*
[3]*Department of Applied Mathematics and Theoretical Physics, University of Cambridge, Wilberforce Road, Cambridge CB3 0WA, United Kingdom*
[4]*Levich Institute and Department of Chemical Engineering, CUNY City College of New York, New York, NY 10031 USA*

Summary Shear jamming and discontinuous shear thickening are phenomena observed in granular materials or dense suspensions, and have been extensively studied in recent years using experiments and numerical simulations. It has become increasingly clear that frictional contacts between particles are necessary for these shear-induced transitions. We have recently developed a theoretical framework that analyzes the collective behavior of dry grains and suspensions using a representation in which, in addition to positions of grains, forces appear as independent statistical variables. In this talk we will present results of application of this framework to shear-induced transitions and demonstrate that in a force-space, which is dual to real space, these transitions show signatures of symmetry breaking and co-existence of phases.

INTRODUCTION

A dense suspension may act as a liquid material that flows with relative ease under slow forcing, while fast forcing can cause an abrupt increase by orders of magnitude in its effective viscosity: this is known as *discontinuous shear thickening* (DST). DST has become broadly known through internet popularizations[1], which show a person running across a bath of cornstarch suspension, into which they sink if they stand still.

Flow property transition, much like classical phase behavior, has great practical relevance, as it determines the processing conditions for a material in engineering contexts. As in classical phase transitions, the key question is how interactions between microscopic constituents give rise to a macroscopic transition. Here, the transition depends upon external forcing, and a developed statistical mechanics framework is not available to guide us. Development of understanding that would ultimately allow prediction, manipulation, and control of the properties of these mixtures would benefit greatly from a theory-guided framework for description of the interaction of various forces in the critical regime when the solid volume fraction ϕ approaches its maximum packing value $\phi_{\max}$.

The shear-thickened state created by DST is a non-equilibrium, flowing steady state. Upon increase of the solid volume fraction, the transition becomes sharper[2] and beyond ϕ_{max} the suspension jams into a solid state. The defining feature of a solid is its ability to resist shear. In most solids, crystalline and amorphous, clearly defined density modulations emerge at low temperature or high density, distinguishing them from liquids, and signaling the breaking of continuous translational symmetry. A consequence of this symmetry breaking is that solids, unlike their liquid counterparts, can resist shear deformations: it costs free energy to distort the patterns encoded in the density modulations. This well-known paradigm breaks down for dry grains and dense suspensions since (i) the concept of a free energy is ill defined for dissipative, frictional grains, and (ii) breaking and formation of frictional contacts can lead to large changes in forces and disrupt the rigidity implied by positional density patterns.

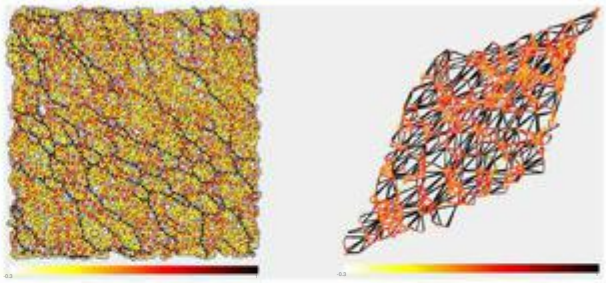

Figure 1: Configurations close to the DST transition in a stress-controlled simulation at $\phi = 0.78$. (Left) The force network with contacts color coded according to the magnitude of the contact force (Yellow: low values to Black: high values). (Right) The corresponding Maxwell-Cremona tiling (FTN) with edges color coded in the same manner as the force network. The force localization in the left figure manifests itself as variations in the density of tile vertices in the tiling.

In previous work on shear jamming in dry grains[3], we have shown that onset of shear-rigidity is related to broken translational symmetry in the space of forces, not positions of grains. More precisely, in 2D, the Maxwell-Cremona tilings[4] develop correlations between the vertices. Maxwell-Cremona tilings represent force-balanced configurations of grains in 2D. Any tiling represents a hypothetical force-balanced state. The tilings, however,

*Corresponding author. Email: bulbul@brandeis.edu

also need to satisfy the constraints of torque balance and the Coulomb condition of static equilibrium relating the magnitude of the tangential forces f_t to that of the normal forces f_N: $f_t \leq \mu f_N$, where μ is the friction coefficient of grains. These introduce correlations between the vertices of the Maxwell tiles, and changes in these correlations mark the shear-jamming transition.

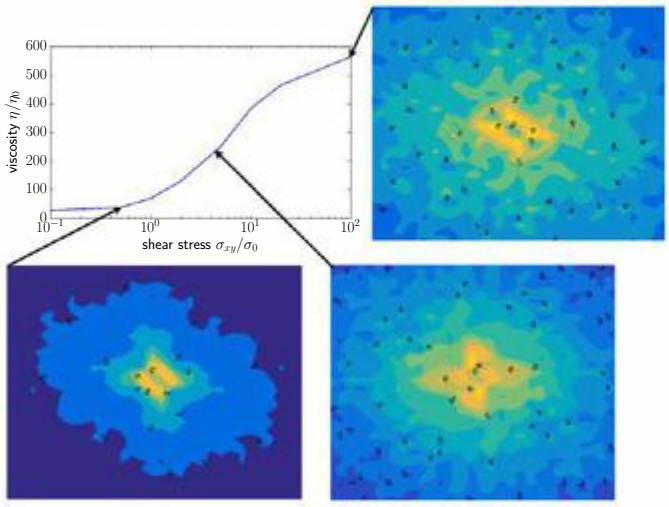

Figure 2: Evolution of structure factor of the *vertices of FTNs* across the DST transition, showing marked changes in both symmetry and form. Similar measures of the positions of grains in the suspension fail to exhibit any marked changes across the DST transition. The structure factors are averaged over the stationary regime of the flowing states in these stress-controlled simulations.

In this talk, we will present analysis of simulation data on DST, and show that there are clear signatures of a phase transition in the statistical properties of the Maxwell-Cremona tilings (FTNs).

FTN ANALYSIS OF DST

We analyzed the FTNs constructed from 2D simulations of suspensions undergoing DST[2] using an algorithm developed by Sumantra Sarkar[5]. A typical FTN is shown in Fig. 1. Each grain is represented as a polygon in the tiling with the edges of the polygon corresponding to the forces acting on that grain. The length of an edge gives the magnitude, and the direction gives the direction of the force but rotated by $\pi/2$. Two grains that are in contact share an edge because of Newton's third law. The ensemble of all tiles from a configuration of grains in force and torque balance thus leads to a tiling: a FTN. The bounding box of the FTN is completely determined by the stresses imposed at the boundary of a sample. Large contact forces lead to large tiles, therefore, force chains manifest themselves as regions of large tiles (black in Fig. 1). The strict edge-matching requirement constrains how tiles of different sizes are organized in a pattern. As seen in Fig. 1, a roughly lamellar structure is one possibility and indicates force chains in the compressive direction of the sheared suspension. One important aspect of the force tiles is that frictional contacts give rise to non-convex polygons whereas frictionless contacts can only lead to convex polygons. The density of non convex polygons provides a clear signature of shear jamming in dry grains[5]. In suspensions, the changes in the concentration of the polygons with stress leads to changes in the point pattern of the vertices of the FTN.

The patterns of vertices in FTNs can be analyzed using all of the tools available for analyzing point patterns such as the pair correlation function and the corresponding structure factor. As Fig. 2 shows, the structure factor evolves across the DST transition: there is a change in symmetry of the pattern and in the decay scale. The focus of this talk will be on the interpretation of this evolution and a theory of the DST transition based on correlations of vertices in FTNs. We will also connect measurables in the FTN space, which is a new way of analyzing suspension microstructure and rheology, to the standard measures in terms of stresses and microstructure in real, positional space.

CONCLUSIONS

We have developed a new representation that is adding insight to the nature of shear thickening in dense suspensions. The new representation illustrates the effects of particle contacts and friction, and especially the constraints of local force and torque balance on the organization of *forces* not just positions of grains. In this talk, we will illustrate the power of this technique and present a statistical theory of the DST transition based on this representation.

References

[1] http://www.pbs.org/wgbh/nova/education/tech/outsmarting-oobleck.html

[2] R. Mari, R. Seto, J. F. Morris, and M. M. Denn, *J. Rheol.* **58** (2014) no. 6, 1693–1724.

[3] S. Sarkar, D. Bi, J. Zhang, R. P. Behringer, and B. Chakraborty, *Physical Review Letters* **111** (2013) 068301.

[4] J. Maxwell, Statistical mechanics framework for static granular matter. *Phil. Mag*27:250,1864 .

[5] S. Sarkar, D. Bi, J. Zhang, J. Ren, R. P. Behringer, and B. Chakraborty, *arXiv: 1509.00678* (2015) .

NUMERICAL SIMULATION OF THE FORMATION OF SHOCK INDUCED PARTICLE JETS USING DEM

Kun Xue[a)], Haoran Cui
[1]*State Key Laboratory of Explosive Science and Technology, Beijing Institute of Technology, Beijing, China*

Abstract The dispersal of a cylindrical particle ring by a blast or shock wave induces the formation of coherent structures which take the form of particle jets. By the discrete element method (DEM), we performed a quasi-two-dimensional numerical simulation of the shock dispersal of the short cylindrical particle rings. Our study found that during the first hundreds of microseconds, particles around the inner ring surface begin to exhibit the velocity discrepancy. The fast moving particles squeeze into the interior regions, constituting the incipient particle jets. During the outward propagation, the tips of particle jets become blunt, even branch into multiple sub-jets, leading to the increase of the jet number which is a function of the impulsive pressure. The origin of particle jets can be attributed to the heterogeneous network of stress chains which precipitates the non-uniform distribution of particle velocities along the circumference.

INTRODUCTION

When a layer of solid particles is dispersed by a blast or shock wave, the expanding particle cloud typically forms a non-uniform structure comprised of coherent jets [1-9]. A growing body of photographic and radiographic evidence suggests that the jets form early during the dispersal process, on the timescale of the propagation of the shock wave through the particle layer [2, 3]. The fact that the timescale of the jet formation is consistent with the shock wave transit times excludes the hydro-dynamic instabilities, such as Rayleigh-Taylor or Kelvin-Helmholtz, as the governing mechanisms since the particle jets were observed well before the growth time associated with these mechanisms [2, 3, 7, 10]. Some investigations attempt to introduce a brittle fragmentation mechanism to explain the jet formation [2, 5]. But in contrast with the solid, particles cannot sustain tensile stresses. Nor does the surface energy exist in the particle medium. However the tension and the surface energy constitute the fundamentals of the brittle fragmentation mechanism.

To understand the formation of shock induced particle jets, it is of essence to reveal the early stage of the jet formation. The numerical simulation of the shock interaction with particle rings based on the discrete element method (DEM) provides the particle-scale information regarding the particle velocity and contact force, which can track the evolution of the velocity and stress profiles.

NUMERICAL SIMULATION

All simulations are carried out using the LIGGGHTS computational code based on a soft-particle DEM. The physical model is the replica of the quasi-two-dimensional experimental setup in ref [4, 9]. The particle packing is done by first letting the particles with the average diameter of 200 μm settle by gravity in the annular simulation box with the inner and outer radii equal to 0.02 and 0.04 m, respectively. The shock loading of the particle rings is performed by exerting a constant pressure p_0 on the innermost layer of particles shaded red in figure 1 for a period time of t_0 (see the inset of figure 1(a)), t_0 = 2 ms, mimicking the sustained shock wave used in ref[4, 9].

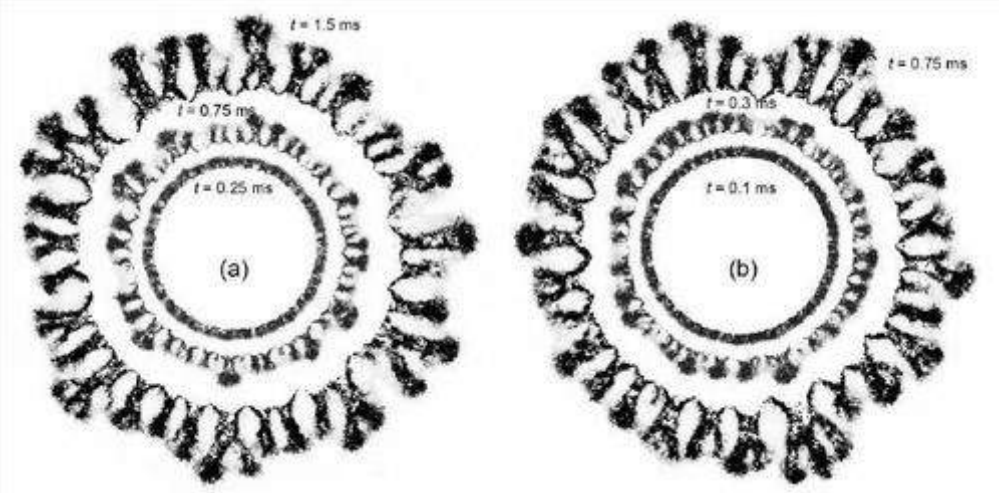

Figure 1. Evolution of the particle ring submitted to the pressure pulses with p_0 = 5 bar (a) and p_0 = 20 bar (b). Note that only particles behind the shock fronts are displayed in the figure. Particles are shaded according to the magnitude of particle velocities.

The evolutions of velocity profiles in the particle rings subject to the pressure pulses with different p_0 are shown in figure 1, both exhibiting resembling features. For the particle ring subject to the pulse with p_0 = 5 bar, at t = 0.25 ms, we can

[a)] Corresponding author. Email: xuekun@bit.edu.cn.

detect an alternate arrangement of particles clusters with low and high velocities. Particles with velocities well above the average are entrained into the interior and evolve into the precursors of the particle jets. These precursors grow into well recognizable particle jets at t = 0.75 ms (see figure 1(a)). The particle jet typically has a mushroom-like blurred tip and the tip becomes increasingly blunt, eventually splitting into multiple branches. Figure 1(a) shows that a number of jets bifurcate well before t = 1.5 ms with some sub-jets converging together. The particle ring subject to the pressure pulse with p_0 = 20 bar undergoes a resembling evolvement except that every signature stages begin at earlier times. In this case, not only can we observe more bifurcation of particle jets, but also a few well-defined trifurcation.

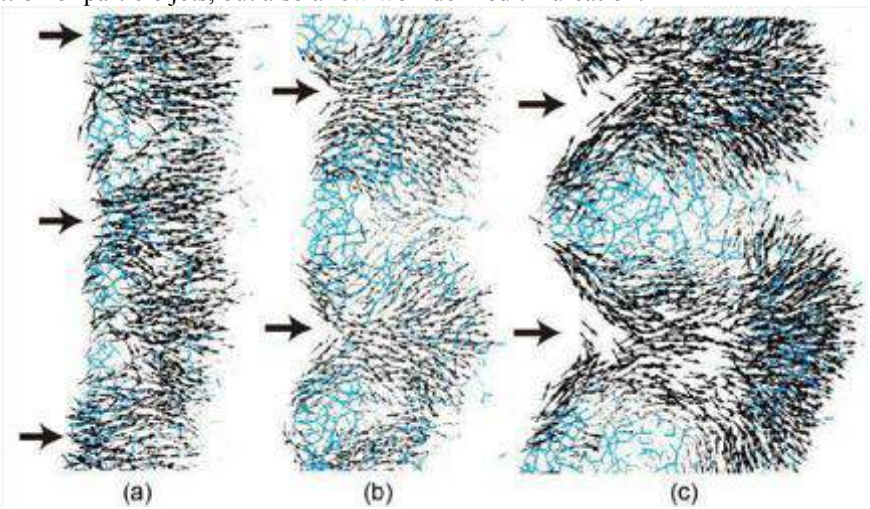

Figure 2. The velocity profile coupled with the network of stress chains in a segment of the particle ring subject to the pressure pulse with p0 = 5 bar at t = 0.25 ms (a), 0.4 ms (b) and 0.75 ms(c). The particle velocities are denoted by the arrows whose size and shade scale with the magnitude of velocity.

In contrast with the solid, stresses in the granular medium are mainly transmitted along the network of stress chains which carry most of load. The heterogeneous nature of the network of stress chains dictates the non-uniform transmission of the momentum. As shown in figure 2 (a), denser and stronger the stress chains are, faster and more efficient the transmission of the momentum. Otherwise the momentum cannot be transferred effectively.

The non-uniform radial transmission of momentum initiates the localized particle flows where the particle jets nucleate. The fast moving particle jets undergo significant transverse expansion with flaring out front (see figure 1 and figure 2), squeezing and compacting the neighboring slow moving particle clusters. These slow moving particle blocks thus are enclosed by the strong shear flows (see figure 2(b) and (c)). The particle shear flows destroy the sustained particle contacts, thus the network of stress chains in the slow moving particle blocks are segmented, disrupting the transmission of the momentum though these blocks. Subsequently these slow moving particle blocks increasingly lags behind the fast penetrating particle jets.

CONCLUSIONS

DEM simulations of the shock dispersal of the particle rings reveal the formation of the shock induced particle jets which are initiated by the non-uniform distribution of the particle velocities on the inner surface. The latter is dictated by the heterogeneous network of the stress chains. The incipient particle jets can disperse, bifurcate/ trifurcate, and coalesce while they are penetrating the particle rings, leading to the variation of the jet number which is also depends on the pulse pressure.

References

[1] D L Frost, C Ornthanalai, Z Zarei, V Tanguay and F Zhang 2007 J. App. Phys. 101 (11), 113529.
[2] A M Milne, E Floyd, A W Longbottom and P Taylor 2014 Shock Waves 24 (5), 501-513.
[3] A M Milne, C Parrish and I Worland 2009 Shock Waves 20 (1), 41-51.
[4] V Rodriguez, R Saurel, G Jourdan and L Houas 2013 Phy. Rev. E 88 (6), 063011.
[5] F Li, K Xue, C Bai 2013 Eur. Phys. J. E 36, 8.
[6] F Zhang, D L Frost, P A Thibault and S B Murray 2001 Shock Waves 10 (6), 431-443.
[7] F Zhang, R C Ripley, A Yoshinaka, C R Findlay, J. Anderson and B. von Rosen 2014 Shock Waves 25 (3), 239-254.
[8] D L. Frost, Y. Grégoire, O. Petel, S. Goroshin and F. Zhang 2012 Phy. Fluids 24 (9), 091109.
[9] V Rodriguez, R Saurel, G Jourdan and L Houas 2014 Phy. Rev. E 90 (4), 043013.
[10] T Xu, F-S Lien, H Ji and F Zhang 2013 Shock Waves 23 (6), 619-634.

DENSITY WAVES IN THE GRAVITATIONAL FLOW OF GRAINS IN NARROW PIPES

Carlos A. Alvarez*[1] and Erick de Moraes Franklin[1]
[1]*Faculty of Mechanical Engineering, University of Campinas - UNICAMP, Campinas, São Paulo, Brazil*

Summary The wavelengths and celerities of density waves in granular materials flowing down in a vertical tube are experimentally investigated using spatiotemporal diagrams. The granular flow was filmed with a high-speed camera, and the diagrams were constructed by digital image processing, using a numerical code developed in the course of this work. Experimental results show the existence of two wave regimes. The first one is characterized by density waves with constant celerity, and the second one by periodic oscillations of the wave system.

INTRODUCTION

Granular materials are a widespread research topic because of their many areas of practical application [1], being frequently observed in nature and industry. Nonetheless, the behavior of granular flows is not well understood. An important problem is the flow of granular materials in pipes. When the grains and the tube diameters are size-constrained, some instabilities may appear in the granular flow. These instabilities consist of alternate high- and low-compactness regions known as plugs and air bubbles, respectively (Figs. 1b and 1c), and may present intermittency, oscillating patterns, and even blockages [2, 3]. Although this instability may appear in vacuum [4, 5], in the specific case of fine grains these patterns are recognized as the product of the interaction between falling grains of small dimension and trapped air. In the present paper we analyze experimentally the formation of density waves that appear when fine grains fall through vertical narrow tube. In our experiments, performed in a laboratory with controlled temperature and relative humidity, grains flowed through a transparent pipe, and the flow was filmed by a high-speed camera. The wavelengths and celerities of the density waves were determined by digital image processing using a numerical code developed in Matlab environment.

EXPERIMENTAL PROCEDURE

The experimental device is schematically presented in Fig. 1a. It consisted of 1.0-m-long vertical glass tube with an internal diameter D of 3 mm. It was attached to a reservoir and a conical hopper with an opening angle of $60\,^{\circ}$. At the bottom of the tube a variable constraint (valve) was disposed, which could be moved across the pipe allowing the outflow adjustment. The hopper entrance and the exit of valve were at atmospheric pressure. The grains consisted of spherical glass beads (specific mass ρ_s = 2500 kg/m^3) divided into two populations: with diameter d between 106 and 212 μm and between 212 and 300 μm.

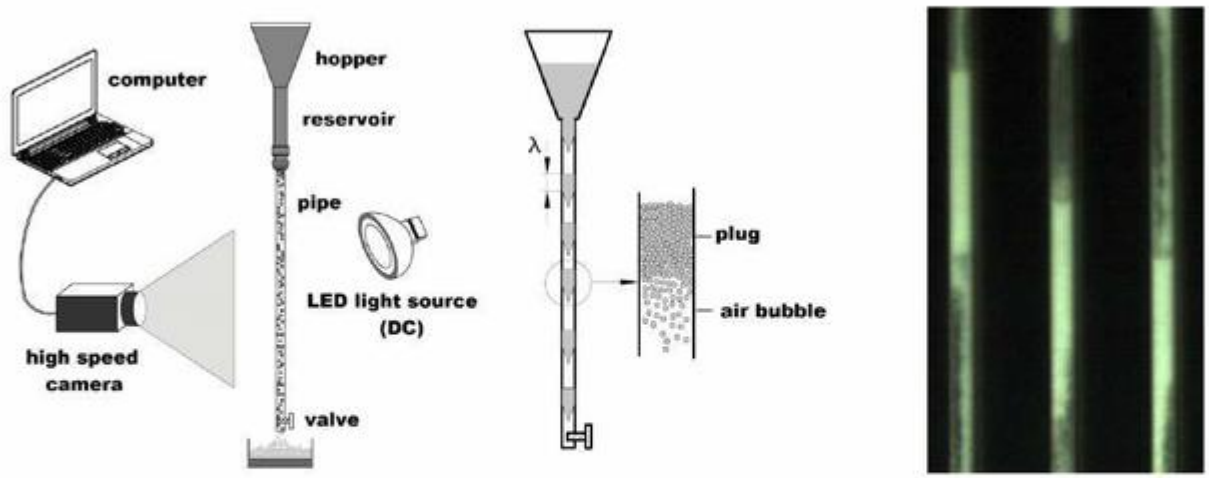

Figure 1: (a) Experimental setup. (b) Schematic view of the density waves. (c) Images acquired during the tests.

The temperature and the humidity were measured within $\pm$ 0.5 $^{\circ}C$ and $\pm$ 2.5%, respectively. The experiments were performed with grains of both smooth and rough surfaces, and the mass flow rate was determined from the time variation of

*Corresponding author. Email: calvarez@fem.unicamp.br

the measured mass, using a chronometer and a balance. The flow of grains and the dynamics of density waves were filmed with a $1280\,px \times 102\ \ px$ high-speed camera (maximum frequency of $1000\,Hz$). In order to provide the necessary light for low exposure times while avoiding beating between the light source and the camera frequency, LED (Low Emission Diode) lamps were connected to a continuous current source. For the present experiments, the camera frequency was set to $250\,Hz$. After the tests, a large number of images (in the order of thousands) in RGB format was obtained, therefore a numerical code was developed in order to calculate the wavelengths and the celerities of the density waves. The waves characteristics are measured from spatiotemporal diagrams generated by the code.

RESULTS

Two wave regimes were observed, the first corresponding to density waves that propagate at a constant celerity, and the second to oscillating waves. The oscillating regime appeared when the experiments were conducted using a batch of glass spheres with rough surface and diameters between 212 and 300 μm. A key observation concerns the direction of propagation: in the constant celerity wave regime, the density waves propagated upward, contrary to flow direction. This flow regime appeared with grains of both smooth and rough surfaces, and diameter between 106 and 212 μm. In the oscillating wave regime, the density waves propagated downward with a modulated drift celerity.

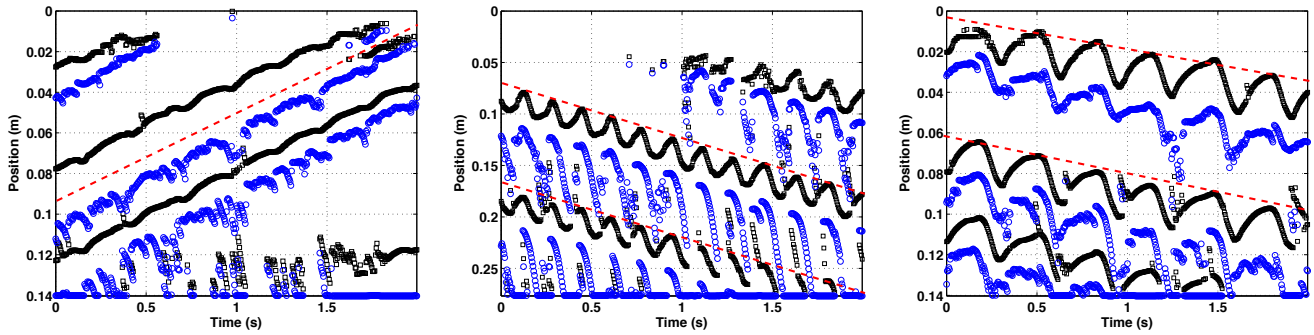

Figure 2: Spatiotemporal diagrams: the plugs positions as a function of the time at several mass flow rates $\dot{m}$. The plugs upper and the bottom positions are shown by squares and circles, respectively. The mean celerity of the plugs v_p is shown in dashed line. (a) v_p = -0.0408 m/s , $\dot{m}$ = 0.40 g/s. (b) v_p = 0.0501 m/s, $\dot{m}$ = 0.37 g/s. (c) v_p = 0.0190 m/s, $\dot{m}$ = 0.21 g/s.

In Fig. 2, the variations as functions of time for the upper and bottom positions of plugs are shown by squares and circles, respectively. The mean celerity of the plug, v_p, can be determined by the slope obtained for the upper zone. The mean wavelength of the plugs λ can be determined by calculating the difference between upper and bottom positions: λ provides the mean size of plugs. Previous works [2, 3] reported that the density waves appeared when the mass flow rate $\dot{m}$ was within 1.5 g/s - 5 g/s. In the present study, the density waves appeared for values of $\dot{m}$ ten times smaller than previously reported. The size of plugs calculated was $\lambda/D \approx 10$, and it is independent of mass flow rate and of flow regime.

CONCLUSIONS

This paper presented an experimental investigation on the density waves of granular flows in narrow tubes. When varying the mass flow rate, two wave regimes occurred: the density waves either propagated at a constant celerity or oscillated over a mean drift celerity. The oscillations suggest a stick-slip displacement of the plugs. The density waves appeared with mass flow rates between 0.1 and 0.95 g/s, ten times smaller than previous reported values. The size of plugs is the same for the two flow regimes and it is independent of the mass flow rate. The flow regimes are affected by the surface state (smooth or rough) and by the diameter of the grains.

References

[1] Duran J.: Sands, powders and grains: an introduction to the physics of granular materials, 2nd Edition, Springer, 1999.

[2] Raafat T., et al.: Density waves in dry granular media falling through a vertical pipe, Phys. Rev. E 53, 4345 - 4350, 1996.

[3] Bertho Y., et al.: Powder flow down a vertical pipe: the effect of air flow, J. Fluid Mech 459: 317-345, 2002.

[4] Savage S. B.: Gravity flow of cohesionless granular materials in chutes and channels, J. Fluid Mech 92: 53-96, 1979.

[5] Wang C. H., et al.: Instabilities of fully developed rapid flow of granular material in channel, J. Fluid Mech 342: 179-197, 1997.

WALL-MEDIA INTERACTIONS IN VIBRATIONALL FLUIDIZED GRANULAR FLOWS

Lucas da Silva Maciel[1], Jan K. Spelt[1a)]
[1] *epartment of echanical and Industrial Engineering, University of Toronto, Toronto, ntario, Canada*

A vibrationally-fluidized granular flow (VFGF) presents a fluid-like bulk flow behaviour superimposed on local velocity fluctuations due to particle collisions and the vibrating container walls. The impacts between particles and workpieces are utilized in manufacturing processes such as vibratory surface finishing, although process control and optimization remain mostly experience-based due to the complexity of VFGF. Recent studies have shown encouraging agreement between experiments and discrete element predictions of bulk and local velocities in VFGFs, enabling extensive observations on how container wall motion and the resulting contact forces influence the bulk and local properties of the granular bed. The present work used discrete element modelling to examine the wall-media contact forces and their connection to both the formation of bulk convection and the local impact velocity distribution throughout a VFGF. The results have explained the development of steady-state VFGF, and have been used to calibrate a model for normal wall forces.

GRANULAR FLOWS IN VIBRATOR FINISHING

Vibratory finishing is a process that employs flowing, vibrating granular media to process a variety of components. The local, small-scale vibrations of the abrasive particles can be used to polish, deburr, harden and burnish surfaces. Due to the complexity of motion and geometries, process control and optimization remain largely based on trial-and-error and industrial experience [1]. Recent studies have shown an encouraging agreement between discrete element modelling (DEM) and experimental measurements of vibratory finishing systems [2]. The present work examined the forces exerted by the vibrating walls on the media and their relation to the bulk convection and local impact velocities throughout the granular bed. The system studied is a tub-like container (Fig. 1a) with vibration in three degrees-of-freedom: two linear oscillations and a rocking motion. Figure 1b shows the motion of the tub wall during one cycle of vibration. The tub is coated with polyurethane and is filled with 6.3 mm diameter smooth steel balls. The vibrational amplitudes were 0.85 mm, 0.66 mm and 0.244° in the horizontal, vertical and rocking oscillations, respectively. This configuration resulted in a counterclockwise bulk flow and the formation of a free surface as shown in Fig 1a.

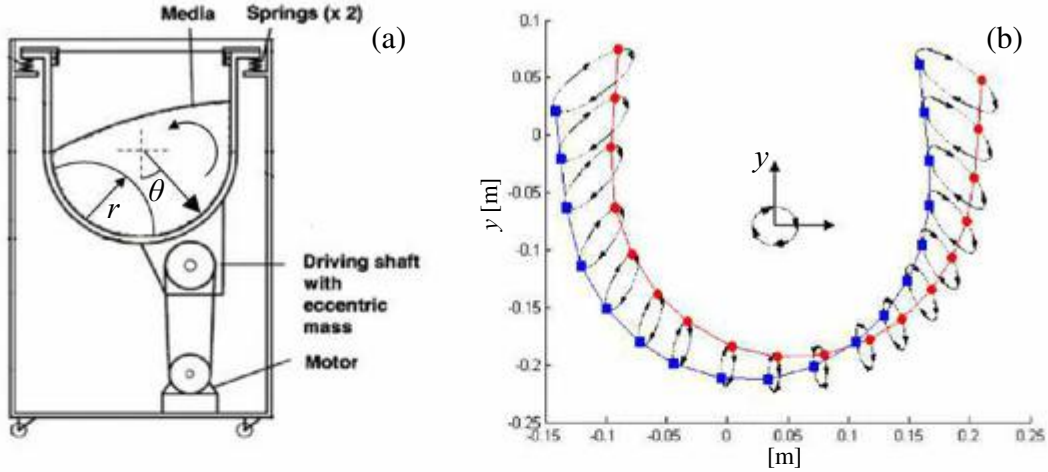

Figure 1 – (a) Vibratory finishing tub showing inclined free surface and bulk flow direction at steady state; (b) tub motion paths (exaggerated scale) at different points on the wall during one cycle.

MODELLING AVERAGE WALL-MEDIA CONTACT FORCES

Wall-media contact forces were modelled analytically in the x-y plane of the tub, and were compared with discrete element models that assumed four particle layers in the z-direction, which has been shown to accurately describe the flow in actual tubs [2]. The normal force exerted by the wall on the granular media at instant t is proportional to the effective media mass and acceleration at a tub point p; i.e. $_n{}^t = m_{eq}\, a_n{}^t$, where m_{eq} is the effective media mass, and $a_n{}^t$ is the positive acceleration of point p (positive coordinate normal to wall toward media). The analytical model assumes the media acceleration to be that of the wall. The effective mass was modelled as that of the media within a radius r from point p (Fig. 1a) with $r = d(C_1 + \ /\Gamma)$, where d is the particle diameter, Γ is a response factor that increases with the vibrational frequency, $= (h/d)C_2$ is a packing factor that scales with the local media depth, h, and C_1 and C_2 are, as yet, unknown functions of particle geometry that can be

a) Corresponding author. Email: spelt@mie.utoronto.ca

calibrated using DEM. Therefore, the normal forces depend on the hydrostatic pressure, the media response time to the wall movement and the wall acceleration towards the media. The model represents an average m_{eq} throughout many vibration cycles of the wall rather than an instantaneous value of r and hence m_{eq} at any moment during a cycle. This was justified by the highly stochastic nature of the wall contact conditions as seen in experiment and DEM simulations.

COMPARISON WITH DEM SIMULATIONS

By varying the phase difference φ between the horizontal and vertical tub oscillations it was possible to vary the distribution of normal wall forces throughout the tub of Fig. 1a. Figures 2a and 2b show the average normal forces plotted against coordinate θ, presented in Fig. 1a, as predicted by the force model and as averaged from 25 DEM simulations of the granular flow during the transient phase before the formation of a steady-state bulk flow and an inclined free surface. The constants C_1=2 and C_2=1.3 were calibrated using the DEM data shown in Figure 2. The model was able to match the local wall force minimum at the bottom of the tub and the asymmetry that varied with φ. Similarly good fits were achieved with the DEM data for φ=1.8 and 2.0. It is recognized that this model assumes a wall force during the portion of the cycle when $a_n{}^t$ is positive but the wall is moving away from the media. However, more recent results have shown that the wall acts upon the media only when moving toward it regardless of its own acceleration. The current predictions are reasonable because velocity and acceleration are linear functions of the amplitude of motion, and the frequency was held constant. Also, the intervals of positive acceleration and positive velocity are both half a cycle.

Thus, another interpretation of the wall-media forces replaces $m_{eq}a_n{}^t$ with two terms: (i) $m_{eq}{}^t(\Delta v^t/t_C)$, where Δv^t is the relative velocity between wall and media at time t and t_C is the average media-wall contact time; i.e. the average acceleration of the media by the wall, and (ii) $[v\ dm_e\ /dt\ ]^t$ because the effective mass changes during one cycle. Therefore, this variant of the analytical model accounts for the media motion and changes in the effective mass throughout a tub cycle. At the time of writing, this updated model has not been tested.

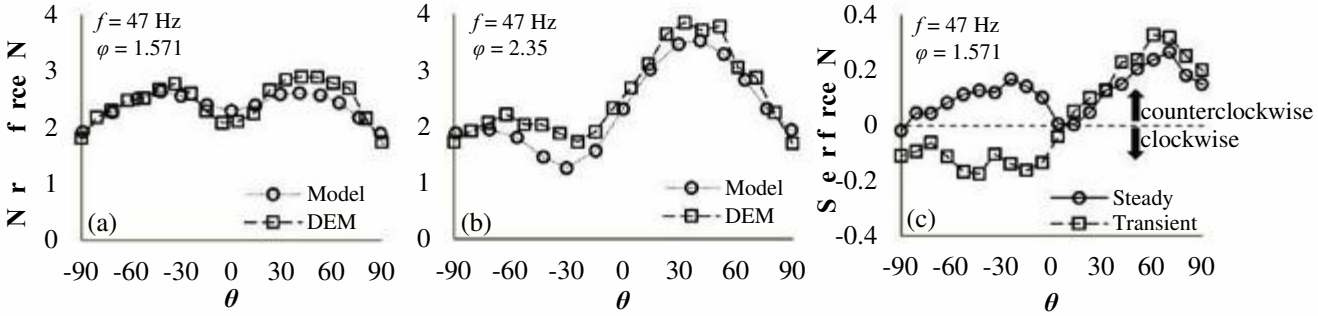

Figure 2 – (a,b) Model and DEM predictions of average normal force distributions during early transient regime as a function of location on the tub wall, θ defined in Fig. 1a; (c) DEM results for tangential force distribution during early transient and steady-state regimes.

Figure 2c shows the tangential forces on the tub wall for the early, transient stages of the process and for the fully-developed steady state after the formation of a stable inclined free surface (Fig. 1a). During the transient phase beginning with a horizontal free surface, the average wall shear forces act in opposite directions, the left side pushing the media clockwise (negative forces) while the right side applies counter-clockwise (positive) tangential forces. However, after reaching steady state with an inclined free surface, both sides of the tub exert an average counter-clockwise force on the media. Since the tub motion is the same in both cases, this significant change in wall shear forces can only be due to changes in the media. Although some of these changes may be due to the formation of an inclined free surface, the directional change in the shear forces suggest that the relative velocity between the walls and the media must evolve during the transient regime. These changes are neglected by the model that uses only the wall acceleration to estimate wall forces, whereas the later model considers the media velocity in calculating the approaching wall velocity Δv^t and could, therefore, account for changes in media motion.

CONCLUSIONS

A model has been proposed to describe the average normal wall forces between a vibrating container and the granular media. DEM simulations have been used to calibrate the model and explore its relation to velocity fluctuations throughout the media. On-going work is focusing on understanding the physical significance of the two calibration parameters in the model, and to develop a tangential force model. An improved understanding of normal and tangential wall forces provides an essential step in predicting bulk and local behaviours in vibratory finishing and supporting the continuum modelling of such systems.

References

[1] W. Li, S. Yang, X. Li, and W. Li, "Development Status and Trends of Mass Finishing Processes," *ey Eng ater* , vol. 621, pp. 111–120, 2014.

[2] K. Hashemnia and J. Spelt, "Particle impact velocities in a vibrationally fluidized granular flow: Measurements and discrete element predictions," *Chem Eng Sci* , vol. 109, pp. 123–135, 2014.

DISCHARGE FLOW OF A GRANULAR MEDIA FROM A SILO: EFFECT OF THE PACKING FRACTION AND OF THE GEOMETRY

Meberika Benyamine[1], Blanche Dalloz-Dubrujeaud [*2], and Pascale Aussillous[2]

[1]*Laboratoire FIMAS, Université de Béchar, Algeria*
[2]*Aix-Marseille Université, CNRS, IUSTI UMR 7343, France*

Summary We present experimental results on discharge of a rectangular silo. We varied two main parameters: the geometry of the silo, and the bulk packing fraction of the granular material. The results are discussed on the base of a physical model proposed by Janda *et al.* [1], which has been modified to predict the the flow rate of bi-dipserse mixtures and different geometric hopper configurations.

INTRODUCTION

The prediction of the mass flow rate of a granular media discharged from a silo has been widely studied because of its practical interest in several industries. However, the control parameters of the flow are not well understood. Through our configuration, several parameters have been explored.
The experimental setup is made of a rectangular silo (height H, width L=60 mm, and thickness W which can be varied from 3.5 to 10 mm). The rectangular outlet located at the centre of the bottom spans the thickness W and its length D can be varied from 1.8 to 26 mm. The discharge angle θ of the outlet can also be varied from θ=0° to θ=80° (Fig. 1). When opening manually the outlet, the grains fall out of the silo and are collected in a vessel. The temporal evolution of the mass $m(t)$ is recorded using an electronic scale. A typical temporal evolution of the flow rate $Q(t)$ is presented on figure 2.

The granular material consists of smooth spherical glass beads with different diameters d from 80 to 4500 μm. With the particles and aperture available, the number of beads in the aperture (D/d) ranges between 1 and 325. In order to control the bulk volumic fraction, different binary mixtures combinations were tested (size ratio of coarse particles diameter on fine particules diameters r=d_c/d_f between 2.2 to 6.3). Controlling the mass fraction X_f of the fine particles, the bulk volumic fraction varies from 0.58 to 0.73. (Fig. 3). Mono-disperse and bi-disperse experiments have been carried out, for the bi-disperse mixtures, all the experiments have been performed with an angle $\theta = 0^o$.

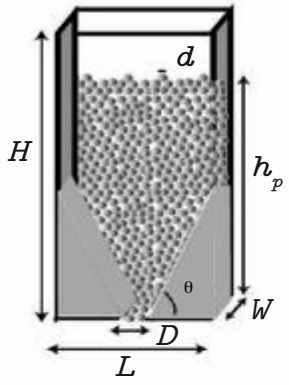

Figure 1: Rectangular silo

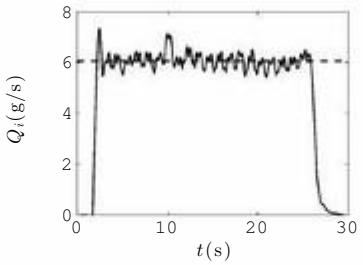

Figure 2: Typical temporal evolution of the instantaneous mass flow rate

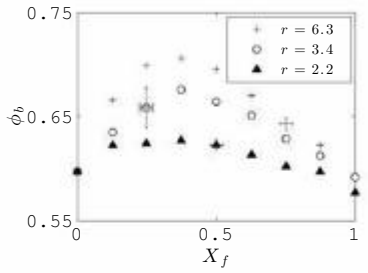

Figure 3: Bulk compacity ϕ_b versus volumic fraction of fine particles X_f

RESULTS AND DISCUSSION

All experiments show that the flow rate is controlled by the outlet diameter D. To predict the flow rate, one of the simplest and widely used expression is the one proposed by Berverloo [3]. It is based on the dimensionless analysis with the concept of a free fall arch at the outlet and the "empty annulus" [4] considering the reduced outlet length due particle size diameter. In our configuration the Beverloo law becomes:

$$Q = C\rho\phi_b g^{1/2} W (D - kd)^{3/2} \tag{1}$$

*Corresponding author. Email: blanche.dalloz@univ-amu.fr

Where ϕ_b is the initial bulk particle volume fraction, C and k, the fitting parameters.
This expression fits well all our experimental results for mono-disperse experiments, but it is difficult to modify this expression in the case of a binary mixture. In all cases we observe that the flow rate always exceeds the rate predicted by a simple mixture law between the flow rate of the purely coarse particles and the purely fine particles (Fig. 4).

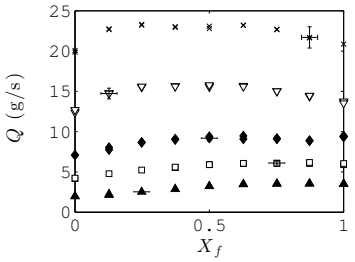

Figure 4: Flow rate versus X_f for binary mixtures (r= .3) with $D(mm)$: 3.5(▲), 5. (□), . (♦), 10(▽), 3.3(×).

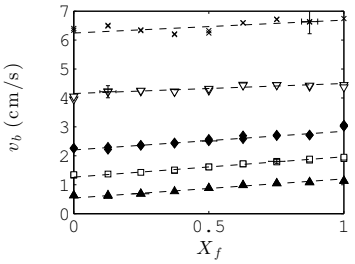

Figure 5: Bulk velocity v_b versus X_f. The dashed lines is the best fit excluding the pure cases X_f=0 and 1 (same legend as fig. 4).

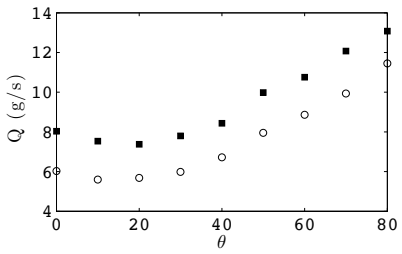

Figure 6: Flow rate versus θ for $D_o = 8\ mm$ with $d = 1.\ \ mm$ (■) and $d = 2\ mm$ (○)

Thus, to interpret our results, we have adapted the model proposed by Janda *et al.* [1] which suggests that for a given outlet diameter, the particles velocities are the same whatever the particle diameter (scaling with $\sqrt{gD}$) and that a dilatancy occurs at the outlet, introducing a geometrical parameter y_d, describing this dilatancy which is d dependent.We adapted this model to propose a new expression for the flow rate :

$$Q = C'\rho\phi_b \mathrm{y}_d \sqrt{gD^3} W = C'\rho\phi_b [1 \nearrow \alpha e^{-\beta \frac{D}{d}}] W \sqrt{gD^3} \tag{2}$$

Assuming that for a bidipserse mixture, the same hypothesis are still and independently valid for each size of particles d_i, each size has his own dilatancy factor y_{di}, and the flow rate for a bidisperse mixture becomes :

$$Q = C'[X_f \mathrm{y}_{d_f} + (1 \nearrow X_f)\mathrm{y}_{d_c}]\rho\phi_b W \sqrt{gD^3} \tag{3}$$

Equation 3 suggests that the dilatancy is D/d_i dependent and that the density profile at the outlet, is a simple mixture law between the volumic fraction of the fine X_f and the coarse X_c particles. Notes that ϕ_b is also given by a mixture law, which implies a complex variation of the flow rate with X_f, this is compatible with our experimental results (Fig. 4). These hypothesis have been tested, measuring the bulk velocity at the free surface $v_b = Q/\rho\phi_b WL$. Numerical discret experiments present results compatible with our assumptions [5].

Following the same ideas, experiments have been carried out with mono-disperse glass beads, varying the discharge angle. For a given outlet D, the flow rate increases rapidly when increasing the θ angle (Fig. 6). Thus, the expression of the flow has to be modified taking into the angle discharge. A simple expression of the outlet diameter as a function of θ is not sufficient to interpret our results. The dilatancy factor has also to be modify.

CONCLUSION

We have experimentally studied the flow discharge in a rectangular silo with mono-diperse and bi-diperse mixture. To interpret our results we have proposed a modification of the Janda model [1] which is in adequation with our experimental results and has been validated numerically by [5]. Modifying the geometry of the hopper (discharge angle), the interpretation of our experimental results are based on the same hypothesis and the influence of the discharge angle on the particle velocity and on the dilatancy factor have been studied.

References

[1] A. Janda, I. Zuriguel, and D. Maza, Phys. Rev. Lett. 108, 248001 (2012)
[2] M. Benyamine and M. Djermane, B. Dalloz-Dubrujeaud and P. Aussillous, PRE 90, 032201 (2014)
[3] W. A. Beverloo, H. A. Leniger, and J. V. de Velde, Chem. Eng. Sci. 15, 260 (1961)
[4] R. L. Brown and J. C. Richards, Trans. Instn. Chem.Engrs. 38, 243 (1960)
[5] Y. Zhou, P. Ruyer, and P. Aussillous, PRE 92, 062204 (2015)

PARTICLE STIFFNESS INFLUENCE ON GRANULAR RHEOLOGY

Adeline Favier[1], Mehdi Bouzid[1,2], Bruno Andreotti[1], Philippe Claudin[1], and Eric Clément[1]
[1]*Laboratoire de Physique et Mécanique des Milieux Hétérogènes, ESPCI, Paris, France*
[2]*Department of Physics, Institute for Soft Matter Synthesis and Metrology,Georgetown University, Washington, D.C., U.S.A.*

Summary We investigate the role of particle stiffness on granular rheology by means of numerical simulations. We discuss under which conditions localized plastic events are present or not when the system is sheared. We also study the different contributions to energy dissipation and the grain coordination number, in order to draw a diagram separating a region where the grains flow in a liquid-like manner and another where their behavior is more akin to solid-like plasticity.

The local rheology of granular flows was first established for dry and rigid particles and relates the effective friction coefficient μ to the inertial number I [1, 2]. It has been generalized for athermal [3, 4] and Brownian [5] dense suspensions. Non-local effects in these granular flows have been evidenced [6, 7], where creeping zones are difficult to conciliate with the simple local rheology. However, the precise identification and understanding of the mechanisms at the origin of these non-local effects is still an open question [8].

Here we address the role of particle stiffness k_n on the granular rheology by means of numerical simulations using the Discrete Element Method (DEM). With for set-up a two-dimensional shear cell at imposed pressure P and shear rate $\dot{\gamma}$, we discuss under which conditions the ratio k_n/P controls the presence or not of localized plastic events during the shearing (Figure 1). To do so, we have in particular built a coarse-grained field $\dot{\mathrm{y}}(\vec{r},t)$ reflecting, at time t, the local contribution to $\dot{\gamma}$ of a small region around the position $\vec{r}$, defined as

$$\dot{\mathrm{y}}(\vec{r},t) = \frac{\sum_{j=1}^{N} [u_i(\vec{r},t) \nearrow u_j(\vec{r},t)][z_i(t) \nearrow z_j(t)] \;\; \mathrm{xp}(\frac{-||\Delta\vec{r}||^2}{2\delta^2})}{\sum_{j=1}^{N} [z_i(t) \nearrow z_j(t)]^2 \;\; \mathrm{xp}(\frac{-||\Delta\vec{r}||^2}{2\delta^2})}, \tag{1}$$

where $u_i(\vec{r},t)$ is the velocity of the grain i and $||\Delta\vec{r}|| = \sqrt{[z_i(t) \nearrow z_j(t)]^2 + [x_i(t) \nearrow x_j(t)]^2}$ denotes the distance between the grains i and j. δ is the coarse-graining length, typically on the order of the grain size d.

We also study the different contributions to energy dissipation as well as the grain coordination number, in order to eventually draw a diagram separating a region where the grains flow in a liquid-like manner and another where their behavior is more akin to solid-like plasticity.

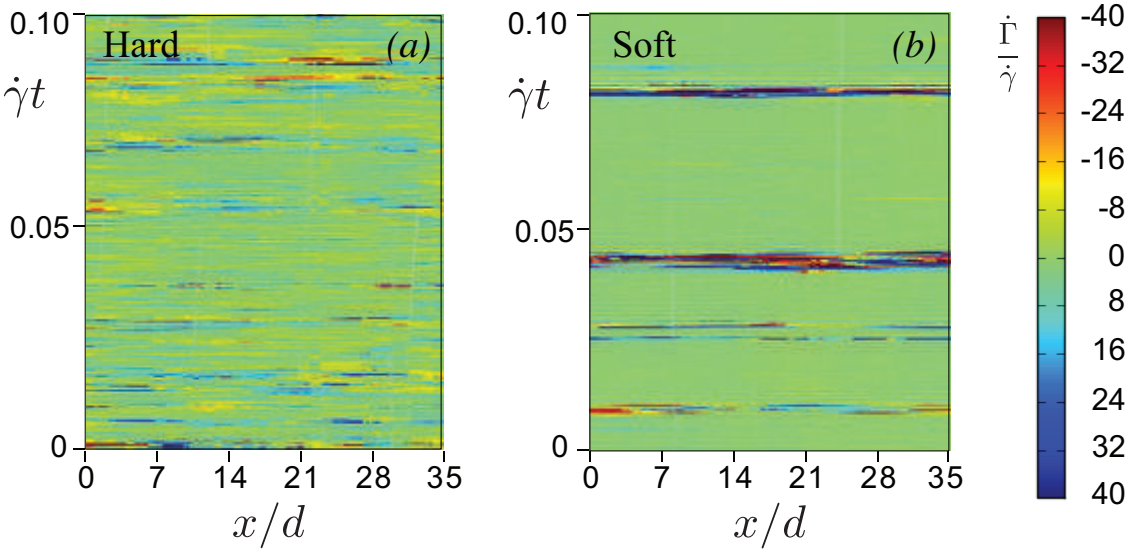

Figure 1: *Space-time diagrams showing the local contribution of* $\dot{\mathrm{y}}$ *to the shear rate* $\dot{\gamma}$*, measured on the central line of the cell, for a system of sheared hard* (a) *and soft* (b) *grains. For this example, the ratio of the grain contact stiffness* k_n *to the overall pressure* P *is* 2.10^4 *and* 10 *respectively; the shear rate corresponds to an inertial number* $I = 5.10^{-4}$*. Color code from blue (*$\dot{\mathrm{y}} = \nearrow 0\dot{\gamma}$*) to red (*$\dot{\mathrm{y}} = \;\; 0\dot{\gamma}$*).*

References

[1] GDR MiDi : On dense granular flows. Eur. Phys. J. E **14**, 341 2004.

[2] Jop P., Forterre Y., Pouliquen O. : A constitutive law for dense granular flows. Nature. **441**, 727 2006.

[3] Boyer F., Guazzelli E., Pouliquen O., Phys. Rev. Lett. **107**, 188301 2011.

[4] Trulsson M., Andreotti B., Claudin P. : Unifying Suspension and Granular Rheology. Phys. Rev. Lett. **109**, 118305 2012.

[5] Trulsson M., Bouzid M., Claudin P., Andreotti B. : Dynamic compressibility of dense granular shear flows. Europhys. Lett. **103**, 38002 2013.

[6] Reddy K.A., Forterre Y., Pouliquen O. : Evidence of Mechanically Activated Processes in Slow Granular Flows. Phys. Rev. Lett. **106**, 108301 2011.

[7] Bouzid M., Trulsson M., Claudin P., Clément E., Andreotti B. : A non-local rheology for granular flows across yield conditions. Phys. Rev. Lett. **111**, 238301 2013.

[8] Bouzid M., Izzet A., Trulsson M., Claudin P., Clément E., Andreotti B. : Non-local rheology in dense granular flows. Europhys. Lett. **109**, 24002 2015.

THE ROLE OF THE PARTICLE STRESS IN THE SIMULATION OF FLUIDIZED BEDS

Mohammad Reza Haghgoo*[1], Donald J. Bergstrom[1], and Raymond J. Spiteri[2]

[1]*Mechanical Engineering, University of Saskatchewan, Saskatoon, Saskatchewan, Canada*
[2]*Computer Science, University of Saskatchewan, Saskatoon, Saskatchewan, Canada*

Summary A two-fluid model based on the kinetic theory of granular flow, for the rapid-flow regime, and the Coulomb friction law, for the slow-plastic regime, is applied to predict the hydrodynamics of dense gas-particle flow in a large-scale three-dimensional fluidized bed. Two different models for the particle stress tensor, in the elastic-inertial regime, are examined to assess their ability to predict the dynamics of the bed. The numerical results are validated against published experimental data and demonstrate the significance of the stress tensor in the elastic-inertial regime. Different flow regimes are identified, in the context of fluidized beds, through the dimensionless Inertial number and the main characteristics of each regime are discussed to better understand the complex dynamics of fluidized beds.

INTRODUCTION AND NUMERICAL MODELING

Fluidization of a dense system of particles by a fluid is widely employed in industry for processes involving drying, separation, and mixing of particles and chemical reactions. In turbulent fluidized beds, where the interstitial fluid plays a significant role in the dynamics of the system, the major challenge is to model the complicated interaction of particles and the turbulence of the fluid. In such systems, the granular particles rarely reach a volume fraction where the friction between particles starts to play a role, i.e., ε_p^{min}. Consequently, the particle stress tensor can be described by the kinetic theory of granular flows. However in bubbling fluidized beds, where the turbulence of the fluid, if any, is damped by the inertia of the particles, not only does the particle volume fraction reach to ε_p^{min}, but it is also very likely to succeed the packed bed limit, i.e., ε_p^{max}. Therefore in bubbling beds, in addition to the rapid flow regime, a quasi-static slow regime is likely to happen. Obviously, there are some regions in the bed where the granular flow undergoes a transient regime that is neither rapid nor slow in nature. Accordingly, in modeling of bubbling beds, the main challenge is to have a comprehensive model that is able to distinguish the different behaviors of the granular flow under each regime and appropriately describe the stresses.

The two-fluid model along with the constitutive relations from [1] are used to simulate an isothermal gas-particle system. There is no general consensus in modeling the stresses in dense regions where there is sustained contact between particles. In one approach, referred to as the Schaeffer model in the literature, Syamlal et al. [1] proposed that frictional stresses need to be considered only for regions where the solid volume fraction is higher than the maximum packing limit, ε_p^{max}. On the other hand, Srivastava and Sundaresan [3] proposed another model, referred to as the Princeton model, that adds the frictional stress to the kinetic-collisional stress tensor in the intermediate regime. Note that both the Princeton and Schaeffer models use the same granular rheology for the rapid and slow regimes.

The height of the simulated bed is 160 cm with a diameter of 30.6 cm. The air is injected at the very bottom of the bed at a velocity of 63 cm/s. All simulations were performed in parallel using 60 cores. The first 10 seconds of the fluidization process is simulated. The numerical code Multiphase Flow with Interphase eXchanges (MFIX) is used to perform the simulations [1]. The results are validated against published experimental data by Laverman et al. [2]

RESULTS AND DISCUSSION

Figures 1a and 1b represent the azimuthally and time-averaged axial velocity profiles for particles at three different heights. At the lowest section, there is an overall downward flow of the particles near the center and a small upward flow in the near-wall region. At the highest section, i.e., for a height of 31 cm, the particle flow is opposite. The results from using the Princeton model are closer to the experimental data than the results from using the Schaeffer model.

To understand the differences between the results predicted by each model, it is helpful to discuss the behaviour of the granular materials under different circumstances. At a large applied stress, particles deform at the contact point(s) and are compressed into the interparticle vacant space. In this quasi-static regime, the particle pressure, p, and shear stresses, τ are independent of the strain rate, $\dot{\gamma}$. In contrast, at high shear strain rates for the rapid flow regime, the momentum transport is due to the instantaneous binary collisions as well as the inertia of the interparticle motions. Therefore in this regime, the rheology of the particles is described by the coefficient of restitution and granular temperature and $p, \tau \sim \dot{\gamma}^2$. Between these two asymptotic regimes is the so called intermediate or elastic-inertial regime [4], where $p, \tau \sim \dot{\gamma}^n$, with $0.5 \leq n \leq 1$. In the rapid-flow regime, the collisions are assumed to be infinitely rigid. However, it is obvious that once a particle is in multiple contact with surrounding particles, the elastic forces do play a role in the momentum transport. Therefore, to understand and quantify the dynamics of dense gas-particle flows, it is helpful to define a dimensionless parameter whose value can help

*Corresponding author. Email: reza.haghgoo@usask.ca



(a) Princeton model (b) Schaeffer model

Figure 1: Averaged axial particle velocity profiles at different heights

identify the regime of the flow. Following da Cruz et al. [5], the Inertial number, $I = |\dot{\gamma}|d_p/(p/\rho_p)^{0.5}$ is defined to be the ratio of the inertial timescale to the macroscopic deformation timescale. For the rapid or inertial regime, I has large values on the order of unity, whereas for the quasi-static regime, I has small values in the order of 10^{-3}; values in between belong to the elastic-inertial regime. Figure 2 shows instantaneous values of the particle volume fraction, the Inertial number, and the particle viscosity in a single plane. Both models predict that the flows inside the bubbles and free-board have the largest value of I corresponding to the rapid-flow regime and, lowest value of the particle viscosity. For the regions around and between the bubbles, i.e., mostly near the center and lower part of the bed, I has moderate values, mapping the flow to the elastic-inertial regime. In these regions, the values of viscosity are also moderate. The regions in dark blue indicate slow flow corresponding to the highest values of viscosity. The slow-flow regime predicted by the Princeton model is mostly located near the wall region, whereas the Schaeffer model predicts one region above the highest bubble and another one at the height of 40 cm. Note that the extent of the regions in which the flow is elastic-inertia is considerable. However, the Schaeffer model treats these regions as a rapid flow, whereas the the Princeton model tries to improve their treatment by adding a frictional stress to the kinetic stresses. Although the Princeton model predicts a more realistic behaviour, there remains a need to introduce the elastic properties of the particles into the constitutive equations of the elastic-inertial regime.

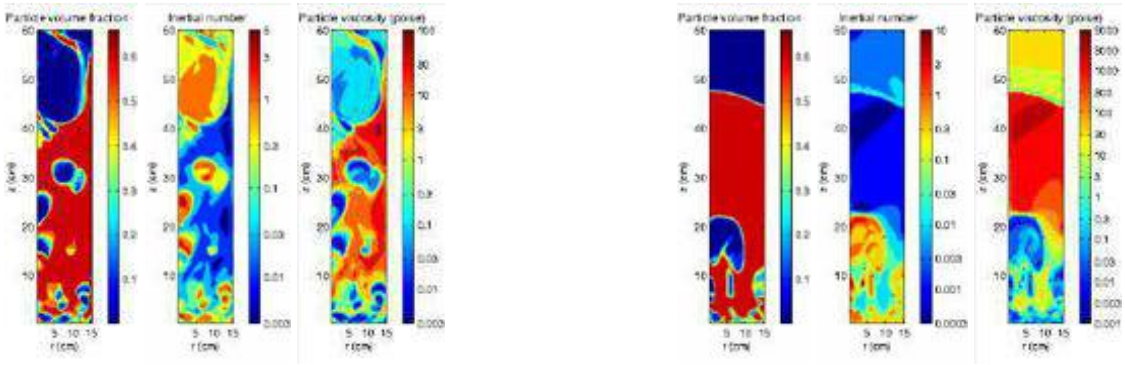

(a) Princeton model (b) Schaeffer model

Figure 2: Particle volume fraction, Inertial number, and particle viscosity at $t = 5\ s$

CONCLUSIONS

This study demonstrates the significance of the particle stress in prediction of dense gas-particle flows. It shows that the Princeton model yields more realistic results compared to the Schaeffer model because it differentiates between the rapid and intermediate regimes. Further study is required to investigate the effects of elastic collisions in the intermediate regime.

References

[1] Syamlal M., et al.: MFIX documentation: theory guide. Technical Note DOE/METC-94/1004, Morgantown Energy Technology Centre, 1993.
[2] Laverman J., et al.: Experimental study on the influence of bed material on the scaling of solid circulation patterns. Powder Technol., 224, 2012.
[3] Srivastava A., Sundaresan S.: Analysis of a frictional-kinetic model for gas-particle flow. Powder Technol.,129:72-85, 2003.
[4] Campbell, C. S.: Granular shear flows at the elastic limit. J. Fluid Mech., 465:261-291, 2002.
[5] F. da Cruz, et al.: Rheophysics of dense granular materials: discrete simulation of plane shear flows. Phys. Rev. E, 72:021309, 2005.

NUMERICAL RESEARCH ON WIND-BLOWN SAND WITH SEMI-BURIED CHECKERBOARD SAND BARRIERS BELT

Hao-jie Huang[1a)], Tian-li Bo[1] & Xiao-jing Zheng[2]
[1]*Key Laboratory of Mechanics on Environment and Disaster in Western China, Ministry of Education, Lanzhou University,Lanzhou 730000, China*
[2]*School of Electronic and Mechanical Engineering, Xidian University, Xi'an, 710071, China*

Abstract

How to inhibition the expansion of the desert edge to the oasis is a major challenge for all over the world, and laying the semi-buried checkerboard sand carriers belt is an effective way to mitigate it. An spatio-temporal development mathematical model of wind-blown sand based on the coupling of wind field and sand grain is established, by laying the semi-buried checkerboard sand carriers belt in the model, the 3D wind field of the internal and rear region of the semi-buried checkerboard sand barriers belt, the sand streamer and sand flux of the sand-laden wind-blown sand, and grain-sand barriers-wind field interaction law are investigated. The results show that the semi-buried checkerboard sand carriers belt has an effect on the mean velocity, turbulence intensity and other turbulence statistics which helps us to establish the theoretical foundation for the effective control of expansion of the desert edge.

Introduction

In general, researchers have tried different ways to study the interaction of saltation particles with the wind field and reveal particle influence on the turbulent characteristics, especially turbulence modification in the internal and rear region of the semi-buried checkerboard sand barriers belt. Obviously, inhibition the expansion of the desert edge to the oasis is always an open-ended question, disputed question is more evidence the challenge. And it forces us to carry forward the real 3D wind-blown sand simulation with the semi-buried checkerboard sand carriers belt, and focus on the influence of saltation particles on the turbluenc characteristics which helps us to cognize the nature of desertification.

Model and Equations

Using the large eddy simulation method in ARPS, the momentum equation of 3D N-S equation after filted is:

$$\frac{\partial \tilde{u}_i}{\partial t}+\tilde{u}_j\frac{\partial \tilde{u}_i}{\partial x_j}=-\frac{1}{\overline{\rho}_f}\frac{\partial}{\partial x_i}(\tilde{p}-\nu\frac{\partial \overline{\rho}_f\tilde{u}_j}{\partial x_j})-\frac{\partial \tau_{ij}}{\partial x_j}-\delta_{i3}g(\frac{\tilde{\theta}}{\overline{\theta}}-\frac{c_p}{c_v}\frac{\tilde{p}}{\overline{p}})+\frac{F_i}{\overline{\rho}_f} \qquad (1)$$

Where, i = 1, 2 and 3 correspond to the streamwise, spanwise and wall-normal directions (i.e., $x_1=x,\ x_2=y,\ x_3=z, u_1=u,\ u_2=v, u_3=w$), respectively; $\tilde{u}_i$, $\tilde{p}$ and $\tilde{\theta}$ represent the filtered wind speed, pressure and potential temperature, respectively; v is a damping coefficient meant to attenuate acoustic waves; ρ_f is the air density; g is the acceleration of gravity; F_i is the feedback force of sand particles; $\delta_{ij}=1$ if $i=j$, otherwise $\delta_{ij}=0$; $\tau_{ij}=u_iu_j-\tilde{u}_i\tilde{u}_j$ are the sub-grid-scale (SGS) stresses [1]; c_p and c_v are the specific heat of air at constant pressure and volume, respectively.

In order to solve above equations, the SGS stresses can be closed as follows:

$$\tau_{ij}-\frac{1}{3}\tau_{kk}\delta_{ij}=-\nu_t(\frac{\partial \tilde{u}_i}{\partial x_j}+\frac{\partial \tilde{u}_j}{\partial x_i}) \qquad (2)$$

Where $\nu_t=(C_{sgs}\Delta)^2\frac{1}{\sqrt{2}}\left|\frac{\partial \tilde{u}_i}{\partial x_j}+\frac{\partial \tilde{u}_j}{\partial x_i}\right|$ is the turbulent viscosity of SGS; Δ is the grid scale; C_{sgs} depends on the Germano subgrid-scale closure method [2,3].

And, the particle movement equation of three direction can be expressed as:

$$m_p\frac{d^2x}{dt^2}=F_{Dx}=\frac{C_D\pi D^2\rho_f}{8}(\tilde{u}-\frac{dx}{dt})^2 \qquad (3)$$

a) Corresponding author. Email: huanghj13@lzu.edu.cn

$$m_p \frac{d^2 y}{dt^2} = F_{Dy} = \frac{C_D \pi D^2 \rho_f}{8} (\tilde{v} - \frac{dy}{dt})^2 \quad (4)$$

$$m_p \frac{d^2 z}{dt^2} = -F_g + F_{Dz} = -\frac{\pi \rho_p D^3}{6} + \frac{C_D \pi D^2 \rho_f}{8} (\tilde{w} - \frac{dz}{dt})^2 \quad (5)$$

Where m_p is the mass of sand particles; $C_D = (0.63 + 4.8 / \mathrm{Re}_p^{0.5})^2$ is the drag coefficient of sand particles [4]; ρ_p and ρ_f are the density of sand particles and air respectively; $\mathrm{Re}_p = (V_f \rho_p D / \mu)[(\tilde{u} - dx/dt)^2 + (\tilde{v} - dy/dt)^2 + (\tilde{w} - dz/dt)^2]^{1/2}$ is the particle Reynolds number; $V_f = 1 - \sum_{k=1}^{k=n} V_P / \Delta V$ is the bulk fraction which is the total sand volumes within grid to the bulk of unit grid; ΔV is the bulk of unit grid; μ is the kinetic viscosity coefficient of air.

The whole computational regions see Figure 1.

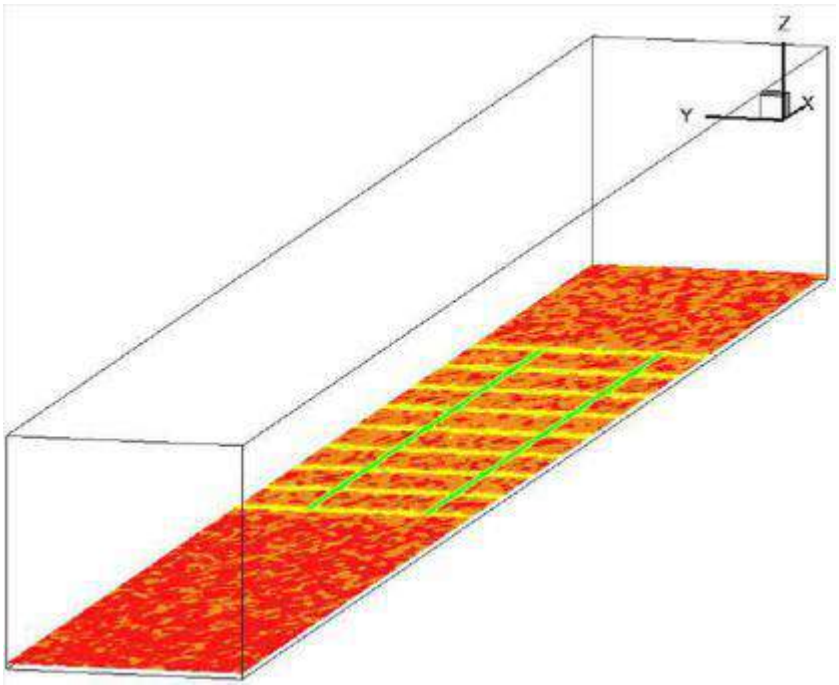

Figure 1. Schematic diagram of wind-blown sand with the semi-buried checkerboard sand barriers belt.

Preliminary Result

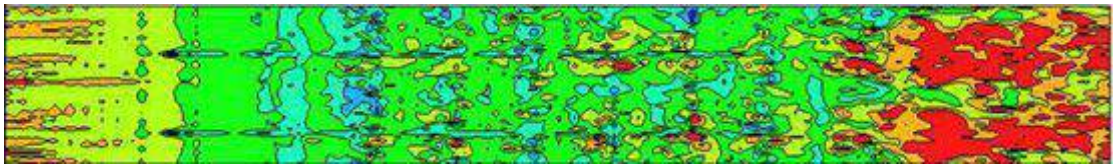

Figure 2.streamwise velocity with the semi-buried checkerboard sand barriers belt

References

[1] Smagorinsky J. General circulation experiments with the primitive equations: I. the basic experiment*[J]. Monthly weather review, 1963, 91(3): 99-164.

[2] Germano, M., Piomelli, U., Moin, P. & Cabot, W. 1991 A dynamic subgrid-scale eddy viscosity model. Phys. Fluids A 3, 1760-1765.

[3] Lilly, D. K. 1992 A proposed modification of the Germano subgrid-scale closure method. Phys.Fluids A 4, 633-635.

[4] Cheng N S. Simplified settling velocity formula for sediment particle[J]. Journal of hydraulic engineering, 1997, 123(2): 149-152.

A CONSTANT HEAT FLUX BOUNDARY CONDITION FOR CFD-DEM SIMULATIONS

Aaron M. Lattanzi[1], Christine M. Hrenya[1,*]
[1] University of Colorado at Boulder, Dept. of Chemical and Biological Engineering, Boulder, CO, USA

Summary The modeling of multiphase flows with a constant heat flux boundary is of great practical and fundamental significance. Assessing the feasibility of a unit operation often requires the prediction of wall temperature gradients, which can induce mechanical failure if they become too large. A numerical technique for modeling such a boundary condition (BC) is proposed for gas-solids flows, and directly applied within a computational fluid dynamics and discrete element method (CFD-DEM) software. This same technique can be extended to polydisperse systems and the two-fluid model.

Computational Methodology

All simulations were performed via MFIX, an open-source software developed by the U. S. National Energy Technology Laboratory for multiphase flows. Specifically, the hydrodynamics and heat transfer of a gas and monodisperse solids were modeled with the CFD-DEM framework within MFIX. The governing equations pertinent to heat transfer are outlined below for both phases.

The gas phase is treated as a continuum via the following thermal energy balance [1]:

$$\frac{\partial}{\partial \mathrm{t}}\left(\varepsilon_g \rho_g C_{p,g} T_g\right) + \mathbf{v_g} \cdot \nabla\left(\varepsilon_g \rho_g C_{p,g} T_g\right) = -\nabla \cdot \mathbf{Q"_g} - \sum_{\mathrm{i}=1}^{\mathrm{n}} h_{g,s,i}\left(T_g - T_{p,i}\right) \quad \textbf{(1)}$$

where ε_g is the gas fraction, ρ_g is the gas density, $C_{p,g}$ is the gas specific heat, T_g is the (thermal) gas temperature, $T_{p,i}$ is the temperature of particle i, n is the number of particles within a fluid cell, $h_{g,s,i}$ is the interphase heat transfer coefficient for particle i, $\mathbf{Q"_g} = -\varepsilon_g K_g \nabla T_g$ is the gas heat flux, and K_g is the gas thermal conductivity.

In contrast to the continuum representation of the gas phase, the solid phase is treated as discrete particles via DEM. The time evolution of each particle property takes the form of an initial value problem. Since the time step for numerical integration must be smaller than the duration of a collision (soft-sphere method), the DEM time step is generally orders of magnitude smaller than the continuum time step; i.e., the DEM solver completes many time steps per one continuum solver (CFD) time step. With regard to heat transfer, radiation is not considered and thus the resulting conductive and convective mechanisms under consideration are: particle-particle (PP) conduction, particle-fluid-particle (PFP) conduction, particle-wall (PW) conduction, particle-fluid-wall (PFW) conduction, and interphase convection. The resulting governing equation for the internal energy of a particle is [3]:

$$m_{p,i} C_{p,i} \frac{\partial}{\partial \mathrm{t}}\left(T_{p,i}\right) = \sum_{\mathrm{j}} \left(\dot{Q}_{i,j}^{PP} + \dot{Q}_{i,j}^{PFP}\right) + \dot{Q}_i^{PW} + \dot{Q}_i^{PFW} + h_{g,s,i}\left(T_g - T_{p,i}\right) \quad \textbf{(2)}$$

where $m_{p,i}$ is the mass of particle i, $C_{p,i}$ is the specific heat of particle i, $\dot{Q}_{i,j}$ is the heat flow between particle i and particle j, and $\dot{Q}_i$ is the heat flow between particle i and a wall. Since the aim of this work is directed at a new boundary condition for use in CFD-DEM simulations, only the mechanisms pertaining to heat transfer with a wall ($\dot{Q}_i^{PW}$ and $\dot{Q}_i^{PFW}$) will be of significance. Rigorous treatments of the PW [2] and PFW [4] mechanisms provide closures for individual particle heat transfer coefficients ($h_{pw,i}$ and $h_{pfw,i}$).

Development of Heat Flux Boundary Condition

When considering a constant heat flux wall BC for multiphase flows, the current state-of-the-art is for a constant flux to *each phase* be specified. Practically speaking, it is often the *total* wall flux which remains constant, while the flux to each phase can vary. For the latter case of a constant total heat flux at the wall, we assume here that all phases experience the same wall temperature and that the heat transfer to each phase occurs in parallel. Therefore, the wall heat flux can be written as a sum of the heat fluxes to each phase, which may vary with time and space ($Q"_w = Q"_g(\mathbf{x}, t) + Q"_s(\mathbf{x}, t)$). Note that the solution for the internal energy of the fluid at the wall yields a single temperature over the numerical cell. To describe the heat transfer of a discrete particle, the wall temperature used for the particle heat transfer is dictated by the fluid cell it resides in (i.e., wall temperature gradients smaller than the fluid cell and arising from the discrete nature of the particles cannot be resolved within a fluid cell). Therefore, the heat flux to the gas phase and solid phase must be given in terms of continuum variables (on a fluid grid basis). For the gas, the flux in terms of continuum variables is readily available ($-\varepsilon_g K_g \nabla T_g$). However, the heat flux to each particle is resolved in DEM. Since the size of a particle is much smaller than the size of a CFD fluid cell, the continuum analog is the average solids heat flux across the fluid cell wall on the boundary:

$$\overline{Q"_s}(\mathbf{x},t) = \frac{1}{mA_c}\sum_{j=1}^{m}\sum_{i=1}^{k_j} H_{s,i}\left(T_w - T_{p,i}\right) = /T_w A - B/// \tag{3}$$

$$A = \sum_{j=1}^{m}\sum_{i=1}^{k_j}\frac{H_{s,i}}{mA_c} ////// B = \sum_{j=1}^{m}\sum_{i=1}^{k_j}\frac{H_{s,i}}{mA_c}T_{p,i} ////// H_{s,i} = h_{pfw,i} + h_{pw,i} \tag{4}$$

where m is the number of DEM time steps within a continuum time step, A_c is the area of the fluid cell plane, k_j is the number of particles undergoing heat transfer in a given DEM time step, T_w is the continuum wall temperature, and $H_{s,i}$ is the total particle-wall heat transfer coefficient. By summing the closures for the heat fluxes ($Q"_w = -\varepsilon_g K_g \nabla T_g \cdot N + T_w A - B$) and discretizing, a Robin type (mixed) BC which couples the phases and satisfies the assumed description of a constant heat flux wall BC is found.

$$\frac{\left(T_{g,i} - T_{g,i-1}\right)}{dx_i} + \frac{A}{\varepsilon_g K_g}T_{g,i-1/2} = \frac{Q"_w + B}{\varepsilon_g K_g} \tag{5}$$

Results

Simulations were completed on four vertical heat exchangers with internal baffles, a constant mass inflow at the top, and constant wall heat fluxes. Wall temperature predictions from the simulations are consistent with qualitative expectations. Areas with high solids concentrations near a wall, and thus high solids heat transfer coefficients, result in low wall temperatures (Figure 1 (a) below). As evidence that the physical description for the BC is upheld, the heat flux data for the first configuration (far left) is given in more detail. Namely, the heat fluxes are extracted along the height of the right domain wall. The simulated wall flux is nearly constant along the column wall and the contribution from each phase changes. A close inspection shows that the oscillations in the solids heat flux correspond to baffle positions, and that they are out of phase with oscillations in the gas heat flux (i.e., the boundary conditions for each phase are coupled).

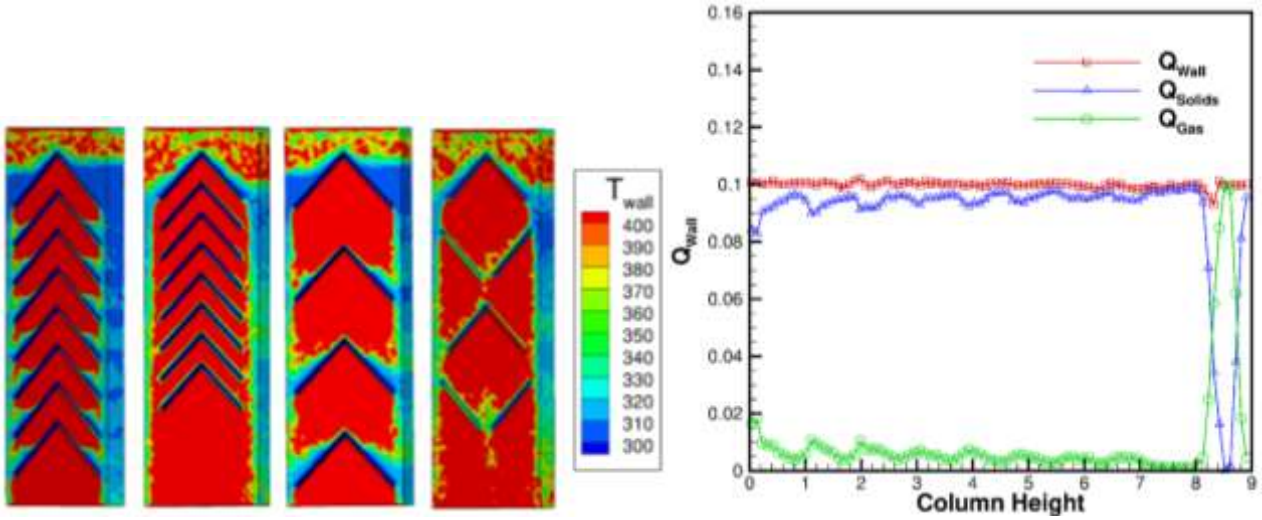

(a) (b)

Figure 1. The temperature [K] profile (a) and extracted heat flux [cal/cm^2s] data (b).

References

[1]Anderson, T.B., and Jackson, R., (1967), "A Fluid Mechanical Description of Fluidized Beds," *Ind. Eng. Chem. Fundamen.*: 527-534.

[2]Batchelor, G. K., and R. W. O'brien, (1977), "Thermal or Electrical Conduction Through a Granular Material," Proceedings of the Royal Society A: Mathematical, *Physical and Engineering Sciences*: 313-33.

[3]Morris, A. B., S. Pannala, Z. Ma, and C. M. Hrenya, (2015), "A conductive Heat Transfer Model for Particle Flows Over Immersed Surfaces," *International Journal of Heat and Mass Transfer: 1277-1289*.

[4]Rong, D. and Horio, M., (1999), "DE simulation of char combustion in a fluidized bed," Second International Conference on CFD in the Minerals and process Industries: 65-70.

POST-FAILURE ANALYSIS OF SLOPE BY SMOOTHED PARTICLE HYDRODYNAMICS

Hideto Nonoyama[1a)] & Yoshihisa Miyata[1)]
[1]*Department of Civil and Environmental Engineering, National Defense Academy, Yokosuka, Kanagawa, Japan*

Summary Assessment of slope stability is a fundamental and important problem. Analysis method to judge the stability has been well developed by application of computational mechanics. Based on this judgment, various geotechnical countermeasure are examined. However the development of analysis on post failure has not been discussed enough. This type analysis is require to predict the large deformation and to consider non-linear material properties. This research investigate applicability of Smoothed Particle Hydrodynamics (SPH) for the analysis. This paper show the results for simple cases. As the result, SPH is useful for analysis post-failure deformation of slope.

INTRODUCTION

Assessment of slope stability is a fundamental and important problem. Analysis method to judge the stability has been well developed by application of computational mechanics. Based on this judgment, various geotechnical countermeasure such as earth reinforcement, control of drainage, and treatment of slope surface, etc. are examined. However the development of analysis on post failure has not been discussed enough. If we can predict how far or how fast collapsed soil moves or how much the soil deform after the collapse, we can easily make plans to save the human life and to re-assessment of the collapse slope. This type analysis is require to predict the large deformation and to consider non-linear material properties. This research investigate applicability of Smoothed Particle Hydrodynamics (SPH) for the analysis. This paper examines outline of the analysis method and show the results for simple cases. The authors will emphasize usefulness of SPH to analysis post-failure deformation of slope.

OUTLINE OF ANALYSIS

Smoothed Particle Hydrodynamics for slope stability analysis

The governing equations used in this study are based on solid mechanics. The equations of continuity and motion can be expressed as follows (Nonoyama et al., 2015),

$$\frac{d\rho}{dt} = -\rho \frac{\partial u_i}{\partial x_i} \tag{1}$$

$$\frac{du_i}{dt} = \frac{1}{\rho}\frac{\partial \sigma_{ij}}{\partial x_j} + F_i \tag{2}$$

where u_i is the velocity vector, ρ is the density, σ_{ij} is the stress tensor and F_i is the external force vector. Applying the SPH interpolation, the governing equations can be written as

$$\frac{d\rho^\alpha}{dt} = -\sum_\beta^N m^\beta \left(u_i^\beta - u_i^\alpha\right)\frac{\partial W^{\alpha\beta}}{\partial x_i} \tag{3}$$

$$\frac{du_i^\alpha}{dt} = \sum_\beta^N m^\beta \left(\frac{\sigma_{ij}^\alpha}{{\rho^\alpha}^2} + \frac{\sigma_{ij}^\beta}{{\rho^\beta}^2} + C_{ij}^{\alpha\beta} \right)\frac{\partial W^{\alpha\beta}}{\partial x_j} + F_i^\alpha \tag{4}$$

where C_{ij} is the sum of the artificial viscosity term (Monaghan and Gingold, 1983) and the artificial stress term (Gray et al., 2001). Bui et al. (2011) is a pioneer achievement in the area.

Analysis case

A great achievement of classical soil mechanics for slope assessment is the stability chart (ex., Janbu, 1954). Using the chart, we can judge the slope stability by using geometric information of the slope, strength and unit weight of the soil. By leaning this, we set the analysis cases. Typical analyzed case is shown in Fig.1. For each geometric condition of the slope, a series of analysis was performed by changing un-drained strength of soil. Then, analyzed deformation was normalized by height of slope and the results was shown as similar as the classical stability chart for slope. On the deformation, maximum depression of the top surface, horizontal movement of the slope surface and uplift deformation of the base foundation.

[a)] Corresponding author. Email: nonoyama@nda.ac.jp

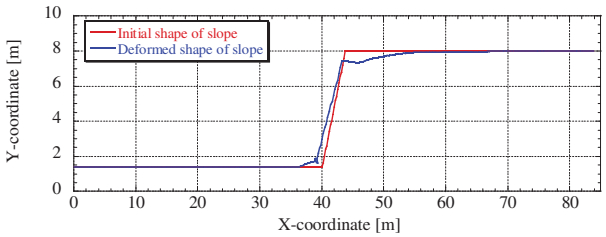

Fig.1 Analysed case (*Fs*=0.95)

RESULTS AND DISCUSSION

Relationship between normalized deformations and slope angle are shown in Fig.2 (a)-(c). Where, safety factor in each figure is the ratio of stability number of critical case and analysis case. Except vertical slope, effect of geometry of slope is relatively small. The safety factor of analysis case, that is soil strength, has most influence to the slope stability. Simulated geometry and shear strain distribution for typical case are shown in Fig.3 (a)-(c). Position of localization is always at the toe of slope and wideness of shear zone depends the safety factor.

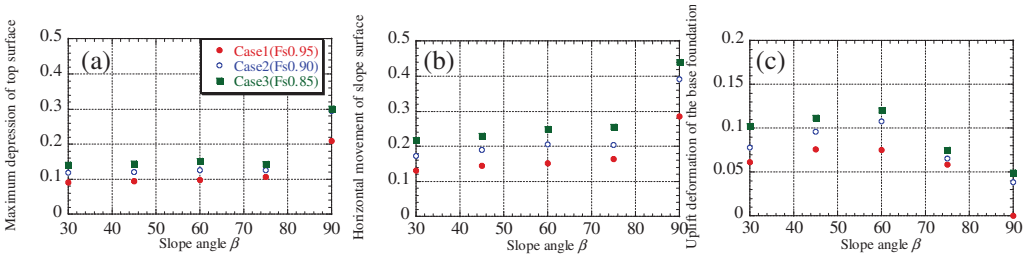

Fig.2 Relationship between normalized deformations and slope angle

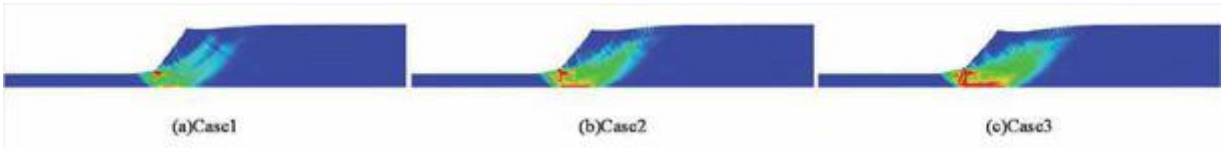

Fig.3 Simulated geometry and shear strain distribution

CONCLUSIONS

SPH is useful for analysis post-failure deformation of slope. The analysis may useful to predict the deformation by considering site condition such as complicated geometry and strength distribution. And it should be also powerful tool to develop the new safety chart defined by the post-failure deformation.

References

[1] Nonoyama, H., Moriguchi, S., Sawada, K. and Yashima, A.: Slope stability analysis using smoothed particle hydrodynamics (SPH) method. *Soils and Foundation* **55**(2):458-470, 2015.

[2] Monaghan, J.J. and Gingold, R.A.: Shock simulation by the particle method SPH. *J. Comput. Phys.* **52**,374-389, 1983.

[3] Gray, J.P., Monaghan, J.J. and Swift, R.P.: SPH elastic dynamics. *Comput. Methods Appl. Mech. Eng.* **190**,6641-6662, 2001.

[4] Bui, H.H., Fukagawa, R., Sako, K. and Wells, J.C.: Slope stability analysis and discontinuous slope failure simulation by elasto-plastic smoothed particle hydrodynamics (SPH). *Geotechnique* **61**(7),565-574, 2011.

[5] Janbu, N.: Stability Analysis of Slopes with Dimensionless Parameters. *Soil Mechanics Series* No.46, Harvard University, January, 81p, 1954.

RIPPLE FORMATION IN A LIBRATING CYLINDER FILLED WITH FLUID

Veronika Dyakova, Victor Kozlov, and Denis Polezhaev *
Laboratory of Vibrational Hydromechanics, Perm State Humanitarian Pedagogical University, Perm, Russia

Summary The dynamics of granular medium in filled with fluid librating horizontal cylinder is experimentally studied. When the cylinder rotated sufficiently rapidly, the granular medium develops the annular layer near the cylindrical wall. The interface between fluid and sand is smooth and axisymmetric. Librations of the cylinder provoke the appearance of quasi-steady relief on the sand surface in the form of regular dunes with crests oriented parallel to the axis of rotation. It is found, that the threshold of ripple formation is determined by the dimensionless librational amplitude. In the supercritical domain, the existence of azimuthal drift of dunes is revealed. Dependently on experimental conditions, the dune migration can be directed either parallel or anti-parallel with respect to the cylinder rotation.

The longitudinal libration corresponds to periodic oscillations of the rotation rate of a rotating body: $\Omega = \Omega_r + \varphi_0 \Omega_l \cos \Omega_l t$, here Ω_r is the mean rotation rate, φ_0 is the amplitude of libration, and Ω_l is the angular libration frequency. Despite the fact that librations are time-dependent, it has been proved that they can generate a steady axisymmetric flow in the liquid interior through the Ekman boundary layer [1]. Thus, in the rotating frame, the fluid undergoes oscillations superimposed on steady rotation. This flow is similar to the motion of annular fluid layer with free surface inside a rapidly rotating horizontal cylinder [2], where fluid oscillations and steady streaming are generated by gravitational force. The oscillatory flow is found to be responsible for the onset of regular dunes with crests oriented parallel to the axis of rotation. In nature, the qualitatively similar fluid flow is in the near shore waters. Surface waves near shore waters provoke the onset of quasi-stationary relief and bring ripples to the continuous drift. We first report experimental results for the stability of liquid – granular medium interface and supercritical dynamics of migrating dunes in a librating horizontal cylinder.

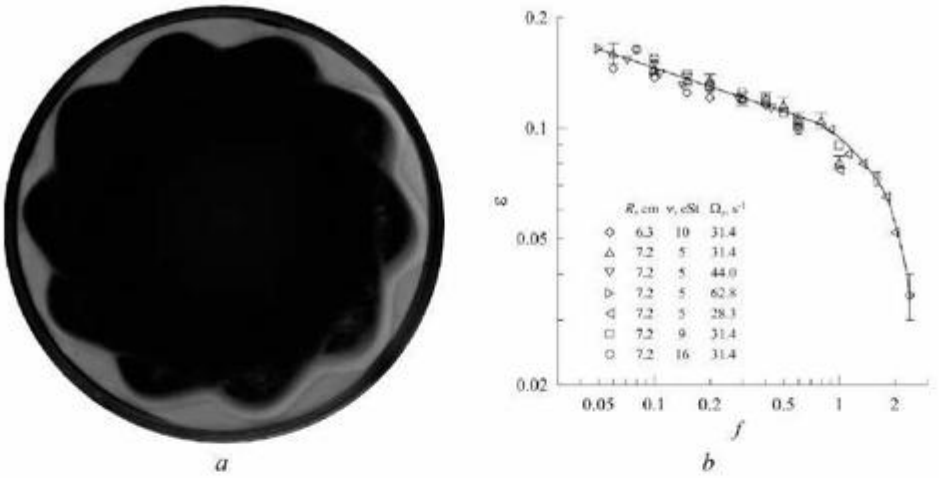

Figure 1. Regular dunes inside a librating cylinder (front view): $f = 0.40$, ϵ = 0.163; the cylinder rotates anti-clockwise (*a*). Dependence of dimensionless libration amplitude ϵ on dimensionless frequency f at the threshold of the onset of quasi-steady relief (*b*)

The experiments are carried out in the a hollow transparent cylinder of inner radius R = 6.3 or 7.2 cm and corresponding length L = 7.8 or 2.2 cm. The cylinder is filled with water-glycerol solution (ν = 5 – 16 cSt) and seeded with glass spheres of density 2.5 g/cm^3. The experiments are carried out with particles, which diameter d varies in the 0.02 ± 0.01 cm range. The mass of granular medium is equal to 80 g in the cylinder of length L = 2.2 cm and 200 g in the cylinder of length L = 7.8 cm.

The cylinder is coupled to the stepper motor which provides rotation with a mean angular velocity Ω_r up to 75 s^{-1}. The radian frequency Ω_l of the cylinder oscillations is chosen between 2 and 75 s^{-1}. In terms of dimensionless numbers, we have explored the following ranges: the ratio between the libration frequency and rotation rate $f \equiv \Omega_l / \Omega_r \in [0.05; 2.5]$ and the dimensionless libration amplitude $\epsilon \equiv \varphi_0 f \in [0; 0.5]$.

*Corresponding author. Email: polezhaev@pspu.ru

While the horizontal cylinder is stationary, the granular medium is at rest at the bottom of the cylinder. When the cylinder rotates with a low to moderate angular velocity its rising side drags out spherical particles from the bottom. After a few revolutions, a concentrated almost uniform suspension of glass spheres in rotating low-viscosity fluid originates. Inside a rapidly rotating cylinder, the annular granular layer develops. In the absence of librations, fluid and granular medium undergo a solid body rotation, and the interfacial surface is axisymmetric. Librations of the cylinder initiate the azimuthal oscillations of the fluid near the granular medium, and the initially axisymmetric interface between fluid and granular medium becomes unstable to the growth of quasi-steady relief (Fig. 1*a*).

According to the observations, the onset of regular dunes is determined by dimensionless libration amplitude: the threshold value of ϵ obtained at different values of Ω_r, Ω_l, and ν favourably agree with each other in the plane f, ϵ (Fig. 1*b*). In the limit $f \ll 1$, experimental data obey the law $\epsilon \sim f^{-1/6}$.

The spatial period of dunes is determined by the amplitude of fluid oscillations: relative period $\lambda/(\varphi_0\epsilon) \sim \varphi_0^{-1.2}$, where λ is the angular distance between two successive dunes. It has also been found that the ripples are flattened off at $\epsilon > 0.5$.

In the supercritical regime, the existence of azimuthal migration of dunes is revealed. Noteworthy, the direction of dune migration is parallel or anti-parallel to the steady rotation. In near-threshold region, dunes migrate in the direction of steady rotation. The increase of ϵ is followed by deceleration of drift and further transition to the reverse migration. Typical migration rate is a few degrees per minute.

The work is supported by Grant 14-11-00476 of the Russian Scientific Foundation.

References

[1] Noir, J., Calkins, M.A., Lasbleis, M., Cantwell, J., and Aurnou, J.M. Physics of the Earth and Planetary Interiors. 2010. 182(1). 98-106.

[2] Dyakova, V., Kozlov, V., and Polezhaev, D. Shock and vibration. 2014.

CONTINUUM DESCRIPTION OF SIRMAS-RADULESCU SHOCK WAVE INSTABILITY IN DISSIPATIVE GASES

Nick Sirmas*[1] and Matei Radulescu[1]

[1]*Department of Mechanical Engineering, University of Ottawa, Ottawa, Ontario, Canada*

Summary Euler and Navier-Stokes simulations are performed to look at the problem of piston driven shock waves through granular gases undergoing viscoelastic collisions. The shock structure predicted by the continuum formulation is found in good agreement with the structure obtained by MD. Introducing strong perturbations to the incoming density field, in accordance with the spacial fluctuations in the upstream state seen in MD, yields similar instabilities as those observed in MD. While the inviscid model predicts a highly turbulent structure from these perturbations, the inclusion of diffusive terms yields comparable pattern formations to those resulting from MD.

INTRODUCTION

Shock waves driven through granular media have been shown to become unstable. For example, experiments have identified unstable formations of finger-like jets in granular media dispersed by shock waves driven through air [1]. Similar formations are observed for granular media that is subjected to a vertically oscillating bed [2]. The complex dynamics involved in these past configurations have prevented the authors to clearly identify the mechanisms controlling the instability.

To address this problem we previously developed a Molecular Dynamics (MD) model to look at the classical problem of a piston propagated shock wave into a system of 2D particles [3]. Particles were assumed to be smooth disks that collide inelastically if the impact velocity of binary collisions exceeded some threshold, which is a simple treatment for viscoelastic collisions. By allowing for finite dissipation within the shock wave, instabilities were found in the form of distinctive high density non-uniformities and convective rolls within the shock structure.

The present study looks for the conditions that such a shock structure and instability can be recovered at the continuum level. Specifically, we investigate the role that diffusion and rarefied effects have on the shock wave. This is done by modelling the problem via the Euler and Navier-Stokes (N-S) equations for a granular gas, and introducing perturbations in the flow field to account for statistical fluctuations.

MODELLING DETAILS

The model involves a piston propagating into a system of disks at velocity u_p. Smooth discs collide inelastically with a constant coefficient of restitution ε if the impact velocity of two colliding disks exceeds some threshold u^*. In the present study we only look at the dilute regime, with the initial packing fraction of disks $\eta = N\pi d^2/A = 0.012$, where N is the number of disks, d is the particle diameter, and A is the area of the domain.

We solve the N-S and Euler equations for a 2D granular gas [4] with the software package *MG*, courtesy of Sam Falle (University of Leeds). The transport coefficients from Jenkins and Richman [5] are used and the energy sink term accounting for inelastic collisions, present in both the Euler and N-S descriptions, has been modified to include u^*, taking the form:

$$\zeta^* = \nearrow\!\!\!

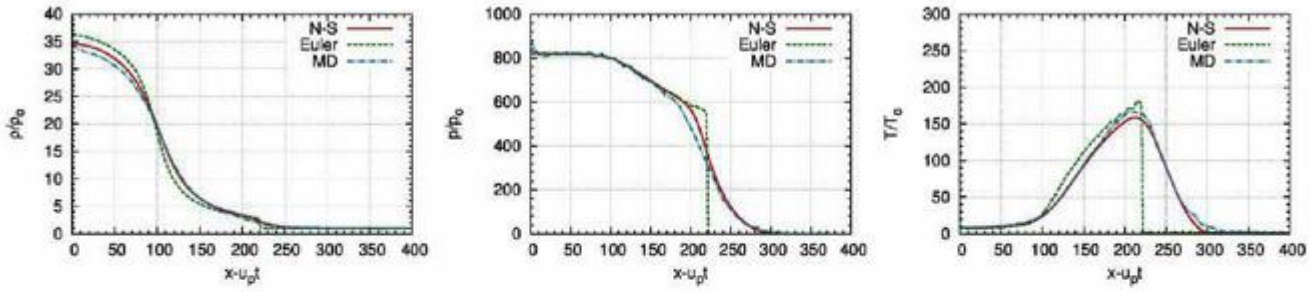

(a) Density (b) Pressure (c) Temperature

Figure 1: Distributions of density, pressure, and temperature in the piston frame of reference obtained from MD, N-S, and Euler simulations, where $u_p/u^* = 2.0$, $u^*/u_{rms(o)} = 10$, and $\varepsilon = 0.95$. Length scales are normalized by disk diameter d.

The 2D structure is obtained from Euler and N-S simulations with incoming density perturbed in accordance with (2). Figure 2 shows the morphology of density for the case considered in Fig. 1. For this case, the N-S results are in good agreement with the overall structure seen in MD, recovering the same wavelength and amplitude of pattern formations at the piston face. The inviscid solution yields a chaotic structure extending from the piston, however the bulk spacing of features is similar to what we see from MD and N-S. Similar results are also observed for varying u_p and ε.

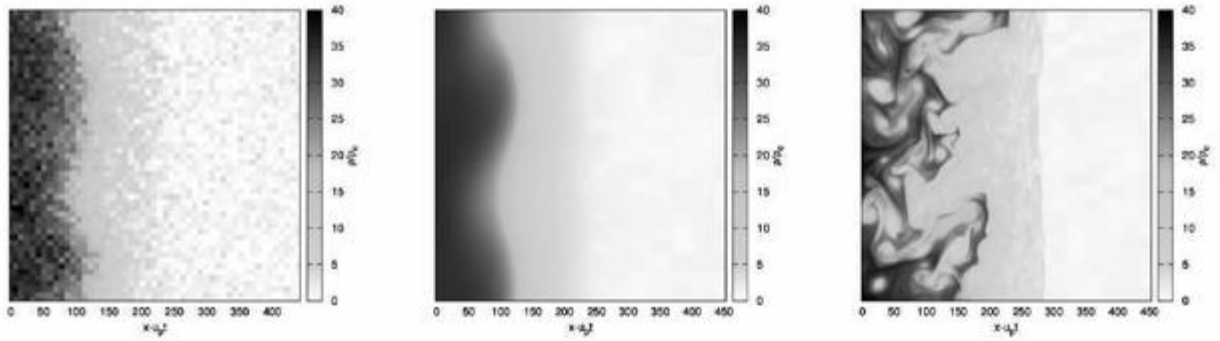

(a) MD (b) N-S (c) Euler

Figure 2: Two-dimensional profile of density in the piston frame of reference obtained from MD, N-S, and Euler simulations, where $u_p/u^* = 2.0$, $u^*/u_{rms(o)} = 10$, $\varepsilon = 0.95$, and $\Delta = 22.5$. Length scales are normalized by disk diameter d.

CONCLUSIONS

The present study recovers the relaxing shock structure in granular gases at the continuum level, which is in agreement with MD results. Introducing strong perturbations to the incoming density field to account for the statistical fluctuations seen in MD yields comparable instabilities as those previously observed from MD. While the inviscid model predicts a highly turbulent structure, the inclusion of viscosity and thermal conductivity yields similarly sized pattern formations to those from MD. With the instability recoverable at the continuum level, future work will now look at theoretical tools to predict and further characterize this phenomena.

References

[1] V. Rodriguez, R. Saurel, G. Jourdan, and L. Houas. Solid-particle jet formation under shock-wave acceleration. *Phys. Rev. E*, 88:063011, Dec 2013.

[2] C. Bizon, M. D. Shattuck, J. B. Swift, W. D. McCormick, and Harry L. Swinney. Patterns in 3d vertically oscillated granular layers: Simulation and experiment. *Phys. Rev. Lett.*, 80(1):57–60, 1998.

[3] N. Sirmas and M. I. Radulescu. Evolution and stability of shock waves in dissipative gases characterized by activated inelastic collisions. *Phys. Rev. E*, 91:023003, Feb 2015.

[4] N. Brilliantov and T. Pöschel. *Kinetic theory of granular gases*. Oxford University Press, Oxford, 2004.

[5] J. Jenkins and M. Richman. Kinetic theory for plane flows of a dense gas of identical, rough, inelastic, circular disks. *Phys. Fluids*, 28(12):3485–3494, 1985.

RHEOLOGICAL PROPERTIES OF GRANULAR SUSPENSIONS AT MODERATE DENSITIES

Francisco Vega Reyes and Vicente Garzó *
Departamento de Física and Instituto de Computación Científica Avanzada (ICCAEx), Universidad de Extremadura, E-06071 Badajoz, Spain

Summary Non-Newtonian transport properties of a granular suspension under uniform shear flow are studied. The suspended particles are modeled as a fluid of smooth hard spheres with inelastic collisions and the interstitial gas is modeled with a volume drag force. The suspension model is based on the Enskog kinetic equation and hence, our results apply for moderate densities. The model is solved by means of two complementary routes: Grads moment method (analytical) and Monte Carlo simulations of the Enskog equation (computational). Unlike in previous works on granular dense suspensions, Grad's solution includes nonlinear terms in the kinetic stress tensor in the evaluation of the momentum transfer from the Enskog collision operator. This allows us to calculate the (nonzero) normal stress differences in the plane normal to the laminar flow. Comparison between theoretical and numerical results shows in general good agreement even for conditions of strong inelasticity and/or moderate densities.

INTRODUCTION

Granular matter under rapid flow conditions can be modeled as a gas of hard spheres (of mass m and diameter σ) with inelastic collisions. In the simplest model, the spheres are assumed to be completely smooth and so, the inelasticity in collisions is only accounted for by a (positive) constant coefficient of normal restitution $\alpha \leq 1$ which only affects to the translational degrees of freedom of grains. The case $\alpha = 1$ refers to elastic collisions. In spite of the simplicity of the model, it has been able to capture many of the trends observed in real granular flows especially those associated with collisional dissipation. On the other hand, although granular particles in nature are usually surrounded by an interstitial fluid (like the air, for instance), the influence of the latter on the dynamic properties of solid particles has been frequently neglected in most theoretical and computational works. However, the impact of the surrounding gas on solid particles turns out to be important in a wide range of practical applications, such as for instance species segregation [1]. For this reason, the study of granular suspensions has attracted the attention of engineering and the physics community in the last few years [2].

Needless to say, the kinetic theory of granular suspensions is an intricate problem since it involves two different phases (solid particles and interstitial gas) and hence, it would require in principle to solve a set of two coupled kinetic equations for each one of the velocity distribution functions of the different phases. Nevertheless, due to the mathematical difficulties involved in the above approach, a different strategy is usually followed and one considers a single kinetic equation for solid particles where the effect of the surrounding gas is accounted for by means of an effective external force. Recently, a new suspension model has been proposed [3]. The model accounts for three sources of particle acceleration due to the gas phase: (i) mean drag (via a term involving a coefficient β and the difference between the mean flow velocities of solid $\mathbf{U}$ and gas $\mathbf{U}_g$ phases), (ii) "thermal" drag (via a term involving a coefficient γ and the granular temperature, or a measure of particle velocity fluctuations), and (iii) particle neighbor effects (via a term involving a coefficient ξ and stochastic Wiener process increment). In the case that $\mathbf{U} = \mathbf{U}_g$, mean drag and neighbor effects (first and third terms of the effective external force) disappear and only the drag force interaction remains. This will be the simplified suspension model considered here.

The objective of this paper is to determine the rheological properties of a granular suspension under uniform (or simple) shear flow (USF). At a macroscopic level, this state is characterized by a constant number density n, a constant (granular) temperature T and a linear velocity field (that is $U_y = U_z = 0$ and $\partial U_x/\partial y \equiv a = \text{const}$). In addition, in the case of granular suspensions, it is usually assumed [4, 5] that $\mathbf{U} = \mathbf{U}_g$ and so, the fluid force is given by the drag viscous force. In the steady state, the viscous heating term is exactly compensated by the cooling terms arising from collisional dissipation and viscous friction. Thus, the (scaled) shear rate $a^* = a/\nu(T)$ (where $\nu(T) \propto \sqrt{T}$ is an effective collision frequency for hard spheres) is a function of the coefficient of restitution α and the (scaled) friction coefficient $\gamma^* \equiv \gamma/\nu$. It is important to remark that the USF state falls beyond Newtonian hydrodynamics [6] since the presence of shearing induces non-zero normal stress differences $P_{xx} - P_{yy}$ and $P_{yy} - P_{zz}$ [7]. The evaluation of the above quantities in terms of α, γ^* and the solid volume fraction ϕ is the main target of the present contribution.

THEORETICAL BACKGROUND

At a microscopic level, the USF is generated by Lees-Edwards boundary conditions which are simply periodic boundary conditions in the local Lagrangian frame $\mathbf{V} = \mathbf{v} - \mathsf{a} \cdot \mathbf{r}$ and $\mathbf{R} = \mathbf{r} - t\mathsf{a} \cdot \mathbf{r}$. Here, a is the tensor with elements $a_{ij} = a\delta_{ix}\delta_{jy}$.

*Corresponding author. Email: vicenteg@unex.es

In terms of the above variables, the velocity distribution function is uniform (namely, $f(\mathbf{r},\mathbf{v}) = f(\mathbf{V})$) and the Enskog kinetic equation for the granular suspension becomes

$$-aV_y\frac{\partial f}{\partial V_x} - \frac{\gamma}{m}\frac{\partial}{\partial \mathbf{V}}\cdot\mathbf{V}f = J_{\mathrm{E}}[\mathbf{V}|f,f], \tag{1}$$

where $J_{\mathrm{E}}[\mathbf{V}|f,f]$ is the Enskog collision operator. The pressure tensor has kinetic and collisional transfer contributions, i.e, $\mathsf{P} = \mathsf{P}^k + \mathsf{P}^c$ where $\mathsf{P}^k = \int \mathrm{d}\mathbf{V} m\mathbf{V}\mathbf{V}f(\mathbf{V})$ and

$$\mathsf{P}^c = \frac{1+\alpha}{4}m\sigma^d\chi\int \mathrm{d}\mathbf{V}_1\int \mathrm{d}\mathbf{V}_2\int \mathrm{d}\widehat{\boldsymbol{\sigma}}\,\Theta(\widehat{\boldsymbol{\sigma}}\cdot\mathbf{g})(\widehat{\boldsymbol{\sigma}}\cdot\mathbf{g})^2\widehat{\boldsymbol{\sigma}}\widehat{\boldsymbol{\sigma}}f(\mathbf{V}_1 + a\sigma\widehat{\sigma}_y\widehat{\mathbf{x}})f(\mathbf{V}_2). \tag{2}$$

Here, χ is the (constant) pair correlation function, d is the dimensionality of the system ($d = 2$ for disks and $d = 3$ for spheres), $\widehat{\boldsymbol{\sigma}}$ is a unit vector along the centers of the two colliding spheres, Θ is the Heaviside step function and $\mathbf{g} = \mathbf{V}_1 - \mathbf{V}_2$ is the relative velocity.

The kinetic contribution P^k can be obtained from Eq. (1) by multiplying both sides of this equation by mV_iV_j and integrating over velocity. The result is

$$a_{i\ell}P^k_{\ell j} + a_{j\ell}P^k_{\ell i} + \frac{2\gamma}{m}P^k_{ij} = \Lambda^{\mathrm{E}}_{ij}, \tag{3}$$

where $\Lambda^{\mathrm{E}}_{ij} \equiv \int \mathrm{d}\mathbf{V}\; mV_iV_jJ_{\mathrm{E}}[\mathbf{V}|f,f]$. The exact forms of the collisional moment $\Lambda^{\mathrm{E}}_{ij}$ and the collisional contribution P^c are not known, even for elastic collisions. However, a good estimate of both quantities can be obtained by using Grad's approximation

$$f(\mathbf{V}) \to f_{\mathrm{M}}(\mathbf{V})\left(1 + \frac{m}{2T}V_iV_j\Pi_{ij}\right), \tag{4}$$

where $f_{\mathrm{M}}(\mathbf{V}) = n\left(m/(2\pi T)\right)^{d/2}e^{-mV^2/2T}$ is the local equilibrium distribution function and $\Pi_{ij} = P^k_{ij} - nT\delta_{ij}$ is the traceless part of the kinetic contribution to the pressure tensor. Upon writing the distribution function (4) we have taken into account that the heat flux vanishes in the USF and have also neglected the contribution to f coming from the fourth-degree velocity moment. The expressions of P^c and $\Lambda^{\mathrm{E}}_{ij}$ can be derived when the trial Grad's distribution (4) is inserted into Eqs. (2) and (3), respectively. The algebra involved in evaluating the velocity integrals is tedious but straightforward and we have expressed the (scaled) pressure tensor $\mathsf{P}/(nT)$ in terms of the parameter space of the problem (the coefficient of restitution α, the scaled friction coefficient γ^* and the solid volume fraction $\phi = (\pi/6)n\sigma^3$ for spheres). In addition, in contrast to previous attempts [5], our calculations have been obtained by retaining nonlinear terms in the (traceless) pressure tensor Π_{ij} and hence, our Grad's solution is able to detect the influence of both viscous friction and inelasticity on the normal stress difference $P_{yy} - P_{zz}$ (which was assumed to be zero in Ref. [5]).

To gauge the reliability of our theoretical predictions for rheological properties, we have also numerically solved the Enskog equation by means of the direct simulation Monte Carlo (DSMC) method [8] applied to inelastic hard spheres under USF. In addition, we have also added the drag force coming from the interaction between the solid particles and the surrounding interstitial gas. After a short transient period, the system achieves a steady state where the elements of the pressure tensor can be computed from the simulations. As in the case of dilute granular suspensions [7], good agreement between theory and simulations is found for conditions of practical interest. In particular, the theory is able to reproduce quantitatively well the dependence of both the shear stress (P_{xy}) and the normal stress differences ($P_{xx} - P_{yy}$ and $P_{yy} - P_{zz}$) on α and/or the density ϕ for not too large values of γ^*.

References

[1] Möbius M. E., Lauderdale B. E., Nagel S. R., Jaeger H. M.: Brazil-nut effect: Size separation of granular particles. Nature 414: 270, 2001.

[2] Koch D. L., Hill R.: Inertial effects in suspension and porous-media flows. Annu. Rev. Fluid Mech. 33: 619-647, 2001.

[3] Garzó V., Tenneti S., Subramaniam S., Hrenya C. M.: Enskog kinetic theory for monodisperse gas-solid flows. J. Fluid Mech. 712: 129-168, 2012.

[4] Tsao H.-K., Koch D. L.: Rapidly sheared, dilute gas-solid suspensions. J. Fluid Mech. 296: 211-245, 1995.

[5] Sangani A. S., Mo G., Tsao H.-K., Koch D. L.: Simple shear flows of dense gas-solid suspensions at finite Stokes numbers. J. Fluid Mech. 313: 309-341, 1996.

[6] Vega Reyes F., Santos A., Garzó V.: Non-Newtonian granular hydrodynamics. What do the inelastic simple shear flow and the elastic Fourier flow have in common?. Phys. Rev. Lett. 104: 028001, 2010.

[7] Chamorro M. G., Vega Reyes F., Garzó V.: Non-Newtonian hydrodynamics for a dilute granular suspension under uniform shear flow. Phys. Rev. E 92: 052205, 2015.

[8] Bird G. I.: Molecular Gas Dynamics and the Direct Simulation of Gas Flows. Clarendon, Oxford 1994.

FS09 - Foams and Cellular Materials

TS.FS09-1.01	Combescure, Christelle - In-plane loading of hexagonal honeycombs: Post-bifurcation and stability behavior (INVITED)	3418
TS.FS09-1.02	Gaitanaros, Stavros - The effect of polydispersity on the crushing of open-cell random foams (INVITED)	3420
TS.FS09-1.03	Berinskii, Igor - Effective elastic properties of some cellular auxetic materials	3422
TS.FS09-1.04	Blanc, Baptiste - Electro osmosis at liquid interfaces	3424
TS.FS09-1.05	Giustiniani, Anaïs - Silicon polyHIPES (High Internal Phase Emulsions) via reactive emulsion stabilization	3426
TS.FS09-1.06	Jacques, Nicolas - A continuum approach to micro-inertia effects in closed-cell solid foams	3428
TS.FS09-2.01	Leroy, Valentin - Acoustical properties of liquid foams (INVITED)	3430
TS.FS09-2.02	Jullien, Marie-Caroline - Thermocapillary Forced-drained Foam: Effect of Surface Rheology	3432
TS.FS09-2.03	Kraiem, Omar - Modelling the crushing behavior of a ceramic brittle foam	3434
TS.FS09-2.04	Krödel, Sebastian - Phononic Microlattices for Ultrasonic Applications	3436
TS.FS09-2.05	Li, Yaning - Auxetic effects induced by re-entrant angle and chirality with large deformation	3438
TS.FS09-2.06	Liebscher, André - Why Laguerre tessellations are good approximations of foams	3440
TS.FS09-3.01	Lorenceau, Elise - Imbibition of dry aqueous foams by oil (INVITED)	3442
TS.FS09-3.02	Liu, Lu - Failure mechanisms in AlSi10Mg lattices via in-situ compression tomography	3444
TS.FS09-3.03	Ryvkin, Michael - Brittle fracture of hierarchical self-similar honeycombs	3446
TS.FS09-3.04	Wang, Dong-Wei - Sound transmission through composite sandwich plate with pyramidal truss cores	3448
TS.FS09-3.05	Xu, Hang - Stiff and strong Octet lattice with tunable coefficient of thermal expansion	3450
TS.FS09-3.06	Zheng, Zhijun - Dynamic behavior and crashworthiness design of graded cellular structures	3452
PO.FS09-1.01.346	Abueidda, Diab - Elasticity and Conductivity of Foams Based on Triply Periodic Minimal Surfaces	3454
PO.FS09-1.02.347	Lu, Tianjian - Sandwich panel with honeycomb-corrugation hybrid core: evaluation of concept	3456
PO.FS09-1.03.348	Ma, Li - Design and Mechanical Response of Assembled 3D Periodic Auxetic Cellular Structures	3458
PO.FS09-2.01.278	Martinez Pavetti, Belen - Quasi-lattice dynamics of random skeletal structures	3460
PO.FS09-2.02.279	Sahraoui, Sohbi - Fractional derivatives model to predict high frequency moduli of acoustic foams	3462
PO.FS09-2.03.280	Wyatt, Hayley - Optimising Material Density of Cellular Bodies in High Elastic Deformation	3464

IN-PLANE LOADING OF HEXAGONAL HONEYCOMBS: POST-BIFURCATION AND STABILITY BEHAVIOR

Christelle Combescure[1,2], Nicolas Triantafyllidis[2], and Ryan S. Elliott *[1]
[1]*Department of Aerospace Engineering and Mechanics, University of Minnesota, Minneapolis, MN USA 55455*
[2]*Laboratorie de Mechanique des Solides (CNRS UMR 7649), Ecole Polytechnique, Route de Saclay, 91128 Palaiseau, France*

Summary Buckling of honeycombs is an important problem. We identify three open questions: (i) How does the mechanical response depend on the applied loading device? (ii) What can the *Bloch wave representation* of all bounded perturbations contribute to our understanding of the stability of post-bifurcated equilibria? and (iii) How does material nonlinearity affect the critical bifurcation load? We model the honeycomb as a 2D infinite perfect periodic medium and use group theory (instead of the imperfection method) to study its bifurcation behavior under various far-field loadings. We evaluate stability using two criteria: rank-one convexity and Bloch wave stability. We find that the post-bifurcation behavior is extremely sensitive to the loading device, and confirm that the *flower mode* is unstable. Our (first ever) Bloch wave stability analysis of the post-bifurcated equilibria shows that the flower mode is stable for all sufficiently short wavelength perturbations, explaining its observation by *Papka and Kyriakides* (1999).

METHODS AND RESULTS

In this work we revisit the problem of in-plane equi-biaxial compression of a regular hexagonal honeycomb structure. There is an extensive literature for this problem: from the seminal experiments of *Papka and Kyriakides* (1994, 1999), to the characterization of the onset of failure by *Triantafyllidis and Schraad* (1998) and *Ohno et al.* (2002), to the study of honeycomb post-bifurcation behavior using an intuitive approach by *Okumura et al.* (2002) and the more systematic group-theory methods of *Saiki et al.* (2005). However, our literature review has identified three open theoretical questions about honeycomb post-bifurcation behavior: (i) How does the mechanical response of a honeycomb depend on the applied loading device? (ii) What can the *Bloch wave representation* of all bounded perturbations contribute to our understanding of the stability of post-bifurcated equilibria? and (iii) What effect does material nonlinearity have on the critical bifurcation load?

Our investigation pays special attention to the effects of the loading device on the post-bifurcation and stability behavior. We consider the equilibrium and bifurcation behavior of the infinite perfect hexagonal honeycomb structure subjected to (i) displacement, (ii) dead load (Biot), and (iii) live load (*two-dimensional pressure*) control. We adopt a purely elastic model and employ linear and nonlinear elastic material constitutive responses. Based on the results of *Triantafyllidis and Schraad* (1998), the (initial) post-bifurcation equilibrium and stability behavior predicted by our model is applicable to all real hexagonal geometry honeycomb structures composed of rate-independent solids subjected to equi-biaxial compressive loadings.

We use a systematic branch-following and bifurcation technique for the perfect structure, complemented by analytical group theory results to identify and compute the bifurcation and post-bifurcation behavior of a perfect hexagonal honeycomb structure. An important feature of this methodology is that it does not use the imperfection method. (The imperfection method is a simple heuristic numerical method encountered in engineering practice that often works well for the study of bifurcation behavior associated with equilibrium paths with widely separated bifurcation points. However, the method is highly unreliable for problems with a high degree of symmetry.) For the evaluation of an equilibrium configuration's stability, we employ only strictly necessary stability conditions that are applicable to all boundary value problems. In particular, we use the Rank-One Convexity (RK1) criterion (to evaluate stability with respect to long wavelength perturbations) and the Bloch wave criterion (to evaluate stability with respect to all bounded perturbations).

With these techniques, we obtain the equilibrium, stability, and bifurcation behavior of the honeycomb subjected to various in-plane (compressive) stress states and identify an infinite set of bifurcation points along the principal equilibrium path. We investigate the honeycomb's 1×1, 1×2, and 2×2 unit cell bifurcation behavior and confirm previous results from the literature. However, we go further in our study of the post-bifurcation behavior and identify the path's stability relative to the RK1 and Bloch wave stability criteria. We also identify a common but *ad-hoc* energy-based stability criterion (that is not generally necessary for all boundary value problems). We show that in many cases the ad-hoc criterion provides erroneous predictions. We further obtain a few representative and interesting examples of previously unreported equilibrium configurations associated with 2×2 and 3×3 unit cells. Finally, we show that relative to the linear stress–strain material behavior the critical bifurcation load *increases* for strain-hardening nonlinearities and *decreases* for strain-softening nonlinearities. However, this effect of material nonlinearity is only observed for appropriately-oriented, predominately uniaxial loading devices.

Our results confirm that, for equi-biaxial loading, the Mode III flower pattern obtained under displacement control conditions is RK1 unstable (as first reported by *Okumura et al.* (2002), but unfortunately dismissed by these authors). Further, we use the Bloch wave stability criterion to gain a deeper understanding of the stability properties of the Mode III bifurcated equilibrium path (Fig. 1). We find that although this mode is unstable with respect to very long wavelength perturbations,

*Corresponding author. Email: relliott@umn.edu

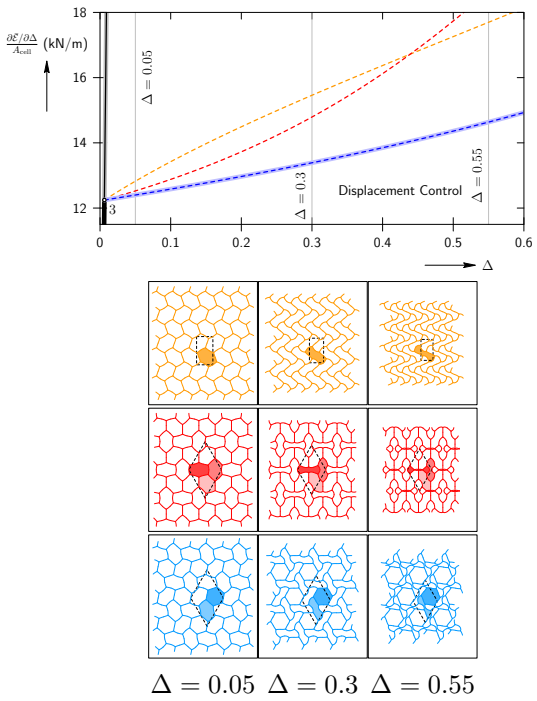

Equi-biaxial displacement control bifurcation diagram and deformed configurations associated with the triple Bloch wave bifurcation of a hexagonal honeycomb structure with linear stress–strain behavior. The bifurcation diagram shows Mode I (orange), Mode II (red), and Mode III (blue) equilibrium paths. All three modes are found to be unstable with respect to the RK1 and Bloch wave criteria. In contrast, the ad-hoc criterion predicts that Mode III is stable. The deformed equilibrium configuration at three loading parameters ($\Delta = .5$, $.3$, and $.55$) is shown for Mode I (first row), Mode II (second row) and, Mode III (third row).

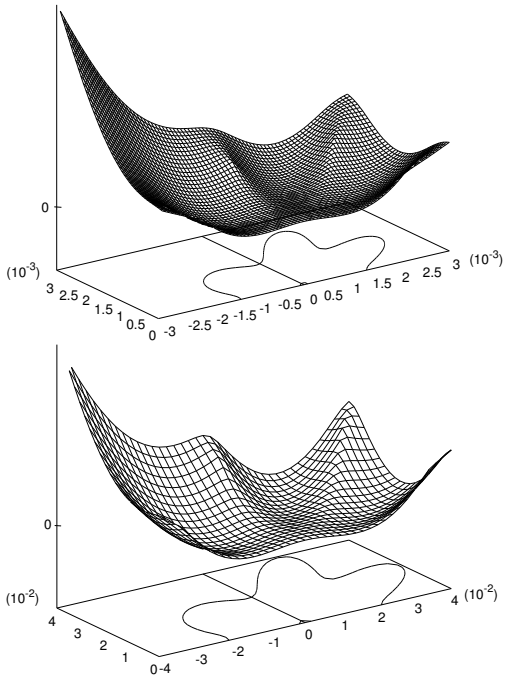

Bloch wave minimum eigenvalue surfaces near the Γ-point, for the equi-biaxial displacement control bifurcated equilibrium Mode III path. Note the significantly different scales used for the axes of the graphs. (Top: $\Delta = .62$) Almost immediately after bifurcation there exist long wavelength Bloch wave modes (with $|\mathbf{k}| < 2.5 \times 1^{-3}$) that are unstable. (Bottom: $\Delta = .386$) Somewhat later in the post-bifurcation evolution the domain of unstable long wavelength Bloch wave modes ($|\mathbf{k}| < 4. \times 1^{-2}$) has increased in size by more than an order of magnitude.

Figure 1: (left) Bifurcation diagram and configurations; (right) Bloch wave stability eigenvalue surfaces for Mode III.

it is stable with respect to short and moderate wavelength perturbations. This provides an explanation for how *Papka and Kyriakides* (1999) were able to observe this mode: the 18×21 unit cell specimens used in their experiments were well within the Mode III moderate wavelength stability range identified in this work. A full description of this study (for the case of equi-biaxial loading and linear stress–strain behavior) may be found in *Combescure et al.* (2016).

ACKNOWLEDGMENTS

The authors thank Stelios Kyriakides for his helpful suggestions, discussions, and encouragement. This work was partially supported by: National Science Foundation (NSF) grant PHY-0941493 and grant CMMI-1462826, the Andre Citroen Chair at the Ecole Polytechnique and the Solid Mechanics Laboratory (LMS) of the Ecole Polytechnique. We also acknowledge support by the University of Minnesota Supercomputing Institute.

References

C. Combescure, P. Henry, and R. S. Elliott. Post-bifurcation and stability of a finitely strained hexagonal honeycomb subjected to equi-biaxial in-plane loading. *Int J Solids Struct*, 2016. In press.

N. Ohno, D. Okumura, and H. Noguchi. Microscopic symmetric bifurcation condition of cellular solids based on a homogenization theory of finite deformation. *J Mech Phys Solids*, 50(5):1125–1153, 2002. doi:10.1016/S0022-5096(01)00106-5.

D. Okumura, N. Ohno, and H. Noguchi. Post-buckling analysis of elastic honeycombs subject to in-plane biaxial compression. *Int J Solids Struct*, 39(1314):3487–3503, 2002. doi:10.1016/S0020-7683(02)00165-8.

S. Papka and S. Kyriakides. In-plane compressive response and crushing of honeycomb. *J Mech Phys Solids*, 42(10):1499–1532, 1994.

S. Papka and S. Kyriakides. Biaxial crushing of honeycombs—part I: Experiments. *Int J Solids and Struct*, 36(29):4367–4396, 1999. doi:10.1016/S0020-7683(98)00224-8.

I. Saiki, K. Ikeda, and K. Murota. Flower patterns appearing on a honeycomb structure and their bifurcation mechanism. *Int J Bifurcat Chaos*, 15(02):497–515, 2005. doi:10.1142/S021812740501217X.

N. Triantafyllidis and M. W. Schraad. Onset of failure in aluminum honeycombs under general in-plane loading. *J Mech Phys Solids*, 46(6):1089–1124, 1998.

THE EFFECT OF POLYDISPERSITY ON THE CRUSHING OF OPEN-CELL RANDOM FOAMS

Stavros Gaitanaros[1a)], Stelios Kyriakides[2] & Andrew M. Kraynik[3]
[1]*Civil Engineering, Johns Hopkins University, Baltimore, Maryland, USA*
[2]*Research Center for Mechanics of Solids, Structures & Materials, University of Texas at Austin, Austin, Texas, USA*
[3]*Sandia National Laboratories (retired), Albuquerque, New Mexico, USA*

Summary Open-cell foams, both natural and synthetic, made from most categories of base materials (e.g., metals, polymers, ceramics) exhibit superior energy absorption characteristics under both low and high velocity impact. In our work micromechanically accurate models generated using the *Surface Evolver* software are used to study how the characteristics of the cellular microstructure affect the crushing response of open-cell foams under quasi-static and impact loadings. Recent results demonstrated that both the collapse stress and the strain-energy absorbed scale with the relative density of the foam. The present work examines the effect of cell-size variations (polydispersity) on the quasi-static and dynamic crushing responses. The results indicate that polydispersity reduces the initial strength of foam but has less influence of the overall energy absorption capacity.

INTRODUCTION

Cellular materials in general and foams in particular are widely used in energy absorption and impact mitigation applications because of the low stress and extended plateau that characterizes their crushing. Connecting the cellular microstructure to these attractive material properties is an essential step in the adoption of cellular materials in engineering design [1]. In the case of foams this task is complicated by the randomness of their cellular microstructure. The challenge is met by using a numerical process involving molecular dynamics, tessellations and the Surface Evolver software to generate a skeletal form of random foams [2] that are subsequently appropriately "dressed" with the desired solid material. We have shown that such micromechanically accurate models can reproduce all aspects of their quasi-static crushing behavior from the onset of localization and propagation of collapsed cells to densification [3]. Similar success has been demonstrated in the modeling of crushing under impact including shock formation [4]. The present work uses a similar modeling framework to further connect the foam microstructure to these mechanical properties. This includes the effect of the foam relative density [5] and cell size variations (polydispersity) [6] on the mechanical behavior under quasi-static and impact loadings.

POLYDISPERSE FOAM MODELING

Briefly, the polydisperse topologies start as Laguerre tessellations coming from dense packings of polydisperse spheres [2]. These tessellations are used as initial conditions in *Surface Evolver* to generate soap froth that satisfies Plateau's laws. The resulting structures are further relaxed through additional topological transitions produced by large deformation tension-compression cycles. The amount of polydispersity is controlled through the probability distribution of the sphere diameters in the original sphere packings. In the present results we report the standard deviation of the foam cell radius R, ($R \equiv$ is the radius of a sphere with the volume of the cell)

$$\sigma = \sqrt{\sum_{i}^{N} \left(\quad_i - \bar{R} \right)^2 / N}.$$

These microstructures are subsequently dressed with shear deformable beam elements, with a non-uniform material distribution that mimics measured values from existing aluminum alloy open-cell foams (see [3]). In an effort to more efficiently model the wider distribution of cell sizes, ligaments are grouped based on the ratio of their length over the mean ligament length. Discretization is based on the same ligament groups, by using 7-18 beam elements per ligament.

A relative density of 8% is assigned to all models through an iterative numerical process starting with an initial density between 7.5 - 8.5%

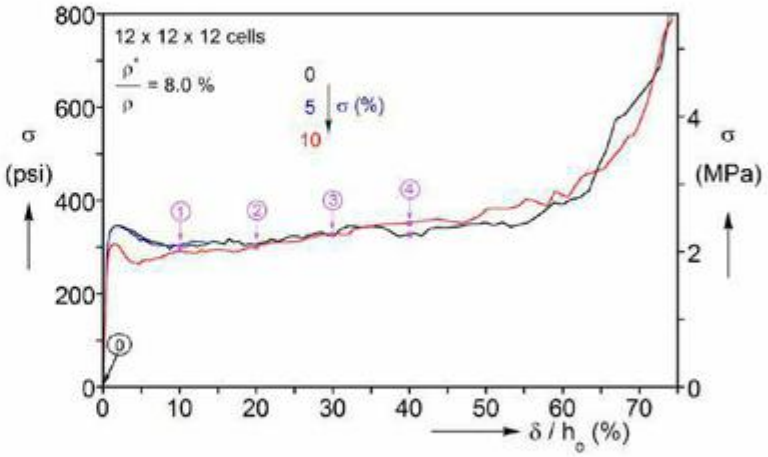

Figure 1 Quasi-static crushing responses of monodisperse (black) and polydisperse (blue and red) foam models of 1728 cells.

a) Corresponding author. Email: stavrosg@jhu.edu.

that takes into account material overlap at the nodes [3,4] and then scaling the ligaments' cross-sectional areas until the exact prescribed value is achieved and checked numerically through finite element simulations.

RESULTS

Random foam models of 12^3 cells, with increased amount of polydispersity are used in crushing simulations to examine the effect of the cell-size variation on the foam's compressive properties (elastic modulus, strength, plateau stress, energy absorption capacity). Typical quasi-static responses from a polydisperse foam with a cell radius standard deviation equal to approximately 10% and a monodisperse foam are shown in **Fig. 1**. They both exhibit an initial linearly elastic regime, a local stress maximum that represents the strength of the foam, followed by an extended stress plateau that ends with densification at an average strain of about 60%. The polydispersity lowers the strength by about 13%. However, the response then picks up and follows the corresponding monodisperse indicating that the plateau stress is less sensitive to the cell-size distribution; it is instead governed by the relative density of the foam [5].

Fig. 2 shows deformed configurations at displacements of $\delta / h_o = \{0, 0.1, 0.2, 0.3, 0.4\}$ marked on the response of **Fig. 1**. The images correspond to cross-sections of approximately one-cell thickness along the cubical model's diagonal. Crushing patterns in the monodisperse foam are similar to previous experimental and numerical observations: localization initiates in the "weakest" zone in the domain developing into of a non-planar band of collapsed cells; the band(s) subsequently gradually propagates crushing the remaining undeformed cells. The patterns in the polydisperse foam on the other hand show highly irregular paths that follow locations of large cells, which are more prone to collapse. Note for example, that initial collapse in the polydisperse model, shown in images ①-②, occurs in the neighborhood of a cluster of large cells evident in the undeformed image ⓪.

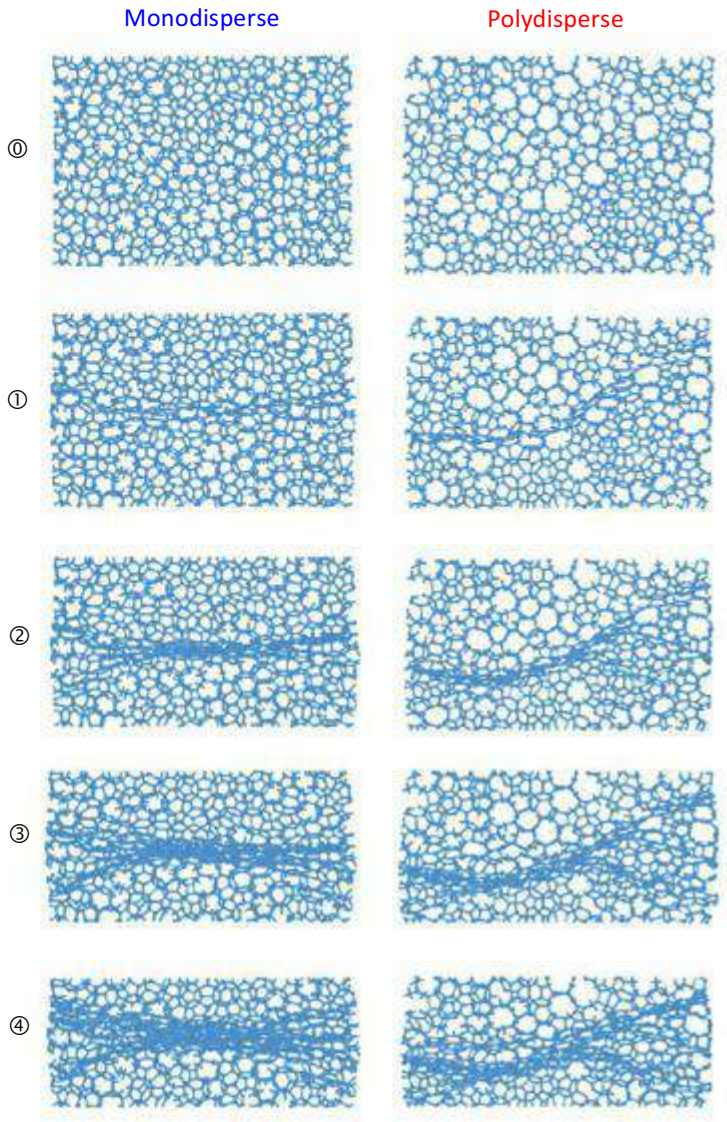

Figure 2. Deformed configurations from the quasi-static crushing of a monodisperse (left) and a polydisperse foam (right).

The presentation will include additional results from quasi-static crushing of polydisperse foam models as well as results from foam models crushed under impact. The dynamic crushing results are used to establish the effect of polydispersity on the foam Hugoniot and predict its effect on the dynamic stresses and on the associated energy absorption dynamic enhancement [6].

References

[1] Gibson, L.J., Ashby, M.F. Cellular Solids: Structure and Properties, 2nd Ed. Cambridge University Press, 1997.

[2] Kraynik A.M., Reinelt D.A., van Swol, F.: Structure of random foam. *Phys. Rev. Lett.* **93**/20, 208301/1-4, 2004.

[3] Gaitanaros S., Kyriakides S., Kraynik A.M.: On the crushing response of random open-cell foams. *Int'l J. Solids Struct.* **49**, 2733-2743, 2012.

[4] Gaitanaros S., Kyriakides S.: Dynamic crushing of aluminum foams Part II – Analysis. *Int'l J. Solids Struct.* **51**, 1646-1661, 2014.

[5] Gaitanaros S., Kyriakides S.: On the effect of relative density on the crushing and energy absorption of open cell foams under impact. *Int'l J. Imp. Engr.* **82**, 3-13, 2015.

[6] Gaitanaros S., Kyriakides S., Kraynik A.M.: On the crushing response of polydisperse foams (in preparation), 2016.

EFFECTIVE ELASTIC PROPERTIES OF SOME CELLULAR AUXETIC MATERIALS

Igor Berinskii*[1]

[1]*School of Mechanical Engineering, The Iby and Aladar Fleischman Faculty of Engineering, Tel Aviv University, Tel Aviv, Israel*

Summary A two–parametric mechanical model is proposed to describe a class of auxetic cellular materials. The microstructure of these materials varies from the regular to re–entrant honeycombs with change of the angle between the nodes of material's lattice. An interaction among the nodes is described by combination of longitudinal and torsional springs. Effective properties of the solid material corresponding to the given microstructure are determined. It is shown that re–entrant honeycomb structures demonstrate the auxetic properties at any combination of parameters whereas the usual honeycombs can have both positive and negative Poisson's ratios.

AUXETIC PROPERTIES OF THE HONEYCOMBS

Most of known materials undergo transverse contraction at longitudinal extension in one direction and a transversal expansion when compressed. However, from physical point of view the opposite behaviour is permissible. The materials called "auxetics" become thicker perpendicular to the applied stretching force and thinner under compression. Usually this feature is connected with a special microstructure of the material that also makes auxetics more subject to the bulk deformation than to the shear one. A broad interest to auxetics appeared after the publication of Lakes [1] where he proposed the three–dimensional re–entrant structures to model polymer foams with negative Poisson's ratios. Even earlier two–dimensional structures were proposed to model auxetic properties of materials by Almgren [2] and Kolpakov [3]. Nowadays a lot of two–dimensional auxetic structures are studied, however re–entrant honeycombs (REH) proposed by Almgren and Kolpakov (Fig. 1) is one of the most common. It is used for design and fabrication of auxetic materials at different scale levels starting form molecular structures to engineering materials. In this paper the springs model is used with another homogenization method to determine the full tensor of elasticity for the effective continuum. As a result, macroscopic elastic constants depend on one geometrical (angle) and two mechanical (stiffness of longitudinal and rotational springs) parameters only. A main purpose of this work is to find out the combinations of these three parameters standing for the auxetic properties of honeycomb structures.

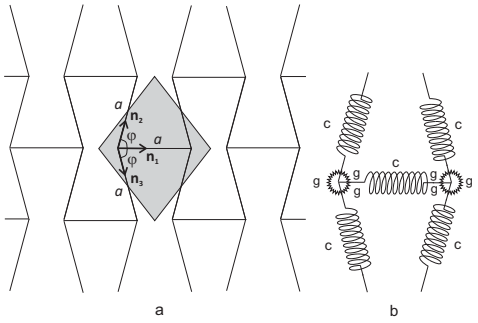

Figure 1: Re-entrant honeycombs (REH) structure (a) and its mechanical model (b)

SYMMETRY OF HONEYCOMB STRUCTURES AND CORRESPONDING SOLID MATERIAL

Let us consider the two-dimensional structure shown at Fig. 1. Let us represent the structure as the nodes connected by linear and torsional springs. For the sake of simplicity consider the interaction among the nearest neighbours only. Denote the longitudinal spring stiffness as c and the torsional spring effective stiffness as g (Fig.1). Suppose that c and g have the same dimension (N/m). For the sake of simplicity the linear springs are considered. In addition, an angle φ connecting the adjacent linear springs is introduced. Two mechanical parameters and angle φ determine the linear elastic properties of the effective continuum corresponding to the material at the macroscale.

A structure has two orthogonal planes of symmetry. For two-dimensional material it corresponds to the orthotropic material with the following matrix of stiffness

$$C = \begin{pmatrix} C_{11} & C_{12} & 0 \\ C_{12} & C_{22} & 0 \\ 0 & 0 & C_{33} \end{pmatrix} \tag{1}$$

*Email: igorbr@post.tau.ac.il

Here the Voight notation was used to represent the 4 independent components of the stiffness tensor: $C_{11} = C_{1111}, C_{22} = C_{2222}, C_{12} = C_{1122}, C_{33} = C_{1212}$. The stiffness matrix (1) must be positive definite for the strain energy density to be positive. This give the following conditions:

$$C_{11} > 0 \qquad C_{11}C_{22} - C_{12}^2 > 0 \qquad C_{33} > 0 \tag{2}$$

Note, in case of orthotropic 2D material these conditions do not give any limits for the Poisson's ratios unlike the 2D isotropic material where $-1 < \nu < 1$.

EFFECTIVE ELASTIC PROPERTIES OF RE–ENTRANT AND REGULAR HONEYCOMBS

The uniform strain of the REH structures and corresponding solid material were considered. Effective elastic properties were found as functions of c and g from the comparison of the resulting deformation energies. Let us do not bring out the general formulae but consider some partial cases instead.

Honeycomb structure

The honeycomb structure can be received from REH structure by substitution $\varphi = 2\pi/3$. As expected, the symmetry of the structure is changed from orthotropic to isotropic. The non-zero components can be found as

$$C_{11} = \tfrac{\sqrt{3}c(c+18g)}{6(c+6g)} \quad C_{12} = \tfrac{\sqrt{3}c(c-6g)}{6(c+6g)} \quad C_{11} = C_{22} \quad C_{33} = \tfrac{1}{2}(C_{11} - C_{12}) \tag{3}$$

This results coincides with the results obtained for graphene crustal lattices that have the same structure [4]. It is easy to check that conditions (2) are satisfied for any positive c and g.

Triangular structure

The elastic constants for this case ($\varphi = \pi/3$) are given by

$$C_{11} = \tfrac{\sqrt{3}c(c+18g)}{18(c+6g)} \quad C_{22} = \tfrac{\sqrt{3}\left(c^2+14cg+16g^2\right)}{2(c+6g)} \quad C_{12} = -\tfrac{\sqrt{3}(c^2+4cg+36g^2)}{6(c+6g)} \quad C_{33} = \tfrac{\sqrt{3}g(5c+6g)}{3c+2g} \tag{4}$$

As C_{11}, C_{22} are the positive defined quadratic forms of positive c and g and C_{12} is a negatively one, the material will always demonstrate auxetic properties.

Rectangular structure

A value $\varphi = \pi/2$ corresponds to the rectangular structure. The following elastic moduli can be obtained:

$$C_{11} = \tfrac{6cg}{c+12g} \quad C_{22} = c \quad C_{12} = 0 \quad C_{33} = 12g \tag{5}$$

These formulae give the zero values for Poisson's ratios, and hence, the rectangular structure is a boundary case between the auxetic and non-auxetic materials.

CONCLUSIONS

The 2-parametric mechanical model was proposed to determine the auxetic properties of two–dimensional materials with a periodic microstructure. The model was used to determine the effective elastic properties of re–entrant honeycomb structure. Some special cases (isotropic honeycombs, rectangular, and triangular lattices) were considered.

References

[1] Lakes R. Foam structures with a negative Poisson's ratio. Science 235 (4792):1038–1040, 1987.

[2] Almgren R. F. An isotropic three-dimensional structure with Poisson's ratio = -1. J. Elasticity 15:427–430, 1985.

[3] Kolpakov A., Determination of the average characteristics of elastic frameworks. J. App. Math. Mech. 49 (6): 739–745, 1985.

[4] Berinskii I., Borodich F. M. Elastic in-plane properties of 2D linearized models of graphene. Mech. Mat. 62:60–68, 2013.

ELECTRO-OSMOSIS AT LIQUID INTERFACES

Baptiste Blanc*[1,2], Oriane Bonhomme[2], Laurent Joly[2], Christophe Ybert[2], and Anne-Laure Biance[2]

[1]*Department of Physics, Brandeis University, Waltham, MA 02454, USA*
[2]*Institut Lumière Matière, UMR5306 Université Lyon 1-CNRS, Université de Lyon 69622 Villeurbanne, France*

Summary Electrokinetic (EK) transport couples hydrodynamics and electrostatics at liquid interfaces. In particular, it is possible to generate a flow near a charged interface in a liquid by applying an electric field, due to the drag force exerted on counter ions near the interface, a phenomenon referred to as electro-osmosis (EO). We propose here to use EO in the context of liquid foams, the charges being carried by the surfactants used to stabilize the foam. The main challenge of the project is to achieve a complete understanding of EK transport in a 3D liquid foam. To do so, we used a multiscale approach combining experimental and theoretical (molecular dynamics (MD) simulation) tools. In this article, we present our newest results on this general project.

ELECTRO OSMOSIS: AN OVERVIEW

Electroosmotic (EO) flow refers to the motion of a fluid generated by an electric field. Close to a charged interface in a liquid, an ionic double layer of opposite charge is established which is dragged by an applied electric field. Far from the interface, the neutral bulk liquid is then set in motion via viscous diffusion, leading to a plug flow at a velocity v.

Such ionic and massic coupled transports, as their streaming current and potential counterparts, are actually encountered in many natural systems and diverse applications, from biology and physiology-with the key role of electrokinetic transport through nanopore in cell regulation- to liquid flow through macro scale porous materials, relevant to building industry, water treatment [1], filtration and energy conversion [2]. From a technological point of view, electric driving of liquids in micro and nano channels has shown excellent integration capability and has become a standard tool for species separation, sorting, and lab on chip application [3]. In all these applications, the interface where EO effects take place can be rather liquid/solid (energy conversion devices for example) or liquid/gas (water treatment by ion flotation through electrically driven bubbles), the plug flow velocity v verifying the relation set by Smoluchovski [4]:

$$v = \frac{\zeta \epsilon E}{\mu} \tag{1}$$

The peculiar nature of the charged interface is accounted for in the so-called ζ-potential. Indeed, this latter potential depends not only on the electrostatic environment in the vicinity of the surface, characterized by the surface electrostatic potential V_s, but also on the hydrodynamic boundary condition. In the case of solid interface where slippage could occur, it has been shown theoretically and experimentally [5] that the ζ potential writes

$$\zeta = V_0(1 + \frac{b}{\lambda}) \tag{2}$$

with b the so-called slip length [4] at the solid/liquid interface. The magnitude of the EO flow will increase if a large surface potential is achieved together with a large slip at the surface. Ionic surfactant laden interfaces seem to gather these two properties, as surfactant density can be relatively large, and the hydrodynamic boundary condition can be tuned by orders of magnitude, as shown by drainage experiments in soap films. Recent MD simulations [6] confirm that an infinitely long soap films display an EO flow resulting from a coupled effect of slippage and counter ion binding. In this numerical work, the relative motion between the water and the surfactant is recorded, neglecting the effect of the surfactant (i.e the charges) mobility along the interface, which has proven to play a crucial role on EO magnitude near hydrophobic surfaces. The experimental study of an electro osmotic flow on a surfactant interface is a first step towards the understanding of a more complex system: the EO flow in foam.

This talk is divided in two parts. We will first present an experimental study of the EO flow generated by one interface. Then we will show preliminary results concerning the behaviour of foam under an electric field.

ELECTRO OSMOSIS CLOSE TO A SOAPY INTERFACE

The present work is dedicated to study the influence of the peculiar hydrodynamic condition on the EO flow near a surfactant laden interface. We therefore built a new experimental method to measure the ζ potential near a surfactant laden interface. The general principle of the measurement is to probe the fluid displacement under electric forcing near a surfactant laden

*Corresponding author. Email: bblanc@brandeis.edu

interface via particle tracking in the liquid. Fluorescent bead displacements are recorded via a confocal inverted microscope (Leica TCS SP5 DMI6000) for various distance to the interface. The full amplitude profile gives access to a measure of the surfactant zeta potential we can compare to the surface charge of the interface. Based on these experimental results we discuss the distribution of surfactants at the interface. In fact, we measure experimentally an EO motion of water compatible with a zeta potential value of the order of around 100mV, and which is decreasing as surfactant concentration increases. By analytical study, we show that the surfactants at the interface are expected to be immobile, and then that the results obtained are compatible with previous MD simulations [6]. The hydrodynamic contribution of the zeta potential can be estimated by using a new optical method (SHG) [7] to probe the static surface potential.

This idea is then put to the test by studying with numerical simulations an electrokinetic phenomenon in a confined system: the electrophoresis motion of nanobubbles covered by surfactant. In this system, we observe that the electric field generates an inhomogeous repartition of surfactant on the bubble (figure 1), confirming our idea that a Marangoni stress prevents surfactant mobility at the interface.

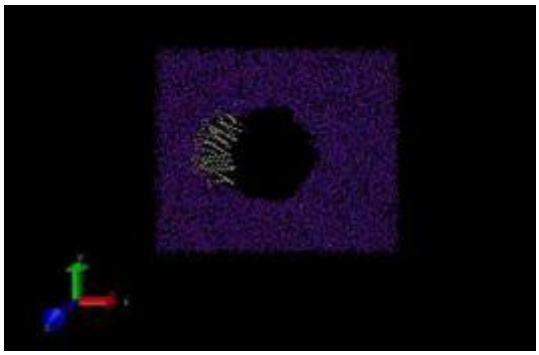

Figure 1: Slice in the z direction of a 24 angstroms radius bubble covered with 30 SDS surfactant (depicted in white) in a salty aqueous solution when an electric field E=0.1V.nm^{-1} is applied in the x direction. SDS molecules are accumulating on one side of the bubble

ELECTRO OSMOSIS IN LIQUID FOAM

In addition to these simple geometry experiment, we study electro-osmotic transport in a class of materials where it has not been explored so far : liquid foams. Liquids foams are gas bubbles trapped in a network of films, plateau border and nodes. EO flow have already been studied in a porous solid media with fixed geometry. The main difference in foam is the deformability of the structure. Though part of our daily lives and important in many industrial processes, foams are short-lived materials. Being strongly out of equilibrium, they irreversibly evolve and, as everybody has observed in a foam bath, they eventually collapse. An important mechanism at play in this process is the drainage induced by gravity, which is unavoidable. A way to cancel and reverse this gravity-driven drainage would be to provoke a counter-gravity EO flow in the foam.

We design then an experimental setup to observe the quantity of water in the plateau Border while an electric field is applied to the foam. The first observations show that an electrical current passing through the system damages dramatically the foam structure. The ions released by electrolysis destabilize the system, its time life being related to the applied electric field. We overcome this difficulty by using special home made electrode and present promising preliminary results on EO in foam, together with hydrodynamic calculation of EO flow in this peculiar deformable porous system.

This work has been funded through french ANR project EFOAM.

References

[1] R. Lemlich. Adsorptive bubble separation techniques. Elsevier, 2012.
[2] A. Siria, P. Poncharal, A.-L. Biance, R. Fulcrand, X. Blase, S. T. Purcell, and L. Bocquet. Giant osmotic energy conversion measured in a single transmembrane boron nitride nanotube. Nature, 494(7438):455-458, Feb. 2013.
[3] L. Bocquet and P. Tabeling. Physics and technological aspects of nanofluidics. Lab on a Chip, 14(17):3143-3158, 2014.
[4] L. Bocquet and E. Charlaix. Nanofluidics, from bulk to interfaces. Chemical Society Reviews, 39(3):1073-1095, 2010.
[5] M. Audry, A. Piednoir, P. Joseph, and E. Charlaix. Amplification of electro-osmotic flows by wall slippage: direct measurements on ots-surfaces. Faraday Discussion, 146:113-124, 2010.
[6] L. Joly, F. Detcheverry, and A.-L. Biance. Anomalous ζ potential in foam films. Physical review letters, 113(8):088301, 2014.
[7] E. Benichou, A. Bruyre, A. Forel, O. Bonhomme, P.-F. Brevet. Molecular organization and phase transition at the air-water interface investigated by second-harmonic generation, SPIE, 2015, p 9360.

SILICONE POLYHIPES VIA REACTIVE EMULSION STABILIZATION

Anaïs Giustiniani*[1], Philippe Guégan[2], Manon Marchand[1], Christophe Poulard[1], and Wiebke Drenckhan[1]
[1]*Laboratoire de Physique des Solides, CNRS, Univ. Paris-Sud, Université Paris-Saclay, Orsay, France*
[2]*Institut Parisien de Chimie Moléculaire, Université Pierre et Marie Curie, 3, rue Galilée, 94200 Ivry sur Seine, France*

Summary We show here how macro-cellular polymers may be obtained by solidification of the continuous phase of a PDMS (polydimethylsiloxane) emulsion, which contains tightly packed PEG (polyethyleneglycol) drops of sub-millimetric dimensions. Coalescence is prohibited by a reactive blending approach which creates a visco-elastic skin around the PEG drops upon contact with the PDMS. We correlate the properties of the PEG/PDMS interface with the emulsion stability in order to optimise the formulation. This is then used with millifluidic methods to obtain explicit control over the structural properties of the final cellular polymer in terms of size, organisation and volume fraction of the cells.

Macro-cellular polymers are highly searched-for materials thanks to their rich mechanical properties. These arise from the internal structuration of the material, in which discrete cells of a fluid or of a solid polymer are tightly packed within a continuous polymeric solid matrix. The size, shape, organisation and volume fraction of these cells have an important influence on the overall material properties. Commonly, the cellular organisation is the signature of an initially liquid state, in which gas bubbles (foam) or liquid droplets (emulsion) are compacted within a continuous liquid monomer/polymer matrix which is solidified to obtain the final material. Understanding and controlling the cellular organisation of the initially liquid template is therefore of utmost interest in order to control the properties of the cellular solid. This requires the control over the size, organisation and volume fraction of the cells, and also over the stability of the liquid system with respect to ageing affects like cells coalescence. While such questions have been investigated successfully for different types of polymers [1], only few advances have been made for materials with a silicone matrix [2], due to the difficulty of stabilizing the liquid template.

Here we use a model system which consists of PEG (polyethyleneglycol) drops in a liquid PDMS (polydimethylsiloxane) which we stabilise against coalescence using a reactive approach which forms a skin around the droplets upon contact with the PDMS phase (see insert Figure 1a). We correlate the properties of the PEG/PDMS interface with the emulsion stability and show that the optimised formulation can be used to generate macro-porous solids with well-controlled structural properties.

To stabilize the emulsion of PEG/PDMS, we use a reative PDMS and add in the PEG phase a crosslinker containing 0.1 M of a catalyst which is active at room temperature. As the PEG and reactive PDMS are in excess compared to the crosslinker, we believe the interfacial properties to depend only on the temperature and the crosslinker concentration C in the PEG phase.

We measure the interfacial tension with a pendant drop device (Tracker from TECLIS) at constant temperature of $25°C$. A drop of the PEG and crosslinker mixture is generated in PDMS, and we follow the evolution in time of the interfacial tension using the Laplacian profile method for different initial crosslinker concentrations C between 0 and 1 mol%.

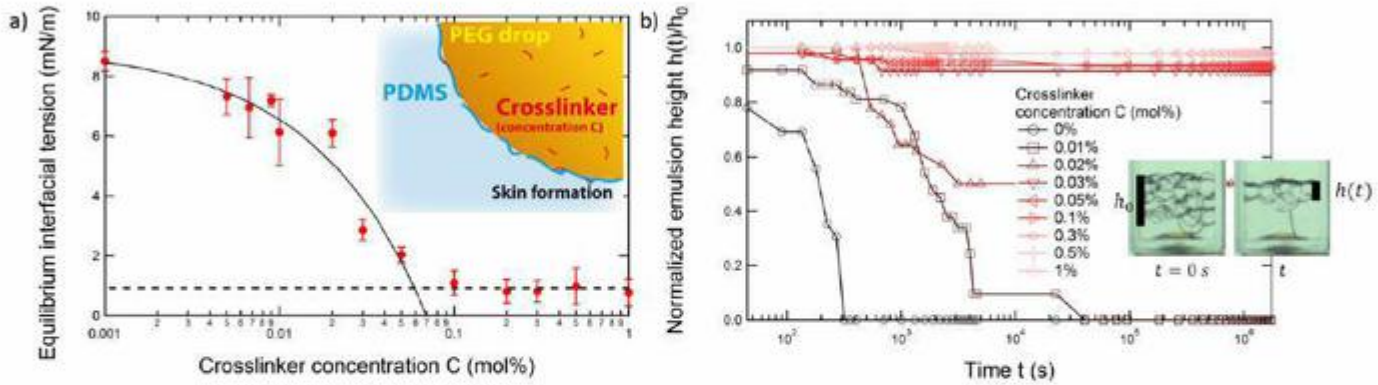

Figure 1: a) Equilibrium interfacial tension at the interface between a reactive PDMS and PEG for different concentrations of crosslinker C in the PEG phase. Insert is a scheme of the skin formation round the PEG drop. b) Evolution of emulsion stability with time for different concentrations of crosslinker C. Insert are pictures of the experiment with the definition of the emulsion height $h(t)$ and h_0, for $C = 0.01$ mol%.

Figure 1a shows the equilibrium interfacial tension for each crosslinker concentration, showing a non linear decrease with C down to 1 mN/m at 0.1 mol% beyond which the interfacial tension is independant of C at long times. We asign the decrease

*Corresponding author. Email: anais.giustiniani@u-psud.fr

of surface tension to the temporary formation of amphiphilic block-copolymers at the interface and the begining of the plateau to the formation of a skin around the PEG drop for $C > 0.05$ mol% [3].

To link these interfacial properties to the emulsion stability, we use a simple protocol. In a cuvette filled with the reactive PDMS, we generate drops of the PEG and crosslinker mixture one by one at a constant rate. They pile at the bottom of the cuvette, and we observe for different concentrations C the emulsion stability, given by the emulsion height $h(t)$ in the cuvette at time t normalized by the initial height h_0. The emulsion generation is prior to the beginning of the imaging at time t=0 s, so the h_0 is different for every concentration since the emulsion has already started evolving. Figure 1b shows the graphical representation of the evolution of the normalized emulsion height for every C. We see that there is a critical concentration 0.03 mol% $\leq C^* \leq$ 0.05 mol% which corresponds to the skin formation and beyond which the emulsions are stable indefinitely.

Using these results, we optimize the formulation needed to generate ultra-stable PDMS emulsions. To be able to vary the drop sizes, we use different techniques: millimetric droplets are generated by a needle connected to a syringe on which a constant flow rate is applied by a syringe pump (Figure 2a), whereas for smaller drops we use millifluidic techniques such as a flow-focusing device (Figure 2b) or a T-junction device [4]. With these different techiques, we generate stable emulsions with drop radii from 100 μm up to several millimeters, with different volume fractions of internal phase (Figure 2c to g), and with disorganized (Figure 2d, e, f and g) or organized (Figure 2c) structures. By solidifying the PDMS phase, one obtains a macro-cellular polymer, which we call a "solid emulsion" (Figure 2f and g).

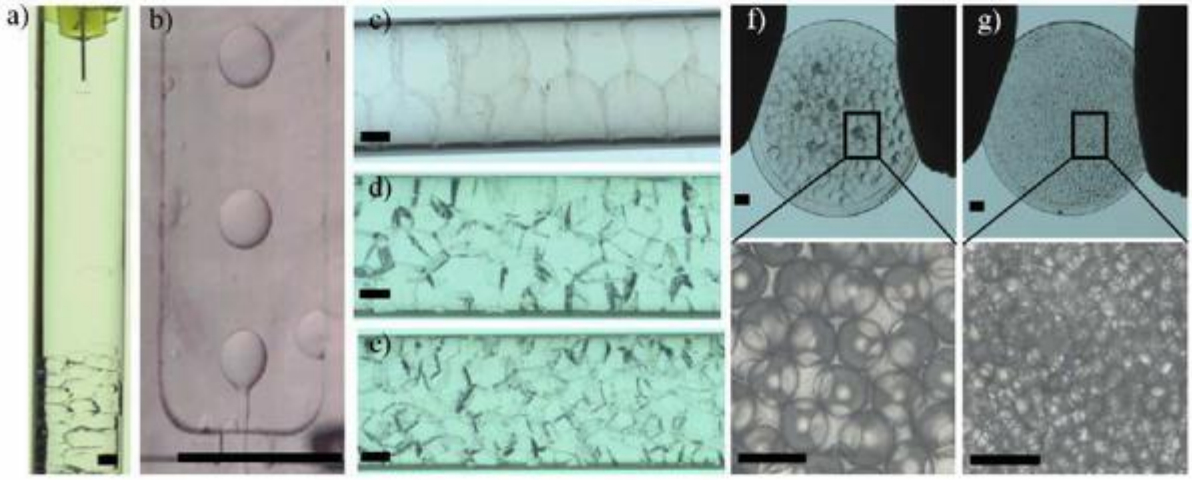

Figure 2: a) Generation of millimeter sized drops by simple dripping from a needle using a syringe pump. b) Generation of drops with a flow-focusing device. c) Liquid emulsion with high drop content and structured organization. d) and e) Liquid emulsions with high drop content and disorganized organization. f) and g) solid emulsions with their respective close-ups. The scale bars are 4 mm.

The obtained materials, either in the liquid state or solidified, present original structures as compared to hard granular materials or soft materials such as foams, because of their deformable but frictional interface [5, 6]. The presence of the liquid drops inside a purely elastic matrix modifies greatly the mechanical properties of the material as compared to the ones of the bare PDMS matrix. The size, organisation and volume fraction of the drops can be used to fine-tune the mechanical properties of the solid emulsion. Future work will concentrate on the control of the emulsion structure and its relationship with its visco-elastic properties.

References

[1] Silverstein M. S.: PolyHIPEs: Recent advacnces in emulsion-templated porous polymers. Progress in Polymer Science 39:199-234, 2014.

[2] Grosse M-T., Lamotte M., Birot M., Deleuze H.: Preparation of Microcellular Polysiloxane Monoliths. Journal of Polymer Science: Part A: Polymer Chemistry, 2008, 46.

[3] Giustiniani A., Guégan P., Marchand M., Poulard C., & Drenckhan, W.: Generation of silicone poly-HIPEs with controlled pore sizes via reactive emulsion stabilization. Submitted.

[4] Garstecki, P., Fuerstman, M. J., Stone, H. A., & Whitesides, G. M.: Formation of droplets and bubbles in a microfluidic T-junction - scaling and mechanism of break-up. Lab on a Chip, 6(3): 437-446, 2006.

[5] Jerkins M., Schröter M., Swinney H.L.: Onset of Mechanical Stability in Random Packings of Frictional Spheres. Physical Review Letters, 2008, 101.

[6] Van der Net A., Drenckhan W., Weaire D., Hutzler S.: The Crystal Structure of Bubbles in the Wet Foam Limit. Soft Matter, 2006, 2.

A CONTINUUM APPROACH TO MICRO-INERTIA EFFECTS IN CLOSED-CELL SOLID FOAMS

Romain Barthélémy[1,2], Nicolas Jacques[1a)], Steven Kerampran[1] & François Vermeersch[2]
[1]*ENSTA Bretagne, Laboratoire Brestois de Mécanique et des Systèmes, Brest, France*
[2]*MBDA France, Le Plessis-Robinson, France*

Summary The present work is devoted to the modelling of the behaviour of solid foams under dynamic loading conditions. Using micromechanics, a continuum model for micro-inertia effects in closed-cell foams is proposed. This simple model is aimed at improving constitutive models for foams by incorporating the contribution of micro-inertia. An application of the proposed modelling to shock wave propagation in metal foams is proposed. The influence of micro-inertia is found to be significant.

INTRODUCTION

Foams are highly porous materials with a relative density (ratio between the density of the foam and the density of its base material) generally lower than 0.3. Metal foams exhibit interesting mechanical properties. In particular, they have excellent energy absorption capabilities and are used in impact protection and shock mitigation applications. The dynamic behaviour of foams is generally different from the one observed under quasi-static loading, even for foams made of materials having a low strain-rate sensitivity (like some aluminium alloys) [1]. In fact, the macroscopic rate-dependency of metal foams is not necessarily related to the viscoplastic behaviour of the base material, but can be due to local inertia effects induced by the rapid crushing of the cells of the foam microstructure during deformation (micro-inertia effects) [2]. This finding was corroborated by the results of recent micromechanical finite element foam models (in which the microstructure is represented explicitly) [3,4].

In this contribution, we propose a continuum description of micro-inertia effects in closed-cell foams. The proposed model is based on a multiscale approach: a unit-cell of the foam microstructure is considered and the macroscopic foam response is obtained using a dynamic averaging procedure. An application of the proposed modelling to shock wave propagation is presented.

MICROMECHANICAL MODELLING

General dynamic homogenisation framework

The present model is based on the dynamic homogenisation technique introduced by Molinari and Mercier [5]. Here, this method is recast in a Lagrangian framework. We consider a Representative Volume Element (RVE) of porous medium that occupies the domain Ω_0 in the initial configuration. The macroscopic nominal stress tensor P_{ji} is defined as the conjugated quantity of the deformation gradient through the virtual work principle:

$$\delta F_{ij} P_{ji} = \langle \delta f_{km} p_{mk} \rangle + \langle \rho_0 \ \delta u_k \gamma_k \rangle \tag{1}$$

where γ_k and p_{mk} respectively denote the components of the acceleration and (nominal) stress fields within the RVE and ρ_0 is the initial (local) mass density. δF_{ij} is a virtual increment of the macroscopic deformation gradient, δu_k is a microscopic virtual displacement field and $f_{km} = \partial u_k / \partial x_m^0 + \delta_{km}$ (with δ_{km} being the Kronecker delta).
With this formalism, the macrostress is the sum of two contributions: a static stress P_{ji}^{sta} related to the behaviour of the constitutive material of the RVE and a dynamic stress P_{ji}^{dyn} induced by local inertia effects within the RVE.

$$P_{ji} = P_{ji}^{sta} + P_{ji}^{dyn} \tag{2}$$

The use of the virtual work principle is very convenient for an analytical characterisation of micro-inertia effects. Indeed, it is often possible to obtain a closed-form expression of the dynamic stress by adopting a suitable trial displacement (or velocity) field [5,6].

A model for closed-cell foams

A model for micro-inertia in closed-cell foams has been developed using the framework described in the previous section. For the derivation of the dynamic stress, we have considered an initially spherical shell as a RVE of the foam, see Fig.1. Because foams have large porosity, we suppose that the thickness of the cell t_c is smaller than its radius R_c and that the mass of the material is distributed over the reference surface Γ_m of the shell. The motion of this surface is defined by the relation: $x_i = F_{ij} x_j^0$. With these assumptions, the following expression for the dynamic stress has been obtained:

$$P_{ji}^{dyn} = \frac{1}{3} \overline{\rho_0} R_c^2 \ddot{F}_{ij} \tag{3}$$

a) Corresponding author. Email: nicolas.jacques@ensta-bretagne.fr

where $\overline{\rho_0}$ is the average initial mass density of the foam. It should be noticed that the dynamic stress is proportional to the second time derivative of the deformation gradient. This means that micro-inertia leads to macroscopic rate effects (even if the base material of the foam has a rate-insensitive behaviour).

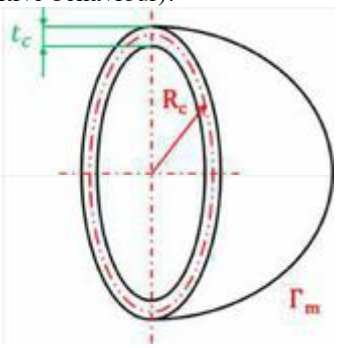

Fig. 1. Scheme of the Representative Volume Element (RVE) considered in the present approach. In the initial configuration, the RVE is a spherical shell of radius R_c and thickness t_c.

APPLICATION TO SHOCK WAVE PROPAGATION

The present model has been applied to the propagation of shock waves in metal foams. We have considered the configuration adopted in [4]. A foam specimen with a relative density of 0.1 and a length of 3 cm impacts a rigid wall. Several impact velocities have been considered. In all cases, a shock wave is generated at the impact surface.

Figure 2 presents a comparison between the results of the proposed continuum model and those of the 3D micromechanical finite element simulations presented in [4]. The results of a continuum simulation in which micro-inertia is not taken into account are also portrayed. It appears that micro-inertia has a significant influence on the features of shock waves. First, micro-inertia induces a shock structure: the shock front has a finite thickness and a continuous evolution of the velocity is observed (Fig. 2-a). Micro-inertia also leads to a reduction of the shock celerity (Fig. 2-b). The results of the proposed modelling are in close agreement with those of the micromechanical finite element simulations.

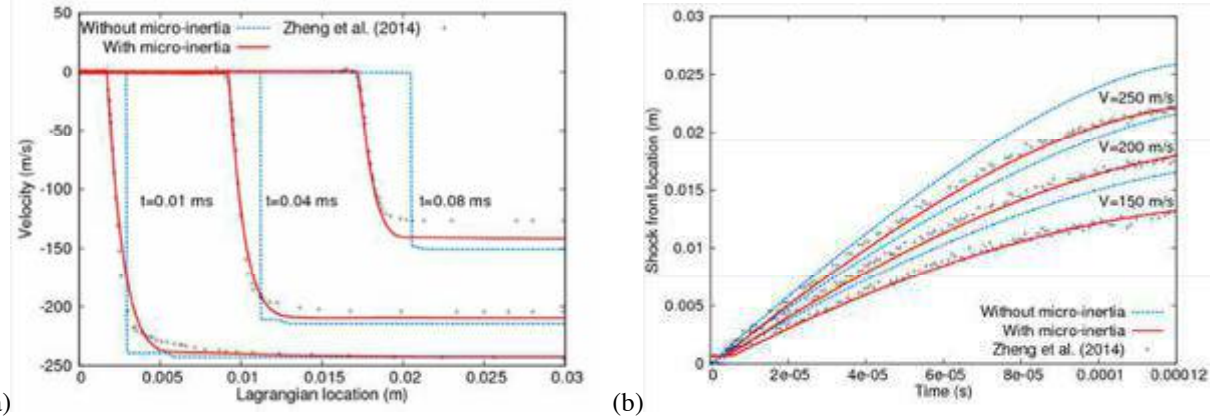

(a) (b)

Fig. 2. Illustration of the influence of micro-inertia on shock propagation. The impact of a foam specimen with a length of 0.03 m against a rigid wall is considered. (a) Velocity distribution along the specimen at several times for an impact velocity of 250 m/s. (b) Time evolution of the shock front position for different impact velocities. The results obtained with and without micro-inertia are compared to the results of the micromechanical finite element simulations of Zheng et al. [4]

References

[1] Barnes A.T., Ravi-Chandar K., Kyriakides S., Gaitanaros S. Dynamic crushing of aluminum foams: Part I–Experiments. *Int J Solid Struct* **51**:1631-1645, 2014.

[2] Tan P.J., Reid S.R., Harrigan J.J., Zou Z., Li S. Dynamic compressive strength properties of aluminium foams. Part I - experimental data and observations. *J Mech Phys Solid* **53**:2174-2205, 2005.

[3] Gaitanaros S., Kyriakides S. Dynamic crushing of aluminum foams: Part II–Analysis. *Int J Solid Struct* **51**:1646-1661, 2014.

[4] Zheng Z., Wang C., Yu J., Reid S.R., Harrigan J.J. Dynamic stress–strain states for metal foams using a 3D cellular model. *J Mech Phys Solid* **72**:93-114, 2014.

[5] Molinari A., Mercier S. Micromechanical modelling of porous materials under dynamic loading. *J Mech Phys Solid* **49**:1497-1516, 2001.

[6] Molinari A., Jacques N., Mercier S., Leblond J.B., Benzerga A.A. A micromechanical model for the dynamic behaviour of porous media in the void coalescence stage. *Int J Solid Struct* **71**:1-18,2015.

ACOUSTICAL PROPERTIES OF LIQUID FOAMS

J. Pierre[1,3,4], V. Leroy*[1], R.-M. Guillermic[2,5], W. Drenckhan[2], A. Saint-Jalmes[3], B. Dollet[3], and F. Elias[1]

[1]*CNRS/Université Paris-Diderot/UPMC, laboratoire MSC, Paris, France*
[2]*CNRS/Université Paris-Sud, LPS, Orsay, France*
[3]*CNRS/Université Rennes 1, IPR, Rennes, France*
[4]*CNRS/UPMC, d'Alembert, Paris, France (Present affiliation)*
[5]*University of Manitoba, Department of Physics and Astronomy, Winnipeg, Canada (Present affiliation)*

Summary Sound velocity and attenuation measurements in well-characterized liquid foams were performed over a wide frequency range (1-600 kHz). The study was limited to the long wavelength case: even for the highest frequencies explored, the wavelength was larger than the typical size of the micro-structure of the foams. Typical results are shown, for a foam with a liquid volume fraction of 10%. A strongly dispersive behavior was found, with three regimes of propagation: at low frequencies, the effective velocity was 33 m/s, as predicted by Wood's law; at high frequencies, the velocity was of the order of 220 m/s; in the intermediate regime, velocity and attenuation varied strongly with frequency, presenting the typical features of a low frequency resonance. A new model is proposed, based on the coupled displacements of films, liquid channels and gas in the foam.

Solid foams and fibrous media have been extensively studied for their acoustical properties, in particular in the scope of sound attenuation. Liquid foams, on the other hand, have received much less attention from acousticians and, as such, they still exhibit unexplained acoustical properties. For instance, it has not been clear whether the high acoustic attenuation measured in liquid foams was mainly due to viscous losses [1] or thermal losses [2]. Moreover, evidence of a low frequency resonance had been reported, but the mechanism of this resonance was not identified [3, 4, 5]. The influence of the chemical composition (*e.g.*, the surfactant used to stabilized the foam) had not been investigated [6]. Here we focus on another open question: what is the effective sound velocity in a liquid foam? According to Wood's law, sound should propagate in a mixture of air and water with a velocity given by the approximate formula: $v_W = 10\,\mathrm{m.s}^{-1}/\sqrt{\Phi(1 \nearrow \Phi)}$ where Φ is the liquid volume fraction (for $2\% < \Phi < 98\%$, this simple formula gives a good approximation of Wood's law, within 3% of relative error, for a mixture of water and air, assuming an isothermal behavior for the air). Some experiments had shown that Wood's law was correct for liquid foams [7, 8], but others had revealed significant deviations [9, 2].

To shed light on this question, we performed experiments with two main improvements compared to previous studies:

- We covered an extended range of frequencies (from 1 to 00 kHz). The low frequency regime was investigated by using an impedance tube [10], while broadband air transducers were used to explore the ultrasonic regime [11].
- We worked with well-characterized foams, *i.e.* we controlled their chemical composition and liquid volume fraction (Φ), and were able to precisely determine the bubble size distribution [12]. Lognormal distributions were found, with average radii of the order of 20 to 0 μm, and a polydispersity index (normalized standard deviation) of about 0. .

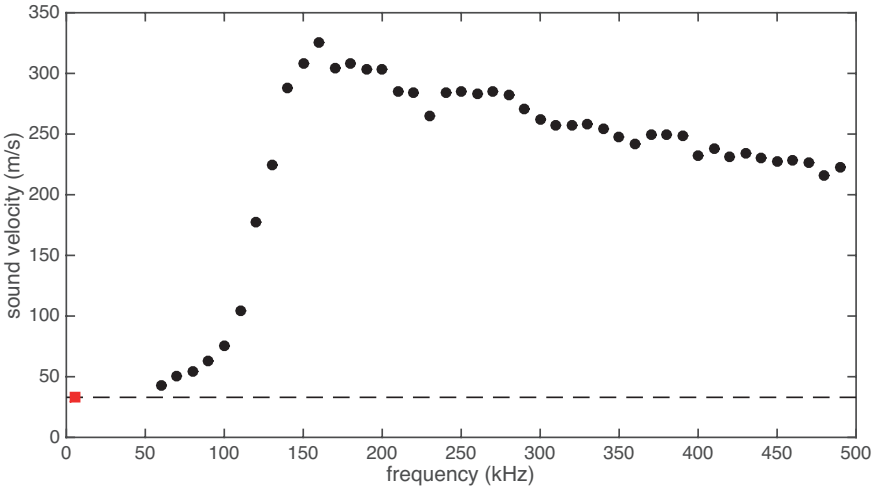

Figure 1: Measured sound velocity, as a function of frequency, in liquid foams with a liquid volume fraction of $\Phi = 10\%$. **Square**: low frequency results (impedance tube) for an average bubble radius of 22 μm and a polydispersity index of 0. . **Circles**: high frequency results (broadband air-transducers) for an average bubble radius of 5 μm and a polydispersity index of 0. 2. **Dashed line**: velocity predicted by Wood's law for $\Phi = 10\%$ (33 m/s).

Figure 1 shows a typical measurement we obtained for the sound velocity as a function of frequency, in a $\Phi = 10\%$ foam. Sound propagation is clearly dispersive, with a Wood's velocity at low frequency, and a higher speed ($\simeq$ 220 m/s) at high

*Corresponding author. Email: valentin.leroy@univ-paris-diderot.fr

frequencies. Dispersion is accompanied by a strong attenuation (not shown), which peaks at 120 kHz (*i.e.*, the frequency at which the increase of sound velocity is steeper in Fig. 1).

We propose a new model to explain our experimental findings [13]. It is based on the particular structure of liquid foams. Foams can be viewed as an assembly of struts (or liquid channels, in the liquid case) connected together to form a network. But contrary to solid foams, which can be either opened-cell or closed-cell, liquid foams are necessarily closed-cell. Indeed, their mechanical stability depends on the existence of the thin films that maintain the tension through the liquid network. These thin films that separate neighboring bubbles appear to be key ingredients to explain the acoustical properties of the foam, because they strongly couple the air and the liquid network displacements. At low frequency, all the components (air, films, struts) move together and Wood's law is recovered. But, at higher frequency, only the air and the films move; the inertia of the struts being too high to let them vibrate. As a consequence, the effective density of the foam is reduced, which explain the high sound velocity observed experimentally. In the intermediate regime, the strong attenuation is explained by a low frequency resonance of the strut-film system, which even gives rise to a regime of negative effective density [13].

Acknowledgement

Support from the French "Agence Nationale de la Recherche" is gratefully acknowledged (ANR-11-BS09-001, project SAMOUSSE supervised by F. Elias).

References

[1] Orenbakh Z. and Shushkov G.: Velocity and dissipation of sound in gas-liquid foams. Soviet physics Acoustics 38, 1992.

[2] Mujica N. and Fauve S.: Sound velocity and absorption in a coarsening foam. Physical Review E 66: 021404, 2002.

[3] Ding J., Tsaur F.W., Lips A., and Akay A.: Acoustical observation of bubbles oscillations induced by bubble popping. Physical Review E 75: 041601, 2007.

[4] Bretagne A., Tourin A. and Leroy V.: Enhanced and reduced transmission of acoustic waves with bubble meta-screens. Applied Physics Letters 99: 221906, 2011.

[5] Salem I.B., Guillermic R.-M., Sample C., Leroy V., Saint-Jalmes A. and Dollet B.: Propagation of ultrasound in aqueous foams: bubble size dependence and resonance effects. Soft Matter 9, 1194-1202, 2013.

[6] Pierre J., Giraudet B., Chasle P., Dollet B. and Saint-Jalmes A.: Sound propagation in liquid foams: unravelling the balance between physical and chemical parameters. Physical Review E 91: 042311, 2015.

[7] Orenbakh Z. and Shushkov G.: Acoustical characteristics of water-air foams. Acoustical Physics 39: 63-66, 1993.

[8] Shreiber I., Ben-Dor G., Britan A. and Feklistov V.: Foam self-clarification phenomenon: An experimental investigation. Shock Waves 15: 199-204, 2006.

[9] Zamashchikov V. and Kakutkina N.: Experimental investigations of the acoustical properties of foams. Soviet physics Acoustics 37: 248-250, 1991.

[10] Pierre J., Guillermic R.-M., Elias F., Drenckhan W. and Leroy V.: Acoustic characterisation of liquid foams with an impedance tube. The European Physical Journal E 36: 1-10, 2013.

[11] Pierre J., Elias F. and Leroy V.: A technique for measuring velocity and attenuation of ultrasound in liquid foams. Ultrasonics 53: 622-629, 2013.

[12] Gaillard T., Honorez C., Jumeau M., Elias F. and Drenckhan W.: A simple technique for the automation of bubble size measurements. Colloids ans Surfaces A: Physicochemical and Engineering Aspects 473: 68-74, 2015.

[13] Pierre J., Dollet B. and Leroy V.: Resonant acoustic propagation and negative density in liquid foams. Physical Review Letters 112: 148307, 2014.

THERMOCAPILLARY FORCED-DRAINED FOAM: EFFECT OF SURFACE RHEOLOGY

Vincent Miralles[1], Emmanuelle Rio[2], Isabelle Cantat[3], and Marie-Caroline Jullien*[1]
[1]*MMN, UMR CNRS 7083, PSL research University, ESPCI ParisTech, 10 rue Vauquelin, 75005 Paris, France.*
[2]*Laboratoire de Physique des Solides, UMR CNRS & Université Paris-Sud 8502, 91405 Orsay Cedex, France.*
[3]*IPR, UMR CNRS 6251, Université de Rennes 1, 35000 Rennes, France.*

Summary In this paper, we show that a thermocapillary stress induces a surface flow which can be sufficient to counteract the bulk gravity drainage, *i.e.* it is possible to stop, or even reverse, the drainage of a liquid foam. We report experiments using either a soluble (SDS) or poorly soluble (DOH) surfactant in a model system, a 2D microfoam, in which the full geometry of the liquid phase is known, leading *a priori* to accessible modeling. In the former case, surface rheology can be disregarded and a model considering mass conservation allows recovering the experimental results. In the later case, the boundary condition includes Gibbs elasticity (non homogeneous surface concentrtaton of surfactant) and both shear and dilational surface viscosities. In this case, investigating surfactant transport mechanisms could not allow extracting a dominant contribution leading to the conclusion that all surface rheology properties have to be considered.

INTRODUCTION

The development of controlled discrete materials (containing packed gas inclusions) covers a large variety of applications such as scaffolds for tissue engineering [1], enhanced oil recovery [2], optics [3] and phononic crystals [4] to cite a few. Controlling gravity drainage leading to non homogeneous gas inclusions is thus an issue to develop controlled materials. Foam drainage models have been steadily refined since the pioneering work of Leonard and Lemlich [7], either considering surface shear viscosity or Gibbs elasticity without leading to a general consensus on a dominant mechanism [5]. In this work, we propose to investigate surface viscoselasticity in a model system which is a 2D microfoam. The advantages are manifold: at microscales, there is no film between adjacent bubbles, the liquid fraction is constant for a cavity smaller than the capillary length, and together with a monolayer of bubbles, allows extracting the 3D liquid fraction of the foam. This configuration may thus appear as a building block experiment for modeling. We first present drainage experiments using a soluble surfactant, SDS, which will be considered as a reference experiment. We show that for a soluble surfactant it is possible to predict the drainage dynamics using mass conservation arguments, while the addition of a small amount of non soluble surfactant, DOH, sufficiently complexifies the boundary condition at the interface to prevent from simple modeling.

EXPERIMENTAL SETUP

The experimental setup is made of a Polydimethylsiloxane (PDMS) Hele-Shaw cell fabricated using soft lithography, of dimensions $L \times w = 2000 \times 1500\,\mu\text{m}^2$ in the plane, and thickness $e \in \{19.3\,;\,5\ .2\}\,\mu$m, see inset of Fig.1.a. Optimized resistors placed below the cell generate a linear temperature profile [6], leading to a constant thermocapillary stress throughout the foam: $\mathrm{d}_x\gamma = \partial_x T\ \partial_T\gamma$. The foaming solution consists of SDS (Sigma-Aldrich, 16 mM - 2 cmc - at 25°C) with DOH (Fluka, the concentration will be precised throughout the paper) mixed with glycerol (5.68 wt%, Aldrich) in deionized water (Millipore). In the following, the DOH bulk concentration will be noted either $[DOH]$ in the graphs, or simply c in the equations. The cavity can be placed either horizontally, undergoing both gravity drainage and the thermocapillary pumping, or horizontally, undergoing solely the thermocapillary pumping. We quantify the drainage dynamics by following the time evolution of the liquid fraction ϕ, by image processing [8]. The drainage dynamics is shown on Fig.1.b.c.d. At initial time the bubbles do not touch Fig.1.b, as drainage is processed, bubbles come into contact Fig.1.c, then the contact point stretches to extend as a contact line Fig.1.d. Drainage dynamics is quantified during the stages c and d.

SOLUBLE SURFACTANT

The liquid fraction as a function of time for a SDS solution is plotted on Fig.1.e. In these experiments, the cell is placed vertically, the liquid flow results from the combination of a bulk flow driven by gravity and a surface flow driven by the thermocapillary stress. Without any temperature gradient, the liquid drains towards the bottom of the cavity over a typical time of 15 s. By switching on the temperature gradient at 3.1 K.mm^{-1}, the liquid fraction is kept constant all along the experiment, stopping gravity drainage is successfully achieved. While increasing the temperature gradient at 7 K.mm^{-1}, the liquid exits the cavity towards the top of the cavity, showing that it is even possible to counteract gravity drainage. A simple model can be derived considering that the liquid flux exiting the cavity results from a thermocapillary flux and a gravity flux. In this model, the boundary condition at the interface is reduced to $\eta\frac{\partial v_x}{\partial n} = \not{\frac{\partial\gamma}{\partial x}}$. It is found that the liquid fraction evolves exponentially, $\phi : \phi_0\ \ \mathrm{xp}(\not{t}/t_d)$ where ϕ_0 is the initial liquid fraction and t_d a typical drainage time, which is found to be robust as compared to the experimental data (see Fig. 1.e).

*Corresponding author. Email: marie-caroline.jullien@espci.fr

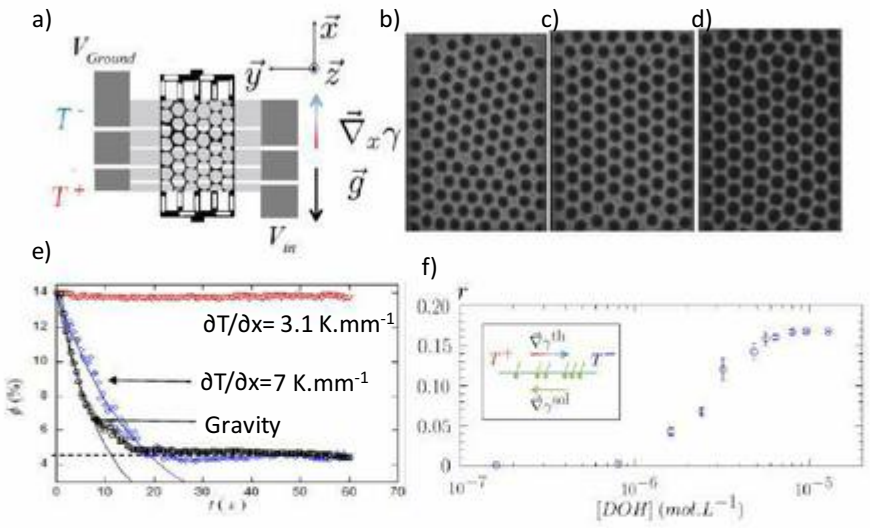

Figure 1: a) Sketch of the experimental setup, b-c-d) Snapshots of the foam during drainage, e) time evolution of the liquid fraction for a SDS solution, f) damping factor r for different [DOH] concentration.

POORLY SOLUBLE SURFACTANT

By adding a small amount of DOH in the solution, the boundary condition is strongly modified to:

$$\eta\frac{\partial v_x}{\partial n} = -\left[\frac{\partial\gamma}{\partial x} + \kappa\frac{\partial}{\partial x}\left(\frac{\partial v_t}{\partial t} + \frac{\partial v_x}{\partial x}\right) + \epsilon\left(\frac{\partial^2 v_x}{\partial t^2} + \frac{\partial^2 v_x}{\partial x^2}\right)\right] , \tag{1}$$

The first term on the right hand side (RHS) is the Marangoni contribution containing both the thermocapillary stress, the driving term, and a solutocapillary contribution (Gibbs elasticity) stemming from an accumulation of surfactants at the front the bubbles (see insert if figure 1.f), leading to a Marangoni stress antagonist to the thermocapillary stress. The second and third term of the RHS of the equation are respectively the surface dilational and shear viscosities. As a whole, these three additional mechanisms lead to a damping of the thermocapillary pumping as sketched on figure 1.f, where r is a damping factor defined by $^- = {}^-{}_0(1-r)$, where v is the mean liquid velocity and v_0 is the mean velocity for a solution containing only SDS. It is clear that the addition of DOH leads to a slowing down of the drainage dynamics. In order to estimate the relative contribution of the three surface rheology properties, we investigate the different surfactant transport mechanisms (diffusion across the meniscus, convection along the film, diffusion across adjacent bubbles) and we cannot extract a clear dominant effect, showing the importance of taking into account the whole surface properties to fully understand drainage dynamics.

CONCLUSIONS

In this work, we present drainage experiments in a model system which is a 2D micro foam which allows, *a priori* to simple modeling as the geometry of the foam is fully accessible. We show that if the solution contains soluble surfactants, drainage dynamics can be easily modeled, while the addition of a poorly soluble surfactant sufficiently complexify the problem to prevent from any prediction.

References

[1] Wang C.-C., Yang K.-C., Lin K.-H., Liu H.-C., Lin F.-H.: Biomaterials 32, 7118, 2011.
[2] FarajzadehR. , Andrianov A., Krastev R., Hirasaki G.J., Rossen W.R.: Advances in Colloid and Interface Science 183-184, 1-13, 2012.
[3] Hashimoto M., Mayers B., Garstecki P., Whitesides G. M.: Small 2, 12921298, 2006.
[4] Leroy V., Bretagne A., Fink M., Willaime H., Tabeling P., Tourin A.: Appl. Phys. Lett. 95, 171904, 2009.
[5] Cohen-Addad S., Höhler, R.:Current Opinion in Colloid & Interface Science 19, 536–548, 2014.
[6] Selva B., Cantat I., Jullien M.-C.: Phys. Fluids 23, 052002, 2011.
[7] Leonard, Lemlich: AICHE J. 11, 18-25, 1965.
[8] Miralles V., Selva B., Cantat I., Jullien M.-C.: Phys. Rev. Lett. 112, 238302, 2014.

MODELLING THE CRUSHING BEHAVIOR OF A CERAMIC BRITTLE FOAM

Omar Kraiem *[1], Nicolas Schmitt[1], Amine Neffati[2], and Han Zhao[1,3]
[1]*LMT-Cachan UMR 8535, ENS Cachan, CNRS, Université Paris Saclay, Bâtiment Léonard de Vinci, 61 avenue du Président Wilson, 94230 Cachan,*
[2]*TN International, 1 Rue des Hérons, 78180 Montigny-le-Bretonneux,*
[3]*Sorbonne Universités, UPMC Univ Paris 06, UFR 919, 75005 Paris, France.,*

Summary This paper presents some experimental results and numerical computations carried out to model the quasi-static crushing behavior of an open-cell ceramic foam (OCCF). The aim was to identify a continuum model able to predict the mechanical response under complex compression loading paths. Different multiaxial compression tests have been performed to characterize the 3D-response of the material, which is slightly anisotropic, strongly non-linear and dependent on the compaction level. It has been shown that the Deshpande-Fleck (DF) yield criterion which depends on both the mean stress and the von Mises effective stress fit the experimental data well. The original DF model developed for foams has been modified by introducing a dependence of the plastic Poisson's ratio with the plastic volumetric strain to improve the prediction of the radial expansion. It has been implemented into the finite-element code LS-Dyna via an usermat subroutine. Results of a simulation of a lab-scale shock absorber subjected to compression are in close agreement with the experimental results and validate the model robustness.

INTRODUCTION

Open-cell ceramic foams (OCCF) constitute a new promising lightweight materials combining interesting physical and thermo-mechanical properties [1]. In particular their ability to accommodate large deformation when it is confined makes them good candidates for energy absorption engineering applications. When subjected to an impact, a confined foam part is subjected to a multiaxial stress state, which is more complex than the uniaxial compression state. Consequently, there is a need to characterize the behavior under multiaxial loadings to identify a mechanical model.

METHODS

To do that, an experimental campaign including multiaxial compression tests was conducted to reproduce the stresses present during the crushing impact. In addition, SEM and X-ray tomographic observations were made. In this paper only quasi-static loadings are described. The experimental results were obtained on cylindrical and cubical specimens of OCCF ($\rho = 280$ g·cm^{-3}). Uniaxial compression tests with and without lateral confinement on the cylindrical specimens were performed with universal hydraulic testing machine (Instron). An ex-situ quasi-static compression test was also performed on an cylinder. To investigate their failure mechanisms, 3D images of the progressive degradation of the sample are reconstructed using X-ray micro-computed tomography analysis. The multiaxial loadings program consisted of three types of triaxial tests such as hydrostatic compression, oedometric compression and proportional compression. These tests were conducted with Canto's compaction device [4] installed in the triaxial testing machine ASTREE. This machine comprises six independent actuators paired up along the three perpendicular directions pushing the blocks to reduce the hole, each one sliding relative to the others. During the triaxial tests, the imposed displacements on the cubical specimen in each direction were measured by laser displacement sensors. Based on the experimental data a slightly modified Deshpande-Fleck model [2] has been identified. The modification of the model has been implemented as a user-defined material model subroutine in the finite element code LS-DYNA [3]. Then simulations by finite element method of crushing tests on a metallic confined OCCF part have been carried out in order to validate this model.

RESULTS AND DISCUSSION

For the multiaxial characterization, under hydrostatic compression loading (ISOU), it was observed that the compressive strength in the foaming direction is higher than that on the two other directions indicating an isotropic transverse behavior of the ceramic foam. Common to most ductile foams, when lateral displacement was prevented by metallic confinement (OEDO conditions), OCCF showed a typical compressive response with the three distinctive regions: at first a short elastic range with a brittle failure, then a crushing plateau and finally a densification with an increase in stiffness and stress (Fig. 1(a)). The confining pressure remained constant after the first damage of the specimen and then it increased as the volumetric strain increase. This result indicates also that the foam displays a non-constant plastic Poisson's ratio. The non-proportional compaction tests (TRIAX) consisted to impose an axial displacement at a constant rate while keeping constant the lateral force. For different confining pressures, this loading path permitted to show that the load-carrying capacity of the OCCF increases significantly with the confining pressure. The analysis of the 3D macroscopic images and SEM micrographs has enabled tracking the mechanisms of deformation during the test (Fig. 1(b)). The images have shown that the non linear deformation of the OCCF are controlled by the appearance of crushing bands in the sample which resulted from the fragmentation of the foam sample into parts becoming more and more smaller until they are transformed into powder at the end of the densification. These observations were also confirmed by a 2D microscopic observation at small fine scale using SEM. In order to estimate the failure surface of the ceramic foam in the different multiaxial loading conditions, the experimental data from all the tests

*Corresponding author. Email: kraiem@lmt.ens-cachan.fr

may be plotted on a $\sigma_m - \sigma_e$ diagram where σ_e is the Von Mises effective stress and σ_m is the mean stress(Fig. 2(a)). The obtained behavior are well described by the elliptic yield criterion in the compressive zone of the space $\sigma_m - \sigma_e$ defined by the Deshpande-Fleck proposal

$$\Phi = \hat{\sigma}^2 - Y^2 = \frac{1}{[1 + (\frac{\alpha(\varepsilon_v)}{3})^2]}[\sigma_e^2 + \alpha(\varepsilon_v)^2\sigma_m^2] - Y^2 \quad (1)$$

where the parameter α defines the shape of the yield surface. To account for a good description of the hardening of the material during the densification, the initial Deshpande-Fleck model was modified to better predict the radial inelastic expansion in the plastic domain by introducing a dependence of the variable shape factor of the yield surface on the volumic plastic strain. To assess the model identification, the crushing of a small metallic confined OCCF part has been simulated by the finite element model and the numerical results compared with the experimental data obtained during a crushing test under quasi-static condition. Fig.2(b) shows the comparison of the force versus displacement curves from both the testing and the simulation. A good realistic description of the test has been obtained.

CONCLUSIONS

It is found that the presence of a crushing plateau at high level of stress under confined case permits to the open-cell ceramic foam to absorb a significantly quantity of energy during an impact. Its non-linear mechanical behaviour is slightly transversely isotropic but it can well described with the isotropic DF model under compressive loadings. Further investigation will be required to model the transversely isotropically behavior of the OCCF and more specifically the strong tension-compression asymmetry observed for this material before this model can be used in engineering studies.

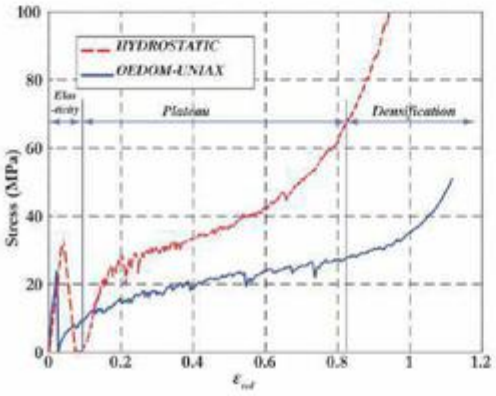

(a) *Stress-strain curves under uniaxial (OEDO) and hydrostatic compression (ISOU) tests*

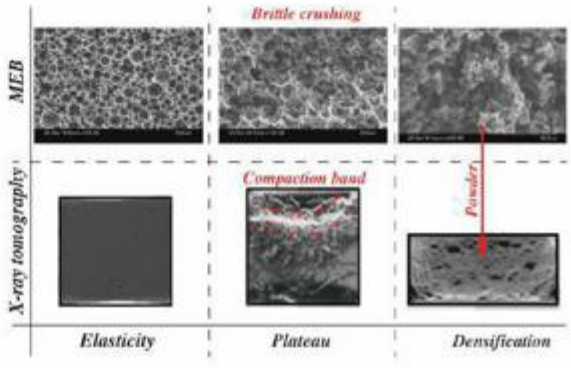

(b) *SEM and X-ray tomography observations of the failure deformation mechanisms under confined uniaxial compression*

Figure 1: *Experimental results of the OCCF material*

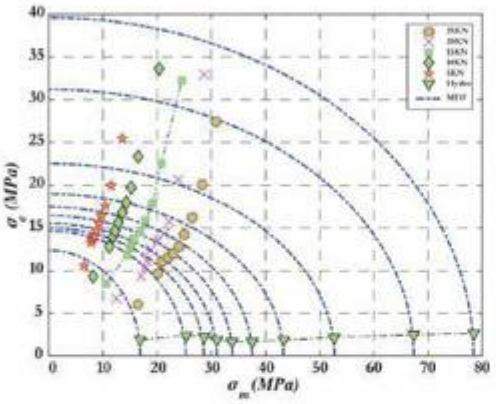

(a) *Yield surface of the DF model*

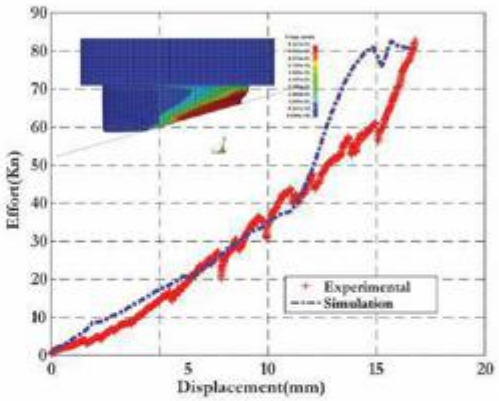

(b) *Comparison of experimental and numerical force-displacement curves from inclined crushing test*

Figure 2: *Numerical results obtained with the DF model*

References

[1] Michael Scheffler, Paolo Colombo: Cellular Ceramics: Structure, Manufacturing, Properties & Applications. Weinheim: Wiley-VCH, 2005.

[2] V.S. Deshpande and N.A. Fleck: Isotropic constitutive models for metallic foams. Journal of the Mechanics and Physics of Solids 48:1253 - 1283, 2000.

[3] J.O.Hallquist,Ls-dyna theoretical manual,1998

[4] Rodrigo C.: Theoretical and experimental study of the compaction and sintering processes of polytetrafluoroethylene (PTFE). Joint PhD thesis, ENS Cachan / USP, Cachan (France), 1983.

PHONONIC MICROLATTICES FOR ULTRASONIC APPLICATIONS

Sebastian Krödel[1a)], Chiara Daraio[1]
[1] *Department of Mechanical and Process Engineering, ETH Zürich, Zürich, Switzerland*

Abstract: Microlattice materials are assembled from slender, truss-like elements arranged in different three-dimensional geometries on a microscale. Recent advances in microfabircation tecniques allowed to obtain extreme properties in this new class of materials. Ultimately their periodicity and micro-size suggests to find applications in dynamic applications, especially in ultrasonic wave propagation. In this work, we study the response of microlattices to ultrasonic excitations, and tailor their acoustic transmission properties independently of the lattice's quasi-static response. We fabricate polymeric microlattices using 3D direct laser writing and test their response experimentally. The studied microlattices are acoustically transparent in water over large frequency regions, due to their water-like acoustic properties. Our findings can be applied in biomedical imaging devices, targeted cell surgery and for the protection of sensitive MEMS.

INTRODUCTION

Most design approaches for determining static properties of periodic microlattices rely on either selecting the lattice material or the variation of the unit cell geometries. To change the constitutive law of the base material polymeric microlattices have been coated with ceramics and metals to create composites [1]. Another approach is the coating an subsequent etching of the poilymer to create hollow lattice materials [2,3]. The obtained materials have shown to be extremely lightweight, while maintaining an unusually high strength, due to size effects that become important for nanometer thick walls. Microlattices have also been proposed as lightweight structures and for impact impact absorbsorption. More importantly their periodic architecture at the microscale allows them to naturally interact with ultrasonic waves (~10-100 MHz), which are of great technological importance. Acoustic waves in phononic crystals exhibit large and omnidirectional acoustic band gaps [4,5]. These band gaps typically occur when the wavelength is on the order of the lattice constant.

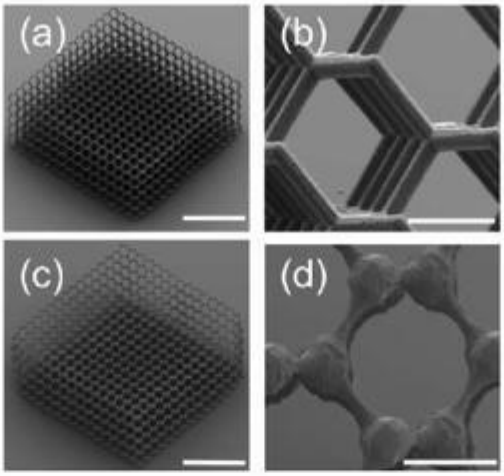

Figure 1: SEM micrographs of the analyzed microlattices materials with straight (a,b) and tapered (c,d). The scale bars are 250 μm in (a,c) and 25 μm in (c,d).

Here, we focus on the band structure engineering of ultrasonic frequencies using micro-architected, polymeric microlattices as phononic crystals. The structures are fabricated using 3D direct laser writing with a commercial Nanoscribe™ system. We vary the acoustic impedance in the lattice parametrizing the single truss elements in the unit cell, instead of variations in the unit cell geometry. We study a diamond-like lattice symmetry (Fig. 1) with a lattice constant of a = 70 μm. The unit cell is constructed from 4 trusses that are connected in one central joint. We study two different parameterizations: Straight trusses with a fixed truss radius of 3.5 μm (see Fig 1(a,b)) and tapered trusses with a radius between 6 μm and 1.5 μm (see Fig. 1(c,d)). These two lattices were chosen to have the same global, quasi-static effective stiffness, however they dramatically differ int their acoustic properties.

[a)] Corresponding author. Email: skroedel@ethz.ch.

NUMERICAL MODELING

We study one-dimensional chains of truss elements using Comsol Multiphysics© to gain analyze the fundamental building blocks of the unit cell. We draw analogies of the one-dimensional systems to the band structure of the full lattices (see Fig. 2(a,b) and derive their band structure for waves propagating in the *z*-direction. Furthermore, these numerical results are compared with the experimental findings.

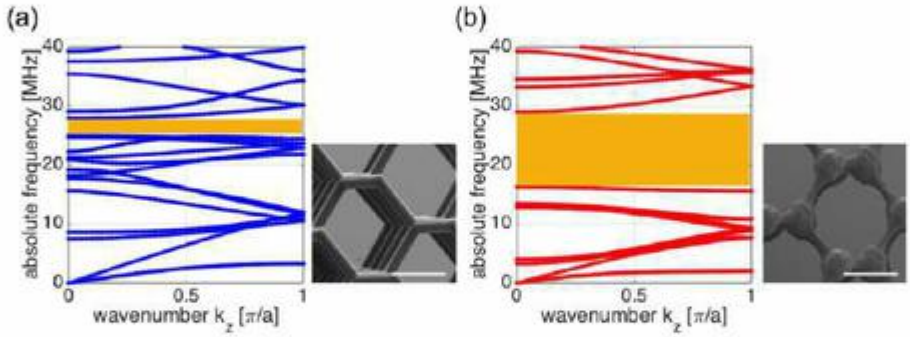

Figure 2: Dispersion relation in z-direction for the straight (a) and tapered (b) lattice materials. Scale bar represents 25 μm.

EXPERIMENTAL METHODS

To test the ultrasonic transmission properties within the lattices we designed a customized ultrasonic water tank (see Fig. 3(a)). The experimental setup is assembled in three main components: (1) a broadband ultrasonic transducer to generate the acoustic excitation; (2) a needle hydrophone to measure the pressure in the far field; (3) the sample and sample holder, positioned between the transducer and the needle sensor. To validate the experimental findings we calculate the frequency response of the two lattices immersed in fluid using the solid-acoustic interaction module in Comsol Multiphysics©. The experimental results (Fig. 3(b,c)) agree well with the numerical simulation.

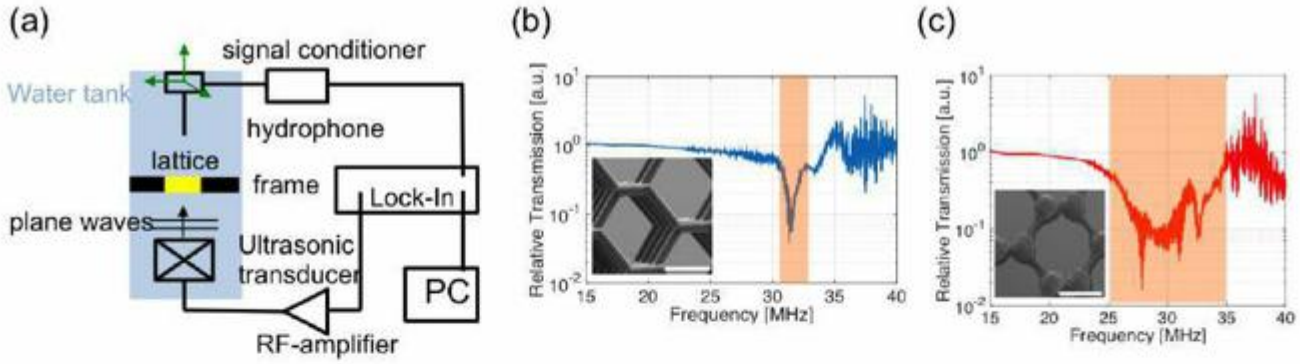

Figure 3: (a) Schematic of the experimental setup. Transmission results for straight (b) and tapered (c) lattice geometries. Scale bar represents 25 μm.

CONCLUSIONS

In summary, we have shown that parameterizing single truss members can effectively control the mechanical and acoustic properties of polymeric microlattice systems. This approach enables the engineering of the acoustic band structure independent of the static properties, such as stiffness. Moreover, the obtained lattices show extremely high acoustic transparency over broad frequency ranges in water, making them advantageous for ultrasonic applications where low reflectivity and narrow working frequencies are a primary need.

References

[1] J. Bauer, S. Hengsbach, I. Tesari, R. Schwaiger, O. Kraft. (2014). *Proc. Natl. Acad. Sci.*, **111**, 7, 2453-8

[2] L. R. Meza, A. J. Zelhofer, J. R. Greer. (2014). *Science,* **345**, 6202, 1322-1326

[3] L. R. Meza, A. J. Zelhofer, N. Clarke, A. J. Meteos, D. M. Kochmann, J. R. Greer. (2015). *Proc. Natl. Acad. Sci.,* **112**, 37, 11502-11507

[4] S. Yang, J. Page, Z. Liu, M. Cowan, C. Chan, P. Sheng. (2002). *Phys. Rev. Lett.*, **88**, 104301.

[5] O. Vasseur, P. a. Deymier, B. Chenni, B. Djafari-Rouhani, L. Dobrzynski, D. Prevost. (2001). *Phys. Rev. Lett.*, **86**, 3012.

AUXETIC EFFECTS INDUCED BY RE-ENTRANT ANGLE AND CHARALITY WITH LARGE DEFORMATION

Yunyao Jiang & Yaning Li[a)]
Department of Mechanical Engineering, University of New Hampshire, Durham, NH03824, USA

Summary The two basic mechanisms of the auxetic effects for open-cell structures are: (1) re-entrant angle, and (2) cell rotation. To explore and compare the auxetic effects caused by the two mechanisms under large deformation, representative structures from each category (the re-entrant honeycombs and chiral cells) were studied. Analytical analysis, finite element (FE) simulations and experiments on 3D printed specimens were integrated to explore the finite deformation of these structures. Thorough Finite Element (FE) simulations were performed to study the influences of independent non-dimensional geometric parameters on the deformation mechanisms including auxetic effects and instability of these structures. The limiting strains for preserving auxetic effects were obtained. Compared with the re-entrant honeycomb, the chiral structures were shown to be able to preserve auxetic effects for much larger deformation. Also, by adding a reinforced core to the basic chiral structure, the auxetic effects can be effectively enlarged.

Introduction

The auxetic open-cell structures have many engineering advantages due to their superior properties. For example, compared with the conventional materials, auxetic materials have increased indentation resistance, shear resistance and energy absorption capability. They also have variable permeability, and were used as fasteners, to achieve synclastic curvature, and to develop shape memory materials. In addition, auxetic materials have better acoustic and vibration properties over their conventional counterparts.

Based on different deformation mechanisms, existing auxetic cellular structures can be roughly classified into two categories, (1) two-dimensional and three-dimensional structures with re-entrant angles [1], and (2) chiral structures that deform by the rotation of cells [2]. Models beyond these two categories can be found in [3, 4]. Extended reviews of all of them can be found in [5, 6]. The classic re-entrant structure was proposed in [1]. The re-entrant structures are usually symmetric so that the negative Poisson's ratio can only be maintained within very small deformation (<~5%); then the structure will lose stability due to the breakage of symmetry. While, due to the non-symmetric rotational deformation mechanism, the chiral structures [2] have the potential to preserve negative Poisson's ratio for large deformation. In this investigation, three types of representative structures [1, 2], the re-entrant honeycomb, a basic chiral structure, and a chiral structure with reinforced core, were used to compare the auxetic effects induced by the two different mechanisms.

AUXETIC EFFECTS AND INSTABILITY OF RE-ENTRANT HONEYCOMBS

For the 2D re-entrant honeycombs, as shown in Fig.1a, the geometry is determined by two non-dimensional parameters, h/l and θ (the rib thickness to rib length ratio is fixed to be 10 for all geometries) and θ is negative. During uni-axial compression, it is well-known that for very small overall strain, the Poisson's ratio is negative. However, when the strain is large, two phenomena will occur within each cell: (1) contact between the ribs, and (2) instability (only micro-instability is considered here). After either of the two stages, the Poisson's ratio of the re-entrant honeycomb will become non-negative, therefore, auxetic effects are lost. Based on this analysis, the limiting strain to lose auxetic effect ε^* can be derived as a function of h/l and θ. From the kinematics, the limiting strain for contact within a cell is derived in this paper as a function of h/l and θ:

$$\varepsilon_{cr}^{c} = \frac{/ -2sin(-\theta)}{/ -2sin(-\theta)}. \tag{1}$$

Based on the Euler-Bernoulli beam theory, the critical strain for the micro-instability of a cell can be also derived as a function of h/l and θ[7]:

$$\varepsilon_{cr}^{i} = \frac{n^2\pi^2 l^2 cos^2\theta}{24h^2(/ +sin\theta)}, \tag{2}$$

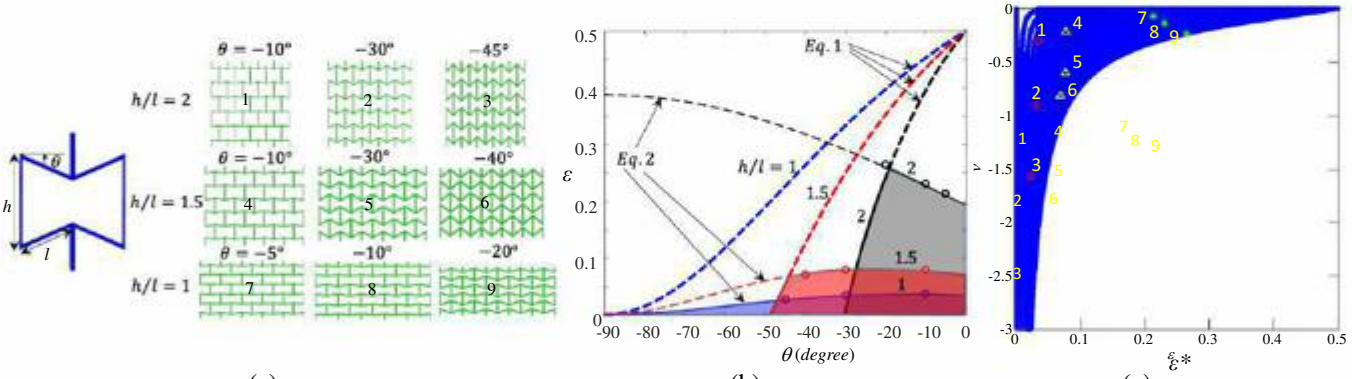

(a) (b) (c)

Fig.1 (a) The geometry of re-entrant honeycombs, (b) the limiting strain for auxetic effect, and (c) the limiting strain vs. Poisson's ratio for re-entrant honeycombs with arbitrary geometry.

[a)] Corresponding author. Email: yaning.li@unh.edu.

where, n is the end constraint factor [7], depending on the degree of constraint to rotation at the ends of the ribs. Thus, the limiting strain to lose auxetic effect is $\varepsilon^* = min(\varepsilon_{cr}^c, \varepsilon_{cr}^i)$ and the Poisson's ratio are expressed as a function of h/l and θ: $\nu_{21} = \frac{\left(\frac{h}{l}+sin\theta\right)sin\theta}{cos^2\theta}$ [7]. Fig. 1b shows the influences of the scale-independent parameter *h/l* and θ on the critical strain to contact (Eq.1) and instability (micro-instability)(Eq.2), and therefore the limiting strain to lose auxetic effects. The intersection points of the two set of curves from the two phenomena indicate the simultaneous contact and instability. The shaded areas underneath the two set of curves represent the parametric space with auxetic effects.

To verify the analytical solutions of the limiting strain and Poisson's ratio, nine 2D plane stress finite element models were set-up in ABAQUS-V6.13, by varying h/l and θ, as shown in Fig.1a. Periodic boundary conditions were used in all simulations. The markers in Figs. 1b and 1c represent the FE results. It can be seen that the analytical results can accurately predict both the limiting strain to lose auxetic effects and the Poisson's ratio. To further explore the relation between the limiting strain to lose axuetic effects and Poisson's ratio, ε^* vs. v_{21} for all possible h/l and θ were plotted in Fig.1c. It can be seen that for the re-entrant honeycombs, to obtain strong auxetic effects, the overall strain needs to be within ~5%. When the strain is larger than this value, the auxetic effects will become dramatically weaker or disappear. This indicates a serious drawback of auxetic structures designed based on the mechanism of re-entrant angle.

MICRO INSTABILITY AND MACRO INSTABILITY

To further explore the instability of these structures, mechanical experiments were performed on 3D printed specimens. Fig.2 shows the experimental results of a 3D-printed re-entrant honeycomb specimen. Uni-axial compression were performed on both x and y directions. In both experiments, the structure lost stability before contact between ribs. Two different instability modes were observed (1) micro-instability when compressed along y direction, and (2) macro-instability when compressed along x direction. Finite element simulations further confirmed the two instability modes. The instability modes is determined by h/l and θ, and the number of cells in the model.

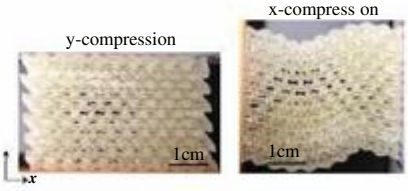

Fig. 2 Two instability modes from the mechanical experiments

AUXETIC EFFECTS OF A CHIRAL STRUCTURE

To further compare the auxetic effects under large deformation of the two basic mechanisms, FE simulations were performed for the cell for isotropic re-entrant honeycomb (h/l=2, θ=-30°), a basic chiral cell, and a chiral cell with reinforced core under vertical uni-axial compression, as shown in Fig.3 (right). 2D plane stress elements and periodic boundary conditions were used in all three cells. The representative volume elements (RVE) of the three cells have the same area, and the thickness of ribs in each cell is the same.

The curves of Poisson's ratio vs. overall compressive strain are shown in Fig.3 (left). It can be seen that for the cell of re-entrant honeycomb, the Poisson's ratio starts from ~-1, and when the overall strain reaches ~2%, the Poisson's ratio dramatically increases to ~0, indicating losing of auxetic effects. However, for the chiral cell, the Poisson's ratio starts from ~-0.4, and this value is preserved/slightly increases towards very large strain (>40%). If the reinforced core is added, the Poisson's ratio will be significantly reduced to ~-1, and this value will increases to~-0.55 for strain ~40%. The auxetic effcts are also well preserved for large overall strain.

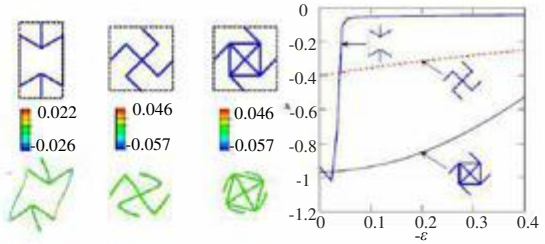

Fig.3 FE results of the three auxetic cells(The legend is for the in-plane principle strain. The overall strains are 12%, 48% and 40%, respectively.).

CONCLUSIONS

For the re-entrant honeycombs, the limiting strain for auxetic effects were derived and further explored by FE simulations and mechanical experiments on 3D printed specimens. It shows that the limiting strain to lose auxetic effects is due to either contact or instability (either micro or macro instability). Based on the results, re-entrant honeycombs can only preserve strong auxetic effects under very small overall strain (<~5%). However, the chiral structures can preserve auxetic effects for very large strain. For the chiral structures, to obtain stronger auxetic effects, a reinforced core can be added to the center of the basic chiral cell. FE simulations showed that by adding a reinforced core to the basic chiral cell, the Poisson's ratio of chiral structure decreases significantly; and this strong auxetic effect can also be preserved for a very large strain.

References

[1] Lakes R. S.: Foam structures with a negative Poisson's ratio. Science 235, 1038–1040, 1987.

[2] Smith, C.W., Grima, J.N., Evans, K.E.:A novel mechanism for generating auxetic behaviour in reticulated foams: missing rib foam model. Acta. Mater., 4349-4356, 2000.

[3] Wojciechowski K. W.: Two-Dimensional Isotropic System with a Negative Poisson Ratio. Phys. Lett. A 137, 60–64, 1989.

[4] Grima J. N., Alderson A. and Evans K. E.: Auxetic Behaviour from Rotating Rigid Units. Phys. Status Solidi B 242, 561–575, 2005.

[5] Evans K. E. and Alderson A.: Auxetic Materials: Functional Materials and Structures from Lateral Thinking! Adv. Mater. 12, 617–628, 2000.

[6] Greaves G. N., Greer A. L., Lakes R. S. and Rouxel T.: Poisson's Ratio and Modern Materials. Nat. Mater. 10, 823–837, 2011.

[7] Gibson L. J., Ashby M. F.: Cellular Solids: Structure and Properties. Oxford: Pergamon Press. 1988.

WHY LAGUERRE TESSELLATIONS ARE GOOD APPROXIMATIONS OF FOAMS

André E. Liebscher*[1], Andrew M. Kraynik[2], and Claudia Redenbach[1]
[1]*Department of Mathematics, University of Kaiserslautern, Kaiserslautern, Germany*
[2]*Physics Department, University of Erlangen-Nuremberg, Erlangen, Germany*

Summary Stochastic models are valuable tools to study the mechanical behaviour of low-density foams. Owing to a similar cellular morphology, Laguerre tessellations have turned out to be the natural model for such foams. Laguerre tessellations are additively weighted generalisations of Voronoi tessellations, where polyhedral cells are formed through interaction of spheres. However, the cell curvature of foams allows only an approximation by Laguerre tessellations. This work studies the error in elasticity induced by the approximation based on simulated random foams. For low polydispersities, Young's modulus is overpredicted with an almost constant error of at most 5 % by the Laguerre approximations. With increasing polydispersity the prediction error increases following a cubic function.

INTRODUCTION

Low-density foams can be perceived as a subdivision of space into random (slightly curved) polyhedral cells whose edges form an interconnected network. Its local structure obeys Plateau's laws, that is, only three faces may intersect at a dihedral angle of exactly 120°. In stochastic geometry a subdivision of space with this topology is known as normal tessellation. It can be shown that any normal tessellation of the three-dimensional Euclidean space $\mathbb{R}^3$ is a Laguerre tessellation [1].

A Laguerre tessellation is an additively weighted generalisation of the well known Voronoi tessellation. The latter is generated by a locally finite set $\varphi = \{x_1, x_2, \dots\} \subset \mathbb{R}^3$ by assigning to each point $x \in \varphi$ the polyhedron $C(x, \varphi)$ composed of those points in space that have x as nearest neighbour in φ. To generalise this notion, we attach to the points of φ positive weights. Each pair $[x, r] \in \varphi$ can then be interpreted as a sphere with centre x and radius r, whose corresponding *Laguerre polyhedron* is defined by

$$C\big([x,r],\varphi\big) = \left\{ y \in \mathbb{R}^3 : ||y-x||^2 - r^2 \le ||y-x'||^2 - r'^2 \quad \text{with} \quad [x',r'] \in \varphi \right\}. \tag{1}$$

If all radii are equal, we obtain the Voronoi polyhedron as special case.

Random Laguerre tessellations appear to be the natural model for low-density foams as both share the same topology and a similar random cellular morphology. However, the cell curvature of foams allows only an approximate representation by Laguerre tessellations. To answer the question how good such an approximation can be, we follow the approach in [2]. Its main idea is to find a set of spheres φ whose Laguerre tessellation best fits the cell system (and thus the edge system) of the foam by minimising the discrepancy between the individual cells of the foam and the Laguerre tessellation. We call such a tessellation Laguerre approximation.

The results in [2] show that the cellular morphology as well as the local topology are reproduced quite well by Laguerre approximations. In this work, we focus on the error in elasticity induced by the approximation based on simulated random foams. The foams were produced with the Surface Evolver [3] by minimising the surface area of Laguerre polyhedra generated from dense polydisperse sphere packings. We then computed the Laguerre approximations of the foams, calculated Young's moduli of the resulting tessellations by finite element analysis, and compared them to the moduli of the foams. The result of this comparison is shown in Figure 1.

ELASTICITY OF APPROXIMATED OPEN CELL FOAMS

For our study we used 8 foams with 1728 and 51 foams with 2197 cells. Their polydispersities ranged from 0 to 0.6, whereas values up to 0.3 are commonly found in real foams. The polydispersity p is defined as the quotient of the standard deviation σ_r and the mean $\bar{r}$ of the equivalent sphere radius r, i. e. $p = \sigma_r / \bar{r}$, where r is determined from the volume $V = \frac{4}{3}\pi r^3$ for each cell of the foam. Note that p equals zero only for monodisperse foams.

The foams were approximated using the method presented in [2]. This method provides an exact reconstruction of a tessellation if it is known to be a Laguerre tessellation. However, as foams cells (especially in foams with high polydispersity) have curved surfaces, an exact representation by Laguerre polyhedra is impossible. To measure the goodness-of-fit of the approximation, we compare the individual foam cells with their approximations and count the number of extra or missing cell neighbours. We denote this quantity as $\mathcal{F}_{\text{diff}}$.

The lower part of Figure 1 shows the mean goodness-of-fit of the Laguerre approximations, grouped into eight classes with respect to polydispersity. Between a polydispersity of 0 and 0.45 the approximation error stays below 5 % with a minimum of about 1 % around $p \approx 0.2$. For polydispersities above 0.45 the error increases to about 14 % at $p \approx 0.6$. This result is not surprising as Plateau's laws have great influence on the morphology of foams, whose cells necessarily need curvature to maintain their local topology.

*Corresponding author. Email: liebscher@mathematik.uni-kl.de

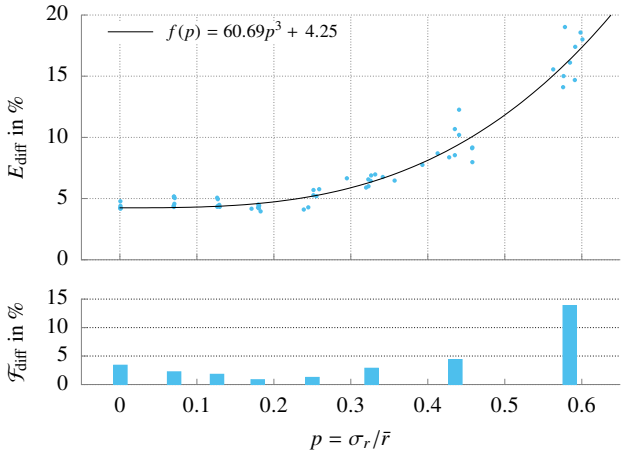

Figure 1: Increase in Young's modulus E_{diff} when approximating foams by Laguerre tessellations with respect to polydispersity p. $\mathcal{F}_{\text{diff}}$ is the mean error in local topology between a foam and its approximation, that is, the number of extra or missing cell neighbours.

To study the influence of the approximation error on elasticity, we determined the difference E_{diff} of Young's modulus for each foam and its corresponding Laguerre approximation. In both cases, Young's modulus was computed by connecting the vertices with straight beam elements of uniform Plateau-border cross section. The Young's moduli of the foams were always softer than then the ones of the Laguerre approximations. This effect is caused by the definition of faces in Laguerre polyhedra, where vertices must lay in a common plane. Owing to cell curvature this restriction does not hold for foams.

E_{diff} is depicted in the upper part of Figure 1. Up to a polydispersity of about 0.25, the error induced in Young's moduli by the Laguerre approximations is relatively insensitive with respect to polydispersity. Within this range it is almost constant and smaller than 5 %. The error then rapidly increases to about 17 % with increasing polydispersity. This relation is well described by a cubic function of the polydispersity p, more precisely

$$f(p) = 60.69p^3 + 4.25\,. \tag{2}$$

The coefficients of Equation (2) were determined by regression analysis using weighted least squares.

CONCLUSIONS

It was shown in [2] that the cellular morphology of foams is reproduced quite well by Laguerre approximations. For polydispersities below 0.45, the lower part of Figure 1 illustrates that even the local topology of the approximations is in astonishing agreement with the simulated foams. Within this range we observed at most 5 % incorrectly assigned cell neighbours in the complete structure. Hence, we may conclude that from a geometric point of view Laguerre tessellations are good approximations for low- to mid-polydisperse low-density foams.

In the presented study we additionally considered the mechanical response of open cell foams. For low-polydisperse foams with $0 \leq p < 0.25$, we found the elastic behaviour of the Laguerre approximations in very good agreement with the one of the simulated foams. The Young's moduli of the approximations were at most 5 % stiffer than the ones of the simulated foams. For mid-polydisperse foams with $0.25 \leq p < 0.5$, the error in Young's modulus increases to 12 % following a cubic function, despite the good geometric approximation. This result is not surprising as with increasing polydispersity the influence of cell curvature on the elastic behaviour becomes predominant.

In practice, however, foams barely exceed a polydispersity of 0.3. Laguerre tessellations are then able provide realistic models for low-density (open cell) foams. Even for higher densities Laguerre tessellations provide reasonable models for the mechanical behaviour of foams [4]. Moreover, the approach presented in this work can be applied to establish bounds for certain mechanical properties of foams as the isotropic Plateau polyhedra theory does for geometric ones [5]. An according study is subject of ongoing research.

References

[1] Lautensack C., Zuyev S.: Random Laguerre tessellations. *Adv. Appl. Probab.* **40**:630–650, 2008.

[2] Liebscher A.: Laguerre approximation of random foams. *Philos. Mag.* **95**:2777–2792, 2015.

[3] Brakke K. A.: The Surface Evolver. *Exp. Math.* **1**:141–165, 1992.

[4] Liebscher A., Andrä H., Kabel M., Merkert D., Redenbach C.: Modelling open cell foams based on 3d image data. In *Proceedings of the 20th International Conference on Composite Materials*. Copenhagen, Denmark 2015.

[5] Hilgenfeldt S., Kraynik A. M., Reinelt D. A., Sullivan J. M.: The structure of foam cells: Isotropic plateau polyhedra. *Europhys. Lett.* **67**:484–490, 2004.

IMBIBITION OF DRY AQUEOUS FOAMS BY OIL

Rémy Mensire[1], Jesse T. Ault[2], Keyvan Piroird[1], Howard A. Stone[2], and Elise Lorenceau [*1]
[1]*Université Paris-Est, Laboratoire Navier, UMR 8205 CNRS-ENPC-IFSTTAR - 2 allée Kepler F-77420 Champs-sur-Marne, France*
[2]*Department of Mechanical and Aerospace Engineering, Princeton University, Princeton, New Jersey 08544, United States*

Summary When put in contact with a liquid, dry foams may wick owing to surface-tension-driven flows until reaching equilibrium. This work is devoted to the dynamics of this imbibition process. We consider imbibition of non-wetting liquid, by putting the dry foam into contact with organic oils. Indeed, with the appropriate choice of surfactants, oil spontaneously invades the liquid network of the foam without damaging it. We consider two geometries for the oil: a large oil slick and a filled oil pore. Our experiments show original dynamics for the imbibition which are discussed using the framework of foam drainage.

INTRODUCTION

Dry liquid foams are biphasic systems constituted of a dense assembly of bubbles. These bubbles are separated by liquid foaming solution, distributed between the thin films, the slender liquid-filled channels, called Plateau borders, and the nodes [1, 2]. The flow of foaming solution throughout the different elements of foam, commonly referred to as foam drainage, has been investigated in various geometries. For example, when a dry liquid foam is put into contact at its bottom with its constitutive foaming solution, the liquid spontaneously rises within the liquid network following a $t^{1/2}$ law as experimentally observed in microgravity conditions [3, 4, 5]. On Earth (as opposed to microgravity conditions), theoretical predictions concerning semi-infinite foams with an initial liquid fraction equal to zero report that the capillary rise continues indefinitely despite gravity, following a $t^{1/3}$ law [6] that recalls capillary rise observed in corners [7, 8]. Dry aqueous foams can therefore be seen as soft liquid porous media in which imbibition processes can occur. This spongelike feature is of obvious practical importance in cleaning industries or Enhance Oil Recovery providing that the remarkable imbibition ability of foam holds for the liquid of interest.

EXPERIMENTS

We therefore consider the interaction of an aqueous foam with an immiscible oil. We first highlight the conditions under which the oil is not a defoaming agent. It appears that using oil and surfactant that ensures negative value of the Entry (E) and Spreading (S) coefficient, is a sufficient condition [9]. Those coefficient, derived from thermodynamics considerations are given by: $E = \gamma_{wa} + \gamma_{wo} \nearrow \gamma_{oa}$ and $S = \gamma_{wa} \nearrow \gamma_{wo} \nearrow \gamma_{oa}$, where γ_{wa},γ_{wo} and γ_{oa} are the interfacial tension of the water/air, water/oil and oil/air interfaces.

Then, we experimentally consider the foam ability to pump oil when trapped in different geometries corresponding to common configurations in geological media such as a reservoir and a soil pore as depicted in figure 1. We generate the foam into a rectangular column with a removable upper part. Thus, we can extract at the top of the column a foam sample for which

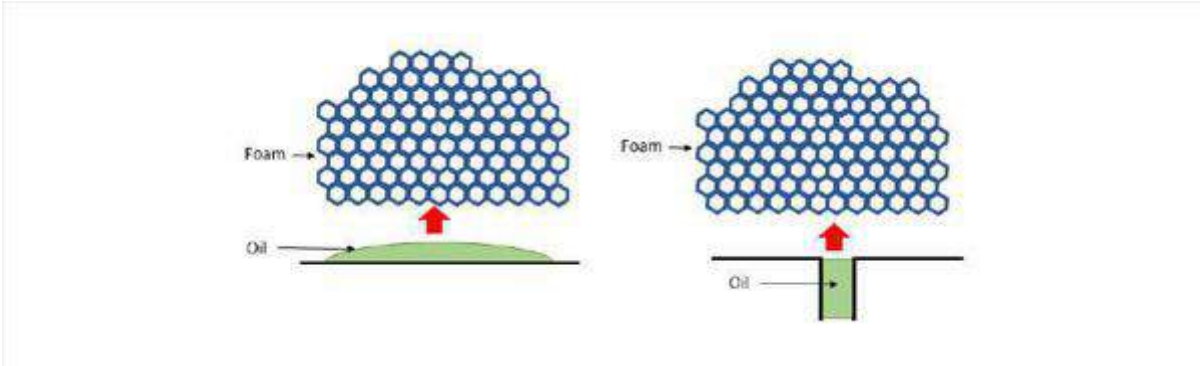

Figure 1: Geometries considered in this work. The dry foam is connected to a horizontal oil slick (left) or to a single pore (right)

*Corresponding author. Email: elise.lorenceau@ifsttar.fr

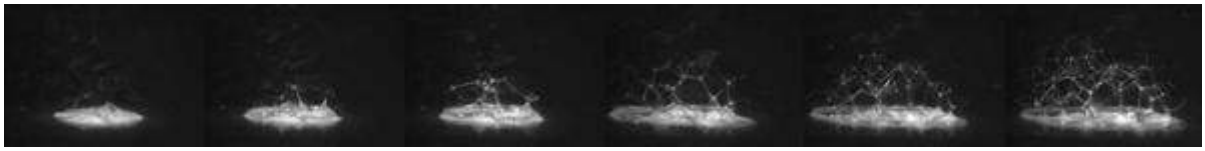

Figure 2: Imbibition of a fluorescent oil drop sitting on a flat surface by a dark aqueous foam placed above (see Figure 1 left). The oil drop is initially 2cm large and the time interval between the images is 5 s.

the liquid fraction can be measured. The foam sample is put into contact with the oil in situations depicted in Figure 1. Given that the contrast of optical indexes between the foam and the liquid is small or null, we add a small quantity of fluorescent dyes to the liquid. Those fluorescent markers, which are trapped in the liquid, provide a means of visualizing the swollen part of the foam. With this set-up and under illumination with excitation at 488 nm, the oil is luminous while the aqueous foam - only constituted of air and foaming solution - is not visible. Then, we use the fluorescence intensity to extract the dynamics of the imbibition front as can be seen in Figure 2.

DISCUSSION

We describe our experimental results using the non-linear foam drainage equation: Dynamics is driven by the capillary pressure and resisted by the viscous and gravity forces in the liquid microchannels. Assuming a constant pressure in the imbibing liquid reservoir, we show that the imbibition front advances and flattens out in time due to gravity, the effect of which is quantified by introducing the Bond number B, which compares the gravitational and capillary pressures using the mean bubble radius as a characteristic length. Theory, numerics and experiments are in good agreement [10, 11].

From our results, we also identify different criteria to predict which imbibing oil-foam couple makes imbibition possible. First, the capillary depression in the foam must overcome the oil depression to set the oil into motion. This condition is fulfilled in the limit of dry foam and small bubbles. Then, the entry and spreading coefficient must be negative and the ratio between the oil-water must be smaller than a critical value.

Last, we discuss the long term evolution of these oil-laden foams under classical ageing processes such as coalescence and topological rearrangements [12].

References

[1] Stevenson P.: Foam Engineering: Fundamentals and Applications Wiley, 2012.

[2] I. Cantat, S. Cohen-Addad, F. Elias, F. Graner, R. Hohler, O. Pitois, F. Rouyer, and A. Saint-James, Foams: Structure and Dynamics (Oxford University Press, Oxford), 2013.

[3] A. Saint-Jalmes, S. Marze, H. Ritacco, D.Langevin, S. Bail, J. Dubail, L. Guingot, G. Roux,P. Sung and L. Tosini, Phys. Rev. Lett., 98 (2007) 058303.

[4] H. Caps, S. Cox, H. Decauwer, D. Weaire, and N. Vandewalle, Colloids Surf. A 261, 131 (2005).

[5] S. Cox, D. Weaire, and G. Verbist, Eur. Phys. J. B 40, 119 (2004).

[6] S. A. Koehler, H. A. Stone, M. P. Brenner, and J. Eggers, Phys. Rev. E 58, 2097 (1998).

[7] A. Ponomarenko, D. Quere, and C. Clanet, J. Fluid Mech. 666, 146 (2011).

[8] T. Cambau, J. Bico, and E. Reyssat, Europhys. Lett. 96, 24001 (2011).

[9] P. Garrett, Defoaming: Theory and Industrial Applications (CRC, Boca Raton, FL, 1992).

[10] K. Piroird and E. Lorenceau, Phys. Rev. Lett. 111, 234503 (2013).

[11] R. Mensire, K. Piroird and E. Lorenceau, Phys. Rev. E. 92, 053014 (2015).

[12] K. Piroird, E. Lorenceau, and A.-L. Biance, Soft Matter 10, 7061 (2014).

FAILURE MECHANISMS IN ALSI10MG LATTICES VIA IN-SITU COMPRESSION TOMOGRAPHY

Lu Liu[1], Francisco Garcia-Moreno[2], John Banhart[2], Damiano Pasini[1a)]
[1] *Department of Mechanical Engineering, McGill University, Montreal, Quebec, Canada*
[2] *School of Processing Sciences and Engineering Department of Materials Science and Technology,Technical University of Berlin, Berlin, Germany*

Summary We use a non-destructive imaging technique to examine the mechanisms of damage initiation and failure evolution of aluminium alloy lattices with either rhombicuboctahedron or regular octet topology under quasi static compression. Results show that each lattice exhibits its own failure mechanism. For the rhombicuboctahedron topology, failure initiates on the top layer of the lattice sample before propagating into the neighbouring layers, thereby resulting in a layer-by-layer crushing mechanism. For the regular octet lattice, damage initiates at the interior surfaces , thus generating an apparent dislocation plane that splits the sample into two portions along a 45 degree plane. From tomography image reconstruction, geometrical imperfections, originated during the manufacturing process, were extracted, morphologically identified and statistically quantified. The probability values of each set of deviations were subsequently used to build realistic full-size finite element models that help elucidate the failure mechanisms and damage evolution observed during the experiments.

INTRODUCTION

Recent development in metal additive manufacturing (AM) enables the fabrication of lightweight metallic lattices with any cell shape and at multiple length scale. Lattices built with AM processes are not defect-free; geometrical imperfections generally emerge during the process, and inevitably lead to a change in the expected mechanical performance [1-2]. As a subset of periodic cellular materials, metallic lattices are structurally more efficient than stochastic metal foams due to their regular arrangement of cells [3]. Their cell topology is one of the main factors controlling their mechanical response, including stiffness, strength and failure mode. A number of experimental studies have been performed to study the mechanical properties of metallic lattices. While several failure modes were observed experimentally [4-5], the explanation of some failure mechanisms of metallic lattices built with AM are still unclear. In particular the role manufacturing deviations in the mechanisms of damage initiation and failure evolution of metallic lattice is still not well understood. This works proposes a combined approach of in-situ experiment and numerical simulations to address this issue.

EXPERIMENTAL INVESTIGATION

Two sets of prismatic lattice samples (size: 20*20*30 mm^3) with either rhombicuboctahedron or regular octet cells were manufactured via selective laser melting (SLM) of aluminium alloy powder AlSi10Mg. Each set contains five samples with identical design. Scanning electron microscopy and micro-computer tomography of each specimen were used to characterize their structural geometry. The former revealed the presence of surface beads resulting from partially melted metal particles. The latter pointed out a clear geometric deviation between the *as-designed* geometries of the lattices and their *as-manufactured* counterparts. In-situ mechanical testing through a miniature loading stage placed within a tomography apparatus was carried out on both set of samples under quasi static compression. After each loading step, the damage evolution was monitored in each slice of the samples through non-destructive imaging techniques.

Results from tomography and mechanical testing show that each lattice exhibits its own mechanism of failure. For the rhombicuboctahedron topology, failure initiates on the top layer of the lattice sample before propagating into the neighbouring layers, thereby resulting in a layer-by-layer crushing mechanism. For the regular octet lattice, on the other hand, damage initiates at the interior surfaces of the sample, thus generating an apparent dislocation plane. At a later stage of the deformation, the propagation of dislocation plane causes a shear fracture that splits the sample into two portions along a 45 degree plane.

The results from in-situ compression tomography were interpreted by considering metallic lattices as solid crystalloid materials, which have a periodic arrangement of atoms that resemble the periodic tessellation of cells in a lattice. The effective stiffness matrix of both the rhombicuboctahedron and the regular octet lattices was obtained via asymptotic homogenization theory. The symmetry of the stiffness matrix, controlled mainly by the cell topology, as well as the presence of slip planes were considered to interpret the directional deformation response of the two sets of lattices. For the rhombicuboctahedron, the response is orthogonal isotropic, whereas for the regular octet is quasi-isotropic. In addition, the regular octet lattice has a typical FCC unit cell with four active slip planes. Under compression, the shear stress on the slip surface causes dislocation which finally leads to a shear fracture. The rhombicuboctahedron lattice, on the other hand, has no active slip system and fails by crushing.

[a)] Email: damiano.pasini @mcgill.ca.

NUMERICAL ANAYSIS

Geometrical imperfections, originated during the manufacturing process，are classified into two categories: i) non-straightness of the struts, and ii) dimensional deviation of the strut cross section. Probability functions of both classes of imperfections are extracted from the tomography images, and are used to reconstruct numerical models which capture the statistics distribution of defects. Each reconstructed geometry is analysed via non-linear FEA model of beam elements. Each node in the FEA model is offset from its original position by the value generated by the probability function of non-straightness. The radius of the cross section of each element is assigned from the probability function of the radius. The stress-strain curve predicted by the simulations show good agreement with that of experiment in both the linear elastic region and the nonlinear plateau region. The simulations reveal other important observations on the damage initiation. Initial plastic hinges form at the end of the struts subjected to bending, cause joint rotation with a consequent drop in stiffness, that subsequently leads to strut local instability. This process induces a crush failure mode of the rhombicuboctahedron lattice and a shear failure mode of the regular octet lattice.

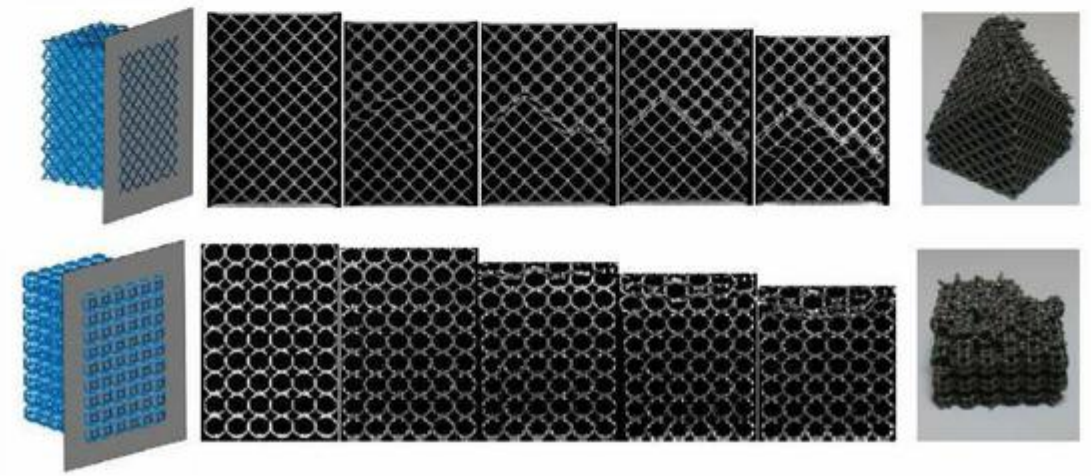

(a) (b)

Figure 1. Failure mechanism of metallic lattices under compression: (a) Damage evolution in the first slice obtained by CT tomography; (b) Failure modes after testing

CONCLUSIONS

Metallic lattices with either rhombicuboctahedron or regular octet topology fabricated by SLM have been compressed under in-situ tomography and their mechanical properties and failure mechanism interpreted with a set of numeric simulations and statistical analysis. The results have revealed that the damage initiates on the top layer of the rhombicuboctahedron lattice and propagates into the neighbouring layers, thereby resulting in a layer-by-layer crushing mechanism. For the regular octet lattice, the damage initiates at the interior surfaces of the sample and generates an apparent dislocation plane. From the tomography image reconstruction, geometrical imperfections were extracted and then introduced into a full-size finite element analysis. Both the failure modes and the stress-strain curves predicted by the nonlinear analysis show good agreement with those obtained from experiments.

References

[1] Vayre, B., F. Vignat, and F. Villeneuve, Metallic additive manufacturing: state-of-the-art review and prospects. Mechanics & Industry, 2012. 13(2): p. 89-96.

[2] Yan, C., et al., Evaluations of cellular lattice structures manufactured using selective laser melting. International Journal of Machine Tools and Manufacture, 2012. 62: p. 32-38.

[3] Vigliotti, A., V.S. Deshpande, and D. Pasini, Non linear constitutive models for lattice materials. Journal of the Mechanics and Physics of Solids, 2014. 64: p. 44-60.

[4] Dong, L., V. Deshpande, and H. Wadley, Mechanical response of Ti–6Al–4V octet-truss lattice structures. International Journal of Solids and Structures, 2015. 60-61: p. 107-124.

[5] Xiao, L., et al., Mechanical behavior of open-cell rhombic dodecahedron Ti–6Al–4V lattice structure. Materials Science and Engineering: A, 2015. 640: p. 375-384.

BRITTLE FRACTURE OF HIERARCHICAL SELF-SIMILAR HONEYCOMBS

Michael Ryvkin[a] & Raz Shraga
School of Mechanical Engineering, Tel Aviv University, Israel

Summary Brittle fracture of hierarchical self-similar honeycombs caused by propagation of a semi-infinite crack is considered. The stress state is obtained by the novel multiscale analysis method allowing to address only one repetitive cell. The critical stress criterion for the fracture toughness analysis is adopted. A parametric study is carried out and optimal crack arresting parameters for hierarchical layout are determined.

FRACTURE TOUGHNESS EVALUATION

The tunable overall mechanical properties of hierarchical honeycombs received recently a considerable attention in the literature (e.g., [1]), but their fracture behaviour yet was not investigated and this issue is the subject of the present paper. Two-dimensional isotropic self-similar hierarchical honeycombs with hexagonal based layout are considered. The periodic patterns corresponding to the different hierarchy orders are depicted in Fig.1. Brittle fracture caused by a macrorack which is formed by broken ligaments is examined, honeycombs are modelled as beam lattices and it is assumed that the crack propagates when the maximal tensile stress in a beam reaches the rupture stress of the parent material σ_{fs}. Thus, the fracture toughness in terms of σ_{fs} can be determined by the analysis of the self-similar crack tip field. This field corresponding to a semi-infinite crack can be obtained by considering of a sufficiently large portion of honeycomb with an embedded crack, however, for hierarchical microstructure this problem may be rather computationally expensive due to a large number of degrees of freedom. In order to overcome this difficulty a novel multiscale analysis method based on the discrete Fourier transform is employed.

A rectangular domain $H_1 \times H_2$ surrounding the crack tip which includes a large number N of rectangular repetitive $h_1 \times h_2$ cells is considered, $N = 4M_1M_2$ where $M_i = H_i/(2h_i),\ i = 1,2$. The cells are identified by the vector index $\mathbf{k} = \{k_1, k_2\}$, $k_i = -M_i, -M_i+1, .., M_1-1$. The stress state in each cell is completely defined by the vector of its nodal displacements $\mathbf{u}^{\mathbf{k}} = \{\mathbf{u}^1, \mathbf{u}^2, .., \mathbf{u}^n\}^{\mathbf{k}}$, each node possesses one rotational and two translational degrees of freedom.

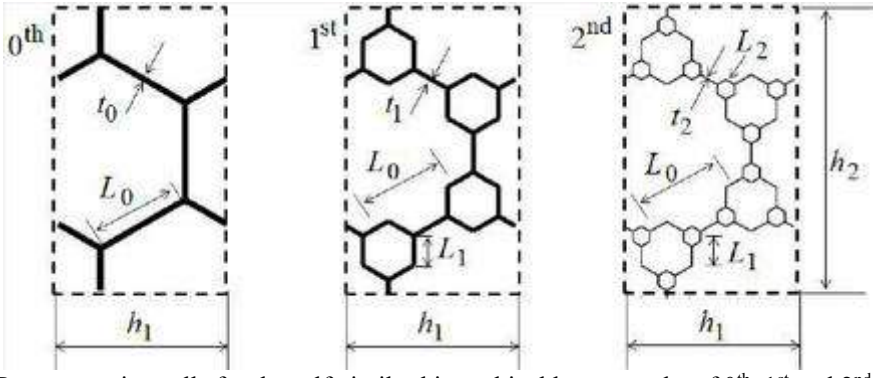

Fig.1. Representative cells for the self-similar hierarchical honeycombs of 0th, 1st and 2nd orders.

The governing equations for the considered problem include the equilibrium equations for each cell, the continuity conditions at the neighbouring cell interfaces and zero traction conditions at the crack faces. The external loading is defined by the conditions at the rectangular domain boundaries which are determined from the K-field solution for homogeneous elastic material possessing effective elastic properties of the honeycomb. Similar to [2], these conditions are formulated in the form of jumps in both displacements and traction components between the opposite sides of the rectangle. The above formulation allowed to reduce the problem for the periodic domain consisting of many cells to the problem for a single representative cell by application of the discrete Fourier transform. The unknowns in this problem are the complex valued Fourier transforms of the cell displacements $\mathbf{u}^* = \mathbf{u}^*(\varphi_1, \varphi_2),\ \varphi_r = \pi q_r / M_r,\ q_r = -M_r, -M_r+1, .., M_r-1;$ $r = 1,2.$ After solving of the representative cell problem $4M_1M_2$ times for each combination of the parameters q_1, q_2 the inverse transform is applied and nodal displacements in all cells of the considered domain are determined. The analysis

[a] Corresponding author. Email: arikr@eng.tau.ac.il

of the stress state in the beam elements in the crack tip vicinity shows where the maximal tensile stress σ_{tip} is developed which allows to determine the fracture toughness

$$K_{IC} = \frac{\sigma_{fs}}{\sigma_{tip}} K$$

where K is an amplitude of the K-field used for the formulation of boundary condition at the remote boundaries.

THE HIERARCHY EFFECT

The influence of the hierarchy on the fracture behaviour is illustrated by a comparison of the Mode I fracture toughness values $K_{IC}(0)$ and $K_{IC}(\gamma)$, for 0th and 1st order layouts, respectively. The dependence of their ratio upon the hierarchy parameter $\gamma = L_1 / L_0$ is presented in Fig.2. The case of fixed relative density $\rho = 0.115$ and constant elements thickness for each hierarchical order is considered, consequently, $t_1 < t_0$, i.e., for the 1st order hierarchy layout the thickness is lower

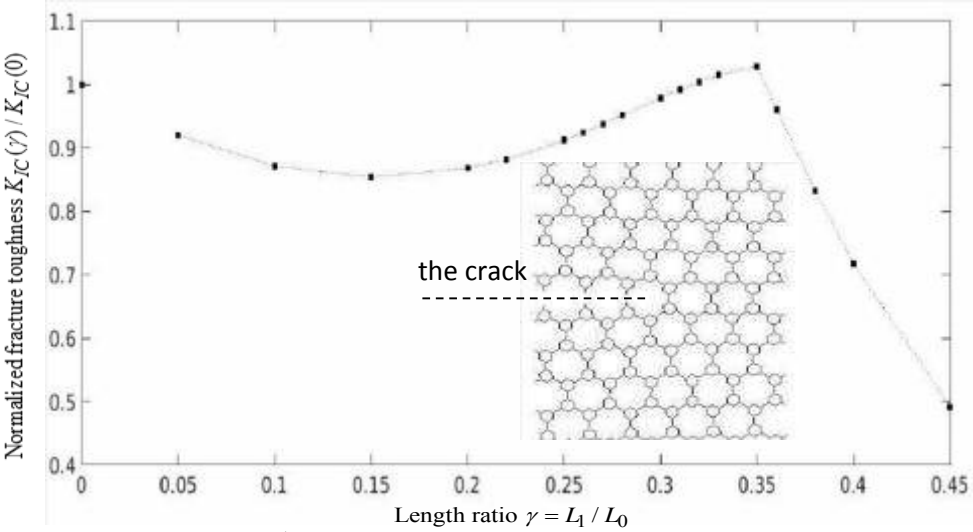

Fig.2. Fracture toughness for the 1st order hierarchical honeycombs for layouts with fixed density and different length ratios of the elements. The inset shows the near-tip region of deformed honeycomb for a specific length ratio.

than for the 0th order case. It appeared, however, that for the optimal length ratio $\gamma = 0.35$ the value of the fracture toughness not only does not decrease but somewhat increases. Note, that the same optimal ratio was reported in the study of elastic modulus of hierarchical honeycombs[1]. The existence of the above optimal value can be explained by the influence of the hierarchy on the bending dominated behaviour of the considered honeycombs. The parametric study for the 2nd order hierarchy has shown that further increase of the toughness up to 9% with respect to the 0 order case is possible for the specific combination of length parameters L_0, L_1 and L_2.

CONCLUSIONS

The fracture toughness of hexagonal honeycomb of fixed relative density decreases with decreasing cell size being inversely proportional to the square root of the length scale $K_{IC} \propto 1/\sqrt{L_0}$. However, if instead of simple scaling with decreased cells size one employs more sophisticated hierarchical layouts, it is possible not only to avoid toughness decrease but even to increase it for optimal values of geometric parameters. These values are found to be close to that which maximise the effective elastic modulus of hierarchical honeycombs.

References

[1] Ajdari, A., Jahromi, B.H., Papadopoulos, J., Nayeb-Hashemi, H., Vaziri, A. Hierarchical honeycombs with tailorable properties.: *International Journal of Solids and Structures*, **49**, 1413-1419, 2012.

[2] Ryvkin, M. and .Hadar, O..: Employing of the discrete Fourier transform for evaluation of crack-tip field in periodic materials. *International Journal of Engineering Science*, **86**, 10-19, 2015 .

SOUND TRANSMISSION THROUGH COMPOSITE SANDWICH PLATE WITH PYRAMIDAL TRUSS CORES

Dong-Wei Wang & Li Ma[a)]
Center for Composite Materials, Harbin Institute of Technology, Harbin, 150080, China

Summary: Lattice sandwich structure is a burgeoning multifunctional material since it is lightweight, designable, etc. It also has the potentialities in sound insulation, which is vital for the safety and stability of service, for its high porosity. In the paper, sound transmission characteristics of pyramidal truss core sandwich panel are investigated. The structure consists of two face-sheets and a core composed of trusses and sound absorbing material filling in the space. The structure is surrounded by acoustic fluid and an incident wave is imposed on the panel. Fluid–structure coupling is considered. The accurate periodic model with pyramidal truss cores repeating in two dimensions is established and analysed. Using the numerical calculation, the sound transmission characteristics of structure is studied. Finally, the effects of parameters of structure and incident wave are discussed for thorough understanding and system design.

INTRODUCTION

Sandwich structure commonly consisting of two thin but stiff skin layers separated by the lightweight core material has broad application prospects in the fields of aviation, shipping and transportation as a novel kind of multifunctional lightweight structure. It has superior properties of low density, high strength, high modulus and potential application in heat transfer, impact resistance, energy absorbing, etc. Vibration and acoustic properties are also very important for the service stability and safety which attract wide attention. Folds[1] studied the transmission and reflection of waves in layered media by elasticity theory. Since then, many authors researched the problem of lattice structure by obtaining the equivalent model using homogenization theory. However, when the wavelength is the on same order as the intervals in the core, it is suitable to regard the structure as a spatially periodic structure with the connection of trusses rather than a multilayer orthotropic plate. Mead [2] expanded the structural response of the periodic structure into a series of space harmonics to investigate structural responses of periodically stiffened beams. Lee [3] studied the wave propagation of periodically rib-stiffened plates based on the former work. Further, Wang[4]and Xin[5] investigated the periodic partitioning and rib-stiffened sandwich structure respectively. The studies above are outstanding but focused on the equivalent model or simplified one with one-dimensionally repeating cell and an accurate model to characterize the sound transmission is desirable. To address the aforementioned deficiencies, we establish the complete model and aim to fill the gap of sound transmission of two-dimensionally periodic lattice with pyramidal truss cores. All possible motions of face-sheet and trusses are taken into account. The sound transmission loss is numerically calculated to demonstrate the properties of the structure. Moreover, investigations are conducted to research the influence of parameters of the wave, material, geometry and layout of truss on sound insulation, which are helpful for the practical design of the structure with acoustic requirements.

MODEL AND THE SYSTEM EQUATION

In the paper, the infinite two-dimensional sandwich structure with pyramidal truss cores is investigated, as shown in Figure 1. x- and y-directions are alone the panel and z-direction is perpendicular to it. The structure is surrounded by acoustic fluid.

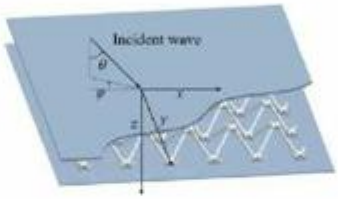

Figure 1. Lattice structure with pyramidal truss cores (absorbing material in core is not shown)

The displacements w(x,y) of the face panel at corresponding points in different periodic elements should have the relationship of transfer constant e^{μ}. The wavenumber and length of cell L should satisfy $kL=\mu$. Then, the motion of panel is expressed as

$$w_i = \sum_{n=-\infty}^{\infty} \sum_{m=-\infty}^{\infty} W_i^{n\,m} e^{-j\left[\left(\mu_x+2n\pi\right)/L\ x+\left(\mu_y+2n\pi\right)/L\ y-wt\right]}, \quad i=1,2.$$

The space is split into three parts: incident field (incident and reflect waves), field in the core, and radiated field. Waves in each room can be expressed by velocity potential function Φ_i as the same pattern of w(x,y). Fluid-structure coupling is considered by imposing velocity continuity condition at fluid–panel interfaces. Combining with the wave equation in the acoustic fluid and absorbing material, the relationships between amplitudes of the motion and parameters in wave potential function are established.

a) Corresponding author. Email: mali@hit.edu.cn

The forces and moments exerted by the trusses and wave pressures are applied on the panel. The truss is regard as Euler-Bernoulli beam and the stiffness of force K_z and moments K_{rx}, K_{ry} caused by compression and bend are obtained easily. Then the governing equations for panels vibration are given by

$$\left(D_1\frac{\partial^4}{\partial x^4}+D_2\frac{\partial^4}{\partial y^4}+2D_3\frac{\partial^4}{\partial x^2\partial y^2}\right)w_1+\left(m_1+\frac{4M_l}{L^2}\right)\frac{\partial^2 w_1}{\partial t^2}-j\omega\rho(\Phi_1-\Phi_2)$$

$$=-2\left(K_z+K_{rx}\frac{\partial^2}{\partial x^2}+K_{ry}\frac{\partial^2}{\partial y^2}\right)(w_1-w_2)\sum_{n=-\infty}^{+\infty}\sum_{m=-\infty}^{+\infty}\left[\delta(x+nL)\delta(y+mL)+\delta(x+nL)\delta(y-L+mL)\right]$$

$$\left(D_1\frac{\partial^4}{\partial x^4}+D_2\frac{\partial^4}{\partial y^4}+2D_3\frac{\partial^4}{\partial x^2\partial y^2}\right)w_2+\left(m_2+\frac{4M_l}{L^2}\right)\frac{\partial^2 w_2}{\partial t^2}+4\left(K_z+K_{rx}\frac{\partial^2}{\partial x^2}+K_{ry}\frac{\partial^2}{\partial y^2}\right)(w_2-w_1)\sum_{n=-\infty}^{+\infty}\sum_{m=-\infty}^{+\infty}\left[\delta\left(x+nL-\frac{L}{2}\right)\delta\left(y+mL-\frac{L}{2}\right)\right]-j\omega\rho(\Phi_2-\Phi_3)=0.$$

The principle of virtual work and the modal orthogonality are used in one cell to gain the motion w_i and the modal amplitudes of waves. Then the sound transmission loss (STL) could be work out by numerical calculation.

RESULTS

The convergence was check out and the result was truncated in limited terms. Also, the theoretical results were compared with those of FEM simulation. The STL curves show the trend, properties of sound insulation and different kinds of resonance. The incident wave and the effects of parameters are discussed for thorough understanding and system design, such as the material, size and layout. The curves arise with the enlargement of the oblique angle θ (confirmed φ=45˚), as shown in Figure 2. Vertical incident meets the best sound isolation in brief. While the azimuth angle φ exerts little influence on the result. Curves coincide in the front half and seem like small oblique translation in some degree in latter half. On the other hand, the increase of modulus of elasticity of truss causes the promotion of the previous resonance frequencies but less effect in high frequency range. But enhancing modulus of elasticity of panel could increase the transmission loss as a whole. The area and shape of cross-section of truss have little impact overall and altering the support angle influences the result which has the similar trend in affecting equivalent density. The parameters of panels and layout of truss are the most important to watch in system design.

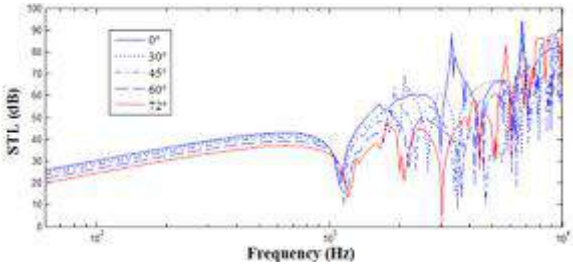

Figure 2. STL curves with respect to varies elevation angle θ of incident wave at confirmed azimuth angle φ=45˚.

CONCLUSION

The accurate two dimensionally periodic model of composite lattice structure with pyramidal truss cores and fillers was established and validated. The dynamic equations were derived using the space harmonic approach and the virtual energy principle. The sound transmission was studied with the surrounding acoustic fluids and wave pressures. The results were received by numerical computation. The characteristics and properties about sound insulation were analysed. The lattice structure is designable and potential in sound insulation. Some parameters were studied for further comprehension which is useful for system design.

References

1 Folds D., Loggins C.: Transmission and reflection of ultrasonic waves in layered media. *The Journal of the Acoustical Society of America* **62**: 1102, 1977.
2 Mead D. J., Pujara K. K.: Space-harmonic analysis of periodically supported beams: response to convected random loading. *Journal of Sound and vibration* **14**: 525-541, 1971.
3 Lee J. H., Kim J.: Analysis of sound transmission through periodically stiffened panels by space harmonic expansion method. J*ournal of Sound and Vibration* **251** (**2**): 349–366, 2002.
4 Wang J., Lu T.J., Woodhouse J., R.S. Langley, Evans J.: Sound transmission through lightweight double-leaf partitions: theoretical modeling. *Journal of Sound and Vibration* **286:** 817–847, 2005.
5 Xin F.X., Lu T.J.: Analytical modeling of fluid loaded orthogonally rib-stiffened sandwich structures: Sound transmission. *Journal of the Mechanics and Physics of Solids* **58**: 1374-1396, 2010.

STIFF AND STRONG OCTET LATTICE WITH TUNABLE COEFFICIENT OF THERMAL EXPANSION

Hang Xu[1] & Damiano Pasini[1a)]
[1]*Mechanical Engineering, McGill University, Montreal, Quebec, Canada*

Summary In this paper, we present two versions of a bi-material Octet lattice, and show that its coefficient of thermal expansion (CTE) can be regulated in designated spatial directions without compromising its structural efficiency. Proof-of-concept lattices are fabricated by laser cutting and assembled by a pretension snap-fit method. Via experiments, simulations and theory, we prove that their CTE can be tailored to low-to-zero or even negative. In particular, digital image correlation is used to measure the CTEs of the two versions of the Octet lattice, whereas asymptotic homogenization theory and finite element simulations are used to calculate their thermomechanical properties. The results are plotted into thermomechanical charts that illustrate the merit of the Octet lattices over other concepts existing in literature.

INTRODUCTION

Systems in space are vulnerable to large temperature changes when travelling into and out of the Earth's shadow. Variations in temperature can cause geometric distortions that are particularly undesirable in structures that must retain their dimensions within acceptable prescribed tolerances, such as in antenna sub-reflectors and optical telescopes. To satisfy thermal-control requirements, materials with a low CTE are generally sought for structures operating over a wide temperature range. Besides low CTE, these materials should also provide desirable stiffness, strength and extraordinarily low mass. One strategy among others, to search for promising material concepts, is to resort to architected materials. Recent works in advanced materials have shown that material architecture can be carefully tailored in periodic lattices to obtain a low-to-zero, or even negative, CTE. While the majority of the concepts existing in literature are planar, those that are in three dimensions have generally low structural efficiency because obtained from cell topologies that are bend dominated. In this paper we present two 3D versions of the Octet truss, a stretch dominated lattice with high structural efficiency, and show strategies to achieve low CTE stability over a wide range of temperature.

DESIGN METHODOLOGY

Fig 1a shows a bi-material tetrahedron with its mechanism of thermal deformation, well-known in literature to attain low CTE. It is based on a stationary node scheme, where the location of the peak node (top) is kept stationary during the thermal expansion. [1] In this work, we introduce an alternative mechanism (Fig 1b), which extends the stationary node concept to stationary lines. The scheme that uses stationary lines indicates that the overall positional relation, including angle and distance, between the two red horizontal beams (thin red line in Fig 1b) remain constant during the thermal expansion. In Fig 1b-I, the material with higher CTE, α_1, is highlighted in red, whereas the material with lower-but-positive CTE, α_2, in blue. Fig 1b-II shows that one of the two visually uncoupled deformation modes is the height increase, ΔH_1, caused by the thermal expansion of the blue elements. The other depicted in Fig 1b-III is a height decrease that originates from the turning of the blue elements at the nodes, a mechanism induced by the greater expansion of the horizontal red bars. As a result, the top red beam is drawn down with a consequent decrease ΔH_2 of the tetrahedron height. By combining these two modes of deformation (Fig 1b-IV), the height increase of the tetrahedron triggered by the blue element expansion is offset by the lowering of its top beam due to the thermal expansion of the red one. By a careful choice of α_1 and α_2, or the skew angle, θ, we can tailor the overall tetrahedron CTE in the vertical direction to any desired value.

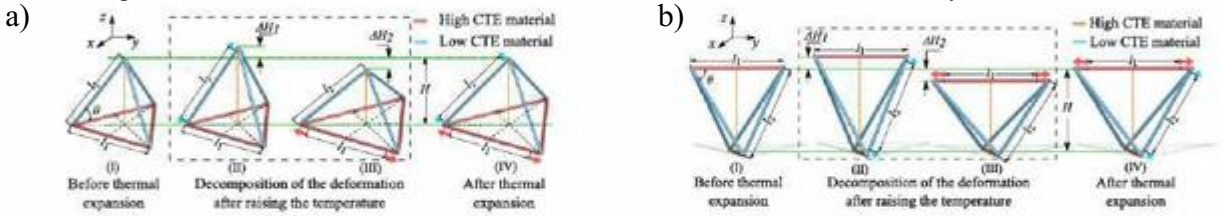

Figure 1: Thermal mechanisms for tetrahedrons with (a) a stationary node and (b) stationary lines.

In this paper, both the strategies in Fig 1, i.e. stationary point (Fig 1a) and stationary lines (Fig 1b), are used to assemble an Octet cell with tailored CTE and high structural efficiency. The former scheme is used to generate the Octet cell in Fig 2a-I, where the assembly of eight tetrahedrons, each with a stationary node, can yield an equivalent low CTE in all directions. Upon heating, the octahedron in the center with high CTE (red) expands outward, and each of its face, being a base of one of the eight tetrahedrons, can drag the peak points of each tetrahedron. Since the eight (blue) vertices, at the upper and low faces of the octet-truss, are stationary nodes, the overall CTE of this version of the octet-truss is isotropic and can be low upon a careful choice of the material properties of the constituents (blue and red). On the other hand, the stationary lines scheme applied to eight tetrahedrons is used to assemble the Octet cell in Fig 2a-II. Upon heating, the high thermal expansion of the horizontal beams (red) causes an inclination change of the skewed beams (blue), a mechanism that preserves stationary the relative position of the planes where the red struts lie. With a proper material choice, a potentially

a) Corresponding author. Email: damiano.pasini@mcgill.ca.

eformation c in a specific
s become ben

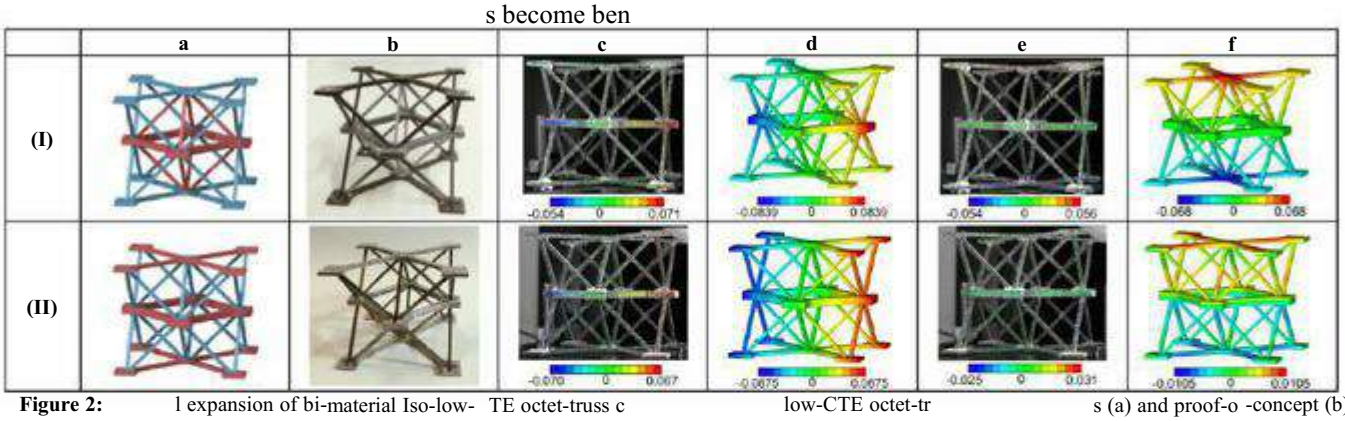

Figure 2: l expansion of bi-material Iso-low- TE octet-truss c low-CTE octet-tr s (a) and proof-o -concept (b) Grade 5; Color d via FEA (d); a and via FEA (f).

, THERMAL ULATION

rategies, we p d theoretical analysis on
ts. We first o predict the
or the Iso-low .03×10^{-5}/℃ -low-CTE Oct ×
10^{-7}/℃ in Fig 2. The 3D cells wer fabricated fr ing a pretensi
le snap-fit m thod [2]. A 3 as used to test
for Iso-low-CTE Octet (9.83×10^{-6}/℃) a d for Aniso-l in z (1.71×10^{-7}/), which
ose obtained escription of t
we generated charts that can erties on com
where the fo (with positive
trength (with downward po t of the two v
the Octet lattic ed, in compari re. [3, 4]

CLUSIONS

er, we have resented two ulate their C E in designa
alues higher t
theory, we h ve shown
that their ther can be tailore ithout weak
iency.

a) b)

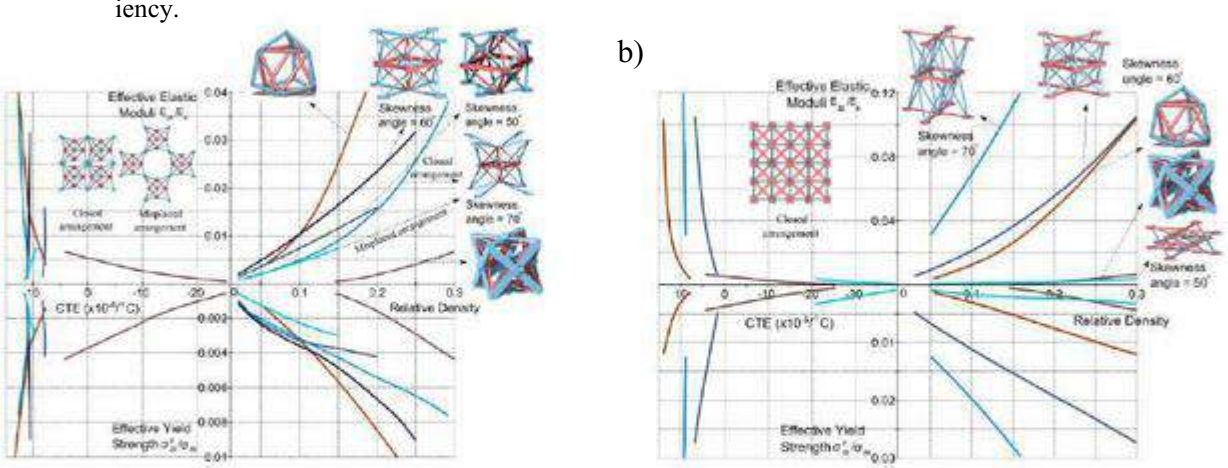

Figure 3: Four-q momechanical pr Aniso-low-CTE (ect to relative de sity. [3, 4]

References

[1] Steeves, C.A., et al., al investigation of the thermal rties of tailored pansion lattices. I . Des., 2009. 5(2) 195-202.
Wadley, Mechan –6Al–4V octet-tr truct., 2015. 60: p
. J. Mech. Phys.
p. 1803-1822.
attice-structures gle Patents.

DYNAMIC BEHAVIOR AND CRASHWORTHINESS DESIGN OF GRADED CELLULAR STRUCTURES

Zhijun Zheng[a], Jie Yang, Xiaokai Wang & Jilin Yu
CAS Key Laboratory of Mechanical Behavior and Design of Materials,
University of Science and Technology of China, Hefei, Anhui 230026, P. R. China

Summary Dynamic behavior of density-graded cellular structures under mass impact is investigated with cell-based finite element models and continuum-based shock wave models. A varying cell-size distribution method is introduced to construct 2D and 3D graded cellular structures. Deformation feature and stress history of 2D graded cellular structures under mass impact are obtained from the cell-based finite element models and they are compared well with the predictions of the shock model. The design of the relative density distribution of graded cellular structures is preformed with the shock model considering the deceleration of the striker as a constant and verified by a 3D graded cellular model. It is illustrated that the shock model could be used to guide the crashworthiness design of graded cellular structures.

INTRODUCTION

Deformation localization and strength enhancement are typical features of cellular metals under dynamic impact and they could be explained by the shock model [1]. Introducing a density gradient to cellular metals may further improve their dynamic mechanical properties [2-5]. Most researches in the literature [2-5] were focus on the dynamic responses of graded cellular metals but few on the crashworthiness design. The present study aims to improve the dynamic crushing models and to present some ideas about the crashworthiness design of graded cellular structures.

CELL-BASED FINITE ELEMENT MODELS

We have developed a varying cell-size distribution method based on Voronoi technique to construct 2D graded cellular models [3,4]. Recently, we have extended this method to construct 3D graded cellular models. The main contribution is about presenting a new principle of random seeding nuclei, i.e. the distance between any two nuclei i and j is required to be

$$\delta_{ij} \geq \begin{cases} (1 \quad) \; 2 \; / \; _{ij}, & \text{for 2D} \\ (1 \quad) \; 2.90h / \; _{ij}, & \text{for 3D} \end{cases}, \tag{1}$$

where k is the cell irregularity, h the cell-wall thickness and ρ_{ij} the local relative density at the middle point between the two nuclei i and j. Two samples are presented in Figs. 1a and 2a. Mass impact of graded cellular structures with an increase relative density along the loading direction, $\rho(X)$, is considered, see Fig. 1a and Fig. 2b. The impact tests are performed by using finite element (FE) method with ABAQUS/ Explicit code [4]. Specimens are hold behind a stationary platen and impacted by a rigid striker with mass M and initial velocity V_0. The cell-wall material is taken to be elastic-perfectly plastic with Young's modulus E = 69 GPa, yield stress σ_{ys} = 170 MPa, Possion's ratio ν = 0.3 and mass density ρ_s = 2700 kg/m^3.

CONTINUUM-BASED SHOCK WAVE MODELS

For the impact scenario considered, there is one shock front propagates in the specimens, as schematically presented in Fig. 1b. For simplicity, the specimens are considered to be made of the rigid–perfectly plastic–locking (R-PP-L) idealization with the plateau stress $\sigma_0(\rho)$ and the locking strain $\varepsilon_L(\rho)$, which are related to the local relative density. From the conservation relations of mass and momentum across the shock front, the shock wave speed and the stress behind the shock front could be given by $\Phi \quad = \quad \varepsilon_L \; \rho \; \Phi$ and $\sigma_B = \sigma_0 \; \rho \; \Phi \; + \rho_s \rho \; \Phi \; v \quad \varepsilon_L \; \rho \; \Phi$ respectively, where Φ is the Lagrangian location of the shock front, v the velocity of the striker and t the time. The motion of the striker together with the deformed portion of the specimen is governed by $v \quad t = -\sigma_B / (m + \rho_s \int_0^{\Phi} \rho \; X \quad X$, where $m = M/A_0$ with A_0 being the cross-sectional area of the specimen. For a given relative density distribution $\rho(X)$, these equations with initial conditions $v = V_0$ and $\Phi = 0$ at $t = 0$ could be solved numerically. Inversely, if given the deceleration history of the striker, the relative density distribution may be determined from these equations. For example, taking the deceleration of the striker as a constant a_0, we have $v^2 = \left(m a_0 + \rho \; a \int_0^{\Phi} \rho \; X \quad X - \sigma_0 \right) \frac{\varepsilon_L}{\rho_s \rho}$. Considering $\frac{\mathrm{d}v^2}{\mathrm{d}\Phi} = 2v \frac{\mathrm{d}v}{\mathrm{d}\Phi} = 2v \frac{v}{\mathrm{d}t} / \frac{\Phi}{\mathrm{d}t} = -2a_0 \varepsilon_L$, we obtain

$$\frac{\mathrm{d}}{\mathrm{d}\Phi} \left[\left(m a_0 + \rho \; a \int_0^{\Phi} \rho \; X \quad X - \sigma_0 \; \rho \; \Phi \quad \right) \frac{\varepsilon_L \; \rho \; \Phi}{\rho_s \rho \; \Phi} \right] = - \; \varepsilon_L \; \rho \; \Phi \quad a_0 . \tag{2}$$

Solving the above equation could give the relative density distribution of graded cellular structure.

[a] Corresponding author. Email: zjzheng@ustc.edu.cn.

RESULTS AND DISCUSSION

The mass impact of a 2D graded cellular structure with a linear relative density distribution in the X-axis $\rho(X) = \rho_{\text{avg}} + \gamma(X - L/2)]$ is first considered, see Fig. 1a, where ρ_{avg} is the average relative density, L the length, W the width and γ the density-gradient parameter. In this case, we take $\rho_{\text{avg}} = 0.1$, $\gamma = 1.0$, $k = 0.2$, $h = 0.26$ mm, $L = 383$ mm, $W = 100$ mm, $M = 5$ g and $V_0 = 120$ m/s. Compared to uniform cellular structures under mass impact, the graded cellular structure has an more obvious feature of deformation localization. Good agreements between the numerical results and the theoretical predictions of the stresses are illustrated in Fig. 1c. In the R-PP-L shock model, $\sigma_0/\sigma_{\text{ys}} = 0.417\rho^2$ and $\varepsilon_{\text{L}} = 0.725(1-\rho)$ [4] are used. It is found that the nominal stress at the proximal end drops quickly and the nominal stress at the distal end increases gradually until the striker reaches zero velocity.

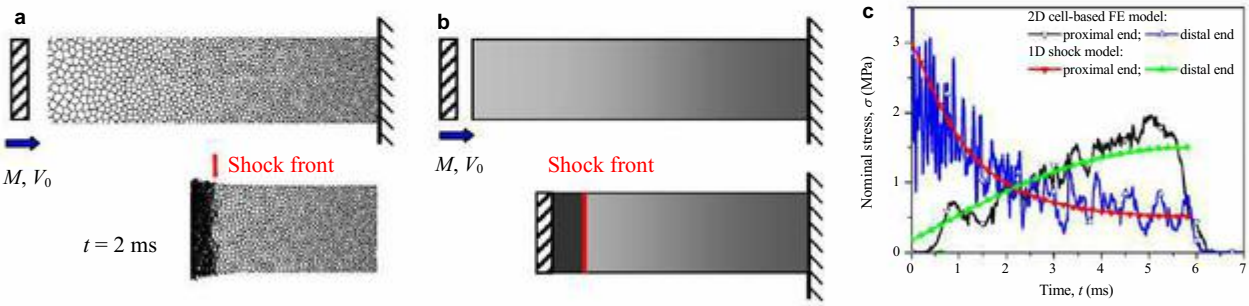

Fig. 1. Mass impact of 2D graded cellular structures: (a) a cell-based FE model, (b) a shock model and (c) the nominal stress history curves.

Consider the striker with $M = 100$ g, $A_0 = 31\times31$ mm^2 and $V_0 = 70$ m/s having a constant deceleration $a_0 = 76.5$ mm/ms^2. Then, the relative density distribution of graded cellular structure could be determined from Eq. (2) with material parameters $\sigma_0/\sigma_{\text{ys}} = 0.833\rho^{1.38}$ and $\varepsilon_{\text{L}} = -\rho$ for closed-cell foam models. The length of the 3D graded cellular specimen is determined to be $L = 50.3$ mm. Applying the least square fitting method, we can have the relative density distribution $\rho(X) = + X - L_0 + X - L_0^2$, in which $L_0 = 62.4$ mm determined from the R-PP-L shock model when using a uniform cellular structure with relative density 0.1 [4]. The deceleration history curve of the striker obtained from the cell-based FE model is compared well with that of the R-PP-L shock model, see Fig. 2c. Thus, the shock model could be used to guide the crashworthiness design of graded cellular structures.

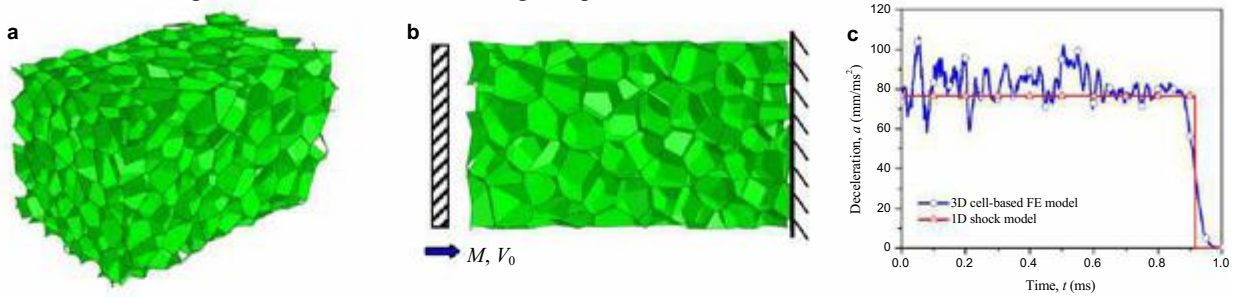

Fig. 2. Mass impact of 3D graded cellular structures: (a) a 3D sample, (b) a cell-based FE model and (c) the deceleration history curves of the striker.

CONCLUSIONS

A varying cell-size distribution method based on Voronoi technique is extended to construct 3D graded cellular structures. The R-PP-L shock model is extended to guide the crashworthiness design of graded cellular structures. Predictions obtained from the shock model are compared well with the results of the cell-based finite element models.

References

[1] Reid S. R., Peng C.: Dynamic Uniaxial Crushing of Wood. *Int. J. Impact Eng.* **19**: 531-570, 1997.

[2] Ajdari A., Nayeb-Hashemi H., Vaziri A.: Dynamic Crushing and Energy Absorption of Regular, Irregular and Functionally Graded Cellular Structures. *Int. J. Solids Struct.* **48**: 506-516, 2011.

[3] Wang X.K., Zheng Z.J., Yu J.L., Wang C.F.: Impact Resistance and Energy Absorption of Functionally Graded Cellular Structures. *Appl. Mech. Mater.* **69**: 73-78, 2011.

[4] Wang X.K., Zheng Z.J., Yu J.L.: Crashworthiness Design of Density-Graded Cellular Metals. *Theor. Appl. Mech. Letters* **3**(3): 031001(1-5), 2013.

[5] Liu J.G., Hou B., Lu F.Y., Zhao H.: A Theoretical Study of Shock Front Propagation in the Density Graded Cellular Rods. *Int. J. Impact Eng.* **80**: 133-142, 2015.

ELASTICITY AND CONDUCTIVITY OF FOAMS BASED ON TRIPLY PERIODIC MINIMAL SURFACES

Diab W. Abueidda[1], Rashid K. Abu Al-Rub[2], Ahmed S. Dalaq [3], Dong-Wook Lee [2], Iwona Jasiuk [1a)]
[1]*Department of Mechanical Science and Engineering, University of Illinois at Urbana-Champaign, Urbana, Illinois, USA*
[2]*Institute Center for Energy, Mechanical and Materials Engineering Department, Masdar Institute of Science and Technology, Abu Dhabi, UAE*
[3]*Department of Mechanical Engineering, McGill University, Montreal, Quebec, Canada*

Summary: Several triply periodic minimal surfaces (TPMS) are used to form novel foams. Unit cells are generated and then their effective elastic moduli and thermal/electrical conductivities are studied using a finite element method under periodic boundary conditions. The uniaxial, bulk and shear moduli, elastic anisotropy and Poisson's ratio of these TPMS-foams are investigated. The CLP-foam possesses highest anisotropy among the TPMS-foams under study. Furthermore, the Neovius-, IWP-, and Primitive-foams have highest bulk moduli whilst the Primitive-foam has highest shear modulus among all studied foams. The conductivities are found to vary linearly with relative density. The conductivities of the IWP-, Gyroid-, Primitive-, Neovius-, and S-foams are very close to each other. The conductivity of the CLP-foam needs to be quantified by two values while the other foams are found to be isotropic and can be quantified by one value.

INTRODUCTION

TPMS considered in this study are Schoen IWP, Schwarz Primitive, Schoen Gyroid, Fischer-Koch S, Neovius, and Schwarz CLP surfaces as shown in Figure 1. These TPMS were used by the authors to create interpenetrating phase composites (IPCs) and study their mechanical and physical properties [1-4]. In this paper, TPMS are utilized to create cellular materials and then to study computationally their elastic properties, thermal/electrical conductivities and anisotropy as proposed in [5].

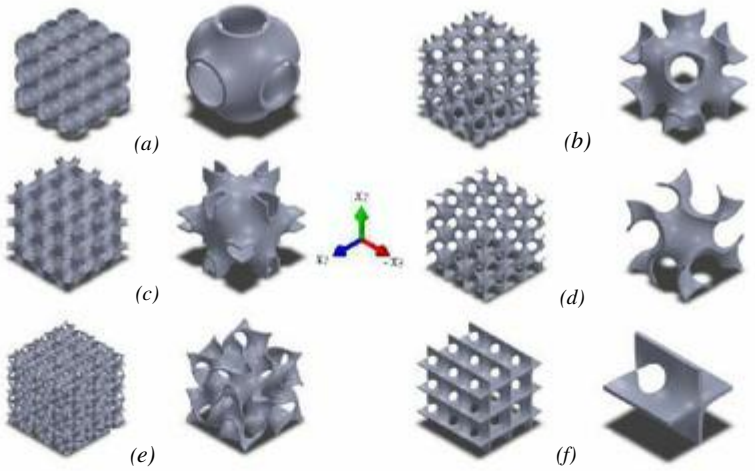

Figure 1: Architectures of foams that are based on TPMS; (a) Primitive, (b) IWP, (c) Neovius, (d) Gyroid, (e) Fischer-Koch S, (f) CLP. The pictures on the left show the three-dimensionally repeated unit cells while the pictures on the right represent one unit cell of the structure.

RESULTS AND DISCUSSIONS

Mesh sensitivity study is performed for the different TPMS-foams in order to ensure objective results. Figure 2 portrays the elastic properties [(a) uniaxial modulus, (b) shear modulus, (c) bulk modulus]. Figure 3 represents the electrical/thermal conductivities of TPMS-foams. Figure 4 illustrates the universal anisotropy indices for the elasticity and conductivity tensors. Within the simulated range of relative densities, generally, the CLP-foam in the x_3-direction has the highest uniaxial modulus and conductivity while the Primitive-foam has the highest shear modulus. On the other hand, the Primitive-, Neovius-, and IWP-foams have the highest bulk modulus. Furthermore, one can observe that CLP-foam has the highest elastic and conductivity anisotropies. Other TPMS-foams have the same anisotropy index for the conductivity with a value of zero which indicates that they are isotropic. For the elastic anisotropy index, there is an observable variation between the different foams. The lowest elastic anisotropy is noticed with Gyroid- and S-foams.

[a)] Iwona Jasiuk. Email: ijasiuk@illinois.edu.

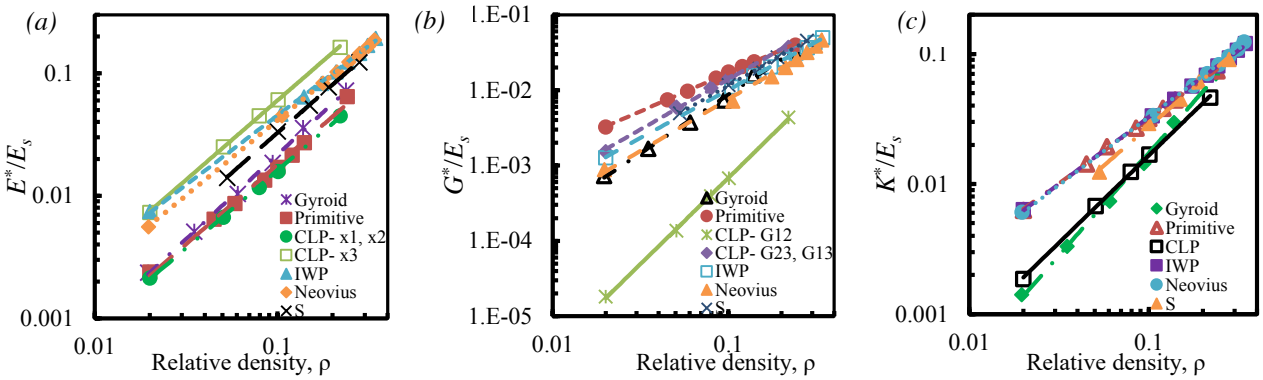

Figure 2: Elastic properties of TPMS-foams: (a) uniaxial modulus, (b) shear modulus, (c) bulk modulus.

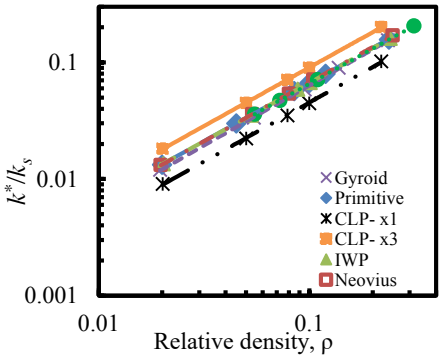

Figure 3: Thermal/electrical conductivity of TPMS-foams.

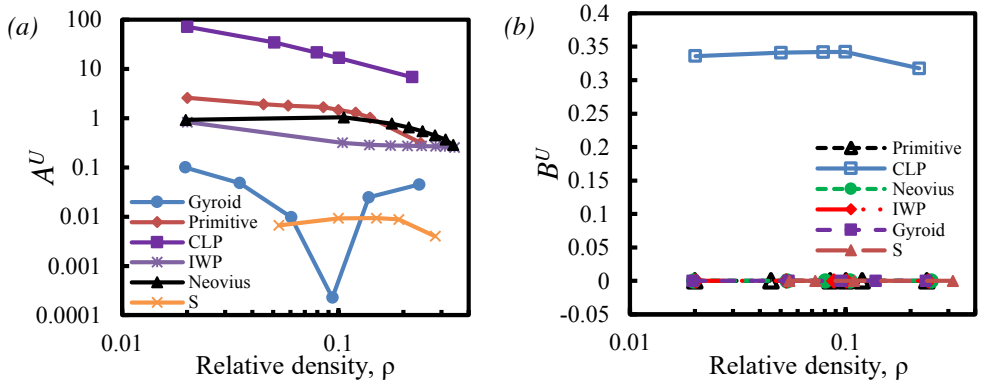

Figure 4: Anisotropy of TPMS-foams. Universal anisotropy index for (a) elasticity (b) conductivity

CONCLUSIONS

In this paper, six types of TPMS are used to create novel cellular materials in order to study their elastic properties, conductivity, and anisotropy based on a finite element method. It is shown that the elastic moduli and the conductivity of these cellular materials is dependent on their internal structure (architecture). Due to the high continuity and connectivity of TPMS, it is expected that the performance of TPMS-foams to be superior as compared to other stochastic and lattice based cellular materials.

References

[1] Abueidda DW, Abu Al-Rub RK, Dalaq AS, Younes HA, Al Ghaferi AA, Shah TK. Electrical conductivity of 3D periodic architectured interpenetrating phase composites with carbon nanostructured-epoxy reinforcements. Composites Science and Technology. 2015;118:127-134.
[2] Abueidda DW, Dalaq AS, Abu Al-Rub RK, Jasiuk I. Micromechanical finite element predictions of a reduced coefficient of thermal expansion for 3D periodic architectured interpenetrating phase composites. Composite Structures. 2015;133:85-97.
[3] Abueidda DW, Dalaq AS, Al-Rub RKA, Younes HA. Finite element predictions of effective multifunctional properties of interpenetrating phase composites with novel triply periodic solid shell architectured reinforcements. International Journal of Mechanical Sciences. 2015;92:80-89.
[4] Abu Al-Rub RK, Abueidda DW, Dalaq AS. Thermo-Electro-Mechanical Properties of Interpenetrating Phase Composites with Periodic Architectured Reinforcements. From Creep Damage Mechanics to Homogenization Methods: Springer; 2015. p. 1-18.
[5] Ranganathan SI, Ostoja-Starzewski M. Universal elastic anisotropy index. Physical Review Letters. 2008;101(5):055504.

Sandwich panel with honeycomb-corrugation hybrid core: evaluation of concept

Tian Jian Lu[1,2a)], Bin Han[1,3]
[1]*MOE Key Laboratory for Multifunctional Materials and Structures*
Xi'an Jiaotong University, Xi'an, PR China
[2]*State Key Laboratory for Strength and Vibration of Mechanical Structures*
Xi'an Jiaotong University, Xi'an, PR China
[3]*School of Mechanical Engineering, Xi'an Jiaotong University, Xi'an, PR China*

Summary The concept of novel lightweight sandwich construction with honeycomb-corrugation hybrid core is evaluated. The hybrid core is manufactured by filling the interstices of aluminum corrugations (folded plates) with precision-cut trapezoidal aluminum honeycomb blocks, bonded together using epoxy glue. The out-of-plane quasi-static compressive performance of such hybrid-cored sandwich panels is experimentally and numerically investigated. Both the compressive strength and energy absorption capacity of the sandwich are dramatically enhanced, compared to those of a conventional sandwich with empty corrugation or single honeycomb core having similar mass. The enhancement is attributed to strong constraints caused by honeycomb-corrugation interaction on deformation and buckling as well as altered failure modes at large deformation.

INTRODUCTION

Hexagonal honeycombs fabricated from thin aluminum (Al) sheets by an in-plane expansion process are widely employed for sandwich constructions due to their high stiffness, strength, and energy absorption as well as great saving in weight. However, existing experimental studies about honeycombs are mostly restricted to relative densities less than 3%, as debonding of the honeycomb from the faceplates will occur at higher relative densities, which limits the load-bearing and energy absorbing capacity of traditional Al honeycombs [1-2].

Like honeycombs, corrugations (folded plates) also have fairly high specific stiffness and specific strength. Unlike honeycombs, however, the energy absorption capacity of the corrugations is typically low. Under quasi-static compression, for instance, a metallic corrugated sandwich core deforms by stretching of its core webs and collapses by Euler or plastic buckling, with sharp softening immediately after the peak load is reached. Consequently, because large forces are transferred while limited amount of energy is absorbed, metallic corrugations are less attractive for energy absorption [3].

To increase further the specific strength and specific absorbed energy (SAE) of honeycombs or corrugations, this study proposes to combine them to form a new sandwich core as shown in Fig. 1(a). A preliminary study of the out-of-plane compression behavior of honeycomb-corrugation hybrid sandwich is carried out, both experimentally and numerically.

SPECIFICATION

As shown in Fig. 1(a), the honeycomb-corrugation hybrid core is manufactured by filling the interstices of corrugations with precision-cut trapezoidal honeycomb blocks, with epoxy used for bonding. Folded plates made of Al-3003-H24 and honeycomb blocks made of Al-3003-H18 are employed. The geometric parameters used for sandwich construction are: honeycomb cell length l_H=2mm, single wall thickness t_H=0.05mm, corrugated plate length l_C=17mm, corrugation angle α=63.5^o, width of corrugation platform d=4mm, core height h=15.3mm, corrugated plate thickness t_C=0.2mm, and faceplate thickness t_f=1.1mm.

RESULTS AND DISCUSSIONS

Quasi-static out-of-plane compression tests are performed for sandwich specimens having the empty corrugated core, the honeycomb core, and the hybrid core. The measured compressive stress versus strain curves along with the captured deformation processes are presented in Fig. 1(b). The flow stress of the hybrid-cored sandwich is significantly higher than that obtained by summing the constituent contributions, i.e., curve 'Sum' in Fig. 1(b). The interaction effect between the curves of 'Honeycomb–corrugation hybrid' and 'Sum', represented by the shaded area in Fig. 1(b), is strong. This implies that the compressive stiffness, strength and energy absorption of both constituents (i.e., honeycomb and corrugation) are significantly enhanced. Different from the honeycomb core, the stress versus strain curve of the honeycomb-corrugation core after the initial peak stress exhibits little fluctuations and enters gradually a stress strengthening region at $\varepsilon_n \approx 0.25$, which is much smaller than the densification strain of honeycomb. With the typical deformation images of empty corrugation and hybrid cores at ε_n=0.25 captured by a video camera additionally presented in Fig. 1(b), the corrugated-core sandwich is seen to collapse by Euler buckling with asymmetric deformations, causing the formation of plastic hinges. In contrast, the hybrid-cored sandwich maintains approximately symmetric deformation during crushing, significantly different from that of the empty corrugation [3] or honeycomb alone [2]. However, as the deformation of honeycomb blocks in the hybrid core could not be clearly identified from the digital images, detailed finite element (FE) analysis is employed to complement the images presented in Fig. 1(b) and to explore further the mechanisms underlying the superior performance of hybrid-cored sandwiches.

[a)] Corresponding author. Email: tjlu@xjtu.edu.cn

Figure 1(c) compares the simulated compressive response of the hybrid with that measured experimentally, and Fig. 1(d) presents typical deformation at ε_n=0.25. The deformation features predicted by the FE analysis appear to be in qualitative agreement with those observed from experiments (Fig. 1(b)). The simulation reveals that, at the early compressive stage, the empty corrugation and the single honeycomb alone both collapse by elastic buckling. In contrast, the initial collapse of the hybrid is dominated by material yielding of corrugated plate and buckling of honeycomb cell wall, with a much higher critical compressive stress than that required by the single honeycomb, leading to remarkably enhanced compressive strength (Fig. 1(c)). The enhancement is attributed to the mutual constraints of corrugation and honeycomb on deformation, which stabilize the corrugated plate and honeycomb cell wall against elastic buckling, and thus greatly increase the critical stress of both constituents. At relatively large compressive strains, as shown in Fig. 1(d), the crushing of the hybrid is dominated by two main deformation mechanisms: (1) conventional progressive folding of honeycomb cell walls [1,2] in Region I; (2) interaction between the twisted folding of honeycomb cell wall and the rotation of multiple plastic hinges formed on corrugated plate in Region II, where the deformation is quite different from the empty corrugation and single honeycomb. For hybrid-cored sandwiches considered in the present study, when ε_n exceeds 0.25, interaction between corrugation and honeycomb in Region II becomes increasingly important, causing sustained strengthening and greatly enhanced energy absorption of the sandwich; Figs. 1(b~c).

CONCLUSIONS

The out-of-plane compressive performance of a novel sandwich panel with honeycomb-corrugated hybrid core is experimentally and numerically studied. Both the strength and energy absorption capacity of the hybrid-cored sandwich are greatly improved relative to a conventional empty corrugated or honeycomb-cored sandwich having similar mass, which is attributed to the constraint on deformation and buckling as a result of strong interaction between corrugated plate and honeycomb cell wall, as well as altered crushing mode at large deformation.

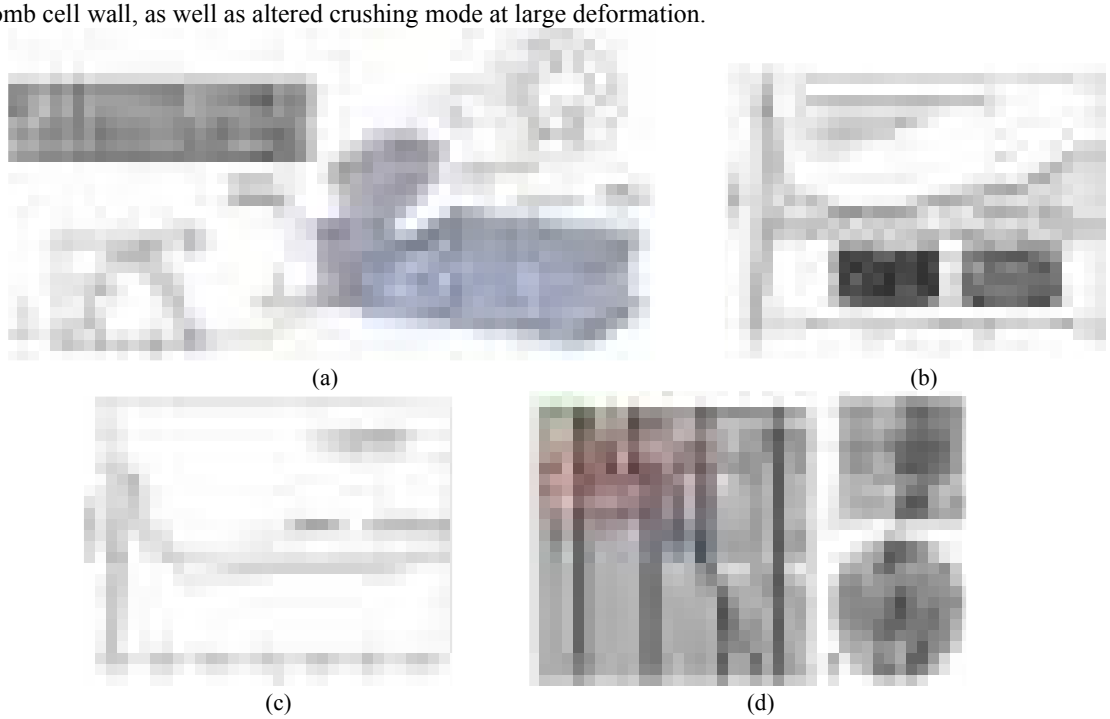

Fig. 1. (a) Schematic of honeycomb-corrugation hybrid-cored sandwich; (b) Experimentally measured compressive stress-strain curves; (c) Comparison between numerically calculated and experimentally measured compressive responses; (c) Numerically simulated crushing of hybrid-cored sandwich at ε_n=0.25, with two different deformation mechanisms highlighted.

References

[1]− Mohr D., Doyoyo M.: Deformation-induced folding systems in thin-walled monolithic hexagonal metallic honeycomb. *Int. J. Solids Struct.* **41**:3353-3377, 2004.

[2]− Wilbert A., Jang W.Y.: Buckling and progressive crushing of laterally loaded honeycomb. *Int. J. Solids Struct.* **48**(5):803-816, 2011.

[3]− Cote F., Deshpande, V.S.: The compressive and shear responses of corrugated and diamond lattice materials. *Int. J. Solids Struct.* **43**:6220-6242, 2006.

DESIGN AND MECHANICAL RESPONSE OF ASSEMBLED 3D PERIODIC AUXETIC CELLULAR STRUCTURES

Li Ma, Xin-Tao Wang & Lin-Zhi Wu
Center for Composite Materials, Harbin Institute of Technology, Harbin 150080, China

Summary As promising metamaterials, 3D periodic auxetic cellular structures (PACSs) have attracted great interest in recent years. However, they usually consist of intricate geometries which make the fabrication of them a significant challenge. The present paper is focused on introducing an interlocking assembly method to fabricate 3D PACSs. There are distinct advantages of the proposed method compared with the additive manufacturing methods used before. The dependences of mechanical properties of the structures on the re-entrant angle were investigated through a combination of experiments and numerical simulations. Results show that the compression modulus of the structures will monotonic decreasing with the increase of re-entrant angle, but there exists an extreme value for Poisson's ratio with the re-entrant angle which is difference with former studies. The effects of the strut thickness and the ratio of the vertical strut length to oblique strut length on the mechanical properties of the structure were also investigated.

INTRODUCTION

Auxetic means that the material or structure possesses negative Poisson's ratio. That is, they will expand in lateral direction when stretched and contract when compressed, which is contrary to common materials and structures. Three dimensional periodic auxetic cellular structures (3D PACSs) have attracted considerable interest and become a focus of auxetic material and structure research in recent years [1, 2]. From these researches, it can be found that nearly all 3D PACSs were manufactured by additive manufacturing methods due to their complicated structure. There are a lot of advantages of additive manufacturing, such as its ability to produce structures of arbitrary geometry in a well-defined manner, decreased lead time from concept to product, ease of design and process modification and so on [2, 3]. However, additive manufacturing method will introduce some defects to the structure such as rough surface [2], irregular cross sections [2], and defects caused by stair stepping effect [4]. Additionally, mass production and cost are also problems for additive manufacturing method, and the materials can be used as well as the scale of the structures are also limited by the additive manufacturing equipment. Till now, fabrication of fiber reinforced plastic composite structure is still a challenge for additive manufacturing method. So, in the development of complicated 3D PACSs both additive manufacturing and traditional manufacturing methods are need.

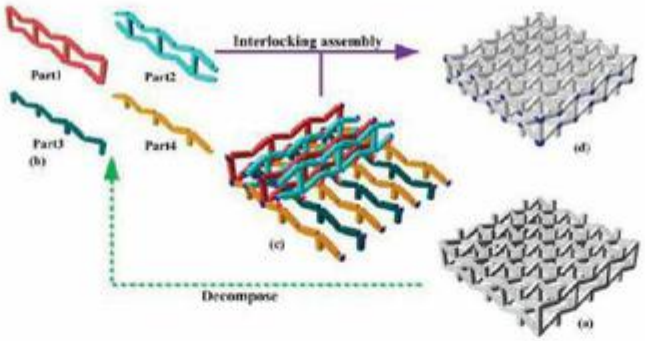

Figure 1. Schematic of interlocking process of 3D PACSs

In this paper, a novel manufacturing method which adopts the interlocking assembly concept was proposed. The interlocking assembly process is schematically described in Figure 1. The 3D PACS was interlocking assembled from four types of 2D re-entrant component parts. As the 2D component parts can be manufactured with conventional machining methods, the struts will have high quality compared with that manufactured by additive manufacturing method. In additionally, as mentioned in the reference each component part can be individually qualified [5]. So, the whole 3D PACS will avoid the defects caused by additive manufacturing method.

RESULTS AND DISCUSSIONS

The specimens for mechanical testing were built with the interlocking assembly method introduced above using metal, polymer and fiber reinforced composite materials respectively. The auxetic responses of proposed structure were investigated experimentally and numerically. The effects of the re-entrant angle, the strut thickness and the ratio of the vertical strut length to oblique strut length on the mechanical properties of the structure were discussed.

Corresponding author. Email: mali@hit.edu.cn.

The Young's modulus of the 3D PACSs will monotonic decreasing with the increase of re-entrant angle can be observed from Figure 2(a), and the experimental results match well with the Finite Element Method results though slightly lower than it. There exists an extreme value for Poisson's ratio with the re-entrant angle around 45° can be observed from Figure 2(b). The absolute value of the Poisson's ratio will decrease (less auxetic) with the increase of the re-entrant angle when the angle is larger than the extreme point, conversely the absolute value of the Poisson's ratio will also decrease with the decrease of the re-entrant angle when the angle is smaller than the extreme point. This phenomenon can be interpreted as follows: when the angle is larger than the extreme point, with the increase of the angle the structure will become less re-entrant, though the re-entrant character is the source of auxetic, so with the increase of the angle the structure will become less auxetic. When the angle is smaller than the extreme point, with the decrease of the angle the oblique struts will more inclined to the vertical strut and will bear more axial load and less bending load, though the main mechanism causing the auxetic character of the structure is the flexure of the oblique struts, so with the decrease of the angle the structure will become less auxetic.

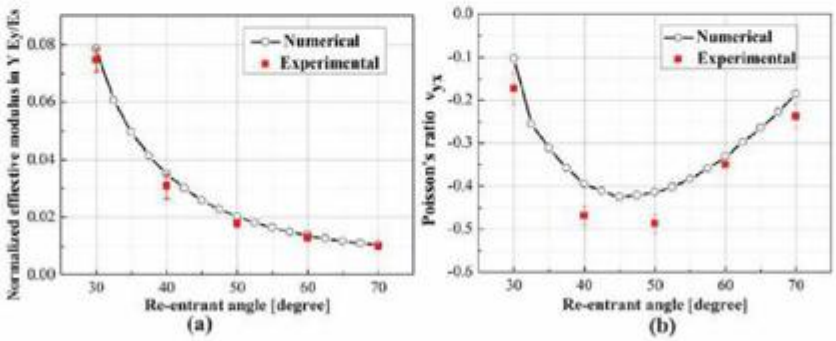

Figure 2. Variation of effective modulus and Poisson's ratio of 3D PACS with re-entrant angle

Using the experimentally verified numerical model, the effects of the strut thickness and the ratio of the vertical strut length to oblique strut length on the mechanical properties of the structure were investigated. The results shown that with the thickening of the struts the compression modulus of the structure monotonously increases and the Poisson's ratio of the structure will gradually change from negative to positive then gradually approaches to the Poisson's ratio of the parent material. The vertical strut length to oblique strut length ratio plays fewer roles on the mechanical properties compared with the re-entrant angle and the strut thickness.

CONCLUSIONS

A novel method which adopts the interlocking assembly concept was proposed to manufacture 3D periodic auxetic cellular structures in present work. This manufacturing method will overcome the defects of additive manufacturing method and has the potential for mass production and automatic manufacturing, at the same time it will greatly reduce the manufacturing expenses. In addition, the method is suitable for any kind of material that can be adhesive bonded (e.g. plastic and fiber reinforced composite) or welded (e.g. metal). The auxetic responses of these structures were investigated through a combination of experiments and numerical simulations, and excellent qualitative and quantitative agreement was found.

References

[1] Schwerdtfeger J., Wein F., Leugering G., et al.: Design of auxetic structures via mathematical optimization. Adv. Mater. **23**:2650-2654, 2011.

[2] Yang L.: Structural Design, Optimization and Application of 3D Re-entrant Auxetic Structures. PhD Thesis, NC State Ind. Eng. Dept., Raleigh, 2011.

[3] Schwerdtfeger J., Heinl P., Singer R.F., et al.:. Auxetic cellular structures through selective electron-beam melting. Phys. Status. Solidi. B. **247**:269-272, 2010.

[4] Schwerdtfeger J., Schury F., Stingl M., et al.: Mechanical characterisation of a periodic auxetic structure produced by SEBM. Phys. Status. Solidi. B. **249**:1347-1352. 2012.

[5] Cheung K. C. and Gershenfeld N.: Reversibly Assembled Cellular Composite Materials, Science. **341**:1219-1221, 2013.

QUASI-LATTICE DYNAMICS OF RANDOM SKELETAL STRUCTURES

Belen Martinez Pavetti[1], Shoji Imatani[1a)]
[1]*Department of Energy Conversion Science, Kyoto University, Kyoto, Japan*

Summary A computational microscopic model is adopted to represent open-celled foam materials as three-dimensional random skeletal structures. The structure is generated by Voronoi tessellation, and it is considered as composed by rod-beam members with six degrees of freedom. A combination of continuum mechanics equations and finite element analysis is applied to evaluate the model response when undergoing dynamic external input. Specifically, the significance of wave propagation modes is studied with main interest in twisting waves.

INTRODUCTION

Skeletal structures are very common in the nature; plant tissues and trabecular bones are examples of this kind of arrangement. Their particular configuration of beam-like members and hollow portions results in outstanding characteristics of lightweight and high energy absorption, which are of great interest for engineering applications. These beam-like members can transmit not only forces but also moments from one point to another[1]. Thus, when analysing the mechanical behaviour of skeletal structures, not only longitudinal and transverse waves are to be considered, twisting waves might also represent a significant wave propagation mode.

The evaluation of the rod-beam branches in terms of mechanical variables is done in order to study the macroscopic response of the arrangement. Using the spatial decomposition technique of Voronoi tessellation and a three-dimensional rod-beam finite element method with six degrees of freedom per node the microscopic computational model is generated. In this model, the significance and effects of twisting waves can be analysed, and a continuum representation for materials with complex internal structure can successfully be constructed.

MATERIAL MODEL

Despite the complex characteristics of shape and dimension related to real skeletal materials, we assume that the structure is composed of rod-like members following a simple elastic law. This limits our approach into open-celled structures. Since we use longitudinal interconnected members, the external action does not have the same effect on each one of them. Although the macroscopic response can easily be deduced by simple inspection of the action, the microscopic effect is more complex. Due to the interconnection between members, the role of the signal changes every time it reaches a connecting point, between axial forces, shear forces, bending moments and twisting moments, which is schematically shown in Fig.1.

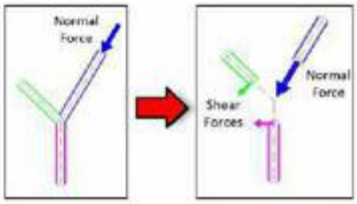

Figure 1. *Example of load role changing when arriving at a connecting point.*

For the rod members, we consider (a) elastic material with elasticity coefficients E and G and mass density ρ, and (b) straight beam/rod with diameter d of circular cross-section, whose length is sufficiently long compared with the cross-section. It implies that rods follow the beam/axes deformation mode. Neither anisotropy nor warping effects are taken into account. Skeletal materials are modelled via the computational geometry technique of Voronoi tessellation, generating an assembly of such one-dimensional interconnected rods. We do notice that these assumptions may be too simple to capture the mechanical response of the skeletal materials. The total displacement vector $\boldsymbol{u}(\boldsymbol{x},t)$ in the rods can be determined by the displacement vector $\boldsymbol{u}(\bar{\boldsymbol{x}},t)$ and the infinitesimal rotation vector $\theta(\bar{\boldsymbol{x}},t)$ along the beam/rod-axis as:

$$\boldsymbol{u}(\boldsymbol{x},t) = \boldsymbol{u}(\bar{\boldsymbol{x}},t) + \theta(\bar{\boldsymbol{x}},t) \times \boldsymbol{r} \tag{1}$$

where $\boldsymbol{r}$ denotes the vector perpendicular to the rod axis. The vectors $\boldsymbol{u}(\bar{\boldsymbol{x}},t)$ and $\theta(\bar{\boldsymbol{x}},t)$ along the rod axis are interpolated in the discretization process. And so kinematical variables at arbitrary position $\boldsymbol{x}$ in the members are discretized and finally determined by the nodal displacement $\{\boldsymbol{u}^n\}$ and nodal rotation $\{\theta^n\}$ in the finite element scheme. Then, the material can be regarded as a kind of generalized continuum, in which not only translation but also rotation influence on the microscopic mechanical behaviour.

In general, the vector wave equation has two types of wave speed: the longitudinal or dilatation wave, and the shear or bending wave. Since the infinitesimal rotation has no dilatation, i.e. divθ=0, we may observe one more kind of wave speed in the media, the twisting wave, which is one of our main interests in this study. One of the key assumptions at this stage is that the substantial material (i.e. ingredient material) is a beam-like simple material.

We assume the Timoshenko mode of deformation in the beam, and simple linear deformation in rod and axis. If we take the z-axis as the longitudinal axis of rods in the local coordinate system and a vector $\{\boldsymbol{r}\}=[x\ y\ 0]^{\mathrm{T}}$ in the cross-section, the displacement $\{\boldsymbol{u}_e\}$ in an element with shape function $[\phi]$ is interpolated as:

$$\{\boldsymbol{u}_e\} = [\phi]\{u^n\} + [\phi]\{\theta^n\} \times \{\boldsymbol{r}\} \tag{2}$$

a) Corresponding author. Email: imatani@energy.kyoto-u.ac.jp

Then, the strain $\{\varepsilon_e\}$ and the stress $\{\sigma_e\}$ in the element are computed via the nodal displacement $\{\boldsymbol{u}^n\}$ and angle $\{\theta^n\}$. The finite element equation is finally reduced to:

$$[M]\{\ddot{U}^n\}+[K]\{U^n\}=\{f^n\} \tag{3}$$

Where $\{f^n\}$ is the nodal force vector, $[M]$ is the mass matrix, and $[K]$ is the stiffness matrix[2,3]. The unknown vector is $\{U^n\}=[\boldsymbol{u}^n\ \theta^n]^T$ representing the generalized displacement. We note that two types of kinematical variables transmit the media. Equation (3) is solved step-by-step via Newmark-β method[2,3].

MODEL PERFORMANCE

We first generate the structure or objective domain by means of Voronoi tessellation technique[4], specifying the desired number of cells. Cells are constructed at random in four dimensions to control the variety of skeletal geometry, and their edges are assigned as the rod/beam members for the skeletal structure, with diameters proportional to their lengths. Each edge is subdivided into several elements with appropriate length. Then, boundary conditions and other simulation parameters are set. The analysis is repeatedly carried out for several mesh patterns with different cell sizes, varying the simulation parameters. This enables us to capture the macroscopic response of the materials.

As an example, a cylindrical embedded sample of diameter D=0.1 and length L=1 is displayed in Fig. 2. When generating this random structure we used 300 cells, giving 7496 nodes and 8177 elements. Common material properties as shear modulus G=1, Young's modulus E=2.6, mass density ρ=1 were set. Then, we applied a prescribed displacement parallel to the "Z" axis given by the pulse $0.17(1-\cos 10\pi t)$ for $0 \le t \le 0.2$, 0 for t>0.2, distributed on the points located at the free end of the cylinder. The time step for the numerical integration is Δt=0.005.

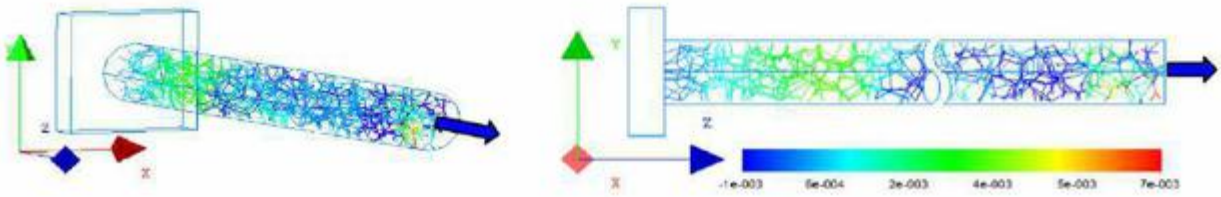

***Figure 2**. Nodal displacements parallel to "Z" axis in a cylindrical skeletal beam undergoing a pulse displacement along "Z". The color legend corresponds to the global nodal displacements along the "Z" axis.*

In Fig. 2 we observe highly deformed members not only near the surface where the disturbance has been applied but also in thin members even a little far from it. Such irregular deformations are caused by the dimension as well as the configuration of the skeletal members. Besides, wave fronts can be tracked which permits the estimation of wave propagation velocities.

Figure 3 shows the typical response obtained with our model. In Fig. 3, RMS values of local longitudinal strain ε_z denoted by EZ, rotation around local "z" axis θ_z designated by OZ, and total local rotations around "x" and "y" axes computed as $\theta_{xy}=(\theta_x^2+\theta_y^2)^{1/2}$ here called OXY are compared. These magnitudes can be considered as representatives of the longitudinal, twisting and bending waves respectively. In Fig. 3 we can see that local twisting has significant values when compared to longitudinal strain. Local twisting actually represents the highest strain value.

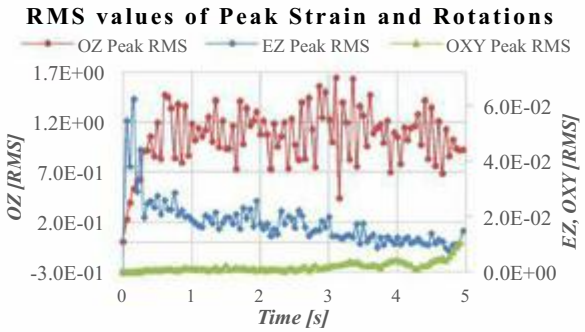

***Figure 3**. Comparison of RMS values of peak local longitudinal strain EZ, peak rotation OZ around local z axis, and peak of com osition o rotations OXY around local x and axes.*

CONCLUDING REMARKS

Micro-deformation in skeletal structures is investigated through the finite element analysis, and the transmission of forces and moments is discussed. The randomness in geometry has essential influence on the microscopic level of deformation. Such a fundamental observation helps us to formulate a macroscopic constitutive model for skeletal materials, for which it is observed that twisting waves should not be despised as they constitute the dominant response. For further analysis, it is expected to adopt the concepts of Cosserat theory on this basic model and to generate a representative sample structure with a 3D printer to compare the proposed model with its response.

References

[1] D. Weaire, and S. Hutzler, The Physics of Foams, Oxford Univ. Press, (2001).
[2] O.C. Zienkiewicz, and K. Morgan, Finite Elements and Approximation, Dover (2006).
[3] K.J. Bathe, Finite Element Procedures, Prentice Hall (1995).
[4] F.P. Preparata and M.I. Shamos, Computational Geometry: An Introduction, Springer-Verlag (1990)

FRACTIONAL DERIVATIVES MODEL TO PREDICT HIGH FREQUENCY MODULI OF ACOUSTIC FOAMS

Sohbi Sahraoui[1a)], Xinxin Guo[1], Guqi Yan[1], Lazhar Benyahia[2]
[1] *LAUM, CNRS UMR 6613, Université du Maine, Av. O. Messiaen, Le Mans, France*
[2] *IMMM, CNRS UMR 6283, Université du Maine, Av. O. Messiaen, Le Mans, France*

Summary This paper presents a time domain method to determine viscoelastic properties of open-cell foams on a wide frequency range. This method is based on the adjustment of the stress-time relationship, obtained from relaxation tests on polymeric foams samples under static compression, with the four fractional derivatives Zener model. The experimental relaxation function, well described by the Mittag-Leffler function, allows to predict straightforward the frequency-dependence of complex modulus of polyurethane foams. A curve was reconstructed on the reduced frequency range (0.1Hz – 1 MHz) using the time-temperature superposition principle. Very good agreement was obtained between experimental complex moduli values and the fractional Zener model predictions. The proposed time domain method may constitute an improved alternative to resonant and non-resonant techniques often used for dynamic characterization of polymers for the determination of viscoelastic moduli on a broad frequency range.

INTRODUCTION

To characterize the mechanical behavior of viscoelastic materials, experiments can be carried out either in frequency or in time domains. In the linear regime, the two results are connected to each other. For example, the relaxation or retardation time function is extracted from experimental curves of complex moduli versus frequency.[/1/] To avoid the long and sometimes difficult series of measurements at several temperatures[/2/] or in a wide frequency range in vacuum,[/3/] this paper is focused on the experimental determination of the relaxation function $R(t)$ and the computation of the complex modulus in frequency domain through a single relaxation test. The originality of the present method lies with the fitting of the relaxation function $R(t)$ and the resolution of the stress–strain relationship in time domain. In addition, it has been shown that the use of Mittag-Leffler function, more appropriate for the fitting process, allows to predict straightforward the frequency-dependence of complex modulus.

The analysis of the fractional Zener model (FZM) in frequency domain[/4/] highlights its mathematical and physical background and its ability to describe the viscoelastic behavior of materials in a wide frequency range. Thus, the frequency dependence of the viscoelastic moduli were calculated on a very broad range of frequency and compared to experimental value obtained by time temperature superposition (TTS) method from isotherm dynamic measurements on a narrow frequency and temperature domains.

FZM IN TIME AND FREQUENCY DOMAIN

The αth order fractional derivative of the function $\varepsilon(t)$ is defined with the gamma function as

$\frac{d^{\alpha}}{dt^{\alpha}}\varepsilon = \frac{1}{\Gamma(1-\alpha)}\frac{d}{dt}\int_0^t \frac{\varepsilon(\tau)}{(t-\tau)^{\alpha}}d\tau$, where τ is an integral variable.[/5/]

For the special case of FZM, the stress-strain relation is written as $\left[1 + a\frac{d^{\alpha}}{dt^{\alpha}}\right]\sigma(t) = \left[m + b\frac{d^{\alpha}}{dt^{\alpha}}\right]\varepsilon(t)$,

and $\left[1 + a(j\omega)^{\alpha}\right]\hat{\sigma}(\omega) = \left[m + b(j\omega)^{\alpha}\right]\hat{\varepsilon}(\omega)$ .in time and frequency domain respectively[/6/]. The complex modulus is

defined as $G^{*}(\omega) = \hat{\sigma}(\omega)/\hat{\varepsilon}(\omega) = G' + jG''$.

EXPERIMENTS AND RESULTS

The polyurethane (PU) foam, kindly provided by Tramico Company, is considered for relaxation tests in time domain and for dynamic measurements in frequency domain. The foam samples were cylinders of 20 mm of radius, and 40 mm or 20 mm length for the relaxation experiments or dynamic measurements respectively. In relaxation tests, a constant strain was applied to the foam sample in the linear regime. The chosen relaxation duration was determined by some tests in the time range (1min - 8 hours); the relaxation function obtained in just 10 min and the FZM are able to predict the measured stress at long time as shown by Fig. 1; the insert is a zoom of the ten first minutes. Following Mainardi[/6/], the relaxation

[a)] Corresponding author. Email: sohbi.sahraoui@univ-lemans.fr

function is $R(t) = m + (b/a - m)E_\alpha(-t^\alpha/a)$ where $E_\alpha(-t^\alpha/a)$ is the classical Mittag-Leffler function. The relative error of the fitted curve is less than 2%.

In dynamic tests the frequency sweep was fixed between 0.16 and 16 Hz. and the strain at 0.1% is in the linear response of the foam. The temperatures of the experiment were fixed at 20, 10, 0, -10 and -20 °C. The TTS is used to compute the complex shear modulus at a reference temperature (20 °C) over a broader frequency range.[7] This method consists in translating horizontally and vertically the curves of *G*' and *G*" versus frequency obtained on a reduced frequency range at different temperatures, in order to superimpose them at a given temperature.

The comparison between experimental measurements and the prediction of the viscoelastic moduli over a wide range of frequency using FZM is presented in Fig. 2. For the studied foam, the agreement is very good both on *G*' and *G*" even though the prediction of the storage modulus is better than for the loss one.

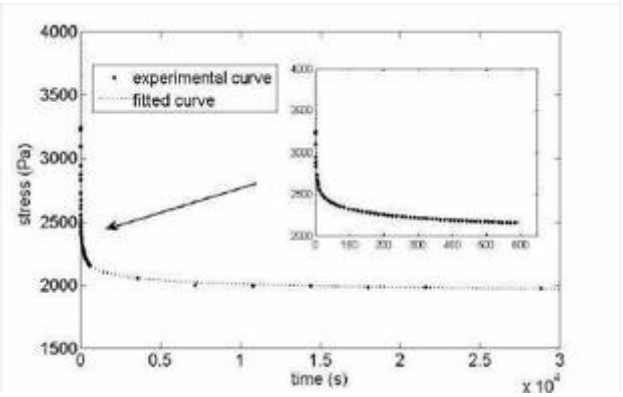

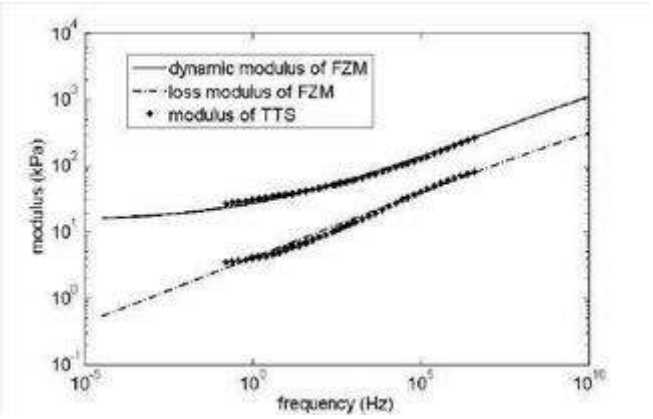

Fig; 1: Stress relaxation (experimental and FZM fitted curves). Fig. 2: Storage and loss moduli comparison

CONCLUSIONS

In this work, by adjusting the FZM on the stress relaxation experiments of acoustic foams, we were able to extract the four parameters of the model. It has been shown that the relaxation function obtained in just 10 min in a single static compression test was sufficient to calculate the complex modulus at any frequency. This model was analyzed and its mathematical and physical backgrounds have been outlined. To verify the applicability and the accuracy of the present procedure, the complex modulus was obtained on a wide frequency range using the TTS principle. The comparison between the experimental results and the predicted values of the FZM has shown a good agreement in a frequency range between 0.1 Hz and 10^6 Hz. The proposed method may be considered as an improved alternative to characterize the frequency dependence of polymeric foams especially at high frequencies and could be generalized for other materials.

References

[1] Soula M., Vinh T., Chevalier Y.: J. Sound Vib. **205**, 185-203, 1997

[2] Etchessahar M., Sahraoui S., Benyahia L., Tassin J. F. : J. Acoust. Soc. Am.117 (3), 1114–1121, 2005

[3] Cuenca J., Van der Kelen C., Goransson P.: J. Appl. Phys. **115**, 084904-11, 2014

[4] Pritz T.: J. Sound Vib. **195**, 103–115, 1996

[5] Ross B.: A brief history and exposition of the fundamental theory of fractional calculus, Lecture notes in mathematics, 457, Springer Verlag, New York, 1975

[6] Mainardi F.: Fractional calculus and waves in linear viscoelasticity. An introduction to mathematical models, Imperial College Press, London, 2010

[7] Williams, M.L., Landel, R.F., Ferry, J.D.: J. Am. Chem. Soc.**77**, 3701–3706, 1955

OPTIMISING MATERIAL DENSIT OF CELLULAR BODIES IN HIGH ELASTIC DEFORMATIONS

Hayley Wyatt[1a)], Khulud Alayyash[1] & L. Angela Mihai [1]
[1]*School of athematics, Cardiff University, Cardiff, United ingdom*

Summary For cellular bodies with uniform cell size, wall thickness, and shape, an important question is whether the same volume of material has the same effect when arranged as many small cells or as fewer large cells. Numerically, we assess the independent impact of cell size and number of cells on the mechanical behaviour of finite element models of periodic, honeycomb-like structures of neo-Hookean or Mooney-Rivlin material, and obtain that the mean non-linear elastic modulus and Poisson 's ratio in the cell walls increase as the number of cells increases while the total volume of solid material remains fixed. This is due to the enhanced elasticity of the cell walls when the material is distributed more uniformly throughout the structure. The results presented here provide valuable information in understanding the behaviour of cellular structures of non-linear elastic material and can be used to optimise their design for various applications.

INTRODUCTION

Cellular bodies are strong, pliable structures, built from seemingly fragile materials. Among the best known mechanical qualities of these structures are their high strength-to-weight ratio and energy absorption capacity, which arise from the inextricable relation between the geometric architecture and the non-linear elastic responses of their constituents. In many natural load-bearing structures, support requirements are typically met through a combination of increase in cell number or size and sustained sclerification (thickening and lignification) of the cell wall. For example, dicotyledon stems (*e g* magnolia, oak, sycamore) increase their diameter primarily by cell division which ultimately form the characteristic annual rings, while monocotyledon stems (*e g* lily, palm, reed) prevent mechanical failure through a combination of initiation of growth with a stem that is sufficiently wide for future supply and support demands, and increase in stem diameter and strength by sustained cell wall expansion and lignification, predominantly toward the stem periphery and base. Even though some monocot plants attain tree stature comparable with arborescent dicotyledons and conifers, their stems are relatively slender. By contrast, tall dicot trees have bigger stem diameters relative to their height than small trees, although the wood density representing the relative quantity of the cell wall in a given volume of wood tissue does not vary significantly among wood species. For living cellular structures, there are many physiological and ecological factors that affect their mechanical properties, and they also change over time. Nevertheless, for structures with uniform cell size, wall thickness, and shape, the fundamental question arises whether the same volume of cell wall material has the same effect when arranged as many small cells or as fewer large cells. In the case of small strain elastic deformations, thresholds on stiffness or strength can be set as constraints in the mechanical design or developmental process [1]. When large strains occur during functional performance, finding suitable criteria that account for the non-linear properties of the deforming cell walls is needed [2].

NON-LINEAR ELASTIC EFFECTS

In our study, finite element modelling was used to investigate the mechanical responses of periodic, honeycomb-like structures with regular geometry, such as square, diamond-shape, and hexagonal cells of non-linear hyperelastc material subject to large strain deformations. The models structures were created in SolidWorks, meshed in Gmsh, and imported into the FEBio software suite [3]. Each structure was made from a single piece of elastic material which occupied a thin square domain of (dimensionless) side 1 in the X- and Y- directions, and 0.1 in the Z-direction. Cells were equal size throughout the structure. The lower external horizontal face was free to slide in the X- and Z-directions, and fixed in the Y-directions. The upper external horizontal face was subject to a prescribed vertical stretch of 50% in the Y-direction, and was free to slide in the X- and Z-directions. The remaining external and internal cell faces were allowed to deform freely (see Figure 1).

For structures made from neo-Hookean or Mooney-Rivlin material, the numerical results show that the non-linear elastic modulus computed as the ratio between the mean effective Cauchy stress and the mean effective logarithmic strain and the non-linear Poisson's ratio defined as the negative ratio between the mean logarithmic strain in the horizontal and vertical direction, respectively, increase as the wall thickness increases while the number of cells is fixed, or as the number of cells increases while the total volume of solid material remains unchanged (see Figure 2). The mean value was calculated as the sum of the values on all the finite elements divided by the number of elements. These effects are due to the enhanced elasticity of the cell walls when more material is added or when the same material is distributed more uniformly throughout the structure.

[a)] Corresponding author. Email: wyatthl@cardiff.ac.uk

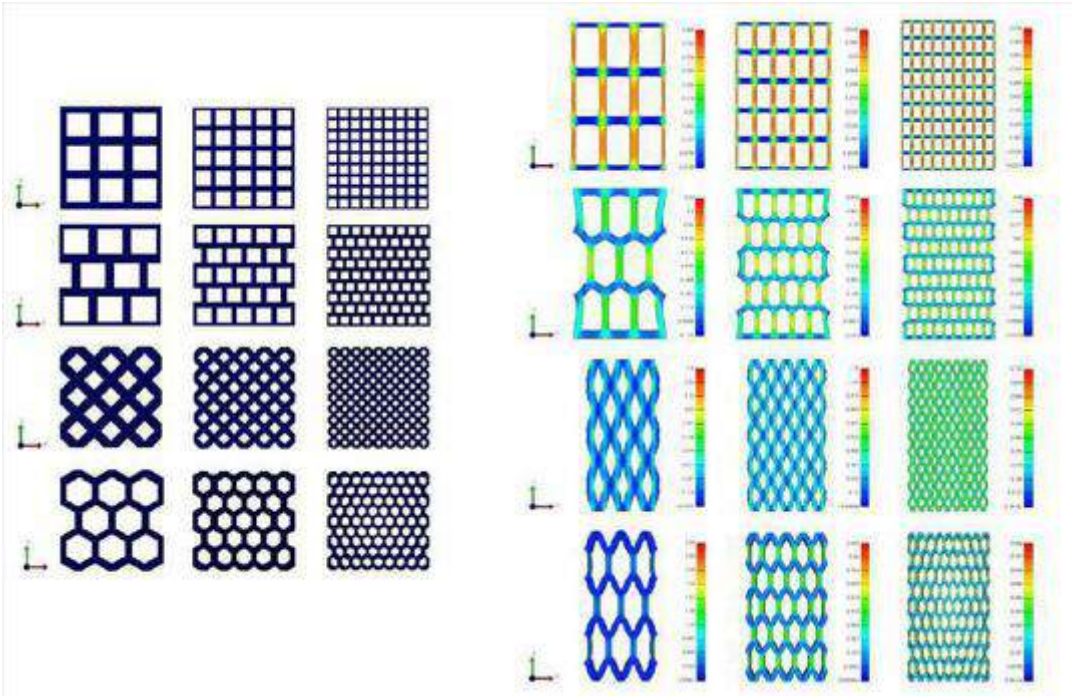

Figure 1. Undeformed model structures with different cell geometries and increasing number of cells while the volume of solid material is fixed (left) and deformed structures subject to 50% stretch in the vertical direction, showing the non-homogeneous Green-Lagrange vertical strains (right). For stacked and diamond cells, the ratio between the thickness and the length of the cell walls also remains unchanged, while for staggered and hexagonal cells, this ratio increases slightly.

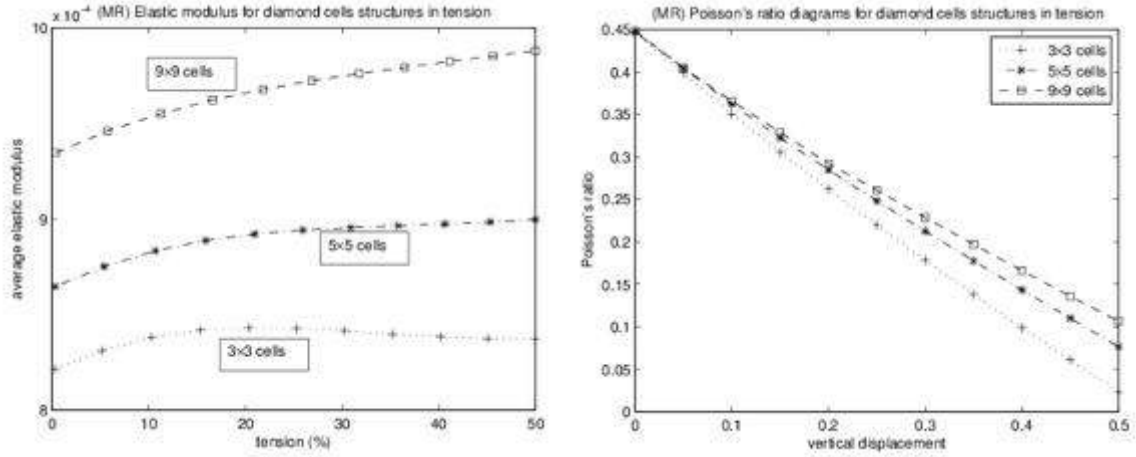

Figure 2. The non-linear elastic modulus (left) and non-linear Poisson's ratio (right) for the diamond cells of Mooney-Rivlin material with the different curves corresponding to structures with a different number of cells while the volume of elastic material is fixed.

CONCLUSION

Thanks to their monotonic behaviour, the non-linear elastic modulus and Poisson's ratio analysed here can be used as indicators for finding the optimum wall thickness or number of cells in similar structures.

Ac n e e en s The support for L.A.M. and H.W. by the Engineering and Physical Sciences Research Council of Great Britain under research grant EP/M011992/1 is gratefully acknowledged.

References

[1] Gibson L.J., Ashby M.F., Harley B.A.: Cellular Materials in Nature and Medicine, Cambridge University Press, 2010.

[2] Mihai L.A., Alayyash K., Goriely A.: Paws, pads and plants: The enhanced elasticity of cell-filled load-bearing structures. *roc Soc A,* 471, 20150107, 2015.

[3] Maas SA, Ellis BJ, Ateshian GA, Weiss J.: FEBio: Finite Elements for Biomechanics, J Biomech Engine 134, 2012.

FS10 - Education in Mechanics

TS.FS10-1.01	Gilchrist, Michael - Use of student competitions to reinforce the learning experience in freshman mechanics education	3467
TS.FS10-1.02	Shimomura, Yutaka - Mechanics for liberal arts students (INVITED)	3469
TS.FS10-1.03	Bigoni, Davide - Teaching structural mechanics with models	3471
TS.FS10-1.04	Chemisky, Yves - Interactive learning experience in mechanics of materials : The 'simmit' project	3473
TS.FS10-1.05	Constantinescu, Andrei - Symbolic Computations: Changing the teaching paradigm for continuous mechanics	3475
TS.FS10-2.01	Stern, Catalina - Teaching physics through experimental projects (INVITED)	3477
TS.FS10-2.02	Wiercigroch, Marian - Nonlinear mechanics for undergraduates (INVITED)	3479
TS.FS10-2.03	Pustovalova, Olga - FlexPDE as a teaching tool in the field of mechanics and mathematical modelling	3481
TS.FS10-2.04	Wilson, Helen - The fluid dynamics of the chocolate fountain: An engaging project	3483
PO.FS10-1.01.350	Da Silva Neto, José Luiz - Optimization of the dynamics of a constant-temperature anemometer	3485
PO.FS10-1.02.351	Shrivastava, Gyan - Fluid Mechanics Education at The University of The West Indies	3487

USE OF STUDENT COMPETITIONS TO REINFORCE THE LEARNING EXPERIENCE IN FRESHMAN MECHANICS EDUCATION

Michael D. Gilchrist
Mechanical & Materials Engineering, University College Dublin, Belfield, Dublin 4, Ireland

Summary The author has been teaching a compulsory introductory *Engineering Mechanics* course for the past decade. This is taken by all Bachelor of Engineering students at University College Dublin in their first university semester. The syllabus topics that students study in this module include vectors, Newton's laws, equilibrium in two and three dimensions, friction and motion in rectilinear and curvilinear coordinate systems. This paper describes a variety of different, low-cost, team competitions that have been organised in past years for each cohort of approximately 300 students annually. It is hoped that these examples of student competitions may be of interest to academics teaching similar mechanics modules elsewhere.

INTRODUCTION

The understanding and application of Newton's laws of motion is fundamentally important in all university level engineering programmes. A solid foundation in these concepts is needed to understand more complex subjects such as mechanics of materials, fluid mechanics, dynamic systems, machine design and control theory. In a university environment, it can be common to teach Newtonian mechanics through theoretical analyses and from a mathematical basis, ignoring many of the tangible everyday connections that students actually have with this subject. By introducing team-based competition assignments, where fundamental mechanics principles are experienced personally, a stronger mental connection can be made with theory, thereby reinforcing students' understanding.

Students studying engineering mechanics at University College Dublin are required to participate in a competition assignment, working in small group sizes (4-5 per group). This competition assignment counts for 20% of the overall module. Other coursework constitutes two laboratory practicals, each counting for 5%. An end of semester written examination counts for the remaining 70%. This approach to teaching blends methods for concept-based learning [1,2] and problem-based learning [3-5]. This firstly promotes a student's understanding of concepts in engineering science and then develops their ability to visualise real-world problems in terms of underlying fundamentals, and subsequently empowers them to quantitatively analyse and obtain solutions to physical problems. In the 21st Century, it remains an imperative that engineering students are provided with a foundation on which to build, and a place in which they can explore the physical manifestation of theoretical concepts [6].

TEAM ASSIGNMENTS

An open design problem with some given constraints is assigned to the class, and they are allowed to solve the problem by any means necessary as long as it complies with given guidelines. The class of 300 students is randomly divided into groups of 5 students which compete against each other. The assignment is typically scheduled during weeks 7-9 of a 12-week semester and teams compete against each other at the end of this three-week period. Such group projects can be used to further enhance the involvement of the students with the theory learned in lectures, and to encourage their creativity, teamwork, and communication skills, which are very important for any working environment. A friendly competitive environment between the groups is created to further motivate the quality of the results and to encourage each student's interest in the results from other groups. A mechanics problem can be analysed on many levels, depending on the knowledge of the person. A theoretical explanation, as detailed as the student's knowledge allows, is required to establish the mental connection between

theoretical analyses and everyday life. Students are also encouraged to research more advanced concepts personally, in order to enhance their understanding and analysis of the mechanical phenomena in these project. Examples of these are summarized below; the corresponding talk will present a selection of videos from these assignments and will discuss student participation and pass rates.

Fastest Egg Race: Design and construct a vehicle to transport a medium sized chicken's egg (uncooked). The vehicle should travel down a ramp and stop as close as possible to the wall at the end of the track in the least amount of time without breaking the egg.

Pasta Bridge: Design and build a freely supported bridge to span a 1 m width using only pasta and glue. The mass of the bridge should not exceed 4 kg. The design should seek to maximize the ratio of total weight carried to self-weight of the bridge.

Paper Tower: Using only A4 sheets of paper, each team of students must build a structure that is at least 1 metre high. The finished tower cannot include any other materials (e.g., adhesive, sellotape, glue, etc.). On the date of the challenge, each team will have one hour to construct their tower. The tower will be required to support a mass of 1 kg at its top for a minimum of 10 seconds. The minimum weight ratio (weight of tower to weight of applied mass) will determine the best performing tower.

Mini Curling: Design and build a mechanical device to launch a polished aluminium puck along a linoleum floor and stop as close to a finish line as possible. The puck will be approximately 20mm thick and 70mm in diameter, and will weigh between 150 and 250g. Since the exact mass of the puck will be unknown until the day of the challenge, students are advised to calculate the sliding distance of a puck impacted by their device as a function of its mass in order to ensure best accuracy.

Mini Basketball: Design and build a mechanical device to throw a tennis ball from variable throwing distances into a basket of 20 cm diameter and 80 cm above the ground. Teams should estimate the trajectory of the ball and calibrate their device to ensure accuracy as a function of throwing distance.

CONCLUSIONS

The use of competition assignments that use real-world examples to emphasise mechanics concepts are shown to enhance participation rates and strengthen levels of engagement for freshman engineering students. There are no additional financial costs to including such activities in engineering mechanics modules, even for large student numbers.

References

1. Redish E.F., *Amer. J. Physics*, **62**:796-803, 1994.
2. Evans D.L., *Proc. Frontiers in Ed. Conf.*, US, November 6-9, 2002.
3. Musto J.C., *Int. J. Mech. Engng Ed.*, **32**:243-257, 2004.
4. Podhorodeski R.P., Sobejko P., *Int. J. Mech. Engng Ed.*, **33**:319-338, 2005.
5. Forero Rueda M.A., Gilchrist M.D., *Int. J. Engng Ed.*, **27**:821-830, 2011.
6. Sheppard S.D., Macatangay K., Colby A., Sullivan W.M., Educating Engineers: Designing for the Future of the Field, Jossey-Bass, 2009.

MECHANICS FOR LIBERAL ARTS STUDENTS

Yutaka Shimomura
Department of Physics, Hiyoshi Campus, Keio University, Yokohama, Japan

Summary From my quarter-century experience of educating liberal arts students of Keio University in Japan, who are generally not good at mathematics, I believe that mechanics is a very effective subject for them to learn scientific approaches through observations and experiments on mechanical phenomena: they develop a study skill of how to find a problem, form a hypothesis for the solution, validate it, and finally solve the problem. This is because many phenomena in mechanics are comparatively simple but attractive, ubiquitous, easily observable, sometimes intuitively understandable and sometimes mysterious.

INTRODUCTION

I am a professor of physics in the faculty of law, Keio University [1], Japan, which was established in 1858 by Yukichi Fukuzawa, whose face is printed on a ten-thousand yen bill. The founder Fukuzawa was one of the pioneers of modern Japan, who noticed the importance of learning that is based on "jitsugaku", or science. It was the demonstrational feature of science that he thought important, as is compactly expressed in the Royal Society's motto 'Nullius in verba' [2]. In fact, he incorporated physics in curriculum at early days of Keio as a basic preparatory subject for all students to learn before other subjects. In 1886, as the first introductory book on science in Japan, he published "Kinmou Kyuuri Zukai" with many Japanese illustrations, which introduces phenomena explained by thermal, solid, fluid mechanics and geoscience.

Succeeding the founder's spirit of science, I have been teaching physics with experiments in Keio University for 25 years to the liberal arts students who belong to the faculties of letters, economics, law, or business and commerce. Most of them are not strong at mathematics, and some are even allergic to mathematical formulae, so that in my physics class I try to avoid using mathematics as much as possible and explain theories in physics with ordinary words.

Since 2006, I also have been teaching to a small study group of three- or four-year level students belonging to the faculty of law, who physically research natural phenomena in the class. Up to now, I have been taking up phenomena mainly in solid and fluid mechanics for this study class.

Here, I review how my liberal arts students in both classes learnt scientific approaches through their experiments and observations of natural phenomena in mechanics to see whether mechanics is effective for their learning.

PHYSICS CLASS

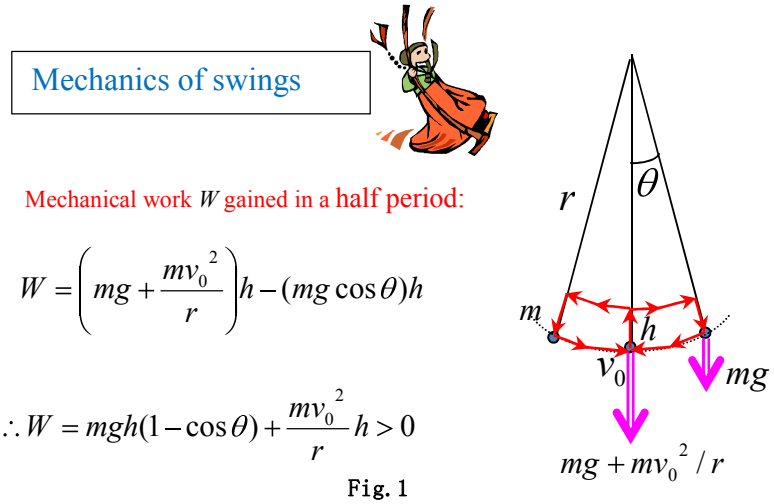

Fig. 1

In the physics class, I call into question the mechanics of swings in playgrounds, which are so familiar to them and simple amusing ride. I often ask students why they can pump their legs just by the repeat of flexing and extending motions, though the repeat does not seem to generate any mechanical energy. Most liberal arts students can't answer this question at once, and I let them think and discuss in a small group. Then, given some hints, they notice the timing of flexing and extending is important and start remembering how they actually move riding on a swing. So, they try to draw a trajectory pattern of their navels on a swing, and finally find that they could give a positive energy to the swing by extending when the swing is in the lowest position and flexing when it is in the highest position because the extending motion should need the force against the centrifugal force in addition to the gravity and the flexing one would not be vertical, as shown in figure 1. As the last topic in this class, I discuss about the possibility for going into a 360-degree roll of a swing, based on their finding. In this class, students really enjoy thinking and discussing about the physical mechanism of a swing without any complex formula and learn the importance of observation and clearly answering the question.

STUDY CLASS

Corresponding author. Email: yutaka@phys-h.keio.ac.jp

In the study class, I have been teaching students for 10 years through observations and experiments on phenomena in solid and fluid mechanics, and so far, I have taken up the flip of a Japanese sword [3], the power-law behaviors of rolling disks [4], the precessions of a gyroscope [5], and the dancing sphere as the former, and the propulsion of water striders [6], the Pen Sue Xi's water spray [7], and the polygonal boundaries formed in rotating fluids [8] as the latter. I will talk about these studies as many as possible at my oral presentation in ICTAM2016, but here, I focus only on the topic the flip of a Japanese sword [3].

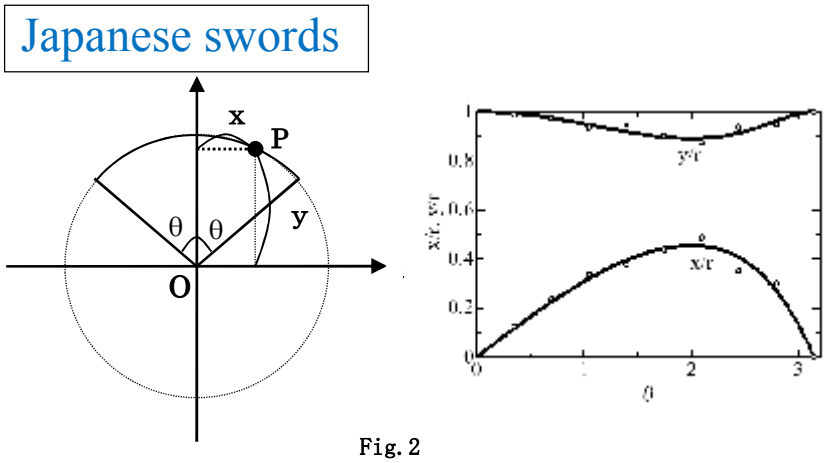

Fig. 2

It is known to some of kendo (Japanese art of fencing) masters that a Japanese sword stably laid on a horizontal table will rotate to take up the other stable position with the cutting side of the blade down when it is quasi-statically pulled to the side of the haft, being horizontally held by a supporting force acting on the edge of the haft, and the length of the part of blade in touch with the table is shortened to a certain length. This simple phenomenon is an exchange of stable positions and there is a critical point on the blade, or the edge of the blade in touch with the table that gives rise to the exchange. I introduced this curious but easily observable phenomenon to my students and questioned about the origin of the exchange: the sword's elliptical cross section, or its warpage of the blade? The students made a straight toy sword with an elliptical cross section and pulled it on a table in the classroom and find it does not show the exchange. Then they cut and reform a wire in the shape of a circular arc and did the same experiment to find it does show the exchange. So they concluded that the exchange of stable positions is caused by the warpage of the blade. They further confirmed that theoretically-predicted positions of the critical points of various circular arcs agree well with the observed counterparts, as shown in figure 2. With their conclusion, I also found that the critical point is the centre of percussion of the blade, which explains the empirically-based advantage of cutting things at the critical point with the Japanese sword.

This class was very successful in developing student's study skill of how to find a problem, form a hypothesis for the solution, validate it, and finally solve the problem through the simple experiments, which are easily executed in a classroom with a few stationery products: a ruler, a protractor, a compass, and a wire.

CONCLUSION

Liberal arts students, who are generally not good at mathematics, can effectively learn scientific approaches through observations and experiments on natural phenomena in mechanics. This is because mechanics can treat phenomena that are comparatively simple but attractive, ubiquitous, easily observable, sometimes intuitively understandable and sometimes mysterious.

References

[1] Keio University, web site http://www.keio.ac.jp/index-en.html

[2] The Royal Society, web site https://royalsociety.org/about-us/history/

[3] Shimomura Y., Hisa S., Shibuya T., Yasuda Y.: The exchange of stable positions for Japanese swords and their centers of percussion. Kyoyo-Ronso **129**(2008)1-11.

[4] Yokoyama E., Ito Y., Shimomura Y.: An experimental study of the exponents in the power-law behaviors of rolling disks. The Hiyoshi Review of Natural Science **48**(2010)1-9.

[5] Hashimoto K., Kanesaka Y., Otogasako A., Takeshita Y., Shimomura Y.: Validation of a formula for precessional motions by analyzing 3D moving images of a gyroscope. The Hiyoshi Review of Natural Science, Keio University **54**(2013)11-23.

[6] Shimomura Y., the students in his seminar: Reexamination of Denny's Paradox. The Hiyoshi Review of Natural Science **42**(2007)17-25.

[7] Tawaki S., Takeshita Y., Shimomura Y.: The Wave Patterns on the Surface of Water in a Horizontally Vibrated Circular Cylinder. The Hiyoshi Review of Natural Science **52**(2012)69-78.

[8] Kakino H., Chen Q., Morita T., Yanagawa M., Shimomura Y.: Similarity between the structures of the polygonal boundaries formed in rotating fluids and hydraulic jumps. The Hiyoshi Review of Natural Science 58(2015)1-10.

TEACHING STRUCTURAL MECHANICS WITH MODELS

Davide Bigoni[1], Francesco Dal Corso[1], Diego Misseroni,[1]
[1]*DICAM, University of Trento, Trento, Italy*

Summary Several models are presented to help teaching structural mechanics at all levels to engineering and physics students. The simpler models have been developed to explain the concepts of elastic beam, segmental arch, truss structure, elastic frame, and Euler buckling. More sophisticated models have been designed to introduce advanced concepts such as flutter instability under tangential follower load and configurational forces under bending and torsion.

INTRODUCTION

In the last decade we have developed physical teaching models to improve the presentation and understanding of scientific results, especially to engineering and physics students (at undergraduate and graduate level), but also to all levels, ranging from untrained audiences to peers in the scientific community.

Digital technology has indisputable merits and is of crucial importance in teaching. However, it tends to reduce physical intuition in students generally and for students used to an intuitive approach (such as those involved in engineering studies) it can be difficult to understand how principles are applied in the real world. This is particularly true in mechanical engineering, probably the hardest discipline in engineering studies.

Several mechanical models developed in our laboratory have been shown to be of primary importance (i) as proof-of-concepts of newly discovered phenomena; (ii) as teaching tools at different levels, including PhD programs; (iii) as demonstrators at public exhibitions, even for untrained public.

Our models have been conceived, designed, and realized to give tangible, vivid evidence of non-intuitive mechanical phenomena. Some of them have been invented for illustrating results obtained within EU financial schemes, others have been addressed to scientific presentations, and others have been designed to help students in understanding basic and advanced concepts of mechanics.

Our results and findings provide a breakthrough innovation in engineering education, through a simplification in the teaching of mechanics. We will continue developing our methods, thus contributing, through engineering education, to a sustainable and equal opportunities human development.

MODELS FOR BASIC STRUCTURAL ANALYSIS

Cross and Morgan wrote in 1932: '*the ability of a designer of continuous structures is measured chiefly by his ability to visualize the deformation of the structure under load. If he cannot form a rough picture of these deformations when he begins the analysis he will probably analyse the structure in some very awkward and difficult way; if he cannot picture these deformations after he has made the analysis, he doesn't know what he is talking about*'. This statement remains valid today. However, the visualization of the deformation of a structure is more complex than it may appear and for this reason, teaching models are fundamental to stimulate students' interest and to simplify learning. We have developed several structural models for Civil engineering students, for elastic beam, segmental arch, truss structure [1], elastic frame [2], and Euler's buckling, Fig. 1.

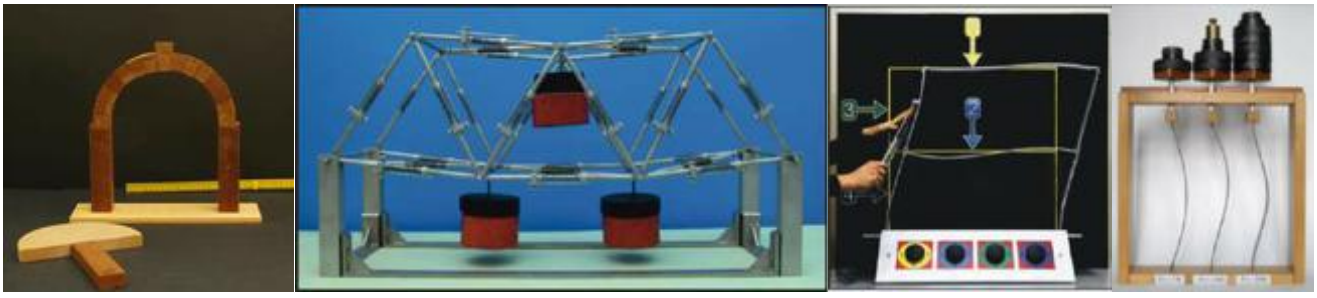

Fig. 1 from left to right, models for: Segmental arch; Truss structure; Elastic frame and Euler's buckling

[a)] Corresponding author. Email: davide.bigoni@unitn.it

ADVANCED MODELS FOR FLUTTER INSTABILITY & CONFIGURATIONAL FORCES

Proof-of-concept-models have been designed by us to give evidence to previously unknown mechanical phenomena. These include: buckling of an elastic rod under tensile dead load [3], flutter instability induced by dry friction [4], effects of curvature constraint on instability [5], existence of configurational forces [6], effects of configurational forces on instability [7], the elastica arm scale [8], the torsional gun [9], Fig. 2. All these phenomena are so innovative that it is hard to imagine their real world implications without a working physical model.

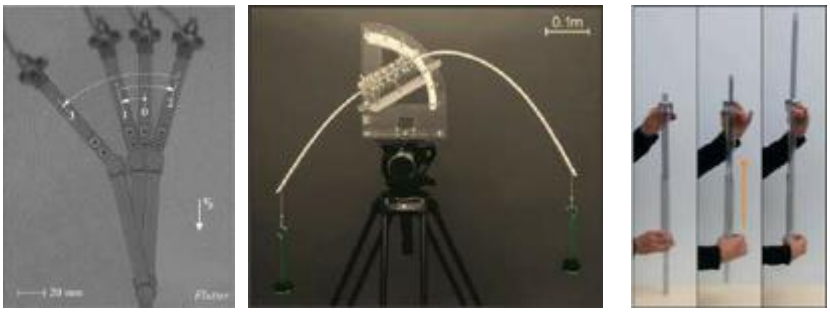

Fig. 2 From left to right, models for: Flutter instability; The elastica arm scale; The torsional gun

CONCLUSIONS

Usually engineers face the problem of characterizing new materials of unknown properties and this is done using standard testing machines. Our models originate from an of 'inverted approach': first we develop a theory to describe a phenomenon and then we build a model which will behave physically according to the theory. In this sense, our laboratory is unique: we use our testing machines with data acquisition to fully define the behaviour of our physical models to see how well it fits the theoretical models. We have thus been able to show complex nonlinear instabilities such as flutter instability in the real world which were previously only demonstrated mathematically. We have discovered and demonstrated buckling instability of a bar in tension and the existence of configurational forces. We have invented a new type of elastically deformable arm balance and a torsional actuator, each one with its associated model. These models have been used to engage both our peers and the public in our discoveries. Teaching models of truss structures and frame structures have been developed to enhance teaching at the undergraduate level.

ACKNOWLEDGEMENT

The authors gratefully acknowledge financial support from the ERC Advanced Grant 'Instabilities and nonlocal multiscale modelling of materials' FP7-PEOPLE-IDEAS-ERC-2013-AdG (2014-2019).

References

[1] Bigoni, D., Dal Corso, F., Misseroni D. and Tommasini, M. A teaching model for truss structures. *Eur. J. Phys.* **33**:1179–1186, 2012.

[2] Misseroni D., Bigoni, D. and Dal Corso, F. A model for teaching elastic frames. *J. Materials Education*, **36**:169-174, 2014.

[3] Zaccaria, D., Bigoni, D., Noselli, G. and Misseroni, D. Structures buckling under tensile dead load. *Proc. Royal Soc. A* **467**:1687-1700, 2011.

[4] Bigoni, D, Noselli, G. Experimental evidence of flutter and divergence instabilities induced by dry friction. *J. Mech. Phys. Solids* 59:2208–2226, 2011.

[5] Bigoni, D., Misseroni, D., Noselli, G. and Zaccaria, D. Effects of the constraint's curvature on structural instability: tensile buckling and multiple bifurcations. *Proc. Royal Soc. A* **468**:2191-2209, 2012..

[6] Bigoni, D., Dal Corso, F., Bosi, F. and Misseroni, D. Eshelby-like forces acting on elastic structures: theoretical and experimental proof. *Mech. Materials* **80**: 368–374, 2015.

[7] Bigoni, D., Bosi, F., Dal Corso, F. and Misseroni, D. Instability of a penetrating blade. *J. Mech. Phys. Solids* **64**:411-425, 2014.

[8] Bosi, F., Misseroni, D., Dal Corso, F. and Bigoni, D. An elastica arm scale. *Proc. Royal Soc. A* **470**:20140232, 2014.

[9] Bigoni, D., Dal Corso, F., Misseroni, D. and Bosi, F. Torsional locomotion. *Proc. Royal Soc. A* **470**:20140599, 2014.

INTERACTIVE LEARNING EXPERIENCE IN MECHANICS OF MATERIALS: THE 'SIMMIT' PROJECT

Yves Chemisky*[1], George Chatzigeorgiou[1], and Fodil Meraghni[1]

[1]*Arts et Métiers ParisTech, LEM3 UMR 7239 CNRS, France*

Summary This communication presents a methodology and tools that take advantage of research projects developments in the field of mechanics of materials for education outreach. Such new learning experience should meets the requirements of efficient interactive learning : ease of use, hands-on oriented, interactive exposure to theoretical concepts. It also has to be linked to state-of-the art scientific and industrial design numerical tools. Based on the new generations students audience expectations, an interactive method has been developed to facilitate the exposure of student to theoretical concepts and hands-on experience. Interactive learning notebooks are utilized, combined with high-efficiency scientific libraries wrapped in the widely-utilized Python language. Such methodology thus allows to easily link the theoretical concepts to industrial softwares and numerical tools, through their Python language scripting interfaces.

INTRODUCTION

Interactive Learning is a pedagogical approach that incorporates interactive experience into course design and delivery. It has evolved over the years, and benefits of the state-of-the art digital technology in terms of human-machine interaction and communication. Among the tremendous number of digital tools available (video and audio support, online communication, serious games), interactive coding is an efficient choice to expose students to basic scientific computing while learning theoretical concepts with a hands-on oriented approach. Such a different learning angle necessitate a paradigm shift in education. In particular, the new audience skills and expectations, and the new technology capabilities have to be included in the design of courses and preparation. A second aspect of interactive content is the interaction and compatibility with up-to-date simulation tools and numerical analysis packages in the field of mechanics of structures and materials. Also, compatibility with optimization methods, data mining, analytics and machine learning is necessary to explore the wide toolbox available to the new generation of engineers and scientists. Concerning the adaptation to new audience, such courses have to match with the Z generation of students expectations [**?**]. Their members have indeed grown up with internet and communication technologies, and they have a savvy use of interactive human-machine tools [**?**]. They therefore naturally highly expect tailored learning, sharing content within a community, and human-machine interaction at any stage of their learning experience. To adapt to such audience, new courses require a quick access to interactive, technology-oriented hands-on experience to facilitate the learning process of theoretical concepts in physics. On the second hand, the design of courses need also to be oriented towards the deep understanding of simulation methods in engineering. Indeed, students should be very familiar with finite element analyses (FEA) packages, material science libraries, optimization algorithms and workflows. Most of the advanced techniques for the simulation of materials nowadays relies on third-party packages dedicated to the behavior of materials, such as DIGIMAT, Z-Mat, MOOSE or SMART+. According to which concepts in mechanical of materials are approached, such transition from numerical research tools to educational material invite us to review the learning experience we propose. Indeed, since the development and/or use of efficient integrated numerical tools is a new requirement for engineers in Mechanics and Materials, a proper paradigm in education must be adopted. We have summarised three important features of an innovative interactive tool: (i) It must be compatible with integrated tools and solutions for the analysis of a material or mechanical system; (ii) the tools and knowledge exposed must be adapted to numerical simulation methods commonly utilized in industry (iii) it must easily interact with other numerical and/or scientific libraries and analytics

SIMMIT : AN INTERACTIVE TOOL

Such conclusions have led to the definition of an interactive learning package, named *simmit* which stands for "*Simulation in mechanics and Materials : interactive tools*". Such tool is proposed in an open-access format, to build a community of contributors around it and facilitate exchanges between users. The objective is eventually to facilitate the transmission of knowledge, concepts and contents that are traditionally utilized in advanced numerical simulation in Mechanics of Materials, from theoretical concepts to practical use of numerical tools for simulation and analytics.

The learning experience of students is typically depict in Figure **??** in dashed lines. Theoretical concepts in mechanics of materials and continuum mechanics are assimilated in one hand, and in a second hand they learn the use of software as well as high-level programming language to connect and interoperate input/outputs of such softwares and build workflow to analyse, optimise, present results. The two aspects are usually disconnected, since there are no tools to combine them. One way to connect the two aspect is to develop a library in a high-level language, such as Python, that will allow to develop an interactive

*Corresponding author. Email: yves.chemisky@ensam.eu

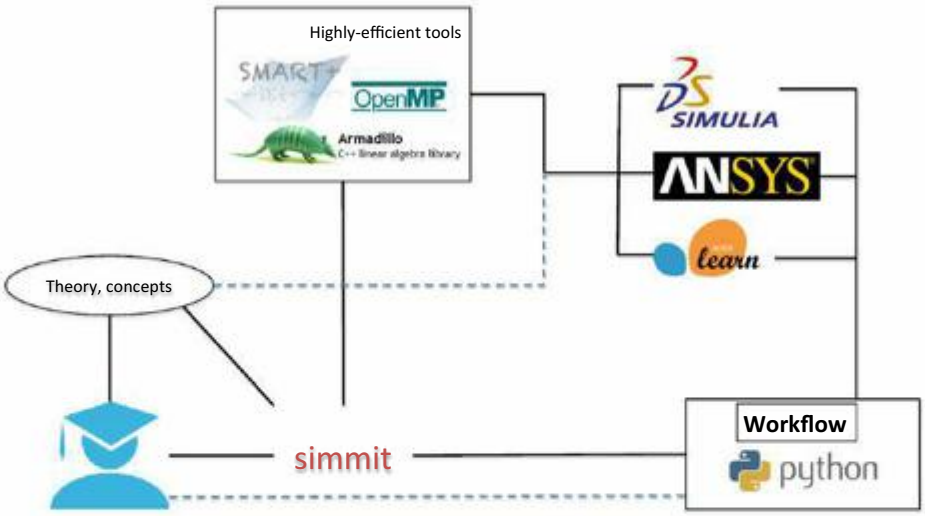

Figure 1: Flowchart describing the learning process of numerical simulation tools, and theoretical concepts in mechanics of materials. Blue Dashed lines present the actual experience and blue plain line represent the interactive experience with simmit

learning experience of theoretical concepts. Python language is a general-purpose, high-level programming language [**?**]. It is widely utilized in the scientific community, notably thanks to scientific packages such as Numpy and Scipy. Moreover, the integration of numerical tools in interactive notebooks has been possible using IPython notebooks since, as an interactive computational environment, they combine code execution, rich text, mathematics, plots and integration of other media. Thus, to propose an interactive learning of Mechanics of Materials using Python blocks in notebooks, the *simmit* library has been developed to expose functions commonly utilized in continuum mechanics, solid materials constitutive relations, non-linear response of materials, physical strain mechanisms, and multi-scale analysis. Note that many python libraries can be utilized for data science, linear algebra, optimization and machine learning to produce a comprehensive set of numerical tools for the analysis of the mechanical behavior of Materials.

Moreover, since most of the research tools rely now on computationally efficient APIs (Application Programming Interface), a good solution is to expose some of the functions proposed in such APIs to be able to integrate them in interactive Python notebooks. In such a case, the efficiency of the original library is maintained (i.e. since it relies on robust linear algebra libraries and multithread packages). The simmit toolbox thus highly relies on a scientific library, named Smart+ [**?**] that regroups a whole set of tools for the numerical simulation of materials. Smart+ has been primarily developed to interact with FEA packages, for instance *Abaqus*, thus focusing in computational efficiency rather than ease of use. The simmit toolbox include Smart+ and Python wrappers developed to allow an easy access in interactive notebooks. As a result, such library will allow learn and use theoretical functions that are usually not accessible in efficient APIs of simulation packages. Moreover, simmit allows to interoperate with such packages, to build tailored solutions in the field of mechanics of materials, as depicted in in Figure **??**.

CONCLUSION

New methods and tools in the field on interactive learning experience are required, according to the next generation audience and societal demand. We have demonstrated that the *simmit* toolbox fulfill those requirements, being compatible with integrated tools and solutions for the analysis of a material or mechanical system, adapted to numerical simulation methods commonly utilized in industry, and can easily interact with other numerical and/or scientific libraries and analytics. It also contains all the necessary tools required for the study of mechanics of materials. The development of a full interactive course based on this tool is ongoing, and will be proposed as a massive open online course.

References

[1] Levit, Alexandra (2015-03-28). "Make Way for Generation Z". The New York Times. Retrieved 2015-12-14.
[2] Prensky, Marc (2001). "Digital Natives, Digital Immigrants Part 1". On the Horizon.
[3] TIOBE Software Index (2015). "TIOBE Programming Community Index Python"
[4] The RedMonk Programming Language Rankings: June 2015 tecosystems". Redmonk.com. 1 July 2015.
[5] SMART+, Smart Materials Algorithms and Research Tools: A Scientific Library for the Analysis of the Thermomechanical Behavior of Heterogeneous Materials, http://www.lem3.fr/chemisky/smartplus/, Retrieved 2016-01-12

SYMBOLIC COMPUTATIONS CHANGING THE TEACHING PARADIGM FOR CONTINOUS MECHANICS

A. Constantinescu *[1] and A.M.Korsunsky[2]
[1]*Laboratoire de Mécanique des Solides - CNRS UMR 7649, École Polytechnique, 91128 Palaiseau cedex, France*
[2]*Department of Engineering Science, University of Oxford, Parks Road, Oxford, OX1 3PJ UK*

Summary The backbone of engineering education is based on the presentation of the fundamental principles, mathematical and physical models embedded in a series of challenging and inspiring examples of applications.

In the last decades, traditional educational paradigms have been challenged an easy access to numerical solutions eroding the fundamental knowledge in mathematics, the access to libraries and knowledge, communication technologies, etc. As a consequence, we witness an important evolution of the way students learn and of the student-teacher interaction.

The paper presents a novel way of understanding continuum mechanics theory using symbolic computations and discusses the combination of symbolic and numeric method for solving the indentation problem of a mulilayer structure.

INTRODUCTION

The backbone of engineering education is based on the presentation of the fundamental principles, mathematical and physical models embedded in a series of challenging and inspiring examples of applications. Ideally, part of the illustrations should come from table-top experiments presented during the lectures. Mastery of the subject will finally arrive with practical skills acquired through experience by solving exercises, doing experiences, analyzing data.

In the last decades, traditional educational paradigms have been challenged from different directions: the explosion of computational power has brought into play an easy access to numerical solutions eroding the fundamental knowledge in mathematics and the capacity to compute closed-form solutions, the internet has changed human interactions and the access to libraries and knowledge, etc. As a consequence, we witness an important evolution of the way students learn and of the student-teacher interaction based on the new communication technologies. Almost all top universities are struggling to shape the new tools of learning and to overcome these difficulties. Most of the effort [3, 4] goes into massive open online courses, shortly denoted as MOOC, which can give easy access to conceptual and technical content, shrink geographical distances and foster interdisciplinary research. However, the explosive popularity of MOOC learning, does not solve the question of how to teach the practical skills of science ? as practical skills have to be acquired through hands-on experiences: problem-solving activities, laboratory courses, field trips, internships and project work etc., see the discussion in [5].

Our aim is to addresses the question of teaching the fundamental concepts and the practical skills of continuous mechanics by taking advantage of capabilities of combining symbolic and numeric computations in programs like MATHEMATICA [6]. The advantages of manipulating a high level symbolic computer code are of different nature. It facilitates computational burden of applying partial differential operators to vector and tensor field in general and especially in non Cartesian coordinate systems and it is therefore a new mean of approaching classical closed-form solution. One can easily check the validity of existing formulas, graphically and numerically manipulate the result and create numeric approximations of the solutions. Moreover, the rigor of a computer code obliges to respect a certain formalism in manipulating the expressions which insures a good understanding of the underlying concepts. Therefore the description of mechanics with such a tool brings the balance between theory, classical closed-form solutions and numerical computational.

The paper presents a novel way of understanding theory using symbolic computations as presented in [1] and discusses the combination of symbolic and numeric method for solving the indentation problem of a mulilayer structure as discussed in [2].

UNDERSTANDING THEORY

The easy manipulation of differential operators on vector and tensor fields opens up a series of subjects in continuous mechanics: kinematic of motion and the concept of deformation, equilibrium of stress fields and their efficient representation using potentials, anisotropy of elasticity tensors, computation of closed-form and approximate solutions for elasticity equilibrium, vibration or buckling problems, approcimate solution using energy minimization principles etc. In order to keep the presentation concise, only few subjects will be select to illustrate the topics included in this treatment.

Kinematics of motion serves as a vehicle for introducing the concept of deformation as a transformation map, leading naturally to the concept of deformation gradient and polar decomposition into rotation and translation. The definition of strain then follows, and particular attention is focused on the concept of small strain. The procedure for *reconstructing the*

*Corresponding author. Email: constant@lms.polytechnique.fr

displacement field from a given distribution of small strains is constructed based on rigorous arguments, and implemented in the form of an efficient MATHEMATICA module. In the process of developing this constructive approach, the conditions for small strain integrability are identified (also known as the Sain Venant strain compatibility conditions) and the significance of the second order incompatibility operator, `inc`.

An arduous subject is the introduction and use of the method of displacement potential. Firstly, the harmonic scalar and vector Papkovich-Neuber potentials are introduced, and the representation of simple deformation states in terms of these potentials are found. Next, the fundamental solution of three-dimensional elasticity is derived, the Kelvin solution for a force concentrated at a point within an infinitely extended isotropic elastic solid. The Kelvin solution serves as the basis for deriving solutions for force doublets, or dipoles, with or without moment, and also for centers of dilatation and rotation which easily be developed starting from this basic brick.

COMBINING SYMBOLIC-NUMERIC SOLUTIONS

Indentation experiments have recently become the standard testing method for hard materials like thin films and surface coatings or soft biological materials like cells. The identification of material properties is based on the indentation curve $P \nearrow h$ representing the applied load P on the indenter with respect to its penetration's depth h during loading/unloading test and various phenomenological formulas are used to relate the apparent indentation modulus to the elastic properties of the different layers.

The solution method discussed here[2] is based on the introduction of Neuber-Papkovich potentials for representing the displacement fields in each layer and the substrate and the application of the Hankel transforms. As such the problem is reduced to the boundary conditions at each interface and at the upper face where the contact takes place. The symbolic manipulation of the complex analytical expression permit to created automatically a linear system equations defining a stress distribution for a given contact radius and indentor shape and to couple it with a nonlinear solver which determines the contact radius of solution the indentation problem.

This construction of the solution method combining the symbolic and numerical part present several advantages over classical methods: it keeps a clear form of the solution method and assures an better control of errors when transposing complex formulas and when adding up further developments and it permits compiling of pre-computed expressions insuring a 10-50 times acceleration of the computing time. Moreover, the style of presentation premits a better understanding of the solution and the possibility to survey the calculations by non-specialists.

PERSPECTIVES

The presentation of several subjects in continuous mechanics using the combined power of symbolic and numeric computations show that arduous subjects can be transformed in a virtual laboratory game. The next step is to connect this tool to other teaching experiments and transform an old and computational intensive subject is a fuzzy elegant play.

References

[1] Constantinescu, A. and Korsunsky, A. *Elasticity with Mathematica*. Cambridge University Press, 2007.

[2] Constantinescu, A., Korsunsky, A., Pison, O., and Oueslati, A. Symbolic and numerical solution of the axisymmetric indentation problem of a multi-layered elastic coating. *International Journal of Solides and Structures*, 50(18):2798–2807, 2013. dx.doi.org/10.1016/j.ijsolstr.2013.04.017.

[3] Waldrop, M Mitchell. 2013. Online Learning: Campus 2.0. Nature 495 (7): 16063. doi:10.1038/495160a.

[4] Crow, M M. 2013. Digital Learning: Look, Then Leap. Nature 499 (7458): 27577. doi:10.1038/499275a.

[5] Waldrop, M Mitchell. 2013. Education Online: the Virtual Lab. Nature 499 (7): 26870. doi:10.1038/499268a.

[6] `http://www.wolfram.com/`

TEACHING PHYSICS THROUGH EXPERIMENTAL PROJECTS

Catalina Stern, Carlos Echeverria & David Porta
Department of Physics, Facultad de Ciencias, UNAM, Mexico City, Mexico

Summary We present the methodology we have used to teach and motivate Physics students to work in experimental projects even in the theoretical courses. We believe this form of teaching forces students to integrate their previous knowledge, encourages their initiative and helps them develop self-confidence. We show some of the projects and discuss our point of view about the relationship between teachers and students.

MOTIVATION

The program to obtain a Bachelor's Degree in Physics at the School of Science of the National University of Mexico has a strong theoretical orientation even though it includes seven compulsory traditional laboratory courses: mechanics, collective phenomena, electricity and magnetism, optics, electronics and contemporary physics I and II. Students comment that they are bored in the labs, that they do not learn, that the equipment is old and does not work so they waste their time and experiments do not come out as expected. This reinforces the myth that physics students do not like to do experiments. In most of these courses, experiments are used to "illustrate" or "prove" concepts seen in the theoretical part of the class. However, in my experience with the two theoretical courses I teach at the sophomore and senior levels, 85% of the students choose an experimental subject for their final project. The rest of the class does either computational work or review theoretical papers.

METHODOLOGY

In general, a team of three students presents the experiments even though sometimes students prefer to work alone. The students dedicate many hours to search for a topic (it is usually a published experimental paper), justify their choice, design and set-up an experiment, obtain results, prepare an oral presentation and write a term paper. This work is additional to traditional homework and partial examinations.
When the projects are very good and the students wish to continue working on them after the semester is over, they get to present their results in the education section of the National Congress of Physics or at the Congress of the Division of Fluid Dynamics of the Mexican Physical Society. We also have a channel in you tube where some of the edited videos can be seen, and we recently started a web page.
Students are free to work elsewhere, but most of the experiments are set up at the Taller de Hidrodinámica y Turbulencia (Hydrodynamics and Turbulence Laboratory) where they can use the techniques and equipment that we use in our research, in particular lasers, high-speed video cameras, frequency generators, spectrum analyzers and power supplies.
The teaching assistants assigned to the course and my graduate students help me guide the younger students through the process. The students present a written proposal of their project, and once it is accepted there is a constant interaction between teachers and students that has proven to be most effective. The environment is friendly, there are many discussions, and the truth is that we all learn with each new project.

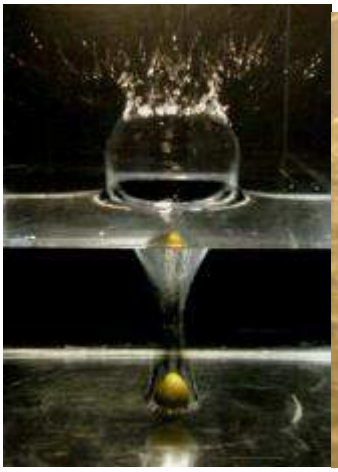
Splashing

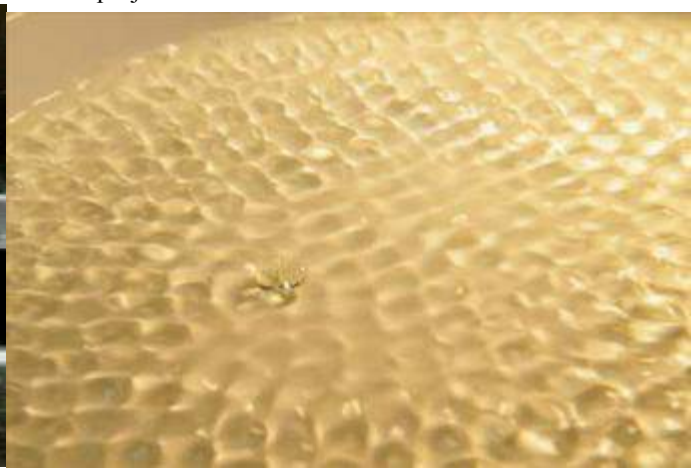
Faraday Waves

[a] Catalina Stern. Email: catalina@ciencias.unam.mx

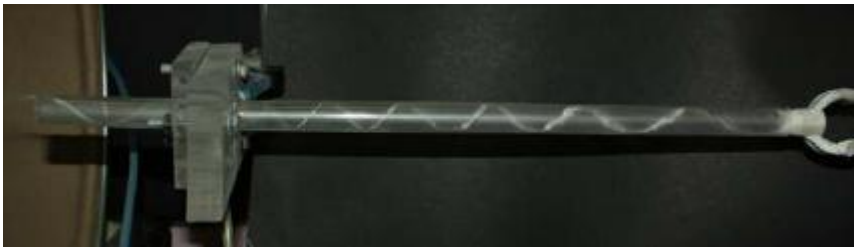

Ranque Hilsch Tube

CONCLUSIONS

We believe that this form of teaching is very important even for students that are theoretically oriented. To work in the laboratory, students have to integrate what they have learned before in mechanics, optics, electricity and electronics, thermodynamics and quantum mechanics. It is one of the few times that they see physics as a whole in a classroom. They also understand the concepts involved in measuring and the physical principles that involved in measuring devices like voltmeters, photodetectors, etc. They learn to design experiments, recognize the important variables and understand concepts like repeatability, precision and uncertainty, and realize the importance of statistics and probability, and data analysis.

Finally, they learn to work as a team, to express themselves orally and by writing, to search for bibliography, to defend their point of view, to present their results. It is also an important experience for the teaching assistants who have to use their imagination in a wide variety of proposals.

This method has influenced the experimental courses of the new program of biomedical physics and some groups of the contemporary physics labs, where students learn through projects starting on the first semester. With the collaboration of some researchers and professors, students spend four weeks in a research lab doing a project and then they switch to another. The following team continues with the work, and at the end, all the groups discuss their work and make a presentation of the evolution of the project. The main advantage is that the students get to work with modern equipment in current research topics close to researchers.

The results exceed our expectations. Students learn more and are very motivated, they are independent and feel free to present their points of view and participate in discussions. We hope to convince our colleagues that all experimental courses should be taught through projects.

NONLINEAR MECHANICS FOR UNDERGRADUATES

Marian Wiercigroch[1]

[1]*Centre for Applied Dynamics Research, University of Aberdeen, Aberdeen, Scotland, UK*

Summary Nonlinear mechanics is fundamental discipline which drives developments in science and engineering. However, there is only one comprehensive nonlinear mechanics course in all English speaking countries offered to the undergraduate students. The course was developed in 2013 at the University of Aberdeen and was given for the first time to a class of over 70 students in 2014. The course introduces the fundamentals of nonlinear mechanics, which are essential for understanding and modelling nonlinear engineering systems using computational mechanics methods such as finite element method, computational nonlinear dynamics and computational fluid dynamics. This paper describes the course and shares some initial teaching experience.

INTRODUCTION

Undoubtedly, main advances in mechanics are driven by the state of the art in various areas of nonlinear mechanics including solid mechanics, fluid mechanics and dynamics. In 2005, I have initiated a conference series names as *Recent Advances in Nonlinear Mechanics*, where the first was held in Aberdeen (2005), the second in Kuala Lumpur (2009); the third one in Harbin (2013) and the next one is to be held in Warsaw in 2017. The main aim of this series is to learn about the developments in each of these distinct areas of nonlinear mechanics and stimulate research interactions. Hence these conferences have programmes with three symposia on dynamics, fluids and solids and general sessions with talks from these three areas are mixed. The experience gain from running this conference series has been valuable in developing a new undergraduate course at the University of Aberdeen.

Nonlinear mechanics is taught mostly at graduate level with many excellent but specific courses including solid mechanics and materials, fracture and fatigue, fluid mechanics and turbulence, and nonlinear dynamics and chaos. It worth noting here that many of these courses have a significant computational element which may even dominate the contents, for example, Computational Fluid Dynamics (CFD). However to my knowledge, there is no single graduate course, which takes a holistic approach to nonlinear mechanics.

Elements of nonlinear mechanics can be found in some undergraduate programme at the senior level, but again there no a single course which would provide students, which would treat nonlinear mechanics in comprehensive manner. Hence, my aim has been to develop a course which would equip senior undergraduate students some fundamental knowledge of nonlinear dynamics. Specifically, the course aims are to: (i) familiarise the student with the concept of nonlinearity and nonlinear behaviour of engineering systems, structures and materials and (ii) enable the student to understand, analyse and interpret the nonlinear behaviour of engineering systems, structures and materials by means of computational mechanics. The course description and my initial experience of teaching it will form the rest of the paper.

COURSE DESCRIPTION AND SYLLABUS

This course introduces the fundamentals of nonlinear mechanics, which is essential for understanding and modelling nonlinear engineering systems using computational mechanics methods such as finite element method, computational nonlinear dynamics and computational fluid dynamics. The course is comprised of six complementary parts. In the first three, an introduction to nonlinear mechanics, the main modelling approaches, the basics of nonlinear dynamics are discussed. Illustrative examples from engineering are given. The fourth part focuses on nonlinear materials and micro-mechanics. In the remaining two parts, the fundamentals and engineering application examples of the Finite Element Method (FEM) and Computational Fluid Dynamics (CFD) are given.

The course has been taught over 11 weeks with 2 lectures and one tutorial per week. By the end of the course students should have a knowledge and understanding of:

- the importance and sources of nonlinear behaviour in engineering systems, structures and materials,
- the fundamental principles behind analytical and computational methods used in nonlinear mechanics,
- the main analytical and computational methods used in nonlinear mechanics,
- the main nonlinear dynamics concepts and tools such as multi-stability, Poincare maps, bifurcations diagrams, Lyapunov exponents and basin of attractions,
- the importance and sources of multiscale plasticity,
- fundamentals of plastic deformation in materials,
- multi-axial yield criteria, associated flow, hardening for materials

The course syllabus has been structured into six modules with increasing complexity and difficulties. The description of the modules is given below:

1. **Preliminaries of nonlinear mechanics.** Role and type of nonlinearities in engineering systems, structures and materials. Difference between linear and nonlinear mechanics. Geometrical and material nonlinearities. Limits of linearisation and example of strongly nonlinear engineering systems. Laboratory demonstration of nonlinear effects (e.g. nonlinear dynamical systems).
2. **Modelling of systems and structures with weak and strong nonlinearities.** Selected analytical and numerical methods used in nonlinear mechanics. Asymptotic expansion and direct numerical simulation. Spatial and time discretisation, computational errors.
3. **Basic concepts of nonlinear dynamics.** Stability, bifurcations and chaos. Computation of phase portraits, Poincare maps and bifurcation diagrams. Numerical analysis of complex dynamic responses of a driven pendulum.
4. **Nonlinear materials and micro-mechanics**. Material related phenomena: yield, associated flow, plasticity, hardening models. Small and large deformations, heterogeneity, polycrystalline microstructure, dislocations, slip systems, Schmid rule, slip rule, statistically stored and geometrically necessary dislocations.
5. **Fundamentals of Finite Elements Methods.** Discretisation and shape functions for 2D and 3D; higher order element formulations. Assembly and solution of matrix equations for a 2D cantilever beam, FEM analysis of 2D problems with geometrical and material nonlinearities.
6. **Fundamental of Computational Fluid Dynamics**. Conservation laws and constitutive equations. Reynolds number, boundary layers and turbulence. Discretisation methods. The finite volume method. Newtonian and non-Newtonian flows, flows with heat transfer. CDF analysis of 2D flows through a pipe with Newtonian and non−Newtonian flows for various Reynolds numbers.

CLOSING REMARKS

As has been stated, nonlinear mechanics is fundamental discipline which drives development of science and engineering. It is difficult to find any cutting edge technology which would not operate in nonlinear regimes. Nonlinear mechanics is taught mostly at graduate level with many excellent but specific courses including solid mechanics and materials, fracture and fatigue, fluid mechanics and turbulence, and nonlinear dynamics and chaos. However, there is only one comprehensive nonlinear mechanics course in all English speaking countries offered to the undergraduate students. The course was developed in 2013 at the University of Aberdeen and was given for the first time to a class of over 70 students in 2014. The course introduces the fundamentals of nonlinear mechanics, which are essential for understanding and modelling nonlinear engineering systems using computational mechanics methods such as finite element method, computational nonlinear dynamics and computational fluid dynamics.

The initial feedback from the students has been encouraging with complementary comments from the best students saying that the course provides them with a platform to understand and investigate complex problems in engineering. The course is being taught now for the second time and we welcome new comments to make this unique course even stronger.

.

FLEXPDE AS A TEACHING TOOL IN THE FIELD OF MECHANICS AND MATHEMATICAL MODELLING

Mikhail Karyakin[1a)] & Olga Pustovalova[1]
[1]*I.I.Vorovich Institute of Mathematics, Mechanics and Computer Science, Southern Federal University, Rostov-on-Don, Russia*

Summary The paper describes some features of finite element package FlexPDE that makes it a very suitable tool for teaching such courses as continuum mechanics, strength of materials, elasticity theory, mathematical modelling etc. Unlike the majority of modern FEM software it is concentrated mostly on equations describing the physical process allowing deeper understanding underlying mathematics, easy switching to new models, and conducting numerical experiments to test the material and functional characteristics of these models. Some examples which can be of use in student labs are presented. They demonstrate not only the nice way from the physical object to numerical result through mathematical modelling but also the problems that are intended to inspire students for independent work, self-study and research activities.

INTRODUCTION

Finite element program FlexPDE [1–2] stays apart of the typical modern FEM packages being oriented not on the engineering design but serving as a tool for numerical analysis of equations with partial derivatives arising in many fields of natural sciences. Flexibility of FlexPDE scripting language allows user easily describe the system of differential equations, boundary conditions, and shape of the region and set up the required quantities to be calculated. The proven effectiveness of this package in the area of elasticity theory makes it very useful for designing and implementation courses on strength of materials, continuum mechanics, the theory of elasticity and plasticity etc.

EXAMPLE 1. METRONOME VIBRATIONS

As an example the scheme for analysis of the frequency of the metronome vibrations is presented below. This problem is not complicated for modelling. At the same time obtained results can be easily compared with known data, or even with a full-scale experiment. Students also can study the dependence of frequencies on various parameters of the construction [3].

Real Object	3D Scheme
	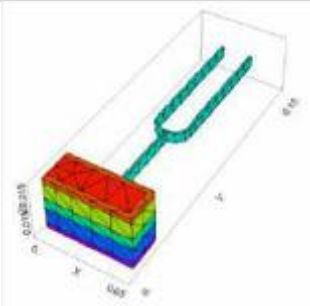

Mathematical Model	
Equilibrium Equations	$\nabla \cdot \boldsymbol{\sigma} + \rho \mathbf{f} = \rho \dfrac{\partial^2 \mathbf{u}}{\partial t^2}$
Cauchy Relations	$\varepsilon_{ij} = \dfrac{1}{2}\left(\dfrac{\partial u_i}{\partial x_j} + \dfrac{\partial u_j}{\partial x_i} \right)$
Hooke's Law	$\sigma_{ij} = \lambda\theta + 2\mu\delta_{ij}\varepsilon_{ij}$
Boundary Conditions	$\mathbf{n} \cdot \boldsymbol{\sigma} = 0$ $\mathbf{u} = 0$
Oscillations	$\mathbf{u}(x, y, z, t) = \mathbf{u}(x, y, z)\cos(\omega t)$

FlexPDE Realisation (Fragment)

```
VARIABLES       U1 U2 U3
DEFINITIONS     h=0.11 rho=7800 ...

EQUATIONS
     U1:    dx(S_11) + dy(S_12) + dz(S_31) + lambda*rho*U = 0
     U2:    dx(S_12) + dy(S_22) + dz(S_32) + lambda*rho*V = 0
     U3:   dx(S_13) + dy(S_23) + dz(S_33) + lambda*rho*W = 0

EXTRUSION
     z = 0, h
BOUNDARIES
       region 1
       start(0,0) load(U1)=0 load(U2)=0 load(U3)=0 line to…

PLOTS
     grid(x+U1, y+U2, z+U3) as "Shape"
     summary
          report lambda
END
```

[a)] Corresponding author. Email: karyakin@sfedu.ru

EXAMPLE 2. NONLINEAR BENDING

The wide range of specific features of hyperelastic bodies [4] can be demonstrated by means the problem of pure bending. Even the simple scheme of analysis presented below opens a number of tasks for individual student research. Amongst them are the calculation of geometrical parameters of computational scheme that guarantee the state of pure bending, and analysis of physical and geometrical nonlinearities. The latter task itself includes several stages – deriving the nonlinear equations, the automation of obtaining such equations for new nonlinear constitutive relations, setting up the correct boundary conditions in the case of large strains, analysis of the effect of the geometrical and material parameters, the use of refined methods of calculation to obtain the best convergence of numerical schemes and so on.

Traditional Scheme	Real Computational Scheme
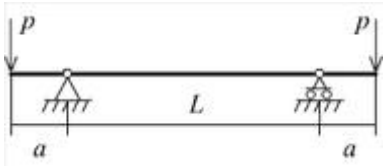	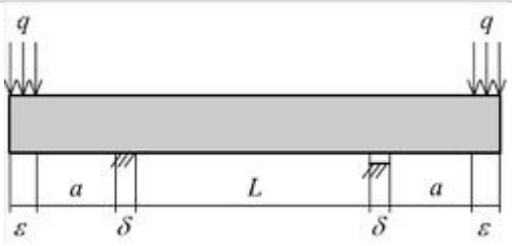

Nonlinear Problem	
Equilibrium Equations for the Piola Tensor	$\frac{\partial D_{11}}{\partial x_1}+\frac{\partial D_{21}}{\partial x_2}=0\ \ \frac{\partial D_{12}}{\partial x_1}+\frac{\partial D_{22}}{\partial x_2}=0$
Blatz & Co Material (Simplified Case) [3]	$W=\frac{1}{2}\mu\left(\frac{I_2}{I_3}+2\sqrt{I_3}-5\right),\quad I_k=I_k(\mathbf{G})$
Boundary Conditions for the Tracking Load	$D_{21}=-q\frac{\partial u_2}{\partial x_1}\ \ D_{22}=-q\frac{\partial u_1}{\partial x_2}$

Deformed Shape	Bending Diagram
	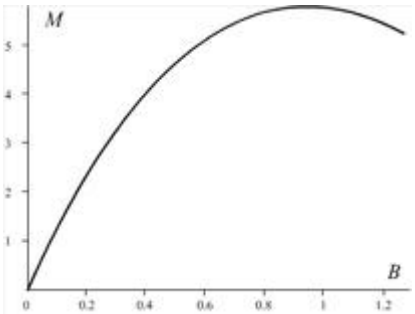

CONCLUSIONS

Nowadays different types of engineering software accompany the teaching process. Using the finite element package FlexPDE when teaching mechanics and mathematical modelling related courses allows students to better absorb the course material, to understand the essence of the problem, to propose new ideas and methods of solution and to attract additional math for solving complex problems.

References

[1] FlexPDE 6. Problems Solving Environment Since 1995, web site http://www.pdesolutions.com/.
[2] Backstrom G.: Deformation and Vibration by Finite Element Analysis. Stockholm: GB Publishing, 2007.
[3] Timoshenko S.: Engineering Education in Russia. New York: McGraw-Hill, USA 1959.
[4] Lurie A.I.: Nonlinear Theory of Elasticity. Horth-Holand: Amsterdam, 1990.

THE FLUID DYNAMICS OF THE CHOCOLATE FOUNTAIN: AN ENGAGING PROJECT

Adam K. Townsend and Helen J. Wilson *

Department of Mathematics, UCL, London, UK

Summary We present a study of the chocolate fountain, carried out as an undergraduate project. Immediately engaging as a topic of conversation (and for public engagement activity), the chocolate fountain also presents opportunities to introduce key concepts of fluid mechanics and of applied mathematics research.

Flow up the central column can be modelled as a pressure-driven pipe flow, and presents an ideal introduction to non-Newtonian fluid mechanics. Flow over the dome is a thin-film flow, whose analysis can introduce a student to scaling considerations and dimensional analysis. Finally, the falling curtain flow is analytically intractable but may nonetheless be partially understood by recourse to the literature on water bells: and the conclusion that the curtain falls inwards due (largely) to surface tension is a beautiful demonstration of physics in action – difficult to guess, but comprehensible (even obvious) once explained.

THE CHOCOLATE FOUNTAIN

We are all familiar with the chocolate fountain (figure 1), a popular attraction at wedding receptions and even conference banquets. As well as being attractive in its own right, it has the potential to be an engaging introduction to various aspects of advanced fluid mechanics, through the different geometries of flow and the complex nature of the fluid itself.

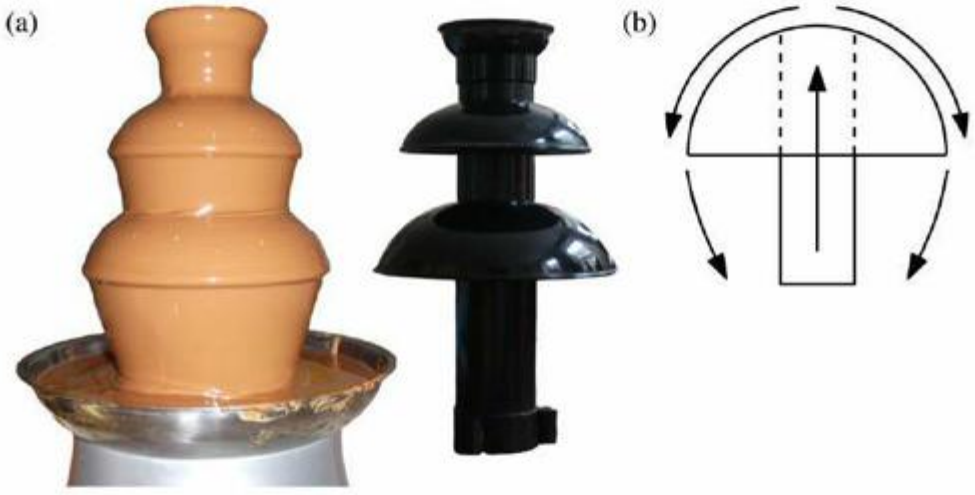

Figure 1: The chocolate fountain: (a) Our fountain both with and without chocolate; (b) Schematic flows used in the project. Taken from [1].

We investigated the chocolate fountain as a final-year undergraduate project (offered by HJW; AKT was the student); this resulted in a paper [1] which attracted media attention from the Daily Mail [2] to the Washington Post [3] and was downloaded over 7500 times in its first two months after publication.

PIPE FLOW

The true flow in the pipe (at least for our tabletop chocolate fountain) is driven by the rotation of a helical screw. It is fully three-dimensional and well outside the remit of an undergraduate project.

Instead, we idealised to a situation in which the pump simply applies an excess pressure at the base of the pipe. The flow becomes unidirectional and this is then an excellent first problem in which to investigate non-Newtonian fluid mechanics. Indeed, in earlier years HJW has sometimes offered a project on non-Newtonian fluid mechanics which did nothing more than investigate this flow and a couple of others like it with a few sample constitutive equations. However, here the choice of constitutive equation is motivated by a real fluid, and the student can engage with current research literature to find viscosity laws to fit chocolate. We found Casson's model and the power-law model (with a Newtonian fluid as an obvious special case); a wider range could easily be considered.

*Corresponding author. Email: helen.wilson@ucl.ac.uk

DOME FLOW

The layer of chocolate flowing over the plastic dome has a very small aspect ratio (its depth is much smaller than its other dimensions) which makes it an archetypal thin-film flow. The scaling concepts involved are new to – and tricky for – many undergraduates; this system is a good introduction to scaling arguments. The leading-order system obtained is a simple balance of viscous and gravitational forces, which can be solved analytically for the power-law model.

CURTAIN FLOW

The freely-falling curtain of chocolate is a much less tractable problem: as such, it presents the most valuable challenge for a strong student. The theory of water bells (see figure 2) is relevant, but is most developed for inviscid fluids.

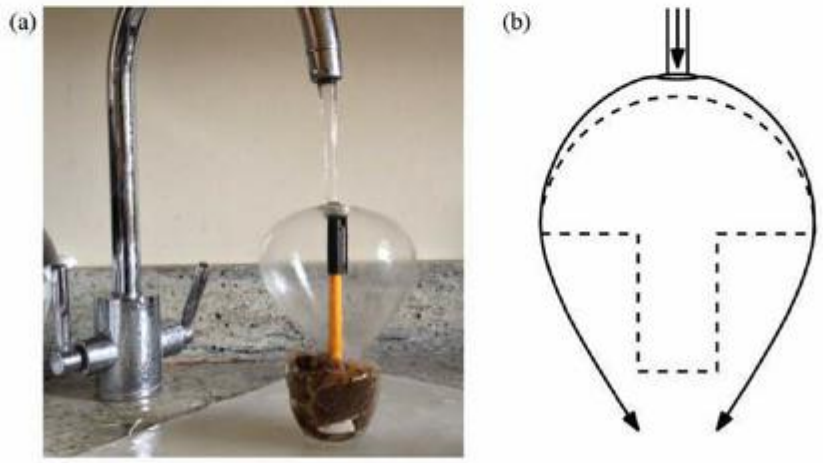

Figure 2: Water bells: (a) Home-made water bell; (b) Mapping the water surface onto the chocolate fountain. Taken from [1].

We were able to use inviscid theory and then compute an energy budget to show that viscous effects are, in fact, important; the most advanced research work in the project was the discovery of a paper [4] which mapped inviscid results onto simulation results for a viscous fluid.

The most accessible conclusion from this section of the project (and the one picked up on by the media) is that the mechanism for the inward trajectory of the falling sheet is primarily surface tension, as both the outer and inner surfaces feel the "hoop stress" of a cylindrical film.

CONCLUSION

The chocolate fountain provides a wide range of opportunities to discover the mathematical tools and physical concepts of fluid mechanics. Two of the geometries lead to analytically tractable problems, the first of which should be accessible even to weak students; the third geometry offers the potential to introduce everything from dimensional analysis to energy budgets and even a first foray into research literature. The fountain is a very cheap piece of experimental equipment, and has also been a fantastic tool for public engagement.

References

[1] Townsend A.K., Wilson H.J.: The fluid dynamics of the chocolate fountain. Eur J. Physics 37:015803, 2015.

[2] Mail Online, http://www.dailymail.co.uk/sciencetech/article-3332276/

[3] Washington Post, https://www.washingtonpost.com/news/speaking-of-science/wp/2015/11/24/someone-finally-looked-into-the-physics-of-chocolate-fountains/

[4] Gilio M., Al-Bender F., Kruth J.-P. The dynamics of a moving sheet of liquid, part I: derivation of the 2D equations of motion. Eur. J. Mech B 24:55571, 2005.

OPTIMIZATION OF THE DYNAMICS OF A CONSTANT-TEMPERATURE ANEMOMETER

José Luiz da Silva Neto[1,3a)], Juliana Braga Rodrigues Loureiro[2,3], Laert Ferreira da Silva Neto[1,3], Daniel Onofre de Almeida Cruz[2,3]

[1] *Department of Electrical Engineering, Federal University of Rio de Janeiro, Rio de Janeiro, Brazil*
[2] *Department of Mechanical Engineering, Federal University of Rio de Janeiro, Rio de Janeiro, Brazil*
[3] *Interdisciplinary Center of Fluid Dynamics, Federal University of Rio de Janeiro, Rio de Janeiro, Brazil*

Summary This work presents the experimental arrangement of the laboratory activities for the graduated Instrumentation course at the Interdisciplinary Center of Fluid Dynamics, in which the technique based on a Constant-Temperature Hot-Wire Anemometer is explored. The main purposes will be discussed. The central contribution is to propose a methodology to numerically obtain the value of the parameter responsible for the optimization of the frequency response of the instrument.

IINTRODUCTION

In any Mechanical Engineering program, either at the undergraduate or graduate level, the basic principles of the discipline are only truly comprehended through hands-on and laboratory activities. Experimental fluids dynamics is essentially an interdisciplinary area. Although the main purpose of an experiment could be to study or address a specific phenomenon, there is much more to the procedure of acquiring and processing the variables of the physical world. At the Interdisciplinary Center of Fluid Dynamics (**NIDF**-Federal University of Rio de Janeiro, Rio de Janeiro, Brazil), the basics of turbulent flow velocity measurement are taught in two main graduate courses. In these courses the approach is that to alternate the theoretical and practical aspects, in a way to cover the fundamental concepts of the principal available techniques. The students are not only put in contact with state-of-the-art equipment, but also, design, construct and analyze the performance of some instruments. Through these courses, **NIDF** have been receiving students from different engineering areas: mechanical, electrical, naval and chemical.

This work regards the measurement of turbulent flow velocity by means of a Constant-Temperature Hot-Wire Anemometer (CTA) [1] as one of the fewest available technics to address the problem. The CTA is relatively simple to construct but particularly difficult to be dynamically calibrated. Viewed as a system to be designed, it covers a great variety of engineering and physics concepts, predominantly: thermodynamics, electronics, nonlinear and linear systems analysis and control and digital signal processing.

The main contribution of this work is to present a methodology to numerically obtain the value of a parameter – the DC offset voltage V_O applied to the Wheatstone Bridge – in order to optimize the frequency response of the CTA. The proposed methodology is based on the assumption that a second order dynamic model is sufficient to characterize the behavior of the CTA. It's a reasonable simplification for most of the modern electronics solutions and unidirectional probes geometries, as long as the modified King's Law holds.

MATERIALS AND METHODS

In the scope of the courses of Instrumentation and Signal Processing, a prototype of a CTA instrument is designed and constructed. As a two months assignment, the students must: construct the hot-wire probe; model the hot-wire behavior; simulate the electronic servo circuit with the hot-wire dynamics; model the nonlinear servo system; linearize the dynamical equations; numerically assess the problem of the dynamical calibration; program a Digital Signal Controller (DSC) for data acquisition; design an environment based on the National Instruments LabWindows CVI software in order to interface with the DSP; compare the experimental performance of the instrument with those obtained by linear and nonlinear simulation.

In order to fabricate the hot-wire probe a micro-manipulator, shown in Figure 1 [2], was designed and constructed at **NIDF**. The servo circuit is designed and assembled according to the simplified circuit presented in Figure 2, where the summing and power stages were lumped into a single unity gain amplifier, while the main gain stage has gain G. Figure 2 shows, also, the variables of the system including the normal flow velocity vector. The CTA circuit electrical variables are acquired by a DSC card based on the Texas Instrument TMS320F28335 Microcontroller.

Based on the system shown in Figure 2 the dynamical nonlinear equations (Equations 1) can be written by assuming a third order system. A first order equation is obtained from the hot-wire dynamics. The first order Low-Pass input filter contributes to a time constant τ_i. The electronic amplification stages introduce, of course, some dynamics that are, in general, very difficult to be completely estimated. However, it is reasonable to assume that the time constant τ_g of the highest gain stage dominates, for the gain-band width product is constant. The input instrumentation amplifier stage usually is set with the larger gain, and the time constant (defined by the 3dB frequency) for this gain can be fairly estimated on the manufacturer's data sheet of the integrated circuit. As long as the remaining integrated circuits have equivalent speed to that of the input amplifier, this simplification have shown to be a very good approximation.

[a)] Corresponding author. Email: zluizneto@gmail.com.

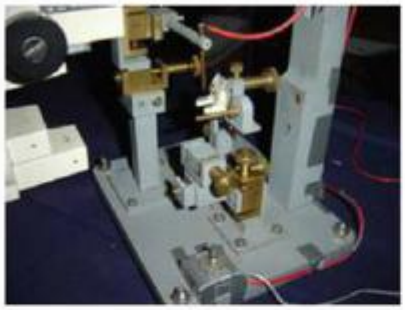

Figure 1. Micro-manipulator.

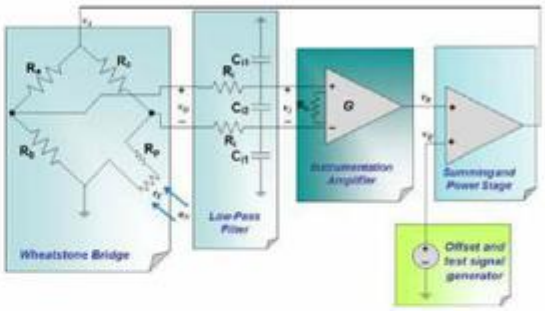

Figure 2. CTA simplified circuit.

$$\frac{dr_F}{dt} = \frac{(B_0 - r_F)}{H}(X + YU_N^n) + \frac{(v_Q + v_B)^2}{(B_a + B_p + r_F)^2}\frac{r_F}{H} \quad (1.a)$$

$$\frac{dv_B}{dt} = \frac{-1}{\tau_g}v_B + \frac{G}{\tau_g}v_I \quad (1.b)$$

$$\frac{dv_I}{dt} = \frac{-1}{\tau_i}v_I + \frac{1}{\tau_i}(v_Q + v_B)\left(\frac{B_b}{B_b + B_c} - \frac{B_p + r_F}{B_a + B_p + r_F}\right) \quad (1.c)$$

In the Equations 1: X and Y are experimental constants; R_0 is the wire resistance at the fluid temperature; H is a constant that depends on the wire geometry and material. This system has three state variables and two inputs: u_N and v_Q. The experimental constants can be obtained by a static calibration $V_A \times U_N$ using the relation $V_A{}^2 = A + B \cdot U_N{}^n$ and then recalculating for the voltage across the wire. The system can then be modelled in the OrCAD EE PSpice electronic circuits simulation software that has a vast components library and, also, all the fundamental blocks to model the hot-wire nonlinear dynamics. By performing the nonlinear frequency response of the simulated system, the very accurate result gives an important insight on the real CTA performance.

The original dynamic equations can be linearized to the first order around some operating point defined by the average values U_N and V_Q. Equation 2 shows the equivalent linear system matrix having r_f, v_b and v_i as the perturbative state variables while V_Q is held constant. The latter is chosen to be the dynamical calibration parameter and is tuned in order to optimize the frequency response.

$$M = \begin{pmatrix} -\frac{X + YU_N^{0.45}}{H} - \frac{2B_F(V_B + V_Q)^2}{H(B_F + B_a + B_p)^3} + \frac{(V_B + V_Q)^2}{H(B_F + B_a + B_p)^2} & \frac{2B_F(V_B + V_Q)}{H(B_F + B_a + B_p)^2} & 0 \\ 0 & -\frac{1}{\tau_g} & \frac{G}{\tau_g} \\ \frac{\left(\frac{B_F + B_p}{(B_F + B_a + B_p)^2} - \frac{1}{B_F + B_a + B_p}\right)(V_B + V_Q)}{\tau_i} & \frac{\frac{B_b}{B_b + B_c} - \frac{B_F + B_p}{B_F + B_a + B_p}}{\tau_i} & -\frac{1}{\tau_i} \end{pmatrix} \quad (2)$$

The characteristic polynomial of the system's matrix has coefficients such that the third degree term coefficient is negligibly smaller than the others. Consequently, this term is neglected and the remaining second degree polynomial equation can be put into the form: $s^2 + a_1 s + a_B = 0$, where a_1 and a_0 are both functions of the operating point and the system's parameters. One must note that the parameter V_Q has not been defined yet and so the operating point is unknown. Nevertheless, the characteristic equation can always be written as $s^2 + \frac{\omega_0}{Q}s + \omega_B = 0$, where Q is the quality factor and ω_0 the natural frequency of the equivalent second order system. By defining Q the pass band of the CTA can be determined, where

$$Q = \frac{\sqrt{a_0}}{a_1} \quad (3)$$

By solving simultaneously Equation 3 and Equations 1 for the static state and the desired Q, the necessary V_Q is obtained. Applying this average voltage to the nonlinear circuit simulation and to the prototype, the theoretical and experimental frequency responses can be obtained and compared. Moreover, the procedure can be repeated for different probes and/or different average flow velocities.

CONCLUSIONS

An experimental setup for the study of the principles of thermal anemometry with a CTA prototype was presented. A methodology to numerically obtain the value of the parameter responsible for the optimization of the frequency response of the instrument was proposed.

References

[1] H.H.Brun, "Hot-Wire Anemometry: Principles and Signal Analysis", Oxford University Press, 1995.

[2] SILVA NETO, J. L.; FREIRE.A.P.S ; LOUREIRO. J.B.R ; MONTEIRO.A.S ; LACERDA. A . Experimental Investigation of the Dynamical Response of a Hot-wire Anemometer Developed to Industrial Applicayions. In: II International Symposium on Industrial Electronics, 2006, Montreal. Anais do ISIE 06 International Symposium on Industrial Electronics, 2006. v. 4. p. 2863-2863.

FLUID MECHANICS EDUCATION AT THE UNIVERSITY OF THE WEST INDIES

Gyan Shrivastava[1a)]
[1]*Department of Civil Engineering, University of the West Indies, St. Augustine, Trinidad, West Indies*

Summary Fluid Mechanics Education for the undergraduate civil engineering students, for the Islands of the Commonwealth Caribbean, is influenced by the need for a robust design of infrastructure for withstanding the forces of nature associated with hurricanes, storm surges, and tsunamis. Against the foregoing background, this paper describes the Fluid Mechanics Education in the Department of Civil of Engineering at the University of the West Indies.

INTRODUCTION

Fluid Mechanics forms the theoretical base for coastal, environmental and hydraulic engineering and plays a critical role in the design of civil engineering infrastructure. In the Caribbean islands, there is a need for protection of critical lifeline infrastructure from high winds and storm surges during the frequent passage of hurricanes. Moreover, these islands are also vulnerable to tsunamis, and there is a need for the construction of tsunami shelters. It should also be noted that most of these islands have a mountainous terrain, and that the major roads, urban areas, airports, water pipelines and hotels are located along the coastline. Therefore, a clear and deep understanding of fluid mechanics is essential for the wind resistant design of buildings and wave resistant design of coastal roads, breakwaters, pipelines, sea walls, shoreline revetments and tsunami shelters. This short paper provides a glimpse of fluid mechanics education for civil engineering students at the University of the West Indies, hereafter abbreviated as the UWI.

THE UNIVERSITY OF THE WEST INDIES (UWI)

The UWI has four campuses - in the Bahamas, Jamaica, Barbados and Trinidad – across the Caribbean Region (Figure 1). It is an autonomous regional institution and currently has a total enrolment of approximately 40,000 students. It started as Imperial College of Tropical Agriculture of the University of London in 1948 and at present is supported by, and serves, the following 17 islands: Anguilla, Antigua and Barbuda, the Bahamas, Barbados, Bermuda, the British Virgin Islands, the Cayman Islands, Dominica, Grenada, Jamaica, Montserrat, St. Kitts, Nevis, St. Lucia, St. Vincent and the Grenadines, Trinidad and Tobago, and Turks and Caicos Islands. These islands have a combined population of about 5 million people, a total land mass of approximately33,000 km^2, and are spread over an oceanic area of approximately $2.25x10^6$ km^2.

The Department of Civil Engineering, which is a part of the UWI Faculty of Engineering, is located at St. Augustine in Trinidad. Its undergraduate programme in Civil Engineering commenced in 1961 in a special relationship with Imperial College, London. Moreover, the Department has maintained academic links with the United Kingdom through a formal accreditation of its programmes by with the UK Engineering Council through the Joint Board of Moderators (JBM), which comprises the UK based Institutions of Civil, Structural and Highway Engineers.



Figure 1: The Caribbean

The central objective of striving for a clear, and deep, understanding of Fluid Mechanics among the undergraduate students is to develop an ability for correctly, and fully, interpreting the codes of practice/design guidelines relating to wind/structure and wave/structure interactions for the design of hazard resistant infrastructure. At the UWI this objective is achieved through a specially designed syllabi and a continuous learning thread [3], which puts the fluid mechanics education at the centre of the relevant issues, as shown in Figure 2.

a) Corresponding author. Email: shrivastava.gyan@gmail.com.

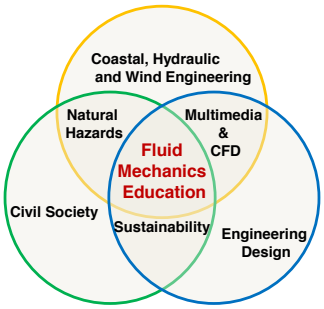

Figure 2: Fluid Mechanics Education for Natural Hazards Mitigation

LEARNING THREAD

The learning thread in Fluid Mechanics for the undergraduate civil engineering students at the UWI begins with an introductory course in Fluid Mechanics in their first year. In this course, principles of hydrostatics, the conservation laws of mass, energy and momentum and their applications are first introduced. These are followed by an introduction to boundary layers. In the second year, the students take another course in Fluid Mechanics which concentrates on flow in open channels, potential flow and atmospheric boundary layer. Thereafter, in the third year, the students take a course in Coastal Engineering where mechanics of wave motion, sediment transport and design of coastal structures are covered. Finally, all undergraduate students are required to carry out a final year capstone design project which - given the oceanic setting of the Commonwealth Caribbean - invariably requires consideration of wind and wave forces. The capstone design project, *inter alia*, requires, and develops, skills of analysis and synthesis, and in it the students come to appreciate the need for clarity, and depth, of their knowledge in Fluid Mechanics for correctly interpreting the physical processes involved as well as the various codes of practice and guidelines mentioned earlier. A clear and deep understanding leads to optimal design and construction of infrastructure, and thus enhances its sustainability.

The aforementioned learning thread is underpinned by closely supervised tutorial sessions, site visits, laboratory experiments, text and reference books, multimedia and Computational Fluid Dynamics (CFD. It is said that those of us who teach fluid mechanics are fortunate, as are our colleagues in some other fields such as optics, that our subject is easily visualized. Moreover, the literature of fluid mechanics has many beautiful and revealing photographs which can be used as a valuable resource for teaching. Thus, conventional lectures are supplemented by “An Album of Fluid Motion” by Van Dyke [4]. Moreover, the advantages of the aforementioned visual nature of Fluid Mechanics, in the learning process, are further strengthened by the use of an interactive multimedia DVD [2].

Integration of Computational Fluid Dynamics (CFD) in the undergraduate fluid mechanics courses can considerably enhance learning [1]. Specifically, classroom CFD demonstrations and home assignments help students to learn the basic concepts of Fluid Mechanics. Moreover, it also shows CFD simulations as a powerful design tool for examining alternative designs. It should be noted, however, that only simple applications of CFD, rather than numerical algorithms, are emphasized, e.g. flow separation around a bluff body.

CONCLUSIONS

Fluid Mechanics Education, for Civil Engineers, in the Commonwealth Caribbean islands needs to specifically address, with clarity and depth, its role in the sustainable design of infrastructure for withstanding the fluid dynamic forces associated with hurricanes, storm surges, and tsunamis. This objective is achieved at UWI through: (a) a specially designed syllabi, and (b) the concurrent use of traditional lectures, tutorials and site visits as well as use of multimedia and CFD in a learning thread through its undergraduate civil engineering curriculum.

Acknowledgements

The author is grateful to the late Professor J. R. D. Francis at Imperial College, London, UK, for creating in him a lifelong interest in Fluid Mechanics.

References

[1] Cengel, Y. A. and Cimbala, J. M.: Fluid Mechanics: Fundamentals and Applications. McGraw-Hill, NY 2006.
[2] Homsby, G. M., (ed): Multi-Media Fluid Mechanics, DVD-ROM. Cambridge University Press, 2008.
[3] Shrivastava, G. S., 2004, Fluid Mechanics and the Undergraduate Civil Engineer, Journal of Hydraulic Engineering, 130(10): 953-956
[4] Van Dyke, M.: An Album of Fluid Motion. Parabolic Press, 1982.